ICTP 2021

FORMING THE FUTURE

Proceedings of the
13th International Conference
on the Technology of Plasticity

EDITED BY

Glenn Daehn · Jian Cao · Brad Kinsey
Erman Tekkaya · Anupam Vivek
Yoshinori Yoshida



TMS

Springer

The Minerals, Metals & Materials Series

Glenn Daehn · Jian Cao · Brad Kinsey ·
Erman Tekkaya · Anupam Vivek ·
Yoshinori Yoshida
Editors

Forming the Future

Proceedings of the 13th International Conference on the Technology of Plasticity

TMS

Springer

Editors
Glenn Daehn
The Ohio State University
Columbus, OH, USA

Jian Cao
Northwestern University
Evanston, IL, USA

Brad Kinsey
University of New Hampshire
Durham, NH, USA

Erman Tekkaya
Technical University of Dortmund
Dortmund, Germany

Anupam Vivek
The Ohio State University
Columbus, OH, USA

Yoshinori Yoshida
Gifu University
Gifu, Japan

ISSN 2367-1181 ISSN 2367-1696 (electronic)
The Minerals, Metals & Materials Series
ISBN 978-3-030-75380-1 ISBN 978-3-030-75381-8 (eBook)
https://doi.org/10.1007/978-3-030-75381-8

© The Minerals, Metals & Materials Society 2021
This work is subject to copyright. All rights are solely and exclusively licensed by the Publisher, whether the whole or part of the material is concerned, specifically the rights of translation, reprinting, reuse of illustrations, recitation, broadcasting, reproduction on microfilms or in any other physical way, and transmission or information storage and retrieval, electronic adaptation, computer software, or by similar or dissimilar methodology now known or hereafter developed.
The use of general descriptive names, registered names, trademarks, service marks, etc. in this publication does not imply, even in the absence of a specific statement, that such names are exempt from the relevant protective laws and regulations and therefore free for general use.
The publisher, the authors and the editors are safe to assume that the advice and information in this book are believed to be true and accurate at the date of publication. Neither the publisher nor the authors or the editors give a warranty, expressed or implied, with respect to the material contained herein or for any errors or omissions that may have been made. The publisher remains neutral with regard to jurisdictional claims in published maps and institutional affiliations.

This Springer imprint is published by the registered company Springer Nature Switzerland AG
The registered company address is: Gewerbestrasse 11, 6330 Cham, Switzerland

Preface

Dear Colleague,

The "lucky" thirteenth International Conference on the Technology of Plasticity (ICTP) was the meeting that just was not destined to happen live. The COVID-19 pandemic forced us to move it from July 2020 to July 2021, and now as I write, the world is starting to recover, vaccinations are coming, but the end of July 2021 is just too early for extensive international travel. This represents the archive of peer-reviewed papers that accompany this meeting.

This is a meeting series with the strongest of international traditions. Meetings have been held in Tokyo, Japan (1984); Stuttgart, Germany (1987); Kyoto, Japan (1990); Beijing, China (1993); Columbus, Ohio, USA (1996); Nuremberg, Germany (1999); Yokohama, Japan (2002); Verona, Italy (2005); Gyeongju, Korea (2008); Aachen, Germany (2011); Nagoya, Japan (2014); and Cambridge, England, and this meeting was to be held in Columbus, Ohio, USA.

This meeting has a strong tradition, and we hope that the papers here and the remote meeting format will maintain the ICTP's traditions of innovation impact and collegiality across the globe.

This meeting is noteworthy also for several special symposia for pioneers of metal forming:

Taylan Altan, The Ohio State University, USA
Niels Bay, Technical University of Denmark, Denmark
Xue-yu Ruan, Shanghai Jiao Tong University, China (memorial symposium)
Yasuhisa Tozawa, Nagoya University, Japan
Rob Wagoner, The Ohio State University, USA
Zhongren Wang, Harbin Institute of Technology, China

I am grateful for the many hours of planning (much for events that are not to be realized) by the planning committee:

Glenn Daehn, The Ohio State University, USA
Jian Cao, Northwestern University, USA
Brad Kinsey, University of New Hampshire, USA
Erman Tekkaya, Technical University of Dortmund, Germany

Anupam Vivek, The Ohio State University, USA
Yoshinori Yoshida, Gifu University, Japan

Despite the unusual circumstances, I think you will agree that this series of full papers (246) shows great quality and innovation in keeping with the spirit of ICTP. The papers are arranged topically and then alphabetically.

The organizers wish to thank the various people and institutions that supported us in organizing the ICTP and in preparing the proceedings. Our sincere thanks go to all authors who submitted excellent papers and who make our (metal) forming community so strong. Secondly, we wish to thank all our reviewers who carefully and constructively evaluated all the submitted papers. The bulk of this reviewing was carried out by the international scientific committee, which is named below and the members of my research group who skillfully filled in several gaps. We are also grateful to the members of the scientific committee and the standing advisory board for their valuable help and advice.

I hope you find these innovative papers useful and enjoy the online conference.

With best wishes,



Glenn Daehn
Mars G. Fontana Professor of Metallurgical Engineering
The Ohio State University
Columbus, OH, USA

ICTP 2021 International Scientific Committee:

Tatsuhiko Aizawa, Shibaura Institute of Technology
Julian Allwood, University of Cambridge
Birgit Awiszus, TU Chemnitz
Tudor Balan, LCFC, Arts et Métiers ParisTech—Metz Campus
Markus Bambach, BTU Cottbus–Senftenberg
Dorel Banabic, Technical University of Cluj-Napoca
Francois Bay, MINES ParisTech
Niels Bay, Technical University of Denmark
B-A Behrens, Leibniz Universitat Hannover
Yan Beygelzimer, Donetsk Institute for Physics and Engineering
Regis Bigot, Ecole Nationale Supérieure d'Arts et Métiers
Pierre-Olivier Bouchard, MINES ParisTech
Jose Divo Bressan, University of Santa Catarina State
Alexander Brosius, Technische Universität Dresden
Stefania Bruschi, University of Padova
Sergio Button, State University of Campinas

Demircan Canadinc, Koç University
Jian Cao, Northwestern University
Jianguo Cao, University of Science and Technology Beijing
Oana Cazacu, University of Florida
Elisabetta Ceretti, University of Brescia
Jose Cesar de Sa, University of Porto
Paulo Roberto Cetlin, Federal University of Minas Gerais
Yvan Chastel, Renault
Francisco Chinesta, Arts et Metiers Institute of Technology
László Cser, Corvinus University of Budapest
Elías Cueto, University of Zaragoza
Zhenshan Cui, Shanghai Jiao Tong University
Glenn Daehn, The Ohio State University
Prashant P. Date, Indian Institute of Technology Bombay
Joost Duflou, KU Leuven
Gang Fang, Tsinghua University
Luigino Filice, University of Calabria
Livan Fratini, Università degli Studi di Palermo
Lander Galdos, Mondragon Unibertsitatea
Andrea Ghiotti, University of Padova
Sergey F. Golovashchenko, Oakland University
Zbigniew Gronostajski, Wroclaw University of Science and Technology
Gerhard Hirt, RWTH Aachen
Werner Homberg, Paderborn University
Sung-Tae Hong, School of Mechanical Engineering, University of Ulsan
Odd Sture Hopperstad, Norwegian University of Science and Technology
Yujie Huang, Korea Advanced Institute of Science and Technology
Hoon Huh, Korea Advanced Institute of Science and Technology
Y-T Im, Korea Advanced Institute of Science and Technology
Shohei Kajikawa, The University of Electro-Communications
Celalettin Karadogan, Institute for Metal Forming Technology—University of Stuttgart
Hyunok Kim, EWI
Brad Kinsey, University of New Hampshire
Antti Korhonen, Helsinki University of Technology
Toshihiko Kuwabara, Tokyo University of Agriculture and Technology
Da Yong Li, Shanghai Jiaotong University
Jian-Jun Li, Huazhong University of Science and Technology
Mathias Liewald, Institute for Metal Forming Technology—University of Stuttgart
Lars-Erik Lindgren, Lulea University of Technology
Gang Liu, Harbin Institute of Technology
Hui Long, The University of Sheffield
Evripides Loukaides, Bath University
Lukasz Madej, AGH University
Ryo Matsumoto, Osaka University

Takashi Matsuno, Tottori University
Marion Merklein, Universität Erlangen-Nürnberg
Wojciech Misiolek, Lehigh University
Pierre Montmitonnet, CEMEF—Centre de Mise en Forme des Matériaux
Y. H. Moon, Pusan National University
Ken-ichiro Mori, Toyohashi University of Technology
Omer Music, TED University
Thomas Neitzert, Auckland University of Technology
Gracious Ngaile, North Carolina State University
Takeshi Nishiwaki, Daido University
Takahiro Ohashi, Kokushikan University
Mats Oldenburg, Luleå University of Technology
Masaaki Otsu, University of Fukui
Hengan Ou, University of Nottingham
Aleksandr Pesin, Magnitogorsk State Technical University
Jean-Philippe Ponthot, University of Liege
Warren Poole, University of British Columbia
Alexandre Rocha da Silva, Federal University of Rio Grande do Sul
Andrzej Rosochowski, University of Strathclyde Glasgow
Jinn-Jong Sheu, National Kaohsiung University of Science and Technology
Kazunari Shinagawa, Kyushu University
Andreas Sterzing, Fraunhofer IWU
Erman Tekkaya, Technische Universität Dortmund
Miklós Tisza, University of Miskolc
Hiroshi Utsunomiya, Osaka University
Ton van den Boogaard, University of Twente
Anupam Vivek, The Ohio State University
Frank Vollertsen, Bremer Institut fur angewandte Strahltechnik
Robert Wagoner, The Ohio State University
Zhigang Wang, Gifu University
Michael Worswick, University of Waterloo
Jian-xin Xie, University of Science and Technology Beijing
Dong-Yol Yang, Gwangju Institute of Science and Technology
Yoshinori Yoshida, Gifu University
Hai Liang Yu, Central South University
Mei Zhan, Northwestern Polytech University
Shihong Zhang, Institute of Metal Research, Chinese Academy of Sciences
Guoqun Zhao, Shandong University
Zhen Zhao, Shanghai Jiaotong University

Contents

Part I Honorary Symposium: Taylan Altan

Self-optimized, Intelligent Open-Loop-Controlled Steel Strip Straightening Machine for Advanced Formability 3
Fabian Bader, Lukas Bathelt, Eugen Djakow, Werner Homberg, Christian Henke, and Ansgar Trächtler

A Vision of Numerically Controlled, Autonomous Manufacturing and Metal Forming 13
Glenn S. Daehn

Investigation of Effects of Part Features in Single Point Incremental Forming of Narrow Channels 25
Suwat Jirathearanat, Dharmesh Kumar, Kai Soon Fong, Atsushi Danno, and A. Senthil Kumar

Enhancing Tool Life by Manipulating the Die Elastic Strain Field During Extrusion 37
Gracious Ngaile and Daniel Santiago

Part II Honorary Symposium: Niels Bay

Oscillation-Free Determination of Material Properties at High Strain Rate 53
Xiangfan Fang

Tribological Conditions in Hot Bending of 22MnB5 Tubes 67
Enrico Simonetto, Andrea Ghiotti, and Stefania Bruschi

In Search of the Perfect Sheet Metal Forming Tribometer 81
L. Schell and P. Groche

A Contact and Friction Model for Forming of Galvanized Steel Sheet Based on Fractal Theory 97
Yao Huang, Leigang Wang, Mingxiao Shi, and Xiang Ma

On the Characterization of Fracture Loci in Thin-Walled Tube Forming 113
J. P. Magrinho, M. B. Silva, and P. A. F. Martins

Deformation Mechanisms in Tool–Workpiece Asperity Contact in Metal Forming 127
Chris Valentin Nielsen, Xiaodan Zhang, Marcel Moghadam, Niels Hansen, and Niels Bay

Welding of Aluminium in Chip Extrusion 139
André Schulze, Oliver Hering, and A. Erman Tekkaya

Part III Honorary Symposium: Xue Yu Ruan

Bulk Microforming from Sheet Metal—A Promising Approach for the Mass Production of Cold-Formed Metallic Micro Parts 151
Martin Kraus and Marion Merklein

Machine Learning (ML)-Based Prediction and Compensation of Springback for Tube Bending 167
J. Ma, H. Li, G. Y. Chen, T. Welo, and G. J. Li

Ductile Fracture Prediction of Hot-Stamped Boron Steel 22MnB5 with Modified Mohr–Coulomb and Hosford–Coulomb Models 179
Fangxing Wu, Bingtao Tang, Ning Guo, Huiping Li, and Qiaoling Wang

Understanding the Microscale Plastic Behavior and Deformation Mechanism of Magnesium Alloy via Ex Situ Experiments and Full-Field Crystal Plasticity Modeling 189
Haiming Zhang, Shuai Xu, Xiaoqing Shang, and Zhenshan Cui

Part IV Honorary Symposium: Yasuhisa Tozawa

A Plasticity Framework for Forming Applications 201
Frédéric Barlat and Toshihiko Kuwabara

Hole Expansion Simulation of Steel Sheet Considering Differential Hardening 209
Shunya Nomura and Toshihiko Kuwabara

Surface Quality of Extruded Sidewall in Cold Backward Cup Extrusion with Low-Frequency Torsional Oscillation 217
Ryo Matsumoto, Seiji Takatsuka, and Hiroshi Utsunomiya

Anisotropic Ductile Fracture Estimation of Diagonal Cracks in Flange-Shaped Parts 227
Atsuo Watanabe, Kunio Hayakawa, Shinichiro Fujikawa, Tatsumi Takeshita, and Mika Furutani

Prediction of Microstructure Behavior During Large-Scale Hot Forging of Ni-Based Superalloy 239
Nobuki Yukawa, Chihiro Osawa, Takayuki Yamada, and Eiji Abe

Part V Honorary Symposium: Rob Wagoner

Simulated Microstructure Effects on Macroscopic Mechanical Properties Based on Multiscale Crystal Plasticity 253
Yoshiteru Aoyagi, Ryota Kobayashi, and David L. McDowell

Experimental Study on Texture Evolution of Mg-Y Magnesium Alloy in Extrusion 263
Dayong Li, Weiqin Tang, Ding Tang, and Yinghong Peng

Advancing the Accuracy of Computational Models for Double-Sided Incremental Forming 271
Newell Moser, Dohyun Leem, Shuheng Liao, Kornel Ehmann, and Jian Cao

Nonlinearity of the Crystal Yield Function in the Rate-Independent Crystal Plasticity and Its Effect on the Evolution of Anisotropy 283
Taejoon Park, Ji Hoon Kim, Hojun Lim, Sobhan Alah Nazari Tiji, Amir Asgharzadeh, and Farhang Pourboghrat

Experimental Study and Analysis on the Effects of Cyclic Bending on the Stress-Strain Curves of Aluminum Plate 291
Yongjun Wang and Pengyan Tong

Part VI Honorary Symposium: Zhongren Wang

Professor Z. R. Wang's Contributions to Metal Forming Theory, Technology, and Education 303
Gang Liu, Shijian Yuan, and Kaifeng Zhang

Adding Value by Advancing Metal Forming Technology 319
Trevor Dean, Bo-Zhou Di, and Li-Liang Wang

A Study of the Forming Quality of Magnesium Alloy Cylindrical Parts with Inner Ribs by Induction-Heating-Assisted Spinning 333
Qinxiang Xia, Jinchuan Long, Gaozhu Huang, Shuai Yuan, and Yi Qin

A Porosity Closure Model for the Integrated Casting and Forging Process of Aluminum Alloy and Its Application 343
Qi Zhang, Liqun Niu, Zhenglong Liang, and Miao Cao

Robust Hydroforming Technologies to Enhance the Formability of Sheet and Tube 353
Shi-Hong Zhang, Da-Yong Chen, Yong Xu, and Yan Ma

Part VII Agile Metal Forming

Recent Investigations on Incremental Sheet Forming: From Fundamentals to Industrial Application Technologies 369
Jun Chen and Zhidong Chang

The Effect of Ultrasonic Vibration on Material Movement in Incremental Sheet Forming 383
Randy Cheng, Ankush Bansal, Jiarui Kang, Xun Liu, and Alan Taub

Investigation of an Integrated Process for Bending and Cross-Section Forming of Tubular Lightweight Parts Based on a Working Media Made of Materials with High Plasticity 395
Matthias Hermes and Viktor Holstein

Instability Analysis in Incremental Rotary Forming of Tube Flanges 403
Bhaskaran Krishnamurthy, Olga Bylya, Kyle Watt, Alastair Conway, Martin Tuffs, and Paul Blackwell

Incremental Collar Forming Process for the Manufacturing of Branched Tubes and Pipes 417
André Leonhardt, Peggy de Witt, Matthias Rehm, Holger Schlegel, and Verena Kräusel

Deformation Analysis in Ultrasonic-Assisted Multi-stage Incremental Sheet Forming 429
Zinan Cheng, Yanle Li, Fangyi Li, and Jianfeng Li

A New Test Method for Sheet Metal Deformation Subject to Tension Under Cyclic Bending and Compression (TCBC) 441
H. Long, S. Ai, F. Tian, B. Lu, J. Chen, and H. Ou

Numerical Modelling and Deformation Mechanics of the English Wheel Process 457
Daniel T. Bowen, Omer Music, A. Alaz Erdinc, Alborz Shokrani, and Evripides G. Loukaides

The Dieless Drawing Process for the Elongation of Ultrafine Copper and Brass Wire 467
Andrij Milenin, Piotr Kustra, Miroslaw Wróbel, Valeriy Pidvysots'kyy, and Marek Packo

Robotic Roller Forming Process and Strategies to Eliminate Geometrical Defect of Edge Waves 479
Yi Liu, Junying Min, and Jianping Lin

Numerical Modelling of the Flow Forming Process: Computation Time Optimization and Accuracy Analysis 493
Ahmed Mehdi Roula, Katia Mocellin, and Pierre-Olivier Bouchard

On the Geometrical Accuracy in Incremental Sheet Forming 507
Gerhard Hirt, Roman Kordtomeikel, Thomas Bremen, Marvin Laugwitz, and David Bailly

Tube Roll Forming Flower Design and Flexible Roll Adjustment with CAE Simulation 523
Jinn-Jong Sheu, Bao-Shan Wang, and Cheng-Hsien Yu

Open Die Forging of Copper Cone 537
A. Shirizly, G. Harpaz, and A. Shmuel

Flexible Manufacturing of Concave–Convex Parts by Incremental Sheet Forming with Active Medium 549
Sebastian Thiery and Noomane Ben Khalifa

Manufacturing of Tailored Blanks with Pre-shaped Involute Gearings by Using a Flexible Rolling Process and Its Application in a Sheet–Bulk Metal Forming Process 563
Manfred Vogel, Robert Schulte, Onur Kaya, and Marion Merklein

Roll Forming of Cup with Curved Rotary Profile 577
Baohong Zhang, Bin Hu, Chunyu Wei, and Xi Zhao

Part VIII Big Data and Metal Forming

Investigation of Machine Learning Models for a Time Series Classification Task in Radial–Axial Ring Rolling 589
Simon Fahle, Thomas Glaser, and Bernd Kuhlenkötter

Toward Neural Network Models to Model Multi-phase Solids 601
Maysam B. Gorji, Julian N. Heidenreich, Mojtaba Mozaffar, and Dirk Mohr

Comparison of Linear Regression and Neural Networks as Surrogates for Sensor Modeling on a Deep Drawn Part 611
Matthias Ryser and Markus Bambach

Development of Mechanical Cards for Finite Element Analysis of Mild Steels by Parameter Optimization 625
M. Emin Tamer, Eda Çapa Kızıltaş, and B. Celal Seyalıoğlu

Part IX Characterization of Plasticity and Ductile Fracture of Metals under Proportional and Non-proportional Loading

Cyclic Loading Tests Based on the In-Plane Torsion Test for Sheet Metal 635
Chong Zhang, Yanshan Lou, Till Clausmeyer, and A. Erman Tekkaya

Plastic and Fracture Characteristics of WE43 Mg Alloy Under Complex Stress States 647
Pengfei Wu, Chong Zhang, Yanshan Lou, Qiang Chen, and Haiqing Ning

Strain Hardening of AA5182-O Considering Strain Rate and Temperature Effect 657
Hongchun Shang, Pengfei Wu, and Yanshan Lou

New Methods for Fracture Detection of Automotive Steels 667
J. Noder, P. Samadian, J. Dykeman, A. Abedini, A. Zhumagulov, M. Worswick, and C. Butcher

Evaluation of Isotropic and Anisotropic Constitutive Models on Plasticity Prediction of AA7075 Extruded Tube Under Tension–Tension and Tension–Compression 681
Sobhan A. Nazari Tiji, Amir Asgharzadeh, Taejoon Park, Madhura Athale, and Farhang Pourboghrat

Estimation and Prevention of Strain Localization in Shear Tests 691
Heinrich Traphöner, Till Clausmeyer, and A. Erman Tekkaya

Experimental and Numerical Studies on Plastic Deformation and Failure Behavior of Carbon Nanotube-Reinforced Al Composite Sheet Under Uniaxial Loading Condition 709
Zhenming Yue, Xinrui Min, Zhanqiu Tan, Junyan Ni, Zhiqiang Li, Jun Gao, and Jie Zhang

Experimental Study on Uniaxial Strain Cyclic Behavior of GS-20Mn5 719
Zongyuan Zou, Shuting Han, Hongzhong Wang, Qun Li, Baofeng Guo, and Shiyan Zhao

Part X Constitutive Behavior

Influence of Deformation on Texture Development During Cold Drawing of Tubes 729
P. Bella, P. Burik, P. Bucek, and M. Ridzon

Dynamic Recrystallization Behaviors of 5083 Aluminum Alloys with Different Initial Microstructures Under Hot Compression 739
Sheng Ding and Jun Yanagimoto

Application of Barlat's Yld 2000-2d Yield Criterion to Predict the Anisotropic Response of Stainless Steel 749
Mauricio Vicente Donadon and José Divo Bressan

Evaluation of Press Forming Technique for Bent Automotive Body Parts Using In-Plane Shear Deformation 763
Yusuke Fujii, Masaki Urabe, Yuji Yamasaki, and Yoshikiyo Tamai

Simulation of Cold Forging Processes Using a Mixed Isotropic-Kinematik Hardening Model 773
Lander Galdos, Julen Agirre, Nagore Otegi, Joseba Mendiguren, and Eneko Saenz de Argandoña

Analysis of the Thermomechanical Flow Behavior of Carburized Sheet Metal in Hot Stamping 789
Alexander Horn and Marion Merklein

Effect of Short Pulsed-Current on Stress Relaxation in Uniaxial Tensile Test 801
Ichsan Indhiarto, Qiu Zheng, Tetsuhide Shimizu, Tsuyoshi Furushima, and Ming Yang

Experimental Study on Mechanical Response of Q235 Steel Under Cyclic Stress Loading 811
Qingling Zhang, Miao Jin, Baofeng Guo, and Qun Li

The Effect of Trace Nitrogen on Microstructure and Property of Cr-Mo-V Hot-Working Die Steel 829
Jinbo Gu, Jingyuan Li, and Lihao Li

Rate-Dependent Hardening Behavior of Autobody Sheet Metals in Tension and Compression 839
H. Huh, G. Joo, and M. K. Kim

Analysis of Creep Behavior of Magnesium Alloy Sheet (AZ31B) in Warm Forming 847
JaeHyeong Yu and Chang-Whan Lee

The Effect of Electroplasticity on the Flow Behavior of AA7075 in T6 Temper 857
Dong Hongrui, Li Xiaoqiang, Wang Haibo, Li Dongsheng, and Yang Yanfeng

Effect of Pulse Current on Mechanical Properties and Microstructure of Ultrahigh-Strength Steel 867
Xin Chen, Dongkai Xu, Lei Shi, Hua Xiao, Xifeng Li, and Jun Chen

Experimental Study and Modelling of Stress Relaxation Ageing Behaviour and Post-form Mechanical Properties in Creep Age Forming of Al-Zn-Mg Alloy 877
Yong Li, Fenggong Lyu, Zhusheng Shi, Yuansong Zeng, Xia Huang, and Jianguo Lin

Flow Behavior and Processing Map of a Nickel-Based Superalloy During Hot Plastic Deformation Process 891
Baoyun Zhang, Shuo Huang, Wenyun Zhang, Beijiang Zhang, and Yongquan Ning

Hot Deformation Behavior and Constitutive Modeling of a Novel Ni-Based Superalloy 901
Hao Yu, Hao Yang, Qi Liu, Baoyun Zhang, Bingchao Xie, and Yongquan Ning

Accurate Modelling of Flow Stress of AISI1025 at Room Temperature and Its Application to Precision Forging Simulation 911
M. S. Joun, M. K. Razali, J. B. Byun, and K. H. Lee

Stress-Relaxation Age Forming of a Component with Complex and Large Curvatures: Simulation and Manufacturing 921
Qi Rong, Zhusheng Shi, Yong Li, and Jianguo Lin

Toward an Efficient Industrial Implementation of W-temper Forming for 7xxx Series Al Alloys 935
Ricardo Trân, Lukas Kertsch, Sebastian Marx, Shreyas Hebbar, Verena Psyk, and Alexander Butz

Calibration and Validation of Stress–Strain Curve in High-Strain Region of Mild Steel Sheet 949
Hideo Tsutamori, Takeshi Nishiwaki, and Hiroaki Onishi

Influence of the Quenching Rate and Natural Ageing Duration on the Formability and Mechanical Properties of EN AW-7075 959
B.-A. Behrens, S. Hübner, H. Vogt, O. Golovko, S. Behrens, and F. Nürnberger

Constitutive Model and Plate Forging Ability of 5052 Aluminum Alloy Under Different Temperatures 973
Yantao Li, Wenzheng Dong, Qiquan Lin, and Zhigang Wang

Research on Rolling Process and Superplasticity for 5A90 Al–Li Alloy 983
Li Xiaoxing, Chen Yangkai, Lang Lihui, and Xiao Rui

Part XI Extrusion and Drawing

Co-Extrusion of Compound-Cast AA7075/6060 Bilayer Billets at Various Temperatures 993
Hui Chen, Danai Giannopoulou, Thomas Greß, Tim Mittler, Jonas Isakovic, Wolfram Volk, and Noomane Ben Khalifa

Reducing Aluminum Extrusion Transverse Weld Process Scrap 1003
Gregory J. Oberhausen, Anselm A. A. Christopher, and Daniel R. Cooper

Introduction of a New Method for Continuous Aluminum Hot Extrusion 1021
Johannes Gebhard, Patrick Kotzyba, Oliver Hering, and A. Erman Tekkaya

Study on Complex Extrusion of Multi Billets: Evaluation of Mechanical Properties of Butt-Joined Products and Analysis of Joining State 1033
Michihiko Hoshino and Izuru Otake

Effect of Expansion Ratio on Formability in Tube Drawing with Diameter Expansion 1043
H. Kawaguchi, T. Kuboki, I. Akasaka, Y. Terashita, M. Akiyama, and S. Kajikawa

Investigation of Forward–Backward–Radial Extrusion Process of Aluminum Alloy Wheel Hub 1055
Qiang Wang, Mu Meng, Xubin Li, and Zhimin Zhang

Part XII Forging

Galling-Free Micro-Forging of Titanium Wire with High Reduction in Thickness by β-SiC Dies 1065
Tatsuhiko Aizawa, Koh-Ichi Ito, and Tatsuya Fukuda

Deformation Mechanism of the Tooth Material Filling for Precision Forging of Spur Gears 1077
Wei Feng, Zengjie Feng, Mengjuan Zhou, Ling Mao, and Xiangyang Jia

Compression of Printed CFRT Composite: Shaping Parameters and Material Health 1087
Eric Becker, Victor Haguenauer, Ludovic Freund, Damien Félix, and Régis Bigot

Influences of Key Forging Parameters on Cold Orbital Forging of Thin Parts with High Circular Ribs 1099
Wuhao Zhuang, Xinghui Han, Lin Hua, and Wei Feng

FE-Based Investigation on the Influence of Inhomogeneously Heated Billets on Subsequent Forging Processes 1107
Arne Jagodzinski, Hendrik Gerland, Mareile Kriwall, Jan Langner, Malte Stonis, and Bernd-Arno Behrens

Development of Automatic Design System for Closed Die Forging Process of Disk-Shaped Products 1121
Yoshihiko Kobayashi, Eiji Sakamoto, and Tetsuya Yagami

A FE Billet Model and A Spring-Mass-Damper Model for the Simulation of Dynamic Forging Process: Application to a Screw Press 1131
Jean-François Mull, Camille Durand, Cyrille Baudouin, and Régis Bigot

Optimization of Open-Die Forging Using Fast Models for Strain, Temperature, and Grain Size in the Context of an Assistance System 1145
Fridtjof Rudolph, Martin Wolfgarten, Viktor Keray, and Gerhard Hirt

General Step Reduction and Enlargement Method for Knowledge-Based Process Planning of Totally Non-axisymmetric Forged Products with Blanking and Punching 1161
Masanobu Umeda, Yuji Mure, Keiichi Katamine, and Kazuya Matsunaga

Investigation of Failure Mechanisms of Cemented Carbide Fine Blanking Punches by Means of Process Forces and Acoustic Emission 1173
Herman Voigts, Rafael Hild, Andreas Feuerhack, and Thomas Bergs

Microstructural Evolution of Ti-55511 Titanium Alloy During Quasi-Beta Forging 1189
Yu-Qiang Jiang, Y. C. Lin, and Guo-Dong Pang

Part XIII High Speed and Impulse Forming

High-Speed Material Characterization Using an Instrumented Forging Hammer 1201
Julen Agirre, David Abedul, Angel Oruna, Nagore Otegi, and Lander Galdos

Advancements in the Simulation of Magnetic Pulse Forming Processes with FORGE® 1217
José Alves, François Bay, Ugo Ripert, Julien Barlier, and Nicolas Poulain

The High-Speed Deformation Behavior of High-Strength Lightweight Al-Li Alloy Sheets 1231
Ali Abd El-Aty, Shi-Hong Zhang, Xunzhong Guo, Yong Xu, Ma Yan, Dayoung Chen, and Jie Tao

The Effects of the High-Velocity Shearing Speed on the Sheared Edge Quality and Edge Cracking 1245
J. Gu, F. Alamos, D. Schoch, J. Bornhorst, and H. Kim

Local Microscopic and Integral Macroscopic Analysis of Magnetic Pulse Welds and Deformations for Dissimilar Metal Joints 1255
Frank Huberth, Balaji Ragupathi, Christian Scheffler, Verena Psyk, and Johannes Preußner

Computational Modeling of Magnetic Pulse Dissimilar Alloys Welding: Aluminum Alloy 6082-T6 and HC420LA Steel 1269
N. Rodriguez-Barrio, E. Iriondo, D. Jouaffre, and F. A. Girot

Influence of Ultrasonic Assistance on the Forming Limits of Steel 1281
Manuel Jäckisch and Marion Merklein

Design and Fabrication of a High-Performance Magnetic Actuator for Magnetic Pulse Welding of Metal Tubes with Large Diameters 1291
Xiaoxiang Li, Quanliang Cao, Zhipeng Lai, Yiliang Lv, Siyuan Chen, Yi zhang, Xiaotao Han, and Liang Li

Deformation Behavior in Magnetic Pressure Parallel Seam Welding 1305
Takashi Ichimura, Yusuke Ito, Makoto Miyazaki, and Akira Hatta

Shaping of Sharp-Edged Design Elements by Electromagnetic Forming 1315
Verena Psyk, Christian Scheffler, Albrecht Stalmann, and Martin Goede

Augmentation of Plasma-Based Impulse Generation with Rapid Chemical Reactions 1329
Brian Thurston, Yu Mao, Troy Lewis, Anupam Vivek, and Glenn Daehn

Recent Developments of Vaporizing Foil Actuator Technique for Manufacturing Applications 1341
K. Sajun Prasad, Jianxiong Li, Blake Barnett, Yu Mao, Glenn S. Daehn, and Anupam Vivek

Grain Size Effect on Formability in Electromagnetically Assisted Micro-Bulging of Pure Titanium Sheet 1351
Chengxi Zhu, Jie Xu, Haiping Yu, Debin Shan, and Bin Guo

Mathematical Model and Quantitative Analysis of Residual Stress Hole During Laser Shock Peening 1361
Xiuquan Cheng, Junhao Zhang, Sizhu Cheng, Chang Yan, and Qinxiang Xia

Part XIV Joining by Forming and Deformation

Simulation and Experimental Analysis of Electromagnetic Pulse Spot Welding of Sheet Metal with a Field Shaper 1373
Hang Zhang, Ning Liu, Qingjian Wang, and Hongfa Ding

Mechanical Properties of Aluminium/Stainless Steel Bimetal Composite Fabricated by Extrusion Process 1383
Kai Soon Fong, Danno Atsushi, Dharmesh Kumar, Wee Kiat Ong, and Suwat Jirathearanat

From Bridge to Bumper: Utilization of Pre-stressing During Manufacturing of Hybrid Sheet Metal Structures 1395
Henning Husmann and Peter Groche

Computer-Aided Modeling of the Hot Forming Staking Process Based on Experimental Data 1411
Sebastian Härtel, Eric Brückner, Birgit Awiszus, and Michael Gehde

Fatigue Characteristics and Failure Mechanism of Self-piercing Riveted Joints of DP590 and AA6061 Plates 1423
Zhichao Huang, Yinglian Jia, and Jiamei Lai

Fretting Damage and Fatigue Property Analysis of Self-piercing Riveted Joints of AA5052 Aluminium Alloy 1437
Zhichao Huang, Yongchao Zhang, and Jiamei Lai

Elastoplastic Finite-Element Analysis of Multi-Body Processes for Joining Mechanical Parts 1451
SukHwan Chung, Jaedong Yoo, and ManSoo Joun

A New Non-destructive Testing Method Applied to Clinching 1461
Rémi Lafarge, Alexander Wolf, Christina Guilleaume, and Alexander Brosius

Investigation on the Strain Induced Oxide Layer Fracture and Bonding During Cold Rolling of Aluminum Alloys 1469
Mahsa Navidirad, Wojciech J. Stepniowski, Elijah Cartier, Tyler Christ, Masashi Watanabe, and Wojciech Z. Misiolek

Ultrasonic Forming—Alternative to Orbital Riveting for Small Bimetallic Components 1479
Wojciech Presz

Self-Piercing Riveting Using Rivets Made of Stainless Steel with High Strain Hardening 1495
Benedikt Uhe, Clara-Maria Kuball, Marion Merklein, and Gerson Meschut

Numerical and Experimental Investigations on Riveting Assembly Processing Parameters of Hub Bearing Unit 1507
You Wang, Wei Xiong, Jia-hua Zhou, and Peng Ren

Part XV Lubrication and Surface Effects

Evaluation of Lubricant Performance for Thick Sheet Ironing Process by Ball Ironing Test 1519
Nuttakorn Sae-eaw and Yingyot Aue-u-lan

Development of Oil-Type Lubricants for Cold Forging Using Phase Transition Behavior Under High-Pressure Conditions 1529
Tomoaki Okano, Nobuhide Tanino, and Kazuhiko Kitamura

Analysis of Work Hardening and Tribological Changes After a Gap Controlled Drawbead Passage 1537
Harald Schmid and Marion Merklein

Investigations on Dynamic Characteristics of a Mechanical Press Considering Both Translational Clearance Joint and Lubrication Effect 1549
Xuze Wu and Yu Sun

Part XVI Microstructure and Damage Development and Characterization

Temperature-Dependent Fracture Loci of AZ31 Magnesium Alloy Sheets 1563
R. Bertolini, Q. Wang, A. Ghiotti, and S. Bruschi

Influence of Specimen Preparation Methods on the Mechanical Properties and Superplastic Behavior of AA5083 Sheets 1573
Mohammad S. Dastgiri, Leo Kiawi, Iman S. Sarraf, Eugene Ryzer, and Daniel E. Green

Application of the Nondestructive Evaluation (NDE) Method to Evaluate the Sheared Edge Quality and Edge Cracking 1585
J. Gu, N. Pathak, S. Freed, E. Todorov, and H. Kim

An Extended Ductile Fracture Prediction Model Considering Hydrostatic Stress and Maximum Shear Stress 1595
Zhe Jia, Lei Mu, Ben Guan, and Yong Zang

Full-Field Strain Measurement in Multi-stage Shear Cutting: High-Speed Camera Setup and Variational Motion Estimation 1605
Christoph Hartmann and Wolfram Volk

A Novel Continuum Damage Constitutive Model for Predicting the Formability of AA7075 Alloy at Elevated Temperatures 1617
Hai Rong, Liang Ying, Ping Hu, and Wenbin Hou

The Influence of Temperature and Strain Rate on the Superplastic Deformation Behavior and Microstructure Evolution of TNW700 Alloy 1623
Lixia Ma, Min Wan, Weidong Li, Jie Shao, and Xuepiao Bai

Finite Element Simulation of Edge Fracture by Mapping the Shear-Induced Ductile Damage into Hole-Expansion Simulation 1633
Lei Mu, Zhe Jia, Ben Guan, and Yong Zang

Relaxation Characteristics of Creasing Process of Scored Paperboard for Liquid Container 1643
Shigeru Nagasawa, Takaomi Nagumo, Azusa Sakamoto, and Kazuki Umemoto

Hot Cutting of Press-Hardened Parts in Different Heat Treatment Regimes 1655
R. Schmidt, A. Rautenstrauch, and V. Kräusel

High-temperature Properties of Hot-Work Tool Steel (AISI H13) Deposited via Direct Energy Deposition 1665
Jongyoun Son, Gwangyong Shin, Kiyong Lee, Chang-hwan Choi, and Dosik Shim

The Study of Energy Absorption of Dual-Material Tailored Plane Strain Sheet 1677
Pengfei Ying, Yulong Ge, and Yong Xia

Cyclic Hardening/Softening of a TRIP Duplex Stainless Steel 1691
Miao Jin, Lei Chen, Zongyuan Zou, Shuo Hao, Qun Li, and Shiyan Zhao

The Local Strain Evolution for Structured Sheet Metals During Uniaxial Deformation 1701
Evgenia Ermilova, Alexander Nikitin, and Sabine Weiß

Part XVII Microstructure Development by Forming

Development and Implementation of Static Recrystallization Model of 6XXX Aluminum Alloy Using Industrial Experiments 1715
Artem Alimov, Ivan Kniazkin, and Nikolay Biba

The Effect of T8 Heat Treatment on Wear Behaviour and Microstructure of 6063 Aluminium Alloy Deformed by Cryo and RT ECAP 1727
Srinivasulu Arnuri and Swami Naidu Gurugubelli

Metal Foils for Bipolar Plates—Correlation of Initial Grain Size and Forming Behavior of 316L 1743
Alexander Bauer, Thomas Mehner, Birgit Awiszus, and Thomas Lampke

Study of the Influence of the Mixed-Grain Structure on the Microscopic Deformation Behavior of 316LN Steel 1757
Y. Q. Li, H. M. Zhang, M. X. Liu, and Z. S. Cui

Dependence of Mesoscale Structure of Drawn High-Carbon Steel Wire on Wire Diameter 1767
Shiori Gondo, Rena Tanemura, Ryuki Mitsui, Satoshi Kajino, Motoo Asakawa, Kosuke Takemoto, Kenichi Tashima, and Shinsuke Suzuki

Thermomechanical Analysis and Experimental Validation of ECAP for Aluminum Sheet Metal 1775
Maximilian Gruber, Yiheng Yang, Christian Illgen, Philipp Frint, Martin F.-X. Wagner, and Wolfram Volk

Transformation of α→β During Hot Deformation in the Two-Phase Region of Ti–6Al–2Zr–1Mo–1V Alloy 1791
Lei Chen, Qifei Zhang, Qun Li, Miao Jin, Shiyan Zhao, and Baofeng Guo

Formability Improvements of AA5754-H32 at Room Temperature via Continuous Bending Under Tension (CBT) and Pre-forming Heat Treatment 1805
Jinjin Ha, Antonio Piccininni, Yannis P. Korkolis, Gianfranco Palumbo, Marko Knezevic, and Brad L. Kinsey

Microstructure Evolution During Isothermal Forging of 7A85 Aluminum Aviation Component 1813
Jian-Liang Hu, You-Ping Yi, Miao Jin, and Hong Bo

The Deformation and Microstructure Analysis of Medium Carbon Steel During Die Forging Process and the Effect of Microalloying Elements 1827
Bo Jiang, Guoning He, Chengcheng Zhang, Xiaolei Ma, Chaolei Zhang, and Yazheng Liu

Effect of Ferrite Rolling Temperature on the Microstructure and Properties of an Ultra-Low Carbon Steel Produced by CSP Process 1841
Guoning He, Xuewen Hu, Bo Jiang, Chaolei Zhang, Haibo Wang, and Yazheng Liu

The Effect of Temperature on the Strain-Induced Austenite to Martensite Transformation in SS 316L During Uniaxial Tension 1853
Elizabeth M. Mamros, M. Bram Kuijer, Mohammad Ali Davarpanah, Ian Baker, and Brad L. Kinsey

Energy-Dependent Surface Integrity of Stainless Steel AISI 304 After Robot-Based Machine Hammer Peening 1863
Robby Mannens, Lars Uhlmann, Andreas Feuerhack, and Thomas Bergs

Non-isothermal Modeling of Static Recrystallization in Hydroformed Steel Tube Using a Coupled Cellular Automata and Finite Element Model 1879
Amir Asgharzadeh, Sobhan Alah Nazari Tiji, Taejoon Park, and Farhang Pourboghrat

Fast Development of New Alloys for Metal Forming Using Additive Manufacturing 1893
Alexander Sviridov, Irina Sizova, and Markus Bambach

Effects of Residual Strain on Grain Growth of Extruded Aluminum Micro-channel Tubes During Heat Treatment 1903
Wenli Fang, Xiaole Chen, Ding Tang, Huamiao Wang, Dayong Li, and Yinghong Peng

Forming of Parts with Locally Defined Mechanical and Ferromagnetic Properties by Flow-Forming 1913
Eugen Wiens, Werner Homberg, Bahman Arian, Kerstin Möhring, and Frank Walther

Constitutive Modeling and Processing Map of Ti–5Al–5Mo–5V–3Cr–1Zr Alloy During Hot Deformation 1925
Yuting Zhou, Jie Zhou, and Peng Wang

Part XVIII Mini-Symposia Characterization of Plasticity and Ductile Fracture of Metals under Proportional and Non-proportional Loading

Establishment of Sheet Plastic Wrinkling Instability WLD and Study on Strain Distribution Characteristics in Instability Region 1939
Bing Du, Han Li, Jun Xie, Pengfei Song, and Changcai Zhao

Plasticity and Fracture Characterization of Advanced High-Strength Steel: Experiments and Modeling 1947
Fei Han, Changwei Lian, Jichao Zhang, and Haomin Jiang

Design of a New Cruciform-Like Specimen for Combined Tension and Shear of Metal Sheets 1961
Minki Kim, Jinjin Ha, Samantha Bonica, and Yannis P. Korkolis

A Study of Anisotropic Yield Function Based on J_2 and J_3 Invariants 1969
YoungSuk Kim, PhuVan Nguyen, and JinJae Kim

Experimental Implementation of SS 316L Cruciform Testing to Achieve Various Deformation Paths 1981
Elizabeth M. Mamros, Sarah M. Mayer, Jinjin Ha, and Brad L. Kinsey

An Application of Homogeneous Anisotropic Hardening Model to the Prestrained Hole-Expansion Experiment 1991
Jinjin Ha and Yannis P. Korkolis

Work Hardening and Fracture Strain Evaluation of Hardened SKD11 Steel Using Shear Punching Test 1999
Takashi Matsuno, Kouta Nakagiri, Hiroto Shoji, and Mitsuru Ohata

Deformation of Metals Under Complex Loading 2009
R. A. Abirov

Part XIX Novel Processes

Numerical Simulation of Tube Bending Supported by Hydraulic Pressure for Manufacturing Butt-Welding Fittings 2019
Josef Domitner, Peter Auer, and Christof Sommitsch

Fluidity of Wood Composite Combined with Natural Binder on Injection Molding 2031
Shohei Kajikawa, Masaya Horikoshi, Takashi Kuboki, Soichi Tanaka, Kenji Umemura, and Kozo Kanayama

Accurate Mapping of Thermal Camera Measurements on Planar Deformations 2041
Celalettin Karadogan and Mathias Liewald

Effect of Bending Intensity on Straightness in Spinner Straightener 2055
Keiichiro Kawasaki, Shohei Kajikawa, Hiromichi Matumura, Tetushi Ono, Hikaru Seimiya, and Takashi Kuboki

Using Local Heat Treatment for Producing Uniform Profile Hollow Components by Radial Rotation Profile-Forming 2067
Robert Laue, Sebastian Härtel, and Birgit Awiszus

Analysis of Tube Spinning 2077
E. C. Sarıyarlıoğlu, O. Music, and M. Bakkal

Transcription of Mirror-Finished Surface onto A5083 Aluminum Alloy Plate by Friction Stir Forming 2089
Takahiro Ohashi, Kento Okuda, Hamed Mofidi Tabatabaei, and Tadashi Nishihara

Combined Computed Tomography and Numerical Modeling for the Analysis of Bending of Additively Manufactured Cellular Sheets 2099
S. Rosenthal, E. Jost, C. Saldana, T. Clausmeyer, M. Hahn, and A. E. Tekkaya

Cutting Blades for Food Processing Applications Manufactured Using Innovative Spin Forming 2115
Tim Rostek, Hanna Makeieva, and Werner Homberg

Influence of Axial Feed Rate on Shape and Thickness Changes During Multi-Pass Tube Spinning: Experiments and Modelling 2127
Biplov K. Roy, Yannis P. Korkolis, Yoshio Arai, Wakako Araki, Takafumi Iijima, and Jin Kouyama

A Brief Review on Theoretical Aspects of Bar Straightening with Recent Developments in Its Modelling, Simulation, Control System, and Stabilization 2135
Sanjib Roy, Arun Kiran Pal, and N. K. Das Talukder

Development of Anti-Loosening Bolts Based on Innovative Double Thread Mechanism 2155
Teruie Takemasu, Toshinaka Shinbutsu, Shuichi Amano, and Jyo Shimura

Study on Precision Forging Methods of Difficult-to-Knockout Components with Non-parallel Internal Grooves 2167
Luyi Han, Guangchun Wang, Xin Wang, and Zhao Liu

Incremental Grooving of Thin-Walled Tubes Filled with Discrete Media 2179
Hao-Xing Tang, Tong Wen, and Xia Chen

Vacuum Hot-Roll Bonding of Titanium and Carbon Steel Using Pure Iron Interlayer 2189
Chao Yu, Hong Xiao, and Xiao Liu

Investigation on the Whole Forming Process of Super-Large Flat Ring 2201
Dan Xie, Wujiao Xu, Yu Wang, and Rui Chen

Development of a New Printing Method Using Soft Material Tools 2211
Yasuharu Yoshikawa and Yusuke Masegi

Plasticity Improvement of CNTs/Mg Nanocomposite Materials Processed by Combining Friction Stir Processing and Ultrasonic-Assisted Extrusion 2221
Qian Zhang, Lehua Qi, Jiming Zhou, Jun Luo, and Junhao Liang

Part XX Residual Stresses in Metal Forming

Complementary Methods for Assessment of Residual Stress Fields Induced by Rotary Swaging of Steel Bars 2233
Dhia Charni, Svetlana Ishkina, Jérémy Epp, Marius Herrmann, Christian Schenck, and Bernd Kuhfuss

Investigations and Improvements in 3D-DIC Optical Residual Stress Analysis—A New Temperature Compensation Method 2249
Frederik Dahms and Werner Homberg

Formation of Residual Stresses in Austenitic Stainless Steels by Infeed and Recess Rotary Swaging 2261
Holger Hoche, Fabian Jaeger, Alessandro Franceschi, Matthias Oechsner, and Peter Groche

Influence of Material Delivery Condition on Residual Stresses and Part Properties During Forward Rod Extrusion 2277
Andreas Jobst and Marion Merklein

Experimental and Numerical Investigations on the Development and Stability of Residual Stresses Arising from Hot Forming Processes 2289
Bernd-Arno Behrens, Jörg Schröder, Hendrik Wester, Dominik Brands, Sonja Uebing, and Christoph Kock

Analysis of Cylindrically and Spherically Embossed Flux Barriers in Non-oriented Electrical Steel 2303
Ines Gilch, Simon Vogt, Tobias Neuwirth, Benedikt Schauerte, Kay Hameyer, Michael Schulz, Alex Gustschin, Wolfram Volk, and Hannes Alois Weiss

Analysis of Influencing Factors on the Achievability of Bistable Fully Closed Shells by Semi-Analytical Modeling 2319
Pavlo Pavliuchenko, Marco Teller, and Gerhard Hirt

Influence of Shear Cutting Process Parameters on the Residual Stress State and the Fatigue Strength of Gears 2331
Daniel Müller, Jens Stahl, Isabella Pätzold, Roland Golle, Thomas Tobie, Wolfram Volk, and Karsten Stahl

Residual Stresses in Hot Bulk Formed Parts—A Phenomenological Approach for the Austenite-to-Martensite Phase Transformation 2345
S. Uebing, D. Brands, L. Scheunemann, C. Kock, H. Wester, B.-A. Behrens, and J. Schröder

Local Creation of Uniform Residual Stresses Into Sheet Metal Components by Means of Multiple One-Side Embossing 2357
Stefan Walzer, Nicola Simon, Mathias Liewald, and Jens Gibmeier

Part XXI Rolling

Hot Ring Rolling and Cold Expanding Strengthening of Mn18Cr18N Thick-Wall Hollow Ingots 2371
Huiqin Chen, Huihua Wen, Jinliang Wang, Fei Li, and Wenwu He

Achieving an Interference Fit Between Two Rings During Composite Ring Rolling 2381
Christopher J. Cleaver and Julian M. Allwood

Advanced Design of Work Roll Contours for Different Roll Mill Types 2395
Xiawei Feng, Xiaochen Wang, Quan Yang, and Zedong Wu

Study on the Transferability of Rolling with Ordered Texturing Roll 2405
Yasuyuki Fujii, Yasushi Maeda, and Hiroshi Utsunomiya

Fundamentals of Continuous Helicoid Auger Flighting Rolling—Deformation Mechanics, Kinematics, and Applications 2419
Ming He

Evaluating an Automated Avoidance of Ring Climbing in Radial–Axial Ring Rolling 2453
Simon Husmann and Bernd Kuhlenkötter

Effect of Delivery Angle on Longitudinal Buckling in Temper Rolling of Thin Steel Strips 2467
Toshiro Okazaki, Yukio Kimura, Hideo Kijima, and Masaru Miyake

A Fast Computational Model for the Local Stress Distribution and Mechanical and Thermal Work Roll Deformations with Effects on Strip Profile and Flatness During Hot Rolling of Strip in Four-High Mills 2483
Christian Overhagen

Investigation of a Novel Constructive Hot Ring Rolling Process for Double Metal Composite Ring 2497
Jiadong Deng, Zhe Cheng, Dongsheng Qian, Jikang Liu, and Rongwen Wu

Effect of Feed Rate on Texture Evolution of 42CrMo Casting Blank During Hot Ring Rolling 2507
Huiping Qi, Fangcheng Qin, Yongtang Li, Huiqin Chen, Chongyu Liu, and Haiquan Qi

A Novel Flexible Skew Rolling Process for Step Shafts: Feasibility Study 2521
Longfei Lin, Baoyu Wang, and Jinxia Shen

A Computational Study on the Producible Rolling Thickness in Ultra-Thin Strip Rolling 2533
Xiao Liu, Chao Yu, and Hong Xiao

Forming Surface Texture on Copper Sheets by Electrically Assisted Micro-Rolling 2547
Zhenhai Xu, Shaoxi Xue, Chunju Wang, Rui Xi, Debin Shan, Guo Bin, and Baosheng Liu

Decoupling of Adverse Effect of Inter-Roll Thrust Force on Steering Control During Strip Rolling 2557
Kazuma Yamaguchi and Atsushi Ishii

Part XXII Sheet Forming

Evaluating the Reliability of a Nondestructive Evaluation (NDE) Tool to Measure the Incoming Sheet Mechanical Properties 2573
Fernando J. Alamos, Jiahui C. Gu, and Hyunok Kim

Study on the Effect of Embossing on the Bending Properties of High-Strength Sheet Metals 2585
David Briesenick, Stefan Walzer, and Mathias Liewald

On the Determination of the Forming Limits by Necking and Fracture of Polycarbonate Sheet 2597
A. Rosa-Sainz, G. Centeno, M. B. Silva, J. A. López-Fernández, A. J. Martínez-Donaire, and C. Vallellano

The Effects of Press Ram Vibrations on the Production Quality 2609
Bernd-Arno Behrens, Kai Brunotte, Richard Krimm, and Oliver Commichau

Localized Contact Pressure of Blankholder for Stamping Irregular Sheet Parts by Configuring the Height of the Supporting Elements 2619
Kuang-Jau Fann, Mathias Liewald, and Kim Rouven Riedmüller

Evaluating 980GEN-3 Steel with Tested and Numerical Forming Limit Curves 2631
T. Feister, L. Zoller, J. Gu, and H. Kim

Formability of Functional Corrugated Cup 2639
Y. Harada and Y. Nishikubo

Experimental and Numerical Investigations into the Influence of the Process Parameters During the Deep Drawing of Fiber Metal Laminates 2649
T. Heggemann, H. Sapli, and W. Homberg

Experimental Analysis on Granular Media-Based Tube Forming with Active Axial Feed 2661
E. Hoffmann, C. Löbbe, and A. E. Tekkaya

Finite Element Simulation and Punch Design for Tube Hydro-Piercing 2671
Yeong-Maw Hwang, Wei-Han Dai, and Pin-Chen Lin

Novel Roll-Bonded Stainless Steel/Boron-Steel Multilayer Under Hot Stamping Conditions 2683
Mike Kamaliev, Marco Teller, Christian Löbbe, Gerhard Hirt, and A. Erman Tekkaya

Effect of Machining Induced Microstructure Changes on the Edge Formability of Titanium Alloys at Room Temperature 2695
J. S. Kwame, E. Yakushina, and P. Blackwell

Investigation on Springback Behavior of Multi-intersecting High Stiffened Structure in Die Forming 2705
Qiyuan He, Weidong Li, Min Wan, Cailing Li, and Chao Cui

Size Effect on Cyclic Deformation Behavior and Springback Prediction of Ultrathin Superalloy Sheet 2719
Weilin He, Bao Meng, Bingyi Song, Rui Zhao, Li Zhang, and Min Wan

Hydro-Mechanical Deep Drawing of Locally Solution-Treated Aluminum Alloy Sheets 2729
Takeshi Nishiwaki, Ryota Sako, and Hideo Tsutamori

Development of Adhesion Preventing Method During Deep Drawing of Titanium Alloy Sheets 2741
Yusuke Okude, Taku Iwaoka, and Isao Nakamura

Development of Warm Press Forming Process Method of Ti–6Al–4 V Alloy Sheet 2751
Yusuke Okude, Taku Iwaoka, Isao Nakamura, and Takashi Katagiri

Research on New Hot Stamping Tool with Low-Cost and High-Efficiency Cooling 2759
Shixin Peng, Jie Zhou, Mengmeng Zhang, Kemin Zhang, and Jie Liu

Formability Analysis of a Local Heat-Treated Aluminium Alloy Thin-Walled Tube 2767
A. Piccininni, J. P. Magrinho, M. B. Silva, and G. Palumbo

Analysis of Material Work Hardening and Fracture Strains for Sheet Metal Stamping Processes 2777
Sergey Golovashchenko, Srecko Zdravkovic, Natalia Reinberg, Saeid Nasheralahkami, and Weitian Zhou

A New Approach for the Production of Burr-Free Sheet Metal Components Having Significantly Increased Residual Formability 2789
Sergei Senn and Mathias Liewald

Fine-Piercing of Electrical Steel Sheets by Edge-Sharpened Diamond Punch 2807
Tatsuhiko Aizawa and Tomomi Shiratori

An Investigation on Formability of Ti6Al4V Alloy in the Three-Layer Sheet Hot Stamping Process 2819
Xiaoming Yang, Baoyu Wang, and Chuanbao Zhu

The Effects of Servo Press Forming on Various Strain Path Failures 2829
L. Zoller, T. Feister, and H. Kim

Part XXIII Technologies to Speed Innovation

Recent Advances on Modeling Plastic Deformation of Textured Metals with Applications to Metal Forming 2839
Oana Cazacu and Benoit Revil-Baudard

Experimental Investigation of Different WAAM (Wire-Arc Additive Manufacturing) Processes and Their Influence on the Component Properties and Formability 2853
Pascal Colditz, Marcel Graf, André Hälsig, Sebastian Härtel, Keval P. Prajadhiama, Yupiter P. Manurung, and Birgit Awiszus

Validation of Automatically Generated Forging Sequences by Using FE Simulations 2867
Yorck Hedicke-Claus, Mareile Kriwall, Jan Langner, Malte Stonis, and Bernd-Arno Behrens

Tube Forming and Fabricating Technologies for Contributing Society by Tackling Problems of Environment and Aging Population 2883
Takashi Kuboki, Atsushi Shirayori, Masaaki Mizumura, Noah Utsumi, and Yeong-Maw Hwang

Multi-objective Sizing Optimization of Elbow-Bar Driving Mechanism of Cold Forging Press 2899
Xinyu Dong and Yu Sun

Pre-forging Shape Design Using Conformal Mapping Method 2909
Chengshang Liu, Wujiao Xu, and Minyao Liu

Part XXIV Value of, and Limits to, Simulation

Constitutive Law Parameter Identification for Hot Forging Using Compression Experiments on Forging Presses 2919
Gabriel Venet, Cyrille Baudouin, and Tudor Balan

FE Simulations of Piercing and Trimming of AL and AHSS Alloys 2925
David Diaz-Infante, Advaith Narayanan, Adam Groseclose, and Taylan Altan

Finite Element Method Based on Space Mesh 2939
Gang Yang and Atsushi Kinoshita

Comparison on the Processing of Height Deviations of Disks from FEM and Real Rollings in Radial-Axial Ring Rolling 2947
Thomas Glaser, Patrick Schwarz, Simon Fahle, Kai Uwe Paffrath, and Bernd Kuhlenkötter

PID Controller Integrated with FEM Model to Generate Boundary Conditions for Free Tube Bulging for Tubular Material Characterization 2959
Sobhan Alah Nazari Tiji, Taejoon Park, Hyunki Kim, Amir Asgharzadeh, Madhura Athale, Ji Hoon Kim, and Farhang Pourboghrat

Author Index 2969

Subject Index 2979

Part I
Honorary Symposium: Taylan Altan

Self-optimized, Intelligent Open-Loop-Controlled Steel Strip Straightening Machine for Advanced Formability



Fabian Bader, Lukas Bathelt, Eugen Djakow, Werner Homberg, Christian Henke, and Ansgar Trächtler

Abstract Innovative self-correcting process control techniques which adapt to the initial geometric characteristics of the strip are a promising approach to fix the local varying distortion of coiled strips by optimizing the leveling process. This paper presents an innovative strategy to improve straightening of AHSS materials (1.4310). This implies optimized leveling, adding minimal plastic deformation, and, thus, strain hardening. Therefore, an "intelligent straightening machine" is being developed which will be presented. To operate an intelligent straightening machine a reliable online measurement of the surface defects is fundamentally essential. This paper describes an approach towards the measurement of a bent steel strip for an automatic straightening process. Therefore, various ways of measuring the bending curvature are investigated. Optical, tactile, and the electromagnetic induction testing MagnaTest are compared with each other. The bending measurement is linked to open-loop control, providing an optimal straightening result in regards of formability, leveling, and reduced strain hardening.

Keywords Intelligent straightening machine · Innovative measurement system · Residual stress · Degeneration of elastic modulus

1 Introduction

As a result of increasing globalization and rising quality requirements, the steel and metal processing industry is facing growing cost and innovation pressure to meet market demands. Not least because of their high lightweight construction potential, high-strength steel materials meet the growing material requirements of steel and metal processing, such as geometrical and dimensional accuracy in various fields of the industry, including aerospace, medical, and electrical connectivity technology.

F. Bader (✉) · E. Djakow · W. Homberg
Department of Forming and Machining Technology, Paderborn University, Paderborn, Germany
e-mail: fb@luf.upb.de

L. Bathelt · C. Henke · A. Trächtler
Fraunhofer IEM, Paderborn, Germany

© The Minerals, Metals & Materials Society 2021

G. Daehn et al. (eds.), *Forming the Future*, The Minerals, Metals & Materials Series,
https://doi.org/10.1007/978-3-030-75381-8_1

The especially narrow tolerances and dimensional accuracy required in processing high-strength steel strip materials present economic and ecological challenges. These are best addressed by improving the processability of high-strength steel materials using straightening devices with setup assistance systems to significantly increase their potential to compete with other materials in the market. These system configurations achieve a higher amount of acceptable formed parts, reducing the quantity of rejects, thus requiring less material and financial resources. The setup assistance systems require additional information regarding material behavior during straightening as well as the straightening process in general.

Numerous publications regarding various topics of investigation of the straightening process have been conducted. To achieve a straightened steel strip, it is first necessary to correctly set up and adjust the straightening machine while its input parameters are changing, which naturally takes place while the material is uncoiled and the curvature of the steel strip changes. Therefore, it is necessary to analyze the material and its forming history as the subsequent forming behavior of the steel strip is directly linked to the state of residual stresses. Hence, [4, 6, 11, 13] analyzed the residual stresses of the steel strip to increase the accuracy of a following FEM calculation. These numerical investigations are used to identify a suitable setup of the straightening roll infeed and the state of stress within the material [3, 5, 10, 12]. But not only numerical calculations are expedient, analytical models can help as well to provide information concerning the infeed of the straightening rolls, as shown in [1, 2, 7, 8]. Morris et al. [9] show the impact that the different adjustable machine rolls have, and demonstrate that the second adjustable roll of the often used seven roll straightening machine has the most impact on curvature, and, consequently, the straightening process. In order to use the calculation results and to straighten a steel strip, an electro-mechanical automated straightening machine is required.

2 Intelligent Straightening Process

In order to meet the requirements of the economical and ecological challenges, the process chain must be modified. Rather than adjusting the rolls of the straightening machine by hand, it needs to be automated. Consequently, there are several different matters that need to be developed/investigated. The test rig setup is shown in Fig. 1.

Live measurement of the steel strip curvature is essential for an automated straightening machine. Continuously gathering the curvature and other surface defects of the steel strip facilitates an automated response to eliminate the curvature. Process steps (straightening roll setup) to react on the changing curvature are indispensable for the automated straightening machine. Therefore, a finite element model is required. The results from the numerical calculation at the first step are fed to a database, which provides the control of the straightening machine with data regarding the roll setup. There is a possibility of using a (semi-) analytical model live, as it may be fast enough to calculate the roll setup after receiving the measured curvature of the sensors, but until that is developed, and its accuracy is meeting the numerical model,

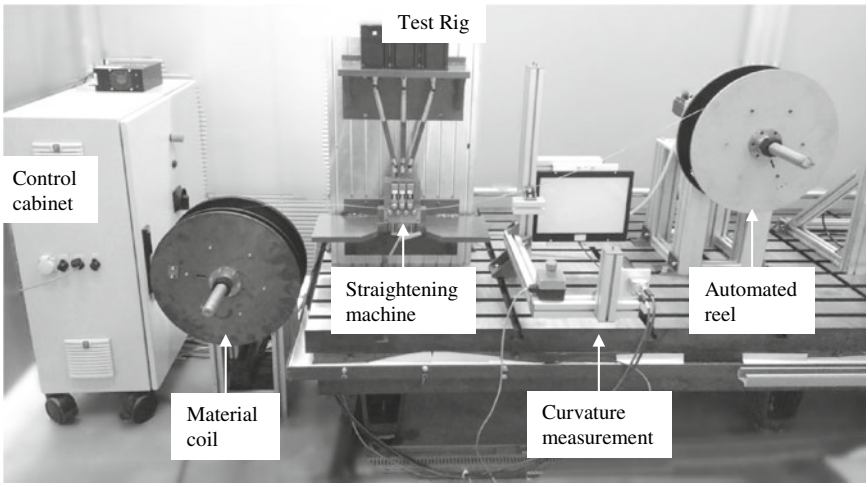


Fig. 1 Test rig setup

the finite element model will be used. The straightening rolls of the straightening machine are connected to guide rails, which are powered by stepper motors. This holistic approach of straightening a steel strip leads to an increased formability and a reduced degeneration of the yield limit, which is preferable for subsequent forming operation.

3 Sensors

The sensor technology includes an upstream detection for the fluctuations in material properties. For this purpose, a magnetic inductive eddy current measurement of the steel strip is carried out using the MagnaTest D system of the Foerster company. The physical principle of this measurement is based on the combination of two coil windings around a die into which the component to be tested is inserted. A switched alternating current in the transmitter winding results in a magnetic field, which induces eddy currents in the material under test. These eddy currents induce another magnetic field, the secondary field, and its influence on the second coil, the receiving sensor, is measured. This influence is evaluated by determining the phase and amplitude shift of the received signal compared to the transmitted signal, and is displayed by the evaluation unit in the impedance plane (Fig. 2a). The evaluation unit enables the measuring points of different components to be categorized, making it possible to detect components that are made of different materials.

For the measurement of the steel strip, the dependency of the residual stresses of the steel strip on the secondary field and thus the measurement results at the receiving sensor are used. As shown in Fig. 2b, the steel strip curvature is indirectly dependent

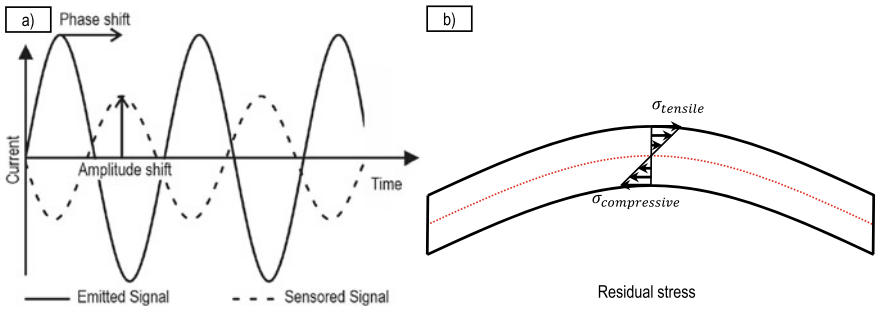


Fig. 2 **a** Phase and amplitude shift **b** residual stresses within the steel strip while bending. (Color figure online)

on the residual stresses in this way, so that the MagnaTest can be used to determine a change in curvature.

The measurement results of a test run are shown in Fig. 3. The test procedure is simple. Up until 25 s the steel strip, as it is, was pulled through the magnetic induction sensor. Then the straightening device was adjusted that one roll was changing the curvature of the steel strip. As indicated, the imaginary part as well as the real part decreases, which can directly be linked to the change of curvature. Since it is not yet possible to assign the magneto-inductive measurement to absolute radii of curvature, a setup procedure for the straightening apparatus is necessary. Hence, the current steel strip curvature is determined at the beginning with the help of a camera-based

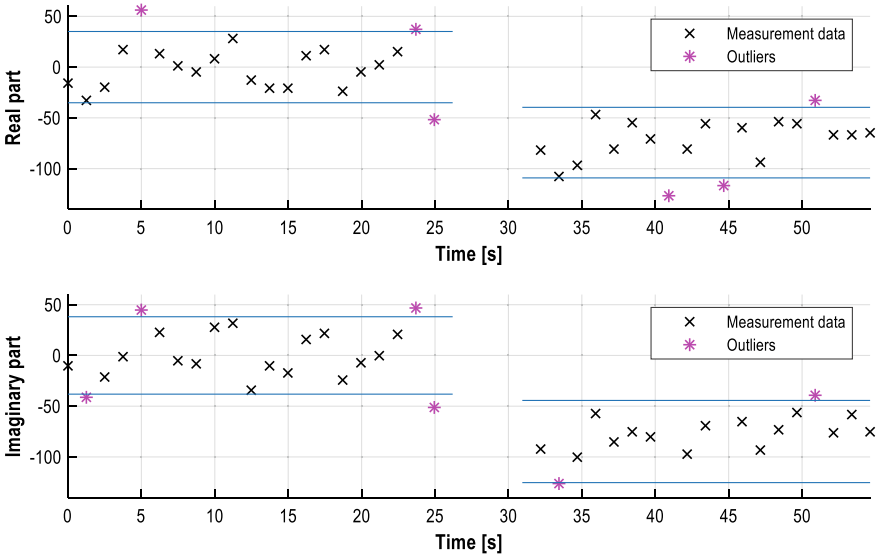


Fig. 3 Measurement results of a curvature change. (Color figure online)

recognition. A camera system from Balluff is used for this purpose, which enables a semi-automated evaluation and curvature determination at the free end of the wire. With this information, the straightener is initially set using the model-based values. The property changes in the material over the entire length of the coil are recorded by MagnaTest D. Thus, the straightening machine is adjusted accordingly. In addition, three load cells determine the forces transmitted by the straightening rolls into the material at each point in time, thus monitoring the process.

When a new coil is inserted, the straightening process begins by optically detecting the current curvature in the wire via the camera. For this purpose, the gravity force is calculated, its influence is subtracted from the optical image, and thus the current steel strip curvature is determined. This curvature value is then fed to the model together with the material parameters and the geometry data. Consequently, the target positions of the straightening rolls, which are then adjusted, are calculated, and the unwinding of the coil can begin. The magnetic induction measurement records the changes in the material properties with the continuous decoiling of the steel strip. Based on this change, the position of the straightening rolls is constantly readjusted so that the straightening result is as uniform as possible.

4 Finite Element Calculation of the Straightening Process

Finite element simulations of the straightening process were conducted to build a database where the significance and the influence of various parameters can be determined. The yield limit from a tensile test of the virgin 1.4310 material is 1719 MPa, while the ultimate tensile strength reaches1939 MPa and Young's modulus is 176 GPa.

The steel strip is subject to a non-linear strain path by alternating bending, and, consequently, it is crucial to describe the material behavior precisely. Hence, it is important to take the Bauschinger effect into account, which describes the early re-yielding of the material in case of pressure loading, which is the case at alternating bending. The Yoshida-Uemori (Y-U) material model [14] accounts for the Bauschinger effect. This model has two yield surfaces. One yield surface represents the kinematic hardening, which upon reaching a certain threshold, affects the isotropic hardening. In this model the isotropic hardening is regarded by the bounding surface, which surrounds the kinematic yield surface [14]. In LS-Dyna, there are different types of material cards that are either the standalone Y-U-model (Mat125) or a combination of the Y-U and Barlat model (Mat226 and Mat 242). For this work, the material type 125 will be used. Additionally, the elastic modulus, which is degenerating under plastic loading, will be taken into account in this material model.

The parametrization of this complex material model requires the testing of three different types of load for the material. A tensile test, a tensile-pressure test (Fig. 4a) to identify the early re-yielding phenomenon, and a cyclic loading-unloading test in the tensile domain, to identify the degeneration of the elastic modulus (results

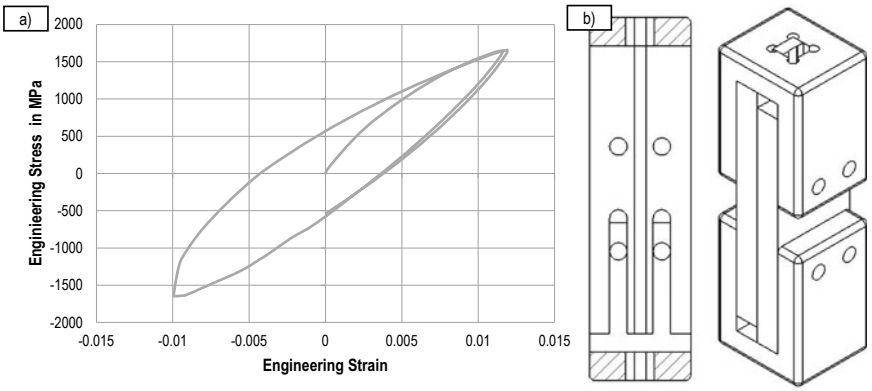


Fig. 4 **a** Tensile-pressure curve. **b** Anti-buckling device for pressure tests

in 176 GPa). Tests were carried out in the department of forming and machining technology lab of Paderborn University. In order to identify the material parameters for the Yoshida-Uemori material card, these exact tests need to be modeled in LS-Dyna for the parameter identification using the LS-Opt tool from Dynamore.

To run a tensile-pressure test, it is necessary to prevent the steel strip from buckling under pressure. For this purpose, an anti-buckling device was manufactured, as shown in Fig. 4b, whereby the steel strip is held in position by the device through the recess. The results of the tensile-pressure test are depicted in Fig. 4a. Since the 1.4310 is advanced high-strength steel, with a yield limit to ultimate tensile strength ratio of 0.886, the elasto-plastic deformation is limited to a small margin. This is reflected by the tensile-pressure curve, where no distinctive shift from the elastic domain to the elasto-plastic domain is visible.

The determination of the material parameters for advanced high-strength steel is not yet completed, however it will be conducted in the near future.

The model is described by the following formula:

$$E = E_0 - (E_0 - E_A)\left[1 - \exp\left(-\xi * \varepsilon^p\right)\right]$$

where E represents the depending elastic modulus, E_0 is the virgin elastic modulus, E_A stands for the asymptotic elastic modulus at a large strain, ξ is a constant, and ε^p is the current plastic strain. This underlines the complex behavior of the advanced high-strength steel material that is used in alternating bending processes, which requires a sound model description to capture the increasing elastic domain with plastic pre-strain.

5 Database

A database is built with the results of the finite element model. Its primary parameters are the current curvature of the steel strip and the setup position for the straightening rolls for a desired final shape, which most of the time will be a straightened steel strip. Additionally, parameters necessary for the calculation of the final curvature are needed, such as the shape of the steel strip, since a round steel strip requires a different straightening approach than a square cross-sectional area. Height, width, diameter, and the orientation of the steel strip in regards to the straightening machine, like a concave or convex inlet into the straightening machine, are all important to take into account.

A database like this can be fed by different sources, such as the mentioned finite element calculation, an analytical model, or recorded experimental data. An interpolation function is planned for missing data between given data. Thus, the control of the straightening machine is able to transfer the data from the database towards the actuators, dependent on the measured values of the curvature.

6 Actuators

The intelligent straightening machine essentially has three actuators. These are the three stepper motors (Beckhoff AM8031 0F20) with a maximum torque of 1.4 Nm that control the straightening rolls. Each straightening roll is controlled individually and independently of the others. Their position is determined at any time by means of the encoders on the stepper motors. In this way, they can be moved independently of each other under position control, and constantly react to the necessities in the process.

7 Conclusion

The subject of this paper is to introduce the work on the intelligent straightening machine and its various facets. The measurement of the curvature with MagnaTest D while superposing tensile stress by the decoiling process is shown. This online measurement system, which links the state of residual stress and its change to the curvature, enables the possibility to set up corrective strategies while running the process. This presents opportunity for a major transition from the manual adjusted straightening machine towards the intelligent automated straightening machines.

Additionally, it is shown that the finite element calculation requires three different types of testing in order to parametrize the material card 125 of LS-Dyna, which is promised to be the most accurate material model for this kind of alternating bending process. The tensile-pressure curve underlines the complex behavior of the advanced

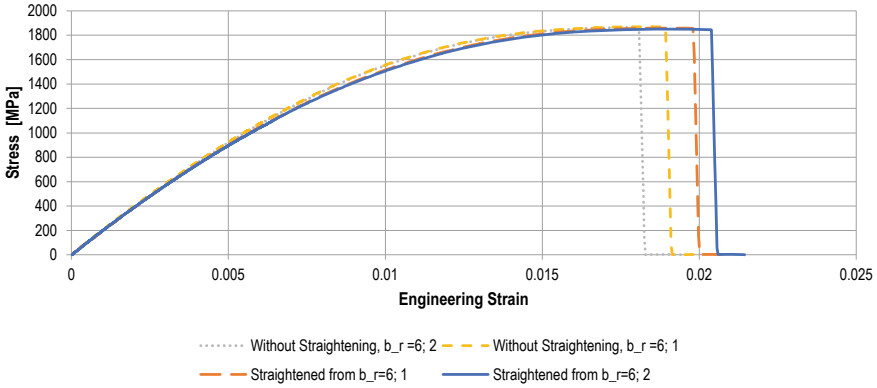


Fig. 5 Results of a tensile test, with and without straightened steel strip. (Color figure online)

high-strength steel and the need for the combined isotropic and kinematic hardening material description.

The results of the numerical calculation and the experimental work will be combined in a database that provides the correct straightening roll setup dependent on the current curvature, the material type, and its geometry, as long as a live calculation is not yet feasible.

This approach of an online measurement leading to an online setup of the straightening machine results in a fully automatic straightening machine. This method promises improved results compared to conventional straightening machines, with first results showing an increased formability of the straightened steel strip of up to 12% compared to the unstraightened steel strip as shown in Fig. 5. There are four different tensile test results shown, where two steel strips have a slight curvature of $0.00053 \frac{1}{\text{mm}}$ and two steel strips are straightened, with the same curvature prior to straightening. The results show that although there is no visible increase to the ultimate tensile strength the deformability increases after a steel strip is straightened.

References

1. Behrens B-A, El Nadi T, Krimm R (2011) Development of an analytical 3D-simulation model of the levelling process. J Mater Process Technol 211(6):1060–1068. https://doi.org/10.1016/j.jmatprotec.2011.01.007
2. Doege E, Menz R, Huinink S (2002) Analysis of the levelling process based upon an anlatic forming model. Institute for Metal forming and Metal Forming Machine Tools, Hannover Germany
3. Grüber M, Hirt G (2016) Numerical investigation of a process control for the roller levelling process based on a force measurement. MSF 854:249–254. https://doi.org/10.4028/www.scientific.net/MSF.854.249
4. Grüber M, Hirt G (2017) A strategy for the controlled setting of flatness and residual stress distribution in sheet metals via roller levelling. Procedia Eng 207:1332–1337. https://doi.org/10.1016/j.proeng.2017.10.892

5. Grüber M, Oligschläger M, Hirt G (2014) Adjusting of roller levellers by finite element simulations including a closed-loop control. AMR 1018:207–214. https://doi.org/10.4028/www.scientific.net/AMR.1018.207
6. Grüber M, Oligschläger M, Hirt G (2015) The effect of the initial stress and strain state in sheet metals on the roller levelling process. KEM 651–653:1023–1028. https://doi.org/10.4028/www.scientific.net/KEM.651-653.1023
7. Lutz-Stefan Henrich (1993) Theoretische und experimentelle Untersuchungen zum Richtwalzen von Blechen. Dissertation. Institut für Mechanik und Regelungstechnik. Universität-Gesamthochschule Siegen, Siegen
8. Liu Z-f, Luo Y-x, Yan X-c, Wang Y-q (2015) Boundary determination of leveling capacity for plate roller leveler based on curvature integration method. J Cent South Univ 22(12):4608–4615. https://doi.org/10.1007/s11771-015-3011-y
9. Morris JW, Hardy SJ, Thomas JT (2005) Effects of tension levelling process parameters on cold rolled strip characteristics using a designed factorial analysis approach. Ironmaking Steelmaking 32(5):443–448. https://doi.org/10.1179/174328105X48089
10. Pernía A, Martínez-de-Pisón FJ, Ordieres J, Alba F, Blanco J (2010) Fine tuning straightening process using genetic algorithms and finite element methods. Ironmaking Steelmaking 37(2):119–125. https://doi.org/10.1179/030192309X12549935902301
11. Schleinzer G, Fischer FD (2000) Residual stress formation during the roller straightening of railway rails. Institute of Mining and Metallurgy, Leoben
12. Wang XG, Huang QX, Wang JM (2010) Research on leveling model of combination leveler. AMR 145:453–457. https://doi.org/10.4028/www.scientific.net/AMR.145.453
13. Yamashita T, Yoshida K (2005) Tensile straightening of superfine wine and residual stress measurement using focused ion beam. Department of Precision Mechanics, Tokio
14. Yoshida F, Uemori T (2002) A model of large-strain cyclic plasticity describing the Bauschinger effect and workhardening stagnation. Int J Plast 18(5–6):661–686. https://doi.org/10.1016/S0749-6419(01)00050-X

A Vision of Numerically Controlled, Autonomous Manufacturing and Metal Forming



Glenn S. Daehn

Abstract Here I lay out a vision for hybrid autonomous manufacturing. Imagine you have a robot-automaton machinist who really likes and knows deformation. What would this enable? What's needed to get there? Use cases and brief research agenda are presented.

Keywords Agile · Metamorphic manufacturing · Open-die forging · Forging · Microstructure

1 Introduction

I hope you will give me some leeway for violating some conventions here. I will organize and write this paper differently than the typical, and I will be the sole author, despite foundational contributions from many in the acknowledgements list. This hopefully provides a single voice and lays responsibilities with shortcomings to me. I do also want to use this as an opportunity to acknowledge and thank those who have really opened my eyes to the magic in metal forming and manufacturing with simultaneous room for creativity and rigor. When I came to the Ohio State University over 30 years ago, the Engineering Research Center on Net Shape Forming, run by Prof. Taylan Altan, was one of the biggest and most influential centers for thought and innovation in the university. This taught me the value in solving real industry problems and mentorship by Prof. Rob Wagoner (who, with Altan is honored at this ICTP) taught me a rigorous approach to describing plasticity. Beyond this, I have also been influenced by the European research I've seen, particularly the work in Dortmund under Prof. Erman Tekkaya, where there is much more activity in re-thinking processes and equipment than we typically have in the US. From these roots and being able to take part in the formation of a Manufacturing USA Institute (LIFT, in Detroit), and interactions with many great colleagues here, we have developed a slightly different approach to the role metal forming may play in the future, as a

G. S. Daehn (✉)
Department of Materials Science and Engineering, The Ohio State University, 140 West 19th Avenue, Columbus, OH 43210, USA
e-mail: daehn.1@osu.edu

© The Minerals, Metals & Materials Society 2021

G. Daehn et al. (eds.), *Forming the Future*, The Minerals, Metals & Materials Series,
https://doi.org/10.1007/978-3-030-75381-8_2

dual process for shaping components and refining materials and microstructures to optimize their properties.

The key question I hope to address with this short note is what would manufacturing look like if we started from first principles and did not have our imaginations corrupted by all the analysis and reverence we have for the existing processes. Are there other ways of doing things? And can we get away without all these complex and expensive, product-specific tools and dies?

2 A Bit of History

We material scientists are well aware that our "ages" are named for materials, copper (~5000 BC), bronze (~3000 BC), iron (1500 BC), steel (~0 AD), and sometimes silicon ages. Extraordinary components and shapes were produced in these time periods. We also know that swords with remarkable properties were produced in Damascus, Syria, and Japan from around 1000 AD, without detailed understanding of metallurgy. The artisan skill of blacksmithing grew from this and provided components that were supremely functional and beautiful. Examples of items about 500 years old are shown in Fig. 1.

In the early 1900s, there was a distinct shift to high productivity metalworking processes, including rolling, extrusion, and stamping. These technologically important processes became the focus of academic and practical study. Further, with the growth of the steel, aluminum, and other specialty metal industries in the early 1900s, there was a great emphasis on the development of thermomechanical processes to achieve desirable performance and processing objectives. High-strength steels, magnetic alloys for transformers, and alloys with the right texture and ductility to create aluminum cans were notable achievements in this period.

The next major wave of "manufacturing science" was centered on computer numerical control (CNC) machining. In the 1920 and 30s, systems of cams and templates were used to move cutting heads to develop complex shapes. It was the confluence of the development of servomechanisms that were first used in artillery gun control and early computer technology that led to CNC machining. The need to economically produce complex airfoil shapes for helicopter and aircraft applications led to the formal birth of CNC machining systems in the late 1940s from collaborations between Parsons Corporation, MIT, and Sikorsky Helicopter. Since then, there have been remarkable advances in tool path planning, tool changes, lubrication, closed-loop control, and fast precision locating mechanisms. Over time, a number of industry standards have emerged in this field including the widespread use of G-code and standard practices have evolved for efficiently converting designed shapes to practical tool paths. CNC is now a strong foundational element in the creation of low-volume and custom components as well as in tool and die and machine manufacturing. CNC machining represented the first wave in digitally controlled manufacturing.



Fig. 1 Examples of artisan blacksmiths' products large and small, all about 500 years old. Top shows a Japanese national treasure: thirteenth-century katana produced by Masamune. Left center shows an Italian embossed steel Burgonet (helmet sculpture, weighing about 3.75 lb) from about 1540. Bottom left shows an Italian steel shield (overview and detail) from about 1560. Right shows "Armors for Man and Horse," German etched steel and leather from about 1548. (Color figure online)

One could argue that additive manufacturing has been with us since civilization or before. Bees and paper wasps create their hives using basically an additive process. Mud huts, adobe, and brick structures were created by the progressive addition of material to meet a desired shape. The modern age of additive manufacturing is described well by a 2014 Wohlers Associates report [1] that both describes the early technical underpinnings that preceded commercial additive manufacturing by decades, as well as chronicles the many commercial starts (and failures) in this field. Like CNC machining, most of the fundamental precursor work was carried out well before the base technologies were assembled into "additive manufacturing" equipment in the US and the first commercial companies were based in the US. The central idea of the additive manufacturing is the ability to add or solidify material to create a physical object that is first defined in the virtual space, often again using G-code as a guide. A number of technologies ranging from light-curing of polymers to robotic hot glue guns and molten metal addition by welding-like processes have all been developed that led to the creation of the ASTM committee (F-42) for developing

common standards in the area, in 2009. Additive manufacturing is the second wave of digital manufacture.

While these methods that were very amenable to academic analysis were being created and refined, the tradition of the blacksmiths in creating small numbers of custom components was continuing and being extended, and variants of G-code have been used for incremental sheet metal forming [2]. For bulk deformation, the blacksmith's tradition ran strong and human force has been augmented with hydraulic presses and power hammers. Very large components have been formed using massive presses and robotic manipulators in open-die forging. Sheet metal forming for most custom parts is carried out with hydroforming and more artistic parts, or lower volume components, are often created by artisans using hand tools such as English wheels, stretcher and shrinker elements in presses, hammers, sandbags, and ingenuity. There are hours and hours of fascinating YouTube videos of very clever artisans making motorcycles, cars, art, and aircraft parts using these methods. A key enabling differentiator between this artisan approach and high productivity methods is that the artisan can check the workpiece in progress against a form and correct the shape by further bending, stretching, or shrinking, and then checking against the form again. This kind of correction is central to the fabrication metallic aircraft sheet metal components after forming close to shape in hydroforming. It also enables dieless forming. Whereas predicting a precise sheet metal shape in bending is difficult, requiring correct assumptions and stable material properties, achieving a precise bend angle, for example, is a trivial matter if one can bend, measure, correct in a re-bend, and repeat until the part has the correct shape.

In the following paragraphs, I will discuss a vision for taking the kinds of processes used by an artisan and executing them using automated systems.

3 A Vision of Metamorphic Manufacturing

A previous paper with Alan Taub, from our LIFT collaboration [3], and an international expert study (http://tms.org/metamorphicmanufacturing) have developed a vision of what is sometimes called the easily understood term Robotic Blacksmithing or my preferred term of metamorphic manufacturing which emphasizes that both the component shape and microstructure are transformed by the process. The key idea is to transfer the essential tasks of a blacksmith and his tools to an automated system that can shape components and optimize microstructure, much the way a blacksmith might, but using greater forces, power, sensing ability, dimensional precision, and most importantly potential reproducibility. The ability to sense, record, and reproduce actions gives a powerful gateway to the possible production of standardized components that can be used in safety-critical applications (Fig. 2).

Most important are the variety of fundamental tools that can be assembled to create a metamorphic manufacturing system. The key difference between the metamorphic approaches and those based on dies is that the final punch and die usually dictates the full shape of the final component. Metamorphic methods use incremental forming and

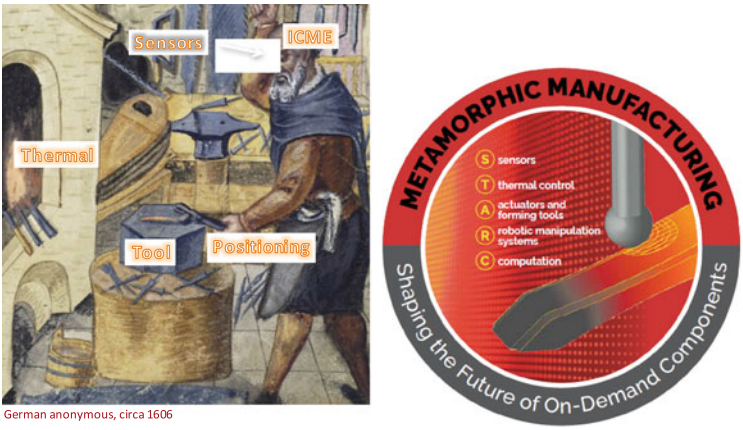


Fig. 2 Key concepts in blacksmithing that can be automated and a "mission badge" resulting from the TMS report that calls out the key aspects that must be considered (Sensors, Thermal control, Actuators and forming, Robotic manipulation, and Computation), giving the STARC moniker. (Color figure online)

numerically positioned or controlled tools (for example, a robot locating a workpiece between the punches of a hydraulic press and repeatedly deforming a programmed amount, moving the workpiece and repeating). There are a large number of processes that can be adapted to this fundamental framework. These are indicated in Fig. 3. In all cases, the incremental deformation of the forming tool introduces displacement that can also be seen as plastic strain. These plastic strains simultaneously provide the ultimate shape of the component, but we also know that they introduce important changes in material microstructure that change (usually improve) properties. These changes can include closing porosity, providing work hardening, introducing texture, or refining large phases that may be the result of a solidification process. Such processes may be very effective at taking a pre-form that may be produced by casting (as is commonly done with billets in open-die forging) or a numerical weld deposit or 3-D printed material and refining the microstructure and setting details of component shape. In short, there are numerous methods that can be used in an incremental fashion, with lightweight tools to at once control shape and microstructure, and the main constraint is our imagination. The blacksmith has demonstrated this for us and the next obvious task is to automate this process with modern deformation tools, robotic control, and optical sensing for dimensions and strains.

4 A Bigger Vision

Imagine taking this concept of an autonomous artisan and take it to its logical conclusion. Artisans are not bound by their processes, but the tools at their disposal. A



Fig. 3 Examples of motivations and possible tools for metamorphic manufacturing, as classed by sheet, bar, bulk, axisymmetric, and profile shapes. There is, of course, much room for interplay among these limiting shapes, and this figure may give some inspiration for new processes. Sheet row shows from left to right: incremental forming example from mechmining.uq.edu, English wheel used for thinning from Desert Precision, a press and robot concept from [4], and a sheet shrinker from Heliotech. Similar sheet stretchers are also available. Bar row shows from left to right: a CNC shaping concept [5], an open-die forging example from Scott Forge, the concept of thread rolling, which can be generalized, from madehow.com, and CNC bending of bar from tradeindia.com, Bulk row shows: shape required for a Joint Strike Fighter bulkhead, general process of use of a hammer with humanoid control, concept for use of a punch in forging to develop recessed shapes, and implementation of turret punches to give agility, from SAMIN Turret Punch Press. Axisymmetric row shows: typical manual example of spinning against a form, ring rolling, and concept for agile CNC-controlled two-sided spinning [6]. Profile row shows: left two images show concept for flexible roll forming of metallic strip, schematic of a CNC 3-D profile bending system from the IUL in Dortmund, Germany, and right shows profile stretch-bending from Fairmount Technology [7, 8]. (Color figure online)

skilled artisan with a relatively small set of simple hand tools can do amazing things, as blacksmiths have shown. These can rival the size, complexity, and utility of components from large presses. If we examine the detailed work of one of these artisans, we notice that they cheat. They are not simply metal forming but will use whatever tricks they can to get the job done, including bending or hammering out to straighten a component out or welding in filler metal and hammering it smooth to take care of a divot.

Just as one small example of how rapidly maturing technologies can be merged to create something new, consider that wire-arc additive can create components with rough geometry and easily locally modify composition by changing wires. This component can then be forged to final shape while improving properties. This deposition and forming can both be incremental.

If we think about the tools that an artisan has at their disposal, they really fall into a very limited number of classes:

- *Deposition and solidification.* Methods such as casting, welding, extrusion-deposition, and so forth are used to physically deposit materials into place. This is largely the heart of additive manufacturing.
- *Material Removal*. This can take place by cutting, grinding, ablation, etc. This is at the heart of CNC machining.
- *Deformation.* Forging, bending, stretching, peening, and so forth are high productivity and highly effective methods to create components.
- *Material Transformation.* Thermodynamic properties such as temperature, pressure, and controlled chemical potentials are used for sintering, curing, carburizing, heat treatment, and so forth. This is often done in concert with deformation in thermomechanical processing.
- *Inspection and sensing*. Are usually currently used post-process to assess quality. New processes for automated bending, incremental forming, and welding, for example, can use dimensional sensing during the process for optimal control.

These kinds of processes all are amenable to agile and incremental fabrication. We can imagine a suite of tools that can be used to carry out the kinds of processes described above, and in situ sensing can provide input for quality assurance and control. We can imagine automated workstations with extreme levels of sensing and tool kits that include general-purpose tools such as hammers, cutting tools, torches and induction coils, deposition nozzles or arc welding equipment, robotic control for positioning and a suite of sensors to monitor shape, temperature, and possibly other properties of the structure or material(s). The most important next element is an intelligent computational system to oversee, manipulate the tools, and make decisions. This tool would take on a role analogous to a blacksmith's brain and execute the myriad of decisions required to create a component that is sufficient for service. This can include aspects such as controlling torch angle, motion, and gap in a welding operation, deciding when given operations are needed—for example, might we need to deform a part to make it fit. And this system can also record all the steps, settings, and data. These data can be used in assessing reproducibility and are essential in qualifying a component for service. These tools quickly move into the

realm of artificial intelligence, where disparate data from position, force, temperature, and part configuration must be brought together to make decisions. This problem of sensor fusion leads to forward predictions, and from there we can monitor and correct for issues. One key issue will be how to transfer the part from one operation to another while maintaining dimensional fidelity and locating datums. Furthermore, the base algorithms should be able to be transferred from one physical automated workshop to another, where the tool set may be somewhat different but perform the same essential functions. Operations may be done on a single "workbench" or the component could be transferred from one piece of equipment to another while maintaining dimensional information.

Again, if we take this idea to its logical conclusion, we can imagine a fully autonomous system for manufacturing that can manufacture a wide range of products with a limited, but versatile set of tools. The production rate of such systems would not rival those of mass production stamping, forging, die casting, and so forth, but because robots can work 24/7, lights out, they could be far more productive than a human-run machine shop and the data produced, provide a digital thread that can be used to assure quality. Formal quality systems would need to be developed around this approach. A pathway to autonomy is shown in Fig. 4 that is inspired by SAE Standard J3016. One could imagine that most of this exists inside a controlled automated factory environment, but it would also have interfaces to supply chains to source optimal raw materials, preforms, and possibly specialized cutting or deformation tools. All of this is a strong analogy to what a human artisan might do.

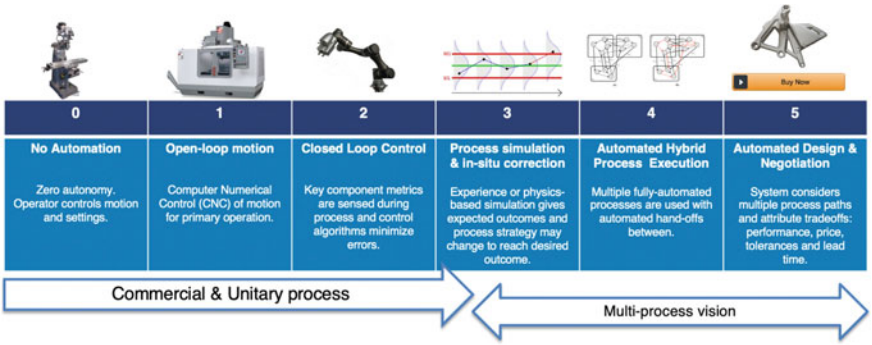


Fig. 4 Analogous to the levels defined for autonomous driving, autonomous manufacturing may move through a progression, gradually becoming more autonomous. This is modeled after SAE Standard J3016. Levels 0–2 are already commercially available. (Color figure online)

5 What Can This Enable? Some Use Cases

Imagine we could build something like this. What would the uses and benefits be? Brief comments on a few use cases that show that there would be substantial value in building automated manufacturing systems that feature plastic deformation.

a. Rapid forgings; near-optimal properties

One of the most obvious uses of closely controlled digital open-die forging is in rapidly producing components similar to those that may have been created by closed-die forging. Forgings are the gold standard for high-quality components and this "robotic blacksmithing" approach should be able to develop essentially the same shapes and strain distributions as closed-die forging. One outstanding challenge will be developing thermal control that approximates that of closed-die forging.

b. Point of Care Medical Manufacturing

Often when patients undergo trauma surgery with bone damage metallic plates are required to hold bones together for healing. Facial impact, for example, can produce multiple fractures requiring many plates of varied forms (see, for example, Arce et al. [9]). These are often created in the operating room by bending plates to the form of the patient. This is slow and imprecise and misfitting can increase stresses, leading to failure. Additive manufacturing is recently being considered to replace the manual bending of standard parts. The numerical bending, with error correction, could be a far faster solution to providing components than additive manufacturing and more precise with less time with the patient in surgery than the manual bend, test, and re-bend procedure now used. The process would be optimal if the fitting could be to a numerical file (as developed in CAT scanning, for example) rather than to a patient or physical form.

c. Novel structures and materials (additive plus deformation)

There are a number of processes to create shapes from metals: casting, wire-arc additive, net-shape powder consolidation, welding of plates, etc. These processes generally produce components with properties that are inferior to those from forging, but these all are candidate processes for developing preforms that can then be forged. This can close voids, develop texture, refine microstructure, and control shape among other benefits.

d. Ultralarge forgings

Because incremental forming uses many small bites to form a part, the press that is used could be dramatically smaller than those in common use. One of the most interesting potential uses of metamorphic manufacturing may be to use preforms and systems with large robots and modestly sized presses to develop very large forgings. The basic work of the blacksmith, again, shows that this is basically possible. This kind of application can have great utility in aircraft and other large structures. This

movie about the US Air Force Heavy Press Program from the early 1960s shows the great utility that this can have [10] and we are largely limited to our ingenuity as to how this might be done. Note that the basic tools used then are essentially unchanged to those used now, except that dies are designed computationally and cut with CNC machining.

6 What Do We Need? A Brief Research Agenda

I hope I have been able to convince you gentle reader that it is worthwhile to develop a coordinated program to develop what a group of us here at Ohio State refer to as hybrid autonomous manufacturing. It's a big area, with potentially a big payoff and would require coordinated work of many people to get there. The metamorphic manufacturing study had some near-term recommendations to jump-start the technology. This echoes some of this and adds some others.

The first thing we probably need are some simple tools and ways to disseminate them. Brian Thurston has been developing a system (during the pandemic) in his living room that is suited for forming plasticine, as an early model material. This system is capable of making complex shapes with interchangeable general-purpose forming tools and by upgrading the press, it can be easily adapted for metal forming. This system can be replicated for under $7000 and it is our intent to share this design so that schools can develop this approach (Fig. 5).

As deformation is at the core, we need a new language (physical and computational) to plan and execute singular deformation steps to create targeted shapes. All of our work as children with modeling clay and more formal work with Plasticine

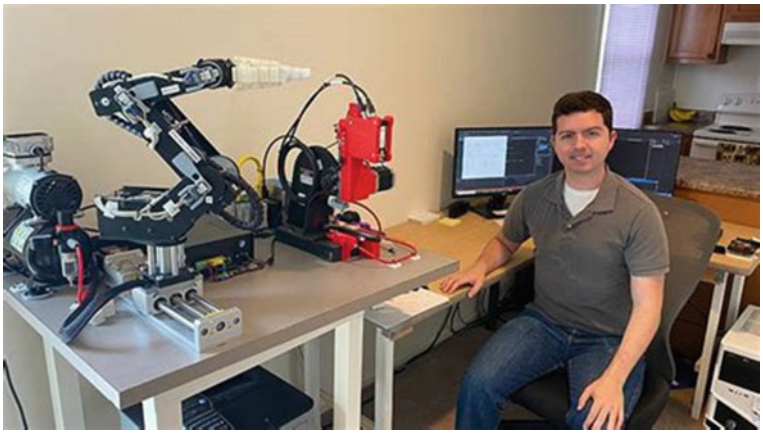


Fig. 5 Physical Exploration and Training Factory Automaton Box system (PET-FAB) being developed by Brian Thurston, including positioning an automated arbor press, optical scanning, and numerical control scheme. (Color figure online)

and the LIFT Prize program showed this is basically possible. This should become akin to computer-aided manufacturing and path planning now done for machining but has very different physics at its core.

Next, we need to add modules for heating, inspection, planning, surface quality, and so on. This requires sensor fusion and artificial intelligence. These tools need to be integrated, abstracted, and essential properties tracked so that common approaches can be used in varied locations and learning shared from one autonomous location to another.

Acknowledgments These ideas have been in development with many colleagues, including those from the TMS study group and local colleagues at Ohio State including Michael Groeber, Steve Niezgoda, David Dean, and Nate Ames. From my group, particularly Brian Thurston has been very active and Anupam Vivek and Sajun Prasad have helped with ideas and putting this in final form.

References

1. Wohlers T, Gornet T (2014) History of additive manufacturing. Wohlers Report 2014—3D Print Addit Manuf State Ind 1–34
2. Emmens WC, Sebastiani G, Antonius H (2010) The technology of incremental sheet forming-a brief overview of the history. J Mater Process Technol (8):81–997
3. Daehn GS, Taub A (2018) Metamorphic Manufacturing: the third wave in digital manufacturing. Manuf Lett 15:86–88
4. Operitescu D, Volk W (2015) Automated driving for individualizd sheet metal part production—a neural network approach. Robort Comput Integr Manuf 35:144–150
5. Groche P, Fritsche D, Tekkaya EA, Allwood JM, Hirt G, Neugebauer R (2007) Incremental bulk metal forming. CIRP Ann—Manuf Technol 56(2):635–656
6. Music O, Allwood JM (2015) Flexible asymmetric spinning. 60 Excell Invent Met Form 60:173–178
7. Becker C, Tekkaya AE, Kleiner M (2014) Fundamentals of the incremental tube forming process. CIRP Ann—Manuf Technol 63(1):253–256
8. Grzancic G, Becker C, Ben Khalifa N (2016) Basic analysis of the incremental profile forming process. J Manuf Sci Eng 138(9):1–6
9. Arce K, Waris S, Alexander AE, Ettinger KS (2018) Novel patient-specific 3-dimensional printed fixation tray for mandibular reconstruction with fibular free flaps. J Oral Maxillofac Surg 76(10):2211–2219
10. rdwaynes (2017, August 11) Air force heavy press program (USAF film) by D.O.D. [Video]. YouTube. https://youtu.be/iZ50nZU3oG8

Investigation of Effects of Part Features in Single Point Incremental Forming of Narrow Channels



Suwat Jirathearanat, Dharmesh Kumar, Kai Soon Fong, Atsushi Danno, and A. Senthil Kumar

Abstract Narrow channels or ribs can be commonly found in sheet metal products. These narrow with high length-to-width aspect ratio channels are often integrated into sheet metal panels for functional features such as stiffeners or guide rails of various topographies, i.e. straight line or composite of curves. This work focused on the development of Single Point Incremental Forming (SPIF) as a cost-efficient forming alternative to stamping or embossing of these features in short-series production. These channels present unique forming challenges, i.e. effects of channel spline geometry, varying cross section, end geometries on part formability, and geometrical accuracy. SPIF of SS316L 0.5-mm-thick narrow channels of three different geometries with a maximum width of 20 mm and its length-to-width aspect ratio larger than 5, i.e. (1) straight channel, (2) taper channel, and (3) curvature channel, was investigated. Based on the experimental results, 5 mm dia. carbide tool and 0.1 mm step-down size were recommended to optimize SPIF of these narrow channels. The effects of the different part features and their interactions with SPIF forming parameters on part formability and deviations are presented and analyzed for further development of die-less narrow channel forming for sheet metal industry.

Keywords Single point incremental forming · Rib forming · Channel forming · Embossing · Maximum wall angle · Pillow effect · Stainless steel

1 Introduction

Narrow channels or ribs can be commonly found in sheet metal products. These narrow with large length-to-width aspect ratio features are often integrated into sheet metal panels for functional features such as stiffeners and guide rails of various

S. Jirathearanat (✉) · D. Kumar · K. S. Fong · A. Danno
Singapore Institute of Manufacturing Technology, Agency for Science Technology and Research (A*STAR), Singapore, Singapore
e-mail: suwatj@SIMTech.a-star.edu.sg

A. Senthil Kumar
Department of Mechanical Engineering, National University of Singapore, Singapore, Singapore

© The Minerals, Metals & Materials Society 2021

G. Daehn et al. (eds.), *Forming the Future*, The Minerals, Metals & Materials Series,
https://doi.org/10.1007/978-3-030-75381-8_3

topographies. Embossing using dedicated geometry-dependent stamping tools is traditionally employed to form these channels. Most embossing operates far from the sheet metal drawing limit ratios, thus a fully stretching process. The resultant channels are typical of small depth and small wall angle. Recently, CNC turret punching machine with roller tools can form shallow ribs of straight or gentle curvatures on flat sheet metal. Similar to embossing, these roller tools can only form ribs with limited depth. In this work, the focus was on application of SPIF as a forming alternative of these channels with deeper depth and larger wall angel in short-series production. Incremental Sheet Forming (ISF) is a die-less and cost-efficient sheet metal forming owning to its use of a generic small hemispherical-tipped tool and CNC-controlled movements [1]. Single Point Incremental Forming (SPIF) is the most basic variation of ISF processes as it requires minimum tooling, i.e. a generic forming tool, fixture table with a dedicated backing plate, and with or without a blank holder. Due to its localized deformation mode, ISF can form sheet metal products far exceeding its material drawing limit ratios [2]. SPIF of sheet metals has been studied by many researchers. Formability of SPIF is largely represented in terms of maximum achievable wall angles (i.e. θ_{max}) determined experimentally either by SPIF of truncated cones with fixed wall angles or varying wall angle cones, which tends to give θ_{max} slightly larger than those obtained from fixed wall angle truncated cones [3]. It was also revealed that SPFI of truncated square pyramids would fracture around the corner of the part due to larger deformation as compared to that happens on flat areas [3]. This information is typically used in process planning for SPIF forming process of various part geometries. In terms of effects of step-down size and tool size on max. wall angle, generally speaking, it was shown that decreasing both step-down size and tool size would increase $\theta_{max,}$ [4]. However, there is an optimum tool size, below which forming instability (i.e. surface cutting) would take place, following a critical tool radius to blank thickness ratio of about 2.2, regardless of sheet metal materials [5]. Pillow effect, metal squeezing, or corner fold are another type of defect normally happen in unformed bottom area of the part. These directly contribute to low part dimensional accuracy and may adversely affect the part formability. Al-Ghamdi et al. studied this pillow effect and pointed out that smaller tool size, smaller step-down size, and strong strain hardening materials would worsen this pillow effect [6]. Based on this knowledge, one must understand interactions between defect characteristics, part features, and material in order to design and optimize process parameters for successful SPIF of any specific part geometry. There is a limited study done on SPIF of any narrow channels in the literature. Afonso et al. studied SPIF of channels and developed special tool path strategies for the forming [7]. However, these channels investigated have large channel widths and open ends, thus not quite applicable to typical narrow channels or ribs with closed ends of this study. Therefore, this investigation focused on SPIF of SS316L 0.5 mm-thick long and narrow channels (20 mm wide) of various features to reveal forming behaviors and optimize SPIF process parameters for this class of geometry.

2 Experimental Procedure

In this investigation, two sets of experiments were conducted, as shown in Tables 1 and 2. Stainless steel sheet SS316L 0.5 mm-thick was incrementally formed into cones (Table 1) and narrow channels of three different shapes (Table 2) using both SKD11 and carbide hemispherical forming tools with diameter of 3, 5, and 15 mm. In Table 1, SPIF of varying wall angle cones was conducted to determine material formability or material maximum achievable wall angles with respect to tool size and tool material. Forming feed rate and spindle speed of 70 mm/min and 2000 rpm were used, respectively. Step-down size of 0.2 mm was applied in forming with tool 5 and 15 mm dia., while for 3 mm dia. tool was used with 0.1 mm step-down size as 0.2 mm step-down size would cause unacceptable surface finish. The varying wall angle cone geometry has the base diameter of 120 mm and the wall angle from 20 to 80°.

In the second set of experiments, three different narrow channels were investigated—(a) straight channel with round and flat ends, (b) taper channel with round ends, and (c) curvature channel with three reducing turning inner radii (i.e. R15, R10, and R5). These channels were formed with various wall angles from 45° to 70°

Table 1 Experimental matrix—SPIF of varying wall angle cones of SS316L 0.5 mm

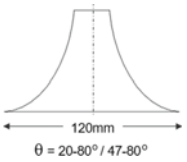
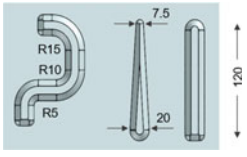
Geometry	Tool dia. (mm)/Tool material	Step-down size (mm/rev)	Feed rate (mm/min)	Spindle speed (RPM)
 Varying wall angle cone	3 mm carbide	0.1	2000	70
	5 mm carbide	0.2		
	5 mm SKD11	0.2		
	15 mm SKD11	0.2		

Table 2 Experimental matrix—SPIF of narrow channels of SS316L 0.5 mm. (Color figure online)

Geometry	Tool dia. (mm)/Material	Wall angle (°)	Step-down size (mm/rev)	Feed rate (mm/min)	AVG spindle speed (RPM)
 3 narrow channels	3 mm carbide	45–70	0.1	1000	170
	5 mm carbide	45–70	0.1	1000	100
			0.2		

as summarized in Table 2. The forming feed rates and spindle speeds used in this set of studies were adjusted to provide rolling condition to the tool-sheet contact. In the experiments, only 3 mm dia. carbide tool was used with 0.1 mm step-down size, while 5 mm dia. carbide tool was used with both 0.1 and 0.2 mm step-down sizes. All parts were formed using SPIF tooling set up in a heavy-duty CNC milling center. UX software was used to generate forming tool paths with a z-level strategy. Parts thicknesses were measured by a handheld ultrasonic device with 0.001 mm accuracy. Part dimensions were laser scanned and measured using GOM inspect software.

3 Results and Discussion

3.1 Effects of Tool Size and Tool Material on SPIF of Varying Wall Angle Cone

Based on the results from first set of experiments, Table 1, the maximum achievable wall angles of SS316L 0.5 mm cones formed with various conditions are plotted in Fig. 1. The avg. max. wall angle of each sample was calculated based on the measured heights (i.e. lowest and highest fracture points), and the cone geometry employed. Photos of the formed parts are shown and compared in Fig. 2. Max. wall angle of 62° was obtained from using SKD11 tool of size 15 mm dia. There was a slight improvement in formability gained when reducing the SKD11 tool size from 15 to 5 mm—max. wall angle of 65° was obtained. It was observed that SKD11 tool of 5 mm dia. caused significant galling on the tool-sheet contact surface. This galling defect, which was caused by higher contact pressure on the surface of 5 mm dia. tool as compared to 15 mm dia. tool, seems to have caused premature fracture earlier than expected. A significant formability improvement was observed when switching the forming tool material from SKD11 to carbide in the case of 5 mm

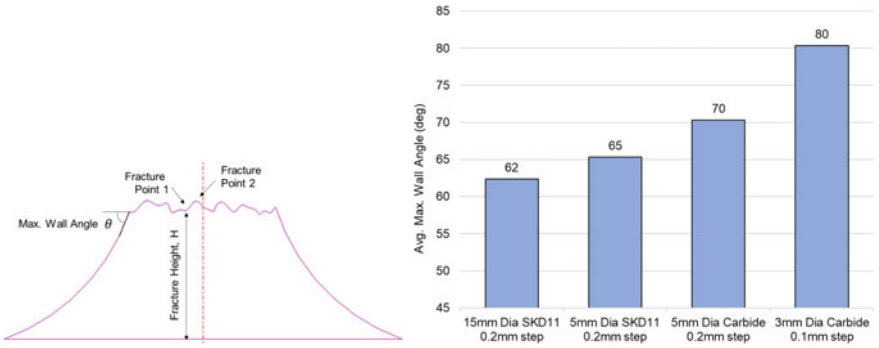


Fig. 1 Effect of tool size and material on maximum wall angle of SS316L 0.5 mm varying wall angle cone. (Color figure online)

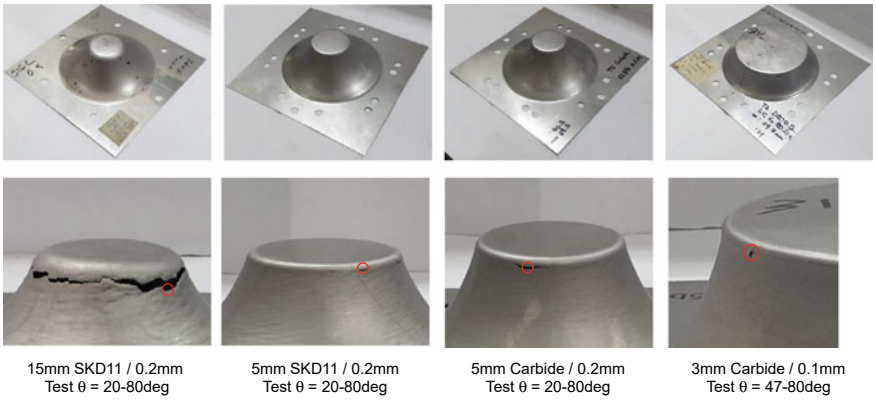


Fig. 2 Varying wall angle cones at maximum wall angle formed by different tool size and material. (Color figure online)

dia. tool, the maximum wall angle increased from 65° to 70°, and there was not any galling defect observed. In order to further investigate the effect of tool size on the stainless steel formability, an even smaller carbide tool of 3 mm dia. was considered. It should be noted that the starting wall angle of the cone geometry used for 3 mm dia. tool was 47° instead of 20°, which was used in the earlier cases (see Fig. 2), to avoid severe pillow formation in the unformed area, which was observed in other experiments conducted. The step-down size had to be reduced from 0.2 to 0.1 mm as to avoid bad surface finish. As a result, the maximum wall angle was markedly increased to 80° as compared to 70° seen in 5 mm dia. carbide tool. Based on the results of varying wall angle cone forming experiments, it can be concluded for SPIF of SS316L 0.5 mm-thick that smaller tools (i.e. 3 and 5 mm dia. Tool) can improve the formability given that surface galling defect can be minimized by using harder tool material such as carbide. It should also be pointed out that these results were obtained by using specific cone geometry that does not lead to any pillow formation during the forming, see Fig. 2. Interestingly, this condition may be difficult to design for SPIF of other part geometries, such as narrow channels.

3.2 Formability of Narrow Channels

Based on the results from second set of experiments, Table 2, max. wall angles of the channels (i.e. straight, taper, and curvature) are plotted and compared in Fig. 3. It can be observed that 3 mm tool with 0.1 mm step-down performed the worst as compared to those of 5 mm tool with 0.1 and 0.2 mm step-down. This finding does not agree with the results from the cone tests presented. With the 3 mm carbide tool, even the straight channel of 45° wall angle could not be formed successfully, and the curvature channel could only be formed up to 55° wall angle, which is much <80° the

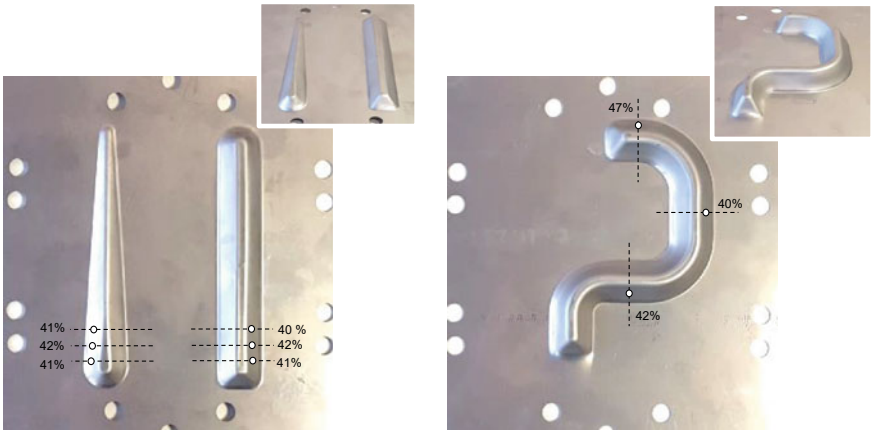


Fig. 3 Maximum wall angles of 3 channels formed by 3 and 5 mm carbide tools 0.1 mm step-down. (Color figure online)

max. wall angle observed in the corresponding cone test. From Fig. 3, there appears to be some interaction between channel geometry and achievable max. wall angle at least in the case of 3 and 5 mm tools with 0.1 mm step-down size, where the straight channels have the smallest max. wall angle and the curvature channels have the largest max. wall angle. Interestingly, by increasing the step-down to 0.2 with 5 mm tool, this interaction disappeared and all the three channels formed equally well at 55° max. wall angle. Generally, increasing step-down size will decrease formability. This is true for the curvature channel as its max. wall angle dropped from 60° to 55° for 0.2 mm step-down. However, increasing step-down to 0.2 mm had caused max. wall angle to increase from 50° to 55° for the straight channel.

Figure 4 compares in detail formability and part height of the channels formed by 5 mm tool and 0.1 mm step-down in order to gain some insights into the interaction of channel geometry and formability. From Fig. 4, it can be seen that fracture site is different for each channel geometry. It is well known for SPIF that part will typically fracture at tighter corner areas, where large deformation is more likely to occur as compared to that at more "open" areas. While the taper and curvature channel fractured at their tight corner as expected (see Fig. 4b and c), the straight channel fractured along the straight "open" side rather than at any of its tight corners, see Fig. 4a. This will be further investigated in the next section.

Max. wall thinning measurements of channels formed successfully using 5 mm tool and 0.1 mm step-down are shown in Fig. 5. Taper and straight channel (Fig. 5a and b) at 50° wall angle have roughly the same max. wall thinning of 41%, while curvature channel at 60° wall angle shows a larger wall thinning of 47% around its top corner. These thinning values agree with most findings in literature.

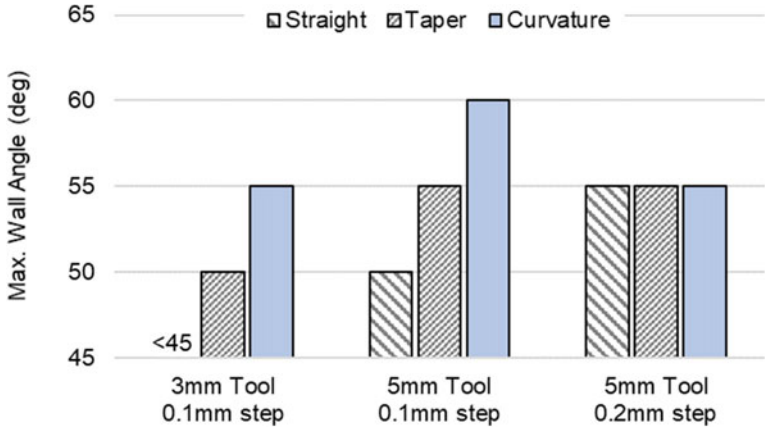


Fig. 4 Channel wall angles and heights formed by 5 mm carbide tool 0.1 mm step-down for **a** straight channel, **b** taper channel, and **c** curvature channel. (Color figure online)

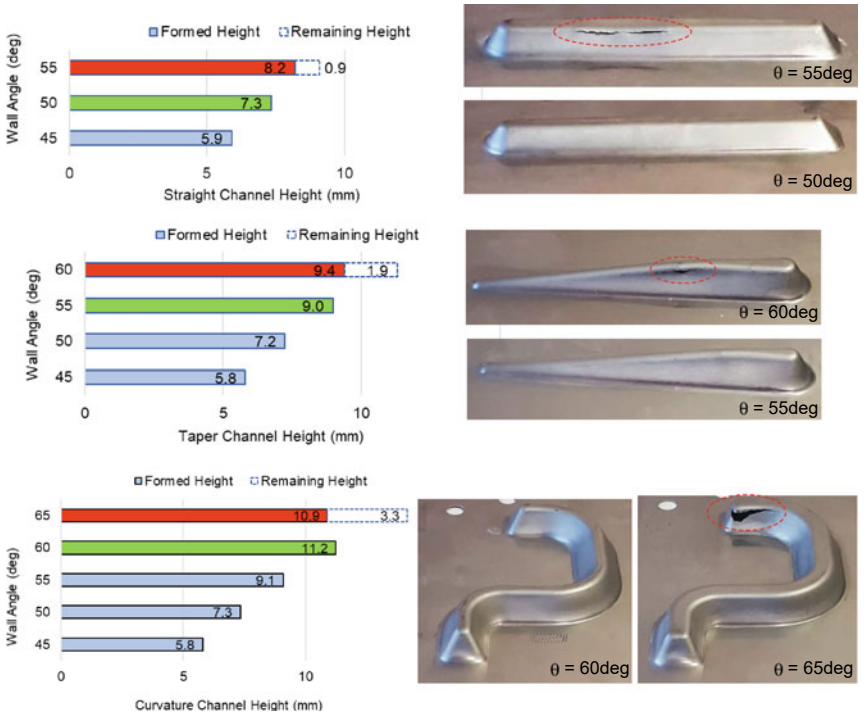


Fig. 5 Channels and wall thinning measurements formed by 5 mm dia. tool with 0.1 mm step-down **a** taper channel 50°, **b** straight channel 50°, and **c** curvature channel 60°. (Color figure online)

3.3 *Effect of Part Features on Formability*

Upon a closer examination of the parts, it was noticed that pillow effect was quite pronounced on top area in some of the straight channels. This particular pillow defect may have caused premature fracture along the straight sidewall of straight channel. Figure 6 displays pillow depths measured and calculated along profile section cuts on scanned surfaces of the channels formed by 5 mm tool and 0.1 mm step-down. It can be seen that the straight channel has the largest pillow depth (i.e. 0.17 mm). Though quite small, these pillow depths may play a significant role in part formability considering they occur over a tight narrow land of the straight channel top (i.e. 5 mm in this case). This pillow, or inverse bulge of the unformed flat top area, folds and in fact wraps around forming tool tip causing a "tight" corner condition, which may lead to premature sidewall fracture. When compared with forming tool radius, this max. pillow depth of the straight channels is approximately 6% of 5 mm tool and as much as 11% of 3 mm tool. It is believed that this pillow effect had caused 3 mm carbide tool to prematurely fracture the straight channel ($\theta_{max} < 45°$), see Fig. 3, and 5 mm carbide tool to premature fracture the part along the straight open sidewall ($\theta_{max} = 50°$), see Fig. 4a. From further pillow depth measurements, it was revealed that this max. pillow depth was reduced to 0.10 for 0.2 mm step-down. This reduced pillow depth may explain the increase in max. wall angle from 50° to 55° for SPIF forming of the straight channel using 5 mm tool with 0.2 mm step-down, see Fig. 3.

As for the taper channel, there appears to be very small pillow (max. 0.05 mm). Therefore, the fracture occurred at the highest tight corner, see Fig. 4b. The pillow formation in the curvature channel is rather complex, Fig. 6. It can be seen that the pillow is quite shallow in the bend sections, but becomes deeper in the straight sections. Though the max. pillow depth (i.e. 0.16 mm) in the lower straight section is just as deep as that of the straight channel, it only happens over a small length bounded by the bends where the pillow seems to shallow up. It is postulated that curvature channels can sustain a larger wall angle as they tend to alleviate the pillow effect

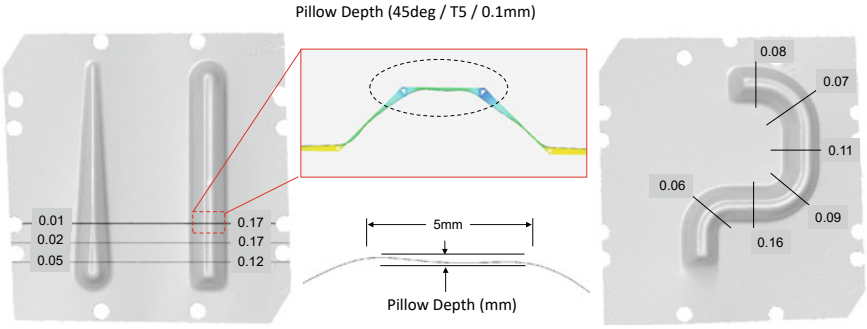


Fig. 6 Pillow depth measurements of channels at 45° wall angle formed by 5 mm carbide tool and 0.1 mm step-down. (Color figure online)

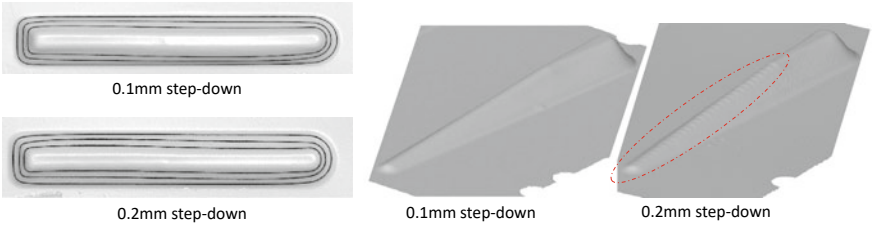


Fig. 7 Part deviation characteristics of **a** straight, and **b** taper channel with 50° wall angle formed by 5 mm carbide tool and different step-down sizes of 0.1 and 0.2 mm. (Color figure online)

around each bend. Therefore, they only fail around the tight corner, see Fig. 4c. Nevertheless, it is possible that premature fracture along a straight section may happen if that straight section is long enough. In another word, a narrow channel of a complete circle may never fail prematurely by the pillow effect.

3.4 Effect of Part Features on Part Dimensional Accuracy

Some interesting characteristics of part geometry deviations are shown in Fig. 7. There appears to be some waviness in the sidewalls of straight channel, Fig. 7a, as can be observed by wavy level contour lines on the channels. This waviness seems to be more pronounced when the step-down size is increased from 0.1 to 0.2 mm. It seems to have been caused by residual stress induced by pressing of the forming tool over a large flat area of the walls. Figure 7b shows a well-known stairs-stepped surface defect on the ridge of taper channel formed with 0.2 mm step-down. This defect can be corrected by decreasing the step-down size to 0.1 mm for this case. In terms of the geometry deviations, its sidewalls are quite flat and symmetrical. This might be due to its rigid triangle-shaped wall.

Part deviation measurements from the curvature channel are shown in Fig. 8. It was observed that cross-sectional profiles of this channel geometry are quite unsymmetrical, especially around the bend sections. Figure 8 plots normal max. deviations of inner and outer wall around each bend section of curvature channels with different wall angles from 45° to 60°. It can be seen that this curvature channel is mostly under formed. For low channel wall angles ($\theta = 45$–$55°$) the part deviations seem to be stable, but become quite sensitive at high wall angle ($\theta_{max} = 60°$). As the channel wall angle increases to maximum at 60°, part deviations seem to be larger for the sidewall on the top side (R35, R30, and R5), and smaller for the sidewall on the bottom side (R15, R10, and R25), Fig. 8. Initially, it was postulated that part deviations around each bend might be correlated to its bend radius, outer bend, and inner bend just, as how stress state of the wall can be related to tensile state and compressive state in curved profile flanging process, respectively, then it would be easier and

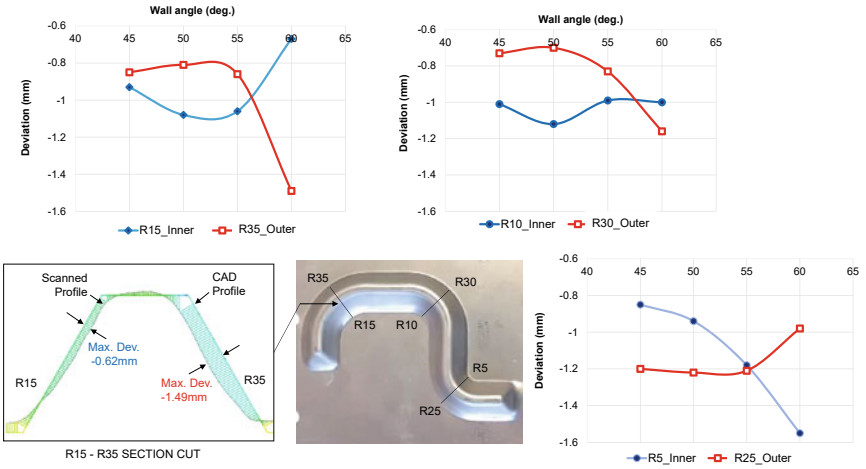


Fig. 8 Maximum part deviation measurements at different turning radii of curvature channels with wall angles from 45 to 60° formed by 5 mm carbide tool and 0.1 mm step-down size. (Color figure online)

systematic to correct such deviations by tool path compensation approach. Unfortunately, there does not appear to be any obvious patterns of part deviations based on the deviation measurements, thus difficult to minimize the deviations by tool path compensation. Heat treatment approach such as pre-annealing of SS316L blank to reduce forming stress levels might be more effective than tool path compensation approach in minimizing part deviations for this class of geometry.

4 Conclusions

This work investigated Single Point Incremental Forming (SPIF) as a forming alternative to stamping of narrow channels or ribs in short-series production. SPIF forming experiments on SS316L 0.5 mm-thick sheet metal were conducted using two sets of part geometries (i) varying wall angle cone and (ii) three different narrow channels—straight, taper, and curvature. The main findings are as the followings:

1. Smaller hemispherical carbide tool will increase formability of SS316L varying wall angle cone—3 mm dia. carbide tool can form the cone up to $\theta_{max} = 80°$, while 5 mm dia. carbide tool can form the cone up to $\theta_{max} = 70°$.
2. Unlike the varying wall angle cone, the smallest tool does not increase but rather decreases the formability of narrow channels. SPIF of narrow channels inherently induces pillow formation, which seems to adversely affect the formability—3 mm dia. carbide tool fails to form even a straight channel of $\theta = 45°$.

3. Formability of narrow channels can be improved by using a bigger tool of 5 mm dia. with 0.2 mm step-down—all the 3 narrow channels can be formed at $\theta_{max} = 55°$. Nevertheless, SPIF of narrow channels seems to yield max. wall angles which are still much smaller than those observed in larger parts such as the cones.
4. Some part deviations in the straight and taper channel are more pronounced when using a large step-down of 0.2 mm. Therefore, 5 mm dia. carbide tool and 0.1 mm step-down size is recommended for SPIF of these particular channel geometries.

References

1. Jeswiet J, Micari F, Hirt G, Bramley A, Duflou J, Allwood J (2005) Asymmetric single point incremental forming of sheet metal. CIRP Ann—Manuf Technol 54(2):88–114
2. Behera AK, De Sousa RA, Ingarao G, Oleksik V (2017) Single point incremental forming: an assessment of the progress and technology trends from 2005 to 2015. J Manuf Process 27:37–62
3. Hussain G, Gao L, Dar NU (2007) An experimental study on some formability evaluation methods in negative incremental forming. J Mater Process Technol 186(1–3):45–53
4. McAnulty T, Jeswiet J, Doolan M (2016) Formability in single point incremental forming: a comparative analysis of the state of the art. CIRP J Manuf Sci Technol 16:43–54
5. Al-Ghamdi KA, Hussain G (2015) Threshold tool-radius condition maximizing the formability in SPIF considering a variety of materials: experimental and FE investigations. Int J Mach Tools Manuf 88:82–94
6. Al-Ghamdi KA, Hussain G (2019) Bulging in incremental sheet forming of cold bonded multi-layered Cu clad sheet: influence of forming conditions and bending. Trans Nonferrous Met Soc China (English Ed.) 29(1):112–122
7. Afonso D, De Sousa RA, Torcato R (2017) Incremental forming of tunnel type parts. Procedia Eng 183:137–142

Enhancing Tool Life by Manipulating the Die Elastic Strain Field During Extrusion



Gracious Ngaile and Daniel Santiago

Abstract A die design architecture for axisymmetric forgings which minimizes the residual contact pressure at the die–workpiece interface during the ejection stroke is proposed. The underlying principle of this die design is that during the forging stroke a tapered die can move in the direction of the forging load thus inducing negative radial elastic strain on the die. When the forging load is removed, the elastic strain energy stored in the die is released thus reposition the die to its initial state. With this design architecture the workpiece can be ejected at no load. Finite element (FE) warm forging simulations for constant velocity joint and pinion gear blank were successfully carried out to evaluate the viability of the process. In addition to reducing residual contact pressure which enhances tribological conditions, the FE simulations conducted have shown that a total energy saving of up to 15% can be achieved with the proposed die designs.

Keywords Extrusion · Die design · Die–workpiece contact pressure · Tool life · Ejection load

1 Introduction

Tool life is a major factor in the cost of forgings, productivity, and part integrity. Forging tools are usually subjected to mechanical, thermal, chemical, and tribological loads. Subjecting dies and punches to severe loading will bring about their eventual failure. The three common modes of failure are tool wear, fatigue fracture, and plastic deformation. In hot forging, tool wear accounts for approximately 70%, whereas the primary mode of failure in cold forging is fatigue fracture [1–4]. A multitude of parameters influence die failure in cold, warm, and hot forging. The interaction of these parameters is complex, as a result, enhancement of tool life has always been a challenge, and strategies to increase tool life can vary greatly from one forging operation to another. Strategies to reduce tool failure which have been

G. Ngaile (✉) · D. Santiago
Department of Mechanical and Aerospace Engineering, North Carolina State University, Raleigh, NC, USA
e-mail: gngaile@ncsu.edu

© The Minerals, Metals & Materials Society 2021

G. Daehn et al. (eds.), *Forming the Future*, The Minerals, Metals & Materials Series,
https://doi.org/10.1007/978-3-030-75381-8_4

adopted over the years include improved lubrication and cooling systems; selection of the tool materials and adequate thermal treatments; surface treatment of the tools via thermochemical reactions such as nitriding which involve diffusion of atomic nitrogen in the steel surface; utilization of hard materials like ceramics; tool shape optimization which at present is carried out with the aid of numerical simulations; and modern tool work supervision where certain parameters can be monitored on the forging machine [5–8].

Lubricants play a critical role in the success of the forging operation. It reduces the friction stress at the tool–workpiece interface, the forming loads, and energy expended in the process. Good lubricant is also critical for the longevity of the tool and surface integrity of the forgings. A wide range of lubricants based on mineral oils and grease are available for simple forging. However, for severe cold forging operations, which exhibit high interface pressures and larger surface expansion, the choices of effective lubricants are limited. For example, the most common lubrication systems for steel and aluminum used in industry today are based on conversion coatings. The conversion coatings adhere to the billet by chemical reactions that create a pre-coat which has proven to bond well with various lubricants such as metal soaps [9]. The conversion coating process, however, involves heavy metal sludge that is difficult to dispose and thus poses health risk to workers [10–13]. The demand for environmentally benign lubrication systems for cold forging prompted the development of less toxic lubricants as an alternative to conversion coatings. Detail review of environmentally friendly lubrication systems can be found in Ref. [13].

On the other hand, lubrication for hot forging operation presents a different set of challenges to those observed in cold forging. For example, high thermal loading at the die–workpiece interface in hot forging precludes the use of many lubricants. One of the attributes of a good lubricant for hot forging is that it should lubricate and cool the die as well. This is crucial because the temperature of the dies needs to be kept below certain levels to prevent die thermal softening. To that effect, the most widely used lubricant in hot forging is water-based graphite. Graphite provides good anti-galling performance due to lower friction and heat resistance. However, graphite oxidizes at 370 °C, thus, it starts losing its performance. It should be noted that graphite lubricants pollute the atmosphere, so it is considered a non-environmentally benign lubricant. Environmental and safety concerns prompted the growth of research on white lubricants. There are three classes of white lubricants that are used in industry today; water-soluble polymer base, carboxylic acid base, and liquid glass base. These lubricants, however, exhibit low lubricity compared to graphite and pose difficulties in releasing the dies [13]. A detailed review of white lubricants used in hot forging can be found in [14]. Another way of enhancing die life is through thermochemical surface treatment. Efforts for developing die coatings for both cold and hot forging operations have been going on for the past 20 years. Physical Vapor Deposition (PVD) and Chemical Vapor Deposition (CVD) are the major methods that are used to diffuse chemical elements into the lattice of the tool material. With recent advances in additive manufacturing, a variety of materials can be sintered together without the need for additional processes. Using powder metallurgy technology,

the matrix phase of a pure metal or alloy can be sintered together with a solid lubricating material, making an antifriction compound. These compounds are called self-lubricating materials. Researchers have studied the effect of adding CaF_2 to a matrix of H13 steel, a steel widely used for tooling in hot forging, and they observed friction reduction when CaF_2 is added up to 10% [15].

As discussed above, there are different ways that could be used to enhance the life of the forging tool. Each of these methods, however, has its limitations. This paper discusses a different approach for improving tool life by manipulating the elastic strain field during the forging cycle. The forging cycle can be divided into two steps: (1) the forging stroke, where forging takes place and (2) the tool–workpiece disengagement stroke, where the workpiece is disengaged from the tooling. The tool–workpiece disengagement part of the cycle can exhibit a substantial tool–billet "residual contact pressure" with potential for galling and tool wear. The goal of this study is to explore innovative tooling designs, which are capable of reducing or eliminating the residual contact pressure via manipulation of the elastic strain field of the dies during the forging cycle.

2 Concept Development

Prior to discussing the concept pertaining to manipulation of elastic strain field in extrusion die design, the mechanics of a typical extrusion tool setup for backward cup extrusion were examined as shown in Fig. 1. The tooling has a compounded die arrangement, with one stress ring and a die press-fitted together. A forging cycle will be regarded as consisting of a "forging stroke" and a "workpiece disengagement stroke." The tool–contact pressure evolution along the boundary of the deforming body *a-b-c-d-e-f-g-h-a* plays a major role in wearing of die and punch (Fig. 1). Due to the elastic deformation characteristics of the tool and the billet, it can be shown that

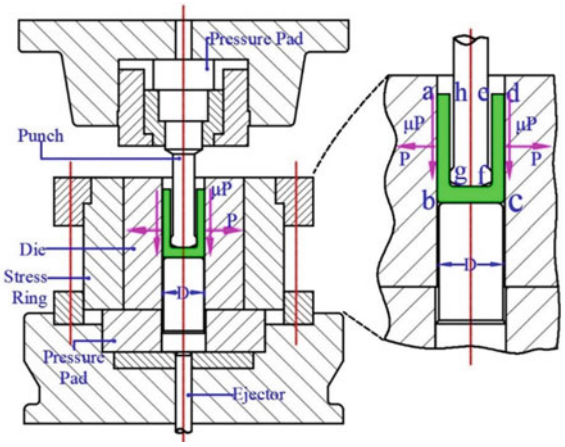


Fig. 1 A typical extrusion tooling setup. (Color figure online)

the contact pressure is exhibited during both the forging stroke and the workpiece disengagement stroke. During the forging stroke, the diameter of the die D will expand to D + Δd. As soon as the load is removed, the expanded die will spring back to D causing a secondary deformation to the forged part. This is the reason for the occurrence of residual die-workpiece contact pressure.

Similarly, as the punch load is removed at the punch–workpiece, the forged cup will attempt to spring back, thus compressing the punch, causing residual contact pressure at the punch land. In addition to causing this mechanical loading, the tool contact pressure has a cascading effect in intensifying thermal and tribological loads.

This paper proposes an extrusion tool architecture that will minimize or eliminate die–billet contact pressure during the disengagement stroke. This can be achieved by modulating the elastic strain field during the forging cycle. The die-workpiece contact pressure domain can be reduced, thereby enhancing tribological conditions, reducing/eliminating ejection load, and ultimately increasing tool life. The tooling architecture shown in Fig. 2 for forward–backward extrusion is design in a way that during the forging stroke, the die will shrink as the tapered die slides along the taper. After releasing the extrusion load, the compressive strain field in the die will be relaxed causing the die to expand (spring back) creating a gap in the order of few microns between the die and the workpiece. If the gap is created along with the whole tool–workpiece interface, residual contact pressure will be zero. Else, very little contact pressure will be exhibited at the interface. With optimization, there is potential to eliminate residual contact pressure during the ejection stroke.

The positive attributes of the tooling architecture given above include the potential to drastically reduce wear, reduce thermal loading to the dies, increase the quality of parts' surfaces, and reduce the possibility of lubricant breakdown as total sliding distance under high pressure is reduced. Manipulation of elastic strain field can be done on the punch by segmenting the punch into two parts thus the contact stress at the punch–workpiece interface is eliminated during the ejection stroke. Details on this technique can be found in an earlier publication by one of the authors [16].

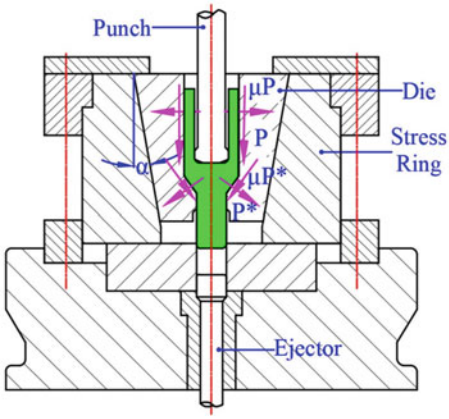


Fig. 2 Taper die design for manipulating die elastic strain field. (Color figure online)

3 Analysis of Tool Loading in Typical Forging Process: Constant Velocity (CV) Joint

This section will present finite element analysis of a constant velocity joint aimed at establishing loading characteristics during forging cycle. Assessment is then made on how the tool load evolution path predetermines the tool life. The forging sequence for manufacturing of a CV joint (outer race) consists of a forward extrusion stage, an upsetting stage, a backward–forward extrusion stage, and sizing stage. Details on forging sequences can be found elsewhere [17]. It is common that the first three stages are performed in a warm or hot workpiece condition, while the sizing stage is performed as cold forming. For this analysis, the geometry will be considered axisymmetric and therefore a preform without the grooves is considered as a final workpiece (Fig. 3). The simulations were carried out with 2D DEFORM Software package. AISI 1045 was used as workpiece material and warm forging conditions were investigated. The flow stress of this material was obtained from DEFORM Software database. Other common parameters entered in DEFORM are given in Table 1. Only the forward extrusion stage will be presented.

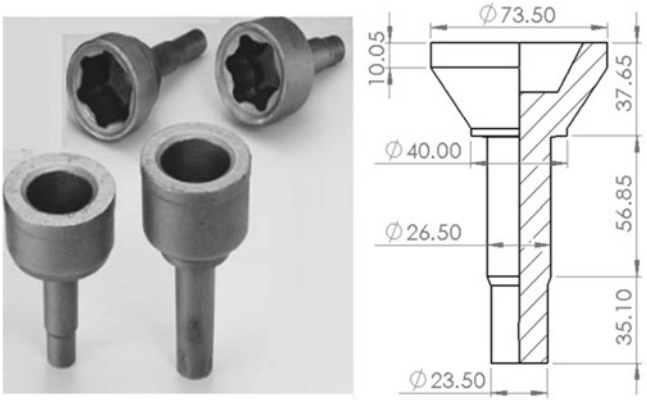


Fig. 3 CV joint preforms and dimensions used in the FE model

Table 1 Common parameters used in the FE simulations

Simulation 2D	Axisymmetric
Shrink fit amount	Uniform 0.1 mm
Die material	H-13
Die temperature	300 °C
Workpiece behavior	Plastic, billet temp 900 °C
Die behavior	Elastic
Friction	Shear factor $m = 0.25$

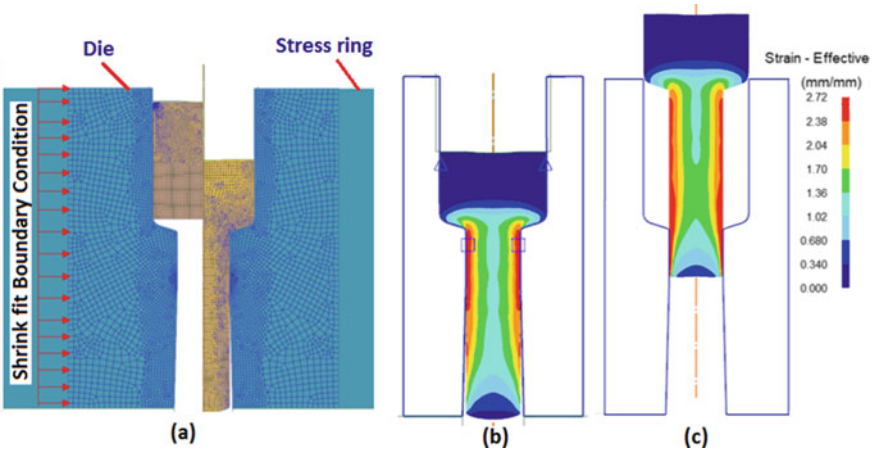


Fig. 4 **a** FE model. **b** Effective strain before ejection. **c** Effective strain after ejection. (Color figure online)

Forward Extrusion Stage

The FE model with representative meshes for the die and the workpiece are shown in Fig. 4a. The stress ring is present in the simulation and by definition; it must be elastic and meshed. The mesh of the ring is similar to the one of the dies, and it is not shown to facilitate the visualization. The shrink-fit boundary condition is applied as a uniform 0.1 mm interference.

Effective strain: Fig. 4b shows the effective strain at the end of the extrusion process. The maximum strain in the material is 2.7. A gradient in the strain distribution occurs on the surface of the extruded part along the axis of the workpiece and it varies from 1.0 to 2.7. During the ejection process, a secondary deformation takes place as clearly seen in Fig. 4c. The effective strain on the surface of the extruded shaft is now about 2.7 along the whole length. It should be noted that the secondary deformation is not an intended operation, but rather it occurs because the dies spring back after removing the extrusion load. This deformation is thus the consequence of residual pressure at the die–workpiece interface.

Forging load and ejection load: Fig. 5a shows the forming and ejection load. The sharp reduction in the cross section causes the load to increase rapidly to its maximum value, close to 250 t. After reaching its maximum, the load stabilizes and slightly decreases with stroke since the die–workpiece contact surface is also decreasing. The interface pressure during the extrusion stage is shown in Fig. 5b. Then, the extrusion load is removed, and the workpiece must be ejected. At this moment the die springs back and thus compresses the workpiece causing a residual pressure. This pressure state is defined as the pressure the die exerts on the part when no load is being applied. The initial residual pressure (just before the ejection starts) can be seen in Fig. 5b. This pressure mainly causes the required load during ejection, Fig. 5a. During FE simulation, the same shear friction parameters were used during forward extrusion

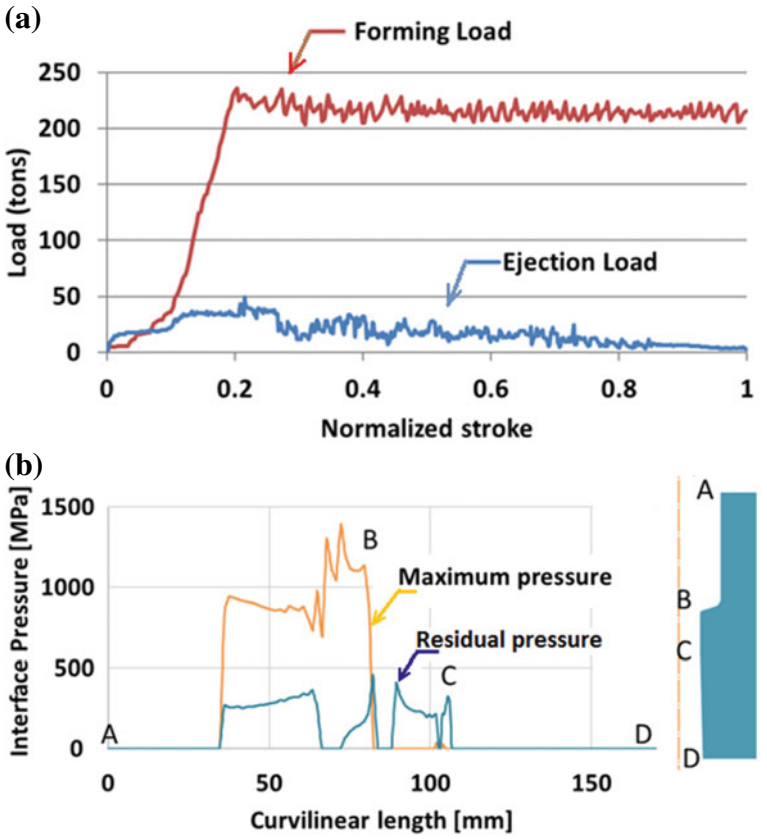


Fig. 5 **a** Load curves for forward extrusion stage of CV joint. **b** Tool–workpiece interface pressure profiles for forward extrusion stage. (Color figure online)

and ejection stroke. In practice, however, the lubricant may have thinned/depleted implying that the friction during ejection may be higher.

Residual pressure: As stated above the residual pressure is the pressure the die exerts on the workpiece when there is no load being applied. As seen in Fig. 5b this pressure is substantial, it is about 30% of the maximum pressure. During ejection, the contact surface area decreases. This may cause contact pressure in certain locations to increase dictated by the overall elastic strain energy stored in the die. This behavior can also be reflected on the ejection load profile. Note that as the ejection progresses; the land of the die (B–C) will exhibit a significant larger residual pressure up to the end of the ejection stroke. This region is thus bound to endure significant die wear. In short, this residual pressure hinders the ejection of the workpiece and plays an important role in the overall wearing of the die. The goal of this study is therefore to devise a methodology to reduce or eliminate residual pressure.

4 Reduction of Residual Contact Pressure in Extrusion by Manipulating Die Elastic Strain Field

As discussed in section two a tooling setup is designed which stores elastic strain energy during the forging stroke. As soon as the extrusion load is removed, the stored elastic energy is released thus repositioning the die such that the residual contact pressure is at its minimum or eliminated. The storage of elastic strain energy is facilitated by compressing the die during the forging stroke. Upon release of the extrusion load the die springs back in accordance with Hooke's law ($\sigma = E\varepsilon$), where E is Young's modulus and ε is the elastic strain. Note that the workpiece which was also under compression will spring back as well, but because the yield stress of the deforming material is smaller compared to that of the tooling, the magnitude of spring back, δ, for the workpiece will be smaller than that of the die. The optimal tooling design regarding the part ejection should generate $\delta_{die} - \delta_{billet} > 0$ along the contact surface. For this condition, the residual contact pressure is zero and the forged part can be ejected by only overcoming the weight of the part.

This tool design is applied to the CV joint forging simulations discussed in Sect. 3. Due to the new tool setup, the workpiece should be formed in a similar manner as in conventional dies, i.e. using same press, devices, and developing the same levels of plastic strain on the workpiece as well as the extrusion load. The new tooling setup would ease the ejection of the workpiece from the die thus reducing the forging energy to be expended, wear on the tool, and potentially reducing overall stresses on the forging tooling setup.

4.1 Constant Velocity (CV) Joint—Forward Extrusion: Proposed Tooling Design

As shown in Sect. 3, a substantial residual pressure was received at the die–workpiece interface. This pressure caused a high ejection load. Moreover, this pressure was present during the entire ejection stroke, and therefore a higher force was required to remove the workpiece throughout the ejection stroke. The retained contact stress has detrimental effects on tool life, as it intensifies tool wear, increases temperature dissipation from the workpiece to the tools, and worsens the tribological conditions.

The proposed tooling concept is aimed at improving the technical challenges during the ejection process. To manipulate the elastic strain, a set of die and sleeve with a taper angle of 7° is designed as shown in Fig. 6. The FE simulation conditions remained the same as that discussed in Sect. 3 for conventional tooling setup. The only exception was imposition of a friction coefficient of 0.1 at the interface between the die and the sleeve. During the extrusion process, the insert slid about 0.7 mm downward as shown in Fig. 6. This movement causes the insert to undergo radial compression storing elastic energy, while at the same time compressing the workpiece radially. When the load is removed, the stored elastic energy is used to return the die

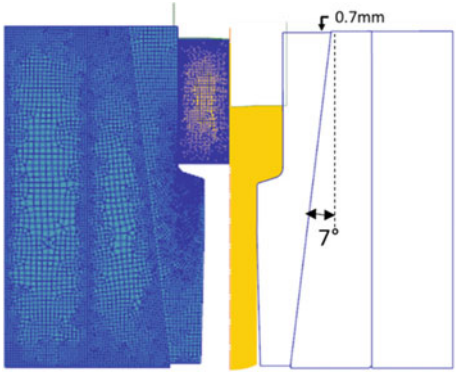


Fig. 6 FE model CV Joint forward extrusion—New die design. (Color figure online)

back to its initial position, creating a gap between die and workpiece in the order of few microns (Fig. 7). This gap allows the workpiece to be removed with minimum load.

The effective stress induced in the new die setup is shown in Fig. 8. The maximum stress attained is at the same level as what was observed in the conventional tooling setup. The new tooling setup, however, provides better stress distribution. The plastic strain distribution of the workpiece at maximum stroke can be seen in Fig. 9a, which is similar to the strain, obtained from the conventional tooling shown in Fig. 4b. Contrary to the conventional tooling, the strain distribution after ejection remains the same for the new tooling (Fig. 9b). This implied that in the new tooling setup no secondary deformation took place during ejection.

Figure 10 shows the extrusion load and ejection load. As expected, the ejection load with this new tooling setup is lower. This implies that during ejection the workpiece is barely in contact with the die. This is also evident for the residual pressure plotted in Fig. 11.

4.2 Comparison Between Conventional and New Tooling Designs

The residual pressure profiles for the conventional and new design at beginning of the ejection process is shown in Fig. 12. The average pressure along the area A–B–C is about 300 MPa for conventional die design. In the new setup, the pressure is almost zero everywhere except a small region. From a tribological point of view, an interface pressure of 300 MPa is substantial. In the absence of appropriate lubrication, friction can increase drastically leading to die wear. Therefore, the new tooling setup has the potential to increase tool life substantially. Due to reduction in the residual stress, the ejection load decreased significantly as seen in Fig. 13. Through integration on

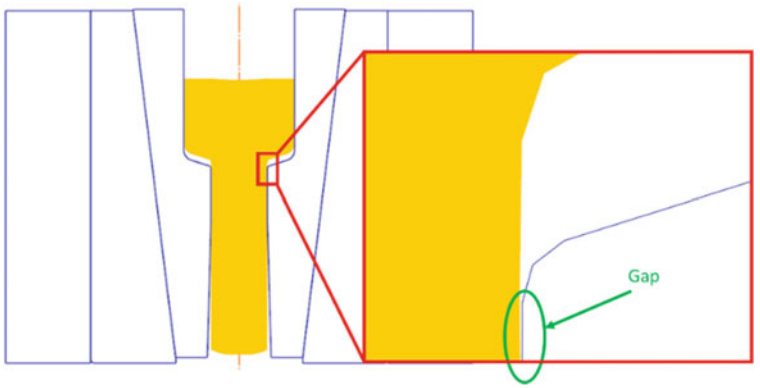


Fig. 7 Illustration of gap created at the land of the die ($\delta_{die} - \delta_{billet} > 0$). (Color figure online)

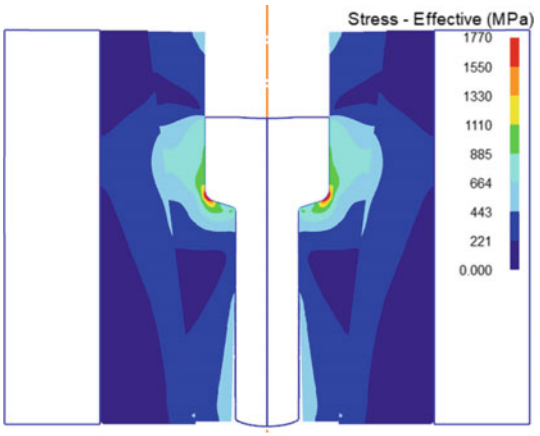


Fig. 8 Effective stress distribution for proposed die/sleeve for forward extrusion. (Color figure online)

the load curves, the total energy saving can be quantified. This case study shows an energy saving of 15% if a new die setup is used.

Another benefit of reducing/eliminating residual pressure is the reduction in heat transfer from the workpiece to the die. In hot forging, die–workpiece contact time is kept at a minimum to prevent thermal softening of the die, which is bound to reduce the hardness of the dies. If the hardness of the dies is reduced below acceptable levels, the tool life will be compromised. Thus, by reducing the residual contact pressure, the amount of heat that can be transferred to the die will be reduced. In turn, the potential for die softening can substantially be reduced.

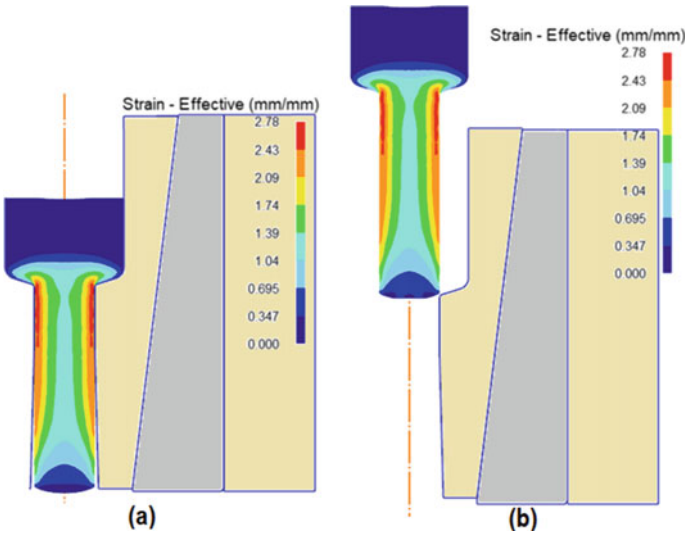
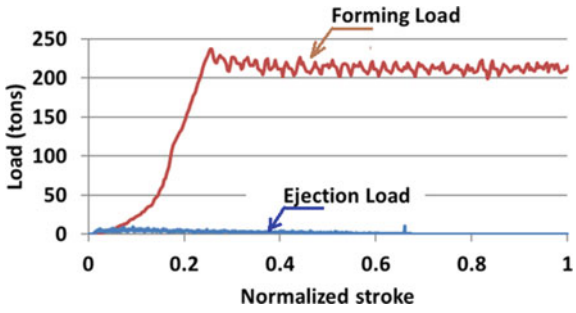


Fig. 9 Same strain distribution **a** before and **b** after ejection. (Color figure online)

Fig. 10 Load curves for the extruding stage for the new tooling setup. (Color figure online)



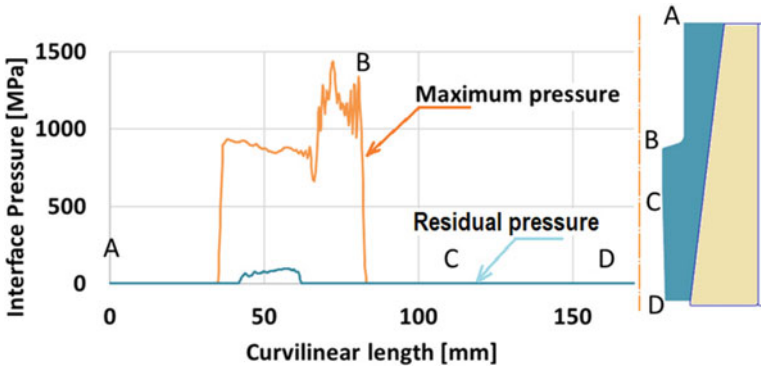


Fig. 11 Pressure profiles for the extrusion stage for the new tooling setup. (Color figure online)

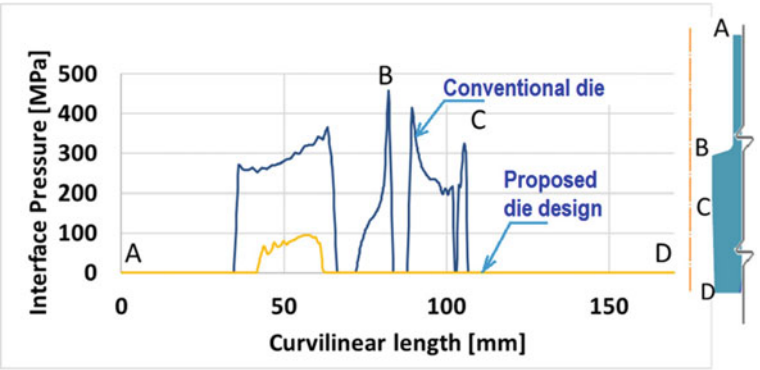
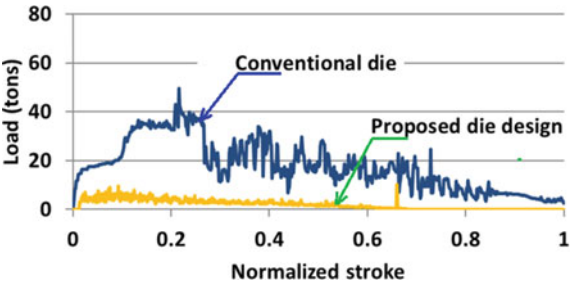


Fig. 12 Comparison in residual pressure between conventional and new tooling setup for forward extrusion. (Color figure online)

Fig. 13 Comparison in ejection load between conventional and new tooling setup for the forward extrusion. (Color figure online)



5 Conclusions

This paper presented a new methodology for designing extrusion dies which result in minimal contact pressure at the interface between the die and the extruded part during the ejection stroke. The proposed die setup is bound to enhance tool life since the tribological loads are substantially reduced. The methodology is based on manipulating elastic strain energy of the dies during extrusion. To demonstrate the viability of the proposed tool design, finite element extrusion simulations for a CV joint were carried out. The major conclusions drawn from this study are:

- Manipulation of the die elastic strain energy is achieved by segmenting a die into a tapered insert and a sleeve. During the extrusion stroke, the tapered die insert can move downward, whereas the sleeve is constrained. Since it is moving on a tapered wall, compressive strains are induced on the die insert, storing elastic energy. During ejection, the die insert sprang back allowing the forged part to be released with minimal load. For the simulation cases studied, a die taper angle of 7° was enough to reduce the contact pressure to insignificant levels.

- The FE simulations conducted have shown that the residual pressure in the range of 400–500 MPa received in conventional dies can be eliminated when the new die setup is used. From the tribological point of view, this level of interface pressure is substantial. In the absence of appropriate lubrication, friction can increase drastically leading to die wear. Therefore, the new tooling setup has the potential to increase tool life substantially.
- Reducing the residual contact pressure results in the reduction of heat transfer from the workpiece to the die, a condition that is critical in hot forging where die–workpiece contact time needs to be kept at a minimum to prevent die thermal softening, which is bound to reduce the hardness of the dies. If the hardness of the dies is reduced below acceptable levels, the die life will be compromised.
- The simulated case studies have shown that a total energy saving of up to 15% can be achieved with the proposed die setup designs.

Acknowledgments The authors would like to acknowledge the Forging Industry Education Research Foundation (FIERF) for supporting this work.

References

1. Cser L, Geiger M, Lange K, Hansel M (1993) Tool life and tool quality in bulk metal forming, IMechE. Proc Inst Mech Engrs 207:223–237
2. Altan T, Ngaile G, and Shen G (2004) Cold and hot forging, fundamentals and applications. ASM Int., Materials Park, OH
3. Behrens B-A, Bouguecha A, Luken I, Mielke J, Bistron M (2014) Tribology in hot forging. Compr Mater Process (5):211–234
4. Hawryluk M (2016) Review of selected methods of increasing the life of forging tools in hot die forging processes. Arch Civil Mech Eng 16:845–866
5. Podgornik B, Hogmark S, Sandberg O (2006) Proper coating selection for improved galling performance of forming tool steel. Wear 261:15–21
6. Dubar M, Dubar L, Dubois A (2005) Wear analysis of tools in cold forging: PVD versus CVD TiN coatings. Wear 259:1109–1116
7. Geiger M, Popp U, Engel U (2002) Excimer laser micro texturing of cold forging tool surfaces—influence on tool life. CIRP Ann 51(1):231–234
8. Dobrzański LA, Labisz K, Klimpel A (2003) Effect of laser alloying on thermal fatigue and mechanical properties of the 32CrMoV12-20 steel. Achiev Mater Manuf EngVolume 19(1):83–90
9. Bay N (1994) State of the art in cold forging lubrication. J Mater Process Technol 46:19–40
10. Ngaile G, Cochran J, Stark D (2007) Formulation of polymer-based lubricant for metal forming. Proc IMechE, B: J Eng Manuf 221:559–568
11. Sagisaka Y, Nakamura T, Hayakawa K, Ishibashi I (2013) Evaluation of environmentally friendly lubricant for aluminum cold forging using friction test based on spline extrusion. J Manuf Processes 15(1):96–101
12. Gariety M, Ngaile G, Altan T (2007) Evaluation of new cold forging lubricants without zinc phosphate pre-coat. Int J Mach Tools Manuf 47(3–4):673–681
13. Bay N, Azushima A, Groche P, Ishibashi I, Merklein M, Morishita M, Nakamura T, Schmid S, Yoshida M (2010) Environmentally benign tribo-systems for metal forming. CIRP Ann: Manuf Technol 59(2):760–780

14. Wan S, Kiet Tieu A, Xia Y, Zhu H, Cui S (2016) An overview of inorganic polymer as potential lubricant additive for high temperature tribology. Tribol Int 102:620–635
15. Rao R, Wang H, Li M, Yao Z, Liu Q, Yan S, (2019) Research on high temperature friction and wear characteristics of H13-Cr_2C_3-CaF_2 self-lubricating materials. IOP Conf Ser: Mater Sci Eng 472
16. Lowrie J, Ngaile G (2016) New punch design for the elimination of punch ejection load through manipulation of the elastic strain field in the punch nose. J Manuf Processes 22:49–59
17. Ku TW, Kim L, Ho Kang BS (2013) Multi-stage cold forging and experimental investigation for the outer race of constant velocity joints. Mater Des V49:368–385

Part II
Honorary Symposium: Niels Bay

Oscillation-Free Determination of Material Properties at High Strain Rate



Xiangfan Fang

Abstract The determination of the plastic deformation properties of materials under high-speed loading is a challenge. The system ringing in a conventional servo-hydraulic tensile machine deteriorates the quality of force measurement. A precise determination of the plasticity and damage is thus difficult. In this work, the system ringing effect of the entire test system, including machine, sample, etc., was analyzed. We found that the system ringing is location- and geometry-dependent. Inspired by the principle of the split-Hopkinson bar, a new type of tensile sample has been developed. In a certain restricted area of this new sample, the tensile forces can be measured without any oscillation effect. The plastic deformation and damage behavior can be determined by using this type of specimen for a wide strain rate range of $10^{-4}-10^{3}$/s. To explain the functionality of the sample and sample design, a one-dimensional stress wave model has been developed.

Keywords Specimen geometry · High-speed tensile test · Servo-hydraulic testing machine · Stress wave · Stress-strain curve · Strain hardening rate

1 Introduction and State of the Art

During a vehicle crash event, large multi-axial plastic deformation occurs. The strain rate of this deformation ranges from 10^{-4} to 10^{3}/s [1, 2]. The material behavior must be correctly described for the FE simulation, which is commonly used in the vehicle development process.

In order to determine flow curves in the strain rate ranging from 10^{-4}/s to 10^{3}/s, three different measuring techniques are generally used: a quasi-static testing machine with 80 mm tensile specimen for 10^{-4}/s to 10^{-2}/s; a servo-hydraulic high-speed testing machine with 20–25 mm smaller tensile specimens according to SEP

X. Fang (✉)
Institute of Automotive Lightweight Design, University of Siegen, Breite Straße 11, 57076 Siegen, Germany
e-mail: Xiangfan.fang@uni-siegen.de

© The Minerals, Metals & Materials Society 2021

G. Daehn et al. (eds.), *Forming the Future*, The Minerals, Metals & Materials Series,
https://doi.org/10.1007/978-3-030-75381-8_5

1230 or ISO 26203-2 standards [3, 4] for a range of up to 1000/s; and the Split-Hopkinson Bar (SHB) for the range >1000 1/s with very small 5–10 mm specimens [5]. The experimental techniques and conditions (i.e., the measurement of force, deformation, specimen geometry and size, as well as the specimen fixation) are different for the various strain rate ranges and produce an apparent discontinuity in material behavior [6].

The use of the different experimental techniques is the result of force signal oscillations at high strain rates, the so-called system ringing effect [7, 8]. It is well known that a sudden force application on a solid body induces a stress impulse σ that is directly proportional to the loading speed V, the material density ρ and its sound speed C according to the Eq. (1) [7].

$$\sigma = V \cdot \rho \cdot C \tag{1}$$

Xiao et al. [8] stated that the insertion of a rubber damper in the force introduction increases the force rise time in such an experiment so that the stress wave has time to move back and forth at least three times within the specimen. This allows a quasi-equilibrium of the force within the specimen to be approximated and the oscillation of the force signals to be reduced. Zhu et al. [9] used the mode analysis of the entire system to filter out the force signal oscillations by using the eigen-frequencies and amplitudes of the system. While the method in [8] also reduces the maximum achievable strain rate and counteracts the goal of the high-speed test, signal filtering is an important intervention in the measurement data. In [3, 4, 10], suitable specimen geometries, measuring techniques and filtering were developed and recommended by extensive investigations. With the SEP 1230/ISO 26203-2 [3, 4], a specimen with a measuring length of 20 mm is given the highest possible natural frequency in order to reduce the vibration amplitude. In addition, the force measurement should be carried out as closely as possible to the gauge length of the specimen at the specimen shoulder area by the use of strain gauges instead of a load cell [10]. With this method, flow curves with reduced oscillations can be obtained up to approximately 200/s.

Using a split-Hopkinson bar (SHB), the force signals can be measured without any oscillation for the range $>10^3$/s. However, the results of such experiments by different research groups for one and the same material are considerably different. Verleysen stated [11] that in an SHB experiment, many of the fundamental assumptions for the evaluation of the test results are not valid in reality. The stress and strain in the very small specimens are not homogeneous as assumed, and the achievement of a quasi-static equilibrium is not always given. This is a contributing factor to the overestimation of the deformations and deviation of the determined stresses. Therefore, many efforts have been made to extend the application range of the servo-hydraulic high-speed tensile machine.

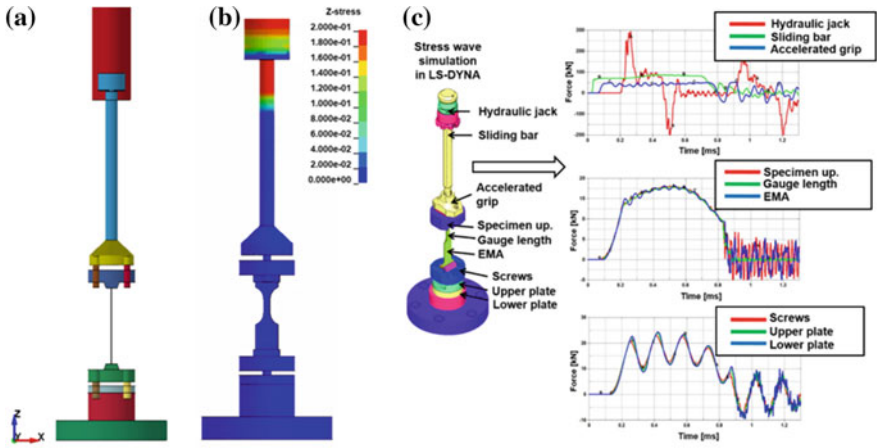


Fig. 1 Loading condition between hydraulic jack and sliding bar (**a**) and the stress wave there at 20 m/s speed (**b**); **c** Force fluctuations at different positions of the test system (EMA: Elastic Measurement Area). (Color figure online)

2 Stress Wave Propagation and System Ringing Analysis

In a high-speed tensile test using the servo-hydraulic tensile machine by the Zwick Roell Group (here a HTM5050 machine), a stress wave with $\sigma \approx 4-500$ MPa occurs on the contact area between the hydraulic jack and the sliding bar when the hydraulic jack hit the sliding bar at 20 m/s (Fig. 1a). Based on the CAD data provided by Zwick, an FEM model was developed in [1, 12] and validated.

There, as can be seen in Fig. 1c, a phenomenon was discovered—the oscillations in the area of the sliding bar are extremely large, they are very large in the area of the load cell and they are very small in the gauge length of the specimen.

3 Development of the New Specimen for Ringing Free Force Measurement

The above conclusion is used as a starting point for the development of a new specimen geometry. Since the force oscillations in the area of the specimen with large plastic deformation are almost zero, it is assumed that the stress waves may be absorbed by the plastic deformation.

Böme reported in [10] that the force vibration is smaller in the sample clamping area of the SEP 1230/ISO 26203-2 sample in comparison to the measurement in the load cell of the tensile machine. The SEP sample is modified in [1, 12] to a so-called Generation I (Gen. I) sample (see Fig. 2). In the test results in [1, 12], the force

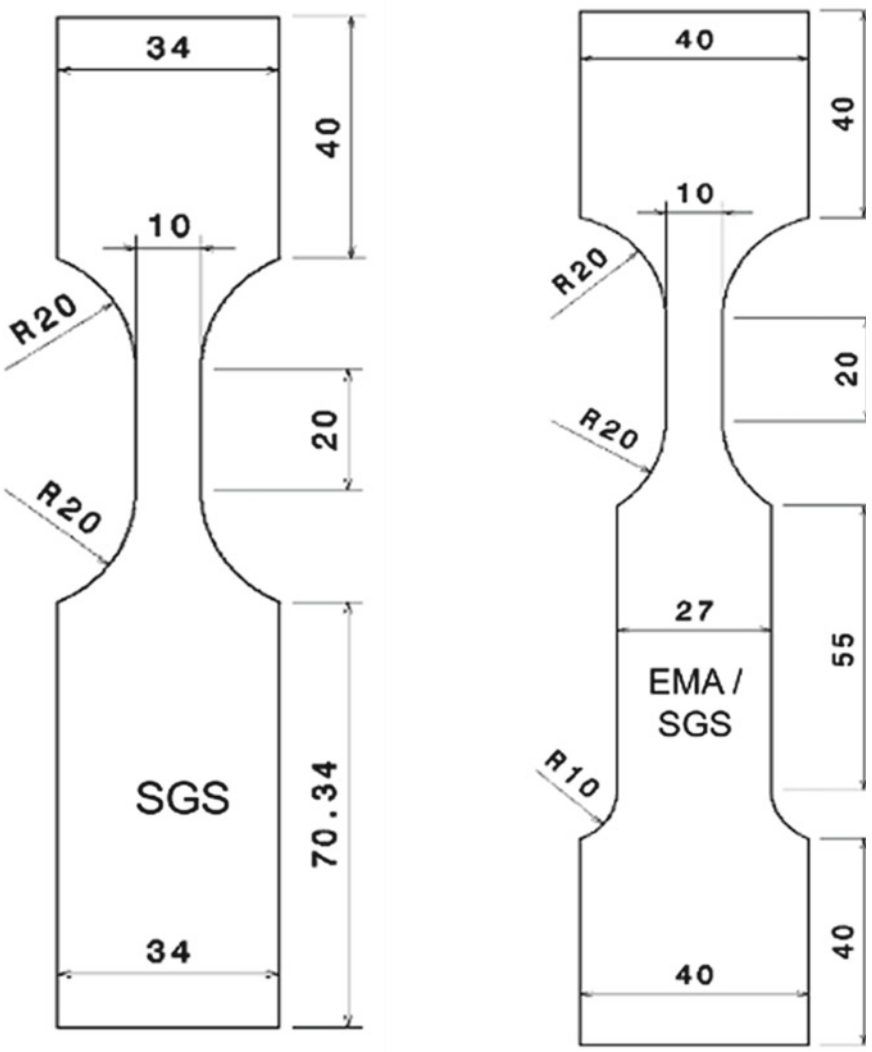


Fig. 2 Comparison of different specimens. Left: SEP 1230; right: Generation I specimen (Gen. I); SGS: strain gauge sensor measurement; EMA: elastic force measurement area

vibration in the area of strain gauge sensor (SGS) in the Gen. I sample is smaller than that of the SEP/ISO sample.

If the force oscillations in the strain gauge sensor (SGS) measurement or elastic measurement area (EMA) of the specimen could be significantly reduced further, a solution for force vibration may be found. Therefore, the geometry of the Gen. I sample has been further modified in different ways, and it ends up at the discovery

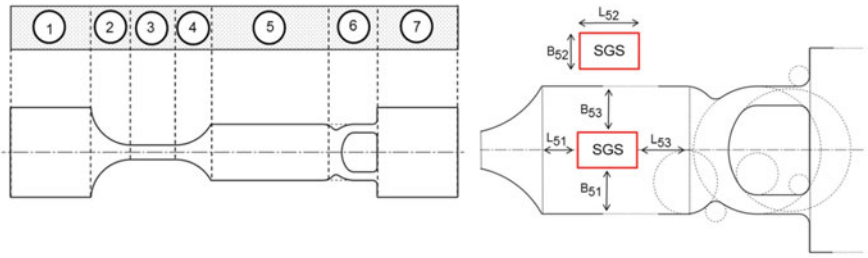


Fig. 3 Gen. III specimen geometry and its characteristics. (Color figure online)

of the Gen. III sample (Fig. 3). In the Gen. III sample, a cut-off (area 6 in Fig. 3) has been introduced in the EMA area of the Gen. I specimen. We hoped to create a kind of geometric filter which may prevent the stress waves from reflecting back to the strain gauge measurement (SGS or EMA) of area 5 when the rightward stress waves coming from area 1 pass areas 5 and 6 and are reflected at the end of area 7.

With a decreasing cross section in the weakening area of 6, a decreasing system ringing could be observed in area 5 which is between the weakened area 6 and the specimen's major plastic deformation, area 3. In the end, the best results could be achieved when a slight plastic deformation occurs in the weakening area 6 in the EMA. The effect of the slight plastic deformation is much larger than the pure geometric changes, i.e., the cross-section reduction between areas 5 and 6.

It seems that in the lower specimen area, the plastic deformation in the weakening area 6 results in the absorption of the elastic waves. This assumption was confirmed by Tasdemirci and Hall [13] and Maurel et al. [14], who analyzed the interaction between stress waves and dislocations in metals and came to the conclusion that dislocation movement may result in wave scattering and attenuate the stress wave [14].

The conditions for an almost vibration-free force measurement in the EMA area of the specimen are now described in detail with the help of Fig. 3. At the same time, it is ensured that the actual major plastic deformation of the specimen in the gauge length remains undisturbed.

The specimen geometry with the best results, the so-called Gen. III specimen (Fig. 3), has five sections (Sect. 2, 3, 4, 5 and 6) with different widths in addition to the two specimen clamping areas (Sects. 1 and 7). The force in the tensile test is applied in Sect. 1, while the specimen is firmly clamped and is immovable in Sect. 7. In Sect. 3, the actual major plastic deformation up to fracture takes place. Section 5 is larger in dimensions than Sect. 3. Next to Sect. 5, another Sect. 6 with geometric weaknesses is introduced. The geometrical dimensions of the specimen must fulfill different conditions:

$$\text{Section 3:} \quad \frac{R_{mB3} \cdot A_{B3}}{R_{mB6} \cdot A_{B6}} < 1 \tag{2}$$

$A_{B(n)}$: Cross section in section (n) with $(n) = 1$–7 (Fig. 3); $R_{mB(n)}$: Tensile strength of the material in section (n)

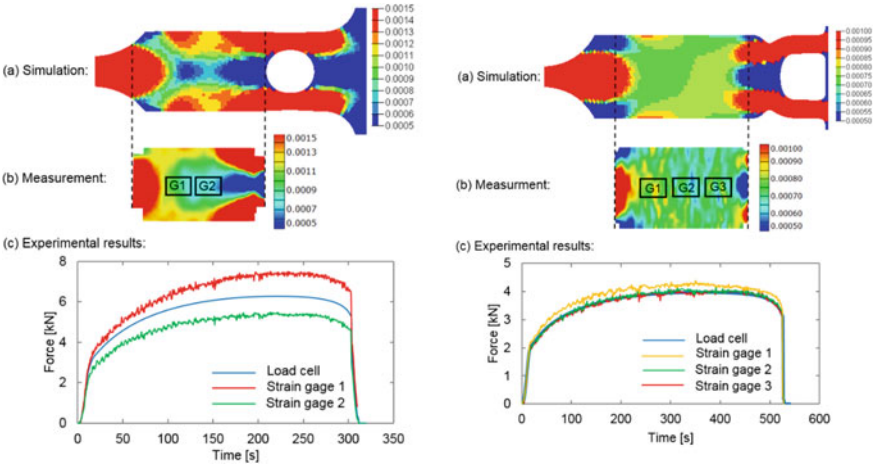


Fig. 4 Influence of the geometry of weakening area 6 on stress homogeneity in area 5 (G1–3: Strain gauge sensor area). FEM and experiment results are both quasi-static tests. Left: sample with a simple hole with in-homogeneous stress in area 5; right: Gen III sample with properly designed cut-outs for homogeneous stress in area 5. (Color figure online)

This ensures that mainly Sect. 3 is deformed. In this section, the specimen deformations are measured to calculate the strains. For a homogeneous quasi-isotropic material, $R_{p0.2}$ and R_m are the same in all sections. The following condition must apply in the force measurement area:

$$\text{Section 5:} \quad \frac{R_{mB3} \cdot A_{B3}}{R_{p0.2B5} \cdot A_{B5}} \leq 1 \tag{3}$$

$R_{p0.2B(n)}$: Yield strength of the material in section (n)

This ensures that only purely elastic deformations occur in Sect. 5. The force is measured locally via strain gauges or via digital image correlation (DIC).

The following conditions must be met in Sect. 6 of the specimen:

$$\text{Section 6:} \quad \frac{R_{p0,2B6}}{R_{mB3}} \leq \frac{A_{B3}}{A_{B6}} < \frac{R_{mB6}}{R_{mB3}} = 1 \quad \text{for homogeneous materials} \tag{4}$$

This is to ensure that Sect. 6 is slightly plastically deformed during the test while Sect. 3 undergoes the major deformations.

Extensive investigation shows that the shape and position of the local weakening in Sect. 6 must be designed appropriately in accordance with Sect. 5. Figure 4 *left* shows that a simple hole may reduce the system ringing, but the stresses in area 5 are inhomogeneous and thus the strain field is also inhomogeneous. The forces measured in G1 are different from G2 and the load cell of the test machine.

Using FEM, this inhomogeneity could be removed, as shown in Fig. 4 *right*. If the strain gauge is placed in G2 or G3, repeatable results can be obtained. The results

are the same as the load cell measurements. Since only the quasi-static material data is required for this sample geometry optimization, this work can be done without any difficulties. Fang and Grams [15] show that the homogeneity of the strain field remains during the whole deformation and that it is valid for both steel and aluminum.

The results of the high-speed tests on two steels in the following section prove that oscillation-free force measurement up to nominal strain rates of $\dot{\varepsilon} = 1000/s$ has now become possible.

4 Experimental Results

With the above-mentioned method, the strain rate dependencies of the flow curves of steel DC 04 and DP 600 are measured and systematically investigated. A Zwick Z100 testing machine was used for the quasi-static tests. The deformations were measured with a GOM 5 M CCD camera (max. frame rate: 29 Hz; max. resolution: 2448 × 2050). The high-speed tests were carried out using a Zwick HTM 5020 testing machine. A PHOTRON SA 5 camera (max. frame rate: 1 MHz; max. resolution 1024 × 1024) was used for the deformation measurement. However, the resolution of the camera had to be limited to 128 × 240 pixels in order to achieve the required high frequency of 150 kHz in the high-speed test up to 1000/s. The measurement data was all post-processed with the GOM ARAMIS software and then evaluated using our own corresponding software. More details can be found in [15].

The nominal strain rates of 4.4×10^{-4}/s, 25/s, 100/s, 200/s, 300/s, 500/s and 1000/s were realized. The same Gen. III specimen was used for all strain rates so that any specimen geometry effects were excluded. The entire strain rate range from 4.4×10^{-4} to 10^3/s could be measured with a single specimen geometry and measurement technique.

The force-time curves for two steels (DC04 and DP600) are plotted in Fig. 5. Force values measured by the load cell of the machine show increased vibrations when strain rate increases. However, the force values measured by strain gauge in

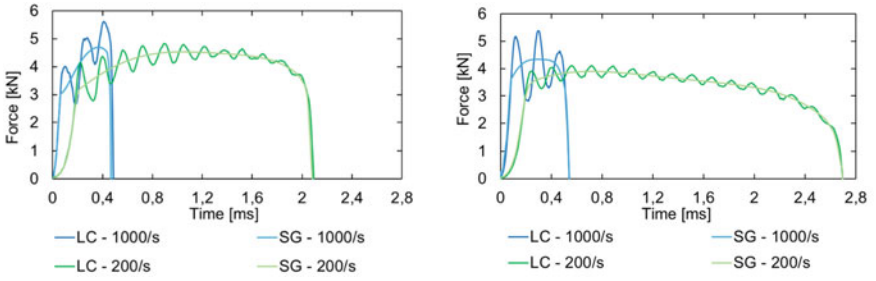


Fig. 5 Force-time signal for **a** DC04 and **b** DP600 steel. LC = force measured directly by the load cell of the machine; SG = force measured by the strain gauge sensor. (Color figure online)

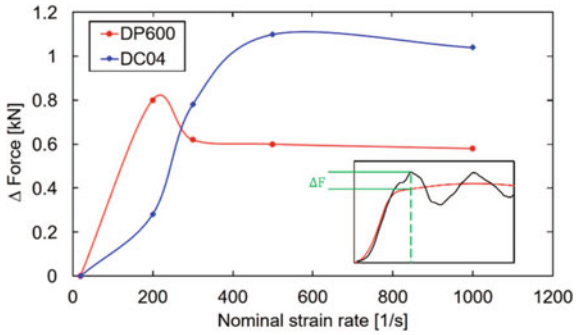


Fig. 6 Force difference between the first peak of the force measured by load cell and the force determined by strain gauge in area 5 of the Gen. III sample. (Color figure online)

area 5 of the sample (Fig. 3) show a very slight oscillation at the beginning that disappears after a certain very short time. This time is dependent on steel grade.

To quantify the effects that system ringing has on force measurements (Fig. 5) by the load cell of the test machine, the difference between the first force peak (as measured by the load cell from the force determined by SG in the EMA) was determined for both DC 04 and DP 600 steel (Fig. 6). The maximum force difference caused by system ringing in DC04 was 1107 N at a nominal strain rate of 500/s. By considering the cross-section area of the sample (6.5 mm width × 1.5 mm thickness), this difference corresponded to a stress difference of 113.5 MPa. In DP600, the maximum force difference was 820 N. Because the thickness of the DP 600 steel was 1.0 mm, the corresponding stress difference was 124 MPa, which is similar to that of DC04. However, using the Gen. III sample, the force value vibration reduces to about 10 N, which corresponds to a stress vibration of only 1 MPa [15], which is nearly negligible.

The stress-strain curves of DC04 are calculated from the Gen. III force data in Fig. 5 and are shown in Fig. 7. Three tests were performed for each strain rate. The fluctuations of the flow curves are small. It should be emphasized that all flow curves are pure measurement data without any filtering.

After these three flow curves are approximated using a cubic spline function, averaging and differentiation take place, which results in a clear hardening behavior (hardening rate $d\sigma/d\varepsilon$). The hardening rate increases with increasing strain rate. This is particularly pronounced in the area of higher stresses. However, there is an anomaly at 500/s that cannot yet be explained. On the other hand, the unusual flow and hardening curves at 100/s can be explained by the conditions of the Zwick testing machine (insufficient energy input at lower speed and readjustment of the hydraulic cylinders).

Figure 8 summarizes the strain rate dependence of the yield strength and the tensile strength of the two steels on a half-logarithmic scale. It should be noted that the strain rates can increase by up to more than 7 times due to the uncontrolled test machine and the increasing localization of the plastic deformation zone at the specimen due to necking (Fig. 9).

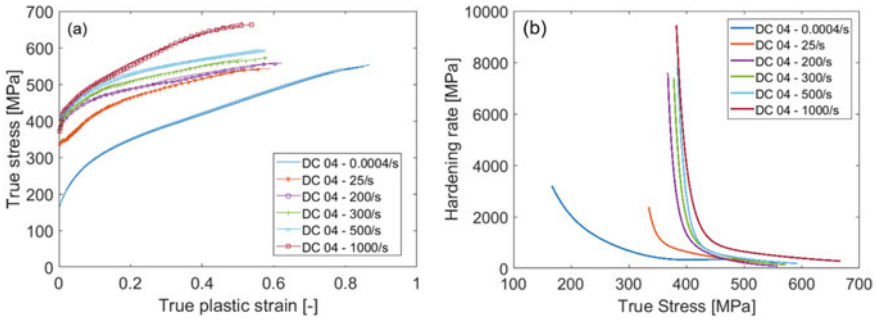


Fig. 7 True stress-strain curves of steel DC 04 (**a**) and the corresponding strain hardening curves (**b**). (Color figure online)

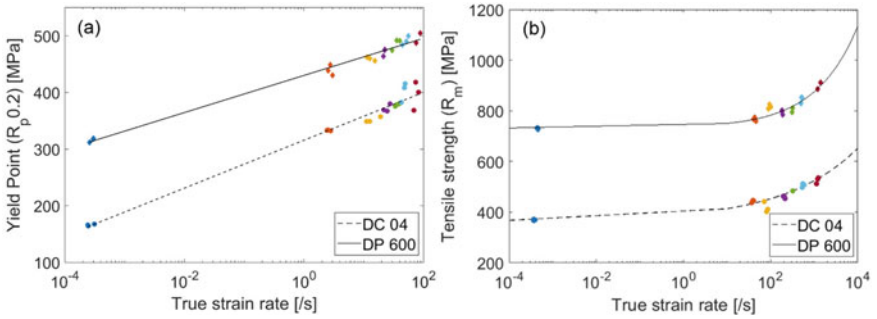


Fig. 8 Strain rate dependence of the yield strength (**a**) and the tensile strength (**b**) of DC 04 and DP 600. (Color figure online)

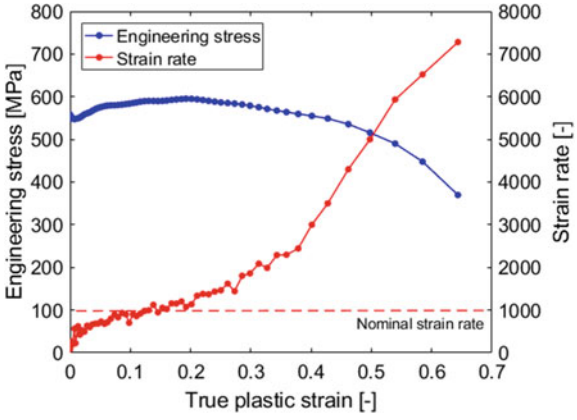


Fig. 9 Strain rate changes of HX 340 steel at 1000 1/s nominal strain rate due to the increasing localization of the plastic deformation (necking). (Color figure online)

At the beginning when yield strength is reached, the pre-set nominal strain rates have not yet been reached, whereas these are already exceeded when measuring

the tensile strength. Therefore, the yield strengths and tensile strengths in Fig. 8 are plotted against the real strain rates, which can be measured by using DIC and calculated using Eq. (5):

$$\dot{\varepsilon}_{\mathrm{yy-real}} = \frac{\in_{\mathrm{yy}}\ (t = t_{n+1}) - \in_{\mathrm{yy}}\ (t = t_n)}{t_{n+1} - t_n} \tag{5}$$

For the yield strength, the slope for DC 04 was slightly larger than the average for DP 600. The tensile strength of the steels also first increased almost linearly in the half-logarithmic scale. However, the increase was much greater at strain rates larger than 100/s. According to [10], these behaviors may be described by using a bi-potential function, and the behavioral change of the strength increase from linear to non-linear may be explained by the change of the thermal activation of the deformation processes from lower to higher strain rates. The strain rate dependence of tensile strength in DP 600 was larger than in DC 04. However, in [10], the dependence of strength on strain rate was only discussed in regard to the nominal strain rate. Based on the results of the present work, data of the dependence on the real strain rate is available.

5 A Physical Model for Gen. III Sample

The Gen. III sample was developed by FEM through trial and error. Meanwhile, a physical model was developed based on theory and equations for a one-dimensional stress wave. As stated in Sect. 1, if a bar is impact loaded, a stress wave with the stress amplitude σ_I will occur according to Eq. (1). This incident stress amplitude is dependent on the material properties $\rho \cdot c$, which is called impedance. The impedance can also be rewritten as $\sqrt{\rho \cdot d\sigma/d\varepsilon}$, where $d\sigma/d\varepsilon$ is the hardening rate of the material. In the case of elastic deformation, it is equal to Young's modulus. In plastic deformation, it is the slope of the stress-strain curve.

When the elastic stress wave created by an impact loading propagates on the bar with different cross sections and impedance, the stress wave may be reflected and transmitted on the cross-section or impedance change areas. The transmitted (σ_T) and reflected (σ_R) stress wave amplitudes are according to Eqs. (6) and (7) [7]:

$$\sigma_T = T \cdot \sigma_I \cdot \frac{A_1}{A_2} \tag{6}$$

$$\sigma_R = F \cdot \sigma_I \tag{7}$$

with n, F and T being defined by Eq. (8a) and (8b):

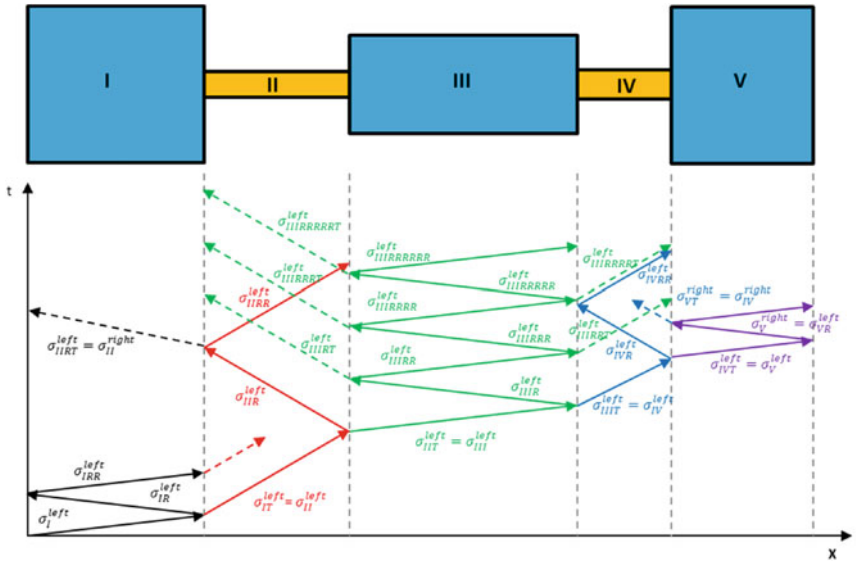


Fig. 10 A simplified one-dimensional beam model of Gen. III sample. (Color figure online)

$$n = \frac{(\rho_0 C_0 A)_1}{(\rho_0 C_0 A)_2} = \frac{\left(\sqrt{\frac{d\sigma}{d\varepsilon} \cdot \rho} \cdot A\right)_1}{\left(\sqrt{\frac{d\sigma}{d\varepsilon} \cdot \rho} \cdot A\right)_2} = \frac{A_1}{A_2} \cdot \alpha \tag{8a}$$

$$F = \frac{1-n}{1+n} \tag{8b}$$

$$T = \frac{2}{1+n} \tag{8c}$$

where α is the ratio between impedance in area 1 to area 2 or between elastic Young's modulus and plastic work hardening rate according to Eq. (9), if the waves are transmitting from a material section in elastic state into a material section in plastic deformation state. If both sections are in elastic state, $\alpha = 1$.

$$\alpha = \frac{(\rho C)_{el}}{(\rho C)_{pl}} \tag{9}$$

It is thus obvious that the transmitted (σ_T) and reflected (σ_R) stress wave amplitudes are different for the incident stress σ_1.

Based on this, a simple one-dimensional stress wave model has been proposed to understand the Gen. III sample [16]. Figure 10 shows the principle of the model: the areas 1 and 2 of the sample in Fig. 3 are unified as beam I in Fig. 10, area 3 as beam II, areas 4 and 5 as beam III, area 6 as beam IV and area 7 as beam V.

The beams have different cross sections $A_I - A_V$. They may have different elastic or elastic-plastic properties. Beams I, III and V should always be in elastic state (characterized by Young's modules E), while beams II and IV are initially in elastic state and change into elastic-plastic state when the specimen is loaded (characterized by work hardening $d\sigma/d\varepsilon$. The impulse load comes from left side (beam I), and beam V on the right side is fixed on the load cell.

As the lower part of Fig. 10 shows, the incident stress wave σ_I^{left} passes though beam I and is transmitted into beam Sect. 2 at the boundary between the two beams. This $\sigma_{IT}^{\text{left}} = \sigma_{II}^{\text{left}}$ can be easily determined using Eqs. (6), (8a) and (8b). Parallel to the wave transmission, σ_I^{left} is also reflected on the same boundary as $\sigma_{IR}^{\text{left}}$ which can be calculated by Eqs. (7), (8a) and (8b).

The same transmission and reflection happens on the boundary between beams II and III as $\sigma_{IIT}^{\text{left}} = \sigma_{III}^{\text{left}}$ and $\sigma_{IIR}^{\text{left}}$, between beams III and IV as $\sigma_{IIIT}^{\text{left}} = \sigma_{IV}^{\text{left}}$ and $\sigma_{IIIR}^{\text{left}}$ and between beams IV and V as $\sigma_{IVT}^{\text{left}} = \sigma_{\text{V}}^{\text{left}}$ and $\sigma_{IVR}^{\text{left}}$.

There are also many second to N-order reflections, such as $\sigma_{IIR}^{\text{left}}$ reflected on boundary II to I as $\sigma_{IIRR}^{\text{left}}$ and $\sigma_{IIIR}^{\text{left}}$, reflected on boundary III to II as $\sigma_{IIIRR}^{\text{left}}$. The same thing happens in beam IV. When considering beam Sect. 3, $N = 6$ times reflections are drawn, with the last one as $\sigma_{IIIRRRRRR}^{\text{left}}$.

Due to the assumptions that plastic deformation in beams II and IV absorbs the stress waves [13, 14] (see also Sect. 3), the second-order reflections $\sigma_{IRR}^{\text{left}}$ in beam I and the $\sigma_{IIRR}^{\text{left}}$ in beam II are not further followed, which is the same as the second-order reflected waves in beams IV and V.

With a number of additional simplifications [16] and the condition that all reflected and transmitted stress waves on the beam boundaries in Fig. 10 should be smaller or much smaller than the incident stress waves, as well as the fact that the transmitted and reflected stresses in beam III $\sigma_{IIIR\ldots R}^{\text{left}}$ are captured in beam III due to the very fast stress wave attenuation in beams II and IV, the number of reflections N for $\sigma_{IIIR\ldots R}^{\text{left}}$ can be calculated until a certain percentage p of the incident stress σ_I remains in beam III. If p is small, the oscillation in beam III is negligible. The design target for the Gen. III sample should be the minimization of N-value.

This analytical one-dimensional model was thus coupled with mathematical optimization (here a sequential quadratic programming SQP [17]), which can predict the sample geometry [16]. Starting with $A_I = A_V = 50\ \text{mm}^2$ and $p = 3\%$, $5 < A_{II} < 7\ \text{mm}^2$, $10 < A_{III} < 60\ \text{mm}^2$, $6.5 < A_{IV} < 7.5\ \text{mm}^2$, the optimization software developed in [16] shows the optimal results with $N = 1$ at $A_{II} = 6.27\ \text{mm}^2$, $A_{II} = 32\ \text{mm}^2$ and $A_{IV} = 6.5\ \text{mm}^2$. These geometric sizes are very close to the Gen. III sample sizes of $A_{II} = 6.5\ \text{mm}^2$, $A_{II} = 25\ \text{mm}^2$ and $A_{IV} \approx 7.5\ \text{mm}^2$.

For the original Gen. III sample sizes of $A_I = A_V = 50\ \text{mm}^2$, $A_{II} = 6.5\ \text{mm}^2$, $A_{II} = 25\ \text{mm}^2$ and $A_{IV} \approx 7.5\ \text{mm}^2$, a reflection number $N = 7$ was produced, which corresponds to the reflection time of 0.06 ms. The experimental results on a ferritic steel FSS439 show that the force oscillation is negligible after approximately 0.12 ms (10–12 reflections), and for a DC04 steel it is almost zero. Therefore, the reflection number N is dependent on steel grade if the same sample geometry is used.

It is also possible to adapt the sample geometry slightly to achieve a minimum N value.

The Gen. III sample can thus be well described and understood by a one-dimensional stress wave model.

6 Summary and Conclusion

Through the FEM modeling of the entire servo-hydraulic test system in combination with physical mechanical ideas, a novel Gen. III specimen geometry with a corresponding measurement method was developed in this work. This allows for an oscillation-free force measurement at strain rates of up to 5000/s. The geometry of the sample can be approximately predicted by a one-dimensional stress wave model which also explains the physical background of the new sample. Using SQP which is implemented in MATLAB tools, the optimal sample geometry for different materials can be predicted.

This new sample can be used for the entire strain rate range of 4.4×10^{-4}–10^{3}/s and enables a continuous determination of material properties for crash calculation. Measurements on steel materials confirm the method and show a clear strain rate dependence.

Acknowledgments This work was partly supported by the German Research Foundation (Deutsche Forschungsgemeinschaft) to which I am indebted. The author also thanks the technical support of Mr. Jens Olschewski and Chongyang Zeng.

References

1. Fang XF, Li J (2014) Numerical stress wave analysis in LS-DYNA and force measurement at strain rates up to 1000/s of a high-speed tensile machine (paper presentation. In: Proceeding 13th LS-DYNA Forum, Bamberg
2. Gese H, Dell H, Reisner M, Brenner F (2014) Improved prediction of material fracture with CrachFEM. In: Paper presentation, 3rd MATFEM conference, Hohenkammer, Germany
3. Ermittlung mechanischer Eigenschaften an Blechwerkstoffen bei hohen Dehraten im Hochgeschwindigkeitszugversuch (SEP 1230)
4. Metallic materials—Tensile testing at high strain rates—Part 2: Servo-hydraulic and other test systems (ISO 26203-2)
5. Metallic materials—Tensile testing at high strain rates—Part 1: Elastic-bar-type systems (ISO 26203-1
6. Cloetea TJ, Stander M (2012) Refinement of the wedge bar technique for compression tests at intermediate strain rates. In: Proceeding EPJ web of conferences 26, 01025 (2012), DYMAT 2012
7. Wang L-L (2007) Foundations of stress waves. Elsevier
8. Xiao X (2008) Dynamic tensile testing of plastic materials. Polym Test 27:164–178

9. Zhu D, Rajan S, Mobasher B, Peled A, Mignolet M (2011) Modal analysis of a servo-hydraulic high speed machine and its application to dynamic tensile testing at an intermediate strain rate. Exp Mech 51:1347–1363
10. Böhme W (2008) FAT-Richtlinie Dynamische Werkstoffkennwerte für die Crashsimulation. Mater Test 50:199–205. https://doi.org/10.3139/120.100865
11. Verleysen P (2009) Numerical study of the influence of the specimen geometry on split Hopkinson bar tensile test results. Latin Am J Solids Struct 6:285–298
12. Li J, Fang XF (2014) Stress wave analysis and optical force measurement of servo-hydraulic machine for high strain rate testing. Exp Mech 54:1497–1501
13. Tasdemirci, Hall IW (2007) The effects of plastic deformation on stress wave propagation in multi-layer materials. Int J Impact Eng 34(11):1797–1813
14. Maurel A, Mercier J-F, Lund F (2004) Elastic wave propagation through a random array of dislocations. Phys Rev B 70: https://doi.org/10.1103/PhysRevB.70.024303
15. Fang XF, Grams R. A novel oscillation-free force measurement for the determination of material properties during high-speed tests. ASTM J Test Eval https://doi.org/10.1520/jte20180887
16. Fang XF. A one-dimensional stress wave model for analytical design and optimization of oscillation free force measurement in high speed tensile test specimens, to be published
17. Boggs PT, Tolle JT (1995) Sequential quadratic programming. Acta Numerica 4:1–51

Tribological Conditions in Hot Bending of 22MnB5 Tubes



Enrico Simonetto, Andrea Ghiotti, and Stefania Bruschi

Abstract Thanks to the high stiffness-to-weight ratio given by the closed-section geometry, tubular components are particularly suitable for automotive applications that require extreme lightness to reduce energy consumption and increase crash-worthiness. Tube bending processes are traditionally performed in cold conditions, but to overcome the dramatic problems of accuracy and formability that the new high-strength steels present, a novel draw bending set at high temperature has been proposed. This paper presents the results of the investigations carried out on the tribological conditions of the hot draw bending of 22MnB5 tubes to obtain tubular parts with tailored mechanical properties. Investigation about the process thermal cycle has been performed with focus on the influence of the contact pressure on the heat transfer. The results show the practicability of the new process chain to obtain hot stamped tubular parts.

Keywords Tube draw bending · High-strength steels · Heat transfer

1 Introduction

The most recent trends of sustainable mobility require the reduction of the hazardous pollutants related to engine emissions. To this aim, the reduction of vehicle weight to decrease the fuel consumption and to increase their autonomy still represents a challenge due to strong requirements in terms of frame stiffness and passenger safety [1]. The last decade saw the development of several manufacturing technologies to further fulfil these needs. The hot stamping of High-Strength Steel (HSS) sheets was one of the most successful ones as it allowed increasing the geometrical complexity

E. Simonetto · A. Ghiotti (✉) · S. Bruschi
Department of Industrial Engineering, University of Padua, via Venezia 1, 35131 Padua, Italy
e-mail: andrea.ghiotti@unipd.it

E. Simonetto
e-mail: enrico.simonetto.1@unipd.it

S. Bruschi
e-mail: stefania.bruschi@unipd.it

© The Minerals, Metals & Materials Society 2021

G. Daehn et al. (eds.), *Forming the Future*, The Minerals, Metals & Materials Series,
https://doi.org/10.1007/978-3-030-75381-8_6

of the components and, at the same time, tailoring their final microstructure [2]. In this way, it made it possible to significantly reduce the thickness of body-in-white sheet components and therefore their weight [3]. A further improvement may be achieved by changing the design of many vehicle parts by substituting sheet-based components with tubular profiles. This could increase the component strength-to-weight ratio, thanks to the better mass distributions allowed by closed hollow cross-sections [4]. Tube bending processes are traditionally carried out at room temperature showing strong limits when applied to HSS such as (i) high forming loads, (ii) low formability, and (iii) high springback. While the former point can be solved by increasing the power of the bending machine actuators, the others limit both the complexity of the obtainable shapes and the accuracy of the processes and their repeatability. As of now, there are not any industrially available technologies to produce bent HSS tubes hardened during the process [5, 6] and with tailored microstructure and mechanical properties [7]. This paper presents experimental investigations carried out to assess the feasibility of new Direct Hot Bending (DHTB) processes of 22MnB5 tubes with focus on the thermal cycle and on the thermal boundary conditions that affect the final workpiece mechanical properties. Experimental measurements of the cooling rates that can be achieved in typical DHTB processes are carried out to evaluate the Heat Transfer Coefficients (HTC) with the tools. The results of the bends performed in hot conditions show that the proposed apparatus allows bending the HSS workpiece exploiting the increased formability of the austenite microstructure. Furthermore, the bent tubes show that different microstructures were obtained on different points according to the applied thermal boundary conditions.

2 Materials

The material used in the investigation is the 22 MnB5 steel grade, provided a sheet with 2 mm thickness and straight tubes having an outer diameter of 40 (±0.1) mm and a thickness of 2 (±0.05). The chemical properties are reported in Table 1.

The tool steel grade is the EN X38CrMoV5-1 alloyed steel, commercially available with the name Böhler W300 (nominal chemical composition in Table 2). To

Table 1 Nominal chemical composition of a 22MnB5 tube (mass continent in %)

Material	C	Mn	Si	Cr	Ti	B
22MnB5	0.21–0.25	1.1–1.4	0.15–0.35	0.15–0.30	0.02–0.05	0.003–0.005

Table 2 Nominal chemical composition of the tool grade (mass content in %)

C	Si	Mn	P	S	Cr	Mo	Ni	V
0.39	0.97	0.43	0.015	0.006	5.01	1.14	0.21	0.35

improve its wear resistance at the hot stamping temperatures, the tool steel is heat-treated to the hardening temperature of 1040 °C and then oil-quenched to obtain a surface hardness of 51 (±1) HRC.

3 Direct Hot Tube Bending (DHTB)

A novel apparatus specifically developed for the rotary draw bending at high temperature of 22MnB5 tubes is hereafter presented. The apparatus is based on a traditional cold tube Rotary Draw Bending (RDB) machine, see Fig. 1, to assess the feasibility of the tube Direct Hot Tube Bending (DHTB) process. Figure 1 shows the main tools and kinematics of RDB.

3.1 DHTB Equipment

A resistance heating system is embedded within the bending machine, in order to limit the thermal loss during the handling stage, and to have the maximum flexibility in the application of thermal cycles to different zones of the tube. A DC generator with a maximum power of 60 kW (6000 A at 10 V) is used as a heating device as shown by Fig. 2a. Two couples of copper electrodes connect the tube with the DC generator; these can be opened or closed to grip the tube, by means of two pneumatic actuators with a maximum force of 950 N each. A couple of electrodes is mounted on a fixed frame (see Fig. 2b), positioned near the pressure die to limit the distance between the heating zone and the dies, to decrease both the handling time and the

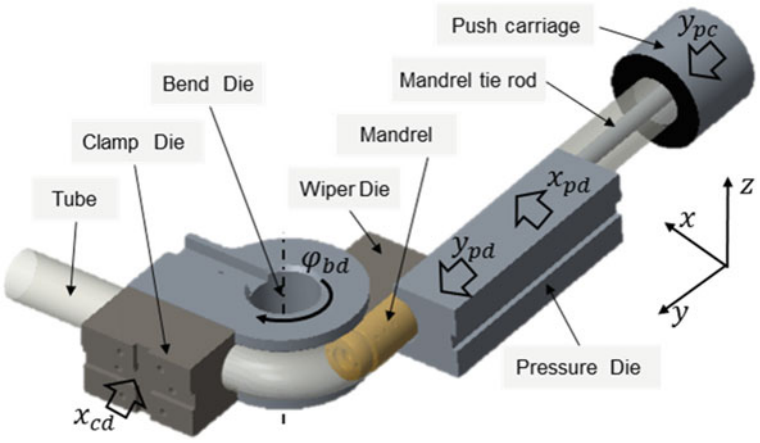


Fig. 1 Kinematics and tools in rotary draw bending process. (Color figure online)

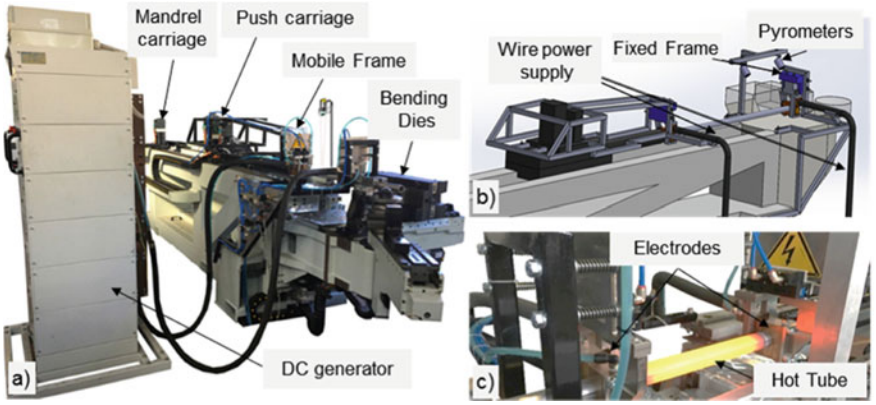


Fig. 2 **a** Overall view of the bending machine equipped with the heating apparatus for DHTB process, **b** model of the heating electrodes, and **c** hot tube heated by resistance heating. (Color figure online)

minimum distance between two subsequent bends. The other couple of electrodes is mounted on a mobile frame linked to the push carriage. This design allows moving the electrodes along the tube axis to change the heated length and adjust the length of the heat-treated zone to the bend angle. The tube temperature is monitored in-line by means of a pyrometer during the heating and holding stages allowing to control the applied electrical power in a closed-loop configuration. Figure 2c shows the copper electrodes and the tube heated at 950 °C during the austenitization stage. This solution has been preferred to others, such as induction heating, since it allows greater flexibility in terms of heating length without hindering the handling stages. The equipment has been tested, by heating the 22MnB5 tubes up to 950 °C, with a heating rate of 5.25 °C/s and a holding time of 60 s with different heated length, namely 200, 300, 400, and 500 mm, to assess the temperature gradient along the treated zone.

3.2 Thermal Cycle

By applying a thermal field to the workpiece, it possible to (i) increase the material formability to obtain more complex shapes, (ii) to reduce the springback angles, and (iii) modify the steel microstructure and so the mechanical properties. To achieve these results, the thermal cycle applied to the tube must be controlled. Figure 3 shows the proposed thermal cycle for the DHTB process, which includes the following steps:

i. Austenitization stage: the tube is heated up until (T_{Aust}) over the Austenitization temperature (Ac1) to obtain an austenitic structure. The heating rate can be increased and so the heating time reduced according to the capabilities of the power supply, in order to reduce the overall process time, while the holding

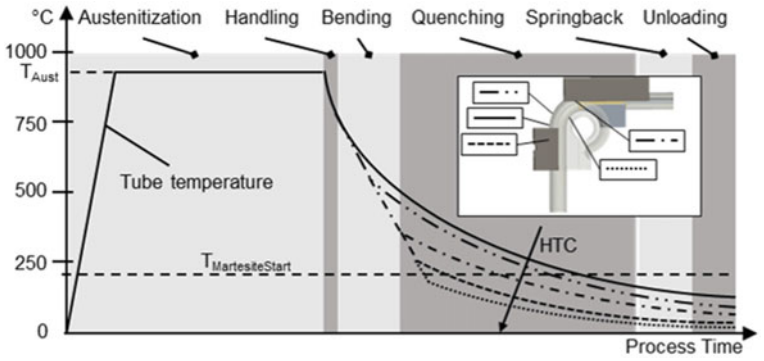


Fig. 3 Thermal cycle applied during the subsequent DHTB process stages. (Color figure online)

time at T_{Aust} is a function of the material properties in order to obtain a partially or fully austenitic structure according to the desired final mechanical properties of the component.

ii. Handling stage: the heated zone is moved from the heating system to the dies group in order to bend the tube. This stage is particularly critical as it is necessary to limit heat loss.

iii. Bending stage: the tube is bent while its temperature is still inside the process temperature window. In fact, all the forming stage should be completed while the tube microstructure is sitll austenite in order to allow an increased formability. At the end of the process, the mandrel is withdrawn from the bending zone.

iv. Quenching stage: after the bending stage is over, the tube is not unloaded as the tools are kept closed in order to maintain higher cooling rates.

v. Springback: when the tube cools down under the lower martensite transformation temperature, in order to reach the highest mechanical strength, the forming loads are released and the tube undergoes the springback phenomenon. However, the springback effect is greatly reduced by the thermal effects.

vi. Unloading: the bent zone is unloaded from the bending machine.

3.3 Boundary Conditions

As shown from the process model in Fig. 1, the thermal boundary conditions during the bending and quenching stages are not constant along the bent zone as the tools move during the process. Consequently, the thermal boundary conditions are not constant during the process forming stage. The chart in Fig. 3 shows different cooling paths that different points along the bending zone undergo during the process according to the evolution of the thermal boundary conditions. Figure 4 shows the contact conditions along several sections of the bending zone, in different moments of the bending stage. At the beginning of the bending stage, as shown by Section

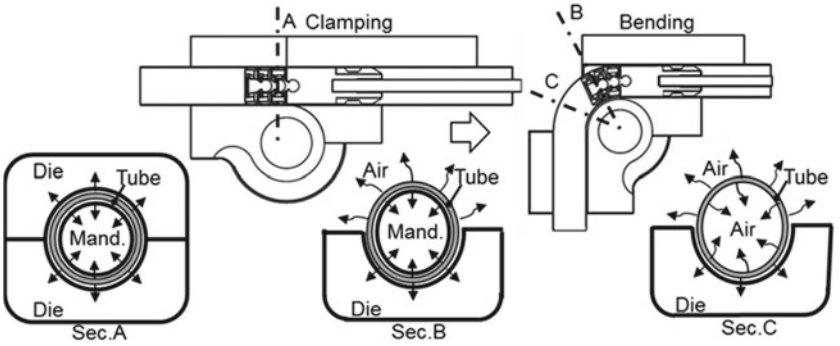


Fig. 4 Main boundary conditions during the quenching stage

A, the thermal exchange is mainly due to conduction since both the inner and outer tube surfaces are in contact with the dies or with the mandrel. Sections B and C are considered after the bending: in the former, the tube inner surface is still in contact with the mandrel and the tube intrados is in contact with the bend die but it is exposed to the air at the extrados. In the latter, the tube is in contact only with the bend die at the intrados, while there is air at the extrados and inside the tube. Therefore, the thermal conditions change during the bending stage and are different point by point, making the process difficult to control.

3.4 HTC Equipment

Figure 5a shows the developed experimental setup to test the different heat transfer conditions between the boron steel specimens and the dies, and between the boron

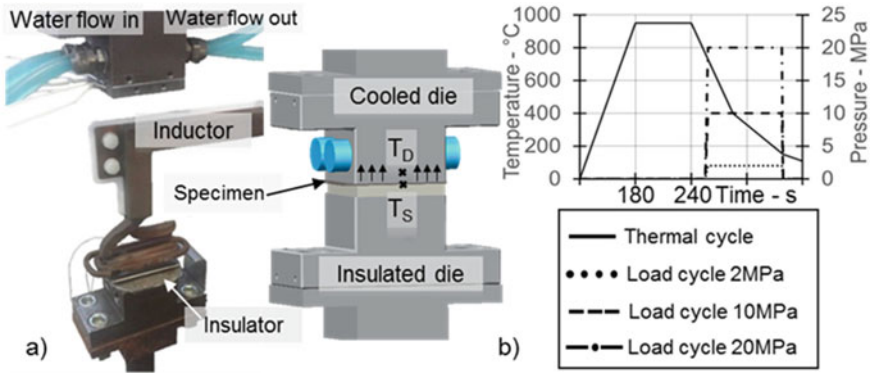


Fig. 5 **a** Experimental setup and the 3D model of the apparatus, **b** load and thermal cycles of the cooling tests. (Color figure online)

Table 3 Experimental plan

Case	1	2	3	4	5	6	7
Normal pressure (MPa)	0	2	10	20	2	10	20
Cooling condition	Calm air	Metal die	Metal die	Metal die	Cooled die	Cooled die	Cooled die
Fluid temperature (°C)	20	–	–	–	10	10	10
Flow per channel (l/s)	–	–	–	–	0.3	0.3	0.3

steel specimen and the air. A 22MnB5 flat sample (size equal to 45 × 50 × 2 mm) is heated by a frontal inductor head, according to the thermal cycle shown in Fig. 5b. The volume and the thickness of these flat samples are consistent with the dimension of the tube bent zone, to replicate a sample with similar thermal inertia and thermal boundary conditions.

Both the die temperature (T_D) and the specimen temperatures (T_S) are measured during the entire test by K-type thermocouples. To replicate the air cooling on the inner surface and with the bending tool on the outer surface, an insulating layer of trathermic® Silcem 1300 is interposed between the specimen and the lower die. Both dies are manufactured with the Böhler W300 steel as indicated in Sect. 2, with embedded cooling channels. The dies are mounted on a hydraulic press MTS322®, capable of a maximum load of 50 kN. The equipment was used to perform different cooling tests, according to Table 3, applying different levels of normal pressure consistent with the values undergone by the tube during the process. The tests were carried out with and without water flow on the upper die channels.

4 Numerical Model

To determine the heat transfer coefficients between the 22MnB5 sheet and the dies, a numerical inverse analysis was performed [8]. Figure 6a shows the 3D numerical model, developed with the commercial software Forge Nxt™, while Fig. 6b shows the temperature profile of the 22MnB5 sheet when the measured temperature T_S reaches the T_M value for a pressure of 2 MPa without water cooling. The thermal exchange between the sheet and the cooled die has been determined in order to fit the simulated temperature with the cooling paths measured during the real tests.

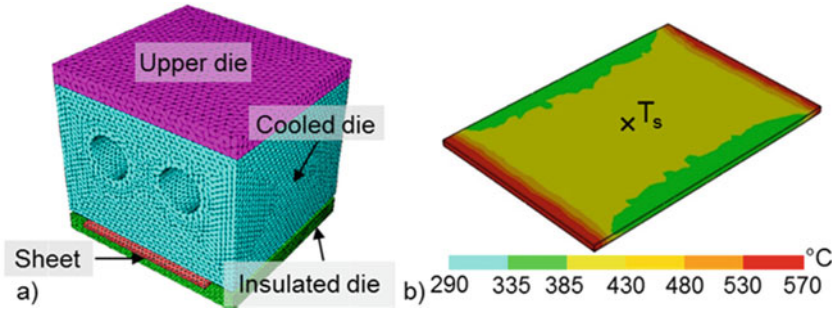


Fig. 6 **a** 3D numerical model of the test system, **b** sample temperature profile when reaching the phase changing temperature TM on the measuring point TS (Case 2). (Color figure online)

5 Results

5.1 Thermal Profile

The typical austenitization process for the 22MnB5 requires a temperature of 950°C, and so the electrodes are water-cooled below 100 °C to avoid excessive oxidation. As the cooled electrodes are in contact with the tube, also the tube is cooled down leading to a certain thermal gradient along the heated length as shown in Fig. 4c. A FLIR^{TM} A40 infrared thermal-camera (measurement range 20–1200 °C) was used to assess the temperature distribution along the tube axis for different heating lengths. Figure 7 shows its distribution for different lengths: 200, 300, 400, and 500 mm. It is possible to notice that the central part of the heated zones has a constant and uniform temperature, with a maximum deviation of ±5 °C, while the end zones of the tubes are at lower temperature due to the presence of the cooled electrodes. The length of these transient zones near the electrodes has a constant value of 50 (±10) mm.

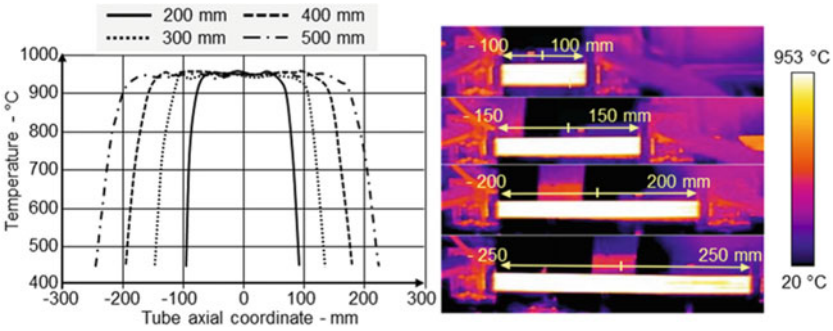


Fig. 7 Temperature profile along the tube axis at the end of the austenitization stage for different heated length. (Color figure online)

5.2 HTC Determination

Figure 8 shows the cooling rate obtained in still air. Figure 8a shows the bent tube at the end of the forming process, where the outer tube surface in the extrados cools down in still air, as shown by Sections B and C in Fig. 3. The cooling path in still air starts from T_A, see Fig. 8b, which is the temperature after the heating. It is worth noticing that the slope change around 600 °C is due to the latent heat release during the bainitic transformation.

The cooling paths measured during the die cooling tests are shown in Fig. 9. The first part of the cooling corresponds to the transfer time from the heating zone to the bend dies, starting from T_A down to the bending starting temperature T_{BS}. Then the dies are closed, with different pressures, leading to a faster temperature drop until T_M. The dies are then kept closed until the unloading temperature T_U is reached. In the case of water-cooled dies, the contact pressure between the dies and the specimen is less influential as shown in Fig. 9b.

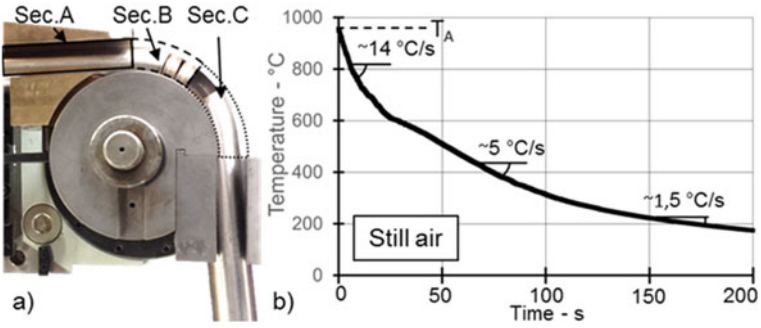


Fig. 8 **a** Tube and tool position at the end of the bending step, **b** specimen cooling path in still air from austenitization temperature. (Color figure online)

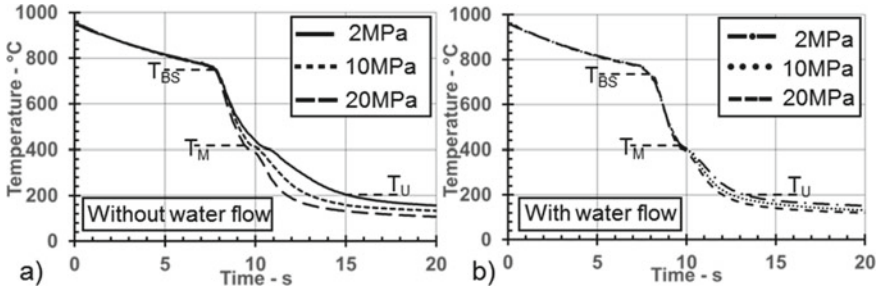


Fig. 9 **a** Specimen cooling path in die cooling without water flow, **b** specimen cooling path in die cooling with a water flow of 0.3 l/s per channel

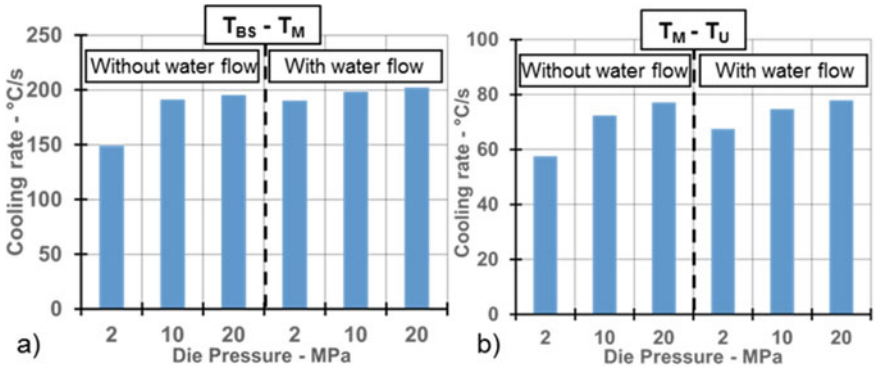


Fig. 10 **a** Cooling rates measured in die cooling tests, from TBS to TM, **b** cooling rates measured in die cooling tests, from TM to TU. (Color figure online)

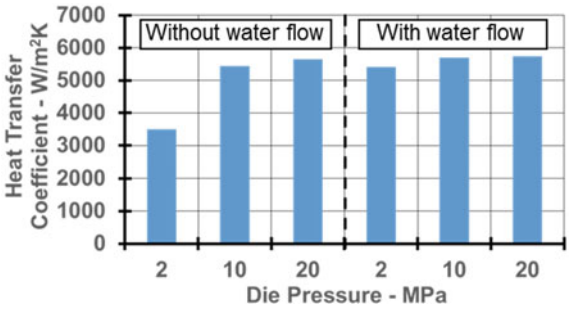


Fig. 11 Heat transfer coefficient obtained from the inverse analysis from T_{BS} to T_U for the die cooling conditions. (Color figure online)

The measured cooling paths were used to calculate the cooling rate varying both the contact pressure and the cooling conditions of the dies. Figure 10a shows the different cooling rates measured before the martensitic transformation while Fig. 10b shows the cooling rate down to T_U.

The experimental data were used to calculate the HTCs, see Fig. 11, between the die and the specimen by the numerical reverse analysis as discussed in Sect. 4. It was seen that HTC is almost stable for contact pressure values over 10 MPa without water flow, while it appears almost negligible with proper water flow.

5.3 Process Time

The duration of each process stages affects the thermal cycle and leads to changes in the workpiece final properties. As discussed in Sect. 3, the tube must be bent before any changes in the microstructure occur in order to avoid any loss of formability or increase in forming loads due to the presence of Martensite or Bainite. Figure 12 shows the position of the bending machine main axes during the process, starting

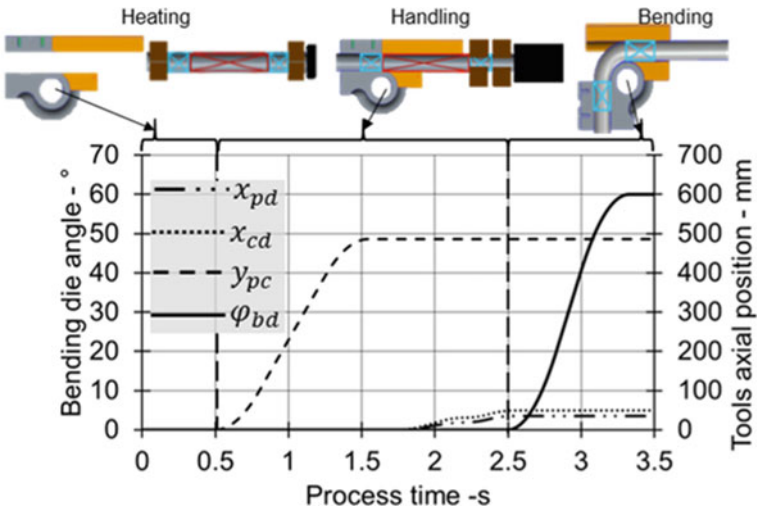


Fig. 12 Position of the bending machine main axes during the DHTB process. (Color figure online)

from the end of the Austenitization stage when the workpiece reaches the thermal profile shown in Fig. 7. During the handling stage, the pneumatic actuators open the copper electrodes and the tube gripped by the push carriage is moved along the axial direction to take the heated zone in the bending position; this operation requires 1.25 s. As shown in Fig. 4, the tube is gripped by the bend and clamp dies in the transient zones as this part is not deformed during the process, while the zone of the tube uniformly heated at 950 °C is positioned between the pressure and the wiper die to be bent. When the tube is in the right axial position, the dies are bought in contact with it, in 0.75 s as shown in Fig. 12. Then the tube is bent with an angular rate of 80°/s, taking 0.75 s to perform a 60° bend as reported in the chart. The cooling rate in still air for a 2 mm thickness tube can be estimated around 15 °C/s while in the case of cooling rate due to conductivity with a die, the cooling rate reaches maximum values of 200 °C/s for a pressure of 20 MPa. Therefore, as the tube is cooled in still air for 0.75 s and then it is in contact with the dies for 1.5 s until the end of the bending state, it is possible to say that the bending operation can be safely carried out before any microstructural changes occurs within the tube.

5.4 Mechanical Properties

After the bending stage the tube is cooled inside the dies, but during the quenching stage different zones of the bent tube undergo different cooling rates. The differences between the thermal boundary conditions on the tube intrados and extrados lead to non-uniform cooling rates and so different final microstructures are obtained. Figure 13a shows a bent tube by means of the DHTB process and highlights two

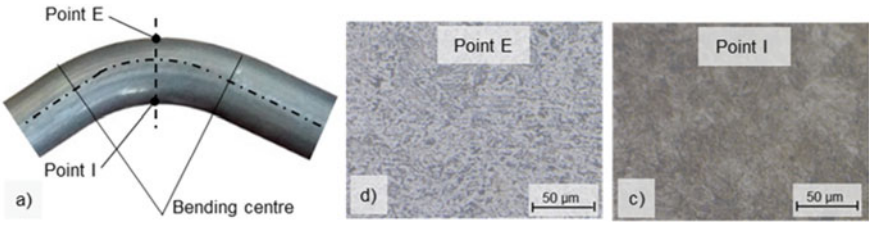


Fig. 13 **a** Tube bent with DHTB process, **b** microstructure at the extrados side, and **c** microstructure at the intrados side. (Color figure online)

different points on the extrados (Point E) and intrados (Point I). The microstructures of these two points were analysed showing that on the extrados side (Point E) a ferrite-perlite-based structure is still present due to the low cooling rate (Fig. 13b). On the other hand, Fig. 13c shows the martensitic microstructure obtained in point I, thanks to the highest cooling rate, greater than the 27 °C/s required to obtain the martensitic transformation.

6 Conclusions

This paper presents an investigation about the Tribological conditions in Direct Hot Bending of a hollow profile. In particular, it focuses on the thermal cycle and on the influence of the thermal boundary conditions between the workpiece and the machine tools. A DHTB prototype was developed to bend 22MnB5 after heating them up to the austenitization temperature, and a simplified experimental equipment was developed to determine the cooling rates and the HTCs as a function of different process parameters. The developed prototype uses a DC generator linked to the workpiece by means of two couple of cooled copper electrodes to apply the thermal field using the Joule effect. The thermal profiles measured at the end of the heating stage, using an infrared thermal-camera, show how the developed system allows to heat up different workpiece lengths in a homogeneous way, with a transition zone of 50 ($\pm$10) mm near the electrodes. Furthermore, the cooling rate and HTCs between the workpiece, the environment, and the dies were determined using the experimental equipment presented in Sect. 5.2 as a function of the contact pressure and of the die cooling channel water flow. These data, together with the process time measured in the DHTB operation allowed to estimate the process temperature windows. The process time was minimized to perform the forming operation at high temperature avoiding any phase transformation and any related formability decrease due to microstructural changes. Then the final microstructures of two different reference points were analysed to evaluate the influence of the different thermal boundary conditions, along the bent tube. The results show that two different microstructures are obtained, as a consequence of the different thermal boundary conditions, in particular a martensitic

structure was obtained on the intrados side, while a ferrite-perlite-based structure was obtained on the bend outer side. The technology proved to be promising to manufacture bent tube with tailored microstructure and mechanical behaviour.

References

1. Tekkaya AE, Khalifa NB, Grzancic G, Holker R (2014) Forming of lightweight metal components: need for new technologies. Procedia Eng 81:28–37
2. Bariani PF, Bruschi S, Ghiotti A, Turetta A (2008) Testing formability in the hot stamping of HSS. CIRP Ann 57:265–268
3. Merklein M, Wieland M, Lechner M, Bruschi S, Ghiotti A (2016) Hot stamping of boron steel sheets with tailored properties: A review. J Mater Process Technol 228:11–24
4. Hea Y, Heng L, Zhiyong Z, Mei Z, Jing L, Guangjun L (2012) Advances and trends on tube bending forming technologies. Chinese J Aeronaut 1–12
5. Hu Z, Li JQ (1999) Computer simulation of pipe-bending processes with small bending radius using local induction heating. J Mater Process Technol 91:75–79
6. Zhang XL, Yang H, Li H, Zhang ZY, Li L (2014) Warm bending mechanism of extrados and intrados of large diameter thin-walled CP-Ti tubes. Trans Nonferrous Met Soc China 24:3257–3264
7. Simonetto E, Venturato G, Ghiotti A, Bruschi S (2018) Modelling of hot rotary draw bending for thin-walled titanium alloy tubes. Int J Mech Sci 148:698–706
8. Simonetto E, Bruschi S, Ghiotti A, Savio E (2015) Prediction of distortions in hot forged martensitic stainless steel turbine blades by numerical simulation. Procedia Manuf 1:804–813

In Search of the Perfect Sheet Metal Forming Tribometer



L. Schell and P. Groche

Abstract Due to increasing variant diversity and mass customization, time and cost-efficient process design has gained importance for several years. Tribological investigations are playing a key role as part of the process design. In particular, the desires for extended process limits, reduction of lubricant amount, and reliable determination of friction coefficients for FE simulations place high requirements on tribometers in sheet metal forming. For quite some time, the strip drawing test with several variations has been considered as an efficient and meaningful method for tribological investigations. This paper summarizes the development of the strip drawing test to date. In particular, design principles for experimental modelling of tribological conditions of deep drawing processes and approaches for friction measurement are described. Moreover, the current state and future requirements for the development of the "perfect" tribometer are discussed in this review paper.

Keywords Strip drawing test · Bending under tension · Tribometer · Friction coefficient · COF · Tribology · Sheet metal forming · Deep drawing

1 Introduction

A trend to shorter product life cycles and increased variant diversity can be observed for various industries [1] especially for the automotive industry [2]. Simultaneously, the growing demand for customized goods is boosted by manufacturing processes like additive manufacturing [3]. These trends are particularly challenging for forming technologies like deep drawing, which typically shine in high volume manufacturing [4]. To address these challenges, production flexibility [1] thus time and cost-efficient process design are important optimization methods. In deep drawing, tribological investigations play a key role in efficient and accurate process design [5]. In particular,

L. Schell · P. Groche (✉)
Institute for Production Engineering and Forming Machines, Darmstadt, TU, Germany
e-mail: groche@ptu.tu-darmstadt.de

L. Schell
e-mail: schell@ptu.tu-darmstadt.de

© The Minerals, Metals & Materials Society 2021

G. Daehn et al. (eds.), *Forming the Future*, The Minerals, Metals & Materials Series,
https://doi.org/10.1007/978-3-030-75381-8_7

the desires for extended process limits, reduction of lubricant amount, and reliable determination of friction coefficients for FE simulations place high requirements on tribometers in sheet metal forming.

Tribological investigations of sheet metal forming processes are the main topic of many scientific publications. A recent overview of sheet metal forming tribometers is given in a review paper from Trzepiecinski et al. [6]. Comprehensive treatise with analyses of the individual tribometers can be found in dissertations of different research institutes [7–13]. This paper provides an extensive overview of the individual methods in form of a literature review including specific comparisons of the individual testing methods. The focus is on both design principles for modelling tribological conditions with tribometers and approaches for the determination of friction coefficients for deep drawing processes. Moreover, the current state and future requirements for the development of the "perfect" friction-focused sheet metal forming tribometer are discussed.

2 Tribological Test Methods

Tribological test methods can be classified into four different groups shown in Fig. 1 [14]: There is a contradiction between metrological accessibility and transferability to real forming processes.

Test methods of category 6 can be used to investigate basic tribological phenomena in a wide range of applications from gasoline engines [15] to prosthetics in the human body [16]. The main advantages of category 6 tribometers are their level of standardization (DIN 51350, DIN 51834, ASTM D5707, ASTM D1894, ASTM G99), although even results from category 6 tribometers with the same operation principle can show different results [17]. Disadvantages are the low transferability to sheet metal forming processes due to different contact conditions [18]. The contact area is typically small, which affects friction coefficients under lubricated conditions [19,

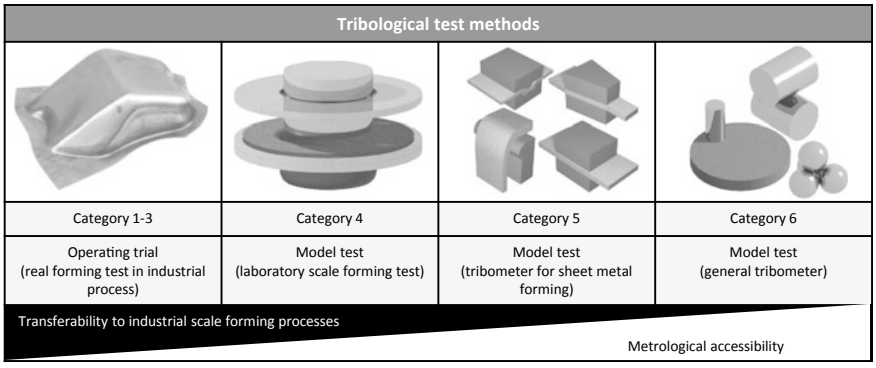


Fig. 1 Categories of tribological test methods for sheet metal forming (cf. [14] and DIN 50322)

20]. Additionally, sliding contact usually occurs repeatedly at the same surface area which is normally not the case in sheet metal forming processes [12]. Last but not least, plastic deformation of sheet metal affects its tribological boundary conditions (e.g., increasing surface roughness [21]) which is not considered in tribometers of category 6.

In contrast, "tribometers" of category 1 to 3 are rather in-situ test methods integrated in press shop forming operations of real parts under conditions of series production. Since the real forming operation is used in the test procedure, there is no need to transfer results. Disadvantages are both the limited options to change tribological loads and the implicit measurement of tribological variables like friction coefficients [12]. Furthermore, expenses of such tribological tests are typically high and should not affect current serial production [14].

Due to the extreme characteristics and distinct disadvantages of the mentioned test methods (categories 1-3 & 6), these test methods cannot be considered as perfect sheet metal forming tribometers. To select the most promising candidates from the remaining categories, it must be clarified what exactly is the objective of the investigation. When it comes to sheet metal forming, two different investigation objectives are conceivable, cf. [14, 22]:

(A) Investigation of tribological systems (e.g., lubricants) concerning their suitability in certain forming processes. Such studies mainly aim at qualitative comparisons and proof of feasibility.
(B) Investigation of frictional behaviour under specific tribological conditions (contact pressure, sliding velocity, temperature, …). Such studies mainly aim at quantitative results in form of friction coefficients.

For objective A, tests from category 4 (e.g., deep drawing of cylindrical cups) can be used but typically lack direct measurement of friction forces or friction coefficients [23]. Friction coefficients have to be derived from FE-based inverse analysis [23] or analytically using Siebel's formula [24]. In both cases, material models directly influence the determined friction coefficients which leads to inaccuracies [11]. For objective B, tests from category 5 are most suitable (e.g., various tests utilizing metal strips). A big advantage of category 5 tribometers over category 4 is the ability to easily adjust tribological conditions independently of each other [12]. Additionally, most category 5 tribometers are independent from material modelling. In order to decide whether the perfect sheet metal forming tribometer is searched in either category 4 (objective A) or category 5 (objective B), the current role of tribometers in sheet metal forming has to be discussed.

3 The Current Role of Tribometers in Sheet Metal Forming

Increasing importance of FE simulations in sheet metal forming results in higher demands for FE modelling accuracy and reliability. Advances in computational power enable more detailed thus more complex FE models; but even a complex

FE model can only be as accurate as its assumptions and input variables. Important and powerful input variables are friction coefficients [5] which, among others, affect simulation results regarding spring back [25], punch force, and sheet thinning [26]. Additionally, numerical modelling of friction gains importance in the industrial use of FE simulations for sheet metal forming [27]. In spite of the promise, friction models could "reduce the demand for experimental friction testing" [28], those numerical models are developed with the help of experiments, either for fitting or for validation purposes [28, 29]. Current publications show that there is still a scientific [18, 30, 31] and commercial [32] interest in sheet metal forming tribometers.

4 Discussion

To determine reliable friction coefficients, tribometers should meet exact requirements concerning homogeneous and stationary conditions (e.g., contact pressure, temperature, sliding velocity, and lubrication regime). In a perfect tribometer, it should be possible to adjust all conditions independently and therefore determine friction coefficients as function of these conditions. Furthermore, models for both sheet deformation or material behaviour should not be necessary when deriving friction coefficients from other measurement parameters [11]. The mentioned requirements are best met by the diverse types of strip drawing tests from category 5. These tests stay as close as possible to the sheet metal forming process (e.g., reproduction of forming conditions). An overview of different category 5 tribometers is shown in Fig. 2. The most promising ones are presented in the top row and will be discussed in detail in this paper.

The reasons to exclude the four tribometers in the bottom row of Fig. 2 are as follows. The draw bead test features both a highly inhomogeneous contact pressure at the draw beads [12] and differences in sliding velocity due to thinning of the strip [11]. It resembles three bending under tension tests connected in series while tribological conditions (e.g., lubrication, sheet surface roughness, contact pressure) are different in each contact zone. The strip-tension test also resembles a bending under tension test, though it shows transient contact pressure with a limited adjustment range and varying sliding speed in the contact zone [11]. The fundamental characteristics of both the draw bead test and the strip-tension test can be checked in the bending under tension paragraph. Hemispherical stretching resembles the strip-tension test though its three-dimensional design leads to even more inhomogeneous and transient contact conditions. Last but not least, the strip reduction test simulates tribological conditions in ironing and is typically used to investigate both lubricant break down [33] and onset of galling [34]. Investigation of friction coefficients in the strip reduction test is difficult [35] and coefficients are given as a function of pulling force rather than a homogeneous contact pressure.

The intention of the following paragraphs is not to list all variants of tribometers from different research institutes (cf. [6]) but to focus on both design principles to reproduce tribological conditions and approaches for the determination of friction

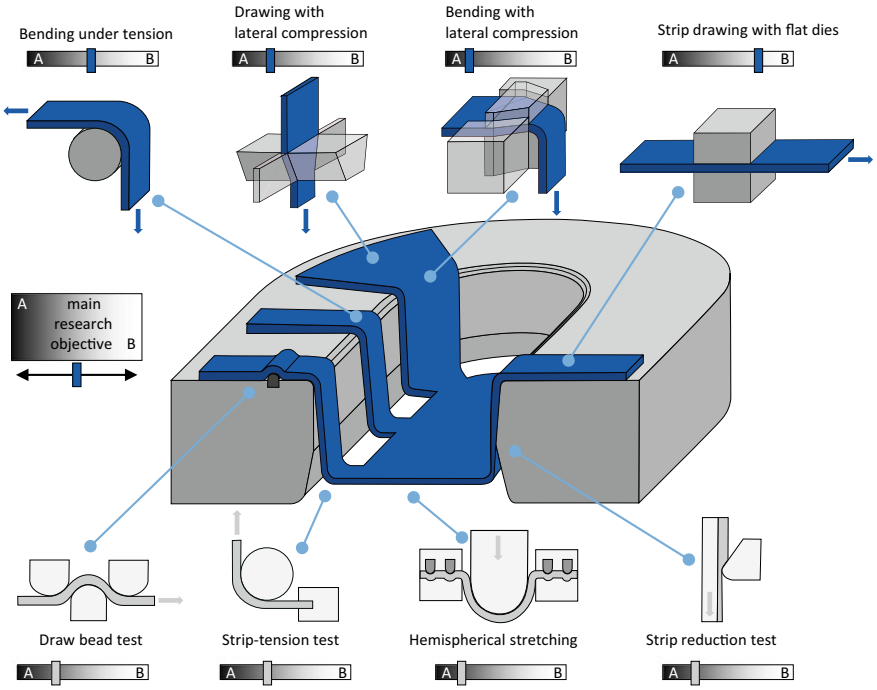


Fig. 2 Overview of sheet metal forming tribometers from category 5 (pictures after [36]). The main research objective is rated by the authors based on theoretical assessment, literature research, and actual experience with various tribometers. (Color figure online)

coefficients. The evaluation is ordered from the tribometer closest to the deep drawing process to the tribometer with the best metrological accessibility.

5 Bending with Lateral Compression

In a critical review of tribometers, Schey [22] tends to assign higher transferability to the more complex tribometers which include some sort of plastic deformation. One of the most complex tests of this kind is based on bending with lateral compression, which is rarely used, because of its complex dies.

Investigations from Lassen and Bay [37] show that besides complex dies, three different experimental setups are necessary to calculate the friction coefficient at the die radius based on the belt friction theory (Fig. 3). A downside of this approach is that measuring errors and variations in boundary conditions are added up. Furthermore, friction at the die radius affects both the bending procedure and forces for plastic deformation. This leads to the demand to derive friction coefficients from one single experiment [11]. Since bending with lateral compression is a combination of both

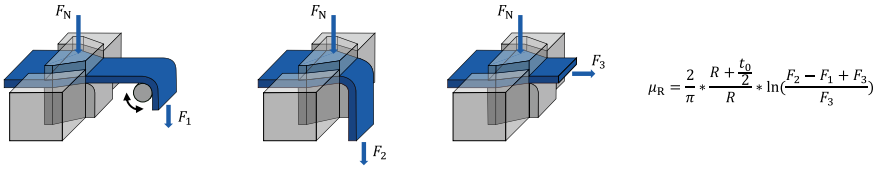


Fig. 3 Bending with lateral compression – test principle and calculation of friction coefficients based on the belt friction theory (cf. [37]). μ_R = friction coefficient at the die radius R, t_0 = initial sheet thickness, $F_\#$ = pulling forces in the different experimental setups, F_N = normal force. (Color figure online)

drawing with lateral compression and bending under tension, an in-depth analysis is performed separately in the respective paragraphs.

6 Drawing with Lateral Compression (Wedge Drawing Test)

The wedge drawing test was first published by Sachs in 1930 [38]. He investigated the drawability of different sheet materials and lubricants without measuring or calculating friction coefficients. His investigations were pursued by Loxley and Swift [39] and taken up again by Reihle [7]. Reihle extensively investigated the influence of contact pressure, lubricant, sheet material, surface roughness, and plastic deformation on the friction coefficient. Although he had a wedge drawing test available, he performed most of his tests with narrow strips without lateral compression because of the difficult to perform experimental procedures. The few tests with lateral compression yield the same friction coefficients as his flat die tests.

Around 20 years later, Ng [40] and Bluemel [41] took up the wedge test again. Bluemel used big diameter rollers to minimize friction and wear at the sheet edges (Fig. 4a), but both authors used the wedge test to investigate maximum drawing ratios but without dedicated studies of the frictional behaviour. In contrast, Kawai et al. developed a complex apparatus to separate friction forces from forming forces and

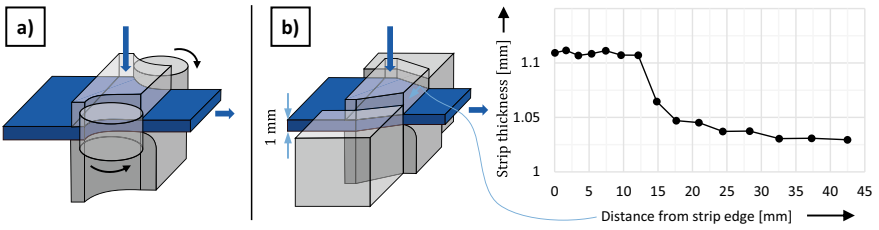


Fig. 4 Wedge drawing test: **a** Test principle from Bluemel (cf. [41]); **b** Numerical investigation of the sheet thickness distribution from Recklin (cf. [21]). (Color figure online)

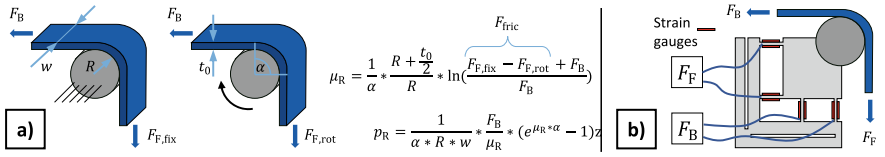


Fig. 5 **a** Test Principle of the traditional BUT test (pictures after [51]) and calculation of the friction coefficient μ_R and the mean contact pressure $\bar{p}_R$ at the die radius (cf. [8]); **b** force measuring method in the BUT test (cf. [49, 50]). (Color figure online)

claimed to quantify friction coefficients with high accuracy [42]. However, occurrence of bulging indicates that homogeneous distribution of contact pressure is not ensured [43]. In the 90 s, Netsch [10] describes problems in the wedge drawing test execution due to canting of thin sheets in the edge region. Miguel et al. developed a wedge test to reproduce deep-drawing-like flange stresses [44] and to investigate formability in pure shear deformation [45]; again, friction coefficients have not been evaluated in the flange region under lateral load. Recklin [21] summarizes the problems in the practical application of the wedge test with severe wear at the sheet edges and tools as well as an uneven sheet thickness distribution (Fig. 4b).

Reviewing all characteristics and disadvantages, the wedge drawing test is not eligible to be a perfect sheet metal forming tribometer. As alternative Recklin et al. [46] used an in-situ method to measure friction in the wedge-shaped blank holder region.[1] They showed that plastic deformation affects sheet roughness and friction in the blank holder region. Although they determined friction coefficients it was not possible to ensure a homogeneous contact pressure distribution.

7 Bending Under Tension (BUT Test)

The BUT test was introduced by Littlewood and Wallace [48]. They investigated friction coefficients dependent on lubricant viscosity and sheet surface roughness. The widely used procedure in the BUT test consists of two successive tests: Drawing both over a rotating cylindrical pin and a fixed cylindrical pin [36] (Fig. 5a). The difference in the front pulling forces $F_{F,fix}$ and $F_{F,rot}$ is assumed to be the friction force F_{fric}. Disadvantages of this dual-test-procedure are stated in the paragraph "Bending with lateral compression". The friction coefficient μ_R at the die radius R is derived from the theory of belt friction using the calculated friction force F_{fric} and the back pulling force F_B (Fig. 5a). A disadvantage of this approach is the assumption that the sheet material behaves as a membrane without resistance to bending [11] which simplifies the assumed contact pressure distribution. An approach from Witthueser [8] to investigate the mean contact pressure $\bar{p}_R$ is also shown in Fig. 5a.

[1] A similar in-situ measurement of friction in the blank holder region was conducted previously by Kasuga et al. [47].

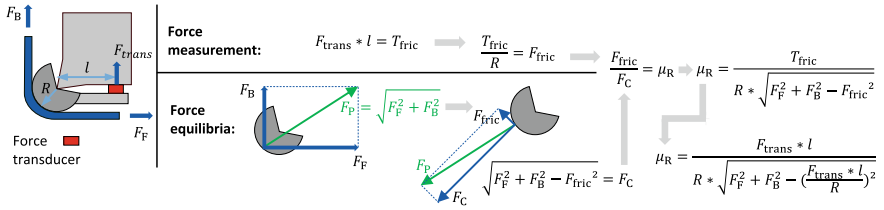


Fig. 6 Test principle of the integrative BUT test after Sniekers and calculation of the friction coefficient μ_R at the die radius (cf. [Sni96]), T_{fric} = friction torque at the die radius, F_{fric} = friction force tangential to the die radius. (Color figure online)

Advancements in the measurement of the front and back forces were achieved by Kernovsky and Weinmann [49, 50]. Strain gauges on the horizontal webs measure vertical forces and strain gauges on the vertical webs measure horizontal forces (Fig. 5b).

A different so-called integrative approach to investigate friction coefficients is presented by Sniekers [11]. He uses a BUT test with integrated force measurement to measure frictional load F_{trans} (cf. Figure 6). The calculation of the friction coefficient μ_R requires the determination of a contact force F_C by force equilibria. Additionally the friction force F_{fric} tangential to the die radius R is derived from the friction torque T_{fric}. Sniekers [11] compares the integrative approach with the belt friction approach in a numerical validation and concludes that the results from the integrative approach are superior to those of the belt friction approach. A big advantage of the integrative approach is the investigation of friction coefficients in a single experiment.

Another single-experiment BUT test was developed by Andreasen et al. [51]. Their approach uses the force measurement from Fig. 5b and a torque transducer in combination with a cylindrical tool pin (Fig. 7). The derivation of the friction stress τ and the mean surface pressure $\bar{p}$ is described by Andreasen et al. [51] and Sulonen et al. [52].

When reviewing the BUT test, it is noticeable that the calculation procedures to quantify the friction coefficients are relatively complicated (compared to the flat die test from a following paragraph). Additionally, the investigation of the mean normal pressure differs from author to author (cf. Figs 5a and 7) or is not made

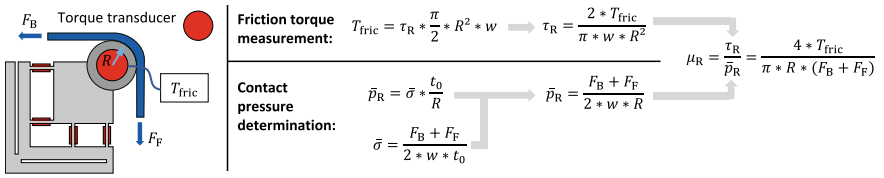


Fig. 7 Test principle of the BUT test after Andreasen (cf. [51, 52]) and calculation of the friction coefficient μ_R at the die radius, $\bar{\sigma}$ = mean tensile stress in the strip, $\bar{p}_R$ = mean contact pressure at the die radius, w = strip width, t_0 = initial strip thickness, τ_R = friction stress at the die radius. (Color figure online)

at all (cf. Fig. 6). Haruff et al. performed a mathematical sensitivity analysis of the calculation procedures in the traditional BUT test. Taking into account the uncertainty in force and geometrical measurements, they ascribe an inaccuracy of $+-0.01$ to the evaluated friction coefficients [53]. However, their investigations do not question the use of the belt friction theory and inhomogeneous conditions in general.

A BUT test procedure that differs from the previous ones is presented by Wenzloff et al. [54]. They use a linearly increasing back force in combination with normalized force values (normalized via dividing measured forces with the strip tensile yield load) to calculate friction coefficients. This approach assumes that the friction coefficient is independent of the contact pressure. According to the author of this paper, this is an unacceptable assumption (cf. [5]) and therefore the test method is not described here in detail.

All the above-mentioned BUT test setups have in common that contact pressure can be adjusted via the back force. Alternatively, contact pressure can be adjusted via changing the die radius, though changing the die radius also changes the contact length [51] and thus the lubrication regime. Speaking of contact pressure: One major concern of the BUT test is inhomogeneous pressure distribution [10, 11]. Netsch found that the degree of homogeneity depends on the bending angle, the die radius, and to a lesser extent on the friction coefficient. He recommends performing BUT tests at a 90° angle and with a die radius of at least 10 mm to achieve acceptable homogenity [10]. Sniekers, however, attributes a much worse contact pressure homogeneity to the BUT test [11], while Witthueser [8] is more confident in a homogeneous distribution. Though, Witthueser's analytical verification is based on the belt friction approach (no bending resistance) and still ascertains a deviation of 9.5% between mean- and calculated local surface pressure.

In further investigations of the BUT test Hortig states that contact pressure distribution at the drawing radius varies depending on whether a back pulling force is applied as a pure tensile force or by a blank holder [55]. Woska developed a variant of the BUT test with a flat blank holder [56] while Reissner used a tensile force in combination with two rollers to reproduce realistic contact pressure distribution [57]. Compared to the traditional BUT test, the tests by Reissner and Woska are more accurate in simulating contact pressure distribution of real forming processes but extraction of friction coefficients is more difficult [22]. Furthermore, contact pressures are highly inhomogeneous over the die radius compared to the traditional BUT test [12, 55].

All in all, the BUT test enables the investigation of average friction coefficients at the die radius, but it has disadvantages in homogeneous contact pressure distribution. Furthermore, it is unfavourable that contact pressure cannot be adjusted directly by a dedicated actuator. The average contact pressure is limited by the yield strength of the strip [10, 11]. The strip drawing test with flat dies, depending on its version, can address these disadvantages and is reviewed in the following paragraph.

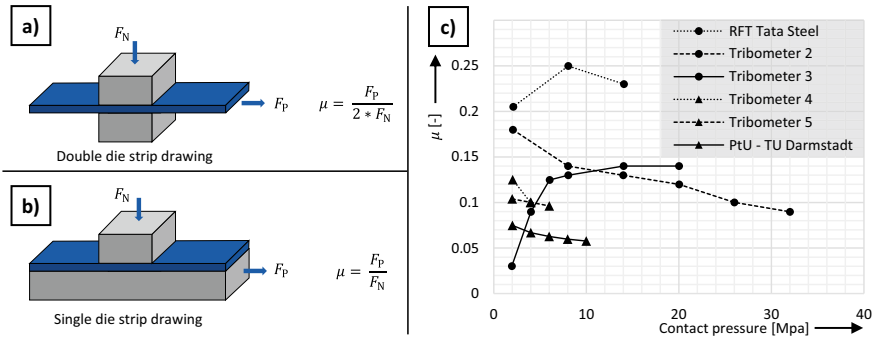


Fig. 8 **a**, **b** Test principles of the strip drawing test with flat dies; **c** round robin test of seven flat die strip drawing tests (from [28] after [59], F_p = pulling force, F_N = normal force, μ = friction coefficient between strip and die(s). (Color figure online)

8 Strip Drawing with Flat Dies (FD Test)

One can assume that the FD-test is the most basic and straightforward sheet metal forming tribometer from Fig. 2. Two basic variants of the FD test are shown in Fig. 8a and b. This depiction emphasizes the simplicity of the test method, especially the derivation of friction coefficients. Still, results are transferable to actual forming processes [58]. Parameters like contact size, contact pressure, drawing speed, tool surface configuration, and drawing length can be adjusted easily and directly. However, in-depth analyses show that a meticulous test stand design is key for reliable tribological investigations with the FD test [13]. Even recently developed FD tests reveal challenges in providing consistent results [18]. A round robin test of seven different FD tribometers in 2013 shows a large scatter of the investigated friction coefficients (Fig. 8c). Possible reasons for such a large scatter are reviewed in the following paragraphs. Most of the considerations and some of the design principles can be transferred to the design process of all kinds of tribometers.

Early tribological investigations with the FD test were performed by Wojtowicz in the 1950s [60]. Wojtowicz investigated several lubricants with different sheet materials and quantitatively described the influence of lubricant viscosity to friction coefficients. His test apparatus worked according to the double die principle (Fig. 8a) and was mounted on a tensile testing machine which provided the pulling force. The normal force on the dies was applied by a screw which was loaded with a torque wrench. Despite the simple test setup, friction coefficients were within 5% of the mean value in consecutive tests.

A short review of design-based limitations of the FD test was performed by Emmens [13] and is supplemented with possible solutions below. Most of the solutions have already proven to be useful in the strip drawing test of the PtU[2] at the TU Darmstadt, which (in its first version) is described by Frontzek [9] and Netsch [10]

[2]Institute for Production Engineering and Forming Machines.

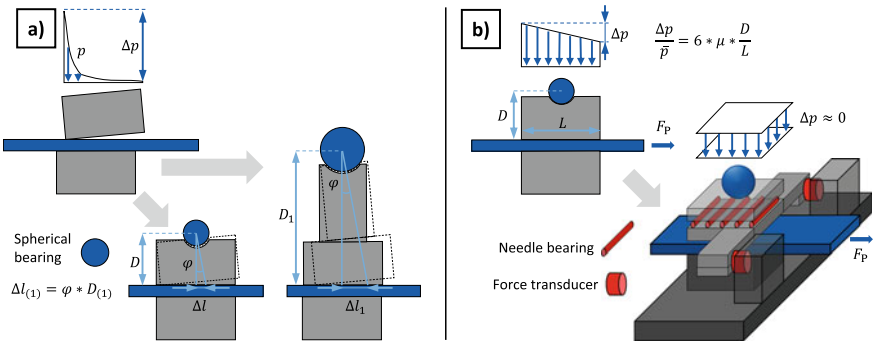


Fig. 9 **a** Misalignment of the dies in the FD test and compensation with a spherical bearing, **b** possible measuring system for friction forces (equation from [13]), p = contact pressure distribution, $\bar{p}$ = mean contact pressure. (Color figure online)

and has been continuously developed since then. The test stand has good transferability to actual forming processes and thus was used to build the testing guideline of the VDA (Federation of the German Automobile Industry) for prelubes [58, 61].

Misalignment of the dies in the FD test (Fig. 9a) causes uneven contact pressure distribution p [8], which leads to wrong contact pressure-dependent friction coefficients. Severe flaws in test results can be evoked by ploughing of the die edges through the strip material. Misalignment should be less than the roughness depth of the contacting surfaces (e.g., 1 μm), even during elastic deformation of the construction caused by the pulling force [13].

A proven solution is provided by spherical bearings to enable self-alignment of the dies (Fig. 9a). When using spherical bearings, it is worthwhile to arrange them as close as possible to the sheet surface in order to reduce the movement of the dies Δl during the aligning process. In other words, the distance D should be minimized without negatively affecting the stiffness of the device. Additionally, the deviation of the contact pressure distribution Δp decreases with decreasing D and increasing die length L (Fig. 9b). To minimize Δp even further, it is favourable to support the dies on the level of the sheet, where the friction force occurs. Thus a tilting of the dies caused by the friction force is avoided. In combination with a linear bearing, the die support can be used as a friction force measuring system (Fig. 9b).

Figure 10a shows the basic influence of the thickness of the dies on the contact pressure distribution. In general, the whole construction of a tribometer should be as stiff as possible. Besides positive effects on uniform contact pressure distribution, high stiffness reduces the appearance of stick slip effects [13]. Especially the design of spring-loaded elements should be done with great care considering possible oscillation effects (cf. [18]). The limitation of the maximum examinable mean contact pressure $\bar{p}_{\max}$ in the double die FD test is shown in Fig. 10b. Possible solutions to increase $\bar{p}_{\max}$ are both the single-sided FD test and the use of two or more stacked strips in the double die FD test (Fig. 10b). However, due to different tension stresses in the strips, both solutions represent a greater abstraction of sheet forming

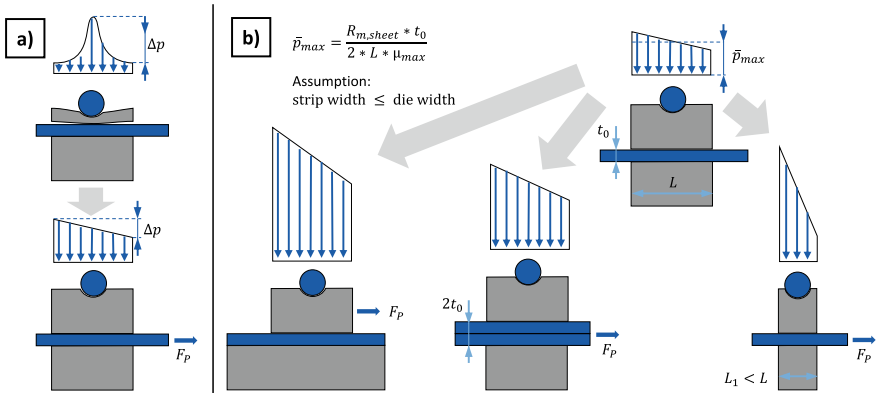


Fig. 10 **a** Effect of the die thickness in the FD test; **b** possibilities to raise the maximum mean contact pressure $\bar{p}_{max}$ in the FD test, L-R single-sided FD test, FD test with stacked strips, FD test with smaller dies. $R_{m,sheet}$ = sheet tensile strength, μ_{max} = maximum friction coefficient. (Color figure online)

processes than the double die FD test with a single strip. Another possibility to increase maximum contact pressure is using smaller dies, though independent investigations from several authors on different FD tribometers show that die size affects results from the FD test [10, 13, 20, 62]. The authors conclude that friction coefficients increase with decreasing die size (only under lubricated conditions [20]). However, Emmens and Netsch do not agree on whether die width or die length is the more pronounced factor of influence. Recklin et al. [62] use an analytical model to describe die size dependent lubricant behaviour in the FD test. The model was validated by measuring the lubricant amount on the dies after the FD experiments. In their investigation, smaller dies lead to increased volume flow and squeezing of lubricant out of the contact zone. Choosing the die size for a FD tribometer should be under consideration of the real forming process. It is important to keep in mind that smaller dies (especially dies with shorter length L or L_1 tend to cause tilting and uneven contact pressure distribution (Fig. 9b and Fig. 10b).

All in all, the FD test makes it possible, like no other sheet metal forming tribometer, to set parameters separately and to ensure homogeneous and stationary conditions. However, despite its apparent simplicity, a thorough dimensioning is necessary. Since one can assume that not every FD test is well designed, it is no surprise that in some publications transferability is rated rather low [22].

9 Conclusion

The search for the perfect sheet metal forming tribometer gathered pace in the mid-twentieth century. Since then, two test methods, namely, the bending under tension



Fig. 11 Logos of the sponsors of the "RAmP" project, in which a tribometer for aluminium hot forming is further developed. (Color figure online)

test (BUT) and the strip drawing test with flat dies (FD test), have proven to be the most promising candidates, although their transferability is controversially discussed [22, 58, 63]. Much of the difference in opinion about these and other tribometers is assumed to be due to poor tribometer design and sloppy execution of experiments. A quote from 1997 is still valid: "Tribotesting suffers from the problem that a result is always obtained, but its relevance to real situations is open to doubt. […] The design and construction of equipment […] have vital importance." [22]

This statement should be kept in mind when designing and using tribometers of any kind at any time. The aim in the development of the "perfect" sheet metal tribometer should be to reproduce the forming process conditions in the tribometer as precise as possible while ensuring metrological accessibility. This paper mainly summarizes different variants of the BUT test and gives advice for the design of FD tests that can be transferred to other tribometers. Furthermore, an orientation is given which test method fits to which research goal.

Future tribometer developments are aimed at the investigation of forming processes like hot stamping which offer demanding tribological challenges [64, 65]. Especially hot forming die quenching of aluminium requires complex tribometer designs, since non-steady-state temperature profiles add "time" as a new investigation dimension. At the PtU of the TU Darmstadt, an aluminium hot forming tribometer is under development as part of the "RAmP" project. Besides friction coefficients, it is planned to investigate wear phenomena of high strength aluminium alloys. These kinds of investigations complicate the search for the perfect sheet metal forming tribometer which will not be over anytime soon (Fig. 11).

The analyses in this paper were carried out as a part of the "RAmP" project. This project (HA project no. 822/19-142) is financed with funds of LOEWE – Landes-Offensive zur Entwicklung Wissenschaftlich-ökonomischer Exzellenz, Förderlinie 3: KMU-Verbundvorhaben (State Offensive for the Development of Scientific and Economic Excellence).

References

1. Roland Berger Strategy Consultants (2012) Mastering product complexity, Düsseldorf
2. Sabadka ID (2014) Impacts of shortening product life cycle in the automotive. Transfer inovácií 29(2013):251–253
3. Hu SJ (2013) Evolving paradigms of manufacturing: from mass production to mass customization and personalization. Procedia CIRP 7:3–8. https://doi.org/10.1016/j.procir.2013.05.002

4. Lange K (ed) (1990) Blechbearbeitung, 2., völlig neubearb. und erw. Aufl. Umformtechnik, Handbuch für Industrie und Wissenschaft/hrsg. von Kurt Lange; Bd. 3. Springer, Berlin
5. Filzek J, Ludwig M, Groche P (2011) Improved FEM simulation of sheet metal forming with friction modelling using laboratory tests. Proceedings of the IDDRG, Bilbao, Spain: 5–8
6. Trzepiecinski T, Lemu HG (2020) Recent developments and trends in the friction testing for conventional sheet metal forming and incremental sheet forming. Metals 10(1):47. https://doi.org/10.3390/met10010047
7. Reihle M (1959) Verhalten des Gleitreibungskoeffizienten von Tiefziehblechen bei hohen Flächenpressungen: Dissertation, Technische Hochschule Stuttgart
8. Witthüser K-P (1980) Untersuchung von Prüfverfahren zur Beurteilung der Reibungsverhältnisse beim Tiefziehen: Dissertation, Universität Hannover
9. Frontzek H (1990) Beitrag zur Bestimmung der Reibungsverhältnisse in der Blechumformung: Dissertation, Technische Hochschule Darmstadt
10. Netsch T (1995) Methode zur Ermittlung von Reibmodellen für die Blechumformung. Zugl.: Darmstadt, Techn. Hochsch., Diss., 1995, Als Ms. gedr. Berichte aus Produktion und Umformtechnik, vol 27. Shaker, Aachen
11. Sniekers RR (1996) Friction in deep drawing: Dissertation. Technische Universiteit Eindhoven. https://doi.org/10.6100/IR458460
12. Filzek J (2004) Kombinierte Prüfmethode für das Reib-, Verschleiß- und Abriebverhalten beim Tief- und Streckziehen: Dissertation. Zugl.: Darmstadt, Techn. Univ., Diss., 2004. Berichte aus Produktion und Umformtechnik, vol 62. Shaker, Aachen
13. Emmens WC (1997) Tribology of flat contacts and its application in deep drawing: Dissertation, University of Twente
14. Staeves J (1998) Beurteilung der Topografie von Blechen im Hinblick auf die Reibung bei der Umformung. Zugl.: Darmstadt, Techn. Univ., Diss., 1998, Als Ms. gedr. Berichte aus Produktion und Umformtechnik, Bd. 41. Shaker, Aachen
15. Barros Bouchet MI de, Kano M (2007) Superlubricity of Diamond/Glycerol Technology Applied to Automotive Gasoline Engines. In: Superlubricity. Elsevier, pp 471–492. https://doi.org/10.1016/b978-044452772-1/50056-1
16. Haider H (2009) Tribological Assessment of UHMWPE in the Knee. In: UHMWPE Biomaterials Handbook. Elsevier, pp 381–408. https://doi.org/10.1016/b978-0-12-374721-1.00026-2
17. Jünemann H (1995) Systematische Betrachtungen tribologischer Prüfverfahren: Reibungs-und Verschleissmessungen. Tribol Schmierungstech 42(4):199–205
18. Kirkhorn L, Frogner K, Andersson M et al (2012) Improved Tribotesting for sheet metal forming. Procedia CIRP 3:507–512. https://doi.org/10.1016/j.procir.2012.07.087
19. Guo B, Gong F, C-j WANG et al (2009) Flow stress and tribology size effects in scaled down cylinder compression. Transactions of Nonferrous Metals Society of China 19:s516–s520. https://doi.org/10.1016/S1003-6326(10)60100-8
20. Guo B, Gong F, Wang C et al (2010) Size effect on friction in scaled down strip drawing. J Mater Sci 45(15):4067–4072. https://doi.org/10.1007/s10853-010-4492-6
21. Recklin V (2020) Untersuchung des Einflusses dehnungsinduzierter Oberflächenevolution in der Blechumformung, 1. Auflage. Berichte aus Produktion und Umformtechnik, vol 121. Shaker, Düren
22. Schey JA (1997) A critical review of the applicability of tribotesters to sheet metal working. In: SAE Technical Paper Series. SAE International, Warrendale, PA, United States. https://doi.org/10.4271/970714
23. Kim H, Sung JH, Sivakumar R et al (2007) Evaluation of stamping lubricants using the deep drawing test. Int J Mach Tools Manuf 47(14):2120–2132. https://doi.org/10.1016/j.ijmachtools.2007.04.014
24. Grüner M, Merklein M (2014) Determination of friction coefficients in deep drawing by modification of Siebel's formula for calculation of ideal drawing force. Prod Eng Res Devel 8(5):577–584. https://doi.org/10.1007/s11740-014-0551-1

25. Gil I, Mendiguren J, Galdos L et al (2016) Influence of the pressure dependent coefficient of friction on deep drawing springback predictions. Tribol Int 103:266–273. https://doi.org/10.1016/j.triboint.2016.07.004
26. Olguner S, Bozdana AT (2016) The effect of friction coefficient on punch load and thickness reduction in deep drawing process. Int J Mater 3:64–68
27. Autoform GmbH (2016) TriboForm Joins AutoForm
28. Hol J, Wiebenga JH, Hörning M et al. (2016) Advanced friction simulation of standardized friction tests: a numerical and experimental demonstrator. J. Phys.: Conf. Ser. 734: 32092. https://doi.org/10.1088/1742-6596/734/3/032092
29. Nielsen CV, Martins PAF, Bay N (2016) Modelling of real area of contact between tool and workpiece in metal forming processes including the influence of subsurface deformation. CIRP Ann 65(1):261–264. https://doi.org/10.1016/j.cirp.2016.04.126
30. Dilmec M, Arap M (2016) Effect of geometrical and process parameters on coefficient of friction in deep drawing process at the flange and the radius regions. Int J Adv Manuf Technol 86(1–4):747–759. https://doi.org/10.1007/s00170-015-8225-5
31. Mehic B, Engler S, Huskic A (2015) Entwicklung einer Streifenziehversuchsanlage zur Untersuchung des Reib-und Verschleißverhaltens von tribologisch beanspruchten Oberflächen. 9. Forschungsforum der Österreichischen Fachhochschulen
32. Raziol GmbH (2020) Tribometer 5000, Iserlohn
33. Olsson DD, Bay N, Andreasen JL (2004) Prediction of limits of lubrication in strip reduction testing. CIRP Ann 53(1):231–234. https://doi.org/10.1016/S0007-8506(07)60686-6
34. Üstünyagiz E, Nielsen CV, Christiansen P et al (2017) Continuous strip reduction test simulating tribological conditions in ironing. Procedia Eng 207:2286–2291. https://doi.org/10.1016/j.proeng.2017.10.996
35. Aleksandrović S, Đorđević M, Stefanović M et al (2014) Different ways of friction coefficient determination in stripe ironing test. Tribol Industry 36(3):293–299
36. Bay N, Olsson DD, Andreasen JL (2008) Lubricant test methods for sheet metal forming. Tribol Int 41(9–10):844–853. https://doi.org/10.1016/j.triboint.2007.11.017
37. Lassen S, Bay N (1993) Evaluation of tribology tests for sheet metal forming. EFB-kolloquim: Reibung. Schmierung, Tribologie in der Blechbearbeitung T12:98–104
38. Sachs G (1930) Ein neues Prüfgerät für Tiefziehbleche. Metall Wirtschaft Wissenschaft und Technik 9(10):213–217
39. Loxley EM, Swift HW (1945) The wedge drawing test. Engineering 159:38–40, 77–80, 136–138
40. Ng P, Chakrabarty J, Mellor PB (1976) A reappraisal of the wedge-drawing test. Int J Mech Sci 18(5):249–259. https://doi.org/10.1016/0020-7403(76)90007-2
41. Blümel KW (1981) Untersuchungen zum Umformverhalten von Stahlfeinblech. Thyssen Technische Berichte 13(1):16–24
42. Kawai N, Nakamura T (1974) The Frictional mechanism on surface of metals plastically deformed: 2nd Report, design and calibration of drawing-type friction testing machine and some preliminary experiments. Bull JSME 17(108):810–827. https://doi.org/10.1299/jsme1958.17.810
43. Kawai N, Nakamura T (1974) The frictional mechanism on surface of metals plastically deformed : 3rd report, effects of the bulk plastic deformation on the frictional shear stress. Bull JSME 17(110):1105–1112. https://doi.org/10.1299/jsme1958.17.1105
44. Miguel V, Benet J, Coello J et al. (2007) Slip line field applied to deep drawing. In: AIP Conference Proceedings. AIP, pp 823–828. https://doi.org/10.1063/1.2740912
45. Miguel V, Martínez A, Coello J et al. (2013) A new approach for evaluating sheet metal forming based on sheet drawing test. Application to TRIP 700 steel. J Mater Process Technol 213(10):1703–1710. https://doi.org/10.1016/j.jmatprotec.2013.04.010
46. Recklin V, Dietrich F, Groche P (2017) In-situ-measurement of the friction coefficient in the deep drawing process. J Phys Conf Ser 896:12027. https://doi.org/10.1088/1742-6596/896/1/012027

47. Kasuga Y, Yamaguchi K, Kato K (1968) Friction and lubrication in the deformation processing of metals : 2nd report, surface texture and coefficient of friction. Bull JSME 11(44):354–360. https://doi.org/10.1299/jsme1958.11.354
48. Littlewood M, Wallace JF (1964) The effect of surface finish and lubrication on the frictional variations involved in the sheet-metal-forming process. Sheet Metal Indus 41(452):925–930
49. Kernosky SK, Weinmann KJ, Michler JR et al (1998) Development of a die shoulder force transducer for sheet metal forming research. J Manuf Sci Eng 120(1):42–48. https://doi.org/10.1115/1.2830109
50. Weinmann KJ, Kernosky SK (1996) Friction studies in sheet metal forming based on a unique die shoulder force transducer. CIRP Ann 45(1):269–272
51. Andreasen JL, Olsson DD, Chodnikiewicz K et al (2006) Bending under tension test with direct friction measurement. Proc Inst Mech En Part B: J Eng Manuf 220(1):73–80. https://doi.org/10.1243/095440505X32913
52. Sulonen M, Eskola P, Kumpulainen J et al. (1981) A reliable method for measuring the friction coefficient in sheet metal forming. Proceedings of IDDRG WG-Meeting: 1–15
53. Haruff JP, van Tyne CJ, Matlock DK (1995) The sensitivity of lab-measured friction coefficients. JOM 47(7):50–52. https://doi.org/10.1007/BF03221232
54. Wenzloff GJ, Hylton TA, Mattock DK (1992) Technical note: a new test procedure for the bending under tension friction test. JMEP 1(5):609–613. https://doi.org/10.1007/BF02649242
55. Hortig DM (2001) Werkzeugbeschichtungen mit Trockenschmierstoffeigenschaften für das Tiefziehen. Zugl.: Darmstadt, Techn. Univ., Diss., 2000. Berichte aus Produktion und Umformtechnik, vol 47. Shaker, Aachen
56. Woska R (1982) Einfluß ausgewählter Oberflächenschichten auf das Reib- und Verschleißverhalten beim Tiefziehen: Dissertation, Technische Hochschule Darmstadt
57. Reissner J (1983) Optimale Reibbedingungen beim geschmierten Tiefziehprozess. In: Grundlagen der Umformtechnik—Stand und Entwicklungstrends/Fundamentals of Metal Forming Technique—State and Trends. Springer, pp 151–165
58. Filzek J, Groche P (2001) Assessment of the Tribological Function of Lubricants for Sheet Metal Forming. In: Totten GE (ed) Bench testing of industrial fluid lubrication and wear properties used in machinery applications: Papers presented at the Symposium on Bench Testing of the Lubrication and Wear Properties of Industrial Fluids Used in Machinery Application held in Seattle, Washington in 26–27 June 2000. ASTM, West Conshohocken, Pa., 97-97-12. https://doi.org/10.1520/stp10502s
59. GDDRG (2013) Reibwertbestimmung: VDEH Round robin test: Arbetsgruppe Oberflächentopographie und Umformbarkeit, IDDRG working group meeting
60. Wojtowicz WJ (1955) Sliding friction test for metalworking lubricants. Lubr Eng 11(3):174–177
61. Verband der Automobilindustrie e.V. (2008) VDA 230-213: Prüfverfahren für die Produktklassen Prelube, Prelube 2, Hotmelt, Spot lubricant, Frankfurt
62. Recklin V, Dietrich F, Groche P (2018) Influence of test stand and contact size sensitivity on the friction coefficient in sheet metal forming. Lubricants 6(2):41. https://doi.org/10.3390/lubricants6020041
63. Ranta-Eskola A, Kumpulainen JO, Sulonen M (1982) Comparison of strip drawing tests used for measuring surface interactions in press forming. 12 th Biennial Congress–International Deep Drawing Research Group 1: 165–174
64. Venema J (2019) Tribological interactions and modelling of friction in hot stamping: Dissertation, University of Twente. doi: 10.3990/1.9789036548175
65. Zheng K, Politis DJ, Wang L et al (2018) A review on forming techniques for manufacturing lightweight complex—shaped aluminium panel components. Int J Lightweight Mater Manuf 1(2):55–80. https://doi.org/10.1016/j.ijlmm.2018.03.006

A Contact and Friction Model for Forming of Galvanized Steel Sheet Based on Fractal Theory



Yao Huang, Leigang Wang, Mingxiao Shi, and Xiang Ma

Abstract Galvanized steel sheets are increasingly used in the automotive industry due to excellent corrosion resistance, sufficient weldability, and formability. During sheet forming of galvanized metals, material failures such as exfoliation and cracking can be found in the zinc coated layers of the sheet under severe friction. Thus, the evaluation of the influences of surface topography, pressure, and lubrication on friction could provide valuable guidance in forming of galvanized metals. A hot-dip galvannealed sheet and a hot-dip galvanized sheet are chosen in this tribology study. The surface topographies of the materials are measured using profile meter and the fractal parameters are calculated using the fractal theory. The contact model between the sheet and the die is established using the real contact area. The friction model concerning the surface topography of galvanized sheet and the pressure is thus formulated. The friction coefficients of the theoretical values are in reasonable agreement with the experimental.

Keywords Galvanized steel · Contact and friction model · Sheet forming · Fractal theory

Y. Huang · L. Wang
School of Materials Science and Technology, Jiangsu University, Zhenjiang 212013, China
e-mail: lgwang@ujs.edu.cn

M. Shi
School of Materials Science and Engineering, Jiangsu University of Science and Technology, Zhenjiang 212003, China

X. Ma (✉)
SINTEF Industry, POB 124, Blindern, 0314 Oslo, Norway
e-mail: xiang.ma@sintef.no

© The Minerals, Metals & Materials Society 2021

G. Daehn et al. (eds.), *Forming the Future*, The Minerals, Metals & Materials Series,
https://doi.org/10.1007/978-3-030-75381-8_8

1 Introduction

Galvanized steel sheets are widely used in the automotive industry to make car panels and bodies due to good weldability and formability, excellent corrosion resistance, and superior coating properties [1–3]. Especially the Japanese cars have been mostly using galvanized steel sheets [4]. Their applications in the United States and Europe are constantly increasing as well. Currently, there is increasingly demanding on durability performance of cars by auto consumers. This requires higher quality and superior performance of galvanized sheets, which is calling for more research focusing on the galvanizing process, the surface quality, and friction characteristics during sheet stamping.

The galvanized sheet refers to the sheet made of ordinary cold-rolled sheet coated with a layer of zinc, so that steel corrosion can be prevented and the lifetime of the material can be extended [4]. Galvanized sheets are consisted of three parts: the steel sheet substrate, the buffer layer, and the galvanized layer. With dissimilar mechanical properties in elastic modulus and yield limits of the coated zinc layer to that of the substrate steel, not only the formability of galvanized steel sheets is more difficult, but also the contact and friction between the galvanized steel and the die tool is more complex than seen in forming ordinary cold-rolled steels. The conditions of contact and friction directly influence the surface quality, the springback, and forming limit of galvanized sheets. At present, more finite element-based numerical simulations have been applied to the sheet plastic deformation analysis. To obtain reliable simulation results, it is necessary to employ an accurate contact model and friction model in examining the formability of galvanized steels.

Depending on the galvanizing process, galvanized sheets can mainly be classified as hot galvanized, electro-galvanized, and mechanically galvanized. Among them, most widely used in industries are hot-dip galvanized and electro-galvanized [5]. Hot dip galvanized coating can be made thick, with very good corrosion resistance and formability at low cost. But the uniformity of coating surface might be quite poor, easily creating zinc tumor and other defects. On the other hand, electro-galvanized coating can provide a superior surface quality and a better coating uniformity. However, the coating is relatively thin with a high production cost. With fast technology development of hot-dip galvanizing, it is possible to produce a more homogeneous zinc coating. Thus, the hot-dip galvanizing process has been widely applied to make galvanized sheets for automotive industry. In this study, two different hot-galvanized coated sheets were chosen for tribology study, i.e., a hot-dip galvannealed sheet and a hot-dip galvanized sheet.

Any friction pair surface is rough at micro-scale. This surface feature has a significant impact on the phenomena such as micro-contact, friction, abrasion, thermal conductivity, and lubrication [6, 7]. As a result, research on the influences of parameters of rough surfaces in tribology is always of immense importance. During the earliest study, Hertz elastic contact theory was used in the contact surface to study a single point contact behavior. Hertz then simplified the contact surface asperities into two elastic spheres contact problem, thus solving the problem of the distribution

of pressure after the compression. Hertz contact model is by far the most classical contact mechanics model, up to now still being used to analyze the two surfaces contact. An elastic-plastic contact model was established in 1954 by introducing the statistical theory [8]. Another classical elastic contact model was further developed by including statistical theory and standard contact mechanics [9]. Their study showed that the actual contact area and the number of asperities were closely linked to the density distribution function of profile height of the contact surface. The applications of these models, however, are limited by the resolution of the measuring instruments and the sample length, as well as uncertainty [10, 11]. Until 1990s, a modified Weierstrass fractal function was introduced and the fractal contact model, i.e., Majumdar-Bhushan or M-B model was established, in which the deformation properties of the contact surface could be determined with a more proper relationship between the real contact area and the load [12].

With the development of the fractal theory in tribology, fractal parameters have been widely used in characterization of rough surface topography and establishment of contact model with self-similarity and scale invariance. A complicated contact model of fractal rough surfaces was developed later [13]. The results showed that the relationship between the contact load and the real contact area was linear. The plastic deformation region decreased, and the contact stiffness increased as the contact area increased. Another modified elastic-plastic contact model with a single fractal asperity was established [14]. The revised model showed that as the load and contact area increased, a transition from elastic to plastic contact mode took place. Furthermore, a fractal contact model was developed based on base length considering asperity deformation properties, fractal theory, and friction effect [15]. The relationship between the fractal dimension, contact force, and real contact area was studied as well by using numerical simulation analysis.

In this study, the surface topography of the galvanized sheet was measured by using optical profile meter. Based on the fractal theory, the fractal parameters were calculated using MATLAB. The real contact between the galvanized sheet and the die was then simplified in order to establish a fractal contact model. Eventually, the friction model was developed and experimentally verified.

2 Surface Topographies and Fractal Features of Galvanized Sheets

2.1 Materials and Methodology

Two different hot-dip galvanized coated sheets are chosen for tribology study, i.e., a hot-dip galvannealed (GA) sheet and a hot-dip galvanized (GI) sheet, supplied by Shanghai BaoSteel Group Corporation. Their product identifications are given as *SP781BQ* for GA sheet and *HC420/780DPD* + *Z* for GI sheet. The coating material in GA sheet is a zinc-iron alloy, while in GI is pure zinc. This gives a much

shinier surface in GI than in GA sheet. A Veeco Wyko NT1100 optical non-contact profile meter is used to measure the surface topography of the galvanized sheets. A rectangular sheet sample in dimension of $30 \times 100\ mm^2$ is cut from the original large sheet for such purpose. All samples are treated with anhydrous ethanol to keep surface finish. In the sample, three micro areas are selected randomly as the measurement area for plotting of the surface profile curve and determining the surface roughness value, as well as the 3D surface topography.

To study the friction behavior of the galvanized sheet, a sliding friction test under flat die is carried out using a testing device from Shanghai BaoSteel Group Corporation. Each of the contact surface areas of the sheet interfacing with the top and bottom of the flat dies is approximately $2 \times 30\ mm^2$ (more details can be found in Figs. 2.3, 2.4, 2.5, 2.6 and 2.7 of [16]). The material is pulled with a sliding speed of 150 mm/min, under a normal load of 1000 N. The surface roughness values (Ra) of the dies are varied between 0.4 μm, 0.8 μm, and 1.2 μm. Both dried and lubricated frictions are applied, while only the results under dry conditions are reported in this paper.

To reduce the experimental errors, each sample and each measurement are repeated three times. An average value of the measured data is given correspondingly.

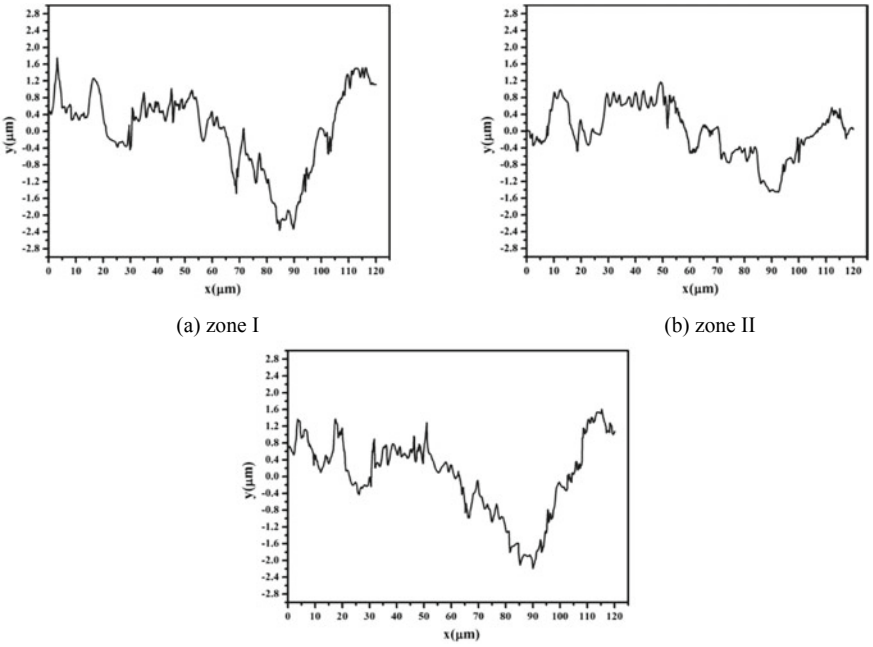
2.2 *Surface Profiles and 3D Topographies of Galvanized Sheets*

The typical surface profile curves of the GI and GA sheets from the three randomly chosen regions on each sample sheet are shown in Figs. 1 and 2, respectively. This clearly shows that a larger fluctuation of surface roughness is seen in the GA sheet than in the GI sheet. The surface roughness values (Ra) of the GA sheet and the GI sheet are measured as 0.889 μm and 0.525 μm, respectively, based on averaging the measured data. This difference might be due to the fact that in the GA sheet, the zinc layer is formed with hard and brittle Zn-Fe alloy; while in the GI sheet, the coating is composed of a relatively soft zinc. Thus, the surface of the GA sheet is much rougher than the GI sheet.

Figure 3 shows the three-dimensional topographies of the galvanized steels. Clearly more uneven asperities are found in the GA sheet surface, while the hot-dip pure zinc coated surface is much smoother.

2.3 *Fractal Characterization of Galvanized Sheets*

In Majumdar-Bhushan model [12], two rough contact surfaces can be simplified by an equivalent rough surface and an ideal rigid flat surface. The height of the asperity on the rough surface is defined as



(a) zone I (b) zone II

(c) zone III

Fig. 1 The surface profiles of GA sheet (SP781BQ) at three zones

$$\delta = G^{(D-1)} a^{\left(\frac{2-D}{2}\right)} \tag{1}$$

where D is fractal dimension, G is the fractal roughness parameter, and a is the contact area.

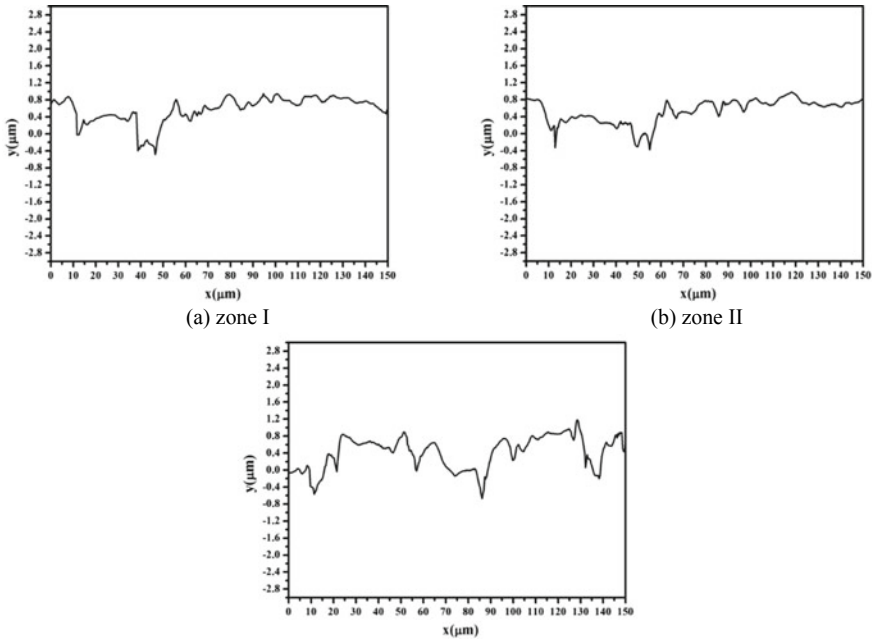
The surface profile curves are used to assess if the fractal characteristics is found in the galvanized sheets, i.e., at the level $1 < D < 2$ when the surfaces have fractal features. Thus the group of the points in the surface profile curves in Figs. 1 and 2 are processed and computed using the root-mean-square method [17].

The calculations are carried out in the MATLAB platform using the relation below:

$$\sigma(\tau) = C\tau^{(2-D)} \tag{2}$$

where the correlation length τ is similar to the discrete values of the displacement variable x in Figs. 1 and 2; $\sigma(t)$ is corresponding to the Weierstrass-Majumdar fractal function [12]; and C is a constant.

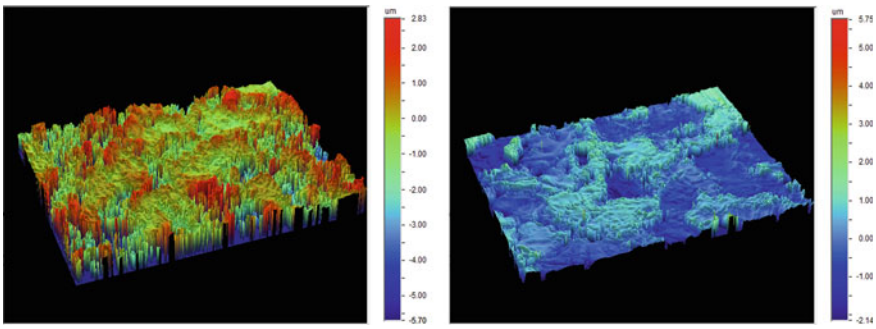
The double logarithm charts of the covariance of the measurement $\sigma(t)$ versus the correlation length τ are given in Fig. 4. It can be seen that the logarithm of root-mean-square measurement is in near linear relation with the logarithm of correlation length. Denoted α as the slope of this linear line, the fractal dimension D is thus determined by [17]:



(a) zone I (b) zone II

(c) zone III

Fig. 2 The surface profiles of GI sheet (HC420/780DPD + Z) at three zones

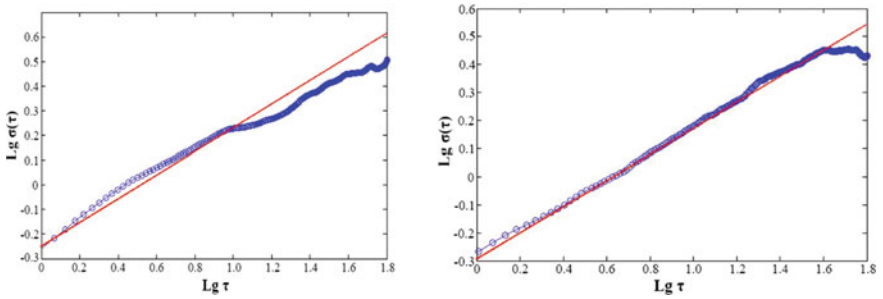


(a) GA sheet (b) GI sheet

Fig. 3 Initial 3D surface topographies of galvanized sheets. (Color figure online)

$$D = 2 - \alpha \tag{3}$$

The calculated fractal dimension and fractal roughness parameter based on Figs. 1 and 2 are given in Table 1. It can be seen that both of the fractal dimensions meet the range $1 < D < 2$. Hence, the surfaces of galvanized sheets have fractal characteristics. The average fractal dimension seen in the GA sheet is smaller than in the GI sheet,



(a) GA sheet (b) GI sheet

Fig. 4 The double logarithm chart of galvanized sheets. (Color figure online)

Table 1 The fractal parameters of galvanized steels

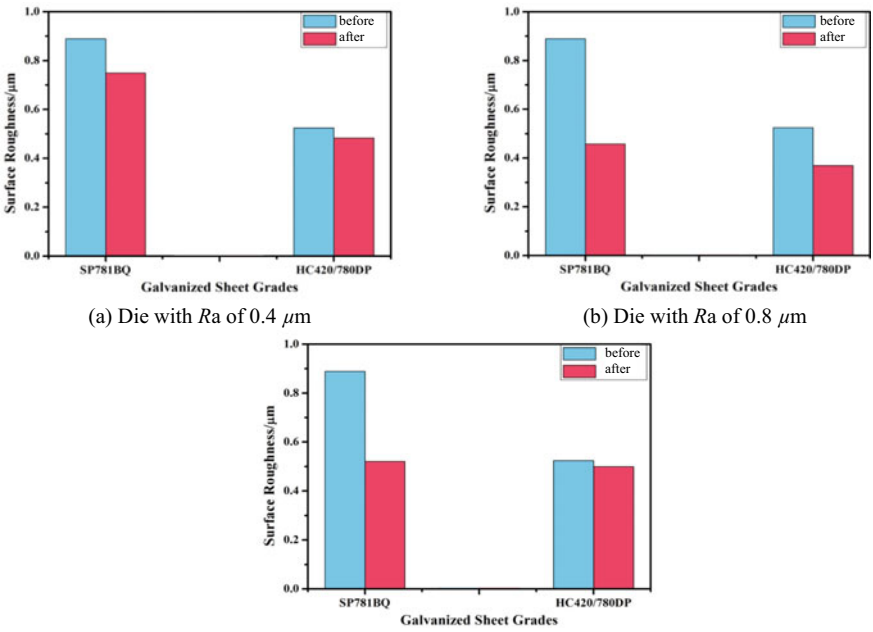
Types of sheet	Fractal dimension D	Fractal roughness parameter G (μm)	Average of D	Average of G (μm)
GA (SP781BQ)	1.522	0.227	1.52	0.23
	1.528	0.229		
	1.497	0.232		
GI (HC420/780DPD+)	1.597	0.114	1.6	0.11
	1.604	0.111		
	1.601	0.112		

while the fractal roughness parameter is obviously larger in the coarse surface of the GA sheet. This may be due to that a smooth surface is generally more delicate, with a deep self-similar fine structure which gives a higher fractal dimension.

2.4 Fractal Change of Galvanized Sheets After Friction

After the sliding friction experiments under a normal load of 1000 N, similar measurements of the surface profile curves and topographies are made using Wyko NT1100 optical profiler meter. The fractal dimension parameter can thus be calculated as before the friction tests. Figure 5 compares the changes in the surface roughness of the sheets before and after friction test. The surface roughness value is less than that before the test. And with the die surface roughness increasing, the surface roughness of the sheets reduces first before increasing again. This is because that the high peaks are worn out after friction.

The roughness of the GA sheet (*SP781BQ*) decreases more than that of the GI sheet (*HC420/780DP*), as seen from Figs. 5 and 6, shows that the fractal dimension of galvanized sheets after friction is greater than that before tests.



(a) Die with *R*a of 0.4 μm

(b) Die with *R*a of 0.8 μm

(c) Die with *R*a of 1.2 μm

Fig. 5 Changed roughness of galvanized sheets before and after friction test. (Color figure online)

3 Fractal Contact Models of Galvanized Sheets

When the largest contact area a_l is larger than critical contact area a_c (i.e., plastic deformation occurs), Majumdar-Bhushan model [12] gives a relation between the real contact area and the pressure or the total contact load P as

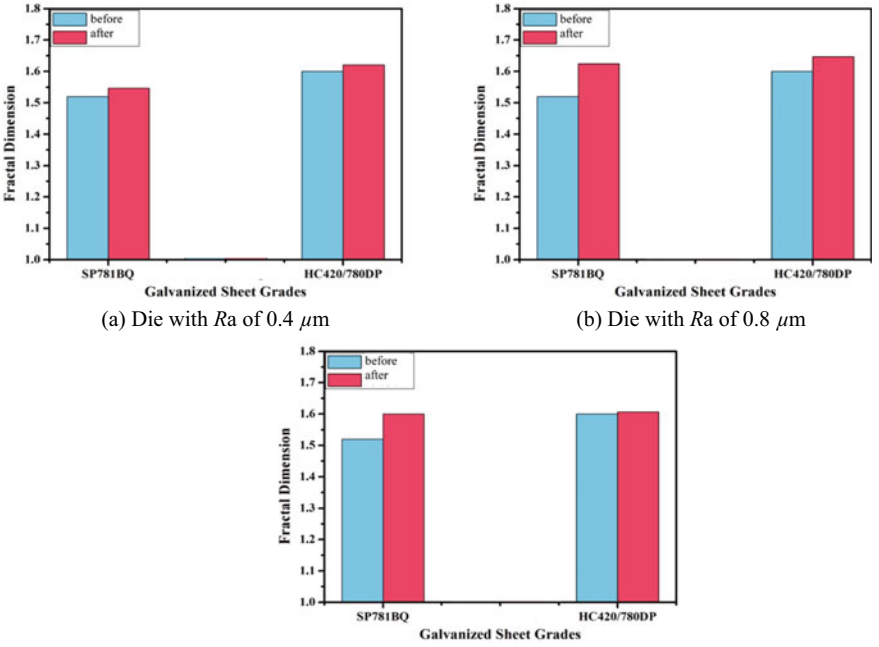
(a) If $D \neq 1.5$:

$$P^* = \frac{4}{3}\sqrt{\pi}\left(G^*\right)^{(D-1)} g_1(D)\left(A_r^*\right)^{\frac{D}{2}} \left\{\left[\left(\frac{D-2}{D}\right)A_r^*\right]^{\frac{3-2D}{2}} - \left(a_c^*\right)^{\frac{3-2D}{2}}\right\} + K\phi g_2(D)\left(A_r^*\right)^{\frac{D}{2}}\left(a_c^*\right)^{\frac{2-D}{2}} \tag{4}$$

(b) If $D = 1.5$:

$$P^* = \sqrt{\pi G^*}\left(\frac{A_r^*}{3}\right)^{\frac{3}{4}} ln\left(\frac{A_r^*}{3a_c^*}\right) + \frac{3}{4}K\phi\left(\frac{A_r^*}{3}\right)^{\frac{3}{4}}\left(a_c^*\right)^{\frac{1}{4}} \tag{5}$$

In Eqs. (4) and (5), the parameters are non-dimensional, i.e.,



(a) Die with *R*a of 0.4 μm

(b) Die with *R*a of 0.8 μm

(c) Die with *R*a of 1.2 μm

Fig. 6 Changed fractal dimension of galvanized sheets before and after friction test. (Color figure online)

$$P^* = \frac{P}{A_a E};\ G^* = \frac{G}{\sqrt{A_a}};\ A_r^* = \frac{A_r}{A_a};\ a_c^* = \frac{a_c}{A_a} = \frac{(G^*)^2}{\left(\frac{K\phi}{2}\right)^{\frac{2}{D-1}}};$$

$$g_1(D) = \frac{D}{3-2D}\left(\frac{D-2}{D}\right)^{\frac{D}{2}};\ g_2(D) = \left(\frac{2-D}{D}\right)^2 \tag{6}$$

where A_a is the nominal contact area, E is the equivalent Hertzian elastic modulus; K is defined as a factor related to the hardness H as well as yield strength σ_y, namely, $K = H/\sigma_y$; ϕ is a factor related to the yield strength σ_y and the elastic modulus E by $\phi = \frac{\sigma_y}{E}$; and A_r is the total real contact area.

Similarly, if $a_1 < a_c$, the contact load is given as

$$P^* = K\phi A_r^* \tag{7}$$

3.1 Contact Model of Hot-Dip Galvannealed (GA) Sheet

The mechanical properties and the surface morphology parameters of the GA sheet can be determined as follows.

For mechanical properties, the collective Young's modules is described as

$$E = \left(\frac{1-\upsilon_2^2}{E_1} + \frac{1-\upsilon_2^2}{E_2}\right)^{-1} \tag{8}$$

where E_1 and υ_1 are Young's modules and Poisson's ratio of the galvanized surface (the values are 0.27 and 130 GPa, respectively); and E_2 and υ_2 are Young's modules and Poisson's ratio of the die surface (the values are 0.3 and 200 GPa, respectively). Inserting these values into Eq. (8) gives Young's modules of 85.6 GPa. Please be noted that the values of the basic material properties (such as Youngs's modules and Poisson's ratio) are provided by the supplier, i.e., Shanghai BaoSteel Group Corporation.

The parameter of material performance is given as

$$K\phi = \frac{H}{E} = 0.022$$

The surface morphology parameters can be determined as follows.

The fractal dimension D is 1.52, the fractal roughness parameter G is 0.23 μm, and the nominal contact area $A_a = 2 \times 30$ mm^2.

Based on the mechanical properties and surface morphology parameters of the GA sheet, the relevant parameters can be calculated using the equations above as

$$G^* = \frac{G}{\sqrt{A_a}} = \frac{0.23 \times 10^{-3}}{\sqrt{2 \times 30}} = 0.0000296$$

$$P^* = \frac{P}{A_a E} = \frac{P}{2 \times 30 \times 85605} = \frac{P}{5136300}$$

$$a_c^* = \frac{a_c}{A_a} = \frac{G^{*2}}{\left(K\phi/2\right)^{2/(D-1)}} = 0.03$$

$$g_1(D) = \frac{D}{3-2D}\left(\frac{D-2}{D}\right)^{\frac{D}{2}} = -15.82$$

$$g_2(D) = \left(\frac{2-D}{D}\right)^{\frac{2-D}{2}} = 0.7583$$

After substituting above parameters into Eq. (4), the relation between the real contact area A_r^* and the load P can be obtained in the following form:

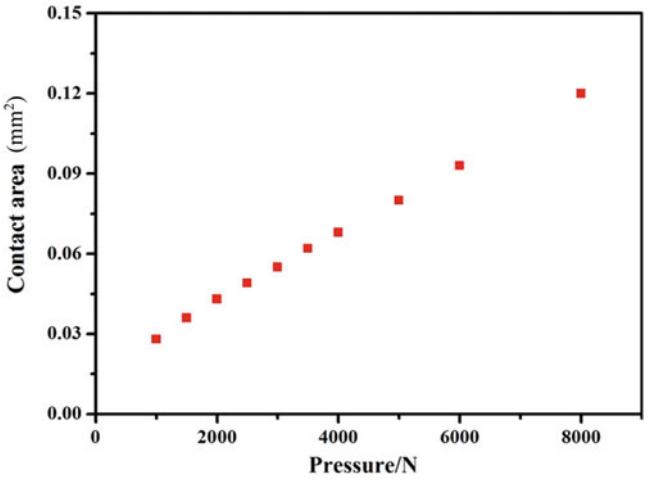


Fig. 7 Relation of real contact area and pressure between the galvanized sheet and the die (GA sheet). (Color figure online)

$$P = 948202A_r^{*0.76} - 869061A_r^{*0.74} \tag{9}$$

The relation between the real contact area and the pressure is shown in Fig. 7, from which it can be concluded that the real contact area rises as the pressure increases.

3.2 Contact Model of Hot-Dip Galvanized (GI) Sheet

The collective Young's modules is 85.6 GPa, same as the GA sheet.

With a different hardness, the parameters of material performance are $K\phi = 0.013$.

Considering that the fractal dimension D is 1.60, the fractal roughness parameter G is 0.11 μm, and the nominal contact area $A_a = 2 \times 30$ mm^2, the other parameters can be calculated as

$$G^* = \frac{G}{\sqrt{A_a}} = \frac{0.11 \times 10^{-3}}{\sqrt{2 \times 30}} = 0.0000142$$

$$P^* = \frac{P}{A_a E} = \frac{P}{2 \times 30 \times 85605} = \frac{P}{5136300}$$

$$a_c^* = \frac{a_c}{A_a} = \frac{G^{*2}}{(K\phi/2)^{2/(D-1)}} = 0.00393$$

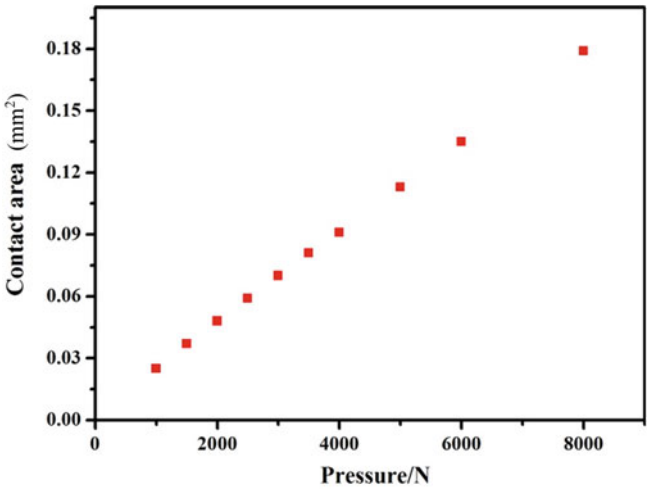


Fig. 8 Relation of real contact area and pressure between the galvanized sheet and the die (GI sheet). (Color figure online)

$$g_1(D) = \frac{D}{3-2D}\left(\frac{2-D}{D}\right)^{\frac{D}{2}} = -2.6391$$

$$g_2(D) = \left(\frac{2-D}{D}\right)^{\frac{2-D}{2}} = 0.75785$$

After above parameters are substituted into Eq. (4), the relation between real contact area A_r^* and the load P can be given in the following form:

$$P = 84460A_r^{*0.8} - 4531A_r^{*0.7} \tag{10}$$

Similarly, the relation between the real contact area and the pressure is shown in Fig. 8 for this GI sheet.

4 Friction Models of Galvanized Sheets

According to the theory of adhesive friction, the friction can be described as

$$F = F_a + F_e = A_r\tau_b + F_e \tag{11}$$

where F is the friction resistance, F_a is the adhesion force, and F_e is the plowing force, A_r is the real contact area, and τ_b is the shear strength of softer material. With

a relatively smooth material surface and a moderate contact pressure, the contribution of plowing force to friction could be neglected. In consequence, the simplified formula of friction coefficient μ is given as

$$\mu = \frac{F}{P} = \frac{A_r \tau_b}{P} \tag{12}$$

4.1 Friction Model of the Hot-Dip Galvannealed (GA) Sheet

When the shear strength of zinc coating is 113 MPa, the friction coefficient according to Eq. (11) is given as

$$\mu = \frac{\tau_b A_r}{P} = \frac{113 A_r}{P} \tag{13}$$

4.2 Friction Model of the Hot-Dip Galvanized (GI) Sheet

When the shear strength of HC420/780DPD + Z zinc coating is 90 MPa, the friction coefficient is

$$\mu = \frac{\tau_b A_r}{P} = \frac{90 A_r}{P} \tag{14}$$

The relation between friction coefficient and positive pressure is shown in Fig. 9, which indicates that the friction coefficient decreases with the increasing pressure. Moreover, the friction coefficient of hot-dip galvannealed sheet shows a massive decline at first. Then tendency of decline becomes slow as the pressure reaches 3000 N. By contrast, the friction coefficient of hot-dip galvanized sheet is slightly decreased.

4.3 Experimental Verification of Friction Model

Flat plate sliding friction experiment is conducted to measure friction coefficients of galvanized sheets under different pressures. The friction coefficients are calculated using the friction model and details of the experiment are shown in Tables 2 and 3.

It can be seen from Tables 2 and 3, friction coefficients of theoretical values are close to experimental values, and the error between them is less than 10%. Due to the ignored plowing force, theoretical values are slightly smaller than experimental

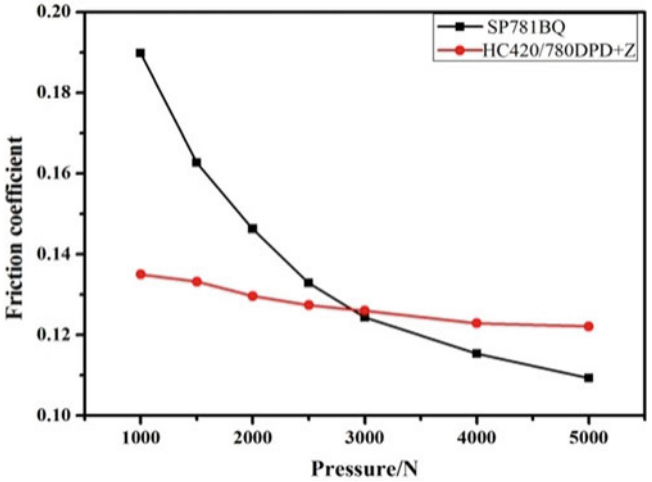


Fig. 9 Friction coefficient calculated by friction model under different pressures. (Color figure online)

Table 2 Friction coefficients of theoretical and experimental value (for SP781BQ sheet)

Pressure/N	1000	1500	2000
Theoretical value	0.1898	0.1627	0.1463
Experimental value	0.2055	0.1793	0.1584
Error	7.6%	9.2%	7.6%

Table 3 Friction coefficients of theoretical and experimental value (for HC420/780DPD + Z sheet)

Pressure/N	1000	1500	2000
Theoretical value	0.135	0.1332	0.1296
Experimental value	0.1501	0.1439	0.1375
Error	10%	7.4%	5.7%

values. It should be noted that in the experiment with a medium normal force, no full adhesion is expected. However, the theoretical model assumes a full adhesion for simplicity.

5 Conclusions

The following conclusions can be drawn from the study:

(1) It has been shown that the galvanized sheet has fractal characteristics. The fractal dimension and fractal roughness parameter for the SP781BQ hot-dip galvannealed sheet are 1.52 and 0.23 μm, respectively. Likewise, the fractal

dimension and the fractal roughness parameter for the HC420/780DPD + Z hot-dip galvanized sheet are 1.6 and 0.11 μm accordingly.

(2) Based on the fractal theory, the elastic-plastic contact model has been developed and the relation between real contact area and pressure has been obtained. The model shows that the real contact area rises with the increase of contact pressure.

(3) Friction model is established based on the fractal contact model. Experimental verification is carried out using the flat plate sliding friction experiment. The results indicate that the error between theoretical and experimental friction coefficients is within 10%. Thus, the friction model developed is relatively accurate.

Acknowledgments This work is supported by the National Natural Science Foundation of China (Project numbers: 51275216 and 51775249).

References

1. Safaeirad M, Toroghinejad MR, Ashrafizadeh F (2008) Effect of microstructure and texture on formability and mechanical properties of hot-dip galvanized steel sheets. J Mater Process Technol 196(1–3):205–212
2. Dong S, Zhou N (2005) Effect of TiC coating on electrode tip surface on electrode degradation during resistance spot welding zinc coated steel. Chinese J Nonferrous Metals 15(2):184–191
3. Zhang Q, Liu B (2002) Recent development in study of effect of coating phase structure of IF galvannealed steel sheet on its properties. Iron Steel 37(12):65–68
4. Xu X, Wang S (2007) Development and prospect of continuous hot-dip galvanized process (in Chinese). Surface Technol 36(1):71–74
5. M. H (2002) Principle and application of mechanical plating (in Chinese). Machinery Industry Publishing House, Beijing
6. Wu J (2000) Characterization of fractal surfaces. Wear 239(1):36–47
7. GC, SG (1998) Some issues about fractal characterization of engineering surfaces (in Chinese). Lubrication Eng (3):3–7
8. Bowden FP, DT (1954) Friction and lubrication. Oxford University Press, Oxford
9. Greenwood JA, Williamson JBP (1966) Contact of nominally flat surfaces. Proc R Soc Lond A 295(1442):300–319
10. Sayles RS, Thomas TR (1978) Surface topography as a nonstationary random process. Nature 271(5644):431–434
11. Majumdar A, Bhushan B (1990) Role of fractal geometry in roughness characterization and contact mechanics of surfaces. J Tribol 112(2):205–216
12. Majumdar A, Bhushan B (1991) Fractal model of elastic-plastic contact between rough surfaces. J Tribol 113(1):1–11
13. Miao X, Huang X (2014) A complete contact model of a fractal rough surface. Wear 309(1–2):146–151
14. Morag Y, Etsion I (2007) Resolving the contradiction of asperities plastic to elastic mode transition in current contact models of fractal rough surfaces. Wear 262(5–6):624–629

15. Ding X, Yan R, Jia Y, Construction and analysis of fractal contact mechanics model for rough surface based on base length (in Chinese). Tribology 34(4):341–347
16. Xu Y (2015) Research on contact model and friction model of galvanized sheet in sheet metal forming (in Chinese). Master thesis, Jiangsu University
17. Ge S, Tonder K (1997) The fractal behavior and fractal characterization of rough surfaces (in Chinese). Tribology 17(1):73–80

On the Characterization of Fracture Loci in Thin-Walled Tube Forming



J. P. Magrinho, M. B. Silva, and P. A. F. Martins

Abstract This paper is focused on the formability limits by fracture of thin-walled tubes. It provides, for the first time ever, the fracture forming limit lines associated with crack opening by tension (mode I), by in-plane shear (mode II) and by mixed-mode consisting of crack opening by modes I and II of fracture mechanics. This is accomplished by an experimental methodology that combines digital image correlation (DIC) and determination of gauge length strains in double notched tensile test (DNTT) specimens, staggered DNTT specimens and shear test specimens. Results are plotted in principal strain space and the crack opening modes are confirmed by fractography analysis performed with a scanning electron microscope (SEM). DNTT specimens are also used to determine fracture toughness in specimens that failed by tension. Results show that the use of DNTT, staggered DNTT and shear tests allow obtaining the strain loading paths and fracture loci across a wide range of forming conditions, ranging from plane strain to pure shear. The fracture forming limit (FFL) line, the shear fracture forming limit (SFFL) line and the transition region between these two lines are similar to those recently published for sheet and strip materials, and their use is of paramount importance for the design and optimization of tube forming processes.

Keywords Tube forming · Thin-walled tubes · Formability limits · Fractography · Fracture toughness

J. P. Magrinho (✉) · M. B. Silva · P. A. F. Martins
IDMEC, Instituto Superior Técnico, Universidade de Lisboa, Av. Rovisco Pais, Lisboa 1049-001, Portugal
e-mail: pmartins@tecnico.ulisboa.pt

M. B. Silva
e-mail: joao.magrinho@tecnico.ulisboa.pt

P. A. F. Martins
e-mail: beatriz.silva@tecnico.ulisboa.pt

© The Minerals, Metals & Materials Society 2021

G. Daehn et al. (eds.), *Forming the Future*, The Minerals, Metals & Materials Series,
https://doi.org/10.1007/978-3-030-75381-8_9

1 Introduction

Growing demand for the design and fabrication of high-strength lightweight structures is pushing forward the utilization of thin-walled tubes in transportation vehicles, buildings and design appliances, among other applications. This trend combined with the development of new tube forming processes has been driving the need to perform accurate characterization and determination of the formability limits by necking and fracture in thin-walled tubes [1].

In recent years, several experiment-based investigations have been carried out to determine the forming limits of thin-walled tubes by means of tube bulging [2, 3] and tube hydroforming [4, 5]. However, none of these studies analyzed the crack opening modes associated with the formability limits.

In contrast, the formability limits in sheet metal forming are nowadays well-understood. Failure by necking in principal strain space is characterized by the forming limit curve (FLC), which was originally proposed by Keeler [6] and Goodwin [7]. Failure by fracture is characterized by the fracture forming limit line (FFL), originally proposed by Embury and Duncan [8] for cracks opening by tension (mode I of fracture mechanics [9]) and by the shear fracture forming limit line (SFFL), recently disclosed by Isik et al. [10] for cracks opening by in-plane shear (mode II of fracture mechanics). The mechanics and physics behind these two fracture lines are comprehensively discussed by Martins et al. [11].

The attempt to extend the methods and procedures that are commonly utilized in sheet metal forming to tube forming leads the authors to recently propose an experimental methodology to obtain the strains at fracture and to determine the critical values of ductile damage by means of tube expansion with rigid dies [12]. In a subsequent work, the authors enhanced their methodology by adding a broader range of testing conditions ranging from pure tension to biaxial stretching. This was done by performing additional experiments in tube expansion with elastomers [13] and allowed determining, for the first time ever, the formability limits of thin-walled tubes by necking and fracture. The resulting FFL was recently confirmed in a numerical and experimental independent investigation focused on the utilization of external inverted tubes as energy absorbers [14].

Despite the above-mentioned advances in the characterization of fracture in thin-walled tubes, the determination of the SFFL (mode II) and of the transition between the FFL and the SFFL (mixed-mode, consisting of crack opening by combination of tension and in-plane shear), is still an open research topic.

Similar to what was previously said about the limited number of research publications on the formability limits by fracture of thin-walled tubes, there are almost no publications connecting fracture toughness and formability testing. In fact, the prevalence is on the determination of fracture toughness in specific applications such as the work of Leitch [15], who analyzed fracture in axially cracked pressure tubes by means of compact fracture toughness test specimens cut out from the tube wall. As a result of this, the number of publications in manufacturing is surprisingly low despite

the importance of fracture toughness [16] and its relationship to fracture loci in principal strain space [17]. This is important because fracture toughness and fracture forming limits are basically two different approaches of the same phenomenon.

Under these circumstances, this paper is focused on thin-walled tubes and has a two-fold objective: (i) to extend the previous methods and procedures developed by the authors [18] for the characterization of the SFFL and the transition between the FFL and the SFFL in principal strain space, and (ii) to propose a new methodology for the determination of the fracture toughness in crack opening by tension (mode I). The first objective made use of new double edge notched tension [19], staggered [20] and shear test specimens [21] with geometries adapted from sheet metal tests and cut-out from the supplied tubes in the longitudinal and transversal directions. The second objective was accomplished by determining the essential work of fracture and made use of double edge notched test specimens cut out and loaded by tension in the longitudinal and transversal tube directions.

2 Experimentation

2.1 Material Characterization

The experimental work was performed on commercial AA6063-T6 aluminum tubes with an outer radius $r_0 = 20$ mm and an average thickness $t_0 = 1.9$ mm. The mechanical properties and flow curve of the material were determined by means of tensile tests along the longitudinal and transversal tube directions. The longitudinal tensile test specimens were prepared in accordance to the ASTM E8/E8M-16 standard [22] and the transversal tensile test specimens were prepared in accordance to a sub-size geometry of the same standard in order to avoid bending effects [23]. Both tests were performed at room temperature in a universal testing machine Instron 5900R.

The longitudinal tensile tests utilized special fixing clamps at the extremities of the specimen to prevent deformation. The transversal tensile test specimens made use of two 'D-shaped blocks' to allow tension in the transverse direction. The specimens were lubricated with polytetrafluoroethylene (teflon®) sheets to reduce friction [13]. The mechanical properties obtained from the tensile tests performed in the longitudinal and transversal directions are summarized in Table 1.

Table 1 Summary of the mechanical properties and constants of Swift's material strain hardening model for the AA6063-T6 aluminum tubes in the longitudinal and transversal directions

Test geometry	Thickness (mm)	σ_Y (MPa)	σ_{UTS} (MPa)	A (%)	r_{avg}	K (MPa)	n	ε_0
TL - Longitudinal	1.90	164.4	204.1	44.10	0.58	300.0	0.125	0.002
TT - Transversal	1.90	163.5	238.2	58.60	1.19	408.5	0.216	0.008

In Table 1, the symbol σ_Y denotes the yield stress, σ_{UTS} is the ultimate tensile strength and A is the elongation at fracture. The anisotropy coefficients ($r = \varepsilon_{width}/\varepsilon_{thickness}$) were directly obtained from the principal strains provided by the digital image correlation system (DIC) for a point located at the center of the tensile specimens. The r_0 and r_{90} coefficients correspond to r_{avg} in the longitudinal (L) and transversal (T) directions, respectively.

The flow curves resulting from the longitudinal and transversal tensile tests were approximated by Swift's material strain hardening model with pre-strain $\tilde{\sigma} = K(\bar{\varepsilon} + \varepsilon_0)^n$. The constants are provided in Table 1.

The formability limits by necking (FLC) and fracture in opening mode I (FFL) were determined by means of tensile tests (TT), expansion with rigid punches (EP), inversion with rigid punches (IP) and bulging with elastomers (BE). Figure 1 shows the results in principal strain space and the light gray dashed lines defined for $\beta = d\varepsilon_2/d\varepsilon_1$ equal to $-1/2$ and 1 are included for reference purposes.

Figure 1a presents the analytical expression of the FFL and the limiting necking ε_1^{*n} and fracture ε_1^{*f} strains in plane strain deformation that resulted from the experiments. Details on the methods and procedures that were utilized to obtain the formability limits and the failure strains are available in previous publications by the authors [13, 14].

2.2 Tube Formability Tests

The formability limits of the tube material by fracture were determined by means of double notched tension (DNTT), staggered DNTT and shear tests. The specimens were cut out from the longitudinal (L) and transverse (T) directions of the tubes, and the tests were performed at room temperature with a cross-head speed of 5 mm/min (quasi-static operating conditions) in the same testing machine where the mechanical characterization had been performed.

Table 2 summarizes the experimental work plan and includes schematic drawings of the different test specimens with information on the geometries, dimensions and corresponding states of stress and strain.

3 Methodology

The strain measurements on the fracture surface of the specimens that were needed to characterize the formability limits and to determine fracture toughness of the tube material were obtained by using a digital image correlation (DIC) system from Dantec Dynamics—model Q-400 3D (Fig. 2).

The surfaces of the specimens were sprayed with a stochastic black speckle pattern on a previously painted uniform white background. The specimens were illuminated

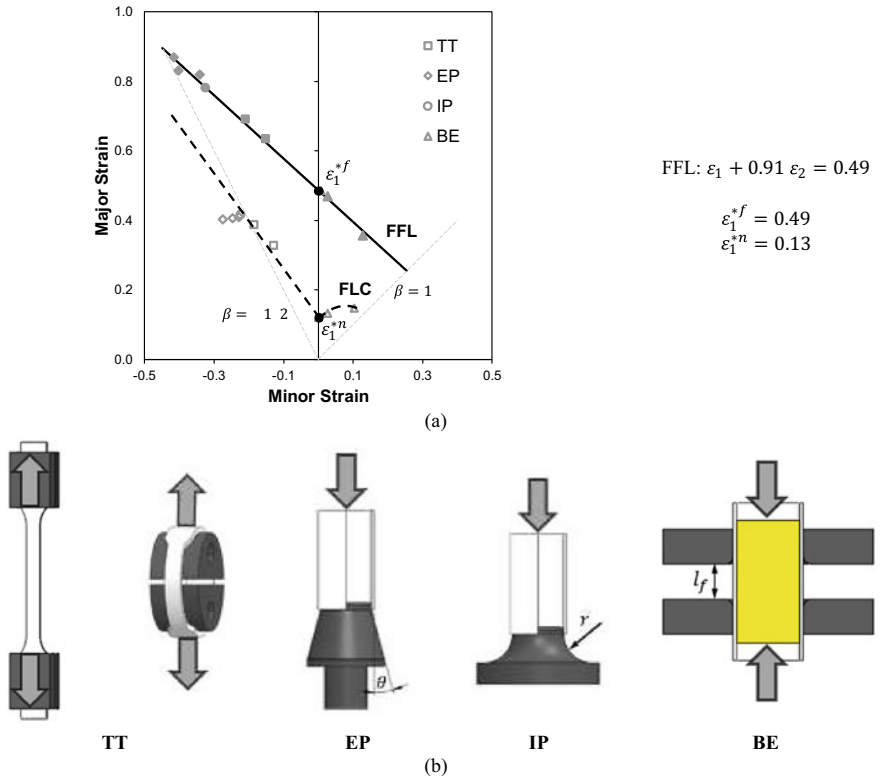


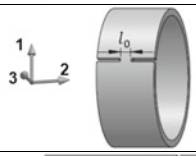
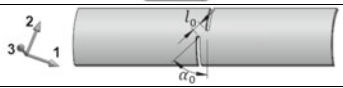
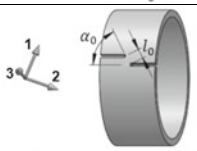
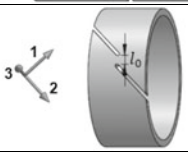
Fig. 1 **a** Formability limits by necking (FLC) and fracture (FFL) of AA6063-T6 aluminum tube in principal strain space obtained from **b** longitudinal and transversal tensile tests (TT), expansion with rigid punches (EP), inversion with rigid punches (IP) and bulging with elastomers (BE) [13, 14]. (Color figure online)

with a spotlight and the DIC system was equipped with 2 cameras with 6 megapixels of resolution and 50.2 mm of focal lenses with an aperture of f/8. The frequency of image acquirement was set to 20 frames per second, and the correlation algorithm was performed with the INSTRA 4D software. A facet size of 13 pixels with a spacing grid of 7 pixels was considered.

3.1 Fracture Strains

The surface strains obtained by DIC near the fracture cannot be considered the fracture strains due to inhomogeneous deformation at the neighborhood of the crack. In other words, the strains provided by DIC are very sensitive to the location of the selected measuring points. As a result of this, the experimental procedure for

Table 2 Experimental work plan with schematic representation of the experimental tube formability tests performed in the aluminum AA6063-T6 tube

Test			Dimensions (mm)	State of Stress	State of Strain
Double Notched Tension Test (DNTT)	L		$l_0 = 5\ to\ 14$	$\sigma_1 > 0$ $\sigma_2 < 0$ $\sigma_3 = 0$	$\varepsilon_1 > 0$ $\varepsilon_2 = 0$ $\varepsilon_3 < 0$
	T		$l_0 = 3\ to\ 7$		
Staggered DNTT	L		$\alpha_0 = 45°\ to\ 80°$ $l_0 = 3\ to\ 7$	$\sigma_1 > -\sigma_2$ $\sigma_3 = 0$	$\varepsilon_1 > -\varepsilon_2$ $\varepsilon_3 < 0$
	T		$\alpha_0 = 45°\ to\ 80°$ $l_0 = 2\ to\ 4$		
Shear Test	L		$l_0 = 2\ to\ 6$	$\sigma_1 = -\sigma_2$ $\sigma_3 = 0$	$\varepsilon_1 = -\varepsilon_2$ $\varepsilon_3 = 0$
	T		$l_0 = 1.5\ to\ 3.5$		

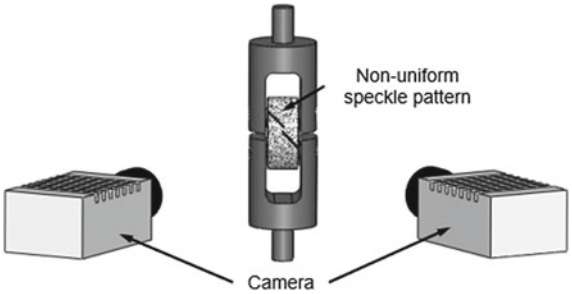


Fig. 2 Schematic representation of the experimental setup utilized by the DIC system for measuring the strains in a transversal shear test

constructing the formability limits by fracture cannot be solely based in DIC and requires additional information of the specimen's thickness at cracking in order to obtain the 'gauge length' strains [13]. For this purpose, individual measurements of thickness t_F were taken along the cracks with a stereomicroscope Mitutoyo TM-505B with a magnification of 30x.

The thickness strain at fracture ε_{tF} was calculated by

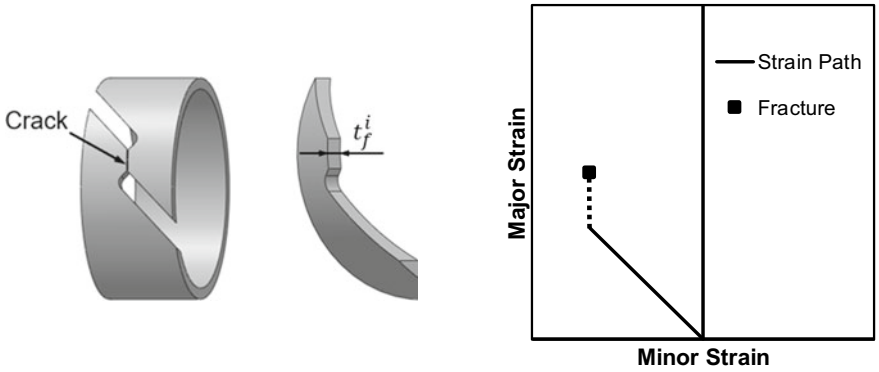


Fig. 3 Schematic representation of the methodology that was utilized to determine the formability limits by fracture. **a** Measuring the thickness along the crack. **b** Fracture strain pair with an indication of the strain loading path (solid line) up to the last measurement obtained by DIC

$$\varepsilon_{tF} = ln\left(\frac{t_F}{t_0}\right) \tag{1}$$

where t_0 was the initial thickness and $t_F = \frac{1}{n}\sum_{i=0}^{n} t_F^i$ was the average thickness at the center of the fracture surface of the specimens (Fig. 3a).

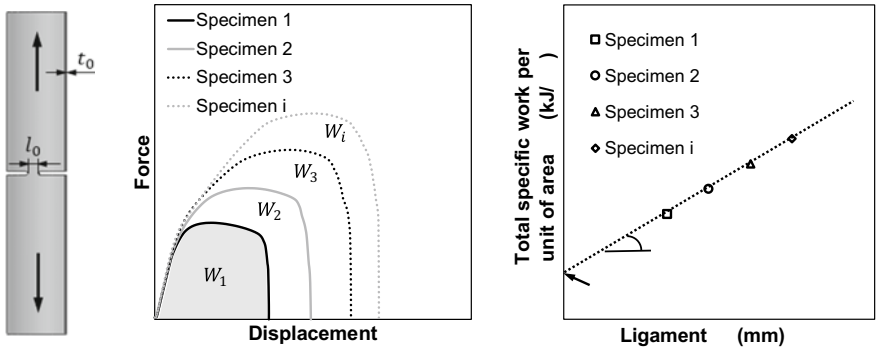
The minor strain ε_2 (meridional strain) was assumed to remain constant after the last measurement by DIC, and the major strain ε_1 (circumferential strain) and was obtained by incompressibility under plane strain deformation conditions,

$$\varepsilon_{1F} = -(\varepsilon_{2F} + \varepsilon_{tF}) \tag{2}$$

Figure 3b illustrates the overall procedure that was utilized to plot the fracture strain in principal strain space (refer to the solid square marker).

3.2 Fracture Toughness

The commonly utilized procedure for determining fracture toughness R requires calculating the total work W_T (Fig. 4b), the total specific work per unit of area w_T (Fig. 4c) and the specific essential work of fracture for DNTT specimens with several ligament sizes l_0 (Fig. 4a) [19]. The specific essential work of fracture (also known as fracture toughness, R) is obtained by extrapolating the total specific work per unit of area w_T to the limiting condition where the starting ligament length l_0 is zero, and the work related to plastic deformation is null (Fig. 4c).



(a) (b) (c)

Fig. 4 Schematic representation of the method utilized to determine fracture toughness R. **a** DNTT test specimen. **b** Typical force–displacement evolution for DNTT specimens with different ligaments sizes l_0. **c** Total specific work per unit of area w_T and extrapolation to obtain fracture toughness R

This paper extends, for the first time ever, the above-described methodology to DNTT specimens obtained from the thin-walled tubes in the longitudinal and transversal directions (Table 2).

4 Results and Discussion

4.1 Fracture Limits

Figure 5 presents the formability limits and the corresponding failure strains for the AA6063-T6 aluminum tubes. The formability limits by necking (FLC) and the fracture forming limit by tension (FFL) were retrieved from a previous work of the authors [13].

The strain paths for the DNTT, staggered DNTT and shear test specimens aligned in the longitudinal (L) and transversal (T) directions were obtained by DIC, and the fracture strain pairs were determined in accordance with the procedure that was described in Sect. 3.1.

As shown in the figure, the strain paths and fracture strain pairs of the longitudinal and transversal DNTT and shear test specimens revealed near-plane strain and pure shear deformation conditions, respectively.

The staggered DNTT specimens with different inclination angles α_0 allowed obtaining fracture strains at the transition zone between the FFL and the SFFL. Results also show that the minor fracture strain decreases with the increase of the inclination angle α_0, in good accordance with previous investigations in sheet formability [18].

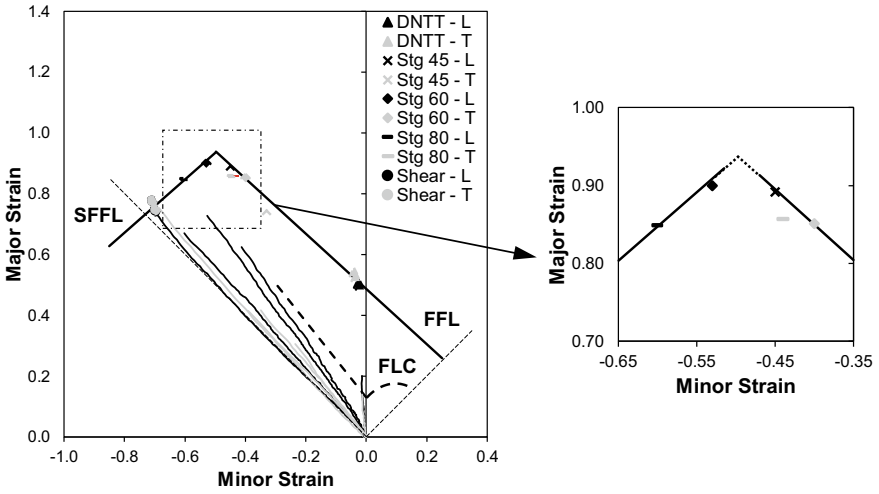


Fig. 5 Strain loading paths and formability limits of the AA6063-T6 aluminum tubes by necking (FLC) and fracture (FFL and SFFL) in principal strain space. The detail is a magnification of the transition region. (Color figure online)

Moreover, the longitudinal staggered DNTT specimen allowed obtaining fracture strains closer to pure shear than the transversal staggered DNTT specimen. This result is due to the strain hardening coefficient n obtained from tensile tests ($n = 0.125$ for the longitudinal direction and $n = 0.216$ for the transversal direction; refer to Table 1). In fact, a larger strain hardening coefficient gives rise to wider plastic deformation regions near the ligaments and, therefore, to smaller localization effects. In other words, a larger strain hardening coefficient gives rise to smaller absolute values of strain at the onset of fracture. A similar effect was recently observed in sheet formability tests [18].

The fractography analysis performed on the fracture surface of each test specimen allowed investigating the crack opening mode and correlating the experimental observations with the fracture forming limits shown in Fig. 5. The images were obtained in a scanning electron microscope (SEM) Hitachi S-2400 with a magnification of 1500X and are representative of the entire length of the fracture surface of the longitudinal and transversal DNTT, staggered DNTT and shear test specimens (Figs. 6 and 7).

As shown in both figures, the fracture surface evolves from a circular dimpled structure typical of a normal fracture caused by remote loading orthogonal to the fracture surface in case of the DNTT specimen, to an elongated parabolic dimpled structure typical of fracture by sliding caused by in-plane shear, in case of the shear test specimens. These results are consistent with the fracture strains of the DNTT and shear test specimens being located on the FFL and SFFL (Fig. 5) corresponding to crack opening modes I and II, respectively.

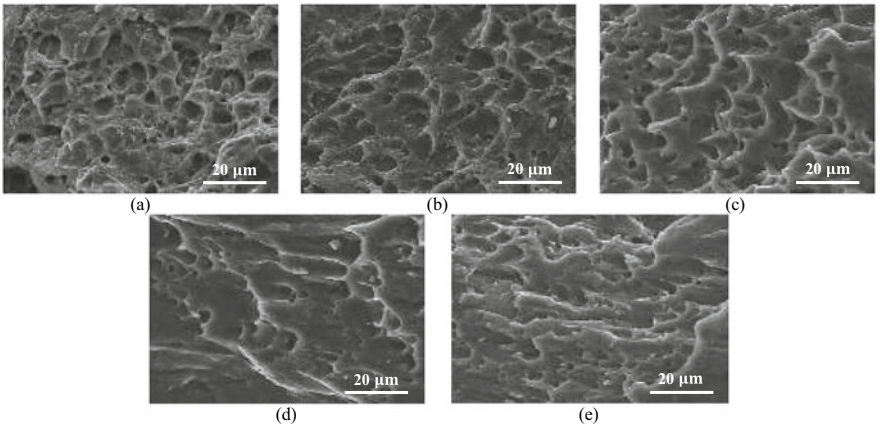


Fig. 6 SEM fractographies of the aluminum AA6063-T6 obtained for the longitudinal **a** DNTT, **b** staggered DNTT with $\theta = 45°$, (d) $\theta = 60°$, (e) $\theta = 80°$ and (f) shear test specimens

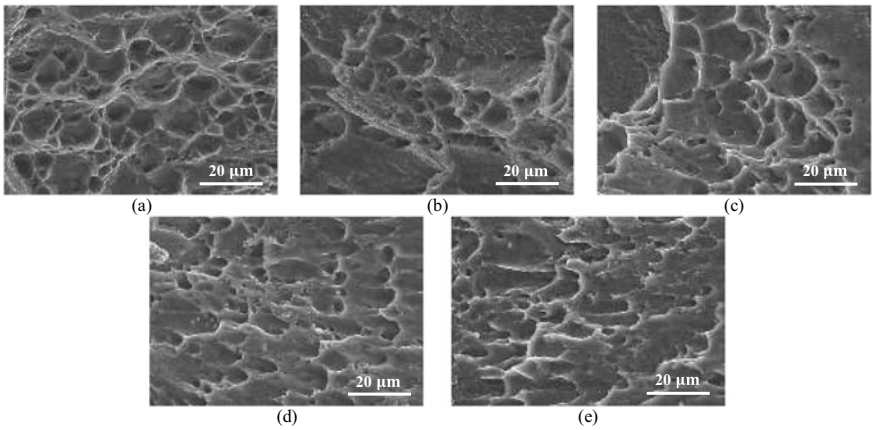


Fig. 7 SEM fractographies of the aluminum AA6063-T6 obtained for the transversal **a** DNTT, **b** staggered DNTT with $\theta = 45°$, (d) $\theta = 60°$, (e) $\theta = 80°$ and (f) shear test specimens

The SEM images included in Figs. 6 and 7 also confirm that staggered DNTT specimens with ligament angles α_0 varying from 45 to 80º have a fracture surface made of circular dimples that are progressively replaced by increasing elongated parabolic dimples. This result is consistent with the fracture strains of the staggered DNTT specimens being in the transition region between the FFL and SFFL (Fig. 5). In other words, the result is consistent with failure by means of a fracture mixed-mode consisting of crack opening by modes I and II.

Moreover, the fractography analysis of the longitudinal (Fig. 6) and transversal (Fig. 7) staggered DNTT specimens also confirms the influence of strain hardening in failure. This is because the fracture surfaces are closer to pure shear and mainly

consist of elongated parabolic dimples in case of the longitudinal DNTT specimens, which have the smallest strain hardening coefficient ($n = 0.125$).

Finally, it is worth mentioning that the experimental work plan allowed obtaining a wide range of strain paths and fracture strains, from plane strain ($\beta = 0$) to pure shear ($\beta = -1$) loading conditions. This allowed an independent confirmation of the FFL that had been previously obtained by the authors [13, 14] and the determination of the SFFL of thin-walled tubes for the first time ever,

$$\varepsilon_{1F} = 0.88\varepsilon_{2F} + 1.38 \tag{3}$$

The FFL and SFFL are approximated by straight lines with a negative slope -0.91 (Fig. 1) and a positive slope + 0.88, respectively. These slopes are different from the theoretical estimates of −1 and + 1 because the experimental conditions deviate from the simplifying assumptions proposed in the theoretical models proposed by Martins et al. [11]. However, the perpendicularity between the FFL and the SFFL maintains, despite these deviations.

4.2 Fracture Toughness

The determination of fracture toughness R followed the methodology that was previously described in Sect. 3.2. Different longitudinal and transversal DNTT specimens with varying ligaments were utilized and the resulting force versus displacement evolutions are shown in Fig. 8a.

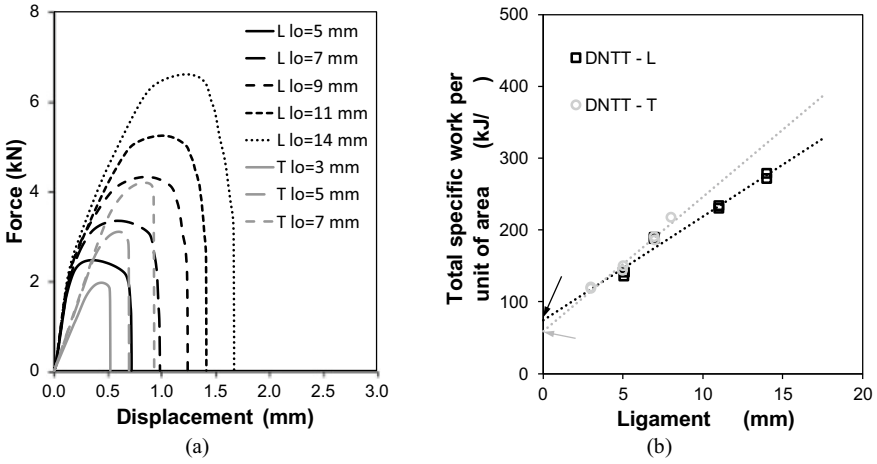


Fig. 8 Fracture toughness R in crack opening mode I for aluminum AA6063-T6 tubes obtained from DNTT specimens: **a** experimental force versus displacement evolution and **b** determination of fracture toughness in longitudinal (L) and transversal (T) directions

The total specific work of fracture per unit of area w_T obtained for several ligaments l_0 in the longitudinal and transversal directions are presented in Fig. 8b. The evolutions are linear, and the fracture toughness in the longitudinal and transversal directions are, respectively, equal to $R_L = 74.5kJ/m^2$ and $R_T = 60.0kJ/m^2$. The difference in the longitudinal and transversal fracture toughness values is related to the difference in strain hardening coefficients, which are higher for the transversal DNTT specimens. This also explains the larger slope γ of the linear fitting of the total specific work per unit of area of these specimens in Fig. 8b.

5 Conclusions

Methods and procedures that were recently developed for the characterization of the fracture limits and for the determination of fracture toughness in sheet metal forming can be easily extended to tube forming. In particular, the combination of digital image correlation (DIC) and thickness measurements at the cracked regions is suitable to determine the strain loading paths and the strains at fracture in double notched tensile test (DNTT) specimens, staggered DNTT specimens and shear test specimens.

Under these circumstances, the main conclusions associated with this investigation on the formability limits of thin-walled tubes are the following:

- Formability by fracture in thin-walled tube forming is limited by the fracture forming limit (FFL) line, the shear fracture forming (SFFL) line and the transition region between these two lines in principal strain space.
- Fractography analysis confirms that the fracture surfaces associated with the FFL consist of circular dimpled structures typical of normal fracture, whereas those associated with the SFFL consist of elongated parabolic dimpled structures typical of fracture by sliding caused by in-plane shear.
- Mixed-modes consisting of crack opening by modes I and II of fracture mechanics entail a combination of circular and elongated parabolic dimpled structures.
- Strain hardening influences the crack opening mode because of its influence on the relative size of the plastic deformation region near the fracture surface.
- Fracture toughness in thin-walled tubes can be determined by a methodology based on the total specific work of fracture per unit area and similar to that commonly utilized in sheet metal forming.
- Anisotropy influences the results and must be taken into account in future investigations on the formability limits of thin-walled tubes.

Acknowledgments The authors would like to acknowledge the support provided by Fundação para a Ciência e a Tecnologia of Portugal and IDMEC under PDTC/EMS-TEC/0626/2014 and UIDB/50022/2020. The work of João Miguel Gago on the material characterization is greatly acknowledged.

References

1. Jeswiet J, Geiger M, Engel U, Kleiner M, Schikorra M, Duflou J, Neugebauer R, Bariani P, Bruschi S (2008) Metal forming progress since 2000. CIRP Ann Manuf Technol 1:2–17
2. Yoshida K, Kuwabara T, Narihara K, Takahashi S (2005) Experimental verification of the path-independence of forming limit stresses. Int J Form Process 8:283–298
3. Hu G, Yang L, Liu J (2013) Determination of forming limit diagram for tube hydroforming based on the strain rate change criterion. AIP Conf Proc 1567:390–393
4. Chen X, Yu Z, Hou B, Li S, Lin Z (2011) A theoretical and experimental study on forming limit diagram for a seamed tube hydroforming. J Mater Process Technol 211:2012–2021
5. Li S, Chen X, Kong Q, Yu Z, Lin Z (2012) Study on formability of tube hydroforming through elliptical die inserts. J Mater Process Technol 212:1916–1924
6. Keeler SP (1968) Circular grid system—A valuable aid for evaluation sheet metal formability. SAE Technical Paper 680092.
7. Goodwin G (1968) Application of strain analysis to sheet metal forming problems in the press shop. SAE Technical Paper 680093.
8. Embury JD, Duncan JL (1981) Formability maps. Annu Rev Mater Sci 11:505–521
9. Silva MB, Skjoedt M, Atkins AG, Bay N, Martins PAF (2008) Single point incremental forming and formability-failure diagrams. J Strain Anal Eng Design 43:15–36
10. Isik K, Silva MB, Tekkaya AE, Martins PAF (2014) Formability limits by fracture in sheet metal forming. J Mater Process Technol 214:1557–1565
11. Martins PAF, Bay N, Tekkaya AE, Atkins AG (2014) Characterization of fracture loci in metal forming. Int J Mech Sci 83:112–123
12. Centeno G, Silva MB, Alves LM, Vallellano C, Martins PAF (2016) Towards the characterization of fracture in thin-walled tube forming. Int J Mech Sci 119:12–22
13. Magrinho JP, Silva MB, Centeno G, Moedas F, Vallellano C, Martins PAF (2019) On the determination of forming limits in thin-walled tubes. Int J Mech Sci 155:381–391
14. Magrinho JP, Centeno G, Silva MB, Vallellano C, Martins PAF (2019) On the formability limits of thin-walled tube inversion using different die fillet radii. Thin-Walled Struct 144
15. Leitch BW (1999) Fracture analysis of an internally pressurized tube containing an Axial, through-wall crack. In: Panontin TL, Sheppard SD (eds) Fatigue and fracture mechanics: twenty ninth Volume, ASTM STP 1332. American Society for Testing and Materials, West Conshohocken, PA
16. Atkins T (2018) The importance of toughness in manufacturing. J Mater Process Technol 261:280–294
17. Silva MB, Isik K, Tekkaya AE, Atkins AG, Martins PAF (2016) Fracture toughness and failure limits in sheet metal forming. J Mater Process Technol 234:249–258
18. Magrinho JP, Silva MB, Reis L, Martins PAF (2019) Formability limits, fractography and fracture toughness in sheet metal forming. Materials 12(9):1493
19. Cotterell B, Reddel JK (1977) The essential work of plane stress ductile fracture. Int J Fract 13(3):267–277
20. Cotterell B, Reddel JK, Mai YW (1982) Mixed mode plane stress ductile fracture. Int J Fract 20(4):243–250
21. ASTM Standard B831–11 (2005) Standard test method for shear testing of thin aluminium alloy products. West Conshohocken, USA:ASTM International
22. ASTM Standard E8/E8M (2016) Standard Test Methods for Tension Testing of Metallic Materials. West Conshohocken, USA:ASTM International
23. Dick C, Korkolis YP (2014) Mechanics and full-field deformation study of the Ring Hoop Tension Test. Int J Solids Struct 51(18):3042–3057

Deformation Mechanisms in Tool–Workpiece Asperity Contact in Metal Forming



Chris Valentin Nielsen, Xiaodan Zhang, Marcel Moghadam, Niels Hansen, and Niels Bay

Abstract The contribution to friction stemming from dissipation of plastic energy is studied by numerical simulations and experiments. The geometrical setup consists of a single model asperity, which is first flattened against a tool with grooves on a smaller length scale. Relative, tangential sliding between the model asperity and the tool is induced subsequently until a steady state is reached. The flank angle of the grooves on the tool is varied. Comparison between the simulations and the experiments leads to validation of the simulations at low tool flank angles, while the current numerical implementation cannot handle the complicated flow around the tool grooves with a large flank angle. At low flank angles, the simulated tangential tool force is in agreement with experiments when keeping one determined friction factor. This proves that the change in tangential force, corresponding to a change in apparent friction factor, is only due to the dissipated energy from the plastic waves. The validated numerical model can be used to determine a wider range of apparent friction factors for strain hardening materials.

Keywords Friction · Asperity contact · Plastic waves

1 Introduction

Bowden and Tabor [3] described the influence of asperity contact on friction and started the intense analysis on asperity flattening among several research groups over the following decades. One path goes through Shaw et al. [12], who suggested a smooth transition from Amontons–Coulomb's friction model to the constant friction model due to asperity flattening being individual at low normal pressures while

C. V. Nielsen (✉) · X. Zhang · M. Moghadam · N. Bay
Manufacturing Engineering, Department of Mechanical Engineering, Technical University of Denmark, 2800 Kgs, Lyngby, Denmark
e-mail: cvni@mek.dtu.dk

N. Hansen
Materials Science and Characterization, Department of Wind Energy, Technical University of Denmark, 4000 Roskilde, Denmark

© The Minerals, Metals & Materials Society 2021

G. Daehn et al. (eds.), *Forming the Future*, The Minerals, Metals & Materials Series,
https://doi.org/10.1007/978-3-030-75381-8_10

being interacting at higher normal pressures, and Wanheim and Bay [17] who quantified the development of real contact area by slip-line analysis under frictional sliding. Sutcliffe [14] also analyzed asperity flattening by slip-line analysis taking into account subsurface deformation but not the asperity interaction at high normal pressures. Lately, Wang et al. [15] and Nielsen et al. [10, 11] analyzed asperity flattening while taking both strain hardening and subsurface deformation into account by a combined experimental and numerical study.

Common for the majority of research on asperity flattening is the focus on model asperities that are scaled up for practical reasons when evaluating real contact area. The real contact area resulting from these analyses is, however, overestimating the true real contact area due to the existence of multiple orders of asperities. In fact, the typical flat plateaus of the first-order asperities contain second-order asperities, and hence, the true real contact area is smaller than that estimated by first-order asperities. Such an approach can continue on the flat plateaus of the second-order asperities, and so forth. Steffensen and Wanheim [13] did such an analysis and concluded that the reduction of the true real contact area due to second-order asperities on the first-order plateaus is rather insensitive to normal pressure and friction on the plateaus. This is justifying the analyses that are being done on model asperities, which represent the first-order asperities of a real surface. It is justified by the higher order effects on the real contact area being rather constant, which leaves the possibility of having this effect hidden in the friction factor that is assumed on the flat plateaus of the first-order asperities.

A number of mechanisms have been proposed as contributions to the friction that appears in the real contact. Bay and Wanheim [1] presented an overview of the origins of friction. Bowden and Tabor [3] identified the shearing of layers due to adhesion and micro welds as well as dragging or plowing of a harder material through a softer material. Wanheim and Abildgaard [16] later added the mechanism of plastic waves in the softer material induced by the roughness of the harder tool material upon relative sliding. They showed the existence of the plastic wave mechanism by an experiment and gave by slip-line analysis the apparent friction factor as function of the real friction factor along the tool grooves and the groove angle on the harder tool material.

Plastic waves have also been analyzed by other groups. Challen and Oxley [4] modeled one hard asperity in relative sliding against a softer material. Depending on the angle of the hard asperity, this gave rise to a steady-state standing wave, wear, or cutting. Challen et al. [5] presented experiments verifying the modeling, and Challen and Oxley [6] presented slip-line analyses with more than one hard asperity and in the full range from zero to full filling of the grooves in the hard material.

Luo et al. [8] applied upper bound analysis to the moving wave mechanism by assuming contact with the tool only on one side. They found that for low flank angles, the wave may disappear after some sliding and confirmed that by experiments. Bin and Luo [2] applied finite element analysis to the analysis of one hard asperity sliding against a softer workpiece material and found good agreement with their simulation and experiments previously published by Challen and Oxley [4].

In the present paper, the focus is on the deformation mechanisms due to plastic waves on top of workpiece asperities that are flattened by a hard tool and subjected to relative sliding against it. First-order asperity flattening is considered by imposing the plastic waves on top of a model asperity. The deformation mechanisms are analyzed by experiments, numerical simulation, and metallurgical analysis.

2 Experimental Setup

The tool–workpiece contact in metal forming is considered by taking into account first-order asperities on the workpiece surface and a tool surface, which in comparison to the workpiece, is smooth. Such an interface is illustrated in Fig. 1a with the identification of a single asperity that is taken out for analysis. The single asperity is shown in a schematic illustration of an experiment in Fig. 1b. At this scale, the tool surface is assumed to have asperities as well, but with a wavelength much smaller than that of the workpiece surface. The experiment illustrated in Fig. 1b has a single model asperity (A) with flank angle γ in contact with a tool (T) with many, smaller asperities with flank angle β. A normal pressure between the asperity and the tool can be induced by the punch (P) resulting in asperity flattening against the tool under plane strain deformation (zero strain perpendicular to the figure due to tool blocks that are not shown in the illustration).

The tool (T) can move tangentially to emulate relative sliding in the tool–workpiece interface. The tangential force will be the sum of the apparent friction against the model asperity and the friction against the base (B), which is minimized by a

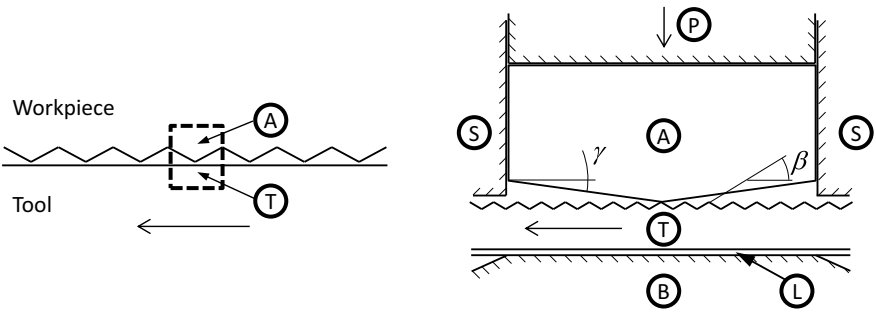


Fig. 1 Schematic illustration of the asperity contact. **a** Workpiece and tool interface represented by first-order workpiece asperities in contact with a smooth tool with relative movement given by the arrow. The dashed rectangle identifies a single asperity (A) and the contacting tool (T). **b** Experimental setup with a single model asperity (A) supported against rotation by (S) and pressed towards a tool (T) by the punch (P). Notice that the tool in this magnification also has asperities. The tool (T) is separated from the base (B) by a layer of Teflon (L) to minimize friction when moved tangentially to the asperity

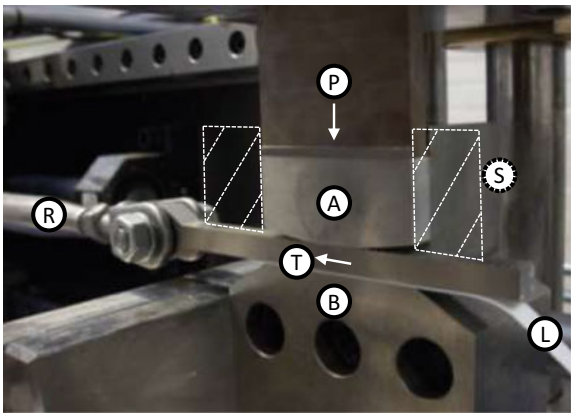


Fig. 2 Experimental setup with labels corresponding to Fig. 1 with the addition of (R) identifying the rigging screw connected to a movable horizontal axis that is used to pull the tool (T). The support is given by four blocks surrounding the model asperity. The two blocks indicated by white dashed lines were removed for taking the photograph. Of the two other blocks, which are used to ensure plane strain deformation, one was also removed for taking the photograph. (Color figure online)

separating layer of Teflon (L). The apparent friction against the model asperity is due to true friction, where workpiece material is in relative sliding along the tool asperities, and due to plastic power dissipation in the plastic waves that the tool induces in the workpiece model asperity.

Figure 2 shows a photograph of the real experiment after having removed a few supporting blocks to allow the photograph to show the model asperity and tool contact. The photograph is taken after an experiment and therefore Fig. 2 shows a flattened model asperity. The normal load applied by the punch (P) is measured by a piezoelectric load cell above the punch. The tangential load on the tool (T) is measured through a pre-compressed piezoelectric load cell connected to the rigging screw (R). Both load cells are outside the photograph.

The model asperity (A) is machined with a flank angle $\gamma = 10^\circ$ and a width $w = 60\,\text{mm}$ representing the model asperity wavelength. The thickness of the specimen is $t = 10\,\text{mm}$ (in the direction of plane strain). The model asperities are made from aluminum 1050, while the tool (T) is made of cold work tool steel, hardened and tempered to 58–60 HRC. Three tools were made with flank angles $\beta = 5^\circ$, $\beta = 10^\circ$, and $\beta = 15^\circ$, respectively. The wavelength of the tool asperities is $l = 1.5\,\text{mm}$. The tool asperities were polished to a roughness $R_a \leq 0.25\,\mu\text{m}$ and the tool asperity tip radii were measured to around $R = 1.4\,\text{mm}$. Zinc stearate was used for lubrication by applying a thin layer to both the workpiece and tool surfaces. The aluminum workpieces were pickled in a NaOH bath prior to rubbing zinc stearate to the surface.

Aluminum 1050 used for the model asperities is characterized by the flow stress curve shown in Fig. 3. The flow stress has been tested at large strains due to heavy local deformation in the experiments. The flow stress curve is based on simple upsetting until an equivalent strain of 0.5. In order to achieve experimental data at large strains,

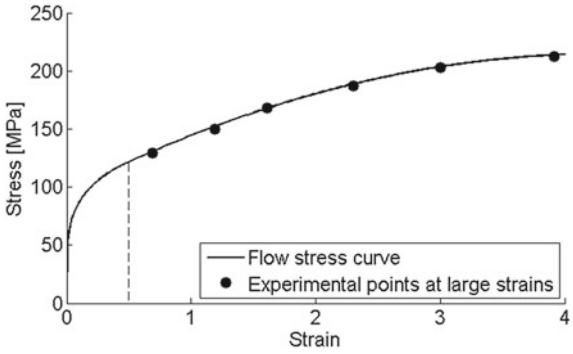


Fig. 3 Flow stress curve based on simple upsetting below an equivalent strain of 0.5 and scaled tensile tests of rolled samples above 0.5

the original 1050 plate was rolled with different thickness reductions and tensile samples were cut from the rolled plates. The yield stress found by tensile testing gave rise to a flow stress at the equivalent strain dictated by the amount of rolling. The data points stemming from rolling and subsequent tensile testing have been multiplied by an estimated factor of 1.18 [7] taking into account the strength anisotropy of the lamellar structure, especially formed at the medium and large strains in the present study. The strength in the normal direction is typically higher than that of the lamellar direction when a lamellar microstructure forms with surface deformation by different processing methods, e.g. due to friction or particle bombardment [18]. By doing this, comparison to compression stress from aluminum 1050 cylinders in our previous research [19] revealed good agreement with the compression stress from the aluminum 1050 cylinders at strains up to 2. The flow stress between equivalent strains of 0.5 and 3.9, which was the maximum strain obtained by rolling, is a best fit by a second-order polynomial through the end point of the upsetting test and the experimental data points at large strains after scaling. Above an equivalent strain of 3.9, the flow stress is assumed constant. The flow stress curve used for numerical modeling can be summarized as

$$\sigma[MPa] = \begin{cases} 141\varepsilon^{0.21} & \text{for} \quad \varepsilon \leq 0.5 \\ 96.1 + 54.7\varepsilon - 6.31\varepsilon^2 & \text{for } 0.5 < \varepsilon \leq 3.9 \\ 214 & \text{for} \quad \varepsilon > 3.9 \end{cases} \tag{1}$$

3 Numerical Model

The deformation mechanisms on the flattened model asperity are simulated by the numerical model shown in Fig. 4. The initial mesh for one model asperity with flank angle $\gamma = 10°$ is shown in Fig. 4a with boundary conditions on the sides that only allow vertical movement and with a nominal normal pressure q stemming from the applied load by the punch. After plain strain asperity flattening against the tool, which

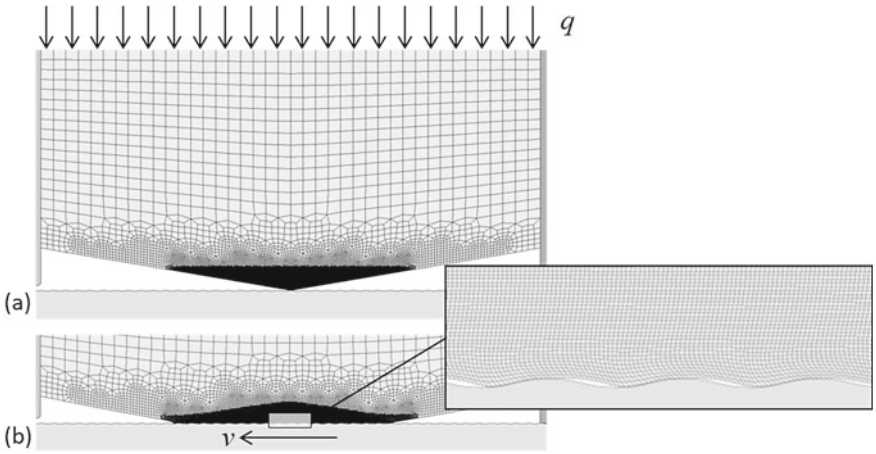


Fig. 4 Finite element mesh consisting of 26,084 quadrilateral elements for simulation of model asperity shown **a** in initial condition and **b** after flattening due to normal pressure q and after sliding with relative velocity v against the hard, rough tool

is shown for the case having tool asperities with flank angle $\beta = 15°$ and wavelength $l = 1.5\,\text{mm}$, relative sliding by a constant velocity $v = 1\,\text{mm/s}$ is imposed. The mesh refinement on the asperity tip allows an initial element size being 3% of the tool asperity wavelength.

The numerical calculations are based on discretization by quadrilateral finite elements and an underlying irreducible flow formulation by minimization of the following functional

$$\Pi = \int_V \bar{\sigma}\dot{\bar{\varepsilon}} dV + K \int_V \dot{\varepsilon}_v^2 dV + \int_{S_f} \left(\int_0^{|u_r|} \tau du_r \right) dS \tag{2}$$

where the energy rate due to plastic deformation is integrated over volume V in the first term consisting of the effective stress $\bar{\sigma}$ and the effective strain rate $\dot{\bar{\varepsilon}}$. Incompressibility is enforced by penalizing volumetric strain rate $\dot{\varepsilon}_v$ by the penalty factor K in the second term. The last term includes the frictional stress τ between the workpiece and the tool by integration over relative sliding velocity u_r on the shared surface S_f. The applied finite element computer program is iform, which is an in-house numerical code shared between the University of Lisbon and the Technical University of Denmark. Additional information is given by Nielsen et al. [9].

4 Results and Discussion

The resulting tangential load from the experiments with flank angle $\beta = 5°$ is shown in Fig. 5 as function of the sliding length. Corresponding simulation results are included in the figure for a variation of the friction factor m in the sliding along the tool grooves. A friction factor $m = 0.1$ in the simulations is found appropriate when comparing to the experiments. Increasing the tool flank angle β, while keeping the friction factor constant will increase the necessary tangential load due to additional dissipation of plastic energy by plastic waves. This is shown by the results in Fig. 6 by simulation results and experiments. The results for $\beta = 5°$ are the same as in

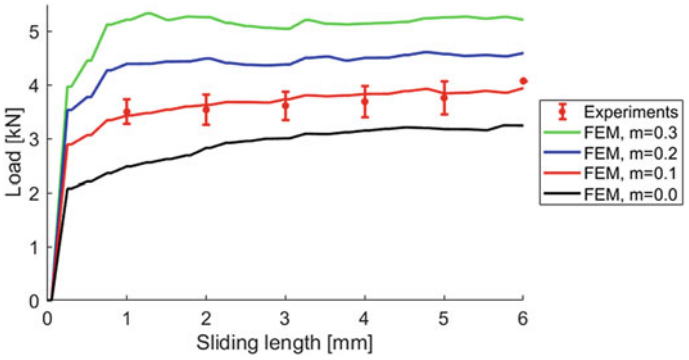


Fig. 5 Tangential load as function of sliding length in case of tool asperity flank angle $\beta = 5°$ for experiments and numerical simulation with variation of the friction factor m. The error bars correspond to one standard deviation based on three repetitions, except for the last point which was only obtained in one of the experiments. (Color figure online)

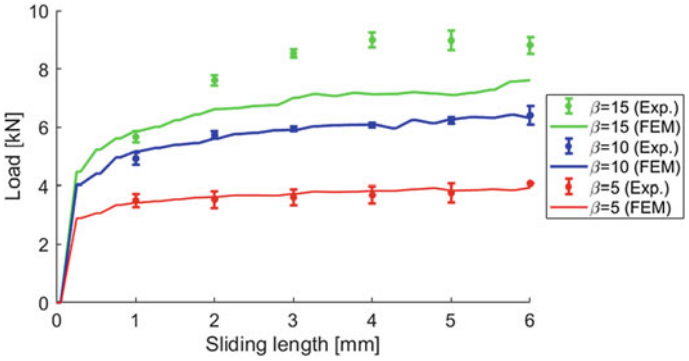


Fig. 6 Tangential load as function of sliding length for different flank angles including experimental results and numerical simulation with friction factor $m = 0.1$. The error bars correspond to one standard deviation based on three repetitions, except for the last point with $\beta = 5°$ which was only obtained in one of the experiments. (Color figure online)

Fig. 5. The simulations with $m = 0.1$ are seen also to match the experiments well for $\beta = 10°$, indicating that the only contribution to the increase of the tangential force is the plastic waves. When increasing the tool flank angle further to $\beta = 15°$ the simulation does not match the experiments any longer. This difference is explained by a difference in the local flow along the grooves. The finite element discretization still results in a smooth and continuous flow, while the experiments reveal workpiece material sheared off and deformed as a third body between the remaining workpiece and the tool. This gives rise to a higher tangential force than the ideal force predicted by simulation of an ideal flow.

All cases show that the tangential force is building up to a rather constant level corresponding to steady-state sliding. From Fig. 6 it is noticed that steady state is obtained later for larger tool flank angle due to larger extend of the deformation field. During the initial transient build-up of the tangential force, the first-order real contact area increases due to the change in stress state. The induced shear on the flattened workpiece asperity reduces the necessary yield pressure, which is compensated by further deformation of the overall asperity as the normal load is kept constant. For the different tool flank angles, Fig. 7a shows the first-order real contact area ratio after deformation due to the applied normal load (dashed curves) and after additional sliding until steady state (solid curves). Both experimental results (blue curves) and simulated results (black curves) are included in the figure for comparison. A slight overestimation of the contact area is noticed for all the simulations. In order to focus on the effect of the additional sliding, Fig. 7b shows the relative change in first-order contact area for the three tool flank angles. Here, the simulations match the experiment for the tool flank angles $\beta = 5°$ and $\beta = 10°$, while the simulation underestimates the relative change for $\beta = 15°$ in agreement with the differences between simulation and experiment discussed in relation to Fig. 6.

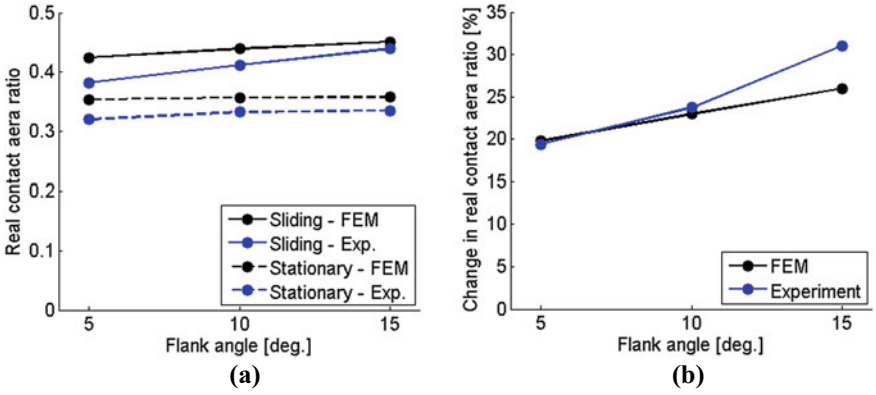


Fig. 7 First-order real contact area between model asperity and tools with three different flank angles by experiments and numerical simulations. The contact area corresponding to stationary contact and to the developed contact area during sliding are shown in (**a**), while the change from stationary to sliding contact area is shown in (**b**). (Color figure online)

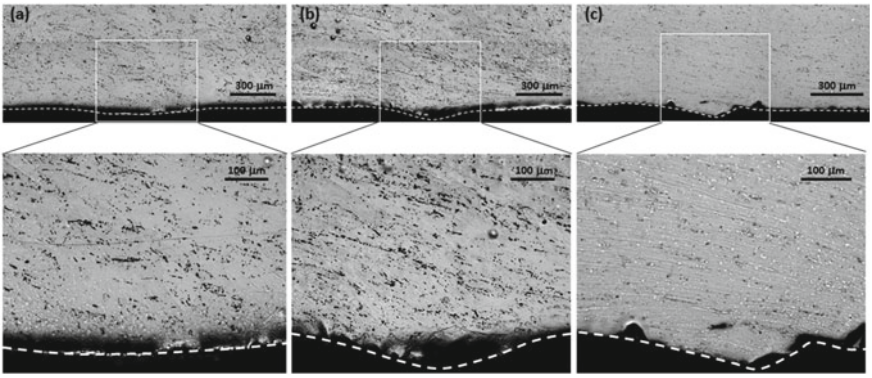


Fig. 8 Cross-sectional LOM pictures of the workpiece material after reaching steady state sliding for tool flank angles **a** $\beta = 5°$, **b** $\beta = 10°$ and **c** $\beta = 15°$. Enlarged pictures are shown from the workpiece tips of the pictures above. Tool movement is in this figure from left to right

Cross-sectional photographs of the deformed workpiece surfaces are shown in Fig. 8 based on light optical microscopy (LOM). For each tool flank angle, a corresponding cross section of the workpiece is shown from the center of the flattened plateau of the first-order asperity. The photographs span just above one wavelength of the tool asperity, while the enlarged photos span around 40% of a tool asperity wavelength near a local tip of the workpiece (valley of the tool). The edges are unfortunately unclear after the grinding, polishing, and etching. White dashed lines have therefore been added manually along the edges. The identified edges for the cases with tool flank angles $\beta = 5°$ and $\beta = 10°$ are smooth waves, while the edge identified for the tool flank angle $\beta = 15°$ is a non-smooth wave due to a flow with much more shear and also induced cracks in the surface. This difference supports the above discussion, where simulations represent the results for the low tool flank angles, $\beta = 5°$ and $\beta = 10°$, while the simulations cannot be validated for the larger tool angle, $\beta = 15°$. It would require both further mesh refinement and handling of microcracks with resulting new contacts in the simulations to deal with the larger flank angle.

5 Conclusions

Plastic waves, as a suggested deformation mechanism in the contact between workpiece asperities and tool surfaces by Wanheim and Abildgaard [16], have been studied by numerical simulations and experiments by an enlarged asperity which is flattened against a tool with smaller grooves representing tool surfaces asperities. The simulations have been successfully validated for low tool flank angles, $\beta = 5°$ and $\beta = 10°$, while the metal flow around the tool grooves for the larger tool angle, $\beta = 15°$, was too complicated for the present numerical implementation as it involved heavy shear

and microcracks with new surfaces getting under compression. This paper leaves the numerical model ready for studying a wider range of friction factors along the tool grooves, a wider range of workpiece materials in terms of strain hardening behavior and a higher resolution of tool flank angles up to at least 10°. Wanheim and Abildgaard [16] already mapped the apparent friction factor as a function of the local friction factor and the tool flank angle for ideal plastic materials. Further work with the presented numerical model allows extending that mapping to include strain hardening materials. Variations of workpiece flank angle is another future extension to the present work. Experiments at smaller scales and numerical modeling based on crystal plasticity with effects of grain sizes and orientation to account for real surface scales are also future work.

Acknowledgments The authors would like to thank Mr. A. Ferfecki for experimental work and The Danish Council for Independent Research (Grant number: DFF-1335-00230) for financial support. Xiaodan Zhang acknowledges support from the European Research Council (ERC) under the European Union Horizon 2020 research and innovation program (grant agreement No 788567-M4D) and support by a research grant (00028216) from VILLUM FONDEN.

References

1. Bay N, Wanheim T (1990) Contact phenomena under bulk plastic deformation conditions. Adv Technol Plasticity 4:1677–1691
2. Bin F, Luo Z-J (1988) Finite element simulation of the friction mechanism in plastic-working technology. Wear 121:41–51
3. Bowden FP, Tabor D (1942) Mechanism of metallic friction. Nature 50(3798):197–199
4. Challen JM, Oxley PLB (1979) An explanation of the different regimes of friction and wear using asperity deformation models. Wear 53:229–243
5. Challen JM, McLean LJ, Oxley PLB (1984) Plastic deformation of a metal surface in sliding contact with a hard wedge: its relation to friction and wear. Proc Royal Soc London A 394:161–181
6. Challen JM, Oxley PLB (1984) A slip line field analysis of the transition from local asperity contact to full contact in metallic sliding friction. Wear 100:171–193
7. Jiang Z, Xu X, Zhu C, Mao Q, Zhang T, Wang H, Jia W (2019) Anisotropy of microstructure and properties of high strength hot extruded processed aluminum alloy. Mater Res Express 6:
8. Luo ZJ, Tang CR, Avitzur B, Van Tyne CJ (1984) A model for simulation of friction phenomenon between dies and workpiece. Appl Math Mech 5(3):1297–1307
9. Nielsen CV, Zhang W, Alves LM, Bay N, Martins PAF (2013) Modelling of thermo-electro-mechanical manufacturing processes with applications in metal forming and resistance welding. Springer, London, UK
10. Nielsen CV, Martins PAF, Bay N (2016a) General friction model extended by the effect of strain hardening. Paper presented at the 7th International Conference on Tribology in Manufacturing Processes, Phuket, Thailand, 35–44
11. Nielsen CV, Martins PAF, Bay N (2016b) Modelling of real area of contact between tool and workpiece in metal forming processes including the influence of subsurface deformation. CIRP Ann Manuf Technol 65:261–264
12. Shaw MC, Ber A, Mamin PA (1960) Friction characteristics of sliding surfaces undergoing subsurface plastic flow. J Basic Eng, 342–346
13. Steffensen H, Wanheim T (1977) Asperities on asperities. Wear 43:89–98

14. Sutcliffe MPF (1988) Surface asperity deformation in metal forming processes. Int J Mech Sci 30(11):847–868
15. Wang ZG, Yoshikawa Y, Suzuki T, Osakada K (2014) Determination of friction law in dry metal forming with DLC coated tool. CIRP Ann Manuf Technol 63:277–280
16. Wanheim T, Abildgaard T (1980) A mechanism for metallic friction. Paper presented at the 4th International Conference on Production Engineering, Tokyo, Japan, 122–127
17. Wanheim T, Bay N (1978) A model for friction in metal forming processes. Ann CIRP 27:189–194
18. Zhang X, Hansen N, Gao Y, Huang X (2012) Hall-Petch and dislocation strengthening in graded nanostructured steel. Acta Mater 60:5933–5943
19. Zhang X, Nielsen CV, Hansen N, Silva CMA, Martins PAF (2019) Local stress and strain in heterogeneously deformed aluminum: a comparison analysis by microhardness, electron microscopy and finite element modelling. Int J Plast 115:93–110

Welding of Aluminium in Chip Extrusion



André Schulze, Oliver Hering, and A. Erman Tekkaya

Abstract The reduction of energy consumption and CO_2 emissions in aluminium profile production can be achieved by solid-state recycling. By direct hot extrusion, aluminium chips can be directly processed into semi-finished or near-net-shape products requiring relatively low energy and having a high material yield. Since the mechanical properties of the extruded profiles highly depend on the welding of the individual chips, the main focus is to achieve a sufficient bonding between the chips. For this, the oxide layer covering the aluminium surface has to be broken. In order to predict the welding of the individual chips and estimate the process success a weld prediction model is developed. The influence of process parameters such as extrusion ratio, temperature, and speed is analysed. The weld model is applied to further profiles and validated by experimental tryouts.

Keywords Solid-state bonding · Chip extrusion · Aluminium

1 Introduction

Currently, most aluminium scrap, including machining swarf, i.e. small chips, is remelted in furnaces and recycled into ingots or die-casting products. However, the conventional recycling method is associated with two main disadvantages. The remelting process requires significantly large amounts of energy, which is unfavourable in terms of energy conservation. In addition, the metal yield rate is very low. These limitations drive the development of alternative technologies for the recycling of aluminium scrap [1]. Recently, solid-state recycling, which involves direct recycling of metal scrap into bulk material by using severe plastic deformation (SPD), has emerged as a potential alternative to the conventional remelting and recycling techniques [2]. Different processes using severe plastic deformation to recycle aluminium scrap of different alloys, mainly AA6XXX alloys, were developed. Examples are cyclic extrusion compression [3], high-pressure torsion [4], compressive

A. Schulze (✉) · O. Hering · A. Erman Tekkaya
Institute of Forming Technology and Lightweight Components, TU Dortmund University, Dortmund, Germany
e-mail: andre.schulze@iul.tu-dortmund.de

© The Minerals, Metals & Materials Society 2021

G. Daehn et al. (eds.), *Forming the Future*, The Minerals, Metals & Materials Series,
https://doi.org/10.1007/978-3-030-75381-8_11

torsion [5], or equal channel angular pressing (ECAP) [6]. The direct recycling of aluminium chips using hot extrusion was first proposed and patented by Stern in 1945 [7]. Gronostajski et al. investigated the production of aluminium and aluminium-based composites using this methodology [8]. Additional works were carried out by Fogagnolo [9] who extruded AA6061 reinforced with Al_2O_3 or Allwood [10] who analysed the recycling of aluminium scrap by cold bonding during cold extrusion and rolling processes. Tekkaya et al. reported on the influence of chip type and compaction strategy on the mechanical properties of hot extruded profiles based on AA6060 chips when using a porthole die [11]. The process parameters extrusion ratio, die design (material flow), and temperature have the most significant influence on the microstructure and the mechanical properties [12]. The underlying mechanism of the chip consolidation is the solid-state welding which due to its importance for different manufacturing processes has been investigated in detail to understand the ongoing physical relationships. In order to be able to make predictions about the welding, two types of weld models are considered in the literature: On the one hand, qualitative models based on the *energy barrier theory*, which are also known as welding criteria, on the other hand, physically motivated models based on the *film theory* for the prediction of an absolute weld strength.

In order to predict the quality of the longitudinal weld seam in porthole die extrusion, weld criteria based on the energy barrier theory were developed. First of all, Akeret assumed that the ratio between the normal contact pressure and the local flow stress of the material in the welding zone must be larger than a critical threshold value [13]. Plata and Piwnik proposed that the value should be integrated over the contact time [14]. Donati and Tomesani introduced the local velocity as an additional variable to the existing model [15]. In the Yu model, the strain rate is integrated over the time considering pressure and local flow stress and a weighing factor which takes diffusion into account [16]. There is only one criterion solely dedicated to the prediction of chip weld quality in hot extrusion of aluminium chips. Güley et al. assumed that an accumulation of bond strength increments starts after a certain critical shear stress is reached, which leads to breakage of the oxide layers [12].

Most of the before-mentioned weld criteria do not take into account the local surface expansion in the contact region. This is, however, an important influencing factor for metal-to-metal solid bonding which was identified by Bay [17]. He developed a physically motivated model to predict the bond strength. The metallic surfaces have to come into direct contact to reach bonding. Concerning aluminium, the oxides covering the surface must be broken. An expansion of the two contacting surfaces is required for this. After local breakage of the oxides, the presence of contact pressure leads to micro extrusion of base metal through the cracks in the broken layers. This leads to the bonding of two contacting surfaces (Fig. 1) [17].

The latest development of the model by Bay was conducted by Cooper and Allwood [18]. This model allows for a prediction of the absolute bond strength σ_b as a function of the normal stress σ_n, shear stress τ and strain, according to

$$\frac{\sigma_b}{\sigma_f} = \left(\frac{0.8}{\sigma_f}\sqrt{\sigma_n^2 + 3\tau^2}\right) \cdot v \cdot \left(0.8\frac{\sigma_n - p_{ex}}{\sigma_f}\right) \tag{1}$$

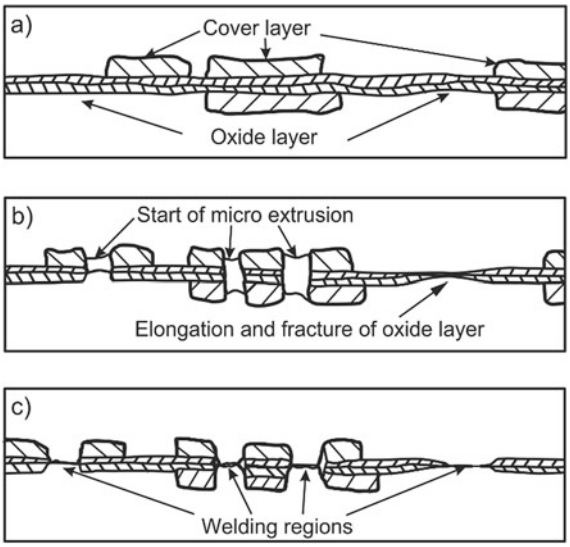


Fig. 1 Schematic steps in solid bonding: **a** Initial contact situation, **b** Elongation and cracking of cover and oxide layer, **c** Local welding (adapted from Bay [17])

The model can be divided into three terms:

1. The first term considers the true microscopic contact surface of the two contacting partners. It is affected by the normal stress σ_n and the shear stress τ, because of microscopic plastic deformations at the interface.
2. The necessary strain to initiate oxide fracture of the oxide layer, so the base material can get into direct contact is included by the second term v.
3. By means of the third term, the microextrusion pressure p_{ex} which is essential for the micro extrusion of base metal through the cracks in the fractured oxide layer is regarded. It depends on a number of geometric and material parameters.

The Cooper and Allwood model was chosen to be adapted for weld quality prediction in aluminium chip extrusion for AA6060 alloy due to its physically motivated background by Kolpak et al. [19]. Some changes have been made in order to apply the model in chip extrusion:

1. The welding between the individual chips is a complex three-dimensional process. Thus, to homogenize the local weld quality, the effective plastic strain ε is set as the relevant strain. The hydrostatic pressure p, which is responsible for the densification of material is defined as the relevant stress measure for welding.
2. Due to the high porosity of the chip-based billets, the encapsulated amount of oxygen drastically increases. Since this is the main driving factor to break oxides and allow base metal to flow through the resulting cracks, an additional factor is added to calculate the additional surface expansion necessary to fully turn the oxygen captured in the pores into oxides on the chip surface.

3. Since no additional oxygen is introduced in the system, it is assumed, that the amount of oxygen captured in the pores of the billets during compaction does not change during the extrusion.

The above-mentioned changes have been implemented in the model leading to the weld quality calculation model given in Fig. 2.

The model works as follows: conventional FE simulation is conducted utilizing the standard material behaviour used for as-cast material because investigations suggest that the material has a density of nearly 100% before flowing in the die cavity (Fig. 2a). Particles are defined on the profile cross-section in order to extract the necessary field quantities. The particles are tracked to calculate their path during the extrusion (Fig. 2b). All necessary field quantities are extracted along each investigated particle line (Fig. 2c). Along each particle line, the weld quality is calculated individually for n points. The weld quality can only increase because within the container no negative pressure (positive hydrostatic stress) exists. This was implemented by assuming the local weld quality to be the maximum weld quality achieved up to the current point i (Fig. 2d) [19].

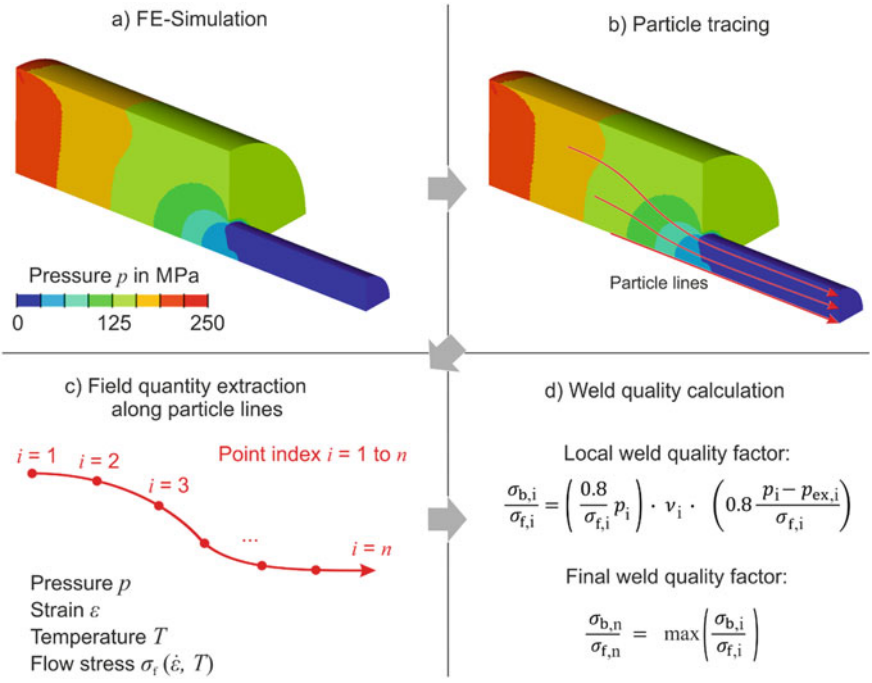


Fig. 2 Adjusted weld model for application in hot extrusion of chip-based billets [19]. (Color figure online)

2 Influence of Process Parameters on the Weld Quality Factor

To verify the model capability different extrusion process parameters which, according to literature influence, the welding of the chips and thus the process success was varied in the simulations. The major parameters are extrusion ratio R, billet temperature T, and ram speed v. For this, an initial diameter of $d_0 = 66$ mm, an initial length $l_0 = 78$ mm, and the extrusion of a round bar were assumed. Starting from a reference set (Fig. 3), the process parameters were varied within a range of industrially relevant limits. For three points over the cross-section, the chip weld quality factor was calculated. The weld quality model is shown to explain the influence of the variation of the extrusion parameters. The influence is indicated with a green arrow if it is positive and with a red arrow if it is negative. As known from the literature the extrusion ratio shows a major influence on the weld quality factor. Starting from a low weld quality factor of $0.5 < \sigma_b/\sigma_f < 0.75$ for $R = 6$, with increasing extrusion ratio the weld quality saturates towards the maximum achievable value of $\sigma_b/\sigma_f = 1$, for all three investigated points. The increase in the weld quality is due to the simultaneous increase in local strain and pressure. The higher strain leads to a higher surface expansion and thus to a larger region where welding is possible. An increase in the billet temperature has no significant influence on the welding of the chips. The local flow stress is reduced by the temperature increase which facilitates the material to flow through the cracked oxide layer. The reduced flow stress also leads to a decrease in the pressure. Since these two effects balance out, the calculated weld quality shows no influence for all three investigated points. Similar observations are made for the influence of the ram speed. The increase of the strain rate would lower the weld quality but, in contrast, the pressure is increased. These two

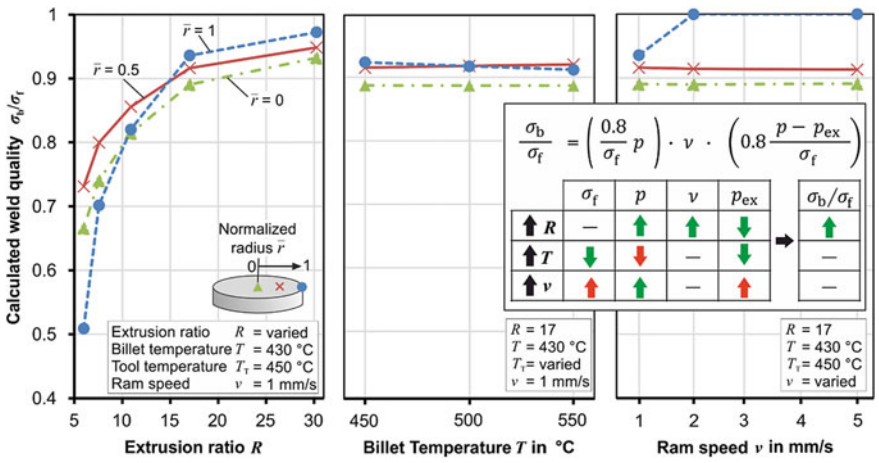


Fig. 3 Influence of extrusion ratio R, extrusion temperature T, and ram speed v on the weld quality factor [19]. (Color figure online)

opposing effects balance out for the inner points of the profile. However, the weld quality is increased in the surface region because the material which ends up at the profile surface, has travelled along the dead metal zones, which leads to large shear strains.

The calculated weld quality resulting in the weld model was validated against a variety of literature results as well as against the results of additional hot extrusion experiments utilizing flat-face dies to produce round bars. Additionally, the stresses at the die exit have to be considered since a velocity gradient leads to positive normal stresses and shear stresses which can cause a delamination of the chips on the profile surface. To withstand the given die exit stresses and to ensure the process success, a minimum weld quality factor of $\sigma_b/\sigma_f > 0.95$ is required. The minimum weld quality factor depends on the chip size and also chip shape because the amount of oxygen captured in the billet is a function of the ratio between the overall chip surface and volume as well as on the (unknown) amount of dissolved oxygen in the pores.

3 Weld Quality Prediction and Experimental Validation

To further validate the weld model and verify the influence of the strain on the welding of the chips during the extrusion process, it was applied to predict the weld quality for the extrusion of two profiles. Both profiles were simulated with HyperXtrude and then the weld quality model was used to calculate the weld quality. The experimental tryouts have been carried out with a hydraulic extrusion press Collin PLA250 t with a maximum ram force of 2.5 MN. The aluminium alloy AA6060 was used for all investigations. The chips were produced by turning of cast bars and then cleaned and cold compacted with a maximum force of 550 kN into chip-based billets with a diameter of 60 mm and an average length of 90 mm resulting in an overall density of 78%. Prior to extrusion the chip-based billets were homogenized at 550 °C for 6 h and then extruded through preheated dies with a temperature of 450 °C.

The first profile is a cross profile with a low extrusion ratio of $R = 7$. A flat-face die with a small pre-chamber was used resulting in low strains during the extrusion. This can be seen in the simulation results (Fig. 4 left). Due to the homogenous material flow through the flat-face die only low strains are achieved over the profile cross-section which means the surface expansion of chips is low and thus the areas of pure aluminium being able to be welded. Solely at the inner edges, higher strains occur. Using the weld quality model to generate a contour plot of the calculated weld quality similar observations can be made indicating a strong correlation between strain and weld quality since the strain has a high influence on the welding of the chips. The contour plot shows insufficient welding for the majority of the profile cross-section solely the inner edges show a calculated weld quality of over 95% (Fig. 4 right).

By evaluating the calculated weld quality along two paths of the cross-section, it can be seen that the calculated weld quality is very low in the centre of the profile (Fig. 5 left). It increases drastically towards the inner edges of the cross (Path 2), however, along Path 1 a sufficient value is not reached. Due to the low calculated

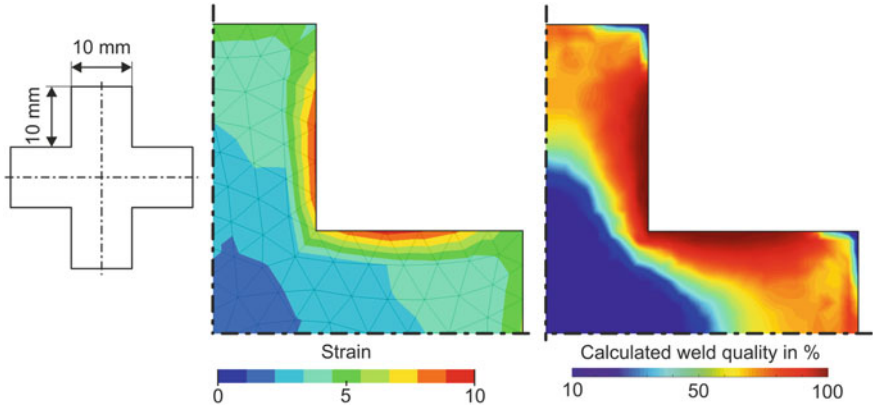


Fig. 4 Cross profile, simulation, and calculated weld quality for a quarter profile. (Color figure online)

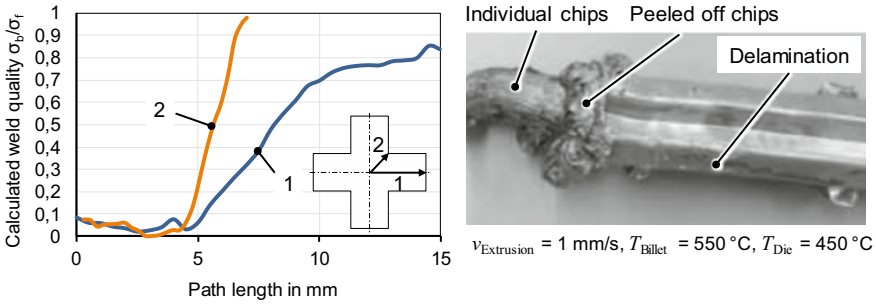


Fig. 5 Calculated weld quality along path 1 and 2, delamination of chips in experimental tryouts. (Color figure online)

weld quality, an insufficient welding will be expected. The experiment shows a strong delamination of the chips because of the poor welding in the profile centre. As a consequence of friction at the die bearing, the outer chips which are welded are peeled off from the centre where individual chips can be detected. Moreover, minor delaminations occur at the profile surface. The experiment corresponds to the calculated weld quality according to Fig. 5 in which a strong delamination of the chips can be observed which validates the weld quality model.

The second profile is an asymmetrical rectangular hollow profile with different wall thicknesses (Fig. 6). A porthole die with two inflows is used in order to divide the material flow and create the profile cross-section. The profile has an extrusion ratio of $R = 14$ which in combination with the porthole die leads to higher strains. The effect of the strain on the welding of the chips can be estimated comparing the contour plot of the simulation (Fig. 6 left) to the weld quality model (Fig. 6 right). In the areas of high strains (near the surface), a good welding of the chips is estimated.

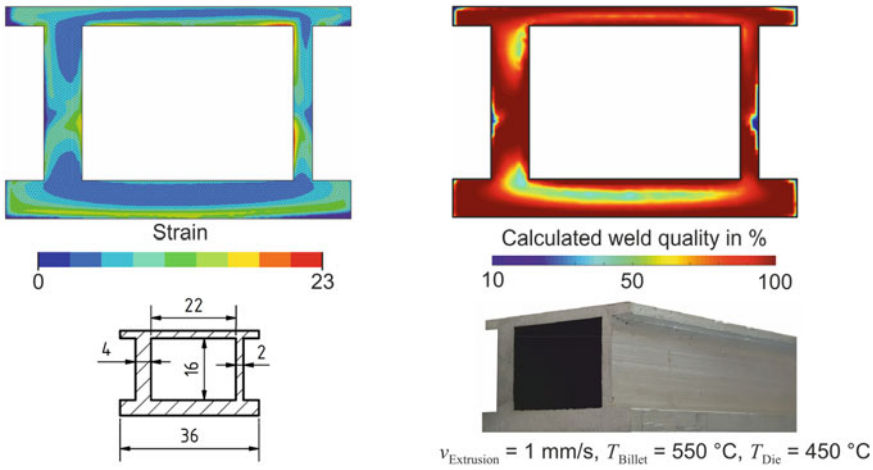


Fig. 6 Asymmetrical rectangular hollow profile: simulation, calculated weld quality and experiment. (Color figure online)

In the middle of the horizontal bridges, the values decrease. Overall a good welding of the chips is predicted which results in profiles without delamination during the experiments (Fig. 6 bottom right). It can be concluded that the distribution of the strain correlates with the calculated weld quality. Nevertheless, the calculation of the weld quality is inevitable to estimate the process success. Despite the strain also the pressure has a major influence on the welding of the chips. Hence, to take all influencing field quantities into account, only the calculated weld quality can give an indication of the welding of the chips during extrusion.

4 Conclusion

In order to numerically predict the process success, a weld model was developed which allows for an estimation of the local chip weld quality depending on the die type and hot extrusion parameters for different profile geometries. In general, a process success is assumed if a minimum weld quality factor of about 95% is reached and the stresses at the die exit region are minimized. For the process success, high strain and pressure are needed to cause oxide breakage and thus welding of the individual aluminium chips. A strong correlation between strain and weld quality is given since high strains lead to high surface expansions of the chips which enable welding of the bare aluminium. The weld model can be used to assess the process success in chip extrusion when designing new profile geometries and dies. In further investigations, it has to be proofed that the weld model also works for other alloys for example AA2XXX, AA5XXX, or AA7XXX series.

References

1. Chiba R, Yoshimura M (2015) Solid-state recycling of aluminium alloy swarf into c-channel by hot extrusion. J Manuf Process 17:1–8
2. Allwood JM, Cullen JM, Cooper DR, Milford RL, Patel ACH, Carruth MA (2010) Conserving our metal energy. WellMet2050, University of Cambridge, Cambridge
3. Peng T, Wang QD, Han YK, Zheng J, Guo W (2010) Consolidation behavior of Mg–10Gd–2Y–0.5Zr chips during solid-state recycling. J Alloys Compd 503:253–9
4. Abd El Aal MI, Yoo Yoon E, Seop Kim H (2013) Recycling of AlSi8Cu3 alloy chips via high pressure torsion. Mater Sci Eng A 560:121–128
5. Kanetake N, Kume Y, Ota S, Morimoto R (2014) Upgrading in mechanical properties of high performance aluminum alloys by compressive torsion process. Proc CIRP 18:57–61
6. Haase M, Ben Khalifa N, Tekkaya AE, Misiolek WZ (2012) Improving mechanical properties of chip-based aluminum extrudates by integrated extrusion and equal channel angular pressing (iECAP). Mater Sci Eng A 539:194–204
7. Stern M (1945) Method for treating aluminum or aluminum alloy scrap. U.S. Patents, p 2391752
8. Gronostajski JZ, Marciniak H, Matuszak A (1996) Production of composites on the base of AlCu4 alloy chips. J Mater Process Technol 60:719–722
9. Fogagnolo JB, Ruiz-Navas EM, Simón MA, Martinez MA (2003) Recycling of aluminium alloy and aluminium matrix composite chips by pressing and hot extrusion. J Mater Process Technol 143–144:792–795
10. Allwood JM, Huang Y, Barlow CY (2005) Recycling scrap aluminium by cold-bonding. In Proceedings of the 8th ICTP, Verona, Italy
11. Tekkaya AE, Schikorra M, Becker D, Biermann D, Hammer N, Pantke K (2009) Hot profile extrusion of AA-6060 aluminum chips. J Mater Process Technol 209:3343–3350
12. Güley V, Güzel A, Jäger A, Ben Khalifa N, Tekkaya AE, Misiolek WZ (2013) Effect of die design on the welding quality during solid state recycling of AA6060 chips by hot extrusion. Mater Sci Eng A 574:163–175
13. Akeret R (1992) Extrusion welds-quality aspects are now center stage. Proceedings of the 5th International Aluminum Extrusion Technology Seminar, vol 1, 319–336
14. Plata M, PiwnikJ (2000) Theoretical and experimental analysis of seam weld formation in hot extrusion of aluminium alloys. Proceedings of the 7th International Aluminium Extrusion Seminar 205–212
15. Donati L, Tomesani L (2004) The prediction of seam welds quality in aluminum extrusion. J Mater Process Technol 153–154:366–373
16. Yu J, Zhao G, Chen L (2016) Analysis of longitudinal weld seam defects and investigation of solid-state bonding criteria in porthole die extrusion process of aluminum alloy profiles. J Mater Process Technol 237:31–47
17. Bay N (1979) Cold Pressure Welding-The Mechanisms Governing Bonding. J Eng Ind 101:121–127
18. Cooper DR, Allwood JM (2014) The influence of deformation conditions in solid-state aluminium welding processes on the resulting weld strength. J Mater Process Technol 214:2576–2592
19. Kolpak F, Schulze A, Dahnke C, Tekkaya AE (2019) Predicting weld-quality in direct hot extrusion of aluminium chips. J Mater Process Technol 274:116–294

Part III
Honorary Symposium: Xue Yu Ruan

Bulk Microforming from Sheet Metal—A Promising Approach for the Mass Production of Cold-Formed Metallic Micro Parts



Martin Kraus and Marion Merklein

Abstract Every year billions of micro parts are produced. In mass production, cold bulk forming offers considerable technological, economical, and ecological potentials compared to alternative production methods. Due to the occurrence of scale effects, high tool stresses, and handling problems, cold bulk forming is not used for the mass production of multi-stage formed metallic micro parts. Within this paper, multi-stage bulk microforming from sheet metal is investigated on the laboratory scale with the material Cu-OFE. Throughout this process, the sheet metal strip serves both as a semi-finished product and as a handling aid. In the first forming stage, a pin is extruded from sheet metal, which is then extruded in a cup during the second stage. For the identification of size effects and the evaluation of such effects on the part quality, the tests are carried out on macro- and micro-scale. In the first step, the process-influencing variable of the blank holder pressure is investigated in the first forming stage in order to derive measures for the highest possible material utilization. The two-stage forming of the pin with cup is compared with a single-stage process to assess the part quality and material utilization depending on the process strategy. Using the correct geometric scaling, size effects are identified and their effects on the forming process are evaluated. The experimental results reveal that it is possible to fabricate micro parts with a diameter of 470 μm and a minimum wall thickness of 36 μm reproducible by using the presented cold bulk microforming process strategy.

Keywords Bulk microforming · Pin extrusion · Material flow · Metallic micro parts · Size effects · Sheet metal

M. Kraus (✉) · M. Merklein
Friedrich-Alexander-Universität Erlangen-Nürnberg, Institute of Manufacturing Technology (LFT), Egerlandstraße 13, 91058 Erlangen, Germany
e-mail: martin.kraus@fau.de

M. Merklein
e-mail: marion.merklein@fau.de

© The Minerals, Metals & Materials Society 2021

G. Daehn et al. (eds.), *Forming the Future*, The Minerals, Metals & Materials Series,
https://doi.org/10.1007/978-3-030-75381-8_12

1 Introduction

The ongoing miniaturization and the continuous development of microproduction technologies enable the production of ever smaller products with an extended functional range. This applies especially to microcomputers, electronics, telecommunication devices, and microelectromechanical systems (MEMS). The MEMS include, for example, acceleration and pressure sensors, which have a wide range of applications in the automotive industry [1]. Further applications of MEMS sensors are in the energy industry, medical technology, and consumer electronics, like flow meters, blood pressure monitors, or video game consoles [2]. Due to the numerous possible applications, the market share is growing continuously [3] and the demand for metallic microcomponents increases rapidly. Besides MEMS, typical examples of metallic micro parts are IC carriers, fasteners, micro-screws, leadframes, sockets, and any kind of connecting elements [4].

In mass production, metal forming processes offer economical, technological, and ecological advantages compared to other production methods. However, scaling down forming processes into the micro-scale can result in the occurrence of size effects, which may have a negative impact on the part quality as well as on the repeat accuracy of the process [5]. Size effects are classified into physical and structural causes. Despite these size effects, high volumes of metallic micro parts, such as leadframes, springs, and micro cups, are nowadays produced in industry using metal forming technology [6]. These components are mainly produced by sheet metal forming processes, as here the transport of the micro parts between the forming stages in multi-acting tool can be realized precisely with the help of the sheet metal strip. For the identification, understanding, and minimization of size effects, numerous of research projects were carried out in the past [7]. A major challenge in micro sheet metal forming is the high, unpredictable springback during bending due to scale effects. Ruan's research group [8] has investigated the influence of size effects on bending thin metal foils with different grain sizes. By using a simplified constitutive model, it was possible to predict the springback angle after microbending.

At present, cold bulk microforming is mainly used in industry for wire bending to produce filaments and springs in large quantities, as it allows to form directly from the wire [6]. For complex, multi-stage formed micro parts, cold bulk microforming is barely used in industry since additional handling challenges arise due to the small part size. As a result of the relative large surface area in relation to the part volume, adhesive forces dominate, which is why the micro parts stick to the gripper systems [6]. To meet these challenges, handling devices, which reduce the contact surface between the gripper and the workpiece, and thus the adhesion force, have been developed. These handling devices are based on vacuum pipettes and iris grippers [6]. The use of such systems improves the micro part transport but reduces the production rate considerably. Another challenge consists in the occurrence of size effects, which have a negative influence on the forming processes and the part quality [9]. Bulk microforming of metallic micro parts from sheet metal strip offers the potential to meet the handling challenges by using the strip as a transport aid between the forming

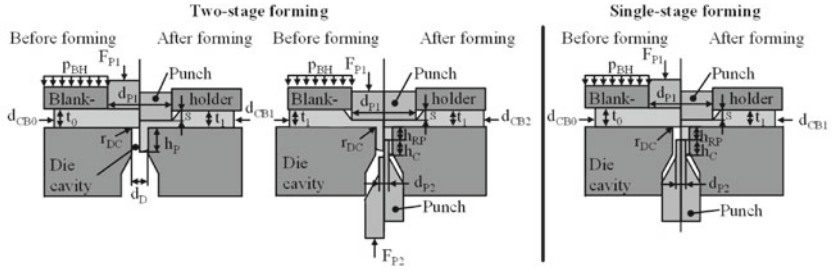
steps in a multi-acting tool system, like in sheet microforming [10]. Size effects might be reduced by a grain refinement during the multi-stage forming process. The principle feasibility of bulk microforming from sheet metal has already been demonstrated in numerous studies by Meng et al. [11], Ghassemali et al. [12], Hirota [13] und Merklein et al. [14]. In the first forming stage, material is extruded, e.g. in the shape of a pin, which is then formed further in several subsequent forming stages. In the last forming stage, the micro part is separated from the metal strip by blanking. One major challenge of this process is the material utilization. Due to the lack of lateral boundaries, a large amount of the displaced material flows laterally into the sheet metal plane and is not available for further forming steps. Ghassemali et al. [12] have shown that the pin height does not increase linearly with the punch stroke. At the end of the process, extrusion is dominant and the pin height in relation to the punch stroke increases rapidly. Hirota [13] has observed with aluminum and Merklein et al. [14] with cooper that the material utilization can be significantly increased by a harder material state. It was also shown that the use of thinner sheets improves the material utilization. The effects of different punch and die diameters on the material flow and the mechanical properties of the pins have been investigated by Ghassemali et al. [15]. Despite a low material utilization, the process has the potential to contribute resource savings if it is integrated into existing progressive processes and uses the offcuts [13].

Within this study, the basic feasibility of the production of micro parts by multi-stage bulk microforming from sheet metal is analysed. For this purpose, a single-stage and two-stage forming strategy for the extrusion of a pin with cup is fundamentally investigated. In order to identify size effects and to evaluate their impact on the process and the micro part, the experiments are carried out in macro- and micro-scale. In the single-stage variant, the micro part is directly formed by a combination of direct impact extrusion (DIE) and direct impact cup extrusion (DICE). For the two-stage variant, a pin is formed by direct impact extrusion (DIE) in the first forming stage and the material is then provided for indirect impact cup extrusion (IICE) in the second forming stage. Additionally, a process-influencing variable on the pin forming is investigated with the blank holder pressure in order to enable recommendations with respect to the material utilization and the process quality.

2 Experimental Setup and Material Characteristics

2.1 Experimental Setup

Figure 1 shows schematically the extrusion processes from sheet metal plane with all relevant process parameters, which are analysed experimentally in this study. A multi-action tool system, which allows a separate control of the blank holder pressure and the extrusion punches, is used for the tests. For the identification of size effects, the processes are investigated in the macro- and micro-scale. Thus, all tool



Scaling factor: $\lambda = \frac{Micro\ sheet\ thickness}{Macro\ sheet\ thickness} = 0.356$

Parameters		Unit	Values	
			Macro	Micro
Process-related parameters				
Relative punch stroke	s/t_0	[%]	75	
Blank holder pressure	p_{BH}	[MPa]	0; 20; 50; 100; 200;	
Workpiece-related parameters				
Sheet thickness	t_0	[mm]	1.32	0.47
Blank diameter	d_{CB0}	[mm]	15.00	5.34
Restpin height	h_{RP}	[mm]	1.000	0.356
Tool-related parameters				
Punch diameter 1	d_{P1}	[mm]	4.00	1.42
Punch diameter 2	d_{P2}	[mm]	0.920; 1.120;	0.328; 0.399;
Die diameter	d_D	[mm]	1.32	0.47
Die radius	r_{DC}	[mm]	0.14	0.05

Fig. 1 Process schematics and process parameters for cold bulk macro- and microforming from sheet metal

geometries are scaled down according to the similarity theory of Geiger et al. [16]. The scaling factor is based on the ratio of the available sheet thicknesses and is $\lambda = 0.356$. The dimensions of all active tool elements are given in Fig. 1. Since the grain size of the metallic structure cannot be scaled exactly geometrically, the occurrence of size effects is expected. For all tests, the extrusion oil Dianol ST in a ratio of 10 g/m^2 is used for lubrication. A constant forming speed of 5 mm/min is chosen for all forming steps, analogous to the upsetting tests for material characterization. The process sequences for single-stage and two-stage forming of a pin with cup are described below.

2.2 Two-Stage Forming (1. DIE; 2. IICE)

DIE. In the two-stage forming process for fabricating the demonstrator part (pin with cup), the first forming stage uses DIE to accumulate material in form of a pin. The pin provides the material for the following forming stages. In this forming stage (DIE), the tooling system consists of a die, a blank holder, and a DIE-punch. At the beginning of the process, the workpiece is axially constrained by the blank holder to prevent the sheet metal from bulging. Afterwards, the DIE-punch is moved downwards, causing a material flow axially and radially into the die as well as radially outwards into the sheet metal plane. The aim of this forming stage is to increase the material flow into

the die cavity in order to provide as much material as possible for further forming stages. For this reason, the effects of different blank holder pressures on the pin and blank shape, process quality, and stability are investigated in this work.

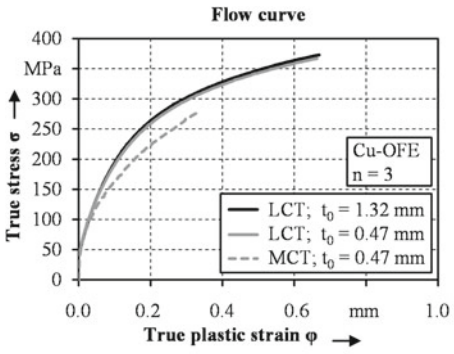
IICE. In the second process stage, a cup is extruded on the pre-formed pin from the first process stage by IICE. For this purpose, the tool system remains closed after the first forming stage. During the process, an IICE-punch is moved up until the desired residual pin height (h_{RP}) is reached. As a result, the cup is formed due to the displaced material of the pin.

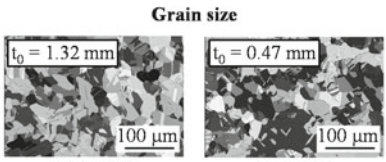
2.3 Single-Stage Forming (DIE/DICE)

DIE/DICE. In the single-stage forming, the demonstrator part is formed by a combination of DIE and DICE. The process sequence is similar to the DIE. The only difference is the fixed positioning of the DICE-punch in the forming zone at the position of the desired residual pin height (h_{RP}). By forming the pin, a cup is formed when it reaches the DICE-punch. The single-step variant is investigated in this study to determine if the material utilization and the mould filling can be increased by multi-stage bulk microforming from sheet metal.

2.4 Material Characteristics

For all the tests, the copper material Cu-OFE is used. Due to its high purity, the absence of oxide inclusions and its single-phase microstructure, this material is well suited as a model material for the fundamental investigation of the multi-stage bulk microforming process from the sheet metal. Moreover, the material is widely used for electrical components due to its high conductivity of at least 101% IACS. In order to exclude the influence of batch fluctuations on the material properties, the sheet metal is taken from the same melt for the investigations in the macro- and micro-scale. For macro-scale, the material was available with a sheet thickness of 1.32 mm and 0.47 mm for micro-scale. Due to the different pass reductions, the material properties, such as pre-hardening, anisotropy, or grain size, are not identical for the two sheet thicknesses in the as-rolled delivery condition. As the different material states may result in incorrect interpretations during the detection of size effects, the material is heat-treated prior to testing. The heat treatment is carried out in a tube furnace under a protective gas atmosphere (argon) at a temperature of 650 °C. This temperature is held for one hour. The cooling took place slowly over several hours in the furnace keeping the protective gas atmosphere. Through heat treatment, it is possible to reduce the anisotropy of the grains almost completely. The heat treatment resulted in cubic grains with almost no measurable anisotropy. The grain size is 24.0 ± 13.8 µm for $t_0 = 1.32$ mm and 27.5 ± 18.0 µm for $t_0 = 0.47$ mm. Thus, the grain size is almost identical and comparable for both sheet thicknesses (Fig. 2). Due





Initial true stress

	LCT	LCT	MCT
t_0 [mm]	0.47	1.32	0.47
σ_{ys} [MPa]	41.1	40.8	35.7
r_b	0.9	1.0	0.9

Fig. 2 Flow curves from LCT and MCT, grain sizes and grain structure as well as the initial yield stress and biaxial anisotropy for both sheet thicknesses

to the similar stress state to the investigated forming process, the strain hardening behaviour is analysed by layer compression tests (LCT) according to Merklein and Kuppert [17]. The evaluated flow curves and the initial yield stresses are shown in Fig. 2. The diagram confirms that the strain hardening behaviour is approximately identical for both sheet thicknesses.

Additional micro compression tests (MCT) are carried out for a better understanding of the forming behaviour of the material in micro-scale. The specimen diameter and height are each 0.47 mm. The samples are produced with the TruMark3020 Nd: YAG laser from Trumpf. The contour of the samples is exposed in several successive cycles, which results in a removal of the surface. Due to the focused laser beam, with a focus diameter of 30 µm and the short recurring pulses, no measurable heat penetration on the grain structure can be detected in micrographs, since the heat of the laser beam is immediately dissipated into the surrounding material. Figure 2 shows that the work hardening decreases for a smaller sample size at a constant grain size. Thus, the strain hardening behaviour is not only dependent on the grain size itself, there is also a dependence on the sample geometry. Ruan's research team already documented this finding in 2006 [18]. The reason for the decrease of the work hardening due to the miniaturization of the samples can be explained by the surface layer model [4]. Due to miniaturization, the proportion of surface grains gets larger in relation to the sample volume. The surface grains on the curved surface area are not subject to any external compatibility conditions and can thus be more easily displaced radially outwards during upsetting. As a result, the required forming force is reduced. In addition, the number of grains in the micro-sample and thus the absolute grain boundaries are lower. This means that fewer dislocations accumulate at the grain boundaries resulting in a softening effect.

3 Results

The influence of the blank holder pressure on the mould filling (pin height) and the material utilization is investigated in a first step. Based on these results, an appropriate blank holder pressure is selected to analyse the single-stage and two-stage forming strategies.

3.1 Influence of the Blank Holder Pressure

The blank holder pressure is investigated in five gradations between 0 MPa and 200 MPa (Fig. 1). After forming, the pin height is measured tactile by a digital absolute digimatic indicator from Mitutoyo. Figure 3a displays the resulting pin height in relation to the blank holder pressure. It is evident that the pin height increases in the macro- as well as in the micro-scale with increasing blank holder pressure.

According to the Coulomb friction law (1), the friction force increases linearly as a result of the increase of the blank holder pressure and thus the contact force (F_N). Due to the higher friction force between the blank holder and the die in the passive forming zone, the lateral material flow outside in the sheet metal plane is inhibited, which leads according to the condition of continuity to an increase of the lateral material flow towards the die cavity and thus to an increase of the pin height.

$$F_{\text{Friction}} = \mu \times F_N \,(\text{Coulomb fricton law}) \tag{1}$$

The further processing of the pin in subsequent forming stages in a progressive die requires not only the greatest possible material utilization but also the lowest possible deformation of the sheet metal strip in order to realize a precise handling of the strip. The qualitative influence of the blank holder pressure on the sheet metal geometry is presented in Fig. 4 by micrographs. Without the use of a blank holder

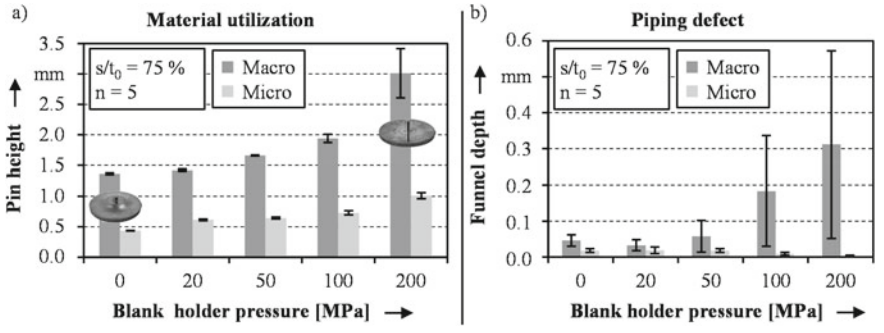


Fig. 3 Influence of the blank holder pressure on pin height and piping defect

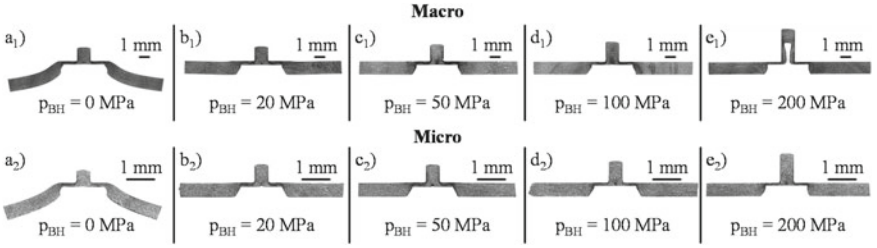


Fig. 4 Micrographs of the pin cross section after DIE in macro- and micro-scale for different blank holder pressures

Table 1 Average blank diameter after forming in relation to the blank holder pressure; n = 5

p_{BH} [MPa]	20	50	100	200
d_{CB1} [mm] (Macro)	15.411	15.462	15.615	15.927
d_{CB1} [mm] (Micro)	5.508	5.521	5.557	5.645

(0 MPa) or if the blank holder pressure is too low (20 MPa), the sheet metal strip is bulging strongly outside the forming zone.

The bulge is reduced with an increasing blank holder pressure and can be completely avoided if the blank holder pressure is sufficient. Regarding the qualitative evaluation of the bulge, there are no differences and thus no size effects between macro- and micro-scale detectables.

For blank holder pressures $p_{BH} > \sigma_{ys}$ the sheet is compressed and plastically deformed by the blank holder. This results in a larger radial expansion of the blank, as shown in Table 1. This enlargement of the blank has a negative effect on the handling in progressive tools. Thus, the blank holder pressure should be selected as high as possible, but always slightly below the yield stress. For the subsequent experiments in this paper, the blank holder pressure of $p_{BH} = 50$ MPa is chosen, as it is the closest to the initial yield stress of Cu–OFE and prevents bulging of the sheet.

The extrusion of pins from sheet metal can result in unwanted piping defects if the process parameters are not selected appropriately [13]. This is the case when the axial material flow velocity (DIE-punch velocity) is lower than the lateral material flow velocity towards the die cavity. As a result, the material detaches from the DIE-punch and a funnel is formed. Figure 3b quantifies the resulting piping defect by the funnel depth in relation to the blank holder pressure. The funnel depth is measured by confocal microscopy on the μSurf from NanoFocus. In macro-scale, the funnel depth increases with rising blank holder pressure. This is not the case in micro-scale. A size effect is present due to the decrease of the funnel depth with increasing blank holder pressure. Besides this, generally smaller funnel depths are observed in micro-scale than in macro-scale, even considering the scaling factor. The shape of the funnel and thus the funnel depth is strongly dependent on the grain structure. Hence, there are also size effects which result in increasing scattering for greater funnel

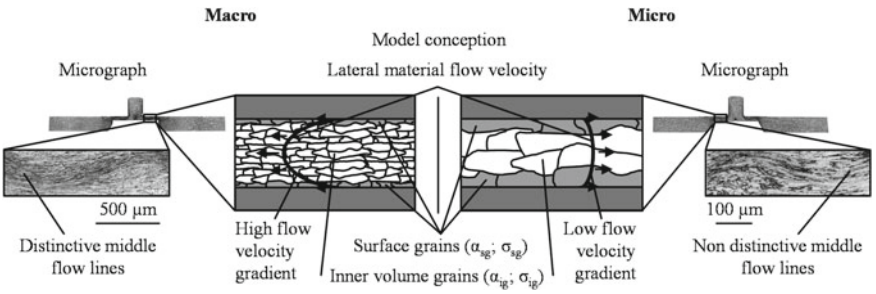


Fig. 5 Surface layer model for the validation of size effects regarding the piping defect

depth. In Fig. 4, the effect of funnel formation is also compared qualitatively for the marco- and micro-scale. Figure 4e_1, e_2 show a large piping defect in macro-scale and no piping defect in micro-scale. This size effect can be explained by transferring the surface layer model [4] to the investigated bulk microforming process from sheet metal. Figure 5 illustrates the surface layer model for the analysed process in macro- and micro-scale as well as the plausibility check based on micrographs of the cross section. Due to the same grain size for macro- and micro-scale, the ratio of surface grains in relation to the total volume is smaller in macro- than in micro-scale, according to the scaling factor.

Surface grains are in direct contact with the forming tools. Thus, the surface friction is transferred into the workpiece through these grains. This results in a large material flow velocity-gradient across the sheet thickness, which can be also observed in conventional DIE-processes. The surface-near grains flow slower than the grains in the middle of the sheet due to the frictional force transferred from the surface grain over the grain boundaries. In micro-scale, the ratio of surface grains is significantly higher than in macro-scale due to the lower grain count. Since there are only a few grains over the cross section, the middle grains are stronger influenced by the surface friction and thus the material flow velocity-gradient is significantly lower than in the macro-scale. As a result, the material flows more homogeneously radially towards the die cavity and does not flow ahead at higher speed in the middle. The more homogeneous material flow results in a reduced piping defect, since there is sufficient material available for an entire mould filling. The described material flow behaviour can be checked for plausibility using the micrographs in Fig. 5. In macro-scale, distinct flow lines in the middle of the sheet can be observed in the micrograph. This indicates a greater deformation in the middle of the sheet and thus a higher material flow velocity. In micro-scale, the flow lines are homogeneously distributed over the entire sheet thickness. The reason for the increase of the funnel depth in macro-scale and the decrease in micro-scale can also be explained by the grain count using the surface layer model. As already mentioned, the lateral material flow outwards into the sheet metal plane is inhibited by increasing blank holder pressure. Thus, the lateral material flow towards the die cavity is enhanced in accordance to volume constancy. The DIE-punch force (active forming zone) increases as a consequence

of the laterally higher flow restriction outwards into the sheet metal plane (passive forming zone). Due to the higher DIE-punch force, the frictional force in the active forming zone increases according to the Coulomb friction law (2). This results in an increase of the lateral material flow velocity-gradient in macro-scale towards the cavity, which favours the forming of piping defects (Fig. 3b). In micro-scale, funnel formation is less than in macro-scale and decreases further with increasing blank holder pressure. This size effect can also be explained by the surface layer model. As less grains are located over the pin cross section and thus the wall friction at the die has a greater influence on the material flow in the centre of the pin, the axial material flow velocity-gradient is also lower in micro-scale than in macro-scale. This is why the funnel depths of the piping defects are relatively smaller in micro-scale. Additionally, the deflection of the grains at the die radius into the die cavity is inhibited in micro-scale due to the lower number of grains. With increasing blank holder pressure and thus higher DIE-punch force, the compatibility condition of the surface grains in the transition area between die/punch and cavity/punch rises. Thus, the deflection and the entry of the material into the die cavity are impeded additionally. This result in a decrease of the funnel depth with increasing blank holder pressure (Fig. 3b).

Figure 6 displays the force–displacement curves for DIE in relation to the punch surface and the sheet thickness in macro- and micro-scale. Without size effects, both curves should be identical. At the beginning of the process, the contact pressure at the DIE-punch is lower in micro-scale than in macro-scale. It can also be observed that the contact pressure increases stronger in micro-scale than in macro-scale during the forming process, causing both curves to converge. At the end of the process, the maximum related punch force in micro-scale is 1238 MPa even slightly higher than in macro-scale with 1212 MPa.

The characteristic of the force–displacement curves can also be explained by the theory of the surface layer model. According to Meßner [19], the yield stress in the surface layer model is calculated by accumulating the yield stresses of the surface and inner volume grains (2). In micro-scale, the yield stress is initially lower due to the fact that the surface grains have lower compatibility conditions due to their free surface and therefore lower yield stresses than the inner grains, which are completely surrounded by neighbouring grains (Fig. 2). Thus, the related process force at the beginning of the process is lower in micro-scale. During the forming process, the contact pressure and thus the frictional force in the process increases. This leads to higher compatibility conditions of the surface grains between workpiece

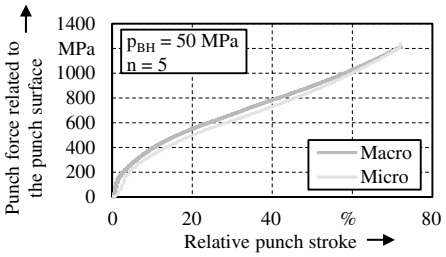


Fig. 6 Force–displacement curves for DIE in relation to the punch surface and the sheet thickness

and tool. In this state, the rigid tool at the contact workpiece-to-tool is more resistant to dislocations than inner grain boundaries. Thus, the related punch force is greater in micro-scale than in macro-scale at the end of the process.

$$\sigma = \alpha_{ig} \times \sigma_{ig} + \alpha_{sg} \times \sigma_{sg} \text{(Surface layer model)} \quad (2)$$

α = Volume share; σ_{ig} = True stress of inner grains; σ_{sg} = True stress of surface grains;

3.2 *Influence of the Process Strategy*

The influence of the process strategy on the material utilization and the mould filling during DIE of a pin with cup is investigated in this study in macro- and micro-scale. The specimens are formed by a single-stage (DIE/DICE) and a two-stage (DIE and IICE) process strategy. The cup height and the residual pin height are measured with the confocal laser-scanning microscope VK-X210 from Keyence. The position of punch 2 (DICE; IICE) is set identically for all configurations. The residual pin height is fixed at $h_{RP} = 1.004 \pm 0.015$ mm in macro- and at $h_{RP} = 0.379 \pm 0.018$ mm in micro-scale according to the scaling factor. Figure 7 compares the measured total heights (cup and residual pin heights) depending on the process strategy and the wall thickness (WT).

First, it can be seen that clearly higher cup heights are achieved for the two-stage process strategy in macro- as well as in micro-scale. In macro-scale, the two-stage process control strategy increases the cup height by 295% for WT = 200 µm and by 264% for WT = 100 µm. In micro-scale, the cup height can be increased by 266% for WT = 71 µm and by 291% for WT = 36 µm. Thus, the increase in material utilization due to the two-stage process strategy is comparable in macro- and micro-scale. Based on this assumption, size effects can be excluded in relation to the process strategy. The reason for the significantly higher material utilization by the two-stage forming process can be traced back to the narrow flow gap between the DICE-punch and

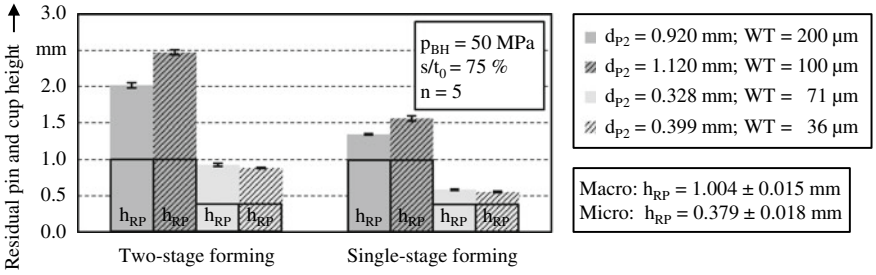


Fig. 7 Total heights (cup and residual pin height) depending on the process strategy and the WT

the die cavity. This gap is clearly smaller than the residual sheet thickness between DIE-punch and the die during forming. Additionally, the wall friction (static friction) caused by the DICE-punch changes the position of the neutral plane radially towards the cavity. Consequently, more material flows radially outwards into the sheet metal plane during single-stage forming. In the two-stage process, the IICE starts after the pin extrusion process (DIE) is completed. At this point, the flow gap between the DIE-punch and the die is $0.25*t_0$, which is significantly smaller than for DIE/DICE (single-stage). The narrow flow gap between DIE-punch and die and the deflection of the axial material flow from the pin by 90 ° into the sheet metal plane cause the material to flow dominantly into the cup wall. Furthermore, the relative velocity of the IICE-punch favours the cup forming in the two-stage process, as the sliding friction at the inner cup wall is lower than the static friction at the die and DIE-punch. As a result, almost the entire displaced material in the pin is used to form the cup.

In the following, only the two-stage process will be discussed, since no size effects occur with regard to the process strategy for the investigated material. In macro-scale, the highest cup height of $h_C = 1.475 \pm 0.028$ mm is achieved for the lower WT = 100 µm. For the WT = 200 µm the cup height is $h_C = 1.013 \pm 0.025$ mm. This is due to the fact, that the used IICE-punch has a larger diameter for smaller WT and thus more material is displaced. Furthermore, due to the small WT, the annular cross-section of the cup is smaller, which is why the cup height is greater in accordance to the volume constancy. In micro-scale, the cup height for the smaller WT = 36 µm is with $h_C = 0.517 \pm 0.009$ mm lower than for the WT = 71 µm with $h_C = 0.561 \pm 0.020$ mm. In contrast to the macro-scale, higher cups for larger WTs are achieved in micro-scale. Thus, a size effect is present here, which can be explained with the aid of the micrographs of the cross sections in Fig. 8 and the surface layer model. In macro-scale, there are 4–11 grains located across the minimum WT = 100 µm. In micro-scale there are only 1–5 grains at WT = 36 µm. Due to the small grain count in micro-scale there are nearly exclusively surface grains through which the frictional force at the active surfaces is transferred into the material. Due to the

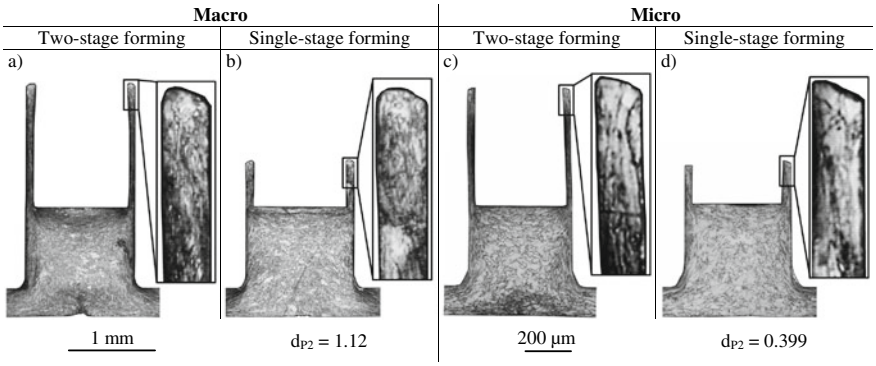


Fig. 8 Micrographs of the cup cross-section after two-stage and single-stage extrusion in macro- and micro-scale

few or non-existent grain boundaries in the material and the very strong hindrance to surface deformation at the rigid tool, the required forming force to fill the cup increases. This means, that the lower the WT and thus the grain count, the higher is the flow resistance to form the cup. Thus, the material is increasingly displaced laterally into the sheet metal plane by the flow gap between DIE-punch and die in micro-scale as the WT decreases. This results in lower cup heights for smaller WTs.

The process standard deviation of the total component length is with 1.52% (macro) and 1.60% (micro) low. Besides, the percental deviation with regard to the cup shape is almost identical in the macro- and micro-scale. In this context, it is shown that the identified size effects do not affect the process variation and thus the process stability. In earlier research studies, uneven cup edges were observed as a size effect during micro cup forming [4]. Due to the process-related grain orientation, the cup edge is formed homogeneously with a maximum tolerance of 0.3 μm (micro). On behalf of the low process variation and the homogeneous forming of the micro part, the investigated process is in principle suitable for the mass production of metallic micro parts.

4 Summary and Outlook

Within this research, extrusion processes from sheet metal plane are investigated in order to produce a micro pin with a cup. To identify size effects, the investigations are carried out in macro- and micro-scale under consideration of a correct geometric scaling. The influences of the blank holder pressure, the single-stage and two-stage process strategies as well as different cup wall thicknesses on the forming of the micro part and the process variation are investigated. The key findings of this study can be summarized as follows:

- The pin height and thus the material utilization increases with increasing blank holder pressure. This also makes it possible to react to fluctuating process parameters such as the sheet thickness or different strengths by adjusting the blank holder pressure.
- The blank holder pressure should be selected as high as possible, but always just below the yield stress in order to prevent plastic deformation of the sheet metal by bulging or thinning.
- In macro-scale, a larger piping defect occurs with increasing blank holder pressure. In micro-scale, the funnels become smaller. This size effect is explained in the article by using the surface layer model.
- The work-hardened pin from the first process stage can be further formed to a cup in macro- and micro-scale.
- The two-stage process strategy enables an increase of the cup heights up to 295% and thus a significant higher material utilization. Single-stage forming results in low cup heights, which is why the multi-stage version with material accumulation in form of a pin and further forming steps is more effective.

- The process strategies have no influence on the occurring size effects.
- In micro-scale, deeper cups are obtained for greater wall thicknesses due to size effects.
- The size effects have no impact on the process variation. The standard deviation is in average 1.52% (macro) and 1.60% (micro). Thus, the process is in principle suitable for the mass production of metallic micro parts for the investigated part dimensions.

In future research work, the investigations will be extended to other materials such as steel and aluminium to ensure the transferability of the scientific findings of this study. Furthermore, the shearing of the micro part by blanking will be studied in a third forming stage. Further studies will focus on the forming of more complex geometries. In this context, the cold bulk microforming process from the sheet metal will be analysed in order to produce metallic micro gears below the current module limit for cold bulk forming.

Acknowledgments The authors would like to thank the Deutsche Forschungsgemeinschaft (DFG, German Research Foundation) which founded this work within the project DFG ME 2043/79-1 'Basic research and determination of process limitations in bulk forming processes of microgears from sheet metal'. The authors would also like to show their gratitude to Mr. Manuel Backer, who participated in this experimental study within the scope of his master thesis.

References

1. Fassi I, Shipley D (2017) Micro-manufacturing technologies and their applications: a theoretical and practical guide. In: Springer Tracts in Mechanical Engineering. Springer International Publishing Switzerland
2. Bouchaud J (2011) High value MEMS market overview. Paper presented at the Conference Design, Test, Integration & Packaging of MEMS/MOEMS, Marseilles, 12 May 2011
3. Mounier E (2014) Future of MEMS: a market & technologies perspective. Paper presented at MEMS Teck Seminar, October 2014
4. Engel U, Eckstein R (2002) Microforming from basic research to its realization. J Mater Process Technol 125–126:35–44
5. Vollertsen F, Schulze Niehoff H, Hu Z (2006) State of the art in micro forming. Int J Mach Tools Manuf 46:1172–1179
6. Geiger M, Kleiner M, Eckstein R, Tiesler N, Engel U (2001) Microforming. CIRP Ann 50(2):445–462
7. Vollertsen F, Biermann D, Hansen H, Jawahir I, Kuzman K (2009) Size effects in manufacturing of metallic components. CIRP Annals—Manufacturing Technology 58:566–587
8. Hezong L, Xianghuai D, Qian W, Yu S, Diehl A, Hagenah H, Engel U, Merklein M (2011) Determination of material intrinsic length and strain gradient hardening in microbending process. Int J Solids Struct 48:163–174
9. Vollertsen F, Biermann D, Hansen H, Jawahir I, Kuzman K (2009) Size effects in manufacturing of metallic components. CIRP Ann Manuf Technol 58(2):566–587
10. Hirota K, Michitsuji K (2015) Deformation behavior in boss forming with small punch/die diameter ratio. J Mater Process Technol 216:294–301

11. Meng B, Fu M, Shi S (2018) Deformation characteristic and geometrical size effect in continuous manufacturing of cylindrical and variable-thickness flanged microparts. J Mater Process Technol 252:546–558
12. Ghassemali E, Tan M, Jarfors A, Lim S (2013) Progressive microforming process: Towards the mass production of micro-parts using sheet metal. Int J Adv Manuf Technol 66:611–621
13. Hirota K (2007) Fabrication of micro-billet by sheet extrusion. J Mater Process Technol 191(1–3):283–287
14. Merklein M, Stellin T, Engel U (2012) Experimental study of a full forward extrusion process from metal strip. Key Eng Mater 504–506:587–592
15. Ghassemali E, Jarfors A, Tan M, Lim S (2013) On the microstructure of micro-pins manufactured by a novel progressive microforming process. IntJ Mater Form 6(1):65–74
16. Geiger M, Messner A, Engel U (1997) Production of microparts—size effects in bulk metal forming, similarity theory. Prod Eng Res Devel 4(1):55–58
17. Merklein M, Kuppert A (2009) A method for the layer compression test considering the anisotropic material behavior. IntJ Mater Form 2:483
18. Shen Y, Yu H, Ruan X (2006) Discussion and prediction on decreasing flow stress scale effect. Trans Nonferrous Metals Soc China 16(1):132–136
19. Meßner A (1998) Kaltmassivumformung metallischer Kleinstteile—Werkstoffverhalten, Wirkflächenreibung. Prozessauslegung, Meisenbach, Bamberg

Machine Learning (ML)-Based Prediction and Compensation of Springback for Tube Bending



J. Ma, H. Li, G. Y. Chen, T. Welo, and G. J. Li

Abstract Bent tubes are extensively used in the manufacturing industry to meet demands for lightweight and high performance. As one of the most significant behaviors affecting the dimensional accuracy in tube bending, springback causes problems in tube assembly and service, making the manufacturing process complex, time-consuming, and difficult to control. This paper attempts to present an accurate, efficient, and flexible strategy to control springback based on Machine Learning (ML) modeling. An enhanced PSO-BP network-based ML model is established, providing a strong ability to account for the influences of material, geometry, and process parameters on springback. For supervised learning, training sample data can be collected from the historical production process or, alternatively, finite element simulation and laboratory-type experiments. Using the cold bending of aluminum tubes as the application case, the ML model is evaluated with high reliability and efficiency in springback prediction and compensation strategy of springback.

Keywords Springback · Tube bending · Machine learning · Compensation

J. Ma · H. Li (✉) · G. Y. Chen
State Key Lab of Solidification Processing, School of Materials Science and Engineering, Northwestern Polytechnical University, Xi'an 710071, China
e-mail: liheng@nwpu.edu.cn

J. Ma
e-mail: jun.ma@ntnu.no

J. Ma · T. Welo
Department of Mechanical and Industrial Engineering, Norwegian University of Science and Technology, Trondheim 7491, Norway

G. J. Li
Chengdu Aircraft Industry (Group) Co., Ltd, Chengdu 610092, China

© The Minerals, Metals & Materials Society 2021

G. Daehn et al. (eds.), *Forming the Future*, The Minerals, Metals & Materials Series,
https://doi.org/10.1007/978-3-030-75381-8_13

1 Introduction

As one of the crucial structures for mass/heat transferring and load bearing with enormous quantities and diversities, bent tubular parts have attracted increased application in most industrial fields, such as automobile, aerospace, energy, and so on [1–3]. Springback is a significant issue for tube bending. It refers to the changes of both angles and curvatures after removing the applied tools, leading to a series of problems such as increased tolerance limit, variabilities in assemble, and, sometimes, service performance [3, 4]. From the point of the manufacturing system, springback makes the forming process complex, significantly affecting the process flexibility [5] as well as the adaptive design of control strategies [6]. In addition, this critical problem becomes more dramatic in the manufacturing of complex 3D structures, as well as small production batches with diverse bending angles and curvatures [7]. Thus, achieving accurate control of springback is of importance to high-precision products and integrated design of smart manufacturing systems. However, springback is the "closing work" in a forming process, meaning that all possible factors from the aspects of material property, geometry, and processing conditions can make an impact on springback, thus making it difficult to control dimensional accuracy in tube bending.

Accurate prediction is the premise to achieve effective control of springback. In the past decades, analytical, experimental, and numerical methods have been widely used to estimate springback in metal forming [3, 4]. The analytical method allows fast springback calculation for simple forming cases, offering an advanced understanding of springback characteristics and mechanisms. The finite element (FE) numerical approach can simulate the actual forming process, in particular, with modeling of the complex contact/friction conditions and nonlinear material properties, thus providing accurate predictions of forming defects, such as thinning, distortion as well as springback once high reliability can be ensured. FE-assisted optimization of tooling and process parameters is widely used in the design stage of the forming process. The experimental approach, however, is generally based on "trial-and-error" to search for a satisfactory result. Furthermore, in recent years, several Deep Learning (DL) methods also emerge in springback analysis to explore the control of dimensional accuracy [8–10].

To this date, most FE-based works and DL-based attempts on springback are focused on sheet metal forming, yet with much less concern on the tube bending processes. The "trial-and-error" approach still acts as the main strategy for springback compensation in tube bending production [1, 3], in which at least 2–3 times bending trials are commonly needed to find out an acceptable compensation solution. It causes some critical problems, including production downtime, high costs, waste of materials, scrap, and increased process uncertainties. This is particularly true for the industrial production of bent tubular parts with small batches and multiple part configurations. Even though FE simulation can be used as the virtual "trial-and-error" to reduce the physical trials, it is also a non-added value operation to simulate all the possible forming conditions. In addition, FE simulation with the deterministic target

springback problem can hardly meet the need for process flexibility. To address these problems, it is a need to develop a feasible and effective strategy that can provide a reliable and fast evaluation of compensation for springback, at the same time, with the possibility for the integrated design of closed-loop-control to improve the product accuracy and enhance the process flexibility for tube bending.

To this aim, this work attempts to develop a flexible strategy for springback prediction and compensation in tube bending based on the ML modeling framework. Training datasets for supervised learning can come from the historical production process, alternatively laboratory-type experiments, and FE simulation. Using the cold bending of aluminum alloy (Al-alloy) tubes as the application case, the ML model is verified in both springback prediction and compensation. Based on this research, an outlook on the future development and industrial application of the ML-based springback control strategy is presented.

2 Methodology

2.1 Overview of ML-Based Modeling for Springback

As mentioned above, almost all the possible factors throughout the forming process can make a difference in springback. In fact, as shown in Fig. 1, in addition to springback, the other geometry dimensions, such as wall thickness, ovalization, etc., as well as product performance, such as working pressure, fatigue, etc., are closely related to the above-mentioned influential factors from the aspect of material, geometry, and process. To this end, a "bridge" can be built to link the various input and/or in-process

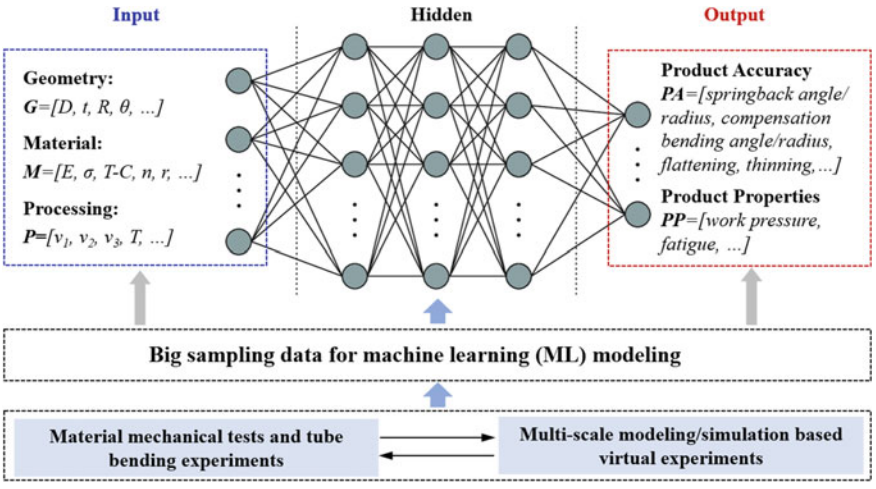


Fig. 1 Overview of the ML-based modeling for tube bending

variables and different output indexes based on big-data mining and analysis, thus achieving better control of product quality and forming process, as well as reducing the manufacturing investment.

However, the accuracy and reliability of the "bridge" model highly depend on the number and quality of sampling data. If the data is all from physical experiments, it will uncourtly cause dramatic time consumption and high cost, especially in small production batches with diverse angles, radius, and spatial structures. Therefore, the idea of this model is to establish the sampling data source by combining typical experiments, such as material property tests and forming experiments, and the multi-scale simulation-based virtual experiments, such as through-process FE simulation of bending–springback. Based on the big-data analysis, a machine learning model can be constructed to map the relation between multiple input variables and springback, thus achieving accurate compensation for springback in tube bending.

2.2 *Rotary Draw Bending and Springback*

Rotary draw bending (RDB) is taken as the forming process in the application. RDB is the most commonly used method for the manufacturing of bent tubes with high dimension accuracy. As shown in Fig. 2a, the whole tube is subjected to the multi-tool constraints; viz., bend die, clamp die, pressure die, wiper die, and flexible mandrel die. Under the joint action of a multi-tool, the tube is drawn around the bending center to form a bent tube with a certain bending radius and angle. Then, the tube is unloaded upon removal of the tools, and springback occurs, as shown in Fig. 2b. Springback in tube bending can cause both changes of released bending angle and radius. For a targeted bending geometry, the processing conditions are always pre-determined after optimization.

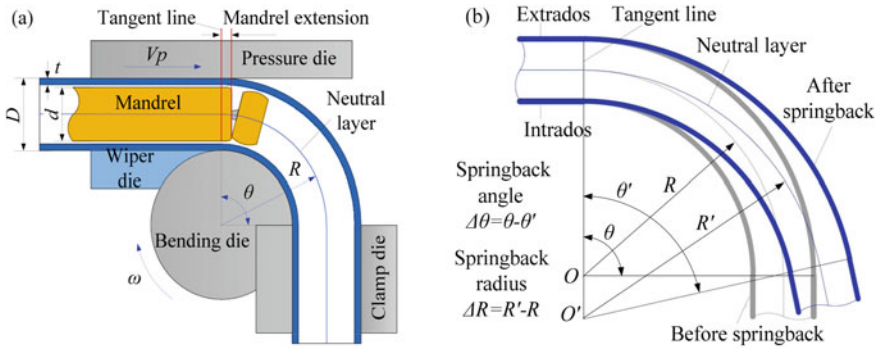


Fig. 2 Schematic view of rotary draw bending: **a** forming principle and tooling system; **b** unloading springback. (Color figure online)

In order to characterize the springback under different bending angles, a springback ratio coefficient is defined as follows:

$$\eta = \Delta\theta \big/ \theta_{\mathrm{b}} = (\theta_{\mathrm{b}} - \theta_{\mathrm{a}}) \big/ \theta_{\mathrm{b}} \tag{1}$$

where η is the springback ratio coefficient, $\Delta\theta$ denotes the amount of springback angle, θ_{b} and θ_{a} represent the bending angle before unloading and actual angle after springback, respectively.

As for springback compensation, a compensation coefficient is also defined as shown in Eq (2):

$$C = \Delta\theta_{\mathrm{c}} \big/ \theta_{\mathrm{t}} = (\theta_{\mathrm{c}} - \theta_{\mathrm{t}}) \big/ \theta_{\mathrm{t}} \tag{2}$$

where C is the compensation coefficient, θ_{t} is the targeted bending angle, and $\Delta\theta_{\mathrm{c}}$ is the amount of compensation angle. Here, θ_{c} is the compensated bending angle, which can further be calculated as follows:

$$\theta_{\mathrm{c}} = (1 + C)\theta_{\mathrm{t}} \tag{3}$$

If the compensation coefficient can be identified, the springback compensation thus can be realized. However, achieving this coefficient presumes an accurate prediction of the springback angle under different bending conditions.

3 Machine Learning Modeling

A myriad of ML algorithms has been developed to address the problems with different features. Among these algorithms, the backpropagation (BP) neural network is the most widely used due to its advanced algorithm structure, which shows a strong ability and potential in recognizing the underlying complicated patterns in engineering tasks [11]. Furthermore, there is a number of successful experiences with utilizing the BP neural network in manufacturing processes, such as stamping, additive manufacturing [12]. Therefore, in this work, the BP neural network is employed as the base to model the relationship between the input variables and springback for tube bending process.

3.1 BP Neural Network

The BP neural network is a multi-layer feedforward network algorithm that is trained according to an error backpropagation scheme [13]. A three-layer BP network with the input layer, the hidden layer, and the output layer is selected as the baseline to construct the ML model. The Hecht–Nelson method is used to determine the node

number of the hidden layer; that is, the node number of the hidden layer is (2n + 1) times the node number of the input layer. For the output, only the springback ratio or compensation coefficient is the objective in this work, which implies that the node number is just set as one.

The basic procedure of the BP network is described as follows:

Step 1: Calculation of hidden layer output:

$$H_j = f\left(\sum_{i=1}^{n} w_{j,i} \cdot x_i + a_j\right) \tag{4}$$

where $w_{j,i}$ represents the connection weight from input node i to hidden node j, a_j is the bias of the neuron j, H_j is the output of hidden layer node j, and f is the activation function of a node.

Step 2: Calculation of the final output:

$$O_k = f_{\mathrm{o}}\left(\sum_{k=1}^{m} w_{k,j} \cdot H_j + b_k\right) \tag{5}$$

where $w_{k,j}$ represents the connection weight from hidden node j to output node k, b_k is the bias of the neuron k, O_k is the output data, and f_{o} is the activation function of output layer nodes.

Step 3: Global minimization of error by training the algorithm:

$$e_k = \sum_{k=1}^{m} |y_k - O_k| \tag{6}$$

where e_k is the error and y_k represents the experimental result of output node k.

Step 4: Check of error tolerance and update of weight coefficients.

3.2 PSO Algorithm

Particle swarm optimization (PSO) was proposed by Kennedy and Eberhart [14], representing an evolutionary computation algorithm inspired by the flocking behavior. In the PSO algorithm, a swarm of particles keeps moving around in a problem space according to the best-known positions of each particle and the entitle swarm, in searching for the optimal solution. The position and moving velocity of the particles in the D-dimensional space are described as follows:

$$\begin{cases} V_i^{t+1} = w^t V_i^t + c_1 r_1 \left(p_{\mathrm{best},i}^t - X_i^t\right) + c_2 r_2 \left(g_{\mathrm{best},i}^t - X_i^t\right) \\ X_i^{t+1} = X_i^t + V_i^{t+1} \end{cases} \tag{7}$$

where X_i^t is the position of particle i in at the t^{th} iteration, V_i^t represents the velocity of this particle, c_1 and c_2 are the learning factors controlling how far a particle can move in a single iteration, and r_1 and r_2 are two random number within [0, 1]. In Eq. (7), $p_{\text{best},i}^t$ and $g_{\text{best},i}^t$ are the optimal position of the particle and the global optimal position of all particles at the tth iteration, respectively, and the w^t is the inertia weight coefficient that makes a balance of the local and global search ability.

In the PSO algorithm, the linearly decreasing inertia weight is commonly used. However, the linear decreasing weight has two drawbacks; viz., the low velocity of convergence when the best point can be detected at an early computation state, and the decreased global search ability with decreasing the weight [15]. Thus, in this model, a nonlinear inertia weight is used to improve the search ability, as shown in Eq. (8):

$$w^t = w_{\max} - \left(w_{\max} - w_{\min}\right) \cdot \tan\left(t \Big/ t_{\max} - \pi \Big/ 4\right) \tag{8}$$

where $w_{\max}$ and $w_{\min}$ are the maximum and minimum inertia weight, and $t_{\max}$ is the maximum iteration, respectively.

In addition, to further improve the global search ability of the PSO algorithm, a crossover operator can be applied after each iteration [16]. According to a given crossover probability, a certain number of particles will be chosen for random hybridization, and then the same number of offspring particles are generated. The position of the offspring particle is determined as

$$X^t = r X_I^t + (1 - r) X_{II}^t \tag{9}$$

where r is a random value within [0, 1], and the subscript "I" and "II" are two parent particles.

The velocity of the offspring particle is calculated by Eq. (10) from their parent particles.

$$V^t = \left|V_I^t\right|\left(V_I^t + V_{II}^t\right) \Big/ \left|V_I^t + V_{II}^t\right| \tag{10}$$

Through the crossover operator, the offspring particles can avoid falling into the local optimization, thus improving the global search ability.

3.3 Enhanced PSO-BP-Based ML Model

By combining the BP neural network and the PSO algorithm with a crossover operator, an enhanced PSO-BP-based machine learning model is thus established. Figure 3 demonstrates the computation flowchart of the proposed ML model. Based on Matlab, the model is numerically implemented for the application in the next section.

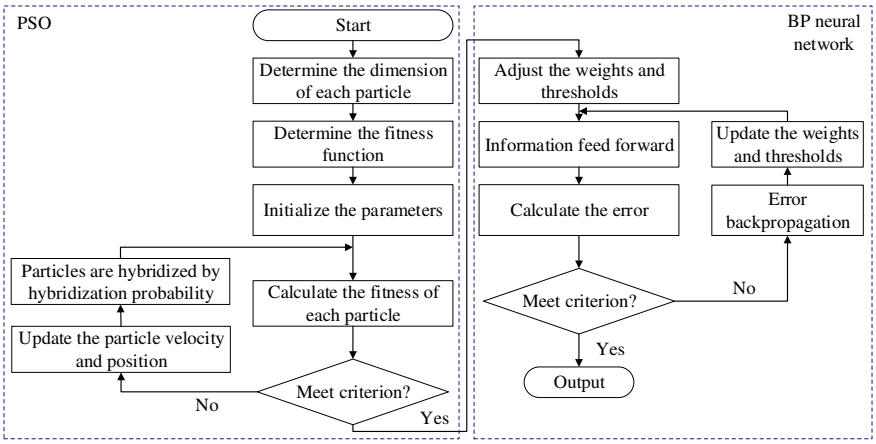


Fig. 3 Flowchart of the enhanced PSO-BP neural network model. (Color figure online)

4 Application and Evaluation

In this application, AA5052-O tubes with eight types of specifications (diameter and thickness) are used. Even though the material grades are the same, variations exist in the mechanical properties between different specifications. Table 1 shows the mechanical properties obtained by uniaxial tension tests, indicating a significant variation in the elastic modulus, yield strength, working hardening, etc. Springback magnitude is determined by the bending moments, elastic modulus, and residual stress after unloading, etc. All the mechanical parameters listed in Table 1 can cause an influence on the stress/strain distribution, further affecting the springback. Therefore, the above material parameters are set as the independent input variables in the ML model. Besides, the geometry parameters—viz., outer diameter, thickness, the

Table 1 Mechanical properties of Al-alloy tubes by uniaxial tension experiments

No.	Outer diameter [mm]	Thickness [mm]	Elastic modulus [MPa]	Yield strength [MPa]	Ultimate tensile strength [MPa]	Fraction elongation [%]	Working hardening exponent	*r*-value
#1	8	1	67244	45	216	22.48	0.328	0.500
#2	10	1	62485	81	220	16.09	0.315	0.929
#3	16	1	67428	70	250	28.57	0.286	0.858
#4	22	1	76190	67	247	25.66	0.302	0.924
#5	30	1	73267	43	180	27.11	0.316	0.628
#6	38	1	73642	81	300	24.14	0.341	0.599
#7	50	1.5	63368	31	128	24.98	0.330	0.635
#8	70	1.5	65671	47	182	26.17	0.346	0.486

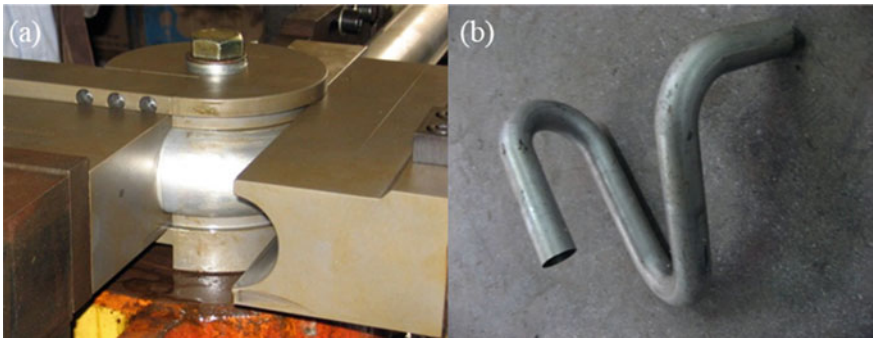


Fig. 4 Rotary draw bending experiment: **a** forming process; **b** Φ50 × t1.5 × 2D bent part. (Color figure online)

ratio of bending radius to outer diameter, and bending angle—are also set as independent input variables. As the tooling/process parameters are generally determined after optimization and then keep constant in production, these parameters are not considered in this work. Figure 4 shows the rotary draw bending process and the typical experimental part.

For the supervised machine learning of this model, the training sample set should be first established. In this application case, only the experimental data collected from the historical tube bending production in a company be used to establish the big-data source, and further to explore the feasibility of the ML model. The training sample data source is comprised of 46 sets of experimental input and springback data, which is acquired from the industrial production process in the company. The training set covers different bending geometries of the above-described eight types of tubular materials, in which the range of bending angle is $\theta = 9$~$122.2°$, and the range of relative bending radius is $R = 2$~$3D$. As shown in Table 2, five sets of experimental inputs are chosen as the test samples to evaluate the prediction accuracy. According to the description in Sect. 3, the parameters related to the ML model are determined

Table 2 Springback prediction based on the ML model

Input				Sp. prediction output + actual result			
D [mm]	t [mm]	Relative bending radius, R/D	Bending angle, θ_b [°]	Exp. sp. angle, $\Delta\theta_{exp}$ [°]	Pred. sp. angle, $\Delta\theta_{pred}$ [°]	Absolute error [°]	Relative error [%]
10	1.0	3	34.20	2.20	2.39	0.19	8.50
16	1.0	2	34.50	1.10	1.02	0.08	7.45
22	1.0	2	66.20	1.30	1.26	0.04	3.31
30	1.0	2	91.20	1.70	1.55	0.15	9.00
70	1.5	2	52.50	1.70	1.65	0.05	3.18

Table 3 Springback compensation based on the ML model

Input				Sp. compensation output + actual result			
D [mm]	t [mm]	Relative bending radius, R/D	Target bending angle, θ_t [°]	Exp. comp. angle, $\Delta\theta_{c,exp}$ [°]	Pred. comp. angle, $\Delta\theta_{c,pred}$ [°]	Absolute error [°]	Relative error [%]
10	1.0	3	32.00	2.20	2.11	0.09	3.91
16	1.0	2	33.40	1.10	0.81	0.29	26.10
22	1.0	2	64.90	1.30	1.21	0.09	7.08
30	1.0	2	89.50	1.70	1.91	0.21	12.53
70	1.5	2	50.80	1.70	1.65	0.05	2.82

as follows: the number of particles: 40, learning coefficient: 2.05, maximum weight: 0.9, minimum weight: 0.4, maximum velocity: 1, hybrid probability: 0.7.

After 34 iterations within 300 s, the prediction results can be calculated, as shown in Table 2. It can be found that the maximum absolute error is 0.188°, the average relative error is 6.29%. Compared with the traditional PSO-BP model, by introducing the crossover operator, not only the prediction accuracy is greatly improved but also the computation time is significantly reduced from 1.5 h to 300 s. For the springback compensation, the computation is completed after 32 iterations within 200 s. As shown in Table 3, the predicted compensation angles can agree with the experimental ones except for one abnormal case. The average absolute error and relative of the compensation angle are 0.15° and 10.49%, respectively. The maximum absolute error is 0.29°, which also meets the tolerance of $\pm$ 0.3° in many application cases.

However, we can find from the predictions of both springback angles and compensation angles, as shown in Tables 2 and 3, that there is still a pronounced variation in the prediction errors, which indicates a probability that an unacceptable prediction occurs. The reason for this variation might be attributed to the sample data used for training the ML model. In this application, the tube specifications (i.e., outer diameter and thickness), and bending geometries (i.e., bending angle and bending radius) vary significantly, however, training data only comprise 46 sets of experimental data from the historical production process. The accuracy of machine learning is sensitive to the number of samples and enlarging the high-quality datasets with a certain range can improve the performance [10, 17]. Thus, for the problem in this work, increasing the size of high-quality training datasets may be helpful to the improvement of springback prediction and compensation. However, it does not mean that the more data of samples, the better performance of the model. The large size of datasets always means an increased computation time. Besides, machine learning can show effectiveness when it is applied to limited types and size of data and well-defined tasks [10]. It needs further exploration to find an optimal size of datasets, thus ensuring the performance as well as balancing the efficiency of the ML model.

5 Conclusions and Outlook

This paper presents a Machine Learning framework for springback prediction and compensation in tube bending towards the improvement of product dimensional accuracy, and process flexibility. The model is based on an enhanced PSO-BP algorithm, which enables a strong ability to address the complex influences of material properties, bending geometries and process parameters on springback, at the same time, has a high computation efficiency. Using the cold rotary draw bending process of Al-alloy tubes, the ML model is verified with high accuracy and efficiency in both springback prediction and compensation. In this application case, the experimental data that are collected from the historical production process in a company is applied for model training. Both the flexible bending geometries (i.e., tube diameter, thickness, bending radius, and bending angle) and the variations of material properties (elastic modulus, yield strength, work hardening exponent, etc.) of the Al-alloy tubes with respect to different specifications are considered to accommodate their influences on springback. The process parameters, however, are not yet considered due to the limited real-time data collection in the forming process.

In future research work, FE simulation-based virtual experiments in combination with typical physical experiments will be used to provide a big-data source for supervised learning of the model, thus improving the prediction/compensation accuracy and reducing the manufacturing investment. In addition, the model will be integrated into the manufacturing system of tube bending, thus seeking a self-adaptive enhancement of the model capability by training with the real-time production data. Finally, a close-loop-control strategy of springback in tube bending will be explored based on the ML model with both offline and online learning.

Acknowledgments Financial assistance of the Commercial Aircraft Research & Development Project of China (MJ-2016-G-64), National Science Funds of China (51522509, 51775441) and NTNU Aluminum Product Innovation Center (NAPIC) is acknowledged.

References

1. Li H, Yang H, Ma J (2018) Tube bending forming technologies: advances and trends. In: Totten GE et al (eds) Encyclopedia of aluminum and its alloys. CRC Press, Boca Raton, pp 2732–2750
2. Li H Fu MW (2019) Deformation based processing of materials: behavior, performance, modeling, and control. Elsevier
3. Li H, Ma J, Liu BY et al (2018) An insight into neutral layer shifting in tube bending. Int J Mach Tools Manufac 126:51–70
4. Wagoner RH, Lim H, Lee MG (2013) Advanced issues in springback. Int J Plast 45:3–20
5. Yang DY, Bambach M, Cao J et al (2018) Flexibility in metal forming. CIRP Ann 67(2):743–765
6. Welo T (2012) Intelligent manufacturing systems: controlling elastic springback in bending. IFIP Int Conf Adv Prod Manag Syst, Rhodes, Greece, 24–26 Sept 2012
7. Allwood JM, Duncan SR, Cao J et al (2016) Closed-loop control of product properties in metal forming. CIRP Ann 65(2):573–596

8. Dezelak M, Pahole I, Ficko M et al (2012) Machine learning for the improvement of springback modelling. Adv Prod Eng Manag 1:17–26
9. Nasrollahi V, Arezoo B (2012) Prediction of springback in sheet metal components with holes on the bending area, using experiments, finite element and neural networks. Mater Des 36:331–336
10. Wang JJ, Ma YL, Zhang LB et al (2018) Deep learning for smart manufacturing: methods and applications. J Manuf Syst 48:144–156
11. Lecun Y, Bengio Y, Hinton G (2015) Deep learning. Nature 521(7553):436–444
12. Qi X, Chen G, Li Y et al (2019) Applying neural-network-based machine learning to additive manufacturing: current applications, challenges, and future perspectives. Engineering 5(4):721–729
13. Li J et al (2012) Brief introduction of backpropagation (BP) neural network algorithm and its improvement. Adv Comput Sci Inf Eng, Zhengzhou, China, 19–20 May 2012
14. Kennedy J, Eberhart, R (1995) Particle swarm optimization (PSO). IEEE Int Conf Neural Networks, Perth, Australia, 27 Nov–1 Dec 1995
15. Bansal JC et al (2011) Inertia weight strategies in particle swarm optimization. IEEE 3rd World Cong Nature Biol Inspir Comp, Salamanca, Spain, 19–21 Oct 2011
16. Chen Y, Li L, Xiao J et al (2018) Particle swarm optimizer with crossover operation. Eng Appl Artif Intel 70:159–169
17. Zhang Y, Ling C (2018) A strategy to apply machine learning to small datasets in materials science. Comput Mater 4(1):1–8

Ductile Fracture Prediction of Hot-Stamped Boron Steel 22MnB5 with Modified Mohr–Coulomb and Hosford–Coulomb Models



Fangxing Wu, Bingtao Tang, Ning Guo, Huiping Li, and Qiaoling Wang

Abstract With the increasing demand for the reduction in energy consumption and enhancement of automobile safety, ultra-high-strength steel are widely used in the automobile industry. Due to the high achievable strength, hot stamping process can be used to supply promising automobile components. The increasing use of high-strength steels provides particular challenges to fracture modeling due to their microstructures and processing conditions. This paper is concerned with plasticity and ductile fracture modelling of hot-stamped boron steel 22MnB5, where martensite phase with high yield strength, work hardening, and ductility are present. The modified Mohr–Coulomb criteria as well as Hosford–Coulomb criteria are implemented using VUMAT in ABAQUS. Parameters of the selected fracture criteria are determined using calibration tests with various kinds of specimen. Fracture properties and flow curves up to large strains are determined from single-phase tensile experiments using digital image correlation. The final hole expansion test shows that the Mohr–Coulomb ductile fracture criterion is more suitable to model ductile fracture in metal forming proc

Keywords Ductile fracture · Boron steel · Hot stamping

1 Introduction

It is critically important to accurately model and predict the failure and fracture behavior with the increased use of high-strength steel components of automobile body structure [1]. Ductile fracture is widely believed to be the main reason for failure

F. Wu · B. Tang (✉) · N. Guo
School of Mechanical and Automotive Engineering, Qilu University of Technology (Shandong Academy of Sciences), Jinan 250353, China

H. Li
School of Materials Science and Engineering, Shandong University of Science and Technology, Qingdao 266590, China

Q. Wang
Department of Industrial Engineering, University of Padova, Padua 35131, Italy

© The Minerals, Metals & Materials Society 2021

G. Daehn et al. (eds.), *Forming the Future*, The Minerals, Metals & Materials Series,
https://doi.org/10.1007/978-3-030-75381-8_14

during forming of advanced high strength steels, aluminum alloys, titanium alloys, and magnesium alloys [2, 3]. Similarly, it is critical to ensure accurate prediction when modeling crash loading sequences [4, 5]. More and more ductile fracture criteria were proposed in the last decade to model ductile fracture behaviors of these advanced metals [6–8].

In this study, the plasticity and ductile fracture of hot-stamped boron steel 22MnB5 are modeled. Four different fracture criteria including two modified Mohr–Coulomb (MMC) and two Hosford–Coulomb (HC) have been implemented in ABAQUS/Explicit using users' subroutine VUMAT. Experiments are conducted on hot-stamped boron steel 22MnB5 (t = 1.8 mm) to calibrate ductile fracture criteria under various stress states, including in-plane shear, uniaxial tension, plane strain tension, and verified by hole expansion test. Digital Image Correlation (DIC) method is applied to monitor the surface pattern and record the strain evolution of the specimen surface during the experiment. Testing of dogbone specimens made in various directions shows that the von Mises criterion with isotropic strain hardening criterion is a simple and accurate choice [9]. Fracture strains of these specimens are calculated by hybrid numerical-experimental method [7] and used to calibrate the parameters of the four different fracture criteria. The calibrated criterion is then utilized to model the dependence of ductile fracture under various loading conditions. Finally, different ductile fracture criteria are compared with experimental results to evaluate their accuracy.

2 Modified Mohr–Coulomb Fracture Criterion

Three-dimensional principal stress vector $(\sigma_{1,}\sigma_{2,}\sigma_3)$ is used to define the stress state. Two stress invariants η and $\overline{\theta}$ are usually used to identify the stress state. The stress triaxiality η is defined as the ratio of the mean stress σ_m to the von Mises equivalent stress $\overline{\theta}_{VM}$:

$$\eta = \frac{\sigma_m}{\overline{\theta}_{VM}} \text{with} \sigma_m = \frac{tr(\boldsymbol{\sigma})}{3} \text{and} \overline{\theta}_{VM} = \sqrt{\frac{3}{2}\boldsymbol{\sigma}' : \boldsymbol{\sigma}'} \tag{1}$$

where $\boldsymbol{\sigma}'$ is the deviatoric stress and the normalized Lode angle $\overline{\theta}$ ranging from -1 to 1 is expressed as

$$\overline{\theta} = 1 - \frac{2}{\pi}\arccos\left(\frac{27}{2}\frac{det(\boldsymbol{\sigma}')}{\overline{\theta}^3_{VM}}\right) \tag{2}$$

Bai and Wierzbicki [10] modified the Mohr–Coulomb (MC) criterion to describe ductile fracture behavior of metals. The modified MC (MMC) criterion was expressed in the space of $\left(\eta, \bar{\theta}, \bar{\varepsilon}^p\right)$. The modified Mohr–Coulomb criterion (MMC4) with four fracture parameters c_1, c_2, $c_3$and c_θ to be calculated by experimental data is expressed

in Eq. (3):

$$\bar{\varepsilon}_f = \left\{ \frac{K}{c_2} \left[c_3 + \frac{\sqrt{3}}{2-\sqrt{3}} (c_\theta - c_3) \left(\sec\left(\frac{\pi \bar{\theta}}{6} \right) - 1 \right) \right] \times \left[\sqrt{\frac{1+c_1^2}{3}} \cos\left(\frac{\pi \bar{\theta}}{6} \right) + c_1 \left(\eta + \frac{1}{3} \sin\left(\frac{\pi \bar{\theta}}{6} \right) \right) \right] \right\}^{-\frac{1}{n}} \tag{3}$$

In case of $c_\theta = 1$, the MMC4 criterion is reduced to MMC3 in a form shown below:

$$\bar{\varepsilon}_f = \left\{ \frac{K}{c_2} \left[c_3 + \frac{\sqrt{3}}{2-\sqrt{3}} (1 - c_3) \left(\sec\left(\frac{\pi \bar{\theta}}{6} \right) - 1 \right) \right] \times \left[\sqrt{\frac{1+c_1^2}{3}} \cos\left(\frac{\pi \bar{\theta}}{6} \right) + c_1 \left(\eta + \frac{1}{3} \sin\left(\frac{\pi \bar{\theta}}{6} \right) \right) \right] \right\}^{-\frac{1}{n}} \tag{4}$$

with K and n related to strain hardening properties.

3 Hosford–Coulomb Fracture Criterion

Mohr and Marcadet [11] modified the Mohr–Coulomb criterion by expressing it as a linear combination of the Hosford equivalent stress and the normal stress acting on the plane of maximum shear stress reaching a critical value b [12]:

$$\bar{\sigma}_{HF} + c(\sigma_1 + \sigma_3) = b \tag{5}$$

Here σ_1,σ_2, and σ_3 are the principal stresses ($\sigma_1 \geq \sigma_2 \geq \sigma_3$), c is the friction coefficient in the Mohr–Coulomb criterion. The Hosford equivalent stress can be expressed as

$$\bar{\sigma}_{HF} = \left\{ \frac{1}{2} \left((\sigma_1 - \sigma_2)^a + (\sigma_1 - \sigma_3)^a + (\sigma_2 - \sigma_3)^a \right) \right\}^{\frac{1}{a}} \tag{6}$$

Equation (6) can be transformed to the space of $\left(\eta, \bar{\theta}, \bar{\varepsilon}^p\right)$. Thus, Hosford–Coulomb fracture criterion for a strictly proportional loading can be expressed as

$$\bar{\varepsilon}_f^{pr}\left[\eta, \bar{\theta}\right] = b(1+c)^{\frac{1}{n_f}} g\left[\eta, \bar{\theta}\right] \tag{7}$$

With

$$g\left[\eta,\bar{\theta}\right]=\left(\left\{\frac{1}{2}\left((f_1-f_2)^a+(f_1-f_3)^a+(f_2-f_3)^a\right)\right\}^{\frac{1}{a}}+c(2\eta+f_1+f_3)\right)^{-\frac{1}{n_f}} \tag{8}$$

The Lode angle parameter-dependent functions can be written as

$$f_1\left[\bar{\theta}\right]=\frac{2}{3}\cos\left[\frac{\pi}{6}\left(1-\bar{\theta}\right)\right] \tag{9}$$

$$f_2\left[\bar{\theta}\right]=\frac{2}{3}\cos\left[\frac{\pi}{6}\left(3+\bar{\theta}\right)\right] \tag{10}$$

$$f_3\left[\bar{\theta}\right]=-\frac{2}{3}\cos\left[\frac{\pi}{6}\left(1+\bar{\theta}\right)\right] \tag{11}$$

In this paper, if the transformation coefficient n_f is always set to 0.1, the criterion is named HCI, while if it is involved in the calibration of the fracture criterion, the criterion is called HCII. Therefore, there are three parameters, a, b, and c to be identified for HCI, while four parameters, a, b, c, and n_f to be determined for HCII.

The two uncoupled fracture models assume that the evolution of damage has no effect on the effective stress–strain response of the material before fracture occurs. Within this framework, damage is depicted using the scalar variable D, and its increase $dD \geq 0$ is defined through the increment of the equivalent plastic strain $\overline{\varepsilon}^p$ with respect to a stress-dependent reference failure strain $\hat{\varepsilon}$ [13].

$$dD=\frac{d\overline{\varepsilon}^p}{\hat{\varepsilon}(\boldsymbol{\sigma})} \tag{12}$$

It is assumed that the material is in its unreformed state in case of $D = 0$ and in fracture initiation process when $D = 1$.

4 Experiments for Hot-Stamped Boron Steel 22MnB5

Experiments are conducted for hot-stamped boron steel 22MnB5 to characterize the plastic and fracture behaviors of the alloy. The in-plane shear specimens are used in experiments to figure out the stress–strain curve. The material work hardening behavior at large strain is obtained by the reverse engineering approach.

The fracture behavior is investigated by five types of specimens: specimens with a central hole, notched specimens (R2.5, R5, R10), in-plane shear, and equi-biaxial test specimens. Stretching processes are recorded by a three-dimensional GOM Aramis

Table 1 Fracture stains of hot-stamped boron steel 22MnB5 and its Lode parameter and stress triaxiality by hybrid method

Specimens	Lode parameter (L)	Lode angle (θ)	Normalized lode angle ($\bar{\theta}$)	Stress triaxiality (η)	Fracture strain (ε_f)
Central hole	− 0.8460	0.0692	0.8678	0.4826	0.6904
Notched R5	− 0.0515	0.4939	0.0568	0.6891	0.5155
In-plane shear	− 0.0457	0.4972	0.0504	0.0183	0.8516
Equi-biaxial	0.9741	1.0359	− 0.9784	0.6330	0.3765

system for the experimental measurement of fracture strains. The von Mises equivalent plastic strains are calculated right before the onset of ductile fracture for these tests and considered as the fracture strains. The normalized Lode parameter and stress triaxiality as well as the ductile fracture strain are recorded in Table 1 for various specimens.

5 Application of the Ductile Fracture Criterion to Hot-Stamped Boron Steel 22MnB5

According to the experimental data shown in Table 1, four different fracture loci are constructed in Fig. 1a–d, respectively in the coordinate of Lode parameter and stress triaxiality. The related experimental data is also plotted in the

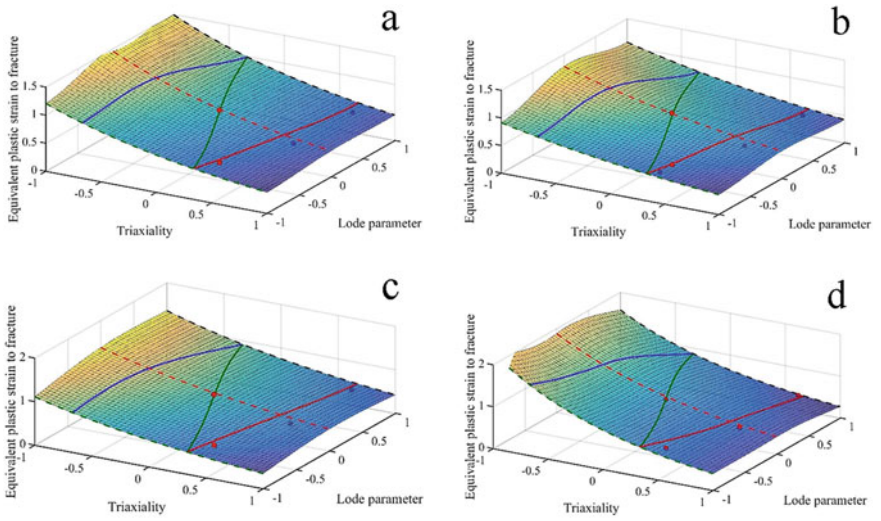


Fig. 1 The constructed fracture loci optimized with the fracture strains **a** HCI; **b** HCII; **c** MMC3; **d** MMC4. (Color figure online)

figures. The constructed fracture loci meet most of the experimental data. The fracture parameters for MMC3 are optimized as K = 1710.8MPa, n = 0.05, c_1 = 0.0133, c_2 = 843.44and c_3 = 0.8624, while for MMC4 are optimized as K = 1710.8MPa, n = 0.05, c_1 = 0.0219, c_2 = 866.27, c_3 = 0.8830and c_θ = 1.0428, and for HCI are optimized as $a = 2.5036, b = 0.5466, c = 0.0295$. Finally, the parameters for HCII are optimized as $a = 2.2542, b = 0.4892, c =$ 0.0077and $n_f = 0.0328$.

The calibrated and constructed fracture loci are implemented using user's subroutine VUMAT in ABAQUS/Explicit. The evolution of ductile fracture is simulated for the central hole, notched R5, in-plane shear as well as hole expansion test specimens. The evolution of load–stroke curves for experiments and numerical simulations for specimen of hot-stamped boron steel 22MnB5 are described in Fig. 2. Table 2 shows the comparison of the calculated fracture displacement with the averaged experimental displacement with four types of fracture criteria. The error functions can be written as

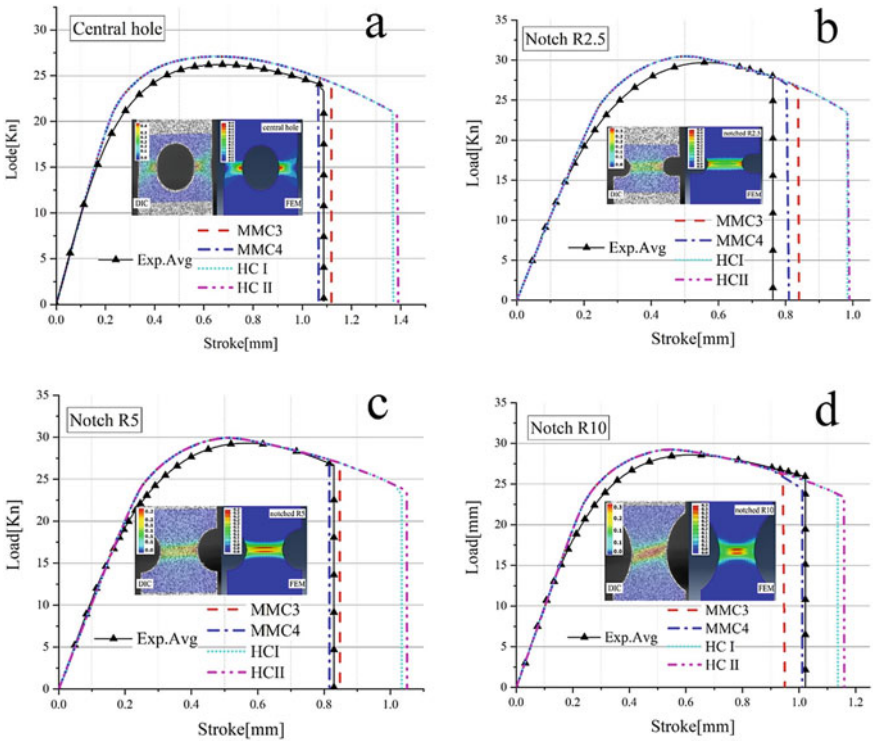


Fig. 2 FE simulation results of tensile process for **a** central hole; **b** notched R2.5; **c** notched R5; **d** notched R10; **e** in-plane shear; **f** hole expansion test. (Color figure online)

Table 2 Comparison of the calculated fracture displacement with the averaged experimental displacement

Specimens	Exp. average (unit:mm)	MMC3(Err)	MMC4(Err)	HCI(Err)	HCII(Err)
Central hole	1.105	1.118(1.19%)	1.066(3.51%)	1.366(23.64%)	1.384(25.27%)
Notched R2.5	0.751	0.840(11.82%)	0.810(7.83%)	0.984(31.03%)	0.983(30.89%)
Notched R5	0.814	0.848(4.24%)	0.816(0.30%)	1.034(22.00%)	1.049(28.87%)
Notched R10	1.072	0.950(11.40%)	1.011(5.69%)	1.137(6.06%)	1.159(8.12%)
In-plane Shear	1.547	1.390(10.18%)	1.440(6.94%)	2.179(40.85%)	2.410(55.79%)
Hole expansion	20.553	21.232(3.30%)	20.514 (0.19%)	38.090(85.33%)	34.906(69.83%)

$$Err = \frac{\left|d_{Expave} - d_f\right|}{d_{Expave}} \tag{13}$$

where d_{Expave} is the averaged experimental displacement,d_f is calculated displacement by fracture criterion.

The plastic deformation and fracture evolution of central hole specimen, three notched specimens, in-plane shear specimen as well as hole expansion test specimen are simulated with four ductile fracture criteria. The comparison of load–stroke curves between FE simulation and experimental data in Fig. 2 shows that the MMC3 and MMC4 ductile fracture criteria meets the experiments quite well. In case of the fracture displacement predicted by the MMC4 fracture criterion, its Err is less than 8%. For the MMC3 fracture criterion, the prediction accuracy is not as good as the MMC4 fracture criterion and its Err is less than 12%. Figure 2 shows that the stroke predicted by two HC models is significantly exceeding the one of the experiment. The reason is due to the overestimation of fracture strains shown in Table 2. It shows that two HC models are not proper to predict the fracture evolution of hot-stamped boron steel 22MnB5.

In case of in-plane shear specimen, the fracture stoke is slightly underestimated by the calibrated ductile fracture models even using MMC4 fracture model. The reason is that, for in-plane shear specimen, the used shear strain to calibrate the fracture criterion is not the true equivalent plastic strain at fracture stroke. Because the change of the Lode parameter and the triaxiality is more severe, the predicted ductile fracture strain by hybrid numerical–experimental method is of a little discrepancy compared with that of experimental data. But the predicted load–stroke evolution of the specimens is still acceptable, showing the wide applicability of the MMC4

fracture model when the stress state ranges from uniaxial tensile to plane strain tensile state.

6 Conclusions

In this paper, four types of fracture criteria, MMC3, MMC4, HCI, and HCII, are applied to predict the fracture behavior of hot-stamped boron steel 22MnB5. Five types of specimens are used to determine the parameter values of fracture criteria and evaluate the their prediction accuracy under different stress states. Hole expansion tests are carried out to investigate their accuracy in case of non-proportional loading conditions. It proves the modified Mohr–Coulomb criteria, especially MMC4 can accurately predict the fracture of high strength steels such as hot-stamped boron steel 22MnB5 under a wide range of stress condition not only in proportional but also in non-proportional loading process.

Acknowledgments This research was funded by the National Natural Science Foundation of China grant number 51875295, the Joint International Research Project of Qilu University of Technology (Shandong Academy of Sciences) grant number QLUTGJHZ2018007, Research Leader Studio in Colleges and Universities of Jinan grant number 2018GXRC026.

References

1. Tang B, Yuan Z, Cheng G, Huang L, Zheng W, Xie H (2013) Experimental verification of tailor welded joining partners for hot stamping and analytical modeling of TWBs rheological constitutive in austenitic state. Mater Sci Eng A 585:304–318
2. Bao Y, Wierzbicki T (2004) On fracture locus in the equivalent strain and stress triaxiality space. Int J Mech Sci 46(1):81–98
3. Lou Y, Chen L, Clausmeyer T, Tekkaya AE, Yoon JW (2017) Modeling of ductile fracture from shear to balanced biaxial tension for sheet metals. Int J Solids Struct 112:169–184
4. Tang B, Wang Q, Wang Z, Zheng W (2013) The influence of deformation history on microstructure and microhardness during the hot stamping process of boron steel B1500HS. Int J Mater Prod Technol 46(4):255–268
5. Pack K, Marcadet SJ (2016) Numerical failure analysis of three-point bending on martensitic hat assembly using advanced plasticity and fracture models for complex loading. Int J Solids Struct 85:144–159
6. Lou Y, Huh H, Lim SJ, Pack KH (2012) New ductile fracture criterion for prediction of fracture forming limit diagrams of sheet metals. Int J Solids Struct 49:3605–3615
7. Lou Y, Huh H (2013) Prediction of ductile fracture for advanced high strength steel with a new criterion: experiments and simulation. J Mater Process Technol 213:1284–1302
8. Bai Y, Wierzbicki T (2008) A new model of metal plasticity and fracture with pressure and Lode dependence. Int J Plast 24:1071–1096
9. Tang B, Wu F, Wang Q, Liu J, Guo N, Ge H, Wang Q, Liu P (2020) Damage prediction of hot stamped boron steel 22MnB5 with a microscopic motivated ductile fracture criterion: Experiment and simulation. Int J Mech Sci 169:

10. Bai Y, Wierzbicki T (2010) Application of extended Mohr-Coulomb criterion to ductile fracture. Int J Fract 161:1–20
11. Mohr D, Marcadet SJ (2015) Micromechanically motivated phenomenological Hosford-Coulomb model for predicting ductile fracture initiation at low stress triaxialities. Int J Solid Struct 67:40–55
12. Cerik B, Lee K, Park SJ, Choung J (2019) Simulation of ship collision and grounding damage using Hosford-Coulomb fracture model for shell elements. Ocean Eng 173:415–432
13. Grolleau V, Roth CC, Lafile V, Galpin B, Mohr D (2019) Loading of mini-Nakazima specimens with a dihedral punch: Determining the strain to fracture for plane strain tension through stretch-bending. Int J Mech Sci 152:329–345

Understanding the Microscale Plastic Behavior and Deformation Mechanism of Magnesium Alloy via Ex Situ Experiments and Full-Field Crystal Plasticity Modeling



Haiming Zhang, Shuai Xu, Xiaoqing Shang, and Zhenshan Cui

Abstract Magnesium alloys have been of growing interest for their low density and high specific strength, but their applications are impeded by their poor formability at room temperature. This work employs the state-of-art experimental and modeling techniques to understand the joint effect of thickness and grain size on the plastic behavior and deformation mechanism of wrought Mg alloy. Equal channel angle pressing was applied to AZ31 Mg alloy to fabricate billets with different grain sizes but the similar basal texture. Interrupted micro-tensile tests combined with ex situ EBSD characterizations were carried on the fine-polished specimens with different grain sizes and thicknesses. It shows that mechanical twinning is significantly affected by both grain size and thickness. In particular, the volume fraction of extension twins decreases with the number of grains in the thickness. Full-field crystal plasticity simulations demonstrate that both the contributions of basal slip and twinning are rather sensitive to grain size.

Keywords Size effect · Deformation twinning · Crystal plasticity · Magnesium alloys · Ex situ EBSD

1 Introduction

For their high specific strength and excellent biocompatibility, magnesium (Mg) alloys are of great application in fabricating micro-parts using in the fields of biological medicine and MEMS, etc. [1, 2]. However, it is challenging to form Mg alloy parts at room temperature, as Mg alloys generally exhibit poor room temperature formability and strong anisotropy for their low-symmetric hexagonal close-packed (HCP) crystal structure. Compared with the cubic metals, e.g., aluminum and copper, Mg alloys show more complex plasticity behaviors. Mg alloys essentially have two types of deformation modes, i.e., dislocation slip and deformation twinning [3]. As regards dislocation slip, the deformation of Mg alloys is mainly accommodated by

H. Zhang (✉) · S. Xu · X. Shang · Z. Cui
School of Materials Science and Engineering, Institute of Forming Technology and Equipment, Shanghai Jiao Tong University, Shanghai 200030, China
e-mail: hm.zhang@sjtu.edu.cn

© The Minerals, Metals & Materials Society 2021

G. Daehn et al. (eds.), *Forming the Future*, The Minerals, Metals & Materials Series,
https://doi.org/10.1007/978-3-030-75381-8_15

basal $\langle a \rangle$ slip and conditionally by prismatic $\langle a \rangle$ slip, pyramidal $\langle a \rangle$ slip, and non-basal $\langle c + a \rangle$ slip. For deformation twinning at room temperature, Mg alloys have $\{10\bar{1}2\}\langle 10\bar{1}\bar{1}\rangle$ extension twinning (ET) accommodating the resolved tensile deformation in $\langle c \rangle$ axis and $\{10\bar{1}1\}\langle 10\bar{1}\bar{2}\rangle$ contraction twinning (CT) accommodating the compressive deformation in $\langle c \rangle$ axis [4]. The deformation mechanism of Mg, therefore, is a complex association of the slip systems with $\langle a \rangle$ and $\langle c+a \rangle$ Burgers vectors as well as various twin systems.

Grain refinement is an important way to overcome the strength–ductility dilemma of Mg alloys. Many works have been carried out to study the grain size effect on mechanical property and deformation mechanism concerning the competition and interaction between dislocation slip and deformation twinning [5, 6]. Barnett et al. [7] reported the inhibition of twinning in an AZ31 alloy with sub-micron grain size. It is attributed to the decrease of the pile-up dislocations, which reduces the local stress at grain boundaries below the threshold of twin nucleation. Based on crystal plasticity (CP) simulations, Jian et al. [8] explained that the Hall–Petch relationship of an AZ31B sheet is primarily due to the grain size dependence of the CRSS of the prismatic slip systems.

Except the grain size effect, the geometrical constraints, such as thickness of foils/sheets, also significantly affect the plastic behaviors and mechanical responses of polycrystalline metals when the dimension of components/specimens decreases to microscale. Understanding the influence of microstructures and geometrical constraints on the deformation mechanism of Mg alloys hence is important for the design of alloys and forming processes. Unlike the cubic metals, for HCP metals, the joint effect of the intrinsic/extrinsic constraints on the deformation and failure mechanisms are still not well understood. In this study, ex situ EBSD characterizations combined with full-filed crystal plasticity (CP) simulations were employed to explore the influence of grain sizes (d) and specimen thicknesses (t) on the plastic behaviors and deformation mechanisms of Mg alloy foils subjected to micro-tensile deformation.

2 Experiment and Modeling Framework

2.1 Micro-Tensile Tests and Ex Situ EBSD Characterizations

The studied material is a commercial extruded AZ31 Mg alloy. The equal channel angular pressing (ECAP) process followed by annealing processing was used to obtain billets with different grain sizes but similar texture. The ECAP was operated with a multi-temperature step-down technology under the Bc route. The refined billets then were annealed under different heat treatments and cut into lath-shaped specimens with length of 28 mm and width of 6 mm, but different nominal thicknesses

Table 1 Average grain size and thickness of the studied AZ31 Mg alloy foils machined from ECAP billets underwent different annealing operations

No.	Annealing temperature (°C)	Annealing time (hour)	Grain size (d) (μm)	Thickness (t) (mm)	λ (t/d)
1	450	10	40	0.2	5
2				0.5	13
3				1.0	25
4	250	2	7	0.2	28
5				0.5	71

($t = 0.2$, 0.5 and 1.0 mm). Table 1 presents the details of the annealing treatments and the obtained grain size (calculated from EBSD maps subsequently) of the studied AZ31 Mg alloy foils.

Uniaxial tensile tests at room temperature were performed on the specimens listed in Table 1 via an in-house micro-tester system with the load cell of 5000 N, as shown in Fig. 1a; the speed of the crosshead is 0.3 mm/min. The tensile direction is along the extrusion direction (ED) of the ECAP operation. The tensile tests were interrupted at the design strain levels, i.e., $\varepsilon_{ED} = 2, 4, 8, 12, 16\%$, and up to fracture. Figure 1b shows the miniature rectangular specimens for the interrupted tensile tests and ex situ EBSD characterizations of microstructure evolution. The microstructure evolution in the region of interest was observed using a MIRA3 field emission SEM equipped with an Oxford EBSD system operating at 20 kV. The region of interest was ground with 600, 1200, 2000, 3000, and 5000 grit SiC papers, and then electro-polished at 15 V voltage in a solution of 3% perchloric acid and ethanol solution chilled to −40 °C. The region of interest was examined again when the specimens were deformed to the designed strain levels.

Figure 2 shows the initial microstructures of the specimens in the form of EBSD maps with ED inverse pole figure (IPF) coloring and (0001) pole figures (PFs). Figure 2a shows the representative microstructure of the coarse grain (CG) specimens (No. 1, 2, and 3 shown in Table 1), and Fig. 2b the fine-grain (FG) specimens (No.4 and 5). The average grain size (d) of the CG specimens is 40 μm and that of the FG

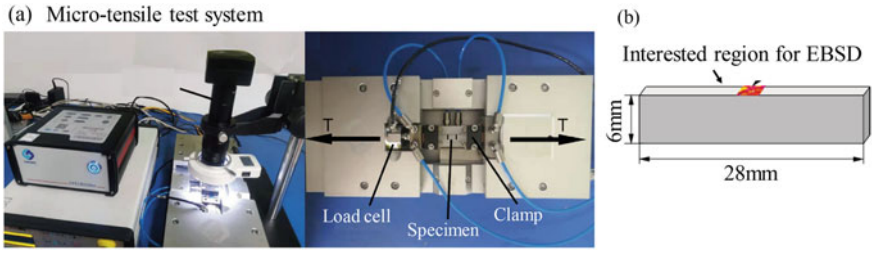


Fig. 1 **a** Micro-tensile test system and **b** the geometrical dimension of the specimens for interrupted tensile tests. (Color figure online)

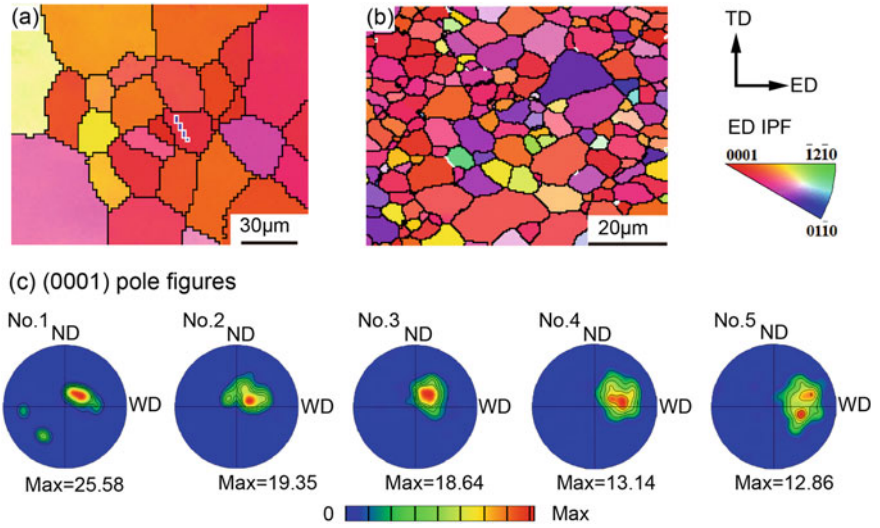


Fig. 2 The initial microstructures of the specimens in form of EBSD maps with ED inverse pole figure (IPF) coloring, **a** the coarse grain specimen and **b** the fine grain specimen. **c** shows the (0001) pole figures (PFs) of all the studied specimens. (Color figure online)

specimens is 7 μm. The (0001) PFs shown in Fig. 2c tells that both the CG and FG specimens show strong basal texture, i.e., a strong ED fiber texture along the basal (0001) pole. It means that extension twinning can be easily activated to coordinate the elongation along *c* axis during the tension deformation. Because of the fewer grains in the region of interest, the texture intensity of the CG specimens is slightly higher than that of the FG specimens.

2.2 CP Constitutive Model Incorporating Dislocation Slip and Deformation Twinning

Full-field CP simulations were complementally used to study the micro-mechanical behaviors of the Mg alloy foils. The CP constitutive model incorporates the plastic deformation models of both dislocation slip and deformation twinning. The twinning model formulating in the form of pseudo slip, referring to Salem et al. [9]. The plastic velocity gradient resulted from both dislocation slip and twinning is expressed as

$$L^p = \sum \dot{\gamma}^{\alpha}_{sp} S^{\alpha}_{sp} + f_{tw} \sum \dot{\gamma}^{\beta}_{tw} S^{\beta}_{tw} \tag{1}$$

Here, S^{α}_{sp} and S^{β}_{tw} are the Schmid tensors of the potential slip systems and twinning systems, $\dot{\gamma}^{\alpha}_{sp}$ and $\dot{\gamma}^{\beta}_{tw}$ denote the plastic shear rates associated with the slip and

twinning on the αth slip system and the βth twinning system, respectively. f_{tw} is the accumulated volume fraction of the twinned areas.

The power-law constitutive relation was adopted to describe the plastic shear rates resulted from both slip and twinning. It is written as

$$\dot{\gamma}_{sp}^{\alpha} = \dot{\gamma}_{sp}^{0} \left| \frac{\tau_{sp}^{\alpha}}{g_{sp}^{\alpha}} \right|^{1/m_{sp}} \operatorname{sign}\left(\tau_{sp}^{\alpha}\right), \text{ and } \dot{\gamma}_{tw}^{\beta} = \dot{\gamma}_{tw}^{0} \frac{\tau_{tw}^{\beta}}{g_{tw}^{\beta}}^{1/m_{tw}} \tag{2}$$

where $\dot{\gamma}_{sp}^{0}$ and $\dot{\gamma}_{tw}^{0}$ are the reference shearing rate, m_{sp} and m_{tw} the rate sensitivity parameters, g_{sp}^{α} and g_{tw}^{β} the slip resistance and twinning resistance. The evolutions of g_{sp}^{α} and g_{tw}^{β} are formulated as follows [9]:

$$\begin{cases} \dot{g}_{sp}^{\alpha} = h_{sp}^{0}(1 + c_1 \cdot f_{tw}) \sum_{\xi} \left(1 - \frac{g_{sp}^{\xi}}{g_{sp}^{\infty}}\right)^{n} \dot{\gamma}_{sp}^{\xi} \\ \dot{g}_{tw}^{\beta} = h_{tw}^{0}(f_{tw})^{c_2} \sum_{\zeta} \dot{\gamma}_{tw}^{\zeta} + h_{tw-sp}^{0} \left(\sum_{\alpha} \gamma_{sp}^{\alpha}\right)^{c_3} \sum_{\xi} \dot{\gamma}_{sp}^{\xi} \end{cases} \tag{3}$$

The material parameter h_{sp}^{0} represents the initial hardening modulus of slip systems, and g_{sp}^{∞} denotes the saturated slip resistance. h_{tw}^{0} and h_{tw-sp}^{0} denote the initial twin hardening moduli due to twin-twin interactions and slip-twin interactions, respectively. The parameters n, c_1, c_2, c_3, and s_{pr} are estimated constants. In particular, c_1 describes the effect of the Basinski mechanism on the slip resistance. Mg alloys have various slip systems and twinning systems to coordinate the plastic deformation. In this work, the CP constitutive model considers $\{0001\}\langle 11\bar{2}0\rangle$ basal $\langle a\rangle$ slip, $\{10\bar{1}0\}\langle 11\bar{2}0\rangle$ prismatic $\langle a\rangle$ slip, $\{1\bar{2}12\}\langle \bar{1}2\bar{1}3\rangle$ pyramidal $\langle c+a\rangle$ slip, and $\{10\bar{1}2\}\langle \bar{1}011\rangle$ extension twinning. The material parameters for the alloy are listed in Table 2.

The CP model was implemented into the open-source spectral method solver DAMASK. The EBSD data of the initial structures shown in Fig. 1 were directly used to construct the studied representative volume elements (RVEs); the periodic boundary condition of uniaxial tension was enforced on the RVEs [10].

Table 2 The material parameters of the CP model for AZ31 Mg alloy. The unit of the stress-type parameters is MPa

Systems	m	n	g^0	g^∞	h_{sp}^0	h_{tw}^0	h_{tw-sp}^0
Basal	0.05	1.088	20	30	332	/	/
Prismatic		1.07	90	140	887		
Pyramidal		2.2	90	165	4500		
Extension twin		/	30	/	/	50	100

3 Results and Discussion

Figure 3 present the EBSD maps of specimens No. 1 (the smallest λ), No. 3, and No. 5 (the largest λ) strained to 0.04 and 0.08, respectively. The white lines depict twinning boundaries (TBs), while the black lines grain boundaries (GBs). It should be noted that all the twins characterized in Fig. 3 are $\{10\bar{1}2\}\langle 10\bar{1}\bar{1}\rangle$ extension twins (ETs), as the reorientation angles are found around 86.3°. Plentiful twins are clearly seen in CG specimens No. 1 and No. 3; this is consistent with the report of Jiang et al. [11] that ETs occur firstly in the deformation of 0.02 ~ 0.04. By contrast, twins are scarcely found in FG specimen No. 5 only few twin embryos appear at GBs. When the specimens were strained to 0.08, the CG ones experienced prominent twinning, especially for specimen No.1 in which most grains are occupied by large ETs. InFG specimen No. 5 the extension twinning is still significantly suppressed. Another observation is that the width of twins in the CG specimens is much larger than that is the FG specimens.

To explore the size effects on the twin behaviors quantitatively, the twin area fractions of the specimens at different deformation stages were counted and are shown in Fig. 4. Both grain size and specimen thickness (or λ) significantly affect the evolution of ETs. The fraction of ETs increases with the decrease of λ. At strain level of 0.08, the twin area fraction of the specimen No.1 is about 17 times that

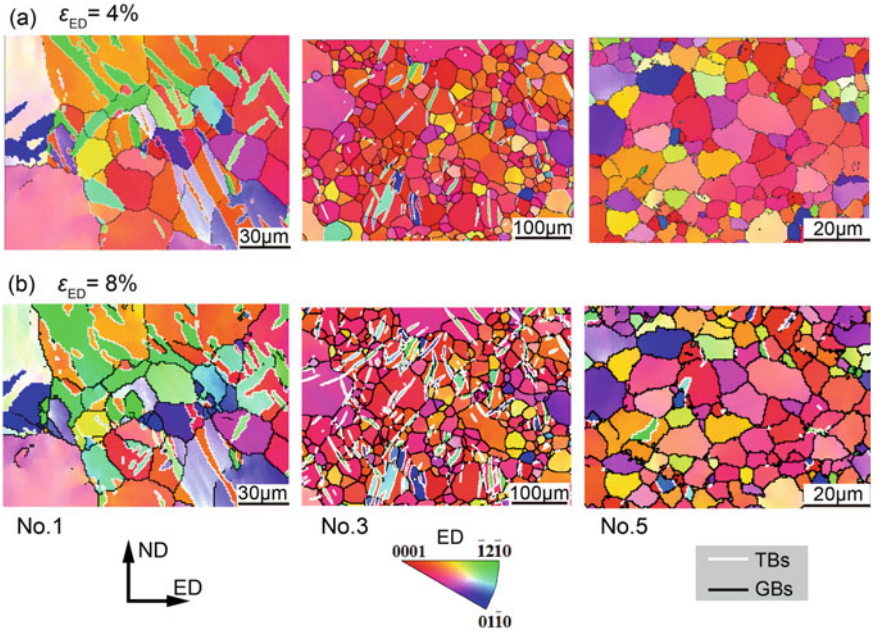


Fig. 3 The microstructures of the specimens No. 1, No. 3, and No. 5 strained to 0.04 and 0.08. (Color figure online)

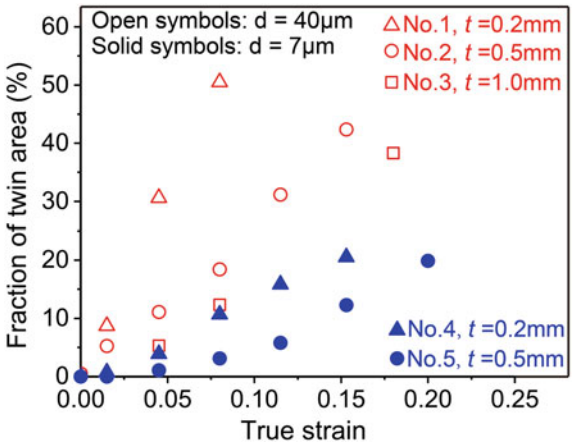


Fig. 4 The evolution of the area fraction of extension twins with respect to the global strain. (Color figure online)

of the specimen No. 5. For the specimen No. 5, even at a relative large fracture strain, the twin area fraction occupies only about 20%, and the activation of ETs is significantly suppressed in the early deformation stage. Consequently, both grain size and thickness soundly affect the extension twinning of the studied AZ31 foils, and it is concluded that λ plays an important role in affecting the nucleation and growth of deformation twinning.

Figure 5 shows the simulated results obtained from the CP simulations; the volume fraction (f_{tw}) of ETs and the total shear of basal slip of the specimens No.1, No. 3, and No. 5 at the strain levels of 0.04 and 0.08, respectively. Since the extension twinning was treated as a pseudo slip in this work, the instantaneous transformation of ETs is viewed to accomplish gradually; $f_{tw} = 1.0$ means that the twinning process has been completed. The predicted ETs essentially agree well with the experimental results shown in Fig. 3, which verifies the accuracy of the full-field CP model. Figure 5 shows that there is obvious competition between the activation of basal slip and extension twinning in the early stage of deformation, i.e., $\varepsilon_{ED} = 0.04$. The activation of ETs is significantly suppressed by the activation of basal slip. However, at the strain level of 0.08, as the work hardening of basal slip the localized shear strain due to the activation of basal slip are changed dramatically. Shear localizations appear in the grains with high volume fraction of ETs, which implies the micromechanical cooperation between basal slip and extension twinning.

To analyze the contribution of individual deformation modes, shear strain due to three slip systems with respect to the total shear of dislocation slip as well as shear strain due to extension twinning were counted, respectively, as shown in Fig. 6. As shown in Fig. 6a, b, basal slip is the dominant slip system to coordinate the plastic deformation of the studied specimens, while the contribution of non-basal slips is distinctly limited. Moreover, the activation of basal slip is influenced by grain size. The contribution ratio of basal slip in the FG specimens is slightly less than that in the CG specimens, while the contribution ratio of non-basal slips is higher which complementally coordinates the plastic deformation effectively. Figure 6a

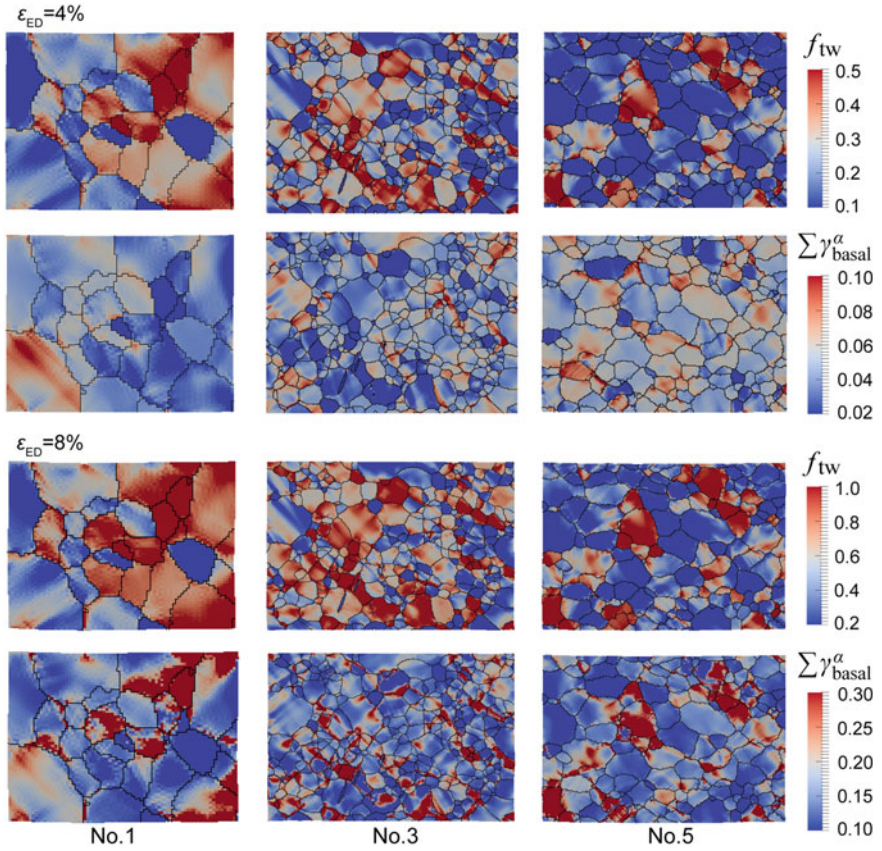


Fig. 5 The simulation results of the volume fraction of extension twins in the specimens at the strain level of 8%. (Color figure online)

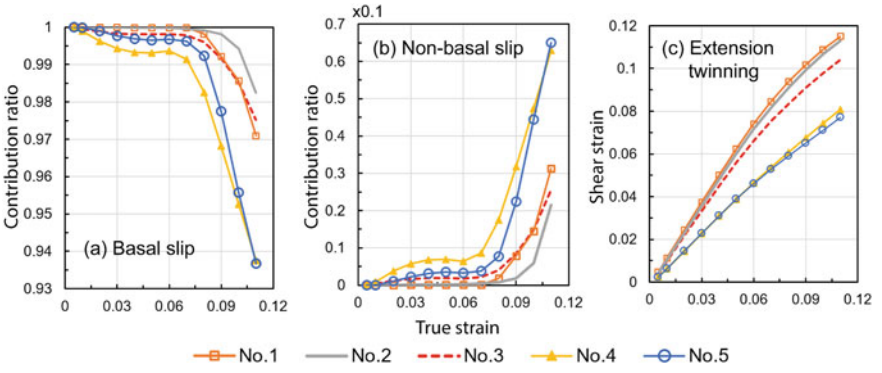


Fig. 6 The contributions of the different deformation modes during the tension deformation. **a** basal slip, **b** non-basal slip, and **c** extension twinning. (Color figure online)

further shows that the contribution ratio of basal slip for both FG specimens and CG specimens, decreases abruptly as the deformation exceeds a threshold strain (i.e. $\varepsilon_{ED} = 0.07–0.09$); Meanwhile, the contribution ratio of prismatic slip increases rapidly to compensate for the decrease of basal slip. Figure 6c shows the evolution of shear strain due to extension twins which agrees well with the experimental results that more extension twins are activated to coordinate the deformation in the CG specimens. Figure 6 also verifies that basal slip and extension twin are two main deformation mechanisms to coordinate the plastic deformation in this study.

4 Conclusion

A series of micro-tensile tests and ex situ EBSD characterizations combined with full-field crystal plasticity (CP) simulations were performed to study the deformation mechanism and microstructure evolution of AZ31 Mg foils with different grain size and thickness. The grain size and thickness distinctly affect the evolution of deformation twins. The twins observed in all the studied foils are $\{10\bar{1}2\}\langle 10\bar{1}\bar{1}\rangle$ extension twins. The area fraction of extension twins increases with deformation, and the increase rate decreases with the number (λ) of grains in thickness. For the coarse grain foils with small λ, extension twins nucleate early and grow quickly. For the fine-grain specimens with large λ, extension twinning is significantly suppressed in the early deformation stage. The full-field CP simulations successfully capture the evolution of extension twinning and show that the dislocation slip is affected by λ. The simulation results confirm that the basal slip contributes mostly to the shear deformation of dislocation slip, while the non-basal slip contributes little even at large deformation.

Acknowledgments The authors acknowledge the funding support from the National Natural Science Foundation of China with the projects of Nos. 51635005 and 51705317. This work is also carried out with support of the Program of Shanghai Academic Research Leader (Grant No. 19XD1401900).

References

1. Liu F, Chen C, Niu J, Pei J, Zhang H, Huang H, Yuan G (2015) The processing of Mg alloy micro-tubes for biodegradable vascular stents. Mater Sci Eng C Mater Biol Appl 48:400–407
2. Wang X, Xu J, Shan D, Guo B, Cao J (2017) Effects of specimen and grain size on electrically-induced softening behavior in uniaxial micro-tension of AZ31 magnesium alloy: experiment and modeling. Mater Design 127:134–143
3. Pandey A, Kabirian F, Hwang J-H, Choi S-H, Khan AS (2015) Mechanical responses and deformation mechanisms of an AZ31 Mg alloy sheet under dynamic and simple shear deformations. Int J Plas 68:111–131
4. Suh B-C, Shim M-S, Kim D-W, Kim NJ (2013) Twinning behavior of Mg–4Zn–1Gd alloy sheet during longitudinal tensile deformation. Scripta Mater 69:465–468

5. Shi BQ, Cheng YQ, Shang XL, Yan H, Chen RS, Ke W (2019) Hall-Petch relationship, twinning responses and their dependences on grain size in the rolled Mg-Zn and Mg-Y alloys. Mater Sci Eng A 743:558–566
6. del Valle JA, Carreño F, Ruano OA (2006) Influence of texture and grain size on work hardening and ductility in magnesium-based alloys processed by ECAP and rolling. Acta Mater 54:4247–4259
7. Barnett MR, Keshavarz Z, Beer AG, Atwell D (2004) Influence of grain size on the compressive deformation of wrought Mg–3Al–1Zn. Acta Mater 52:5093–5103
8. Jain A, Duygulu O, Brown DW, Tomé CN, Agnew SR (2008) Grain size effects on the tensile properties and deformation mechanisms of a magnesium alloy, AZ31B, sheet. Mater Sci Eng A 486:545–555
9. Salem AA, Kalidindi SR, Semiatin SL (2005) Strain hardening due to deformation twinning in α-titanium: constitutive relations and crystal-plasticity modeling. Acta Mater 53:3495–3502
10. Zhang H, Liu J, Sui D, Cui Z, Fu MW (2018) Study of microstructural grain and geometric size effects on plastic heterogeneities at grain-level by using crystal plasticity modeling with high-fidelity representative microstructures. Int J Plas 100:69–89
11. Jiang L, Jonas JJ, Mishra RK, Luo AA, Sachdev AK, Godet S (2007) Twinning and texture development in two Mg alloys subjected to loading along three different strain paths. Acta Mater 55:3899–3910

Part IV
Honorary Symposium: Yasuhisa Tozawa

A Plasticity Framework for Forming Applications



Frédéric Barlat and Toshihiko Kuwabara

Abstract This presentation reviews the key features of a macroscopic plasticity framework applicable to numerical simulations of practical forming processes in industry. The constitutive relationships are developed for anisotropic materials with an anisotropic hardening assumption. The framework relies on mathematical concepts, physical understanding of deformation mechanisms, and experimental results. Lower scale simulation results are essential for the introduction of relevant features in the macroscopic framework. The experimental investigations on plasticity conducted by Professor Tozawa in the 1960s and 1970s is of fundamental importance for the development and validation of the theory.

Keyword Plasticity · Yield condition · Yield surface · Flow rule · Hardening behavior

1 Background

In sheet metal forming simulations for process design and optimization, a plasticity theory is necessary to model the material deformation behavior. The flow theory of plasticity is a well-established and reliable approach to model the inelastic behavior of materials with a yield condition defined by an effective stress and a hardening function, and a flow rule. For each material, these three characteristics should be defined mathematically and measured experimentally, as explained in [1]. Since plasticity is a highly non-linear phenomenon, assumptions are needed to define suitable mathematical descriptions. For metals, the isotropic hardening assumption is often adopted with an anisotropic yield condition and the associated flow rule. The latter indicates that the strain increment is normal to the yield surface. Isotropic hardening means that

F. Barlat (✉)
Graduate Institute of Ferrous Technology, Pohang University of Science and Technology, 77 Cheongam-ro, Nam-gu, Pohang, Gyeongbuk 37673, Republic of Korea
e-mail: f.barlat@postech.ac.kr

F. Barlat · T. Kuwabara
Institute of Global Innovation Research, Tokyo University of Agriculture and Technology, Tokyo, Japan

© The Minerals, Metals & Materials Society 2021

G. Daehn et al. (eds.), *Forming the Future*, The Minerals, Metals & Materials Series,
https://doi.org/10.1007/978-3-030-75381-8_16

the yield surface associated with the yield condition, expands while keeping the same shape. This approach is reasonably accurate for linear or pseudo-linear strain paths. However, when drastic strain path changes occur, additional hardening phenomena are observed such as the Bauschinger effect during strain reversal. This behavior is often captured using the kinematic hardening assumption, in which the yield surface translates in stress space. Sometimes, kinematic hardening is supplemented by distortional plasticity effects. In this article, the isotropic hardening approach for pseudo-linear strain paths, and a purely distortional plasticity description for non-linear strain paths are outlined. In both cases, the work of Professor Tozawa was essential to validate the concepts with high levels of confidence.

2 Linear Strain Path

Tozawa [2] developed a biaxial compression testing device to deform cubic specimens made of stacked sheets. By applying various compressive stress states on specimens with different orientations and assuming that the hydrostatic pressure had no influence on yielding, he determined the yield surfaces of many materials over the entire deviatoric plane, with axes corresponding to the normal stresses in the three characteristic directions of a sheet, namely, rolling (RD), transverse (TD), and normal (ND). As an example, the yield surfaces of commercially pure aluminum alloys, determined with a 0.2% offset strain, are represented in Fig. 1a&b for different amounts of plastic strain [2, 3]. This figure indicates that all the contours have similar

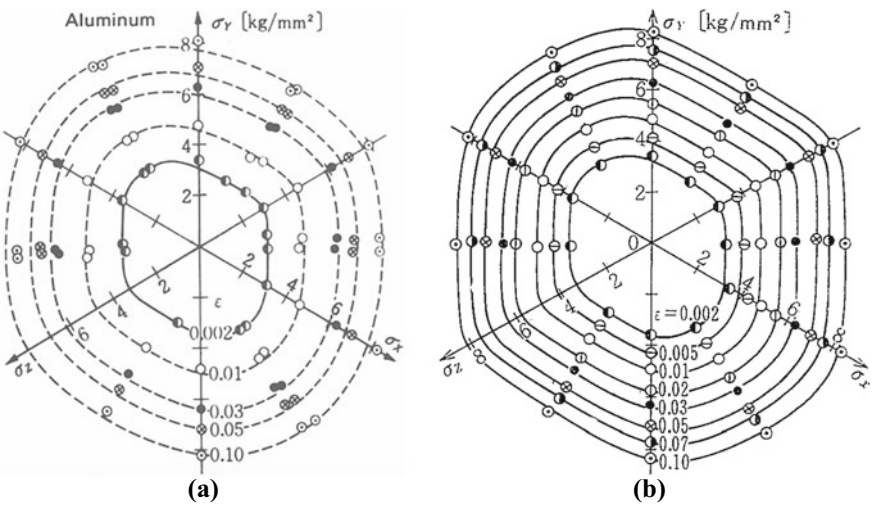


Fig. 1 Yield surfaces of commercial purity aluminum sheet samples measured using biaxial compression tests and projected in the deviatoric plane with the normal stresses σ_x, σ_y, and σ_z in the RD, TD, and ND directions, respectively; **a** from Ref. [2] and **b** from Ref. [3]

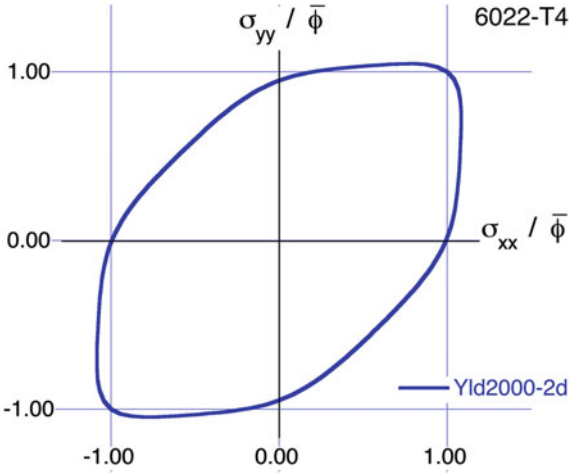


Fig. 2 Normalized plane stress yield surface for 6022-T4 aluminum alloy represented in plane of variables $\sigma_{xx}/\overline{\phi}$ and $\sigma_{yy}/\overline{\phi}$ (normal stresses in rolling and transverse directions, respectively). (Color figure online)

shapes, which is consistent with the isotropic hardening assumption. In addition, each contour exhibits areas with high and low curvatures. Note that Kuwabara [4] observed similar behavior using biaxial testing with cruciform and tubular specimens.

In the flow theory of plasticity, under the assumption of isotropic hardening, the yield condition is defined as

$$\overline{\phi}(\mathbf{s}) = \sigma_r(\overline{\varepsilon}) \tag{1.}$$

where $\overline{\phi}$ is an effective stress that accounts for plastic anisotropy, $\mathbf{s}$ the stress deviator, σ_r a reference stress–strain curve and $\overline{\varepsilon}$ the work-equivalent effective strain. A number of effective stresses or the corresponding anisotropic yield functions are described in [1]. Figure 2 represents the yield surface of a 6022-T4 aluminum alloy sheet sample calculated using the plane stress Yld2000-2d yield condition (see [1] for a brief review). The line represents the intersection of the normalized yield surface with the plane of the ND stress $\sigma_{zz}/\overline{\phi} = 0$. This line is unique because isotropic hardening is assumed and Eq. (1) implies that all the subsequent yield surfaces are superimposed. In Fig. 2, the material of the Al-Mg-Si series is not the same as in Tozawa's work. In addition, the intersection plane is different from the deviatoric plane featured in Fig. 1. In spite of these drawbacks, it is clear that areas of high and low yield surface curvatures can be observed in Fig. 2, in qualitative agreement with Fig. 1. However, the isotropic von Mises and anisotropic Hill [5] yield conditions would not show these features because the curvature would be more uniform, while the yield condition of Tresca would lead to sharp corners. The anisotropic Yld2000-2d yield condition was developed to provide a good representation of crystal plasticity simulation results, which also show the presence of curvature effects on the yield surface [6]. Therefore, it may be said that Yld2000-2d qualitatively captures important features observed

either experimentally by Tozawa or predicted by crystal plasticity simulations, which provide a strong support for its validity.

3 Pre-strained Material

Tozawa [2] conducted experiments similar to those described above for pre-strained materials. For instance, Fig. 3 show the yield surfaces, determined using a 0.2% offset strain, of an Al-stabilized steel that was first subjected to various amounts of pre-strains in uniaxial tension in the rolling direction. This figure shows that the subsequent yield surfaces flatten roughly in the direction opposite to the pre-load, i.e. towards a plane indicated by the dashed line in Fig. 3. In fact, a more accurate description of the distortion is that the yield surface flattens towards a plane parallel to the plane tangent to the yield surface during pre-straining, which corresponds to the two parallel solid lines in Fig. 3.

Kinematic hardening is commonly used to account for the effects of a pre-strain on plastic flow as, for instance, in the modeling of the Bauschinger effect after a load reversal. However, in this article, a pure distortional plasticity model, called HAH, is employed to capture the additional hardening effects due to a strain path change. In the HAH model, the yield condition in Eq. (1) was extended to [7]

$$\overline{\sigma}(\mathbf{s}) = \left\{\overline{\phi}(\mathbf{s})^q + \phi_x(\mathbf{s})\right\}^{\frac{1}{q}} = \sigma_R(\overline{\varepsilon}) \tag{2.}$$

with

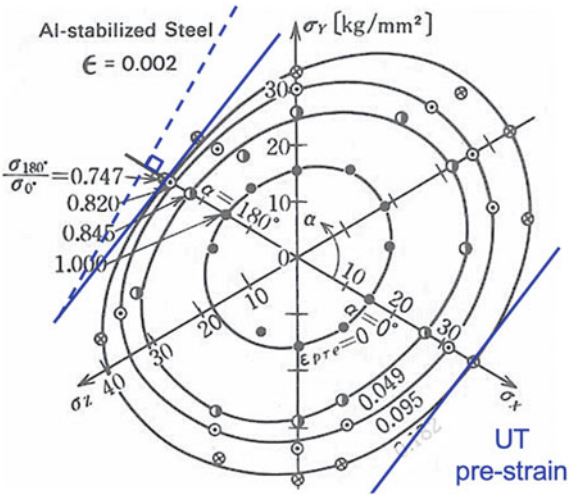


Fig. 3 Yield surfaces for an anisotropic steel pre-strained in RD uniaxial tension by various amounts, showing the yield surface flattening in a region at the opposite side of the load during pre-strain, toward a plane orthogonal to the pre-strain increment. (Color figure online)

$$\phi_x(\mathbf{s}) = \phi_h(\mathbf{s}) = f_-^q \left| \widehat{\mathbf{h}} : \mathbf{s} - \left| \widehat{\mathbf{h}} : \mathbf{s} \right| \right|^q + f_+^q \left| \widehat{\mathbf{h}} : \mathbf{s} + \left| \widehat{\mathbf{h}} : \mathbf{s} \right| \right|^q \tag{3.}$$

and q a constant exponent. An alternate form of $\phi_x(\mathbf{s})$ was proposed later [8]

$$\phi_x(\mathbf{s}) = \phi_\varepsilon(\boldsymbol{s}) = f_-^q \left| \frac{\hat{\dot{\boldsymbol{\varepsilon}}}_h : \mathbf{s} - \left| \hat{\dot{\boldsymbol{\varepsilon}}}_h : \mathbf{s} \right|}{\hat{\dot{\boldsymbol{\varepsilon}}}_h : \widehat{\mathbf{h}}} \right|^q + f_+^q \left| \frac{\hat{\dot{\boldsymbol{\varepsilon}}}_h : \mathbf{s} + \left| \hat{\dot{\boldsymbol{\varepsilon}}}_h : \mathbf{s} \right|}{\hat{\dot{\boldsymbol{\varepsilon}}}_h : \widehat{\mathbf{h}}} \right|^q \tag{4.}$$

Equation (2) is a generalization of Eq. (1), with an additional term $\phi_x(\mathbf{s})$ to introduce the distortion of the yield condition described by Eq. (1). In fact, the material responses obtained by Eqs. (1) and (2) are exactly the same if the boundary conditions applied to Eq. (2) leads to a linear strain path. $\widehat{\mathbf{h}}$, the so-called microstructure deviator, is a tensorial state variable indicating the distortion orientation and $\hat{\dot{\boldsymbol{\varepsilon}}}_h$ the associated yield surface normal. f_+ and f_- are two scalar state variables that control the amount of distortion. In this article, the role of $\widehat{\mathbf{h}}$ is only to define the direction of the pre-strain. The expression of $\phi_x(\mathbf{s})$ in Eq. (3) was selected because it is simpler and contains only stress terms in addition to $\widehat{\mathbf{h}}$. However, this function leads to a distortion with $\hat{\dot{\boldsymbol{\varepsilon}}}_{-h}$ parallel to $\widehat{\mathbf{h}}$ where $\hat{\dot{\boldsymbol{\varepsilon}}}_{-h}$ is the yield surface normal corresponding to $-\widehat{\mathbf{h}}$. In contrast, the expression of $\phi_x(\mathbf{s})$ in Eq. (4) leads to a distortion with $\hat{\dot{\boldsymbol{\varepsilon}}}_{-h}$ parallel to $\hat{\dot{\boldsymbol{\varepsilon}}}_h$. Figure 4 shows, in the deviatoric plane, the yield surfaces calculated using either Eq. (3) or Eq. (4) in the yield condition of the HAH model. This work indicates that Eq. (4) leads to a flattening orientation, which is in excellent qualitative agreement with Tozawa's experimental results.

Note that the complete HAH model requires additional state variable evolution equations. However, this detailed description is out of the scope of the present article, which concentrates on the yield condition only.

4 Discussion

For isotropic hardening, Hershey [9] proposed an isotropic yield condition leading to regions of low and high curvatures that were reintroduced later by Hosford [10]. Logan and Hosford [11] generalized this yield condition to restricted cases of plastic anisotropy. More importantly, using crystal plasticity simulations, they firmly established the existence of high and low curvature areas in the yield surface of a cubic metal. Both Tozawa's experimental results and crystal plasticity simulations led to consistent yield surfaces curvature variations that motivated the development of well-formulated non-quadratic yield conditions such as Yld2000-2d for anisotropic materials.

The so-called HAH distortional plasticity model was developed to describe the plastic behavior of metals subjected to arbitrary loading histories. The first version [7] was constructed on the basis of Eq. (3), mostly to capture the Bauschinger effect.

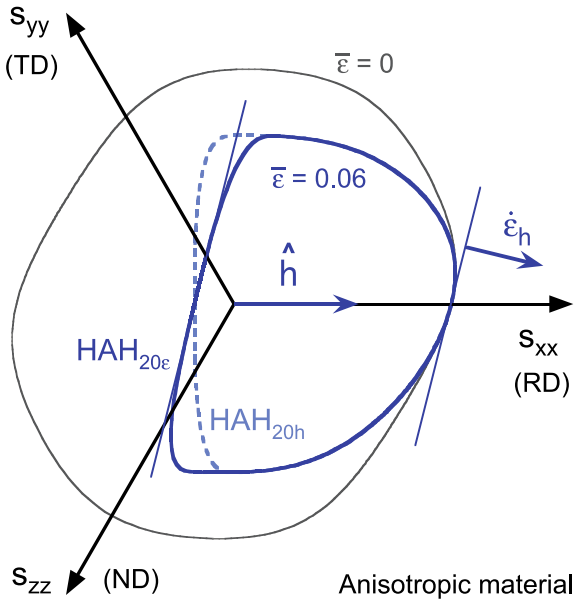


Fig. 4 Illustration of the yield surface of metallic material in deviatoric plane after a pre-strain of about 0.06 in RD uniaxial tension using either Eq. (3) [labeled HAH_{20h}] and Eq. (4) [labeled] $HAH_{20\varepsilon}$ in distortional plasticity model. (Color figure online)

The most recent version, called HAH_{20} [12] offers Eq. (4) as an alternative, as well as better state variable evolution equations to describe a number of anisotropic hardening effects. In fact, Eq. (4) was suggested as a result of crystal plasticity simulations coupled with strain path-dependent dislocation density evolutions to model strain hardening. The excellent qualitative agreement between Eq. (4) and Tozawa's results was observed in retrospect after the crystal plasticity simulations were analyzed. The HAH_{20} model was implemented in finite element (FE) code [13] and used successfully for the forming simulations of the B-pillar of an autobody structure [14]. Nevertheless, the qualitative agreement between Tozawa's experiments, the results of crystal plasticity simulations, and this new distortional plasticity model sets a direction paving the way to future macroscopic constitutive description of plasticity that will lead to even more accurate forming process simulation results.

Acknowledgments FB is grateful to POSCO and the Institute of Global Innovation Research, Tokyo University of Agriculture and Technology for support.

References

1. Barlat F, Kuwabara T (2016) Anisotropic yield conditions in mathematical theory of plasticity. J Jpn Soc Tech Plast 57:230–243
2. Tozawa Y (1978) Plastic deformation behavior under the conditions of combined stress. In: Koistinen DP, Wang NM (eds) Mechanics of sheet metal forming. Plenum Press, pp 81–110
3. Shirai H, Tozawa Y (1975) Yield surface of prestrained initial anisotropic materials. J Jpn Soc Tech Plast 16:1041–1048
4. Kuwabara T (2007) Advances in experiments on metal sheets and tubes in support of constitutive modeling and forming simulations. Int J Plast 23:385–419
5. Hill R (1948) A theory of the yielding and plastic flow of anisotropic metals. Proc R Soc London A193:281–297
6. Barlat F, Richmond O (1987) Prediction of tricomponent plane stress yield surfaces and associated flow and failure behavior of strongly textured fcc sheets. Mat Sci Eng 95:15–29
7. Barlat F, Gracio JJ, Lee MG, Rauch EF, Vincze G (2011) An alternative to kinematic hardening in classical plasticity. Int J Plast 27:1309–1327
8. Barlat F (2018) Advanced constitutive modeling for application to sheet forming. J Phys Conf Ser 1063, Numisheet 2018. https://doi.org/10.1088/1742-6596/1063/1/012002
9. Hershey AV (1954) The plasticity of an isotropic aggregate of anisotropic face centred cubic crystals. J Appl Mech 21:241–249
10. Hosford WF (1972) A generalized isotropic yield criterion. ASME J Appl Mech 39:607–609
11. Logan RW, Hosford WF (1980) Upper-bound anisotropic yield locus calculations assuming pencil glide. Int J Mech Sci 22:419–430
12. Barlat F, Yoon SY, Lee SY, Wi MS, Kim JH (2020) Distortional plasticity framework for advanced high strength steels. Int J Solids Struct 202:947–962
13. Yoon SY, Lee SY, Barlat F (2020). Numerical integration algorithm of updated homogeneous anisotropic hardening model in finite element framework. Comput Meth Appl Mech Eng 372:113449
14. Yoon, SY, Lee, SY, Barlat, F (2020). Finite element implementation of pressure-sensitive plasticity model and its application to distortional hardening and sheet metal forming simulation. J Mat Proc Techn (submitted)

Hole Expansion Simulation of Steel Sheet Considering Differential Hardening



Shunya Nomura and Toshihiko Kuwabara

Abstract Finite element analysis (FEA) of hole expansion forming is investigated to clarify the effects of material models on the predictive accuracy of the FEA. The multiaxial plastic deformation behavior of a hot rolled steel sheet with a tensile strength of 440 MPa was measured using biaxial tensile tests with cruciform specimens (ISO 16842, 2014) and tubular specimens subjected to servo-controlled axial force and internal pressure. Many linear stress paths in the first quadrant of stress space are applied to the specimens to measure the contours of plastic work (CPW) and the directions of plastic strain rate (DPSR) up to a reference plastic strain of 0.22. It is found that the Yld2000-2d yield function (Barlat et al., 2003) accurately reproduces both the CPW and DPSR. Isotropic (IH) and differential hardening (DH) models are determined using the Yld2000-2d yield function; in the DH model the values of exponent and eight material parameters of the Yld2000-2d yield function change as functions of reference plastic strain. Moreover, a hole expansion forming experiment was performed. The thickness strain distribution along the hole edge was measured and compared with the FEA results obtained using selected yield functions. The DH model correctly predicts the minimum thickness position that matches the fracture position of the specimen in experiment. It is concluded that the yield function best capturing both the plastic work contours and the directions of plastic strain rates leads to the most accurate FEA results.

Keywords Biaxial tension · Steel sheet · Anisotropy · Yield function · Finite element analysis

S. Nomura
Graduate School of Mechanical Systems Engineering, Tokyo University of Agriculture and Technology, 2-24-16 Naka-Cho, Koganei-Shi, Tokyo 184-8588, Japan
e-mail: s187900t@st.go.tuat.ac.jp

T. Kuwabara (✉)
Division of Advanced Mechanical Systems Engineering, Institute of Engineering, Tokyo University of Agriculture and Technology, 2-24-16 Naka-Cho, Koganei-Shi, Tokyo 184-8588, Japan
e-mail: kuwabara@cc.tuat.ac.jp

© The Minerals, Metals & Materials Society 2021

G. Daehn et al. (eds.), *Forming the Future*, The Minerals, Metals & Materials Series,
https://doi.org/10.1007/978-3-030-75381-8_17

1 Introduction

The establishment of trial-and-error-less manufacturing enhanced by numerical forming simulations has been strongly desired in industry to shorten the product development period and reduce costs for prototype manufacturing. The accuracy of forming simulations is significantly affected by the material models used in the simulation [1]. Therefore, it is crucial to use a proper material model that accurately reproduces the deformation behavior of the material in finite element analysis (FEA) in order to improve the accuracy of the simulation [2].

The authors investigated the effects of material models on the predictive accuracy of hole expansion forming simulation of steel sheet [3–5]. In particular, Kuwabara and Ichikawa [5] performed biaxial tensile tests using cruciform specimens [6, 7] and multiaxial tube expansion tests (MTET) with tubular specimens subjected to servo-controlled axial force and internal pressure [8, 9] for the test material to identify proper material models to be used in the FEA of the hole expansion forming. Both isotropic hardening (IH) model and differential hardening (DH) model, which can reproduce the change in the shapes of plastic work contours with work hardening, were applied to the FEA. It was found that the Yld2000-2d yield function [10] gives a more accurate description of the biaxial deformation behavior of the test material than the von Mises and Hill's quadratic yield functions. However, even the calculated results by the Yld2000-2d yield function showed some deviation from the measured thickness strain distribution in the vicinity of the hole edge.

The objective of this study is to further investigate the effects of material models on the accuracy of the hole expansion forming simulation. The test material used in this study is a hot rolled steel sheet with a tensile strength of 440 MPa. An objective function is introduced and the parameters of the Yld2000-2d yield function are determined so that the difference between the measurement and prediction for both the plastic work contours and the directions of plastic strain rates, $\mathbf{D}^{\mathrm{p}}$, can be minimized. Both IH and DH models based on the Yld2000-2d yield function are applied to the FEA of the hole expansion forming. It is found that the DH model correctly predicts the minimum thickness position that matches the fracture position of the specimen in experiment.

2 Experimental Methods

The test material used in this study was a 1.6-mm-thick hot rolled steel sheet with a tensile strength of 440 MPa. The rolling (RD), transverse (TD), and normal to the sheet plane (ND) directions of the sheet sample are referred to as the x-, y-, and z-axes, respectively.

Biaxial tensile tests using cruciform specimens and tubular specimens were performed to measure the plastic deformation behavior of the test material under biaxila tension. Figure 1a shows a schematic of the cruciform specimen used for the

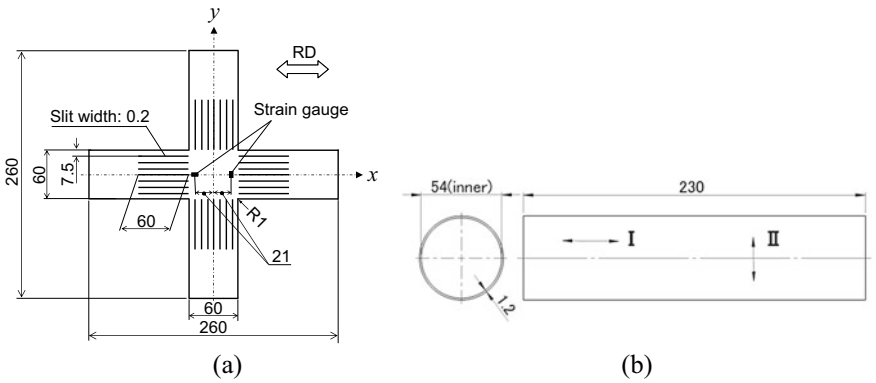


Fig. 1 Specimens used for the biaxial tensile tests (dimensions in mm). **a** Cruciform specimen. **b** Tubular specimen. The mark ↔ indicates the RD of the original sheet sample

biaxial tensile tests of the as-received sheet sample. The geometry of the specimen was the same as that developed in [6] and followed ISO 16842 [7]. The specimen arms were parallel to the RD and TD of the material. The slits were fabricated by laser machining. A couple of strain gauges (YFLA-2, Tokyo Sokki Kenkyujo Co.) were mounted at ± 21 mm from the center along the maximum loading direction and measure the normal strain components, ε_x and ε_y. See [7] for the details of the experimental methods. Using FEAs, Hanabusa et al. [11, 12] estimated that the stress measurement error is less than 2% when the strain components are measured at the positions shown in Fig. 1a.

Figure 1b shows the tubular specimen used for the MTETs. The specimens were fabricated by bending and laser welding into a cylindrical shape with an inner diameter of 54 mm and a length of 230 mm. Two types of tubular specimens were fabricated; type I specimen had the RD in the axial direction and type II specimen had the RD in the circumferential direction. Type I specimens were used for the tests with $\sigma_x \leq \sigma_y$ and type II for the tests with $\sigma_x \geq \sigma_y$; the maximum principal stress direction was always taken to be in the circumferential direction of the specimen. See [9] for the details of the experimental method. Both the cruciform and tubular specimens were subjected to linear stress paths with true stress ratios $\sigma_x : \sigma_y = 4{:}1$, 2:1, 4:3, 1:1, 3:4, 1:2, and 1:4. Standard uniaxial tensile specimens (JIS 13 B-type) were used for the uniaxial tensile tests with $\sigma_x : \sigma_y = 1{:}0$ and 0:1.

The concept of the contour of plastic work in stress space [13] was introduced in order to evaluate the work hardening behavior of the test material under biaxial tension. The stress–strain curve obtained from a uniaxial tensile test along the RD was selected as a reference datum for work hardening; the uniaxial true stresses σ_0 and the plastic work per unit volume W_0 corresponding to particular values of offset logarithmic plastic strains $\varepsilon_0^{\mathrm{p}}$ were determined. The uniaxial tensile true stress σ_{90} in

the TD and the biaxial true stress components (σ_x, σ_y) obtained from biaxial tensile tests were then determined at the same plastic work as W_0. The stress points $(\sigma_0, 0)$, $(0, \sigma_{90})$, and (σ_x, σ_y) form a contour of plastic work associated with a particular value of $\varepsilon_0^{\mathrm{p}}$.

3 Material Testing Results and Material Modeling

Figure 2a, b shows the measured stress points forming contours of plastic work and the direction of the plastic strain rate for $\varepsilon_0^{\mathrm{p}} = 0.22$. In Fig. 2(a), the stress values are normalized by the σ_0. Also depicted in Fig. 2 are the data calculated using the von Mises, Hill's quadratic (Hill'48) [14], and the Yld20000-2d yield functions [10]. The anisotropic parameters of the Hill'48 were determined using r_0,r_{45}, r_{90}, and σ_0, where r_θ is the r-value measured by a tensile test at an angle of θ from the RD. The anisotropic parameters α_i $(i = 1\text{–}8)$ and exponent M of the Yld2000-2d yield function were determined to minimize the cost function given by Eq. (1):

$$F = \frac{1}{N}\sum_{i=1}^{N}\left\{w_{\sigma,i}\left(l_{\mathrm{M},i} - l_{\mathrm{C},i}\right)^2 + w_{\beta,i}\left(\beta_{\mathrm{M},i} - \beta_{\mathrm{C},i}\right)^2\right\}, \tag{1}$$

where N $(= 14)$ is the number of linear stress paths for the biaxial tensile tests with linear stress paths of $\sigma_x : \sigma_y = 4{:}1$, 2:1, 4:3, 1:1, 3:4, 1:2, 1:4, and the uniaxial tensile tests for every 15° from RD. $l_{\mathrm{M},i}$ is the distance between the origin of the normalized principal stress space and the stress point on the i th stress path and $l_{\mathrm{C},i}$ is the distance between the origin of the normalized principal stress space and

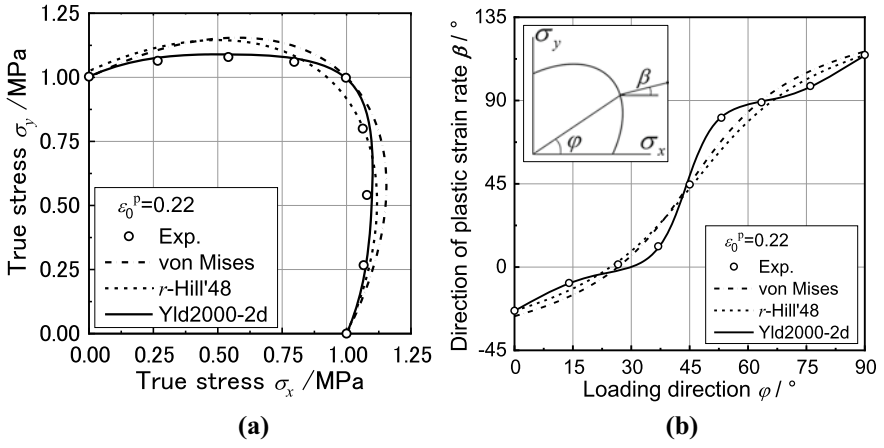


Fig. 2 Measured data of **a** the stress points forming contours of plastic work, and **b** the directions of plastic strain rate

the calculated yield locus along the i th stress path. $\beta_{M,i}$ is the direction of the $\mathbf{D}^p$ measured for the i th stress path and $\beta_{C,i}$ is the value of β calculated using the yield function and the normality flow rule at the i th stress path. $w_{\sigma,i}$ and $w_{\beta,i}$ are the weighting factors for l_i and β_i, respectively. Real-coded genetic algorithm (GA) was used to minimize the cost function and to avoid a local optimum solution. Details of the calculation procedures for minimizing F are given in [15]. The calculated results by the Yld2000-2d yield function are consistent with the experimental data for both work contour and β.

Moreover, a DH model was made using the Yld2000-2d yield function, in which the variation of α_i ($i = 1$–8) and M with the increase of ε_0^p were taken into account as functions of ε_0^p.

4 Hole Expansion Forming Experiment and FEA Simulation

Hole expansion forming experiments using a flat-headed punch were performed to quantitatively evaluate the effect of the material models on the predictive accuracy of the hole expansion forming simulation. The tool geometry used for the hole expansion forming is shown in Fig. 3a. The punch and die hole diameters were 100 mm and 130 mm, respectively. The initial hole with a diameter of 30 mm was fabricated at the center of a circular blank using a wire-electrical discharging machine. The periphery of the blank was clamped using a triangular draw-bead with a diameter of 195 mm. The interface between the blank and punch head was lubricated with Vaseline and 0.3-mm-thick Teflon sheet, while no lubricant was applied to the interfaces between the blank and the die/blank holder. The punch velocity was approximately 0.1 mm/s, which gave an average strain rate of 10^{-3} s^{-1} to the hole edge, and is comparable to those for the biaxial material tests. The forming was terminated at a punch stroke of $h = 28$ mm. The sheet thickness along the hole edge (at positions 2 mm distant from the hole edge on the undeformed blank) was measured using a digital micrometer with a minimum readout of 0.001 mm.

FEA of the hole expansion forming was carried out using Abaqus/Standard Ver. 6.14. Figure 3b shows the initial mesh division of a blank used in the FEA. The increment of element divisions in the circumferential direction was 3.0° The increment of element divisions in the radial direction was 1 mm. One quarter of a blank was analyzed, owing to the orthotropic material symmetry. Reduced 4-node shell elements (S4R) with five integration points in the thickness direction were used for the blank.

The punch, die and blank holder were defined as rigid bodies. The coefficients of friction were assumed to be 0.03 between the punch and blank and 0.15 for the other contact areas, as no lubricant was applied to the surfaces of the die and blank holder. The displacement of the blank edge (a diameter of 195 mm) was fixed at the bead

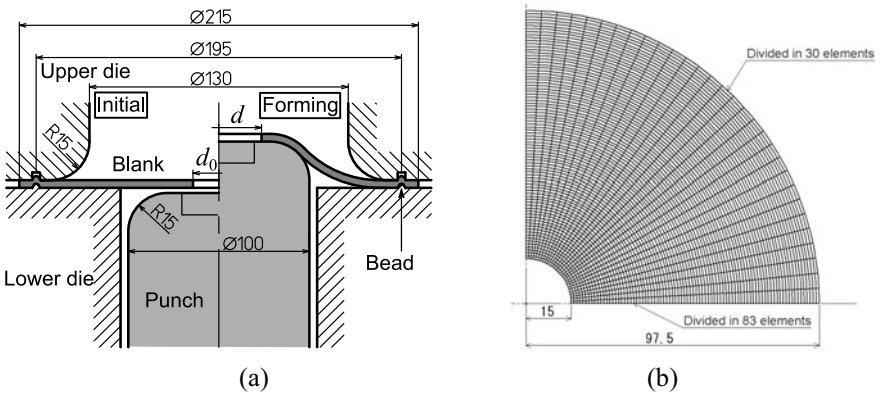


Fig. 3 Schematic illustration of the hole expansion test: **a** tool geometry, and **b** initial mesh division of a blank used in the FEA of the hole expansion forming

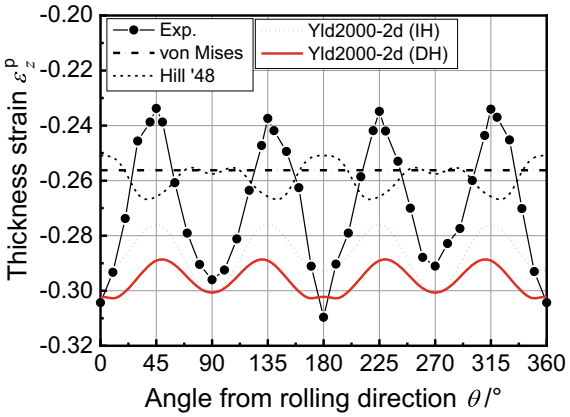


Fig. 4 Thickness strains along the hole edge compared with those calculated using selected yield functions. The thickness strains were measured at positions 2 mm away from the hole edge. (Color figure online)

position. The material was unloaded when the punch stroke reached 30 mm, and the FEA was terminated.

The material models used in the FEAs were the IH models based on the von Mises and Hill'48 yield functions shown in Fig. 2a, and those based on the Yld2000-2d shown in Fig. 2b.

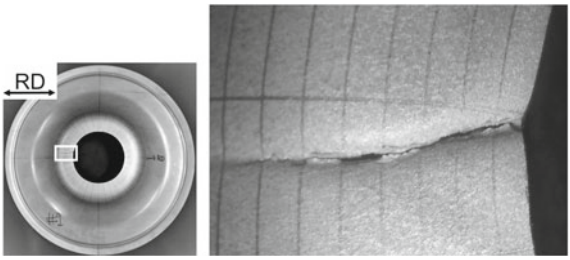


Fig. 5 Top view of a specimen with fracture at the hole edge

5 Results of the FEA of Hole Expansion Forming

Figure 4 shows the experimental results of the logarithmic thickness plastic strains $\varepsilon_z^{\mathrm{p}}$ along the hole edge at a punch stroke $h = 28$ mm. They take a minimum in the RD, a second local minimum in the TD, and a maximum in 45° (DD) from the RD. The figure also shows the FEA predictions calculated using the IH and DH models based on the Yld2000-2d yield function. Both the DH and IH models predicts that a maximum is in DD, which is consistent with the expriment. The DH model shows a good agreement with the measurement in the vicinity of the RD and TD and it also correctly predicts that $\varepsilon_z^{\mathrm{p}}$ becomes minimum in the RD. On the otherhand, the IH model predicts a minimum in the TD. The Hill'48 predicts that they take a minimum in the vicinity of the DD and a maximum in the RD; therefore, the prediction is the exact opposite of the experimental trend.

In the hole expansion experiment fracture occurred at a punch stroke of 32 mm near the hole edge along the RD, see Fig. 5. The position of fracture is consistent with the minimum thickness position as prediction by the DH model. The DH model correctly predicts the minimum thickness position that matches the fracture position of the specimen in experiment. It is concluded that the yield function best capturing both the plastic work contours and the directions of plastic strain rates leads to the most accurate FEA results.

6 Conclusions

Hole expansion forming of a 440 MPa hot-rolled steel sheet is investigated both experimentally and analytically to clarify the effects of material models on the predictive accuracy of the FEA of the forming process. The DH model correctly predicts the minimum thickness position that matches the fracture position of the specimen in experiment. It is concluded that the yield function best capturing both the plastic work contours and the directions of plastic strain rates leads to the most accurate FEA results.

References

1. Banabic D, Barlat F, Cazacu O, Kuwabara T (2010) Advances in anisotropy and formability. Int J Mater Form 3:165–189
2. Barlat F, Kuwabara T (2016) Anisotropic yield conditions in mathematical theory of plasticity. J Jap Soc Technol Plast 57:230–243
3. Kuwabara T, Hashimoto K, Iizuka E, Yoon JW (2011) Effect of anisotropic yield functions on the accuracy of hole expansion simulations. J Mater Process Technol 211:475–481
4. Hashimoto K, Kuwabara T, Iizuka E, Yoon JW (2010) Effect of anisotropic yield functions on the accuracy of hole expansion simulations for 590 MPa grade steel sheet. Tetsu-to-Hagané 96:557–563
5. Kuwabara T, Ichikawa K (2015) Hole expansion simulation considering the differential hardening of a sheet metal. R J Technol Sci Appl Mech 60:63–81
6. Kuwabara T, Ikeda S, Kuroda T (1998) Measurement and analysis of differential work hardening in cold-rolled steel sheet under biaxial tension. J Mater Process Technol 80(81):517–523
7. ISO 16842: 2014 Metallic materials −Sheet and strip −Biaxial tensile testing method using a cruciform test piece
8. Ishiki M, Kuwabara T, Hayashida Y (2011) Measurement and analysis of differential work hardening behavior of pure titanium sheet using spline function. Int J Mater Form 4:193–204
9. Kuwabara T, Sugawara F (2013) Multiaxial tube expansion test method for measurement of sheet metal deformation behavior under biaxial tension for a large strain range. Int J Plast 45:103–118
10. Barlat F, Brem JC, Yoon JW, Chung K, Dick RE, Lege DJ, Pourboghrat F, Choi SH, Chu E (2013) Plane stress yield function for aluminum alloy sheets—part 1: Theory. Int J Plast 19:1297–1319
11. Hanabusa Y, Takizawa H, Kuwabara T (2010) Evaluation of accuracy of stress measurements determined in biaxial stress tests with cruciform specimen using numerical method. Steel Res Int 81:1376–1379
12. Hanabusa Y, Takizawa H, Kuwabara T (2013) Numerical verification of a biaxial tensile test method using a cruciform specimen. J Mater Process Technol 213:961–970
13. Hill R, Hecker SS, Stout MG (1994) An investigation of plastic flow and differential work hardening in orthotropic brass tubes under fluid pressure and axial load. Int J Solids Struct 31:2999–3021
14. Hill R (1948) A theory of the yielding and plastic flow of anisotropic metals. Proc R Soc London A193:281–297
15. Hakoyama T, Kuwabara T (2015) Effect of biaxial work hardening modeling for sheet metals on the accuracy of forming limit analyses using the Marciniak-Kuczynski approach. In: Altenbach H, Matsuda T, Okumura D (eds) From creep damage mechanics to homogenization methods. Springer, Heidelberg, pp 67–95

Surface Quality of Extruded Sidewall in Cold Backward Cup Extrusion with Low-Frequency Torsional Oscillation



Ryo Matsumoto, Seiji Takatsuka, and Hiroshi Utsunomiya

Abstract The effect of torsional oscillation on the surface quality of an extruded sidewall of a workpiece was investigated in backward cup extrusion with an extrusion ratio of 2.0 at room temperature. In this extrusion process, a cylindrical aluminum workpiece lubricated with mineral oil was extruded in the axial direction and simultaneously twisted in the circumferential direction between extrusion and knockout punches. The two punches were controlled with an axial speed of 0.1 mm/s, an alternating amplitude of 5°, and a maximum angular speed of 0.5 rpm. The torsional oscillation tilted the traction direction at the container–workpiece from the radial direction to the circumferential direction with approximately 25% lower contact pressure on the container. As the result, the surface of the extruded sidewall was uniformly smoothed.

Keywords Forging · Extrusion · Torsion · Friction · Surface

1 Introduction

To reduce axial load in the forging process, the authors developed forging process with torsional oscillation. In this process, torsional oscillation around the forging axis was superposed with axial deformation. According to the theory of plasticity, plastic deformation of metals can be promoted by the combination of normal and shear stresses [1]. In our previous studies, the maximum reduction in axial load was attained with larger than 20% under torsion/axial speeds higher than 60°/mm in cold forging and cold backward cup extrusion [2, 3].

On the other hand, the authors aim not only to reduce the axial load but also to improve the properties of the forged products such as surface qualities, shape accuracy, and microstructure in forging process with torsional oscillation. This is because the superposition of torsional moment during axial deformation is a well-known method to change the stress and strain distributions in the workpiece. For

R. Matsumoto (✉) · S. Takatsuka · H. Utsunomiya
Division of Materials and Manufacturing Science, Osaka University, 2-1 Yamadaoka, Suita 565-0871, Osaka, Japan
e-mail: ryo@mat.eng.osaka-u.ac.jp

© The Minerals, Metals & Materials Society 2021

G. Daehn et al. (eds.), *Forming the Future*, The Minerals, Metals & Materials Series,
https://doi.org/10.1007/978-3-030-75381-8_18

example, crystallographic grain refinement of workpiece by applying large shear strain was reported in KOBO-type forming with torsional moment in die forging [4]. The superposition of torsional moment during axial deformation was also applied to friction test [5, 6] because the contact and sliding conditions between die and workpiece can be controlled. In forging process, the application of torsional moment is expected to change friction, lubrication, and surface qualities of the forged product.

In this study, the effect of torsional oscillation on surface quality of extruded workpiece was investigated in cold backward cup extrusion. The relationship between the torsional oscillation conditions and the surface qualities is investigated through extrusion experiment on an originally designed equipment. The change in contact state between the die and the workpiece is discussed using the results of finite element simulation.

2 Extrusion Process with Torsional Oscillation and Procedures of Experiment

Figure 1 shows the schematic illustration of the die layout, the punch shape, and the surface groove of the punches for backward cup extrusion with torsional oscillation. A cylindrical workpiece inserted in the container was extruded by the extrusion punch in the z-direction (the axial direction or height direction) and simultaneously twisted by the knockout punch in the θ direction (the circumferential direction) around the z-axis. The extrusion punch was moved downward in the z-direction, while the knockout punch was rotated or rotationally oscillated in the θ direction (not moved in the z-direction). The diameter of the workpiece, the inner diameter of the container, and the diameter of the extrusion punch were ϕ 13.9 mm, ϕ14 mm, and ϕ10 mm, respectively. The extrusion ratio was 2.0.

Backward cup extrusion with torsional oscillation was performed using originally designed equipment. Due to the capacities of the maximum load and torque of the

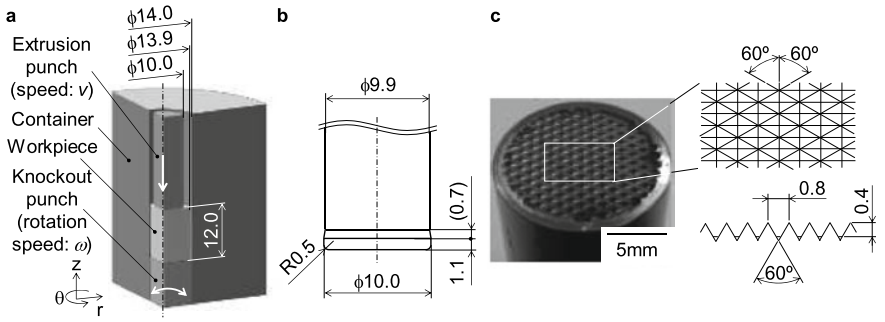


Fig. 1 **a** Layout of dies and workpiece, **b** Detail of end shape of extrusion punch, **c** Groove on end surface of punches

apparatus, JIS A1070 aluminum cylinder was selected as the workpiece. The initial surface roughness of the outer surface of the workpiece was $Ra = 0.30$–0.50 μm. The mineral oil with a kinematic viscosity of 32 mm^2/s (at 313 K) was applied with a thickness of approximately 90 μm to the outer surface of the workpiece. The dies were made of JIS SKH51 high-speed tool steel (63 HRC). In the experiment, when the axial extrusion stroke reached 0.5 mm, the knockout punch started to rotate circumferentially around the extrusion axis. To grip and twist the workpiece by the two punches, knurled grooves with a depth of 0.4 mm and a vertical angle of 60° were prepared with a crossing angle of 120° and a pitch of 0.8 mm on the end surfaces of the punches, as shown in Fig. 1c. From our previous report of upsetting with torsional oscillation [2], the axial extrusion speed was set to $v = 0$–0.1 mm/s, while the rotation speed and amplitude were set to $\omega = 0$–0.5 rpm (0–0.05 rad) and 5° (π/36 rad), respectively. The maximum frequency of the torsional oscillation was 0.15 Hz.

3 Experimental Results

3.1 Appearance and Surface Roughness of Outer Surface of Extruded Workpiece

Figure 2 shows the appearance of the outer surface of the extruded workpiece. The surface defects of the extruded workpiece were caused by turning marks in the initial workpiece because the adhesion of the workpiece was not observed at the surface

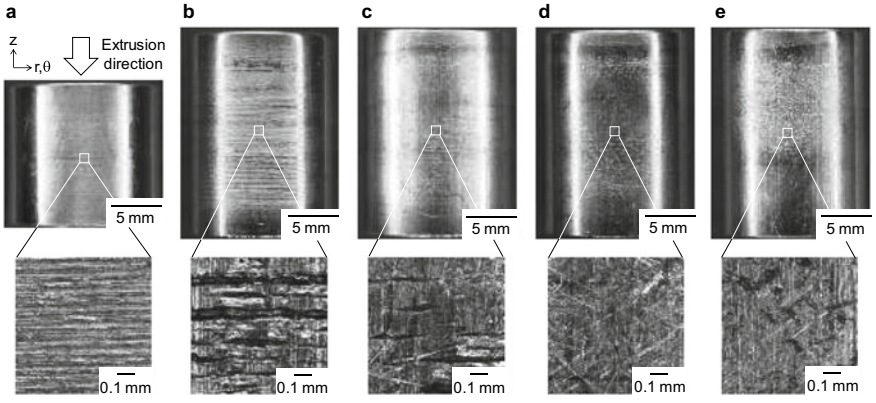


Fig. 2 Photographs of outer surface of the extruded workpiece in backward extrusion with torsional oscillation ($v = 0.1$ mm/s, axial stroke: 6.0 mm), **a** Initial workpiece, **b** $\omega = 0$ rpm, **c** $\omega = 0.3$ rpm ($\theta_{acc} = 83°$), **d** $\omega = 0.5$ rpm ($\theta_{acc} = 165°$), **e** $\omega = 0.5$ rpm ($\theta_{acc} = 165°$, one-way) (θ_{acc}: accumulative rotation angle of knockout punch)

of the container. The surface defects were stretched in the extrusion (z)-direction of the workpiece in extrusion without torsional oscillation. On the other hand, the length of the surface defects was shortened in the circumferential direction and was tilted from the radial direction to the diagonal direction in extrusion with torsional oscillation. It means that the surface defects are elongated and shallowed by the torsional oscillation.

The surface profile of the outer surface of the extruded workpiece in the circumferential direction is shown in Fig. 3. The surface profile was measured by a 2D stylus type profilometer along the extrusion direction. The surface was roughened due to the stretching of the surface defects as above described in extrusion without torsional oscillation, while the surface was smoothed as the rotation speed increased in extrusion with torsional oscillation.

Figure 4 shows the relationship between the surface roughness on the outer surface of the extruded workpiece and the accumulative rotation angle of the knockout punch (accumulative twisted angle of the workpiece, θ_{acc}). The surface roughness was measured at 16 locations of which four places every 4.0 mm in the extrusion direction of the extruded workpiece and four places every 90° in the circumferential direction. The average and standard deviation of the surface roughness decreased with increasing accumulative rotation angle in the range of $0° < \theta_{acc} < 360°$. The average and standard deviation of the surface roughness were lower than the initial in the range of $200° < \theta_{acc} < 360°$. It was confirmed that the outer surface of the workpiece was flattened and the unevenness of the surface roughness was reduced by applying torsional oscillation during extrusion. This implies that torsional oscillation was effective for reducing the unevenness of the lubrication state because the lubricant was squeezed not only in the extrusion direction but also in the circumferential direction between the container and the workpiece. However, excessive torsion deteriorated the surface qualities of the extruded workpiece because the average and standard deviation of the surface roughness increased with increasing accumulative rotation angle in the range of $\theta_{acc} > 360°$.

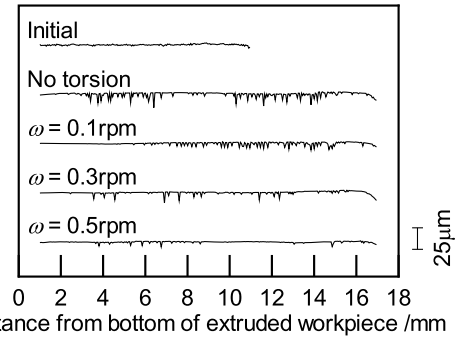


Fig. 3 Surface profile of the outer surface of extruded workpiece in backward extrusion with torsional oscillation ($v = 0.1$ mm/s, axial stroke: 6.0 mm)

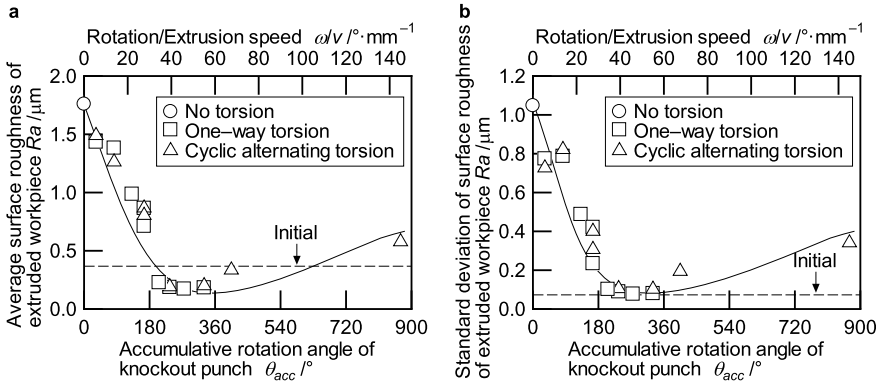


Fig. 4 Relationship between surface roughness at the outer surface of extruded workpiece and rotation angle of knockout punch in backward extrusion with torsional moment ($v = 0$–0.1 mm/s, $\omega = 0.5$ rpm, axial stroke: 6.0 mm), **a** Average surface roughness, **b** Standard deviation of surface roughness

3.2 *Deformation Behavior of Indentation of Outer Surface of Workpiece During Extrusion*

To investigate the sliding behavior of the workpiece at the container–workpiece interface, four hemispherical indentations were prepared at a height of 6.0 mm from the bottom and 90° intervals in the circumferential direction in the outer surface of the initial workpiece using a Rockwell hardness tester. The diameter and depth of the indentation were approximately 0.56 mm and maximum 0.13 mm, respectively.

Figure 5 shows the photograph of the indentation of the extruded workpiece. The indentation was deformed to ellipse slightly stretched in the extrusion direction in extrusion with/without torsional oscillation (Fig. 5b, c). The indentation was deformed to an ellipse with a high aspect ratio tilted toward the torsional direction in extrusion with a one-way torsional moment (Fig. 5d). The relationship between the indentation shape of the extruded workpiece and the accumulative rotation angle of the knockout punch is shown in Fig. 6. Here, the indentation shape was measured

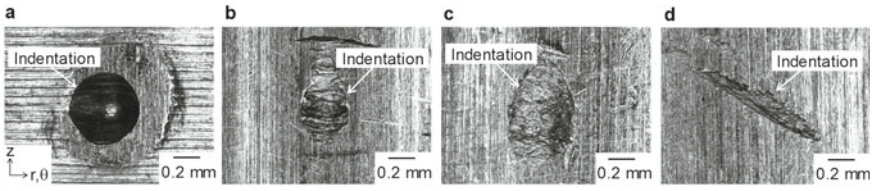


Fig. 5 Photographs of hemispherical indentation at outer surface of extruded workpiece in backward extrusion with torsional oscillation ($v = 0.1$ mm/s, axial stroke: 6.0 mm), **a** Initial workpiece, **b** $\omega = 0$ rpm, **c** $\omega = 0.5$ rpm ($\theta_{acc} = 165°$), **d** $\omega = 0.5$ rpm ($\theta_{acc} = 165°$, one-way)

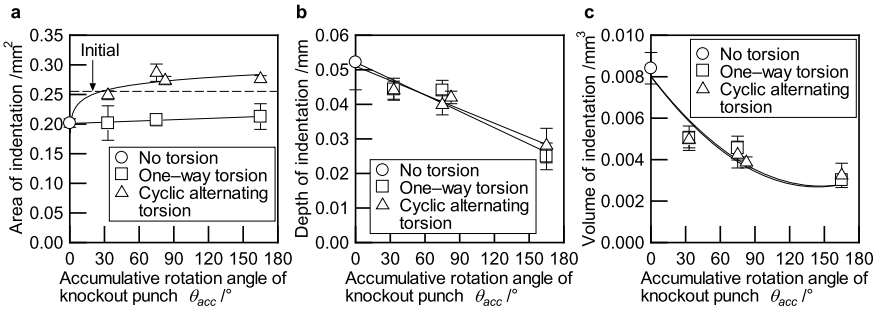


Fig. 6 Relationship between hemispherical indentation shape at outer surface of extruded workpiece and accumulative rotation angle of knockout punch in backward extrusion with torsional moment ($v = 0.1$ mm/s, axial stroke: 6.0 mm), **a** Cross-sectional area, **b** Maximum depth, **c** Volume

by a laser microscope with an image processing function. The accumulative rotation angle of the knockout punch was equal to the accumulative twisted angle of the workpiece because the workpiece was twisted by the knurled grooves of the punches without slipping. The cross-sectional area of the indentation became large in extrusion with torsional oscillation, while the depth of the indentation became shallow with increasing accumulative rotation angle. As the result, the volume of the indentation decreased with increasing accumulative rotation angle. It was confirmed that the outer surface of the workpiece was smoothed by applying torsional oscillation during extrusion.

4 Discussions by Finite Element Analysis

4.1 Finite Element Analysis Conditions

The elastic–plastic deformation and temperature change of the workpiece in extrusion were analyzed by a commercial three-dimensional finite element code, Simufact Forming ver. 15.0 (MSC Software Company). In the analysis, the material properties of the aluminum workpiece were employed from the built-in database of material properties in Simufact Forming ver. 15.0. The model of the flow stress was an isotropic hardening model. The temperature dependences of the flow stress, Young's modulus, the thermal conductivity, and the specific heat were taken into account in the analysis, and the strain rate sensitivity of the flow stress was also taken into account.

The dies were treated as rigid bodies under an isothermal state, and the end surfaces of the punches were assumed to be flat (no knurled grooves). To grip the workpiece for circumferential twisting, the frictional condition at the end surface of the punch–workpiece interface was assumed to be sticking (no sliding), while the frictional condition at other parts of the container–workpiece interface was shear

friction factor $m = 0.2$. The heat transfer coefficients on the die–workpiece interface and the free surfaces of the workpiece were assumed to be 5000 W/(m^2·K) and 50 W/(m^2·K), respectively.

4.2 Rotation Speed and Contact Pressure Between Container and Workpiece

Figure 7 shows the calculated circumferential rotation speed of the outer surface of the workpiece in backward extrusion with the one-way torsional moment. The rotation speed of the workpiece gradually decreased from the bottom of the workpiece to the height position of the end surface of the punch, while the rotation speed of the extruded sidewall of the workpiece (the distance from the bottom of the workpiece: longer than 8 mm) was constant at 20–40% of the rotation speed of the knockout punch. It is found that the part of the workpiece sandwiched between the extrusion and knockout punches were circumferentially twisted during extrusion, while the sidewall part of the extruded workpiece was not twisted during extrusion.

The calculated contact pressure between the container and the workpiece in backward extrusion with torsional moment was shown in Fig. 8. The contact pressure in extrusion with torsional moment was reduced by approximately 25%. This is due to the traction direction at the container–workpiece is tilted from the radial direction to the circumferential direction by torsional moment during extrusion.

The above circumferential sliding of the workpiece and the reduction in contact pressure at the container–workpiece are suggested to influence the surface quality of the outer surface of the extruded workpiece. It was also reported that surface

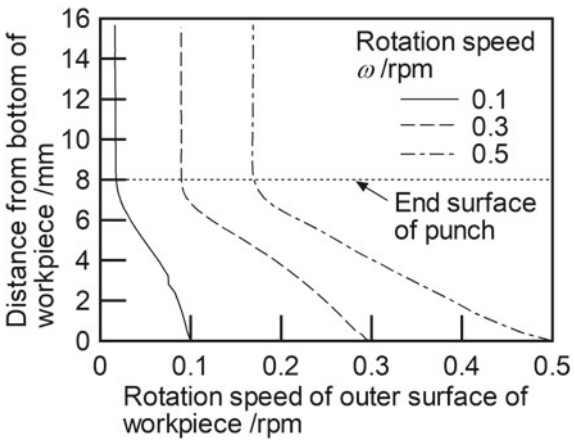


Fig. 7 Circumferential rotation speed of the outer surface of workpiece in backward extrusion with one-way torsional moment (axial stroke: 4.0 mm, FEM)

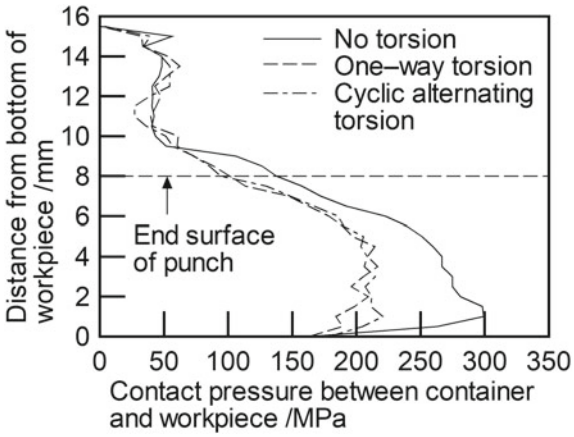


Fig. 8 Contact pressure between container and workpiece in backward extrusion with torsional moment (axial stroke: 4.0 mm, $\omega = 0.5$ rpm, FEM)

roughness of JIS A1050 aluminum was smoothed to approximately 10% in sliding with longer than 0.25 mm under contact pressure with higher than 150 MPa [7]. Therefore, the changes of the indentation shape in Sect. 3.1 and the surface roughness in Sect. 3.2 are reasonable.

5 Conclusions

In this study, the effect of torsional oscillation on surface quality of extruded workpiece was investigated in cold backward cup extrusion. Torsional oscillation with a maximum frequency of 0.15 Hz around the extrusion axis was applied on axial extrusion. The relationship between the torsional oscillation conditions and the surface properties was investigated by experiment and the finite element simulation. The following remarks were obtained.

(1) The torsional oscillation tilts the traction direction at the container–workpiece from the radial direction to the circumferential direction. The contact pressure between the container and the workpiece is reduced by approximately 25%.
(2) The average and standard deviation of the surface roughness of the outer surface of the extruded workpiece are lower than the initial by applying the torsional oscillation with accumulative torsion angle of 200°–360°.

Acknowledgments This work was financially supported in part by the Japan Society for the Promotion of Science (JSPS) with a Grant-in-Aid for Scientific Research (C) (15K06504), the Amada Foundation (AF-2016005), and the Light Metal Educational Foundation, Inc.

References

1. Bridgman PW (1964) Studies in large plastic flow and fracture. Harvard University Press, pp 247–278. https://doi.org/10.4159/harvard.9780674731349
2. Matsumoto R, Kou J, Utsunomiya H (2017) Reduction in axial forging load by low-frequency torsional oscillation in cold upsetting. Int J Adv Manuf Technol 93:933–943. https://doi.org/10.1007/s00170-017-0553-1
3. Matsumoto R, Takatsuka S, Utsunomiya H (2019) Reduction in axial extrusion load by low-frequency torsional oscillation in cold backward cup extrusion. In: Proceedings of 52nd International Cold Forging Group Plenary Meeting (ICFG 2019) 143–148
4. Korbel A, Bochniak W (2004) Refinement and control of the metal structure elements by plastic deformation. Scr Mater 51:755–759. https://doi.org/10.1016/j.scriptamat.2004.06.020
5. Hansen BG, Bay N (1986) Two new methods for testing lubricants for cold forging. J Mech Work Technol 13:189–204. https://doi.org/10.1016/0378-3804(86)90065-3
6. Sawamura M, Yogo Y, Kamiyama M, Iwata N (2014) Measurement of friction coefficient by backward extrusion with rotating tool under severe forming conditions. Proc Eng 81:1866–1871. https://doi.org/10.1016/j.proeng.2014.10.247
7. Nakamura T, Kondo K, Nishigaya T (1990) Smoothing conditions of workmetal surface in metalworking processes (effects of contact pressure and relative slip displacemetnt). Trans Jpn Soc Mech Eng Ser C 56:2794–2801 (in Japanese). https://doi.org/10.1299/kikaic.56.2794

Anisotropic Ductile Fracture Estimation of Diagonal Cracks in Flange-Shaped Parts



Atsuo Watanabe, Kunio Hayakawa, Shinichiro Fujikawa, Tatsumi Takeshita, and Mika Furutani

Abstract Inclined rotary forming (IRF) combines bending and axial compression with rotation and is employed for forming flange shaft-structured parts from round rod billets. Although the forming load is smaller than the one in conventional processes, cracks may develop during this process. However, it is difficult to predict the onset of cracks using conventional ductile fracture prediction equations. In this paper, an equation for predicting ductile fractures is proposed, which considers anisotropic ductile damage. The proposed equation is expressed as a second-rank tensor resulting from the inner product of the stress tensor and the strain increment tensor. Referring to the previously published results on the compression of cylindrical specimens, the difference between diagonal and longitudinal sidewall cracks was clarified by considering the anisotropy of ductile damage. The proposed equation was then applied to the IRF process, wherein diagonal cracks developed at the outer rim of flange. Consequently, it was possible to estimate the requirements for reducing diagonal cracks by controlling lubrication conditions.

Keywords Ductile fracture · Finite element analysis · Anisotropic damage · Rotary forming

A. Watanabe (✉) · S. Fujikawa
Nissan Motor Co., Ltd, Yokosuka, Japan
e-mail: at-watanabe@mail.nissan.co.jp

S. Fujikawa
e-mail: s-fujikawa@mail.nissan.co.jp

A. Watanabe · K. Hayakawa
Graduate School of Science and Technology, Shizuoka University, Hamamatsu, Japan
e-mail: hayakawa.kunio@shizuoka.ac.jp

T. Takeshita · M. Furutani
JATCO Ltd., Fuji, Japan
e-mail: tatsumi_takeshita@jatco.co.jp

M. Furutani
e-mail: mika_furutani@jatco.co.jp

© The Minerals, Metals & Materials Society 2021

G. Daehn et al. (eds.), *Forming the Future*, The Minerals, Metals & Materials Series,
https://doi.org/10.1007/978-3-030-75381-8_19

1 Introduction

Cold forging processes of complex parts offer weight and cost reduction and are widely used in the automotive industry [1, 2]. Ductile fracture defects often define the forming limit of cold-forged parts. Therefore, accurate prediction of ductile fractures using the tools of the finite element analysis is necessary; this can help reduce the cost associated with trial-and-error design.

As the near-net shaping of forged parts progresses and material deformation becomes increasingly complicated, it is necessary to further improve the prediction accuracy of ductile fractures. Considering anisotropic damage associated with ductile fractures, the generation and growth of microscopic voids and cracks in the material depends on the direction of the applied stress and/or strain. In other words, the damage profile is essentially anisotropic. Therefore, prediction accuracy can be likely improved by accounting for this damage anisotropy.

In this paper, we propose to use damage anisotropy during the evolution of ductile fractures to improve the prediction accuracy of ductile fractures. The proposed equation is validated for the inclined rotary forming (IRF) process, wherein diagonal cracks develop at the outer rim of flange. Consequently, requirements for reducing diagonal cracks by controlling lubrication conditions were identified.

2 Ductile Fractures in IRF

IRF as a forming process is shown schematically in Fig. 1. In this process, the free part of the shaft is thickened by setting a steel billet to both the pushing and receiving dies, and by rotating the dies while inclining the receiving die [3–5]. This process allows thickening of the free part of the billet using a lower load, owing to a locally high forming pressure caused by the inclined rotary forming, such as orbital forming. The authors have been developing this method to apply to a part called a pulley that constitutes a part of the automatic transmission mechanism in modern automobiles [5].

The studied material was SCr420H (JIS) and spheroidizing annealing was performed before forming. The spheroidizing annealing was performed at the holding temperature of 690 °C and for the holding time of 10 h. After that, phosphate coating was applied for lubrication. Cold multi-stage forward extrusion was conducted before the IRF process, to shape the product (Fig. 2). In the IRF process, the forming force was 2600 kN, the rotation speed was 60 rpm, and the angle of the inclining die was 4°. During the forming, oil was poured for the auxiliary lubrication. The diameter expansion ratio, which is the ratio of the final diameter to the initial diameter, was 2.8.

Figure 2 shows the formed samples during the IRF process. After the process, diagonal cracks at the outer rim of flange (Fig. 2) were observed. When investigating factors that could suppress these diagonal cracks, it was confirmed that these

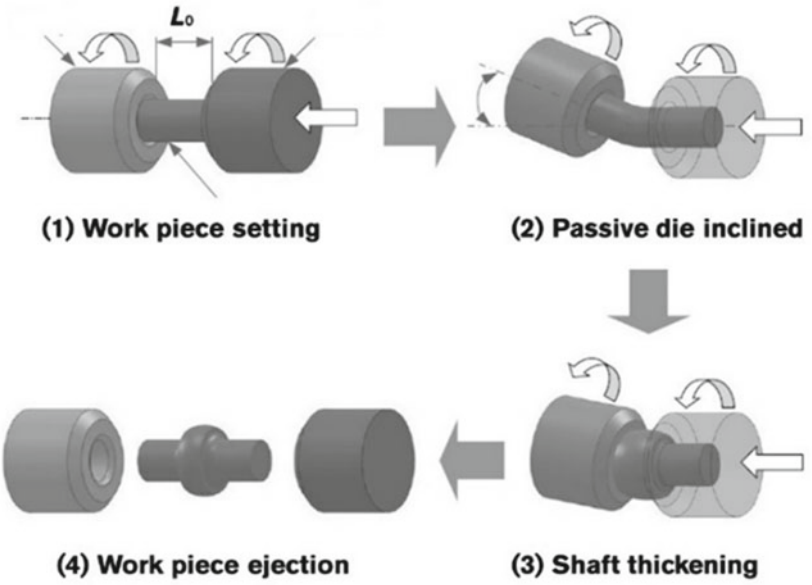


Fig. 1 Inclined rotary forming process

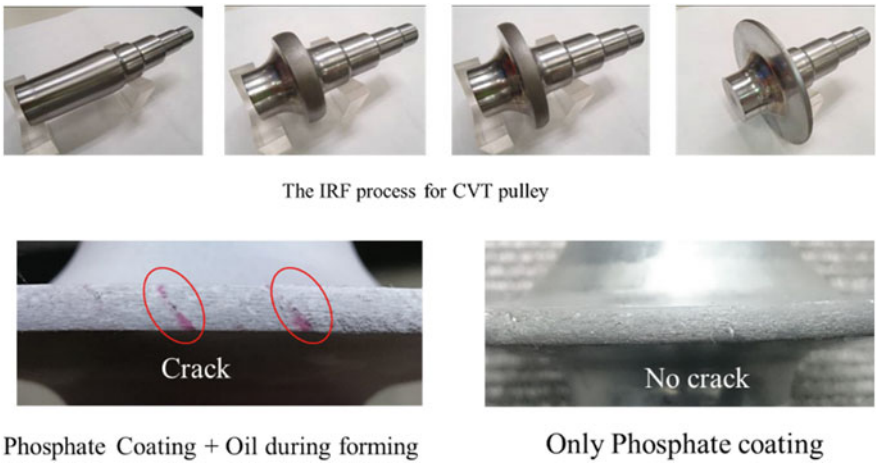


Fig. 2 Cracks in flange-shaped parts. (Color figure online)

diagonal cracks could be alleviated by stopping the oil supply for lubrication during the forming. In this paper, the occurrence and suppression of the diagonal cracks were clarified using the anisotropic ductile fractures theory and finite element analysis. The finite element analysis was performed using the dedicated finite element software DEFORM-2D, DEFORM-3D (SFTC), and their user subroutine functions.

3 Proposed Equations for Ductile Fracture Prediction Using Anisotropic Ductile Damage

Isotropic ductile fractures criteria by Cockcroft and Latham [6] in Eq. (1) were used for the ductile damage evaluation; these criteria are widely used in the finite element analysis of cold forging. I_1 is the threshold on the ductile fracture, $\sigma_{\max}$ is the maximal principal stress, $\bar{\sigma}$ is the equivalent stress, and $d\bar{\varepsilon}$ is the equivalent strain increment. Equation (1) assumes isotropic damage and cannot capture the damage direction. To capture the damage direction, the anisotropic ductile fracture theory was proposed and applied to ductile fractures in the forward extrusion [7].

The inner product of the stress tensor and the strain increment tensor represents the specific strain energy increment, as given by Eq. (2), where σ_{ij} is the stress tensor, $d\varepsilon_{ij}$ is the strain increment tensor, and δ_{ij} is the Kronecker delta. Based on Eq. (2), a ductile damage model of the second-order tensor is given by Eq. (3), which can be considered as a possible modification of Eq. (1).

Equations (1) and (3) are based on the idea of evaluating the accumulation of the strain energy expressed by the product of the stress and strain increments as material ductile damage. In the case of Eq. (3), the effect of the stress/strain direction on the ductile damage evolution can be considered.

When discussing anisotropic ductile damage, it is often convenient to use principal values. However, because Eq. (3) features an asymmetric tensor, the principal values may be complex numbers, in which case physical interpretation is difficult. Therefore, with reference to the effective stress method [8] in the framework of continuum damage mechanics, symmetrized variables were adopted as the proposed equation, as shown in Eq. (4). In the cylindrical coordinate system O-$r\theta z$, the principal values $\bar{\bar{D}}_{\mathrm{I}}$, $\bar{\bar{D}}_{\mathrm{II}}$, and $\bar{\bar{D}}_{\mathrm{III}}$ are calculated according to Eq. (5).

$$D_{\mathrm{CL}} = I_1,\ D_{\mathrm{CL}} \equiv \int \left(\frac{\sigma \max}{\bar{\sigma}} \right) d\bar{\varepsilon} \tag{1}$$

$$dE = \sigma_{ij} d\varepsilon_{ij} = \delta_{ij} \left(\sigma_{ik} d\varepsilon_{kj} \right) \tag{2}$$

$$\bar{\bar{D}}_{ij} = \int \frac{\sigma_{ik}}{\bar{\sigma}} d\varepsilon_{kj} \tag{3}$$

$$\bar{\bar{D}}_{ij} = \frac{1}{2} \int \left(\frac{\sigma_{ik}}{\bar{\sigma}} d\varepsilon_{kj} + \frac{\sigma_{jl}}{\bar{\sigma}} d\varepsilon_{li} \right) \tag{4}$$

$$\left. \begin{matrix} \bar{\bar{D}}_{\mathrm{I}} \\ \bar{\bar{D}}_{\mathrm{II}} \end{matrix} \right\} = \frac{1}{2} \left(\bar{\bar{D}}_r + \bar{\bar{D}}_z \right) \pm \sqrt{\left(\frac{\bar{\bar{D}}_r - \bar{\bar{D}}_z}{2} \right)^2 + \bar{\bar{D}}_{rz}^2},\ \bar{\bar{D}}_{\mathrm{III}} = \bar{\bar{D}}_\theta \tag{5}$$

4 Application of the Anisotropic Ductile Damage Model to Side Cracks in the Cylindrical Compression Test

4.1 Investigation of Diagonal Cracks in Compression Tests

To study the effect of the anisotropic damage model on diagonal cracks in flange-shaped parts as in the IRF process, we used the previously published result of the cylindrical compression test [9]; that study also reported the formation of diagonal cracks. In that experiment, when compression was performed using conical-type dies as in Fig. 3, diagonal cracks appeared on the side of the cylinder. When compression was performed using boundary-restrained dies as shown in Fig. 4, longitudinal cracks appeared. W and H are the initial diameter and the initial height. In this condition, the finite element analysis was conducted axisymmetrically using DEFORM-2D. The Coulomb friction coefficient was 0.1 for the compression test with conical-type dies, and the shear friction coefficient was 0.5 for the compression test with boundary-restrained dies, to match previously reported stress changes. The flow stress data were taken from the literature [9]. Figures 5 and 6 show the change in the stress at the center of the height of the cylinder side. The horizontal axis shows the compressive logarithmic strain, $\ln(H/h)$, where h is the current height. The direction of the maximal principal stress of both types was the θ direction in cylindrical coordinates. This

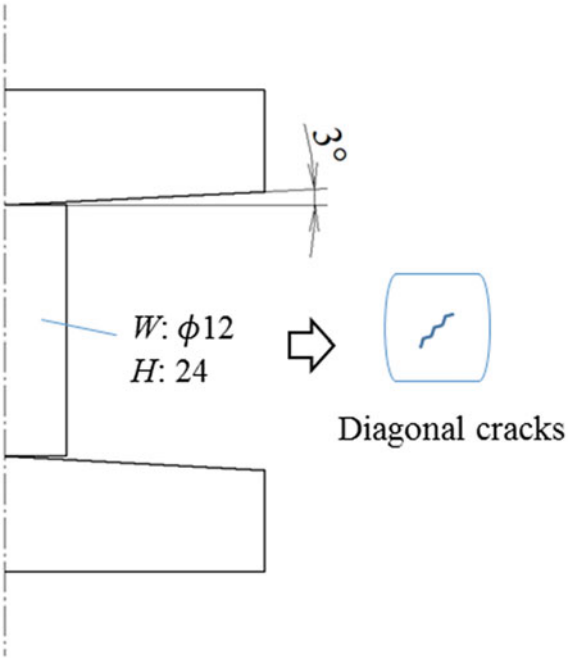


Fig. 3 Diagonal cracks in the compression test. (Color figure online)

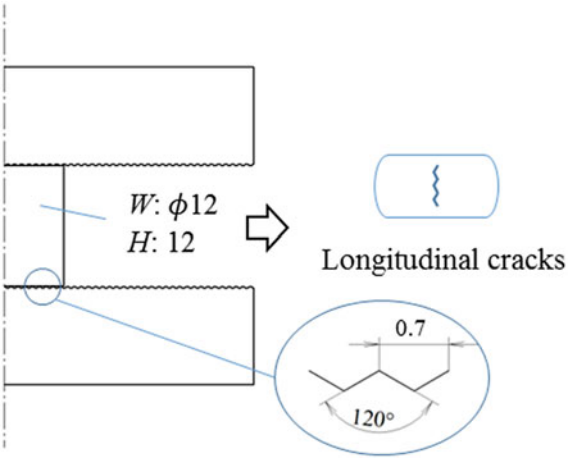


Fig. 4 Longitudinal cracks in the compression test. (Color figure online)

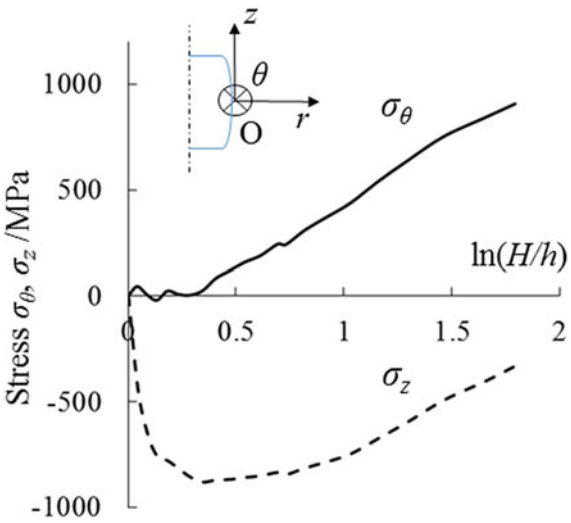


Fig. 5 Change in the stress in the compression test (Fig. 3). (Color figure online)

fracture formation model is based on the maximal shear stress theory in the literature [9].

The developed anisotropic damage model was applied to the results of this experiment. Equation (4) was implemented into the DEFORM-2D by using user subroutines. The value in Eq. (4) varies depending on the system of coordinates. D_θ quantifies the damage in the θ direction in cylindrical coordinates, that is, the direction perpendicular to the vertical crack. $D_{\theta 45^\circ}$ quantifies the damage in the direction of 45° around the r axis, that is, in the direction perpendicular to the diagonal crack. For the compression test with conical-type dies in which diagonal cracks occurred, $D_{\theta 45^\circ}$

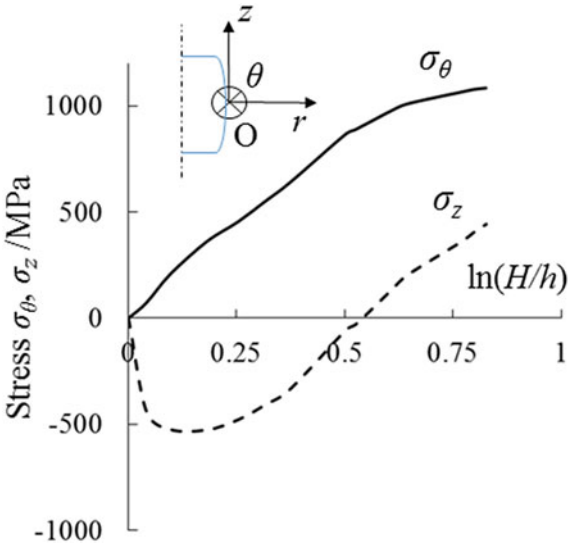


Fig. 6 Change in the stress in the compression test (Fig. 4). (Color figure online)

(perpendicular to the crack) was larger than D_θ, as shown in Fig. 7. For the compression test with boundary-restrained dies in which longitudinal cracks occurred, D_θ was larger than $D_{\theta 45^\circ}$, as shown in Fig. 8. It is confirmed that the proposed model can properly assume the direction of the damage on each compression condition.

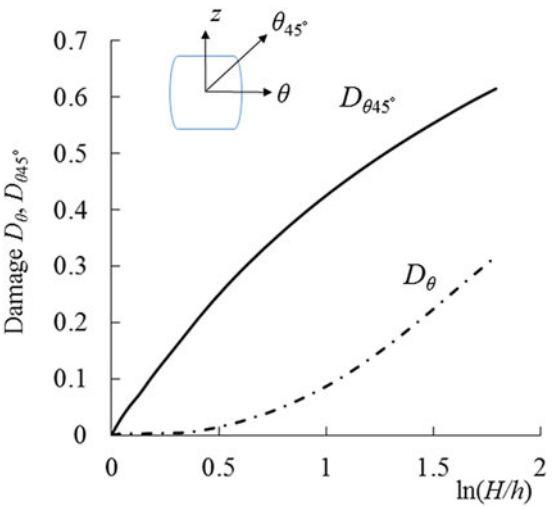


Fig. 7 Change in the damage in the compression test (Fig. 3). (Color figure online)

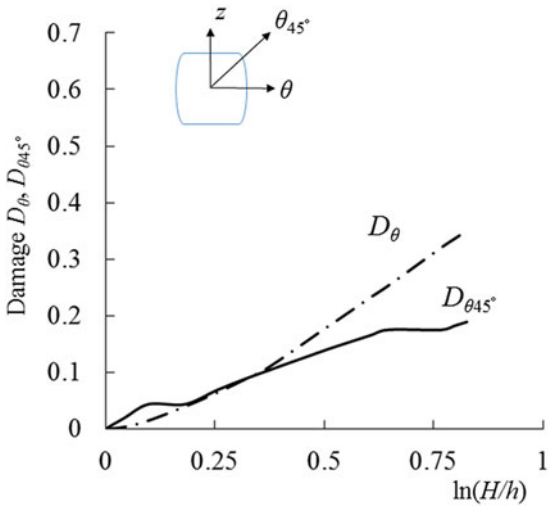


Fig. 8 Change in the damage in the compression test (Fig. 4). (Color figure online)

4.2 Application of the Anisotropic Damage Model in the Principal Direction

To study the formation of diagonal cracks using Eqs. (4) and (5), a principal value was added in the shear direction, in addition to the principal value in the vertical direction. The damage equation for the principal value in the shear direction was given in Eq. (7), based on the same concept as Mohr's stress circle. The concept underlying the damage energy in Eq. (2) is that the damage becomes positive when both the stress and strain rates are negative. As shown in Fig. 9, the stress in the z-direction at the diagonal crack is negative, but the damage is positive, and it is estimated to be small when calculating the principal value in the shear direction. Therefore, Eq. (6) is proposed for calculating the principal value in the shear direction. C_{ij} takes the value of -1.0 if

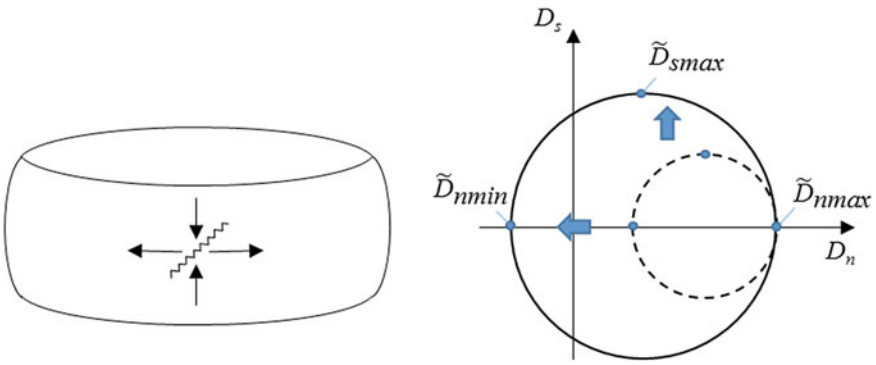


Fig. 9 Conceptual depiction of damage in the shear principal direction. (Color figure online)

the stress σ_{ij} is negative and 1.0 if the stress is positive. The damage value is basically a positive value with directionality, but only when calculating the principal value in the shear direction, and the principal value in the shear direction $\tilde{D}_{smax}$ is calculated from $\tilde{D}_{ij}$ as Eq. (7). This calculation model was applied to the compression test with conical-type dies (Fig. 3), and the principal value, $\tilde{D}_{smax}$ coincided with the change in $D_{\theta 45^\circ}$ in Fig. 7. The value of $\tilde{D}_{nmax}$ coincided with that of D_θ. The anisotropic damage model with principal values in the shear direction can be used for calculating actual parts.

$$\tilde{D}_{ij} = C_{ij}\bar{\bar{D}}_{ij} \cdot \text{no sum on } i \text{ and } j \tag{6}$$

$$\tilde{D}_{smax} = \frac{1}{2}\left(\tilde{D}_{nmax} - \tilde{D}_{nmin}\right) \tag{7}$$

5 Simulation of the IRF Process with the Anisotropic Ductile Damage Model

To reproduce the diagonal cracks in the outer rim of flange of the CVT pulley in the IRF process as described in Sect. 1, the finite element analysis using DEFORM-3D was performed. The material was SCr420H (JIS). Table 1 shows the chemical composition of the material. The spheroidizing annealing temperature was 690 °C. Microstructure is ferrite perlite structure. The flow stress was measured using a tensile test on the material and was used for calculations. Material constants of flow stress data are shown in Table 2. The forming force was 2600 kN, the rotation speed was 60 rpm, and the angle of the inclining die was 4°, the same as for the conditions for which crack generation was observed, as described in Sect. 1. The axial length of the bar was 243.0 mm and the maximal diameter was 48.2 mm before forming, as shown in the left panel of Fig. 10. The simulation terminated when the diameter expansion ratio reached 2.8. The element size was about 2 mm in the flange-formed

Table 1 Chemical composition of SCr420H

Material	C	Si	Mn	P	S	Cr
SCr420H	0.20	0.25	0.73	0.03	0.03	1.05

Table 2 Material constants of Swift's law of SCr420H

Plasticity coefficient F/MPa	Work hardening exponent n	Material constant ε_0
889	0.17	0.003
		$\sigma = F(\varepsilon + \varepsilon_0)^n$

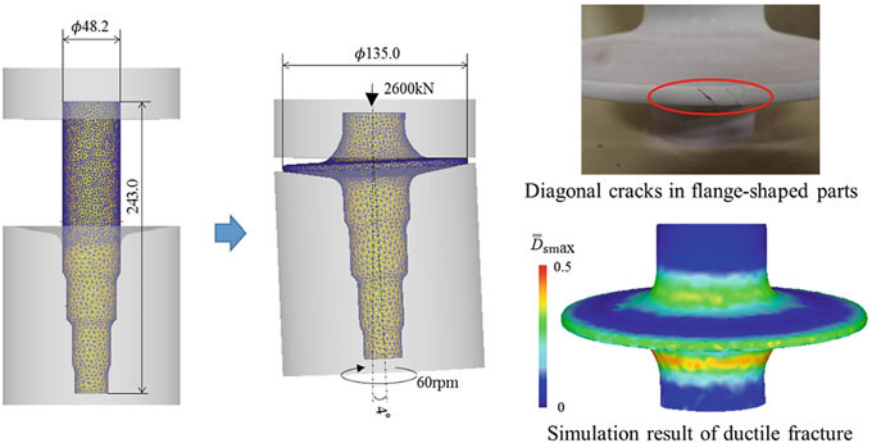


Fig. 10 CVT pulley in the simulation of the IRF process. (Color figure online)

part. The step was 2°, according to the rotating dies. To reproduce the formation of cracks owing to the difference in the lubrication state, as described in Sect. 1, the friction coefficient was set to 0.02, to capture phosphate coating and oil pouring, corresponding to the condition of good lubrication. The friction coefficient was 0.3 to capture phosphate coating only, corresponding to the condition of insufficient lubrication. Figure 10 shows the analysis model and the analysis results for damage calculation.

Equations (4)–(7) were incorporated into the DEFORM-3D user subroutine, to quantify the damage. Figure 11 shows the change in $\tilde{D}_{smax}$ at the outer rim of the flange, where diagonal cracks occurred. Because the calculation results exhibited

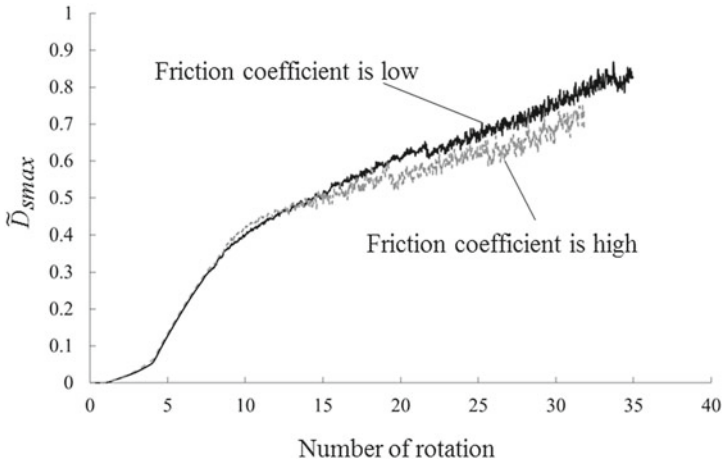


Fig. 11 Difference in $\tilde{D}_{smax}$ at the fracture point

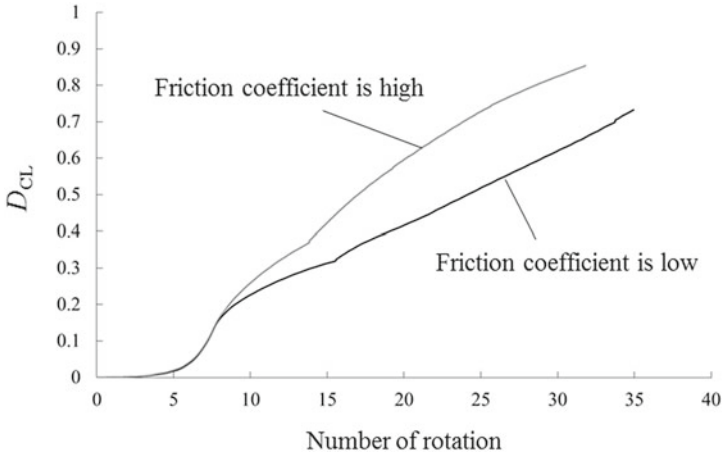


Fig. 12 Difference in D_{CL} at the fracture point

some dispersion along the circumferential direction of the outer rim, we averaged the 12 points on the outer circumference (every 30°). The damage value $\tilde{D}_{smax}$ was higher for the low friction coefficient. This demonstrates that diagonal cracks can be formed, similar to the experiment in Sect. 1. Because the coefficient of friction was lower, the material flow along the radial direction was larger. Because the axial compression at the outer rim of the flange was larger, the damage in the shear direction was stronger.

It is considered that ductile fracture occurs when the damage value reaches fracture threshold. This fracture threshold depends on the type of material and heat treatment condition, and is determined by tensile tests. In addition, the threshold must be verified whether it can be applied to the actual parts, which are complexly formed [7]. In this case, it is considered that fracture threshold was between 0.7 and 0.8, based on the actual occurrence of cracks in the parts and Fig. 11.

Figure 12 shows the change in the damage value, calculated using the normalized Cockcroft–Latham equation, Eq. (1), under the same conditions. In the conventional predictive equation that assumes isotropic damage, the contribution to the damage along the θ direction, which is the maximal principal stress, increases. Consequently, the damage value for the insufficient lubrication condition increases. This suggests that anisotropic predictive modeling is necessary to properly infer the formation of diagonal cracks owing to the shear of the flange phenomenon, as is the case here.

6 Conclusion

A novel equation for quantification of the ductile fracture-related damage, which accounts for anisotropy, was proposed in this paper. In the case of a complex material flow such as the IRF process, the conventional isotropic ductile failure damage equation does not accurately predict the position of the onset of ductile failures. In light of this, the conclusions of this study obtained are summarized as follows.

1. For the proposed equation of ductile fracture generation that accounts for anisotropy, the amount of damage was expressed as the inner product of the stress tensor and the strain tensor increment.

2. The proposed anisotropic ductile damage model was applied to the phenomenon of diagonal cracks and longitudinal cracks on the side of a cylinder, which were observed in cylinder compression experiments, as described in the literature. The effectiveness of this model was verified. The analysis concluded that the principal value of damage along not only the vertical direction but also the shear direction should be considered.

3. The anisotropic ductile damage model was applied to describe the onset of diagonal cracks in the IRF process. The effect of lubrication condition on the onset of diagonal cracks was properly predicted by employing the proposed model.

References

1. Nakajima M, Arai S, Kondo K (2009) Practical use by precision forging of toothed gears utilizing divided flow method. J Jpn Soc Technol Plast 50–587:20–24 (in Japanese)
2. Ishikawa T (2011) Trend of numerical simulation in metal forming. Denki-Seiko 82–2:133–141 (in Japanese)
3. Kuwahara Y, Okabe N, Ikuta F (2010) J Jpn Soc Technol Plast 51–592:460–464 (in Japanese)
4. Kuwahara Y, Okabe N, Ikuta F (2010) J Jpn Soc Technol Plast 51–592:455–459 (in Japanese)
5. Fujikawa S, Watanabe A, Nakazawa K, Takeshita T, Okamoto M, Terada H (2017) Damage value estimation for inclined rotary forming. In: The proceedings of ICFG2017, pp 72–77
6. Cockcroft MG, Latham DJ (1968) Ductility and workability of metals. J Inst Met 96:33–39
7. Watanabe A, Hayakawa K, Fujikawa S, Shiga N (2019) Prediction method of ductile fracture in cold forging using anisotropic ductile fracture criterion. In: The proceeding of ICFG2019, pp 19–27
8. Murakami S (2012) Continuum damage mechanics. Springer, pp 111–138
9. Kudo H, Aoi K (1967) Effect of compression test condition upon fracturing of a medium carbon steel. J Jpn Soc Technol Plast 8–72:17–27 (in Japanese)

Prediction of Microstructure Behavior During Large-Scale Hot Forging of Ni-Based Superalloy



Nobuki Yukawa, Chihiro Osawa, Takayuki Yamada, and Eiji Abe

Abstract For the production of large heat-resistant components, improving the prediction accuracy of microstructural behavior by the finite element method leads cost and time reduction in process optimization. To perform this task, it is essential to predict the recrystallization behavior accurately, during hot forging and heat treatment of Ni-base superalloys. So far, many researchers have used the Avrami equation to predict the recrystallization behavior. However, this uses experimental coefficients determined empirically for each process, so it is not suitable for predicting the microstructure of large-scale hot forged parts with different complex deformation and thermal histories at different locations. Because the recrystallization behavior is considered to depend on the path, and on the temperature, strain, and strain rate at that time. Therefore, an incremental form of a prediction model based on the Avrami equation has been developed as a solution. Optimized parameters for the incremental model were obtained by using a genetic algorithm which is an adaptive heuristic search algorithm. At this time, it is not enough to use only the results of small tests at the laboratory level as training data for genetic algorithm. This is because the thermal histories and distributions have a large difference between the small specimens and the large parts. In this study, 1,500 and 50,000 t class forging tests were performed, and the parameters in the prediction model were determined using these results as learning data. As a result, the average error of prediction was reduced to about half.

Keywords Ni-based superalloy · Microstructure · Recrystallization · FEM

1 Introduction

In recent years, the demand for aircraft has increased and there is a need to increase the combustion temperature of gas turbines in order to improve fuel efficiency. To achieve this, the gas turbine material must have high strength and fracture toughness

N. Yukawa (✉) · C. Osawa · T. Yamada · E. Abe
Department of Materials Science and Engineering, Nagoya University, Nagoya, Japan
e-mail: yukawa@nagoya-u.jp

© The Minerals, Metals & Materials Society 2021

G. Daehn et al. (eds.), *Forming the Future*, The Minerals, Metals & Materials Series,
https://doi.org/10.1007/978-3-030-75381-8_20

at high temperatures. Alloy 718 superalloy is a Ni-based superalloy that is used widely in gas turbines to satisfy these demands [1].

Alloy 718 turbine disks are manufactured through casting, multiple hot forging, and heat treatment. The microstructure changes induced during the manufacturing process affect the heat resistance of the alloy during the service. In order to guarantee the high-temperature strength, for example, it is necessary to control the grain size within a certain range. Alloy 718 is an austenite single-phase material, so grain refinement due to phase transformation cannot be expected [2]. Therefore, only grain refinement by recrystallization during hot forging and heat treatment is an effective means.

The recrystallization behavior has been studied so far. The Avrami equation is often used to predict softening phenomena caused by dynamic, post-dynamic, and static recrystallization [3]. In order to predict the fraction of recrystallization by the Avrami equation, it is necessary to determine some parameters in the equation. An assumption is made in recrystallization prediction by the Avrami equation using the Arrhenius plot method. The assumption is that the temperature, strain, and strain rate of the material does not change from the initial values during the process. The assumption has been used for simple forgings such as small free upsetting tests in the 10 t class.

However, in an actual hot forging, even if it is a small test piece in a modeled experiment, deformation at each location is complicated due to shape and friction, and the temperature is not constant and uniform due to heat release to the atmosphere and heat removal to the dies. This is even more pronounced in turbine disk forgings about 2 m in diameter. In the case of large forging, the temperature difference between the surface layer and the central part increases because the material to be forged is exposed to the cold atmosphere after it is removed from the heating furnace until the forging is completed. Also, the strain distribution inside the material is large because it is formed by multiple complex die forgings. In such complicated and non-uniform forging, the above assumption do not hold and it is difficult to accurately predict recrystallization using the parameters obtained on above assumption.

Therefore, in this research, a prediction model and a parameter optimization method that can respond to change and distributions during process were developed. Avrami equation is changed to an incremental form, and a genetic algorithm is used to determine the parameters in the prediction models. At this time, it is not enough to use only the results of small tests at the laboratory level as training data for genetic algorithm. This is because there is a difference in temperature change and deformation behavior during hot forging and heat treatment between small test specimens at the laboratory level and large real forgings. These differences are due to the difference in surface area to volume ratio of these materials. The volume that stores heat is the cube of the dimension, but the surface area that releases heat is the square. Specifically, the surface area/volume ratio of a large forging is about 1/60 of that of a small laboratory specimen, and the heat histories and distributions are completely different between the two.

In this study, in addition to the small forging test, tests using a 1,500 t class hot forging simulator (about 380 t) and tests using a 50,000 t forging press (about 13000 t)

Table 1 Chemical composition of tested material (mass %)

Ni	Cr	Mo	Fe	Nb(+Ta)	Ti	Al
54.0	18.0	3.0	18.5	5.1	0.9	0.5

were performed. Based on the results obtained from these tests, the parameters in the dynamic recrystallization prediction model and the post-dynamic/static recrystallization prediction model were determined using a genetic algorithm, respectively, and the recrystallization behavior of a large forging with a shape close to that of a turbine disk product was predicted. As a result of verifying the accuracy of the prediction model by comparing the experimental values and the prediction values, it is shown that the accuracy was improved by optimizing including the results of 1,500 and 50,000 t forging tests.

2 Experimental Procedure

2.1 Materials

Alloy 718 was used in the tests. The specimens were machined from a triple melted ingot (vacuum induction melting followed by electro-slag remelting and vacuum arc remelting). The chemical composition of the tested material is shown in Table 1.

2.2 Small Forging Test

Isothermal compression tests were done using THERMECMASTER-Z (FTZ-203A, Fuji Electric Industrial Co., Ltd). The shape of the specimen is a cylinder with 8 mm in diameter and 12 mm in height. The specimens were heated in a vacuum to the testing temperature in a few seconds by high-frequency induction heating, held for 60 s at the test temperature, and then compressed axially while maintaining temperature. At this time, the mica plates were used on the upper and the lower end surface as heat insulators. The ranges for test temperature, average strain rate, compression rate, and initial grain diameter is 960–1020 °C, 0.02–0.2 s^{-1}, 33–60%, and 18–539 μm, respectively.

After forging, cooling was performed in three different processes. Details are shown as small A test, small B test, and small C test, respectively.

- Small A test

In order to determine the parameters in the dynamic recrystallization prediction model, the specimens were cooled by N_2 gas immediately after hot forging to realize the quench condition.

- Small B test

In order to determine the parameters in the post-dynamic/static recrystallization prediction model, the specimens were held at the forging temperature after hot forging. The holding time was 15 s, 30 s, 60 s, and after holding, it was quenched with N_2 gas.

- Small C test

In order to determine the parameters in the post-dynamic/static recrystallization prediction model, the specimens were cooled to 500 °C at a rate of -15 °C $\cdot$ min^{-1} after hot forging. Then cooled with N_2 gas.

2.3 1,500 T Forging Test

Free upsetting hot forging tests were done using a large hot forging simulator installed at National Institute for Materials Science. This is a device that integrates an atmospheric furnace, a press (HCF-1,500, Sumitomo Heavy Industries, Ltd.), the cooling control devices, temperature measurement devices, and a manipulating robot. The shape of the specimen is a cylinder with 80 mm in diameter and 140 mm in height and has a corner radius of 3 mm at each end edge of the cylinder. The specimens were heated to the testing temperature in the furnace, held for 3600 s at the test temperature, moved to the compression die by the manipulator, and then compressed axially while maintaining temperature. At this time, glass lubricant was used between the specimen and the upper and lower dies. The testing temperature range, strain rate, compression rate, and initial grain diameter are 900 and 980 °C, 0.1 s^{-1}, 50%, and 160 μm, respectively. After compression, the specimens were removed from the die and cooled at a rate of -15 °C $\cdot$ min^{-1}.

2.4 50,000 T Forging Test

Two types of large forging tests were conducted using a 50,000 t hydraulic forging press. The first is the No.1 shape used for parameter determination, and the second is the No.2 shape used for accuracy verification. For both shapes, two-stage tests were conducted: rough forging and finish forging. The initial shape of the specimen for the No.1 test is a cylinder with 258 mm in diameter and 538 mm in height, and the



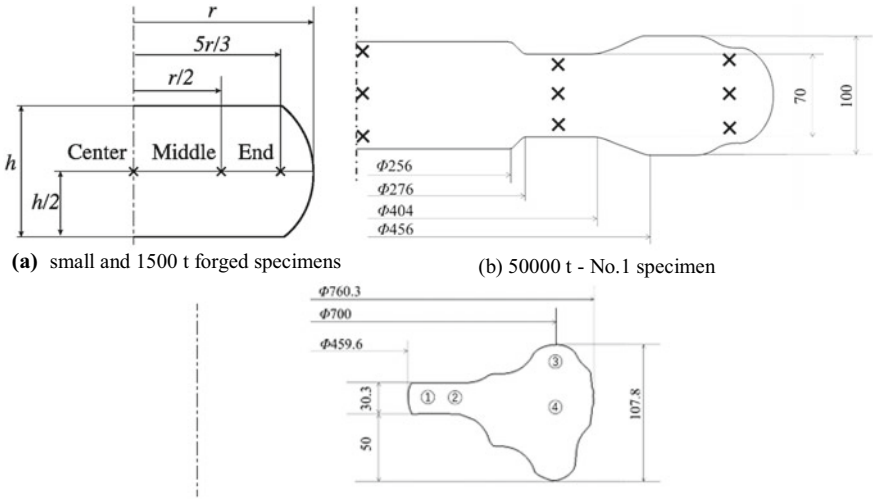
Fig. 1 Appearances of each shape specimens after rough forging and finish forging. (Color figure online)

No.2 test is a cylinder with 258 mm in diameter and 760 mm in height, before the rough forging. The No.2 shape specimen was machined to ring shape between rough forging and finish forging. Figure 1 shows the appearances of each shape specimen after rough forging and finish forging. The specimens before rough forging and finish forging were heated to 980 °C in a heating furnace in about 15 h, transported to the press machine by a robot arm, and then forged. After that, the forged specimens were taken out from the press machine with a robot arm and air-cooled on two metal bars.

2.5 Microstructure Observation

The microstructure of the specimen after cooling was observed in the vertical -section and the area fraction of recrystallization and recrystallized grain size was measured by EBSD method. In this study, the average grain size is calculated by the image processing method on the cut surface. Generally, grains have various shapes, and the average grain size is evaluated to be smaller than the actual size by image processing method on the cut surface as the grains have a shape that deviates greatly from the spherical shape. However, since the recrystallized grains are often equiaxed, the effect of shape-related errors in this study is considered to be small. On the other hand, it should be noted that even with equiaxed grains, the two-dimensional grain size is only a characteristic value of the cross section of the three-dimensional structure [5], and a value smaller than the three-dimensional grain size can be obtained.

The observation positions of small forged specimens and 1,500 t forged specimens are several areas of 1/2 in height, shown in Fig. 2a. The observation positions of 50,000 t No. 1 and No. 2 forged specimens are shown in Fig. 2b and c, respectively.



(a) small and 1500 t forged specimens

(b) 50000 t - No.1 specimen

(c) 50000 t - No.1 specimen

Fig. 2 Observation positions of each specimen

3 Prediction Model

3.1 Incremental Form of the Avrami Equation

In order to predict the fraction of dynamic recrystallization during the complex unstable deformation process, an incremental form of the Avrami equation was developed [4]. Equations (1) and (2) show the prediction model of dynamic recrystallization grain diameter.

$$D_{new} = a_3 \cdot \varepsilon^{p_1} \cdot Z^{-m_3} \tag{1}$$

$$Z = \dot{\varepsilon} exp(Q/RT) \tag{2}$$

where D_{new} is the nucleation particle size of dynamic recrystallization, ε is the amount of residual strain in the region, $\dot{\varepsilon}$ is the equivalent strain rate, T is the temperature, and a_3, p_1, m_3, Q are material constants. Total 21 parameters are contained in the equations. The parameters in these prediction models were optimized using the results of small A tests under 39 conditions as learning data.

Both post-dynamic recrystallization and static recrystallization are recrystallizations occurring after hot forging. Therefore, it is difficult to distinguish between post-dynamic recrystallized grains and static recrystallized grains in the microstructure observed after the small B, small C, 1,500 t and 50,000 t-No. 1 forging tests.

In this study, the recrystallization that occurs after hot forging is summarized as post-dynamic/static recrystallization.

Prediction models for area fraction of recrystallization after heat treatment, $X_{post,static}$, are shown in Eq. (3) [6].

$$X_{post,static} = 1.0 - exp\left[-\beta_s\left(\frac{t}{t_{0.5}}\right)^{K_s}\right] \tag{3}$$

where t is the holding time, $t_{0.5}$ is the time for 50% post-dynamic/static recrystallization, and β_s, K_s are material constants. The incremental form of this equation was expressed as shown in Eqs. (4)–(7).

$$X^{n+1}_{post,static} = X^{n}_{post,static} + d\left(X^{n}_{post,static}\right) \tag{4}$$

$$d\left(X^{n}_{post,static}\right) = \frac{\partial X}{\partial t}dt + \frac{\partial X}{\partial t_{0.5}}dt_{0.5} \tag{5}$$

$$\frac{\partial X}{\partial t} = \frac{-\beta_s \cdot K_s \cdot \left(\frac{t}{t_{0.5}}\right)^{K_s-1.0} \cdot exp\left[-\beta_s\left(\frac{t}{t_{0.5}}\right)^{K_s}\right]}{t_{0.5}} \tag{6}$$

$$\frac{\partial X}{\partial t_{0.5}} = \frac{-\beta_s \cdot K_s \cdot t \cdot \left(\frac{t}{t_{0.5}}\right)^{K_s-1.0} \cdot exp\left[-\beta_s\left(\frac{t}{t_{0.5}}\right)^{K_s}\right]}{(t_{0.5})^2} \tag{7}$$

For $t_{0.5}$, Eq. (8) has been proposed by previous research [6].

$$t_{0.5} = a_1 \cdot (d_0)^b \cdot \varepsilon^{-m_1} \cdot \dot{\varepsilon}^{-p_1} \cdot exp\left(\frac{Q_1}{RT}\right) \tag{8}$$

where d_0 is the initial grain diameter, $\dot{\varepsilon}$ is the equivalent strain rate during hot forging, and a_1, b, m_1, $p_1$and Q_1 are constants. The residual strain calculated by the dynamic recrystallization prediction model are used as initial values. In this equation, $t_{0.5}$ depends on the initial grain diameter. However, in this study, it is not appropriate to use a constant initial grain diameter when calculating $t_{0.5}$ at each calculation step because the calculation is performed in an incremental form. Therefore, the grain boundary length at each step was used instead of the initial grain diameter.

$$t_{0.5} = a_1 \cdot L^{-n_1} \cdot \varepsilon^{-m_1} \cdot \dot{\varepsilon}^{-p_1} \cdot exp\left(\frac{Q_1}{RT}\right) \tag{9}$$

L is the grain boundary length of the target region.

These equations contain a total of 17 parameters. The parameters in these prediction models were optimized using the results of small B (9 data), small C (3 data), 1,500 t (12 data), and 50,000 t-No. 1 tests (9 data) as learning data.

3.2 Overview of Parameter Optimization

The parameters in the dynamic and post-dynamic/static recrystallization prediction models were optimized by using genetic algorithm. First, the history of the temperature and the strain rate inside the material during forging and cooling was acquired by finite element analysis and used as input data. Next, using the input data and randomly generated parameters, the fraction of recrystallization and recrystallized grain size were calculated in a prediction model. Then, the calculated values were compared with the experimental values, the genetic operations were performed to reduce the error, and a new parameter group was generated. This operation was repeated, and the generation parameter group that is converged empirically enough was determined as the optimal value.

4 Results of Prediction Model

4.1 Calculation Accuracy

Figure 3 shows the calculation results when the parameters in the dynamic recrystallization prediction model were optimized using the results of the small A tests.

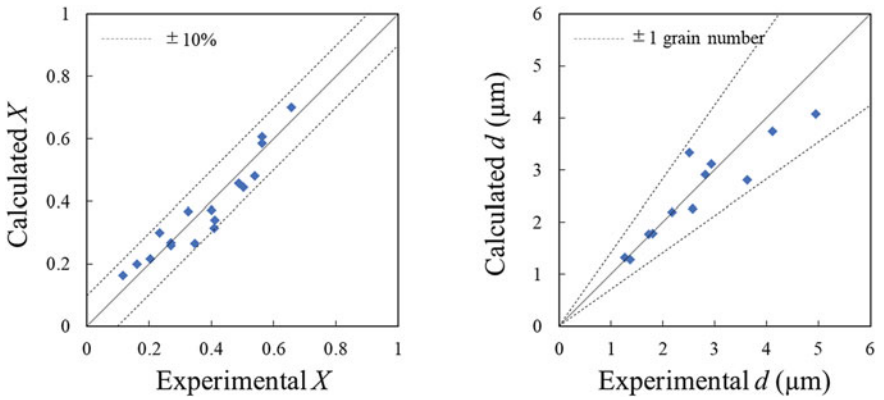


Fig. 3 Calculation results of dynamic recrystallization to decide parameters. **a** the fraction of recrystallization, **b** the recrystallized grain size. (Color figure online)

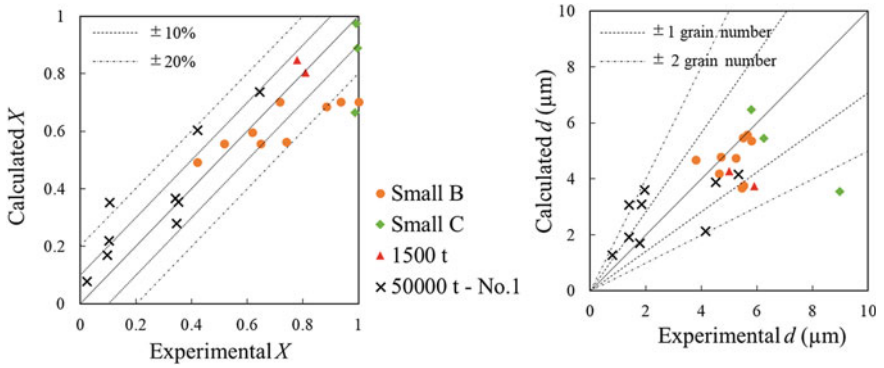


Fig. 4 Calculation results of post-dynamic/static recrystallization. **a** Fraction of recrystallization, **b** Recrystallized grain size. (Color figure online)

Figure 3a shows the fraction of recrystallization, and Fig. 3b shows the recrystallized grain size. The dotted lines in the figure indicate the range of the fraction of ± 10% for the fraction of recrystallization and ± 1 ASTM grain size number for the recrystallized grain size, respectively. From these figures, it can be seen that the errors were within the range of ±10% for the fraction of recrystallization and ±1 ASTM grain size number for the recrystallized grain size in all results, and the calculated values agreed well with the experimental values. The average error is 4.4% for the fraction of recrystallization and 10% for the recrystallized grain size.

Figure 4 shows the calculation results when the parameters in the post-dynamic/static recrystallization prediction model were optimized using the results of the small B, small C, 1,500 t, and 50,000 t-No. 1 forging tests. The dashed lines indicate the error range of ±20% for the fraction of recrystallization and ±2 ASTM grain size number for the recrystallized grain size. From this figure, it can be seen that most of the results were within the error range of ±20% for the fraction of recrystallization and ±2 ASTM grain size number for the recrystallized grain size. The average error was 11.0% for the fraction of recrystallization and 30.7% for the recrystallized grain size.

4.2 Prediction Accuracy

In order to verify the accuracy of the constructed recrystallization prediction model and the optimized parameters, a prediction was conducted for the 50,000 t-No. 2 forging test. Figure 5 shows the EBSD map obtained at each observation position shown in Fig. 2c after forging.

Figure 6 shows the comparison between the experimental results (blue bar) and the predicted results (red bar) using the small A, B, C, 1,500 t, and 50,000 t-No. 1 tests for parameter optimization. From these results, the average error for the four

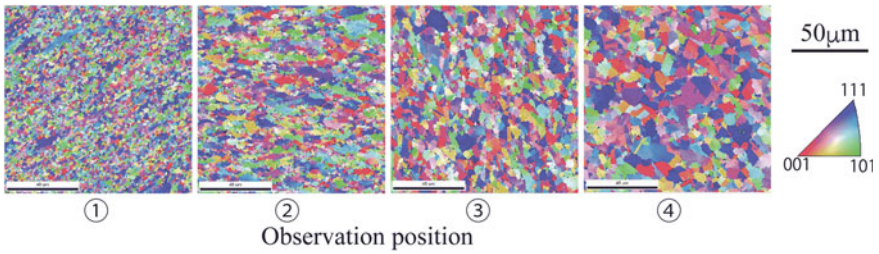
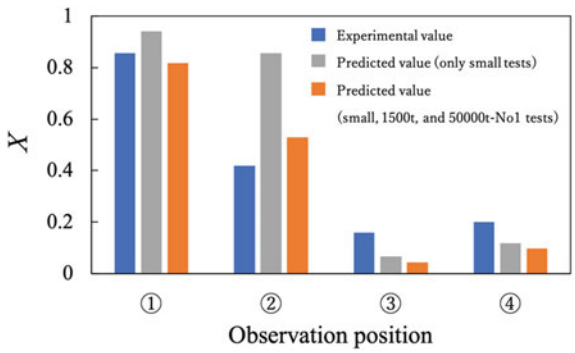


Fig. 5 EBSD map at each observation position in 50000t-No. 2 forging test. (Color figure online)

Fig. 6 Prediction results of the fraction of recrystallization in 50000 t-No. 2 forging test. (Color figure online)



observation positions was 9.2%. Predicted results using only the small tests are also shown in this figure (gray bar). In this case, the average error of the prediction results was 17.4%. The prediction accuracy was improved by optimizing the parameters using the results of the 1,500 t forging test and the 50,000 t forging test, as compared to the conventional method using only the small forging tests. In this figure, it can be seen that the error of the predicted results using small, 1,500 t, and 50,000 t-No. 1 tests are slightly larger than the result using only the small tests at positions 3 and 4. In these areas, the strain rate is very small compared to the experimental tests that are used for the parameter optimization, and it is considered that this caused the error.

The fraction of post-dynamic/static recrystallization depends on the residual strain after forging and the temperature during cooling. As a result of finite element analysis, there was almost no temperature distribution inside the small C specimens cooled at a rate of -15 °C · min^{-1}, whereas the maximum temperature difference was 92 °C inside the 1,500 t forged specimen. The maximum temperature difference inside the 50,000 t-No. 1 forged test specimen was 241 °C. By determining the parameters in the post-dynamic/static recrystallization prediction model in consideration such a temperature distribution, it is thought that the prediction accuracy for 50,000 t-No. 2 forged test, which also has a large temperature difference (maximum temperature difference 179 °C), was improved.

Figure 7 shows the prediction results for the recrystallized grain size. Comparing the experimental values with the predicted values using optimized the parameters

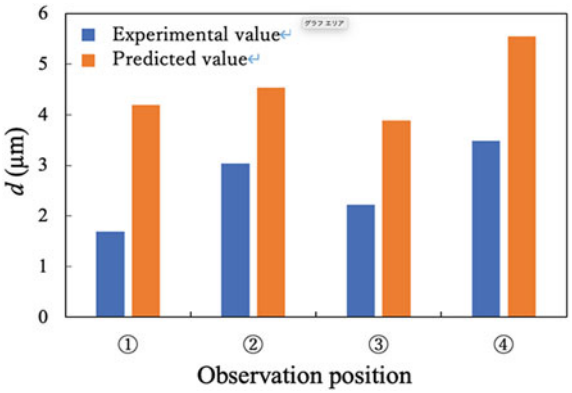


Fig. 7 Prediction results of the recrystallized grain size in 50000 t-No. 2 forging test. (Color figure online)

by the results of the 1,500 t forging test and the 50,000 t-No. 1 forging test for each position, the error was within ±2 ASTM grain size number, but the predicted values exceeded the experimental values.

The reason why the predicted value of the recrystallized grain size exceeded the experimental value may be that the calculation during the 50,000 t – No. 2 forging was in the extrapolated range. The dynamic recrystallization nucleation grain size is a function of the residual strain, the strain rate, and the temperature, as shown in Eqs. (1) and (2). In this study, the strain rate during 50,000 t-No. 2 forging obtained by finite element analysis was less than one-tenth of the strain rate in the small A test used for parameter determination. As a result, the prediction for the 50,000 t-No. 2 forging test was in the extrapolated range, and the difference between the experimental value and the predicted value may have increased. Furthermore, the post-dynamic/static recrystallization behavior is calculated using these values, and it is considered that the error from the experimental value was widened in the calculation of grain growth.

5 Conclusion

In this study, 1,500 t forging test and 50,000 t-No. 1 forging test were performed in addition to small forging tests, and a recrystallization prediction system was developed using the results. The results are shown below.

1. As a result of post-prediction in a forging test assuming a turbine disk, the average error in the fraction of recrystallization was about half that in the case of prediction using a model constructed using only small tests.
2. In the prediction result of the recrystallized grain size, although the error was within ±2 ASTM grain size number, the calculated value was larger than the experimental value. This is thought to be because post-prediction is in the extrapolated range. In the future work, it is necessary to determine the parameters using the results of forging performed under low strain rate conditions.

References

1. Chang S-H, Lee S-C, Tang T-P, Ho H-H (2006) Influences of soaking time in hot isostatic pressing. Mater Trans 47(2):426–432
2. Hatta T, Hironaka T, Yoshida H, Isogawa,S, Masunaga A (2007) Process Modeling of INCONEL alloy 718 for Free Forging. Denki Seiko 78(3):215–220
3. Matsui T (2013) High temperature deformation and dynamic recrystallisation behavior of Inconel 718. Mater Trans 54:512–519
4. Yamada T, Abe E, Osawa C, Yukawa N (2018) Prediction on microstructure and mechanical properties of hot forged Ni-based super alloy by optimization using genetic algorithms. Proc. Manuf 15:356–363
5. Takayama Y, Tozawa T, Kato H, Kato S, Furushiro N, Hori S (1988) Change in the grain size distribution during grain growth in recrystallized aluminum. J Jpn Inst Met Mater 52(5):465–471
6. Gangshu Shen SL, Semiatin RS (1995) Modeling microstructural development during the forging of Waspaloy. Metall Mater Trans A 26:1795–1803

Part V
Honorary Symposium: Rob Wagoner

Simulated Microstructure Effects on Macroscopic Mechanical Properties Based on Multiscale Crystal Plasticity



Yoshiteru Aoyagi, Ryota Kobayashi, and David L. McDowell

Abstract In this study, we investigated the influence of microscopic structures of highly cold-rolled pure aluminum A1050 on macroscopic mechanical properties based on the crystal plasticity finite element (FE) analysis. Uniaxial tensile tests and biaxial tensile tests were performed, and the contours of plastic work were plotted. The comparison of experimental results and results obtained by the crystal plasticity FE simulation with a small number of grains indicates that the yield strength for the rolling direction was higher than that for the transverse direction of the rolled sheet; however, the experimental and numerical yield surfaces did not agree. Extreme value analysis was used to estimate the variation of mechanical properties in simulated results due to the combination of crystal orientation in the computational models employed.

Keywords Crystal plasticity · Finite elements analysis · Contour of plastic work · Extreme value analysis

1 Introduction

Sheet metals produced by severe rolling show high specific strength and anisotropy of mechanical properties depending on the strong rolling texture [1, 2]. It is difficult to predict the yield behavior precisely using standard yield functions developed for isotropic materials. In order to approximate the yield behavior of the anisotropic materials, anisotropic yield functions [3, 4] obtained by extension of theories for isotropic materials have been proposed. These methods require complex experimental procedures such as biaxial tensile tests [5] and compression–torsion tests [6] to determine the yield surface. Crystal plasticity simulations reproducing various

Y. Aoyagi (✉) · R. Kobayashi
Department of Finemechanics, Tohoku University, Sendai, Miyagi 980-8579, Japan
e-mail: aoyagi@tohoku.ac.jp

D. L. McDowell
Materials Science and Engineering, Georgia Institute of Technology, Atlanta, GA 30332-0245, USA

© The Minerals, Metals & Materials Society 2021

G. Daehn et al. (eds.), *Forming the Future*, The Minerals, Metals & Materials Series,
https://doi.org/10.1007/978-3-030-75381-8_21

phenomena [7] have attracted attention because of the development of microscopic observation of metals using the electron backscattered diffraction pattern (EBSD) method [8, 9]. However, uniaxial tensile tests are commonly used to estimate hardening properties for calibration of parameters used in crystal plasticity simulations without consideration of the mechanical anisotropy.

In this study, crystal plasticity simulations are carried out for highly deformed aluminum to investigate the effects of microstructure on mechanical properties. The yield surface predicted by the crystal plasticity analyses based on the microstructure of the aluminum sheet is compared with the experimental result obtained by uniaxial and biaxial tensile tests. Moreover, the extreme value analysis for mechanical properties provides an understanding of the role of microstructure and size of the volume elements used in simulations on the variance of material responses.

2 Macroscopic Mechanical Properties of an Aluminum Sheet

2.1 Experimental Procedures

Experimental procedures are the same as in a previous work [10], whereas some experimental results are updated. A highly cold-rolled pure aluminum A1050 sheet with a reduction ratio of 93.3% was used as a sample. Microstructures of the sample were observed by the EBSD method, and uniaxial and biaxial tensile tests were performed. Test specimens for the uniaxial tensile tests were cut out from the aluminum sheets so that the loading direction is parallel to the transverse direction (TD) or the rolling direction (RD). Ten specimens were prepared for each direction to estimate the reliable difference between strength for RD and TD. The tensile tests were performed under the static condition: the strain rate is 1.0×10^{-3}. Note that two outliers were omitted. TD and RD correspond, respectively, to the x-axis direction and the y-axis direction in the stress space. The thickness of the specimen is 0.2 mm, and the shape of the specimen is the same as the half size of the ISO6892-1 type specimen. The shape of the uniaxial tensile test specimen and the cruciform specimen for the biaxial tensile test [4] are depicted in Fig. 1. The cruciform specimens were cut out so that the longitudinal directions of the cruciform were parallel to the RD and TD of the rolled sheet. The thickness of the specimen is 0.2 mm, the length is 90 mm, the length of the arm is 30 mm, and the measurement area is a square of 20 mm $\times$ 20 mm. The seven silts were provided in the arm part to reduce the in-plane shear stress. The biaxial tensile tests were performed under sufficiently static condition, and the stress ratio σ_x:σ_y was set in the nine different patterns: σ_x:σ_y = 4:1, 3:1, 2:1, 1.5:1, 1:1, 1:1.5, 1:2, 1:3, 1:4, where σ_x and σ_y correspond to the normal stress for the TD and RD, respectively. The stress was calculated by dividing the test load by the width of the measurement area and thickness of the cruciform specimen. In the case of biaxial tensile tests, since arm parts fracture in the early stage of the

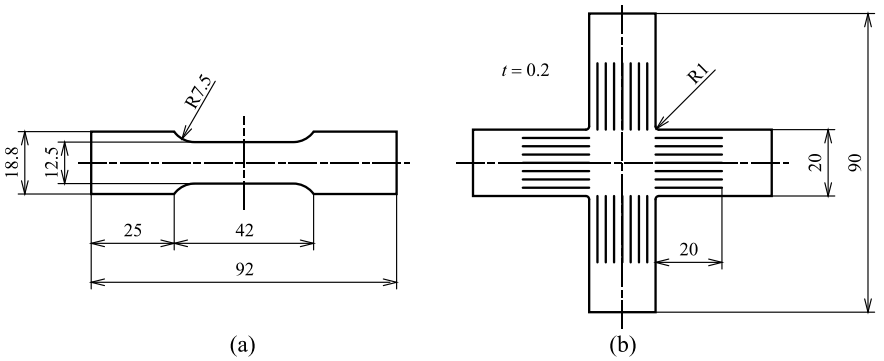


Fig. 1 Specimens for **a** uniaxial tensile test and **b** biaxial tensile test

deformation, the maximum strain is about 0.4%. Thus, the strain was measured using strain gages attached along TD and RD orientations in the measurement area. In this study, the value of the plastic work was calculated from the area under the stress–strain curves obtained by the uniaxial and biaxial tensile tests. At each stress ratio, the contours of plastic work instead of the yield surface were obtained by plotting the stress components (σ_x, σ_y) on the principal stress space when the plastic work reaches a determined value.

2.2 *Experimental Results*

The crystal orientation map and <111> pole figure obtained by the EBSD observation are shown in Fig. 2. It can be seen that the preferred orientation is Brass orientation {110} <112> and Copper orientation {112} <111> from the crystal orientation map, and S orientation is also preferred orientation from the pole figure. The average grain size is approximately 3.48 μm. The averaged 0.2% proof strength of each specimen

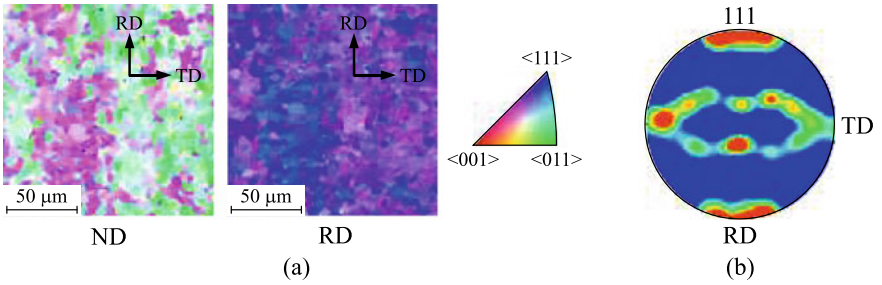


Fig. 2 **a** The crystal orientation maps and **b** the pole figure measured by EBSD observation. (Color figure online)

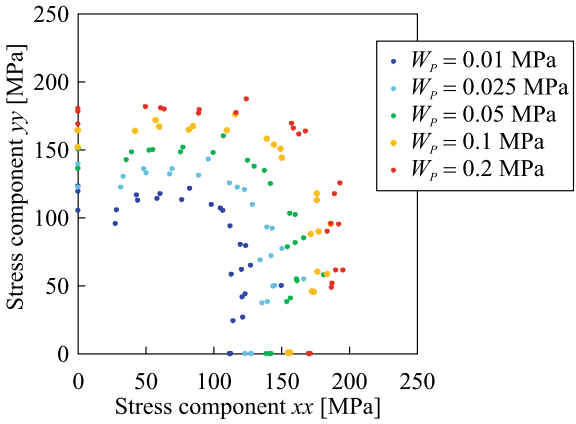


Fig. 3 Measured stress points corresponding to contours of constant plastic work. (Color figure online)

obtained by the uniaxial tensile tests are, respectively, 175.09 ± 33.65 MPa and 184.19 ± 15.02 MPa for TD and RD and averaged Young's modulus for TD and RD are, respectively, 72.90 ± 8.31 GPa and 72.59 ± 12.38 GPa. The value of 0.2% proof strength tends to be higher in RD. The contours of plastic work obtained by the uniaxial and the biaxial tensile tests are plotted in Fig. 3.

3 Crystal Plasticity Finite Element Simulations

3.1 Multiscale Crystal Plasticity Modeling

In this study, the following elasto-viscoplastic constitutive equation proposed by Pierce et al. [11] is used.

$$\overset{\nabla}{\mathbf{T}} = \mathbf{C}^e : \mathbf{D} - \mathbf{C}^e : \sum_{\alpha} (\mathbf{s}^{(\alpha)} \otimes \mathbf{m}^{(\alpha)})_S \dot{\gamma}^{(\alpha)} \tag{1}$$

where $\overset{\nabla}{\mathbf{T}}$ is the corotational rate of Cauchy stress, $\mathbf{C}^e$ is the anisotropic elastic modulus tensor, $\mathbf{D}$ is the deformation rate tensor, $\mathbf{s}^{(\alpha)}$ is the slip direction vector, $\mathbf{m}^{(\alpha)}$ is the normal direction vector to the slip plane, $(\ )_S$ means the symmetric part of second-order tensor, and $\dot{\gamma}^{(\alpha)}$ is the slip rate. In order to consider the hardening effect caused by the interaction of dislocations, following slip rate hardening law [12] is used.

$$\dot{\gamma}^{(\alpha)} = \dot{\gamma}_0^{(\alpha)} \left(\frac{\tau^{(\alpha)}}{g^{(\alpha)}} \right) \left| \frac{\tau^{(\alpha)}}{g^{(\alpha)}} \right|^{\frac{1}{m}-1} \tag{2}$$

where $\dot{\gamma}_0^{(\alpha)}$ is the reference slip rate, $\tau^{(\alpha)}$ is the resolved shear stress, $g^{(\alpha)}$ is the flow stress, and m is the strain rate sensitivity. The evolution equation of the flow stress is represented as

$$g^{(\alpha)} = \tau_0^{(\alpha)} + \sum_{\beta} \Omega^{(\alpha\beta)} a \mu \tilde{b} \sqrt{\rho_d^{(\beta)}} \tag{3}$$

where $\tau_0^{(\alpha)}$ is the reference value of $g^{(\alpha)}$, $\Omega^{(\alpha\beta)}$ is the dislocation interaction matrix, a is a numerical factor whose order is 0.1, μ is the elastic shear modulus, $\tilde{b}$ is the magnitude of the Burgers vector, and $\rho_d^{(\beta)}$ is the dislocation density. The rate of dislocation density $\dot{\rho}_d^{(\beta)}$ presented by authors [13] is given by

$$\dot{\rho}_d^{(\beta)} = \dot{\rho}_a^{(\beta)} - \dot{\rho}_r^{(\beta)} = \frac{r\rho_f}{\tilde{b}} \left| \dot{\gamma}^{(\beta)} \right| - k\rho_d^{(\beta)} \dot{\rho}_a^{(\beta)} = \left(1 - k\rho_d^{(\beta)}\right) \frac{r\rho_f}{\tilde{b}} \left| \dot{\gamma}^{(\beta)} \right| \tag{4}$$

where k is the annihilation ratio and corresponds to the inverse of the saturated density of dislocation, r is the mean length of remaining dislocation lines, and ρ_f is the density of forest dislocations.

3.2 *Uniaxial Tensile Simulation for Determination of Material Parameters*

In order to identify some material parameters, we carried out the uniaxial tensile simulation. The crystal orientation measured by the EBSD method at 27 or 216 points was randomly assigned to each grain for the computational model with an ensemble of grains, as depicted in Fig. 4. The average grain size of the computational model is 3.48 μm, and the number of grains is 27. In the analysis, periodic boundary conditions are applied. TD is parallel to the x-axis and RD is parallel to the y-axis. We carried out the numerical simulations assuming uniaxial tensile tests in this section and the biaxial tensile or compression tests in the following section by controlling the displacement at the three vortexes of the computational model.

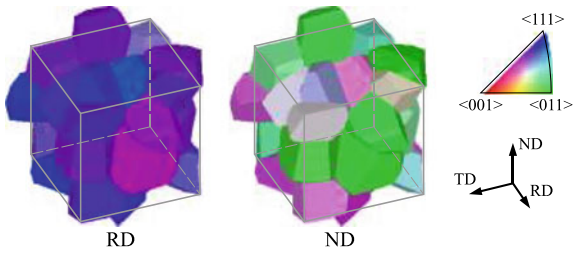


Fig. 4 Computational model with 27 grains. (Color figure online)

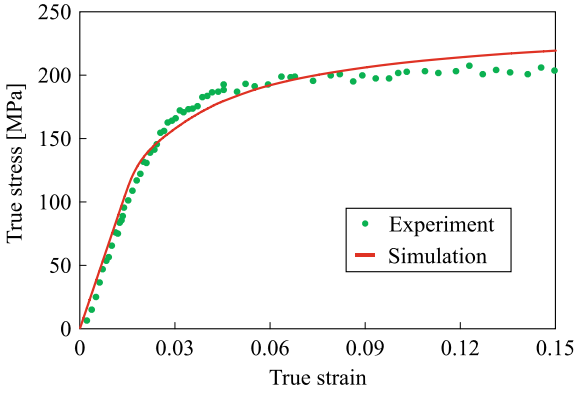


Fig. 5 Stress–strain cuves obtained by experiment and simulation for identification of material parameters. (Color figure online)

Table 1 The identified material parameters for the following simulations

Initial dislocation density	$\rho_d^{(\beta)}$	2.345×10^{12} m^{-2}
Annihilation ratio	k	7.13×10^{-14} m^{-2}
Mean length of accumulated dislocation	r	1.83 μm

The material parameters were identified by fitting the stress–true strain curves obtained by numerical analysis to that measured by the uniaxial tensile test for RD, as shown in Fig. 5. The identified initial dislocation density, annihilation rates of dislocations, and mean accumulated dislocation length are summarized in Table 1.

3.3 Biaxial Tensile and Compression Simulations for the Prediction of the Yield Surface

We performed biaxial tensile and compression simulations to predict the yield surface of cold-rolled aluminum. The computational model is the same as Fig. 4. The strain rate averaged in the analysis region $\dot{\varepsilon}_{xx}$ and $\dot{\varepsilon}_{yy}$ was varied in 28 combinations assuming biaxial stress states. The stress components σ_{xx} and σ_{yy} averaged in the analysis region when the plastic work W_p reaches the specified value are plotted in the stress space. The plastic work was calculated by integrating the plastic work at the integration points over the entire analysis region.

The contours of plastic work calculated from the results of the numerical analyses are compared to the experimental results as shown in Fig. 6. The value of plastic work $W_P = 0.01$ MPa corresponds to the macroscopic yielding estimated by the 0.2% proof strength. From the comparison between the experimental and numerical results, we find that the crystal plasticity simulation underestimates the strength for TD when the plastic work is 0.2 MPa. Anisotropic strength of metals depends strongly

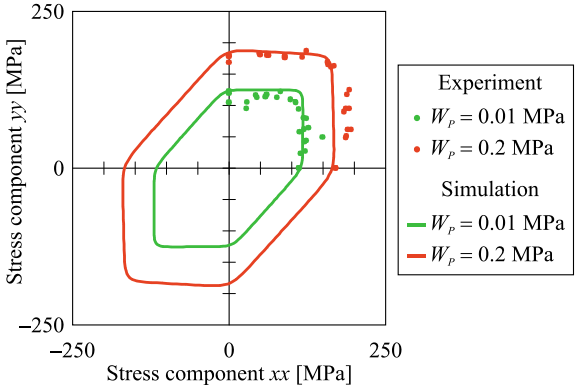


Fig. 6 Measured stress points corresponding to contours of constant plastic work obtained by experiments and simulations. (Color figure online)

on the initial crystal orientation, and 27 grains may be insufficient to represent the macroscopic mechanical behavior of severely cold-rolled aluminum.

3.4 Extreme Value Analysis of Mechanical Properties

In the crystal plasticity simulation, a large number of grains, which is enough to reproduce the effects of the microstructure is required to predict the macroscopic mechanical behavior of polycrystalline metals. In this section, we investigate the effect of the number of grains and the rolling texture of aluminum. We conducted 100 simulations with the 27 grains model and 30 simulations for the 216 grains models. Different combinations of the random crystal orientation extracted from the EBSD measurement are assigned in each simulation model.

We use the extreme value theory [14] to process mechanical properties such as the 0.2% proof strength and Young's modulus obtained by the crystal plasticity simulation using each computational model. The extreme value theory denotes that the distribution of maximum or minimum values in different assemblies selected from a set follows a specific distribution. We assume that the values of the mechanical properties calculated with each computational model show the Gumbel distribution [14] because the weakest point in materials should determine the strength of the materials. The Gumbel distribution is given by

$$P_i = 1 - \exp\left[-\exp\{\alpha(y_i - u)\}\right] \tag{5}$$

where y_i is the i-th ranked minimum value, P_i is the cumulative distribution function, i.e., the probability that minimum value in a assemble is greater than or equal to y_i, α is the inverse of parameter expressing variance, and the u is the mode value. Equation (5) can be written as

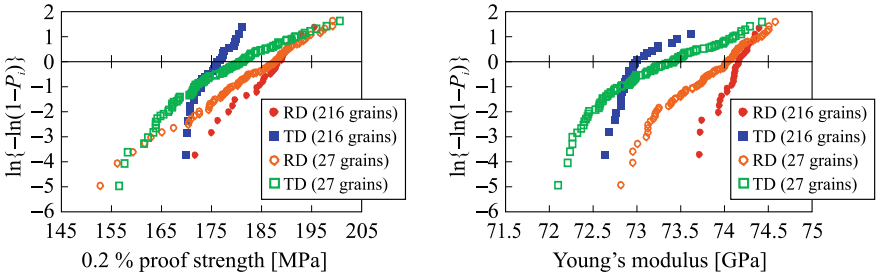


Fig. 7 The 0.2% proof strength and Young's modulus determined from the simulations. (Color figure online)

$$\ln\{-\ln(1-P_i)\} = \alpha(y_i - u) \tag{6}$$

The cumulative distribution function of each mechanical property is calculated by [15].

$$P_i(x_i) = \frac{i - 0.3}{n + 0.4} \tag{7}$$

where x_i corresponds to the values of the 0.2% proof strength σ_i and Young's modulus E_i of each computational model, i is the rank of each data, and n is the total number of models.

The 0.2% proof strength and Young's modulus values obtained by the crystal plasticity simulations are summarized in Fig. 7. It is considered that 100 simulations for the 27 grains model are reasonable because the distribution of extreme values is similar to normal distributions of extreme values. On the other hand, in the case of the computational model with 216 grains, the variance of the extreme value is smaller than that obtained using the model with 27 grains. A total of 30 simulations are enough to estimate a reliable distribution of extreme values for the 216 grains model. Note that such numbers of simulations do not indicate the necessary and sufficient number of simulations. When we apply linear approximation to the distribution of Fig. 7, the gradient of the line and the cross-section of the linear line and the horizontal axis correspond to the inverse of parameter expressing variance α and the mode value u, respectively. The mode values of the 0.2% proof strength and Young's modulus for RD are higher than that for TD regardless of the number of grains. This trend agrees with the experimental results. The mode values are almost independent of the number of grains. This result predicts that the extreme value analysis with a small number of grains can estimate the mode value of the mechanical properties. On the other hand, when we focus on the gradient of the distribution, we find that the variance of the mechanical properties is significant when the number of grains is small. It can be said that it is difficult to estimate the macroscopic mechanical properties using only one combination of crystal orientation with a small number of grains. The influence

of the crystal orientation on the macroscopic strength increases when the number of grains is small.

4 Conclusion

In this study, the effects of the microstructure on the macroscopic mechanical properties of the severely cold-rolled pure aluminum A1050 were investigated by the uniaxial and biaxial tensile tests and the crystal plasticity simulation. In the extreme value analysis based on the crystal plasticity simulations, the mode values of the mechanical properties for the computational models with the different number of grains agree well. It is difficult to estimate the macroscopic mechanical properties using only one combination of crystal orientation with a small number of grains. However, the extreme value analysis with a small number of grains can estimate the mode value of the mechanical properties.

Acknowledgments This work was performed with the support of JSPS KAKENHI Grant Numbers JP16H06059, JP17KK0108, JP18H05453, and the Japan Science and Technology Agency (JST) Grant Number JPMJSK1413.

References

1. Dillamore IL et al (1971) An experimental study of the mechanical anisotropy of some common metals. Int J Mech Sci 13:1049–1061 (Pergamon Press)
2. Li ZJ, Winther G, Hansen N (2004) Anisotropy of plastic deformation in rolled aluminum. Mater Sci Eng A 387–389:199–202
3. Barlat F et al (2003) Plane stress yield function for aluminum alloy sheets part1: theory. Int J Plast 19:1297–1319
4. Hill R (1948) A theory of the yielding and plastic flow of anisotropic metals. Proc R Soc Lond A 193:281–297
5. Kuwabara T, Ikeda S, Kuroda K (1998) Measurement and analysis of differential work hardening in cold-rolled steel sheet under biaxial tension. J Mater Process Technol 80–81:517–523
6. Yoshida K, Ishii A, Tadano Y (2014) Work hardening behavior of polycrystalline aluminum alloy under multiaxial stress paths. Int J Plast 53:17–39
7. Aoyagi Y, Kaji Y (2012) Crystal plasticity simulation considering oxidation along grain boundary and effect of grain size on stress corrosion cracking. Mater Trans 53:161–166
8. Inal K, Mishra RK, Cazacu O (2010) Forming simulation of aluminum sheets using an anisotropic yield function coupled with crystal plasticity theory. Int J Solids Struct 47:2223–2233
9. Aoyagi Y et al (2018) Crystal plasticity simulation considering microstructures of austenitic stainless steel on macroscopic yield function. Mater Sci Forum 941:212–217
10. Aoyagi Y, et al (2019) Multiscale simulation based on macroscopic deformation model predicted by microstructure information of ultrafine-grained metals. In: Proceedings of the 10th pacific rim international conference on advanced materials and processing, pp 879–871
11. Peirce D, Asaro RJ, Needleman A (1983) Material rate dependence and localized deformation in crystalline solids. Acta Metall 31–12:1951–1976

12. Pan J, Rice JR (1983) Rate sensitivity of plastic flow and implications for yiels-surface vertices. Int J Solids Struct 19–11:973–987
13. Aoyagi Y, Tsuru T, Shimokawa T (2014) Crystal plasticity modeling and simulation considering the behavior of the dislocation source of ultrafine-grained metal. Int J Plast 55:43–57
14. Gumbel EJ (1958) Statistics of extremes. Columbia University Press
15. Przybyla CP, McDowell DL (2010) Microstructure-sensitive extreme value probabilities for high cycle fatigue of Ni-base superalloy IN 100. Int J Plast 26:372–394

Experimental Study on Texture Evolution of Mg-Y Magnesium Alloy in Extrusion



Dayong Li, Weiqin Tang, Ding Tang, and Yinghong Peng

Abstract The low lattice symmetry and limit deformation modes of wrought magnesium (Mg) alloys restrain it from wide use in aerospace and automobile industries. Addition of rare earth (RE) elements has been used as the texture modifier to improve the formability of Mg alloys. Mg-1Al and Mg-4Y extruded alloys were investigated to probe the effects of the Y addition on the texture and microstructure of Mg alloys. It is demonstrated that the non-RE alloys exhibit a $\{10\bar{1}0\}$ or $\{10\bar{1}0\} - \{11\bar{2}0\}$ texture depending on the recrystallized fraction, whereas the yttrium (Y) Mg alloys develop a $\{11\bar{2}1\}$ "RE texture" component. The mechanism of "RE texture" component's formation was studied by using the electronic backscattered diffraction (EBSD) technique. The results indicate that the formation of both $\{11\bar{2}0\}$ and $\{11\bar{2}1\}$ texture components is closely related to the continuous dynamic recrystallization (CDRX) of the grains which nucleate in the mantle regions of the original grains.

Keywords Magnesium · Rare earth · Texture · Dynamic recrystallization

1 Introduction

Extrusion is an efficient process for fabricating high-performance Mg alloy components, and can significantly refine microstructure and improve mechanical properties [1, 2]. However, the strong anisotropy and limited ductility of extruded Mg alloys still pose great challenge to their applications in automotive and aerospace industries. Such limitations are mainly attributed to the strong basal or fiber-type texture originated from extrusion process. Therefore, extensive works on texture modification and ductility improvement have been performed in recent years [3, 4].

Rare earth (RE) elements, such as Ce, Gd, Y, and Nd, have been used to change texture evolution, thus reducing the anisotropy and enhancing the ductility of extruded Mg alloy. It is suggested [3, 5, 6] that the texture modification or weakening for RE-Mg alloys extrusion shifts the peak intensity from the conventional

D. Li (✉) · W. Tang · D. Tang · Y. Peng
State Key Laboratory of Mechanical Systems and Vibration, Shanghai Jiao Tong University, 800 Dongchuan Road, Shanghai 200240, China
e-mail: dyli@sjtu.edu.cn

© The Minerals, Metals & Materials Society 2021

G. Daehn et al. (eds.), *Forming the Future*, The Minerals, Metals & Materials Series,
https://doi.org/10.1007/978-3-030-75381-8_22

$\{10\bar{1}0\}$ pole toward a new texture component near to $\{11\bar{2}1\}$ pole, which is called "RE texture," instead of producing an ideal randomized texture.

A significant number of researches have been devoted to explaining the formation mechanism of such kind of "RE texture" component. Some researchers [7, 8] attributed the weakened texture to the particle stimulated nucleation (PSN) of recrystallization. However, this particle-related mechanism is questionable since many conventional (non-RE) Mg alloys have stable particles but still develop a strong basal texture [9]. Precipitates, which can affect the recrystallization and the textures of Al–Mn alloy, have been proved that the critical RE content required to weaken texture is below the expected bulk solid solubility [10]. Relevant experiments showed that RE elements can strongly segregate to grain boundaries [11, 12]. Furthermore, a size misfit between RE and magnesium atoms can result in a solute drag effect [9], which is believed to be related to the "RE texture" formation. Yttrium (Y) is known to produce pronounced solute drag effect due to its strong tendency to segregate to boundaries [11, 13]. However, there is still controversy on the formation mechanism of $\{11\bar{2}1\}$ "RE texture" component, due to the differences in alloy composition and extrusion conditions for various studies. Therefore, it is still of necessity to explore the influential mechanism of RE elements additions.

2 Material and Experimental Procedure

Mg-1Al and Mg-4Y were fabricated by melting pure magnesium with pure aluminum or with a master alloy of Mg-25 wt%Y in the appropriate proportions. The as-cast billets were solution treated in a furnace for 16 h at 535 °C followed by an immediate water quench.

Round bars with the diameter of 20 mm were extruded using a vertical extrusion press. The solid solute billets were lubricated with MoS_2 paste, preheated to the temperature of 400 °C, held for 1 h, and then pushed by a ram through a die. The ram was set to move with a low speed of 2 mm/s and a high speed of 10 mm/s, respectively. The extruded bars were immediately quenched into water to preserve the microstructure in its as-deformed state.

Labotex texture analysis software was used to generate orientation distributions and full pole figures. Grain sizes, recrystallized volume fraction, twin volume, misorientation distribution, and micro-textures were examined using the Channel 5 electron backscattered diffraction (EBSD) system equipped with a Nova NanoSEM^{TM} 230 scanning electron microscope. All of the EBSD data were processed with the HKL Channel 5 software.

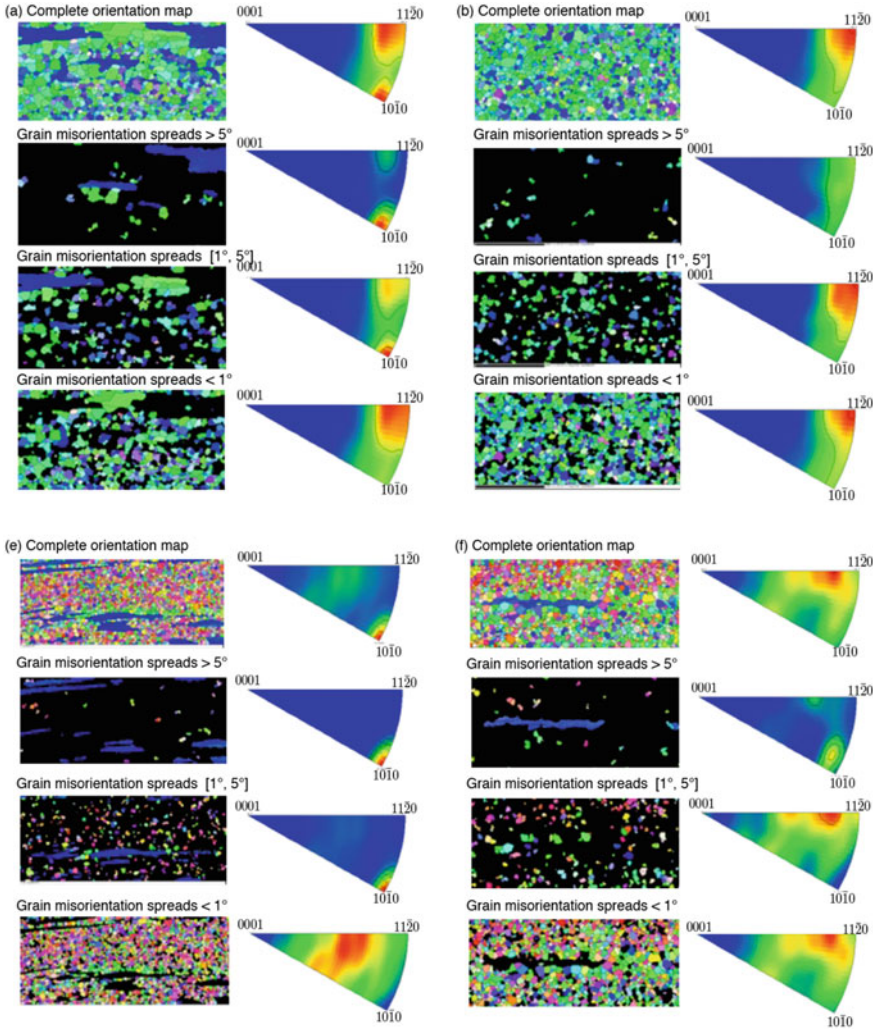


Fig. 1 Grain orientation maps and inverse pole figures for longitudinal section of extrusions: **a** Mg-1Al (v = 2 mm/s), **b** Mg-1Al (v = 10 mm/s), **c** Mg-4Y (v = 2 mm/s), and **d** Mg-4Y (v = 10 mm/s). (Color figure online)

3 Results and Discussion

3.1 The Effect of Y Addition on the Formation and Growth of DRX Grains

Figure 1 shows the grain orientation maps and the corresponding micro-textures for longitudinal section of extrusions. According to Bohlen et al. [6] and Stanford et al. [14], the grain misorientation is employed to distinguish the unrecrystallized grains from the recrystallized grains. The grains with misorientation less than 1° are regarded as "recrystallized grains"; the grains with misorientation greater than 5° are considered to be "original grains"; and the grains with misorientation between 1° and 5° are described as "intermediate grains."

Figure 1a indicates the typical $\{10\bar{1}0\} - \{11\bar{2}0\}$ texture is formed in 2 mm/s extruded Mg-1Al. The elongated "unrecrystallized grains" are mainly responsible for the $\{10\bar{1}0\}$ component. Most "recrystallized grains" are oriented around the $\{11\bar{2}0\}$ pole to form the $\{11\bar{2}0\}$ texture component. The "intermediate grains" have a wider orientation spread along the arc between the $\{10\bar{1}0\}$ and $\{11\bar{2}0\}$ poles. For 10 mm/s extrusion speed (Fig. 1b), a fully recrystallized microstructure is developed. The elongated unrecrystallized grains and the corresponding $\{10\bar{1}0\}$ texture component disappear. Both the "intermediate grains" and the new "recrystallized grains" are oriented around the $\{11\bar{2}0\}$ pole.

Figure 1c shows that the $\{10\bar{1}0\} - \{11\bar{2}1\}$ texture and partially recrystallized microstructure can be observed in 2 mm/s extruded Mg-4Y. The "recrystallized grains" produces a new $\{11\bar{2}1\}$ "RE texture" component that lies between the $\{11\bar{2}0\}$ and the {0001} poles. Some of the "recrystallized grains" even appear in the $\{10\bar{1}1\}$ pole. The "unrecrystallized grains" and most "intermediate grains" are oriented around the $\{10\bar{1}0\}$ pole to develop a sharp $\{10\bar{1}0\}$ texture component. Interestingly, the $\{10\bar{1}0\}$ component exists in the 10 mm/s extruded Mg-4Y (Fig. 1d) in which case a fully recrystallized microstructure and a single $\{11\bar{2}1\}$ texture component is expected. This indicates that the formation of the recrystallized grains is retarded by the Y addition.

The Y addition also retarded growth and broadened orientation spreads of the recrystallized grains. In fact, these two aspects are intertwined with each other during the development of texture and microstructure. If further DRX occurs repeatedly within the recrystallized grains, a much weaker texture is expected.

3.2 *The Effect of Y Addition on "RE Texture" Component in Terms of Twin*

To evaluate the effect of twins on the texture development, the high angle grain boundaries, twin boundaries, and their misorientation axes distribution of 10 mm/s extruded Mg-4Y alloy are presented in Fig. 2.

It can be found that the main contributors to the peaks of the misorientation distribution are not the twin variants, but those grain boundaries having almost as large as the misorientation of twins. Take the $\{10\bar{1}2\}$ extension twin, for example, the twin boundaries with 86 ± 5° $11\bar{2}0$ rotation only accounts for 0.991% of all the boundaries, while the grain boundaries associated with 86 ± 5° misorientation angle have an area fraction of 12%. The misorientation axes of the grain boundaries distribute in the 81–91° section randomly, instead of developing clusters around $\bar{1}2\bar{1}0$ axis like the twin boundaries. Very similar behaviors appear for the other two twin variants, contraction twin and double twin.

Based on the above analysis, the twin variants could be the origin of the broadened orientation spread and weakened texture of the recrystallized grains in the RE containing alloys. However, the twin variants are not be responsible for the development of the $\{11\bar{2}1\}$ "RE texture" component, which is based on a special case assuming a grain with $\{10\bar{1}0\}$ or $\{11\bar{2}0\}$ planes aligned with the extrusion direction. Similarly, the possibility for the contraction twin and double twin to develop the "RE texture" component can be eliminated.

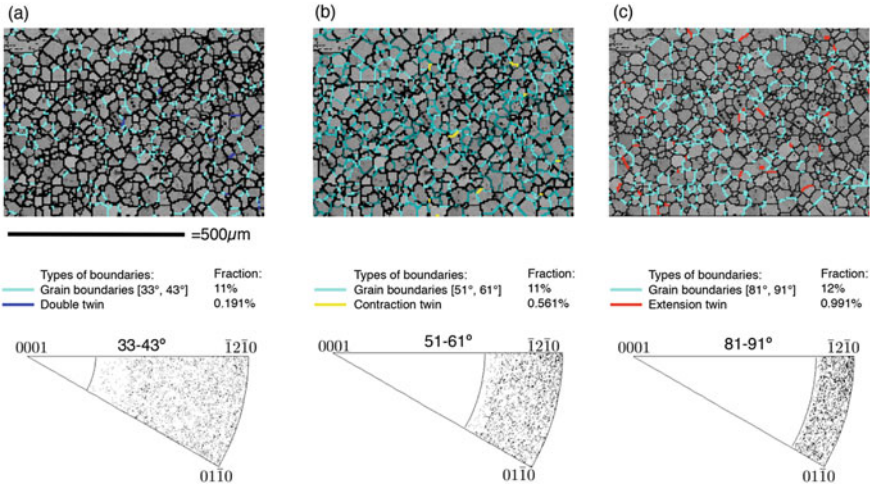


Fig. 2 **a** 38 ± 5° grain boundaries and the double twin boundaries, **b** 56 ± 5° grain boundaries and the contraction twin boundaries, and **c** 86 ± 5° grain boundaries and the extension twin boundaries of 10 mm/s extruded Mg-4Y. (Color figure online)

3.3 *The Effect of Y Addition on Texture Development in Terms of DRX Mechanisms*

Figure 3 gives a view of the continuous transition of the crystalline orientations from unrecrystallized grains to DRX grains in detail. A strong $\{10\bar{1}0\}$ texture component is retained in the subset 1 with elongated unrecrystallized grains. Subset 2 in the vicinity of subset 1 has its prismatic pole intensity along the arc between the $\{10\bar{1}0\}$ pole and the $\{11\bar{2}0\}$ pole. Subset 3 develops much smaller recrystallized grains as a consequence of DRX occurring. DRX grains are preferentially formed near the original grain boundaries where dislocations accumulate, and then grow and form new grain boundaries by absorbing the dislocations generated by further plastic deformation, thus changing the misorientations of grains. The original grain region coordinates the strain by slipping. Therefore, DRX and slip mechanisms are responsible for the misorientations between recrystallized grains and unrecrystallized grains in Mg-1Al.

The CDRX behavior of 2 mm/s extruded Mg-4Y alloy is presented in Fig. 4. Like Mg-1Al alloy with extrusion speed of 2 mm/s, subset 1 develops a strong $\{10\bar{1}0\}$ texture and subset 2 inclines to $\{11\bar{2}0\}$ pole. However, the grains in set 3 tend to form {0002} pole instead of $\{11\bar{2}0\}$ pole in Mg-1Al alloy. As a result, the recrystallized grains in the mantle regions of the original grains create a new $\{11\bar{2}1\}$ "RE texture" component. It turns out that Mg-Y alloy develops the recrystallization texture different from Mg–Al alloy during the extrusion process. The grains in the interiors of the original grains, however, develop textures similar to the non-RE Mg-1Al alloy.

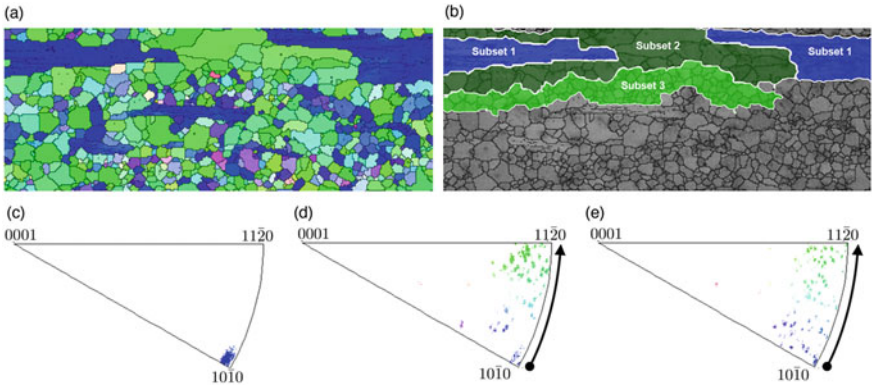


Fig. 3 EBSD maps of 2 mm/s extruded Mg-1Al alloy: **a** orientation map, **b** boundary map, **c** inverse pole figure of subset 1, **d** inverse pole figure of subset 2, and **e** inverse pole figure of subset 3. (Color figure online)

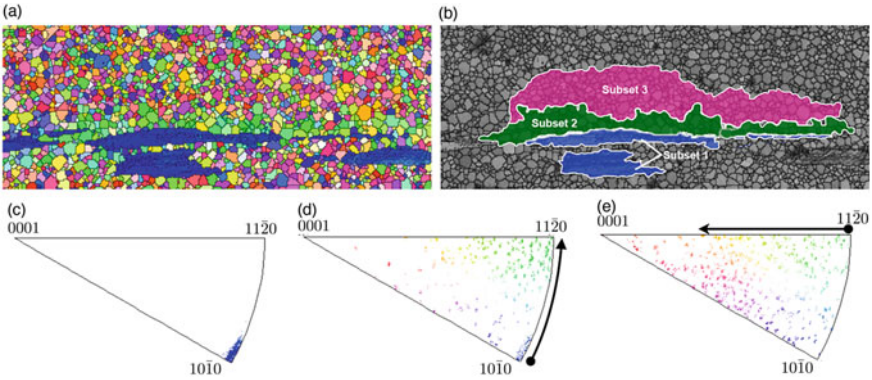


Fig. 4 EBSD maps of 2 mm/s extruded Mg-4Y alloy: **a** orientation map, **b** boundary map, **c** inverse pole figure of subset 1, **d** inverse pole figure of subset 2, and **e** inverse pole figure of subset 3. (Color figure online)

4 Conclusions

The microstructure and texture evolution of Mg-1Al and Mg-4Y were experimentally investigated during the extrusion. The effect of Y addition on microstructure and texture developments is concluded as follows:

(1) The Y addition suppresses the DRX of Y containing alloys during the extrusion.
(2) The Y addition leads to a greater propensity for extension and contraction twins. However, the twin variants are irrelevant with the $\{11\bar{2}1\}$ "RE texture" component.
(3) The $\{11\bar{2}1\}$ "RE texture" component in RE containing alloy is attributed to the DRX grains in the mantle regions of the original grains.

Acknowledgments The authors from SJTU would like to acknowledge the support of the National Natural Science Foundation of China (Nos. 51775337, 51675331). This paper is partly supported by the Materials Genome Initiative Center, Shanghai Jiao Tong University.

References

1. Chen L, Zhang J, Zhao G, Wang Z, Zhang C (2018) Microstructure and mechanical properties of Mg-Al-Zn alloy extruded by porthole die with different initial billets. Mater Sci Eng A 718:390–397
2. Yang Q, Jiang B, Tian Y, Liu W, Pan F (2013) A tilted weak texture processed by an asymmetric extrusion for magnesium alloy sheets. Mater Lett 100:29–31
3. Mishra RK, Gupta AK, Rao PR, Sachdev AK, Kumar AM, Luo AA (2008) Influence of cerium on the texture and ductility of magnesium extrusions. Scr Mater 59:562–565
4. Minárik P, Král R, Pešička J, Daniš S, Janeček M (2016) Microstructure characterization of LAE442 magnesium alloy processed by extrusion and ECAP. Mater Charact 112:1–10

5. Minárik P, Drozdenko D, Zemková M, Veselý J, Čapek J, Bohlen J, Dobroň P (2019) Advanced analysis of the deformation mechanisms in extruded magnesium alloys containing neodymium or yttrium. Mater Sci Eng A 759:455–464
6. Bohlen J, Yi S, Letzig D, Kainer KU (2010) Effect of rare earth elements on the microstructure and texture development in magnesium–manganese alloys during extrusion. Mater Sci Eng A 527:7092–7098
7. Davis B, Humphreys FJ, Lorimer GW (2007) The deformation, recrystallisation and texture of three magnesium alloy extrusions. Mater Sci Technol 23:1173–1180
8. Yu Z, Tang A, He J, Gao Z, She J, Liu J, Pan F (2018) Effect of high content of manganese on microstructure, texture and mechanical properties of magnesium alloy. Mater Charact 136:310–317
9. Robson JD (2014) Effect of rare-earth additions on the texture of wrought magnesium alloys: The role of grain boundary segregation. Metall Mater Trans A 45:3205–3212
10. Stanford N (2010) Micro-alloying mg with Y, Ce, Gd and La for texture modification-A comparative study. Mater Sci Eng A 527:2669–2677
11. Hadorn JP, Hantzsche K, Yi SB, Bohlen J, Letzig D, Wollmershauser JA, Agnew SR (2012) Role of solute in the texture modification during hot deformation of Mg-rare earth alloys. Metall Mater Trans A 43:1347–1362
12. Stanford N, Sha G, Xia JH, Ringer SP, Barnett MR (2011) Solute segregation and texture modification in an extruded magnesium alloy containing gadolinium. Scr Mater 65:919–921
13. Barrett CD, Imandoust A, Kadiri HE (2018) The effect of rare earth element segregation on grain boundary energy and mobility in magnesium and ensuing texture weakening. Scr Mater 146:46–50
14. Stanford N, Callaghan MD, Jong B (2013) The effect of rare earth elements on the behaviour of magnesium-based alloys: part 1—hot deformation behavior. Mater Sci Eng A 565:459–468

Advancing the Accuracy of Computational Models for Double-Sided Incremental Forming



Newell Moser, Dohyun Leem, Shuheng Liao, Kornel Ehmann, and Jian Cao

Abstract Double-Sided Incremental Forming (DSIF) is a rapid-prototyping manufacturing process for metal forming that, for low-volume production, is competitively energy-efficient. However, controlling the DSIF process in terms of accuracy and formability is an ongoing challenge. These control challenges arise due to a lack of understanding of the underlying deformation mechanisms in DSIF, which finite element simulations can help to unravel. However, DSIF pushes the limits of modern finite element formulations due to true strains that approach one, finite rotations, nonlinear contact, and triaxial stress states that range across multiple length scales. To confidently develop a finite element model of DSIF, an extensive verification process must be considered, which is the objective of this study. In this work, different finite element types and varying amounts of artificial acceleration are investigated, and recommendations based on efficiency and accuracy are summarized. A simplified, axisymmetric geometry was considered to reduce simulation time. For this geometry, accelerating the explicit finite element simulation by a mass factor of 10^5 or greater affected the stress triaxiality in the sheet by as much as 40% in some locations with respect to the quasi-static case. Additionally, the ratio of the kinetic energy to internal energy of the sheet was not a reliable indicator of whether a DSIF simulation is approximately quasi-static.

N. Moser (✉)
Applied Chemicals and Materials Division, National Institute of Standards and Technology, 325 Broadway, Boulder, CO 80305, USA
e-mail: newell.moser@nist.gov

D. Leem · S. Liao · K. Ehmann · J. Cao
Department of Mechanical Engineering, Northwestern University, 2145 Sheridan Rd, Evanston, IL 60201, USA
e-mail: dohyunleem2021@u.northwestern.edu

S. Liao
e-mail: shuhengliao2023@u.northwestern.edu

K. Ehmann
e-mail: k-ehmann@northwestern.edu

J. Cao
e-mail: jcao@northwestern.edu

© The Minerals, Metals & Materials Society 2021

G. Daehn et al. (eds.), *Forming the Future*, The Minerals, Metals & Materials Series,
https://doi.org/10.1007/978-3-030-75381-8_23

Keywords Metal forming · Simulation · Finite element · Verification · Mass scaling

1 Introduction and Motivation

Double-Sided Incremental Forming (DSIF) is a flexible metal forming process that uses two numerically controlled tools—one above and one below the sheet—that move along a predefined toolpath [1]. In addition to flexibility, parts formed by DSIF demonstrate a marked improvement in formability relative to conventional forming processes like stamping [2]. More specifically, failure strains in DSIF surpass those observed in stamping, which are usually defined by the necking limit and are characterized by forming limit diagrams.

Although DSIF has great potential toward the rapid production of freeform sheet metal parts, the use of a secondary tool also contributes to additional challenges that can affect process control. Similar to Single-Point Incremental Forming (SPIF), the principal technical challenges in DSIF are related to process control: geometric accuracy, surface quality, process throughput, and excessive thinning or fracture [3]. In order to improve process control, there is a need to develop accurate, efficient models of DSIF in order to better understand the mechanics of the process, as well as to quantify values which cannot be easily measured (e.g., residual stresses).

There are numerous challenges associated with simulating DSIF. Even forming a simple geometry, like a funnel, involves large-strain deformations, finite rotations, cyclic loading-unloading histories, nonlinear material behavior, contact-impact interfaces, and a range of triaxial stress states. To overcome these challenging nonlinearities, state-of-the-art techniques within the finite element method are commonly used [4–7].

Without any artificial acceleration, a finite element simulation of DSIF could readily require *months* to finish [8]. One strategy to speed up a simulation is to choose a simpler geometry, like an axisymmetric part, and develop a reduced model [7]. Though, for large finite element problems, explicit (transient) integrators with artificial acceleration tend to scale better than implicit (equilibrium) integrators, particularly if strong nonlinearities are present like contact interfaces. For a more detailed discussion on explicit and implicit finite element methods, the interested reader is referred to Belytschko et al. [9] and Wriggers [10]. Since full-scale simulations of DSIF often involve a large number of finite elements (greater than 10^6 degrees of freedom), explicit methods are a popular choice to model the process [6, 11].

To artificially accelerate an explicit finite element model, either mass scaling or velocity scaling can be used. By increasing the mass in the model, the stable time step associated with explicit simulations increases, thereby necessitating fewer time steps to complete the simulation. Researchers simulating incremental sheet forming commonly use a mass scaling factor of 10^5, or more [6, 11, 12]. On the other hand, researchers must be careful not to use too much artificial acceleration. Otherwise,

the model will no longer be a fair approximation of the real process, which is usually quasi-static depending on the tool speed. However, for a given DSIF model, it is currently unclear what a safe upper limit is in terms of mass scaling.

In this study, we develop a simplified finite element model of DSIF in order to verify the relative effects of varying key parameters in the model. By changing the parameters in the model, like mass scaling, the predicted stresses and strains will be shown to significantly change relative to the baseline quasi-static simulation. As a result, recommended values and methods related to mass scaling and finite element type are given and discussed.

2 Verification Model of DSIF

In order to vary a wide range of finite element parameters within a practical time span, a simplified DSIF model was created which is still capable of capturing the predominant forming mechanics of DSIF. As shown in Fig. 1, an axisymmetric, partially preformed part was chosen, and only half of the model was meshed by using a symmetry boundary condition. In DSIF, shear distortion occurs tangential to the toolpath, so a 10 mm extension was created to distance any erroneous effects of the symmetry boundary condition from the conical region of interest. Although the symmetric boundary condition is not strictly true in DSIF, it is assumed to be a fair assumption since the region of interest is far away from the boundary and the dominant mechanics of DSIF are highly localized. To clarify, the region of interest is within the center of the toolpath's arc just as the tool crosses the X-axis.

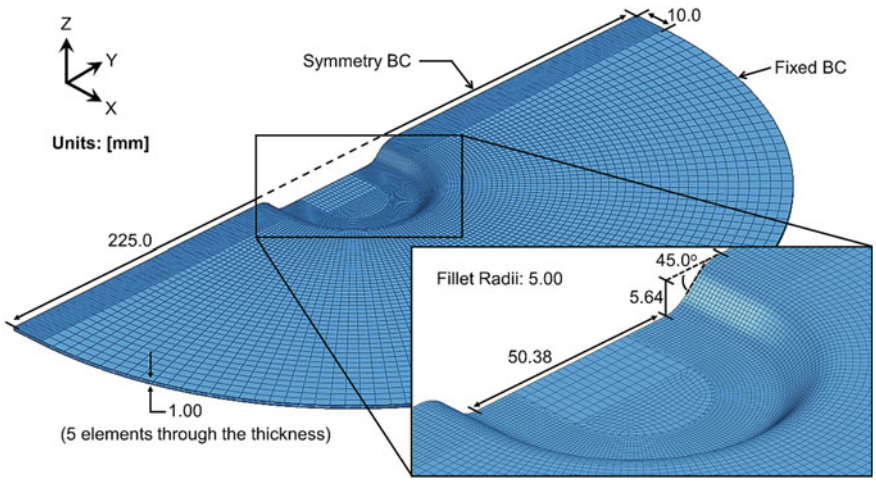


Fig. 1 Shown is the finite element mesh used for the verification DSIF model. (Color figure online)

For each revolution in the spiral toolpath, a "jump" has been added so that the tools lift-off and then regain contact while traversing along the symmetry boundary condition. By reducing the domain size and performing only five toolpath revolutions for a total length of 731 mm, this simplified model serves as an efficient testbed for comparing finite element procedures in DSIF. However, the proposed verification model is only suggested for investigating *relative* comparisons between simulations.

A total of 55,096 reduced-integration, linear brick elements with stiffness-based hourglass controls [13] were used to model the sheet in Fig. 1, while the hemispherical tools—10 mm in diameter—were modeled with rigid shell elements. Although reduced-integration elements were ultimately chosen, other element formulations were trialed, which will be discussed in the next section. In the forming region, elements were approximately 0.5 mm $\times$ 0.5 mm $\times$ 0.2 mm in size. A node-to-surface contact constraint was enforced using the penalty formulation, and friction was neglected. The material of the sheet was modeled after aluminum alloy 5754-O using J_2 flow theory, also commonly referred to as von Mises plasticity with isotropic hardening. A Voce strain hardening model was used within the material model, based on the same parameters used by Moser et al. [4].

All of the verification simulations were performed using Abaqus FEA[1] (version 2017). Since this verification model is simplified and less costly in computational resources than a full-scale model of DSIF, it was reasonable to solve this representative DSIF problem using an implicit (equilibrium) scheme. This static case was used to establish a baseline. Then, the verification model was solved using an explicit (transient) scheme with successive increases in artificial acceleration.

3 Finite Element Type

Different hexahedral element technologies were trialed using the verification model shown in Fig. 1 while assuming static conditions. Shell element formulations were not considered in this work due to the underlying assumptions in shell elements related to stresses and strains in the thickness direction, which can be inaccurate for double-sided contact [14]. A summary of the key findings is given in Table 1. Abaqus nomenclature is used as shorthand for the different types of elements: C3D20R is a 20-node, second-order serendipity element that uses reduced integration and stiffness-based hourglass controls; C3D8 is an 8-node, first-order element based on a selectively reduced integration scheme; C3D8I is an 8-node, first-order, fully integrated element that is enhanced by incompatible modes; and C3D8R is an 8-node,

[1]Certain commercial equipment, software, and/or materials are identified in this paper in order to adequately specify the experimental or simulation procedure. In no case does such identification imply recommendation or endorsement by the National Institute of Standards and Technology, nor does it imply that the equipment and/or materials used are necessarily the best available for the purpose.

Table 1 Results of trialing different solid continuum elements in the verification DSIF model. Wall time is defined as the elapsed "wall-clock" time required to complete the simulation. HG is short for hourglass, and SR for selectively reduced

Type of hexahedral solid continuum element	Shear locking	Volumetric locking	Wall time × Number of computer cores (CPU · hr)
C3D20R (w/HG Controls)	Minimal	Severe	(256.3 h) × (72 CPU) = 18,454
C3D8 (SR Integration)	Severe	None	(52.5 h) × (24 CPU) = 1,260
C3D8I (Incompatible Modes)	Severe	Moderate	(86.2 h) × (24 CPU) = 2,069
C3D8R (w/HG Controls)	None	None	(60.2 h) × (24 CPU) = 1,446

reduced-integration element that utilizes stiffness-based hourglass controls. In an effort to be comprehensive, shear locking, volumetric locking, and hourglass controls are briefly summarized next; more details are discussed by Belytschko et al. [9].

Shear locking occurs in first-order, fully integrated elements that are subjected to bending. The numerical formulation of these elements gives rise to shear strains that do not really exist—the so-called parasitic shear. Therefore, these elements are too stiff in bending. Volumetric locking (sometimes termed pressure locking) occurs in fully integrated elements when the material behavior is incompressible, such as von Mises materials. Spurious pressure stresses develop at the integration points, causing an element to behave too stiffly for deformations that should cause no volume changes (see Fig. 2). Reduced integration, or under-integrated, refers to using fewer Gaussian integration points than are necessary to integrate the element matrices exactly for an undistorted element. A linear (i.e., first-order) element with reduced integration implies that a single integration point is used, which is located at the element center.

Referring to Table 1, fully integrated hexahedral elements (C3D8I) fall victim to volumetric locking and shear locking. However, a reduced-integration (or selectively reduced integration) scheme for the element stiffness matrix not only greatly reduces running time, but these formulations can also alleviate volumetric locking and shear locking. Though, under-integrated elements can result in spurious zero-energy modes of deformation, which are commonly termed "hourglass" modes. Thus, hourglass controls must be employed to artificially stiffen the response of the element against these zero-energy deformation modes. Moreover, hexahedral elements usually provide a solution of equivalent accuracy at less cost compared to tetrahedral elements [9]. However, hexahedral elements are more sensitive to severe mesh distortions, so a structured mesh should be used wherever possible. For these reasons, the C3D8R element with a structured mesh was chosen for this simplified DSIF model.

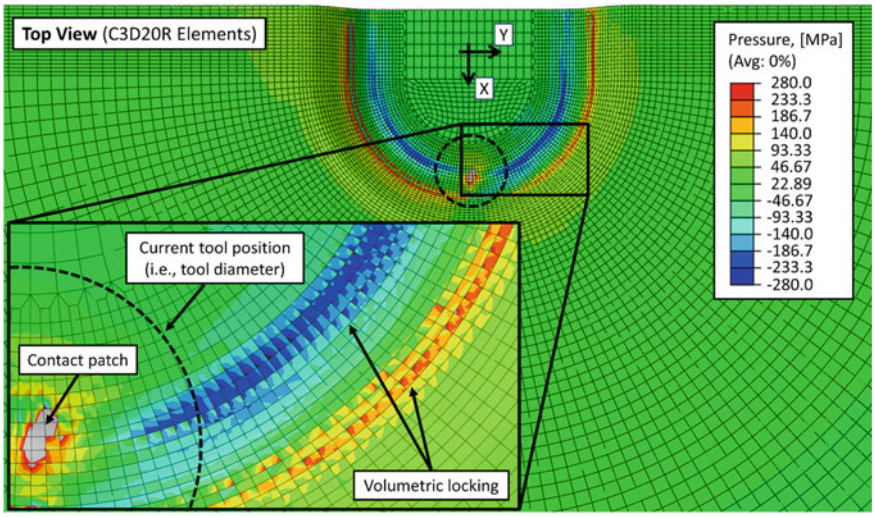


Fig. 2 An example of volumetric locking in the pressure (i.e., negative mean stress) field when using quadratic C3D20R elements. Notice the strong discontinuities across element edges. The top and bottom tools (currently hidden) are traversing counterclockwise. (Color figure online)

4 Effects of Mass Scaling

An explicit finite element simulation can be sped up by artificially increasing the mass or scaling the velocity of moving entities. More specifically, increasing the velocity by a factor of k reduces the simulation time by a factor of k, but also artificially increases the kinetic energy by k^2. Increasing the mass (or density) by a factor of k reduces the simulation time by $\sqrt{k}$, but artificially increases the kinetic energy by k. For a given artificial increase in kinetic energy, the effects of accelerating the simplified DSIF model will be similar whether it is achieved through mass or velocity scaling. So, only mass scaling is discussed here.

Referring to Table 2, four cases were considered in evaluating the effects of mass scaling: (1) the Implicit Static case based on solving the static equations using an implicit load-stepping algorithm, (2) the Quasi-static case based on no mass scaling, (3) the Mass-1 case based on a mass-scaling factor of 1.0×10^3, and (4) the Mass-2 case based on a mass-scaling factor of 1.0×10^5. The tool velocity was set to be constant for all cases involving mass scaling.

Table 2 Mass scaling factors considered in the verification DSIF model. Except for the Implicit Static model, all models utilize an explicit time-stepping algorithm

Nickname	Implicit static	Quasi-static	Mass-1	Mass-2
Mass scaling Factor	1.0	1.0	1.0×10^3	1.0×10^5
Tool velocity	~	250 mm/s	250 mm/s	250 mm/s
Wall time (72 cores)	20.1 h	256.5 h	8.7 h	0.9 h

The stress triaxiality through the thickness during the final toolpath revolution is shown in Fig. 3 for each simulation case. Note, the stress triaxiality is defined as the hydrostatic stress divided by the von Mises equivalent stress. With mass scaling, the stress triaxiality lessens in magnitude (becomes more compressive) near regions of contact. More specifically, adding mass by a factor of 10^5 changed the stress triaxiality by 41% near the tip of the top tool, and by 23% near the bottom tool. Mass-1 utilized a moderate amount of mass scaling, and the trends and magnitudes in the stress triaxiality are not significantly altered relative to the Quasi-static case. Although not shown here, increasing amounts of mass scaling had less of an effect on kinematic quantities—like the equivalent plastic strain—compared to kinetic quantities, like the stress triaxiality and the Lode angle parameter.

Another interesting observation to take note of in Fig. 3 is that the Quasi-static case, based on explicit time-stepping, predicts higher stress triaxialities compared to the Implicit Static case; ideally, they should closely match. We believe these differences are largely due to the numerical implementations of the explicit and implicit procedures, and not because of the physics of the problem at hand. The largest differences in the predictions occurred near regions of contact, which supports the assumption that these effects could be due to the difference in the implementation of the implicit and explicit contact algorithms. Both the implicit scheme (dependent on the iterative Newton's method) and the explicit scheme (based on the central

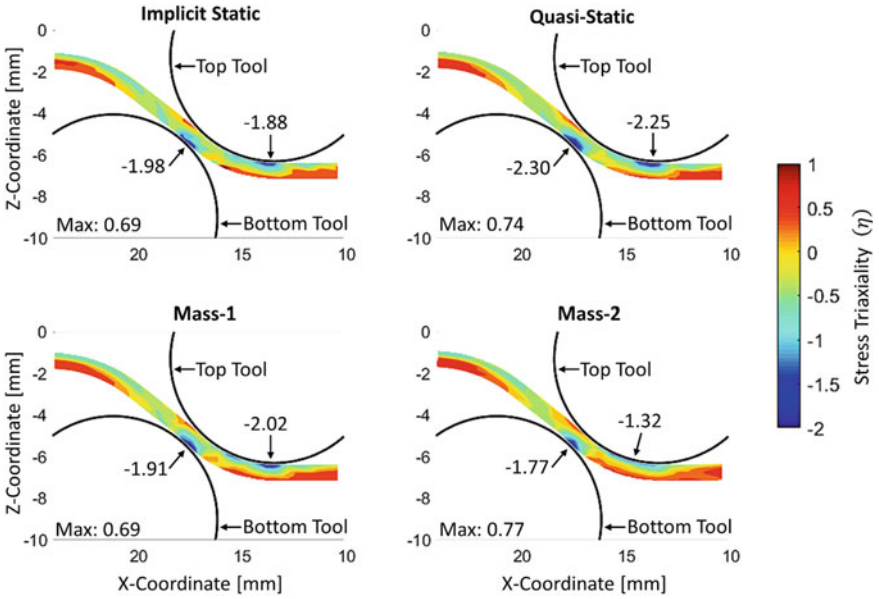


Fig. 3 The relative effects of mass scaling on the stress triaxiality. Shown in each case is the cross-sectional side view of the sheet while the tools pass over the X-axis (see Fig. 2). The black partial circles represent the perimeter of the tools at this time in the simulation. The minimum (i.e., most compressive) stress triaxialities are pointed out near the regions of contact. (Color figure online)

difference method) are second-order accurate in time regarding the truncation error [9]. However, the iterative Newton scheme inherent to implicit methods requires that the energy and displacement residual errors be within a specified tolerance in order to meet convergence requirements. Explicit methods, on the other hand, do not directly enforce the energy balance; they take a small step forward in time without the need for iterations. Furthermore, explicit methods rely on lumping (i.e., diagonalizing) the mass matrix rather than using the consistent mass matrix, and the lumping procedure is generally performed in an ad hoc fashion [15]. Although we can speculate why these differences in the stress triaxialities are appearing, we cannot be certain which is more accurate since this study is limited to relative comparisons. Still, it is interesting to note that, with everything else being equal, the implicit and explicit schemes predicted different magnitudes in the stress triaxialities; though, they do predict similar trends.

The average forming forces and their corresponding standard deviations are given in Table 3. Although the average magnitudes of the forming forces vary due to mass scaling, the results do not exhibit strong trends. This suggest that increasing the amount of artificial acceleration does not consistently change the average magnitude of the forming forces. On the other hand, increasing the amount of artificial acceleration does result in larger standard deviations of the predicted contact forces. Since the Mass-2 case is not quasi-static based on the changes in the mechanics, as shown in Fig. 3, the average forming force is not a good indicator of whether a DSIF simulation is quasi-static or not.

The likely reason that the average forming forces do not significantly differ in Table 3 is because the overall summation of the contact pressures do not significantly change with additional inertial effects. Even though the magnitude of the (compressive) stress triaxialities do change, the total compressive area also changes in such a way to make up for this. Then, when the contact stresses are integrated over the area to calculate the contact forces, the average resultant forces will not change significantly.

One way to determine if a metal forming simulation is quasi-static is to analyze the ratio between the kinetic energy and the internal energy of the deforming metal. In sheet metal forming, the internal energy is usually dominated by the accumulation of plastic strains. If the kinetic energy approaches the internal energy in magnitude, then the deforming sheet is no longer quasi-static. This rule-of-thumb is a reasonable

Table 3 The Z-forces (i.e., axial forces) in the top tool are compared between the verification simulations. The average (Avg.) and standard deviation (Std. Dev.) values are calculated from the force histories throughout the final toolpath revolution

Simulation case	Avg. Z-Force (N)	Std. Dev. Z-Force (N)
Implicit Static	471.0	± 40.9
Quasi-static	606.1	± 30.4
Mass-1	551.5	± 63.0
Mass-2	608.6	± 89.2

Table 4 The internal energy (I.E.), kinetic energy (K.E.), and standard deviation (Std. Dev.) in the kinetic energy of the deformable sheet are compared during the final toolpath revolution. All energy units are in, N·mm

Simulation case	Sheet I.E.	Sheet K.E.	Std. Dev. in K.E.
Implicit static	1.11×10^4	0.00	$\pm$ 0.00
Quasi-static	1.25×10^4	0.111	$\pm$ 0.088
Mass-1	1.36×10^4	22.4	$\pm$ 10.6
Mass-2	1.54×10^4	366	$\pm$ 118

assumption when the entire sheet is deforming, but it does not hold well for DSIF (see Table 4). In DSIF, the localized zones of the sheet will deform as the tools travel along the toolpath, and in effect, the (global) internal energy of the sheet continues to increase over time as new locations experience plastic straining. However, the kinetic energy remains approximately constant over time. Notice in Table 4 that the kinetic energy is at least an order of magnitude less than the internal energy for all cases. However, as stated before, the Mass-2 case is not quasi-static based on Fig. 3.

5 Conclusions and Recommendations

The result of this verification study is a set of finite element parameters that strike a balance between computational efficiency and (relative) accuracy. The following recommendations can be considered for new, full-scale simulations of DSIF. Though this study is not extensive, there are additional finite element parameters, like the material model, that should be validated in any new finite element model. Moreover, it is important to recall that a simplified geometry was chosen for this verification study, and consequently, we cannot guarantee that the following conclusions can be extended for all possible toolpaths in DSIF. Rather, these conclusions and recommendations should be considered as reasonable starting points, but further investigation may be necessary for specific geometries. Our conclusions and recommendations are as follows:

- As a starting point for new DSIF models, we recommend scaling the mass between a factor of 10^2 and 10^4, and in general, not above 10^5. Depending on the toolpath and mesh, adding more artificial acceleration can degrade the accuracy of the solution, specifically for kinetic terms like the stress triaxiality and Lode angle parameter.
- In choosing an element type, first-order solid continuum hexahedral elements with reduced-integration and hourglass controls are recommended. They are robust at handling the many sources of nonlinearity that arise in DSIF. However, for improved accuracy, it is important to create a structured mesh that limits element

distortion at finite strains. Also, more studies using different finite element technologies should be explored, such as B-bar formulations [16] and hexahedral thick-shell elements.

- The ratio between the global internal energy and global kinetic energy of the sheet should not be used to determine whether a simulation of DSIF is quasi-static. This energy ratio is not applicable because the nature of DSIF involves highly localized deformations. Moreover, the average contact forces are also not a good indicator of whether a DSIF simulation is quasi-static. In future work, it would be worthwhile to formulate a local energy ratio by defining a characteristic length, which could be based on the area of the contact patch between the tools and the sheet. For now, the surest method of evaluating the effects of artificial acceleration is to directly examine the changes in the mechanics, such as the stress triaxiality and Lode angle parameter.

References

1. Moser N, Zhang Z, Ren H, Zhang H, Shi Y, Ndip-Agbor EE, Lu B, Chen J, Ehmann KF, Cao J (2016) Effective forming strategy for double-sided incremental forming considering in-plane curvature and tool direction. CIRP Ann Manuf Technol 65:265–268. https://doi.org/10.1016/j.cirp.2016.04.131
2. Lu B, Fang Y, Xu DK, Chen J, Ai S, Long H, Ou H, Cao J (2015) Investigation of material deformation mechanism in double side incremental sheet forming. Int J Mach Tools Manuf 93:37–48. https://doi.org/10.1016/j.ijmachtools.2015.03.007
3. Li Y, Chen X, Liu Z, Sun J, Li F, Li J, Zhao G (2017) A review on the recent development of incremental sheet-forming process. Int J Adv Manuf Technol 92:2439–2462. https://doi.org/10.1007/s00170-017-0251-z
4. Moser N, Pritchet D, Ren H, Ehmann KF, Cao J (2016) An efficient and general finite element model for double-sided incremental forming. J Manuf Sci Eng 138. https://doi.org/10.1115/1.4033483
5. Smith J, Malhotra R, Liu WK, Cao J (2013) Deformation mechanics in single-point and accumulative double-sided incremental forming. Int J Adv Manuf Technol 69:1185–1201. https://doi.org/10.1007/s00170-013-5053-3
6. Esmaeilpour R, Kim H, Park T, Pourboghrat F, Mohammed B (2017) Comparison of 3D yield functions for finite element simulation of single point incremental forming (SPIF) of aluminum 7075. Int J Mech Sci 133:544–554. https://doi.org/10.1016/j.ijmecsci.2017.09.019
7. Henrard C, Bouffioux C, Eyckens P, Sol H, Duflou JR, Van Houtte P, Van Bael A, Duchêne L, Habraken AM (2011) Forming forces in single point incremental forming: Prediction by finite element simulations, validation and sensitivity. Comput Mech 47:573–590. https://doi.org/10.1007/s00466-010-0563-4
8. Ren H, Moser N, Zhang Z, Ndip-Agbor E, Smith J, Ehmann KF, Cao J (2015) Effects of tool positions in accumulated double-sided incremental forming on part geometry. J Manuf Sci Eng Trans ASME 137:1–8. https://doi.org/10.1115/1.4030528
9. Belytschko T, Liu WK, Moran B, Elkhodary K (2014) Nonlinear finite elements for continua and structures, 2nd ed. Wiley
10. Wriggers P (2008) Nonlinear finite element methods. Springer, Berlin Heidelberg
11. Malhotra R, Xue L, Belytschko T, Cao J (2012) Mechanics of fracture in single point incremental forming. J Mater Process Technol 212:1573–1590. https://doi.org/10.1016/j.jmatprotec.2012.02.021

12. Shin J, Bansal A, Nath M, Cheng R, Banu M, Taub A, Martinek B (2018) Prediction of negative bulge in two point incremental forming of an asymmetric shape part. J Phys: Conf Ser 1063: https://doi.org/10.1088/1742-6596/1063/1/012057
13. Flanagan DP, Belytschko T (1981) A uniform strain hexahedron and quadrilateral with orthogonal hourglass control. Int J Numer Methods Eng 17:679–706. https://doi.org/10.1002/nme.1620170504
14. Lee PS, Bathe KJ (2005) Insight into finite element shell discretizations by use of the "basic shell mathematical model". Comput Struct 83:69–90. https://doi.org/10.1016/j.compstruc.2004.07.005
15. Tekkaya AE (2000) State-of-the-art of simulation of sheet metal forming. J Mater Process Technol 103:14–22. https://doi.org/10.1016/S0924-0136(00)00413-1
16. Hughes T (1980) Generalization of selective integration procedures to anisotropic and nonlinear media. Int J Numer Methods Eng 15:1413–1418. https://doi.org/10.1002/nme.1620150914

Nonlinearity of the Crystal Yield Function in the Rate-Independent Crystal Plasticity and Its Effect on the Evolution of Anisotropy



Taejoon Park, Ji Hoon Kim, Hojun Lim, Sobhan Alah Nazari Tiji, Amir Asgharzadeh, and Farhang Pourboghrat

Abstract In typical crystal plasticity framework, the constitutive functions for the slip rate is commonly described by the rate-dependent formulation to avoid the non-uniqueness of the active slip systems due to the interdependency of the slip systems. These rate-dependent models are computationally expensive as these models impose numerically stiff, highly nonlinear equations that need to be solved at every integration point. Alternatively, the rate-independent crystal plasticity model uses the crystal yield function to describe the slip deformation and plastic spin by the active slip systems without the non-uniqueness problem. In this study, the effect of nonlinearity between resolved shear stress and slip rate on the shape of the crystal yield function in the formulation of the rate-independent crystal plasticity was rigorously investigated. In addition to the effects of the crystal plasticity model, the influence of the nonlinearity of the single crystal yield function on the evolution of anisotropy for various polycrystalline materials was evaluated.

Keywords Crystal plasticity · Anisotropy · Yield stress surface · Strain-rate potential

1 Introduction

In the crystal plasticity (CP), the plastic deformation is described by the shear deformations of the slip systems. The activation of each slip system and the resulting slip rate are determined based on the resolved shear stress for a given stress state. In typical crystal plasticity framework [1–4], a hypothetical rate-dependent formation is commonly adopted to account for the slip rate of each slip system. Since numerically

T. Park (✉) · S. A. N. Tiji · A. Asgharzadeh · F. Pourboghrat
The Oho State University, Columbus, OH 43210, USA
e-mail: park.2417@osu.edu

J. H. Kim
Pusan National University, Busan 46241, Republic of Korea

H. Lim
Sandia National Laboratories, Albuquerque, NM 87185, USA

© The Minerals, Metals & Materials Society 2021

G. Daehn et al. (eds.), *Forming the Future*, The Minerals, Metals & Materials Series,
https://doi.org/10.1007/978-3-030-75381-8_24

stiff, highly nonlinear equations are needed to be solved at every integration point, these rate-dependent models are computationally expensive. Alternatively, the rate-independent crystal plasticity model uses the crystal yield function to describe the slip deformation and plastic spin by the active slip systems without the non-uniqueness problem [5, 6]. When the plastic deformation determined by the crystal yield function, the slip rate that satisfies the consistency condition is iteratively obtained by the derivative of the crystal yield function based on the normality rule. Since a scalar variable is determined by the iteration rather than multiple variables, the non-uniqueness problem can be avoided.

In this study, the difference of the rate-independent formulation from the rate-dependent formulation was investigated. Specifically, the effect of nonlinear relationship between the resolved shear stress and slip rate on the shape of the yield stress and strain-rate potential surfaces as well as the crystal rotation was evaluated. For the comparison, a single face-centered cubic (FCC) crystal was considered.

2 Crystal Plasticity Models

The rate-independent crystal plasticity model uses the crystal yield function:

$$f(\sigma) = \frac{1}{\rho} \ln \left\{ \sum_{\alpha=1}^{N} \exp\left[\rho \left(\frac{|\tau^{\alpha}|}{g^{\alpha}} - 1 \right) \right] \right\} \tag{1}$$

Here, N is the number of the slip systems, g^{α} is the slip resistance, τ^{α} is the resolved shear stress, and ρ is a parameter to control the nonlinearity of the crystal yield function of the α-th slip system. If $f(\sigma) \geq 0$, plastic deformation by the slip occurs.

The slip rate, $\dot{\gamma}^{\alpha}$, of the α-th slip system is determined by the derivative of the crystal yield function:

$$\dot{\gamma}^{\alpha} = \dot{\lambda} \frac{\partial f(\sigma)}{\partial \tau^{\alpha}} \tag{2}$$

Here, $\dot{\lambda}$ is the rate of the Lagrange multiplier that satisfies the consistency condition ($f(\sigma) = 0$).

As for the typical rate-dependent crystal plasticity framework, the slip rate is commonly described by the following power-law type formulation:

$$\dot{\gamma}^{\alpha} = \dot{\gamma}_0^{\alpha} sign\left(\tau^{\alpha}\right) \left(\frac{|\tau^{\alpha}|}{g^{\alpha}} \right)^{\frac{1}{m}} \tag{3}$$

Here, $\dot{\gamma}_0^{\alpha}$ is the reference slip rate and m is the rate sensitivity parameter for the α-th slip system.

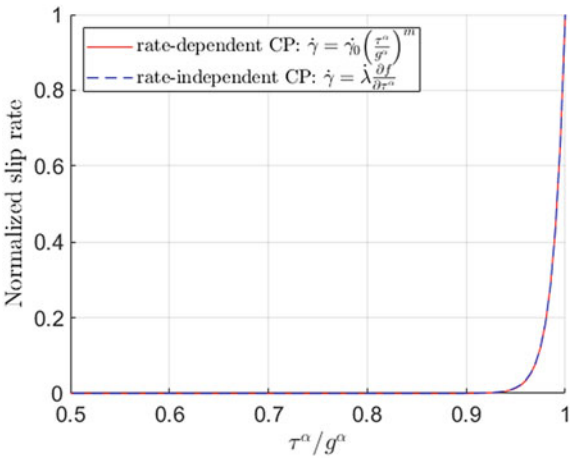


Fig. 1 Comparison of the normalized slip rate of the rate-dependent and rate-independent crystal plasticity models. (Color figure online)

The nonlinearity parameter, ρ, and the rate sensitivity parameter, m, define the nonlinear relationship between the slip rate, $\dot{\gamma}^\alpha$, and the ratio of the resolved shear stress over the slip resistance, $\frac{\tau^\alpha}{g^\alpha}$, in the rate-independent crystal plasticity and the rate-independent crystal plasticity, respectively. For comparison, the nonlinearity parameter, ρ, of the rate-independent crystal plasticity model was adjusted to match the slip rate of the rate-dependent crystal plasticity model in a quasi-static condition as shown in Fig. 1.

Both for the rate-independent and rate-dependent CP models, the slip resistance, g^α, was assumed as a function of the evolution of the dislocation density:

$$g^\alpha = A\,\mu\,b\sqrt{\sum_{\beta=1}^{n} h^{\alpha\beta}\rho^\beta} \tag{4}$$

Here, A is a material constant, μ is the shear modulus, b is the Burgers vector, and ρ^β is the dislocation density for the β-th slip system. The components of the dislocation interaction matrix, $h^{\alpha\beta}$ were calculated based on the slip plane normal of the α-th slip system and the line direction of the β-th slip system [2].

The evolution of the dislocation density for the α-th slip system was calculated based on the slip rate of the α-th slip system and the accumulated dislocation density:

$$\dot{\rho}^\alpha = \frac{1}{b}\left(\frac{\sqrt{\sum \rho^\beta}}{k_a} - k_b\rho^\alpha\right)|\dot{\gamma}^\alpha| \tag{5}$$

Here, k_a and k_b are material constants.

3 Comparison of the Crystal Plasticity Models

For the comparison of the crystal plasticity models, the yield stress and strain-rate potential surfaces were calculated for a single FCC crystal. The same plastic work increment of 0.4 MPa, which corresponds to the 0.2% offset yield stress in the uniaxial tension test, was considered to determine the equivalent yield stresses and their conjugate plastic strain increments in various deformation modes. It is worth noting that the shapes of the normalized yield stress and strain-rate potential surfaces are insensitive to the amount of the plastic work increment selected. Figures 2 and 3 show the normalized yield stress and strain-rate potential surfaces calculated based on the rate-independent and rate-dependent CP models, respectively. Both CP models showed nearly identical yield stress and strain-rate potential surfaces for the single FCC crystal.

Distributions of the numbers of activated slip systems, normalized initial yield stresses, and evolution of the tensile directions in the uniaxial tensile test were also calculated based on the rate-independent and rate-dependent CP models as shown in Figs. 4 and 5, respectively. Again, both CP models showed nearly identical results for the single FCC crystal.

In order to evaluate the effect of the heterogeneous distribution of the resolved shear stresses on the FCC slip systems, numerical simulations for the uniaxial tensile test were performed for the single FCC crystal. Based on the Newton–Raphson method, the slip rate and increment of the dislocation density for each slip system as well as the resulting increase in stress and plastic strain were iteratively calculated for each increment of the plastic work. The uniaxial tensile stress was applied to

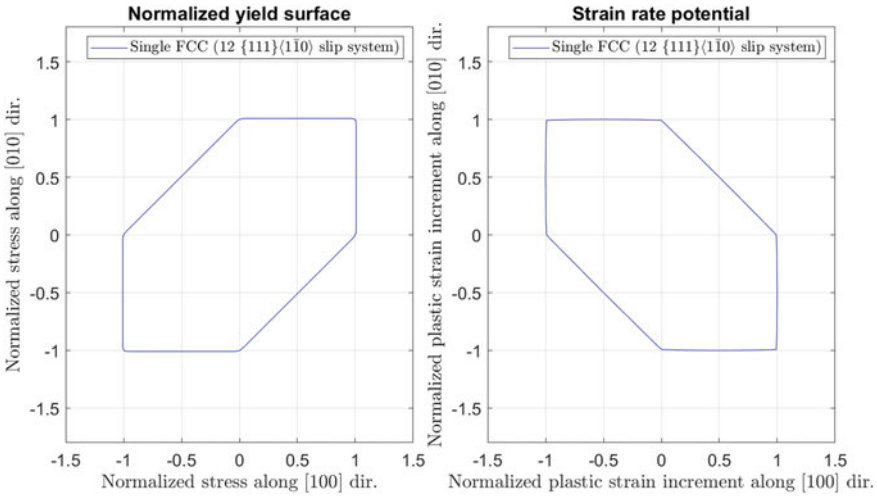


Fig. 2 Normalized yield stress and strain-rate potential surfaces of a single FCC crystal (rate-independent CP model). (Color figure online)

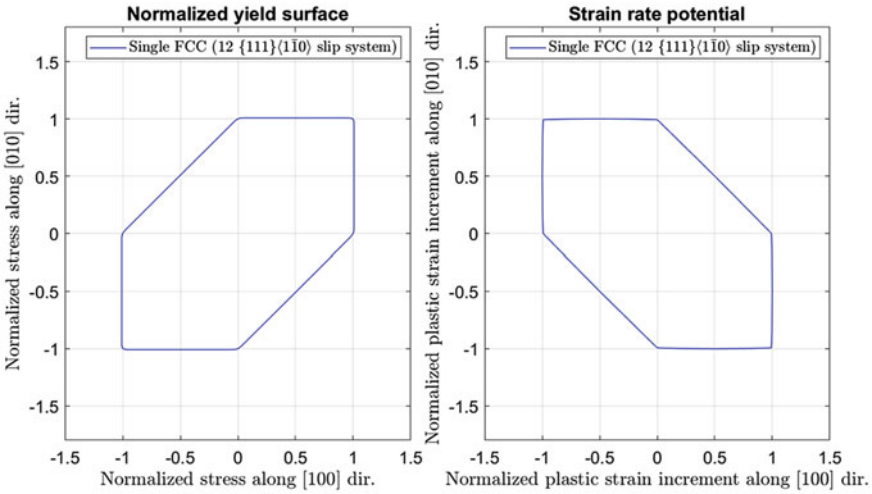


Fig. 3 Normalized yield stress and strain-rate potential surfaces of a single FCC crystal (rate-dependent CP model). (Color figure online)

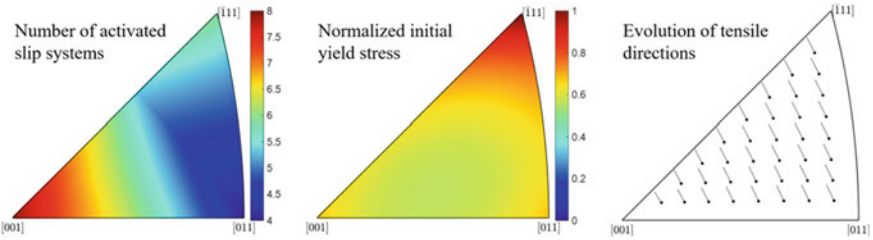


Fig. 4 Distributions of the numbers of activated slip systems, normalized initial yield stresses, and evolution of the tensile directions during the uniaxial tensile test (rate-independent CP model). (Color figure online)

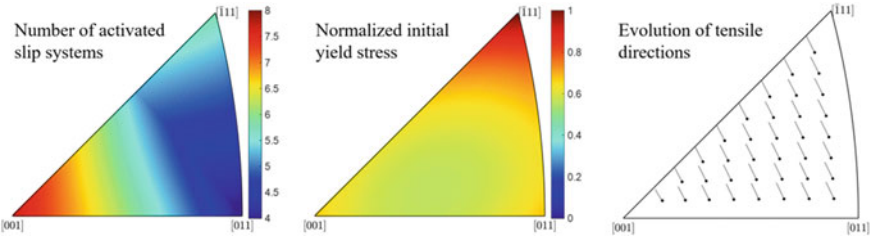


Fig. 5 Distributions of the numbers of activated slip systems, normalized initial yield stresses, and evolution of the tensile directions during the uniaxial tensile test (rate-dependent CP model). (Color figure online)

the single FCC crystal, and rotation of the crystal about the tensile direction was accounted for by the plastic spin. The [110] direction in which the lowest number of the slip systems are activated in the uniaxial tensile test, as shown in Figs. 4 and 5, was selected as the tensile direction. The tensile simulations were performed until the accumulated plastic work reached 10 MPa. Figures 6 and 7 compare the shapes of the yield stress and strain-rate potential surfaces before and after the uniaxial tension

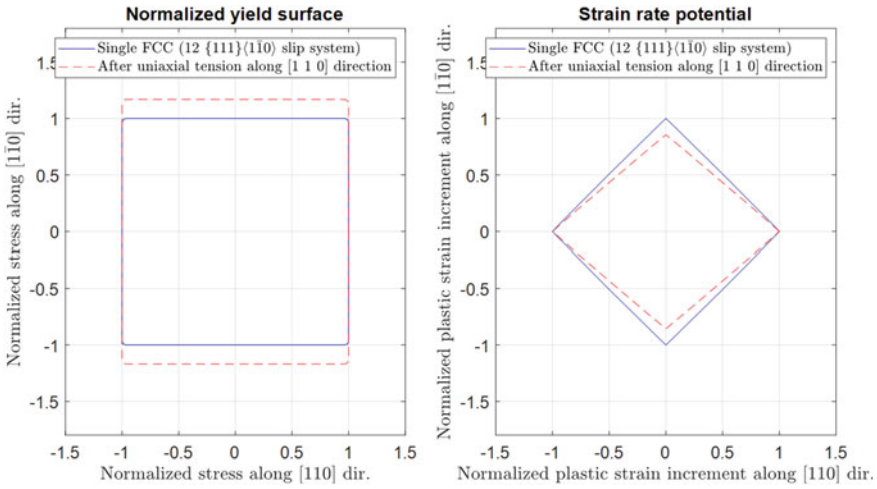


Fig. 6 Evolution of yield stress and strain-rate potential surfaces after uniaxial tension along [110] direction (rate-independent CP model). (Color figure online)

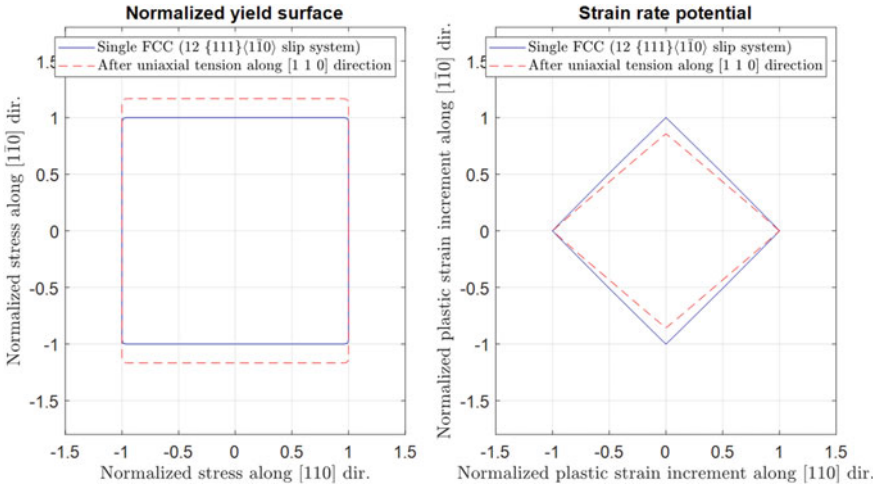


Fig. 7 Evolution of yield stress and strain-rate potential surfaces after uniaxial tension along [110] direction (rate-dependent CP model). (Color figure online)

along the [110] direction for the rate-independent and rate-dependent CP models, respectively. In spite of the heterogeneous distribution of the resolved shear stresses caused by the activated slip systems during the uniaxial tension test in the [110] direction, the yield stress and strain-rate potential surfaces of the two CP models are nearly identical.

4 Conclusions

In this study, the effect of the nonlinearity in the relationship between the resolved shear stress and slip rate was investigated. The nonlinearity parameter, ρ, of the rate-independent crystal plasticity model was adjusted to match the slip rate of the rate-dependent crystal plasticity model. For the comparison, normalized yield stress and strain-rate potential surfaces for a single FCC crystal were generated based on the rate-independent and rate-dependent formulations. Uniaxial tension simulations were also performed for the single FCC crystal to evaluate the effect of the heterogeneous distribution of the resolved shear stresses on the FCC slip systems. From the comparison of the yield stress and strain-rate potential surfaces, it could be concluded that the rate-independent and rate-dependent crystal plasticity models show nearly identical behavior when the nonlinearity in the formulation of the slip rate is about the same.

References

1. Peirce D, Asaro RJ, Needleman A (1981) Material rate dependence and localized deformation in crystalline solids. Acta Metall 31(12):1951–1976
2. Lee MG, Lim H, Adams BL, Hirth JP, Wagoner RH (2010) A dislocation density-based single crystal constitutive equation. Int J Plast 26:925–938
3. Kim JH, Lee MG, Kang JH, Oh CS, Barlat F (2017) Crystal plasticity finite element analysis of ferritic stainless steel for sheet formability prediction. Int J Plast 93:26–45
4. Lim H, Battaile CC, Bishop JE, Foulk JW III (2019) Investigating mesh sensitivity and polycrystalline RVEs in crystal plasticity finite element simulations. Int J Plast 121:101–115
5. Zamiri AR, Pourboghrat F (2010) A novel yield function for single crystals based on combined constraints optimization. Int J Plast 26:731–746
6. Park T, Hector LG Jr, Hu X, Abu-Farha F, Fellinger MR, Kim H, Esmaeilpour R, Pourboghrat F (2019) Crystal plasticity modeling of 3rd generation multi-phase AHSS with martensitic transformation. Int J Plast 120:1–46

Experimental Study and Analysis on the Effects of Cyclic Bending on the Stress-Strain Curves of Aluminum Plate



Yongjun Wang and Pengyan Tong

Abstract The true stress-strain curves of 2024 aluminum alloy plate are investigated under different deformation conditions through the cyclic bending and uniaxial tensile tests. Under this condition, the equivalent strain limit is improved with the increase of the times of circle bending, which is linear accumulated along the line that is perpendicular to the neutral layer on which the bending strain is zero. Furthermore, the tensile test with the cyclic bended plate samples were carried out. The equivalent strain of layer is calculated and compared with original tensile test. It is found that the ultimate strain limit of average equivalent strain of the layers on section is extended with a significant value.

Keywords Cyclic bending · Stress-strain curve · Aluminum plate · Ultimate strain limit

1 Introduction

The localized necking and ductile fracture are two distinct failure mechanisms for sheet metal deformation processes, shows path dependent, geometry dependent, and texture dependent properties. The forming limit diagram (FLD) of sheet metal is typically gained by bulge testing, of which the strain is a monotonous increasing condition, is widely used in sheet metal forming field. In order to describe the FLD, many predictive mathematical models were built with respect to the stress-strain curve and were applied in a lot of forming process simulation.

The forming limit of sheet metal is sensitivity with stain path, different forming condition has different forming limit, especially the cyclic loading. Bambach [1] noticed this cyclic straining and the possible effect on material behavior. Emmens [2, 3] investigated the ultimate strain limit of Bending-under-tension, which means that the stress is not uniform over the thickness of the sheet with simultaneous bending and stretching, as a result that the uniform elongations of up to 430% were obtained

Y. Wang (✉) · P. Tong
School of Mechanical Engineering, Northwestern Polytechnical University, Xi'an, Shaanxi 710072, China
e-mail: wyongjun@nwpu.edu.cn

© The Minerals, Metals & Materials Society 2021

G. Daehn et al. (eds.), *Forming the Future*, The Minerals, Metals & Materials Series,
https://doi.org/10.1007/978-3-030-75381-8_25

with mild steel. Ma et al. [4] adopted strain hardening exponent, stress triaxiality, and strain lode parameters to build a model to predict the initiation of fracture of St14 steel sheets. Li et al. [5] theoretically investigated the failure models of sheet metals under hybrid stretch-bending loadings with the system instability and local material behavior as two different failure mechanisms for forming limits and ductile fracture. Song et al. [6] investigated the characterization of forming limits at fracture of DP600 steel sheets under in-plane biaxial loadings with three ductile fracture criteria and found that the Oyane criterion with two parameters gives the best prediction. Steffen Gerke et al. [7] carried out non-proportional biaxial experiments and corresponding numerical simulations to analyze the load-history dependence on damage and fracture behavior of ductile metals with consistent anisotropic continuum damage model considering the effect of stress triaxiality and Lode parameter on damage behavior. Klingbeil [8] combined a hyperelasticity-based elasto-plastic model for non-linear isotropic as well as kinematic hardening with a modified Gurson model for ductile damage and failure during cyclic and non-proportional loading at large deformation. Harald Schmid [9] found that the forming ability reduced after a drawbead under uniaxial stress state with a conventional tensile test setup and an optical measurement system. Peng [10] found that there is a significant reduction of forming limit with the increase of grain size of copper sheet metals under different deformation paths with traditional setup of forming limit experiments. Kengo Yoshida et al. [11] investigated the effect of changing strain paths on the forming limit stresses of sheet metals using the Marciniak–Kuczynski model and a phenomenological plasticity model with non-normality effects. Jun Cao et al. [12] investigated the fracture loci containing fracture forming limit diagrams (FFLDs) in sheet metal using a modified elliptical fracture criterion based on two kinds of strain energy density to predict the ductile fracture behavior of AA2024-T351 and AA7050-T7451.

This paper focuses on the strain path on the stress-strain curves of aluminum plate with cyclic bending and tensile test, to investigate the effect of equivalent strain of cyclic bending on the tensile equivalent strain and the change of forming limit under different cyclic bending to build basement for next step research on the ductile fracture model.

2 Analytical Model

In order to build the cyclic bending analytical model, assume that the sheet metal strip is cyclically bended as shown in Fig. 1.

In Fig. 1. The radius of cylinder mold is ρ, the thickness of the sheet strip is t. After n times of bending and revers bending, the strain on the section of plate is accumulated as shown in Fig. 2.

In Fig. 2. The equivalent strain on layers is linear to the y coordinate, and it can be expressed as follows:

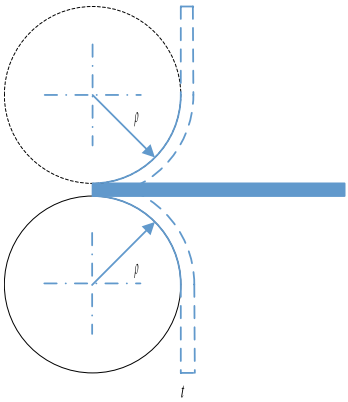


Fig. 1 Schematic of set up for cycle bending. (Color figure online)

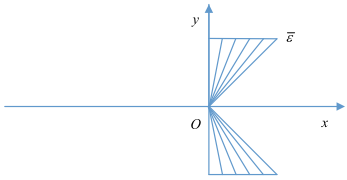


Fig. 2 Schematic of the equivalent strain after cyclic bending. (Color figure online)

$$\varepsilon_x = \frac{y}{\rho} \tag{1}$$

Assume that the width of sheet plate is not changing during bending process. Thereby it is a planar strain state, so there are the following relations.

$$\varepsilon_y = \varepsilon_x,\ \varepsilon_z = 0$$

where ε_z is the strain in the width direction.

So the equivalent strain on layer y is

$$\bar{\varepsilon}_x(y) = \frac{2}{3}\frac{y}{\rho} \tag{2}$$

After bending and revers bending times of m, the equivalent strain becomes

$$\bar{\varepsilon}_{x,n}(y) = \frac{4}{3}m\frac{y}{\rho} \tag{3}$$

When the samples were undergone uniaxial tension, the equivalent strain on layers are shown as Fig. 3.

In Fig. 3, the average equivalent strain of layer can be expressed as follows:

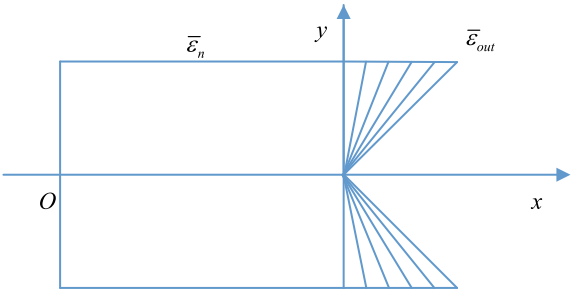


Fig. 3 Tensile after cyclic bending. (Color figure online)

$$\bar{\varepsilon} = \frac{1}{2}\bar{\varepsilon}_{out} + \bar{\varepsilon}_n = \frac{1}{3}m\frac{t}{\rho_n} + \bar{\varepsilon}_n \tag{4}$$

where the $\bar{\varepsilon}_{out}$ is the equivalent strain of outer layer, and $\bar{\varepsilon}_n$ is the equivalent strain of the neutral layer.

Assumption the material work hardening behavior obeys common power function model, so the equivalent stress is

$$\bar{\sigma} = K\bar{\varepsilon}^n \tag{5}$$

where K is the strain hardening coefficient, and n is the strain hardening exponent.

So the stress on axial can be express as follows:

$$\sigma_x = \frac{2}{b*t}K\int_0^{\frac{t}{2}}\left(\frac{4}{3}m\frac{y}{\rho} + \varepsilon_n\right)^n bdy = \frac{3}{2}\frac{K\rho}{tm(n+1)}\left(\frac{2}{3}\frac{mt}{\rho} + \varepsilon_n\right)^{n+1} \tag{6}$$

3 Experimental Work

3.1 Experiment Setup

The aluminum adopted for experiment is Al2024-O with supply state, and its thickness is 0.02 inch. The dimension of sample for uniaxial tension test is shown in Fig. 4. The capacity of the test machine is 100KN. The diameter of bending mold is 80 mm (Fig. 5).

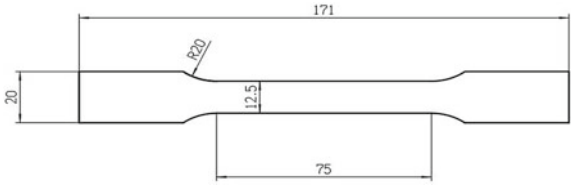


Fig. 4 Dimension of sample for uniaxial tension test

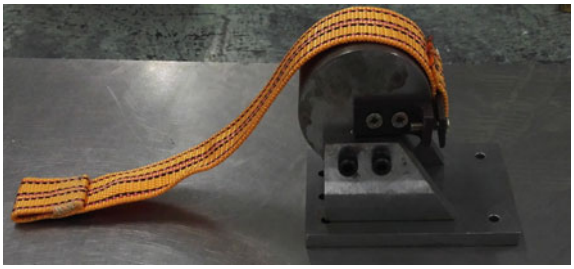


Fig. 5 Cyclic bending mold. (Color figure online)

3.2 Experiment Procedure

The experiment steps are as follows:

Firstly, machine the tensile test samples according to Fig. 4.
Secondly, number and measure the dimension of samples.
Thirdly, cyclically bend the sample according to Fig. 6.
Fourthly, uniaxial tension test.
Fifthly, test data fitting with origin software.

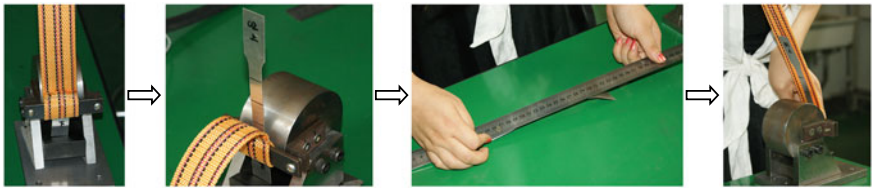


Fig. 6 Cyclic bending procedure. (Color figure online)

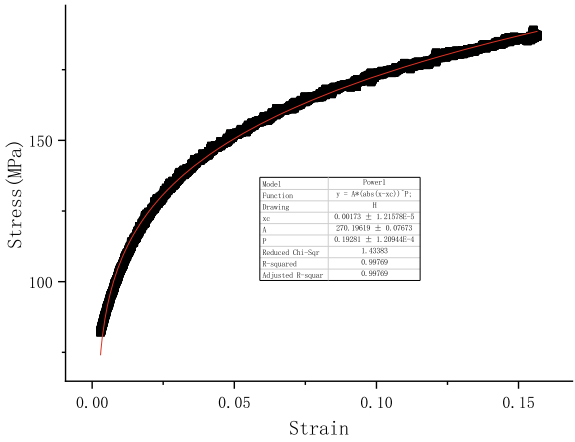


Fig. 7 Fitting for true stress-strain data of original Al2024-O. (Color figure online)

3.3 Experiment Results

The samples undergone 10, 20, 30, 40, and 50 rounds of cyclic bending,respectively, and then subjected to uniaxial tensile test. The test data of true stress–strain were fitted by origin soft ware. One set of true stress-strain data is fitted as shown in Fig. 7.

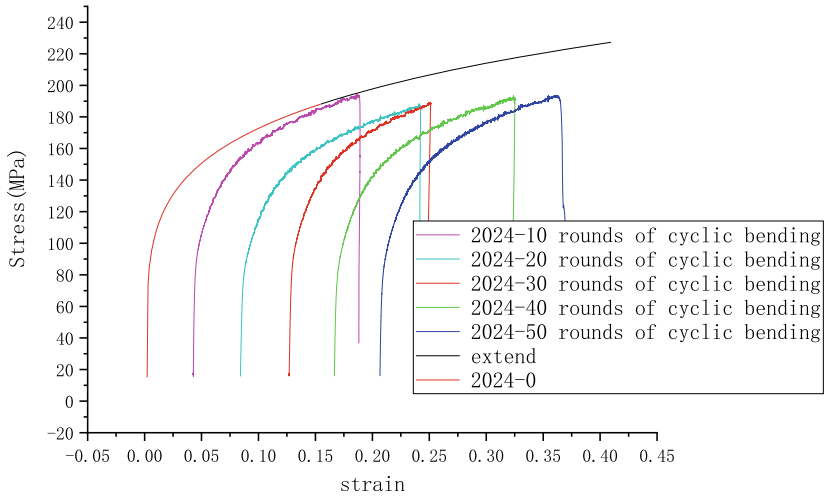
The true stress-strain curves for different rounds of cyclic bending are shown in Fig. 8. Initial material without bending is fitted by power low. The red part of original Al2024-O is the test data, and the dark part is extended according the fitted parameters, which are 0.19281 for n and 270.19619 for K. Other lines are true stress-strain curves of 10, 20, 30, 40, and 50 rounds cyclic bendingrespectively, with (for a) and without (for b) the beginning point translated to right a distant which is equal to the average equivalent strain of cyclic bending.

The material properties of curves in Fig. 8. fitted for power function are listed in Table 1.

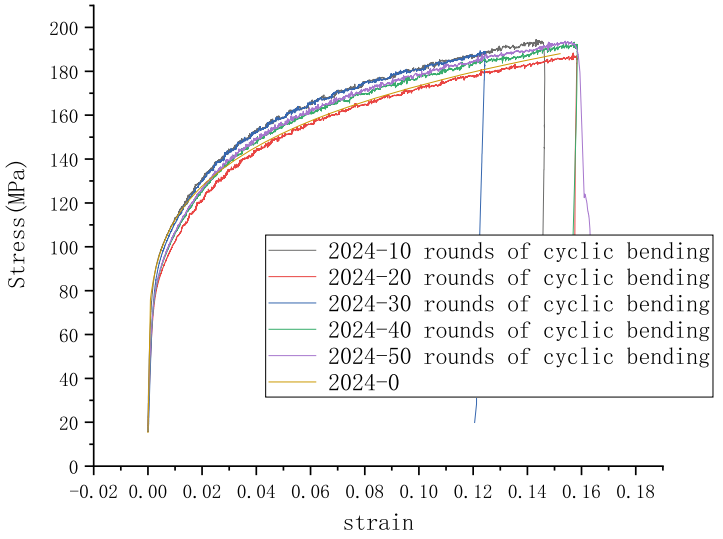
4 Discussion

From Table 1, it can be found that the ultimate limit strain, the strength limit, and also the strain hardening exponent, as well as strength coefficient of the cyclically bended sample, is similar with original one which is not bended. However, the Young's modulus decreases significantly for cyclically bended samples, and the more rounds of cyclic bending the more notably the decrease. But the strain hardening exponent and the strength coefficient reach the biggest only when the sample undergoes 30 rounds of cyclic bending.

From Fig. 8, It can be found that the shape of the true stress-strain curves are similar with each other between bended and non-bended.



(a)



(b)

Fig. 8 True stress-strain curves for different rounds of cyclic bending. (Color figure online)

Table 1 Material properties of samples undergone cyclic bending

Cyclic number	Young's modulus/GPa	Strain hardening exponent n	Strength coefficient K	Average equivalent strain of cyclic bending	Equivalent strain limit after cyclic bending	Total ultimate equivalent strain limit
0	68.679	0.19281	270.19619	0	0.15631	0.15632
10	56.692	0.18759	279.95331	0.04283	0.14520	0.18803
20	36.456	0.19461	270.40107	0.08417	0.15797	0.24214
30	36.639	0.19694	286.64736	0.12675	0.12405	0.25080
40	24.232	0.18826	274.6957	0.16667	0.15820	0.32486
50	19.567	0.18702	276.40787	0.20667	0.15694	0.36361

The result means that the damage occurred when the sheet metal was cyclically bended, as a result Young's modulus decreases with the rounds of cyclic bending, of which the average equivalent strain is accumulated with the increase of the bending times which leads to the total average equivalent strain increase significantly.

5 Conclusions

The true stress-strain curves of Al2024-O aluminum alloy plate are investigated under different deformation conditions through the cyclic bending and uniaxial tensile tests.

The ultimate limit strain, the strength limit, and also the strain hardening exponent, as well as strength coefficient of the cyclically bended sample, is similar with original one which is not bended.

Considering the equivalent strain of cyclic bending, the total equivalent strain limit is improved with the increase of the times of circle bending.

The Young's modulus decreases significantly for cyclically bended samples, and the more rounds of cyclic bending the more notably the decrease.

Acknowledgments The support from the National Nature Science Foundation of China (51790171) are gratefully acknowledged.

References

1. Bambach M, Hirt G, Junk S (2003) Modelling and experimental evaluation of the incremental CNC sheet metal forming process. In: Proceedings 7th COMPLAS. Barcelona, Spain, April 7–10
2. Emmens WC, Boogaard AHVD (2009) An overview of stabilizing deformation mechanisms in incremental sheet forming. J Mater Process Technol 209(8):3688–3695

3. Emmens WC, van den Boogaard AH (2008) Extended tensile testing with simultaneous bending. In: Proceedings IDDRG 2008 International Conference. Olofstrom, Sweden, June 16–18, pp 219–229
4. Ma X, Li F, Li J Analysis of forming limits based on a new ductile damage criterion in St14 steel sheets. Mater Design 68:134–145
5. Theoretical failure investigation for sheet metals under hybrid stretch-bending loadings. Int J Mech Sci 2015, 104:75–90
6. Song X, Leotoing L, Guines D et al (2017) Characterization of forming limits at fracture with an optimized cruciform specimen: application to DP600 steel sheets. Int J Mech Sci 126:35–43
7. Gerke S, Zistl M, Brünig M (2019) Experiments and numerical simulation of damage and fracture of the X0-specimen under non-proportional loading paths. Int J Solids Struct 163:157–169
8. Klingbeil D, Svendsen B, Reusch F (2016) Gurson-based modelling of ductile damage and failure during cyclic loading processes at large deformation. Eng Fract Mech 160:95–123
9. Harald S et al (2019) Failure behavior of different sheet metals after passing a drawbead. Procedia Manuf
10. Peng LF, Xu ZT, Fu MW (2016) Forming limit of sheet metals in meso-scale plastic forming by using different failure criteria. Int J Mech Sci 120:190–203
11. Yoshida k, Kuwabara T, Kuroda M Path-dependence of the forming limit stresses in a sheet metal. Int J Plast 23(3):361–384
12. Cao J, Li F, Ma X et al (2017) A modified elliptical fracture criterion to predict fracture forming limit diagrams for sheet metals. J Mater Process Technol 252:116–127

Part VI
Honorary Symposium: Zhongren Wang

Professor Z. R. Wang's Contributions to Metal Forming Theory, Technology, and Education



Gang Liu, Shijian Yuan, and Kaifeng Zhang

Abstract Professor Wang once served as the president of the China Society for Technology of Plasticity (CSTP). He also hosted and chaired the 4th International Conference of Technologies of Plasticity (ICTP) in Beijing, in 1993, to bring the event for the first time to China. During the 60 years' academic career life on metal forming, he has published 17 books and more than 300 academic papers, and won international and national Awards 5 times, including invention award and science & technology progress award, etc. The main contributions of Professor Wang include: developing the engineering plasticity theory and promoting its applications, inventing the dieless hydroforming method for large-scale spherical shells, solving the technological problems of several key national projects of China, leading internationalization of Chinese community of plasticity engineering, and supervising a group of talents on metal forming.

Keywords Engineering plasticity · Dieless hydro-bulging · Flexible multi-point forming · Low load precision bending

1 Introduction

Professor Z. R. Wang (1934.5.10–2019.4.25) was a full-time professor at Harbin Institute of Technology (HIT), China. Professor Wang is a famous research scientist in the field of international plasticity engineering. He received his Bachelor's degree from the Department of Metal Plastic Processing in Beijing Institute of Iron and Steel Technology, in 1955, and then obtained his Master's Degree in the Department of Metal Plastic Processing in HIT under the supervision of a former Soviet Union professor. In 1957, after his master's degree, he stayed in Harbin Institute

G. Liu (✉) · S. Yuan · K. Zhang
National Key Laboratory for Precision Hot Processing of Metals, Harbin Institute of Technology, Harbin 150001, China
e-mail: gliu@hit.edu.cn

G. Liu
Institute of High Pressure Fluid Forming, Harbin Institute of Technology, Harbin 150001, China

© The Minerals, Metals & Materials Society 2021

G. Daehn et al. (eds.), *Forming the Future*, The Minerals, Metals & Materials Series,
https://doi.org/10.1007/978-3-030-75381-8_26

of technology to teach. In 1985, he was promoted to Professor and doctoral supervisor. From 1987 to 1997, he served as the director of the metal forming division. Within that decade, under his excellent leadership, the metal forming team has made a great progress in education, research, and educational discipline construction. He has carried out research into aspects of metal forming theory and technology, primarily hydroforming. Within his research career of about 60 years, Professor Wang has published 17 monographs, textbooks, manuals, and collections, as well as more than 300 academic papers. Remarkably, the monograph *Engineering Plasticity Theory and Applications in Metal Forming* was published by Wiley in 2018, when he was 84 years old.

As a representative of metal forming community in China, Professor Wang served as the president of the China Society for Technology of Plasticity (CSTP) from 1991 to 1994, and successfully hosted the 4th International Conference on Technology of Plasticity (ICTP) in Beijing, in 1993. He has successively served as the Standing Advisory Board of ICTP and made significant contributions to the conference series. Professor Wang also served as the Chairman of the International Conference on Rotary Forming in 1989 and the 1st International Conference on New Forming Technology in 2004. Furthermore, he was also the editorial board member of several well-known international journals, such as *Journal of Material Processing Technology* (JMPT). In recognition of his contribution to Chinese plasticity engineering, CSTP awarded him the *Golden Anvil Award*.

Based on deep mechanical knowledge, Professor Wang proposed the innovative forming method of spherical shells, and won the Brussels Eureka Gold Medal of World Fair Invention in 1987 and the Chinese National Technology Invention Award in 1992. Over the past 40 years, he has won National Technology Invention Awards and National Science and Technology Progress Awards four times in total, and more than 10 other science and technology awards. Meanwhile, as a successful teacher, he had supervised or co-supervised PhD candidates over 40, postgraduate and undergraduate students over hundred. Most of them has become experts or scholars in metal forming community of China, USA, UK, Japan, Canada, Germany, and Singapore (Fig. 1).

2 Research on Plasticity Theory and Its Applications

2.1 A Consistent Sequence Law of Stress-Strain Components

Through the mechanical analysis based on the classical incremental strain theory or the total strain theory, the quantitative relationship between the components of deviatoric stress and strain increments or the total strain can be directly obtained. However, the quantitative determination of stress distribution in a deforming body is difficult, and it is nearly impossible to compute the total strain using the total strain theory. Professor Wang presented the simplified consistent sequence law considering



Fig. 1 Professor Z. R. Wang and dieless hydro-bulged sphere for the 80th anniversary of HIT. (Color figure online)

the relations between the stress and strain components in line with the incremental theory and the total strain theory. It has been verified that, qualitative results from the consistent sequence law have great value to deal with complex problems in engineering practice, when quantitative data could be determined experimentally. The proposed law can be described as follows [1]:

(1) In the process of metal forming, if the associated principal strain axis directions are unchanged with the magnitude sequence of the principal stress components given as: $\sigma_1 > \sigma_2 > \sigma_3$, then, the principal strain sequence is similar, that is $\varepsilon_1 > \varepsilon_2 > \varepsilon_3$ ($\varepsilon_1 > 0$, $\varepsilon_3 < 0$).

(2) An unvaried relationship: $\sigma_2 > (\sigma_1 + \sigma_3)/2$ gives $\varepsilon_2 > 0$, $\sigma_2 = (\sigma_1 + \sigma_3)/2$ gives $\varepsilon_2 = 0$, $\sigma_2 < (\sigma_1 + \sigma_3)/2$ gives $\varepsilon_2 < 0$.

The first expression of the proposed law describes the sequential relationship between the stresses and strains, while the second expression is the unvaried relationship based on the intermediate principal stress either close to σ_1 or to σ_3. The proposed consistent sequence law supports a qualitative judgment on the basis of increment strain theory and can be used to determine the relative magnitude of strain components in various directions when the stress changes within a certain range,

though the quantitative strain components can not be calculated. Thus, the tendency of dimensional variation in the body subjected to deformation during forming can be known presumably.

For engineering applications of metal forming, the law can be elucidated in the following aspects:

(1) The greatest increase of strain occurs in the direction where acts the algebraically maximal principal stress (i.e., positive-tensile and negative-compressive) of the whole stressed body in all directions, and the greatest decrease in the direction where the minimum stress acts.
(2) The variations of dimensions are consistent with the principal stress in the direction that acts the intermediate principal stress. Then the dimensions get close to the maximum or the minimum. The dimensional variation stated above refers to the total strain.

2.2 Division of Stress and Strain on the Yield Locus

Based on the consistent sequence law between stress and strain, for specific metal forming operations, Professor Wang proposed an approach to express the relations graphically between yield criterion and the theory of plastic stress and strain relationships. Two steps are needed and given as follows:

(1) Based on the force analysis of process, identify the position corresponding to specific forming process on the yield surface, and then determine the loading locus in different areas of the deformation zone.
(2) Divide the stress state on the yield locus into different zones with various strain types according to the consistent sequence law, then determine the tendency of size variation in particular part of the workpiece [2, 3].

The stresses of some sheet and tube forming processes are able to be zoned on the yield locus in the axisymmetric plane-stress state, and the loading locus of typical plane-stress deforming processes can be determined. On this situation, the normal stress through workpiece thickness may be neglected, $\sigma_t = 0$. The projection of the Mises cylinder on the coordinate plane with $\sigma_t = 0$ is an ellipse, described by Eq. (1) involving the radial stress and the circumferential stress, where Y is the flow stress. Equation (1) is graphically represented using Fig. 2. There are three circles outside the elliptical yield locus, viz. the inner circle, the middle circle, and the outer circle. These circles separately denote the normal through-thickness strain increments, the axial (radial) strain increments, and the circumferential strain increments.

$$\sigma_\theta^2 - \sigma_\rho \sigma_\theta + \sigma_\rho^2 = Y^2 \tag{1}$$

The proposed figure is the first attempt to integrate yield locus, stress zoning, tendency of strain increment variation, and plane-stress metal forming processes

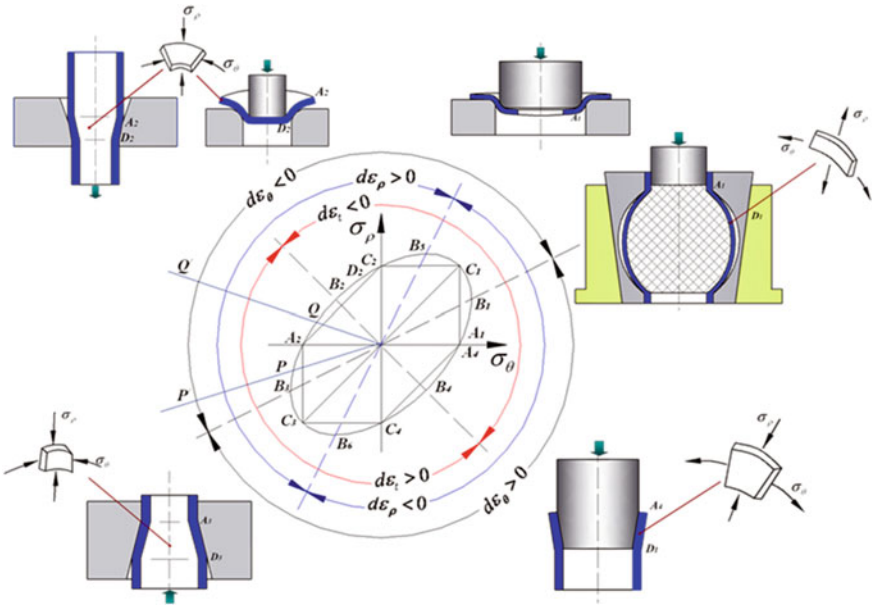


Fig. 2 Zoning of Mises yield ellipse at typical plane stress states. (Reproduced from Wang 1980 Ref [3]). (Color figure online)

using a single graph, which can be used to determine the dimensional variation tendency of a workpiece being deformed conveniently.

Using the similar approach to graphically describe the relations of plane-stress states, various metal forming operations with three-dimensional stress states are shown in Fig. 3. The figure is constructed based on the unfolded Mises yield cylinder [1, 4]. Any stress state in the deforming body dominated by the particular location on the Mises yield cylinder surface can be found in the Fig. 3. The three principal stress components of each stress state can be identified by the distance from the point to the π-plane, viz. mean stress σ_m, and a vector on the π-plane with a radius and an angle θ. In Fig. 3, the lower the position of metal forming process, the higher the compressive stress and the plasticity of the material. Again, one deformation type may correspond to different stress states. Normally, the force that tools exert on the workpiece directly related to one or two principal stresses. Because the relative positions among σ_m, σ_1, σ_2, and σ_3 can be found from Fig. 3, the force can be evaluated according to the position of the stress state [5].

Reference [6] claims Figs. 2 and 3 as important contributions to the theory of metal forming. Firstly, such graphic approach proposed a new way to integrally and simultaneously show the stress, the strain, and the yield locus. Moreover, the tendency of dimensional change in various metal forming processes is able to be presented based on a unified solution to integrate multiple indicator functions into a single diagram.

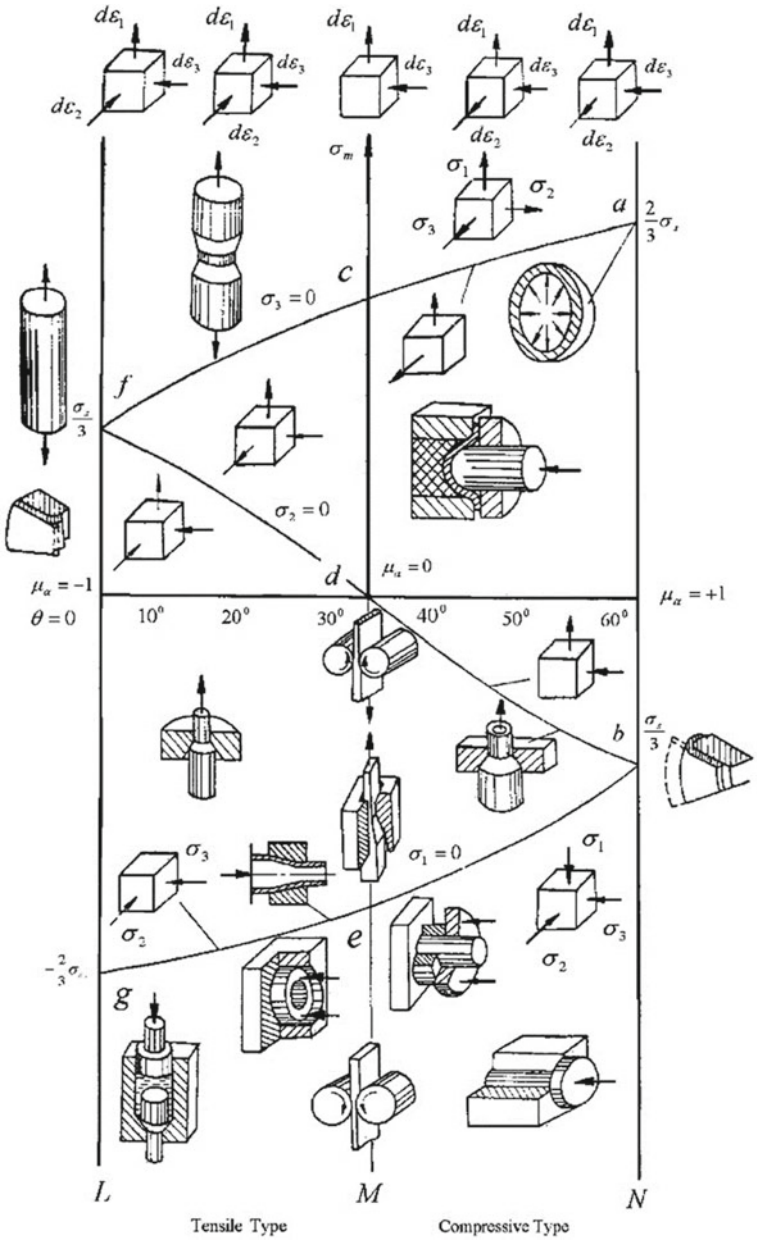


Fig. 3 Locations of metal forming processes with three-dimensional stress states on the Mises cylinder (Reproduced from Wang. 1993 Ref [4])

3 Dieless Hydro-Bulging Technology

3.1 Principle of Dieless Hydro-Bulging of Spherical Shells

Stamping using rigid dies has been the traditional technology to manufacture spherical vessels. The biggest disadvantage of conventional process is the need for presses with large-scale bed and forming dies. Moreover, the complicated stamping and trimming procedure resulted in a severely high production cost. To address above limitations, Professor Wang, for the first time, proposed the dieless hydro-bulging technology in 1985, which has gained great popularity in various industries [7, 8].

The typical dieless hydroforming process of spherical shells begins with assembling the steel plates and/or roll-bent plates with single curvature into a closed polyhedral shell followed by welding. Then the closed shell is deformed gradually into a spherical shape by filling liquid (usually pure water) to exert internal pressure [9–11]. Since the used shells are of single curvature, the preparation is consisted of blanking, bending, and/or plate rolling, assembling and welding, hydroforming is comparably simple (see Fig. 4). It excels at (1) the total manufacture cost is significantly reduced resulting from the avoidance of large-scale dies and presses; (2) the production period is shorten because of obviating the need for exchanging dies;

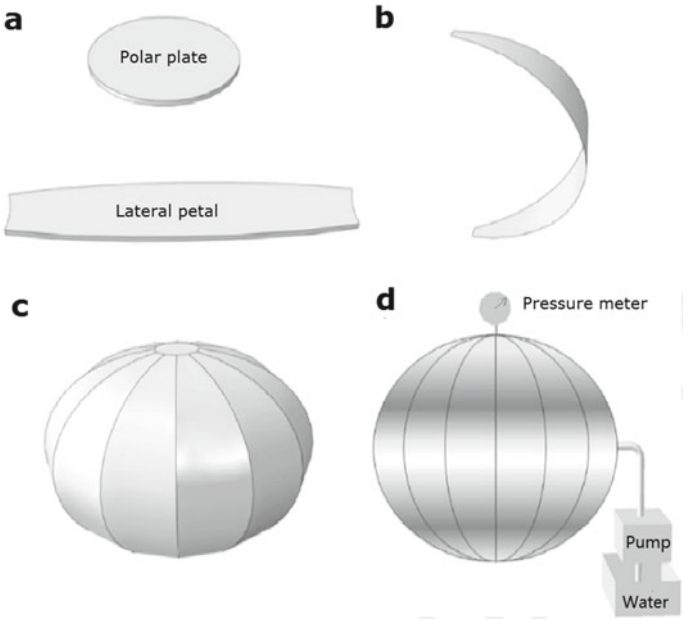


Fig. 4 Schematic of the main operations of hydro-bulging process of spherical shell: **a** blanking, **b** roll-bending of lateral petals, **c** assembling and welding, **d** hydro-bulging (Reproduced from Wang et al. 2018 Ref [12])

and (3) the welding-induced residual stresses are greatly reduced using the overload hydro-bulging.

Hydro-bulging of spherical shell is an automatic spheroidizing process under the action of the increasing internal pressure because the shape of preform is a polyhedral shell inscribed in an ideal spherical shell. Using the earth coordinate system, the principal stresses on the shell are defined as longitudinal stress σ_ρ and latitudinal stress σ_θ. Based on the Laplace equation, which describes a shell that is internally pressurized in the normal direction, the relationship between the stress, internal pressure, and radii of the shell can be written into Eq. (2).

$$\frac{p}{t} = \frac{\sigma_\theta}{R_\theta} + \frac{\sigma_\rho}{R_\rho} = \frac{p_\theta}{t} + \frac{p_\rho}{t} \tag{2}$$

where, p is the internal pressure, t is the nominal thickness of the shell, p_ρ is the forming pressure calculated with longitudinal curvature, and p_θ is the forming pressure calculated with latitudinal curvature (Fig. 5).

During the shell hydroforming, the workpiece can be regarded as a deformed object sustaining a balance force simultaneously. The force exerted on one half is balanced by the other half of the workpiece. It is understandable that the shape of the shell preform is gradually changing into a sphere neglecting the difference to the final product. Two mechanisms in forming the spherical shells are revealed as follows:

(1) Geometry Adjustment Mechanism: with the increase of internal pressure, the larger curvature radius decreases and vice versa.
(2) Physical Adjustment Mechanism: In the process of spheroidizing, strain hardening occurs in the deformed area, resulting in the stop of deformation. With the increase of pressure, the adjacent undeformed area begins to deform. This

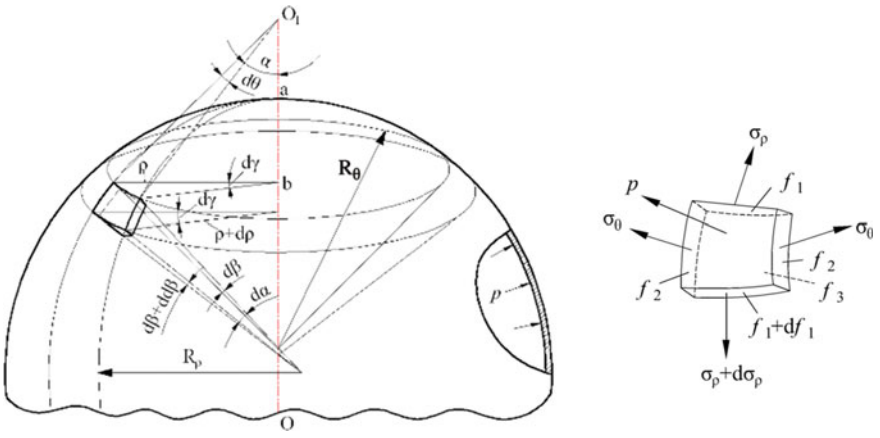


Fig. 5 Hydro-bulged shell and the element for stress analysis. (Reproduced from Wang et al. 2018 Ref [12]). (Color figure online)

mechanism contributes to avoiding the strain concentration and achieving uniform deformation.

3.2 Applications of the Dieless Hydro-Bulging Technology

Since 1985, three series of dieless hydro-bulging products have been developed: (1) spherical water tower and water supply tank; (2) pressure vessel and liquefied gas tank; (3) architectural decoration ball.

The shell made by dieless hydro-bulging technology has been successfully applied in the spherical water tower (Fig. 6a) of railway industry and urban water supply, the spherical storage tank of liquefied petroleum gas (Fig. 6b), and the spherical and ellipsoidal launch tower of communication, radio, and television; the spherical ornaments formed by this technology have also been widely used in the architecture decoration; the flight simulation ball curtain with a diameter of 7 m is also used in the field of pilot training.

Comparing to the traditional manufacturing technologies, the dieless hydro-bulging shell exhibits the following advantages:

- Flexibility. Because shells can be formed without press and dies, dieless hydro-bulging is especially suitable for small volume production.
- Shorter production cycle, lower cost, and easier manufacturing in construction site.
- Lower residual stress along the welds due to over-loading effect during bulging.

Professor Wang won the Brussels Eureka Gold Medal of World Fair Invention (1987) and the Chinese National Invention Award (1992) with the dieless hydro-bulging technology. Professor H. Sekiguchi from Tokyo University published a paper

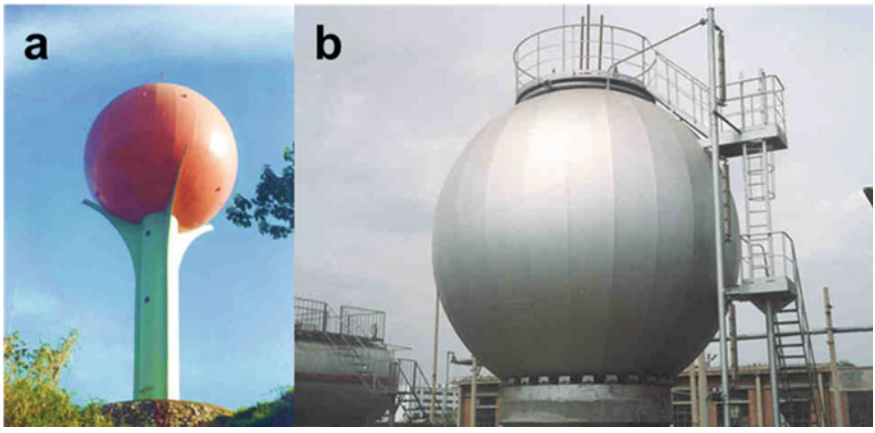


Fig. 6 **a** Spherical water tower (200 m^3), **b** Storage tank of liquefied petroleum gas (200 m^3) (Reproduced from Wang et al. 2014 Ref [13]). (Color figure online)

titled "The First Patent (?) in China" in *Journal of Japan Society for Technology of Plasticity* [14]. In 1990, the journal *American Machinist* reported new achievements selected by the 18th North American Machining Research Institute, among which the dieless hydro-bulging technology was listed as one of the top three highlights [15].

4 Contributions to Key National Projects in China

Professor Z. R. Wang exhibited great talent and skills in applying plastic theory to solve complex engineering problems. He could play the roles of scholar, engineer, and team leader. Through combining theory with engineering practice, he led the team to creatively solve a series of technical problems in national key engineering projects, such as large-scale space environment simulator and large-scale wind tunnel.

4.1 Large-Scale Space Environment Simulator

The large-scale space environment simulator of China Manned Space Engineering Program is a large-scale device for simulating the space environment and testing Shenzhou spacecraft [16]. Figure 7 shows the appearance and loading process of the spacecraft. The main vessel had a diameter of 12 m, a height of 22.4 m, and a total volume of about 3000 m^3 [17]. At that time, the device was the largest space environment simulator in Asia and the third largest in the world. The simulator was capable of simulating the space environment characteristics, such as ultra-low

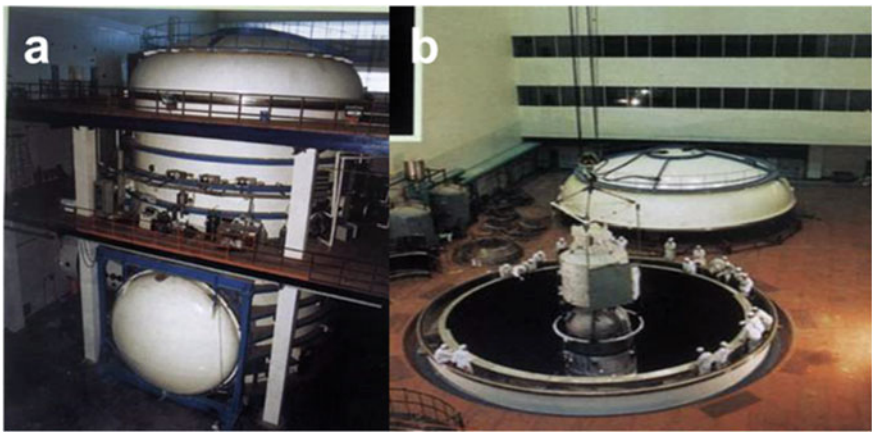


Fig. 7 **a** Appearance of vacuum vessel, **b** put into spacecraft (Reproduced from Zhi et al. 1998 Ref [16]). (Color figure online)

temperature, high vacuum and strong solar radiation, which can be regarded as to an artificially created small space.

Figure 7 shows the top cover with a diameter of 12 m on the vessel. Driven by the stringent requirement of vacuum degree of 10^{-5} Pa, a high reliability sealing needs to be realized between the cover and the vessel flange.

Therefore, the accuracy of flange forming and machining are extremely high. As the chief engineer of this project, Professor Wang led the team to accomplish a number of technology breakthroughs. A series of technical difficulties involved in the manufacture of this simulator, such as low load precision bending, machining deformation control, dynamic control of clamping mode, welding deformation control, and on-site precision machining, have been successfully solved [18]. The large-scale space environment simulator has been used in Shenzhou spaceship experiments for many times, made significant contributions to the continuous successful launches of spaceships in China.

4.2 Large-Scale Wind Tunnel

Professor Wang also served as the chief engineer of the FL-9 low speed pressurized wind tunnel construction project, which was the largest wind tunnel with low speed and high Reynolds number in Asia, in 2005 [19]. The maximum outer dimension of the wind tunnel was 86 m, the maximum diameter of the pressure-bearing shell was 14.5 m, and the volume of the tunnel was about 13000 m^3. Resulting from the characteristics of complex structure and huge size, it is very difficult to manufacture. The cross-section shapes of the large-scale shrinkage shell (Fig. 8) along the axis varies significantly, which is composed by hundreds of curved plates with different profiles. If the conventional stamping process is adopted, hundreds of dies sets are

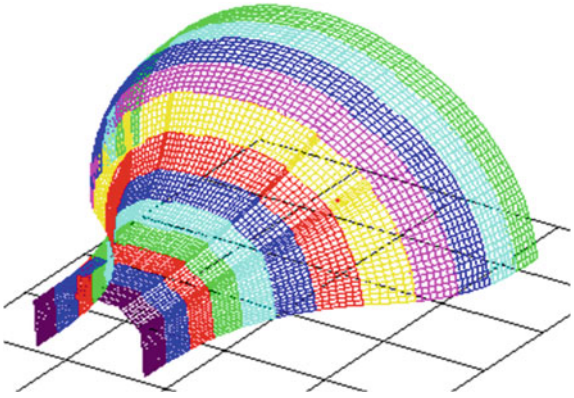


Fig. 8 Structure of the part in a wind tunnel (Reproduced from Wang et al. 2004 Ref [19]). (Color figure online)

needed resulting in a huge manufacture cost. Therefore, Professor Wang proposed the flexible multi-point forming technology enabling the low-cost and high-efficiency manufacturing of various curved plates to be achieved [20].

The die set for flexible multi-point forming consists of an elastic punch and an adjustable female die assembly. The adjustable die is composed of nearly one hundred scattered dies. By adjusting the height of each die, different shapes of die surfaces can be obtained. The elastic base plate was mounted on the mold to avoid the uneven surface of the workpiece. The flexible multi-point forming technology is used to manufacture all kinds of curved components needed for wind tunnel shrink shell, which greatly saved the use of die material and cycle time of processing, resulting in significantly reduced engineering cost. Figure 9 is a shrinkage body assembled with formed parts. In September 2006, the first test run was successful, and all aspects of quality examination obtained the expected results [21].



Fig. 9 Assembling of the workpieces formed by flexible reconfigurable die (Reproduced from Wang et al. 2006 Ref [20]). (Color figure online)

5 Contribution to Internationalization of Chinese Community of Plasticity Engineering

5.1 Chair of the 4th ICTP in Beijing

Professor Z. R. Wang was the representative of leading Chinese plasticity engineering scholars to the international community communication. As the president of CSTP, he introduced Chinese academic research progress and industry development of metal forming to the international plasticity engineering community, and organized the national plasticity engineering community to win the right to host the 4th ICTP for the first time in China.

In September 1993, CSTP successfully hosted the 4th ICTP in Beijing, and Professor Wang, served as the conference chair (Fig. 10). There were approximately 450 delegates from 32 countries and regions attended the conference, including about half from oversea. Famous research scientists and experts of metal forming from all the major industrial organization and research institutes attended the conference, e.g., T. Altan and B. Avitzur from the USA, H. Kudo, T. Nakagawa and M. Kiuchi from Japan, R. Kopp and K. Lange from Germany, and P. Standring from UK. Mr. G.Y. He, the Minister of the Ministry of Machinery Industry of China, attended the opening ceremony and delivered a speech. Fruitful academic exchanges were generated on the schemes of sheet metal processing, forging, extrusion, rolling, tube forming, drawing, rotary forming, powder forming, superplastic forming, and new plastic processing technologies, with 260 oral presentations and 83 posters given in this conference. As an innovation in the schedule of ICTP, two special free discussion



Fig. 10 Opening ceremony of 4th ICTP (G.Y. He, H. Kudo, Z.R. Wang, T. Altan). (Color figure online)

sessions were organized with the topics of: the development trend of metal forming and training of young talents.

5.2 *Launching International Conference on New Forming Technology (ICNFT)*

It is a precondition for the development of new technologies to understand the meaning of the elementary plastic processes. This is also of greatest interest, if processing windows have to be expanded to more complex, more precise or smaller geometries. Meanwhile, to form advanced high-performance materials, new forming technologies have been developed and promoted to practical applications. Therefore, in 2004, Professor Wang, Professor T.A. Dean, Professor F. Vollertsen, and Professor S.J. Yuan launched the new conference series called International Conference on New Forming Technology (ICNFT). The first ICNFT was successfully hold in Harbin, China, in Sep. 2004. More than 100 delegates from over 20 countries attended the conference (Fig. 11).

ICNFT has been organized in China, Germany, and UK alternatively for 6 times, and great success has been achieved. To date, the conference has become an inspiration forum for researchers and professional engineers to exchange innovative ideas and research experience and to discuss cutting-edge novel forming technologies potentially to be applied in the manufacturing industry in present and future years. The next 7th ICNFT will be held in Changsha, China.



Fig. 11 Opening speech from Professor Z.R. Wang in the 1st ICNFT. (Color figure online)

References

1. Wang ZR (1979) The sequential correspondence law between stress and strain, and comment on Gubkin's minimum resistance law. Forg Stamp Technol 4(5):19–21
2. Wang ZR, Li SD, Liu LJ (1982) On division of stress on the yield locus and correspondence between the regions on the yield locus and the size variation of workpieces during metal forming. Acta Metall Sin 18(4):433–438
3. Wang ZR (1980) The rules of correspondence between strain and stress order and its application in metal forming process of plane stress. J Harbin Inst Technol 3:56–61
4. Wang ZR, He YX (1993) The present situation of forging and stamping techniques in China, advanced technology of plasticity-Proc. 4th ICTP, International Academic Publishers: 3–10
5. Wang ZR (1994) Comprehensive analysis of stress–strain in typical metal forming processes. J Harbin Inst Technol 2:62–66
6. Hu WL, He ZB, Fang Y (2004) Uniform principle on stress, strain and yield locus for analysing metal forming processes: the contribution of Prof. Z.R. Wang. J Mater Process Technol 151(1–3):27–32
7. Wang ZR, Wang T, Kang DC et al (1989) The technology of the hydro-bulging of whole spherical vessels and experimental analysis. J Mech Work Technol 18(1):85–94
8. Zhang SH, Wang ZR, Wang T (1990) The integrally hydroforming process of spherical vessels. Int J Press Vessel Pip 42(1):111–120
9. Yuan SJ, Teng BG, Dong XY et al (2004) Progress in large vessel forming: introduction of some innovations of Prof. Z. R. Wang. J Mater Process Technol 151:12–17
10. Wang ZR, Liu G, Yuan SJ et al (2005) Progress in shell hydroforming. J Mater Process Technol 167(2–3):230–236
11. Wang ZR, Yuan SJ (2006) New forming technologies used in manufacturing large vessels. Int J Mach Tool Manuf 46:1180–1187
12. Wang ZR, Hu WL, Yuan SJ, Wang XS (2018) Engineering plasticity-theory and applications in metal forming. Higher Education Press, Beijing
13. Wang ZR (2014) Theory and key techniques of hydro-bulging spherical vessels. Harbin Institute of Technology Press, Harbin
14. Sekiguchi H (1986) The first patent (?) in China. J Japan Soc Technol Plast 27(306):819
15. Jablonwskl J (1990) What's new in metalworking research. Am Mach 7:67–70
16. Zhi YS (1996) Research on key technology of vacuum vessel forming for space environment simulator. PhD thesis, Harbin Institute of Technology
17. Zhi YS et al (1998) A study of the sealing flange manufacturing of a huge vacuum vessel. Press Vessel Technol 1:43–47
18. Wang ZR, Zhang Q (2010) Less loading and approaching uniform forming theory and application. Higher Education Press, Beijing
19. Dong GQ, Wang ZR et al (2007) FEM analysis and gas pressure intensity test of FL-9 low-speed compressed-air wind tunnel. J Exp Fluid Mech 21(4):77–82
20. Wang RW, Dong XY (2004) Some key technologies used in manufacturing the space environmental simulator and a large wind tunnel. J Plast Eng 11(2):35–40
21. Wang ZR, Dong GQ, Teng BG et al (2006) Multipoint sandwich forming and its applications in manufacturing contraction of wind tunnel. Acta Aeronautica et Astronautica Sinica 37:989–992

Adding Value by Advancing Metal Forming Technology



Trevor Dean, Bo-Zhou Di, and Li-Liang Wang

Abstract The metal forming industry is responding to changing technical and commercial demands of customers and increasingly stringent legislative restrictions. In addition, on demand delivery requires lead times having to contract. Also Original Equipment Manufacturers are demanding deliveries just-in-time on changeable schedules and for many products batch quantities have become smaller than they were a few years ago. Thus, lead times must be shortened. To meet these challenges, in the metal forming industry, the rate at which new and existing process technologies and production practices are being developed is increasing. Computer-aided design and manufacturing systems have been allied to computer process simulation, to form powerful Cloud based, knowledge-based tools for producing parts right-first-time through identifying the customers' needs. The purpose of this paper is to illustrate the contribution made by the authors to enhance the added value of metal formed parts, through advancing scientific process knowledge and developing software to support computer-aided manufacture.

Keywords Metal forming · Added value

1 Automotive Industry

1.1 Weight Reduction Versus Cost Effectiveness

The main market for component manufacturers is the automotive industry and developments in this market are a gauge by which the technological requirements for mass produced parts may be assessed across the whole board of metal formed manufacture. Automotive Original Equipment Manufacturers (OEMs) are tending to become essentially designers, assemblers, and wholesalers of complete automobiles. They

T. Dean
Department of Mechanical Engineering, University of Birmingham, Birmingham B15 2TT, UK

B.-Z. Di · L.-L. Wang (✉)
Department of Mechanical Engineering, Imperial College London, London SW7 2AZ, UK
e-mail: liliang.wang@imperial.ac.uk

© The Minerals, Metals & Materials Society 2021

G. Daehn et al. (eds.), *Forming the Future*, The Minerals, Metals & Materials Series,
https://doi.org/10.1007/978-3-030-75381-8_27

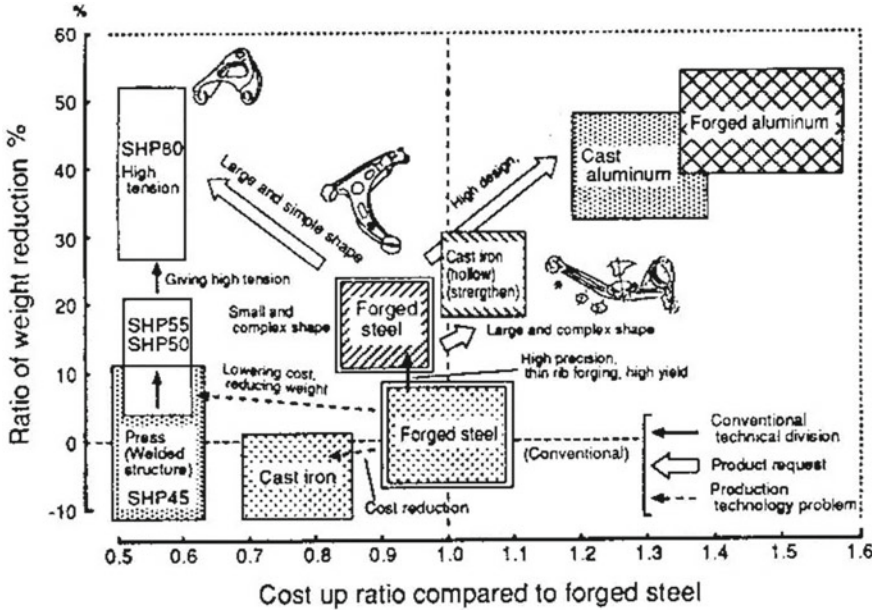


Fig. 1 Effect of processing technology and material on weight and cost of a suspension arm [1]

are reducing in-house parts manufacture and Tier 1 suppliers are being called upon to be proactive at the design stage through concurrent (simultaneous) engineering activities. Ultimately they will be responsible for component design and manufacture within and OEM's specification, which can include, material, aspect of geometry, and performance characteristics. To meet legislative and market competitive demands for improved performance, components are being made lighter in weight and with high strength/rigidity, by design and by using low-density material, and to net or near net shape to increase yield and productivity while reducing cost. The effect of reducing weight saving on component cost is illustrated for a suspension arm in Fig. 1 [1]. It is shown that, compared with a traditional forged part, lighter parts can be made by other methods some at greater and some at lower cost, the benefit of sheet metal fabrication is apparent, particularly when high strength steel is used. The sheet and tubular metal industry is engaged in forming and fabrication of a range of components for the automotive industry, with the introduction of bearings and bushes, to produce lightweight, rigid sub-assemblies such as, steering arms and linkages. The introduction of hydroforming has enabled feasible shape complication to be increased, resulting in commercial manufacture of net shape and nearer to net-shape parts. The bulk forming industry is producing nearer to net shape, often by reducing processing temperatures and engaging in finish machining and sub-assembly operations and new methods for forging products with reduced weight are being sought.



Design	Weight (kg)	Cost US$
Conventional Steel	5.8	38
Al 5xxx (5 pieces)	3.3	94
HFQ (one piece)	2.5	53

Fig. 2 Cost and weight estimation for 3 door inner panel designs

1.2 Hot Forming and Quenching Sheet Aluminium Alloy

Reducing designed weight of a part by using low-density material often results in increased cost. But Hot Form Quench (HFQ), a hot sheet metal forming process relatively recently introduced by the authors and colleagues [2], which combines forming and heat treatment, enables high strength lightweight aluminium alloy parts of complex shape to be made at acceptable cost. The car door inner panel shown in Fig. 2 is an example of an HFQ product. Aluminium door panels, usually of 5xxx series alloy, are used in some premium cars and because of the low formability of the alloy and the impossibility of forming the part in one piece, they comprise an assembly of several components and compared with the cost of a standard steel one piece product, a weight reduction of 43% increases cost by 150%. For the HFQ product, made as a single piece, a weight reduction of 57% increases cost by 40%. The latter cost although higher, is recouped by greater environmental friendliness and lower outgoing costs, in the driving cycle.

1.3 Forging Net-Shape Gears

Forming net-shape gears has been the subject of research and development for many years [3–5]. Two major process characteristics can add value to mono-alloy net-shape gears. Compared with conventional forged gear blanks, expensive post-formed machining is eliminated or much reduced and material yield is greatly increased; both facts reduce costs. In addition, it has been shown that gears with formed teeth have high dynamic mechanical properties, exemplified by toughness and fatigue strength. Small size compact gears can be forged or extruded cold and the authors have expended much work on process development for forging large spur and helical gears (too large for cold forming) on single action presses, the type most commonly found in UK forge shops. The starting point of the work was the production of traditional gear blanks, as shown in Fig. 3. When hot forged, these parts are inaccurate, have a poor surface, because of flash have a low yield and are not close to finished form.



Fig. 3 Progression toward net-shape forged gear. (Color figure online)

Therefore, they are of low added value. An advance in added value is achieved by warm forming (to improve dimensional accuracy) in completely closed tools, gear blanks with synchro dog teeth. Apart from the synchro teeth which are cold formed to size, all-over machining of the blanks is necessary. The next advance was to near net-shape to forge the gears with involute running teeth. This brought the parts nearer to net shape, but difficulty in locating gears for fine machining the running teeth to size severely undermined the added value.

To form net-shape involute gear teeth which are ready for service, a warm/cold process was envisaged in which the teeth were forged near to net shape, which is oversize with an 0.1 mm envelope in completely closed dies and subsequently, after cleaning and lubricating, cold ironed to bring them to net shape. Essentially, the tool consists of a punch with mandrel and a pre-stressed die containing a tooth form in its bore and the ironing operation consists merely of pushing the oversize warm forged gear, positioned on punch and mandrel, through the die. This is a simple process but die design is complicated as elastic distortion of the gear and the tooling has to be considered and geometry of the die teeth is not conventional involute.

Tooth form of the ironing die was obtained using FE (Finite Element) and an elastic plastic model. Tooth flank profiles within specification can be formed and utilising the changing tool/work-piece interface pressure, natural crowning of the teeth can be obtained, as is required for high performance gears.



(a) Two-part Billet (b) Section through Forged Gear

Fig. 4 Bimetallic billet and forged gear. (Color figure online)

1.4 Forging Bimetallic Gears

Figure 4 shows a gear forged in a development program the aim of which is to enable production of gears with reduced weight using two metals [6]. The gear comprises an outer band of heat treatable steel and a core of lightweight metal; aluminium, maybe magnesium, alloy, that fit loosely together.

Usually they are preheated separately to appropriate temperatures, fitted together in a tool, as shown in Fig. 4a, and forged in one operation. Bonding of the two workpiece components is achieved by mechanical locking in both vertical and horizontal planes and if the temperature at the bimetallic interface is sufficient, by metallurgical bonding. The added value of this product is that it enables lighter designs of mechanical power transmissions for vehicles.

1.5 Forging High Performance Pistons from Powder

One way to reduce the environmental impact of internal combustion engines is to increase their running efficiency and this requires increased combustion temperature and pressure. The extra loading is taxing the strength of conventional die cast pistons, so investigations into the manufacture of pistons with higher properties was undertaken at University of Birmingham. An aluminium alloy was made from powder, having a composition possessing high mechanical properties at high temperature, which was consolidated into bar using the 'Conform', continuous extrusion process. The bar was cut into billet which was heated and forged, in one operation, to form a fully dense and near net-shape piston. Added value was achieved in the higher service performance properties of the pistons and also the high yield of nearly 90%, obtained through forging. Figure 5 shows forged and machined pistons.

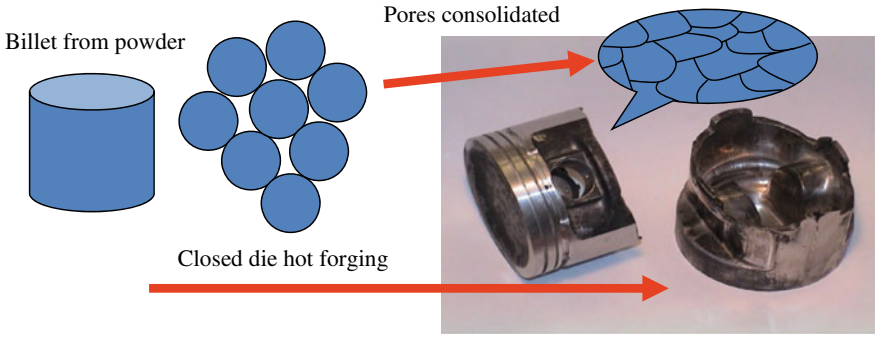


Fig. 5 Near net-shape forged high performance piston. (Color figure online)

2 Mining Industry

2.1 Forging Cast Preforms

Forging of cast iron preforms, to improve mechanical properties and geometric accuracy, has been the subject of intermittent research for many years, as exemplified by the patent Schlegel [7]. In contrast, the considerable potential for added value arising if scrap metal can be cheaply recycled to prime raw material and formed into high specification components has not yet been thoroughly addressed. Such an opportunity occurred for these authors with a British company manufacturing edge tools for agricultural use. The main aim was to melt scrap alloy steel, made both in-house and bought in (at 1/10th the cost of prime metal) cast it into preforms for forging a range of components, utilising the residual casting heat. The processing route is shown in Fig. 6.

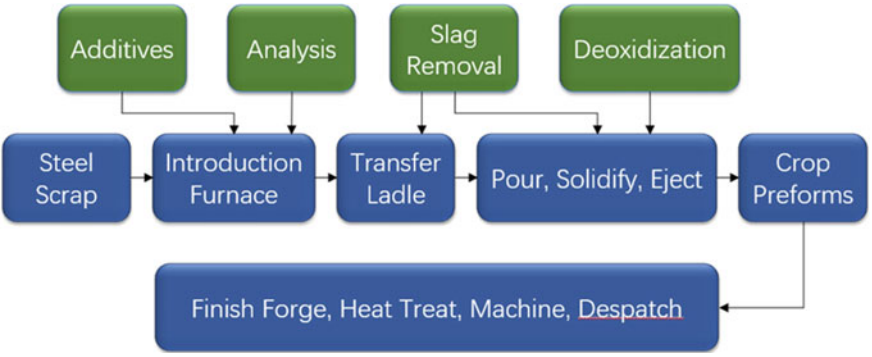
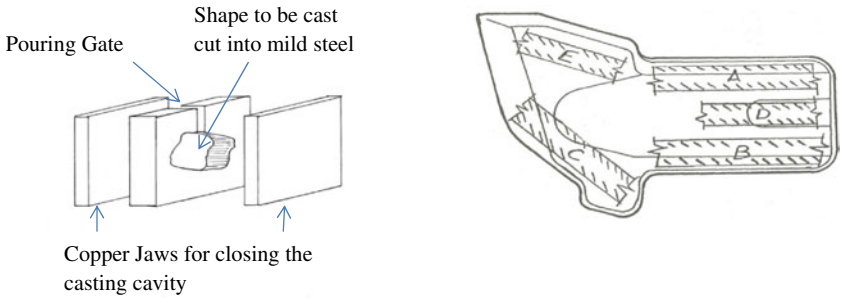


Fig. 6 Processing route for hot forging cast preforms. (Color figure online)



(a) Mould Components (b) Forged Cast Preform

Fig. 7 Coal cutter pick forged from cast preform. (Color figure online)

A key feature of the process is that the casting moulds should be cheap, reusable, and enable rapid production. They were made by flame cutting an outline of the shape to be cast, plus pouring gate, through a mild steel slab of thickness of the casting, (or castings), to be made in it. When the slab is sandwiched between two water-cooled copper jaws, a cavity is formed into which molten metal is poured. The metal solidifies rapidly in the moulds and then the copper jaws are retracted and the mould moves to an ejector stage and is followed to the pouring stage by an empty mould. Figure 7 is a sketch of the main mould components and a forged, cast preform, with positions of test-pieces shaded. The part chosen for trials was a coal cutter pick in alloy steel BS 817 M40, weighing 1 kg. Also shown are the regions from which tensile and impact test-pieces were machined. It was discovered that for a reduction in thickness of about 60% in forging, not all casting voids were closed. Mechanical properties of cast/forged parts depended on orientation, relative to casting direction, of the cast preform in the die and on the degree of deformation. However, the toughness and tensile properties in the cast/forged parts, on average could be as high as that in conventionally forged parts. Overall, because preforms of 'ideal shape' could be cast, the amount of flash produced in the finishing die was only about 10%. In addition it was estimated that the cost of the cast preform could be from about 30 to 60% less than that formed from rolled bar stock, depending on output and steel composition.

3 Aircraft Industry

3.1 Hot Die Forging Aerofoil Blades

Nearly half the production cost of forged engine aerofoil blades can be due to shape correction after forging. A major reason for post-forging distortion is thermal gradients in the forgings due to their thin section and heat loss to dies. A means to overcome

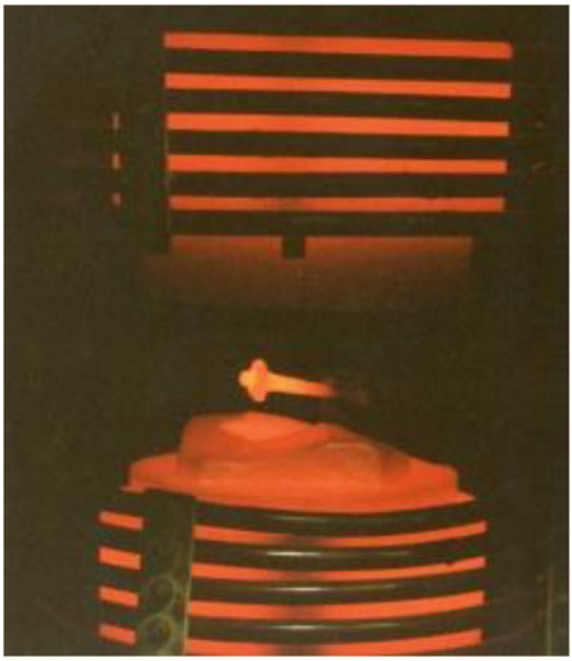


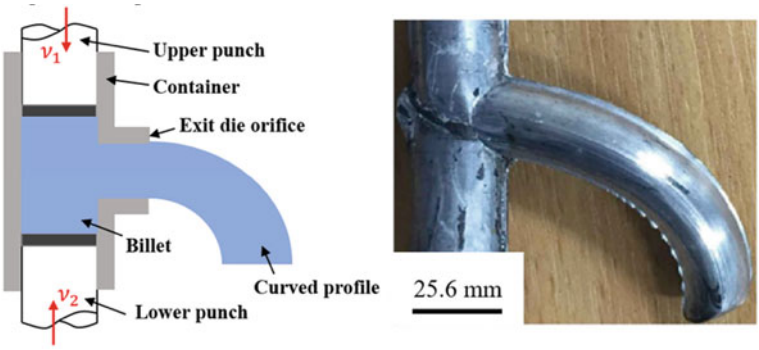
Fig. 8 Heated blade preform between heated dies. (Color figure online)

this is isothermal forging, but this process is time-consuming and reduces productivity unacceptably. The idea was conceived to undertake forging in hot dies while heating work-pieces in a conventional furnace. Figure 8 is a photograph of a preform about to be placed between dies heated by induction coils. The specification of mechanical and metallurgical properties of blades is strict and the consequence of this new technology on the properties has to be predictable through material modelling and process simulation. Added value is through shortening and cheapening of the production process.

4 Railway and Architectural Industries

4.1 Forming Curved Complex-shaped Profiles

For structural and aerodynamic reasons, curved profiles are widely used in the transport industry for manufacturing lightweight structures. Conventionally, the profiles are made from straight extruded bar, which is curved by form bending or cutting and welding. In addition to adding cost and time to manufacture, the first method degrades section geometry and the second impairs mechanical properties also. A new method introduced by the authors, differential velocity sideways extrusion, termed DVSE, in which bar is extruded using two opposing pistons, enables profiles with



(a) Deformation Kinematics (b) Extruded Curved Bar

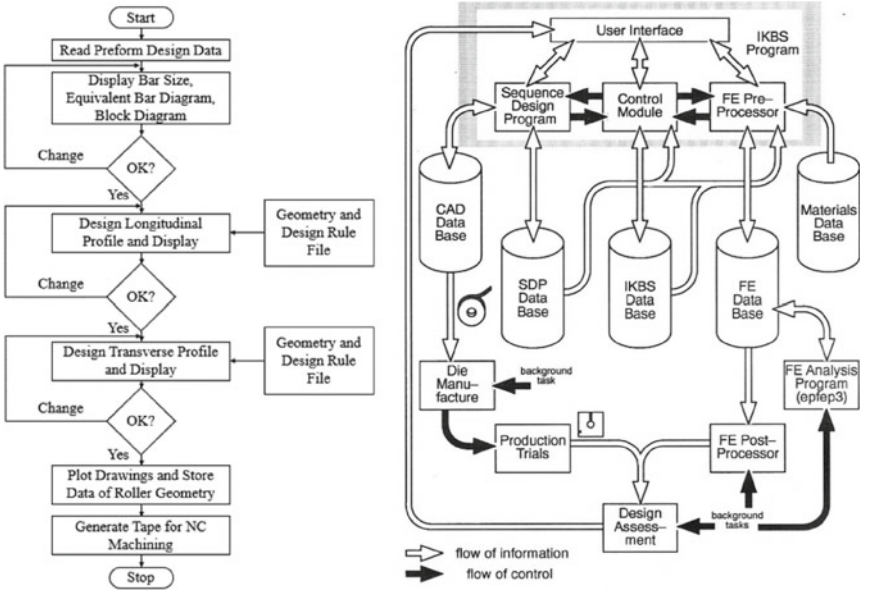
Fig. 9 Differential velocity sideways extrusion. (Color figure online)

prescribed curvature to be extruded directly [8]. The basis of the process is shown in Fig. 9. It has been demonstrated that not only can curved profiles be extruded accurately, but also, for AA1050, compared with the billet, grain refinement and increases in hardness, yield strength, and ultimate tensile strength by 134.8%, 354.0%, and 116.8%, respectively, were achieved in the formed curved bar [9]. Added value is in provision of higher strength profiles with undistorted section geometry utilising a more efficient production process.

5 Computer-Based Production Systems

Computer-based facilities can add value to formed parts; by reducing lead times, through speeding up product and process design, by reducing cost through process optimisation and by maximising product qualities through modelling and simulation.

Research and development of computer-based aids for the metal forming industry, initially undertaken at the University of Birmingham in the late 1970s, was ahead of its time in that the UK industry was only in an early stage of adopting the rudimentary computer-based modelling software being introduced commercially. Nevertheless, this software led to component design being expressed digitally instead of hand drawn graphics and paved the way for subsequent computer-based aids to process and production. Integration of the rapidly developing modelling software with empirical design rules, based on best industrial practice, enabled researchers at Birmingham to produce computer-aided design (CAD) programs usable by inexperienced workers to design acceptable tooling and processes. The structure of these 'knowledge-based' systems (KBS) is exemplified by [10–12] and an example of the linear structure of the programs can be seen in Fig. 10a, which shows that data for CNC (Computer Numerically Controlled) machining of tools could be generated also. Earlier, work was centred on the hot forging industry, which was experiencing



(a) Knowledge-based system (b) Intelligent knowledge-based system (IKBS)

Fig. 10 Program structures for computer-aided design and manufacture

shortage of experienced engineers, including the company that had adopted the net-shape gear forging process. When numerical computing methods and FE simulation software became available, by enabling tool designs to be validated and if necessary modified in a virtual environment, they allowed CAD programs to be expanded to become, intelligent knowledge-based systems, which could not only be used to rapidly design process and tools using well tried rules, but also optimise processes and deal with new types of components by using simulation only when necessary. The new information resulting from simulation is added to the database. An example of the structure of an Intelligent knowledge-based system (IKBS) for forging dies is shown in Fig. 10b [13].

The structure of the IKBS comprises 3 essential programs: (a) Sequence design program, which will deal with part families governed by the same set of design rules, (b) FE pre-processor to create data files for simulation, and (c) Control module to supervise the other two modules. An important aspect of the IKBS is that it compares a component to be designed for with previously dealt with cases in the same family. The degree of similarity for each operational stage is based on a 'success indicator', which shows how satisfactory is a particular designed stage and a 'confidence indicator', which shows how strongly information in the knowledge-base supports the evaluation of the success indicator. The reasoning is given in detail in [11].

6 Cloud Based Multi-objective FE Simulation Technology

In recent years, a Cloud based multi-objective FE simulation technology was developed at Imperial College London [14–16]. This Cloud based system is forging a gateway to financially reward academic innovations, e.g. published data and advanced models, etc. in collaboration with a renowned FE code provider, AutoForm, leading to the direct applications of frontier knowledge in industry and academia. As shown in Fig. 11, the structure of the Cloud based multi-objective FE simulation system includes three essential layers: (a) Resource layer, which will collect resources contributed by researchers from academia and industry, (b) Cloud platform layer, which will host functional modules and portfolios and execute these numerical models online, and (c) Application layer. Users from industry and academia will visualise the FE simulation results via user interface to enable process optimisation.

Added value of the Cloud based multi-objective FEA (Finite Element Analysis) system is in provision of interoperable functional modules (advanced models and testing data) and portfolios (bundles of FE models and functional modules), to avoid repeated lab-scale research. The reuse of knowledge could lead to a 50 to 85% cost reduction in research and development, depending on the forming technologies. Moreover, added value can be realised via the Internet of Things of supply chains

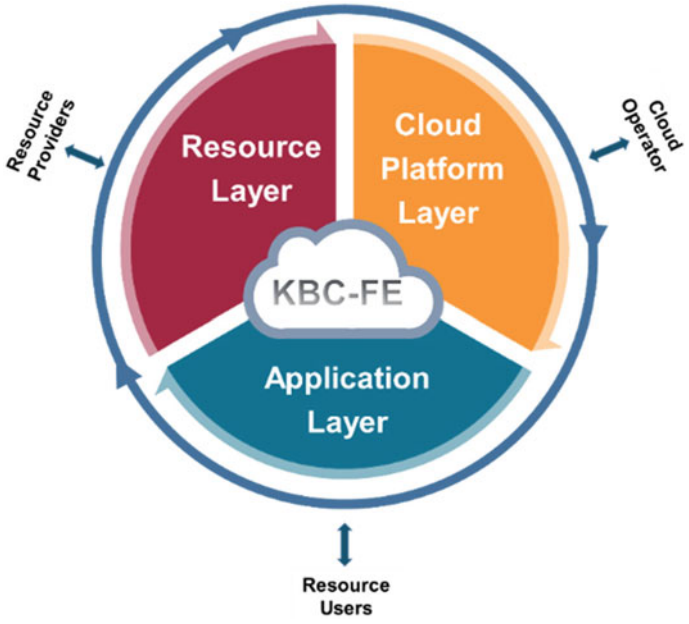


Fig. 11 The framework of cloud based multi-objective fe simulation system. (Color figure online)

for future metal forming industry, i.e. the Cloud based FEA system will enable data exchange and the data-guided production right-first-time through identifying the customers' needs.

7 Concluding Remarks

In this paper, the authors presented a review of research conducted in the past forty years within the research group to enhancing the added value of metal formed parts. Development of advanced manufacturing technologies has reduced the efforts for post-form fabrications, enhanced post-form strength of the metal formed parts, and enabled recycled materials to be used in manufacture, adding value to metal formed parts. In addition, digital technologies can add value to formed parts by reducing lead times, by reducing cost through process optimisation, and by maximising product qualities through modelling and simulation. In the future, added value of metal formed parts can be further enhanced through the identification of customers' needs and the production of mass-customised products.

Acknowledgments This paper was written in fond memory of Professor Z.R. Wang, a sound scientist, excellent engineer, and warm friend.

References

1. Hayashi M (1993) Current trends in automotive forging industry. In: Proc. 26th ICFG Plenary Meeting. Osaka: 11.1–11.12
2. Wang L, Strangwood M, Balint D, Lin J, Dean TA (2011) Formability and failure mechanisms of AA2024 under hot forming conditions. Mater Sci Eng A 528:2648–2656
3. Dean TA (2000) The net-shape forming of gears. Mater Des 21:271–278
4. Sadeghi MH, Dean TA (1994) Precision forging straight and helical spur gears. J Mater Process Technol 45:25–30
5. Kondo K, Ohga K (1995) Precision cold die forging of a ring gear by divided flow method. Int J Mach Tools Manuf 35(8):1105–1113
6. Politis DJ, Lin J, Dean TA (2012) Investigation of material flow in forging bi-metal components. In: Proceedings 14th International metal forming conference-steel research international, September 16–19. Krakow, Poland, pp 231–234
7. Schlegel FJW (1956) Nov. 21st, Working of cast iron utilising dies, Patent No. 761, 654
8. Zhou W, Lin J, Dean TA, Wang L (2017) A novel application of sideways extrusion to produce curved aluminium profiles: feasibility study. Procedia Eng 207:2304–2309
9. Zhou W, Yu J, Lin J, Dean TA (2019) Manufacturing a curved profile with fine grains and high strength by differential velocity sideways extrusion. Int J Mach Tool Man 140:77–88
10. Choi SH, Dean TA (1984) Computer-aided design and machining of roller dies for forging hammers. Int J Mach Tool Des Res 24:121–131
11. Gokler MI, Dean TA, Knight WA (1981) Computer-aided sequence design for hot upset forgings. In: Proceedings of the 22nd International machine tool design and research conference, pp 457–466

12. Yu GB, Dean TA (1985) A CAD/CAM Package for axisymmetric forging dies. In: Proceedings of the 25th International machine tool design and research conference, pp 459–464
13. Bakhshi-Jooybari M, Pillinger I, Dean TA, Hartley P (1996) Development of product and process criteria for an intelligent knowledge-based system for forging die design. Proc Instn Mech Engrs 210:565–578
14. Wang A, Zheng Y, Liu J, El Fakir O, Masen M, Wang L (2016) Knowledge based cloud FE simulation a multi-objective FEA system for advanced FE simulation of hot stamping process. In: The 10th International conference and workshop on numerical simulation of 3D sheet metal forming processes, Numisheet
15. Dhawan S, El Fakir O, Zhang Q, Wang A, Zheng Y, Wu G, Wang L An online database for hosting and executing numerical models, patent filed: Application Number: 201911116210.6
16. Wang Ailing, Liu Jun, Gao Haoxiang, Wang Li-Liang, Masen Marc (2017) Hot stamping of AA6082 tailor welded blanks: experiments and knowledge-based cloud–finite element (KBC-FE) simulation. J Mater Process Technol 250:228–238

A Study of the Forming Quality of Magnesium Alloy Cylindrical Parts with Inner Ribs by Induction-Heating-Assisted Spinning



Qinxiang Xia, Jinchuan Long, Gaozhu Huang, Shuai Yuan, and Yi Qin

Abstract Magnesium alloy cylindrical parts with inner ribs (MACPIR) are attractive as lightweight components for improving the performance of high-end equipment in various industrial sectors. Induction-heating-assisted spinning (IHAS), an effective way to manufacture cylindrical parts made of difficult-to-deform materials, was used to form the MACPIR. However, when using this process for MACPIR, nonuniform deformation and other forming defects can easily occur between the cylindrical wall and inner ribs. A FEM model of MACPIR during IHAS was developed via ABAQUS, and experimental verification was conducted. Forming defects that occurred during the spinning process of MACPIR were analyzed, and evaluation indexes of forming quality were proposed. The results show that the concavity of rib back, and nonuniform distribution of rib height along tangential and axial directions are the main forming defects. Additionally, the influence of process parameters on the forming quality was discussed. The results indicate that the forming quality of MACPIR can be improved under a forming temperature of $T = 300 \sim 350$ °C, roller feed rate $f = 0.4 \sim 0.6$ mm/r, and thinning ratio of wall thickness $\Psi_t = 65 \sim 75\%$. The simulation results confirm well with experimental ones.

Keywords Magnesium alloys · Cylindrical parts with inner ribs · Induction-heating-assisted spinning · Forming quality · Forming defects

Q. Xia · J. Long · G. Huang · S. Yuan (✉)
School of Mechanical and Automotive Engineering, South China University of Technology, Guangzhou 510640, China
e-mail: 591361599@qq.com

Q. Xia
e-mail: meqxxia@scut.edu.cn

J. Long
e-mail: long.jc@mail.scut.edu.cn

G. Huang
e-mail: 2810909156@qq.com

J. Long · Y. Qin (✉)
Centre for Precision Manufacturing, DMEM, University of Strathclyde, Glasgow G1 1XQ, UK
e-mail: qin.yi@strath.ac.uk

© The Minerals, Metals & Materials Society 2021

G. Daehn et al. (eds.), *Forming the Future*, The Minerals, Metals & Materials Series,
https://doi.org/10.1007/978-3-030-75381-8_28

1 Introduction

Magnesium alloys are being widely applied in the automobile, aviation and aerospace fields due to their light weight [1]. Cylindrical parts with inner ribs can also be used to reduce weight and enhance overall product performance [2, 3]. Thus, magnesium alloy cylindrical parts with inner ribs (MACPIR) become one of the most promising lightweight components. The formability of magnesium alloys is limited at room temperature due to their hexagonal close packed (HCP) crystal structure, but it can be greatly enhanced at an elevated temperature [4]. As an effective method of forming cylindrical parts made of difficult-to-deform metals, induction-heating-assisted spinning (IHAS) was used for manufacturing the MACPIR. However, differences in the required amount of deformation between the inner ribs and the cylindrical wall can result in nonuniform deformation during the spinning process. Also forming defects such as cracks and bulges occur easily because of unwise selection of process parameters [5]. Therefore, it is of significance to study the forming quality of MACPIR formed by IHAS and explore the optimal process parameters to decrease the forming defects.

Investigations on power spinning of cylindrical parts with inner ribs (CPIR) have been reported in recent years. Jiang et al. [6] simulated the backward ball spinning of 5A02 aluminum alloy CPIR via DEFORM-3D and conducted a verification experiment. The results show that increasing the size of the balls can contribute to the formability of inner ribs. Xia et al. [7] simulated the power spinning of a Q235 cup-shaped thin-walled inner gear via MSC.MARC and compared this with experimental results. They found that the thinning ratio is the dominant factor which determines the filling height of gear teeth. Meanwhile, Zhang et al. [8] simulated the hot flow forming of AZ31B magnesium alloy cylindrical parts via ABAQUS and carried out an experiment. The results showed that wrinkles occur at the top edge of the spun workpiece under a large thinning ratio of wall thickness $\Psi_t = 45\%$ when the forming temperature $T = 420$ °C and roller feed rate $f = 0.1$ mm/r.

ZK61 magnesium alloy is a typical wrought magnesium alloy with good comprehensive mechanical properties [9]. In the previous work of the authors [10], the constitutive model of ZK61 alloy considering compensation of strain was developed and the predicted flow stress values of this showed good agreement with that obtained by a high-temperature axial compression test (HTACT). Furthermore, Xia et al. [5, 11] simulated the IHAS process of ZK61 MACPIR via MSC.MARC to analyze the material flow of a spun workpiece with inner ribs (SWIR) during the spinning. Corresponding experimental and metallographic tests were carried out to investigate the microstructure evolution of SWIR under different process parameters as well. The results indicate that a large thinning ratio of wall thickness Ψ_t or a high forming temperature T can facilitate the filling of inner ribs and increase the rib height; they also indicate that Ψ_t plays an important role in grain refinement of SWIR.

In this paper, the FEM model of ZK61 MACPIR during the IHAS process was developed via ABAQUS and the IHAS experiment was conducted. The forming defects that occurred during the spinning process were analyzed, and the influence of the process parameters on the forming quality of SWIR was investigated.

2 Development and Verification of FEM Model

2.1 Development of FEM Model

The geometric model was developed via ABAQUS, the geometric parameters of which are listed in Table 1. The trapezoidal-shaped inner ribs were selected to improve the stiffness of the cylindrical parts and facilitate the material flow within the ribs [12]. The number of inner ribs was designed as a multiple of 3 to ensure the stability of the adopted three-roller stagger spinning [13]. The height and width of inner ribs were designed according to the standard JB/T9177-1999 [14]. In the simulation, the bottom of the blank was fixed with a snap ring and its opening was a free end, and the inner ribs form under three rollers during the IHAS. Figure 1 shows the FEM model via ABAQUS, the cylindrical blank was defined as a deformable body meshed with a C3D8RT element which is suitable for hot deformation analysis, while the rollers and mandrel were all defined as rigid bodies. Moreover, four elements were meshed along the direction of the wall thickness to obtain the radial deformation information. The total number of elements were 90000.

The true stress and strain data of solution-treated ZK61 alloy during hot deformation were obtained via HTACT [9], which was conducted under a temperature of

Table 1 Geometric parameters of FEM model

Mandrel parameters			Roller parameters			Blank parameters		
Diameter /mm	Number of rib grooves	Depth of rib groove /mm	Diameter /mm	Roundness radius /mm	Forming angle /°	Internal diameter /mm	Thickness /mm	Length /mm
60	12	4	100	6	25	60	8	50

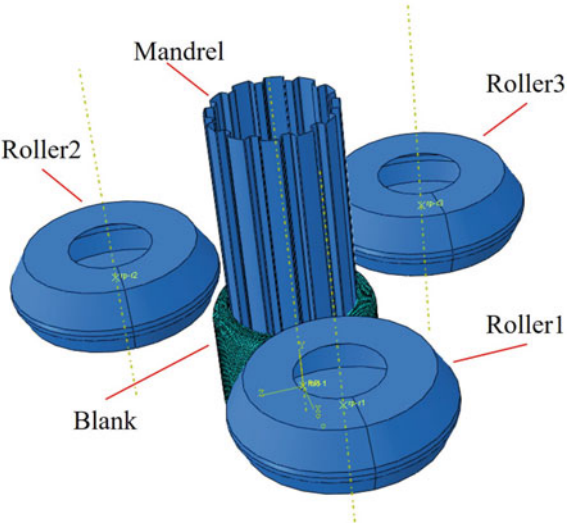


Fig. 1 FEM model of IHAS. (Color figure online)

Table 2 Thermodynamic parameters of ZK61 alloy

Temperature/(°C)	250	300	350	400
Elastic modulus E/(GPa)	24.43	23.45	22.51	20.31
Heat conduction coefficient λ/(W/m·°C)	111.8	116.7	120.7	125.3
Specific heat $c(\times 10^3)$/(J/Kg·°C)	1.277	1.284	1.303	1.325
Thermal expansion coefficient a $(\times 10^{-5})$/(°C)	2.33	2.34	2.39	2.41

250–450 and strain rate of 0.001–10/s. These data were imported into ABAQUS in the form of true stress and plastic strain. Since the blank meshed by the solid element has no rotational degrees of freedom, the coupling constraint is applied to a reference point located at the bottom of the blank, by which the rotations of both the blank and the mandrel can be realized. The isotropy Coulomb friction model was chosen in this study, and the friction coefficients between rollers and blank, and mandrel and blank are set as 0.1 and 0.15 [15], respectively. Also, the forming temperature during IHAS is influenced by not only heat conduction between blank, rollers, snap ring, and mandrel, but also heat radiation between the blank and the outer environment. The thermodynamic parameters of ZK61 alloy including elastic modulus, heat conduction coefficient, specific heat, and thermal expansion coefficient were obtained by dynamic thermomechanical analysis (DMA), a hot disk thermal conductivity instrument, differential scanning calorimetry (DSC), and thermal dilatometer (DIL402PC) under $T = 250$–450, to simulate the actual spinning forming process, as shown in Table 2.

2.2 Experimental and Simulation Conditions

Reasonable process parameters are essential to guarantee the forming quality of the spun workpiece. Ψ_t is generally selected as 40–70% during power spinning of CPIR, and large thinning ratio can be beneficial for the radial flow of material and filling of inner ribs, and Ψ_t of 60–75% is chosen in this study. Moreover, T of 250–400 °C is usually suitable for plastic deformation of magnesium alloys [16], and f is normally selected within 0.1–1.0 mm/r for IHAS [17]. Table 3 shows the process parameters for IHAS of ZK61 alloy CPIR. The experiment was carried out on a HGQX vertical spinning machine, as shown in Fig. 2.

2.3 Verification of Finite Element Model

The verification experiment was conducted under $T = 300$ °C, $f = 0.4$ mm/r, and $\Psi_t = 60\%$. As shown in Fig. 3a, the wave-shaped opening-end appears during both

Table 3 Process parameters of IHAS

Thinning ratio of wall thickness ψ_t/%	Reduction/reduction of each roller ⊿/mm	Roller feed rate f/(mm/r)	Forming temperature T/°C
60	4.8/(1.65, 1.6, 1.55)	0.4, 0.6, 0.8, 1.0	250, 300, 350, 400
65	5.2/(1.8, 1.75, 1.65)		
70	5.6/(1.95, 1.9, 1.75)		
75	6/(2.15, 2, 1.85)		

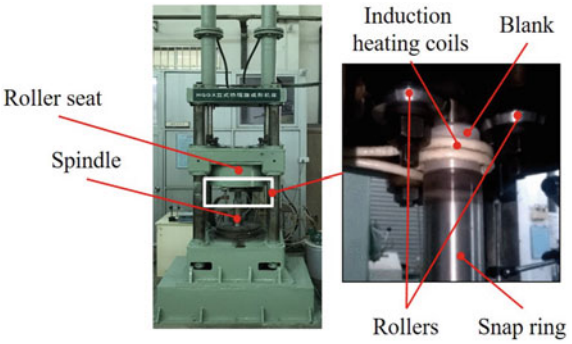


Fig. 2 IHAS experiment. (Color figure online)

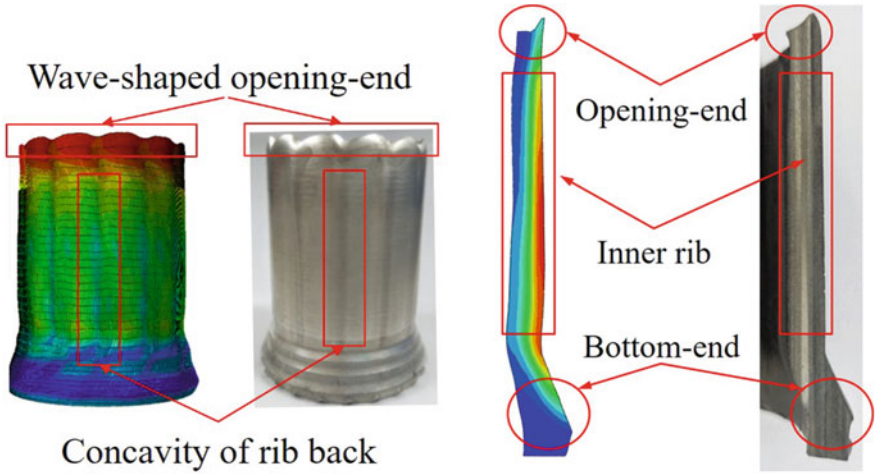


Fig. 3 Result comparison between the simulated SWIR and experimental one under $T = 300$ °C, $f = 0.4$ mm/r, and $\Psi_t = 60\%$. (Color figure online)

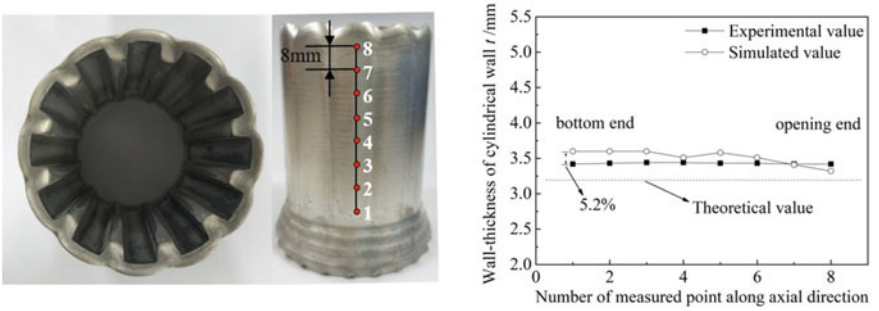


Fig. 4 Result comparison between simulated wall thickness and experimental one under $T = 300$ °C, $f = 0.4$ mm/r, and $\Psi_t = 60\%$. (Color figure online)

simulation and the experiment, where the concavity of the inner ribs occurred at the outer surface of the spun workpiece. As shown in Fig. 3b, the simulated opening-end and bottom-end of the spun workpiece are similar to that of the experiment, where the rib height near the bottom-end is higher than that near the opening-end. Therefore, the simulation results confirm well with the experimental ones. Additionally, the ultrasonic thickness gauge was adopted to obtain the wall-thickness distribution of spun workpiece. Figure 4a shows the measured points of wall thickness along the axial direction at the cylindrical wall, and Fig. 4b show the result comparison between simulated values and experimental ones, where the maximum relative error between them is only 5.2%. This indicates the developed FEM model for MACPIR during IHAS is reliable.

3 Evaluation Indexes of Forming Quality for SWIR

Figures 3 and 5 show the forming defects that occurred during IHAS of ZK61 alloy CPIR, including the concavity of the outer wall at the rib back, nonuniform distribution of rib height along the longitudinal and tangential directions. To evaluate the

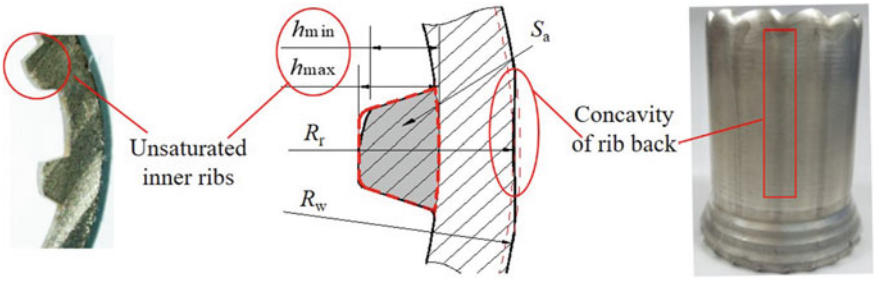


Fig. 5 Experimental result under $T = 300$ °C, $f = 0.4$ mm/r, and $\Psi_t = 60\%$. (Color figure online)

forming quality of SWIR, the indexes such as the saturation degree of inner rib S, inhomogeneity of rib height λ, and concavity ratio of rib back η were put forward, as shown in Fig. 5, and these indexes can be calculated by the following equations.

$$S = \frac{S_a}{S_t} \times 100\% \tag{1}$$

$$\lambda = \frac{h_{max} - h_{min}}{h} \times 100\% \tag{2}$$

$$\eta = \frac{R_w - R_r}{R_w} \times 100\% \tag{3}$$

where S_a and S_t are the actual and theoretical cross-section areas of inner ribs, respectively; h_{max} and h_{min} are the maximum and minimum heights of inner ribs, respectively; R_w and R_r are the outer radii at the cylindrical wall and inner rib, respectively.

4 Results and Discussion

4.1 Influence of Temperature on Forming Quality

Figure 6 shows the influence of T on forming quality of SWIR when $f = 0.4$ mm/r and $\Psi_t = 60\%$. As shown in Fig. 6a, the S increases gradually at the bottom-end as T initially increases and then decreases at the opening-end. The S_{max} occurs at the bottom-end under $T = 400$ °C, while the S_{min} occurs at its opening-end, which indicates the filling of inner ribs along the axial direction is nonuniform. Although S at the bottom-end under $T = 300 \sim 350$ °C is smaller than that under $T = 400$ °C, the differences of S between the bottom-end and opening-end under $T = 300 \sim 350$ °C is smaller, i.e., the filling of inner ribs along the axial direction within this temperature range tends to be more uniform. As shown in Fig. 6b, the λ decreases firstly and then increases with the increase of T, and λ_{min} occurs at both the opening-end and bottom-end under $T = 350$ °C, which means the filling of inner ribs can be enhanced

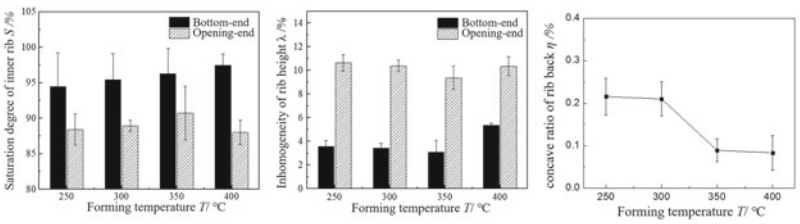


Fig. 6 Influence of T on forming quality of SWIR under $f = 0.4$ mm/r and $\Psi_t = 60\%$

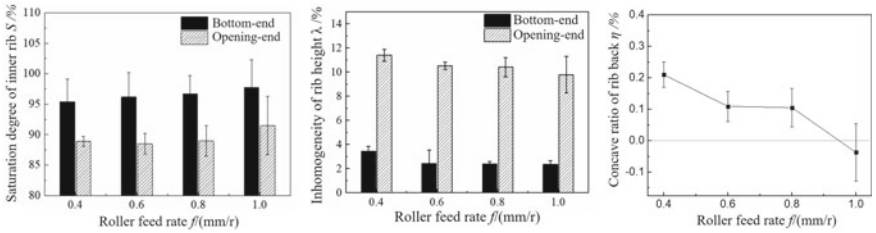


Fig. 7 Influence of f on forming quality of SWIR under $T = 300$ °C, $\Psi_t = 60\%$

effectively under $T = 350$ °C. As shown in Fig. 6c, the η decreases gradually with the increase of T, which is almost steady under $T = 350$ °C. Therefore, $T = 300 \sim 350$ °C is more beneficial for improving the forming quality of SWIR.

4.2 *Influence of Roller Feed Rate on Forming Quality*

Figure 7 shows the influence of f on forming quality of SWIR under $T = 300$ °C and $\Psi_t = 60\%$. As shown in Fig. 7a, S tends to increase as f increases. This is because the deformation degree increases by increasing the f per unit of time, material flow decreases along the axial direction and increases along the radial direction, which can facilitate the filling of inner ribs. As shown in Fig. 7b, the λ decreases gradually as f increases which indicates the filling of inner ribs tends to be uniform under a large f. However, as shown in Fig. 7c, the η decreases firstly and then increases along the negative direction as f increases. The value of η is negative when $f = 1.0$ mm/r, i.e., part of the rib back is higher than that of the cylindrical wall at both sides, and the concavity transfers into the cylindrical wall from the rib back. This is because axial flow of material at the cylindrical wall decreases and tangential flow of the material increases with the increase of f; this makes more material flow into the inner ribs and leads to the occurrence of concavity at the cylindrical wall. Meanwhile, the material flow accelerates and flow instability occurs easily under large f; this can often result in a crack defect. Therefore, a small range of f within 0.4–0.6 mm/r is more suitable for IHAS of SWIR.

4.3 *Influence of Thinning Ratio on Forming Quality*

Figure 8 shows the influence of Ψ_t on forming quality of SWIR when $T = 300$ °C and $f = 0.4$ mm/r. As shown in Fig. 8a, S increases gradually with the increase of Ψ_t, and the filling of inner ribs is more uniform along the axial direction. The S is more than 99.5% under $\Psi_t = 75\%$, i.e., the inner ribs can be filled up under this thinning ratio. As shown in Fig. 8b, the λ decreases with the increase of Ψ_t,

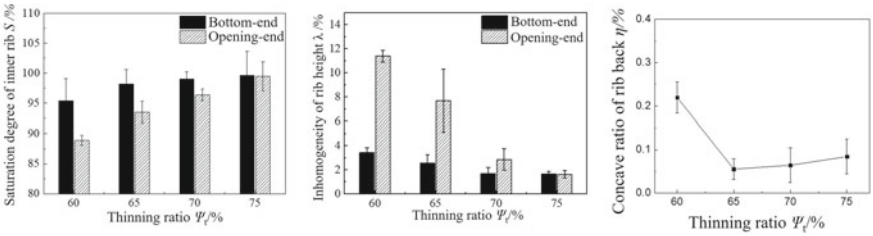


Fig. 8 Influence of Ψ_t on forming quality of SWIR under $T = 300$ °C and $f = 0.4$ mm/r

and the λ_{min} about 1.6% can be obtained under $\Psi_t = 75\%$, where the values of λ are basically consistent along the axial direction. This indicates that a large Ψ_t is beneficial for the filling of inner ribs as well as improvement of forming quality for SWIR. However, as shown in Fig. 8c, the η decreases firstly and then slightly increases with the increase of Ψ_t, and the η_{min} about 0.06% was obtained under $\Psi_t = 65\%$. This indicates that increasing Ψ_t can lead to the decreasing of η. In fact, the filling of the inner rib is insufficient under a small Ψ_t of 60%, and the concavity of the rib back is therefore severe at the inner ribs. However, the ratio of inner rib height to the cylindrical wall thickness increases when $\Psi_t \geq 65\%$, and thus springback of the material at the cylindrical wall is more obvious than that at the inner ribs; these are responsible for the slight increase of η. Therefore, a suitable thinning ratio of 65–75% is also helpful for improving the forming quality of SWIR.

5 Conclusions

The induction-heating-assisted spinning (IHAS) process of ZK61 magnesium alloy cylindrical parts with inner ribs (MACPIR) was investigated via FEM simulation and an experiment. The influence of process parameters on the forming quality of spun workpieces with inner ribs (SWIR) was studied. Some conclusions can be drawn as follows:

(1) Forming defects occurred during IHAS of ZK61 MACPIR. These mainly included concavity of the outer wall at the rib back and nonuniform distribution of rib height along longitudinal and tangential directions. These can be improved by decreasing the ratio of inner rib height to cylindrical wall thickness and increasing the filling of the inner ribs.

(2) The proposed indexes including the saturation degree of an inner rib S, inhomogeneity of rib height λ, and concavity ratio of rib back η can be used to evaluate the forming quality of SWIR. Process parameters which are beneficial for the improvement of forming quality for SWIR are forming temperature $T = 300 \sim 350$ °C, roller feed rate $f = 0.4 \sim 0.6$ mm/r, and thinning ratio of wall thickness $\Psi_t = 65\% \sim 75\%$.

Acknowledgments This project is financially supported by National Natural Science Foundation of China (No. 51775194). One of the authors, Jinchuan Long, also would like to acknowledge financial support from the Chinese Scholarship Council (CSC).

References

1. Liu BY, Liu F, Yang N, Zhai XB, Zhang L, Yang Y, Li B, Li J, Ma E, Nie JF, Shan ZW (2019) Large plasticity in magnesium mediated by pyramidal dislocations. Science 365(6448):73–75
2. Luo W, Chen F, Xu BB, Yang ZJ, Guo YM, Lu B, Huang T (2018) Study on compound spinning technology of large thin-walled parts with ring inner ribs and curvilinear generatrix. Int J Adv Manuf Technol 98(5–8):1199–1216
3. Zeng X, Fan XG, Li HW, Zhan M, Gao PF, Chen Q (2019) Recent developments in spinning of complex thin-walled parts with inner ribs. J Netshape Form Eng 11(5):21–31 (in Chinese)
4. Hadadzadeh A, Wells MA (2017) Analysis of the hot deformation of ZK60 magnesium alloy. J Magn Alloys 5(4):369–387
5. Xia QX, Long JC, Yuan S, Cheng XQ (2019) Numerical investigation on the material flow of magnesium alloy cylindrical parts with inner ribs during hot power spinning. Paper presented at the 13th International Conference on Numerical Methods in Industrial Forming Processes, Portsmouth, New Hampshire, 23–27 June 2019
6. Jiang SY, Zheng YF, Ren ZY, Li CF (2009) Multi-pass spinning of thin-walled tubular part with longitudinal inner ribs. Trans Nonferrous Met Soc China 19(1):215–221
7. Xia QX, Yang MH, Hu Y, Cheng XQ (2006) Numerical simulation and experimentation cup-shaped thin-walled inner rectangular gear formed by spinning. Chin J Mech Eng 42(12):192–196 (in Chinese)
8. Zhang YL, Wang FH, Dong J, Jin L, Liu CH, Ding WJ (2018) Grain refinement and orientation of AZ31B magnesium alloy in hot flow forming under different thickness reductions. J Mater Sci Technol 34(7):1091–1102
9. Dong S, Yu Q, Jiang YY, Dong J, Wang FH, Jin L, Ding WJ (2017) Characteristic cyclic plastic deformation in ZK60 magnesium alloy. Int J Plast 91:25–47
10. Xia QX, Long JC, Xiao GF, Cheng XQ (2019) Constitutive model of extruded ZK61 magnesium alloy at high temperature considering compensation of strain. Paper presented at the 16th National Annual Conference on Plastic Engineering, Taiyuan, Shanxi, 18–20 October 2019
11. Xia QX, Yuan S, Long JC, Huang GZ, Cheng XQ (2019) Microstructure evolution of magnesium alloy cylindrical parts with inner ribs during hot power spinning. Paper presented at the 2nd Asian Pacific Symposium on Technology of Plasticity. Tokyo, Japan, 31 July-3 August 2019
12. Xia QX, Li XM, Li XL, Zhou C, Zhang SJ (2008) Experimental research and numerical simulation on cup-shaped thin-walled trapezoidal inner gear formed by spinning. Forg Stamp Technol 33(6):57–62 (in Chinese)
13. Xia QX, Hu Y, Sun LY, Ye BY (2007) Numerical simulation of influence of roller working surface on spin forming of rectangular inner meshing gear. J S China Univ Technol Nat Sci Ed 35(8):1–6 (in Chinese)
14. JB/T9177-1999. Structural main factors for steel die forgings
15. Xia QX, Long JC, Zhu NY, Xiao GF (2019) Research on the microstructure evolution of Ni-based superalloy cylindrical parts during hot power spinning. Adv Manuf 7(1):52–63
16. Li JQ, Liu J, Cui ZS (2014) Characterization of hot deformation behavior of extruded ZK60 magnesium alloy using 3D processing maps. Mater Des 56:889–897
17. Xiao GF, Zhu NY, Long JC, Xia QX, Chen WP (2018) Research on precise control of microstructure and mechanical properties of Ni-based superalloy cylindrical parts during hot backward flow spinning. J Manuf Process 34:140–147

A Porosity Closure Model for the Integrated Casting and Forging Process of Aluminum Alloy and Its Application



Qi Zhang, Liqun Niu, Zhenglong Liang, and Miao Cao

Abstract Integrated casting and forging process (ICFP) is a feasible manufacturing method which significantly improves the mechanical properties of casting due to forging process eliminating porosity defects. In this study, a new model that predicts the law of porosity closure during forging is proposed, which considered the variation of stress triaxiality ratio, Lode parameter and effective strain, was implemented into finite element package FORGE2.1. A356 was used as specimen materials subjected to X-ray computed tomography (CT) scanning. The comparison between the simulation results and the experimental results shows that the proposed model can accurately predict the maps of porosity closure volume in the forging process of A356 aluminum alloy. With the model, the ICFP design and optimization will be convenient.

Keywords Integrated casting and forging process · Porosity closure model · Lode stress parameter · Stress triaxiality ratio

1 Introduction

With the rapid development of the automobile manufacturing industry, higher requirements have been put forward for structure lightweight, energy saving and emission reduction, and there is a need for lightweight metal materials, especially advanced manufacturing methods for aluminum alloys. Integrated casting and forging process (ICFP) combines the advantages of casting and forging, which is a feasible method and means for eliminating porosity defects, as reported by [5]. However, the optimization of the ICFP process is determined by the conventional trial-and-error method, with a large workload and low efficiency. Mathematical model is one of the effective ways to solve this problem. Therefore, there are many researches which have concentrated on the porosity closure model and closed index in the last decades. Saby et al. [4] reviewed the various criteria or models for

Q. Zhang (✉) · L. Niu · Z. Liang · M. Cao
School of Mechanical Engineering, Xi'an Jiaotong University, Xi'an 710049, Shaanxi, China
e-mail: henryzhang@mail.xjtu.edu.cn

© The Minerals, Metals & Materials Society 2021

G. Daehn et al. (eds.), *Forming the Future*, The Minerals, Metals & Materials Series,
https://doi.org/10.1007/978-3-030-75381-8_29

predicting the void closure in industrial applications. They pointed out that the use of Lode stress parameter will be a huge improvement.

In this paper, the influence of stress triaxiality ratio and Lode stress parameter on porosity closure is quantitatively assessed and a new model (called STLB model) is defined in the following section. The new prediction model is implemented in the finite element software FORGE and is compared to the stress triaxiality based (STB) model by P. Lasne and detailed in [3]. The third section presents an evolution of the STLB model for a case of the ICFP process.

2 Prediction Model for Porosity Closure

In this section, the mesoscale approach used to perform explicit simulations is adopted, which takes into account the effect of Lode stress parameter u and stress triaxiality ratio Tx. For more details, the reader can refer to [1]. In order to study the evolution of porosity, the strain ratio of porosity radius ε_P was defined. The expression is as follows:

$$\varepsilon_P = \frac{R}{R_0} \tag{1}$$

where R_0 denotes the initial radius of the spherical porosity, and R corresponds to the radius after deformation. The $\varepsilon_{P_{max}}$ represents in the main direction of the stress, and the $\varepsilon_{P_{max}} = 0$ corresponds to a threshold value of porosity closure.

2.1 Influence of Lode Stress Parameter and Stress Triaxiality Ratios

In this section, different stress triaxiality ratios $T_X \in (0, -0.5, -1, -1.5)$ and different Lode stress parameters $u \in (0, 0.25, 0.5, 0.75, 1)$ are used to illustrate the effect of the Lode parameter on spherical porosity closure. The relationship between the strain ratio of porosity radius $\varepsilon_{P_{max}}$ and effective strain ε_e is illustrated in Fig. 1. When T_X is kept constant, different u value has an effect on porosity closure; the larger the u value is, the smaller is the critical strain value. In Fig. 1a, where $T_X = 0$, when $u = 1$ and $\varepsilon_{P_{max}} = 0$, the strain value is equal to 1.049. In Fig. 1b, where $T_X = -0.5$, when $u = 1$ and $\varepsilon_{P_{max}} = 0$, the strain value is equal to 0.747. Then, looking at Fig. 1c, where $T_X = -1$, when $u = 1$ and $\varepsilon_{P_{max}} = 0$, the strain value is equal to 0.612. The same behavior, concerning the influence of T_X on porosity closure, is noted again so that the strain value is still decreasing for the case $Tx = -1.5$ (Fig. 1d) with $\varepsilon_e = 0.529$. The data reveals that the stress triaxiality ratio T_X and Lode parameter u have

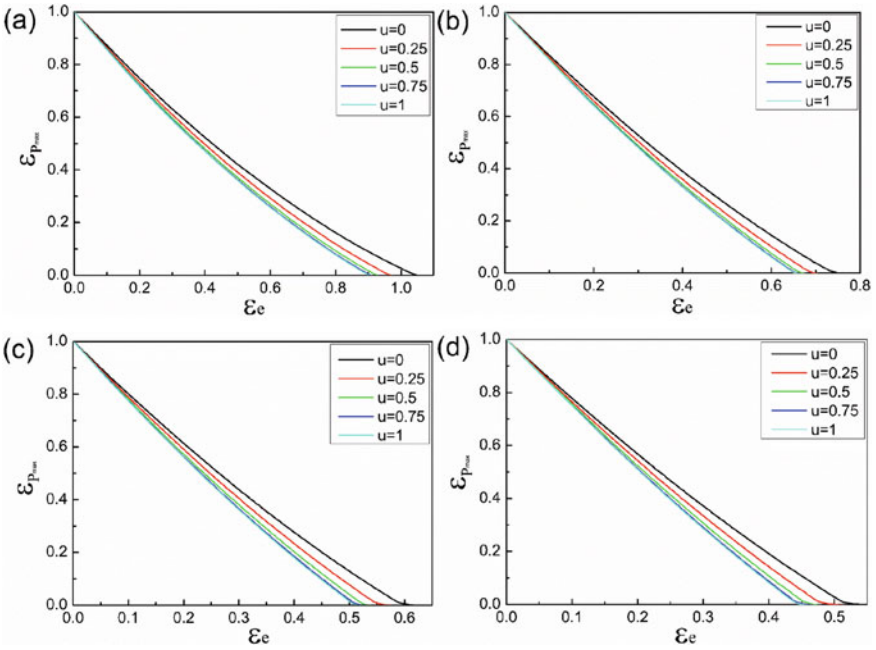


Fig. 1 Relationship between porosity ratio $\varepsilon_{P_{max}}$ and effective strain ε_e: $T_X = 0$; **a** $T_X = -0.5$; **b** $T_X = -1$; **c** $T_X = -1.5$. (Color figure online)

a significant influence on porosity closure. The effective strain value required for porosity closure decreases as the stress triaxiality level increases, as reported by [6].

2.2 A New Porosity Closure Model

A new model for predicting maps of porosity closure volume was defined, including the stress triaxiality ratio T_X and the Lode stress parameter μ. The ε_c represents the critical effective strain of the RVE surface when the porosity is completely closed. The new model can be expressed as follows:

$$\varepsilon_c = \left[D_1 + D_2 \exp(D_3 T_X)\right](1+u)^{D_4} \tag{2}$$

$$D_4 = A(T_X)^2 + BT_X + C(u)^2 + Eu + FT_X u + G \tag{3}$$

The regression coefficients can be determined by the regression method and the results are shown in Table 1. The comparison between model data and compute data is illustrated in Fig. 2, where the STLB model can accurately fit the compute data.

Table 1 The regression coefficients of the STLB model

D_1	D_2	D_3	A	B	C	E	F	G
0.448	0.599	1.341	−0.022	−0.047	−0.017	0.202	0.028	−0.389

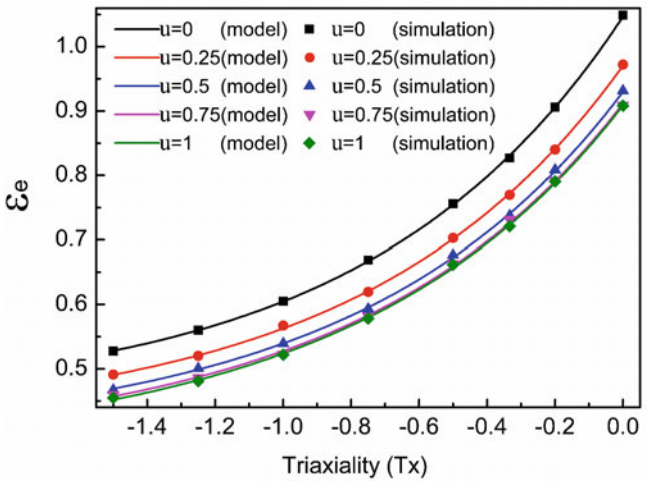


Fig. 2 Comparison between the simulation data and model data. (Color figure online)

To assess the precision of the STLB model, the average error between the model calculated strain ε_m and RVE simulation obtained ε_s can be computed as follows:

$$\text{error} = \frac{1}{\mathrm{N}} \sum_{\mathrm{i}=1}^{\mathrm{N}} |(\varepsilon_{\mathrm{m}} - \varepsilon_{\mathrm{s}})/\varepsilon_{\mathrm{s}}| \times 100\% \tag{4}$$

The porosity closure strain values of both model calculation results and the simulation data are extracted at different stress triaxiality ratios Tx∈ (0, −0.2, −0.333, −0.5, −0.75, −1, −1.25, −1.5) and different values of Lode stress parameters u ∈ (0, 0.25, 0.5, 0.75, 1). The error can be calculated by Eq. [4], and the error of the STLB model is 2.35%.

2.3 Validation of the Porosity Closure Model

Cylindrical specimens (Ø6 mm ×H9mm) are machined from the shrinkage zone of casting parts, which is conducive to subsequent porosity measurement and analysis. The hot forging experiments were carried out on a Gleeble 3800 thermal system simulator. The experimental scheme of hot forging is shown in Table 2. A high-

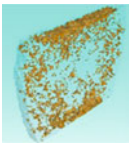
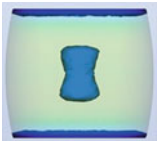
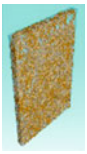
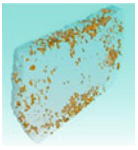
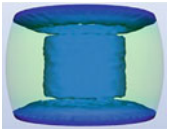
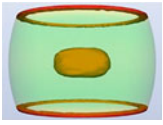
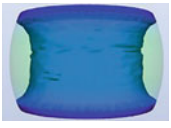
Table 2 Hot forging experimental scheme

Name	Billet size (mm)	Temperature (°C)	Strain rate (s^{-1})	Reduction (mm)	Reduction ratio (%)
Case1	Φ6.0 × H9.0	400	0.1	2.7	30
Case2				3.6	40
Case3				4.5	50

resolution and micro-focus X-ray CT system YXLON Y. Cheetah was used to reveal the porosity distribution before and after hot forging.

The 3D X-ray CT images with a thickness of 1 mm were cut along the central plane to better display its maps of micro-porosity closure. The semi-transparent display of the X-ray CT images can better reveal the distribution of internal porosities. The material is represented in virescent and the porosity is represented in yellow. The numerical and CT experimental results are shown in Table 3. When the reduction is 30%, there is no porosity closure zone in the STLB model, which is consistent with the experimental results. However, porosity closure zone exists in the STB model. When the reduction is 40%, there is a porosity closure zone in the STLB model and the STB model. The STLB model is less than the predicted porosity closure area of the STB model, which is in better agreement with the experimental results. With the amount of reduction increasing, the significant porosity closure zone exists in Case3. Evidently, the numerical results obtained from the STLB model can well predict the experimental results.

Table 3 Comparison of porosity closure area at CT, STB and STLB. (Color figure online)

	Cast-CT	Forged-CT	STB	STLB
Case1				
Case2				
Case3				

3 Applications to Integrated Casting and Forging Process (ICFP)

Process principle of ICFP mainly includes four procedures: casting, solidification, forging, and opening die, which was studied and is presented in [5]. First, casting procedure ensures that the die cavity is fully filled. Then, molten metal in the die cavity is completely solidified under a certain static pressure. Forging is the key procedure of the ICFP, which makes full use of the latent heat of solidification to further compensate the porosity and cavity of the part.

One type of automobile control arm which was made from A356 aluminum alloy is used as the research object. The thermodynamic properties of A356 alloy refers to [2]. The casting and solidification are simulated by software THERCAST. The Niyama criterion is an estimation of the risk of porosity in the THERCAST. The high risk of presence of porosity is then indicated by high values of the criterion, where 0 is the minimum value that indicates the absence of porosity. Figure 3a shows the high risk area of the presence of porosity distribution of the control arm after solidification. Typical regions are selected for microstructure observation; there are some porosities in the red region, as shown in Fig. 3b. Therefore, the result indicated by THERMCAST match the high values of the criterion at high risk for the presence of porosity.

According to the distribution results of porosities, the composite die of ICFP for automobile control arm is designed, as shown in Fig. 4. The punch is moved down to forge the parts after a certain forging waiting time. In order to design and optimize the process of ICFP, the STLB model was implemented into finite element (FE) analysis software FORGE2.1.

Figure 5 shows the evolution of Niyama distribution in the control arm during forging. It can be seen that with the increase of the reduction, Niyama value on the control arm gradually decreases, and the area of porosity distribution gradually decreases.

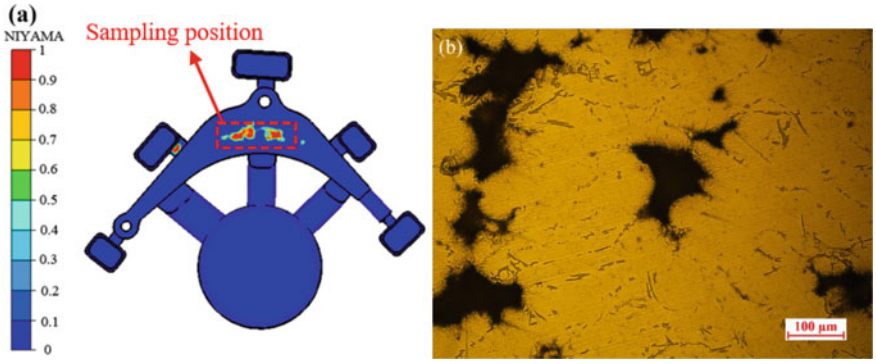


Fig. 3 **a** The sampling position of automobile control arm; **b** Microstructure of sample in **a**. (Color figure online)

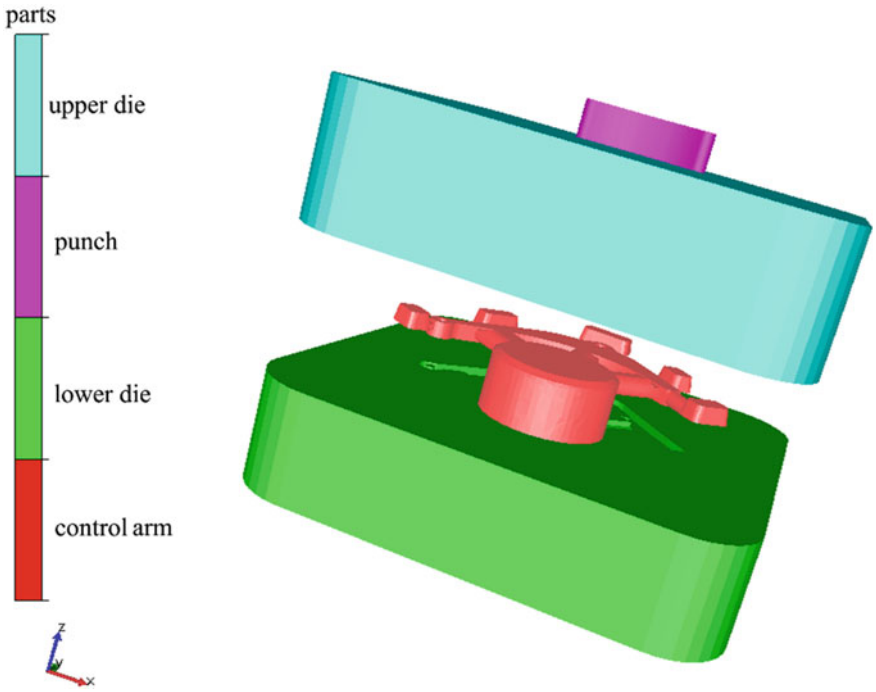


Fig. 4 The composite die of ICFP for automobile control arm. (Color figure online)

Figure 6 shows the sampling position and microstructure of ICFP for automobile control arm. Through the microstructure, it can be observed that there are no porosities in the sampling position. Obviously, the numerical results obtained from the STLB model well agree with the experimental results.

4 Conclusions

(1) The stress triaxiality ratio and Lode stress parameter-based (STLB) model is proposed. In comparison with the STB model, the new model used the Lode stress parameter that defines the stress state accurately. The average error of the STLB model is 2.35%. X-ray CT scan results show that the STLB model can predict porosity closure more accurately than the STB model.

(2) Integrated casting and forging process (ICFP) was used as validation cases. The experimental results well agree with the simulated results obtained from STLB models, which indicates that the new model for process design and optimization will be convenient.

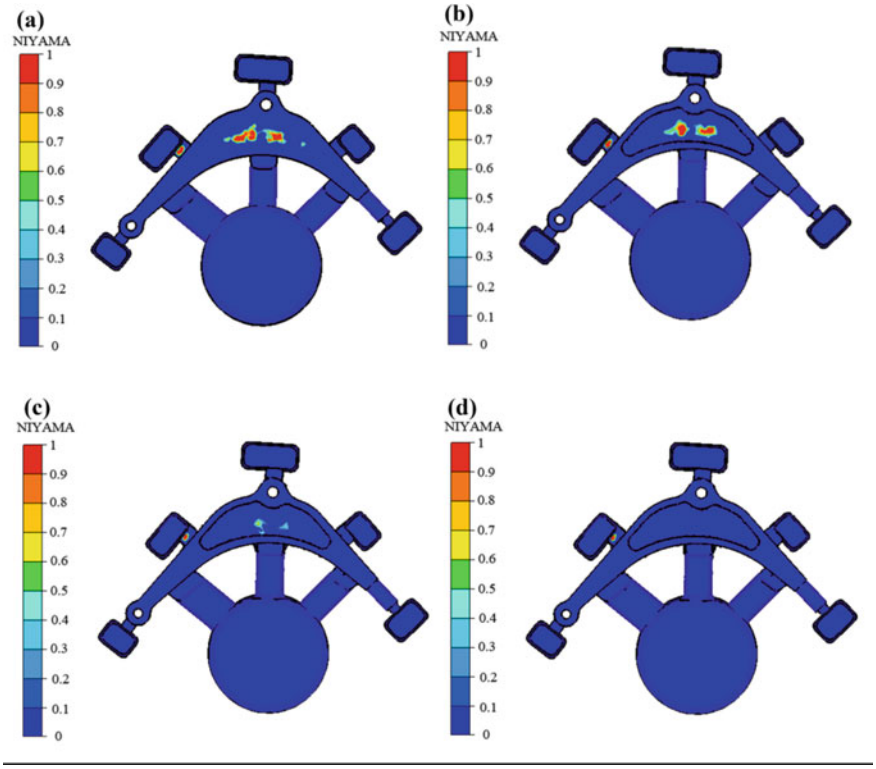


Fig. 5 The evolution of Niyama distribution for different compression values. **a** 0 mm; **b** 1 mm; **c** 2 mm; **d** 2.5 mm. (Color figure online)

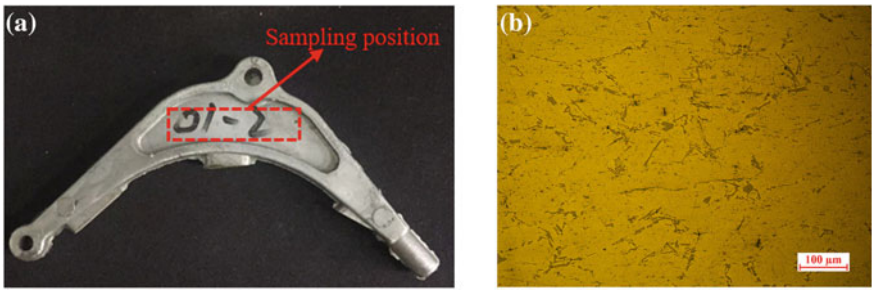


Fig. 6 The sampling position and microstructure of ICFP for automobile control arm. **a** The sampling position of automobile control arm; **b** Microstructure of sample in **a**. (Color figure online)

Acknowledgments The project was supported by the National Natural Science Foundation of China (Nos. 51875441), and by the Shaanxi province Natural Science Basic Research Program (Nos. 2019JQ-598), and by the Fundamental Research Funds for the Central Universities (No. zrzd2017027).

References

1. Chbihi A, Bouchard PO, Bernacki M, Pino Muñoz D (2017) Influence of lode angle on modelling of void closure in hot metal forming processes. Finite Elem Anal Des 126:13–25
2. Liang Z, Zhang Q (2018) Quasi-static loading responses and constitutive modeling of Al–Si–Mg alloy. Metals 8:838
3. Saby M (2013) Understanding and modeling of void closure mechanisms in hot metal forming processes. PhD Thesis, Mines ParisTech
4. Saby M, Bouchard PO, Bernacki M (2015) Void closure criteria for hot metal forming: a review. J Manuf Process 19:239–250
5. Zhang Q, Cao M, Zhang S, Zhang DW, Zhao SD, Liu Q (2014) Integrated casting and forging process for aluminum alloy automobile wheel. Adv Mech Eng, 1–12
6. Zhang X-X, Cui Z-S, Chen W, Li Y (2009) A criterion for void closure in large ingots during hot forging. J Mater Process Technol 209:1950–1959

Robust Hydroforming Technologies to Enhance the Formability of Sheet and Tube



Shi-Hong Zhang, Da-Yong Chen, Yong Xu, and Yan Ma

Abstract Pulsating hydroforming and impact hydroforming are two advanced technologies to increase the formability of material compared with other traditional forming technologies. They were systematically investigated from aspects of technical principle, forming mechanism, equipment, and applications. Pulsating hydroforming can improve the forming ability by altering the friction condition of sheet/tube parts or by utilizing the effect of transformation induced plasticity of stainless steels under the pulsating loading. As for impact hydroforming, the strain rate can reach 10^3–10^4/s and the instantaneous pressure can be GPa level, which can obviously increase the elongation of hard-to-form material by 20–60%. The effect of flexible liquid and impact impulse was investigated by both experiment and simulation, while the mechanisms were related to the compatible deformation of the second phase, strain decentralization, and defect stabilization. The technologies have been used on the manufacturing of complex, thin-walled components for the fields of aeronautics and aerospace, automobile, nuclear power, etc.

Keywords Pulsating hydroforming · Impact hydroforming · Sheet and tube · High strain rate · Formability

1 Introduction

Nowadays, complex components are needed in the fields of automobile, aeronautical and astronautical, nuclear power, etc. These components are characterized with thin-wall, large size, complex and curved surface, deep cavity. So, it is very difficult to use the conventional processes such as rigid punching, rolling, and forging to manufacture the complex parts; especially, some of them are made of low formability materials such as aluminum, magnesium, and titanium alloy. As an advanced lightweight forming process, hydroforming has been widely used in these fields to manufacture the complex and hard-to-form components during recent decades. Especially, Wang

S.-H. Zhang (✉) · D.-Y. Chen · Y. Xu · Y. Ma
Institute of Metal Research, Chinese Academy of Sciences, Shenyang 110016, China
e-mail: shzhang@imr.ac.cn

© The Minerals, Metals & Materials Society 2021

G. Daehn et al. (eds.), *Forming the Future*, The Minerals, Metals & Materials Series,
https://doi.org/10.1007/978-3-030-75381-8_30

et al. innovatively used hydroforming to manufacture spherical vessels as a polyhedral shell from polygons. The final product had a reasonable structure and need not be pressed and shaped by dies [1]. Zhang has summarized the new development of hydroforming including flat sheet hydroforming, hydro-bulging, hydromechanical deep drawing, shell forming, viscous pressure forming, etc. early in the 1990s [2]. The hydroforming presents many advantages over conventional stamping and welding processes including the reduction in the number of dies, manufacturing costs, and the increase in dimensional accuracy.

However, there are still some defects such as the wrinkling, buckling, and bursting due to the improper relationship between inner pressure and axial feed during the hydroforming process. And higher and higher standard is proposed for hydroforming especially for the hard-to-form material, such as aluminum, and magnesium alloy which is widely used in the aeronautical and astronautical field.

In recent years, a new process referred to as pulsating hydroforming of tubes had been developed based on the simulation and experiment. It is characterized by decreasing the local thinning ratio and increasing the uniform expansion, which could effectively improve the formability of the tube component [3]. It was found that both pulsating loading effect and microstructure evolution contributed to the increasement of formability based on the investigation of Mori and Xu on the mechanism of formability improvement [4, 5]. The mechanisms of formability improvement were systematically investigated, and the corresponding machine was designed and manufactured according to the study [6].

In recent decades, it was found that high speed forming could improve the formability effectively which includes the electromagnetic forming (EMF), the electrohydraulic forming (EHF), the explosive forming, and so on [7, 8]. As one of the high strain rate (HSR) forming processes, impact hydroforming (IHF) could enhance the formability of sheet metals [9]. It is proposed that the sheet is formed by high pressure and transient loading which combines the advantages of high speed forming and the flexible adaptation of liquid medium [10]. The high pressure of liquid is produced by the impact of the projectile, and the sheet is formed under this high-pressure pulse. The strain rate can reach the level of 10^3–10^4/s and the instantaneous pressure even can be more than 1 GPa in some conditions under IHF [9, 11].

In this study, both of the pulsating hydroforming and impact hydroforming are systematically investigated from the aspects of the mechanisms of the formability improvement, machine designing and manufacturing and the application of these novel technologies.

2 Pulsating Hydroforming

2.1 The Mechanism of Formability Improvement

As it was illustrated in Fig. 1, the formability of SS 304 was investigated using the loading and unloading experiment. And the experiment was done under the in situ XRD observation to study the procedure of phase transformation. It was found that the elongation and ultimate tensile strength of SS 304 was increased by 24.3% and 9.2%, respectively, by pulsating loading compared with traditional hydroforming [5].

The in situ XRD observation was conducted when the unloading strain was 0.3, 0.4, 0.5, 0.6, and near fracture, respectively. The diffraction degree (2θ) was in the range of 40–100°, and the main peaks were γ(111), γ(200), γ(220), γ(311), (110), (200), and (211), respectively, in the XRD spectra. Furthermore, it was found that the initial specimen contained only austenite (γ) from the results of X-ray diffraction as illustrated in Fig. 2. However, the diffraction of the γ phase shifted to a higher angle due to the stress of deformation. It was found that the ratio of the γ phase to the integrated intensity of phase increased gradually when the strain was enhanced, especially for γ(111) and (110). Meanwhile, it was discovered that the martensitic

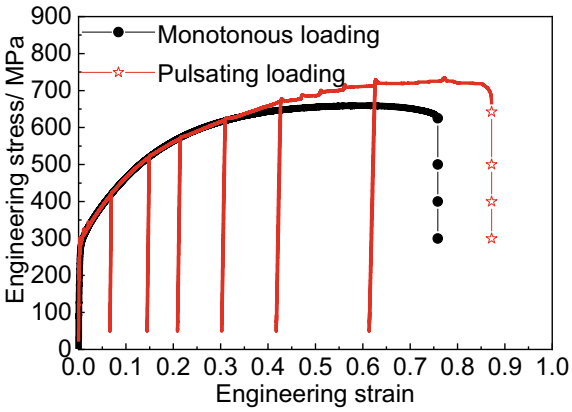


Fig. 1 Stress-strain curve and phase analysis under the pulsating loading [5]. (Color figure online)

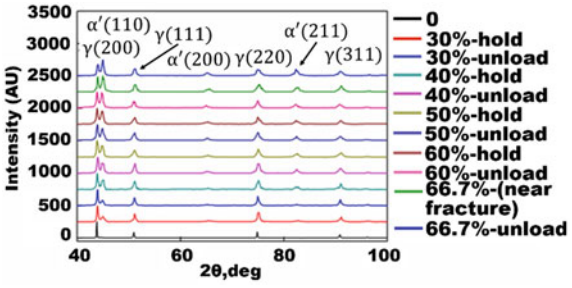


Fig. 2 The diffraction peak of each phase obtained by in situ XRD under loading and unloading tension [12]. (Color figure online)

transformation started at the first stage of deformation. The variation of martensitic fraction coincided well with previous findings before the strain of 0.4. The unloading procedure had minor influence on the kinetics of martensitic transformation at small strains (strains are not more than 0.3), while the fraction of the martensitic phase were characterized with a sudden increase at unloading points when the strain surpassed 0.4. The content of the martensitic phase increased after each procedure of unloading at large strains. By calculation, the martensitic fraction could be extremely increased by approximate 10% through single cyclic loading and unloading [12].

It was found that the plasticity of the austenitic steel was obviously improved under the pulsated loading according to the results of experimentation. The pulsated loading could increase the fraction of the martensite induced by the strain from the observation of in situ XRD. The possible explanation was that the unloading process made the dislocation density low and the austenite matrix soften, which contributed to promote the nucleation and growth of the martensite induced by strain. Consequently, the transformation induced plasticity (TRIP) effect was enhanced and the necking was delayed.

2.2 *The Design and Manufacture of the Pulsating Hydroforming Machine*

The main investigation focused on the process principle and deformation mechanism by the previous scholars. The study was rarely made on the aspect of designing and manufacturing for the pulsating hydroforming machine. In China, the first THF-300 pulsating machine was developed and manufactured by Institute of Metal Research, Chinese Academy of Sciences, in 2010. As illustrated in Fig. 3, the machine is mainly composed of three sub-systems which include the lateral feeding, the liquid filling,



Fig. 3 Novel machine of pulsating loading (THF-300): **a** Hydraulic power station; **b** Control system [13]. (Color figure online)

and the pressurization system. The exact controlling of the internal pressure was realized in the cavity of the component by using the system of closed-loop control. Several different loading modes can be achieved which include single linear, multiple-stage linear, sinusoidal, and step loading, respectively. Typically, the maximum of output pressure can be at the level of 300 MPa with the pulsating loading. The wave amplitude is in the range of 0.5–30 MPa, the frequency is not more than 0.5 Hz, and the precision is ±2 MPa, which illustrate the high precision of the machine [13].

2.3 *The Process Investigation of Pulsating Hydroforming*

Engine cradle is an important part of front axle of the chassis in automobile. It is difficult to be manufactured by the conventional hydroforming process due to the structure of hollow cross section with different dimensions. Multiple procedures are required to manufacture the complicated component (like engine cradle) including the tube bending, preforming, hydroforming, etc. But, only two steps are required to manufacture the engine cradle which include the bending and the pulsating hydroforming. It was illustrated in Fig. 4 that different amplitudes were adopted in the experiment of pulsating hydroforming compared with the monotonic loading path. It was found that the bursting would happen before internal pressure reached 120 MPa

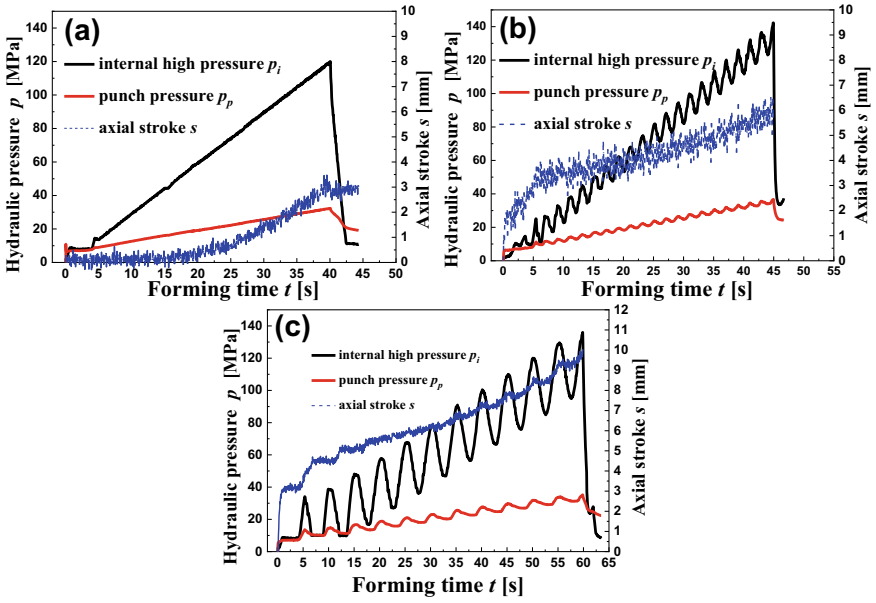


Fig. 4 Experimental data curves acquired by tube hydroforming: **a** monotonic loading path; **b** amplitude = 10 MPa; **c** amplitude = 20 MPa [5, 6]. (Color figure online)

under the monotonic loading. However, the defect could be refrained if the pulsating loading was employed by which the internal pressure could reach the pre-setting value under the condition of two different amplitudes.

The axial stroke was found only to be 3 mm from the result illustrated in Fig. 4a, which was inappreciable during the beginning stage of loading. The bursting was found to concentrate in the corner zone with 95degree angle under the situation of the monotonic loading path. Furthermore, the crack possibly occurred on the both inside and outside surfaces of the tube [5, 6].

However, more axial strokes could be obtained by using the pulsating loading compared with the common one. The loading path lead to the reduction of friction between the tube and die, which made axial strokes increase variably when the amplitudes were large. It could be found that the axial strokes displayed a stepped increase with the load pulsation during hydroforming, and the total stroke for single-side punch is nearly 10 mm when the amplitude was 20 MPa as illustrated in Fig. 4c. On the other hand, it had been proved that the TRIP effect in austenitic stainless steel could be remarkably enhanced by the process of loading and unloading resembled pulsating load according to the previous work. Therefore, the formability was drastically improved by pulsating load, and the bursting could be effectively restrained even under the homogeneous deformation [5, 6].

Consequently, the Integral engine cradle was successfully manufactured by this novel IHF using the material of 304 stainless steel without any defects, such as cracks and wrinkles. The thinning ratio was less than 30%, which could be considered safe in hydroforming. The final component was illustrated in Fig. 5 [5, 6].



Fig. 5 Integral component of engine cradle with good quality [5, 6]

3 Impact Hydroforming

3.1 The Principle of Impact Hydroforming

The process principle of IHF is illustrated in Fig. 6. The projectile is driven by the energy of source, then it shocks the liquid of the chamber; therefore, the liquid is accelerated to form the blank suddenly by means of impact wave which characterizes with high pressure and velocity; afterwards, the blank is shaped to be the final component with certain structure and size. In this procedure, the pressure can even be 500–1000 MPa and the forming time is in the range of 500 μs. As a high-speed forming means, it can increase the formability of material, especially the one which has low plasticity [9, 14].

3.2 The Design and Manufacture of High Energy-Efficiency IHF Press

Based on the research on the propagation of wave under the impact hydroforming, and also, according to the investigation on the energy source, sealing, and controlling, a novel impact hydroforming press is designed and manufactured as illustrated in Fig. 7. The composite of gas-liquid energy source was innovatively used to solve the problem of energy insufficiency. The impact energy could reach 225 kJ under the affect of the liquid which has been accelerated by the high speed projectile that drove by the energy source. Meanwhile, the energy could be controlled exactly by the method of composite energy source. Moreover, the resistance of impact forming was reduced by the design of no seal ring in the high-speed cylinder, no oil pressure under the travel route of the impact bar, and the optimization of exhaust hole. In addition,

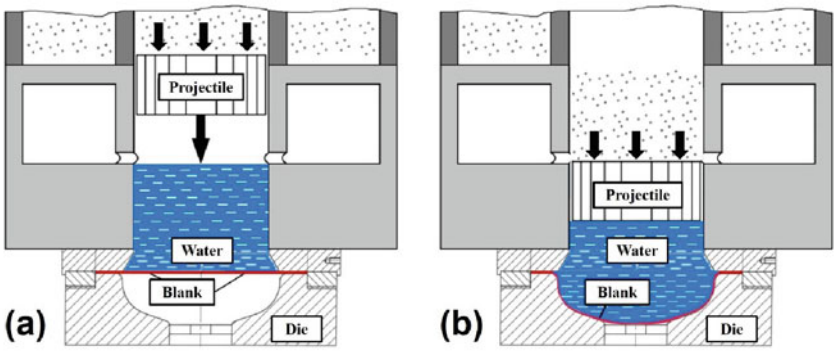


Fig. 6 Process principle of impact hydroforming: **a** Before IHF; **b** After IHF. (Color figure online)



Fig. 7 Impact hydroforming press and system [11]. (Color figure online)

the dynamic model locking was realized by employing a servo system and by the exacted control of the operating platform. The IHF machine mainly includes the energy source, accelerate zone, forming zone, and controlling system [9]. The IHF press can be used to form the tube and sheet component and evaluate the formability of metal material by providing the dynamic measure system. The basic parameters of this novel IHF press is illustrated in Table 1.

Table 1 The parameter of the novel IHF machine [9]

Parameters of IHF press	Parameter value
Impact mode	Single projectile
Principle of acceleration	Composite of gas and liquid
Max accelerate energy	18 MPa
The mass of the projectile	60, 90, 120 kg, Adjustable
Max impact speed	80 m/s
Max energy of projectile	225 kJ
Max pressure in chamber	1000 MPa
The diameter of chamber	250 mm

3.3 The Evaluation of High Strain Rate Formability

The dynamic formability of metal material is valuably investigated because the procedure of IHF finishes instantaneously. The solid-liquid coupling finite element modeling (FEM) was employed as one efficient method to evaluated the formability in the limit forming time. The Gruneisen equation of state (EOS) was used to describe the behavior of the forming liquid which could reflect the wave effect on the blank. The modified John-Cook (J-C) constitutive model was established to present the special hardening behavior of material which could offer more accurate value of elongation and strength. In addition, the Fluid-Structure-Interaction (FSI) algorithm was employed to realize the coupling between the projectile and the liquid, as well as, the liquid and the blank [11, 15, 16].

The forming ratio is defined as the ratio of initial diameter of the blank with the diameter of die cavity. And the forming height ratio is defined as the ratio of the depth of the formed part with the diameter of die cavity. The evaluation of formability should consider the influence of impact energy and forming ratio on the forming behavior of the part. Hence, the different diameters of blank were designed and adopted in both FEM and experiment, which is listed in Table 2.

The corresponding experiment was employed to verify the validity of solid-liquid coupling FEM. And the relative die was designed as illustrated in Fig. 8. The die mainly includes the upper die, fixing ring, locating ring, lower die, die set, and centering plate. The diameter of die cavity is designed as 38.5 mm, the radius of die

Table 2 The initial diameters and corresponding forming ratios for formability evaluation testing

Initial diameter of blank/mm	51.2	54.7	57.8	63.9	70.5	77.0	83.6
Forming ratio	1.42	1.51	1.60	1.77	1.95	2.13	2.31

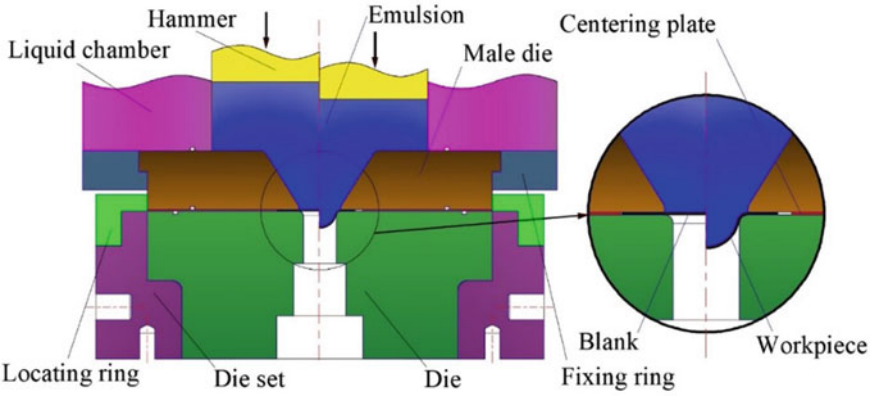


Fig. 8 The geometrical model for formability evaluation of impact hydroforming [11]. (Color figure online)

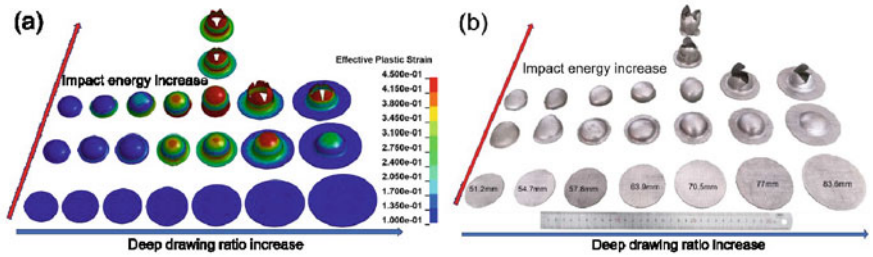


Fig. 9 The specimen of formability evaluation under impact hydroforming: **a** Solid-liquid coupling FEM; **b** Experiment of IHF [11]. (Color figure online)

corner is 5 mm, and the diameter of the chamber is 48.5 mm. As for the material, AA 2A06 is adopted considering its wide application in the aeronautic field [11].

The FEM was conducted under different impact energies and forming ratios to realize incomplete forming (with flange), complete forming (without flange), and crack. The different parts were listed as in Fig. 9a based on the solid-liquid coupling FEM. The blank can be completely drawn into the die cavity without the drawback of crack if the impact energy is large enough when the forming ratio is less than 1.77. However, the blank had the possibility to be not only completely formed if the energy was controlled reasonably but also easily cracked if the energy was little higher when the forming ratio is 1.95. The blank would crack directly if the energy was little high or incompletely deformed if the energy was not enough when the ratios were 2.13 and 2.31. The component would crack to be 3–4 parts when the forming ratio was larger than 2.02 in the same time that the energy is too high. The area of large effective plastic strain was located at the bottom and round corner of the part from the analysis of FEM. 3–5 parts were formed under each condition as used in FEM. As illustrated in Fig. 9b, the results from experiment coincide well with the one of FEM from aspects of crack features, shape, and size [11].

According to the previous FEM and experiment, the formability curve was established describing the relationship between impact engergy and forming ratio, forming height ratio, and forming ratio, which was illustrated in Fig. 10a and b. The limit forming ratios were 1.99 and 2.02 as for FEM and the experiment, respectively, which were larger than the ratio of 1.95 that is gotten from rigid punch deep drawing. Furthermore, three areas were distinguished to stand for the uncomplete forming, complete forming, and crack. At the same time, the forming height ratios were confirmed as 1.04 and 0.95 by FEM and experiment, respectively. The corresponding equations were established which stand for the relationship of impact energy, forming height ratio with forming ratio, as listed in Eqs. (1) and (2). Both of the curves and equations were very useful to quantitatively design the process of IHF [11].

$$E_{\text{impact}} = \begin{cases} -18807.21 + 38792.44 * D_{\text{ratio}} - 27104.02 * D_{\text{ratio}}^2 \\ +6488.88 * D_{\text{ratio}}^3, & \text{when} D_{\text{ratio}} \leq 1.99 \\ 800.47 + 8.35e7 * 0.00402^{D_{\text{ratio}}}, & \text{when} D_{\text{ratio}} \geq 1.99 \end{cases} \quad (1)$$

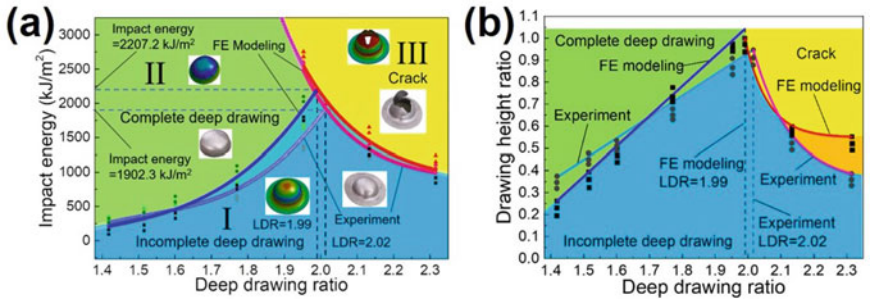


Fig. 10 The curve of formability evaluation for IHF: **a** Relationship between impact energy and forming ratio; **b** Relationship between forming height ratio and forming ratio [11]. (Color figure online)

$$D_{\text{hratio}} = \begin{cases} -1.67 + 1.36 * D_{\text{ratio}}, & \text{when} D_{\text{ratio}} \le 1.99 \\ 0.55 + 2.15E12 * (4.27E - 7)^{D_{\text{ratio}}}, & \text{when} D_{\text{ratio}} \ge 1.99 \end{cases} \quad (2)$$

3.4 The Application of IHF on the Complex Sheet Component

The complex sheet component characterizes with two chambers whose deep drawing ratio is more than 3.5, which is usually used in the aeronautic field. It is difficult to be formed by the conventional drop hammer technology because of the problems of multiple heat treatment and forming steps. The forming pressure will be more than 90 MPa and the defects of crack and wrinkle will be obvious if the common hydroforming process is employed. According to the investigation, the previous preforming and impact hydroforming are adopted as the final forming scheme of this component. The dies used for preforming and impact hydroforming are illustrated in Fig. 11a [9].

The solid-liquid coupling FEM was employed to optimize the process of IHF and the corresponding forming parameters. And the impact wave loading and the feasible liquid were applied to promote the material feeding and enhancement of the formability. Hence, the defects of crack and wrinkle were effectively avoided. The filling of the small corner of the part was especially prominent compared with the conventional forming method. And the procedure was shortened from 8 to 2 compared with the traditional drop hammer forming. The final component is illustrated in Fig. 11 [17, 18].

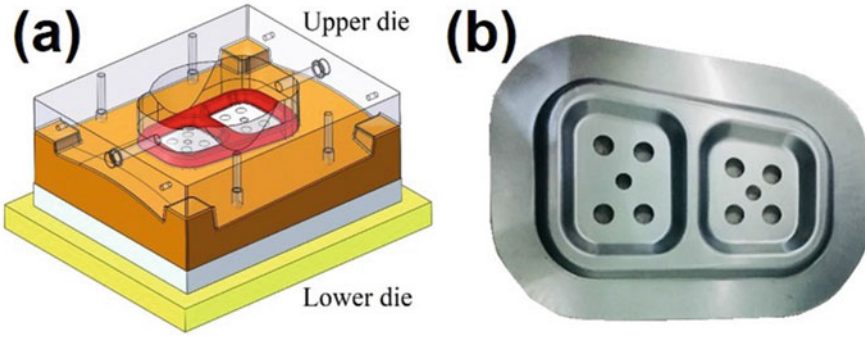


Fig. 11 The die of impact hydroforming and the deformed component: **a** Die of IHF; **b** Frame component. (Color figure online)

4 Conclusion

(1) Experimental results indicate that the fraction of strain-induced martensite increases due to the alternation of internal structure involving the internal stress and dislocation configuration when unloading occurs. It is revealed that nucleation and growth of martensite are facilitated, known as transformation induced plasticity (TRIP) under the pulsating load. Both axial feeding and TRIP effect finally contribute to the formability improvement of austenite steel.

(2) A novel high energy-efficiency IHF machine was designed and manufactured by solving the problems of energy source mode, dynamic resistance reduction, and dynamic locking of die. And a novel method was established to evaluate the dynamic formability of sheet material based on the impact hydroforming. Moreover, the complex sheet component was successfully manufactured with good surface quality and accurate size by IHF.

(3) The two novel technologies can be utilized to manufacture the components in aeronautics and astronautics, automobile, and nuclear power fields which characterize thin-wall, large size, deep cavity and complex structure.

Acknowledgments This paper is supported by National Natural Science Foundation of China (No. 51875548), Natural Science Foundation of Liaoning Province of China (Grand No. 20180550851), Project for transfer and transformation of scientific and technological achievements, Chinese Academy of Sciences, Henan Province (No. 2020204).

References

1. Wang ZR, Wang T, Kang DC, Zhang SH, Fang Y (1989) The technology of the hydro-bulging of whole spherical vessels and experimental analysis. J Mech Work Technol 18:85–94
2. Zhang SH (1999) Developments in hydroforming. J Mater Process Technol 91:236–244
3. Hama T, Asakawa M, Fukiharu H et al (2004) Simulation of hammering hydroforming by static explicit FEM. ISIJ Int 44(1):123–128
4. Mori K, Maeno T, Maki S (2007) Mechanism of improvement of formability in pulsating hydroforming of tubes. Int J Mach Tool Manu. 47:978–984
5. Xu Y, Zhang SH, Cheng M et al (2012) In situ X-ray diffraction study of martensitic transformation in austenitic stainless steel during cyclic tensile loading and unloading. Scripta Mater 67:771–774
6. Xu Y, Zhang SH, Song HW et al (2011) The enhancement of transformation induced plasticity effect on austenitic stainless steels by cyclic tensile loading and unloading. Mater Lett 65:1545–1547
7. Psyk V, Risch D, Kinsey BL, Tekkaya AE, Kleiner M (2011) Electromagnetic forming—a review. J Mater Process Technol 211(5):787–829
8. Golovashchenko SF, Gillard AJ, Mamutov AV (2013) Formability of dual phase steels in electrohydraulic forming. J Mater Process Technol 213(7):1191–1212
9. Ma Y, Xu Y, Zhang SH, Banabic D, El-Aty AA, Chen DY, Cheng M, Song HW, Pokrovsky AI, Chen GQ (2018) Investigation on formability enhancement of 5A06 aluminum sheet by impact hydroforming. CIRP Ann Manuf Technol 67:281–284
10. Lang LH, Wang SH, Yang CL (2013) Investigation on the innovative Impact Hydroforming Technology. Paper presented at the 11th International Conference on Numerical Methods in Industrial Forming Processes, Shenyang, China
11. Chen DY, Xu Y, Zhang SH, et al (2019) A novel method to evaluate the high strain rate formability of sheet metals under impact hydroforming. J Mater Process Technol. https://doi.org/10.1016/j.jmatprotec.2019.116553
12. Xu Y, Zhang SH, Cheng M et al (2013) Effect of loading modes on mechanical property and strain induced martensite transformation of austenitic stainless steels. Acta Metall Sinica. 49(7):775–782
13. Zhang SH, Xu Y, Cheng M et al (2013) Technology and equipment of the pulsating hydroforming technology. J Mech Eng 49(24):1–6
14. Shang J, Daehn G (2011) Electromagnetically assisted sheet metal stamping. J Mater Process Technol 211(5):868–874
15. Zhang SH, Chen DY, Xu Y, et al (2019) High strain rate formability of AA2B06-O alloy during impact hydroforming. Paper presented at the 13th international conference on numerical methods in industrial forming processes. New Hampshire, pp 349–352
16. Xu Y, ABD EL-ATY A, Zhang SH, et al (2019) Effect of novel impact hydroforming technology on the formability of Al alloys. In: IOP Conference Series Materials Science and Engineering 651:012053
17. Zhang SH, Ma Y, Xu Y, et al (2018) Experimental investigation of novel impact hydroforming technology on sheet metal formability. In: IOP Conference Series Journal of Physics 1063:012173
18. Zhang SH, Ma Y, Xu Y, et al. (2018) Effect of impact hydroforming loads on the formability of AA5A06 sheet metal. In: International deep drawing research group 37th annual conference. IOP Conference Series Materials Science and Engineering 418:012114

Part VII
Agile Metal Forming

Recent Investigations on Incremental Sheet Forming: From Fundamentals to Industrial Application Technologies



Jun Chen and Zhidong Chang

Abstract Incremental sheet forming (ISF) is a promising flexible forming process in fabricating low-batch or customized sheet metal parts, and has potentials in reduced process lead time and cost, and increased formability. In the plenary talk, recent investigations on ISF fundamentals and the technologies for ISF industrial application will be presented, which cover tool path algorithms, forming tool development, surface roughness and forming load predictions, new variants of ISF, deformation mechanism of different ISF variants, and several industrial application cases. Finally, an outlook about ISF will be made as well.

Keywords Incremental sheet forming · Tool path · Surface quality · Geometric deviation · Deformation mechanism

1 Introduction

ISF is one of the advanced flexible forming processes appropriate for small batch production of sheet metal parts. Research in the ISF field has been extended to different aspects in recent years, including forming limit, deformation mechanism, forming force, geometric accuracy, surface roughness, and tool path. Duflou et al. [1] found that the dimensional accuracy and formability for a range of materials can be improved through laser-assisted incremental forming process. Araghi et al. [2] proposed a new hybrid forming process by combining ISF and stretch forming, and indicated that noticeable reduction of cycle time and more uniform thickness distribution can be obtained. Silva et al. [3] proposed an analytical model of contact stress based on membrane analysis in the ISF process, by which the cracks were claimed to be caused by meridional tensile stress instead of in-plane shearing stress. Emmens et al. [4] presented an overview of deformation mechanisms that were suggested to explain the enhanced formability of the ISF process. Six mechanisms were suggested

J. Chen (✉) · Z. Chang
Department of Plasticity Technology, Shanghai Jiao Tong University, Shanghai 200030, P.R. China
e-mail: jun_chen@sjtu.edu.cn

© The Minerals, Metals & Materials Society 2021

G. Daehn et al. (eds.), *Forming the Future*, The Minerals, Metals & Materials Series,
https://doi.org/10.1007/978-3-030-75381-8_31

as follows: contact stress, bending under tension, shearing, cyclic straining, geometrical inability to grow, and hydrostatic stress. To obtain a better understanding of the shear effect, Lu et al. [5] developed an analytical model based on the analysis of stress state in ISF deformation and proposed an explicit relationship between stress state and forming parameters. Eyckens et al. [6] investigated the straining behavior in the ISF process based on Digital Image Correlation and numerical simulation. Experimental results demonstrated that the dominant mechanism for the cone with a low wall angle is through-thickness shearing, while bending for the cone with a large wall angle. Silva et al. [7] proposed a link between plastic flow, void coalescence and growth, ductile damage, crack opening modes, and fracture toughness in ISF, and proposed an analytical framework to estimate the location of the fracture loci in the principal strain space. Duflou et al. [8] investigated the effects of tool radius, sheet thickness, wall angle, and step depth on forming load, and indicated that the slope of the force curve can be used as a failure prediction indicator. Mulay et al. [9] studied the effects of feed rate, step depth, tool diameter, and sheet thickness on surface roughness, and found that the step depth and tool diameter have significant effects on the surface roughness. Li et al. [10] investigated dimensional accuracy of straight-wall cylinders in multi-stage incremental forming based on an experiment method and mathematic analysis. Besides, some advanced materials have been applied in this field, such as titanium alloy[11], polymers [12], and composite sheets [13].

Although there have been lots of researches targeting to reveal the deformation mechanism, there is a lack of new experimental researches output in recent years. This paper attempts to present systematic investigations of the current state of the art in the ISF process over the last 2 years explored by our team, with the target of throwing light on the future development that can take place using this manufacturing process.

2 Tool Path Algorithm

Different from linear interpolation of conventional tool path, a novel quadratic spiral tool path (QSTP) generation algorithm was proposed by Chang et al. [14]. The new tool path can be generated based on the quadratic interpolation of three neighboring contour lines as shown in Fig. 1, and the points on the tool path can be obtained through the calculation of Lagrange quadratic interpolation.

For better understanding of the impact of QSTP, the thickness thinning and geometric accuracy were case-studied by forming typical parts with varied wall angles and compared with conventional spiral tool path (CSTP). Two different materials AA5052 and DC05 were used to evaluate the influences of sheet material properties. As shown in Fig. 2a, the results of two sheet materials indicate similar tendencies but with different deviations, and the part formed by QSTP has better geometric accuracy than that formed by CSTP. Thinning tendencies are similar in both parts and both materials, but better thickness distribution can be obtained in the part formed

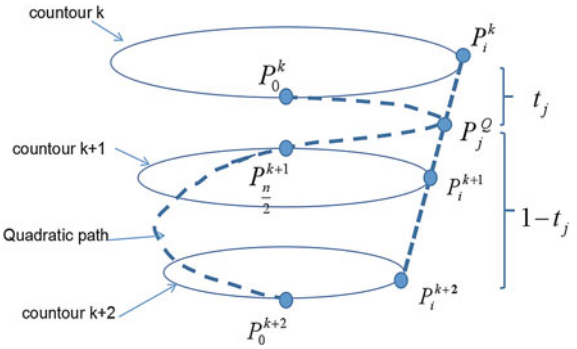
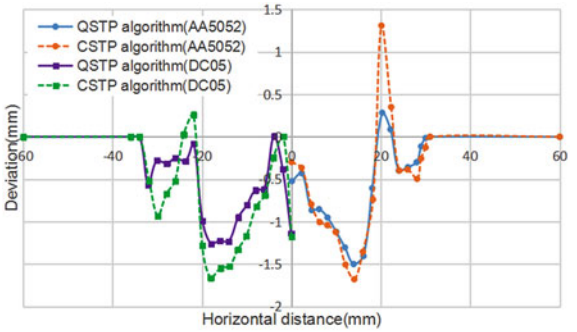
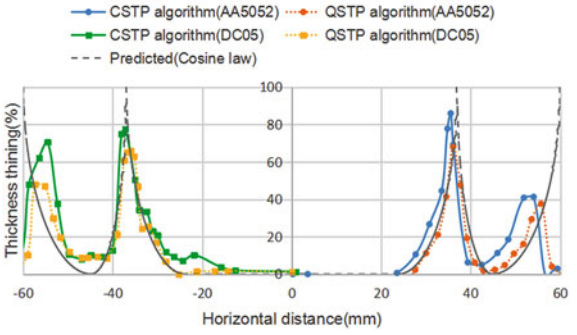


Fig. 1 Quadratic Lagrange interpolation based on three neighboring contour lines. (Color figure online)



(a)



(b)

Fig. 2 Experimental results for different sheet materials using QSTP and CSTP: (**a**) geometric deviation; (**b**) thickness thinning. (Color figure online)

by QSTP as shown in Fig. 2b. Experimental results confirm that QSTP can improve geometric accuracy, and reduce severe thickness thinning for different sheet materials compared with CSTP.

3 Analytical Prediction Model

3.1 Analytical Model of Forming Force

In order to overcome the problems of the widely used empirical models for load prediction, other than the regression method by experimental results, the new analytical models to predict the forming force were developed by Chang et al. [15] based on the analytical calculations for the contact area and the through-thickness stress. As shown in Fig. 3, the contact area is an ellipsoid crown surface, and the updated models for calculating the contact area can be developed by sliding the tool configuration along meridional and circumferential directions.

To calculate the through-thickness stress, the membrane approach was conducted as shown in Fig. 4. Along the directions of thickness, circumference, and meridian, the corresponding stress components were considered during membrane analysis. The stress components of a small element at the contact zone were analyzed for the solution of the through-thickness stress in the contact area. By multiplying the updated calculations of contact area with the through-thickness stress, the analytical force models of ISF can be represented by,=

$$F = \sigma_t S = \frac{2}{\sqrt{3}} \frac{2t}{r + 2.5t} \overline{\sigma} \frac{\pi r}{2} (h_1 + r(1 - \cos\alpha) \frac{\alpha + \arccos \frac{r - hs}{r}}{\arccos \frac{r - h_1}{r}}) \qquad (1)$$

A series of experiments of typical sheet metal parts with different geometries for different materials with varied process parameters including wall angle, step depth, tool radius, and sheet metal thickness in different typical ISF processes were used to validate the proposed analytical models. It can be seen from Fig. 5 that the predicted forces with different materials in different ISF processes are in good agreement with the measurements. It is concluded that the proposed analytical models are derived from the forming principle of ISF, have wider applicability than the empirical model,

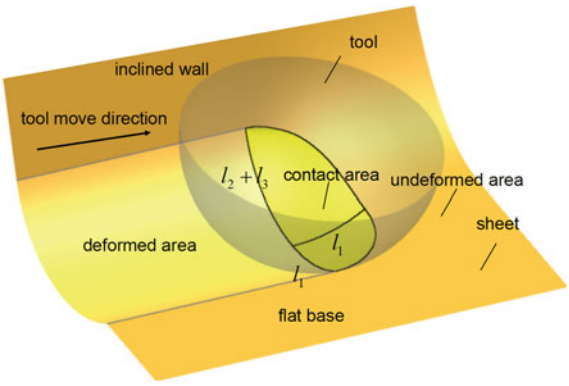


Fig. 3 Schematic illustration of contact area. (Color figure online)

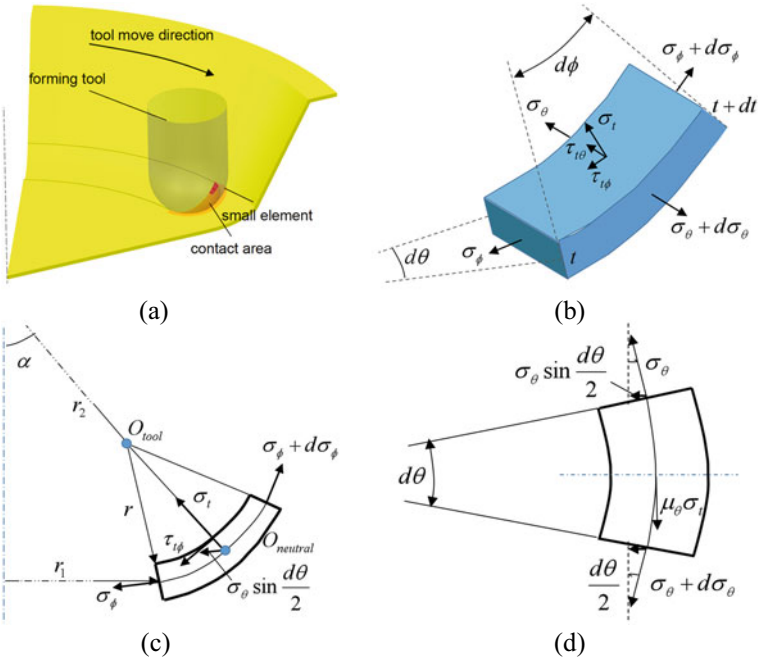


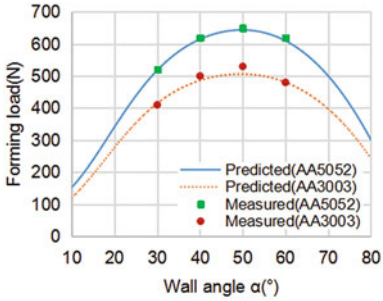
Fig. 4 Membrane approach of ISF process: (**a**) Overview; (**b**) stress components; (**c**) meridional view; (**d**) circumferential view. (Color figure online)

and can be used to calculate the forming force and force components along the axial, tangential, and radial directions for SPIF, MPISF, and IHF processes.

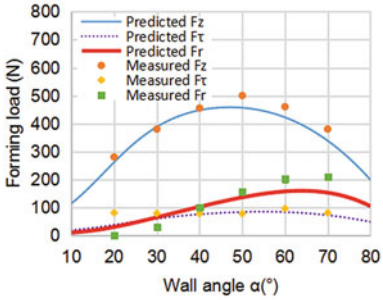
3.2 Analytical Model of Surface Roughness

In order to set up an analytical model to predict the surface roughness of the parts formed by ISF, a new mechanism about the evolution of surface roughness was assumed by Chang et al. [16] based on the forming principle of ISF as shown in Fig. 6. The "scallop" on the sheet surface is considered to be related to the uneven distribution of sheet thickness along the meridian direction, which considers elastic deflection and plastic deformation. The uneven distribution of sheet thickness under the tool head was calculated through the geometric relationship between the tool and the sheet as shown in Fig. 7. The surface roughness of the part surface can be calculated by the thickness difference of the "scallop",

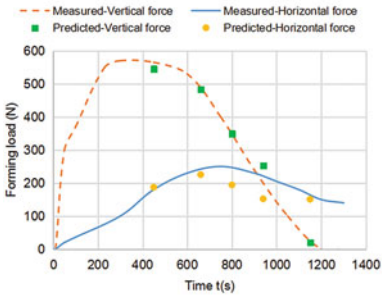
$$Ra = 0.268Rz = 0.268\left(\frac{t_2}{e^{\frac{\sqrt{3}}{2}\left(\frac{1}{K}\bar{\sigma}^{B}\right)^{\frac{1}{n}}}} - t\cos\alpha\right) \qquad (2)$$



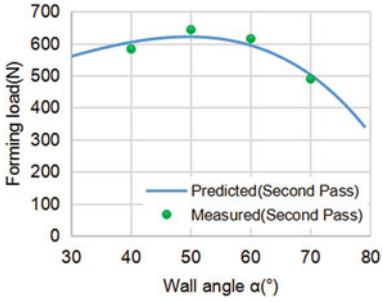
(a) single-point ISF



(b) force components



(c) incremental hole-flanging



(d) multi-pass ISF

Fig. 5 Analytical predictions of forming force with varied process parameters in typical ISF processes. (Color figure online)

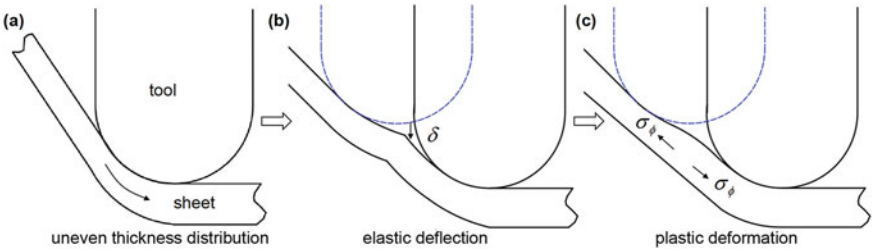


Fig. 6 Three steps of surface roughness evolution during incremental sheet forming. (Color figure online)

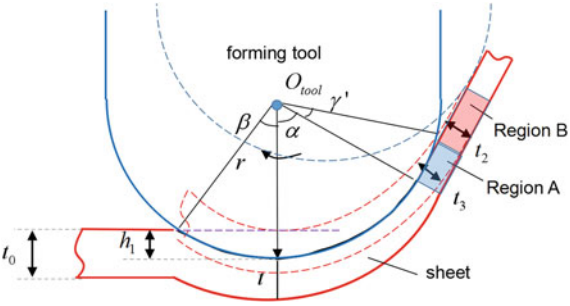


Fig. 7 Actual relationship between tool and sheet. (Color figure online)

A series of experiments for surface roughness of a conical part with varied process parameters for different materials have been conducted to validate the proposed models. As shown in Fig. 8, the predicted values of surface roughness are in good agreement with the measurements. The comparison between the calculated and measured results shows that the proposed analytical models maintain high prediction accuracy, which considered the effects of tool radius, wall angle, step depth, sheet thickness, and material properties. Besides, the new models are more accurate with wider applicability than the current geometry-based models, and can be used to calculate the surface roughness Ra and Rz under different process parameters and sheet materials.

3.3 Analytical Model of Twisting Angle

Revealing the twisting mechanism in ISF is of great importance for understanding the deformation mechanism and controlling the deformation stability. As shown in Fig. 9, the mechanism of the twisting phenomenon, proposed by Chang et al. [17], is that the uneven through-thickness stress distribution under the tool head leads to the uneven distribution of circumferential friction stress along the meridional direction, which

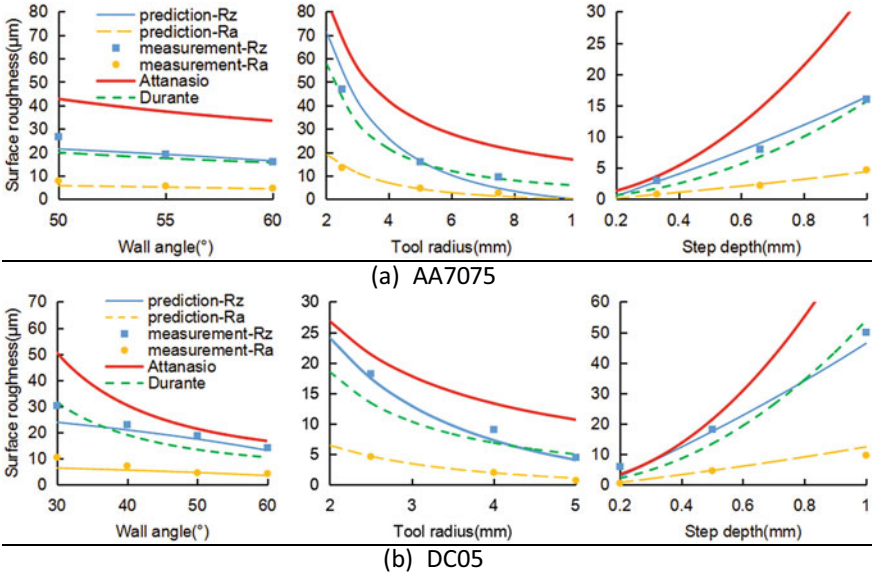


Fig. 8 Variation of surface roughness under varied process parameters for different materials. (Color figure online)

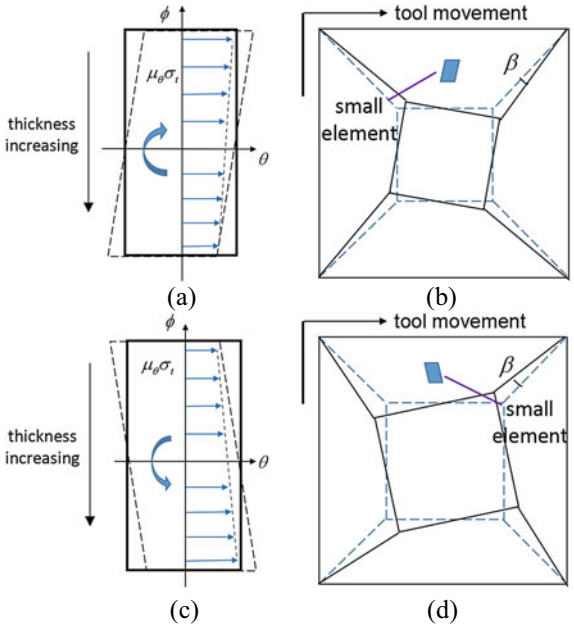


Fig. 9 Schematic view of twisting phenomena: (**a**) 40° wall angle; (**b**) forward twisting; (**c**) 65° wall angle; (**d**) reverse twisting. (Color figure online)

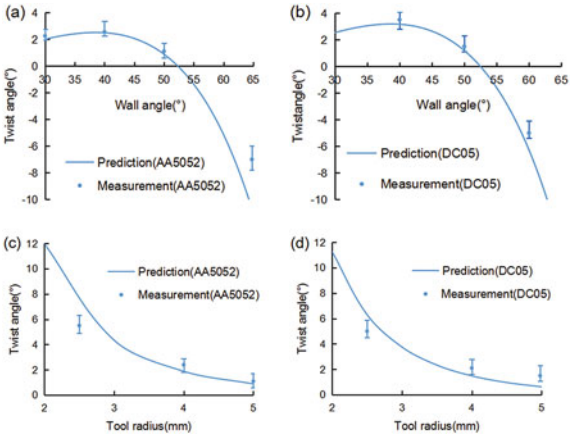


Fig. 10 Variations of twisting angle for different process parameters and materials: (**a**) varied wall angles (AA5052); (**b**) varied wall angles (DC05); (**c**) varied tool radius (AA5052); (**d**) varied tool radius (DC05). (Color figure online)

generates a torque that causes the twisting of the elements on the sheet metal. The value of dσt/dα determines the direction of the torque and the direction of twisting.

An analytical model in predicting twisting angle was developed based on membrane analysis, which can be represented as

$$\beta = \frac{\sqrt{3}\mu_\theta \ln\cos\alpha}{2}\frac{d\sigma_t}{d\alpha}$$

$$= \frac{2r_t t_o \mu_\theta \sin\alpha(\ln\cos\alpha + n) + 2.5nt_0^2\mu_\theta \sin(2\alpha)}{(r_t + 2.5t_0\cos\alpha)^2} K\left(\frac{2}{\sqrt{3}}\ln\frac{1}{\cos\alpha}\right)^n \quad (3)$$

A series of experiments on the twisting angle of truncated pyramid parts with varied process parameters and different materials have been conducted to validate the analytical model. As shown in Fig. 10, for a specified part, a small wall angle causes positive twisting angle, while a large wall angle causes negative twisting angle. It is also found that the analytical value is in good agreement with the measured values for varied process parameters and different materials, with the average numerical measurement error of 15.6%.

4 New Variants of ISF

To improve the surface quality and formability of low-ductility metallic sheets, a novel three-sheet incremental forming (TSIF) process was proposed. As shown in Fig. 11, the idea of the TSIF process is to put a target sheet with lower ductility between the upper auxiliary (UA) sheet and lower auxiliary (LA) sheet, then the three sheets are fixed together and formed by the forming tool to a geometry. The

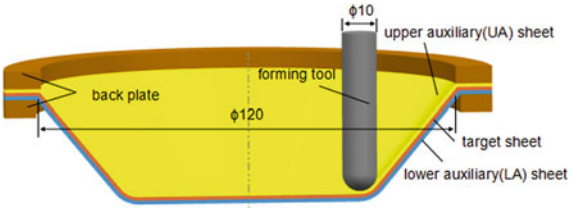


Fig. 11 Schematic of TSIF. (Color figure online)

existence of the UA sheet aims to avoid the direct contact between the tool and target sheet, and the LA sheet is prepared to provide the extra compressive stress to the target sheet and improve the stress state in the contact zone.

For better understanding forming characteristic of TSIF, the surface quality and forming limit of the target sheet were investigated by experiments for different sheet materials and compared with the conventional single point incremental sheet forming (CISF) process. As shown in Fig. 12, experimental results demonstrate that the surface roughness can be significantly reduced by an average of 80% in the TSIF process compared with that by CISF. Ra of the part formed by TSIF always keeps at a small value with the variation of step depth, indicating that the effect of step depth on Ra of TSIF is obviously less sensitive than that of CISF. Results also prove that the forming limit and fracture strains of AA2024 and AA7075 sheets can be improved dramatically with the extra compressive stress from the LA sheet, which is helpful for low-ductility sheet metal component fabrication.

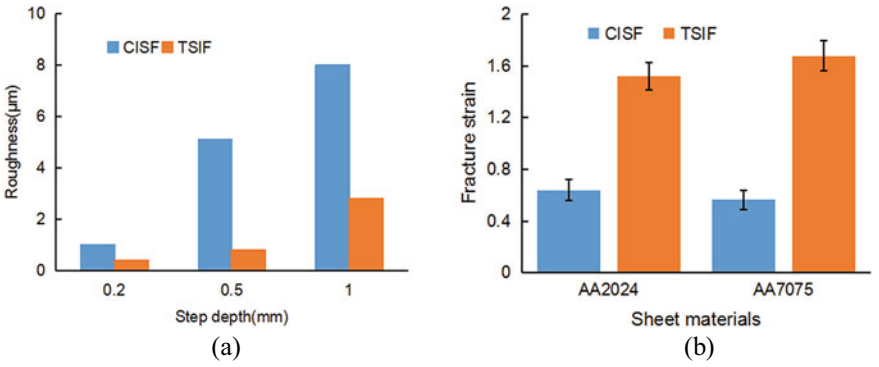


Fig. 12 Experimental results of different materials for CISF and TSIF: (**a**) surface roughness; (**b**) fracture strain. (Color figure online)

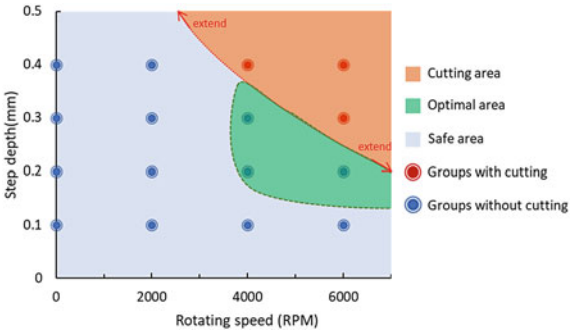


Fig. 13 Process window. (Color figure online)

5 Process Window

5.1 Formability for ISF with High-Speed Tool Rotation

ISF with high-speed tool rotation is another promising alternative for forming low-ductility sheet metals. but high-speed friction between the tool and the deforming sheet metal might cause bad surface quality, and process parameters have contradictory effects on formability and surface quality. To solve this puzzle, the effects of four factors on forming temperature and surface quality were analyzed by Wang et al. [18] through orthogonal experiments for a truncated cone with a constant wall angle of AA2024-T. A process window for ISF with high-speed tool rotation was obtained to have a higher forming temperature for better formability with reasonable surface quality. Orthogonal analysis results on forming temperature show that rotating speed has the greatest influence, followed by step depth.

By collecting the experimental results of cutting (red point) and no cutting (blue point), Fig. 13 demonstrates the safe area (blue area) and the cutting area (orange area), which shows that the ranges of rotating speed and step depth can be used to define the process window to avoid cutting. Thus, the optimal area (green area) which can guarantee high forming temperature without cutting is provided in Fig. 13. Besides, the applicability of the process window proposed was verified by another truncated cone with varied wall angles using AA2024-T and AA5052-H32. Figure 14 shows the maximum wall angle with process parameters set within the optimal area, and the formability of two aluminum alloy sheets was improved.

5.2 Geometric Deviation

One of the key challenges for ISF is geometric accuracy, especially for complex sheet metal parts. A typical non-axisymmetric part of AA5052 with the stepped feature

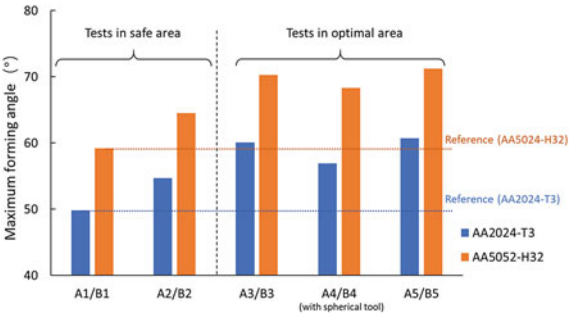


Fig. 14 Measured maximum wall angles of AA2024-T3 and AA5052-H32. (Color figure online)

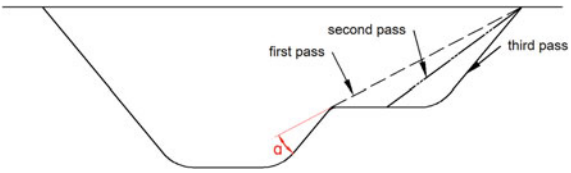


Fig. 15 Three-pass ISF of the stepped feature. (Color figure online)

was studied by Dai et al. [19] through orthogonal experiments with 4 parameters in 4 levels to determine the optimal process parameters for better geometric accuracy.

Three-pass ISF was developed to form the stepped feature as shown in Fig. 15. An attempt was made to change the forming process sequence, in which the stepped flank is formed prior to the stepped plane, and later the stepped plane is formed in several passes. Experiments demonstrate that a larger angle is helpful in subsequently forming the upper sidewall and the stepped plane, respectively.

To further improve the local geometric accuracy, the angle of the stepped flank and the height of the stepped plane need to be compensated in Multi-pass ISF. Based on the local geometric deviation and the deflection mode at the corner between the stepped plane and the stepped flank, the compensation scheme of the intermediate configuration in each pass is shown in Fig. 16. Based on the proposed methodology, the geometric accuracy of the non-axisymmetric part with the stepped feature has been obviously improved, particularly at the stepped feature as shown in Fig. 17.

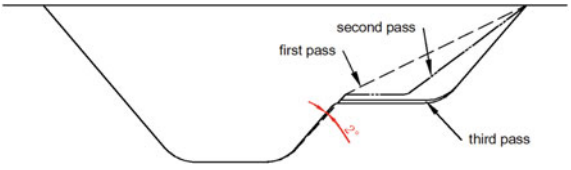


Fig. 16 Compensation scheme of the intermediate configuration for each pass. (Color figure online)

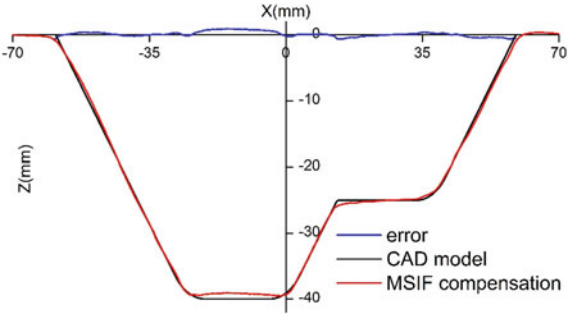


Fig. 17 Sectional profile and the error of new multi-pass ISF with toolpath compensation. (Color figure online)

6 Outlook

A systematic review of the latest developments of the ISF process was conducted, and this provides a feasible direction for future research. The process fundamentals in terms of process window, analytical models, tool paths and new variants of ISF were systematically introduced. The new tool path and variants of ISF have the capability of extending the process window for industrial application and obtaining parts with some specific requirements. Analytical models developed based on membrane analysis have the ability to accurately predict the forming force, surface roughness, and twisting angle, and provide feasible solutions to better control the forming quality of parts formed by ISF. The investigations on the process window are significant for improving the formability and geometric accuracy of sheet metal for further industrial application. The application of ISF has increased significantly, which will provide directions for the development of flexible industrial systems based on ISF.

Acknowledgments The authors are grateful for the financial support from National Natural Science Foundation of China through grant #U1737210 and the Program of Shanghai Excellent Academic Research Leadership through grant #19XD1401900.

References

1. Duflou JR, Callebaut B, Verbert J, Baerdemaeker HD (2007) Laser assisted incremental forming: formability and accuracy improvement. CIRP Ann–Manuf Technol 56:273–276
2. Araghi BT, Manco GL, Bambach M, Hirt G (2009) Investigation into a new hybrid forming process: incremental sheet forming combined with stretch forming. CIRP Ann-Manuf Technol 58:225–228
3. Silva MB, Skjoedt M, Martins P, Bay N (2008) Revisiting the fundamentals of single point incremental forming by means of membrane analysis. Int J Mach Tools Manuf 48:73–83
4. Emmens WC, Boogaard AHVD (2009) An overview of stabilizing deformation mechanisms in incremental sheet forming. J Mater Process Technol 209:3688–3695
5. Lu B, Fang Y, Xu DK, Chen J, Ou H, Moser NH, Cao J (2014) Mechanism investigation of friction-related effects in single point incremental forming using a developed oblique roller-ball tool. Int J Mach Tool Manuf 85:14–29

6. Eyckens P, Belkassem B, Henrard C, Gu J, Sol H, Habraken AM, Duflou JR, Bael AV, Houtte PV (2011) Strain evolution in the single point incremental forming process: digital image correlation measurement and finite element prediction. Int J Mater Form 4:55–71
7. Silva MB, Isik K, Tekkaya AE, Atkins AG, Martins PAF (2016) Fracture toughness and failure limits in sheet metal forming. J Mater Process Technol 234:249–258
8. Duflou J, Tunckol Y, Szekeres A, Vanherck P (2007) Experimental study on force measurements for single point incremental forming. J Mater Process Technol 189:65–72
9. Mulay A, Ben S, Ismail S, Kocanda A (2017) Experimental investigations into the effects of SPIF forming conditions on surface roughness and formability by design of experiments. J Braz Soc Mech Sci 39:3997–4010
10. Li Z, Lu S, Chen P (2017) Improvement of dimensional accuracy based on multistage single point incremental forming of a straight wall cylinder part. Int J Precis Eng Manuf 18:1281–1286
11. Palumbo G, Brandizzi M (2012) Experimental investigations on the single point incremental forming of a titanium alloy component combining static heating with high tool rotation speed. Mater Design 40:43–51
12. Silva MB, Alves L, Martins P (2010) Single point incremental forming of PVC: experimental findings and theoretical interpretation. Eur J Mech-A/Solids 29(4):557–566
13. Jackson K, Allwood J, Landert M (2008) Incremental forming of sandwich panels. J Mater Process Technol 204:290–303
14. Chang Z, Li M, Li M, Chen J (2019) Investigations on a novel quadratic spiral tool path and its effect on incremental sheet forming process. Int J Adv Manuf Tech 103:2953–2964
15. Chang Z, Li M, Chen J (2019) Analytical modeling and experimental validation of the forming force in several typical incremental sheet forming processes. Int J Mach Tool Manuf 140:62–76
16. Chang Z, Chen J (2019) Analytical model and experimental validation of surface roughness for incremental sheet metal forming parts. Int J Mach Tool Manuf 146:103453
17. Chang Z, Chen J (2020) Mechanism of the twisting in incremental sheet forming process. J Mater Process Technol 276:116396
18. Wang Z, Cai S, Chen J (2020) Experimental investigations on friction stir assisted single point incremental forming of low-ductility aluminum alloy sheet for higher formability with reasonable surface quality. J Mater Process Technol 277:116488
19. Dai P, Chang Z, Li M, Chen J (2019) Reduction of geometric deviation XE “geometric deviation” by multi-pass incremental forming combined with tool path compensation for non-axisymmetric aluminum alloy component with stepped feature. Int J Adv Manuf Tech 102:809–817

The Effect of Ultrasonic Vibration on Material Movement in Incremental Sheet Forming



Randy Cheng, Ankush Bansal, Jiarui Kang, Xun Liu, and Alan Taub

Abstract Applied mechanical vibration in various manufacturing processes, usually at ultrasonic frequencies of 20 kHz, has been shown to influence the forming and friction forces. The material softening behavior under superimposed ultrasonic vibrations is known as acoustoplasticity. This paper investigates the effect of acoustoplastic softening phenomenon on material movement in incremental forming of AA7075 sheets. A 45° cone is formed using a two-point incremental forming strategy (TPIF). Added ultrasonic vibration shows higher amount of material movement, which is supported through quantitative measurements including greater bulge height, surface profilometry, and thickness distribution around the tool contact area. Surface roughness measurements, relative to the depth of the geometry, increase with progressive forming. This coincides with the notion of greater material movement, accumulation, and surface deformation.

Keywords Incremental sheet metal forming · Acoustoplasticity effect · Aluminum alloy 7075 · Material movement · Bulge · Ultrasonic assisted · Vibration assisted

1 Introduction

Incremental sheet forming (ISF) has garnered interest for its unique manufacturing advantages such as design flexibility and increased formability of sheet metal parts [1]. The process involves a hemispherical-ended tool which travels along a tool path and locally deforms a blank until the desired 3D geometry is completed. Typical

R. Cheng (✉) · A. Taub
Department of Material Science and Engineering, University of Michigan, Ann Arbor, MI 48109, USA
e-mail: randyjfc@umich.edu

A. Bansal · A. Taub
Department of Mechanical Engineering, University of Michigan, Ann Arbor, MI 48109, USA

J. Kang · X. Liu
Department of Material Science and Engineering, The Ohio State University, Columbus, OH 48210, USA

© The Minerals, Metals & Materials Society 2021

G. Daehn et al. (eds.), *Forming the Future*, The Minerals, Metals & Materials Series,
https://doi.org/10.1007/978-3-030-75381-8_32

manufacturing machinery, such as CNCs, lathes, and robotic arms, can implement an ISF strategy utilizing already existing G code generating software and standard fixtures. Single-point (SPIF) and two-point (TPIF) incremental forming are covered in this work [1, 2]. SPIF does not require a die which aids in its flexibility. TPIF uses partial or half-dies to aid in supporting the sheet; this prevents additional plastic deformation away from the local contact area. The tool can also push the sheet against the die, referred to as squeeze, effectively changing the through thickness strain.

With all deformation processes, adjustments are usually required depending on the material and the design to satisfy product outcomes. The agile attribute in ISF arises from its ease of modifying the tool path which leads to quick turnaround times compared to stamping or hydroforming [3]. Higher formability in ISF can be achieved as instability and necking are suppressed from the localized nature of the deformation [1]. Although ISF offers these advantages, the process also has some compromises. Local deformations on the sheet surface leads to added tribological wear and higher roughness compared to conventionally formed parts [4]. Furthermore, unlike stamping where springback predictive models are available, ISF still requires tool path adjustments to obtain comparable dimensional accuracy [1, 2, 5].

A multitude of assistive methods have been proposed to address these process constraints [5–7]. Ultrasonic vibration assistance is a new method which takes advantage of acoustoplasticity. Langenecker and Blaha [8] first experimentally demonstrated the acoustoplastic effect (APE) during tensile deformation of aluminum and zinc crystals and noted large reduction in force. Langenecker [9] proposed an acoustic energy interaction with pinned dislocations leading to a reduction in flow stress. This phenomenon was later coined as acoustoplasticity. Various reports have illustrated a compelling argument for this softening phenomenon. Siu et al. [10] conducted hardness tests with ultrasonic excitation perpendicular to the loading axis and showed an increased plastic zone and subsequent increase in low angle grain boundary formation. Kang and Liu [11] conducted tensile experiments on pure copper with an ultrasonic excitation parallel to the loading axis. The deformed microstructure displayed a reduction in stored dislocations in grain interiors and greater geometrically necessary dislocations located near grain boundaries. Zhou et el. observed similar stress reduction effects correlated with ultrasonic vibration amplitude and frequency [12]. After a period of ultrasonic activation, the material, loaded quasi-statically in compression, may exhibit residual softening or hardening. Based on the reported work, there is substantial evidence to support the notion that ultrasonic vibration impacts the resulting microstructure and therefore, the deformation behavior.

The application of acoustoplasticity in ISF has been limited. Amini et al. [13] performed ultrasonic-assisted incremental forming (UA-ISF) on AA1050 with a straight groove geometry and noted improvements in formability, reduction in forming forces, and improved springback. Cheng et al. [14] performed ultrasonic-assisted SPIF and TPIF on AA 7075. In those experiments, the effectiveness in SPIF operations was minimal which was attributed to a loss in transmission of acoustic

energy to elastic vibration of the sheet. The UA-TPIF process showed force reductions of 11–18% accompanied by thickness reductions in the formed parts. The literature has yet to address the acoustoplastic effect on material movement, geometric accuracy, and roughness.

We examined three ISF variants: SPIF, TPIF, and TPIF + UA. The effect of ultrasonic vibration on the in-plane forces and on material movement was quantified through measurements of the bulge height, approximated from surface profilometry, and from the thickness distribution around the tool contact area at the end of the forming process.

2 Experimental Setup

Incremental forming experiments were performed on a Cincinnati HMC 400-EP CNC milling machine. A truncated cone die, with a wall angle of 45°, was selected for two-point incremental forming (TPIF) experiments. A hemispherical-ended tool with 8 mm diameter was employed to deform 1.63 mm thick AA 7075 sheets. The sheets were cut out into 200 × 200 mm blanks and held at the edges using a binder plate as shown in Fig. 1. An internal piezoelectric ceramic generates the ultrasonic frequency in the device, and an operating frequency of 20,200 Hz is maintained by a Dukane iQ-LS series wave form generator. Additional information regarding ISF parameters are listed in Table 1.

A multi-squeeze tool path strategy illustrated Fig. 2a was employed to investigate the effect of squeeze factor *SF* on part fabrication. The sine law, shown in Eq. 1, is typically used to estimate the final thickness, t_f, of the sheet in ISF forming, given the forming angle, α [1]. In TPIF, the squeeze factor is defined as the extra displacement

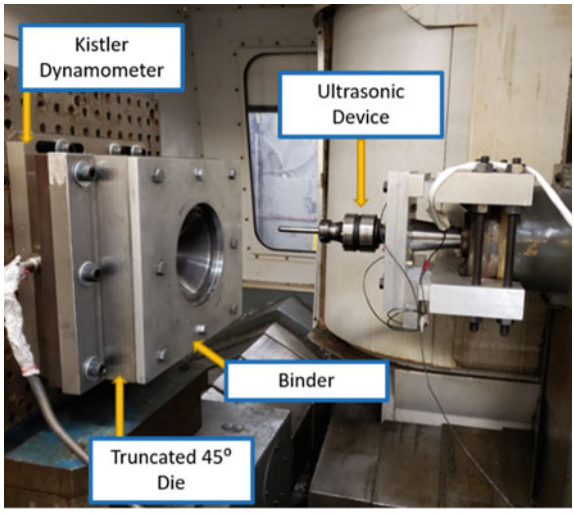


Fig. 1 Incremental forming setup. Ultrasonic input is supplied using a 20 kHz, Dukane generator. The ultrasonic device is held a custom clamp fixture. A conical 45° sits on a Kistler force dynamometer. (Color figure online)

Table 1 Incremental forming parameters

ISF process parameters	
Lubricant	Molybdenum Disulfide (MoS_2)
Tool diameter	8 mm
Blank thickness	1.63 mm
Resonant frequency	20,200 Hz
Feed rate	42.3 mm/s
Step size	0.25 mm
Spindle rotation	Locked

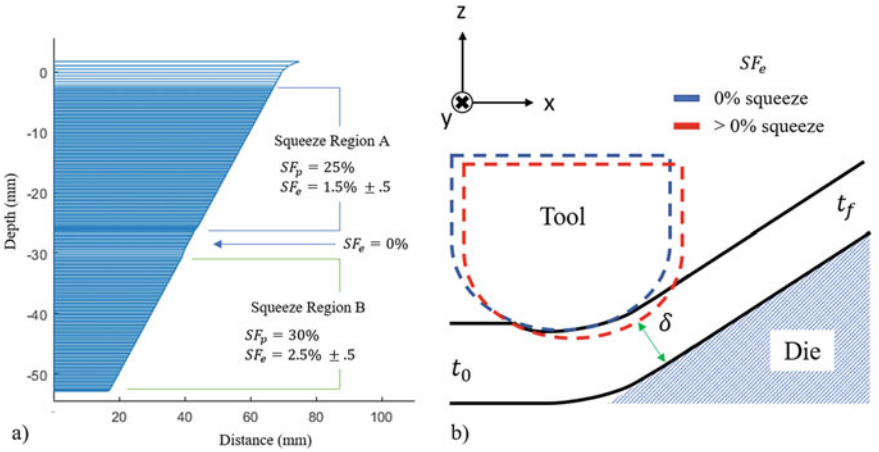


Fig. 2 Geometric illustrations for tool path strategy and programmed squeeze. **a** tool path representation showing squeeze region A, squeeze region B, and the transition in between. **b** Visual representation of effective squeeze. (Color figure online)

of the tool into the sheet, defined as the percentage of the final thickness (t_f) that is squeezed between the tool and die surfaces. A visualization of programmed squeeze is presented in Fig. 2b. The programmed squeeze factor, SF_p, is defined as in Eq. 2 [15]:

$$t_f = t_0 \cdot \sin(90 - \alpha) \tag{1}$$

$$SF_p = \left(1 - \frac{\delta}{t_f}\right) \cdot 100 \tag{2}$$

δ represents the intended distance of the tool, from die surface. A $SF_p = 100\%$ is when the tool is programmed to touch the die surface and a $SF_p = 0\%$ implies that there is no material being squeezed. The tool path strategy, Fig.2a, uses two regions of programmed squeeze factors, designated as regions A ($SF_p = 25\%$) and B ($SF_p = 30\%$). It is important to note that the programmed squeeze in the tool path

is not the same as the actual squeeze which is referred to as the effective squeeze, SF_e. Bansal et al. [15] showed that the tool deflection and machine compliance have a large impact on squeeze. The effective squeeze factor can be represented through Eq. 3. If the sum of the desired squeeze, δ, and deflection from machine compliance and tool deflection, Δ, is larger than t_f, the sheet is not being squeezed. In this case, a negative SF_e can be thought of as a degenerative SPIF.

$$SF_e = \left(1 - \frac{\delta + \Delta}{t_f}\right) \cdot 100 \tag{3}$$

Δ is the compensation factor for machine compliance and tool deflection.

The effective squeeze in our TPIF experiments ranges from $SF_e = 1 - 3\%$. Squeeze region A has a squeeze factor $SF_e = 1.5 \pm .5\%$ and squeeze region B has a squeeze factor of $SF_e = 2.5 \pm .5\%$. These squeeze factors will be referred to as $SF_e = 1.5\%$ and 2.5% for brevity. The effective squeeze factors were chosen based on the previous work of Bansal et al. [15]. There are two methods of verifying a positive effective squeeze factor. First, TPIF parts formed with $SF_e = 0\%$, like in SPIF, have an orange peel surface finish on the side of the sheet facing the die [16]. With$SF_e > 0\%$, the surface finish will be similar to that of the die surface. Second, the forming force should be greater when the sheet is being squeezed. Both conditions are satisfied in the TPIF experiments in this study.

A Hexagon laser CMM, 7525SI series, was used to measure the wall angle of the incrementally formed parts. The cross-sectional data was extracted using Polywork's inspection software. Surface roughness and profilometry data were measured on an Olympus DSX510 optical microscope.

3 Results and Analysis

The planar forming force is the resultant X and Y force. Figure 3 shows the planar forming force for the three conditions: SPIF, TPIF, and TPIF + UA. The initial increase in force, 100—200 s, is where the tool first contacts the filet region of the die. This is a common transient region, and the force stabilizes when the tool reaches a constant 45° wall angle which is referred to as the steady state. The average steady-state force in SPIF is roughly 300 N and the forming force for both TPIF and TPIF + UA conditions is greater, as expected. In the first squeeze region, $SF_e = 1.5\%$, the steady-state force is 550 ± 100 N. The spread in force is due to a slight eccentricity in the die. This minor deviation from a perfect 45° cone create sregions with slightly higher and lower squeeze so a range is provided. The planar force increases from $SF_e = 1.5\%$ to $SF_e = 2.5\%$ squeeze factor. The + UA planar force gradually increases in $SF_e = 1.5\%$ region and sharply increases in the higher $SF_e = 2.5\%$ region. The forming process of the + UA specimen was stopped at a lower depth to avoid damage to the tool/die. In the transition region between the two squeeze

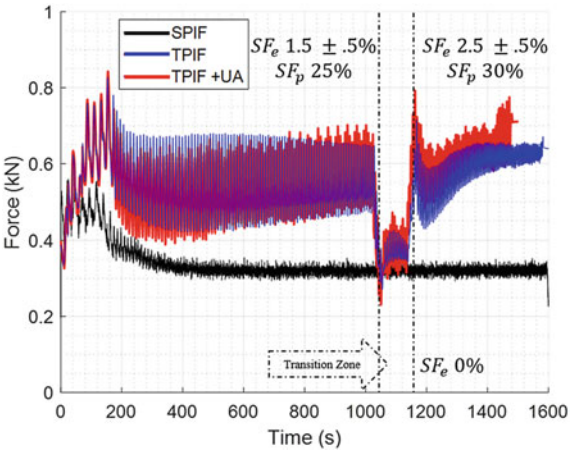


Fig. 3 Planar forming force of incrementally formed specimens in SPIF, TPIF, and TPIF + UA variants. The tool path strategy applies two regions of programmed squeeze with a gradual transition in between. (Color figure online)

conditions, the tool retracts to $SF_e = 0\%$ over several tool passes, forms the sheet at $SF_e = 0\%$, and gradually increases the squeeze to $SF_e = 2.5\%$. The forming forces during the transition region maintain a similar range of values as that during SPIF.

Geometric accuracy was measured from laser CMM profiles and EDM cut cross sections in Fig. 4. The sheet experiences some springback along the bend around −

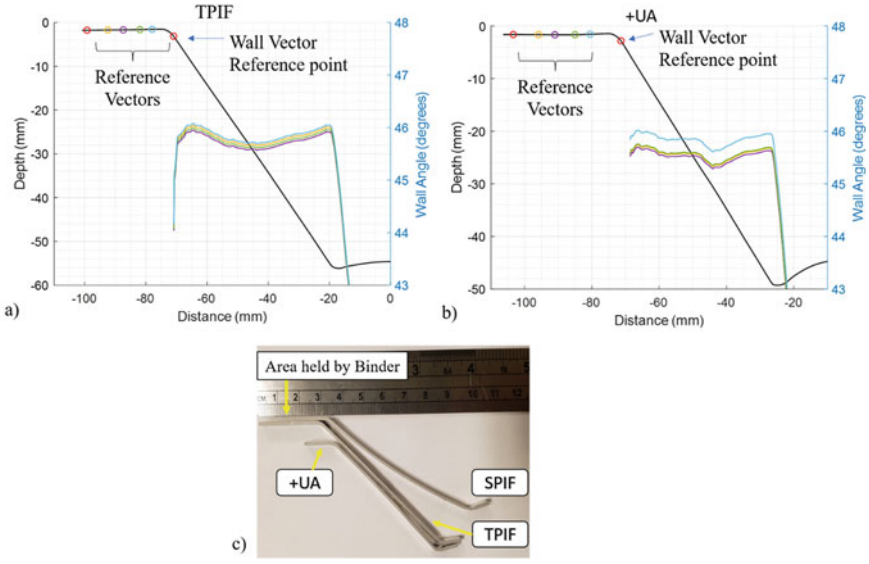


Fig. 4 Comparing wall angles of cross-sectioned ISF specimens **a** TPIF wall angle relative to the depth of the part, **b** + UA wall angle relative to the depth of the part, and **c** cut cross sections of ISF parts after forming. (Color figure online)

75 mm. Therefore, several reference vectors along the binder of the sheet were used as indicated in Fig. 4a, b. The wall vector is calculated using a point along the depth of the wall with respect to the fix point at -70 mm. The UA specimen has an average wall angle of 45.5° ± 0.2 and the TPIF specimens has a wall angle of 45.7° ± .3. The SPIF wall angle was comparable to the 45° designed tool path prior to cutting; however, after cutting, the specimen cross section curves upwards from releasing stored residual stress as shown in Fig. 4b.

In incremental forming, the sheet locally conforms to the concavity or shape of the tool due to the localized plastic deformation. This creates wavy-like surface features, which are referred to as scallops as shown in Fig. 5a. The SEM images show a higher density of flake-like features in the TPIF surface and more defined tool striation lines in the + UA specimen. Figure 5b is a cross-sectional representation of these scallop features. The spacing of the scallop feature are related to the step size (Δz) and forming angle (α) by $\Delta z/\sin(\alpha)$. This equates to a spacing of roughly 350 μm. Roughness measurements should exclude this periodic feature. A cutoff frequency of 350 μm was found to be sensitive to roughness values at the peaks, so a smaller cutoff wavelength of 80 μm was used instead. The surface roughness relative to the forming depth is plotted in Fig. 5c. The + UA specimen has a higher roughness throughout the depth of the sample. The SPIF shows relatively consistent roughness with respect to forming depth while the TPIF and + UA roughness slightly increase relative to depth.

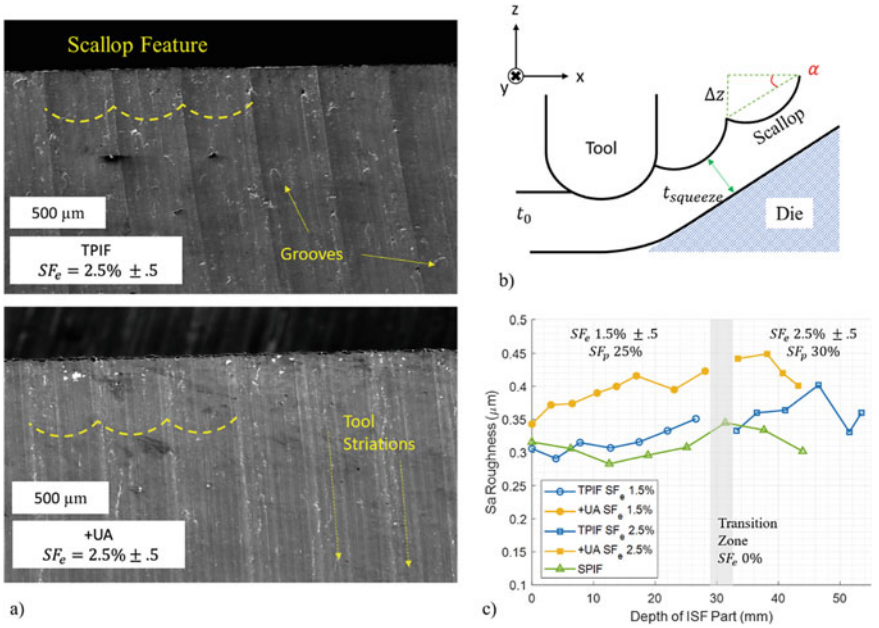


Fig. 5 Surface measurements **a** SEM images of TPIF and + UA surface indicating scallop geometry and spacing,**b** cross-section diagram of scallop feature, and **c** surface roughness, Sa, measurements relative to ISF part depth. (Color figure online)

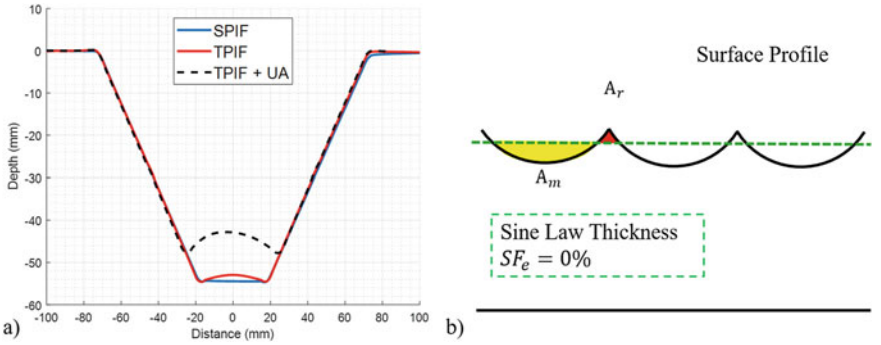


Fig. 6. **a** Cross sections extracted from laser CMM scans of pre-cut ISF parts, **b** representation of material movement in ISF given that Am > Ar. (Color figure online)

Cross-sectional scans, shown in Fig. 6a, indicate the presence of a geometric defect called a bulge at the bottom of the part. The + UA specimen has a bulge height of 4.90 mm while the TPIF bulge height is 1.61 mm. Jae et al. [17] suggested that material is moved forward in incremental forming operations under sufficient amount of squeeze, leading to a bulge. They quantified the moved material by taking the difference in thickness relative to the sine-law thickness for an individual scallop represented in Fig. 6b. If the area in the region above the line of the sine law, Ar, is equal to the material below the sine law, Am, the effective thickness coincides with the sine law. Assuming material conservation, Am > Ar indicates the material had been pushed ahead of the tool. With each Δz increment, the material is continually pushed toward the center of the part and accumulates ahead of the tool. To approximate the total amount of material moved, the area, Am-Ar, is multiplied by the number of tool passes or the number of steps in the depth direction. Using this method, material accumulation was calculated using an average Am-Ar value taken from three points in each squeeze region and plotted in Fig. 7a. As shown with the TPIF specimen, with increasing squeeze, the total volume of moved material increases. Adding ultrasonic vibrations increases the material accumulation in the $SF_e = 1.5\%$ region. Since the + UA forming was stopped at a smaller forming depth, an equivalent approximation was calculated for TPIF at $SF_e = 2.5\%$. Adding ultrasonic vibration also shows a greater amount of material accumulation in the $SF_e = 2.5\%$ region. Material accumulation can be compared using measured cross sections. The last tool contact region from the cross sections in Fig. 6a was overlayed and plotted in Fig. 7b. This cross section can be partitioned into three regions: bulge, tool contact, and wall regions. Along the wall region, both samples have a similar $t_f = 1.15\text{mm} \pm 0.02$. The thickness in the bulge or center region of the part is equal to $t_0 = 1.63\text{mm} \pm 0.01$. The thickness in the tool contact region shows a gradient between t_0 and t_f. The thickness distribution of the + UA is greater than the TPIF sample around the tool contact area suggesting greater material accumulation. A macroscopic image of each part is shown in Fig. 8. The parts in Fig. 8 are flipped upside-down and the die-side of the sheet is being shown. Both parts show evidence of squeeze as machining marks,

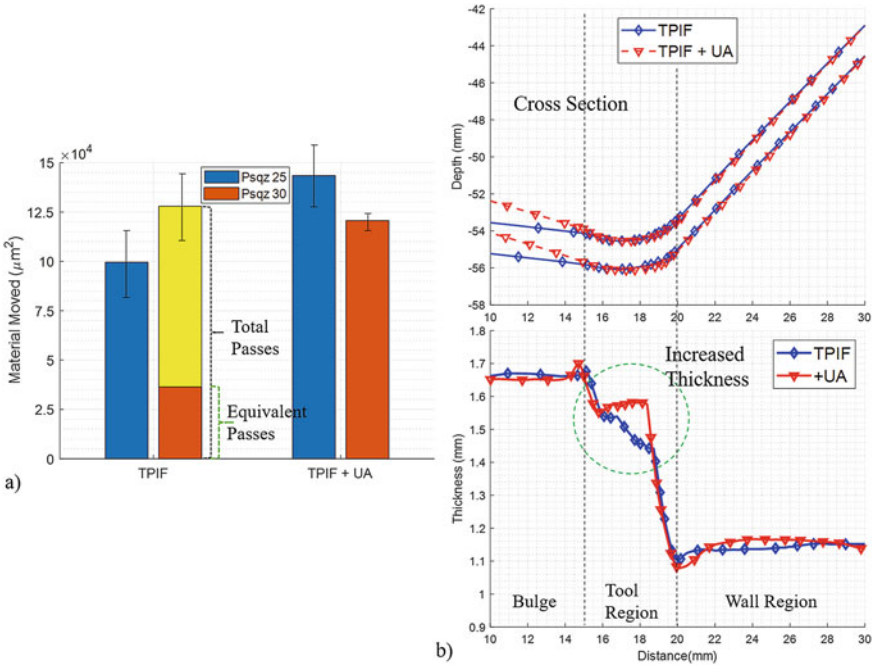


Fig. 7. **a** Material accumulated in TPIF and + UA specimens within their respective squeeze regions, **b** thickness distribution around the tool contact region of the last pass. Squeeze region $SF_e = 2.5\% \pm 0.5$. (Color figure online)

from the die, are imprinted onto the die-side of the sheet. The bulge is evident based on the depression shown in Fig. 8b.

4 Discussion

The geometric accuracy of ISF parts were measured using laser CMM scanning and post-cutting measurements. All parts achieved close to the desired 45° taper in the pre-cut measurement. Once cut, the stored residual stress is relieved, and the wall angle is measured again. TPIF and + UA specimens retain the desired wall angle while the SPIF part shows considerable springback. Springback occurs when a residual stress gradient is present in the specimen. Since TPIF and + UA utilize the back support of the die, both surfaces of the sheet can experience compressive deformation in the through thickness direction when squeezed. In single-point forming, the sheet's "die-side" experiences tensile stresses while the tool-side experiences compressive stresses underneath the tool, similar to bending. Upon cutting, the stored tensile and compressive forces cause the cross section to bend upwards.

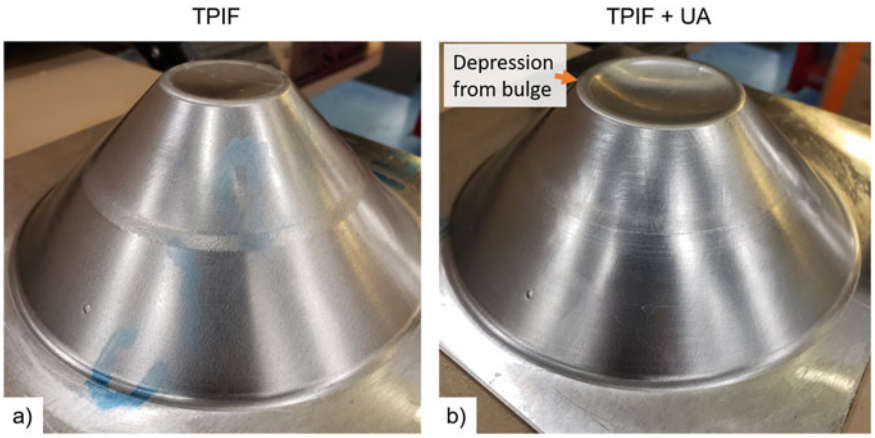


Fig. 8 Two-point incrementally formed cones **a** with effective squeeze and **b** with ultrasonic vibrations. (Color figure online)

From the planar force data, it is shown that both TPIF and + UA specimens achieved a positive effect squeeze as indicated by the greater forming force relative to SPIF. Increasing the squeeze from $SF_e = 1.5\%$ to $SF_p = 2.5\%$ increased the planar forming force as expected. The TPIF forming force was maintaining a steady mean force within their respective squeeze factor. Adding ultrasonic vibrations leads to a gradual increase in planar force in both squeeze regions. This was attributed to the formation of a macro-defect feature called a bulge. Through laser CMM scans, the + UA specimen has a larger bulge height compared to the TPIF specimen. The maximum bulge height values are 4.9 mm and 1.6 mm for + UA and TPIF samples, respectively.

The bulge formation is correlated to material movement in ISF. The sheet conforms to the geometry of the tool through the localized deformation and creates a surface feature called a scallop. In the conditions where the effective thickness of one scallop deviates from the sine law, as shown in Fig. 6b as $A_m - A_r > 0$, material must have been moved based on the material conservation law. Approximating the net material movement based on scallop geometry suggests a positive correlation with increasing squeeze. The addition of ultrasonic vibration creates deeper scallops and therefore greater material movement. Material conservation theory suggest that the displaced material should accumulate at the bottom of the part. This coincides with the gradual increase in force. With every pass, the material ahead of the tool continues to build and therefore, the force increases. The greater thickness around the last tool position in + UA sample compared to the TPIF sample supports this notion.

Coinciding with increased material movement, both TPIF and + UA samples show a slightly increasing surface roughness relative to forming depth. This is expected as greater material deformation leads to higher roughness. Maintaining same process parameters, the added ultrasonic vibration showed different outcomes of the ISF

formed parts. The results suggest that added vibrations led to greater material movement as shown by the larger bulge height and greater thickness distribution around the last tool contact area. Although the planar forming forces did not indicate acoustic softening, effects of ultrasonic vibration are reflected on the material movement. The application of ultrasonic vibrations has previously been shown to reduce forming force [14]. However, this work suggests that adding ultrasonic vibration can lead to differences in part outcomes without direct force reductions. In the same conclusion, effects of the acoustoplasticity phenomenon on ISF process closely depend on the specific forming conditions. A few key areas will be addressed in future work. Specifically, equivalent transmission of acoustic energy needs to be studied and compared to uniaxial tensile test + UA in literature. The effects of tool diameter, feed rate, and step size are all related to the total acoustic energy transmitted during incremental forming. This should further expand our understanding of how to utilize the acoustoplasticity phenomenon.

5 Conclusion

In this work, the effect ultrasonic vibration on material movement in incremental sheet metal forming was studied. Three variants of ISF were explored: single-point (SPIF), two-point (TPIF), and two-point with aided ultrasonic vibration (+UA). The + UA specimen showed a gradual increase in force with progressive forming. This greater forming force is due to an increase in material movement, resulting in the formation of a macro-defect called a bulge. The material moved is represented by the difference in thickness between the sine law thickness and measured thickness. Several quantitative measures support the increase in material movement with added vibration including the greater bulge height, approximated material movement from scallop profiles, and a greater thickness distribution from the last tool contact area. In addition, the surface roughness increased with progressive forming.

Acknowledgments This material is based upon work supported by the National Science Foundation under CMMI No. 2018963.

References

1. Duflou JR, Habraken AM, Cao J, Malhotra R, Bambach M, Adams D, Jeswiet J (2018) Single point incremental forming: state-of-the-art and prospects. Int J Mater Form 11:743–773
2. Silva MB, Martins PAF (2014) Incremental Sheet Forming. Compr Mater Process pp 7–26. Elsevier
3. Daehn GS, Taub A (2018) Metamorphic manufacturing: The third wave in digital manufacturing. Manuf Lett 15:86–88
4. Kumar A, Gulati V, Kumar P (2018) Effects of Process Parameters on Surface Roughness in Incremental Sheet Forming. Materials Today Proceedings 5(14):28026–28032

5. Ren H, Xie J, Liao S, Leem D, Ehmann K, Cao J (2019) In-situ springback compensation in incremental sheet forming. CIRP Ann 68(1):317–320
6. Duflou JR, Callebaut B, Verbert J, De Baerdemaeker H (2007) Laser Assisted Incremental Forming: Formability and Accuracy Improvement. CIRP Ann 56(1):273–276
7. Cao T, Lu B, Xu D, Zhang H, Chen J, Long H, Cao J (2015) An efficient method for thickness prediction in multi-pass incremental sheet forming. Int J Adv Manuf Technol 77(1–4):469–483
8. Langenecker B (1961) Work-softening of metal crystals by alternating the rate of glide strain. Acta Metall 9(10):937–940
9. Langenecker B (1966) Effects of Ultrasound on Deformation Characteristics of Metals. IEEE Transactions on Sonics and Ultrasonics 13(1):1–8
10. Siu KW, Ngan AHW, Jones IP (2011) New insight on acoustoplasticity—Ultrasonic irradiation enhances subgrain formation during deformation. Int J Plast 27(5):788–800
11. Kang J, Liu X, Xu M (2020) Plastic deformation of pure copper in ultrasonic assisted micro-tensile test. Materials Science and Engineering: A, p 139364
12. Zhou H, Cui H, Qin QH (2016) Influence of ultrasonic vibration on the plasticity of metals during compression process J Mater Process Technol 251:146–159
13. Amini S, Gollo AH, Paktinat H (2017) An investigation of conventional and ultrasonic-assisted incremental forming of annealed AA1050 sheet Int J Adv Manuf Technol 90:1569–1578
14. Cheng R, Wiley N, Short M, Liu X, Taub A (2019) Applying ultrasonic vibration during single-point and two-point incremental sheet forming. Procedia Manufacturing 34:186–192
15. Bansal A, Cheng R, Banu M, Taub A, Ni J (2020) Experimental analysis of material squeeze factor in two-point incremental forming of AL 7075-O. Manufacturing Science and Engineering Conference (MSEC)
16. Nath M, Shin J, Bansal A, Banu M, Taub A (2018) Comparison of texture and surface finish evolution during single point incremental forming and formability testing of AA 7075. In: Martin O. (eds) Light Metals 2018. The Minerals, Metals & Materials Series. Springer, Cham
17. Shin J, Bansal A, Nath M, Cheng R, Banu M, Taub A, Martinek B (2018) Prediction of Negative Bulge in Two Point Incremental Forming of an Asymmetric Shape Part J Phys Conf 1063(1):2057

Investigation of an Integrated Process for Bending and Cross-Section Forming of Tubular Lightweight Parts Based on a Working Media Made of Materials with High Plasticity



Matthias Hermes and Viktor Holstein

Abstract Thin-walled steel profiles are the key to cost efficient lightweight structures. Structure parts and design elements in cars and trucks are often based on curved and hydroformed profiles. The possible production chains for those parts are often long and complex, and the machines and tools are expensive, and the flexibility is low. For smaller production lots, e.g., for applications in aircraft industry, these processes are not efficient. This paper shows a solution for smaller and middle-sized production lots realized by an integrated process for bending and cross section forming of tubular lightweight parts by a forming operation based on a working media made of metal alloys with high plasticity. The paper shows the process idea, fundamental mechanisms, the process analysis, and the process limits. Furthermore, a strategy is given to find a practical process windows.

Keywords Tube forming · Roll forming · Profile bending · Hydroforming · Lightweight design · High strength steel

1 Introduction

Hydroforming has been an important production technology for many years. The basics are explained in [1]. Complex thin-walled lightweight components, for example, for automotive applications, can be produced in one process step on special hydroforming presses. For smaller parts, this technology is often inefficient because of high machine costs and the relatively high process time. Moreover, the process parameters pressure axial force and positioning of the axial punch tools have to be controlled simultaneously. The preliminary process development for each work piece is difficult, and a lot of simulation and experimental work has to be done to

M. Hermes (✉) · V. Holstein
Chair for Forming and Joining Technology, South Westphalia University of Applied Sciences, Jahnstraße 23, 59872 Meschede, Germany
e-mail: Hermes.matthias@fh-swf.de

V. Holstein
e-mail: Holstein.Viktor@fh-swf.de

© The Minerals, Metals & Materials Society 2021

G. Daehn et al. (eds.), *Forming the Future*, The Minerals, Metals & Materials Series,
https://doi.org/10.1007/978-3-030-75381-8_33

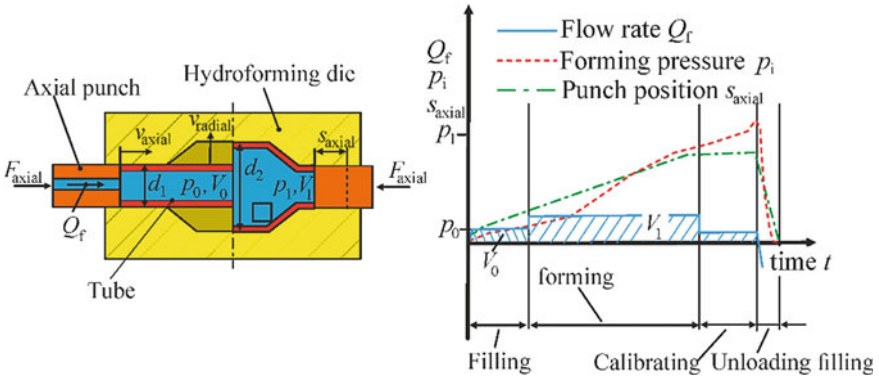


Fig. 1 Complex process parameters of a simple THF process. (Color figure online)

find a robust process window. In Fig. 1, the process parameters for a simple tube hydroforming (THF) are shown. Typical curves describe the interaction between the flow rate Q_f of the filling medium, the forming pressure p_i, and the axial position of the punch s_{axial}. Because of this complexity, it is not efficient to use THF for smaller production lots. But the trend in future production industry is to realize a flexible production down to batch size one. Another problem is hat the process chain for THF parts does not end with the THF process. Often preliminary bending or preforming steps are necessary to get the final work piece. Looking at the interesting geometries that can be manufactured with THF, a solution for smaller production lots with a simple tool design and a robust process behavior should be found. An interesting idea is shown in [2]. The work describes investigations for the use of granular medium for a hot THF process. The process idea seems to be interesting, but the granular medium has complex behavior in its inner pressure distribution. This has to be calculated to get a sufficient forming result.

Moreover, the idea explained in [3] is interesting as well. The new draw forging process couples deep drawing and cold forging in one process. It combines a sheet blank (e.g., steel) with a cylindrical core (e.g., aluminum). The sheet material defines the surface properties of the component. Inspiring is the use of two different materials and two different forming operations in one hybrid process design.

Those hybrid and flexible process designs are the vision of the modern production technology, especially metal forming technology. This paper shows a forming process for tubes that does use the combination of a THF process and a bulk metal process.

2 Process Idea and Pre-investigations

The process idea is based on different thoughts regarding problems of existing processes for common THF processes. The Idea is to use metal alloys with low melting temperatures instead of water and create a quasi-bulk metal part. This method

has been in use for bending for many years, e. g., in the field of music instruments production. The new idea is to combine the bending step with an axial tube forming process to get complex tubular lightweight parts in one production step. The plastic material works in the first step as a plastic mandrel to protect the cross section of the tube of necking in and wrinkling; at the following tube forming step, the plastic material in the tube is used as a working media. For that, it is compressed by axial punches and forms the tube into a closed die geometry. Finally, the working media is heated together with the finished work piece and is melted out of the hollow structure. Some opportunities of this process idea compared to conventional THF can be expected:

- Less sealing problems because the working media is made of solid material.
- The process should be more robust than THF. The typical effect of THF is that the thinnest or weakest area of the shape shows at first a local thinning. That should not occur with TFPW because of the solid core that should show a homogeneous forming.
- Material should behave like a bulk metal forming part, so less wrinkles should occur.
- No complex and cost intensive control system gives the opportunity to use the process as a "low budget hydroforming process", e.g., for lower production batches.

At first, a concept how such process chain of a TFPW (Tube forming with plastic working media) can be realized. So in Fig. 2, a thinkable process chain is explained in detail: The first step is coating the inner and outer tube wall to define the friction behavior and to reduce abrasive contact of the outer tube wall with the die. Different types of coatings were investigated: silicone oil, a graphite alcohol mixture, Molikote MoS_2 grease, lubricant varnish C 220, and a pure PTFE-foil.

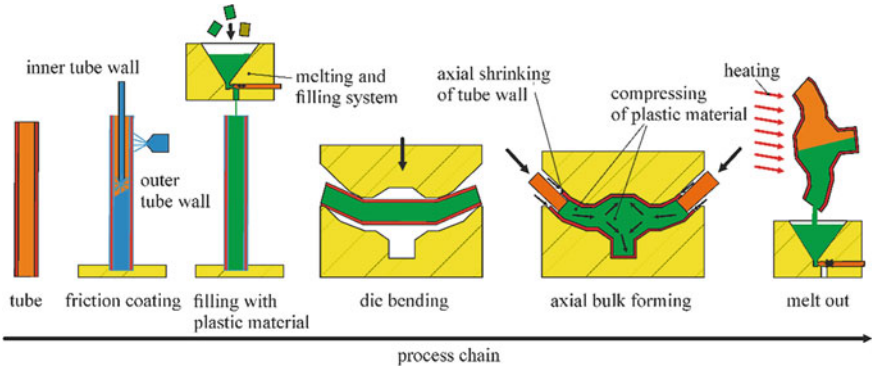


Fig. 2 Process chain for new process chain of tube forming based on a working media made of materials with high plasticity. (Color figure online)

The next step is the filling of the tube by a special melting and filling system. Because of the low temperatures, it is easily possible to use a simple valve system for that. Different alloys were investigated and the ideal for typical technical materials are:

- 75Sn25Bi (melting point at about 182 °C, for copper and aluminum alloys)
- 72Bi28In (melting point at about 115 °C, for mild steels like S 235)
- 100Bi (melting point at about 271 °C, for stronger materials like high-strength steels and stainless steels).

(It is alternatively possible to use preliminarily cast cylindrical cores made of the material that fit to the inner diameter of the tube, and mount it by sticking the core into the tube.) After that, the filled tube is cooled down to room temperature and installed into the die that has similar design like a THF die. The die can be closed without collapsing of the tube cross section because of its quasi-bulk metal behavior. The cross section can be preformed by that. The die has to be closed by a high force built up by a hydraulic press or a similar system. The next step is the axial compression of the inner material from both sides of the tube ends by hydraulic driven punches. At the same time the tube wall moves driven by friction between the tube and the core into the forming zone together with the plastic filling material that works like a working media. When the die geometry is filled with the tube wall and the inner material, the die can be opened and the work piece is heated. Because of the low melting point, the inner material runs out of the hollow shape back into the filling system and can be used for the next part.

In Fig. 3, some early results are shown. These experiments were done to realize a proof of concept. In the left picture, two double-wall tubes were bent by rotary draw bending. To reduce the cross section deformation in one tube, sand was used as filling material. For the second tube, 75Sn25Bi was used to fill the complete cross section of the double tube. This work piece was investigated for aircraft industry and shows the positive effect for bending with such filling materials very well. The sand-filled tube has wrinkles on the inner bending radius, while the second tube has

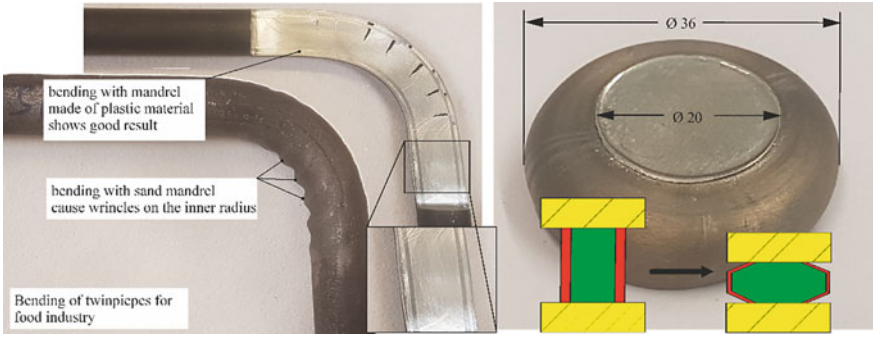


Fig. 3 Proof of concept of the filling with plastic materials. (Color figure online)

a very good bending result. At the outer radius, the filling material has some cracks that are not important for the result of the crack-free bend twin pipe.

On the right picture, a bulging test was made with a stainless steel tube 1.4571 (X6CrNiMoTi17-12–2), 20 × 1 mm filled with 75Bi25Bi. It was possible to bulge the part to an outer diameter of Ø 36 mm what means an expansion of about 80%.

These interesting results became the motivation for further work and the stepwise analyzation of the process. Filling up tubes or profiles by alloy with plastic behavior is well known in industry. So the question of how the mechanisms work in cross section forming are not clear and are explained in the following.

In Fig. 4, the main differences between THF and the TFPW are explained. In THF the fluid is pumped into the tube and expands the tube by the inner fluid pressure p_{Fluid}. At the same time, the axial force F_{axial} on the punch compresses the tube in the longitudinal direction for sealing and for pushing the material axial into the forming zone. Against this force works the friction force $F_{\text{R,die}}$ that arises by the lateral force of the forming pressure that presses the tube wall against the inner die surface and is additionally defined by the friction coefficient. On the right side, the TFPW process is analyzed. Similar to hydroforming, $F_{\text{R,die}}$ works against the movement of the tube wall into the die. Additionally, the working media made of material with high plasticity, that is filled into the tube like a core, has to move along the inner tube wall. Both forces work against the axial forming force F_{axial} of the forming punch. To get a good result, the friction circumstances of the tube, the die and the material have to be analyzed. Additionally, the forming behavior of the highly plastic working media is a strongly influencing parameter. In the following, the interdependencies of the friction coefficient influenced by the use of different coatings is shown. For the working media, the alloy 72Bi28In was used in all experiments to analyze the behavior of a seamless mild steel tube (Ø 22 × 1 mm, S235). Aim of the investigations was to learn about first interaction of the parameters to find a strategy to identify practical process windows.

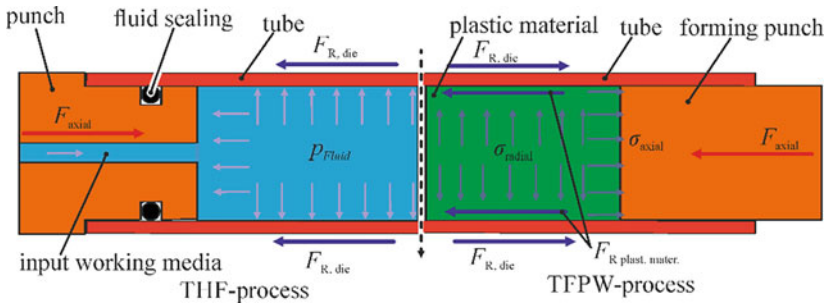


Fig. 4 Differences between a conventional THF process and the TFPM process. (Color figure online)

3 Analysis of the Influence of Coatings on Friction Parameters and Process Limits

In Fig. 5, the experimental setup and a good work piece and two failure parts are shown. The experimental setup consists of a die similar to a simple THF die. In the middle, the die has a hollow shape that makes it possible to expand a tube of Ø 22 mm to an outer diameter of Ø 35 mm. On both sides of the die, there are strong hydraulic cylinders mounted that can apply a maximum axial force of 180kN. For closing the die, a 1000kN hydraulic press was used.

The failure parts show two typical process limits: A tangential crack caused by too little axial flow into the forming die and a wrinkle caused by too much material flow in axial direction or to less radial expansion by the bulged plastic material. These parameters can be influenced by different lubrication methods on the inner and the outer tube wall.

To find a working process window for a good forming result, a variety of combinations of lubricants mentioned above were investigated. The friction coefficient that arises during the process is difficult to analyze experimentally. So, to understand the process in a better way, an axisymmetric simulation model with Abaqus FEM software with rigid bodies for the punches and the die and a 0.5 mm net for the tube and a 2 mm net for the plastic material core was built up. The forming characteristics of the tube was given by a tensile test of a sheet metal strip of the same material. For the characteristics of the 72Bi28In, a tensile specimen was made by casting and tested by tensile test. The typical process limits of wrinkles in the tube wall could be shown in FE-simulation model in principle.

In Fig. 6, two examples of the results of the numerical analysis are shown. The specimen on the right has a good forming result. The shape of the die is filled very well and the tube shows no wrinkles or cracks. The calculation was done with a friction parameter on the outer tube wall of $\mu_a = 0.01$ and on the inner tube wall with $\mu_a = 0.05$. The material flow of the tube wall into the forming zone can be

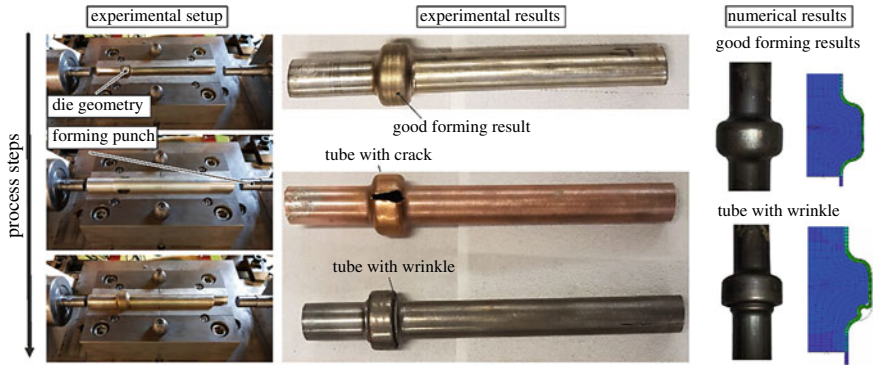


Fig. 5 Experimental setup and process limits in FEM and experiment. (Color figure online)

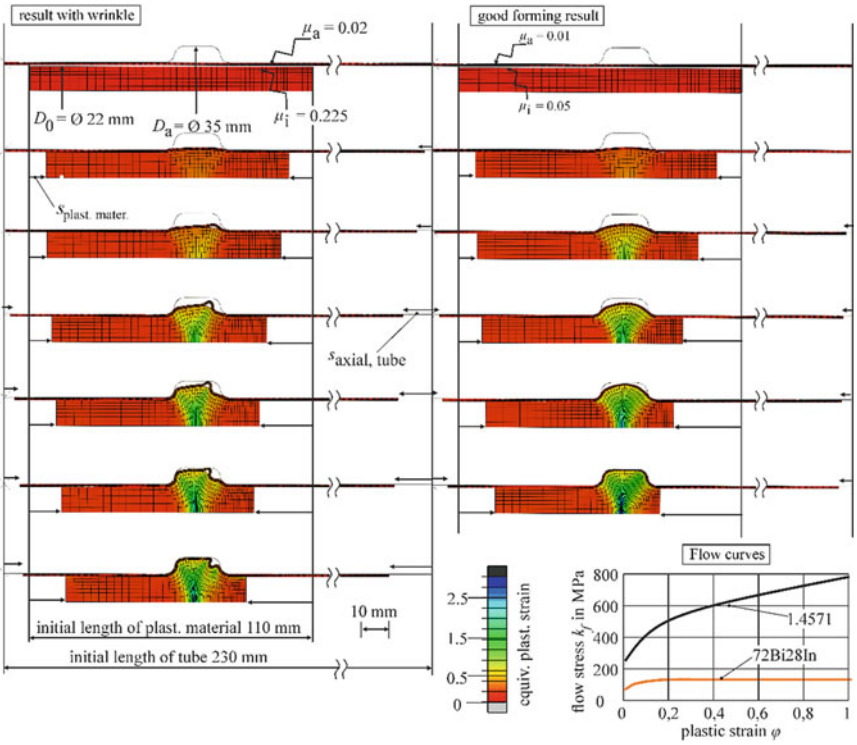


Fig. 6 Example results of the FE-model of the process with variation of the friction coefficient at the inner and the outer tube wall. (Color figure online)

detected in the diagram. The specimen on the left has a bigger difference between the friction coefficients and shows a wrinkle. The reason is less material flow of the filling material into the die shape to expand the tube. Similar significant results could be seen in experiments. To simulate the failure by localization or cracks, a FLC (Forming Limit Curve) was used. It is difficult to get FLCs from tubular materials, so an approximation according to [4] was used. With this model a range of calculations with a variation of the friction coefficients were made to find a process window.

In Fig. 7, the numerical results of these investigations are shown. To get a good forming result, the right combination of friction coefficients on the inner and the outer tube wall has to be determined. If the combination is not sufficient, a wrinkle occurs, because the tube flows too much into the die. The other failure is local thinning or a crack. This was detected by the FLC. Regarding the experimental results on the right diagram, a rough comparison can be made. The experiments show only one good combination of lubricant that lead to a good result; this combination can be found in the numerical investigations too. So, the model overestimates the process window. This shows that the model has to be developed further and other influencing parameters have to be considered in future investigations.

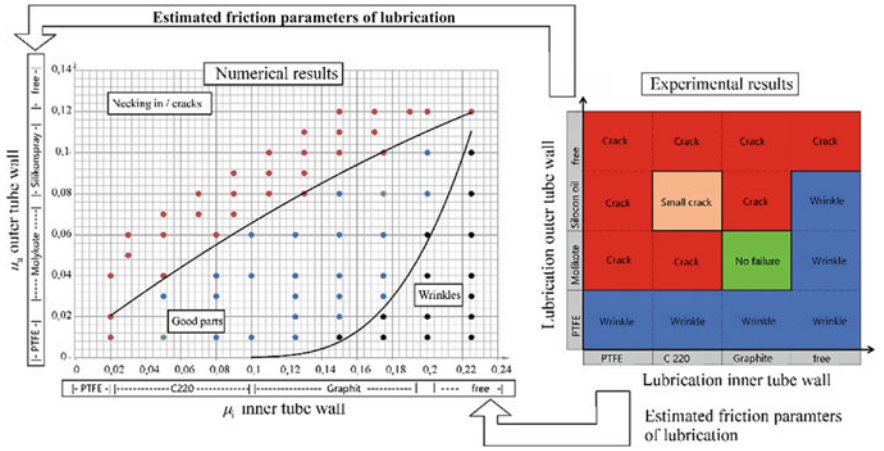


Fig. 7 Process window investigated by numerical and experimental methods. (Color figure online)

4 Summary and Outlook

The paper shows a process idea for a tube forming method for bending and cross section forming for lightweight parts using a working media made of material with high plasticity. The used materials are alloys made of Sn, Bi, and In, with low melting points. The process principle and some applications were explained. In the analysis part, the results of investigations of the influence of friction on the process limits were shown first. Following this, the process was developed further to get a better understanding of how the interaction between working media material, tube, work piece, and die works. The tool technology has to be developed and more materials and work piece geometries have to be tested.

Acknowledgments This paper was supported by the federal ministry for economic affairs and energy based on a decision of the German parliament.

References

1. Neugebauer R (2007) Hydro-Umformung. Springer. ISBN-13 978–3–540–21171–6
2. Chen H, Hess S, Haeberle J, Pitikaris S, Born P, Güner A, Sperl M, Tekkaya AE (2016) Enhanced granular mediumbased tube and hollow profile press hardening. CIRP Ann Manuf Technol 65:273–276
3. Napierala O, Izydorczyk M, Hering O, Dahnke C, Tekkaya AE, Process for the production of composite parts by combination of sheet expansion, deep drawing, and forward rod extrusion. patent application number DE 10 2019 002 851.1 Patent applicant TU Dortmund University, Status: Filed
4. Banabic D, A review on recent developments of Marciniak-Kuczynski model. A tribute to Professor Zdzislaw Marciniak. Comput Methods Mater Sci 10:225–237

Instability Analysis in Incremental Rotary Forming of Tube Flanges



Bhaskaran Krishnamurthy, Olga Bylya, Kyle Watt, Alastair Conway, Martin Tuffs, and Paul Blackwell

Abstract Rotary forming is an exciting route for forming flanges of different angles from seamless tubes of high-strength materials. True to its incremental nature, the process offers great flexibility, but the issues encountered are atypical and complex. One such issue observed in experimental trials is the internal buckling of tubes during specific instances of flange formation. The origin of this instability is non-trivial, and ordinarily, finite-element (FE) models fail to capture this instability. To analyse and understand the problem, systematic experimental trials were carried out using different tube thicknesses, tube materials, and tool kinematics. This paper summarises the results from a critical analysis to establish (1) a criteria for quantifying the instability and identifying the instances of its occurrence, (2) a validation methodology to fine-tune FE models for the process, and (3) use of FE models to understand the influence of tool path in the flange forming stage.

Keywords Rotary forming · Flange forming · Incremental bulk forming · Process instabilities · Tool kinematics

1 Introduction

Rotary forming is an incremental bulk forming process that affords the possibility to form a wide range of tubular components using simple sets of tools prescribing a complex tool path [5, 10]. The high degrees of freedom (DoF) and highly localised area of deformation makes it a very flexible process. For instance, the components

B. Krishnamurthy (✉) · O. Bylya · K. Watt · A. Conway
Advanced Forming Research Centre, University of Strathclyde, 85 Inchinnan Drive, Inchinnan P49LJ, UK
e-mail: bhaskaran.krishnamurthy@strath.ac.uk

P. Blackwell
Design, Manufacturing and Engineering Management, University of Strathclyde, James Weir Building, 75 Montrose St, Glasgow G1 1XJ, UK

M. Tuffs
Rolls-Royce plc, PO Box 31, Derby D24 8BJ, UK

© The Minerals, Metals & Materials Society 2021

G. Daehn et al. (eds.), *Forming the Future*, The Minerals, Metals & Materials Series,
https://doi.org/10.1007/978-3-030-75381-8_34

shown in Fig. 1a were all made from a simple conical top tool and a hollow cylindrical bottom tool (shown in Fig. 1b, c). By forming the flanges from a seamless tube, there is a significant reduction in material wastage as opposed to traditional machining operations; and by using incremental loading, it is possible to produce very high deformations (50–100%) in high-strength materials with limited ductility (12%) at room temperature using a small machine, as opposed to traditional flaring operations.

The complex tool path and the localised deformation, although advantageous when it works, poses a big challenge in understanding the mechanics and modelling of the process [3, 6]. The loading and resulting stress–strain state is non-monotonous, cyclic and significantly triaxial. This, in turn, renders the design for the processing and shaping of tool kinematics a significant challenge. Previous studies in this area are limited [1, 7, 8, 10] and stock commercial finite element software packages are not well suited to model this process, due in large part to the big uncertainty in having an appropriate material model and assumptions on boundary conditions. This problem comes to the fore when trying to shape the process for forming near-net shape components. Tubes with flanges of specific angles are a common requirement in the aerospace and automobile industry and are seen as viable components to be produced by rotary forming. With the optimal forming programme, it is possible to form these flanges in a single step without any intermediate processing or heat treatment. However, with no established industrial practise, even establishing the first framework for shaping the process is non-trivial. Choosing an appropriate starting material condition, tool kinematic parameters and tool path are complex problems which are impractical to solve by a trial and error method. This is due not only to the fact that the number of parameters are quite large for design of experiments approach, but the parameters are interdependant with no readily obvious relations with each other. This results in many process instabilities and failures which are hard to predict and plan against (as shown in Fig. 2), and some of these failures can be expensive as they have the potential to not only damage the workpiece, but the tools, as well as the machine.



Fig. 1 Representation of the **a** versatile range of components that can be formed using rotary forming using a simple set of **b** conical top tool and **c** hollow bottom tool. (Color figure online)

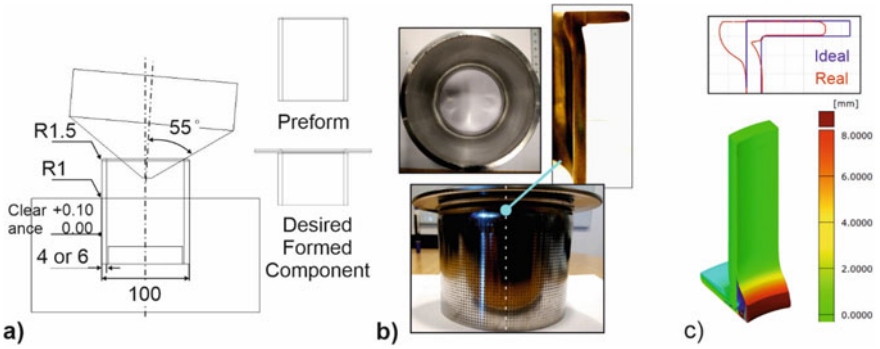


Fig. 2 Representation of the **a** preform geometry and desired formed component (**b**–**c**) and the internal buckling issue studied; **b** Actual formed component, with the slice used for further study; **c** Comparison of the formed component with ideal expected geometry using proprietary GOM Inspect software. (Color figure online)

Herein, the focus is on a single-step rotary forming of a 90° flange onto hollow tubular components and understanding the instability termed 'internal buckling' observed therein. As shown in Fig. 2a, the need is to form a 90° flange onto an initially straight tube with minimal defects or deviation along the fold. However, in reality, a notable internal flow of material can occur along the inner edge of the fold as shown in Fig. 2b, c. Three aerospace materials, namely JETHETE M152 steel, nickel-chromium-cobalt alloy C263, and INCONEL718 have been tested with varying parameters of tube thickness, upstand height, forming method, and forming depth. The internal buckling was observed under all conditions to varying degrees. This paper outlines the authors' attempts to quantify the instability, identify the instance of its occurrence, and develop process models to predict it.

2 Methodology

2.1 Geometry

All preforms used for the trials were of outer diameter 100 mm and length 110 mm. Two different tube thicknesses of 6 and 4 mm were used. Fillets of 1.5 mm radius were machined on both edges at the top end (forming end) of the workpiece to ensure smooth initial contact with the top tool. A 55° ($\boldsymbol{\beta}$) top tool was used as it affords possibility for nutation of 35° to the horizontal datum and thereby high flexibility without compromising on the strength of the tool [10]. A hollow bottom tool with a cylindrical cavity of a depth of 75 mm, maximum clearance of 0.1 mm with the O.D. of the workpiece and a fillet of 1 mm radius along the top edge was machined to hold the workpiece as shown in Fig. 2a.

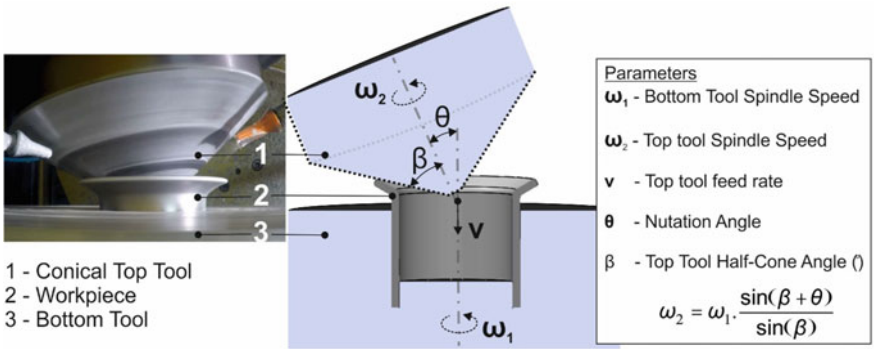


Fig. 3 Schematic representation of the rotary forming process with the key kinematic parameters highlighted. (Color figure online)

2.2 Machine

The Advanced Forming Research Centre of the University of Strathclyde, Scotland, is one of the High Value Manufacturing Catapult (HVMC) centres established to bring together academic research and industrial expertise to drive innovation in the UK. In line with this, state-of-the-art rotary incremental bulk forming machines have been installed specifically for industrial-scale research. The MJC RFN 200 T-4 machine is one such custom-designed spin-nutation type rotary forging machine. As opposed to the more common orbital type of rotary forging/forming machine, the spin-nutation-type design enables nutation angles ($\boldsymbol{\theta}$) in the range 0°–45°, with the ability to change it at any time during the process, and also apply a maximum load of 200 T at any point in this range. This is especially suited for forming flanges of different angles onto hollow tubes.

The machine has 4 DoF—the top tool can translate vertically, rotate about its own axis and also rotate along the axis perpendicular to the horizontal (termed 'nutation'), while the bottom tool can rotate about its own axis translating this rotation in turn to the workpiece. In order to maintain a rolling contact, the top tool is rotated at a higher velocity ($\boldsymbol{\omega}_2$) proportional to the rotational velocity of bottom tool ($\boldsymbol{\omega}_1$), half-angle of the cone ($\boldsymbol{\beta}$), and the nutation angle ($\boldsymbol{\theta}$) as shown in Fig. 3c.

2.3 Kinematics

The required rotation speed of the bottom tool, the Z position, X position (which gets translated to the nutation angle), rotation speed, and feed rate of the top tool were input in the form of CNC codes to the MJC RFN 200 T-4 machine. These values were chosen based on know-how and the fact that they have yielded successful results in the past.

2.4 Forming Method

One of the key aspects that needs to be decided as part of the process design is the forming method to be used. As previously mentioned, owing to the flexibility afforded by the machine, the flanges can be formed in different ways using different top tool paths. Two of the preferred methods are summarised in Fig. 4. In Method 1, during Stage I (flaring stage), the top tool is allowed to translate towards the workpiece with a small nutation angle to a depth of 14 mm. Following this in Stage II, the top tool is nutated from that depth without any change in the Z position of the top tool. Method 2 differs from 1 in that the top tool is made to translate to a larger depth in Stage I, and then prescribed a simultaneous nutation and vertical translation to achieve the final shape in Stage II as shown in Fig. 4.

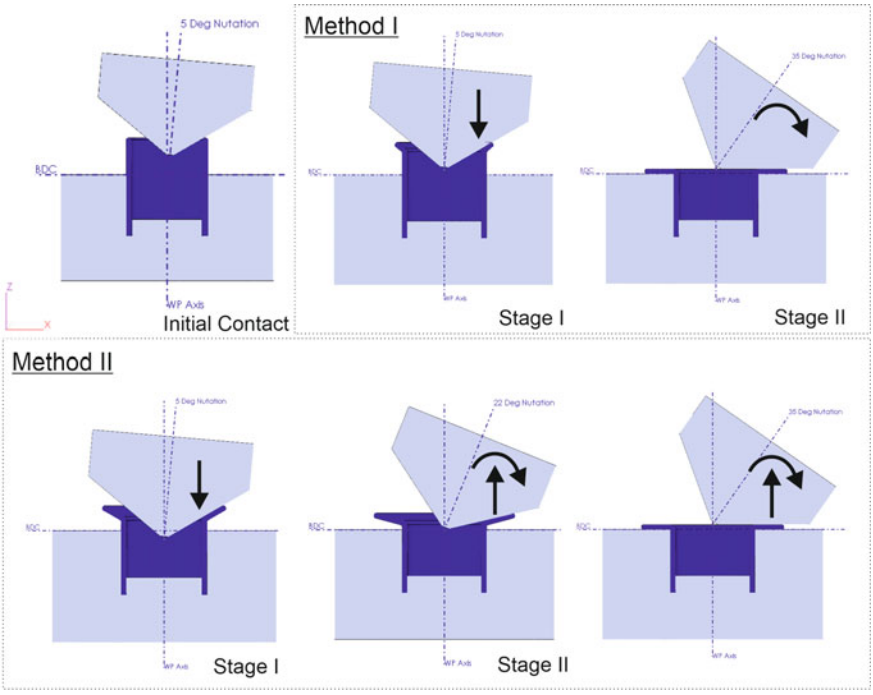
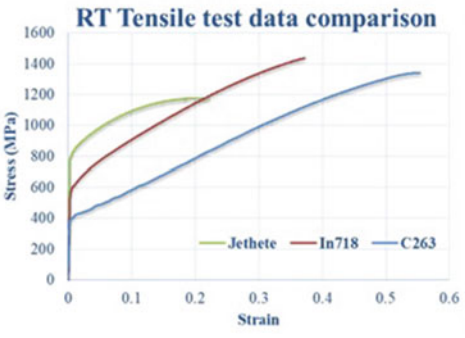


Fig. 4 Schematic representation of the different forming routes adopted. Method I involves only nutation in the second stage, while Method II involves both nutation and upwards translation. (Color figure online)

2.5 Process Modelling and Validation

Finite-element process models were developed in the commercial metal-forming software, QForm, for the project. The kinematic parameters used in the trials were input to the software, and standard friction and heat transfer parameters available in the software database were used in the setup of the model. The problem was formulated as a 3D elasto-plastic one owing to the localised complex cyclic and incremental loading observed in the process. An isotropic hardening material model was used for the three materials, which were developed using the RT tensile data shown in Fig. 5. Experimental observation of the temperatures in the component did not exceed the range 100–150 °C. It has been reported that the mechanical properties of steels and nickel alloys tended to be nearly strain-rate insensitive at such low temperatures [4], Special [9] and this was further verified in separate tensile tests. Hence, RT material data was deemed to be representative enough. The detailed modelling methodology used and the challenges faced in modelling rotary forming processes are summarised in earlier works [2, 6, 10].

To validate the model, the load, geometry, strain, and temperature data obtained from the experiments were used. The calibration procedure is summarised in Fig. 6, wherein the geometry and temperature profile generated through the trials, as observed from a high-definition video and thermal image capture, respectively, were used to validate the values obtained in the process models. Similarly, the forming load traces recorded on the machine were used for validating those obtained from the process models. The output geometry obtained from the full and interrupted trials were measured as well as scanned for analysis. To get a clear image of the region of folding, thin slices of width 20 mm were cut (as shown in Fig. 2b) from the tubes and then photographed. These were then processed and compared with those obtained from the process models (exported as .STL files) in proprietary GOM Inspect software (Fig. 6c).



Properties	Jethete	IN718	C263
Young's Modulus, E (GPa)	216	189	220
Yield Stress, σ_y (MPa)	787	574	404
Ultimate tensile, stress, σ_u (MPa)	1175	1437	1341
Normalised strain hardening/softening factor, γ	0.12	0.30	0.44
Limiting tensile elongation, δ	0.22	0.37	0.55

Fig. 5 Summary of room temperature tensile test data for the three materials studied. (Color figure online)

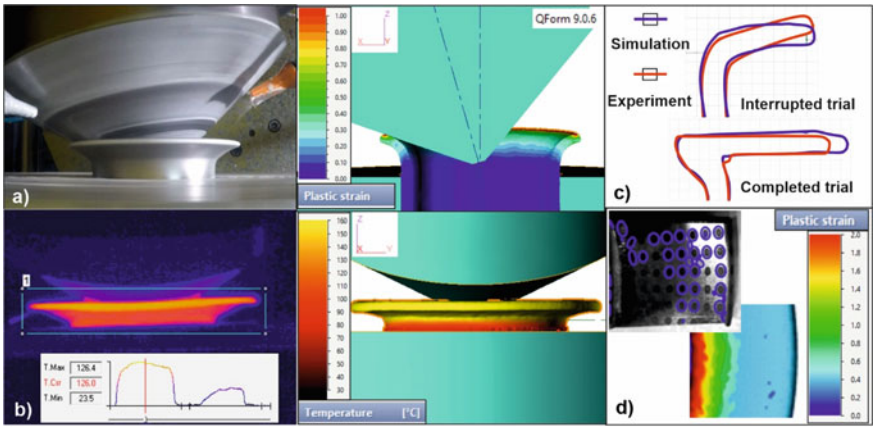


Fig. 6 Validation methodology used for the process models—validation with through-process recording **a** metal flow with the high-definition video and **b** temperature profile with that of the thermal camera recording; and validation of **c** output geometry by GOM comparison and **d** strain profile using the image processing method. (Color figure online)

In addition, an electrochemically etched rectangular dot grid system, commonly used in sheet metal forming limit identification, was used to determine the strain on the deformed surface of the tubes here. These were then used for validating the strain profile observed in the FE simulation (Fig. 6d).

3 Results and Discussion

3.1 Identification and Quantification of Instability

To identify the origin of the instability, interrupted trials were planned, i.e. the trials were stopped at the instance of starting of the instability. To determine this point, videos obtained for preliminary trials from the high-definition cameras were processed using a commercial video processing software. The videos were trimmed to the exact duration of the process, following which linear guidelines were used to identify the exact instance of the commencement of instability, as shown in Fig. 7. This was then compared with the machine data and process simulation to translate this point in time to the nutation position of the top tool. As can be observed in Fig. 7, the onset of instability is early in the nickel alloys (at 22° nutation in stage II), while it happens at a later stage in Jethete (at 26° nutation in stage II). Interrupted trials were carried out for the materials where the process was stopped at the points identified.

The interesting aspect to be noted here is the profile formed by Jethete and C263 at the onset of instability. This profile could also be observed in the completely formed geometry, as well as can be derived from Table 1, and gives clues to understanding

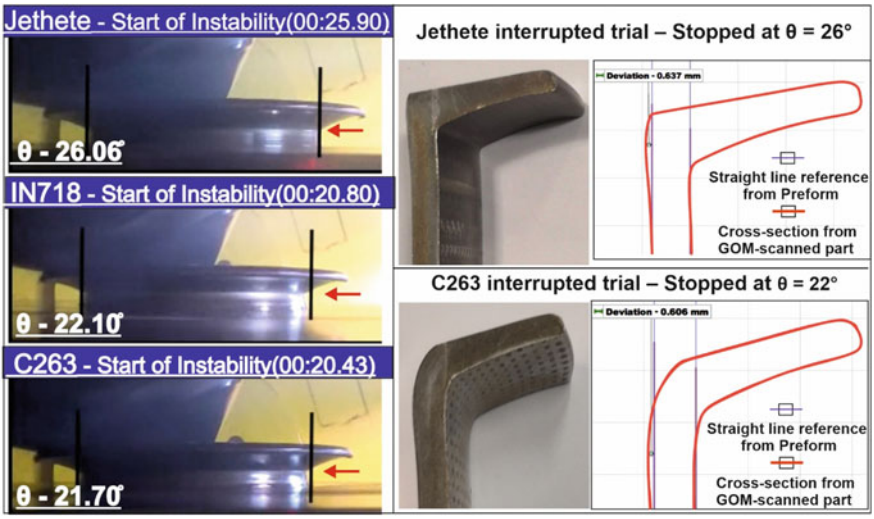


Fig. 7 Representation of the high-definition video capture analysis carried out to identify the instances of instability in the three different materials. (Color figure online)

Table 1 Comparison of the output geometries for difference material and thickness

Thickness	Part no.	I.D	Int. hoop strain	O.D	Ext. hoop strain
Jethete					
6	223-5	82.49	(−)0.06	141.89	0.42
4	232-5	80.30	(−)0.13	140.92	0.41
C263					
6	223-12	80.6	(−)0.08	141.2	0.41
4	232-3	77.54	(−)0.18	134.63	0.35
IN718					
6	223-17	78.6	(−)0.11	139.7	0.40
4	232-1	75.8	(−)0.18	133.08	0.33

the prevalent buckling in Nickel alloys compared to that in Jethete. More study on this aspect is needed to understand completely the origin of such a buckling effect and how to avoid it for new materials.

To quantify the instability, the key features of the formed component, outer diameter and inner diameter of the flange and the thickness at the outer and inner part of the flange, were measured using a Vernier Calliper. Three measurements were taken each time and the average of the three measurements were used for analysis. The hoop strain values were then calculated with respect to the initial circumference. These are summarised in Table 1. In addition, thin slices of 20 mm width were also

cut from the specimens and analysed with respect to the ideal expected geometry as shown in Fig. 2c.

3.2 Fine-Tuning of Process Models

Validation and prediction of the output geometry was one of the most challenging aspects of developing a more robust model for the rotary forming process. More specifically, the ability to capture the buckling effect observed in the forming trials is non-trivial and required a few unconventional techniques. Using the conventional method for modelling such a finite deformation process—specifically, a strain-based remeshing technique—material flow behaviour near the fold in the flange could not be captured in the process model. Modification of the hardening behaviour in the material models did not yield positive results and the process model was still unable to capture the internal flow of material during the nutation stage. The use of a standard tetrahedral solid element mesh and remeshing technique was later identified to be the reason for this effect. Through remeshing, wherein the Finite-Element (FE) software continuously tries to realign and change the local mesh elements in the areas of high deformation, somehow rendered the material 'soft' and flow in an ideal way to help in the convergence of results.

The prevalent buckling effect observed in the trials carried out with the thinner (4 mm) tubes was very helpful in fine-tuning the process model. Figure 8 provides a summary of the stages in the fine-tuning of the model. As a first step, a brick (rectangular) shell mesh element was used without remeshing criteria. This seemed to yield better geometry prediction and was able to predict the output geometry with the buckling effect. In addition, it was also possible to capture the difference in the flow behaviour around the fold between Jethete and C263, as seen in Fig. 8. In addition, using the brick mesh without remeshing, it was possible to bring down the simulation time considerably, from 3 weeks to 3 days.

However, this method was still prone to some inaccuracy in geometry prediction, as was observed when validating the process model with interrupted trials. While the process model was able to predict the final output geometry, it still predicted the metal flow in intermediate stages of forming with error as shown in Fig. 8.

The use of a solid tetrahedral mesh, without remeshing, however, seemed to improve the geometry prediction in intermediate stages as well, and was found to provide better representation of the material flow. The use of this method did seem to increase the simulation time compared to that of the brick mesh. Therefore, the suggestion would be to run initial simulations with a brick mesh without remeshing for preliminary iterations to test hypotheses, while a solid tetra mesh without remeshing is recommended for final simulations. The lack of remeshing seemed to cause some problems while simulating Method 2 type of forming, as the tool path tends to produce a highly distorted mesh in stage II. In such a case, it was found to be useful to stop the simulation at the start of mesh distortion, remesh the

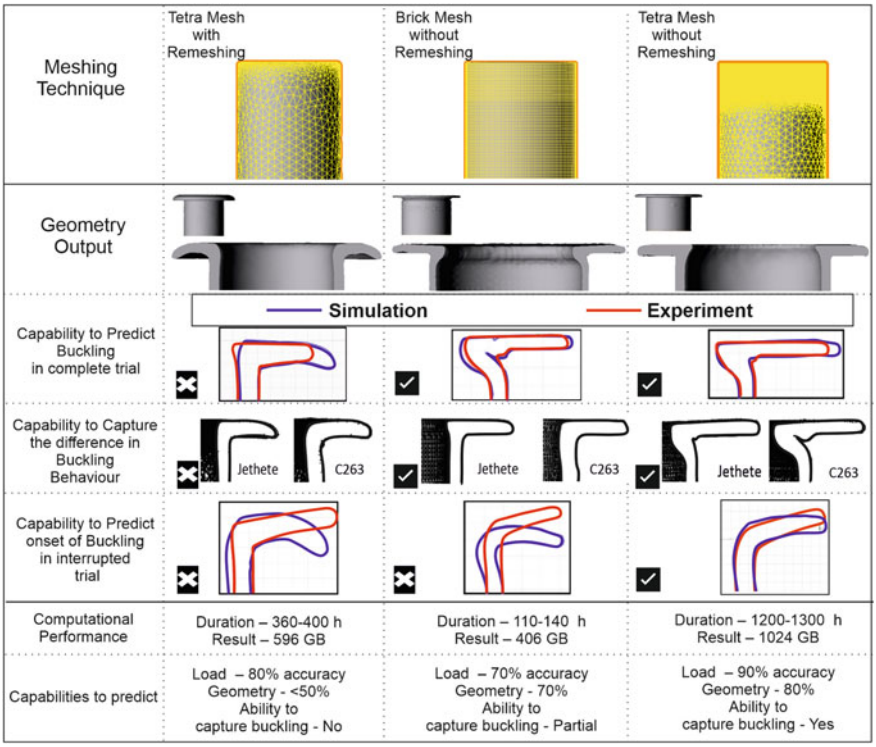
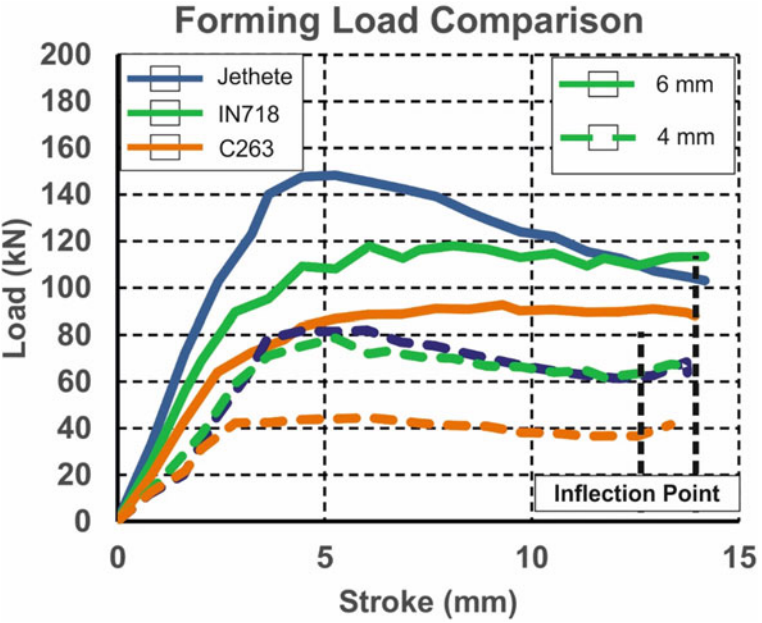


Fig. 8 Representation of the increase in maturity of geometry prediction in the process models **a** preliminary stage, **b** intermediate stage using a brick mesh without remeshing and **c** improved state using a tetra mesh without remeshing. (Color figure online)

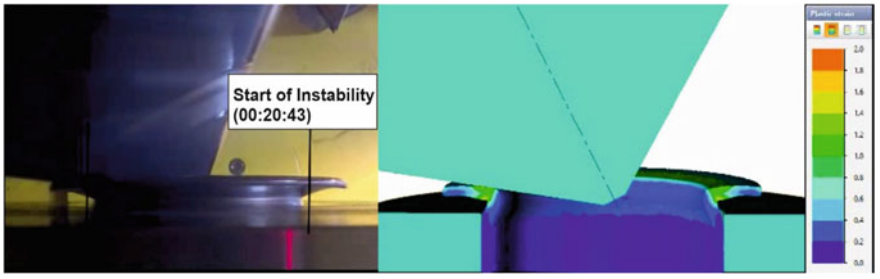
local region for a short while, and then continue the simulation without remeshing until further inacceptable distortion of the mesh.

3.3 Preliminary Improvements Through Process Models

The validated process model was used to glean some insight into the mechanics of rotary flange forming and devise some recommendations to eliminate or at least reduce the internal buckling. As shown in Fig. 9, the load trace and geometry development were analysed using the process model. The load trace in conjunction with the geometry observed in the process model provided some hints to the start of internal buckling. It is hypothesised that at the trough of the load trace, the forming mechanism changes. This critical point, termed as the 'inflection point' herein, is shown for the three materials and two different thicknesses in Fig. 9a. This was used in the shaping of our process (as shown in Fig. 9b), but further in-depth study on



(a)



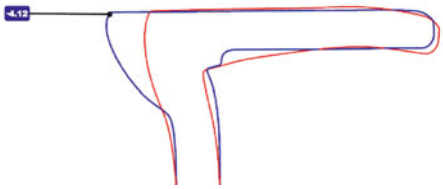
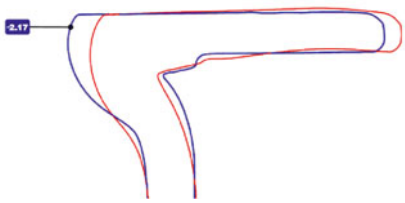
(b)

Fig. 9 Preliminary results from the improved process model **b** comparison of the forming load trace for Jethete, IN718, and C263, **c** Prediction of the start of instability using the process model. (Color figure online)

the process mechanics will be useful to translate the results to new materials and geometry.

The geometry prediction capability of the process model (as shown in Fig. 9b) were used to shape the process and compare the results for the different forming methods. Table 2 shown, compares the output geometry obtained using the improved process using Method 2 with that of the initial process using Method 1. As can be seen from the measurements and GOM scan analysis shown in Table 2, the use of Method 2 seems to result in reduced buckling than that observed with Method 1.

Table 2 Comparison of the output geometries for trials carried out using Method 1 and 2. (Color figure online)

Material	Measure	Method 1	Method 2	GOM section comparison
Jethete	I.D	78.91	86.46	 Comparison – Method 1 (Blue) and 2 (Red)
	O.D	139.95	141.48	
C263	I.D	77.45	81.96	 Comparison – Method 1 (Blue) and 2 (Red)
	O.D	134.73	138.31	

Only Jethete and C263 were tested in this case, as a representative for steel and nickel alloy. In both cases, there were pronounced improvements in the output geometry. The combination of Z motion and nutation of the top tool seemed to prevent the drastic internal movement of the workpiece. Although the thickness distribution in the formed component seemed to be non-uniform in the case of Method 2, it did result in a better forming along the inner edge (part in contact with the bottom tool) of the flange. The lack of fold along the inner edge was a positive sign and the component could easily be subjected to a further machining operation to achieve the end result.

4 Conclusions

Herein, a systematic analysis of internal buckling observed in rotary forming of a 90° flange using different aerospace-grade alloys with different tube thicknesses were carried out. Methods for quantifying the instability and identifying the instances of its occurrence were identified and novel validation methodology was developed to fine-tune an FE model for the process, which were lacking hereinbefore. The main contribution from the present work were the use of validated process models to gain some basic understanding of the mechanics of rotary forming and to assist in the shaping of the rotary forming process to yield improved results.

The use of a combined nutation-translation type top tool motion (Method 2) during the flange forming stage was found to result in reduced buckling than that observed with only nutation (Method 1) for both Jethete and C263. This can be used to inform

forming strategies for the future. Furthermore, buckling was observed to be more prevalent, to happen earlier, and to occur in a different way in nickel alloys than in Jethete steel. The aspects of the material properties that leads to this effect need to be studied further to help effect successful trials using material preparation techniques such as heat treatment.

Acknowledgments The authors would like to acknowledge Rolls Royce Plc for funding this work from their Innovate UK: Aerospace Technology Institute Strategic R&D Project grant (application no. 66733-263147) titled "Manufacturing Portfolio Project 2: Manufacture of Advanced Materials". We would also like to thank the AFRC's Forging and Incremental Processes team for their excellent support, guidance, and provision of resources throughout the project. Most importantly, we greatly appreciate the time spent by key staff in both Rolls-Royce and AFRC in support of this project.

References

1. Appleton E, Slater RAC (1973) Effects of upper platen configuration in the rotary forging process and rotary forging into a contoured lower platen. Int J Mach Tool Des Res 13(1):43–62. https://doi.org/10.1016/0020-7357(73)90030-9
2. Bylya OI, Ward M, Krishnamurty B, Tamang S, Vasin RA (2017) Modelling challenges for incremental bulk processes despite advances in simulation technology: example issues and approaches. Procedia Eng 207(September):2358–2363. https://doi.org/10.1016/j.proeng.2017.10.1008
3. Bylya OI, Timur Khismatullin PB, Rudolf AV (2018) The effect of elasto-plastic properties of materials on their formability by flow forming. J Mater Process Technol 252 (Sept 2017): 34–44. https://doi.org/10.1016/j.jmatprotec.2017.09.007
4. Dieter GE (1988) Mechanical Metallurgy, 3rd ed. In: Mechanical Metallurgy, 3rd revise, vol 23. McGraw-Hill Book Company (UK) Limited, London, pp 194–194. https://doi.org/10.1002/crat.2170230211.
5. Groche P, Fritsche D, Tekkaya EA, Allwood JM, Hirt G, Neugebauer R (2007) Incremental bulk metal forming. CIRP Ann Manuf Technol 56(2):635–656. https://doi.org/10.1016/j.cirp.2007.10.006
6. Krishnamurthy B, Bylya O, Muir L, Conway A, Blackwell P (2017) On the specifics of modelling of rotary forging processes. Comput Methods Mater Sci 17(1):22–29
7. Montoya I, Santos MT, Pérez I, González B, Puigjaner JF (2008) Kinematic and sensitivity analysis of rotary forging process by means of a simulation model. IntJ Mater Form 1(SUPPL. 1):383–386. https://doi.org/10.1007/s12289-008-0075-3
8. Oudin J, Ravalard Y, Verwaerde G, Gelin JC (1985) Force, torque and plastic flow analysis in rotary upsetting of ring shaped billets. Int J Mech Sci 27(11–12):761–780. https://doi.org/10.1016/0020-7403(85)90008-6
9. Special Metals (2007) IN718 Datasheet, 1–28. SMC-066
10. Tamang S, Bylya O, Ward M, Luo X, Halliday S, Tuffs M (2017) Comparison between rotary and conventional flaring processes. AIP Conf Proc 1896:1–8. https://doi.org/10.1063/1.5008047

Incremental Collar Forming Process for the Manufacturing of Branched Tubes and Pipes



André Leonhardt, Peggy de Witt, Matthias Rehm, Holger Schlegel, and Verena Kräusel

Abstract Beside the manufacturing of finished parts by Incremental Sheet Metal Forming (ISF), final operations within the process chain can also be realized with this technology. The technological capabilities of performing incremental (hole-)flanging operations for sheet metal parts has been investigated in research context. The current topic focusses on the transfer of the incremental forming technology to manufacture tubular parts. An incremental collar forming process was developed where all motions are executed by the forming tool. Due to the fixed position of the workpiece, tubes, as well as pipes can be branched. Stainless steel tubes made of 1.4404 (316L) with an outer diameter of 54 mm and a wall thickness of 1.5 mm were used for experimental evidence of functional capability of the incremental collaring process. The influence of different pre-hole geometries and forming tool shapes on the properties of the collar (e. g. geometrical accuracy, wall thickness) was investigated.

Keywords Incremental forming · Collar forming · Branched tube

1 Introduction and State-Of-The-Art

Incremental forming technologies are characterized by high flexibility due to the small forming storage of the used tools enabling a fast and cost-efficient small batch production. In ISF, the sheet metal is kinematically formed by the numerical controlled motion of a simple tool causing plastic deformation of the material in a tightly limited, partial forming zone. In addition to the incremental forming of the final shape of sheet metal parts, finishing operations performed by ISF within a process chain are the context of scientific and industrial research. Taleb-Araghi et al. [1] investigated the process combination of stretch forming with a subsequent

A. Leonhardt (✉) · V. Kräusel
Professorship Forming and Joining, Institute for Machine Tools and Production Processes, Chemnitz University of Technology, Chemnitz, Germany
e-mail: andre.leonhardt@mb.tu-chemnitz.de

P. de Witt · M. Rehm · H. Schlegel
Professorship Production Systems and Processes, Institute for Machine Tools and Production Processes, Chemnitz University of Technology, Chemnitz, Germany

© The Minerals, Metals & Materials Society 2021

G. Daehn et al. (eds.), *Forming the Future*, The Minerals, Metals & Materials Series,
https://doi.org/10.1007/978-3-030-75381-8_35

ISF of specific part features in a single machine setup, improving the geometrical accuracy and the sheet thickness distribution as well as shortening the process time. Moreover, a lot of research effort has been spent to show the technological capabilities of incremental flanging operations being performed by ISF. The works of Voswinckel et al. [2] and López-Fernández et al. [3] involve the stretch and shrink flanging of open (cut) edges using an incremental forming approach. Investigations on the incremental hole-flanging have been carried out by Cui et al. [4], Centeno et al. [5], Cristino et al. [6], Bambach et al. [7], and Cao et al. [8]. The focus of all these studies was the so-called "forward flanging" approach in which the flanged wall is bent downward by the tool. Different tool and blank holder setups, as well as tool path strategies, are used to optimize the final flange. In contrast to these findings, Petek et al. [9] proposed an upward bending of a hole flange applying a ball headed tool—the so-called "backward flanging" method. Wen et al. [10] present a tool with tapered shoulders allowing a combination of forward and backward flanging as well as open edge and hole-flanging.

Besides the use of ISF in the flanging of flat sheet metal parts, the approach of incremental forming is already utilized for the industrial production of tubular parts, e. g. for the incremental tube end forming. These process variants are used for the thickening, closing, reducing, expanding, and profiling of the tube ends. In addition to the tube end forming with an open (cut) edge, the hole-flanging of the tube shell surface, the so-called collar forming, is applied to produce branched tubing. Branches are needed if one media flow shall be divided into different pipelines or vice versa. On the one hand, branched pipes can be produced by connecting the single tubes with T-fittings. On the other hand, the branch can be manufactured from the pipeline itself. In industry, branching is mainly produced by casting, joining or forming technologies, whereas high efforts have been undertaken to substitute casted or joined branches with formed ones [11]. The reasons for this can be summarized as follows:

- decreasing post processing of parts due to near-net-shape-forming
- increasing surface quality
- streamlined transitions between the pipelines
- decreasing part weight due to elimination of additional components
- producing of branches on long pipelines and existing pipe systems.

Collar forming can be realized by rigid or elastic tools as well as by hydroforming. In the latter case, a dome is first formed by applying internal pressure via the medium and axially pushing the pipe ends. Subsequently, the cap is cut off, so that the collar emerges. Furthermore, an elastic tool made of rubber can be applied in collar forming. At first, a pre-hole is cut in the shell surface and the elastomer is put into the tube. The elastic core is then axially compressed by two punches so that it moves into the die hole, forming the collar. Due to the long cycle times, the high investment costs for the plant and the required tools, these processes are not widely used in industry. For this reason, the collar forming with rigid tools has become established in industrial practice. Typically, this is implemented by means of a translational tool movement. A punch or a ball with an appropriate diameter is used to form the collar in one step.

A mechanical or hydraulic device, which applies the necessary forming force, is inserted laterally into the tube and positioned under the previously inserted hole. The collar is then made by pressing out the punch or the ball. With this process variant, only collar diameters smaller than the tube diameter can be formed. Alternatively, the punch can be pulled out of the tube by applying a tensile force via a tie rod. This process variant is used, especially for cold collar forming of thin-walled tubes [11].

There are only a few approaches in which the incremental flanging of sheet metal is transferred to the collar forming of tubular parts combining a translational and rotational tool movement. The T-Drill process is an industrial used incremental collar forming method needing special tooling with two forming pins. At first, a round pre-hole is drilled in which the collar forming head is inserted. After this, the forming pins are extended and the collar is formed with a superimposed rotational pull-out movement of the tool. Then the collar is trimmed to the desired height and the branch pipe is attached to the main pipe by butt welding [11]. In the craft sector, installers for heating, ventilation, and air conditioning use tools from Rothenberger with special extractor hooks for collar forming of copper pipes [11]. Further investigations and process variants of incremental collar forming were presented by Teramae et al. [12] and Yang et al. [13]. Teramae et al. used a simple bar tool with a hemispherical tip for forming the branched tube. The areas of the major and minor axis of the elliptical pre-hole are formed one after the other, whereby the forming tool is partially inclined. Thinning in particular is examined with the aim of harmonizing the thickness distribution through the special process sequence [12]. An improved bar tool with a conical pre-forming zone and a cylindrical shaping zone is presented in [13]. The collar forming of 316L tubes with a wall thickness of 0.5 mm is realized in a multi-stage forming process divided into pre-and collar forming. During the forming process, the tool moves in a sequence of translational and rotational motions which are partly superimposed. Accordingly, the objective of the current study is to present a new incremental collar forming method with simple tooling for the manufacturing of branched tubes and pipes (patented in [14]). Experimental results are presented as evidence of functional capability of the new process.

2 Description of Incremental Collar Forming Process

The basis for the new process is a tube with a defined pre-hole which is firmly clamped during the entire forming process (Fig. 1a). A simple forming mandrel is used as a tool, whose dimensions and shape can vary depending on the requirements of the collar forming task. First, the tool, which is set at a defined angle, is axially inserted into the pre-hole (Fig. 1b). Then, the forming mandrel is advanced radially to the pre-hole by a defined value (Fig. 1c). The forming of the pre-hole edge and the setting up of the collar takes place through a rotational movement of the tool around the pre-hole axis, which is superimposed with a translational outward movement along the pre-hole axis (Fig. 1d). In addition to the active rotation around the pre-hole axis, which is generated by an electric motor, a passive rolling of the active

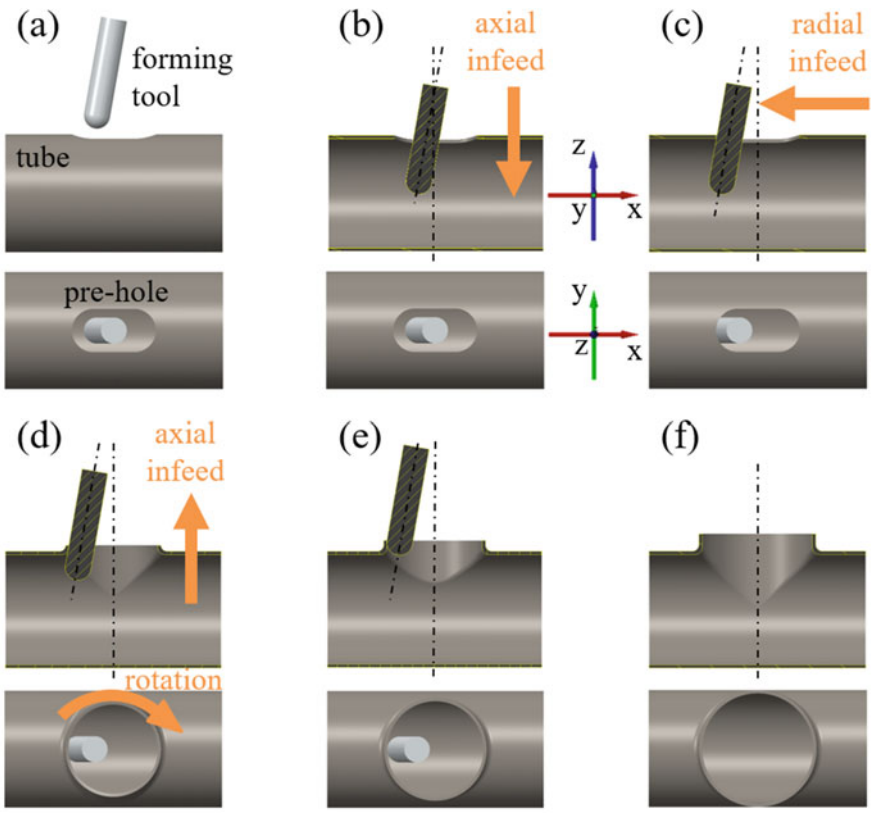


Fig. 1 Steps of tool movement for one forming cycle **a**–**e**, 1:1 collar formed after several cycles. (Color figure online)

part on the pre-hole or collar contour takes place due to friction, since the forming mandrel is mounted to rotate around the tool longitudinal axis. After the mandrel has moved out of the tube (Fig. 1e), the process steps are repeated. In the first steps of the multi-stage process, the pre-hole areas of the shorter pre-hole axis are formed. The sequence of steps, consisting of axial and radial movements, is repeated until the collar has reached its target diameter (Fig. 1f).

Due to the process kinematics, a simple low-cost tool can be used to produce different collar geometries within a defined diameter range. Since all movements are performed by the tool alone, not only shorter pipe sections (T-fittings), but also larger pipes and even entire pipe systems can be formed in this way. In addition to T-fittings, cross pieces can also be produced, whereby only one-sided accessibility is necessary. In contrast to pressing with a punch, so-called 1:1 collars can also be formed, where the collar diameter corresponds to the pipe diameter. Due to this high flexibility, the process allows the forming of small lot sizes up to a quantity of 1. Furthermore, when arranged in a corresponding plant concept with several necking stages, economic production of medium to large quantities is also possible.

3 Experimentation

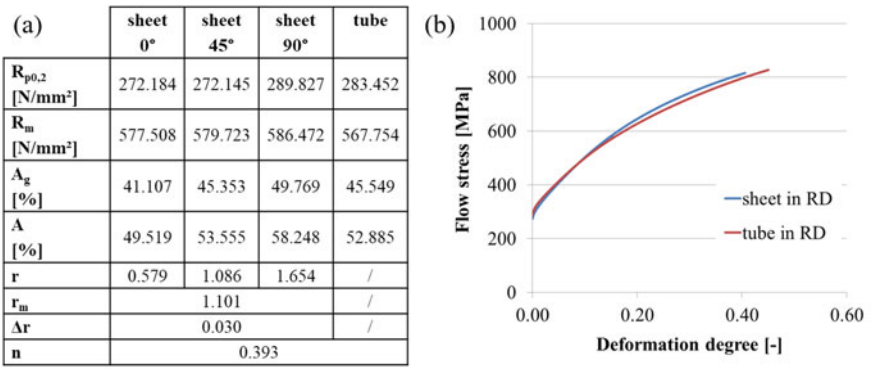
3.1 Investigated Tube Material

Stainless steel tubes made of 1.4404 with a wall thickness of 1.5 mm and an outer diameter of 54.0 mm were used for the experimental investigations of the incremental collar forming process. The chemical composition of the alloy X2CrNiMo17-12–2 is shown in Table 1. The tubes were manufactured from sheet metal by roll forming and subsequent longitudinal induction welding.

Tensile tests were performed according to ISO 6892–1:2016 in order to receive the mechanical properties. Samples were taken from the semi-finished sheet metal in 0°, 45°, and 90° to the rolling direction, as well as from the tube in the direction of tube axis opposite the welding seam. For the tensile specimens, the same geometry was used both for specimens from the sheet metal and for specimens from the tube with a gauge width of 12.5 mm, an original gauge length of 50 mm and a parallel length of 75 mm. At least five samples were prepared by abrasive water jet cutting. The samples taken from the tube were not straightened, but only flattened at the ends due to the clamping force. Figure 2 summarizes the results of the mechanical properties for all four testing conditions and shows the flow curves for the samples from the sheet metal in rolling direction as well as from the tube. The strain hardening exponent n was determined by the flow curve data according to SWIFT.

Table 1 Chemical composition of investigated alloy X2CrNiMo17-12–2

C	Si	Mn	P	S	Cr	Ni	Mo	N
0.020	0.45	1.31	0.035	0.001	16.90	10.60	2.34	0.023



	sheet 0°	sheet 45°	sheet 90°	tube
$R_{p0,2}$ [N/mm²]	272.184	272.145	289.827	283.452
R_m [N/mm²]	577.508	579.723	586.472	567.754
A_g [%]	41.107	45.353	49.769	45.549
A [%]	49.519	53.555	58.248	52.885
r	0.579	1.086	1.654	/
r_m	1.101			/
Δr	0.030			/
n	0.393			

Fig. 2 Mechanical properties **a** and flow curves **b** of 1.4404 specimens, taken from sheet metal and tube. (Color figure online)

3.2 Experimental Setup and Testing Procedure

The forming tests were performed on a machine from ATG Automations-Technik-Gröditz GmbH & Co. KG, which was developed for the presented collar forming process. The basic structure of the machine concept is shown in [14]. All necessary movements of the forming tool are realized by various drives. Two mandrel geometries were used in the tests (Fig. 3) and the angle of the active surface was varied: a conically reducing mandrel with a negative angle of 8° and a conically enlarging mandrel with a positive angle of 4°. This results in different diameters at the spherical tooltip, which is in contact with the material at the end of every forming cycle. The additional inclination of the mandrel in the tool clamping of the machine in combination with the angle of the tool active surface create an undercut. The undercut determines the diameter increase of the collar in each forming cycle in addition to the axial infeed of the mandrel into the pre-hole and the radial infeed. An advantage of the conically enlarging tool is the possibility of a larger infeed even with smaller pre-holes. The tip of the mandrel, which has the largest dimensions, can be inserted into the tube at the centre of the pre-hole. The tool can subsequently perform a larger radial infeed, since the diameter decreases towards the tool clamping. The mandrels were manufactured from the material CPM Rex M4 by turning, hardening, and grinding.

Different pre-hole calculations were taken from the literature (Fig. 4), since circular holes cannot be used for the collar forming of tubes. However, these geometries have been calculated and designed for collar forming with punch or ball. A collar height of 4.5 mm was assumed for all pre-hole shapes. The basket arch according to NASS [15] was calculated from geometrical parameters without taking into account the tube wall thickness and the die radius of the clamping. These two geometrical parameters were included in the design for ellipse I according to HENTRICH [11], whereby the die radius was 2.0 mm. Not only the geometry, but also material parameters such as tensile strength, uniform elongation and strain hardening exponent were considered in the calculation of ellipse II according to HENTRICH [11]. The required mechanical parameters were determined from the results of the tensile tests for the sheet metal as well as the tube in rolling direction. The two axis values of the ellipse II were transferred to a slotted hole (slotted hole II according to HENTRICH) to investigate the influence of the pre-hole shape. The reason for this was that only one

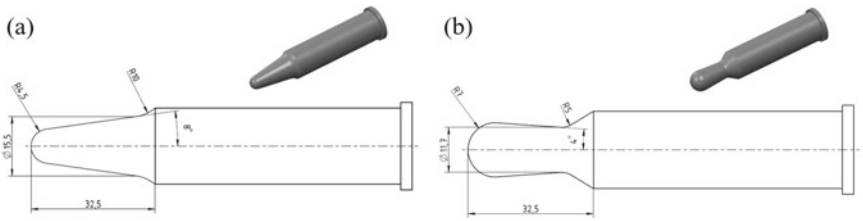


Fig. 3 Conical reducing a and conical enlarging tool for incremental collar forming process

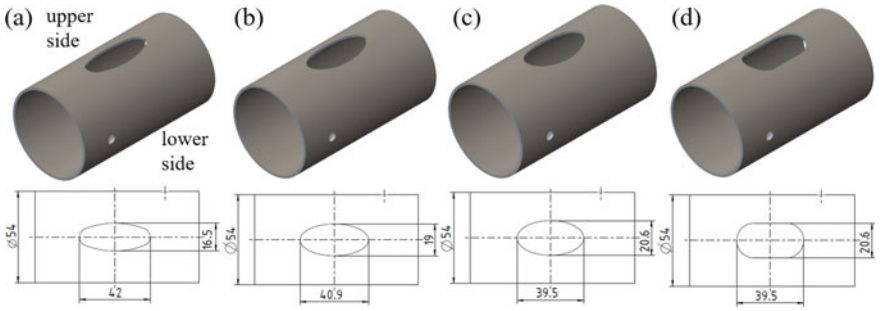


Fig. 4 Pre-hole geometries for incremental collar forming process: basket arch acc. to NASS **a**, ellipse I acc. to HENTRICH **b**, ellipse II acc. to HENTRICH **c,** and slotted hole acc. to HENTRICH **d**

axis is needed in a possible machine concept for milling a slotted hole. The pre-holes were positioned opposite the welding seam and inserted into the tube by milling. The material within the pilot hole was first removed in several roughing cycles before the final contour was produced with a finishing pass. The edge of the pre-hole had to be deburred afterwards. In addition to the pre-holes, a hole was drilled in the tube shell surface serving both to position the tube in the clamping and for subsequent referencing during evaluation. The tube was clamped between two half-shells after positioning.

A rotational speed of 86 min^{-1} and a feed rate of 3 mm/s was set for the collar forming steps (Fig. 1d, e) as well as a constant infeed of the mandrel of 1.1 mm for each cycle. All tests were performed without the use of lubricants. This avoids expensive cleaning processes after collar forming for tubes used in the food industry. The aim of the experiments was to form a 1:1 collar. The number of forming cycles had to be varied depending on the starting point for the first cycle and the projection length of the mandrels. Fifteen cycles were, therefore, required using the conically reducing mandrel and 13 cycles using the conically enlarging tool to achieve an inner diameter of 51 mm.

Besides the investigation of different pre-hole geometries, the calculation for ellipse II was used to determine the influence of the collar height and the maximum expansion ratio (Table 2). Due to the mandrel dimensions, the maximum collar height was limited to 6.5 mm. Test series were conducted for both mandrel geometries, using the same collar forming programs as before. Pre-forming cycles had to be realized for the pre-holes with collar heights between 5.0 and 6.5 mm when using the conically reducing mandrel.

Table 2 Dimensions of the ellipse axes and expansion ratio of the ellipse II according to HENTRICH for different collar heights

Collar height [mm]	Dimension of larger pre-hole axis a [mm]	Dimension of smaller pre-hole axis b [mm]	Expansion ratio (axis b to inner diameter of collar) [%]
3.0	44.0	24.1	111.62
4.5	**39.5**	**20.6**	**147.57**
5.0	38.0	19.4	162.89
5.5	36.5	18.2	180.22
6.0	35.0	17.0	200.00
6.5	33.5	15.8	222.78

3.3 Optical Measurement and Analysis of Incrementally Formed Collars

The inner and outer surfaces of the collar and the tube were scanned by the optical measurement system GOM ATOS (Fig. 5a). For this purpose, the branched tube was clamped between two cones and scanned using the optical sensor. The recorded images were referenced to each other and merged into a virtual model. For the evaluation, the tubes were first aligned using a fitting cylinder of the outer tube surface and the positioning hole. The collar height for the investigated tube diameter according to DIN 11,852, which describes tee-fittings for the food and chemical industry, is given as 3.5 mm. In industry, however, face milling is usually performed after forming in order to obtain a flat collar edge for subsequent butt welding. Therefore, the evaluation was executed at a collar height of 1.5 mm (Fig. 5b). The roundness, straightness and cylindricity of the inner and outer collar surface were determined besides the collar diameter. In addition, the collar height and wall thickness (distribution) were analyzed.

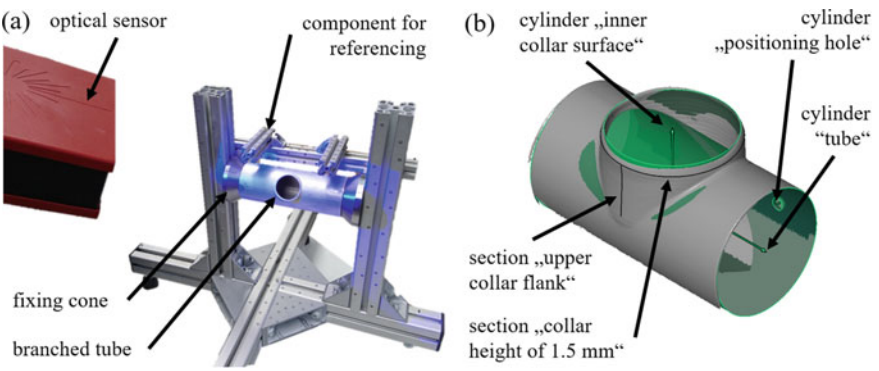


Fig. 5 Measurement setup for scanning of branched tubes **a** and scanned tube with evaluation features **b**. (Color figure online)

4 Results

4.1 Properties of an Incrementally Formed Collar

DIN 11852 provides the basis for the evaluation of the collars. In the following, the collars with pre-hole "ellipse II according to HENTRICH" will be analyzed for both mandrel geometries. The values determined from the optical measurement are summarized in Table 3. The collar height of 4.5 mm assumed for the pre-hole calculations was reached and even exceeded, taking into account the deviation of ± 1.0 mm permitted in the standard. The collar height of 3.5 mm specified in DIN 11,852 was fulfilled. The maximum and minimum height varies by more than 1.0 mm along the collar circumference. This can be improved by further optimizing the pre-hole geometry. Furthermore, a 1:1 collar was achieved as the target diameters were reached. A too large total infeed can be derived, which has to be adjusted in the machine program, due to the values for the inner diameters. Both roundness and

Table 3 Obtained heights, diameters, and shape tolerances for the collar with pre-hole ellipse II according to HENTRICH for both tool geometries

Parameter	Value for conical reducing tool	Value for conical enlarging tool
Max. collar height [mm]	5.40	5.22
Min. collar height [mm]	4.26	4.94
Difference in heights [mm]	1.14	0.28
Mean inner diameter [mm]	51.58	51.53
Mean outer diameter [mm]	54.17	53.96
Inner roundness [mm]	0.78	0.60
Outer roundness [mm]	0.57	0.40
Inner straightness [mm]	0.61	0.50
Outer straightness [mm]	0.51	0.49
Inner cylindricity [mm]	1.60	1.47
Outer cylindricity [mm]	1.14	1.08

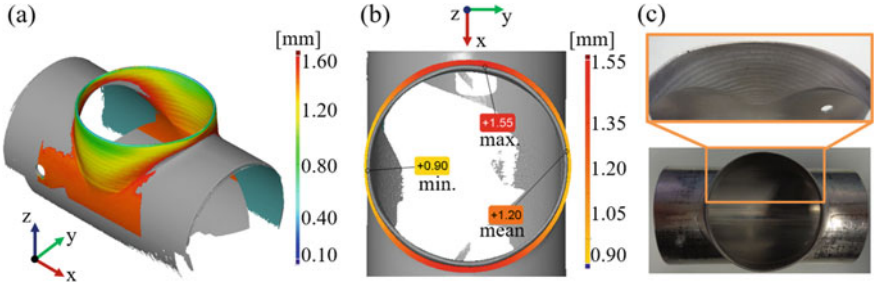


Fig. 6 Sheet thickness distribution within the collar **a** and at a collar height of 1.5 mm **b** for ellipse II formed with conically enlarging tool, inner collar surface **c** for ellipse II formed with conically reducing tool. (Color figure online)

cylindricity are lower for the outer surface, as the metal is formed against the die hole. In contrast, there is only punctual contact between the mandrel and the inner surface. The values for straightness reflect the mean value for the upper and lower flank, respectively. In some cases, the values for the upper side are twice as large as those for the lower side. The reason for this is the clamping of the tube between two half-shells. While the forming forces are transferred into the machine table at the lower side, the resiliency in the upper area leads to higher deviations. Only tolerances according to ISO 2768-c are specified in the standard with permissible deviations of ± 0.8 mm for the given tube diameter, which are maintained when transferred to the form tolerances.

The minimum sheet thickness with values between 0.8 mm and 1.0 mm is obtained along the larger pre-hole axis a, as this area is formed more severely (Fig. 6a, b). According to these values, the maximum permitted wall thickness reduction of 25% from DIN 11,852 is exceeded. An increase in thickness up to 1.6 mm occurs along the short axis b, which is caused by an initial compression of the pre-hole edge by the mandrel. The average sheet thickness is approx. 1.2 mm. Further optimization with regard to pre-hole and mandrel geometry, as well as the forming parameters such as infeed and number of cycles, will contribute to achieve a more homogeneous sheet thickness distribution.

Material abrasion occurs during collar forming, especially when using the conically reducing mandrel. This is caused by the initial compression and a subsequent chip removal of the pre-hole edge along the short axis. The larger undercut of the conically enlarging tool minimizes chip formation, since the bending ratio is increased within a cycle. Furthermore, the tool path is formed in the collar wall (Fig. 6c). The surface can be improved by a final finishing cycle with low feed rate and small infeed. In addition, the surface roughness can be enhanced through higher infeeds per cycle causing less contact cycle between material and tool. A coating of the mandrel can also optimize the tribological conditions, whereby the use of lubricants should be avoided due to targeted application in the food industry.

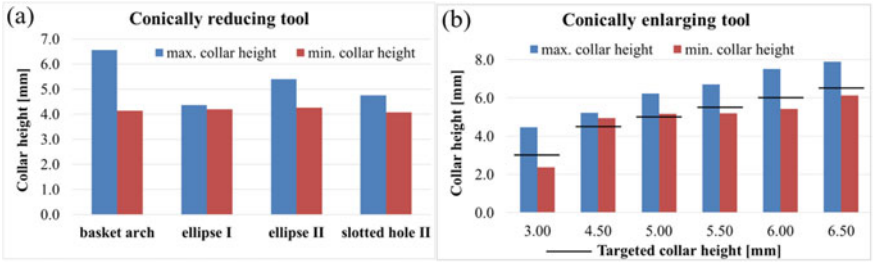


Fig. 7 Results for collar heights using various pre-hole geometries **a** and different targeted heights according to the calculation for ellipse II **b**. (Color figure online)

4.2 Influence of Pre-hole

The required collar height according to DIN 11,852 is also achieved with the other pre-hole shapes. The maximum height for the pre-hole according to NASS clearly exceeds the assumed calculation value of 4.5 mm (Fig. 7a). The range of minimum collar heights is smaller compared to the maximum values. The smallest difference between the minimum and the maximum value is obtained with ellipse I achieving a flat collar edge. The comparison between the ellipse II and the designed slotted hole II clearly indicates that the pre-hole shape also has a great influence, in addition to the dimensions of the axes. The maximum value of the collar height is reduced by adapting the shape, particularly with the conically reducing tool.

The ellipses II being calculated for different targeted collar heights were formed without continuous edge cracks. A maximum expansion ratio of over 220% was achieved. Only collars with a targeted height of 6.5 mm show necking and slight cracks visible at the neck edge. In correlation to the theoretical calculation, an increase in the values of the maximum collar height is obtained (Fig. 7b). All maximum values exceed the nominal values. With the help of the pre-hole calculation used, a range (collar height between 4.5 and 5.5 mm) with the best collar results can be determined with regard to the final minimum height as well as the flatness of the collar edge.

5 Conclusion and Outlook

A novel process for incremental collar forming of tubes made of 1.4404 was presented, with which 1:1 collars were achieved. The collars obtained were optically scanned and analyzed with regard to sheet thickness and geometrical accuracy and compared with an applicable standard for the food industry. The pre-hole calculations for collar forming with punch or ball were transferred to incremental forming variant. Four different calculation methods were examined and compared in terms of final collar height. In addition, pre-hole dimensions were determined for different targeted collar heights for a selected calculation method. A maximum collar height

of over 6.0 mm and a maximum expansion ratio of over 220% was achieved. The presented process enables the flexible production of T-pieces as well as the collar forming for large tubes and piping systems. Additional forming parameters such as infeed and feed rate will be investigated for further process optimization achieving a more homogeneous sheet thickness distribution. The number of forming cycles with regard to surface quality and cycle time should be reduced. Process simulation with numerical methods will be performed and compared with experimental results.

Acknowledgments We gratefully acknowledge the cooperation of our project partners ATG Automations-Technik-Gröditz GmbH & Co. KG and SANHA GmbH & Co. KG as well as the financial support of the "Central Innovation Programme for SMEs" (ZIM) of the Federal Ministry for Economic Affairs and Energy.

References

1. Taleb-Araghi B, Manco G, Bambach M, Hirt G (2009) Investigation into a new hybrid forming process: incremental sheet forming combined with stretch forming. CIRP Ann 58(1):225–228
2. Voswinckel H, Bambach M, Hirt G (2015) Improving geometrical accuracy for flanging by incremental sheet metal forming. Int J Mater Form 8(3):391–399
3. López-Fernández JA, Centeno G, Martínez-Donaire AJ, Morales-Palma D, Vallellano C (2018) Experimental and numerical analysis of the flanging process by SPIF. IOP Conf Ser: J Phys: Conf Ser 1063
4. Cui Z, Gao L (2010) Studies on hole-flanging process using multistage incremental forming. CIRP J Mater Process Technol 2:124–128
5. Centeno G, Silva MB, Cristino V, Vallellano C, Martins PAF (2012) Hole-flanging by incremental sheet forming. Int J Mach Tools Manuf 59:46–54
6. Cristino VAM, Montanari L, Silva MB, Martins PAF (2015) Towards square hole-flanging produced by single point incremental forming. Proc IMechE Part L: J Mater: Des Appl 229(5):380–388
7. Bambach M, Voswinckel H, Hirt G (2014) A new process design for performing hole-flanging operations by incremental sheet forming. Procedia Eng 81:2305–2310
8. Cao T, Lu B, Ou H, Long H, Chen J (2016) Investigation on a new hole-flanging approach by incremental sheet forming through a featured tool. Int J Mach Tools Manuf 110:1–17
9. Petek A, Kuzman K (2012) Backward hole-flanging technology using an incremental approach. J Mech Eng 58:73–80
10. Wen T, Zhang S, Zheng J, Huang Q, Liu Q (2016) Bi-directional dieless incremental flanging of sheet metals using a bar tool with tapered shoulders. J Mater Process Technol 229:795–803
11. Hentrich C (2002) Untersuchungen zum Aushalsen von Rohren mit starrem Werkzeug unter besonderer Berücksichtigung der Vorlochgeometrie. PhD thesis, Otto-von-Guericke-Universität Magdeburg
12. Teramae T, Manabe K, Ueno K, Nakamura K, Takeda H (2007) Effect of material properties on deformation behavior in incremental tube-burring process using a bar tool. J Mater Process Technol 191(1–3):24–29
13. Yang C, Wen T, Liu LT, Zhang S (2014) Dieless incremental hole-flanging of thin-walled tube for producing branched tubing. J Mater Process Technol 214:2461–2467
14. Keil, U (2019) Erzeugung eines Abgangs an einem Hohlkörper. Offenlegungsschrift DE 10 2018 112 845 A1 2019.12.05
15. Nass R (1964) Das Aushalsen von Blechen und Rohren in kaltem Zustand bei Wanddicken zwischen 3 und 9 mm. PhD thesis, TH Stuttgart

Deformation Analysis in Ultrasonic-Assisted Multi-stage Incremental Sheet Forming



Zinan Cheng, Yanle Li, Fangyi Li, and Jianfeng Li

Abstract The multi-stage incremental sheet forming is a promising forming strategy to fabricate complex shapes through the rational design of intermediate shapes. To further improve the formability, the ultrasonic-assisted multi-stage incremental sheet forming is proposed. The present work aims to reveal the effect of ultrasonic vibration (UV) on the thickness distribution, strain–stress state and the forming force variation. First, the finite element (FE) model is established through ABAQUS software, in which the trajectory of the forming tool with the high-frequency vibration is defined via the user subroutine VUAMP. Then, after the verification of the FE model, the thickness evolution, the stress–strain state and the forming force are comprehensively analyzed. It is found that the thickness distribution can be effective improved by introducing UV. In addition, the stress concentration in the bending area is effectively alleviated and the equivalent plastic strain is obviously increased under the UV. Final, the application of UV can lead to a notable reduction of forming force and smoother forming force curves at the latter two stages. The findings of this work provides evidences that ultrasonic assistance is an effective strategy to improve the incremental forming process.

Keywords Ultrasonic vibration · Multi-stage incremental forming · Finite element model · Thickness evolution · Stress–strain analysis

Z. Cheng · Y. Li (✉) · F. Li · J. Li
Key Laboratory of High Efficiency and Clean Mechanical Manufacture, Ministry of Education
School of Mechanical Engineering, Shandong University, Jinan 250061, China
e-mail: yanle.li@sdu.edu.cn

National Demonstration Center for Experimental Mechanical Engineering Education, Shandong University, Jinan 250061, China

School of Mechanical Engineering, Shandong University, Jinan 250061, China

© The Minerals, Metals & Materials Society 2021

G. Daehn et al. (eds.), *Forming the Future*, The Minerals, Metals & Materials Series,
https://doi.org/10.1007/978-3-030-75381-8_36

1 Introduction

During the last two decades, great importance has been attached to incremental sheet forming (ISF) which is featured with high flexibility, great customization, small-scale production and low cost [1, 2]. In the ISF process, the three-dimensional shape is dispersed into a large amount of layers of plane shape, and the forming tool is controlled by a computer numerically controlled (CNC) machine to finish the target shape incrementally according on the prescribed trajectory. Due to the gradual accumulation of the local plastic deformation, ISF possesses a better formability compared to other traditional forming processes [3]. However, during the forming of difficult-to-form parts by ISF, the serious thickness reduction and fractures are inevitable by using traditional single-stage toolpath [4]. Therefore, the multi-stage incremental forming has been proposed. Moreover, the ultrasonic vibration (UV) was introduced to many manufacturing process (e.g. compression [5], upsetting [6] and spinning [7], etc.) due to the improvement of geometric accuracy [8] and formability [9], and the reduction of both the flow stress [10] and the surface roughness [11].

Kitazawa et al. [12] attempted to adopt the two-stage incremental forming to produce a hemi-ellipsoidal shape. Kim and Yang [13] proposed a double-pass incremental forming process and it was found that the shear-dominate deformation has an essential influence on the thickness reduction. Therefore, the final thickness strain can be predicted and the intermediate shape could restrain the serious shear deformation. Iseki and Naganawa [14] established a multi-stage incremental sheet metal bulging machine using spherical and cylindrical rollers for manufacturing shapes with vertical walls, and the final thickness distribution was calculated based on the forming limit diagram. Particularly, Skjoedt et al. [15] proposed various four-stage forming strategies including the down-up-down-down (DUDD) and down-down-down-up (DDDU) forming direction. The result showed that the strain distribution is not only depending on the toolpath geometry but also on the forming direction (upwards and downwards). Similarly, to overcome the limitation of maximum forming angle, Duflou et al. [16] implemented a five-stage incremental forming method and the maximum thickness reduction during the multi-stage is lower than that in the single-stage forming process, implying an increase of the formability. Ndip-Agbor et al. [4] relieved the stepped feature of the multi-stage forming through the prediction of the rigid body motion (RBM) and the application of the 3D contact patch toolpath. After a seven-stage forming of the developed strategies, a 15° increase of the maximum forming angle and a more evenly thickness distribution were obtained.

In terms of the application of UV in ISF process, existing studies have been focused on the single-stage incremental forming process. Amini et al. [17] found that plain strains of the parts formed by ultrasonic-assisted ISF are obviously higher than that without UV. Through a series of ultrasonic-assisted groove forming experiments, Vahdati et al. [18] found that the forming force and the surface roughness of formed parts can be reduced, and the forming depth and the geometric accuracy were enhanced. To reveal the influence mechanism of UV, Li et al. [19, 20] proposed the novel constitutive model and the material flow model to further reveal the influence

mechanisms of vibration field. The results showed that the UV can decrease the deformation flow stress and increase the equivalent plastic strain and the material flow area. Li et al. [21] found that when the vibration frequency is less than 40 kHz, the increase of the frequency can effectively reduce the vertical forming force. Through a series of experiments, Zhai et al. [22] found that the UV can effectively reduce the surface roughness and increase the surface bearing ability.

In the present work, the UV was applied to the multi-stage incremental forming process to further improve the formability. Furthermore, forming force, strain, stress and thickness evolution were analyzed through FE model to reveal the influence of UV on the deformation process. The rest of the paper is organized as follows. Section 2 describes the establishment of the FE model and the experimental platform. Section 3 interprets the simulation results and provides corresponding discussion. Final, the main conclusions of the present work are drawn in Sect. 4.

2 Methods

2.1 Finite Element Modeling

The FE model of ultrasonic-assisted incremental forming was established in ABAQUS/Explicit module based on the working principles shown in Fig. 1. In the FE model, the thickness of the sheets was defined as 1.0 mm and the material properties of AA1050-O are listed in Table1. In particular, to fully reflect the softening effect of UV, a self-developed constitutive model [19] was employed. In addition,

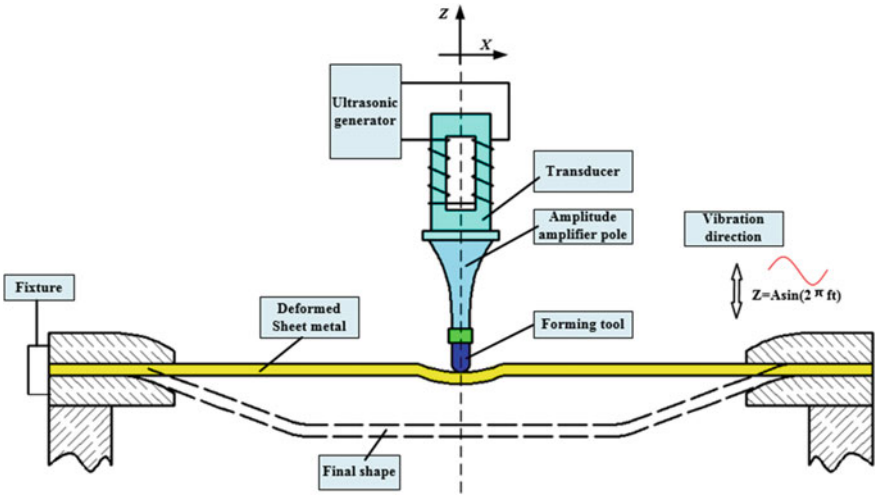


Fig. 1 Schematic diagram of the ultrasonic-assisted incremental forming. (Color figure online)

Table 1 Material properties of AA1050-O

Material property	Value (unit)
Density	2.7×10^{-9} (g/mm^3)
Yield strength	31.40 (MPa)
Ultimate tensile strength	69.68 (MPa)
Young's modulus	69.12 (GPa)
Elongation at break	52.43 (%)
Poisson's ratio	0.33

since the material of previous is different, the parameters in constitutive model were determined through the same method. The diameter of the forming tool was 5 mm. Furthermore, the sheet and the forming tool were set as the deformable shell and the discrete rigid, and the corresponding element type were determined as S4R and R3D4, respectively. The mesh strategy is shown in Fig. 2, in which the sheet was divided into the central deformed area and the surrounding fixed area. All freedoms of elements at the fixed area were constrained. The surface to surface contact condition between the forming tool and sheet was employed, and the forming tool was defined as the master surface while the sheet was set as the slave surface.

The shape of truncated cone was chosen as the forming target and the spiral toolpath was employed to avoid the stress concentration. The designed spiral toolpath and intermediate stages of the multi-stage forming are shown in Fig. 3. It is noticed that along the vertical direction, the forming tool has a continuous feed and high-frequency vibration. Therefore, the spiral toolpath needs to be analyzed as a function of the step time. The formula derivation process is shown in Fig. 4. Take an example of a single point P in the spiral toolpath, the forming depth can be determined through the following formula:

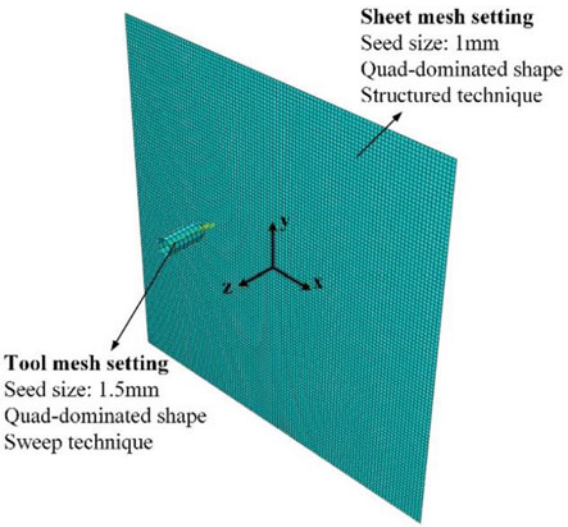


Fig. 2 The mesh setting and the mesh sketch of the sheet and forming tool. (Color figure online)

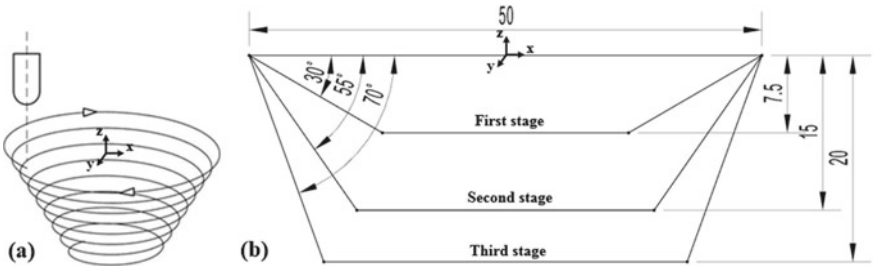


Fig. 3 **a** The spiral toolpath **b** The trajectory design of multi-stage forming

$$h = t \cdot V_h \tag{1}$$

where h is the forming depth (along the Z coordinate), t is the forming time, $V_h = H/T$ is the vertical feed speed of the forming tool. H is the total height of the truncated cone and T is the total step time. Subsequently, the radius of the spiral $R^{'}$ can be expressed as:

$$R^{'} = R - h/\tan\alpha \tag{2}$$

where R and α are the upper initial radius and the wall angle of the designed truncated cone, respectively. Then, the coordinates of a spatial point at time t can be written as follows:

$$\begin{cases} X = R^{'}\cos(\omega t) \\ Y = R^{'}\sin(\omega t) \\ Z = V_h t + A\sin(2\pi f t) \end{cases} \tag{3}$$

where $\omega = 2k\pi/T$ is the angular velocity, k is the number of spiral toolpath layers, A and f are the vibration amplitude and the frequency of UV, respectively. Then, the toolpath of the forming tool can be applied through the user subroutine VUAMP. For convenience, three forming stages were analyzed in a single FE model with three corresponding steps.

2.2 Experiments

To verify the developed FE models, corresponding experiments for ultrasonic-assisted multi-stage incremental forming were performed. As shown in Fig. 5, the experimental platform consists of an ultrasonic system, a machining center

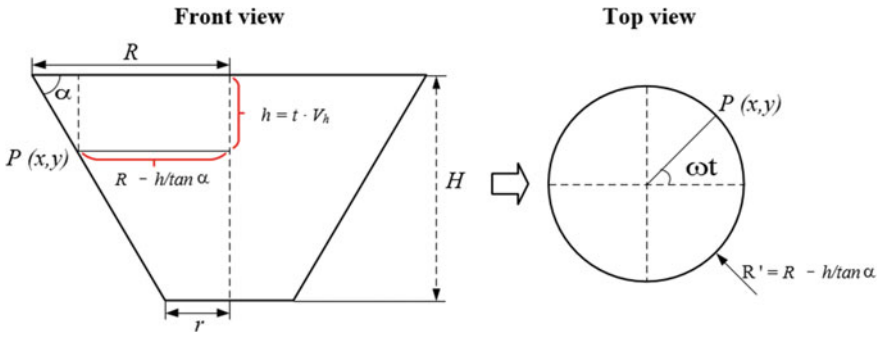


Fig. 4 The schematic diagram for the derivation process of the spiral toolpath. (Color figure online)

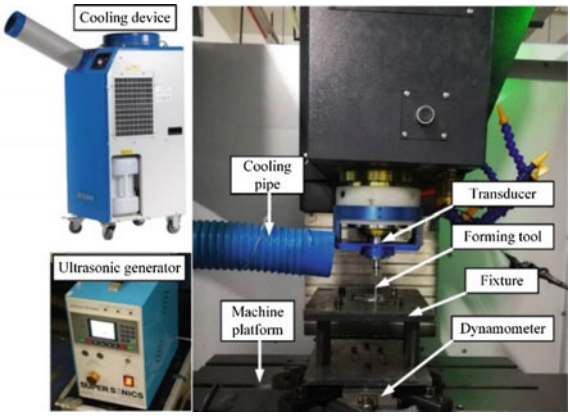


Fig. 5 Experimental platform of ultrasonic-assisted incremental forming. (Color figure online)

(DAEWOO ACE-V500), a fixture and a dynamometer (Kisler 9257B). The ultrasonic system includes an ultrasonic generator, a transducer, a forming tool, and a cooling device. Moreover, the experimental parameters are same as the simulation and the forming toolpath of three forming stages were generated in UG-NX software.

3 Results and Discussion

3.1 FE Model Verification

The comparison of forming force was shown in Fig. 6. Both force values and the evolution trend show reasonable agreement to corresponding experimental results. Without UV, the average errors in each stage are 5.8, 7.2 and 15.4%, and for UV

condition, the values are 6.9, 7.4 and 17.3%, respectively. Therefore, the developed FE model can be employed to further investigate the deformation behavior of the multi-stage forming process.

It can be noticed from Fig. 6 that the changing trend of forming force is similar under different UV condition, but the force value decreases obviously under UV

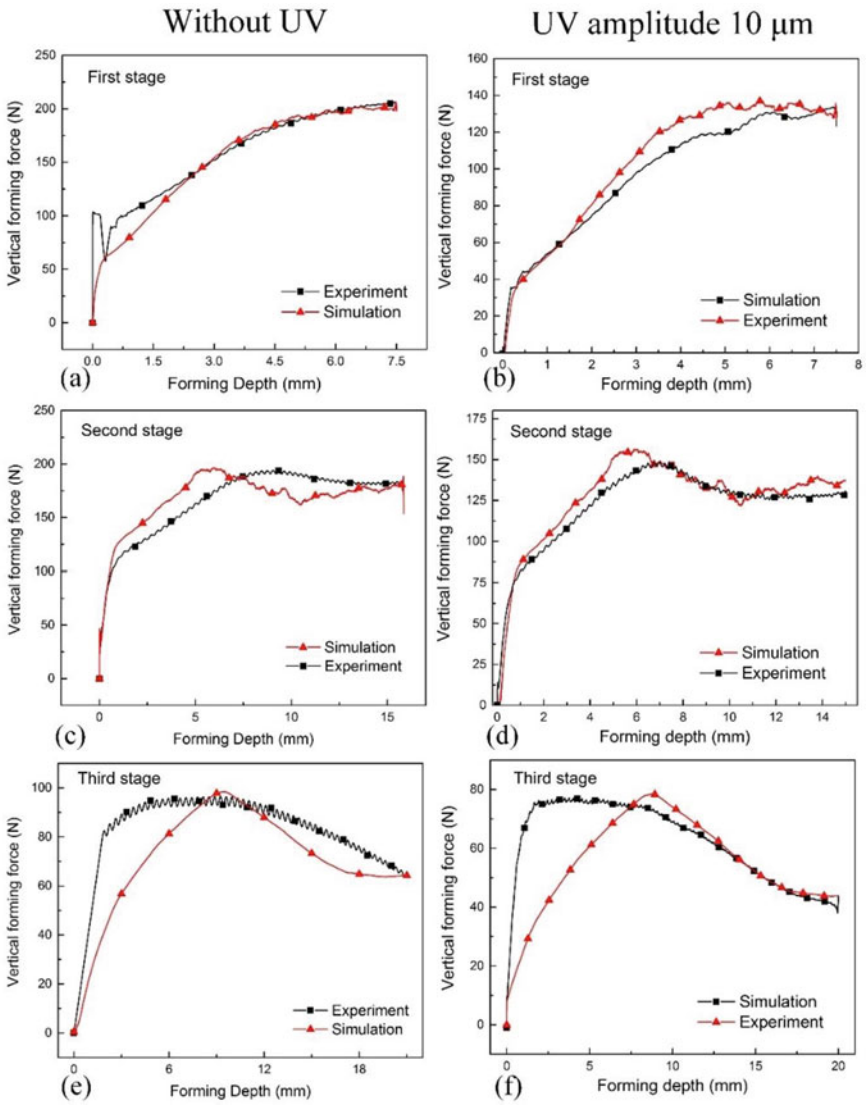


Fig. 6 Forming force comparison between simulation and experiments: Without UV: **a** First stage **c** Second stage **e** Third stage. UV amplitude 10 μm: **b** First stage **d** Second stage **f** Third stage. (Color figure online)

condition. In addition, the maximum force reduction rates caused by UV in three forming stages are 30.2, 26.1, and 20.4%. Then, due to the larger plastic deformation in the second stage, the material becomes completely yielded and then reaches the ultimate tensile strength. After that, considering the tensile property of AA1050-O material, the strength and the deformation resistance of material begins to reduce. As a result, the forming force first increases and then decreases to a relative stable value in the second stage. However, it can be observed that the force is much smaller in the third stage compared to the first two stages. There are two main factors accounting for this distinct change. First, under the serious plastic deformation condition, the thickness of the sheet metal reduces significantly. Furthermore, with the increase of the forming angle (70° in third stage), the normal contact area between the tool and the sheet gradually decreases. Consequently, the resistant force applied on the forming tool is reduced obviously.

3.2 Thickness Distribution

The thickness distribution of three forming stages under different UV condition are shown in Fig. 7. The maximum thickness reduction occurs in the side wall, while the minimum value takes place in the bottom area. Furthermore, it can be noticed that the application of UV can decrease the maximum thickness reduction in the side wall and the increase the thickness reduction in the bottom area. The maximum thickness reduction rates of three stages reduced by 2.1, 5.9 and 8.4%, respectively, and in the severe deformation condition of the third stage, the positive effect of UV becomes more obvious. Moreover, under the same volume of material, UV can make the material flow from the bottom area to the side wall so that the material distribution becomes more uniform.

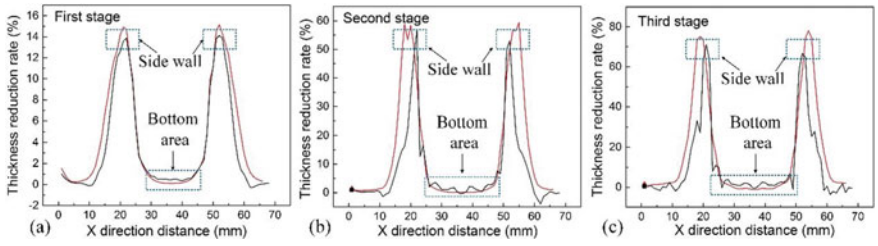


Fig. 7 Thickness evolution of cross section during the multi-stage incremental forming process: **a** First stage **b** Second stage **c** Third stage. (Color figure online)

3.3 Stress and Strain Analysis

The stress distribution of the sheet material during the multi-stage forming process is shown in Fig. 8. It can be noticed that in both UV condition, the maximum stress always occurs in the contact area of the forming tool and the sheet, and the maximum values of three stages are basically the same. However, the application of UV can effective decrease the stress during the forming process, and the maximum stress values are reduced by 47.1, 47.5, and 48% for three forming stages, respectively. Moreover, the strain evolution during the forming process is shown in Fig. 9, in which, ε_{11}, ε_{22} and ε_{33} are the strain of depth direction, circumferential and thickness direction. It can be clearly noticed that compared to ε_{11} and ε_{33}, the value of ε_{22} is

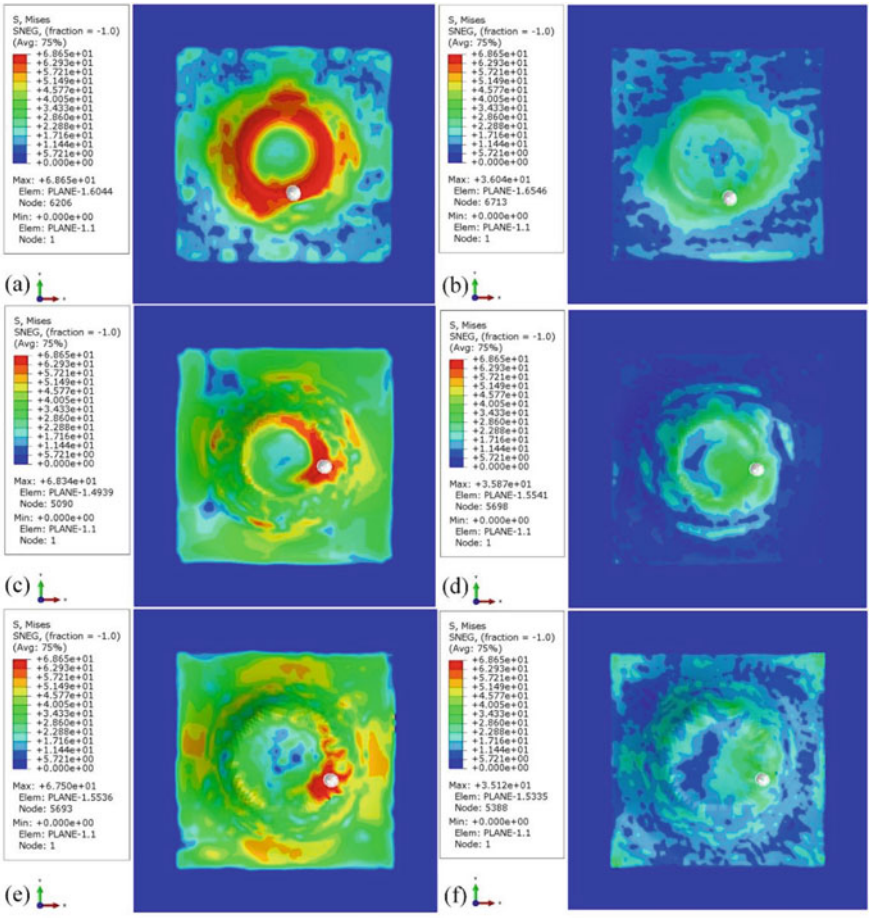


Fig. 8 Distribution of Mises stress, Without UV: **a** First stage **c** Second stage **e** Third stage. With UV: **b** First stage **d** Second stage **f** Third stage. (Color figure online)

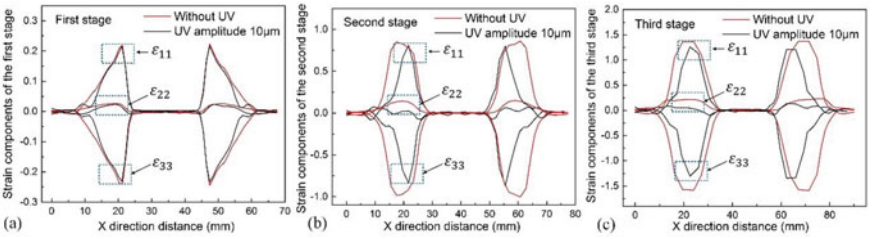


Fig. 9 Strain components of cross section: **a** First stage **b** Second stage **c** Third stage. (Color figure online)

much smaller to ignore, which indicates that the deformation in plane is the main forming mode of ISF. Moreover, in the first stage, values of strain components under different UV conditions are almost the same, while in the second and third stages, the application of UV can reduce the strain components of the formed part, especially the maximum strain value of ε_{11} and ε_{33}, which is consistent with the evolution of thickness.

4 Conclusions

In the present work, FE models for the ultrasonic-assisted multi-stage incremental forming are established and experimentally verified, in which the high-frequency vibration is loaded by the user subroutine VUAMP and a self-developed constitutive model is employed. Then, the forming force simulated thickness evolution and the stress–strain state are analyzed in detail. The main conclusions are summarized as follows:

1. The established FE model was verified through the comparison of forming force between simulation and experiment, and error between simulation and experiment is under 10%, which indicates that the FE model can be applied to further study of the forming process. Moreover, the maximum force reduction rates caused by UV in three forming stages are 30.2, 26.1, and 20.4%.
2. The thickness distribution of the cross section was analyzed through simulation results. It is noticed that the maximum thickness reduction rates of three stages reduced by 2.1, 5.9 and 8.4%, respectively. Furthermore, the maximum thickness reduction in the side wall reduce, meanwhile, the thickness reduction in the bottom area slightly increases. The results show that along the cross section, material distribution becomes more uniform under UV condition.
3. The application of UV can effective decrease the stress during the forming process, and the maximum stress values are reduced by 47.1, 47.5, and 48% for three forming stages, respectively. Furthermore, in the second and third stages, maximum values of strain components of ε_{11} and ε_{33} reduce by 12.3 and 9.1%, respectively, which is consistent with the thickness evolution.

Acknowledgments This work is supported by National Natural Science Foundation of China (51975328), Postdoctoral Innovation Project of Shandong Province (201701011), and Young Scholars Program of Shandong University (2018WLJH55).

References

1. Duflou JR, Habraken A-M, Cao J, Malhotra R, Bambach M, Adams D, Vanhove H, Mohammadi A, Jeswiet J (2017) Single point incremental forming: state-of-the-art and prospects. Int J Mater Form 11(6):743–773. https://doi.org/10.1007/s12289-017-1387-y
2. Li Y, Chen X, Liu Z, Sun J, Li F, Li J, Zhao G (2017) A review on the recent development of incremental sheet-forming process. Int J Adv Manuf Technol 92(5–8):2439–2462. https://doi.org/10.1007/s00170-017-0251-z
3. Reddy NV, Lingam R, Cao J (2015) Incremental metal forming processes in manufacturing. 411–452. https://doi.org/10.1007/978-1-4471-4670-4_45
4. Ndip-Agbor E, Cheng P, Moser N, Ehmann K, Cao J (2019) Prediction of rigid body motion in multi-pass single point incremental forming. J Mater Process Technol 269:117–127. https://doi.org/10.1016/j.jmatprotec.2019.02.007
5. Deshpande A, Hsu K (2018) Acoustic energy enabled dynamic recovery in aluminium and its effects on stress evolution and post-deformation microstructure. Mater Sci Eng A 711:62–68. https://doi.org/10.1016/j.msea.2017.11.015
6. Yao Z, Kim G-Y, Wang Z, Faidley L, Zou Q, Mei D, Chen Z (2012) Acoustic softening and residual hardening in aluminum: Modeling and experiments. Int J Plast 39:75–87. https://doi.org/10.1016/j.ijplas.2012.06.003
7. Rasoli MA, Abdullah A, Farzin M, Tehrani AF, Taherizadeh A (2012) Influence of UVs on tube spinning process. J Mater Process Technol 212(6):1443–1452. https://doi.org/10.1016/j.jmatprotec.2012.02.006
8. JQ Xie TF Zhou Y Liu T Kuriyagawa XB Wang 2016 The effects of UV in hot pressing for microgrooves Mater Sci Forum 861 121 126. https://doi.org/10.4028/www.scientific.net/MSF.861.121
9. Yang M, Bai L, Li Y, Yuan Q (2019) Influences of vibration parameters on formability of 1060 aluminum sheet processed by UV-assisted single point incremental forming. Adv Mater Sci Eng 2019:1–12. https://doi.org/10.1155/2019/8405438
10. Langenecker B (1966) Effects of ultrasound on deformation characteristics. IEEE TRANSACTIONS SONICS ULTRASONICS su-13, No 1
11. Sun S, Tang J, Shao W, Chen C, Liu Y (2019) Research on the matching relationship between ultrasonic-assisted grinding parameters and workpiece surface roughness. Int J Adv Manuf Technol 102(1–4):487–496. https://doi.org/10.1007/s00170-018-3195-z
12. Kitazawa K, Nakane M (1997) Hemi-ellipsoidal stretch-expanding of aluminum sheet by CNC incremental forming process with two path method. J Jpn Inst Light Metals 47:440–445
13. Kim TJ, Yang DY (2000) Improvement of formability for the incremental sheet metal forming process. Int J Mech Sci 42(7):1271–1286. https://doi.org/10.1016/S0020-7403(99)00047-8
14. Iseki H, Naganawa T (2002) Vertical wall surface forming of rectangular shell using multistage incremental forming with spherical and cylindrical rollers. J Mater Process Technol 130–131:675–679. https://doi.org/10.1016/S0924-0136(02)00735-5
15. Skjoedt M, Bay N, Endelt B, Ingarao G (2008) Multi stage strategies for single point incremental forming of a cup. Int J Mater Form 1 (1):1199–1202
16. Duflou JR, Verbert J, Belkassem B, Gu J, Sol H, Henrard C, Habraken AM (2008) Process window enhancement for single point incremental forming through multi-step toolpaths. CIRP Ann 57(1):253–256. https://doi.org/10.1016/j.cirp.2008.03.030

17. Amini S, Hosseinpour Gollo A, Paktinat H (2016) An investigation of conventional and ultrasonic-assisted incremental forming of annealed AA1050 sheet. Int J Adv Manuf Technol 90(5–8):1569–1578. https://doi.org/10.1007/s00170-016-9458-7
18. Vahdati M, Mahdavinejad R, Amini S (2015) Investigation of the UV effect in incremental sheet metal forming process. Proc Inst Mech Eng Pt B: J Eng Manuf 231(6):971–982. https://doi.org/10.1177/0954405415578579
19. Li Y, Cheng Z, Chen X, Long Y, Li X, Li F, Li J, Twiefel J (2019) Constitutive modeling and deformation analysis for the ultrasonic-assisted incremental forming process. Int J Adv Manuf Technol 104(5–8):2287–2299. https://doi.org/10.1007/s00170-019-04031-3
20. Li Y, Zhai W, Wang Z, Li X, Sun L, Li J, Zhao G (2019) Investigation on the material flow and deformation behavior during ultrasonic-assisted incremental forming of straight grooves. J Market Res. https://doi.org/10.1016/j.jmrt.2019.10.072
21. Li P, He J, Liu Q, Yang M, Wang Q, Yuan Q, Li Y (2017) Evaluation of forming forces in ultrasonic incremental sheet metal forming. Aerosp Sci Technol 63:132–139. https://doi.org/10.1016/j.ast.2016.12.028
22. Zhai W, Li Y, Cheng Z, Sun L, Li F, Li J (2020) Investigation on the forming force and surface quality during ultrasonic-assisted incremental sheet forming process. Int J Adv Manuf Technol. https://doi.org/10.1007/s00170-019-04870-0

A New Test Method for Sheet Metal Deformation Subject to Tension Under Cyclic Bending and Compression (TCBC)



H. Long, S. Ai, F. Tian, B. Lu, J. Chen, and H. Ou

Abstract A new test method for sheet metal deformation, *Tension under Cyclic Bending and Compression (TCBC)*, is developed in this study. The TCBC method is capable of testing material deformation under tension, bending, and compression with cyclic loading. The effect of each deformation mode can be independently controlled by adjusting corresponding parameters. Using the TCBC test rig developed, aluminium alloy AA5251-H22 is tested under four different testing conditions: simple tension, tension under cyclic compression, tension under cyclic bending, and tension under cyclic bending and compression. The maximum elongation of the tested specimen at fracture and the tensile force required for material plastic deformation are evaluated. The results show that the maximum elongation increases significantly under the TCBC condition due to localised plastic deformation under compression that delays the fracture. Finite element modelling of the TCBC test is developed to obtain stress distributions to explain the enhanced formability. The new TCBC method may be used for testing material formability that resembles double-side incremental forming.

Keywords Incremental sheet forming · Formability · Material testing

1 Introduction

Incremental sheet forming (ISF) is a flexible, cost-effective, and energy-efficient process, particularly suitable for high-value manufacturing of small-batch and prototype products. In the ISF process, a simple tool with a hemispherical head moves

H. Long (✉) · S. Ai · F. Tian · B. Lu
Department of Mechanical Engineering, University of Sheffield, Sheffield S1 3JD, UK
e-mail: h.long@sheffield.ac.uk

J. Chen
Department of Plasticity Technology, Shanghai Jiao Tong University, Shanghai 200030, China

H. Ou
Department of Mechanical, Materials and Manufacturing Engineering, University of Nottingham, Nottingham NG7 2RD, UK

© The Minerals, Metals & Materials Society 2021

G. Daehn et al. (eds.), *Forming the Future*, The Minerals, Metals & Materials Series,
https://doi.org/10.1007/978-3-030-75381-8_37

along predefined tool paths to deform a sheet blank incrementally into desired geometry. The ISF does not require any dedicated forming moulds or dies, thus it is flexible to manufacture small-batch products of different geometries and dimensions. The forming forces required in ISF are relatively small because the material is deformed locally and incrementally, thus there is no need to use heavy-duty forming equipment which further improves manufacturing flexibility. Furthermore, it has been widely reported that a variety of materials, when processed under ISF, has exhibited greater formability than that obtained by conventional sheet forming processes. Double-side incremental forming (DSIF), first reported by Meier et al. [1] and Smith et al. [2], has been developed to further enhance the material formability and to improve the process accuracy, compared to the conventional ISF using single-point incremental forming (SPIF). Figure 1 shows the basic concepts of single-point incremental forming (SPIF) and double-side incremental forming (DSIF). DSIF uses two simple tools at each side of the sheet blank; one tool acting as a master tool moves along predesigned tool paths to deform the material incrementally, while another tool moves synchronously acting as a support tool.

Forming limit curves (FLCs) are widely used to evaluate the material formability in conventional sheet metal forming processes. Banabic [3] reported that the dome test, hydraulic bulge test, and the Nakajima test were the commonly adopted testing methods to obtain the FLCs for various materials in the industry. An FLC defined the boundary of the stable deformation and unstable deformation of a material under various strain paths, such as uniaxial tension, plane strain, and equal biaxial tension. Materials generally exhibit much higher formability in ISF processes than that in the conventional forming processes. The FLCs obtained from SPIF experiments also show very different strain limit values and distributions upon the fracture occurrence, as illustrated in Fig. 2. The significantly enhanced formability in SPIF was demonstrated by testing various materials, including aluminium alloys used by Shim and Park [4] and Filice et al. [5], copper, steel, and aluminium alloys used by Fratini et al. [6]. For DSIF, both Malhotra et al. [7] and Lu et al. [8] reported that the material formability was further enhanced due to the compressive loading employed in DSIF in comparison with SPIF.

Emmens et al. [9] stated that FLCs could only be an effective method to predict the formability under the pre-condition that the material deformation is plane stress

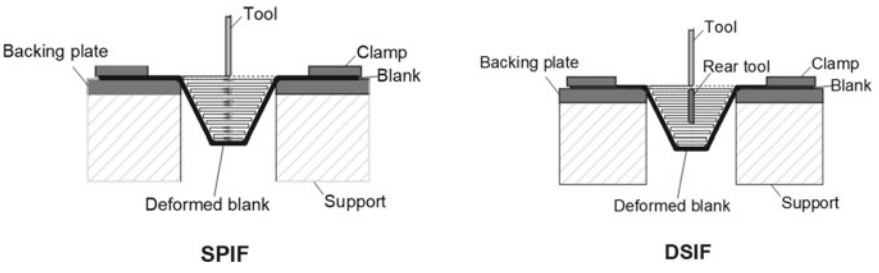


Fig. 1 Illustrations of single-point (SPIF) and double-side incremental forming (DSIF)

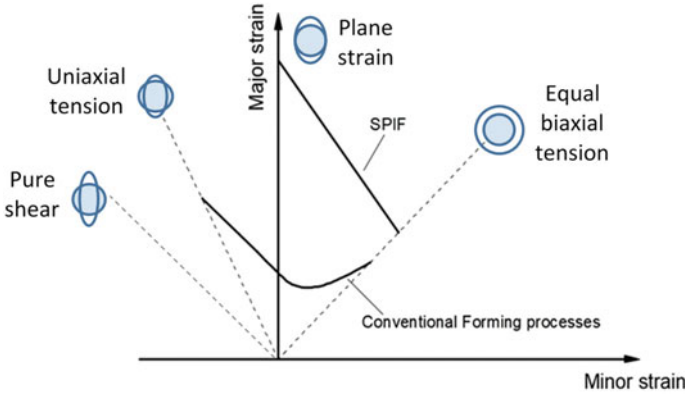


Fig. 2 Comparison of forming limit curves in conventional forming and SPIF processes. (Color figure online)

with a linear strain path, without bending and through thickness shear. In the conventional forming processes, the critical areas of the deforming part are generally under simple deformation conditions. However, the strain paths of SPIF deforming parts are generally between plane strain and equal biaxial tension [4, 10], where the material deformation is accumulated incrementally. It is widely acknowledged that the material deformation in SPIF is limited to the contact area between the tool and deforming sheet. Both experimental study and finite element (FE) simulation confirm that the material deformation in SPIF is a combination of stretching, bending, and shearing. Smith et al. [2] confirmed the effect of these deformation modes in ISF by comparing stress and strain distributions of the material elements in the thickness direction obtained from FE simulations. Eyckens et al. [11], Jackson and Allwood [12] investigated the influence of through-thickness-shear of the ISF formed parts on the material formability and identified the existence of stretching, bending, and shearing deformation modes. Furthermore, progressive toolpaths in ISF create cyclic and non-monotonic loading conditions. Consequently, the ISF formability can be affected by specific tool paths and process parameters, which makes it difficult to predict the onset of the fracture accurately. Emmens et al. [13] explained the stabilised deformation mechanisms in SPIF and concluded that the fracture could eventually occur at the weak spot of the material under continuous tensile loading. As a result, any deformation mode that suppresses the damage propagation at the weak spot improves the material formability. By applying a loading condition of cyclic bending onto the material, Emmens and von den Boogaard [14] performed the continuous bending under tension (CBT) test, in which the weakest spot in the test specimen changed constantly, leading to a significantly increased maximum elongation of 430% for material DC04.

The published studies on ISF material deformation, fracture, and formability are mostly conducted by performing the ISF test itself, as reviewed by Li et al. [15], Gatea et al. [16], and Sheng et al. [17]. However, owing to the complexity of the ISF process, including the complex loading conditions and localised contact and

cyclic deformation, it is not easy to evaluate the individual and interactive effects of different deformation modes as well as the cyclic loading condition on the material deformation and fracture by simply conducting SPIF or DSIF tests. The traditional formability evaluation methods, such as FLCs, as shown in Fig. 2, are unable to explain the experimental observation of material formability enhancement achieved in the ISF processes.

In this study, a new test method named *tension under cyclic bending and compression* (TCBC) is developed to investigate the material deformation in incremental forming processes, such as SPIF and DSIF. This test method is a further development of the CBT test method [14] owing to the introduction of compression deformation mode in addition to the deformation modes of tension and bending with cyclic loading. Using the developed TCBC test rig, four different testing conditions—simple tension (ST), tension under cyclic compression (TCC), tension under cyclic bending (TCB), and tension under cyclic bending and compression (TCBC)—are performed to investigate the bending effect, compression effect, and combined effect of bending and compression on the formability enhancement. Finite element models of TCB and TCBC tests are also developed to explain the effect of the localised material deformation and interaction of bending and compression on the formability enhancement.

2 TCBC Test Concept Development

The focus of this study is to develop a material testing method capable of applying various loading conditions such as tension, bending, and compression, with the cyclic loading effect. In the CBT test developed by Emmens and van den Boogaard [13, 14], the sheet specimen was stretched in the longitudinal direction while the cyclic bending was also applied, thus the material deformation under tension and bending with cyclic effect was investigated. To facilitate the superimposed compressive loading generated by the additional tool employed in DSIF, the new test method needs to provide a compressive force from the other side of the sheet specimen, moving synchronously with the bending tool. Figure 3 illustrates the different deformation zones at the contact between the master and slave tools because of the introduction of the compressive loading in DSIF.

Figure 4 presents the design concept of tension under cyclic bending and compression (TCBC) test. It consists of a bending roller, a compression roller, and two support rollers to enable the application of tension, bending, and compression deformation with cyclic loading effect. To develop the detailed design of the test rig, an analytical model based on the elementary plasticity theory is developed to characterise the effect of tension, bending, and compression on the initiation of material plastic deformation [18]. By considering an infinitely small element of the specimen material within the compressive deformation zone, as shown in Fig. 4, based on the force equilibrium condition and the Tresca yield criterion, the contact stress between the specimen and bending roller, σ_t, can be derived as

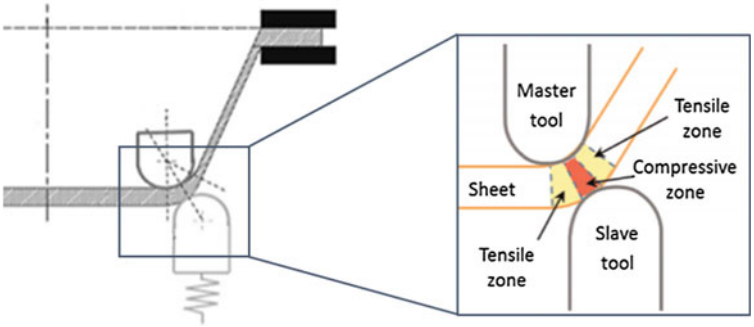


Fig. 3 Different deformation zones at the contact between master and slave tools in DSIF. (Color figure online)

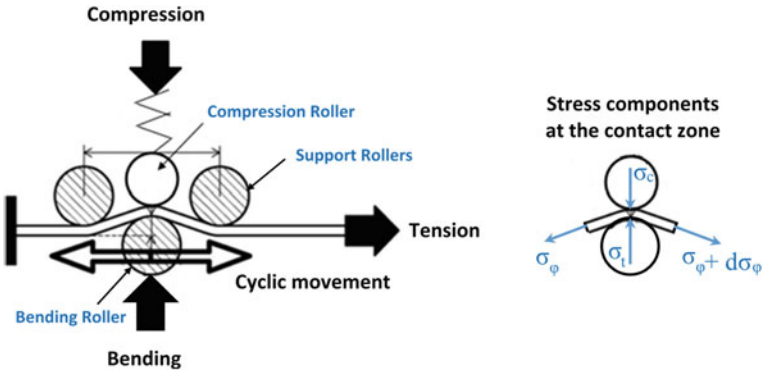


Fig. 4 Design concept of tension under cyclic bending and compression (TCBC) test. (Color figure online)

$$\sigma_t = \frac{\sigma_s + \sigma_c \frac{r_t}{t}}{1 + \frac{r_t}{t}}$$

where σ_s is the material flow stress, σ_c is the contact stress between the specimen and the compression roller, as shown in Fig. 4; r_t is the radius of the bending and compression rollers, and t is the thickness of the specimen under deformation. The tensile stress of the specimen in its longitudinal direction, σ_φ, can be derived as

$$\sigma_\varphi = \frac{(\sigma_s - \sigma_c) \frac{r_t}{t}}{1 + \frac{r_t}{t}}$$

By varying the radius of the rollers from 8 to 12 mm, using sheet thickness from 1 to 2 mm, it has been shown that the ratio of roller radius to sheet thickness only varies from 4 to 12. To illustrate the effect of compressive stress σ_c and contact stress due to bending roller σ_t on the variation of the tensile stress $\sigma_{\varphi,}$ the rollers with a

radius of 10 mm and the sheet blank thickness of 1, 1.2, 1.5, and 2 mm are tested. The ratio of the compressive stress to the flow stress, σ_c/σ_s, is varied as 0.3, 0.5, 0.7, and 0.9 to evaluate the variation of the tensile stress to the flow stress ratio, σ_φ/σ_s, as shown in Fig. 5. The analysis clearly shows that higher compressive stress will result in a much lower tensile stress required to reach the desired plastic deformation of the material, thus delaying the occurrence of fracture. Using the roller radius and sheet thickness values tested, the ratio of roller radius to sheet thickness only shows the minimal effect on the variation of the tensile stress ratio. As also shown in Fig. 5, the tensile stress ratio σ_φ/σ_s reduces proportionally while the contact stress ratio due to

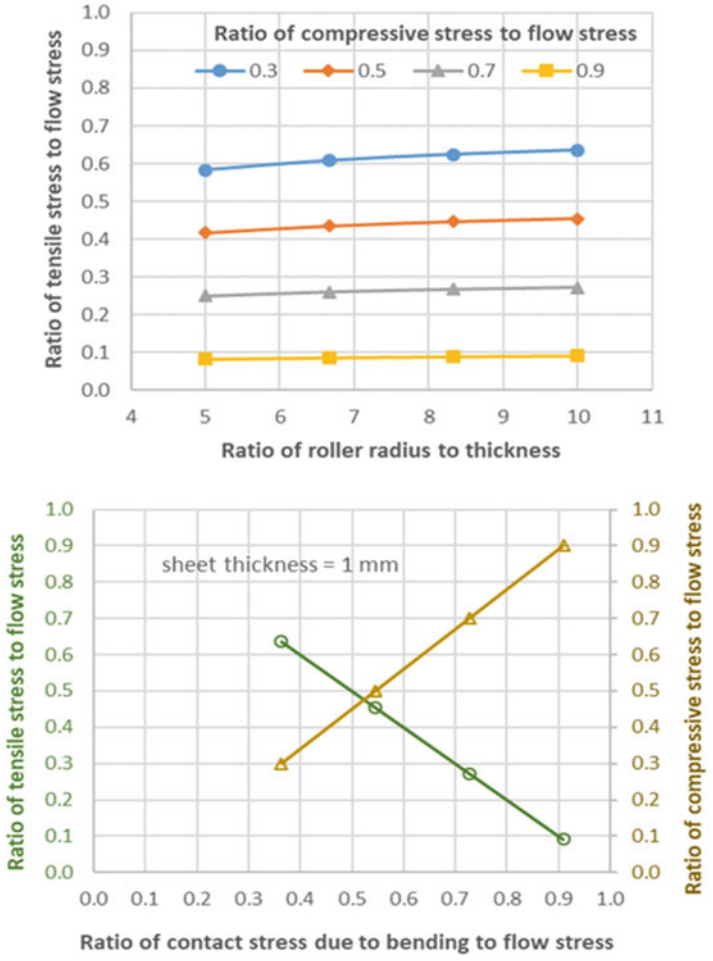


Fig. 5 Effect of compressive stress ratio (σ_c/σ_s) and bending contact stress ratio (σ_I/σ_s) on tensile stress ratio (σ_φ/σ_s). (Color figure online)

bending σ_t/σ_s increases; however, the compressive stress ratio σ_c/σ_s also increases with the increasing contact stress ratio due to bending σ_t/σ_s, which may result in high stresses in the localised areas of the specimen-tool contact, thus leading to early fracture.

3 TCBC Test Rig Design and Manufacturing

Based on the TCBC test concept developed and the analysis of the effect of the bending and compressive loading on the material plastic deformation, a test rig is designed and manufactured. The CAD model and completed TCBC test rig are shown in Fig. 6.

Various loading conditions can be applied onto the sheet specimen by using the developed loading device, mounted on a uniaxial tensile test platform as shown in Fig. 6. Both ends of the sheet specimen are clamped and the specimen is stretched from one end by the movement of the linear screw mechanism driven by a DC motor. Bending and compression loadings onto the specimen can be applied by the loading device where the specimen can be inserted through and bent from the below by the bending roller and compressed from the above by the compression roller. The compression roller is supported by two cylindrical springs to provide the required level of the compression force as well as to maintain the contact between the compression roller and the specimen. In order to ensure the bending being applied to

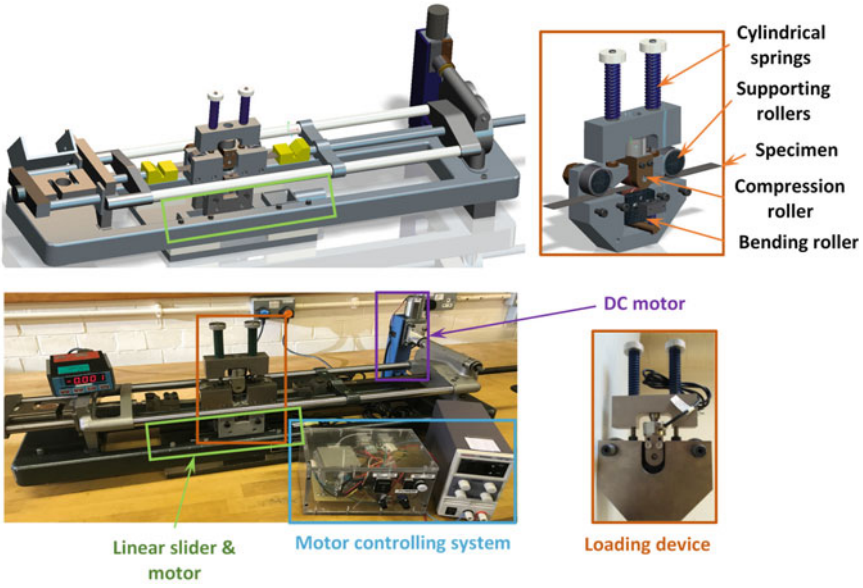


Fig. 6 Tension under cyclic bending and compression (TCBC) test rig and loading device. (Color figure online)

the target deformation zone and maintain the bending effect during cyclic loading, the specimen is kept in position by two supporting rollers positioned at a constant distance. All rollers can rotate freely around their own axis to reduce friction. The loading device can move along a slider track that is mounted on the base of the uniaxial tensile test platform and driven by another DC motor. On both ends of the slider track, a micro switch is placed; once the loading device hits the switch, the rotating direction of the DC motor will be reversed, creating a cyclic movement of the loading device. Using the motor controlling system, the stroke speed of the slider, the tensile speed, the bending depth, and the compression force can be independently controlled and varied. These correspond to the effect of each deformation mode in DSIF, including cyclic effect, tension effect, bending effect, and compression effect.

4 TCBC Experiment and Results Discussion

Using the test rig developed, four different types of experiments, representing various loading conditions, are performed. These include tests of simple tension (ST), tension under cyclic compression (TCC), tension under cyclic bending (TCB), and tension under cyclic bending and compression (TCBC). Material AA5251-H22 is used and sheet specimens with a thickness of 1, 1.2, and 1.5 mm are tested. Five test parameters are investigated where the compressive force is varied from 0 to 1700 N, bending depth from 1 to 13 mm, stroke speed from 0 to 2.5 mm/s, and stretching speed from 0 to 4 mm/min.

4.1 Effect of Various Loading Conditions on Material Deformation

Figure 7 shows the tensile force time history when the sheet thickness is 1.5 mm, the compression force 906 N, bending depth 9 mm, stroke speed 1.5 mm/s, and stretching speed 3.2 mm/min. Significant tensile force reduction is recorded under TCC, TBC, and TCBC conditions when compared to that under simple tension. The maximum tensile force under TCBC condition is only 50% of that required under simple tension. Figure 8 shows the maximum elongation ratio at fracture of the specimens tested under these conditions. The maximum elongation ratios of the specimen under TCC, TCB, and TCBC are significantly higher than that under simple tension. The specimen elongation is the greatest under TCBC while the elongation under TCB is higher than that under TCC. The fracture behaviour of the specimens is also different under different testing conditions. In the simple tension test, the crack of the specimen occurs at an approximate angle of 45° to the elongation direction of the specimen. While in other tests of TCC, TCB, and TCBC, the cracks of the specimen are all perpendicular to the elongation direction. The

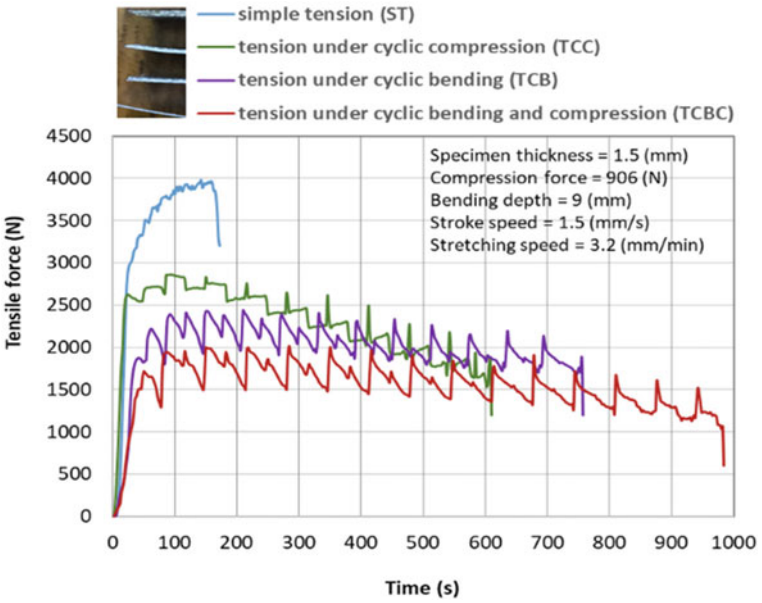


Fig. 7 Tensile force time history under four different testing conditions. (Color figure online)

difference in the cracking orientation of the specimens resulted from the difference in stress distributions due to different loading conditions, as discussed in Sect. 4.3.

4.2 Effect of Bending Depth and Compression Force on Material Deformation

To investigate the bending effect on material deformation, different values of the bending depth, varied from 1 to 13 mm, are used under the TCB testing conditions, while all other parameters remain constant. Figure 9 shows variations of the maximum elongation ratio and maximum tensile force when different values of the bending depth are applied. It shows that the maximum elongation ratio increases with the increasing bending depth; at the bending depth of 12 mm, the maximum elongation ratio achieved is 70%, i.e. equivalent to an increase of 42 mm elongation from the original gauge length of 60 mm. However, when the bending depth is further increased to 13 mm, the maximum elongation ratio starts to reduce which was explained by Emmens et al. [19] as a fracture mechanism under cyclic loading effect. Figure 9 also shows that the maximum tensile force reduces considerably when the bending depth is increased. The tensile force reduction trend levels out and remains almost constant after the bending depth reaches to and is >10 mm.

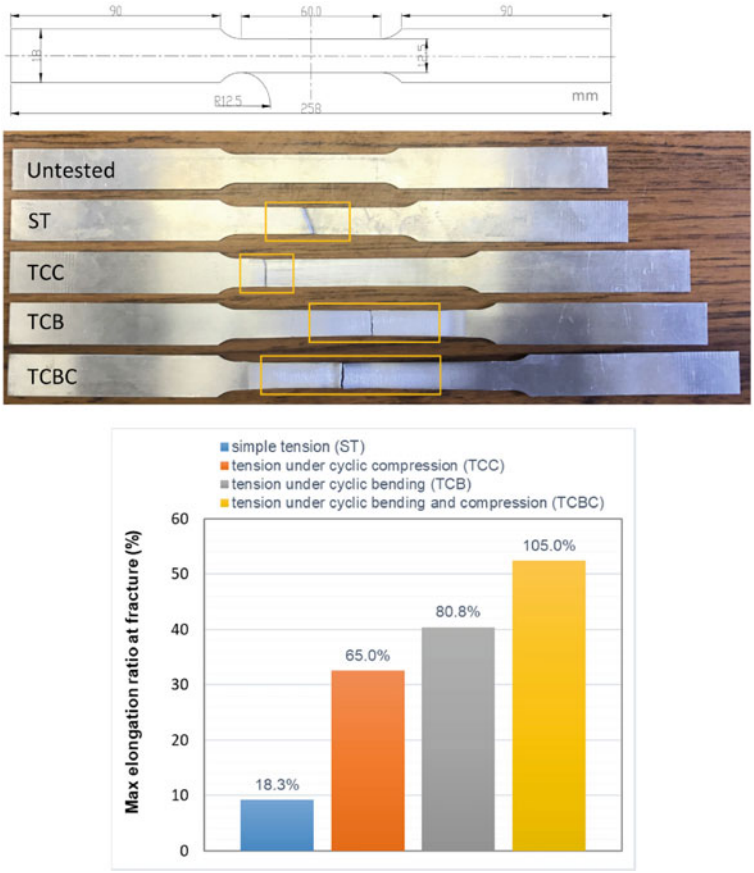


Fig. 8 Maximum elongation of tested specimens under four different testing conditions (thickness 1.5 mm, compression 906 N, bending 9 mm, stroke speed 1.5 mm/s, and stretching speed 3.2 mm/min). (Color figure online)

To investigate the compression effect on material deformation, different values of the compression force, varied from 100 to 1700 N, are applied under TCBC testing condition while all other parameters remain constant. Figure 10 shows variations of the maximum elongation ratio and maximum tensile force when different values of the compression force are used. At the compression force of 906 N the maximum elongation ratio reaches 80%; with further increases of the compression force from 906 to 1359 N the maximum elongation ratio increases significantly to peak at 142%. However, with further increase of the compression force, the maximum elongation ratio starts to decrease. When the compression force increases, Fig. 10 shows a steady decrease of the tensile force required for achieving the material plastic deformation.

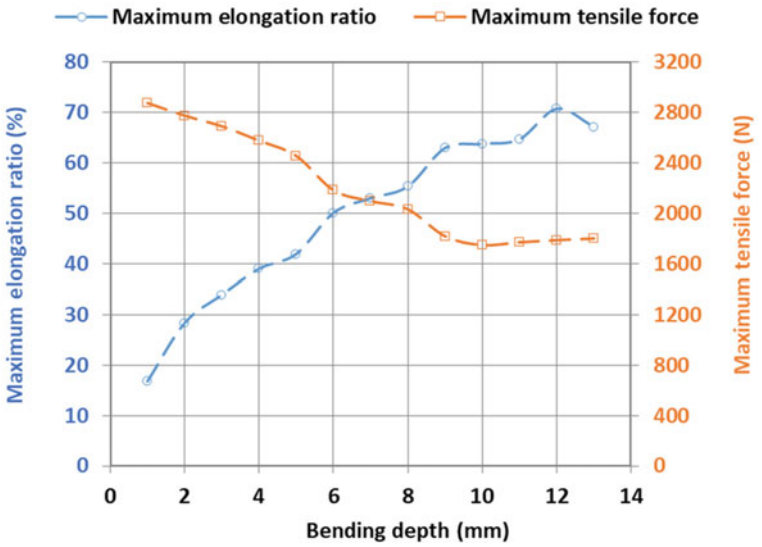


Fig. 9 TCB tests with variable bending depth (thickness 1 mm, compression force 0, stroke speed 1 mm/s, and stretching speed 2.4 mm/min). (Color figure online)

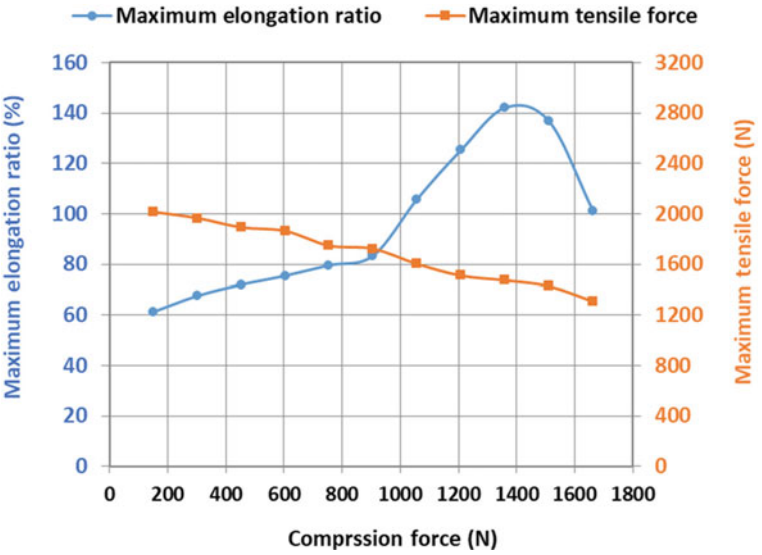


Fig. 10 TCBC tests with variable compression force (thickness 1.2 mm, bending 9 mm, stroke speed 1.5 mm/s, and stretching speed 3.2 mm/min). (Color figure online)

4.3 FE Modelling of Material Deformation Under TCB and TCBC Conditions

To understand the material deformation characteristics of the significantly increased elongation of the specimen under TCB and TCBC testing conditions, the FE models of TCB and TCBC tests are generated to simulate the experimental tests using the developed test rig. In FE modelling, a stroke speed of 1.5 mm/s and stretching speed of 2.4 mm/min are applied to the specimen thickness of 1 mm under bending depth of 9 mm. For the TCBC model, an additional compression force of 600 N is applied; while for the TCB model it is zero. The details of the FE modelling can be found in [18]. Figures 11 and 12 show the FE stress distributions on two surfaces of the specimen in the longitudinal direction at the uniform material deformation stage, under the TCB and TCBC testing conditions, respectively. Under both testing conditions, for the surface in contact with the compression roller the material is under tension and subjected to the highest plastic deformation. On the other hand, for the surface in contact with the bending roller the material is under compression.

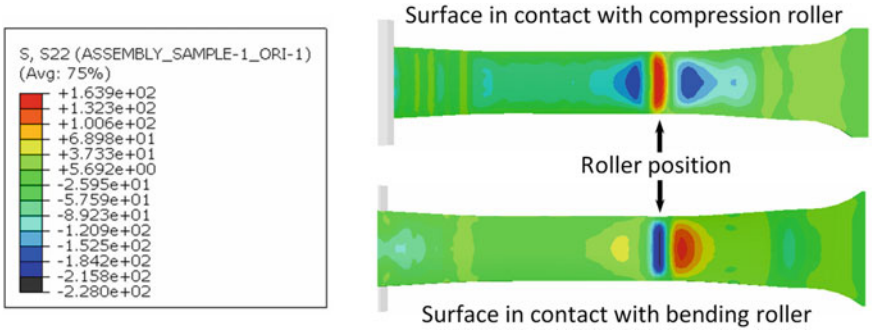


Fig. 11 TCB test—stress distributions of deformation zones around compression and bending rollers. (Color figure online)

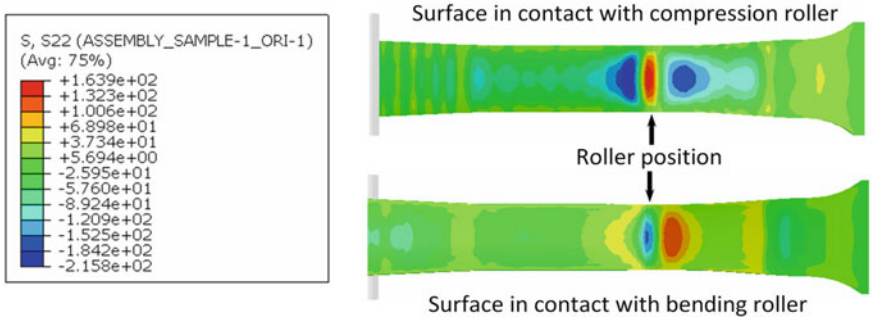


Fig. 12 TCBC test—stress distributions of deformation zones around compression and bending rollers. (Color figure online)

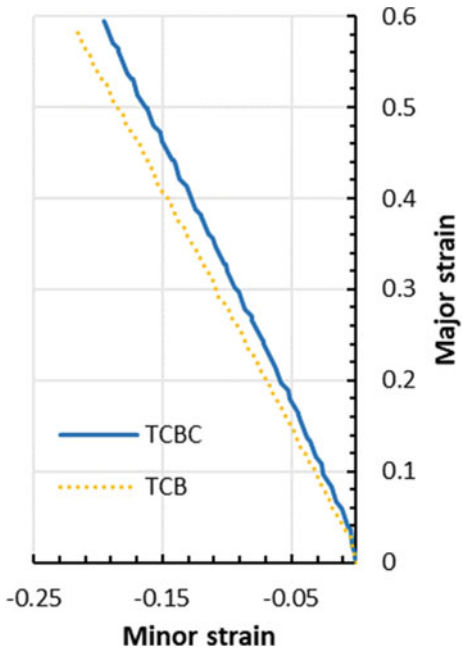


Fig. 13 Strain paths of elements in FE modelling of TCBC and TCB tests. (Color figure online)

The additional compressive force in the TCBC test reduces the difference of the stresses on these two surfaces leading to a more uniform stress gradient through the specimen thickness. The more homogeneous stress distribution in the specimen thickness allows the material to undertake a greater plastic deformation, thus delays the occurrence of fracture.

Figure 13 shows the strain paths of the elements located on the outer surface in the centre of the specimen of the TCBC and TCB FE models. The strain component in the longitudinal direction of the specimen is a major strain and the strain component in the specimen's width direction is a minor strain. The nonlinear strain paths reflect the effect of cyclic loading on the material deformation. For TCBC test, the introduction of the compressive force reduces the material deformation in the lateral direction than that in the TCB test, while elongations of the specimens in the longitudinal direction are the same. In the TCBC and TCB tests, as shown in Fig. 13, the material deformation is approximately between the plane strain and uniaxial tension, as illustrated in Fig. 2. However, in the ISF processes, the material is approximately under a strain state between the plane strain and equal biaxial tension. The difference could be caused by two factors, first due to the difference of the geometric constrains between the TCBC tests and the ISF processes, and secondly, how the tension is applied onto the specimen material. In the TCBC and TCB tests, tension is applied by continuous stretching force from the clamp. By comparison, in the ISF processes, the sheet blank is only clamped on its outer edges, once the tool(s) moves away from

the sheet-tool contact area, the tension applied on that area of the material would be partially released. As a result, the strain paths obtained from the TCBC and TCB tests are different from the ISF processes.

5 Conclusions

The new TCBC test method has successfully produced results to evaluate the material deformation under four different conditions: simple tension (ST), tension under cyclic compression (TCC), tension under cyclic bending (TCB), and tension under cyclic bending and compression (TCBC). The following conclusions may be drawn:

- The compressive force shows a significant effect on the increase of the maximum elongation of the tested specimen and a significant reduction of the tensile force required to achieve the material plastic deformation. However, high compression forces greater than a certain limit may reduce the maximum elongation, thus have a negative effect on formability.
- The bending depth displays a considerable effect on the increase of the maximum elongation even under a small value of bending depth tested. However, when the bending depth is increased above a certain limit, it may result in higher tensile stresses on the specimen surface in contact with the compression roller, thus causing early fracture of the specimen.
- The maximum elongation increases significantly under TCBC condition due to cyclic alternations of localised plastic deformation zone that delays the occurrence of fracture. The experimental testing and FE modelling results also show the effects of complex interactions between compression and bending on the material deformation and fracture.

Acknowledgments The authors would like to acknowledge the research funding support received from UK EPSRC (EP/T005254/1) and EU FP7 Marie Curie Actions (FP7-PEOPLE-2013 IIF 628055). They are also grateful to senior mechanical technician David Webster in Department of Mechanical Engineering of the University of Sheffield for his support in developing and manufacturing the TCBC test rig.

References

1. Meier H, Magnus C, Smukala V (2011) Impact of superimposed pressure on dieless incremental sheet metal forming with two moving tools. CIRP Ann Manuf Technol 60(1):327–330
2. Smith J, Malhotra R, Liu W, Cao J (2013) Deformation mechanics in single-point and accumulative double-sided incremental forming. Int J Adv Manuf Technol 69(5–8):1185–1201
3. Banabic D (2000) Formability of metallicmaterials: plastic anisotropy, formability testing, forming limits. Springer Science & Business Media
4. Shim M-S, Park J-J (2001) The formability of aluminium sheet in incremental forming. J Mater Process Technol 113(1):654–658

5. Filice L, Fratini L, Micari F (2002) Analysis of material formability in incremental forming. CIRP Ann Manuf Technol 51(1):199–202
6. Fratini L, Ambrogio G, Di Lorenzo R, Filice L, Micari F (2004) Influence of mechanical properties of the sheet material on formability in single point incremental forming. CIRP Ann Manuf Technol 53(1):207–210
7. Malhotra R, Cao J, BeltranM X, Magargee J, Kiridena V, Xia ZC (2012) Accumulative-DSIF strategy for enhancing process capabilities in incremental forming. CIRP Ann Manuf Technol 61(1):251–254
8. Lu B, Fang Y, Xu D, Chen J, Ai S, Long H, Ou H, Cao J (2015) Investigation of material deformation mechanism in double side incremental sheet forming. Int J Mach Tools Manuf 93:37–48
9. Emmens WC, van der Weijde D, van den Boogaard AH (2009) The FLC, enhanced formability, and incremental sheet forming. In: Proceedings of the international deep drawing research group IDDRG 2009 international conference, pp 1–3
10. Martins P, Bay N, Skjødt M, Silva M (2008) Theory of single point incremental forming. CIRP Ann Manuf Technol 57(1):247–252
11. Eyckens P, Van Bael A, Van Houtte P (2009) Marciniak-Kuczynski type modelling of the effect of through-thickness shear on the forming limits of sheet metal. Int J Plast 25(12):2249–2268
12. Jackson K, Allwood J (2009) The mechanics of incremental sheet forming. J Mater Process Technol 209(3):1158–1174
13. Emmens WC, Van den Boogaard AH (2009) An overview of stabilizing deformation mechanisms in incremental sheet forming. J Mater Process Technol 209(8):3688–3695
14. Emmens WC, Van den Boogaard AH (2009) Incremental forming by continuous bending under tension—an experimental investigation. J Mater Process Technol 209(14):5456–5463
15. Li Y, Chen X, Liu Z, Sun J, Li F, Li J, Zhao G (2017) A review on the recent development of incremental sheet-forming process. Int J Adv Manuf Technol 1–24
16. Gatea S, Ou H, McCartney G (2016) Review on the influence of process parameters in incremental sheet forming. Int J Adv Manuf Technol 87(1–4):479–499
17. Ai S, Long H (2019) A review on material fracture mechanism in incremental sheet forming. Int J Adv Manuf Technol 104(1–4):33–61
18. Ai S, Dai R, Long H (2020) Investigating formability enhancement in double side incremental forming by developing a new test method of tension under cyclic bending and compression. J Mater Process Technol 275:
19. Emmens WC, Van den Boogaard AH (2011) Cyclic stretch-bending: mechanics, stability and formability. J Mater Process Technol 211:1965–1981

Numerical Modelling and Deformation Mechanics of the English Wheel Process



Daniel T. Bowen, Omer Music, A. Alaz Erdinc, Alborz Shokrani, and Evripides G. Loukaides

Abstract The mechanisation of traditional craft processes can serve as a starting point for novel process development in the increasingly topical field of flexible metal forming. This approach presents several challenges, including understanding the underlying mechanics, mechanisation, and providing suitable control methods for such processes. Here, we focus on the underlying mechanics of the process known as the English wheel. In this work, the process is studied through validated numerical modelling techniques. The influence of various geometrical parameters is examined and the possible patterns of plastic deformation are presented.

Keywords English wheel · Craft · Finite element · Metal forming · Stretch-bending · Tool force

1 Introduction

The environmental and economic benefits of eliminating part-specific tooling have resulted in increasing interest in developing additional flexible metal forming processes over the past few years [1]. This is defined as extending the range of attainable part geometries from a single process. The motivation for flexible forming comes from the environmental and economic benefits of eliminating part-specific tooling. The advent of Industry 4.0 signals that manufacturing is beginning to move away from traditional mass production and towards mass customisation [1, 2]. At the same time, the route to reliable new flexible processes presents many challenges.

A skilled craftsperson has the ability to form a diverse range of part geometries from a blank using just a small set of universal tooling. Such craft processes often serve as starting points for novel flexible forming process development. Some

D. T. Bowen · A. Shokrani · E. G. Loukaides (✉)
Department of Mechanical Engineering, University of Bath, Bath, UK
e-mail: E.Loukaides@bath.ac.uk

O. Music · A. Alaz Erdinc
Department of Mechanical Engineering, TED University, Ankara, Turkey

© The Minerals, Metals & Materials Society 2021

G. Daehn et al. (eds.), *Forming the Future*, The Minerals, Metals & Materials Series,
https://doi.org/10.1007/978-3-030-75381-8_38

examples include flexible asymmetric spinning [3] and more recently, the "folding-shearing" process [4]. One craft process that has not received much attention in the literature is the English wheel (EW).

The EW was first used by panel beaters in the early 1900s to create compound curves in metal sheets [5]. The process incrementally stretches sheets of metal by passing the material through two dissimilarly shaped and sized roller anvils. Wheeling (the act of using the EW) is a labour-intensive and complex process. Nevertheless, the EW remains popular with job shops and hobbyists. It is capable of producing a vast range of doubly curved surfaces with an extremely limited set of tooling, and at a very low cost, whilst delivering an excellent surface finish. For the same reasons, it is an attractive candidate for mechanisation and automation. Existing attempts of mechanisation use a data-intensive approach without considering the underlying mechanics and typically employ a robotic arm to actuate the sheet [6]. Previous work in understanding the mechanics of the English wheel is scarce. Music and Allwood [7] measured and compared the instantaneous deformation of workpieces for a number of processes, including the EW. Their focus was on the comparison between processes; hence, no in-depth information for the EW was presented.

For human operators, the ability to create sheet metal geometries with limited tooling comes from years of training and practice, which provide intuition and understanding of the craft process. However, existing craft experience is difficult to translate to a technical understanding of the process and seldom provides sufficient information for automation. The processes that require a skilled worker to initiate and continually update the manufacturing strategy are slow and costly. Deskilled processes allow for large-scale industrial adaptation, which can translate into mass customisation of parts with doubly curved surfaces.

Disappointingly, there is almost no mention of the EW process in the metal forming literature. This paper presents the first steps in comprehensively understanding the English wheel process. We employ an FEA model to examine the mechanics of the local deformation. A parametric study qualifies how different process parameters influence deformation. Our results further the understanding of the underlying mechanics; an essential step towards future attempts of mechanisation.

2 Overview of Manual Wheeling

A conventional EW is shown in Fig. 1. The frame (1) can be either fabricated from three welded bars or cast as one single piece. Cast frames are more desirable as they are stiffer and suffer less bending during the process. The upper anvil (2) has a flat radial profile and an outer radius approximately twice that of the lower anvil (3). The lower anvil is mounted on a lead screw so that the gap between the anvils can be adjusted (4). A selection of lower anvils is usually used, each with varying profiles. These profiles are defined as having various *blow radii,* as shown in Fig. 1. The blow

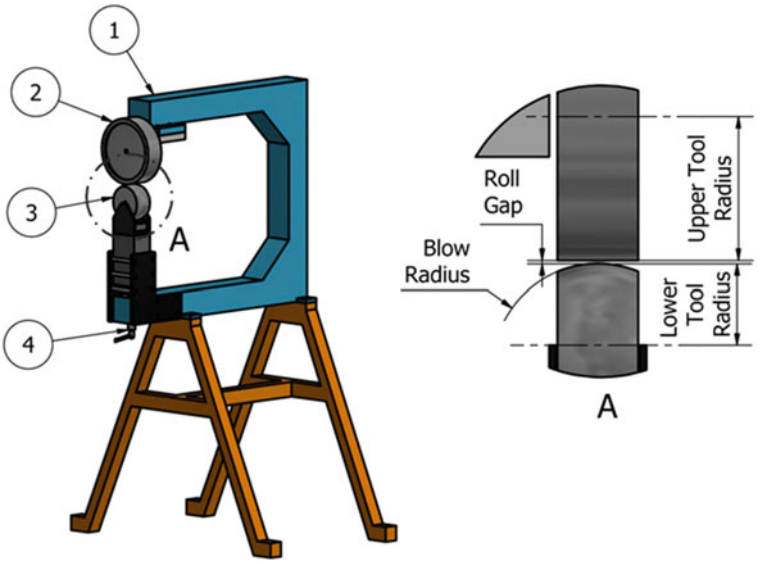


Fig. 1 Typical English wheel. (Color figure online)

radius is required to allow curved parts through the gap, but it also has a function in controlling the curvature produced, which we examine later in this paper.

During the process of manual wheeling, the sheet is not constrained around the outer edges by a supporting fixture. Instead, the sheet is held in a variety of different ways by the operator. With both roller tools free to rotate, the actuation force required to drive the sheet through the tools is provided by the worker. Between forward and backward passes, a slight yaw angle, φ, is introduced so as to work across the desirable area in a zig-zag pattern, as shown in Fig. 2. Care is usually taken not to wheel the boundaries of the sheet. The exact function and influence of this undeformed boundary on the final product is also an open question.

3 Finite Element Model

A finite element model was created in Abaqus FEA package. In this work, non-zero yaw angles were not considered, i.e., only tool paths along a single straight line were considered. This allowed a number of simplifications, including making use of symmetry to reduce computation time. A schematic of the model is shown in Fig. 3, where the relevant directions and the plane of symmetry are labelled. We also show the hold region where the boundary conditions are applied, and a central region on the sheet with a refined mesh.

The model uses an implicit time scheme solver. Upper and lower anvils are defined as analytical rigid parts. The sheet is modelled using full integration

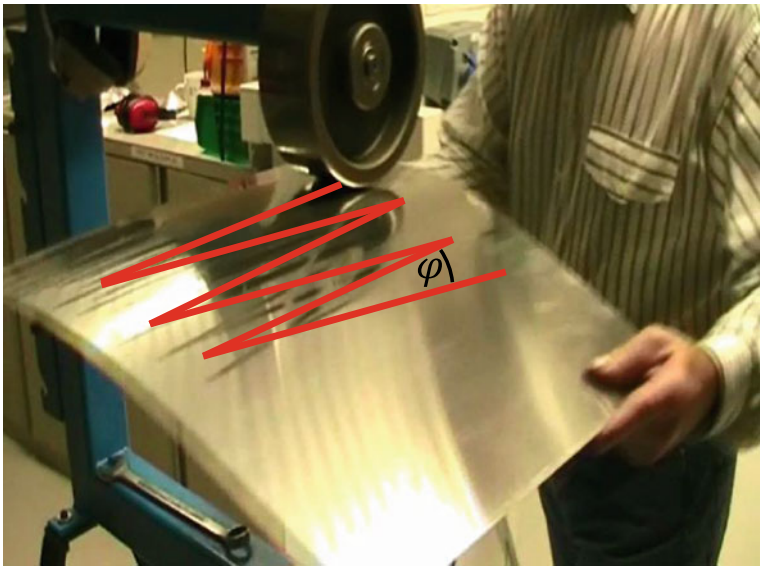


Fig. 2 Tracking pattern used during wheeling. (Color figure online)

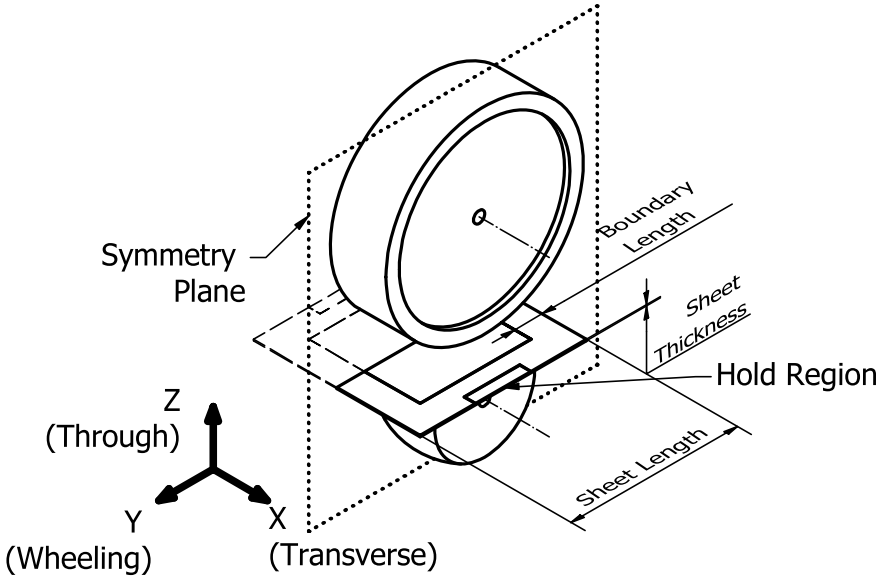


Fig. 3 Model configuration

C3D8 elements. The mesh has four through-thickness elements to capture through-thickness behaviour and the element sizes in-plane are smaller towards the plane of symmetry, with the centre elements having an in-place length of 0.5 mm. The sheet material is modelled as aluminium 5251 with Young's modulus of 70 GPa, Poisson's ratio of 0.3, and density of 2700 kg/m^3 with plastic hardening data prescribed from unidirectional experimental testing. A standard surface-to-surface contact method was specified between the anvils and sheet with a Coulomb friction coefficient of 0.2. The anvils were assigned inertia values calculated based on their shape and material (steel of density 8000 kg/m^3) and are free to rotate, similar to the real process.

Firstly, the effect of simple indentation was tested. This model was composed of two Abaqus steps, one where a vertical motion was prescribed for the tools so that the sheet was squeezed in the through-thickness direction, and one where this motion was reversed. A second model was developed to include a third step between the aforementioned two, where the sheet was actuated along the y-direction, to emulate the physical process of wheeling.

One of the major challenges in modelling the process is identifying and applying suitable boundary conditions. In practice, the worker manoeuvres and drives the sheet through the tools by grasping the outer edges. As the sheet develops curvature, they will react to this by adapting the grip based on experience. Replicating these conditions numerically requires extensive study of manual wheeling by experts to formulate the process. For this study, boundary conditions have been prescribed to have as little influence near the deformation region as possible. This was done by constraining a small region—the *hold region,* far from the deformation zone to drive the sheet through in the wheeling direction only; the remaining two directions (transverse and through) are unconstrained.

To verify the model, results from a straight line back and forth wheeling pass were compared with a physical trial on an EW. Sheet geometry was measured using a GOM ATOS optical three-dimensional coordinate measurement system. For the sheet size used in this study (150 mm × 150 mm), the measurement error is ±0.01 mm or ±3% of the maximum profile height measured. Results are displayed in Fig. 4 and show that the z-direction displacement in the numerical model is within 15% of the physical measurements.

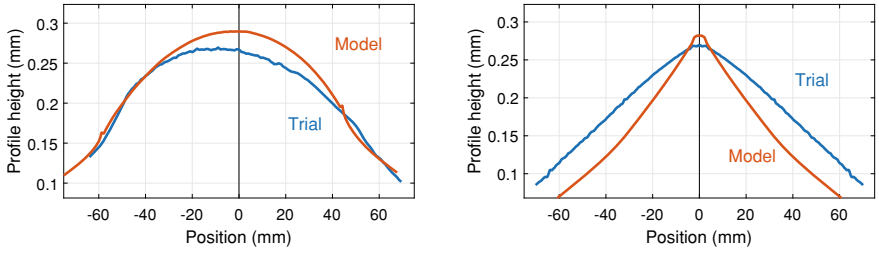


Fig. 4 Comparison of sheet geometry for physical trials and numerical model. (Color figure online)

4 Results and Discussion

4.1 English Wheel Mechanics

We first look at one base case (see Table 1), to describe the typical deformation during the process of wheeling. Initially, when the rollers first make contact with the sheet and squeeze the material, the material both thins and thickens, as shown in Fig. 5i. The thinning occurs in the region between the tool and the sheet (the contact region) as well as the region immediately surrounding it. Some of the region

Table 1 Parameters for all the simulations. Dimensions given in mm

Parameter		Base case	Variant			
			1	2	3	4
Reduction ratio, q		4%	3%	4%	5%	6%
Blow radius, R (mm)		150	50	100	150	200
Sheet thickness	1	Upper tool radius			101.6	
Sheet length	150	Lower tool radius			50.8	
Boundary length	37.5	–				

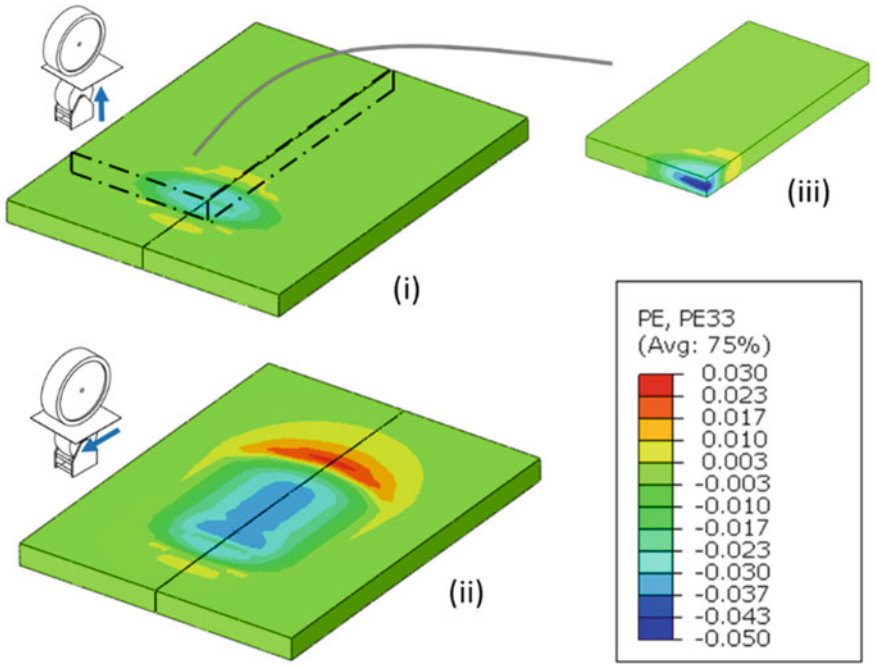


Fig. 5 Through-thickness strain mirrored along the symmetry plane during (i) initial indentation and (ii) wheeling. (iii) Cross section shown during indentation. (Color figure online)

beyond this, however, thickens. The material beyond the plastic region provides the compressive stresses that stop the material from spreading outward further and force it to thicken. This thickening of the material is not axisymmetric due to the dissimilar roller profiles.

As the sheet is driven through the rolls, material builds up in front of the anvils, in the direction of the wheelpath. The increase in thickness in this region is far greater than the thickening of material observed in the transverse direction. As shown in Fig. 5ii, this build-up can be displayed prominently at the end of the pass.

For further understanding, a section of a sheet that has been wheeled is considered far away from the initial squeeze contact area and the edge of the sheet. In this region, strains appear uniform over a short length along the wheeling path. At the locations of contact with the tools, the sheet shows both through-thickness thinning (Z) and expansion of material in the transverse direction (X). This implies that the material is being pushed outwards.

When wheeling, the curvature is developed mostly in the transverse direction. The magnitude and mechanism by which this deformation occurs can be analysed by considering the upper and lower transverse strains, ε_X. These are plotted for various points along the X direction in Fig. 6. Close to the wheeling path, high values of positive strain indicate the sheet is stretching at this point. The difference between strains (Δ) in the top and bottom surfaces shows that the sheet is also bending making for a combined mechanism of deformation.

Away from the wheelpath, these strains reduce and eventually start to compress the material. Around the region of maximum compression, the magnitude of bending also rises; the difference between upper and lower surface strains is largest here. This is the location of maximum bending in the transverse direction, and not directly under the tools. Beyond this point, plastic strains diminish. Springback was not notable, likely due to the free sheet boundaries in the process.

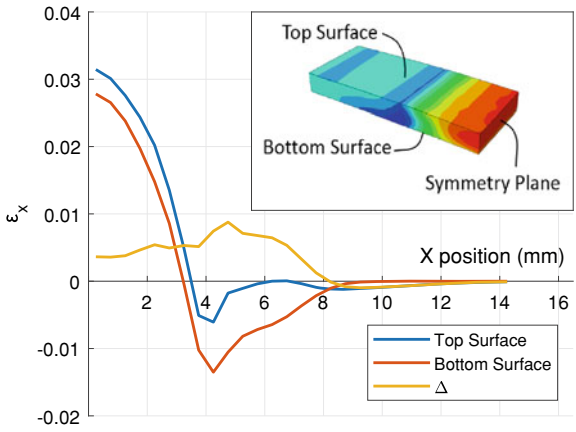


Fig. 6 Strains in X direction for wheeled section of sheet. (Color figure online)

5 Parametric Study

The base case in the previous section served to give an initial description of the process mechanics. Here, we expand our understanding with a number of trials that examine how configurable parameters affect the mechanics of the process. We define the reduction ratio, q, as the ratio of the indentation depth travelled by the tool and the original sheet thickness. Blow radius, R, is also varied with values and other default values shown in Table 1.

One set of trials focuses on the initial squeezing of the sheet. This pushes material outward and causes thickening of material around the tool contact area. In a similar process of driving, the tool is typically axisymmetric and thus the spread of material outward is the same in all directions from the bite point. In the case of the EW, the dissimilar upper and lower anvils, and their non-axisymmetric geometries cause the material to be formed in a more complex way, as seen in Fig. 5iii. The effect of the reduction ratio and the lower tool profile on the through-thickness strain, ε_z, is investigated in Fig. 7 for the indentation step. A quarter model with a refined mesh size is used for these trials; element size at the centre is reduced to 0.2 mm.

A manual on EW operation suggests that lower tools should be selected purely to adjust the contact area with the sheet, accommodating curvature in the transverse direction [5]. However, these results show that for a flat sheet, the lower tool profile can affect the thickening profile of the sheet as well. The reduction ratio also has a

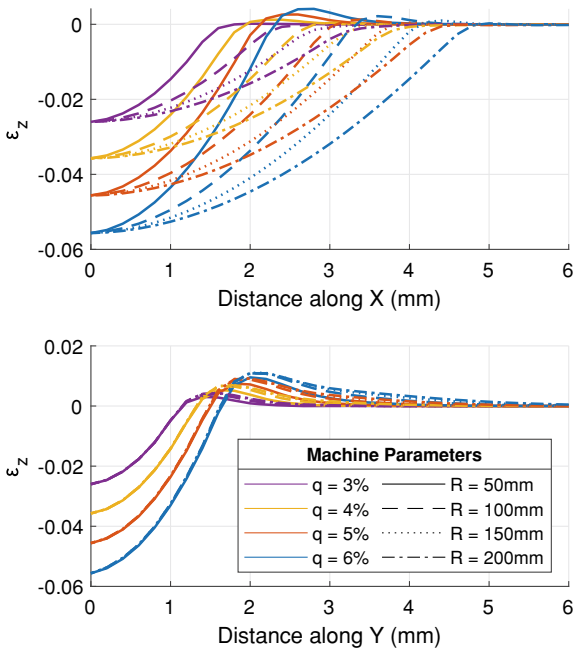


Fig. 7 Through-thickness strains after squeezing and releasing the sheet. (Color figure online)

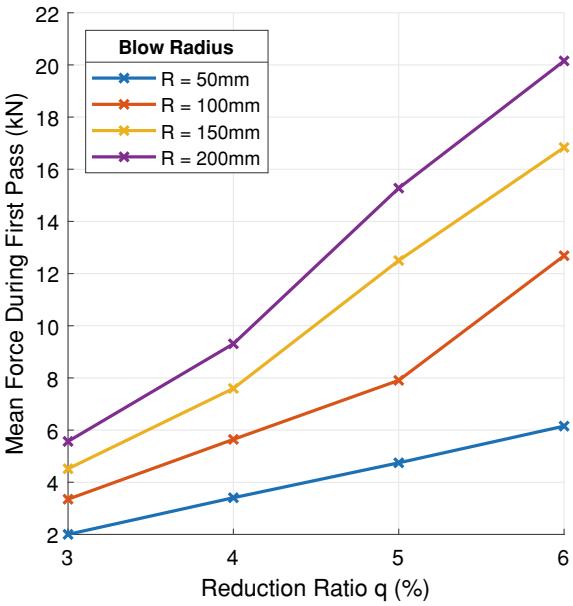


Fig. 8 Average tool reaction force in z-direction. (Color figure online)

significant effect on the magnitude of the peak strains seen in both directions. Furthermore, some threshold exists for roll gap and tool radius, whereby no thickening takes place in the transverse direction. It is acknowledged that this is not indicative of the process as a whole; it does not take into account the effect of tool rotation and sheet movement during wheeling. However, this does demonstrate that both lower tool selection and roll gap affect the through-thickness strain profile of the sheet.

The anvil reaction force in the Z-direction during wheeling was observed to change with different lower tool profiles and roll gaps. A plot of the mean force, with bars showing the standard deviation of force throughout an initial pass for different profiles, is shown in Fig. 8. When the sheet was rolled both forward and backward through the tools, the force dropped by 70%. This has implications for the accuracy of the model. For a given tool force the frame will experience some bending, causing the roll gap to increase. As the tool force is shown to be dependent on the roll gap, these coupled variables should come to an equilibrium state, resulting in a new gap and force. This change in roll gap, as previously shown, can have an effect on the characteristics of the material deformation, and not only on its magnitude.

6 Conclusions

This paper presented the first parameterised examination of the mechanisms of deformation experienced by the sheet during the wheeling process. We showed that curvature is produced locally, with the curvature in the transverse direction dominating.

We explored the influence of tool geometry and tool gap on the deformation. Other subtle effects, like the possible thickening of the workpiece immediately past the area of contact, were observed for the first time.

Future work will concentrate on identifying the best approach to accurately represent realistic boundary condition for this process in simulation. Alternative boundary conditions and actuation methods to those normally employed in traditional wheeling will be explored and their effect on the deformation mechanics will be investigated. Finally, frame deformation and the yaw angle were not accounted for in our model but will be addressed in further efforts.

References

1. Yang DY, Bambach M, Cao J, Duflou JR, Groche P, Kuboki T, Sterzing A, Tekkaya AE, Lee CW (2018) Flexibility in metal forming. CIRP Ann 67(2):743–765
2. Allwood JM, Utsunomiya H (2006) A survey of flexible forming processes in Japan. Int J Mach Tools Manuf 46(15):1939–1960
3. Music O, Allwood JM (2011) Flexible asymmetric spinning. CIRP Ann 60(1):319–322
4. Allwood JM, Cleaver CJ, Loukaides EG, Music O, Nagy-Sochacki A (2019) Folding-shearing: shrinking and stretching sheet metal with no thickness change. CIRP Ann 68(1):285–288
5. Longyard WH (2014) Learning the English wheel. Wolfgang Publications
6. Nicholas P, Rossi G (2018) Modelling a complex fabrication system: new design tools for doubly curved metal surfaces fabricated using the English wheel. In: Proceedings of eCAADe 2018: computing for a better tomorrow, pp 811–820
7. Music O, Allwood JM (2012) The use of spatial impulse responses to characterise flexible forming processes with mobile tools. J Mater Process Technol 212(5):1139–1156

The Dieless Drawing Process for the Elongation of Ultrafine Copper and Brass Wire



Andrij Milenin, Piotr Kustra, Miroslaw Wróbel, Valeriy Pidvysots'kyy, and Marek Packo

Abstract In this study, a new method of ultrafine copper and brass wires production was proposed. The proposed technology is based on the dieless drawing. The workpiece for the dieless drawing is a thin wire (100–200 μ) obtained by a conventional drawing method. The proposed technology is based on the implementation of a multi-pass incremental deformation. Moreover, in each pass, strain and strain rate sensitivity of flow stress should be positive and significant. The deformation parameters in each pass are determined based on the flow stress dependency on the strain, strain rate, and temperature. Therefore, plastometric tests of copper and CuZn37 alloy were performed. To estimate the temperature of deforming wire the FE modeling of dieless drawing was performed. The obtained data were used in the practical implementation of incremental dieless drawing technology. Roughness analysis was performed for brass samples. In the performed experiments tests, the dieless drawing will lead to an increase of roughness of the wire surface. However, this increase is relatively small. The value of R_a before the dieless drawing was 1.73 μ, and after deformation, it was 2.23 μ.

Keywords Dieless drawing · Copper · Wire · Roughness · Workability

1 Introduction

The ultrafine wire is widely used in the microelectronic industry, microrobotic, filtration, and other technical areas. The conventional manufacturing technology of fine wire is based on a cold drawing in dies with diamond cores. It was shown by Kraft [1] that using an expensive die significantly increases the cost of the process. The workability of the wire decreases due to strain hardening in the multi-pass drawing process. For some materials, this requires a process shutdown and heat treatment.

A. Milenin (✉) · P. Kustra · M. Wróbel · M. Packo
AGH University of Science and Technology, Kraków, Poland
e-mail: milenin@agh.edu.pl

V. Pidvysots'kyy
Institute for Ferrous Metallurgy, ul. K. Miarki, 12-14, 44-100 Gliwice, Poland

© The Minerals, Metals & Materials Society 2021

G. Daehn et al. (eds.), *Forming the Future*, The Minerals, Metals & Materials Series,
https://doi.org/10.1007/978-3-030-75381-8_39

For example, as Seitz et al. have shown in their work [2], this should be done when drawing wire from magnesium alloys. In this case, additional heat treatment lasts for several hours in a vacuum or inert gas. This significantly increases the cost of the process and makes it less productive. On the other hand, the lubricants used in wire drawing and their removal by chemical treatment degrade the surface quality of the wire and further increase the cost of the process. These and other disadvantages of conventional wire drawing limit the ability to produce fine wire and increase the cost of the process.

A potential solution to the above problems could be the usage of the dieless drawing process. Generally, the process of dieless drawing is a stretching of a wire, rod, or tube with its simultaneous local heating in the deformation zone. The heat source is usually represented by an electric furnace, inductor, or laser beam. The first studies of this process were performed by Weiss and Kot [3] and devoted to the production of wire. Dieless drawing allows elongation of the wire without using a deforming die. This fact is important since in the conventional drawing process the cost of the die is very high. Additionally, dieless drawing has several other advantages. For example, Supriadi et al. [4] have shown that it is possible to vary the stretching and cross-sectional shape of the tubes along their length, which is impossible to obtain with conventional drawing or extrusion. Another advantage is the achievement of a relatively large elongation in one pass. In the process of continuous dieless drawing of carbon steel wire, Tiernan and Hillery [5] achieved uniform reductions of cross-section up to 72% in a single pass. They have shown that the drawing method is more fracture-resistant than the corresponding wire drawn conventionally with dies.

One of the promising possibilities of dieless drawing is the production of fine and ultrafine wire. Li et al. [6] have shown that by laser dieless drawing it is possible to elongate the wire with initial diameters of 125–500 μ from commercial-grade pure nickel. The maximum achieved reduction in the area was 30–40%. It was discovered that workability increases in an inert gas atmosphere.

Potentially, dieless drawing may allow obtaining a wire with a smaller diameter than the industry produces. However, the implementation of dieless drawing for the production of ultrafine wire requires a solution to two important problems that define the purpose of this paper. The first is the optimal choice of temperature and deformation parameters to achieve maximum forming limit and uniformity of diameter along the length of the wire. The concept of dieless drawing, which allows solving this problem, was proposed by Milenin [7] using the example of a magnesium alloy. The idea behind this approach is to perform multi-pass dieless drawing. Moreover, in each pass, the material must be in conditions of maximum hardening. This approach allows us to reduce the irregularity of the diameter along the length of the wire and to increase the workability of material in the technological process. However, its effectiveness depends on the sensitivity of the flow stress of the deformable material to strain and strain rate. With high sensitivity, the method becomes more efficient. By the effectiveness (E) of a multi-pass dieless drawing process, we mean the ratio of the maximum achievable elongation with multi-pass deformation to this value obtained by a single-pass process.

The second problem is the increase of roughness during dieless drawing. Furushima and Manabe [8] have shown that the surface roughness during dieless drawing increases with increasing elongation. Furthermore, the rate of increase of roughness depends on the grain size of the initial materials. Further studies by Furushima et al. [9] showed that the evolution of roughness significantly affects the workability of the material during dieless drawing. This problem has become more important for the production of the ultrafine wire because the resulting roughness can be comparable to the diameter of the wire, and significantly reduce the workability.

Thus, the solution to these problems requires both plastometric studies of the material and laboratory dieless drawing tests to predict the workability and roughness of the wire under conditions of dieless drawing.

2 Material Properties

This paper studies two materials—technically pure copper and CuZn37 alloy (brass). Plastometric studies of these materials were performed at a temperature range of 20–90 °C (copper) and 400–650 °C (CuZn37). The experiments were carried out on GLEEBLE (copper) and Zwick 250 (CuZn37) machines.

The choice of a GLEEBLE physical simulator for the study of copper was made because at high temperatures, copper has a complex dependence of flow stress on the strain. For example, this was shown by Garcia et al. [10]. Due to this fact, it is difficult to apply the inverse analysis method, which requires an accurate approximation of the dependence of stress on strain using analytical functions [11]. The GLEEBLE machine minimizes the influence of friction and controls the temperature with high accuracy, but the cost of testing is high. In experiments with the GLEEBLE, the hardware stabilization of the material temperature was carried out during the test. The accuracy of this temperature control for strain rates of 0.01 and 0.1 s^{-1} was about 1 °C. The tested samples had an initial diameter of 8 mm and a height of 10 mm. Typical flow stress–strain curves for copper are shown in Fig. 1.

In compressive tests on the Zwick 250 machine, such a correction was impossible; therefore, an inverse analysis was applied based on modeling strain-induced heating of the sample and friction. As it was shown by Chandra et al. [12], brass is characterized by monotonic dependencies of flow stress–strain. For this reason, a more simple machine (Zwick 250) was used and the subsequent processing of the results by the inverse analysis method. The used samples had an initial diameter of 5 mm and a height of 6 mm. Each experiment was repeated 2–3 times. The experiments were carried out for strain rates of 0.1, 0.5, and 1.0 s^{-1}.

The methodology of inverse analysis was adapted for the deformation conditions in the Zwick 250 machine. In the inverse analysis, the compression load (P) was calculated using an analytical model of yield strength in the form of an equation:

$$\sigma = A\exp(-m_1 t)\varepsilon^{m_2}\dot{\varepsilon}^{m_3}\exp(-m_4\varepsilon)t^{m_5} \quad (1)$$

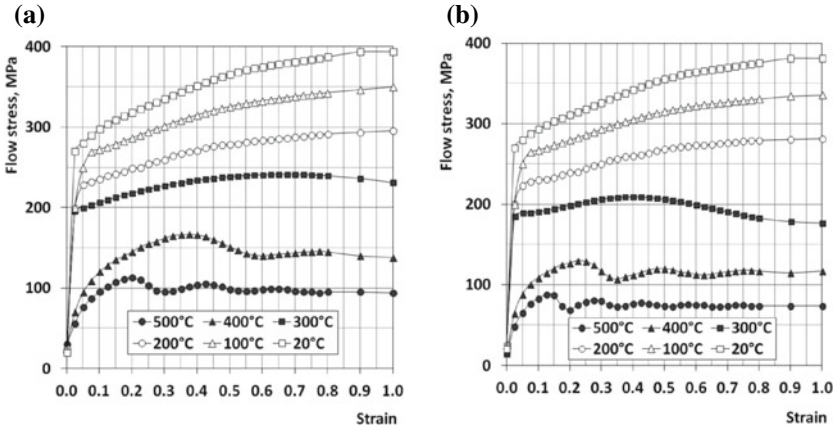


Fig. 1 Experimental dependence of flow stress on strain for commercial copper at temperatures of 20–500 °C: **a** for strain rate 0.1 1/s; **b** for strain rate 0.01 1/s

where A, m_1–m_5 = empirical coefficients, ε = strain, $\dot{\varepsilon}$ = strain rate, and t = temperature.

Equation (1) is used in the compression test model, which takes into account deformation heating, friction, and changing the shape of the sample during compression. This model, adapted for the test conditions in the machine Zwick 250, is described in the paper of Milenin et al. [13].

The squared difference of the calculated and measured compression load is taken as the objective function. The objective function was minimized by variation of empirical coefficients in Eq. (1). As a result of minimizing the objective function, the following coefficients of Eq. (1) are determined: $A = 2148.29$; $m_1 = 0.00615030$; $m_2 = 0.181711$; $m_3 = 0.155512$; $m_4 = 0.643115$; $m_5 = 0.156934$.

The average error in load approximation was 3.8%. A comparison of the calculated and experimental values of the load depending on the displacement of the tool for a strain rate of 0.5 is shown in Fig. 2. Figure 3 shows the results of the calculation of flow stress according to formula (1) using determined coefficients.

In the experiments on GLEEBLE and Zwick 250, samples of various geometries were used; however, in both cases, no signs of uneven deformation up to a strain of 0.5–0.6 were observed. Therefore, the stress state of the samples was close to linear, and the results are relevant.

3 Setup for Dieless Drawing and Experiments

For the practical implementation of the process parameters, a special experimental setup was developed (Fig. 4). The setup described here can continuously produce wire with the dieless drawing method. The setup software controls the linear rotation

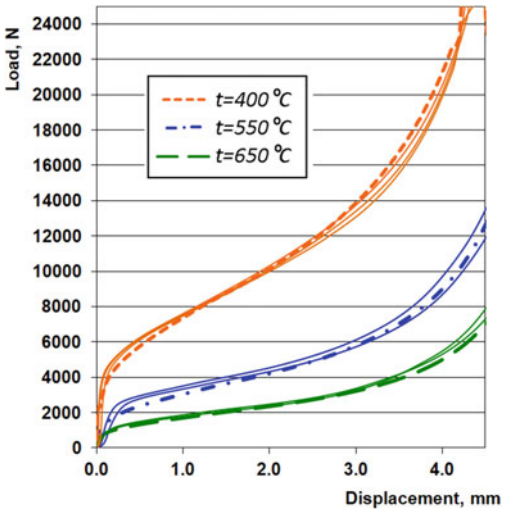


Fig. 2 Dependence of the load during plastometric compressive tests of a sample of CuZn37 alloy on the displacement of a tool: thin solid lines—experiments; thick dashed lines—calculation of load based on Eq. (1). (Color figure online)

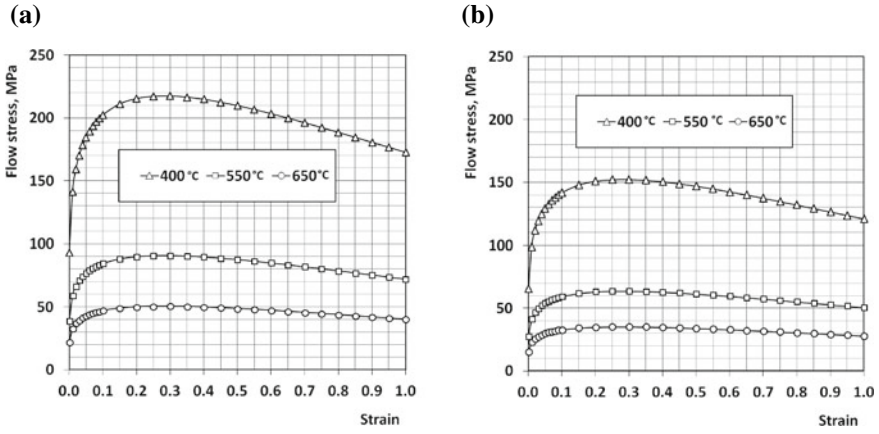


Fig. 3 The flow stress of CuZn37 alloy: **a** for strain rate 0.1 1/s; **b** for strain rate 0.01 1/s

rates of the rollers (V_1 and V_2). The designed setup allows for continuous multi-pass dieless drawing without removing the wire. In this case, after the completion of the current pass, the roller velocities V_1 and V_2 are reversed.

In the setup software the amount of strain of the wire in the heated zone during pass $\varepsilon_{\text{pass}}$ is calculated from the condition of constant volume for $V_2 > V_1$:

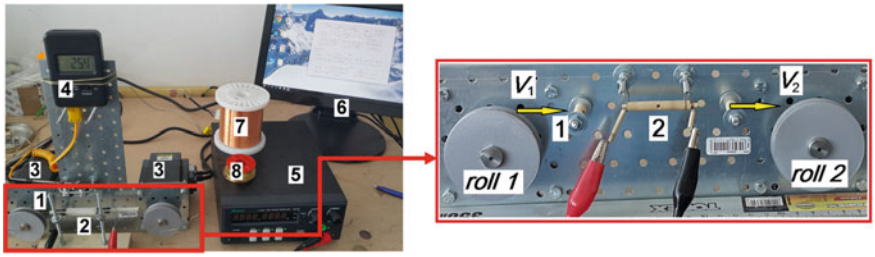


Fig. 4 Setup for dieless drawing of wire: 1—wire; 2—heating device; 3—engines; 4—module for measurement of temperature inside the heating device; 5—power supply for the heating device; 6—control computer with setup software; 7, 8—initial wire made of CuZn37 and copper. (Color figure online)

$$\varepsilon_{\text{pass}} = 1 - \frac{V_1}{V_2} \tag{2}$$

FE model of temperature in the wire is implemented in setup software. This model is based on the solution of a one-dimensional axisymmetric unsteady heat problem. Since measuring the temperature of a thin wire is extremely difficult, this software is designed to calculate the temperature in a wire.

The thermal problem in the metal was solved as non-stationary heat transport problem:

$$k\left(\frac{\partial^2 t}{\partial r^2} + \frac{1}{r}\frac{\partial t}{\partial r}\right) = c\rho\frac{dt}{d\tau} \tag{3}$$

where c is the specific heat, ρ is the alloy density, τ is the time, and k is the thermal conductivity coefficient.

Equation of non-steady-state heat exchange (3) is treated using the Galerkin method and standard FEM procedure. One-dimensional linear finite elements were used. A grid of 50 finite elements was used. Thus, the FE model of temperature is based on considering the passage of the wire cross-section through the deformation zone. This made it possible to obtain a solution in real time on the control computer of the setup (MODECOM microcomputer with processor Intel® Atom™ Z3735F was used).

As the boundary conditions, the temperature in the heating device t_d and the heat transfer coefficient α_d are used. In practical modeling α_d was taken at 300 W/m^{2}K, and t_d was measured by a thermocouple (K-type thermocouple and device TM-902C Lutron was used). When modeling, the following values of density (ρ), thermal conductivity (k), and heat capacity (c) were adopted:

$$\text{Cu: } \rho = 8650\ \text{kg}/\text{m}^3;\quad k = 250\ \text{W}/\text{mK};\quad c = 390\ \text{J}/\text{kgK};$$
$$\text{CuZn37: } \rho = 8115\ \text{kg}/\text{m}^3;\quad k = 140\ \text{W}/\text{mK};\quad c = 380\ \text{J}/\text{kgK}.$$

The conditions and results of the experiments are presented in Table 1. In Table 1, d_{wp}=initial diameter of wire; n=number of passes; ε_d=the logarithmic strain of diameter: $\varepsilon_d = ln\left(\frac{d_{\text{final}}}{d_{wp}}\right)$; E=effectiveness of a multi-pass process.

The calculated temperature of the wire for the conditions listed in Table 1 is shown in Fig. 5. The presented results show that at given wire diameters and drawing speeds, the wire temperature always reaches the temperature in a heating device with an accuracy of several degrees Celsius. Thus, the measured temperature of the heating device can be considered the deformation temperature.

For all cases listed in Table 1, the dieless drawing was carried out until the wire was broken. The final diameter of the wire was taken from the previous passage. Thus, the data presented in Table 1 characterize the conditions of a stable process. In single-pass processes ($n = 1$), the velocity V_2 increased stepwise until a wire break was reached.

The choice of strains in each pass for multi-pass processes was carried out using the dependences of flow stress on the strain, strain rate, and temperature (Figs. 1 and 3). The general rule states that the strain in one pass should correspond to the maximum strain hardening of the material. The idea of increasing workability is that high strain hardening of the material blocks the development of the neck, which increases the overall deformation of the material to failure. Since the hardening of the material decreases with the increasing strain (Figs. 1 and 3), the efficiency of the multi-pass process should increase with decreasing elongation in one pass. This was shown, for example, in [7]. However, since the maximum hardening corresponds to very small strains, there is always a trade-off between process productivity (small strains per pass increase the number of passes) and the maximum achievable strain in the process. A deeper analysis of this issue was performed in [7]. Two levels of strains in one pass are practically accepted—0.047 (positions 1, 2, 6 of the table) and 0.093 (position 5). The choice of only two strains for the study is due to the limited time and high cost of the study. Further research, however, should be carried out to establish the dependence workability on strains in each pass.

It should be noted that with these strains, brass has a much more intense hardening (Fig. 3) than copper (Fig. 1). For this reason, it can be expected that the use of multi-pass deformation for copper will be less efficient.

4 Discussion

The results obtained for copper (positions 6 and 7 of the table) allow us to formulate two conclusions. First, the total elongation of the wire is small (0.21–0.23) and significantly lesser than that of brass wire (0.31–0.63). The second conclusion is that using a multi-pass process instead of a single-pass process does not significantly increase workability. The effectiveness of the multi-pass process was 1.11. One of the reasons for this result may be the complex nature of the dependence of flow stress on strain for copper. A deeper analysis of this problem will be made in future studies.

Table 1 Conditions and results of experiments

N	Material	d_{wp} (mm)	V_1 (mm/s)	V_2 (mm/s)	ε_{pass}	n	d_{final} (mm)	t_d (°C)	Strain rate (1/s)	ε_d	ε_{final}	E
1	CuZn37	0.2	24.3	25.5	0.047	13	0.147	530	0.383	−0.308	0.616	1.97
2	CuZn37	0.2	24.3	25.5	0.047	13	0.146	590	0.392	−0.315	0.629	1.54
3	CuZn37	0.2	24.3	35.5	–	1	0.171	530	0.234	−0.157	0.313	–
4	CuZn37	0.2	24.3	41.2	–	1	0.163	590	0.335	−0.205	0.409	–
5	CuZn37	0.5	2.43	2.68	0.093	4	0.415	400	0.024	−0.186	0.373	–
6	Cu	0.1	24.3	25.5	0.047	5	0.089	300	0.145	−0.117	0.233	1.11
7	Cu	0.1	24.3	30.9	–	1	0.090	300	0.145	−0.105	0.211	–

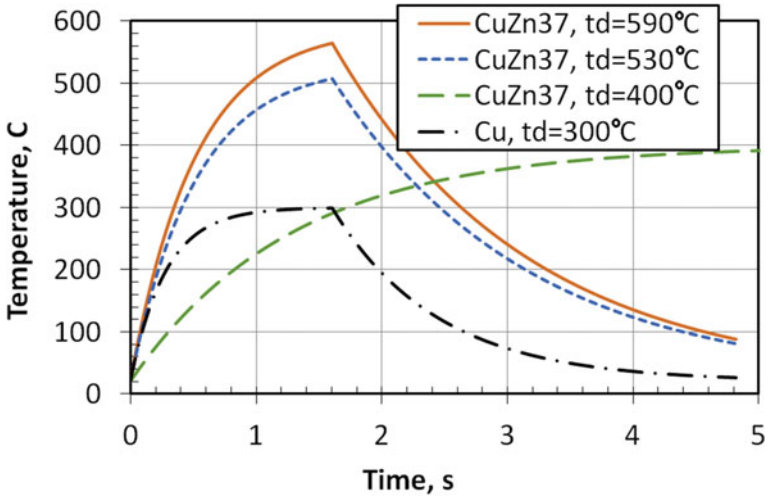


Fig. 5 The FEM calculated dependences of the temperature of the wire during the experiments (t_d is a temperature in the heating device; $t_d = 590$ °C corresponded to positions 2 and 4; $t_d = 530$ °C—to positions 1 and 2; $t_d = 400$ °C—to position 5; $t_d = 300$ °C—to positions 6 and 7 from Table 1). (Color figure online)

The surface of the wire before and after the dieless drawing is shown in Fig. 6. On the surface of the wire after deformation cracks are observed on the grain boundaries (Fig. 6c).

The results obtained for brass are more optimistic. The effectiveness of the multi-pass process at a temperature of 530 °C is 1.97 (position 1 in Table 1). At the same time, increasing the temperature to 590 °C reduces the effectiveness to 1.54 (position 2 in Table 1). This is because with increasing temperature workability in a single-pass process (positions 3 and 4 in the table) increased faster than in the multi-pass process (positions 1 and 2 in the table). The resulting wire has a defect-free surface (Fig. 7), both in the case of a single-pass (Fig. 7b) and a multi-pass process (Fig. 7c).

The result obtained at 400 °C (position 5 in Table 1) is characterized by significantly lower workability ($\varepsilon_{\text{final}} = 0.373$) and the appearance of cracks network at

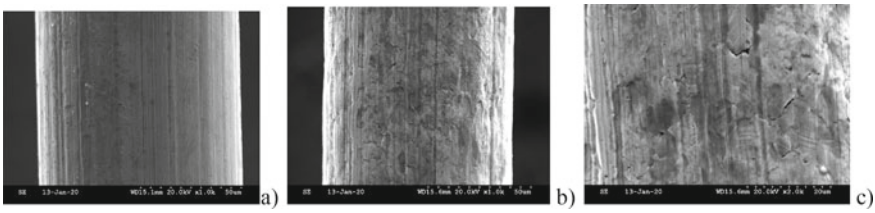


Fig. 6 SEM images of copper wire before (**a**) and after (**b**) multi-pass dieless drawing; **c** surface of wire after deformation (position 6 in Table 1)

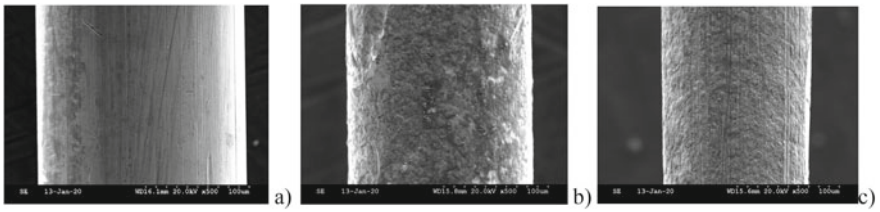


Fig. 7 SEM images of CuZn37 alloy wires before deformation (**a**), after conventional dieless drawing (**b**) (position 3 in Table 1), and after incremental multi-pass dieless drawing (**c**) (position 1 in Table 1)

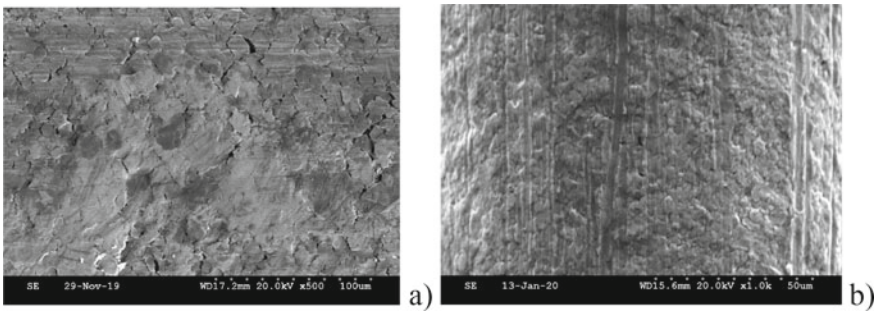
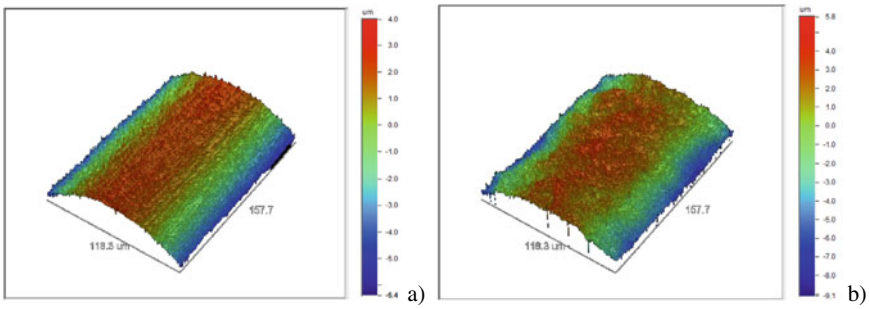


Fig. 8 SEM images of CuZn37 alloy wires after multi-pass deformation at 400 °C (**a**) and 530 °C (**b**)

the grain boundaries (Fig. 8a). For the dieless drawing at a temperature of 530 °C, no cracks are observed (Fig. 8b), although the achieved deformation is much larger ($\varepsilon_{\text{final}} = 0.616$). Figures 6, 7, and 8 have different magnifications, and the scales are shown at the bottom of each image.

Roughness analysis was performed for brass samples. In the general case, the dieless drawing will lead to an increase of roughness (Fig. 9). However, this increase is relatively small. For example, the value of R_a before the dieless drawing was 1.73 μ, and after deformation, it was 2.23 μ. In other experiments, the change in roughness was lesser. It is possible that the strain in each pass affects the roughness similar to the effect on the unevenness of the diameter of tubes, studied in [7]. It can be assumed that with a small increment of elongation in one pass, the roughness will decrease compared to a single-pass process. However, this assumption should be interpreted with caution, because at the moment we do not have theoretical and experimental evidence for this statement.



a) b)

Fig. 9 Surface profile of CuZn37 alloy wire before (**a**) and after (**b**) multi-pass dieless drawing at temperature of 400 °C (position 5 in Table 1). (Color figure online)

5 Conclusions

1. An experimental setup for the multi-pass dieless drawing of an ultrafine wire was designed and commissioned to produce a reduction in the cross-sectional area of a copper and brass wire without the use of conventional wire drawing dies. A designed setup can continuously produce wire using the dieless drawing method without limitation in wire length.
2. The flow stress of technical copper and brass was studied. The results showed that brass has a more stable hardening interval on the stress-strain curve. That is why this material is more promising for multi-pass incremental dieless drawing. The dieless drawing experiments confirm the above statement. The effectiveness of the multi-pass dieless drawing process for brass wire at 530 °C was close to 2.0. Irreversible defects on the wire surface were not observed.
3. The result obtained at 400 °C is characterized by significantly lower workability of brass wire and the appearance of a cracks network at the grain boundaries.
4. The total elongation of the thin copper wire was small (0.21–0.23) and significantly lesser than that of brass wire (0.31–0.63). Using a multi-pass process instead of a single-pass process does not significantly increase workability. One of the reasons for this result may be the complex nature of the dependence of flow stress on strain for copper. A deeper analysis of this problem will be done in future studies.

Acknowledgments The work was supported by the NCN of Poland, Project No. 2017/27/B/ST8/01471.

References

1. Kraft FB (1980) Three fine wire drawing systems—an economic comparison. Wire J 13(7):103–105
2. Seitz JM, Utermohlen D, Wulf E, Klose C, Bach FW (2011) The manufacture of resorbable suture material from magnesium—drawing and stranding of thin wires. Adv Eng Mater 13:1087–1095
3. Weiss V, Kot RA (1969) Dieless wire drawing with transformation plasticity. Wire J 9:182–189
4. Supriadi S, Furushima T, Manabe K (2011) Development of precision profile control system with fuzzy model and correction function for tube dieless drawing. J Solid Mech Mater Eng 5(12):1059–1070
5. Tiernan P, Hillery MT (2004) Dieless wire drawing—an experimental and numerical analysis. J Mater Process Technol 155–156:1178–1183
6. Li Y, Quick NR, Kar A (2002) Dieless laser drawing of fine metal wires. J Mater Proc Technol 123:451–458
7. Milenin A (2018) Rheology-based approach of design the dieless drawing processes. Arch Civil Mech Eng 18:1309–1317
8. Furushima T, Manabe K (2007) Dieless drawing process of extruded non-circular aluminum alloy tubes with double hollow section. JJILM 57(8):351–356
9. Furushima T, Imagawa Y, Manabe K, Sakai T (2015) Effects of oxidation and surface roughening on drawing limit in dieless drawing process of SUS304 stainless steel microtubes. J Mater Process Technol 223:186–192
10. Garcia V, Cabrera JM, Prado JM (2007) Effects of precipitation during dynamic recrystallization of copper with different oxygen levels. Mater Sci Forum 558–559:511–516
11. Szeliga D, Matuszyk P, Kuziak R, Pietrzyk M (2002) Identification of rheological parameters on the basis of various types of plastometric tests. J Mater Proc Technol 125–126:150–154
12. Chandra T, Jonas JJ, Taplin DMR (1976) The mechanical behaviour of cerium-modified alpha-beta brass at high temperatures. J Mater Sci 11:1843–1848
13. Milenin A, Kustra P, Paćko M (2010) Mathematical model of warm drawing of MgCa0.8 alloy accounting for ductility of the material. Comp Meth Mater Sci 10:69–79

Robotic Roller Forming Process and Strategies to Eliminate Geometrical Defect of Edge Waves



Yi Liu, Junying Min, and Jianping Lin

Abstract Robotic roller forming (RRF) is a new dieless and flexible forming process using a roller mounted on an industrial robot to form sheet metal products by multiple passes with predefined tool paths. In this study, DP590 (dual-phase) steel sheets are formed to bent specimens having a right angle by RRF with three passes, and edge waves are observed at the flange of DP590 specimens. Finite element analysis is utilized to reproduce the edge waves. According to finite element simulation, longitudinal plastic strains are generated at the flange edges due to excessive tensile and compressive stresses, which results in severe edge waves. Two strategies are introduced to eliminate edge waves. One has to optimize forming parameters, and the effects of forming angle increment and moving direction of the roller on longitudinal peak strains at the flange edges are evaluated. Another strategy to eliminate edge waves is to apply laser heating in RRF, where the heating spot is 25 mm in front of the roller. Experimental results demonstrate that laser heating reduces forming forces, eliminates edge waves as well as the required number of forming passes.

Keywords Robotic roller forming · Edge waves · Longitudinal peak strain · Laser heating

1 Introduction

Sheet metal bending is an important process used in the manufacturing of thin-walled components. Flanging is a typical bending process, which involves drawing or stretch forming with the assistance of die and punch. It is difficult to form ultra-high-strength steels by one step due to their small ductility. Roller forming, which progressively bends metal sheet to the desired shape by successive sets of rotating rollers [1], is applied in industry to bending some materials with high strength and low ductility for its incremental nature. Some defects, such as longitudinal bow, are prone to happen, and some research has been investigated on the optimization of process and

Y. Liu · J. Min (✉) · J. Lin
School of Mechanical Engineering, Tongji University, Shanghai 201804, China
e-mail: Junying.Min@tongji.edu.cn

© The Minerals, Metals & Materials Society 2021

G. Daehn et al. (eds.), *Forming the Future*, The Minerals, Metals & Materials Series,
https://doi.org/10.1007/978-3-030-75381-8_40

part shape parameters [2]. Edge waves are also typical defects in the conventional roller forming process; it is difficult to eliminate in subsequent processes. Previous studies were mainly forced on the occurrence of edge waves and the effect of forming parameters on the severity of edge waves. Farzin et al. [3] suggested that the edge waves were due to the plastic local buckling of the rim, and a buckling limit strain (BLS) of 0.9% was introduced and employed to avoid edge waves. The BLS was then used by Zeng et al. [4] to design the forming angle increment and roller radius for cold roller forming, and the desired section was produced by a minimum roller station to avoid edge waves. Tehrani et al. [5] stated that longitudinal strain in the first station should be below a critical value, and the influence of varying the fold angle in subsequent rolling stations on the occurrence of edge waves can be neglected. Roller forming can be used to fabricate various thin-walled profiles by a proper design of rollers at present; however, it is applied in some situations with mass production due to lack of flexibility and high cost of forming rollers.

In recent years, flexible sheet metal forming processes have been developed due to rapidly changing customer demands [6]. To meet the demand for small-batch and variable cross-section profiles, researchers have paid much attention to flexible bending process, especially on flanging. Wen et al. [7] utilized improved bar tools with tapered shoulders to perform forward and backward flanging of open edges and hole rims of Al 6061 sheets. Voswinckel et al. [8] analyzed the technological capabilities of conducting flanging of DC04 mild steel by incremental sheet forming. Zhang et al. [9] studied the deformation mechanics in the hole-flanging process of AA5754-O by double-sided incremental forming and found enhanced formability in shrink flanging due to meridional tensile strain and the localized deformation mode. Han et al. [10] used a rotary tool to perform the straight flanging process of AA2024-O on an incremental forming machine. The deformation process in incremental flanging is quite different from that in conventional flanging formed by press-working, and some defects such as plate warpage and buckling at flange onset might happen [7]; besides, severe thinning or even fracture could be observed in the incremental hole-flanging process of 1060 aluminum sheets [11].

Sheet metal flanging is an important finishing operation in manufacturing processes, and the surface quality of flanging has a significant impact on the subsequent joining and assembling processes. Therefore, a flexible flanging process combining the incremental nature of conventional roller forming and incremental flanging is proposed here with the aid of industrial robots and roller tools, namely robotic roller forming (RRF) process. This paper presents the details of RRF process and a typical defect, i.e. edge waves, was observed in experiments. Two strategies are proposed to eliminate edge waves in RRF: one is to optimize the forming parameters of RRF through finite element simulation, and the other is to form the parts with synchronized laser heating.

2 Robotic Roller Forming (RRF) Process

The robotic roller forming (RRF) platform has been developed at Tongji University as presented in Fig. 1. The RRF platform is composed of a roller driven by a KR600 R2830 industrial robot and a fixture frame. It can be extended to a greater RRF system collaborated by multiple industrial robots to form parts with more complex shapes. The RRF process is illustrated in Fig. 2. The sheet material used in this work is a high-strength dual-phase steel, DP590, with a thickness of 1.2 mm. The sheet specimens were firmly clamped on the fixture frame, and the roller having a diameter of 50 mm and a height of 25 mm moved along the longitudinal direction of the sheet specimen with several forming passes. The sheet specimen is incrementally formed in each pass until its final shape. Forming parameters, such as number of forming passes, forming paths, etc., can be numerically programmed into the controlling system of the industrial robot. In contrast to the flanging by stamping and conventional roller forming process, the forming roller is independent of clamping geometries, and the roller results in a small and limited deformation zone so that the required forming forces are much lower.

In the preliminary research, an L-shaped part was formed by three passes (3P); for example, the forming angle increment in each pass was 30°. The length of the specimen is 250 mm and the widths of the web and flange are 40 mm and 20 mm,

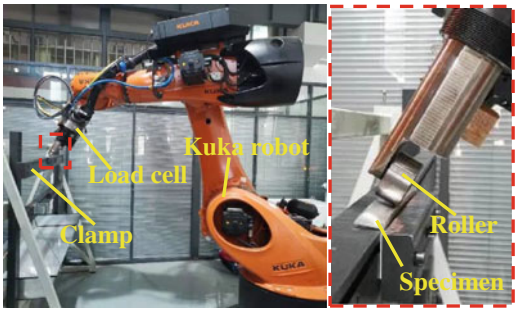


Fig. 1 Experimental setup of RRF process. (Color figure online)

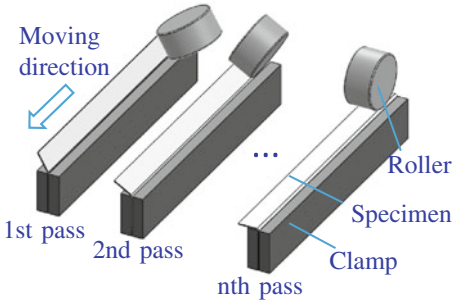


Fig. 2 An illustration of RRF process. (Color figure online)

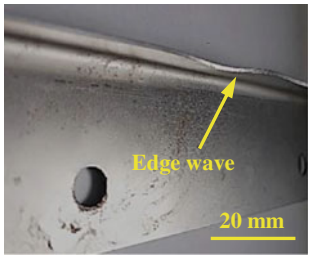


Fig. 3 An RRF specimen with three forming passes. (Color figure online)

respectively. The L-shaped part after three passes is presented in Fig. 3, and the obvious edge waves were noted at the flange edges.

3 Optimization of Forming Angle Increment and Moving Direction of Roller to Eliminate Edge Waves in RRF

3.1 Finite Element Simulation

To obtain RRF specimens with higher geometrical accuracy, a finite element model of RRF is established with Ls-Dyna as presented in Fig. 4. The geometry of the simulation model was the same as the dimension mentioned above. The fixture and roller were set as rigid. Shell element was applied for the metal sheet due to a low thickness to width ratio. The element size for the clamping area (constrained for six degrees-of-freedom) was 1 mm × 1 mm, and the element sizes of the deformation zone and the flange were 1 mm × 0.25 mm and 1 mm × 0.5 mm, respectively. A material model of MAT133 was adopted for the sheet steel DP590, and the parameters of the DP590 steel were obtained by uniaxial tensile testing and biaxial tensile testing, as listed in Table 1. A contact type of forming_one_way_surface_to_surface was applied and the friction coefficient value was set to 0.27 according to experimental results. The duration of each forming pass was set to 0.01 s to accelerate the solution,

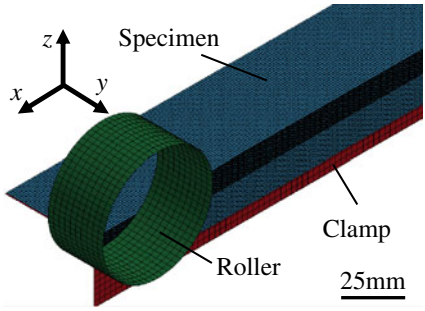


Fig. 4 Finite element model of RRF. (Color figure online)

Table 1 Material parameters of DP590 steel used in finite element simulation (MAT133 in Ls-Dyna)

Density (kg/m^3)	E (MPa)	Poisson's ratio	K (MPa)	ε_0	n	Hardening law	A
7.84e3	2.022e5	0.3	1015	0.002	0.172	1	6
α_1	α_2	α_3	α_4	α_5	α_6	α_7	α_8
1.0148211	0.9735020	0.8346100	0.9894840	0.9877220	0.9540490	0.9646920	1.0707800

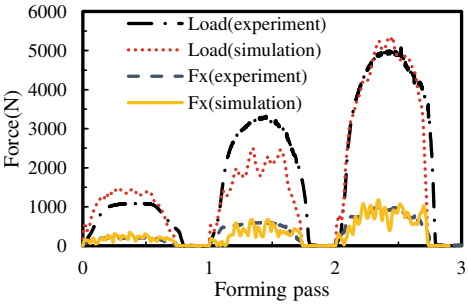


Fig. 5 Comparison of experimental and simulation results of RRF. (Color figure online)

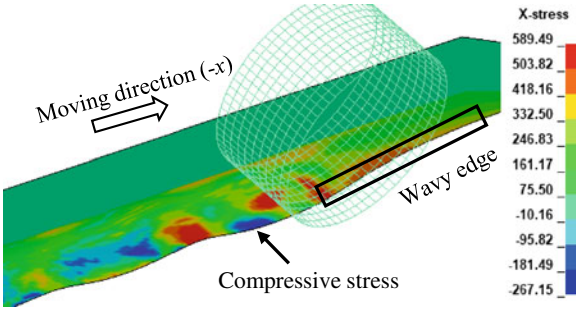


Fig. 6 Edge waves on an RRF specimen reproduced by finite element simulation. (Color figure online)

which corresponds to ~1000 times the moving speed in experiments. A normalization method is used to compare between the simulation and experimental results, and Fig. 5 indicates a good agreement between the forming load perpendicular to the contact interface as well as force along the moving direction (Fx) recorded by the load cell Omega 191 equipped on the KR600 robot and the simulation results. Edge waves are reproduced by FE simulation as shown in Fig. 6. The elements in front of the roller are elongated to a 3D curve; afterwards, the elements suffer from compressive stresses after the roller leaves to keep the edge straight. The compressive stresses increase at larger longitudinal plastic strains. The edge buckling occurs as the compressive stresses exceed a threshold value, i.e. the limit of compression instability.

3.2 Optimization of Forming Parameters

Longitudinal peak strain is closely bound up with the geometries of formed parts and forming parameters. Lindgren [12] developed a model to calculate longitudinal peak strain at the flange of a U-Channel with consideration of flange length, forming angle, yield stress, sheet thickness as well as roller radius. Abeyrathna et al. [13] proved that longitudinal peak edge strain in roller forming increases with an increase of forming angle and a decrease of flange length. Considering the specific part formed by RRF in this study, the material properties and the flange length are fixed. The roller is

a universal tool, thus the radius should be constant for each forming pass to avoid changing tools frequently, and the angle increment in each forming pass, as well as the moving direction of the roller, can be optimized by programming.

A simple method to reduce edge waves is to increase forming passes and decrease angle increment in each forming pass; therefore, two cases of forming by six passes (15° for each pass) and eight passes (12° for the first two passes and 11° for the later six passes) were studied by FE simulation. However, the longitudinal peak strain will increase in the case with a constant angle in each forming pass. By taking into account forming efficiency (i.e. minimizing the pass number), a downhill method was applied to the FE simulation to limit the accumulation of the longitudinal peak strain. In this study, the optimization target for the downhill method was to control the longitudinal peak strain in each forming pass to 0.009 [3, 4]. The longitudinal peak strain was determined by the maximum strain along the x-axis (ε_x) of elements at flange edges during this forming pass. In this simulation model, the maximum ε_x were extracted at a distance of 50 mm away from the section edge (Fig. 7) to eliminate any effect of end flare [14]. Longitudinal peak strain of forming angle increment from 12° to 19° as well as 30° for the first forming pass is obtained by simulation, as shown in Fig. 8. A linear relation between longitudinal peak strain and

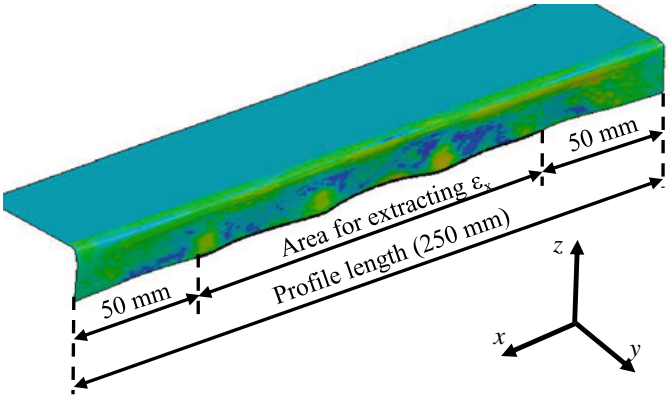


Fig. 7 Definition of area for extracting ε_x. (Color figure online)

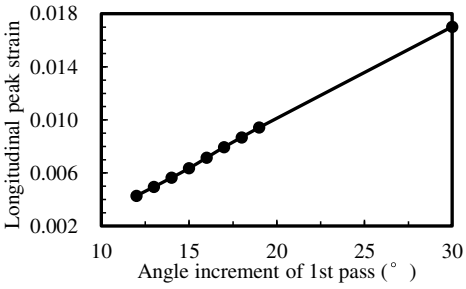


Fig. 8 Effects of forming angle increment on longitudinal peak strain at the first forming pass

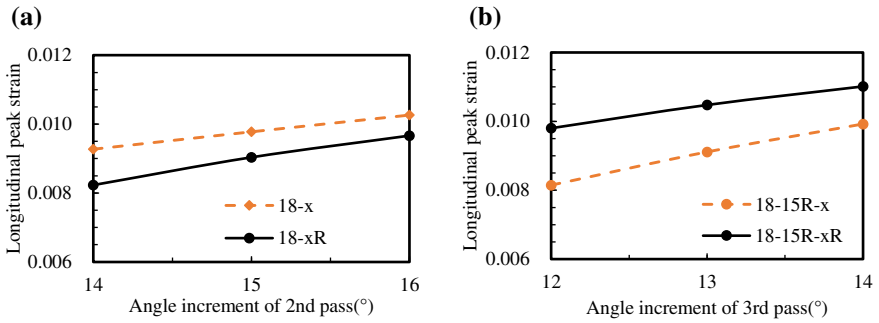


Fig. 9 Effect of angle increment on longitudinal peak strain. **a** Second forming pass; **b** Third forming pass. (Color figure online)

forming angle increment can be observed, and an angle increment of 18° is chosen to control the longitudinal peak strain to a limit of 0.009.

For the second forming pass, a factor of the moving direction of the roller is also considered. For the moving direction opposite to the first forming pass, the forming parameter is designated as forming angle plus "R". (For instance, 15R indicates an angle increment of 15°, and the moving direction reverses to that in the first forming pass.) Six forming parameters are studied by FE simulation, and the effects of forming angle increment on longitudinal peak strain are exhibited in Fig. 9a. It can be concluded that a linear relation between longitudinal peak strain and forming angle increment still exists for both moving directions, and it is depicted that the longitudinal peak strain of forming by reciprocating motion is smaller than forming by the same direction. The forming procedure for the first two passes is 18-15R. A similar phenomenon can also be observed in the simulation results for the third forming pass in Fig. 9b, and the forming procedure for the formal three passes is set as 18-15R-12. To save solution time for simulation and also increase efficiency in RRF, reciprocating motion is applied for the following analysis, and a similar operation is conducted for the following forming passes till the forming angle reaches 90°. Eventually, the forming parameter to constrain the longitudinal peak strain to a limit of 0.009 is 18-15R-12-10R-10-10R-10-5R.

3.3 Results and Discussion

In this study, five RRF processes are analyzed by FE simulation, including three passes with a constant angle increment of 30° in each forming pass (3P, 30-30-30), six passes with a constant angle increment of 15° in each forming pass (6P, 15-15-15-15-15-15), eight passes with similar angle increment in each forming passes (8P, 12-12-11-11-11-11-11-11), downhill method by one direction with variable angle increment (8P-D, 18-15-12-10-10-10-10-5) and downhill method by reciprocating

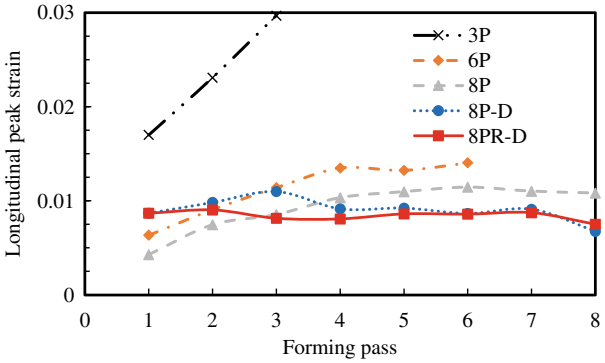


Fig. 10 Longitudinal peak strain for each forming pass of different forming processes. (Color figure online)

motion (8PR-D, 18-15R-12-10R-10-10R-10-5R). The longitudinal peak strain of each forming is presented in Fig. 10. Longitudinal peak strain increases obviously at the first three forming passes with constant angle increment of 15° or 30°, while the longitudinal peak strain is limited below ~0.01 by using the downhill method.

To evaluate the severity of edge waves, the average height of edge waves ($\bar{h}$) and the maximum height of edge waves ($h_{\max}$) are introduced and illustrated in Fig. 11. The y-coordinate of the nodes at the flange edges are extracted by each millimeter (except the nodes at a distance of 50 mm away from section edge), and a deviation between the average y-coordinate value and actual y-coordinate value is defined as the height of edge wave (h). $\bar{h}$ and $h_{\max}$ are defined as average value and maximum value of h, respectively. The edge profiles are compared in terms of $\bar{h}$ and $h_{\max}$ which are listed in Table 2, and the formed specimens of 3P, 6P, and 8PR-D are compared in Fig. 12. The optimization method to constrain the longitudinal peak strain can

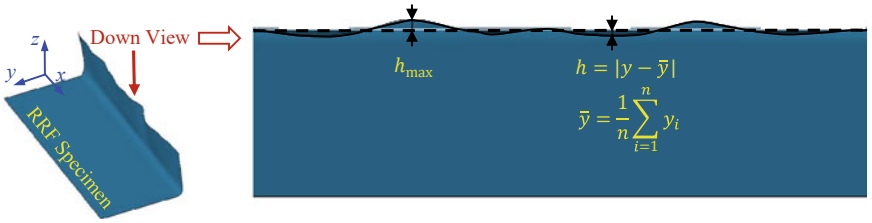


Fig. 11 Schematic of the average height and maximum height of edge waves. (Color figure online)

Table 2 Comparison of severity of edge waves for five processes

	3P	6P	8P	8P-D	8PR-D
$\bar{h}$ (mm)	0.972	0.344	0.177	0.140	0.116
$h_{\max}$ (mm)	2.172	0.766	0.499	0.387	0.344

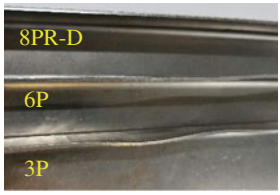


Fig. 12 RRF specimen. (Color figure online)

be used to obtain straight edge specimens without visible edge waves compared with forming by three passes and six passes. Additionally, the average height and maximum height of edge waves of 8PR-D are decreased by 10–35% in comparison with the forming process by one direction (8P-D) and by a constant angle increment (8P).

4 Application of Laser Heating to Eliminate Edge Waves in RRF

4.1 RRF with Local Laser Heating

In RRF, the essence of edge waves is the excessive plastic deformation at flange edges resulting from bending moment generated at the bending radius. Therefore, it is feasible to eliminate edge waves by decreasing bending moment, e.g. by decreasing the angle increment of each forming pass, by softening the deformation zone through local heating.

Although the forming force of RRF is relatively low compared with stamping, the process is still constrained by the load capability of industrial robots, especially when forming ultra-high-strength sheet materials. A new concept of RRF with laser heating (LRRF) as illustrated in Fig. 13 is developed to deal with these problems. In LRRF, a laser beam is introduced 25 mm in front of the roller to locally heat the to-be-deformed area, and the roller follows the heat source synchronously and a flange is then formed by multiple forming passes. The experimental setup of LRRF illustrated in Fig. 14 was used to form DP590 steel sheets by three passes (30° in

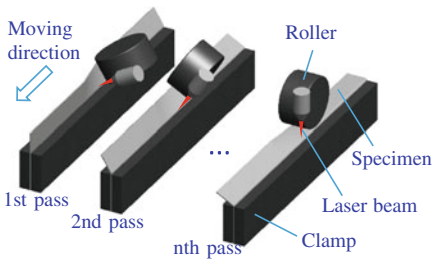


Fig. 13 An illustration of RRF with laser heating. (Color figure online)



Fig. 14 Experimental setup of RRF with laser heating. (Color figure online)

each pass) and by six passes (15° in each pass). The laser spot had a rectangle shape with a dimension of 4 mm × 2 mm, and the 4 mm edge was perpendicular to the moving direction. Laser power for LRRF was set to 1200 W and a forming velocity was 30 mm/s.

4.2 Results and Discussion

Forming forces are compared in Fig. 15 with the results from RRF experiment at room temperature. From Fig. 15, it is demonstrated that the application of laser heating reduces forming forces by 20% at the same forming parameters. The formed specimens are compared in Fig. 16, and with laser heating, edge waves are eliminated

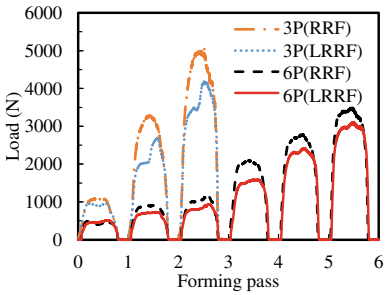


Fig. 15 Comparison of forming forces by RRF and LRRF. (Color figure online)

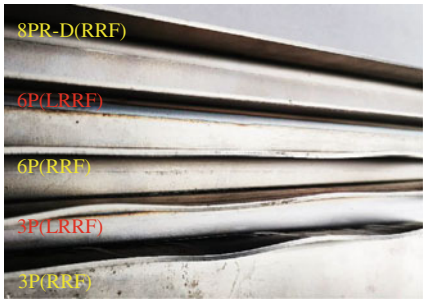


Fig. 16 Comparison of RRF and LRRF specimens. (Color figure online)

when using six forming passes with a constant angle increment of 15°. It is observed that the edge of LRRF-6P specimen is nearly identical to the specimen formed by the downhill method by reciprocating motion.

Although LRRF eliminates edge waves with fewer forming passes, the forming process parameters (e.g. moving speed of the roller, heating temperature, angle increment in each forming pass, etc.) are still required to be optimized to further minimize the number of forming passes and increase forming efficiency.

5 Conclusions

In this study, a robotic roller forming (RRF) process is proposed and developed. Experimental and numerical researches were conducted to increase the geometrical accuracy of formed specimens. Two strategies to eliminate edge waves are introduced, and the following conclusions can be drawn.

(1) The newly developed robotic roller forming process that combines advantages of the conventional roller forming process, incremental forming, and industrial robot can be used to bend high strength steel with a single roller without fracture. However, edge waves caused by excessive plastic deformation were observed on the formed specimens as geometrical defects.
(2) Edge waves can be eliminated by optimizing forming parameters. The effects of angle increment and moving direction of the roller on geometrical accuracy are investigated, and an optimal forming parameter of forming for eight passes by reciprocating motion is proposed to limit the longitudinal peak strain and consequently eliminate edge waves.
(3) It is experimentally demonstrated that edge waves can also be eliminated by applying synchronized laser heating in RRF. Results reveal that the peak forming forces are reduced by 20%, and high geometrical accuracy is achieved with fewer forming passes in comparison with RRF at room temperature.

Acknowledgments The authors would like to acknowledge the financial support for this research provided through the Fundamental Research Funds for the Central Universities.

References

1. Panton SM, Zhu SD, Duncan JL (1994) Fundamental deformation types and sectional properties in roll forming. Int J Mech Sci 36(8):725–735
2. Safdarian R, Naeini HM (2015) The effects of forming parameters on the cold roll forming of channel section. Thin-Walled Struct 92:130–136
3. Farzin M, Tehrani S, Shameli E (2002) Determination of buckling limit of strain in cold roll forming by the finite element analysis. J Mater Process Technol 125–126:626–632

4. Zeng G, Li SH, Yu ZQ, Lai XM (2009) Optimization design of roll profiles for cold roll forming based on response surface method. Mater Des 30(6):1930–1938
5. Tehrani MS, Hartley P, Naeini HM, Khademizadeh H (2006) Localised edge buckling in cold roll-forming of symmetric channel section. Thin-Walled Struct 44(2):184–196
6. Yang DY, Bambach M, Cao J, Duflou JR, Lee CW (2018) Flexibility in metal forming. CIRP Ann—Manuf Technol 67(2):743–765
7. Wen T, Zhang S, Zheng J, Huang Q, Liu Q (2016) Bi-directional dieless incremental flanging of sheet metals using a bar tool with tapered shoulders. J Mater Process Technol 229:795–803
8. Voswinckel H, Bambach M, Hirt G (2015) Improving geometrical accuracy for flanging by incremental sheet metal forming. Int J Mater Form 8(3):391–399
9. Zhang H, Zhang ZX, Ren HQ, Cao J, Chen J (2018) Deformation mechanics and failure mode in stretch and shrink flanging by double-sided incremental forming. Int J Mech Sci 144:216–222
10. Han K, Li XQ, Peng XY, Wang HB, Li DS, Li YL, Li Q (2019) Experimental and numerical study on the deformation mechanism of straight flanging by incremental sheet forming. Int J Mech Sci 160:75–89
11. Cui Z, Gao L (2010) Studies on hole-flanging process using multistage incremental forming. CIRP J Manuf Sci Technol 2(2):124–128
12. Lindgren M (2007) An improved model for the longitudinal peak strain in the flange of a roll formed u-channel developed by FE-analyses. Steel Res Int 78(1):82–87
13. Abeyrathna B, Rolfe B, Weiss M (2017) The effect of process and geometric parameters on longitudinal edge strain and product defects in cold roll forming. Int J Adv Manuf Technol 92:743–754
14. Badr OM, Rolfe B, Weiss M (2018) Effect of the forming method on part shape quality in cold roll forming high strength Ti-6Al-4V sheet. J Manuf Process 32:513–521

Numerical Modelling of the Flow Forming Process: Computation Time Optimization and Accuracy Analysis



Ahmed Mehdi Roula, Katia Mocellin, and Pierre-Olivier Bouchard

Abstract Flow forming is an incremental forming process during which a roller tool deforms a rotating sheet metal by applying a force which is local and evolving during the entire process. The finite element software FORGE® is used in order to model this process. The local tool-workpiece contact conditions and the high rotation speed make the modelling of this process difficult with high computation time. It is, therefore, necessary to develop optimization strategies aiming to reduce the computation time whilst maintaining a sufficient level of results accuracy. A first configuration optimization method consists of reducing the geometry of the initial blank and using symmetry planes. The final reduced geometry obtainable is 36° wide. This method is then associated with a second one which consists of reducing the number of calculation time steps during the entire process. The calculation time steps removed are those occurring when the roller tool is not in contact with the deformable sheet metal anymore. The two combined methods give the ability to drastically reduce the computation time compared to the reference case. In addition, the global and local results of the reference case are mostly conserved when applying the configuration optimization methods.

Keywords Flow forming · Incremental forming · Numerical modelling · Computation time · Optimization

1 Introduction

Incremental sheet forming (ISF) processes refer to processes during which the plastic deformation takes place due to repeated contacts between the sheet metal and the tool. The contact zone evolves during the entire process. During these processes, high strain levels can be reached without fracture. Furthermore, the ISF processes

A. M. Roula (✉) · K. Mocellin · P.-O. Bouchard
CEMEF Mines ParisTech, PSL Research University, CNRS, UMR 7635, CS 10207, 06904 Sophia-Antipolis Cedex, France
e-mail: ahmed.roula@mines-paristech.fr

© The Minerals, Metals & Materials Society 2021

G. Daehn et al. (eds.), *Forming the Future*, The Minerals, Metals & Materials Series,
https://doi.org/10.1007/978-3-030-75381-8_41

make it possible to form complex 3D parts with limited machining operations so that it limits the material loss. Thus, ISF has become of great interest in the last few decades.

Flow forming (or spinning) is a specific type of ISF process. During flow forming, a metal sheet is placed over a rotating mandrel and is incrementally deformed by a roller which follows a specific trajectory to stick and compress the sheet on the mandrel. Consequently, the complex local and cyclic loading conditions allow reaching high plastic strain levels with reduced involved forces compared to the ones required in a conventional metal forming process. Despite these advantages, the ISF processes have some drawbacks. For example, strain localization (necking) can occur, leading to premature damage. This problem is misunderstood in the literature and slows down the development of new products.

Numerical modelling of ISF processes allows a better understanding of the material behaviour during the forming operation, which could improve the fracture predictions. However, the local tool-workpiece contact conditions and the high rotation speed make the modelling of these processes difficult with high computation time.

In this study, the finite element software FORGE® is used. A configuration optimization is sought in order to reduce the computation time while maintaining a sufficient level of results accuracy.

In the first section of the current work, a description of the process modelling and the principle type of results is presented. The second section describes the methods developed to reduce the calculation time. In the last section, the results obtained with this optimized model will be discussed and compared to a reference case.

2 Numerical Modelling of the Flow Forming Process

The finite element software FORGE® is used in this study. With this software, several forming processes like forging, rolling, and deep-drawing can be modelled. FORGE® uses linear tetrahedral elements with an implicit resolution using velocity–pressure mixed formulation.

The flow forming process is usually split into three main categories [1] as illustrated in Fig. 1. These categories are:

- Conventional spinning, during which the blank thickness remains nearly constant during the process;
- Shear spinning, where the thickness decreases. The final thickness depends on the angle between the part wall and the rotation axis;
- Tube spinning, during which one or more rollers deform a tubular piece to reduce the wall thickness.

The flow forming process studied in the current work differs from these processes. In fact, it could be related to conventional spinning with a reduction in the wall thickness.

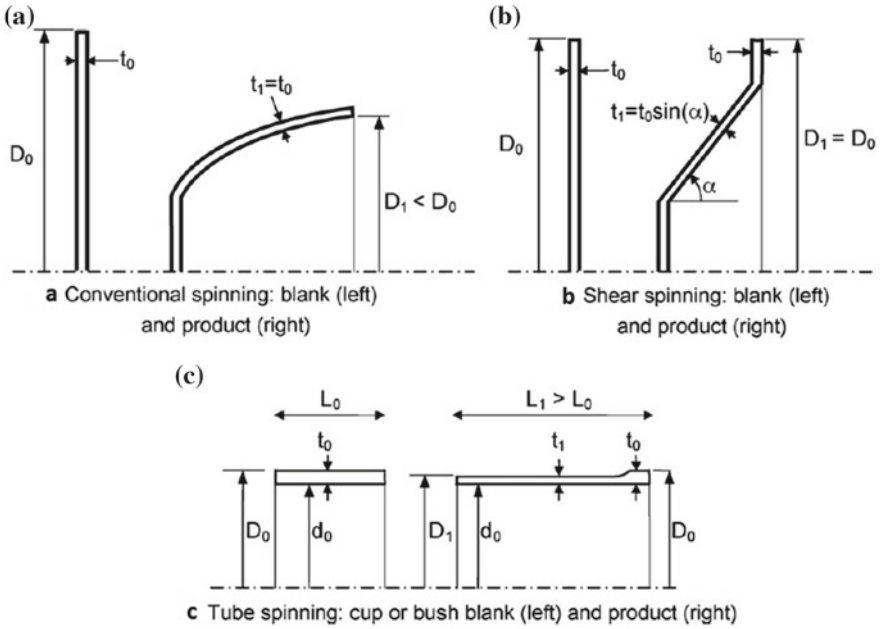


Fig. 1 Spinning configurations: **a** conventional spinning, **b** Shear spinning, **c** Tube spinning [1]

In this process, a sheet metal is maintained between a tailstock and a mandrel. All of these elements turn with a high rotation speed around a vertical axis while a roller tool, which describes a complex planar path, deforms locally the sheet metal (Fig. 2). The wall thickness is reduced during this process.

The inner shape of the metal at the end of the process is given by the outer shape of the mandrel. Meanwhile, the outer shape of the metal is given by the roller path.

As mentioned in the introduction, the high computation time is a major problem in the modelling of the flow forming process. This high computation time is due to the fine mesh size and the small-time calculation step, both required to manage the local tool-workpiece contact and the high rotation speed. An example of the mesh used is given in Fig. 3.

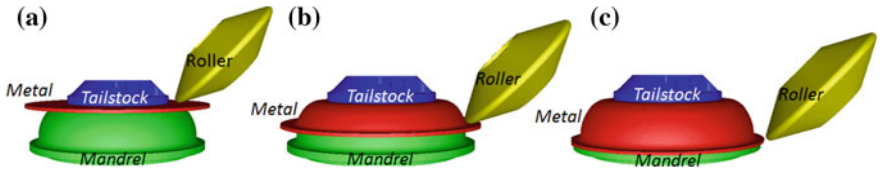


Fig. 2 Numerical modelling of flow forming process using FORGE® software: **a** initial state, **b** intermediate state, **c** final state. (Color figure online)

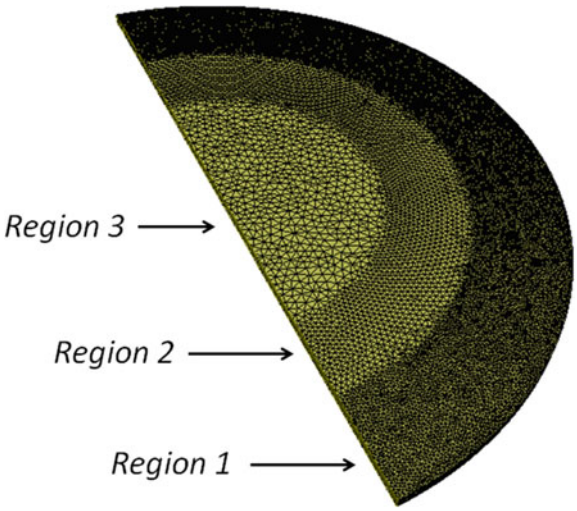


Fig. 3 Mesh used to model the flow forming of a 4.5 mm thick disc with a 280 mm diameter. The regions 1, 2 and 3 are meshed with a mean mesh size of 1, 2 and 3 mm, respectively. The disc is truncated for the illustration. (Color figure online)

Region 3, which is in contact with the tailstock, is not deformed during the process. As a consequence, it is meshed coarsely. Region 1 is the one which will be deformed; therefore, it is meshed finely. Region 2 is a transition zone between the two regions previously mentioned. A pre-study showed that for this modelling configuration, remeshing is not necessary, so it is disabled.

The material is an aluminium alloy modelled through an elastic-plastic power law given by:

$$\sigma = k\ \bar{\varepsilon}^n \tag{1}$$

where σ is the flow stress, $\bar{\varepsilon}$ the equivalent strain, and k and n material parameters whose values are 165 MPa and 0.22, respectively. The Young modulus value is 69 GPa. A tensile test, whose flow curve is shown in Fig. 4, is used to obtain these parameters.

As the strains in flow forming reach much higher values than those in tensile test, the extrapolation of the stresses at higher strain values is needed. The validity of this extrapolation has been verified for this material with the in-plane torsion test [2] (results not shown here). This test allows reaching strains as high as those met in flow forming.

Results (that will be discussed in the last section) are of two kinds: global and local results. Among the global results, can be mentioned:

– Geometrical information like the wall thickness distribution;
– Mechanical values like the roller global forces needed in the flow forming process.

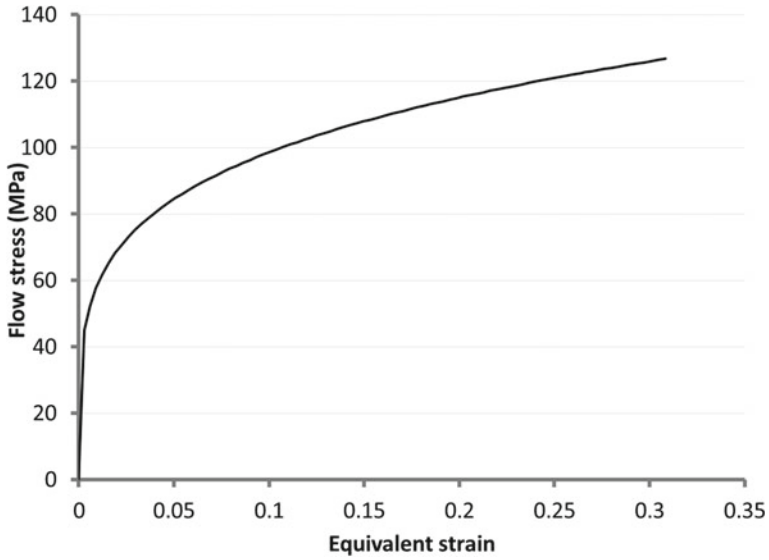


Fig. 4 Tensile flow curve of the used aluminium material

The local results concern those stored locally on sensors assumed to be linked with the material. A sensor tracks and records the local mechanical state like the equivalent strain and the Rice & Tracey damage variable. These two mechanical quantities will be defined in the last section. The evolution of the temperature on the sensors is also recorded.

3 Configuration Optimization Methods

A pre-study on the modelling of the flow forming process showed that a little CPU time can be saved if the roller is chosen to be rotating instead of the blank (which is driven by the mandrel and the tailstock). Thus, the roller adopts a helical trajectory. This change in the roller kinematics does not affect at all the accuracy of the results, the types of which are given in the end of the previous section.

Consequently, after applying this change in the roller kinematics, the modelling of the complete 3D configuration with refined mesh in the deformed zone (called hereinafter *reference case*, Fig. 3) has been launched on 30 CPUs of a calculation computer.[1] This case has a computation time of approximately 1500 h. This computation time is obviously too long and the purpose of the current section is to introduce methods to reduce it while preserving a sufficient level of results accuracy. The unique

[1]CPU: Intel(R) Xeon(R) CPU E5-2630 v3 @ 2.40 GHz.

configuration that will be studied in the following is the flow forming of a 4.5 mm thick disc having a 280 mm diameter.

3.1 Geometry Reduction

This approach (Fig. 5) consists of reducing the original complete geometry (360°). Consequently, the flow forming modelling is performed on *reduced geometries*. Nevertheless, the complete geometry of the non-deformable tools (tailstock, roller, and mandrel) is conserved as it does not impact the CPU time nor computation conditions.

An important feature of this approach is the use of two symmetry planes. These planes are placed on two lateral edges of the sheet as illustrated in Fig. 5. Obviously, applying such symmetry conditions does not correspond to the real 3D process since it adds edge effects due to the symmetry actions of the roller. For this reason, symmetry planes are not generally used in ISF modelling. However, the novelty is that due to the very small contact area between the roller and the workpiece (<4° wide), the local action of the roller on the sheet far enough from the symmetry faces could be the representative of the real process conditions.

Being equidistant from the two symmetry faces of the reduced geometry, the median plane is the most distant area from these faces. Consequently, in order to avoid edge effects, this plane is chosen to analyse geometrical and mechanical results. Actually, further research shows that the accuracy of the global and local results is conserved within a 10° wide area around the median plane.

As shown in Fig. 5c, the final geometry is the 36° one. Further geometry reduction is not possible because in such a case, the elements of the mesh are too deformed, causing non-convergence issues. The number of nodes in the reference case is approximately 191,000 while the final 36° geometry has approximately a tenth of this

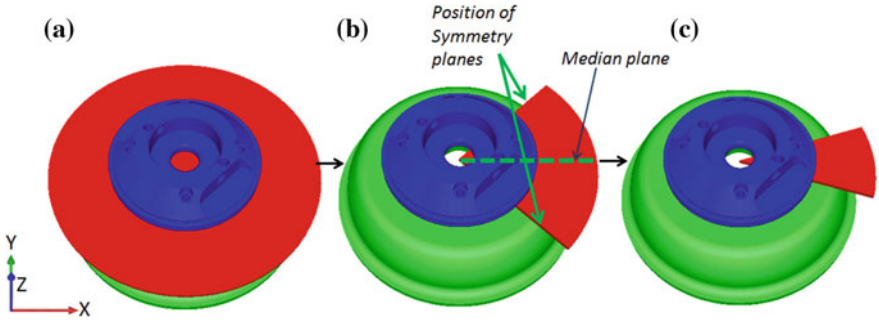


Fig. 5 Geometry reduction approach: **a** initial geometry (360°), **b** example of intermediate geometry (90°), **c** final geometry (36°). (Color figure online)

number. This final geometry will be used in the second configuration optimization method.

3.2 Calculation Time Steps Reduction

The use of the previously described approach reduces, theoretically, the calculation time by reducing the number of elements. Nevertheless, this approach involves that the roller kinematics will be unchanged so that it describes a helical path during the entire process, as explained at the beginning of the current section. This helical path of the roller is associated with a constant and fine calculation time step (10^{-4} s), used even though the roller is not in contact with the metal sheet.

The aim of the current second approach is to remove unnecessary calculation time steps when using reduced geometries. Unnecessary calculation time steps are those during which mechanical and thermal calculations are done, despite the roller is out of contact with the deformable reduced geometry.

The first step towards this configuration optimization technique is to identify and remove those unnecessary calculation time steps. For a given reduced geometry with a helical roller path during the whole process, determining those calculation time steps is equivalent to determine the times when all the forces measured on the roller are equal to zero. After that, the previously used roller kinematics is maintained (time–velocity control), so as the calculation time steps in the deformable zone (10^{-4} s).

The modelling of the flow forming process using this new optimization technique can now be performed by selecting, a priori, the calculation time steps during which the roller will be in contact with the deformable reduced geometry. This method allows avoiding approximately 18,600 unnecessary calculation time steps, which represent 79% of total calculation time steps done before applying this optimization method.

Figure 6 depicts the roller planar path after the process modelling using the reference case (without geometry and calculation time steps reductions). After applying both reduction techniques, a process modelling with a 36° reduced geometry is performed and the final roller planar path is also given in Fig. 6.

A maximum error of 0.05% between the two cases (along the X and Z axes) shows that there is an excellent match of the paths. This shows that applying the two reduction techniques does not impact the roller kinematics description. In the last section, the results obtained after implementing both configuration optimization methods will be shown and compared with a reference case.

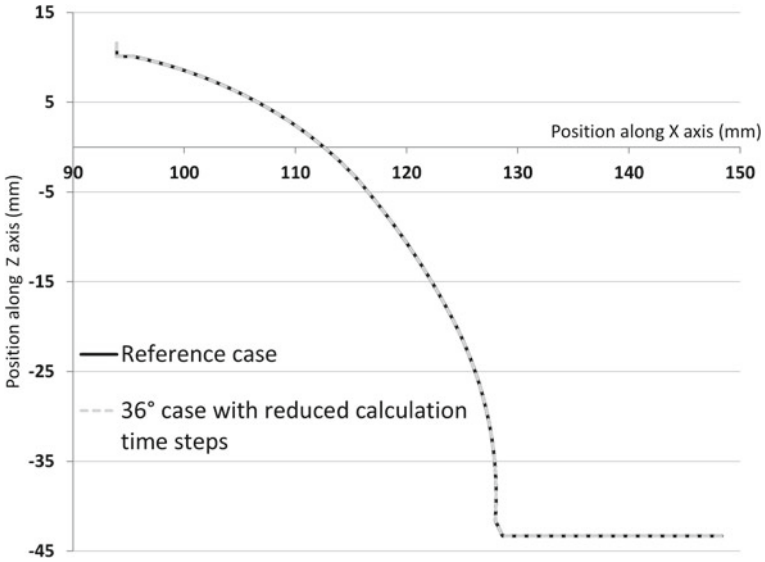


Fig. 6 Comparison of roller planar paths after the process modelling

4 Discussion

The aim of this section is to present the main results obtained after implementing the configuration optimization methods explained above. Therefore, a process modelling with a 36° reduced geometry is performed. The restriction area (area outside of which the roller will not be in contact with the sheet metal anymore) related to this reduced geometry is a little bit bigger than 36°. Therefore, it is 68° wide. This is due to the persistent contact between the blank and the roller that is not negligible. This case has been launched on 6 CPUs of a calculation computer[2] (which is different from the previous one), with a computation time of approximately 45 h.

4.1 Global Results

4.1.1 Geometrical Results

The geometrical results correspond to the wall thickness distribution after the flow forming process modelling.

Figure 7 shows the wall thickness distribution along the Z-axis (mandrel axis) in a 36° reduced geometry case (taken into the median plane) compared with the

[2]CPU: Intel(R) Xeon(R) CPU E5-2650 v3 @ 2.30 GHz.

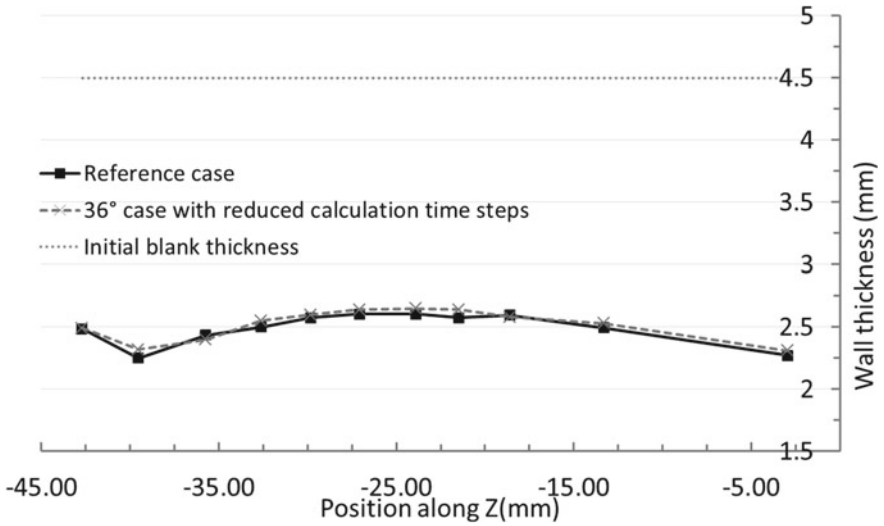


Fig. 7 Wall thickness distribution in a 36° reduced geometry compared to the reference case

reference case. The position along the Z-axis in this figure is the same as the one shown in Fig. 6.

As shown in this figure, the initial blank thickness is 4.5 mm. Therefore, even with a significant reduction ratio of approximately 45%, the use of the configuration optimization methods allows producing a wall thickness distribution very close to the one reached with the reference case (maximum error of 3%). Intermediate reduced geometries (45°, 60°, and 90°) show the same trend. Excessive thinning (necking) [3] is not expected for this configuration (4.5 mm thick disc having a 280 mm diameter).

4.1.2 Flow Forming Forces

The flow forming forces are the ones applied by the roller tool on the deformable sheet metal. These forces influence strongly the local behaviour of sheet metal, especially the stress states. Consequently, it will have a great impact on mechanical behaviour and also fracture predictions.

Figure 8 shows the norm of the flow forming force (global force in the three directions) for the 36° reduced geometry case with the calculation time steps reduction method compared to the reference case.

In this figure, it is clear that applying the two optimization methods does not influence the profile forces during the whole process. Thus, this feature could be helpful within an inverse analysis approach aiming to calibrate hardening or damage models using the experimental data.

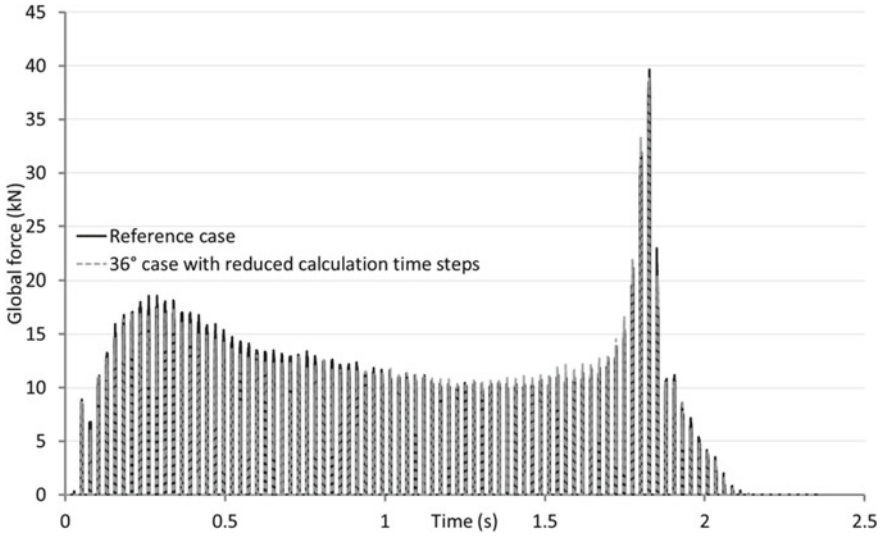


Fig. 8 Flow forming force profiles for a 36° reduced geometry compared to the reference case

4.2 Local Results

As mentioned in the first section, the local results concern information stored locally on different sensors. In this section, attention will be given to equivalent strain, Rice and Tracey damage variable [4], and temperature.

There are multiple ways of predicting ductile fracture in the ISF processes, using either coupled damage variables or uncoupled failure criteria. There is not a single damage model which is able to accurately predict the failure occurrence for all the ISF processes. As the stress triaxiality ratio is considered as one of the most important parameters with respect to ductile damage growth, it has been decided in the current work to estimate damage through the Rice and Tracey failure criteria. In addition to the stress triaxiality ratio, maximal principal stress or maximal shear stress are other important parameters regarding ductile damage. This will be addressed in a future study.

More information regarding the comparison of damage models in metal forming can be found in [3, 5].

The Rice and Tracey damage variable D, as implemented in FORGE®, is defined as

$$D = \int_0^{\bar{\varepsilon}} 0.283 e^{(1.5\eta)} d\bar{\varepsilon} \tag{2}$$

where $\bar{\varepsilon}$ is the equivalent strain and η is the stress triaxiality ratio. At any moment of the process, the value of this variable in a given element indicates the damage

occurring within this element. Thus, D reaches the critical value D_c when $\bar{\varepsilon}$ reaches $\bar{\varepsilon}_f$ (equivalent strain at fracture).

The evolution of these quantities will be studied on three sensors positioned, in the initial blank, at a radius of 105 mm and on three different positions through the thickness (Fig. 9). One sensor is located on the outer surface in contact with the roller (roller sensor). Another is located on the inner surface in contact with the mandrel (mandrel sensor). The last sensor is located at the mid-thickness (mid-sensor). These sensors are located initially in the median plane.

Figures 10 and 11 show, respectively, the final values of equivalent strain and Rice and Tracey damage variable stored on these three sensors.

It is clear from Fig. 10 that, for both cases, the highest strains are reached for the metal in contact with the roller. Strains reach, for every position through the thickness, high values (up to nearly 2). This feature is typical of ISF processes so that high final strains are reached due to progressive cumulative and localized plastic strains during the entire process [6]. These strains are far above those observed for simple tests like the tensile test. This is due to the specific stress states (negative stress triaxiality) observed in this process. Despite such strains, the progressive incremental deformation and the compressive stress state have a stabilizing effect permitting to avoid fracture [6], which is not observed experimentally during the flow forming of the current configuration (4.5 mm thick disc having a 280 mm diameter).

The higher strains are reached for the roller position. Despite that, Fig. 11 shows that the higher final value of the Rice and Tracey damage variable is the one achieved for the mandrel position. This is due to the stress state in the mandrel position, which is characterized by high positive triaxiality values when the roller passes by the sensor's position (bending visible in Fig. 9). At the same moment, the stress state near the roller position is compressive. This stress state is more stabilizing, leading to less damage, as presented in [7, 8].

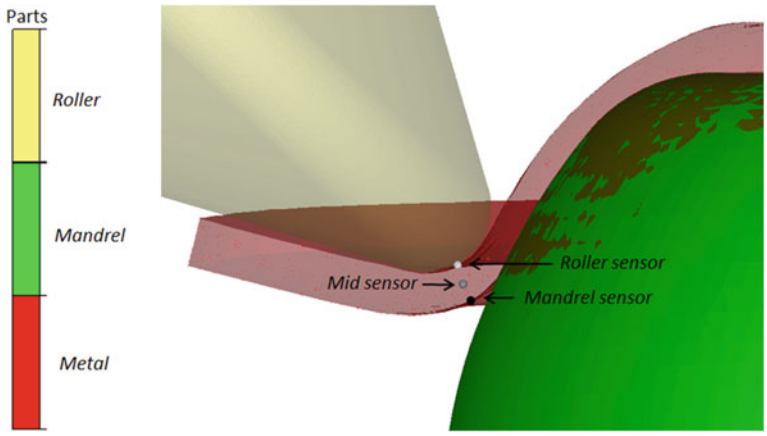


Fig. 9 Three sensors initially positioned at a radius of 105 mm. The roller is passing by the position of these sensors. (Color figure online)

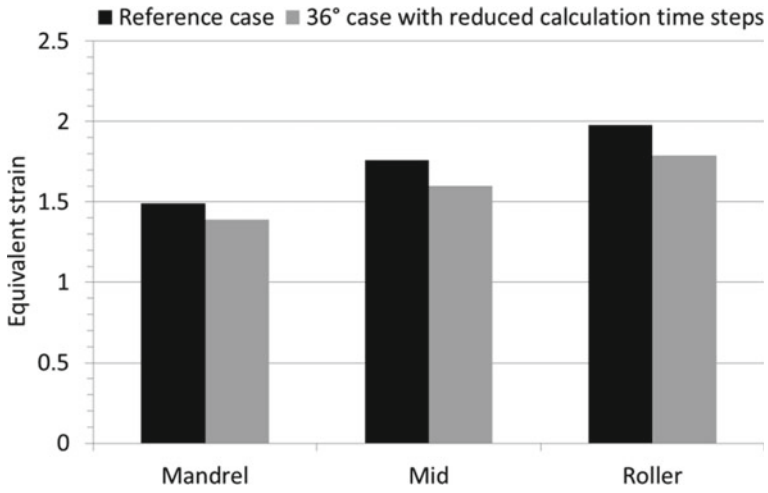


Fig. 10 Final equivalent strain values given on three sensors positioned at a radius of 105 mm

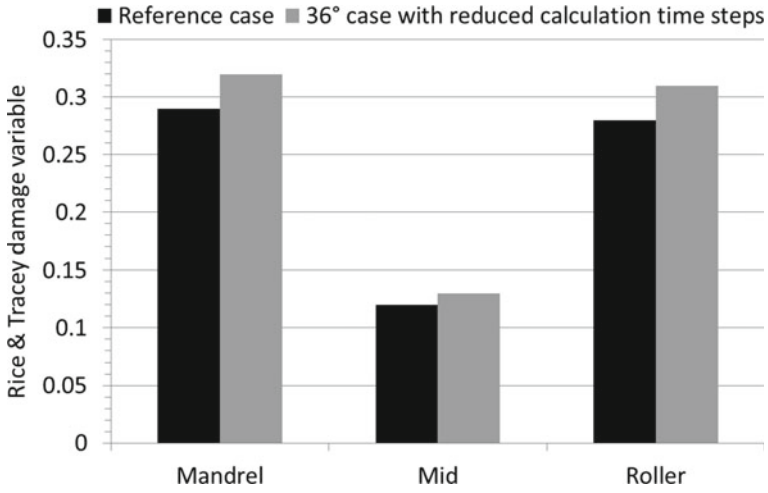


Fig. 11 Final Rice and Tracey damage variable values given on three sensors positioned at a radius of 105 mm

The mid position shows less damage than the other ones (Fig. 11). This is due to the values of stress triaxiality in this position, which are smaller than those in the other positions.

Compared to the reference case, the final equivalent strain in the case of the reduced geometry is underestimated whatever the position through the thickness (Fig. 10). Nevertheless, the difference between the two cases is <10% (9.6% for the "roller" position, 9.1% for the "Mid" position, and 6.7% for the "mandrel" position). The same observation could be done for the Rice and Tracey damage variable

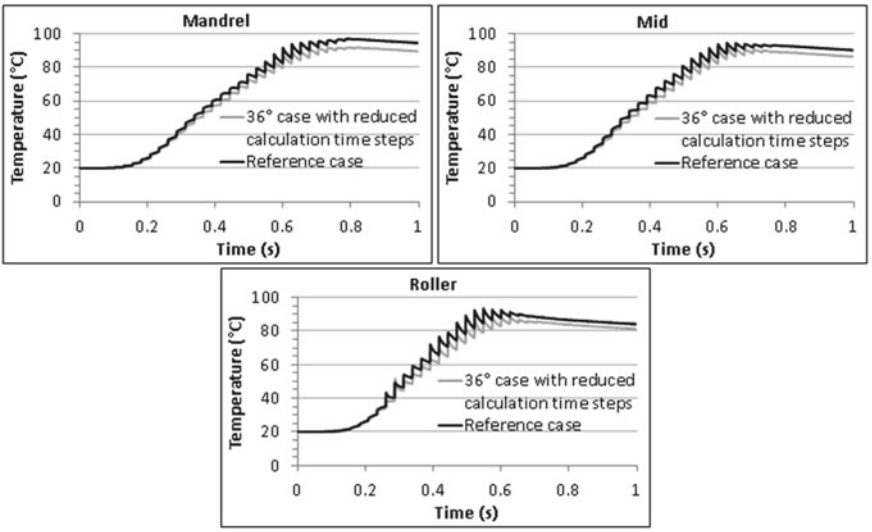


Fig. 12 Evolution of the temperature on three sensors initially positioned at a radius of 105 mm

(Fig. 11), which is this time overestimated compared to the reference case. This overestimation is due to an overestimation of the stress triaxiality in the case of the reduced geometry compared to the reference case. Nevertheless, the differences between the two configurations are 9.3% for the "roller" position, 7.7% for the "Mid" position, and 9.7% for the "mandrel" position. The same trends can be observed at other radii.

Figure 12 depicts the evolution of the temperature during the flow forming process on the sensors shown in Fig. 9.

The increase in the temperature is due to the plastic deformation caused by the cyclic action of the roller. The temperature decreases when the roller is far enough from the sensors, before increasing again, cyclically. With the evolution of the process, the roller becomes far enough from the sensors and the plastic deformation ends, leading to a progressive decrease of the temperature (this happens between 0.6 and 0.78 s depending on the considered sensor). The decrease of temperature is faster for the roller sensor compared to the two others, thanks to the heat exchange with air. Adiabatic heat transfer condition is imposed between the workpiece and the tools.

As for the equivalent strain, the temperature is underestimated for the reduced case compared to the reference case, for all of these sensors. However, the maximum difference in temperature between the two cases is less than 5%. This means that thermal properties are mostly conserved with the reduced geometry.

These results show that applying the two configuration optimization methods allows having good and representative results of the reference case (<10% error) with a huge gain in CPU time.

5 Conclusion

Process modelling has great importance in the comprehension of specific problems occurring during the ISF processes, such as premature fracture. Nevertheless, the modelling of a complete configuration (reference case) is a time-consuming task and choices have been made in order to reduce this process computation time.

In the current work, configuration optimization and time step adaptation were studied with respect to CPU time reduction and accuracy of the results. A first method, which uses reduced geometries with symmetry planes, allows reaching a minimally reduced geometry of 36° while maintaining the accuracy of the results into the median plane. Further geometry reduction causes non-convergence issues. A second approach consists of removing unnecessary calculation time steps (i.e. time steps during which mechanical and thermal calculations are done despite the roller is not in contact with the metal sheet). With the combination of the two approaches, the roller path is preserved.

Applying both approaches together enables to mostly conserve major global and local results, with a calculation time considerably reduced. This interesting outcome could make the prediction of final parts geometry or failure initiation faster. Furthermore, it could be helpful in order to determine quickly the influence of different process parameters (lubrication, rotation speed, etc.) on the final global and local results.

References

1. Music O, Allwood JM, Kawai K (2010) A review of the mechanics of metal spinning. J Mater Process Technol 210:3–23. https://doi.org/10.1016/j.jmatprotec.2009.08.021
2. Yin Q, Soyarslan C, Isik K, Tekkaya AE (2015) A grooved in-plane torsion test for the investigation of shear fracture in sheet materials. Int J Solids Struct 66:121–132. https://doi.org/10.1016/j.ijsolstr.2015.03.032
3. Ai S, Long H (2019) A review on material fracture mechanism in incremental sheet forming. Int J Adv Manuf Technol 104:33–61. https://doi.org/10.1007/s00170-019-03682-6
4. Rice JR, Tracey DM (1969) On the ductile enlargement of voids in triaxial stress fields. J Mech Phys Solids 17:201–217. https://doi.org/10.1016/0022-5096(69)90033-7
5. Cao TS, Bobadilla C, Montmitonnet P, Bouchard P-O (2015) A comparative study of three ductile damage approaches for fracture prediction in cold forming processes. J Mater Process Technol 216:385–404. https://doi.org/10.1016/j.jmatprotec.2014.10.009
6. Malhotra R, Xue L, Belytschko T, Cao J (2012) Mechanics of fracture in single point incremental forming. J Mater Process Technol 212:1573–1590. https://doi.org/10.1016/j.jmatprotec.2012.02.021
7. Bao Y, Wierzbicki T (2005) On the cut-off value of negative triaxiality for fracture. Eng Fract Mech 72:1049–1069. https://doi.org/10.1016/j.engfracmech.2004.07.011
8. Wu PD, Chen XX, Lloyd DJ, Embury JD (2010) Effects of superimposed hydrostatic pressure on fracture in sheet metals under tension. Int J Mech Sci 52:236–244. https://doi.org/10.1016/j.ijmecsci.2009.09.014

On the Geometrical Accuracy in Incremental Sheet Forming



Gerhard Hirt, Roman Kordtomeikel, Thomas Bremen, Marvin Laugwitz, and David Bailly

Abstract The industrial application of incremental sheet forming (ISF) still stays behind the expectations due to the low geometrical accuracy of the produced parts as well as the insufficient predictability of the forming result. This is due to the fact that some mechanisms which cause the geometrical deviations are not fully understood. Many investigations have already been carried out to determine which types of stresses induced by ISF influence the forming result. This paper tries to systematically categorize selected typical geometric deviations and to review their underlying mechanisms based on current literature as well as their own experience. The intention is to provide a structured basis for future scientific discussion and to stimulate an exchange of experience, with the goal that a better understanding may help to improve the geometrical accuracy of parts manufactured by incremental sheet forming.

Keywords Incremental sheet forming · Geometrical accuracy · Process understanding

1 Introduction

Incremental sheet forming (ISF) has been a focus of worldwide research efforts since the turn of the millennium. The aim is to develop a sheet metal forming process that can manufacture complex sheet metal parts economically, even as individual parts or in small quantities, with a minimum of component-specific tooling. Since then, several process variants have been developed, with which a large number of prototype parts, some of which are very demanding, have been produced to prove their feasibility. However, their use in industrial applications falls short of expectations,

G. Hirt · R. Kordtomeikel (✉) · T. Bremen · M. Laugwitz · D. Bailly
Institute of Metal Forming, RWTH Aachen University, Intzestr. 10, 52072 Aachen, Germany
e-mail: roman.schmitz@ibf.rwth-aachen.de

G. Hirt
e-mail: hirt@ibf.rwth-aachen.de

© The Minerals, Metals & Materials Society 2021

G. Daehn et al. (eds.), *Forming the Future*, The Minerals, Metals & Materials Series,
https://doi.org/10.1007/978-3-030-75381-8_42

although economic calculations can prove profitability advantages over other prototype processes despite longer required process time. According to the authors, there are two main reasons for this:

1. The part geometries were designed for other processes and cannot be processed by ISF.
2. The required geometrical accuracy is not achieved, or at least not without time-consuming series of tests.

This paper focuses on the second topic. Geometrical inaccuracies also occur in any other sheet metal forming processes. However, based on many years of experience and using modern simulation methods, some of these can be predicted and compensated by suitable countermeasures. Such countermeasures usually require more or less complex and cost-intensive modifications of the forming tools. In the case of incremental sheet forming, compensation could largely be achieved by programming a different tool path alone, or at least the modification of tooling is less cost-intensive. However, this advantage cannot be used as long as the interaction between the tool path and the geometric deviations are not fully understood. In the end, two questions arise in each specific case:

1. Does a tool path exist that can achieve the desired target geometry from a flat sheet by incremental sheet forming keeping the required accuracy?
2. If so, how can this path be identified from the infinite number of possible tool paths?

A partial aspect of the first question, namely whether the part can be manufactured without material failure, can today be answered quite reliably with known criteria, like fracture forming limit line (FFL) and the "sine law" [1–3], or other approximate formulas relating sheet thinning to the part geometry. It is more difficult to answer the question which accuracy level can be achieved? The aim of this paper is therefore to collect, propose and describe physical mechanisms leading to selected typical geometrical deviations observed in the authors' experience or described in the literature. The intention is to provide a structured basis for future scientific discussion, with the goal that a better understanding may help to improve the geometrical accuracy of parts manufactured by incremental sheet forming. This article is therefore structured as follows: In Sect. 2, the geometric requirements for sheet metal parts are briefly described, as they represent the target definition to be fulfilled by the process. Section 3 explains the focus of the paper regarding process variants and defect types. Section 4 describes the fundamentals of the mechanics of incremental sheet forming to the extent necessary for understanding the following section. The fifth section postulates physical mechanisms for the formation of geometrical defects.

2 Geometrical Tolerances for Sheet Metal Parts

As in other areas of manufacturing technology, the geometrical tolerances that must be adhered to for sheet metal parts depend on the part size and the area of application. For example, in the automated mass production of automotive bodies with narrow gaps, much tighter tolerances must be maintained in comparison to those required for facade construction or large aerospace components. Whenever only small quantities are produced for large parts, detailed adjustments can be made individually, sometimes manually, during assembly. From the authors' experience, tolerances in the range of ±0.5 mm can be reported for OEMs in the automotive sector even for prototype production for doors, hoods or fenders. Allwood et al. [4] have surveyed the geometrical tolerances for various products by means of a questionnaire with various sheet metal component manufacturers in the UK, and here it comes to a tolerance range of ±0.15 to ±1.0 mm for the automotive sector, ±5.0 mm for shipbuilding and ±0.13 to ±5.0 mm for the aerospace sector, depending on component size and complexity. If the literature on incremental sheet forming provides information on the achieved geometrical accuracy, in many cases the above limits are not reached [5, 6]. And even when using algorithms to compensate observed or expected deviations by modifying the tool path, the tolerances often cannot be met. Thus, it is necessary to pay more attention to the topic of geometrical accuracy in ISF.

3 Focus and Objectives

Focusing with regard to the considered process variants: There are different process variants of incremental sheet forming, which are described in [7]. There are also various hybrid process variants, such as the combination of stretch forming with subsequent incremental sheet forming [8] or the superposition of a hydrostatic pressure [9, 10]. Even though it has been shown that stretch forming can improve geometrical accuracy in many cases [11–13], the subsequent incremental forming process still follows the mechanisms of the general ISF process and influences the final geometry. Thus, stretch forming is not discussed in this paper. Also, methods with two moving tools are excluded, since this significantly increases the variety of possible causes for geometrical deviations and the number of variables [14]. Nevertheless, it can be assumed that at least some of the mechanisms and defect types discussed in Sects. 4 and 5 are also valid for this process. The focus of the paper is on the process variants a) single-point incremental forming (SPIF) and b) two-point incremental forming (TPIF) shown in Fig. 1. For variant b) it has to be distinguished whether it is a full or partial die.

Focusing with regard to the considered causes for geometrical deviations: A considerable part of the literature from the field of incremental sheet forming deals with the question of how precisely the forming tool follows the given tool path. Especially when using industrial robots with limited structural stiffness, elastic deflection

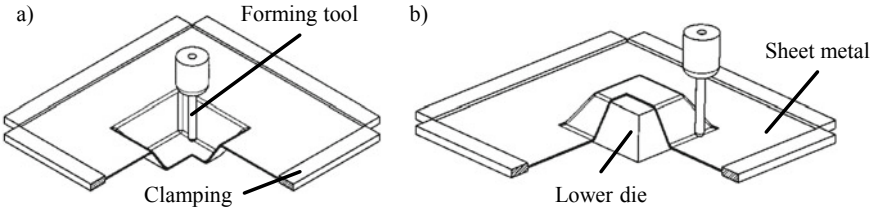


Fig. 1 Variations of the incremental sheet forming based on [15]. **a** SPIF. **b** TPIF with a full die

has to be expected due to the forming forces. The causes of this problem are at least theoretically describable and can be corrected with suitable algorithms [16–18]. In addition, when sufficiently rigid machine tools are used, the resulting geometrical tool displacements are generally significantly smaller than the geometrical inaccuracies of the product generated by the forming process [19]. Accordingly, the effects of insufficient machine accuracy are not considered in this paper; instead, it is assumed that the machine follows the given tool path exactly. Also, the geometrical deviations resulting from unsuitable tool geometry are not taken into account. This would be the case, for example, if a narrow radius in the part cannot be formed simply because the radius of the forming tool is larger. Excessive thinning, necking, and finally failure of the sheet during forming can also be seen as geometrical defects. However, there are numerous Refs. [20–22] related to the forming limits, and the existing models allow a relatively reliable prediction for many materials. Therefore, this topic is explicitly not considered further in this article. Nevertheless, it must be kept in mind that applying compensation methods to increase accuracy, such as over bending, might also increase the risk of material failure.

In this paper, the authors focus on those defects that occur despite a perfectly maintained toolpath in geometries that generally can be realized by incremental sheet forming with sufficient remaining wall thickness. The defects also include those that appear or intensify after unclamping and trimming. The aim is to derive the causes of these defects as far as possible from mechanisms that can be explained by continuum mechanics and material physics. Therefore, the next chapter provides a brief description of metal flow in ISF.

4 Deformation Modes in Incremental Sheet Forming

Various articles have discussed the "mechanics" of incremental sheet forming, mainly with the target to identify forming limits. Both, analytical considerations as well as sophisticated FE models have been used. With respect to the origins of geometrical deviations, the following considerations are to be considered.

Geometric deviations may be a consequence of generally non-adequate metal flow or a result of residual stresses, which are induced during the forming operation, or most likely both. For the following, we assume a local coordinate system in the

forming zone with the axis oriented (i) normal to the sheet surface, (ii) in the sheet plane in tool movement direction, and (iii) in the sheet plane perpendicular to the tool movement. Then generally the following deformation modes may occur: strain (compression or stretching) in all axis directions as well as shear in the direction of the tool path or perpendicular to the tool movement. The latter is usually referred to as "through thickness shear". Also bending modes occur, which basically means that "in-plane strains" vary across the thickness of the sheet.

According to Maqbool and Bambach [23] the deformation modes "membrane stretching", "bending" and "through-thickness shear" are dominant under the geometrical conditions of their numerical study. Also, Malhotra et al. [24] already postulated these three different deformation modes with the aid of FE models. Experimental investigations by Jackson and Allwood [25] also showed that stretching and shear perpendicular to the path direction and shear in the path direction are major deformation mechanisms in SPIF and TPIF. Shear in the path direction is a consequence of the friction between tool and sheet metal and is an essential strain component under the chosen experimental conditions.

As residual stresses in the material may cause elastic deformation during and after the process, it is important to understand how they develop during the process. Residual stresses are always caused when plastic deformation is spatially inhomogeneous. The most prominent example is bending, where in-plane strains vary across the thickness. Accordingly, various authors, among others Tanaka et al. [26], Maqbool and Bambach [23], study how the deformation modes can be influenced by the process parameters and especially how the bending mode can be reduced. According to Maqbool and Bambach [23], the deformation mechanism in SPIF is always a combination of the three modes mentioned in the previous paragraph. Within a numerical simulation study, shell elements (with through-thickness strain) are used to show that the relative proportion of the modes is dependent on different process parameters. According to the results, an increase in the wall angle results in an increased percentage of the "bending" mode, a decrease leads to a larger percentage of the "shear" mode. Increasing the tool radius and vertical pitch increases the global deformation and increases the portion of the bending mode accordingly. An increase in sheet thickness, friction, and a reduction in tool diameter stabilize the forming by increasing the percentage of (through-thickness) shear mode. This is in good accordance with the experimental results from Eyckens et al. [27] using digital image correlation.

These deformation modes are also helpful in discussing the origins of geometric deviations not only considering conventional springback.

5 Mechanisms of the Formation of Geometrical Defects in Incremental Sheet Forming

In the context of the geometrical accuracy of sheet metal parts, the term springback is often used. This term easily evokes the association that the geometrical defects are only caused by elastic springback, which can be well described, for example, in bending. In this case, the elastic deformation after unloading is directed against the direction of loading. In incremental sheet forming residual stresses are induced by a wide variety of reasons, leading to elastic deformation after unclamping of the sheet or trimming. The direction of these deformations is not always in the opposite direction to the intended forming. In this article, the term springback is therefore used more narrowly and refers exclusively to the fact that the elastic part of the previous deformation is completely or partially reversed when the load is removed. The paper tries to differentiate other effects than this from the general term "springback". Other effects might be for example a plastic material flow, which deviates from the theoretical assumption of pure material projection. Also, the release of elastic residual stresses of other causes, e.g. due to deformation-induced phase transformations, is not referred to as "springback" here.

Beyond the mechanisms already excluded in Sect. 3 the following sections describe five different mechanisms, which lead to typical geometrical inaccuracies. This selection makes no claim to completeness but tries to provide a substantial basis and structure, to which further mechanisms may be added.

In some cases, a simple FE model is used for illustration. It is based on the explicit solver of LS-DYNA R901 from Livermore Software Technology Corporation using four fully integrated type 2 solid elements discretized over the sheet thickness of 1 mm. The elastic-plastic material model, 24-piecewise linear plasticity, is used as material model for the sheet metal, taking into account a stored flow curve for 1.0338. The tools are assumed to be rigid and the tool path is based on time and coordinates. The ball-headed forming tool has a diameter of 20 mm. The sheet is fixed on its outer element edges and all degrees of freedom are restrained here.

5.1 Plastic Deformation Outside the Contact Zone

During an ISF process the location of the applied force (tool position) moves along the workpiece. Since the occurring forces must be large enough to form the local area, they can cause significant reaction forces or bending moments elsewhere in the part. These can lead to undesired plastic deformation at locations, which were not intended to be formed. A well-known example is the so-called draw-in, which can be seen in Fig. 2. If no contour-near support plate is used on the backside of the sheet, forming also takes place outside the contact zone of the tool. The FE model confirms plastic strain in this region, see Fig. 2a) and b). This effect, however, may occur also in any other location of a more complicated component, for example at

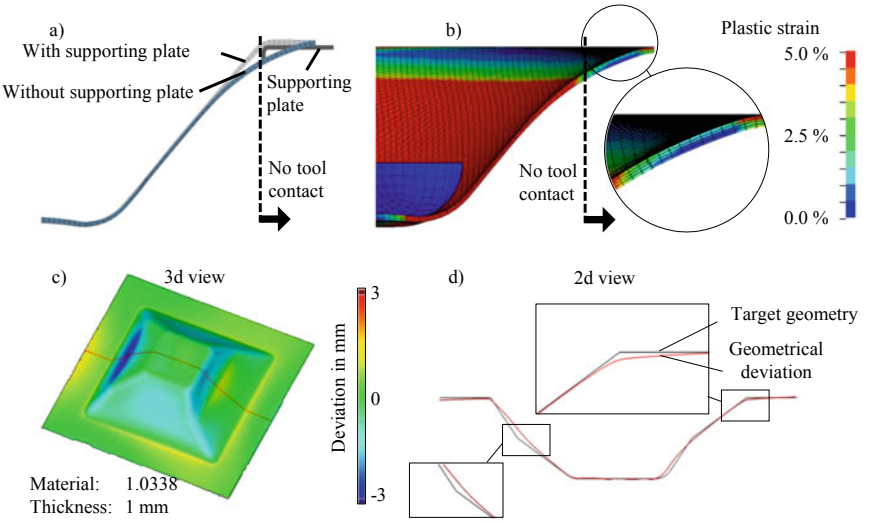


Fig. 2 **a** Comparison of FE results with and without supporting plate; **b** Strain plot (FE model) during forming shows plastic strain even in the area without tool contact; **c** Deviation plot for an experimental formed pyramid; **d** Section through the formed pyramid. (Color figure online)

previously formed locations as demonstrated by a section (Fig. 2d) cut through a formed pyramid (Fig. 2c).

5.2 Elastic Part Deflection During the Process

The entire part undergoes a continuous elastic deflection during the process as a result of the moving point of deformation force, which means that the material partially "escapes" the intended forming. Due to the often cyclic tool paths, this can also be described as tumbling. Such elastic deflection may result in the following:

- Transversely to the tool path, locally only a part of the initially intended feed per tool revolution is realized in plastic deformation.
- In the circumferential direction, this may result in the fact that the required circumferential extension is not fully achieved.

The tumbling is demonstrated by means of the forming of a hole flange. Figure 3 shows the simulation as well as experimental results of a hole-flanging process using ISF. During forming, the forming head employs a circular downward movement to realize the hole flange. The aim is a hole flange with an angle of 90° ($\alpha = \beta = 90°$). During the process it can be observed that the flange opposite to the side of the tool has a smaller angle than the side with tool contact, see Fig. 3a). This tumbling

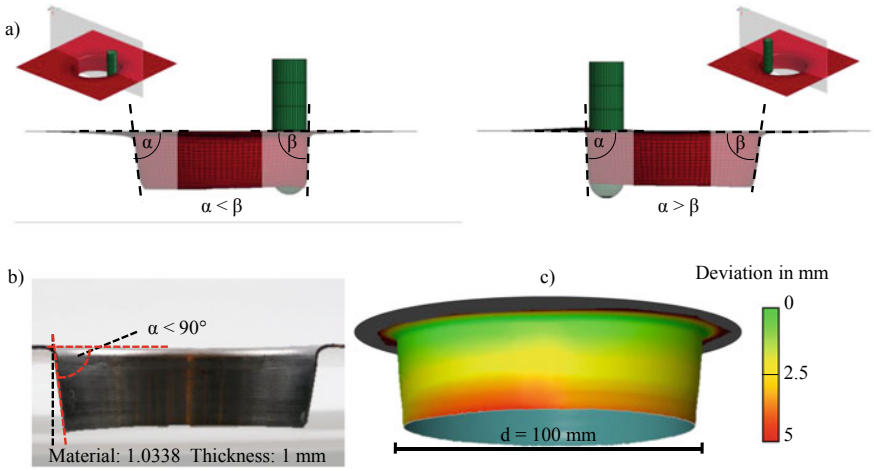


Fig. 3 **a** Illustration of the tumbling hole flange during forming (FEM simulation); **b** Trimmed conical hole flange after forming; **c** Deviation plot for the formed hole flange [28]. (Color figure online)

is noticeable throughout the entire process and ultimately results in a conical hole flange, which is well confirmed by the experimental result, see Fig. 3b) and c).

Methods to minimize this deviation are, on the one hand, a reduction of the deflection movement by additional support via dies or multiple tools [29] or, on the other hand, compensation of the previously calculated deflection movement by a modified tool path, as suggested by Cao [19].

5.3 Release of the Regular Elastic Part of the Local Deformation

"In-plane"-springback of the stretching deformations as well as springback related to homogeneous through thickness shear is usually small compared to the global deformation. Problematic, however, are changes in angle or curvature. These mainly result from a variation of residual stresses across the sheet thickness caused by a variation of strain across the sheet thickness, which was called "bending mode" in Sect. 4. With respect to the chronological occurrence of springback, it makes sense to distinguish between three cases:

1. During the process: A locally limited elastic springback occurs continuously in the follow-up of the tool tip (Fig. 4) [30, 31]. The remaining bulge c) may, however, also be caused by other reasons explained in Sect. 5.5.1.
2. After unloading and unclamping (Fig. 5): The entire component elastically springs back until it is in global mechanical equilibrium. This happens at the

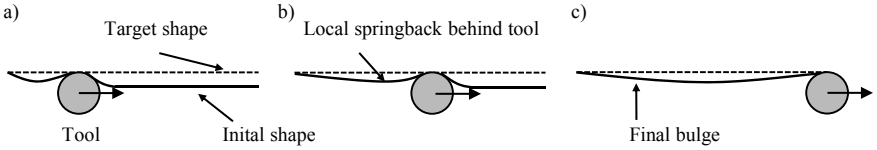


Fig. 4 Elastic springback behind the forming tool in the process according to Bambach [30]. **a** Sheet is pushed into the target position, **b** local springback behind the tool, **c** the local springback contributes to global deviations



Fig. 5 Elastic springback after ISF process for unloading, unclamping and cutting/trimming [30]

end of the process as soon as the contact between the forming tool or clamping system and the sheet metal is removed [30, 32, 33] or during the process, whenever the tool is lifted as part of the programmed tool path.

3. After trimming (Fig. 5): By trimming the component to its final contour, the (residual) stress state is changed and the part springs back elastically until it has found a new mechanical equilibrium [31–33].

However, the bending mechanism already mentioned in Sect. 4 is not the only mechanism resulting in a strain variation across the thickness. Depending on the selected feed rate, component geometry, and sheet thickness, it is also possible that such strain gradients occur like in shot peening. This can lead to residual compressive stresses in the previous contact surface. During unclamping or trimming, such residual stresses may cause changes in the curvature, which in extreme cases can result in curling of the surface. One example of curling is presented in Fig. 6. Here, curling is a result of the tool path pattern and the forming tool intruding the sheet by $i = 0.1$ mm. Intruding the sheet with the forming tool may happen during forming, for example in TPIF when thinning is considered incorrectly in the tool path design. Experiments with varying intrusion depths and tool path directions have shown that the forming result differs significantly, even for changes of the intrusion depth by a tenth of a millimeter [34]. In the presented case, a flat specimen with dimensions of 260 mm $\times$ 40 mm $\times$ 1 mm is clamped at the two short opposing sides and is formed according to a tool path pattern presented in Fig. 6b). The tool path follows the blue lines alternating parallel to the longest sheet side with a pitch of 1 mm parallel to the shorter sheet sides. The black arrows are meant to clarify the tool path strategy.

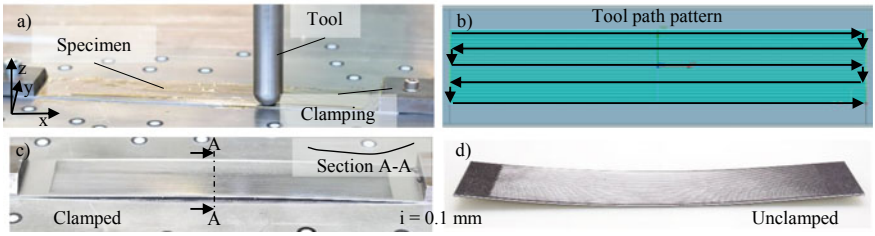


Fig. 6 **a** Experimental setup; **b** Tool path pattern for forming a flat surface; **c** Clamped sheet with surface section through part; **d** Unclamped sheet [34]. (Color figure online)

Although a flat surface is formed, it can be already seen in the clamped state that the result deviates from a flat sheet. The long edges of the sheet are clearly curved upwards, see surface section A-A in Fig. 6c). After unclamping the sheet is curling in a way that the short sides tend to upwards, as presented in Fig. 6d).

5.4 Geometry Changes Due to Transformation-Induced Residual Stresses

Further causes of residual stresses may lie in microstructural changes in the material. If materials locally change their microstructure as a result of forming (e.g. deformation-induced martensite transformation), the resulting change in the specific volume leads to considerable residual stresses, which was demonstrated by Hedström et al. on the basis of tensile tests [35]. Katajarinne and Kivivuori [36] verified the presence of a significant fraction of strain-induced martensite in ISF for different stainless steels, depending on the forming speed and steel grade. Such residual stresses may cause excessive deflections, far beyond those of usual springback, which is shown in Fig. 7 by Bambach [30] after laser cutting an incrementally formed stainless steel component.

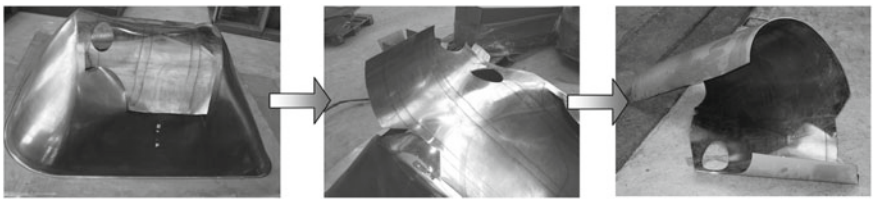


Fig. 7 Excessive elastic deflections during (left and middle) and after (right) laser cutting due to deformation-induced martensite [30]

5.5 *Geometry Inaccuracies Induced by the Local Material Flow*

Tool path planning typically follows strategies that are known from CNC-machining. However, other than in CNC-machining material is not removed but displaced. The algorithms might nevertheless work, as long as the only deformation mode would be perfectly homogeneous through-thickness shear. However, in Sect. 4, it was pointed out that among others also in-plane stretching, both, parallel or transversal to the tool path, frequently occurs. This may cause geometry deviations at least as follows.

5.5.1 Disproportional Enlargement of the Surface

An enlargement of the surface that exceeds the amount required by the geometric projection leads to compressive stresses in the sheet if this enlargement is restricted by stiffened elements (i.e. corners) of the component. If these compressive stresses are larger than the buckling stress, bulges occur, which can be directed inwards or outwards. The excessive enlargement of the surface can be a result of strains in one or two directions:

(a) If the sheet is stretched in the direction of the tool path, this necessarily results in longer "fibers" in the path direction than assumed by the pure material projection, see Fig. 4c).
(b) If the overall strain in the feed direction, i.e. transverse to the path direction, is greater than required an excessive "fiber length" in the feed direction occurs.

Even though no general quantitative relation is known describing the evolution of these excessive stretches, it can be assumed that the relevant influencing factors are the process parameters feed rate, tool radius, sheet thickness, and wall angle, as well as the component geometry and the friction between tool and sheet. Bulges that form in this way cannot be avoided simply by overcompensating the tool path, as is attempted in various publications [15, 30, 37]. Hirt et al. [15] and Junk [37] proposed a compensation, where the measured deviation of the actual geometry is mirrored to the target geometry, see Fig. 8a). Depending on the chosen "scaling factor c" a significant reduction of geometrical deviations could be realized, see Fig. 8b). However, as the compensated tool path is longer than the original one, the length of the fiber along the considered pyramid wall is not shortened but further stretched. Thus the larger bulge is replaced by smaller waves. Rather, a "shorter" tool path should have been defined for compensation, which is impossible for flat surfaces as there is no shorter path than the original straight line.

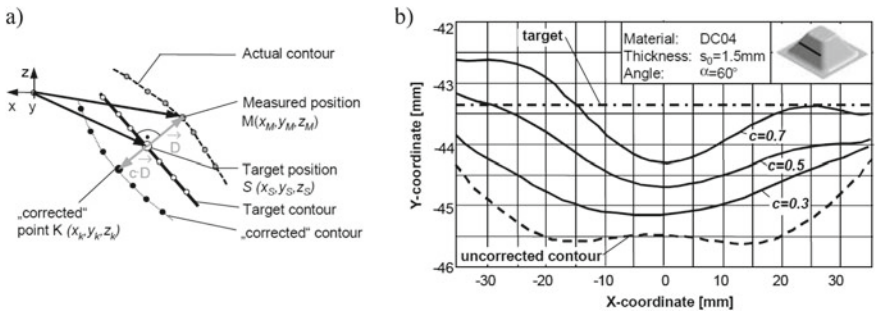


Fig. 8 **a** The correction algorithm proposed by Hirt et al. [15] and Junk [37]; **b** The resulting reduction of total deviation and the formation of waves [37]

5.5.2 Forwarding a Bulge in Front of the Tool

If a bulge is formed as a result of the mechanisms under Sect. 5.5.1, it can be pushed in front of the tool during the process. This effect is possible both in the path direction and in the feed direction. A defect often discussed in the literature [38–40] and occasionally referred to as the "pillow effect" is shown in Fig. 9a). One possible reason for this effect can be the pushing of a bulge in the feed direction. At least it is obvious that in such cases there is more material at the bottom surface of the part than theoretically foreseen by the assumption of pure material projection. Another possible reason is the geometrical stiffness of a component, which might hinder the bottom surface from simply following the circumferential forming.

Excessive pushing of material in front of the tool can lead to the formation of wrinkles and overlaps, among other things, see Fig. 9b). In general, geometrical stiffening features such as corners foster buckling, because the excessive surface cannot spread due to these constraints.

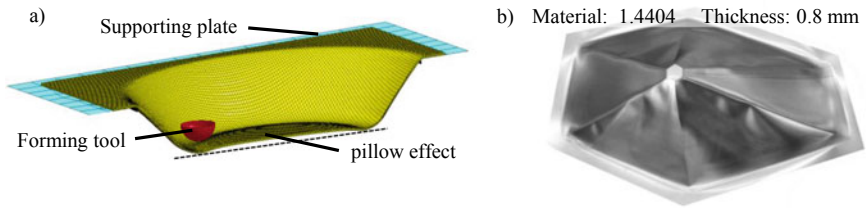


Fig. 9 **a** FE-model showing the pillow effect; **b** ISF formed pyramid made of 1.4404 showing wrinkles and overlaps [41]. (Color figure online)

6 Summary and Conclusions

Even if the forming machine perfectly follows the specified tool path, geometrical deviations may occur during incremental sheet forming. A significant part of these geometrical defects can be divided into typical categories and explained by the mechanisms summarized below:

1. The forming zone is not always limited to the local contact area (Sect. 5.1).
2. The sheet partially escapes the plastic deformation intended by the tool path, because the emerging component is elastically deflected by the moving local forming force (Sect. 5.2).
3. The release of residual stresses after unclamping and trimming leads to elastic deformations.
    a. On the one hand, these residual stresses can be a result of inhomogeneous deformation, i.e. due to the bending fraction over the sheet thickness (Sect. 5.3).
    b. Other residual stresses, such as deformation-induced microstructure transformations, can cause considerable elastic deformation in different directions during trimming (Sect. 5.4)
    c. Both types of elastic recovery (a, b) are not necessarily directed against the forming direction.
4. If the local in-plane stretches lead to an excessive increase in surface area, buckling and bulges can occur, especially in combination with geometrical constraints (Sect. 5.5).

Even if the mechanisms mentioned can at least explain the origin of the described types of defects qualitatively to some extent, a reliable quantitative description of the correlations is still lacking. With regard to efficient identification of suitable tool paths, it is also not sufficient that the numerical process simulation can correctly map these defects already in various cases. The computing times that are still far too long for complicated components do not allow a large number of process variants to be tested in simulation, especially if even the tool path should be optimized. Therefore, it will be important for future economic application of ISF to be able to decide quickly whether and with which tool path strategy a given part can be produced appropriately and precisely. Therefore, powerful process planning methods are mandatory that allow for a fast and precise accuracy prediction and must be based on a profound process understanding. For this purpose, the collection of mechanisms described above must be further sharpened and extended. It could also be helpful to create a wider experience base, e.g. a public collection of well-documented tool paths and the part geometries generated by these.

References

1. Jeswiet J (2005) Asymmetric incremental sheet forming. Adv Mater Res 6–8:35–58
2. Isik K, Silva MB, Tekkaya AE, Martins PAF (2014) Formability limits by fracture in sheet metal forming. J Mater Process Technol 214(8):1557–1565
3. Silva MB, Skjoedt M, Bay N, Martins PAF (2009) Revisiting single-point incremental forming and formability/failure diagrams by means of finite elements and experimentation. J Strain Anal Eng Des 44(4):221–234
4. Allwood JM, King GPF, Duflou J (2005) A structured search for applications of the incremental sheet-forming process by product segmentation. Proc Inst Mech Eng Part B-J Eng Manuf 219(2):239–244
5. Gupta P, Szekeres A, Jeswiet J (2019) Design and development of an aerospace component with single-point incremental forming. Int J Adv Manuf Technol 103(9–12):3683–3702
6. Meyer W, Bons J, Schmitz RUC (2019) Use of incremental sheet metal forming to enable an agile development process in automotive engineering. In: ASK Umformtechnik "Ideen Form geben", Aachen, Germany, 33, pp 389–398, 28–29 March 2019
7. Bambach M, Hirt G, Junk S (2003) Modelling and experimental evaluation of the incremental CNC sheet metal forming process. In: VII international conference on computational plasticity, COMPLAS2003
8. Taleb Araghi B, Bambach M, Hirt G, Zettler J (2011) Investigation into the process mechanics of the hybrid process combination of stretch forming and incremental sheet forming. In: Steel research international, Special Edition: 10th ICTP (2011), S. 519–24
9. Kumar Y, Kumar S (2019) Experimental and analytical evaluation of incremental sheet hydro-forming strategies to produce high forming angle sheets. Heliyon 5:6
10. Ben Khalifa N, Thiery S (2019) Incremental sheet forming with active medium. CIRP Ann 68(1):313–316
11. Taleb Araghi B, Göttmann A, Bambach M, Hirt G, Bergweiler G, Diettrich J, Steiners M, Saeed-Akbari A, Taleb Araghi B, Göttmann A, Bambach M, Hirt G. Review on the development of a hybrid incremental sheet forming system for small sizes and individualized production. Review on the development of a hybrid incremental sheet forming system for small batch sizes and individualized production
12. Galdos L, Chinesta F, Sukia A, Chastel Y, Otegi N, El Mansori M, Ortubay R, Ruiz de la Torre A, Forgas A, Rastellini F (2011) Enhancement of incremental sheet metal forming technology by means of stretch forming. In: 13th international conference on advances in materials and processing technology 2011
13. Taleb-Araghi B, Göttmann A, Bergweiler G, Saeed-Akbari A, Bültmann J, Zettler J, Bambach M, Hirt G (2011) Investigation on incremental sheet forming combined with laser heating and stretch forming for the production of lightweight structures. Key Eng Mater 473:919–928
14. Kwiatkowski L, Urban M, Sebastiani G, Tekkaya AE (2010) Tooling concepts to speed up incremental sheet forming. Product Eng Res Dev 4(1):57–64
15. Hirt G, Ames J, Bambach M, Kopp R, Hirt G (2004) Forming strategies and process modelling for CNC incremental sheet forming. CIRP Ann—Manuf Technol 53(1):203–206
16. Meier H, Laurischkat R, Zhu J (2011) A model based approach to increase the part accuracy in robot based incremental sheet metal forming. In: 13th international conference on advances in materials and processing technology 2011
17. Meier H, Buff BO, Laurischkat R, Smukala V (2009) Increasing the part accuracy in dieless robot-based incremental sheet metal forming. CIRP Ann—Manuf Technol 58(1):233–238
18. Meier H, Laurischkat R, Bertsch C, Reese S. Prediction of path deviation in robot based incremental sheet metal forming by means of an integrated finite element. multi body system model
19. Ren H, Xie J, Liao S, Leem D, Ehmann K, Cao J (2019) In-situ springback compensation in incremental sheet forming. CIRP Ann 68(1):317–320
20. Ambrogio G, Filice L, Gagliardi F, Micari F (2005) Sheet thinning prediction in single point incremental forming. Adv Mater Res 6–8:479–486

21. Bambach M (2010) A geometrical model of the kinematics of incremental sheet forming for the prediction of membrane strains and sheet thickness. J Mater Process Technol 210(12):1562–1573
22. Buffa G, Ingarao G, Fratini L, Micari F (2011) Shape distortion and thickness distribution during SPIF processes: expermental and numerical analysis. Key Eng Mater 473:913–918
23. Maqbool F, Bambach M (2018) Dominant deformation mechanisms in single point incremental forming (SPIF) and their effect on geometrical accuracy. Int J Mech Sci 136:279–292
24. Malhotra R, Xue L, Belytschko T, Cao J (2012) Mechanics of fracture in single point incremental forming. J Mater Process Technol 212(7):1573–1590
25. Jackson K, Allwood J (2009) The mechanics of incremental sheet forming. J Mater Process Technol 209(3):1158–1174
26. Tanaka S, Nakamura T, Hayakawa K, Nakamura H, Motomura K (2007) Residual stress in sheet metal parts made by incremental forming process. In: Proceedings numiform 07, Portugal, 17–21 June 2007, S. 775–80
27. Eyckens P, Belkassem B, Henrard C, Gu J, Sol H, Habraken AM, Duflou JR, van Bael A, van Houtte P (2011) Strain evolution in the single point incremental forming process: digital image correlation measurement and finite element prediction. Int J Mater Form 4(1):55–71
28. Abschlussbericht zum Forschungsvorhaben: Untersuchung der Verfahrensgrenzen beim inkrementellen Abkanten und Kragenziehen mithilfe eines CNC gesteuerten Umformwerkzeugs, HI 790/38, Institut für Bildsame Formgebung der RWTH Aachen (2015)
29. Laugwitz M, Voswinckel H, Hirt G, Bambach M (2017) Development of tooling concepts to increase geometrical accuracy in high speed incremental hole flanging. Int J Mater Form 11(4):471–477
30. Bambach M (2007) Process strategies and modelling approaches for asymmetric incremental sheet forming. Dissertation, Aachen
31. Bambach M, Taleb Aragi B, Hirt G (2009) Strategies to improve the geometric accuracy in asymmetric single point incremental forming. Prod Eng Res Dev 3(2):145–156
32. Zhang Z, Zhang H, Shi Y, Moser N, Ren H, Ehmann KF, Cao J (2016) Springback reduction by annealing for incremental sheet forming. Procedia Manuf 5:696–706
33. Maqbool F, Bambach M (2019) Experimental and numerical investigation of the influence of process parameters in incremental sheet metal forming on residual stresses. J Manuf Mater Process 3:2, S. 31
34. Schmitz RUC, Bremen T, Bailly DB, Hirt GKP (2020) On the influence of the tool path and intrusion depth on the geometrical accuracy in incremental sheet forming. Metals 10:5, S. 661
35. Hedström P, Lienert U, Almer J, Odén M (2007) Stepwise transformation behavior of the strain-induced martensitic transformation in a metastable stainless steel. Scripta Mater 56(3):213–216
36. Katajarinne T, Kivivuori S (2012) Strain induced martensite in incremental forming—formation. Effect and control: advances in materials and processing technologies, XV
37. Junk S (2003) Inkrementelle Blechumformung mit CNC-Werkzeugmaschinen. Verfahrensgrenzen und Umformstrategien. Dissertation, Saarbrücken
38. Ambrogio G, Cozza V, Filice L, Micari F (2007) An analytical model for improving precision in single point incremental forming. J Mater Process Technol 191(1–3):92–95
39. Essa K, Hartley P (2010) An assessment of various process strategies for improving precision in single point incremental forming. Int J Mater Forming 4:401–412
40. Isidore BBL, Hussain G, Shamchi SP, Khan WA (2016) Prediction and control of pillow defect in single point incremental forming using numerical simulations. J Mech Sci Technol 30(5):2151–2161
41. Bailly D, Bambach M, Hirt G, Pofahl T, Herkrath R, Trautz M (2014) Analysis into differences between the buckling in single-point and two-point incremental sheet forming of components for self-supporting sheet metal structures. Key Eng Mater 622–623:367–374

Tube Roll Forming Flower Design and Flexible Roll Adjustment with CAE Simulation



Jinn-Jong Sheu, Bao-Shan Wang, and Cheng-Hsien Yu

Abstract The roundness and the angle of the edges on the cross-sectional profile at the exit of the fin pass are crucial for the welding quality of the ERW tube. In this paper, the adjustment of the bending angles of the cage rolls was proposed to make a 9-inch tube. The proposed roll forming machine layout is capable of making tubes in a specific range of outside diameters without changing rolls. The CAE simulations were carried out to verify the proposed roll flower designs and the bending angle control strategies of the cage roll stations. The CAE simulations had verified the proposed flower design using different roll adjustments, and proper bending angle control strategies are able to make the demonstrated tube.

Keywords Cold roll forming · Tube forming · Flexible roll forming · Cage roll

1 Introduction

Roll forming is suitable for making long tubes quickly and efficiently. The process and the tool designs for tube roll forming are mostly depending on the experiences of the engineers. The try-out and tool modifications are not only time-consuming but also expensive. The application of flexible and adjustable tools is capable of dealing with the tool modification problems but the adjustment of tools is painful due to the high degree of freedom of the tools.

Naeini et al. [1] had investigated the weight of longitudinal out-of-plane bending energy for roll forming of symmetric channel sections considering different bend angles and flange widths. The decrease of the dimensionless work ratios indicates that the longitudinal out-of-plane bending energy is less significant. Woo et al. [2] had studied the defects of the flexible roll forming process via the experimental works for different materials. The double-layer material could cause problems at the interface.

J.-J. Sheu (✉) · B.-S. Wang · C.-H. Yu
National Kaohsiung University of Science and Technology, No. 415, Jiangong Road, Kaohsiung, Taiwan
e-mail: jjsheu@nkust.edu.tw

© The Minerals, Metals & Materials Society 2021

G. Daehn et al. (eds.), *Forming the Future*, The Minerals, Metals & Materials Series,
https://doi.org/10.1007/978-3-030-75381-8_43

Chen et al. [3] proposed a roll flower design method for ERW pipes cage roll forming with the blank edge modeling of cubic equations. The FEM software LS-DYNA was used to simulate the forming process and study the effects of the roll positions and forming angles. Wen et al. [4] had studied the phenomenon of strip edge instabilities in the downhill forming process considering the lift of the end of the strip. The roll gap should be adjusted to prevent the rotation of the strip segment and avoid the occurrence of the edge instabilities of ERW tube roll forming. Kasaei et al. [5] had compared the contour roll forming (CORF) process using BD (break down) and side rolls with the cage roll forming (CARF) process using small cage rolls. The curvature distributions of the CORF process are more uniform than the CARF process for HWF tube forming. Jiang et al. [6] had proposed a cage roll forming mill and studied the effects of the non-bending areas. The analysis of the strain distribution is likely to find the areas of buckling. In this paper, the tool adjustment method and the effect of different settings on the edge deformation of the strip were studied. The proposed roll forming machine is composed of different types of breakdown (BD) rolls,cage rolls, and fin pass as shown in Fig. 1. The tools can be adjusted flexibly to make tubes in a specific range of dimensions and thickness. There are three breakdown passes, nine cage passes, three fin passes, and one squeeze pass.

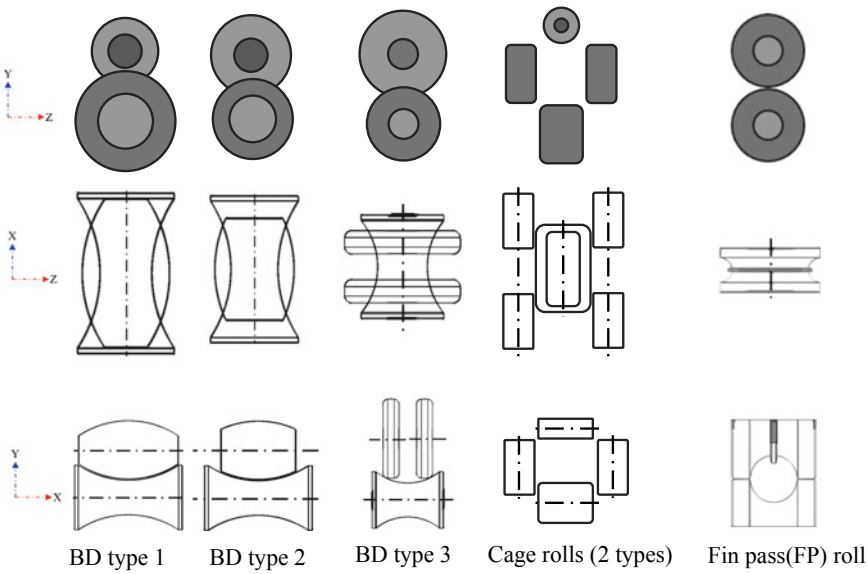


Fig. 1 Different types of tools designed to construct a tube roll forming machine. (Color figure online)

2 Design of the Tube Roll Forming Process and Tool

The roll adjustment for each pass of the roll forming machine is based on the process design or the roll flower pattern used. The forming process is generated with the virtual cross-sectional changes of the strip from the inlet break down station to the final exit of the fin pass stands. The flower pattern is the arrangement of the section profiles of the long strip according to the specific guiding line.

2.1 Roll Flower Design

The roll flower was designed to distribute the bending angle of the strip from the entrance station to the exit station (fin pass). There are three stages of flower pattern, tube bottom curvature creation by stations BD1 to BD3, edge lift, and U–O shaping by cage forming, precision control of the tube dimension, and the curvature. A roll flower designed with the assumption of the equal strip width (constant arc length of each station) was given in Fig. 2. The blank will be deformed during the forming process; as a result, the thickness, width, and the length of the strip will be changed. This virtual flower is the reference for the roll geometry design and the roll position adjustment.

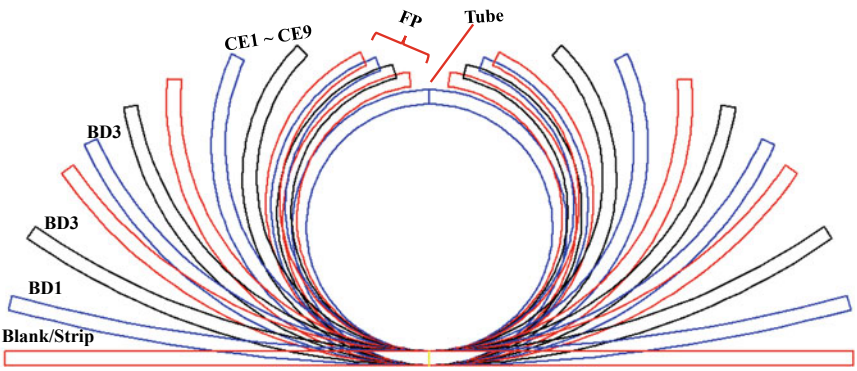


Fig. 2 Flower pattern of a tube roll forming with the assumption of constant arc length. (Color figure online)

2.2 Roll Design and Adjustment

The breakdown (BD) rolls were applied to clamp the strip and break the flat blank into a certain curvature for further roll forming pass feeding and designed according to the section profiles of the corresponding roll flower. The cage rolls were applied to lift and to press the edge of the strip to shape the curved strip into a round shape for smooth feeding of the first fin pass station. The cage roll pairs were arranged either horizontally or vertically to control the lifting angles of the strip edge and the curvature of the entire section profile. The fin pass rolls were applied to control the curvature of the final product and to grind the strip edge using the center fins for better contact of the welding station. The adjustments of the roll gap and the relative position of the roll were determined using the virtual section profile given by the roll flower. The parameters of the roll geometry design and the roll adjustment were given in the following sections.

2.3 Roll Adjustment with Respect to Roll Flower

The adjustment of the rolls for each pass of the universal roll forming machine is determined according to the roll flower pattern which presents the virtual cross section of the forming process at each pass. The vertical positions of the virtual cross sections could be aligned referring to the bottom, the gravity of the center, or any chose locations. The centers of the section profile were aligned along the roll forming direction and formed a horizontal guiding line as shown in Fig. 2. The adjustment of the breakdown rolls was adjusted to cope with the inlet strip thickness and width for feeding and curving purposes as shown in Fig. 3. Type 1 BD roll was applied in the first station for clamping and breaking the flat strip into a curved shape with

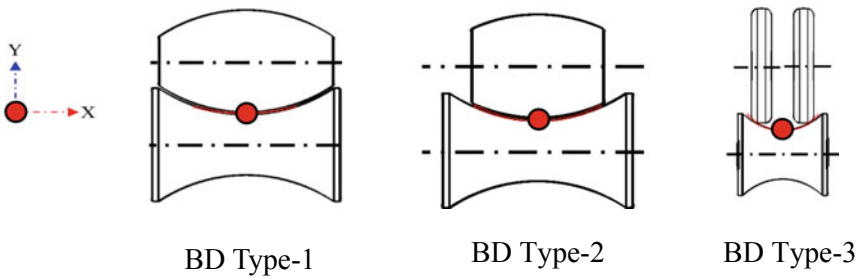


Fig. 3 The adjustment of the breakdown roll type 1, type 2, and type 3. (Color figure online)

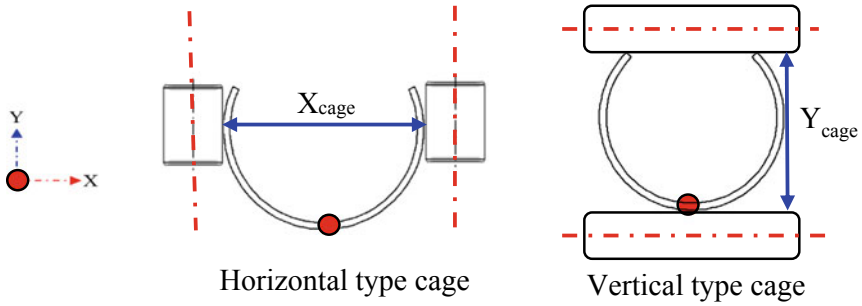


Fig. 4 The adjustment of roll distance for the horizontal cage rolls and the vertical cage rolls. (Color figure online)

small curvature. Type 2 BD roll was applied to bend the center of the strip again to increase the curvature of the blank. Type 3 BD roll was applied to bend the edge of the strip to form a better contact region for the cage rolls.

The adjustment of the vertical and the horizontal cage rolls was a sequence of the strip width and height changing to cope with the roll flower profiles. The horizontal roll distance, X_{cage}, and the vertical roll distance, Y_{cage}, as shown in Fig. 4 were adjusted to cope with the required section profiles of the roll flower. The fin pass rolls were designed to form the strip into a round tube using the shaping rolls and the center fin. The gap between the upper and lower rolls can be adjusted to cope with the extra width of the strip blank.

2.4 Roll Forming Machine Layout

The tube roll forming machine could be built by selecting different numbers of rolls with the combinations of different types of stations. The roll forming machine shown in Fig. 5 is composed of 15 stands that were arranged with a distance of 600 mm in the roll forming direction. There are two bending angle designs based on the proposed roll flower design, and the combinations of the bending angle accumulation were shown in Table 1. The cage roll forming stands were divided into three segments for different bending angle control strategies: “group” design keeps the same bending angle in the same group; “individual” design gives a higher bending angle for horizontal cage rolls in the same group to compensate the spreading out effect of the vertical cage roll.

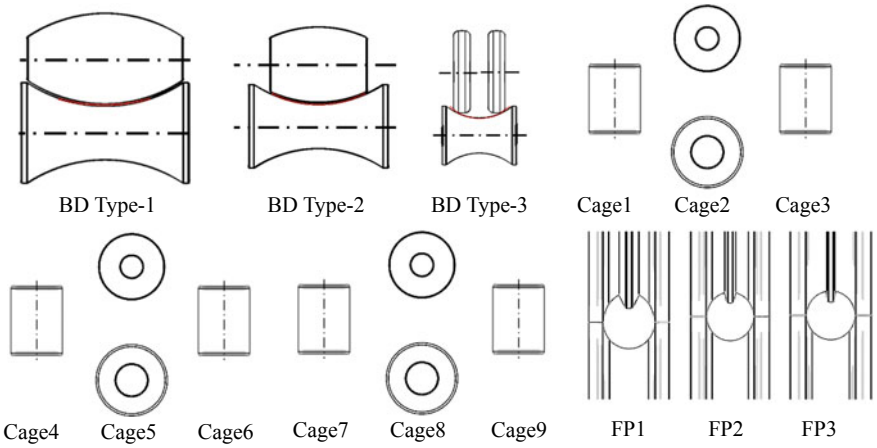


Fig. 5 Layout of the tube roll forming mill with breakdown, cage, and fin pass rolls. (Color figure online)

3 CAE Simulation of the Tube Roll Forming Process

The tube roll forming process was simulated using 3D FEM software (*simufact.forming*) to predict the forming results of the different roll adjustments. The blank material adopted is the API 5CT K55 grade sheet with 9 mm in thickness. The yield stress is 379 MPa for the K55 grade API tube. The power-law model was used for the flow stress calculation. The coefficient of the strength and the strain hardness exponent are 1004 MPa and 0.15, respectively. The outside diameter of the tube is 330 mm. The symmetry model was built to do the simulations. The width, the thickness, and the length of the blank are 520 mm, 9 mm, and 1800 mm, respectively. The three-dimensional hexagonal mesh was used to create the blank FEM model; the mesh sizes in the forming direction and the lateral direction were 20 mm and 9 mm, respectively. The number of the blank mesh is 13,680 as shown in Fig. 6. The roll forming speed is 250 mm/s. The Coulomb friction coefficient assumed is 0.14.

4 Results and Discussion

The tube roll forming process with flexible roll adjustment relies on the setup of the cage rolls to make a sound tube. The bending angle accumulations of the designed data and the simulated results were shown in Table 2. The forming process with the segment group control strategy was not able to finish the forming process due to the insufficient lifting angle to enter station 10 cage roll. The forming process with the individual cage roll control strategy was able to finish forming process successfully.

Table 1 The accumulated bending angles for the tube roll forming process design

Design	Station														
	1	2	3	4	5	6	7	8	9	10	11	12	13	14	15
Group	15	55	95	115			135			155			160	165	170
Individual	15	65	99	120/115/120			140/135/140			160/155/160			160	165	170

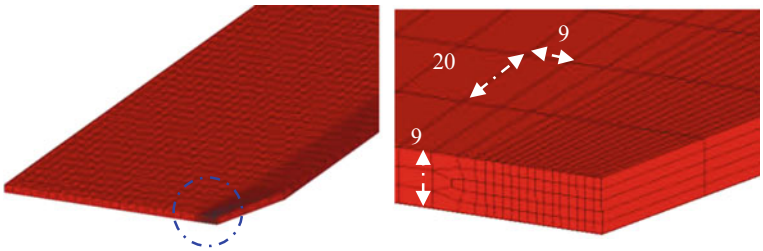


Fig. 6 The dimensions of the entire blank and the mesh refinement of the strip edge. (Color figure online)

4.1 Geometrical Control of the Cage Rolls

The main purpose of the cage rolls is to change the curvature of the strip gradually to feed into the final fin pass forming. The mean section profile curvatures of the strip from cage 1 to cage 9 were shown in Fig. 7. The final radius of the tube is 165 mm (the corresponding curvature is 0.006/mm). The average curvature of the cage roll stations was distributed in the range 0.003–0.006. The second cage roll station and the final cage roll station had shown a significant variation of curvature which indicates the roll adjustment of these two stations maybe not proper.

4.2 Strain and Stress Distributions of the Breakdown Stations

The breakdown stations should be able to form a curved blank to feed into the cage stations. The effective strain and the equivalent stress distributions of BD stations were shown in Fig. 8. The effective stress of the entire curved blank was larger than the yield stress until station 3; the spring back of the blank had decreased the bending angle and resulted in the forming difficulty of cage rolls.

4.3 Strain and Stress Distributions of the Cage Roll Stations

The cage roll stations are the width and the height control process of the blank using cylindrical rolls. The effective strain and the effective stress distributions of station 4 (cage 1) to station 12 (cage 9) were shown in Figs. 9 and 10. The effective strain is mainly distributed at the edges and the center bottom of the blank since the contacts of the rolls and the blank occurred at these areas. Stations 11 and 12 had larger strains and stresses that indicated the deformations of blank at these stations are more severe.

Table 2 The predicted bending angles of the two control strategies

Design	Station														
	1	2	3	4	5	6	7	8	9	10	11	12	13	14	15
Cage rolls were controlled in three segment groups															
Designed	15	55	95	115			135			155			160	165	170
Results	15	55	80	89/93/89			101/105/111			–			–	–	–
Cage rolls were controlled individually															
Designed	15	65	99	120/115/120			140/135/140			160/155/160			160	165	170
Results	15	65	85	114/112/112			122/118/126			132/128/130			160	165	170

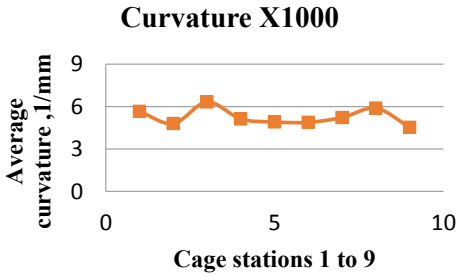


Fig. 7 The average curvature distribution of the cage roll stations. (Color figure online)

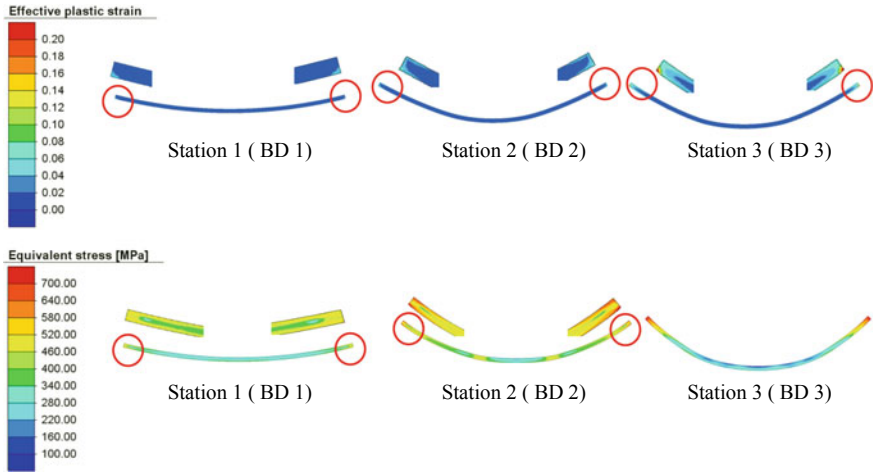


Fig. 8 The effective plastic strain (top) and the equivalent stress (bottom) distributions. (Color figure online)

4.4 Strain and Stress Distributions of the Fin Pass Stations

The fin pass (FP) stations compressed the entire blank to contact with the rolls and form the round tube. The effective plastic strain and the effective stress distributions of station 13 (FP 1) to station 15 (FP 3) were shown in Figs. 11 and 12. The effective strain distribution at the FP 1 station is similar to the previous station (cage 9) but the geometry of the blank had been changed dramatically. The equivalent stress distributions revealed that the deformations of the FP 2 and the FP 3 stations are in the vertical and the horizontal directions, respectively.

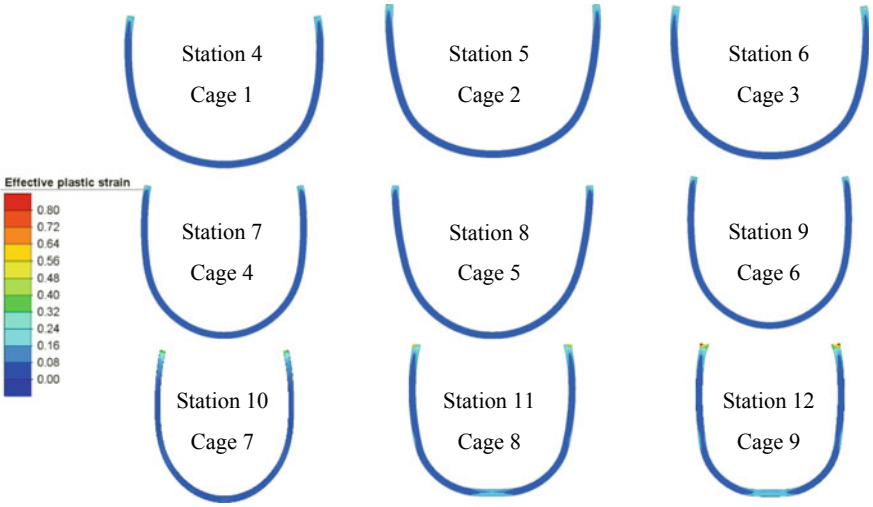


Fig. 9 The equivalent stress distributions of the cage roll stations. (Color figure online)

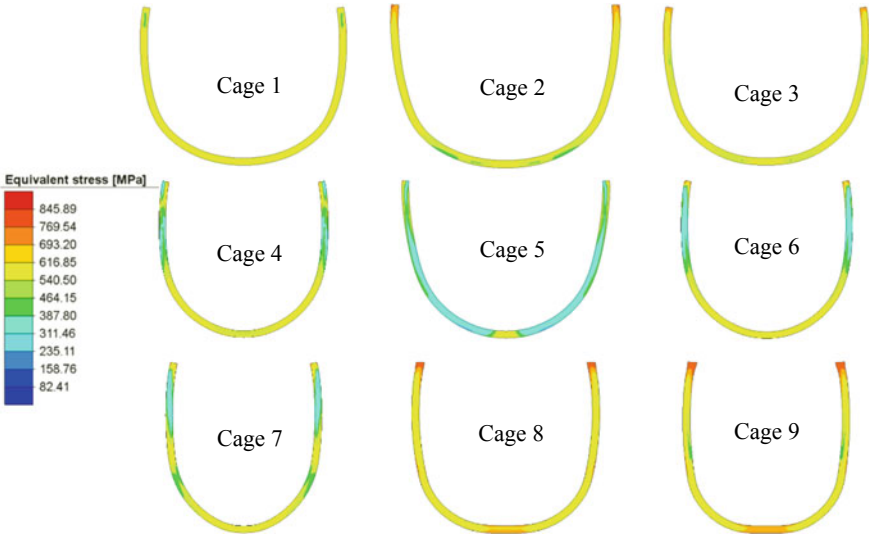


Fig. 10 The effective plastic strain distributions of the cage roll stations. (Color figure online)

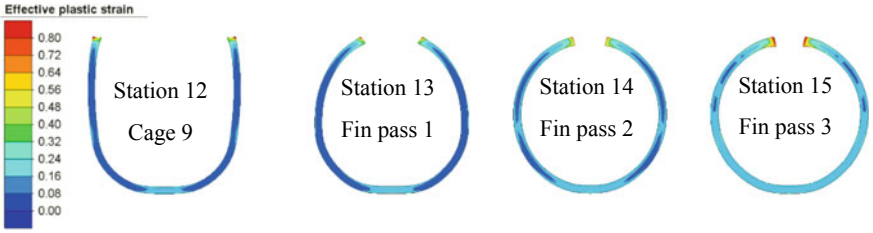


Fig. 11 The effective plastic strain distributions of the fin pass stations and the cage 9 station (left). (Color figure online)

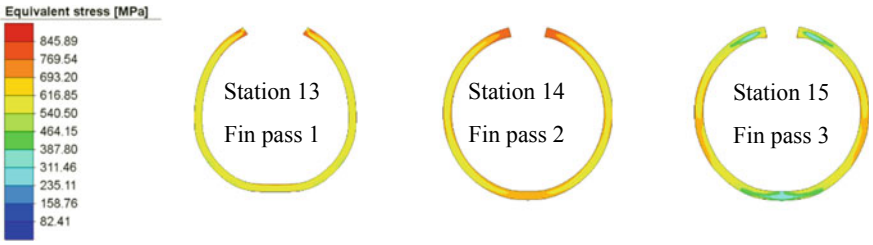


Fig. 12 The equivalent stress distributions of the fin pass stations. (Color figure online)

5 Conclusions

The proposed cage roll forming process was simulated using three-dimensional FEM successfully. The control strategies of the cage roll and the roll position adjustment were crucial for sound product making. The strip edge should be bent properly to avoid the spread-out phenomenon in the cage roll forming zone. The arrangement of the bending angles in the cage roll forming zone is essential and the roll adjustment should take into consideration the spring back in the previous station.

Acknowledgments The authors would like to thank the Ministry of Science and Technology of Taiwan for the financial support of the granted project number MOST-108-2221-E-992-070.

References

1. Moslemi NH, Salmani TM, Safdarian R (2008) Investigating the weight of longitudinal out-of-plane bending energy in prediction deformation. In: Proceedings of the metal forming conference 2008, vol 12, pp 141–144
2. Woo Y, Kang P, Ilyeong Oh, Moon Y (2018) Flexible roll forming of double layered blank. Procedia Manuf 15:775–781

3. Chen W, Jiang J, Li D, Zou T, Peng Y (2019) Flower pattern and roll positioning design for the cage roll forming process of ERW pipes. J Mater Process Tech 295–312
4. Wen B, Pick RJ (1994) Modelling of skelp edge instabilities in the roll forming of ERW pipe. J Mater Process Technol 41:425–446
5. Kasaei MM, Moslemi Naeini H (2011) Comparison of strip deformation between the contour roll forming (CORF) process and cage roll forming (CARF) process of HFW pipes. In: 3rd International conference on manufacturing engineering, ICME2011, Tehran, Iran, pp 27–29
6. Jiang J, Li D, Peng Y, Li J (2009) Research on strip deformation in the cage roll-forming process of ERW round pipes. J Mater Process Technol 209:4850–4856

Open Die Forging of Copper Cone



A. Shirizly, G. Harpaz, and A. Shmuel

Abstract The open die forging/upsetting of bulk material to a cone shape involves high plastic deformation. The plastic strain causes major changes in the material's mechanical and metallurgical characteristics. In order to gain a better understanding of these characteristic changes, experimental, analytical, and numerical models were developed and studied. First, sample material properties and friction conditions (with several lubricants) were measured. Next, analytical models (upper bound and slab method) simulated the forging forces and the results were compared to results from a finite element (FE) model. These were then compared with the experimental findings using C101 copper. The preformed samples were surface etched with a grid pattern and the strain caused by the forming operations was measured from the grid changes. The flow pattern was inspected and compared with the outcomes using a similar material and a numerical model. A good resemblance was found between the experimental results and the theoretical models.

Keywords Open die forging · Upper bound · Lower bound · Finite element · Copper

1 Introduction

Open die forging is one of the most common processes found in the metal forming industries. The compression of a solid cylinder is well explored as a forging process. Among the early solutions for cylinder forging were the works of Kobayashi [1], Avitzur [2], Hosford [3], and a velocity for an upper bound solution was introduced. Yang and Lee [4] expanded the upper bound method to three-dimensional problems, and Dixit 2002 [5] examined the effects of barreling in a compression test. In 1989, Kobayashi et al. [6] published a finite element (FE) book with an emphasis on metal forming and presented the results for the compression of a solid cylinder. Additional work has been done to investigate compressible materials. Shirizly et al. [7, 8] investigated the open die forging of porous materials based on limit analysis and an

A. Shirizly (✉) · G. Harpaz · A. Shmuel
Rafael – Advanced Defense Systems Ltd., 3102102 Haifa, Israel

© The Minerals, Metals & Materials Society 2021

G. Daehn et al. (eds.), *Forming the Future*, The Minerals, Metals & Materials Series,
https://doi.org/10.1007/978-3-030-75381-8_44

experimental procedure. Lichtenberger [9] described the warm forging process with temperatures below the recrystallization temperature for a cone liner material and a few forging steps than needed for the production of cold-forged cones. However, open die forging of a cone is still obscure. Engineering experience has provided some knowledge but many of the process parameters remain in obscurity. The universal models developed in this work cover a wide spectrum of cone angles (from a solid cylinder to a sharp cone), material properties, and friction conditions.

2 Analytical, Numerical, and Experimental Models

Two analytical models were developed for the open die forging of a cone: (i) the slab method that assesses the stress distribution and the applied force and (ii) the upper bound method that gives an upper limit approximation for the applied force. ABAQUS\Explicit software was used for FE modeling of the process. All models were used to analyze the process parameters (forging speed, lubrication, material hardening, etc.). The outcomes of the above models were compared with the experimental results.

2.1 Material Properties

The raw material used in this study was copper C101. To model the material's behavior, a number of uniaxial tensile tests were performed at different loading rates. The tensile samples were prepared in the longitudinal direction of an Ø50 mm extruded bar, according to the ISO-6892-1 [10]. The loading velocity of 18 [mm/min] was chosen to represent the raw material properties and matched the strain rate during the product forging process.

The Ludwik power law of strain-hardening model [11] was used to describe the plastic behavior of the raw material, according to the following expression:

$$\sigma = C\varepsilon^{n} \tag{1}$$

where σ is the true stress, C is a material constant, known as the "strength coefficient", ε is the true plastic strain, and n is the strain-hardening exponent.

The material properties derived from the tensile experiments are given in Table 1.

Table 1 Uniaxial tensile material properties (average of three samples)

Yield stress σ_y [MPa]	Ultimate tensile stress σ_{UTS} [MPa]	Elongation [%]	Reduction of area [%]	Material constant C [MPa]	Hardening coefficient n
58.5	216.7	61.5	85.2	486.9	0.5113

2.2 Slab Analysis

Slab analysis of plasticity for incompressible materials is based on balancing forces on a differential slab of material. The slab analysis relies on several assumptions:

1. The principal axes are in the directions of the applied loads,
2. The deformation is homogeneous so that the plane sections remain plane,
3. The effects of friction do not alter the directions of the principal axes or cause internal distortion,
4. The material obeys the incompressibility condition under yielding.

Figure 1 illustrates *open die forging of cone*. A force F is applied on the material via a cone punch (upper die), and the material is compressed with a constant coefficient of friction m versus the lower die.

Balancing the forces on the differential slab in the radial direction and applying the circumferential symmetry conditions gives

$$\left(\sigma_r + \frac{\partial \sigma_r}{\partial r} dr\right)(r + dr)hd\theta - \sigma_r rhd\theta + (P\cos\alpha - P\cos\alpha)rd\theta\frac{dr}{\sin\alpha} - 2\tau\sin\alpha rd\theta\frac{dr}{\sin\alpha} - 2\sigma_\theta \sin\frac{d\theta}{2}hdr = 0 \quad (2)$$

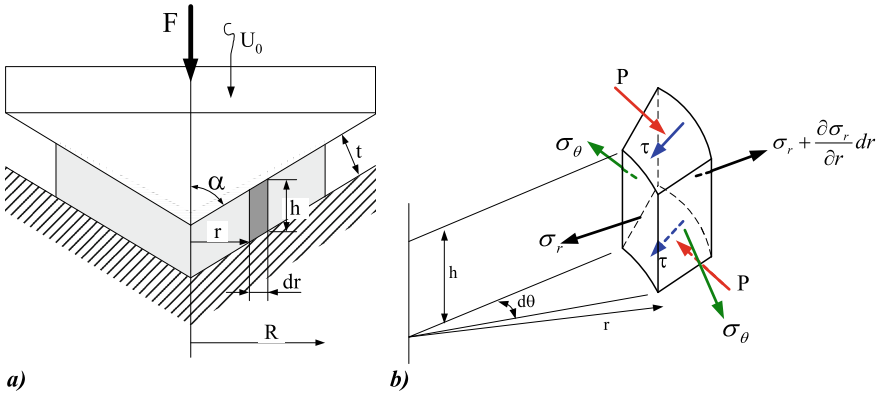


Fig. 1 Slab method model: **a** Cone model; **b** Slab used for force balancing. (Color figure online)

where $\tau = m\bar{\sigma}$ is the shear stress strength of the interface, m is the friction coefficient, and $\bar{\sigma}$ is the equivalent stress.

Simplifying by substituting $\sin\left(\frac{d\theta}{2}\right) \sim \frac{d\theta}{2}$ and neglecting second-order differentials gives

$$\frac{\partial \sigma_r}{\partial r} + \frac{\sigma_r - \sigma_\theta}{r} - \frac{2\tau}{h} = 0 \tag{3}$$

For axially symmetric flow, $\varepsilon_\theta = \varepsilon_r$; therefore, $\sigma_\theta = \sigma_r$.

Applying the von-Mises yield criteria gives

$$\bar{\sigma}^2 = \frac{1}{6}\left[(\sigma_r - \sigma_\theta)^2 + (\sigma_\theta - \sigma_z)^2 + (\sigma_z - \sigma_r)^2\right] \tag{4}$$

Solution of Eq. (3), and using yield criterion 4, as well as the axisymmetric and the radial boundary conditions $\sigma_r = 0@r = R$, leads to the stress distributions:

$$\sigma_r = \frac{2m\bar{\sigma}(R-r)}{h} = \frac{2m\bar{\sigma}(R-r)}{t}\cos\alpha;\ \sigma_\theta = \sigma_r;\ \sigma_z = \bar{\sigma} + \sigma_r \tag{5}$$

and the applied force: $F = \int\limits_A \sigma_z dA = \int\limits_0^R \sigma_z 2\pi r dr$

$$F = -2\pi R^2 C\left\{\left(1 + \frac{1}{12}\frac{\cos^2\alpha}{\sin^2\alpha}\right)^{1/2} ln\frac{h_0}{h}\right\}^n \left(1 + \frac{2m}{3}\frac{R}{h}\right) \tag{6}$$

In the case of disk upsetting ($\alpha = \pi/2$), the above solution is identical to the axially symmetric compression solution [1–3].

2.3 Upper Bound Solution

The upper bound approach is used to predict the maximum power required for deformation during a metal forming action. The upper bound solution is based on satisfying yield criteria, geometric self-consistency, kinematically admissible velocity fields, and velocity boundary conditions.

The geometry and process parameters for the upper bound solution are shown in Fig. 2a, and the relevant surfaces and velocities are shown in Fig. 2b

The admissible strain rate and velocity field for the cone are given by

$$U_r^* = \frac{U_0}{2}\frac{r}{h};\ U_\theta^* = 0;\ U_z^* = -U_0\left(\frac{z}{h} - \frac{r}{2h}\frac{\cos\alpha}{\sin\alpha}\right)$$

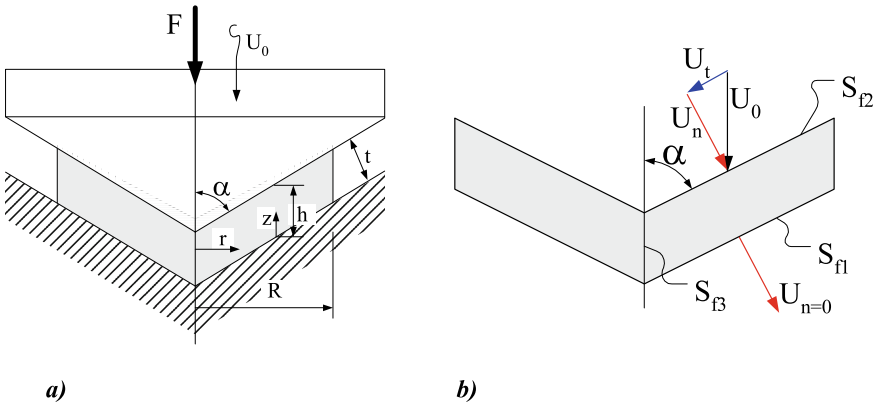


Fig. 2 Upper bound model: **a** Model parameters; **b** Contact surfaces (S_{f1}, S_{f2}, S_{f3}), applied velocity U_0 and corresponding velocities (U_n, U_t,). (Color figure online)

$$\dot{\varepsilon}_r^* = \frac{\partial U_r^*}{\partial r} = \frac{U_0}{2h}; \dot{\varepsilon}_\theta^* = \frac{U_r^*}{r} = \frac{U_0}{2h}; \dot{\varepsilon}_z^* = \frac{\partial U_z^*}{\partial z} = -\frac{U_0}{h}$$
$$\dot{\varepsilon}_{rz}^* = \frac{1}{2}\left(\frac{\partial U_r^*}{\partial z} + \frac{\partial U_z^*}{\partial r}\right) = \frac{1}{4}\frac{U_0}{h}\frac{\cos\alpha}{\sin\alpha}; \dot{\varepsilon}_{r\theta}^* = \dot{\varepsilon}_{\theta z}^* = 0 \tag{7}$$

The superscript * indicates the admissible strain rate and velocity field, and not necessarily the actual velocity field.

The upper bound of the power consumption J* is composed of:

$$J^* = \dot{W}_{def}^* + \dot{W}_f^* + \dot{W}_\Gamma^* - \dot{W}_T^* \; J^* > J \tag{8}$$

where J is the actual power and F is the actual force $F = J/U_0$.

The work rate of deformation is given by

$$\dot{W}_{def} = \int_V \sigma_{ij}\dot{\varepsilon}_{ij} dv = \int_V \bar{\sigma}\ \dot{\bar{\varepsilon}}\, dv \tag{9}$$

Applying the strain rates (7) and the Ludwik power law of strain-hardening to Eq. (1) yields the rate of deformation:

$$\dot{W}_{def}^* = \pi C R^2 U_0 \left(1 + \frac{1}{12}\frac{\cos^2\alpha}{\sin^2\alpha}\right)^{\frac{n+1}{2}} \left(ln\frac{h_0}{h}\right)^n \tag{10}$$

The work rate dissipated over the boundary between the material and the tools, S_{f1} and S_{f2} are given by

$$\dot{W}_f^* = \int_{S_f} \tau \left|\Delta U^*\right| dS_f$$

$$\dot{W}_f^* = 2\pi m C U_0 R^2 \left(1 + \frac{1}{12}\frac{\cos^2\alpha}{\sin^2\alpha}\right)^{\frac{n}{2}} \left(ln\frac{h_0}{h}\right)^n \left(\frac{R}{h}\frac{1}{3\sin^2\alpha} - \frac{1}{2} - \frac{\cos\alpha}{\sin\alpha}\right) \quad (11)$$

The work rate along the discontinuity line S_{f3} is $\dot{W}_\Gamma^* = \int_{S_\Gamma} \tau |\Delta U^*| dS_\Gamma = 0$, and on the traction surfaces $\dot{W}_T^* = \int_{S_T} T_i u_i dS_T = 0$.

Applying the upper bound force is achieved by inserting Eqs. (10) and (11) into (8) and dividing by the press velocity U_0.

2.4 Finite Element (FE) Solution

FE simulations were performed to simulate cone forging and to validate and compare with the analytical models and the experimental results. The simulations included predictions of the flow mechanism, stress and strain distributions, and the punch force throughout the forging process. The FE simulations were performed using ABAQUS\Explicit software. The preformed cone raw material was meshed using C3D8R (8-node linear brick, reduced integration with hourglass control). The upper and lower dies were meshed using R3D4\R3D3 (two-dimensional rigid elements). The typical size of all the elements in the simulation was 1 mm.

During the simulation, the kinetic and internal energies were compared to the forging process values, limiting their ratio to between 5% and 10% throughout the process. Under this constraint, the forging process was assumed to be quasi-static and the dynamic effects can be neglected relative to the plastic deformation so that the results are plausible. The preformed mesh and the setup tools in the FE simulation are presented in Fig. 3.

In all FE simulations, the lower die is fixed and the punch presses the cone against the die. The die is closed at the bottom so that toward the end of the forging process

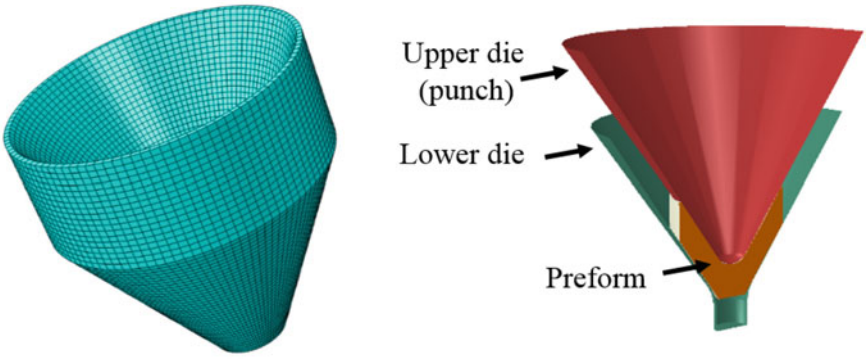


Fig. 3 Preform mesh and tools setup in the FE simulation. (Color figure online)

the material flow is inhibited to match the analytical solutions and the subsequent experiments.

2.5 *Experimental Study*

A series of experiments was conducted on copper C101 with the material properties described in Sect. 2.1. A double-action 600-ton hydraulic press was used to perform the forging tests (the major press axis was used for the forming operation and the secondary axis was used for the part release). The specimen geometry is shown in Fig. 4. Prior to the forming operation, the preform and the tolls were lubricated with a lubrication oil for "yellow" materials, such as F3118 (synthetic drawing oil) or graphite-based mineral oil. The preform samples were surface etched with a grid

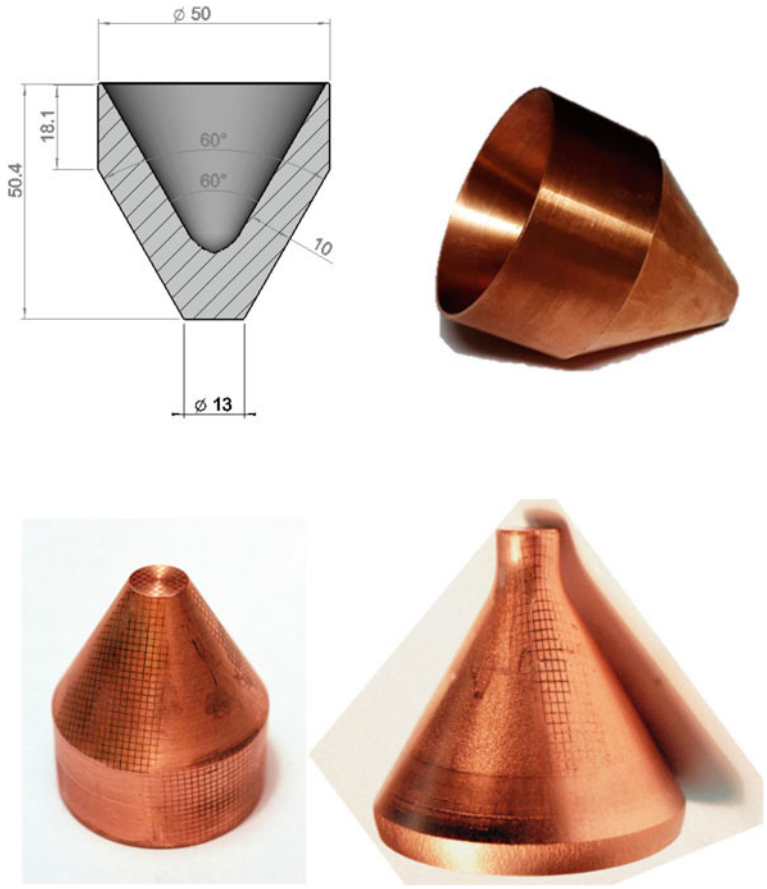


Fig. 4 The forging preform geometry prior and after surface etched with a grid pattern and grid changes due to the deformation process. (Color figure online)

pattern and the strain caused by the forming operations was measured from the grid changes. The measured strains were compared with the simulations, and the flow patterns were inspected and compared using a similar material and a numerical model.

3 Results and Discussion

The prediction of the loading paths by using a rigorous bound (slab method without friction and upper bound with the maximal friction coefficient) is given in Fig. 5, where the sample height is normalized by the initial height and the force is normalized by the force $F_0 = \pi R^2 \sigma_0$. The large difference between the bounds is due to the bound theory [2]; however, it may be more practical for the process designer to update the friction factors so that the results match the laboratory conditions. The experimental results of cone forging ($2\alpha = 60^\circ$) with two different lubricants are shown in Fig. 6. All experiments were conducted under laboratory conditions; the average results of each set of tests are scattered along the loading path and located between the bounds (with $m = 0.2$ for the upper bound approximation and $m = 0.1$ for the slab solution) and the FE simulation results (with $m = 0.1$). At the beginning of the forging process the measured force fits the FE results and was lower than the predicted bound. When the forging process progresses, the FE model and the experimental results are located between the analytical approximations.

In order to examine the influence of friction on the applied force, several coefficients of friction were used in simulations of the forging process, as shown in Fig. 7 for a cone with $2\alpha = 60^\circ$. As expected, when the friction is higher the required forging force increases and rapidly rises when the thickness becomes less than 0.6 of the initial thickness. In all the FE simulations, toward the end of the forging process

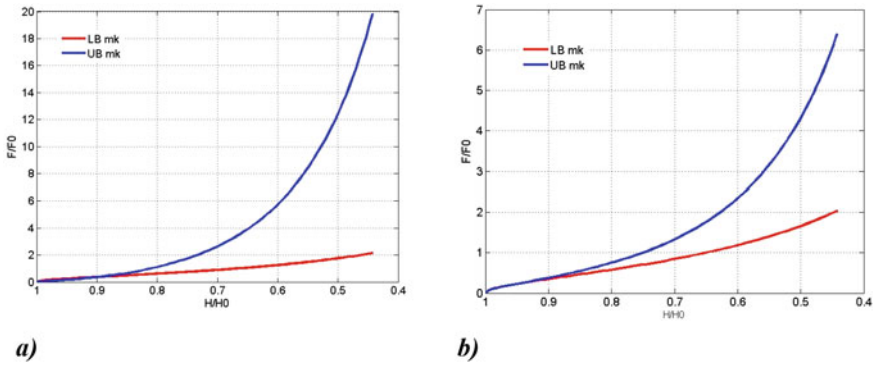


Fig. 5 The effect of the cone angle a on the predicted bounds using the slab method without friction ($m = 0$) and the upper bound with the maximal friction coefficient ($m = 1$): **a** $2\alpha = 60^\circ$—cone compression; **b** $2\alpha = 180^\circ$—compression of solid cylinder between flat dies. (Color figure online)

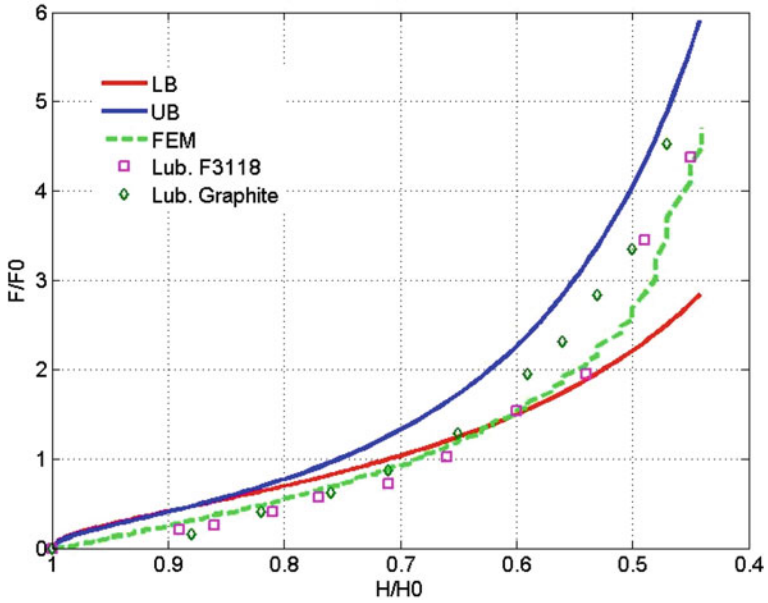


Fig. 6 Comparison between cone forging ($2\alpha = 60^{o}$) experiments (with two different lubricants), approximate limit analysis and numerical FE solution. The approximate bound solutions and the FE were obtained by different coefficients of friction for each model (0.1 for slab and FE, 0.2 for the upper bound). (Color figure online)

there is an increase in the reaction force because the flowing material is blocked at the bottom of the die, as defined in the analytical models. The radial principal stress and the displacements found in the FE simulation are presenting in Fig. 8 for $m = 0.1$ and $t/t_0 = 0.43$. It can be seen that, unlike the analytical model (purely cone), the material initially filled the cylindrical part at the bottom of the cone and then continued to deform the cone thickness. When the simulation applies to the thickness change, the simulation results are between the dual bounds (Fig. 6).

A qualitative comparison between the FE tangential strain and the results for a similar material is shown in Fig. 9. In order to present the material flow with a similar material, several layers of plasticine (with different colors and uniform thickness) were placed, layer by layer, and deformed in a Bakelite die. Then, the look-alike material was cut to represent the material flow. It can be seen that even though the Bakelite die was open at the cone edge, the material flow is very similar to the simulation.

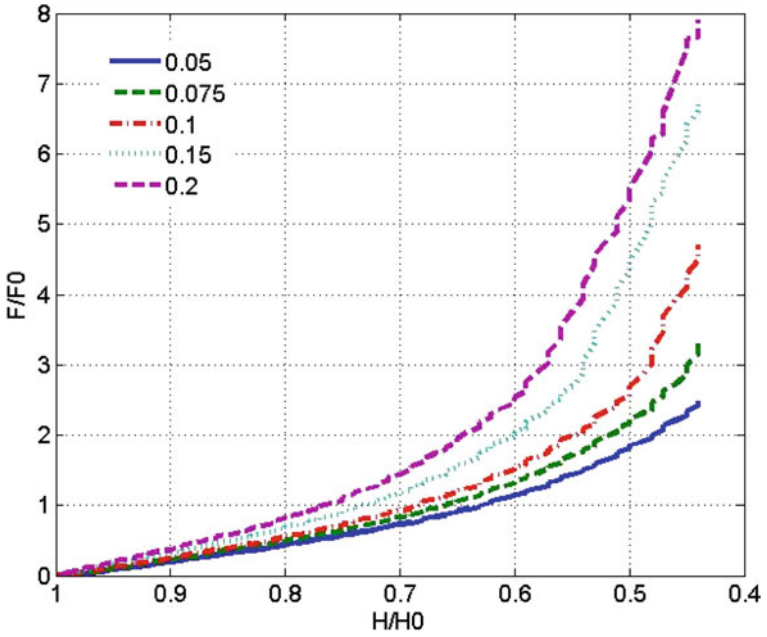


Fig. 7 The effect of coefficient of friction on the applied load as predicted by FE solution for cone forging ($2\alpha = 60°$). (Color figure online)

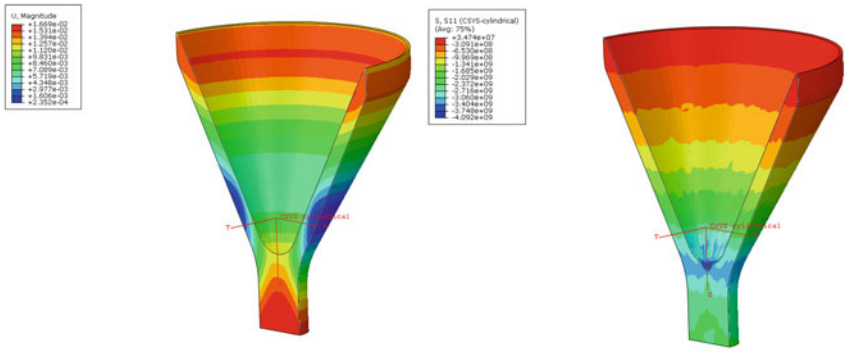


Fig. 8 Displacements [meter] and radial principal stress [Pascal] found in FE simulation of the copper cone, with friction coefficient ($m = 0.1$), at $t/t_0 = 0.43$: **a** $2\alpha = 60°$ cone compression; **b** Radial principal stress. (Color figure online)

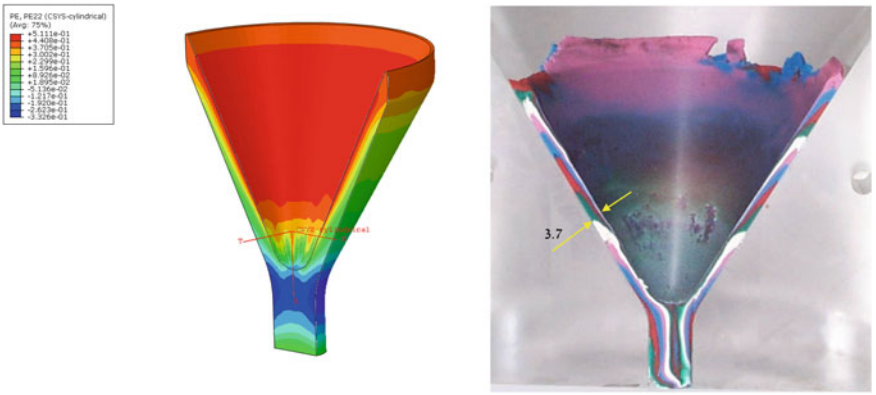


Fig. 9 Qualitative comparison between the FE tangential strain and a similar material: **a** FE tangential strain; **b** Layers of similar material after deformation. (Color figure online)

4 Summary and Conclusions

Three simulation techniques were used to simulate the open die forging of a cone: two analytical models—upper bound and slab analyses of plasticity—and an Abacus FE simulation. The models were compared with the experimental results in the forging of a copper cone. The analytical universal models were developed for a wide range of angles of axisymmetric open die forging. The semi cone angle α was used as a parameter, and for $\alpha = \pi/2$ the solution coincides with that for disk upsetting. A good resemblance was found between the models and the subsequent experiments for the applied force and specimen deformation.

References

1. Kobayashi S (1964) Upper bound solution of axisymmetric forming problems. Trans ASME 86:112–126
2. Avitzur B (1968) Metal forming: Processes and analysis. McGraw-Hill, New York, p 1968
3. Hosford WF Caddell RM (2007) Metal forming: mechanics and metallurgy. Cambridge University Press. ISBN-13 978-0-521-88121-0
4. Yang DY, Lee CH (1978) Analysis of three-dimensional extrusion of sections through curved dies by conformal transformation. Int J Mech Sci 26:541–552
5. Dixit R, Ngaile G, Altan T (2002) Measurement of flow stress for cold forging, engineering research center for net shape manufacturing, ERC/NSM-01-R-05
6. Kobayashi S, Oh S-I, Altan T (1989) Metal forming and the finite-element method. Oxford University Press, New York

7. Shirizly A, Rittel D, Rubinski L, Tirosh J (1999) On damage distribution in the upsetting process of sintered powder materials. Int J Fract 97:321–336. https://doi.org/10.1023/A:1018332431030
8. Shirizly A, Tirosh J, Rubinski L (1998) Open die forging of porous materials. Mater Sci Eng A 249:55–61. https://doi.org/10.1016/s0921-5093(98)00563-2
9. Lichtenberger A (1983) Process for the elaboration of shaped charge liner, French Patent No 8608377
10. ISO-6892-1:2016 Metallic materials—Tensile Testing Part 1: Method of test at room temperature
11. Ludwik P (1909) Elements der Technologischen Mechanik. Springer, Berlin

Flexible Manufacturing of Concave–Convex Parts by Incremental Sheet Forming with Active Medium



Sebastian Thiery and Noomane Ben Khalifa

Abstract Incremental sheet forming with active medium (IFAM) is a flexible manufacturing process that creates concave–convex sheet metal parts in one clamping without needing a counter tool or a die. In the first study of this new process (Ben Khalifa and Thiery in CIRP Ann 68(1):313–316, 2019, [1]), a conventional hemispherical tool has been used in interaction with pressurised air to manufacture concave–convex parts. Since the geometric accuracy was not satisfying, within the present study, a conical tool with a dedicated angle is introduced to IFAM. The idea behind this tool concept is to restrict the inclined part wall to a target angle. At first, results from the numerical investigation show an improvement of the accuracy when a conical tool is used to manufacture a truncated convex pyramid. Subsequently, experiments validate the numerical model and reveal increased process reliability. The experimental investigations of truncated convex cones and concave–convex parts close the paper and underline the feasibility of the tool concept.

Keywords Incremental forming · Active medium · Tool geometry · Concave–convex · Geometric accuracy

1 Introduction

Nowadays, the manufacturing industry has to deal with different challenges that arise from climate change and global competition. Automotive lightweight construction is an important solution to produce safe and fuel-efficient vehicles but is subject to economic restrictions. In this context, high-strength materials are continuously developed and applied for lightweight structures. The increase in material strength comes often along with reduced formability and thus forming processes have to be

S. Thiery (✉) · N. Ben Khalifa
Institute of Product and Process Innovation, Leuphana University of Lüneburg, Universitaetsallee 1, 21335 Lueneburg, Germany
e-mail: sebastian.thiery@leuphana.de

N. Ben Khalifa
Institute of Materials and Process Design, Helmholtz-Zentrum Hereon, Max-Planck-Straße 1, 21502 Geesthacht, Germany

© The Minerals, Metals & Materials Society 2021

G. Daehn et al. (eds.), *Forming the Future*, The Minerals, Metals & Materials Series,
https://doi.org/10.1007/978-3-030-75381-8_45

optimised simultaneously. Hydroforming has become an important technology in this field by having a great potential for processing high-strength materials.

All processes belonging to the hydroforming technology have in common that a working medium is engaged to shape metal parts [2]. Differing in the shape of workpieces, this technology can be distinguished into tube and sheet hydroforming [3]. Furthermore, there is the option either to replace the punch or die of the tool by working medium [3]. No matter which process type is selected, the forming operation by working medium happens form-based by being restricted through contact with the tool. The main advantages of hydroforming are reduction of friction, improved forming limits, and increased surface quality.

Nevertheless, one drawback of hydroforming is a more complex process design than it is required for conventional stamping tools [4]. It needs dedicated tools and is for this reason more suitable for mass production [5]. Small-batch production needs, instead, a flexible forming technology like incremental sheet forming [6].

Hydroforming and incremental sheet forming can be combined leading to a great variety of applications while saving the flexibility of incremental sheet forming. For example, pressurised oil can be used by acting as a punch to create a preform that is formed to a truncated cone in a subsequent step by incremental forming [7]. Another possible option is to use pressurised oil as a soft support during SPIF, acting as a liquid die, to produce high wall angles in a multistage forming process [8]. Being even more flexible, the highest level of interaction between pressurised medium and incremental forming is achieved by a novel process called incremental sheet forming with active medium (IFAM) [1]. By adapting the tool path to move in the horizontal plane, it allows the medium to act as counter tool [1]. This strategy extends the product range to complex concave–convex shapes without a die, a customized setup, or intermediate turning of the blank [1].

IFAM can use the same hemispherical tools as those that are applied for single-point incremental forming (SPIF) [1]. Hemispherical tool heads provide the advantages of an easy tool path generation and a uniform contact area even if a part with varying wall angle is to be formed [9]. An important parameter is the tool diameter that has a direct influence on the process capability [10]. However, a hemispherical tool shape is not a mandatory requirement for incremental forming. Tool heads can be conical with an angular profile and can affect the formability of the process [11]. Furthermore, tool heads might also have a flat end and improve profile accuracy [12]. Not only the macroscopic geometry of tools but also the surface on microscopic scale has to be considered. Textured surfaces on the tool heads enhance lubrication and change friction at the tool–workpiece interface [13].

Because the tool path is long in incremental forming processes, simulating the process by the finite element method takes a long time [14]. For simulation, either explicit or implicit time integration algorithms can be used [15]. Mass scaling and time scaling are methods to reduce the computational time for an explicit solver [16]. However, both the methods have an effect on the accuracy of the simulation [15]. Depending on the scope of simulation, one can decide to use shell elements for global modelling or solid elements for revealing local forming mechanism [17].

Using solid elements for simulating IFAM, it is shown that stress concentration and sheet thinning occur in the contact zone between the tool and the blank [1].

Because plastic deformation only happens in a small region, as it is typical for incremental forming processes, IFAM requires only very small pressures in contrast to hydroforming. Using aluminium AA1050 of thickness 1 mm for their experiments, Ben Khalifa and Thiery [1] showed that a very low-pressure level of 0.035 MPa is sufficient to cause plastic deformation due to stress concentration in the local forming zone. In comparison to IFAM, hydroforming operations require a hundred times higher pressure level, up to 5 MPa, for a homogenous plastic bulging of similar material [7].

Form-based hydroforming processes have dedicated tools, which restrict bulging of the blank and shape the blank into its target geometry. Instead, the final geometry of the blank in IFAM is the result of an interaction of the dominant process parameters pressure and tool path as well as contact conditions between tool and blank. Tool path and target shape in IFAM are not as strongly connected to each other as in SPIF. For this reason, suitable process strategies have to be developed to reach the target shape in IFAM. Approaches might be based on controlling pressure during the forming process, adapting tool path to compensate deviations, or changing contact conditions between the tool and the blank. This paper focuses on the latter strategy by introducing a tool with a dedicated angle to IFAM.

In the following section, general information for conducting IFAM experiments and simulations is provided. It includes a description of the setup and the tool geometry as well as a strategy to generate tool paths under considerations of the tool geometry. Furthermore, the material properties and the settings for the numerical model are addressed. In the third section, the numerical model is used to prove the feasibility of the conical tool shape and to determine the required pressure level for manufacturing truncated pyramids. Based on the same process parameters, the truncated pyramids are manufactured in experiments and their accuracy towards the target shape is analysed. Additionally, the accuracy of truncated cones and concave–convex parts are experimentally investigated.

2 Investigation Methods

2.1 Equipment and Tool Geometry

The experimental setup, which is placed on the machine bench of a high-speed portal milling machine, is depicted in Fig. 1a. Generally in IFAM, a blank is fixed by a blank holder on the top of a pressure chamber and a forming tool, which is attached to the spindle of the milling machine, shapes the blank either concavely or convexly into a part. The pressurised air is used as an active medium in the range 0–0.6 MPa. The pressure control valve is placed outside of the milling machine and connected by a tube to the pressure chamber. A sensor measures the actual pressure inside the

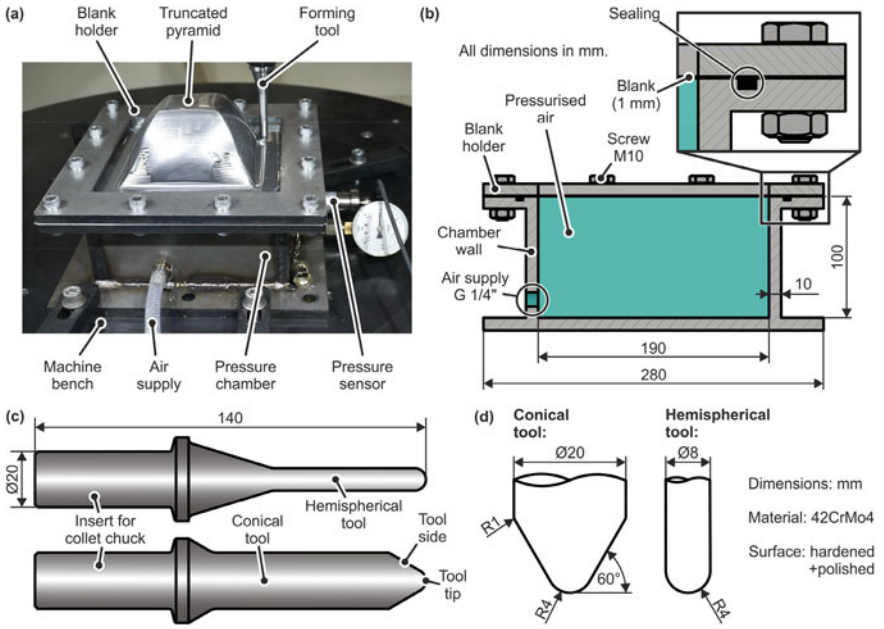


Fig. 1 **a** Experimental setup of IFAM showing the manufacturing process of a truncated pyramid, **b** half-section of the pressure chamber including a blank before forming, **c** full view of the hemispherical and the conical tool, **d** detail view and dimensions of the tooltips. (Color figure online)

chamber in relation to atmospheric pressure throughout the whole forming process. Figure 1b shows the half-section of the pressure chamber with a blank fixed by the blank holder onto the top. The pressure chamber has a depth of 100 mm and provides sufficient space to be used for SPIF if the air is released. In SPIF, the blank is shaped by the tool downwards and this progress is defined as negative or concave forming. An upward movement of the blank instead, like it is shown for the manufacturing of a truncated pyramid in Fig. 1a, is defined as positive or convex forming. The bulging is caused by the pressure acting on the bottom surface of the blank and can be controlled by tool movement to achieve a certain shape.

The full geometries of the hemispherical and the conical tool are shown in Fig. 1c; both tools have an identical length, and the shafts to connect the tools to collect the chuck of the tool holder are the same. The differences between the tools come from the changed geometry of the tooltip, whose detailed view is depicted in Fig. 1d. The tooltip of both tools has a radius of 4 mm to keep the contact conditions as comparable as possible. The radius of the shaft and the tip of the hemispherical tool are the same and the tip merges tangentially with the shaft, which is comparatively thin for this reason. At the conical tool instead, the tip is smoothly connected to a cone with an angle of 60° that is corresponding to the wall angle of the later discussed target geometry. The aim of using this conical shape is to restrict the bulging of the

blank to the target angle and to increase the geometric accuracy. Another striven side effect is an improvement of process reliability because excessive thinning is avoided and tool forces are distributed to a larger surface. To have a sufficient contact area between the cone and the blank, a large radius of the shaft is chosen. A small radius between the cone and the shaft prevents damaging the blank by a sharp edge.

2.2 Tool Path Design

The procedure for generating a tool path with its main steps is illustrated in Fig. 2a–c. A target shape has to be designed at first; the truncated pyramid that is shown in Fig. 2a with a height of 75 mm and a wall angle of 60° is the target shape for the following investigations. The origin of the coordinate system is placed at the centre of the upper surface of the blank. In the second step, the target shape is cut into horizontal layers and the contours are connected from the top to the bottom of a lengthy path, see Fig. 2b. In this step, the path resembles paths of other incremental sheet forming processes. The special feature of the IFAM tool path is created in the last step, as depicted in Fig. 2c, by projecting the three-dimensional tool path in the *XY*-plane. For simple applications, it is sufficient to move the tool to the initial position of the blank surface and afterwards only to change its position in the *XY*-plane. Only for difficult applications, it is necessary to adapt the vertical tool position during the

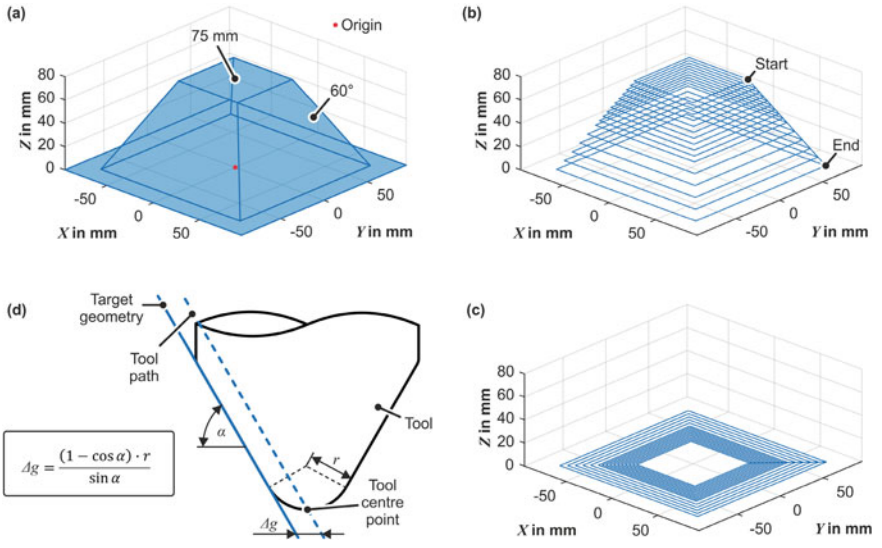


Fig. 2 **a** Creating a target shape as previous step before generating tool paths, **b** cutting target shape into layers and connecting the outer contours, **c** projecting the tool path into the *XY*-plane, **d** tool compensation. (Color figure online)

process but this can only happen inside a small range restricted by elastic bulging of the blank. The final tool path defines only the width of the truncated pyramid and does not define the height or the wall angle. By varying the pressure, it is possible to create truncated pyramids with different heights and with changing wall angles by using the same tool path.

The tool path in Fig. 2c is a reduced representation of the tool path used for the simulation and the experiments but its core message is the same. The first 41 cycles have a horizontal step size of 0.5 mm and the last 24 cycles have a larger horizontal step size of 1 mm. It would not be possible to achieve a part height of 75 mm with a large horizontal step size throughout the whole process because the convex bulging at the beginning of the process is weak. A smaller horizontal step size and a higher number of cycles increase the convex bulging [1]. Therefore, a smaller step size has been selected at the beginning of the process to enhance convex bulging and to keep it approximately constant between the first half and the second half of the forming process. This strategy allows us to use the same tool path and the same pressure level for both tools and to ensure comparability between the results. Furthermore, all the results are based on a feed rate of 1500 mm/min and a rotational speed of 60 1/min.

For generating the tool paths, a tool compensation is taken into account as shown in Fig. 2d because both conical and hemispherical tools are not perfectly sharp. The tool centre point is not located at the intersection of the conical sides but on the round tip and therefore follows the target shape with a horizontal offset Δg. Because the CNC programme is manually written, the horizontal offset Δg is calculated depending on the tool radius and the wall angle, thus resulting in $\Delta g = 2.309$ mm. This tool compensation counts for both tool shapes. Regarding the forming strategy, it can be distinguished in inner compensation for SPIF and outer compensation for IFAM.

2.3 Material Properties and Numerical Model

The experimental setup allows processing of pure aluminium blank in a range from 0.5 to 2.0 mm thickness and of deep drawing steel DC04 blank with a thickness of 1 mm. Aluminium in half-hard state, AA1050A-H24, is chosen as blank material for the following experiments. The blanks have a quadratic shape and an overall width of 280 mm; blank area inside the clamping is 190 mm $\times$ 190 mm. The rolling direction of the blank is always aligned at the X-axis of the milling machine. The surface of the blanks was lubricated during experiments. The material properties are determined by the tensile test with specimen cut in the rolling direction and the flow curve for simulation is extrapolated by Swift, see Fig. 3a. The material thickness is 0.96 mm and is accordingly considered in the numerical model.

The aim of the numerical investigation is to simulate a complete manufacturing process. The model is build up in the simulation software Abaqus 6.14-6, and an explicit solver is chosen. A rigid tool and an elastic-plastic blank are the two components of this model, which is illustrated in Fig. 3b. The blank holder and the part of the blank in direct contact with the blank holder are not included in this model,

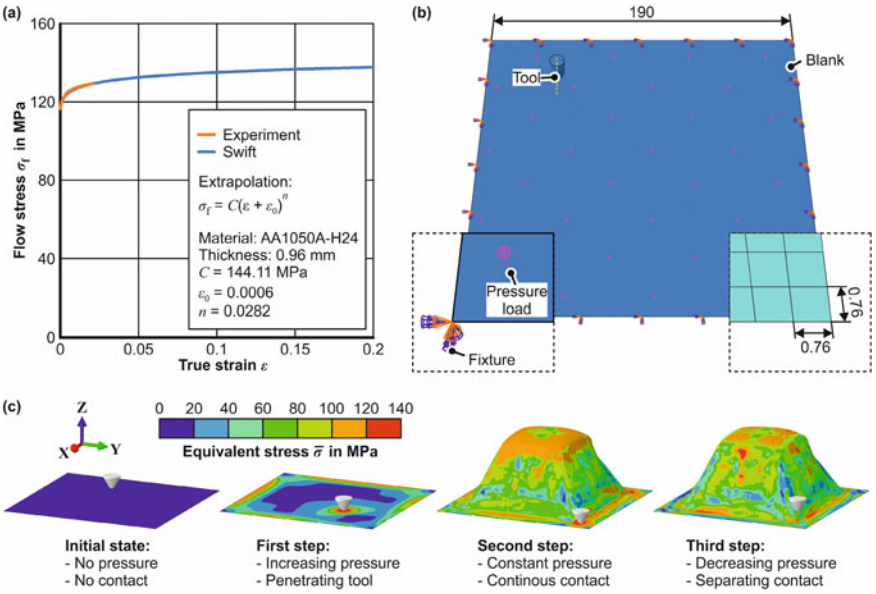


Fig. 3 **a** Extrapolation of the material's flow curve, **b** numerical model of IFAM representing the initial state, **c** equivalent stress $\bar{\sigma}$ at the end of each simulation step showing the manufacturing process of a truncated pyramid. (Color figure online)

and the blank is reduced to the area inside the clamping. Instead, the clamping of the blank is implemented as an idealised boundary condition on the edges. Because the overall shape of the final part is the focus of the investigation without analysing mechanism through the blank thickness, shell elements S4R are applied with five thickness integration points. With a constant element size of 0.76 mm, the homogenous mesh consists of 62,500 elements in total. The plastic material properties of the blank are defined with combined hardening and the number of backstresses is set to five. The contact between blank and tool is frictionless and the rotational speed of the tool is neglected. Not the entire tool but only the tooltip is considered in the model and its geometry is adapted according to Fig. 1d for the different simulation runs. The tool path of Fig. 2c is integrated as the displacement boundary condition of the tool. The last important component of the experimental setup, the pressurised air, is defined as mechanical load on the bottom surface of the blank and the pressure level is the process parameter to be optimized by simulation for later experiments.

The process simulation is divided into three steps (Fig. 3c). First, the pressure is applied and the tool penetrates the blank. The second step covers the forming process. In the last step, the tool removes from the blank and the pressure is released. When the pressure is increasing, the blank immediately reacts with upwards movement and elastic bulging. To simulate this kinematic process properly, mass scaling is deactivated in the first step as well as in the last step for a similar reason. In contrast to this, mass scaling is used moderately during the second step to ensure a time increment

of at least 2×10^{-7} s. However, the biggest amount of reducing computational time is achieved by a time scaling factor of 40 leading to a feed rate of 1000 mm/s in the simulation.

3 Results and Discussion

3.1 Influence on Geometrical Accuracy

Initially, the numerical model with the conical tool was used to determine the pressure level that is necessary to manufacture a truncated pyramid with a height not less than the height of the target shape. A pressure level of 0.425 MPa satisfies this requirement, and with this pressure level, the simulation of the manufacturing process with a hemispherical tool was repeated. The geometry of the deformed meshes of both simulations has been exported and then compared with the CAD files of the target shape. Figure 4a shows the absolute deviation between the simulation and the target geometry on the basis of the deformed mesh. In general, it can be seen that the deviations are heterogeneous within one part and that the trends of deviation are opposite between both simulations. The lateral surfaces of the part simulated with the hemispherical tool are in good agreement with the target shape but its corners do not fit well. The other way round, the part simulated with the conical tool has

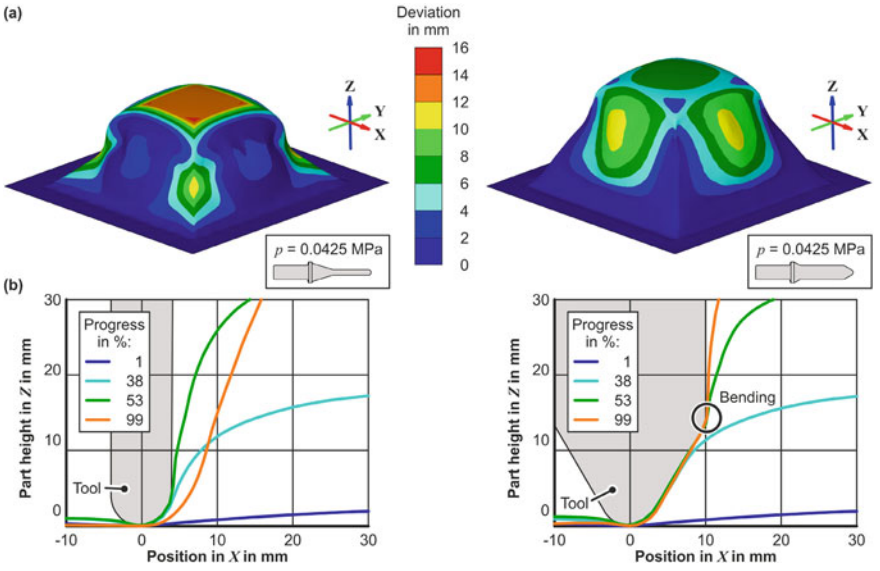


Fig. 4 **a** Absolute deviation between the simulated parts and the target shape, **b** development of the part geometry in contact region between the tool and the blank. (Color figure online)

good accuracy at the corners but not at the lateral surfaces. However, both truncated pyramids have the greatest differences towards each other on their upper face. Using the hemispherical tool, the part is with a height of 62.7 mm lower than the target shape and has a deviation of 12.3 mm. In the case of conical tool, the part grew up to a height of 82.4 mm and was 7.4 mm bigger than the target shape. The maximum deviation is smaller when using the conical tool; it can be concluded from this numerical investigation that not only the geometrical accuracy improves when a conical tool is used but also the convex bulging is facilitated under the condition of constant pressure.

This leads to the question of why the conical tool that was intended to restrict the convex bulging causes a higher part height than the tool that is not restricting the convex bulging. To answer this question, the development of the contact condition during the process has been analysed. Figure 4b shows the part geometry at different time points during the forming process by aligning the cross-sections in the *ZY*-plane in relation to the current tool position. For both simulations, a continuous change of the part wall can be observed but the tool geometries are causing different effects. In the beginning, the wall angle increases unrestricted on interaction with the hemispherical tool but after the horizontal step size changes to 1 mm, the wall angle flattens again, resulting in a smaller part. On the contrary, if it comes into full contact between the conical tool and the part wall, it remains unchanged until the end of the process. Additionally, a second bending of the part wall emerges with progress in the ongoing process and thus the target wall angle and the target height exceed.

3.2 Experimental Validation

After the general feasibility of using the conical tool was proved by simulation, experiments have been conducted with the same pressure level of 0.0425 MPa. The manufacturing of the truncated pyramid by using the conical tool directly succeeded. However, during the experiment with the hemispherical tool, a crack occurred and the experiment had to be stopped because in this case the pressure cannot be kept up and further convex forming is not possible. A new experiment with reduced pressure of 0.0405 MPa could be carried out successfully. The geometry of the manufactured parts was digitalised by a 3D scanner and the cross-sections in the *YZ*-plane, as well as the cross-section through the corners, have been analysed, see Fig. 5a and b. The part with the greatest deviation was the one with the crack manufactured by the hemispherical tool and pressure of 0.0425 MPa. The wall angle increased rapidly, and the crack occurred in the contact region between the lateral surface and the tooltip in the 38th cycle. The final height was 33.1 mm. Even when the pressure was reduced and the part could be produced completely with the hemispherical tool, the deviation remained high for both the lateral surfaces and in the corner because the convex bulging flattens out in the second part of the forming process with a horizontal step size of 1 mm. Only by using the conical tool, it was possible to create a part in the desired dimension. Especially, the accuracy in the corners

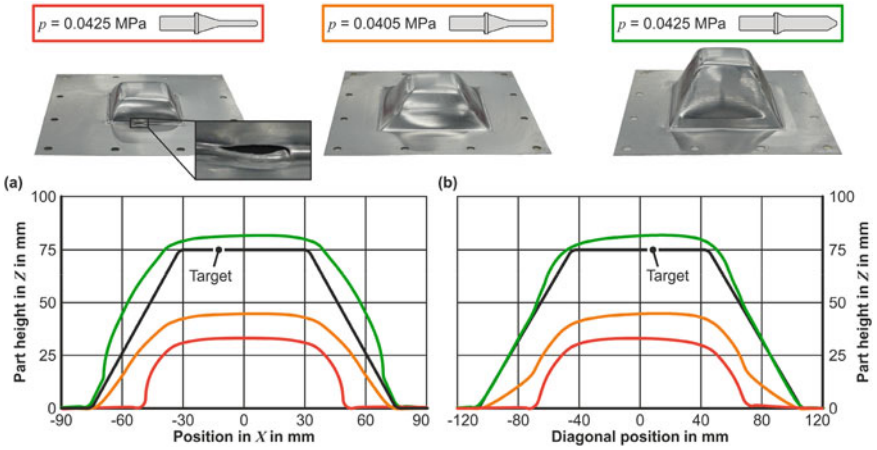


Fig. 5 **a** Cross-sections in the *XZ*-plane, **b** cross-sections of diagonal cut. (Color figure online)

was remarkable. In conclusion, the experiments not only validated the findings of the numerical investigation but also reveal that the conical tool shape increases the process reliability.

Because the manufacturing process with the hemispherical tool failed, it was only possible to compare the results between simulation and experiment concerning the conical tool. Figure 6a shows that the simulation delivered realistic results. Based on these results, the horizontal cross-sections of the truncated pyramid have been analysed at different height levels, as depicted in Fig. 6b. In the lower regions where the part is in contact with the tool, the part has a good accuracy both at the lateral surfaces and at the corners. The corners still have good accuracy in the middle region, but results in an outer bulging at the lateral surfaces. At the top region, the part deviates outwards from the target shape in all regions. The radial force of the pressure might be the reason for the deformation of the angular geometry into a round shape.

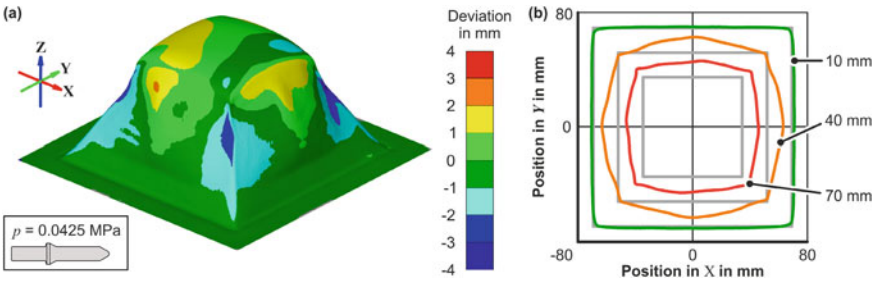


Fig. 6 **a** Comparison of the simulated part and the real experiment, **b** horizontal cross-sections at different height levels of the simulated part. (Color figure online)

3.3 Analysis of Rotationally Symmetric and Concave–Convex Geometries

To see the effect of the tool geometry in interaction with a circular tool path, truncated cones and concave–convex parts have been manufactured. Using the same strategy for these tool paths, the horizontal tool step size was 0.5 mm for the first half and 1 mm for the second half of the forming process. By analogy with the truncated pyramids, three experiments have been conducted for each geometry. The corresponding cross-sections are compared with each other in Fig. 7a and b.

At a pressure level of 0.0525 MPa, a truncated cone could be manufactured by the conical but not by the hemispherical tool. This time, the crack occurred at the transition region from one cycle to the next one shortly before the process ends. The truncated cone could be manufactured with the hemispherical tool at a pressure level of 0.0515 MPa resulting in a similar part as has been created by using the conical tool. For the latter one, the effect of the horizontal step size on the wall angle is less obvious than for the hemispherical tool. In this case, the differences between the hemispherical tool and the conical tool are not as strong as for the truncated pyramid.

The complex parts combine a concave truncated pyramid with a convex truncated cone. The truncated pyramid, which is located in the inner region, was manufactured at first by SPIF with neither pressure nor a back-plate and the vertical step size

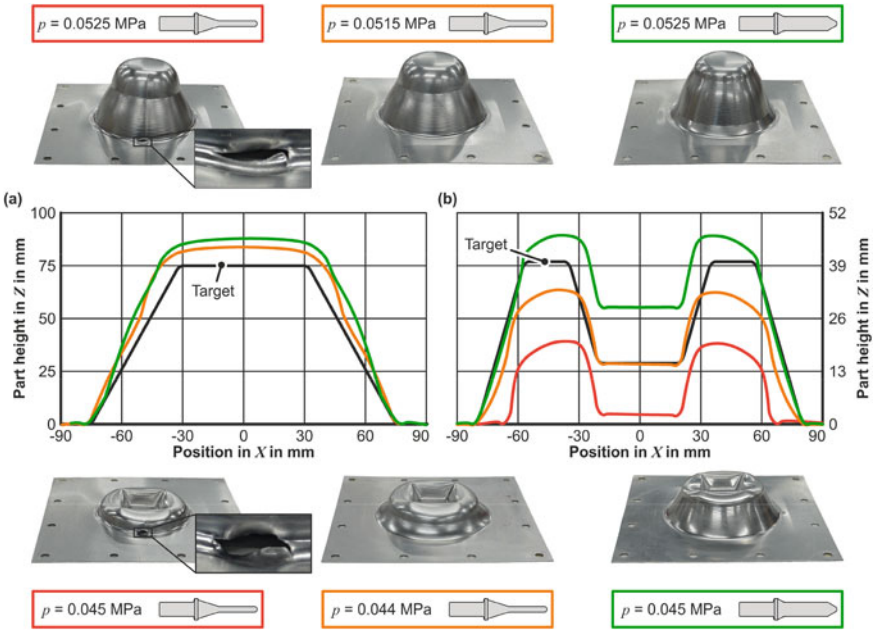


Fig. 7 **a** Cross-sections of the truncated cones, **b** cross-sections of the concave–convex parts. (Color figure online)

was 1 mm. Secondly, the pressure was applied and the outer truncated cone was manufactured. With a pressure of 0.045 MPa, the truncated cone was created with good accuracy by the conical tool. However, through unintended convex bulging of the blank in the area between the inner and the outer feature, the truncated pyramid vertically deviates from its target position. The accuracy in the outer regions of the part created by the hemispherical tool and a pressure of 0.044 MPa lags behind the accuracy of the part produced by the conical tool. When the same pressure of 0.045 MPa was used in combination with the hemispherical tool, a great wall angle emerged and the part failed during the transition from one to the next cycle like the previous truncated cone. The example of these concave–convex parts shows that the positive effects of the conical tool at least account for rotationally symmetric geometries in complex shapes.

4 Conclusions

The geometry of parts manufactured by incremental sheet forming with active medium (IFAM) is a result of interacting pressure, tool path, as well as tool geometry. All of these factors have a significant influence on the geometric accuracy. To achieve a target shape more easily, this paper pursues the approach to change the tool geometry into a conical shape, which restricts the convex bulging. The feasibility of this approach was proven by numerical investigation on the example of a truncated pyramid. The simulated processes have been repeated in experiments and the manufacturing of truncated cones and concave–convex parts completed the analysis. The following conclusions can be drawn:

1. The improvement of geometrical accuracy is dependent on the target shape. The difference is small for truncated cones, which have a rotational symmetric geometry. However, conical tools have a positive influence on the geometric accuracy for truncated pyramids and concave–convex parts.
2. Conical tools increase process reliability for any target shape. The pressure levels that can be applied in combination with the conical tools cause cracks when a hemispherical tool is used. In comparison, the manufacturing with hemispherical tools needs a reduced pressure level by at least 0.001 MPa.
3. A side effect, which is observable in simulation, is facilitated by convex bulging through conical tools. This effect is not verifiable in experiments because cracks might occur when using a hemispherical tool.
4. A second bending of the lateral part wall can emerge and cause additional bulging and exceeding of target height. However, corners of truncated pyramids have better geometrical accuracy than lateral surfaces.
5. Changing the contact conditions by adapting the tool geometry is not a stand-alone solution for overall accuracy. Investigations on pressure control and tool path design are necessary for further improvement.

Acknowledgments The authors would like to express their gratitude to the German Research Foundation (DFG) for funding the research project (grant number BE 5196/14-1) that led to the present results.

References

1. Ben Khalifa N, Thiery S (2019) Incremental sheet forming with active medium. CIRP Ann 68(1):313–316
2. Tolazzi M (2010) Hydroforming applications in automotive: a review. IntJ Mater Form 3(1):307–310
3. Lang LH, Wang ZR, Kang DC, Yuan SJ, Zhang SH, Danckert J, Nielsen KB (2004) Hydroforming highlights: sheet hydroforming and tube hydroforming. J Mater Process Technol 151(1–3):165–177
4. Celeghini M (2004) Wirkmedienbasierte Blechumformung: Grundlagenuntersuchungen zum Einfluss von Werkstoff und Bauteilgeometrie. PhD thesis, Friedrich-Alexander-Universität Erlangen-Nürnburg
5. Bambach M (2008) Process strategies and modelling approaches for asymmetric incremental sheet forming. PhD thesis, RWTH Aachen University
6. Jeswiet J, Micari F, Hirt G, Bramley A, Duflou J, Allwood J (2005) Asymmetric single point incremental forming of sheet metal. CIRP Ann 54(2):88–114
7. Shamsari M, Mirnia MJ, Elyasi M, Baseri H (2018) Formability improvement in single point incremental forming of truncated cone using a two-stage hybrid deformation strategy. Int J Adv Manuf Technol 94(5–8):2357–2368
8. Kumar Y, Kumar S (2019) Experimental and analytical evaluation of Incremental Sheet Hydro-Forming strategies to produce high forming angle sheets. Heliyon 5(6):
9. Jadhav S (2004) Basic investigations of the incremental sheet metal forming process on a CNC milling machine. University of Dortmund
10. Jackson K (2008) The mechanics of incremental sheet forming. PhD thesis, University of Cambridge
11. Cawley B, Adams D, Jeswiet J (2012) Examining tool shapes in single point incremental forming. Proc. NAMRI/SME 26:201–206
12. Ziran X, Gao L, Hussain G, Cui Z (2010) The performance of flat end and hemispherical end tools in single-point incremental forming. Int J Adv Manuf Technol 46(9–12):1113–1118
13. Xu D, Wu W, Malhotra R, Chen J, Lu B, Cao J (2013) Mechanism investigation for the influence of tool rotation and laser surface texturing (LST) on formability in single point incremental forming. Int J Mach Tools Manuf 73:37–46
14. Hadoush A, van den Boogaard AH (2012) Efficient implicit simulation of incremental sheet forming. Int J Numer Methods Eng 90(5):597–612
15. Hadoush A (2010) Efficient simulation and process mechanics of incremental sheet forming. PhD thesis, University of Twente
16. Surech K, Regalla SP (2014) Effect of time scaling and mass scaling in numerical simulation of incremental forming. Appl Mech Mater 612:105–110
17. Bambach M, Hirt G, Junk S (2003) Modelling and experimental evaluation of the incremental CNC sheet metal forming process. In: 7th international conference on computational plasticity, pp 1–16

Manufacturing of Tailored Blanks with Pre-shaped Involute Gearings by Using a Flexible Rolling Process and Its Application in a Sheet–Bulk Metal Forming Process



Manfred Vogel, Robert Schulte, Onur Kaya, and Marion Merklein

Abstract Nowadays, the efficient manufacturing of functional components in short process chains is important due to the goal of a further reduction of greenhouse gases. Additionally, there are also technical demands like functional integration combined with an improvement of the component's properties. Previous investigations have shown that the application of tailored blanks with a defined thickness profile can lead to an improvement of the geometrical and mechanical properties of functional components. However, common forming processes reach their limits. A promising approach to enlarge these process limits is the application of bulk forming operations to sheet metals, the so-called sheet–bulk metal forming (SBMF). Within this process class, one possibility for manufacturing such blanks is a flexible rolling process. As a result of movement of two rolling tools in combination with a die cavity in the lower tool, a defined geometry can be manufactured perpendicular to the sheet plane. In order to raise the complexity combined with a shorter process chain and thus to fulfil the requirements defined by the subsequent forming operations, a new design that contains a preform of involute gearings is introduced. In order to acquire process knowledge, the mild deep drawing steel DC04 with an initial sheet thickness of $t_0 = 2.0$ mm is used. Furthermore, the subsequent application of the tailored blanks in a combined deep drawing and upsetting process is shown, with a characterization of the geometrical and mechanical properties.

Keywords Sheet forming · Flexible rolling · Tailored blank

M. Vogel (✉) · R. Schulte · O. Kaya · M. Merklein
Friedrich-Alexander-Universität Erlangen-Nürnberg, Institute of Manufacturing Technology (LFT), Egerlandstraße 13, 91058 Erlangen, Germany
e-mail: manfred.vogel@fau.de

R. Schulte
e-mail: robert.schulte@fau.de

O. Kaya
e-mail: onur.kaya@fau.de

M. Merklein
e-mail: marion.merklein@fau.de

© The Minerals, Metals & Materials Society 2021

G. Daehn et al. (eds.), *Forming the Future*, The Minerals, Metals & Materials Series,
https://doi.org/10.1007/978-3-030-75381-8_46

1 Introduction

The responsibility and awareness regarding the threat of climate change led to the approval of the Paris Agreement by the international community in 2015. In order to not exceed the global average temperature rise above 1.5–2 °C, a reduction of greenhouse gas emissions is mandatory [1]. Studies have shown that the most produced global greenhouse gas (GHG) emissions take place in agriculture, energy supply, industry, and transport [2]. According to a report of Greenpeace in 2018, 9% of the total annual GHG emissions is caused by the car industry [3]. Due to a high traffic volume of more than one billion vehicles, which are currently driven mainly by internal combustion engines, this sector offers great potential for saving CO_2 [4]. Therefore, on the one hand, the automotive industry develops new alternative powertrains like battery or fuel electric driving systems [5]. On the other hand, lightweight construction is a key technology for the reduction of the vehicle's weight. Based on the requirements for functional components, e.g. synchronizer rings, the conventional bulk and sheet metal forming processes reach their limits. To satisfy the increasing demand for complex functional components and resource-efficient manufacturing, the innovative process class of sheet–bulk metal forming (SBMF) was developed. Due to a process combination, the advantages of both sheet and bulk forming operations can be used [6]. Depending on the forming process, process-adapted semi-finished parts with customized geometrical and mechanical characteristics, the so-called tailored blanks can be manufactured to increase the local material volume and thus the die filling of functional elements [7]. Previous investigations in [7] have shown that a flexible rolling process can be used for manufacturing tailored blanks with a homogeneous thickness profile. To realize a high variety of geometries, different die cavities can be mounted on the rotary table. By applying such semi-finished products in a subsequent process combination of deep drawing and upsetting, the die filling of different functional elements (e.g. gearings) can be increased. However, this process improvement reaches the limit as soon as the material is ironed due to a too large material volume and thus a too high sheet thickness. In order to extend the process limits combined with a shorter process chain, the manufacturing of tailored blanks with pre-shaped functional elements perpendicular to the sheet plane is mandatory. Thus, new challenges regarding a defined control of the material flow and strain hardening arise. Subsequently, a combined deep drawing and upsetting process is shown for applying such tailored blanks. For the investigations presented in this paper a mild deep drawing steel DC04 with an initial sheet thickness of $t_0 = 2$ mm is used.

2 Experimental Setup

This chapter gives an overview of the machine setup for the flexible rolling process as well as the target geometry. Subsequently, the manufactured tailored blanks are applied in a combination of a deep drawing and upsetting process. This experimental

setup and the geometry of the functional components are also presented in this chapter.

2.1 Flexible Rolling of Tailored Blanks and Target Geometry

The main parts of the flexible rolling machine are the two rolling tools, which are assembled on the upper construction in the x-direction as well as the rotary table in the lower construction in the z-direction. A partial view of the working area and the geometrical dimensions of the rolling tools is shown in Fig. 1. The rolls have a diameter of $d_{tool} = 80$ mm and are positioned with an offset of 180°, whereby the right roll is used as the forming roll and the left roll as the smoothing roll. Geometrically, double-tap rolls with defined forming-(α) and smoothing-angle (β) are used. The rolling tool has always a width of b = 20 mm divided into b_1 = 15 mm and b_2 = 5 mm. They are not actively driven for rotation. Only the friction between the rolling tools and the workpiece led to a rotational movement. In order to be able to induce a defined material flow, the rolling tools are driven translationally in the x-direction. During the whole forming process the blank is clamped by the blank holder with a maximum pressure of p = 100 bar. Additionally, in order to guarantee the centring of the sheet metal, it is clamped by a screw on the rotary table. A more detailed description of the flexible rolling machine regarding the construction and the kinematic process limits can be found in [6]. The rotational and vertical movement of the rotary table in addition to the horizontal movement of the rolling tools causes a radial, axial, and tangential material flow. Depending on the applied process strategy, defined tailored blank geometries with different thickness profiles can be achieved.

Due to the increasing complexity of functional components and a required reduction of the process chain length, the aim of these investigations is the manufacturing of tailored blanks with a preform of involute gearings with a subsequent deep drawing

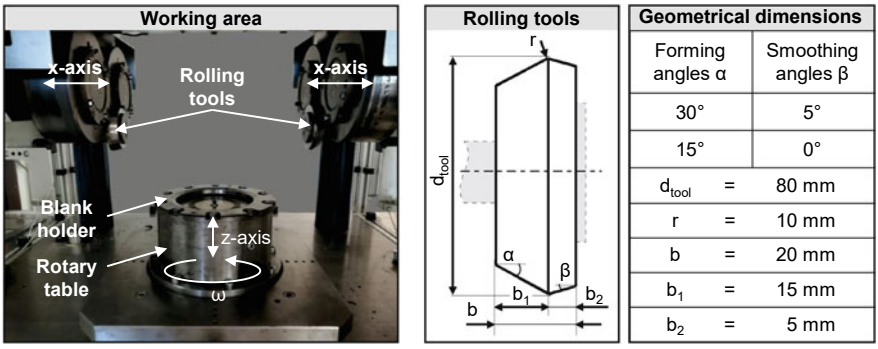


Fig. 1 Working area of the flexible rolling machine and geometrical dimensions of the tools. (Color figure online)

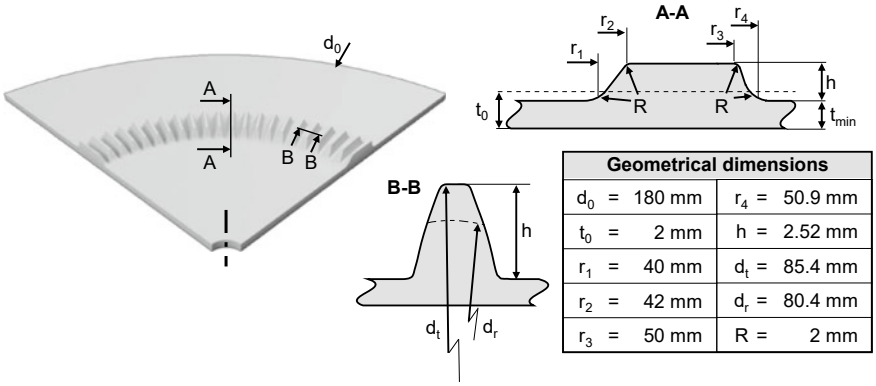


Fig. 2 Target tailored blank geometry—geometry of the die cavity

and upsetting process. In Fig. 2, the target geometry of the tailored blank is schematically shown, which also defines the die cavity as the negative form in the rotary table. Due to planned investigations regarding the application behaviour of functional components manufactured by sheet–bulk metal forming processes, the mild deep drawing steel DC04 with an initial sheet thickness of $t_0 = 2$ mm and a diameter $d_0 = 180$ mm is used. The functional elements are arranged rotational perpendicular to the sheet plane at a radial position between $r_1 = 40$ mm and $r_4 = 50.9$ mm and consist of 84 gear teeth. In order to enable a high die filling through a homogenous material flow, there is an inlet area starting at a radial position of $r_1 = 40$ mm with a horizontal width of 2 mm. In addition, the continuous transition prevents stress concentration during the manufacturing of the final geometry. In the outlet area also a transition zone has to be inserted to reduce the notch effect and thus tool loads in the die cavity. However, to inhibit the material flow out of the die cavity, the transition zone has only a width of 0.9 mm starting at $r_3 = 50$ mm. The edges themselves are rounded with a radius of $R = 2$ mm. The gearing itself is designed with a module $m = 1$, whereby a tip diameter of $d_t = 85.4$ mm and a root diameter of $d_r = 80.4$ mm are realized. Due to this geometric definition of the involute gearing, the tailored blank has a gearing height of $h = 2.52$ mm. A schematic representation of one gearing element is also shown in Fig. 2. For an application of these semi-finished products in the subsequent forming process, there is a laser cutting process at a radial position of $r_3 = 50$ mm.

2.2 Manufacturing Process and Target Geometry

To manufacture the final component, a combined deep drawing and upsetting process is applied. During the deep drawing operation the basic shape of the part is formed, whereas the functional elements of the tailored blank are formed in the subsequent

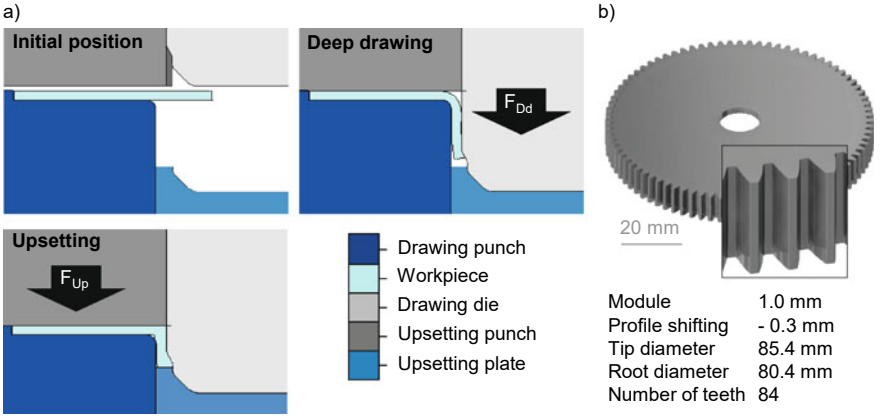


Fig. 3 **a** Process setup of the combined sheet–bulk metal forming process and **b** geometric properties of the functional component with involute gearings. (Color figure online)

upsetting stroke due to a reduction of the cup height. The process proceeds force-controlled, whereby the upsetting force exceeds the drawing force considerably. The process combination is applied in a single press stroke and therefore requires a triple-acting press. Therefore, a hydraulic press of the type TZP400-3 by Lasco with a conventional press ram and two die cushions is used. The maximum press force amounts to 4,000 kN. The tool setup developed for this sheet–bulk metal forming process consists of four active components, two in the upper and two in the lower tool. The active components in the upper tool are the drawing die and upsetting punch, whereas the drawing punch and upsetting plate are part of the lower tool. Schematic tool setup and kinematics are presented in Fig. 3a. In the initial position the semi-finished product is placed on the drawing punch and then clamped by the upper tool. Afterwards, the drawing die moves downwards to draw the cup and proceeds until it is in contact with the upsetting plate. The drawing punch radius is $r_{Dp} = 1$ mm and the external diameter amounts to $d_{Dp} = 80$ mm. As already shown in [8], the positioning of the semi-finished product in relation to the thickening direction of the tailored blank plays a decisive role for a possible component failure. Subsequently, the cup and drawing punch are displaced by the upsetting punch under the upsetting force F_{Up}. The maximum upsetting force in this investigation was set to $F_{Up} =$ 1,000 kN. For conventional blanks with an initial sheet thickness of $t_0 = 2$ mm, the upsetting force induces a radial material flow towards the gear cavity, whereas for rolled tailored blanks the upsetting force is applied to increase the die filling of the gear teeth manufactured within the flexible rolling process. The target geometry has an external involute gearing with a module of $m = 1$, corresponding to the cavity used for the manufacturing of the tailored blanks. For the final component, the tip diameter is $d_t = 85.4$ mm and the root diameter is $d_r = 80.4$ mm. The total amount of teeth is 84, as presented in Fig. 3b. As the material volume in the geared section is

different for conventional semi-finished products and tailored blanks, the resulting cup height varies under the equal upsetting force.

3 Manufacturing of Tailored Blanks

In order to analyse the benefits of manufacturing and application of tailored blanks with discrete functional elements and for increasing the process knowledge of the flexible rolling process, experimental tests were carried out. Subsequently, the semi-finished products were characterized regarding their resulting contour, sheet thicknesses, and material volumes, as well as the mechanical properties by analysing the hardness distribution.

3.1 Process Strategy and Resulting Geometry

In previous investigations in [8], a process strategy was introduced which could be used to manufacture rotational symmetric tailored blanks with a circular material thickening. The challenge was to concentrate the material flow purposefully in the thickening profile in order to achieve a homogeneous thickening. In contrast to previous investigations, the challenge regarding the manufacturing of functional elements perpendicular to the sheet plane is the die filling of local interrupted material thickening geometries. Thus, a defined control of the direction-dependent material flow is mandatory. Therefore, a new process strategy has to be developed under consideration of individual process parameters. Through process analysis for the manufacturing of tailored blanks with a rotationally symmetric thickness profile in [7], the process parameter of the vertical roll displacement (VRD) could be identified as an essential process variable for achieving a high material volume in the thickening zone. Within this paper the transferability by variation of this process parameter is analysed by taking the process limits into account. However, the geometry of the die cavities influences the direction-dependent material flow back to the centre of the blank. For this reason, in combination with investigations for manufacturing cyclic-symmetric tailored blanks in which a vertical roll displacement of VRD = 0.8 mm could be identified as appropriate [9], eight steps in the linear distribution in an interval between VRD = 0.1 mm and VRD = 0.8 mm are analysed in this paper. Additionally, an overview of all the relevant process parameters of the flexible rolling process is shown in Table 1.

In this case, the target values are both the largest possible die filling as well as a small bulging of the tailored blank, consequently resulting in the flexible rolling process. For the development of a new process strategy, the experimental tests have been geometrically measured. For a deeper analysis, the semi-finished products are digitized by a strip light projection process using the optical 3D scanner ATOS (GOM GmbH). The final results after the first stroke by using different process parameters

Table 1 Process parameters

Process parameters		Factor level
Rotary table RPM [rot/s]		0.5
Feed rate [mm/s]		0.15
Vertical roll displacement [mm]	Stroke 1	0.1/0.2/0.3/0.4/0.5/0.6/0.7/0.8
	Stroke 2	0.8/0.9/1.0

are shown in Fig. 4. In order to achieve the highest die filling, the rolling path of the forming roll starts at a radius of r = 14 mm and moves up to a radial position of r = 55 mm. The radial positions of the rolling paths are relatively referred to the transition zone between the forming and the smoothing angle of the rolling tool. The innermost position is a system-related process limit.

A radial in-feed causes a material accumulation in front of the forming roll, whereby the sheet bulges due to the tool contact in the forming roll, similar to flow forming processes [10]. In order to get this material accumulation specifically into the thickening area, there is also a rolling tool at a radial position of r = 50 mm with an offset of 180°, which points to the forming angle in the direction of the blank centre. The results of the tailored blank contours are shown in Fig. 4a as a function of different vertical roll displacements. Due to a higher reduction of the sheet thickness,

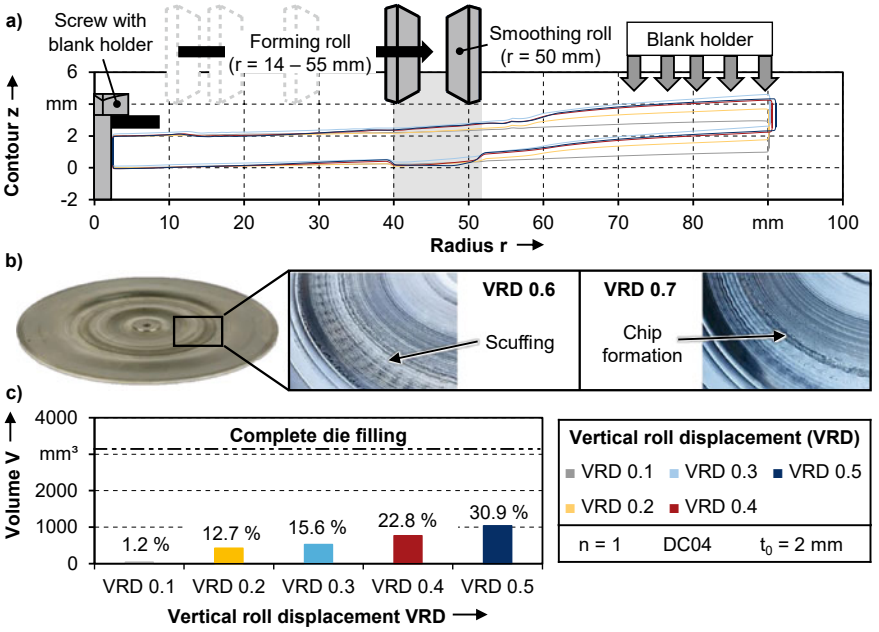


Fig. 4 Results after the first stroke: **a** contour, **b** process limits, and **c** volume in the die cavity. (Color figure online)

the material volume in the die cavities and also the bulging of the semi-finished product increase. By varying the pass reduction from VRD = 0.1 mm to VRD = 0.3 mm the bulge also rises from 1.2 to 2.3 mm in the outer diameter. However, the bulging height no longer increases with a higher vertical roll displacement. Therefore, for VRD = 0.5 mm there is also a bulging of 2.3 mm detectable. This correlation is due to the forming process and the gradient of the stress conditions in the sheet thickness direction. By increasing the vertical roll displacement, the contact pressure between the tool and the workpiece increases, which results in a more homogenous material flow and thus reduces the difference in the stress conditions between the rolling and the die side. These stresses are discharged after releasing the blank holder, which leads to the characteristic bulging of the tailored blank.

A further increase of the vertical roll displacement up to VRD = 0.7 mm leads to process failures on the surface of the tailored blank, as shown in Fig. 4b. During the flexible rolling process, the material in the primary forming zone is subjected to a three-dimensional stress and strain state due to tool contact. Consequently, the radial material flow leads to an accumulation in the secondary forming zone in front of the rolling tool, resulting in predominant compressive stress conditions. This material volume is used for the die filling of the target geometry. With a value of VRD = 0.6 mm, the accumulated material is too large in relation to the cyclic symmetric interruptions between the functional elements, so the material flow is not completely directed into the die cavities. The remaining material volume is radially displaced in front of the forming roll, which results in a material overlap. Due to further processing of the rolling path, suffering of the surface occurs. Especially for an application of the tailored blanks in subsequent processes, these defects represent damage potential through notch effects. Due to an increase of VRD = 0.7 mm, the material overlap in combination with another tool contact leads to chip formation. Depending on the flexible rolling machine, there is no significant change between VRD = 0.5 mm and VRD = 0.6 mm detectable. Thus, the vertical roll displacement of VRD = 0.5 mm represents a process limit for the first rolling stroke.

For geometric reasons, however, an increase of the vertical roll displacement also leads to a higher material volume to be achieved in the die cavities. Based on the target geometry, the complete material volume of the gearing elements is 3360 mm^3. While a vertical roll displacement of VRD = 0.1 mm leads to a material volume of only 40.3 mm^3, which is 1.2% of the target volume, VRD = 0.5 mm leads to an increase of up to 30.9%. This correlation is shown in Fig. 3c. Due to the maximum die filling at this setting and the process limit at VRD = 0.5 mm, this setting is used as the basis for a subsequent rolling stroke.

However, to shorten the process chain, a further increase of the material volume in the individual functional elements is mandatory. With the objective of a higher die filling, a second stroke is applied with an increased vertical roll displacement. In order to be able to analyse the material flow, experimental tests with adapted vertical roll displacements were carried out. Due to previous investigations in [9], the correlation between the strain hardening by the first rolling stroke and increased roll displacements in a second stroke could be clarified. For this analysis, values between VRD = 0.8 mm and VRD = 1.0 mm are considered with an interval of $\Delta =$

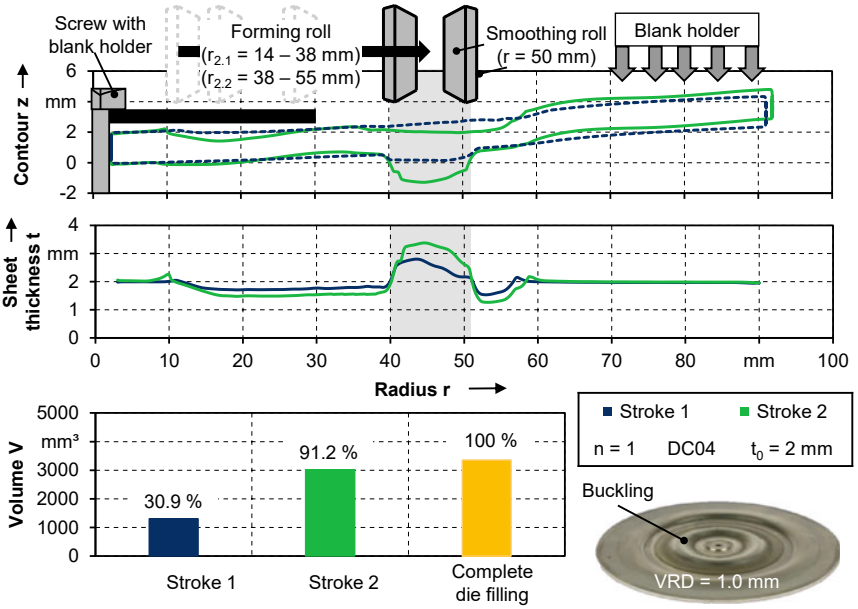


Fig. 5 Final geometric results after two rolling strokes regarding **a** contour and sheet thickness and **b** volume. (Color figure online)

0.1 mm. However, despite the previous forming stroke, buckling occurs with a rising vertical roll displacement, as seen in Fig. 5. Due to the material accumulation in front of the forming roll combined with the levelling of the smoothing roll, which is offset by 180°, material reflux occurs at the centre of the blank in addition to an increase of the outer diameter. Thus, the tailored blank buckles in the inner rolling zone between the inner blank holder and the rolling tool due to the free buckling length and the stiffness of the material. This correlates with an increase of the vertical roll displacement. As a result, in the second stroke, an enlarged blank holder is used in the tailored blank centre and the rolling path of the forming roll is divided in order to achieve an optimum ratio between a high material volume and the geometric dimensional accuracy. The forming roll moves from r = 14 mm to r = 38 mm with a vertical roll displacement of VRD = 0.8 mm. Subsequently, the inner blank holder with a heightened diameter is mounted when the outer blank holder is still clamped. Then the rolling stroke is continued with the same set of parameters until the forming roll has reached a radial position of r = 55 mm. The final geometry with regard to the semi-finished product contour and the achieved sheet thickness and material volume is shown in Fig. 5. It can be observed that the second stroke not only leads to a further thinning of the material in the inner rolling zone but also levelling of the material in the thickening area. While in the first rolling stroke a maximum sheet thickness of t = 2.8 mm is achieved, a maximum of t = 3.4 mm is possible after the second stroke. However, the volume in the die cavity increases up to 91.2%. This

new process control can thus be used for the manufacturing of functional elements with interrupted die cavities, whereby a limit of the forming behaviour of the used material must be taken into account. Furthermore, due to the orientation of the rolling strokes from inside to outside, this process strategy can be used for the manufacturing of tailored blanks with a smaller diameter and thus without a cutting operation.

3.2 *Mechanical Properties*

In order to increase the process knowledge and for evaluation of the mechanical properties for the subsequent *forming* process, the hardness distribution is a relevant parameter for the quality of the tailored blanks. Due to the high perpendicular process forces, which occur during the flexible rolling process, there is strain hardening of the material. For qualifying the final tailored blank geometry, the Vickers' hardness at the cross-sections of the functional elements and the intermediate area was measured for both strokes with a test force of F = 0.05 kp, a measuring point distance of 0.3 mm across the sheet thickness, and 0.6 mm in the radial direction. The results of the evaluation regarding hardness plots and sections of the microstructure are shown in Fig. 6.

The qualitative contour plots of the first stroke show a tendency of increase in the hardness values on the radial position of the die cavities. This can be confirmed by the grain orientation of the microstructure. During the forming stroke material

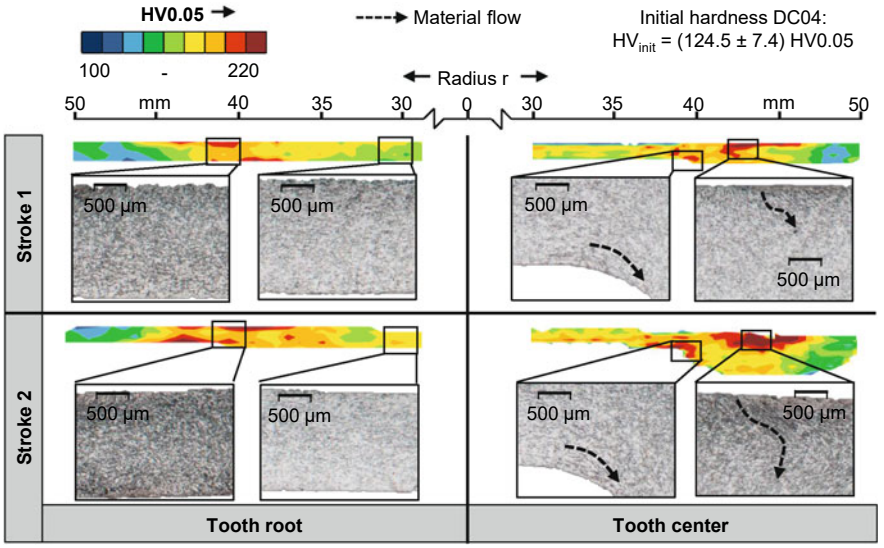


Fig. 6 Mechanical properties of the tailored blank in the tooth root and canter after each stroke. (Color figure online)

is accumulated in front of the rolling tool. Due to the levelling by the smoothing roll, there is a kind of upsetting process in the thickening area which leads, on the one hand, to the filling of the cavities and, on the other hand, to a strain hardening in this area. While in the tooth root the highest hardness values are (228.9 ± 19.8) HV0.05, the hardness values in the tooth centre are 21% higher. This is caused by the direction-dependent material flow. The tool contact of the rolling tool in addition to the rotary movement of the rotary table leads to a tangential material flow. Thus, the material accumulation in the intermediate area of the tooth root is displaced into the die cavities. Superimposed on the translational movement of the rolling tools and the resulting radial material flow, the material is higher strain hardened in the thickening area of the tooth centre, thereby hardness values of up to (279.9 ± 25.1) HV0.05 are reached. The same effect can be seen after the second stroke. Due to the higher vertical roll displacement and thus increased process forces, the quantity of material flow rises which leads to a stronger strain hardening. Due to the direction-dependent material flow, these areas must be considered for other materials for an application in the subsequent forming process to prevent failures.

4 Manufacturing of Functional Components

The manufactured tailored blanks are used in the process combination presented in Sect. 2.2. For an analysis of the volume of the functional components, the parts are also digitized by the strip light projection method for each forming step.

The resulting geometries after the deep drawing and upsetting process are shown in Fig. 7a. In the first step, the blank with the involute gearings is deeply drawn to form a cup. After the drawing process, the cup has a resulting height of $h_{d\text{-}tb}$ = 12.34 mm and the material volume in the teeth of the involute gearings amounts to V_G = 1,107.50 mm^3. Subsequently, the cup is formed with the adjusted upsetting force of F_{Up} = 1,000 kN. Thus, the component's height is reduced by about 40% to $h_{u\text{-}tb}$ = 7.43 mm, but the material volume in the functional elements grows up to V_G = 2,299.69 mm^3, as shown in Fig. 7b. In order to quantify the advantages of the application of semi-finished products with discrete functional elements, the same parts were manufactured using sheet metals with a thickness of t_0 = 2 mm. A comparative analysis of the cup height between the conventional and the tailored blank shows $h_{d\text{-}c}$ = 12.85 mm and Δ = 0.51 mm, a higher shape of the component with t_0 = 2 mm after the deep drawing process. This difference can be explained by the increased ironing caused by the drawing die in the area of the tooth root of the functional component. Due to the lack of an adapted thickness profile using the discrete functional elements, the volume in the gearing for the conventional sheet is 84% lower than for the tailored blank. After the upsetting process, the cup height of the part using a flat sheet amounts to $h_{u\text{-}c}$ = 7.89 mm and a material volume of V_G = 1,772.46 mm^3 in the involute gearing. Compared to the application of the tailored blank, a 23% lower die filling of the functional elements is reached. In addition to the geometric shapes of the functional elements, the strain hardening represents a

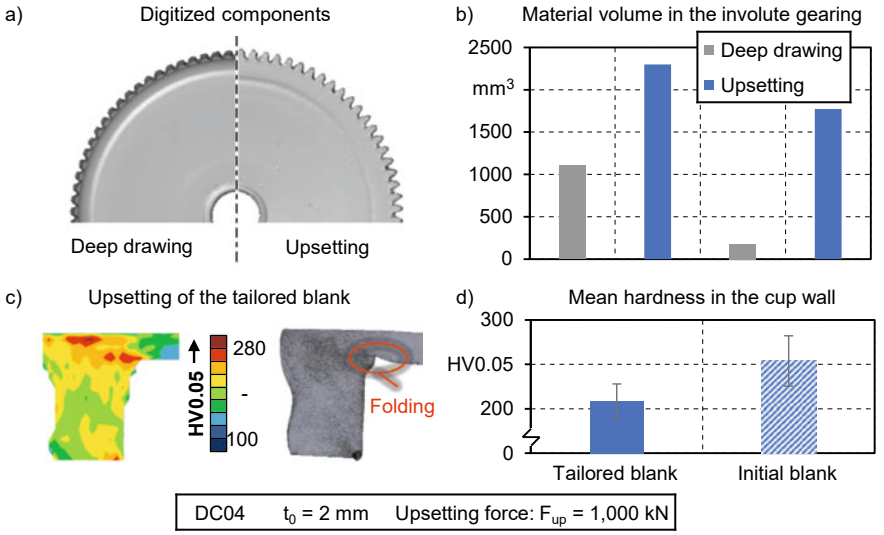


Fig. 7 Analysis of the functional components regarding **a** digitized components, **b** material volume in the involute gearing, **c** strain hardening and microstructure and **d** mean hardness in the cup wall. (Color figure online)

decisive result, especially with regard to the usability and tolerable load capacity of the functional components. For this reason, an analysis of the strain hardening and microstructure of one tooth was carried out after the upsetting process. In Fig. 7c higher hardness values of up to 263.4 HV0.05 are detectable in the area of the drawing radius compared to the tooth tip. This can be explained by the material flow into the cup bottom, which occurs during the upsetting process and results in a folding of the material. This can also be seen in the analysis of the microstructure. Previous investigations in [9] have shown that despite the application of tailored blanks, the folding cannot be prevented. However, the qualitative evaluation of the hardness distribution shows a homogenization of the strain hardening compared to the semi-finished product with the discrete functional elements. During the upsetting process of the cup wall, a radial material flow primarily takes place in the direction of the functional elements. Hence, there is a higher forming level in the inlet area of the involute gearing, which results in an increase in the strain hardening circumferential. This effect can also be seen in Fig. 7d, in which the mean hardness in the cup wall is compared for using a tailored blank and a flat sheet in the upsetting process. Due to the lower deformation by using tailored blanks with discrete functional elements, an average hardness distribution of (208.7 ± 19.3) HV0.05 is reached. This is about 18% less compared to the application of conventional semi-finished products. The significantly lower geometrical moment of inertia per unit by applying a sheet metal with $t_0 = 2$ mm in the upsetting process leads to an average hardness value of (253.8 ± 28.2) HV0.05.

Furthermore, within the framework of the investigations, it has to be taken into account that for the manufacturing of functional components with such a large material volume, tailored blanks with a circumferential material thickening as presented in [7] cannot be used for production in the combined deep drawing and upsetting process. Due to the negative shape of the gear geometry in the drawing die and the resulting process control, the material is ironed in the drawing gap, whereby a process limit is reached.

5 Summary and Outlook

For manufacturing functional components with higher complexity in short process chains, tailored blanks with discrete functional elements are introduced in this paper to improve the intended material flow. For achieving the target die filling of the functional elements in a flexible rolling process, a new process strategy with two rolling strokes is evolved. The orientation of the single strokes is one-directional from inside to outside. Thus, a material volume of up to 91% can be reached in the die cavities of the involute gearing. Hereby, the rolling process and the die cavities influence the strain hardening of the final tailored blanks geometry. Due to the tool contact and the interrupted thickening areas, the highest strain hardening occurs on the rolling side in the thickening area. These manufactured tailored blanks were applied in a combined deep drawing and upsetting process. It could be shown that the die filling of the involute gearing after the forming process can be increased significantly up to 84% compared to the application of conventional semi-finished products, due to the application of tailored blanks with a preform. However, the functional elements are not yet completely filled with material. Furthermore, it could be seen that the combined deep drawing and upsetting process leads to folding in the drawing radius. In this context, further research and an adaptation to the tailored blank layout are necessary. Additionally, it has to be investigated whether a complete die filling of the functional elements in the manufacturing of the tailored blanks is possible by using semi-finished products with a higher initial sheet thickness in order to shorten the process duration by using a calibration process only. To ensure widespread use and an increase in applicability towards the resistance of higher component loads, the transferability of the process regarding the application of higher strength steel materials or other classes of materials for both the flexible rolling and the deep drawing and upsetting process has to be analysed.

Acknowledgments This work was supported by the German Research Foundation (DFG) within the scope of the Transregional Collaborative Research Centre on sheet–bulk metal forming (SFB/TR 73, https://www.tr-73.de) in the subproject A1 “Process combination for manufacturing teethed, thin-walled functional components out of tailored blanks”.

References

1. United Nations (2015) Paris agreement. Paper presented at the 21st session of the conference of the parties to the united nations framework convention on climate change, Paris, 30 November–13 December 2015
2. United Nations Climate Change (2019) Climate action and support trends. https://unfccc.int/sites/default/files/resource/Climate_Action_Support_Trends_2019.pdf. Accessed 23 November 2019
3. Stephan B, Lee I, Kim J (2019) Crashing the climate: How the car industry is driving the climate crisis. Greenpeace East Asia and Germany
4. Canzler W, Knie A (2019) Autodämmerung: Experimentierräume für die Verkehrswende. Heinrich-Böll-Stiftung
5. Bratzel S, Thömmes J (2018) Alternative Antriebe, Autonomes Fahren, Mobilitätsdienstleistungen - Neue Infrastrukturen für die Verkehrswende im Automobilsektor. Heinrich-Böll-Stiftung. https://www.boell.de/sites/default/files/heinrich-boell-stiftung_alternative-antriebe-autonomes-fahren_v01_kommentierbar.pdf. Accessed 24 Nov 2019
6. Opel S (2013) Herstellung prozessangepasster Halbzeuge mit variabler Blechdicke durch die Anwendung von Verfahren der Blechmassivumformung. PhD thesis, Friedrich-Alexander-Universität Erlangen-Nürnberg
7. Hildenbrand P, Lechner M, Merklein M (2016) A new strategy for manufacturing tailored blanks by a flexible rolling process. In: Kawalla R, Ullmann M, Neh K (eds) Production and further processing of flat products. materials science forum. Trans Tech Publications, pp 99–105
8. Hildenbrand P, Schneider T, Merklein M (2015) Flexible rolling of process adapted semi-finished parts and its application in a sheet-bulk metal forming process. In: Key engineering materials, vol 639. Trans Tech Publications Ltd., pp 259–266
9. Vogel M, Lechner M, Hildenbrand P, Schulte R, Merklein M (2017) Manufacturing of tailored blanks by flexible rolling and its application in a sheet-bulk metal forming process. In: Proceedings SCT2017. Verlag Stahleisen GmbH
10. Ufer R (2006) Modellierung und Simulation von Drückwalzprozessen. In: Technische Universität Chemnitz

Roll Forming of Cup with Curved Rotary Profile



Baohong Zhang, Bin Hu, Chunyu Wei, and Xi Zhao

Abstract In order to improve the production efficiency and material utilization rate of metal cup with a curved rotary profile, a new method of roll forming (RF) is proposed. That is, a roll forming equipment with a set of pre-forming rollers and a set of shaping rollers is mounted on the drawing hydraulic press to form a curved rotary profile of cup. The influence of roller number on the roll forming was studied by numerical simulation. The results show that the open end of the rolled part is extremely uneven when two rollers are used. In addition, metal flows into the gaps between rollers, forming thin flashes which must be cut off after the pre-forming step. The open end of the rolled part is relatively even when three rollers or four rollers are used. No metal flows into the gaps between pre-forming rollers, and no folding is found after shaping. The accuracy of numerical simulation is verified by experiments, and aluminum cups with a curved rotary profile that meet the requirements were successfully formed.

Keywords Cup with rotary curve shape · Roll forming · Numerical simulation · Pre-forming · Shaping

1 Introduction

In modern manufacturing, metal cup parts with a curved rotary profile not only have extensive applications but also need large-scale production of parts, such as drill pipe joints and projectile bodies, whose final shape or the shape in a certain step during the forming process needs to be a curved rotary profile. In order to meet the requirements of high mechanical properties and mass production, cup with a curved rotary profile is usually traditionally manufactured using the production process of plastic forming

B. Zhang (✉) · B. Hu · C. Wei
School of Materials Science and Engineering, North University of China, Taiyuan 030051, China
e-mail: zhangbh@nuc.edu.cn

X. Zhao
Engineering Research Center for Magnesium-Base Material Processing Technology, Ministry of Education, North University of China, Taiyuan 030051, China

© The Minerals, Metals & Materials Society 2021

G. Daehn et al. (eds.), *Forming the Future*, The Minerals, Metals & Materials Series,
https://doi.org/10.1007/978-3-030-75381-8_47

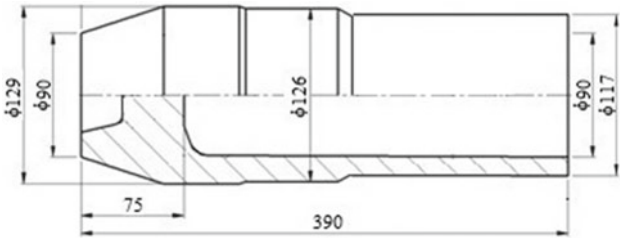


Fig. 1 Cup with curved rotary profile

and then machining [1–6]. However, the material utilization rate is relatively low using this traditional production process for cup with a curved rotary profile, and the longer the smaller-diameter section(s) of the part, the lower the material utilization rate. In order to improve the material utilization rate, Xu Hengqiu et al. used the hot-spinning method to form the curved rotary profile of cup and formed ideal samples [7, 8]. However, the production efficiency of hot-spinning is low, which cannot meet the requirements of mass production, and the mandrel is difficult to put out from the workpiece after hot-spinning. Therefore, the production of cup with a curved rotary profile does not use the hot-spinning process.

In order to increase the material utilization rate of cup with a curved rotary profile and meet the requirements of its production efficiency, a roll forming (RF) method is proposed in this paper. A kind of cup with a curved rotary profile is taken as an example (as shown in Fig. 1), and the influence of the number of rollers on the quality of the cup after roll forming was studied.

2 Principle of Roll Forming

On the basis of the analysis of forming methods such as roll forging and drawing, a method of RF for cup with curved rotary profile was proposed and the schematic of RF is shown in Fig. 2 [9–12]. At the time of RF, the punch is installed under the movable ram of the hydraulic press. The billet, which is pushed by the downwardly moving punch, makes the pre-forming rollers rotate, and the curved rotary profile of the cup is formed by the specific groove shape on the surface of the rollers. During the RF process, some metal will flow into the gap between the rollers and form a thin flash, which will make it difficult to do subsequent machining (as shown in Fig. 3). In order to avoid the formation of a thin flash, a triangular flash groove is designed between the adjacent pre-forming rollers. As a result, the metal that flows into the gap between the rollers will form a triangular flash, which can be eliminated by the shaping rollers installed below the pre-forming rollers. The shaping rollers rotate at an offset angle with respect to the forming rollers (as shown in Fig. 4). The essence of RF is to achieve wall thickness reduction and axial elongation of thick-walled

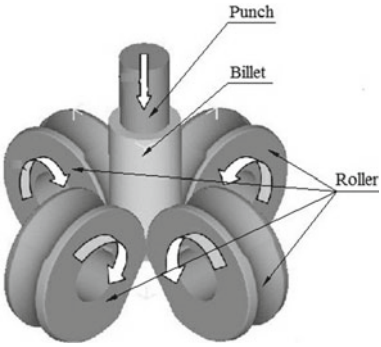


Fig. 2 Schematic diagram of RF

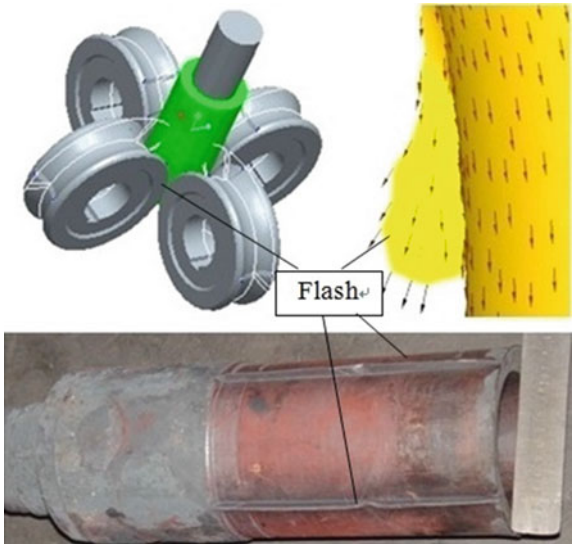


Fig. 3 Flash between rollers. (Color figure online)

cups through the rotary extrusion of the roller. At the time of RF, two, three, or four rollers can be used, but the number of rollers will influence the flowing of metal and the quality of the rolled cup.

3 Numerical Simulation of RF

3.1 Model of Numerical Simulation

The Deform-3D finite element software was used to simulate RF with three kinds of roller number, which is two-roller, three-roller, and four-roller. The model of numerical simulation for RF is shown in Fig. 5, which consists of punch, billet,

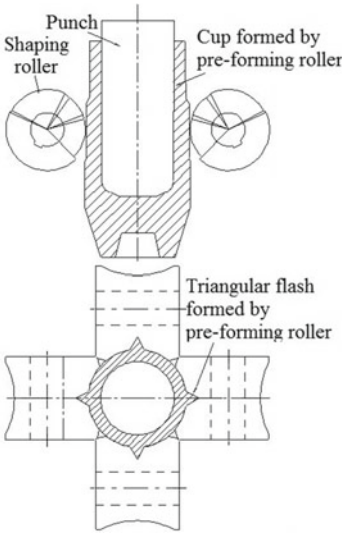
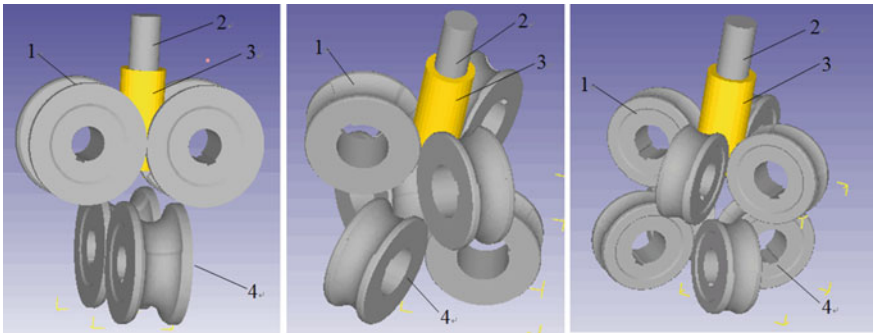


Fig. 4 Shaping of RF



(a) Two-roller (b) Three-roller (c) Four-roll

Fig. 5 Model of numerical simulation. (1: Pre-forming roller; 2: Punch; 3: Billet; 4: Shaping roller). (Color figure online)

and rollers. The billet is a plastic body, and the rollers and punch are rigid bodies. The speed of punch is 10 mm/s. The material is pure aluminum 1060. The friction between the billet and the rollers and punch is based on a shear friction model and the friction coefficient is set to 0.3. The initial element of the billet is 28143, and the number of nodes is 129073. The initial temperature of the billet and the ambient temperature are 20 °C. The billet for RF is shown in Fig. 6.

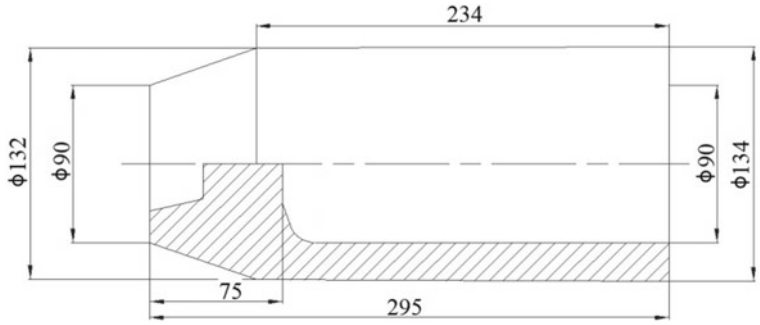
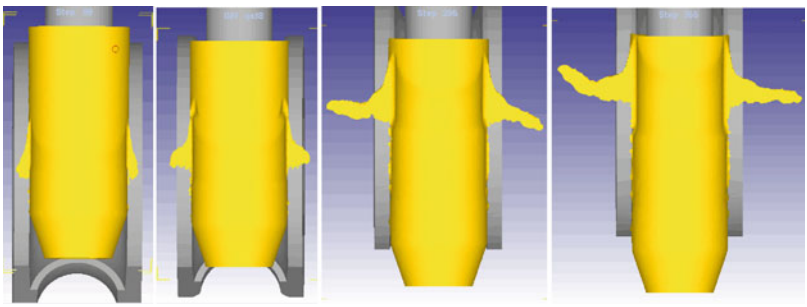


Fig. 6 Billet for RF

3.2 Results of Numerical Simulation

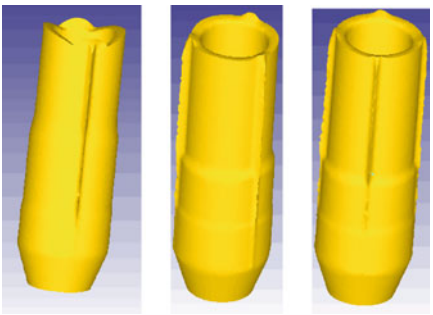
3.2.1 Pre-forming of RF

The pre-forming process of two-roller RF is shown in Fig. 7. It can be seen from Fig. 7 that during the process of two-roller pre-forming RF, the metal fills the flashing groove between the rollers and then flows into the gap between the rollers, which causes the forming of thin flashes. As the RF progresses, the flashes are cut off. During the pre-forming process of three-roller and four-roller, the metal did not completely fill the flash groove between the rollers, so the metal did not flow into the gap between the rollers to form a thin flash. The rolled part and the open end of the rolled part after pre-forming of RF are, respectively, shown in Figs. 8 and 9. It can be observed from Figs. 8 and 9 that the open end of the rolled part is extremely uneven when the two-roller is used. Due to large amount of metal flowing into the gap between rollers, the open end of the rolled part has a high boss at the corresponding position of the flash groove between rollers. The open end of the three-roller rolled part also formed a boss at the corresponding position of the flash groove between



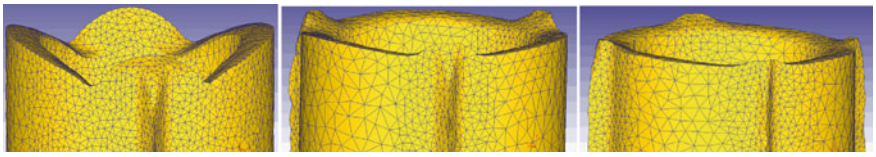
(a) Step99 (b) Step 120 (c) Step 295 (d) Step 355

Fig. 7 Pre-forming process of two-roller RF. (Color figure online)



(a) Two-roller (b) Three-roller (c) Four-roller

Fig. 8 Rolled part after pre-forming of RF. (Color figure online)



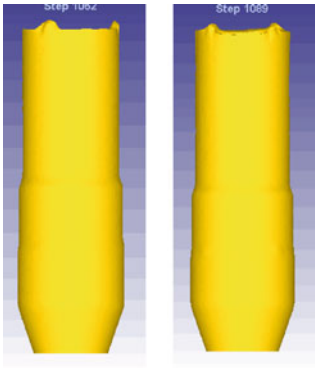
(a) Two-roller (b) Three-roller (c) Four-roller

Fig. 9 Open end of rolled part after pre-forming of RF. (Color figure online)

rollers, but the height of the boss is lower than that of the two-roller rolled part, and the open end is more even; the open end of the four-roller rolled part also formed a boss at the corresponding position of the flash groove between rollers, but the height of the boss is the lowest among the three kinds of rolled parts, and the open end is the most even. The difference between the two-roller and three- or four-roller is very obvious, but the difference between three-roller and four-roller is not obvious. The main reason for this phenomenon is that as the number of roller increases, the number of gaps between the rollers increases accordingly, so the metal is more uniformly deformed in the circumferential direction. The number of gaps between rollers for three- and four-roller, respectively, increased by 50% and 100% compared to that of two-roller, while the number of gaps between rollers for four-roller increased by only 33% compared to that of three-roller, which causes the differences of roller number is obvious or not.

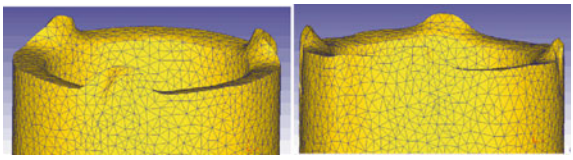
3.2.2 Shaping of RF

The thin flash at the gap between the rollers was cut off during the pre-forming of two-roller, which not only wastes the metal but also will affect the RF of the next workpiece as the flash remains in the gap between the rollers. Therefore, the two-roller is not suitable for RF of the cup with a curved rotary profile, and the numerical



(a) Three-roller (b) Four-roller

Fig. 10 Rolled part after shaping of RF. (Color figure online)



(a) Three-roller (b) Four-roller

Fig. 11 Open end of rolled part after shaping of RF. (Color figure online)

simulation of shaping with two-roller was not performed. The rolled parts of three-roller and four-roller after shaping of RF are shown in Fig. 10. It can be observed from Fig. 10 that the flashes formed by pre-forming of RF were eliminated after the shaping of RF; the surface of rolled part is smooth and there are no defects such as folding and cracking in the rolled part; new flash wasn't formed at the gap between the shaping rollers. It can be observed from Fig. 11 that the height of the boss at the open end of the rolled parts increases slightly after shaping of RF compared with the pre-forming of RF.

4 Experiment

As the difference between the simulation results of three-roller and four-roller is relatively small, and the three-roller RF equipment is simpler and easier to control than that of four-roller, experiments were carried out with the three-roller equipment. The three-roller RF equipment shown in Fig. 12 was used to perform the RF experiment on a hydraulic press. The RF equipment has three pre-forming rollers and three shaping rollers. At the time of RF, the speed of the hydraulic press is 10 mm/s. The



Fig. 12 RF equipment of three-roller. (Color figure online)

material of billet is pure aluminum 1060 and it is carried out at room temperature. The cup with a curved rotary profile obtained by RF is shown in Fig. 13. It can be observed from Fig. 13 that the cup with a curved rotary profile has no defects such as folding and cracking. The error between the roll-formed parts and the simulation results at the length in the axial direction and the height of the open end is less than 10%. The other dimensions and shapes of the roll-formed parts obtained in the experiments were consistent with the simulation results.

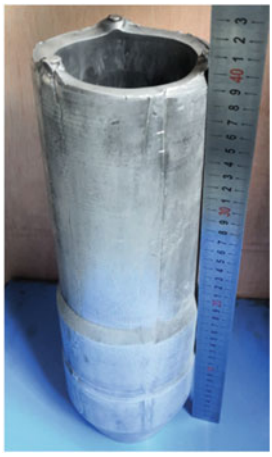


Fig. 13 Roll-formed parts. (Color figure online)

5 Conclusion

Roll forming can be used for the production of cup with a curved rotary profile to improve the material utilization rate and production efficiency, and thus it reduces machining and production costs. The thin flash at the gap between the rollers is formed and cut off during the pre-forming of two-roller, which will affect the roll forming of the next workpiece. Therefore, the two-roller is not suitable for roll forming. Three-roller or four-roller can form ideal parts and they are recommended for roll forming of cup with a curved rotary profile.

Acknowledgments This work was supported by National Natural Science Foundation of China under grant No. 51775519.

References

1. Zhu XH, Zhang Z (2017) Design of an ultra-high torque double shoulder drill-pipe tool joint for extended reach wells. Nat Gas Ind B 4(5):374–381
2. Dong LL, Zhu XH, Yang DS (2019) Study on mechanical behaviors of double shoulder drill pipe joint thread. Petrol 5(1):102–112
3. Kang BS, Lee JH, Kim SH (1997) Development of a methodology to form net-shape nosing shells by the backwards tracing scheme of the rigid-plastic FEM. Int J Mach Tools Manuf 37(6):737–750
4. Hwang SM, Kobayashi S (1987) Preform design in shell nosing at elevated temperatures. Int J Mach Tools Manuf 27(1):1–14
5. Zhu J (1997) A new approach to preform design in shell nosing. J Mater Process Technol 63(1–3): 640–644
6. Li CL, Wang YS, Zhang ZB, Zhu LL, Xiao J (2018) Review of the characteristics of ammunition of gustav 84 mm calibre recoilless of Sweden. J Ord Equip Eng 39(4):72–80
7. Xu HQ, Zhang R, Wang DL, Huang T, Guo L, Zheng HW, Gao WL (2014) Research on technology of hot spinning forming of parts of 60Si2Mn steel with curvilinear. New Technol New Process 3:14–16
8. Zhan M, Yang H, Guo J, Wang XX (2015) Review on hot spinning for difficult-to-deform lightweight metals. Trans Nonferrous Met Soc China 25(6):1732–1743
9. Wang HW, Zhang BH, Zhang ZM (2014) Research on the new technology of the no-flash roll-die drawing of cylinder parts with curvilinear rotating shape. J Plast Eng 21(3):31–35
10. Zhao X, Zhang ZM,Zhang BH (2014) Research on rolling-extrusion forming of variable wall thickness cylinder parts. Mater Res Innov 18(Sup2): 931–936
11. Sun H, Zhang BH, Li XB, Zhang ZM, Duan ZY (2019) Influence of roller number on quality of cylinder parts in roll extrusion forming. Forging Stamp Technol 44(5):73–81
12. Zhao X, Zhang ZM,Zhang BH (2013) Finite element simulation on rolling-extrusion forming of variable wall thickness cylinder parts. J Chem Pharm Res 5(9): 536–541

Part VIII
Big Data and Metal Forming

Investigation of Machine Learning Models for a Time Series Classification Task in Radial–Axial Ring Rolling



Simon Fahle, Thomas Glaser, and Bernd Kuhlenkötter

Abstract The great potential of machine learning models in different domains has been shown in recent years. Based upon initial research regarding preprocessing methods for time series classification in the hot forming technology of radial–axial Ring Rolling, this paper takes the next step to further investigate the suitability of different machine learning models for a classification task regarding the ovality of a formed ring. This is achieved by implementing several models of the time series classification domain in machine learning and training them on actual production data of thyssenkrupp rothe erde Germany. The data set consists of different production days and ring geometries, and thus includes a plurality of challenges of radial–axial ring rolling real-world data. Different experiments will be performed and their results will be analyzed regarding performance, interpretability, and usability in the production environment. Thus, a suitable model for the underlying task will be investigated, which is essential for a future model deployment to improve the radial–axial ring rolling process further.

Keywords Ring rolling · Machine learning · Quality prediction

1 Introduction

In times of evolving amounts of time series data being produced in different industries such as wind energy [1], health care [2, 3], as well as remote sensing [4, 5], a transformation toward an application in the hot forming sector is necessary. Time series data is different in contrast to tabular data as it is not only independent and identically distributed but also has a time dependence [6] requiring different approaches when being analyzed. Thus, a time series classification (TSC) approach is used to analyze production data from radial–axial ring rolling (RARR). RARR is a well-established hot forming process capable of forming highly durable axial symmetrical products. Its complexity is high due to the instability of the hot forming aspect (temperatures up

S. Fahle (✉) · T. Glaser · B. Kuhlenkötter
Chair of Production Systems, Ruhr-University Bochum, Bochum, Germany
e-mail: fahle@lps.rub.de

© The Minerals, Metals & Materials Society 2021

G. Daehn et al. (eds.), *Forming the Future*, The Minerals, Metals & Materials Series,
https://doi.org/10.1007/978-3-030-75381-8_48

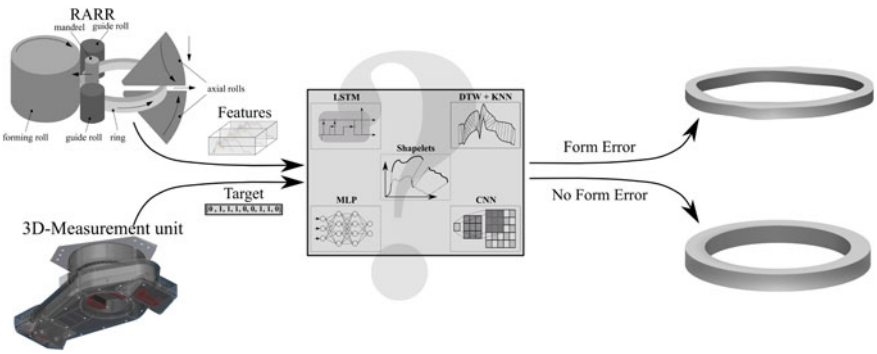


Fig. 1 Evaluation process of the conducted research toward a suitable model for quality prediction in RARR. (Color figure online)

to 1200 °C), the two opposing rolling gaps (radial and axial), as well as imperfections in stock material and previous production steps such as heating or punching. A study conducted in 2019 shows that process data from RARR in Germany has not been used to its full potential [7] and initial studies for the usability of machine learning have been presented. The aim of this research is to advance on the latest research regarding machine learning methods from TSC for quality prediction in RARR and evaluate the best-suited algorithm regarding its classification performance. Further, an initial study related to the interpretability of selected algorithms is conducted to extract information to improve the actual forming process by analyzing the algorithm's decision and derive process control strategies. Moreover, this study is based on actual production data from thyssenkrupp rothe erde Germany GmbH. The data set was acquired during different production days and inherits different geometries, thus representing typical samples of a RARR company. The data set is subject to a confidentiality agreement and must therefore not be made available to the public. This study compares several traditional, newer, and SOTA algorithms in the domain of TSC with hyperparameter tuning for their applicability to the underlying problem of predicting ring ovality. On the way to developing a whole framework for quality prediction and prevention, the next step of a most suitable model has to be taken since initial analysis regarding data acquisition and preprocessing has been conducted earlier by Fahle et al. [7, 8]. Figure 1 reflects the conducted experiments to find a suitable model to accurately predict quality in RARR and gain insights into decision interpretation of the used model.

2 Related Work

We start the related work section by giving examples of current advances regarding the relevant topics within this research. This will provide a deeper insight into the fields of RARR as well as TSC.

2.1 Radial–Axial Ring Rolling

Current research in RARR is pointed in different directions, such as simulation, process control, and innovations, as well as data analysis in recent years. With respect to simulations, many approaches use finite-element simulations to simulate and improve the process such as Allegri et al. with their research resulting in newly proposed milling curves that achieved good quality results with reduced process time and loads [9]. Another simulation-based approach toward an intelligent simulation for the rolling process of titanium alloy rings is proposed by Liang et al. They implemented a model using Abaqus/Explicit to control roll motions with regard to the material's temperature [10]. Regarding new process innovations and different combinations of the traditional RARR with other processes, Kuhlenkötter et al. investigated the suitability to combine the RARR process with thermal spraying to compact coatings in an innovative manner. The results show that by rolling thermally sprayed coatings a higher compressed residual stress can be induced, yet a final intact coating could not be established in the initial experiments [11]. Another approach where RARR has been combined with a different process is shown by Michl et al. They explored whether the use of additive manufacturing in the form of a wire arc additive manufacturing is suitable to produce better near-net shape preforms. Their results show that wire arc additive manufacturing shows promising results to lower process expenses and improve process efficiency [12]. Regarding the second core topic of this contribution, the machine learning in the form of TSC is currently researched by the aforementioned research by Fahle et al. in the RARR domain. One aspect of their research focused on data utilization and data analysis methods in RARR in 2019 for a variety of German ring rolling companies. Moreover, a framework for the RARR process was proposed to enable the RARR process to use data-driven methods such as machine learning for problems like quality prediction [7]. Furthermore, Fahle et al. investigated different preprocessing methods for TSC in RARR using common approaches as well as a domain-specific approach: using individual scaling with regard to RARR-specific rolling phases [8]. Moreover, another data-driven approach in the form of a meta-model is proposed by Havinga et al. within the metal forming mass production process of sheet bending. They mention several advantages by using data-driven techniques in metal forming as well as remaining research questions such as the model uncertainty and measurement accuracy in metal forming [13].

2.2 Time Series Classification

TSC is a highly researched area within data mining and is considered an important problem within data mining [14]. As temporal data became available [15], many algorithms, especially different deep learning architectures, have been proposed in the subdomain of TSC within the machine learning area. Examples for such deep learning

approaches are convolutional model based on the inception architecture named inception time [16] and a multivariate approach using long short-term memory cells and fully convolutional networks named MLSTM-FCN [17]. All these approaches try to establish the SOTA results using deep learning approaches as in recent years the SOTA performances were reached by using an ensemble of different TSC algorithms named HIVE-COTE. [18] Yet, according to Fawaz et al., this ensemble is not applicable to real-world problems because of its high training time complexity and thus unscalability into bigger data sets [16].

In order to compare the results of different classifiers, benchmark databases have been established within different domains of machine learning. A common representative for the task of image recognition was ImageNet [19] by providing a comparable base to validate performances of different models. With regard to TSC there is the UEA & UCR Time Series Classification Repository [20]. Different studies have been conducted searching for domain agnostic best models within the TSC domain [21]. A later study enhanced the said research by implementing deep learning models and their results on the benchmark repository [22]. Furthermore, there are different implementations for a variety of models and algorithms such as *tslearn* [23] and *sktime(-dl)* [6] that are partly used within the implementation for the proposed research in the domain of RARR.

3 Evaluation of Suitable Models for Quality Prediction in RARR

In this section, the core part of the contribution as well as all the corresponding information will be provided. We start by describing the data set used to evaluate the usability of the implemented TSC models for an application in RARR. We further discuss the used approach to include multivariate inputs as well as the model tuning performed within this research. We close this part by defining the initial requirements a suitable model has to offer.

3.1 Data Set

The current data set consists of 1078 samples from different production days of thyssenkrupp rothe erde Germany. The data set is preprocessed using different approaches, which have been explored by Fahle et al. for the application in RARR. The used data set is multivariate and provides up to five input features for this study. Those features range from radial and axial forces, ring growth rates, and motor current to several geometrical features from the process. During the evaluation not only parameter tuning within the algorithms is performed but also the number of features $(1, 3, 5)$ and their impact are explored. The inputs are limited as an even higher degree

of input features will be investigated in future research where up to 46 input features will be compared regarding their added benefit in a multivariate approach. Moreover, this will be analyzed with regard to potential computational drawbacks for online predictions, as the prediction time has to meet certain criteria from industrial control technology. The features are part of an actual ring rolling machine at thyssenkrupp and are accessed through their log files. The inputs used are the centering force on the inlet side, axial current, values for the diameter describing the radial rolling gap, and height describing the axial rolling gap, both derived through machine positions and the laser value. These features resulted in the highest univariate performances in an earlier study, which is described in the multivariate approach section. The features are stacked in the order they are listed for the multivariate approach with three and five features. Additional inputs that will be investigated in future research are, for example, revolution speeds, torques, and forces of the axial and radial rolls up to process-specific quantities such as the ring growth rate. Finally, an independent 3D measurement unit that is placed directly after the ring rolling process measures the target for each sample.

Due to a non-disclosure agreement, the data set must not be made available to the public and is still an object to grow, as the data acquisition process is still ongoing. The data set is almost evenly distributed, as the threshold for "ovality" is set such that the quality of produced rings will be increased, and only highly qualitatively rings will be produced. Rings that would break the threshold will be classified and, in a future process using an online (early) time series classification approach, immediately improved by assisting the worker in giving suggestions for parameter settings for the specific rolling process. The used preprocessing steps are standardization and phase-scaling, which are both described and evaluated by Fahle et al. [8]

The data set is split into a train and test split with an 80/20 ratio. Within the train split, there is another 80/20 split to form a validation or sometimes-called development set. This is done following the best practices because the process of hyperparameter tuning should not be done on the test set, as it would already induce some form of bias in the evaluation. Hence, the hyperparameter search will be conducted using five-fold cross-validation with random splits regarding the train and validation splits. After that, all tuned models will be retrained once on the whole training set and will predict the entirely separated test set they have never seen before. The results, both, tuning as well as testing, are shown in Tables 2 and 3.

3.2 Multivariate Approach

Moreover, the data set was split into different levels regarding multivariate inputs. All models were trained on a univariate data set only using a geometric input feature for the axial-slide, and different multivariate sets with three and five features. This experiment was conducted to evaluate whether different kinds of algorithms exceed the growing size of dimensions in the input space as well as to gain information about the benefit to include more than just one single input feature. The inputs are chosen

with respect to an earlier study regarding single feature performances on an earlier version of the data set that did not consist of the actual 1078 samples. The most important feature at that time was the inlet-sided centering force (Channel IFzE166 in the log) is in the univariate data set split. As feature inputs increase, features such as the current of the axial rolling parts and direct and indirect geometric features of the rolling gaps and the laser value are stacked to form the multivariate approach.

Some models do support a multivariate approach from the start, yet others do not. Two common approaches presented by Löning et al. within their *sktime* implementation are chosen and briefly described. One approach is to concatenate all input features to one long vector and use it as a single univariate input, whereas the other uses an ensemble where the classifier is trained on each dimension individually and all individual trainings are used to form an ensemble prediction where the majority vote is used, called column-wise-ensemble [6]. These approaches are implemented where needed, i.e. TSF and kNN.

3.3 Models and Methods

The implemented models are mainly derived from the *sktime* [6], *tslearn* [23] tools as well as individual implementation of their initial authors, i.e. Karim et al. [17]. All used models are shown in Table 1 and represent different TSC algorithm types.

Manual optimization was chosen for hyperparameter optimization. To start with, all baseline implementations were used as their initial authors provided them. For kNN, TSF, and Shapelet a grid-like search was conducted. The rocket transformer uses random kernels by default as to why it was not tuned. For all deep learning models, a random tuning with regards to author's statements for tuning was performed as this should result in better performances according to Bergstra et al. [24]. The values in brackets in Table 1 display the values with regard to each layer for each set. All other parameters were not changed and implemented as suggested by the authors or the corresponding implementation in *sktime(-dl)* and *tslearn.* No hyperparameter was tuned regarding ROCKET as the transformer implementation offered none.

The training was performed using five differently shuffled train-/test-/validation-splits, using the cross-validation approach to strengthen the validity of our conducted model training. All models were trained using the train data set, then the differently tuned models were evaluated on the validation split and the final "best" models parameters were lastly used to predict the test sets to have an unbiased result. For the deep learning models, a model checkpoint was used to ensure that the best iteration of all epochs was chosen in terms of validation loss. Epochs were only increased for larger architectures, as this was not necessary due to the size of the dataset in relation to the other architectures and their learning curves.

Table 1 Hyperparamter tuning

Used model	Type	Parameters	Values
KNN	Distance-based	Metric neighbors	dtw, ddtw, wdtw, lcss, erp, msm, twe 1, 3, 10
TimeSeriesForest	Intervals-based	Estimators Criterion Max_features	50, 100 gini, entropy auto, sqrt, log2, None
Shapelet	Shapelet-based	L: Fraction of length used for base shapelet R: No. of different shapelets lengths Batch size:	0.1, 0.2 2, 3 16, 32
ROCKET	Transformer	/	/
MLP	Deep-Learning	Dropout Dense layer neurons	[0.1, 0.2, 0.2, 0.3], [0.2, 0.25, 0.25, 0.3] [500, 500, 500], [250, 250, 250], [100, 100, 100]
InceptionTime	Deep-Learning	Filter number Kernel size Epochs	16, 32 21, 41 100, 500
CNN	Deep-Learning	Filter number Kernel size	[6, 12], [3, 6] [7], [5]
FCN	Deep-Learning	Filter number Kernel size Batch size	[128, 256, 128], [64, 128, 64], [64, 128, 32] [3, 5, 8], [1, 3, 4] 8, 16, 32
LSTM-FCN	Deep-Learning	LSTM Filter number Kernel size Batch size Epochs	8, 32, 64, 128 [64, 128, 64], [128, 256, 128], [128, 256, 64] [3, 5, 8], [1, 3, 4] 16, 32 100, 500

3.4 Requirements

For the underlying use case of a quality prediction and in a future version quality prevention model, the model has to have different properties. It has to reach a sufficiently high performance regarding classification accuracy to ensure that no unnecessary production process deceleration occurs where it was not needed because the rolled ring was achieving given quality standards either way. Moreover, the decision should be interpretable by the worker as a productive deployment in a production line highly benefits through process improvements triggered by the model's decision. There is literature to support the urge for the process of gaining trust in machine learning or artificial intelligence (AI) systems such as Siau and Wang [25] as well as

Linkov et al. [26], yet trust in an AI-driven decision-making system may be advantageous. An explainable decision in RARR would be needed for constant process improvement. The decisions made by the system could then be interpreted by an experienced technologist and give insights that might not have been looked at.

An open question is to what extent a prediction performance regarding sensitivity, sensibility, and accuracy should be reached to justify the effort and a potential process delay due to the automatic algorithmic interactions with the process control unit.

4 Results

The results for all the summarized validation accuracies throughout the splits for each of the best-tuned classifiers are shown in Table 2. The results show the mean accuracies as well as the standard deviation of all best hyperparameter tuned models for each classifier trained on the aforementioned five-fold split. It is apparent that most models preferred higher dimensionality, i.e. more input features than lower degrees of dimension, as the five best working models used five input features for their best mean prediction accuracy on the validation splits. Surprisingly, the TSF-Model, which is used only as a univariate time series for the best parameter set, reached the highest mean validation accuracy with a classification accuracy of 0.895. The second best was the FCN with 0.894 and the MLSTM-FCN with 0.892. The standard deviations of all classifiers were in the same range with MLP and kNN on the higher end with 0.030.

All model trainings and evaluation runs showed that for the case of RARR, a column-wise-ensemble method for every single feature is superior to the approach where all features are appended and one long vector is chosen as all best results originated from the column-wise-ensemble method for multivariable inputs.

From all tuned models, the ones with the best validation accuracy within each classifier are chosen and used to predict the classes for the unseen test data split,

Table 2 Validation performances of all classifiers

		Validation accuracy	
Classifier	nFeatures	Mean	Std
InceptionTime	3	0.890	0.025
FCN	5	0.894	0.023
MLP	5	0.829	0.030
CNN	3	0.874	0.025
MLSTM-FCN	5	0.892	0.025
RocketRidge	5	0.886	0.026
Shapelet	3	0.854	0.025
TSF	1	0.895	0.023
kNearestNeighbor	5	0.868	0.030

the split that every model sees only once. These results are displayed in Table 3. The results on the test set represent an unbiased generalized performance on the set. It can be observed that the TSF worked second best with a test accuracy of 0.875, outperforming all other models besides the MLST-FCN model with its test set accuracy of 0.880, keeping in mind it is only used as a univariate representation of the data set with the inlet-sided centering force IFzE166 as its only feature to predict ovality.

Two things are worth noting: for once, Hive-Cote was not regarded as its high-time complexity made the model unfeasible for the application at hand. Secondly, the inception time model managed to perfectly overfit the training set, thus reaching training accuracies (neither validation nor test) of 1.00, and leading toward an estimation that a substantial amount of effort put into fine-tuning that architecture could lead to better results with regard to generalization.

As for the interpretability of the given models is concerned, there are different methods to visualize each model's prediction or at least parts of their prediction process. For k-nearest-neighbor models, there is the visualization of the distances and their differences, which could somewhat loosely be interpreted by a human. For

Table 3 Final test results showing best generalization capabilities

Classifier	Test accuracy	Set of hyperparameters
MLSTM-FCN	0.880	LSTM: 64 Filter number: [64, 128, 64] Kernel size: [3, 5, 8] Batch size: 32 Epochs: 500
TSF	0.875	Estimators: 250 Criterion: entropy Max features: log2
RocketRidge	0.870	/
FCN	0.866	Filter number: [64,128,32] Kernel size: [3, 5, 8] batch size: 8
Inception	0.856	Filter number: 32 Kernel size: 21 Epochs: 100
Shapelet	0.852	L: 0.1 R: 3 Batch size: 32
CNN	0.852	Filter number: [6, 12] Kernel size: [5]
NearestNeighbor	0.843	Metric: wdtw Neighbors: 10
MLP	0.824	Dropout: [0.1, 0.2, 0.2, 0.3] Dense: [500, 500, 500]

the TSF, as far as the authors know, there is no direct representation such as the discovered shapelets by a shapelet model that can be visualized and interpreted regarding the production process. Similar to the discovered shapelets for some network architectures with a specific layer (global average pooling), there is the class activation map (CAM) that can be used to gain insights into where or what part of the data was significant [27]. This feature can be implemented for a TSC approach, as shown by Fawaz et al. [22]. This can be applied to the MLSTM-FCN architecture and thus be used to gain more insights into the model's prediction.

5 Conclusion

Concluding the conducted experiments, it can be stated that for the use case of quality prediction problems focusing on ovality, using time series classification in RARR, the MLSTM-FCN model seems to be the most suitable. With respect to the requirements in this domain, it has the highest test accuracy along with a promising method called class activation map to make the decision given by the model more interpretable. Nevertheless, especially the TSF with its second-best performance in terms of test accuracy should not be completely neglected, as its accuracy is only slightly worse than that of the MLSTM-FCN model, especially in view of the sparse univariate input of the TSF compared to the five multivariate features with the MLSTM-FCN. This leads to the conclusion to focus on those two models while building the final framework for the quality prediction task.

6 Future Work

Further research needs to be conducted to analyze the impact of even higher dimensional input data or a preferred selection of those on the prediction performance as well as the analysis of aforementioned CAMs produced by a model to gain more insights on to what extend or what part of a feature contributed to the classification prediction. The initial steps toward an analysis have been conducted, which showed promising results to deduce new insights from such visualizations. Moreover, an early prediction of time series will be investigated so that failure can not only be predicted but also prevented, as a prediction could be made before the rolled ring is finished and potential counter-measures can be activated.

Acknowledgments This work is funded by the Deutsche Forschungsgemeinschaft (DFG, German Research Foundation)—404517758. The authors would like to additionally thank Dr. Andreas Kneißler and thyssenkrupp rothe erde Germany GmbH for their support and access to their real-world data.

References

1. Yuan B, Wang C, Jiang F, Long M, Yu PS, Liu Y WaveletFCNN: a deep time series classification model for wind turbine blade icing detection, pp. 1–9 (Preprint). http://arxiv.org/pdf/1902.05625v1
2. Fawaz HI, Forestier G, Weber J, Idoumghar L, Muller P-A (2018) Evaluating surgical skills from kinematic data using convolutional neural networks. 0302-9743 11073 (9), pp 214–221
3. Forestier G, Petitjean F, Senin P, Despinoy F, Huaulmé A, Fawaz HI, Weber J, Idoumghar L, Muller P-A, Jannin P (2018) Surgical motion analysis using discriminative interpretable patterns. Artif Intell Med 91:3–11
4. Rußwurm M, Körner M (2020) Self-attention for raw optical Satellite Time Series Classification. ISPRS J Photogramm Remote Sens 169:421–435
5. Pelletier C, Webb G, Petitjean F (2019). Temporal convolutional neural network for the classification of satellite image time series. Remote Sens 11 (5: 523):1–25
6. Löning M, Bagnall A, Ganesh S, Kazakov V, Lines J, Király FJ (2019) Sktime: a unified interface for machine learning with time series (Preprint), pp 1–9
7. Fahle S, Kuhlenkötter B (2020) A framework for data integration and analysis in radial-axial ring rolling. In: Nyhuis P, Herberger D, Hübner M (eds), Proceedings of the 1st conference on production systems and logistics (CPSL 2020). Institutionelles Repositorium der Leibniz Universität Hannover, Hannover, pp 127–136
8. Fahle S, Kneißler A, Glaser T, Kuhlenkötter B (2021) Research on preprocessing methods for time series classification using machine learning models in the domain of radial-axial ring rolling. In: Behrens B-A, Brosius A, Hintze W, Ihlenfeldt S, Wulfsberg JP (eds) Production at the leading edge of technology. Springer, Berlin, pp 487–496
9. Allegri G, Giorleo L (2020) Ring Rolling speed rolls optimization to improve ring quality and reduce production time. JMES 14(1):6272–6284
10. Liang L, Guo L, Wang Y, Li X (2019) Towards an intelligent FE simulation for real-time temperature-controlled radial-axial ring rolling process. J Manuf Process 48:1–11
11. Kuhlenkötter B, Glaser T, Fahle S, Husmann S, Abdulgader M, Tillmann W (2020) Investigation of compaction by ring rolling on thermal sprayed coatings. Procedia Manuf 50:192–198
12. Michl D, Sydow B, Bambach M (2020) Ring rolling of pre-forms made by wire-arc additive manufacturing. Procedia Manuf 47:342–348
13. Havinga J, Mandal PK, van den Boogaard T (2019) Exploiting data in smart factories: real-time state estimation and model improvement in metal forming mass production. Int J Mater Form 207(3):663–673
14. Yang Q, WU X (2006) 10 challenging problems in data mining research. Int J Info Tech Dec Mak 05(04):597–604
15. Silva DF, Giusti R, Keogh E, Batista GE (2018) Speeding up similarity search under dynamic time warping by pruning unpromising alignments. Data Min Knowl Disc 32(4):988–1016
16. Fawaz IH, Lucas B, Forestier G, Pelletier C, Schmidt DF, Weber J, Webb GI, Idoumghar L, Muller P-A, Petitjean F (2020) InceptionTime: finding AlexNet for time series classification. Data Min Knowl Disc 34(6):1936–1962
17. Karim F, Majumdar S, Darabi H, Harford S (2019) Multivariate LSTM-FCNs for time series classification. Neural Netw Off J Int Neural Netw Soc 116:237–245
18. Lines J, Taylor S, Bagnall A (2018) Time series classification with HIVE-COTE. ACM Trans Knowl Discov Data 12(5):1–35
19. Deng J, Dong W, Socher R, Li L-J, Li K, Fei-Fei L (2009) ImageNet: a large-scale hierarchical image database. In: 2009 IEEE conference on computer vision and pattern recognition. 2009 IEEE computer society conference on computer vision and pattern recognition workshops (CVPR workshops), Miami, FL. 20.06.2009–25.06.2009. IEEE, pp 248–255
20. Dau HA, Keogh E, Kamgar K, Yeh C-CM, Zhu Y, Gharghabi S, Ratanamahatana CA, Yanping Hu B, Begum N, Bagnall A, Mueen A, Batista G, Hexagon-ML (2018). The UCR time series classification archive

21. Bagnall A, Lines J, Bostrom A, Large J, Keogh E (2017) The great time series classification bake off: a review and experimental evaluation of recent algorithmic advances. Data Min Knowl Disc 31(3):606–660
22. Fawaz IH, Forestier G, Weber J, Idoumghar L, Muller P-A (2019) Deep learning for time series classification: a review. Data Min Knowl Disc 33:917–963
23. Tavenard R, Faouzi J, Vandewiele G, Divo F, Androz G, Holtz C, Payne M, Yurchak R, Rußwurm M, Kolar K, Woods E (2020) Tslearn, a machine learning toolkit for time series data. J Mach Learn Res 21, 118(21):1–6
24. Bergstra James, Bengio Yoshua (2012) Random search for hyper-parameter optimization. J Mach Learn Res 13(10):281–305
25. Siau K, Wang W (2018) Building trust in artificial intelligence, machine learning and robotics. Cut Bus Technol J 31(2):47–53
26. Linkov I, Galaitsi S, Trump BD, Keisler JM, Kott A (2020) Cybertrust: from explainable to actionable and interpretable artificial intelligence. Computer 53(9):91–96
27. Zhou B, Khosla A, Lapedriza A, Oliva A, Torralba A (2016) Learning deep features for discriminative localization. In: 2016 IEEE conference on computer vision and pattern recognition (CVPR), Las Vegas, NV, USA. 27.06.2016–30.06.2016. IEEE, pp 2921–2929

Toward Neural Network Models to Model Multi-phase Solids



Maysam B. Gorji, Julian N. Heidenreich, Mojtaba Mozaffar, and Dirk Mohr

Abstract In this study, a neural network model is developed to describe the large deformation response of a multi-phase material, i.e., a two-dimensional perforated plate. Using the finite element, virtual experiments are performed to generate stress–strain data for monotonic biaxial loading paths. Subsequently, a combination of fully connected and recurrent neural network models are trained and validated using the results from the virtual experiments. The predictions of a network show a remarkable good agreement with all the experimental data. The suggested neural network-based constitutive model does provide a robust solution to the problem at hand, providing a fully anisotropic, three-dimensional material model capable of covering all physical material properties. The suggested procedure promises to be generally applicable to any material class and can be paired with any numerical method.

Keywords Artificial intelligence · Fully connected neural network · Recurrent neural network · Plasticity · Multi-phase material

1 Introduction

An appropriate constitutive model to describe the plastic material flow behavior especially in sheet metal has always been a challenging assignment. In the framework of this research, we show the potential of a machine learning-based modeling framework for the homogenization of multi-phase material properties, which lends itself to different applications such as modeling of composite materials, granular materials used in (e.g.) lithium-ion batteries, metamaterials, and porous structures. The theory

M. B. Gorji (✉) · J. N. Heidenreich · D. Mohr
Impact and Crashworthiness Laboratory, Department of Mechanical Engineering, Massachusetts Institute of Technology, Cambridge, MA, USA
e-mail: gorji@mit.edu

Department of Mechanical and Process Engineering, Chair of Computational Modeling of Materials in Manufacturing, ETH Zurich, Zurich, Switzerland

M. Mozaffar
Department of Mechanical Engineering, Northwestern University, Evanston, IL 60201, USA

© The Minerals, Metals & Materials Society 2021

G. Daehn et al. (eds.), *Forming the Future*, The Minerals, Metals & Materials Series,
https://doi.org/10.1007/978-3-030-75381-8_49

of homogenization uses the asymptotic expansion to approximate the relevant field variables like displacements. This introduces an additive split of all field variables on average, constant value, and its perturbations as a result of heterogeneities on a microscopic level. Despite all the studies carried out and the progress that has been made so far, the homogenization of material properties still remains a challenge nowadays. Every new class of materials and categories of physical interaction of components requires a rigorous investigation and formulation of new mathematical formulations. Additionally, material sciences still advance much faster than the research regarding material characterization. In this study, we suggest a machine learning and especially neural network-based constitutive model to describe the plasticity response of a multi-phase material.

Machine learning (ML) offers superior alternatives to traditional approaches for modeling and decision-making. This especially applies to adaptive environments where a fixed set of rules cannot sufficiently predict the behavior or in cases where alternative modeling approaches are computationally expensive or too complex to make and maintain [1]. Fully connected neural networks (FCNNs) are a class of multilayer artificial neural networks (ANNs), in which each neuron receives the values of all neurons in its previous layer as inputs to perform its calculations. The FCNNs are used to predict the behavior of the materials in sheet forming processes [2, 3]. While FCNNs offer fast calculations and a simplistic implementation, their predictions are limited to a fixed number of time steps and allow restricted predictability of history-dependent features. Meanwhile, recurrent neural networks (RNNs) are a special class of ANNs that incorporate a recursive history signal in the network architecture that enables temporal predictions [4]. Training RNNs has long been considered a challenge due to extreme cases of vanishing and exploding gradients in the backpropagation process [5]. The long short-term memory (LSTM) [6] and the gated recurrent units (GRU) [7] are two successful formulations of RNNs that resolve the notorious training issues associated with RNNs. RNNs are used in [8] to predict the behavior of composites representative volume element (RVE) by combining temporal and non-temporal features under nonlinear loading. It is worth mentioning that aside from the versatile applications of ML as well as computing outputs explicitly from the inputs, ML starts to flourish extraordinarily when a large amount of data is accessible. In practice, a robot-assisted automated testing system is a reliable way to provide a large experimental data set [9]. In this work, the studied alloy is a 1.0 mm thick high-formable AA5182 sheet, which is widely used in the automotive body panels and reinforcement members due to its high strength and formability as well as its good corrosion resistance. Its material properties are obtained from Peters [10].

2 Artificial Neural Network

In this study, two approaches have been discussed to mimic the history-dependent, mechanical response of the material. The first architectures are based on FCNNs:

the key objection of using these structures is that they tend to neglect any notion of time order; the network is amnesic to the deformation history, i.e., the FCNN just learns, remembers, and predicts based on the formative moments of the training. The second approach relies on RNN: they manage to capture stress state evolutions by adding hidden state variables known as memory cells to the ANN architecture. Unlike the FCNN, the RNN output at time t is directly connected to its prior decisions by ingesting its own previous output at time $t - \Delta t$ as a new input into the sequence. So, the same strains as inputs, but with different deformation histories generate different outputs. In this work, we deploy GRUs as a gated mechanism by taking into account two sources of present inputs and recent past ones.

The training procedure of ANN can be summarized as the sequential feeding of samples as input vectors and adjustment of the network's weights and biases, learning the underlying function. The goal is to minimize the computed error of the network calculated between the desired and the actual response of the output layer. This type of learning is known as supervised learning, which originates from the fact that there is an external teacher to control and subsequently achieve the desired output. One path through the entire range of the training set is called an epoch. The error is calculated at the end of each epoch; weights and biases will then be updated with the new values. To measure the accuracy of the network, we define the so-called cost function with respect to the weights and biases of the network. The cost function in our feed-forward model is a mean squared error (MSE) defined by the difference between the predicted ANN outputs $\mathbf{Y}_i$ and given target responses $\widehat{Y}_i$. It reads as $\mathrm{MSE}(\Omega) = \frac{1}{n}\sum_{i=1}^{n}\left(\overline{Y}_i - Y_i\right)^2$, where Ω stands for all trainable parameters, including weight matrixes and bias values.

3 Results and Discussion for the Structural Application

3.1 Round Hole Staggered Perforated Plate

In this section, we demonstrate the ANN-based constitutive model of a perforated plate featuring a direction-dependent, anisotropic material response upon external loading. For this purpose, a round-hole staggered square plate is designed. As sketched in Fig. 1a, the perforation is introduced via a 10×10 grid. Holes are randomly distributed in the grid to lower the relative density, which is defined as the ratio of a solid area over the area of the 10×10 grid. In order to limit the number of possible perforated configurations, we introduce a four-fold rotational symmetry. In the smaller 5×5 grid (top left quadrant of Fig. 1a) 13 holes are randomly placed. The rotation of this structure around the center point yields the final 10×10 structure with a relative density of 0.74 resulting in 48 solid- and 52 hole-cells.

The training and testing datasets required for successful parameter identification are created with the help of numerical simulations using the implicit solver of FE-package LS-DYNA in conjunction with the Yld2000-2d plasticity model. The

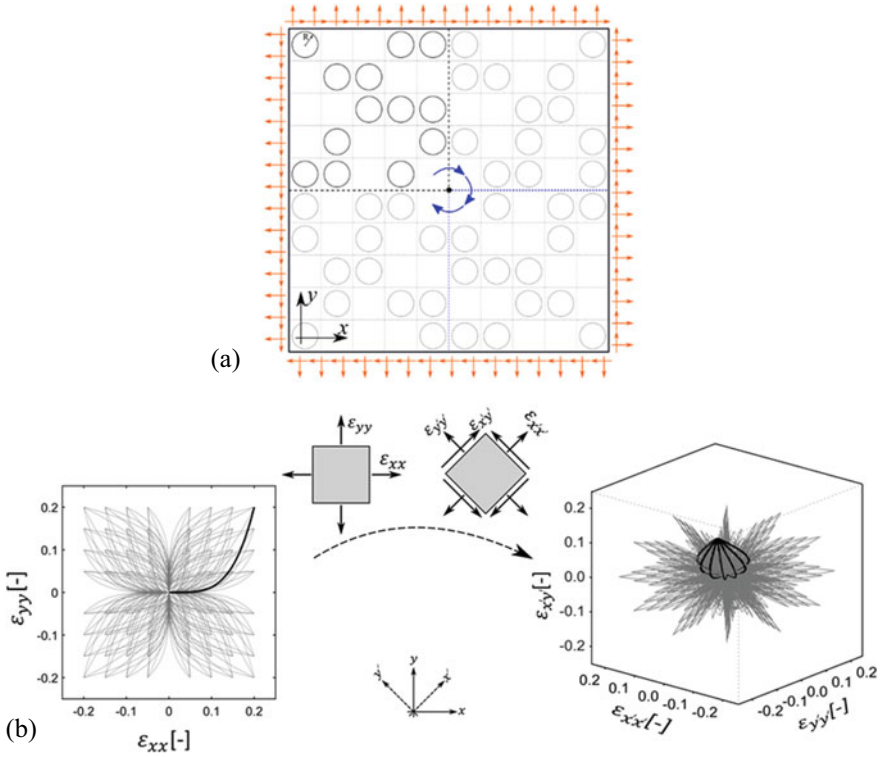


Fig. 1 **a** Unit cell of two-dimensional perforated plate structure with the randomly distributed holes. Generation of loading paths for training in 2D and 3D strain space. (Color figure online)

AA5182 structure is discretized with the linear four-node shell elements and five integration points through the thickness; the total number of elements is about 40,000. The representative volume element (RVE) displayed in Fig. 1a is extended to an infinite medium using periodic boundary conditions, linking the displacements of the nodes at the outer perimeter to the applied displacement gradient. To do so, the local displacement field $\boldsymbol{u}$ is decomposed into $\widehat{u}$, the applied deformation on the unit cell, and $\widetilde{u}$, which can be interpreted as local fluctuations. The applied displacement field is linearly approximated using the displacement gradient $\mathbf{H}$:

$$\mathbf{u}(x) \widehat{=} \widehat{\mathbf{u}}(x) + \widetilde{\mathbf{u}}(x) \approx \mathbf{u_0} + \mathbf{H}x + \widetilde{\mathbf{u}}(x). \tag{1}$$

An additional constraint on the local fluctuations is introduced to enforce periodicity of the unit cells leads:

$$\tilde{u}(x) = \tilde{u}(x + nl_i e_i) \forall n \in Z. \tag{2}$$

.

These equations yield a translatoric invariance of the deformation response by shifts by a multiple of the unit cell dimension l_i along with the principal directions e_i of the structure. The mesh of the square unit cell is designed in a way that every node on the perimeter has a corresponding node on the opposite side of the unit cell at a distance of l_i along the unit face normal $\boldsymbol{n}$. Combining Eqs. 1 and 2 leads to the following relationship between each pair of nodes:

$$\boldsymbol{u}(x_1) - \boldsymbol{u}(x_2) = l_i \boldsymbol{H}\boldsymbol{n}. \tag{3}$$

Two control nodes are considered to control the deformation of each set of opposite faces of the two-dimensional unit cell. Hereby, the translatoric degrees of freedom of the control nodes represent the components of the applied displacement gradient. Equation 3 is implemented in the FE simulation via linear kinematic constraints on the nodal displacements. The resulting forces applied to the control nodes are equal to the components of the first Piola-Kirchhoff stress $\boldsymbol{P}^I$ tensor. Note that the sampled strain paths represent components of the Hencky strain tensor. The displacement gradient, which is applied to the RVE is determined via polar decomposition of the deformation gradient assuming rotation-free deformations.

3.2 Non-proportional Monotonic Loading

The 140 deformation paths in the normal strain space $\varepsilon_{xx} - \varepsilon_{yy}$ with the squared-length of 0.08 are delineated in Fig. 1b. The strain evolution follows the power-law function ($y = Ax^n$) with seven values for the exponent $\in [0.1, 0.25, 0.5, 1, 2, 4, 10]$. The three-dimensional input strain vector in $x' - y'$ space is thereupon simply computed using the rotational matrix $([\cos(\alpha) - \sin(\alpha); \sin(\alpha)\cos(\alpha)])$ for nine different angles $\alpha \in [0 : 10 : 80]$. For reference, the transformation of one exemplarily loading path ($\varepsilon_{xx} = 0.04$,$\varepsilon_{yy} = -0.04$ with the power law's exponent 10) to $x' - y'$ space is highlighted with the solid black lines in Fig. 1b.

The simulation results of one of the exemplary deformation patterns are shown in Fig. 2. Plot (a) depicts the strain inputs, while plots (b) and (c) illustrate the resulting stresses based on the forces in the x and y directions on the control points DN1 and DN2. Following the nomenclature used for introducing the deformation and displacement gradient, the evaluation of node DN1 yields the components $\boldsymbol{P}^I_{xx}$ and $\boldsymbol{P}^I_{yx}$ of the first Piola-Kirchhoff tensor and DN2 yields the components $\boldsymbol{P}^I_{yx}$ and $\boldsymbol{P}^I_{yy}$, respectively. Note that despite the fact that the input strains are based on monotonic functions, the resulting stresses do not necessarily conform to that rule. In an extreme case, this can lead to load reversal. For instance, the component $\boldsymbol{P}^I_{xx}$ in Fig. 2b starts out as compressive stress and changes to a tensile force after approximately one-third of the deformation has been applied to the structure. The contour plots in Fig. 2d depict the equivalent plastic strain throughout the deformation. As expected, we observe strain concentrations near the holes. The overall global change in geometry is dominated by the local deformation around the holes. Keep in mind that throughout

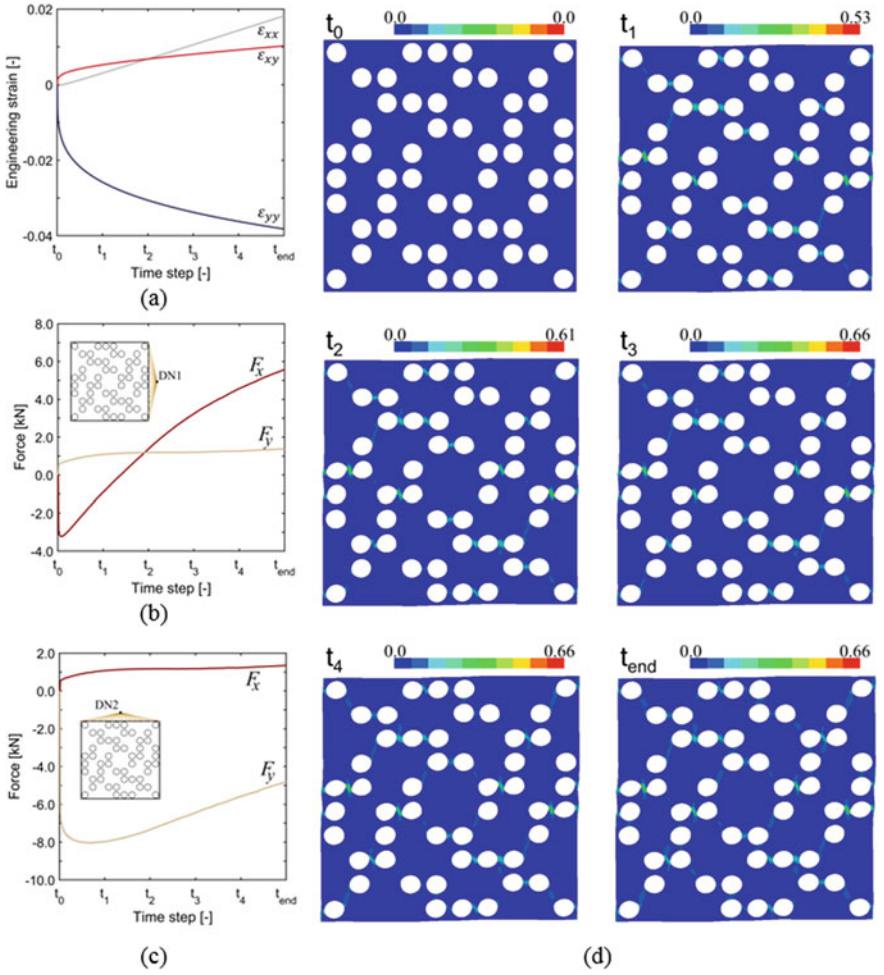


Fig. 2 Results from a representative virtual experiment (unit cell simulation): **a** Imposed strain histories and computed force histories for **b** control points DN1 and **c** DN2. **d** Deformed unit cells for selected time steps. The contour plot shows the equivalent plastic strain. (Color figure online)

this study and for all performed simulations, it is assumed that the local equivalent plastic strain stays below the fracture threshold.

3.3 Post-processing and Dataset Preparation

For consistency and later implementation in the numerical simulation scheme, the neural network is trained based on Hencky strains E_{Hencky} and Cauchy stresses σ.

Hence, the obtained displacement gradient and first Piola-Kirchhoff stress tensor have to be converted. In order to obtain the full three-dimensional displacement gradient, we need to monitor the Hencky strain in the thickness direction at each integration point. An effective measure of thickness strain is determined by averaging the extracted strains. The averaged effective strain is transformed into the engineering strain space and serves in the following as the zz-component of the displacement gradient. The Hencky strain tensor, as well as the Cauchy stress tensor, is calculated based on the following formulas:

$$\boldsymbol{E}_{\text{Hencky}} = \frac{1}{2}\ln\left(\boldsymbol{F}^{\mathrm{T}}\boldsymbol{F}\right) = \frac{1}{2}\ln\left((\boldsymbol{H}+1)^{\mathrm{T}}(\boldsymbol{H}+1)\right), \tag{4}$$

$$\boldsymbol{\sigma} = (\det(\boldsymbol{F}))^{-1}\boldsymbol{P}^{\mathrm{I}}\boldsymbol{F}^{\mathrm{T}} = (\det(\boldsymbol{H}+1))^{-1}\boldsymbol{P}^{\mathrm{I}}(\boldsymbol{H}+1)^{\mathrm{T}}. \tag{5}$$

3.4 A Neural Network-Based Constitutive Model

The final network is an assembly of two GRU cells with 100 neurons followed by one time-distributed fully connected layer. This structure is capable of predicting the elastoplastic behavior of the studied meta-material for over 500 time steps. The strains $\{\varepsilon_{xx}, \varepsilon_{yy}, \varepsilon_{xy}\}$ are defined as the input, while the stresses along with the thinning $\{\sigma_{xx}, \sigma_{yy}, \sigma_{xy}, \varepsilon_{zz}\}$ represent the output of the ANN model. Moreover, 945 loading paths out of the 1260 generated ones are used to train the RNN (75% of all generated paths), while the rest, 315 loadings (25% of all generated paths), are used to test the model. The network is trained for 1000 epochs, which leads to an MSE of 3.36E-4 and 6.70E-4 on training and test sets, respectively.

Figure 3a shows the evolution of an exemplarily untrained strain vector as a function of time for validation purposes. The target outputs are presented in Fig. 3b as solid black lines. The predicted ANN results are shown by dashed red lines, i.e., the progression of stresses is in excellent agreement with the numerical results. The explicit stress values at the last time step are $\sigma_{xx} = 94.19MPa$, $\sigma_{yy} = 87.97MPa$, and $\sigma_{xy} = 7.00MPa$. Accordingly, the prediction of the neural network is $\sigma_{xx}^{RNN} = 94.54MPa$, $\sigma_{yy}^{RNN} = 87.07MPa$, and $\sigma_{xy}^{RNN} = 7.07MPa$.

Developing the neural network model assists in predicting the stress distribution for any arbitrary non-proportional monotonic deformation. As an example, the stress evolution of 36 proportional monotonic loadings in the normal strain space $\varepsilon_{xx}, \varepsilon_{yy}, \varepsilon_{xy} = 0$ is predicted by the trained ANN model, which is shown as black solid lines in Fig. 3c. The total work (per unit volume) is computed based on the stresses derived from the ANN model alongside the input strains as

$$\psi(t) = \int_0^t \left(\sigma_{xx}\varepsilon_{xx} + \sigma_{yy}\varepsilon_{yy}\right)dt \tag{6}$$

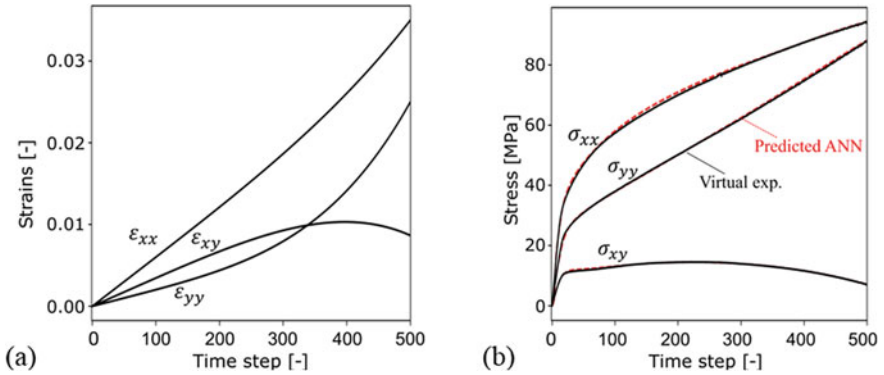


Fig. 3 **a** Testing of the trained GRU100-FCNN100 model for the 2D perforated plate: **a** shows the imposed strain histories, while **b** shows the corresponding stress histories predicted by the unit cell model (black curves) and the neural network model (red lines). (Color figure online)

With the help of these results, the energy surface of the studied perforated plate at three distinct levels, $\psi(t) = 0.10mj$, $0.75mj$, and $2.0mj$, are computed. The derived curves are sketched in Fig. 4a. Interestingly, all of the derived surfaces are convex, i.e., $\left(\sigma_{ij} - \sigma^*_{ij}\right).d\varepsilon_{ij} \geq 0$, where σ_{ij} is the present loading state in an elementary material system. This equation is valid for every σ^*_{ij}, which means that loading state σ_{ij}, associated with the present plastic increment of strain $(d\varepsilon_{ij})$ maximizes the infinitesimal total work. The red contour in Fig. 4a represents the total energy of $\psi(t) = 0.10mj$ and is assumed to represent the onset of plastification of the studied perforated plate. Taking this into account, the uniaxial tension along the x and y directions exhibits yield stress of about 48 MPa and 46.6 MPa, respectively. Under equi-biaxial loading, the studied perforated plate plastifies at $\sigma_{xx} = \sigma_{yy} = 45MPa$. In addition to that, Fig. 4b illustrates the NN approximation of the effective stress at an energy level of $\psi(t) = 0.10mj$. We define the effective stress as $\overline{\sigma}_{eff} = \sqrt{\sigma^2_{xx} + \sigma^2_{yy} + \sigma_{xx}\sigma_{yy}}$. The predicted maximum strength of the material reaches $\overline{\sigma}^{EBC}_{eff} = 78.5MPa$ under equi-biaxial compression, which is just 1% higher than the stress at equi-biaxial tension $\overline{\sigma}^{EBT}_{eff} = 78MPa$.

The perforated plate behaves almost identically when it is subjected to the uniaxial tension or compression loading. The lowest stress value is observed under shear loading with the $\overline{\sigma}^{SH}_{eff} = 32MPa$. The designed ANN model is also capable of delivering highly accurate results for the thickness reduction ε_{zz}. Thus, the NN approximation allows us to calculate a Lankford anisotropic coefficient as the ratio of the contractile strain in the width to the thickness direction. Under linear load paths and at a total energy of $\psi(t) = 0.10mj$, the Lankford ratios in the x and y directions are $r_x = 0.957$ and $r_y = 0.939$, respectively. Additionally, $r_{EBT} = \varepsilon_{yy}/\varepsilon_{xx} = 0.978$ when the perforated plate is subjected to equi-biaxial tensile loading.

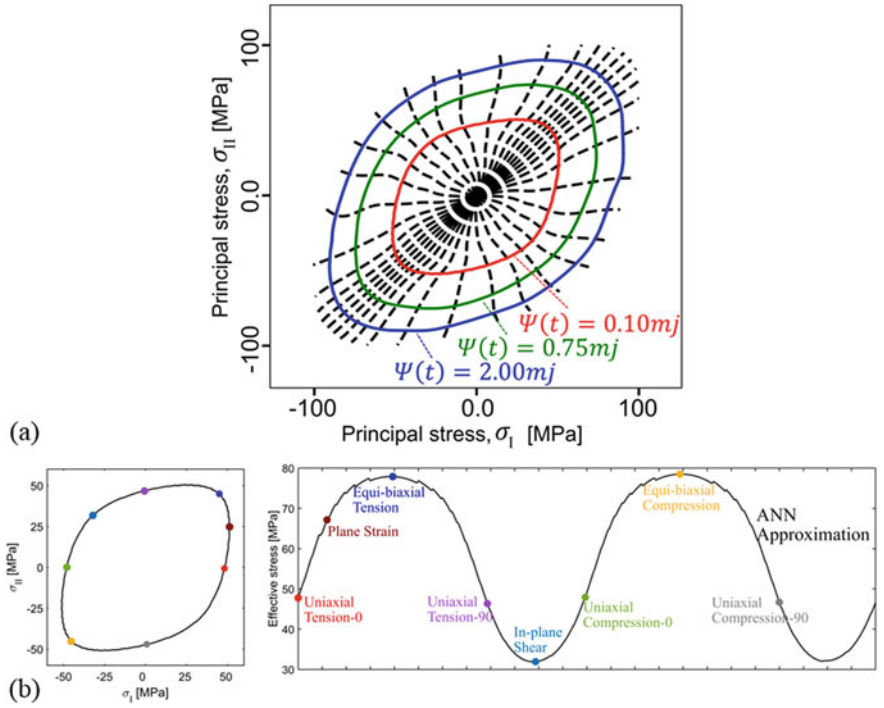


Fig. 4 **a** The predicted energy surface using neural network model (colored lines), the target outputs of implemented strains are drawn with the solid black lines. **b** The effective stress along the energy surface $\psi(t) = 0.10mj$. (Color figure online)

4 Summary and Conclusions

In this study, we show that ANNs are alternative tools that can assist in modeling a material response and predicting mechanical responses. The obtained multi-axial responses of the multi-phase material are then modeled by one of the two different ANN classes: (i) FCNN, fully connected neural network, or (ii) RNN, recurrent neural network. Simplicity in architecture and the low number of parameters in the FCNN approach make this network more facile. However, the RNN architectures are required in cases when the history of the input variables plays a critical role. The comparison illustrates that the RNN-based predicted results show a good agreement with the experimental targets. With this research, we would like to re-emphasize the tremendous potential of machine learning to generate a homogenized model of heterogeneous material properties. The structural behavior of a perforated plate with a relative density of 0.74 is studied under the non-proportional monotonic loadings. An RNN model is trained to retrieve the constitutive parameters of the studied material. The neural network model serves as a strong tool to define the yielding of the structure under different loading evolutions and loading directions.

Acknowledgments Special thanks are due to Prof. Cao for valuable discussions.

References

1. Géron A (2017) Hands-on machine learning with Scikit-Learn and TensorFlow: concepts, tools, and techniques to build intelligent systems. O'Reilly Media, Inc
2. Gorji M, Mohr D (2019) A basic neural network model describing the plasticity of sheet metal. IDDRG2019, Portsmouth, New Hampshire, USA
3. Gorji M, Mohr D (2019) Towards neural network models for describing the large deformation behavior of sheet metal. IOP Conf Ser: Mater Sci Eng 651:012102
4. Hopfield JJ (1982) Neural networks and physical systems with emergent collective computational abilities. Proc Natl Acad Sci 79(8):2554–2558
5. Hochreiter S, Bengio Y, Frasconi P, Schmidhuber J (2001) Gradient flow in recurrent nets: the difficulty of learning long-term dependencies
6. Hochreiter S, Schmidhuber J (1997) Long short-term memory. Neural Comput 9(8):1735–1780
7. Cho K, Van Merriënboer B, Gulcehre C, Bahdanau D, Bougares F, Schwenk H, Bengio Y (2014) Learning phrase representations using RNN encoder-decoder for statistical machine translation. arXiv preprint arXiv:1406.1078
8. Mozaffar M, Bostanabad R, Chen W, Ehmann K, Cao J, Bessa MA (2019) Foundations for computational plasticity with deep learning. Submitted for publication
9. Jordan B, Gorji M, Mohr D (2019) Neural network model describing the temperature- and rate-dependent stress-strain response of polypropylene. Submitted to Int J Plast
10. Peters PR (2015) Yield functions taking into account anisotropic hardening effects for an improved virtual representation of deep drawing processes. Doctoral dissertation, ETH Zurich

Comparison of Linear Regression and Neural Networks as Surrogates for Sensor Modeling on a Deep Drawn Part



Matthias Ryser and Markus Bambach

Abstract Several developments in deep drawing aim at systematically determining modifications during tool tryout. Recent work deals with a simulation-based method to discover the current state parameters based on characteristic measurement quantities and infer a tryout proposal by comparing with the simulated robust optimum. While the simulation provides an accurate model of the drawing process, a low fidelity surrogate model is required to predict the influence of process parameters on the targets in a computationally efficient manner. In this work, training data is generated by a stochastic finite element simulation in AutoForm. The data points are used to fit and evaluate linear models as well as neural networks for regression. These models use process parameters as predictors to estimate the target parameters draw-in and local blank holder forces. Results show that simple models outperform complex models. No evidence was found that the model accuracy increases by using neural networks.

Keywords Deep drawing · Surrogate modeling · FE simulation · Regression · Bias-variance-tradeoff

Nomenclature

FEM	Finite element method
MLP	Multilayer perceptron
Elastic-net	Elastic-net regression
kNN	k-nearest neighbor algorithm
Spacer	Drawing aid used in the deep drawing tool

M. Ryser (✉) · M. Bambach
Institute of Virtual Manufacturing, Swiss Federal Institute of Technology, Technoparkstrasse 1, 8005 Zurich, Switzerland
e-mail: ryser@ivp.mavt.ethz.ch

© The Minerals, Metals & Materials Society 2021

G. Daehn et al. (eds.), *Forming the Future*, The Minerals, Metals & Materials Series,
https://doi.org/10.1007/978-3-030-75381-8_50

1 Introduction: On the Bias-Variance-Tradeoff in Modeling

Stochastic finite element simulations are used for different purposes in deep drawing. Despite the usage in the robustness analysis of the process, stochastic finite element simulations are also used for sensitivity analysis of process parameters on the process itself [1] or for predictive quality estimation [2]. Additionally, the ongoing work deals with inverse parameter modeling in deep drawing [3]. In each of these use cases, surrogate models describing relevant process quantities, like draw-ins or local blank holder forces dependent on the input parameters of the stochastic finite element simulation, are required.

Approaches, which are often used for this regression problem, are linear regression with ordinary least squares loss or other loss functions or artificial neural networks like the multilayer perceptron. In the core of the choice of modeling approach as well as its model parameters lies the bias-variance-tradeoff, which is visualized qualitatively in Fig. 1. The bias-variance-tradeoff describes the conflict of minimizing the estimator error during supervised learning, which can be decomposed into the error due to bias, variance, and the irreducible error due to noise. However, the latter results from the noise in the problem itself and cannot be reduced. The errors due to bias as well as variance are in competition with each other, meaning that, in general, a reduction of the error due to variance leads to a higher bias and vice versa. The analysis of the error components provides a framework to select the optimal model complexity for a given problem with a defined amount of data and can thus be used to identify suitable regression models for sensor modeling in deep drawing. The left part of the graph in Fig. 1 corresponds to simple models; for example, models with only a few degrees of freedom or models whose coefficients are determined using strong regularization. The prediction error of these models consists mainly of the model bias, which is the error occurring since the model is not capable of describing the underlying relationship in the data. On the other hand, the right-hand side in Fig. 1 belongs to models with very high complexity. These models are capable of describing the underlying functional relationship, but due to their high flexibility, they also tend to overfit to noise in the training data, leading to a high variance in the prediction among different training datasets. The model complexity best suited for

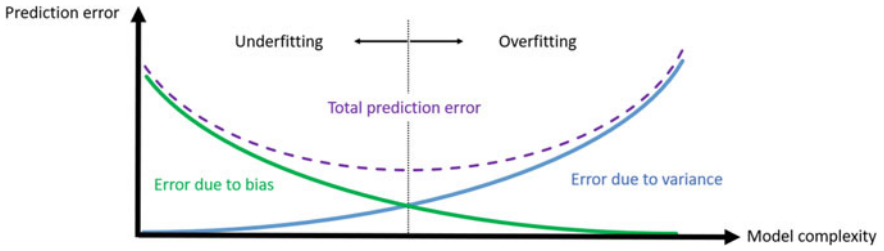


Fig. 1 Qualitative illustration of the bias-variance-tradeoff and its consequence on the choice of model complexity. (Color figure online)

a specific problem is found by a tradeoff between these two extrema and identified by the minimum total prediction error in the middle of Fig. 1. Note that the optimal model complexity does not only depend on the underlying relationship but also on the amount of available training data. In general, using more data points for training leads to less variance of the trained model, which therefore moves the minimum total prediction error to the right, and to higher model complexity in the optimum case [4].

Bishop [4] provides a mathematical description and more in-depth analysis about the bias-variance-tradeoff for the use in pattern recognition and machine learning. Although advanced mathematical understanding of the bias-variance-tradeoff is available, no analysis on draw-in or drawing aid force modeling in deep drawing has been found. In this work, the bias-variance-tradeoff is examined on a deep drawn part. For the modeling, draw-in as well as drawing aid force signals generated by stochastic finite element simulations are used for the evaluation of different modeling approaches. All programming is done in python using scikit-learn 0.24.0 for all machine learning-related tasks. The following questions are answered:

- What does the curve depicted in Fig. 1 applied on draw-ins and spacer forces of a deep drawn part look like in reality?
- How well do neural networks as highly parameterized models perform in sensor modeling compared to linear regression as a low parameterized modeling approach?
- What modeling complexity of the two mentioned approaches leads to the highest model accuracy of draw-ins or drawing aid forces in deep drawing?

2 Approaches Used for Sensor Modeling in This Work

2.1 Unregularized and Regularized Linear Regression

The very basic approach for regression problems is linear regression, representing a linear or nonlinear mapping from the predictor variable X on the target variable y. Such models are linearly dependent on the model coefficients ω. In this case, the model complexity depicted in Fig. 1 can be either controlled by adding a regularization term with an additional model parameter λ to the loss function or by using a preceding feature transformation into higher dimensions. In case of the simultaneous use of the L_1 and the L_2 norm on the model coefficients, elastic-net regression results are obtained, whose loss function for model training is given in Eq. 1, where ω are the model coefficients, λ is the regularization strength, M is the number of model coefficients, and N is the number of data points used for training. This formulation is also used in this work.

$$L(\omega) = \frac{1}{2}\sum_{n=1}^{N}(x_n\omega_n - y_n)^2 + \lambda\left(\frac{1-\alpha}{2}\sum_{m=1}^{M}\omega_m^2 + \alpha\sum_{m=1}^{M}|\omega_m|\right) \tag{1}$$

2.2 *Artificial Neural Networks*

Another approach for the regression problem is the use of artificial neural networks. In its simplest form, the input of the multilayer perceptron X is fully connected to the output y by several hidden layers with a given number of neurons, and the information is only fed in the forward direction. The simple case with three hidden layers and four neurons (circles) in each hidden layer is depicted in Fig. 2. Each neuron contains an activation function which is applied on the input from the previous layer. In the case of neural networks, the model complexity is controlled mainly by the number of hidden layers as well as neurons in each hidden layer. Additionally, model complexity can also be controlled again by a regularization term on the model coefficients or by further methods like drop-out which are not used in this work. As nonlinearity, the ReLu-activation function is consistently used in this work. Goodfellow et al. [5] motivate the use of neural networks in contrast to linear regression models for two reasons: First, whereas approaches like linear regression require the manual definition of a feature map into nonlinear features in the nonlinear case before model fitting, neural nets automatically train the feature map with the model parameters by using different levels of hidden layers. Therefore, no manual decision on the feature mapping has to be made. Second, due to the inherent hierarchical structure, neural nets are also capable of solving problems with hierarchical information structure, for example in computer vision analyzing pixels in an image for detection of edges, then detection of contours, and finally type of objects.

3 Simulation Setup

During data generation, a stochastic finite element simulation is performed on a mini engine hood. The process is a single action drawing process using punch, blank holder, and die, which are depicted in Fig. 3. The tool contains three drawbeads as well as five drawing aids, as illustrated in Fig. 3. The drawing aids are modeled as elastic blocks with a stiffness of 400 kN/mm, allowing a local reduction of the

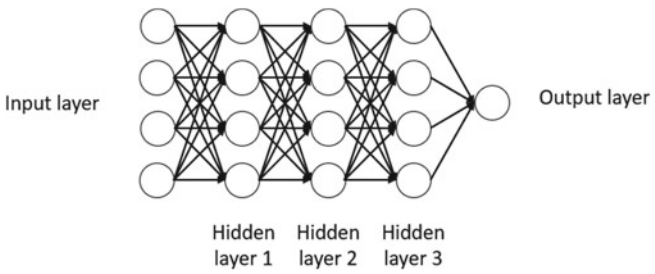


Fig. 2 Architecture of the multilayer perceptron with three hidden layers and four neurons per hidden layer

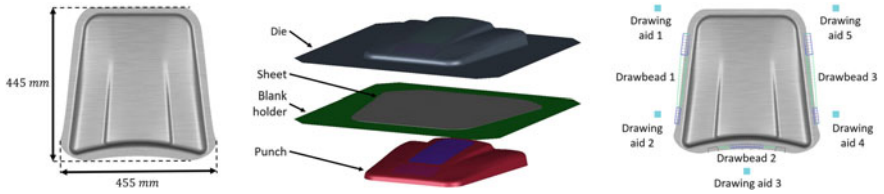


Fig. 3 Setup of the stochastic finite element simulation used in this work. **a** Mini engine hood geometry, **b** Setup of tools in simulation: die, blank holder, sheet and punch, **c** Drawbeads and drawing aid positions relative to the part. (Color figure online)

pressure between the blank holder and the sheet, and thus adjusting the local draw-in. The height of the drawing aids is variable and varied throughout the stochastic finite element simulation as will be shown later. The blank holder force is produced by columns, which allow small tilting angles of the blank holder due to an eccentric pressure distribution between the blank holder and the die. The total blank holder movement from upper to lower dead center is 75 mm. The simulations are performed in AutoForm R8.

3.1 Material Description

The material used for the forming operation is Aluminum EN AW-6016 with a thickness of 1.0 mm. The material data was taken from the material database from AutoForm R8 (6016_T4P) without any modification. The flow behavior is described using a combined approach with Swift [6] and Hockett-Sherby [7]. For the description of the yield locus, the anisotropic formulation according to Barlat and Lian [8] is used. For the yield locus, the exponent $M = 8$ was used.

3.2 Setup of Stochastic Finite Element Simulation

In the finite element simulation, material, tool, and process parameters are varied to account for uncertainties inherent in the deep drawing process. Regarding material parameters, yield stress, tensile strength, and the R-values in all three directions are varied. To reduce the number of independent parameters and thus the number of total simulations, these material parameters are all varied fully correlated. In the tool, the height of all three drawing aids as well as the drawbeads are varied independently. As process parameters, the friction coefficient and the global blank holder force are also varied. Variation in blank thickness is considered too. As a reference, the values of the variation range are chosen experience-based and in a way that results in no defective parts. All varied parameters as well as their nominal value and variation range are given in Table 1. The setup of the simulation leads to 12 independent parameters in

Table 1 Input parameters and range used for the stochastic finite element simulation

Parameter description	Nominal value	Min value	Max value	Correlated with
Friction coefficient μ	0.14	0.09	0.15	–
Blank thickness t_{sheet}	1.00 mm	0.99 mm	1.01 mm	–
R-value R_0	0.64	0.62	0.66	–
R-value R_{45}	0.50	0.48	0.52	R_0
R-value R_{90}	0.71	0.69	0.73	R_0
Yield stress $Rp_{0.2}$	127.4 MPa	117.4 MPa	137.4 MPa	R_0
Tensile strength R_m	241.4 MPa	226.4 MPa	256.4 MPa	R_0
Blank holder force F	690 kN	552 kN	828 kN	–
5 Drawing aid heights (independent)	1.05 mm	1.00 mm	1.15 mm	–
3 Drawbead heights (independent)	6.0 mm	4.5 mm	6.0 mm	–

total. The design of experiments for the stochastic finite element simulation is finally obtained by using Latin hypercube sampling. To make sure a well-grounded dataset is generated for the following experiments, 300 simulations are performed.

3.3 Extraction of Sensor Data

The extracted data from the simulation consists of three parts: First, the independent parameters varied in the design of experiments are stored. Second, the draw-in at the boundary of the blank is extracted for each simulation at 120 locations, uniformly distributed around the part. The draw-in is measured perpendicular to the part boundary as in optical measurement and not in the direction of material flow. To take into account the evolution over time, the draw-in is not only extracted in the bottom dead center but extracted over time in 12 steps at blank holder position 74, 60, 50, 40, 30, 25, 20, 15, 10, 5, 2, and 1 mm before the bottom dead center. An example of such a draw-in signal is given in Fig. 4 on the left side. In addition to

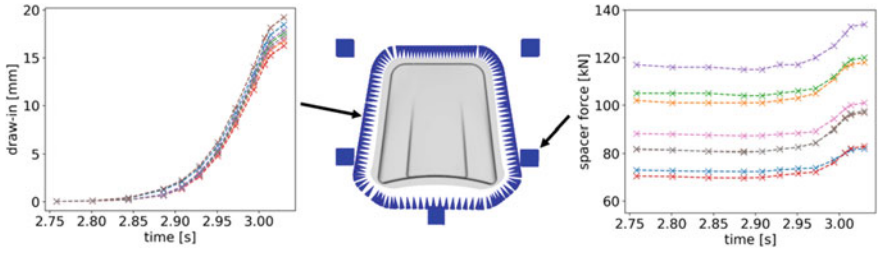


Fig. 4 Example data for draw-in (cones) and spacer (cubes) force signals for one sensor each and seven simulations, evaluated at 12 blank holder positions. (Color figure online)

the draw-in signal, the force in each drawing aid is also used as output. The force signal is not available in the current Version R8 in the GUI, but AutoForm stores the acting force for each drawing aid and each increment in the output file, which can be then read using an external script. The force signal is also extracted at the same blank holder positions as the draw-ins. As an example, a force signal over time is given in Fig. 4 on the right side.

4 Surrogate Modeling of Sensor Signals

For the modeling of the sensor signals obtained in the finite element simulations, the parameters from the design of experiments are used as input and the signal for each sensor as output variable. Independent models are then fitted for each timestep on a training set, whose size in terms of data points is calculated as the training point ratio R_{train} times the total number of simulations. The models are then evaluated on the test set of size $(1 - R_{train})$ times the total number of simulations. For each sensor signal, the evaluation metric is averaged over all 12 timesteps, resulting in one scalar for each sensor describing its modeling accuracy. As an evaluation metric, the R^2 metric is used which describes the proportion of explained variance by the model relative to the total variance in the output data. Before training the models, the datasets are standardized by subtraction of the mean value and division by the standard deviation.

4.1 Surrogate Modeling of Draw-Ins

For the draw-in modeling, the elastic-net is used with preceding feature transformation of first up to sixth order. Four multilayer perceptrons are trained with one hidden layer and one neuron, one hidden layer with 12 neurons (equals number of input parameters), two hidden layers with 12 neurons, and three hidden layers with 12 neurons each. Additionally, a k-nearest-neighbor model is used which simply looks for the nearest point in the train set and predicts its value, assuming k is set to one (only 1 neighbor).

The kNN model is used as a reference since it represents a model that simply memorizes but is inherently not able to learn functional relationships. The results of the draw-in models are illustrated in Fig. 5. The left column contains the results for the elastic-net regression and the right column the results for the MLP; the results are separated for better visibility. For a small dataset for training, for example 30 simulations, the linear elastic-net shows the highest score on the test set. At approximately 60 data points, the elastic-net with quadratic features outperforms the linear. This result is remarkable since the fully quadratic model for a 12-dimensional input contains 92 model coefficients (including intercept), which means that the model coefficients are still not uniquely defined. The standard deviation between the model

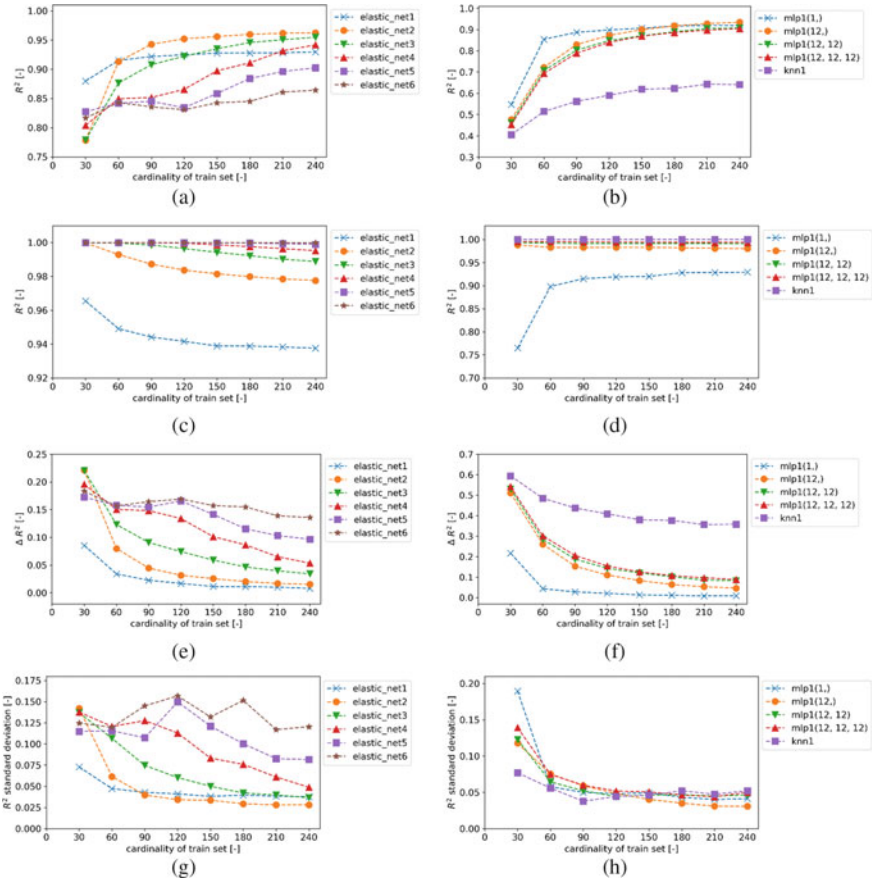


Fig. 5 Evaluation of the modeling results of the draw-in based on the R^2 metric (number in parentheses denotes size of hidden layers of MLP, numbers directly after algorithm name denote order of feature transformation). **a** R^2 on the test set while using elastic-net, **b** R^2 on the test set while using MLP and kNN, **c** R^2 on the training set while using elastic-net, **d** R^2 on the training set while using MLP and kNN, **e** Difference between training and test set for elastic-net, **f** Difference between training and test set for MLP and kNN, **g** Standard dev. of R^2 between draw-ins for elastic-net, **h** Standard dev. of R^2 between draw-ins for MLP and kNN. (Color figure online)

quality of the quadratic model on the bottom left, which also includes the variance of the estimators due to the choice of training points, shows that for 90–120 training points, the variance starts to flatten and remains approximately constant. From this amount of training data, the parameters of the quadratic model are fully defined and lead to the best modeling score from this point. Comparison with higher-order models of the elastic-net shows clear overfitting, due to the low test score (1st row) but high training score (2nd row), thus a high difference between these two which is denoted as bad generalization ability (3rd row) and larger variance as can be seen in the 4th row. On the other side, the high training error on the first-order model

shows clear signs of underfitting, since the model is not capable, in contrast to the quadratic model, of capturing quadratic functional relations as well as interactions between input parameters. All models lead to a higher test score compared to the nearest neighbor method, meaning that learning of the underlying relationships has improved the modeling accuracy.

Since the neural network in the right columns contains much more parameters, the test score is worse (1st row). Note that the version with one hidden layer containing one neuron has a similar structure compared to the linear elastic-net since a multi-dimensional mapping is only done from the input to the hidden layer, leading to a similar result on the test score between these two. The MLP does not significantly benefit by adding more complexity, which leads to overfitting as can be seen by the high training score (2nd row) but low test score (1st row) and therefore bad generalization (3rd row).

4.2 Surrogate Modeling of Drawing Aid Forces

For the modeling of the drawing aid forces, the same modeling approaches are chosen as for the draw-in signals. The result is shown in Fig. 6. High modeling quality is already reached by using elastic-net regression and linear features only. For the linear elastic-net, an almost perfect test score of 0.999 is obtained at 240 data points for training. All elastic-net models show low test error (1st row), similar training error (2nd row) compared to the test error, and therefore good generalization ability (lower values in the 3rd row). Independent of the degree of features, the elastic-net leads to similar prediction accuracy. A comparison of the result of feature transformations from 1st order to 6th order shows a monotonically decreasing model quality if only 30 data points are used for training. Again, the most complex MLPs are overfitting, which results in a low test score but high training score. As can be seen on the data in the right column, the modeling of spacer forces does not benefit from the use of more complex models like the neural network with multiple hidden layers neither.

An explanation for this result can be found by studying the influence of the process parameters on the resulting drawing aid forces by analyzing the force distribution between the blank holder and the die. The most influential quantity on the drawing aid force is the height of the same drawing aid. The secondary influential quantities are the blank holder force, which on increase will increase the drawing aid forces globally; the sheet thickness on reduction increases the drawing aid forces; and the drawbead height on reduction results in less drawbead uplift force, thus shifting more force to the drawing aids. Since the drawing aid height is by far the most influential quantity and the drawing aid is modeled purely elastic with constant stiffness, it results in almost linear behavior. The same also holds for the blank thickness since a reduction of blank thickness has a comparable effect with the increase of the drawing aid height.

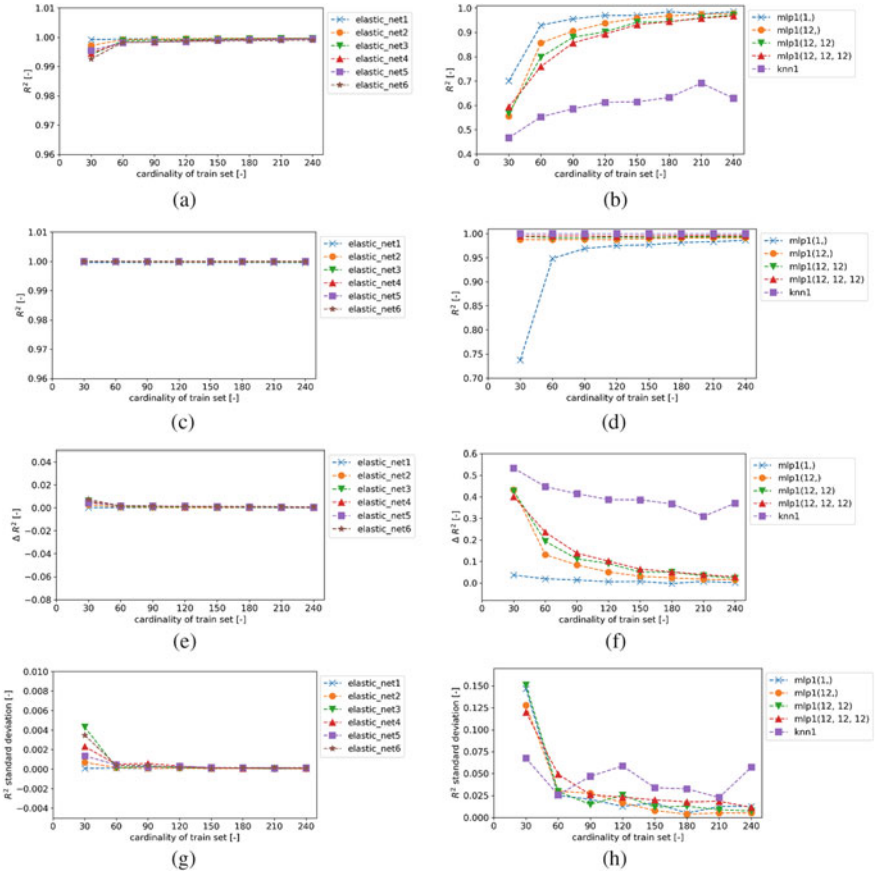


Fig. 6 Evaluation of the modeling results of the drawing aid forces based on the R^2 metric (number in parentheses denote size of hidden layers of MLP, numbers directly after algorithm name denote order of feature transformation). **a** R^2 on the test set while using elastic-net, **b** R^2 on the test set while using MLP and kNN, **c** R^2 on the training set while using elastic-net, **d** R^2 on the training set while using MLP and kNN, **e** Difference between training and test set for elastic-net, **f** Difference between training and test set for MLP and kNN, **g** Standard dev. of R^2 between draw-ins for elastic-net, **h** Standard dev. of R^2 between draw-ins for MLP and kNN. (Color figure online)

4.3 Comparison of Training Duration

Another point of interest during model selection is the time required for training. Figure 7 contains the training times for one sensor signal for the models used above, which is calculated as the average over all sensors (draw-in and drawing aid force). Since each signal contains 12 timesteps, in fact 12 independent regression models are trained for each sensor. Each duration that is mentioned thus corresponds to fitting 12 models. The kNN algorithm needs only a minimum amount of time since it does not perform any modeling steps. With an average of 0.008 s, the elastic-net with

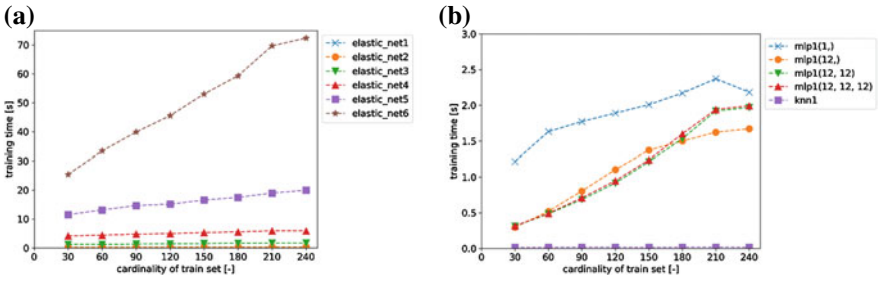


Fig. 7 Comparison of training time for the models used. **a** Training time for elastic-net estimators, **b** Training time for kNN and MLP estimators. (Color figure online)

linear features is the fastest model, followed by the elastic-net with second-order features (0.29 s). All MLPs except the simplest require around 1.1 s on average and are already faster than the elastic-net with third-order features (1.5 s). Figure 7 also shows a dramatic increase in training time if high feature orders are used, especially if the training set gets larger, which can make the use of these models impractical. Analysis of the training time for the $mlp1(1,)$ shows that the model requires much more iterations during training, leading to an increased training time although the number of parameters is significantly smaller compared to the other MLPs.

4.4 Visualization of Model Quality Dependent on Model Complexity

In the introduction, the bias-variance-tradeoff was illustrated in a qualitative manner. The data gained in this study allows determining the discrete values for the modeling quality dependent on model complexity and expressing the relationship, as shown in Fig. 1, with real data in a quantitative manner. The analysis is done on the elastic-net of the draw-in modeling. Since the y-axis in Fig. 1 is an error-like quantity (the lower the better), $\left(1 - R^2\right)$ is used on the y-axis which leads to the same qualitative behavior. The result is shown in Fig. 8. The lowest error corresponds to second-order features, except for the blue curve representing the use of only 30 training points. Note that the result of only 30 data points for training leads to only poor models; therefore, it is of very limited expressiveness from a statistical point of view.

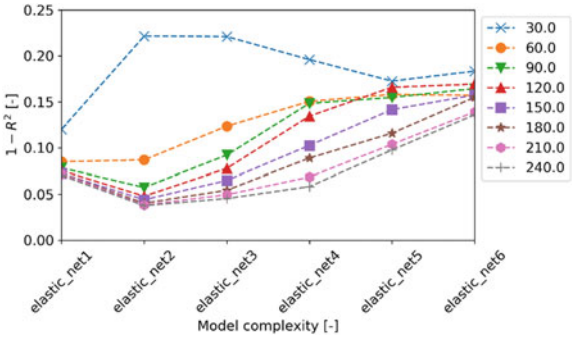


Fig. 8 Model error dependent on its complexity (draw-in data). (Color figure online)

5 Conclusion

In this work, the bias-variance-tradeoff in modeling of draw-in as well as drawing aid force signals was analyzed in a quantitative manner on a deep drawn part. The following conclusions are drawn:

- Given the range of number of training samples used to train surrogate models, the quadratic model showed the highest modeling score if the ratio between number of training points and model coefficients exceeds 0.62 for the draw-in signal.
- Linear models are in general not sufficient to describe the draw-in accurately. The only exception where linear models perform best is the case if only a very small amount of training data is available.
- For the modeling of drawing aid forces on the part examined above and with the given amount of training data, linear models have proven to be sufficient, independent of the ratio of training data compared to model coefficients.
- The result shows no evidence that the modeling quality increases by using either features of higher order than 2 or more complex approaches like neural networks, which is true for draw-ins as well as drawing aid forces. It cannot be ruled out that these more complex models perform better in a more complex case, for example if splits or wrinkles occur.

In summary, the result from this study shows that linear regression approaches provide a powerful tool for surrogate modeling in practical use in deep drawing. The linear regression models lead to high model quality combined with short training periods. Additionally, it is also worth mentioning that the simple regression models also allow the interpretation of model coefficients, which is not possible anymore for more complex models like MLPs with multiple hidden layers.

References

1. Schwarz C, Ackert P, Mauermann R (2018) Principal component analysis and singular value decomposition used for a numerical sensitivity analysis of a complex drawn part. Int J Adv Manuf Tech 94(5):2255–2265
2. Neuhauser FM, Struck R, Mautz H, Manopulo N, Hora P (2019) Sensor placement strategy and quality estimation in modern car body production using stochastic finite element methods. Proc Manuf 27:104–111
3. Neuhauser FM (2020) Potentials of artificial intelligence in production. PhD thesis, ETH Zurich
4. Bishop CM (2006) Pattern recognition and machine learning. Springer, New York
5. Goodfellow I, Bengio Y, Courville A (2016) Deep learning. MIT Press, Cambridge
6. Swift HW (1952) Plastic instability under plane stress. J Mech Phys Solids 1(1):1–18
7. Hockett JE, Sherby OD (1975) Large strain deformation of polycrystalline metals at low homologous temperatures. J Mech Phys Solids 23(2):87–98
8. Barlat F, Lian K (1989) Plastic behavior and stretchability of sheet metals. Part I: a yield function for orthotropic sheets under plane stress conditions. Int J Plast 5(1):51–66

Development of Mechanical Cards for Finite Element Analysis of Mild Steels by Parameter Optimization



M. Emin Tamer, Eda Çapa Kızıltaş, and B. Celal Seyalıoğlu

Abstract Material card generation has a significant role for characterizing the mechanical behaviour to estimate accurate deformation in finite element analysis. Regarding this, the most commonly used characterization test for sheet metals is the uniaxial tension test due to its simplicity and well-defined testing standards. The mechanical properties such as ultimate tensile strength can be determined by tensile tests. However, the strain level can reach to a specific value which is low as compared to strain levels reached in cold forming operations. In this paper, the experimental data is optimized with finite element analysis and a good consistency between experimental and simulation results is achieved. Parameter optimization is used as a guiding tool to extend strain levels according to 3 mechanical equations: Swift, Hockett-Sherby, and Combined material model. The user interface is designed with the detailed graphs and optimized parameters with the help of MATLAB tool.

Keywords Material cards · Optimization · Mechanical characterization

1 Introduction

Nowadays, finite element (FE) modelling in the automotive industry has a potent influence on sheet metal forming. Numerical simulations allow the reduction of expensive and time-consuming trials, before mass production of a stamping component on press line. Furthermore, finite element analysis is used for optimizing the design of sheet metal forming processes. The robustness of the analysis has been developed recently to integrate process deviations and material disperse in the analysis [1]. The significant point in numerical simulations is proper mechanical characterization. The predictive capabilities of simulations, especially in deep drawing process are entirely prompted by the quality of the material characterization. The researcher can analyze the problems due to the influence of characterization and

M. Emin Tamer (✉) · E. Ç. Kızıltaş · B. Celal Seyalıoğlu
Borçelik Çelik Sanayi Ticaret A.Ş., R&D Center, Gemlik 16601, Bursa, Turkey
e-mail: emint@borcelik.com

© The Minerals, Metals & Materials Society 2021

G. Daehn et al. (eds.), *Forming the Future*, The Minerals, Metals & Materials Series,
https://doi.org/10.1007/978-3-030-75381-8_51

improve the reliability of the results with the help of optimization of the mechanical parameters [2].

Mechanical characterization tests are vital requirement for numerical simulations to obtain efficient deformation results and process design. There are several studies to model the constitutive equations and characterization parameters. The effect of material property is accurately modelled when the variations and correlations in the input parameters are represented with values close to the physically observed ones [3, 4]. The Hill quadratic function is corresponded with strain ratios commonly used in industrial applications, on the contrary, the yield function doesn't describe material anisotropy in a wide perspective [5, 6]. The reliability of the numerical analysis is limited since the engineers use incomplete material knowledge in FE analysis. In the literature, there are also sufficiently flexible non-quadratic yield functions [7–9]. Moreover, new researches are performed to improve the flexibility of the yield functions [10–12].

In this study, the mechanical characterization test datum was evaluated and optimized with finite element analysis by a new algorithm with the help of MATLAB tool. The usage of two material models for the calculation of the flow curves and the optimization of the parameters with tensile test simulation is the new way explained in this study. Regarding this, tensile and compression tests are performed, and this novel algorithm processed those data using three material equations: Swift, Hockett-Sherby, and Combined material model. This study depends on quick data processing, generally when raw data obtained there several methods to process and prepare for simulations. In the first part of this study, the raw data were measured from mechanical tests and the second part includes the optimization with finite element analysis program. The evaluation of finite element analysis is done at Ls-Dyna environment (Fig. 1a). For the validation of the calculated material model parameters, tensile test simulation was performed, and force-displacement data is compared with experimental results. According to ASTM-E8 standard, a tensile test specimen was used for the analysis. Before the simulation, the new algorithm processes and evaluates

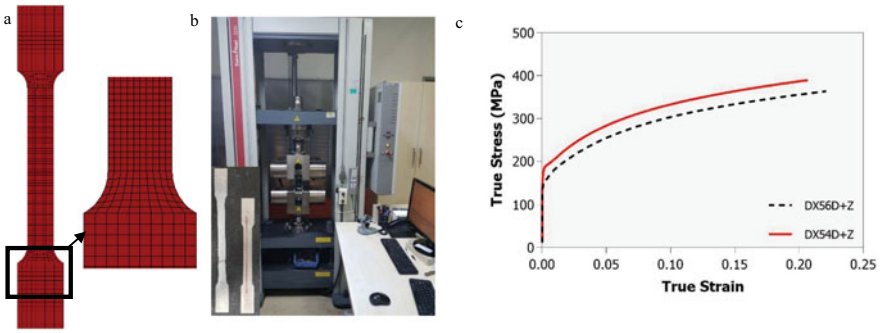


Fig. 1 **a** The mesh of tensile specimen having 2 mm of element size at gauge area, **b** Tensile testing device in Borcelik and test specimen before and after deformation, and **c** Average true stress and true strain curves. (Color figure online)

the data and creates flow curve. Afterwards, the novel algorithm exports the material card including flow curve and 3 material equation parameters. After the several tensile test simulations, the algorithm prepares and exports final material card for sheet metal forming processes. The validation is done with the real measurement's force-displacement curve.

2 Experimental Study

To evaluate the mechanical tests DX54D + Z and DX56D + Z tensile specimens were performed. The DX54D + Z and DX56D + Z material, continuous annealed and hot dip galvanized IF steels, were chosen owing to its wide application range in automotive industry. The nominal thickness of the sheet materials was 0.7 mm, in contrast the individually measured thicknesses were in the range of 0.68–0.72 mm for DX54D + Z and 0.69 - 0.71 mm for DX56D + Z, respectively. The whole tests were performed with three repetitions in each direction (rolling, diagonal, and transverse) with Euro norm test speed. The average values with standard deviation of the test results in three directions are demonstrated in Table 1. Displacement, force, true strain, and stress values were exported form ZwickRoell TestXpert software and used in the algorithm as input values. The average true stress versus true strain curves and the test setup is shown in Fig. 1b, c.

To obtain biaxial flow curve and anisotropy the stack compression and compression tests were executed in this study. The stack compression test was first proposed by Pawelski [13], in which an alternative experiment for acquiring flow curve in a wide range of strain values due to its deformation state. This method is not standardized and different researches are still being made [14, 15]. The stack compression test made use of multi-layer cylinder like specimens (Fig. 2) that were assembled by gathering up circular discs cut from the same material by electric discharge machine. The preparation of the circular flat specimens was critical for ensuring that all the layers were concentric and had identical cross-sectional area provided with frictionless conditions along the contact interface. The tests were performed as 3 repetitions for each sample including 5 circular discs each. The tests are conducted at ZwickRoell 250 kN tension compression testing device with the speed of 2 mm/min.

Table 1 The average mechanical properties of DX54D + Z and DX56D + Z

Material	t (mm)	Yield stress(MPa)	Tensile stress (MPa)	A_g (%)	A_{80} (%)	n	r
DX54D + Z	0.70 ± 0.02	184.7 ± 3	316 ± 5.3	18.6 ± 0.8	39 ± 2.2	0.22	2.1 ± 0.017
DX56D + Z	0.70 ± 0.01	154.3 ± 4.2	298 ± 4.5	22.1 ± 1.2	42 ± 3.1	0.23	2.44 ± 0.04

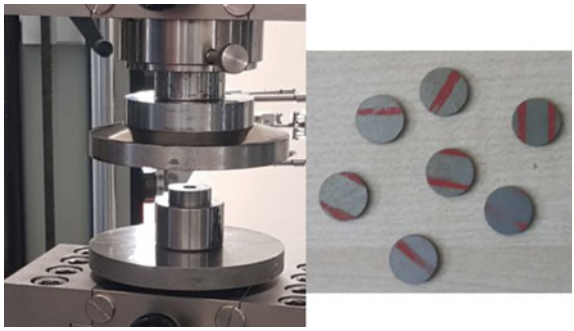


Fig. 2 Stack compression test setup and circular specimens. (Color figure online)

3 Material Optimization Interface

Based on material equations, a new interface for quick material card generation has been developed by authors that consists of three major modules:

- Displays tensile test results in three directions including yield stress, strain hardening coefficient, and anisotropy values.
- Extends and displays three material equation graphs up to 1 strain value.
- The comparison of force-displacement graphs and combined model's material equation parameters.

The algorithm involves two major parts; the first part evaluates the raw material data and calculates flow curves according to Swift, Hockett-Sherby, and Combined model (consists of Swift and Hockett-Sherby material equations with a coefficient) up to 1 strain value. The second part optimizes the equation parameters executing the series of tensile test simulation. The structure of the new interface is illustrated

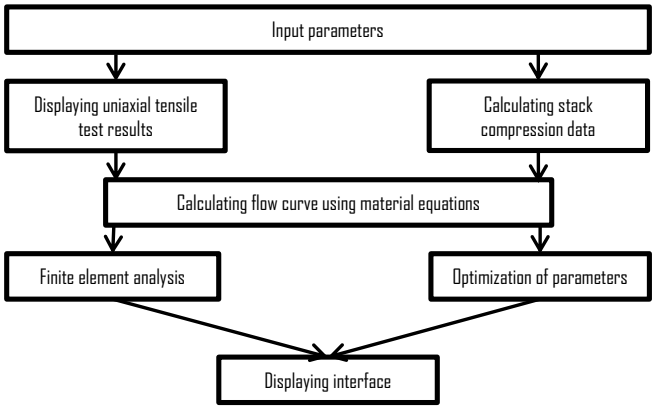


Fig. 3 Structure of the new interface

in Fig. 3, where the structure presents the process of the material card generating interface, as well as their interaction.

The tensile and stack compression test datum from ZwickRoell Z250 kN are exported which involves true stress and true strain data. Then the algorithm imports this raw data and evaluates by using strain hardening material equations. The unknown coefficients are calculated according to the true stress–true strain curve by curve fitting methods using MATLAB. In curve fitting method, it was implemented linear regression type curve fitting due to convenience with the objective functions. The fitted curve is adapted according to minimum error target with least square and gradient descent approach. In this method, R-Square values are aimed to be over 0.9 for appropriate equation fitting. The unknown parameters stated in the paper are related with extended true stress-strain curve. The aim is to find most convenient (Swift, Hockett-Sherby, and Combined material equations) parameters for best fitting equation according to true stress-strain curve. Therefore, data set is extended both true strain and true stress pairs. The true strain points were configured as training set and applied curve fitting algorithm through real output true stress. The linear regression type curve fitting was implemented due to suitability with those equations mentioned above. The fitted curve is adapted according to minimum error target with least square and gradient descent approach. The mentioned minimum error is based on sum of the square of errors; which is the objective function for optimization, that is, sum of difference between calculated stress and observed stress. The gradient descent approach is followed while updating parameters in each iteration by integrating error according to strain values. After an approximate result, the true stress–strain curves were extended to 1 strain value. For the sake of user experience, both experimental and calculated curves were overlapped through graph. After obtaining extended flow curves according to the all strain hardening model, the optimization was held for combined model. The other material equations can be preferable, however, the combined model is the best fitted equation for optimization with its parameter variety. Optimization part was run in Ls-Dyna software to decide most appropriate parameter combinations by reducing overall difference in force-displacement outcomes of numerical and experimental results. K (Strength coefficient), SS (Saturation stress), a (Strength hardening law exponent), and p (Strength hardening law exponent) are the parameters that are iteratively changed through this new algorithm.

The equations used in this method are given below:

Swift equation: $\sigma = K(\varepsilon_0 + \varepsilon)^n$
Hockett-Sherby Equation:$\sigma = SS - (SS - \sigma_0) * e^{-a\varepsilon^p}$
Combined Equation: $\sigma = (1-\alpha)\left[K(\varepsilon_0 + \varepsilon)^n\right] + \alpha[S - (SS - \sigma_0) * e^{-a\varepsilon^p}]$

The basis of iterations depends on evaluated values in the beginning of the algorithm. These parameters were chosen taking the following bases into account:

– Decreasing the running time due to iterations.
– The effects towards the equations.

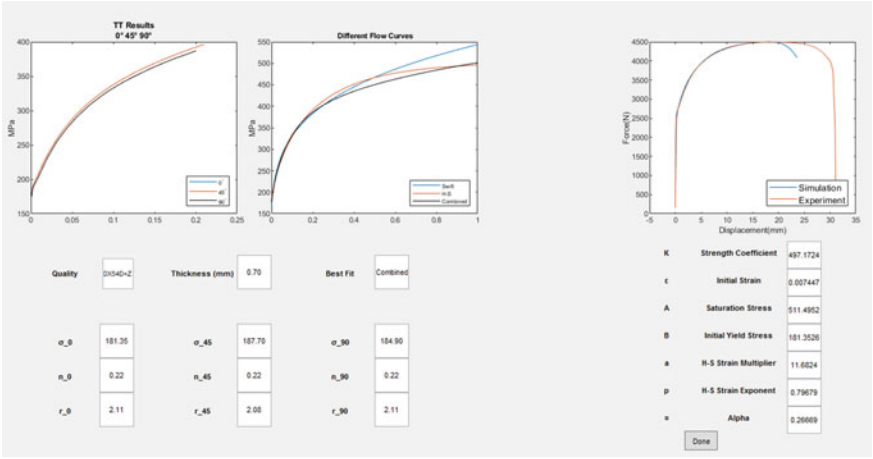


Fig. 4 The interface of the material card generating algorithm. (Color figure online)

To sum up, the final numerical and experimental force-displacement graphs that optimized parameters are published in interface result window (Fig. 4).

In Fig. 4, the different flow curves with different material models are obtained only in rolling direction (00-direction). Moreover, at the right-hand side of the figure, the force-displacement graph includes 0 directional experimental and finite element analysis results.

To compare the results of new algorithm and conventional material model, a real car body component was analyzed for the validation. A rear side of inner door panel has been used for the case study (Fig. 5). The deep drawing analyses were performed in Autoform environment.

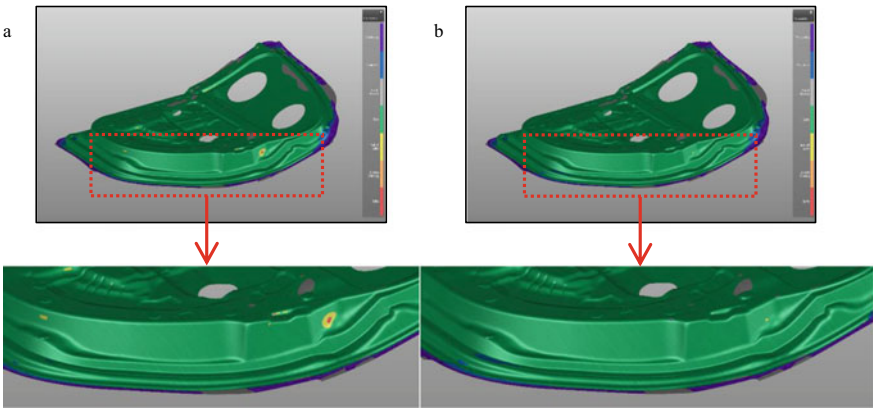


Fig. 5 The comparison of formability results between the new algorithm and conventional material model. (Color figure online)

The model illustrated in Fig. 5a was analyzed by BBC yield surface and non-optimized Swift and Hockett-Sherby material model. As can be seen in the figure, there are some tearing tendencies and critical regions at certain locations. On the contrary, In Fig. 5b, the potential tearing regions were disappeared. As mentioned above, the new algorithm calculates the unknown parameters using curve fitting method in MATLAB. Therefore, the simulation with new material card including optimized parameters improved the formability.

4 Conclusion

In this paper, a new algorithm for material characterization with optimizing the mechanical parameters of material equations was presented. Despite limited levels in flow curve measuring tests, higher trusted values are achieved with material equations by this new interface. Material card generation has a major role for characterizing the mechanical behaviour to obtain reliable simulation results. The calculated material data is used in series of tensile test simulation. The algorithm runs up to the force-displacement data of experimental and simulation results are convenient, in other words; with the optimization of the material parameters such as strength coefficient, strain law exponents (a and p), and saturation stress, material card based on extended virtual data has converged to the real-life measurement. In conclusion, the algorithm can be used for improving the reliability of the finite element analysis of sheet metal forming operations.

5 Future Work

Future investigations are necessary to validate these kinds of conclusions that can be drawn from this study. Future research should assist the investigation of the effects on the results upon the application of new steel grades. Also, this new interface should be developed taking the effects of other material equations into account and by increasing the iterations on parameter optimization. It appears from the current work that further attempts will be beneficial to retest the reliability of numerical simulations in sheet metal forming analysis.

References

1. An YG, Eyckens P, Boterman R, Atzema E, Abspoel M, Scholting M (2017) An improved polycrystal plasticity model and its deployment in stretch forming for highly formable sheet steels. Proc Eng 207:197–202
2. Beyer HG, Sendhoff B (2007) Comput Methods Appl Mech Eng 196:3190–3218

3. Gödel V, Merklein M (2011) Variation of deep drawing steel grades' properties in dependency of the stress state and its impact on FEA. Mater Form 4:183–192
4. Aspenberg D, Larsson R, Nilsson L (2012) An evaluation of the statistics of steel material model parameters. Mater Process Technol 212:1288–1297
5. Hill R (1948) A theory of the yielding and plastic flow of anisotropic metals. Proc R Soc London A 193:281–297
6. An YG, Vegter H, Carless L, Lambriks M (2011) A novel yield locus description by combining the Taylor and the relaxed Taylor theory for sheet steels. Int J Plast 27(11):1758–1780
7. Hill R (1990) Constitutive modelling of orthotropic plasticity in sheet metals. J Mech Phys Solids 38:405–417
8. Barlat F, Brem JC, Yoon JW, Chung K, Dick RE, Lege DJ, etc (2003) Plane stress yield function for aluminum alloy sheets-part 1: theory. Int J Plast 19:1297–1319
9. Banabic D, Aretz H, Comsa DS, Paraianu L (2005) An improved analytical description of orthotropy in metallic sheets. Int J Plast 21:493–512
10. Vegter H, van den Boogaard AH (2006) A plane stress yield function for anisotropic sheet material by interpolation of biaxial stress states. Int J Plast 22:557–580
11. Barlat F, Aretz H, Yoon JW, Karabin ME, Brem JC, Dick RE (2005) Linear transformation-based anisotropic yield functions. Int J Plast 21:1009–1039
12. Comsa D, Banabic D (2008) Plane stress yield criterion for highly anisotropic sheet metals. In: Hora P (ed) Proceedings of the 7th international conference and workshop on numerical simulation of 3d sheet metal forming processes, Numisheet, Interlaken, Switzerland
13. Pawelski O (1967) Über das stauchen von holzylindern und seine eignung zur bestimmung der formänderungsfestigkeit dünner bleche. Arch Eisenhüttenwes 38:437–442
14. Merklein M, Kuppert A (2009) A method for the layer compression test considering the anisotropic material behaviour. Int J Mater Form 12:483–486
15. Hochholdinger B, Grass H, Lipp A, Hora P (2009), Determination of flow curves by stack compression tests and inverse analysis for the simulation of hot forming. In: 7th European LS-DYNA Conference, Salzburg, Austria

Part IX
Characterization of Plasticity and Ductile Fracture of Metals under Proportional and Non-proportional Loading

Cyclic Loading Tests Based on the In-Plane Torsion Test for Sheet Metal



Chong Zhang, Yanshan Lou, Till Clausmeyer, and A. Erman Tekkaya

Abstract In-plane torsion test has attracted a lot of attention recently. As a novel shear test, it can avoid unwanted reaction torque compared with the traditional in-plane shear test. The in-plane torsion test with circular groove specimens can avoid early fracture at the free edges, and thus achieve actual fracture strain under pure shear state because it has no free boundaries. In this study, digital image correlation is implemented to measure the torsion angle to obtain the precise torque-torsion angle curves. For specimens with slits, strain hardening is calibrated by inverse engineering approach. The strain path at the center of the shear zone during the torsion test is observed to be very close to a pure simple shear state. Cyclic shear loading tests are carried out for twin bridge shear specimen. The combined isotropic-nonlinear kinematic hardening model, Yoshida–Uemori two-surface model, and homogeneous anisotropic hardening model are evaluated to characterize the cyclic loading behaviors.

Keywords Bauschinger effect · Cyclic shear loading · In-plane torsion test · Kinematic hardening · Distorted hardening

1 Introduction

A proper material model considering the forward–reverse loading behavior has become necessary particularly for the springback prediction of materials like high strength steels and aluminum alloys. There are two main types of phenomenological models to model the forward–reverse loading behavior which including the bauschinger effect, transient behavior, permanent softening, and unloading modulus. One is the well-accepted kinematic hardening models with back-stress such as

C. Zhang · Y. Lou (✉)
School of Mechanical Engineering, Xi'an Jiaotong University, 28 Xianning West Rd, Xi'an 710049, Shaanxi, China
e-mail: ys.lou@xjtu.edu.cn

T. Clausmeyer · A. E. Tekkaya
IUL, TU Dortmund University, Baroper Str. 303, Dortmund 44227, Germany

© The Minerals, Metals & Materials Society 2021

G. Daehn et al. (eds.), *Forming the Future*, The Minerals, Metals & Materials Series,
https://doi.org/10.1007/978-3-030-75381-8_52

nonlinear kinematic (NLK) hardening approaches [1–3], Yoshida–Uemori (YU) model, including the yield surface and bounding surface [4–6]. The other alternative to account for the forward–reverse loading behavior is the distortional plasticity models without considering the back-stress such as homogeneous anisotropic hardening (HAH) model [7, 8].

Two main types of testing procedure are widely accepted to evaluate the forward–reverse loading behavior, including the widely used in-plane tension–compression [5, 9, 10], and in-plane forward–reverse simple shear tests [11–13]. The in-plane tension–compression tests need the clamping tools to avoid buckling, which occurs during the compressive process. However, the clamping tools make strain measurement difficult by digital image correlation (DIC) and need extra efforts to eliminate the influence of friction between the specimen and clamping tools. The in-plane forward–reverse simple shear test provides a large strain range without clamping tools to prevent the buckling occurs. The strain distribution fields can be measured during the forward–reverse loading processes by DIC. However, inhomogeneous strain deformation at the edge of shear zone make it difficult to calculate the forward–reverse stress–strain data analytically. The inverse method is recommended to eliminate errors caused by inhomogeneous strain deformation. There is another novel shear test: in-plane torsion test has attracted a lot of attention recently [12–15]. It can avoid unwanted reaction torque compared with the traditional in-plane shear test including twin bridge shear specimen, stress-adjusted groove specimen, etc. The in-plane torsion test with stress-adjusted groove specimen can achieve continuous strain measurement in the stress-adjusted groove. Therefore, the stress–strain data can be calculated analytically as a standardized specimen. Zang et al. also proposed a new approach to calibrate the hardening parameters inversely from the springback profiles of three-point bending tests with pre-strained sheets [16].

In this study, the cyclic loading tests of twin bridge shear specimen based on the in-plane torsion test are conducted for an AA5182 aluminum alloy. The combined isotropic-nonlinear kinematic hardening (IH + NLK) model, YU, and HAH models are evaluated to characterize the cyclic loading behavior.

2 Phenomenological Models

The anisotropic study for the AA5182 aluminum alloy is not involved in this article. Yld2000-2d yield function is employed with its isotropic form for body-centered cubic (BCC) material. Hardening models for cyclic loading behavior evaluation are employed as below.

2.1 Isotropic Hardening (IH) Model

Voce hardening law is employed in this study to describe the isotropic hardening behavior of AA5182 as below

$$\tilde{\sigma} = A - (A - B)exp\left(-C\overline{\varepsilon}^{p}\right) \tag{1}$$

where $\tilde{\sigma}$ is the effective stress, $\overline{\varepsilon}^{p}$ is the equivalent plastic strain, and A, B, and C are parameters.

2.2 Combined Isotropic-Nonlinear Kinematic Hardening Model

The IH+NLK model is a mixed hardening rule as a superposition of nonlinear isotropic and kinematic hardening.

$$f = \phi(\boldsymbol{S} - \boldsymbol{\alpha}) - R - \sigma_0 = 0 \tag{2}$$

where $\boldsymbol{S}$ is stress deviator tensor, $\boldsymbol{\alpha}$ is back-stress, σ_0 is initial yield stress, and R is the isotropic part of the hardening. R enlarges with the increment of effective plastic strain dp as

$$dR = b(Q - R)dp \tag{3}$$

where b and Q are parameters of isotropic hardening part.

Several back-stresses are developed as below

$$\boldsymbol{\alpha} = \sum_{m=1}^{M} \boldsymbol{\alpha}^{(m)} \tag{4}$$

$$d\boldsymbol{\alpha}^{(m)} = \frac{2}{3}c^{(m)}d\boldsymbol{\varepsilon}^{\boldsymbol{p}} - \gamma^{(m)}\boldsymbol{\alpha}^{(m)}dp \tag{5}$$

where $c^{(m)}$ and $\gamma^{(m)}$ are parameters of nonlinear kinematic hardening part.

2.3 Yoshida-Uemori (YU) Model

YU model [4] belongs two-surface model which including the yield surface f and bounding surface F as below

$$f = \phi(\boldsymbol{S} - \boldsymbol{\alpha}) - \sigma_0 = 0 \tag{6}$$

$$F = \phi(\boldsymbol{S} - \boldsymbol{\beta}) - R - B = 0 \tag{7}$$

where $\boldsymbol{\beta}$ denotes the center of the bounding surface, and B and R are its initial size and isotropic hardening. Back-stress $\boldsymbol{\alpha}$ consists of two components as

$$\boldsymbol{\alpha} = \boldsymbol{\alpha}_* + \boldsymbol{\beta} \tag{8}$$

where $\boldsymbol{\alpha}_*$ is the relative motion of the yield surface with respect to the bounding surface F.

$$\boldsymbol{\alpha}_* = c(\frac{a}{\sigma_0}(\boldsymbol{S} - \boldsymbol{\alpha}) - \sqrt{\frac{a}{\|\boldsymbol{\alpha}_*\|}}\boldsymbol{\alpha}_*)\dot{p} \tag{9}$$

where c is the parameters, $\dot{p}$ is the effective plastic strain rate, and a is the difference between the size of bounding surface and yield surface.

$$\dot{p} = \sqrt{\frac{2}{3}\left\|\varepsilon^{\dot{p}}\right\|} \tag{10}$$

$$a = B + R - \sigma_0 \tag{11}$$

$$\dot{R} = m(R_{sat} - R)\dot{p} \tag{12}$$

where B and R_{sat} are parameters.

Kinematic hardening $\boldsymbol{\beta}$ for the bounding surface F is developed as

$$\dot{\boldsymbol{\beta}} = m(\frac{b}{Y}(\boldsymbol{S} - \boldsymbol{\alpha}) - \boldsymbol{\beta})\dot{p} \tag{13}$$

Since the work hardening stagnation is not exhibited for the studied material, the surface g to modify the evolution of the bounding surface F is not presented in this study.

YU model also considers the variable Young's modulus and as a function of the accumulated plastic strain p

$$E = E_0 - (E_0 - E_a)(1 - e^{-\xi p}) \tag{14}$$

where E_0 and E_a are the values of Young's modulus for initial and infinitely large pre-strained material, and ξ is a material parameter.

2.4 Homogeneous Anisotropic Hardening (HAH) Model

Barlat et al. proposed an approach without considering the back-stress which is called homogeneous yield function-based anisotropic hardening model. In this model, the yield surface does not translate in stress space, but its shape distorted. The original HAH model [7] is defined as

$$\begin{aligned}\phi(\boldsymbol{s}) =&(\phi^q + \phi_h^q)^{\frac{1}{q}} \\ =& (\phi^q(\boldsymbol{s}) + f_1^q \left|\widehat{\boldsymbol{h}}^{\boldsymbol{s}} : \boldsymbol{s} - \left|\widehat{\boldsymbol{h}}^{\boldsymbol{s}} : \boldsymbol{s}\right|\right|^q + f_2^q \left|\widehat{\boldsymbol{h}}^{\boldsymbol{s}} : \boldsymbol{s} + \left|\widehat{\boldsymbol{h}}^{\boldsymbol{s}} : \boldsymbol{s}\right|\right|^q)^{\frac{1}{q}} = \tilde{\sigma}(\overline{\varepsilon}^p)\end{aligned} \tag{15}$$

where $\phi^q(\boldsymbol{s})$ is the component of the stable yield function, ϕ_h^q is the fluctuating component to controls the distortion of yield surface for the prediction of Bauschinger effect. q is a constant, f_1 and f_2 are state variables, and $\widehat{\boldsymbol{h}}^{\boldsymbol{s}}$ is the normalized microstructure deviator.

$$\widehat{h}_{ij}^s = \frac{h_{ij}^s}{\sqrt{\frac{8}{3} h_{kl}^s h_{kl}^s}} \tag{16}$$

The state variables f_1 and f_2 can be expressed as a function of other variables g_1 and g_2

$$f_1 = (g_1^{-q} - 1)^{\frac{1}{q}} \text{and} f_2 = (g_2^{-q} - 1)^{\frac{1}{q}} \tag{17}$$

.

When plastic deformation occurs, the evolution laws for the state variables g_1 and g_2 are detailed in [7].

3 Experiments

Cyclic twin bridge shear tests are conducted based on the in-plane torsion test as illustrated in Fig. 1. The rotation speed is set to 0.043°/s which results in a quasi-static strain rate of about 0.005 s^{-1} on the center of shear zone. The shear anisotropy is not studied in this paper and specimens are tested along the rolling direction.

One forward–reverse shear test results with three different pre-strain are conducted as show in Fig. 2. When the torsion angle reaches 0.5°, 1°, and 1.5° degrees, respectively, the reversal begins until failure. The equivalent mises strain along the transverse section cut at different torsion angle is plotted in Fig. 1b, which indicate that 0.5°, 1°, and1.5° correspond to a pre-strain of 0.05, 0.1, and 0.15, respectively. Cyclic forward–reverse shear tests also are conducted. Figure 3 shows the torsion angle-time curves during cyclic shear test. The angle is measured by DIC and the slope of the angle vs. time is about 0.04°/s, which is slightly lower than the control speed. The DIC measurement method for torsion angle is recommended because it calculates torsion angles based on the speckle pattern on the sheet surface. Therefore, the measurement error caused by transmission clearance of the transmission system and elastic deformation of the tool can be avoided.

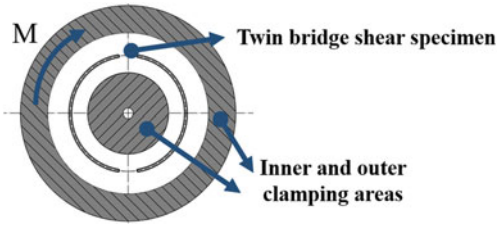


Fig. 1 Twin bridge shear tests based on in-plane torsion test. (Color figure online)

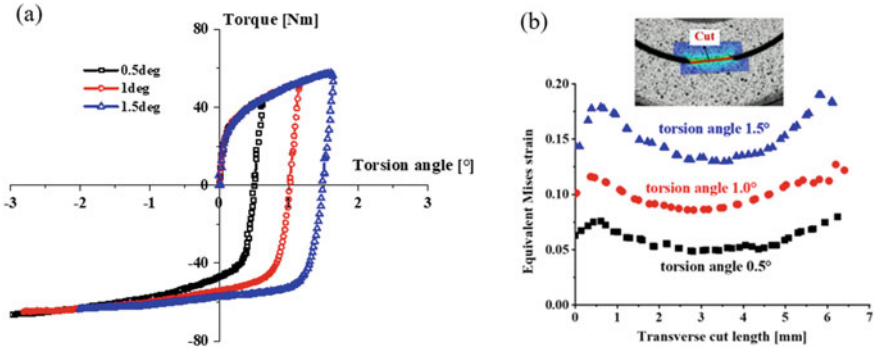


Fig. 2 One forward–reverse shear tests with different pre-strain: **a** torque–angle curves; **b** strain distribution along cut. (Color figure online)

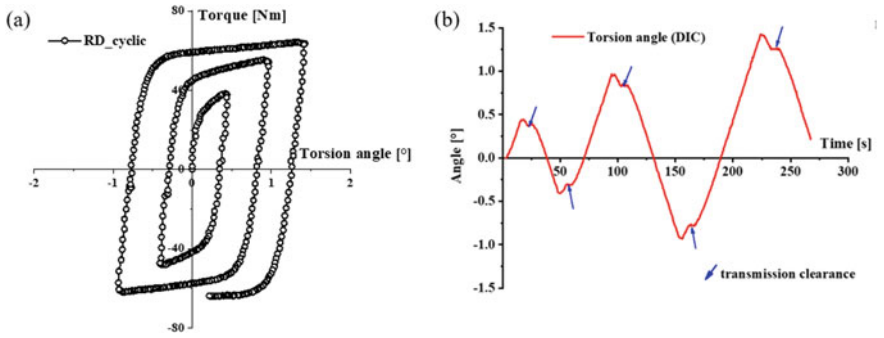


Fig. 3 Cyclic forward–reverse shear test results: **a** torque–angle curves; **b** torsion angle versus time curves. (Color figure online)

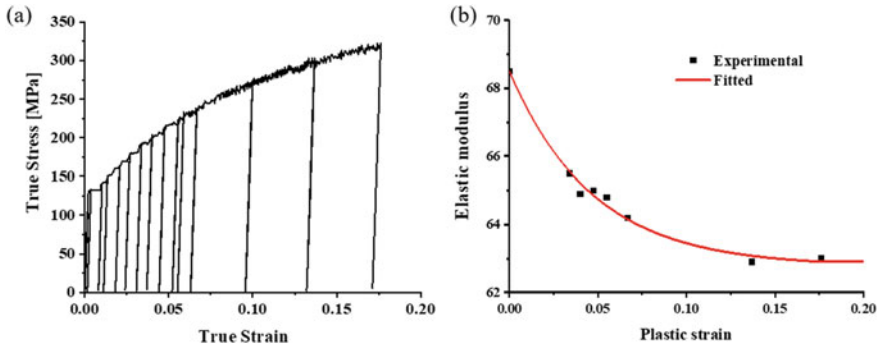


Fig. 4 Cyclic loading–unloading uniaxial tensile tests: **a** true stress versus true strain curves; **b** unloading modulus versus plastic strain curves. (Color figure online)

Cyclic loading–unloading uniaxial tensile tests are also conducted to obtain the unloading modulus under different plastic strain as show in Fig. 4 and the data are fitted according to Eq. (14).

4 Calibration and Results

Since the strain distribution on the shear zone is not uniform as mentioned in Sect. 3. The cyclic shear stress–strain curves cannot be calculated analytically. The inverse engineering method is recommended to calibrate the constitutive models by conducting the reliable numerical simulation. Schematic of the inverse engineering calibration method for twin bridge shear test is shown in Fig. 5. The difference $Total_error$ between the simulated torque-torsion angle curves and experimental data is taken as objective function to minimize as Eq. (18). Optimized model parameters are finally determined through multiple iterations as shown in Table 1.

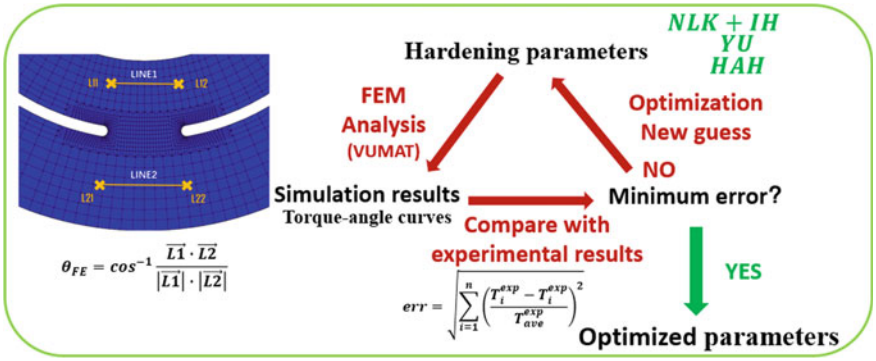


Fig. 5 Schematic of the inverse engineering calibration for twin bridge shear test. (Color figure online)

$$Total_error = {err_m}^{0.5deg} + {err_m}^{1.0deg} + {err_m}^{1.5deg} \tag{18}$$

$$err_m = \sqrt{\sum_{i=1}^{n} \left(\frac{T_i^{exp} - T_i^{num})}{T_{ave}^{exp}} \right)^2} \tag{19}$$

where n is the number of samples, T_i^{exp} and T_i^{num} are the experimental and numerical simulated torque values corresponding to the i sample, and T_{ave}^{exp} is the average torque values of the experimental torque-torsion angle curves.

The predicted torque–angle curves are compared with the experiments for one forward–reverse shear tests in Fig. 6. It can be seen that, when compared with the IH model, the other three models consider the bauschinger effect can better simulate the cyclic loading behavior of materials. The comparison of $Total_error$ shows that HAH and YU models perform better than the NLK + IH model which cannot accurately predict the "re-yielding" and transient behavior of the material. For cyclic forward–reverse shear tests, predicted torque–angle curves are consistent with the experimental data until the final third reversal. The transient behavior and permanent softening are not correctly predicted by all models. That's probably because the calibration procedure is based on the one forward–reverse tests, but the cyclic forward–reverse experimental data are not included (Fig. 7).

5 Conclusions

Cyclic shear tests are completed based on the twin bridge shear tests for an aluminum alloy. The inverse engineering approach is recommended to calibrate the hardening models by conducting multiple simulations. After multiple iterations, the difference between the predicted curves and experimental results are finally minimized. The

Table 1 Calibrated parameters for constitutive models

Hardening model	IH			IH+NLK					Variable Young's modulus		
parameters	$A[Mpa]$	$B[Mpa]$	C	$Q[Mpa]$	b	$c_1[Mpa]$	γ_1	$c_2[Mpa]$	$E_0[Gpa]$	$E_a[Gpa]$	ξ
values	338	128	12.36	131.8	17.78	1558.9	508.6	159.3	68.5	62.7	21.2
Total_error	/			3.58					/		
Hardening model	YU					HAH					
parameters	$B_{YU}[Mpa]$	$R_{sat}[Mpa]$	m	c	$b_{YU}[Mpa]$	q	k	k_1	k_2	k_3	k_4	k_5
values	153.7	184.2	7.56	291.3	30.09	2	26.6	141.3	82.2	0.018	0.9	33.0
Total_error	3.19					2.42						

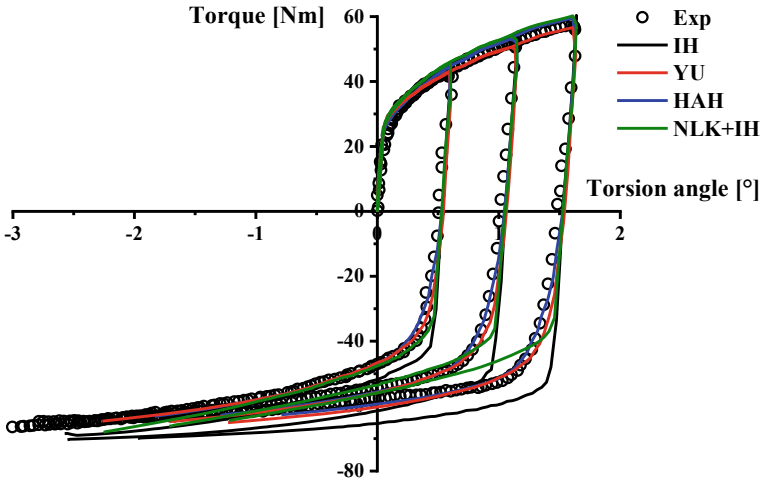


Fig. 6 Predicted torque–angle curves for one forward–reverse shear tests. (Color figure online)

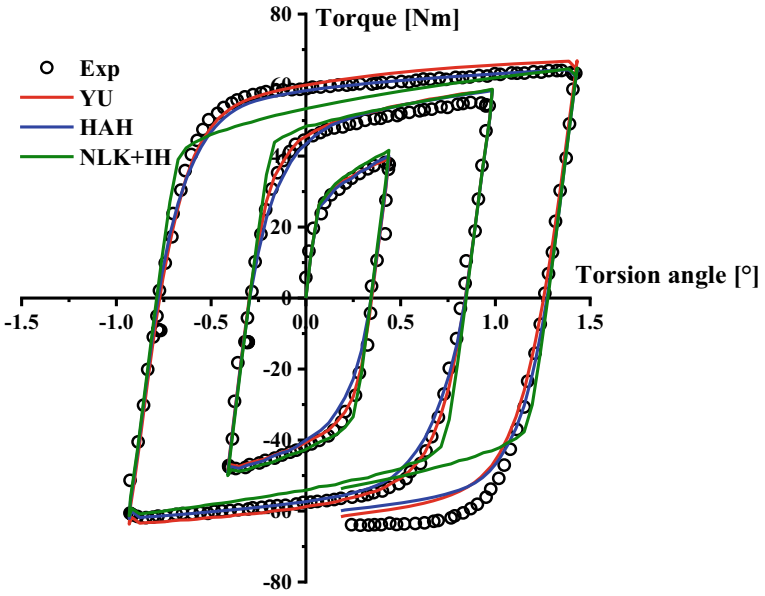


Fig. 7 Predicted torque–angle curves for cyclic forward–reverse shear tests. (Color figure online)

calibrated results show that models considering the kinematic hardening or distorted hardening can better describe the cyclic loading behavior than isotropic hardening. HAH model and YU model perform better than the NLK + IH model. For cyclic forward–reverse shear tests, all models cannot predict the transient behavior and

permanent softening correctly about the final third reversal. The cyclic forward–reverse experimental data must be included in calibration procedure.

Acknowledgments The authors acknowledge the financial support by the National Natural Science Foundation of China (Grant No. 52075423), the State Key Laboratory of Mechanical System and Vibration (Grant No. MSV202009), and the State Key Laboratory of High Performance Complex Manufacturing (Grant No. Kfkt2019-02).

References

1. Armstrong PJ, Frederick CO (1966) A mathematical representation of the multiaxial Bauschinger effect. Technical Report RD/B/N 731
2. Chaboche JL (1986) Time-independent constitutive theories for cyclic plasticity. Int J Plast 2:149–188
3. Chaboche JL (2008) A review of some plasticity and viscoplasticity constitutive theories. Int J Plast 24:1642–1693
4. Yoshida F, Uemori T (2002) A model of large-strain cyclic plasticity describing the Bauschinger effect and workhardening stagnation. Int J Plast 18:661–686
5. Yoshida F, Uemori T, Fujiwara K (2002) Elastic-plastic behavior of steel sheets under in-plane cyclic tension-compression at large strain. Int J Plast 18:633–659
6. Yoshida F, Hamasaki H, Uemori T (2015) Modeling of anisotropic hardening of sheet metals including description of the Bauschinger effect. Int J Plast 75:170–188
7. Barlat F, Gracio JJ, Lee MG, Rauch EF, Vincze G (2011) An alternative to kinematic hardening in classical plasticity. Int J Plast 27:1309–1327
8. Barlat F, Yoon SY, Lee SY, Wi MS, Kim JH (2020) Distortional plasticity framework with application to advanced high strength steel. Int J Solids Struct 202:947–962
9. Joo G, Huh H, Choi MK (2016) Tension/compression hardening behaviors of auto-body steel sheets at intermediate strain rates. Int J Mech Sci 108–109:174–187
10. Chang Y, Wang BT, Li XD, Wang CY, Zhao KM, Dong H (2020) A new continuous tensile-compressive testing device with friction-counteracting and anti-buckling supporting mechanism for large strain. J Mater Process Technol 278:116540
11. Lee JW, Lee MG, Barlat F (2012) Finite element modeling using homogeneous anisotropic hardening and application to spring-back prediction. Int J Plast 29:13–41
12. Yin Q, Soyarslan C, Güner A, Brosius A, Tekkaya AE (2012) A cyclic twin bridge shear test for the identification of kinematic hardening parameters. Int J Mech Sci 59:31–43
13. Yin Q, Tekkaya AE, Traphöner H (2015) Determining cyclic flow curves using the in-plane torsion test. CIRP Ann Manuf Technol 64:261–264
14. Traphöner H, Clausmeyer T, Tekkaya AE (2021) Methods for measuring large shear strains in in-plane torsion tests. J Mater Process Technol 287:116516
15. Grolleau V, Roth CC, Mohr D (2019) Characterizing plasticity and fracture of sheet metal through a novel in-plane torsion experiment. IOP Conf Ser Mater Sci Eng 651:012101
16. Zang SL, Lee MG, Sun L, Kim JH (2014) Measurement of the Bauschinger behavior of sheet metals by three-point bending springback test with pre-strained strips. Int J Plast 59:84–107

Plastic and Fracture Characteristics of WE43 Mg Alloy Under Complex Stress States



Pengfei Wu, Chong Zhang, Yanshan Lou, Qiang Chen, and Haiqing Ning

Abstract This paper investigates the deformation behavior and fracture characteristics of WE43 Mg alloy under various stress states, including tension, compression, and shear. The digital image correlation technique is adopted to obtain highly accurate experimental data and stress–strain curve. The result indicates that the plastic deformation behavior under different stress states has a great difference and fracture already obviously occurs before necking. After calibrating the material constants of yield function and hardening equation, numerical and experimental result are compared. The result shows that the prediction accuracy of FE is very high. The fracture strain under different loading states is ensured through a hybrid experimental-numerical method. The fracture locus is constructed based on DF2016 criterion and the predicted fracture strain is compared with the experimental result. The result reveals that DF2016 ductile fracture criterion can correctly predict the fracture limit strain under various stress states.

Keywords Deformation behavior · Hybrid experimental-numerical method · Fracture characterization · Various loading states

1 Introduction

Magnesium (Mg) alloys are applied in the industry of transportation, chemistry, aerospace, and medicine due to their high strength-to-density ratio, enhanced specific stiffness, and excellent process property [1, 2]. However, as a hexagonal close-packed metal, the deformation mechanism during plastic flow is very complex due to a variety of slip systems and twinning modes, resulting in the tension–compression

P. Wu · C. Zhang · Y. Lou (✉)
School of Mechanical Engineering, Xi'an Jiaotong University, 28 Xianning West Road, Xi'an, Shanxi 710049, China
e-mail: ys.lou@xjtu.edu.cn

Q. Chen · H. Ning
Southwest Technology and Engineering Research Institute, 33 Yuzhou Road, Chongqing 400039, China
e-mail: 2009chenqiang@163.com

© The Minerals, Metals & Materials Society 2021

G. Daehn et al. (eds.), *Forming the Future*, The Minerals, Metals & Materials Series,
https://doi.org/10.1007/978-3-030-75381-8_53

asymmetry [3–6]. In addition, the forming capacity of Mg alloys is poor, which limits its application [7]. For the purpose of overcoming these disadvantages, an alloying method, namely adding rare earth (RE) elements to Mg crystal, becomes one of the effective ways [8]. As one of Mg-RE system, WE43 alloy has outstanding strength and plasticity at room temperature [9].

The paper aims to characterize the plastic and fracture behavior of WE43 alloy. Mechanical experiments under different stress states are carried out including tension, compression, and shear. The plastic flow is simulated using Drucker yield function and Swift-Voce hardening equation. Ductile fracture behavior is characterized through DF2016 criterion. The numerical result is compared with the experimental data to verify the accuracy of established model on the plastic flow and fracture behavior of WE43 alloy.

2 Experiment

The chemical composition of WE43 alloy is shown in Table 1, and five types of specimens are manufactured along rolling direction (RD) of raw material with the structure illustrated in Fig. 1. These specimens include uniaxial tension (UT), uniaxial compression (UC), plane strain tension (PT), plane strain compression (PC), and in-plane torsion for shear (TS). All experiments are conducted in 100kN INSTRON

Table 1 Chemical composition of WE43 alloy material (wt%)

Y	Nd	Ce	La	Zr	Si	Fe	Cu	Ni	Mg
3.7 ~ 4.3	2.4 ~ 3.0	0.3	0.2	0.5	0.001	0.015	0.001	0.001	REM

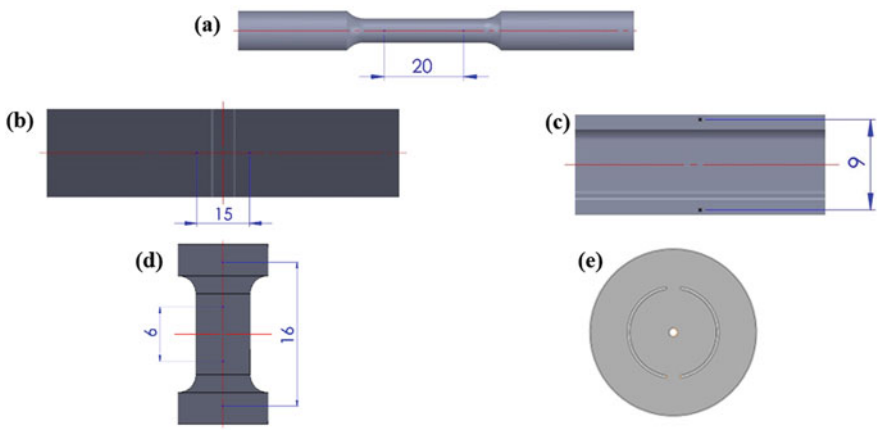


Fig. 1 Two-dimensional size of specimens [unit: mm]: **a** UT, **b** PT, **c** PC, **d** UC, and e TS. (Color figure online)

machine and self-developed torsion device. The loading process from initial to fracture is recorded through the XTOP optical non-contact digital image correlation system. The data of force, stroke, and engineering strain is measured. Each experiment is carried out with a constant loading velocity at least three times to ensure the accuracy of mechanical testing.

3 Results

Force-stroke curves of UT and UC specimens are shown in Fig. 2a. The 20 mm length medially on the region of φ6 mm along the axial is selected as the gauge of UT specimen. The center-symmetric 6 mm length along the axial is the gauge of UC specimen. It can be clearly seen that the load gradually rises with the increase of loading stroke. The deformation process of WE43 alloy is from elastic to elastic-plastic and till to fracture. Besides, the loading force drops immediately when the load reaches to the maximum value, which indicates that fracture obviously occurs before necking [10]. Through the corresponding calculation using the equation of stress–strain, true stress-plastic strain relationships under uniaxial tension and compression are presented in Fig. 2b. It is clearly indicated that WE43 alloy possesses smaller tension-compression asymmetry comparing with traditional Mg alloys, such as AZ31 [11]. The ultimate stress and plastic strain are higher than some common Mg alloys, which reflects the effectiveness of this alloying method.

The macroscopic fracture morphologies of UT and UC specimens are shown in Fig. 3. It can be seen that the fracture is a gray and dark cup-cone shape with an oblique angle under uniaxial tension. Under uniaxial compression, the fracture surface presents the 45° shear fracture. The phenomenon indicates that the fracture of WE43 alloy belongs to the ductile fracture.

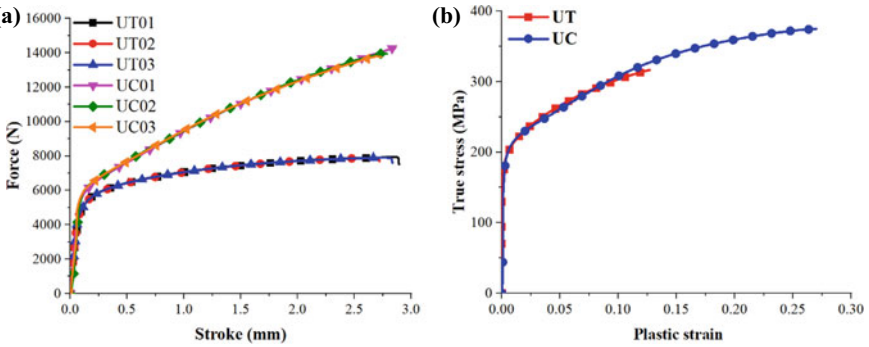


Fig. 2 Experimental results of UT and UC specimens: **a** force-stroke curve and **b** stress–strain relationship. (Color figure online)



Fig. 3 Fracture morphology of WE43 alloy: **a** UT and **b** UC. (Color figure online)

4 Material Model

4.1 Yield Function

As shown in Fig. 2b, the yield stress of WE43 alloy under uniaxial tension and compression is identical. Therefore, the Drucker isotropic equation [12] is selected as the yield function of finite element (FE) simulation. The yield criterion considers the effect of second and third deviatoric stress invariants J_2, J_3 and the equation of that is expressed as below

$$f(\sigma_{ij}) = a[(J_2^3 - cJ_3^2)^{1/6}] \tag{1}$$

where a and c are two material constants. Equation (1) is transformed to von Mises yield function when the value of parameter c is 0. Drucker yield function also can be written as

$$\bar{\sigma} = a\left\{\frac{1}{27} - c\frac{4L^2(L^2-9)^2}{729(L^2+3)^2}\right\}^{1/6}\sigma_{Mises} \tag{2}$$

with

$$L = \frac{2\sigma_2 - \sigma_1 - \sigma_3}{\sigma_1 - \sigma_3} = \frac{(\sigma_2 - \sigma_3) - (\sigma_1 - \sigma_2)}{\sigma_1 - \sigma_3} \tag{3}$$

$$a = \left\{\frac{1}{27} - c\frac{4}{729}\right\}^{-1/6} \tag{4}$$

where σ_1, σ_2, and σ_3 are three principal values of stress tensor $\boldsymbol{\sigma}$, L denotes the Lode parameter, and σ_{Mises} represents the von Mises stress. In this paper, the value of parameter c is set as 2.0 and the value of parameter a is calculated as 1.8652 through Eq. (4) [13].

Table 2 Material constants of yield function and hardening equation for WE43 alloy

Material constants	F-E
a	1.8652
c	2
k (GPa)	22.0957
ε_0	0.0004
n	0.0017
A (GPa)	−21.1186
B (GPa)	−21.5116
C	3.2921
α	0.5

4.2 Hardening Equation

At room temperature, the metallic material during the plastic deformation mainly possesses the hardening behavior. Generally, the plastic flow of metal is described by a hardening equation. There are several material models, such as Swift, Voce, and Swift-Voce with the form of

$$\sigma = k(\varepsilon_0 + \varepsilon)^n \tag{5}$$

$$\sigma = A - (A - B)\exp(-C\varepsilon) \tag{6}$$

$$\sigma = \alpha k(\varepsilon_0 + \varepsilon)^n + (1 - \alpha)(A - (A - B)\exp(-C\varepsilon)) \tag{7}$$

where σ is the equivalent stress, ε is the equivalent plastic strain (PEEQ), and k, ε_0, n, A, B, C, and α are material constants calibrated from the material tests. The Swift-Voce model is selected as the hardening equation in this study due to the multi-parameter flexibility.

Based on the experimental result presented in Fig. 2b, these material constants in Eq. (6) are calibrated and listed in Table 2.

4.3 Fracture Criterion

In order to characterize ductile fracture under various loading conditions, DF2016 fracture criterion [14, 15] is adopted, which is expressed as follows:

$$\left(\frac{2\tau_{\max}}{\sigma_{Mises}}\right)^{C_1}\left(\frac{f(\eta, L, C)}{f(1/3, -1, C)}\right)^{C_2}\varepsilon_f^p = C_3 \tag{8}$$

where C, C_1, C_2 , and C_3 are four material constants, η denotes the stress triaxiality, and ε_f^p is the fracture limit strain. The function $f\ (\eta, L, C)$ is suggested to write in this form of

$$f(\eta, L, C) = \frac{\sigma_1}{\overline{\sigma}} + C = \eta + C_4 \frac{(3 - L)}{3\sqrt{L^2 + 3}} + C \tag{9}$$

C_4 is also a constant considering the effect of L on the torsion voids coalescence.

5 Fracture Prediction

Adopting the unconstrained nonlinear optimization method of MATLAB software, the formula of error is defined with the form of

$$err = \sum_1^n \left(\frac{S_{cal}^i}{S_{\exp}^i} - 1\right)^2 \tag{9}$$

where n denotes the number of calculation, and $S_{\exp}^i$ and S_{cal}^i are the experimental and calculated value.

In order to obtain the result of mechanical property under different stress states, a hybrid experimental-numerical method is adopted. It is assumed that the FE predictions of the whole field of stress and strain tensors in the specimen are in agreement with the corresponding actual ones if the FE simulation predicts coincident load-displacement curve [16]. Other assumption is also followed that the fracture first appears inside the gauge center. The comparison of FE prediction and experimental result is shown in Fig. 4, which indicates that the prediction has a high accuracy.

Based on the acquired data, material constants of DF2016 fracture criterion are calibrated and summarized in Table 3. The fracture locus of DF2016 ductile fracture

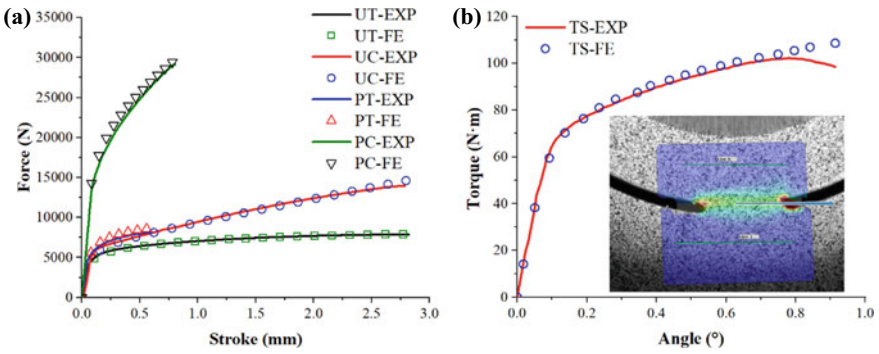


Fig. 4 Comparison of FE prediction and experimental result: **a** UT, UC, PT, and PC, and **b** TS. (Color figure online)

Table 3 Summary of material constants for DF2016 fracture criterion

C	C_1	C_2	C_3	C_4
−0.0819	1.4020	1.2803	0.2421	6.2456

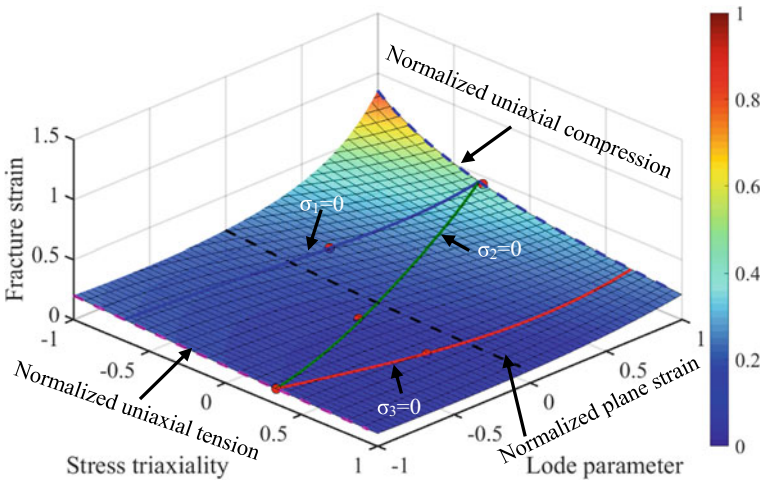


Fig. 5 DF2016 fracture locus for WE43 alloy. (Color figure online)

criterion is constructed, as shown in Fig. 5. It can be seen that prediction accuracy is high. Besides, the fracture locus in the principal stress space of (σ_I, σ_{II}) is constructed, as illustrated in Fig. 6.

6 Conclusion

In this work, experiments under various stress states are conducted and deformation behavior of tension and compression is investigated. The result indicates that WE43 alloy possesses the lower tension-compression asymmetry. The fracture belongs to the ductile fracture through the analysis of macroscopic fracture morphology. In the situation, the Drucker yield function, Swift-Voce hardening equation, and DF2016 fracture criterion are selected as the theoretical model. After calibrating material constants of these models, the plastic deformation under various stress states is simulated by a hybrid experimental–numerical method. By the comparison of numerical and experimental results, the result indicates that the predicted accuracy of model is high. It also implies that the established model can be used in the FE simulation of plastic deformation for WE43 alloy.

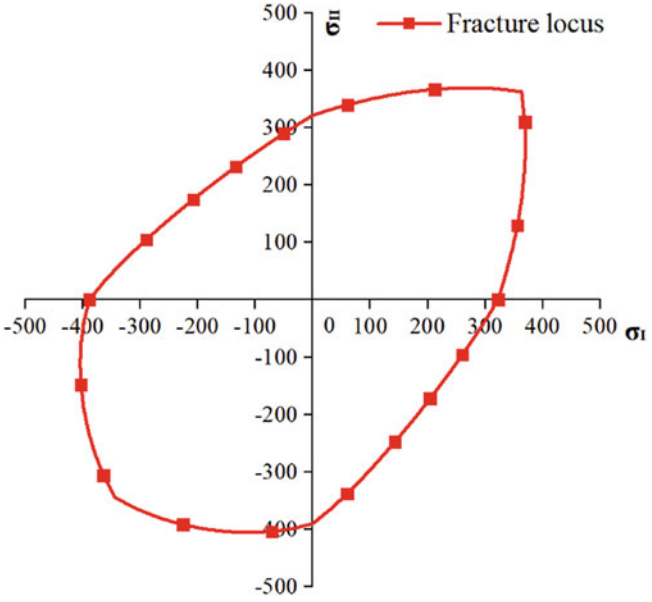


Fig. 6 Fracture locus under plane stress constructed in the principal stress space of (σ_I, σ_{II}). (Color figure online)

Acknowledgments The authors acknowledge the financial supports by the National Natural Science Foundation of China (Grant No. 52075423), the State Key Laboratory of Mechanical System and Vibration (Grant No. MSV202009), and the State Key Laboratory of High Performance Complex Manufacturing (Grant No. Kfkt2019-02).

References

1. Tokunaga T, Ohno M (2019) Microstructure evolution during superplastic deformation of an Al-coated Mg alloy sheet. J Alloys Compd 805:436–443
2. Kabirian F, Khan AS, Gnäupel-Herlod T (2015) Visco-plastic modeling of mechanical responses and texture evolution in extruded AZ31 magnesium alloy for various loading conditions. Int J Plast 68:1–20
3. Wang L, Fang G, Leeflang S, Duszczyk J, Zhou J (2014) Investigation into the hot workability of the as-extruded WE43 magnesium alloy using processing map. J Mech Behav Biomed Mater 32:270–278
4. Gangireddy S, Gwalani B, Liu K, Faierson EJ, Mishra RS (2019) Microstructure and mechanical behavior of an additive manufactured (AM) WE43-Mg alloy. Addit Manuf 26:53–64
5. Fu P, Peng L, Jiang H, Zhang Z, Zhai C (2008) Fracture behavior and mechanical properties of Mg-4Y-2Nd-1Gd-0.4Zr (wt.%) alloy at room temperature. Mater Sci Eng A 486(1):572–579
6. Feather WG, Ghorbanpour S, Savage DJ, Ardeljan M, Knezevic M (2019) Mechanical response, twinning, and texture evolution of WE43 magnesium-rare earth alloy as a function of strain rate: Experiments and multi-level crystal plasticity modeling. Int J Plast 120:180–204

7. Jahedi M, Mcwilliams BA, Knezevic M (2018) Deformation and fracture mechanisms in WE43 magnesium-rare earth alloy fabricated by direct-chill casting and rolling. Mater Sci Eng A 726:194–207
8. Hantzsche K, Bohlen J, Wendt J, Kainer KU, Yi SB, Letzig D (2010) Effect of rare earth additions on microstructure and texture development of magnesium alloy sheets. Scr Mater 63(7):725–730
9. Nie JF (2012) Precipitation and hardening in magnesium alloys. Metall Mater Trans A 43(11):3891–3939
10. Lou Y, Yoon JW, Huh H (2014) Modeling of shear ductile fracture considering a changeable cut-off value for stress triaxiality. Int J Plast 54:56–80
11. Lan YT, Zhong XC, Quan GF, Lin RC, Zhang KS (2015) Crystal anisotropy of AZ31 magnesium alloy under uniaxial tension and compression. Trans Nonferrous Metals Soc China 25(1):249–260
12. Drucker DC (1949) Relations of experiments to mathematical theories of plasticity. J Appl Mech 16:349–357
13. Lou Y, Yoon JW (2018) Anisotropic yield function based on stress invariants for BCC and FCC metals and its extension to ductile fracture criterion. Int J Plast 101:125–155
14. Lou Y, Yoon JW (2017) Anisotropic ductile fracture criterion based on linear transformation. Int J Plasticity Plast 93:3–25
15. Lou Y, Chen L, Clausmeyer T, Tekkaya AE, Yoon JW (2017) Modeling of ductile fracture from shear to balanced biaxial tension for sheet metals. Int J Solids Struct 112:169–184
16. Xiao X, Mu Z, Pan H, Lou Y (2018) Effect of the Lode parameter in predicting shear cracking of 2024-T351 aluminum alloy Taylor rods. Int J Impact Eng 120:185–201

Strain Hardening of AA5182-O Considering Strain Rate and Temperature Effect



Hongchun Shang, Pengfei Wu, and Yanshan Lou

Abstract Strain hardening properties of AA5182-O metal sheet are experimentally studied and analytically modeled at different temperature in this research using a dogbone specimen. The strain rate hardening and thermal softening behaviors are then modeled by popular analytical models to consider the strain rate and thermal effects. The high nonlinear strain hardening with the effect of strain rate and temperature is also illustrated by artificial neural network. The results show that the strain hardening with strain rate and thermal effect can be accurately modeled by the neural network compared with the conventional models, but its computation efficiency is much lower than the analytical models.

Keywords Strain rate · Thermal softening · Neural network

1 Introduction

Aluminum alloy has become the main lightweight material to replace automotive steel, due to its high specific strength, corrosion resistance, and many other advantages. However, the room-temperature formability of aluminum sheet is lower than that of steel sheet, so its application in automobile body and chassis components is greatly restricted [1–4]. In order to solve this problem, the warm forming process of aluminum alloy sheet has received extensive attention. The problem of concern in engineering applications is how to accurately model the influence of temperature and strain rate on the forming performance of aluminum sheet.

This paper experimentally investigates the effect of strain rate and temperature on strain hardening behavior of AA5182-O alloy. Their effects are analytically modeled by the Johnson–Cook, Zerilli—Armstrong, and Lim–Huh models. The artificial neural network (ANN) is also used to model the coupled strain rate and thermal effect of the alloy. The traditional constitutive and ANN models are all implemented in numerical simulation to predict the reaction force of the alloy at different stretching

H. Shang · P. Wu · Y. Lou (✉)
School of Mechanical Engineering, Xi'an Jiaotong University, 28 Xianning West Road, Xi'an, Shaanxi 710049, China
e-mail: ys.lou@xjtu.edu.cn

© The Minerals, Metals & Materials Society 2021

G. Daehn et al. (eds.), *Forming the Future*, The Minerals, Metals & Materials Series,
https://doi.org/10.1007/978-3-030-75381-8_54

velocity and temperature. The predicted load-stroke curves are compared with experimental results to evaluate their prediction accuracy with strain rate and thermal effect.

2 Experiments

The samples were obtained by milling an aluminum plate with a size of 500 × 500 mm along the rolling direction. The samples were widely known as dogbone specimens as shown in Fig. 1. The tensile tests were conducted on INSTRON universal testing machine. Five specimens were tested for each loading conditions to ensure the repeatability of experiments. The experiment covered a wide temperature range (300–573 k), and the strain rate range is 0.001–0.5/s. The gauge length was 20 mm for the stroke measurement by XTOP digital image correlation system.

The measured force-displacement curve before necking was then used to calculate the stress-strain curves of AA5182-O at different strain rates and temperatures, as shown in Fig. 2. It can be observed that at 300 k, when the strain rate increases from 0.001/s to 0.5/s, this material exhibits a slight negative strain rate sensitivity. It can be observed that at 300 k, when the strain rate increases from 0.001/s to 0.5/s, this material exhibits a slight negative strain rate sensitivity. The DSA effect shows that as the stretching speed increases, the stress intensity decreases. We have confirmed this conclusion through repeated experiments. When the temperature is 373 k, the flow stress is the highest at 0.01/s and the lowest at 0.5/s. When the temperature is 423 k, the flow stress at 0.001/s has been significantly reduced, compared to the other three curves. For the temperature after 473 k, with the increase of strain rate, the change trend of flow stress is consistent. The experimental results show a significant strain rate strengthening effect and the flow stress increases as the stretching rate increases. And with the increase in temperature, the gap between the four groups of experimental curves with different strain rates becomes larger and larger. Finally, we compare the experimental results at different temperatures under the same strain rate. As the temperature increases, the strain before the maximum force becomes smaller and smaller. This shows a significant temperature softening effect. When the

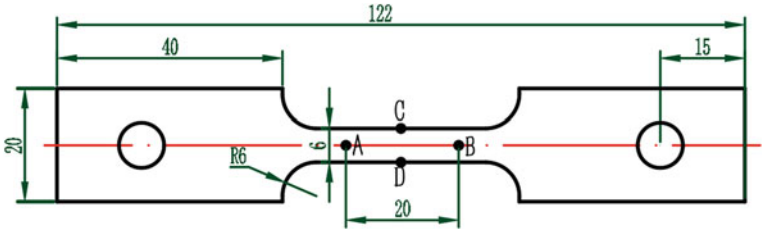


Fig. 1 Dogbone specimen geometries. (Color figure online)

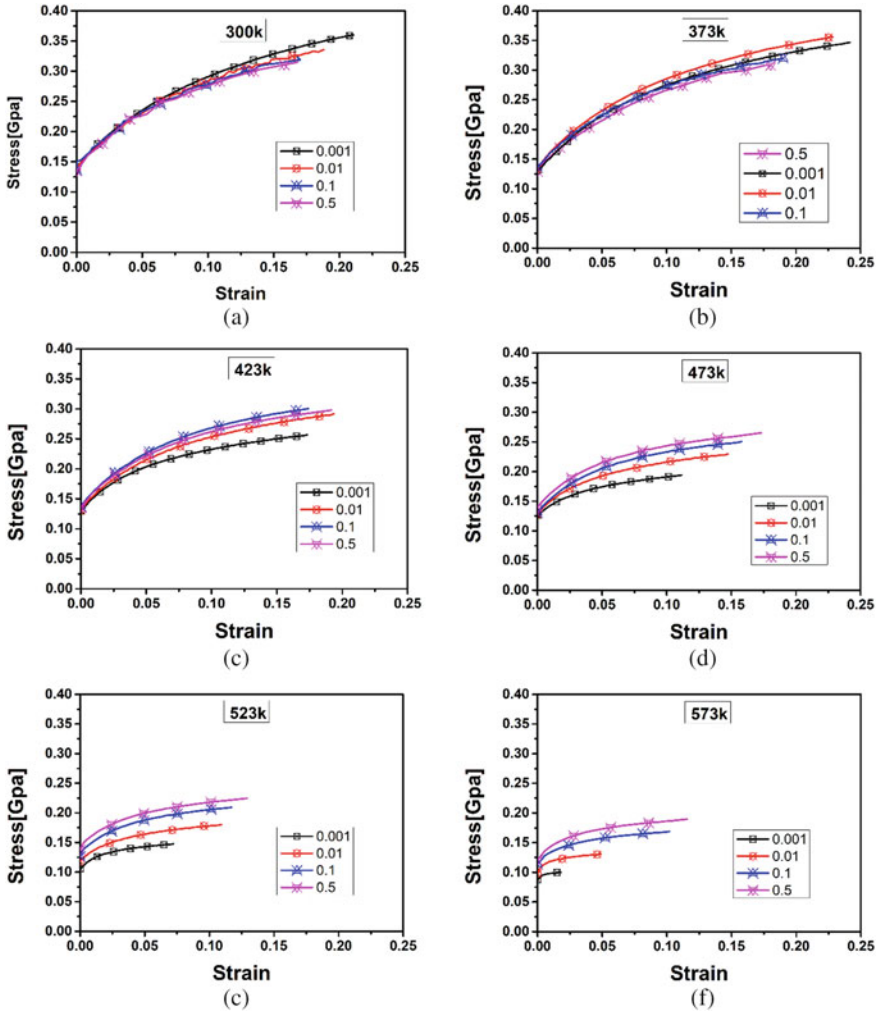


Fig. 2 Experimental true stress–true strain curves at different strain rates and temperatures. (Color figure online)

temperature reaches 573 k, the strain with a strain rate of 0.001/s is only 0.018. To sum up, through the comparison of 24 sets of experiments, it is found that AA5182-O exhibits a strong temperature and strain rate coupling effect.

3 Constitutive Model

Johnson and Cook (1983) [5] proposed a dynamic hardening model for metal deformation under high strain, high strain rate, and high temperature conditions. This model is highly accepted in computer simulation programs due to its simple form and easy accessibility of material constants for wide range of materials in literature. Moreover, JC model is available in many FE simulation platforms such as ABAQUS, DEFORM, etc. The original Johnson–Cook constitutive model can be expressed as

$$\begin{aligned}\sigma(\varepsilon, \dot{\varepsilon}, T) =& [\sigma_{\mathrm{r}}(\varepsilon)] \cdot [\sigma_{\dot{\varepsilon}}(\dot{\varepsilon})] \cdot [\sigma_{\mathrm{T}}(T)] \\ =& \left[A + B(\varepsilon)^n\right] \cdot \left[1 + C \ln \frac{\dot{\varepsilon}}{\dot{\varepsilon}_0}\right] \cdot \left[1 - \left(\frac{T - T_{\mathrm{r}}}{T_{\mathrm{m}} - T_{\mathrm{r}}}\right)^m\right]\end{aligned} \tag{1}$$

Zerilli and Armstrong (1987) [6] proposed a material dynamic constitutive model based on the dislocation mechanism. Through their observations, it is found that different crystal structures have different dislocation mechanisms. Therefore, the Z-A constitutive model gives different flow stress expressions for the two crystal structures:

$$\sigma = C_0 + \left[C_1 + C_2\sqrt{\varepsilon}\right]\exp[-C_3 T + C_4 T \ln \dot{\varepsilon}] + C_5 \varepsilon^n \tag{2}$$

For FCC,($C_1 = C_5 = 0$): $\sigma = C_0 + C_2 \varepsilon^{-1/2} \exp(-C_3 T + C_4 T \ln \dot{\varepsilon})$

Huh et al. (2014) [7–9] tested 4340 steel, OFHC copper, and Ti6Al4V alloy at different strain rates, and compared and verified different types of dynamic hardening models. However, its hardening behavior at high temperatures has some shortcomings. In order to express the thermal softening effect at high temperature, Piao et al. [8] added a thermal softening term involving rate to the Lim–Huh model, expressed as

$$\begin{aligned}\sigma_{(\varepsilon,\dot{\varepsilon},T)} =& [\sigma_{\mathrm{r}}(\varepsilon)] \cdot [\sigma_{\dot{\varepsilon}}(\varepsilon, \dot{\varepsilon})] \cdot [\sigma_{\mathrm{T}}(T, \dot{\varepsilon})] \\ =& A(\varepsilon + \varepsilon_0)^n \cdot \left[\frac{1 + q(\varepsilon)\dot{\varepsilon}^{p(\varepsilon)}}{1 + q(\varepsilon)\dot{\varepsilon}_r^{p(\varepsilon)}}\right] \cdot \left[1 - \left(\frac{T - T_{\mathrm{r}}}{T_{\mathrm{m}} - T_{\mathrm{r}}}\right)^{m(\dot{\varepsilon})}\right]\end{aligned} \tag{3}$$

where $q(\varepsilon) = \frac{q_1}{(\varepsilon + q_2)^{q_3}}$, $p(\varepsilon) = \frac{p_1}{(\varepsilon + p_2)^{p_3}}$, $m(\dot{\varepsilon}) = m_1 + m_2 \cdot \ln \frac{\dot{\varepsilon}}{\dot{\varepsilon}_{\mathrm{r}}}$, $\dot{\varepsilon} > \dot{\varepsilon}_r$ and $T_{\mathrm{r}} \leq T \leq T_{\mathrm{m}}$.

Artificial Neural Network (ANN) [10–12] is a data-driven nonlinear mapping model constructed according to the principle of human brain organization and activity. The basic idea of BP neural network is that the learning process is composed of two processes: forward propagation of signals and back propagation of errors. In forward propagation, samples are imported from the input layer, processed by various hidden layers, and finally passed to the output layer. Error back propagation is to pass the output error back to the input layer by layer through the hidden layer in some

form, and apportion the error to all units in each layer. The process of constant weight adjustment is the network training process. This process continues until the error of the network output is reduced to an acceptable level, or until the preset number of learning times.

Data normalization is a preprocessing technology. MinMaxscaler technology is selected to project all input variables onto the interval [0,1], which is defined as follows:

$$\overline{x}_i = \frac{x_i - x_{\min}}{x_{\max} - x_{\min}} \tag{4}$$

Each neuron in each layer is connected to the neuron of the next layer with a different weight. When the connection is passed, the weight will change.

$$H_i^{(k)} = tanh\left[\sum_{j=1}^{p} W_{ij}^{(k-1)} H_j^{(k-1)} + b_i^{(k-1)}\right] \tag{5}$$

The hyperbolic tangent is selected as the activation function to calculate the output layer.

$$\overline{y} = tanh\left[\sum_{j=1}^{p} W_l^{(k)} H_l^{(k)} + b^{(k)}\right] \tag{6}$$

Finally, the output variable is scaled linearly from [0,1]. The mean square error (MSE) defined by the following equation quantifies the ability of the neural network to predict flow stress:

$$MSE = \frac{1}{N}\sum_{i=1}^{N}\left(\frac{\sigma_{exp} - \sigma_{pred}}{\sigma_{exp}}\right)^2 \tag{7}$$

4 Results and Discussion

The predicted stress-strain curves are compared with experimental results at different strain rates and temperatures in Fig. 3. The yield stress comparison between the experiment and each model is compared in Fig. 4. The comparison shows that the LH model predicts better accuracy than JC and ZA FCC models. The artificial neural network's prediction matches with experimental results with the highest accuracy.

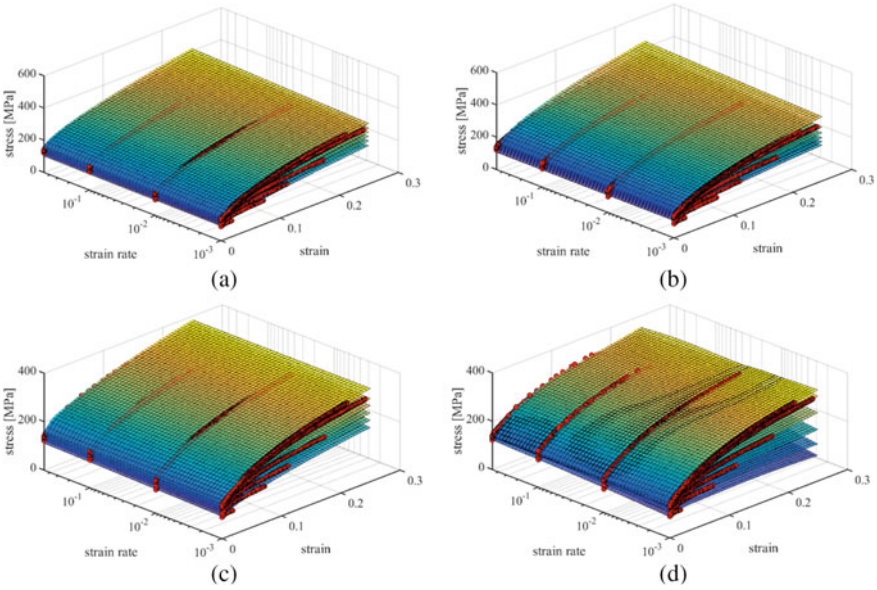


Fig. 3 Comparison of calculated flow stress with experimental data: **a** JC; **b** ZA FCC; **c** LH; **d** Artificial neural network. (Color figure online)

ABAQUS user material subroutines (ABAQUS/Explicit VUMATs) are developed and tested, including JC, ZA, and LH hardening functions, and the developed artificial neural network constitutive model [13]. It can be observed from Fig. 5a that the finite element simulation results of the artificial neural network are completely consistent with the experimental results. In addition, it can accurately calibrate the influence of negative strain rate at 300 k. It is found from Fig. 5c that the calibration results of the four traditional models except the artificial neural network are lower than the experimental values. The theoretical calibration results of the artificial neural network are exactly the same as the experimental results, but the finite element simulation results are slightly lower than the theoretical results in the second half. This is because the stretching speed is faster and the thermal effect is more obvious. The results shown in Fig. 5e are performed in the highest temperature environment in this batch of experiments. The theoretical calibration results of the neural network are still completely consistent with the experimental values. Because of the thermal softening effect, the finite element simulation results of the neural network are still slightly lower than the theoretical calibration results. It can be seen from Fig. 5f that only the curve predicted by the artificial neural network can pass the experimental points.

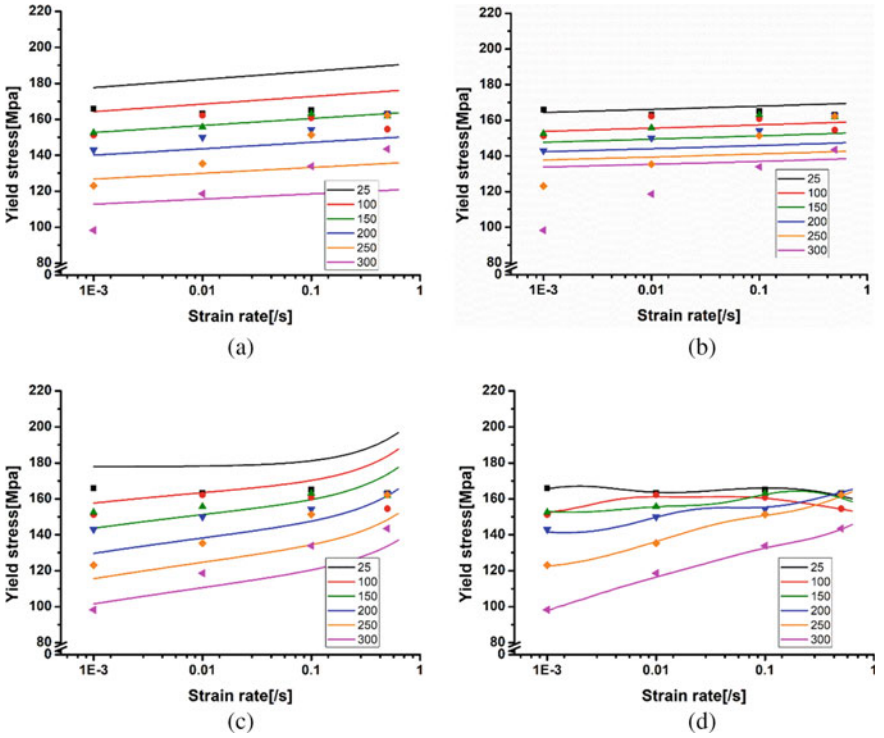


Fig. 4 Comparison of calculated yield stress with experimental data at a plastic strain of 0.01: **a** JC; **b** ZA FCC; **c** LH; **d** Artificial neural network. (Color figure online)

5 Conclusions

This paper studies the flow behavior of AA 5182-O in the temperature range of 300–573 k and the strain rate range of 0.001–0.5/s. ABAQUS user material subroutines are developed and tested for JC, ZA, LH hardening functions, and the ANN model. The calibration results of each model are quantitatively compared by MSE error. The results show that the new constitutive model can well describe the negative strain rate effect and the non-monotonic temperature effect. But its computational cost is much larger than traditional models.

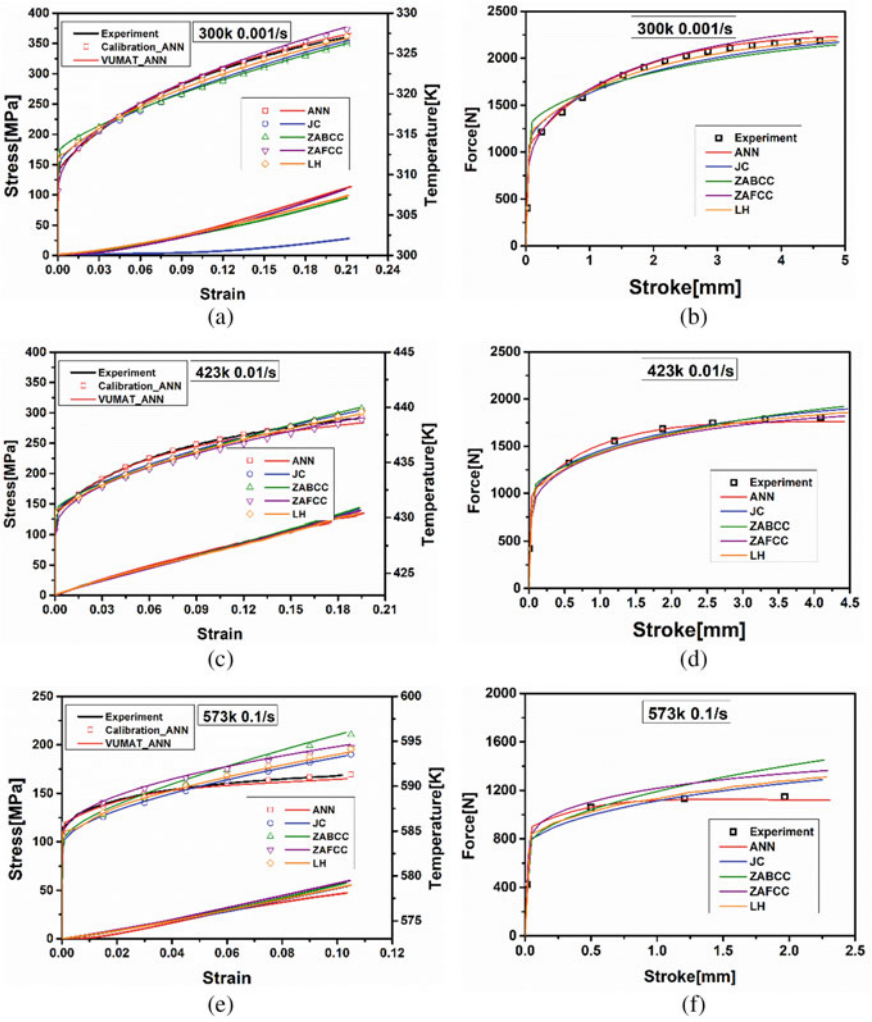


Fig. 5 Different constitutive models: Comparison of model predictions with experiments on dogbone specimens for **a**, **b** 300 k 0.001/s, **c**–**d** 423 k 0.01/s, **e**–**f** 573 k 0.1/s. (Color figure online)

References

1. Huh H, Lee HJ, Song JH (2012) Dynamic hardening equation of the auto-body steel sheet with the variation of temperature. Int J Autom Technol 13(1):43–60
2. Wang L, Li YL, Suo T et al (2013) Research on dynamic tensile mechanical properties of aluminum alloy used in aviation. J Aeronaut Mater 33(4):71–77
3. Paresi PR, Lou YS, Narayanan A et al (2019) Enhanced constitutive model for aeronautic aluminium alloy (AA2024-T351) under high strain rates and elevated temperatures. Int J Autom Technol 20(1):79–87

4. Dai J, Li X, Lu SQ et al (2014) Study on constitutive equation of TC21 titanium alloy at high temperature deformation. J Netshape Form Eng 6(6):116–121
5. Johnson GR, Cook WH (1983) A constitutive model and data for metals subjected to large strains, high strain rates and high temperatures. Eng Fract Mech 21:541–548
6. Zerilli FJ, Armstrong RW (1987) Dislocation-mechanics-based constitutive relations for material dynamics calculations. J Appl Phys 61(5):1816–1825
7. Huh H, Ahn K, Lim JH et al (2014) Evaluation of dynamic hardening models for BCC, FCC, and HCP metals at a wide range of strain rates. J Mater Process Technol 214(7):1326–40
8. Piao MJ, Huh H, Lee IJ (2016) Characterization of hardening behavior at ultra-high strain rate, large strain, and high temperature. Key Eng Mater 725:138–142
9. Huh H, Kang WJ, Han SS (2002) A tension split hopkinson bar for investigating the dynamic behavior of sheet metals. Exp Mech 42(1):8–17
10. Li X, Roth CC, Mohr D (2019) Machine-learning based temperature- and rate-dependent plasticity model: application to analysis of fracture experiments on DP steel. Int J Plast
11. Jenab A, Sarraf IS, Green DE et al (2016) The use of genetic algorithm and neural network to predict rate-dependent tensile flow behaviour of AA5182-O sheets. Mater Design 94:262–273
12. Shen FH, Münstermann S, Lian JH (2020) An evolving plasticity model considering anisotropy, thermal softening and dynamic strain aging. Int J Plast 2020:102747
13. Shang HC, Wu PF, Lou YS, et al Strain hardening of AA5182-O considering strain rate and thermal effect: experiments, analytical/ANN modeling and computations. Under review

New Methods for Fracture Detection of Automotive Steels



J. Noder, P. Samadian, J. Dykeman, A. Abedini, A. Zhumagulov, M. Worswick, and C. Butcher

Abstract The VDA 238-100 tight radius bend test has received significant attention from industry over the past decade because it provides a proportional plane strain–plane stress state until fracture. It will be demonstrated that the adoption of the vertical punch force as the unique metric for failure detection can lead to false positives. The punch force will reduce at large bend angles due to the mechanics of the test even in the absence of material failure. Two novel detection methods based on the nominal principal stress and the plastic work were evaluated on six different steel grades with a nominal ultimate tensile strength of approximately 590 MPa. Three 590R advanced high-strength steels provided by three different suppliers and three variants of the Ductibor® 500 are studied. The stress-based metric can be seen as an improvement over the VDA 238-100 load methodology since it accounts for thinning of the specimen cross-section and can identify false positives when the material forms a full bend in the absence of fracture but drops at bend angles greater than 160°. For performance ranking of materials with the same strength level, the plastic work metric is found to be sufficiently sensitive to distinguish between various 590 MPa steel grades since the material hardening rate is directly embedded.

Keywords VDA 238-100 tight radius bend test · Folding over · Plastic work · Stress metric · Ductibor® 500 · 590R

1 Introduction

Accurate plane strain fracture characterization is paramount for failure prediction in bending-dominated forming processes and energy-absorbing crash structures. During bending of sheet metals, the neutral axis divides the material cross-section

J. Noder (✉) · P. Samadian · A. Abedini · A. Zhumagulov · M. Worswick · C. Butcher
Department of Mechanical and Mechatronics Engineering, University of Waterloo, Waterloo, ON, Canada
e-mail: jnoder@uwaterloo.ca

J. Dykeman
Honda R&D Americas Inc., 21001 State Route 739, Raymond, OH 43067-9705, USA

© The Minerals, Metals & Materials Society 2021

G. Daehn et al. (eds.), *Forming the Future*, The Minerals, Metals & Materials Series,
https://doi.org/10.1007/978-3-030-75381-8_55

into layers that undergo plane strain tensile stretching (above the neutral axis) and material layers below the neutral axis that are compressed in plane strain compression. The induced through-thickness strain gradient mitigates the formation of a through-thickness neck prior to fracture, thus the effective forming limit becomes the fracture limit [1].

A popular approach to characterize the material behavior in plane strain tension involves notched tensile specimens which accommodate testing in a regular tensile frame. On the downside, notched tensile tests suffer from tensile instabilities since fracture occurs under a triaxial stress state on the specimen mid-plane where strains cannot be measured with Digital Image Correlation (DIC) techniques [2–4]. Therefore, inverse Finite Element (FE) analysis is required to extract the strain history and stress state of the element in the neck. The VDA 238-100 [5, 6] tight radius bend test offers an attractive alternative; the specimen is deformed over a sharp punch tip radius of 0.2 mm or 0.4 mm and a roller spacing of about twice the sheet thickness. Since the material is deformed in a plane strain bending mode, necking is suppressed and fracture is initiated on the convex (outer) specimen surface where strains can directly be measured utilizing the inverted V-bend test frame with full-field stereoscopic DIC measurements developed at the University of Waterloo [7].

Following the VDA 238-100 specification, the vertical punch load is adopted as the unique metric for failure identification and the bend angle serves as the performance metric for material ranking. In light of the inverted V-bend test frame adopted for this study, which incorporates DIC, the failure strains will be reported as well. Depending on the material type and sheet thickness, a reduction of 30 N or 60 N from the peak punch load is adopted for failure identification. It will be shown in this study that the punch force will decrease at large bend angles (>100°) due to kinematic boundary conditions even in the absence of material failure thus resulting in potentially too conservative failure strains and bend angles. A novel proposed methodology by Noder et al. [8] considers a stress-based metric that accounts for sheet thinning measured using DIC or an empirical equation that can successfully detect false positives. The primary advantage of the methodology of Noder et al. [8] is that the stress metric can be readily calculated using the available data in the VDA bend test. If a fracture occurs due to cracking, then the results obtained using the stress metric are in agreement with the VDA load drop criterion. A comprehensive evaluation of seven automotive steels with a strength level from 270 MPa to 1500 MPa revealed that the stress metric can successfully be utilized to identify materials that fold over or lose contact with the punch, referred to as punch lift-off. Further, Noder et al. [8] proposed a plastic work metric that has the material hardening rate directly embedded and served to rank the performance of alloys with similar strength levels. In this study, the alternative detection methods of Noder et al. [8] are applied to six steel grades with a nominal ultimate tensile strength of approximately 590 MPa to determine if the differences between similar grades can be detected. Additionally, AHSS of 590 MPa ultimate strength are particularly challenging since their moderate strength and relatively high ductility can lead to folding over in the bend

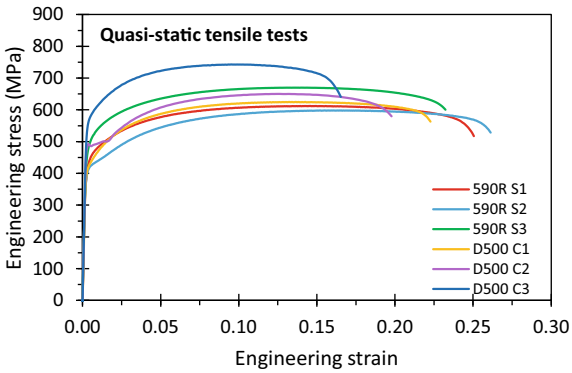


Fig. 1 Tensile performance of studied steel grades in the sheet transverse direction obtained in quasi-static tensile tests utilizing JIS No. 5 tensile geometries. A virtual extensometer length of 50 mm was adopted. (Color figure online)

test or cracking at large bend angles. It was found that the plastic work metric can be used to distinguish the material performance in the tight radius bend test even when the material performs a full bend and does not exhibit clear fracture.

2 Material Selection

Automotive steel grades with an ultimate tensile strength (UTS) of approximately 590 MPa are commonly used for energy-absorbing structures in the body-in-white owing to their superior formability and moderate strength level. Six steel grades were selected. Three JAC590R alloys were provided by different suppliers, hereinafter referred to as 590R S1, 590R S2, and 590R S3. Three variants of the hot stamping steel, Ductibor® 500, were created by changing the die pressure and die temperature for quenching. The blank was austenized at a temperature of 930 °C and held for 5 min followed by rapid transfer (10 s) into the die set where the blank was quenched and held for 15 s. The first condition (i), hereinafter referred to as D500 C1, was quenched at a die temperature of 25 °C and a pressure of 15 MPa, (ii) D500 C2 corresponds to a die temperature of 150 °C and a pressure of 26 MPa, and (iii) D500 C3 was quenched in 7 °C chilled dies at a pressure of 26 MPa.

The quasi-static constitutive response of the six steel grades was studied in the sheet transverse direction using JIS No. 5 tensile specimens. Full-field stereoscopic DIC strain measurements using the Vic-3D® software from Correlated Solutions Inc. were adopted. The stress–strain response is depicted in Fig. 1 and the mechanical properties and sheet thicknesses are recorded in Table 1.

3 Experimental Procedure

The conventional VDA 238-100 tight radius bend apparatus does not consider the use of optical strain measurements on the convex specimen surface and its design is not readily amenable for camera access of the convex surface where fracture will be initiated. The V-bend frame utilized for this study has been inverted and

Table 1 Tensile mechanical properties of the studied 590 MPa steel grades. The values in brackets correspond to the standard deviation. The uniform and total elongation are based on a virtual extensometer length of 50 mm. The R-value was obtained over a plastic strain range of 2–18.4% for the 590R S1, 2–19.5% for the 590R S2, 2–10% for the 590R S3, 2–12.4% for D500 C1, 2–11.7% D500 C2, and 2–9.6% for the D500 C3

	Yield stress (0.2% offset) (MPa)	Ultimate tensile Stress (MPa)	Uniform elongation UE (%)	Total elongation TE (%)	R-value
590R S1, 1.6 mm	435 (± 3)	607 (± 4)	19.6 (± 0.7)	24.7 (± 0.6)	0.80 (± 0.01)
590R S2, 1.6 mm	422 (± 19)	598 (± 12)	20.3 (± 1.6)	26.3 (± 2.5)	0.78 (± 0.04)
590R S3, 1.4 mm	490 (± 2)	671 (± 1)	13.4 (± 0.1)	23.7 (± 0.4)	0.90 (± 0.02)
D500 C1, 1.6 mm	354 (± 20)	618 (± 11)	12.8 (± 0.5)	18.4 (± 3.0)	0.75 (± 0.03)
D500 C2, 1.6 mm	486 (± 11)	661 (± 6)	12.8 (± 0.4)	18.6 (± 3.0)	0.80 (± 0.01)
D500 C3, 1.6 mm	585 (± 23)	744 (± 32)	10.0 (± 0.7)	16.3 (± 3.2)	0.84 (± 0.02)

was developed by Cheong et al. [7] to facilitate full-field stereoscopic DIC of the entire bending width. The primary difference in the VDA 238-100 set-up lies in the stationary punch and the chamfered rollers (30 mm diameter) which descent to bend the specimen. A schematic of the V-bend test frame is shown in Fig. 2a and the reader is referred to Cheong et al. [9] for further details.

Following the VDA 238-100 guidelines, a gap size of two times the sheet thickness plus 0.5 mm was selected for all tested steel grades. In light of the advanced ductility of the studied alloys, the sharper punch tip radius of 0.2 mm (0.21 mm as-fabricated) was selected instead of the 0.4 mm radius punch. A test velocity of 20 mm/min was selected for all tests. The VDA bend angle is computed such that

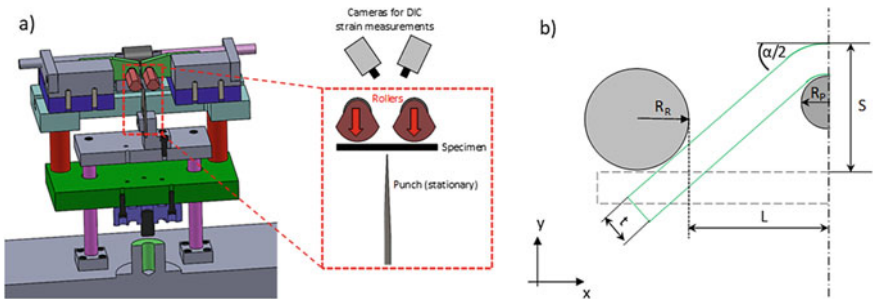


Fig. 2 Schematic of inverted V-bend test frame at the University of Waterloo (**a**) and for computation of the bend angle (**b**). The variable *L* refers to half of the roller gap width. (Color figure online)

$$\alpha_{VDA}(R_R, t, L, S) = 2\left(-\tan^{-1}\left(\frac{1}{d}\sqrt{c^2-(d+b)^2}-(c-S)\right)\frac{180^\circ}{\pi}\right) \quad (1)$$

where $b = R_R + \frac{L}{2}$, $c = R_R + t$, $g = b^2 + (c-S)^2$, $d = \frac{-\sqrt{h^2-4gi}-h}{2g}$

$$h = -2c^2b + 2b^3 + 2(c-S)^2b$$

$$i = c^4 - 2b^2c^2 - c^2(c-S)^2 + b^2(c-S)^2 + b^4$$

where the reader is referred to Fig. 2b for clarification of the adopted variables.

Specimens were machined to a width and length of 60 mm except for the D500 C2 and D500 C3 which were machined to a width and length of 50 mm to provide a plane strain bending condition for all tested steel grades. The specimens were tested in the transverse direction to be aligned with the primary loading condition. For full-field logarithmic strain measurements, a random black speckle pattern with white background paint was created and images were collected at a frequency of approximately 10 frames per second. The Vic-3D® software from Correlated Solutions Inc. was adopted with a strain filter of 7 pixels and a step size of 2 which resulted in a virtual strain gage length (VSGL) of approximately 0.5 mm. Five line slices perpendicular to the crack location were extracted from the specimen and imported into a custom MATLAB® script following the ISO12004-2 standard [10] for formability analysis. Based on the work of Cheong et al. [9], the peak strain was identified for each line slice and the average value reported. Figure 3 representatively shows the uniform strain distribution in the bending zone and highlights the proportional plane strain condition throughout the test for the 590R S3.

4 Detection Methods in the VDA 238-100 Tight Radius Bend Test

4.1 V-Bend Mechanics

Prior to exploring different failure detection methods, it is paramount to establish a fundamental understanding of the bending mechanics in the tight radius bend test. Figure 4 schematically illustrates the evolution of the bend angle and the force components. For low bend angles (α_1-α_2), the assumption of a three-point bending scenario with the punch force, F_y, as the primary force component is reasonable. For large bend angles, however, the contact points between the specimen and the punch are gradually shifted from the initial punch center to the left and right edge of the punch tip radius, causing a tangential force component. The transition to a four-point bending condition illustrated for bend angle α_3 is reflected by an almost horizontal resultant force for which the horizontal force component dominates and the

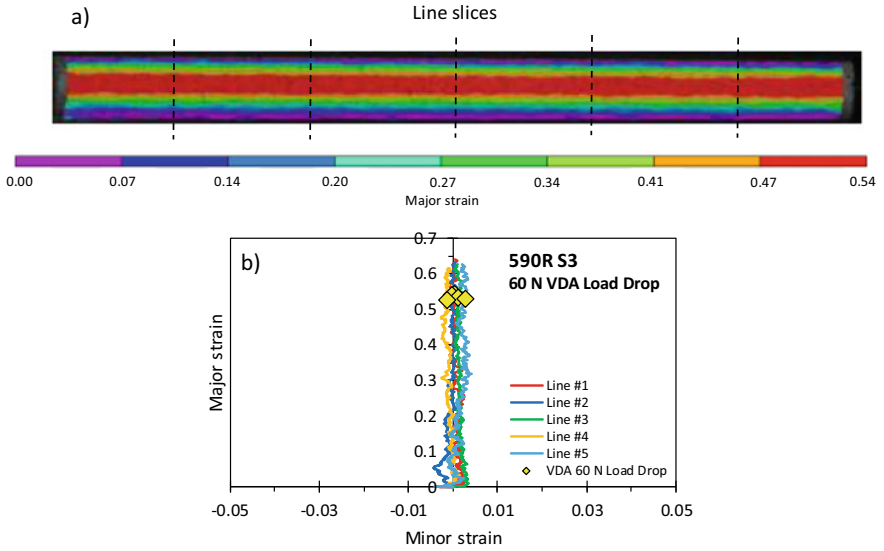


Fig. 3 Strain distribution (**a**) and strain path evolution obtained in the V-bend test representatively shown for the 590R S3 (**b**). (Color figure online)

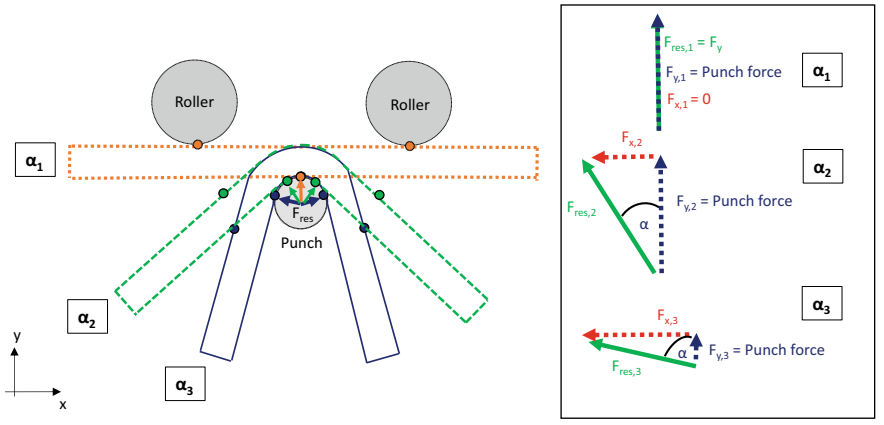


Fig. 4 Evolution of the bend angle and resultant force and evolution of the force components. A decrease in the punch force does not necessarily indicate material failure but can result as a natural consequence of the kinematic boundary conditions in the test set-up. (Color figure online)

punch force is minor. Consequently, a reduction in the load drop does not necessarily indicate material failure and requires additional efforts such as optical inspection of tested specimens.

Adoption of the bending moment of the cross-section naturally accounts for the decrease in the punch force by consideration of the resultant force and the change in

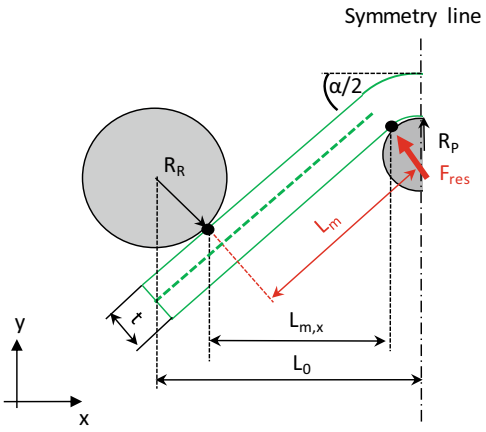


Fig. 5 Schematic of mechanics in the VDA 238-100 tight radius bend test for the derivation of the bending moment methodology. Note that the dashed green line refers to the position of the neutral axis that is assumed to remain aligned with the sheet mid-plane for a rigid perfectly plastic material and that punch lift-off does not occur. (Color figure online)

the contact points reflected in the resultant moment arm. Following the procedure of Troive [11] and referring to Fig. 5, the bending moment of the cross-section can be approximated from the resultant force, F_{res}, and the moment arm, L_m such that

$$M = F_{res} L_m = \frac{F_y}{2\cos\left(\frac{\alpha}{2}\right)} \frac{L_{m,x}}{\cos\left(\frac{\alpha}{2}\right)} \tag{2}$$

where $L_{m,x}$ approximately corresponds to the moment arm in the x-direction, assuming a straight flange as

$$L_{m,x} \approx L_0 - (R_R + R_P)\sin\left(\frac{\alpha}{2}\right) \tag{3}$$

and R_R and R_P are the roller radius and the punch radius, respectively. Half of the width of the roller gap including the roller radius, denoted as L_0, yields

$$L_0 = (t + 0.25) + R_R \tag{4}$$

Assembly of Eqs. (2)–(4) yields the following expression for the bending moment of the cross-section

$$M = F_{res} L_m = \frac{F_y}{2}\left(\frac{t + 0.25 + R_R - (R_R + R_P)\sin\left(\frac{\alpha}{2}\right)}{\cos^2\left(\frac{\alpha}{2}\right)}\right) \tag{5}$$

and the total energy associated with deformation of the cross-section is

$$U = \int_0^{\alpha} M d\alpha \tag{6}$$

The evolution of the bending moment can now be readily calculated with Eq. (5) using the same experiment data available in the conventional V-bend test. Note that Eq. (5) is for the bending moment of the cross-section and that the hardening response and through-thickness strain gradient are embedded. The plastic response within the cross-section is complex due to the severe bending strain gradient, a shifting of the neutral axis toward the concave specimen side, and a stress reversal of some layers from being initially in compression into tension. An integration of the material response at each layer of material through-thickness would produce the moment of the cross-section. Nevertheless, adoption of the bending moment is a rather non-intuitive quantity compared to using a nominal stress or punch force. Noder et al. [8] also highlighted potential complications for alloys with a low hardening rate that can produce an approximately constant bending moment. A stress-based metric is preferable since it accounts for the sample dimensions and avoids the ambiguity of using force-based thresholds. Fortunately, adopting the closed-form solution for a *rigid, perfectly plastic* material [12], the bending moment can be related to the yield stress, σ_y, and a stress metric, Σ, can be defined, where w corresponds to the specimen width such that

$$M_{rigid-plastic} = \frac{\sigma_y t^2 w}{4} = \text{constant} \tag{7}$$

It is important that the instantaneous specimen thickness in Eq. (8) is used. Larour et al. [13] showed that the specimen undergoes thinning of up to 30% during the bending process which was in reasonable agreement with DIC measurements for a series of alloys presented by Noder et al. [8]. Owing to the stationary punch in the V-bend frame at the University of Waterloo, thinning of the cross-section can be retrieved from the out-of-plane displacement. The amount of thinning is material dependent and is directly linked to the hardening response. Noder et al. [8] also provided a basic phenomenological equation for approximation of the engineering thinning strain

$$\Sigma = \frac{4}{t^2 w} M(F_y, \alpha) \tag{8}$$

$$\varepsilon_t = A - A \exp\left(-B(\alpha)^C\right) \tag{9}$$

where $A = 0.2110$, $B = 0.0012$, and $C = 1.4636$. Note that Eq. (9) does not account for the effect of bend severity which will be the subject of future work.

The volume of the deformed material is estimated using the bend radius at the mid-thickness as

$$V = wt\left(\frac{R_o + R_i}{2}\right)\alpha(rad) \tag{10}$$

where R_i and R_o correspond to the inner and outer sheet radius, respectively. Assuming that the inner radius of the bend corresponds to the punch, the approximate plastic work of the cross-section can be readily determined from the total energy of Eq. (6) and the volume of Eq. (10) as

$$W = \int \sigma d\varepsilon = \frac{U}{V} = \frac{\int_0^{\alpha} M d\alpha}{wt\left(1 + \frac{t}{2R_p}\right) R_p \alpha(rad)} \tag{11}$$

5 Results and Discussion

For baseline comparison of the new methodologies, the 60 N load threshold upon the peak punch force was adopted for failure identification following the VDA 238-100 specification. One representative load curve for each tested steel grade is depicted in Fig. 6a and clearly indicates a reduction in the punch force at VDA bend angles ranging from 110° to 123° in Fig. 7a, while optical inspection at the load threshold in Fig. 8 confirmed the absence of visible cracks on the specimen convex surface. Since the regular VDA 238-100 V-bend apparatus does not consider DIC strain measurements, the bend angle is commonly adopted as a unique metric for material ranking. Following this procedure, the performance of the 590R S3 would be ranked first and the D500 C3 last. Cheong et al. [9] demonstrated that the bend angle at failure is dependent upon the bend severity, t/R_p, and that the plane strain failure strain is the unique metric which governs the bend performance. Interestingly, the major strain at failure summarized in Fig. 7b identifies the D500 C3 to be superior and the D500 C1 to be at the lower end with a major strain of 0.59 and 0.50, respectively.

Consideration of the stress metric indicates that the observed reduction in the punch force was caused as a natural consequence of the kinematic boundary conditions in the V-bend frame. The evolution of the stress metric in Fig. 6b shows an increasing trend past the 60 N VDA load threshold but drops at bend angles

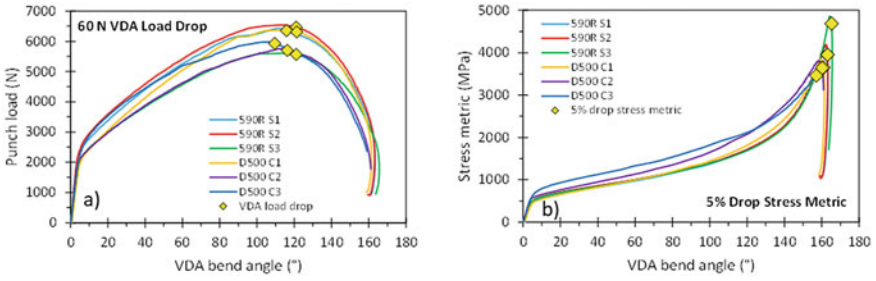


Fig. 6 Evolution of the punch load (**a**) and the stress metric (**b**) representatively shown for one repeat per tested alloy. (Color figure online)

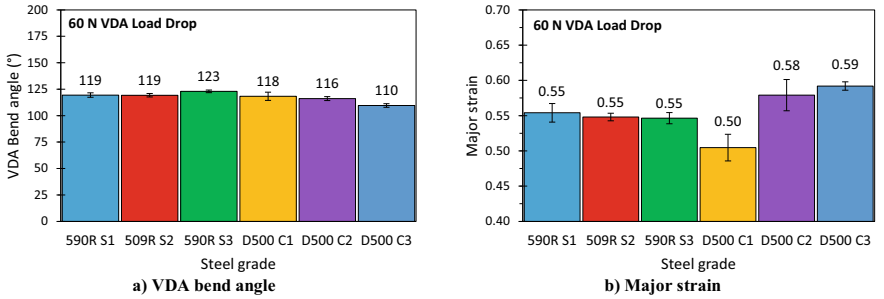


Fig. 7 VDA bend angle and major strain adopting the 60 N load threshold recommended by the VDA 238-100 specification. (Color figure online)

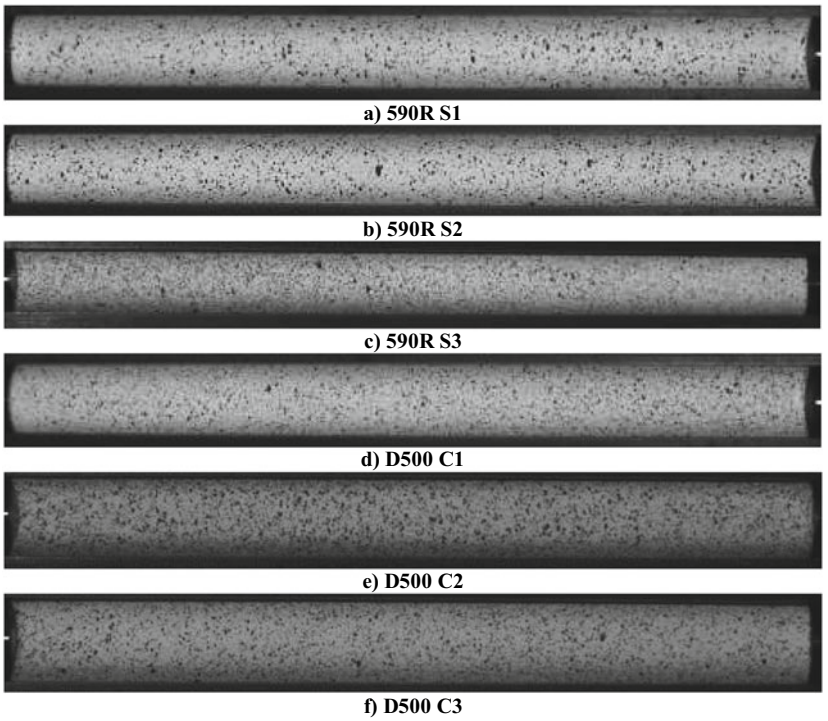


Fig. 8 Optical inspection of the specimen surface at the 60 N VDA load drop for the tested steel grades

exceeding approximately 160° as summarized in Fig. 9a. Comparison of the failure strains in Fig. 9b using a 5% reduction in the stress metric records failure strains that are approximately 0.26-40 strain higher than recorded by the VDA 238-100 specification.

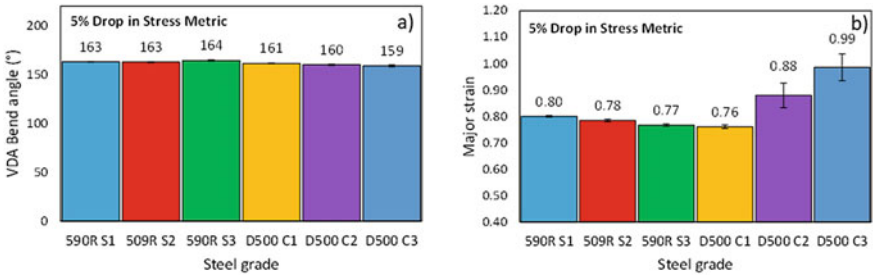


Fig. 9 VDA bend angle (**a**) and major strain (**b**) adopting a 5% drop in the stress metric. (Color figure online)

A viable concern in the V-bend test is potential punch lift-off which renders the test invalid since the inner bend radius does no longer conform to the punch tip radius and the effective bend severity increases and fracture occurs at a lower bend angle. For plane strain fracture characterization, the strain state remains plane strain bending on the outer surface and the measured fracture strain remains valid. Since the punch is stationary in the current set-up, the evolution of the out-of-plane displacement in Fig. 10 was utilized to determine punch lift-off. Note that the displacement is assumed to be positive, thus thinning is represented by an increase in the out-of-plane displacement which is observed up to a bend angle of approximately 147°. Interestingly, the punch force decreased much earlier at bend angles of about 123°, indicating that the reduction in the punch force appears to occur prior to punch lift-off for the considered steel grades. The stress metric correctly indicates the absence of failure until bend angles larger than 160° but needs to be limited to the maximum bend angle when punch lift-off occurs. The same restriction applies to instantaneous

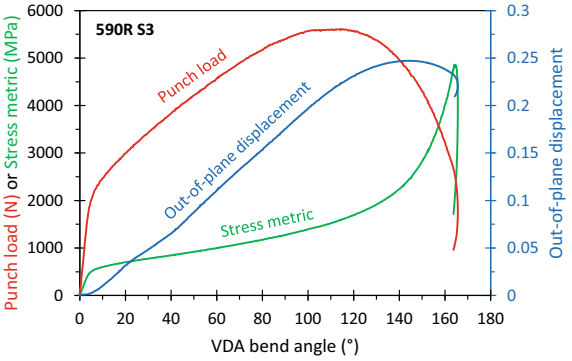


Fig. 10 Visualization of the shortcomings of the VDA 238-100 failure detection method representatively shown for the 590R S3. The reduction in the punch force is not related to material failure that was correctly captured by the stress metric. The out-of-plane displacement indicates that punch lift-off occurred at a bend angle of approximately 147°. (Color figure online)

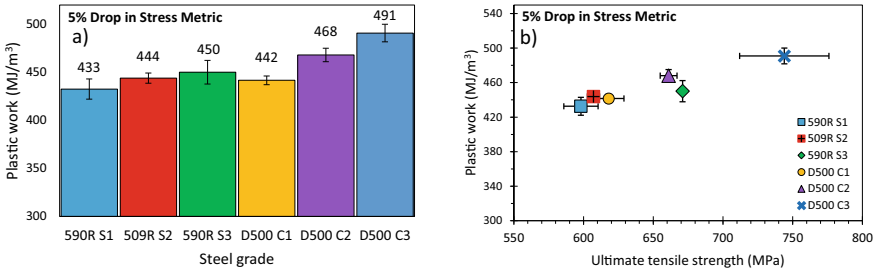


Fig. 11 Comparison of plastic work (**a**) and correlation with the material UTS (**b**) for the studied steel grades. (Color figure online)

thinning from DIC measurements, which is only valid prior to punch lift-off. For empirical thinning in Eq. (9), a limitation to bend angles of 140° is recommended.

While the stress metric provided a noticeable improvement over the VDA 238-100 load threshold methodology, it drops at bend angles greater than 160° when the punch force has decreased by about 80%. To differentiate the performance of alloys of the same nominal strength level, the work per volume using Eq. (11) can be adopted. The advantage of a plastic work metric lies in the hardening behavior which is directly embedded in the bending moment evolution. Comparison of the plastic work clearly demonstrates the superior performance of the D500 C3 followed by the D500 C2 and the 590R C3 that correlates well with the strength level shown in Fig. 11.

6 Conclusion

This paper provided a comprehensive study on the material plane strain fracture performance of six steel grades with a strength level of approximately 590 MPa using various metrics for performance ranking. The primary conclusions are as follows:

- Adoption of the VDA 238-100 load methodology resulted in false positives for the studied steel grades since the reduction in the load drop was not associated with material fracture but the kinematic boundary conditions of the test frame.
- The novel stress metric accounts for thinning of the cross-section and can detect false positives but drops at bend angles greater than 160°.
- Computation of the plastic work allowed clear distinction between the studied material grades and has the hardening rate embedded in the bending moment.

Acknowledgments Financial support for this study was provided in part by the Natural Sciences and Engineering Research Council of Canada, the American Iron and Steel Institute (AISI), and Honda Research Americas (HRA). The authors would particularly like to thank Willie Bernert and Chris Brown from ArcelorMittal, Dr. Hesham Ezzat of AISI, and Dr. Kishore Pydimarry of HRA

for their support of the project. We would also like to gratefully acknowledge Kenneth Cheong from the University of Waterloo for his valuable discussion on V-bend experiments.

References

1. Stoughton TB, Yoon JW (2011) A new approach for failure criterion for sheet metals. Int J Plast 27:440–459. https://doi.org/10.1016/j.ijplas.2010.07.004
2. Mohr D, Henn S (2007) Calibration of stress-triaxiality dependent crack formation criteria: a new hybrid experimental-numerical method. J Exper Mech 47:805–820. https://doi.org/10.1007/s11340-007-9039-7
3. Dunand M, Mohr D (2010) Hybrid experimental-numerical analysis of basic ductile fracture experiments for sheet metals. Int J Solids Struct 47:1130–1143. https://doi.org/10.1016/j.ijsolstr.2009.12.011
4. Pack K, Ahn K, Huh H, Lou Y (2014) Fracture modelling of DP780 sheets using a hybrid experimental-numerical method and two-dimensional digital image correlation. Int J Mater Product Technol 48, https://doi.org/10.1504/IJMPT.2014.059029
5. VDA 238-100 (2010) Test specification: plate bending test for metallic materials
6. VDA 238-100 (2017) Test specification: plate bending test for metallic materials
7. Cheong K, Omer K, Butcher C, George R, Dykeman J (2017) Evaluation of the VDA 238-100 tight radius bending test using digital image correlation strain measurements. IOP Conf Ser J Phys
8. Noder J, Butcher C, Dykeman J (2020) New methodlogies for Fracture Detection of Automotive Steels in Tight Radius Bending: Application to the VDA 238-100 V-Bend Test. J Exp Mech. https://doi.org/10.1007/s11340-020-00627-z
9. Cheong K, Butcher C, Dykeman J (2018) The influence of the through-thickness strain gradients on the fracture characterization of advanced high-strength steels. SAE Int J Mater Manuf 11(4). https://doi.org/10.4271/2018-01-0627
10. International Organization for Standardization, (2008). ISO/DIC 12004-2:2008. Metallic materials sheet and strip —Determination of forming limit curves—Part 2: determination of forming limit curves in the laboratory
11. Troive L (2017) New method for evaluation of bend ability based on three-point-bending and the evolution of the cross-section moment. IOP Conf Ser J Phys 896(2017)
12. Hill R (1950) Mathematical theory of plasticity. Oxford University Press
13. Larour P, Hackl B, Leomann F (2013) Sensitivity analysis on the calculated bending angle in the instrumented bending test. IDDRG conference, Zurich, Switzerland

Evaluation of Isotropic and Anisotropic Constitutive Models on Plasticity Prediction of AA7075 Extruded Tube Under Tension–Tension and Tension–Compression



Sobhan A. Nazari Tiji, Amir Asgharzadeh, Taejoon Park, Madhura Athale, and Farhang Pourboghrat

Abstract Plasticity of AA7075-O extruded tube under tension–tension (T-T) and tension–compression (T-C) was characterized using multiaxial tube expansion test method. Three different yield functions, von-Mises, Hill's 1948, and Yld2004 were considered to model the anisotropic plasticity of the AA7075-O tubes under T-T and T-C. The anisotropic models were calibrated based on the measured biaxial stresses and the conjugate plastic strain rates as strain-rate potential based on plastic work equivalency. As shown, this calibration method is an accurate and more flexible way of calibrating the advanced yield functions with no necessity for having proportional loading paths. It was also shown that the three yield functions predict the strain paths under T-C conditions almost similarly, however, the strain paths under T-T conditions are predicted better as the number of anisotropy parameters in the yield functions increases.

Keywords AA7075 · Tube bulging · Anisotropic plasticity · Multiaxial loading

1 Introduction

Multiaxial testing has been considered in different studies as an accurate method to characterize the anisotropic plasticity of different materials [1–4]. Tube-free bulging as one of the multiaxial testing methods has been widely used for plasticity characterization of tubular materials [1, 5–9]. Except for the very recent studies conducted by Zhang et al. [6] and the authors of this paper [1], in all other studies either the first quadrant (Tension–Tension) or the second quadrant (Tension–Compression) of the

S. A. Nazari Tiji · A. Asgharzadeh · T. Park · F. Pourboghrat (✉)
Department of Integrated Systems Engineering, The Ohio State University, 210 Baker Systems, 1971 Neil Avenue, Columbus, OH 43210, USA
e-mail: pourboghrat.2@osu.edu

M. Athale · F. Pourboghrat
Department of Mechanical and Aerospace Engineering, The Ohio State University, 201 W 19th Ave, Columbus, OH 43210, USA

© The Minerals, Metals & Materials Society 2021

G. Daehn et al. (eds.), *Forming the Future*, The Minerals, Metals & Materials Series,
https://doi.org/10.1007/978-3-030-75381-8_56

stress space was characterized and used for anisotropic plasticity modeling of tubular materials. However, characterizing tubular materials under both Tension–Tension and Tension–Compression provides sufficient and accurate data for calibration of advanced anisotropic yield functions to accurately predict tubular materials behavior under complex loading. Moreover, to account for the strain data for anisotropic plasticity characterization of the tubular materials, the Lankford coefficients (R values) in three cases, r_0 (R value in longitudinal direction), r_{90} (R value in hoop direction), and r_b (R value in balanced biaxial condition) were generally considered so far in all the previous studies. The R value in tubular materials longitudinal direction, r_0, is easy to measure using standard uniaxial tensile test; however, measuring the R values in hoop direction, r_{90}, and balanced biaxial condition, r_b, has always been challenging because of the geometrical constraints of the tubular materials. Different techniques have been used to measure r_{90} and r_b. Ring hoop tension test [10] has been used as a technique to measure the R value in hoop direction of the tubular materials. However, because of the friction issue in this technique, its reliability has always been questioned. In other studies [5, 6, 8] r_{90} and r_b were measured by performing a controlled tube bulging experiments that require a sophisticated and expensive feedback control system that would control the deformation of the bulging tube to maintain the deformation mode throughout the test in real time.

In the authors' previous study [1], an experimental tube expansion test setup was developed for plasticity characterization of tubular materials under biaxial tension and tension–compression. In that study, AA7075-O extruded tube was characterized both in stress space (Yield Surface) and plastic strain rate space (Strain-rate Potential) under biaxial tension and tension–compression. It was shown that, unlike all the other previous studies, it is not necessary to generate proportional loading using a sophisticated and expensive real-time feedback control system to characterize the yield surface for tubular materials. The authors showed that any nonlinear or linear loading paths can be used to characterize the yield surface of the tubular materials based on plastic work equivalency. Therefore, the authors suggested that, considering the linear and nonlinear loading paths during tube expansion, the data in the stress space and their conjugate plastic strain rates as the strain-rate potential to account for the strain data can be used directly from the biaxial tests to characterize the plasticity of the tubular materials without any need for ring hoop tension test or any real-time sophistical and expensive controlled tube expansion tests. In this study, the data obtained after characterization of the AA7075-O tube in both stress and plastic strain rate spaces in [1] are used to calibrate Hill's 1948 and Yld2004 anisotropic yield functions. Then, the calibrated yield functions are used to predict the strain paths evolved based on the internal pressure and axial feed that were used during the experiments. It must be mentioned that the VUMAT developed by Esmaeilpour et al. [11] was used for the FEM simulations using the Yld2004 yield function.

2 Experimental Procedure

AA7075-O extruded tubes with an outer diameter (OD) of 38.1 mm, thickness (t_0) of 1.67 mm, and bulge length (L_B) of 88 mm were used in this study. Figure 1 shows the schematic of the tube with the clamping.

First, the uniaxial tensile test was performed based on the ASTM E8 standard on the dog-bone specimen cut along the longitudinal direction of the tube. Then, tube bulging simulations with von-Mises yield function based on the uniaxial tension test flow curve using FEM with a proportional–integral–derivative (PID) controller algorithm (as a user-subroutine) integrated with it were performed to generate the required boundary conditions (Internal pressure and axial feed profiles) for eight different biaxial tests. To generate the boundary conditions, first, the desired strain paths at the pole of the tubes were defined in the user-subroutine. Then the PID user-subroutine integrated with the tube bulging FEM model would generate the internal pressure and the axial feed in a way that would result in the desired strain paths at the pole of the tubes. The details of this boundary condition generation method can be found in [1]. The boundary conditions generated and used for the experiments are shown in Fig. 2. As can be seen, eight biaxial tests were performed, four biaxial tension tests (a, b, c, and d) and four tension–compression tests (e, f, g, and h). 3D DIC system was used for all the experiments in order to capture the strain evolution of the bulging tube. The internal pressure and the axial stroke/load over time were also recorded by the control station of the tube hydroforming machine. Figure 3a shows the experimental setup and Fig. 3b shows the surface of the bulging tube with the evolved Mises strain map on it measured by the 3D DIC system.

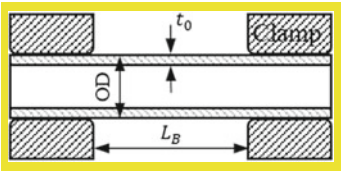


Fig. 1 Schematic of the tube for the bulging tests. (Color figure online)

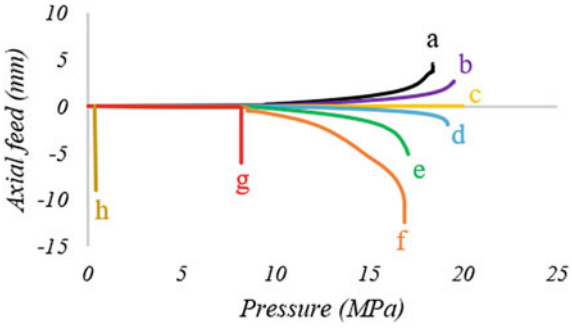


Fig. 2 Prescribed boundary conditions for the eight biaxial tests. (Color figure online)

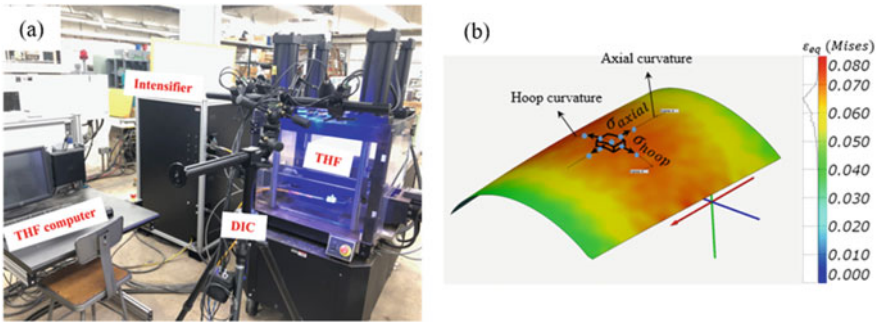


Fig. 3 **a** The experimental setup and **b** the DIC measurement of the Mises strain evolving on the bulging tube. (Color figure online)

3 Modeling

3.1 Principal Stresses Calculation

As Fig. 3b shows, the principal stresses at the pole of the tube were calculated based on the force equilibrium on a membrane using Eqs. (1) and (2).

$$\sigma_{axial} = \frac{P\pi\left(r_{hoop} - t\right)^2 - R_{F_{axial}}}{2\pi\left(r_{hoop} - \frac{t}{2}\right)t} \tag{1}$$

$$\sigma_{hoop} = \frac{(r_{axial} - t)\left(2r_{hoop} - 2t\right)}{(2r_{axial} - t)t}P - \frac{2r_{hoop} - t}{2r_{axial} - t}\sigma_{axial} \tag{2}$$

In Eqs. (1) and (2), P is the internal pressure, $R_{F_{axial}}$ is the axial reaction force on the actuators, r_{hoop} and r_{axial} (shown in Fig. 4) are the bulging tube curvature at the pole section of the tube in hoop and axial directions, respectively, and t is the thickness of the tube at the pole which is calculated using the initial thickness (t_0) and the major and minor strains at the pole (Eq. 3).

$$t = t_0 e^{-\left(\varepsilon_{axial} + \varepsilon_{hoop}\right)} \tag{3}$$

It also has to be mentioned that the axial and hoop curvatures of the bulging tubes at the pole section are calculated based on the least mean square method to fit a circle to the points on the surface of the tube at the pole section in axial and hoop directions.



Fig. 4 Schematic of the bulged tube with axial and hoop curvatures

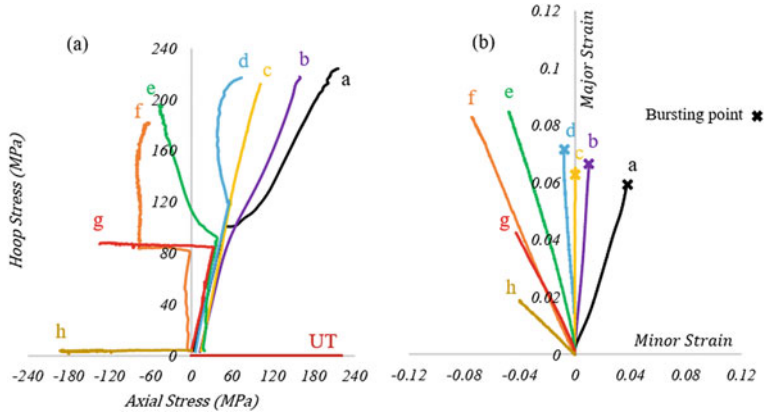


Fig. 5 **a** Stress paths at the pole of the tubes under T-T (a-d) and C-T (e-h) and **b** Strain paths at the pole of the tubes under T-T (a-d) and C-T (e-h). (Color figure online)

Figure 5a shows the principal stresses calculated at the pole of the tubes for all the eight biaxial tests plus the uniaxial tensile test, and Fig. 5b shows the measured principal strains at the pole of the tubes.

3.2 Yield Functions Calibration

In this study, three different yield functions, von-Mises, Hill's 1948, and Yld2004 were considered for the elastoplastic modeling of the AA7075-O tubes under tension–tension and tension–compression. In Eq. (4) (Hill's 1948), $\overline{\sigma}$ is the effective stress, F, G, H, L, M, and N are anisotropic coefficients, and in Eq. (5) (Yld2004), $\widetilde{S}_i'$ and $\widetilde{S}_i''$ are the principal values of two tensors defined by two linear transformations on the stress deviator. In Eq. (5), a is considered 6 for BCC materials and 8 for FCC materials. Details of the Yld2004 model can be found in [12].

$$\begin{aligned}\varphi^2 =& F(\sigma_{22}-\sigma_{33})^2 + G(\sigma_{33}-\sigma_{11})^2 \\ &+ H(\sigma_{11}-\sigma_{22})^2 + 2L\sigma_{23}^2 + 2M\sigma_{31}^2 + 2N\sigma_{12}^2 = \overline{\sigma}^2\end{aligned} \tag{4}$$

$$\varphi = \varphi(\bar{S}', \bar{S}'') = \left|\bar{S}_1' - \bar{S}_1''\right|^a + \left|\bar{S}_1' - \bar{S}_2''\right|^a + \left|\bar{S}_1' - \bar{S}_3''\right|^a + \left|\bar{S}_2' - \bar{S}_1''\right|^a + \left|\bar{S}_2' - \bar{S}_2''\right|^a + \left|\bar{S}_2' - \bar{S}_3''\right|^a + \left|\bar{S}_3' - \bar{S}_1''\right|^a + \left|\bar{S}_3' - \bar{S}_2''\right|^a + \left|\bar{S}_3' - \bar{S}_3''\right|^a = 4\bar{\sigma}^a \tag{5}$$

A single tensile test is enough to calibrate von-Mises yield function. However, to calibrate the anisotropic coefficients of Hill's 1948 and Yld2004, first, the principal stresses at a particular plastic work level as an equivalent hardening state for all the loading paths were characterized in stress space as well as their conjugate plastic

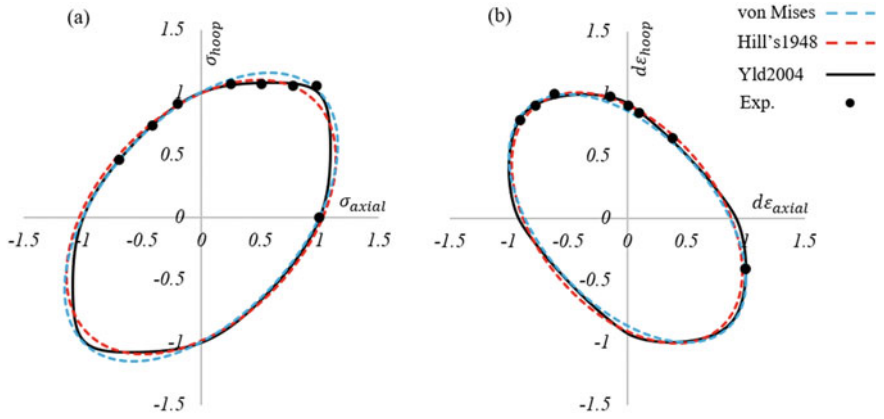


Fig. 6 **a** Normalized yield surface (Stress values were normalized to the uniaxial tension stress) and **b** Normalized strain-rate potential (Strain rates were normalized to the axial plastic strain rate in uniaxial tension) at plastic work level of 7 MPa. (Color figure online)

strain rate in strain rate space as can be seen in Fig. 6. It has to be mentioned that the plastic strain rates were calculated by calculating the derivative of the plastic strain with respect to the plastic work at a particular plastic work level considered as the equivalent hardening state. To determine the anisotropic coefficients of Hill's 1948 and Yld2004 yield functions, the error function given in Eq. (6) was minimized. In Eq. (6), c' and c'' represent the anisotropic parameters, q represents the number of experimental flow stresses, l represents the number of experimental conjugate plastic strain rate ratio, and W_q and W_l are the weights for the flow stresses and plastic strain rate ratios, respectively.

It also has to be mentioned that $\frac{\partial\varphi/\partial\sigma_{ii}}{\partial\varphi/\partial\sigma_{jj}}_{l}$ in Eq. (6) represents the direction of the plastic strain rate based on the normality rule for yield function φ based on associated flow rule assumption.

$$E\left(c'_{ij}, c''_{ij}\right) = \sum_{q} W_q \left(\sigma_q\big|_{pr} - \sigma_q\big|_{ex}\right)^2 + \sum_{l} W_l \left(\frac{\partial\varphi/\partial\sigma_{ii}}{\partial\varphi/\partial\sigma_{jj}}_{l} \big|_{pr} - \frac{d\varepsilon^p_{ii}}{d\varepsilon^p_{jj}}_{l} \big|_{ex} \right) \quad (6)$$

As Eq. (6) shows, to calibrate the anisotropic Hill's 1948 and Yld2004 yield functions, the stress space data as well as the plastic strain rate space data in the form of strain-rate potential are used. Figure 6a shows the calibrated von-Mises, Hill's 1948, and Yld2004 yield functions' yield surfaces and Fig. 6b shows the calculated strain-rate potentials' for the three yield functions. It must be mentioned that since it is experimentally very difficult to measure the out-of-plane parameters, and also because, in the thin-walled tube-free bulging tests, the out-of-plane stresses are negligible, the isotropic parameters were considered for the out-of-plane anisotropic parameters of the Hill's 1948 (L = 1.5, and M = 1.5) and Yld2004 ($c'_{55} = c'_{66} = c''_{55} = c''_{66} = 1$). Tables 1 and 2 show the calibrated anisotropic parameters for Hill's 1948 and Yld2004, respectively.

Table 1 Calibrated Hill's 1948 anisotropic parameters

F	G	H	N	L	M
0.59647	0.52675	0.42054	1.0201	1.5	1.5

Table 2 Calibrated Yld2004 anisotropic parameters ($c'_{55} = c'_{66} = c''_{55} = c''_{66} = 1$)

c'_{12}	c'_{13}	c'_{21}	c'_{23}	c'_{31}	c'_{32}	c'_{44}
0.8368	0.7596	0.8303	0.6864	0.8986	0.9296	1.0490
c''_{12}	c''_{13}	c''_{21}	c''_{23}	c''_{31}	c''_{32}	c''_{44}
1.0085	1.2167	1.0679	1.2332	0.9799	1.0129	1.0490

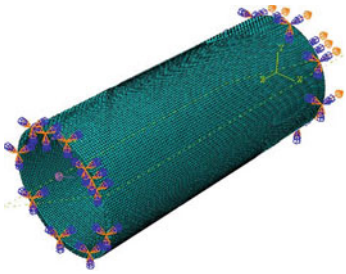


Fig. 7 FEM model of the tube for multiaxial expansion test. (Color figure online)

3.3 FEM Modeling

The calibrated yield functions were used for FEM simulations of the tube expansion tests under biaxial tension and tension–compression. In the FEM model, the eight-node linear brick element with reduced integration (C3D8R) was used, and three through-thickness elements were considered for the tube. The dimensions of the tube in the FEM model were also identical to the actual tubular samples' size. As for the boundary conditions, the same internal pressure and axial feed that were used in the experiments were also applied to the tube in the FEM model. Figure 7 shows the FEM model of the tube with the boundary conditions. As can be seen, one end of the tube is fixed and the other end can move axially, which is identical to how the tests were performed experimentally.

4 Results and Discussion

Figure 8 shows the strain paths measured compared to the ones predicted by the FEM simulations using von-Mises, Hill's 1948, and Yld2004 yield functions.

As can be seen in Fig. 8, with no surprise, as the material model gets more sophisticated with more parameters to be calibrated from von-Mises to Hill's 1948

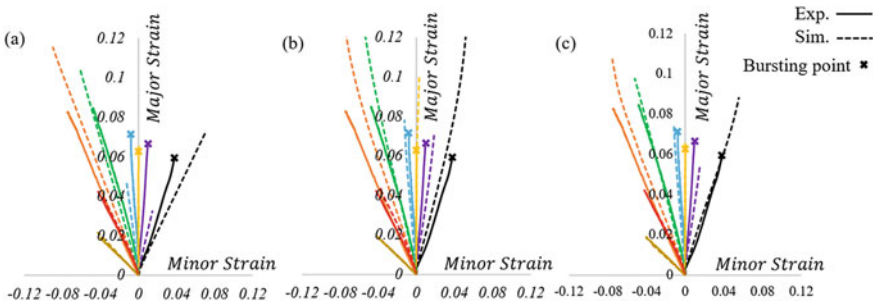


Fig. 8 FEM simulation results compared to the experiments for **a** von-Mises, **b** Hill's 1948, and **c** Yld2004 yield functions. (Color figure online)

to Yld2004, the FEM results show a better agreement with the measured strain paths. The point that is proven with these results is that proportional loading is not necessary for plasticity characterization, and as shown in Fig. 5, not all the loading paths are necessarily proportional; however, the yield functions can be calibrated using these experimental data based on plastic work equivalency. Also, it can be seen in Fig. 8 that using strain-rate potential, which was directly calculated based on the biaxial data, to account for the strain data in the calibration process is an accurate and flexible method and results in reasonable prediction instead of using R values for particular cases ($r_{0,}$ $r_{90,\text{ and}}$ $r_{b)}$ that are difficult to obtain for tubular materials or are not reliable and enough for advanced anisotropic yield functions with a high number of coefficients such as YLD2004. The other point to mention is that, as can be seen in Fig. 8, the isotropic von-Mises yield function is predicting the strain paths in tension–compression as good as Hill's 1948 and Yld2004, which means that this material shows isotropic behavior under tension–compression, while the anisotropic plasticity is significant under tension–tension, where Hill's 1948 and Yld2004 are predicting better with Yld2004 predicting the maximum elongation limit also better than Hill's 1948.

5 Conclusions

- It was shown that direct use of the biaxial data in the stress and strain rate spaces for the calibration of the yield functions is an accurate and flexible method, especially for the yield functions with a high number of coefficients.
- R value measurement in different directions for yield function calibration is very difficult for tubular materials. However, strain-rate potential that is the conjugate to the stress data for a particular plastic work can be used with any linear or nonlinear loading paths to account for the strain data for yield functions calibration.
- All the yield functions from simple isotropic quadratic von-Mises to anisotropic quadratic Hill's 1948 to anisotropic non-quadratic Yld2004 almost similarly

capture the isotropic plasticity of AA7075-O extruded tube under tension–compression. While, the anisotropic plasticity of the AA7075-O tube, which is significant under tension–tension, is captured more accurately with the yield function with a higher number of coefficients compared to the others.

Acknowledgments The authors wish to thank the U.S. Department of Energy for the support of this project through the DOE award DE-FG02-13ER41974 and DOE DE-EE000597, with the United States Automotive Materials Partnership LLC (USAMP), and Lightweight Innovations for Tomorrow (LIFT) for the support through the grant number GRT00045017.

References

1. Nazari Tiji SA, Park T, Asgharzadeh A, Kim H, Athale M, Kim JH, et al. (2020) Characterization of yield stress surface and strain-rate potential for tubular materials using multiaxial tube expansion test method. Int J Plast 133. https://doi.org/10.1016/j.ijplas.2020.102838
2. Kuwabara T, Sugawara F (2013) Multiaxial tube expansion test method for measurement of sheet metal deformation behavior under biaxial tension for a large strain range. Int J Plast 45:103–18. https://doi.org/10.1016/j.ijplas.2012.12.003
3. Korkolis YP, Kyriakides S (2008) Inflation and burst of aluminum tubes. Part II: an advanced yield function including deformation-induced anisotropy. Int J Plast 24:1625–37
4. Deng N, Kuwabara T, Korkolis YP (2015) Cruciform specimen design and verification for constitutive identification of anisotropic sheets. Exp Mech 55:1005–22. https://doi.org/10.1007/s11340-015-9999-y
5. Wang X, Hu W, Huang S, Ding R (2019) Experimental investigations on extruded 6063 aluminium alloy tubes under complex tension-compression stress states. Int J Solids Struct 168:123–37. https://doi.org/10.1016/j.ijsolstr.2019.03.022
6. Zhang K, He Z, Zheng K, Yuan S (2020) Experimental verification of anisotropic constitutive models under tension-tension and tension-compression stress states. Int J Mech Sci 178. https://doi.org/10.1016/j.ijmecsci.2020.105618
7. He Z, Zhang K, Lin Y, Yuan S (2020) An accurate determination method for constitutive model of anisotropic tubular materials with DIC-based controlled biaxial tensile test. Int J Mech Sci 181. https://doi.org/10.1016/j.ijmecsci.2020.105715
8. Kuwabara T, Yoshida K, Narihara K, Takahashi S (2005) Anisotropic plastic deformation of extruded aluminum alloy tube under axial forces and internal pressure. Int J Plast 21:101–17. https://doi.org/10.1016/j.ijplas.2004.04.006
9. Asgharzadeh A, Nazari Tiji SA, Esmaeilpour R, Park T, Pourboghrat F (2020) Determination of hardness-strength and -flow behavior relationships in bulged aluminum alloys and verification by FE analysis on Rockwell hardness test. Int J Adv Manuf Technol 106:315–31. https://doi.org/10.1007/s00170-019-04565-6
10. Dick CP, Korkolis YP (2014) Mechanics and full-field deformation study of the ring hoop tension test. Int J Solids Struct 51:3042–57. https://doi.org/10.1016/j.ijsolstr.2014.04.023
11. Esmaeilpour R, Kim H, Park T, Pourboghrat F, Mohammed B (2017) Comparison of 3D yield functions for finite element simulation of single point incremental forming (SPIF) of aluminum 7075. Int J Mech Sci 133:544–54. https://doi.org/10.1016/j.ijmecsci.2017.09.019
12. Barlat F, Aretz H, Yoon JW, Karabin ME, Brem JC, Dick RE (2005) Linear transfomation-based anisotropicyield functions. Int J Plast 21:1009–39

Estimation and Prevention of Strain Localization in Shear Tests



Heinrich Traphöner, Till Clausmeyer, and A. Erman Tekkaya

Abstract The localization of strain in conventional shear tests and in-plane torsion tests is analysed for three different materials, namely CP1000, DP1000, and DC04. The influence of material properties, such as strength, strain hardening, and strain gauge length on the measurement of shear strains is investigated experimentally and by a new analytical approach. The weakly hardening high-strength complex-phase steel CP1000 shows experimental and analytical deviations up to 25% of the determined strain depending on the evaluation strategy. Such deviations will lead to crucial errors for the calibration of fracture curves and damage models. By a new grooved in-plane torsion test specimen shear tests can be performed without the influence of the localization of strain. Strain measurements can thus be performed more exactly nearly regardless of the strain gauge length and hardening behaviour. In the first experimental results, the deviation is below 4.6% for CP1000 and below 0.5% for DC04.

Keywords Strain localization · DIC · Flow curve · Shear test · In-plane torsion test · Hardening

1 Introduction

Numerical simulations as well as the optical measurement of strains are based on a discretization of the surface of a continuum into individual areas. Local strains within these single "elements" can only be determined for the entire area. Local differences within the elements are not measured. One characteristic of shear tests, such as the Miyauchi shear test [1] or the in-plane torsion test [2], is the increasing stress gradient, which leads to the localization of shear strain in a narrow area of the sample. The intensity of the localization is influenced by the shape of the specimen and the mechanical properties of the materials. For some applications, such as the characterization of the Bauschinger effect using the in-plane torsion test, this stress

H. Traphöner (✉) · T. Clausmeyer · A. E. Tekkaya
Institute of Forming Technology and Lightweight Components (IUL), TU Dortmund University, Baroper Str. 303, 44227 Dortmund, Germany
e-mail: heinrich.traphoener@iul.tu-dortmund.de

© The Minerals, Metals & Materials Society 2021

G. Daehn et al. (eds.), *Forming the Future*, The Minerals, Metals & Materials Series,
https://doi.org/10.1007/978-3-030-75381-8_57

gradient is useful for efficient material characterization. Cyclic flow curves can be determined at different positions of the sample and thus with different strains during load reversal [3]. For many conventional shear tests, a locally varying cross-section, and hence a gradient of stress, is even necessary to produce the desired simple shear deformation in the test area [4]. For other applications, such as determining flow curves with very little or no strain hardening, the strain gradient is a major issue [5]. Strain localization in a narrow range around the position of maximum stress occurs, which can no longer be accurately measured by the discretization of the optical strain measurement. This work pursues three objectives:

- a sensitivity analysis for the relation between strain hardening and the resulting strain field in shear tests.
- an analytical calculation of the error due to discretization in shear tests for conventional shear tests and the in-plane torsion test.
- a presentation of a new grooved sample for the in-plane torsion test exhibiting no localization of the strain.

2 Experimental Analysis of Strain Localization in Shear Tests

2.1 Materials

Three materials were characterized to analyse the influence of strain localization to evaluate the amount of localization and the differences in the determined strain by a defined variation of the discretization size (strain gauge length). The study examined the ductile and strongly strain hardening DC04 steel, the high-strength dual-phase steel DP1000, and the complex-phase steel CP1000. The flow curves of the investigated materials are shown in Fig. 1. These were determined in the tensile test in the rolling direction according to the SEP1240 standard and extrapolated with flow curves from the in-plane torsion test. DC04 has a pronounced strain hardening (n

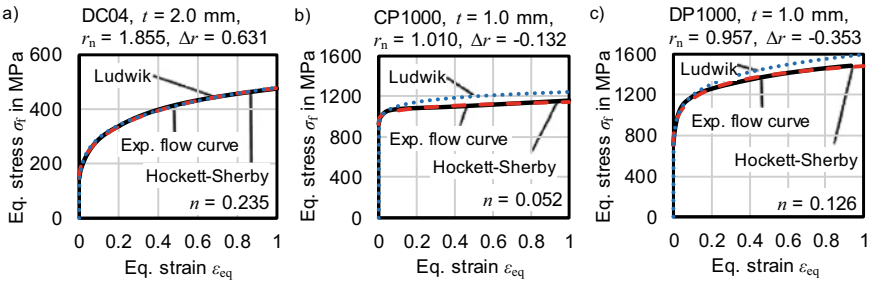


Fig. 1 Experimental flow curves and hardening exponent n for the investigated materials **a** DC04, **b** CP1000, and **c** DP1000. (Color figure online)

= 0.235). The initial yield stress is low at approx. 200 MPa and increases by approx. 150% at $\varphi = 1$. For CP1000, a slight hardening ($n = 0.052$) can be seen. After a high initial strength of 1000 MPa, the yield stress increases rapidly to about 1150 MPa and then rises only very slightly. DP1000 combines high initial strength with moderate strain hardening ($n = 0.126$). Due to the different strength and hardening levels, in principle, different localization properties are expected for these materials. The experimental flow curves were approximated using Hockett–Sherby and Hollomon equation. The hardening exponent n from the Hollomon approximation is a measure of the rate of increase in strength of the materials and is directly taken from the tensile test results. The approximated curves are applied in the analytical calculations in Sects. 3.3 and 4.1.

2.2 Experimental Setup and Specimen

Three different shear test samples shown in Fig. 2 were used to illustrate the localization behaviour. These are a conventional shear test with a shear length L_0 of 4 mm and a radius R_l of 1 mm (Fig. 2a) and the in-plane torsion test with the planar specimen (Fig. 2b) and with circular groove (Fig. 2c). The conventional shear test is loaded linearly parallel to the shear zone with the force F in a uniaxial testing machine. The in-plane torsion test is loaded with a torque M between inner and outer clamping. The inner clamping radius r_I is 15 mm and the outer clamping radius r_O is 30 mm. The groove has a radius r_{groove} of 4 mm and half the sheet thickness at the root of the groove. Details of the in-plane torsion test setup can be found in [6]. The strain on the specimen surface is measured by a 3D-DIC system.

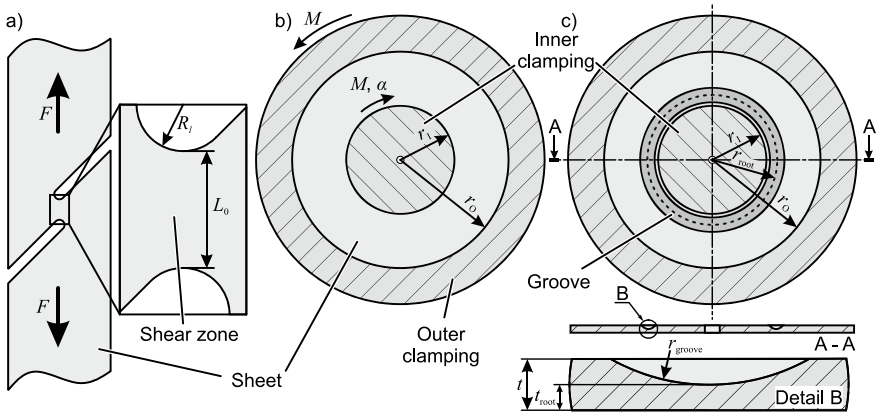


Fig. 2 Specimen shapes and dimensions for **a** conventional shear test with linear load application, **b** planar in-plane torsion test, and **c** grooved in-plane torsion test

2.3 *Influence of Strain Gauge Length on Strain Measurements Using DIC*

The specimen shown in Fig. 2 was tested and the strain field is measured using DIC. The strain gauge length was adjusted successively to defined values after the test by varying the DIC facet size and distance. A detailed description of the DIC settings is given in [5]. Each of the three specimens was evaluated with a different strain gauge length l_0 between 0.15 and 0.5 mm, and the mean strain along a line is measured at an equal position on the specimen.

2.3.1 Strain Distribution in Conventional Shear Tests

The influence of strain gauge length on the optical strain measurement between 0.15 mm and 0.5 mm is shown in Fig. 3 for the conventional shear test. The mean equivalent strain along the position of maximum strain and the deviation of the measured strain from the reference configuration ($l_0 = 0.15$ mm) are shown in each DIC strain field. DC04 shows only slight differences in the measured strain. A wide area of high strains is observed. Even larger strain gauge lengths do not lead to significant deviations. For CP1000, a very narrow deformation band and a strongly decreasing gradient of strain result. The measured strains for a strain gauge length of 0.5 mm are 16% smaller than for a gauge length of 0.15 mm. Strain measurement for CP1000 therefore shows a strong sensitivity to the strain gauge length. The deviation in the measured strain (7–8%) for DP1000 falls between the measured

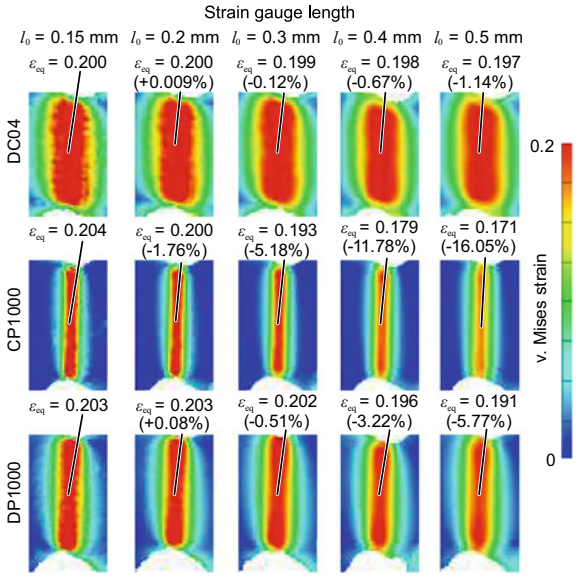


Fig. 3 Experimental deviations of the strain measurement with variation of the strain gauge length in the conventional shear test. (Color figure online)

ranges for DC04 and CP1000. Measurement deviations show a strong correlation with the hardening coefficient *n*. The smaller the hardening coefficient, the higher the deviation of the measured strains.

2.3.2 Strain Distribution in In-plane Torsion Tests

In-plane torsion tests were performed analogous to the conventional shear test. The strain gauge length is varied between 0.2 and 0.5 mm as shown in Fig. 4a. The radially decreasing strain gradient is comparable to the conventional shear test. In correlation with the work hardening of the materials, the intensity is stronger or weaker. In addition, for larger strain gauge lengths, the points close to the inner clamping can no longer be determined correctly, since the larger facets also make it

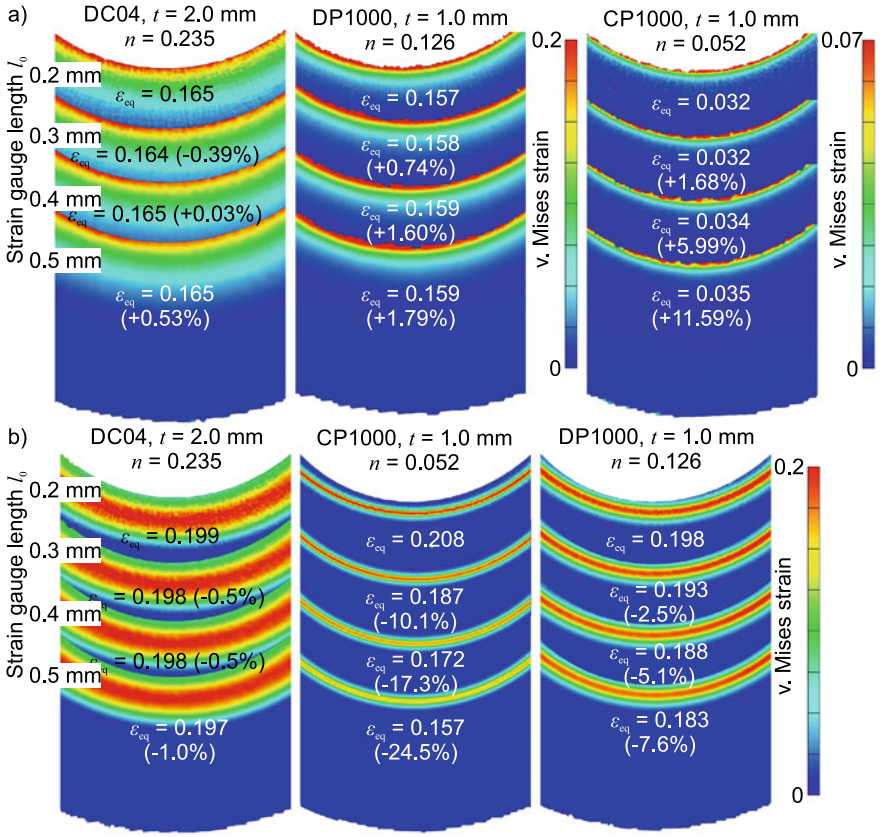


Fig. 4 Results of the strain measurement for DC04, CP1000, and DP1000 using different strain gauge lengths in the in-plane torsion test with **a** planar specimen and **b** conventional groove according to Fig. 3b [5]. (Color figure online)

impossible to measure a larger area near the inner clamping (at least ½ facet distance to the inner clamping). For this reason, the strain measurement was performed at a distance of 0.5 mm from the inner clamping ($r = 15.5$ mm). In comparison to the conventional shear test the measured strains increase with increasing gauge length. For the CP1000, an increase of the measured strain of approx. 11.6% can be seen.

The radially decreasing stress and strain gradient are even more pronounced when using a specimen with a circular groove. Figure 4b shows the equivalent strain for one specimen each of DC04, CP1000, and DP1000. Especially, the CP1000 steel with low hardening exhibits up to 25% deviation of the measured strain with respect to the smallest gauge length due to the strong localization of strain ($n = 0.052$) in a narrow range. DC04 ($n = 0.235$) shows only deviations of 1% of the measured strain. The larger the hardening of the materials, the lower the deviation is as the strain gauge length is increased, since the gradient of the strain at the maximum does not decrease so much. The smaller the strain gauge length, the more precise the strain measurement. The exact strain of highly localizing materials with strong strain gradients is therefore reasonably measurable only with very small optical facets.

3 Analytical Estimation of Measurement Errors Due to Strain Localization in Shear Tests

The experimental results from Sect. 2.3 show that the material-dependent localization of strain has a major impact on DIC-based shear strain measurement. In the following section, the error caused by the discretization is estimated analytically depending on the specimen geometry, the material properties, and the strain gauge length. With the described method, on the one hand, it is possible to analytically predict the measurement deviation and, on the other hand, to derive approaches for improving the measurement accuracy using DIC-based measurement of shear strains. The discretization error is defined as the ratio of measured shear strain for a discrete region γ_{dis} of size l_0 to the exact local strain γ:

$$\zeta = \frac{\gamma_{\mathrm{dis}}}{\gamma} - 1. \tag{1}$$

The discretization error ζ may have positive or negative values depending on whether the discrete strains γ_{dis} are larger or smaller than the exact strain γ. Figure 5a shows the deformation of an initially straight line for the conventional shear test. When the sample is loaded, the line deforms depending on the local stress in the test area. The exact local strain corresponds to the local shear angle η. The shear angle $\eta(l_0)$ for the discrete element of size l_0 is an integral measure resulting from the displacement dy along l_0. With nonlinear deformation of the line, there will be deviations of the measured shear angle from the exact local shear angle ($\eta \neq \eta(l_0)$). For $l_0 = 0$, the discretization error ζ is 0 and the strain measurement is exact. Figure 5b and c shows the deformation of a radial line for the in-plane torsion test

without groove and with groove. The discrete shear angle is here an integral measure over the circumferential angle θ.

For the subsequent analytical estimation of the discretization error, some assumptions are made as follows:

1. There is ideal simple shear in the test area, meaning that the cross-section (shear length and local sheet thickness) of the sheared area does not change.
2. There are no edge effects or inhomogeneity. Shear stress and shear strain are constant along the shear plane (for shear test: $\tau(x) = \text{const}$; for in-plane torsion: $\tau(\theta) = \text{const}$).
3. The shear stress can be calculated exactly from the force and the cross-section.
4. There is an isotropic material behaviour following the v. Mises yield criterion.
5. The flow curve of the material is known and can be approximated analytically.

3.1 Calculation of Local Shear Strains

With known elastic–plastic material properties, the local strain can be calculated analytically from the local shear stress τ. The shear strain γ is

$$\gamma(\tau) = \gamma_{\text{el}}(\tau) + \gamma_{\text{pl}}(\tau). \tag{2}$$

The elastic shear strain γ_{el} results from Hooke's law in dependency of the shear modulus *G*. The plastic shear strain $\gamma_{\text{pl}}(\tau)$ results from any hardening law:

$$\gamma_{\text{el}}(\tau) = \frac{\tau}{G} \text{ and } \gamma_{\text{pl}} = f(\tau). \tag{3}$$

The von Mises yield criterion is used to calculate shear stress and shear strain from the equivalent stress and strain:

$$\varepsilon_{\text{eq}} = \frac{\gamma_{\text{pl}}}{\sqrt{3}} \text{ and } \sigma_{\text{y}} = \sqrt{3} \cdot \tau. \tag{4}$$

The hardening law according to Ludwik,

$$\sigma_{\text{y,Ludwik}} = \sigma_0 + C \cdot \varepsilon_{\text{eq}}^n, \tag{5}$$

for example, results in the plastic shear strain.

$$\gamma_{\text{pl}}(\tau) = \sqrt{3} \cdot \left(\frac{\sqrt{3} \cdot \tau - \sigma_0}{C} \right)^{\frac{1}{n}} \text{ for } \tau > \frac{\sigma_0}{\sqrt{3}} \cdot \tag{6}$$

The shear stress τ is the force *F* referred to the cross-section in the shear region *A*.

$$\tau = \frac{F}{A}. \tag{7}$$

3.1.1 Conventional Shear Tests

For conventional shear tests as shown in Fig. 2a, the force F is directly measured and for the cross-section A follows:

$$\begin{aligned} A(x) &= t(x) \cdot L(x) \\ &= t \cdot \left(L_0 + 2 \cdot \left(R_l - \sqrt{R_l^2 - x^2} \right) \right). \end{aligned} \tag{8}$$

3.1.2 In-plane Torsion Test

The radius-dependent force *F,*

$$F(r) = \frac{M}{r}, \tag{9}$$

in in-plane torsion tests is calculated from the torque *M,* and the cross-section is calculated as

$$A(r) = 2 \cdot \pi \cdot r \cdot t(r) \tag{10}$$

with a constant sheet thickness t for the planar specimen (Fig. 2b) and a radius-dependent sheet thickness.

$$t(r) = t_{\text{root}} + r_{\text{groove}} - \sqrt{r_{\text{groove}}^2 - (r_{\text{root}} - r)^2} \tag{11}$$

for the grooved specimen according to Fig. 2c. With Eqs. (2)–(11) and known material parameters, the local shear strain can be determined exactly for all presented specimen shapes.

3.2 Calculation of Measured Discrete Shear Strains

The discrete shear strain is determined by integrating the displacements along the deformed lines. Due to the different coordinate systems (Cartesian and polar), the conventional shear test and the in-plane torsion test are to be considered separately.

3.2.1 Conventional Shear Tests

The local shear strain

$$\gamma = \tan(\eta) = \frac{dy}{dx} \tag{12}$$

is calculated from the local slope of the deformed line. For a discrete element with initial edge length l_0 follows from Eq. (12):

$$\gamma_{\text{dis}} = \frac{\Delta y}{\Delta x} = \frac{\Delta y}{l_0} \tag{13}$$

with

$$\Delta y = \int_{x_1}^{x_2} dy = \int_{x_1}^{x_2} \gamma(x) \cdot dx. \tag{14}$$

Inserting Eq. (14) into Eq. (13) follows for the discrete strain.

$$\gamma_{\text{dis}} = \frac{1}{l_0} \cdot \int_{x-\frac{l_0}{2}}^{x+\frac{l_0}{2}} \gamma(x) \cdot dx. \tag{15}$$

The required exact local strain $\gamma(x)$ is defined as described in previous Sect. 3.1.

3.2.2 In-plane Torsion Test

The calculation of the integral shear strain as a function of the strain gauge length for the in-plane torsion test is analogous to the conventional shear test. Shear strain is calculated from the local slope of the radial line:

$$\gamma = \tan(\eta) = r \frac{d\alpha}{dr}. \tag{16}$$

The discrete strain for a radial section $\Delta r = l_0$ is

$$\gamma_{\mathrm{dis}} = r\frac{\Delta\alpha}{\Delta r} = r\frac{\Delta\alpha}{l_0} \tag{17}$$

with the angular difference $\Delta\alpha$ from the integral of the incremental angle change $\mathrm{d}\alpha$.

$$\Delta\alpha = \int_{r_1}^{r_2} d\alpha = \int_{r-\frac{l_0}{2}}^{r+\frac{l_0}{2}} \frac{\gamma}{r} dr. \tag{18}$$

It follows for the discrete strain.

$$\gamma_{\mathrm{dis}} = \frac{1}{l_0} \cdot \int_{r-\frac{l_0}{2}}^{r+\frac{l_0}{2}} \frac{\gamma(r)}{r} dr. \tag{19}$$

$\gamma(r)$ is defined as described in Sect. 3.1.

3.3 Example Calculations for the Experimental Materials

The estimation of the measurement deviation was carried out for the materials investigated in Sect. 2. For this purpose, the flow curves of the materials were approximated according to Hockett and Sherby

$$\sigma_{\mathrm{y,HS}} = \sigma_\infty - (\sigma_\infty - \sigma_0) \cdot e^{-m\varepsilon_{\mathrm{eq}}^n} \tag{20}$$

as shown in Fig. 1 and the discretization error ζ is calculated according to Eq. (1). Figure 6 shows the discretization error in dependence of the equivalent strain for the conventional shear test. The strain gauge length l_0 was varied from approximately 0 mm (1×10^{-5} mm) to 0.5 mm in 0.1 mm steps.

3.3.1 Measurement Deviations During Elastic–plastic Transition

Figure 6 shows a strong increase of the discretization error at low strain for all materials. This is due to the measurement of test areas, which experience partially elastic and partially plastic strain as schematically illustrated in Fig. 7. If, for example, the local strain at the radius r is to be determined and this is just elastic, but the regions of the smaller radius within the same discrete element are already plastically

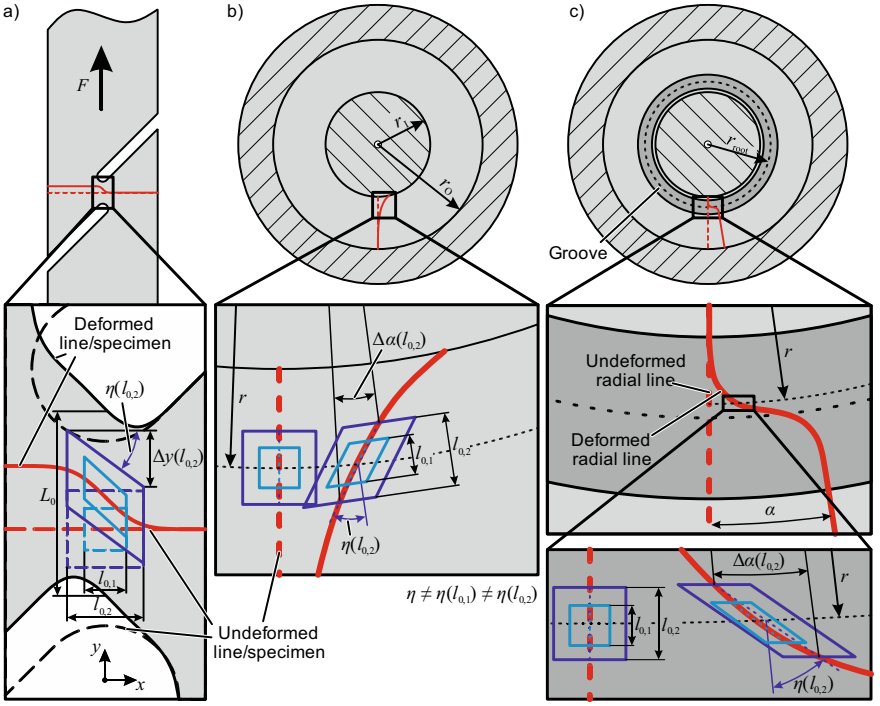


Fig. 5 Idealized deformation of an initially linear line in **a** the ASTM shear test, **b** the full in-plane torsion specimen, and **c** the in-plane torsion test with a grooved geometry. (Color figure online)

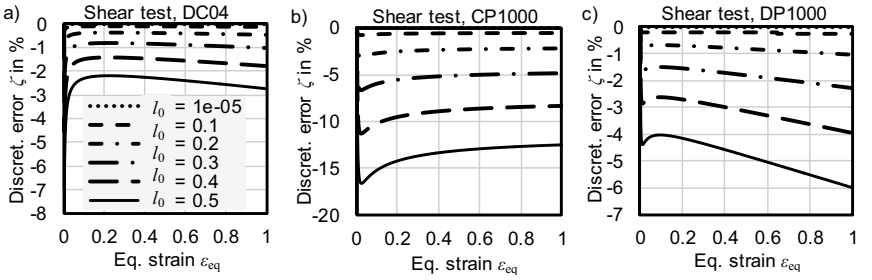


Fig. 6 Analytical calculated discretization errors for the investigated materials **a** DC04, **b** CP1000, and **c** DP1000 for conventional shear tests according to Fig. 2a

deformed, then the total distortion of the element in relation to the local distortion at the radius r is significantly greater and thus also the measured strain. The plastic strain is significantly greater than the elastic strain so that the integral determination of the strain always leads to an averaging of very small and in comparison very large strains and thus leads to large errors to the real local strain. The greater the proportion of the

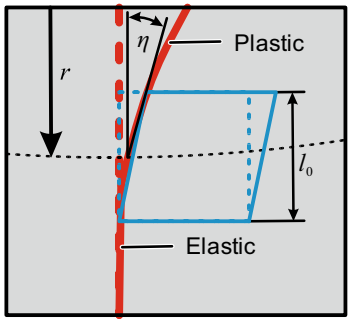


Fig. 7 Illustration of measurement deviation during elastic–plastic transition within the discrete element. (Color figure online)

purely elastic or subsequently the plastic region of the discrete measuring element, the lower the measurement deviation. The greatest deviation occurs when reaching the elastic–plastic transition at radius r, in which half of the range is elastic and the other half is already plastic. The softer the elastic–plastic transition, the lower the measurement deviation.

4 Prevention of Measurement Errors Due to Strain Localization in Shear Tests

It has been shown that measurement errors occur depending on the material properties, the sample geometry, and the settings of the DIC system. To reduce or avoid measuring errors using measuring systems with discrete measuring ranges, the following strategies can be used:

1. The strain gauge length must be reduced so far that errors are negligible.
2. The sample shape must be designed in a manner that localization does not occur. Both methods are briefly presented below.
   Furthermore, other methods are possible. These are not part of the present work.
3. Determine the error and then correct the measured strain by the error. For this, all sample-specific, material-specific, and system-specific parameters must be known exactly. Since the purpose of performing shear tests is to quantify the material-specific parameters, these are usually not available a priori.
4. Alternative measuring methods can be used. These include, e.g., the evaluation of the shear strain from the grain structure or, in the case of the in-plane torsion test, the determination of the shear strain from torque and angle of rotation [5].

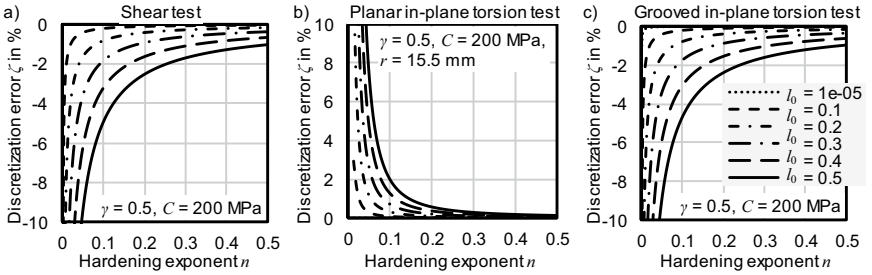


Fig. 8 Discretization error in dependency of the hardening exponent n for **a** the conventional shear test, **b** the planar in-plane torsion test at radius $r = 15.5$ mm, and **c** the grooved in-plane torsion test

4.1 Definition of Strain Gauge Length Based on the n*-Value*

Assuming the Hollomon (1945) hardening law

$$\sigma_{\mathrm{y}} = C \cdot \varepsilon_{\mathrm{eq}}^{n} \tag{21}$$

and neglecting elastic strains, the estimated measurement error in dependency of the hardening exponent n can be derived. It can be shown that the measurement deviation is nearly independent of the linear parameter C and independent of the shear strain γ, but mainly on the hardening exponent n. Figure 8 shows the expected measurement error as a function of the hardening exponent n and the strain gauge length l_0 for the three specimen types shown in Fig. 2. Using the given information, an estimation of the expected measurement deviation can already be made with knowledge of the n-value from the tensile test or the other way around, a suitable setting of the DIC system can be selected for which the deviation is sufficiently small.

4.2 Prevention of Strain Localization Using a New Grooved Specimen for In-Plane Torsion Tests

For the classic design of a groove, the shape of the groove is first defined, and then the resulting stress and strain along the groove contour result. The stress and strain state can then be further improved by inverse modification of the geometry. With the following new design method, the desired radial stress or strain profile is first defined, and then the local sheet thickness is defined based on it. Figure 9a shows the principle of the design for the new stress-adjusted groove in comparison with the stress distribution for the planar specimen and the specimen with conventional circular groove. The stress profile of the novel groove shape represents the following requirements:

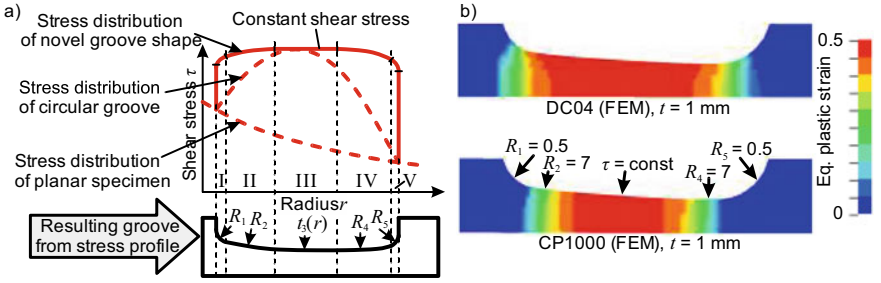


Fig. 9 **a** Principle of stress-adjusted groove shape. The local sheet thickness is defined depending on the required stress distribution. **b** Numerical analysis of the strain distribution for the stress-adjusted groove contour for DC04 and CP1000 in $t = 1$ mm sheet thickness [5]. (Color figure online)

1. The stress in the test area (zone III) of the groove should be constant along a radial section: $\tau(r) = \text{constant}$. The resulting strain will be constant as well. Thereby, the influence of the strain gauge length on the strain measurement (see Fig. 4b) can be avoided since no strain localization will occur. As long as the strain gauge length is not larger than the radial section with constant strains (size of zone III), the strain gauge length should have no influence on the measured strains.
2. Inside (zone II) and outside (zone IV), the gradient of stress should be weak to avoid locating the strain at transitions between the zones.
3. At the transitions to the surface of the sheet, a strong stress gradient is desirable to minimize the width of the groove. The wider the groove, the lower the maximum stress.
4. The stress profile should be continuous.

As a result, the shape of the groove results directly from the given requirements. The radius-dependent sheet thickness $t(r)$ can be calculated analytically from the calculation of stresses:

$$\tau(r) = \frac{M}{2 \cdot \pi \cdot t(r) \cdot r^2} \stackrel{!}{=} \text{constant}. \tag{22}$$

The sheet thickness $t(r)$ in the area of constant stress Δr_{const} (Zone III) results in

$$t(r) = \frac{t_{\text{mean}} \cdot r_{\text{mean}}^2}{r^2}. \tag{23}$$

A finite-element analysis is performed and the equivalent plastic strain for a section through the novel groove with radially constant stress is shown in Fig. 9b. The used flow curves correspond to the investigated DC04 (Fig. 1a) and CP1000 (Fig. 1b) materials as presented in Sect. 2. The element size is 0.05 mm. The sheet thickness

t is 1 mm and the width of Zone III Δr_{const} of 1.5 mm is arbitrary and should be at least the size of the strain gauge length of the measurement settings. On both sides, circular transitions with initially low stress gradient (radius 7 mm) and then strong stress gradients (radius 0.5 mm) complete the groove. There is a continuous transition between all zones. The strain in the centre of the groove (Zone III) is almost constant and homogeneous. Both materials show no difference in this area. A difference in the strain distribution due to the different amounts of localization can only be observed at the radii R_1–R_5.

The first experimental determined strain fields for the in-plane torsion test with the new groove manufactured by electro-discharge machining (EDM) are shown in Fig. 10. The investigated materials DC04, CP1000, and DP1000 are equal to the previous sections. Each specimen was evaluated with a different strain gauge length l_0 between 0.2 and 0.5 mm and the averaged strain along a circumferential circular line at the mean radius r_{mean} was measured. For CP1000, the deviation at 0.5 mm strain gauge lengths is reduced to 4.6% for the illustrated specimen at v. Mises strains of approx. 0.2 (Fig. 10b). The conventional circular groove shows 25% deviation (Fig. 4b). For an equivalent strain of approx. 0.5, the deviation is even reduced to 1.4%. The deviation for DC04 and DP1000 is below 0.7%. The remaining difference can be attributed to production-related deviations from the target local sheet thickness. The measured groove contour does not agree exactly with the analytical design, the stress along the radius is no longer perfectly constant,

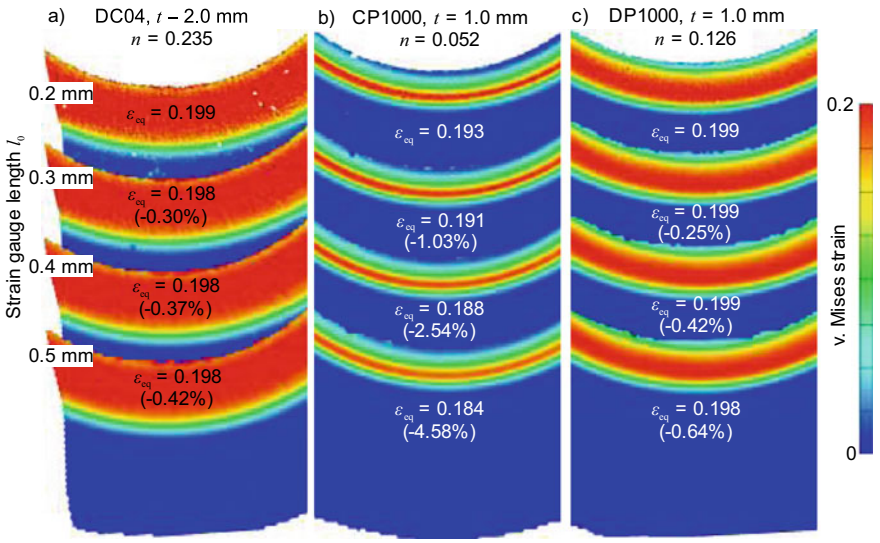


Fig. 10 Experimentally determined strain field for **a** DC04, **b** CP1000, and **c** DP1000 using the new stress-adjusted grooved specimen evaluated with different strain gauge lengths at $\varepsilon_{eq} = 0.2$ equivalent strain. (Color figure online)

and errors due to localization occur. In addition, other factors, such as the planar anisotropy, may influence the homogeneous strain field. Although this influence was negligible for the materials examined, it could be relevant for other materials and should therefore be examined in future works.

5 Conclusion

The influence of strain gauge length on the measurement of shear strains using DIC was investigated for three materials. The lower the work hardening of the material, the greater the measurement error due to the optical elements selected too large. Deviations up to 25% were measured for CP1000 material while DC04 only exhibits 1% deviation using the same setting. Through the presented analytical approach, the error can be estimated depending on the material properties and the specimen shape for conventional shear tests as well as for the in-plane torsion test. From the analytically determined dependence of the measurement deviation on the hardening exponent n, a material-specific setting of the measuring system can be defined. The necessary information can be taken directly from the results of the tensile test. The newly presented in-plane torsion test specimen with a stress-adjusted groove can also completely avoid the shear strain localization. However, this requires the exact production of the necessary groove contour. Any deviation from the ideal contour leads to a deviation from the homogeneous strain profile. Other influences on the test results, such as the planar anisotropy, must be examined in future works.

Acknowledgments The authors acknowledge funding from the German Research Foundation (DFG) for project 327544970 “Novel in-plane torsion specimen for the characterization of damage and hardening”.

References

1. Miyauchi K (1984) A proposal for a planar simple shear test in sheet metals. Sci Pap Inst Phys Chem Res (Jpn) 78:27–40
2. Marciniak Z (1961) Influence of the sign change of the load on the strain hardening curve of a copper test piece subject to torsion. Archiwum Mechaniki Stosowanej 13:743–752
3. Yin Q, Tekkaya AE, Traphöner H (2015) Determining cyclic flow curves using the in-plane torsion test. CIRP Ann Manuf Technol 64:261–264
4. Roth CC, Mohr D (2018) Determining the strain to fracture for simple shear for a wide range of sheet metals. Int J Mech Sci 149:224–240

5. Traphöner H, Clausmeyer T, Tekkaya AE (2019) Methods for measuring large shear strains in in-plane torsion tests. J Mater Process Technol. https://doi.org/10.1016/j.jmatprotec.2019.116516
6. Traphöner H, Clausmeyer T, Tekkaya AE (2018) Material characterization for plane and curved sheets using the in-plane torsion test—an overview. J Mater Process Technol 257:278–287

Experimental and Numerical Studies on Plastic Deformation and Failure Behavior of Carbon Nanotube-Reinforced Al Composite Sheet Under Uniaxial Loading Condition



Zhenming Yue, Xinrui Min, Zhanqiu Tan, Junyan Ni, Zhiqiang Li, Jun Gao, and Jie Zhang

Abstract The carbon nanotube (CNT) reinforced aluminum has been expected as one ideal metal matrix composite characterized by superior strength and high elastic modulus. However, the reduction of its ductility is often a serious drawback. Nonuniformity in the microstructure makes it difficult to maintain the structural integrity during the deformation. In this study, the mechanical property of CNT/Al2024 composite sheet of 1.0 mm will be investigated through uniaxial tensile tests. Meanwhile, the simulations based on micro- and macro-mechanical constitutive are conducted to reveal the relationship between the evolution of microstructure, like grain size, dislocation density and interfacial bonding, and macro deformation responses. This work can be helpful to better understand the key factors that influence the plastic deformation and failure of CNT/Al2024 composite under complex loading conditions.

Keywords Carbon nanotubes (CNTs) · Carbon nanotube-reinforced aluminum · Plastic deformation and failure

Z. Yue (✉) · X. Min · J. Gao
Associated Engineering Research Center of Mechanics and Mechatronic Equipment, Shandong University, Weihai 264209, China
e-mail: yuezhenming@sdu.edu.cn

Z. Yue · Z. Tan · Z. Li
State Key Laboratory of Metal Matrix Composites, Shanghai Jiao Tong University, 800 Dongchuan Road, Shanghai 200240, China

J. Ni
Department of Electrical Energy, Metals, Mechanical Constructions and Systems, Faculty of Engineering and Architecture, Ghent University, Ghent 9000, Belgium

J. Zhang
Sino-French Institute of Computing Technology for Advanced Materials (CTAM), Shanghai 200002, China

© The Minerals, Metals & Materials Society 2021

G. Daehn et al. (eds.), *Forming the Future*, The Minerals, Metals & Materials Series,
https://doi.org/10.1007/978-3-030-75381-8_58

1 Introduction

Carbon nanotubes (CNTs) are a kind of ideal reinforcement for metal matrix composites with the advantages of high modulus, good toughness, and stable structure. After the addition of CNTs, the metal matrix composites can be improved in strength and modulus at the same time to obtain excellent specific strength, specific stiffness, shock absorption, and other characteristics [1]. So the composite material has been widely used in aerospace, ship, automobile, electronics, and other fields. At present, the research on carbon nanotube-reinforced aluminum matrix composites mainly focuses on the production process, mechanical properties, microstructure, and so on.

Kwon et al. [2] used the method of hot pressing and sintering before extrusion to achieve uniform distribution of carbon nanotubes (CNTs). The results showed that the strength of CNT/Al composites increased with the increase of CNTs volume fraction. Kuzumaki et al. [3] conducted uniaxial tension tests on carbon nanotube-reinforced aluminum matrix composites, and the results showed that carbon nanotubes had a significant effect on the improvement of mechanical properties of the aluminum matrix. Esawi et al. [4] prepared the carbon nanotube-reinforced aluminum matrix composite by powder metallurgy, and the test results showed that the tensile strength of the composite was 21% higher than that of the aluminum matrix. With the breakthrough of preparation technology, the research on plastic deformation and damage fracture mechanism of carbon nanotube-reinforced aluminum matrix composites is just beginning. How to explain the mechanical strength and fracture damage failure mechanism of composite materials from the perspective of microstructure has become an urgent problem to be solved. Jian et al. [5] established a cohesive force model based on interfacial atomic van der Waals force interaction and studied the relationship between interfacial stress and interfacial displacement. Tan et al. [6] studied the macroscopic mechanical properties of carbon nanotube-reinforced composites based on the cohesion model and the theoretical basis of micromechanics. Finite element simulation analysis is a common method to analyze the mechanical characteristics of materials. Combined with the representative volume element (RVE) method, the mechanical responses of composites with different reinforcement bodies randomly distributed can be studied. But the plastic deformation and damage behavior of the composites are still less studied through the crystal model.

In this paper, the two-dimensional mesoscopic model of CNT/Al composites was established by the Voronoi algorithm based on the representative volume element (RVE) method. The mechanical properties of the Al matrix were studied by the crystal plastic model. The interface properties of carbon nanotube composites are represented by the cohesive model, and the plastic deformation and damage behavior of CNT reinforced aluminum matrix composites were studied.

2 Crystal Plasticity Model

Carbon nanotube reinforced aluminum matrix composites can be regarded as composed of two parts: the homogeneous matrix phase of aluminum alloy and the influence zone phase of carbon nanotube reinforcement. The matrix phase will be described by crystal plasticity, so as to obtain the effect of microstructure on plasticity and damage, and the plastic deformation and damage evolution of carbon nanotube-reinforced aluminum matrix composites will be studied at the mesoscopic level. Taylor [7] first introduced the concepts of slip and lattice rotation. Subsequently, Hill [8], Rice [9], and Asaro [10] established and developed the crystal plasticity theory to describe the plastic deformation of crystals. Crystal plastic constitutive model is widely used to characterize the macroscopic and microscopic evolution of polycrystalline materials, especially the evolution of crystal structure. The single crystal plastic constitutive equation [11, 12] adopted in this paper is as follows:

$$\dot{\sigma} = C : D - \sum_{\alpha=1}^{n} R_a \cdot \dot{\gamma}_\alpha \tag{1}$$

$$R_\alpha = C : P_\alpha - \sigma \cdot Q_\alpha + Q_\alpha \cdot \sigma \tag{2}$$

$$P_\alpha = \frac{1}{2}(s_\alpha \otimes m_\alpha + m_\alpha \otimes s_\alpha) \tag{3}$$

$$Q_\alpha = \frac{1}{2}(s_\alpha \otimes m_\alpha - m_\alpha \otimes s_\alpha) \tag{4}$$

$$\dot{\gamma}_\alpha = \dot{\gamma}_0 \left(\frac{\tau_\alpha}{g_\alpha} \right)^n sign(\tau_\alpha) \tag{5}$$

where $\dot{\sigma}$ is the Jaumann rate of the Cauchy stress tensor, C is the fourth-order elastic tensor, $\dot{\gamma}_\alpha$ is the plastic sliding shear rate, s_α denotes the slip direction, m_α denotes the normal direction of the slip surface, and g_α denotes the strain hardening state of the crystal. In the cubic system, the hardening law can be expressed as follows:

$$\dot{g}_\alpha = \sum_{\beta=1}^{n} h_{\alpha\beta} \left| \dot{\gamma}_\beta \right| \tag{6}$$

$$h_{\alpha\beta} = q h_0 (1 - \frac{g_\alpha}{g_s})^a \tag{7}$$

In the formula, $h_{\alpha\beta}$ is the hardening modulus matrix containing the self-hardening modulus and the latent hardening modulus, q is hardening matrix parameters, g_s is the saturation slip resistance, and h_0 and a are the hardening parameters for constitutive details.

3 Geometrical Modeling Based on Voronoi

To accurately predict the mechanical response of composites material, it is necessary to describe the microstructure accurately. In this study, a geometric model close to the microstructure of carbon nanotubes is established based on the Voronoi diagram. The Voronoi diagram is a spatial partition structure based on the proximity principle [13]. This model provides a more realistic microstructure for the simulation of polycrystalline materials and has more advantages in characterizing the random crystal orientation of polycrystalline materials.

3.1 CNT/Al Composite Material Model Based on Voronoi Diagram

In this paper, a two-phase polycrystalline model of Al alloy matrix and CNT/Al influence region was established based on the ABAQUS platform and the RVE model combined with the basic algorithm of the Voronoi diagram. The model dimension is 1×1 μm, as shown in Fig. 1. The crystal orientation was randomly assigned to each grain in the generated Voronoi diagram. Table 1 shows the parameters of the Al alloy matrix in the crystal plasticity model.

The properties of the affected zone of CNTs were expressed by the elastoplastic model individually, and Table 2 shows the CNT material parameters. In the table,

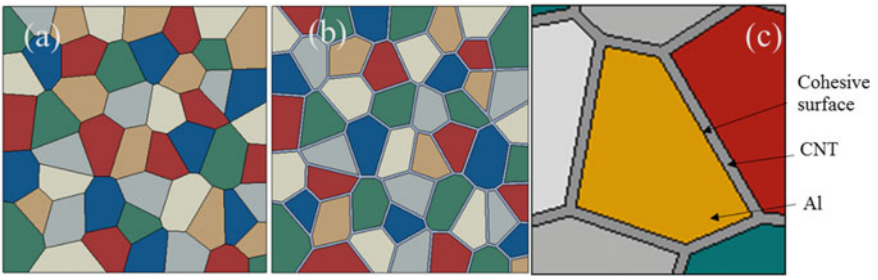


Fig. 1 The RVE model based on the Voronoi diagram. **a** Only the Al alloy matrix is considered in the RVE model, **b** Both matrix Al and reinforcement CNT are considered in the RVE model, **c** A schematic diagram considering the cohesion relationship between the CNTs and Al interfaces. (Color figure online)

Table 1 Some parameters of Al in the crystal plasticity model

Material	Elastic constants/MPa			ν	$\dot{\gamma}_{\alpha 0}$	n	h_0 MPa	g_s MPa	a	q
	C_{11}	C_{12}	C_{44}							
Al	106750	60410	28340	0.3	0.001	10	85	75	2.25	1

Table 2 The material parameters of CNT

Material	ν	E/GPa	σ_b/GPa	ρ/(g/cm^3)
CNT	0.2	1000	100	2.25

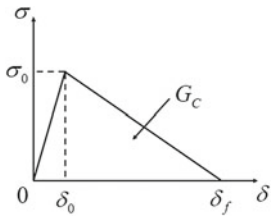


Fig. 2 Constitutive relation of bilinear cohesive elements

Table 3 Interface property parameters of cohesion model

Parameter	E/GPa	σ_0/MPa	δ_0/μm	δ_f/μm	G_C/(N/m)
Value	100	550	0.002	0.01	2.75

ν is Poisson's ratio, E is the elastic modulus, σ_b is the tensile strength, and ρ is the density.

The interfacial strength between the affected zone and the matrix phase was expressed by the cohesion model. In this paper, the bilinear cohesion model is adopted based on the ABAQUS platform, as shown in Fig. 2.

Where σ_0 is the initial stress of damage, δ_0 is the initial displacement of damage,δ_f is the displacement of damage failure, and G_C is the normal fracture energy. The interface property parameters of the cohesion model are shown in Table 3.

3.2 Boundary Conditions

During the loading process, in order to avoid the phenomenon of neck constriction and uneven distribution of strain, the boundary nodes of the constructed RVE model were restricted to make the distribution of strain more uniform, so as to obtain more accurate average strain and stress. As shown in Fig. 3, it is a schematic diagram of the boundary conditions of the RVE model after meshing. In Fig. 3, Top and Bottom are the set of nodes on the horizontal edge, Left and Right are the set of nodes on the vertical edge. A, B, C, and D are the nodes of the four corners, respectively. RP-1 and RP-2 are two reference points. The general constraint equation between nodes is shown below:

$$A_1 u_i^1 + A_2 u_j^2 + \cdots + A_N u_{\mathrm{k}}^{\mathrm{N}} = u \tag{8}$$

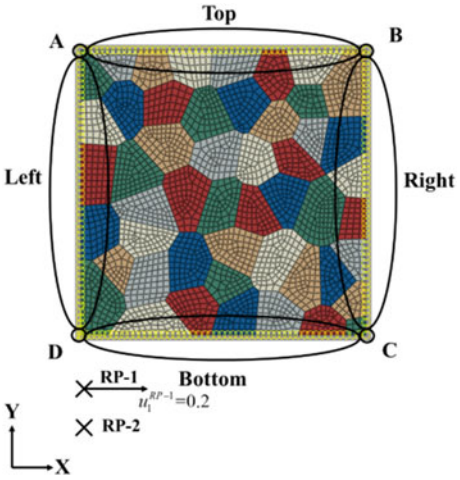


Fig. 3 Schematic diagram of the boundary conditions of the RVE model after meshing. (Color figure online)

where A_1, A_2, and A_N are the node coefficients, $u^1, u^2 \cdots u^N$ are the displacement of the corresponding node, i, j, and k are the degrees of freedom of the node, and u is the displacement of the reference point. In this paper, the simulation is performed in the X-axis direction. Therefore, the nodes A, D, and the node set Left have the same displacement in the X-axis direction, as do the nodes B, C, and the node set Right. The nodes constraint equation are shown below:

$$u_1^A = u_1^D = u_1^{Left} \tag{9}$$

$$u_1^B = u_1^C = u_1^{Right} \tag{10}$$

$$u_1^{Right} - u_1^{Left} = u_1^{RP-1} \tag{11}$$

In the Y-axis direction, the displacements of nodes A, B, and node set Top are the same and the displacements of nodes C, D, and node set Bottom are also the same. The nodes constraint equation are shown below:

$$u_2^A = u_2^B = u_2^{Top} \tag{12}$$

$$u_2^C = u_2^D = u_2^{Bottom} \tag{13}$$

$$u_2^{Top} + u_2^{Bottom} = u_2^{RP-2} \tag{14}$$

where u_1^{RP-1} is the displacement of the reference point RP-1 in the X-axis direction; u_2^{RP-2} is the displacement of the reference point RP-2 in the Y-axis direction. In this study, $u_1^{RP-1} = 0.2$ and $u_2^{RP-2} = 0$.

4 Results and Analysis

In order to show the effect of CNTs on the overall mechanical properties of composites, the mechanical response comparison curves of Al alloy matrix and CNT/Al composites in the uniaxial tensile simulation are presented in Fig. 4. The results showed that with the introduction of CNT into the Al matrix, its mechanical properties are significantly improved. The yield strength and elasticity modulus of CNT/Al composites have been increased correspondingly, which also proves that the reinforcement has a strengthening effect on the mechanical properties of the composite material.

Figures 5 and 6 show the distribution cloud diagram of stress and strain of Al matrix and CNT/Al composites under different tensile strain variables, respectively. By comparing the stress–strain distribution cloud map in Figs. 5 and 6, it can be found that with the addition of CNTs, the overall stress–strain cloud map of the composite material is more uniform. Meanwhile, the strain of CNTs is always the minimum, while the stress is always the maximum. The reason is that CNT has a larger elastic modulus than Al, so in the whole deformation process of composite materials, the deformation of CNT is the lowest, but the stress is the highest. By comparing the maximum stress and strain values, it can be clearly found that the maximum strain of CNT/Al composite material is lower than that of Al matrix, while the maximum stress is higher than that of Al matrix, indicating that the addition of CNTs makes the

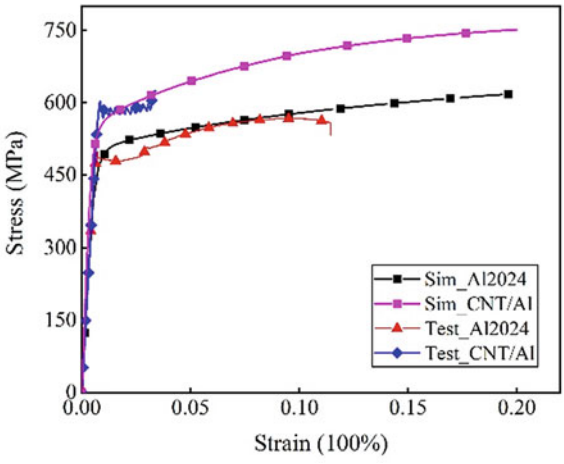


Fig. 4 Stress–strain curves of Al matrix and CNT/Al composites. (Color figure online)

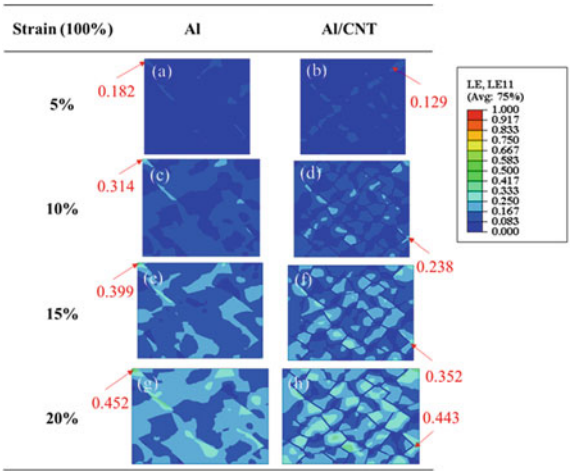


Fig. 5 Cloud diagram of strain distribution. (Color figure online)

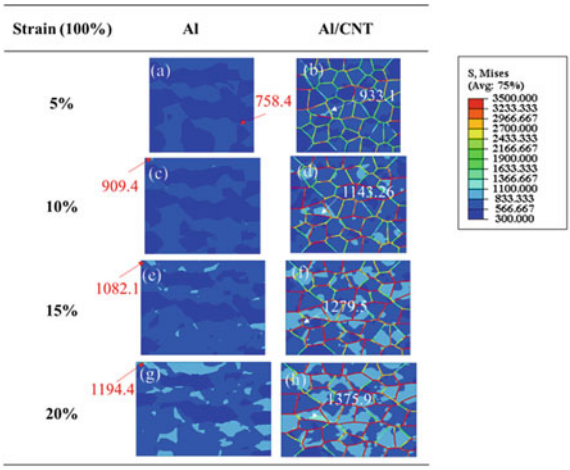


Fig. 6 Cloud diagram of equivalent stress distribution. (Color figure online)

deformation of Al matrix in the composite material more consistent and the plastic strain distribution more uniform. At the same time, it also shows that CNTs play a major bearing role in composite materials.

Through the setting of cohesive surface in ABAQUS, the whole process of damage and destruction of CNT/Al composite material can be viewed more clearly. In the elastic bearing stage, as the amount of deformation increases, the strength of the CNTs affected zone gradually increases and reaches the maximum value. In this stage, there is no damage in the affected zone (SDEG = 0), as shown in Fig. 7a. At this point, the strength of the affected zone plays a role in stress transfer between the CNTs and Al, so that the stress is more distributed on the CNTs. Therefore, the ductility of CNT/Al composites can be improved to some extent by increasing the

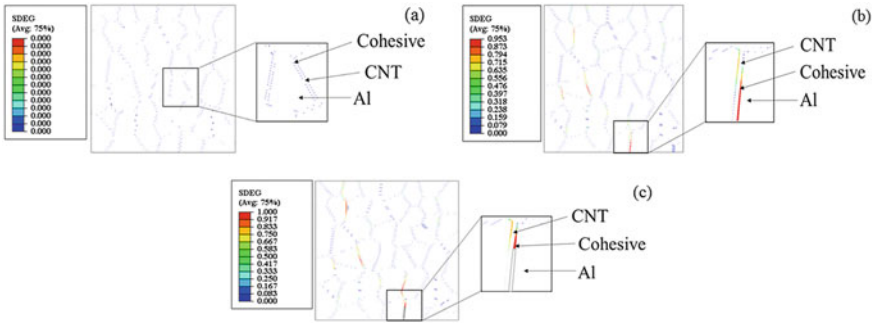


Fig. 7 The process of interface damage. **a** The diagram of elastic bearing stage, **b** The diagram of damage accumulation stage, **c** The diagram of crack propagation stage. (Color figure online)

strength of the interface. After the strength of the affected area reaches the maximum value, the affected zone enters the damage accumulation stage. With the increase of deformation, the damage gradually accumulated, as shown in Fig. 7b. In this stage, the interface strength gradually decreases, the stress transferred at the interface decreases, and the bearing capacity of CNTs and Al decreases. When SDEG = 1, the CNTs affected zone is completely damaged, and at this time, the affected zone enters the crack propagation stage. As the amount of deformation increases, the crack gradually expands, as shown in Fig. 7c. The failure zone no longer plays the role of transferring stress, and the CNTs and Al around the failure interface lose their bearing capacity.

5 Conclusions

In this paper, the elastoplastic and damage behaviors of CNT/Al composites were studied. A two-dimensional RVE model of composites was constructed in combination with the Voronoi algorithm. The mechanical behavior of the aluminum alloy was described by crystal plasticity theory. The cohesive model is used to describe the bonding ability of the matrix phase and the enhanced phase. The following conclusions are obtained through simulation studies.

During the entire deformation process of CNT/Al composites, the strain in the affected zone of CNTs was always the minimum and the stress was always the maximum. The addition of CNTs made the plastic strain distribution of matrix phase in the composites more uniform, playing a major bearing role in composite materials. The damage evolution of CNT/Al composites during loading deformation can be roughly divided into three stages: the elastic loading stage, the damage accumulation stage, and the crack propagation stage. In the elastic bearing stage, the interface plays a role in transferring stress, and the stress is mainly distributed in the affected zone of CNTs. In the damage accumulation stage, the strength of the interface gradually decreases, the stress transferred from the interface decreases, and the bearing capacity

of the CNTs affected zone and Al matrix phase decreases. In the crack propagation stage, the crack gradually develops and expands, the interface completely fails, and the CNT affected zone and Al matrix phase lose the bearing capacity. Increasing the interface strength between the CNT affected zone and the Al matrix phase can improve the overall ductility of the CNT/Al composite to a certain extent.

References

1. Deng K-K, Wang C-J, Nie K-B, Wang X-JJAMS (2019) Recent research on the deformation behavior of particle reinforced magnesium matrix composite: a review 32(4):413–425
2. Kwon H, Estili M, Takagi K, Miyazaki T, Kawasaki A (2008) Combination of hot extrusion and spark plasma sintering for producing carbon nanotube reinforced aluminum matrix composites. Carbon 47(3)
3. Kuzumaki T, Miyazawa K, Ito HIK (1998) Processing of carbon nanotube reinforced aluminum composite. J Master Res 13(9):2445–2449
4. Esawi AMK, Morsi K, Sayed A et al (2009) Fabrication and properties of dispersed carbon nanotube-aluminum composites. Mater Sci Eng A 508(1):167–173
5. Jiang LY, Huang Y, Jiang H et al (2006) A cohesive law for carbon nanotube/polymer interfaces based on the van der Waals force. J Mech Phys Solids 54(11):2436–2452
6. Tan H, Jiang LY, Huang Y et al (2007) The effect of van der Waals-based interface cohesive law on carbon nanotube-reinforced composite materials. Comp Sci Tech 67(14):2941–2946
7. Taylor GI, Elam CF (1925) The plastic extension and fracture of aluminum crystals. Proc Royal Soc London 108(745):28–51
8. Hill R, Rice JR (1972) Constitutive analysis of elastic-plastic crystals at arbitrary strain. J Mech Phys Solids 20(6):401–413
9. Rice JR (1971) Inelastic constitutive relations for solids: An internal-variable theory and its application to metal plasticity. J Mech Phys Solids 19(6):433–455
10. Asaro RJ, Rice JR (1977) Strain localization in ductile single crystals ☆. J Mech Phys Solids 25(5):309–338
11. Peirce D, Asaro RJ, Needleman A (1982) An analysis of nonuniform and localized deformation in ductile single crystals. Acta Metall 30(6):1087–1119
12. Hutchinson JW (1976) Bounds and self-consistent estimates for creep of polycrystalline materials. Proceedings of the royal society of London
13. Ghoshal G, Turner JA (2009) Numerical model of longitudinal wave scattering in polycrystals. IEEE Trans Ultrason Ferroelectr Freq Control 56(7):1419–1428

Experimental Study on Uniaxial Strain Cyclic Behavior of GS-20Mn5



Zongyuan Zou, Shuting Han, Hongzhong Wang, Qun Li, Baofeng Guo, and Shiyan Zhao

Abstract Due to the common discontinuity of the structure and non-uniform load, local high stress phenomenon tends to appear in the mechanical structure under repeated loading, and even local small plastic deformation may occur. In this case, the cyclic elastic–plastic mechanical properties of the structural steel are the key elements for the reasonable and accurate assessment of structural safety. In order to study the cyclic mechanical properties of GS-20Mn5, which is a commonly used steel in load-bearing mechanical equipment, corresponding strain cyclic loading tests were performed. The cyclic elastoplastic deformation characteristics under strain-controlled cyclic loading with different strain ratios ($R = -1, 0.5$) are studied, and the cyclic hardening/softening and mean stress relaxation features are revealed. The results show that the cyclic hardening/softening features are affected by the strain amplitude and cycles. This test material tends to show cyclic hardening at higher strain amplitudes. The cyclic stress–strain curve is obtained by the incremental step test, and the corresponding yield strength is about 4.8% larger than that under uniaxial tension. When $R = 0.5$, the test material exhibits obvious mean stress relaxation. When the strain amplitude is 0.16%, 0.30%, and 0.40%, the mean stress decreases and then stabilizes at about 25 MPa, −3 MPa, and −6 MPa, respectively. For the mechanical equipment made of GS-20Mn5 with local small plastic deformation under cyclic loading, the obtained cyclic mechanical performance of GS-20Mn5 can provide a reference for the analysis and evaluation of the structural safety.

Keywords GS-20Mn5 · Cyclic loading · The cyclic stress–strain curve · Cyclic hardening/softening · Mean stress relaxation

Z. Zou (✉) · S. Han · H. Wang · Q. Li · B. Guo · S. Zhao
Key Laboratory of Advanced Forging & Stamping Technology and Science of Ministry of Education, Yanshan
University, Qinhuangdao, China
e-mail: zzy@ysu.edu.cn

Q. Li
e-mail: qunli@ysu.edu.cn

© The Minerals, Metals & Materials Society 2021

G. Daehn et al. (eds.), *Forming the Future*, The Minerals, Metals & Materials Series,
https://doi.org/10.1007/978-3-030-75381-8_59

1 Introduction

Most mechanical structures and components are often subjected to cyclic load when they are in service. Due to the complexity of the load and structure, the local high stress phenomenon occurs frequently during loading, and even local small plastic deformation happens. The elastoplastic properties of materials under cyclic loading are different from those under monotonic loading, such as cyclic hardening/softening and mean stress relaxation. More and more scholars pay attention to the cyclic deformation characteristics of materials and their influence on the fatigue life and loading capacity of structures. The cyclic hardening and softening characteristics of low-yielding steel BLY160 under cyclic loading were investigated, and the constitutive model to describe the cyclic deformation characteristics of the material was established [1]. The cyclic deformation response of 9–12% Cr steel under different loading conditions and its influence on fatigue life were analyzed [2]. The low cycle fatigue tests on 2121-t851 aluminum alloy with different strain ratios were conducted, and the effects of strain amplitude and strain ratio on low cycle fatigue behavior and micromechanism were analyzed [3]. Furthermore, the uniaxial cyclic elastoplastic deformation and fatigue failure of API-5L X65 steel under different loading conditions were studied [4]. Many researchers demonstrate that the cyclic hardening/softening characteristics, mean stress relaxation, and other cyclic plasticity properties of materials have significant effects on load-bearing capacity and life of structures. Therefore, clarifying the cyclic deformation characteristics of materials is important for rational mechanical structure design, analysis, and safety evaluation.

The cast steel GS-20Mn5(conforming to Germany standard DIN17182-1992) is commonly used for the column, beam, workbench of press, subjected to repeated load when the press is working. The studies of GS-20Mn5 mostly focused on its welding technology, and yet, the cyclic hardening/softening under cyclic loading and the mean stress relaxation characteristics have not been found in academic literature. In this work, the monotonic tension test and cyclic loading tests for strain ratio of -1 and 0.5 with different strain amplitudes were performed for GS-20Mn5, then the cyclic hardening/softening characteristics and the mean stress relaxation were studied, and the mechanical properties and deformation laws under cyclic loading of GS-20Mn5 were analyzed, which can provide a reference for strength and safety evaluation of mechanical structure made of GS-20Mn5.

2 Specimen and Equipment

The uniaxial tension specimen and cyclic loading specimen are shown in Figs. 1 and 2, respectively. The test equipment used, as shown in Fig. 3, is Instron 8801 hydraulic servo fatigue testing machine.

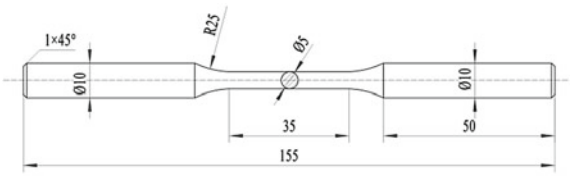


Fig. 1 Uniaxial tension specimen's size

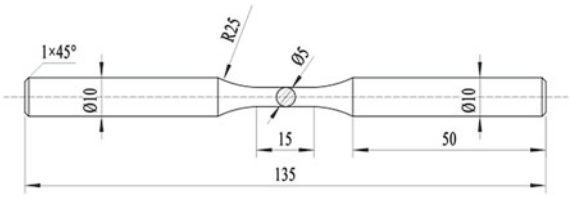


Fig. 2 Cyclic loading specimen's size



Fig. 3 The photo of test. (Color figure online)

3 Experimental Investigation

3.1 Uniaxial Tension Test

In the test, the contact extensometer (Instron 2620-601) was used to measure the strain of the uniaxial tension process in real time, the strain rate is 0.1%/s, three repeated tests were carried out, and the resulted uniaxial tension stress–strain curve of GS-20Mn5 material is shown in Fig. 4. The test results show that GS-20Mn5 has an obvious yield platform in the uniaxial tensile deformation process, with a strain range of about 0.00156–0.0099 mm/mm, the yield limit is about 310 MPa, and the elastic modulus is about 212GPa.

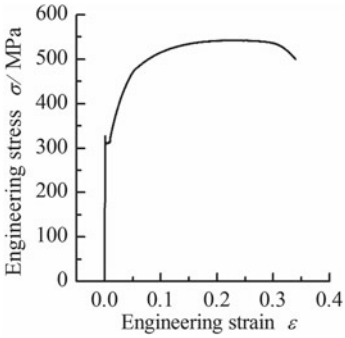


Fig. 4 Uniaxial tensile stress–strain curve

3.2 Experimental Study on Cyclic Hardening/Softening Characteristics

In the cyclic loading test, Instron's Wavematrix software was applied to set up the strain-controlled loading program to realize the closed-loop control and data acquisition of the test. Triangular wave was selected for the loading waveform, and the loading rate was 0.1%/s.

3.2.1 Single Step Cyclic Loading Test

Strain-controlled cyclic loading tests with strain ratio $R = -1$ were performed under three different strain amplitudes of 0.16%, 0.30%, and 0.40%, respectively. The number of cycles is 300 per strain amplitude. The response curves of stress amplitude with cycles of different strain amplitudes are shown in Fig. 5. It can be seen that when the strain amplitude is 0.16%, the stress amplitude decreases with the increase of the cycles, and finally stabilizes, in other words, the material shows cyclic softening characteristics during the initial cycles (about 200 cycles), and finally reaches cyclic stabilization; when the strain amplitude is 0.30%, the stress amplitude decreases first

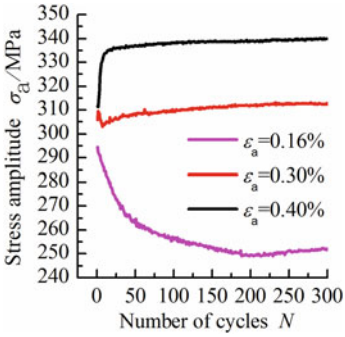


Fig. 5 Response curve of stress amplitude with cycles. (Color figure online)

and then increases with the increase of the cycle numbers, and finally stabilizes, that is, the material undergoes a slight cyclic softening first, then exhibits cyclic hardening characteristics, and finally tends to cyclic stabilization; and when the strain amplitude is 0.40%, the stress amplitude increases with the increase of cycles, and finally stabilizes, that is, the material first exhibits cyclic hardening characteristics, and finally reaches cyclic stabilization. That is to say, under cyclic loading conditions with different strain amplitudes, the response stress amplitude of the test material changes with the cycles differently. Both the strain amplitudes and the cyclic numbers are the factors that affect the cyclic hardening/softening characteristics. For the test material, a cyclic softening/hardening transition occurs with a strain amplitude in the range of [0.16%, 0.40%], and the cyclic softening gradually transforms to cyclic hardening with the increase of strain amplitude.

3.2.2 Incremental Step Cyclic Loading Test

Cyclic stress–strain curve of materials can be measured by the incremental step test [5, 6], and the cyclic stress–strain curve is used to reflect the mechanical properties of the material after cyclic loading. By comparing the cyclic stress–strain curve with the uniaxial tensile stress–strain curve, the cyclic hardening/softening characteristics of the material can be analyzed. The strain amplitudes of the incremental step test in this paper are 0.04%, 0.08%, 0.12%, 0.16%, 0.20%, 0.25%, 0.30%, 0.35%, 0.40%, 0.45%, and 0.50%. In order to obtain the hysteresis loop of steady state, 300 cycles of each strain amplitude is performed. The cyclic stress–strain curve of GS-20Mn5 is shown in Fig. 6.

According to the comparison between the cyclic stress–strain curve and the uniaxial tensile stress–strain curve in Fig. 6, it can be seen that when the strain amplitude is less than 0.30%, the cyclic stress–strain curve is lower than that of the uniaxial tensile stress–strain curve. That is to say, compared with the monotonic tension, the cyclic stabilization state of the material is characterized by cyclic softening. When the strain amplitude is greater than 0.30%, the cyclic stress–strain curve is higher than the uniaxial tensile stress–strain curve, and the material shows cyclic

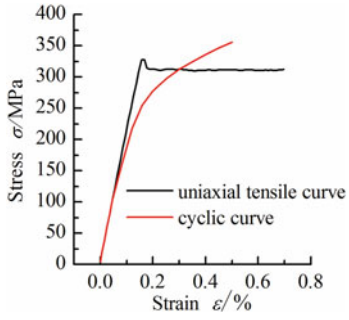


Fig. 6 Comparison of uniaxial tensile and cyclic stress–strain curve. (Color figure online)

hardening characteristics. The yield strength corresponding to the cyclic stress–strain curve is 325 MPa, which is about 4.8% higher than the yield strength corresponding to the uniaxial tensile stress–strain curve.

3.3 Experimental Study on Mean Stress Relaxation

The asymmetric strain-controlled cyclic test with strain ratio R of 0.5 was performed under different amplitudes of 0.16%, 0.30%, and 0.40% respectively to study the mean stress relaxation characteristic. About 2400 cycles were conducted for each strain amplitude. The mean stresses along with cycles of different strain amplitudes are shown in Fig. 7. It can be seen from that, under the three strain amplitudes, the material shows obvious mean stress relaxation characteristic. With the increase of cycles, the mean stress gradually decreases and tends to stabilization. When the strain amplitude is 0.16%, 0.30%, and 0.40% respectively, the mean stress eventually stabilizes to about 25 MPa, −3 MPa, and −6 MPa. It is worth noting that dimensionless form of mean stress is adopted as σ_{mn}/σ_{m1} to reflect the relaxation more clearly, and the curves of mean stress ratio with cycles are shown in Fig. 8. Here, σ_{mn} is the mean stress of the N_{th} cycle and σ_{m1} is the initial mean stress. It can be seen from Fig. 8 that the greater the strain amplitude is, the greater the mean stress relaxation rate is.

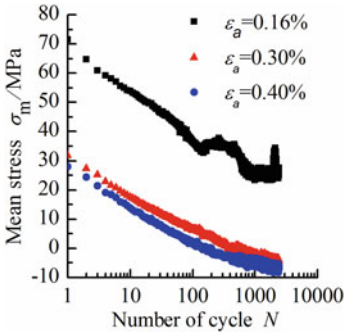


Fig. 7 Evolution of mean stress with cycles. (Color figure online)

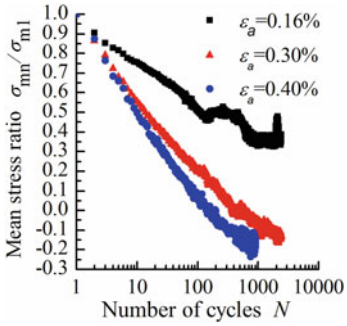


Fig. 8 Evolution of mean stress ratio with cycles. (Color figure online)

4 Conclusion

By uniaxial tensile test and strain-controlled cyclic loading test of GS-20Mn5, the following conclusions are concluded:

(1) The cyclic hardening/softening characteristics are affected by strain amplitude and cycles. Within the condition of experiment research, the experimental material is characterized by cyclic hardening behavior under larger strain amplitude (0.40%), while it is characterized by cyclic softening characteristic under lower strain amplitude (0.16%). In addition, under the strain amplitude (0.30%), the cyclic softening and hardening shift with the increase of cycles.

(2) According to the cyclic stress–strain curve with a strain range of [0−0.50%] obtained from the symmetrical strain incremental step test, when the strain amplitude is less than 0.30%, the stable state of the test material is characterized by cyclic softening compared with the monotonic tension, while when the strain amplitude is greater than 0.30%, the material is characterized by cyclic hardening. The yield strength corresponding to the cyclic stress–strain curve is 325 MPa, which is about 4.8% higher than the yield strength of 310 MPa under uniaxial tension.

(3) Under the asymmetric strain-controlled cyclic loading (strain ratio 0.5, strain amplitude 0.16%, 0.30% and 0.40%), the larger the strain amplitude is, the larger the mean stress relaxation rate and the smaller the mean stress stable value are.

Acknowledgments The authors gratefully acknowledge support provided by the National Natural Science Foundation of China (No.51905467) and State Key Laboratory of Materials Processing and Die & Mould Technology, Huazhong University of Science and Technology, China (P2019-018).

References

1. Xu L, Nie X, Fan J et al (2016) Cyclic hardening and softening behavior of the low yield point steel BLY160: experimental response and constitutive modeling. Int J Plasticity 78:44–63
2. Wu DL (2016) Effect of control mode on high temperature low cycle fatigue behavior of 9–12% Cr steel and cyclic constitutive modeling. PhD thesis, Shanghai: East China University of Science and Technology
3. Hao H (2018) A study on the mean stress relaxation and fatigue life estimation under random load of 2124-T851 aluminum alloy. PhD thesis, Zhejiang University
4. FatobaO AkidR (2018) Uniaxial cyclic elasto-plastic deformation and fatigue failure of API-5L X65 steel under various loading conditions. Theor Appl Fract Mec 94:147–159
5. Hsu TYJ, Wang Z (2014) Cyclic stress–strain response and microstructure evolution of polycrystalline Cu under pure compressive cyclic loading condition. Mat Sci Eng A-Struct 615:302–312
6. Marohnic T, Basan R, Franulovic M (2015) Evaluation of the possibility of estimating cyclic stress-strain parameters and curves from monotonic properties of steels. Procedia Eng 101:277–284

Part X
Constitutive Behavior

Influence of Deformation on Texture Development During Cold Drawing of Tubes



P. Bella, P. Burik, P. Bucek, and M. Ridzon

Abstract Cold drawing of tubes is a metal forming process that allows manufacturers to produce high precision tubes. The anisotropy is a natural phenomenon in the tube wall thickness, in this method of manufacture. The EBSD measurements have been made on several Ferritic–pearlitic steels (8.9 wt% pearlite content) with different deformations for the detection of the effect composition has on the texture formation. The development of the crystallographic texture can be clearly explained by the stress–strain state at the material flow. This article was pointed out and connected between the development of the texture and stress state during the cold drawing process by turning the body-centered K8 grid (BBC). A significant influence on the texture change is also the heat treatment, where grains have the different ability of recrystallization. The cognition of this process will make it possible to achieve a tube with the optimum texture for the cold drawing process.

Keywords Cold drawing · Texture · Finite-element method

1 Introduction

Cold tube drawing is a metalworking process used to produce high-quality seamless tubes with precise dimensions, good surface finish, and high mechanical properties. Seamless tubes are used for applications where the homogeneity of strength, microstructure, and extended product life are important design parameters. For this particular technology, a hot rolled seamless steel tube serves as a feedstock for multiple cold drawing operations with intermediate heat treatment [1]. There are two processes employed for cold drawing seamless steel tube: drawing with the fixed plug and hollow sinking process (Fig. 1). Drawing with the fixed plug reduced outer diameter and wall thickness. The fixed cylindrical or fixed conical plug is used depending on the thickness of the input feedstock. The conical plug allows to use

P. Bella (✉) · P. Burik · P. Bucek · M. Ridzon
ŽP Research and Development Centre, Kolkáreň 35, 976 81 Podbrezová, Slovak Republic
e-mail: bella@zelpo.sk

© The Minerals, Metals & Materials Society 2021

G. Daehn et al. (eds.), *Forming the Future*, The Minerals, Metals & Materials Series,
https://doi.org/10.1007/978-3-030-75381-8_60

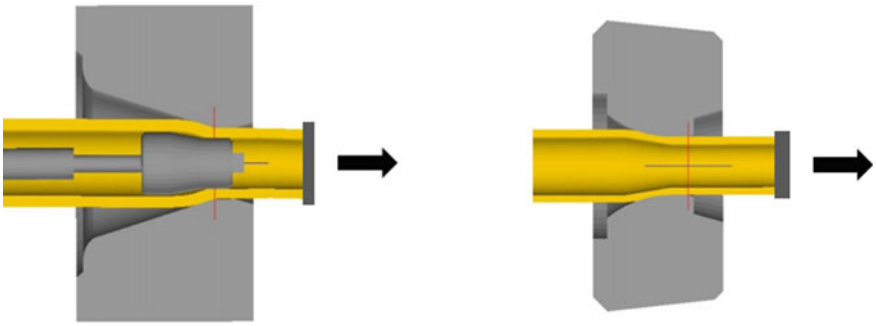


Fig. 1 Numerical scheme of drawing with the fixed plug (left) and hollow sinking process (right). (Color figure online)

higher drawing speed thanks to its geometry which provides a better flow of material. Hollow sinking is the final process in which the wall thickness remains the same, and the outer dimension is reduced [2, 3]. The change in wall thickness during deformation depends on the input dimensions of the tube and die geometry [4].

The low temperature during the cold drawing process does not allow dynamic recrystallization and thus the material hardening occurs due to the accumulation of dislocations. During the forming process, individual grains are elongated in the direction of the main deformation. Too high level of deformation and hardening is associated with a depletion of material plasticity and the risk of defects, and therefore recrystallization annealing is required. During annealing, the new deformation-free equiaxial grains are formed and the material is further deformed [5–7]. Given the demanding nature of the production process and strict requirements placed on tube diameters, the process was being looked into by means of the finite-element method (FEM) in DEFORM-3D simulation software. This numerical method provides an insight into the plastic deformation process and enables to investigate different physical fields in the modeled body, e.g., mechanical stress, deformation, deformation rate, damage criteria, material flow, etc. The technological process can be further optimized based on simulation results [8, 9]. For material flow analysis, sophisticated approach was chosen. By means of electron backscattering diffraction (EBSD), the texture of cold-drawn tubes was observed in cylindrical coordinates with respect to the drawing direction. Different grain orientations have different forming abilities. It is assumed that material with an optimal texture achieves high formability. Sample analysis for the EBSD method is very demanding and time consuming. We try to find a connection between the development of the texture and the stress state during plug drawing and hollow sinking process by rotation of the body-centered K8 grid (BBC). The cognition of this process will make it possible to achieve a tube with the optimum texture for cold drawing process. According to the literary overview, there has been little attention focused on this topic. This issue was solved in the works [10, 11]. The change of grain orientation by means of a tensile or compress stress was explained according to the scheme in Fig. 2. When the [100]–[110] boundary

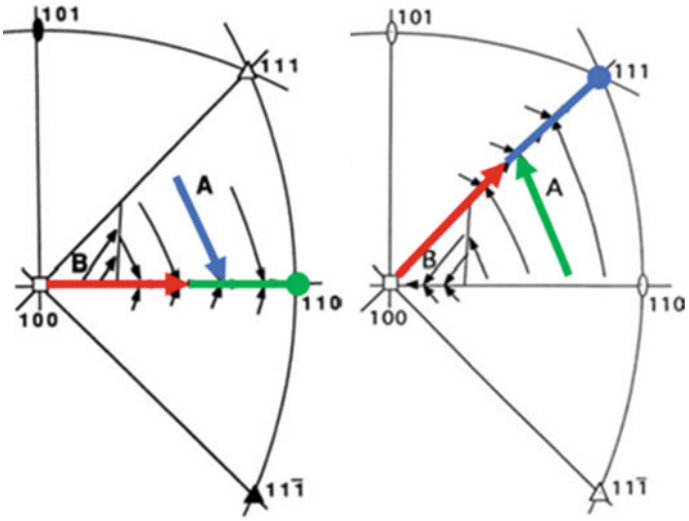


Fig. 2 Lattice rotation for BCC crystals: in tension (left); in compression (right). (Color figure online)

is reached, the combined slip in the [11–1] and [111] directions will cause rotation toward the [110] orientation, which is the stable end orientation (Fig. 2a). For a BCC crystal with pencil glide slip systems, the crystal atoms (CA) rotates away from the active slip direction. If the CA lies in region A, it will end up rotating toward the [111] end stable orientation (Fig. 2b), whereas if the CA lies initially in region B, it will rotate toward the [100] end orientation [12].

2 Material, Simulation, and Experiment

Technological exams were carried out on drawing bench TS 400. The used material was of grade E235 (Ø22 × 1.25 → Ø18 × 0.9 mm). The output diameter of the die land was 18 mm. The plug with outer diameter of 16.2 mm was used to achieve the required wall thickness. The outer diameter and the wall thickness were measured immediately after the pass. After that, the hollow sinking pass (Ø18 × 0.9 → Ø12 × 0.95 mm) which was carried out on drawing bench TS 3P–125 was selected from the same technological process. The output diameter of the die land was 12 mm. During the drawing process, the oil was being injected constantly. The outside diameter and the wall thickness of the tube were measured immediately. Forming tools were created in CAD program according to drawing setting and they were imported into the software DEFORM-3D with suitable file. Forming tools were defined as rigid objects. The tube was defined as a plastic object, which is suitable for modeling cold forming processes under certain conditions. In order to shorten the calculation

time, it is possible to use the 1° symmetry for the modeled domain. The tube was defined by FEM brick mesh. The wall thickness was described by ten elements due to high precision. Material data were defined by means of tensile tests. The tensile test defines the true strain to only $\varepsilon = 0.2$. The curve of flow stress was calculated by extrapolation to deformation $\varepsilon = 0.7$ according to [13]. This value is typical for cold-drawn tubes. The material temperature was 20 °C and no heat transfer between the material and the tools was considered. The friction boundary condition between the feedstock and the tools has been estimated according to a plant trial during which we recorded the electrical power of the bench and calculated the corresponding drawing force. In Table 1, there is a comparison of drawing force obtained from the plant trial and from DEFORM-3D simulation. A good agreement between experimental and simulation results confirmed that the material data and the friction coefficient were estimated correctly and also a good agreement between calculated dimensions and measured dimensions from technology has been achieved (Tables 2 and 3). The FEM formulation was of a Lagrangian incremental type. The drawing carriage was given the drawing velocity of $v = 400$ mm/s (as in technology). The results were evaluated in postprocessor DEFORM-3D in a steady state of the simulation (Eulerian point of view), which inherently oscillated due to the numerical nature of the model. Particular areas were described according to the cylindrical coordinate system for transparent analysis $[R, \theta, Z]$ (Fig. 3).

The crystallographic orientation of grains with individual orientations was examined by means of the EBSD method. The samples were taken from the longitudinal section of the tube. ESBD maps were acquired on an area ~ 200 × 150 μm using

Table 1 Comparison of drawing force F

Drawing pass	Ft [kN]	Fs [kN]	Difference [kN]	Difference [%]	Friction coefficient
22 × 1,25 → 18 × 0,9	44	44.21	0.21	0.48	0.06
18 × 0,9 → 12 × 0,95	9	9.1	0.1	1.1	0.045

Table 2 Comparison of dimensions—Outer diameter (OD)

Drawing pass	ODt [mm]	ODs [mm]	Difference [mm]	Difference [%]
22 × 1,25 → 18 × 0,9	18	17.94	−0.06	−0.21
18 × 0,9 → 12 × 0,95	12,02	11.97	−0.05	−0.42

Table 3 Comparison of dimensions—Wall thickness (WT)

Drawing pass	WTt [mm]	WTs [mm]	Difference [mm]	Difference [%]
22 × 1.25 → 18 × 0.9	0.92	0.91	−0.01	−0.51
18 × 0.9 → 12 × 0.95	0.98	0.97	−0.01	−1.02

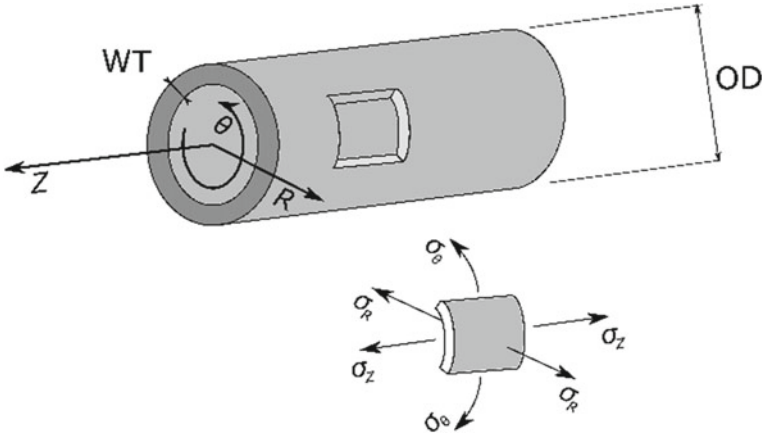


Fig. 3 Illustration of cylindrical cores on tube

a step size of 1 μm and applying a sample tilt angle of 70° at accelerating voltages 20 kV. The obtained EBSD data were processed by HKL Channel 5 software. The samples were also evaluated in cylindrical coordinate system.

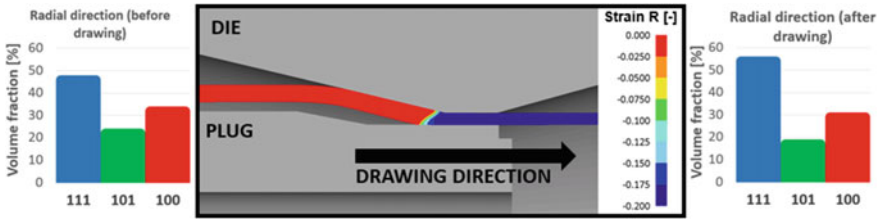


Fig. 4 Radial strain (middle) and texture before (left) and after plug drawing (right). (Color figure online)

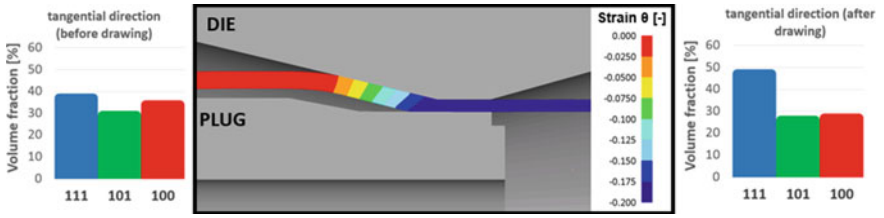


Fig. 5 Tangential strain (middle) and texture before (left) and after plug drawing (right). (Color figure online)

3 Results and Discussion

Figures 4, 5, and 6 show results cold drawn with fixed plug from tube dimensions Ø22 × 1.25 mm to the dimensions of Ø18 x 0,9 mm. In the radial direction, the plug reduced wall thickness (Fig. 4). The radial strain was calculated by the value $\varepsilon_R = -0.27$ after the deformation zone. According to the rotation scheme of lattice that compress stress has caused an increase in the volume fraction of grain orientation <111> at the expense of grain orientation <101> and <100>. In the tangential direction (Fig. 5) was recorded compress strain ($\varepsilon_\Theta = -0.19$) because of reduction of the outer diameter of the tube. The change in the volume fraction is similar to that in the radial direction. In the axial direction (Fig. 6), there is a dominant effect on the axial strain $\varepsilon_Z = 0.50$. The grain orientation in the axial direction rotated by effect tensile stress into a stable grain orientation <101> in the BCC grid. Figures 7, 8, and 9 show results of hollow sinking process from dimensions Ø18 × 0.9 mm to Ø12 × 0.95 mm. In the radial direction, low tensile strain values ($\varepsilon_R = 0.08$) and the absence of compress stress are observed, since it is a hollow sinking process and there is no reduction in the wall thickness (Fig. 7). The low tensile component caused a low roughen of wall thickness. Just in the radial direction was observed a considerable change of development in the grain orientation in comparing to the plug drawing. The tensile stress in the radial direction caused a roughen/thicken of wall thickness. We can declare, according to volume fracture of grain orientation, that tensile stress has an influence on increasing grain orientation (101) from (111) and

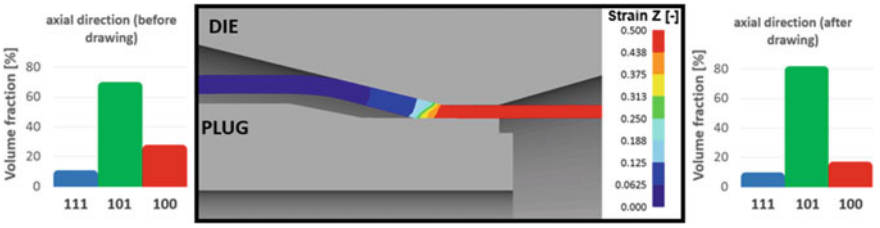


Fig. 6 Axial strain (middle) and texture before (left) and after plug drawing (right). (Color figure online)

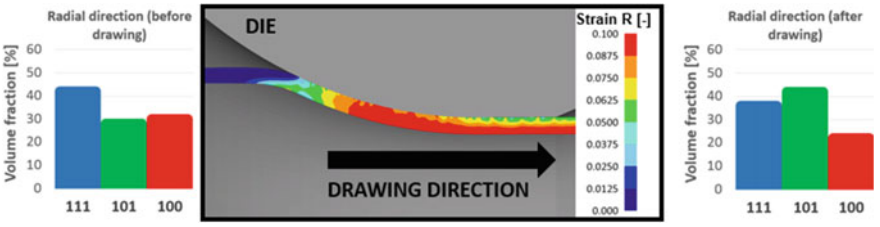


Fig. 7 Radial strain (middle) and texture before (left) and after hollow sinking (right). (Color figure online)

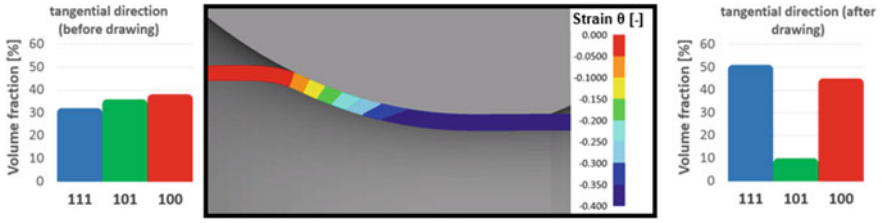


Fig. 8 Tangential strain (middle) and texture before (left) and after hollow sinking (right). (Color figure online)

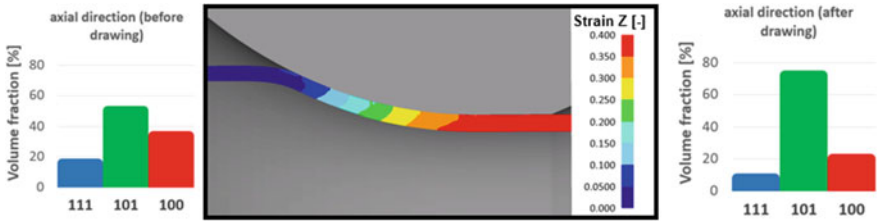


Fig. 9 Axial strain (middle) and texture before (left) and after hollow sinking (right). (Color figure online)

(100). In the tangential direction was the tube loaded by dominant compress strain $\varepsilon_\Theta = -0.44$ as illustrated in Fig. 8. The dominant effect of compress stress caused a reduction in the outer diameter of the tube after drawing. And also, compress stress caused increasing density of poles in texture (111). In the grain orientation (101), the density of poles was reduced. In the axial direction (Fig. 9) was the tube loaded by dominant tensile strain $\varepsilon_Z = 0.37$. The dominant tensile stress caused an increasing volume fraction of grain orientation (101) at the expense of grain orientation (111) and (100). The crystal plane (101) in the body-centered cubic (BCC) lattice of ferrite is most densely occupied by atoms and therefore the deformation occurs by sliding in this orientation.

On the basis of the results obtained, it is possible to create a simple model of texture development when cold steel tubes are drawn.

3.1 Scheme of Texture Development During Drawing with the Fixed Plug

Grain orientations in radial and tangential direction rotated by effect compress the stress into a stable orientation (111) in the BCC grid. Grain orientations in the axial direction rotated by effect tensile stress into a stable orientation (101) in the BCC grid (Fig. 10).

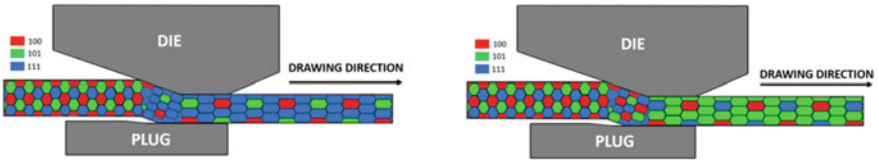


Fig. 10 Scheme of texture development during plug drawing in radial, tangential (left), and axial directions (right). (Color figure online)

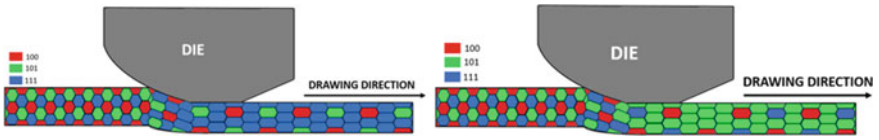


Fig. 11 Scheme of texture development during hollow sinking in tangential (left), axial, and radial directions (right). (Color figure online)

3.2 Scheme of Texture Development During Hollow Sinking Process

Grain orientations in tangential direction rotated by effect compress the stress into a stable orientation (111) in the BCC grid. Grain orientations in the axial direction rotated by effect tensile stress into a stable orientation (101) in the BCC grid. The texture development in radial direction depends on the change of wall thickness. If the wall thickness roughens/thickens, the orientation (101) will increase (Fig. 11).

4 Conclusions

We were able to find a connection between the development of the texture and the stress state during plug drawing and hollow sinking process by rotation of the body-centered K8 grid (BBC). We tried to estimate the value of stresses that cause rotation of the crystallographic grid, and thus change the percentage of the preferred crystallographic grid (or orientations) in the given direction of the cylindrical coordinate system. To simplify the concepts, we have developed models of texture development for plug drawing and hollow sinking process. Mastering this process will make the optimum texture for cold drawing process possible. Our next goal will be to confirm these models with further experiments.

Acknowledgments This work was supported by the Slovak Research and Development Agency under the contract No. APVV-15-0319 and No. APVV-18-0418.

References

1. Hyeong-Min H, Jun-Hwhan K, Sung-Ho K, Jong-Ryoul K (2018) Evaluation of workability on the microstructure and mechanical property of modified 9Cr-2 W steel for fuel cladding by cold drawing process and intermediate heat treatment condition. Metals 8, 193
2. Ridzon M (2016) Production technology for precision seamless steel tubes from the perspective of Microhardness changes. Eng Mater https://doi.org/10.4028/www.scientific.net/KEM.716.988
3. Neves F, O (2005) Residual stress on stainless steel a304 tube drawn with fixed plug. 18-th international congress of mechanical engineering, November 6–11, Ouro Preto, MG
4. Pernis R (2006) Calculation of wall thickness at tube sinking. Acta Metallurgica Slovaca 12:191–201
5. Loharkar PK, Pradhan MK (2017) Modeling and analysis of cold drawing process. Handbook of research on manufacturing process modeling and optimization strategies. https://doi.org/10.4018/978-1-5225-2440-3.ch003
6. Raji NA, Oluwole O (2011) Influence of degree of cold-drawing on the mechanical properties of low carbon steel. Mater Sci Appl. https://doi.org/10.4236/msa.2011.211208
7. Belyakov A et al (2004) Microstructure evolution in ferritic stainless steels during large strain deformation materials transactions 45(9):2812–2821
8. Boutenela F, Delhommeb M, Velaya V (2018) Finite element modelling of cold drawing for high precision tubes. Comptes rendus mécanique 348(8):665–677
9. Kuboki T, (2008) Effect of plug on levelling of residual stress in tube drawing. J Mater Process Technol. https://doi.org/10.1016/j.jmatprotec.2007.11.029
10. Parilák L, Burik P, Bella P, Kejzlar P (2018) Evolution of deformation texture in cold drawing of steel tubes using EBSD analysis and FEM simulation. IOP conference series: materials science and engineering. https://doi.org/10.1016/j.jmatprotec.2007.11.029
11. Parilák L, Burik P, Bella P, Kejzlar P (2018) Texture evolution cold drawing seamless steel tube. Proceedings of the expert conference ZP VVC, pp 121–127
12. Hosford WF (2010) Mechanical behavior of materials, Second edition, Cambridge university press, pp 121–123
13. Fischer Ch (2016) Derivation of $\sigma = K.\varepsilon^n$ curve from yield and UTS Data, Scientific Forming Technologies Corp, Manual Deform System Documentation

Dynamic Recrystallization Behaviors of 5083 Aluminum Alloys with Different Initial Microstructures Under Hot Compression



Sheng Ding and Jun Yanagimoto

Abstract To study the dynamic softening behaviors of 5083 aluminum alloys with different initial microstructures under hot compression, hot compression tests of extruded and homogenized specimens were conducted at a strain rate ranging from 0.1 to 10/s and deformation temperatures ranging from 350 to 450 °C. The obtained true stress–strain curves of homogenized specimens were lower than those of extruded specimens especially at the initial deformation stage, suggesting that the effect of different initial microstructures on flow stress is significant especially at the initial deformation stage. Electron backscatter diffraction (EBSD) was used to observe the microstructure evolution process. The characteristics of continuous dynamic recrystallization, particle-stimulated recrystallization, and discontinuous dynamic recrystallization were confirmed. The experiments deformed at the same temperature and strain rate but with different strains showed the transition from continuous to discontinuous recrystallization. The recrystallization mechanism of 5083 aluminum alloys with different initial microstructures is thus finally illustrated.

Keywords Aluminum alloy · Hot compression · Dynamic recrystallization · Microstructure evolution

1 Introduction

Hot working is an important method in manufacturing to change the mechanical and geometrical properties of metals and alloys, especially for non-heat treatable ones [1]. During hot working, dynamic softening behaviors including dynamic recovery (DRV) and dynamic recrystallization (DRX) contribute greatly in decreasing the flow stress and thus lowering the load in manufacturing. Generally, the metals and alloys with high stacking fault energy seldom experience dynamic recrystallization during hot working, because dynamic recovery is enough for reducing the stored energy during deformation [2]. Aluminum alloys which have high stacking fault

S. Ding (✉) · J. Yanagimoto
Department of Mechanical Engineering, The University of Tokyo, Hongo 7-3-1, Bunkyo 113-8656, Tokyo, Japan
e-mail: sheng.ding@cem.t.u-tokyo.ac.jp

© The Minerals, Metals & Materials Society 2021

G. Daehn et al. (eds.), *Forming the Future*, The Minerals, Metals & Materials Series,
https://doi.org/10.1007/978-3-030-75381-8_61

energy are exceptions. They were revealed to experience dynamic recrystallization, including different series: 2xxx [3], 5xxx [4], 6xxx [5], and 7xxx [6] series. However, the mechanism of how the dynamic recrystallization process evolves for metals and alloys with high stacking fault energy in the previous research is still unclear, as there should be a difference compared with conventional dynamic recrystallization process. Moreover, homogenized initial microstructure is usually adopted to study the dynamic recrystallization process because the simple initial microstructure makes the research much easier. It is more challenging and meaningful to study the dynamic recrystallization process starting with a complicated initial microstructure, such as an extruded or rolled one, as they more often appeared in the manufacturing process.

In this study, hot compression tests of extruded and homogenized specimens deformed at different strain rates and temperatures were conducted to obtain the true stress–strain curves and study the deformation behaviors. For understanding the dynamic recrystallization process during deformation, hot compression tests deformed at different strains were also conducted. The following electron backscatter diffraction (EBSD) analysis identified the different mechanisms of dynamic recrystallization process during deformation.

2 Experimental Procedures

A commercial extruded rod of A5083BE-O aluminum alloy was used to prepare the test specimens for compression tests, whose chemical composition is 0.1Si, 0.15Fe, 0.04Cu, 0.82Mn, 4.5 Mg, 0.09Cr, 0.03Zn, 0.01Ti, and balanced Al. Two types of test specimens with different initial microstructures (extruded and homogenized) were prepared. The extruded test specimens with 8 mm diameter and 12 mm height were directly cut from the extruded rod. For preparing the homogenized test specimens, billets with 20 mm diameter and 45 mm height were first cut from the original extruded rod. Then a homogenizing treatment including a cold compression up to a true strain of 0.3 and a furnace homogenizing at 520 °C for 4 h was applied to these billets. Finally, the homogenized test specimens with 8 mm diameter and 12 mm height were cut from these homogenizing treated billets. The initial microstructures of extruded and homogenized test specimens are shown in Fig. 1.

Hot compression tests were conducted by the Thermecmastor-Z machine. Different temperatures (350, 400, and 450 °C) and strain rates (0.1, 1, and 10/s) were selected to obtain flow curves under various experimental conditions. To reveal the microstructure evolution during deformation, hot compression tests at the same experimental conditions (400°C and 1/s) but with different strains (0.1, 0.5, 0.9) were conducted.

To identify the DRX grains in EBSD observations, grains with lower grain orientation spread (GOS) and within a desired grain size range are considered as recrystallized grains [7], while the other grains are thus to be deformed grains.

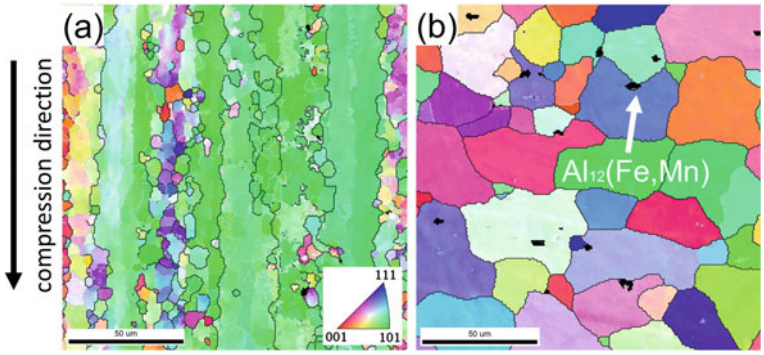


Fig. 1 Inverse pole figure (IPF) maps presenting the **a** extruded and **b** homogenized initial microstructures. (Color figure online)

3 Results and Discussion

3.1 True Stress–Strain Curves

True stress–strain curves of extruded and homogenized specimens obtained from hot compression tests are presented in Fig. 2. Flow stress decreases during deformation can be observed for all conditions, suggesting that dynamic recrystallization occurs during deformation. Flow stress level decreases with increasing temperature or decreasing strain rate. It is worth noting that at the initial deformation stage, as highlighted in dashed elliptical areas, the flow stress of extruded specimens is always higher, proving that different initial microstructures have a big influence on flow curves at the initial deformation stage. In contrast, at the final deformation stage, flow stress levels of extruded and homogenized specimens tend to be similar.

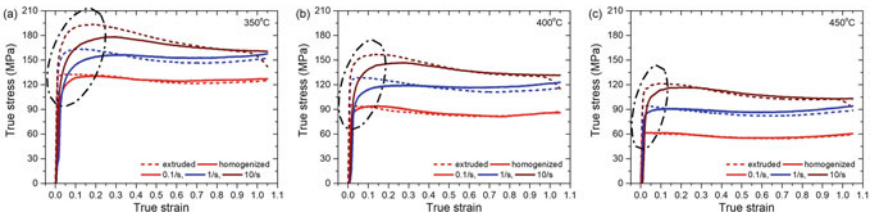


Fig. 2 True stress–strain curves deformed at **a** 350 °C, **b** 400 °C, and **c** 450 °C. (Color figure online)

Table 1 Arrhenius material constants

Initial microstructure condition	α MPa	n_{cst}	ln A_{cst} s^{-1}	Q kJ/mol
Extruded	0.008	6.80	35.71	205.46
Homogenized	0.008	7.43	36.83	211.26

3.2 Activation Energy of Deformation

Generally, the influence including both strain rate and temperature on flow behaviors can be expressed by only one parameter, i.e., the Zener–Hollomon parameter Z [8], as

$$Z = \dot{\varepsilon}\exp\left(\frac{Q}{RT}\right) \tag{1}$$

where R is the universal gas constant and Q is the activation energy of deformation (kJ/mol). Besides, the relationship between the Zener–Hollomon parameter Z and flow stress can be expressed by using an Arrhenius type equation as

$$Z = A_{cst}[\sinh(\alpha\sigma)]^{n_{cst}} \tag{2}$$

where α, n_{cst} , and A_{cst} are Arrhenius material constants. However, considering the flow stress range, the relationship between the Zener–Hollomon parameter Z and flow stress can also be expressed in power and exponential equations, respectively:

$$Z = \begin{cases} A'_{cst}\sigma^{n'_{cst}} & \alpha\sigma < 0.8 \\ A''_{cst}\exp(\beta\sigma) & \alpha\sigma > 1.2 \end{cases} \tag{3}$$

where A'_{cst}, n'_{cst}, A''_{cst} , and β are material parameters in different equation forms. These Arrhenius material constants can be obtained by regression analysis from stress–strain data, and they are summarized in Table 1. The activation energy of extruded specimens is smaller, suggesting that the dynamic recrystallization process of extruded specimens is easier compared with that of homogenized specimens. This can be confirmed by the later microstructure observations.

3.3 Microstructure Evolution

(1) Under different temperatures and strain rates

Under the whole experimental conditions, a fully recrystallized microstructure cannot be obtained, indicating that despite dynamic recrystallization, dynamic recovery is

still active and not replaced by dynamic recrystallization at the final deformation stage. When deformed at the same temperature with different strain rates, as shown in Fig. 3e, f for extruded specimens and Fig. 3m, n for homogenized specimens, a higher volume fraction of DRX can be observed under a lower strain rate condition, suggesting that a lower strain rate promotes the dynamic recrystallization process. When deformed at the same strain rate with different temperatures, as shown in Fig. 3e, g for extruded specimens and Fig. 3m, o for homogenized specimens, a higher volume fraction of DRX can be observed under a higher temperature condition, suggesting that a higher temperature promotes the dynamic recrystallization process. The reason for this is that a lower strain rate offers more time for energy accumulation

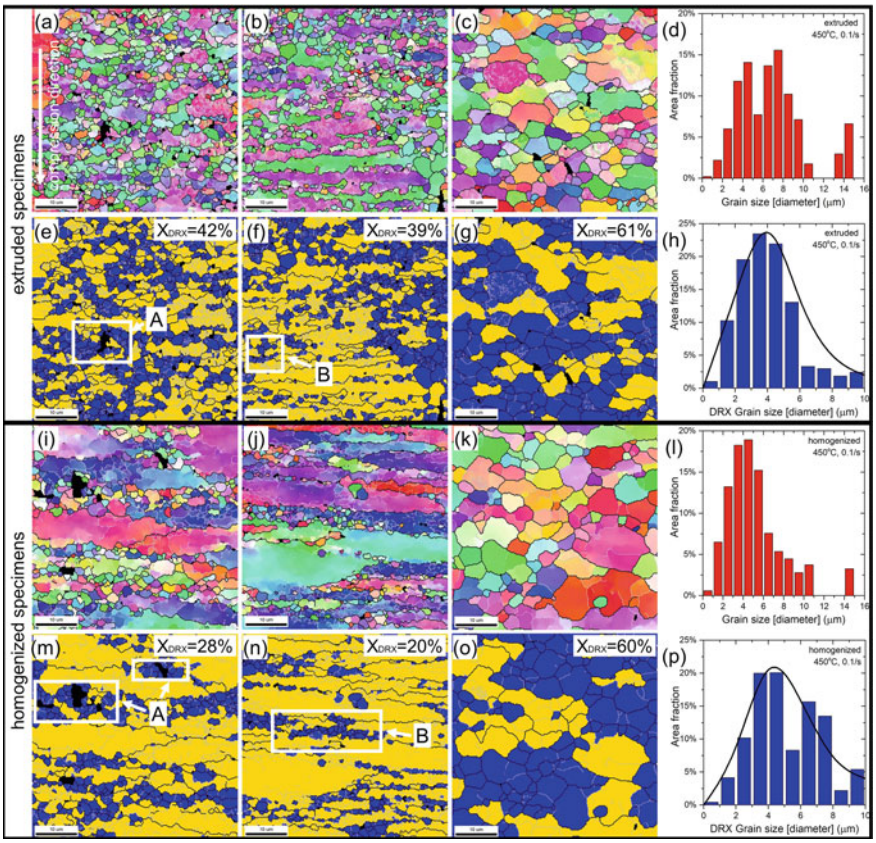


Fig. 3 IPF maps of extruded specimens deformed at **a** 350 °C, 0.1/s; **b** 350 °C, 10/s; and **c** 450 °C, 0.1/s, **e**–**g** corresponding to microstructures partitioned by GOS (grains in blue and yellow are recrystallized and deformed grains, respectively). IPF maps of homogenized specimens deformed at **i** 350 °C, 0.1/s; **j** 350 °C, 10/s; and **k** 450 °C, 0.1/s, (m-o) corresponding to microstructures partitioned by GOS. **d**, (l) grain size distributions of extruded and homogenized specimens deformed at 450 °C, 0.1/s, respectively. **h**, (p) grain size distributions of DRX grains of extruded and homogenized specimens deformed at 450 °C, 0.1/s, respectively. (Color figure online)

and a higher temperature provides more mobility of grain boundary, which both can enhance the dynamic recrystallization process [9].

It is worth noting that when the Zener–Hollomon parameter value Z is relatively low, which means dynamic recrystallization is more active, as shown in Fig. 3c, k for extruded and homogenized specimens, and no big differences between these two deformed microstructures can be observed, especially when compared with Fig. 3a, i, or b, j. The reason is that the average grain sizes of recrystallized grains for extruded and homogenized specimens are almost the same, as compared in Fig. 3h, p, i.e., initial microstructure has less effect on DRX grain size. Besides, when the volume fraction of DRX is relatively high, DRX grains become dominant. As a result, the grain size distributions of compressed microstructures, although start with different initial microstructures, are almost the same, as shown in Fig. 3d, i.

(2) Under different strains at the same temperature and strain rate

To reveal the microstructure evolution during a specific deformation process, compression tests at the same temperature and strain rate but with different strains were conducted including the major deformation stages from initial deformation stage (before critical strain, $\varepsilon = 0.1$), intermediate deformation stage (after critical strain, half of total strain, $\varepsilon = 0.5$) to final deformation stage (approach total strain, $\varepsilon = 0.9$).

At the initial deformation stage, as shown in Fig. 4a, d, no recrystallized grains can be observed in the homogenized specimen, while just a few recrystallized grains can

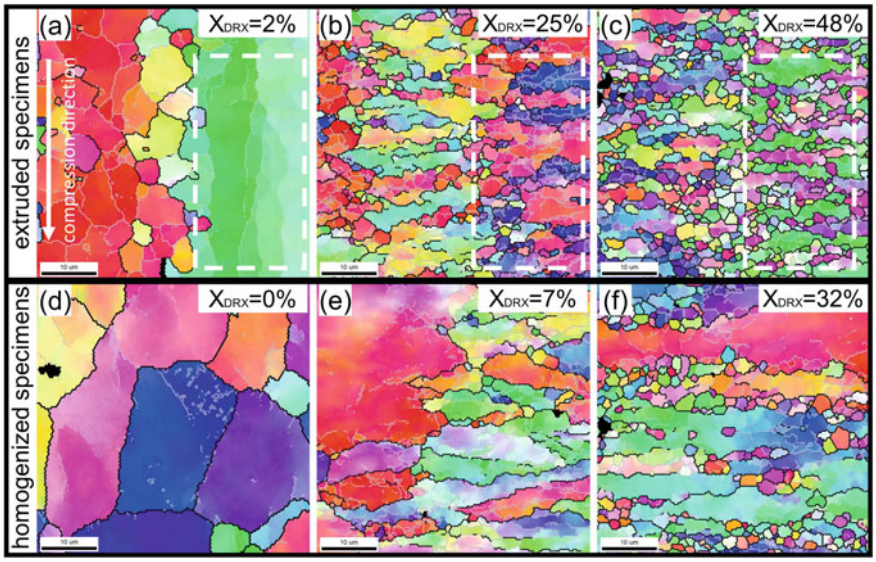


Fig. 4 IPF maps of extruded specimens deformed at 400 °C, 1/s with a true strain of **a** 0.1, **b** 0.5, **c** 0.9. IPF maps of homogenized specimens deformed at 400 °C, 1/s with a true strain of **d** 0.1, **e** 0.5, **f** 0.9. (Color figure online)

be observed in the extruded specimen. Sub-grain boundaries start to generate within the original grains. And the original grain boundaries become serrated with further compression. When the stored deformation energy is enough for dynamic recrystallization to occur, i.e., after critical strain, small equiaxed recrystallized grains can be observed, as shown in Fig. 4b, e. At the final deformation stage, a partially recrystallized microstructure including pancaked deformed grains and equiaxed recrystallized grains is observed for both extruded and homogenized specimens, as shown in Fig. 4c, f. And the recrystallized volume fraction of extruded specimen is always higher than that of homogenized specimen.

Besides, from the crystallographic directions shown in the IPF maps of extruded specimens, the prior elongated structure can still be distinguished, as shown in the dashed frames highlighted in Fig. 4a–c, and the similar colors in these areas suggest that these pancaked deformed grains are originated from a same elongated grain.

3.4 *Mechanism of Dynamic Recrystallization with Different Initial Microstructures*

Figure 5 presents the dynamic recrystallization process of extruded and homogenized specimens during compression. Intermetallic particles exist in both extruded and homogenized specimens. During deformation, dislocation density and misorientation can easily increase around these particles since they do not deform. As a result, recrystallized grains occur much more easily at these places (particle-stimulated recrystallization, PSN-DRX) [10], as shown in region A in Fig. 3e, m.

For the extruded specimens, its initial microstructure mainly consists of large elongated grains and small equiaxed grains. Sub-grain structures already exist within

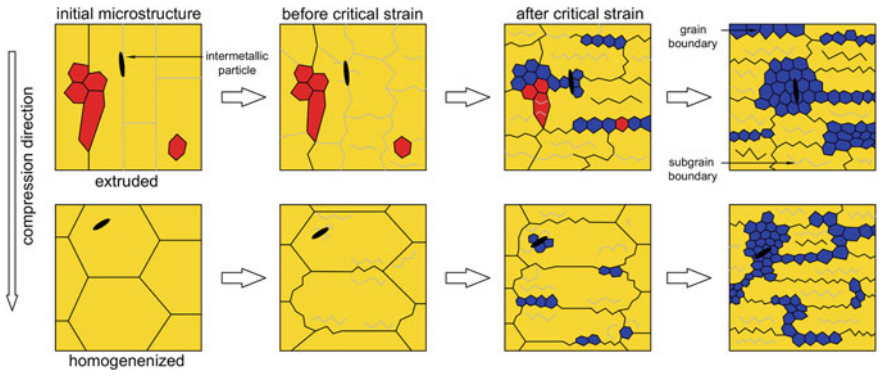


Fig. 5 Illustration of dynamic recrystallization process for A5083 aluminum alloys of extruded and homogenized specimens (Yellow grains: original grains/deformed grains; red grains: small grains exist in extruded initial microstructure; blue grains: recrystallized grains). (Color figure online)

elongated grains, some of these sub-grain boundaries progressively evolve to high-angle grain boundaries during deformation, and thus divide the original large elongated grain into pancaked deformed grains. Meanwhile, some of those sub-grains boundaries transfer to become recrystallized grains by progressive lattice rotation (continuous dynamic recrystallization, cDRX) [11]. With further deformation, grain boundaries of pancaked deformed grains become serrated, supporting a potential area for recrystallization by grain boundary bulging (discontinuous dynamic recrystallization, dDRX) [2], as shown in region B in Fig. 3f.

For the homogenized specimens, its initial microstructure is simple with only homogenized grains. There are almost no sub-grain structures within its initial microstructure. When deformation starts, sub-grain structures generate, especially near the original grain boundaries and triple junctions. With further deformation, original grains become pancaked, and their grain boundaries become serrated. sub-grain structures at these serrated grain boundaries and triple junctions can transform into new grains, as shown in the region B in Fig. 3n.

To conclude, sub-grain structures transfer to high-angle grain boundaries by cDRX, and further compression creates serrated grain boundaries, these serrated grain boundaries together with the areas around particles and triple junctions offer potential areas for dDRX. More sub-grain structures in extruded specimens make the dynamic recrystallization process faster than in homogenized specimens.

4 Conclusions

Hot compression tests of extruded and homogenized specimens were conducted at different strain rates, temperatures, and strains to study deformation behaviors and dynamic recrystallization process of 5083 aluminum alloy under different initial microstructures. The major conclusions can be summarized as follows.

(1) Flow stress of extruded specimens during deformation is always higher than that of homogenized specimens, especially at the initial deformation stage, showing the effect of different initial microstructures on flow stress.
(2) Microstructural observations confirmed the occurrence of dynamic recrystallization including particle-stimulated, continuous, and discontinuous dynamic recrystallization. Besides, the dynamic recrystallization process with different initial microstructures was illustrated.

References

1. Ding S, Khan SA, Yanagimoto J (2018) Constitutive descriptions and microstructure evolution of extruded A5083 aluminum alloy during hot compression. Mater Sci Eng A 728:133–143
2. Sakai T, Belyakov A, Kaibyshev R, Miura H, Jonas JJ (2014) Dynamic and post-dynamic recrystallization under hot, cold and severe plastic deformation conditions. Prog Mater Sci 60:130–207
3. Huang X, Zhang H, Han Y, Wu W, Chen J (2010) Hot deformation behavior of 2026 aluminum alloy during compression at elevated temperature. Mater Sci Eng A 527:485–490
4. Jeong HT, Han SH, Kim WJ (2019) Effects of large amounts of Mg (5–13 wt%) on hot compressive deformation behavior and processing maps of Al-Mg alloys. J Alloys Compd 788:1282–1299
5. Zhang H, Li L, Yuan D, Peng D (2007) Hot deformation behavior of the new Al–Mg–Si–Cu aluminum alloy during compression at elevated temperatures. Mater Charact 58(2):168–173
6. Rokni MR, Zarei-Hanzaki A, Roostaei AA, Abedi HR (2011) An investigation into the hot deformation characteristics of 7075 aluminum alloy. Mater Des 32(4):2339-2344
7. Krämer T, Eisenhut L, Germain L, Rupp D, Detemple E, Motz C (2018) Assessment of EBSD analysis and reconstruction methods as a tool for the determination of recrystallized fractions in hot-deformed austenitic microstructures. Metall Mater Trans A 193:108873
8. McQueen HJ, Spigarelli S, Kassner S, Evangelista E (2016) Hot deformation and processing of aluminum alloys. CRC Press
9. McQueen HJ (2004) Development of dynamic recrystallization theory. Mater Sci Eng A 203-208
10. Robson JD, Henry DT, Davis B (2009) Particle effects on recrystallization in magnesium-manganese alloys: particle-stimulated nucleation. Acta Mater 57(9):2739-2747
11. Jata KV, Semiatin SL (2000) Continuous dynamic recrystallization during friction stir welding of high strength aluminum alloys. Scr Mater 43(8):743-749

Application of Barlat's Yld 2000-2d Yield Criterion to Predict the Anisotropic Response of Stainless Steel



Mauricio Vicente Donadon and José Divo Bressan

Abstract The plastic anisotropic response of stainless steel materials is investigated in this paper by using Barlat's Yld 2000-2d yield criterion. A new set of anisotropy coefficients is proposed and calibrated based on material experimental data. The new set of coefficients for the Lankford anisotropy coefficient, normalized yield stress, and equal biaxial stress were numerically obtained using the Newton–Raphson method. Study cases for AISI 409L and AISI 430 materials are presented and discussed. Correlations between predictions and experimental results indicate that Barlat's yield stress criterion and plastic stress potential for stainless materials are not coincident. Hence, the Barlat's non-associate flow rule gives better fitting with the experimental Lankford's coefficient of anisotropy results.

Keywords Stainless steel · Plastic anisotropy · Barlat's Yld 2000-2d yield criterion

1 Introduction

Anisotropy is a very commonly observed phenomenon whereby properties of material vary, depending on the direction along which they are measured. This obviously cannot apply to volumetric properties like density or specific heat, but virtually all other types of behaviour are susceptible to being anisotropic [1]. These can even include some chemical behaviour such as corrosion rates, but for the sake of simplicity, within the paper content it will be restricted to mechanical properties, particularly the yielding behaviour of metals. In general, the materials in the family of stainless steel such as austenitic and ferritic grades are isotropic materials. The existence of anisotropy behaviour in the stainless steel plates by a small amount is unavoidable due to the manufacturing process of a plate such as rolling. For instance,

M. V. Donadon (✉)
Instituto Tecnológico de Aeronáutica-ITA, São José dos Campos, SP, Brazil
e-mail: donadon@ita.br

J. D. Bressan
Universidade do Estado de Santa Catarina-UDESC, Joinville, SC, Brazil
e-mail: josedivo.bressan@udesc.br

© The Minerals, Metals & Materials Society 2021

G. Daehn et al. (eds.), *Forming the Future*, The Minerals, Metals & Materials Series,
https://doi.org/10.1007/978-3-030-75381-8_62

the mechanical properties of Duplex stainless steel vary significantly with respect to the different directions due to the presence of both ferrite and austenite phases in its matrix [2, 3], where the orientation of the grains on the rolled plate plays a major role in the variation of mechanical properties. There are two types of anisotropy possibilities in any material, i.e. crystallographic anisotropy produced by severe plastic deformation during the rolling and the mechanical fibering due to the second phases present in the direction of working.

In order to address yield modelling in metals, several yield criteria can be found in the open literature. For instance, Tresca yield criterion [4], von Mises yield criterion [5], and modified versions of von Mises yield criterion proposed by Hershey [6] and Hosford [7] are widely used for isotropic materials. Despite their accuracy to predict yielding behaviour of isotropic materials in general, they do not account for material directionality effects such as changes in mechanical properties induced by the rolling process, where high anisotropy can be observed in the longitudinal and transverse directions of the elongated grains. The first theoretical studies on yield modelling of anisotropic material date back to 1948 where Rodney Hill [6] proposed a yield stress criterion for anisotropic material with orthotropic anisotropy in metal forming operations. The criterion was further improved in [7] to accommodate metals with normal anisotropy $R < 1$, introducing seven anisotropy parameters in the yield function. Bassani [8] proposed a different form of yield criterion for anisotropic polycrystalline metals which covers a wide range of transversely isotropic properties or planar isotropy, but material with normal anisotropy. Ferron et al. [9] proposed a parameterized yield stress criterion for planar anisotropy, which involves nine parameters for describing the plastic anisotropy of sheet metals. Barlat et al. [10] presented, in 1997, a phenomenological yield stress function asserting that it was more suitable for anisotropic aluminium alloy sheets, the Yld96 yield stress function. Based on Hershey [6] and Hosford [7] yield stress criteria for isotropic material and on Yld96 yield stress criterion, Barlat et al. [11] proposed the Yld 2000-2d anisotropic yield stress criterion applied to sheet metal forming under plane stress condition for pressure-independent metals exhibiting orthotropic anisotropy.

The present paper investigates the plastic anisotropic response of stainless steel materials by using Barlat's Yld 2000-2d yield criterion [11] and the correspondent Barlat's non-associated flow rule to calculate the Lankford's coefficient of anisotropy, r_θ values. Comparisons between theoretical predictions and experimental results for AISI 409L and AISI 430 are presented and conclusions are drawn.

2 Barlat's Yld 2000-2d Anisotropic Yield Stress Criterion

The Barlat's Yld 2000-2d anisotropic yield stress criterion can be written in terms of Cauchy stress tensor components for plane stress conditions as follows:

$$\varphi(\sigma_{xx},\ \sigma_{yy},\ \tau_{xy}) = \frac{1}{2^m}\left|a_1\,\sigma_{xx} + a_2\,\sigma_{yy} + \left[\left(a_3\,\sigma_{xx} - a_4\,\sigma_{yy}\right)^2 + \left(2a_8\tau_{xy}\right)^2\right]^{1/2}\right|^m + \\ + \frac{1}{2^m}\left|a_1\,\sigma_{xx} + a_2\,\sigma_{yy} - \left[\left(a_3\,\sigma_{xx} - a_4\,\sigma_{yy}\right)^2 + \left(2a_8\tau_{xy}\right)^2\right]^{1/2}\right|^m + \\ + \left|\left(a_5\,\sigma_{xx} - a_6\,\sigma_{yy}\right)^2 + \left(2a_7\tau_{xy}\right)^2\right|^{m/2} = 2\bar{\sigma}^m = 2\sigma_o^m(1+\bar{\varepsilon}/\varepsilon_o)^{n\,m} \quad (1)$$

where a_i are the coefficients of plastic anisotropy. Assuming Barlat's yield stress criterion as the flow stress potential, the strain increments $d\varepsilon_{ij}$ can be calculated from the associated flow rule as [12]

$$d\varepsilon_{ij} = d\lambda\,\frac{\partial\,\varphi\left(\sigma_{xx},\sigma_{yy},\tau_{xx}\right)}{\partial\,\sigma_{ij}} \quad (2)$$

where σ_{ij} are the stress components and $d\varepsilon_{ij}$ are the strain increments in the principal anisotropy directions: $d\varepsilon_{xx}$ is in the rolling direction RD and $d\varepsilon_{yy}$ is in the transverse direction TD. For a standard tensile test specimen cut at angle θ to RD, under the uniaxial tensile stress σ_θ in x′-axis of the specimen tensile direction and y′-axis of the width direction, for plane stress condition, the stress components and strain increments in the anisotropy (x,y)-axis or (RD,TD)-axis can be obtained through a coordinate transformation matrix $T(\theta)$ that relates the global (specimen) stresses to local stresses in the anisotropy axes (x,y). By doing so, assuming associate flow rule and applying the Euler's identity theorem for a homogeneous stress function of degree 'm' to the Barlat's yield stress criterion function $\varphi\left(\sigma_{xx},\sigma_{yy},\tau_{xy}\right)$ one can demonstrate that the Lankford's coefficient of anisotropy can be calculated by

$$r_\theta = \frac{d\varepsilon_{widh}}{d\varepsilon_{thickness}} = -\frac{sen^2\theta + \left(d\varepsilon_{yy}/d\varepsilon_{xx}\right)\cos^2\theta - 2\left(d\varepsilon_{xy}/d\varepsilon_{xx}\right)sen\theta\cos\theta}{1+\left(d\varepsilon_{yy}/d\varepsilon_{xx}\right)} \\ = \frac{2m\,\bar{\sigma}^m}{\left[1+\left(d\varepsilon_{yy}/d\varepsilon_{xx}\right)\right]\sigma_\theta\frac{\partial\,\varphi}{\partial\,\sigma_{xx}}} - 1 \quad (3)$$

In addition, the balanced biaxial coefficient of anisotropy is calculated by

$$r_b = \frac{d\varepsilon_{TD}}{d\varepsilon_{RD}} = \frac{d\varepsilon_{yy}}{d\varepsilon_{xx}} = \frac{\partial\varphi/\partial\sigma_{yy}}{\partial\varphi/\partial\sigma_{xx}} \quad (4)$$

For a tensile test specimen under a uniaxial tensile stress σ_θ, the equivalent stress can be expressed as $\bar{\sigma} = A\,\sigma_\theta$, where $A = \left\{2^m F + |B + C|^m + |B - C|^m\right\}^{1/m}/2^{1+1/m}$ and the Lankford's coefficient of anisotropy calculated from the associate flow rule is simplified to

$$r_\theta = \frac{2m\, A^m \sigma_\theta^{m-1}}{\frac{\partial \varphi}{\partial \sigma_{xx}} + \frac{\partial \varphi}{\partial \sigma_{yy}}} - 1 \tag{5}$$

The derivatives of the yield stress function $\varphi\left(\sigma_{xx}, \sigma_{yy}, \tau_{xy}\right)$ are obtained from Eq. (1), including the derivative sign for the modulus function, and are obtained as

$$\begin{aligned}\frac{\partial \varphi}{\partial \sigma_{xx}} &= mE\sigma_\theta^{m-1} a_5 + \frac{m}{2^m}|B + C|^{m-1}\{a_1 + D\, a_3\}\sigma_\theta^{m-1} \\ &\quad + \frac{m}{2^m}|B - C|^{m-2}(B - C)\{a_1 - D\, a_3\}\sigma_\theta^{m-1}\end{aligned} \tag{6}$$

$$\begin{aligned}\frac{\partial \varphi}{\partial \sigma_{yy}} &= mE\sigma_\theta^{m-1}(-a_6) + \frac{m}{2^m}|B + C|^{m-1}\{a_2 - D\, a_4\}\sigma_\theta^{m-1} \\ &\quad + \frac{m}{2^m}|B - C|^{m-2}(B - C)\{a_2 + Da_4\}\sigma_\theta^{m-1}\end{aligned} \tag{7}$$

Finally, substituting Eqs. (6) and (7) into Eqs. (4) and (5), the generalized Lankford's coefficient of anisotropy r_θ and the balanced biaxial coefficient of anisotropy r_b are calculated by

$$r_\theta = \frac{2^m F + |B + C|^m + |B - C|^m}{2^m E(a_5 - a_6) + |B + C|^{m-1}(a_1 + a_2 + D_{34}) + |B - C|^{m-2}(B - C)(a_1 + a_2 - D_{34})} - 1 \tag{8}$$

$$r_b = \frac{2^m (a_5 - a_6)^m + |(a_1 + a_2) + |a_3 - a_4||^m + |G|^m}{2^m (a_5 - a_6)^{m-1} a_5 + |(a_1 + a_2) + |a_3 - a_4||^{m-1}(a_1 + a_3) + |G|^{m-2} G\,(a_1 - a_3)} - 1 \tag{9}$$

where

$$B = a_1 \cos^2\theta + a_2 sen^2\theta,\; C = \left[\left(a_3 \cos^2\theta - a_4\, sen^2\theta\right)^2 + 4a_8^2\, sen^2\theta \cos^2\theta\right]^{1/2} \tag{10a}$$

$$D = \left(a_3 \cos^2\theta - a_4\, sen^2\theta\right)/C,\; D_{34} = D(a_3 - a_4) \tag{10b}$$

$$E = \left|\left(a_5 \cos^2\theta - a_6\, sen^2\theta\right)^2 + 4a_7^2\, sen^2\theta \cos^2\theta\right|^{(m/2)-1}\left(a_5 \cos^2\theta - a_6\, sen^2\theta\right) \tag{10c}$$

$$F = \left|\left(a_5 \cos^2\theta - a_6 sen^2\theta\right)^2 + 4a_7^2\, sen^2\theta \cos^2\theta\right|^{m/2} \tag{10d}$$

$$G = (a_1 + a_2) - |a_3 - a_4| \tag{10e}$$

For a uniaxial tensile test specimen under loading at 0° RD, the stress components are $\sigma_{xx} = \sigma_0$ and $\sigma_{yy} = \tau_{xy} = 0$, where σ_0 is the yield stress. Then, the Barlat's Yld 2000-2d anisotropic yield stress criterion, Eq. (1), is further reduced to

$$|2\,a_5\,|^m + |a_1 + a_3\,|^m + |\,a_1 - a_3\,|^m = 2^{1+m}\left(\frac{\bar{\sigma}}{\sigma_o}\right)^m \tag{11}$$

Imposing the condition that the equivalent stress at any yielding stress condition in uniaxial tensile test at nominal strain rate condition should be $\bar{\sigma} = \sigma_o(1 + \bar{\varepsilon}/\varepsilon_o)^n$, thus

$$|2\,a_5\,|^m + |a_1 + a_3\,|^m + |\,a_1 - a_3\,|^m - 2^{1+m}(1 + \bar{\varepsilon}/\varepsilon_o)^n = 0 \tag{12}$$

However, it is possible to assume a different plastic stress or strain condition, as for example $\bar{\sigma} = \sigma_b$ at balanced biaxial stress state. For a sheet metal specimen under plane stress and equal biaxial stress condition and aligned to RD, $\sigma_{xx} = \sigma_{yy} = \sigma_b$ *and* $\tau_{xy} = 0$, hence Eq. (1) becomes

$$2^m(a_5 - a_6)^m + |(a_1 + a_2) + |a_3 - a_4|\,|^m + |\,(a_1 + a_2) - |a_3 - a_4|\,|^m = 2^{1+m}\left(\frac{\bar{\sigma}}{\sigma_b}\right)^m \tag{13}$$

Assuming that the equivalent stress is equal to the current flow stress, $\bar{\sigma} = \sigma_o(1 + \bar{\varepsilon}/\varepsilon_o)^n$, at current yielding condition, thus the normalized equi-biaxial stress is calculated by

$$\frac{\sigma_b}{\sigma_o} = \frac{2^{1+1/m}(1 + \bar{\varepsilon}/\varepsilon_o)^n}{\left\{2^m(a_5 - a_6)^m + |(a_1 + a_2) + |a_3 - a_4|\,|^m + |\,(a_1 + a_2) - |a_3 - a_4|\,|^m\right\}^{1/m}} \tag{14}$$

For tensile test specimens under uniaxial tensile stress σ_θ, the equivalent stress of Eq. (1) is simplified to $\bar{\sigma} = A\,\sigma_\theta$. Consequently, the normalized yield stress at any angle θ to RD is

$$\frac{\sigma_\theta}{\sigma_o} = \frac{\left\{|2\,a_5\,|^m + |a_1 + a_3\,|^m + |\,a_1 - a_3\,|^m\right\}^{1/m}}{\left\{2^m F + |\,B + C\,|^m + |\,B - C\,|^m\right\}^{1/m}} \tag{15}$$

For a specimen under pure shear stress test, the stress components are $\sigma_{xx} = \sigma_{yy} = 0$ and $\tau_{xy} = \tau_o = k$, where $\tau_0 = k$ is the material shear yield stress. Then, Eq. (1) is reduced to

$$a_7 = \pm 2^{(1/m)-1}\frac{\sigma_o}{\tau_o} = \pm 2^{(1/m)-1}\frac{\sigma_o}{k} \tag{16}$$

2.1 Determination of the Anisotropic Coefficients a_i Values

In order to solve the set of nonlinear equations in terms of a_i, i=1,…8, Eqs. (8), (9), (12), (14), and (15) can be rearranged as follows:

$$s_o(a_i) = |2\,a_5\,|^m + |a_1 + a_3\,|^m + |\,a_1 - a_3\,|^m - 2^{1+m}(1+\bar{\varepsilon}/\varepsilon_o)^n = 0 \quad (17)$$

$$s_\theta(a_i,\sigma_\theta) = \frac{\left\{|2\,a_5\,|^m + |a_1 + a_3\,|^m + |\,a_1 - a_3\,|^m\right\}^{1/m}}{\left\{2^m F + |\,B + C\,|^m + |\,B - C\,|^m\right\}^{1/m}} - \frac{\sigma_{\theta\,\exp}}{\sigma_o} = 0 \quad (18)$$

$$s_b(a_i) = \frac{2^{1+1/m}(1+\bar{\varepsilon}/\varepsilon_o)^n}{\left\{2^m(a_5 - a_6)^m + |(a_1 + a_2) + |a_3 - a_4|\,|^m + |\,G\,|^m\right\}^{1/m}} - \frac{\sigma_{b\,\exp}}{\sigma_o} = 0 \quad (19)$$

$$r_\theta(a_i,\theta) = \frac{2^m F + |\,B + C\,|^m + |\,B - C\,|^m}{2^m E(a_5 - a_6) + |\,B + C|^{m-1}(a_1 + a_2 + D_{34}) + |B - C|^{m-2}(B - C)(a_1 + a_2 - D_{34})} - 1 - r_{\theta\,\exp} = 0 \quad (20)$$

$$r_b(a_i) = \frac{2^m(a_5 - a_6)^m + |(a_1 + a_2) + |a_3 - a_4|\,|^m + |G|^m}{|(a_1 + a_2) + |a_3 - a_4||^{m-1}(a_1 + a_3) + |G|^{m-2}G\,(a_1 - a_3) + 2^m(a_5 - a_6)^{m-1}a_5} - 1 - r_{b\,\exp} = 0 \quad (21)$$

This set of nonlinear equations can be rewritten in a compact matrix form given by Eq. (22)

$$\{\psi(\{a\})\}^T = \left\{ \{s_\theta(\{a\})\}^T \; \{r_\theta(\{a\})\}^T \; s_b(\{a\}) \; r_b(\{a\}) \right\} = \{0\}$$

$$\{a\}^T = \left\{ a_1 \; a_2 \; a_3 \; a_4 \; a_5 \; a_6 \; a_7 \; a_8 \right\} \quad (22)$$

where $\{s_\theta(\{a\})\} \in \mathbb{R}^p$, $\{r_\theta(\{a\})\} \in \mathbb{R}^q$; defining p and q as the number of experimental yield stresses and r-values of interest such that $(p+q) = 8$. According to Barlat recommendation [38] to calculate the coefficients of anisotropy a_i, the definition of the set of equations to be solved should have equal numbers of r-values and yield stresses, s-values, which are defined by the following parameters:

$$\{\psi(\{a\})\}^T = \left\{ s_o(\{a\}) \; s_{45^0}(\{a\}) \; s_{90^0}(\{a\}) \; r_o(\{a\}) \; r_{45^0}(\{a\}) \; r_{90^0}(\{a\}) \; s_b(\{a\}) \; r_b(\{a\}) \right\}$$
$$\{a\}^T = \left\{ a_1 \; a_2 \; a_3 \; a_4 \; a_5 \; a_6 \; a_7 \; a_8 \right\} \quad (23)$$

The linearization of the function $\{\psi(\{a\})\}$ about the point $\{a\}$ leads to

$$\{\psi(\{a\} + \{\delta a\})\} = \{\psi(\{a\})\} + [J(\{a\})]\{\delta a\} \quad (24)$$

where $[J(\{a\})]$ is the Jacobian matrix (of size 8×8) made up of the partial derivatives

$$J_{ij} = \frac{\partial \psi_i}{\partial a_j} \quad (25)$$

By setting $\{Z(\{a\} + \{\delta a\})\} = \{0\}$ and letting $\{a\} + \{\delta a\}$ be the improved solution, we find the following expression for the iterative predictor $\{\delta a\}$:

$$\{\delta a\} = [J(\{a\})]^{-1}\{\psi(\{a\})\} \tag{26}$$

In order to improve accuracy and achieve converge to solve convex unconstrained problems, a relaxation factor can be added to find the correction between successive iterations. For this case the new correction predictor can be rewritten as follows:

$$\{\delta a\} = \eta[J(\{a\})]^{-1}\{\psi(\{a\})\} \tag{27}$$

where $\eta = 1/2^N$ is the relaxation factor. N is an user-defined integer number defined within the interval $N \in [0, N_{\max}]$, where no general rule can be given for the choice of an optimum N and suitable values for a particular set of nonlinear equations are usually defined by using a trial and error procedure. The set of nonlinear equations are iteratively solved by using the following procedure:

1. Estimate the initial solution vector $\{a\}$;
2. Evaluate $\{\psi(\{a\})\}$.
3. Compute the Jacobian matrix $[J(\{a\})]$ from Eq. (25).
4. Compute $\{\delta a\}$ from Eq. (12).
5. Let $\{a\} \leftarrow \{a\} + \{\delta a\}$ and repeat steps 2–5 until $\|\{\delta a\}\| < \varepsilon$, where ε is the assumed error tolerance.

3 Materials Anisotropy Parameters

The coefficients of plastic anisotropy, a_i, of Barlat's Yld 2000-2d yield criterion were calibrated based on material experimental data for simple uniaxial tension, biaxial stress, and compression in-plane tests available in the literature, and listed in Tables 1 and 2. The plastic anisotropy parameters of the stainless steels used to calibrate the

Table 1 Mechanical plastic anisotropy parameters of the stainless steels

Metal alloy	*Anisotropy coefficients, r-values* r_o r_{15} r_{30} r_{45} r_{60} r_{75} r_{90} r_b							
Steel AISI 409L [13]	1.58	1.68	1.61	1.93	2.46	2.54	2.49	0.90
Steel AISI 430 [13]	1.06	1.04	0.98	0.88	1.15	1.31	1.30	0.90

Table 2 Normalized yield stress of the stainless steels

Metal alloy	*Normalized yield stress, s-values* ($=\sigma_\theta/\sigma_o$ or σ_θ/σ_b) σ_o σ_{15} σ_{30} σ_{45} σ_{60} σ_{75} σ_{90} σ_b							
Steel AISI 409L [13]	0.908	0.915	0.931	0.952	0.962	0.959	0.936	1.00
Steel AISI 430 [13]	0.887	0.886	0.896	0.911	0.921	0.916	0.898	1.00

model were: Lankford's coefficient of anisotropy r-values, normalized tensile yield stress s-values ($=\sigma_\theta/\sigma_o$), and equal biaxial stress parameters r_b and σ_b.

4 Analyses and Discussion

Tables 3 and 4 show the calculated plastic anisotropy coefficients of Barlat's Yld 2000-2d yield stress criterion for the AISI 409L and AISI 430 stainless steels for different combinations of normalized yield stress (s-values) and anisotropy coefficients (r-values).

The results for AISI 409L and AISI 430 are plotted in Figs. 1 and 2, respectively, for different normalized yield stress (s-values) and anisotropy coefficients (r-values).

Figure 1a, e, f indicate a fairly good agreement between experimental and the predicted normalized yield stress and r-values obtained using the Barlat's Yld 2000-2d yield stress criterion for different theta values with respect to the rolling direction. Despite of a good agreement in terms of normalized stresses, a very poor correlation was found for the r-values depicted in Fig. 1b, c, d. This poor correlation indicates that the assumption of the yield stress criterion and the plastic flow stress potential functions does not hold for this kind of material due to its anisotropic nature. The same behaviour was also depicted in Fig. 2c–d for the AISI 430, where a significant discrepancy between the predicted r-values obtained using the Barlat's Yld 2000-2d yield stress criterion and the experimental results was found. Conversely, Fig. 2e, f show good agreement between the predicted and the experimental r-values but poor correlation between the predicted and experimental results in terms of s-values. This implies that additional experimental anisotropy parameters are required in order to improve the accuracy of the Barlat's Yld 2000-2d yield stress criterion for the AISI 409L and AISI 430 stainless steel alloys studied herein.

5 Concluding Remarks

A detailed study on the applicability of the Barlat's Yld 2000-2d yield stress criterion to predict the anisotropic behaviour of stainless steel alloys was presented herein. The main conclusions of the present work are listed as follows:

1. A new set of equations to calculate the Lankford's and equal biaxial coefficients of anisotropy (r-value), and the normalized yield stress (s-value) for uniaxial and equal biaxial stress testing, and plastic anisotropy a_i values were proposed to describe the Barlat's Yld 2000-2d yield stress criterion.
2. Results from the present study indicate the Barlat's Yld 2000-2d yield stress criterion and the plastic flow stress potential of examined stainless steels were not coincident. This implies that a non-associated plastic flow rule is required to describe the anisotropy parameters, r-values.

Table 3 The calculated plastic anisotropy coefficients of Barlat's Yld 2000-2d yield stress criterion $\varphi\,(\sigma_{xx},\ \sigma_{yy},\ \tau_{xy})$ for AISI 409L

Experim.	m	a_1	a_2	a_3	a_4	a_5	a_6	a_7	a_8
4 s + 4r	6	1.002668	0.814219	0.939474	0.938629	1.025273	1.033327	1.000546	0.877389
6 s + 2r	6	1.23189	−0.09101	0.976622	1.874141	0.756158	0.801293	0.984190	1.263480
7 s + 1r [a]	6	1.870454	−0.77238	0.334143	1.257714	0.296260	0.911328	0.977399	1.029339
7 s + 1r [b]	6	1.555577	−0.51133	0.006901	1.001280	0.453036	0.755077	0.786751	0.594560
3 s + 5r	6	1.338375	0.055217	0.860478	1.180594	0.784888	1.079154	0.971424	1.131844
2 s + 5r	6	0.711262	0.173284	1.483571	1.261118	0.793738	1.120401	0.786467	1.614420

Table 4 The calculated plastic anisotropy coefficients of Barlat's Yld 2000-2d yield stress criterion $\varphi\,(\sigma_{xx},\ \sigma_{yy},\ \tau_{xy})$ for AISI 430

Experim.	m	a_1	a_2	a_3	a_4	a_5	a_6	a_7	a_8
4 s + 4r	6	0.934720	0.839496	1.111037	1.111041	0.974158	0.999642	0.937283	1.121714
5 s + 3r	6	1.270937	0.350750	0.938187	1.283656	0.754091	1.075696	0.918650	1.191723
6 s + 2r	6	1.069910	0.096838	1.048180	1.872673	0.915595	0.877161	0.816077	1.474634
7 s + 1r	6	1.870454	−0.77238	0.334143	1.257714	0.296260	0.911328	0.977399	1.029339
1 s + 7r	6	−0.90022	2.451174	1.128144	0.936817	0.984731	−0.85149	1.416227	−2.45255
2 s + 6r	6	−0.99487	2.213079	0.754523	0.867442	1.076023	0.166716	0.856082	−1.34457

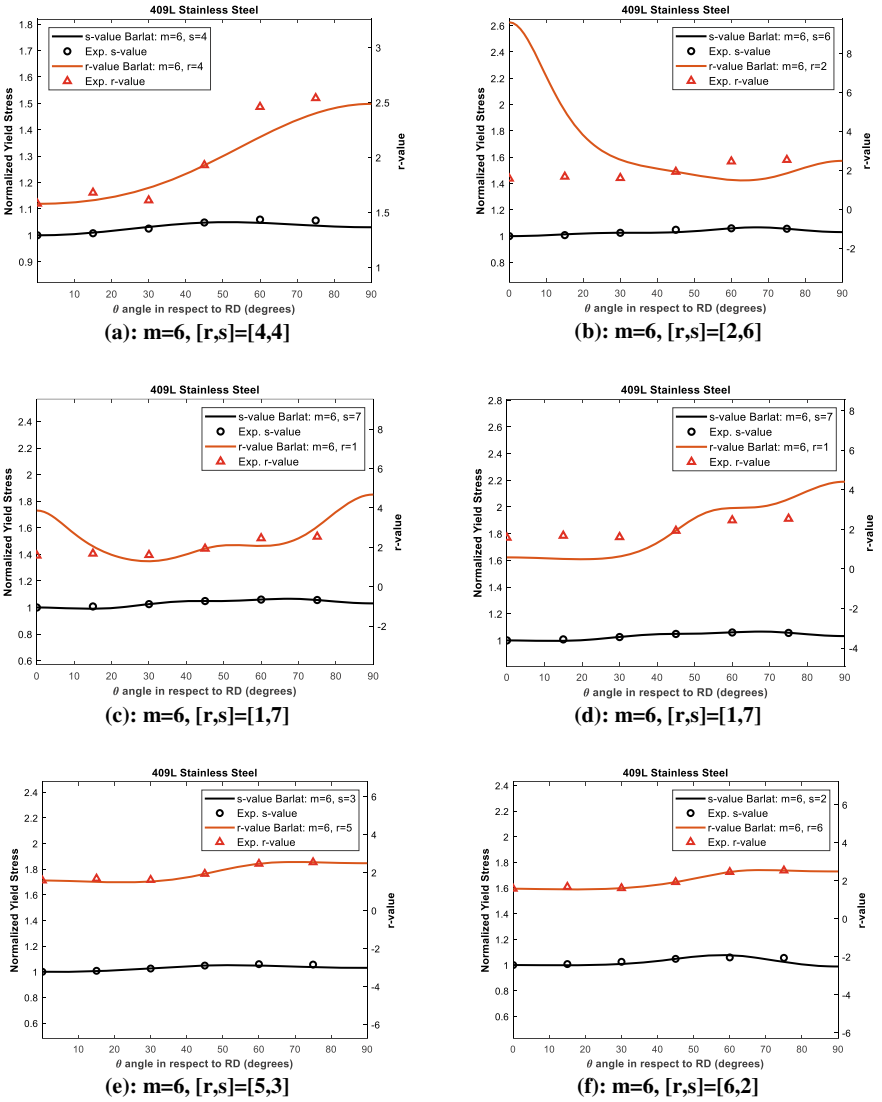


Fig. 1 Comparison of Barlat's Yld 2000-2d prediction curves with the experimental results for tensile tests of AISI 409L. (Color figure online)

3. Barlat's Yld 2000-2d stress function can be employed to characterize suitably both the yield stress criterion and the flow stress potential, but they are not coincident for the stainless steel alloys studied herein. This implies that additional experimental anisotropy parameters are required for accurate curve fitting.

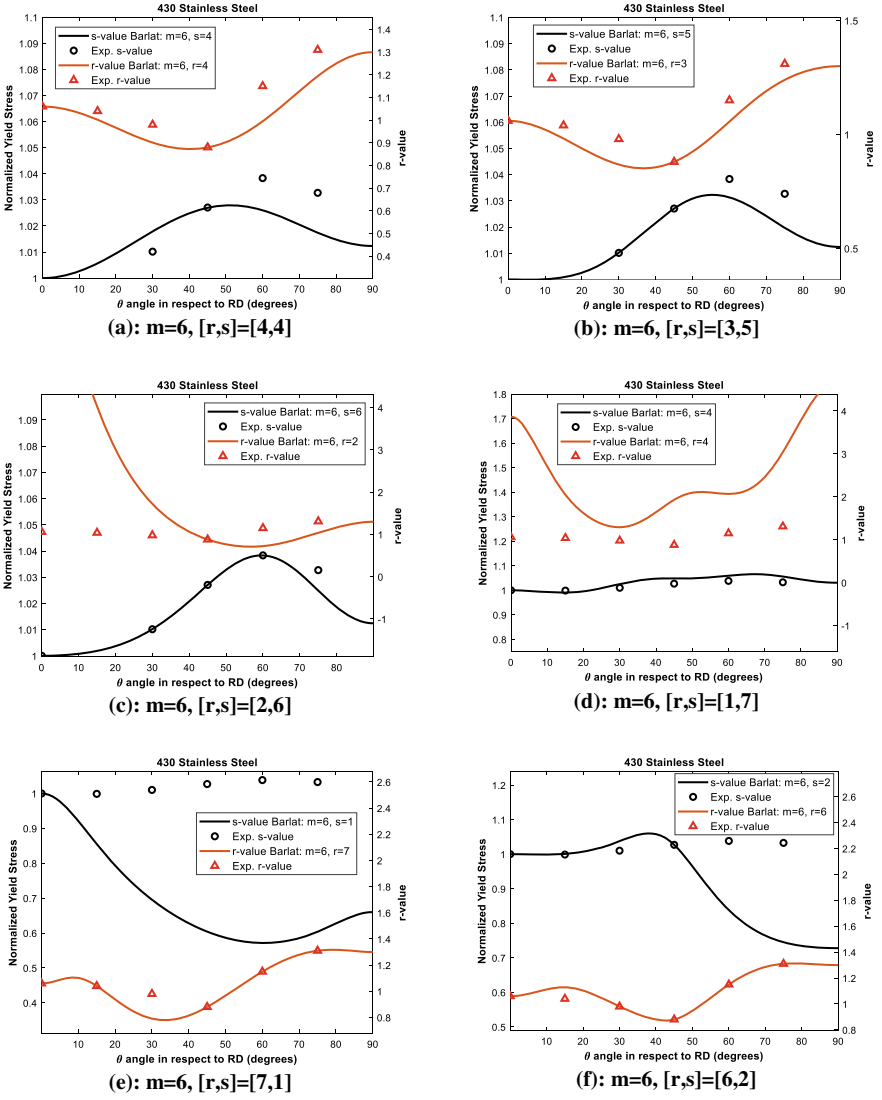


Fig. 2 Comparison of Barlat's Yld 2000-2d prediction curves with the experimental results for tensile tests of AISI 430. (Color figure online)

4. Thus, the accuracy of Barlat's Yld 2000-2d stress function, which requires eight anisotropy coefficients, is similar to Barlat's Yld 2004-18p three-dimensional yield stress criterion that requires 18 anisotropy coefficients.
5. The proposed Newton–Raphson method with relaxation has shown to be a robust and accurate method to determine the plastic anisotropy a_i values.

Acknowledgments The authors would like to gratefully acknowledge University of Santa Catarina State—UDESC and Instituto Tecnológico de Aeronáutica—ITA, CAPES of Brazil and CNPq through grant no. 301069/2019-0 for their support.

References

1. Hutchinson B (2015) Critical Assessment 16: Anisotropy in metals. Mater Sci Technol 31(12):1393–1401. https://doi.org/10.1179/1743284715Y.0000000118
2. Mateo A, Llanes L, Akdut N, Stolarz J, Anglada M (2003) Anisotropy effects on the fatigue behaviour of rolled duplex stainless steels. Int J Fatigue 25:481–488
3. Lippold JC, Kotecki DJ (2005) Welding metallurgy and weldability of stainless steels. Wiley publications
4. Johnson W, Sowerby R, Venter RD (1982) Plane-strain slip-line fields for metal deformation processes. Ed. Pergamon Press, Oxford
5. von Mises R (1913) Mechanik der festen köper im plastischen deformablen zustand. Gött. Nachr. Math. Phys. Klasse, pp 582–592
6. Hershey AV (1954) The plasticity of an isotropic aggregate of anisotropic face centred cubic crystals. J Appl Mech Trans ASME 21:241–249
7. Hosford WF (1972) A generalized isotropic yield criterion. J Appl Mech Trans ASME 39:607–609
8. Ferron G, Makkouk R, Morreale J (1994) A parametric description of orthotropic plasticity in metal sheets. Int J Plasticity 10:431–449
9. Bassani JL (1977) Yield characterization of metals with transversely isotropic plastic properties. Int J Mech Sci 19:651–660
10. Barlat F, Maeda Y, Chung K, Yanagawa M, Brem JC, Hayashida Y, Lege DJ, Matsui K, Murtha SJ, Hattori S, Becker RC, Makosey S (1997) Yield function development for aluminium alloy sheets. J Mech Phys Solids 45:1727–1763
11. Yoon JW, Barlat F, Chung K, Pourboghrat F, Yang DY (2000) Earing predictions based on asymmetric nonquadratic yield function. Int J Plasticity 16:1075–1104
12. Bressan JD, Barlat F (2010) A shear fracture criterion to predict limit strains in sheet metal forming. Int J Mater Form 3 Suppl 1:235–238
13. Xu L, Barlat F, Ahn DC (2010) Constitutive modelling of ferritic stainless steel. Int J Mater Form 3:135–145

Evaluation of Press Forming Technique for Bent Automotive Body Parts Using In-Plane Shear Deformation



Yusuke Fujii, Masaki Urabe, Yuji Yamasaki, and Yoshikiyo Tamai

Abstract A basic evaluation of a new press forming technique using in-plane shear deformation was carried out to suppress fracture and wrinkle of parts bent in the height direction, supposing auto body parts such as the front side member rear. This two-step technique comprises two processes. The first process is deep draw forming with a rectangular blank to induce in-plane shear strain in the blank. The second process is bending the pre-formed blank into a part shape with a U-shaped cross section. According to experiments, in-plane shear deformation was induced in the blank in the first process when the press stroke changed along the part longitudinal direction, and increasing the induced in-plane shear deformation made it possible to form a part with a higher bent angle in the height direction in the second process. The results suggested that complex bent parts which were difficult to form by the conventional press forming technique can be formed without fracture or wrinkle when appropriate in-plane shear deformation is induced in the blank in the first process.

Keywords Press forming technique · In-plane shear deformation · Pre-forming

1 Introduction

To achieve both weight reduction and collision safety in automobiles, strengthening of auto body parts by using ultra-high-strength steel sheets is effective [1]. However, two major problems in press forming of ultra-high-strength steel sheets are fracture, which occurs due to the low ductility of the steel, and wrinkles due to its high yield strength [2]. For example, draw forming is generally applied to auto body parts which are bent in the height direction, as shown in Fig. 1. In draw forming, the

Y. Fujii (✉) · M. Urabe · Y. Tamai
Steel Research Laboratory, JFE Steel Corporation, 1, Kawasaki-Cho, Chuo-Ku, Chiba 260-0835, Japan
e-mail: yus-fujii@jfe-steel.co.jp

Y. Yamasaki
Steel Research Laboratory, JFE Steel Corporation, 1, Koukan-Cho, Fukuyama 721-8510, Japan

© The Minerals, Metals & Materials Society 2021

G. Daehn et al. (eds.), *Forming the Future*, The Minerals, Metals & Materials Series,
https://doi.org/10.1007/978-3-030-75381-8_63

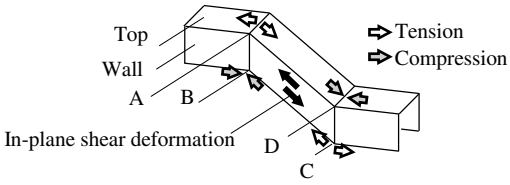


Fig. 1 Schematic of bent parts and deformation caused in conventional press forming

outer side portions of the blank are held with a die during press forming, and tensile deformation on the outer side of the bent portions in the side view (portions A and C) and compressive deformation on the inner side (portions B and D) occur in the blank. Fracture and wrinkle caused, respectively, by this tensile and compressive deformation are major problems when applying higher strength steel sheets to parts with geometries of this type.

The proposed countermeasures against fracture include reducing the tension of the punch shoulders by reducing the frictional resistance or deformation resistance of the material [3, 4] and enhancing the strength of the material at the punch shoulder [5]. However, the effects of these countermeasures are insufficient for ultra-high-strength steel sheets due to their low ductility and high deformation resistance. As a countermeasure against wrinkles, generally, there is a method in which some additional shapes are provided at the bottom of the punch to absorb the excessive material surplus [6], but this is not applicable when there are restrictions on the punch shape.

During forming of parts bent in the height direction, in-plane shear deformation also occurs in the wall defined by ABCD in the straight portion (Fig. 1), and when this in-plane shear deformation occurs, tensile and compressive deformation can be reduced corresponding to the size of the deformation. Therefore, in this study, we evaluated a new press forming technique for bent parts by adding a pre-forming process to intentionally induce large in-plane shear deformation in the wall ABCD of the straight portion.

2 Aim of Press Forming Technique Using In-Plane Shear Deformation

In order to form a part which is bent in the height direction without fracture or wrinkle, as described above, it is important to suppress tensile deformation and compression deformation in the bent portions of the part. We considered that the tensile and compressive deformation at bent portions could be *suppressed* by adding a pre-process which induces in-plane shear deformation in the wall ABCD of the straight portion. To induce in-plane shear deformation in this first step, we evaluated a pre-forming process, as shown in Fig. 2a, in which the press stroke direction was the AD direction and the shapes of the die and blank were cylindrical and rectangular, respectively. When the material flowed into the sidewall from the flange side, the timing of inflow in the blank width direction was different. Specifically, the timing

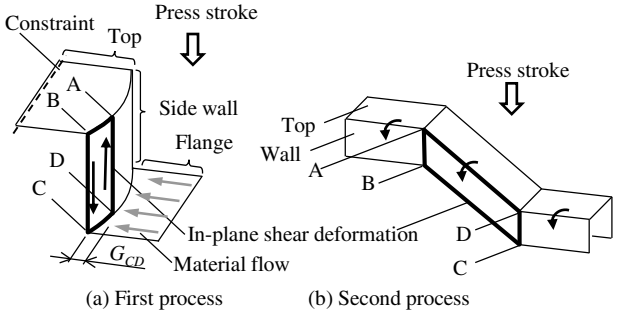


Fig. 2 Schematics of first and second processes in new forming technique

at the width-direction edge was delayed by a distance G_{CD} compared with that at the center. This difference of the inflow velocity between the center and the edges causes shear deformation. In-plane shear deformation is induced in the whole region ABCD because this shear deformation occurs sequentially at the die shoulder. Therefore, in the second process, a part bent in the height direction can be formed easily simply by bending the ridge line AD, as shown in Fig. 2b, because the region ABCD where in-plane shear deformation was induced in the first process is formed into the wall of the straight portion.

In this paper, first, the occurrence of in-plane shear deformation in the first process was confirmed by the finite element method (FEM). Then, experiments were conducted to measure the amount of in-plane shear deformation induced in the first process, and the effect of in-plane shear deformation on the bent angle of the final formed part was investigated by forming in the second process.

3 Prediction of In-Plane Shear Deformation by FEM Analysis

3.1 FEM Analysis Conditions

The amount of in-plane shear deformation caused in the first process was predicted by FEM analysis. Figure 3 shows an analysis model of the die and blank. Four types of punch radius R_p were examined: 12.5, 16.5, 20.0, and 25.0 mm. The blank was a rectangle with a width of 30 mm and length of 180 mm, and was shaped symmetrically at M–M′. The shoulder radii of both the punch and die were 5 mm. The forming height was 50 mm. The solver was LSDYNA® Ver 9.7.1 R5 (Livermore Software Technology Corp.) using the dynamic explicit method. Table 1 shows the mechanical properties of the test material used in the FEM analysis. The blank was a shell element with an element size of 2 mm. The blank holder force was 9.8 kN, and the friction coefficient was 0.15. In this paper, in-plane shear strain was defined as engineering shear strain.

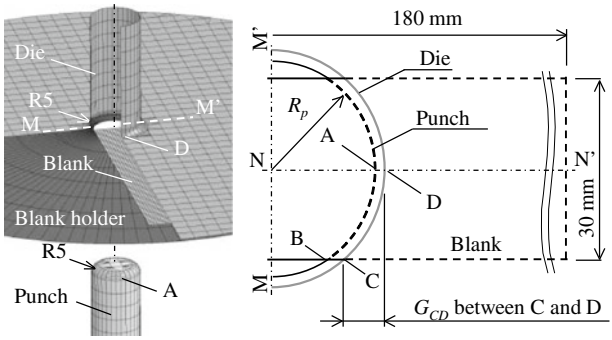


Fig. 3 Details of FEM model used in first process to obtain in-plane shear deformation

Table 1 Mechanical properties of test material

Grade	Thickness (mm)	YS (MPa)	TS (MPa)	El (%)
270	0.5	163	297	50

3.2 FEM Analysis Results

An example of the predicted in-plane shear strain distribution after the first process is shown in Fig. 4. The occurrence of in-plane shear strain in the region ABCD of the sidewall was predicted. Figure 5 shows the distribution of shear strain in cross-section O–O′ in the middle of the sidewall in the width direction. In-plane shear strain was negligible at point O at the center of the blank width and at point O′ at the edge, and displayed its maximum value at the center between those two points. Figure 6 shows the effect of the punch radius R_p on the average value of in-plane shear strain γ_{Ave} generated in the range of positions from 2 to 12 mm from the blank width center in Fig. 5. As the punch radius R_p decreased, in-plane shear strain increased. The reasons for this change are considered in the following section.

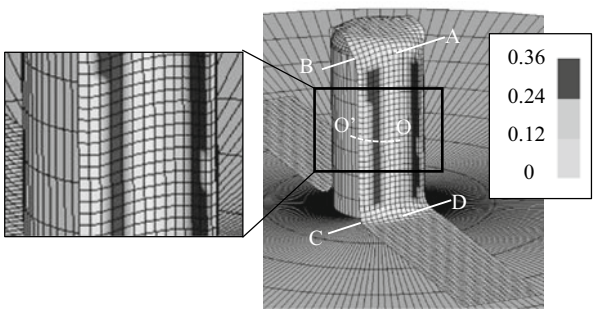


Fig. 4 Calculated distribution of in-plane shear strain at sidewall of punch in case of $R_p = 12.5$ mm and Grade 270 MPa

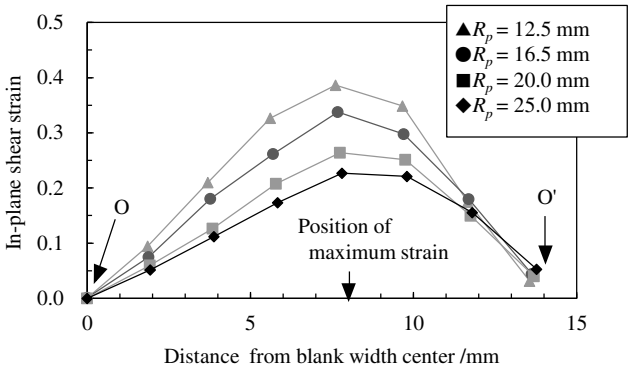
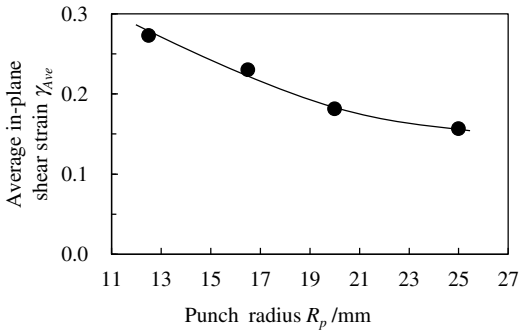


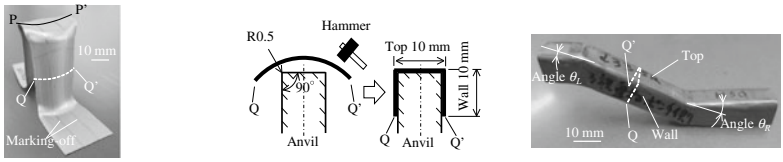
Fig. 5 Calculated distribution of in-plane shear strain in section O–O′ in first process

Fig. 6 Relationship between average in-plane shear strain γ_{Ave} and punch radius R_p in the first process



3.3 Discussion

Since the shapes of the die and blank are symmetrical on the M and M′ sides with respect to N-N′, as shown in Fig. 3, in-plane shear deformation is canceled at point O in the center of the blank width. On the other hand, because the material inflow in the circumferential direction is not restricted at point O′ near the edge, material inflow to the sidewall occurs with size reduction deformation in the circumferential direction. For this reason, it is considered that the difference in the inflow velocity between the edge side and the center in the width direction is reduced, and the in-plane shear deformation is less likely to occur at those points. As a result, it is estimated that in-plane shear strain distribution shown in Fig. 5 is generated between the point O and point O′ and reaches its maximum near the center. Since the distance G_{CD} increases as the punch radius R_p decreases, it is considered that in-plane shear strain becomes larger as the difference of the inflow velocity to the sidewall increases.



(a) Formed panel after first process (b) Forming technique (Q-Q' section) (c)Formed panel after second process

Fig. 7 Forming method in the second process

4 Experimental Method and Results

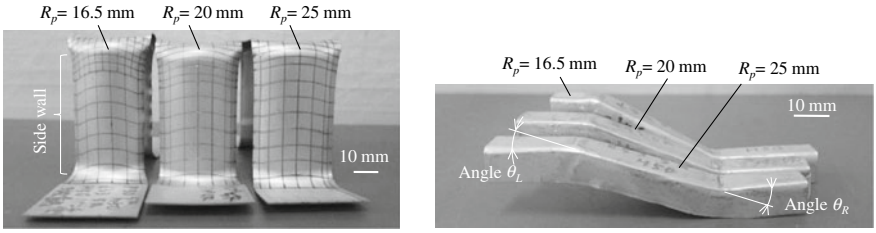
4.1 Purpose and Method of Experiment

In order to evaluate the effect of in-plane shear deformation on the bent angles of formed products bent in the height direction, the formed specimens in which in-plane shear deformation was induced in the first process were bent in the second process, and the bent angles in the height direction were examined.

The die used in the first process was the same as that in the FEM analysis (Fig. 3). The punch radii R_p were 16.5, 20.0, and 25.0 mm, and various in-plane shear deformation was given to the blanks. The blank material was the 270 MPa grade steel sheet in Table 1. The blank was lined with orthogonal grids at intervals of 5 mm, and was then draw-formed using a 500 kN deep-drawing instrument and cut along P-P′, as shown in Fig. 7a. In the second process, the pre-formed part was formed to a part with U-shaped cross-section by sheet metal processing using a hammer and jig, as shown in Fig. 7b. When the second bending process is carried out by press forming using an ordinary die, the pre-formed part is formed to the pre-determined die shape. Because this is not suitable for the purpose of this experiment, in which we investigated the degree of the bent angle in the height direction, sheet metal processing was used as the second process to reproduce the sequence of material deformation during press forming with an ordinary die as closely as possible. First, the pre-formed part was bent along the ridge lines at the positions where the widths of the top portion and vertical walls were each 10 mm. Next, the curved surface was flattened in the order of the top and vertical wall, and then processed so that the angle between the top and walls was 90°. The influence of in-plane shear deformation on the bent angle was determined by measuring angles θ_R and θ_L of the formed parts obtained by sheet metal working as described in Fig. 7c.

4.2 Experimental Results

The formed parts obtained in the first and second processes are shown in Fig. 8. The blanks could be formed without fracture or wrinkle under all conditions. The



(a) First process (b) Second process

Fig. 8 Formed parts in each process

ruled lines were distorted in a parallelogram shape between the width center and the edge portions at the sidewall of the first process, confirming that in-plane shear deformation occurred (Fig. 8a). In the second process, the formed parts bent in the height direction were obtained, and the effect of applying in-plane shear deformation was demonstrated (Fig. 8b).

As shown in Fig. 9, the four areas indicated by the broken lines were selected from the center of the sidewall of the first process, and the average value γ_{Ave} was obtained by calculating the in-plane shear strain from the lattice deformation. The relationship between this average in-plane shear strain γ_{Ave} and the punch radius R_p is shown in Fig. 10. As the punch radius R_p became smaller, γ_{Ave} increased. Moreover, these values were in good agreement with the FEM analysis results. The bent angles θ_L and θ_R after the second process became larger as the punch radius R_p in the first process became smaller. Figure 11 shows the effect of the average in-plane shear

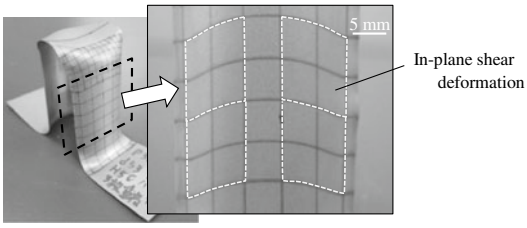


Fig. 9 Draw-formed panel (left) and enlarged view of wall portion (right)

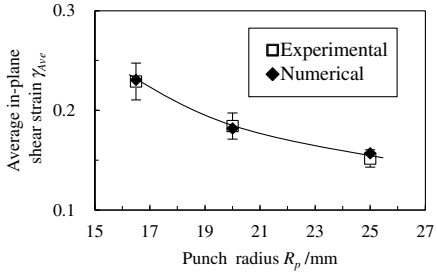


Fig. 10 Relationship between average in-plane shear strain γ_{Ave} and punch radius R_p in the first process

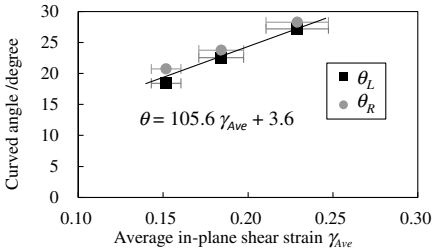


Fig. 11 Effect of average in-plane shear strain γ_{Ave} on bent angle in the height direction

strain γ_{Ave} in the first process on the bent angle after the second process. The bent angle was proportional to γ_{Ave}, and the sizes of bent angles θ_L and θ_R were almost the same.

The degree of contribution of in-plane shear deformation to the bent angle of the formed part measured in the above experiment was verified. Figure 12 shows a schematic diagram explaining the effect of in-plane shear deformation at the straight wall and elongation at the bent portion on the bent angle in the height direction. When the wall portion deforms to a parallel four-sided shape as a result of in-plane shear deformation, an angle change in the height direction occurs. Therefore, using the average in-plane shear strain γ_{Ave}, the bent angle θ_γ in the height direction caused by in-plane shear deformation was geometrically calculated by the following equation. Here, π indicates the circumference ratio.

$$\theta_\gamma = 180/\pi \cdot \tan^{-1} \gamma_{Ave} \tag{1}$$

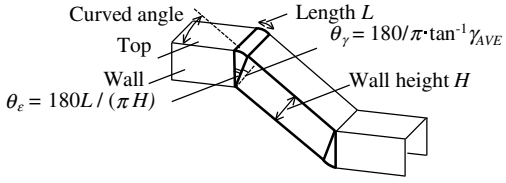


Fig. 12 Schematic of effect of bent angle on in-plane shear strain and stretched deformation

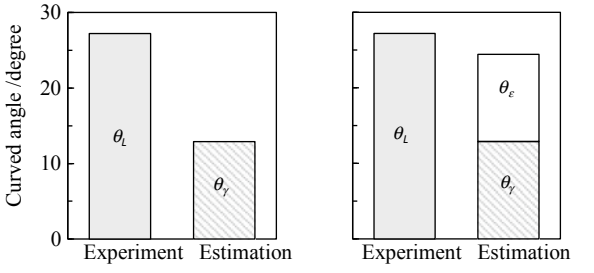


Fig. 13 Experimental and estimated bent angle (R_p = 16.5 mm)

Figure 13a shows the result of a comparison of the calculated bent angle θ_γ and the measured angle θ_L when the punch radius R_p was 16.5 mm. The angle θ_γ calculated from the measured value of in-plane shear deformation was smaller than the measured value θ_L, which was about 47%. This means that another factor also contributes to the angle θ_L of the second formed part. Next, therefore, the contribution of elongation at the bent portion was verified. The elongation in the longitudinal direction caused by tensile deformation by the punch and the shoulder portions in the first process was L, and the angle change θ_ε of the formed part after the second process was geometrically calculated by the following equation. Here, H represents the height of the longitudinal wall of the second formed part.

$$\theta_\varepsilon = 180L/(\pi H) \tag{2}$$

The elongation L predicted by the FEM analysis at the punch shoulder in the first process was substituted into Eq. (2) to obtain the predicted value θ_ε. Figure 13b shows the sum of the predicted value θ_ε and the predicted value θ_γ of angle change due to in-plane shear strain. The sum of θ_ε and θ_γ was almost equal to the measured value θ_L. Based on the above results, it was found that the developed technique for draw forming a rectangular blank in a cylindrical shape in the first process causes the bent angle in the side view of the formed part in the second process due to a combination of in-plane shear deformation of the sidewall and the tensile deformation at the punch and die shoulders in the first process.

5 Conclusion

(1) A press forming technique which enables forming of parts bent in the height direction without fracture or wrinkle by addition of a pre-process to induce in-plane shear deformation in the wall of the straight side of the bent part was proposed, and the possibility of this technique was verified by an FEM analysis and experimental study.
(2) It was possible to induce in-plane shear deformation in the wall by drawing the rectangular blank in the part longitudinal direction, and parts bent in the height direction could be formed easily by using this shear deformation.
(3) It was found that the bent angle increased when the in-plane shear deformation applied in the first process was increased.

References

1. Manabu T (2015) Sheet steel technology for the last 100 years: progress in sheet steels in hand with the automotive industry. ISIJ Int 55(1):79–88
2. Takehide S (2001) Physical metallurgy of modern high strength steel sheets. ISIJ Int 41(6):520–532
3. Ken-ichi M, Yosuke Y, Tetsuya Y (2005) FE Simulation on blank holder control using friction reducing algorithm in deep drawing process. JSME Int J Series A 48(4):341–345
4. Hideki I, Robert S (1995) Determination of the optimum blank shape when deep drawing nonaxisymmetric cups, using a finite-element method: simplified determination of optimum blank shape and limiting drawing ratio by inverse finite-element procedure. JSME Int J Series A 38(4):473–479
5. Kazuyoshi K, Kyoichi O (1975) press formability of an inhomogeneous sheet metal. Bull JSME 18(126):1403–1411
6. Shen YH, Song YL, Hua L, Yang L, Lv ZX (2015) Function relationship between structural characteristics of automotive beam parts and wrinkling in hot stamping. Proc of 2nd international conference on advanced high strength steel and press hardening, 299–304

Simulation of Cold Forging Processes Using a Mixed Isotropic-Kinematik Hardening Model



Lander Galdos, Julen Agirre, Nagore Otegi, Joseba Mendiguren, and Eneko Saenz de Argandoña

Abstract Cold forging is a manufacturing process where a bar stock is inserted into a die and squeezed with a second closed die. It is one of the most widely used chipless forming processes, often requiring no machining or additional operations to get tight tolerances. Because materials to be formed are increasingly harder and the geometrical complexity is greater, the finite element simulation is becoming an essential tool for process design. This study proposes the use of the Chaboche hardening model for the cold forging simulation of a 42CrMoS4Al material industrial automotive ball pin. The material model has been fitted with experimental data obtained from cyclic torsion tests at different reversal plastic strains as well as monotonic torsion tests at different strain rates. Comparison between the classical isotropic hardening and the new mixed hardening model are presented for the different forging steps.

Keywords Cold forging · Numerical simulation · Mixed hardening

1 Introduction

The cold forging is a bulk forming process that aims to obtain near net shape semi-finished components. Unlike the hot forging, the cold forging process produces very precise components having tight geometrical tolerances and good surface finishing.

L. Galdos (✉) · J. Agirre · N. Otegi · J. Mendiguren · E. S. de Argandoña
Advanced Material Forming Processes Research Group, Mondragon Unibertsitatea, Loramendi 4, 20500 Arrasate-Mondragon, Spain
e-mail: lgaldos@mondragon.edu

J. Agirre
e-mail: jagirreb@mondragon.edu

N. Otegi
e-mail: notegi@mondragon.edu

J. Mendiguren
e-mail: jmendiguren@mondragon.edu

E. S. de Argandoña
e-mail: esaenzdeargan@mondragon.edu

© The Minerals, Metals & Materials Society 2021

G. Daehn et al. (eds.), *Forming the Future*, The Minerals, Metals & Materials Series,
https://doi.org/10.1007/978-3-030-75381-8_64

Usually small to medium components are produced by this technology using high production rate horizontal presses. Typical components are bolts, geared shafts and pins among others [1, 2].

Like in many metal-forming processes, cold forging industry is increasingly using the finite element modelling for process and tool design. In this regard, the numerical modelling is becoming state of the art in the cold forging companies and usual outputs are the material flow, used for checking the die filling and folds, and the punch forces. Advanced features that are not fully stablished in the sector are the advanced fracture criteria as proposed by [3, 4] and the analysis of the resulting residual stresses and their influence on the final properties [5, 6].

Because the accuracy level demanded to the numerical models is high during cold forged process definition, take into account that geometrical accuracy is often cents of millimeter, the accuracy of numerical inputs is of high importance. Regardless the mesh quality, the remeshing strategy and the numerical method used to solve the problem, the material and contact definition are critical for getting the desired reliability. Latest works for properly identifying the friction coefficient for cold forging simulation have being led by the "Lubrication" Subgroup of the International Cold Forging Group (ICFG). An inter-laboratory comparison using different friction tests was done by different re-known authors and conclusions were presented in [7]. Regarding the material modelling, Bruschi et al. presented a deep review about the modelling of material behaviour in sheet metal forming [8]. In the paper, relevant hardening models for capturing metals Bauschinger effect are explained. The use of mixed isotropic and kinematic hardening models influence the final accuracy of the numerical models, especially in terms of springback and residual stresses. These hardening models have been rarely employed in the cold forging process simulations.

For this reason, the main objective of this paper is to show the influence the hardening model has on the numerical results of an industrial automotive ball pin forging. The state of the art for cyclic behavior modelling and cyclic material characterization is presented and experimental results obtained by using cyclic torsion tests are presented and discussed by the authors for a cold forging steel.

The Chaboche and Lemaitre mixed hardening model is presented and the material parameters identification procedure is explained using the experimental data obtained in the cyclic torsion tests. Finally, the numerical results obtained using an isotropic hardening material model and the fitted mixed hardening model are shown and compared by using an industrially often-used FEM software.

Table 1 Chemical composition of 42CrMoS4Al case hardening steel

C	Mn	Si	P	S	Cr	Mo	Cu	Al
0.42	0.76	0.14	0.009	0.025	1.03	0.176	0.14	0.024

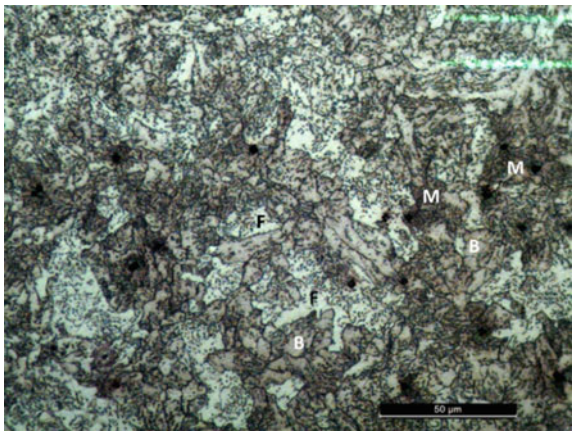


Fig. 1 As received microstructure of 42CrMoS4Al case hardening steel. (Color figure online)

2 Material Cyclic Characterization

2.1 Material Properties

The 42CrMoS4Al case hardening steel used to produce automotive ball pins was selected for the current study. 26 mm diameter steel rods were used for the experimental testing. The material was obtained in the annealed condition, which is the as-received state used in the forging companies for producing the selected component. Material composition is shown in Table 1.

The as received material microstructure is shown in Fig. 1. The edging used for revealing the microstructure was the Nital-Beraha. Ferrite is colored in white, the Martensite is dark brown and Bainite is light brown.

2.2 Monotonic and Cyclic Material Testing: State of the Art

In metal forming operations and cold forging processes, the metals are normally subjected to very complex strain paths that include loading reversal. For this reason, complex phenomenological hardening models are increasingly being introduced in finite element modelling codes to provide accurate predictions of material behavior. Four types of hardening may arise during forming processes: (i) isotropic hardening, which refers to the proportional expansion of the initial yield surface; (ii) kinematic

hardening, if the deforming material shows a yield surface that does not change in form and size, but translates in the stress space; (iii) rotational hardening, which causes the yield locus to rotate; (iv) distortional hardening, which causes the yield locus to distort [8].

Mixed isotropic and kinematic hardening models are becoming of common use in the sheet metal forming simulations since they significantly influence the springback prediction accuracy and are able to reproduce different phenomenon such as the Bauschinger effect, the transient behaviour, the permanent softening and ratcheting [9–11]. The different phenomenon that appear during the reverse loading are illustrated in Fig. 2.

Different authors have proposed several reverse loading tests needed for the cyclic characterization of sheet metals and the analysis of these phenomena. Experimental data using a tension–compression test were obtained for different materials by Silvestre et al. [12]. The test was valid for plastic strain levels up to ±3%. Brunet et al. [13] identified the hardening parameters by using bending tests of a mild steel. The results showed some limitations and uncertainties due to the fact that the strain state in the sample was not exactly a pure strain state of bending. The cyclic three point bending test was also used to determine various hardening laws of DP600 and 220 IF steels by Eggertsen and Mattiasson [14].

Other authors combined different tests, such as Weiss et al. [15], who used bending and simple shear tests for studying the Bauschinger effect of various DP steel grades at high strain levels. Miyauchi et al. presented a very interesting test for cyclic shear

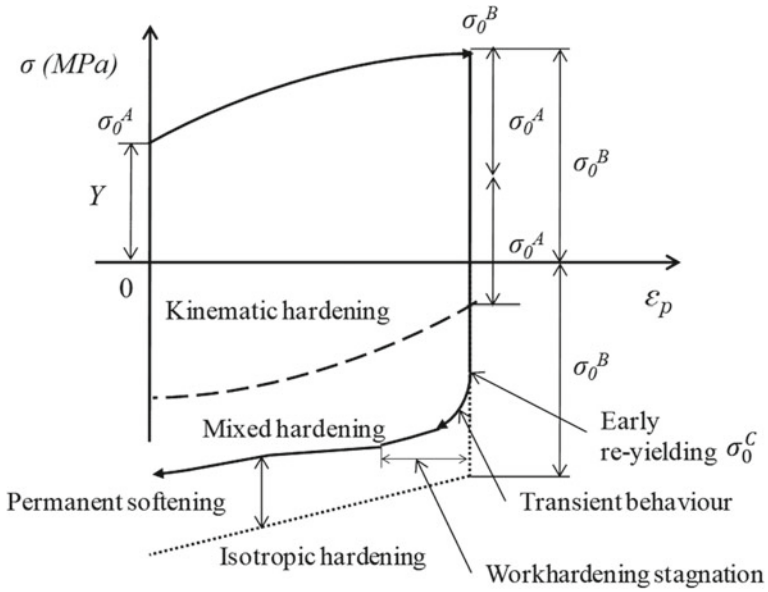


Fig. 2 As received microstructure of 42CrMoS4Al case hardening steel

testing of metal sheets [16] and Tekkaya et al. extended the in plane torsion test for the characterization of sheet metals at very high strain levels [17].

The above-mentioned works show that the sheet metal forming community is well advanced in the cyclic characterization of materials. Many authors used tension-compression tests for the characterization of the kinematic behaviour of solid samples at very low strain levels with the aim to be used in fatigue modelling. However, very few works intended for forming process modelling of bulk material were found during the literature review. Madej et al. used tension-compression tests of solid samples cut from thick sheets for the study of the high temperature levelling of thick plates [18]. Strain levels were small compared to cold forging. Narita et al. used small size shear samples cut from wire to study the influence of the hardening model in the springback prediction of cold forged extruded components [19–21]. Strains up to 35% were achieved before strain reversal and the Yoshida-Uemori model was used in their works for the cyclic behaviour modelling of the initial wires. The estimated final extruded diameter by the Yoshida-Uemori model was more uniform and closer to the experimental results.

Finally, it is worth to mention that torsion tests of solid samples are suitable for high strain level testing of metallic materials. In this regard, Badiola et al. used this experimental procedure to study the cyclic behavior of rods and understand the austenite–ferrite phase transformation in a Nb-microalloyed steel at high temperature [22]. Her et al. recently presented a new method to obtain high strain flow curves for cold forging including kinematic hardening by using a combination of extrusion plus tensile or compression tests [23].

2.3 Cyclic Torsion Tests

Cyclic torsion tests were used for the kinematic characterization of the material at strain levels similar to the ones reached during cold forging. It is well known that torsion tests are capable to reach very high strains due to the stress state that is present in the material during the test as it was mentioned before. The geometry of the sample and the torsion tester are shown in Fig. 3.

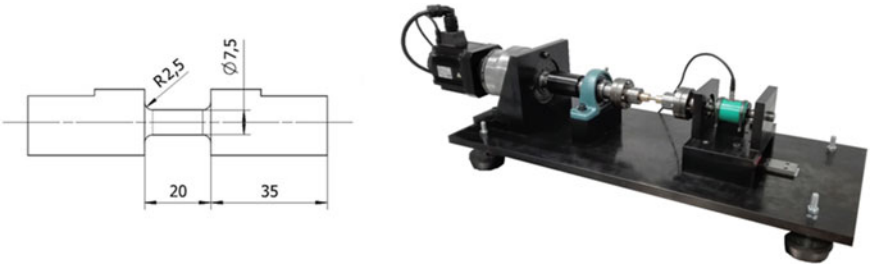


Fig. 3 Torsion sample dimensions and torsion test bench. (Color figure online)

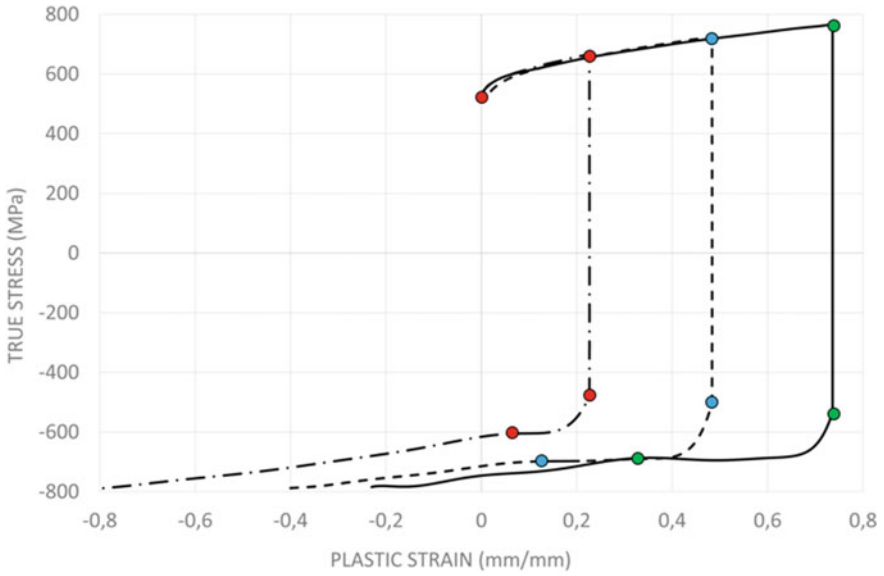


Fig. 4 Experimental stress-strain curves at different reversal angles. (Color figure online)

Cyclic tests were performed using three different reversal angles: 100º, 200º and 300º (approximate equivalent total strains of 0.25, 0.5 and 0.75). After clockwise twisting of the samples up to the desired reversal angle the rotation direction was inversed and the material was twist counterclockwise until rupture occurred. The elastic part of the cyclic curves was removed using the 0.2% offset method, which is equal to approximately 1º offset. Finally the torque–twist angle data was converted into shear stress–shear strain according to the method proposed by Fields and Backofen [24] and then, into true stress–true strain by applying the Von Mises criterion. The experimental stress–strain curves are shown in Fig. 4.

2.4 Evolution of the Kinematic Behavior of the Analyzed Steel

The analysis of the cyclic experimental curves was performed to understand the kinematic behavior of the selected steel. The evolution of the tension and compression yield stress ratio (σ_0^B/σ_0^C) was analysed for the different cyclic reversals. As it is shown in Fig. 5 the Bauschinger effect reaches an asymptotic value after an initial decrease and thus, the isotropic hardening or yield surface expansion suffered by the material is continuously compensated in the same ratio by the kinematic hardening or the translation of the yield surface. The evolution of the transient softening and the work hardening stagnation is shown in Fig. 6. The definition of the measured

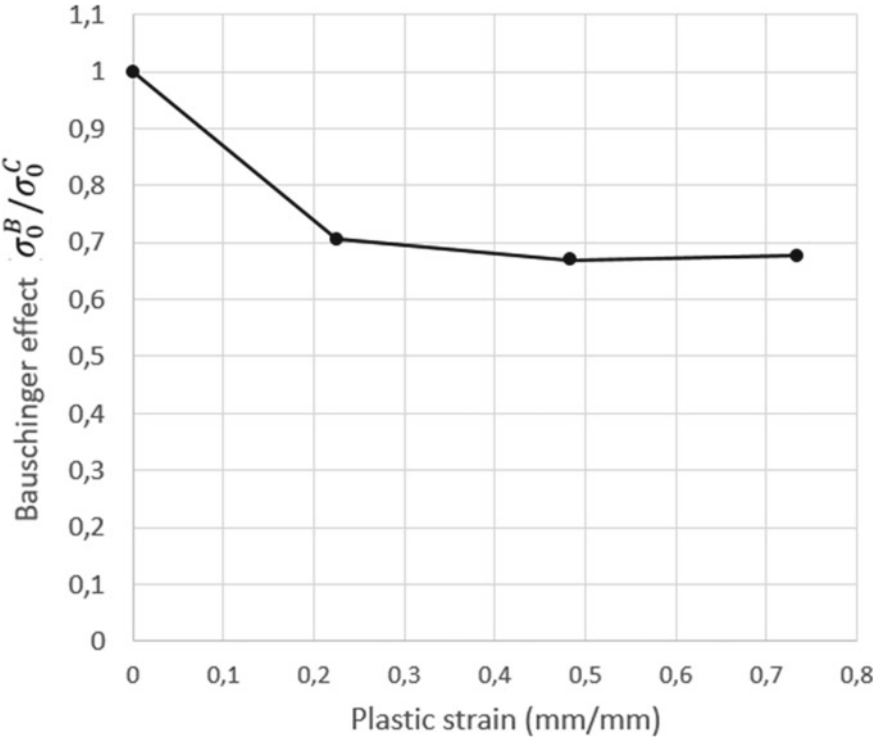


Fig. 5 Evolution of Bauschinger ratio

lengths for both variables are detailed in Fig. 1. The transient softening length or strain is almost constant for all the cyclic reversals while the work hardening stagnation increases with the applied prestrain. This is a well-known phenomena for stress reversal at large strains. Transmission Electron Microscope observations revealed the main features of the evolution of dislocation substructures under stress reversal. During the strain-hardening stagnation, preformed dislocation walls gradually disintegrate. The amount of reverse strain which is necessary for the complete dissolution of these walls increases with the prestrain [25].

Finally, the evolution of the isotropic hardening and the kinematic hardening have been analyzed. From Fig. 7 and for the uniaxial cyclic loading case the values of the isotropic hardening R and the kinematic hardening X can be calculated analytically for the different reversal strains as follows:

$$R = \left(\frac{\sigma_0^B - \sigma_0^C}{2}\right) - \sigma_0^A \tag{1}$$

$$X = \sigma_0^B - \left(\sigma_0^A + R\right) = \frac{\sigma_0^B + \sigma_0^C}{2} \tag{2}$$

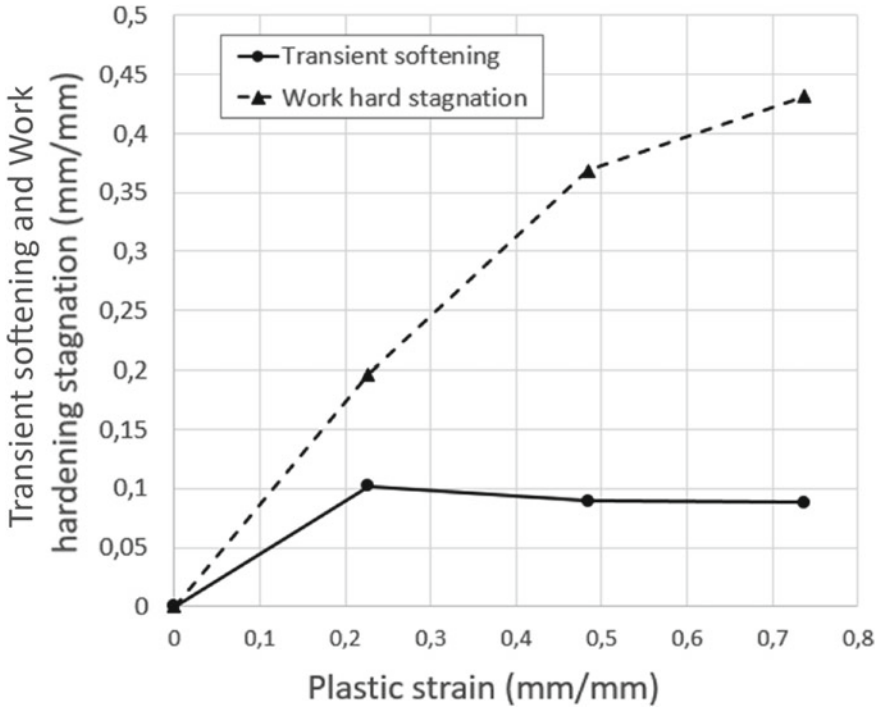


Fig. 6 Evolution of transient softening and stagnation behaviour

Note that σ_0^C is negative in the formulae, as it is the compression yield stress of the material after loading. σ_0^A and σ_0^B are positive being the initial yield stress and yield stress after uniaxial pre-straining.. The evolution of isotropic hardening (R) and the kinematic hardening (X) for the different cyclic tests is shown in Fig. 8. As it is observed, the R follows a linear evolution while X tends to stabilize at a plastic strain of approximately 0.8.

3 Parameter Identification of Mixed Chaboche and Lemaitre Model

The Chaboche and Lemaitre hardening model (1990) [26] was combined with the Von Mises yield criteria, as these are recommended for cyclic plasticity analyses and widely distributed in commercial FE-codes. The Von Mises yield criteria can be expressed.

The Chaboche and Lemaitre hardening model (1990) [25] was combined with the Von Mises yield criteria, as these are recommended for cyclic plasticity analyses and widely distributed in commercial FE-codes. The Von Mises yield criteria can be expressed:

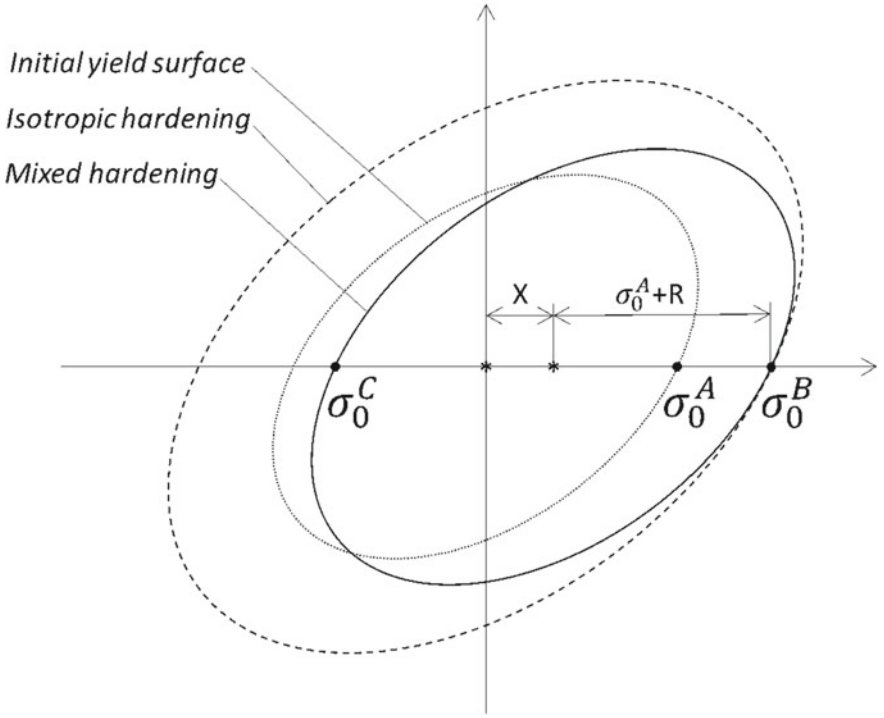


Fig. 7 Representation of isotropic and kinematic hardening

$$\phi(\boldsymbol{\sigma}, \boldsymbol{X}, \sigma y) = \sqrt{3/2(\boldsymbol{\sigma} - \boldsymbol{X}) : (\boldsymbol{\sigma} - \boldsymbol{X})} - \sigma y - R \tag{3}$$

where $\boldsymbol{\sigma}$ denotes the deviatoric stress tensor, $\boldsymbol{X}$ is the deviatoric backstress tensor, σ_y is the initial yield stress and R is the isotropic hardening. An associated flow rule has been considered to define the plastic strain increment.

The Chaboche and Lemaitre hardening model is a mixed isotropic-kinematic hardening formulation. The nonlinear kinematic hardening describes the movement of the yield surface by means of the evolution of the backstress. The change in the size of the yield surface, is related to the isotropic hardening and is introduced by means of the initial value of the yield strength σ_y and the isotropic variable R. In the proposed model, the evolution of the isotropic hardening is defined in function of the accumulated plastic strain $\mathrm{d}\bar{\varepsilon}_p$ by the following law:

$$\mathrm{d}R = b \cdot (Q - R) \cdot \mathrm{d}\bar{\varepsilon}_p \tag{4}$$

where and are material parameters of the model. The kinematic evolution of the yield surface, proposed by Chaboche et al. is presented in Eq. (5). This model is based on a decomposition of the non-linear kinematic hardening rule proposed by Armstrong and Frederik (1966). Chaboche decomposed a stable hysteresis curve in several parts

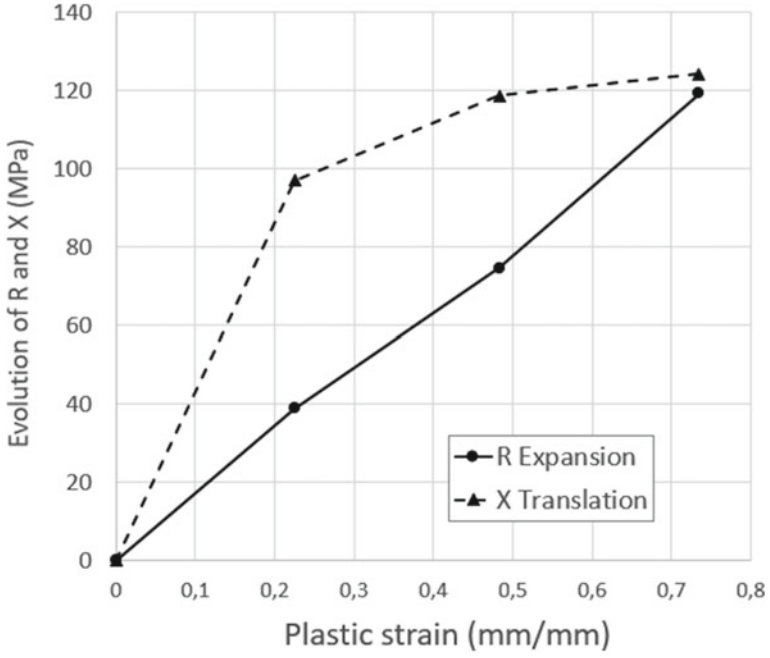


Fig. 8 Evolution of isotropic and kinematic hardening

and it was observed that increasing the material parameters of the hardening rule by the superposition of backstresses, a more accurate model was obtained [16]. However, in this work only one backstress has been considered in the model definition.

$$d\,\boldsymbol{X} = \frac{2}{3} C d\varepsilon_p - \gamma \boldsymbol{X} d\bar{\varepsilon}_p \tag{5}$$

where C and γ are the material parameters to be fitted.

The parameter identification method consisted of an unconstrained non-linear optimization proposed by Nelder and Mead [51] available at Matlab®. First, initial values of Q, b, C and γ where found using the data of Fig. 8. After these first calculation the error function shown in Eq. (6) was minimized using all the experimental data of the three cyclic tests.

$$f_{obj} = \frac{1}{n} \sum_{i=1}^{n} \left| \sigma_i^{exp} - \sigma_i^{model} \right| \tag{6}$$

The results of the fitting are presented in Fig. 9. The model taking into account only the isotropic hardening was labelled as IH while the mixed isotropic and kinematic model with one backstress is labelled as KH. As can be observed, the model was able to predict the cyclic hardening of the material. The model predicted the Bauschinger

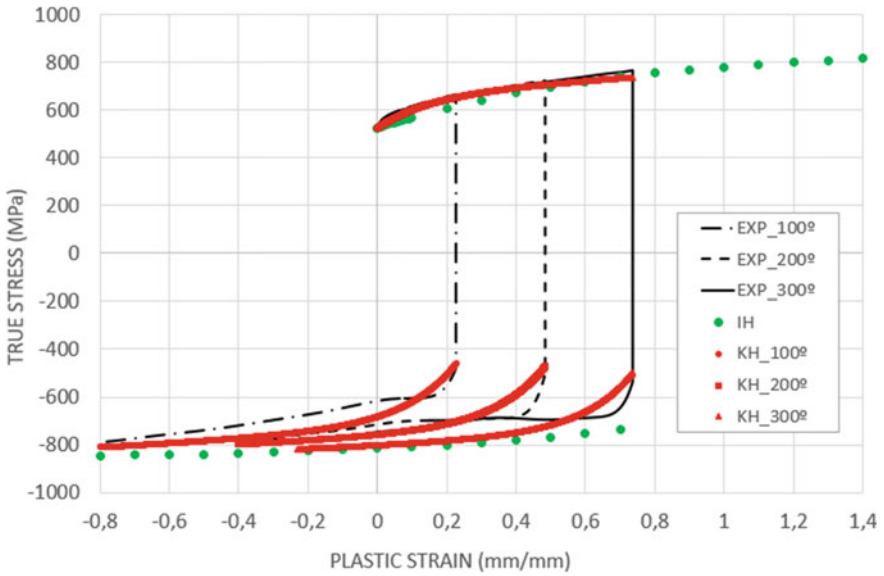


Fig. 9 Fitting of Chaboche and Lemaitre model to experimental curves. (Color figure online)

Table 2 Material parameters of the mixed Chaboche and Lemaitre hardening model

Isoropic model IH			Mixed hardening model IK			
σ_0	Q	b	Q	b	C	γ
525 MPa	335 MPa	1.45	300 MPa	0.5	850	7.0

Effect observed in the experimental results. However, was not able to accurately predict the transient behavior and work hardening stagnation. This can be explained because only one backstress tensor was used in this study and at least two are needed for capturing the transient behavior. The four material parameters involved in the model obtained by means of the explained optimization method are presented in Table 2.

4 Finite Element Modelling of a Ball Pin Cold Forging

In order to quantify the influence the hardening model has on the numerical results, a real cold forging process of a ball pin was simulated. For confidential issues, only the first three operations were simulated; one upsetting, one extrusion operation and the forging of the ball.

FORGE® NxT was used for the process modelling. A full 3D model was used although the model is asymmetric because the material model was coded for a 3D general case. One twelfth of the billet was simulated using two symmetry planes to

avoid excessive computing time. The mesh sensitivity analysis suggested the use of 0.5 mm mesh size in the most strained areas, the transition and rounded zones. For this reason, the billet was meshed using tetrahedral elements with a general mesh size of 1.5 mm and remeshing boxes of 0.5 mm in the transition zones. A friction value of $\mu = 0.05$ was used in the simulations as suggested in [7]. Simulations were run with the two material models, a pure isotropic model and a mixed kinematic hardening model as explained before. For the numerical comparison the material flow, the equivalent Von Mises stress after each process step, the residual stresses after punch-die release and the punch forces were compared.

The material flow analysis, displacement in Z direction, (see Fig. 10) demonstrates that material flow is similar in both material models. The equivalent strain analysis shows similar results and strain levels are similar for both material models. This can be explained because the closed die forging is driven by the die and punch geometries. The material displacement after punch release is higher for the isotropic model. This can be explained because higher residual stresses result when using a isotropic model in the lower part of the ball pin.

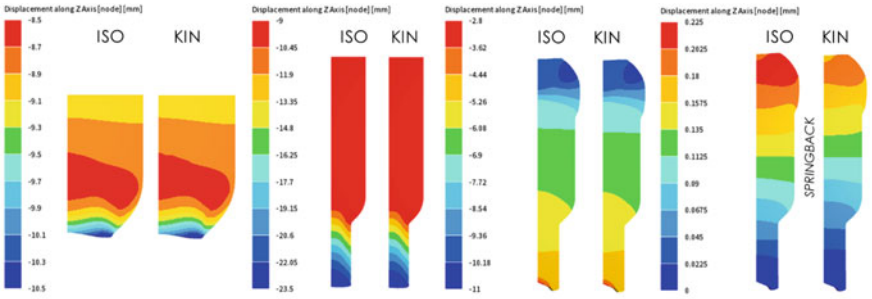


Fig. 10 Material flow results (displacement in Z direction). Upsetting, Extrusion and Ball forging operations together with the final springback. (Color figure online)

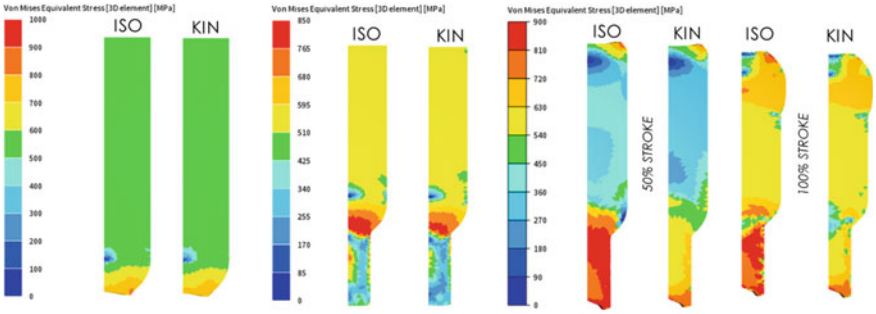


Fig. 11 Material flow results (displacement in Z direction). Upsetting, Extrusion and Ball forging operations together with the final springback. (Color figure online)

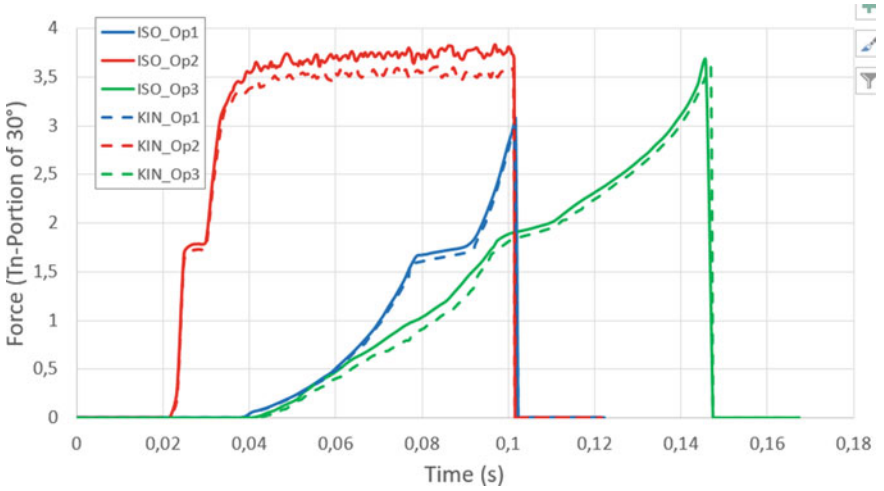


Fig. 12 Punch forces for the different hardening models and operations. (Color figure online)

The equivalent Von Mises stresses after each process step are shown in Fig. 11. The Upsetting and Extrusion operations show similar stress levels for both models. However, the third operation clearly shows that the compression of the lower part after the extrusion operation is highly affected by the hardening model. AT 50% of the punch stroke, when the bottom part of the ball pin is forged, shows significantly higher stress levels for the isotropic model than the kinematic one. This is also observed after the punch reaches the 100% of the stroke at this operation and this explains the higher springback observed after this forging operation in the material flow results.

Finally, punch forces for the different hardening models and operations are shown in Fig. 12. Kinematic model forces are lower than the isotropic model. This is observed principally in the extrusion operation. The difference is not remarkable in the last operation where the kinematic hardening model predicts the biggest differences in terms of stresses. However cam be explained because the biggest amount of work is used for the ball forging where the kinematic hardening effect is not important.

5 Conclusions

The 42CrMoS4Al case hardening steel used to produce automotive ball pins was characterized using torsion cyclic tests. The methodology showed the test is suitable for reaching high strain levels and studying the transient softening and work hardening stagnation phenomena. These two effects could be important for the cold forging process modeling because equivalent strains reached in this process are very high.

The experimental results were fitted to the well-known the Chaboche and Lemaitre hardening model. The mixed hardening model was able to capture the Bauschinger effect but the transient softening and work hardening stagnation were not properly captured. The superposition of more backstress tensors needs to be evaluated to enhance the model accuracy. On the other hand the influence of the temperature needs to be also introduced in the model. This is currently being analyzed by the authors.

Different material flow was observed for the kinematic and isotropic models principally in the final springback of the component. Von Mises stresses are different for the two laws during the forging but the biggest influence was observed during the compression after an extrusion operation, where the path change is important. Although the kinematic hardening showed slightly lower punch forces the difference seems to be not relevant for the analyzed component.

Acknowledgments The authors would like to thank the Gipuzkoa Provincial Council for the funding of the RELASHEET research project (Desarrollo de distintos métodos de alivio de tensiones residuales en chapas metálicas) and the Ecenarro S. Coop. cold forging company for their technical support.

References

1. Sevenler K, Raghupathi PS, Altan T (1987) Forming-sequence design for multistage cold forging. J Mech Working Technol 14(2):121–135
2. Semiatin SL (2005) ASM Handbook vol 14A, Metalworking: Bulk Forming. ASM International, Novelty
3. Bariani PF, Bruschi S, Ghiotti A, Simionato M (2011) Ductile fracture prediction in cold forging process chains. CIRP Ann 60(1):287–290
4. Stebunov S, Vlasov A, Biba N (2018) Prediction of fracture in cold forging with modified Cockcroft-Latham criterion. Procedia Manuf 15:519–526
5. Gerin B, Pessard E, Morel F, Verdu C, Mary A (2015) Effect of cold forming on the high cycle fatigue behaviour of a 27MnCr5 steel. Procedia Eng 133:603–612
6. Tekkaya AE, Allwood JM, Bariani PF, Bruschi S, Cao J, Gramlich S, Lueg-Althoff J (2015) Metal forming beyond shaping: predicting and setting product properties. CIRP Annals 64(2):629–653
7. Groche P, Kramer P, Bay N, Christiansen P, Dubar L, Hayakawa K, Moreau P (2018) Friction coefficients in cold forging: a global perspective. CIRP Annals 67(1):261–264
8. Bruschi S, Altan T, Banabic D, Bariani PF, Brosius A, Cao J, Tekkaya AE (2014) Testing and modelling of material behaviour and formability in sheet metal forming. CIRP Annals 63(2):727–749
9. Lee MG, Kim D, Kim C, Wenner ML, Chung K (2005) Spring-back evaluation of automotive sheets based on isotropic–kinematic hardening laws and non-quadratic anisotropic yield functions, part III: applications. Int J Plast 21(5):915–953
10. Taherizadeh A, Green DE, Ghaei A, Yoon JW (2010) A non-associated constitutive model with mixed iso-kinematic hardening for finite element simulation of sheet metal forming. Int J Plast 26(2):288–309
11. Vladimirov IN, Pietryga MP, Reese S (2010) Anisotropic finite elastoplasticity with nonlinear kinematic and isotropic hardening and application to sheet metal forming. Int J Plast 26(5):659–687

12. Silvestre E, Mendiguren J, Galdos L, De Argandoña ES (2015) Comparison of the hardening behaviour of different steel families: From mild and stainless steel to advanced high strength steels. Int J Mech Sci 101:10–20
13. Brunet M, Morestin F, Godereaux S (2001) Nonlinear kinematic hardening identification for anisotropic sheet metals with bending-unbending tests. J Eng Mater Technol 123(4):378–383
14. Eggertsen PA, Mattiasson K (2010) An efficient inverse approach for material hardening parameter identification from a three-point bending test. Eng Comput 26(2):159–170
15. Weiss M, Kupke A, Manach PY, Galdos L, Hodgson PD (2015) On the Bauschinger effect in dual phase steel at high levels of strain. Mater Sci Eng A 643:127–136
16. Miyauchi K (1984) stress–strain relationship in simple shear of in-plane deformation for various steel sheets. In Efficiency in sheet metal forming, IDDRG 13 th Biennial congress, pp 360–371
17. Yin Q, Tekkaya AE, Traphöner H (2015) Determining cyclic flow curves using the in-plane torsion test. CIRP Ann 64(1):261–264
18. Madej L, Muszka K, Perzyński K, Majta J, Pietrzyk M (2011) Computer aided development of the levelling technology for flat products. CIRP Ann 60(1):291–294
19. Narita S, Uemori T, Hayakawa K, Kubota Y (2016) Effect of hardening rule on analysis of forming and strength of multistage cold forged bolt without heat treatment. J Jpn Soc Technol Plast, 54–670
20. Narita S, Hayakawa K, Kubota Y, Harada T, Uemori T (2017) Effect of hardening rule for spring back behavior of forging. Procedia Eng 207:167–172
21. Fujii T, Hayakawa K, Harada T, Narita S (2018) Cyclic simple shear test of material for cold forging. Procedia Manuf 15:1785–1791
22. Lanzagorta JL, Jorge-Badiola D, Gutiérrez I (2010) Effect of the strain reversal on austenite–ferrite phase transformation in a Nb-microalloyed steel. Mater Sci Eng A 527(4–5):934–940
23. Hering O, Kolpak F, Dahnke C, Tekkaya E (2019) High strain flow curves by mechanical tests on specimens pre-strained by forward rod extrusion. Proceedings of the 52nd ICFG plenary meeting
24. Fields DS, Backofen WA (1957) Determination of strain hardening characteristics by torsion testing. Proc. ASTM 57:1259–1272
25. Hu Z, Rauch EF, Teodosiu C (1992) Work-hardening behavior of mild steel under stress reversal at large strains. Int J Plast 8(7):839–856
26. Lemaitre J, Chaboche JL (1994) Mechanics of solid materials. Cambridge University Press

Analysis of the Thermomechanical Flow Behavior of Carburized Sheet Metal in Hot Stamping



Alexander Horn and Marion Merklein

Abstract The reduction of fuel consumption due to restrictions regarding CO_2 emissions is one of the major driving forces for lightweight design in the automotive industry. In this context, hot stamping of ultra-high-strength steels has developed to a state of the art process for manufacturing safety-relevant components. With regard to passenger safety and weight reduction, further potential lies in the functional optimization of the parts. Prior local carburization followed by hot-stamping is a new process variant for tailored properties, which overcomes the limitations of established processes. Due to the varying carbon content after carburization, the sheets have graded mechanical properties. Within this contribution, the influence of temperature, strain rate and carburization on the flow behavior will be investigated. For this purpose, tensile tests at elevated temperatures are carried out in a physical simulator of type Gleeble. The resulting flow curves of the carburized complex phase steel are modeled with a modified Norton-Hoff hardening law and the influence of the carburization process is analyzed by means of the initial yield stress. Furthermore, the results from tensile tests are correlated with the phase transformation behavior obtained by a laser ultrasonic sensor.

Keywords Hot stamping · Quenching · Carburization

1 Introduction

One of the biggest challenges in today's automotive industry is the reduction of car body weight. This is especially apparent against the background of increasing demands regarding safety standards and expectations of comfort. As a result, the average vehicle weight significantly increased within recent years [1]. To fulfill

A. Horn (✉) · M. Merklein
Friedrich-Alexander-Universität Erlangen-Nürnberg, Institute of Manufacturing Technology (LFT), Egerlandstraße 13, 91058 Erlangen, Germany
e-mail: alexander.horn@fau.de

M. Merklein
e-mail: marion.merklein@fau.de

© The Minerals, Metals & Materials Society 2021

G. Daehn et al. (eds.), *Forming the Future*, The Minerals, Metals & Materials Series,
https://doi.org/10.1007/978-3-030-75381-8_65

the contradictory request of low fuel consumption and governmental requirements concerning CO_2 emissions, lightweight design is of the highest importance. Besides the application of lightweight materials, for instance, aluminum or titanium, the usage of ultra-high-strength steels is a successful strategy. In terms of safety-relevant components, such as b-pillars or bumper plates, hot stamping has developed to a state of the art process for manufacturing [2]. In this process, steel sheets are fully austenitized above their AC_3 temperature for several minutes. Afterward, the sheets are transferred to a press and subsequently formed and in-die quenched [3]. With the conventionally used boron-manganese steel alloy 22MnB5, an ultimate tensile strength of 1500 MPa can be achieved as long as the cooling rate during quenching exceeds the critical value of 27 K/s. Further development of hot stamping steels, for example by increasing carbon content, has led to tensile strengths of up to 2000 MPa [4].

The application of functional optimized components offers further potential regarding passenger safety and weight reduction [5]. The process variants for manufacturing parts with tailored properties can be divided into two groups. One aims to improve the ductility of the parts, while the other strategies locally increase strength. The enhancement of ductility, which is beneficial during crashes, since impact energy can be absorbed, can be realized by means of controlling the microstructure during the process. To prevent the martensitic transformation, which would result in high strength, but low ductility, either the austenitization process [6] or the in-die quenching step can be adapted [7]. Furthermore, it is possible to perform additional heat treatment after hot stamping to receive an annealed microstructure [8]. A fourth strategy to improve ductility are tailor welded blanks, where the joining partner is selected with regard to a high residual elongation after quenching [9]. The second approach for functional optimized components is to locally increase strength, which improves structural integrity. State of the art processes are the application patchwork blanks [10] and tailor rolled [11], or rather tailor forged blanks [12]. A novel process is to locally increase carbon content by carburization. For this purpose, the sheets of a complex phase steel are coated with carbonic material such as graphite prior to a heat treatment [13]. Another approach is to expose the sheets to a carbonic atmosphere, while some areas are masked [14]. It was found, that it is possible to significantly enhance the ultimate tensile strength in carburized areas compared to non-carburized zones with only a small transition zone. After carburization, the semi-finished parts are hot stamped. As with all manufacturing processes, especially thermally assisted ones, a suitable material model is necessary for the numerical process design. Therefore, the thermomechanical flow behavior of a carburized sheet is investigated within this study. In this context, the initial yield stress is compared to samples being hot stamped from as-delivered condition. Furthermore, the flow behavior is modeled using Norton-Hoff hardening law. In addition, the results from tensile tests are correlated with phase transformation obtained by a laser ultrasonic sensor.

2 Methodology

2.1 Investigated Material

The investigated sheet material is a complex-phase steel CP-W® 800 with a sheet thickness of 1.6 mm. This steel alloy can be related to the advanced high strength steels. In the as-delivered condition, it is typically used for safety-relevant car body parts. The initial fine-grained microstructure consists out of ferrite, bainite and martensite. Although CP-W® 800 is usually processed via cold-forming, hot stamping is also applicable. Due to an improved strength after hot stamping, the application potential of this alloy is extended. Since the carbon content in the as-delivered condition amounts to 0.14 wt% [15], a further increase in strength by carburization is possible. As a comparison, the conventionally used hot stamping steel 22MnB5 has a carbon content of 0.25 wt% [16]. For this reason, the CP-W® 800 is particularly suitable for the process combination of carburization followed by hot stamping. Table 1 shows the ultimate tensile strength as a result of various process routes. In this context, it is noteworthy, that the hot stamping process consists of four minutes dwell time at 900 °C for austenitization followed by water quenching. The carburization parameters are three hours of holding time and a carburization temperature of 900 °C as well.

2.2 Uniaxial Tensile Tests at Elevated Temperatures

Within this study, carburized samples, as well as samples being hot stamped from as-delivered condition, are investigated. While the specimens being hot stamped from the as-delivered material do not need additional treatment, carburized samples are coated with graphite and heat-treated for three hours at 900 °C prior to uniaxial tensile tests. The tests are carried out in a physical simulator of type Gleeble 3500® (Dynamic Systems Inc., Poestenkill, NY, USA) with digital image correlation GOM Aramis for optical strain measurement. The samples are heated by an electrical current and temperature is controlled with thermocouples. The evaluation of the strain is done in the center of the samples, where the temperature is homogeneous. For both, carburized samples and samples being hot stamped from as-delivered condition, the

Table 1 Ultimate tensile strength of CP-W® 800 depending on the process route

	Ultimate tensile strength
As delivered	780 MPa [15]
Hot stamped from as-delivered condition	1128 MPa
Carburized and hot stamped	1400 MPa [13]

Table 2 Experimental parameters for uniaxial tensile tests at elevated temperatures

		Temperature				
		500 °C	600 °C	700 °C	800 °C	
Strain rate	0.01 s^{-1}	x	x	xo	x	x Carburized o Hot stamped from as-delivered condition
	0.1 s^{-1}	xo	xo	xo	xo	
	0.5 s^{-1}	x	x	xo	x	

same time-temperature profile is applied. It consists of heating up to the austenitization temperature of 900 °C with a rate of 15 K/s followed by four minutes of holding time. Afterward, a quenching rate of 50 K/s is applied to cool the samples to the testing temperature. Compressed air is used as quenchant. The testing temperatures are 500 °C, 600 °C, 700°C and 800 °C, which corresponds to the temperature range for forming in hot stamping. Furthermore, three different strain rates are applied to investigate the influence of the deformation rate. In the case of carburized samples, a full factorial design is chosen, while samples being hot stamped from as-delivered material are only investigated at selected parameter combinations. The experimental parameters are shown in Table 2.

In the first step, the influence of the carburization process is analyzed. While the ultimate tensile strength is appropriate to investigate the different mechanical properties after carburization and hot stamping, the initial yield surface is more suitable in terms of the thermomechanical flow behavior. Moreover, the temperature and strain rate dependency of the carburized samples are evaluated. Finally, the flow behavior will be modeled using a modified Norton-Hoff hardening law [17].

2.3 Phase Transformation

Besides uniaxial tensile tests at elevated temperatures, also the phase transformation behavior is analyzed to support the findings from tensile testing. This will be done using a laser-ultrasonic sensor. The measuring principle is rested upon the interaction of a laser pulse generated ultrasonic signal with the microstructure of the base material [18]. While conventional dilatation is premised on the temperature and phase-dependent thermal expansion, the principle of laser-generated ultrasound is based on the variation of ultrasonic propagation speed [19]. A generation laser pulse causes ablation on the surface of the samples. Due to the vaporization of the material, the ultrasonic pulse is induced. The ultrasound signal propagates through the sample and gets reflected at the specimen's bottom side. The respective echo is detected by means of an interferometer with the detection laser. By analyzing the variation of the delay between consecutive echoes, phase transformation can be monitored [20]. Besides phase transformation, evaluation of the ultrasonic attenuation allows the in-situ investigation of austenite grain growth [21]. The determined measurands refer to an average of the measured volume, consisting out of a cylinder with the height of

the samples' thickness and the laser spot as base area. Within this study, a sensor of type LUMet® is used. The generation laser is a frequency-doubled Nd:YAG pulse laser with a pulse duration of approximately 6 ns and maximum pulse energy of 72 mJ, while the detection laser is a frequency stabilized Nd: YAG laser with a pulse duration of 90 µs. To verify the findings from the laser-ultrasonic sensor, the transformed fraction is compared to measurement data obtained with an extensometer of type Keyence LS7600. To enable a correlation between the results from the uniaxial tensile tests at elevated temperatures and the phase transformation, the same thermal cycle is applied. The samples are heated to a temperature of 900 °C with 15 K/s, held for four minutes and quenched to room temperature with a quenching rate of 50 K/s.

3 Results

3.1 Uniaxial Tensile Tests at Elevated Temperatures

Contrary to the experimental design shown in Table 2, the evaluation of neither the true stress-strain curve nor the initial yield strength was possible for strain rates of 0.1 s^{-1} and 0.5 s^{-1} at 500 °C, since eccentric failure occurred. Due to the conductive heating, the temperature distribution is inhomogeneous along the sample. Therefore, the applied temperature cycle is only valid for the middle area of the specimens. If the quenching rate is sufficient, phase transformation leads to a gradient in strength at lower temperatures. As a result, the softer eccentric areas fail during testing. As the first part of the results, the initial yield stresses of carburized samples and samples being hot stamped from as-delivered material are presented. Figure 1 shows the respective values.

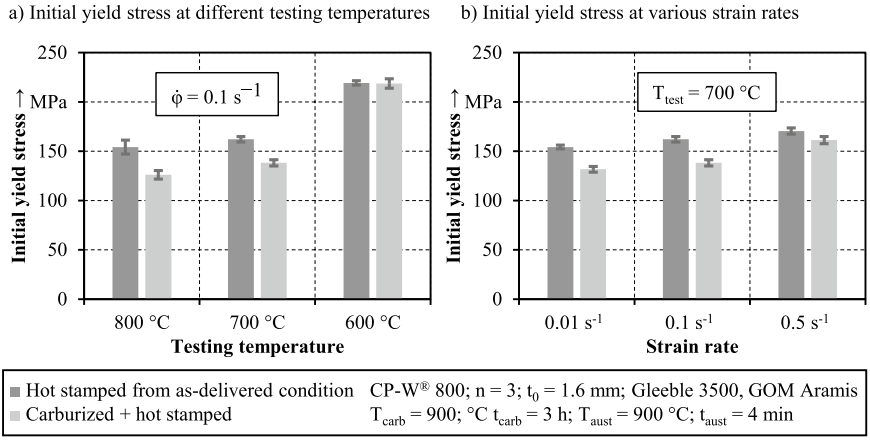


Fig. 1 Initial yield strength of carburized and non-carburized samples at various temperatures and strain rates

It can be seen, that there are temperature and strain rate dependent differences in the initial yield stress. For all tested parameter combinations, the initial yield stress of samples being hot stamped from as-delivered condition is higher compared to carburized specimens. In the case of a testing temperature of 800 °C and 0.1 s^{-1}, the difference amounts to approximately 28 MPa. Lowering the testing temperature, the gap decreases to 14 MPa at 700 °C and nearly 0 MPa at 600 °C. A contrary trend can be seen for the strain rate, which is illustrated in Fig. 1b. Increasing the strain rate from 0.01 s^{-1} to 0.5 s^{-1} leads to a decreasing difference in the initial yield strength between carburized specimens and samples being hot stamped from as-delivered material from 23 MPa to 9 MPa.

Besides the initial yield strength, also the true stress-strain curves of carburized samples are analyzed. During the tensile tests, a degree of deformation of up to 0.9 was achieved. For better comparison, the data is only shown up to a value of 0.3. Moreover, due to the temperature distribution, necking occurs already at low degrees of deformation, which results in an exponential rise of strain rate.

Figure 2a shows the results for testing temperatures of 800, 700, 600 and 500 °C at a strain rate of 0.01 s^{-1}. It can be seen, that not only the initial yield strength increases with decreasing temperature, which was already seen in Fig. 1, but also strain hardening. The rise of both, strain hardening and initial yield strength is especially apparent between 700 °C and 600 °C and between 600 °C and 500 °C. The influence of forming speed can be seen by means of the strain rate, illustrated in Fig. 2b. At a temperature of 800 °C, the initial yield stress of various strain rates is within the range of ±5 MPa, whereas the strain hardening increases with a rising strain rate. For a testing temperature of 600 °C, contrary behavior can be seen. The initial yield stresses are between 168 and 235 MPa. However, the difference in flow

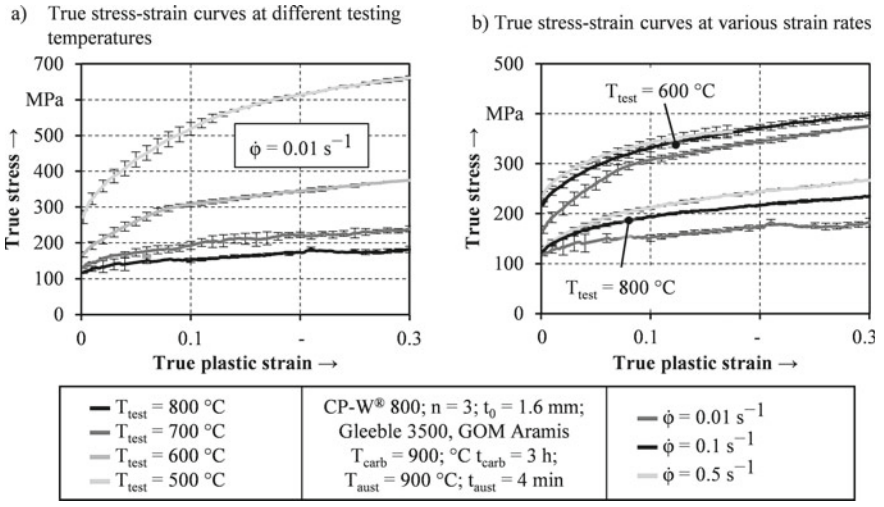


Fig. 2 Flow curves of carburized and non-carburized samples at temperatures between 800 and 500 °C and three different strain rates

stress decreases at higher deformation rates. This is especially apparent for a strain rate of 0.1 s^{-1} and 0.5 s^{-1}, where the flow stress is within the standard deviation for degrees of deformation higher than 0.1.

After analyzing the true stress-strain curves of carburized samples, the flow behavior is interpolated and extrapolated using a modified Norton-Hoff model [17]. According to this approach, the relationship between flow stress σf and degree of deformation φ, strain rate $\dot{\varphi}$ and temperature T can be expressed as

$$\sigma_f(\varphi, \dot{\varphi}, T) = K \cdot e^{\beta/T} \cdot (c + \varphi)^n \cdot \dot{\varphi}^m \tag{1}$$

with K, β, n, m and c as model parameters that have to be fitted to match the experimental data. Besides modeling the flow behavior with fixed model parameters from Eq. 1, two further approaches are pursued. To improve accuracy, the parameters K, β, n and m are also expressed as a function of temperature. Besides an exponential correlation, which was already used by Lechler and Merklein [17] for modeling of the flow behavior of 22MnB5, also a linear relationship is used. The respective equations are presented in Eqs. 2 and 3.

$$\text{Linear correlation}: \; K, \beta, n \text{ and } m \rightarrow f(T) = x_0 + c_x \cdot T \tag{2}$$

$$\text{Exponential correlation}: \; K, \beta, n \text{ and } m \rightarrow f(T) = x_0 \cdot e^{c_x \cdot T} \tag{3}$$

For fitting the parameters to the experimental data, the least square method is applied. To ensure a constant strain rate, input data is limited to a degree of deformation of up to $\varphi = 0.2$. The evaluation of the three different modeling approaches is done by means of the root mean square error, displayed in Fig. 3a. The RMSE relates to all tested temperatures and strain rates. While the average deviation between experimental and analytical data amounts to around 15 MPa in the case of fixed model parameters, it is reduced to 8.4 MPa for temperature-dependent coefficients. The difference of the RMSE between a linear and an exponential correlation is below 0.1 MPa. Therefore, both approaches can be seen as equivalent with regard to the interpolation and extrapolation of true stress-strain curves of a carburized complex phase steel at elevated temperatures. The respective model parameters for all three approaches are listed in Table 3.

In Fig. 3b, the comparison between the experimental data and the analytical approximation using a linear correlation between temperature and the model coefficients, is displayed. The results are exemplarily shown for a temperature of 500 °C and 700 °C and in the case of 700 °C for three different strain rates. It can be seen, that there is a good agreement between experimental and analytical data.

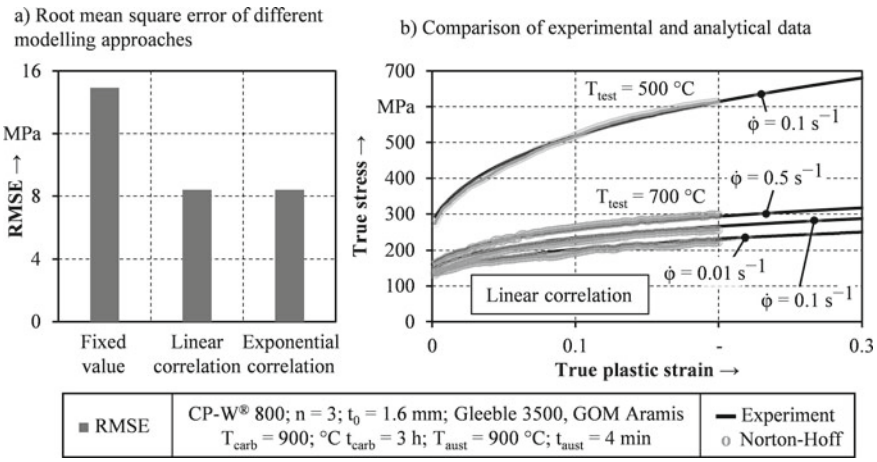


Fig. 3 **a** Root mean square error of different approaches using a modified Norton-Hoff model. **b** Comparison of experimental and analytical true stress-strain data using a modified Norton-Hoff model and linear temperature dependence of model parameters

Table 3 Model parameters for interpolation and extrapolation of true stress-strain curves of a carburized complex phase steel at elevated temperatures

	K_0	c_K	β_0	c_β	n_0	c_n	m_0	c_m	c
Fixed	47.91	–	1537.36	–	0.23	–	0.045	–	0.012
Linear	0.52	0.031	2101.71	−0.065	0.42	−0.00032	−0.095	0.00022	0.011
Exponential	23.37	0.0014	2389.40	−0.00086	0.56	−0.0015	0.0056	0.0033	0.011

3.2 Phase Transformation

Besides the flow behavior, also the occurring phase transformations are investigated by means of a laser ultrasonic sensor. The resulting measurement data is similar to conventional dilatometry curves. A direct comparison of the curves obtained by both measurement principles is not possible, due to different physical quantities determined. While conventional dilatometry refers to longitudinal expansion, the laser ultrasonic sensor measures ultrasonic velocity. Therefore, the transformed fraction is presented in dependence on the temperature during cooling. The transformed fraction is calculated according to Fig. 4a. The phase transformation occurs as a discontinuity in the ultrasonic velocity or rather dilatation curve. With the help of two constructed tangents, the transformed fraction is calculated. The respective results are shown in Fig. 4b. It can be seen, that phase transformation begins between 620 °C and 640 °C. The end of the transformation is approximately between 460 °C and 480 °C. The measurement data obtained by the laser ultrasonic sensor show good repeatability. Compared to the extensometer, the progress of phase transformation

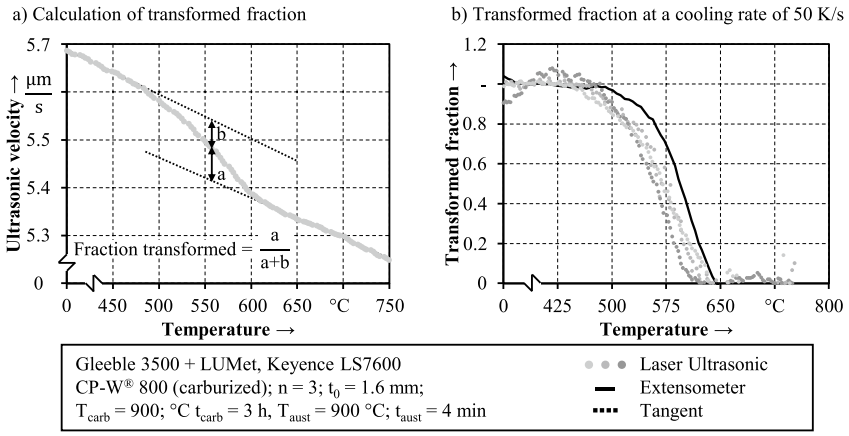


Fig. 4 **a** Procedure for the calculation of transformed phase fraction from measurement data. **b** Comparison of transformed fraction of experimental data measured with laser-ultrasonic and extensometer at a quenching rate of 50 K/s

is of good accordance, especially with regard to the start and end temperatures. Therefore, the applicability of this measurement principle for the determination of phase transformation during hot stamping can be confirmed.

4 Discussion

In the results section, it was illustrated, that the initial yield stress of carburized samples was lower in comparison with specimens being hot stamped from as-delivered condition. These findings indicate a contrary behavior compared to tensile tests at room temperature, where strength is increased due to the carburization process as listed in Table 1. During the carburization process, the carbon content increases. Various authors already investigated the influence of carbon on the stress-strain behavior at elevated temperatures. Wray [22] showed, that carbon content reduces work hardening at temperatures between 850 and 1300 °C. This effect was explained with enhanced dynamic recovery, probably due to an expansion of the austenite lattice. Kong et al. [23] analyzed the flow stress of several austenitic steels with a varying carbon content of up to 0.79 wt%. The results indicated that increasing carbon content leads to an increase in flow stress at low temperatures and high strain rates, while it decreases flow stress at high temperatures and low strain rates. Serajzadeh and Taheri [24] stated that the rate of dynamic recrystallization increases with rising carbon content, while dynamic recovery decreases. As a result, under conditions with dominating dynamic recrystallization such as high temperatures and low strain rates, flow stress is decreased, while a contrary effect can be seen when dynamic recovery is dominating, hence at low temperatures and high strain rates.

These findings are in good accordance with the results from Sect. 3, where the difference in initial yield stress between carburized specimens and samples being hot stamped from as-delivered material decreased at lower temperatures and high strain rates.

Besides the influence of carburization on the initial yield stress, the temperature and strain rate dependent flow behavior was analyzed as well. As expected, flow stress was reduced with rising temperatures and decreasing strain rate, which is an already well know behavior [25]. However, it was depicted in Fig. 2a, that the temperature-dependent rate of increase in flow stress was higher at temperatures below 700 °C. This can be explained with the decomposition of austenite. The experiments with the laser ultrasonic sensors revealed a start temperature for the phase transformation of approximately 620 °C to 640 °C. Since the transformed fraction increases with decreasing temperature, as shown in Fig. 4b, the rate of increase in stress further goes up. In addition, it was shown, that the effect of strain rate decreased at lower temperatures. In the case of 0.1 s^{-1} at 600 °C strain hardening was higher compared to a strain rate of 0.5 s^{-1}. An explanation for this is an ongoing phase transformation. As shown in Fig. 4b, only a small fraction of austenite is already transformed at 600 °C. Since a lower strain rate equals a longer test duration, phase transformation further proceeds, which results in increased strain hardening during deformation.

5 Summary and Outlook

Within this study, the thermomechanical flow behavior of a carburized complex-phase steel at elevated temperatures was investigated. It was shown, that the initial yield stress was reduced due to the carburization process. The influence depends on the respective strain rate and temperature. Furthermore, the flow behavior was analyzed and modeled using a modified Norton-Hoff approach. As expected, the experiments revealed a temperature and strain rate dependent material behavior. By using a linear and exponential dependence of the Norton-Hoff parameters on temperature, accordance between experimental and analytical data was significantly improved. To support the findings from uniaxial tensile tests at elevated temperatures, phase transformation was investigated by means of a laser ultrasonic sensor and correlated with the stress-strain curves.

Within this work, carburized samples were compared to specimens being hot stamped from as-delivered material. To enable a holistic process design of the tailored carburization process by numerical simulation, the flow behavior of non-carburized samples under process conditions, more precisely after a heat treatment of several hours, has to be investigated as well. Furthermore, the phase transformation under various quenching conditions is of high interest.

Acknowledgments The authors would like to thank the German Research Foundation (DFG) for funding the project “Tailored Carburization: Gradierung mechanischer Eigenschaften in der Blechebene und über die Blechdicke” (DFG ME 2043/51-1).

The authors would also like to show their gratitude to Mr. Yaowu Jiang, who participated in this experimental study within the scope of his master thesis.

References

1. The International Council on Clean Transportation Europe, European Vehicle Market Statistics-2018/19, 2018
2. Mori K, Bariani PF, Behrens B-A, Brosius A, Bruschi S, Maeno T, Merklein M, Yanagimoto J (2017) Hot stamping of ultra-high strength steel parts. CIRP Ann 66(2):755–777
3. Karbasian H, Tekkaya AE (2010) A review on hot stamping. J Mater Process Technol 210(15):2103–2118
4. Gerber T, Heckelmann I, Diaz N, Lenze FJ (2013) Efforts in expanding the portfolio of hot forming steel material concepts. In: Oldenburg M, Prakash B, Steinhoff K (eds) 4th International Conference on Hot Sheet Metal Forming of High-Performance Steel—CHS^2. Luleå, Sweden, pp 145–152
5. Merklein M, Wieland M, Lechner M, Bruschi S, Ghiotti A (2016) Hot stamping of boron steel sheets with tailored properties: A review. J Mater Process Technol 228:11–24
6. Mori K, Maeno T, Mongkolkaji K (2013) Tailored die quenching of steel parts having strength distribution using bypass resistance heating in hot stamping. J Mater Process Technol 213(3):508–514
7. Omer K, ten Kortenaar L, Butcher C, Worswick M, Malcolm S, Detwiler D (2017) Testing of a hot stamped axial crush member with tailored properties—experiments and models. Int J Impact Eng 103:12–28
8. Laumann T, Pfestorf M (2008) Crash behaviour of various modern steels exposed to high deformation rates. In Steinhoff K, Oldenburg M, BP (Eds) 1st international conference on hot sheet metal forming of high-performance steel—CHS^2, Kassel, Germany, pp 143–151
9. Duque Múnera D, Pic A, Abou-Khalil D, Shmit F, Pinard F (2008) Innovative press hardened steel based laser welded blanks solutions for weight savings and crash safety improvements. SAE Int J Mater Manf 1:472–479
10. Lei C, Xing Z, Xu W, Hong Z, Shan D (2017) Hot stamping of patchwork blanks: modelling and experimental investigation. Int J Adv Manuf Technol 92(5–8):2609–2617
11. Goeddeke B, Teipel N, Brecht J (2017) Hot Formed Tailor Rolled Products, Lightweight Solutions With Tailored Properties For Modern Vehicle Structure. In: Oldenburg M, Prakash B, Steinhoff K (eds) 6th International Conference on Hot Sheet Metal Forming of High-Performance Steel—CHS^2. Atlanta, USA, pp 481–490
12. Tajul L, Maeno T, Kinoshita T, Mori K-I (2016) Successive forging of tailored blank having thickness distribution for hot stamping. Int J Adv Manuf Technol 89(9–12):3731–3739
13. Horn A, Merklein M (2019) Functional optimization of hot-stamped components by local carburization. Int J Lightweight Mater Manuf
14. Rolfe B, Abdollahpoor A, Wang Y, Pereira M, Kong H, Fabijanic D, Hu K, Han R, Gao K, Liu A, Pan L, Bi Y, Wang ZJ, Zhang YS (2017) Local Patchworking of sheet properties combining carburization and hot stamping. 3rd international conference on advanced high strength steel and press hardening, WORLD SCIENTIFIC, Xian, China, pp 346–351
15. Thyssenkrupp, Product information for complex-phase steels. https://www.thyssenkrupp-steel.com/en/products/sheet-coated-products/multiphase-steel/complex-phase-steel/ (2017). Accessed 12 Oct 2017
16. Thyssenkrupp, Product information for manganese-boron steels for hot forming. https://www.thyssenkrupp-steel.com/en/products/sheet-coated-products/manganese-boron-steel-for-hot-forming/mbw-manganese-boron-steel-for-hot-forming/ (2019). Accessed 5 March 2020

17. Lechler J, Merklein M (2008) Hot stamping of ultra high strength steels as a key technology for lightweight construction. Materials science and technology conference and exhibition, MS and T'08, pp. 1698–1709
18. Davies SJ, Edwards C, Taylor GS, Palmer SB (1993) Laser-generated ultrasound: its properties, mechanisms and multifarious applications. J Phys D Appl Phys 26(3):329
19. Kruger SE, Damm EB (2006) Monitoring austenite decomposition by ultrasonic velocity. Mater Sci Eng A 425(1–2):238–243
20. Dubois M, Moreau A, Bussière JF (2001) Ultrasonic velocity measurements during phase transformations in steels using laser ultrasonics. J Appl Phys 89(11):6487–6495
21. Dubois M, Militzer M, Moreau A, Bussière JF (2000) A new technique for the quantitative real-time monitoring of austenite grain growth in steel. Scr Mater 42(9):867–874
22. Wray PJ (1982) Effect of carbon content on the plastic flow of plain carbon steels at elevated temperatures. Metall Trans A 13(1):125–134
23. Kong LX, Hodgson PD, Collinson DC (1998) Modelling the effect of carbon content on hot strength of steels using a modified artificial neural network. ISIJ Int 38(10):1121–1129
24. Serajzadeh S, Karimi Taheri A (2002) An investigation on the effect of carbon and silicon on flow behavior of steel. Mater Des 23(3):271–276
25. Bruschi S, Altan T, Banabic D, Bariani PF, Brosius A, Cao J, Ghiotti A, Khraisheh M, Merklein M, Tekkaya AE (2014) Testing and modelling of material behaviour and formability in sheet metal forming. CIRP Ann 63(2):727–749

Effect of Short Pulsed-Current on Stress Relaxation in Uniaxial Tensile Test



Ichsan Indhiarto, Qiu Zheng, Tetsuhide Shimizu, Tsuyoshi Furushima, and Ming Yang

Abstract Electricity-assisted metal forming, especially using pulsed-current, was demonstrated to promote a drop in flow stress and improving formability. To investigate the effect of pulsed-current on stress relaxation, a uniaxial tensile test was conducted with different pulsed-current parameters by changing its pulse-width and frequency. Short pulse-width was used in the range of microseconds, while the frequency was arranged under 1 kHz. Different level of temperature was used to consider the effect from joule heating. Stress relaxation in the tensile test was repeated at constant strain interval at 3% strain. This research presents an analysis of stress relaxation influenced by the time-dependent parameter of short pulsed-current.

Keywords Electropulse · Electroplasticity · AZ31B · Stress relaxation

1 Introduction

In recent years, interest in applying pulsed-current to the manufacturing process of metals was increasing. The effect of pulsed-current on reducing the flow stress and promoting metal deformation was reported in many studies. It has been found that on exposure to pulsed DC current, AZ31 plastic behavior was mainly dictated by its current density in its root mean square value, while the peak current can increase its potency [1]. It is also shown that the influence of pulsed-current can reduce flow stress and increase elongation in Al–Mg–Si alloy [2]. Another research shows that pulsed-current did induce dynamic recrystallization at a lower temperature which affects flow stress [3]. Another observation found that the non-deformation test with

I. Indhiarto (✉) · T. Shimizu · M. Yang
Department of Intelligent Mechanical System, Graduate School of System Design, Tokyo Metropolitan University, 6-6, Asahigaoka, Hino-shi, Tokyo 191-0065, Japan
e-mail: indhiarto-ichsan@ed.tmu.ac.jp

Q. Zheng · T. Furushima
Department of Mechanical and Biofunctional Systems, Institute of Industrial Science, University of Tokyo, Komaba 4-6-1, Meguro, Tokyo 153-8505, Japan

© The Minerals, Metals & Materials Society 2021

G. Daehn et al. (eds.), *Forming the Future*, The Minerals, Metals & Materials Series,
https://doi.org/10.1007/978-3-030-75381-8_66

pulsed-current can affect dislocation density, thus affecting its formability properties [4]. Meanwhile, the effect of pulsed-current on stress relaxation conditions was still not properly investigated.

In this study, the effect of electricity on stress relaxation of AZ31 sheet material of thickness 100 μm was investigated. By distinguishing between the thermal and non-thermal effects by regulating the temperature, the effect of electricity can be further analyzed. The relationship between temperature, type of current flow, current density, and frequency can be investigated.

2 Experiment and Methods

2.1 Material and Specimen Preparation

JIS AZ31B with chemical composition as stated in Table 1 was acquired directly from the manufacturer. A workpiece of 100 μm thickness was used in this experiment. The raw material was acquired from Nippon Kinzoku Co., Ltd Itabashi in rolled thin foils. The specimen was manufactured to become dog bone shape, as can be observed in Fig. 1 according to DIN 50125:2009-07 Type H test pieces. All the manufactured specimens were cut at 0° in the rolling direction. The specimen was cleaned with ethanol to remove any oil residue after the manufacturing process. After cleaning, all the specimens were dried, then annealed to remove any residual stress, and normalized then to their conditions. The annealing parameter was 200 °C and

Table 1 Chemical composition of AZ31B

Chemical composition (wt%)								
Al	Zn	Mn	Si	Fe	Cu	Ni	Ca	Mg
3.1	0.88	0.37	0.01	0.002	<0.01	<0.001	0.01	Rem.

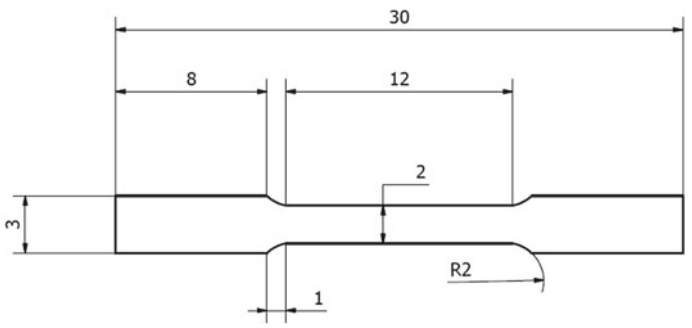


Fig. 1 Shape and dimension of specimen

cooling inside for 1 h until room temperature was also done in a vacuum. To provide constant emissivity, one side of the specimen was sprayed using thermographic spray paint with an emissivity index 0.94.

2.2 Experimental Methods

Uniaxial tensile test was conducted using universal test machine from Zwick Roell Z005 equipped with Zwick Roel LaserXtens as extensometer and Zwick Roell 5 kN load cell. The strain rate was 0.001 s^{-1} for all conditions. Optris infrared thermography camera was used to measure and record the surface temperature of workpiece. The temperature reading was measured by OMRON digital controller in PID mode. This temperature control system was responsible for maintaining the temperature of the specimen during the test. The pulsed-current was generated from PEKURIS PVP 2KV1KA pulse power supply with maximum voltage and current 2 kV and 1 kA, respectively. Schematic and real views of the experimental setup are given in Fig. 2a, b, respectively. Each test was started 1 min after the specimen reaches the desired temperature. The stress relaxation test was started from 3% nominal strain and kept at that level for 20 s. That treatment was repeated every 3% nominal strain increment until break.

Different temperature conditions are used for each electrical condition, as can be observed in Table 2. The temperature was regulated for different electrical conditions to distinguish between thermal and non-thermal effects. The non-thermal effect is commonly referred to as Electroplasticity. Due to Joule heating, the workpiece temperature will increase proportionately with current density. In the case of pulsed-current, there are two types of current density, which is peak current density and root mean square of the peak current density. The root mean square current density is equivalent to the DC current density at the same temperature. In this way, the peak current density at pulsed condition can be applied at a higher magnitude but still

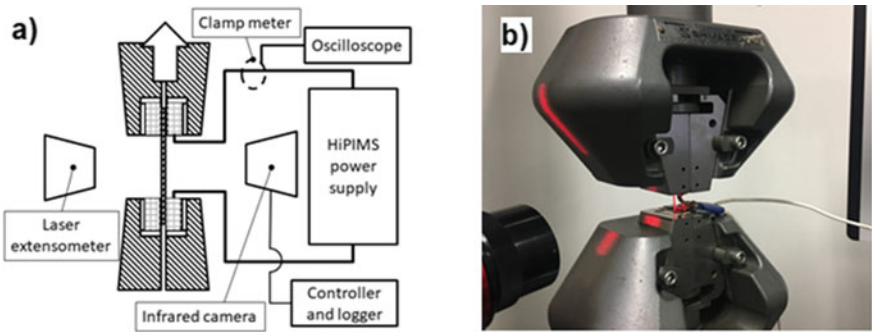


Fig. 2 View of experimental setup **a** schematic and **b** real view. (Color figure online)

Table 2 Experimental conditions

Electrical conditions	Frequency (kHz)	Pulse width (μs)	Temperature (°C)
Pulsed-current	0.5	150	50
			100
			200
	1	150	50
			100
			200
Direct current (DC)	–	–	50
			100
			200

resulting in the same temperature as the DC condition. For comparison purposes, we use the current density from the DC condition and peak current density from the pulsed condition.

3 Results and Discussion

3.1 Finding Stress Relaxation Limit

Due to short time nature of this experiment, the stress relaxation limit was unknown. But, since the initial stress was well recorded, the stress relaxation limit can be predicted using some fitting parameter. Luo et al. [5] provide an equation for parameter fitting with good agreement with their experimental results, as can be seen below.

$$\sigma_t = \sigma_r + \sum_{i=1}^{j} A_i \exp\left(-\frac{t^m}{B_i}\right) \tag{1}$$

σ_t, σ_r, and t are stress at a given time, stress relaxation limit, and time, respectively. A_i, B_i, and m are fitting parameters related to material nature and relaxation conditions. At the beginning of relaxation stage where t is 0,

$$\sigma_t = \sigma_r + \sum_{i=1}^{j} A_i = \sigma_0 \tag{2}$$

where σ_0 is initial stress, then the equation can become

$$\sigma_t = \sigma_0 + \sum_{i=1}^{j} A_i \left(\exp\left(-\frac{t^m}{B_i} \right) - 1 \right) \tag{3}$$

From (3) the fitting parameter can be acquired, as shown in Table 3. The fitting curve and its experimental value are given in Fig. 3. After acquiring the fitting parameter, (1) was used to find the stress relaxation limit. The value of stress relaxation limit is provided in Table 4.

Table 3 Fitting parameter to find stress relaxation limit

Electrical conditions	Frequency (kHz)	Temperature (°C)	A	B	m
Pulsed-current	0.5	50	38.8	3.74	0.65
		100	50.71	4.1	0.6
		200	35.77	4.09	0.78
	1	50	42.35	3.51	0.62
		100	54.22	4.16	0.64
		200	41.07	4.1	0.67
Direct current	–	50	41.91	4.02	0.6
		100	47.87	4.05	0.6
		200	44.92	4.1	0.67

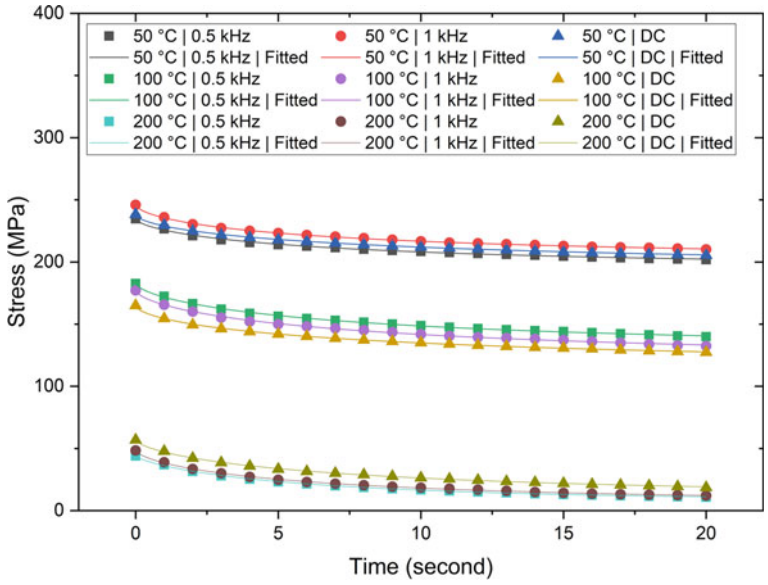


Fig. 3 Time versus nominal stress curve with fitted curve from (3). (Color figure online)

Table 4 Stress relaxation limit and stress exponent

Temperature	σ_r (MPa)			n		
(°C)	0.5 kHz	1 kHz	DC	0.5 kHz	1 kHz	DC
50	198.07	200.78	199.41	29.49	31.44	32.72
100	129.04	128.69	130.35	16.5	16.12	17.67
200	6.28	5.87	11.42	4.29	4.13	4.6

Stress relaxation limit at 50 °C and 100 °C shows no difference despite having different electrical conditions. But, at 200 °C, it is apparent that the stress relaxation limit for DC is slightly higher than the other two. This result agrees with the previous result, which stated that with a high-enough temperature, pulsed-current can produce lower flow stress than DC, given the same operating temperature environment [6]. The stress relaxation limit and initial stress were given in Fig. 4 to produce modified stress–strain curve from each experiment. Disregarding the electrical conditions, the stress–strain curve shows a pattern typical for each temperature group. At 50 °C it shows strain hardening. With increasing temperature, the strain hardening slowly diminishes and at 200 °C it shows thermal softening phenomenon.

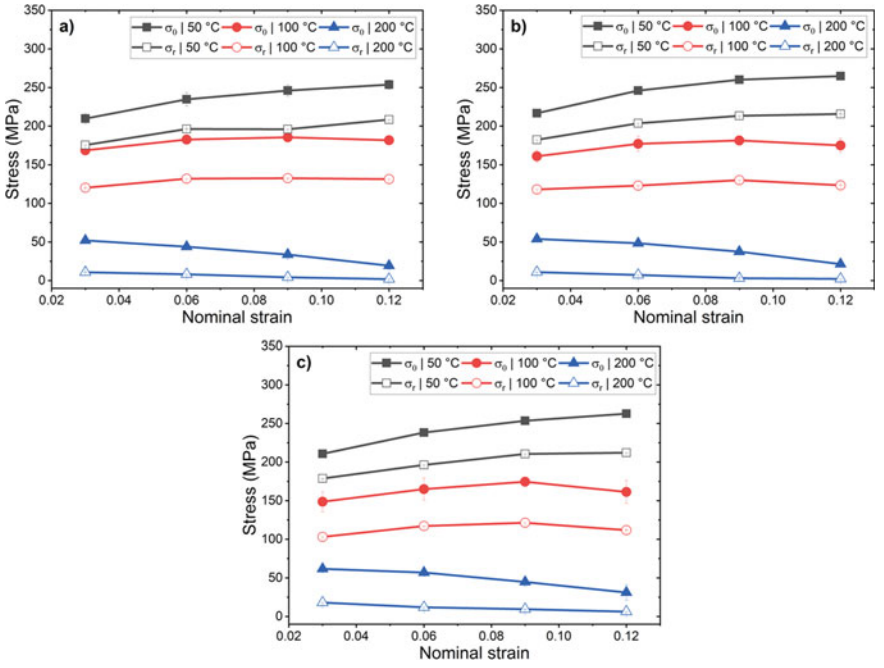


Fig. 4 Modified stress–strain curve with initial stress (σ_0) and stress relaxation limit (σ_r) for **a** 0.5 kHz, **b** 1 kHz, and **c** DC. (Color figure online)

3.2 Stress Exponent

Stress relaxation is regarded as somewhat a kind of plastic deformation where it can be expressed with

$$\varepsilon_0 = \varepsilon_e + \varepsilon_p = constant \tag{4}$$

where ε_0, ε_e, and ε_p represent total strain, elastic strain, and plastic strain, respectively. Considering (4) stress relaxation can also be expressed using creep strain with

$$\dot{\varepsilon}_c = \frac{d\sigma}{dt}\left(-\frac{1}{E}\right) \tag{5}$$

where $\dot{\varepsilon}_c$ is the creep strain rate and E is its elastic modulus. To determine the creep mode at each condition, the stress exponent needs to be calculated. The stress exponent (n) was acquired from the gradient of $\log \dot{\varepsilon}_c / \log \sigma$ [5, 7, 8]. The stress exponent can be seen in Table 4.

The stress exponent did not show a significant difference at the same temperature. It has been stated that the creep mode was mainly regulated by the temperature. At stress exponent n = 1, the creep mechanism is purely diffusive. Grain elongates in the direction of stress due to the diffusion of vacancies through the grain. Vacancies diffusion along grain boundary also contributes to grain elongation. At stress exponent 4–5, climb and annihilation of dislocation mainly control the creep mode. Dislocation climb enhanced by extensive number of vacancies diffusion occurs during stress relaxation [9]. At high stress exponent, it is called power law creep. The power law creep happens at temperature below 50% of its material melting point. In this study, from its low temperature nature, it is apparent that the main mechanism in stress relaxation will be mainly related to dislocation creep. Another consideration is that this study used short time relaxation, meaning it only stays in the first stage of relaxation where most of the diffusion happens rather than in the next stage of relaxation [10]. Also due to this short time nature, the static recovery barely happens and thus grain refining can be avoided [8, 11].

As can be observed from Table 4, this experimental result agrees with the previous law. The stress relaxation at all conditions never goes lower than 4. This means all conditions were subjected to power law creep as its relaxation mechanism. But, as temperature increases, the stress exponent value steadily decreases and approaches 1. At higher temperatures the diffusion rate increases, which also contributes to increased activity of diffusion creep where the dislocation climbs in part due to vacancies diffusion. It is also demonstrated that the stress exponent barely changes with the different electrical conditions at a constant temperature. But it is also worth noting that, despite its minuscule value, DC condition always has higher stress exponent value than the pulsed-current condition.

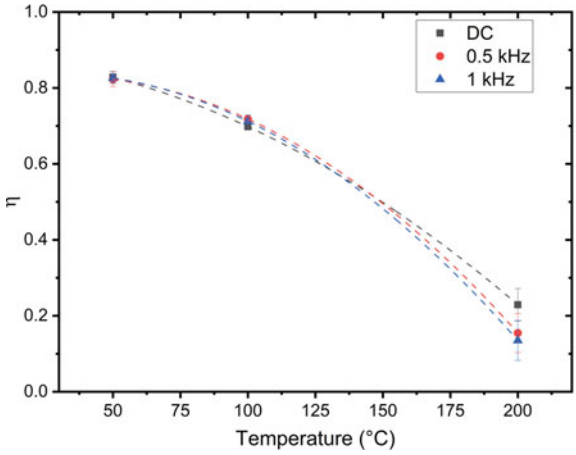


Fig. 5 Relationship between temperature and relaxation resistance at different electricity conditions. (Color figure online)

3.3 Relaxation Resistance

Relaxation resistance (η) can be determined using the ratio between relaxation limit to initial stress. Higher relaxation resistance means it is harder for stress to go down during stress relaxation process [10]. Figure 5 demonstrates the relationship between temperature and relaxation resistance. At 50 °C and 100 °C, the relaxation resistance shows no difference for 0.5 kHz, 1 kHz, and DC. But, at 200 °C the relaxation resistance of DC becomes higher than the other two. From the previous section, it is noted that the relaxation mechanism was mainly dislocation creep. It has been suggested that the movement of dislocation in stress relaxation test was not affected by the flow of current. At 50 °C and 100 °C the thermal effect is the main contributor of movement of dislocation.

At 200 °C, relaxation resistance for DC has a higher value than 0.5 and 1 kHz. As already mentioned before, at higher temperature the value of the stress exponent decreases and becomes closer to 1. It can be said that more diffusion creep mechanisms take effect compared to lower temperature. This result shows that the vacancy diffusion rate is more sensitive to current flow, especially pulsed-current, than dislocation movement, thus promoting dislocation climb. While the DC condition shows higher relaxation resistance, pulsed-current conditions, namely 0.5 kHz and 1 kHz, show no difference in its value.

Several studies state that electropulse can promote dynamic recrystallization and induce grain boundary sliding to take action under relatively poor conditions for AZ31 magnesium alloy [1, 6, 12–16]. It is worth noting that this effect mainly acts near the recrystallization temperature of AZ31, which is around 250 °C. Several prior studies also show that non-basal slip system can be activated at lower temperature, thus further promote the moving of dislocations. Since below 200 °C the main mechanism of relaxation is dislocation creep, the promotion of grain boundary sliding and non-basal slip system at a lower temperature is beneficial to reduce the relaxation resistance.

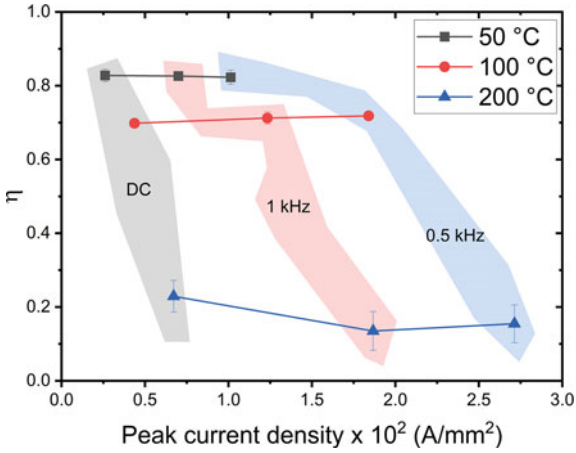


Fig. 6 Relationship between current density and relaxation resistance. (Color figure online)

Figure 6 shows the relationship between current density and relaxation limit. At 50 °C and 100 °C the current density has no effect on the relaxation limit, as already discussed earlier. At 200 °C the current density of 0.5 kHz, 1 kHz, and DC is 271.33 A/mm^2, 186.67 A/mm^2, and 67.18 A/mm^2, respectively. The difference from DC to 1 kHz is nearly three times, while DC to 0.5 kHz is four times. The large distance between the DC and pulsed-current can also be attributed to why the vacancy diffusion rate becomes more active with different electricity conditions. Thus, the relationship between the current density and relaxation mechanism is worth to be discussed as a future study.

4 Conclusions

In this paper, the stress relaxation of AZ31 at different electrical conditions was performed. The mechanism of relaxation at different working temperatures was demonstrated. The stress relaxation mechanism in this study was observed to be mainly law power dislocation at low temperature. The mechanism shifts to corporate more diffusion creep with increasing temperature. Only at 200 °C that the relaxation resistance was found to be different for DC and pulsed-current. But, in pulsed-current, different frequencies did not result in different relaxation limits.

Lower relaxation limit in pulsed-current can be attributed to several mechanisms. First is the promotion of grain boundary sliding induced by dynamic recrystallization which contributes to dislocation creep. The other is increasing the rate of vacancy diffusion, thus enhancing dislocation climb to avoid dislocation to entangle.

Acknowledgments This work was supported by the funding from Tokyo Human Resource Fund for City Diplomacy.

References

1. Bao W, Chu X, Lin S, Gao J (2016) Electro-plastic effect on tensile deformation behaviour and microstructural mechanism of AZ31B alloy. Mater Sci Technol, https://doi.org/10.1080/02670836.2016.1242272
2. Kim MJ et al (2016) Electric current-assisted deformation behavior of Al-Mg-Si alloy under uniaxial tension. Int J Plast, https://doi.org/10.1016/j.ijplas.2016.09.010
3. Xie H, Wang Q, Peng F, Liu K, Dong X, Wang J (2015) Electroplastic effect in AZ31B magnesium alloy sheet through uniaxial tensile tests. Trans Nonferrous Met Soc China, https://doi.org/10.1016/S1003-6326(15)63892-4
4. Liang P, Lin K-L (2017) Non-deformation recrystallization of metal with electric current stressing. J Alloys Compd 722:690–697. https://doi.org/10.1016/j.jallcom.2017.06.032
5. Luo J, Xiong W, Li X, Chen J (2019) Investigation on high-temperature stress relaxation behavior of Ti-6Al-4 V sheet. Mater Sci Eng A 743:755–763, https://doi.org/10.1016/j.msea.2018.11.151
6. Indhiarto I, Shimizu T, Furushima T, Yang M (2018) Effect of DC pulsed-current on deformation behavior of magnesium alloy thin sheets. Procedia Manuf 15, https://doi.org/10.1016/j.promfg.2018.07.270
7. Mitchell TE, Hirth JP, Misra A (2002) Apparent activation energy and stress exponent in materials with a high Peierls stress 50:1087–1093
8. Zong Y, Liu P, Guo B, Shan D (2015) Materials Science & Engineering A Investigation on high temperature short-term creep and stress relaxation of titanium alloy. Mater Sci Eng A 620:172–180. https://doi.org/10.1016/j.msea.2014.10.015
9. Athul KR, Pillai UTS, Srinivasan A, Pai BC (2016) A review of different creep mechanisms in Mg alloys based on stress exponent and activation energy. Adv Eng Mater 18(5):770–794. https://doi.org/10.1002/adem.201500393
10. Oding IA (1965) Creep and stress relaxation in metals. Oliver & Boyd, Edinburgh
11. Liu Y, Yin Z-D, Zhu J-C, Li M-W (2003) Stress relaxation behavior of Ti-6Al-4 V alloy. Trans Nonferrous Met Soc China (English Ed., vol 13, no. 4, pp 881–884
12. Li X, Li X, Zhu J, Ye X, Tang G (2016) Microstructure and texture evolution of cold-rolled Mg–3Al–1Zn alloy by electropulse treatment stimulating recrystallization. Scr Mater 112:23–27. https://doi.org/10.1016/j.scriptamat.2015.09.001
13. Kuang J, Du X, Li X, Yang Y, Luo AA, Tang G (2016) Athermal influence of pulsed electric current on the twinning behavior of Mg–3Al–1Zn alloy during rolling. Scr Mater 114:151–155. https://doi.org/10.1016/j.scriptamat.2015.12.014
14. Liu K, Dong X, Xie H, Peng F (2015) Effect of pulsed current on the deformation behavior of AZ31B magnesium alloy. Mater Sci Eng A, https://doi.org/10.1016/j.msea.2014.11.039
15. Bao W, Chu X, Lin S, Gao J (2015) Experimental investigation on formability and microstructure of AZ31B alloy in electropulse-assisted incremental forming. Mater Des 87:632–639. https://doi.org/10.1016/j.matdes.2015.08.072
16. Xie H, Wang Q, Liu K, Peng F, Dong X, Wang J (2015) Investigation of influence of direct-current pulses on springback during V-bending of AZ31B magnesium alloy sheet. J Mater Process Technol. https://doi.org/10.1016/j.jmatprotec.2014.12.011

Experimental Study on Mechanical Response of Q235 Steel Under Cyclic Stress Loading



Qingling Zhang, Miao Jin, Baofeng Guo, and Qun Li

Abstract The cyclic softening/hardening, ratcheting effect, and Bauschinger effect usually occur in the body structure of large mechanical equipment under cyclic loading. This manuscript focuses on Q235 steel commonly used in the welded frame of large mechanical equipment. The experiments were carried out with mean stress varying from −60 to 60 MPa and stress amplitude varying from 300 to 340 MPa, respectively, and the mechanical responses were analyzed comprehensively. The experimental results show that Q235 steel exhibits cyclic softening characteristics at positive mean stress and cyclic hardening characteristics at negative mean stress. The larger the stress amplitude or the absolute value of the mean stress, the greater the absolute value of ratcheting strain. At the same stress amplitude, when the absolute value of the mean stress is equal, the Bauschinger coefficient is almost equal. Based on the experimental results, the evolution formula of ratcheting strain is established by a phenomenological method.

Keywords Cyclic stress loading · Cyclic softening/hardening · Ratcheting · Bauschinger effect

1 Introduction

Q235 steel is usually used as the raw material of the hydraulic press beam and other structural parts, due to its plasticity, toughness, good weldability, strength, and high-cost performance. In engineering applications, the hydraulic press beam is often subject to cyclic loading in the process of work. Because of its complexity in

Funding Information: Natural Science Foundation of China (51575474); Natural Science Foundation of Hebei Province, China (E2019203560)

Q. Zhang · M. Jin (✉) · B. Guo · Q. Li
School of Mechanical Engineering, Yanshan University, Qinhuangdao 066004, People's Republic of China
e-mail: jmiao@ysu.edu.cn

Key Laboratory of Advanced Forging & Stamping Technology and Science, Ministry of Education of China, Yanshan University, Qinhuangdao 066004, People's Republic of China

© The Minerals, Metals & Materials Society 2021

G. Daehn et al. (eds.), *Forming the Future*, The Minerals, Metals & Materials Series,
https://doi.org/10.1007/978-3-030-75381-8_67

the structure, it is easy to produce stress concentration phenomena and even plastic deformation in the local area. Therefore, to study the deformation behavior of Q235 steel under cyclic loading after plastic deformation is very meaningful.

After plastic deformation of the structure, ratcheting effect, Bauschinger effect, and cyclic softening/hardening behavior will occur under cyclic loading. These cyclic deformation behaviors directly affect the design and safety evaluation of the beam structure of the hydraulic press.

Scholars at home and abroad have done a lot of research on the mechanical response of different materials under cyclic loading [1–6]. They also analyzed the influence of loading rate, stress amplitude, maximum stress, mean stress, and loading history on the cyclic softening/hardening and ratcheting effect about 316L stainless steel, 16Mn, SUS301L stainless steel, and 2024-T3 aluminum alloy. Lee [7] simulated the deformation behavior of two-phase stainless steel S32750 with the new constitutive model, and further verified the influence of positive mean stress, stress amplitude, and loading history on the behavior of uniaxial ratcheting. Segle et al. [8] conducted combined loading tests of the main loading and side loading on ferrite steel P265 and austenite steel 316L simultaneously, and concluded that ratcheting effect increases with the increase of loading level. Zhifeng [9] studied the relationship between ratcheting effect and microstructure of hot-rolled AZ31B magnesium alloy under asymmetric stress cyclic loading. Kang [10–12] explored the influence of mean stress, stress amplitude, and stress ratio on ratcheting strain of SS304 stainless steel at room temperature, and revealed cyclic soft/hardening characteristics and ratcheting deformation behavior of SS304 stainless steel under different loading rates, different holding time, and non-proportional loading paths. Zhang et al. [13] obtained the conditions for ratcheting effect of Q235 steel when the average stress was positive, through cyclic loading tests under different stress combinations.

Mingsen [14] carried out an axial tension-compression cyclic loading test on 7A04 aluminum alloy with four different strain values to explore the Bauschinger effect generated in the plastic deformation process after small pre-stress. Qingling et al. [15] found that under small symmetric strain cyclic loading, the cyclic hardening rate and the change rate of Bauschinger energy parameters of Q235 would eventually reach a stable value with the increase of cycle numbers. Chao [16] found that both QP980 and QP1180 show the Bauschinger effect through the tension-compression cyclic loading test. The authors of [17–19] studied the Bauschinger effect of as-cast A356-T6 aluminum alloy, rolled 7075 aluminum alloy, carbon steel, and X80 steel under different pre-strain, different heat treatment processes, microstructure, and yield ratio. Han [20] carried out the tension-compression loading experiment on low carbon steel, low alloy steel, and duplex steel, and found that the Bauschinger effect on the three materials is related to the pre-strain but not to the strain rate.

Although many researchers have studied the cyclic deformation behaviors of different metal materials in many aspects, studies on Q235 steel in this area are rare, especially under the conditions of zero and negative mean stress. Therefore, the plastic deformation response of Q235 steel was analyzed in this work at positive, zero, and negative mean stress, which can provide more comprehensive experimental data and theoretical basis for the engineering application of Q235 steel.

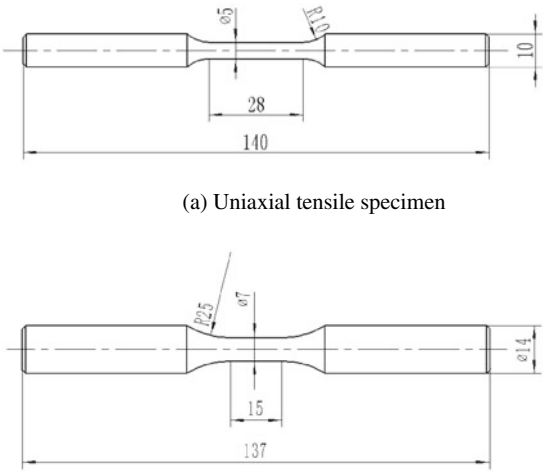
2 Experimental Procedure

All the experimental specimens are solid bars cut from Q235 steel plate in the rolling direction. The thickness of the steel plate is 20 mm. The specimens have a circular section and are processed according to the national standard GB228.1-2010 and GBT 3075-2008. The basic sizes of the uniaxial tensile specimen and cyclic loading specimen are shown in Fig. 1.

All experiments were carried out on Instron 8801 electro-hydraulic servo fatigue testing machine, which was equipped with contact extensometers. The extensometer with a 25 mm gauge was used for uniaxial tensile experiments, and the extensometer with a 12.5 mm gauge was used for cyclic loading experiments. The measurement accuracy of the two extensometers is 0.1 um.

Uniaxial tensile experiments were controlled by strain, and the strain rate was 0.1%. The basic mechanical properties of Q235 steel at room temperature were obtained through three repeated tests, which are shown in Table 1.

According to the properties of Q235 steel obtained from uniaxial tensile and uniaxial compressive experiments, the loading conditions of cyclic stress loading experiments were determined. The specific experimental scheme is listed in Table 2.



(a) Uniaxial tensile specimen

(b) Cyclic loading specimen

Fig. 1 The basic dimension of specimen (unit: mm)

Table 1 The results of uniaxial tensile and compressive experiments

Test	Elasticity modulus (E)/GPa	Upper yield limit (σ_s')/MPa	Lower yield limit (σ_s)/MPa
Tensile	210	310	243
Compressive	206	326	238

Table 2 Various combinations of mean stress and stress amplitude for ratcheting experiments

Sample number	Mean stress (σ_m)/MPa	Stress amplitude (σ_a)/MPa	Number of cycles (N)/c
FYL-01	−20	300	100
FYL -02	−20	320	100
FYL -03	−20	340	100
FYL -04	−40	300	100
FYL -05	−60	300	100
DCYL-06	0	300	100
DCYL-07	0	320	100
DCYL-08	0	340	100
ZYL-09	20	300	30
ZYL-10	20	320	30
ZYL-11	20	340	30
ZYL-12	40	300	30
ZYL-13	60	300	30

In order to keep the loading rate consistent during each cyclic loading process, triangular wave loading was adopted. The loading waveforms under different stress conditions are shown in Fig. 2. The loading rate was set to 40 MPa/s.

3 Results and Discussion

3.1 Analysis of Ratcheting Effect

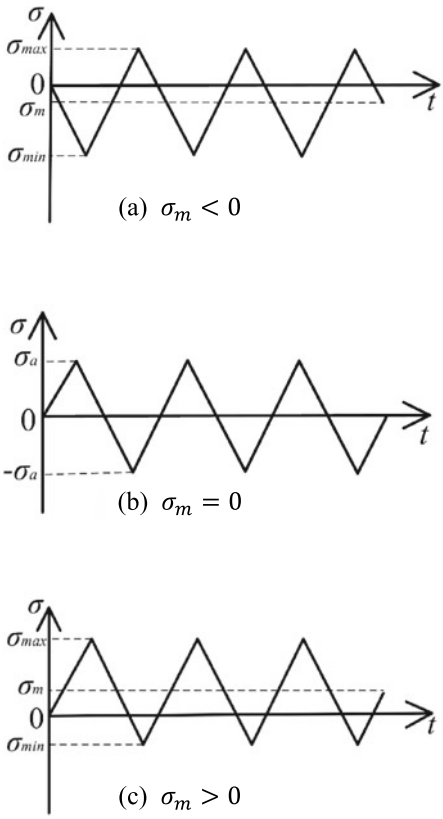
The traditional ratcheting effect is defined as the cyclic accumulation of plastic strain under asymmetric stress loading. However, this phenomenon is also found under symmetric stress loading. In this manuscript, the ratcheting strain $_{\mathrm{r}}$ is calculated by formula 1.

$$\varepsilon_{\mathrm{r}} = \left(\varepsilon^{\mathrm{T}}_{\max} + \varepsilon^{\mathrm{T}}_{\min}\right)/2 \tag{1}$$

where $\varepsilon^{T}_{\max}$, $\varepsilon^{T}_{\min}$, respectively, represent the maximum and minimum true strains in a cycle. The increment of ratcheting strain in each cycle is called the ratcheting strain rate, in terms of $\mathrm{d}_{\mathrm{r}}/\mathrm{d}N$, where N is the cyclic numbers.

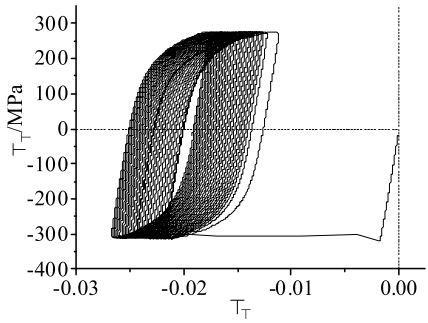
Figure 3 shows the stress–strain hysteretic curve of Q235 steel during cyclic loading with stress amplitude of 300 MPa and mean stress of −20 MPa, 0 MPa, and 20 MPa. In this figure, $_{\mathrm{T}}$ represents the true strain and $_{\mathrm{T}}$ represents the true stress. Since there is yield platform in the hysteretic curve of Q235, the strain in the first

Fig. 2 The loading curves

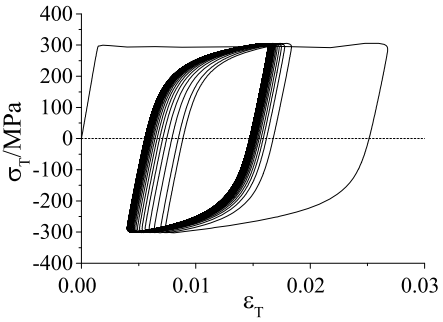


cycle is large. As shown in Fig. 3, no matter the mean stress is positive, negative, or zero, the hysteretic curves of Q235 do not close, which means the ratcheting phenomenon has occurred. When the mean stress is negative, the hysteretic curve moves toward the negative direction of the strain. When the mean stress is zero, the hysteretic curve first moves toward the negative direction of the strain for several cycles and then turns to the positive direction. When the mean stress is positive, the hysteretic curve always moves toward the positive direction of the strain.

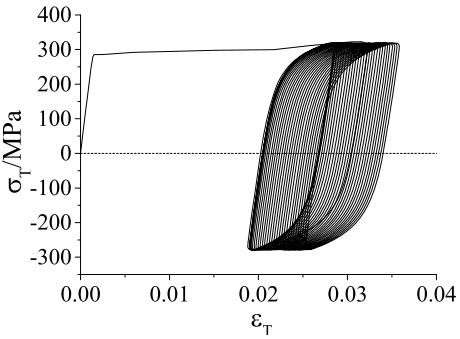
The ratcheting strain under various loading conditions was calculated according to formula (1). Due to the influence of the yield platform, the ratcheting strain in the first cycle should be discarded. The calculation of ratcheting strain starts from the second cycle in this manuscript. The variation curve of ratcheting strain with cyclic numbers under different mean stress at the same stress amplitude of 300 MPa is illustrated in Fig. 4. The ratcheting strain is positive when the mean stress is positive, and the ratcheting strain is negative when the mean stress is negative. The greater the absolute value of average stress, the greater is the absolute value of ratchet strain. The absolute value of ratcheting strain increases as the cycle numbers



（a）-20±300MPa



（b）0±300MPa



（c）20±300MPa

Fig. 3 Cyclic stress–strain curve

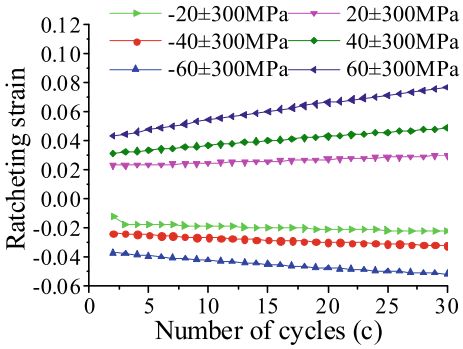


Fig. 4 The ratcheting strain versus cycle numbers at the stress amplitude of 300 MPa. (Color figure online)

increase. Although the variation trend of ratcheting strain under different mean stress is similar, ratcheting strain rate is different. With the increase of cyclic numbers, ratcheting strain rate becomes stable gradually. If the stable value of ratcheting strain rate is higher than the mean stress is, the greater is the ratcheting strain rate. When the mean stress is negative, the ratcheting strain rate increases with the increase of the absolute value of the mean stress also, but it is not as significant as the positive mean stress.

Figure 5 presents the ratcheting strain under different stress amplitudes when the mean stress is positive, zero, and negative. It can be observed that the ratcheting strain and ratcheting strain rate all increase with the increase of stress amplitude, no matter the mean stress value is positive or negative. Under the control of symmetrical cyclic stress loading, the ratcheting strain decreases rapidly in the first ten cycles and then increases gradually. The ratcheting strain rate also increases with the increase of stress amplitude (Table 3).

According to the above analysis, the ratcheting strain of Q235 steel relates to the mean stress, stress amplitude, and cyclic numbers. Based on the phenomenological theory, the following calculation formula of the ratcheting strain is established.

$$\varepsilon_r = \begin{cases} \dfrac{\lambda\eta\sigma_m}{\sigma_s{}'-\sigma_s}\exp(\eta)N + \dfrac{\varepsilon'}{\eta}\sigma_m > 0 \\ \dfrac{\lambda\eta^3}{\sigma_s{}'-\sigma_s}\exp(\eta)N + \dfrac{\varepsilon'}{\eta^2}\sigma_m = 0 \\ \dfrac{\lambda\sigma_m}{(\sigma_s{}'-\sigma_s)\eta}\exp(\eta)N - \dfrac{\varepsilon'}{\eta}\sigma_m < 0 \end{cases} \tag{2}$$

where λ is the material parameter, and it is 3.5 for Q235 which can be obtained by fitting the ratcheting strain with cyclic numbers under stress loading; ε' is the strain in uniaxial tensile stress–strain curve corresponding to the peak stress of applied loading in cyclic stress experiment; $\eta = \sigma_a/\sigma_s$.

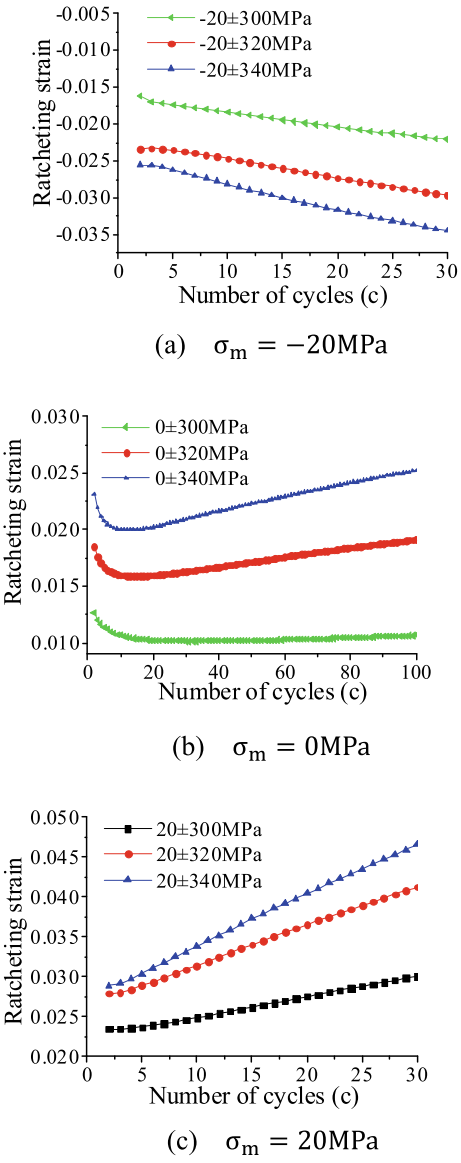


Fig. 5 The ratcheting strain versus cycle numbers at different stress level. (Color figure online)

As shown in Fig. 6, the ratcheting strain calculated by the formula (2) and the data obtained from the test are in good agreement. Therefore, this formula can characterize the ratcheting effect of Q235 steel very well.

Table 3 The ratcheting strain rate at the stress amplitude of 300 MPa

Stress level (MPa)		Ratcheting strain rate (10^{-3}%/c)
Stress amplitude	Mean stress	
300	−60	−0.38
	−40	−0.23
	−20	−0.16
	20	0.25
	40	0.56
	60	1.04

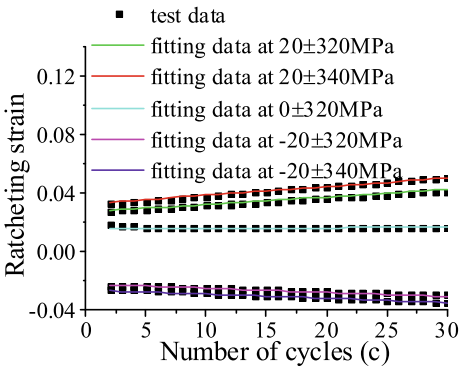


Fig. 6 Comparison of the test data and fitting data. (Color figure online)

3.2 Analysis of Cyclic Softening/Hardening

Q235 steel shows different cyclic softening and hardening behaviors under different stress loading conditions. Figure 7 shows the evolution of strain amplitude with cyclic numbers under the same stress amplitude of 300 MPa and different mean stress. The corresponding cyclic softening and hardening rates are shown in Table 4. Figure 7a and Table 4 illustrate that when the mean stress is negative, Q235 steel presents hardening characteristics with the increase of cyclic numbers eventually, and the smaller the absolute value of the average stress, the greater is the absolute value of the cyclic hardening rate. It can also be observed that when the mean stress is positive, the cyclic softening phenomenon appears, and the greater the mean stress, the higher is the cyclic softening rate.

Figure 8 presents the change of strain amplitude with cyclic numbers under different stress amplitudes, when the mean stress is −20 MPa, 0 MPa, and 20 MPa. As shown in Fig. 8a, when the mean stress is −20 MPa, cyclic hardening occurs after ten cycles of softening. It can be seen from Fig. 8b, when the mean stress is 0 MPa, the strain response is similar to the negative mean stress, which is softening

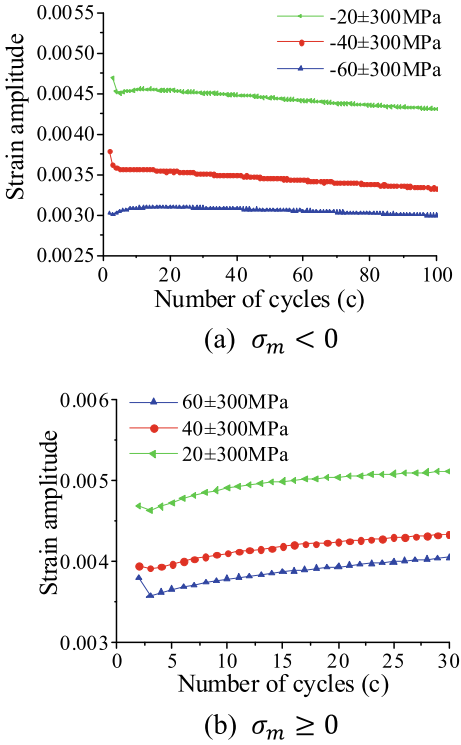


Fig. 7 The strain amplitude versus cycle numbers at the stress amplitude of 300 MPa. (Color figure online)

Table 4 The cycling hardening/softening rate at the stress amplitude of 300 MPa

Stress level (MPa)		Cycling hardening rate (10^{-5}%/c)	Cycling softening rate (10^{-5}%/c)
Stress amplitude	Mean stress		
300	−60	−0.132	–
	−40	−0.263	–
	−20	−0.295	–
	20	–	0.732
	40	–	0.973
	60	–	1.174

before hardening. When the mean stress is 20 MPa, Q235 presents the cyclic softening characteristic. These conclusions are consistent with the foregoing analysis of Fig. 7.

Under these three kinds of loading conditions, there is no cycle hardening saturation in the test cycle. The cyclic softening and hardening rate tends to stabilize to a non-zero constant with the increase of the cycle numbers. The steady rates of cyclic

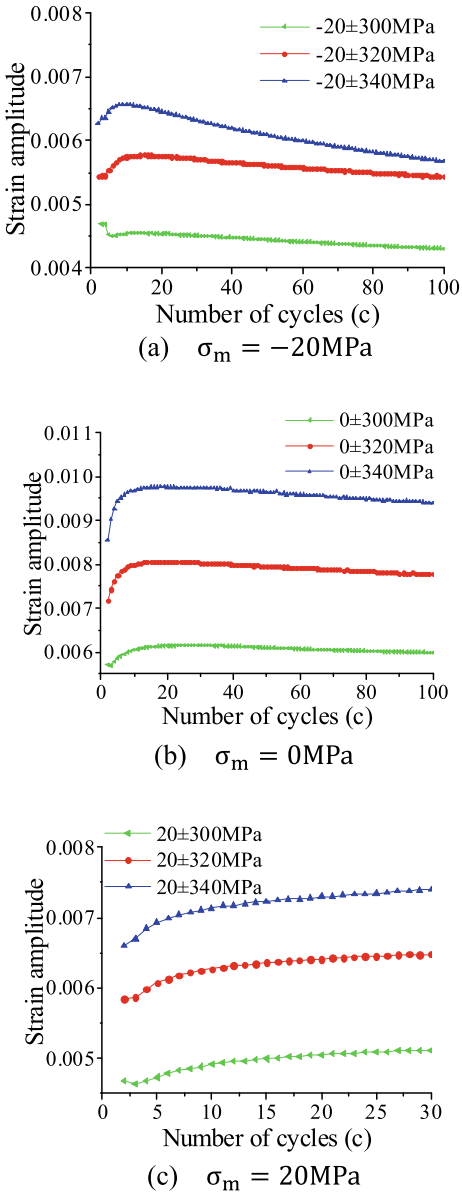


Fig. 8 The strain amplitude versus cycle numbers. (Color figure online)

softening and hardening are listed in Table 5. It is obvious that under the same mean stress condition, the higher the stress amplitude, the higher is the absolute value of cyclic softening or cyclic hardening rate.

Combined with Figs. 7 and 8, when the mean stress is negative, the smaller the absolute value of the mean stress or the larger the stress amplitude, the more

Table 5 The cycling hardening/softening rate at the mean stress of −20 MPa, 0 MPa, and 20 MPa

Stress level (MPa)		Cycling hardening rate (10^{-5}%/c)	Cycling softening rate (10^{-5}%/c)
Mean stress	Stress amplitude		
−20	300	−0.295	–
	320	−0.405	–
	340	−0.947	–
0	300	−0.239	–
	320	−0.378	–
	340	−0.481	–
20	300	–	0.732
	320	–	0.786
	340	–	1.071

obvious is the cyclic hardening. When the mean stress is positive, the cyclic softening phenomenon slightly intensifies with the increase of the mean stress and stress amplitude. When the mean stress is zero, the cyclic softening behavior increases with the increase of stress amplitude.

3.3 Analysis of Bauschinger Effect

Bauschinger effect means that the yield strength decreases obviously compared with the performance of the original pre-deformation direction when the metal deformed in a certain direction in advance and then deformed in the opposite direction. The yield stress in this manuscript is calculated when 0.2% elongation occurs in the material, i.e. $\sigma_{0.2}$, as shown in Fig. 9.

The variation curves of yield stress under different mean stress at the stress amplitude of 300 MPa are illustrated in Fig. 10. As shown in the figure, when the mean stress is negative, the compressive yield stress is greater than the tensile yield stress, and with the increase of the absolute value of the mean stress, the compressive yield

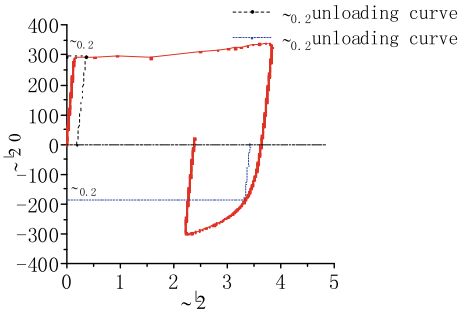


Fig. 9 Method to obtain yield stress $\sigma_{0.2}$. (Color figure online)

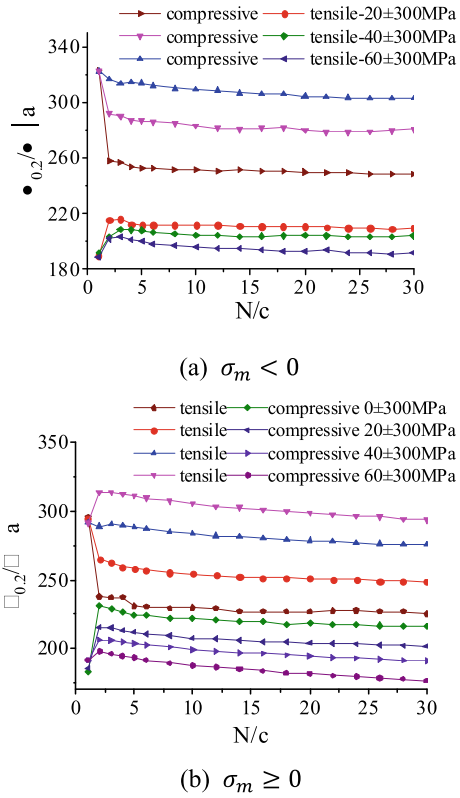


Fig. 10 Yield stress with different mean stress at the stress amplitude of 300 MPa. (Color figure online)

stress increases, while the tensile yield stress decreases. When the mean stress is positive, the tensile yield stress is greater than the compressive yield stress, and with the increase of the mean stress, the tensile yield stress increases, while the compressive yield stress decreases. When the mean stress is zero, the tensile and compressive yield stresses still differ by about 10 MPa due to asymmetrical tensile and compressive properties.

The yield stresses of each cycle under the same mean stress and different amplitude are presented in Fig. 11. It is consistent with the conclusion drawn in Fig. 10 that under the stress loading, the higher the tensile loading or the compressive loading, the higher is the yield stress in the corresponding direction. As the stress loading is symmetrical, the yield stress is not equal due to the asymmetry of tensile and compressive properties. When the mean stress is constant, the yield stress changes slightly with the increase of the stress amplitude. By comparing Figs. 10 and 11, it can be observed that under the same peak stress, the mean stress has a more significant influence on the yield stress than the stress amplitude.

In order to describe the Bauschinger effect more intuitively, the Bauschinger coefficient is introduced. The Bauschinger coefficient relates directly to the change of yield stress after pretension/precompression deformation under cyclic loading.

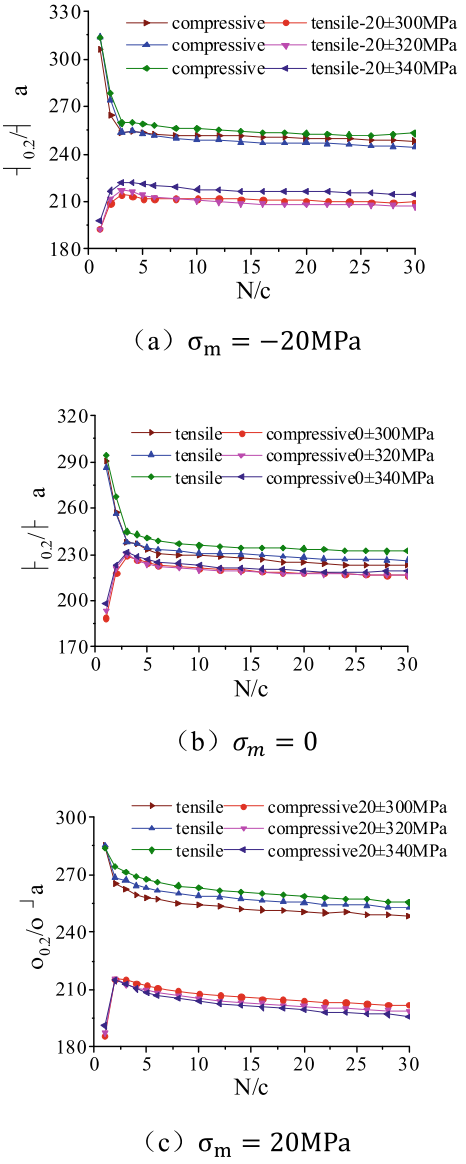


Fig. 11 Yield stress with different stress amplitudes at the same mean stress. (Color figure online)

The more the yield strength decreases, the higher is the Bauschinger coefficient, and the more obvious is the Bauschinger effect. The Bauschinger coefficient is expressed as follows:

$$B = \begin{cases} \frac{\sigma_{0.2}^{+} - \sigma_{0.2}^{-}}{\sigma_{0.2}^{+}} & \sigma_m > 0 \\ \frac{\sigma_{0.2}^{-} - \sigma_{0.2}^{+}}{\sigma_{0.2}^{-}} & \sigma_m \leq 0 \end{cases} \tag{3}$$

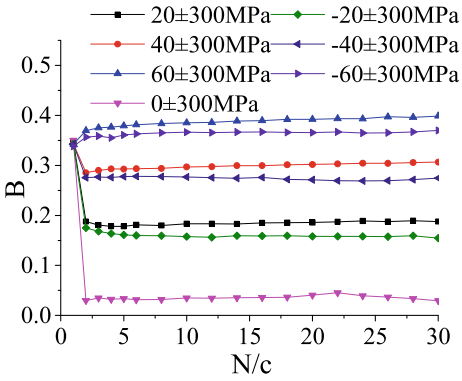


Fig. 12 The variation of Bauschinger coefficient with cyclic numbers at the stress amplitude of 300 MPa. (Color figure online)

where $\sigma_{0.2}^{+}$ is for the tensile yield stress, and $\sigma_{0.2}^{-}$ is for the compressive yield stress.

The variation trend of the Bauschinger coefficient with the cyclic numbers at different mean stress is drawn in Fig. 12, when the stress amplitude is 300 MPa. As can be seen from the figure, the Bauschinger coefficients in the first cycle are nearly equal under different stress loading, but it is greatly different from the second cycle. The larger the mean stress, the larger is the Bauschinger coefficient, which means more obvious the Bauschinger effect. The values of the Bauschinger coefficient in the second cycle under various loading conditions and the change rates in the subsequent cycles are given in Table 6. It can be concluded that if the absolute value of the mean stress is equal, the Bauschinger coefficient is very close, and the Bauschinger coefficient changes little after the second cycle. It is feasible to use the Bauschinger coefficient in the second cycle to describe the influence of Bauschinger effect on the mechanical properties of Q235 steel.

Table 6 Change rates of Bauschinger coefficient with cyclic numbers at different stress levels

Stress level (MPa)		B at the second cycle	Growth rate (10^{-4})
Stress amplitude	Mean stress		
300	−20	0.1750	−1.63
	−400	0.2757	−2.57
	−60	0.3565	−1.88
	0	0.0298	−0.47
	20	0.1876	3.15
	40	0.2853	4.88
	60	0.3696	6.43

4 Conclusions

(1) Ratcheting effect will occur when Q235 is subjected to both symmetric and asymmetric cyclic stress loading.
(2) When the mean stress is the same, the greater the stress amplitude is, the greater the absolute value of ratcheting strain and the ratcheting strain rate; when the stress amplitude is the same, the greater the mean stress is, the greater the absolute value of ratcheting strain and the ratcheting strain rate is.
(3) Q235 steel shows cyclic softening properties, which become more obvious with the increase of the mean stress and the stress amplitude when the mean stress is positive. Q235 steel shows cyclic hardening properties, which become more obvious with the decrease of the absolute value of the mean stress and the increase of the stress amplitude when the mean stress is non-positive.
(4) The Bauschinger coefficient of Q235 steel is nearly equal, when the absolute value of the mean stress is the same, and the Bauschinger coefficient of the second cycle can be used to characterize the Bauschinger effect of the material.

References

1. Xianjie Y, Qing G, Lixun C, Yangkai X (1997) On the ratcheting effects of 316L stainless steel under uniaxial loading. Acta Aeronautica et Astronautica Sinica 4:12–17
2. Jian P, Yi G, Qiao D, Ying W, Kaishang L (2019) Fatigue and cycle plastic behavior of 316L austenitic stainless steel under asymmetric load. Acta Metallurgica Sinica 55(06):773–782
3. Yi Z, Zhixiang Z, Shufang L (2019) Experiment researches for 16Mn steel under proportional and non-proportional stressing. J Chongqing Jiaotong Univ (Nat Sci) 29(02):311–314
4. Yuan X, Yu W, Fu S, Yu D, Chen X (2016) Effect of mean stress and ratcheting strain on the low cycle fatigue behavior of a wrought 316LN stainless steel. Mater Sci Eng A, 677
5. Luo H, Kang G, Kan Q et al (2017) Experimental investigation on the heterogeneous ratchetting of SUS301L stainless steel butt weld joint during uniaxial cyclic loading. Int J Fatigue S014211231730364X
6. Abdollahi E, Chakherlou TN (2017) Numerical and experimental study of ratcheting in cold expanded plate of Al-alloy 2024-T3 in double shear lap joints. Fatigue Fract Eng Mater Struct
7. Lee C-H, Nguyen V, Do V, Chang K-H (2014) Analysis of uniaxial ratcheting behavior and cyclic mean stress relaxation of a duplex stainless steel. Int J Plasticity, 62
8. Segle P, Eklund G, Skog M (2016) A two-rod testing approach for understanding ratcheting in structures. Int J Pressure Vessels Piping, 139–140
9. Zhifeng Y, Denghui W, Wenxian W et al (2018) Ratcheting strain and microstructure evolution of AZ31B magnesium alloy under a tensile-tensile cyclic loading. Materials 11(4):513
10. Kang G, Liu Y, Li Z (2006) Experimental study on ratchetting-fatigue interaction of SS304 stainless steel in uniaxial cyclic stressing. Mater Sci Eng A, 435
11. Kang G, Gao Q, Yang X (2004) Uniaxial and non-proportionally multiaxial ratcheting of SS304 stainless steel at room temperature: Experiments and simulations. Int J Non-Linear Mech 39(5):843–857
12. Qianhua K, Guozheng K, Juan Z, Yujie L (2005) Experimental study on non-proportionally multiaxial time-dependent cyclic deformations of SS304 stainless steel at high temperature. Acta Metall Sin 09:963–968

13. Zhang Q, Jin M, Li Q, Guo B (2019) Thehysteretic curve characteristics on Q235 steel under asymmetrical cyclic loading. J Brazilian Soc Mech Sci Eng 8(9), 41
14. Mingsen C, Jing H, Xia C, Guangze D (2015) Effect of strain capacities on Bauschinger effect of 7A04 aluminum alloy. Hot Working Technol 44(06):55–59
15. Qingling Z, Miao J, Hongsheng Z, Hao Zou Zongyuan D (2017) Experiment research on material characteristics of Q235 under small deformation cyclic loading. J Mech Eng, 53(20):69–76
16. Chao N, Xinping C, Jun C (2019) Theory and application study on springback prediction accuracy for QP steel with different material hardening models. J Plasticity Eng 26(01):221–226
17. Jordon JB, Horstemeyer MF, Solanki K et al (2007) Damage and stress state influence on the Bauschinger effect in aluminum alloys. Mech Mater 39(10):920–931
18. Hemmerich E, Rolfe B, Hodgson PD et al (2011) The effect of pre-strain on the material behaviour and the Bauschinger effect in the bending of hot rolled and aged steel. Mater Sci Eng A 528(9):3302–3309
19. Han SY, Sohn SS, Shin SY et al (2012) Effects of microstructure and yield ratio on strain hardening and Bauschinger effect in two API X80 linepipe steels. Mater Sci Eng A 551(31):192–199
20. Han K, Tyne CJV, Levy BS (2005) Effect of strain and strain rate on the bauschinger effect response of three different steels. Metall Mater Trans A 36(9):2379–2384

The Effect of Trace Nitrogen on Microstructure and Property of Cr-Mo-V Hot-Working Die Steel



Jinbo Gu, Jingyuan Li, and Lihao Li

Abstract The effect of trace nitrogen on microstructure, hardness, toughness, and tempering stability of Cr-Mo-V hot-working die steel was investigated in this study. Results show that trace nitrogen promotes the precipitation of V(C, N), increasing the amounts of undissolved carbides in tempered steel. The undissolved carbides exert a stronger pinning effect on refining austenitic grains during the quenching process and refine the final tempered microstructure. The solid solubility of alloying elements and lattice distortion of matrix decreased obviously by trace nitrogen. Trace nitrogen could increase the hardness and toughness of hot-working die steel by refining the microstructure. However, the tempering stability would be decreased obviously due to the decrease of solid solubility of alloy elements, especially V. The results of this research can be used to provide a scientific basis for applications of nitrogen in hot-working die steel.

Keywords Nitrogen · Die steel · Hardness · Toughness · Tempering stability

1 Introduction

Due to its high hot hardness and toughness, Cr-Mo-V die steel is commonly used in forging, hot-extrusion, and die-casting [1, 2]. There have been many studies on the development of hot-working die steel, including composition adjustment and process improvement. The effect of different alloy elements such as Nb [3, 4] and Re [5] on die steel has been widely investigated. However, there are few reports about the application of nitrogen on this type of steel. On the other hand, it has been widely recognized that nitrogen can be used as a useful alloy element, especially in austenitic stainless steel. Trace nitrogen could enlarge the austenite phase region,

J. Gu · J. Li (✉) · L. Li
School of Materials Science and Engineering, University of Science and Technology, Beijing 100083, China
e-mail: lijy@ustb.edu.cn

J. Gu
e-mail: gujinboustb@163.com

© The Minerals, Metals & Materials Society 2021

G. Daehn et al. (eds.), *Forming the Future*, The Minerals, Metals & Materials Series,
https://doi.org/10.1007/978-3-030-75381-8_68

enhance the solution strengthening effect, and improve the corrosion resistance [6, 7]. Especially, trace nitrogen plays an important role in delaying precipitation and coarsening of carbide which is a benefit to improve the structural stability of steel [8]. Therefore, there is an application prospect of nitrogen on hot-working die steel, according to its strengthening mechanism.

The purpose of the present research is to study the effect of trace nitrogen on microstructure, hardness, toughness. and tempering stability of Dievar (4Cr5Mo2V) hot-working die steel. The results of this research can be used to provide a scientific basis for applications of nitrogen in hot-working die steel.

2 Experimental

Two 50 kg ingots of Dievar steel were prepared in a vacuum induction melting furnace with the measured composition as listed in Table 1. The nitrogen-alloyed steel was melted under the protection of the nitrogen atmosphere. The ingots were heated to 1250 °C and held at that temperature for 3 h for sufficient multi-directional forging between 850 and 1150 °C. After forging, 850–650 °C annealing process at a rate of 10 °C/h was adopted to the ingots, and then air-cooled. Subsequently, the samples were austenitized at 1030 °C for 30 min, quenched in oil to attain martensite, and then tempered at 600 °C for 4 h to produce tempered martensite. A Rockwell hardness tester (TH320, Beijing TIME Group Co., Ltd, China) and impact testing machine (JB-30B, Jinan Hensgrand Instrument Co., Ltd., China) were used to measure the HRC hardness and impact toughness using the Charpy V-notch test method (ASTM A370). The tempered microstructure was observed using scanning electron microscopy (SEM; S-360, CAMBRIDGE, England) equipped with energy-dispersive X-ray spectroscopy (EDS). The effect of nitrogen on precipitates and solid solubility of alloying elements was analyzed by Thermo-Calc software and X-ray diffraction (XRD; DMAX-RB, Rigaku, Japan).

Table 1 Chemical compositions of tested steel (wt%)

Samples	C	Si	Mn	Cr	Mo	V	P	S	N	Fe
Dievar	0.39	0.48	0.38	5.3	2.4	0.68	0.0076	0.0038	0.004	Bal.
Dievar(N)	0.39	0.48	0.40	5.26	2.4	0.70	0.064	0.0032	0.042	Bal.

3 Results and Discussion

3.1 Microstructure

The final tempering microstructure of the two steels consists of tempered martensite, undissolved carbide, and a small amount of residual austenite, as shown in Fig. 1. It is observed that the martensite is uniformly distributed in the original austenite matrix. The major difference between the two steels is that the undissolved carbides measured 100 nm of Dievar(N) steel, which is much more than that of Dievar steel. Further, EDS map (Fig. 2) confirms that the undissolved carbides were enriched with V and little Cr or Mo, indicating that nitrogen addition increased the V-rich carbides. Moreover, the original austenite size of Dievar(N) is 10 μm, much smaller than that of Dievar steel.

To investigate the crystal structure of martensite lath, electron back-scattered diffraction (EBSD) was subjected to tempered samples. As shown in Fig. 3, the tempered martensite slab structure of two steels is clearly visible. The original austenite grain is composed of several slat bundles with different orientations, and each slat bundle includes several slat blocks. The orientation difference of the strip bundles on both sides of the original austenitic grain boundary is obvious, which is attributed to that the martensite strip first grows in the nucleus of the original austenitic grain boundary and then grows on both sides during the quenching process [9, 10]. Further grain size statistics show that the sub-grain of Dievar(N) steel is obviously small, which proves that the grain of the original austenite is small and the degree of martensite strip coarsening is relatively small during the tempering process.

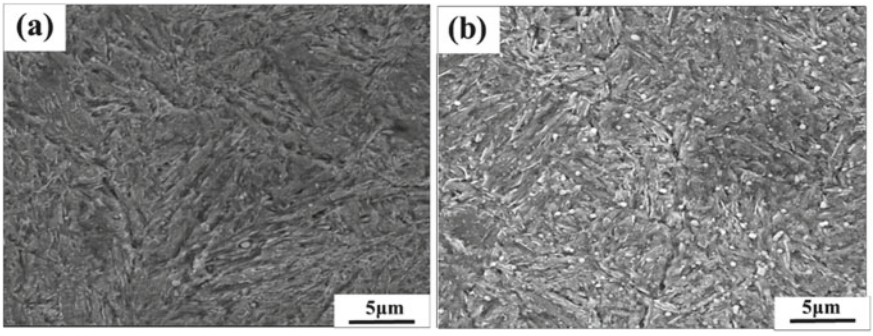


Fig. 1 Microstructure of tempered steel: **a** Dievar; **b** Dievar(N)

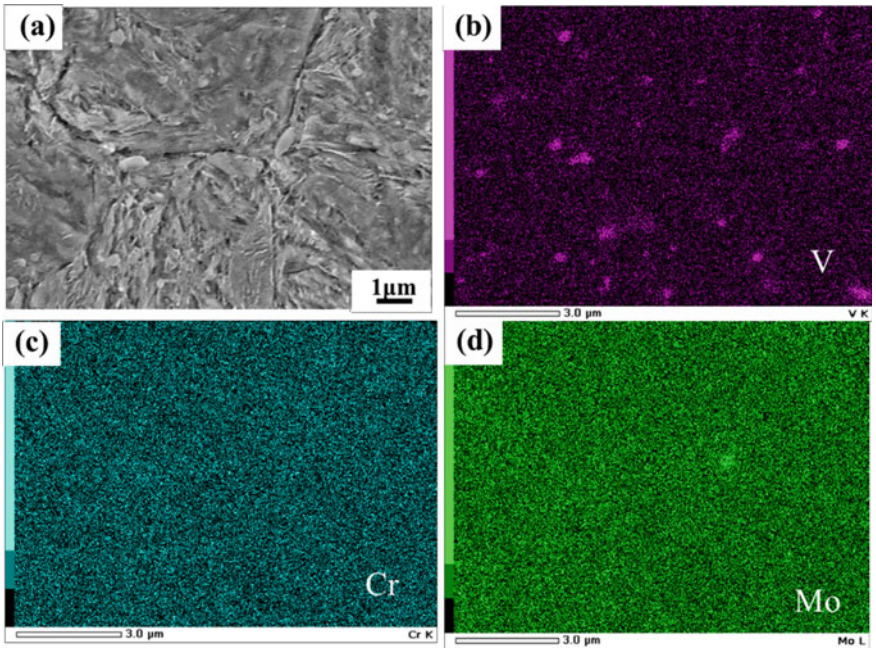


Fig. 2 The EDS map of undissolved carbide. **a** Morphology; **b–d** EDS map of V, Cr, and Mo. (Color figure online)

3.2 Mechanical Properties and Tempering Stability

The mechanical properties of steel were as shown in Fig. 4a. As can be seen, the hardness and toughness of Dievar steel are 49HRC and 18 J cm^{-2}, respectively, while those are 51.5HRC and 21 J · cm^{-2} for Dievar(N) steel. Obviously, trace nitrogen has the benefit of increasing the hardness and toughness of steel. In general, the increase of hardness is easy to result in a decrease of toughness. Obviously, the reason for the above phenomenon was ascribed to the refinement of microstructure, as shown in Fig. 2.

As known to all, tempering stability is another important performance, which is closely related to the service life of die steel. In this study, Dievar steel and Dievar(N) steel exhibited different tempering stability, as shown in Fig. 4b. The initial hardness of the samples at quenched state was 53HRC and 55.5HRC for Dievar and Dievar(N) steel, respectively. The hardness of both steels decreased continuously with the increase of tempering time. The hardness of Dievar(N) steel is higher than that of Dievar steel between 0 and 24 h. But when tempered time increase to 48 h, the hardness of Dievar(N) begins to fall below that of Dievar steel, exhibiting poor tempering stability. Figure 5 shows the microstructure of samples tempered for 24 and 48 h. As can be seen from Fig. 5a and b, the martensite characteristics of the lath are no longer obvious, indicating the recovery of matrix [11]. However, the amount of carbides is not so much different from the samples tempered for 4 h, which means

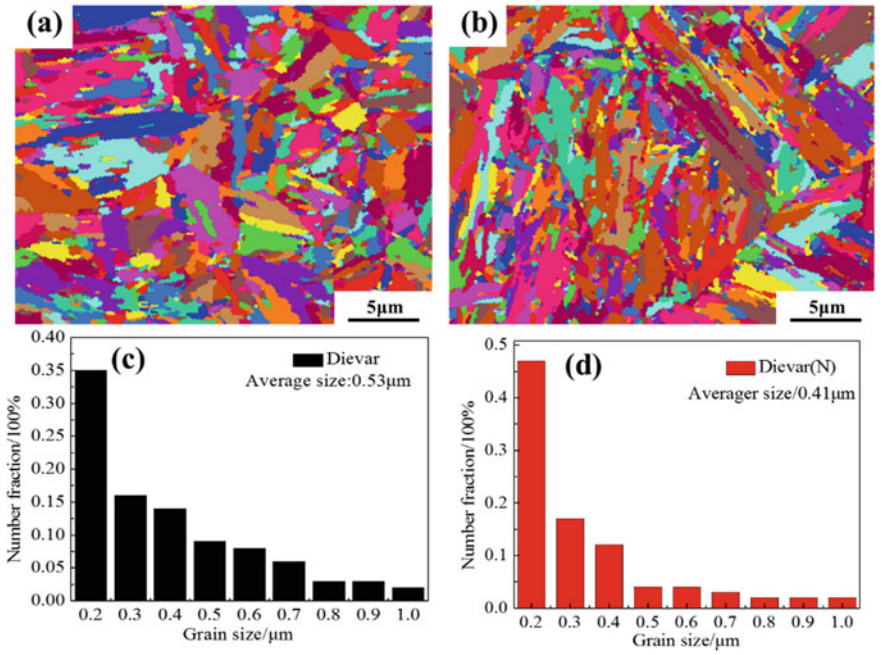


Fig. 3 The crystal structure and grain size distribution. **a** Morphology of Dievar; **b** Morphology of Dievar(N); **c** Grain size distribution of Dievar; **d** Grain size distribution of Dievar(N). (Color figure online)

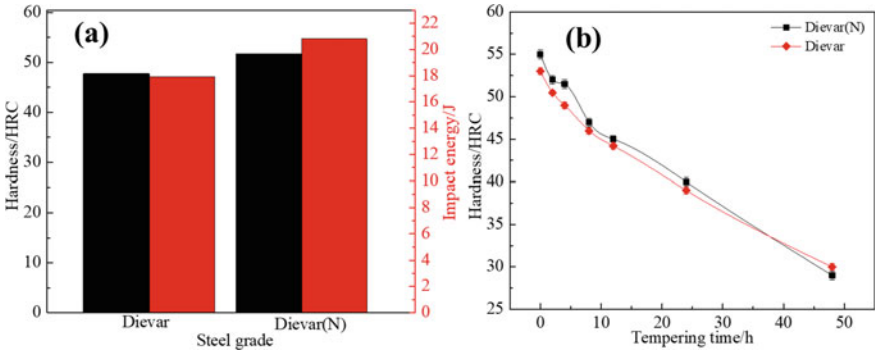


Fig. 4 Mechanical properties and tempering stability of samples: **a** Mechanical properties. **b** Tempering stability. (Color figure online)

that the carbides did not grow significantly during long-term tempering. Further, the morphology exhibits a big difference when the tempering time extended to 48 h, as shown in Fig. 5c and d. A large amount of carbides begin to precipitate in both samples. However, the amount of carbides in Dievar(N) steel is much more than

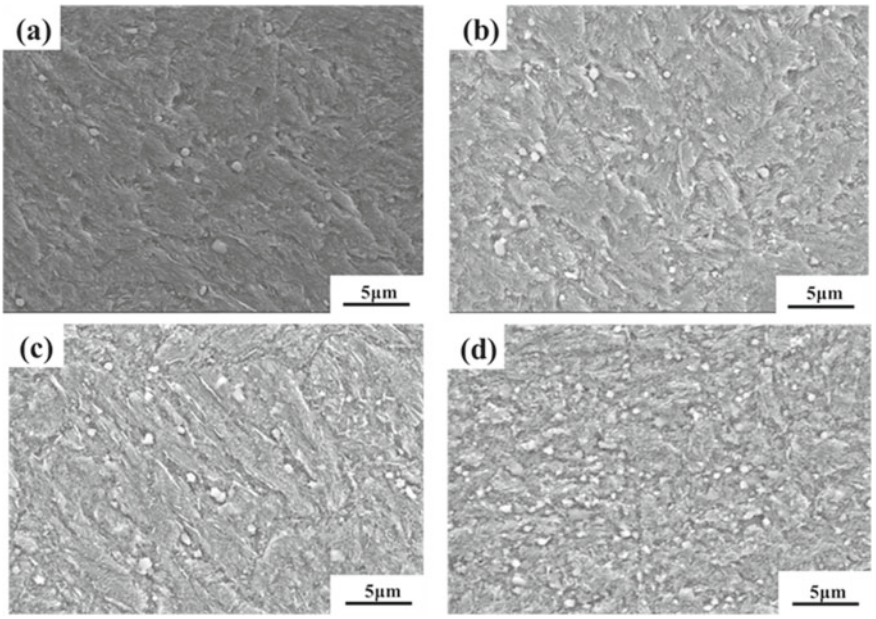


Fig. 5 SEM micrographs of tempered samples: **a** Dievar (24 h); **b** Dievar(N) (24 h); **c** Dievar (48 h); **d** Dievar(N) (48 h)

that of Dievar steel, indicating poor tempering stability, which is consistent with the tempering stability curve. Further, EDS confirms that large Cr-rich carbides begin to precipitate in Dievar(N) steel as shown in Fig. 6. Therefore, the tempering stability of Dievar(N) steel was deteriorated by precipitation of Cr-rich carbides.

3.3 Influence Mechanism

Figure 7 shows the binary phase diagrams of Dievar steel calculated by Thermo-calc software (database TCFE7). As can be observed, the most significant effect of trace nitrogen on phase diagram is the solution temperature change of M(C, N). With the increase of nitrogen content in steel, the solution temperature of M(C, N) increase from 1300 to 1600 K. In other words, trace nitrogen increase the stability of M(C, N) significantly, resulting in that M(C, N) can exist at higher quenching temperatures. It is worth noting that the gas phase will generate when nitrogen increases to 0.07% because of supersolubility. Further, equilibrium precipitation diagrams [12, 13], Figure 8, show that trace nitrogen mainly precipitates as V(C, N) and not only increase the precipitation temperature but also increase the amount of precipitation significantly. These highly stable precipitates were insoluble during austenitization before quenching and then remain in the tempering samples, which is consistent with the SEM observation in Fig. 1.

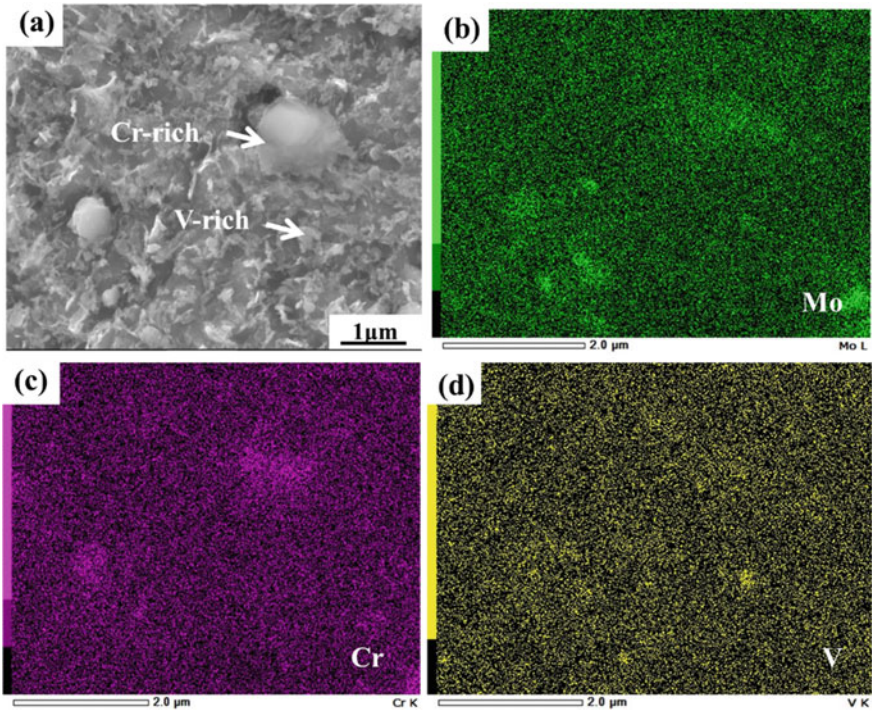


Fig. 6 SEM micrographs and EDS of Dievar(N) tempered for 48 h: **a** SEM micrographs; **b–d** EDS map of V, Cr, and Mo. (Color figure online)

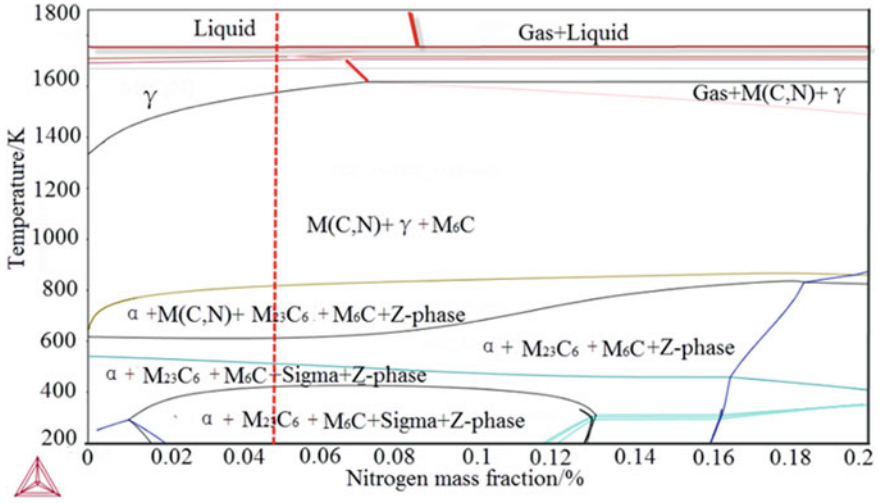


Fig. 7 Binary phase diagrams by Thermo-Calc software. (Color figure online)

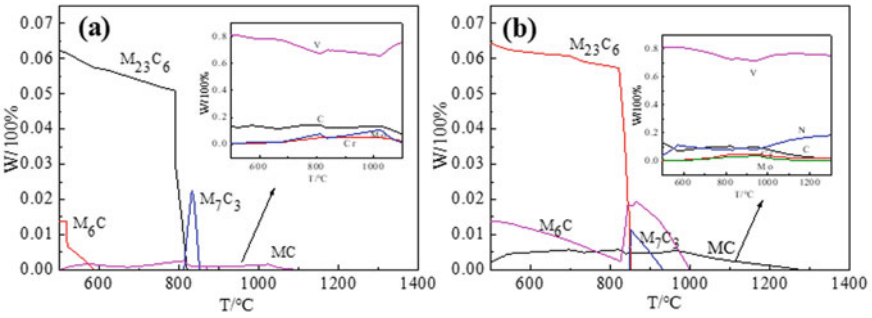


Fig. 8 Equilibrium precipitation calculated by Thermo-Calc software. (Color figure online)

In fact, all performance changes of die steel are attributed to the precipitation of these V(C, N). On the one hand, the precipitation of V(C, N) benefits in inhibiting the growth of original austenitic grains during the quenching process, while refining the final tempered microstructure, as shown in Fig. 2 provide the benefit of increasing the hardness and toughness of steel. On the other hand, these nano-sized carbides cause less loss to toughness because of their small size, guaranteeing high toughness [14]. However, large amounts of undissolved carbides are sure to take up a lot of alloying elements, especially V, thus resulting in that the alloying element could not be fully soluted into matrix, which can be proved by XRD as shown in Fig. 9. As can be observed, the diffraction angles of Dievar steel are shifted toward smaller diffraction angles compared to Dievar(N) steel, indicating a more severe lattice distortion. In other words, trace nitrogen decreases the solid solubility of alloying elements, especially V, which is an important carbide stabilizing element [15]. Reduction of vanadium in quenching matrix leads to decrease of vanadium in tempering metastable precipitates. These metastable precipitates are easy to transform to Cr-rich carbides and coarsening during long temper time due to lack of V, resulting in lower tempering

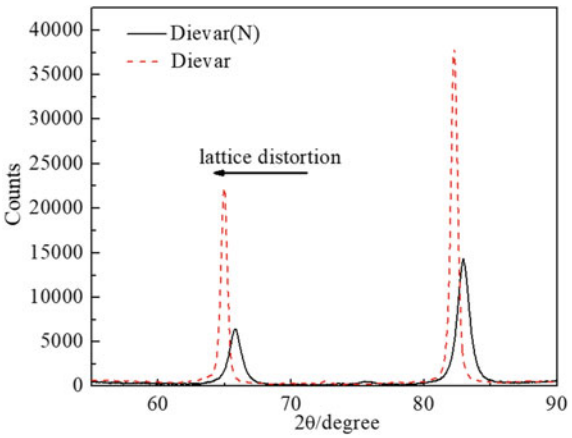


Fig. 9 X-ray diffraction pattern curves of tested steels quenched at 1030 °C. (Color figure online)

stability of steel. Therefore, trace nitrogen decreases the tempering stability of steel through decreasing of vanadium element in the matrix.

4 Conclusions

The effect of trace nitrogen on microstructure and the property of Cr-Mo-V hot-working die steel were studied in this work. The main conclusions are drawn as follows:

(1) Trace nitrogen promotes the precipitation of nano-sized V(C, N), increasing the undissolved carbides in tempered steel.
(2) The undissolved V(C, N) carbides in nitrogen-alloyed steel exert a stronger pinning effect on refining austenitic grains during the quenching process and refine the final tempered microstructure. However, the solid solubility of alloying elements and lattice distortion of matrix decreased obviously.
(3) Trace nitrogen could increase the hardness and toughness of Cr-Mo-V steel by refining the microstructure. However, the tempering stability would be decreased obviously due to the decrease of solid solubility of alloy elements such as V.

Acknowledgments The authors acknowledge financial support from the National Natural Science Foundation of China (Grant No. U1806220), National Natural Science Foundation of China (Grant No. 52027805), Science and Technology Major Project of Shanxi Province (20191102006).

References

1. Wang YL, Song KX, Zhang YM (2019) Microstructure evolution and fracture mechanism of H13 steel during high temperature tensile deformation. Mater Sci and Eng A 746:127–133
2. Podgornik B, Puš G, Žužek B (2018) Heat treatment optimization and properties correlation for H11-type hot-work tool steel. Metall and Mater Trans A 49:455–462
3. Kheirandish S, Noorian A (2008) Effect of niobium on microstructure of cast AISIH13 hot work tool steel. J Iron Steel Res Int 15:61–66
4. Wang M, Ma DS, Liu ZT (2014) Effect of Nb on segregation, primary carbides and toughness of h13 steel. Acta Metall Sin 50:285–293
5. Gao JZ, Fu PX, Liu HW (2015) Effects of rare earth on the microstructure and impact toughness of H13 Steel. Metals 5:383–394
6. Speidel M O (2003) From high-nitrogen steels (HNS) to high-interstitial alloys (HIA). High Nitrogen Steels 1–8
7. Werner E (1988) Solid solution and grain size hardening of nitrogen-alloyed austenitic steels. Mater Sci and Eng A 101:93–98
8. Seifert M, Siebert S, Huth S (2015) New developments in martensitic stainless steels containing C + N. Steel Res Int 86(12):1508–1516
9. Humphreys FJ (2004) Characterization of fine scale microstructures by electronbackscatter diffraction (EBSD). Scripta Mater 51(7):771–776

10. Hiromoto K, Rintaro U, Masato U (2005) Crystallographic analysis of plate martensite in Fe-28.5at% Ni by Fe-SEM/EBSD. Mater Charact 54(4–5): 378–386
11. Xu LQ, Zhang DT, Liu YC (2014) Precipitation behavior and martensite lath coarsening during tempering of T/P92 ferritic heat-resistant steel. Int J Min Met Mater 21:438–447
12. Gu JB, Li JY, Chang RJ (2019) Enhanced refinement of $Cr_{23}C_6$ by heterogeneous nucleation in annealed nitrogen-alloyed 4Cr5Mo2V die steel. Metall Mater Trans A 50:518–522
13. Du JJ, Sun ZL, Zhang X (2018) Effect of nitrogen on impact toughness of vanadium microalloyed steel for high-strength bar. Heat Treat 4:18–23
14. Yang CF, Wang QL (2008) Research, development, and production of V-N microalloyed high strength rebars for building in China. J Iron Steel Res Int 15(2):81–86
15. Yong QL (2006) Secondary phases in steels, 2nd edn. Metallurgical Industry Press, Beijing

Rate-Dependent Hardening Behavior of Autobody Sheet Metals in Tension and Compression



H. Huh, G. Joo, and M. K. Kim

Abstract This paper is concerned with the evaluation of rate-dependent hardening behaviors of autobody metal sheets with novel tension and compression testing devices. Hardening behaviors in tension and compression are indispensable for accurate numerical simulation of sheet metal forming and subsequent spring-back as well as crashworthiness. In addition, it is important to consider the strain rate effect for hardening behaviors in tension and compression because sheet metal deformation prevails at intermediate strain rates up to hundreds per second in press shops of the automotive industry as well as in car crash. Novel in-plane tension and compression testing devices are developed with a servo-hydraulic testing machine to obtain tension–compression hardening curves of autobody metal sheets at intermediate strain rates ranging from 0.001 s^{-1} to 100 s^{-1}. With the testing devices specially developed, hardening behaviors are evaluated in tension–compression for mild steel sheets, TRIP980, TWIP980 steel sheets, and magnesium alloy at various strain rates ranging from 0.001 to 100 s^{-1} in terms of the flow stress considering the Bauschinger effect and the permanent softening. It is observed that the stress offset is dependent on the inherent characteristics of metal sheets as well as the strain rates. It is confirmed from the experiments that the Bauschinger effect decreases as the strain rate increases. The permanent softening defines the stress offset between flow stress curves in tension–compression and monotonic tension with large deformation after loading reversal.

Keywords Hardening behavior · Tension and compression · Rate dependency · Autobody sheet metal · Permanent softening

1 Introduction

In practical sheet metal forming, hardening behaviors of AHSS sheets are subjected to both complicated loading paths and strain rate effects simultaneously. With regards

H. Huh · G. Joo (✉) · M. K. Kim
Korea Advanced Institute of Science and Technology, 291 Dahak-ro, Yuseong-gu, Daejeon 34141, Republic of Korea
e-mail: hijgs@kaist.ac.kr

© The Minerals, Metals & Materials Society 2021

G. Daehn et al. (eds.), *Forming the Future*, The Minerals, Metals & Materials Series,
https://doi.org/10.1007/978-3-030-75381-8_69

to loading path, it is necessary to characterize the material properties for tension and compression because of loading reversal due to bending–unbending process in sheet metal forming. Consideration of the strain rate effect is also necessary to measure the material properties which alter at intermediate strain rates higher than tens per second in automotive sheet metal forming.

In order to observe hardening behaviors of sheet metals under loading reversal, in-plane uniaxial tension–compression tests are preferable because of uniform deformation in the gauge section of a specimen. To realize the in-plane compression test, however, a sheet specimen should be prevented from buckling in accordance with an eccentric load. Many researchers have developed various methods to suppress the buckling of a specimen under the in-plane compression test [2, 4, 5, 9, 13, 14]. The most promising clamping method to prevent buckling is a hydraulic clamping system proposed by many researchers [1, 3, 9–12]. In contrast to the previous work performed at the quasi-static state, in-plane tension and compression material properties have been investigated at intermediate strain rates with servo-hydraulic material testing machines, which can control a constant high velocity during experiments. Joo et al. [7] have developed a novel device for a servo-hydraulic testing machine to obtain tension–compression hardening curves of auto-body metal sheets at intermediate strain rates without fluctuation of the measured force.

This paper proposes novel tension and compression test devices that avoid the fluctuation of the measured force at intermediate strain rates of up to 100 s^{-1}. Hardening behaviors are evaluated with experimental results in tension–compression for various metal sheets such as DQ steel, DP steel, TRIP980, TWIP980 steel sheets, and magnesium alloy at various strain rates ranging from 0.001 to 100 s^{-1} considering the Bauschinger effect and the permanent softening. It is confirmed from the experiments that the Bauschinger effect decreases as the strain rate increases. It is also noted that the permanent softening is observed in the hardening behavior of TWIP980 and DP590, not of DQ steel and TRIP980.

2 Experimental Setup

A novel compression device has been suggested to measure an actual force of a specimen during deformation from a load cell at intermediate strain rates up to 100 s^{-1}. The main concept of a new device is to install a load cell close to a specimen inside the novel devices to measure the actual force during specimen deformation regardless of the vibration mode of a jig system [6, 8]. Figure 1 illustrates schematic diagrams of compression test devices before and after modification. The most important difference between the two test devices is the location of a load cell for the force measurement. Before modification, a load cell was not included inside the test device, whereas it was installed between the jig mount and the fixed block of the HSMTM. After modification, on the other hand, a load cell is installed between the specimen mount and the fixed jig of the test device. According to this modification, the movement of the load cell can be independent of the jig vibration so that the

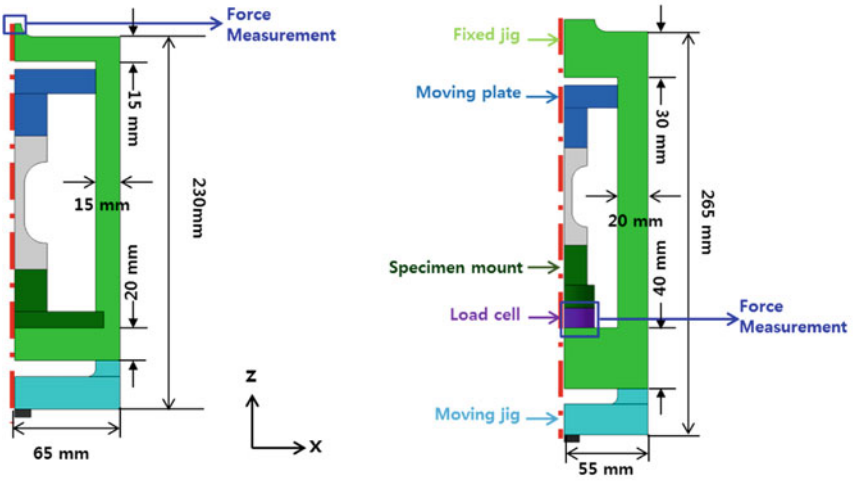


Fig. 1 Schematic diagrams of compression test devices: **a** before modification; **b** after modification. (Color figure online)

measured force can be less vulnerable to the jig vibration. Consequently, the actual force of a specimen during deformation can be measured from the load cell inside the novel test device.

3 Rate-Dependent Tension–Compression Hardening Behaviors of Sheet Metals

3.1 AHSS Steels of TRIP980 and TWIP980

Stress−strain curves of TRIP980 and TWIP980 steel sheets are obtained in tension and subsequent compression with a variation of the strain rate from 0.001 to 100 s^{-1} as shown in Fig. 2. The stress–strain curves confirm the positive strain rate hardening effect of both the materials in tension and subsequent compression. It is not easy to identify the tension–compression hardening characteristics from the obtained result of Fig. 2. Tension–compression hardening, however, can be investigated from a comparison of stress–strain curves in tension–compression and monotonic tension as shown in Fig. 3.

Figure 3 shows true stress–true strain curves in tension and those in subsequent compression at the strain rate of 100 s^{-1}. Solid lines with square and circle symbols indicate tension and subsequent compression test results, respectively, while dotted lines represent monotonic tension test results. It is noted from the comparison that the subsequent compressive yield stress becomes smaller than the flow stress in

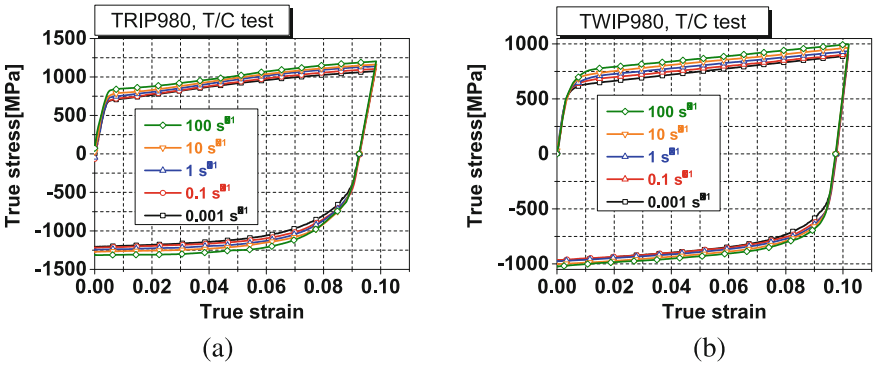


Fig. 2 Rate-dependent hardening curves of AHSS sheets in tension and subsequent compression: **a** TRIP980; **b** TWIP980. (Color figure online)

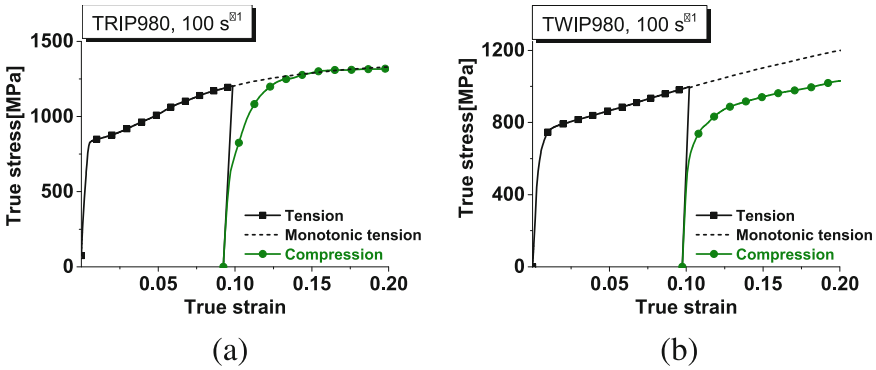


Fig. 3 Comparison of hardening curves of the TRIP980 and TWIP980 steel sheet in tension–compression and monotonic tension at a strain rate 100 s^{-1}: **a** TRIP980; **b** TWIP980. (Color figure online)

monotonic tension because of the Bauschinger effect. After the early re-yielding, in addition, the subsequent compressive curves of the two AHSS sheets exhibit a rapid change of the hardening rate for the transient behavior. The two types of AHSS sheets, however, show distinct hardening behavior at large deformation after the transient behavior. The TRIP980 steel sheet shows a convergence to the monotonic tensile curve, while the TWIP980 steel sheet maintains a constant stress offset showing that its curve remains smaller than that in monotonic tension as found in Fig. 3b, which is explained as the permanent softening.

3.2 AHSS Steels of DQ Steel and DP590

Stress−strain curves of DQ and DP590 steel sheets are obtained in tension and subsequent compression with the variation of the strain rate from 0.001 to 50 s^{-1} as shown in Fig. 4. The stress–strain curves show even more remarkable positive strain rate hardening of the both materials in tension and subsequent compression than the previous TRIP980 and TWIP980 steel.

Tension–compression hardening can be investigated from comparison of stress–strain curves in tension–compression and monotonic tension as shown in Fig. 5. Figure 5 shows true stress–true strain curves in tension and those in subsequent compression at the strain rate of 50 s^{-1}. Solid lines with hollow square and circle symbols indicate tension and subsequent compression test results, respectively, while dotted lines represent monotonic tension test results. The two types of steel sheets show distinct hardening behavior at large deformation after the transient behavior

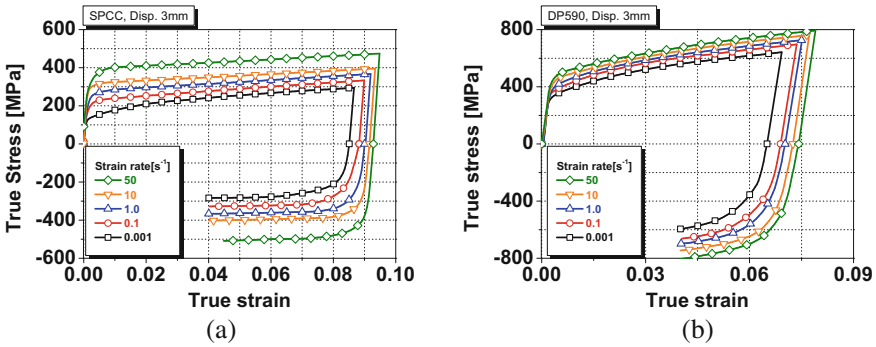


Fig. 4 Rate-dependent hardening curves of steel sheets in tension and subsequent compression: **a** DQ steel; **b** DP590. (Color figure online)

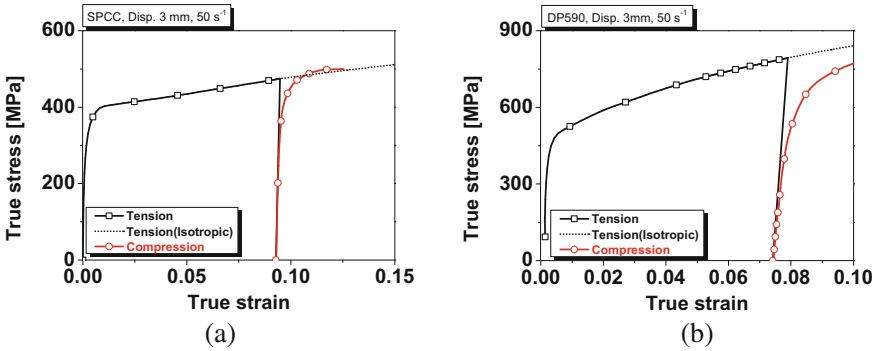


Fig. 5 Comparison of hardening curves of the DQ and DP590 steel sheet in tension–compression and monotonic tension at a strain rate 50 s^{-1}: **a** DQ steel; **b** DP590. (Color figure online)

explained in the previous section. The DQ steel sheet shows a convergence to the monotonic tensile curve while the DP590 steel sheet maintains a constant stress offset showing that its curve remains smaller than that in monotonic tension as found in Fig. 5b, which is explained as the permanent softening. Although the whole curves at various strain rates are not presented in Fig. 5, the hardening behavior of DQ steel in subsequent compression is interesting because they show the permanent softening at low strain rate and gradual convergence to the monotonic tension hardening as the strain rate increases. As a result, the hardening curve at the strain rate of 50 s^{-1} shows a convergence to the monotonic tensile curve in Fig. 5a.

3.3 Magnesium Alloy of AZ31B

Stress−strain curves of a magnesium alloy of AZ31B are obtained in tension and compression with the variation of the strain rate from 0.001 to 100 s^{-1} as shown in Fig. 6. The stress–strain curves are depicted for tension and compression separately because the hardening behavior in compression is exotic and entirely different from that in tension as shown in Fig. 6. The stress–strain curves in subsequent compression show very low compressive yield stress compared to the monotonic tensile curves, which is even different from the Bauschinger effect. After the early re-yielding, the subsequent compressive curves of AZ31B retain their slow hardening rate until a certain amount of deformation regardless of the strain rate showing independence of the strain rate. After some amount of deformation, the hardening rate increases rapidly and then slows down until the deformation reaches a limit strain at fracture. It should be noted that the hardening behavior continues until fracture which takes place even in the compression loading with the side-guide plates. The compressive yield stress is very low and almost half of the expected monotonic tensile flow stress. After the early yielding, the flow stress in compression reaches a very large value

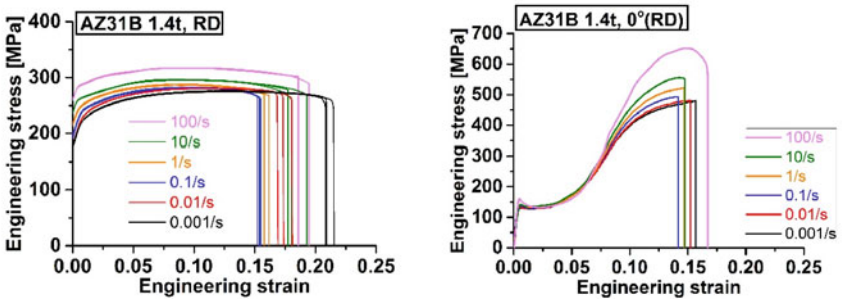


Fig. 6 Rate-dependent hardening curves of AZ31B sheets in tension and subsequent compression: **a** Tension; **b** Compression. (Color figure online)

which is almost four times higher than the compressive yield stress. This phenomenon explains the reason why an experimental result of the hardening curve has not been reported up to now. It is very tricky to conduct the compression test because of the exotic hardening behavior of AZ31B.

4 Conclusion

Rate-dependent hardening behavior of steel sheets and magnesium alloy sheets is evaluated at a wide range of the strain rate with novel tension and compression test devices [6, 8]. Tension–compression hardening behaviors are investigated in terms of the Bauschinger effect and the permanent softening with respect to the strain rate. In addition, asymmetric hardening behaviors are investigated from simple tension and simple compression test results. The main conclusion is summarized as follows:

(1) Novel tension and compression test devices are proposed to measure an actual force of a specimen during deformation at strain rates up to 100 s^{-1}. In the novel test devices, a load cell is installed between the specimen mount and the fixed jig of the novel devices.
(2) Tension–compression hardening behavior of steel sheets is evaluated with the variation of the strain rate in terms of the Bauschinger effect and the permanent softening. As the strain rate becomes higher, the Bauschinger ratio becomes larger with the decrease of the Bauschingher effect. The TWIP980 and DP590 show constant stress offset of the permanent softening at large reverse deformation, which increases as the strain rate increases.
(3) Tension–compression hardening behaviors of magnesium alloy sheet is evaluated with the variation of the strain rate. The hardening behavior of AZ31B shows very exotic and entirely different tendency from that of steel sheets. After the early yielding, the flow stress in compression reaches a very large value which is almost four times higher than the compressive yield stress.

References

1. Ahn K, Yoo D, Seo MH, Park SH, Chung K (2009) Springback prediction of TWIP automotive sheets. Met Mater Int 15(4):637–647
2. Balakrishnan V (1999) Measurement of in-plane bauschinger effect in metal sheet. Master Thesis, The Ohio State University, Columbus, Ohio, USA
3. Boger RK, Wagoner RH, Barlat F, Lee MG, Chung K (2005) Continuous, large strain, tension−compression testing of sheet material. Int J Plast 21:2319–2343
4. Cao J, Lee W, Cheng HS, Seniw M, Wang H, Chung K (2009) Experimental and numerical investigation of combined isotropic-kinematic hardening behavior of sheet metals. Int J Plast 25:942–972
5. Geng L, Wagoner RH (2002) Role of plastic anisotropy and its evolution on springback. Int J Mech Sci 44(1):123–148

6. Joo G, Huh H (2018) Rate-dependent isotropic-kinematic hardening model in tension-compression of TRIP and TWIP steel sheets. Int J Mech Sci 146–147:432–444
7. Joo G, Huh H, Choi MK (2016) Tension/compression hardening behaviors of auto-body steel sheets at intermediate strain rates. Int J Mech Sci 108:174–187
8. Joo G, Huh H, Kwon J (2019) Evaluation of rate-dependent hardening behaviors of AHSS sheets with novel tension and compression test devices. J Mater Proc Tech 270:365–379
9. Kuwabara T, Morita Y, Miyashita S (1995) Elastic−plastic behavior sheet metal subjected to in-plane reverse loading. J Japan Society Tech Plast 36:769–774
10. Lee MG, Kim D, Kim C, Wenner ML, Wagoner RH, Chung K (2005) Spring-back evaluation of automotive sheets based on isotropic-kinematic hardening laws and non-quadratic anisotropic yield functions. Int J Plast 21:833–914
11. Lou XY, Li M, Boger RK, Agnew SR, Wagoner RH (2007) Hardening evolution of AZ31B Mg sheet. Int J Plast 23(1):44–86
12. Piao K, Lee JK, Kim JH, Kim HY, Chung K, Barlat F, Wangoner RH (2012) A sheet tension/compression test for elevated temperature. Int J Plast 38:27–46
13. Tan Z, Magnusson C, Persson B (1994) The Bauschinger effect in compression-tension of sheet materials. Mater Sci Eng A 183:31–38
14. Yoshida F, Uemori T, Fujiwara K (2002) Elastic−plastic behavior of steel sheets under in-plane cyclic tension−compression at large strain. Int J Plast 18(5–6):633–659

Analysis of Creep Behavior of Magnesium Alloy Sheet (AZ31B) in Warm Forming



JaeHyeong Yu and Chang-Whan Lee

Abstract In this study, creep behavior characteristics of magnesium alloy sheet (AZ31B) according to pre-strain during warm forming were analyzed through experiments. In addition, stress relaxation process was analyzed by applying the creep behavior of magnesium alloy sheet to analytical simulation. In the creep test, the strain due to the creep phenomenon of magnesium alloy at room temperature was 0.001 at 1000 s of constant load holding time, whereas it was broken at 8 s at 250 °C. The stress exponent of magnesium alloy at room temperature is 10.60 and the stress exponent is 4.8 at 250 °C. Similarly, in the case of stress relaxation experiments at room temperature, the amount of load reduction was 74 N at 1000 s while the amount of load reduction was reduced by 522 N at 250 °C. The stress exponent and parameters obtained from the experiments were applied to the analysis simulation, and the creep and stress relaxation processes were compared with the experimental results.

Keywords Magnesium alloy sheet (AZ31B) · Warm forming · Uniaxial tensile creep · Stress relaxation · Finite element method · V-bending process

1 Introduction

Magnesium alloys are expected to be used in many applications such as semiconductors, displays, aerospace, and automotive parts due to their superior specific strength [1]. However, when forming at room temperature, it is easy to break due to low elongation and large springback occurs due to high flow stress. Owing to the tensile behavior of magnesium alloy at room temperature work hardening mainly occurs, whereas work softening occurs due to recrystallization and potential rise from 150 °C [2]. For this reason, magnesium alloys are mainly formed in a warm form. Sufficient

J. Yu · C.-W. Lee (✉)
Seoul National University of Science and Technology, Seoul, South Korea
e-mail: cwlee@seoultech.ac.kr

J. Yu
e-mail: jhyu9109@seoulteh.ac.kr

© The Minerals, Metals & Materials Society 2021

G. Daehn et al. (eds.), *Forming the Future*, The Minerals, Metals & Materials Series,
https://doi.org/10.1007/978-3-030-75381-8_70

creep strength is also essential for the application of magnesium alloys in automotive power trains, which are conventionally used in materials such as aluminum and steel. Previous studies on the creep behavior and warm forming of magnesium alloys are as follows.

Reddy et al. [3] performed a deep-drawing process on the various forming temperature of magnesium alloy by analysis simulation and experimental methods. Through this, the LDR value increases with increasing forming temperature in both simulation and experiment, but after 300 °C, the LDR value decreases due to the reduction of a local cross-section of the material. Wang et al. [4] measured the springback of the magnesium alloy sheet as a function of the punch radius and forming temperature in V bending forming. As a result, it was confirmed that the spring back of the magnesium alloy decreases as the forming temperature increases and the punch radius decreases. Also, the springback behavior was analyzed by observing the microstructures of the tension and compression parts with respect to the neutral axis of the specimen. Kim and Kim [5] measured the creep behavior of a magnesium alloy sheet at a temperature of 0.5 T_m or less. As a result, magnesium alloys exhibited different behaviors such as primary creep behavior under low stress and secondary creep behavior under high stress, and each behavior was predicted by the creep model. Kim et al. [6] conducted a three-point bending test in a warm state using a magnesium alloy sheet to investigate the effect of stress relaxation on springback. This shows that the springback decreases as the holding time of the material in the die increases. Kang et al. [7] used an AZ31 magnesium alloy to predict the short-term creep rupture life by the initial strain method (ISM) and a deformation mechanism that led to creep deformation at or below 0.5 times the melting temperature of pure magnesium. Creep experiments were performed at 443 K and stress conditions 109–141 MPa. This confirmed that the creep deformation mechanism of AZ31 is cross slip in the temperature range 423–443 K.

In this study, creep and stress relaxation tests were conducted to analyze the creep characteristics of magnesium alloy sheet (AZ31B) as a function of forming temperature and pre-strain. Creep behavior was analyzed and stress exponent was measured on the various forming temperature and pre-strain. Analytical simulations were performed using the stress exponent and parameters obtained from the experiments, and the results were compared and analyzed. Using the same stress exponent and parameters, the stress relaxation process was analyzed by analytical simulation and compared with the experimental results.

2 Experiment and Simulation Procedure

2.1 Material

In this study, Table 1 shows the chemical composition of magnesium alloy sheets that are used. The flow stress on the various forming temperature of the magnesium

Table 1 The chemical composition of magnesium alloy

Element	Mg	Al	Zn	Mn	Sl	Cu	Ca	Fe	Ni
Content(%)	97	2.5–3.5	0.6–1.4	0.2	0.1	0.050	0.040	0.0050	0.0050

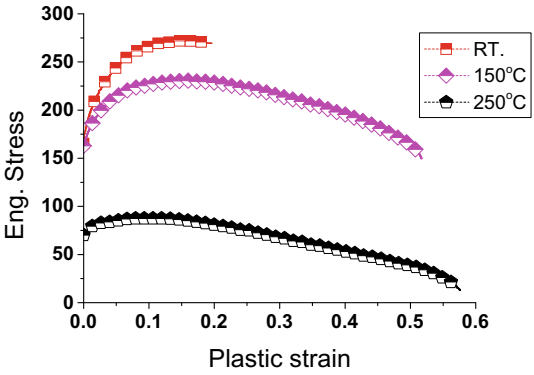


Fig. 1 The stress–strain of magnesium alloy sheet (AZ31B) . (Color figure online)

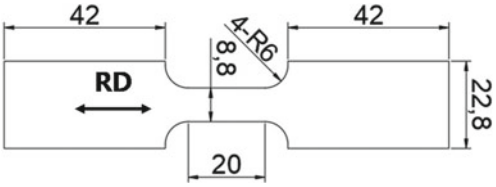


Fig. 2 The specimen of uniaxial tensile creep test

alloy sheet (AZ31B) is shown in Fig. 1. For this flow stress, the specimen shown in Fig. 2 was measured through a tensile test using the material tester INSTRON8516.

Creep test specimens were made in the rolling direction of the sheet (R.D.) and the schematics of the specimens are shown in Fig. 2 [8]. The gauge length of the specimen was 20, 8.8 mm wide and 1 mm thick.

2.2 Uniaxial Tensile Creep Test

In this study, the uniaxial tensile creep test was conducted to analyze the creep behavior of magnesium alloy sheet (AZ31B) according to temperature and pre-strain. Forming temperature is room temperature, 50, 100, 150, 200, and 250 °C. In the case of pre-strain, 50, 75, 90, and 100% of the ultimate tensile strength of the magnesium alloy sheet was defined as the strain when stress was applied. In the case of creep strain measurement, the specimen was tensiled to the target pre-strain, and then the measured strain changes due to constant load. The speed of the crosshead during the pre-strain was set to 12 mm/min and the constant load time was set to 0–1000 s.

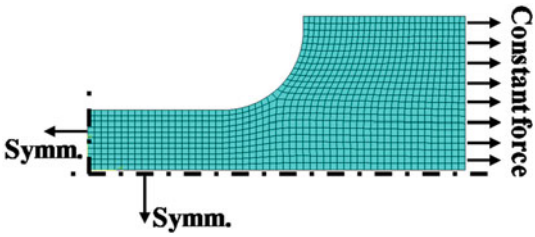


Fig. 3 The FEM model of uniaxial tensile creep process. (Color figure online)

2.3 Simulation

In this study, the creep and stress relaxation processes of magnesium alloy sheets were analyzed using ABAQUS v2016, a commercial finite element analysis program. The schematic of the creep process for the analysis is shown in Fig. 3. To analyze the creep process, *ABAQUS* Visco code was used and the material was modeled using solid elements. In this study, the secondary creep stage was considered and assumed as plane stress. For material properties, plastic strain and yield stress were used at 250 °C using the reference of benchmark # 2 provided by *NUMISHEET* [9]. In the case of creep properties, the parameters obtained from creep experiments were used in this study.

3 Results

3.1 Uniaxial Tensile Creep Test According to Temperature and Pre-strain

In this experiment, the creep test was conducted under constant load conditions to analyze the creep behavior of the magnesium alloy sheet. The creep behavior of magnesium alloy sheet (AZ31B) with pre-strain at forming temperature of 250 °C is shown in Fig. 4. The third creep entry time is 120 s when the pre-strain of the magnesium alloy sheet (AZ31B) is 50% at 250 °C and 8 s when it is 90%. Through this, it can be seen that the larger the pre-strain, the faster the tertiary creep stage and the shorter the rupture time. Also, it can be seen that the creep rupture is abruptly reduced between 50 and 75% of the pre-strain. For this reason, it can be seen that as the pre-strain progresses to the plastic region, the vertical cross-section in the tensile direction decreases and the creep rupture time occurs quickly.

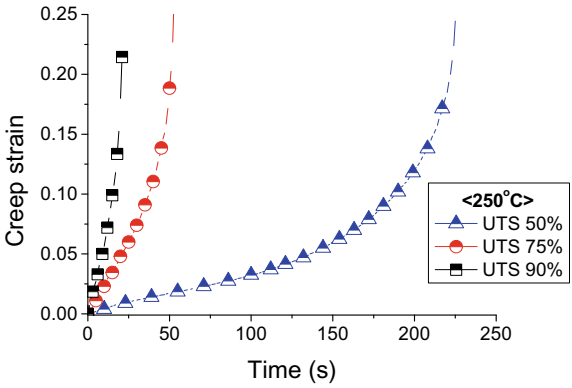


Fig. 4 The creep behavior of AZ31B according to pre-strain at 250 °C. (Color figure online)

3.2 Stress Exponent of Creep Strain

In this study, the creep behavior of magnesium alloy sheet was analyzed according to forming temperature and constant load time. From these results, the stress exponent for creep strain was obtained by the following method. The primary creep stage is characterized by a monotonous decrease in the creep strain rate, and the creep strain rate is constant for the secondary creep stage. In the case of tertiary creep, the creep strain rate increases rapidly. The creep strain can be represented by the simple power law formula

$$\varepsilon_c = A\sigma^n t^m \tag{1}$$

where A, n, m are the temperature-dependent parameters. In this study, the primary and secondary creep stage was considered and the third creep was not considered. In this study, it was found that the primary creep stage is shorter than the secondary creep stage in the magnesium alloy sheet (AZ31B). Especially, the larger the pre-strain, the shorter is the primary creep section and then it immediately enters the secondary creep section. Therefore, the creep strain rate (the slope of the creep strain diagram) in the primary and secondary creep stages is constant. At this time, the empirical formula for expressing the creep strain rate as a function of stress and temperature can be expressed as Eq. (2). Equation (2) shows the dependence on the stress of the normal creep rate (secondary creep).

$$\dot{\varepsilon}_c = A\sigma^n \tag{2}$$

To find the parameters A and n, take the logarithm in Eq. (2) and make it a linear equation.

$$ln(\dot{\varepsilon}_c) = lnA + nln\sigma \tag{3}$$

Table 2 The stress exponent parameter of AZ31B according to forming temperature

	100 °C	150 °C	200 °C	250 °C
Stress exponent (n)	10.60	9.30	7.65	4.80
Parameter A	2.97E-30	8.59E-25	6.08E-20	9.13E-13

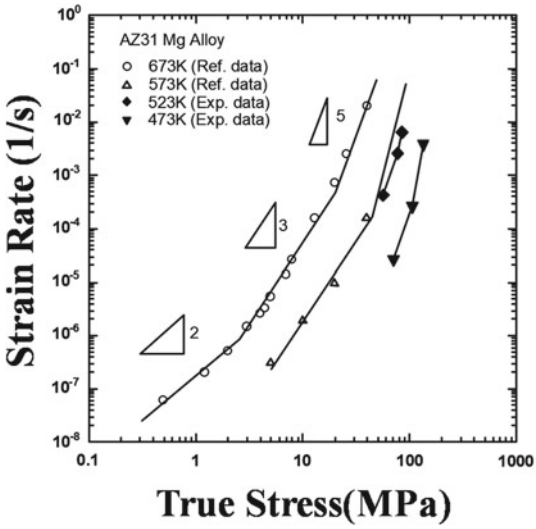


Fig. 5 Steady-state strain rate against stress for specimens tested from 573 to 673 K [10]

The parameters A and n were obtained through Eq. (3) and the experiment. The stress exponent at each forming temperature is shown in Table 2.

The stress exponent obtained in this study is shown in the results of previous studies representing the stress exponent of steady-state creep strain and true stress (Fig. 5) [10]. Figure 5 represents the creep rate for the secondary creep strain corresponding to each temperature when the material is stressed. As can be observed from Fig. 5, the speed of creep test in this study was performed in a range similar to the speed used in the previous study.

3.3 Simulation Results of Creep

At the forming temperature of 250 °C and the 75% of pre-strain of the ultimate tensile strength, the results of the creep strain simulation and the experimental are shown in Fig. 6.

In the case of the experiment at the pre-strain $\varepsilon_{75\%}$, the time to enter the tertiary creep stage from the secondary creep stage is about 40 s. In the case of the analytical simulation, the time taken from the secondary creep stage to the tertiary creep stage is about 39 s, showing a 2% error based on the experimental result. At $\varepsilon_{90\%}$ pre-strain,

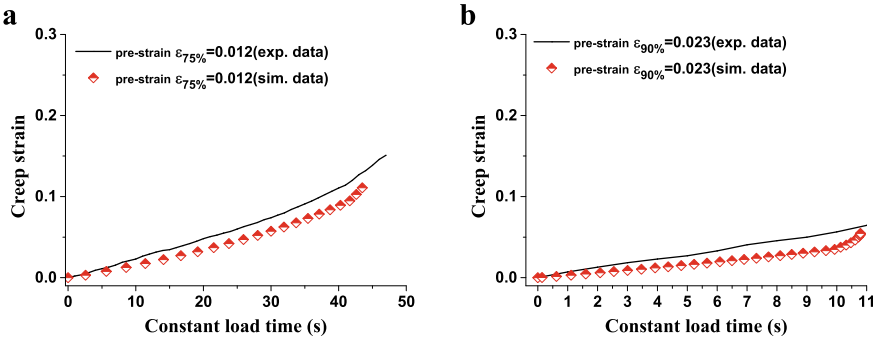


Fig. 6 Creep strain for experimental and simulation under constant load at **a** 75% and **b** 90% of pre-strain. (Color figure online)

the entry time of the tertiary creep section is 10 s for the experiment, and the entry time of the third creep section for the analysis is 11 s, showing a 10% error based on the experimental results. In addition, both experimental and analytical simulations show that the higher the pre-strain, the shorter the tertiary creep entry time and the higher the creep rate in the secondary creep stage. In this study, creep modeling was performed without considering the tertiary creep stage. Therefore, the experimental and the analysis simulation results tend to be different from the tertiary creep.

3.4 Simulation Results of Stress Relaxation

As a result of analytical simulations using the parameters obtained in the previous section of this study, it can be seen that there is a similar trend up to the secondary creep stage considered. In addition, materials having creep characteristics generate stress relaxation characteristics similar to the creep characteristics. In this study, therefore, the stress relaxation process was compared with the experimental and simulations. Figure 7 is the result of the stress relaxation under constant displacement time in the experimental and analytical simulations.

As can be observed from the experimental and analytical simulation results for all pre-strains, the load decreased and converged from about 30 s as the constant displacement holding time increased. At the pre-strain $\varepsilon_{75\%}$, the load reduction amount is 524 N for the experiment, and the load reduction amount is 478 N for the analysis simulation when the constant displacement time is 30 s. This shows an 8% error based on the experimental results. At the pre-strain $\varepsilon_{90\%}$, the load reduction amount is 553 N for the experiment, and the load reduction amount is 496 N for the analysis simulation when the constant displacement time is 30 s. This shows a 10% error based on the experimental results. At pre-strain $\varepsilon_{75\%}$, it takes 14 s for the load relaxation time (time to reach initial load $(F_0) \times 0.37$) for the experiment and 15 s for the analytical simulation. The two results show a difference of about 1 s. At the pre-strain

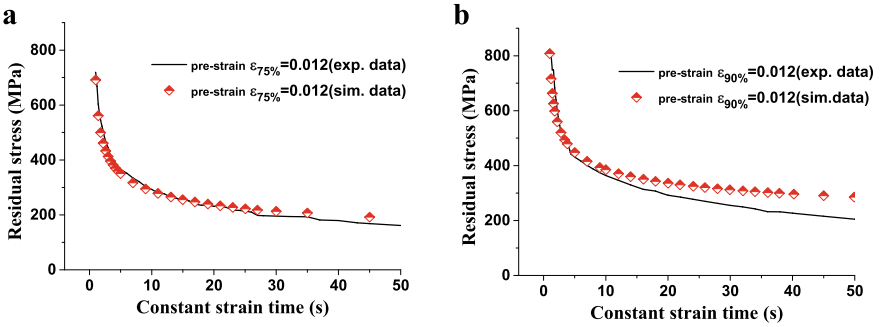


Fig. 7 Residual stress for experimental and simulation under constant strain at **a** 75% and **b** 90% of pre-strain. (Color figure online)

$\varepsilon_{90\%}$, there is a difference of about 7, 19 s for the load relaxation time for the experimental and 12 s for the analysis simulation. When the stress relaxation behavior is applied to the V-bending process, the springback change is shown in Fig. 8.

The springback tended to decrease as material holding time increases in the die at all forming temperatures. This is because the springback decreases due to the stress caused by the deformation of the material relaxation. The springback tends to rapidly decrease the holding time of the material in the die to about 250 s, and then tends to converge. As the forming temperature increased, the amount of springback reduction also increased. This trend is similar to that of the stress relaxation test on the forming temperature in the previous section. In addition, the amount of springback decreased according to the forming temperature is 16.65° and the amount of springback decreased is 19.25° as the holding time of the material in the die increases at 200 °C [11]. As a result, it can be noticed that the amount of springback decrease with increasing material holding time in the die is larger than the amount of springback decrease with increasing forming temperature.

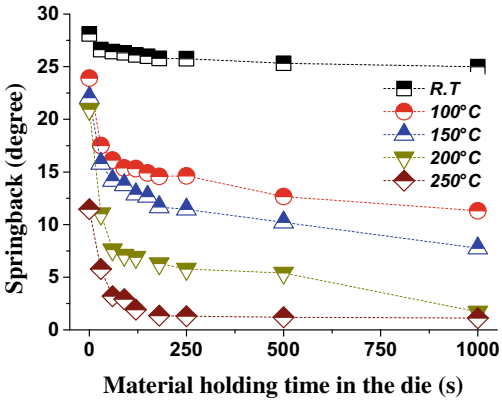


Fig. 8 The springback of V-bending process according to material holding time and forming temperature [11]. (Color figure online)

4 Conclusion

In this study, the creep and stress relaxation behaviors of magnesium alloy sheet (AZ31B) according to temperature and pre-strain were analyzed through experimental and analytical simulations. The research results are as follows.

The stress exponent obtained through the uniaxial tensile creep test was 4.8 at 250 °C and decreased with increasing forming temperature.

Both creep experiments and analytical simulations tended to reduce the time to enter the tertiary creep as the pre-strain increased. In addition, the error in experimental and analytical simulations according to each pre-strain was measured to be <10%.

As a result of stress relaxation simulation after applying the same parameters as the creep simulation, the load tended to converge from about 30 s.

References

1. Friedrich H, Schumann S (2001) Research for a new age of magnesium in the automotive industry. J Mater Process Technol 117(3):276–281
2. Feng F, Huang S, Meng Z, Jianhua H, Lei Yu, Zhou M, Dan W, Yang Z (2014) Experimental study on tensile property of AZ31B magnesium alloy at different high strain rates and temperatures. Mater Des 57(0261–3069):10–20
3. Reddy ACS, Rajesham S, Reddy PR (2015) Experimental and simulation study on the warm deep drawing of AZ31 alloy. Adv Prod Eng Manag 10(3):153–161
4. Wang L, Huang G, Zhang H, Wang Y, Yin L (2013) Evolution of springback and neutral layer of AZ31B magnesium alloy V-bending under warm forming conditions. J Mater Process Technol 213(6):844–850
5. Kim KY, Kim WJ (2007) Creep behavior of AZ31 magnesium alloy in low temperature range between 423 K and 473 K. J Mater Sci 45(15):6171–6176
6. Kim JH, Kim D, Lee YS, Lee MG (2013) Stress relaxation and springback of magnesium alloy sheets. J Korean Soc Prec Eng 1009–1010
7. Kang DM, An JO, Jeon SH, Koo Y, Sim SB (2008) A prediction on the creep rupture life of AZ31 Mg alloy at below 0.5Tm. J Korean Soc Manuf Process Eng 17(8):558–563
8. Bae GH (2011) A study on the tension/compression hardening behavior auto-body steel sheets considering the pre-strain and the strain rate. Ph.D. thesis, KAIST University
9. NUMISHEET 93' proceeding, Benchmark #2
10. Chung CS, Kim HK (2009) Creep properties of AZ31 magnesium alloy at elevated temperature. J Korean Soc Saf 24(6):20–26
11. Yu JH, Lee C-W (2020) Analysis of spring-back characteristics of magnesium alloy sheet (AZ31B) considering time-dependent in warm bending forming "in press". J Korean Soc Prec Eng

The Effect of Electroplasticity on the Flow Behavior of AA7075 in T6 Temper



Dong Hongrui, Li Xiaoqiang, Wang Haibo, Li Dongsheng, and Yang Yanfeng

Abstract Warming forming, or the combination of cold forming, and multiple heat treatment processes are usually used to obtain AA7075 parts in T6 temper. However, the above-mentioned methods increase the forming cycle and cost, and lead easily to change in the microstructure. In this paper, a new forming process is proposed, namely pure electroplastic-assisted thermal forming (PEPATF) process, which can reduce the forming temperature by using pure electroplastic/non-thermal effect to compensate plasticity loss caused by the decrease of temperature. In order to research the mechanism of electroplastic effect, oven-heating uniaxial tension at different temperatures and electrically assisted uniaxial tension test at different temperatures and current densities are performed for AA7075-T6. On the one hand, the results show that at the same temperature, the flow stress obtained by electrically assisted heating is lower than that obtained by oven-heating, indicating that pure electroplasticity exists and is more obvious with the increase of temperature. Moreover, at the same temperature, the flow stress decreases with the increase of current density at the same temperature. On the other hand, the elongation obtained by electrically assisted uniaxial tension is higher than that obtained by oven-heating uniaxial tension. For electrically assisted uniaxial tension, the largest elongation is at 150 °C.

Keywords Oven-heating · Uniaxial tension · Electrically assisted uniaxial tension · Electroplastic effect

D. Hongrui · L. Xiaoqiang (✉) · L. Dongsheng
School of Mechanical Engineering and Automation, Beihang University, Beijing 100191, China
e-mail: lixiaoqiang@buaa.edu.cn

W. Haibo
School of Mechanical and Materials Engineering, North China University Technology, Beijing 100144, China

Y. Yanfeng
Université de Lorraine, Arts et Métiers ParisTech, 57000 Metz, France

© The Minerals, Metals & Materials Society 2021

G. Daehn et al. (eds.), *Forming the Future*, The Minerals, Metals & Materials Series,
https://doi.org/10.1007/978-3-030-75381-8_71

1 Introduction

Modern aerospace equipment is developing toward lightweight, long life, and high reliability, and its service performance tends to be extreme, which requires that its material must have super high strength and low weight correspondingly. AA7075 is widely used in aerospace field because of excellent combination of properties such as high strength to density ratio, fracture toughness, and resistance to stress corrosion cracking [1, 2]. When in T6 temper, its tensile strength can reach 550 MPa, which can be used to manufacture aircraft structures and other parts with high strength. However, poor formability at room temperature limits its application [3].

In order to obtain AA7075 part in T6 temper, the combination of cold forming and multiple heat treatment processes are usually used to form the part, and heat treatment is used to make the part in T6 temper. However, the following problems exist: (1) long process route, long manufacturing cycle, and high cost; (2) large deformation due to heat treatment; (3) large force, large springback, and low forming accuracy. Based on the above problems, Sotirov et al. [4] proposed the warm forming of AA7075 in T6 temper directly, which avoids intermediate heat treatment, significantly reduces the forming cycle, and improves the forming accuracy. In order to improve the formability of AA7075 in T6 temper, it is necessary to make its forming temperature reach 200–230 °C. However, the forming temperature of 200–230 °C will induce the change of microstructure during the forming process, which will decrease the yield strength of the part after forming and affect its service performance. If the forming temperature is decreased, the plasticity of AA7075 will decrease. Therefore, the new forming methods are needed to solve these problems.

Researchers have found that the formability of metal has changed significantly when the current is applied during forming, such as the increase of plasticity and the decrease of deformation resistance [5]. This phenomenon is called electroplastic effect. It has been found that on the one hand, electric current can increase the temperature of the material through the Joule heating effect, which makes the material soften (thermoplasticity/thermal effect). On the other hand, electric current can directly reduce the flow stress of the material (pure electroplasticity/non-thermal effect). Therefore, pure electroplasticity can be used to reduce the forming temperature and make up for the decrease of the plasticity caused by the decrease of the temperature. A novel process is put forward, namely pure electroplastic-assisted thermal forming (PEPATF) process, which can reduce the forming temperature by using pure electroplastic/non-thermal effect to compensate plasticity. It is expected to greatly improve the forming limit and the forming quality of the materials. It is a promising technology to realize the precise forming and manufacturing of the difficult-to-form materials and structures.

In order to use PEPATF process, it is necessary to research the mechanism of electroplastic effect. In this paper, oven-heating uniaxial tension at different temperatures and electrically assisted uniaxial tension test at different temperatures and different current densities are performed for AA7075 in T6 temper and the thermal effect and electroplastic effect are studied.

2 Material and Experiment

2.1 Material and Specimen

The material used in the test is AA7075 with T6 temper, whose chemical composition is shown in Table 1. The size of specimen used in oven-heating uniaxial tension is shown in Fig. 1. During electrically assisted uniaxial tension, the non-uniform temperature distribution on the specimen is mainly caused by the heat conduction between specimen and clamp. Therefore, in order to improve the uniformity of temperature distribution, the contact area between specimen and clamp should be decreased to increase the contact resistance. Therefore, the size of the designed specimen used in electrically assisted uniaxial tension is shown in Fig. 2.

2.2 Oven-Heating Uniaxial Tension

In order to study the influence of electroplasticity and pure electroplasticity on the flow behavior of AA7075-T6, it is first necessary to study the influence of thermal effect on the flow behavior. Therefore, oven-heating uniaxial tensions are carried out at different temperatures (25, 50, 100, 150, and 200 °C) with a strain rate of 0.005/s and each test is repeated three times. During the test, three thermocouples are used to measure the temperature of the upper, middle, and lower area of the specimen, and the strain is measured with a ceramic extensometer. The test equipment is shown in Fig. 3.

Table 1 Chemical composition of AA7075-T6 (wt%)

Zn	Mg	Cu	Si	Fe	Mn	Ti	Cr	Others	Al
05.1–6.1	2.1–2.9	1.2–2	≤0.4	≤0.5	≤0.3	≤0.2	0.18–0.28	0.05–0.15	Balance

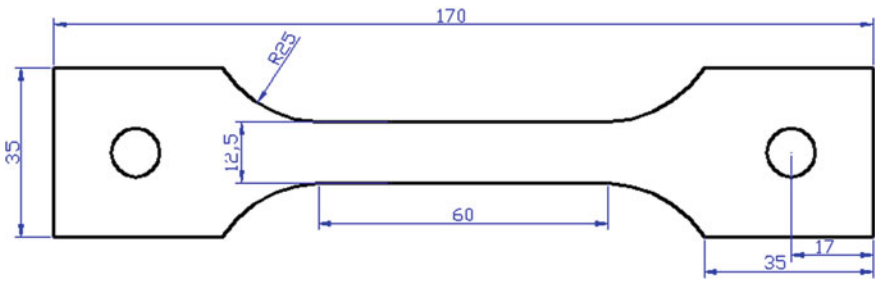


Fig. 1 The size of specimen used in oven-heating uniaxial tension. (Color figure online)

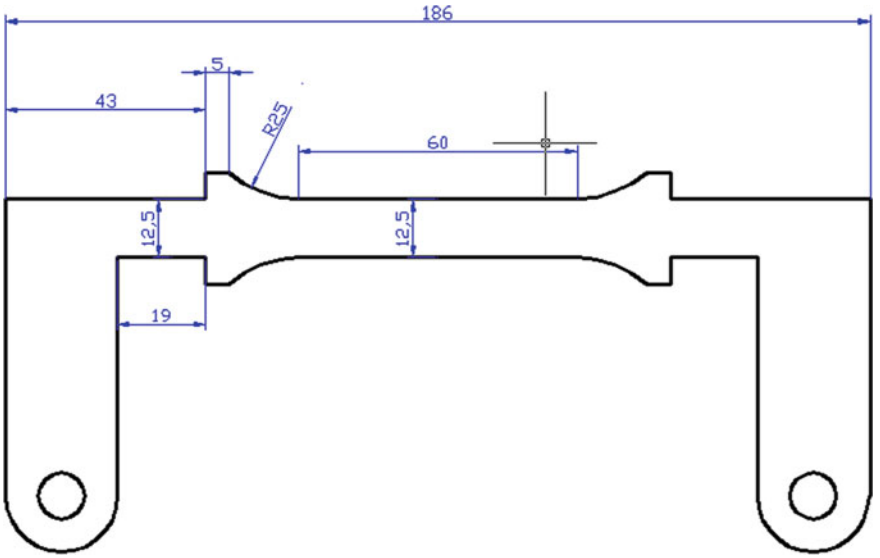


Fig. 2 The size of specimen used in electrically assisted uniaxial tension. (Color figure online)

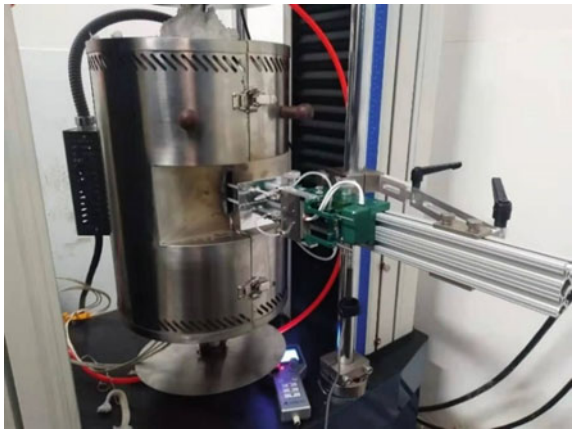


Fig. 3 Test equipment for oven-heating uniaxial tension. (Color figure online)

2.3 Electrically Assisted Uniaxial Tension

In order to study the influence of electrical parameters on the flow behavior of AA7075-T6, electrically assisted uniaxial tensions are carried out with different temperatures and current densities. The test matrix is shown in Table 2 and each test is repeated 3–5 times. The test equipment is shown in Fig. 4. During the test, clampers are insulated with an insulating electrical board. Digital image correlation (DIC) is used to measure the strain, an infrared thermal imaging camera is used to

Table 2 Test matrix for electrically assisted uniaxial tension

No.	Temperature/°C	Current density/A/mm^2	Strain rate/s^{-1}
1	50	5	0.005
2	50	10	0.005
3	100	10	0.005
4	100	15	0.005
5	150	15	0.005
6	150	20	0.005
7	200	15	0.005
8	200	20	0.005

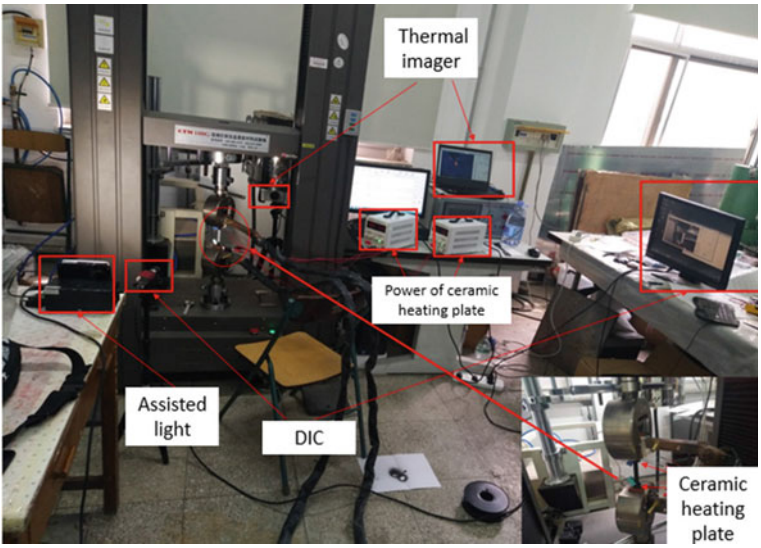


Fig. 4 Test equipment for electrically assisted uniaxial tension. (Color figure online)

measure the temperature, and a blower is used to control the temperature distribution on the specimen. A ceramic heating plate is used to compensate for the lost heat due to the heat conduction between specimen and clamper. In order to stabilize the emissivity of temperature measurement, the specimen is coated with a thin layer of black paint and the emissivity is set to 0.9 [6].

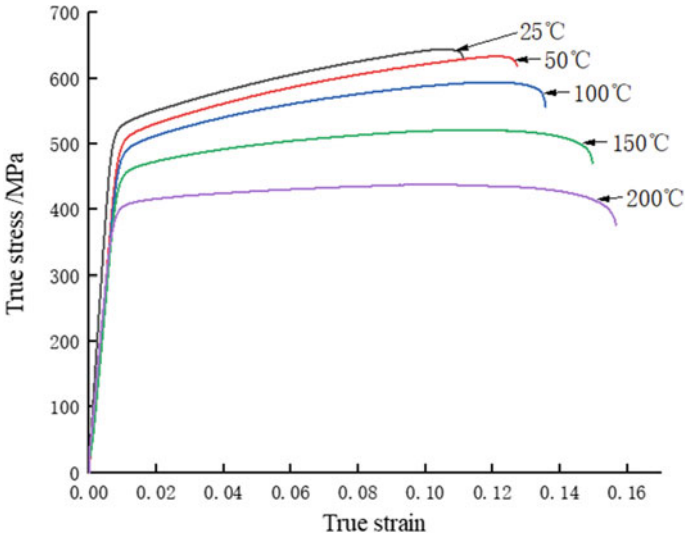


Fig. 5 Flow stress curves at different temperatures (oven-heating). (Color figure online)

3 Results and Discussion

3.1 Results

The flow stress curves for oven-heating uniaxial tension at different temperatures are shown in Fig. 5. The flow stress decreases (600–410 MPa) and the elongation increases with the increase of temperature (25–200 °C). In addition, at the same temperature increment, the higher the temperature, the greater is the decrease of flow stress. The flow stress curves obtained by electrically assisted uniaxial tension are shown in Fig. 6. As observed from Fig. 6, the flow stress decreases with the increase of temperature; at the same temperature, the flow stress slightly decreases with the increase of current density.

3.2 Discussion

In terms of flow stress and yield ratio, the difference ($\Delta\sigma$) of flow stress between oven-heating and electrically assisted heating at the same temperature is shown in Fig. 7, which is expressed as Eq. (1), where σ_O is the stress value obtained with oven-heating and σ_E is the stress value obtained with electrically assisted heating. Because the flow stress values with different current densities are very close at the same temperature, the stress value of one current density is selected to calculate the stress difference at a certain temperature. As observed from Fig. 7, when the temperature

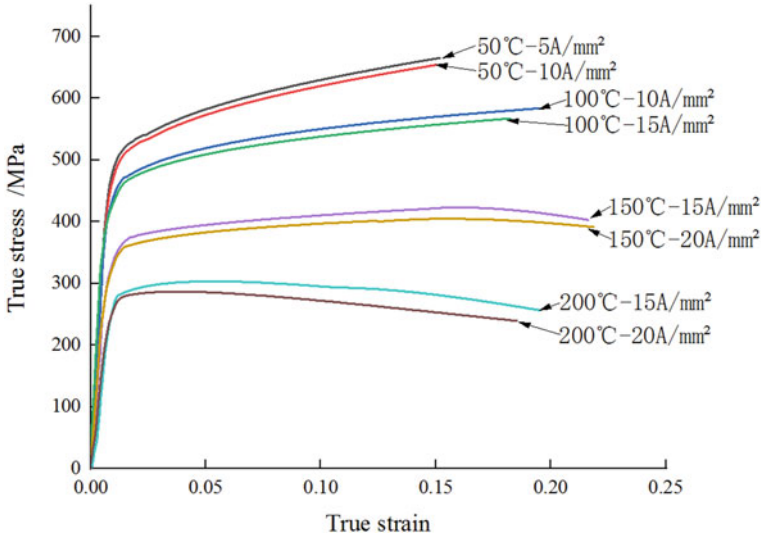


Fig. 6 Flow stress curves at different temperatures and current densities (electrically-assisted). (Color figure online)

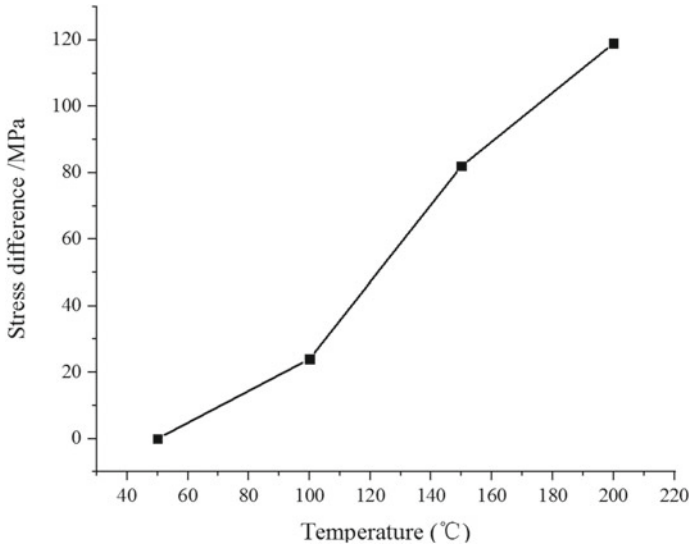


Fig. 7 The difference curves of flow stress for different heating methods at the same temperature

is 50 °C, the $\Delta\sigma$ is close to 0. With the increase of temperature, the $\Delta\sigma$ increases, which shows that pure electroplasticity becomes more obvious with the increase of temperature. In addition, the stress level at 150 °C for electrically assisted heating

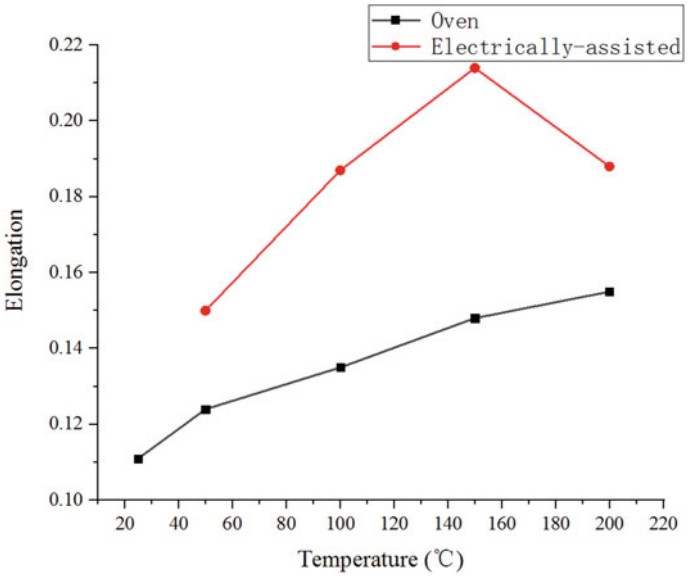


Fig. 8 Change curves of elongation with temperature for different heating methods. (Color figure online)

is close to that at 200 °C for oven heating, and the yield ratio of electrically assisted heating is obviously lower than that for oven heating, which shows that AA7075-T6 has better plastic formability with electrically assisted forming. In addition, for electrically assisted uniaxial tension, the difference of stress obtained by different current densities at the same temperature is very small, which is mainly because the difference of current density at the same temperature is only 5 A/mm^2.

$$\Delta\sigma = \sigma_{\mathrm{O}} - \sigma_{\mathrm{E}} \tag{1}$$

In terms of elongation, the change curves of elongation with temperature for different heating methods are shown in Fig. 8. Attentively, the elongation corresponding to different current densities at the same temperature for electrically assisted uniaxial tension is close, so the elongation under a certain current density at the same temperature is selected when the elongation is compared. As observed from Fig. 8, larger elongation can be obtained with electrically assisted heating. For oven-heating uniaxial tension, the elongation increases with the increase of temperature; for electrically assisted uniaxial tension, the elongation increases with the increase of temperature/current density on the whole. However, the elongation at 200 °C is lower than that at 150 °C, which is because of the obvious high temperature softening effect and non-uniform temperature distribution.

4 Conclusion

1. For AA7075-T6, there is pure electroplasticity. The higher the temperature, the more obvious is the pure electroplasticity.
2. The flow stress level at 150 °C for electrically assisted uniaxial tension is the same as that at 200 °C for oven-heating uniaxial tension. However, the corresponding yield strength ratio of electrically assisted uniaxial tension is lower than that of oven-heating uniaxial tension.
3. The elongation obtained by electrically assisted uniaxial tension is higher than that obtained by oven-heating uniaxial tension. For electrically assisted uniaxial tension within the temperature range of 50–200 °C in this paper, the largest elongation is obtained at 150 °C.

Acknowledgments The authors thank the support from the Fundamental Research Funds for the Central Universities (YWF-19-BJ-J-163) and the National Natural Science Foundation of China (51775023). Also, the authors thank the suggestions of editors and reviewers.

References

1. Heinz A, Haszler A, Keidel C et al (2000) Recent development in aluminium alloys for aerospace applications. Mater Sci Eng A 280(1):102–107
2. Rokni MR, Zarei-Hanzaki A, Roostaei AA et al (2011) An investigation into the hot deformation characteristics of 7075 aluminum alloy. Mater Des 32(4):2339–2344
3. Wang H, Luo YB, Friedman P et al (2012) Warm forming behavior of high strength aluminum alloy AA7075. Trans. Nonferrous Met. Soc. China 22(1):0–7
4. Sotirov N, Simon P, Waltenberger T et al (2010) Towards high strength. In: 7xxx Aluminium sheet components through warm forming. Paper presented at the 12th international conference on aluminium alloys. Yokohama, Japan, 5–9 September 2010
5. Roh J-H, Seo J-J, Hong S-T et al (2014) The mechanical behavior of 5052-H32 aluminum alloys under a pulsed electric current. Int J Plast 58:84–99
6. Zhao K, Fan R, Wang L (2016) The effect of electric current and strain rate on serrated flow of sheet aluminum alloy 5754. J Mater Eng Perform 25(3):781–789

Effect of Pulse Current on Mechanical Properties and Microstructure of Ultrahigh-Strength Steel



Xin Chen, Dongkai Xu, Lei Shi, Hua Xiao, Xifeng Li, and Jun Chen

Abstract The effects of pulse current on the microstructure and mechanical properties of two kinds of ultrahigh-strength steels (UHSS) were studied by electrically assisted tension tests. The elongation of the two UHSS (MS1300 and QP980) moderately increases at relatively low current density, while their microstructures keep almost unchanged. For MS1300 steel, the elongation can be increased from 8.3% at room temperature to 12.4% at the current density of 6.58 A/mm^2. The peak stress of QP980 is reduced to 900 MPa at the current density of 7.46 A/mm^2, and the elongation is increased from 22.3% at room temperature to 38.4%. If the current density is further increased, the tensile strengths of UHSS are greatly reduced. Meanwhile, their microstructures are also obviously varied. Therefore, the appropriate current density should be selected in order to maintain the UHSS grades.

Keywords Pulse current · Ultrahigh-strength steel · Mechanical properties · Microstructure

1 Introduction

Ultrahigh-strength steels can reduce automobile sheet thickness under the premise of ensuring the safety requirements. They are important materials for realizing the automobile lightweight [1]. Ultrahigh-strength steels have some disadvantages, i.e., high yield limit, low elongation, easy cracking during forming, large residual stress after forming, and large springback amount. These drawbacks make them difficult to form complex structures, which limit their application. The hot stamping forming

X. Chen · X. Li (✉) · J. Chen
Department of Plasticity Technology, School of Materials Science and Engineering, Shanghai Jiao Tong University, Shanghai 200030, China
e-mail: lixifeng@sjtu.edu.cn

D. Xu · L. Shi · H. Xiao
Research Institute, Baoshan Iron and Steel Co., Ltd., Shanghai 201900, China

State Key Laboratory of Development and Application Technology of Automotive Steels (BaoSteel), Shanghai 201900, China

© The Minerals, Metals & Materials Society 2021

G. Daehn et al. (eds.), *Forming the Future*, The Minerals, Metals & Materials Series,
https://doi.org/10.1007/978-3-030-75381-8_72

process for high-strength steels is relatively mature now, but it has disadvantages such as high energy consumption, long forming cycle, and high cost [2, 3].

At the same time, some studies show that the pulse current has a significant effect on the regulation of the material microstructure. Pulse current treatment is a processing method of instantaneous high energy input. It has the merits of short time, high energy effect, convenient operation, and efficiency [4]. Additionally, the action of pulse current on various metals is different from the ordinary heating effect. The pulse current is helpful for the metal forming process as follows: (1) reducing the flow stress during plastic forming; (2) improving the forming limit of materials and increasing plasticity; (3) decreasing or eliminating the workpiece springback after forming; and (4) achieving the microstructure regulation and optimization during the forming process [5].

Electrically assisted forming (EAF) is a metal forming technique where the metal workpiece formability is improved owing to the application of electricity that is applied concurrently during plastic deformation [6–8]. Nowadays, it is mainly used in light alloy materials and has achieved remarkable usage effects. However, there are few forming applications for UHSS. Therefore, two kinds of UHSS (MS1300 and QP980) provided by BaoSteel that were chosen for this study. Both have a tensile strength of about 1000 MPa. The electrically assisted tension and microscopic analysis were performed to study the effect of pulse current on their deformation behavior and microstructural evolution.

2 Experimental Methods

The chemical compositions of two AHSS are shown in Table 1. The thicknesses of MS1300 and QP980 steel sheets are 1.4 and 1.2 mm, respectively. The sheet was wire cut to obtain tensile specimens with a gauge length of 35 mm × 6 mm. The electrically assisted tension and pulse current treatment without stretching were carried out on a SANS testing machine. The initial strain rate was 10^{-3} s^{-1}. The pulse current was supplied by TSGZ-2.0KVA capacitor banks. The amount of pulse current was measured by a Tektronix oscilloscope. FLIR-A651 thermal imager was used to record the specimen temperature variation. Each tension under the same condition was repeated with a minimum of three samples to ensure repeatability and reproducibility.

In the microscopic analysis experiment, the microstructure of UHSS was observed by Zeiss optical microscope. The phase analysis of the specimen was performed on

Table 1 Chemical compositions of MS1300 and QP980 sheet (wt%)

Material	C	Si	Mn	P	S	Fe
MS1300	0.18	0.37	1.55	0.011	0.002	Balance
QP980	0.20	1.49	1.80	0.017	0.0043	Balance

the D8 Advance X-ray diffractometer. The XRD measurements were carried out between 30° and 95° at room temperature by using a diffractometer with Cu target and a step size of 0.02°. The fracture morphology was observed by TESCAN Mira3 scanning electron microscope.

3 Results and Discussion

The microstructure of UHSS needs to be finely regulated since the phase transformation easily occurs at high temperatures [9]. Therefore, excessive current should not be introduced into EAF to avoid changing their microstructure. In the following experiment, the output voltage was fixed to 30 V. The current density was changed by adjusting the pulse current frequency to study the influence of pulse current on the tensile behavior of MS1300 steel.

As shown in Table 2, the current density has a significant effect on the tensile properties of MS1300 steel. The elongation under the current density of 5.60– 7.49 A/mm^2 has an increase compared to that tested at room temperature. Under the current density of 6.58 A/mm^2, the elongation can be increased to 12.4%. The result is similar to the conclusions of Xie et al. [10]. The pulse current helps to increase the elongation within a certain range. But when the current density is too large, it generates a higher temperature in the necking region to accelerate the specimen fracture. The elongation declines instead.

As shown in Fig. 1 and Table 2, when the specimen temperature increases the elastic modulus gradually decreases, and the flow stress slightly rises. The peak stress during the tensile process first increases and then decreases in the current density range of 4.99–6.58 A/mm^2. The peak stress of MS1300 steel exceeds that tested at room temperature. Lin and Zhang [11] have carried out high temperature tension tests on MS1400 steel of Baosteel by using Gleeble1500 thermal simulation testing machine. The results showed that the flow stress of martensitic steel monotonously decreased with the increase of temperature. Therefore, the non-thermal effect of pulse current makes the flow stress of MS1300 steel increase. The current density

Table 2 Electrically assisted tension results of MS1300 steel at different current densities

Current density (A/mm^2)	Temperature (°C)	Peak stress (MPa)	Elongation (%)
0	20	1357.7	8.3
4.99	145	1410.1	6.5
5.60	178	1458.5	8.5
6.02	212	1442.3	12.2
6.58	240	1461.2	12.4
7.03	279	1342.6	11.6
7.49	310	1298.8	11.2

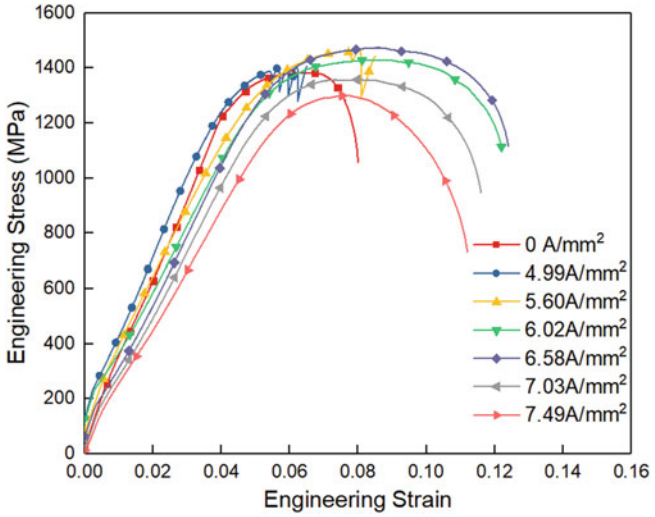


Fig. 1 Engineering stress–strain curves of MS1300 at different current densities. (Color figure online)

is further increased to 7.49 A/mm^2, and the flow stress of MS1300 steel decreases. The joule heating effect dominates, and it increases the temperature and softens the specimens. In addition, when the current density is 4.99 A/mm^2, the temperature of MS1300 specimen only reaches 145 °C. But the elongation is abnormally decreased. It shows that pulse current causes low-temperature temper embrittlement of MS1300 steel [12].

A similar experimental method was selected for QP980 steel, and the output voltage was fixed to 20 V. The testing results are listed in Table 3. The tensile deformation behavior of QP980 steel significantly varies at different current densities. The tensile strength of QP980 in the electrically assisted tension process is lower

Table 3 Electrically assisted tension results of QP980 steel at different current densities

Current density (A/mm^2)	Temperature (°C)	Peak stress (MPa)	Elongation (%)
0	20	1041.7	22.3
3.31	67	970	23.15
5.39	165	890	25.8
6.47	230	890	30.3
7.46	295	900	38.4
8.37	355	923	35.5
9.86	510	1020	23.3
10.78	600	790	15.3

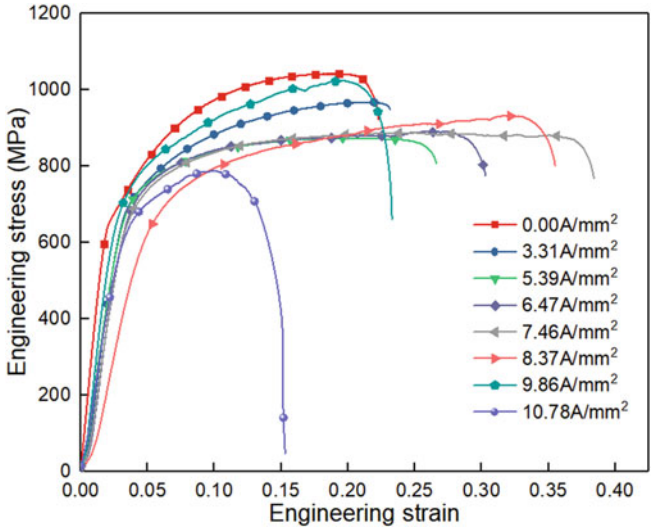


Fig. 2 Engineering stress–strain curves of QP980 at different current densities. (Color figure online)

than that tested at room temperature. But it does not show obvious regularity. It indicates that the effect of pulse current on the deformation behavior of QP980 is not solely caused by the joule heating effect. On the one hand, the temperature increase reduces the strength of QP980 steel. On the other hand, the non-thermal effect of pulse current may increase the flow stress of QP980 steel. Under the pulse current of 9.86 A/mm^2, the peak stress reaches 1020 MPa and it is close to that tested at room temperature. Further increasing the current density, the thermal effect may play a leading role, and the flow stress of QP980 steel decreases rapidly (Fig. 2).

With the increase of pulse current density, the elongation of QP980 steel after electrically assisted tension first increases and then decreases. It rises from 22.3% at room temperature to 38.4% at current density of 7.46 A/mm^2. When the current density is further increased, the elongation decreases instead. The thermal effect of pulse current gradually dominates. The higher current density in necking section results in a local temperature increase that accelerates the fracture process.

The microstructure near the fracture zone of the stretched specimens is shown in Fig. 3. The original microstructure of MS1300 steel is composed of acicular martensite and ferrite. The martensite is the main phase. The ferrite is distributed in the martensite matrix. After electrically assisted tensions with a current density of 4.99–7.49 A/mm^2, the basic phase compositions of the stretched specimen have no significant change. When the current density is controlled in relatively low value ranges, the elongation of MS1300 steel can be increased without destroying its microstructure or reducing its strength. Nevertheless, the elongation variation may result from the direct effect of the drift electrons on dislocation motion [13, 14]. Dislocation pile-ups and tangles are overcome and the plasticity is differently improved by pulse current with various densities.

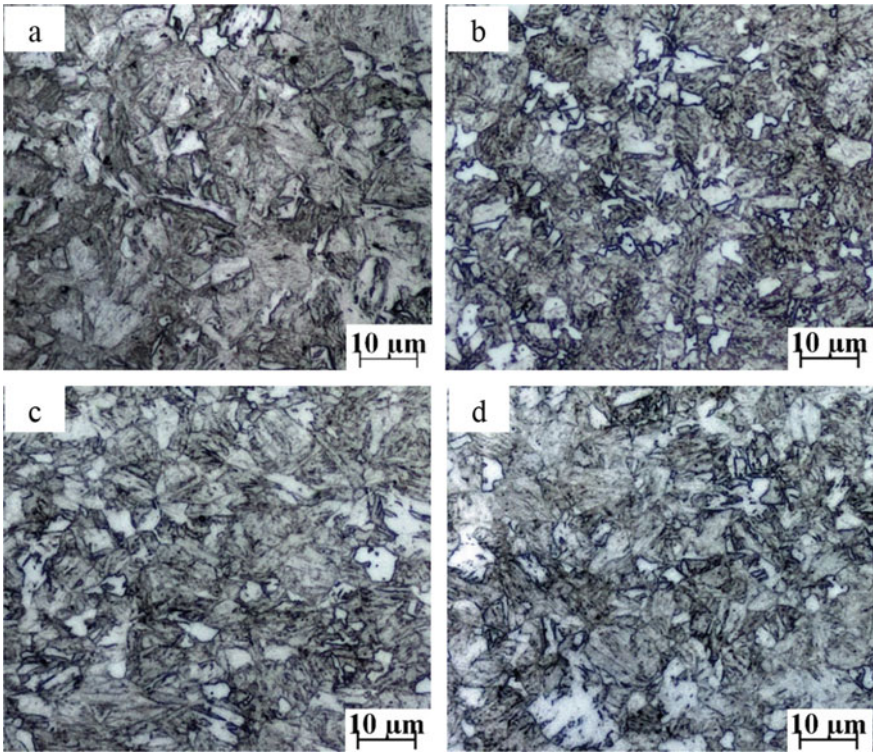


Fig. 3 Microstructure of MS1300 specimens after stretching at different current densities: **a** 0, **b** 4.99 A/mm^2, **c** 6.58 A/mm^2, **d** 7.49 A/mm^2. (Color figure online)

Further increasing the current density to 9.21 and 12.03 A/mm^2, the pulse current treatments were performed on the specimens without stretching for 100 s. Their temperatures reached 427 °C and 706 °C, respectively. As indicated in Fig. 4, there is a significant microstructural change. Figure 4a shows that the boundaries between ferrite and martensite are blurred. The carbide in the martensite matrix precipitates and diffuses into ferrite to form an intermediate phase. Figure 4b shows that the decomposition of martensite and the diffusion rate of carbide increases greatly after the high temperature and electron wind effect produced by pulse current. After 100 s treatment at relatively high current density, the martensite almost disappears. The recrystallization occurs and the new grains tend to be equiaxed.

The microstructure near fracture zones of electrically assisted tension specimens of QP980 was observed in Fig. 5. Figure 5a shows the optical microstructure of QP980 after stretching at room temperature. It contains a large amount of martensite, and the rest is mainly ferrite. The temperature reaches 67 °C at 3.31 A/mm^2. The microstructure is nearly the same as that stretched at room temperature. This indicates that the low-density current can reduce the flow stress without changing the microstructure of QP980 steel. When the pulse current density of 6.47 A/mm^2

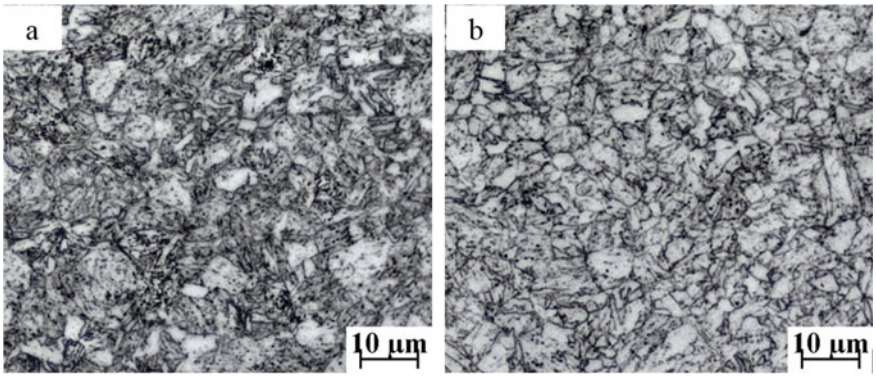


Fig. 4 Microstructure of MS1300 steel after 100 s pulse current treatment without stretching: **a** 9.21 A/mm^2, **b** 12.03 A/mm^2. (Color figure online)

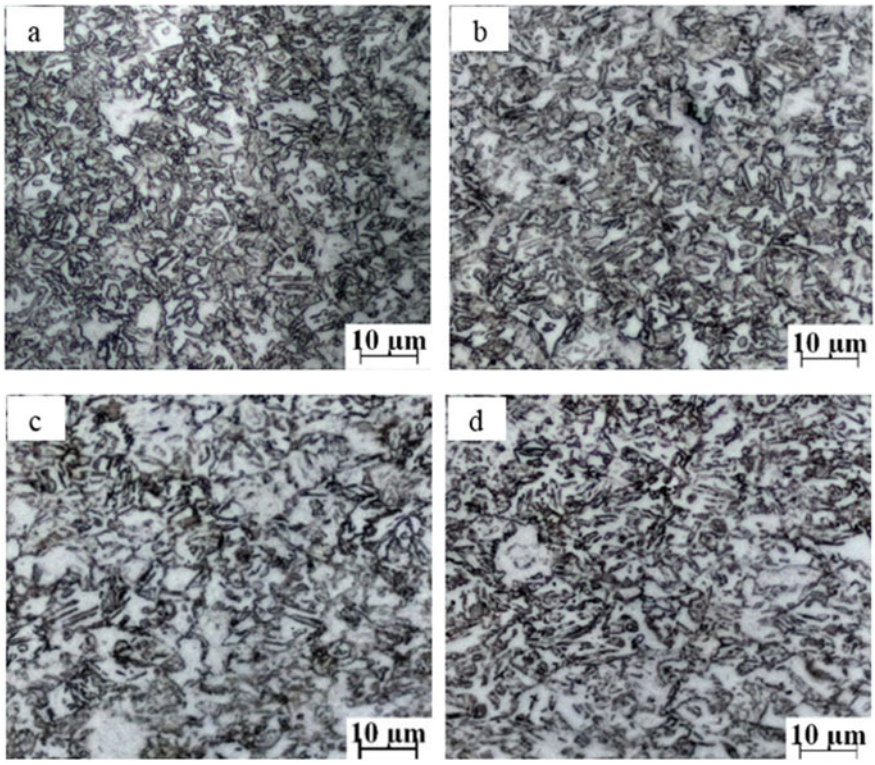


Fig. 5 Microstructure of QP980 specimens after stretching at different current densities: **a** 0, **b** 3.31 A/mm^2, **c** 6.47 A/mm^2, **d** 9.86 A/mm^2. (Color figure online)

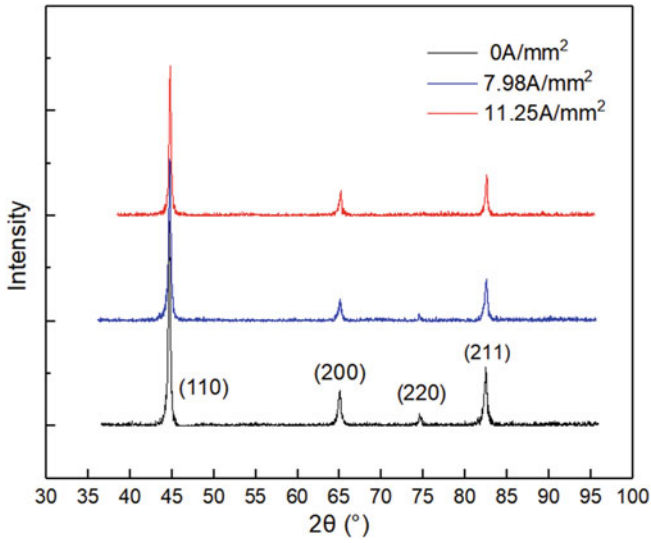


Fig. 6 Diffraction pattern of QP980 steel after pulse current treatment without stretching at different current densities. (Color figure online)

is applied, the temperature reaches 230 °C. Figure 5c shows that its microstructure is changed significantly. The martensite content is obviously reduced, and the ferrite fraction is increased. The deformation process is accompanied by the martensite decomposition, which partly reduces the tensile strength of QP980 steel. A similar transformation appears at 9.86 A/mm^2 as indicated in Fig. 5d.

The retained austenite in QP980 steel can be transformed into martensite during the plastic deformation. Therefore, in order to study the effect of pulse current on the retained austenite of QP980, the undeformed QP980 sheet was treated by pulse current for 100 s. The XRD analysis was carried out to obtain the diffraction patterns as shown in Fig. 6. It can be seen that the XRD diffraction patterns of original QP980 steel mainly consist of four peaks of (110), (200), (220), and (211). The (220) peak corresponds to the austenite. When the current density is 7.98 A/mm^2, the peak intensity of (200) weakens. It indicates that the austenite content is reduced due to the effect of pulse current. When the current density increases to 11.25 A/mm^2, the (200) peak disappears, which indicates that excessive current can cause the decomposition of retained austenite.

Figure 7 shows fracture morphologies of QP980 specimens after stretching at different current densities. For the as-received QP980 steel, large quantities of small voids distribute on the fracture surface, indicating the ductile fracture characteristics. When the current density of 7.46 A/mm^2 is applied, the voids become larger and deeper, which demonstrate better plasticity. Actually, the highest elongation of 38.4% is obtained at 7.46 A/mm^2 as shown in Table 3. Therefore, the fracture morphology observation accords to the electrically assisted tension results.

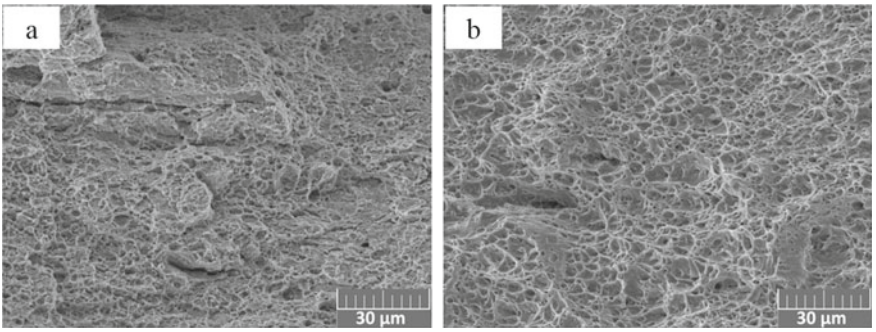


Fig. 7 Fracture morphologies of QP980 specimens after stretching at different current densities: **a** 0, **b** 7.46 A/mm^2

4 Conclusions

(1) Pulse current can improve the tensile deformation behavior of ultrahigh-strength steel. For MS1300 steel, the elongation can be increased from 8.3% at room temperature to 12.4% at a current density of 6.58 A/mm^2. The peak stress of QP980 is reduced to 900 MPa at a current density of 7.46 A/mm^2, and the elongation is increased from 22.3% at room temperature to 38.4%.

(2) The non-thermal effect of current may cause the abnormal rise of flow stress in ultrahigh-strength steel. For MS1300 steel, the peak stress of the electrically assisted tension in the current density range of 4.99–6.58 A/mm^2 exceeds that tested at room temperature. For QP980 steel, its peak stress obviously varies when the current density is increased from 3.31 to 10.78 A/mm^2.

Acknowledgments This work was supported by NSFC-Liaoning Province United Foundation (No. U1908229) and Equipment Pre-research Fund (No. 61409230408). The authors are grateful for this financial support.

References

1. Liu C, Wang L, Liu Y (2012) Development of advanced high-strength steel used for automobile and its application in body design. Spec Steel Technol 18(2):1–4
2. Lin ZG (2016) Research progress and present technique application situation of advanced high-strength automobile steel sheet. Hebei Metallurgy
3. Li Y, Liu HW, Du YH (2011) Applications and developments of AHSS in automobile industry. Mater Rev 25:101–116
4. Ding JH, Li H, Bian TJ (2018) Electroplasticity and electrically-assisted forming: a critical review. Acta Aeronautica et Astronautica Sinica. 39(1):15–32
5. Li XH (2015) Effect of pulse current on the microstructure and properties of different initial state 40Cr steels. Jilin University

6. Bunget CJ, Salandro WA, Mears L (2013) Thermomechanical modeling sensitivity analysis of electrically assisted forming. Proc Inst Mech Eng, Part B: J Eng Manuf 227(8):1089–1098
7. Li XF, Zhou Q, Zhao SJ, Chen J (2014) Effect of pulse current on bending behavior of Ti6Al4 V alloy. Procedia Eng 81:1799–1804
8. Jiang B, Yang WB, Zhang ZY, Li XF, Ren XP, Wang YQ (2020) Numerical simulation and experiment of electrically-assisted incremental forming of thin TC4 titanium alloy sheet. Materials 13(6):1335
9. Zhu XD, Xue P, Li W (2017) Status of the development and application of Baosteel's cold rolled martensitic steel sheets. Baosteel Technology
10. Xie HY, Dong XH, Liu K (2015) Experimental investigation on electroplastic effect of DP980 advanced high strength steel. Mater Sci Eng A 637:23–28
11. Lin X, Zhang QD (2017) Constitutive model of HC1150/1400MS martensitic steel at high temperature. Heat Treat Met 42(10):197–202
12. Liu SF (2009) Grain boundary martensite formation and tempering brittleness at low temperature of steels. Hebei University of Technology
13. Song PC, Li XF, Ding W, Chen J (2014) Electroplastic tensile behavior of 5A90 Al-Li alloys. Acta Metallurgica Sinica (English Letters). 27(4):642–648
14. Li XF, Ji BY, Zhou Q, Chen J, Gao P (2016) Influence of grain size on electrically-assisted tensile behavior of Ti-6Al-4V alloy. J Mater Eng Perform 25(10):4514–4520

Experimental Study and Modelling of Stress Relaxation Ageing Behaviour and Post-form Mechanical Properties in Creep Age Forming of Al-Zn-Mg Alloy



Yong Li, Fenggong Lyu, Zhusheng Shi, Yuansong Zeng, Xia Huang, and Jianguo Lin

Abstract The stress relaxation ageing behaviour and post-form mechanical properties of an Al-Zn-Mg alloy, AA7B04, have been experimentally investigated and modelled. The stress relaxation ageing tests were carried out under different initial stress levels and durations at 165 °C and subsequent tensile tests were performed at room temperature. The detailed effects of stress and time on stress relaxation and main post-form mechanical properties (yield strength, ultimate tensile strength, and uniform elongation) have been analysed and discussed. Based on the results and analysis, a set of unified constitutive equations has been developed for the first time to simultaneously predict stress relaxation ageing behaviour of the aluminium alloy during the creep age forming (CAF) process and the main mechanical properties of the products after CAF. The model comprises three sub-models, including microstructure, stress relaxation ageing and post-form mechanical properties, and has successfully predicted corresponding behaviour. The developed model provides an effective tool to not only predict the forming process but also support possible industrial applications for CAF products.

Keywords Stress relaxation · Ageing · Post-form mechanical property · Al-Zn-Mg alloy · Constitutive model

1 Introduction

Creep age forming (CAF) is an advanced sheet forming technology that combines creep/stress relaxation and artificial ageing processes to concurrently deform and strengthen heat-treatable aluminium alloys, making it an efficient and accurate

Y. Li (✉)
School of Mechanical Engineering and Automation, Beihang University, Beijing 100191, China
e-mail: liyong19@buaa.edu.cn

F. Lyu · Y. Zeng · X. Huang
AVIC Manufacturing Technology Institute, Beijing 100024, China

Z. Shi · J. Lin
Department of Mechanical Engineering, Imperial College London, London SW7 2AZ, UK

© The Minerals, Metals & Materials Society 2021

G. Daehn et al. (eds.), *Forming the Future*, The Minerals, Metals & Materials Series,
https://doi.org/10.1007/978-3-030-75381-8_73

method to manufacture large panels in the aerospace industry, such as wing skins [1, 2]. The integrated creep ageing or stress relaxation ageing (SRA) behaviour of aluminium alloys is a key factor to determine both the final shape and post-form mechanical properties of creep age formed (CAFed) products. Hence, it is important to systematically understand and predict the relationship between creep/stress relaxation and key mechanical properties during and after CAF so as to provide useful guidance for not only accurate forming but also successful applications of the CAFed products.

The creep ageing or stress relaxation ageing behaviour, including both key microstructures and macro-properties, of various heat-treatable aluminium alloys, such as Al-Cu-Mg [3], Al-Zn-Mg [4], and Al-Cu-Li [5], has been widely investigated in the last few decades and based on which many constitutive models have been proposed to predict the evolutions of precipitation, dislocation, creep/stress relaxation and yield strength during creep ageing for CAF process simulation [3, 6]. Except for the yield strength, other post-form mechanical properties of the CAFed materials, such as tensile strength and elongation, which are also key factors concerned for industrial applications, however, have attracted less attention currently. Li et al. [7] and Chen et al. [8] have investigated the work hardening behaviour, tensile strength, and uniform elongation properties of AA2050 and AA7050 materials after CAF, respectively, and the relationship between the microstructures and post-form mechanical properties has been discussed. However, the corresponding modelling work is still unavailable.

Hence, this study tries to perform a systematic investigation of the SRA behaviour during CAF and key post-form mechanical properties after CAF in both experimental and modelling ways. SRA and tensile tests of an Al-Zn-Mg alloy, AA7B04, have been performed for detailed analysis and discussion, and based on which a unified constitutive model to simultaneously predict both stress relaxation and key post-form mechanical properties has been proposed and discussed.

2 Materials and Experiments

The material investigated is AA7B04, with the main chemical composition of Al-5.97Zn-2.48 Mg-1.51Cu (wt%). The material was prepared with a special initial temper, named AA7B04-P, which had undergone solution heat treatment (SHT), water-quenching, pre-stretching, and a single-step artificial ageing to an under-aged state.

A set of SRA tests at 165 °C was performed under different initial stress levels (200, 250, 300, and 350 MPa) at different durations (2, 4, 8, and 16 h) to get the stress relaxation behaviour of the material. In addition, tensile tests at room temperature were also carried out on specimens after SRA tests to investigate the evolutions of main post-form mechanical properties of the material during SRA. The dog-bone specimens were prepared for both SRA and tensile tests, with the key dimension of 8 mm in radius and 50 mm in gauge length. Both kinds of tests were carried out on an

Instron 5584 machine with a furnace to provide a high-temperature environment. In SRA tests, specimens were first heated to 165 °C, then loaded to the initial stress level, and held for designated durations for stress relaxation behaviour characterisation. The quasi-static tensile tests were performed with a strain rate of 10^{-4} s^{-1}. Further details of the material and corresponding test conditions can be found in a previous study [4].

3 Experimental Results and Discussion

Figure 1 shows the stress relaxation curves of AA7B04-P at 165 °C. Higher initial stress leads to a more prominent stress relaxation behaviour, due to the larger creep strains generated at higher initial stress levels [4]. The remained stress after 16 h tests is generally larger with a higher initial stress level from 200 to 300 MPa; however, the remained stress for the initial stress of 350 MPa is lower than that for 300 MPa. This is because 350 MPa already exceeds the 0.01% offset yield point of the material (325 MPa) and the phenomenon may be explained by the additional initial dislocations introduced when loaded to the plastic region [4, 9].

The room temperature flow stress curves of the material after SRA tests under different initial stress levels at different durations have been plotted in Fig. 2. All the flow stress curves of the SRAed materials show a fair level of work hardening behaviour, in which the highest level of work hardening exists in the as-received material. The flow stress level becomes lower with increasing SRA time under the initial stress of 200 MPa. In addition, Fig. 2 compares the flow stress of the material after 16 h SRA tests under 200 and 300 MPa, and the results show that with a higher initial stress, a lower flow stress is observed in the material after the SRA test for the same duration.

Figure 3a shows the detailed ultimate tensile strength (σ_{UTS}) and yield strength (σ_y) values of the materials SRAed under initial stresses of 200 and 300 MPa.

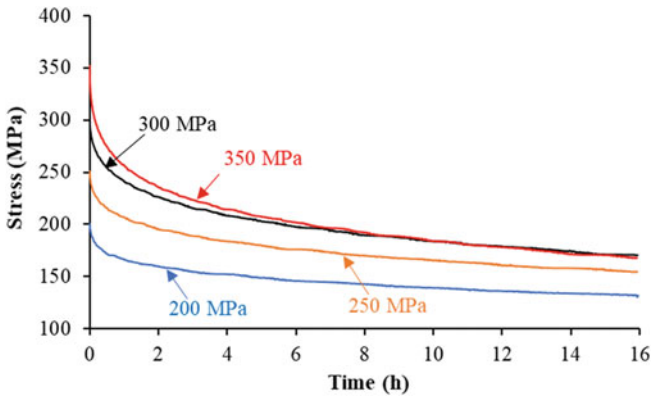


Fig. 1 Stress relaxation curves of AA7B04-P under different initial stress levels at 165 °C. (Color figure online)

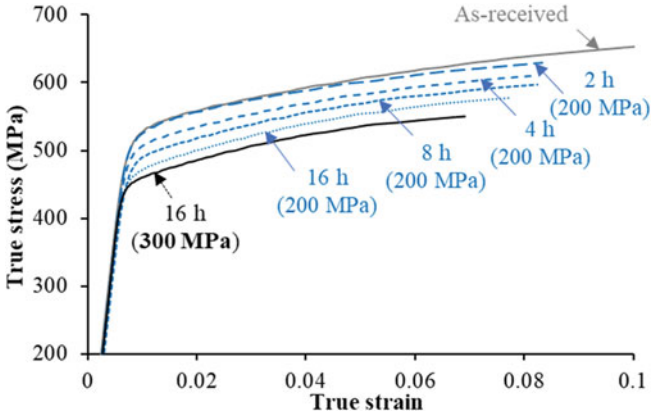


Fig. 2 The stress–strain curves of AA7B04-P after SRA tests at 165 °C for a different duration and under indicated initial stress levels. (Color figure online)

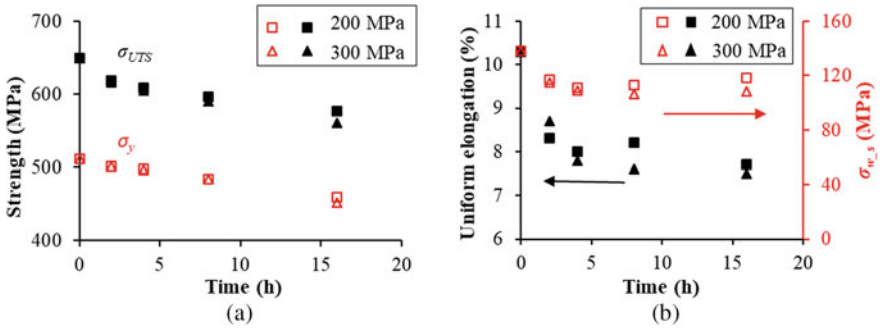


Fig. 3 Evolution of **a** ultimate tensile strength (σ_{UTS}) and yield strength (σ_y), and **b** uniform elongation and saturate work hardening stress (σ_{w_s}) versus SRA time for AA7B04-P at 165 °C. (Color figure online)

Although the as-received material is in an under-aged condition [4], yield strength of the material decreases after 2 h SRA tests and experiences a continuously decreasing trend afterwards, which indicate that over-ageing has already started after 2 h. With higher initial stress, slightly lower yield strength is observed in the SRAed materials under the same testing time and temperature, as higher initial stresses lead to larger stress relaxation/creep, which can accelerate the coarsening of precipitates in the material [10]. Meanwhile, σ_{UTS} shows the same trend with σ_y results.

The uniform elongation, as shown in Fig. 3b, decreases significantly at the first 2 h, which could be related to the depleted solutes in the material from under-ageing to over-ageing within the first 2 h [11]. Figure 3b also shows the saturate work hardening stress ($\sigma_{w_s} = \sigma_{UTS} - \sigma_y$) of the SRAed materials, which demonstrates a similar trend with the uniform elongation. It should be noted that a slight increase of

σ_{w_s} after 8 h SRA tests can be observed in Fig. 3b, which may be due to the size of non-shearable precipitates that grow to a high level after 8 h tests, and the geometrically necessary dislocations accumulated around these fine precipitates become high enough to facilitate the work hardening of the material [12].

4 Modelling

A unified constitutive model that utilises and modifies both the conventional creep-ageing and work hardening equations has been proposed in this study to simultaneously model and predict the stress relaxation behaviour during CAF and main post-form mechanical properties of the alloys after CAF. The developed model is divided into three sub-models, from microstructures to macro-properties, including microstructure, stress relaxation ageing, and post-form mechanical properties sub-models.

4.1 Microstructure Sub-model

The main microstructures related to the stress relaxation ageing behaviour of aluminium alloys include precipitates, solid solutes, and dislocations. The effect of precipitates on SRA behaviour has been generally characterised by its size (r) and volume fraction (f), while the effects from solid solutes and dislocations are represented by solute concentration (c) and dislocation density (ρ), respectively. All the microstructural variables are modelled as normalised values in this study to eliminate the high difficulties in obtaining the actual microstructure values. The evolutions of these main microstructural variables during SRA can be modelled by the following equations [6, 13]:

$$\dot{\overline{r}} = C_r(Q - \overline{r})^{m_1}\left(1 + \gamma_0\overline{\rho}^{m_2}\right) \tag{1}$$

$$\dot{\overline{c}} = -A_1(\overline{c} - \overline{c}_a)\left(1 + \gamma_0\overline{\rho}^{m_2}\right) \tag{2}$$

$$\dot{\overline{\rho}} = A_2(1 - \overline{\rho})|\dot{\varepsilon}_c|^{m_3} - C_p\overline{\rho}^{m_4} \tag{3}$$

$$\overline{f} = \frac{1 - \overline{c}}{1 - \overline{c}_a} \tag{4}$$

$\overline{r}$ in Eq. (1) is the normalised precipitate radius defined as $\overline{r} = r/r_c$, where r_c is the critical radius at peak-ageing state. $\overline{r}$ then evolves from 0 at SHT state to 1 at peak-ageing state, and $\overline{r} \geq 1$ indicates over-ageing states. Q represents the maximum size

of precipitates during SRA of the alloys. $\overline{c}$ in Eq. (2) is the normalised solute concentration defined as $\overline{c} = c/c_s$, in which c_s is the solute concentration at SHT temperature. $\overline{c}_a$ is the normalised value at the test temperature. $\overline{\rho} = (\rho - \rho_0)/(\rho_s - \rho_0)$ is the normalised dislocation density, in which ρ_0 and ρ_s are dislocation density of the material before SRA tests and its maximum level during SRA tests, and thus, $\overline{\rho}$ generally evolves from 0 to 1 during the SRA tests. The accumulation and dynamic recovery effects of dislocations during SRA are considered in the first term on the right-hand side of Eq. (3), while the second term represents the static recovery effect. In addition, the normalised volume fraction of precipitates $\overline{f} = f/f_s$, in which f_s is the final equilibrium value of f during ageing, can be directly modelled by corresponding solute concentrations according to Eq. (4). Other parameters in Eqs. (1) to (4) are material constants and will be determined in Sect. 5.1.

4.2 Stress Relaxation Ageing Sub-model

The stress relaxation ageing sub-model contains two parts, one for the modelling of stress relaxation curves and the other for yield strength evolutions during the SRA tests. It is generally believed that the stress relaxation during SRA comes from creep strains and can be directly modelled according to the evolutions of creep strains. The creep behaviour is determined by related microstructural variables and can be modelled by the following equations [6]:

$$\dot{\varepsilon}_c = A_4 \sinh[B_1(\sigma - \sigma_{th})(1 - H)]\text{sign}(\sigma) \tag{5}$$

$$H = k_1\overline{\rho} + k_2\overline{c} + k_3\overline{r} \tag{6}$$

$$\dot{\sigma} = -E\dot{\varepsilon}_c \tag{7}$$

$\dot{\varepsilon}_c$ is the creep strain rate, which is modelled by the sinh function of applied stress σ, creep threshold stress σ_{th} and a variable H representing the combined effect from key microstructural variables in Eq. (6). E is the Young's modulus of the material, and the stress relaxation rate can be directly related to creep strain rate by Eq. (7). A_4, B_1, k_1, k_2, and k_3 are material constants to be determined in Sect. 5.1.

However, for yield strength (σ_y), it is comprised of three strengthening components from different microstructures, including dislocation hardening (σ_{dis}), precipitation hardening (σ_p), and solid solution hardening (σ_{ss}), which can be modelled as [14]:

$$\sigma_{dis} = A_3\overline{\rho}^n \tag{8}$$

$$\sigma_p = \sigma_r\overline{f}^{m_5} \tag{9}$$

$$\dot{\sigma}_r = C_a \dot{\bar{r}}^{m_7} \left(1 - \bar{r}^{m_8}\right) \tag{10}$$

$$\sigma_{ss} = C_{SS} \bar{c}^{m_{10}} \tag{11}$$

$$\sigma_y = \sigma_{ss} + \sigma_a = \sigma_{ss} + \sqrt{\sigma_{dis}^2 + \sigma_p^2} \tag{12}$$

in which A_3, n, m_5, C_a, m_7, m_8, C_{SS}, and m_{10} are material constants to be determined. A classic law of mixtures is utilised to combine the strengthening components for yield strength in Eq. (12), in which σ_a represents the combined effect from dislocations and precipitates.

4.3 Post-form Mechanical Properties Sub-model

Work hardening behaviour determines the post-form mechanical properties of ultimate tensile strength and uniform elongation. It has been reported that work hardening behaviour of aluminium alloys during plastic deformation is generally attributed to dislocation hardening: the statistically stored dislocations (ρ_{ss}) from interactions with weak obstacles (shearable precipitates) and solid solutes, and the geometrically necessary dislocations (ρ_{gn}) stored around strong obstacles (non-shearable precipitates) [15]. Both parts of dislocations would contribute to the work hardening behaviour during SRA of AA7B04-P in this study according to the results in Sect. 3, and the following equations are utilised to model their evolutions and effects on work hardening [14, 16]:

$$\dot{\bar{\rho}}_{ss} = k_4 * \bar{c}^{n_1} * \left(1 - \bar{\rho}_{ss}\right) \dot{\varepsilon}_p^{n_2} \tag{13}$$

$$\bar{\rho}_{gn} = \frac{k_5}{\bar{r}^{n_3}} \left[1 - \exp\left(-\dot{\varepsilon}_p^{n_4}\right)\right] \tag{14}$$

$$\sigma_d = C_d \sqrt{\bar{\rho}_{ss} + \bar{\rho}_{gn}} \tag{15}$$

$$\sigma_f = \sigma_{ss} + \sqrt{\sigma_d^2 + \sigma_a^2} \tag{16}$$

$$\sigma_w = \sigma_f - \sigma_y \tag{17}$$

The normalised values of ρ_{ss} and ρ_{gn} are used for modelling in Eqs. (13) and (14), and their contributions to work hardening have been represented by σ_d with the classic law of mixtures in Eqs. (15) and (16). The actual work hardening stresses

shown in the stress–strain curves in Fig. 2 then are represented by σ_w in Eq. (17). In addition, k_4, n_1, n_2, k_5, n_3, and n_4 are material constants.

5 Modelling Results and Discussion

5.1 Calibration of the Model

The AA7B04-P material has been reported to achieve the peak-ageing state after artificial ageing at 165 °C for about 4 h, with an average precipitate radius of about 4.5 nm at the as-received state and 5 nm after 165 °C/4 h artificial ageing [4]; hence, the initial value of normalised precipitate radius $\overline{r}_0$ is determined as 0.9. A cell assumption was used to relate the volume fraction and radius of precipitate, as $\overline{f} = (r/r_c)^3$ [6], and the initial value of normalised volume fraction $\overline{f}_0$ was approximately 0.72. $\overline{c}_0$ was then determined by Eq. (4). The initial values of the strengthening components were approximately determined according to [17]. The initial values of all the variables are listed in Table 1.

Based on the initial values determined in Table 1, a combination of manual adjusting and computational curve fitting method was utilised to calibrate all the material constants in the developed constitutive model according to the experimental data in Sect. 3, as detailed in [6, 14]. The determined material constants are listed in Table 2.

Table 1 Initial and equilibrium values of variables in the constitutive model for SRA of AA7B04-P

$\overline{r}_0$ (–)	$\overline{c}_0$ (–)	$\overline{\rho}_0$ (–)	$\overline{f}_0$ (–)	σ_{dis_0} (MPa)	σ_{p_0} (MPa)	σ_{ss_0} (MPa)	σ_{th} (MPa)	$\overline{c}_a$ (–)
0.9	0.356	0	0.72	0	386	120	57.8	0.105

Table 2 Determined material constants in the constitutive model for SRA of AA7B04-P at 165 °C

C_r (h^{-1})	Q (–)	γ_0 (–)	m_1 (–)	m_2 (–)	A_1 (–)	A_2 (–)	m_3 (–)	C_p (–)	m_4 (–)
0.0126	4.8	2.7	1.3	1.88	0.86	68	0.65	0.02	1.02
A_4 (h^{-1})	B_1 (MPa)	k_1 (-)	k_2 (-)	k_3 (-)	A_3 (MPa)	n (-)	m_5 (-)	C_a (MPa)	m_7 (-)
4.2E-5	0.025	0.9	0.3	0.04	128	0.5	0.5	30	0.5
m_8 (–)	C_{SS} (MPa_	m_{10} (–)	k_4 (–)	k_5 (–)	n_1 (–)	n_2 (–)	n_3 (–)	n_4 (–)	C_d (MPa)
0.8	239.7	0.67	1.2	4.6	0.07	0.7	0.08	0.65	282

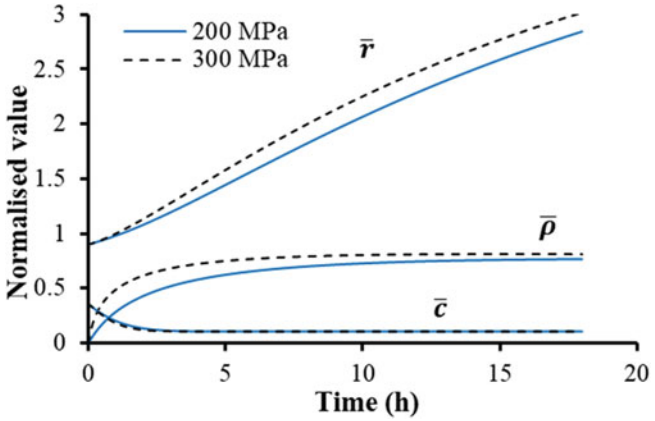


Fig. 4 Modelled evolution of normalised values of dislocation density ($\bar{\rho}$), precipitate radius ($\bar{r}$), and solid solution concentration ($\bar{c}$) in AA7B04-P during 16 h SRA tests at 165 °C under different initial stresses. (Color figure online)

5.2 Microstructural Evolutions

Figure 4 shows the evolution of normalised microstructural variables during SRA tests under 200 and 300 MPa from modelling results according to the material constants in Table 2. The normalised precipitate radius $\bar{r}$ increases continuously along the SRA time, and achieves to 1 (peak-ageing state) within 2 h, which shows the same trend with yield strength results obtained in Fig. 2, indicating the rationality of the modelling results [4]. The accelerated coarsening of precipitates at higher initial stress levels has also been successfully predicted in Fig. 4 [1]. Meanwhile, the normalised solute concentration $\bar{c}$ decreases to a stable level before 2 h, indicating an over-ageing behaviour after 2 h as well. The normalised dislocation density $\bar{\rho}$ increases significantly in the first couple of hours and gradually reaches a saturate level afterwards, which shows the same trend with many previous studies [1, 3]. In addition, more dislocations under higher initial stresses in SRA tests have also been well predicted by the developed model.

5.3 Stress Relaxation Behaviour

The stress relaxation curves under different initial stress levels from experiments and corresponding modelling results are compared in Fig. 5. A good correspondence between them has been achieved, especially for initial stress levels from 200 to 300 MPa, indicating the effectiveness of the model and determined material constants in modelling the stress relaxation behaviour of the alloys in the elastic region. When the initial stress increases to 350 MPa and exceeds the 0.01% offset yield stress, the

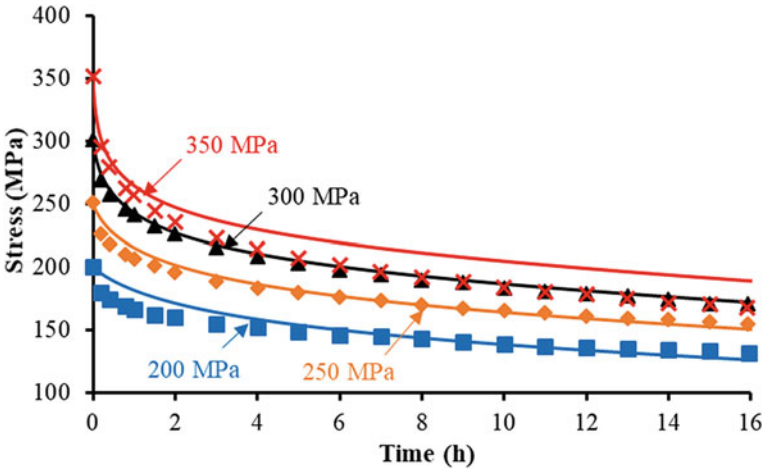


Fig. 5 Comparison of stress relaxation curves of AA7B04-P after 165 °C/16 h SRA tests under indicated initial stress levels from experiments (symbols) and modelling (solid lines). (Color figure online)

model predicts a larger remained stress compared with the experimental results; the reason could be attributed to the different stress relaxation mechanisms in the plastic region as reported in [5], which has not been considered in the model developed in this study.

5.4 Yield Strength Behaviour

Figure 6 compares the experimental and modelling results of the evolutions of yield strength and strengthening components during SRA tests. A good agreement between experiments and models in yield strength has been achieved, indicating the effectiveness of the developed model. A slight increase of yield strength σ_y has been well predicted within the first 2 h of SRA tests, due to the combined effect from precipitation hardening σ_p, dislocation hardening σ_{dis} and solid solution hardening σ_{ss}, as shown in Fig. 6. In addition, the effect of higher initial stress levels in accelerating the softening of the over-aged material has also been successfully modelled in Fig. 6.

5.5 Work Hardening Behaviour

The work hardening stress σ_w versus plastic strain ε_p curves from experiments and modelling results are compared in Fig. 7. Based on the predicted microstructures in Fig. 4 at different time states of SRA tests, the predicted work hardening results

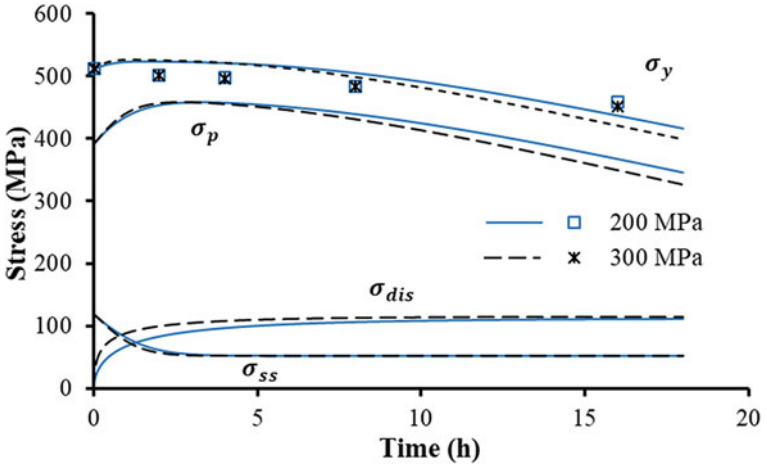


Fig. 6 Evolution of yield strength σ_y and strengthening components from precipitates σ_p, dislocations σ_{dis}, and solid solutes σ_{ss} of AA7B04-P during 16 h SRA tests at 165 °C from experiments (symbols) and modelling (lines). (Color figure online)

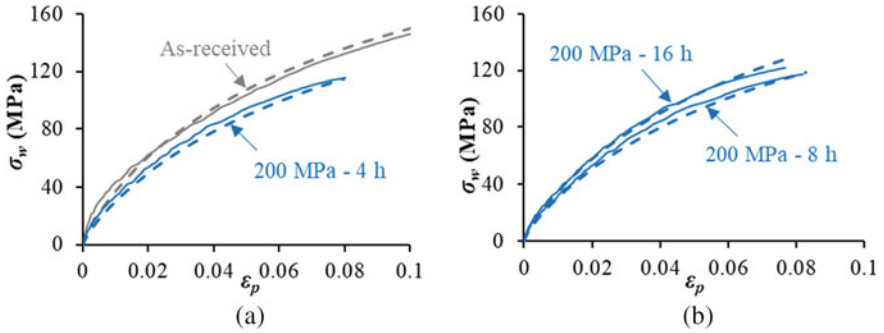


Fig. 7 Comparison of plastic stress versus plastic strain curves of AA7B04-P after SRA tests at 165 °C under initial stress of 200 MPa with indicated time durations from experiments (solid lines) and simulations (dashed lines). (Color figure online)

all correspond well with experimental results for the SRAed alloy with different durations in Fig. 7. In addition, the increase of work hardening stress after 8 h SRA tests has also been well predicted in Fig. 7b. All these results help to demonstrate the effectiveness of the developed model in predicting both microstructures and macro-properties of the alloys during and after SRA tests.

6 Conclusions

The stress relaxation ageing behaviour during CAF and post-form properties after CAF of AA7B04-P material at 165 °C have been experimentally investigated in this study. Higher initial stress leads to more apparent stress relaxation behaviour. Over-ageing occurs within the first 2 h of SRA tests, after which both lower yield strength and ultimate tensile strength can be observed with higher initial stressess. The uniform elongation and saturate work hardening stress show similar trends during SRA, decrease first, and experience a minor increasing trend after 8 h, which may be attributed to the accumulated geometrically necessary dislocations from the well-developed non-shearable precipitates.

A unified constitutive model, which is divided into three sub-models (microstructure, stress relaxation ageing, and post-form mechanical properties), has been developed in this study. The model, for the first time, simultaneously predict the stress relaxation ageing and key post-form mechanical properties in both micro and macro-sides during and after SRA tests, providing a solid and effective tool to predict the forming process and support potential industrial applications. It should be noted that the current model excellently predicts the SRA-related behaviour in the elastic region; however, more work needs to be done to accurately predict the SRA behaviour in both elastic and plastic regions.

Acknowledgments The research in this paper was funded by the National Natural Science Foundation of China (52005020) and Guangdong Basic and Applied Basic Research Foundation (2019A1515110851). The strong support from the Aviation Industry Corporation of China (AVIC) Manufacturing Technology Institute (MTI) for this funded research is much appreciated. The experiments in this study were performed at the AVIC Centre for Structural Design and Manufacture at Imperial College London.

References

1. Zhan L, Lin J, Dean T (2011) A review of the development of creep age forming: experimentation, modelling and applications. Int J Mach Tools Manuf 51(1):1–17
2. Ho K, Lin J, Dean T (2004) Modelling of springback in creep forming thick aluminum sheets. Int J Plast 20(4–5):733–751
3. Yang Y, Zhan L, Shen R, Yin X, Li X, Li W, Huang M, He D (2017) Effect of pre-deformation on creep age forming of 2219 aluminum alloy: experimental and constitutive modelling. Mater Sci Eng, A 683:227–235
4. Lyu F, Li Y, Shi Z, Huang X, Zeng Y, Lin J (2020) Stress and temperature dependence of stress relaxation ageing behaviour of an Al–Zn–Mg alloy. Mater Sci Eng A 773:138859
5. Li Y, Shi Z, Lin J, Yang Y-L, Huang B-M, Chung T-F, Yang J-R (2016) Experimental investigation of tension and compression creep-ageing behaviour of AA2050 with different initial tempers. Mater Sci Eng A 657:299–308
6. Li Y, Shi Z, Lin J, Yang Y-L, Rong Q, Huang B-M, Chung T-F, Tsao C-S, Yang J-R, Balint DS (2017) A unified constitutive model for asymmetric tension and compression creep-ageing behaviour of naturally aged Al-Cu-Li alloy. Int J Plast 89:130–149

7. Li Y, Yang Y-L, Rong Q, Shi Z, Lin J, Said R (2019) Effect of initial tempers on mechanical properties of creep-aged AA2050. Manuf Rev 6:8
8. Chen JF, Zhen L, Jiang JT, Yang L, Shao WZ, Zhang BY (2012) Microstructures and mechanical properties of age-formed 7050 aluminum alloy. Mater Sci Eng A 539:115–123
9. Rong Q, Li Y, Shi Z, Meng L, Sun X, Sun X, Lin J (2019) Experimental investigations of stress-relaxation ageing behaviour of AA6082. Mater Sci Eng A 750:108–116
10. Zhu A, Starke E Jr (2001) Stress aging of Al–xCu alloys: experiments. Acta Mater 49(12):2285–2295
11. Deschamps A, Decreus B, De Geuser F, Dorin T, Weyland M (2013) The influence of precipitation on plastic deformation of Al–Cu–Li alloys. Acta Mater 61(11):4010–4021
12. Ashby M (1970) The deformation of plastically non-homogeneous materials. Philos Mag: J Theor Exp Appl Phys 21(170):399–424
13. Shercliff H, Ashby M (1990) A process model for age hardening of aluminium alloys—I. The Model, Acta Metallurgica et Materialia 38(10):1789–1802
14. Li Y, Shi Z, Lin J (2019) Experimental investigation and modelling of yield strength and work hardening behaviour of artificially aged Al-Cu-Li alloy. Mater Des 183:108121
15. Myhr OR, Grong Ø, Pedersen KO (2010) A combined precipitation, yield strength, and work hardening model for Al-Mg-Si alloys. Metall Mater Trans 41(9):2276–2289
16. Kocks U (1976) Laws for work-hardening and low-temperature creep. J Eng Mater Technol 98(1):76–85
17. Lyu F, Li Y, Huang X, Shi Z, Zeng Y, Lin J (2019) An investigation of creep age forming of AA7B04 stiffened plates: Experiment and FE modelling. J Manuf Process 37:232–241

Flow Behavior and Processing Map of a Nickel-Based Superalloy During Hot Plastic Deformation Process



Baoyun Zhang, Shuo Huang, Wenyun Zhang, Beijiang Zhang, and Yongquan Ning

Abstract Nickel-based superalloys have been widely used to produce high-performance components in advanced engines. In present research, isothermal compression tests of GH4065A nickel-based superalloy were conducted at deformation temperatures of 1020–1140 °C and strain rates of 0.001–1.0 s^{-1}. The deformation temperature and strain rate have a significant effect on the flow curves, from which the intrinsic connection between the flow stress and deformation behavior can be systematically investigated. The deformation activation energy of the studied alloy was calculated to be 521.65 kJ·mol^{-1} at the strain of 0.5 when the flow stress was steady. Meanwhile, the constitutive equation was constructed for modeling the hot plastic deformation, and the prediction accuracy of flow stress was well verified. Based on the combination of processing map and microstructural observation, two instability domains were delineated as follows: Domain #1: 1020–1065 °C/0.25–1.0 s^{-1}; Domain #2: 1130–1140 °C/0.001–0.002 s^{-1}. In addition, the instability mechanism of these two domains was deeply discussed. The results obtained in this research would provide effective theoretical guidance for manufacturing high-performance components in advanced engines.

Keywords Hot plastic deformation · Flow behavior · Processing map

1 Introduction

Nickel-based superalloy GH4065A is a newly developed precipitation strengthening alloy with face-centered-cubic structure, which has been considered as candidate

B. Zhang · Y. Ning (✉)
School of Materials Science and Engineering, Northwestern Polytechnical University, Xi'an 710072, China
e-mail: luckyning@nwpu.edu.cn

S. Huang · W. Zhang · B. Zhang
High-Temperature Materials Institute, Central Iron and Steel Research Institute, Beijing 100081, China

© The Minerals, Metals & Materials Society 2021

G. Daehn et al. (eds.), *Forming the Future*, The Minerals, Metals & Materials Series,
https://doi.org/10.1007/978-3-030-75381-8_74

material for critical rotating components in the range of 700–750 °C of high-performance aero-engines due to its outstanding microstructural stability and excellent mechanical properties. Generally, proper combination of hot deformation parameters such as strain rate and deformation temperature can improve the workability of novel superalloy effectively [1, 2]. However, obtainable information on the hot deformation behavior of GH4065A nickel-based superalloy can be hardly found in the present open literature. Thus, it is vital to investigate the flow behavior and microstructural evolution of the GH4065A nickel-based superalloy during hot plastic deformation.

In present research, uniaxial compression tests were carried out on the GH4065A nickel-based superalloy at different deformation temperatures and strain rates. On the basis of compression results, the flow behavior and constitutive model were deeply investigated. Moreover, processing map was also established to further study the hot workability of alloy GH4065A, and the domains of flow instability were identified.

2 Material and Experiments

The alloy GH4065A investigated in present work was supplied by Central Iron and Steel Research Institute, Beijing. Its chemical composition in weight percent is listed in Table 1. The initial microstructure of the as-received GH4065A nickel-based superalloy is illustrated in Fig. 1a. Small equiaxed recrystallized grains and large agglomerated non-recrystallized grains can be observed before hot deformation, showing a typical mixed grain structure. Figure 1b, c gives out the various morphologies of γ' precipitate in two different regions, respectively. It can be found that coarse γ' phases are mainly distributed at recrystallization regions, while a large number of fine γ' precipitates exist in non-recrystallization regions.

Cylindrical specimens of 8 mm in diameter and 12 mm in height were electro-discharge prepared from the GH4065A nickel-based superalloy experimental billet. With a heating rate of 10 °C/s, compression specimens were heated to deformation temperatures (1020, 1050, 1080, 1110, and 1140 °C) in the Gleeble-3800 thermo-mechanical simulator, held at deformation temperature for 5 min in order to eliminate thermal gradient. Subsequently, the specimens were compressed to 50% reduction in height accounting true strain of 0.69 at four different strain rates (0.001, 0.01, 0.1, and 1.0 s^{-1}). The deformed specimens were quenched immediately, using water, to preserve the microstructure formed during hot deformation. Eventually, the specimens were sliced along the compression axis, and the microstructural observation

Table 1 Chemical composition of the GH4065A nickel-based superalloy (wt.%)

C	Cr	Co	Fe	Ti	Al	Nb	Mo	W	Ni
0.02	16.00	13.00	1.00	3.70	2.10	0.70	4.00	4.00	Bal

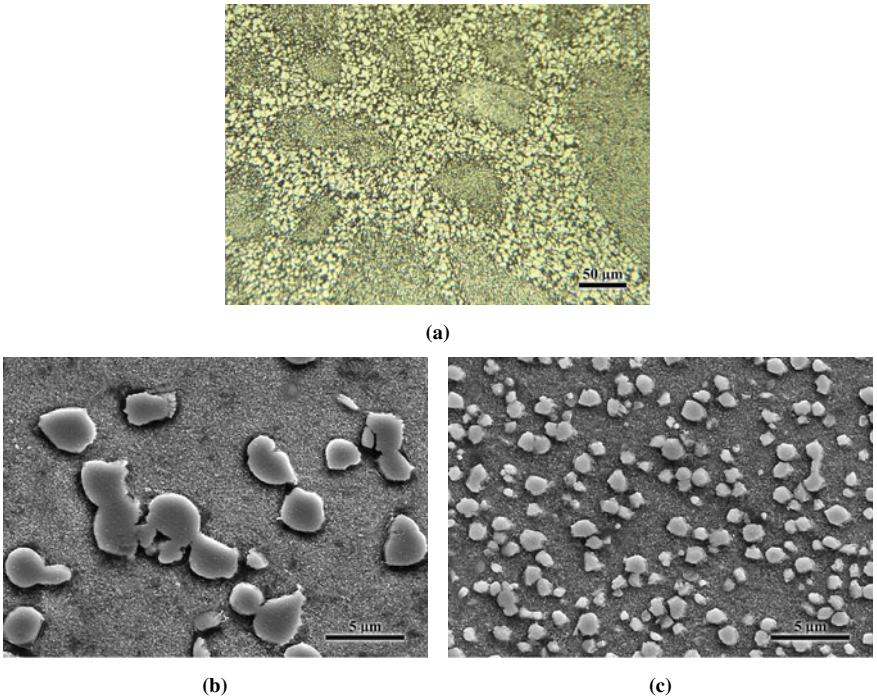


Fig. 1 **a** Initial microstructure of the as-received GH4065A nickel-based superalloy; **b** Coarse γ' phases present at recrystallization regions; **c** Fine γ' precipitates exist in non-recrystallization regions. (Color figure online)

was carried out by optical microscopy (OM) with the chemical etchant of $CuCl_2$ (20 g) + HCl (100 mL) + C_2H_5OH (100 mL).

3 Results and Discussion

3.1 Flow Behavior

The flow curves of the GH4065A nickel-based superalloy obtained via isothermal compression tests under different deformation conditions are illustrated in Fig. 2. Obviously, the effects of deformation temperature and strain rate on the flow behavior of the alloy GH4065A are remarkable. Generally, the curvilinear trend of flow curves is capable of reflecting the inherent relationship between the flow stress and thermal-dynamic behavior. At the beginning of deformation, the strain hardening, which is guided by the generation and multiplication of dislocations [3, 4], results in the sharply increase of the flow stress to a peak value. With the increase of strain, the

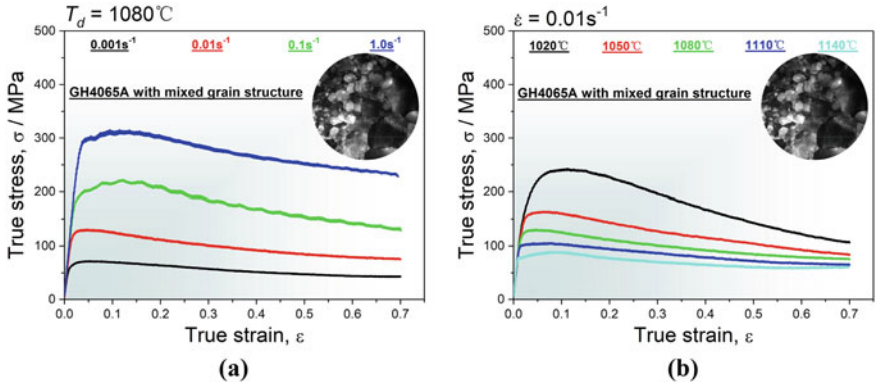


Fig. 2 Selected flow curves of the GH4065A nickel-based superalloy at different deformation conditions: **a** 1080 °C; **b** 0.01 s^{-1}. (Color figure online)

dynamic softening behavior induced by dislocation cross-slip and climb such as dynamic recovery and dynamic recrystallization begin to appear, and thus partially counterbalancing the effect of strain hardening [5, 6]. Consequently, the flow stress gradually reduces to a certain extent after the peak value. With the further increase of deformation degree, dynamic recrystallization becomes the dominant deformation mechanism. Finally, the platform of flow stress occurs at the high-strain zone due to the dynamic equilibrium between strain hardening and dynamic softening is achieved and the dislocation density maintains relatively constant [7].

In addition, it is noteworthy that peak flow stresses increase with the augment of strain rate, whereas they all decrease with deformation temperature increasing. Under relatively high strain rate, the reduction of deformation time increases the strain hardening effect and restrains the nucleation and growth of dynamic recrystallization grains [8]. The average kinetic energy of atoms increases with the augment of deformation temperature. Meanwhile, the elevated deformation temperature provides the higher movability of grain boundaries [9].

3.2 Constitutive Equation

The constitutive equations associated with various deformation parameters such as deformation temperature and strain rate are utilized to depict the flow behavior during hot plastic deformation. In this work, the Arrhenius constitutive equation proposed by Sellars and Mctegart [10] is employed to investigate the deformation behavior of the GH4065A nickel-based superalloy, as follows:

$$\dot{\varepsilon} = A_1 \sigma^{n_1} \exp\left(-\frac{Q}{RT}\right) \alpha\sigma < 0.8 \tag{1}$$

$$\dot{\varepsilon} = A_2 \exp(\beta\sigma) \exp\left(-\frac{Q}{RT}\right) \alpha\sigma > 1.2 \tag{2}$$

$$\dot{\varepsilon} = A[\sinh(\alpha\sigma)]^n \exp\left(-\frac{Q}{RT}\right) \text{ for all } \sigma \tag{3}$$

where $\dot{\varepsilon}$ is strain rate (s^{-1}); σ is flow stress (MPa); T is deformation temperature (K); Q is activation energy of hot deformation ($kJ \cdot mol^{-1}$); R is molar gas constant (8.314 $J \cdot mol^{-1} \cdot K^{-1}$). Moreover, A_1, A_2, A, β, n_1, n, and α ($\alpha = \beta/n_1$) are material constants.

Taking the natural logarithm on both sides of Eqs. (1)–(3), the following equations can be obtained:

$$\ln\dot{\varepsilon} = n_1 \ln\sigma + \left(\ln A_1 - \frac{Q}{RT}\right) \tag{4}$$

$$\ln\dot{\varepsilon} = \beta\sigma + \left(\ln A_2 - \frac{Q}{RT}\right) \tag{5}$$

$$\ln\dot{\varepsilon} = n \ln[\sinh(\alpha\sigma)] + \left(\ln A - \frac{Q}{RT}\right) \tag{6}$$

In this paper, the material constants were calculated at the strain of 0.5 when the flow stress was steady. Based on Eqs. (4) and (5), the values of n_1 and β can be obtained as 4.509 and 0.0369 from linear fitting between the lnσ–ln $\dot{\varepsilon}$ and σ–ln $\dot{\varepsilon}$, which were plotted as shown in Fig. 3a, b. Thus, the α value was calculated to be 0.00819.

Taking the partial derivative on both sides of Eq. (6), the n and Q can be expressed as:

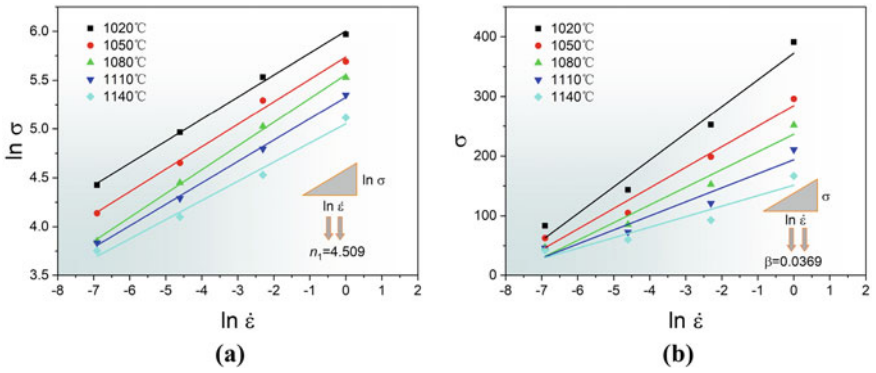


Fig. 3 Relationships between **a** lnσ–ln $\dot{\varepsilon}$; **b** σ–ln $\dot{\varepsilon}$. (Color figure online)

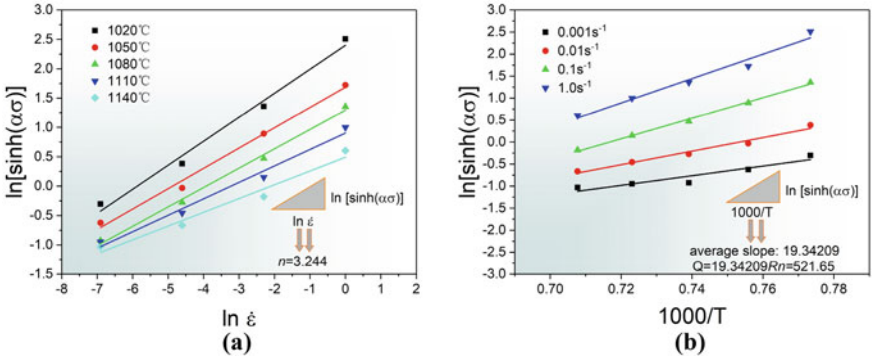


Fig. 4 Relationships between **a** ln[sinh(ασ)]–ln $\dot{\varepsilon}$; **b** ln[sinh(ασ)]–1000/T. (Color figure online)

$$n = \left.\frac{\partial \ln \dot{\varepsilon}}{\partial \ln[\sinh(\alpha\sigma)]}\right|_T \tag{7}$$

$$Q = Rn \left.\frac{\partial \ln[\sinh(\alpha\sigma)]}{\partial(1/T)}\right|_{\dot{\varepsilon}} \tag{8}$$

According to Eqs. (7) and (8), the linear relationships of ln[sinh(ασ)]–ln $\dot{\varepsilon}$ and ln[sinh(ασ)]–1000/T can be given, as shown in Fig. 4a, b, respectively. From Fig. 4, these data can be obtained: $n = 3.244$, $Q/Rn = 19.34209$. Therefore, the activation energy of the GH4065A nickel-based superalloy can be derived as 521.65 kJ·mol^{-1}.

Considering the effects of deformation temperature and strain rate, the Zener–Hollomon parameter is introduced [11]:

$$Z = \dot{\varepsilon} \exp\left(\frac{Q}{RT}\right) = A[\sinh(\alpha\sigma)]^n \tag{9}$$

Treating Eq. (9) by natural logarithm, the following equation can be obtained:

$$\ln Z = \ln A + n \ln[\sinh(\alpha\sigma)] \tag{10}$$

Figure 5 illustrates the linear relationship between ln$Z$ and ln[sinh(ασ)] with the correlation coefficient about 0.98. The intercept of the fitting curve signals the value of ln$A$. Thus A-value can be determined as 2.14×10^{18}.

Eventually, substituting the values of α, n, Q, and A into Eq. (3), the constitutive equation at the strain of 0.5 for the GH4065A nickel-based superalloy can be described by a hyperbolic sine equation as follows:

$$\dot{\varepsilon} = 2.14 \times 10^{18}[\sinh(0.00819\sigma)]^{3.244} \exp\left(-\frac{521650}{RT}\right)$$

In order to verify the credibility of the established constitutive equation, Fig. 6

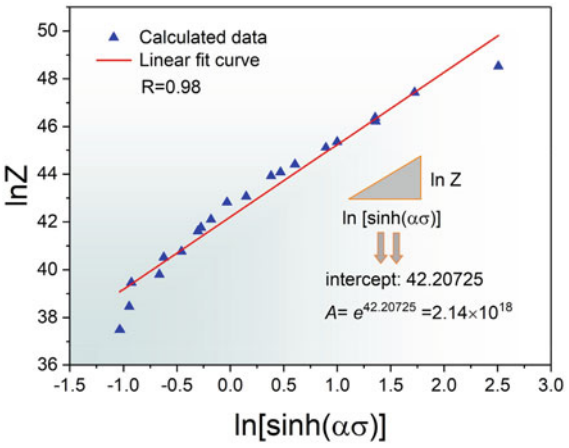


Fig. 5 Relationship between ln*Z*–ln[sinh(ασ)]. (Color figure online)

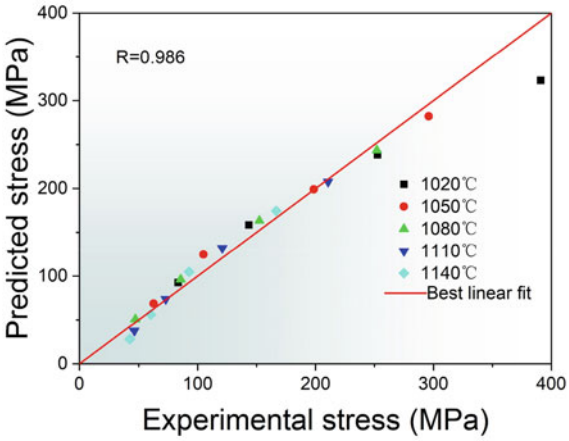


Fig. 6 Comparison between predicted data and experimental results. (Color figure online)

illustrates the comparison between predicted data and experimental results with *R*-value about 0.986. It can be observed that almost all data points are close to the line of best fit. Therefore, the established constitutive equation in this research has a good ability to predict the flow stress of the GH4065A nickel-based superalloy.

3.3 Processing Map

Processing map based on dynamic material model (DMM) has been proven as a powerful method to optimize hot working parameters and control microstructural evolution during the hot plastic deformation of metallic materials [12, 13]. The processing map can be established by the superimposition of instability map on

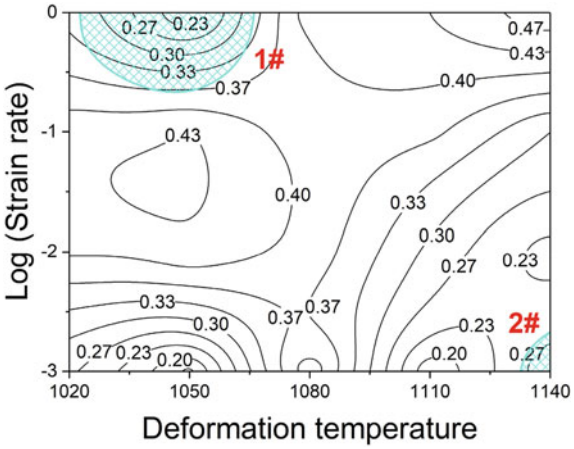


Fig. 7 The processing map of the GH4065A nickel-based superalloy processed at the strain of 0.69. (Color figure online)

power dissipation map, from which unstable region can be determined effectively. Moreover, microstructural observation is necessary to verify the instability mechanism related to the unstable region. With the huge advantages of time and cost saving, processing map is of great significance for practical industrial manufacturing.

The processing map obtained on GH4065A nickel-based superalloy at the strain of 0.69 is illustrated in Fig. 7. The contour numbers in processing map represent the value of power dissipation efficiency. The white and blue regions were identified as stable and unstable domains, respectively. It can be observed that two instability domains are delineated in processing map. The first occurs at the deformation temperature range of 1020–1065 °C and strain rate range of 0.25–1.0 s^{-1}, marked as Domain #1 in the processing map. The corresponding microstructure in this domain under the condition of 1050 °C/1.0 s^{-1} is shown in Fig. 8a. The adiabatic shear band can be

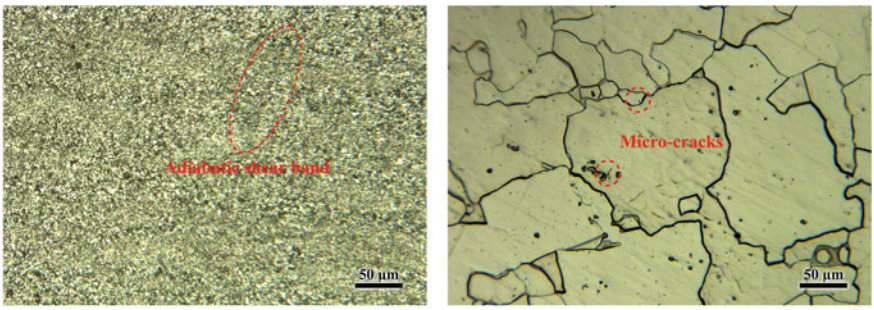


Fig. 8 Typical microstructures of the GH4065A nickel-based superalloy deformed at the condition of **a** 1#: 1050 °C/1.0 s^{-1}; **b** 2#: 1140 °C/0.001 s^{-1}. (Color figure online)

clearly seen under this condition, which is oriented to be about 45° off the compression axis. The second (Domain #2) locates at the deformation temperature about 1130–1140 °C and strain rate about 0.001–0.002 s^{-1}. Figure 8b gives the typical microstructure in this area under the condition of 1140 °C/0.001 s^{-1}. Obviously, the micro-cracks appear. Thus, these two instability domains should be prevented in hot working process of the GH4065A nickel-based superalloy.

4 Conclusions

Isothermal compression tests were carried out on the GH4065A nickel-based superalloy at the deformation temperature range of 1020–1140 °C and the strain rate range of 0.001–1.0 s^{-1} with the deformation degree of 50%. The following conclusions can be drawn from this research:

(1) The flow curves of the GH4065A nickel-based superalloy are sensitive to deformation temperature and strain rate. Flow stress decreases significantly with the increase of deformation temperature or the decrease of strain rate.

(2) The constitutive equation at the strain of 0.5 constructed for modeling the hot plastic deformation of the GH4065A nickel-based superalloy can be expressed as:

$$\dot{\varepsilon} = 2.14 \times 10^{18}[\sinh(0.00819\sigma)]^{3.244} \exp\left(-\frac{521650}{RT}\right)$$

(3) Based on processing map processed at the strain of 0.69, two instability domains can be identified as follows: Domain #1: 1020–1065 °C/0.25–1.0 s^{-1}; Domain #2: 1130–1140 °C/0.001–0.002 s^{-1}. The adiabatic shear band and micro-cracks are responsible for the above-mentioned domains, respectively.

References

1. Jia D, Sun WR, Xu DS, Liu F (2019) Dynamic recrystallization behavior of GH4169G alloy during hot compressive deformation. J Mater Sci Technol 35:1851–1859
2. Qin XY, Huang DW, Yan XJ, Zhang XY, Qi MJ, Yue S (2019) Hot deformation behaviors and optimization of processing parameters for Alloy 602 CA. J Alloys Compd 770:507–516
3. Wen DX, Lin YC, Chen J, Chen XM, Zhang JL, Liang YJ, Li LT (2015) Work-hardening behaviors of typical solution-treated and aged Ni-based superalloys during hot deformation. J Alloys Compd 618:372–379
4. Xie BC, Zhang BY, Ning YQ, Fu MW (2019) Mechanisms of DRX nucleation with grain boundary bulging and subgrain rotation during the hot working of nickel-based superalloys with columnar grains. J Alloys Compd 786:636–647
5. Wu RH, Liu Y, Geng C, Lin QQ, Xiao YF, Xu JR, Kang W (2017) Study on hot deformation behavior and intrinsic workability of 6063 aluminum alloys using 3D processing map. J Alloys Compd 713:212–221

6. Wang YX, Zhao GQ, Xu X, Chen XX, Zhang CS (2019) Constitutive modeling, processing map establishment and microstructure analysis of spray deposited Al-Cu-Li alloy 2195. J Alloys Compd 779:735–751
7. Lin YC, Li LT, Xia YC, Jiang YQ (2013) Hot deformation and processing map of a typical Al–Zn–Mg–Cu alloy. J Alloys Compd 550:438–445
8. Lin YC, Wu XY, Chen XM, Chen J, Wen DX, Zhang JL, Li LT (2015) EBSD study of a hot deformed nickel-based superalloy. J Alloys Compd 640:101–113
9. Liao HC, Wu YN, Zhou KX, Yang J (2015) Hot deformation behavior and processing map of Al-Si-Mg alloys containing different amount of silicon based on Gleebe-3500 hot compression simulation. Mater Des 65:1091–1099
10. Sellars CM, Mctegart WJ (1966) On the mechanism of hot deformation. Acta Metall 14:1136–1138
11. Zener C, Hollomon JH (1944) Effect of strain rate upon plastic flow of steel. J Appl Phys 15:22–32
12. Sun Y, Wan ZP, Hu LX, Ren JS (2015) Characterization of hot processing parameters of powder metallurgy TiAl-based alloy based on the activation energy map and processing map. Mater Des 86:922–932
13. Pu EX, Zheng WJ, Song ZG, Feng H, Dong H (2017) Hot deformation characterization of nickel-based superalloy UNS10276 through processing map and microstructural studies. J Alloys Compd 694:617–631

Hot Deformation Behavior and Constitutive Modeling of a Novel Ni-Based Superalloy



Hao Yu, Hao Yang, Qi Liu, Baoyun Zhang, Bingchao Xie, and Yongquan Ning

Abstract Ni-based superalloys are widely used to manufacture the key components of a gas turbine engine because of their superior mechanical properties at elevated temperatures. In the present work, the hot deformation behavior of a novel Ni-based superalloy was investigated by compression test at temperatures of 1020–1140 °C and strain rates of 0.001–10 s^{-1}. At low temperature and high strain rates, the flow stress rapidly increased to a peak value due to work hardening. However, at high temperatures and low strain rates, the flow curves exhibited a typical dynamic softening stage. The hot deformation activation energy of the studied superalloy is determined to be 735.4961 kJ/mol, and a strain-compensated Arrhenius-type constitutive equation is obtained. On comparing the predicted and experimental values, the developed constitutive equation can accurately describe the deformation mechanism and the flow behavior. Meanwhile, the influence of hot processing parameters on microstructure has been deeply explored, which can optimize the process parameters for manufacturing key components in gas turbine engine.

Keywords Hot plastic deformation · Flow behavior · Constitutive modeling · Microstructure · Ni-based superalloy

1 Introduction

Owing to their excellent high-temperature rupture life, fatigue crack growth resistance, and creep strength, nickel-based superalloys are widely used in advanced turbine engines and other critical components [1–3]. The hot deformation behaviors of nickel-based superalloys were dependent on various factors, including the deformation temperature, strain rate, and strain; in addition, the initial microstructure also affects the hot deformation behaviors and final properties [4–6]. Thus, understanding the deformation behaviors of nickel-based superalloy at high temperatures could optimize the forming process and guide the practical application. In order to

H. Yu · H. Yang · Q. Liu · B. Zhang · B. Xie · Y. Ning (✉)
School of Materials Science and Engineering, Northwestern Polytechnical University, Xian 710072, China
e-mail: ningke521@163.com

© The Minerals, Metals & Materials Society 2021

G. Daehn et al. (eds.), *Forming the Future*, The Minerals, Metals & Materials Series,
https://doi.org/10.1007/978-3-030-75381-8_75

simulate the hot deformation processes accurately, hot compression deformation had been well investigated and various constitutive models had been established [7–9].

In order to understand the hot deformation behavior of the novel nickel-based superalloy, in this paper the alloys were investigated by isothermal compression tests with the wide ranges of deformation temperature and strain rate. Based on the experimental results, the peak stress Arrhenius constitutive relationship of the alloy was established, through verification, and the model can accurately describe the relationship between the flow stress, strain rate, and deformation temperature.

2 Materials and Experiments

The material used in the present work was a disc with a diameter of 260 mm and a height of 25 mm after cogging. The chemical composition (wt.%) of this alloy was shown in Table 1, and the γ' solvus temperature was estimated to be about 1107 °C [10]. Cylindrical specimens with a diameter and height of 8 mm and 12 mm, respectively, were machined from the disc after cogging. Figure 1a presents the microstructure of the studied superalloy before the hot deformation, which is composed of fine equiaxed recrystallized grains and cluster-like non-recrystallized regions. Figure 1b shows the secondary γ' precipitates in the as-received superalloy, and it has been found that the secondary γ' precipitates were a mixture of irregular shape, small spherical, and cluster-like. The compression tests were performed using the Gleeble-1500D thermo-mechanical simulator at the deformation temperatures of 1020, 1050,

Table 1 Chemical composition of the studied alloy (wt.%)

Ni	Fe	Co	Cr	Mo	W	Al	Ti	Nb	B	C	Zr
Base	4	8.5	15.7	3.1	2.7	2.25	3.4	1.1	0.01	0.015	0.03

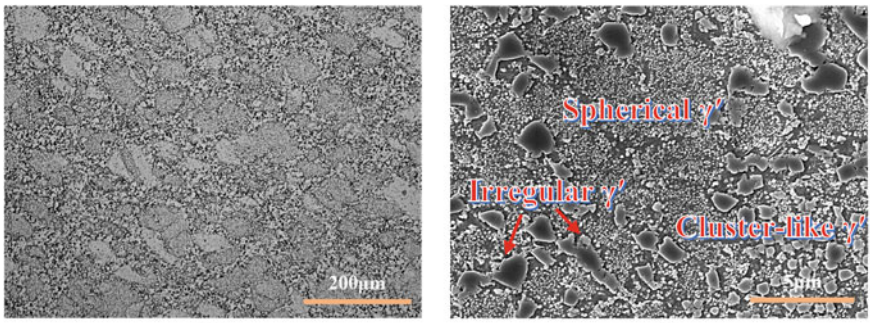


Fig. 1 **a** Microstructure of the studied alloy before the hot deformation, **b** γ' precipitates in the as-received superalloy. (Color figure online)

1080, 1110, and 1140 °C. The strain rates were 0.001, 0.01, 0.1, 1, and 10 s^{-1}, and the height reduction was 50%. Before the compression tests, the end faces of the specimen were coated with graphite lubricate to reduce the impact of contact friction on the stress state. All specimens were heated to the desired temperature at a heating rate of 10 K/s and then soaked for keeping the sample's temperature uniform before loading to eliminate the thermal gradient prior to deformation. The stress–strain data were automatically recorded by the testing system during the hot compression. The specimen after each compression was immediately quenched by the water. After deformation, the specimens were sectioned parallel to the compression axis through the centerline. Specimens for optical microscopy were mechanically polished and etched in a solution consisting of 10 mL HCl + 10 mL CH_3CH_2OH + 1 g $CuCl_2$ at room temperature for 1–3 min. Microstructure examination was performed by using OLYMPUS optical microscope. For scanning electron microscope (SEM), to reveal the morphology of γ' precipitate, the samples were mechanically polished and etched with a solution of 45%H_2SO_4 + 42%HNO_3 + 13%H_3PO_4, with electrolytic etching parameters as 3.5 V and 3–5 s. Morphology of the γ' precipitates was conducted using TESCAN SEM in the secondary electron (SE) or In-beam mode.

3 Results and Discussion

3.1 The True Stress–Strain Curves

Figure 2a–e shows the true stress–strain curves of hot compression of the studied alloy at various temperatures of 1020–1140 °C with strain rates of 0.001–10 s^{-1}. It can be seen that the flow behavior of the alloy is sensitive to deformation temperature and strain rate. The flow stress decreases with the increasing temperature and decreasing strain rate at a constant strain, and the true stress–strain curves exhibited completely different shapes depending on the deformation temperature and strain rate. When the strain was small, the flow stress increases quickly and rapidly increased to a peak value with increasing strain. In this process, the work hardening effect plays a dominant role, the dynamic softening is not enough to compensate for the work hardening caused by the dislocation proliferation. The deformation resistance reached the maximum and the corresponding stress and strain values, which were peak stress and peak strain, respectively. Both the peak stress and the peak strain were found to increase with decreasing deformation temperature or increasing strain rate. After exceeding the peak strain, the flow stress decreases gradually with the increase of strain. The flow curves exhibited an obvious phenomenon of flow softening, and the influence of dynamic softening was predominant. As the strain increases, the rates for the vacancy diffusion in the alloy increase, the ability of dislocations to overcome obstacles increases, and cross-slip of screw dislocations and climb of edge dislocations increase. Thus, dynamic recovery and recrystallization became easy to occur, making the density of dislocations decrease and overcome the work hardening

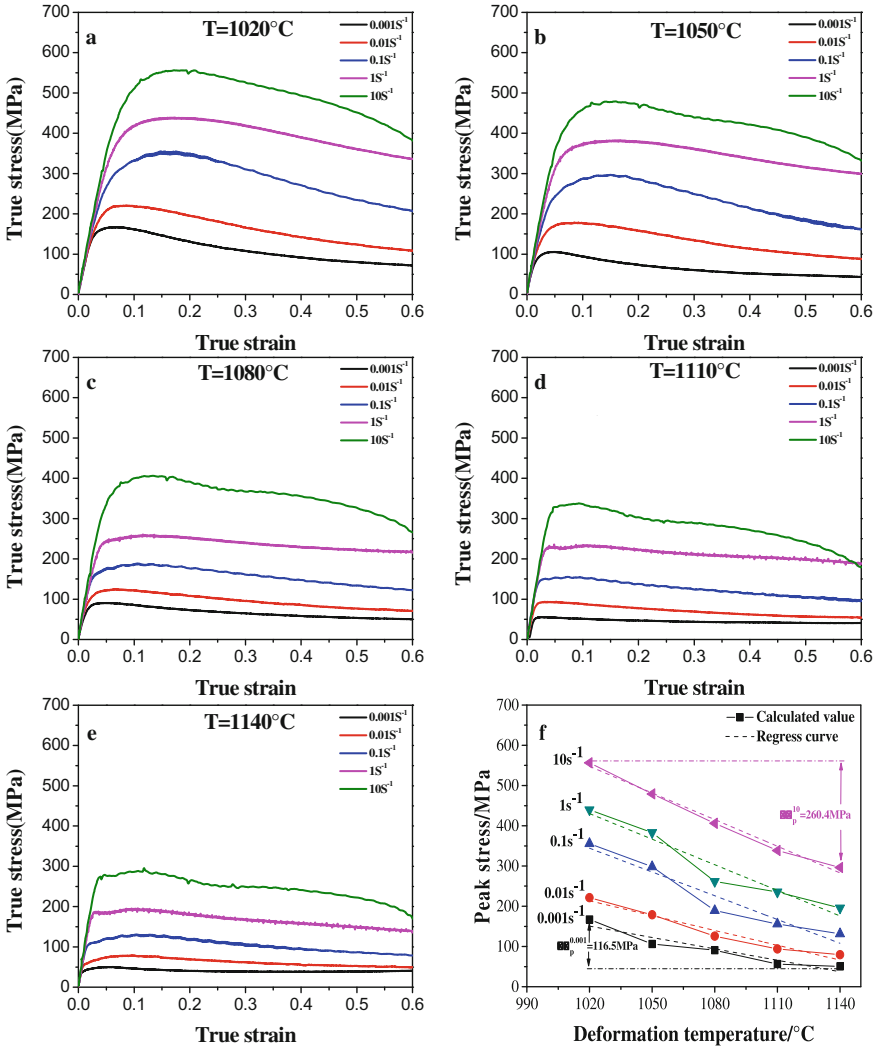


Fig. 2 True stress–true strain curves for the studied superalloy **a** T = 1020 °C **b** T = 1050 °C **c** T = 1080 °C **d** T = 1110 °C **e** T = 1140 °C **f** the peak stress of the studied superalloy. (Color figure online)

caused by the dislocation pile-up and tangling. Finally, the flow stress attains a relatively stable value under high strain, and the stress values were steady-state stress. The dynamic softening and the work hardening effects reach a dynamic balance.

Generally, the flow behavior of the alloy during the hot deformation is a result of the combined strain hardening and dynamic softening. The true stress–strain curves can be divided into three types: have an obvious peak, quasi-steady flow; have an obvious peak, continuous dynamic softening; and no obvious peak, steady flow. The flow softening was mainly associated with deformation heating and microstructure

evolution such as dynamic recrystallization. Figure 2f shows the peak stress gaps as a function of deformation temperature at various strain rates. It can be observed that when the strain rate is 10 s^{-1}, peak stress can be up to 550 MPa at 1020 °C, just 296 MPa at 1140 °C, and the peak stress gap is about 260.4 MPa. The peak stress is close to 170 MPa under the deformation temperature of 1020 °C, just 50 MPa at 1140 °C, and the peak stress gap is about 116.5 MPa. A similar pattern can be found under other strain rates, which shows that the peak stress decreases gradually with the increase of deformation temperature at a constant strain rate. It is because with the increase of deformation temperature, the atom's ability to move increases, the bonding force between atoms decreases, and the critical shear stress of the alloy decreases, which in turn reduces the construction of dislocation motion and crystal ship. In addition, the increase of deformation temperature is beneficial for the mobility of grain boundaries, which promote the nucleation and growth of dynamically recrystallized grains. Thus, the flow stress decrease.

3.2 Constitutive Modeling of Peak Stress

Researches on different materials show that high-temperature deformation of alloys is a process controlled by thermal activation. In order to accurately describe the relationship between the stress, strain rate, and the deformation temperature, the peak stress on deformation temperature and strain rate can be represented by hyperbolic sine-type Arrhenius equation proposed by Sellars and Tegart [11]:

$$\dot{\varepsilon} = A\left[\sinh\left(\alpha\sigma_p\right)\right]^n exp(-Q/RT) \tag{1}$$

In addition, the relationship between flow stress and strain rate can be described by the following models at low and high stress levels:

$$\dot{\varepsilon} = A_1\sigma^{n_1} \quad (\alpha\sigma < 0.8) \tag{2}$$

$$\dot{\varepsilon} = A_2 \exp(\beta\sigma) \quad (\alpha\sigma > 1.2) \tag{3}$$

where $\dot{\varepsilon}$ are the values of n1 (s^{-1}), σ_p is the peak stress (MPa), n is the stress exponent, Q is the apparent activation energy for deformation (J mol^{-1}), T is deformation temperature (K), R is the universal gas constant (8.3145 J mol^{-1} K^{-1}), and A_1, A_2, A, n_1, β, and α are materials constants. After taking the logarithm of Eqs. (1), (2), and (3):

$$\ln\dot{\varepsilon} = \ln A + n\ln[\sinh(\alpha\sigma)] \tag{4}$$

$$\ln\dot{\varepsilon} = \ln A_1 + n_1\ln\sigma \tag{5}$$

$$\ln \dot{\varepsilon} = \ln A_2 + \beta\sigma \tag{6}$$

The values of n_1 and β can be calculated by the linear statistical regression method. The peak stress and strain rate under different deformation temperatures are taken into Eqs. (5) and (6) to get the relationship between $\ln \sigma$ and $\ln \dot{\varepsilon}$ and the relationship between σ and $\ln \dot{\varepsilon}$, which are shown in Fig. 3a, b. It can be obtained that the average value of $n_1 = 5.8912$ and $\beta = 0.0286$. Therefore, $\alpha = \beta/n_1$=0.004852 is obtained. After the value of α was determined, from Eqs. (4) and (1) we get the relationship between $\ln[\sinh(\alpha\sigma)]$ and $\ln\dot{\varepsilon}$ and the relationship between $\ln[\sinh(\alpha\sigma)]$ and 1000/T, which are shown in Fig. 3c, d. Then, the values of n, A, and Q can be obtained by linear fitting of the experimental data and are found to be $n = 4.3098$, $A = 1.0124 \times 10^{27}$, and $Q = 735.4961$ kJ mol^{-1}. According to the values of α, A, n, and Q, the peak stress by hyperbolic sine-type Arrhenius constitutive relationship of the alloy can be expressed as:

$$\dot{\varepsilon} \cdot \exp(735496.1/RT) = 1.0124 \times 10^{27} \cdot [\sinh(0.004852\sigma)]^{4.3098} \tag{7}$$

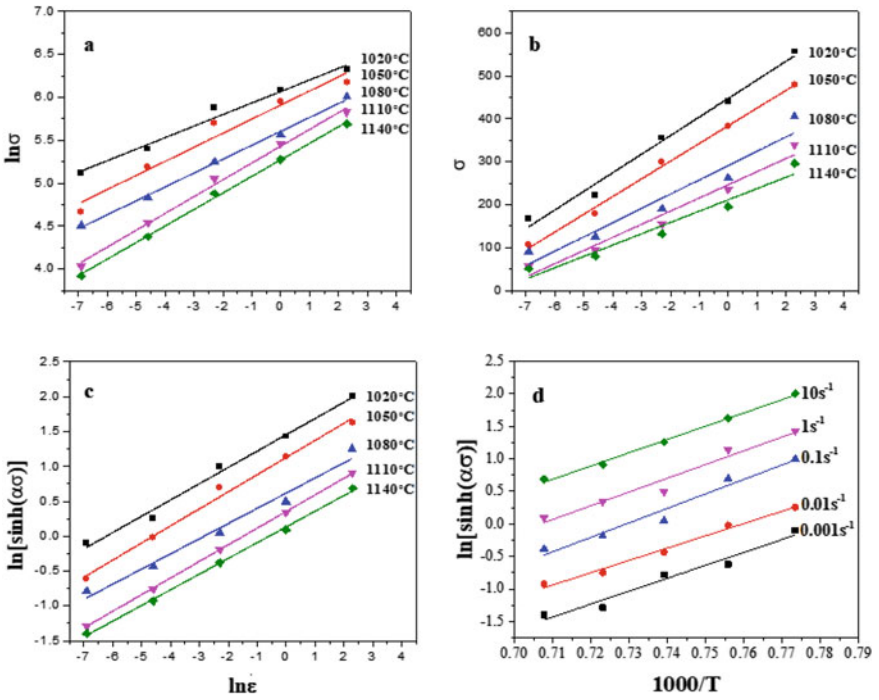


Fig. 3 The relationship between **a** $\ln \sigma$ and $\ln \dot{\varepsilon}$; **b** σ and $\ln \dot{\varepsilon}$; **c** $\ln[\sinh(\alpha\sigma)]$ and $\ln \dot{\varepsilon}$; **d** $\ln[\sinh(\alpha\sigma)]$ and 1000/T. (Color figure online)

Based on the regression analysis on the parameters of the hyperbolic sinusoidal Arrhenius equation, the functional relationship between parameters of the constitutive relationship and the true strain under different strains was established and the values of the parameters in the Arrhenius equation under different strains were calculated. The relationship between the parameters and the strain can be fit using a cubic function, and the third-order functions of each parameter with respect to ε can be obtained. Figure 4 shows the fitting curves, and it can be seen from the figure that the fit curves of each model are constant with respect to the strain variable is very well, and the linear correlation coefficients R are all above 0.99. The third-order functions can be expressed as:

$$\alpha = -4.1463 \times 10^{-4}\varepsilon^3 - 0.0030\varepsilon^2 + 0.0084\varepsilon + 0.0055 \tag{8}$$

$$\mathrm{n} = -10.7969\varepsilon^3 + 17.5480\varepsilon^2 - 8.8785\varepsilon + 4.6118 \tag{9}$$

$$\ln \mathrm{A} = 167.4583 - 182.3092\varepsilon^2 + 14.4139\varepsilon + 61.2625 \tag{10}$$

$$\mathrm{Q} = 1987.1757\varepsilon^3 - 2189.9876\varepsilon^2 + 207.6428\varepsilon + 735.0847 \tag{11}$$

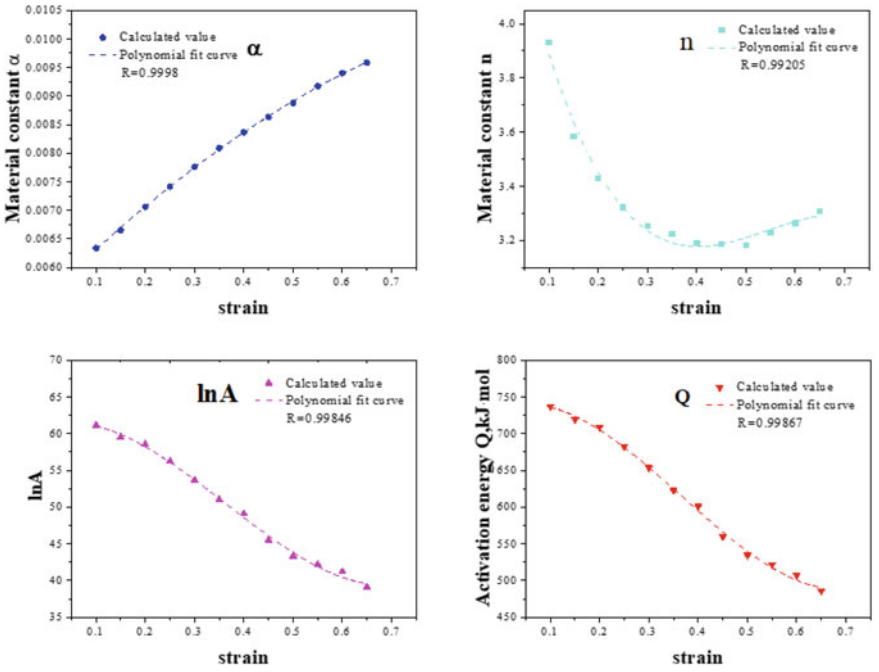


Fig. 4 Relationships between α, n, lnA, and Q and true strain. (Color figure online)

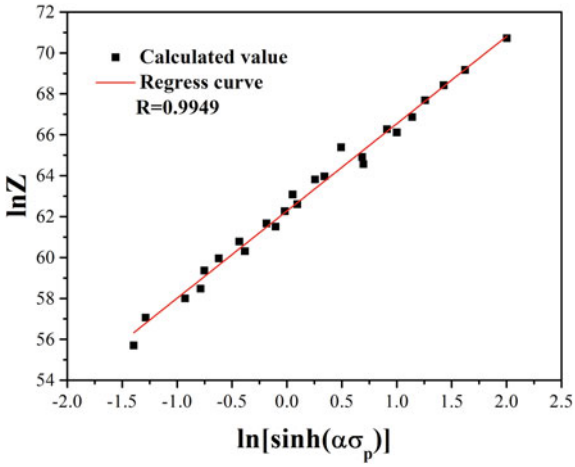


Fig. 5 Relationship between lnZ and $\ln[\sinh(\alpha\sigma_p)]$. (Color figure online)

Figure 5 shows the relationship between lnZ and $\ln[\sinh(\alpha\sigma_p)]$ according to the unary linear regression analysis. It can be seen that the fitting curve shows a good linear relationship, with a linear correlation coefficient of R = 0.9949, indicating that the hyperbolic sine-type Arrhenius constitutive relationship can accurately describe the relationship between the peak flow stress of the alloy and the deformation temperature and strain rate.

3.3 Microstructure and γ′ Precipitate

Figure 6 shows the microstructure of the studied alloy after the hot deformation. When the deformation temperature is 1020 °C, it can be seen that there are still a large number of non-recrystallized regions inside the alloy, the non-recrystallized regions that are elongated, and in the center of the deformation region, dynamic recrystallization has occurred, and the grain is fine, as shown in Fig. 6a. The influence of γ' precipitates on the microstructure evolution of the alloy was important. When the samples deformed at a sub-solvus temperature (1020 °C), the content and size of the γ' precipitates do not change greatly, as shown in Fig. 6b. The existence of the γ' precipitates not only promotes the nucleation of dynamic recrystallization but also inhibits the movement of the grain boundaries. Increasing deformation temperature promotes the occurrence of dynamic recrystallization of the alloy. Complete dynamic recrystallization occurred, and the uniform equiaxed recrystallized grains were obtained at the deformation temperature of 1140 °C (Fig. 6c). This is because at higher deformation temperature, the γ' precipitates are almost dissolved completely (Fig. 6d), and the pinning effect of grain boundaries migration and dislocations movement decreases.

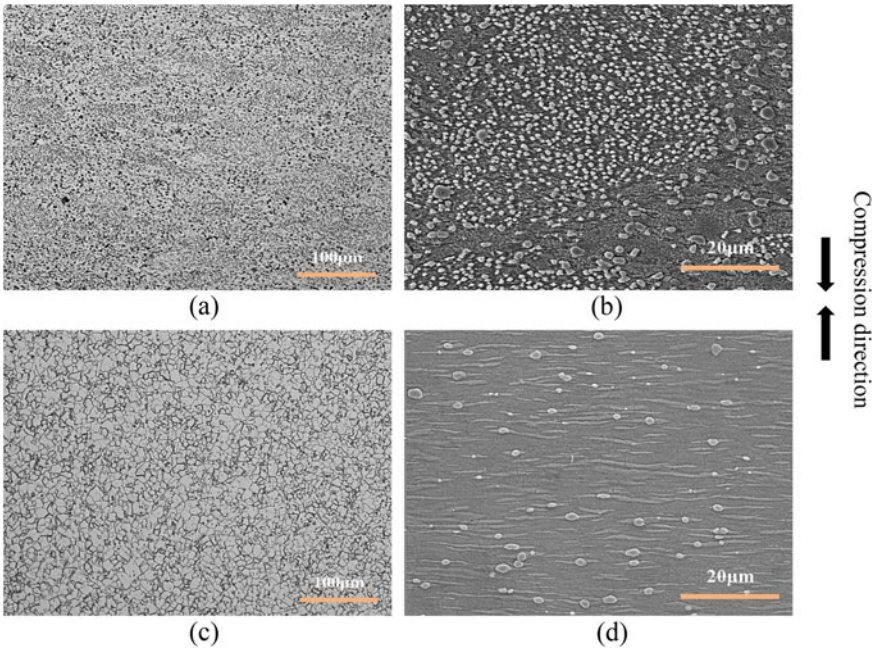


Fig. 6 Microstructure of the studied alloy after the hot deformation, **a** OM 1020 °C, 1 s^{-1}, **b** SEM 1020 °C, 1 s^{-1}, **c** OM 1140 °C, 1 s^{-1}, **d** SEM 1140 °C, 1 s^{-1}. (Color figure online)

4 Conclusions

Based on the hot compression tests of the novel Ni-based superalloy, flow behaviors under the conditions of various deformation parameters were obtained in this work. The main results are summarized as follows:

(1) The experimental data were analyzed, and the true stress–strain curves can be divided into three types: have an obvious peak, quasi-steady flow; have an obvious peak, continuous dynamic softening; and no obvious peak, steady flow.

(2) Based on the regression analysis, the peak stress hyperbolic sine-type Arrhenius equation of this studied alloy was established, the model can accurately describe the relationship between the strain rate, deformation temperature, and true strain of the alloy during high-temperature compressive deformation, and can well predict its hot deformation behavior.

(3) Microstructure of this alloy under various deformation parameters were analyzed, and it shows that the γ' precipitates have an important effect on microstructure evolution. At γ' sub-solvus temperature, γ' precipitates promote dynamic recrystallization nucleation, and the recrystallized grains are tiny;

however, at γ' super-solvus temperature, dissolution of γ' phase is beneficial for the mobility of grain boundaries, completely dynamic recrystallization has occurred, and the uniform equiaxed recrystallized grains were obtained.

References

1. Wen DX, Lin YC, Li HB, Chen XM (2014) Hot deformation behavior and processing map of a typical Ni-based superalloy. Mater Sci Eng A 591:183–192
2. Chang LT, Sun WR, Cui YY, Zhang FQ, Yang R (2014) Effect of heat treatment on microstructure and mechanical properties of the hot-isostatic-pressed Inconel 718 powder compact. J Alloy Compd 590:227–232
3. Satheesh Kumar SS, Raghu T, Bhattacharjee PP, Rao GA, Borah U (2016) Strain rate dependent microstructural evolution during hot deformation of a hot isostatically processed nickel base superalloy. J Alloy Compd 681:28–42
4. Jiang SY, Sun D, Zhang YQ, Zhu XM, Wang M, Zhao CZ (2016) Plastic deformation mechanisms of NiCuCrMoTiAlNb Ni-based alloys at cryogenic temperature. Mater Sci Eng A 664:135–214
5. Sajjadi SA, Chaichi A, Ezatpour HR, Maghsoudlou A, Kalaie MA (2016) Hot deformation processing map and microstructural evaluation of the Ni-based superalloy IN-738LC. J Mat Eng Perform 25:1269–1275
6. Loyda A, Hernández-Muñoz GM, Reyes LA, Zambrano-Robledo P (2016) Microstructure modeling of a Ni-Fe-Based superalloy during the rotary forging process. J Mat Eng Perform 25:2128–2137
7. Ning YQ, Yao ZK, Lei YY, Guo HZ, Fu MW (2011) Hot deformation behavior of the post-cogging FGH4096 superalloy with fine equiaxed microstructure. Mater Charact 62:887–893
8. Liu YH, Yao ZK, Ning YQ, Nan Y, Guo HZ, Qin C, Shi ZF (2014) The flow behavior and constitutive equation in isothermal compression of FGH4096-GH4133B dual alloy. Mater Des 63:829–837
9. Wu HX, Ge CC, Yan QZ, Xia M, Tian T, Zhu ZL, Hu QP (2017) Plastic deformation behavior of spray formed superalloy FGH100. Mater Sci Eng A 699:156–164
10. Masoumi F, Jahazi M, Shahriari D, Cormier J (2016) Coarsening and dissolution of γ' precipitates during solution treatment of AD730™ Ni-based superalloy: mechanisms and kinetics models. J Alloys Compd 658:981–995
11. Sellars CM, Mctegart WJ (1966) On the mechanism of hot deformation. Acta Metall 14(9):1136–1138

Accurate Modelling of Flow Stress of AISI1025 at Room Temperature and Its Application to Precision Forging Simulation



M. S. Joun, M. K. Razali, J. B. Byun, and K. H. Lee

Abstract This paper evaluates and criticizes the Swift model of expressing strain hardening behaviours of metals at room temperature using an experimental tensile test and its FE prediction. A concept of reference flow stress curve composed of two ranges of strain divided by the true strain at the necking point is proposed, which predicts tensile test exactly from the standpoint of engineering and is thus employed to evaluate the Swift model. It has been shown that it has a weak point in describing the flow stress of typical strain hardening material with emphasis on necking. An improved Swift model is applied to obtain accurate flow stress of a commercial steel AISI1025 and it is employed to simulate a sequence of cold forging processes by precision complete analysis for process and die optimal design in terms of die life, which should be conducted under an accurate analysis model.

Keywords Flow stress · Material model · Strain hardening · Accuracy in terms of tensile test · Finite element analysis

1 Introduction

Recently, the implementation of high-strength steels in the automotive industry has become prevailing and desirable owing to their structured integrity and long-lasting properties. However, formability of such materials is unfavourable and thus an appropriate flow stress model for precision engineering together with optimal die and

M. S. Joun (✉)
ERI, School of Mechanical and Aerospace Engineering, Gyeongsang National University (GNU), Gyeongnam, Jinju 52828, Republic of Korea
e-mail: msjoun@gnu.ac.kr

M. K. Razali · J. B. Byun
Graduate School of Mechanical and Aerospace Engineering, Gyeongsang National University (GNU), Gyeongnam, Jinju 52828, Republic of Korea
e-mail: kas2393@afdex.com

K. H. Lee
Pungkang Co., Ltd., Hwaseong-si, Gyeonggi-do 18572, Republic of Korea

© The Minerals, Metals & Materials Society 2021

G. Daehn et al. (eds.), *Forming the Future*, The Minerals, Metals & Materials Series,
https://doi.org/10.1007/978-3-030-75381-8_76

process design is required to amplify the effectiveness of productive effort and cost reduction [1].

Several phenomenological and metallurgical flow stress models for stainless steels and common carbon steels [2] have been widely used in metal forming simulation. The common feature for these types of model is that these models can be expressed as a function of state variables, including strain, strain rate, and temperature. They can be fitted to convenient mathematical functions using macroscopic mechanical tests. Although this is a long-known fact, taking a look at the literature of metal forming simulations reveals that it is often overlooked [3]. This negligence can be related to some difficulties, i.e., the maximum strain that can be achieved in the characterization tests is limited and usually lower than that being reached in the actual bulk-forming processes [1]. Extrapolation of the obtained flow stress curves up to higher strain is essential, which is regarded as a major error source. A model with optimally determined material constants is inevitable to overcome the problems in extrapolation [4].

Research works in modelling flow stress in terms of strain hardening which is dominant in the cold metal forming are represented by well-known models such as the Ludwik model [5], Hollomon model [6], Swift model [7], and Voce model [8]. Nonetheless, it is a matter of fact that strain hardening behaviours at room temperature are greatly influenced by the pre-works, i.e., manufacturing process and heat treatment; by all means, a simple well-known function is not suitable to express flow stress at larger strain for cold forming [9].

Difficulties in material characterization and somewhat complicated and time-consuming remedies may push researchers to choose an easier way to model material behaviours under some assumptions. Flow stress curve at lower strain, normally up to 0.5, can be obtained using tensile, compression, ball indentation, torsion, and notch tensile tests [10]. In bulk metal forming, flow stress prediction exceeding 1.0 is necessary. However, there are no conventional flow stress models with proper material constant determination schemes until Joun et al. [1, 11] presented the practical approach of predicting true stress–strain curves with high accuracy from tensile test data, i.e., engineering stress–strain curve of a simple cylindrical specimen.

In this paper, research on material characterization of a typical strain hardening steel is conducted together with its application to an automatic multi-stage cold forging process.

2 Criticism of the Swift Model

Figure 1 shows the experimental engineering stress–strain curve of commercial steel AISI1025 denoted by a solid line and its corresponding true stress–strain curve in the upper side, called AFDEX-M8. The latter was obtained using a special function of AFDEX [12], which is based on a half and perfect FE model with rigid-plastic finite element method. It was shown [11] that the flow stress curve is also compatible with the predictions of tensile test by elastoplastic finite element method.

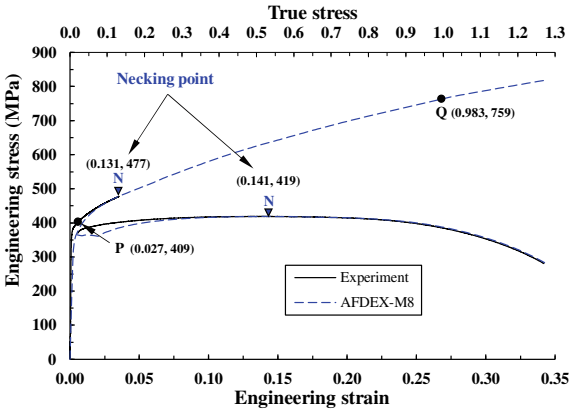


Fig. 1 Experimental and predicted engineering stress–strain curves and its associated true stress–strain curve denoted by AFDEX-M8. (Color figure online)

Figure 1 shows that the predicted tensile test, that is, engineering stress–strain curve is in good agreement with the experiments, especially at larger strain after the necking point, indicating that AFDEX-M8 can be used as a reference flow stress curve (denoted by RFS) after necking point. Note that the flow stress up to the necking point can be calculated from the simple arithmetic formula by relating true values to engineering values of stress and strain. The entire reference flow stress curve which will be used to evaluate the well-known Swift model can thus be defined by two curves, i.e., one for the left side of the necking point by a theoretical curve and the other for the rest by a numerically optimized curve.

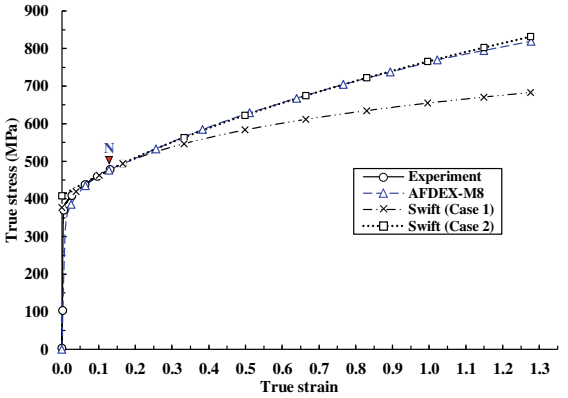
Swift flow stress model [7] is a well-known flow stress model at room temperature, widely used in describing the flow stress curve with respect to strain. It is expressed by three parameters as follows:

$$\sigma = Y_o(1 + \alpha_1 \varepsilon)^{n_1} \tag{1}$$

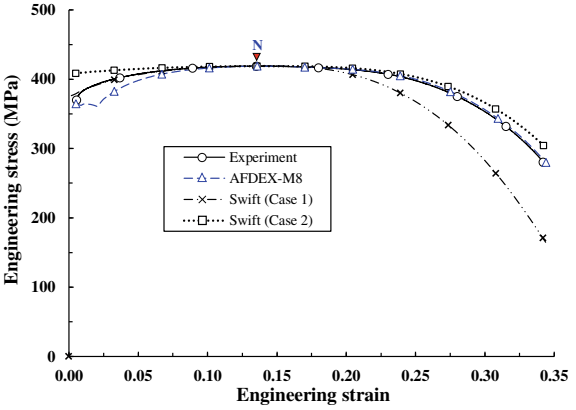
where Y_o is the yield strength of material, and α_1 and n_1 are the first strain hardening constant and the first strain hardening exponent called in this paper, respectively. The necking point is very important when a material model is defined in terms of tensile test. To meet the necking point, two conditions [1] should be satisfied, that is, only one freedom is left to specify the Swift model.

To approximate the reference flow stress curve by the Swift model, two points were chosen, that is, P and Q representing the left and right sides of the necking point denoted by N in Fig. 1, respectively. Two different Swift flow stresses which pass P or Q are shown in Fig. 2a by Cases 1 and 2 for the points P and Q, respectively. Their corresponding material constants of the Swift model are summarized in Table 1.

Figure 2b compares the theoretical tensile tests predicted by three flow stresses, including Case 1, Case 2, and AFDEX-M8, and experimental tensile test. All predictions are in excellent agreement with the experiments around the necking point. It is shown that AFDEX-M8 meets quite well with experiments except at the lower strain.



(a) Flow stress



(b) Tensile test

Fig. 2 Comparison of experiments and predictions by AFDEX-M8, Case 1 and Case 2. (Color figure online)

Table 1 Two Swift models

Swift model	Y_o (MPa)	α_1	n_1
Case 1	376.7	21.50	0.179
Case 2	408.5	3.440	0.422

Of course, the reference flow stress curve can be used for predicting the tensile test almost exactly for the entire region of interested strain.

Cases 1 and 2, however, exhibit greater errors in the right and left sides, respectively, implying that the Swift model cannot satisfy the flow stress of the material before and after the necking point at the same time. Case 1 predicted an accurate engineering stress–strain curve up to the necking point but the curve bent quicker than the experiment because of the underestimated flow stress after the necking point, as can be seen in Fig. 2a. On the contrary, Case 2 showed a better prediction of the

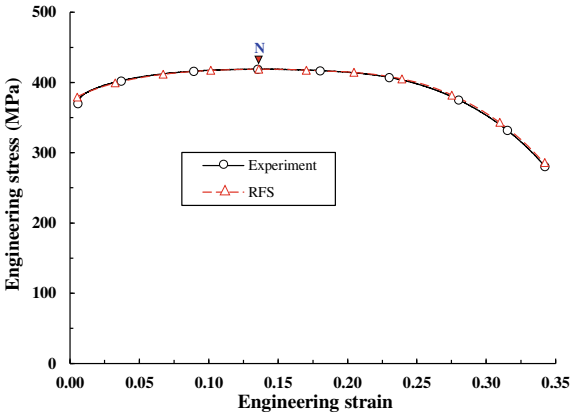


Fig. 3 Comparison of experimental and predicted engineering stress–strain curves by RFS. (Color figure online)

engineering stress–strain curve after the necking point but it overestimated the flow stress at lower strain before the necking point, resulting in non-negligible error.

Figure 3 compares the predicted tensile test obtained by the reference flow stress curve with the experimental tensile test, showing their exact agreement from the standpoint of engineering. It is noted that the reference flow stress was not formulated by a closed-form function and that it is not practical, especially either when it should be extrapolated for much larger strain or when a softening behaviour due to damage accumulation should be dealt with.

3 Introduction of Improved Swift Model

An improved Swift flow stress model developed in a previous study [13] is used, which is formulated as follows:

$$\sigma = Y_o\left(1 + \alpha_1\varepsilon + \alpha_2\varepsilon^{n_2}\right)^{n_1} \tag{2}$$

where α_2 and n_2 are called the second strain hardening constant and the second strain hardening exponent, respectively. Parameters Y_o and α_1 were determined in the same manner as with the Swift model (Case 1), then α_2 was calculated to meet the sampled point marked "Q" in Fig. 1 with n_2 fixed as 3.0. The calculated parameters were summarized in Table 2. Figure 4 shows the calculated flow stress based on the improved Swift model. It can be concluded that the improved Swift model can satisfy

Table 2 Parameters for the improved Swift model

Y_o (MPa)	α_1	α_2	n_1	n_2
376.7	21.50	30.69	0.179	3.0

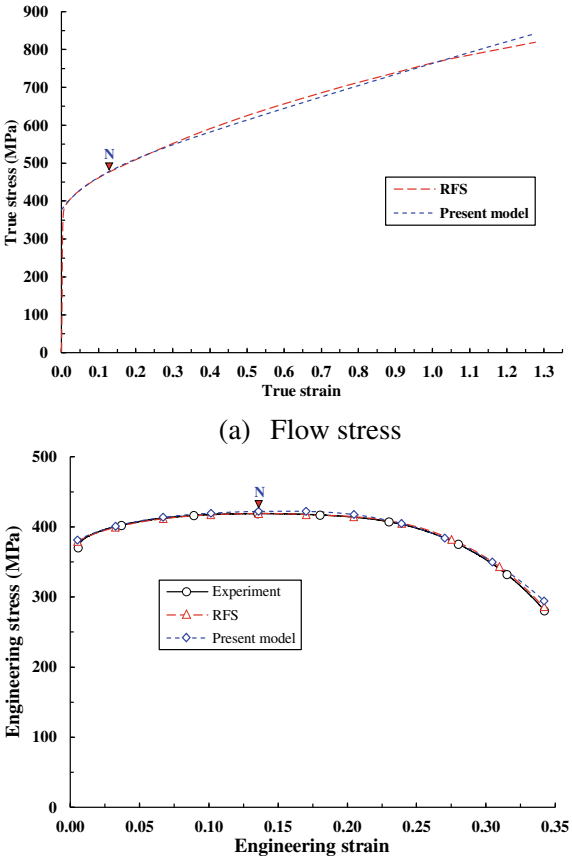


Fig. 4 Comparison of experiments and prediction by RFS and present model. (Color figure online)

both sides before and after the necking point with acceptable accuracy as well as the necking point accurately. Of course, RFS still has the highest accuracy, as can be seen in Fig. 3. On the contrary, the improved Swift model is formulated by a closed-form function with minimized material constants, which is practical and mathematically powerful for further study [14].

4 FE Analysis of an Automatic Multi-stage Cold Forging Process

For successful and competitive mass production of fasteners and auto-parts by an automatic multi-stage cold forging machine [15–18], die life is one of the hot issues to be managed scientifically, which needs high precision simulation of the process.

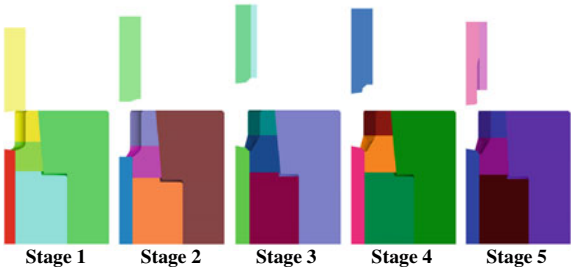


Fig. 5 Process design of the nut cold forging process. (Color figure online)

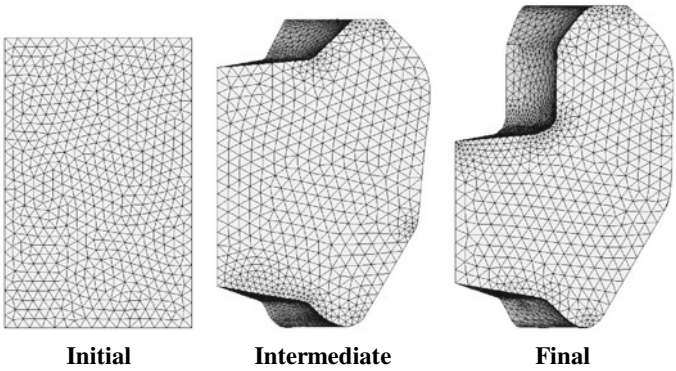


Fig. 6 Tetrahedral finite element mesh systems

A sequence of the typical nut forming process seen in Fig. 5 was simulated by an elastoplastic finite element method [19] with die elastic deformation considered, i.e., by completely coupled analysis. Die deformation due to shrink fit was also considered. The flow stress described in Fig. 4a was used for this purpose. Figure 6 shows typical tetrahedral finite element systems [20] during simulation. The frictional coefficient was assumed 0.05. The dependence of flow stress on the strain rate and temperature was neglected.

Figures 7, 8, and 9 show the predictions of change of metal flow lines, history of deformation with strain and die stresses, respectively. It should be emphasized again that the entire finite element simulation was conducted in a fully automatic way considering all factors affecting the material and die deformations.

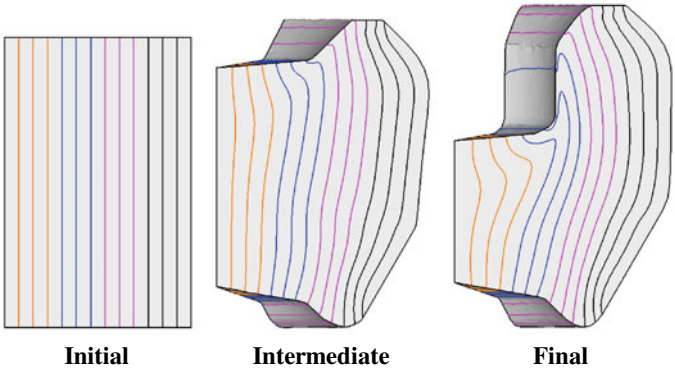


Fig. 7 Change of metal flow lines. (Color figure online)

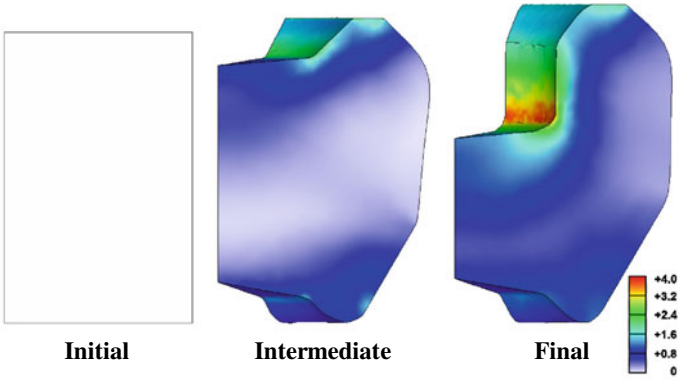


Fig. 8 Change of strain. (Color figure online)

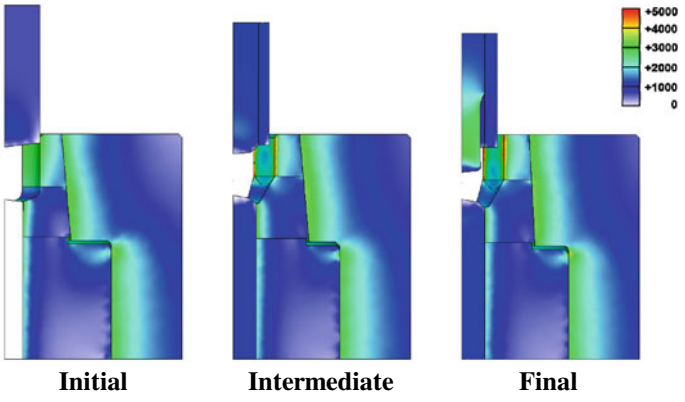


Fig. 9 Effective stresses of die parts. (Color figure online)

5 Concluding Remarks

The Swift model was evaluated and criticized to reveal its dominance and drawback using a tensile test curve of carbon steel. The main advantage of this model is the mathematical simplicity and accurate necking point prediction. On the other hand, the foremost shortage of this model lies in the fact that it cannot satisfy both flow stresses before and after the necking point at the same time in the case of the test example.

A reference flow stress was proposed to be used for material characterization at room temperature, which can describe flow stress at both sides of the necking point with higher accuracy. It was shown that the reference flow stress predicted almost the exact engineering stress–strain curve of the tensile test.

It was shown that the improved Swift model with a minimum number of material constants can depict the entire flow stress curve with high accuracy. It is noted that the improved Swift model is very useful because of its mathematical simplicity and extendability for reflecting the softening effect due to damage accumulation and extrapolating the flow stress at a much larger strain.

The improved Swift model was successfully applied to a precision simulation of an automatic multi-stage cold forging process of nut for the purpose of increase in die life, which needs accurate flow stress information.

Acknowledgments This work was financially supported by the Ministry of Trade, Industry and Energy (MOTIE) as a part of the Joint R&D project (20003950).

References

1. Joun MS, Eom JG, Lee MC (2008) A new method for acquiring true stress–strain curves over a large range of strains using a tensile test and finite element method. Mech Mater 40:586–593
2. Lin YC, Chen XM (2011) A critical review of experimental results and constitutive descriptions for metals and alloys in hot working. Mater Des 32:1733–1759
3. Altan T, Vazquez V (1996) Numerical process simulation for tool and process design in bulk metal forming. CIRP Ann 45:599–615
4. Şimşir C, Duran D (2018) A flow stress model for steel in cold forging process range and the associated method for parameter identification. Int J Adv Manuf Technol 94:3795–3808
5. Ludwik P (1909) Elemente der Technologischen Mechanik. J Springer, Berlin
6. Hollomon JH (1945) Coordinate and amplify the knowledge. AIME Trans 162:268–290
7. Swift HW (1952) Plastic instability under plane stress. J Mech Phys Solids 1:1–18
8. Voce E (1948) The relationship between stress and strain for homogeneous deformation. J Inst Metals 74:537–562
9. Eom JG, Son YH, Jeong SW, Ahn ST, Jang SM, Yoon DJ, Joun MS (2014) Effect of strain hardening capability on plastic deformation behaviors of material during metal forming. Mater Des 1980–2015(54):1010–1018
10. Joun MS, Choi IS, Eom JG, Lee MC (2007) Finite element analysis of tensile testing with emphasis on necking. Comput Mater Sci 41:63–69
11. Eom JG, Chun WJ, Joun MS, Comparison of rigid-plastic and elastoplastic finite element predictions of a tensile test of cylindrical specimens. Key Eng Mater 622–623:611–616

12. Joun MS, Lee MC, Eom JG (2011) Intelligent metal-forming simulation. Paper presented at ASME international manufacturing science and engineering conference, Corvallis, Oregon, USA, June 2011 vol 1, pp 161–168
13. Razali MK, Byun JB, Joun MS (2019) Plastic deformation behaviors of SUS 304 at low and warm temperature and a mathematical model. Paper presented at the Korean society for technology of plasticity, Jeju Island, South Korea, Oct 2019, pp 225–226
14. Razali MK, Irani M, Joun MS (2019) General modeling of flow stress curves of alloys at elevated temperatures using bi-linearly interpolated or closed-form functions for material parameters. J. Mater. Res. Technol. 8:2710–2720
15. Joun MS, Lee SW, Chung JH (1998) Finite element analysis of a multi-stage axisymmetric forging process. Comput Mater Sci 41(1):63–69
16. Lee MC, Chung SH, Joun MS (2009) Automatic and precise simulation of multistage automatic cold-forging processes by combined analyses of two- and three-dimensional approaches. Int J Adv Manuf Technol 41:1–7
17. Sun MC, Tzou GY, Zheng LA (2013) Processing animation simulation and FEM analysis of multi-stage cold forging of stainless automotive battery fastener. Ind J Eng Mater Sci 20:219–224
18. Im CS, Suh SR, Lee MC, Kim JH, Joun MS (1999) Computer aided process design in cold-former forging using a forging simulator and a commercial CAD software. J Mater Process Technol 95:155–163
19. Joun MS, Chung J, Ahn ST (2009) Macroscopic modelling of metal forming processes by FEM. In: Jinseam media; South Korea, pp 311–335
20. Lee MC, Joun MS, Lee JK (2007) Adaptive tetrahedral element generation and refinement to improve the quality of bulk metal forming simulation. Finite Elem Anal Des 43:788–802

Stress-Relaxation Age Forming of a Component with Complex and Large Curvatures: Simulation and Manufacturing



Qi Rong, Zhusheng Shi, Yong Li, and Jianguo Lin

Abstract Stress-relaxation age forming (SRAF) of a component (820 × 300 × 3 mm^3) with complex and large curvatures has been simulated and a corresponding SRAF test of an Al–Mg–Si alloy, AA6082-T6, has been carried out in this study. An FE model is established to simulate the stress-relaxation ageing (SRA) behaviour of AA6082-T6 during SRAF at various stress levels, ranging from elastic to plastic regions, and a unified constitutive model for SRA of the material has been implemented in the finite element (FE) software ABAQUS via the user-defined subroutine CREEP. An optimised tool surface was determined from the FE simulation through springback predication and compensation and was used for manufacturing test. A good agreement of the formed shape has been achieved between the FE simulation and the SRAF test, with a maximum shape error below 4 mm, satisfying the industrial requirement. The hardness results from the formed plate showed an insignificant change of strength during SRAF, and are in good agreement with the simulation. The effects of the initial plastic strain and creep strain generated during loading and stress-relaxation stages on the formed shape have also been analysed.

Keywords Stress-relaxation age forming · Creep age forming · Large and complex curvature · FE simulation · Al–Mg–Si alloy

1 Introduction

Stress-relaxation age forming (SRAF), which is also called creep age forming (CAF), is a sheet metal forming technology combining material deformation and age hardening in one process, and has been widely employed in the production of extra-large panels in the aeronautics industry [1, 2]. For example, the SRAF method has been used for the production of upper wing skins of Airbus A380 superjumbo [3] and

Q. Rong · Z. Shi (✉) · J. Lin
Department of Mechanical Engineering, Imperial College London, London SW7 2AZ, UK
e-mail: zhusheng.shi@imperial.ac.uk

Y. Li
School of Mechanical Engineering and Automation, Beihang University, Beijing 100191, China

© The Minerals, Metals & Materials Society 2021

G. Daehn et al. (eds.), *Forming the Future*, The Minerals, Metals & Materials Series,
https://doi.org/10.1007/978-3-030-75381-8_77

Gulfstram G-IV Aircraft [2]. Because of the advantages of SRAF technology, it is beneficial to broaden its applications to other areas, such as the locomotive industry, where the panels normally have large size and complex shape. However, the current SRAF applications are for the panels with large size but relatively small curvatures and most experimental and modelling investigations so far are mainly focused on the SRA behaviours of the age-hardenable aluminium alloys in the elastic region. Very few studies have been done on SRAF of panels with large curvature, in which the material deformed in the plastic region. Yang [4] manufactured a singly curved stiffened panel with a curvature radius of 650 mm, which is the largest curvature of the SRAFed panel published so far. The unavoidable springback phenomenon occurring during SRAF varies with curvature and thickness of the plate as well as the SRAF process parameters, and to accurately predict it for the formed plate, the development and calibration of the material model for the SRA behaviour are very important. Recently, some modelling work has been carried out to predict the stress-relaxation/creep ageing behaviours in both elastic and plastic regions [5, 6], and both explicit and implicit algorithms have been used in previous studies on the FE simulations of the SRAF process of aluminium alloys [7–9]. However, no reports have been found on the FE simulations and SRAF tests of panels with large and complex curvatures.

Aluminium alloy AA6082 is one of the most used lightweight materials in the locomotive industry due to its good combination of strength and weldability [10, 11]. To broaden SRAF to the panels with large and complex curvatures in the locomotive industry, experimental investigation has been carried out on SRA behaviour of AA6082-T6 with initial loading in both the elastic and plastic regions [12]. The aim of the study is to use the FE simulation to guide the tool surface design for manufacturing a component with complex and large curvature. An FE model is built to simulate the SRA behaviour of AA6082-T6 during SRAF at various stress levels ranging from elastic to plastic regions. An explicit integration method has been used to solve a constitutive material model and implemented into ABAQUS for FE simulation of the SRAF process. The techniques and procedures for the implementation of the developed material model in ABAQUS are described in detail. The FE simulation has been carried out to determine the tool surface for SRAF of a panel with large and complex curvatures that was selected from an in-service high-speed train. The corresponding SRAF test has then been performed to validate the developed FE models in the prediction of springback behaviour during SRAF of the material. The hardness test of the specimens cut from the SRAFed plate has also been carried out to verify the post-form strength predicted by the FE model.

2 FE Simulation

2.1 Material Model

SRA behaviour in both the elastic and plastic regions of AA6082-T6 has been investigated at 160 °C up to 12 h in an earlier study [12], during which there is no significant change in the yield strength within the timeframe, which is important for the application of SRAF of peak-aged material. It was concluded that the enhanced stress relaxation with higher initial strains in the plastic region is mainly due to increased dislocation movement and decreased resistance of the material to stress relaxation deformation. Based on the analysis, the following set of constitutive equations has been developed [13] and employed in this study for the prediction of the stress-relaxation ageing behaviour of AA6082-T6 from elastic to plastic regions:

$$\dot{\sigma} = \mathrm{E}\dot{\varepsilon}_e = -\mathrm{E}\dot{\varepsilon}_c \tag{1}$$

$$\dot{\varepsilon}_c = A_1 \sinh\{B_1[(\sigma - \sigma_{th})(1-\overline{\rho})]\}\mathrm{sign}\{\sigma\} + k_4\dot{\sigma}_{\mathrm{dis}} \tag{2}$$

$$\sigma_{th} = C_{th}\overline{\lambda}^{-1} - C_1\overline{\rho}^{n_4} \tag{3}$$

$$\dot{\overline{\rho}} = A_3(1-\overline{\rho})|\dot{\varepsilon}_c|^{n_1} - C_p\overline{\rho}^{m_4} \tag{4}$$

$$\dot{\bar{l}} = C_L(Q-\bar{l})^{m_2}(1+\gamma_0\overline{\rho}^{m_3}) \tag{5}$$

$$\dot{\overline{\lambda}} = k_3\dot{\bar{l}} \tag{6}$$

$$\sigma_y = \sigma_{\mathrm{ss}} + \sqrt{{\sigma_A}^2 + {\sigma_{\mathrm{dis}}}^2} \tag{7}$$

$$\dot{\sigma}_{ss} = 0 \tag{8}$$

$$\dot{\sigma_A} = C_A(1-\bar{l})\dot{\bar{l}}^{m_1} \tag{9}$$

$$\dot{\sigma}_{\mathrm{dis}} = A_2 n_3 \overline{\rho}^{n_3-1}\dot{\overline{\rho}} \tag{10}$$

where A_1, A_3, B_1, C_p, C_A, C_L, C_{th}, k_3,k_4, m_1, m_2, m_3, m_4, n_1, n_4, Q, γ_0, C_1 are material constants to be determined from the experimental data.

Equation (1) is the relationship between the creep strain rate $\dot{\varepsilon}_c$ and stress-relaxation rate $\dot{\sigma}$, and E is the Young's modulus of the material. Equation (2) describes the evolution of creep strain rate $\dot{\varepsilon}_c$, which is a function of applied stress σ, threshold

stress σ_{th}, and normalised dislocation density $\overline{\rho}$; and the annealing effect on recovery has also been added since greater effect occurs due to the existence of non-shearable precipitates [14–16]. Equation (3) describes the evolution of threshold stress σ_{th}, which is a function of normalised inter-particle spacing $\overline{\lambda}$ and normalised dislocation density $\overline{\rho}$ [17, 18]. Equation (4) describes the evolution of normalised dislocation density $\overline{\rho}$, which is defined as $\overline{\rho} = (\rho - \rho_i)/\rho_s$, where ρ is the instantaneous dislocation density, ρ_i is the dislocation density in the as-received material before loading, and ρ_s is the saturated dislocation density during stress-relaxation ageing [19]. Equation (5) describes the evolution of precipitate size [8], where the normalised precipitate length $\overline{l}$ is used to represent, which is defined as $\overline{l} = l/l_p$, where l is the instantaneous precipitate length and l_p is the precipitate length at the peak-ageing condition, and thus $\overline{l}$ will evolve with an initial value of 1. The use of precipitate length is mainly due to the precipitation coarsening direction along its length direction during SRA of AA6082-T6 at 160 °C up to 12 h [12]. Equation (6) describes the evolution of the normalised inter-particle spacing, which is defined as $\overline{\lambda} = \lambda/\lambda_p$, where λ is the instantaneous inter-particle spacing and λ_p is the inter-particle spacing in the peak-ageing condition. $\overline{\lambda}$ will evolve with an initial value of 1 and follows a similar trend as $\overline{l}$. Equation (7) describes the evolution of yield strength σ_y, which is a function of solution hardening σ_{ss}, precipitation hardening σ_A, and dislocation hardening σ_{dis}. The evolution of these three strength components are described in Eqs. (8–10), respectively. The initial state of the studied material is at peak-aged condition, the solutes concentration and volume fraction of the precipitates will change little during further ageing, and thus the strength that comes from solute hardening is a constant, as shown in Eq. (8) [20, 21].

Since a large number of dislocations has been generated during loading to the plastic region, the initial value of the normalised dislocation density is no longer 0, and so are the initial dislocation hardening strength and threshold stress. The equations to model their initial value are summarised in Eqs. (11–13), respectively [22].

$$\overline{\rho}_0 = k_2 {\varepsilon_0}^{n_2} \mathrm{H}(\sigma_0 - \sigma_y) \tag{11}$$

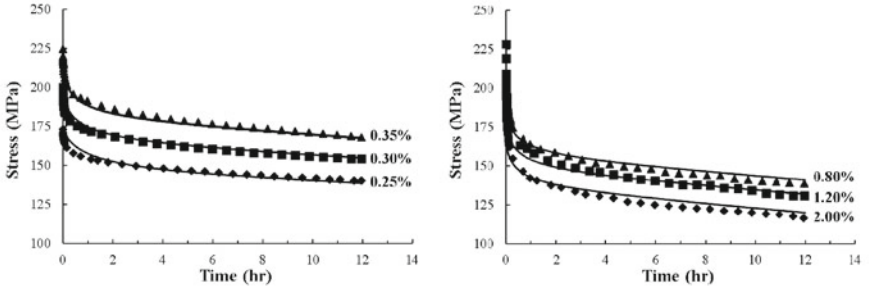
$$\sigma_{dis0} = A_2 \cdot \bar{\rho}_0^{n_3} \tag{12}$$

$$\sigma_{th0} = B_2 - k_1 \cdot \sqrt{\overline{\rho}_0} \tag{13}$$

where k_2,n_2,A_2,n_3,B_2, and k_1 are material constants to be determined from the experimental data. $\mathrm{H}(\sigma_0 - \sigma_y)$ in Eq. (11) is the Heaviside step function; when $\sigma_0 \geq \sigma_y$, $\mathrm{H}(\sigma_0 - \sigma_y) = 1$, representing the dislocation densities generated by loading in the plastic region. Otherwise, $\mathrm{H}(\sigma_0 - \sigma_y) = 0$. Material constants in the equation were determined by fitting the simulated curves to the corresponding experimental results, and the determined material constants are listed in Table 1. Figure 1 compares the computed results with experiments for stress-relaxation behaviour of AA6082-T6 under different initial strain levels ranging from elastic (0.25%, 0.30%, and 0.35%)

Table 1 Summary of the calibrated material constants of the material model for stress-relaxation ageing of AA6082-T6 at 160 °C

A_1 (−)	A_2 (MPa)	$A_3(h^{-1})$	B_1(MPa)	k_3(−)	C_p(−)	C_A(MPa)	n_4(−)
3.1e-6	80	120	0.0685	3.36	0.0645	3	2
k_2(−)	k_1 (MPa)	C_{th}(MPa)	B_2 (MPa)	m_1 (−)	m_2 (−)	C_1 (MPa)	m_4 (−)
12	190	31	95	0.3	2	0.2	0.1
n_1 (−)	n_2 (−)	n_3 (−)	$C_L(h^{-1})$	Q (−)	γ_0 (−)	k_4(MPa^{-1})	m_3 (−)
0.6	1.15	1	0.07	2.1	6	0.3	5



(a) With initial strains in the elastic region (b) With initial strains in the plastic strain

Fig. 1 Comparison of stress-relaxation curves between experiments (symbols) and calibrated models (solid lines) with six initial strain levels in (**a**) elastic and (**b**) plastic regions

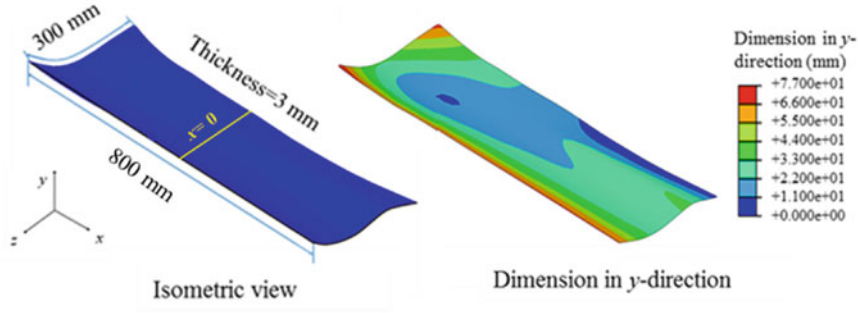
to plastic regions (0.80%, 1.20%, and 2.00%), and good agreement between them has been achieved. Additionally, 75–90% of the total stress relaxation has taken place in the first 5 h ageing process at all tested initial strain levels, and thus the ageing time of the SRAF test performed in this work is determined to be 5 h for better production efficiency.

2.2 Implementation of Material Model

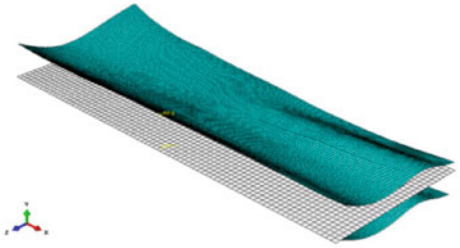
The developed material model is implemented into the commercial FE solver ABAQUS via the user-defined subroutine CREEP for process simulation. Both explicit and implicit methods have been used in previous studies on the FE simulations of the SRAF process of aluminium alloys [7, 23], and the explicit method has been found to be more straightforward and convenient to use, with satisfying results. Therefore, the explicit integration algorithms are used in this work, and all the material constants and initial values are defined in the subroutine. The effectiveness of the developed FE model has been validated by stress-relaxation age forming (SRAF) of a singly curved plate, which deformed in the plastic region with a curvature radius of 700 mm.

The FE model created to simulate the SRAF process of an AA6082-T6 panel with large and complex curvatures is shown in Fig. 2, with the dimension of the objective shape and developed FE model for demonstration plate. The length and width of both upper and bottom tools in this model are, respectively, 800 and 280 mm. The blank is modelled with shell elements (S4R) in ABAQUS with a dimension of 800 × 300 × 3 mm. The penalty friction formulation is used, and the friction coefficient between the tool and the blank is defined as 0.1 [4]. In order to obtain satisfactory results in a more efficient way, the mesh convergence tests have been performed, and the results were obtained with different blank mesh sizes, i.e., 5, 10, 20, 25 mm. The maximum vertical deflections at $x = 0$ on the plate by using different mesh sizes are plotted in Fig. 3. From the point of view of efficiency and computational time, 10 mm was selected as the mesh size of the blank. The basic mesh properties of the model are summarised in Table 2.

For the easier implementation of the FE model, the whole SRAF process is regarded as an isothermal process and the heating and cooling processes are not taken into account since their durations are relatively short compared to the ageing process. Also, due to the slower creep deformation at a lower temperature, and a minor effect of different stress levels on the ageing behaviour of the material in this study, the thermal effects are ignored in the FE modelling. Therefore, the stress–strain



(a) Dimension of the objective shape



(b) Isometric view of the developed FE model

Fig. 2 FE model for SRAF. **a** Dimension of the objective shape. **b** Isometric view of the developed model. (Color figure online)

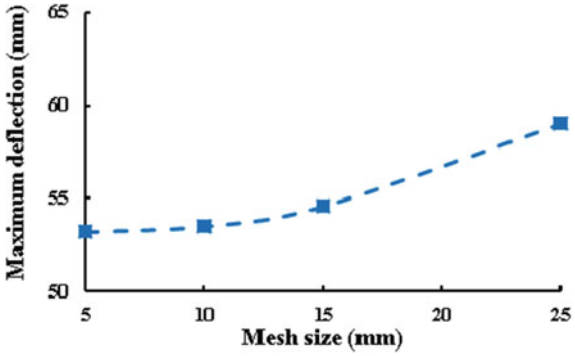


Fig. 3 Mesh convergence test results. (Color figure online)

Table 2 Basic mesh properties of each part in FE model for the panel

Part name	Element type	Element number	Mesh size (mm)
Upper tool	Discrete rigid (R3D4)	9760	5
Bottom tool	Discrete rigid (R3D4)	9760	5
Blank	Shell (S4R)	2400	10

relationship of AA6082-T6 at the ageing temperature 160 °C is used to simulate the material properties evolution during loading in SRAF FE simulations in this study. A Young's modulus of 70 GPa and Poisson's ratio of 0.33 is defined for the elastic property of the material. The plastic part of the experimental stress–strain curve is inputted into the FE models to define the plastic properties of the material, and the inputted initial plastic strain ($\varepsilon_p = 0$) is defined at the point after which $\varepsilon \neq \sigma\ E$.

The numerical simulation of SRAF tests has been divided into five stages according to practical SRAF procedures, including:

1. Initial stage: Define the reference points of the upper and bottom forming tools. The bottom tool is fully constrained, and the upper tool can only move along its thickness direction. The blank is positioned close to the bottom tool at the initial stage.
2. Gravity stage: Position the tools and blank in the FE model automatically through a gravity stage simulation.
3. Loading stage: Apply a predetermined displacement along the thickness direction to fully load the upper tool onto the blank.
4. Stress-relaxation ageing stage: Hold all the parts for a controlled time, for example, 5 h in this study, during which the creep subroutine is activated, and the stress-relaxation ageing behaviour of the blank is simulated.
5. Unloading stage: The upper tool is set to lift to its original location, and the springback of the blank occurs.

The setting of boundary conditions is quite rigorous because of the large and complex deformations needed for the objective shape. The commonly accepted three-node boundary condition setting has been used, and the first node is selected as the first point on the blank contacted with the upper tool during loading, and the other two nodes are selected with the same x or y coordinates as the first node, respectively, in the y- and x-directions to control the translational and rotational movement of the blank.

Due to the difficulty in accurately predicting the springback of the panels after forming, especially for those with large and complex curvatures, springback compensation is an essential step in the tool shape determination process. Generally, springback is compensated by adding the dimensional difference between the objective shape and FE simulated shape of the formed blank to the tool shape used for the last simulation and generating a new tool shape to be used in the next simulation. An accelerated springback compensation method has been used in this study, and more details of the method can be found in an earlier study [24]. The optimised tool shape for producing the demonstration panel was obtained after three iterations of springback compensation that the maximum error between the formed shape by the optimised tool and the objective shape was controlled less than 2 mm.

2.3 Simulation Results

Figure 4 shows the effective stress distribution in the blank after each stage during SRAF by using the optimised tools. The maximum effective stress in the loaded blank was around 229 MPa, which already reaches the plastic region at 160 °C; the

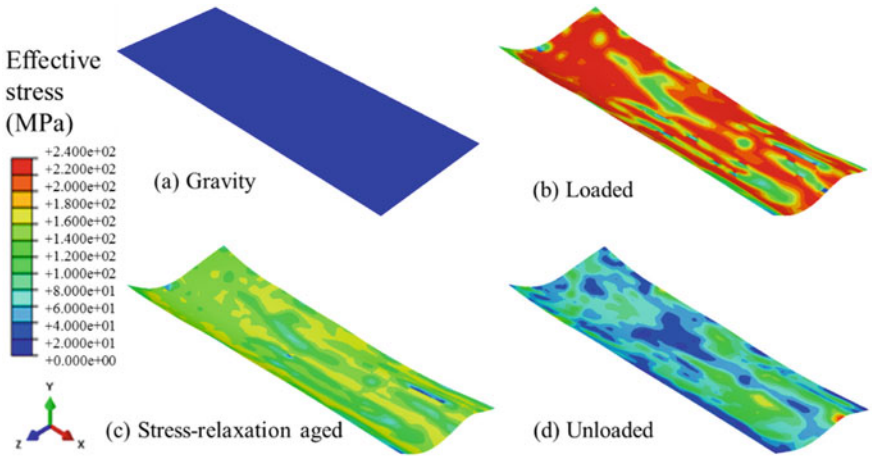


Fig. 4 Numerical results of the effective stress distribution in the blank after each stage during SRAF of the panel. (Color figure online)

minimum effective stress in the blank was around 32 MPa; and the effective stress in most of the loaded blank was in the range of 200–230 MPa. After 5 h of stress relaxation, the majority of the effective stresses decreased to around 160 MPa, with a maximum value of 175 MPa and a minimum value of 17 MPa. After full unloading, the residual stresses left in the blank were mainly in the range of 3–150 MPa, and higher residual stresses were observed at the locations with larger curvatures.

Figure 5 shows the simulated effective plastic strain generated after the loading stage of the SRAF process, and a maximum plastic strain of around 5.5% was achieved after loading.

Creep strain was generated during stress relaxation, and its evolution with ageing time is shown in Fig. 6, with a gradual increase in ageing time. The maximum creep strain generated during stress relaxation was less than 3% of the maximum plastic strain value during the loading stage, indicating the significant effect of the initial plastic strain on the final shape of the SRAFed workpiece.

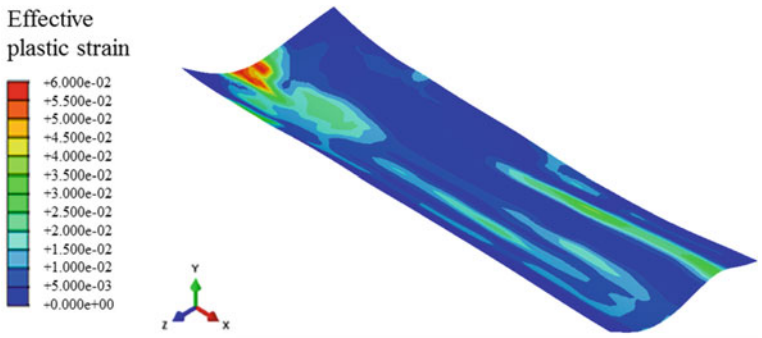


Fig. 5 FE simulated effective plastic strain of the panel after loading. (Color figure online)

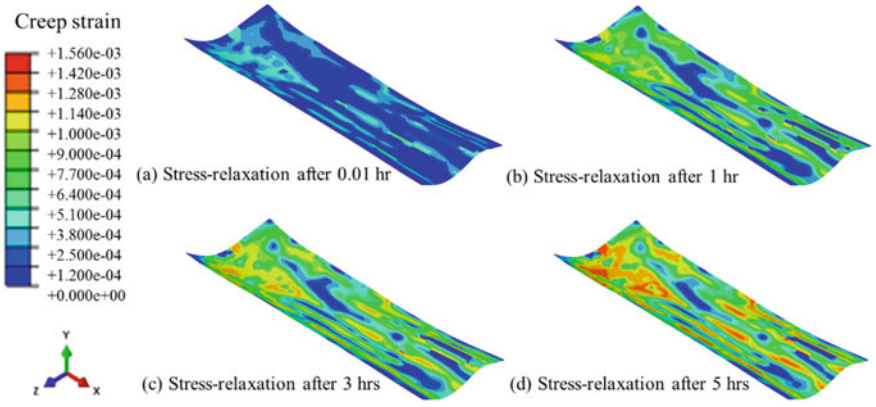


Fig. 6 Evolution of the FE simulated creep strain of the panel during stress-relaxation ageing. (Color figure online)

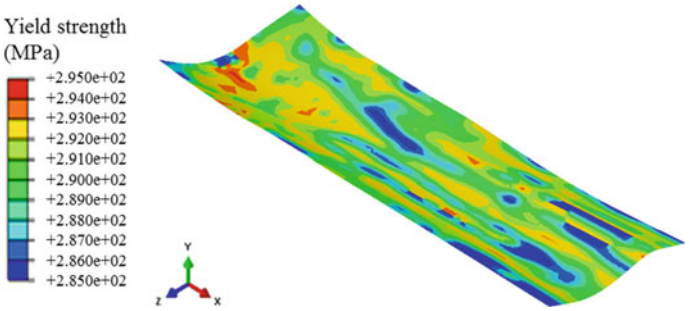
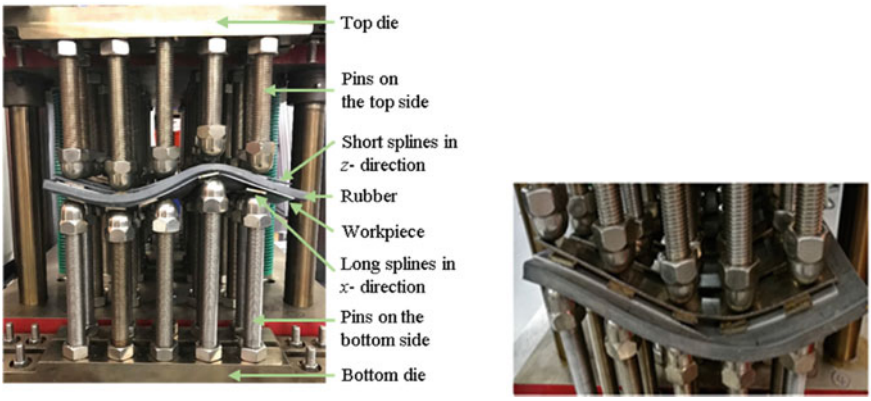


Fig. 7 FE simulated yield strength of the panel after unloading. (Color figure online)

The resultant yield strength of the SRAFed panel at room temperature was predicted to be in the range of 285.5–295 MPa as shown in Fig. 7, with an insignificant variation of yield strength of the SRAFed material compared to its initial state which was set as 290 MPa based on the material model.

3 SRAF Test Verification

SRAF tests were performed using a flexible forming tool with multi-forming pins, as detailed in an earlier study [25]. Figure 8 shows the toolset for SRAF test. The height of each forming pin was determined according to the optimised tool shape, and the blank was prepared with a dimension of $820 \times 300 \times 3$ mm^3. The blank was first loaded to have full contact with the top and bottom pins of the forming tool so



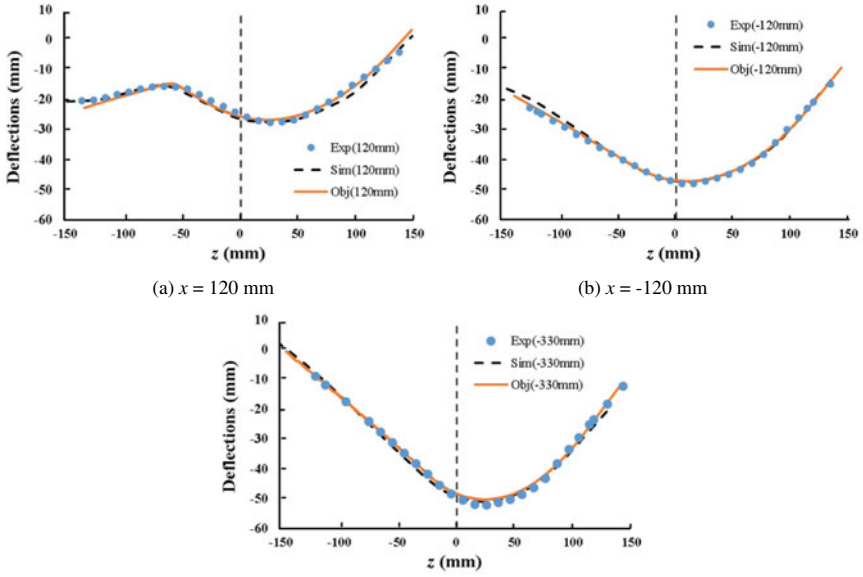
(a) View from x+ direction (b) View from x- direction

Fig. 8 Views of tool setup for SRAF test. **a** View from the $x+$ direction. **b** View from the $x-$ direction. (Color figure online)

that it be deformed to the predetermined shape of the tool surface. The tools were tightened and the whole toolset was moved into a pre-heated furnace. The 5 h SRA was started once the blank reached 160 °C. After the 5 h SRA process, the toolset was moved out of the furnace and unloaded. A 3D coordinate measurement machine CMM LKG90C was employed to measure the deflections of the SRAFed blank.

Figure 9 shows the measured deflections of SRAFed panel (symbols) at selected locations and the results obtained from the FE model (dashed lines) and the objective shape (solid lines). As can be seen, a very good agreement has been achieved among these three sets of data. The maximum deviation among them is within 4 mm, which is less than 5% of the total deflection of the panel and fulfils the general dimensional accuracy requirement for panel assembling in the industry. These deviations may come from the limitations of the lab-scale flexible tool currently used such that the flexible pins are not close enough to generate exactly some specific, large curvature. Such deviations can be further decreased by using the tool with more forming pins or even using solid tools.

The strength of the SRAFed material was evaluated by the hardness test, using Zwick hardness tester with 30 N load (HV3). Six samples were cut from the as-received plate and the SRAFed plate, respectively, five tests for each sample, and the hardness results are shown in Fig. 10, including their variations. It was found that the



(a) x = 120 mm

(b) x = -120 mm

(c) x = -330 mm

Fig. 9 Comparison of the formed shape along the z-direction by using the optimised tool from experiments (symbols) and FE simulation results (dashed lines) with the objective shape (solid lines) of the demonstration panel at cross-sections with the indicated x position. **a** $x = 120$ mm. **b** $x = -120$ mm. **c** $x = -330$ mm. (Color figure online)

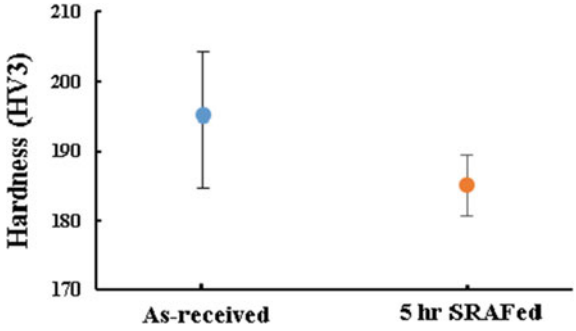


Fig. 10 Hardness results of the as-received and the SRAFed plates. (Color figure online)

average hardness decreased from 195.2 ± 9 HV3 to 185.2 ± 5 HV3 after 5 h SRA at 160 °C. The results correspond well with the simulated results that the SRA process contributes insignificant effect to the strength evolution of AA6082-T6 during SRAF. The current study also shows that sufficient strength has been maintained after SRAF and is adequate for industrial application.

4 Conclusions

Finite element simulation has been carried out on stress-relaxation age forming of AA6082-T6 for a component (820 × 300 × 3 mm^3) with complex and large curvatures. The evolutions of the stress and strain distributions and mechanical property of the blank during SRAF have been predicted by FE simulations. An optimised tool surface was obtained through springback compensation and was used to carry out the corresponding SRAF of an AA6082-T6 panel for verification. It was found that the maximum creep strain generated during stress relaxation was less than 3% of the maximum value of the plastic strain during the loading stage, showing the very significant effect of the initial plastic strain on the final shape for components with large curvature. It was also observed that less springback occurred at the locations with larger curvatures. The successful manufacture of the industrial panel with a maximum shape error of 4 mm and the correct prediction of a minor change in the strength/hardness of the SRAFed plate compared to the as-received plate have proven the feasibility and the accuracy of the developed modelling and springback compensation techniques. It also shows the importance of FE simulation to guide the tool surface design. The work in this study provides a series of numerical and manufacturing tools for the SRAF process of AA6082-T6, which can be applied to other heat-treatable aluminium alloys and guide further industrial manufacturing of panels with complex and large curvatures through SRAF technology.

Acknowledgments Much appreciated is the strong support received from CRRC Qingdao Sifang Co., Ltd. The research was performed at the CRRC Sifang-Imperial Centre for Rail Transportation Manufacturing Technologies at Imperial College London.

References

1. Eberl F, Gardiner S, Campanile G, Surdon G, Venmans M, Prangnell P (2008) Ageformable panels for commercial aircraft. P I Mech Eng G-J Aer. 222(G6):873–886
2. Zhan L, Lin J, Dean TA (2011) A review of the development of creep age forming: Experimentation, modelling and applications. Int J Mach Tool Manu 51(1):1–17
3. Holman MC (1989) Autoclave age forming large aluminum aircraft panels. J Mech Work Technol 20:477–488
4. Yang H (2013) Creep age forming investigation on aluminum alloy 2219 and related studies. Ph.D. thesis. Imperial College London.
5. Ma Z, Zhan L, Liu C, Xu L, Xu Y, Ma P, Li J (2018) Stress-level-dependency and bimodal precipitation behaviors during creep ageing of Al-Cu alloy: Experiments and modeling. Int J Plast 110:183–201
6. Yang Y, Zhan L, Liu C, Wang, X, Wang Q, Tang Z, Li G, Huang M, Hu Z (2019) Stress-relaxation ageing behavior and microstructural evolution under varying initial stresses in an Al–Cu alloy: Experiments and modeling. Int J Plast. 102646.
7. Lin J, Ho KC, Dean TA (2006) An integrated process for modelling of precipitation hardening and springback in creep age-forming. Int J Mach Tool Manu 46(11):1266–1270
8. Zhan L, Lin J, Dean TA, Huang M (2011) Experimental studies and constitutive modelling of the hardening of aluminium alloy 7055 under creep age forming conditions. Int J Mech Sci 53(8):595–605
9. Li Y, Shi Z, Lin J, Yang Y, Saillard P, Said R (2018) FE simulation of asymmetric creep-ageing behaviour of AA2050 and its application to creep age forming. Int J Mech Sci 140:228–240
10. Babu G, Murti K, Janardhana G (2008) An experimental study on the effect of welding parameters on mechanical and microstructural properties of AA 6082–T6 friction stir welded butt joints. ARPN J Eng Appl Sci. 3(5):68–73
11. Edwards GA, Stiller K, Dunlop GL, Couper MJ (1998) The precipitation sequence in Al–Mg–Si alloys. Acta Mater 46(11):3893–3904
12. Rong Q, Li Y, Shi Z, Meng L, Sun X, Sun X, Lin J (2019) Experimental investigations of stress-relaxation ageing behaviour of AA6082. Mater Sci Eng A 750:108–116
13. Rong Q, Shi Z, Li Y, Lin J (2021) Constitutive modelling and its application to stress-relaxation age forming of AA6082 with elastic and plastic loadings. J Mater Proc Tech 295:117168
14 Rollett A, Humphreys F, Rohrer GS, Hatherly M (2004) Recrystallization and related annealing phenomena. Elsevier, United Kingdom
15. Cheng L, Poole W, Embury J, Lloyd D (2003) The influence of precipitation on the work-hardening behavior of the aluminum alloys AA6111 and AA7030. Metall Mater Trans A 34(11):2473–2481
16. Mecking H, Kocks, UF (1979) A mechanism for static and dynamic recovery. In: Strength of metals and alloys. Pergamon, p 345–350.
17. Arzt E, Wilkinson DS (1986) Threshold stresses for dislocation climb over hard particles: the effect of an attractive interaction. Acta Metall 34:1893–1898
18. Zhou D, Zhao W, Mao H, Hu Y, Xu X, Sun X, Lu Z (2015) Precipitate characteristics and their effects on the high-temperature creep resistance of alumina-forming austenitic stainless steels. Mater Sci Eng A 622:91–100
19. Li Y, Shi Z, Lin J, Yang Y, Rong Q, Huang B, Chung T, Tsao C, Yang J, Balint D (2017) A unified constitutive model for asymmetric tension and compression creep-ageing behaviour of naturally aged Al-Cu-Li alloy. Int J Plast 89:130–149
20. Anjabin N, Taheri K (2010) The effect of aging treatment on mechanical properties of AA6082 alloy: modeling experiment. Iranian J. Mater. Sci. Eng. 7:14–21
21. Esmaeili S, Lloyd DJ, Poole WJ (2003) A yield strength model for the Al-Mg-Si-Cu alloy AA6111. Acta mater 51:2243–2257
22. Dunne, F, Petrinic, N (2005) Introduction to computational plasticity. Oxford University Press on Demand.

23. Lyu F, Li Y, Huang X, Shi Z, Zeng Y, Lin J (2019) An investigation of creep age forming of AA7B04 stiffened plates: Experiment and FE modelling. J Manu Proc. 37:232–241
24. Li Y, Rong Q, Shi Z, Sun X, Meng L, Lin J (2018) An accelerated springback compensation method for creep age forming. Int J Adv Manu Tech. 102:121–134
25. Rong Q, Li Y, Sun X, Shi Z, Meng L, Lin J (2018) Experimental studies of the efficient use of flexible tool in creep age forming. MATEC Web of Conferences. EDP Sci 190:13002

Toward an Efficient Industrial Implementation of W-temper Forming for 7xxx Series Al Alloys



Ricardo Trân, Lukas Kertsch, Sebastian Marx, Shreyas Hebbar, Verena Psyk, and Alexander Butz

Abstract Manufacturing technologies for parts made from ultra-high-strength 7xxx series aluminum sheet material have been the focus of research in recent years. A promising approach is W-temper forming, where sheet material is cold formed after heat treatment. Conventional heat treatment routes are very time-consuming and inefficient. In this study, a new more efficient and industry-orientated transfer tool concept has been developed. Heating and cooling of the sheets take place in separate contact tempering stages, which allow superior heating and cooling rates in comparison to conventional methods. To analyze the influences of temperature rates and deformation on microstructure and mechanical behavior, thermo-mechanical experiments in a Gleeble simulator were carried out. The results prove the great potential of the transfer tool concept with inline heat treatment for series production. The process-dependent mechanical properties determine a suitable process window for the industrial application of the W-temper forming of the analyzed alloys.

Keywords 7xxx series aluminum · Contact tempering · Contact heating · W-temper · Retrogression and re-aging · Quench rate sensitivity

1 Introduction

Legal requirements to reduce CO_2 emissions and the resulting demands for lower fuel consumption are prompting the automotive industry to push ahead with lightweight construction strategies, such as material sciences, construction design, and systems engineering, to reduce vehicle weight [1, 2]. Owing to its low density of 2710 kg/m^3, aluminum has great potential for lightweight construction and is therefore already

R. Trân (✉) · S. Marx · V. Psyk
Fraunhofer Institute for Machine Tools and Forming Technology IWU, Reichenhainer Straße 88, 09126 Chemnitz, Germany
e-mail: ricardo.tran@iwu.fraunhofer.de

L. Kertsch · S. Hebbar · A. Butz
Fraunhofer Institute for Mechanics of Materials IWM, Wöhlerstraße 11, 79108 Freiburg, Germany
e-mail: lukas.kertsch@iwm.fraunhofer.de

© The Minerals, Metals & Materials Society 2021

G. Daehn et al. (eds.), *Forming the Future*, The Minerals, Metals & Materials Series,
https://doi.org/10.1007/978-3-030-75381-8_78

being used to replace conventional steel materials to significantly reduce vehicle weight [3, 4].

Currently, precipitation-hardenable alloys of the 7xxx series are increasingly used in the automotive industry, especially EN AW-7020 and EN AW-7075. Different production routes have already been researched in the field of processing semi-finished sheet metal products. However, a breakthrough across industries has been slowed down so far due to the complex tool and system requirements. Especially the use of high-strength aluminum profiles and tubes for the production of complex-shaped components with cross-sections ranging from single-chamber profiles with constant wall thicknesses to multi-chamber profiles with different wall thicknesses and with various flanges is currently a challenge in terms of forming technology due to the limited formability of these semi-finished products.

Temperature-supported processes can be used to significantly increase the forming capacity of high strength, precipitation-hardenable 7xxx series aluminum alloys [5, 6]. In particular, the processes of forming in solution-annealed, quenched and naturally aged state, the so-called W-temper forming [7–10], as well as forming under quenching conditions, the so-called Hot Form Quenching (HFQ®) [11, 12] are subjects of current research and scientific discussion (see Fig. 1) [13]. Both process variations are based on heat treatment in order to distribute the precipitated alloying elements, which are responsible for the high strength, homogeneously in the microstructure by solution annealing and thus to improve the forming behavior. The challenge with Hot Form Quenching® or hot stamping is that the forming process is carried out with a component heated to approximately 500 °C, which requires expensive cooled and temperature-wear resistant tools, heat-resistant lubricants, and extraction equipment [14]. In the case of W-temper forming, which is the focus of this study, the semi-finished product is quenched after heating up to solution annealing temperature. This significantly increases the forming capacity for a short amount of time, which leads to very high possible degrees of deformation in the subsequent cold forming process [9, 13]. At the same time, the advantages of a typical cold forming process, such as the wide range of applicable lubricants and the simpler

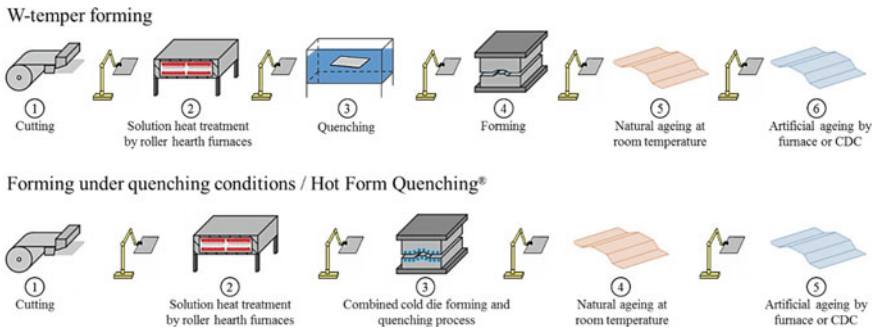


Fig. 1 Process routes for W-temper forming and forming under quenching conditions, the so-called Hot Form Quenching®, according to Ref. [3]. (Color figure online)

tool design, can be used. After forming, the components are cured either over time (natural aging) or in a temperature-supported process (artificial aging). During this process, fine particles are precipitated in the material structure, which has a significant strength-increasing effect [15].

During the solution heat treatment, all soluble precipitate phases dissolve and their constituent elements distribute within the aluminum matrix. In order to provide the potential for the formation of hardening precipitates, the cooling has to be performed at a critical rate or faster to avoid detrimental quench-induced precipitation [16, 17]. From the supersaturated solid solution, the most important precipitation sequence in 7xxx series aluminum alloys involves Mg and Zn-rich phases [18]. Already at room temperature, Guinier–Preston (GP) zones, i.e., Al, Zn, and Mg-rich clusters can form. During typical artificial aging treatments the metastable phase η' with the approximate chemical composition $MgZn_2$ forms. These precipitates are most efficient for hardening. During over-aging or at elevated temperatures, the stable phase η ($MgZn_2$) can form. This is not desirable because these precipitates are less effective for hardening. Further stable phases may precipitate, too, but they are of minor relevance under realistic process conditions [18]. Furthermore, various intermetallic phases are typically present [19]. Although they may have negative effects on the mechanical properties, they usually already form during solidification and cannot be dissolved below the solidus temperature.

Currently, chamber or roller hearth furnaces are commonly used to heat the semi-finished products to approximately 500 °C. These heating concepts work according to the thermal radiation and convection principle and, therefore, transfer the heat to the workpiece very slowly [20]. In addition to the large space requirements of such plants, the heating process is also disadvantageous from an economic point of view. With contact heating, for example, heating times can be reduced by up to 90% compared to conventional furnace heating. However, despite the obvious economic potential, contact heating is currently not used on the W-temper route.

2 Objective

Within this study, the development and construction of a unit for contact heating and contact cooling of sheet metal blanks made of precipitation-hardenable aluminum alloys is presented (see Fig. 2).

Heating and quenching routes are to be identified, which are suitable for setting material states for improved cold forming processes. It is essential that high-strength states comparable to the initial state are achieved even after subsequent aging treatment. The industrial transferability of W-temper forming is to be demonstrated in a meaningful demonstrator scale. To this end, the Fraunhofer Institute for Mechanics of Materials IWM identifies relevant process windows for practical application in extensive material investigations. Based on the temperatures, heating and cooling rates, and holding times that have to be achieved, a tool concept for W-temper forming is

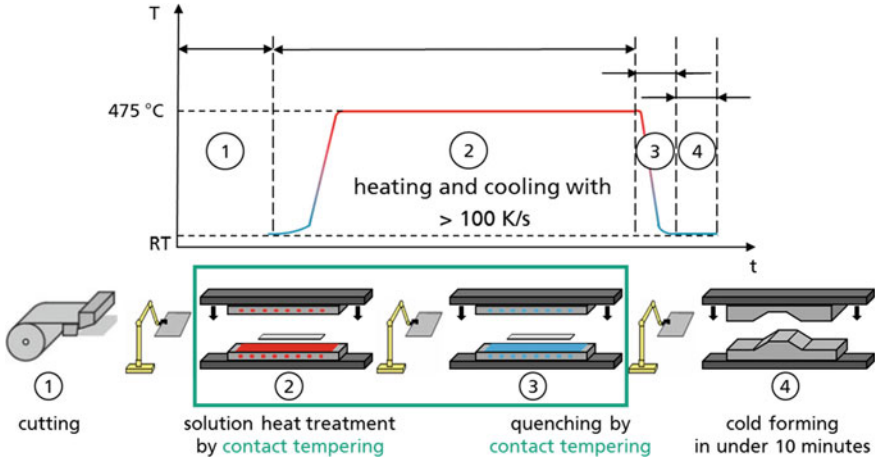


Fig. 2 Process sequence for the processing of heat treatable aluminum alloys by contact tempering. (Color figure online)

developed and tested at the Fraunhofer Institute for Machine Tools and Forming Technology IWU. The results of this study show which heat treatment routes can be used to improve the microstructural properties of the alloys EN AW-7020 and EN AW-7075 for subsequent cold forming by means of contact tempering and demonstrate the potential of contact tempering for industrial applications.

3 Material Characterization and Process Parameter Identification

To define feasible process windows for the W-temper forming of the two Mg-Zn aluminum alloys, sheets of 2.0 mm thickness in a T6 temper state were tested. The alloy EN AW-7020 is practically copper-free, whereas the alloy EN AW-7075 contains a significant amount of Cu and also a higher content of Zn and Mg. The chemical compositions are given in Table 1.

For both alloys, differential scanning calorimetry (DSC) measurements were done using a Netzsch Pegasus 404 °C at various heating and cooling rates. The DSC signals are shown in Fig. 3. In the displayed diagrams, endothermic reactions like the dissolution of a precipitate phase cause upward peaks, whereas exothermic reactions

Table 1 Chemical composition of the analyzed alloys in mass percent

Alloy	Al	Zn	Mg	Cu	Fe	Si	Mn	Cr	Zr	Ti
EN AW-7020	Bal.	4.92	1.27	0.06	0.13	0.05	0.15	0.10	0.09	0.02
EN AW-7075	Bal.	7.26	2.92	1.72	0.11	0.08	0.03	0.19	0.04	0.04

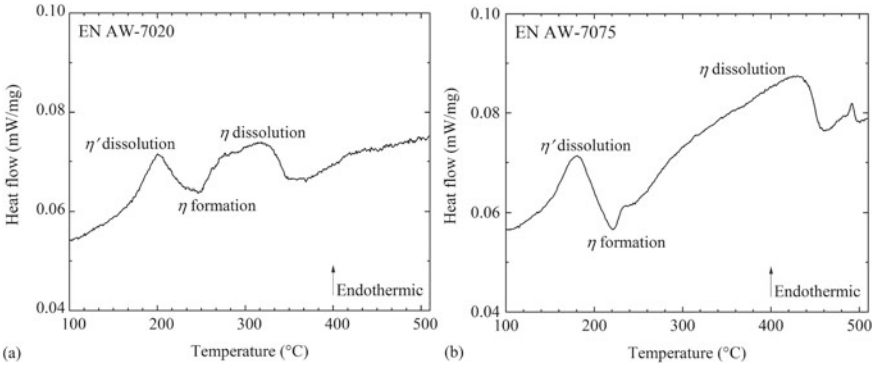


Fig. 3 DSC signals of the alloys **a** EN AW-7020. **b** EN AW-7075 during heating at the rate of 5 K/min

like the formation of a new phase cause downward peaks. By this, the temperature ranges within which precipitate phases are stable as well as suitable heat treatment temperatures can be identified. It has to be taken into account that the reaction temperatures during heating may be slightly overestimated. From the DSC curves, 480 °C was identified as a suitable solution heat treatment temperature for both alloys. Besides, two candidate retrogression temperatures were identified for the alloy EN AW-7020. Already at the relatively low temperature of 225 °C, it can be assumed that all hardening η' precipitates are dissolved, but with the risk of forming undesired equilibrium precipitates, mainly η, during the retrogression heat treatment. At a higher temperature of 360 °C, all Mg–Zn precipitates including η should be dissolved. For the alloy EN AW-7075, too, the lower temperature of 225 °C is a candidate retrogression temperature for the same reason. However, since the dissolution of equilibrium precipitate phases is only completed above 450 °C in this alloy, there is no direct counterpart for the higher retrogression temperature as found for the alloy EN AW-7020. Therefore, several elevated retrogression temperatures for EN AW-7020 between 300 °C and 400 °C were chosen.

To simulate the inline W-temper process, the heat treatments and the subsequent characterization by tensile tests were carried out in the thermo-mechanical simulator Gleeble 3150 using standard tensile test specimens. This makes it possible to heat, quench, and deform without unnecessary interruption due to changing the testing device. In the Gleeble, the specimens are heated by resistance heating. The temperature is controlled with a thermocouple in the specimen center while the jaws are water-cooled resulting in an inhomogeneous temperature along with the specimen. Consequently, only the center region of the specimens, which actually undergoes the simulated process, is further considered. A heating rate of 20 K/s was selected for all heat treatments. Quenching after the heat treatment was done with compressed air. The critical quenching rate to suppress precipitation during cooling is 3 K/s in the temperature range between approximately 320 °C and 180 °C for the alloy EN

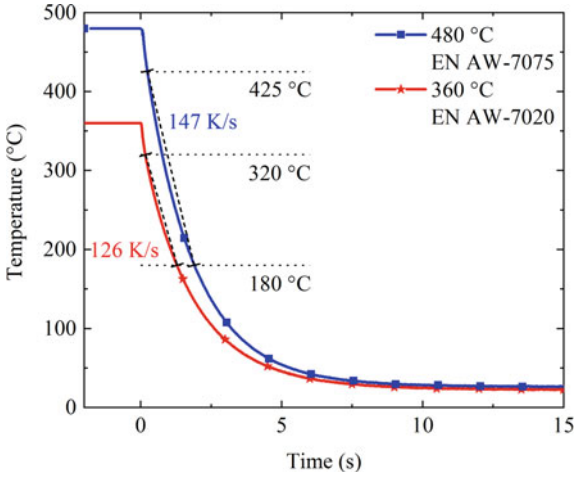


Fig. 4 Temperature over time during air quenching from different temperatures in the Gleeble 3150 and average cooling rates achieved in the critical temperature ranges for the alloys EN AW-7020 and EN AW-7075. (Color figure online)

AW-7020 [17] and 100 K/s between 425 °C and 180 °C for the alloy EN AW-7075 [16].

These critical temperature ranges reported in the literature are consistent with the temperature ranges where the stable precipitates were present in the DSC experiments: The upper limits coincide with the temperatures at the maxima of the respective η dissolution peaks of both alloys taking into account that they are shifted to slightly lower values due to the fast cooling. Below 180 °C, however, the formation of η' is more likely. Figure 4 shows the temperature over time during air quenching in the Gleeble leading to an average cooling rate of 147 K/s between 425 °C and 180 °C as well as 126 K/s between 320 °C and 180 °C. This is faster than the critical rates reported in the literature and should therefore be sufficient to avoid quench-induced precipitation. Various holding times at the solution heat treatment temperature of 480 °C followed by air quenching were tested for the alloy EN AW-7020. The hardness decreased from 121 HV in the as-received state to 56 HV after only 5 s and further to 50 HV after 30 s while it did not significantly change at longer holding times. Therefore, a holding time of 30 s was chosen for all further heat treatments. The suitability of the various selected heat treatment temperatures was evaluated based on the hardness and ductility after quenching as well as on the gain in hardness during the subsequent artificial aging in a furnace at 120 °C. The stress–strain curves of the tensile tests are shown in Fig. 5. For the alloy EN AW-7020, the yield stress could be reduced from 319 MPa in the as-received state to the value of 76 MPa after both solution heat treatment at 480 °C and retrogression heat treatment at 360 °C. The maximum elongation increased significantly and also the strain hardening increased. However, the strain at fracture and ultimate tensile strength could not be quantified after the heat treatments, because the specimens broke outside the gauge length due to the inhomogeneous temperature distribution in the Gleeble heat treatments. For the alloy EN AW-7075, the yield stress dropped from 530 to 160 MPa after the solution heat treatment at 480 °C. Further tests on the alloy EN AW-7075 after solution heat

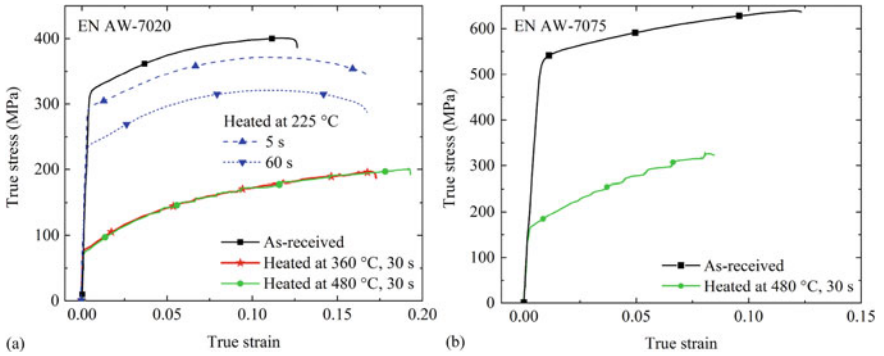


Fig. 5 True stress–strain diagrams of (**a**) EN AW-7020 (as-received, solution heat treated at 480 °C, and retrogression heat treated at 225 °C and 360 °C). **b** EN AW-7075 (as-received and solution heat treated at 480 °C), strain rate is 0.1 s^{-1}. Note that all specimens heat treated at 360 °C and 480 °C broke outside the gauge length. (Color figure online)

treatment in a furnace as well as published experiments [21] suggest that the elongation at fracture is 18–20% for both alloys. The heat treatment at 225 °C, even with longer holding times, results in poor ductility as shown for the alloy EN AW-7020. Therefore this temperature is not further considered. With increasing softening after the heat treatment, the specimens exhibit an increasingly serrated flow behavior due to the Portevin–Le Châtelier (PLC) effect, which might affect the surface quality of formed parts.

Figure 6 shows the hardness evolution during artificial aging. For both alloys, the hardness of the as-received T6 temper could be restored after solution heat treatment and subsequent aging. Besides, a retrogression heat treatment at 360 °C and re-aging led to a very similar behavior for the alloy EN AW-7020 such that this is an interesting

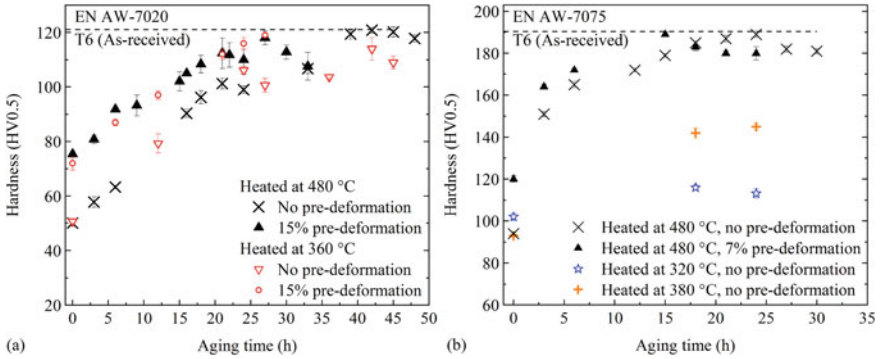


Fig. 6 Hardness evolution during artificial aging at 120 °C in the alloys **a** EN AW-7020 (as-received, solution heat treated at 480 °C, and retrogression heat treated at 360 °C**). b** EN AW-7075 (as-received, solution heat treated at 480 °C, and retrogression heat treated at 320 °C and 380 °C) without and with pre-deformation. (Color figure online)

alternative to the solution heat treatment at a higher temperature. For the alloy EN AW-7075, the solution heat treatment at 480 °C is the only feasible option because the retrogression heat treatments at all investigated temperatures resulted in poor re-aging performance. In addition, the effect of a tensile deformation subsequent to quenching and before aging was studied. As can be seen in Fig. 6, in all considered cases similar peak hardness values as without pre-deformation were achieved. The time to peak hardness, however, was significantly reduced due to the pre-deformation and the rate of hardness loss in the over-aging regime was increased.

Overall, the results can be summarized as follows: For both tested materials, a solution heat treatment at 480 °C followed by quenching at a rate of 147 K/s between 425 °C and 180 °C is suitable to significantly reduce the yield stress and increase the ductility as well as to restore the as-received T6 hardness by artificial aging. For the alloy EN AW-7020, a retrogression heat treatment at 360 °C followed by quenching at a rate of 126 K/s between 320 °C and 180 °C and re-aging leads to very similar results and is, therefore, an interesting alternative. However, for the alloy EN AW-7075 the retrogression heat treatments at all investigated temperatures result in poor material properties and are therefore not suitable for practical applications. A plastic deformation between quenching and aging reduces the time to peak hardness.

4 Tool Design and Experimental Setup

Based on the identified requirements regarding heat treatment temperatures and the required quenching rates, a transfer tool was developed in which sheet metal blanks can first be heated to the target temperature by contact tempering and then be quenched in a second contact tempering tool to set the W-temper state. In the third stage, the heat-treated sheets are then to be cold formed. An electrical heating concept with a total output of 2400 W was used to temper the heating stage. In the heating stage, surface pressures of up to 4.5 MPa can be set for a blank size of 300 × 300 mm. This surface pressure is necessary to ensure sufficient heat transfer. Significantly higher surface pressures could result in the sheet being deformed already during heating. In the quenching tool, the surface pressure is set via the closing force of the press. Investigations by Merklein et al. [14] showed that significantly higher cooling rates can be achieved by increasing the surface pressure during cooling. Saturation of the maximum achievable heat transfer coefficient was achieved at a surface pressure of approx. 30 MPa. Taking into account the sample size used, a press closing force of 2700 kN was set accordingly in the cooling stage. To ensure the highest possible cooling rates, the cooling plates are continuously water-cooled to approximately 20 °C.

Plates with a wall thickness of 2.0 mm are used. In order to determine the heating and cooling rates, a sheet metal plate was fitted with five thermocouples on the front and back. These are each installed in a groove and in different sheet areas. They are located both directly above and between the heating elements and both at the edge and in the center of the sheet (see Fig. 7).

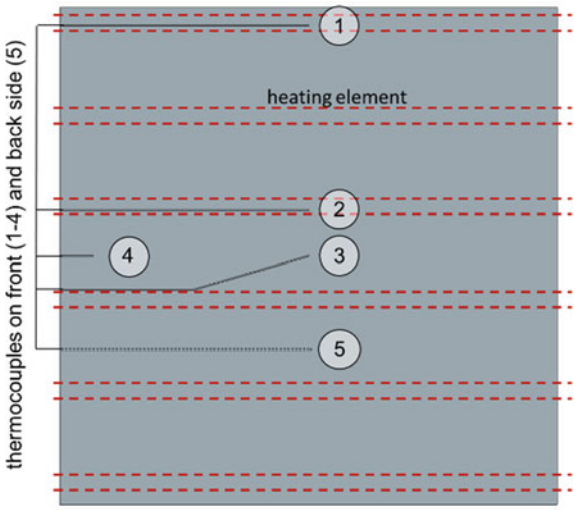


Fig. 7 Arrangement of the thermocouples (type K) in the testing sheet. The position of the heating elements is marked with red dotted lines. (Color figure online)

5 Results of Technological Tests

In order to validate the developed contact heating tool for an industrial application, heating and cooling tests were carried out with the previously prepared test plate (see Fig. 7). First of all, it was investigated how much faster the heating is compared to furnace heating and further whether the critical cooling rates for setting the W-temper state can be achieved by contact cooling. For this purpose, the heating tool was first heated up to 360 °C. A higher tool temperature would result in faster heating of the sheet metal samples due to the higher temperature difference. Figure 8 shows the heating curve of the sheet metal in the tool. The curve represents the averaged

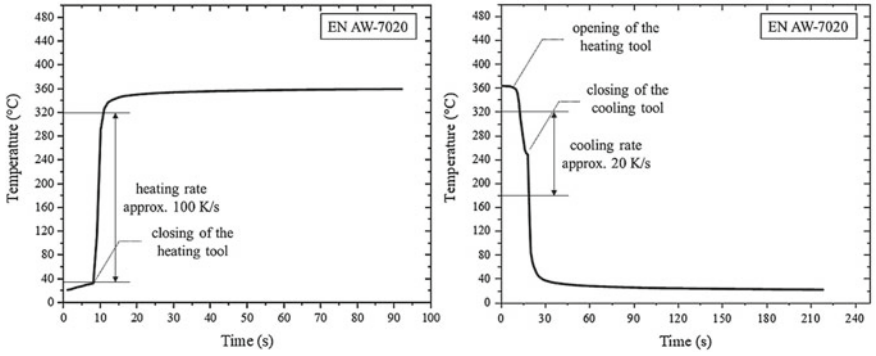


Fig. 8 Temperature profile for heating (left) and cooling (right) of the sheets (EN AW-7020) by contact tempering. Heating tool with a temperature of 360 °C and cooling tool with a temperature of about 20 °C

course of the five recorded thermocouple curves. The deviation of the measured temperatures was in the range of 5 K, which proves the homogeneous temperature distribution within the sheet. Despite the different thermocouple positions, no significant temperature differences were found in the sheet metal, which proves the homogeneous heating of the specimen. From room temperature to 320 °C a heating rate of approx. 100 K/s is achieved. In order to exclude an influence of the heating rate on the material condition, the heating rates determined in the experiment are to be transferred in further Gleeble experiments. To reach 360 °C, considerably more time is required. If the holding time had no influence on the set material condition, the tool could be tempered higher in order to shorten the heating time even further. However, the higher the tool temperature is above the target temperature, the hotter the sheets become, which could be relevant if critical holding times have to be observed. Reference [15] shows that for EN AW-7020, a holding time of only 1 min is sufficient to achieve significantly improved forming properties after subsequent cooling. Increasing the holding time does not improve the material properties. Similar investigations were carried out in Ref. [22] for the alloy EN AW-7075. In this case, too, the holding time could be reduced to 1 min without risking a deterioration of the material properties after cooling and subsequent aging treatment. The results presented in this study confirm these impressions and show that even a holding time of only 30 s is sufficient to both reduce the yield stress and to achieve sufficient strength after artificial aging.

Both in the preliminary investigations and the literature, it became clear that above all the critical cooling rates must be achieved. To determine the actual cooling rates, the heated sheet metal was transferred from the heating stage to the cooling stage. As Fig. 8 shows, significant cooling was already determined by placing the sheet in the lower part of the tool. After closing the tool and applying the closing force of 2700 kN, which equals a surface pressure of 30 MPa, the sheets cooled down rapidly to room temperature. In the test with the contact cooling tool, an average cooling rate of approx. 22 K/s in the temperature range between 320 °C and 180 °C was achieved if an initial temperature of about 360 °C was set. This means that the cooling is much faster than the critical cooling rate of 3 K/s for EN AW-7020 defined in Ref. [17]. The results have shown that by means of contact heating and cooling, the samples can not only be quickly heated to the target temperature of 360 °C but also quickly cooled back to room temperature. Based on the results of the previous Gleeble trials, this allows the inline heat treatment of EN AW-7020 to be carried out exceedingly efficiently on an industrial scale.

In the second series of tests (see Fig. 9), the heating tool was heated up to 480 °C. From the moment the sheet was inserted into the contact heating tool up to 420 °C an average heating rate of approximately 100 K/s was achieved (see Fig. 9). As in the heating tests to 360 °C, the heating time to the target temperature of 480 °C could be significantly reduced by a higher mold temperature. After heating, the sample was transferred to the cooling tool. The sheet metal was already cooled down to about 430 °C by the transfer and placement in the tool (see Fig. 9). The cooling rate is significantly increased by closing the tool. In the critical temperature range from 420 °C to 180 °C, an average cooling rate of approx. 145 K/s is achieved. Thus, the

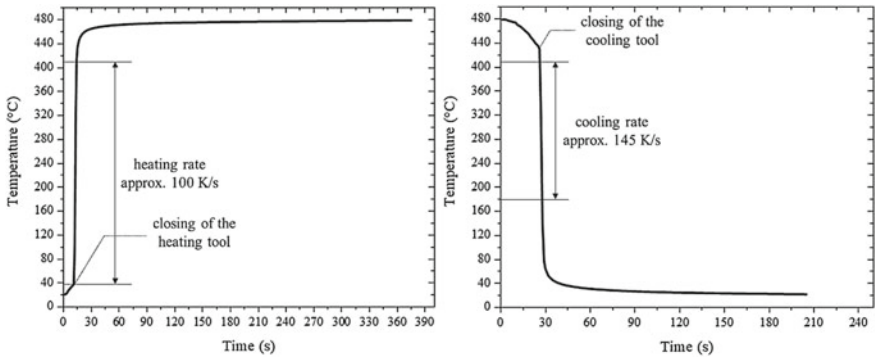


Fig. 9 Temperature profile for heating (left) and cooling (right) of the sheets by contact tempering. Heating tool with a temperature of 480 °C, and cooling tool with a temperature of about 20 °C

cooling rate in the critical temperature range is significantly higher than described in Ref. [15]. Also with reference to the Gleeble tests carried out, it should be possible to set an optimum W-temper condition for a subsequent cold forming process.

As already mentioned, higher tool temperatures and thus higher temperature differences between tool and sheet could significantly increase the heating rates. Lower holding times mean that the heating-up times and thus the cycle times in industrial applications for contact heating can be significantly reduced once again, which increases the efficiency of the entire process chain of W-temper forming by the use of contact tempering. Exemplary heating tests of the same samples as used for the contact tempering trials in a chamber furnace heated to the target temperature have shown that the heating process takes about eight times longer (see Fig. 10).

6 Summary and Conclusions

Within the study, the immense potential of contact tempering was demonstrated and an approach for industrial application was presented. Contact heating and contact cooling could adjust the W-temper state necessary for cold forming of the aluminum alloys EN AW-7020 and EN AW-7075. Gleeble tests have shown that for both EN AW-7020 and EN AW-7075, a solution heat treatment at 480 °C and subsequent quenching is appropriate to obtain sufficient formability and to arrive at similar hardness after aging as in the as-received T6 temper. In addition, for EN AW-7020, heating to 360 °C and subsequent cooling is sufficient to achieve significantly improved forming properties without deteriorating material properties after aging. Further investigations to reduce the holding times are planned. It is also necessary to find out whether the heat treatment parameters determined for the material in the T6 temper and the tool technology developed are also suitable for the use of semi-finished products in the T4 condition. As a next step, a forming tool will be

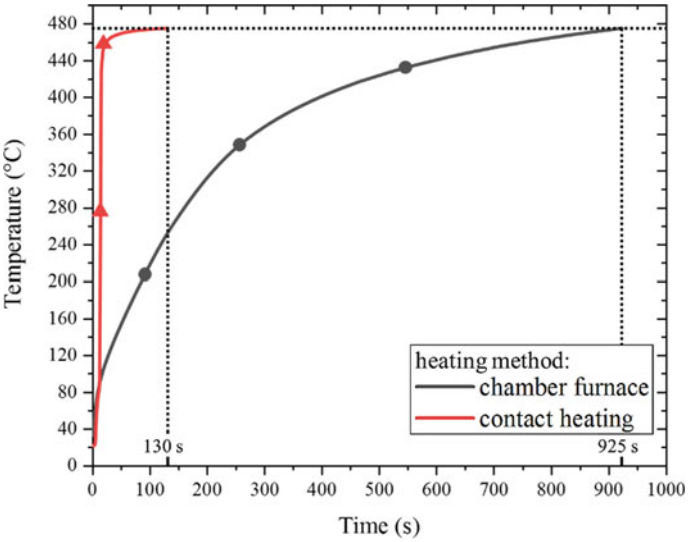


Fig. 10 Comparison between temperature profiles of 2.0 mm sheet material heated by chamber furnace and contact heating. (Color figure online)

developed to produce a demonstrator component after the cooling stage. Furthermore, the tempering concept will be adapted to the use of tubes and hollow profiles.

References

1. Psyk V et al (2015) Structuring by electromagnetic forming and by forming with an elastomer punch as a tool for component optimisation regarding mechanical stiffness and acoustic performance. Manufacturing Rev 2:23
2. Psyk V, Scheffler C, Linnemann M, Landgrebe D (2017) Process analysis for magnetic pulse welding of similar and dissimilar material sheet metal joints. Procedia Eng 207:353–358
3. B-A Behrens, S Hübner, H Vogt (2018) Formability of 7000 aluminum alloys in warm and hot forming condition. IOP Conf Ser: Mater Sci Eng 418:12027
4. J Schlosser et al (2017) Materials and simulation modelling of a crash-beam performance—A comparison study showing the potential for weight saving using warm-formed ultra-high strength aluminium alloys. J Phys: Conf Ser 896:12091
5. B-A Behrens et al (2019) Prozesse zur Umformung von höchstfesten Aluminiumlegierungen der 7xxx-Reihe. EFB-Kolloquium Blechverarbeitung 2019, pp 171–185
6. F Ostermann (2014) Anwendungstechnologie Aluminium. Springer, Berlin
7. T Grohmann (2016) Forming of AMAG 7xxx series aluminium sheet alloys. New developments in sheet metal forming - Hydroforming of sheets, tubes and profiles: international conference in Fellbach, May 10th–11th, Inventum, 2016
8. M Heckmann, D Gernhardt, A Birkert, K Baier (2019) Presswerkseitige Einbringung von Funktionselementen in hochfeste AA7xxx-Aluminiumbauteile. EFB-Kolloquium Blechverarbeitung 2019, pp 143–155
9. Sáenz de Argandoña E, Galdos L, Ortubay R, Mendiguren J, Agirretxe X (2015) Room temperature forming of AA7075 aluminum alloys: W-temper process. KEM 651–653:199–204

10. J Mendiguren, E S de Argandona, L Galdos (2016) Hot stamping of AA7075 aluminum sheets. IOP Conf Ser: Mater Sci Eng 159:012026
11. J Lin, T Dean, R Garrett, A Foster (2008) Process for forming metal alloy sheet components. WO2008/059242A2, Great Britain, 22 May 2008
12. A Foster, T Dean, J Lin (2010) Process for forming aluminium alloy sheet components. WO 2010/032002 Al, Great Britain
13. Kumar M, Kirov G, Grabner F, Mukeli E (2016) Sheet forming processes for AW-7xxx alloys: Relevant process parameters. MSF 879:1036–1042
14. M Merklein, J Degner (2018) Fertigung hochfester Aluminiumbauteile durch Umformen unter Abschreckbedingungen. Europäische Forschungsgesellschaft für Blechverarbeitung, Hannover, EFB-Forschungsbericht EFB-493
15. B-A Behrens et al (2018) Warmumformung von 7xxx-Aluminiumlegierungen. EFB-Forschungsbericht 501
16. Milkereit B et al (2018) Dissolution and precipitation behavior for hot forming of 7021 and 7075 aluminum alloys. Metals 8(7):531
17. Zhang Y, Milkereit B, Kessler O, Schick C, Rometsch PA (2014) Development of continuous cooling precipitation diagrams for aluminium alloys AA7150 and AA7020. J Alloy Compd 584:581–589
18. Löffler H, Kovacs I, Lendvai J (1983) Decomposition processes in Al-Zn-Mg alloys. J Mater Sci 18:2215–2240
19. Andreatta F, Lohrengel MM, Terryn H, de Wit JHW (2003) Electrochemical characterisation of aluminium AA7075-T6 and solution heat treated AA7075 using a micro-capillary cell. Electrochim Acta 48(20–22):3239–3247
20. V Ploshkhin et al (2011) New heating technology for the furnace-free press hardening process. In IDDRG—Tools and technologies for processing ultra high strength materials, pp 191–198.
21. Kumar M (2017) AW-7075-T6 sheet for shock heat treatment forming process. Trans Nonferrous Metals Soc China 27(10):2156–2162
22. N Unger (2017) Untersuchung einer thermisch unterstützten Fertigungskette zur Herstellung umgeformter Bauteile aus der höherfesten Aluminiumlegierung EN AW-7020. Dissertation, Friedrich-Alexander-Universität Erlangen-Nürnberg; Meisenbach KG

Calibration and Validation of Stress–Strain Curve in High-Strain Region of Mild Steel Sheet



Hideo Tsutamori, Takeshi Nishiwaki, and Hiroaki Onishi

Abstract Stress–strain curve in the high-strain region is one of the most important models that must be taken into consideration for high-precision sheet metal forming simulation. In this study, using mild steel sheets, tensile tests were conducted with a necked shape specimen at the center in order to generate non-uniform elongation. Using image analysis, strain–load relationships were obtained using multiple gauge lengths, and stress–strain relationships were obtained by inverse analysis using FE simulation. With a sufficiently small gauge length it is possible to get stress–strain curve in the high-strain region. The advantage of this method is that the experiments can be implemented only with a uniaxial tensile test. For validation, the original hole expansion test model that is not affected by friction is proposed. The thickness strain distribution along the hole with large plastic strain is compared with the experimental and numerical results to indicate the validity of this method.

Keywords Stress–strain curve · Inverse analysis · Uniaxial tensile test · Mild steel sheet

1 Introduction

The stress–strain curve is one of the most essential and fundamental properties for numerical simulation of sheet metal forming. The curve is usually obtained by a uniaxial tensile test. It is well known that a stress–strain curve is correct within the uniform elongation. However, in the non-uniform elongation region of the uniaxial tensile test, stress–strain relationship can be obtained but is not correct. Since the cross-sectional area is not constant, the stress after elongation becomes non-uniform, which means the average value within the gauge length. On the other hand, large plastic strain regions are often seen in the formed sheet panels of mechanical or automotive parts, for example, the edge of holes or bending and unbending regions.

H. Tsutamori (✉) · T. Nishiwaki · H. Onishi
Department of Mechanical Engineering, Daido University, 10-3 Takiharu-cho, Minami-ku, Naogoya 457-8530, Japan
e-mail: h-tuta@daido-it.ac.jp

© The Minerals, Metals & Materials Society 2021

G. Daehn et al. (eds.), *Forming the Future*, The Minerals, Metals & Materials Series,
https://doi.org/10.1007/978-3-030-75381-8_79

That effective plastic strain is larger than the ultimate uniform elongation of stress–strain curve. The stress–strain curve in the high-strain region is an important material model for numerical simulation. So far, there are various studies to obtain the stress–strain relationship in the high-strain region. A method of observing the necking during the test using CCD camera has been proposed [1–3], and there is a study of using optimization software to obtain the stress–strain curve in the tensile test of the bar specimens [4]. A plane share test [5] or bending test [6] may be used to obtain the stress–strain curve in the high-strain region. In this paper, we propose a method for obtaining stress–strain curve in the high-strain region of mild steel sheet by inverse analysis using digital image correlation (DIC) system and FE analysis. Furthermore, an evaluation of the curve in the high-strain region was conducted by hole expansion test using the uniaxial tensile test. Since this hole expansion test does not include friction or bending, it was possible to validate the stress–strain curve in the high-strain region by comparison between the experimental and numerical analysis.

2 Model of Stress–Strain Curve in the High-Strain Region

Before extending a stress–strain curve in the high-strain region, it is necessary to obtain an s–s curve in the uniform elongation range. This is the base s–s curve up to the true strain ε_{ext} at the extension point. In this study, mild steel sheets were used, and ε_{ext} was set to 0.2. Next, upper and lower limit curves are prepared expediently. The upper limit curve uses the Swift hardening model [7] of Eq. (1). The lower limit curve employs the Voce hardening model [8] of Eq. (2). In these equations, σ is a true stress, ε_p is an effective plastic strain, ε_0 is constant, and F, n, σ_0, σ_∞, and D are positive constants.

$$\sigma_{sw} = F\left(\varepsilon_0 + \varepsilon_p\right)^n \tag{1}$$

$$\sigma_{vo} = \sigma_\infty + (\sigma_0 - \sigma_\infty)e^{-D\varepsilon_p} \tag{2}$$

The plastic strain ε_{cnc} ($<\varepsilon_{\text{ext}}$) which is a connection point on the base s–s curve is determined. The base curve, the upper limit curve, and the lower limit curve are smoothly connected at the connection point. In this study, it was set to 0.05. The true stress at the connection point is defined as σ_{cnc}, and the following equations are obtained from the connection conditions at the point (ε_{cnc}, σ_{cnc}) on the base s–s curve.

$$\sigma_{\text{cnc}} = F(\varepsilon_0 + \varepsilon_{\text{cnc}})^n \tag{3}$$

$$\sigma_{\text{cnc}} = \sigma_\infty + (\sigma_0 - \sigma_\infty)e^{-D\varepsilon_{\text{cnc}}} \tag{4}$$

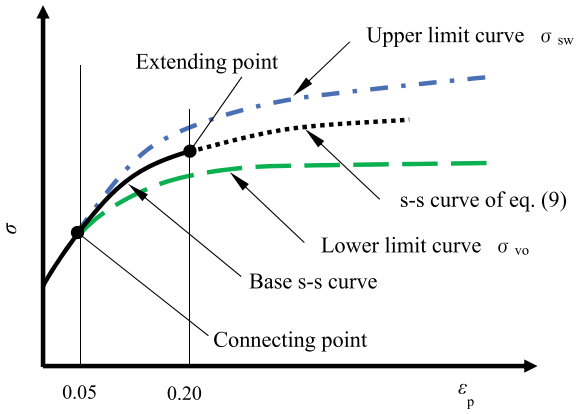


Fig. 1 Model of s–s curve in the high-strain region. (Color figure online)

The following equations are also obtained from the tangent continuous condition:

$$\frac{\mathrm{d}\sigma}{\mathrm{d}\varepsilon_p} = nF(\varepsilon_0 + \varepsilon_{\mathrm{cnc}})^{n-1} \tag{5}$$

$$\frac{\mathrm{d}\sigma}{\mathrm{d}\varepsilon_p} = -D(\sigma_0 - \sigma_\infty)\mathrm{e}^{-D\varepsilon_{\mathrm{cnc}}} \tag{6}$$

The value of $\mathrm{d}\sigma/\mathrm{d}\varepsilon_p$ is given by the base s–s curve. Equation (7) is obtained by the second derivative continuous condition between Eqs. (1) and (2) at the connection point. Equation (8) is obtained by the assumption that the stress value is the average between the upper and the lower limit curves at the extending point. The constants ε_0, F, n, σ_0, σ_∞, and D are obtained by solving the six equations from (3) to (8). Figure 1 shows the above-described curves and the connection and the extending points.

$$\frac{\mathrm{d}^2\sigma}{\mathrm{d}{\varepsilon_p}^2} = n(n-1)(\varepsilon_0 + \varepsilon_{\mathrm{cnc}})^{n-2} = D^2(\sigma_0 - \sigma_\infty)\mathrm{e}^{-D\varepsilon_{\mathrm{cnc}}} \tag{7}$$

$$\sigma_{\mathrm{ext}} = \frac{F(\varepsilon_0 + \varepsilon_{\mathrm{ext}})^n + \left\{\sigma_\infty + (\sigma_0 - \sigma_\infty)e^{-D\varepsilon_{\mathrm{ext}}}\right\}}{2} \tag{8}$$

Further, in Eq. (9), the extension curve is defined by linear interpolation of the upper limit curve σ_{sw} of Eq. (1) and the lower limit curve σ_{vo} of Eq. (2).

$$\sigma = \left(1 - t\left(\varepsilon_p\right)\right)\sigma_{vo} + t\left(\varepsilon_p\right)\sigma_{sw} \tag{9}$$

$t\left(\varepsilon_p\right)$ in Eq. (9) is a function of the effective plastic strain and represented by Eq. (10).

$$t\left(\varepsilon_p\right) = 0.5 + a\left(\varepsilon_p - \varepsilon_{\mathrm{ext}}\right) + b\left\{e^{-c\left(\varepsilon_p - \varepsilon_{\mathrm{ext}}\right)} - 1\right\} \tag{10}$$

Here, $0 \leqq t(\varepsilon_p) \leqq 1$; a, b, and c, are constants. $t(\varepsilon_p)$ is assumed as a linear combination of constant 0.5, a term proportional to the effective plastic strain and a term that decreases exponentially with respect to the effective plastic strain. How to get the value of variables a, b, and c is shown in Sect. 6.

3 Uniaxial Tensile Test

The uniaxial tensile tests were conducted using two geometrical types of specimen. Figure 2 shows the geometries of the specimen. Type A is a specimen that meets the Japanese uniaxial tensile test standard with 25×60 mm straight width and length. This was used for the purpose of measuring the base s–s curve within uniform elongation and identifying anisotropic parameters. Tensile tests were carried out in three directions with respect to the rolling direction, and the repetition number was three for each direction. These mechanical properties are shown in Table 1.

On the other hand, the type B specimen has an arc shape on both sides. This is deformed non-uniformly from the beginning of the tensile test. These are used to

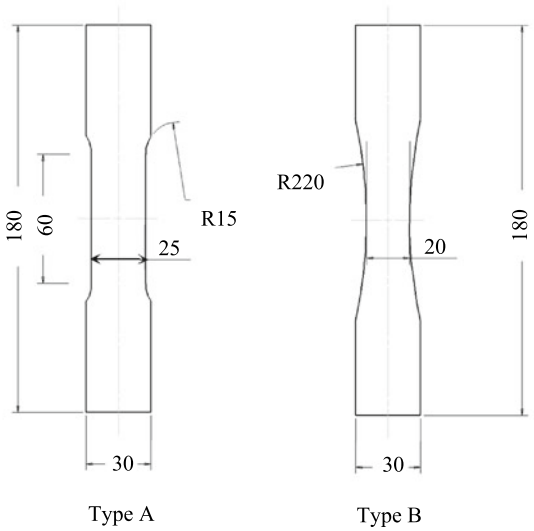


Fig. 2 Geometries of the specimen for uniaxial tensile test

Table 1 Material mechanical properties

Tensile direction/°	YS/(MPa)	TS/(MPa)	n	r value ($\varepsilon_p = 0.2$)
0	199.9	320.2	0.20	1.67
45	205.7	327.7	0.19	1.36
90	202.0	318.3	0.20	2.12

Table 2 Equi-biaxial stress and strain increment

Normalized stress ($\varepsilon^p = 0.2$)	Strain increment ratio ($r_b = \mathrm{d}\varepsilon_y / d\varepsilon_x$) ($\varepsilon^p = 0.2$)
1.038	1.010

Table 3 Anisotropic parameters of YLD2000-2D

α1	α2	α3	α4	α5	α6	α7	α8	m
0.988	1.111	1.051	0.943	0.956	0.924	1.005	0.945	6

calibrate the s–s curve in the high strain region in Sect. 6. The displacements were measured by image analysis, in which the gauge lengths were 2 mm and 5 mm from the center, and the load force was measured by the load cell.

4 Bulge Test

In the high-strain region, even in the uniaxial tensile test, the stress state becomes biaxial stress, and it is important to measure the biaxial stress and employ an appropriate anisotropic yield function. In this study, a hydraulic bulge test was conducted. Table 2 shows the normalized values of the equi-biaxial stress at which the plastic work is equal to the work of 20% plastic strain in the uniaxial tensile test in the rolling direction, and the plastic strain increment ratio at that time.

5 Identification of Yield Function Parameters

In this study, YLD2000-2D [9] was used for the yield function because it can consider equi-biaxial stress state. To calculate the anisotropic parameters, we used flow stresses and r values of the uniaxial tensile tests of 0°, 45°, and 90° in the tensile directions, and the results of the bulge test. The anisotropic parameters α1–α8 were solved by numerical calculation with order m of yield function set to 6. Table 3 shows the results of anisotropic parameters of YLD2000-2D.

6 Calibration of Stress–Strain Curve in the High-Strain Region

Optimization software LS-OPT was used to obtain the s–s curve in the high-strain region. The variables are a, b, and c in Eq. (9). The evaluation functions are the relationship between nominal stress and nominal strain in tensile tests with type

Table 4 Optimization results of variables by LS-OPT

a	*b*	*c*
0.036	−0.378	1.258

B specimen using multiple gauge lengths. The variables are calculated so that the differences between the experiments and the numerical simulation results become minimum by the mean square error method. Table 4 shows the result of variables. Figure 3 shows tensile test using type B specimen. Figure 4 shows the comparison of relationship results between nominal stress and nominal strain with 5 mm of gauge length. For the arc specimens, the nominal stress means the load force divided by the initial section area of the center and nominal strain means the displacement divided

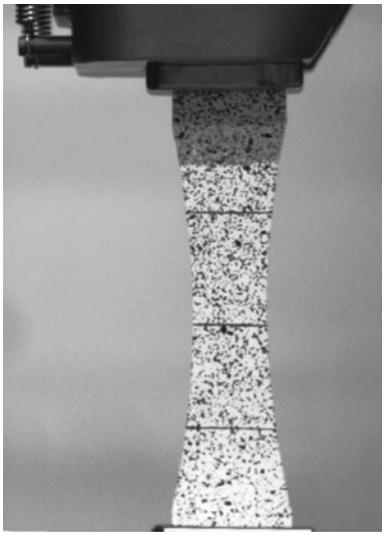


Fig. 3 Experimental photo of type B specimen

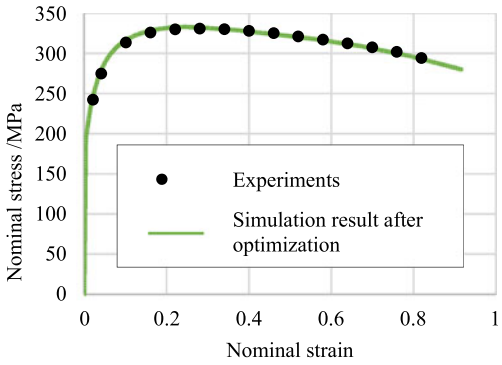


Fig. 4 Comparison result of gauge length 5 mm. (Color figure online)

by the initial length in this study. Dot points are experimental results and solid curve is simulation result after optimization. Figure 5 also shows the same comparison with 2 mm of gauge length. In general, good agreement was obtained although there was some dissociation at a nominal strain of more than 0.6 with a gauge length of 2 mm. Figure 6 shows the s–s curve (true stress-effective plastic strain curve) including the high-strain region by the proposed method.

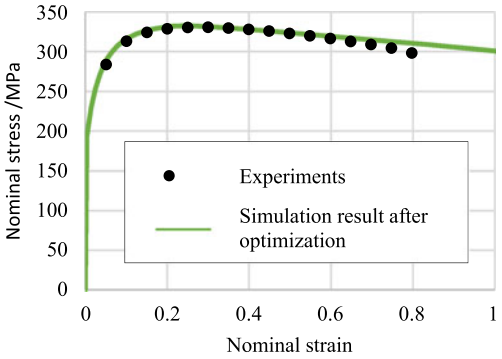


Fig. 5 Comparison result of gauge length 2 mm. (Color figure online)

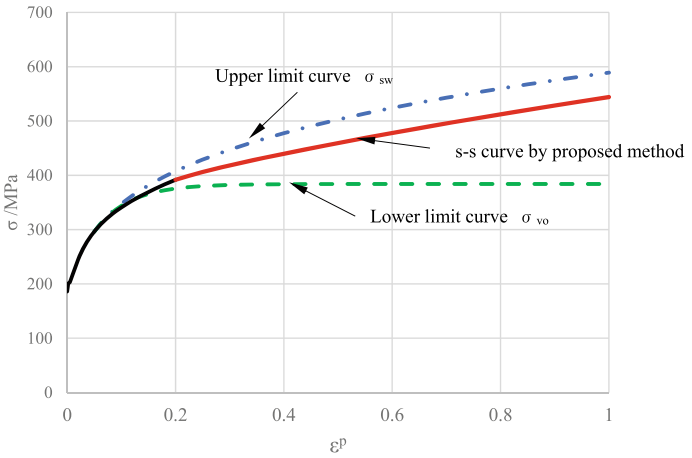


Fig. 6 Stress–strain curve obtained by the proposed method. (Color figure online)

7 Validation of s–s Curve in the High-Strain Region Obtained by the Proposed Method

In order to evaluate the validity of the obtained stress–strain relationship in the high-strain region, a hole expansion test was conducted and the thickness strain distribution along the hole edge was compared. The hole expansion test is often used [10–13] to evaluate the prediction accuracy of the anisotropic yield function. However, it is difficult to separate influences of friction modeling and the Bauschinger effect from the evaluation, since it includes a contact with the dies and bending deformation. Therefore, the original hole expansion test was conducted with a uniaxial tensile tester using a specimen with a notch and a hole in the center as shown in Fig. 7. Accurate evaluation is possible because the proposed method does not need to consider a friction model or bending model. The strain distribution around the hole was measured by the DIC method, and the thickness strain was calculated assuming constant volume during plastic deformation. Figure 8 shows the thickness distribution at 1 mm from the hole edge before the test when the hole diameter is 7.00 mm. The upper and lower limit curves are also shown due to comparison. The proposed method and the experimental results showed good agreement, and the maximum value of the effective plastic strain was 0.29 in this condition. Figure 9 shows a comparison of the thickness distribution when the hole diameter is 7.31 mm. Similarly, the experimental results agreed well with the proposed method. The maximum

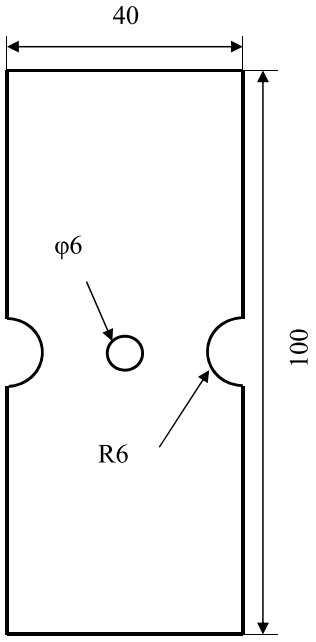


Fig. 7 Geometry of a uniaxial hole deformation test

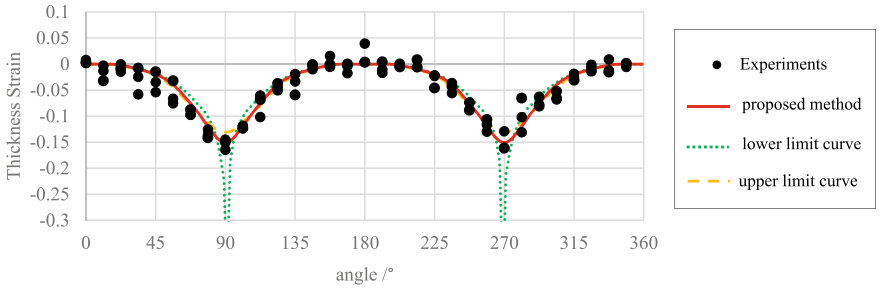


Fig. 8 Comparison of thickness distribution when hole diameter is 7.00 mm. (Color figure online)

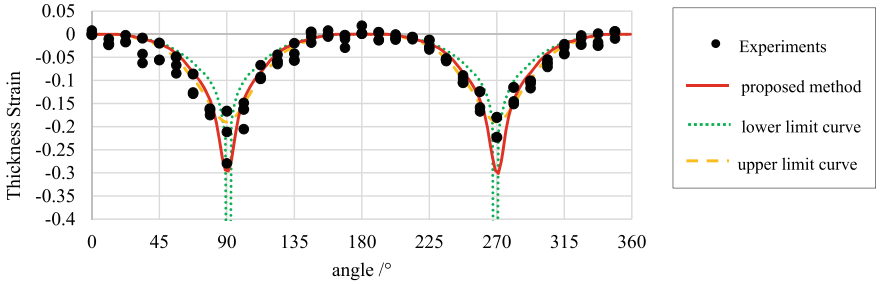


Fig. 9 Comparison of thickness distribution when hole diameter is 7.31 mm. (Color figure online)

value of the effective plastic strain was 0.51. These results revealed the validity of the proposed extending method of the s–s curve.

8 Concluding Remarks

An accurate s–s curve in the high-strain region is one of the important issues for improving the prediction of the sheet metal forming simulation. In this study, we proposed a method to obtain s–s curve in the high-strain region using the uniaxial tensile tester, DIC, and FE simulation. The key messages of this work are summarized as follows:

1. The upper and lower limit curves were defined using the base s–s curve up to uniform elongation, and a s–s curve model in the high-strain region with three variables was proposed.
2. Using the optimization software LS-OPT, three variables were specified, and a s–s curve in the high-strain region was obtained.
3. The hole expansion test which does not include bending or contact with the die was proposed.

4. The validity of the proposed extending method of s–s curve by uniaxial hole expansion test was confirmed.

References

1. Coppieters S, Cooreman S, Sol H, Van Houtte P, Debruyne D (2011) Identification of the post-necking hardening behavior of sheet metal by comparison of the internal and external work in the necking zone. J Mater Process Technol 211:545–552
2. M Vaz Junior, E Lenz Cardoso, P Andres Munoz-Rojas (2012) Further studies on the application of genetic algorithms to identification of inelastic parameters. Proceedings of Material Forming 2012 Congress, 935–938.
3. Yoshida Y, Yukawa N, Ishikawa T (2004) Determination of ductile damage parameters by notched round bar tension test using image analysis. AIP Conf Proc 712:1869–1874
4. Murata M, Yoshida Y, Nishiwaki T (2018) Stress correction method for flow stress identification by tensile test using notched round bar. J Mater Process Technol 251:65–72
5. Sergeboni C, Shrivastava S (1983) Application of the plane simple shear test for determination of the plastic behavior of solid polymers at large strains. J Mater Sci 18:903–918
6. Suzuki T, Okamura K, Capilla G, Hamasaki H, Yoshida F (2018) Effect of anisotropy evolution on circular and oval hole expansion behavior of high-strength steel sheets. Int J Mech Sci 146–147:556–570
7. Swift HW (1952) Plastic instability under plane stresses. J Mech Phys Solids 1:1–18
8. Voce E (1948) The relationship between stress and strain for homogeneous deformation. J Inst Metals 74:537–562
9. Barlat F, Brem JC, Yoon JW, Chung K, Dick RE, Lege DJ, Pourboghrat F, Choi SH, Chu E (2003) Plane stress yield function for aluminum alloy sheets – part 1: theory. Int J Plast 19:1297–1319
10. Iizuka E, Hashimoto K, Kuwabara T (2014) Effects of anisotropic yield functions on the accuracy of forming simulations of hole expansion. Procedia Eng 81:2433–2438
11. Panich S, Uthaisangsuk V, Suranuntchai S, Jirathearanat S (2012) Anisotropic plastic behavior of TRIP 780 steel sheet in hole expansion test. Key Eng Mater 504–506:89–94
12. Kuwabara T, Mori T, Asano M, Hakoyama T, Barlat F (2017) Material modeling of 6016-O and 6016-T4 aluminum alloy sheets and application to hole expansion forming simulation. Int J Plast 93:164–186
13. Kuwabara T, Hashimoto K, Iizuka E, Yoon JW (2011) Effect of anisotropic yield functions on the accuracy of hole expansion simulations. J Mater Process Technol 211:475–481

Influence of the Quenching Rate and Natural Ageing Duration on the Formability and Mechanical Properties of EN AW-7075



B.-A. Behrens, S. Hübner, H. Vogt, O. Golovko, S. Behrens, and F. Nürnberger

Abstract Due to the low density and high tensile strength, the aluminium alloy EN AW-7075 offers a high lightweight potential for structural components. In recent years, 7xxx-aluminium alloys have been the subject of numerous investigations in the field of warm and hot forming and suitable heat treatments to fully use their potential for applications in automotive bodies. Alternatively, forming blanks of these alloys at room temperature in the W-temper state is favourable since conventional tools can be used. However, this condition is unstable. As the ageing duration after quenching increases, the formability decreases due to natural ageing. Hence, the objective of this investigation was to determine the formability of EN AW-7075 as a function of the ageing time. Furthermore, since the quenching rate after solution heat treatment influences the resulting mechanical properties, an adapted process route to manufacture components with tailored properties was explored. For this purpose, samples were partially quenched after solution heat treatment and then artificially aged. To determine the influence of the quenching rate, hardness tests were carried out.

Keywords 7xxx-aluminium alloys · Cold forming · Formability · Tailored tempering

1 Introduction

Nowadays, the most common lightweight material in the automobile industry is aluminium. In car bodies mainly the alloy series 5000 and 6000 are used for structural or shell parts, respectively. However, the highest strength aluminium alloys belong to the 7000 series. These materials have the same specific strength as hot-stamped

B.-A. Behrens · S. Hübner · H. Vogt (✉)
Institut Für Umformtechnik Und Umformmaschinen (Forming Technology and Machines), Leibniz Universität Hannover, An der Universität 2, 30823 Garbsen, Germany
e-mail: vogt@ifum.uni-hannover.de

O. Golovko · S. Behrens · F. Nürnberger
Institut Für Werkstoffkunde (Materials Science), Leibniz Universität Hannover, An der Universität 2, 30823 Garbsen, Germany

© The Minerals, Metals & Materials Society 2021

G. Daehn et al. (eds.), *Forming the Future*, The Minerals, Metals & Materials Series,
https://doi.org/10.1007/978-3-030-75381-8_80

steels and an additional feature of increased elongation at break [1]. In particular, the substitution of hot-stamped steel components by components made of 7000 series aluminium alloys can lead to a significant reduction in body weight. However, these alloys have so far been rarely used in car body construction. The reason for this is the low formability of the materials at room temperature in the highest strength state. Therefore, various approaches are currently being investigated to improve the formability of the alloys.

One approach is the warm forming of the high strength material after quenching and artificial ageing (in T6 condition according to EN 515). The improved formability of this process is based on the dissolution of η' precipitations and dynamic recovery effects at elevated temperatures [2]. Sotirov et al. [1] and Behrens et al. [3] have determined the increased formability for this process route for the alloy EN AW-7075. The influence of the heat treatment condition of the initial material on the formability has also been examined by Kumar et al. [4]. Noder et al. have investigated a process variant for non-isothermal forming [5]. They and Behrens et al. [6] have determined an over-ageing of the aluminium alloys. This is caused by the additional heat treatment for warm forming.

Another approach is the hot forming process route. Therefore, the aluminium blanks are heated to temperatures above the recrystallisation temperature. The sheet material is subsequently transferred into a water-cooled press tool and simultaneously formed and quenched [7]. Argandoña et al. [8] have used this process route to form defect-free B-pillars. However, due to the solution heat treatment process, the formed components have no usable mechanical properties. Therefore, an artificial ageing step must be carried out afterwards. The increase in strength is based on the forming of finely dispersed metastable precipitations [7]. The precipitation sequence determined by Degischer [9] and Löffler [10] describes partially coherent η' precipitations as the main hardening phase for 7000 series aluminium alloys. For the alloy EN AW-7075, Behrens et al. [11] have additionally investigated the influence of the quenching rate on the mechanical properties, which should be chosen according to the copper content of the alloy.

However, warm and hot forming solutions require additional process steps and a complex tooling system in comparison to cold forming processes. Alternatively, the forming of such blanks at room temperature in the W-temper state is favourable since conventional tools can be used. Therefore, in this paper, a cold forming process route is investigated.

2 Cold Forming Process Route

The high strength of the 7000 series aluminium alloys results in a limited formability in T6 condition at room temperature. Therefore, different approaches like the W-temper process are examined to increase the formability. This process is named after the W-temper heat treatment state. This condition is achieved after solution heat treatment and quenching of the material. The alloying elements remain dissolved and

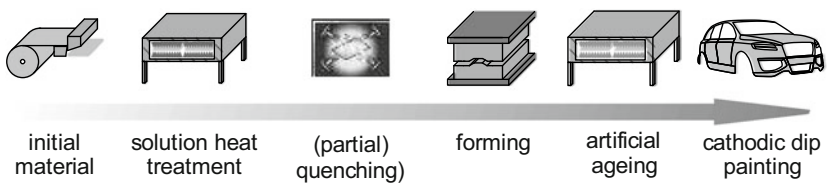


Fig. 1 Cold forming and heat treatment process route for the 7000 series aluminium alloy

a supersaturated state with a high number of solute atoms and vacancies is formed. Due to its high ductility, this heat treatment state allows cold forming. However, the blanks must be formed as soon as possible after quenching; otherwise, the material will age naturally. As a result, the strength of the material increases and thus its formability is reduced. Argandoña [12] investigated the formability of EN AW-7075 at room temperature in the ductile W condition. To set the final mechanical properties of the components, a subsequent heat treatment is necessary [13] which can be a combination of artificial ageing and the cathodic dip painting process, see Fig. 1. An extension of the process route is possible by controlled cooling of the blanks. Since copper-containing alloys of the 7000 series have a sensitivity to the quenching rate, it is possible to produce components with load-optimised tailored properties. For example, a spray field can be used to quench certain areas of the blank rapidly, while the remaining areas cool down slowly [14, 15]. Following artificial ageing, high strengths are achieved in the rapidly quenched areas. In the slowly cooled areas the strength is lower, but the ductility increases.

3 Experimental Setup

For the experimental investigations, the aluminium alloy EN AW-7075 in T6 state was examined. This alloy contains copper and is thus sensible for quench processes [13]. The mechanical properties are listed in Table 1.

Table 1 Investigated aluminium sheet metal material

	Sheet thickness (mm)	Ultimate tensile strength *UTS* (MPa)	Elongation at break *A* (%)	Copper content (wt.%)
EN AW-7075 T6	2.0	569	14.1	1.63

3.1 Formability in W-Temper State

A Nakajima test was carried out to investigate the formability of alloy EN AW-7075 in the W-temper state. This test was used to determine forming limit curves for various heat treatment conditions. Both the influence of the quenching rate and of the natural ageing time between solution heat treatment and the Nakajima test were investigated. For sample preparation, the Nakajima samples were, therefore, first solution heat-treated and then quenched. The solution annealing temperature (T_{SHT}) was 480 °C and was maintained for 10 min (t_{SHT}). For rapid quenching, the blanks were subsequently cooled in a pneumatically operated plate tool. This is shown in Fig. 2 on the left. To ensure uniform cooling of the blanks, the plates of the tool were water-cooled. In addition, and to simulate low cooling rates, the blanks were placed on spacers in the tool to prevent premature cooling. For this slow cooling of the samples, they were cooled down at air. The time–temperature curves for both quenching methods are shown in Fig. 2 on the right. In the pneumatic tool, a quenching rate of 250 K/s is reached in the temperature range of 400 °C–200 °C, at air of 1.11 K/s.

After quenching, the blanks were aged naturally for various times. The ageing duration was varied between 5 min and 30 days after quenching. However, the ageing period was not started until the temperature of the blanks dropped below 50 °C during quenching so that forming at room temperature could be ensured for the samples cooled at air. The different ageing durations were chosen according to the data of Ostermann et al., as shown in Fig. 3. This is based on the increasing hardness of the material with increasing natural ageing time.

The quenched samples were used subsequently to determine a forming limit curve for each quenching rate and ageing duration. A universal testing machine from the Erichsen company was used for this purpose, see Fig. 4 on the left. The tests were

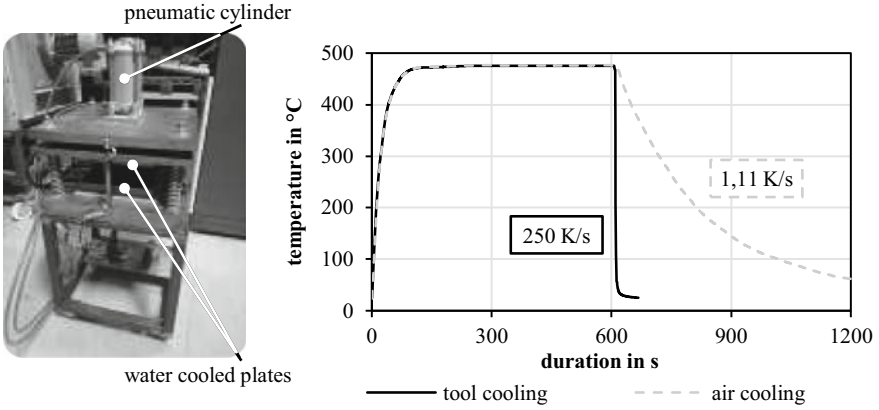


Fig. 2 Pneumatically operated tool (left) and time–temperature diagram of the quenching step for high and low cooling rates (right)

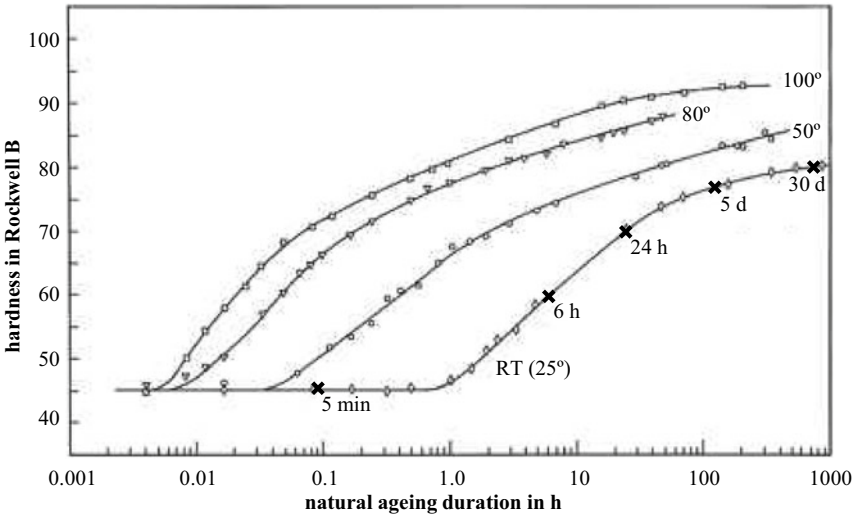


Fig. 3 Hardness development depending on the natural ageing time according to [13] and the selected ageing times according to the hardness evolution

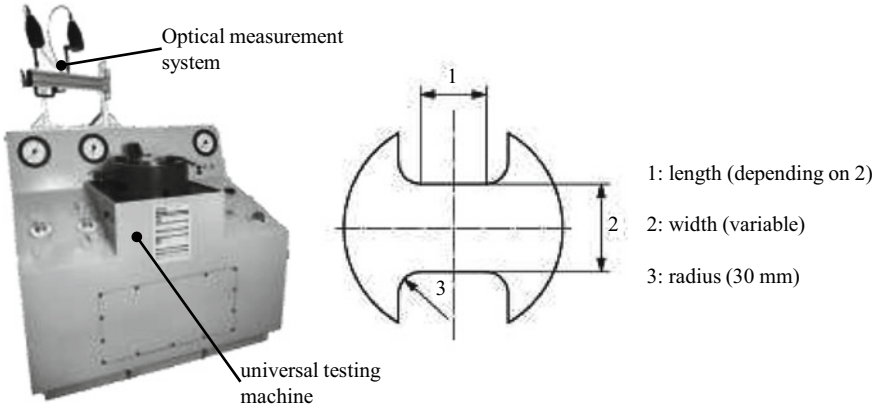


Fig. 4 Nakajima testing rig (left) and shape of the sheet metal samples (right)

carried out according to DIN EN ISO 12004-2. The hemispherical punch had a diameter of 100 mm. The clamping force to prevent the material from flowing was set to 300 kN and the punch speed during the test was 1.5 mm/s. The specimens were prepared according to DIN EN ISO 12004-2. The shape shown in Fig. 4 on the right was used. The rolling direction of the blanks was parallel to the orientation of the crossbar. The width of the crossbar was varied to set different stress states in the sample. A total of five crossbar widths were used, ranging from 30 to 160 mm.

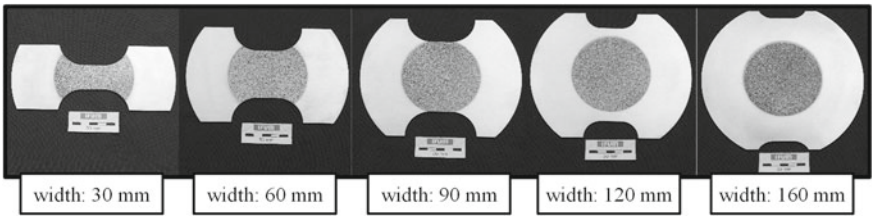


Fig. 5 Overview of the used test samples and the varied width of the crossbar

The optical measuring system Aramis from the company GOM mbH was used to evaluate the samples. For this purpose, a stochastic pattern was applied to the samples, which can be detected by the measuring system. The prepared samples with the varied crossbar widths are shown in Fig. 5. The evaluation of the samples was carried out according to the online method AM3 described in DIN EN ISO 12004-2. The maximum major and minor strain were determined immediately before the crack.

3.2 Tailored Tempering of EN AW-7075

In order to obtain areas with different mechanical properties in one part, the alloy EN AW-7075 was partially quenched after solution heat treatment. An adjustable compressed air-quenching facility as shown in Fig. 6 on the left was used for this purpose. By means of cooling nozzles, it is possible to cool down certain areas of the blank with different quenching rates. These areas achieve a higher strength after the heat treatment. To change the quenching rate, various parameters can be set. On the one hand, these are the number and arrangement of the cooling nozzles. It is either possible to use three nozzles arranged below the blank or a total of six nozzles.

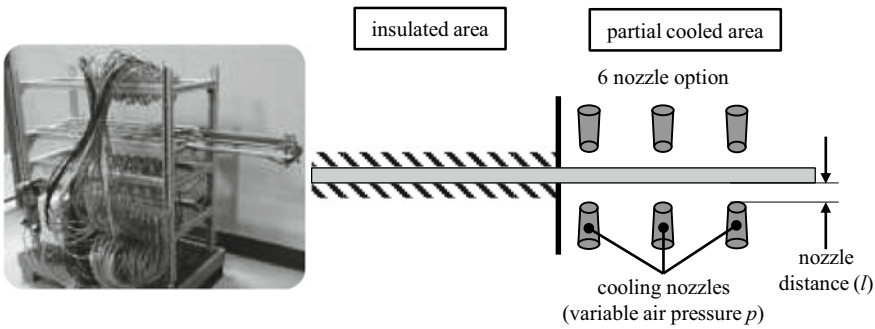


Fig. 6 Compressed air-quenching facility for partial quenching (left) and schematic overview of the adjustable compressed air-quenching facility parameters

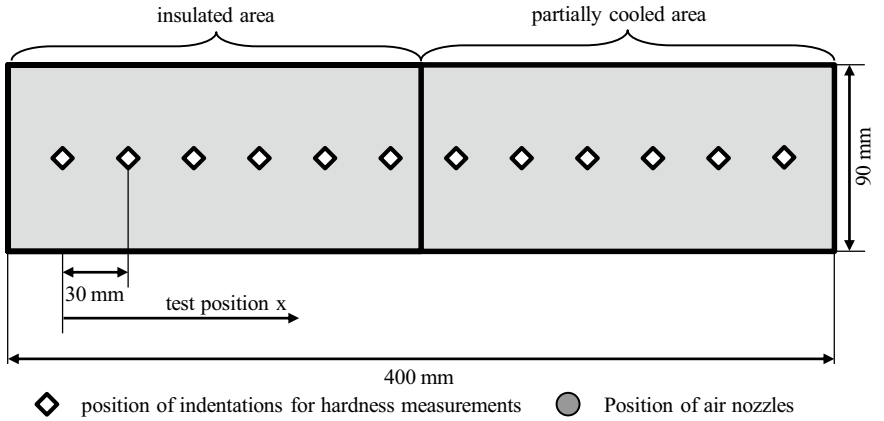


Fig. 7 Indentation positions for the hardness measurements of the partially quenched sheets

Furthermore, the distance (l) between the nozzles and the blank can be either 100 mm or 150 mm. In addition, the air pressure (p) can be adjusted between 1 and 6 bar. On the other hand, a low quenching rate is required for areas where low strength is to be achieved. This can be reached in the test setup used by insulation. A schematic layout of the compressed air-quenching facility is shown in Fig. 6 on the right. The solution heat treatment before quenching was performed at 480 °C for a duration of 10 min.

After solution heat treatment and partial quenching, the heat treatment was continued by artificial ageing of the sheet metal strips at 120 °C for 24 h. A Vickers hardness test was then carried out on the surface of the samples. A ZwickRoell ZHU250 hardness testing machine was used for this purpose. The test was equivalent to the HV10 hardness test. The positions of the hardness test are shown in Fig. 7. Five hardness indentations were made in each of the insulated and quenched areas. The tests were performed at a distance of 30 mm from each other.

The evaluation method shown in Fig. 8 was used to determine the hardness gradient and the transition zone length as a function of the quenching parameters. First of all, the mean value of the hardness of the first four hardness indentations and the last four hardness indentations was determined. These mean values are entered as lines 1 and 2 in the hardness profile. The distance between the intersection points of lines 1 and 2 with the hardness curve describes the transition zone. In addition, the difference between the two mean values along the transition zone is the hardness gradient. The hardness gradient and the transition zone are used as evaluation criteria.

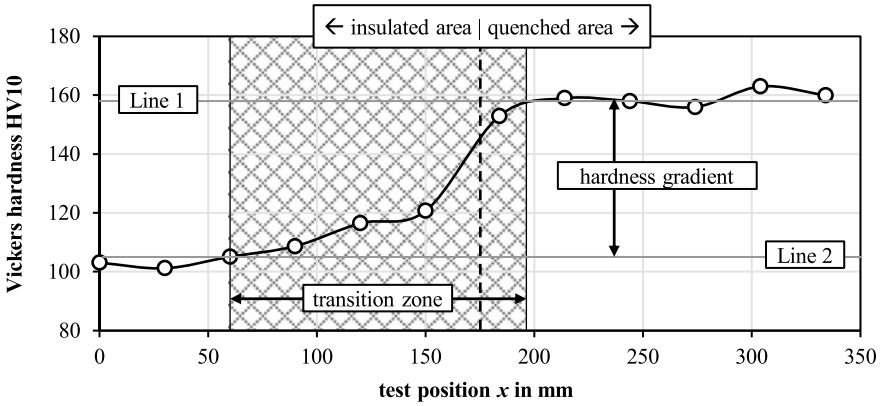


Fig. 8 Analysis method for the partially quenched sheets

4 Results of the Experimental Investigations

4.1 Formability in W Temper State

First, the influence of the natural ageing time on the formability of the alloy EN AW-7075 after quenching was investigated. For this purpose, the Nakajima specimens were either quenched quickly in the pneumatic press or cooled slowly at air. As an example for natural ageing durations of 6 h and 30 days, the forming limit curves of the slowly cooled samples are shown in Fig. 9. As a reference, a forming limit curve for the investigated material in the T6 condition was also determined. The

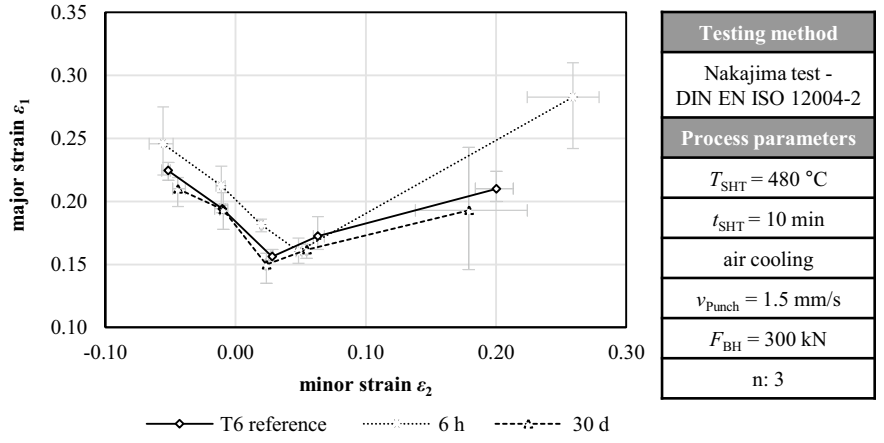
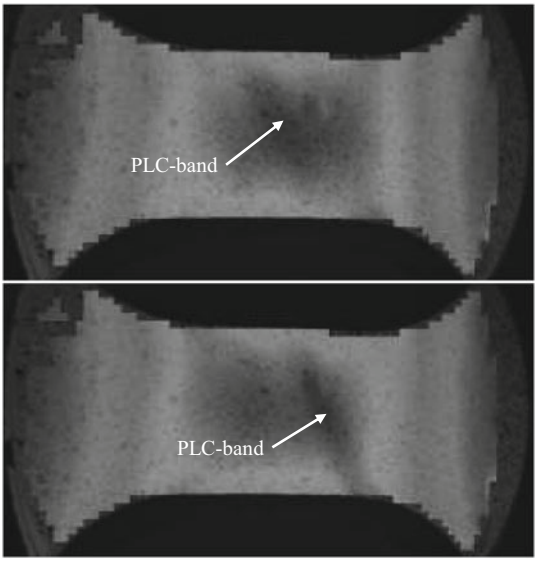


Fig. 9 Influence of the natural ageing time on the formability of EN AW-7075

lowest formability was found for all material states between a major strain degree of 0.14 and 0.16. The minor strain varies between 0.025 and 0.05. For strain states that remain within the range of uniaxial tension, the formability for the natural-aged samples are slightly higher than for the reference state. The highest formability is achieved with decreasing ageing time. The same behaviour can be observed for the biaxial stress state. Only the formability of the samples aged for 30 days is below the reference level. As before, the samples that have been aged naturally for the shortest time have the highest forming capacity. The same behaviour was determined for the rapidly quenched samples.

During the Nakajima experiments, a dynamic strain ageing was determined in the samples. This phenomenon is also known as Portevin–Le Chatelier effect. The plastic deformation occurs unevenly across the formed area. The effect is more pronounced in samples quenched quickly and exposed to a short natural ageing time. This can be explained by the higher amount of solute atoms immediately after quenching. The formation of PLC bands during the Nakajima experiments is shown in Fig. 10. In this figure, the major strain is represented on the sample surface. The dark bands indicate a localised plastic strain in the sample.

In addition to the influence of the natural ageing time, the influence of the quenching rate on the formability was investigated. The results for an ageing duration of six hours are shown in Fig. 11. The obtained results are representative of all ageing durations. The T6 condition of the material EN AW-7075 is shown as a reference. For the area of uniaxial tension up to the lowest major strain, the rapidly quenched samples have a higher forming capacity. This is slightly higher than the reference



Testing method
Nakajima test - DIN EN ISO 12004-2
Process parameters
T_{SHT} = 480 °C
t_{SHT} = 10 min
tool cooling
width= 30 mm
v_{Punch} = 1.5 mm/s
F_{BH} = 300 kN
n: 3

Fig. 10 Portevin–Le Chatelier bands during the Nakajima test

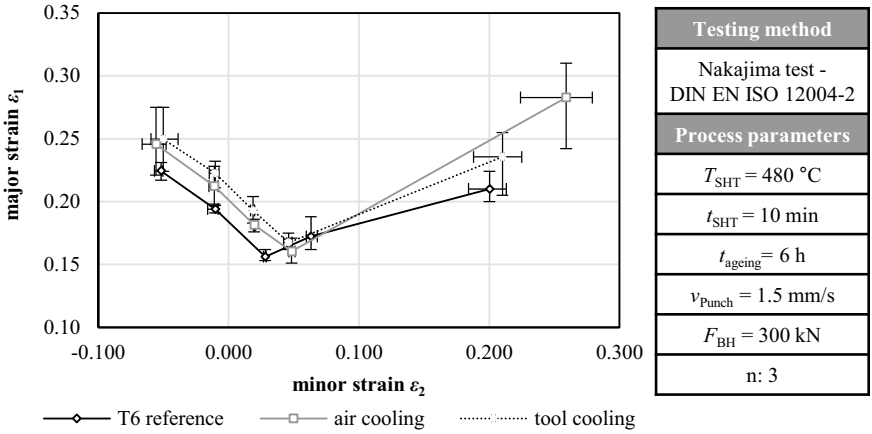


Fig. 11 Influence of the quenching rate on the formability of EN AW-7075

condition. In the biaxial stress state, on the other hand, the formability of the slowly cooled specimens is higher than that of the rapidly quenched.

4.2 Tailored Tempering of EN AW-7075

To achieve partially different mechanical properties in sheet metal strips of the material EN AW-7075, these strips were quenched in a compressed air-quenching facility with varying parameters. In insulated areas with a low quenching rate, zones with reduced hardness should be tailored. In areas with a higher quenching rate, however, a higher hardness has to be obtained. In these areas, the sheet was quenched in the compressed air-quenching facility with varying air pressure, varying nozzle distance from the sheet, and either three or six nozzles. The influence of the number and arrangement of the nozzles is shown in Fig. 12. By quenching the sheet metal on both sides with six instead of three nozzles, the hardness level in the complete sheet metal increases. The quenching rate of the rapidly quenched zone is therefore so strong that the insulation is not fully suited to maintain the reduced hardness level in the insulated area. However, the hardness gradient and the width of the transition zone are only slightly affected by the number and arrangement of the nozzles.

The results of the determined hardness gradients and transition zones are shown in Fig. 13. The air pressure and the distance between the nozzles and the sheet metal were varied. The six nozzle configuration was used for all parameter variations. It was observed that with increasing air pressure the hardness gradient increases. With a nozzle distance of 100 mm the hardness gradient increases from 43 HV10 at 1 bar air pressure to 54 HV10 at 6 bar. For a nozzle distance of 150 mm the determined difference is more distinct. In this case, the hardness gradient increases from 28 HV10 to 53 HV10 when the air pressure increases. For both nozzle distances of 100 mm

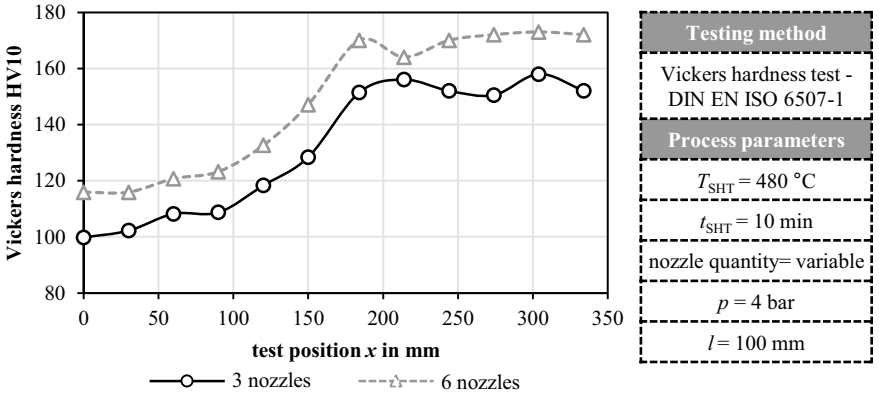


Fig. 12 Hardness profiles of partially quenched sheet metal strips by varied nozzle quantity

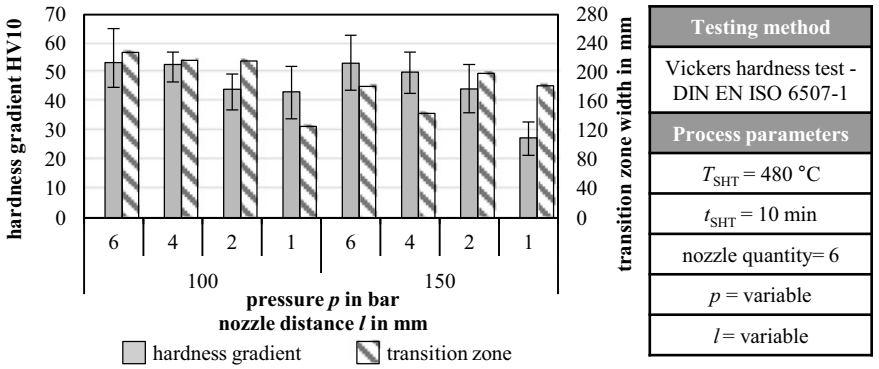


Fig. 13 Results for the hardness gradient and transition zone of partially quenched EN AW-7075

and 150 mm the influence of the air pressure on the transition area is rather small. At 100 mm a reduction of the transition area with decreasing air pressure has been determined. At a distance of 150 mm, on the other hand, no clear influence can be identified.

5 Conclusions and Outlook

The influence of the quenching rate and the natural ageing duration after quenching on the formability of the alloy EN AW-7075 in the W-temper state was investigated. Furthermore, it was determined how a partial quenching process can be carried out to produce components with locally adjusted tailored mechanical properties. It was shown that the W-temper state reaches an increased formability compared to

the T6 state. However, the formability decreases with increasing ageing time. For short ageing times after quenching, PLC bands are formed, which cause localisation of the strain and limit the formability. It has also been shown that in the stress state area of uniaxial tension, a rapid quenching rate after solution heat treatment is advantageous for formability. For the biaxial stress state, however, slow quenching rates are advantageous. In future experiments, the PLC effect will be investigated more closely by tensile tests. In addition, the process of solution heat treatment and quenching with subsequent forming will be transferred to a complex-forming geometry, and formability will be studied at the example of deep-drawing tests.

Additionally, the influence of the quenching conditions on the mechanical properties, particularly the hardness, was determined. By means of a compressed air-quenching facility setup, it was possible to produce sheet metal strips with locally adapted properties. A hardness gradient of up to 54 HV10 was obtained. For example, a transition zone of 144 mm at a hardness gradient of 50 HV10 was achieved. In future researches, the influence of alternative quenching media on others such as water–air mix shall be investigated. The aim will be to reduce the processing time while maintaining the hardness gradient and decreasing the width of the transition zone.

Acknowledgments The project "Tailored Tempering of 7xxx-Aluminum Alloys" Ref.-No. AiF 20190N was financed and supervised by the European Research Association for Sheet Metal Working (EFB). In the scope of the program to promote Industrial Collective Research, it was funded by the German Federation of Industrial Research Associations (AiF) by means of the Federal Ministry of Economic Affairs and Energy (BMWi) on the basis of a decision by the German Bundestag. Furthermore, the authors would like to thank the industrial partners in this research project.

References

1. Sotirov N, Simon P, Waltenberger T, Uffelmann D, Melzer C (2011) Verbessertes Umformverhalten von höchstfesten 7xxx-Aluminiumblechen durch Halbwarmumformen. HTM J. Heat Treatm. Mat. 66(1):37–43
2. Kumar M, Sotirov N, Chimani CM (2014) Investigations on warm forming of AW-7020-T6 alloy sheet. JMatProTec 214(8):1769–1776. https://doi.org/10.1016/j.jmatprotec.2014.03.024
3. J Noder, S DiCecco, C Butcher, M Worswick 2017 Finite element simulation of non-isothermal warm forming of high-strength aluminum alloy sheet. AIP Conf Proc 1896:080017. https://doi.org/10.1063/1.5008097
4. Kumar M, Ross NG (2016) Influence of temper on the performance of a high-strength Al-Zn-Mg alloy sheet in the warm forming processing chain. JMatProTec 231:189–198. https://doi.org/10.1016/j.jmatprotec.2015.12.026
5. Behrens B-A, Hübner S, Vogt H (2018) Formability of 7000 aluminum alloys in warm and hot forming condition. IOP Conf Ser: Mater Sci Eng 418:012027. https://doi.org/10.1088/1757-899X/418/1/012027
6. Behrens B-A, Hübner S, Vogt H (2017) Forming of high-strength aluminum alloys – Influence of the forming temperature on the formability of 7xxx-aluminum alloys. WT Werkstatttechnik 107(10):695–699

7. El Fakir O, Wang L, Balint D, Dear JP, Lin J, Dean TA (2014) Numerical study of the solution heat treatment, forming, and in-die quenching (HFQ) process on AA5754. IJMachTools 87:39–48. https://doi.org/10.1016/j.ijmachtools.2014.07.008
8. Mendiguren J, Saenz de Argandoña E and Galdos L (2016) Hot stamping of AA7075 aluminum sheets. IOP Conf Ser: Mater Sci Eng 159:012026 https://doi.org/10.1088/1757-899X/159/1/012026
9. Degischer HP, Lacom W, Zahra A, Zahra CY (1980) Decomposition process in an Al-5%Zn-1%Mg alloy. Z Met 71(4):231–238
10. Löffler H, Kovács I, Lendvai J (1983) Review: Decomposition processes in Al-Zn-Mg alloys. J Mater Sci 18:2215–2240
11. Behrens B-A, Nürnberger F, Bonk C, Hübner S, Behrens S and Vogt H (2017) Influences on the formability and mechanical properties of 7000-aluminum alloys in hot and warm forming. J Phys: Conf Ser 896:012004 https://doi.org/10.1088/1742-6596/896/1/012004
12. Sáenz de Argandoña E, Galdos L, Ortubay R, Mendiguren J, Agirretxe X (2015) Room temperature forming of AA7075 aluminum alloys: W-temper process. KEM 651–653:199–204
13. Ostermann F (2014) Anwendungstechnologie aluminium, 3rd edn. Springer Vieweg, Berlin.
14. Nürnberger F, Diekamp M, Moritz J, Wolf L, Hübner S, Behrens B-A (2014) Spray cooling of early extracted hot stamped parts. Paper presented at the 143rd TMS Annual Meeting, San Diego, California, 16–20 February 2014, pp 983–990 https://doi.org/10.1002/9781118889879.ch116
15. L Wolf, M Diekamp, T Gretzki, F Nürnberger, F-W Bach, D Rodman, J Moritz, J Schrödter, S Hübner, B-A Behrens 2014 Hot stamping and subsequent spray cooling: A new manufacturing approach. In Plastic deformation of metals. Akzent, Dnipropetrovsk, UA, pp 36–55

Constitutive Model and Plate Forging Ability of 5052 Aluminum Alloy Under Different Temperatures



Yantao Li, Wenzheng Dong, Qiquan Lin, and Zhigang Wang

Abstract The hot tensile deformation behavior of 5052 aluminum alloy is investigated by uniaxial tensile tests with the temperature range of 523–723 K and strain rate range of 0.001–0.1 s^{-1}. The constitutive equation is established based on the Arrhenius-type equation and Zener–Hollomon parameters, which are applied to numerical simulation for solid boss forming by plate forging process. As a result, the flow stresses obtained from the constitutive equation are consistent with the experiments, and the proposed constitutive equation is succeeded to predict the deformation behavior in the plate forging process. The best forming temperature for boss solid forming is 673 K based on the boss forming ability analysis.

Keywords 5052 Aluminum alloy · Constitutive model · Plate forging · Numerical simulation

1 Introduction

In recent years, energy conservation and CO_2 emission have become a serious concern in the world. Under the pressure of energy savings and emission reduction, lightweight plays an important role in the field of automobiles. On the one hand, to reduce the weight of vehicles more lightweight materials such as aluminum alloy and magnesium alloy are used in car bodies [1]. On the other hand, various combined forming processes such as plate forging [2–4] have been proposed to manufacture

Y. T. Li · W. Z. Dong (✉) · Q. Q. Lin
Key Laboratory of Robot and Application Technology of Hunan Province, Xiangtan University, Xiangtan, China
e-mail: wzdong@xtu.edu.cn

W. Z. Dong
State Key Laboratory of Materials Processing and Die and Mould Technology, Huazhong University of Science and Technology, Wuhan, China

W. Z. Dong · Z. G. Wang
Department of Mechanical and System Engineering, Gifu University, Gifu, Japan

© The Minerals, Metals & Materials Society 2021

G. Daehn et al. (eds.), *Forming the Future*, The Minerals, Metals & Materials Series,
https://doi.org/10.1007/978-3-030-75381-8_81

a function lightweight part. Up to now, a great deal of work has been done on the development of plate forging [5, 6].

As the material flow behavior of aluminum alloy during hot formation is complex, the process parameters of temperature, strain rate, and strain significantly influence its microstructure and properties. Many constitutive models such as Mirzadeh [7], Mirzaie et al. [8], Arrhenius-type with Zener–Hollomon parameters [9], Baktash and Mirzadeh [10] were proposed to predict the flow stress during hot formation. In the case of 5052 aluminum alloy, Lin et al. [11] studied the flow stress behavior by hot isothermal compression test. As among the plate forging process, the sheet deformation and the bulk deformation are mixed simultaneously, and more often the stretching or drawing is the main deformation mode. Thus, the hot tensile deformation behavior of 5052 aluminum alloy is investigated in the present work, and the plate forging ability for solid boss forming is also examined by numerical simulation and laboratory experiments.

2 Experimental Procedures

2.1 Uniaxial Tensile Testing

The commercial A5052-H24 with a thickness of 2 mm was prepared in the study. All tensile specimens were machined from the rolling direction as illustrated in Fig. 1, with a gage length of 30 mm. Isothermal uniaxial tension experiments under five deformation temperatures (523, 573, 623, 673, and 723 K) and three strain rates (10^{-3}, 10^{-2}, and 10^{-1} s^{-1}) were carried out on Instron 3369 universal testing machine. Load and displacement data were automatically collected.

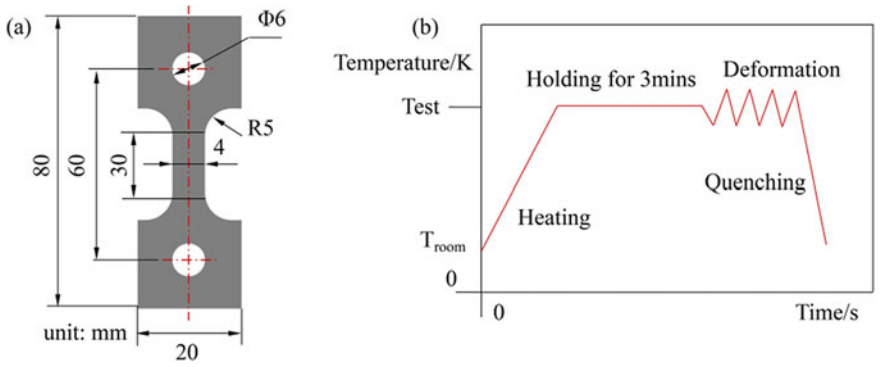


Fig. 1 **a** Size of tensile test specimen **b** Control conditions for hot tensile deformation. (Color figure online)

2.2 Experiment Setup for Solid Boss Forming by Plate Forging Process

Previously, a novel plate forging process named compression-drawing were proposed to form the solid boss on a plate product with a lower forming load [4]. Figure 2a shows the principle of the compression-drawing process. The drawing die moves upward with a velocity V and the blank is drawn when a constant punch load is applied to the bottom of the cup, and then a boss is extruded from the blank when the blank is compressed plastically. Compared with the traditional backward extrusion process, an extra counter-punch would be added to generate the backpressure in the opposite direction as well as bear the total processing load. The plate forging ability for solid boss forming is also examined by laboratory experiments on a hydraulic press, as shown in Fig. 2b. The process parameters used for the experiment are listed in Table 1.

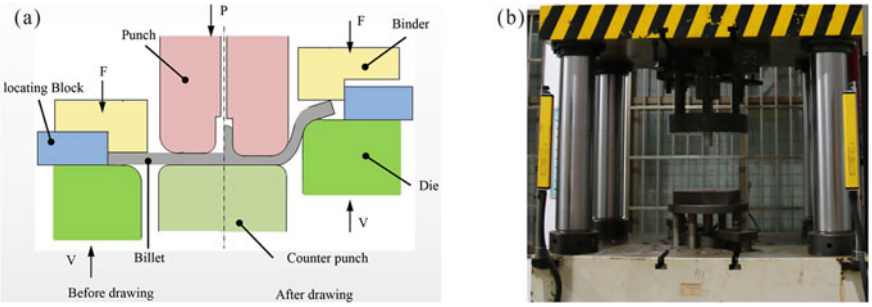


Fig. 2 **a** Principle of solid boss forming by plate forging and **b** Tool setup. (Color figure online)

Table 1 Process parameters for the experiment

Process variables	Values
Workpiece	Diameter: 60 mm/thickness: 2 mm
	Temperature: 298–573 K
Punch	Boss diameter: 1.5 2.5 mm
	Boss fillet radius: 1 mm
Die	Inner diameter: 45.2 mm
	Fillet radius: 8 mm
Counter-punch	Diameter: 40 mm
Counter-punch load	48 ton
Lubricant	Dry

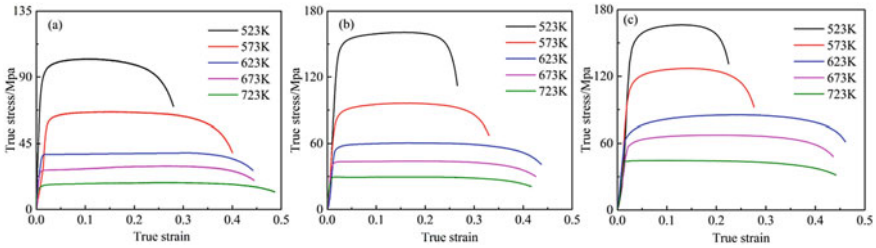


Fig. 3 True stress–strain curves at temperatures 523, 573, 623, 673, and 723 K under strain rate: **a** 0.001 s^{-1}, **b** 0.01 s^{-1}, and **c** 0.1 s^{-1}. (Color figure online)

3 Results and Discussion

3.1 True Stress–Strain Curve

The true stress–strain curves of 5052 aluminum alloy during uniaxial tension tests under different conditions are shown in Fig. 3. Obviously, the flow stress typically increases linearly, gradually reaches the peak at a particular strain, and then saturated approximately due to dynamic softening with dropping in the final stage. It can also be seen that the flow stress decreases with the temperature rising, increases with strain rate rising, which might be summarized as temperature negative and strain rate positive correlation in brief, respectively. Under the lowest strain rate of 0.001 s^{-1}, the total elongation is the highest with the lowest strength simultaneously, for there might be enough time and kinetics to complete dynamic recrystallization.

3.2 Constitutive Modeling

To examine the hot tensile deformation behaviors of 5052 aluminum alloy under different temperatures and strain rates, the Arrhenius-type constitutive equation and Zener–Hollomon parameter in an exponent-type equation were used [12].

$$\dot{\varepsilon} = Af(\sigma)\exp[-Q/(RT)] \tag{1}$$

where

$$f(\sigma) = \begin{cases} \sigma^{n_1}, & \alpha\sigma < 0.8 \\ \exp(\beta\sigma), & \alpha\sigma > 1.2 \\ \sinh(\alpha\sigma)^n, & \text{for all } \sigma \end{cases} \tag{2}$$

$$Z = \dot{\varepsilon}\exp[Q/(RT)] \tag{3}$$

Table 2 Values of material constants at a strain of 0.1

A_3/s^{-1}	α/Mpa^{-1}	n_2	$Q/(KJ \cdot mol^{-1})$
3.14×10^{14}	0.0211	5.055	162.72

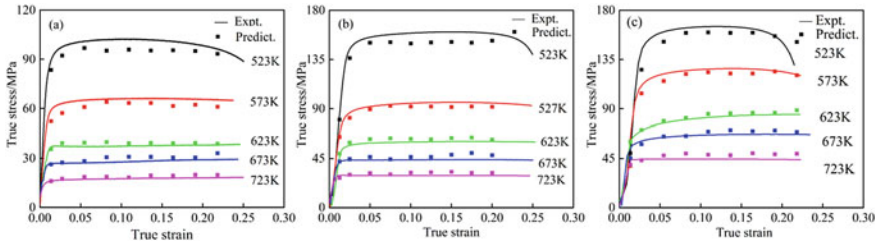


Fig. 4 Comparison of the Arrhenius model prediction with experimental true stress–strain under strain rate: **a** 0.001 s^{-1}, **b** 0.01 s^{-1}, and **c** 0.1 s^{-1}. (Color figure online)

Then, the relationship between strain rate and stress can be described as follows with different flow stress levels:

$$\dot{\varepsilon} = \begin{cases} A_1\sigma^{n_1}\exp\left(-\frac{Q}{RT}\right) & \text{for } \alpha\sigma < 0.8 \\ A_2\exp(\beta\sigma)\exp\left(-\frac{Q}{RT}\right) & \text{for } \alpha\sigma > 1.2 \\ A_3[\sinh(\alpha\sigma)]^{n_2}\exp\left(-\frac{Q}{RT}\right) & \text{for all } \sigma \end{cases} \tag{4}$$

where Q is the active energy for hot deformation, R is gas constant, T is temperature, A_1, A_2, A_3, α, β, n_1, n_2 are material temperature-dependent constants determined by experiment and among them $\alpha = \beta/n_1$.

Based on multivariate linear data analysis, the values of A_3, α, n_2, Q at a true strain of 0.1 are determined and listed in Table 2.

Figure 4 shows the true stress–strain responses of 5052 aluminum alloy with the Arrhenius model predicted curves. It is found that the predicted curves fit well with the experimental results. Moreover, in order to evaluate the deviation between prediction and experiment quantitatively, statistical analysis was conducted. The distribution of relative error, expressed as Eq. (5), is shown in Fig. 5.

$$error(\%) = \frac{\sigma_{\text{exp}} - \sigma_{\text{predict}}}{\sigma_{\text{exp}}} \times 100 \tag{5}$$

where σ_{exp} and σ_{predict} are the experimental and prediction flow stress. From Fig. 5, clearly, most of the absolute relative errors are fewer than 10%, demonstrating the Arrhenius model with excellent predictability. Meanwhile, it is worth noting the deviation is relatively large for a particular inspection point.

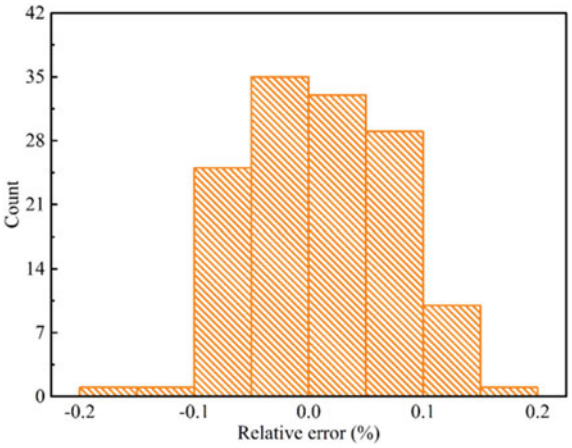


Fig.5 Statistical analysis of the relative error by the Arrhenius model. (Color figure online)

3.3 Application of Constitutive Model in Solid Boss Forming by Plate Forging

To validate the application of tensile model in solid boss forming by plate forging, the established constitutive model was introduced to DEFORM software to carry out the thermal-mechanical simulation. Figure 6 shows the FE model of solid boss forming by plate forging. The billet is defined as rigid plastic meshed by tetrahedral elements with local refinement, while the punch, die, counter-punch, and binder are defined as rigid. Numerical prediction of solid boss forming process during drawing is illustrated in Fig. 7. The bottom metal flows inward the solid boss cavity as well as flows outward the cylindrical wall. The solid boss height gradually increases to the maximum and then remains unchanged.

Figure 8 shows the comparisons of the boss height of the stamped parts obtained

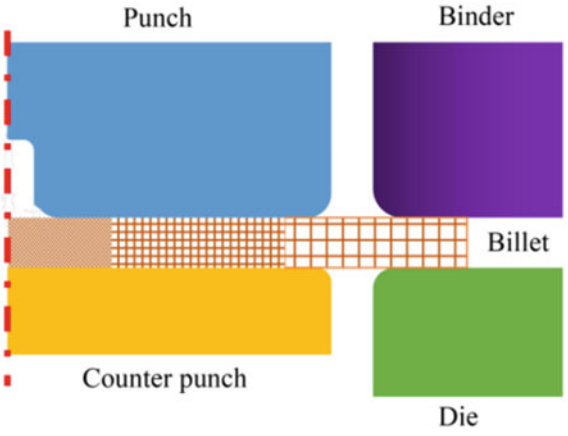


Fig. 6 FE model for solid boss forming by plate forging. (Color figure online)

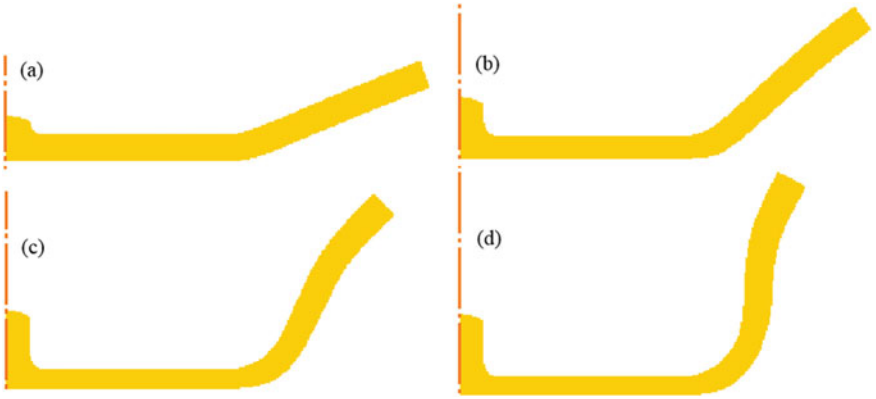


Fig. 7 Solid boss forming process during drawing. **a** Die stroke 5 mm, **b** Die stroke 10 mm, **c** Die stroke 15 mm, and **c** Die stroke 20 mm. (Color figure online)

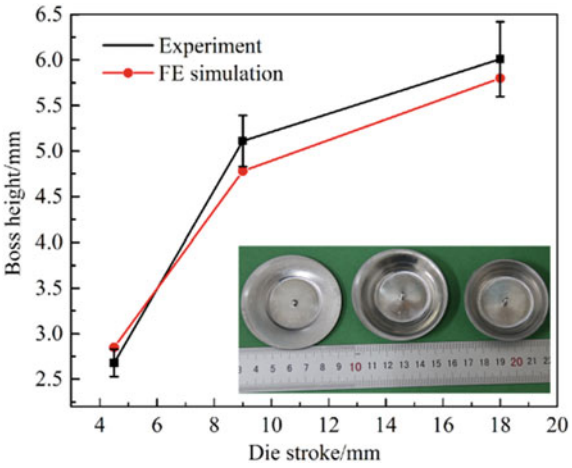


Fig. 8 Boss heights of formed parts obtained from simulation and experiment. (Color figure online)

from numerical simulation and experiment. Obviously, the boss height increases rapidly to the half of punch stroke and then gradually grows slowly. The figure shows that the prediction results based on the tensile model are in good accordance with experiments, with the difference of the boss height less than 15%, and the tensile model satisfies the accuracy demand of plate forging comprehensively. It could be indicated that the Arrhenius model is able to predict the trend of flow behavior and the tensile model is adequate to describe the flow behavior in solid boss forming by plate forging.

3.4 Boss Forming Ability Analysis

As in our previous studies, divided points are an important factor that affects the boss forming ability [4, 13]. To examine the boss forming ability, the decrease in volume of the bottom part and the boss volume are considered, and a dimensionless parameter ζ is defined as described in Eq. (6) to character the boss forming ability.

$$\zeta = \frac{\sigma_s}{p} \cdot \frac{V_b}{V_p} \tag{6}$$

where σ_s is the yield strength, P is the counter-punch pressure at the instant moment, V_b is the volume of the solid boss, and V_P is the volume of materials participating in extrusion deformation, illustrated in Fig. 9. In order to figure out the influence of process parameters on the boss ability analysis, different boss radii (d_b/2), which were found to play an important role in dimple defect, are chosen. The effect of boss radius and temperature on the boss ability is shown in Fig. 10. Obviously, it can be drawn that the boss ability increases with boss radius increasing. However, for the

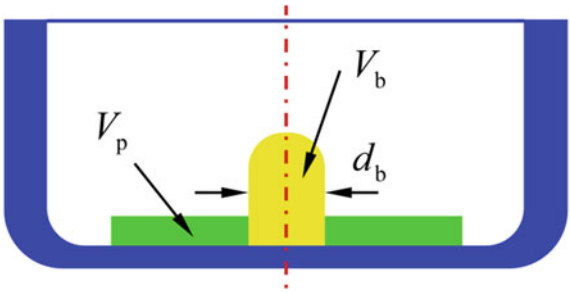


Fig. 9 Schematic drawing of the boss forming ability. (Color figure online)

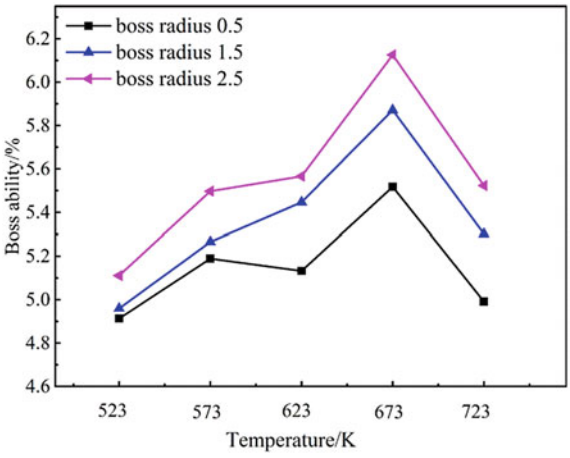


Fig. 10 Effect of boss radius and temperature on the boss forming ability. (Color figure online)

same boss radius, the boss forming ability increases with temperature increasing and reaches its maximum at 673 K.

4 Conclusions

(1) Flow behavior of 5052 aluminum alloy under hot conditions has been investigated by means of uniaxial tensile testing. The flow stress increases with the increasing of strain rate and decreasing of deformation temperature.
(2) The Arrhenius model is adequate to predict the material flow behavior with good accuracy. Tensile model is qualified to describe the flow characteristic in solid boss forming by plate forging.
(3) In the case of boss forming ability, the best forming temperature for solid boss forming is 673 K.

Acknowledgments This work is supported by the Education Department of Hunan Province (No: 18C0112), the Youth Science Foundation of Natural Science Foundation of Hunan Province (No: 2019JJ50604), and the Degree & Postgraduate Education Reform Project of Hunan Province (No: CX20190490).

References

1. Mallick PK (2010) Materials, design and manufacturing for lightweight vehicles. Woodhead Publishing, pp 79–113
2. Wang ZG, Yoshikawa Y, Osakada K (2013) A new forming method of solid bosses on a cup made by deep drawing. CIRP Ann Manuf Technol 62(1):291–294
3. Wang ZG, Hirasawa K, Yoshikawa Y, Osakada K (2016) Forming of light-weight gear wheel by plate forging. CIRP Ann Manuf Technol 65(1):293–296
4. Wang ZG, Dong WZ (2018) A new forming method of flange on a drawn cup by plate forging. Procedia Manuf 15:955–960
5. Merklein M, Allwood JM, Behrens BA et al (2012) Bulk forming of sheet metal. CIRP Annals-Manuf Technol 61(2):725–745
6. Mori K, Nakano T (2016) State-of-the-art of plate forging in Japan. Prod Eng Res Devel 10(1):81–91
7. Mirzadeh H (2015) Constitutive modeling and prediction of hot deformation flow stress under dynamic recrystallization conditions. Mech Mater 85:66–79
8. Mirzaie T, Mirzadeh H, Cabrera JM (2016) A simple Zerilli-Armstrong constitutive equation for modeling and prediction of hot deformation flow stress of steels. Mech Mater 94:38–45
9. Mirzadeh H (2015) A simplified approach for developing constitutive equations for modeling and prediction of hot deformation flow stress. Metall Mater Trans A 46(9):4027–4037
10. Baktash R, Mirzadeh H (2016) A simple constitutive model for prediction of single-peak flow curves under hot working conditions. J Eng Mater Technol 138(2):021004
11. Lin ZY, Jing CW, Da RW, Li JF, Zheng ZQ, Peng ZW (2007) Flow stress behavior of 5052 aluminum alloy under hot compression deformation. Alum Fabr 174(02):17–20 (in Chinese)

12. Sellars CM, Mctegart WJ (1966) On the mechanism of hot deformation. Acta Metall 14(9):1136–1138
13. Dong WZ, Zhang CY, Lin QQ, Wang ZG (2017) Investigation on dimple defect mechanism in solid boss forming process by plate forging. Procedia Eng 207:1159–1164

Research on Rolling Process and Superplasticity for 5A90 Al–Li Alloy



Li Xiaoxing, Chen Yangkai, Lang Lihui, and Xiao Rui

Abstract In order to study the tensile properties of Al–Li alloy 5A90 at high temperature, the Al–Li alloy sheet metal with a thickness of 1.6 mm was obtained by rolling the original plate with the original thickness of 7.3 mm. Universal tensile tests of the previously rolled sheet metals were carried out in the temperature range of 375–450 °C with a strain rate of 0.002 s^{-1}. The experimental results show that the elongation of the material reaches 600% at the temperature of 425 °C, the true strain reaches 2.0, and the peak stress at this temperature is 8.0 MPa.

Keywords Rolling · Superplasticity · 5A90 · Universal tensile

1 Introduction

To overcome the energy crisis, advanced manufacturing technology has been developed to achieve lightweight. The light alloy with low density and high strength is now widely used to replace traditional metal materials in the automotive industry and aerospace field. Al–Li alloy 5A90 has a lower density and higher strength than traditional aluminum alloys and it is an ideal material to replace conventional aluminum alloys. The quality of structural parts reduced by 10–15% and their rigidity increased by 15–20% with the application of 5A90. However, Al–Li alloys have poor plasticity, large springback, easy cracking, poor part accuracy, and surface quality during processing at room temperature. It is difficult to produce complex parts in traditional cold forming processes, which block the application of Al–Li 5A90 [1].

With the development and maturity of hot forming process, several materials, such as TA15, AA5083 aluminum alloy, show superplasticity at particular temperature and strain rate. It makes possible the plastic forming of sheet metal with large deformation and complex profile.

L. Xiaoxing · C. Yangkai (✉) · L. Lihui
School of Mechanical Engineering and Automation, Beihang University, Beijing, China
e-mail: cykangel@126.com

X. Rui
Beijing Hangxing Machinery Manufacturing Co., Ltd., Beijing, China

© The Minerals, Metals & Materials Society 2021

G. Daehn et al. (eds.), *Forming the Future*, The Minerals, Metals & Materials Series,
https://doi.org/10.1007/978-3-030-75381-8_82

Pengchao et al. [2] investigated the thermal tensile and electro-plastic tensile properties of 5A90 Al–Li alloys. They pointed out that the plastic strain increased from about 0.3 to 0.55 with the rising tensile temperature from 110 to 290 °C. Ma et al. [3] researched the constitutive relationship in the temperature range from 200 to 450 and in strain rate range of 0.3×10^{-3} s^{-1} to 0.2×10^{-1} s^{-2}. The result shows that the max plastic strain is lower than 0.55. Zhang et al. [4] examined the superplastic deformation in hot forming for 5A90 Al–Li alloy with 655% elongation. Hongping et al. [5] put forward a rolling process and obtained 765% elongation. However, there are two major defects in the process plan. The serious cracking of the edge of sheet metal by cold rolling results in that only one of the three can be used. The other shortcoming is the serious pollution to the environment.

This paper studies the rolling process and superplastic properties of 5A90 aluminum–lithium alloy sheet metal. An optimal rolling process and relevant process parameters are proposed. This process causes less pollution to the environment. The results of the hot tensile experiment show the plastic strain up to 2.0. 5A90 Al–Li produced in this paper performs well in superplasticity and can satisfy the industrial application.

2 Rolling Process

Raw sheet metal of 5A90 Al–Li alloy is of 7.3 mm thickness. The chemical composition of this sheet metal is shown in Table 1.

Rolling process greatly affects the degree of fine crystallization of sheet metal. Thus there is a great influence of elongation of 5A90 under a high-temperature situation. The effect of reduction on properties of 5A90 has been investigated for each pass at high temperatures. The complete process plan is as follows.

Step 1. Soaking 2 h at 475 °C and then cooling in water.

Step 2. Sheet metal is soaked for 48 h at 300 °C and 4 h at 400 °C.

Step 3. The sheet metal is rolled in five steps at high temperature with a rolling speed of 0.427 m/s, and baked again 20 min after each pass. The thinning of each pass is 15% of the thickness of the previous pass, respectively. After these passes, the thickness of the sheet metal is 45% of the previous thickness.

Step 4. Preheating at 360 °C, then rolling in the transverse direction of the rolling direction in Step 3, the reduction is the same with Step 3; the thickness of sheet metal is 1.5 mm at the end of this step.

Table 1 The chemical composition of 5A90 Al–Li alloy (wt.%)

Si	Fe	Cu	Mg	Na	Li	Ti	Zr	Others	Al
0.15	0.2	0.05	5.4	0.0015	2.1	0.1	0.12	0.05	Margin

Step 5. Soaking 1 h at 500 °C in an air furnace and then water quenched.

The hot mill is shown in Fig. 1. The diameter of the work roll is 350 mm which has the capacity to roll a sheet up to 400 mm in width. Roll speed is in the range of 0–30 r/min. The maximum roll force is 1500 kN. The rolled plate is edge crack free and its surface quality is good. The plate after pickling is shown in Fig. 2.



Fig. 1 The hot mill. (Color figure online)



Fig. 2 The plate after pickling. (Color figure online)

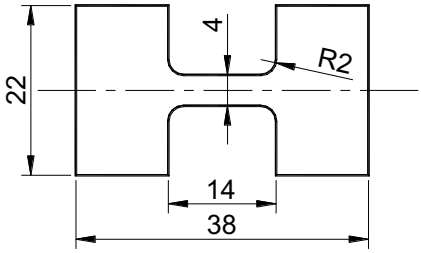


Fig. 3 The geometry of the dog-bone specimen

3 Tensile Experiment and Results

The UTM5504X electronic universal testing machine of Suns with a stroke of 150 mm is used to test the tensile behavior of 5A90 at high temperatures. An approximately constant stretch rate is ensured by controlling the stretch speed step-by-step by MaterialTest4.0 software. The testing machine is equipped with a PID automatic temperature controller for temperature control. The temperature control accuracy of the heating device is in the range of ±3 °C. The maximum experimental temperature of the single pull device is 500 °C. The force–displacement sensor in the range of 0–1000 N is used in these tests. The dimensions of the high-temperature dog-bone specimen are shown in Fig. 3. After processing by wire electric discharge machine, the sides of the specimen were polished with 600# sandpaper.

Xinming et al. [6] pointed out that the conditions for reaching superplasticity are in the strain rate range of 0.0005–0.001 s^{-1} and in the temperature range of 450–500 °C for 5A90 Al–Li alloy sheet metals by multi-pass rolling method. The elongation of 5A90 Al–Li alloy under the temperature of 450 °C and the strain rate of 0.001 s^{-1} is maximum. Ying [7] raised the elongation is considerable under the temperature of 400 °C and three strain rates (0.01 s^{-1}, 0.0025 s^{-1}, and 0.00025 s^{-1}). So, the universal tensile test is performed in the temperature range of 375 to 450 and at the strain rate of 0.002 s^{-1}.

The stress–strain curve of this material is shown in Figs. 4, 5, and 6. As the experimental temperature increases, the maximum true strain increases first and then decreases. The maximum strain reaches its maximum value 2.2 at 425 °C. The relationship between peak stress and temperature is shown in Fig. 7. From the influence of temperature on the elongation of this sheet metal, as shown in Fig. 8, the max elongation is 300% at 425 °C.

4 Conclusion

In this paper, the Al–Li alloy sheet metal of thickness 1.6 mm was obtained by rolling the original plate with the original thickness of 7.3 mm. To obtain the tensile properties of the previous rolled sheet metal, the universal tensile tests were carried

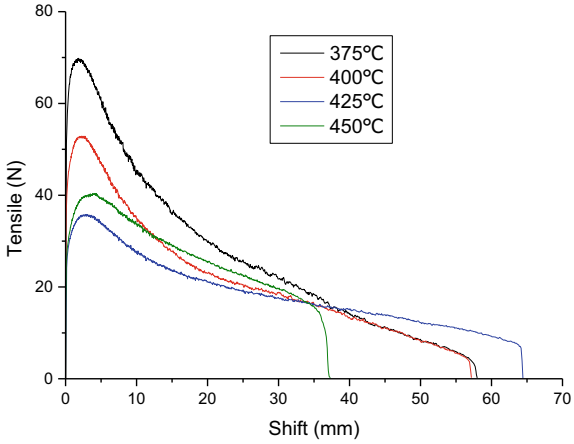


Fig. 4 Tensile–shift curves of 5A90. (Color figure online)

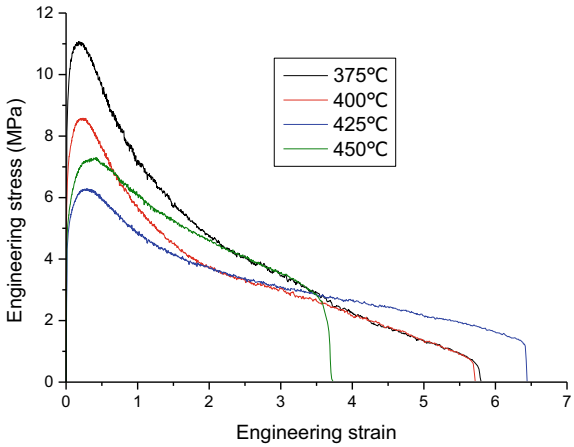


Fig. 5 Engineering stress–strain curves of 5A90. (Color figure online)

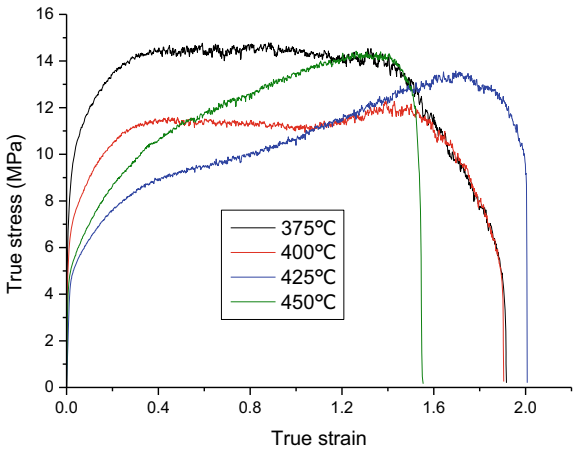


Fig. 6 True stress–strain responses of 5A90. (Color figure online)

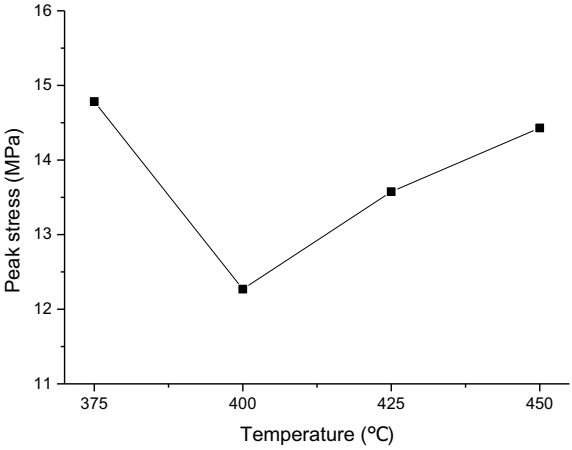


Fig. 7 Peak stress of 5A90

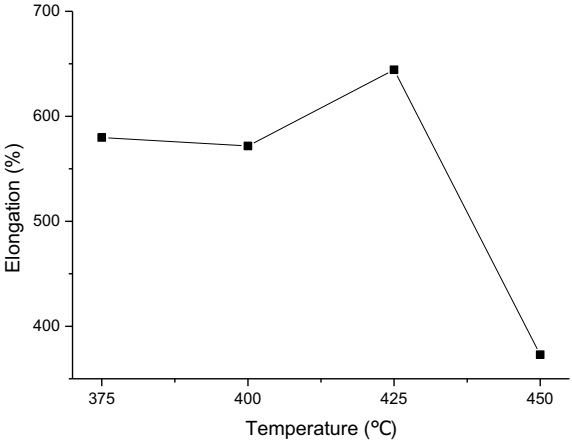


Fig. 8 Elongation of 5A90

out in the temperature range of 375–450 °C with a strain rate of 0.002 s^{-1}. From the above investigation, we can come to the following conclusions.

The 5A90 sheet metal rolled with the parameters of this paper is edge crack free and its surface quality is good.

The experimental results show that the elongation of the material reaches 600% at the temperature of 425 °C, the true strain reaches 2.0, and the peak stress at this temperature is 8.0 MPa. That is to say, the best forming temperature is 425 °C. And the rolled sheet metal shows good superplasticity.

Acknowledgments This work was supported by the Youth Science Foundation Project of China under grant number 51905512.

References

1. Guowei W et al (2017) Superplastic deformation behavior of 5A90 aluminum–lithium alloy. Zhongnan Daxue Xuebao (Ziran Kexue Ban)/J Central South Univ (Science and Technology) 48:1141–1148
2. Pengchao S et al (2014) Electroplastic tensile behavior of 5A90 Al–Li alloys. Acta Metallurgica Sinica (English Letters) 27(4):642–648
3. Gaoshan M, Min W, Xiangdong W (2007) Research on the constitutive relationship of 5A90 aluminum–lithium alloy at hot forming temperature. J Plast Eng 14(3):68–71
4. Pan Z et al (2014) Grain structure and microtexture evolution during superplastic deformation of 5A90 Al–Li alloy. Trans Nonferrous Metals Soc China 24(7):2088–2093
5. Hongping L et al (2014) Microstructure and texture characterization of superplastic Al–Mg–Li alloy. Trans Nonferrous Metals Soc China 24(7):2079–2087
6. Xinming Z et al (2012) Methods of improving superplasticity for 1420 Al–Li alloy sheets. Cast Forg Weld 41(23):9–12
7. Ying Y (2019) Investigation on hot formability of 5A90 Al–Li alloy sheet and its experimental verification. Shandong University

Part XI
Extrusion and Drawing

Co-Extrusion of Compound-Cast AA7075/6060 Bilayer Billets at Various Temperatures



Hui Chen, Danai Giannopoulou, Thomas Greß, Tim Mittler, Jonas Isakovic, Wolfram Volk, and Noomane Ben Khalifa

Abstract A combination of dissimilar AA7075/6060 aluminum alloys benefits the advantages of high strength and good corrosion resistance in one hybrid component. Static compound casting using appropriate casting conditions can achieve intermetallic bonding at the interface of the core AA7075 and sleeve AA6060. The inhomogeneous bonding due to non-uniform thermal conditions during static compound casting can be eliminated by the following co-extrusion procedure. Direct hot extrusion of compound-cast AA7075/6060 bilayer billets at a temperature of 420, 450, and 480 °C is conducted to analyze the influence of extrusion temperature on the interfacial bonding. The evolution of the interfacial bonding properties at different extrusion temperatures of as-cast billets is depicted by light optical metallography and mechanical push-out test.

Keywords Compound casting · Co-extrusion · Bond strength

1 Introduction

The requirement of energy efficiency and emission regulations increased the pressure on automotive OEMs to improve the CO_2 levels, fuel efficiency, and exhaust gas emissions. Lightweight innovation is the countermeasure thus far. A potential strategy in manufacturing lightweight components without scarifying the performance of the components is to use functionally graded composite materials. The components

H. Chen (✉) · N. Ben Khalifa
Leuphana University of Lüneburg, Institute of Product and Process Innovation, Universitätsallee 1, 21335 Lüneburg, Germany
e-mail: Hui.Chen@leuphana.de

D. Giannopoulou · J. Isakovic · N. Ben Khalifa
Helmholtz-Zentrum Hereon, Institute of Material and Process Design, Max-Planck-Straße 1, 21502 Geesthacht, Germany

T. Greß · T. Mittler · W. Volk
Technical University of Munich, Walther-Meißner-Straße 4, 85748 Garching, Germany

© The Minerals, Metals & Materials Society 2021

G. Daehn et al. (eds.), *Forming the Future*, The Minerals, Metals & Materials Series,
https://doi.org/10.1007/978-3-030-75381-8_83

produced by multi-materials with different characteristics provide beneficial advantages such as high strength to weight ratio, high corrosion resistance, and thermal conductivity.

Different approaches have been developed and used to produce composite profiles and semi-finished products by extrusion, which can avoid the disadvantages such as the heat-affected zone, porosity, or grain growth in the conventional fusion joining method [1]. With the aim to increase strength, stiffness, functionality, or the adjustment of certain electrical properties, processes such as co-extrusion, composite extrusion with particle-reinforced extrusion billets, or composite extrusion with the continuous embedding of continuous composite elements have been successfully implemented [2].

Co-extrusion of bimetal billets is the state-of-the-art in manufacturing straight, bar-type, semi-finished products that exhibit an optimal combination of desired properties. Several investigations were focused on predicting the material flow of bimetallic composite [3, 4], which indicates the flow stress ratio, the die angle, and die friction as the key factors [5]. Another important factor in co-extrusion of bimetals is the integrity of the bond between the materials [6]. Most of the materials used in the current bimetal rod extrusion are not bonded before the extrusion process. The extrusion billets are pre-processed by milling, surface cleaning, and brushing, which is time- and energy-consuming [7]. In the work of [8], the aluminum/titanium compound extrusion billets are prepared with a titanium-core integrally molded in the aluminum billet. An intermetallic layer between the joint partners before extrusion was obtained. Comparing with extrusion of composite billet by insertion of the Ti6Al4V core into an AlSi1MgMn billet, the bonding strength of using molded billet is much higher. The billet with inserted core into aluminum sleeve presents an oxide layer that hinders the formation of bonding during plastic deformation [9]. The adhesive and/or cohesive bond between the bimetals interface can be only achieved through plastic deformation under favorable process conditions, e.g., temperature, hydrostatic pressure, etc. [10].

The static compound casting of Al/Al bimetal can fabricate billets with initial intermetallic bonding prior to extrusion. The formation of bonding in an equal material system attributes to the remelting, recrystallization, and diffusion of the partner materials [11]. The metallurgical bonding between AA7075 and AA6060 can be achieved under favorable process conditions using the dendrite coherence point (DCP) as a critical value [12].

In the present work, the influence of the extrusion temperature on interfacial bonding between AA7075/AA6060 compounds is investigated. The AA7075/AA6060 compound billet is fabricated by static compound casting. The interfacial bonding of the compound extrudate after hot extrusion at different temperatures is characterized by metallography and mechanical test.

2 Materials

A rotational geometry was chosen as an analyzing example. As-cast billets are produced by static compound casting methods according to [12]. The core material is a commercial AA7075 aluminum alloy with chemical compositions of 90.5Al–1.63Cu–0.18Si–0.27Fe–2.20 Mg–5.48Zn–0.19Cr in wt.%. The sleeve material is an AA6060 aluminum alloy with chemical compositions of 98.8Al–0.02Cu–0.50Si–0.17Fe–0.48 Mg–0.01Zn–0.02Cr in wt.%. The steel die made of hot-working steel 1.2343 was designed and produced for the static compound casting. Therefore, the steel die can be heated by heating cartridges. The first substrate casting step was to pour the 720 °C ± 10 °C core AA7075 melt into the die mold cavity, while graphite insert was used to mold the sleeve geometry till the solidification of the core. After the core AA7075 solidified and cooled down to 400 °C, the graphite insert was pulled out and the AA6060 melt with a temperature of 750 °C ± 10 °C was poured into the cavity between the core and the die mold. The temperature profiles of the substrate, the sleeve, and the die were recorded by thermal couples. The core AA7075 has a diameter of 35 mm and the sleeve AA6060 has a diameter of 65 mm. Several cast billets were produced under this casting condition. A reference as-cast billet was used for light optical metallography (LOM), SEM/EDS analysis, and mechanical characterization (push-out test and micro-hardness test) of the interfacial bonding. An additional three as-cast billets were used for further hot extrusion experiments.

3 Experimental Conditions

The direct hot extrusion experiments used a flat-face die with a diameter of 28 mm. The container of the hot extrusion setup has a diameter of 50 mm. The as-cast billets were machined to a round bar with a diameter of 49 mm and length of 170 mm from the casting gate (Fig. 1a). The core AA7075 aluminum alloy has a solidus temperature of 476 °C; therefore, the maximum hot extrusion temperature was chosen to be 480 °C. The three hot extrusion experiments were carried out under 480, 450, and 420 °C. The as-cast billets were heated to the target temperatures and homogenized for three hours, respectively. The extrusion container and flat-face die were also heated up to the corresponding forming temperature via heat cartridges. The billets were inserted into the container while the side of the casting gate faced the extrusion die.

After hot extrusion, the cross-sectional samples with a thickness of 2 mm were extracted from three positions of the extrudate by diamond saw cutting. The cross-sectional samples were designated as E1, E2, and E3, which were corresponding to the positions of the cross-sectional samples extracted from the referential as-cast billet (Fig. 1b). The cross-sectional samples extracted by electrical discharge machining from the referential as-cast billet at positions of 50, 90, and 130 mm away to the casting gate were designated as C1, C2, and C3. The cross-sectional samples

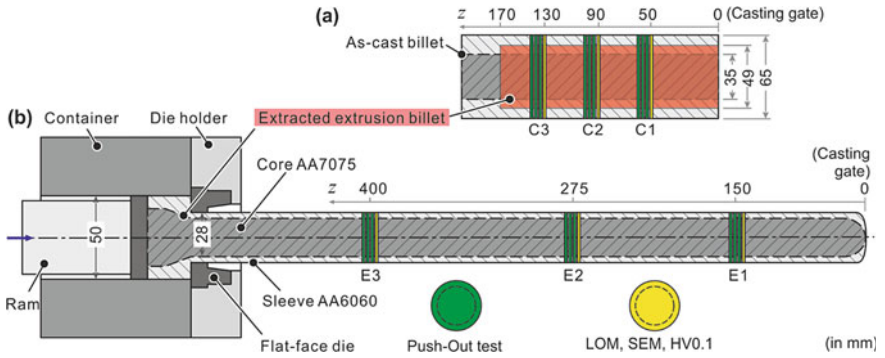


Fig. 1 **a** Dimension of the as-cast billet and extraction of specimens for further work; **b** Hot extrusion setup and the location of cross-sectional specimens for interface characterization. (Color figure online)

were prepared for metallography analysis according to [13]. The Vickers' microhardness of the near interface region was determined with an EMCO test machine using an indentation load of 0.1 kg on those polished cross-sectional specimens. An additional three specimens at the corresponding three positions were extracted for the push-out test to analyze the axial shear bonding strength between the core and the sleeve materials.

The setup and configuration of the push-out test on the as-cast samples were described in [13], which guided a similar configuration in designing the push-out test setup for an extrudate specimen (Fig. 2). The edge of the punch r_p and die r_i was 0.1 mm. The clearance between push-out punch and die $(d_d - d_p)/2$ was 0.5 mm. The core diameter d_i was not constant throughout the whole extrudate since the uniform distribution of the core and sleeve materials can be obtained only in the middle of the extruded profile [6]. Therefore, several pairs of punch and die with different diameters were produced to ensure the distribution of the bonding interface in between the die and the punch. The push-out test setup was installed on a universal test machine Zwick/Roell Z250. The push-out test speed was 1 mm/min. The maximum shear force F_{max} was recorded to calculate the axial shear bonding strength between the core AA7075 and the sleeve AA6060 according to Eq. (1)

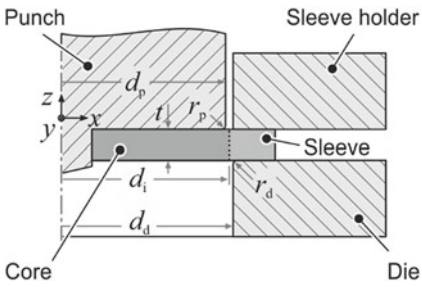


Fig. 2 Configuration of the push-out test

$$\tau_{axial} = \frac{F_{max}}{\pi d_i t} \tag{1}$$

where d_i is the diameter of the interface and t is the thickness of the disc-like sample.

4 Evaluation of the Interface Bonding

4.1 Metallography

A comparison of the bonding interface between the core AA7075 and the sleeve AA6060 in as-cast state and extruded states under different temperatures was presented in Fig. 3. The observation samples were as-cast sample C1 and extrudate sample E1 that were at positions close to the casting gate. The partial cohesive bonding is presented in the as-cast state (Fig. 3a). Many gaps existed at the interface of the core AA7075 and the sleeve AA6060. There were also macroscopic voids

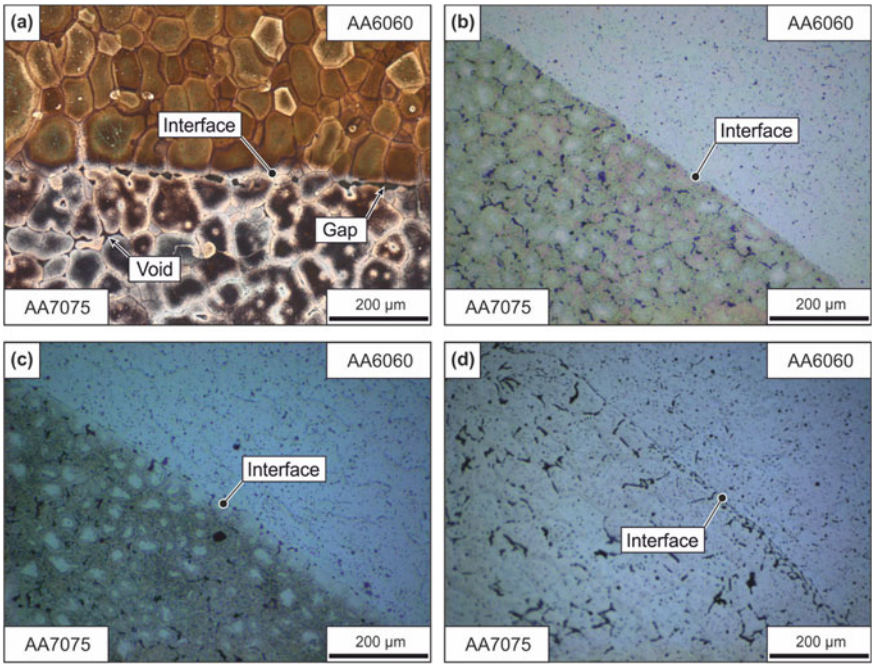


Fig. 3 Microstructure of the near interface region in the cross-section samples at 50 mm to the casting gate: **a** as-cast sample C1; **b** extrudate sample E1 by extrudate temperature of 480 °C; **c** extrudate sample E1 by extrudate temperature of 450 °C; **d** extrudate sample E1 by extrudate temperature of 420 °C. (Color figure online)

inside the core AA7075 due to the thermal stress during the second phase (compound) casting step in fabricating the billets.

After hot extrusion, the serve plastic deformation at high temperatures and high pressure reduced the gaps between the core and the sleeve materials. At a high extrusion temperature of 480 °C, a sufficient cohesive bonding between the core AA7075 and the sleeve AA6060 can be achieved (Fig. 3b). No gaps or macroscopic void at the interface can be observed in a light optical micrograph. The voids inside the core were also eliminated. There were still a few voids at the interface when an extrusion temperature is 450 °C (Fig. 3c). The diffusion zone between the core and the sleeve materials at this extrusion temperature was relatively wider than the other two experimental temperatures. When the extrusion temperature was even lower (420 °C), the clear interface between the core AA7075 and the sleeve AA6060 is presented in the optical metallography (Fig. 3d).

4.2 SEM Analysis

Figure 4 shows SEM images at the near interface region of the extrudate sample E2, i.e., the middle position of the extrudate. The SEM images presented no micro-voids inside the core AA7075 at extrusion temperatures of 480 °C and 450 °C. Few micro-voids still existed after the hot extrusion at 420 °C. Particles existed on the grain boundaries in both core AA7075 and sleeve AA6060. According to the SEM/EDS analysis, those coarse particles in sleeve AA6060 should be α-AlFeSi phase [14]. The α-AlFeSi phase was stable, which was difficult to dissolve into Al matrix and presented after hot extrusion at different temperatures. There were coarse particles and needle-like particles in core AA7075. Under higher extrusion temperature, the coarse particles broke into needle-like particles, which dissolved into Al matrix and then precipitated during extrusion [15]. Higher extrusion temperature enhanced the solubility of the alloying elements [16]. Therefore, few particles were precipitated after hot extrusion [17]. Figure 4 shows that few particles existed in the

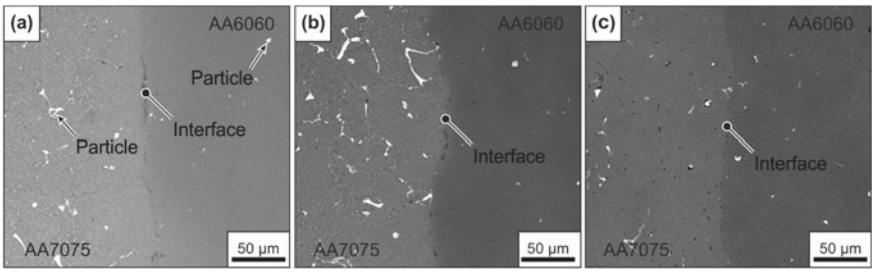


Fig. 4 SEM micrographs of the interface between core AA7075 and sleeve AA6060 after extrusion temperature of **a** 480 °C, **b** 450 °C, and **c** 420 °C

core AA7075 after hot extrusion at high temperature, which means that extrusion at higher temperature reduces the number of particles in the core AA7075 material.

4.3 Mechanical Characterization

A significant improvement of the interfacial bonding strength was achieved for extruded billet by hot extrusion process compared with the initial static compound-casted billets (Fig. 5). The shear strength values of extruded billets by the push-out test showed much higher results at the corresponding positions after hot extrusion compared with the as-cast billet. The initial as-cast billet had the highest bonding strength in the middle (C2, z-position of 90 mm), while a relatively lower interfacial bonding strength is presented at the position close to the casting gate (C1, z-position of 50 mm). The bonding strength of the as-cast billets strongly depended on the z-positon. This was due to the metallurgical interaction and dissolution of the microstructure of AA7075 between the joining partners during the compound casting.

After hot extrusion, the highest bonding strength is still present at the middle of the extrudate. Nevertheless, the bonding strength values along the extrudate were more homogeneous. Higher bonding strength can be expected at the position close to the casting gate. The extrusion temperature played a positive role in enhancing the bonding strength between the core AA7075 and the sleeve AA6060. The axial shear bonding strengths along the whole extrudate increased with the increasing extrusion temperature.

The micro-hardness in the near interface region of the cross-sectional specimens was summarized in Fig. 6. The tests were conducted perpendicular to the AA7075/6060 interface that was indicated as positon of $x = 0$ mm. The micro-hardness at the core material presented a much higher hardness value under higher

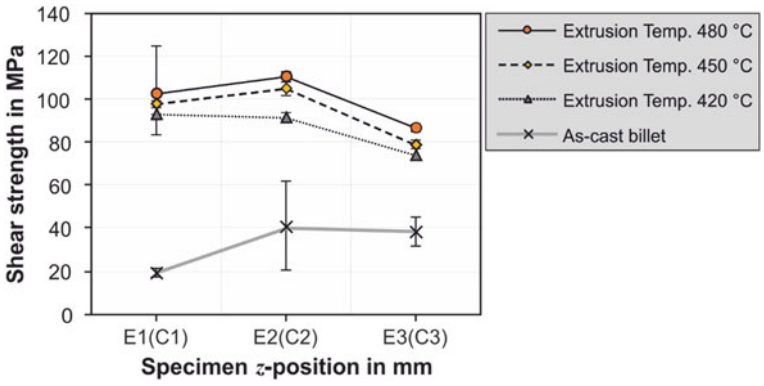


Fig. 5 Shear strength of the interfacial bonding by using push-out test. (Color figure online)

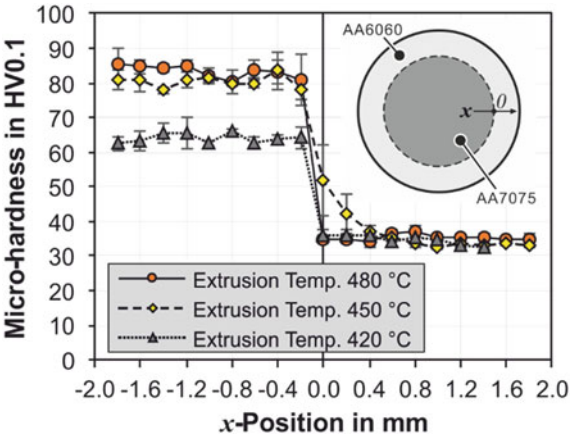


Fig. 6 Micro-hardness in the near interface region of the cross-sectional specimens. (Color figure online)

extrusion temperature, which suggested that the higher temperature improved the mechanical properties of the core material. The hardness of the sleeve showed similar values no matter which extrusion temperatures were used.

The width of the diffusion zones between the core AA7075 and the sleeve AA6060 was 200 μm under extrusion temperatures of 480 and 420 °C. A larger transition area between core and sleeve materials was presented when extrusion temperature was 450 °C, which had been proven by the light optical metallography results, as shown in Fig. 3c.

5 Summary

Co-extrusion of AA7075/AA6060 bimetal billets at different temperatures was conducted in this work. The rotational composite billets were fabricated by static compound casting. Homogeneous interface bonding can be hardly achieved by compound casting. Due to the different thermal expansion ratios of the bimetal, the thermal stress induced voids inside the core AA7075 and gaps at the interface during the solidification and cooling in compound casting. These defects can be improved by hot extrusion. The shear bonding strength between AA7075 and AA6060 increased from 19 to 102 MPa by hot extrusion at 480 °C. Homogenization of the interfacial bonding along the extrudate was another benefit of the consequent hot extrusion process after compound casting. Higher extrusion temperature not only increased the interfacial bonding strength but also improved the mechanical properties of the core AA7075 material, while the void inside the core AA7075 can be eliminated at an extrusion temperature of above 450 °C.

Acknowledgments The German Research Foundation (DFG) kindly supported this work (grant number BE5196/11-1 and VO-1487/25-1). The authors acknowledge the financial funding from the DFG.

References

1. Partridge PG, Ward-Close CM (1989) Diffusion bonding of advanced materials. Met Mater 5(6):334
2. Müller K (2001) Strangpressen von Halbzeugen aus metallischen Verbundwerkstoffen. In: Sauer G, Siegert K (eds) Strangpressen/ Bauser M, 2nd edn. Aluminium-Verlag, Düsseldorf, Düsseldorf, pp 464–483
3. Osakada K, Limb M, Mellor PB (1973) Hydrostatic extrusion of composite rods with hard cores. Int J Mech Sci 15(4):291–307. https://doi.org/10.1016/0020-7403(73)90011-8
4. Tokuno H, Ikeda K (1991) Analysis of deformation in extrusion of composite rods. J Mater Process Technol 26(3):323–335. https://doi.org/10.1016/0924-0136(91)90067-O
5. Alcaraz JL, Gil-Sevillano J, Martinez-Esnaola JM (1996) A fracture condition based on the upper bound method for the extrusion of bimetallic tubes. J Mater Process Technol 61(3):265–274. https://doi.org/10.1016/0924-0136(95)02186-8
6. Kazanowski P, Epler ME, Misiolek WZ (2004) Bi-metal rod extrusion—process and product optimization. Mater Sci Eng A 369(1–2):170–180. https://doi.org/10.1016/j.msea.2003.11.002
7. Haga T, Nakamura R, Kumai S, Watari H (2009) Clad strip casting by a twin roll caster. Arc Mater Sci Eng 37(2):117–124
8. Grittner N, Striewe B, von Hehl A, Bormann D, Hunkel M, Zoch HW, Bach FW (2012) Co-extrusion of aluminium-titanium-compounds. Key Eng Mater 491:67–74. https://doi.org/10.4028/www.scientific.net/KEM.491.67
9. Dietrich D, Grittner N, Mehner T, Nickel D, Schaper M, Maier HJ, Lampke T (2014) Microstructural evolution in the bonding zones of co-extruded aluminium/titanium. J Mater Sci 49(6):2442–2455. https://doi.org/10.1007/s10853-013-7912-6
10. Fan X, Chen L, Chen G, Zhao G, Zhang C (2017) Joining of 1060/6063 aluminum alloys based on porthole die extrusion process. J Mater Process Technol 250:65–72. https://doi.org/10.1016/j.jmatprotec.2017.07.009
11. Papis KJM, Hallstedt B, Löffler JF, Uggowitzer PJ (2008) Interface formation in aluminium–aluminium compound casting. Acta Mater 56(13):3036–3043. https://doi.org/0.1016/j.actamat.2008.02.042
12. Greß T, Mittler T, Schmid S, Chen H, Khalifa NB, Volk W (2018) Thermal analysis and production of as-cast Al 7075/6060 bilayer billets. Int J Metalcast 1–13. https://doi.org/10.1007/s40962-018-0282-8
13. Greß T, Stahl J, Mittler T, Spano L, Chen H, Khalifa NB, Volk W (2019) Mechanical characterization of as-cast AA7075/6060 and CuSn6/Cu99.5 compounds using an experimental and numerical push-out test. Mater Sci Eng A 751:214–225. https://doi.org/10.1016/j.msea.2019.02.080
14. Kuijpers NCW, Kool WH, Koenis PTG, Nilsen KE, Todd I, van der Zwaag S (2002) Assessment of different techniques for quantification of α-Al (FeMn) Si and β-AlFeSi intermetallics in AA 6xxx alloys. Mater Charact 49(5):409–420. https://doi.org/10.1016/S1044-5803(03)00036-6
15. Xu X, Zhao Y, Wang X, Zhang Y, Ning Y (2015) The rapid age strengthening induced by Ag additions in 7075 aluminum alloy. Mater Sci Eng A 648:367–370. https://doi.org/10.1016/j.msea.2015.09.044
16. Chen G, Chen L, Zhao G, Zhang C (2017) Microstructure evolution during solution treatment of extruded Al-Zn-Mg profile containing a longitudinal weld seam. J Alloy Compd 729:210–221. https://doi.org/10.1016/j.jallcom.2017.09.143
17. Tang J, Chen L, Fan X, Zhao G, Zhang C (2018) Co-extrusion of dissimilar AA6063/AA7075 by porthole die at various temperatures. J Alloy Compd 764:162–169. https://doi.org/10.1016/j.jallcom.2018.06.068

Reducing Aluminum Extrusion Transverse Weld Process Scrap



Gregory J. Oberhausen, Anselm A. A. Christopher, and Daniel R. Cooper

Abstract Nearly 20% of the aluminum produced globally is extruded. Up to one-quarter of this aluminum is scrapped in the form of extrusion butts and segments of extruded profiles that contain weak solid-state "transverse" welds that are created between consecutively extruded billets in direct extrusion. In this article, extrusion of differently colored clay billets is used to conduct a parametric study on the effect of extrusion ratio, die angle, friction coefficient, profile shape, and dummy block profile on the transverse weld length. Shorter transverse weld lengths require smaller lengths of the extruded profile to be extracted and scrapped. The results show that the transverse weld length can be reduced by decreasing the extrusion ratio, die angle, or friction coefficient. The profile shape also has a strong influence; the transverse weld length was found to scale with the cross-sectional perimeter to area ratio of the extruded profile. Additionally, it is shown that the dummy block profile (a previously unexplored design variable) can be modified to decrease the weld length. A concave dummy block was designed using an estimated velocity field for axisymmetric extrusion of solid rods, decreasing the weld length by 44%. The industry implications of this work and the need for further research are discussed.

Keywords Transverse weld · Dummy block · Material efficiency · Process scrap

1 Introduction

Aluminum is one of the five materials (steel, cement, paper, plastic, and aluminum) whose production is responsible for over half of all annual greenhouse gas emissions released by industry globally [1]. The energy efficiency of the primary aluminum production process is reaching the thermodynamic limit [2]; therefore, significant emission reductions must be delivered through electricity grid decarbonization and/or material efficiency [3]. Global material flow analyses (MFAs) of the aluminum sector reveal significant ostensible opportunities to increase material efficiency by reducing

G. J. Oberhausen · A. A. A. Christopher · D. R. Cooper (✉)
Mechanical Engineering Department, George G. Brown Laboratory, University of Michigan, 2350 Hayward Street, Ann Arbor, MI 48109-2125, USA
e-mail: drcooper@umich.edu

© The Minerals, Metals & Materials Society 2021

G. Daehn et al. (eds.), *Forming the Future*, The Minerals, Metals & Materials Series,
https://doi.org/10.1007/978-3-030-75381-8_84

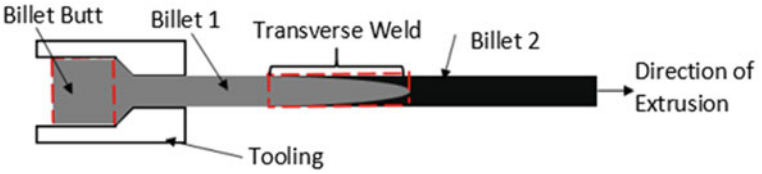


Fig. 1 Major sources of scrap in consecutively extruded billets. (Color figure online)

manufacturing scrap generation. Cullen and Allwood [3] found that 40% of all liquid aluminum is scrapped before reaching a final product, and those billets destined for extrusion account for 20% of all semi-finished aluminum. In their mass balanced MFA, Cullen and Allwood calculated that 25% of the extrusion billet is scrapped during the metal forming process. Elsewhere, the European Aluminum Association (EAA) surveyed 69 extruders (894 kt of product; 32% of European production) and found that between 22 and 24% of the extrusion billet volume is scrapped during the metal forming process [4, 5].

There are many sources of scrap in the aluminum extrusion process. Sheppard [6], in his seminal textbook on aluminum extrusion, identifies many of these sources as insignificant because each accounts for less than 2% of the total initial billet volume. These insignificant scrap sources include the material deformed by the grippers during the stretching process as well as material remaining in the die after a tool changeover. Sheppard identifies the two most significant sources of scrap: removal of the billet butt and the transverse weld. The approximate locations of the billet butt and the transverse weld within the extrusion process are shown in Fig. 1.

The billet butt is scrapped because it contains a concentration of impurities which would reduce the aesthetic, mechanical, and electrical properties of the final profile if it were to be extruded through the die [7]. To prevent this effect, it is a standard industry practice to not press the whole length of the billet through the die; thus, allowing the billet butt to be sheared off between strokes of the main hydraulic ram [6]. The source of the impurities in the billet butt is the billet skin, which contains oxides and solid-phase inclusions, such as spinels ($MgAl_2O_4$), carbides, nitrides, and intermetallics, developed during billet casting [7]. The billet skin impurities concentrate in the billet butt during the extrusion process due to the material flow inside the billet. While the center of the billet flows through the die, the billet skin has a tendency to stick to the container walls due to friction [6, 8], forming a conglomeration of billet skin in the last 5–20% of the initial billet length [6]. To the authors' knowledge, the shearing of billet butts is common place in the industry [9]. An alternative to butt shearing is "Dick's extrusion method" [6] which utilizes a dummy block with a diameter smaller than that of the container walls. After the initial stroke of the press, the billet skin is left intact on the container walls and a second press-stroke is then used to remove the skin in the form of a "skull". Dick's method is less prevalent in current industry practice [9], which is probably because of the extra time that results from the second press-stroke for each billet.

Transverse weld scrap is the segment of the extruded profile that contains the interface between two consecutively extruded billets. This interface forms a solid-state weld that elongates over a significant length of the extruded material and is typically removed from the extruded profile due to concerns of it having lower strength than surrounding material [6]. Reviewing the literature, however, the authors have found only one recorded instance of the transverse weld strength being experimentally tested. Den Bakker et al. [10] test the transverse weld tensile strength of a series of dog-bone samples extracted from a hollow AA6082 extrusion. They find that the weld strength varies by position with respect to length along the weld; dropping to around 75% of the strength of the parent metal. Sheppard [6] does not quantify the contribution of transverse weld removal to total extrusion scrap rates; however, Mahmoodkhani et al. [11] and Hatzenbichler and Buchmayr [12] found that the transverse weld length (TWL) accounted for 20 and 15% of the initial billet volume in profiles for which the billet butt accounted for 12 and 10% of the initial billet volume, respectively. The rest of this article will focus on existing and novel methods of reducing the TWL, as this is the largest source of scrap identified in the extrusion process.

1.1 Previous Work on Reducing the Length of the Transverse Weld Scrap

Parametric studies often use finite element models (FEMs) to investigate methods of reducing the billet butt volume and TWL [8, 11–15]. Extensive experiments are probably avoided due to their high cost and the significant time expended in processing and measuring the TWL. However, it is common for a single extrusion to be performed on the simplest set of parameters, from which the extrusion pressure and experimentally measured billet butt or TWL are used to validate the FEM [8, 11, 12, 14, 15]. The parameters that have been studied by previous researchers include die angle, extrusion ratio, ram velocity, ram-billet friction coefficient, billet length, temperature, and bearing length for solid profiles, in addition to port bridge diameter, welding chamber radius, and baffle plate height of the specialty porthole die used in hollow extrusions [8, 11–15]. The finite element software packages used in these studies are DEFORM™ [8, 11, 12, 14] and HyperXtrude™ [13, 15]. The alloys studied are AA3003 [11], AA6005 [13], AA6063 [8, 14], AA6082 [12], and AA7N01 [15].

The parametric studies found in the literature were performed by making slight alterations to validated finite element simulations such that the effect of individual parameter changes on the TWL could be isolated and measured. Studies on solid, axisymmetric profiles have looked at the effects of die angle, extrusion ratio, ram velocity, ram-billet friction coefficient, bearing length, and billet length on the TWL [11, 12]. Decreasing the extrusion ratio was found to have the largest effect of reducing the TWL [12]. The use of a smaller die angle [11], increasing billet length, or increasing temperature [12] was also found to have a significant effect in reducing

the TWL. Bearing length, ram velocity, and ram-billet friction coefficient were found to have an insignificant effect on the TWL [12]. No studies on non-axisymmetric solid profiles have been found in the literature. The hollow profile studies [13, 15] examined non-axisymmetric profiles (no studies on hollow axisymmetric profiles were found) and also looked at extrusion ratio, temperature, and ram speed, as well as porthole die dimensions, including the port bridge diameter, welding chamber radius, and baffle plate height. It was again found that decreasing the extrusion ratio has a significant impact in reducing the TWL [15]. Increasing the port bridge diameter, welding chamber radius, and baffle plate height were all found to have a significant effect in decreasing the TWL as well [15]. On the contrary to solid profiles, however, it was found that an increase in the ram speed could actually decrease the TWL [13, 15], and that the temperature no longer had a significant impact [15]. Although Zhang et al. [15] suggest that the ram speed would affect the material flow velocity through the die and therefore affect the transverse weld formation, neither they nor Chen et al. [13] offered an explanation for the varying impacts they observed between the solid and hollow profiles.

Previous research on reducing the TWL has examined neither the effect of the profile shape nor the effect of the dummy block profile geometry. In addition, previous work has been focused primarily on FEM studies. This work will examine the effect of common and novel extrusion design variables on the TWL using a multi-colored clay extrusion technique before discussing the significance of the results and the implications for the industry.

2 Methodology

2.1 Equipment

The experiments in this study were conducted on a hydraulic press extrusion setup developed for this research, shown in Fig. 2. The press container is made of aluminum, 127 mm long, with an internal diameter of Ø25.4 mm. The interchangeable dummy block is made of steel and was turned on a lathe to produce a sliding fit with the container. Several sets of dies were also produced for use with this press (Fig. 3). Die sets were machined and polished from a Ø42 mm aluminum rod. The first set is designed for axisymmetric solid rod extrusions of varying diameters corresponding to extrusion ratios of 4, 6.67, 10, and 25. The next set was produced for rectangular profiles of the same extrusion ratios. The third and final set of dies are more complex geometries, one cross and one with dual circles, both with an extrusion ratio of 4. Each die in these three sets has one side with a flat face (a die angle of 90°) and one side with a tapered 45° die angle.

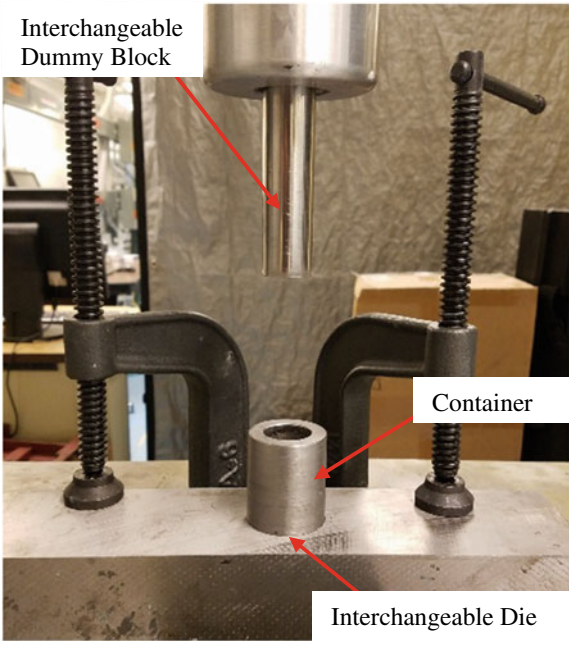


Fig. 2 Experimental plasticine clay direct extrusion press used in this study. (Color figure online)

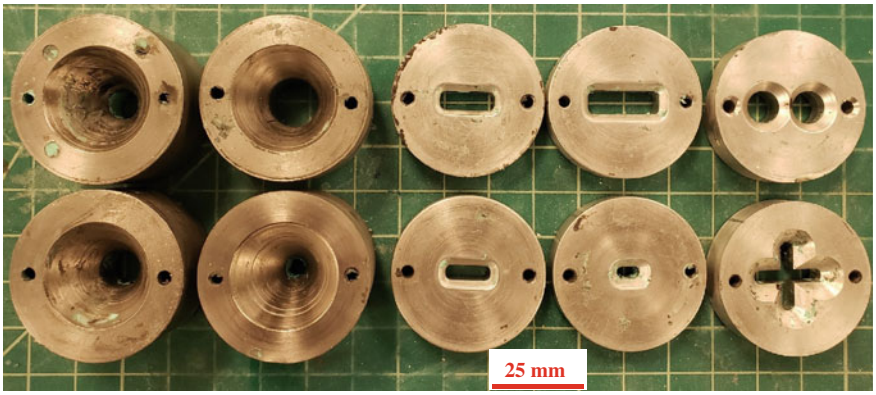


Fig. 3 From left to right: Axisymmetric die set; rectangular die set; complex dies with the dual-circle die on top, cross die at the bottom. (Color figure online)

2.2 Billet Material

The billets used in the experiments were made from plasticine clay, which is a low-cost material that can be used to adequately model hot-metal deformation [16]. In addition, the use of differently colored plasticine for consecutive billets enables the

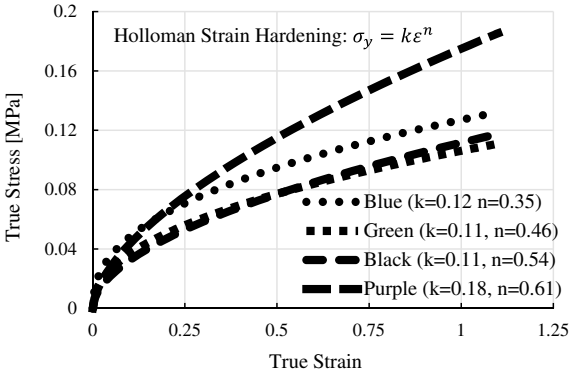


Fig. 4 Flow curves of four different colors of plasticine

transverse weld in an extruded profile to be easily located using a scalpel to section the profiles, as opposed to the lengthy and expensive sectioning, polishing, and etching process that is required for aluminum extrusions.

2.2.1 Billet Flow Curve

The elastoplastic properties of plasticine are dependent on its color [16], which is an indicative of the additives present in the clay. The two colors of plasticine used in this work must have similar mechanical behavior to maintain a consistent material flow through the die, as would be the case in real industrial extrusion of aluminum billets. The flow curve of differently colored plasticine was determined using a uniaxial compression test [16], and fitted to a power-law Hollomon strain hardening model [17], as shown in Fig. 4. Based on these results, the green and black were chosen for the experiments. In each extrusion trial, the green billet was extruded first, followed by the black billet.

2.2.2 Billet-Tool Friction Condition

Plasticine extrusions were conducted using different lubricants to examine the effect of friction on the TWL. Friction ring compression tests were conducted in order to determine the Coulomb friction coefficient (μ) under different lubrication conditions [17, 18].

During a friction test, a ring of plasticine (initially of height $h_0 = 25.4$ mm, inner radius $r_0 = 12.7$ mm, and thickness $t_0 = 9.5$ mm) was covered in lubricant and axially compressed between two platens, reducing the height (h). The test was intermittently paused in order to measure the inner radius (r) of the ring at the mid-plane at different levels of compression. The changing inner radius is indicative of the friction conditions; e.g., if there were zero friction the radius would increase, whereas with sticking friction it would decrease [17, 18]. Green plasticine and aluminum

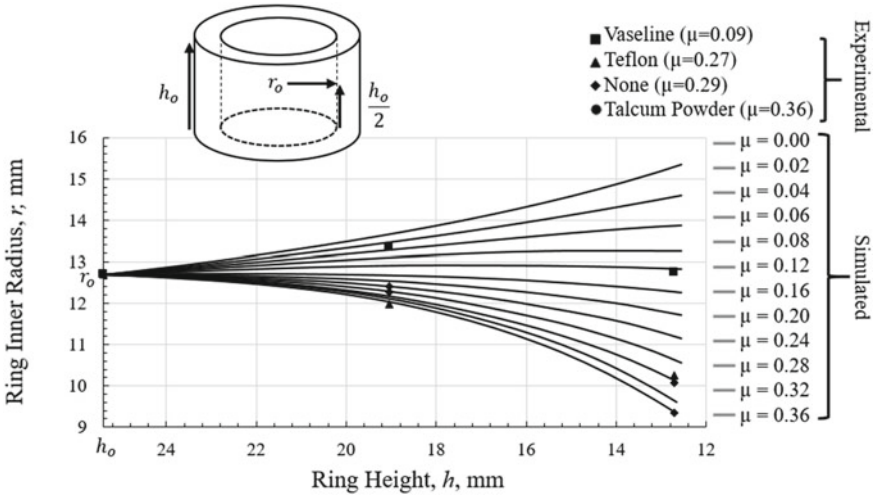


Fig. 5 Friction ring compression test results: experimental data points for different lubricants, and simulated curves for different modeled friction levels

platens of the same surface finish as the extrusion container were used in the friction tests. Additional trials tested the effect of using Vaseline®, Teflon® spray, and talcum powder as lubricants, as well as the use of no lubricants at all. An Abaqus FEM was produced to simulate the change of the inner radius during compression for different contact friction conditions. These FEM results were compared to the experimental results (see Fig. 5) in order to estimate the friction coefficient (μ) associated with each of the different lubricants. The axisymmetric, quarter-sized Abaqus model was meshed using 1,000 linear CAX4 elements with reduced integration and enhanced hourglass control. The validity of the model was confirmed by comparing the simulated and actual compression loads and ensuring that the energy dissipated due to contact stabilization was less than 1% of the internal energy of the model. The interfaces between the billet and the bottom and top plates were modeled using penalty tangential behavior at a range of friction coefficients from 0 to 0.36.

2.3 Dummy Block Geometry

The majority of the experiments conducted in this work used a conventional flat-faced dummy block; however, an attempt was also made to adjust the TWL by changing the geometry of the dummy block face in order to alter the material flow through the die. The material at the center of the billet-on-billet interface travels through the die quicker than the material at the interface periphery, which causes the elongation of the "bullet-shaped" weld. It was hypothesized that the TWL could be reduced by changing to an initially concave billet-on-billet interface geometry (see Fig. 6a). A

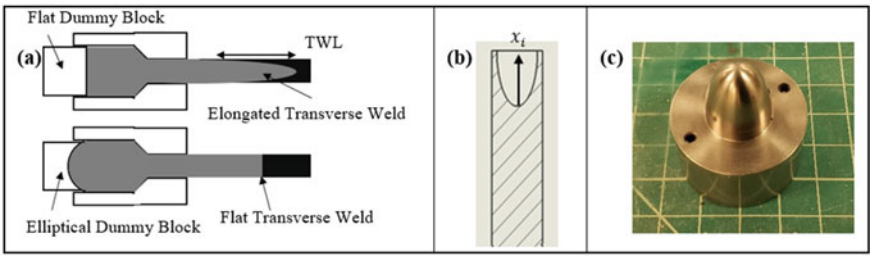


Fig. 6 **a** Transverse weld geometry formed in conventional extrusion (top) and profiled dummy block and billet extrusion (bottom). **b** Section view of elliptical concave ram used in profiled dummy block and billet experiments. **c** The convex forming element used as part of the profiled billet mold. (Color figure online)

trial dummy block and billet geometry were designed using analytical velocity field analysis, as described below.

For axisymmetric profiles, the flow of metal through the die can be estimated using a velocity field first proposed by Avitzur [19], where velocity discontinuities appear as spherical "caps" at the die entry and exit, see Fig. 7. To understand the difference in material flow between the center and outside of the billet, consider two particles (A and O, Fig. 7) both situated at the end of a billet (on the interface with a previously extruded billet) but at different radial positions. A is located near the edge of the billet (next to the container wall) and O is located on the billet center axis. During the extrusion process, both particles enter the velocity field with speed v_i (the ram speed). O then passes through the spherical-cap velocity discontinuity before A. Both particles exit the die at speed v_o, where v_o is equal to the product of v_i and the extrusion ratio (R_i^2/R_o^2). The TWL can be estimated as the difference in the axial positions of A and O once they emerge from the die (A'' and O'').

The velocity field is broken into three regions. The first region, I, contains material traveling at the same speed as the ram, v_i. This region ends at the first spherical-cap velocity discontinuity, along which points A' and O are found. The field line at this

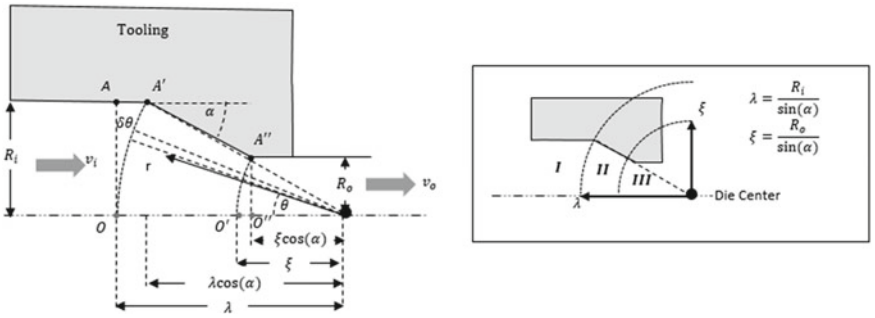


Fig. 7 Estimated velocity field for solid axisymmetric extrusion. Velocity discontinuities are seen as circular arcs on this 2D image

first spherical-cap velocity discontinuity indicates the start of region II, with material traveling at increasing speed in the direction of the die center, labeled on Fig. 7. Region II ends at the second spherical-cap velocity discontinuity, with a smaller radius (on which lie points A'' and O'). The material then enters region III in which all materials (irrespective of their radial positions) travel in the extrusion direction at speed v_o. Point A'' is located at the end of the conical die taper, marking the exit of particle A from the forming region. Point O'' is found within region III, traveling at the velocity of the exiting profile, v_o.

The time taken by particle A to travel through region I, from point A to A', is shown in Eq. 1.

$$t_{AA'} = \frac{\lambda(1 - \cos\alpha)}{v_i} \tag{1}$$

On entry to region II, material flows toward the die center at $v_i\cos\theta$, ensuring that the normal component of velocity is continuous on the velocity discontinuity surface; however, the parallel component of the velocity is discontinuous in this kinematically admissible velocity field [17]. Next, to find the changing velocity in region II, consider a small area of material traced out by $\delta\ \theta$ at a distance r from the die center (Fig. 7). The area of this strip is $2\pi r^2 sin\theta\delta\theta$. Volume conservation, therefore, dictates that the velocity toward the die center at any point along the length, r, from the entrance to the exit of region II is given by Eq. 2.

$$v(r, \theta) = \frac{v_i\lambda^2\cos\theta}{r^2} \tag{2}$$

It follows that the the time taken by particle A to travel through region II, from A' to A'', is given by Eq. 3.

$$\begin{aligned} dt = \frac{dr}{v(r,\ \alpha)} \rightarrow t_{A'A''} &= \int_{\xi}^{\lambda} \frac{r^2 dr}{v_i\lambda^2\cos\alpha} \rightarrow t_{A'A''} \\ &= \frac{1}{3v_i\cos\alpha}\left(\frac{\lambda^3 - \xi^3}{\lambda^2}\right) \quad for\ \theta = \alpha \end{aligned} \tag{3}$$

Similarly, the time taken by particle O to travel through region II, from O to O', is given by Eq. 4.

$$t_{OO'} = \frac{1}{3v_i}\left(\frac{\lambda^3 - \xi^3}{\lambda^2}\right) \tag{4}$$

Lastly, the time taken by particle O to travel through region III, from O' to O'', is given by Eq. 5.

$$t_{O'O''} = \frac{\xi(1 - \cos\alpha)}{v_o} \tag{5}$$

The difference in the time taken for particles A and O to travel from initial to final positions (A'' and O'') can then be used to solve for the total extra distance traveled by particle O into the profile, the TWL, shown in Eq. 6.

$$Transverse\ weld\ length\ (TWL) = v_0 \times (t_{AA'} + t_{A'A''} - t_{oo'} - t_{o'o''}) \quad (6)$$

The difference in distance particles A and O travel into the profile can be reduced by using a billet with a leading concave and trailing convex face, extruded with a concave dummy block. This offsets the initial axial position of A and O; particle O being shifted further back a distance, x_i, toward the ram in region I (Fig. 6b). The offset distance (x_i), which according to the stylized velocity field model above, will result in the axial alignment of A'' and O'' (TWL = 0), as given in Eq. 7.

$$\begin{aligned} x_i &= v_i \times (t_{AA'} + t_{A'A''} - t_{oo'} - t_{o'o''}) \\ &= \frac{Transverse\ weld\ length\ (flat\ billet\ scenario:\ eqn6)}{Extrusion\ ratio} \end{aligned} \quad (7)$$

Using the above analysis, a concave dummy block geometry was designed for axisymmetric extrusion of a solid rod with a die angle of $\alpha = 45°$ (see Fig. 6b). A mold with a convex forming element of identical geometry, shown in Fig. 6c, was machined and used in conjunction with the concave ram to make billets with a concave recess at one end and a convex protrusion at the other end. These profiled billets were then loaded into the extrusion press with the convex end of the billet nested into the concave ram. Multiple billets were then consecutively extruded and the TWLs measured.

Table 1 The values of the parameters studied in each of the sets of experiments

Trials	Extrusion Ratio	Die angle	Friction Coefficient	Profile Shape	Dummy Block & Billet Geometry
Set 1	4, 6.67, 10, 25	Tapered (45°), Flat (90°)	Unlubricated ($\mu = 0.29$), Vaseline ($\mu = 0.09$)	Axisymmetric, rectangular	Conventional (flat)
Set 2	4	Tapered (45°)	Unlubricated	Axisymmetric, rectangular, cross, dual-circle	Conventional (flat)
Set 3	4	Tapered (45°)	Unlubricated	Axisymmetric	Conventional (flat), Profiled (concave)

2.4 Experiments

A parametric study was performed on the TWL as a factor of the extrusion ratio, die angle, friction coefficient, profile shape, and dummy block profile. Table 1 summarizes the 35 different experiments conducted. Each experiment was performed three times in order to increase the reliability of the results. The resulting TWLs were measured using high-resolution photography input into IC Measure computer software [20]. The length of the weld was measured from the tip to the point at which the cross-sectional area of the old billet was just 5% of the total cross-sectional area of the profile. This criterion of 5% area is used in industry as a standard point at which the effect that the transverse weld has on lowering profile strength is deemed to be no longer significant [11]. For the axisymmetric profiles, longitudinal scalpel cuts along the length of the extruded profile revealed the complete weld geometry. For non-axisymmetric shapes, however, a salami-slicing approach was used to determine the weld geometry (see Fig. 8).

3 Results

The TWLs measured in this study ranged from 55 to 570 mm, increasing by a factor of 10 from a Vaseline® lubricated tapered axisymmetric die with an extrusion ratio of 4, to an unlubricated, flat rectangular die with an extrusion ratio of 25. The effects of the extrusion ratio, die angle, and friction coefficient on the TWL are shown in Fig. 9. The effect of the profile shape on the TWL is presented in Figs. 10 and 11.

The effect of the extrusion ratio was studied on both lubricated and non-lubricated, axisymmetric, tapered, and flat die faces. The results from the axisymmetric experiments in Fig. 9 show that as the extrusion ratio increases, the weld length increases significantly. The TWL from using unlubricated, flat dies increased by 500% from 73 mm at an extrusion ratio of 4 to 430 mm at an extrusion ratio of 25.

The results in Fig. 9 also show that the use of the tapered die reduced the TWL in nearly all scenarios. Similarly, the TWL decreased in nearly all the trials where Vaseline® was used to lower the friction coefficient. The influence of lubrication on the TWL was greatest in the case of the tapered dies at higher extrusion ratios. For example, the Vaseline® decreased the TWL associated with the tapered die by an insignificant amount at an extrusion ratio of 4, increasing to a 30% reduction at an extrusion ratio of 25. In contrast, the percent reduction in the TWL caused by using



Fig. 8 Incremental cross-sectional "salami-slicing" cuts of the cross profile. (Color figure online)

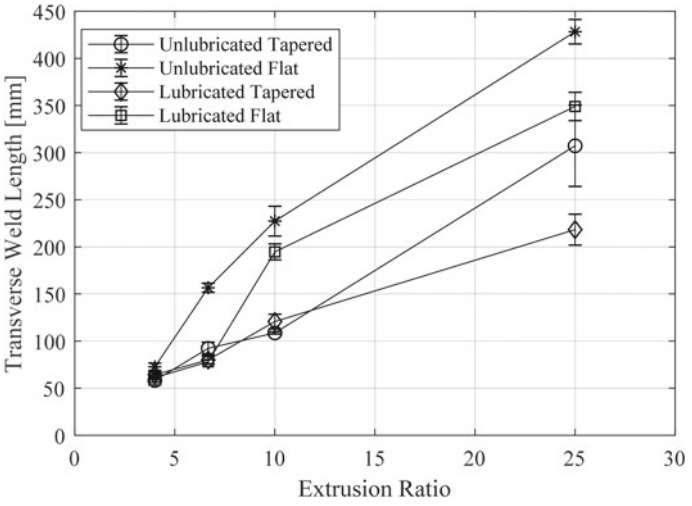


Fig. 9 Transverse weld lengths in axisymmetric solid profiles at varying extrusion ratios, die angles, and friction coefficients

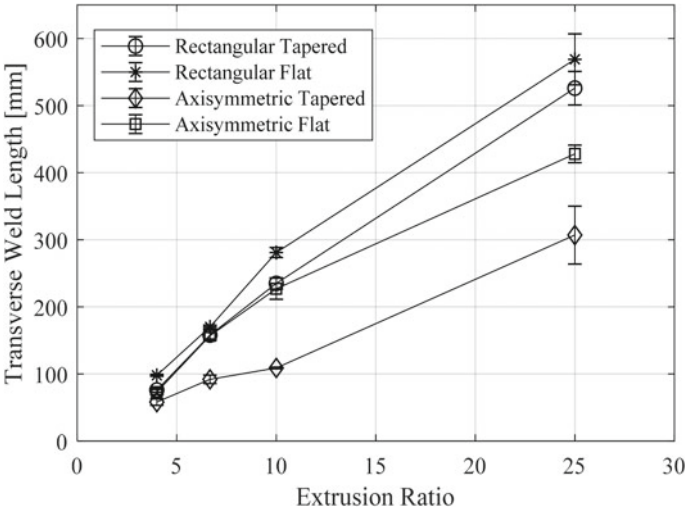


Fig. 10 Transverse weld lengths in axisymmetric and rectangular solid profiles at varying extrusion ratios and die angles (unlubricated friction conditions)

lubrication was relatively constant across different extrusion ratios in the case of the flat dies.

The results in Fig. 10 show that extruding the rectangular profiles produced longer TWLs than extruding the corresponding axisymmetric profiles at the same extrusion ratio. The amount the TWL increased varied by scenario, from 8% in the case of flat

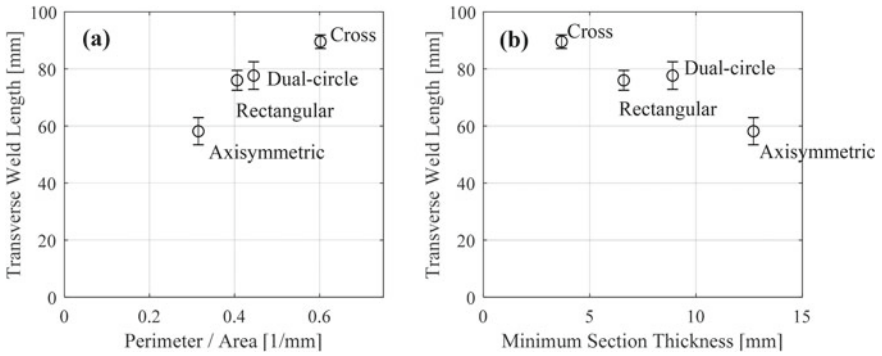


Fig. 11 Transverse weld lengths against **a** the ratio of profile cross-sectional perimeter to area and **b** the profile minimum section thickness. All profiles represent an extrusion ratio of 4

dies at an extrusion ratio of 6.67, to a 110% increase in the case of tapered dies at an extrusion ratio of 10. The second set of profile shape trials included two, more complex profiles both at an extrusion ratio of 4; one cross-shaped, one dual-circle, as shown in Fig. 3. Figure 11 shows the measured TWLs for the various extruded profile shapes when plotted against (a) the ratio of profile perimeter to area and (b) the minimum section thickness of each profile. These plots show that, for the shapes chosen in this research, the TWL increases as the ratio of the perimeter to area increases.

Figure 12 shows that the concave-profiled dummy block and profiled billets produced a TWL of 31 mm, which represents a 44% reduction in weld length from the 55 mm weld that was produced using a flat dummy block and conventional billet geometry. The resulting weld profile is shown to have changed drastically, inverting at the tip.



Fig. 12 Transverse weld profiles produced from **a** flat and **b** concave profiled dummy blocks. (Color figure online)

(a) Weld from flat-profiled dummy block

(b) Weld from concave-profiled dummy block

4 Discussion

In this section, we discuss the physical reasons behind the experimental trends and the implications for reducing process scrap in the industry.

4.1 Extrusion Ratio

The extrusion ratio is a term that equals the cross-sectional area of the press container divided by the cross-sectional area of the extruded profile. A smaller extrusion ratio reduces the TWL by reducing the relative velocity difference between the material flowing at the interior and exterior of the profile (Fig. 7). An extruder has limited flexibility to change the profile geometry requested by a customer; therefore, the extruder can only reduce the extrusion ratio by using a press with a smaller container diameter. Reduced container and therefore billet diameters would, however, reduce plant throughput without a concurrent increase in billet length in order to maintain overall billet volume. A smaller extrusion ratio also reduces the ram force required to push material through the die; however, longer billets would increase the ram force through higher billet-container frictional forces. Chien et al. [21] recently showed that for AA6063 extrusions at 454 °C, decreasing the billet diameter from 254 to 203 mm and simultaneously increasing the length of the billet to maintain a constant volume of aluminum resulted in a 1.9% decrease in extrusion load. This would allow for the length of the billet to be increased even further before the maximum load rating of the press is reached. Chien et al. show that a marginal increase in throughput could be achieved while also decreasing the extrusion ratio, and from this research, it can be reasoned that the transverse weld scrap amount would also be decreased.

4.2 Die Angle and Friction

In the industry and in the literature, it is often assumed that a flat die forms a dead metal zone (DMZ) with a DMZ angle (equivalent in function to the die angle) of close to 45°. The DMZ is a volume of stationary material at the face of the die over which the billet material shears, allowing it to flow through the die. If it were the case that a flat die forms a 45° DMZ angle, then we would expect that the TWL results from using the flat and 45° unlubricated tapered dies might be similar. However, our results show that using a tapered die significantly reduces the TWL, particularly at higher extrusion ratios. Sectioning partially extruded billets from this work (Fig. 13) revealed that the DMZ angle formed on an unlubricated, flat die of extrusion ratio 4 was close to 45° (Fig. 13a) but that this DMZ angle greatly increased at higher extrusion ratios (Fig. 13b) becoming much closer to a truly square/flat material flow. Elsewhere, Sluzalec [22] found that the relationship between the DMZ angle and

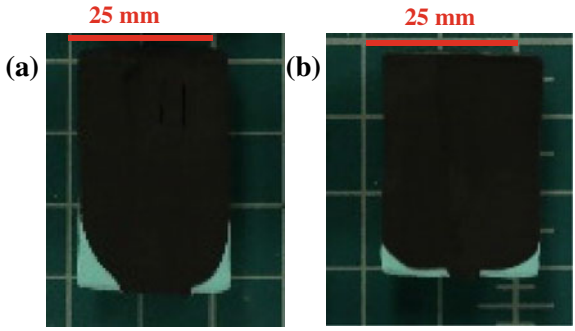


Fig. 13 Longitudinal cross-sectional cut after partial extrusion of the second billet to show DMZ of **a** extrusion ratio = 4, and **b** extrusion ratio = 25. DMZ is in green. Aspect ratio of billets (diameter:initial length) = 1. (Color figure online)

extrusion ratio changes based on the aspect ratio of the billet used (billet length to diameter). He found that for an aspect ratio of 1 (the ratio used in this research), the DMZ angle increases with the extrusion ratio. However, as the aspect ratio is increased through an increase in billet length, the DMZ was found to decrease as the extrusion ratio increases.

When using flat dies, the effect that reducing the friction has on the TWL is relatively constant across the extrusion ratios, whereas the effect that reducing the friction has on the TWL when using tapered dies appears to grow with the extrusion ratio (Fig. 9). One explanation for this observation is that the DMZ angle formed behind the flat die increases as friction is lowered, as observed by Sluzalec [22] for billet aspect ratios of 1. An increasing DMZ angle would act to increase the TWL (analogous to increasing the die angle) and therefore counteracts some of the positive effects of decreasing the TWL through reduced friction. To isolate the effect of friction on TWL (independent of DMZ/die angle), it is therefore recommended to observe the changes in TWL on the tapered dies. This research suggests that adding a lubricant to lower the friction coefficient can significantly reduce TWLs at higher extrusion ratios. However, many extruders are reluctant to use lubricant between the billet and container wall for fear that this could cause surface defects on the extruded profile, including blistering [6].

4.3 Profile Shape

The effect of the profile shape on the TWL has not been previously studied. Figure 11 suggests (for a given cross-sectional area) the TWL scales with the perimeter of the extruded profile cross-section. This may be because a larger perimeter suggests a thinner average section thickness and, locally, this manifests itself as a more extreme material flow; equivalent to a local increase in the extrusion ratio. For example, in the extrusion of the cross profile the old (green) billet can be seen further along the profile in the thin extremities of the cross rather than in the thicker central portion (see

Fig. 8). A larger perimeter also causes greater frictional forces, which, as discussed elsewhere, will lead to a higher TWL.

An extruder may have limited opportunities to influence the shape of the extruded profile requested by a customer. However, designers should be fully aware of the material efficiency and environmental implications of their component designs. There is probably some scope for improved profile shapes that reduce the TWL, which can be found through greater awareness of the process scrap ramifications.

4.4 Dummy Block Profile

This article has presented a simple case study that highlights the potential of using profiled dummy blocks and billets to control material flow through the die and to subsequently reduce the TWL. The TWL decreased by 44% in the case study (Fig. 12). The reason the TWL did not decrease to zero because the velocity field that is used to design the profiled block and billets is an idealization of extrusion and drawing flow through conical dies, neglecting, for example, the effect of friction along the container walls.

Further studies must address the technical feasibility of the profiled dummy block concept across a wider variety of profile shapes as well as the use of real aluminum material rather than a clay proxy. The benefits from reduced scrap generation will have to be reconciled against barriers to industry take-up that may include the costs of the new dummy blocks and new casting molds or forming apparatus that are needed to make the profiled billets.

5 Conclusions and Future Work

The removal of transverse welds between consecutively extruded billets is a key material inefficiency in the aluminum extrusion industry. This study has shown the potential to reduce the TWL through reduced extrusion ratios, die angles, friction coefficients, and profile perimeter to area ratios. Additionally, it has been demonstrated that adjustments to the dummy block profile (a previously unexplored design variable) might be an option to further decrease the weld length. Future work will include defining a process window for the profiled dummy block concept considering more realistic extrusion profiles (e.g., hollow non-axisymmetric shapes) and exploring the potential to reduce the TWL while constraining dummy block stresses to the elastic region and minimizing the costs of any new profile-specific dummy blocks and casting molds or forming apparatus.

Acknowledgments The first author was supported by a funding award from the Michigan Translational Research and Commercialization (MTRAC) program.

References

1. International Energy Agency (2017) Energy technology perspectives 2017—Executive summary. https://webstore.iea.org/download/summary/237?fileName=English-ETP-2017-ES.pdf. Accessed 15 Apr 2020
2. Gutowski TG, Sahni S, Allwood JM, Ashby MF, Timothy GM, Ashby F, Worrell E (2013) The energy required to produce materials: constraints on energy-intensity improvements, parameters of demand. Philos Trans Mathe Phys Eng Sci 371:1–14
3. Cullen JM, Allwood JM (2013) Mapping the global flow of aluminum: From liquid aluminum to end-use goods. Environ Sci Technol 47(7):3057–3064
4. European Aluminum Association (2018) Environmental profile report. https://european-aluminium.eu/resource-hub/environmental-profile-report-2018/. Accessed 13 Apr 2020
5. European Aluminum Association (2013) Environmental profile report. https://european-aluminium.eu/media/1329/environmental-profile-report-for-the-european-aluminium-industry.pdf. Accessed 13 Apr 2020
6. Sheppard T (1999) Extrusion of aluminium alloys. Springer Science + Business Media, Dordrecht
7. Saha PK (2000) Aluminum extrusion technology. ASM International, Materials Park, Ohio
8. Sano H, Ishikawa T, Yukawa N, Yoshida Y, Kaneko T, Sakamoto J (2008) Effect of back end lubricant conditions on billet skin behavior in direct extrusion. Keikinzoku/J Japan Inst Light Metals 58(5):189–193
9. Oberhausen GJ, Cooper DR (2019) Semi-structured interviews with North American Extrusion Industry Experts
10. Den Bakker AJ, Katgerman L, Van Der Zwaag S (2016) Analysis of the structure and resulting mechanical properties of aluminium extrusions containing a charge weld interface. J Mater Process Technol 229:9–21
11. Mahmoodkhani Y, Wells MA, Parson N, Poole WJ (2013) Numerical modelling of the material flow during extrusion of aluminium alloys and transverse weld formation. J Mater Process Technol 214(3):688–700
12. Hatzenbichler T, Buchmayr B (2010) Finite element method simulation of internal defects in billet-to-billet extrusion. Proc Inst Mec Eng Part B: J Eng Manufact 224(7):1029–1042
13. Chen L, Zhao G, Yu J, Zhang W (2015) Evaluation of a pyramid die extrusion for a hollow aluminum profile using FE simulation. J Mech Sci Technol 29(5):2195–2203
14. Sano H, Ishikawa T, Yukawa N, Yoshida Y, Kaneko T (2008) Effect of extrusion mode and die shape on billet skin behavior in aluminum extrusion. Keikinzoku/J Japan Inst Light Metals 58(5):183–188
15. Zhang C, Dong Y, Wang C, Zhao G, Chen L, Sun W (2017) Evolution of transverse weld during porthole extrusion of AA7N01 hollow profile. J Mater Proc Technol 248(January):103–114
16. Sofuoglu H, Rasty J (2000) Flow behavior of plasticine used in physical modeling of metal forming processes. Tribol Int 33(8):523–529
17. Hosford WF, Caddell RM (2007) Metal forming: mechanics and metallurgy. Cambridge University Press, New York
18. Sofuoglu H, Rasty J (1999) On the measurement of friction coefficient utilizing the ring compression test. Tribol Int 32(6):327–335
19. Avitzur B (1963) Analysis of wire drawing and extrusion through conical dies of small cone angle. J Eng Ind
20. The Imaging Source (2019) IC Measure. https://www.theimagingsource.com/support/downloads-for-windows/end-user-software/icmeasure/. Accessed 13 Apr 2020
21. Chien K, Robbins P, Jowett C, Wang Y (2018) Extrusion productivity, Part I – Billet Geometry, Light Metal Age
22. Sluzalec A (1991) Analysis of dead zones in the process of direct extrusion through single-hole flat die. Commun Appl Num Methods 7(4):281–287

Introduction of a New Method for Continuous Aluminum Hot Extrusion



Johannes Gebhard, Patrick Kotzyba, Oliver Hering, and A. Erman Tekkaya

Abstract The new extrusion process combines the conventional methods of direct and indirect aluminum hot extrusion by an innovative container and die setup with a moving or stationary valve. The process enables the continuous extrusion of aluminum profiles without any interruptions. With both variants, moving or stationary valves, the usual dead cycle times can be used for a continuous extrusion process. Furthermore, due to the continuous material flow, a stationary profile exit temperature can be achieved, which leads to constant material properties. As of now, a continuous extrusion press for aluminum is not available. The new process concept is analyzed on the basis of scaled experimental models using the model material plasticine and numerical simulations. The similarity of the model material was validated by aluminum extrusion experiments. Various model material colors were investigated, and the resulting material flow and process forces of the new process were analyzed.

Keywords Hot extrusion · Physical process modeling · Extrusion press

1 Introduction

Hot aluminum extrusion is a common process for producing long semi-finished profiles from cylindrical billets. Particularly for the processing of aluminum alloys, direct and indirect extrusion are of economic importance. Due to increasing product requirements, process control plays an increasingly important role. One of the most important factors in this context is the achievement of a constant profile exit temperature since this has a decisive influence on the mechanical properties of the profiles. The most important process parameters are the billet temperature and ram speed, which influence the temperature in the forming zone and thus the product properties [1]. In order to achieve a temporally constant temperature profile, and consequently stationary forming, the billet can be used with an axial temperature gradient, adjusted

J. Gebhard (✉) · P. Kotzyba · O. Hering · A. E. Tekkaya
Institute of Forming Technology and Lightweight Components, TU Dortmund University, Dortmund, Germany
e-mail: johannes.gebhard@iul.tu-dortmund.de

© The Minerals, Metals & Materials Society 2021

G. Daehn et al. (eds.), *Forming the Future*, The Minerals, Metals & Materials Series,
https://doi.org/10.1007/978-3-030-75381-8_85

to the extrusion speed. Alternatively, the system is locally heated or cooled. In various studies, both the lateral grading of billet temperature [2] and the adjustment of the ram speed [3] were investigated. The process could be controlled in a way that a constant profile exit temperature is reached during the forming of a billet for a certain time window, however, the outlet temperature cannot be kept completely constant. In addition, both the heat generated by forming and the heat dissipation are influenced by the extrusion speed [4]. Associated with the process-related waiting times when loading the billets, there is a transient temperature profile in the forming zone.

The microstructure has a direct influence on the mechanical properties and could be analyzed and characterized by EBSD measurements [5]. Especially when using high-strength AA7xxx alloys, the profile exit temperature must be kept in an operating window, in order to achieve good mechanical product properties [6]. One method to avoid process errors caused by excessive temperatures is active die cooling near the guide surfaces [7]. As a result, productivity can be increased significantly but still, no constant outlet temperature is achieved.

In addition to a constant profile outlet temperature, a continuous process sequence is desirable, especially with regard to the development of new extrusion technologies. From conventional hot extrusion, numerous non-conventional processes have been developed, such as composite extrusion with continuous [8] and discontinuous reinforcement elements [9] and co-extrusion of aluminum and magnesium [10]. Process extensions include curved profile extruding [11] and extrusion with variable wall thicknesses without [12] and with a mandrel [13]. However, the basic procedure is unchanged and consists essentially of the steps billet feeding, billet loading, upsetting, pressing, and removal of the discard. In particular, for the mentioned non-conventional processes, the dead-cycle-time between two billets is of great disadvantage, since the profile exit is interrupted and it leads to a drop of temperature and therefore to unsteady conditions. This can cause quality loss or reduced efficiency. But even for conventional profile extrusion, the resulting dead-cycle-time during block change limits the efficiency and cost-effectiveness of the extrusion process. Hot extrusion is strictly not a continuous or stationary process, but a quasi-stationary process. The development of an uninterrupted, continuous extrusion process offers the potential for a significant increase in economic efficiency as well as an expansion of existing process limits, in particular for non-conventional hot extrusion processes.

Plasticine is a well-known material for visualizing the flow behavior [14] and the process forces [15] of metallic materials. The composition of the material influences the plastic properties. Wanheim [16] investigated both yield stress and hardening behavior with different fractions of wax, hardener, and kaolin. Since it can be colored differently, it is suitable for the visualizing of the material flow [17]. Schöpfer and Zulauf [18] adjusted strain hardening and strain rate-dependent flow properties of Beck's plasticine by adding oil. The similarity can be achieved for flow behavior, friction, and forming heat, with some limitations also for heat transfer [19]. Dicks [20] has shown that the material flow of plasticine and aluminum is similar in hot extrusion.

With increasing computing power and advanced finite element simulation software, numerical methods for process design and analysis are mainly used. The FEM

is a flexible method for describing the complex thermal and mechanical processes involved in extrusion molding [21]. For continuous extrusion, the two methods of direct and indirect extrusion are combined by a moving valve. For a successful numerical simulation, the resulting different boundary conditions must be linked together. This concerns the material flow in the extrusion die, valve, hollow ram, or second container. Usually, only stationary material is considered for aluminum extrusion with an Eulerian approach of discretization. Due to the movement of the valve and the hollow ram, the flow volume changes in the presented continuous extrusion during a cycle. Therefore, the extrusion cycle needs to be split and investigated stepwise. Because no continuous extrusion press exists, the numerical approach cannot be validated experimentally. Therefore, in particular, physical process modeling, while maintaining similarity, can serve to validate the numerical investigation.

2 Continuous Extrusion

In the following, a new method for continuous extrusion is presented in which billets and profiles are comparable to conventional extrusion. The method distinguishes itself from the existing conform process [22] by significantly higher extrusion ratios and higher flexibility. The process considered here, and from now on referred to as continuous extrusion, is a combination of direct and indirect extrusion and allows the production of endless profiles, with the steady material flow in the extrusion die. The process was developed and patented in cooperation between the IUL and the SMS group GmbH [23]. The main components of the press are shown schematically in Fig. 1. Between two containers, a valve is arranged, which allows the material to flow only in the extrusion direction. During extrusion, the press is operated by two main hydraulic cylinders, the first cylinder is used for direct extrusion and the second cylinder for indirect extrusion. Accordingly, the ram for indirect extrusion is designed hollow. The die is positioned in the extrusion direction behind the hollow ram according to Fig. 1.

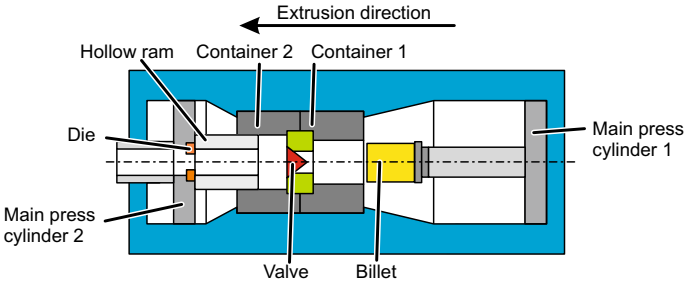


Fig. 1 Schematic of the main components of the continuous extrusion press. (Color figure online)

The process sequence can be subdivided into the two phases of direct and indirect extrusion, with both phases merging smoothly. Before the direct extrusion phase begins, the billet is supplied laterally and inserted into container 1. Then the ram is moved in the extrusion direction. Due to the material flow, the valve is opened and the material flows into container 2 and exits at the die (Fig. 2a). In order to allow indirect extrusion by moving the hollow ram, a part of the material must remain in container 2. For this purpose, the hollow ram is moved in the extrusion direction and the volume of container 2 is increased (Fig. 2b).

For indirect extrusion, the hollow ram is moved against the extrusion direction. The valve is closed by the resulting material flow against the extrusion direction. At the same time, the material from container 2 is pressed through the hollow ram and the extrusion die (Fig. 3a). Since the two containers are spatially separated by the valve, the next billet can be loaded into recipient 1, while indirect extrusion is maintained (Fig. 3b).

As soon as the material from container 2 is extruded and the hollow ram is in its final position, the initial state (Fig. 2a) is reached and the cycle can be repeated. Depending on the volumes of the two containers, the ram velocities can be selected or regulated so that the profile exit velocity remains constant during the whole cycle.

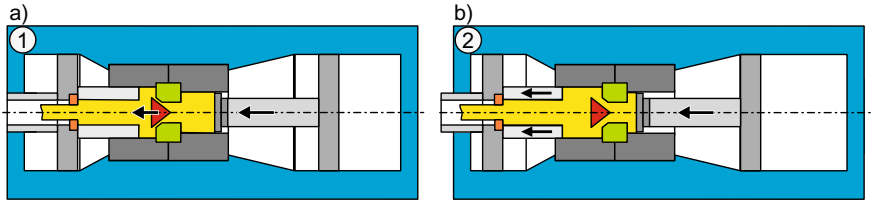


Fig. 2 Schematic sequence of the direct phase of continuous extrusion (steps 1 and 2). (Color figure online)

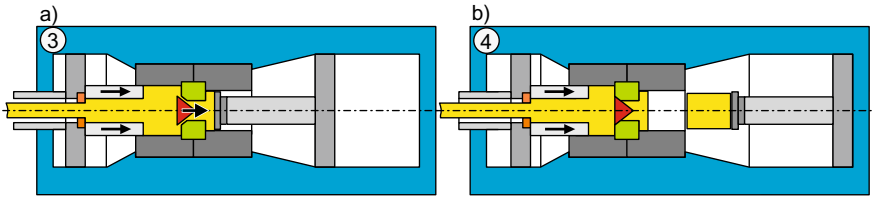


Fig. 3 Schematic sequence of the indirect phase of continuous extrusion (steps 3 and 4). (Color figure online)

3 Similarity of Plasticine and Aluminum

To investigate the continuous extrusion process, physical process modeling and FEM were used. While the commercially available software HyperXtrude can be used to simulate aluminum hot extrusion, the model material must first be characterized to establish the similarity to aluminum. Afterward, physical experiments are conducted on a scaled model of the continuous extrusion press using the characterized material. The used model material is plasticine which was provided by Becks Plastilin. The material behavior was investigated by upsetting tests and a direct comparison for direct aluminum hot extrusion. Figure 4 shows the setup of the compression test and the flow curves for the strain rates $\dot{\varphi} = 0.0067\ s^{-1},\ 0.1\ s^{-1},\ 0.22\ s^{-1}$. The specimens have a diameter of $d = 32$ mm and a height of $h = 50$ mm and are compressed into a cylindrical shape. The specimens were lubricated with talcum powder, compressed, and evaluated until the point of barreling.

The flow curves show a significant dependency of strain rate; also the plasticine shows nearly no strain-dependent hardening. This behavior is comparable to aluminum in hot conditions. Therefore, it is assumed that the chosen plasticine can be used to model the behavior of aluminum for the process of extrusion. Since it was not possible to reach strain rates that are comparable to aluminum extrusion, a comparative experimental setup was chosen to validate the similarity of plasticine.

To directly compare a scaled model with plasticine to the real-sized process of aluminum extrusion, an existing porthole die was scaled by the factor of $d_{\mathrm{I}}/d_{\mathrm{II}} = 3.088$ where d_{I} represents the dimension of the full-size aluminum extrusion die and d_{II} represents the dimensions of the model. The scale factor was also applied to the diameters of the containers to compare the process forces.

The aluminum extrusion experiments were conducted on a 10 MN direct extrusion press with the aluminum alloy AA6060. Billets, die, and container were heated to 450 °C and the profiles were extruded with a ram velocity of 1 mm/s. The setup and die geometry are shown in Fig. 5a. A similar setup was conducted with plasticine and a scale factor of 3.088. All parameters—die dimensions, container diameter, billet

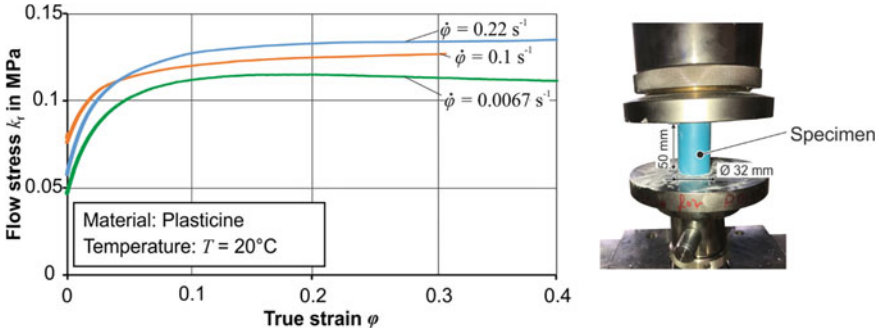


Fig. 4 Flow curves for the used plasticine. (Color figure online)

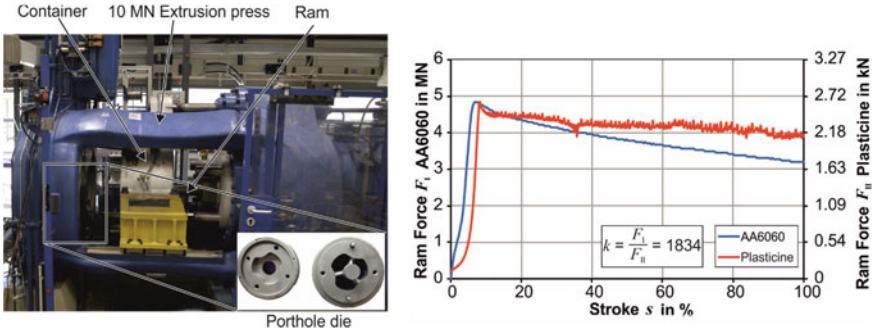


Fig. 5 **a** Experimental setup of extrusion experiments and **b** comparison of ram forces with respect to scale. (Color figure online)

length, and extrusion speed—were scaled accordingly. To compare the ram forces, the force–stroke curve of the model experiments was scaled dependent on flow stress and dimensions. The ratio of the ram forces can be determined by

$$k = \frac{F_{\mathrm{I}}}{F_{\mathrm{II}}} = \frac{d_{\mathrm{I}}^2 \cdot \sigma_{\mathrm{f,I}}}{d_{\mathrm{II}}^2 \cdot \sigma_{\mathrm{f,II}}} = 1834$$

Figure 5b shows the ram forces for aluminum extrusion and the scaled force of plasticine.

With the calculated scaling factor k, the ram forces of the plasticine model and the aluminum extrusion experiment nearly match for the maximum ram force. With advancing ram stroke, the friction in the model experiment between ram and container increases, and therefore, the process force deviates from the real-sized extrusion experiment. This can be explained by uneven sealing since no expanding dummy block was used in the model. Therefore, the validation of the model is done by comparing the maximum extrusion force. For the used plasticine, the model matches the behavior of aluminum AA6060.

4 Analysis of Continuous Extrusion

The introduced process of continuous hot extrusion consists of the direct pressing phase and the indirect pressing phase (Figs. 2 and 3). During the direct phase, the material is pushed through the first container, the valve, the second container, the hollow ram, and finally, the extrusion die. The process was simulated in HyperXtrude with an Eulerian approach. The complete cycle is separated into direct and indirect extrusions. Figure 6 shows the flow volume and contour plot of the continuous extrusion process. The material, AA6060, is modeled with a sine hyperbolic material law based on Zener-Holomon, e.g., Seller-Tergart. For the direct phase of the extrusion

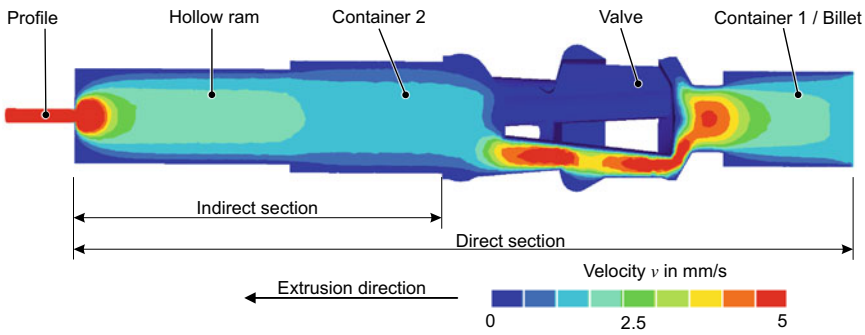


Fig. 6 Flow volume of the continuous extrusion process. (Color figure online)

cycle, the whole flow volume is considered (compare Fig. 6). It is assumed that the valve stops the material flow in the reverse extrusion direction. To compute the indirect pressing phase, only the flow volume of the hollow ram and container 2 are taken into account. The element edge length in the generated mesh in the direct and indirect part is 6 mm. The speed of hollow and direct ram is 1.47 mm/s in order to match the scale of the model experiments. The initial billet temperature and the temperature of the press were set to 450 °C.

The velocity distribution in Fig. 6 shows two major forming zones, the first one is at the valve and the other forming zone is in the hollow ram. The ram force during the direct phase is, therefore, considerably increased. With a diameter of 100 mm for container 1 and the inside of the hollow ram, a profile diameter of 14.7 mm ($R = 64$), the maximum ram force of direct extrusion is $F_{\mathrm{sim,I,direct}} = 6.3$ MN and for the indirect phase $F_{\mathrm{sim,I,indirect}} = 2.6$ MN. The indirect phase is comparable to a conventional extrusion process, where a similar process force would be reached.

The numerical investigations show process forces and material flow but cannot predict the functionality of the moving valve since only stationary forming is considered. Therefore, a model of the continuous extrusion press was constructed with polymer standard parts and additive polymer manufacturing (FDM). The press was scaled to a container diameter of $d_{0,\mathrm{II}} = 34$ mm and installed to a ZWICK universal testing machine with a maximum force of 250 kN. The setup is shown in Fig. 7.

To continuously extrude, two independently moving rams are necessary. Since this is not possible in the testing machine, the continuous cycle is again separated into two steps, the direct and the indirect phase. The direct extrusion phase is achieved by blocking the relative displacement between hollow ram and container 2 with stands and applying load on the ram (Fig. 7). By removing the stands and applying load on container 1, the indirect phase of the continuous extrusion cycle is performed where the hollow ram is pushed into container 2. During both phases, profile extrusion is achieved. To fill container 2, the stands are put between container 2 and the backup plate of the testing machine such that the hollow ram and die are in distance to the backup plate. When a billet is loaded into container 1 and pressed, container 2 is filled with plasticine until the die reaches the backup plate of the machine. When the

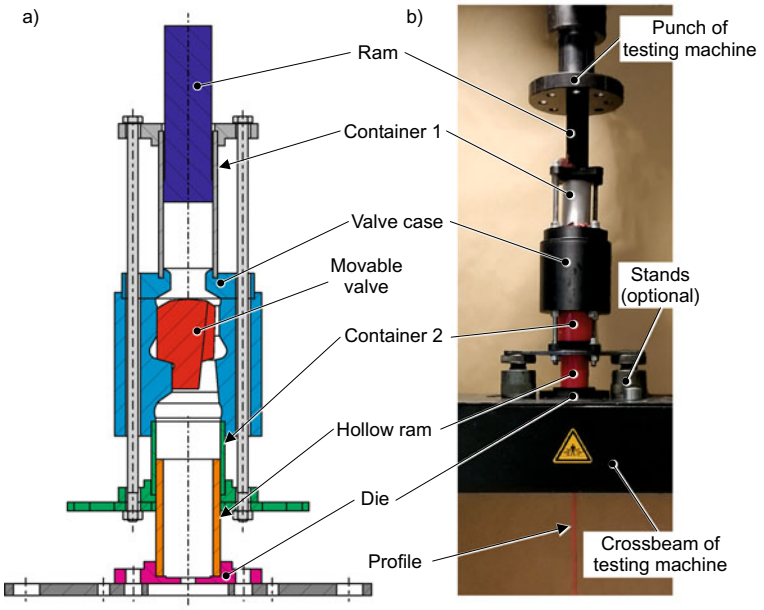


Fig. 7 **a** Model of the continuous extrusion press and **b** setup in the universal testing machine. (Color figure online)

ram is moving further, the material is pushed through the die and the direct extrusion phase continues. With this sequence, the whole cycle of continuous extrusion, except the simulation movement of ram and hollow ram can be investigated.

Figure 8a shows the ram forces of the direct extrusion phase and the indirect phase. Since the material has to flow through the valve, container 2, and hollow ram, the process force is significantly higher than for conventional direct extrusion. The force for the indirect phase is approximately 40% of the ram force during the direct phase. As mentioned earlier, the force of the indirect phase is comparable to conventional

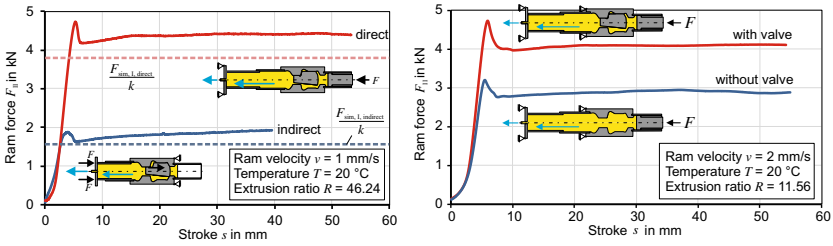


Fig. 8 Process force **a** with movable valve and **b** without valve for the direct and indirect phase of the process. (Color figure online)

aluminum extrusion. This leads to the conclusion that the valve consumes a lot of energy and needs to be examined further.

During the experiments, the material flow was as desired and the valve prevented material flow from container 2 to container 1. However, it was also observed that the valve did not move during the experiments. The position of the valve was measured tactile between the phases from the side of container 1, showing that it is not necessary to spatially separate container 1 and container 2 to enable continuous extrusion. When comparing the forces of the plasticine model and the numerical simulations with aluminum on the real-sized press, the same scaling method can be used as mentioned earlier. The forces ($F_{\mathrm{II,direct}}$ and $F_{\mathrm{II,indirect}}$) can be scaled with the factor $k = 1664$ and compared with the numerical simulations. The numerical forces are approximately 13% lower than the forces obtained with the plasticine model.

Figure 8 b shows the ram force–stroke curve for the direct extrusion step with and without the movable valve for another extrusion ratio and ram velocity. The force can be reduced to approximately 27%. Even without the movable valve, an extrudate is produced in the following indirect phase and just a minor amount of material is flowing from container 2 into container 1. This leads to the conclusion that the chamber between containers 1 and 2 can be designed suitably for the material flow to reduce the force of the direct phase and simultaneously preventing the reflux in the indirect phase.

In addition to the ram forces, the material flow in the continuous extrusion process was examined. To visualize the material flow, differently colored billets, in this case blue and yellow, were pressed in sequence. After pressing the third billet, the process was stopped and the remaining material was removed carefully from the press. Figure 9 shows the removed material and a plot of the material flow in the longitudinal cross-section.

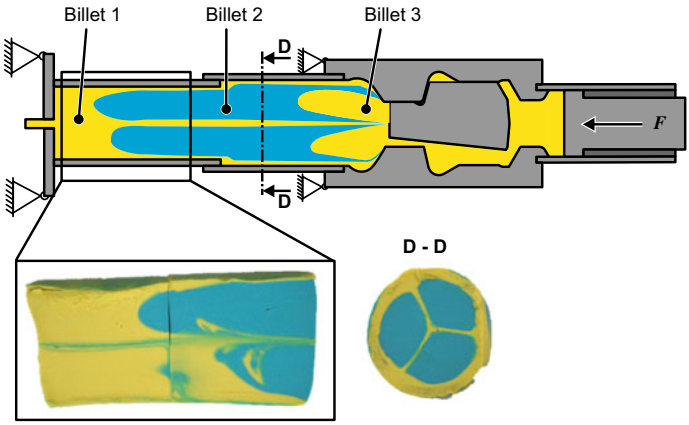


Fig. 9 Material flow visualized with differently colored plasticine during the direct phase of the extrusion cycle. (Color figure online)

The movable valve acts comparable to a porthole die with three bridges, and three longitudinal weld seams can be observed. The depicted flow pattern also applies to the profile. In this case, a symmetrical round profile of 5 mm diameter was produced. The longitudinal and lateral cross-section shown in Fig. 9 is also valid for the final extrudate.

5 Conclusion and Outlook

The process of continuous hot extrusion can be performed with a stationary valve that is adapted to the material flow. The advantages are reduction of the flow volume and no moving parts in the valve. While the reduced flow volume allows a smaller press size and easier cleaning or change of alloys, the usage of stationary parts increases the durability and risk for failures; for example, due to jamming or clamping of the moving valve. To prove the concept of a stationary valve, the model was modified according to Fig. 10.

With the given diameters for die exit and stationary die, direct extrusion and indirect extrusion could be realized. After the indirect phase of extrusion, just a small amount of plasticine has flown back, against the extrusion direction (Fig. 10). Nearly all of the contents in container 2 were extruded to a profile. This leads to the conclusion that the chosen parameters represent the process limit for the indirect phase of the press. When the diameter of the stationary valve is enlarged, more material flows back to container 1.

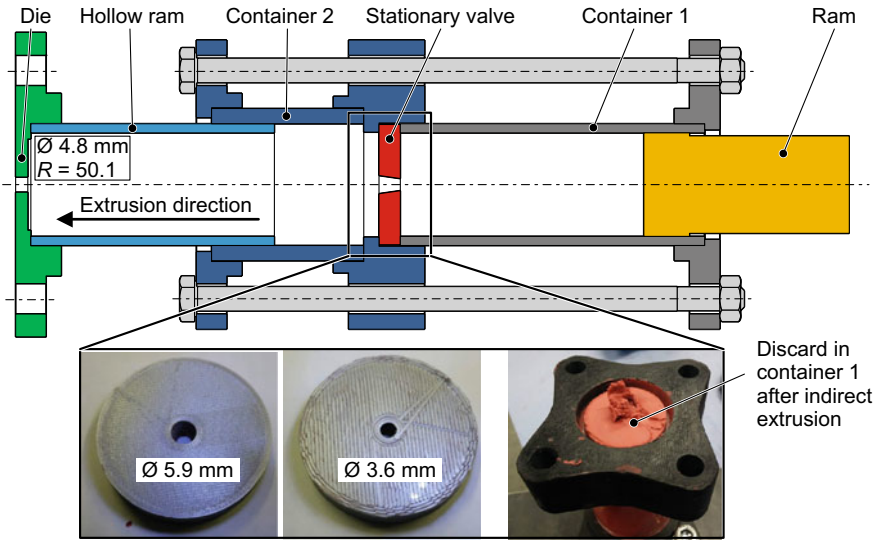


Fig. 10 Schematic of the continuous extrusion press with stationary valve, and result obtained with plasticine. (Color figure online)

With the process of continuous extrusion, constant profile extrusion can be realized. The concept of the process was investigated numerically and, by using the method of similitude, with a scaled model of the press. The model material was compared with aluminum AA6060. It was shown that the chosen material is suitable to represent the material flow of aluminum under the condition of hot extrusion. Since the model was used on an existing universal testing machine with only one moving axis, the continuous pressing cycle was reproduced by moving ram and hollow ram sequentially. By using differently colored plasticine, the material flow was analyzed. In addition, it was shown that the two containers of the press do not necessarily need to be spatially separated by a moving valve. An inter-chamber adapted to the material flow can be utilized to prevent material flowing in the opposite extrusion direction from container 2 to container 1. In summary, the following key points can be concluded:

- The continuous extrusion process can be modeled with Eulerian FEM approaches
- The process forces are more than twice as big during the direct phase compared to conventional extrusion
- The movable valve leads to additional longitudinal weld seams
- Due to the movable valve, the transverse weld will experience higher strain, leading to better welding
- Material flow against the main extrusion direction can be prevented by a moving or stationary valve
- A stationary valve needs to match the used extrusion die to enable continuous extrusion
- The process window for the stationary valve needs to be investigated in more detail.

References

1. Bauser M, Sauer G, Siegert K (2006) Extrusion, 2. Materials Park, Ohio: ASM International
2. Bastani FA, Aukrust T, Brandal S (2011) Optimisation of flow balance and isothermal extrusion of aluminium using finite-element simulations. J Mater Process Technol 211(4):650–667
3. Chanda T, Zhou J, Duszczyk J (2001) A comparative study on iso-speed extrusion and isothermal extrusion of 6061 Al alloy using 3D FEM simulation. J Mater Process Technol 114(2):145–153
4. Li L, Zhou J, Duszczyk J (2004) Prediction of temperature evolution during the extrusion of 7075 aluminium alloy at various ram speeds by means of 3D FEM simulation. J Mater Process Technol 145(3):360–370
5. Kayser T, Klusemann B, Lambers HG, Maier HJ, Svendsen B (2010) Characterization of grain microstructure development in the aluminum alloy EN AW-6060 during extrusion. Mater Sci Eng A 527(24–25):6568–6573
6. Paulisch MC, Lentz M, Wemme H, Andrich A, Driehorst I, Reimers W (2016) The different dependencies of the mechanical properties and microstructures on hot extrusion and artificial aging processing in case of the alloys Al 7108 and Al 7175. J Mater Process Technol 233:68–78

7. Hölker R, Jäger A, Ben Khalifa N, Tekkaya AE (2013) Controlling heat balance in hot aluminum extrusion by additive manufactured extrusion dies with conformal cooling channels. Int J Precis Eng Manuf 14(8):1487–1493
8. Pietzka D, Schikorra M, Tekkaya AE (2008) Embedding of alumina reinforcing elements in the composite extrusion process. Adv Mater Res 43(January):9–16
9. Foydl A, Pfeiffer I, Kammler M, Pietzka D, Matthias T, Jäger A, Tekkaya AE, Behrens BA (2012) Manufacturing of steel-reinforced aluminum products by combining hot extrusion and closed-die forging. Key Eng Mater 504–506(February):481–486
10. Negendank M, Mueller S, Reimers W (2012) Coextrusion of Mg-Al macro composites. J Mater Process Technol 212(9):1954–1962
11. Selvaggio A, Tekkaya AE (2011) Mehrachsiges Runden beim Strangpressen. VDI Fortschritt-Berichte 678(2):3–26
12. Selvaggio A, Haase M, Ben Khalifa N, Tekkaya AE (2014) Extrusion of profiles with variable wall thickness. Procedia CIRP 18:15–20
13. Negendank M, Müller S, Reimers W (2014) Extrusion of aluminum tubes with axially graded wall thickness and mechanical characterization. Procedia CIRP 18:3–8
14. Green AP (1951) XLII. The use of plasticine models to simulate the plastic flow of metals. London, Edinburgh, Dublin Philos Mag J Sci 42(327):365–373.
15. Altan T, Henning HJ, Sabroff AM (1968) The use of model materials in predicting forming loads in metalworking. Army Mater Mech Res Cent, 1–32
16. Wanheim T, Schreiber MP, Gronbaek J, Danckert J (1980) Physical modelling of metal forming processes. J Appl Metalwork 1(3):5–14
17. Sofuoglu H, Gedikli H (2004) Physical and numerical analysis of three dimensional extrusion process. Comput Mater Sci 31(1–2):113–124
18. Schöpfer MPJ, Zulauf G (2002) Strain-dependent rheology and the memory of plasticine. Tectonophysics 354(1–2):85–99
19. Eckerson K, Liechty B, Sorensen CD (2008) Thermomechanical similarity between Van Aken plasticine and metals in hot-forming processes. J Strain Anal Eng Des 43(5):383–394
20. Dicks N (1994) Physikalische Simulation des Strangpressen zur Analyse verscheidener Problemstellungen aus der Fertigung. Verlag Stahleisen mbH, Düsseldorf
21. Schikorra M (2006) Modellierung und simulationsgestützte Analyse des Verbundstrang-pressens. Shaker Verlag, Aachen
22. Etherington C (1974) Conform—a new concept for the continuous extrusion forming of metals. Form Met ASME J Eng Ind 96(3):893–900
23. Muschalik U, Ben Khalifa N, Selvaggio A, Tekkaya AE (2012) Strangpresse sowie Verfahren zum kontinuierlichen Pressen von Metall

Study on Complex Extrusion of Multi Billets: Evaluation of Mechanical Properties of Butt-Joined Products and Analysis of Joining State



Michihiko Hoshino and Izuru Otake

Abstract In recent years, an aluminum double-skin panel, which has a complicated and wide cross-sectional shape, is manufactured by extrusion and used for railway vehicles. It is difficult to manufacture a double-skin panel exceeding 600 mm width in the current forward extrusion process. However, from the viewpoint of weight saving, there is a demand to make a double-skin panel with larger widths. So we propose to manufacture double-skin panel with complex extrusion of multi-billets. Complex extrusion of multi-billets is suitable for producing complicated and wide extruded shapes. We focused that the joint part of the double-skin panel is joined in a plate shape. In this study, industrial pure aluminum A1050 and representative extruded alloy A6063 were extruded into a plate shape, and the joining state was evaluated by tensile test, micro Vickers hardness test, microscopic observation, and numerical analysis.

Keywords Complex extrusion · Double-skin panel · Joining stress

1 Introduction

At present, some railway vehicles have a double-skin structure using a complex and wide cross-sectional shape manufactured by extrusion. Railway cars of this structure are made by welding a number of double-skin panels formed long by direct extrusion. There is a demand to increase the width of the structural panel from the viewpoint of reducing the welding length and reducing the weight. However, by the current extrusion, the width of the structural panel is limited to about 600 [mm]. Because in case of that the diameter of billet is over 600 [mm] and the width of double-skin structure is more than 600 [mm], extrusion ratio is about 50 and extrusion force is more than 100 [MN].

In this study, it is proposed to produce wide double-skin panel using complex extrusion of multi-billets. The complex extrusion of multi-billets is a processing

M. Hoshino (✉) · I. Otake
College of Science and Technology, Nihon University, Tokyo, Japan
e-mail: hoshino@mech.cst.nihon-u.ac.jp

© The Minerals, Metals & Materials Society 2021

G. Daehn et al. (eds.), *Forming the Future*, The Minerals, Metals & Materials Series,
https://doi.org/10.1007/978-3-030-75381-8_86

method in which multiple billets are extruded with a single die and formed into a single product [1, 2]. In this extrusion method, it is possible to extrude the same or different material types of workpieces and to join these workpieces during extrusion [3, 4]. It is important to control the flow of the workpieces by the die with suitable shape in order to manufacture the wide double-skin panel with good joining [5].

In the previous research, a model experiment using oil clay and the numerical simulation for a butt-joining, which is the basic pattern of the joining of the double-skin panel, have been achieved. It is clear that the effects of the ironing shape of the die approach part and the joining angle when the workpieces run across are important to the strength of joining the workpieces [6, 7]. And the extrusion force of complex extrusion of multi billets is letter than one of conventional extrusion.

In this study, complex extrusions of multi-billets of A1050, which is a pure aluminum for industrial use, and A6063, which is a typically extruded alloy, are achieved, and it is possible to manufacture good extruded products. It is understood that these joining strength is satisfactory from the results of tensile test. Furthermore, the joining condition of the workpieces is evaluated by the micro Vickers hardness test of the products and microstructure observation of the joint parts with an optical microscope. The results of the experiments are in good agreements with the estimation of the stress generated in the width direction of the joints of the workpiece by numerical analysis.

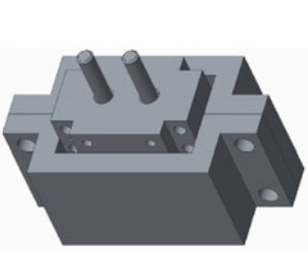
2 Experimental Method

2.1 Aluminum Alloy Extrusion Experiment

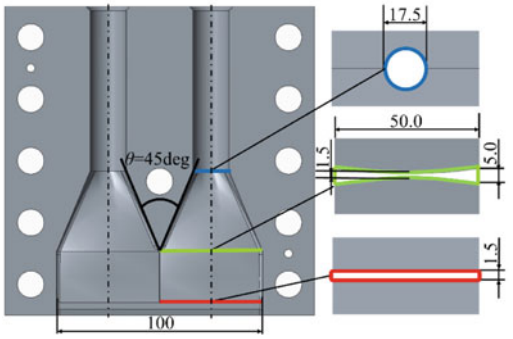
The experimental equipment (dies and two punches without bolts and nuts) used in this experiment and the inner dimensions of the die are shown in Fig. 1, and θ in the figure is defined as the merging angle. In the section from blue line to green line in Fig. 1, ironing in the thickness direction is applied to the center of each axis, and the workpiece flows not only in the extrusion direction but also in the width direction.

The geometry of die is designed in such a way that ironing in the thickness direction is applied at the end of each die approach part in order to achieve good joining between the workpieces.

In this experiment, first, billets of A1050 and A6063 were inserted into the container shown in Fig. 1, and the whole container with billets was heated to 600 °C in an electric furnace. Next, two punches were set in each hollow container and workpieces were extruded with an Amsler compression tester 3MN until just before the workpiece was joined. After the first extrusion process, workpieces were added to the container, and they were reheated to 600 °C in an electric furnace and then pressed. Thereafter, this procedure was repeated four times for every 60 mm of the ram stroke. Table 1 shows the experimental conditions and Table 2 shows the chemical composition of the test materials.



(a) Experimental extrusion device



(b) Internal dimension of dies

Fig. 1 Experimental extrusion device and dies. **a** Experimental extrusion device, **b** Internal dimension of dies. (Color figure online)

Table 1 Experimental extrusion conditions

Material of workpiece	A1050,A6063
Material of tool	SKD61 (HRC50)
Dimensions of workpiece [mm]	φ17.0 × 60.0
Dimension of product cross-section [mm]	t1.5 × w100
Container diameter [mm]	φ17.5
Extrusion speed [mm/s]	0.3
Extrusion ratio [-]	3.2
Joining angle θ [degrees]	45.0
Experiment temperature [°C]	600

Table. 2 Chemical composition of alloy used in experiment (mass%)

Alloy	Si	Fe	Cu	Mn	Mg	Cr	Zn	Ti	Al
A1050	0.25	0.40	0.05	0.05	0.05	-	0.05	0.03	bal
A6063	0.20 - 0.60	0.35	0.10	0.10	0.45 - 0.9	0.10	0.10	0.10	bal

2.2 Tensile Test of Extruded Products

In this test, a tensile test specimen in the width direction was manufactured from the center part, which includes the joint surface, and the base metal part of the extruded plate-shaped product. A uniaxial tensile test result was evaluated by efficiency strength R_{str} which is obtained by dividing the tensile strength of the joint $\sigma_{B,join}$ in the test results by the tensile strength $\sigma_{B,base}$ of the base metal, and efficiency elongation r_e which is obtained by the uniform elongation of the joint e_{join}

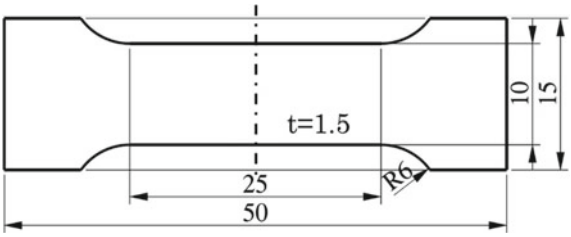


Fig. 2 Dimension of tensile test piece

divided by the uniform elongation of the base metal e_{base}. The bonding condition was evaluated by comparing the ratio R_{str}, r_e, and the proof stress $\sigma_{0.2}$.

The tensile test speed is 0.375 mm/min. The geometries of this specimen shown in Fig. 2 is special in order to match small extruded products.

2.3 Micro Vickers Hardness Test

In this test, a test piece was manufactured by cutting and polishing the workpiece immediately after joining to the plane of symmetry in the thickness direction, and a micro Vickers hardness test was performed at 11 measurement positions in the width direction shown in Fig. 3. The test load was 300 gram-force for A1050, 500 gram-force for A6063, and the load holding time was 15 s. The joint condition was evaluated by comparing the hardness distribution at the joint with one at the other part.

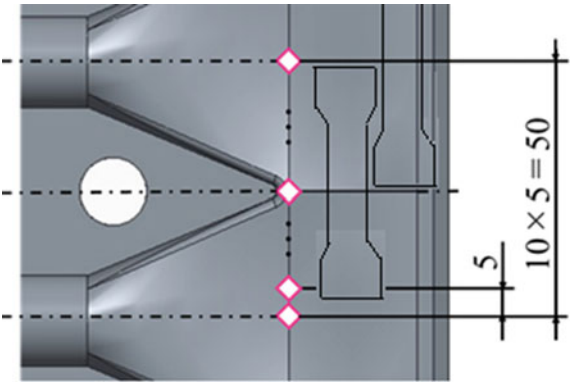


Fig. 3 Measurement position of Vickers hardness test. (Color figure online)

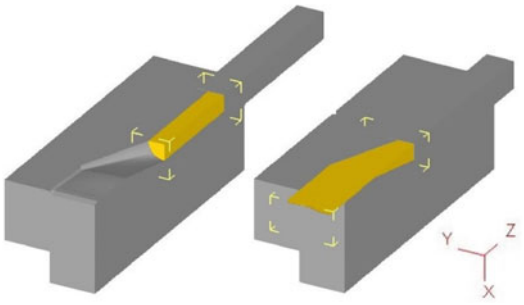
2.4 Microscopic Observation of the Joint

In this observation, the specimen after the micro Vickers hardness test was further polished, then etched with 50 °C NaOH 1.0 mass% aqueous solution for 20 s. The specimen was observed using an optical microscope. From the observation results, the bonding state of the workpiece was evaluated based on the presence or absence of the bonding interface, inclusion of impurities, and roughening of grain surfaces.

2.5 Numerical Analysis

In the numerical analysis, the joining stress (hereinafter referred to as σ_{join}) generated in the width direction of the joint of the workpiece is estimated using DEFORM-3D V11.0 released by Scientific Forming Technologies Corporation, and the bonding state was evaluated based on whether or not the joining stress σ_{join} exceeded the deformation resistance σ_y of the work material.

Figure 4 shows the analysis model of the numerical analysis, Fig. 5 shows the measurement points of the joining stress σ_{join}, and Table 3 shows the analysis conditions. The stress generated in the direction of the arrow in Fig. 5 is defined as the joining stress σ_{join}. For the convenience of the material data, the analysis was performed assuming that the workpiece was A1050 and A6061, and the extrusion temperature was 450 °C. The reason is using A6061 instead of A6063 is that material database of A6061 has higher range of temperature than one of A6063 in DEFORM-3D V11.0.



(a) Before processing (b) After processing

Fig. 4 Analysis model for numerical simulation. (Color figure online)

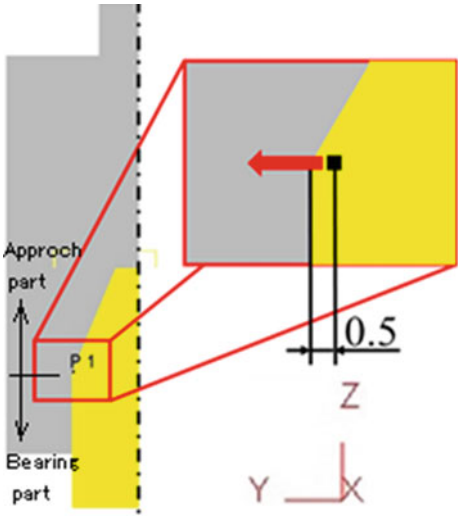


Fig. 5 Measurement point of joining stress. (Color figure online)

Table 3 Analysis conditions of numerical simulation

Material of workpiece	A1050,A6061
Object type	Rigid plastic
Division model	Quarter
Dimensions of workpiece [mm]	φ17.0 × 60.0
Dimension of product cross-section [mm]	t1.5 × w100
Container diameter [mm]	φ17.5
Extrusion speed [mm/s]	0.3
Extrusion ratio [-]	3.2
Joining angle θ [degrees]	45.0
Extrusion temperature [°C]	450
Mesh number [-]	100,000
Shear friction coefficient [-]	0.8
Heat transfer coefficient [W/(m^{2}K)]	5.0

3 Results and Discussion

3.1 Tensile Test of Extruded Products

The nominal stress–nominal strain diagram of A1050 measured in this test is shown in Fig. 6, and the maximum load point of each specimen is shown by the broken line. From Fig. 6, it was found that the proof stress $\sigma_{0.2}$ of A1050 was almost the same between the base metal and the joint, and the joining efficiency R_{str} determined from the tensile strength was 90.9%.

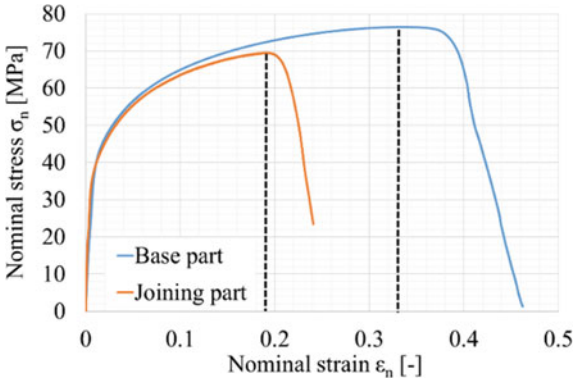


Fig. 6 Stress–strain curve of tensile test (A1050). (Color figure online)

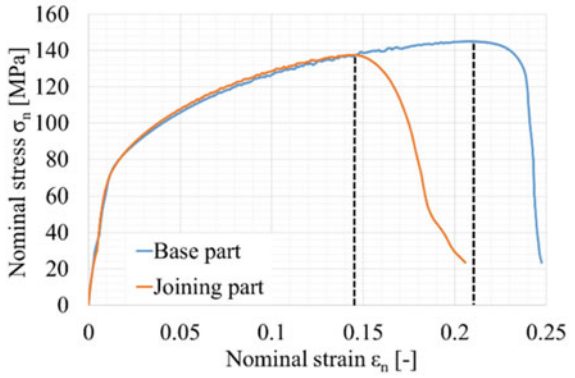


Fig. 7 Stress–strain curve of tensile test (A6063). (Color figure online)

However, the elongation ratio r_e obtained from uniform elongation was as small as 55.9%. The nominal stress–nominal strain diagram of A6063 measured in this test is shown in Fig. 7, and the maximum load point of each specimen is shown by the broken line.

From Fig. 7, it was found that in A6063, the proof stress $\sigma_{0.2}$ showed almost the same value in the base material and the joint, and the joining efficiency R_{str} determined from the tensile strength was 94.8%. However, the elongation ratio r_e obtained from uniform elongation was as small as 74.9%. In addition, it is possible to be confirmed that the serrations seen in the Al–Mg alloy have occurred after yielding.

3.2 Micro Vickers Hardness Test

Figure 8 shows the results of the micro Vickers hardness test for A1050 and A6063 measured in this test. No significant difference in Vickers hardness was found

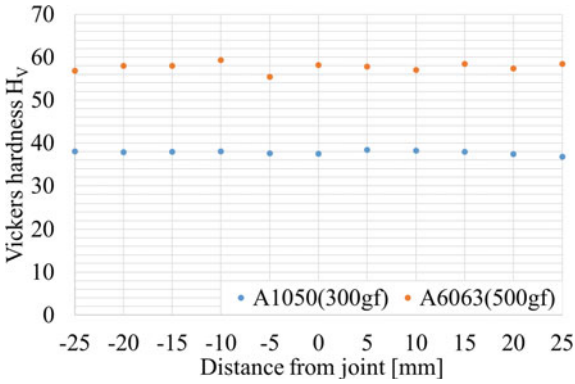
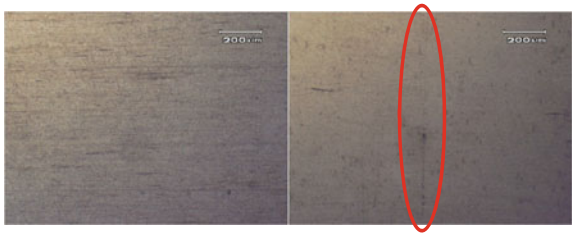


Fig. 8 Hardness distribution of the extruded product in the width direction. (Color figure online)



(a) A1050 (b) A6063

Fig. 9 Enlarged view of a joint interface of extruded product. (Color figure online)

between the workpiece joint and the other parts. Therefore, it was found that there was no difference in strength between the joint and the base material.

3.3 Microscopic Observation of the Joint

Figure 9 shows a photograph of the joint observed with an optical microscope. From Fig. 9, the joint interface cannot be confirmed in A1050, but can be confirmed in the long circle of A6063. This difference is because A6063 has more second phase than A1050, and an additional element exists at the grain boundary of α phase (pure aluminum grain). In both A1050 and A6063, defects such as inclusion of impurities could not be confirmed.

3.4 Numerical Analysis

Figure 10 shows the joining stress–stroke diagram of A1050 and A6061. The broken line shows the average value of the joining stress after a stroke of 10 mm where the joining stress σ_{join} is constantly generated. The stroke was offset to the position

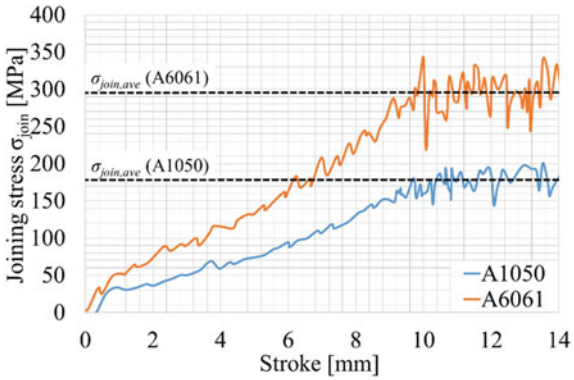
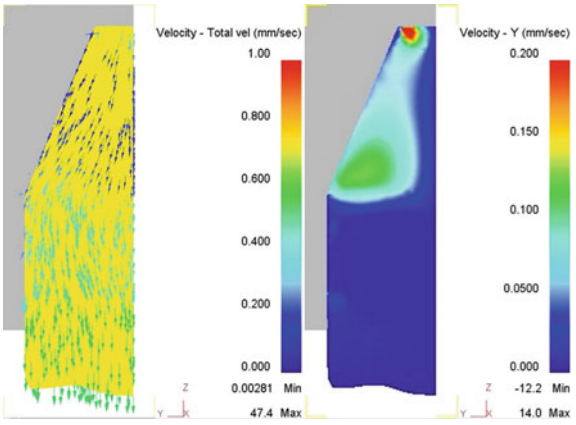


Fig. 10 Joining stress–stroke curve of complex extrusion of multi-billets. (Color figure online)

where the joining stress σ_{join} started to rise. From Fig. 10, the average of the joining stress σ_{join} was 177.7 MPa for A1050 and 296.0 MPa for A6061. This value reaches 9.5 times the deformation resistance of A1050 $\sigma_y = 18.6$ MPa which is calculated at forming temperature from material database of DEFORM-3D V11.0 and 13.0 times the deformation resistance of calculated A6061 $\sigma_y = 22.8$ MPa from the same database at the measurement point of joining stress, and the workpieces have sufficiently yielded. Therefore, it is clear that good joining has been achieved.

Figure 11 shows the velocity vector and the Y-direction velocity distribution of the workpiece in the steady-state of extrusion. Since there was no significant difference between A1050 and A6061 in both the velocity vector and the Y-direction velocity distribution, only the case of A1050 is described. From Fig. 11(a), before the start of joining of the workpiece, the workpiece flows in the Y-direction due to the ironing in the thickness direction at the center of the extrusion axis. In addition, since the flow in the width direction of the workpiece is not completely uniform in the die bearing



(a) Velocity vector (b) Y-direction velocity

Fig. 11 Velocity distribution in the approach part and bearing part of die. (Color figure online)

part, there is room for improvement in the design of the die approach part. From Fig. 11(b), it can be seen that the workpiece in the Y-direction immediately before the start of welding of the workpiece flows in the Y-direction at a speed of about 0.1 mm/s, more than twice the speed after the start of welding. This confirms that the shape of the die approach contributes to the joining of the workpiece.

4 Conclusion

1. From the results of the tensile test, it was found that the proof stress $\sigma_{0.2}$ of the base metal and one of the joint part was almost the same, and the joining efficiency R_{str} was 90.9% for A1050 and 94.8% for A6063.
2. From the results of the micro Vickers hardness test and the microstructure observation with an optical microscope, it is clear that the bonding in multi-billet extrusion with ironing was good.
3. From the numerical analysis, it was found that the joining stress σ_{join} generated in the width direction of the workpiece reached 9.5 times the deformation resistance σ_y of A1050 and 13.0 times the deformation resistance σ_y of A6063.

From the above results, it is possible to produce a wide plate of A1050 and A6063 by using complex extrusion of multi-billets.

References

1. Ikeda K et al (1993) Welding state of 7475 aluminum alloy pipes formed by hot multi-billet extrusion method. J Japan Inst Light Metals 43(2):76–81
2. Xie JX et al. (2005) Fabrication of W/Cu functionally gradient materials by multi-billet extrusion. Mater Sci Forum 475/479(Pt.2):1511–1516
3. Hoshino M (2011) New extrusion of variable cross section shape and curved frame. Paper presented at International Conference of Technology for Plasticity 2011, Aachen, 25–30 September 2011
4. Hoshino M, Narahashi D (2014) Research on the influence of die shape in complex extrusion of multi billets. Key Eng Mater 585:141–148
5. Japan Society for Technology of Plasticity (1992) Extrusion -From basic to advanced technology. Corona, Tokyo
6. Fujisawa K (2018) Effect of the width expansion die shape of the multi billet composite extrusion on the bonding surface pressure. Bull Japan Soc Technol Plas 1(12):68–69
7. Wang M, Hoshino M (2015) Research on the influence of vertical ironing to bonding pressure within multi-billet extrusion for inner ribbed tube. Paper presented at International Conference of Extrusion and benchmark 2015, Firenze, 12–16 May 2015

Effect of Expansion Ratio on Formability in Tube Drawing with Diameter Expansion



H. Kawaguchi, T. Kuboki, I. Akasaka, Y. Terashita, M. Akiyama, and S. Kajikawa

Abstract Conventional tube drawing methods have the disadvantage that thickness reduction in one pass is small. This paper proposed a tube drawing method for overcoming this disadvantage, and the method expands the diameter at the same time of drawing. At first, the tube is flared by pushing the plug into the tube end. After that, the plug is drawn by chucking the flared end, and the entire tube is expanded. Tensile circumferential and axial stress reduces the tube thickness effectively during the plug drawing. In this study, the effect of expansion ratio on formability, such as thickness reduction and dimensional accuracy, was investigated by experiments and finite element analyses (FEA) for verifying the effectiveness of the proposed method. As a result, the thickness reduction increased with an increase in the expansion ratio, and the maximum thickness reduction ratio was 0.3 when an aluminum alloy of AA1070 was used. Furthermore, the deformation mechanism was considered by FEA.

Keywords Expansion drawing · Expansion ratio · Tube forming · Thickness reduction · Overshoot

H. Kawaguchi (✉) · T. Kuboki · S. Kajikawa
Department of Mechanical and Intelligent Systems Engineering, The University of Electro-Communications, 1-5-1 Chofu Gaoka, Chofu 182-8585, Tokyo, Japan
e-mail: kawaguchi@mt.mce.uec.ac.jp

I. Akasaka · Y. Terashita
Miyazaki Machinery Systems Co, Ltd.1 Arai, Kaizuka-shi, Osaka 597-8588, Japan
e-mail: Akasaka@miyazakijp.com

Y. Terashita
e-mail: Terashita@miyazakijp.com

M. Akiyama
Akiyama Research Laboratory2-7-306 Tanaka Sekiden-cho, , Sakyo-ku, Kyoto-shi, Kyoto 606-8203, Japan
e-mail: masayoshiakiyama@ac.auone-net.jp

© The Minerals, Metals & Materials Society 2021

G. Daehn et al. (eds.), *Forming the Future*, The Minerals, Metals & Materials Series,
https://doi.org/10.1007/978-3-030-75381-8_87

1 Introduction

Metal circular tube materials are widely used in industrial machines and automobile parts. It is mainly manufactured by drawing with diameter constriction. At present, there are many studies about drawing with diameter constriction [1, 2]. However, there is a limit of the thickness reduction in one pass in conventional drawing with diameter shrink. Therefore, drawing multiple times is required when manufacturing a thin-walled tube.

Tube drawing with diameter expansion has been proposed as a method to improve the drawing limit [3, 4]. The proposed method is composed of two processes: flaring and drawing, as shown in Fig. 1. At first, form the gripping part in the flaring process (Fig. 1a). After that, grasp the gripping part and draw the plug through the tube into the drawing process (Fig. 1b).

In this method, it is possible to realize efficient thickness reduction compared to the conventional tube drawing with diameter shrink. As shown in Fig. 2, circumferential stress is compressive in the case of the conventional method, while circumferential stress is tensile in the proposed method. Therefore, the proposed method is effective for reducing the thickness, because radial deviatoric stress is large compared to the conventional method. In this study, the thickness reduction obtained by the tube expansion drawing process is investigated and the dimensional accuracy of the molded product is evaluated. The tube expansion drawing was performed, and the thickness reduction and processing accuracy of the molded product were evaluated by measuring the dimensions of the molded product.

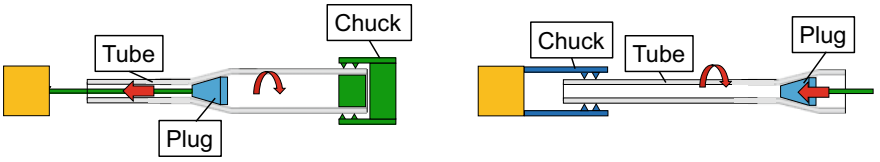


Fig. 1 Process of expansion drawing. **a** Expansion process, **b** Drawing process. (Color figure online)

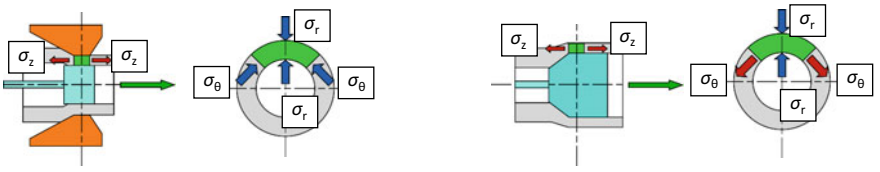


Fig. 2 Deviatoric stress of plug drawing and expansion drawing. **a** Drawing with diameter shrink, **b** Drawing with diameter expansion. (Color figure online)

2 Experimental and Analysis

2.1 Experimental Method and Condition

First, the flaring experiment was performed, and a plug is inserted into the tube as shown in Fig. 3. After that, the drawing experiment was performed. Figures 4 and 5 show a schematic diagram and a photograph of the drawing experiment.

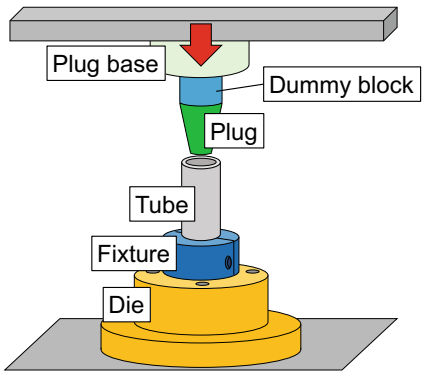


Fig. 3 Expansion pushing machine. (Color figure online)

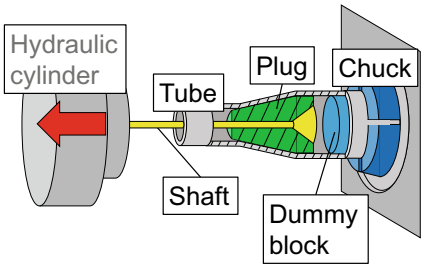


Fig. 4 Drawing machine. (Color figure online)

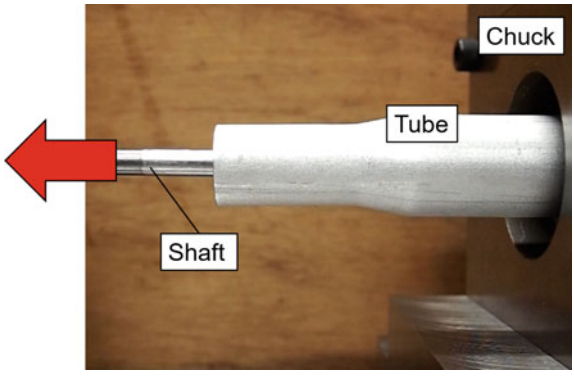


Fig. 5 Photograph of drawing machine. (Color figure online)

Table 1 Tube material conditions

Material	AA1070, STKM13C
Initial thickness t_0/mm	2
Outer diameter d_0/mm	30
Length L_0/mm	200

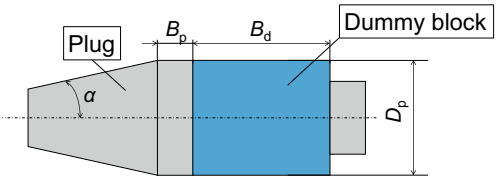


Fig. 6 Geometrical parameters of plug with dummy block. (Color figure online)

Table 2 Plug conditions

Half angle α/°	12
Bearing length B_p/mm	15
Dummy block length B_d/mm	43
Plug diameter D_p/mm (Expansion ratio E)	28, 30, 32, 34, 36 (0.077, 0.15, 0.23, 0.31, 0.38)

Table 1 shows the material conditions. Two types of materials, which are aluminum alloy 1070 and steel of STKM13C (Japan Industrial Standard, JIS G 3445), were used. The deviation between the central axis of the outer and inner diameter of the tube, which indicates the value of eccentricity, is 0.049 mm for AA1070 and 0.028 mm for STKM13C, respectively. Figure 6 shows a schematic diagram of the plug used in the experiment, and Table 2 shows the plug conditions. A dummy block, which becomes a core of the chucked part in the drawing process, was incorporated in the plug. This dummy block prevents the crush of the tube by chucking. The expansion ratio of the tube was varied by changing the plug diameter. From this experiment, the effect of the expansion ratio on the thickness reduction and dimensional accuracy was investigated.

2.2 Analysis Method and Condition

Finite element method (FEM) analysis was performed using the model shown in Fig. 7 in order to consider the experimental results. Table 3 shows the properties of the materials in Swift's law. Swift's law is shown in the following equation.

$$\sigma = F(\varepsilon + \varepsilon_0)^n$$

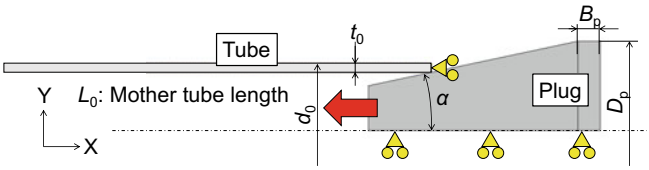


Fig. 7 FEM analysis model. (Color figure online)

Table 3 Mechanical properties in Swift's law

Material	A1100	STKM13C
Strength coefficient F /MPa	121	725
Hardening exponent n	0.048	0.023
Offset of strain ε_0	0.0013	0.0032

The analysis conditions are the same as that of the experiment and are shown in Tables 1 and 2. Furthermore, the friction coefficient was 0.3 [4], and the number of elements was 300 in the axial direction and 13 in the radial direction. The finite element method code "ELFEN", which was developed by Rockfield Software Limited in the UK, was used for numerical analysis. The static implicit method was used for the numerical calculation. The model is two-dimensional with axisymmetry, and the von Mises yield criterion was adopted. The element type was four-node rectangular.

2.3 *Measuring Method*

Figure 8 shows a schematic diagram of the molded product. The thickness and inner diameter of the molded tube were measured. Thickness was measured at 10 mm intervals in the axial direction and measured at 45 intervals in the circumferential direction at each axial position by using an acoustic wavemeter. After measuring the thickness, the tube was cut at 30 mm intervals using a band saw, and the inner

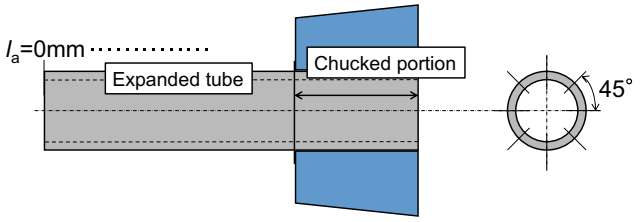


Fig. 8 Measuring method of the expanded tube. (Color figure online)

diameter of each tube piece was measured at 90° intervals in the circumferential direction by using a caliper.

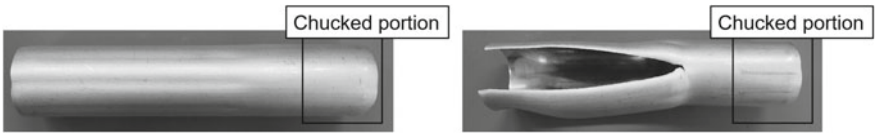
3 Results and Discussion

3.1 Evaluation of Thickness Reduction

Figure 9 shows examples of success and failure, and Table 4 shows the molding results under each condition. When the plug diameter $D_p = 36$ mm for AA1070 and $D_p = 34$ mm for STKM13C, cracks occurred as shown in Fig. 9b. The maximum diameter without cracks is defined as the limit diameter D_{max}.

Figure 10 shows the relationship between distance l_a from the tube end and thickness reduction ratio γ. In both materials, the thickness reduction ratio γ increased as the expansion ratio E increased, and the experiment and analysis matched qualitatively. Under all conditions, the thickness reduction ratio γ was constant in the middle part of the tube, but the thickness reduction ratio γ was low near the tube end compared to the middle part. It is because the axial tensile stress was small near the tube end. Compared to that at the middle part, the thickness reduction ratio γ was also low in the part near the chucked part in the experiment, because the plug applied axial compressive stress to the chucked tube end during the flaring process in the first step. In FEM, thickness reduction did not decrease at the fixed end because only the drawing process was analyzed.

Figure 11 shows the effect of expansion ratio E on the thickness reduction ratio γ, which was averaged in the stable thickness range except for each tube end. In Fig. 11, the experimental and analysis results were compared. In both materials,



(a) Success (b) Failure

Fig. 9 Photograph of the formed product. **a** Success, **b** Failure

Table 4 Molding results

Plug diameter D_p/mm (Expansion ratio E)	28 (0.077)	30 (0.15)	32 (0.23)	34 (0.31)	36 (0.38)
AA1070	○	○	○	○	×
STKM13C	○	○	○	×	

○:Success × :Failure

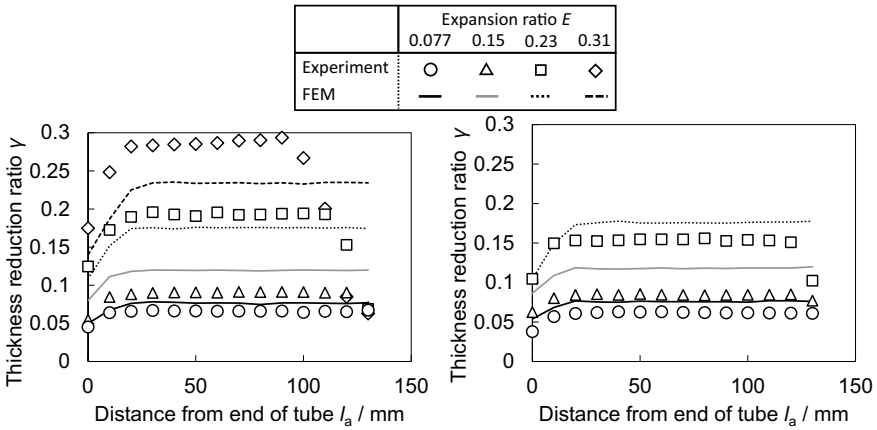


Fig. 10 Relationship between distance from the end of tube l_a and thickness reduction ratio γ. **a** AA1070, **b** STKM13C

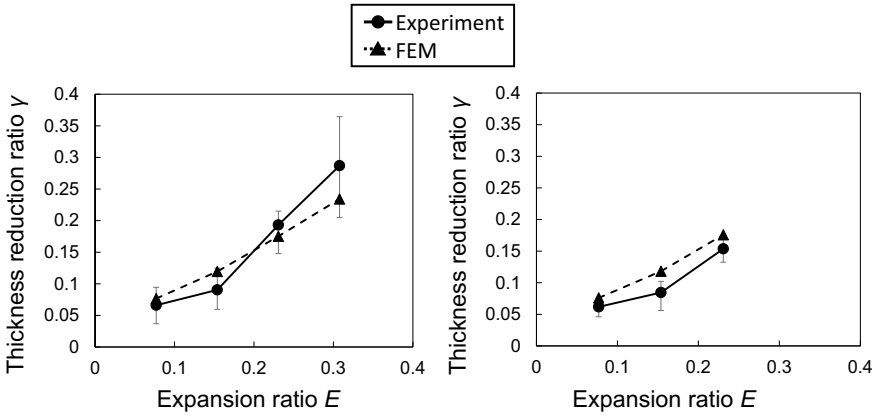


Fig. 11 Effect of expansion ratio E on thickness reduction ratio γ. **a** AA1070, **b** STKM13C

there was no significant difference between the results of the experiment and the analysis. In Fig. 11a of AA1070, when the expansion ratio E was 0.31, thickness reduction ratio γ was approximately 0.3. This value exceeded the thickness reduction ratio γ of 0.2 in the conventional tube drawing [5]. However, this condition had a larger error bar than the other conditions. Figure 12 shows a photograph of the tube draw under the condition of $E = 0.31$. The wall thickness was locally reduced and became unstable in the circumferential direction. This effect increased the error bar in the large expansion ratio.

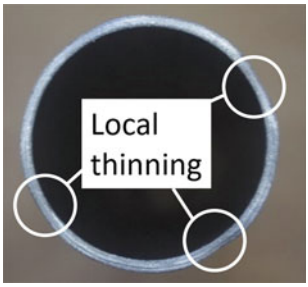


Fig. 12 Molded products locally thinned in the circumferential direction (AA1070, $E = 0.31$). (Color figure online)

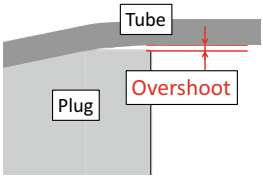


Fig. 13 Overview of overshoot. (Color figure online)

3.2 Evaluation of Tube Inner Diameter

Figure 13 shows "overshoot" in the expansion drawing. There was a gap between the plug diameter D_p and the tube inner diameter d_i after expansion drawing. Overshoot g_o was defined in the following equation.

$$g_o = (d_i - D_p)/2$$

Overshoot g_o should be small for improving the dimensional accuracy of the inner diameter. Figure 14 shows the relationship between distance from the end of the tube l_a and overshoot g_o in the experiment and analysis. The overshoot g_o was low at the tube end, and then increases as the distance from the end of tube l_a increases regardless of the material kind. The overshoot became stable when l_a is larger than 30 mm. The overshoot g_o was the largest when the expansion ratio E was the smallest at 0.077, and the overshoot g_o decreases as expansion ratio E increases.

The average value of the overshoot g_o was calculated for 30 mm $< l_a <$ 90 mm in Fig. 14, and the effect of expansion ratio E on overshoot g_o was summarized in Fig. 15. As a result, it was found that the overshoot g_o of AA1070 was larger than that of STKM13C. It is because the bending radius was larger at the plug corner during the drawing in the case of AA1070, in which the work hardening exponent was large compared to that of STKM13C as shown in Table 3.

The reason why the overshoot g_o becomes large when the expansion ratio E is small is analyzed. Figure 16 shows the axial stress distribution at the expanded straight part. As shown in the part [A] in Fig. 16a, axial tensile stress is applied to the inside of the tube, and compressive stress is applied to the outside of the tube. When the expansion ratio E was small, the tensile stress inside the tube expands to

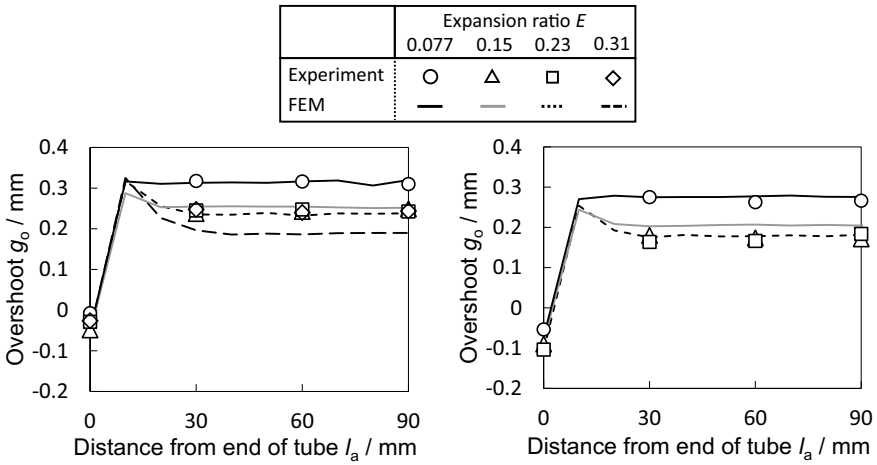


Fig. 14 Relationship between distance from the end of tube l_a and overshoot g_o. **a** AA1070, **b** STKM13C

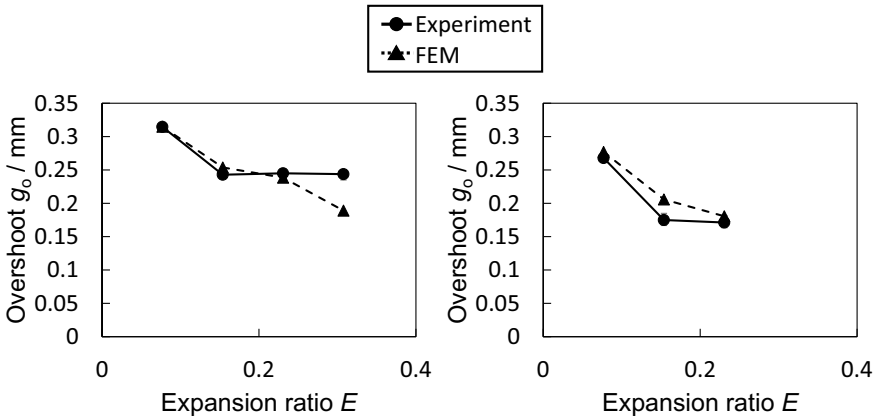


Fig. 15 Effect of expansion ratio E on overshoot g_o. **a** AA1070, **b** STKM13C

the outside with the increase in the expansion ratio E as shown in Fig. 16b, c and d. Furthermore, Fig. 17 shows the relationship between the axial load F_z applied to the fixed tube end and the expansion ratio E during the drawing. As the expansion ratio E increased, the axial load F_z also increased. These results indicated that the large expansion reduces the overshoot g_o by stretching the tube strongly in the axial direction.

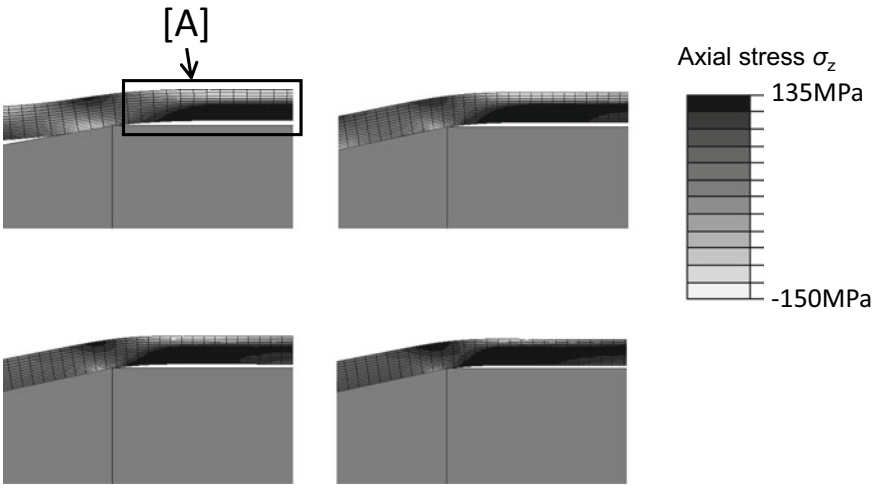
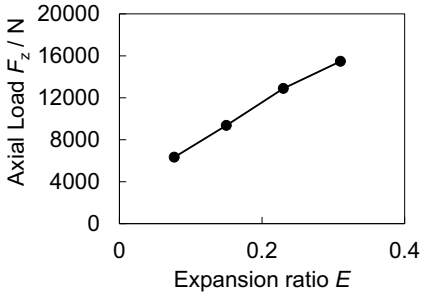


Fig. 16 Axial stress distribution at the expanded straight part (AA1070). **a** $E = 0.077$, **b** $E = 0.15$, **c** $E = 0.23$, **d** $E = 0.31$

Fig. 17 Relationship between axial load F_z and expansion ratio E during the drawing (AA1070)



4 Conclusions

In this study, the thickness reduction and dimensional accuracy were evaluated by experiments and finite element analysis for the realization of the tube expansion drawing. The results can be summarized as follows:

- The effect of the expansion ratio E on the thickness reduction ratio γ was investigated. The thickness reduction ratio γ also increased as the expansion ratio E increased.
- When the expansion ratio E was 0.31, the thickness reduction ratio γ was about 0.3, whose value exceeded the thickness reduction ratio γ in the conventional drawing method. However, local thinning was observed, and the wall thickness became unstable in the circumferential direction.
- The overshoot g_o was generally larger for AA1070 than for STKM13C.

- The overshoot g_o is the largest when the expansion ratio E is the smallest at 0.077, and the overshoot g_o decreases as expansion ratio E increases. It is considered that when the expansion ratio E is large, the axial load increases and the overshoot is suppressed.

Acknowledgments This work was supported by grant no. AF-2018034 from the Amada Foundation.

References

1. Kuboki T, Nishida K, Sakaki T, Murata M (2008) Effect of plug on levelling of residual stress in tube drawing. J Mater Process Technol 204:162–168
2. Kuboki T, Tasaka S, Kajikawa S (2017) Examination of working condition for reducing thickness variation in tube drawing with plug. In: Proceedings of the xiv international conference on computational plasticity: Fundamentals and applications. Barcelona, Spain, pp 57
3. Kajikawa S et al. (2019) Experimental investigation of tube drawing process with diameter expansion. In: Proceedings of the 9th international conference on tube hydroforming. Kaohsung, Taiwan, pp 1821
4. Kajikawa S et al. (2017) Finite element analysis of tube drawing process with diameter expansion. In: Proceedings of the xiv international conference on computational plasticity: Fundamentals and applications. Barcelona, Spain, pp 35
5. The Japanese Society for Technology of Plasticity (1990) Drawing: from fundamentals to up-to-date techniques, Corona Publishing. Tokyo, p 23

Investigation of Forward–Backward–Radial Extrusion Process of Aluminum Alloy Wheel Hub



Qiang Wang, Mu Meng, Xubin Li, and Zhimin Zhang

Abstract As a kind of extrusion process, the forward–backward–radial extrusion (FBRE) process can be used to produce complex-shaped parts with hoop protrusions or flanges. The control of metal flow is the key to affect forming, strain distribution, and forming load during the FBRE process. On the basis of summarizing the research of the FBRE process, this paper presents the numerical and experimental results of aluminum alloy hub production using this method. Material flow behavior and strain distribution within the final product were investigated by finite element methods. The parameters such as billet size, die corner radius, and friction conditions are optimized and determined to control the material flow in different sections. While the uniformity of extrusion deformation is greatly improved, the extrusion forming load is reduced, and the aluminum alloy hub was manufactured by the FBRE process. The comparison between the theoretical and the experimental results shows good agreement.

Keywords Forward–backward–radial extrusion · Aluminum alloy · Metal flow · Equivalent strain

1 Introduction

Nowadays, the extrusion process has been widely used in the manufacturing industries due to minimum material waste, high dimensional accuracy, and better mechanical properties of products [1, 2]. The basic or primary operations of extrusion are forward extrusion, backward extrusion, and radial extrusion according to direct relationships between the material flow and the punch movement [3]. There are combined simultaneous processes in which a billet is extruded simultaneously in the forward, backward, and/or radial directions relative to the punch movement. These combined extrusion processes offer the potentiality of producing a variety of relatively complex-shaped engineering components. Furthermore, combinations of

Q. Wang (✉) · M. Meng · X. Li · Z. Zhang
College of Materials Science and Engineering, North University of China, Taiyuan 030051, China
e-mail: wangqiang@nuc.edu.cn

© The Minerals, Metals & Materials Society 2021

G. Daehn et al. (eds.), *Forming the Future*, The Minerals, Metals & Materials Series,
https://doi.org/10.1007/978-3-030-75381-8_88

extrusion processes can also facilitate eliminating the need for multistep forming and reducing the production cost.

Many researchers have been interested in the study on combined extrusion. Kuzman et al. investigated the influences of tool geometry, friction, and lubrication, as well as workpiece properties, on balanced material flow in a combined backward–forward rod extrusion process [4]. Lee et al. proposed a new forward–backward combined extrusion process of a piston pin for an automobile part which can secure simultaneous filling for elimination of the flow defect [5]. In a study by Ho-Joon Choi et al., the effect of die geometrical parameters and friction factor on the punch load, volume ratio of the flange to can, and workpiece height are analyzed and summarized quantitatively during radial–backward extrusion [6]. Farhoumand and Ebrahimi investigated the effect of geometrical parameters such as die corner radius and gap height, as well as process conditions such as friction, on material flow, forming load, and strain heterogeneity in the FBRE process [7, 8].

In the present study, the forward–backward–radial extrusion (FBRE) process will be used to produce an aluminum alloy hub. Material flow behavior and strain distribution within the final product were investigated by finite element methods. The parameters such as billet size, die corner radius, and friction conditions were optimized to control the material flow in different regions. Finally, forming experiments were conducted and the microstructure and mechanical properties of the extruded hub were investigated, which aims at verifying the validity of the proposed method.

2 FBRE Process of Wheel Hub

Figure 1 shows the three-dimensional model of the hub. The hub is a typical cylindrical part with a flange, circular bosses and ribs on the flange, and side ribs on the cylinder wall. The geometrical shapes are complicated and the deformation is large. The upper and lower cylinders and the flange with bosses and ribs could not accomplish in a single pass by conventional hot forging. Considering the above-mentioned reasons, the FBRE process was adopted for the aluminum alloy hub.

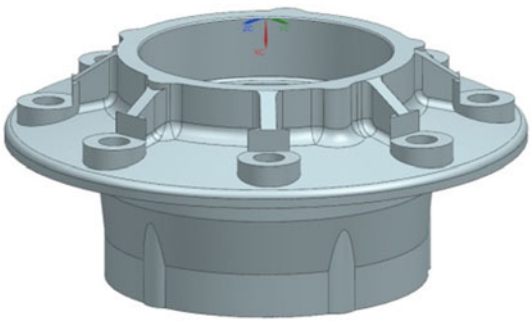


Fig. 1 Three-dimensional model of the wheel hub. (Color figure online)

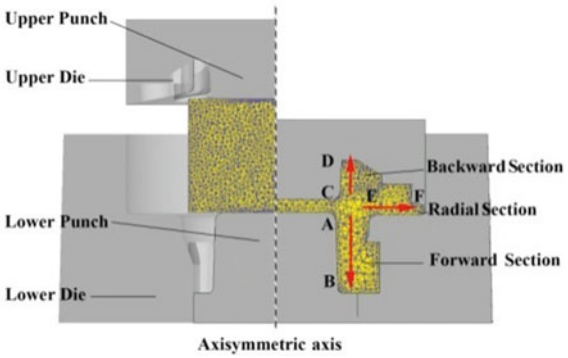


Fig. 2 Schematic diagram of the wheel hub FBRE process. (Color figure online)

Forward–backward–radial extrusion is a forging process in which material flows into the die cavity in the backward, forward, and radial directions by means of punch axial movement. During FBRE process of the aluminum alloy hub, the upper punch and upper die move downward, while the lower punch and lower die are stationary, which causes radial flow into a die cavity, forward and backward flow between the punch and the die—by means of which a flange and can are formed, and backward flow into upper a die cavity—forming circular bosses and ribs on the flange. Different from the common FBRE process, die cavity forming flange is the gap height that changes with the movement position of the upper die. Figure 2 shows the initial (left side) and final (right side) positions of the upper punch and upper die in the process, while the arrows show the direction of material flow in different directions, respectively.

As known, it is possible to restrict the metal flow into the flange and/or can by die geometrical parameters such as die corner radius and gap height, as well as process conditions such as friction. For the FBRE of wheel hub, the parameters of billet size and die corner radius are mainly studied and determined. The parameters are also schematically illustrated in Fig. 2.

3 FE and Experimental Procedure

3.1 Simulation

The commercial finite element software DEFORM 3D-6.1 was used to analyze the FBRE forming process. The employed material in this study was the 7A04 aluminum alloy (Al-6.15wt%Zn-2.63wt%Mg-1.6 wt%Cu). The stress–strain relation of this material, determined from the compression test, was input into the FE software [9]. The material model was defined as elastic–plastic. All die parts were considered as rigid bodies. A tetrahedral element type was used and the mesh sensitivity test was executed. The suitable mesh number was reported to be 100,000. The simulation

type was the Lagrangian incremental. The global re-meshing was chosen and the type of interference depth selected was relative and its value was selected to be 0.7. The conjugate-gradient was chosen as the solver of the simulation. The shear friction model was used to describe the friction behavior between the billet and the tools.

Since the geometrical parameters and friction conditions influence the metal flow into the flange and/or can, different billet size, die corner radius, and friction coefficients are selected in the simulation. The friction coefficient (μ) was 0.08, 0.12, 0.25, 0.3, and 0.4, respectively. The die corner fillets were 5, 10, 15, and 20 mm, respectively. The three different cylindrical billets with the height-to-diameter ratios of 0.38, 0.66, and 1.07 were selected.

3.2 Experimental Procedure

Cylindrical billets with 200 mm diameter, 132 mm length, and height-to-diameter ratio 0.66 were sawed from extruded 7A04 alloy bar. The die corner fillet in the experimental setup was 10 mm. The contact surfaces between the billet and the tools were forehand lubricated with oil-based graphite. The deformation billets were heated to 470 °C, whereas the temperature error was controlled within a divergence of $\pm$ 5 °C. The forming mold was pre-heated to a matching temperature with the billet. The FBRE process was performed in a 12.5MN capacity hydraulic oil press machine with a ram speed of 5 mm/s. The products processed were solution treated at 470 °C for 2 h and then subsequently aged at 125 °C in an air furnace.

Microstructure and mechanical properties specimens were cut from the can and flange and machined into tensile specimens of 5 mm gauge diameter and 25 mm gauge length. Tensile testing was carried out on an Instron-100kN material test machine at a speed of 1 mm/min. Microstructure examination was performed with an optical microscope (OM). The grain size was determined using a linear intercept method from a large number of non-overlapping measurements.

4 Results and Discussion

4.1 Equivalent Strain Analysis

The effect of billet size, die corner radius, and friction coefficient on the effective plastic strain of the FBRE wheel hub was analyzed by finite element methods. In the forward section (from point A to point B), backward section (from point C to point D), and radial section (from point E to point F), one path was considered on their thickness center lines, respectively. Different paths in cross-section of the FBRE sample were defined and mapped in the deformed mesh, as shown in Fig. 2. The effective strain value of 10 points was selected to be used in the forward section,

and the distance of each two points application was 8.5 mm, which is 5 points and 8.5 mm in the backward section and 10 points and 7.0 mm in the radial section.

The equivalent plastic strain for various frictional conditions has been depicted in Fig. 3. The equivalent strain in each region has the same change trend under different friction. In the forward and backward sections, the equivalent strain decreases along extrusion direction as a whole, and reaches the minimum at the end position. But in the radial section, the equivalent strain increases along the extrusion direction. When the friction coefficient is 0.4, the equivalent strain is the smallest in three regions. As the friction coefficient increases from 0.08 to 0.3, the equivalent strain of the same point increases in the forward section, decreases in the backward section, and basically does not change in the radial section.

The effect of various die corner radius on the equivalent strain in forward, backward, and radial sections of the FBRE sample is depicted in Fig. 4. Similarly, the equivalent strain is the maximum in the vicinity of point A which rapidly declines toward point B, point C maximum to point D minimum, and point E minimum to point F maximum. This is due to intense deformation at the corner of the punch which causes localized larger strain. When the die corner radius is 10 mm, the equivalent strain is smaller than that of other die corner radius in three regions. These show a shift in material flow preferences when the die corner radius is 10 mm.

The quantitative values of the effective strain of the FBRE sample for various billet sizes are compared, as shown in Fig. 5. As can be seen from the figure, the

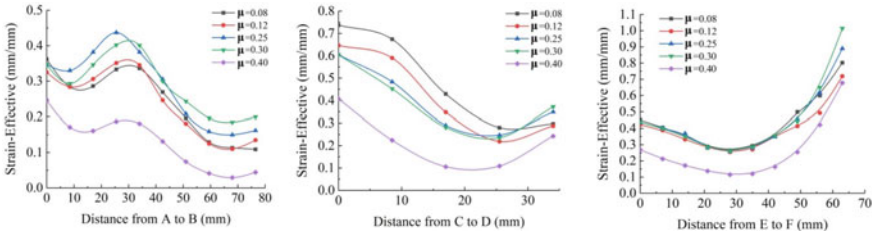


Fig. 3 Effect of friction on the equivalent plastic strain in different sections of an FBRE processed hub (h/d = 0.66, R = 10 mm). (Color figure online)

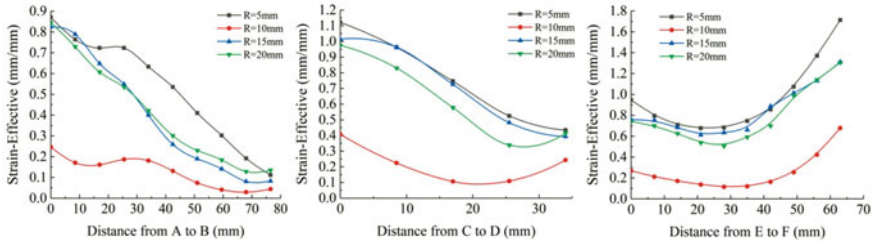


Fig. 4 Effect of die corner radius on the equivalent plastic strain in different sections of an FBRE processed hub (h/d = 0.66,μ = 0.4). (Color figure online)

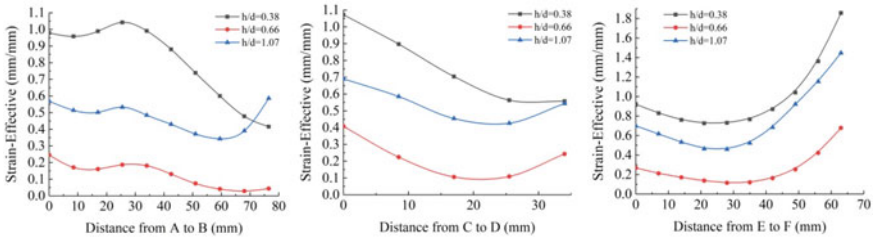


Fig. 5 Effect of billet size on the equivalent strain in different sections of an FBRE processed hub(R = 10 mm, μ = 0.4). (Color figure online)

equivalent strain in the height-to-diameter ratio of 0.38 is larger than those of other billets in three regions. The relatively small equivalent strain is obtained when the height-to-diameter ratio is 0.66, which shows that the material tends to progress more into the forward, backward, and radial sections simultaneously due to an easier flow when the billet diameter is close to the cylinder diameter. Besides, increasing the height-to-diameter ratio to 1.07 enlarges the equivalent strain due to the large upsetting deformation in the early stage.

4.2 Microstructure and Mechanical Properties

The 7A04 alloy wheel hubs were extruded successfully in one step without cracks or discontinuities according to the present technique. Both the extrusion part and finished product are shown in Fig. 6. The FBRE process of aluminum alloy hub can reduce forming operation and production cost compared with conventional hot forging.

The mechanical properties remarkably improved for the 7A04 alloy hub. The UTS and the TYS were over 560 MPa and 480 MPa, respectively, the elongation was above 8% in both can and flange areas. The difference of the UTS and the TYS between the can and the flange was less than 5%. It is noted that the mechanical property anisotropy was obviously reduced due to the relatively uniform deformation. Figure 7



Fig. 6 The wheel hubs by FBRE process. **a** Extrusion part, **b** finished product. (Color figure online)

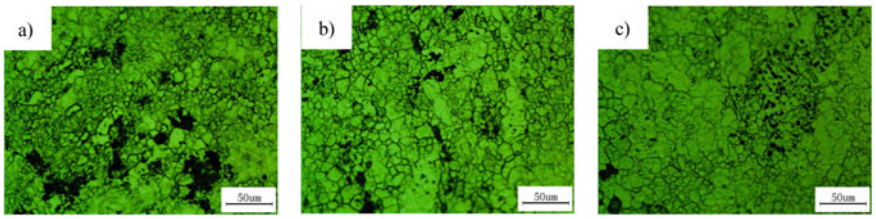


Fig. 7 Microstructure of 7A04 alloy part extruded in. **a** Upper can, **b** lower can, **c** flange areas. (Color figure online)

shows the microstructure of the analyzed areas of the 7A04 alloy hub in the T6 condition. It is obvious that the extrusion specimens have recrystallized and the grains refine greatly. Microscope observation showed that small recrystallized dynamically grains of mean size is about 8 ~ 10 μm, which is connected with localization of strains large values in these areas. At the same time, a large amount of fine and uniformly distributed second-phase particles can be observed in both can and flange areas. A more detailed microstructure and mechanical properties would be necessary to better understand the difference in effective strain amount obtained for the can and flange sections.

5 Conclusions

The forward–backward–radial extrusion process of aluminum alloy hub was analyzed in this paper. The effect of geometrical parameters such as billet size and die corner radius, as well as process conditions such as friction, on material flow and equivalent strain was investigated. It is found that the friction has a different effect on the equivalent strain in the forward, backward, and radial sections of the FBRE sample. When the height-to-diameter ratio of the billet is 0.66 and the die corner radius is 10 mm, the material tends to progress more into the forward, backward, and radial sections simultaneously due to an easier flow. The simulation results were verified experimentally and the 7A04 alloy wheel hubs were manufactured successfully in one step by the FBRE process.

Acknowledgments The authors are grateful for the research support of the Program for the Top Young and Middle-aged Innovative Talents of Higher Learning Institutions of Shanxi.

References

1. Wang Q, Zhang Z, Jianmin Yu, Xue Y (2017) A novel backward extrusion process through rotating die and open punch. Proc Eng 207:383–388
2. Moshksar MM, Ebrahimi R (1998) An analytical approach for backward-extrusion forging of regular polygonal hollow components. Int J Mech Sci 12:1247–1263
3. Ko BD, Kim DJ, Lee SH, Hwang BB (2001) The influence of die geometry on the radial extrusion processes. J Mater Process Technol 113:109114
4. Kuzman K, Pfeifer E, Bay N, Hunding J (1996) Control of material flow in a combined backward can-forward rod extrusion. J Mater Process Technol 60:141–147
5. Lee DJ, Kim DJ, Kim BM (2003) New processes to prevent a flow defect in the combined forward–backward cold extrusion of a piston-pin. J Mater Process Technol 139:422–427
6. Choi H-J, Choi J-H, Hwang B-B (2001) The forming characteristics of radial–backward extrusion. J Mater Process Technol 113(1–3):141–147
7. Farhoumand A, Ebrahimi R (2009) Analysis of forward-backward-radial extrusion process. Mater Des 30(6):2152–2157
8. Farhoumand A, Ebrahimi R (2016) Experimental investigation and numerical simulation of plastic flow behavior during forward-backward-radial extrusion process. Prog Nat Sci 26(6):650–656
9. YongbiaoYang ZX, Zhang Z, Li X (2014) Processing maps for hot deformation of the extruded 7075 aluminum alloy bar: anisotropy of hot workability. Mater Sci Eng A 528:4312–4317

Part XII
Forging

Galling-Free Micro-Forging of Titanium Wire with High Reduction in Thickness by β-SiC Dies



Tatsuhiko Aizawa, Koh-Ichi Ito, and Tatsuya Fukuda

Abstract SiC-coated SiC die and punch were used for forging titanium wire to have a triangular cross-section higher than 30% reduction in wire diameter. Computer numerical control (CNC) stamper was utilized to describe the elasto-plastic behavior of titanium wire in dry forging. Precise analyses on the contact interface between SiC coating punch and titanium work were made to investigate the mass transfer of metallic titanium as well as titanium oxide debris particles onto SiC coating surface. On the basis of these experimental results, how to design the die materials for dry metal forming of titanium was reconsidered for biomedical applications of wrought titanium.

Keywords Galling-free forging · Titanium · SiC-coated dies

1 Introduction

Most light metals and alloys are easy to make adhesion onto the die surfaces without the use of protective coatings during metal forming [1]. Diamond-like carbon (DLC) coating was effective to be free from adhesion of aluminum and aluminum alloys even in mechanical milling and cutting [2]. In particular, nano-laminated DLC coating was useful to sustain low friction and wear in ironing, forging, and stamping [3–5]. Ceramic dies were also useful to dry metal forming [6]; e.g., aluminum alloy and cold-rolled steel sheets were successfully deep-drawn by using the dry SiC or ZrO_2-sintered dies. Among those light metal work materials, pure titanium and titanium

T. Aizawa (✉)
Surface Engineering Design Laboratory, SIT, 3-15-10 Minami-Rokugo, Ota-City 144-0045, Tokyo, Japan
e-mail: taizawa@sic.shibaura-it.ac.jp

K.-I. Ito · T. Fukuda
Tokai Engineering Service Co., Ltd., 31, Miyano-Nishi, Kishoin, Kyoto 601-8306, Japan
e-mail: k-ito@tes2001.com

T. Fukuda
e-mail: t-fukuda@tes2001.com

© The Minerals, Metals & Materials Society 2021

G. Daehn et al. (eds.), *Forming the Future*, The Minerals, Metals & Materials Series,
https://doi.org/10.1007/978-3-030-75381-8_89

alloys are difficult or nearly impossible to be free from galling in metal forming. Under the upsetting of titanium wire, the SKD11 die surface was covered by the titanium films transferred from work material [7]; TiO_2 debris particles splashed around the dies from the oxidized surface of wire in each upsetting process. No improvement was reported in dry deep-drawing of titanium sheet by using any sintered dies of SiC, Si_3N_4, Al_2O_3, and ZrO_2 [6]. In particular, failure in dry deep-drawing by SiC die requires reconsideration on the material compatibility between SiC die and titanium in metal forming [8]. This difficulty is also identified as one of the greatest issues to hinder the near-net shaping of titanium and titanium alloys to biomedical parts and tools [9].

The authors proposed to employ the thick and dense SiC coating as a die material for dry upsetting and forging of pure titanium wires in cold [10–14]. Since SiC-sintered substrates have a porosity of 1.0–0.5% as well as glassy grain-boundary layers, they suffer from the adhesion and mass transfer of titanium. This galling of titanium to sintered SiC die resulted in a severe reduction of deep-drawability in practice [6]. SiC coating by chemical vapor deposition (CVD) is fully dense without any secondary phases. Hence, this SiC coating is a suitable die material to reconsider the material compatibility between its crystalline structure with covalent bonding and the titanium works. After upsetting and forging experiments in the previous studies, no transfer of titanium was detected on the contact interface of SiC coating punch and die. Adhesion of titanium oxide debris particles took place on the punch surface outside of the initial contact zone between SiC punch and titanium work.

In the present study, this SiC-coated SiC die and punch are used for micro-forging of titanium wire to have a triangular cross-section. This forging with a higher reduction of wire diameter than 30% becomes suitable to investigate the possibility of titanium transfer onto the punch and die surfaces and to describe the adhesion behavior of oxide debris particles. Computer numerical control (CNC) stamper is utilized to describe the elasto-plastic behavior of titanium wire in dry forging with up to 35% reduction in diameter. Precise analyses on the contact interface between SiC coating and titanium work are performed to investigate the mass transfer of metallic titanium as well as the titanium oxide debris particles onto SiC coating surface. On the basis of these experimental results, how to design the die materials for dry metal forming of transition metals including titanium is reconsidered for biomedical applications of wrought titanium.

2 Experimental Procedure

A dense, thick SiC layer with a thickness of 3 mm was formed onto the sintered SiC substrate by the thermal CVD process. X-ray diffraction (XRD), laser microscopy, and three-dimensional profilometer were utilized to characterize the deposited SiC coating. CNC stamper was used to make micro-forging of pure titanium wire with the diameter of 0.98 mm by using this SiC-coated SiC die and punch. Scanning electron

microscopy (SEM)–electron dispersive X-ray spectroscopy (EDX) was also utilized to describe the adhesion process on the SiC coating punch.

SiC-coated SiC die. A sintered SiC block with an average porosity of 0.5% was prepared as a substrate for thermal CVD to synthesize and deposit the polycrystalline SiC coating. As depicted in Fig. 1, this coating has a single phase of β-SiC and has 3C–SiC crystallographic structure. The average grain size is 10 μm. Different from other SiC-coatings by CVD and physical vapor deposition (PVD), there are no amorphous phases in this β-SiC coating.

As reported in [15], the thickness of amorphous SiC coating is at most 7 μm by CVD or PVD. In addition, these amorphous coatings have less strength and toughness than needed in cold stamping and forging.

Figure 2a depicts a SiC-coated SiC substrate with a coating thickness of 3 mm. This substrate is directly used as a punch. The femtosecond laser machining system

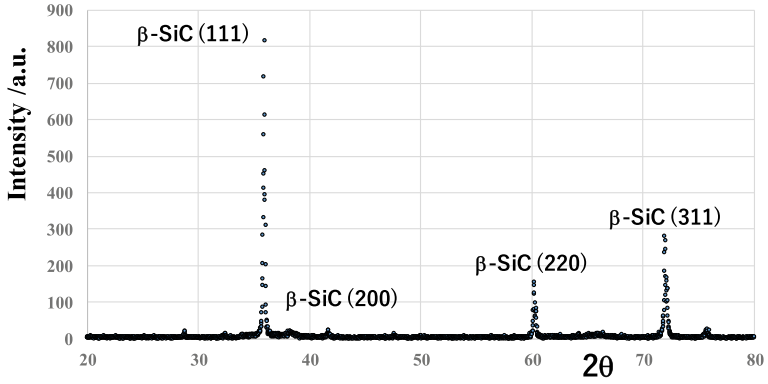


Fig. 1 XRD diagram of CVD-coated SiC thick film onto the sintered SiC substrate. (Color figure online)

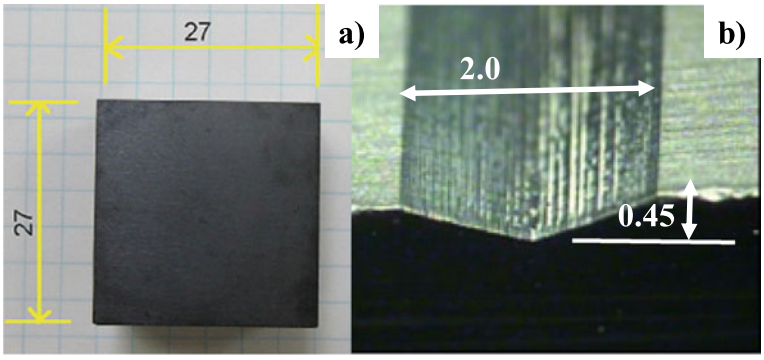


Fig. 2 SiC-coated SiC punch and die. **a** Punch with a flat surface, and **b** die with a triangular groove to fix the titanium wire. (Color figure online)

was utilized to cut a triangular groove into the SiC-coated SiC die as shown in Fig. 2b. The groove depth is 0.45 mm; its width is 2.0 mm. Owing to this thick SiC coating, the titanium wire with a diameter of 0.98 mm is forged into this groove with direct contact to SiC coating to shape the cylindrical wire to the triangular one with a higher than 30% reduction in diameter.

Cassette dies. These SiC punch and core die were fixed into the upper and lower cassette dies, respectively, as shown in Fig. 3. In particular, the cubic SiC punch was locked in the upper die to make micro-forging experiments.

Forging process by CNC stamper. Figure 4 depicts the CNC stamping system for this micro-forging experiment. In this CNC stamper, four loading axes were independently controlled to move upward and downward with less allowable eccentric loading. The maximum load was 50 kN; the loading sequence was controlled by the history of stroke. The sum of powers by four motors as well as the stroke was monitored during stamping.

In the following experiments, the punch was controlled to move down from the height of 80 mm down to 42 mm by 10 mm/s for 3.8 s in the first term. In the second term, the stroke speed was reduced to 0.02 mm/s to precisely decrease the height of 42 to 41.7 mm for 15 s. SiC punch was expected to be in contact with the work during this term, and the work was loaded to the specified height (δ_L) for each reduction; e.g., $\delta_L = 41.5$ mm for 10% reduction, 41.4 mm for 20%, and so forth. In the third term, the stroke was kept constant by δ_L for 0.5 s before the increase of stroke by 10 mm/s.

Observation and measurement. SEM–EDX was utilized to make microstructure and element mapping analyses on the contact surface of SiC-coated SiC punch with the deformed titanium wire.

Titanium wire work. A pure titanium wire of industrial-grade I with a diameter of 0.98 mm and length of 20 mm was employed as a work material in the micro-forging process. Its chemical compositions were listed as follows: hydrogen content was 0.0012 mass%, oxygen 0.097 mass%, nitrogen 0.007 mass%, iron 0.042 mass%, and carbon 0.007 mass%, respectively, for titanium in balance.

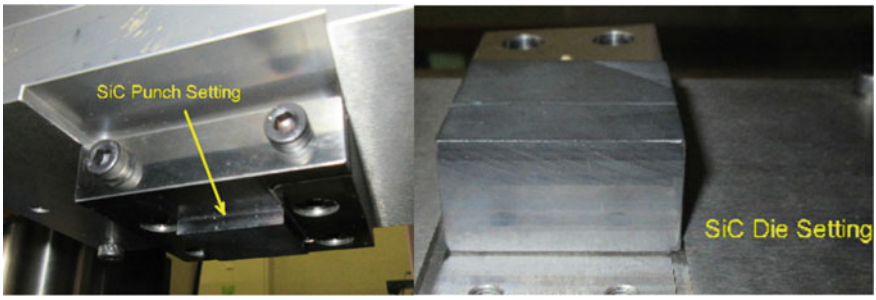


Fig. 3 A cassette die set for upsetting to be fixed between the upper and lower bolsters in the CNC stamper. **a** Upper die set with SiC punch and **b** lower dieset with SiC core die. (Color figure online)



Fig. 4 CNC stamping system for upsetting experiments. (Color figure online)

3 Experimental Results

CNC stamping system is employed to make micro-forging experiments with the use of the SiC-coated SiC punch and die. The relationship between the applied power and stroke is in situ measured to describe the elasto-plastic behavior in forging.

Micro-forging behavior. A cylindrical wire with a diameter of 0.98 mm is forged by lowering the SiC-coated SiC punch with the increasing reduction (r) of wire diameter and shaped into triangular wires. Figure 5 depicts the variation of cross-sections in the forged titanium wire at r = 10, 20, and 35%, respectively. When r = 10%, the top of the wire begins to be flattened by compression in forging. When r increases to 20%, this flattening advances to broaden the contact surface area to the SiC-coating punch. The bottom of the wire partially fills the cavity of the triangular groove in the die. Up to r = 35%, the flattening width at the top of the wire becomes broader than 1 mm. The filling depth of titanium into the triangular groove reaches 0.3 mm. The present forging behavior of titanium wire is governed by the flattening process on contact with the punch surface as well as the filling process into the triangular groove in the die.

Figure 6 depicts the applied power to stroke relationship in forging. The punch commences to be in contact with a titanium wire; the power or the load begins to increase at point A. The wire is compressed in the longitudinal direction up to point B after observation on the forged wire cross-sections. The flattening process of wire advances from point B and the contact area to SiC coating punch broadens monotonously with increasing stroke. At point C, the filling process into a groove

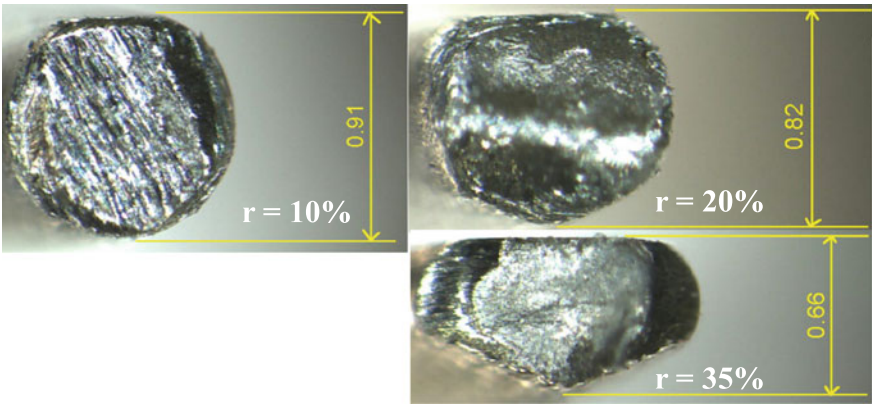


Fig. 5 Forging behavior of a cylindrical wire with the diameter 0.98 mm to shape into triangular wires with the increasing reduction of diameter. (Color figure online)

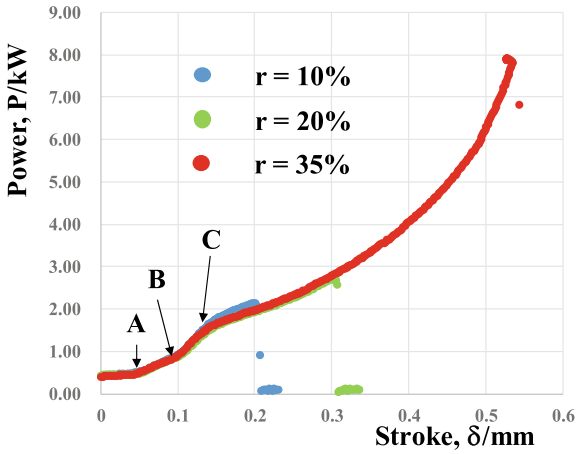


Fig. 6 Power to stroke relationship in forging of titanium wire with the increasing reduction of diameter. (Color figure online)

in die starts. After this point, the work hardening of wires takes place together with flattening along with the SiC coating punch and filling into a groove in die.

SEM analysis on SiC-coated SiC punch. SEM analysis was made on the SiC coating punch surface after cold, dry forging of titanium wire by r = 35%. As shown in Fig. 7a, a contact trace to titanium work is seen on the SiC coating. As closely observed by SEM in Fig. 7b, this trace consists of two layers. Two B-regions neighboring to C-region are colored in white with a difference to the original SiC coating in the A-region, while the C-region is colored in gray with dotted black spots. This trance width, including the C-region and its upper and lower B-regions, just corresponds to the contact interface width around 1.2 mm between the wire and the SiC coating punch at r = 35%. This reveals that the C-region with a width of 0.2 mm is an initial contact surface at r < 10% and that both B-regions are extended

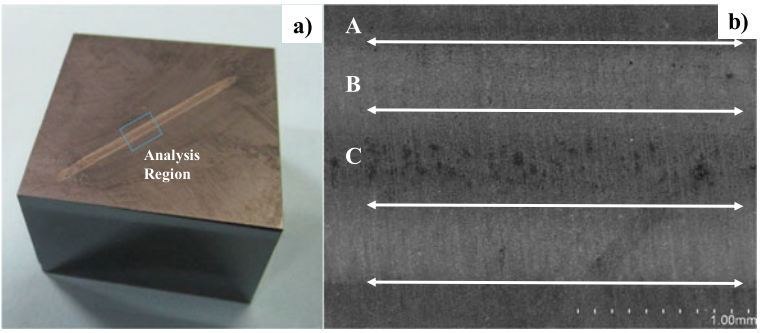


Fig. 7 Observation on the SiC coating punch surface after cold forging in dry at r = 35%. **a** Surface condition of SiC coating punch and **b** SEM analysis on the contact zone and its vicinity. (Color figure online)

contact interfaces by flattening of wire along the punch surface at r > 10%. That is, C-region is an initial contact interface of wire to SiC coating under high compressive stress, and two B-regions are formed by extension of contact area in flattening of wire along with the SiC coating punch.

SEM–EDX analyses on SiC-coated SiC punch. The SEM image and EDX element mapping on the C-region are shown in Fig. 8. The black dots in this C-region, denoted by "a," are isolated carbon from SiC coating. The white layers, denoted by "b," are titanium oxides. No mass transfer of titanium only in metallic is detected in this EDX analysis. This reveals that carbon is isolated from β-SiC crystals under high compressive pressure in initial contact of titanium wire to SiC punch but that

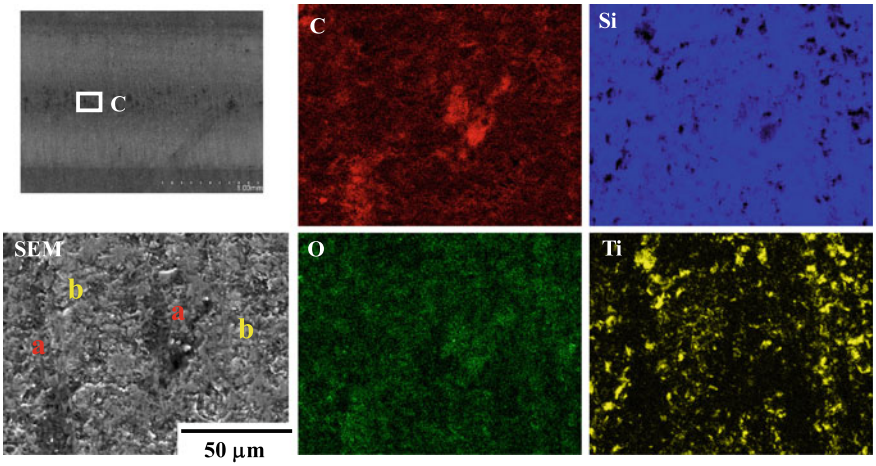


Fig. 8 SEM analysis and EDX element mapping on the C-region in the trace on the SiC coating. Titanium and oxygen mappings are coincident with each other. (Color figure online)

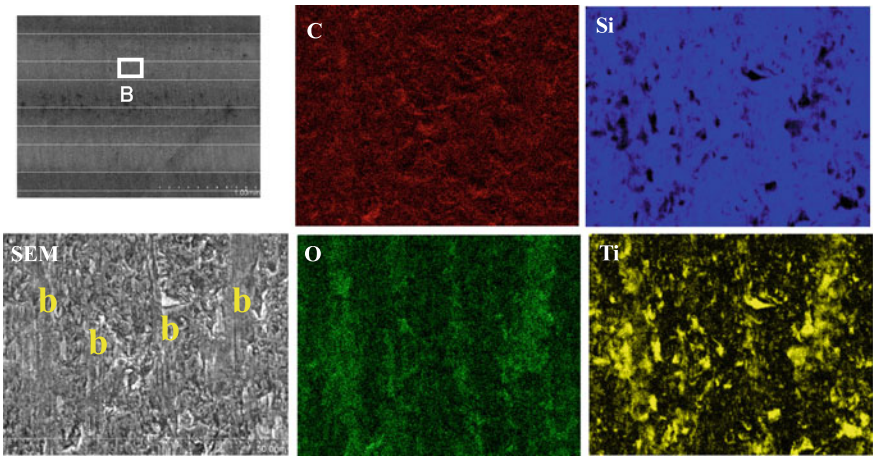


Fig. 9 SEM analysis and EDX element mapping on the B-region in the trace on the SiC coating. Titanium and oxygen mappings are just coincident with each other in a similar manner to Fig. 8. No carbon segregation is seen in the carbon mapping. (Color figure online)

titanium oxide debris particles from the wire deposit onto the SiC coating surface and form the titanium oxide layers in the lateral direction by flattening process.

Figure 9 depicts the SEM image and element mapping on the B-regions, neighboring to the C-region. Since carbon distributes uniformly in these B-regions without segregation, carbon does not isolate from SiC crystalline structure. Titanium and oxygen mappings are coincident with each other; titanium oxide debris particles also deposit on these regions in a similar manner in the C-region. These deposited titanium oxide debris form layers in the lateral directions. This implies that titanium debris deposits form a thin film on the SiC coating and this film grows with flattening of wire on the SiC punch surface. There are no deposits of debris particles outside of these B-regions.

This SEM–EDX analysis proves that metallic titanium does not transfer onto SiC coating punch even at its initial contact interface to titanium wire and that titanium oxide debris particles do not splash over the punch surface but deposit on the punch surface and form the thin layers radially from the initial contact zone together with the flattening process of wire on the punch surface.

4 Discussion

Galling or work material transfer to die surfaces is induced mechanically and chemically in metal forming. The former mechano-chemical galling is often observed in hot stamping and forging. The steel sheets adhere to the tool steel die when the temperature on the interface goes beyond the flash temperature [3]. The oxide glasses are

deformed by mold stamping just above the glass-transition temperature and cemented onto the DLC-coated mold-stamping dies [16]. The latter chemical galling possibly occurs even in cold stamping and forging. Upsetting and deep-drawing of titanium sheets experienced severe galling in practice [6, 7]. As discussed in [11–14], this chemical galling comes from the material compatibility between titanium and die surface material. Pure titanium versus the tool steel die or the sintered SiC die with glassy zones are typical pairs with attractive compatibility to enhance the chemical galling process.

Material compatibility in solid-state contact is often discussed by the classical theory on this compatibility [8, 17]. After this HSAB (hard and soft acid and base) principle, a pair of materials in contact is identified as acid–base pair. In the present case, titanium ions are classified into the hard acid group while the Si-oriented ion is grouped into the hard base one. Then, hard acid and base pair are easy to react on the contact interface. The present experiment proves that no direct transfer of metallic titanium takes place even under the high compressive stress state enough to trigger the isolation of carbon from SiC crystals. The classical treatise is never true to describe the present galling-free material compatibility in solid-state contact condition. New theoretical understanding with the use of computational chemistry [18] is necessary to describe the solid-state interaction between SiC coating and transient metals in metal forming.

After precise EDX analysis on the element mapping, carbon isolates and agglomerates as a black dot on the SiC coating surface only at the initial contact interface of SiC punch to wire. Since titanium is never detected on these high carbon content zones in Fig. 7, this carbon isolation has nothing to do with the attraction of carbon by the direct reaction between carbon and titanium [19]. When SiC single crystal is held at the elevated temperature over 1500 K, carbon is left by isolation of Si on the SiC surface and grows as a graphene layer [20]. In the present situation, the flash temperature on the contact interface between titanium wire and SiC coating is much lower than the critical temperature to ignite Si-isolation from SiC crystals. In the phase diagram for Si–C binary system [21], β-SiC crystalline structure is stable in the higher carbon content regions than 50% from RT and atmospheric pressure up to 2400 K and 50 GPa, respectively. Assuming that titanium wire is elasto-plastically contact on the SiC coating with the area of 100 μm $\times$ 20 μm at the load of 10 kN around the C-region in Fig. 6, the applied pressure on the contact surface reaches 5 GPa. Hence, the Si–C phase diagram teaches that unstable isolation of carbon from β-SiC phase could be never feasible at this low-pressure range and low flash temperature. To be noticed, the carbon supersaturation into SiC 3C-structure drives fast rate growth of β-SiC crystalline layer in CVD coating [22]. Under the high compressive stress state, the carbon could isolate from this supersaturated state in β-SiC 3C-structure and agglomerate at the highly pressurized contact interface. In the present experiment, the carbon agglomerates align in dots on the initial contact zone as shown in Fig. 8. Since this dot size is nearly equivalent to the β-SiC grain size, the isolated carbon atoms from the carbon supersaturated β-SiC crystals form this carbon agglomerate in each β-SiC grain. This predicts that this formation of dotted carbon agglomerates has a superficial grain size effect of β-SiC grains.

5 Summary

Dense, thick, β-SiC coating with cubic structure and covalent bonding has the potential to work as a galling-free die for dry forging of transient metals, including the pure titanium as well as the titanium alloys. The pure titanium circular wire is forged into a triangular bar without metallic titanium transfer onto SiC coating punch and die. Titanium oxide debris particles deposit onto the SiC punch surface and form thin adhesive layers onto SiC punch surface in the lateral direction. This adhesive trace is too thin to hinder the successive forging in mass production. Those debris particles never splash around the atmosphere in forging.

The supersaturated carbon isolates from β-SiC crystals at high contact pressure and agglomerates as a dot on the contact interface. This distribution of free carbon agglomerates has grain size dependence of β-SiC coating. What triggers this isolation of carbon from β-SiC crystallographic structure must be studied by the tribo-testing and metal forming simulations in experiments and by the first principle calculation in the theoretical treatise. These free-carbon agglomerates have no reaction with titanium during forging. This agglomerate is expected to be working as a tribo-film to reduce the friction on the contact interface in the practical application of SiC coating as a die in metal forming.

Acknowledgments The authors would like to express their gratitude to Mr. S. Kurozumi (Nano-Coat Film, LLC.) and Mr. T. Yoshino (Komatsu-Seiki Kosakusho, Co., Ltd.) for their help in the experiment.

References

1. Dohda K, Boher C, Rezai-Aria F, Mahayotsanun N (2015) Tribology in metal forming at elevated temperatures. Friction 3(1):1–27
2. Aizawa T, Masaki E, Morimoto E, Sugita Y (2014) Recycling of DLC-coated tools for dry machining of aluminum alloys via oxygen plasma ashing. Mech Eng Res (41):52–62
3. Morita H, Aizawa T, Yoshida N, Kurozumi S (2012) Dry transfer stamping by nano-laminated DLC-coated tools. Proc 10th ICTP (2012, Germany, September), pp 1103–1107
4. Aizawa T, Morita H (2016) Tribological design and engineering in surface treatment for semi-dry and dry stamping. Proc. 4th ICTMP (2016, Thai, March), pp 14–28
5. Dohda K, Aizawa T (2014) Tribo-characterization of silicon doped and nano-structured DLC coatings by metal forming simulators. Manufac Lett 2:82–85
6. Kataoka S, Murakawa M, Aizawa T, Ike H (2004) Tribology of dry deep-drawing of various metal sheets with used of ceramic tools. Surf Coat Technol 178:582–590
7. Kihara T (2019) Visualization of deforming process of titanium and titanium alloy using high speed camera. Proc 2019 JSTP Conf. pp 41–42
8. Aramaki K (2014) Further consideration on corrosion and inhibition phenomena of anions based on the hard and soft acids and bases principles. Zairyou-to-Kankyo 63:417–428
9. Hanson M (2008) On adhesion and galling in metal forming. Uppsala Dissertations, Uppsala University
10. Aizawa T, Fukuda T (2019) CNC dry micro-forging of pure titanium wire by SiC-coated SiC die. Proc 3rd APSTP, pp 21–26

11. Aizawa T, Ito K, Fukuda T (2020) SiC-coated SiC die for galling-free forging of pure titanium. Mater Trans 61(2):282–288
12. Aizawa T, Ito K, Fukuda T (2021, January) Dense SiC coating die-technology for galling-free forging process. Proc 1st GRGLMM Int Symp (Toyama, Japan; January, 2021), pp 81–86
13. Aizawa T, Yoshino T, Ito KI, Fukuda T (2020) Thick β-SIC CVD-coated SiC die system for dry cold forging of metals. J Crystal, MDPI 10(539):1–13
14. Aizawa T, Yoshino T, Shiratori T, Dohda K (2020) Anti-galling β-SiC coating dies for fine forging of titanium. Proc 3rd Int Conf Mater Strength Appl Mech (MSAM 2020) (Macau, China; December, 2020) (in press)
15. Knoteck O, Loeffer F, Wolkers L (1993) Amorphous SiC PVD coatings. Diamond Rel Mater 2:528–530
16. Aizawa T, Dohda K, Shiratori T (2019) Nano-structured tribo-coating for cold and hot stamping. Proc. 52nd ICFG Plenay Meeting (September 16th, 2019; San Sebastian, Spain), pp 116–123
17. Pearson RG (Ed.) (1973) Hard and soft acids and bases. Dowden Hatchinson & Ross, Inc., Stroudsburg
18. Lewars EG (2016) Computational Chemistry. Springer International Publishing, Switzerland
19. Yokosawa T, Takagi JI, Kataoka S, Tanaka S (2005) Study on polishing of CVD diamond film (1st report). J. Precise Mechanical Eng 71(9):1131–1136
20. Kusunoki M, Norimatsu W (2016) Growth and superiority of epitaxial graphene on SiC. Microscopy 50(1):28–38
21. Haase V, Kirschstein G, List H, Ruprecht S, Sangster R, Schröder F, Töpper W, Vanecek H, Heit W, Schlichting J, Katscher H (1995) The Si–C phase diagram. Gmelin Handbook of Inorganic and Organometallic Chemistry. 8th Ed. Springer
22. Seki K, Alexander, Kozawa S, Harada S, Ujihara T, Takeda Y (2012) Polytype-selective growth of SiC by supersaturation control in solution growth. J Crystal Growth 360:176–180

Deformation Mechanism of the Tooth Material Filling for Precision Forging of Spur Gears



Wei Feng, Zengjie Feng, Mengjuan Zhou, Ling Mao, and Xiangyang Jia

Abstract Spur gears are an important transmission part used widely in many industries. Precision forging of spur gears has a lot of advantages compared with the conventional mechanical cutting method. However, it is very difficult to fill the corner well and the forging load is also very large, especially in the final forming stage during the precision forging of spur gears. So, a three-dimensional (3D) finite element (FE) model for precision forging of spur gears was built by DEFORM-3D software. The stress and strain states in different forming stages and positions of billet have been studied. Also, the Lode parameter μ_σ was calculated, and the metal flow line method was used to reveal the deformation mechanism of the tooth material. Results show that the Lode parameter of the tooth shape is negative at the beginning of the tooth filling and is positive at the final stage of the tooth filling. Also, the stress state changes from two-directional compressive stress and one-directional tensile stress to three-directional compressive stress.

Keywords Spur gears · Precision forging · Deformation mechanism · Lode parameter

1 Introduction

It is well known that precision forging gears have advantages of high efficiency, low cost, as well as increased surface quality, compared with the conventional mechanical cutting methods [1, 2]. However, the corner filling is difficult and the forging load

W. Feng (✉) · Z. Feng · M. Zhou · L. Mao
School of Materials Science and Engineering, Wuhan University of Technology, 430070, Wuhan Hubei, China
e-mail: fengwei@whut.edu.cn

Hubei Key Laboratory of Advanced Technology for Automotive Components, Wuhan Hubei 430070, China

W. Feng · X. Jia
Hubei Engineering Research Center for Green Precision Material Forming, 430070, Wuhan Hubei, China

© The Minerals, Metals & Materials Society 2021

G. Daehn et al. (eds.), *Forming the Future*, The Minerals, Metals & Materials Series,
https://doi.org/10.1007/978-3-030-75381-8_90

is very large, especially in the final forming stage during precision forging of spur gears, which reduces the product quality and shortens the mold life [3].

To solve these problems, many types of research were done, most of which focused on die designs, billet shapes, deformation conditions, etc. An idea of movable cavity die design was proposed by Tuncer and Dean, in which the better friction condition can improve forming quality and reduce forming load [4]. A two-step forging technology was developed by Jung to produce well-shaped helical gears with lower forging load [5]. Zuo performed relief-cavity designs in different sizes and studied the effects of different designs on corner filling, billet stress, die stress, forming load, and material utilization to determine the optimal design [6]. Jin investigated the effects of forging parameters on uniformity in deformation and microstructure of AZ31Bstraightspur gear, concluding that decreasing deformation temperature or increasing strain rate is positive to get fine-grained microstructure but negative to the uniformity in both deformation and microstructure [7]. Sadeghi found that the billet/die interface friction can influence forging pressure through changing metal flow during gear forging [8].

Although the quality of gears produced by precision forging is influenced by various factors besides designs of die and billet, the fundamental solution to spur gears forging problems is to change metal deformation mode, referring to the metal-plastic forming principle.

The Lode parameter μ_σ can reflect the influence of the middle principal stress on the material yielding and failure criterion [9]. So it is used to indicate the directionality of the stress state and the type of the strain state and is also used to study the effect on the localization of plastic flow in a micromechanical model by many scholars [11].

It is well known that the flow line can make mechanical anisotropic properties present in the metal. The better mechanical properties can be obtained along the longitudinal direction and the lower along the transverse direction. Many scholars researched the metal flow law and optimized the forming process by the metal flow line method to control and improve the mechanical properties of the forged product [12].

Forging of spur gears is a complicated metal-plastic forming process. Especially, the corner filling is very different and the forging load is very large. Therefore, it is necessary to explore the metal deformation mechanism in precision forging process of spur gears. In this work, a three-dimensional finite element model for precision forging of spur gears was built, the stress and strain states in different forming stages and positions of corners have been studied, and the material flow law was obtained by metal flow line method. Besides, the Lode parameter μ_σ was calculated to reveal the mechanism of the material deformation by simulating the process.

2 Establishment of 3D FE Model

To analyze the metal deformation mechanism in precision forging process of spur gears, a 3D FE model of a spur gear was established to simulate the precision forging process using the finite software DEFORM-3D, based on the rigid visco-plastic theory with conjugate gradient method and direct iteration, as shown in Fig. 1.

For the spur gear studied in this work, its specifications of a number of teeth, normal module, pressure angle, and teeth width are 18, 2 mm, 20°, and 20 mm, respectively. Also, it is a pitch diameter of 36 mm and a root diameter of 31 mm. The billet is a cylinder with a diameter approximately equal to the root diameter of the spur gear. The height of the billet is defined according to the law of volume constancy of the material in metal plastic deformation. The designed size of the billet is $\varphi 31\ mm \times 26\ mm$ and the material is 20CrMnTiH, a kind of low-carbon gear steel used widely in China. The billet is defined as a plastic body and all the dies are regarded as rigid ones in FE modeling. The flow stress curve introduced in the material library is obtained through the hot compression test of this material [13]. The die material is AISI-H13. In order to save the simulation time, a quarter of the model is built. The element number of the billet is 50000 after using the meshing window. The constant shear friction factor between the dies and the billet is 0.25. Environment temperature is 20°C and the forming temperature of the billet is 850 °C. The punch speed is 10 mm/s.

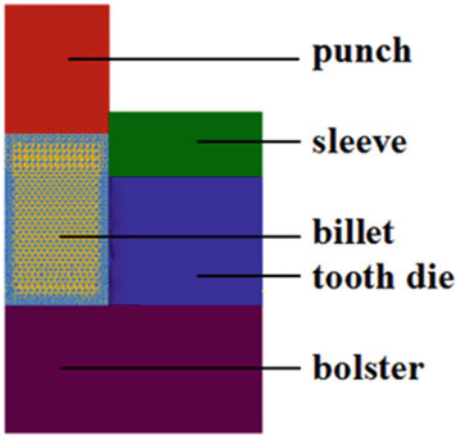


Fig. 1. 3D FE model of precision forging of spur gear. (Color figure online)

3 Results and Discussion

3.1 Decision of Different Forming Stages

Figure 2 gives the variation curves of forming load with stroke of punch. As shown in Fig. 2, the forming load increases gradually with the increasing stroke in the early forming stages and increases quickly in the final forming stage. To study the law of material flowing and deformation mechanism, the whole forging process of spur gears is divided into four stages according to the variation trend of forming load and teeth shape filling condition, as shown in Fig. 2. Points 1, 2, 3, and 4 in Fig. 2 correspond to different filling moments. Point 1 indicates that the deformation degree is 35%, the billet filled the cavity, and the maximum diameter of the billet is equal to the base circle diameter at the moment. Point 2 indicates that the deformation degree is 75%, the billet continued to fill the cavity, and the maximum diameter of the billet is equal to the pitch circle diameter at the moment. Point 3 indicates that the deformation degree is 80%, the billet is almost full of the teeth cavity except for the corner, and the maximum diameter of the billet is equal to the addendum circle diameter at the moment. Point 4 indicates that the deformation degree is 100%, the billet filled the corner, and the forging load reached the maximum at the moment.

The teeth shapes of the billet under different deformation degrees are shown in Fig. 3. It can be seen from Figs. 2 and 3 that the forging force increased gradually at the stage I, II and III. When the billet begins to contact the root of the tooth die, the forming load increases sharply at the final forming stage IV because of the free area reducing and metal flow resistance increasing, in which the tooth filling is very hard and the forming load rises rapidly. Therefore, it is vital to study the deformation mechanism to reveal the cause of corner filling and large forming load during spur gears precision forging.

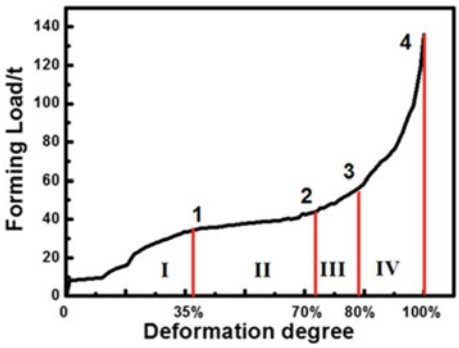


Fig. 2 Load-stroke curve. (Color figure online)

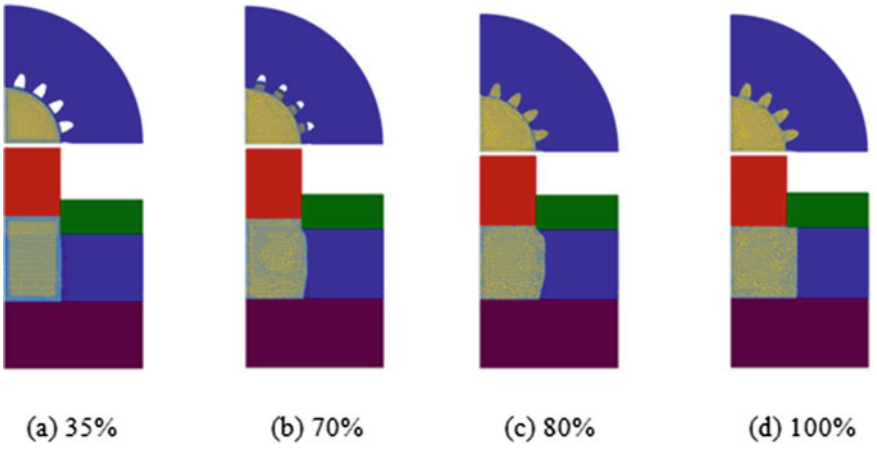


Fig. 3 The teeth shape of the billet under different deformation degrees. (Color figure online)

3.2 Deformation Zones in Different Forming Stages

Based on the forming force and metal flow principle, the spur gears precision forging process can be approximated as two basic deformation modes, namely cylinder upsetting deformation and extrusion deformation.

To illustrate the forming progress in detail, the billet is divided into three deformation zones according to different deformation characteristics and force conditions. All the zones of different forming stages are shown in Fig. 4.

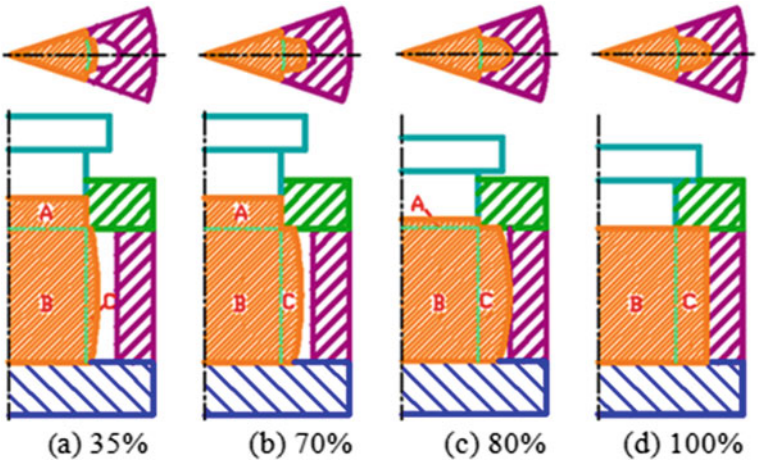


Fig. 4 Deformation zones of different forming stages. (Color figure online)

For zone A, at the forming stages I, II, and III, the plastic deformation of the metal does not occur and only moves down rigidly under the pressing of the punch. And part of metal in zone A flows into zone B and participates in deformation. For zone B, the material is compressed by the material in zone A and filled into the cavity. Metal in zone C is subjected to extrusion deformation and metal filled the tooth cavity due to the radial pushing from the material in zone B and circumferential compression from the teeth cavity. For zone C, the deformation is uneven in the axial direction because of friction from die parts. Deformation in zone C is more complicated compared to the other zones.

3.3 Deformation Characteristics Under Different Forming Stages

To decide the deformation type in spur gears precision forging, a flownet method was used to study the deformation characteristics of each zone in different forming stages. The flownet method is a kind of post-processing method of the DEFORM-3D software, in which the user can be allowed to place some form (2D or 3D) of a grid onto the object and let the simulation track the deformation of the grid throughout the deformation. This is an excellent way in which to visualize any potential irregularities in the grain structure or to view potential surface defects.

Figure 5 shows the deformation characteristics of grids under different forming stages during precision forging spur gears. It can be shown in Fig. 5 that the shape of grids in zone A has not deformed because of the constraint of the sleeve. For zone B, grids are compressed axially and elongated radially with the deformation degree increasing. The distribution of radial elongation is uneven at the forming stages III and IV, which is larger in the middle and smaller at both ends, as shown in Fig. 5 c and d. However, the axial compression is more and more severe with the increasing deformation degree. In addition, the vertical lines of coordinate grids bend into the teeth cavity, respectively. For grids in zone C, the axial compression and radial elongation increased gradually with the increasing deformation degree.

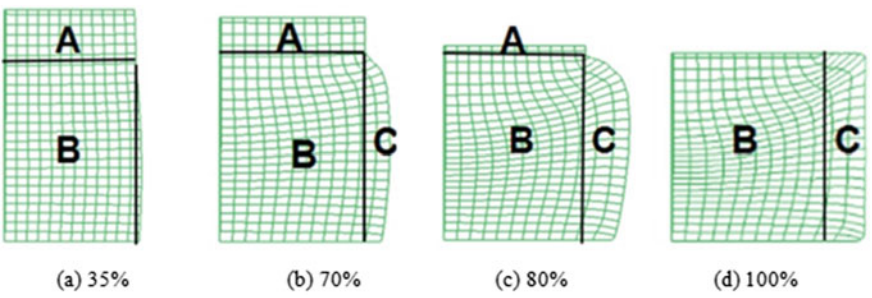


Fig. 5 Deformation characteristics of grids under different forming stages. (Color figure online)

Also, the horizontal lines of coordinate grids continue bending to the top and bottom sides of the billet, and the vertical lines bend to the addendum. Besides, the grid deformation of zone C is more severe than that of zone B.

3.4 The Stress State of Different Forming Stages

In order to research the deformation mechanism in detail, the tooth portion is divided into five regions ①, ②, ③, ④, and ⑤, as shown in Fig. 6. Regions ①, ②, ③, ④, and ⑤ represented zones closing to groove, root, the upper, the middle, and the lower end of the tooth, respectively.

Based on the three-dimensional finite element for precision forging of spur gear, the point tracking method was used to extract stress states and strain states in each forming stage. Table 1 shows the stress state of five regions under different forming stages. From Table 1, it can be found that: (1) The stress state in the groove of a tooth is always three-directional compressive stress under different forming stages; (2) The stress state of the upper and the lower zone of the tooth shape converts from two-directional compressive stress and one-directional tensile stress in forming stages I and II to three-directional compressive stress in forming stages III and IV; (3) The root and the middle of the tooth shape change from two-directional compressive stress and one-directional tensile stress state in forming stage I to three-directional compressive stress state in forming stages II, III, and IV.

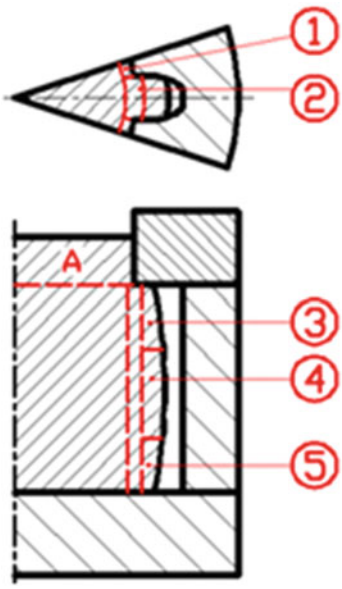


Fig. 6 Five regions of billet with complex deformation. (Color figure online)

Table 1 Stress states of five regions in each stage

Regions	I	II	III	IV
①	0	0	0	0
②	1	0	0	0
③	1	1	0	0
④	1	0	0	0
⑤	1	1	0	0
inline media object				

3.5 The Strain State of Different Forming Stages

In precision forging of spur gear, the metal flow is not only affected by stress state but also the strain state. Generally speaking, the stress state at an arbitrary point of a material can be described using three principal stresses or the three stress invariants [10]. The Lode parameter μ_σ, which varies from -1 to 1, not only can be used to represent the stress state but also to decide qualitatively the type of the strain state for engineering problem [10, 13]. The Lode parameter μ_σ is defined as follows:

$$\mu_\sigma = \frac{2\sigma_2 - \sigma_1 - \sigma_3}{\sigma_1 - \sigma_3} \tag{1}$$

where σ_1, σ_2, and σ_3 are the largest principal stress, the middle principal stress, and the third stress, respectively.

When $\mu_\sigma < 0$ the deformation type is the tensile strain, when $\mu_\sigma > 0$ the deformation type is compression strain, and when $\mu_\sigma = 0$ the deformation type is the plane strain. Therefore, the Lode parameter μ_σ was calculated to reveal the strain type of billet at different stages. All the principal stress information of the selected regions can be obtained according to tracking points, and then the Lode parameter μ_σ can be calculated according to Eq. (1). Table 2 shows the Lode parameter μ_σ calculated under different regions and forming stages according to Table 1.

It can be found that from Table 2: (1) For region ①, ②, $\mu_\sigma < 0$ in the whole forming process, the deformation type is the elongation deformation. (2) For region ③, ⑤, μ_σ

Table 2 Lode parameter μ_σ of five regions in each stage

Regions	I	II	III	IV
①	−0.51	−0.39	−0.63	−0.55
②	−0.22	−0.53	−0.59	−0.46
③	−0.48	−0.46	−0.24	0.21
④	−0.53	0.10	0.26	0.21
⑤	−0.47	−0.46	−0.25	0.23

< 0 in stages I, II, and III, the deformation type is the elongation deformation; $\mu_\sigma > 0$ in stage IV, the deformation type is compression deformation. (3) For region ④ $\mu_\sigma < 0$ in stage I, the deformation type is the elongation deformation; $\mu_\sigma > 0$ in stages II, III, and IV, the deformation type is the compression deformation.

4 Conclusions

A 3D FE model for precision forging of spur gears was established to reveal the mechanism of the material flow. And the stress state, strain states, and the Lode parameter μ_σ in different forming stages and positions of the billet have been studied.

Conclusions can be drawn that the forming load increases quickly in the final forming stage. The Lode parameter μ_σ of the tooth portion is negative at the beginning, meaning tensile deformation, and μ_σ is all positive at the final forming stage, meaning compression deformation. Meanwhile, the stress state of the upper and the lower of the tooth portion changes from two-directional compressive stress and one-directional tensile stress in forming stages I and II to three-directional compressive stress in forming stages III and IV, while the middle of the tooth shape is always three-directional compressive stress state except for the forming stage I.

Acknowledgments The authors would like to thank the National Natural Science Foundation of China (51475344), 111 Project (B17034), and Innovative Research Team Development Program of the Ministry of Education of China (IRT13087) for the support given to this research.

References

1. Kretzschmar J, Stockmann M, Ihlemann J, Schiller S, Hellfritzsch (2015) Experimental–numerical investigation of the rolling process of high gears. Exp Techniques 39(3):28–36
2. Feng W, Hua L, Han XH (2012) Finite element analysis and simulation for cold precision forging of a helical gear. J Cent South Univ 19:3369–3377
3. Wang Q, He F (2004) A review of developments in the forging of connecting rods in China. J Mater Proc Tech 151(1):192–195
4. Tuncer C, Dean TA (1987) Die design alternatives for precision forging hollow parts. Int J Mach Tools Manuf 27(1):65–76
5. Zuo B, Wang BY, Li Z, Zheng MN, Zhu XX (2015) Design of relief-cavity in closed-precision forging of gears. J Cent South Uni 22(4):1287–1297
6. Jung SY, Kang MC, Kim C, Kim CH, Chang YJ, Han SM (2009) A Study on the Extrusion by a two-step process for manufacturing helical gear. Int J Adv Manuf Technol 41(7–8):684–693
7. Jin ZY, Li NN, Zhang Q, Yan K, Cui ZS (2017) Effects of forging parameters on uniformity in deformation and microstructure of AZ31B straight spur gear. Trans Nonferrous Metals Soc China 27(10):2172–2180
8. Sadeghi MH (2003) Gear forging: mathematical modeling and experimental validation. J Manuf Sci Eng 125(4):753–762
9. Li F, Chu GN, Liu XJ (2009) Deformation division of metal flow behavior during extrusion process of 7075 aluminum alloy. J Cent South Univ Technol 16:0738–0742

10. Dunand M, Mohr D (2014) Effect of lode parameter on plastic flow localization after proportional loading at low stress triaxialities. J Mech Phys Solids 66:133–153
11. Zheng Y, Liu D, Zhang Z, Yang YH, Ren LJ (2017) The flow line evolution of hot open ACDG process for titanium alloy discs. Archives Civil Mech Eng 17:827–838
12. Feng W, Fu YH (2014) High temperature deformation behavior and constitutive modeling for 20CrMnTiH steel. Mater Des 57:465–471
13. Wang ZR (2006) The physical essence of Lode parameters and their influence on plastic flow. J Solid Mechan 27(3):277–282 (In Chinese)

Compression of Printed CFRT Composite: Shaping Parameters and Material Health



Eric Becker, Victor Haguenauer, Ludovic Freund, Damien Félix, and Régis Bigot

Abstract EPITHER is an innovative way of shaping composite materials that seek to combine the strength of continuous fibre reinforced thermoplastic (CFRT) composite materials with the high production rates existing in the forging industry. The use of composites in the manufacture of structural parts must make it possible to lighten the driving parts of vehicles and to give part of the solution to the reduction of CO_2 emissions. Good material health is crucial for the production of structural parts, and some of the parameters associated with it are a direct consequence of the shaping conditions and have an influence on the strength of the final product. With a view to controlling and optimizing the shaping parameters, this study begins by defining the relevant material characteristics to be measured in order to judge the quality of the latter, then studying the links between the process and the finished product.

Keywords Composite · Additive manufacturing · Forging · Consolidation · 3D printing

E. Becker · V. Haguenauer (✉) · L. Freund · R. Bigot
Arts Et Metiers Institute of Technology, Université de Lorraine, LCFC, HESAM Université, 57070 Metz, France
e-mail: victor.haguenauer@ensam.eu

E. Becker
e-mail: eric.becker@ensam.eu

L. Freund
e-mail: ludovic.freund@ensam.eu

R. Bigot
e-mail: regis.bigot@ensam.eu

D. Félix
Setforge Engineering, Arts et Métiers - 41, avenue Berthelot, 42152 L'Horme, France
e-mail: damien.felix@setforge.net

© The Minerals, Metals & Materials Society 2021

G. Daehn et al. (eds.), *Forming the Future*, The Minerals, Metals & Materials Series,
https://doi.org/10.1007/978-3-030-75381-8_91

1 Introduction

Actually, automobile, aeronautics, and aerospace industries are the main sectors for the application of composite material and the percentage of composite present inside vehicles is increasing year after year. These materials present interesting characteristics, in particular a very attractive weight/mechanical characteristics ratio. This attractive ratio gives a real interest to integrate composite into vehicles, and it could lead to a reduction of weight and thus CO_2 emissions of made vehicles. Currently, few composite manufacturing processes allow the production of thick composite structure, especially if the matrix of the composite is thermoplastic. The shaping process described in this article is patented by the SETFORGE companies, the Arts et Metiers Institute of Technology and the Institut de Soudure. This process makes it possible to realize oriented-carbon fibre (CF)/thermoplastic composite parts from raw material usually in the form of commingling yarn in order to produce structural and thick parts.

To develop this process, it is important to study the influence of the shaping conditions on the quality of the composite product. In this study, the choice was made to study the material health of composite products with the aim of qualifying them. Numerous studies have looked at the influence of various parameters on the mechanical characteristics of the composite. In particular, concerning the influence of the fibre content [1–3] tends to increase the values of Young's modulus as well as the limit at break of the composite. Tekinalp et al. [3] compared the results of mechanical tests carried out on printed composite test pieces obtained by compression. Thus the tested pieces have different fibre content levels and also a substantial or low presence of porosity. Ashir et al. [4] studied the influence of porosities on the resistance of composite material plates. Increasing fibre content leads to an overall increase in the mechanical characteristics of composite products. Increasing the porosity ratio has the opposite effect [3, 4]. The observed trends are consistent with those described by homogenization methods: "rules of mixture" [5–7]. The main objective of this study is to determine the impact of the shaping conditions on the material health of made samples. Here the tested parameter is the compression ratio and itd influence on porosity ratio and fibre content is presented.

2 Method

2.1 Process Description

The described process can be decomposed into two main steps:

- Printing of the preform, additive manufacturing makes possible the realization of preforms with a mastery of fibres orientation and easy handling.

Table 1 Material datasheet CF/PA12 9 T LABS (Source 9 T LABS)

Composition		
Carbon fibre:	STS40F13(24 k)	Toho Tenax
Matrix system	PA12	ESMChemie
Fibre volume content	50%	
Density of composite	1.405 g/cm^3	

- Shaping step gives the part its final shape with good tolerances and tends to decrease void content.

2.1.1 Drop-Off and Pre-Consolidation of the Raw Material

The device used to manufacture the preforms is a CarbonKit 9 T LABS associated with an Ultimaker2 3D printer. The combination of these two systems allows depositing pre-consolidated composite yarn. This composite yarn is composed of a mixture of long and oriented (planar orientation) carbon fibre associated with a PA12 thermoplastic. Table 1 shows the characteristics associated with the material supplied by 9 T LABS. The used system does not mix the fibre and the matrix during the printing process, while most composite printers do. This difference is related to the format of the material used which is in the form of co-blended yarn. Eichenhofer et al. [8, 9] present a head allowing the printing of several multi-threaded threads, CF/thermoplastic, and allowing the manufacture of robotic continuous mesh. Wang et al. [10] present a review of 3D printing techniques for composite materials.

The composite preforms produced for this study are produced by printing 70 layers of theoretical height 0.27 mm thick for a final thickness of 18.9 mm. The printing temperature is set at 200 °C and the feed rate is 4 mm/s.

2.1.2 Forging Step

The shaping step consists of:

- Placement of the preform (Fig. 2a) in the steel tools.
- Heats tools and preform in a convection oven up to a temperature of 250 °C until the temperature in the composite, controlled by a thermocouple, reaches the set.
- Compression of the part along the stacking axis of the layers with an Instron traction/compression machine until a given height. The compression speed is set to 10 mm/min and the compression force is measured during the process. The part is kept under pressure while cooling.
- Demoulding and deburring of the part.

In this study, five parts with different compression ratios were made. Figure 2a presents a composite preform obtained by 3D printing. This preform is rigid and can be easily handled. Figure 2b shows a part obtained after compression, and the final



Fig. 1 CarbonKit 9 T Labs FC composite long fibre printing system implanted on Ultimaker 3D printer (Source 9 T LABS). (Color figure online)

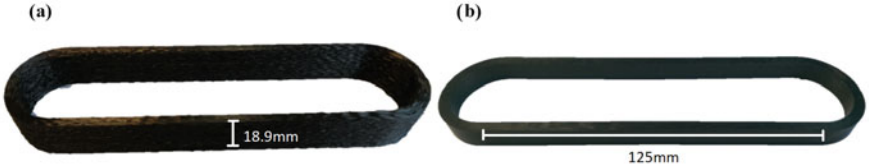


Fig. 2 **a** Printed preform, **b** Forged part. (Color figure online)

height is a function of the displacement command. The objective of this stage is to consolidate the part and suppress as much as possible the porosities present in the preforms.

2.2 Sampling and Analysis

2.2.1 Parts Characteristics

Dimension measurements are made on preforms and finished parts. The purpose is to obtain the shaping ratio τ_c from the height of the preform h_i (18.9 mm) and the final height of the part h_f:

$$\tau_c = 1 - \frac{h_f}{h_i} \tag{1}$$

The composite preforms are also weighted before the forging step in order to obtain the mass of material integrated into the tool m_i. After forging and deburring the finished parts are also weighed so as to obtain m_f, the final mass of the sample. Equation (2) makes it possible to obtain the loss of material τ_l (percentage of material lost during deburring step).

$$\tau_l = 1 - \frac{m_f}{m_i} \tag{2}$$

2.2.2 Micro and Macrographic Analysis

Test parts produced in the frame of this study are then sectioned and polished in order to produce micrographs. The sections produced correspond to the straight part of the forged part. The microscopies are carried out with a KEYENCE VHX-7000 optical microscope. This microscope makes it possible to realize image assemblies automatically. Thus it is possible to observe the entire section of a part with sufficient resolution to observe each of the fibres individually. Figure 3 shows images taken from sample C-PA 42 (described in Table 2).

According to the method presented by Ledru and et al. [11], fibres, matrix, and void content are determined by image analysis of the micrographs. This method is realized in two main stages: (i) binarization and (ii) thresholding of the image in order to separate the fibres from the rest of the image to obtain the volume ratio of fibre or to separate the porosities from the rest in order to get the porosity ratio. To facilitate the separation of porosity, a reduction of image resolution is necessary. Once the images have been processed, software is used to measure the surface of fibres or porosities.

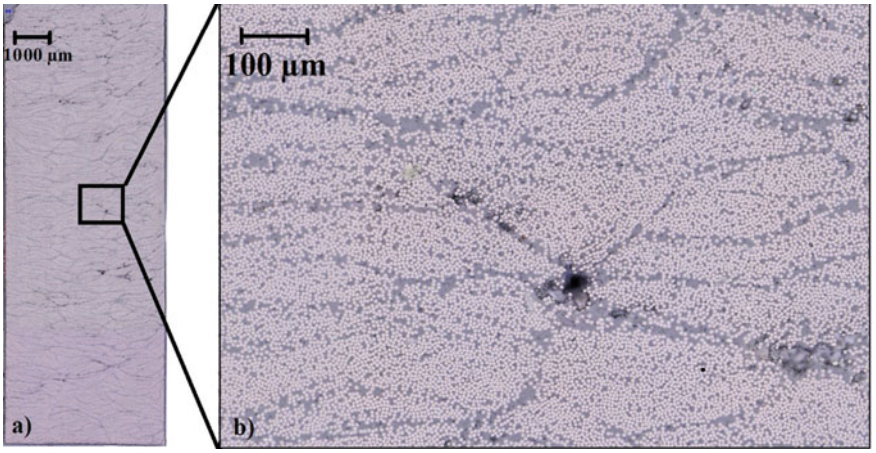


Fig. 3 **a** Image of a complete section of the sample C-PA 42, **b** Zoomed view, fibre appears in white, matrix in light grey, and porosity in grey/black. (Color figure online)

Table 2 Result of the shaping of the five samples

Sample	Ratio of compression [%]	Mass of preform m_i [g]	Mass of final part m_f [g]	Preform height h_i [mm]	Height after compression h_f [mm]	Mass of burr [g]	Loss of material τ_1 [%w]	Max pressure [Bar]
C-PA 0	0	22.87	22.87	19.075	19.075	0	0	0.0
C-PA 31	31.5	23.12	23.07	19.475	13.35	0.05	0.22	1.9
C-PA 42	42.7	23.02	22.74	19.275	11.05	0.28	1.22	13.6
C-PA 46	46.2	23.1	22.01	19.375	10.425	1.09	4.72	104.5
C-PA 54	54.5	22.96	19.31	19.5	8.875	3.65	15.90	204.2

3 Results and Discussion

3.1 Process Analysis

The five parts were compressed at different shaping ratio, thus the pieces have a height h_j different from each other. It is possible to define the theoretical shaping ratio T for these samples. It corresponds to the shaping ratio which makes it possible to fill functional gaps and to remove porosities present initially in the composite preforms integrated into the tool without causing the material to leak out of the tool.

If this shaping ratio is applied, the resulting part should have a very low porosity ratio as well as a non-existent loss of material. The expression of the shaping ratio is given in Eq. (3).

$$T[\%] = 1 - \frac{m_p}{\rho_c \cdot h_i \cdot S} \tag{3}$$

ρ_c is defined in Table 1 and corresponds to the density of the composite for fibre content of 50%v. m_p is the mass of the preform, h_i is the initial height of the preform. S corresponds to the surface of the bottom of the tool, and the value of this parameter was obtained from the measurements made on the tool. Equation (3) is applied for the five preforms. The values of T obtained are in the range from 41.91% to 42.95% for an average of 42.37%. The values of T change little from one preform to another due to the regularity of deposit by the fused filament fabrication (FFF) system.

As described above, the shaping step consists of compressing a preform of known mass and dimensions with rigid tools. Considering a composite preform inside the mould, his volume is containing: (i) a volume of composite, (ii) a volume of air present in the porosities of the preform, as well as (iii) a volume of air between the preform and the walls of the tool (functional gaps).

Considering the following hypothesis true, the evacuation of the material out of the tool only occurs after the complete filling of the tool. A shaping ratio higher than the value of T relating to a preform can result in a part without porosity but with an evacuation of the excess material. The excess material is then deburred which leads to a loss of material that should be minimized. Conversely, a value of shaping ratio lower than T leads to a part with dimensions that do not correspond to those imposed by the tool and/or containing porosities. Table 2 shows the data from shaping obtained for the five samples. The imposed shaping ratios are between 0% (printed preform C-PA 0) and 54.5%. The applied pressure ranged from 0 to 205 bars.

Figure 4 shows the pressure applied during shaping and the loss of material as a function of the compression ratio. The average value of the theoretical compression ratio T of 42.3% is represented by the vertical line.

Phase A described in Fig. 4 corresponds to samples whose shaping ratios were lower than T. The samples present in this field have low shaping pressures as well as a low loss of material. However, the sample C-PA 31 does not have a non-loss of material, and this testifies to the fact that a quantity of material flows outside the tool. Phase B in Fig. 4 corresponds to the area where the applied shaping ratio is higher than T. The material losses observed are substantial (up to 15.9%w), and the same applies to the pressures applied (13–205 bars).

The sample C-PA 42 was shaped with a ratio of shaping close to T. This sample has a loss of material of 1.22% and undergoes a pressure of 13 bars. It might be possible that this sample has a low porosity ratio.

The micrographs used for image processing also testify to the consequences of the displacement of matter. Figure 5 shows the surface condition of the external face of samples C-PA 0, 31, and 42. The observations of these images confirm the previous conclusions:

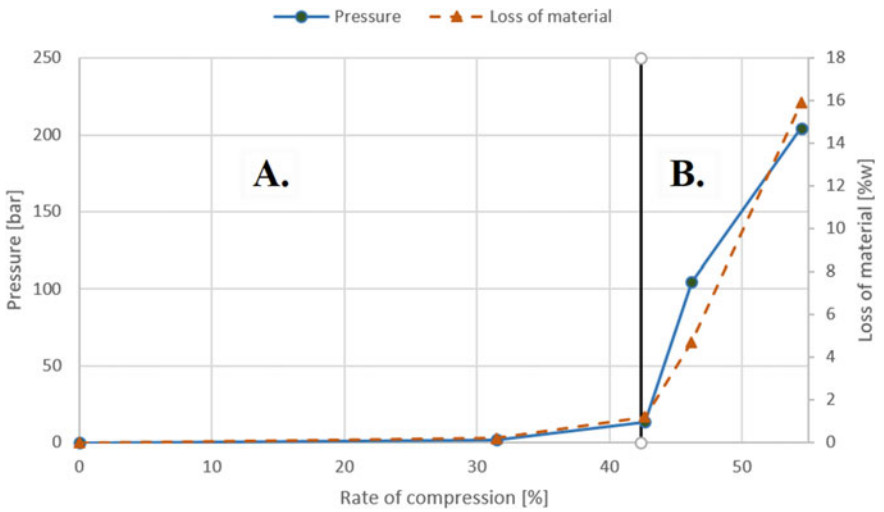


Fig. 4 Pressure and loss of material function of compression ratio. (Color figure online)

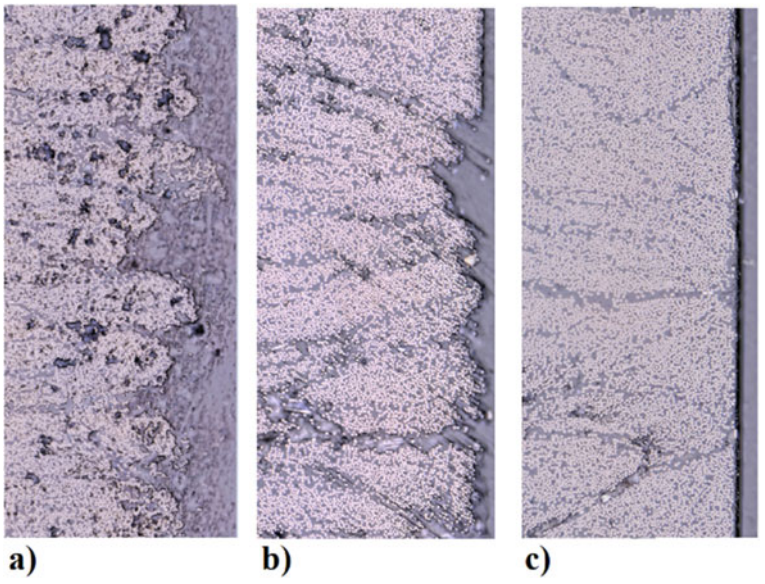


Fig. 5 External surface of samples C-PA 0 (**a**), C-PA 31 (**b**), and C-PA 42 (**c**). (Color figure online)

- The samples C-PA 0 and 31 show a surface condition that is not planar with the ratio of shaping applied did not make it possible to fill the functional clearances.
- The samples C-PA 46 and 52 have a planar surface state which testifies to the filling of the functional clearances.

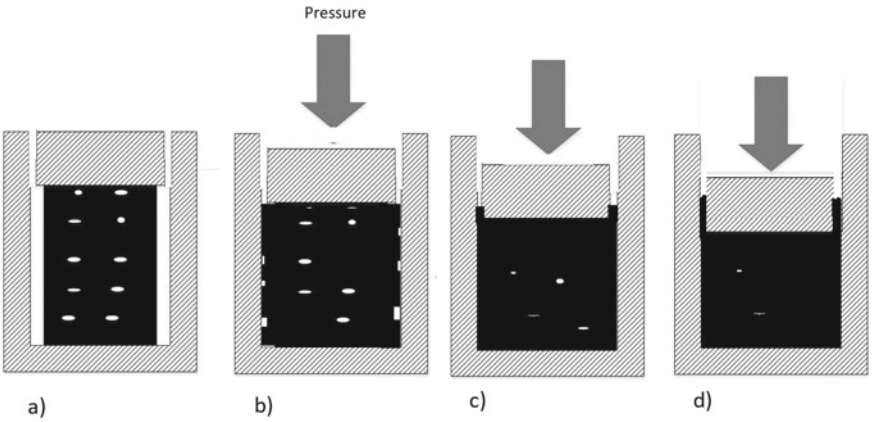


Fig. 6 **a** Initial condition (C-PA 0), **b** Start of compression (C-PA 31), **c** Low porosity and small loss of material (C-PA 42), and **d** Low porosity and high loss of material (C-PA 54)

To resume previous results and observations, during the shaping process the material moves and generates several phenomena: (i) the material flows so as to fill the functional gaps which allow the placement of the printed preforms in the mould. (ii) The material then tends to fill the voids presents in the preform and to evacuate some air. (iii) Once the volume of the tool is mostly filled with material, and if the displacement and the force are sufficient, the material flows outside the tool by the functional gaps of the latter and make a flash. Figure 6 shows the state of the samples at the end of compression. For (b), in view of the results in Table 2 the two phenomena (i) and (ii) occur. For (c) and (d), the functional clearances are filled, so phenomena (ii) and (iii) occur simultaneously.

3.2 Influence of Compression Ratio on Matter Health

This section presents the results of the image processing and their analysis. Table 3 presents values of the fibre volume fraction, the porosity ratio, and the fibre ratio.

Table 3 Fibre, matrix, and porosity volume fraction for each sample

Sample	Ratio of compression [%]	Fibre volume fraction [%v]	Porosity volume fraction [%v]	Fibre ratio [%]
C-PA 0	0 (Printed preform)	42.60	19.42	52.86
C-PA 31	31.5	44.16	12.68	50.56
C-PA 42	42.7	51.39	0.89	51.84
C-PA 46	46.2	51.70	0.68	51.32
C-PA 54	54.5	51.86	0.23	51.98

The results of the fibre ratio for the five samples are in the range from 50 to 53%, and these values are close to the value of 50% given by the supplier (Table 1). This low variability testifies to the fact that from one sample to another the composition of the composite material does not change or little despite an evacuation of material that could have been substantial. Material evacuation, therefore, has no influence on the fibre content of the composite in this tool configuration, and for this type of material, it is possible that different shaping conditions could lead to an increase in the fibre content. Mayer [12] presented results for the use of the same process with a PPS/carbon fibre composite and observed a flash mainly composed of a matrix which could thus lead to an increase in the fibre content in the parts concerned.

Sample C-PA 0 corresponding to a preform at the print outlet has a porosity ratio of 19.42%. This value is quite similar to the results of Tekinalp et al. [3], who also studied the composite parts (oriented short fibres) obtained by the FFF process. The parts presented have a similar appearance to the preforms produced with the 9 T LABS system, and the porosity ratio is estimated between 16 and 27%. In order to check the quality of the image processing results, a transition from the volume percentages to mass percentages is realized. From these values and the densities of the components, the mass of the samples is calculated. Thus the masses of the samples calculated have deviations of the order of 5% with the measured values, which testifies to the good quality of the results of the image processing.

Overall, increasing the shaping ratio tends to decrease the porosity ratio of the forged samples. However, samples C-PA 46 and 54 show a consequent loss of material for a slight reduction in the porosity ratio compared to sample C-PA 42. For a decrease from 0.89 to 0.23% of porosity, the loss of material increase from 1.22 to 15.9%. Given the various parameters studied, the C-PA 42 sample presents the optimal characteristics for this tool configuration. This conclusion is consistent with the conclusions of paragraph 3.1, where the application of a shaping ratio equal to or close to T leads to optimal results.

4 Conclusions and Perspectives

This article presents an innovative shaping process for composite materials. This process makes it possible to (i) produce thick structural parts, (ii) great control of the orientation of the fibres, as well as (iii) good material health of the parts produced within a particular porosity ratio of less than 1%. The objective of this study is to study the influence of the shaping conditions and parameters on the quality of the resulting composite products. If necessary, the variant parameter is the shaping ratio, and the parameters studied are the volume ratio of the fibre as well as the porosity ratio. A theoretical value of the shaping ratio was presented and compared with the experimental case. The results of this study led to the following conclusions:

1. In this tool configuration, the application of high pressure (100–200 bar) leads to a consequent material spin and reduces the porosity ratio up to 0.23%.

2. The results of the image processing, particularly the values of the fibre/matrix ratio compared to the volume of material of the samples allow us to conclude that the spin had no influence on the fibre/matrix ratio of the composite.
3. The C-PA 42 sample has the most interesting characteristics: a porosity ratio of less than 1% for a mass loss of 1.22%. Thus, even in this tool and shaping configuration, it is possible by applying the theoretical compression ratio during shaping, to obtain composite products with interesting material health.

Acknowledgments The authors would like to thank companies SETFORGE and the INSTITUT DE SOUDURE, and more particularly SETFORGE for their financial support.

References

1. Perrot Y (2006) comportement mécanique de matériaux composites verre / polyester utilisés en construction navale de plaisance - Cas des résines polyester limitant les émissions de styrène Contribution à l ' étude des matériaux composites utilisés en construction navale
2. Motahhari S (1998) Fiber prestressed composites: a study of the influences of fibre prestressing on the mechanical properties of polymer matrix composites
3. Tekinalp HL et al (2014) Highly oriented carbon fiber-polymer composites via additive manufacturing. Compos Sci Technol 105:144–150
4. Ashir M, Nocke A, Bulavinov A, Pinchuk R, Cherif C (2019) Influence of defined amount of voids on the mechanical properties of carbon fiber-reinforced plastics. Polym Compos 40(S2):E1049–E1056
5. Chamis CC (1989) Mechanics of composite materials: past, present, and future. J Compos Technol Res 11(1):3–14
6. Rosen BW (1964) Moduli of Fiber-Reinforci, no. 63
7. Younes R, Hallal A, Fardoun F, Hajj F (2012) Comparative review study on elastic properties modeling for unidirectional composite materials. In Composites and Their Properties, InTech
8. Eichenhofer M, Wong JCH, Ermanni P (2017) Continuous lattice fabrication of ultra-lightweight composite structures. Addit Manuf 18:48–57
9. Eichenhofer M, Wong JCH, Ermanni P (2018) Exploiting cyclic softening in continuous lattice fabrication for the additive manufacturing of high performance fibre-reinforced thermoplastic composite materials. Compos Sci Technol 164(May):248–259
10. Wang X, Jiang M, Zhou Z, Gou J, Hui D (2017) 3D printing of polymer matrix composites: a review and prospective. Compos Part B Eng 110:442–458
11. Ledru Y, Piquet R, Michel L, Schmidt F, Bernhart G (2009) 2-D and 3-D void quantification with image analyses in aeronautic composite laminates, Jnc 16:11
12. Mayer P (2017) Contribution à la définition du processus de conception et de réalisation de pièces produitsà hautes caractéristiques spécifiques

Influences of Key Forging Parameters on Cold Orbital Forging of Thin Parts with High Circular Ribs



Wuhao Zhuang, Xinghui Han, Lin Hua, and Wei Feng

Abstract In this paper, a cold orbital forging process is proposed to manufacture thin parts with high circular ribs. First, a FE model was established for the numerical process analysis. Then a verification experiment was performed to verify the validity of the FE model developed above. By using the FE simulation method, the influences of several forging parameters on the cold orbital forging of thin parts with high circular ribs were investigated. The results show that effective strain can be obviously improved by increasing feed velocity of cavity die, but has less change with different friction factors. Synchronism of metal flowing between the inner rib and the outer rib can be improved by decreasing feed velocity of cavity die and friction factor. Moreover, the circumferential metal flowing degree can be slightly reduced by increasing feed velocity of cavity die and friction factor.

Keywords Cold orbital forging · Thin part with high circular ribs · Metal flowing analysis

1 Introduction

Thin part with high circular ribs (Fig. 1) is quite difficult to be fabricated by the conventional forging process. This is because the die cavities of circular ribs are narrow and deep, and metal flowing inside these die cavities is quite difficult. On the other hand, the forging load is huge to forge the thin baseplate by using the conventional forging process. In order to improve the metal flow capacity and reduce forging load, the cold orbital forging process is a good alternative. By now, the forming mechanism of cold orbital forging process has been revealed [1–4]. Cold

W. Zhuang · X. Han (✉) · L. Hua · W. Feng
School of Automotive Engineering, Wuhan University of Technology, Wuhan 430070, China
e-mail: hanxinghuihlp@126.com

Hubei Key Laboratory of Advanced Technology of Automotive Components, Wuhan University of Technology, Wuhan 430070, China

Hubei Collaborative Innovation Center for Automotive Components Technology, Wuhan University of Technology, Wuhan 430070, China

© The Minerals, Metals & Materials Society 2021

G. Daehn et al. (eds.), *Forming the Future*, The Minerals, Metals & Materials Series,
https://doi.org/10.1007/978-3-030-75381-8_92

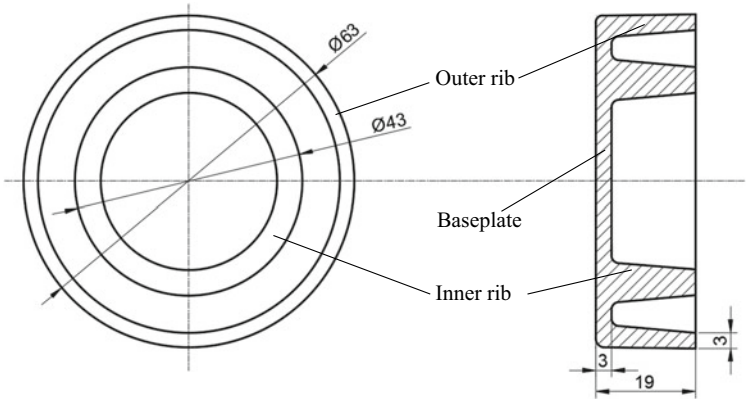


Fig. 1 Drawing of thin parts with high circular ribs

orbital forging processes of cylindrical parts [5], flanged parts [6, 7], deep groove parts [8], and gear parts [9–11] have been developed. However, no research has been reported about cold orbital forging of thin parts with high circular ribs. In this paper, a FE model of the cold orbital forging of thin parts with high circular ribs was established, and the validity of this FE model was verified by experiments. By using this FE model, the influences of several cold orbital forging parameters on effective strain distribution, height difference between the inner rib and outer rib, and circumferential metal flowing degree were revealed comprehensively.

2 Establishment and Verification of FE Model

In order to investigate the influences of key forging parameters on cold orbital forging of thin parts with high circular ribs, a rigid plastic FE model is developed, as shown in Fig. 2. This FE model consists of three parts: orbital die, cavity die, and billet. The orbital die is a tilted cone die, and performs rotational motion during cold orbital forging at the rotational speed of 8π rad/s. The cavity die performs feed motion during cold orbital forging, and the feed velocity of cavity die $v = 4$ mm/s. To simulate the plastic deformation of cold orbital forging, the billet should be set as rigid plastic type, and meshed by using tetrahedral mesh. The total mesh count is set as 100,000. The material of the billet is AISI-1006 steel and the strain–stress curves of this steel are shown in Fig. 3. The lubricating conditions between billet and dies are defined by using shear friction, and friction factor $m = 0.12$.

To verify the validity of FE model developed above, a cold orbital forging experiment of thin parts with high circular ribs was executed under the same forging parameters and a MoS_2 grease was used as a lubricant between the billet and dies. The cold orbital forging parts are shown in Fig. 4. As can be seen from Fig. 4, the

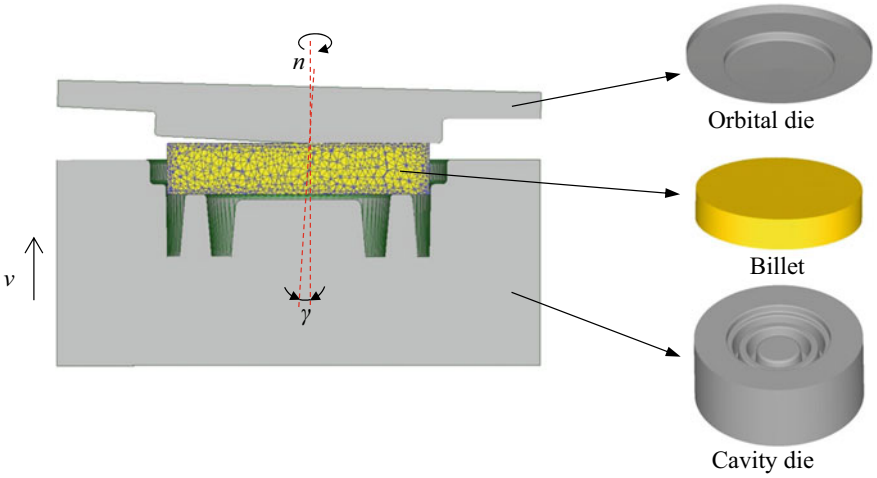


Fig. 2 FE model of cold orbital forging of thin parts with high circular ribs. (Color figure online)

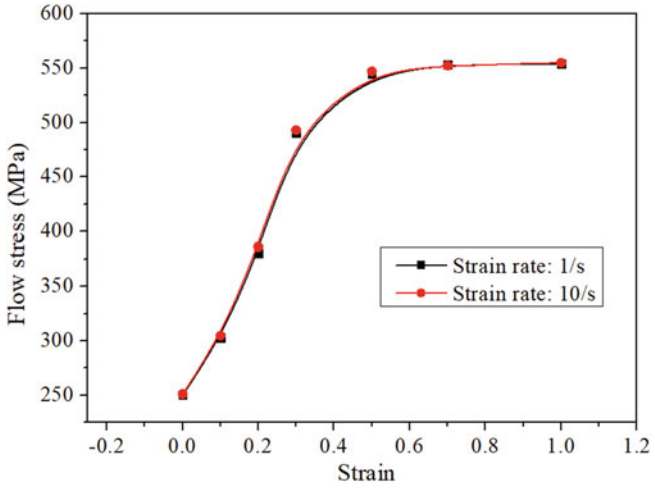


Fig. 3 Strain–stress curves of AISI-1006 steel. (Color figure online)

simulation forged part is quite similar to the experimental forged parts, which can effectively validate the validity of the FE model developed above.



(a) Simulation part (b) Experimental part

Fig. 4 Cold orbital forging dies of thin parts with high circular ribs. (Color figure online)

3 Influences of Key Parameters on Cold Orbital Forging of Thin Parts with High Circular Ribs

3.1 Effective Strain Distribution

Figure 5 shows the evolution of effective strain distribution with different key forging parameters. It can be seen from Fig. 5a that the effective strain of the whole part significantly decreases with increasing feed velocity of cavity die v. The reason is that larger v means less number of revolution circles of orbital die, so the repeated rolling deformation of the billet can be reduced, and the intensity of plastic deformation can be decreased. In Fig. 5b, the distribution of effective strain is weakly affected by

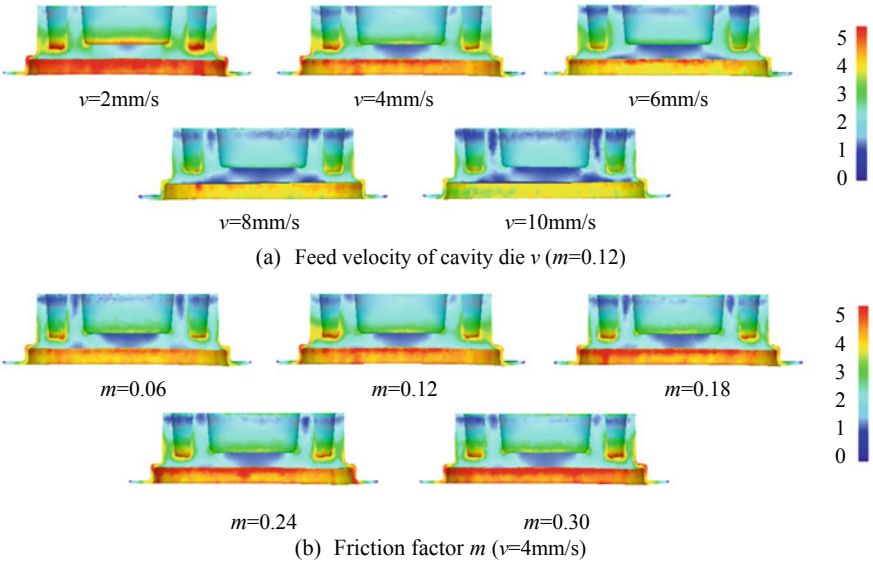
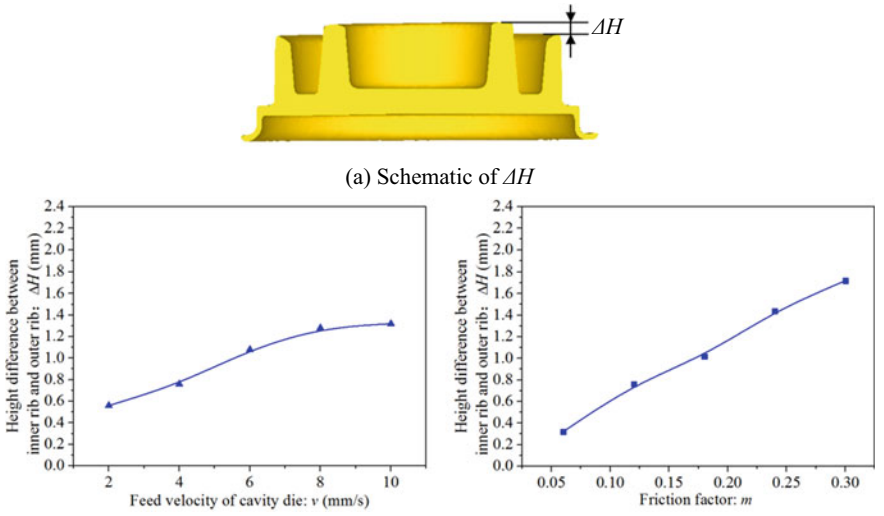


Fig. 5 Effective strain distribution under different forging parameters. (Color figure online)

friction factor *m*. This is because larger *m* only increases the friction resistance on the surface of the billet, but has a little effect inside the billet.

3.2 Height Difference Between Inner Rib and Outer Rib

In cold orbital forging of thin parts with high circular ribs, the metal flowing process of the inner rib and the outer rib is non-synchronous. This non-synchronous metal flowing would cause unbalanced force between the inner rib and the outer rib, which would lead to a high crack risk of cavity die. In this paper, the maximum height difference between the inner rib and the outer rib ΔH is designated to appraise the non-synchronism of metal flowing between the inner rib and the outer rib (Fig. 6a), and the effects of key cold orbital forging parameters on ΔH are revealed in Fig. 6. It can be seen from Fig. 6b, with increasing feed velocity of cavity die v, ΔH gradually increases. This is because that the larger the v is, the less time it takes to execute radial metal flowing so that the outer rid cannot be fully formed owing to less metal flowing in the radial direction. With increasing friction factor m, the metal flow resistance in the radial direction increases, and less metal can flow into the die cavity of the outer rib so that the height of the outer rib is smaller than that of the inner rib and ΔH markedly increases, as shown in Fig. 6c.



(a) Schematic of ΔH

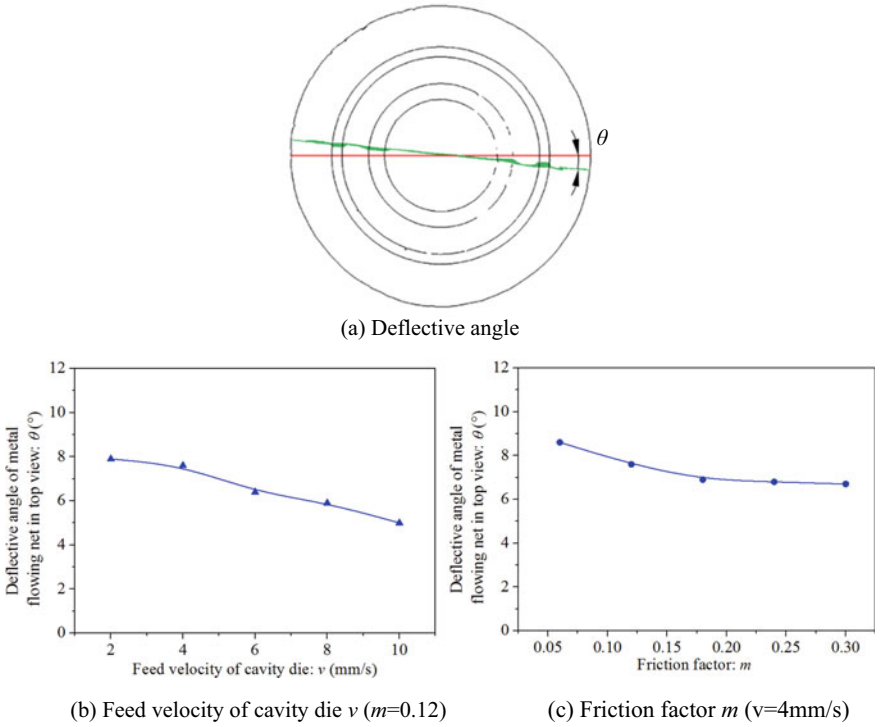
(b) Feed velocity of cavity die v (m=0.12)

(c) Friction factor m (v=4mm/s)

Fig. 6 Height difference between the inner rib and the outer rib under different forging parameters. (Color figure online)

3.3 Circumferential Metal Flowing Degree

In cold orbital forging of thin parts with high circular ribs, the orbital die repeatedly rolls on the surface of the billet, which leads to obviously circumferential metal flowing. In order to intuitively reflect the circumferential metal flowing degree in this cold orbital forging process, a deflective angle θ is defined, as shown in Fig. 7a. In Fig. 7a, the red line is a labeled line on billet before cold orbital forging, and the green line is the final position of the labeled line after cold orbital forging. Figure 7b and c shows the influences of key parameters on deflection angle θ. As observed from Fig. 7b, θ slightly drops with increasing v. This is because that larger v leads to less rolling times of orbital die on the surface of the billet so that less metal is driven in the circumferential direction. In Fig. 7c, θ slightly reduces with increasing m, which is due to larger frictional resistance.



(a) Deflective angle

(b) Feed velocity of cavity die v (m=0.12)

(c) Friction factor m (v=4mm/s)

Fig. 7 Influences of key parameters on circumferential metal flowing degree. (Color figure online)

4 Conclusions

(1) Effective strain can be obviously improved by increasing feed velocity of cavity die, but the fiction factor has a trivial effect on effective strain distribution.
(2) Synchronism of metal flowing between the inner rib and the outer rib can be improved by faster feed velocity of cavity die and smaller friction factor.
(3) Circumferential metal flowing degree can be slightly reduced by larger feed velocity of cavity die and friction factor.

Acknowledgments The authors would like to thank the Natural Science Foundation of China (No. 51575416), Innovative Research Team Development Program of Ministry of Education of China (No. IRT_17R83), 111 Project (No. B17034), and Natural Science Foundation of Hubei Province (No. 2019CFA041) for the support given to this research.

References

1. Standring PM, Moon JR, Appleton E (1980) Plastic deformation produced during indentation phase of rotary forging. Met Technol 7:159–166
2. Nowak J, Madej L, Ziolkiewicz S, Plewinski A, Grosman F, Pietrzyk M (2008) Recent development in orbital forging technology. Int J Mater Form 1:387–390
3. Han XH, Hua L (2011) Prediction of contact pressure, slip distance and wear in cold rotary forging using finite element methods. Tribol Int 44:1742–1753
4. Milutinović M, Baloš S, Plančak M, Movrin D (2017) Comparison of some mechanical properties and micro-topography of a component with non-axisymmetric geometry manufactured by cold orbital and hot forging. J Mater Process Technol. 249:179–192
5. Nam C, Lee M, Eom J, Choi M, Joun M (2014) Finite element analysis model of rotary forging for assembling wheel hub bearing assembly[J]. Procedia Eng. 81:2475–2480
6. Hildenbrand P, Lechner M, Vogel M, Herrmann H, Merklein M (2018) Orbital forming of tailored blanks with two-sided local material thickening. Int J Adv Manuf Tech 97:3469–3478
7. Pérez M (2018) Microstructural and texture evolution of Jethete M152 flanged-test pieces during cold rotary forging. J Mater Process Technol 252:582–594
8. Jin Q, Han XH, Hua L, Zhuang WH, Feng W (2018) Process optimization method for cold orbital forging of component with deep and narrow groove. J Mater Process Technol. 33:161–174
9. Han XH, Hu YX, Hua L (2016) Cold orbital forging of gear rack. Int J Mech Sci 117:227–242
10. Han XH, Hua L, Zhuang WH, Zhang XC (2014) Process design and control in cold rotary forging of non-rotary gear parts. J Mater Process Technol 214:2402–2416
11. Samołyk G (2013) Investigation of the cold orbital forging process of an AlMgSi alloy bevel gear. J Mater Process Technol 213:1692–1702

FE-Based Investigation on the Influence of Inhomogeneously Heated Billets on Subsequent Forging Processes



Arne Jagodzinski, Hendrik Gerland, Mareile Kriwall, Jan Langner, Malte Stonis, and Bernd-Arno Behrens

Abstract Multi-stage forging process chains are often used for the efficient production of complex geometries. Typically, these consist of homogeneous heating, one or more preform stages, and the final forging step. By inhomogeneously heated billets, the process chains can be simplified or shortened. This shall be achieved by setting various temperature fields within a billet, resulting in different yield stresses. These can influence the material flow, leading to easier production of complex parts. In this study, the influence of inhomogeneously heated billets on the forming process is investigated by means of FEA. For this purpose, two process chains including inhomogeneous heating and three homogeneously heated reference process chains are developed and compared. Each process chain is optimized until form filling and no defects occur. Target figures for the assessment are necessary forming force, the amount of material necessary to achieve form filling and die abrasion wear. For process chains with inhomogeneously heated billets, the results showed a small time window of about 5 s for a successful forming in terms of form filling. Forming forces and die abrasion wear increase for inhomogeneously heated billets due to higher initial flow stresses. However, the flash ratio decreases when billets are heated inhomogeneously. Depending on their size, inhomogeneously heated billets show up to 11.8% less flash than homogeneously heated billets. This shows a potential for the use of inhomogeneous heating to make forging processes more efficient. Subsequently, experimental tests will be carried out to verify the results of the simulations.

Keywords Inhomogeneous heating · Forging · FEA · Resource efficiency · Preform operation

A. Jagodzinski (✉) · H. Gerland · M. Kriwall · J. Langner · M. Stonis · B.-A. Behrens
IPH—Institut für Integrierte Produktion Hannover gGmbH, Hollerithallee 6, 30419 Hannover, Germany
e-mail: jagodzinski@iph-hannover.de
URL: https://www.iph-hannover.de

© The Minerals, Metals & Materials Society 2021

G. Daehn et al. (eds.), *Forming the Future*, The Minerals, Metals & Materials Series,
https://doi.org/10.1007/978-3-030-75381-8_93

1 Introduction

In forging technology, the use of materials and energy, especially for heating the billets, is accountable for a large amount of the manufacturing costs [1]. For this reason, it is very important for the forging industry to use manufacturing processes that are as material- and energy-efficient as possible in order to increase their competitiveness and make a contribution to conserving resources. One way of reducing energy consumption and the associated costs is to increase the efficiency of billet heating. Lowering the forming temperature also has a major impact on the manufacturing costs of forgings. By reducing the temperature from 1,200 to 1,080 °C, manufacturing costs can be reduced by approximately 12% [2].

The research project "Use of different flow stresses for forming inhomogeneously heated billets" investigates the influences of inhomogeneous billet heating on subsequent steps of a forging process chain. The aim is to adjust the flow stresses of the billet by means of different temperatures that are set in the billet by inductive heating and thus influence the forming behavior. This enables a more efficient design of production processes with regard to the material and energy input.

The goal of the present study is to investigate an inhomogeneous billet heating with regard to its influence on the necessary flash ratio to achieve form filling as well as on the die abrasion wear and the forming force of subsequent forging process steps. The investigation is carried out purely simulation-based, using a sample part with a geometry based on a common rail geometry. The sample part has two areas in which, due to secondary shape elements, large deformations take place and a lot of material is required to achieve form filling as well as two areas with a low mass.

Furthermore, by replacing a complicated preforming step, such as cross-wedge or forge rolling, with a simple preforming process, such as upsetting or flattening, it has to be examined whether the use of inhomogeneous heating can contribute to a simplification of the manufacturing process. The necessary mass predistribution shall be achieved during the simple preforming by the different flow stresses arising in the differently heated areas.

To achieve this goal, several forging process chains must be designed first. In addition to a realistic reference process chain, a process chain with a simple flattening step as a preform operation and a process chain without a preform operation are created. These process chains are additionally divided into a version with homogeneous heating and one with inhomogeneous heating. This results in a total of five process chains for each billet. Each of the five process chains is further subdivided into two different part sizes so that the scaling effects can be considered later in the investigation. All process chains to be created are optimized with regard to their billet size until a defect-free and form-filling process is achieved, while the flash ratio is decreased to a minimum. Afterward, a parameter study will be conducted to compare the designed process chains and thereby identify the effects of the inhomogeneous heating using the design of experiments (DoE) method. The results of the parameter study will also be used to identify a suitable parameter field for subsequent experimental trials.

2 State-of-the-Art

In forging processes, the combination of induction heating and flash reduced forging can lead to a significant decrease in energy consumption. Behrens et al. investigated the influence of induction heating on the energy consumption of a multi-directional forging process. They designed a flash reduced forging process for a two-cylinder crankshaft including inductive heating and reheating of the part. In the first investigation, they were able to reduce the energy necessary for the heating of the part from 4.85 kWh/part to 4.74 kWh/part, including the reheating [3]. By further optimizing the process, they were able to achieve a further reduction in energy consumption. It was possible to reduce the total energy consumption to 3.27 kWh/part, which corresponds to a reduction of 24% [4]. Both heating and reheating were performed homogeneously for these studies.

Recent research has looked at different approaches and processes for partial heating of billets and their subsequent forming. In the Transregio 30 (TRR 30)—"Process-integrated production of functionally graded structures on the basis of thermo-mechanically coupled phenomena"—different temperatures in a forging billet were considered. In subproject A1, Matzenmiller investigated the possibility of hot/cold forming of a shaft end after partial heating [5]. In subproject B2 of TRR30, Mahnken investigated the thermomechanical die loading during hot/cold forming with partial heating [6].

Özmen, Okman, and Tekkaya investigated the influence of partial heating on the forming of steel, titanium, and aluminum billets in different experiments. For this purpose, they heated the raw parts laterally by means of gas or induction heating and laser irradiation and then carried out a compression process [7, 8]. Merrygold considered hot/cold forming by layering and upsetting solid and hollow cylindrical billets at different temperatures [9].

All the above-mentioned investigations dealt with partial heating, whereas in the research project described in this paper inhomogeneous heating and its influence on the forging process are considered. While partial heating often only heats a certain area of the billet—in industrial practice, for example, it is usual to heat only the head side of a billet to form simple shapes such as screw heads or valves—inhomogeneous heating heats the entire billet (see Fig. 3). For this purpose, the billet is divided into several zones and these are heated to different degrees. The inhomogeneous temperatures lead to different flow stresses and thus to a change in the forming behavior in the temperature zones.

An inhomogeneous billet heating was performed by Kruse et al. [10]. They heated the steel component of a serially arranged friction-welded tailored forming part made of steel and aluminum in an inductor. Due to the heat conduction in the part, this led to an inhomogeneous temperature profile after heating. After the heating, the billet was cross-wedge rolled. For the experiments described in this paper, a monomaterial part was used which is completely heated in an inductor. The inhomogeneous temperature profile was not set by heat conduction but by the coil geometry.

3 Investigations and Results

3.1 Process Design

In this paper, the analysis of the influence of inhomogeneously heated billets on subsequent forging processes is presented. For this study, five different process chains had to be designed using FE simulations. Each of these process chains is divided into a large and a small version, depending on the size of the final geometry. In this chapter, the process chains and the simulation model used are described.

The starting point for the design of all process chains was a sample part that is approximated to the shape of a common rail. As mentioned above, the process chains are each divided into a large and a small version, depending on the size of the final geometry. This is due to the possibility of scaling effects in the later parameter study. The geometry of the final part is shown in Fig. 1. While the lengths (l_f) and diameters (d_f) change for the two different sizes, the ratio of the two remains the same. For both sizes the ratio is $l_f/d_f = 8.35$. The main objective of the process design is to identify suitable billet sizes for all process chains as well as suitable temperature profiles for the inhomogeneously heated process chains, which are required to achieve form filling depending on the different heating and preform operations.

The five process chains developed are divided into two process chains with inhomogeneous billet heating and three reference process chains which contain homogeneous billet heating. Two of the homogeneously heated reference process chains have a forging sequence identical to the two inhomogeneously heated process chains. The third homogeneously heated process chain, hereinafter referred to as the "reference process chain", consists of a preform forging step in a partially closed die, followed by a final forging step in an open die. This process chain serves as a benchmark for the performance of the inhomogeneous heating to a conventional stage sequence for the production of the sample part. The influences of inhomogeneous heating are

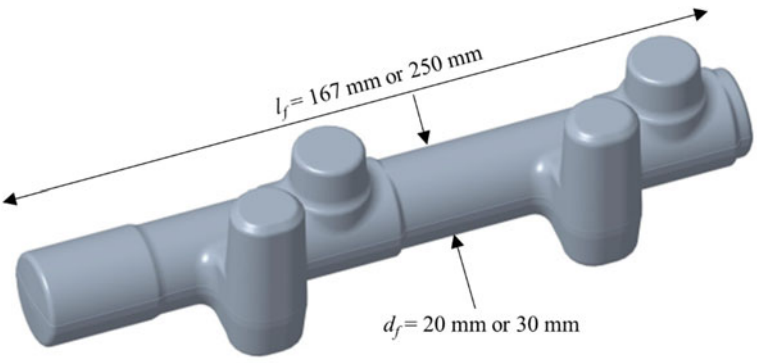


Fig. 1 Geometry of the sample part in two dimensions. (Color figure online)

evaluated in the remaining four process chains. Since two of these process chains only differ concerning the way of heating (homogeneous and inhomogeneous), they are hereinafter referred to as "Process chain I A / B" and "Process chain II A / B". Process chain I consists of a homogeneous (A) or inhomogeneous (B) billet heating, followed by a flattening which serves as a simple preforming operation and the final forging step in an open die. Due to the inhomogeneous temperature profile and the resulting inhomogeneous flow stress distribution in process chain I B, the flattening should lead to a predistribution of mass by forming the hot areas of the component more strongly than the warm areas. Process chain II also starts with a homogeneous (A) or inhomogeneous (B) billet heating. It does not, however, have a preforming step, but only a final forging step after the heating. An overview of the five considered process chains is shown in Fig. 2. In order to be able to evaluate scaling effects in the later course of the investigations, a large and a small version are created for each process chain, which differ in the size of the final geometry (see Fig. 1).

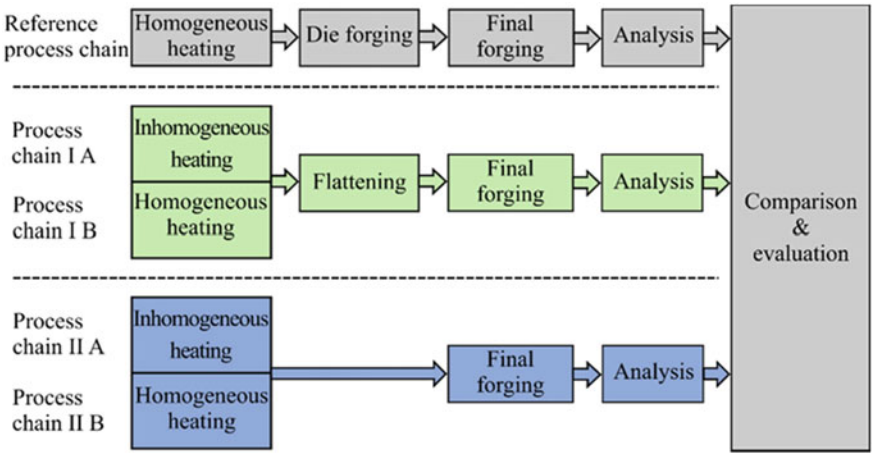


Fig. 2 Investigated process chains. (Color figure online)

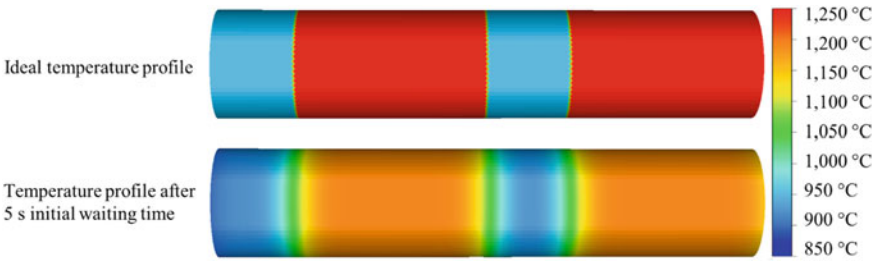


Fig. 3 Inhomogeneously heated billet before and after the initial waiting time. (Color figure online)

Table 1 Regression coefficients of Hensel–Spittel equation for 42CrMo4

A	m_1	m_2	m_3	m_4
Solidity	Dependence of temperature	Dependence of strain hardening	Dependence of equivalent strain rate	Dependence of equivalent strain
1,872.0667 N/mm^2	−0.00289	−0.1123	0.14368	−0.04879

The setup of the FE simulations is identical for the design of all process chains as well as for the parameter study (see Sect. 3.2). The simulations were performed via the FEA-software FORGE NxT 2.1 using the press kinematic of a hydraulic press and non-deformable dies. The material used for the billets is 42CrMo4 (1.7225). Its material description and therefore its flow curves are based on the flow curve equation by Hensel and Spittel. This equation describes a materials' forming behavior as a function of the temperature T, the effective strain ε, the strain rate $\dot{\varepsilon}$, as well as the coefficients A and $m_{1\text{-}9}$ [11]. However, FORGE NxT 2.1 uses a shortened version of the equation only using the coefficients m_1 to m_4 (see Eq. (1)). The necessary regression coefficients are stored within the material database of the program and are shown in Table 1.

$$\sigma_f = A \bullet e^{m_1 T} \bullet \varepsilon^{m_2} \bullet e^{\frac{m_4}{\varepsilon}} \bullet \dot{\varepsilon}^{m_3} \tag{1}$$

The following parameters were used in the FE simulations of the process design (see Table 2).

The temperatures set for the inhomogeneously heated billets were 1,250 °C for the hot parts and 900 °C for the warm parts of the billet. The inhomogeneous heating was achieved in the simulations by assigning the so-called temperature boxes to the desired temperature ranges. This feature of FORGE NxT 2.1 allows assigning certain temperatures to individual nodes of the FE mesh. However, this results in very discrete transitions between the different temperature ranges. These are defined as ideal inhomogeneous heating but can hardly be achieved in a real process due to compensation processes. Therefore, a short waiting time of 5 s was implemented before the start of the first forging step. Figure 3 shows an inhomogeneously heated part before and after an initial waiting time of 5 s.

It was possible to achieve form filling and defect-free forging processes for all investigated process chains. In Fig. 4 the workpieces of all process chains are shown directly before final forging.

Table 2 Simulation input parameters for the process design

Die temperature T_{die}	Ambient temperature T_a	Billet Material	Forming Speed v	Friction coefficient μ	Friction factor m	Mesh size for big billet size/small billet size
250 °C	50 °C	1.7225	100 mm/s	0.15	0.3	1.5 mm/1 mm

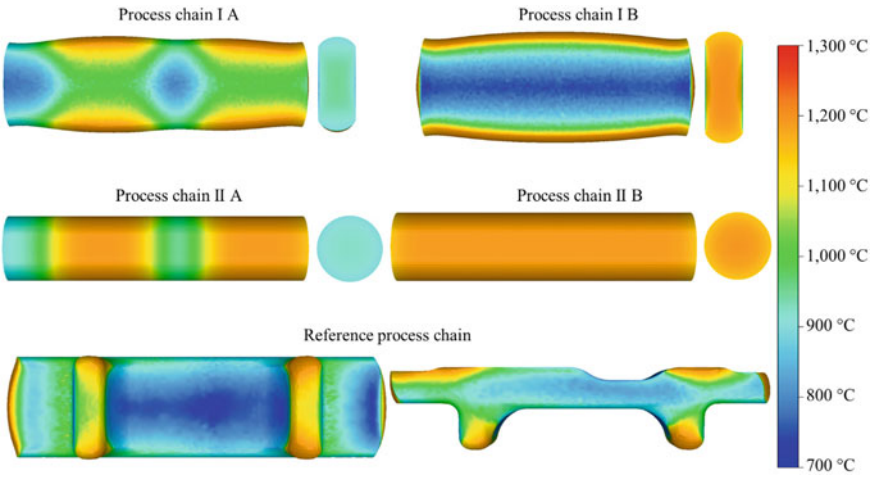


Fig. 4 Workpieces of all process chains before final forging. (Color figure online)

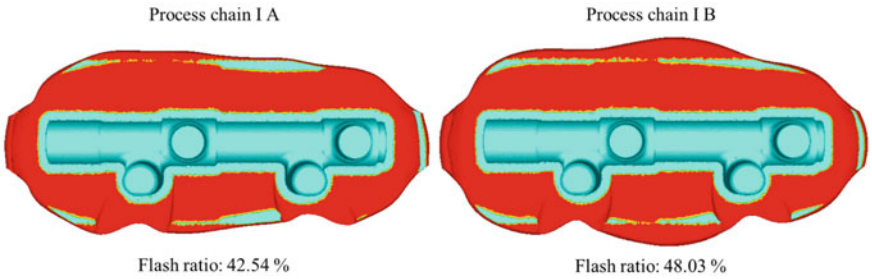


Fig. 5 Contact analysis of final forgings of process chain I. (Color figure online)

Figure 5 shows the contact analysis of the final forgings of process chain I A and process chain I B. It is clearly visible that the flash ratio of process chain I B is higher than the flash ratio of process chain I A.

3.2 Parameter Study

This chapter presents the parameter study that was carried out to determine the influences of the inhomogeneous billet heating on the subsequent steps of the designed forging process chains. The study was designed according to the DoE method as a full factorial two-stage experimental design using the software Minitab 17. With the exception of the forming speed, the simulation input parameters correspond to those of the process chain design (see Table 2). The forming speed was varied as well as

Table 3 Input parameters for the parameter study

Forming speed v	Initial waiting time t_i	Final geometry size d_f, l_f
100–300 mm/s	5–20 s	$d_f = 20$–30 mm, $l_f = 167$–250 mm

the initial waiting time and the final geometry size. The study's input parameters and their levels are shown in Table 3. This results in a total of 40 simulations.

For the evaluation of the parameter study, the comparison of versions A and B of the different process chains is of particular importance. As these process chains differ only in the type of heating selected, they have the greatest significance with regard to the influences of inhomogeneous heating. The comparison of the process chains I and II with each other serves to estimate whether a simple preforming process, such as flattening, is effective for reducing material consumption. The comparison of the two process chains I and II with the reference process chain serves to examine the efficiency of inhomogeneous heating in comparison to a conventional preform optimized process.

Only the final forging stages were compared during the parameter study. This is due to the fact, that the process chains consist of a varying number of stages—some have a preforming step while in others the final forging is undertaken directly after heating. For this purpose, a distinction is made between mandatory evaluation criteria, which must be fulfilled in order to obtain a successful forging process and which can only assume the values "True" or "False" and quantitative evaluation criteria. The mandatory evaluation criteria include the absence of folds and the form filling. The quantitative evaluation criteria are the amount of material required to obtain form filling, the forming force, and the die abrasion wear. For each of them, a minimum value is aimed for.

The simulations showed that no folds occur in any of the investigated process chains. The investigation of the mold filling revealed only a small process window in which a satisfactory process is possible. The inhomogeneously heated process chains, in particular, were very susceptible to the long initial waiting time of 20 s (see Fig. 6, left). In none of these simulated processes form filling could be achieved, while in homogeneously heated processes about 50% of all simulations reached form filling. For the short initial waiting time of 5 s, the chances for form filling were significantly higher. With a slight mass predistribution via flattening, all the simulations containing an inhomogeneous heating reached form filling. Without a preforming step, the proportion of form filling simulations was reduced to 75%. The same result was obtained for simulations with homogeneously heated billets. The size of the final geometry only had a small impact on form filling. The small size had a slightly higher rate of form filling than the bigger geometry. The most probable reason for this is that the billet designed for the bigger final geometry had a smaller flash ratio than the billets for the small geometry, meaning that for the small geometry the amount of material available to fill the form was higher, making it easier to reach form filling. The forming speed did not have any impact on the form filling. 60%

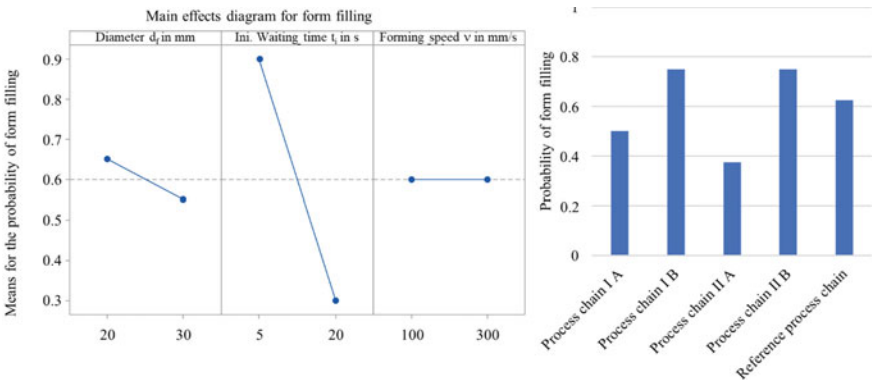


Fig. 6 The main effects for form filling under consideration of all parameter combinations (*left*) and comparison of the investigated process chains (*right*). (Color figure online)

of all simulations reached form filling for both investigated speeds regardless of the heating and preforming. In Fig. 6 on the left, the main effects for the form filling are shown under consideration of all parameter combinations. The right part of Fig. 6 shows the probability of a form filling process for the five investigated process chains.

For the amount of needed forming force, the most significant parameter was the size of the final geometry. The initial waiting time had only a small impact on the forming force, while the forming speed had none (see Fig. 7, left). For parameter combinations using an inhomogeneous heating, an increase in initial waiting time resulted in a decrease of forming force. The reason for the decrease in forming force was the compensation processes that led to a homogenization of the temperature profile. In these, the warm parts of the billet usually increased in temperature leading to a decrease in flow stresses and therefore to a decrease in the forming force. This

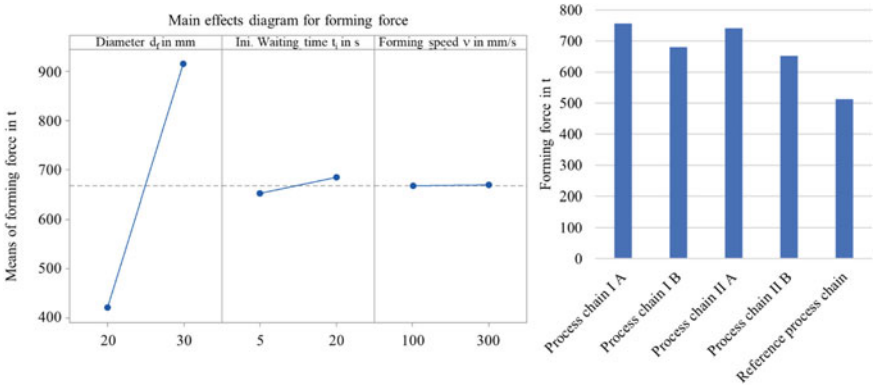


Fig. 7 The main effects for the forming force under consideration of all parameter combinations (*left*) and comparison of the investigated process chains (*right*). (Color figure online)

effect was higher in simulations without preforming since the flattening supports the compensation processes leading to a faster homogenization of the temperature profile. For homogeneously heated billets, the increase in initial waiting time led to an increase in forming force. Since no compensation processes took place and the billet cooled down homogeneously, the flow stresses also increased homogeneously leading to an increase in forming force. The main effects of the forming force, under consideration of all parameter combinations, are shown in Fig. 7, left. Overall, the forming forces were higher for processes with an inhomogeneous heating. In process chain I the inhomogeneously heated simulations showed a mean forming force of 755 t, while the homogeneously heated simulations reached a mean forming force of 680 t resulting in an increase of 75 t for inhomogeneous heating. Without preforming, the difference increases to 90 t with a mean forming force for homogeneous heating of 650 t and for inhomogeneous heating of 740 t. The reference chain showed a mean forming force of 510 t (see Fig. 7, right).

For the die abrasion wear, all parameter combinations qualitatively showed the same qualitative effects. The bigger size of the final geometry and the longer initial waiting time led to an increase in die abrasion wear, while the forming speed led to a decrease (see Fig. 8, left). When comparing the process chains, it becomes clear that flattening led to an increase in die abrasion wear (see Fig. 8, right). Also, an inhomogeneous billet heating led to an increase in die abrasion wear. However, the rate of change was about the same for both. An inhomogeneously heated billet led to an approximately 5% higher die abrasion wear compared to a homogeneously heated billet, while the flattening of the billet generated about 6% more die abrasion wear than a non-preformed billet.

Since not all of the simulations performed for the parameter study reached form filling, the flash ratio was compared using the initially designed processes described in Chap. 3.1 (see Fig. 4). Therefore, an investigation of the influence of the initial waiting time and the forming speed was not performed. The initial waiting time

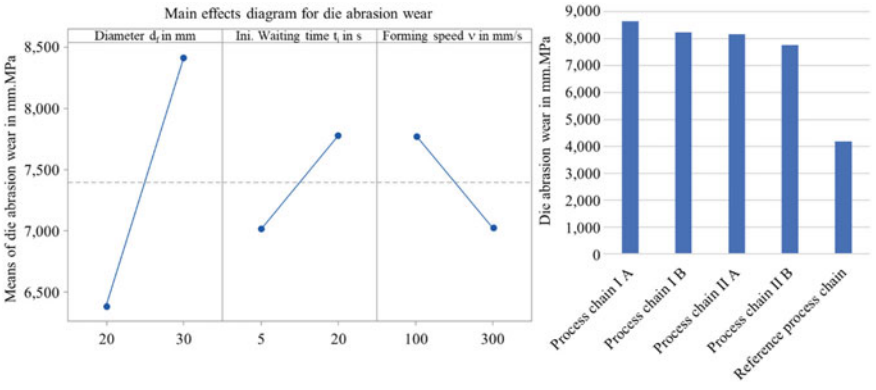


Fig. 8 The main effects for the die abrasion wear under consideration of all parameter combinations (*left*) and comparison of the investigated process chains (*right*). (Color figure online)

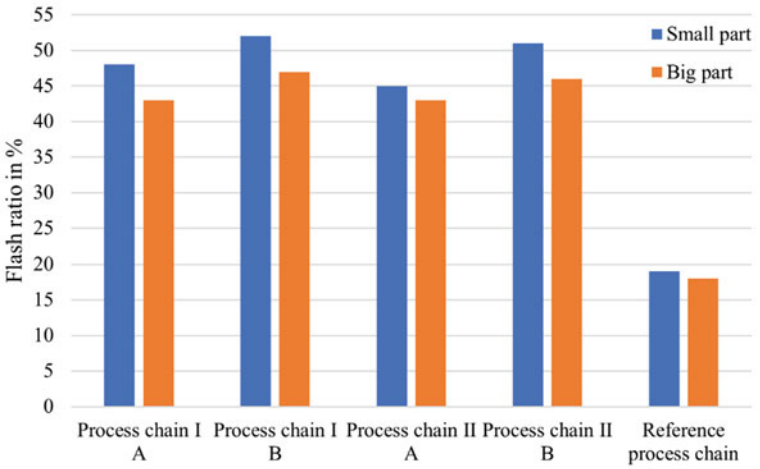


Fig. 9 Comparison of the investigated process chains regarding their flash ratio. (Color figure online)

would, of course, have had a significant influence on the flash ratio, but since the investigation of the form filling showed that the time window for a successful process is very small and clearly below 20 s, a variation of the waiting time would not have been effective. In addition, the forming speed showed no influence on the form filling at all. Therefore, it was found unnecessary to investigate these parameters in correspondence to their influence on the flash ratio. Figure 9 shows the comparison of the investigated process chains in regard to their flash ratio. At first glance, it is obvious that a larger final part results in less flash. This can be explained by the fact that they have less fineness, which made them easier to fill and which reduces the flash ratio. It can also be seen that the process chains containing flattening had a higher flash ratio than those without a preforming step. However, the most important observation that can be made is the reduction of the flash ratio in inhomogeneously heated process chains. The implementation of inhomogeneous heating in a process without a preform step led to a reduction of the flash ratio of 11.8% (6% points). In a process with a preform step, the reduction still corresponded to a reduction of 9.4% (5% points). This shows major potential for increasing the material efficiency of forging processes.

4 Conclusion and Outlook

This paper discusses an FE-based investigation of the influence of inhomogeneously heated billets on subsequent forging processes. The investigation was separated into two stages. In the first stage, the process chains that were investigated had to be designed. In the second stage, a parameter study was conducted to compare the

different process chains and thereby identify the influence of the inhomogeneous heating on them. In this stage, the influence of the forming speed, the initial waiting time on the size of the final geometry on the process chains, and the influence of an inhomogeneous billet heating on the form filling, the forming force, the die abrasion wear, and the flash ratio were studied.

For inhomogeneously heated process chains, a very small process window could be determined with regard to the initial waiting time. The longer the billet cooled down after an ideal inhomogeneous heating, the less likely it was that a form filling could be achieved. It was also found that flattening as a preforming step for inhomogeneously heated process chains is not effective, since compared to processes without preforming, it generally led to a deterioration of all evaluation criteria. The die abrasion and the necessary forming force increased due to higher flow stresses by inhomogeneous heating. An important finding, however, was the possibility of reducing flash by inhomogeneous heating of the billets. It was possible to reduce the flash ratio of an inhomogeneously heated process by 11.8% compared to an identical homogeneously heated process. This shows a high potential of inhomogeneous heating of billets in forging processes. It also shows the need for further investigations. Thus, it should be checked whether the combination of a preform optimized process, as it was carried out in the reference process chain, and an inhomogeneous heating also allows a reduction of the flash ratio.

In addition, the present investigations form the basis for experimental tests. For these, an inductive heating process must first be designed, which allows the smallest possible transition area between hot and warm temperature fields in the billets. Subsequently, forging tests can be carried out to verify the results of the present simulative study.

Acknowledgments The research project "Use of different flow stresses for forming inhomogeneously heated billets" (BE 1691/212-1) was funded by the German Research Foundation (DFG). The authors thank the DFG for its support.

References

1. Herbertz R, Labs R, Langejürgen M (2010) Energiepotenziale in der Massivumformung. Schmiede J (3):16–18
2. Dannenberg M, Charlin F (2012) Auslegung schmiedetechnischer Prozessketten—Ein neuer Ansatz zur Modellierung und softwaregestützten Optimierung von Produktionsprozessketten. Schmiede J (3):34–37
3. Behrens BA, Rüther T, Langner J, Stonis M, Güzey G (2014) Increasing the competitive capacity of SME's be designing a new energy efficient forging process chain. Paper presented at the 7th International Scientific Colloquium "Modelling for Electromagnetic Processing" (MEP), Hannover, Germany, 16–19 September 2014
4. Stonis M, Langner J, Blohm T (2015) Induction reheating of preforms and flash reduced forging of crankshafts. Paper presented at the METEC & 2nd European Steel Technology and Application Days (ESTAD), Düsseldorf, Germany, 15–19 June 2015

5. Matzenmiller A, Bröcker C (2012) Thermo-mechanically coupled FE analysis and sensitivity study of simultaneous hot/cold forging process with local inductive heating and cooling. Int J Mater Form 5(4):275–300. https://doi.org/10.1007/s12289-011-1042-y
6. Mahnken R, Ehlenbröker U, Dieker J (2013) Simulation of hybrid-forming processes to examine thermal shock behaviour in the forming tool and phase transformations in the workpiece. In: Heim HP, Biermann D, Homberg W (eds) Functionally Graded Materials in Industrial Mass Production, vol 2. Verlag Wissenschaftliche Scripten, Auerbach, pp 167–182
7. Okman O, Özmen M, Huwiler H, Tekkaya AE (2007) Free forming of locally induction heated specimens. Int J Mach Tool Manu 47(7–8):1197–1205. https://doi.org/10.1016/j.ijmachtools.2006.08.022
8. Özmen M (2005) Forming of complicated shapes by local heating. Paper presented at the 8th International Conference on Technology of Plasticity (ICTP), Verona, Italy, 9–13 October 2005
9. Merrygold E, Osman FH (1998) Forging of complex geometries with differential heating. J Mater Process Tech 80:179–183. https://doi.org/10.1016/S0924-0136(98)00138-1
10. Kruse J, Jagodzinski A, Langner J, Stonis M, Behrens BA (2019) Investigation of the joining zone displacement of cross-wedge rolled serially arranged hybrid parts. Int J Mater Form. https://doi.org/10.1007/s12289-019-01494-3
11. Hensel A, Spittel T (1978) Kraft- und Arbeitsbedarf bildsamer Formgebungsverfahren. Dt. Verl. für Grundstoffindustrie, Leipzig

Development of Automatic Design System for Closed Die Forging Process of Disk-Shaped Products



Yoshihiko Kobayashi, Eiji Sakamoto, and Tetsuya Yagami

Abstract When designing a closed die forging process, it is necessary to determine the process conditions with respect to various evaluation points such as forging load and shape accuracy. Two examples of process conditions are the number of stages and the die surface shape of each stage. It is particularly difficult to determine the combination of these two process conditions, which is called "process layout" in this paper, because there are numerous potential patterns that lead to a long development period for the design. Our objective is to generate a draft of the process layout for closed die forging. In this study, the authors focus on the forging process for disk-shaped products. To design a die surface shape with high flexibility, the authors propose a new method for die surface shape called the functional surface connection method and have developed an automatic design method for process layout by combining the proposed method with FEM and an optimization algorithm. The evaluation results showed that a process layout in which forging load restriction and forged shape accuracy were satisfied could be generated automatically.

Keywords Automatic process design · Multistage forging process · FEM · Optimization algorithm · Closed die forging · Disk-shaped product

1 Introduction

In the design of a closed die forging process, process conditions such as the number of stages, the die surface shape of each stage, the bottom dead center, and pressing speed need to be determined. These conditions are investigated by considering several evaluation points, including pressing load, forged shape accuracy, metal structure of forged workpiece, and die wear. Generally, these conditions are designed by FEM [1, 2, 3]. However, determining the proper conditions by trial and error is difficult because there is a lot of flexibility in the process design. In particular, the design of a multistage process is difficult. The multistage process is effective when forming in one stage

Y. Kobayashi (✉) · E. Sakamoto · T. Yagami
Hitachi, Ltd. Research & Development Group, 292, Yoshida-cho, Totsuka-ku, Yokohama-shi, Kanagawa-ken 244–0817, Japan
e-mail: yoshihiko.kobayashi.ad@hitachi.com

© The Minerals, Metals & Materials Society 2021

G. Daehn et al. (eds.), *Forming the Future*, The Minerals, Metals & Materials Series,
https://doi.org/10.1007/978-3-030-75381-8_94

process is impossible [4], but as there are numerous combinations of the number of stages and the die surface shape of each stage (which is called "process layout" in this paper), the development period required for designing the process layout is very long. Reduction of the development period for process design is required in the production of many kinds of products.

In this study, the authors focus on the process in which a billet is forged into a disk-shaped product as an example of a closed die forging process. For a disk-shaped product, there are no clues for generating the die surface shape for each stage, so the process designer has to determine the proper die surface shapes from among various options. The conventional approach to die surface shape design has been trial and error based on the experience and intuition of the designer.

Many kinds of support technologies for process design have been developed to improve design efficiency for forging processes [5–8]. Several previous studies have focused on forging process design based on accumulated forging knowledge of a similar target shape. Although some of the previous studies have tried to generate proper process layout without any production rules, the die surface shape, which is important for the process layout design of disk-shaped products, cannot be appropriately determined. Other studies have examined the optimization of process layout or die surface shapes [9–13], but the forging processes were subjected to prerequisites in which the rough process layout and rough die surface shape of each stage were already known. In light of these aspects, a process design method that can generate a proper process layout and proper die surface shape at each stage without accumulated forging knowledge is still a technical challenge.

In this work, to generate a draft of the process layout for closed die forging, the authors investigated an automatic design method for disk-shaped products. Although there are various evaluation points (as mentioned above), as the first step of this attempt for automatic process design, the authors developed a prototype design system to generate process layouts for a net-shape forging part under the forging load restriction.

2 Automatic Design Method for Forging Process Layout of Disk-Shaped Products

2.1 Design of Die Surface Shape by Functional Surface Connection Method

The authors propose a functional surface connection method to generate a die surface. This method is based on the idea that each region of a die surface has its own function. With this method, the entire die surface shape is composed of connected partial die surface shapes that express different functions. These partial surfaces are called functional surfaces.

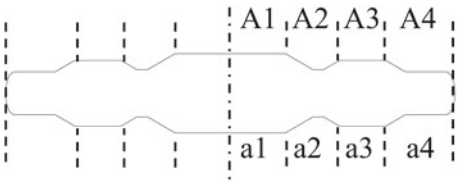


Fig. 1 Domain segmentation based on target shape

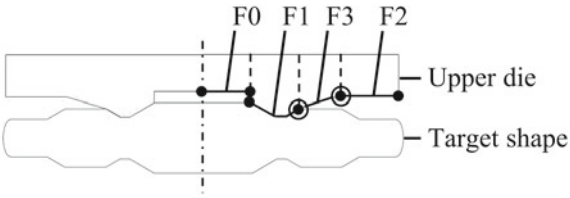


Fig. 2 Upper die shape represented by functional surface connection method

To generate the die surface by the proposed method, first, the authors introduce domain segmentation based on the geometrical features of the target forging shape, as shown in Fig. 1. In the example shown in the figure, domain segmentation is defined as A1 to A4 for the top surface and a1 to a4 for the bottom surface. The domain is divided into a concave shape of the target shape (A2, A4, a2, and a4) and others (A1, A3, a1, and a3). Second, various functional surfaces that express die surface function are assigned to each segment. Then, the entire die surface shape is generated by using four functional surfaces. Functional surface F0 means reducing the forging load by noncontact with the workpiece. Functional surface F1 means forming the workpiece to the target surface shape. Functional surface F2 means forming the workpiece to a flat surface shape. Functional surface F3 means forming the workpiece to a tapered surface shape. To express these functions, the following surface shapes are defined. F0 is a noncontact shape with the workpiece. F1 is the same shape as the target surface. F2 is a flat shape. F3 is a tapered shape. The taper angle of F3 (tapered shape) is set to 30° to the horizon. An entire die surface is generated by connecting these functional surface shapes as shown in Fig. 2, where an example of upper die generation is shown. In this case, the upper die surface is shaped by four connected functional surfaces (F0, F1, F3, and F2). The proposed method can generate various die surface shapes by means of this functional surface connection.

2.2 Automatic Design Flow for Process Layout

To design the process layout automatically, the authors developed the automatic design flow shown in Fig. 3. The design of a process layout depends on the number of stages. Accordingly, in the proposed design flow, the initial number of stages is assumed tentatively, and then the proper die surface of each stage is searched.

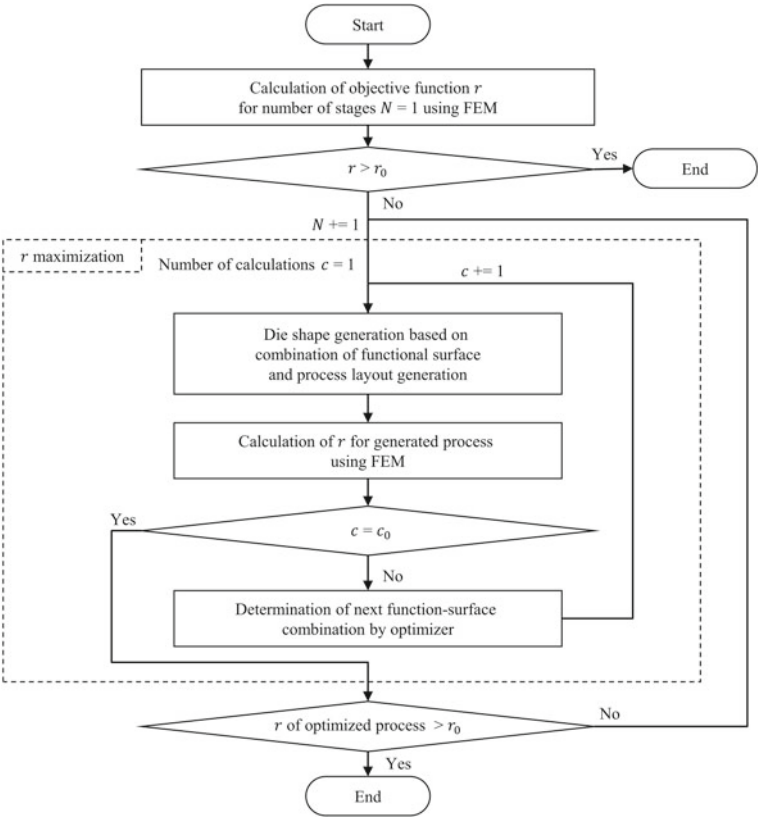


Fig. 3 Flowchart of automatic design for process layout

First, the number of stages is set to one. Objective function r is calculated on the basis of a FEM simulation result. In the FEM simulation, the shape of the entire die surface is the same as the target surface shape. r is given as $r = r_1 – r_2$, where r_1 is a shape concordance percentage between the forged workpiece and the target shape and r_2 is an excess percentage of the forging load compared with the forging load restriction. An r of 100% means that the shape error between the forged workpiece and the target shape is 0% and the forging load is less than the forging load restriction. After r calculation, it is determined whether r is greater than the restrictive value r_0 for objective function r.

If r does not reach r_0, the number of stages is increased before the process layout is searched. In the design of the process layout, the die surface of each stage is generated by the connection of functional surfaces F0 to F3, as shown in Fig. 2. To evaluate the generated process layout, r is calculated on the basis of the FEM result and maximized by repeated calculation using an optimization algorithm. To perform optimization of the process layout, all die surfaces of all stages are represented by a row of symbols that expresses functional surfaces in each segmented domain.

Functional surfaces F0 to F3 are converted into the symbol 0 to 3, respectively. For instance, the vertical symmetric shape; when the number of stages is 3 and the number of domain segmentation is 4 as shown in Fig. 1, the number of symbols which compose the row expressing process layout is 12. The example of this row is [1, 2, 2, 3, 2, 1, 3, 3, 1, 0, 1, 1], where the parts of [1, 2, 2, 3], [2, 1, 3, 3], and [1, 0, 1, 1] express each functional surfaces connections of the die surface shape in each stage. In the repeated calculation, this order of symbols is optimized to maximize the r value. This repetition is continued until the maximum number of available optimizations indicated by the number c_0 is obtained. After repeating calculations, it is determined whether r of the optimized process layout is greater than the restrictive value r_0. If the maximized r is greater than r_0, this process layout is considered to be proper and the design process is completed. On the other hand, if the maximized r is less than that of the previous value r_0, the number of stages is further increased and the search for the proper process layout is continued until maximized r exceeds r_0.

3 Verification of Automatic Design of Process Layout

3.1 Verification Target

In this section, the authors evaluate the effectiveness of the proposed automatic design method for generating the process layout. The method was applied to the target in Fig. 4, where (a) shows the workpiece before forging and (b) is the target shape. The material of the billet was SUS304.

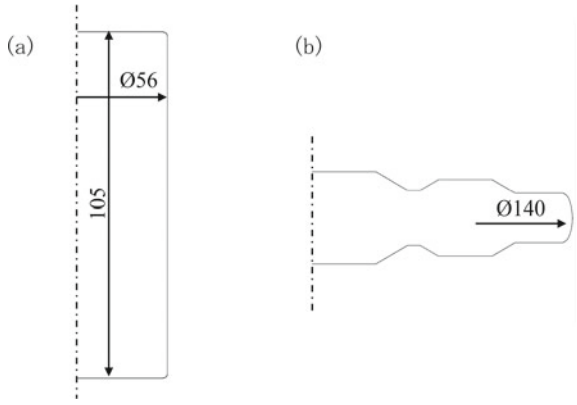


Fig. 4 Application target of the proposed automatic design method

3.2 *Implementation of Automatic Design Flow*

To perform the automatic design flow shown in Fig. 3, the authors developed a prototype system. Its functions include generating the die surface by the functional surface connection method, constructing a FEM model, executing FEM simulation, calculating objective function r, and maximizing r by an optimization algorithm. DEFORM 2D v11.2 was used as a FEM solver. Maximization of r was performed by a genetic algorithm. Load restriction and r_0 were set to 12 MN and 95%, respectively.

4 Results and Discussion

The process layouts in which objective function r became the largest of all the calculation conditions are shown in Fig. 5. The number of stages of these results ranged from one to four. In the case of one and two stages, forging load reached the forging load restriction, 12MN. In these cases, the obtained forged shapes had low accuracy due to an underfill at the outer region. In contrast, in the case of three stages, a process layout without forging load excess or underfill part was obtained. Automatic design calculation was also performed in a case with four stages as a reference. In this case, a process layout without forging load excess or underfill part

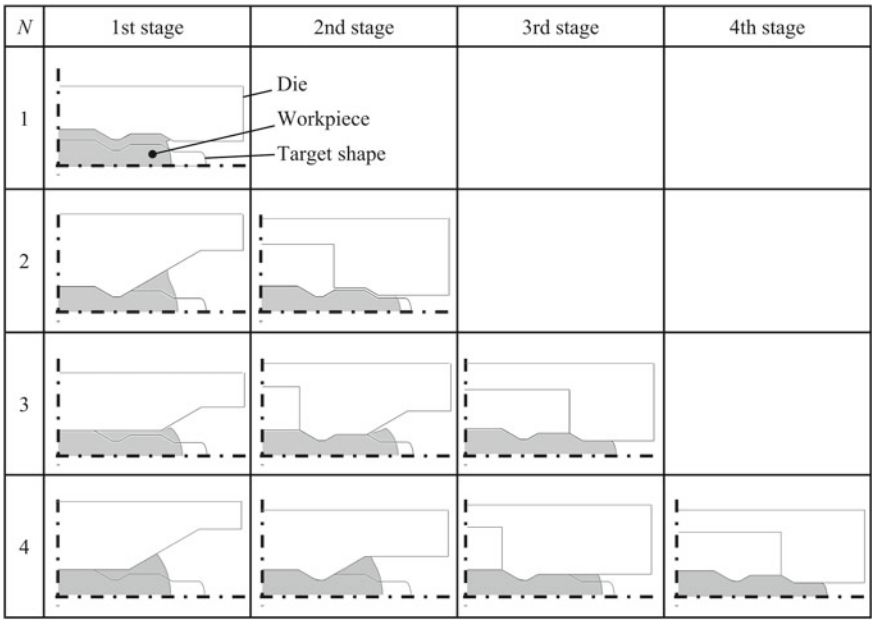


Fig. 5 Obtained processes for each number of stages

was obtained, the same as with the three-stage process. However, the authors found that with four stages, one of them was unnecessary, so the case with three stages is considered more proper. These results demonstrate that a process layout with a small number of stages can be obtained automatically by the proposed automatic design flow using the functional surface connection method.

Next, the authors selected five process layouts from the 250 calculations for the process layout optimization of the three-stage process and compared them. These are shown in Fig. 6 and labeled as layouts i to v. In the figure, forging load is written as a relative value based on forging load restriction. Process layouts i and ii are any samples during the optimization process. In process layout i, the authors found forging load excess and a lap at the outer region (Fig. 7a), which is a defect of the forged shape, at the third stage. In process layout ii, forging load excess occurred at the second and third stages. In process layouts i and ii, various patterns of process layout were evaluated in the optimization process, which indicates that many combinations of the functional surface were calculated for all die shapes of all stages to search for the process layout by maximizing the r value. In addition, two similar process layouts,

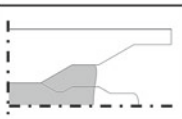
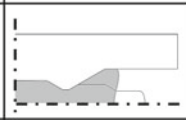
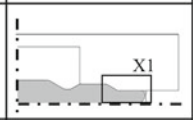
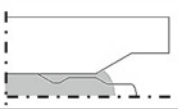
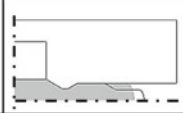
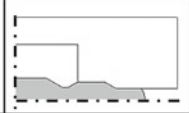
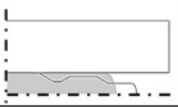
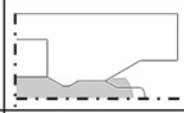
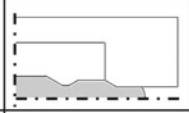
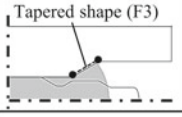
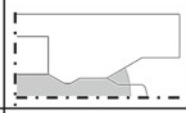
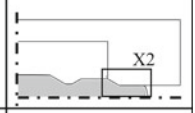
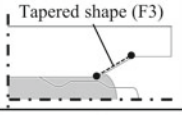
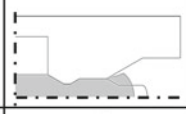
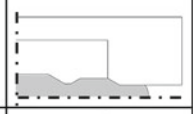
Sample number		1st stage	2nd stage	3rd stage
i	Process			
	Relative load [%]	−42	−39	+32
ii	Process			
	Relative load [%]	−11	+13	+40
iii	Process			
	Relative load [%]	+6	−19	−12
iv	Process			
	Relative load [%]	−38	−18	−13
v (the best result)	Process			
	Relative load [%]	−11	−19	−12

Fig. 6 FEM calculation results in optimization of three-stage process

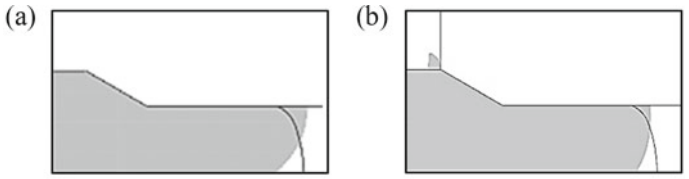


Fig. 7 Enlarged view around area **a** X1 and **b** X2 in Fig. 6

iii and iv, comparing with the process with most maximized r (as shown in Fig. 5) were selected. And then, these process layouts were compared with the process with the most maximized r in detail. The difference between these two process layouts and the process with the most maximized r is the die surface of the first stage.

Process layout v in Fig. 6 is the process with the most maximized r shown in Fig. 5. At the first stage of process layout iii, the die with the flat surface shape pressed the workpiece. The forging load at the first stage, 12.7 MN, exceeded 6% based on the forging load restriction. In contrast, at the first stage of process layout iv, the forging load did not exceed the forging load restriction. However, the shape accuracy of the forged shape became low because a lap at the outer region (Fig. 7b) was found after the third stage. As the examples of process layouts iii and iv, the die surface shape affects forging load and forged shape accuracy. In process layout v (which is the r maximized process), because the position of the tapered shape at the first stage was in the middle (between process layouts iii and iv), the authors could obtain a process layout in which both the forging load restriction and forged shape accuracy were satisfied. This demonstrates that the proposed automatic design method can determine the process layout automatically.

Previously, when there has been no accumulated forging knowledge to help with generating the process design, it is difficult to automatically design a die surface and process layout because these determinations have depended on the experience and intuition of the designer. The proposed method generates a process layout without any knowledge by searching for the proper die shape globally. Incidentally, optimizing the parameters of a die surface is effective when designing a process layout for a net-shape forging part under the forging load restriction. The proposed method can optimize the die surface parameters locally by changing the position of the functional surface. For example, in the case of process layouts iii to v in Fig. 6, the position of F3, which is a tapered shape at the first stage, can be changed and optimized to satisfy the forging load restriction and shape accuracy. Thus, the proposed method can express global and local optimizations.

5 Conclusion

In this work, the authors have proposed an automatic design method to automatically generate a draft layout for the closed die forging process of disk-shaped products.

The evaluation points of the forging process were forging load restriction and forged shape accuracy. Our work can be summarized as follows:

- The authors proposed a functional surface connection method based on die surface functions to generate die surface shapes of the closed die forging process. A prototype automatic design system was developed by combining the proposed die surface generation method with FEM and an optimization algorithm.
- To evaluate the proposed design method, verification was performed for a disk-shaped product. After various combinations of functional surface were evaluated, the proposed design method was able to automatically obtain a process layout with no forging load excess or underfill part.

In the future, the authors plan to investigate expanding application targets. The authors will also finetune the automatic design system so that it can consider additional evaluation points.

References

1. Mohsin Abdullah Al-Shammari, Lutfi Y Zedan, Akram M Al-Shammari (2018) FE simulation of multi-stage cold forging process for metal shell of spark plug manufacturing. 2018 1st International Scientific Conference of Engineering Sciences—3rd Scientific Conference of Engineering Science (ISCES), Diyala, Iraq, 10–11 January 2018
2. Movrin D et al. (2012) Optimization and design of multistage hot forging processes by numerical simulation and experimental verification. J Technol Plast 35:75–89
3. Cheng LV et al. (2008) 3D FEM simulation of the multi-stage forging process of a gas turbine compressor blade. J Mater Proc Technol 198:463–470
4. KS Park, Chester J Van Tyne, YH Moon (2007) Process analysis of multistage forging by using finite element method. J Mater Proc Technol 187–188:586–590
5. Quang-Cherng Hsu, Rong-Shean Lee (1997) Cold forging process design based on the induction of analytical knowledge. J Mater Proc Technol 69:264–272
6. Bariani P et al. (1987) Computer aided design of multi-stage cold forging process: Load Peaks and Strain Distribution Evaluation. CIRP Annals 36:145–148
7. Sevenler K, Raghupathi PS, Altan T (1987) Forming-sequence design for multistage cold forging. J Mechan Work Technol 14:121–135
8. Osamu Takata et al. (2005) A knowledge-based system for process planning in cold forging using the adjustment of stepped cylinder method. International Conference on Applications of Declarative Programming and Knowledge Management (INAP 2005), Fukuoka, Japan, 22–24 October 2005
9. Ryutaro Hino et al. (2008) A new algorithm for reduction of number of press-forming stages in forging processes using numerical optimization and FE simulation. Int J Mechan Sci 50:974–983
10. Xinhai Zhao et al. (2002) Preform die shape design for uniformity of deformation in forging based on preform sensitivity analysis. J Mater Proc Technol 128:25–32
11. Roy S, Ghosh S, Shivpuri R (1995) A new approach to optimal design of multi-stage metal forming processes with micro genetic algorithms. Int J Mach Tools Manufac 37:29–44
12. Zhao GQ et al. (1997) Sensitivity analysis based preform die shape design using the finite element method. J Mater Eng Perf 6:303–310
13. Shahriari D et al. (2008) Optimal closed die finish forgings for nimonic80-A alloy using FEM method. Int J Mater Form 1:29–32

A FE Billet Model and a Spring-Mass-Damper Model for the Simulation of Dynamic Forging Process: Application to a Screw Press



Jean-François Mull, Camille Durand, Cyrille Baudouin, and Régis Bigot

Abstract In forging processes, the determination of blow efficiency is very important, as it quantifies the part of the stroke energy actually transmitted to the billet. Thus, forging processes should be deeply analyzed in order to better understand the stroke energy conversion, accurately estimate blow efficiency, and thus better predict process parameters. In this paper, a spring-mass-damper vibration model is proposed to describe forming operations of a screw press. Parameters specially adapted to the machine-tools system are identified, thanks to a stroke without billet. Thereafter, the experimental upsetting of a copper cylinder is realized, and two independent numerical simulations are performed. First, the billet upsetting is simulated by FE simulation with no consideration of the elastic and damping effect due to the machine-tools behavior in order to determine a relation between the load and the billet height. Then, forging load from the FE simulation is used to perform another simulation of the forging process with the spring-mass-damping model. Results show that the model is relevant to simulate load and ram displacement. Moreover, simulation can predict the distribution of the energy during the simulation and the blow efficiency can be calculated. This new way to obtain blow efficiency might improve productivity in process development and provide a better understanding of energy-driven machines.

Keywords Dynamic · Machine behavior · Process modeling · Numerical simulation · FE simulation

J.-F. Mull (✉) · C. Durand · C. Baudouin · R. Bigot
Arts et Metiers Institute of Technology, Université de Lorraine, LCFC, HESAM Université, 57070 Metz, France
e-mail: jeanfrancois.mull@ensam.eu

C. Durand
e-mail: camille.durand@ensam.eu

C. Baudouin
e-mail: cyrille.baudouin@ensam.eu

R. Bigot
e-mail: regis.bigot@ensam.eu

© The Minerals, Metals & Materials Society 2021

G. Daehn et al. (eds.), *Forming the Future*, The Minerals, Metals & Materials Series,
https://doi.org/10.1007/978-3-030-75381-8_95

1 Introduction

For energy piloted forging machines, the prediction of the energy actually transmitted to the billet for each blow is important in the conception of a forging sequence. Because it allows determining the number of necessary blows and thus optimizes the sequence. Therefore, a deep analysis is required to determine the distribution of the energy during the forging process and calculate the blow efficiency. For that, it is needed to consider billet and machine behavior. Different approaches were proposed to model energy-driven machines. For hammers, studies focused on the impact of the machine foundation [1] or the machine structure [2, 3]. But in every case, the dynamic models proposed were an association of springs, masses, and dampers with a different degree of freedom. In order to perform the simulation of the whole forging process, it is needed to couple the billet model and the machine model. For a hammer, Vajpayee et al. [4] realized simulations of the forging process by considering a press model constituted of one spring and two masses. Billet behavior was modeled by Siebel law allowing the calculation of the forging load during the simulation. The influence of process parameters as impact velocity and model parameters on the process efficiency and clash load was studied. This method is not time-consuming, but it does not allow using FE simulation for complex geometries and obtaining accurate predictions of billet behavior. Three different ways to couple the FE billet model and press model were defined for the forging process: offline coupling, model integration, and co-simulation [5]. Offline coupling simulates the machine and billet behavior in separate environments, the results of one of which is used for the calculation of the other. Model integration simulates the machine and billet behavior in the same environment allowing direct interactions. But simple machine model is required to keep a reasonable calculation time. Furthermore, the co-simulation is a mix of the previous methods, where the machine and billet behavior are simulated in different environments but linked with a third software that manages a synchronized cycle. Kroiß [6] developed an integrated model considering the interactions between billet, tools, and machine for a cold forging application. Optimization was realized on the die dimensions and punch position to obtain high workpiece accuracy. A coupled multibody-finite element simulation (MBS-FEM) for sheet metal forming application was developed [7]. From a 3D CAD of the press structure, the MBS model of a mechanical press was established after several assumptions on press part geometries. A mass was attributed to each element of the press and connection between each of them was defined. Then, the machine model was coupled with the FE simulation of the sheet upsetting to obtain a co-simulation of the whole forging process.

In this study, a spring-mass-damper vibration model is proposed to describe the forming operation of a screw press LASCO SPR400. The model parameters are identified with experimental measurement of load and impact velocity during a stroke without billet allowing to obtain parameters adapted to the machine–tools system. Then, the cold upsetting of a copper specimen is experimentally performed to validate the prediction of the model. Furthermore, two simulations are performed independently. First, a FE simulation of the copper upsetting is realized with no

consideration of the elastic and damping behavior of the machine and tools. This simulation provides a relation between billet height and forging load. Then, a second simulation with the spring-mass-damper model using the relation between load and billet height from FE simulation as input is performed. The results from the second simulation are compared with the experimental measurement concerning load and ram displacement and the simulated energy distribution during the forging process is studied.

2 Method

2.1 Definition of the Model and Identification of Associated Parameters

2.1.1 Experimental Protocol

The screw press of the study is the LASCO SPR400 from the Vulcain platform in Metz, France. The press has a portal frame structure and is equipped with a direct electric drive motor providing the forging energy. A load sensor constituting strain gauges is fixed on the lower toolholder of the press. The lower tool is directly screwed on the load sensor and the upper tool is fixed to the upper toolholder. In order to study the press behavior, a stroke without a billet is performed experimentally; in this case, the shock is generated by the collision between the upper and the lower tools. One stroke settled to reach 9% of the maximum press stroke energy is performed. Load signals from the sensor and ram displacement are recorded during the blow. The ram displacement is obtained with a magnetic coding system integrated into the machine (Fig. 1).

The ram velocity when the upper tool impacts the lower tool is deduced from the ram displacement. The numerical derivative of the ram displacement provides a large error for the evaluation of the ram velocity because of the short time period of the measurement (0.1 ms). One way to reduce this error is to fit the displacement curve with a differentiable function and derive it analytically to obtain velocity [8]. The 20 ms before the impact between the upper tool and the billet is considered. The displacement curve is fitted by a quadratic function with MATLAB® and the function *polyfit*. The derivative of the quadratic function is calculated and is evaluated at the moment of the contact between the tool and the billet. It provides an impact velocity equal to 0.20 m/s.

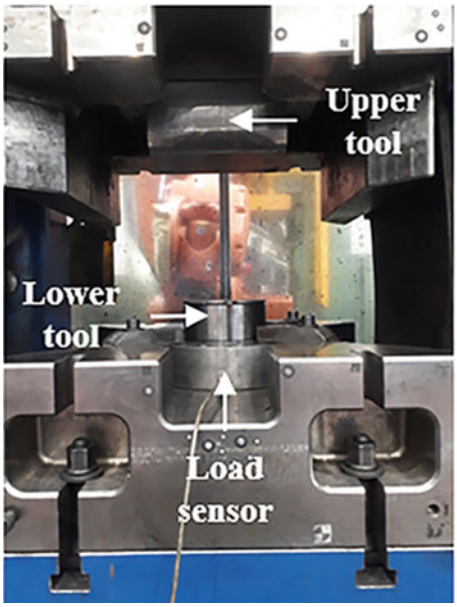


Fig. 1 View of the experimental assembly in upper dead point position. (Color figure online)

2.2 *Model of the Stroke Without Billet*

A two-degree-of-freedom spring-mass-damping vibration model is proposed to describe the press behavior during a stroke without billet (Fig. 2). This model constitutes two masses, two dampers, and three springs. The two masses represent the part in motion in the system (tools, toolholders, ram, screw, and flywheel). The spring k_{Moving} and the damper c_{Moving} link the two masses and model the elastic deformations and damping effects between the parts in motions in the system. The spring k_{Fixed} and the damper c_{Fixed} model the elastic deformations and the damping effects of the frame. During the experiment (cf. Sect. 2.1.1), a load sensor is placed on the stable of the press to be impacted by the upper tool. This sensor has an influence on the system behavior and needs to be considered. Hence, the spring k_{Sensor} is introduced in the model. This spring is linked to mass 1 and the fixed part.

The application of the fundamental principle of the dynamics to the mass 1 and the mass 2 provides the dynamic equations of the system as presented in Eqs. (1) and (2). The spring k_{Sensor} and the Kelvin-Voigt system consisted of the spring k_{Fixed} and the damper c_{Fixed} which are in series. Thus, the load applied to the spring k_{Sensor} and the Kelvin-Voigt system is the same. This equality is written in Eq. (3).

$$m_2\ddot{X}_2 = -k_{\text{Moving}}(X_2 - X_1) - c_{\text{Moving}}\left(\dot{X}_2 - \dot{X}_1\right) \tag{1}$$

$$m_1\ddot{X}_1 = k_{\text{Moving}}(X_2 - X_1) + c_{\text{Moving}}(\dot{X}_2 - \dot{X}_1) - k_{\text{Sensor}}(X_1 - X_{\text{Fixed}}) \tag{2}$$

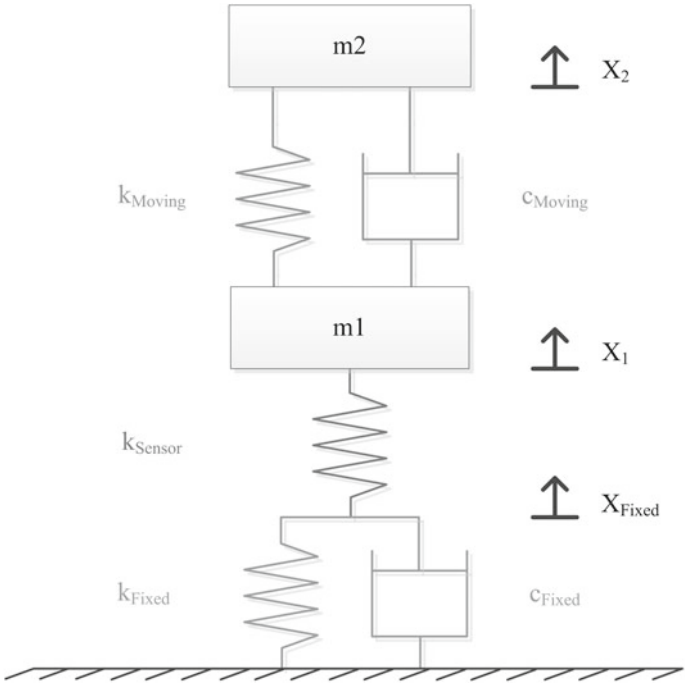


Fig. 2 Model of the screw press and load sensor system for a stroke without billet

$$-k_{\text{Sensor}}(X_1 - X_{\text{Fixed}}) = -k_{\text{Fixed}}X_{\text{Fixed}} - c_{\text{Fixed}}X_{\text{Fixed}} \tag{3}$$

where X_1 is the displacement of the mass 1, X_2 is the displacement of the mass 2, and X_{Fixed} is the displacement of the upper point of the spring k_{Fixed} according to their position at $t = 0$. The stiffness k_{Sensor} is obtained from the sensor manufacturer documentation and is equal to 6.67 GN/m. The initial velocity of the masses 1 and 2 is fixed to 0.20 m/s as in experimental conditions. The model is implemented in MATLAB SIMULINK and the numerical solution of the equations of the model is obtained with the fixed-step solver ode8 (Dormand-Prince method).

2.3 Parameters Identification

The identification of the model parameters is realized with the MATLAB module "Parameter Estimation". The load signal simulated at the spring k_{Sensor} is fitted to the load signal measured with the sensor during the experiment. The program starts to solve the model equations to obtain a numerical solution, and the squared error between the experimental signal and the numerical solution is calculated. This cost

Table 1 Model parameters

m_1	2471 kg
m_2	117 150 kg
c_{Moving}	1.51×10^5 N.s/m
c_{Fixed}	0 N.s/m
k_{Moving}	2.26×10^9 N/m
k_{Fixed}	4.86×10^9 N/m

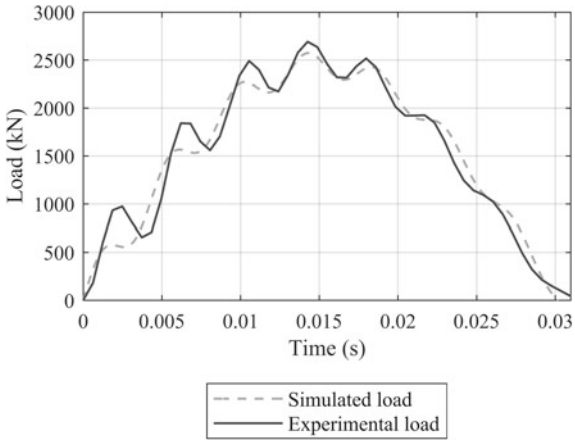


Fig. 3 Experimental and fitted load signals

function is minimized according to the trust-region-reflective algorithm and provides model parameters presented in Table 1.

The experimental load signal and the simulated load to the spring k_{Sensor} with parameters from Table1 are presented in Fig. 3.

2.4 Validation of the Predictive Capacity of the Model for Copper Cylinder Upsetting

2.4.1 Experimental Protocol

The experimental assembly is the same as presented in Sect. 2.1.1, but in this case the cold upsetting of a copper billet is performed. The specimen is a cylinder of 29.9 mm diameter and 59.7 mm length placed on the lower tool. No lubricant is used during the experiment. Concerning process settings, the velocity of the ram is regulated before the impact to provide 60% of the maximum press energy. The load from the sensor and the ram displacement are recorded during the stroke. The method presented in Sect. 2.1.1 is used to estimate the impact velocity equal to 0.51 m/s. The final billet height is measured and is equal to 19.8 mm.

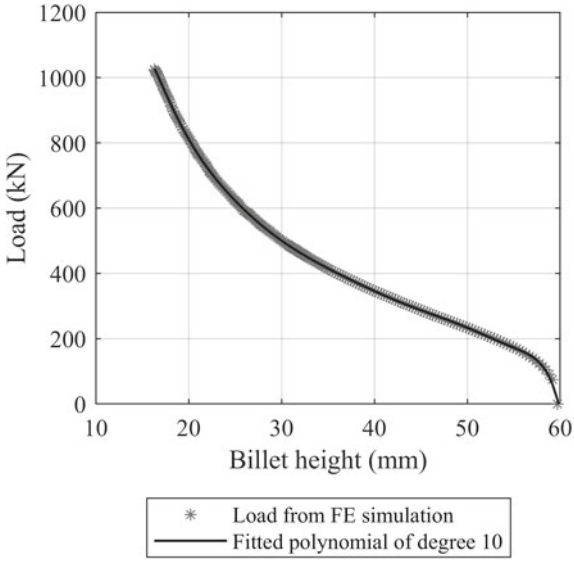


Fig. 4 Load as a function of the billet height from FE simulation and fitted polynomial of degree 10

2.4.2 FE Simulation for the Determination of the Forging Load as a Function of the Billet Height

The upsetting of a copper cylinder of 29.9 mm diameter and 59.7 mm high is simulated with the FE software Forge® NxT 2.1. The material behavior is described by a constitutive law of Hansel-Spittel whose parameters are selected from the database of the software. Friction behavior is modeled by Coulomb limited Tresca model. The friction coefficients are defined and are equal to $\mu/\overline{m} = 0.15/0.26$. Thermal exchanges with air and dies are considered. The associated heat transfer coefficients are, respectively, equal to 10 $W.m^{-2}.K^{-1}$ and 10 $kW.m^{-2}.K^{-1}$. A 2 mm size tetrahedra element is chosen for the mesh. Elastic and damping effects due to the machine–tools system are not considered in this simulation. Results from FE simulation allow obtaining the forging load as a function of the billet height for the interval from 16.3 to 59.7 mm. In order to use the simulated forging load with the spring-mass-damping model, it is required to express the forging load as a continuous function of the billet height. For this purpose, the load from the FE simulation is fitted by a polynomial of degree 10 noted as P (Fig. 4).

2.4.3 Billet-Interface-Machine (BIM) Model

For the simulation of billet upsetting, the spring-mass-damping model is completed as presented in Fig. 5.

The application of the fundamental principle of the dynamics to the mass 1 and the mass 2 provides the dynamic equations of the press system in Eqs. (4) and (5).

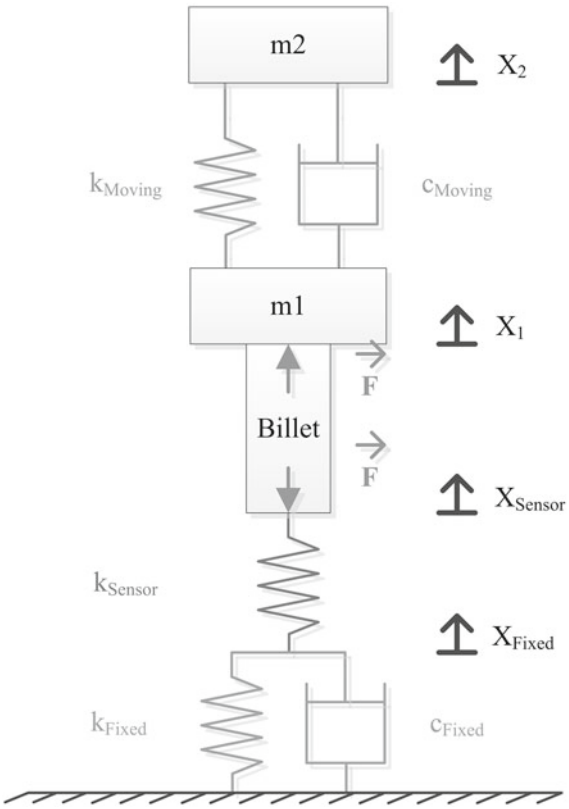


Fig. 5
Billet-Interface-Machine (BIM) model

The spring k_{Sensor} is directly linked to the billet, thus the forging load from the billet is directly applied to the spring, and the relation is written in Eq. (6). Equation (7) is obtained as explained in Sect. 2.2.

$$m_2\ddot{X}_2 + k_{\text{Moving}}(X_2 - X_1) + c_{\text{Moving}}\left(\dot{X}_2 - \dot{X}_1\right) = 0 \tag{4}$$

$$m_1\ddot{X}_1 - k_{\text{Moving}}(X_2 - X_1) - c_{\text{Moving}}\left(\dot{X}_2 - \dot{X}_1\right) = -F \tag{5}$$

$$-k_{\text{Sensor}}(X_{\text{Sensor}} - X_{\text{Fixed}}) = F \tag{6}$$

$$-k_{\text{Sensor}}(X_{\text{Sensor}} - X_{\text{Fixed}}) = -k_{\text{Fixed}}X_{\text{Fixed}} - c_{\text{Fixed}}X_{\text{Fixed}} \tag{7}$$

where X_1 is the displacement of the mass 1, X_2 is the displacement of the mass 2, X_{Sensor} is the displacement of the upper point of the spring k_{Sensor}, and X_{Fixed} is the displacement of the upper point of the spring k_{Fixed} according to their position at $t =$

0. As it can be seen, the reaction force from the billet F is required to perform the simulations of the billet upsetting. F is calculated for each increment of the simulation with the polynomial P identified in Sect. 2.3.2. At each moment, the billet height can be expressed by $X_1 - X_{\text{Sensor}} + h_0$ with h_0 the initial billet height. Thus, the load can be calculated such as $F = P\,(X_1 - X_{\text{Sensor}} + h_0)$.

The model is called "Billet-Interface-Machine" (BIM) model because it allows the coupling of these three aspects in simulation. The billet behavior and the impact of friction at the interface between material and tools are considered, thanks to the expression of the forging load from the FE simulation. Furthermore, the machine–tools behavior is described by the spring-mass-damping model which considers damping effects and elastic strains in the system. The BIM model is implemented on MATLAB® SIMULINK® with the parameters from Table 1. The simulation parameters are the same as presented in Sect. 2.2. The numerical simulation is realized by fixing the initial velocity of both masses to −0.51 m/s as in the experimental conditions.

3 Results and Discussion

The load measured by the sensor and the simulated load for k_{Sensor} are presented in Fig. 6. During the forging process, the simulation underestimates the load compared to the experiment before 0.06 s. Then, a slight difference can be noticed between

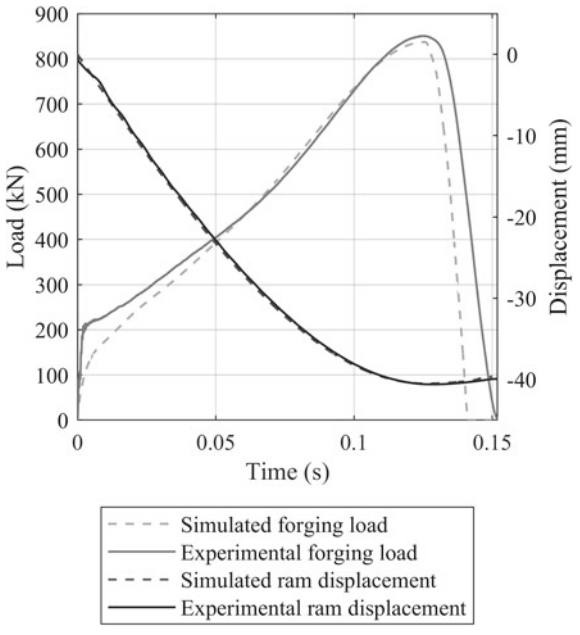


Fig. 6 Forging load and ram displacement measured with the load sensor and press displacement sensor, load in k_{Sensor}, and ram displacement simulated for the upsetting of copper cylinder upsetting

experimental and simulated load until reaching the maximum blow force with a maximum relative deviation of 2.5%. The maximum blow force predicted by simulation is 1.5% lower than the measured value. The forging time, defined as the time to reach the maximum blow force, is equal to 124.7 ms in the experiment and 125.8 ms in the simulation, giving a relative deviation of 0.01%. After reaching the maximum blow force, bigger differences are observed between simulation and experimental results. The simulated spring back time equal to 15.3 ms is smaller than the experimental spring back time equal to 27.8 ms. This means a relative deviation equal to 45%. Figure 6 also shows the ram displacement obtained by experimental measurement and by simulation. 0 corresponds to the initial contact between the tool and the billet. The ram displacement is accurately predicted by the simulation during the whole forging process. The minimum experimental and simulated displacements show a relative deviation of 0.3%. From the moment of the contact between the tool and the billet to 25 ms, damped vibrations can be observed on the experimental ram displacement. The amplitude of the vibration is very low compared to the global signal. No vibrations can be observed on the simulated signal. In the simulation, the final billet height is estimated to be 19.5 mm, meaning a relative deviation of 1.5% compared to the experimental result. It can be noted that the billet height simulated with the BIM model is always in the interval of identification of the polynomial *P*.

The distribution of the energy of the system for each blow is presented in Fig. 7. The model considers four types of energy: the kinetic energy of the masses, the elastic energy stored by the springs, the damped energy dissipated by the dampers, and the billet energy considering the plastic energy and the energy dissipated in the friction between the tools and the material. At the beginning of the stroke, all the energy is coming from the motion of the two masses. Thus, the energy is purely kinetic and can be calculated as $½.(m_1 + m_2).v_0^2$.

It can be observed from Fig. 7 that until reaching the maximum blow force the kinetic energy decreases during the forging process, whereas the billet energy and the elastic energy increase. Then, the billet energy remains constant while the kinetic energy increases and the elastic energy decreases. Concerning damped energy, it never exceeds 0.02% of the total energy. 98% of the initial kinetic energy is converted into billet energy at the end of the forging process. This value represents the efficiency of the stroke. During the blow, 2% of the available energy is turned into elastic energy. After reaching the maximum blow force, the elastic energy is turned again into kinetic energy in the acceleration of masses 1 and 2 in the opposite direction of the stroke.

Results have shown that the forging load and the ram displacement can be predicted by the simulation. The determination of the forging load with FE simulation and a fitted polynomial is suitable to simulate the whole forging process. The FE simulation allows obtaining the forging load in ideal conditions, i.e., with no consideration of the press behavior. Then, the second numerical simulation allows determining the part of the stroke energy transmitted to the machine–tools system and process variables associated with the operation.

In our case, the machine–tools system has a small impact on the forging process. Indeed, only 2% of the initial stroke energy is turned into elastic energy. The experimental study case corresponds to a soft blow, where most of the available energy is

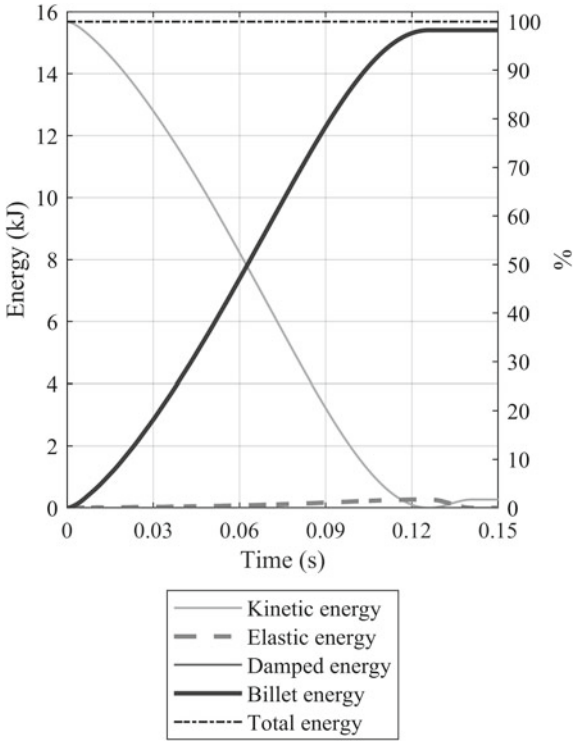


Fig. 7 Distribution of the energy for one simulated blow on a copper specimen

transmitted to the workpiece. For soft blows, small loads and large billet deformations are noticed [9]. Thus, the model provides a good representation of the energy distribution during the forging process. As the energy transmitted to the billet can be predicted by the simulation, it is possible to assess the efficiency of the blow.

It was noticed that the damped energy remains very low compared to the stroke energy. For this given forging operation, the damped energy can be neglected. As can be observed from Table 1, the damping effect is only caused by the relative displacement between the masses because k_{Fixed} is equal to 0. In the case of a soft blow, vibration modes are not activated enough and the relative displacement between the masses is too low to dissipate a significant part of the stroke energy in the damper. For hard blows [9], the damped energy might be more important and could become significant.

In this study, the forging operation is the cold upsetting of a copper cylinder. It simplifies the experimental protocol by allowing to neglect thermal effects, thus the measurement of the billet temperature and the transfer times are not required. Simulations of a more complex workpiece for hot materials could be intended. However, it is needed to keep an axisymmetric geometry for the workpiece because the press behavior is only considered for the vertical axis of the press in the model. Thus, this methodology brings a new way to cross the FE model and spring-mass-damper

press model without the need to couple two softwares. The consideration of the energy dissipated in the dynamic effects in the machine implies an improvement of the accuracy of the numerical simulations and a better prediction of the process variables.

4 Conclusions

This study presents an experimental methodology to model forming operations in the case of a screw press. Model parameters were identified with the measurement of the ram impact velocity and the load during a stroke without billet. Then, independent simulations crossing a FE model and the spring-mass-damper model for copper cylinder upsetting were performed. FE simulation allowed determining a relation between load and billet height used as an input of the simulation performed with the spring-mass-damper model. Experimental copper upsetting was led with the measurement of the load and ram displacement. Simulation results show a good agreement with experimental measurements. The following conclusions were drawn:

1. Measurements of the ram impact velocity and the forging load during a stroke without billet are enough to determine specially adapted model parameters for the screw press.
2. The use of FE simulation to predict the forging load required for the simulation of the forging process with a spring-mass-damper press model is suitable to predict the process variables. It provides a complete representation of the system without developing a coupling between two software.
3. The model of the whole forging process can predict the distribution of the energy in the system during the forging process. Thus, it is possible to determine the part of the stroke energy transmitted to the billet and calculate the blow efficiency for a given forging operation.

Acknowledgments The authors would like to express their sincere appreciation to Sebastien Burgun and Alexandre Fendler for their technical support in the realization of the experimental protocols. Moreover, they wish to thank MANOIR INDUSTRIES for their financial support in this research project.

References

1. Novak M, El Hifnawy L (1983) Vibration of hammer foundations. Int J Soil Dyn Earthq Eng 2(1): 43–53. https://doi.org/10.1016/0261-7277(83)90026-8
2. Gregorian V, Sadek MM, Tobias SA (1976) Noise generated by a laboratory drop hammer and its interrelation with the structural dynamics and process parameters. Int J Mach Tool Des Res 16(4): 301–318. https://doi.org/10.1016/0020-7357(76)90040-8

3. Vajpayee S, Sadek MM, Tobias SA (1982) Prediction of linear noise-load relationship for impact forming machines. Int J Mach Tool Des Res 22(1): 1–6. https://doi.org/10.1016/0020-7357(82)90015-4
4. Vajpayee S, Sadek MM, Tobias SA (1979) The efficiency and clash load of impact forming machines to the second order of approximation. Int J Mach Tool Des Res 19(4): 237–252. https://doi.org/10.1016/0020-7357(79)90013-1
5. Brecher C, Esser M, Witt S (2009) Interaction of manufacturing process and machine tool, chap 5. CIRP Ann 58(2): 588–607. https://doi.org/10.1016/j.cirp.2009.09.005
6. Kroiß T, Engel U, Merklein M (2013) Comprehensive approach for process modeling and optimization in cold forging considering interactions between process, tool and press. J Mater Process Technol 213(7): 1118–1127. https://doi.org/10.1016/j.jmatprotec.2012.09.004
7. Swidergal K et al (2015) Experimental and numerical investigation of blankholder's vibration in a forming tool: a coupled MBS-FEM approach. Prod Eng 9(5–6): 623–634. https://doi.org/10.1007/s11740-015-0640-9
8. Chen R et al (2019) A stereo-vision system for measuring the ram speed of steam hammers in an environment with a large field of view and strong vibrations. Sensors 19(5): 996. https://doi.org/10.3390/s19050996
9. Altan T, Ngaile G, Shen G (2005) Cold and hot forging: fundamentals and applications. ASM International

Optimization of Open-Die Forging Using Fast Models for Strain, Temperature, and Grain Size in the Context of an Assistance System



Fridtjof Rudolph, Martin Wolfgarten, Viktor Keray, and Gerhard Hirt

Abstract Besides achieving the intended final shape, one main aim of open-die forging is the adjustment of the mechanical properties by transforming the cast structure into a fine-grained microstructure. To achieve this, the process needs to be designed in a way that ensures achieving all the required part properties, such as grain size, which up to now often requires a lot of operator experience. This paper presents the concept of a forging assistance system, since during forging small deviations from the previously designed pass schedule might add up to unacceptable errors. Such an assistance system requires the evolution of part geometry and surface temperature as input, which are captured with a thermographic camera. The assistance system then uses fast models for equivalent strain, temperature, and microstructure which allow calculation of these properties for the core fibre within seconds on the basis of semi-empirical and physical formulae. However, in the context of an assistance system, which gives real-time advice in case of process deviations, these calculation times are still fairly long, if the hundreds of iteration necessary for process optimization are taken into account. Therefore, three scenarios of deviations, which have to be solved within different time frames, are examined to explore the limits of the chosen classical optimization algorithm.

Keywords Open-die forging · Fast modelling · Assistance system

F. Rudolph (✉) · M. Wolfgarten · V. Keray · G. Hirt
Institute of Metal Forming, RWTH Aachen University, Intzestraße 10, 52074 Aachen, Germany
e-mail: fridtjof.rudolph@ibf.rwth-aachen.de

M. Wolfgarten
e-mail: martin.wolfgarten@rwth-aachen.de

V. Keray
e-mail: viktor.keray@outlook.com

G. Hirt
e-mail: gerhard.hirt@ibf.rwth-aachen.de

© The Minerals, Metals & Materials Society 2021

G. Daehn et al. (eds.), *Forming the Future*, The Minerals, Metals & Materials Series,
https://doi.org/10.1007/978-3-030-75381-8_96

1 Introduction

The main goal of open-die forging besides achieving the desired geometry is to improve the mechanical properties by transforming the inhomogeneously solidified cast structure into a fine-grained microstructure. In order to guarantee excellent properties, the forging process must be designed in such a way that a certain temperature window is maintained during the process and a sufficiently large deformation needs to be introduced into the part to enable this transformation.

Nowadays, these part properties can be calculated and new open-die forging processes can be designed with the aid of either finite element analysis (FEA) or with fast models based on semi-empirical and physical formulae. FEA enables analysing of all parameters relevant for forming technology, but is very complex and time-consuming, while the fast models calculate only the most important process parameters in open-die forging for the core fibre of the workpiece in short calculation times.

However, in the case of unplanned process deviations, the previously designed process layout may be invalid and the desired properties can only be achieved by adjusting the pass schedule. In this paper, the application of fast models for temperature, equivalent strain, and microstructure in an assistance system is examined on the basis of three different process deviations. These show under which conditions the optimization still provides a satisfying adjustment of the pass schedule, which comprises the term assistance system in the context of this paper.

2 Assistance Systems

Over the last decades, several approaches for assistance systems for open-die forging have been developed. Siemer and Kopp [1] developed a fast model for offline and online calculation of open-die forging processes. The aim of this model is to design processes with a homogeneous equivalent strain distribution and to monitor the correct process sequence online. The calculation system consists of a specially developed spread model, a strain model, and a heat balance calculation. Press force, press velocity, temperatures, manipulator positions, as well as billet length were recorded in order to enable the online calculation of the equivalent strain. Temperature and microstructure are not taken into account.

In [2] and [3] Grisse and Heischeid present the model “Forge to Limit”, which was integrated into the control of a forging manipulator to demonstrate the online capability. The goal is to maximize the increase in length by minimizing the spread. In addition, the model can be used to optimize forging sequences with respect to a reduction of process time. Billet properties such as strain and temperature are not considered.

Elbadan [4] developed an automatic forging cell, which is able to design and implement the appropriate forging sequence inversely based on a defined target geometry.

During the process, a comparison between target and actual geometry is made by measurement with an end-effector after each stroke. If necessary, the process route is adapted fully automatically taking into account the technical boundary conditions. The online adaptation of the forging sequence is based on a fast model for geometry calculation using the upper bound method, therefore this system is limited to geometry adaptation.

The industrially available measuring system "LaCam" from Minteq Ferrotron Division [5, 6] has a fast calculation model for strain in the core for drawing out. The system is capable of displaying the current core consolidation per stroke and for the entire process using the billet geometry and the measurement data of the forging press. With regard to an assistance system, suggestions are made to the press operator as to where the next strokes should be positioned to ensure uniform equivalent strain over the entire length of the ingot. Temperature and microstructure are not taken into consideration.

Pelster and Blei [7] developed a fast model for the design and online monitoring of the geometry change, temperature, and microstructure for radial forging. The models are linked to the "ComForge" pass schedule calculation program. The 1D FEM temperature model is corrected by a heat balance calculation by Paukert [8]. The 2D equivalent strain model is also based on [8] and additional FEM simulations. The software calculates the equivalent strain distribution depending on the bite ratio and the true strain. For the microstructure calculation, the program MatILDa from GMT is used, which is integrated into the FEM software Simufact.

3 Fast Modelling in Open-Die Forging

Four of the presented assistance systems for open-die forging are limited to geometry and strain calculation. The fifth system for radial forging takes the microstructure into account but only for documentation purpose due to the long calculation times [7]. To close this gap for open-die forging, models for temperature, equivalent strain and microstructure with short computation times have been developed in the past. As these models build the foundation of the assistance system presented in this work, they are presented in more detail.

Rosenstock et al. [9] presented a temperature model for open-die forging based on the finite difference method (FDM), which can calculate the 3D temperature field for the entire process and workpiece geometry including cooling. The model takes all relevant phenomena into account: radiation, convection, heat conduction to tools and the environment, as well as dissipation.

One of the first fast models for the equivalent strain in the core fibre during forging was presented by Stenzhorn [10] and it allows the rough estimation of the strain distribution by linear approximation. An extended model was published by Recker et al., who used this model for the calculation of the equivalent strain for more than one pass for three-dimensional forging [11] based on FEM studies. The equivalent

strain for each stroke is described with a $\sin^2$ function which is superpositioned to obtain the distribution of the equivalent plastic strain for the whole process.

The semi-empirical program "StrucSim" for microstructure calculation was developed by Karhausen [12]. Using the input parameters such as temperature, equivalent strain, and equivalent strain rate, material properties such as austenite grain size and recrystallized fraction are calculated based on constitutive equations. The microstructure of the component is divided into a recrystallized and a non-recrystallized fraction at each time step according to the Johnson–Mehl–Avrami-Kalmogorov (JMAK) equation. For process such as open-die forging, the results of the fast models can be used to calculate the microstructure evolution in the core fibre for the whole process. The temperature and equivalent strain models were validated by comparison with results from a validated FEM model [13], while the microstructure model was validated directly with experiments [14].

4 Process Design Using Fast Models

The pass schedule calculation was implemented by coupling the above-presented models for temperature, equivalent strain, and microstructure with a geometry-based pass schedule calculation in MATLAB [11, 15]. This enables manual designing of pass schedules according to part properties. The procedure for process design is as follows.

First, the user defines the general process parameters (bite ratio, final workpiece geometry, material, etc.) as well as starting and boundary conditions (e.g. starting geometry and temperature as well as maximum press force), as is the case for conventional pass schedule calculation programs. Second, the software generates a pass schedule considering all input variables and provides the process sequence on a time axis for the fast models. Third, the fast models calculate the temperature and equivalent strain along with the process, which enables the calculation of microstructure for each stroke. Lastly, the results including a pass schedule and additional information are presented to the user in the graphical user interface (GUI), and the user can decide to repeat this process with different settings to manually optimize the process. As the calculation times for a conventional forging process with 8 passes and 170 strokes are less than 3 s (Intel Xeon E3-1240 v6), many of such cycles are possible in a comparatively small timeframe.

5 Process Monitoring

The fast calculation times allow for the process parallel calculation of temperature, microstructure, and equivalent strain in the core fibre from live measurement data. For this purpose, the change in length per stroke and the spatial billet position are needed as input for the equivalent strain model. Additionally, the surface temperature

is needed to calibrate the temperature model during the process to achieve maximum accuracy for the microstructure calculation. The software can be used either to document the forging process or as a decision support system for the operator by providing additional information or as necessary input data for an assistance system. As a proof-of-concept, Rosenstock et al. [14] connected the fast models via TCIP/IP with a "LaCam" forge system and performed two industrial forging processes. The model results were validated with metallographical grain size measurements of the finished forged billets.

For measurement a high-resolution thermographic camera can also be chosen, as it allows providing information about the elongation via edge detection algorithms and additionally generates surface temperature data to adjust the temperature fields. The measurement results are used as input for the fast models and the results are presented to the user in a GUI seen in Fig. 1. With this, detection and documentation of process deviations are possible, which consequently provides the basis for adjusting the ongoing process if deviations occur.

6 Process Optimization

A process optimization in the context of an assistance system is possible with the presented process planning and monitoring methods, as shown in Fig. 2. In case of a deviation from the planned process sequence, the models could be used to adjust the pass schedule online due to their short calculation time. The fast models may be used to calculate the current properties of the part during the forging process and to compare them with the expected properties of the previously specified pass schedule. Subsequently, in the event of a deviation, e.g. due to an operating error, the pass schedule can be adapted so that the desired properties can still be achieved despite the deviation. It is, however, unknown which process deviation can be solved within a certain time limit. Therefore, in this paper, an optimization approach is investigated regarding solvability and computing times for different process deviations.

Like the manual optimization described above, it is possible to use optimization algorithms for process layout and online optimization. The optimization loop follows the basic structure shown in Fig. 3. The user must provide the optimizer with a starting point and an upper and lower limit for the input parameters. The input parameters are the furnace temperature, transport time from the furnace to press, waiting time between passes, bite ratios as well as height reductions, press speed, and tool temperature. The non-variable process variables, such as start and target geometry, must also be specified. Lastly, the user defines the boundary conditions, e.g. maximum press force or maximum grain size. After a pass schedule is calculated, the corresponding equivalent strain, temperature, and microstructure are determined. After one loop, the algorithm evaluates the process and restarts the calculation with a new set of input parameters if the termination condition, e.g. time limit or finding of an ideal parameter set, is not fulfilled.

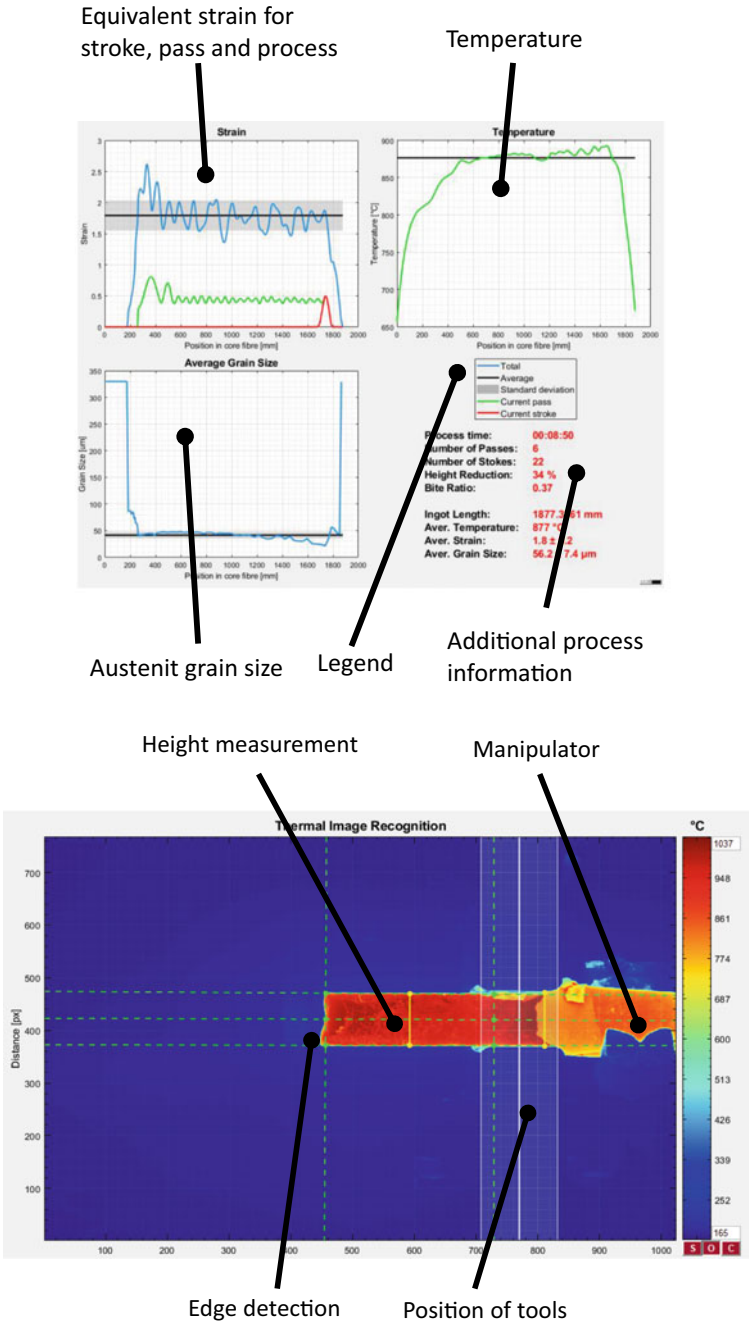


Fig. 1 GUI of the online monitor (top) and edge detection with a thermographic camera (bottom). (Color figure online)

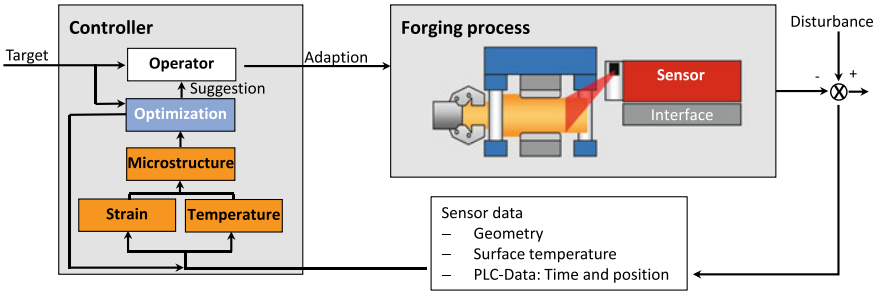


Fig. 2 Concept of an assistance system in open-die forging. (Color figure online)

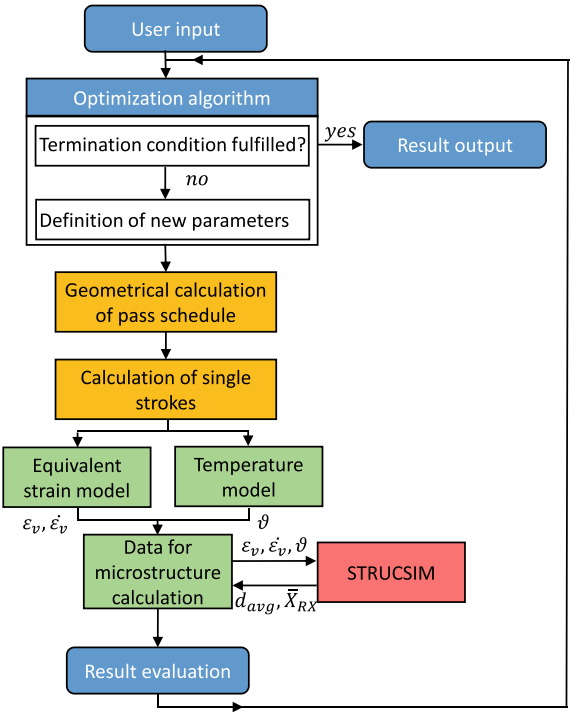


Fig. 3 Optimization loop for property-based pass schedule calculation. (Color figure online)

Since forging is an incremental forming process with up to many hundred forming steps, a single geometry can be achieved with an almost infinite number of process variants, which in turn leads to a very wide range of possible pass schedules. Additionally, the relationship between input parameters and their effect on the final workpiece properties is very complex, since a single parameter might influence the whole process. For example, the bite ratio b_w has an influence on the value as well as the homogeneity of the equivalent strain, press force, the recrystallization of the material, and process time. With a change in process time, the temperature changes

and influences the grain growth and recrystallization kinematic as well. Also, most input parameters such as height reduction, bite ratio, and press speed can be varied individually for each of them up to several hundred forming steps. Therefore, the optimization problem is characterized by the high complexity of open-die forging.

Due to the complex and unsteady transfer function between input and output parameters of the fast model, gradient-based optimization algorithms are not necessarily appropriate since they are fast, but often accept a local minimum as a solution too early. Therefore, the deterministic method "patternsearch" is used, which is integrated into MATLAB and offers a good compromise between solution speed and optimization quality. The method is based on the fact that with each iteration input variables are changed in the positive and negative directions by a step size within the upper and lower limits, and it is checked whether there is an improvement of the objective function. If this check is successful, the determined point is the starting point for the following iteration. If this iteration is not successful, the step size is reduced or increased. Termination conditions for the algorithm include a certain number of iterations, a time span, or if the search pattern falls below a specified minimum step size.

6.1 Definition of the Cost Function

Besides the basic structure of the optimization loop and the selection of the optimization algorithm, the result of the optimization is primarily dependent on the cost function, which was demonstrated for open-die forging in [14]. The cost function is divided into a target function, which assesses the quality of the result, and a penalty function, which punishes the violation of boundary conditions.

The selected targets and boundary conditions are listed in Table 1, where a low value symbolizes a better solution. The aim of the optimization is to achieve good and homogeneous part properties with respect to the microstructure and the equivalent strain as well as general process parameters, such as furnace temperature and process time. The individual terms of the target function are weighted so that parameters with low scalar values such as the equivalent strain are considered equally by the optimizer. The exact values of the different weights are chosen experience based on the user. The overall target function is the sum of the individual target terms. In contrast to a multiplicative operation, this has the advantage that converging a term towards zero does not result in the entire target function striving towards zero.

The possible solutions to the optimization problem are limited by the boundary conditions, which must not be violated. The boundary conditions are weighted with a pre-factor and an exponent. This ensures that the algorithm tries to keep the press limits, the forging temperature window, and the minimal workpiece properties to be achieved. Finally, the quality of the result is evaluated by the sum of the target and penalty function and depending on the result, the optimization is aborted or the next run of the optimization loop is started.

Table 1 Target values and boundary conditions

Target	Target term
High mean equivalent strain in the core fibre $\overline{\varepsilon}$	$c_1 = 1.000 \cdot \frac{1}{\overline{\varepsilon}}$
Low standard deviation of equivalent strain s_ε	$c_2 = 10.000 \cdot s_\varepsilon$
Low mean austenitic grain size in the core fibre $\overline{d}$ in µm	$c_3 = 10 \cdot \overline{d}$
Low standard deviation of austenitic grain size s_d in µm	$c_4 = 100 \cdot s_d$
Short process time t_S in s	$c_5 = t_S$
Low furnace temperature ϑ_F for the forging process depending on the allowed minimum temperature ϑ_{min} in °C	$c_6 = (\vartheta_F - \vartheta_{min})$
Boundary condition	*Penalty term*
Bite width b_w always smaller than tool width B in mm	$s_1 = \left(\sum_{i=1}^{n} \max\left\{\left(b_{w0,i} - B\right), 0\right\}\right)^4$
Surface temperature after forging $\vartheta_{n,O}$ larger than the allowed minimal forming temperature ϑ_{min} in °C	$s_2 = \max\left\{\left(\vartheta_{min} - \vartheta_{n,O}\right), 0\right\}^4$
Maximum ingot temperature during the whole process $\vartheta_{i,Feld}$ smaller than the allowed maximum forming temperature ϑ_{max} in °C	$s_3 = \max\left\{\left(\max\left\{\vartheta_{i,Feld}\right\} - \vartheta_{max}\right), 0\right\}^4$
Forging force F_i always smaller than maximum press force F_{max} in N	$s_4 = 10 \cdot \left(\sum_{i=1}^{n} \max\{(F_i - F_{max}), 0\}\right)^6$
Highest austenitic grain size after cooling d smaller than the maximal allowed grain size d_{max} in µm	$s_5 = 10 \cdot \max\{(\max(d) - d_{max}), 0\}^4$
Smallest equivalent strain ε larger than minimal allowed equivalent strain ε_{min}	$s_6 = 100 \cdot \max\{(\varepsilon_{min} - \min(\varepsilon)), 0\}^4$

6.2 Reference Process Without Deviations

At first, an industrial-scaled open-die forging process was numerically investigated. The chosen process parameters and boundary conditions are summarized in Table 2. As a material the most common tempering steel 42CrMo4/1.7225 was chosen due to its large industrial relevance. The material data, i.e. flow curve and microstructure model, were obtained by experiment, metallography and the remaining properties, such as specific heat capacity, conductivity, and Young's modulus were taken from the literature [16].

No time limit for the optimization algorithm was chosen since this reference pass schedule shown in Table 3 will be used to benchmark the quality of the adapted pass schedules, i.e. the quality of the reaction to process deviations. The maximum forging force limits the maximum available height reduction and bite ratio. Therefore, an average bite ratio of 0.32 and a height reduction of 12.2% were chosen by the algorithm. The total optimization time was 4.7 h.

Table 2 General parameters and boundary conditions for the investigated process

Ingot
Geometry of the ingot (h x w x l): 800 × 800 x 1200 mm
Target geometry (h x w x l): 470 × 470 x 3477 mm
Surrounding temperature: 25 °C
Emissivity: 0.85, Heat transfer coefficient to surrounding: 35 W/(m^2·K)
Forging dies
Assumed die temperature (constant): 300 °C; Press velocity: 100 mm/s
Heat transfer coefficient between forging dies and ingot: 4,000 W/(m^2·K)
Boundary Conditions
Die width: 2000 mm (Radius 200 mm on each side)
Assumed maximum forging force F_{max}: 25 MN
Assumed maximum ϑ_{max}/ minimum forging temperature ϑ_{min}: 1250/850 °C
Minimum allowed equivalent strain ε_{min}: 2.0
Maximum allowed grain size d_{max}: 175 µm

Table 3 Reference pass schedule

Input parameters	Pass									
	1	2	3	4	5	6	7	8	9	10
ε_h in %	12.4	12.1	12.4	12.1	12.3	12.0	12.5	12.2	12.4	12.1
s_{B_0}/h_0	0.31	0.33	0.31	0.33	0.30	0.33	0.30	0.32	0.31	0.33
Force F_i in MN	24.68	23.30	23.28	22.70	22.18	21.33	24.23	23.82	22.88	24.96

Using the target and penalty terms in Table 1, the cost values in Table 4 were calculated. The average equivalent strain is 2.10 with a very small standard deviation of 0.01. Similarly, the grain size is very homogeneously distributed with an average value of 165 µm and a standard deviation of 1.1 µm. The total process time without cooling is 872 s and the furnace temperature of 1034 °C was chosen. The total cost value q_{tot} is 3414 according to the cost function given in Table 1, where a lower value indicates a better optimization result.

All boundary conditions are fulfilled and lead to no penalty for the cost function, which has a high priority since any violation of the boundary conditions results in a very high penalty. A closer evaluation of the boundary conditions shows that each condition is only barely fulfilled. Therefore, the algorithm has very little freedom to adapt process parameters that are directly checked in the boundary conditions, e.g. the temperature.

Table 4 Results and corresponding cost values

	Result	Cost value
Boundary conditions s_1, s_2, s_3, and s_4		0
Mean equivalent strain $\overline{\varepsilon}$	2.10	$c_1 = 476.18$
Standard deviation of equivalent strain s_ε	0.01	$c_2 = 113.01$
Minimal equivalent strain $\varepsilon_{\min}$	2.06	$s_6 = 0$
Mean austenitic grain size $\overline{d}$ in µm	165	$c_3 = 1655.51$
Standard deviation of austenitic grain size s_d in µm	1.1	$c_4 = 113.91$
Maximal austenitic grain size $d_{\max}$ in µm	167	$s_5 = 0$
Process time t_S in s	871.6	$c_5 = 871.60$
Furnace temperature ϑ_F in °C	1034	$c_6 = 183.96$
Total target $\sum c_i$		3414
Total penalty $\sum s_i$		0

6.3 Different Process Deviations

The presented vision of an assistance system for open-die forging can observe the process deviations online during the process. There are many different possible deviations that need to be handled individually in the given timeframe. This means, however, that the assistant system must be able to differentiate the various deviations and chose appropriate optimization settings for each one. Therefore, three different process deviations of the above-optimized process are examined:

(a) Due to an error in one of the hydraulic pumps, the maximum press force is reduced by 20%. The error is known a few hours in advance and the optimizer has time for several thousand iterations. ($F_{\max} = 20$ MN, maximum calculation time: 4 h.)
(b) The manipulator control system crashes and it takes 20 min to fix the problem while the workpiece is already taken out of the furnace. (Transport time + 1200 s, maximum calculation time: 20 min.)
(c) The press operator chooses a height reduction of 8.4% in the third pass instead of 12.4%. The new pass schedule should be calculated as fast as possible since it is unrealistic to stop the process for a significant time. ($\varepsilon_{h,\text{pass3}} = 8.4\%$, calculation time: fastest possible.)

In Scenario (a), the above-presented optimizer can be used with an additional termination condition after 4 h of computing time. The results of the newly started optimization are shown in Table 5. The lower press force of maximal 20 MN is achieved by reducing the average bite ratio from 0.32 to 0.26. As a result, process time increases significantly, and all process objectives, such as minimum grain size, can be met. The calculation time is 3.9 h and the evaluation of the cost function is 3724, which is approx. 10% worse than in the reference process.

Table 5 Results and corresponding cost values for Scenario (a) and (b)

	Scenario (a)		Scenario (b)	
	Result	Cost value	Result	Cost value
Boundary conditions s_1, s_2, s_3 and s_4		0		1.87×10^6
Mean equivalent strain $\overline{\varepsilon}$	2.09	$c_1 = 479.25$	2.22	$c_1 = 450.99$
Standard deviation of equivalent strain s_ε	0.01	$c_2 = 141.53$	0.01	$c_2 = 104.65$
Minimal equivalent strain $\varepsilon_{\min}$	2.04	$s_6 = 0$	2.16	$s_6 = 0$
Mean austenitic grain size $\overline{d}$ in µm	168	$c_3 = 1679.49$	138	$c_3 = 1383.63$
Standard deviation of austenitic grain size s_d in µm	2.9	$c_4 = 285.71$	5.34	$c_4 = 533.91$
Maximal austenitic grain size $d_{\max}$ in µm	172	$s_5 = 0$	142	$s_5 = 0$
Process time t_S in s	942.4	$c_5 = 942.4$	1086	$c_5 = 1086.4$
Furnace temperature ϑ_F in °C	1045	$c_6 = 195.22$	1034	$c_6 = 183.96$
Total target $\sum c_i$		3724		3744
Total penalty $\sum s_i$		0		1.87×10^6

In Scenario (b), the optimization does not achieve a meaningful result in the short computing time. If the optimization is cancelled after 20 min, most of the boundary condition is not fulfilled and the total cost value is above 1×10^9. Therefore, the optimization scheme seen in Fig. 3 is slightly altered. In order to reduce the computation time, the optimization is first performed without calculating the temperature and microstructure. This leads to a pass schedule with a high and very homogeneous strain distribution in less than 180 s. This pass schedule is then used as a starting point for further optimization so that the optimization of temperature and microstructure is completed after 16.4 min.

When analysing the results in Table 5, it is noticeable that the achieved equivalent strain is larger and the grain size is smaller. The small grain size can be explained by the lower grain growth of the cooled billet. The equivalent strain in the core increases due to the pronounced temperature gradient in the forging part. The areas close to the surface have higher flow stress so that in comparison more deformation is introduced into the hotter and softer core. Two additional passes are required for forging, as the force limit of the press is reached due to the lower temperature. The total cost value without boundary conditions is 3744, which is slightly worse than the result without deviation.

Although one boundary condition is unfulfilled, the minimum surface temperature of 813 °C is lower than the lowest permissible forging temperature. This deviation leads to a penalty of 1.87×10^6. Overall, a forging process with the same results after this deviation was not found, and the user must decide whether a deviation from the minimum forging temperature of up to 37 °C in 4.4% of the component is acceptable or whether a new heat is necessary.

Table 6 Results and corresponding target values for Scenario (c) with 211 s and 883 s calculation time

	Scenario (c)—fast		Scenario (c)—slow	
	Result	Cost value	Result	Cost value
Boundary conditions s_1, s_2, s_3 and s_4		0		0
Mean equivalent strain $\overline{\varepsilon}$	2.08	c_1= 480.77	2.12	c_1= 471.83
Standard deviation of equivalent strain s_ε	0.01	c_2= 132.83	0.02	c_2= 212.55
Minimal equivalent strain $\varepsilon_{\min}$	2.03	s_6= 0	2.05	s_6= 0
Mean austenitic grain size $\overline{d}$ in µm	187	c_3= 1865.05	170	c_3= 1704.17
Standard deviation of austenitic grain size s_d in µm	2.15	c_4= 215.46	3.91	c_4= 390.81
Maximal austenitic grain size $d_{\max}$ in µm	189	s_5= 384,160	175	s_5= 0
Process time t_S in s	894.6	c_5= 894.61	890.3	c_5= 890.32
Furnace temperature ϑ_F in °C	1034	c_6= 183.96	1034	c_6= 183.96
Total target $\sum c_i$		3773		3854
Total penalty $\sum s_i$		387,933		0

Lastly, the optimization results of Scenario (c) with two optimization schemes with different calculation times are presented in Table 6. The first optimization was completed in 211 s using the same method for the speed up as in Scenario (b). The significantly shorter calculation time results from more stringent termination conditions and the reduced number of degrees of freedom since the start temperature and the first three strokes are already set. The optimization is successful without consideration of the boundary conditions with a cost value of 3773, but the desired grain size was not achieved and thus the disturbance could not be compensated, including the penalty term for the too height average austenite grain size the total value of the cost function is 387,933.

The failure of the previous optimization is due to the short optimization time limit. In an optimization time of 211 s, 83 full pass schedules including part properties can be calculated, which is too little to explore the complex optimization area. Only after a computation time of 883 s, a solution was found while considering all boundary conditions, which is rated at 3854 by the cost function. The results show that the chosen classical optimizer is suitable to find solutions for different process deviations. However, the computing time is still too long to react to deviations for short open-die forging processes within the concept of an assistance system, as even though

fast models are used to calculate workpiece properties, hundreds of iterations are necessary to achieve satisfying optimizations results.

7 Conclusion

The following conclusion can be drawn regarding optimization of open-die forging using fast models for strain, temperature, and grain size in the context of an assistance system:

- A cost function on the basis of process and optimization experience was developed, which allows evaluating the forging process under consideration of boundary conditions.
- The presented optimization method enables pass schedule modification in reaction to process deviations while keeping previously defined goals such as grain size or minimum equivalent strain.
- Optimization time of 15 min for industrial-scale open-die forging processes are achievable using classical optimization algorithms.

Acknowledgments This work was funded by the Deutsche Forschungsgemeinschaft (DFG, German Research Foundation) under Germany's Excellence Strategy—EXC-2023 Internet of Production—390621612.

References

1. Siemer E (1987) Qualitätsoptimierende Prozeßsteuerung des Reckschmiedens. Düsseldorf. Stahleisen. (also Ph.D thesis, RWTH Aachen)
2. Grisse HJ, Betz H, Dango R (1997) Computer optimized integrated forging. Park U (Pub.). In: 13th international forgemasters meeting: advances in heavy forgings. Pusan. Korea
3. Heischeid C, Betz H, Dango R (2000) Computerised optimisation of the forging on a 3300 tons open die forging press. Verein Deutscher Eisenhüttenleute (Pub.). In: 14th international forgemasters meeting. Wiesbaden. p 132–136
4. Elbadan AM (2004) Adaptive scheduling for an incremental flexible forging cell. Dissertation McMaster University, Hamilton, Canada 30(2): 102–108
5. Kirchhoff S, Lamm R, Müller N, Rech R (2003) Laser measurement on large open die forging (Lacam forge), steel castings and forgings Association of Japan (Pub.). In: 15th international forgemasters meeting. Kobe. Japan
6. Kirchhoff S (2007) Method and apparatus for optimizing forging prosesses. Patent US 7,281,402 B2
7. Pelster H, Borowikow A (2012) Microstructure simulation in forging. Verein Deutscher Eisenhüttenleute (Pub.). In: 1st international conference on ingot casting rolling and forging (ICRF). Aachen
8. Paukert R (1983) Investigations into metal flow in radial-forging. CIRP Ann Manuf Technol 32:211–214. https://doi.org/10.1016/S0007-8506(07)63392-7

9. Rosenstock D, Recker D, Hirt G (2014) Online analysis of cogging processes—evaluation of the equivalent strain. Temperature and grain size distribution. Steel castings and forgings Association of Japan (Pub.). In: 19th international forgemasters meeting. Tokyo Bay Area. Japan. p 507–512
10. Stenzhorn F (1982) Beitrag zur empirisch-theoretischen Vorausplanung des Freiformschmiedens großer Blöcke mit Hohlräumen. PhD thesis. RWTH Aachen
11. Recker D, Franzke M, Hirt G (2011) Fast models for online-optimization during open die forging. CIRP Ann Manuf Technol 60:295–298. https://doi.org/10.1016/j.cirp.2011.03.142
12. Karhausen K, Kopp R (1992) Model for intergrated process and microstructure simulation in hot forming. Steel Res 63(6): 247–256
13. Wolfgarten M, Rosenstock D, Rudolph F, Hirt G (2019) New approach for the optimization of pass-schedules in open-die forging. Int J Mater Form 12(6):973–983. https://doi.org/10.1007/s12289-019-01471-w
14. Rosenstock D, Recker D, Hirt G, Steingeißer K-J, Rech R, Gehrmann B, Lamm R (2013) Application of fast calculation model for the process monitoring of open die forging processes. Key Eng Mater 554–557:248–263. https://doi.org/10.4028/www.scientific.net/KEM.554-557.248
15. Wolfgarten M, Rudolph F, Hirt G (2019) Application of fast models for equivalent strain, temperature and microstructure in open-die forging. In: Metec & 4th ESTAD 2019. European steel technology and application days. Düsseldorf. Germany
16. Spittel M, Spittel T (2009) Landolt-Börnstein—Group VIII advanced materials and technologies. Metal forming data of ferrous alloys—deformation behavior. Steel symbol/number: 42CrMo4/1.7225. https://doi.org/10.1007/978-3-540-44760-3

General Step Reduction and Enlargement Method for Knowledge-Based Process Planning of Totally Non-axisymmetric Forged Products with Blanking and Punching



Masanobu Umeda, Yuji Mure, Keiichi Katamine, and Kazuya Matsunaga

Abstract A forging process planning method, including blanking and punching, termed General Step Reduction and Enlargement (GeneSteR+E), is discussed for cold- and warm-forged products. It is applicable to non-axisymmetric forged products that consist totally of non-axisymmetric shape elements and can generate multiple process plans without relying on design cases. The shape of a forged product is split into outer and inner shapes, which are then split into axisymmetric and non-axisymmetric shape representation units termed basic elements (BEs) according to shape separation rules. Process plans are generated in reverse order from a final forged product by applying shape transformation rules that reduce the number of steps between BEs until a billet (or a blank) is obtained. The shape transformation rules are defined not only for forging, but also blanking and punching. An experimental knowledge base was implemented and applied to several non-axisymmetric forged products, such as an electrical connector. The results show that the GeneSteR+E method is applicable to the design of forging processes including blanking and punching of totally non-axisymmetric products and can generate satisfactory process plans comparable to those developed by an experienced engineer.

M. Umeda (✉) · K. Katamine
Kyushu Institute of Technology, 680-4 Kawazu, Iizuka, Fukuoka 820-8502, Japan
e-mail: umerin@ci.kyutech.ac.jp

K. Katamine
e-mail: katamine@ci.kyutech.ac.jp

Y. Mure
Kagoshima Prefectural Institute of Industrial Technology, 1445-1, Hayato-Oda, Kirishima 899-5105, Japan
e-mail: mure@kagoshima-it.go.jp

K. Matsunaga
Kyushu Institute of Technology, Komatsu Ltd, 3-25-1, Shinomiya, Hiratsuka, Kanagawa 254-0014, Japan
e-mail: kazuya_matsunaga@global.komatsu

© The Minerals, Metals & Materials Society 2021

G. Daehn et al. (eds.), *Forming the Future*, The Minerals, Metals & Materials Series,
https://doi.org/10.1007/978-3-030-75381-8_97

1 Introduction

Process planning for cold- and warm-forged products involves generating a process to form a final product from a billet (or a blank) using forging dies. It significantly affects the quality, cost, and delivery of the forged products. The planning is time-consuming and difficult, even for experienced engineers, because extensive knowledge and experience in plastic forming, forging, blanking, and punching are required. Improvements in the efficiency and quality of the process planning are thus important issues in the design and manufacturing of forged products.

Traditional rule-based approaches [1, 2, 4, 6, 7, 11] and case-based approaches [3, 5, 8] have been proposed for forging process planning. Most are limited to products similar to design cases or are mainly axisymmetric products. In contrast, the General Step Reduction (GeneSteR) method [9] for forging processes does not rely on design cases and is applicable to non-axisymmetric cold- and warm-forged products, such as hexagon-head bolts and universal joint yokes, that consist of axisymmetric and non-axisymmetric shape elements. However, the GeneSteR method is still limited to partially non-axisymmetric forged products that contain axisymmetric shape elements and is not applicable to totally non-axisymmetric products that consist of only non-axisymmetric shape elements.

In this paper, an extension of the GeneSteR method, termed General Step Reduction and Enlargement (GeneSteR+E), is shown to be applicable to totally non-axisymmetric cold- and warm-forged products, such as USB Type-C connectors, without losing GeneSteR generality. In addition, the GeneSteR+E method can support the process planning for blanking and punching, which are often used with forging. To clearly distinguish a non-axisymmetric forged product that consists of only non-axisymmetric shape elements from one that contains axisymmetric shape elements, this paper uses the terms ‘totally’ with respect to the former and ‘partially’ with respect to the latter.

The model representation of totally non-axisymmetric forged products in the GeneSteR+E method is described in Sect. 2. Essential ideas and details to generate process plans via the GeneSteR+E method are described in Sect. 3, and the design procedure for forging process plans is described in Sect. 4. The experimental results applied to several forged products using an experimental knowledge base that implements the GeneSteR+E method are shown in Sect. 5.

2 Model Representation of Forged Products

2.1 Basic Representation Unit of Forged Products

The GeneSteR+E method represents the shape of a forged product using basic shape representation units termed basic elements (BEs), as in the GeneSteR method.

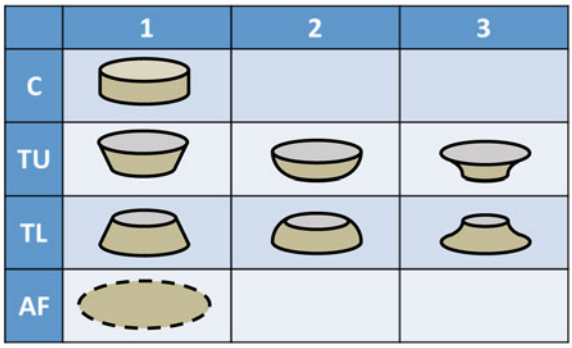


Fig. 1 Basic elements (BEs) for representing the shape of a forged product using shape representation unitsd. (Color figure online)

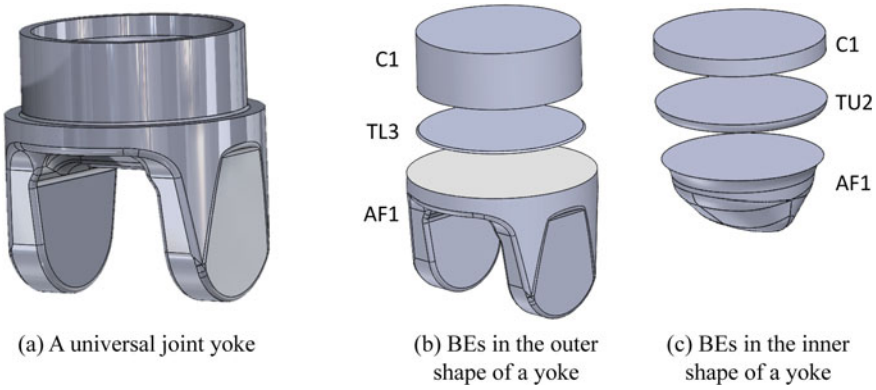


Fig. 2 Example of a partially non-axisymmetric universal joint yoke and its shape representations using BEs in the GeneSteR method. (Color figure online)

Figure 1 lists BEs, where row C and column 1 in the table is denoted C1. C2 defined in [9] was removed because it can be represented by using the pair TU2 and TL2.

Seven of the BEs, such as C1, have strictly defined axisymmetric shapes, such as a cylinder, whereas AF1 has no strictly defined shape and represents any non-axisymmetric shape. BEs have attributes characterizing their geometric outlines, with precise shapes specified by three-dimensional geometric models of a computer-aided design system.

The shape of a forged product is split into outer and inner shapes, which are then split into BEs by vertical planes to a forming direction. The design object model of a forged product represents its outer and inner shapes using two respective series of BEs. Figure 2 is an example of a universal joint yoke, that is partially non-axisymmetric, and its shape representations using BEs. In the GeneSteR method, successive non-axisymmetric shape elements in a forged product are represented using a single non-axisymmetric AF1.

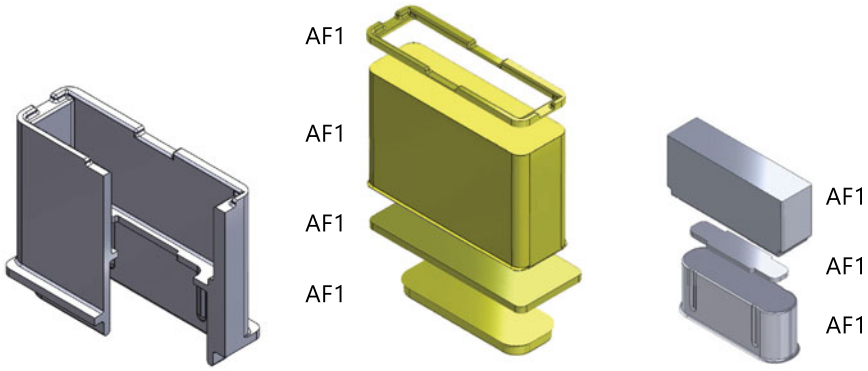
2.2 *Representation of Totally Non-Axisymmetric Forged Products*

The GeneSteR method represents successive non-axisymmetric shape elements using a single AF1. Therefore, a totally non-axisymmetric forged product, such as an electrical connector shown in Fig. 3a, that contains no axisymmetric shape elements, is represented with a single AF1. In such a case, a process plan that consists of only a single forming step is generated, as described in Sect. 3.1, and is generally unrealistic due to design constraints, such as the limit of the forming load.

The GeneSteR+E method introduces new shape separation rules (SRs) to split successive non-axisymmetric shape elements of a forged product into several non-axisymmetric AF1s. The SRs are as follows:

SR1 A plane splitting a forged product must be vertical to a forming direction.
SR2 A plane must split a forged product into exactly two parts.
SR3 A plane must be located at inflection points of the second-order differential function of a cross section.
SR4 A plane must be located at discontinuous points of a cross section function.

Rule SR2 prevents a BE from being separated into isolated parts, as in the universal joint yoke that has a projecting joint structure at the bottom. The shape separation is essential for the process planning of a totally non-axisymmetric forged product like the electrical connector. Figure 3b, c, respectively, shows BEs of the outer and inner shapes of the connector.



(a) An electrical connector

(b) BEs in the outer shape of an electrical connector

(c) BEs in the inner shape of an electrical connector

Fig. 3 A totally non-axisymmetric electrical connector and its outer and inner shape representations using BEs. (Color figure online)

3 General Step Reduction and Enlargement Method

3.1 Process Plan Generation by Step Reduction

As in the GeneSteR method, forged products, billets, and intermediate forged products in a GeneSteR+E process plan are all represented by BEs. Reversed forging process plans are generated by reducing the number of steps between successive BEs until a cylindrical or square billet is obtained. Step reduction is performed by simple step-by-step shape transformations over the BEs. Figure 4 illustrates a shape transformation and its corresponding forming step as the reverse operation of the shape transformation.

A forging process plan is generated by the following procedure. Starting from the forged product, one of the BEs of a post-formed product is selected as a key, indicated in red in Fig. 4. Then, one of the applicable shape transformation rules described in Sect. 3.2 is applied to the key. Several BEs are then selected as targets, which are indicated in blue in Fig. 4, according to an applied rule. The shape of a pre-formed product is created by substituting targets of a post-formed product with new BEs according to an applied rule. Because there are many candidates for a key, an applicable shape transformation rule, and targets, multiple process plans can be generated by an exhaustive search for them. In other words, a process plan consisting of a single forming step is generated if a forged product is represented using a single AF1.

3.2 Shape Transformation Rules

The shape transformation from post-formed to pre-formed products occurs according to simple rules defined for the outer and inner shapes. Figures 5 and 6 illustrate the shape transformation rules for the outer and inner shapes, respectively, and are extensions of those defined in the GeneSteR method.

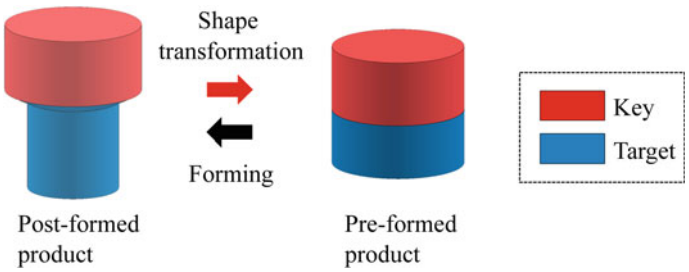


Fig. 4 Example of a shape transformation and the forming step of a process plan. (Color figure online)

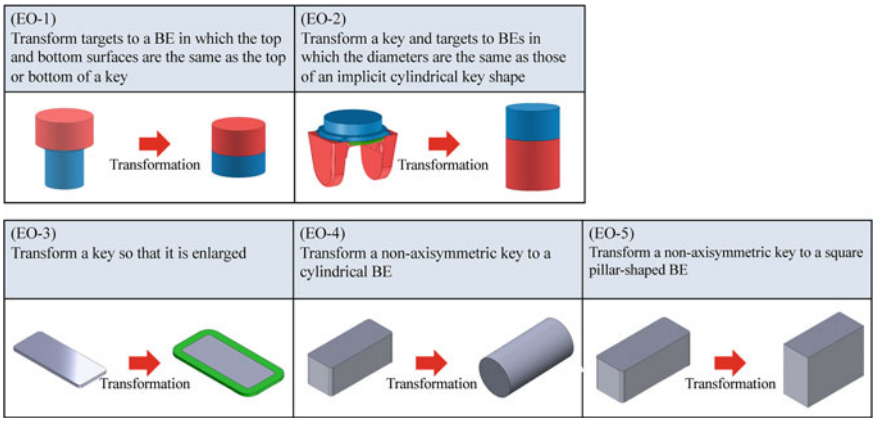


Fig. 5 Shape transformation rules for the outer shapes. (Color figure online)

Rule EO-1 for the outer shape adjusts the top and bottom surfaces of targets to the top or bottom surface of a key, which corresponds to forming via upsetting or forward or backward extrusion. Rule EO-2 adjusts the diameters of a key and targets to that of a cylindrical shape included implicitly in the key. EO-1 and EO-2 are similar to those defined for the GeneSteR method, whereas rules EO-3, EO-4, and EO-5 are new for the GeneSteR+E method. Rule EO-3 enlarges a key to a certain volume, which corresponds to cutting an edge off via blanking. Rule EO-4 restores to a cylindrical billet that is pressed in the direction perpendicular to its rotation axis, while rule EO-5 restores to a square billet.

Similarly, rule EI-1 for the inner shape is to adjust the top and bottom surfaces of targets to the top or bottom surfaces of a key, which corresponds to a forming via forward or backward extrusion. EI-1 and EI-2 are similar to those defined for the GeneSteR method, whereas, rules EI-4, EI-5, and EI-6 are new for the GeneSteR+E method. For example, rule EI-4 fills in a hole, which corresponds to cutting a hole via punching.

Rules O-1 and O-2 defined for the GeneSteR method are unified in rule EO-1 because the O-1 and O-2 geometric transformations are the same except for the surface shapes from an axisymmetric point of view. However, rule O-4 for design constraints regarding the limit of the forming load was eliminated because design constraints are considered in a later design phase as discussed in Sect. 4. A similar rule restructuring was also performed for the inner shapes.

4 Design Procedure for Forging Process Plans

Design constraints, such as the limit of the forming load, are not considered while transforming a shape according to the rules; therefore, some generated process plans may not be applicable to actual production. In addition, the forming steps in generated

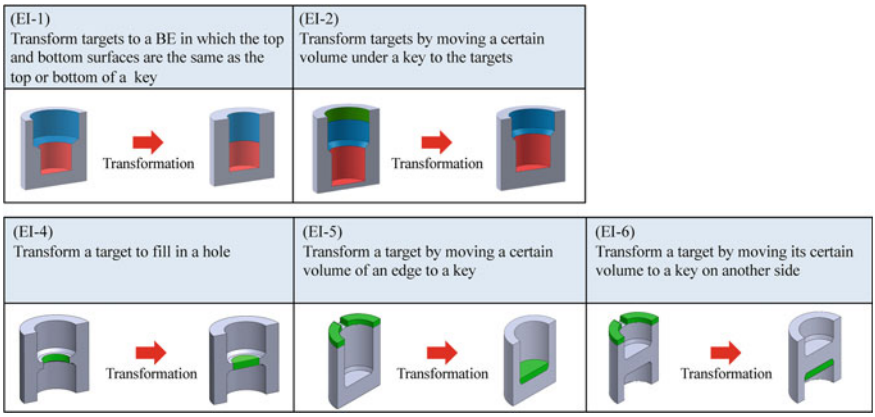


Fig. 6 Shape transformation rules for the inner shapes. (Color figure online)

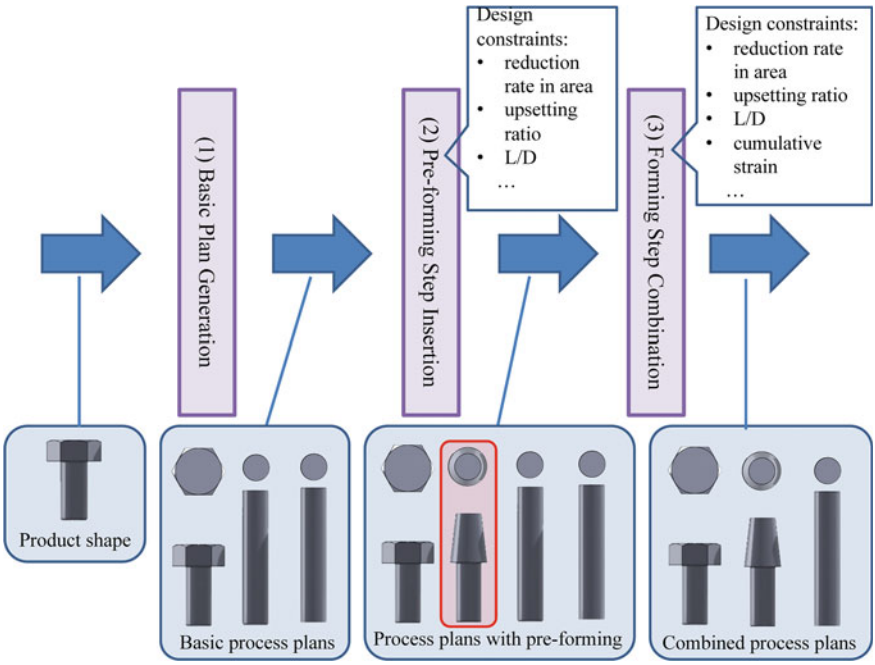


Fig. 7 Design procedure based on the GeneSteR+E method for forging process plans. (Color figure online)

plans may become too long to be practical because the rules are simple and the transformation is performed step by step. Therefore, the design procedure of the forging process is organized into three phases as shown in Fig. 7.

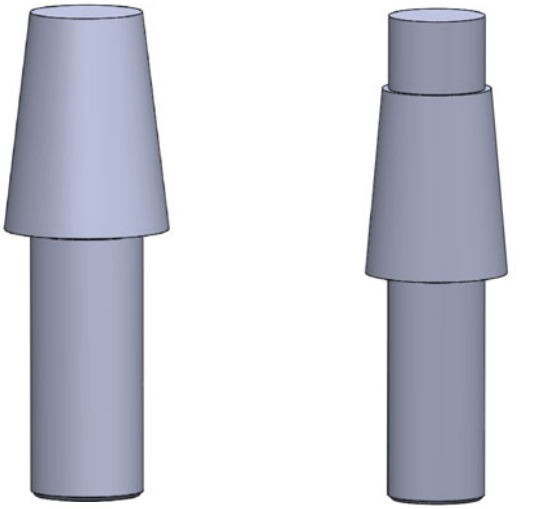


Fig. 8 Corn and bell shapes for preventing work material from being buckled by upsetting. (Color figure online)

First, basic process plans are generated by applying the GeneSteR+E method to a final forged product. The process plans generated in this phase may contain impractical forming steps because design constraints are ignored. Therefore, pre-forming steps are inserted into the plans in the second phase, considering design constraints, such as reduction rate in area, upsetting ratio, and L/D. Corn and bell shapes shown in Fig. 8 can be candidates for pre-forming steps inserted into process plans to prevent work material from being buckled via upsetting. Rule O-4 in the GeneSteR method was defined to prevent increases in the forming load by partly extruding work material forward and is realized in this phase as described in Sect. 3.2. Finally, multiple forming steps are combined into one by considering design constraints related to large shape changes in the third phase. The reduction in the number of forming steps will reduce production costs and lead time.

Because the shape transformation and the design constraints can be handled separately, unlike with the GeneSteR method, the management of the design knowledge becomes easier.

5 System Implementation and Experimental Results

The shape transformation rules are realized by using a set of basic shape operation functions that manipulate three-dimensional geometric models in SolidWorks through its OLE interface. New shape operation functions `CreateCuboid` and `ExpandByVolume` are added to the function set given in [9] for the new shape

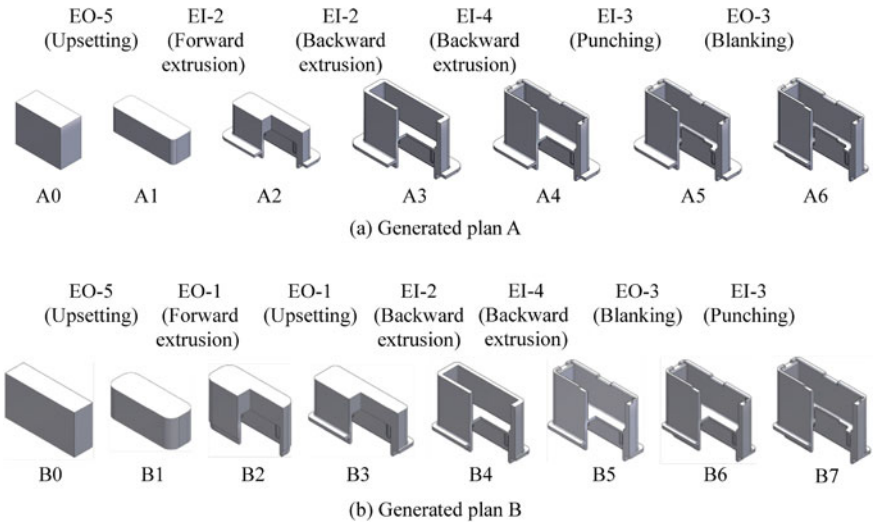


Fig. 9 Examples of generated process plans for an electrical connector. (Color figure online)

transformation rules. An experimental knowledge base, which implements the basic plan generation phase based on the GeneSteR+E method, is developed in the DSP knowledge representation language [10] using these functions.

The knowledge base was applied to cold- or warm-forged products, such as a hexagon-head bolt, a universal joint yoke, and an electrical connector. In the latter case, 162 process plans were generated in 6.55 h. Figure 9 shows two sample process plans generated via the knowledge base, while Fig. 10 shows one designed by an experienced engineer.

Plan A in Fig. 9 is similar to that of the engineer if it is modified by the next design phases described in Sect. 4. That is, the pre-forming step P2 is inserted between A2 and A3 for plastic deformability in the pre-forming step insertion phase, and the forming steps from A2 to P2 and from A3 to A4 are combined into single step to reduce the number of steps in the forming step combination phase. These results show that the GeneSteR+E method is applicable to forging process design, including blanking and punching, of totally non-axisymmetric products and can generate satisfactory process plans comparable to those by an experienced engineer. The execution time could be improved.

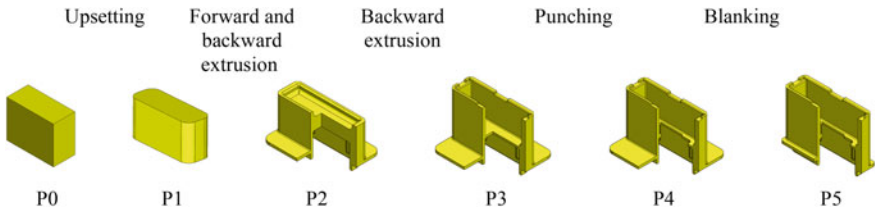


Fig. 10 Example of a process plan designed by an experienced engineer for an electrical connector. (Color figure online)

6 Conclusions and Future Work

This paper proposes a process planning method termed GeneSteR+E for totally non-axisymmetric cold- and warm-forged products that consist of only non-axisymmetric-shaped elements. It can generate plans for forging processes, including blanking and punching, for a forged product without relying on design cases.

An experimental knowledge base was implemented based on the GeneSteR+E method and applied to several forged products. The experimental results for an electrical connector had 162 generated process plans within 6.55 h. The generated plans included a plan comparable to one designed by an experienced engineer if the pre-forming step insertion and the forming step combination were applied to the comparable plan. These results show that GeneSteR+E is applicable to forging process design, including blanking and punching, of totally non-axisymmetric forged products.

The basic plan generation phase based on the GeneSteR+E method does not take care of design constraints; therefore, they have to be considered in the pre-forming step insertion and the forming step combination phases to produce deformable process plans. However, such design constraints have not been well systematized for non-axisymmetric forged products. Further research on this issue is essential to develop a practical knowledge base for forging process planning.

Acknowledgments The authors are grateful to Mr.Tateki Hamasaki who contributed to the establishment and evaluation of the GeneSteR+E method in the early research stage. This research was supported by the Strategic Core Technology Advancement Program by the Ministry of Economy, Trade and Industry, Japan.

References

1. Kim HS, Im YT (1999) An expert system for cold forging process design based on a depth-first search. J Mater Process Technol 95:262–274
2. Kumar S, Singh R (2004) A low cost knowledge base system framework for progressive die design. J Mater Process Technol 153:958–964

3. Lange K, Du G (1989) A formal approach to designing forming sequences for cold forging. Trans NAMRI/SME 17–22
4. Mahmood T, Lengyel B, Husband TM (1990) Expert system for process planning in the cold forging of steel. Expert Plan Syst 322:141–146
5. Numthong C, Butdee S (2012) The knowledge based system for forging process design based on case-based reasoning and finite element method. Asian Int J Sci Technol Prod Manuf Eng 5(2):45–54
6. Sevenler K, Raghupathi PS, Altan T (1987) Forming-sequence design for multistage cold forging. J Mech Working Technol 14:121–135
7. Takata O, Mure Y, Nakashima Y, Ogawa M, Umeda M, Nagasawa I (2005) Knowledge-based system for process planning and die configuration design in cold forging. In: Proceedings of the 8th international conference on technology of plasticity, p 8
8. Takata O, Nakanishi K, Yamazaki T (1990) Forming-sequence design expert system for multi-stage cold forging: forest-d. In: Proceedings of Pacific Rim international conference on artificial intelligence'90, pp 101–113
9. Umeda M, Mure Y, Katamine K, Kawahigashi K (2017) General step reduction method for knowledge-based process planning of non-axisymmetrical forged product. In: Proceedings of the 12th international conference on the technology of plasticity (ICTP 2017), pp 448–453
10. Umeda M, Nagasawa I, Higuchi T (1996) The elements of programming style in design calculations. In: Proceedings of the ninth international conference on industrial and engineering applications of artificial intelligence and expert systems, pp 77–86
11. Xuewen C, Siyu Z, Jun C, Xueyu R (2005) Research of knowledge-based hammer forging design support system. Int J Adv Manuf Technol 27:25–32

Investigation of Failure Mechanisms of Cemented Carbide Fine Blanking Punches by Means of Process Forces and Acoustic Emission



Herman Voigts, Rafael Hild, Andreas Feuerhack, and Thomas Bergs

Abstract Due to the processing of high-strength materials in fine blanking, the lifetime of conventional high-speed steel punches decreases rapidly. Materials with higher wear resistance and compressive strength, such as cemented carbide, are investigated for use in fine blanking processes. However, cemented carbide punches often fracture during the stripping off phase due to the combined tensile and flexural stress collective. The understanding of fracture mechanisms and subsequent fracture prevention supports the application of cemented carbides. The fracture mechanisms during stripping off are mostly unknown. The objective is to identify fracture mechanisms of cemented carbide punches. The fracture mechanism of cemented carbide punches was metrologically monitored by means of acoustic emission (AE) and process forces. The fracture pattern was analyzed related to the measured signals. In order to interpret the AE signal, basic process analyses were performed. Subsequently, a punch fracture of cemented carbide was provoked with the high-strength steel 1.8974. Cemented carbide punches tend to fracture during stripping off as a cause of asymmetrical interactions with the scrap web.

Keywords Fine blanking · Cemented carbide · Acoustic emission · Stripping off

1 Introduction

1.1 Initial Situation

Ecological demands require emissions reduction in the mobility sector. As a result, the automotive industry faces challenges in terms of the application of lightweight solutions in structural and functional components and assemblies. Compared to 2016, the worldwide market volume for lightweight applications is expected to grow from €80 bn to €140 bn in 2020 [1]. In the field of metal processing, lightweight design

H. Voigts (✉) · R. Hild · A. Feuerhack · T. Bergs
Laboratory for Machine Tools and Production Engineering (WZL), RWTH Aachen University, Aachen, Germany
e-mail: H.Voigts@wzl.rwth-aachen.de

© The Minerals, Metals & Materials Society 2021

G. Daehn et al. (eds.), *Forming the Future*, The Minerals, Metals & Materials Series,
https://doi.org/10.1007/978-3-030-75381-8_98

means integration of several functions in one part and structural lightweight design. Lightweight design leads to complex geometry and fine details of the blanked part as well as the processing of lightweight steel with high strength. Fine blanking is a highly productive manufacturing technology used for the manufacture of precise, functional lightweight system parts, e.g., for interior, mechanical, or safety components in combustion and electrical vehicles [2]. Both complex geometry with fine details and the processing of high-strength materials lead to high tool loads with local stress concentration in the punch. High local stresses lead to extensive wear or even plastification on the cutting edge of the punch. Tool failures occur suddenly due to chipping or by increasing abrasive and adhesive wear. Tool materials with higher compressive strength and wear resistance, such as cemented carbide grades, have a high potential for fine blanking of high-strength sheet metal. Nowadays, cemented carbides are successfully applied as tool materials for cutting, forming [3], and machining tools [4], where the high hardness, compressive strength, and wear resistance allow an improvement with respect to conventional tool steels.

1.2 State-of-the-art

In blanking of materials of higher strength and ductility, due to the hydrostatic stress state in the shearing zone, the springback of the sheet metal after the blanking phase causes high clamping forces [9]. The stripping force of high-strength TRIP steel with an ultimate tensile strength (UTS) of 850 MPa increases about the factor 10 compared to a bake hardening steel with a UTS of 320 MPa. The clamping mechanisms of the scrap web on the punch and the stripping force at fine blanking with cemented carbide punches have been investigated using a validated FE model [10]. Cemented carbide punches often fracture during fine blanking of high-strength steels in the stripping off phase. The scrap web clamps on the punch due to elastic springback. An analytic model for the description of the clamping and the stripping force was derived based on the approach of the shaft-hub connection theory. The stripping force increases for high UTS, elasticity, and sheet thickness. The UTS is interdependent on sheet thickness due to dissipated heat during shearing. The investigation was done for circular geometries.

AE has been used for fine blanking process analysis. Evaluation algorithms and signal characteristics in a three-step process, consisting of pre-punching, embossing, fine blanking, and upsetting have been investigated [11]. It was found that very complex interdependencies exist between the individual processes so that a direct correlation between a given signal and product quality is not immediately possible. Effects of workpiece errors on acoustic signals are found to be very small. Nevertheless, with a well-designed application, a process monitoring of the fine blanking process concerning the product quality based on the relative changing of acoustic signals is possible. Investigations for AE analysis of workpiece quality in fine blanking processes with compound dies [12] as well as progressive dies [13] were

published. AE has also been used for the detection of breakages as well as the chipping of cutting tools during machining [14]. Later, AE was used for the detection of catastrophic tool failure of drilling and cutting tools using root mean square (RMS) signals [15]. Tool fracture generates a significant burst of the measured AE signal.

A deep understanding of the interactions between the scrap web and the punch during stripping off can be used for the process design with a balanced load collective and compensated harmful stresses. This will allow for the application of cemented carbide for challenging processes and the processing of high-strength steels.

1.3 Objective

Fracture of the cemented carbide punch during stripping off is a cause of the interaction between the punch and the scrap web. The clamping of the scrap web on the punch as a result of elastic springback has been investigated. Further influence quantities from the cutting line geometry, geometric shape of the scrap web regarding the die roll, and stiffness of the scrap web are not comprehensively researched yet.

The main objective is to find the cause and effect relations between the scrap web and the punch during the stripping off phase in order to explain fracture mechanisms of cemented carbide punches. The evolution of fracture is analyzed using AE and force signals. The course of fracture is then explained with respect to the strip layout and properties of the sheared surface of the scrap web.

1.4 Methodology

AE and force analyses were conducted in order to identify the cause and effect interactions between the scrap web and cemented carbide punches during stripping off. Using a standard analogy geometry in a 2-up fine blanking tool, test strokes with a lower grade sheet metal were conducted. The characteristic of AE and punch force signal was analyzed for standard process settings. During the blanking phase, the scrap web is clamped on the punch. The critical load for cemented carbide punches is during the stripping phase. Both phases have been evaluated for Böhler S390 high-speed steel (HSS) punches with a hardness of 64 HRc. The blanked material was 1.7131 in soft annealed state with a sheet thickness of 6 mm and a UTS of approximately 400 MPa. In the second test, the HSS punches were replaced with a WC–Co cemented carbide grade with 8.5% binder content and submicron-fine average grain size. The sheet metal material was a micro-alloyed high-strength steel 1.8974 with a sheet thickness of 6 mm and a UTS of 715 MPa. This was done in order to provoke a punch face fracture of the cemented carbide punch. The fracture pattern was interpreted using punch force and AE signals in order to explain the fracture mechanisms. Finally, the scrap web was analyzed regarding geometry and

bridge widths. The fracture of cemented carbide punches was explained in context with the interactions between the punch and the scrap web. Elastic deformation of the scrap web during the relative motion with the punch leads to circumferentially uneven seizure and wedging.

2 Experimental Setup

The experiments were conducted on a servo-mechanical fine blanking press FEINTOOL XFT 2500 speed with a decoiler and leveler unit for automatic sheet metal supply. Figure 1a shows the cross-section of the fine blanking tool with the tool elements in the flux of force with the positions of the sensors for force and AE measurement. The fine blanking tool is a simple 2-up compound die producing two analogy geometries in one stroke. The strip layout is presented in Fig. 1b with two shifted and balanced arrow-shape geometries. During the shearing and stripping off phases, the active elements interact with the sheet metal, which is separated into two blanked parts and the scrap web. Hydraulic counter holder and blank holder forces introduce compressive stresses in the shearing zone which allows for larger forming grades during separation and therefore enables a high smooth-cut portion, see Fig. 1c [3].

Both the blanking and the stripping off phases are relevant for the analysis of fracture mechanisms. During the blanking phase, the interference fit of the scrap web and the punch is established, which is determined by the sheared surface quality characteristics. The interference fit leads to clamping and tensile stresses during stripping

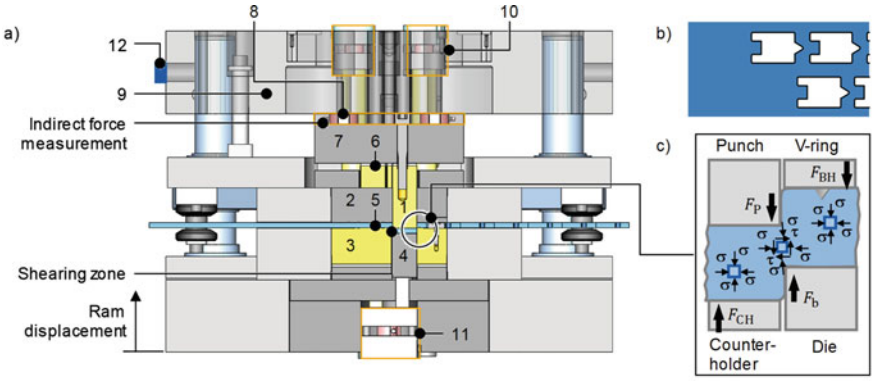


Fig. 1 Section through fine blanking tool with tool elements and positions of AE and force sensors (**a**), stress state in forming area and shearing zone (**b**), and strip layout (**c**). Legend: F_b—blanking force; F_{CH}—counter holder force; F_P—punch force; F_{BH}—blank holder force. (Color figure online)

off. Therefore, the complete fine blanking cycle is analyzed. Forming mechanisms are already known to emit structure-borne noise [12]. Fractures emit a burst in the AE signal [15]. It is also assumed that the tribosystem affects AE during the penetration of the sheet metal in the shearing phase and during the stripping off phase. AE has been used for the analysis of the tribosystem in gears using RMS signals [16]. Structure-borne noise is conducted from the punch through the tool components and measured outside the tool on the lateral top shoe. On each joint connection between components, noise is reflected [17]. Thus, a direct application of the sensor close to the punch is favorable. The only way to apply the sensor was on the top shoe. For the experiments, a sensor of the type KISTLER 8152C with a range of 400 kHz was used. The AE sensor was mounted using an M6-thread on the tool with a defined torque of 9 Nm. The contact surface for noise transmission on the tool surface was flat ground. The contact surface between the top shoe and the AE sensor was covered with ultrasonic transmission gel.

The process forces punch force F_P, blank holder force F_{BH}, and counter holder force F_{CH} were measured using piezo-electric load washers. The sensors were mounted in force shunts for indirect force measurement. Two tactile length gauges of the type HAIDENHAIN Specto with a system accuracy of ± 1 µm were used for the reference distances top shoe-ram and top shoe-guide plate. AE, forces, and displacement were measured in analogous with NATIONAL INSTRUMENTS LABVIEW software and saved in a TDMS format. The AE signal was measured with a sampling rate of 1 MHz which is twice the measuring range in order to avoid aliasing. Forces and displacements were measured with a sampling rate of 10 kHz.

Two experimental test series have been performed. In the first series, blanking strokes without tool fracture were conducted for a process analysis using HSS punches and 1.7131 sheet metal. The goal was the identification and quantification of characteristics in the AE and force signals. Due to the running-in of the fine blanking process, the blanking process was repeated 20 times in automatic mode of the fine blanking press. The 20th stroke was evaluated. The settings were set according to Table 1.

In the second test series, an overload of a cemented carbide punch was provoked using WC-Co cemented carbide punches and 1.8974 sheet metal. The stroke rate was set to 50 min^{-1} with a corresponding averaged blanking velocity v of 47 mm/s. The non-uniform transmission of the double toggle lever press provides for a mostly constant blanking velocity before top dead center (TDC) of the bottom-driven

Table 1 Process settings for fine blanking experiments

Parameter	Symbol	Unit	Value	Parameter	Symbol	Unit	Value
Stroke rate	h	min^{-1}	50	Counter holder force	F_{CH}	kN	300
Averaged blanking velocity	v	mm/s	47	Stripping off timing after TDC	t_{Strip}	mm	0
Blank holder force	F_{BH}	kN	350	Ejecting timing after TDC	t_{Eject}	mm	10

fine blanking press and stripping off velocity after TDC. The fracture surface was analyzed using light microscopy.

3 Results and Discussion of Waveforms of AE and Process Forces

First, the time–amplitude AE and force signals were analyzed with the displacement signals of the ram and the blank holder in order to get an understanding of the AE and force signals. Process variables have been varied in order to identify characteristics in the signals. Subsequently, the AE and force signal from a tool fracture due to material overload during stripping off was measured.

3.1 AE and Force Analysis of an Experimental 2-up Compound Die Fine Blanking Process

In correspondence with the ram and blank holder displacement curves, characteristics from the AE-signal were identified, see Fig. 2. Characteristic events during a fine blanking cycle became obvious.

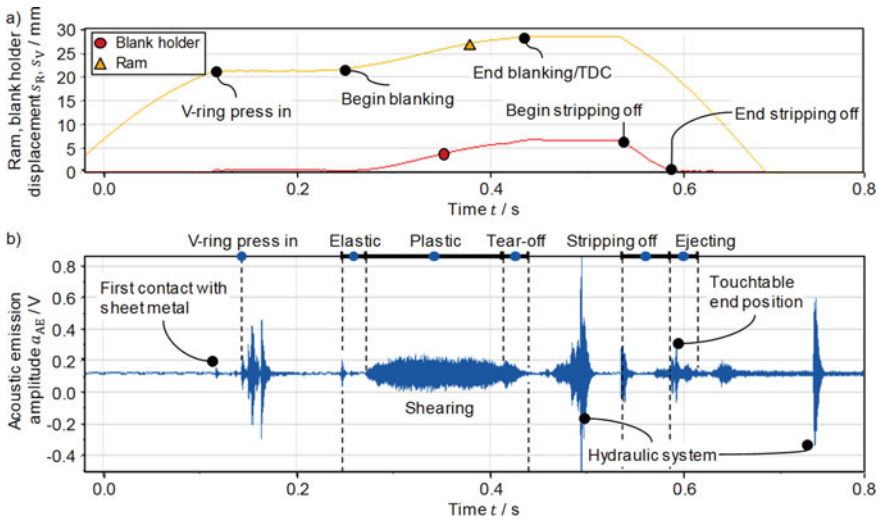


Fig. 2 Displacement (**a**) and AE signal (**b**) of a fine blanking cycle at stroke rate $n = 50\ \text{min}^{-1}$, blank holder force $F_{BH} = 350$ kN, counter holder force $F_{CH} = 300$ kN, stripping off at 0 mm after TDC, ejecting at 10 mm after TDC. (Color figure online)

The first contact between the V-ring and the sheet metal which is supported by the blank holder after the tool closes at 0.1 s is shown by a small peak before the V-ring is pressed into the sheet metal. The press-in of the V-ring and the clamping of the sheet metal while the touch table is moved is presented by peaks before 0.2 s. The plateau of the ram and blank holder displacement curves is due to the lifting of the touch table while the punch cannot apply a counterforce because the punch is not supported.

After the touch table reaches its end position, the punch is supported by the press body and the blanking phase begins. At the beginning of the blanking phase, the deformation is mostly elastic while die roll is formed which does not show high amplitudes in the AE signal. In the plastic portion of the shearing process, the amplitude increases which is due to dislocation movements during the forming operation. The amplitude during the shearing phase was observed to increase when the blank holder and counter holder force were increased according to [12]. Higher process forces induce a higher compressive stress state in the shearing zone, thus increase dislocation movement. At the end of the plastic forming when the cross-section and the forming zone and thus the AE amplitude decrease, the amplitude shortly increases which is explained by tear-off on the sheared surface. The torn-off surface height is about 5–10% of the sheared part thickness and occurs at a similar time compared to the AE peak.

The second plateau of the ram and blank holder displacement signals after reaching TDC at the end of blanking is due to the lowering of the touch table to its lower end position. The tool is opened at rapid traverse after the touch table reaches its end position. The stripping off is conducted immediately at the beginning of the opening of the tool. Peaks in a short distance at the beginning are explained with stick–slip behavior in the beginning. A higher amplitude at the end of the stripping off is observed which is expected to be based on the tribology between punch and scrap web. The amplitudes of the peaks are increased with higher stripping off velocity and decrease during the stripping phase while the contact surface between punch and the scrap web decreases linearly. Other peaks in the AE signal are explained with the behavior of the hydraulic system or reaching of end positions.

The process forces of the punch, blank holder, and counter holder were measured in correspondence to ram and blank holder displacement, see Fig. 3. The forces during the blanking phase are significantly higher compared to the stripping off and ejection phases. However, the stripping off phase is the more critical phase for fine blanking with cemented carbide punches because cemented carbide punches catastrophically fail in this phase [8].

Analogous to the AE analysis, characteristics from the blanking cycle are found in the force signals. When the press closes the tool and the strip is clamped, see Fig. 3a, the first amplitudes are seen in the punch and blank holder force in Fig. 3b. After the touch table is lifted to the end position, the blank holder and counter holder force build. The punch is set 0.1 mm back behind the blank holder such that the punch force builds slightly later than the blank holder force. At the beginning of the blanking phase, the punch force increases linearly. The increase in the punch force is to overcome the elastic deformation and the formation of die roll on the sheared part

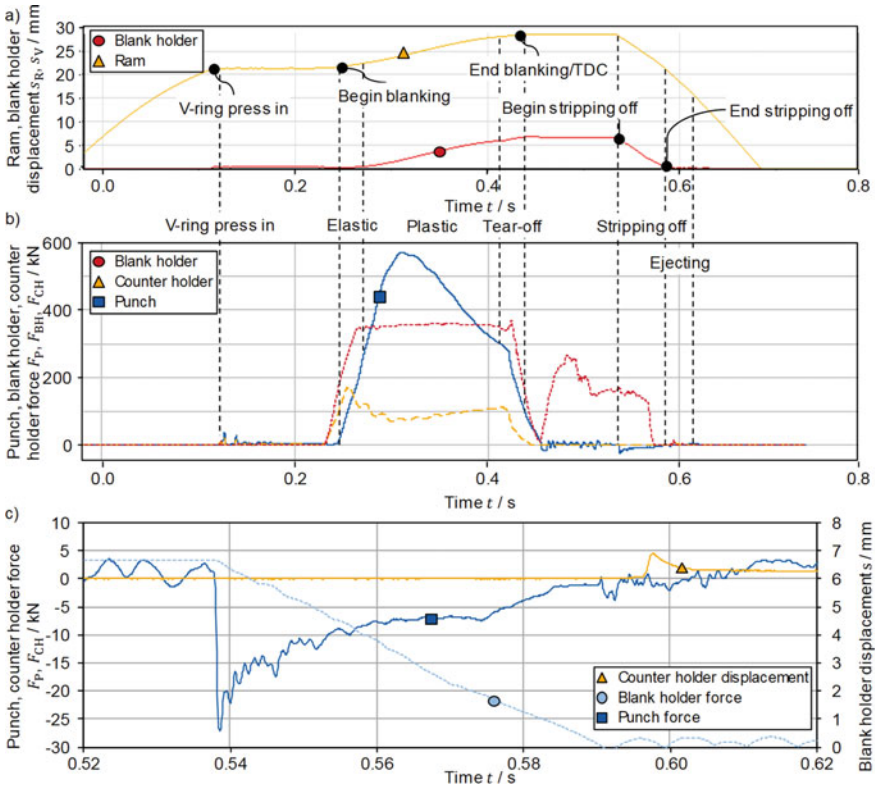


Fig. 3 Displacement (**a**), process force analysis of a fine blanking cycle (**b**), and force analysis during stripping off and ejection phase (**c**) at stroke rate $n = 50\ \text{min}^{-1}$, blank holder force $F_{BH} = 350$ kN, counter holder force $F_{CH} = 300$ kN, stripping off at 0 mm after TDC, ejecting at 10 mm after TDC. (Color figure online)

and the scrap web. The maximum punch force is registered after die roll formation is completed and the shearing zone is still large. After the punch force peak, when the shearing zone thickness decreases linearly with the ram displacement, the punch force decreases linearly correspondingly. At the end of the blanking phase before TDC, the punch force decreases rapidly which is explained by tear-off on the sheared surface of the sheared part and the scrap web. The process forces of the blank holder and the counter holder are controlled and the waveform depends on the hydraulic system. The volatile waveform of the counter holder is explained with the inertia of the hydraulic system.

The stripping off force at the punch and ejection force at the counter holder in Fig. 3c are small compared to the blanking forces. Stripping off timing was set to 0 mm after TDC in order to clamp the sheet metal between the guide plate and the die for better control of the stripping off and to avoid tilting of the scrap web. A tilted scrap web can cause uncontrolled stick–slip and flexural loads with increased

peaks on the punch. The punch tensile force increases rapidly at the beginning of the stripping off until the static friction is exceeded. Then the scrap web starts to slide off the punch with linear blank holder displacement. The punch tensile force decreases roughly linearly with the blank holder displacement as the contact area decreases linearly with the blank holder displacement. The punch force is close to zero before stripping off is completed which is explained with the die roll on the scrap web such that contact ends before the end of the stripping off phase. At the beginning of the stripping off phase, undulations are observed. The undulations increase when stripping off is delayed after TDC such that the scrap web is not clamped between the blank holder and the die. It is assumed that these undulations are due to a stick–slip behavior.

Ejection of the blanked parts from the die was set to 10 mm after TDC and is visualized by the counter holder force in Fig. 3c after the stripping off. Similar behavior compared to the punch during stripping off is observed without the undulations at the beginning and with a lower amplitude.

3.2 A Provoked Fracture of a Cemented Carbide Punch Due to Material Overload

A material overload of a WC–Co cemented carbide grade with submicron-fine average grain size and 8.5% binder content as punch material was provoked. The second punch in the 2-up fine blanking tool was made from HSS. Cemented carbides have high compressive strength but a low tensile and flexural strength compared to HSS [18]. This leads to material overload during stripping off phase in fine blanking of high-strength sheet metal S700MC with 6 mm sheet thickness. AE was measured during tool fracture and analyzed in Fig. 4. The blanking phase (Fig. 4a) is ordinary as with sharp punches. Fracture of the cemented carbide punch was registered as a burst after one-third of the stripping off path (Fig. 4b). The burst indicates catastrophic tool failure equivalent to drilling as investigated in [15].

The punch face was clamped and the face fragment remained in the scrap web. The assumed stripping off path from the measured signal until punch fracture correlated with the position of the face fragment in the scrap web. From the AE two cracks were observed. Two crack initiations were also observed in the fracture pattern on the punch face (Fig. 4c). The fractures confluence in the exposed vertical line close to the point of the second crack initiation.

The punch force during stripping off was analyzed in Fig. 5 analogous to Fig. 3c. Only the cemented carbide punch fractured due to overload. The HSS punch had sufficient ductility to withstand the load collective. Therefore, the force signal is formed by the fractured and the non-fractured punch. However, the force waveform gives information about the course of fracture.

The stripping force with the high-strength sheet S700MC and the cemented carbide punch increased to 70 kN compared to the softer sheet metal 16MnCr5

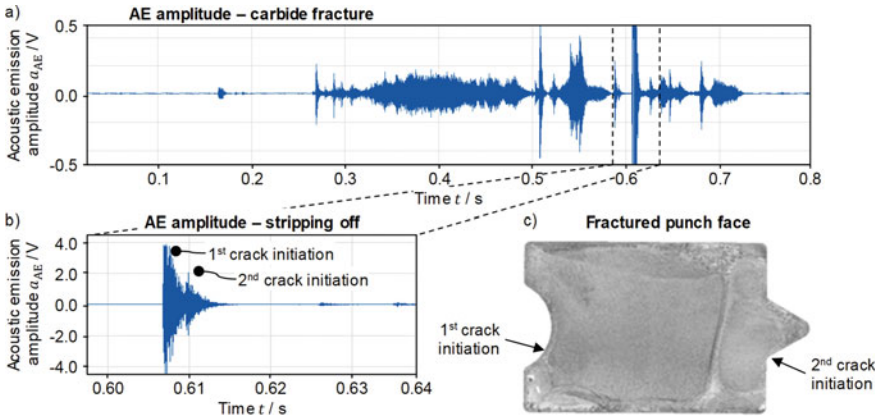


Fig. 4 AE of a fine blanking cycle with a provoked fracture of a cemented carbide punch (**a**), AE burst during stripping off phase (**b**), and fracture pattern of the punch face (**c**). (Color figure online)

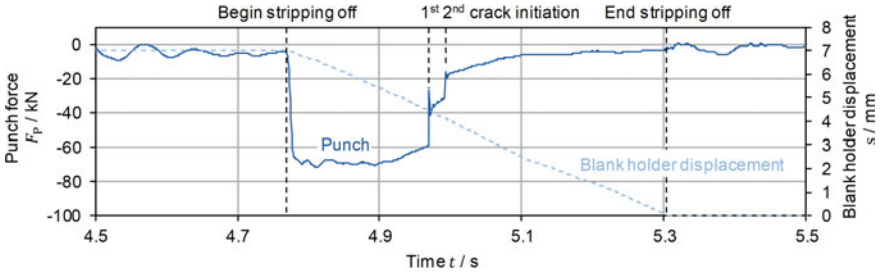


Fig. 5 Punch force of a provoked fracture of a cemented carbide punch during stripping off phase. (Color figure online)

with 25 kN. Instead of a decreasing stripping force, it remains constant for 1 mm of blank holder displacement before the stripping force starts to decrease. After one-third of the stripping path, first crack initiation is observed in the form of a sudden force drop. A second force drop occurred shortly after the first one.

4 Discussion of the Results

The fracture of the cemented carbide punch face during the stripping off phase caused a double peak in the AE signal and two punch force drops that were analyzed in Chapter 3.2. The sudden release of the strained punch after the fracture stimulated the acoustic eigenfrequency of the oscillation system of the punch and the joint tool elements. This caused a high amplitude of the measured AE signal, comparable to crack propagation according to [19].

The fracture pattern on the punch face is explained with the measured punch force and AE signal. On the fractured punch face, two opposing crack initiation points were identified. It is assumed that the punch was clamped on one end of the geometry where the first crack was initiated and flexural stresses were induced. The flexural strength was exceeded locally which led to the first crack initiation. The fracture leads to an asymmetric release of the punch which led to conversed clamping on the opposing side of the geometry. The same procedure occurred again at the point of the second crack initiation, see Figs. 4 and 5.

In previous investigations, the clamping of the scrap web on cemented carbide punches in fine blanking processes was described and explained with elastic spring-back of the scrap web for different materials and sheet thicknesses [10]. However, in industrial processes, the scrap web does not have constant circumferential stiffness at the cutting line due to relatively small bridge widths. Variable stiffness of the scrap web enables the material to locally unload the punch elastically, which results in variable clamping along the cutting line.

Moreover, the sheared surface of the scrap web varies along the cutting line. Different geometry elements are characterized by varying die roll and smooth cut portion as investigated in previous work [20]. This led to locally asymmetric contact areas between the punch and the scrap web on asymmetric cutting lines. Furthermore, the behavior of die roll during stripping off phase needs to be investigated.

Based on the stiffness and the die roll of the scrap web, two approaches for the explanation of fracture of cemented carbide punches in fine blanking have been established. Therefore, the scrap web is further analyzed.

Figure 6 shows the scrap web with the two cavities I and II and the holes from the previous blanking operation. Bridge widths are limited due to the distance to the previous hole of 10 mm and to the strip border of 7 mm. The scrap web right from the cavities and to the strip border is less stiff than on the infeed side. Thus, the clamping of the scrap web on the punch may relax where bridge widths are small. On the other side, the material in the strip on the infeed side has no ability to elude. The unbalanced clamping caused flexural loads in the punch during stripping off.

During the tests, the cemented carbide punch was mounted in cavity I. The scrap web of the provoked fracture experiment was measured with a 3D-sensor GOM

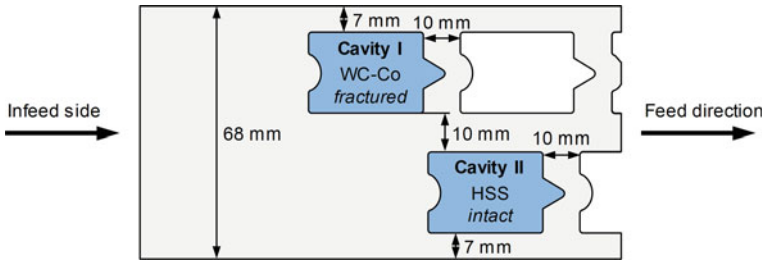


Fig. 6 Measures of the scrap web affecting its stiffness around cavities I and II. (Color figure online)

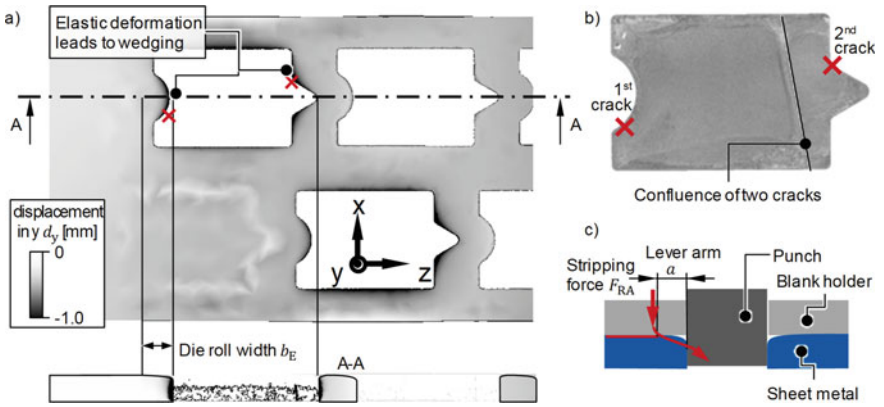


Fig. 7 Deformation of the scrap web in blanking direction (**a**), fracture pattern of the corresponding cemented carbide punch face (**b**), and wedging mechanism between scrap web with die roll and punch (**c**). (Color figure online)

ATOS and converted into an STL mesh. The STL mesh was compared with an ideal rectangular and plane CAD file of the scrap web using the software GOM INSPECT. Deviations in blanking direction (y) are presented in a false-color image in Fig. 7a.

Die roll in convexity radii of the geometry on the scrap side is clearly increased locally along the cutting line. There are convexity radii at the left-sided semicircular notch and right-sided next to the gear tooth, which shows an increased die roll. The die roll height is up to 0.7 mm which is 12% of the sheet metal thickness. The locally reduced die roll height results in lower friction force in convex geometry elements of the scrap web, assuming that the clamping force is constant along the cutting line. Together with locally reduced stiffness due to small bridge widths, concave geometry elements with larger bridge widths undergo larger friction during stripping off. In cavity I, the corner at the infeed side on the sheet metal center has a negligible die roll and large bridge width. However, the explanation with reduced friction due to die roll height is not sufficient for the explanation of crack initiation points.

In convex radii of the scrap web in the semicircular notch and besides the gear tooth, the die roll width is large with approximately 3 mm. The blank holder is used for stripping off the scrap web from the punch. In the die roll area, the scrap web cannot be supported by the blank holder. Thus, the stripping force is introduced into the scrap web over the die roll width as the lever arm as indicated in Fig. 7c. The elastic deformation of the die roll area in the scrap web during stripping off has been investigated in previous work [21]. Figure 8a shows von Mises stresses in a finite element model of the stripping off phase with a circular geometry with a diameter d = 30 mm. The simulation was run linear statical in Abaqus/Standard. The punch was modeled elastic as cemented carbide with Young's modulus E = 480 GPa. The sheet metal was modeled elastic-plastic using flow curves as high-strength steel 1.8974 was used in the experimental test. The non-supported scrap web deforms elastically in the die roll area during stripping off which leads to wedging with the punch as visualized

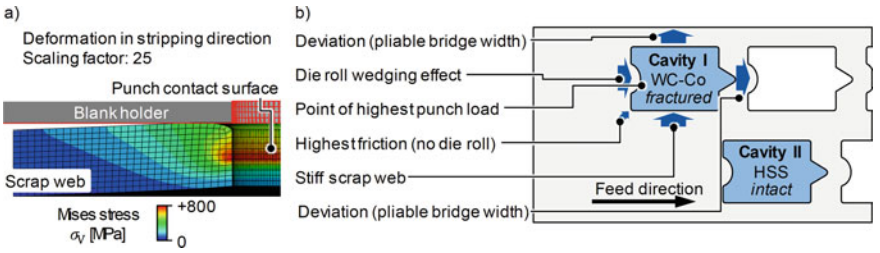


Fig. 8 Visualization of die roll wedging effect according to [21] (**a**) and asymmetric clamping mechanism leading to punch fracture during stripping off due to die roll wedging effect and asymmetric stiffness of the scrap web (**b**). (Color figure online)

in Fig. 8a. The die roll wedging effect results in increased contact normal stresses and subsequently to high stripping forces and clamping of the punch. The failure mechanism of the cemented carbide punch is explained in Fig. 8b. High stripping forces in the semicircular notch and the high stiffness of the sheet metal strip on the infeed side hold the punch back and introduce flexural stress into the punch. The small bridge width at the strip border, which results in lower clamping, enables the punch to slightly move to the strip border. As a consequence, the wedging in the notch was increased on the strip center side, where the first crack initiation point was identified.

5 Conclusion and Outlook

Punch fracture mechanisms during fine blanking of high-strength sheet metal have been investigated. The used tool was a 2-up compound die with an asymmetric geometry. One punch was made of HSS while the other one was made of tungsten carbide. The carbide punch fractured during the stripping off phase. Through process force and AE analysis, the course of fracture could be reconstructed. Two crack initiation points were identified in the measured signals and on the fracture pattern. As a consequence of the punch geometry and the strip layout, the punch was loaded with flexural and tensile stresses during the stripping off.

- Elastic springback due to the hydrostatic stress state in the shearing zone causes the scrap web to clamp on the punch during the stripping phase
- Small bridges in the scrap web are pushed away from the punch such that small bridges cannot hold the clamping force. This effect leads to asymmetric clamping if the scrap web is determined by asymmetric bridge widths. The strip has a high stiffness on the infeed side and small bridge widths in the scrap web. Moreover, the bridge width to strip borders is small.
- Die roll on the scrap web is not supported by the blank holder during stripping off such that the stripping force is introduced to the punch over a lever arm.

The non-supported scrap web in the die roll area deforms elastically. The elastic deformation finally causes a die roll wedging effect between the scrap web and the punch. With asymmetric cutting line geometries, different-sized die roll on opposing sides of the geometry results in a flexural load on the punch or in local exceedance of the material strength.

In future investigations, the stripping phase in a fine blanking cycle with asymmetric cutting line geometry needs to be simulated in order to quantify the observed effects. For example, the punch fractured after one-third of the stripping path. With the gained knowledge, asymmetric clamping of cemented carbide punches need to be compensated by an improved strip layout or die roll control.

References

1. State of Baden Württemberg (2014) Leichtbau—Trends und Zukunftsmärkte und deren Bedeutung für Baden-Württemberg. In: Leaflet, Baden Württemberg, Germany
2. Demmel P, Hoffmann H, Feinschneiden. In: Siegert K (Hrsg.): Blechumformung. Verfahren, werkzeuge und maschinen (Rh. VDI). Berlin, Germany, Heidelberg, Germany: Springer Vieweg 241–256
3. Klocke F (2017) Fertigungsverfahren 4. Springer, Berlin
4. Bonache V, Rayón E, Salvador MD, Busquets D (2010) Nanoindentation study of WC–12Co hardmetals obtained from nanocrystalline powders: evaluation of hardness and modulus on individual phases. Mater Sci Eng A 527(12):2935–2941
5. Ceratizit Deutschland GmbH (2016) Lösungen für den Werkzeugbau. Herausgegeben von Ceratizit Deutschland GmbH
6. Behrens B-A, Krimm R et al (2010) Erhöhung der Verschleißfestigkeit beim Scherschneiden durch aktivgelötete Keramik- und Hartmetall-Schneidstempelinlays. Umformtechnik 3(1):1–12
7. Klaasen H, Kübarsepp J et al (2007) Blanking performance and fatigue endurance of carbide composites. TIC 70(1):14–18
8. Krobath M, Klünsner T et al (2018) Tensile stresses in fine blanking tools and their relevance to tool fracture behavior. Int J Mach Tools Manuf 126: 44–50
9. Escher C, Henke T (2004) Werkzeugwerkstoffe für die Verarbeitung von hochfesten Stahlblechwerkstoffen. In: Siegert K (Hrsg.): Neuere Entwicklungen in der Blechumformung. [Vortragstexte zur Veranstaltung Internationale Konferenz "Neuere Entwicklungen in der Blechumformung" in Fellbach (bei Stuttgart) am 11. und 12. Mai 2004]. Frankfurt [Main], Deutschland: MAT-INFO, Werkstoff-Informationsges 105–124
10. Baer O, Feuerhack A, Voigts H, Bergs T (2019) Investigation of the mechanical punch loads during fine blanking of high-strength steels with cemented carbide. Procedia Manuf 34: 90–100
11. Herres W-U (1991) Prozeßüberwachung beim Feinschneiden. Möglichkeiten der indirekten Qualitätskontrolle durch Auswertung von Werkzeugkräften und akustischen Emissionen, Aachen
12. König W, Herres W-U (1992) Überwachung des Feinschneidprozesses. Werkzeugkräfte und Körperschall liefern auswertbare Informationen. Fertigungstechnik 134(7–8): 77–82
13. König W, Herres W-U, Rentsch C (1992) Überwachung von Feinschneid- und Folgeverbundprozessen. Monitoring of fine blanking and follow on processes—Tool forces and acoustic emission. Blech Rohre Profile 39(10): 791–794
14. Lan MS, Dornfeld DA (1984) In-process tool fracture detection. J Eng Mater Technol 106(2):111–118

15. Jemielniak K, Otman O (1998) Catastrophic tool failure detection based on acoustic emission signal analysis. CIRP Ann 47(1):31–34
16. Raja Hamzah RI, Mba D (2007) Acoustic emission and specific film thickness for operating spur gears. Wear 129(4):860–867
17. Möser M, Kropp W, Cremer L, Heckl M (2010) Körperschall. Physikalische Grundlagen und technische Anwendungen. 3., aktualisierte Aufl., Berlin, Springer
18. Ceratizit Deutschland GmbH (2016) Innovation. The new CF grade family (leaflet). Herausgegeben von Ceratizit Deutschland GmbH
19. Huang M, Jiang L et al (1998) Using acoustic emission in fatigue and fracture materials research. J Minerals, Metals Mater Soc 50(11):1–14
20. Voigts H, Trauth D et al (2018) Dependencies of the die-roll height during fine blanking of case hardening steel 16MnCr5 without V-ring using a nesting strategy. Int J Adv Manuf Technol 95(5–8):3083–3091
21. Bergs T, Bletek T et al (2019) PM-Werkzeuge in der Fertigungstechnik—Anwendungen und Potentiale. Veranstaltung vom 28.–29.11.2019, aus der Reihe “38. Hagener Symposium”, Hagen

Microstructural Evolution of Ti-55511 Titanium Alloy During Quasi-Beta Forging



Yu-Qiang Jiang, Y. C. Lin, and Guo-Dong Pang

Abstract The quasi-beta forging behavior of Ti-55511 alloy is systematically studied by hot compressive deformation experiments and electron back-scattered diffraction (EBSD) tests. The results show that the strain rates have obvious effects on the hot deformation behaviors of the studied alloy. With the increase of strain rate, the flow stress increases. At low strain rates, the work hardening rates hardly change until a critical strain, and then the work hardening rates slightly increase. At a medium strain rate (0.1 s^{-1}), the work hardening rate gradually decreases until a critical strain, and then the work hardening rate shows little variation with strain. However, at high strain rates (1 s^{-1}), the positive work hardening rate indicates the obvious work hardening at the initial deformation stage, and the work hardening rates change to negative and then to positive with strain when the strain rate is further increased to 10 s^{-1}. The main soften mechanism of β grain is DRV. With the increase of strain rate, the fraction of DRX grains and the sub-grains decrease. Too high strain rate leads to the formation of flow localization.

Keywords Microstructural evolution · Ti-55511 alloy · Quasi-beta forging

1 Introduction

Admired for their excellent high specific strength and fracture toughness, titanium alloys are widely used in aircraft industries [1, 2]. However, the narrow TMP parameter ranges and complicated mechanical/microstructural evolution restrict the forming qualities of the titanium alloys [3, 4]. So, the hot deformation behaviors of high-strength titanium alloys were pursued by many authors [5, 6].

According to the relationship between the forging temperature and beta transition temperature, the forging of titanium alloys is split into β and α + β forging. For the α

Y.-Q. Jiang · Y. C. Lin (✉) · G.-D. Pang
School of Mechanical and Electrical Engineering, Central South University, Changsha 410083, China
e-mail: yclin@csu.edu.cn

State Key Laboratory of High Performance Complex Manufacturing, Changsha 410083, China

© The Minerals, Metals & Materials Society 2021

G. Daehn et al. (eds.), *Forming the Future*, The Minerals, Metals & Materials Series,
https://doi.org/10.1007/978-3-030-75381-8_99

+ β forging, the initial grain size, strain, strain rate, and temperature have important effects on the dynamic evolution of the α phase [7–9]. When the temperature is higher than the β transition temperature, namely the β forging, the DRX and DRV of β phases will happen [10, 11]. The processing parameters, such as strain, strain rate, and deformation temperature, also have a remarkable influence on the evolution of β phases [12, 13].

For the high-strength beta alloy, the quasi-beta forging (the deformation temperature slightly exceeded the beta transfer temperature) is put forward to control the β grain size [14, 15]. In this work, the quasi-beta deformation behaviors of Ti-55511 alloys and the microstructural evolutions are systematically studied by the EBSD method. The effects of strain rates on the deformation behavior and microstructural evolution of the studied alloy are investigated. Meanwhile, the deformation mechanism of the studied alloy is discussed.

2 Material and Experiment

A near beta titanium alloy, Ti-55511, was used in this study. The beta transition temperature of the studied alloy is 1148 K obtained by optical examination [16, 17]. Cylindrical specimens (ϕ8mm × 12mm) were prepared from the wrought bar. To get the single beta phase, the specimens were heat-treated at 1173 K for 60 min followed by water quenching. The initial microstructure obtained by the authors of the specimens after heat treatment is shown in Fig. 1. The hot compression tests were conducted at 1163 K on Gleebe-3500 thermal simulation test machine, and strain

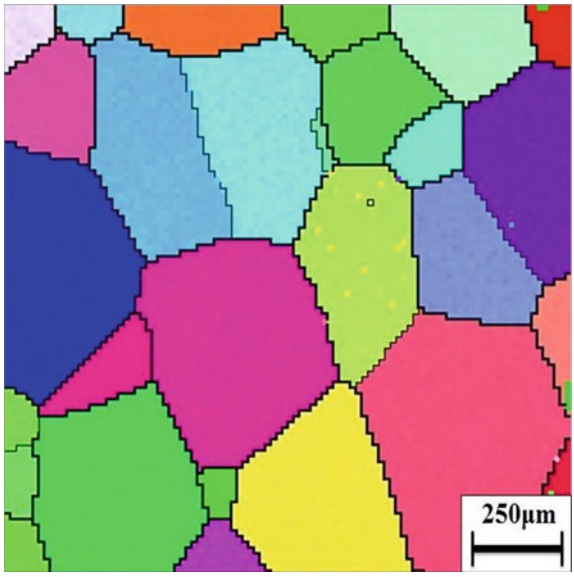


Fig. 1 The initial microscopy image of the studied alloy. (Color figure online)

rates of 0.001, 0.01, 0.1, 1, and 10 s^{-1}. After the hot deformation, the specimens were water quenched for the following EBSD observation.

Prior to the hot deformation, the specimens were heated to the target temperature at 10 K/s, and then kept for 300 s to minimize the differential temperature. After the hot deformation, the specimens were water quenched for the following microstructural observation. Then the specimens were sectioned parallel to the compression axis and prepared for the EBSD observation. The samples for EBSD observation were electrochemical polished in corrosive liquid of 5 ml $HClO_4$ and 95 ml CH_3COOH for 30 s at the voltage of 50–55 V. The step size during the EBSD observation is 10 μm because of the large grain size and to reduce the scanning time.

3 Results and Discussion

3.1 The Quasi-Beta Deformation Behavior

Figure 2 shows the quasi-beta deformation behaviors of the studied alloy. It can be found from Fig. 2 that the strain rates have obvious effects on the hot deformation behavior of the studied alloy. Generally, with the increase of strain, the stress first increases and then almost keeps stable when the saturation stress is reached, which shows the typical DRV feature [4]. Moreover, increasing the strain rate can largely increase the stress. There is enough time for the DRV and DRX, and the relative low flow stress can be found at a low strain rate. However, the short deformation time restrains the DRV and DRX process, and the flow stress is increased at a high strain rate.

Figure 2b shows the relationships between the work hardening rate ($\partial\sigma/\partial\varepsilon$) and true strain. It can be found from Fig. 2b that the coupling between strain and strain

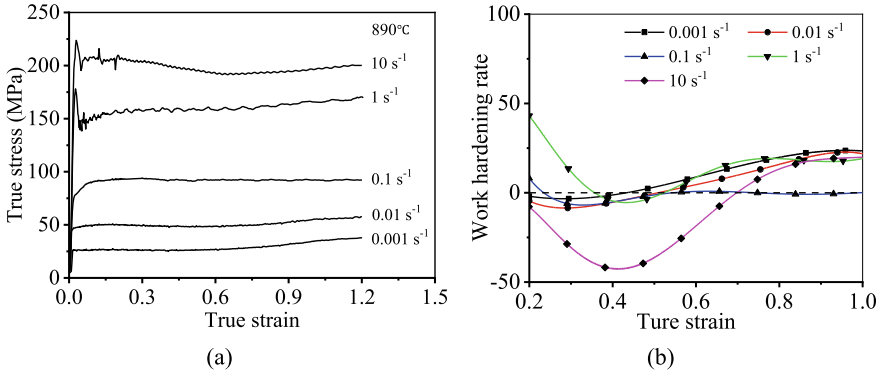


Fig. 2 The quasi-beta deformation behavior of the studied alloy: (**a**) The true stress true strain curves; (**b**) Work hardening rates. (Color figure online)

rate has remarkable effects on the flow stress of the studied alloy. At low strain rates (0.001–0.01 s^{-1}), the work hardening rates hardly change until a strain of 0.6, and then the work hardening rates slightly increase, as shown in Fig. 2b. At a medium strain rate (0.1 s^{-1}), the work hardening rate gradually decreases until the true strain of 0.3, and then the work hardening rate shows little variation with strain. However, at high strain rates (1 s^{-1}), the positive work hardening rate indicates the obvious work hardening. When the strain rate is further increased to 10 s^{-1}, the work hardening rates change from negative to positive, as shown in Fig. 2b.

During the hot deformation of the studied alloy, the strain rate sensitivity factor ($\partial \ln \sigma / \partial \ln \varepsilon$) lies in the range of 0.19–0.23, and the deformation activation energy ranges from 180 to 220 kJ/mol, which is slightly greater than the self-diffusion activation energy of the beta titanium (153 kJ/mol) [18]. So, the main deformation mechanism of the studied alloy is the slip and cross-slip of the dislocation, and the soften mechanism is DRV [19, 20].

3.2 *Microstructural Evolution*

During quasi-beta deformation of Ti-55511 alloy, the complicated microstructural evolution leads to the versatile hot deformation behaviors. In the following parts, the complicated microstructural evolution is discussed and the relationship between microstructural evolution and hot deformation behavior is revealed.

3.2.1 Effect of Strain

Figure 3 shows the inverse pole figures (IPFs) of the studied alloy deformed at true strains of 0.3, 0.6, and 1.2, and the arrows show the compressive direction. In Fig. 3, the LAGBs and HAGBs are marked by thin-gray and thick-black lines, respectively.

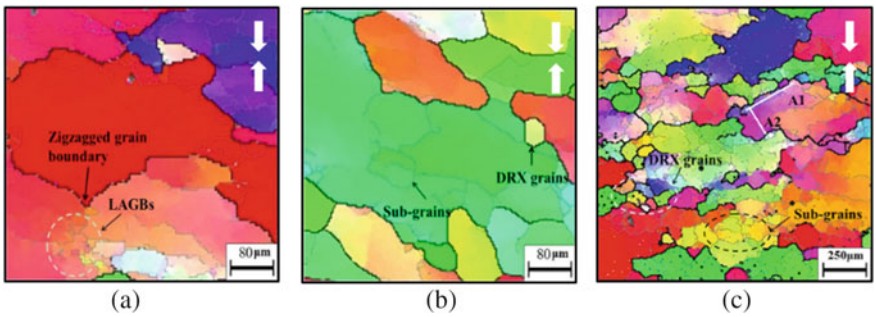


Fig. 3 The IPFs of Ti-55511 alloy deformed at 0.001 s^{-1} and strains of **a** 0.3; **b** 0.6; **c** 1.2. (Color figure online)

It can be found from Fig. 3 that the strain has obvious effects on the evolution of β phases of Ti-55511 alloy. At a relatively low strain (0.3), the initial β grain is slightly elongated, and the β grain boundaries are irregularly zigzagged. Meanwhile, there are plentiful LAGBs in the initial β grains, as shown in Fig. 3a. When the strain is increased to 0.6, some DRX grains are formed in the zigzagged initial β grains, and sub-grains are also formed in the initial β grains, as shown in Fig. 3b. However, when the strain is further increased to 1.2, a great deal of DRX grains are formed in the initial β grains. Within the initial β grains, the number of sub-grains is increased, as shown in Fig. 3c.

3.2.2 Effect of Strain Rate

Figure 4 shows the IPFs of the studied alloy deformed at different strain rates, and the arrows show the compressive direction. It can be found from Figs. 3c and 4 that the strain rates have tremendous effects on the evolution of the beta phase. At a relatively low strain rate (0.001–0.01 s^{-1}), the initial beta grain boundaries are irregularly zigzagged, and some DDRX grains and sub-grains are formed (Fig. 3c). Figure 5a, b illustrates the variations of the local and cumulative misorientations along the lines labeled in Fig. 3c. As indicated in Fig. 5a, b, the local misorientation (point to point) which is greater than 10° is scarcely observed, and the cumulative misorientations (point to origin) along grain boundary, as well as from grain boundary to grain interior, are larger than 15°, which indicates that the DRX is under development stages. Meanwhile, the misorientation mutation can be found in Fig. 5a, b, which indicates the occurrence of sub-grains and the development of DRV.

When the strain rate is increased to 0.1 s^{-1}, the initial beta grains are elongated, and the degree of grain boundary zigzagging is decreased. Meanwhile, the number of DRX grains and sub-grains decreases, as shown in Fig. 4a. The cumulative misorientations along grain boundary, as well as from grain boundary to grain interior, are no more than 10° (Fig. 5c, d), indicating the slow evolution of the DRX process. In

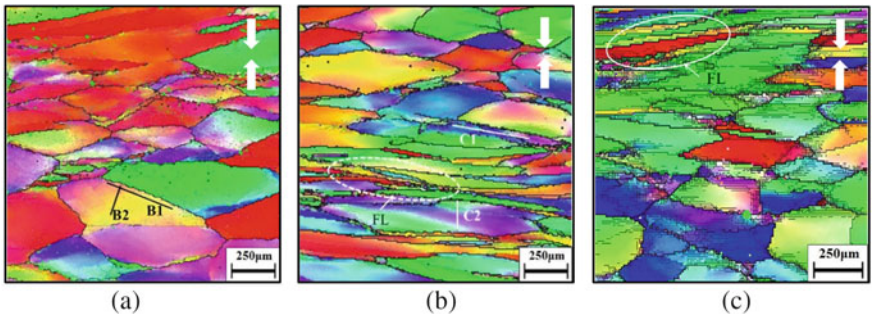


Fig. 4 The IPFs of the studied alloy at a strain of 1.2 and strain rates of **a** 0.1 s^{-1}; **b** 1 s^{-1}; **c** 10 s^{-1}. (Color figure online)

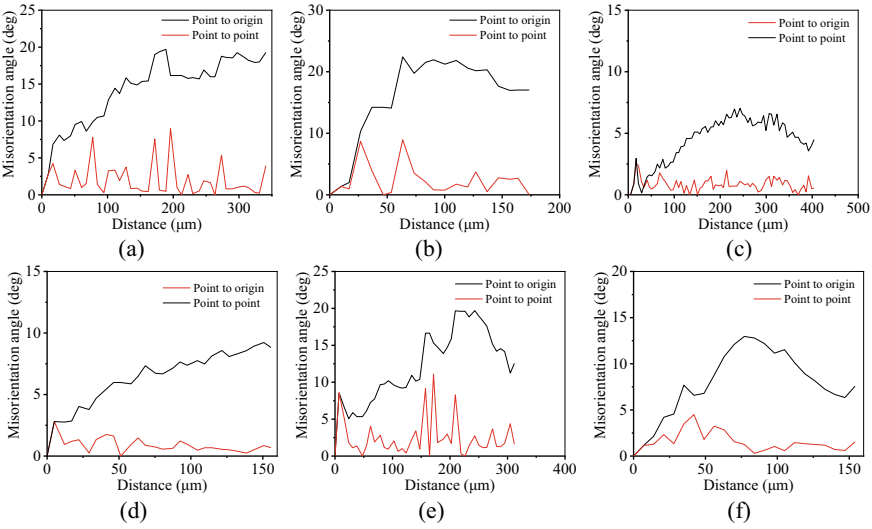


Fig. 5 Evolution of misorientation angles along the lines labeled in Fig. 3c and Fig. 4: **a** A1; **b** A2; **c** B1; **d** B2; **e** C1; **f** C2. (Color figure online)

addition, dense, small sub-grains are formed at the initial β grains boundaries, and the misorientation mutation occurs more frequently (Fig. 5c).

When the strain rate is increased to 1 s^{-1}, the initial beta grains are further elongated, and less irregular zigzagged grain boundaries are formed, indicating the lower degree of DRX, as shown in Fig. 4b. The cumulative misorientations along grain boundary exceed 15°, while the cumulative misorientations from grain boundary to grain interior are no more than 15°, as displayed in Fig. 5e, f. However, with the increase of strain rates, the deformation is accumulated at the local area, and obvious deformation gradient and flow localization are formed (Fig. 4b). When the strain rate is further increased to 10 s^{-1}, more obvious flow localization (FL) and elongated initial beta grains are found, as shown in Fig. 4c. Yamanaka et al. [21] also found the flow localization at high strain rates (1 s^{-1}).

3.3 The Deformation Mechanism of Ti-55511 Alloy

Due to high stacking fault energy, the DRV of β phases is apt to happen. The soften mechanism of β phases is DRV, and only small DRX grains emerged at the initial β grain boundary, as shown in Figs. 3 and 4. Figure 6 shows the kernel average misorientation (KAM) maps of the studied alloy at different strain rates. It can be seen from Fig. 6a that there are many LAGBs within the initial β grain, which indicates the high dislocation density. The high-density dislocations impede the deformation of the studied alloy, and the flow stress is gradually increased, as shown in Fig. 2.

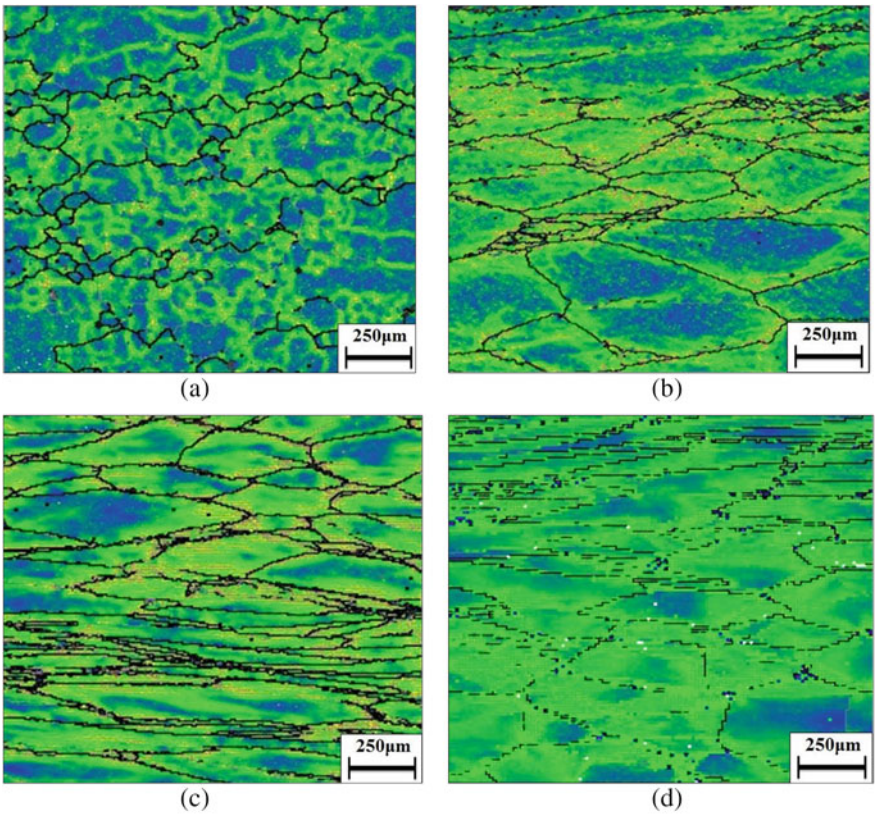


Fig. 6 The KAM maps of the studied alloy deformed at a strain of 1.2 and strain rates of **a** 0.001 s^{-1}; **b** 0.1 s^{-1}; **c** 1 s^{-1}; **d** 10 s^{-1}. (Color figure online)

When the strain rate is increased to 0.1 s^{-1}, many sub-grains are formed at the initial beta grain boundary due to DRV (Fig. 6b) and the balance between work hardening and DRV is obtained. So, the flow stress is almost unchanged with the strains, as shown in Fig. 2. However, when the strain rate is increased to 1 s^{-1}, more dislocations and tiny sub-grains are accumulated at the initial β grain boundary, as shown in Fig. 6c. The deformation of β grain is impeded by the tiny sub-grains and LAGBs, and the flow stress is increased gradually, as shown in Fig. 2. When the strain rate is further increased to 10 s^{-1}, the DRV is further improved, and many tiny sub-grains are formed in the beta grains. The short deformation time restricts the growth of sub-grains, and the DRX grains are seldom found (Fig. 4c). Due to the formation of tiny sub-grains, the degree of dislocation entanglement is increased, and the flow stress is increased with strain (Fig. 2).

Figure 7 shows the schematic diagram of the deformation mechanism of the studied alloy. Due to the work hardening, the dislocations are accumulated within the initial beta grains. With the increase of strain, the DRV is promoted, and some

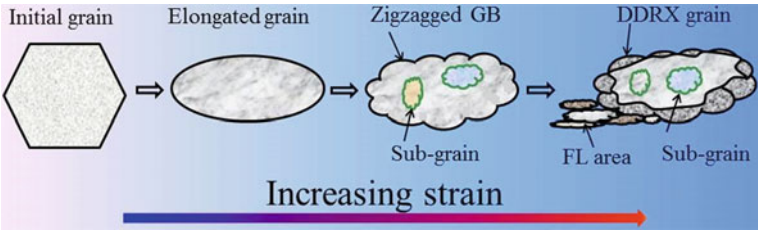


Fig. 7 The deformation mechanism of the studied Ti-55511 alloy. (Color figure online)

sub-grains are formed in the initial beta grains. At the same time, the initial beta grains are elongated and boundaries are zigzagged. On further increasing the strain, the DRX grains are formed at the zigzagged grain boundaries, and the number of sub-grains is increased.

4 Conclusions

The quasi-beta deformation behavior and microstructural evolution of Ti-55511 alloys are systematically studied, and the main conclusions are summarized as follows:

(1) The strain rates and strain have obvious effects on the flow behaviors of Ti-55511 alloy. With the increase of strain rate, the flow stress increases. The coupling between strain and strain rate has remarkable effects on the flow stress of the studied alloy. At low strain rates, the work hardening is not obvious, and work hardening and dynamic softening are the main flow characters at high strain rates.

(2) The main soften mechanism of beta grain is DRV. With the increase of strain, the initial beta grain boundary is zigzagged, and the DRX grains and sub-grains are observed. With the increase of strain rate, the fraction of DRX grains and the sub-grains decrease. Too high strain rate leads to the formation of flow localization.

Acknowledgments This work was supported by the National Natural Science Foundation Council of China (Grant No. 51775564).

References

1. Lin YC, Tang Y, Zhang XY, Chen C, Yang H, Zhou KC (2019) Effects of solution temperature and cooling rate on microstructure and micro-hardness of a hot compressed Ti-6Al-4V alloy. Vacuum 159:191–199

2. Banerjee D, Williams JC (2013) Perspectives on titanium science and technology. Acta Mater 61:844–879
3. Lin YC, Huang J, Li H, Chen DD (2018) Phase transformation and constitutive models of a hot compressed TC18 titanium alloy in the α+β regime. Vacuum 157:83–91
4. Wang QW, Lin YC, Jiang YQ, Liu XG, Zhang XY, Chen DD, Chen C, Zhou KC (2019) Precipitation behavior of a β-quenched Ti-5Al-5Mo-5V-1Cr-1Fe alloy during high-temperature compression. Mater Charact 151:358–367
5. Guo LL, Fan XG, Yu G, Yang H (2016) Microstructure control techniques in primary hot working of titanium alloy bars: a review. Chin J Aeronaut 29:30–40
6. Kolli R, Devaraj A (2018) A review of metastable beta titanium alloys. Metals 8:506
7. Li C, Zhang XY, Li Z, Zhou KC (2013) Hot deformation of Ti-5Al-5Mo-5V-1Cr-1Fe near β titanium alloys containing thin and thick lamellar α phase. Mater Sci Eng A 573:75–83
8. Semiatin SL, Seetharaman V, Weiss I (1999) Flow behavior and globularization kinetics during hot working of Ti-6Al-4V with a colony alpha microstructure. Mater Sci Eng A 263:257–271
9. Lin YC, Jiang XY, Shuai CJ, Zhao CY, He DG, Chen MS, Chen C (2018) Effects of initial microstructures on hot tensile deformation behaviors and fracture characteristics of Ti-6Al-4V alloy. Mater Sci Eng A 711:293–302
10. Sen M, Suman S, Kumar M, Banerjee T, Bhattacharjee A, Kar SK (2018) Thermo-mechanical processing window for β phase recrystallization inTi-5Al-5Mo-5V-3Cr alloy. Mater Charact 146:55–70
11. Jiang YQ, Lin YC, Pang GD, He DG, Kotkunde N (2019) Constitutive model and processing maps for a Ti-55511 alloy in β region. Adv Eng Mater 1900930
12. Lei LM, Huang X, Wang MM, Wang LQ, Qin JN, Lu SQ (2011) Effect of temperature on deformation behavior and microstructures of TC11 titanium alloy. Mater Sci Eng A 528:8236–8243
13. Fan XG, Zhang Y, Gao PF, Lei ZN, Zhan M (2017) Deformation behavior and microstructure evolution during hot working of a coarse-grained Ti-5Al-5Mo-5V-3Cr-1Zr titanium alloy in beta phase field. Mater Sci Eng A 694:24–32
14. Shi XH, Shi CL, Zeng WD, Wang HJ, Jia ZQ (2015) Study on the fatigue crack growth rates of Ti-5Al5Mo-5V-1Cr-1Fe titanium alloy with basket-weave microstructure. Mater Sci Eng A 621:143–148
15. Wang KL, Lu SQ, Dong XJ, Li X, Ouyang DL (2016) Deformation behavior of Ti-5.6Al-4.8Sn-2.0Zr-1.0Mo-0.35Si-0.85Nd alloy in β/quasi-β forging process. J Iron Steel Res Int 23:1297–1302
16. Jiang YQ, Lin YC, Zhang XY, Chen C, Wang QW, Pang GD (2018) Isothermal tensile deformation behaviors and fracture mechanism of Ti-5Al-5Mo-5V-1Cr-1Fe alloy in β phase field. Vacuum 156:187–197
17. Lin YC, Pang GD, Jiang YQ, Liu XG, Zhang XY, Chen C, Zhou KC (2019) Hot compressive deformation behavior and microstructure evolution of a Ti-55511 alloy with basket-weave microstructures. Vacuum 169:108878
18. Ning YQ, Xie BC, Liang HQ, Li H, Yang XM, Guo HZ (2015) Dynamic softening behavior of TC18 titanium alloy during hot deformation. Mater Des 71:68–77
19. Guo HZ, Yao ZK, Ning YQ, Miao XP, Ge MM (2017) Effect of initial alpha lamellar thickness on deformation behavior of a near-α high-temperature alloy during thermomechanical processing. Mater Sci Eng A 682:345–353
20. Yang XM, Guo HZ, Liang HQ, Yao ZK, Yuan SC (2016) Flow behavior and constitutive equation of Ti-6.5Al-2Sn-4Zr-4Mo-1W-0.2Si titanium alloy. J Mater Eng Perform 25:1347–1359
21. Yamanaka K, Matsumoto H, Chiba A (2019) A constitutive model and processing maps describing the high-temperature deformation behavior of Ti-17 alloy in the β-phase field. Adv Eng Mater 21:1800775

Part XIII
High Speed and Impulse Forming

High-Speed Material Characterization Using an Instrumented Forging Hammer



Julen Agirre, David Abedul, Angel Oruna, Nagore Otegi, and Lander Galdos

Abstract Hammer forging is a widely employed manufacturing process to produce parts with excellent mechanical properties. Although the rheological behavior and the microstructural transformation phenomena of metals under hammer forging conditions are of great industrial interest, few materials have been tested in such intermediate strain rates ($10–10^3$ s^{-1}) due to the lack of laboratory machines for intermediate speed testing. With the objective of addressing that gap, this paper presents a novel automatic forging simulator comprising an instrumented forging hammer capable of performing intermediate speed deformations, up to 5 m/s. Three data acquisition approaches were evaluated to select the most appropriate approach and obtain valid rheological data from intermediate strain rate tests performed on the developed hammer. First, the data obtained by both a high-speed camera and a load cell was combined to calculate reference flow curves. Then, two additional data monitoring approaches were then analyzed, employing independently first the high-speed camera and then the load cell data. It was concluded that flow curves obtained utilizing only the load cell data offered accurate results without the need for an expensive and complex high-speed camera.

Keywords Forging · Material characterization · High-speed testing · Hammer · Monitoring

J. Agirre (✉) · D. Abedul · A. Oruna · N. Otegi · L. Galdos
Advanced Material Forming Processes Research Group, Mondragon Unibertsitatea, Loramendi 4, 20500 Arrasate-Mondragon, Spain
e-mail: jagirreb@mondragon.edu

D. Abedul
e-mail: dabedul@mondragon.edu

A. Oruna
e-mail: aoruna@mondragon.edu

N. Otegi
e-mail: notegi@mondragon.edu

L. Galdos
e-mail: lgaldos@mondragon.edu

© The Minerals, Metals & Materials Society 2021

G. Daehn et al. (eds.), *Forming the Future*, The Minerals, Metals & Materials Series,
https://doi.org/10.1007/978-3-030-75381-8_100

1 Introduction

Hammer forging is a widely employed technology that produces parts with superior mechanical properties and with minimum material waste. The initial billet, which usually has a simple geometry, is plastically deformed in one or more operations to produce parts with complex final geometries. The process is attractive from an economic standpoint when a large number of parts must be produced and/or when superior mechanical properties are required [1]. Frequently, such exceptional mechanical properties are achievable only by a hammer forging process.

The most significant characteristic of hammer forging is the high deformation speed, and thus the high strain rates reached when forming the material. Although in other manufacturing processes such as machining operations the material is subjected to higher strain rates (10^3–10^6 s^{-1}) than those reached in hammer forging operations (10–10^3 s^{-1}), deformation speeds in hammer forging are much higher than those of press forging [2]. In the case of mechanical presses, this variable can reach a maximum of only 30 s^{-1}, and no more than 10 s^{-1} in hydraulic presses [2, 3].

Although the rheological behavior and the microstructural transformation phenomena of metals under hammer forging conditions are of great industrial interest, few studies have been carried out, and few materials have been tested in such intermediate strain rates. One of the main reasons is that there are not many commercial experimental facilities that allow testing under such conditions [2]. Conventional servo-hydraulic testing machines are commonly utilized for quasi-static strain rate testing ($\leq$10 s^{-1}), and high strain rate tests (>10^3 s^{-1}) are generally performed in split Hopkinson pressure bar (SHPB) testing machines [2]. However, there is a lack of laboratory testing facilities to perform tests in the gap between quasi-static and high strain rates. Numerous researchers have developed testing machines for intermediate strain rate testing, such as servo-hydraulic machines or modified SHPB systems. However, excessive acquisition noise or limited achievable strain levels are the main drawbacks of these machines [2]. Furthermore, very few of these testing facilities are equipped with a heating system, resulting in a lack of machines capable of performing tests at both intermediate strain rates and high temperatures.

This paper presents a novel automatic forging simulator developed to address this gap. This laboratory-scale testing machine is able to reproduce a wide range of real cold and hot industrial forging conditions, from low strain rates in an isothermal hydraulic press up to intermediate strain rates in an instrumented forging hammer. Additional forging strategies can also be tested, including intermediate heating cycles and combined strain rate deformations. Moreover, by modifying the sample geometry and the tooling of the forming modules, several loading conditions, such as compression, tension, or shear, can also be tested.

As regards the instrumented forging hammer, data acquisition in the intermediate to high-speed range is crucial to obtain valid and representative results. There exist a number of high acquisition-rate techniques to measure the kinematics and

load in these speed ranges. For kinematic data acquisition, non-contact measurement techniques are often used, e.g., high-speed cameras with digital image correlation (DIC), laser displacement sensors, or customized extensometers. The load applied to the specimen is typically measured by a Hopkinson bar or by a piezoelectric load cell connected to an amplifier and an oscilloscope [2]. The instrumented hammer presented in this paper is equipped with two of the aforementioned acquisition devices: a high-speed camera with DIC, and a piezoelectric load cell with an amplifier and an oscilloscope. These two techniques were selected as they offer a good compromise between cost, versatility, and robustness.

In the present paper, three acquisition approaches are evaluated so as to select the most appropriate approach and to obtain valid rheological data from intermediate strain rate tests performed on the instrumented forging hammer. For this purpose, the instrumented hammer was employed to perform cold uniaxial upsetting tests at four intermediate strain rates. The uniaxial compression test is a widely known method to determine the flow stress of a metallic material as a function of the strain applied, by compressing a cylindrical sample between two flat dies [4]. In this case, the tested material was S235JR structural steel.

First of all, data obtained by both the high-speed camera and the load cell was combined to calculate reference flow curves. With the aim of simplifying the data acquisition setup of the instrumented hammer, two additional data monitoring methods were then analyzed. These were data acquired solely by the high-speed camera to analytically calculate the flow curves, and data acquired by only the load cell to calculate the same stress–strain curves.

The suitability of each monitoring technique was evaluated in terms of the correctness and the sharpness of the acquired rheological data as well as the simplicity of the monitoring setup. Results of the three acquisition approaches were compared and evaluated and the most appropriate acquisition technique for the novel instrumented forging hammer was selected. This work forms the basis for future studies in intermediate strain rate testing, not only for flow data acquisition at these underexplored strain rates but also for the study of microstructural transformation phenomena of metallic materials at these strain rates and under cold to hot conditions.

2 Experimental Procedure

2.1 Instrumented Forging Hammer

Very few commercial laboratory machines are capable of testing materials at hammer forging strain rates (up to 300 s^{-1}). To address that problem, a novel automatic forging simulator was developed and constructed (Fig. 1). This automatic forging simulator was designed to perform compression, tension, and shear tests, in addition to crash tests. It comprised four main sections: a heating furnace (max. 1350 ºC), an isothermal hydraulic press, an instrumented hammer and a quenching medium.

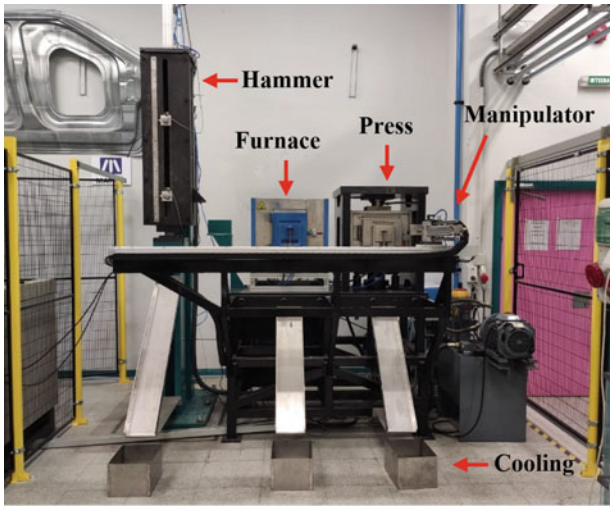


Fig. 1 Overview of the developed experimental forging simulator. (Color figure online)

To minimize human error and optimize manipulation times, the machine is fully automated, and sample manipulation is carried out by an electro-pneumatic system.

In the present paper, we focus on the instrumented hammer, as it was the only deformation module employed in the study. The hammer is pneumatically actuated and capable of performing high-speed deformations, up to 5 m/s. Such elevated speeds mean that upsetting tests at strain rates of up to 300 s^{-1} can be carried out (depending on the geometry of the tested sample), thus covering the range of strain rates commonly reached in industrial hammer processes. In a conventional uniaxial upsetting test, the strain rate at which the sample is deformed is calculated by the following equation (Eq. 1):

$$\dot{\varepsilon} = \frac{v}{h} \tag{1}$$

where v and h are the instantaneous deformation velocity and instantaneous sample height, respectively. As an example, if a strain rate of 300 s^{-1} is sought in a conventional uniaxial upsetting test with an initial deformation velocity of 5 m/s, an initial sample height of 16.67 mm would be needed. If a constant strain rate is required during the straining, a decreasing deformation velocity would need to be applied to the sample.

In the instrumented forging hammer presented in this paper, the sample is deformed by kinetic energy, propelling the upper die downward with a high-pressure pneumatic cylinder. Speed variation is accomplished by modifying the falling height of the upper die; the greater the falling height, the higher the deformation velocity, and thus, the higher the deformation energy. The weight of the upper die is 92 kg, and hence the maximum applicable deformation energy is 1.15 kJ.

2.2 Uniaxial Upsetting Tests and Data Acquisition Setup

With the objective of selecting the most appropriate acquisition approach to generate valid flow data at elevated strain rates, cold uniaxial compression tests were performed with the instrumented hammer at four different speeds (3.3, 4, 4.7, and 5 m/s) which correspond to four different strain rates (150, 200, 235, and 260 s^{-1}, respectively). Cylindrical samples (Ø13,5 × 20 mm) of S235JR structural steel were employed for the tests.

Although correct lubrication is necessary to obtain accurate compression flow data, in the present work neither lubrication nor Rastegaev-type samples were utilized. This is because the aim of this study was not to obtain accurate flow curves of S235JR but to evaluate different acquisition approaches. For the same reason, neither barreling nor temperature corrections were applied.

As regards data monitoring, two techniques were utilized to acquire load and displacement experimental data. For the measurement of the kinematics of the upper die, a Photron Fastcam-APX RS250K high-speed camera with appropriate illumination lamps was used (Fig. 2). This camera offers recording rates of up to 250,000 fps. In this study, experimental measurements were taken at 15,000 fps. Random point patterns were generated in the upper (moving) and lower (static) dies, and the deformation kinematics were obtained with the DIC software GOM Correlate (Fig. 3). For safety reasons, the deformation of the sample was carried out inside a cavity located on the lower side of the upper die. Therefore, for the strain calculation of the sample, the linear displacement of the upper die was taken into account. The upper die was considered rigid, and consequently, the motion of the upper die was determined to be equal to the deformation kinematics of the sample. To acquire the impact force, a piezoelectric load cell connected to an oscilloscope was employed (Fig. 2). This force sensor was mounted directly inside the lower static die of the hammer, and the acquisition frequency was 300 kHz.

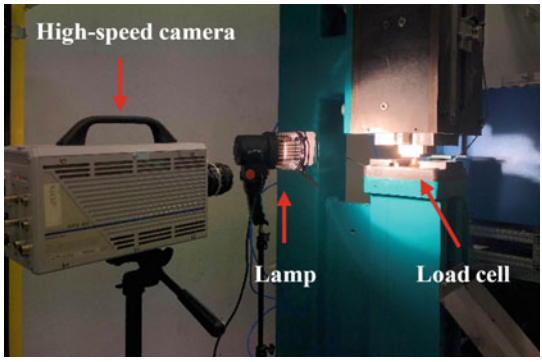


Fig. 2 Data acquisition setup. (Color figure online)

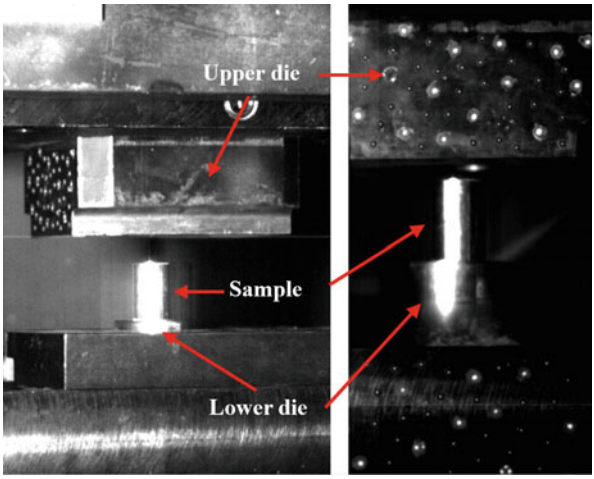


Fig. 3 Upper moving and lower static dies recorded with Photron Fastcam-APX RS250K high-speed camera. (Color figure online)

3 Results and Discussion

In this section, the experimental results are presented. First of all, reference flow curves are discussed, which were generated combining the kinematics obtained by the high-speed camera and the force measured by the load cell. Next, the two analytically calculated flow curves are presented, one using the data obtained by the high-speed camera, and the other is the data acquired by the force sensor. Finally, the flow curves generated by the three acquisition approaches are compared.

Henceforth, the lowest tested strain rate (150 s^{-1}) is referred to as case 1, the strain rate of 200 s^{-1} as case 2, the next higher strain rate (235 s^{-1}) as case 3, and the highest tested strain rate (260 s^{-1}) as case 4. Three repetitions were performed for each of the four velocities and a very low deviation was observed in all cases. Mean values were calculated for each case. As the test was automated, this undoubtedly enhanced the repeatability of the results.

3.1 Reference Curves

Reference flow curves were generated by combining the motion data obtained from the high-speed camera and the force measured by the load cell. As for the high-speed camera results, Fig. 4 shows the DIC technique employed for the acquisition of the kinematics of the upper and lower dies. A mean value of all the measured points was calculated in each of the dies. The displacement and velocity data of the four tested strain rates is presented in Fig. 5. As expected, it is observed that the higher the impact speed, the greater the sample deformation. A velocity peak can be seen at the beginning of each speed curve, at the instant in which the upper die makes

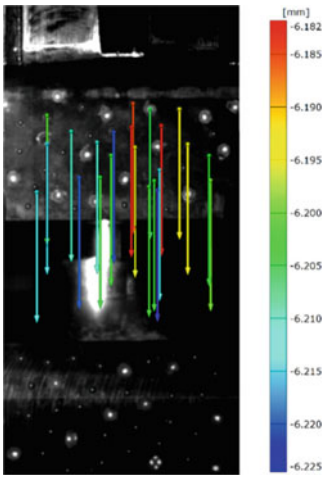


Fig. 4 Displacement of the upper die calculated with GOM Correlate DIC software. (Color figure online)

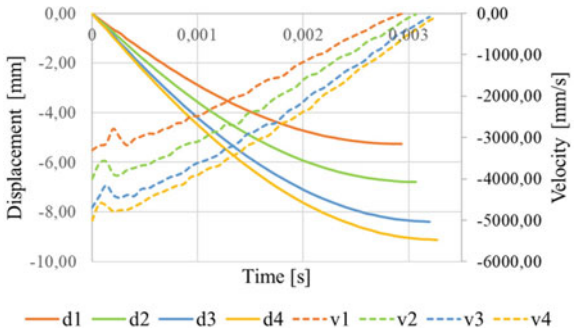


Fig. 5 Displacement and velocity of the upper die acquired with a high-speed camera. (Color figure online)

contact with the sample. This is likely due to the lack of lubrication between both surfaces, and thus the use of lubrication may smooth those peaks. It is also observed that the speed curves follow a relatively linear tendency.

It is important to highlight that only the motion data of the upper die was employed to generate the flow curves, disregarding the displacement of the lower die. In the most unfavorable case, that of the highest velocity, the maximum displacement of the lower die was 0.32 mm, while the maximum displacement of the upper die was 11.67 mm. In this case, the displacement of the lower die is 2.74% of the displacement of the upper die. Figure 6 shows the acceleration of the upper die during the high-speed deformation. Although the tendency is similar from case to case, high levels of noise and significant variations in acceleration values can be observed.

True strain values were calculated taking into account the displacement of the upper die measured by the high-speed camera (Eq. 2). Once true strain was calculated, true strain rate values were also obtained (Eq. 1). With respect to the evolution of strain rates during the uniaxial upsetting tests, once the upper die comes into contact with the sample, the die starts decelerating with a linear trend (Fig. 5). Figure 7

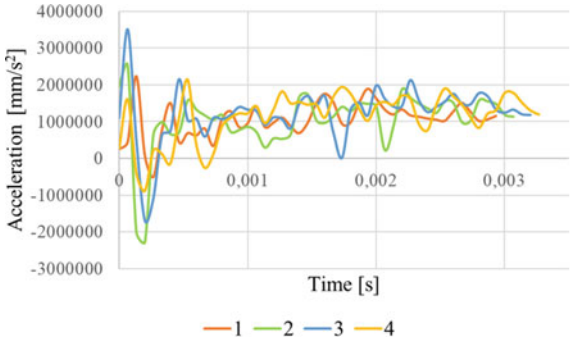


Fig. 6 Acceleration of the upper die acquired with a high-speed camera. (Color figure online)

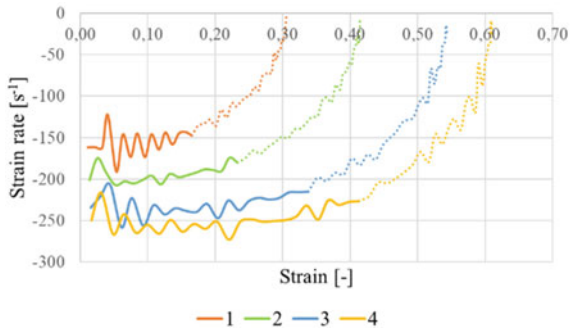


Fig. 7 Strain rates acquired with a high-speed camera. (Color figure online)

shows that the strain rate remains relatively constant up to a certain strain level, and this strain level is higher in the case of the highest deformation speed. Taking this into account, if a constant strain rate is sought, a criterion is needed to specify the strain level until which the test can be considered as strain rate constant. In the case of this work, a constant strain rate was considered until the strain rate dropped below 90% of the initial strain rate value. The constant strain rate ranges are marked as solid lines in Fig. 7 and the non-constant ranges as dotted lines. The figure shows that at the highest speed, strain rates of 250 s^{-1} are reached. In industrial hammer processes strain rates of up to 200 $s^{-1}$are attained, and thus the tests performed with the instrumented forging hammer covered the range of strain rates found in the industry.

As for data obtained by the load cell, Fig. 8 shows the force acquisition during the compression tests. It can be seen that the higher the strain rate, the higher the force needed to deform the material. As in the case of the velocities acquired by the high-speed camera, a peak is observed at the beginning of the force curves. This can be attributed to the first contact between the upper die and the sample and could be smoothed by applying lubrication between both surfaces.

Figure 9 sets out force vs displacement curves generated by combining the displacement captured with the high-speed camera, and the force acquired with

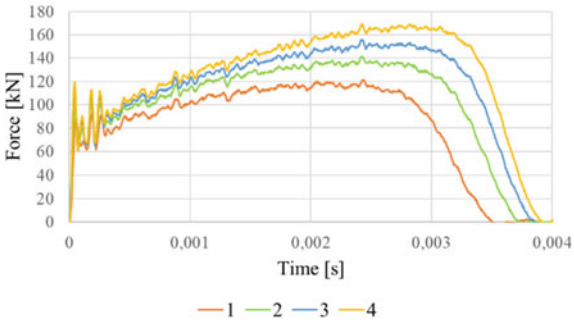


Fig. 8 Force data acquired with load cell. (Color figure online)

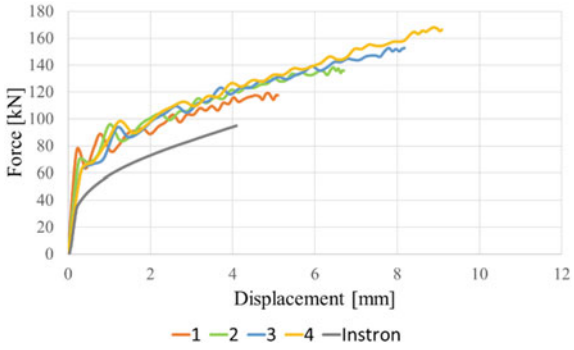


Fig. 9 Reference force versus displacement data. (Color figure online)

the load cell. Additionally, a force vs displacement curve obtained from a quasi-static compression test performed in a universal electro-mechanic drive Instron-4206 testing machine is shown. Compression tests in this standard testing machine were performed at a strain rate of 0.001 s^{-1}, significantly lower than the strain rates of the instrumented forging hammer, hence the difference in force.

To generate a typical stress–strain curve, displacement values were converted into true strain values by Eq. 2, and the force values were converted into stress values using Eq. 3:

$$\varepsilon = \ln\left(\frac{h}{h_0}\right) \tag{2}$$

$$\sigma = \frac{\vec{F}}{A} \tag{3}$$

where h is the height of the sample at each point of the test, h_0 is the initial height; and F and A are the force and transversal area at each point of the test, respectively. The instantaneous transversal area of the sample was calculated based on the following assumption (Eq. 5):

$$V_0 = V \tag{4}$$

$$A = \frac{A_0 \cdot h_0}{h} \tag{5}$$

where A_0 and h_0 are the initial area and initial height of the sample, respectively, and h is the instantaneous height of the sample measured by the high-speed camera. In cases of considerable barreling, this assumption can lead to errors. Little barreling was observed in the uniaxial upsetting tests performed in the current work, and therefore the assumption can be considered as valid (Fig. 10).

Reference true stress vs true strain flow curves is presented in Fig. 11. Interestingly, a maximum valid true strain of 0.42 was achieved at the highest strain rate. Intermediate strain rate flow curves show some noise which could be mathematically smoothed if needed. Quasi-static tensile and compression curves of tests performed in the aforementioned universal Instron testing machine are included in the figure as a reference.



Fig. 10 Tested samples at four different strain rates. (Color figure online)

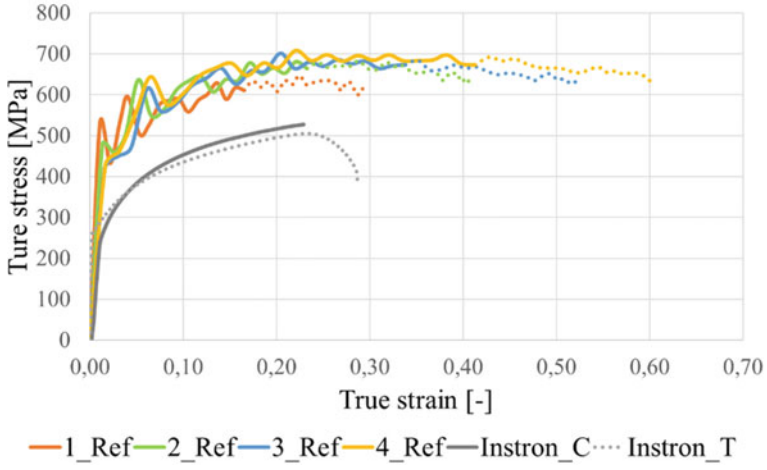


Fig. 11 Reference medium strain rate flow curves, and Intron compression (C) and Instron tensile (T) curves. (Color figure online)

3.2 Curves from High-Speed Camera Data Only

Once the reference flow curves were obtained by combining high-speed camera data and load cell data, a second approach was used to evaluate its ability to calculate valid flow data under hammer forging conditions. For this second approach, stress vs strain curves were generated by employing only data acquired by the high-speed camera. As the kinematics of the upper and lower dies can be directly acquired by the high-speed camera, the true strain is obtained. To analytically calculate the force data from the motion data measured by the high-speed camera, Newton's second law was followed (Eq. 6):

$$\vec{F} = m \cdot \vec{a} \tag{6}$$

where m is the total mass of the moving elements and $\vec{a}$ is the acceleration acquired by the camera. The mass of all the moving elements in the upper die was measured at 92 kg. As an example, in case 3 force acquired by the load cell and the force analytically calculated from camera data is shown in Fig. 12. Although the calculated curve follows the tendency of the reference load cell data, significant noise and a lack of sharpness can be distinguished. Moreover, at the beginning of the curve, at small strains, the calculated curve does not represent the reference curve.

By analytically calculating the force in all the cases (Eq. 6), and converting it into stress (Eq. 3), stress vs strain curves were generated from only the high-speed camera data (Fig. 13). Each case is presented separately as the noise makes differentiation difficult. Although the calculated flow curves follow the reference force tendencies measured by the load cell, significant noise is discernable in all cases. In addition, this monitoring technique is unable to represent the beginning of the flow curve at small strains.

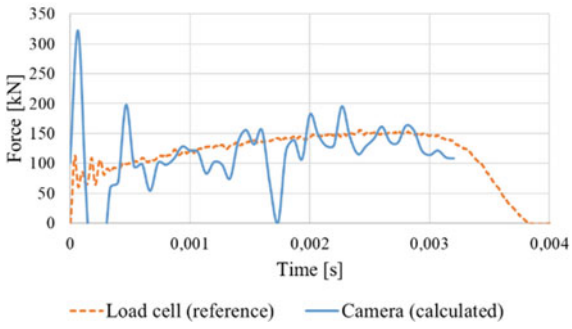


Fig. 12 Load cell (reference) force versus camera (calculated) force for case 3. (Color figure online)

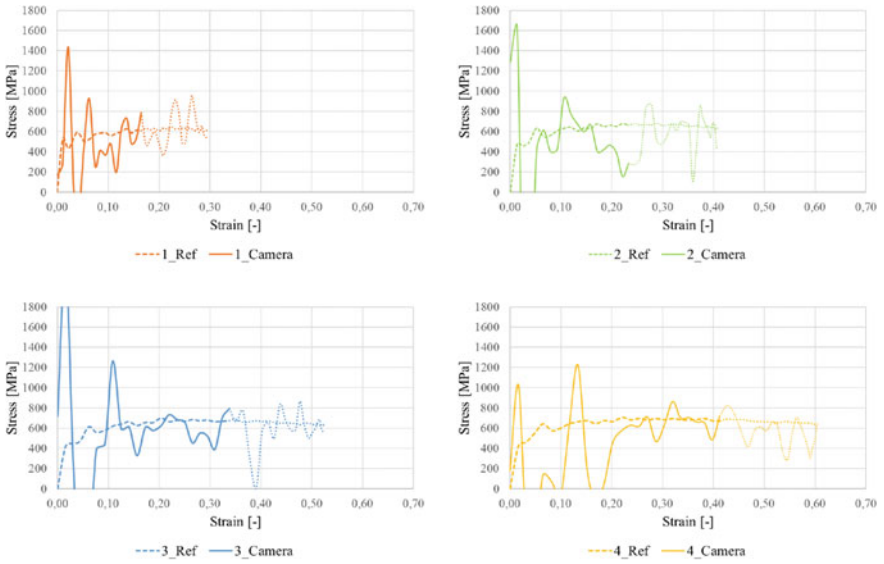


Fig. 13 Reference flow curves versus calculated (camera) flow curves for all tested velocities. (Color figure online)

3.3 Curves from Load Cell Data Only

Finally, a third acquisition approach was analyzed, in which medium strain rate flow curves were generated by only employing data acquired by the load cell. Deformation forces were directly acquired by the load cell, and to extract strain and stress data, acceleration was first calculated with Newton's second law (Eq. 7):

$$\vec{a} = \frac{\vec{F}}{m} \tag{7}$$

where m is the total mass of the moving elements and $\vec{F}$ is the force acquired by the load cell directly. It was known that the mass of all moving elements was 92 kg. Taking case 3 as an example, acceleration acquired by the high-speed camera and acceleration analytically calculated from load cell data is presented in Fig. 14. It can be clearly seen that the calculated acceleration follows the reference tendency. Furthermore, the calculated acceleration signal is significantly smoother and sharper than the acceleration acquired by the high-speed camera.

Once the acceleration was calculated, the equation of an accelerated linear motion was employed to calculate the position of the upper die at each point of the test (Eq. 6):

$$\vec{s} = \vec{s}_0 + \vec{v}_0 \cdot t + \frac{1}{2} \cdot \vec{a} \cdot t^2 \tag{6}$$

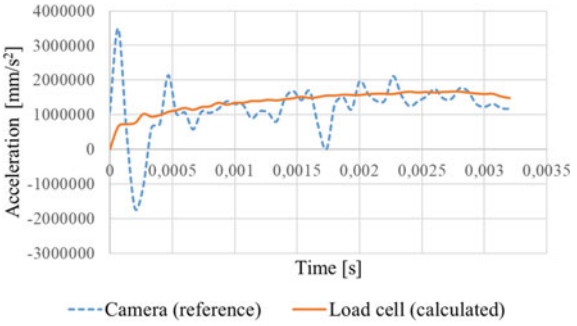


Fig. 14 Camera (reference) acceleration versus load cell (calculated) acceleration for case 3. (Color figure online)

where $\vec{s}_0$ is the initial position of the upper die, $\vec{v}_0$ is its initial velocity, $\vec{a}$ is its acceleration, and t is the time. To calculate position data using this equation, the initial velocity is the only variable that cannot be measured or analytically calculated from load cell data. Thus, in this case the velocity of the upper die just before the impact measured by the high-speed camera was used. However, as a future line, to analytically calculate the displacement of the upper die without employing an expensive and complex high-speed camera, the idea is to equip the hammer with a simple velocity measuring setup. To do so, two electrical switches separated by a known distance and connected to the same oscilloscope of the load cell will be utilized. The two switches will detect the upper die just before impact. Knowing the time difference between the two detectors and the distance between the two switches, the velocity of the upper die just before the impact will be calculated by Eq. 7:

$$\vec{v} = \frac{d}{\Delta t} \tag{7}$$

where d and Δt is the distance between the two detectors and the time difference between the two detections, respectively. By calculating the displacement in all cases (Eq. 6) and converting it into stress and strain data (Eqs. 2 and 3), flow curves were generated utilizing only the load cell data (Fig. 15).

The analytically calculated flow curves utilizing solely data acquired by the load cell and the reference flow curves show very good agreement. Similar noise is discernable in both cases and the deviation between them is minimum.

4 Conclusions

In this study, a novel automatic forging simulator comprising an instrumented forging hammer capable of performing intermediate speed deformations is presented. Three data acquisition approaches were evaluated so as to select the most appropriate

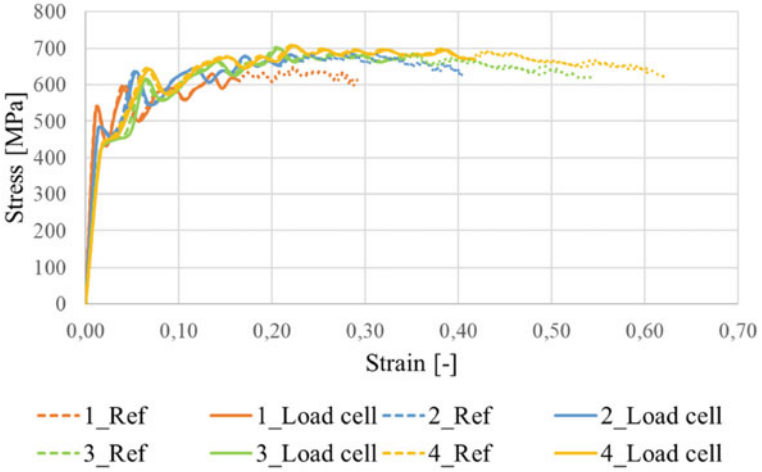


Fig. 15 Reference flow curves versus calculated (load cell) flow curves for all tested velocities. (Color figure online)

technique and obtain valid rheological data from intermediate strain rate upsetting tests. The main conclusions are set out as follows:

- Flow data calculated by employing only the high-speed camera was not sufficiently accurate and significant noise was discernable in all cases.
- Although analytically calculated forces followed reference force tendencies measured by the load cell, this monitoring approach was not sharp enough to precisely represent the beginning of the curve at small strain values.
- Stress vs strain data calculated by only employing data acquired by the load cell showed very good agreement with the reference flow curves without the need for an expensive and complex high-speed camera. Similar noise is discernable in both cases and the deviation between them is minimum. Moreover, no time-consuming DIC post-processing was required, and thus the flow data calculation is considerably faster.
- Based on these conclusions, it was determined that this acquisition approach will be implemented in the instrumented forging hammer for future material behavior analysis at medium strain rates.

Acknowledgments This work was funded by the Basque Government through the OGForge (Piezas forjadas de prestaciones extremas para el sector Oil and Gas mediante procesos de forja eficientes optimizados por modelos complejos de evolución microstructural) and DIGICUT (Estudio fundamental de procesos de corte y definición de las bases para su digitalización) research projects. The authors would also like to thank ULMA Forja S.Coop. and Fagor Arrasate S.Coop. for their economic and technical support.

References

1. Altan T, Ngaile G (2005) ASM cold and hot forging
2. Bhujangrao T, Froustey C, Iriondo E, Veiga F, Darnis P, Mata FG (2020) Review of intermediate strain rate testing devices. Metals (Basel) 10:1–24. https://doi.org/10.3390/met10070894
3. Prasad YVRK, Rao KP, Sasidhara S (2015) Hot working guide—a compendium of processing maps, 2nd edn. https://doi.org/10.1016/B978-0-08-033454-7.50019-X
4. Ye XJ, Gong XJ, Yang BB, Li YP, Nie Y (2019) Deformation inhomogeneity due to sample–anvil friction in cylindrical compression test. Trans Nonferrous Met Soc China (English Ed) 29: 279–86. https://doi.org/10.1016/S1003-6326(19)64937-X
5. Torrente G (2018) Numerical and experimental studies of compression-tested copper: proposal for a new friction correction. Mater Res 21. https://doi.org/10.1590/1980-5373-mr-2017-0905

Advancements in the Simulation of Magnetic Pulse Forming Processes with FORGE®



José Alves, François Bay, Ugo Ripert, Julien Barlier, and Nicolas Poulain

Abstract In this work, the latest developments on the electromagnetic (EM) module of FORGE® and the derived improvements for simulating the magnetic pulse forming process are presented. The following aspects are covered: advanced material description for high-intensity magnetic fields where coupling with the material database software JMatPro® is extended to account for the EM phenomena; integration of the forming limit diagrams (FLD) for analysis of thin sheets forming; improved meshing/remeshing for large displacements in the fully immersed multi-objects approach, where a particular focus is given to the fields transfer stage, showing how the overall CPU time can be reduced by half or more; and introduction of an advanced second-order time-stepping integration method based on an asynchronous interpolation that was previously developed for thermal-shock problems and is now extended to the computation of EM fields showing excellent convergency and stability properties.

Keywords Magnetic pulse forming · Finite elements

J. Alves (✉) · U. Ripert · J. Barlier
Transvalor S.A, 950 avenue Roumanille, CS 40237 Biot, 06904 Sophia Antipolis cedex, France
e-mail: jose.alves@transvalor.com

U. Ripert
e-mail: ugo.ripert@transvalor.com

J. Barlier
e-mail: julien.barlier@transvalor.com

F. Bay
MINES Paris-Tech, PSL- Research University, CEMEF—Center for Material Forming CNRS UMR 7635, CS 10207 rue Claude Daunesse, 06904 Sophia-Antipolis Cedex, France
e-mail: francois.bay@mines-paristech.com

N. Poulain
Transvalor Americas, 17 North State Street, Chicago, USA
e-mail: nicolas.poulain@transvaloramericas.com

© The Minerals, Metals & Materials Society 2021

G. Daehn et al. (eds.), *Forming the Future*, The Minerals, Metals & Materials Series,
https://doi.org/10.1007/978-3-030-75381-8_101

1 Introduction

The interest in high-speed forming processes and especially magnetic pulse forming (MPF) continues to grow due to the benefits these processes bring to forming metallic alloys that show low formability under regular forming conditions when compared to conventional steels. This is the case for aluminum alloys, copper alloys, and in some cases magnesium alloys. For some materials, it has been shown that deformation at high strain rates improves the formability limits [1]. A debate is still ongoing on the exact mechanisms responsible for such phenomena. It is argued that at such strain rates the internal available energy enables a viscous almost fluid-like flow. It is also argued that shock waves traveling within the bulk of the material allow for a very efficient release of elastic deformation and residual stresses [2]. These improvements in formability are not systematically found and thus there is continuous research on the description of material properties. In the case of MPF, it is also necessary to consider the presence of large magnetic fields. For instance, Li et al. [3] recently showed the influence of high pulsed magnetic fields at low strain rates on an Al7055 alloy. In that work, it was shown that between 0 and 3 T the forming limit increases by up to 20%, and the residual stresses decrease by a factor of 10. Beyond that point, and up to 7 T the forming limit decreases with respect to 0 T, and the residual stresses are found at the same levels. In a typical MPF process, the magnetic field can reach values beyond 10 T that, even if for a short period of time,[1] can contribute to the activating movement of dislocations affecting the mechanical behavior during forming and the in-use properties afterward.

Due to the complex multi-physical interactions in this process, it is not obvious how to properly quantify the influence of each physical phenomenon. As experimental research continues to bring more information on the behavior of several kinds of materials, it is also necessary to improve the existing mathematical and numerical models which are the tools for interpreting the underlying phenomena and help in the decision-making process for optimizing energy consumption, material usage, and so on.

In this work, some of the latest developments done within the numerical simulation software FORGE® and its electromagnetic module FORGE®\Induction are presented. After a review of the fundamental physical principles, it is shown how the material data software JMatPro® can be used to obtain a first approximation of rheological and physical properties to carry out complex numerical simulations. Furthermore, the possibility of evaluating forming limit diagrams for high strain rate data is presented. In the following sections, numerical aspects related to time-step integration of the electromagnetic problem, automatic time-stepping on the mechanical side when dealing with impact conditions in MPF, and improvements to the data communication stages needed for the coupling of the several physics involved in the simulation are covered.

[1] A medium-size MPF machine delivers between 5 and 20 kJ of energy which is about the same energy stored in a modern smartphone battery. This energy is delivered in a time laps of less than 100 μs in order to release the power required to plastically deform the materials.

2 Multi-Physical Model

The computational model is based on a loose coupling between a thermo-mechanical dedicated solver and an electromagnetic dedicated solver (Fig. 1).

2.1 Thermomechanical Model

The solid mechanics model takes into account the conservation of linear momentum Eq. (1) and the mass conservation equation for compressible media:

$$\begin{aligned} \nabla \cdot \underline{\underline{\sigma}} + \vec{f} &= \rho \frac{D\vec{v}}{Dt} \\ \nabla \vec{v} &= \frac{1}{\rho}\frac{d\rho}{dt} \end{aligned} \tag{1}$$

where $\underline{\underline{\sigma}}$ denotes the Cauchy stress tensor, ρ the material density, $\vec{f}$ the volumetric force density vector in which the external loadings such as gravity or the Lorentz body forces are defined. Temperature evolution in the workpiece is determined by solving the heat transfer equation:

$$\rho C_p \frac{\partial T}{\partial t} - \nabla \cdot k \nabla T = \dot{Q} \tag{2}$$

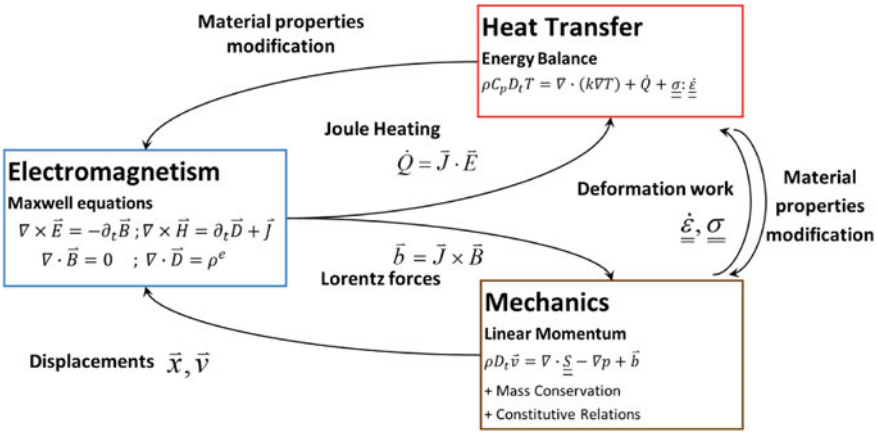


Fig. 1 Global interaction scheme of the physical models for electromagnetically-driven processes. (Color figure online)

where C_p represents the specific heat and k the thermal conductivity. The volumetric heat source term $\dot{Q}$ is made up of the sum of the dissipated heat due to plasticity and of the induced Joule power.

2.2 Electromagnetic Model

The electromagnetic model is based on the quasi-static state approximation of Maxwell equations expressed in the scalar-vector potential form:

$$\begin{aligned} &\sigma \frac{\partial \vec{A}}{\partial t} + \frac{1}{\mu_0} \nabla \times \frac{1}{\mu_r} \nabla \times \vec{A} = -\sigma \nabla \phi \\ &\nabla \cdot \sigma \nabla \phi = 0 \end{aligned} \tag{3}$$

where $\vec{A}$ is the magnetic vector potential, ϕ represents the scalar electric potential, σ denotes the electric conductivity, μ_0 the magnetic permeability of void space, and μ_r the material relative permeability.

2.3 Spatial Discretization

The 3D finite element discretization is carried out using tetrahedral finite elements which have the advantage of enabling automatic and fast remeshing strategies for any complex geometry. This basic geometry is declined in different linear formulations depending on the physical field to be computed as shown in Fig. 2.

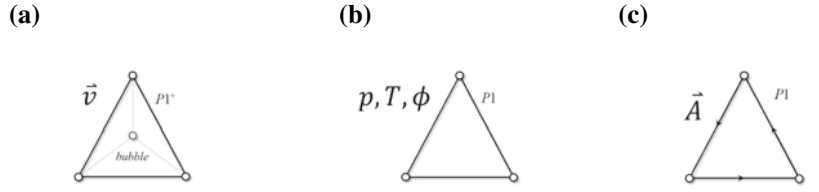


Fig. 2 Type of linear elements used in FORGE®. **a** Bubble linear element for the velocity field. **b** Regular P1 element for pressure, temperature, and electric potential fields. **c** Edge or Nédélec [5] element for the magnetic potential

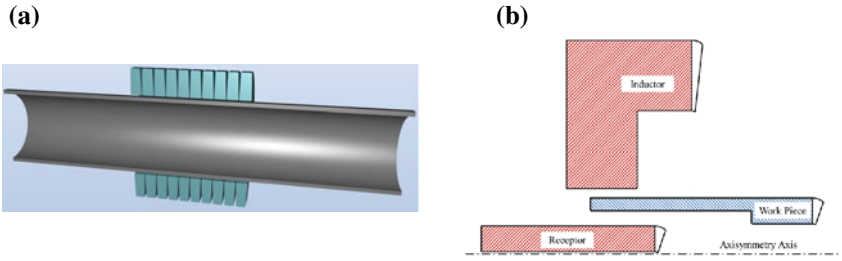


Fig. 3 **a** Free compression test of an Al6066-T6 tube [6]. **b** Magnetic pulse crimping of an aluminum Al2024 tube with a copper cylinder [7]. (Color figure online)

2.4 Test Cases

In order to test the different developments proposed in the following, two formerly introduced test models were used. The first case corresponds to a free compression test case (Fig. 3a)—courtesy of the I^2FG group. The second one consists of a magnetic pulse welding simulation of an aluminum alloy with a copper bar (Fig. 3b)—courtesy of BMAX.

3 Complex Material Behaviors and Strain-Rate-Dependent Forming Limit Diagrams

In order to define a useful material description, it is not only important to consider all the electromagnetic and thermo-mechanical interactions but also to choose the scale at which such interactions are to be represented/analyzed. At the macro-scale either phenomenological behavior laws or homogenization approaches can be used to describe the material behavior with sufficient accuracy and reasonable computational times. From a phenomenological approach, it is common to use rheological behavior models adapted to high strain rates such as the Johnson–Cook model. The disadvantage of such approaches is the need for large experimental tests to fit the model parameters. The advantage is that once fitted these models enable very accurate results within the range of loading conditions at which they were obtained.

Another additional approach typically used as a first estimate for the material description when no experimental data is available or neither possible to obtain is the application of software such as JMatPro® or Thermo-Calc®. These allow generating material behavior models for a large range of physical properties. For instance, within the FORGE® framework, all material parameters are defined as thermo-dependent, i.e., density, heat capacity, thermal conductivity, electrical resistivity, Young's modulus, etc. Furthermore, the magnetic permeability is defined as a function of the magnetic field as well as the temperature $\mu_r = f\left(T, \vec{H}\right)$ within

Table 1 Mean chemical composition of an Al6066-T6 aluminum alloy

Component	Al	Cr	Cu	Fe	Mg	Mn	Si	Ti	Zn
wt%	93.15	0.4	1.2	0.5	1.4	1.1	1.8	0.2	0.25

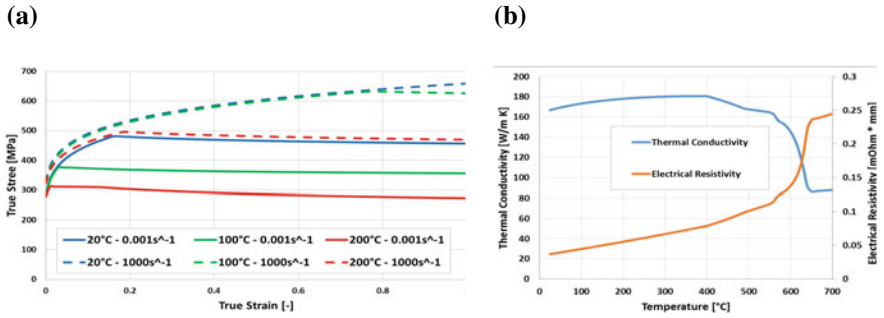


Fig. 4 Rheological data and physical data for the Al6066-T6 as generated by JMatPro® v11. (Color figure online)

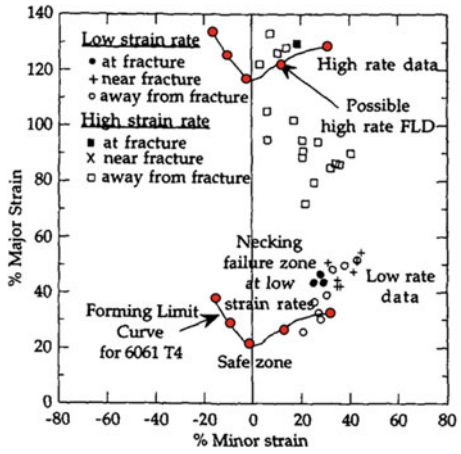
the electromagnetic module.[2] A compressible elasto-viscoplastic (EVP) model is applied for the mechanical representation of the stress–strain interaction in solid mechanics. All these properties can be found for several types of alloys from JMatPro® by entering the chemical composition as input. An example is shown for the Al6066-T6 alloy in Table 1 and Fig. 4.

As mentioned at the beginning, one of the key interests in MPF technologies is the possibility to access increased formability regimes for difficult-to-form materials. It is common practice to characterize formability using forming limit diagrams (FLD) in applications with thin metal sheets or thin tubes. Within this approach, the strain state is projected to a principal reference frame in which it is assumed that only two of the three components are necessary to fully characterize the formability. The third component is assumed to correspond perfectly to the deformation in the thickness direction of the part and to be uniform.

An example of an FLD as reported from the literature is shown in Fig. 5. Here it is shown how the formability of an Al6061-T4 alloy is increased at high strain rates. Nevertheless, it is important to highlight that it is also reported that this behavior is not necessarily incremental, i.e., below some unknown strain rate threshold value no improvements are observed. As this field continues to evolve, the possibility to define experimentally obtained FLDs was introduced in the software allowing the use of simulation for validation/verification purposes.

In order to use 3D volume elements in this context, the total strain tensor is projected on all external surfaces (triangles) of the mesh. The tensor is rotated on a space orthogonal to the normal direction of each surface. Two principal strain components parallel to the surfaces are computed from this rotation. These values

[2] At large magnetic field conditions it is usual to assume full magnetization of the material ($\mu_r = 1$).



$$\varepsilon_I = f(\varepsilon_{II}, T, \dot{\varepsilon})$$

Piece-wise linear file data-base

Fig. 5 Forming limit diagram of Al6061-T4 aluminum alloy as reported in [1]. (Color figure online)

are then used to compute how far away a surface element is from the forming limit curve, giving a factor between (0 and 1) if the element is below the FLC and in the "safe" region or (>1) if the element overpasses the FLC. An example is shown in Fig. 6 where the FLD is computed using a piecewise linear description as shown by the red dots in Fig. 5.

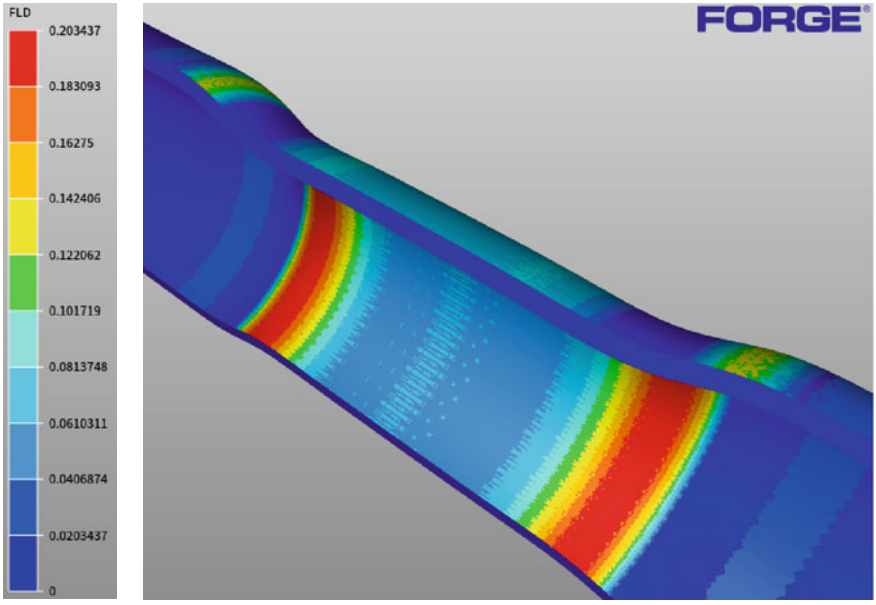


Fig. 6 Distribution of the forming limit criteria for the tube compression test. (Color figure online)

4 Robust Second-Order Time-Stepping

One of the key aspects in modeling evolution problems is how to properly discretize the time dependency. It is needed to have a robust, stable, and consistent method to minimize the divergence between the numerical approximation and the "real" solution. In this work, the use of a family of second-order methods presented previously is introduced in the software FORGE® for the thermal problem and extended to the electromagnetic problem, as described in Eq. (3). A detailed description can be found in [8, 9]. In the following, a brief summary of the method is given:

A system of ordinary differential equations is given as:

$$C\frac{\partial X}{\partial t} + KX = Q \tag{4}$$

It is required to compute X at a future time t_{n+1} assuming all state and input fields are known at the current time t_n and a past time t_{n-1}, where $t_{n+1} > t_n > t_{n-1}$, $\Delta t = t_{n+1} - t_n$ and $\Delta t_0 = t_n - t_{n-1}$ are the current and previous time-steps. An asynchronous time is also introduced as shown in Fig. 7.

The discretization and equilibrium are established at a virtual time as follows:

$$t^* = \alpha_1 t_{n-1} + \alpha_2 t_n + \alpha_3 t^a_{n+1}; \alpha_1 + \alpha_2 + \alpha_3 = 1 \tag{5}$$

$$X^* = \alpha_1 X_{n-1} + \alpha_2 X_n + \alpha_3 X^a_{n+1} \tag{6}$$

$$\frac{\partial X^*}{\partial t} = (1-\gamma)\frac{X_n - X_{n-1}}{\Delta t_0} + \gamma\frac{X^a_{n+1} - X_n}{\Delta t_a} \tag{7}$$

$$C^*\frac{\partial X^*}{\partial t} + K^* X^* = Q^* \tag{8}$$

The assembly of the linear system is written as:

$$\left[C^* + \frac{\alpha_3}{\gamma}\Delta t_a K^*\right]X^* = \frac{\alpha_3}{\gamma}\Delta t_a Q^* + C^*\left(\alpha_2 + \frac{\Delta t_a}{\Delta t_0}(\gamma - 1)\frac{\alpha_3}{\gamma} + \alpha_3\right)X_n$$

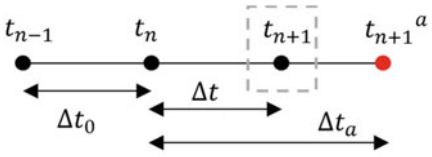


Fig. 7 Discretization of time in the asynchronous time-integration approach. (Color figure online)

$$+\left(\alpha_1 - \frac{\Delta t_a}{\Delta t_0}(\gamma - 1)\frac{\alpha_3}{\gamma}\right)X_{n-1} \tag{9}$$

And the actual solution at t_{n+1} is re-interpolated by:

$$X_{n+1} = \frac{\Delta t}{\alpha_3 \Delta t_a}X^* + \left(1 - \left(1 + \frac{\alpha_2}{\alpha_3}\right)\frac{\Delta t}{\Delta t_a}\right)X_n - \frac{\alpha_1}{\alpha_3}\frac{\Delta t}{\Delta t_a}X_{n-1} \tag{10}$$

For practical purposes $\Delta t_a = \Delta t$ is used, meaning that there are four numerical parameters to define the integration scheme. The method is defined:

- unconditionally stable if

$$\gamma \geq \frac{1}{2}; \alpha_1 > \frac{1}{2}(1 - \gamma)$$

- and consistent if

$$\alpha_2 = 1 - \alpha_1 + \left(\frac{1}{2} - \alpha_1\right)\frac{\Delta t_a}{\Delta t} - \frac{\gamma}{2}\left(1 + \frac{\Delta t_a}{\Delta t}\right)$$

$$\alpha_3 = \left(\alpha_1 - \frac{1}{2}\right)\frac{\Delta t_a}{\Delta t} + \frac{\gamma}{2}\left(1 + \frac{\Delta t_a}{\Delta t}\right)$$

In order to respect both conditions, there are only two free numerical parameters from where to choose α_1 and γ. Otherwise, the consistency condition can be violated as is the case for the classical Euler-implicit method (Table 2).

To evaluate the influence of the integration method on the resolution of the electromagnetic problem, the evolution of the active power (Joule heating) during the discharge using the test case 1 was investigated. The comparison is done by selecting different levels of refinement of the time-step applied to the electromagnetic problem: in this case $dt = [0.1, 0.5, 1]\,\mu$s. As shown in Fig. 8, for the Euler-implicit method the active energy is underestimated as the time-step grows, implying that for a reliable computation it would be necessary to use systematically small time-steps. For the Dupont-implicit method, the estimations are almost identical enabling larger time-steps with higher confidence in the results.

Table 2 List of some known time-integration schemes that can be derived from the proposed method

Name	γ	α_1	α_2	α_3	Observation
Euler-implicit	1	0	0	1	Stable but not consistent
Crank-Nicolson	1	0	1/2	1/2	
Dupont-implicit	3/4	0	0	1	The multiplying factors are the same as the QSSC method previously tested in [4]
Lees	1/2	1/3	1/3	1/3	

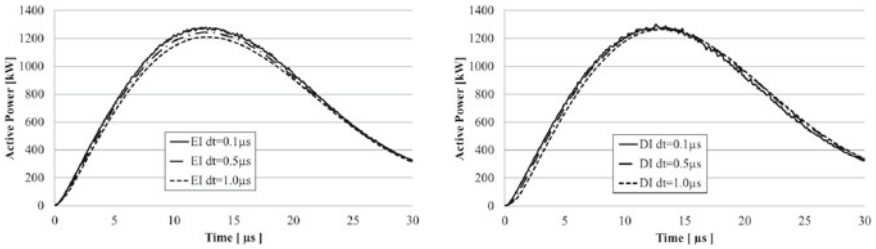


Fig. 8 Comparison of the numerical convergence for three time-step refinements of the active power in the electromagnetic model. (Left) Euler-implicit method. (Right) Dupont-implicit method

5 Field Transport Optimization

Several improvements have been introduced in the meshing/remeshing step necessary to enable the following large displacements and deformations within the resolution of the electromagnetic problem. In the following, some of the strategies that have been adopted and the improvements on the overall computational time are presented.

When talking about numerical computation, one of the key aspects is the fact that communicating information is more computationally costly than executing an algebraic computation. This is also the case for finite element simulations in which it dealt with different meshes to represent different physical phenomena and the communication between the different meshes is mandatory. Within the framework of electromagnetic simulation in FORGE®, there are four stages in which information must be communicated between different meshes. The first one will not be covered here being placed within the thermo-mechanical computation during remeshing. The other three stages (Fig. 9) correspond to (1) the communication from the electromagnetic module to the thermo-mechanical module, (2) the update of the electromagnetic model from the thermo-mechanical one, and (3) the recovering of a previously computed increment within the electromagnetic module if the mesh is modified.

Since a single mesh containing all solids is used in our numerical approach for electromagnetic computation, in some cases the communication between the two stages can be computationally costly. This is especially true in stages (1) and (3). The most time-consuming aspect is to build the acceleration structure which can be thought of as an index that allows a fast look up of a given point within a source mesh. There are several techniques that can be used to build this structure like octrees or the bounding volume hierarchy method. The latter is used with a bottom-up strategy (build containing cells from small to big) in order to build a precise and optimal search tree. However, the computational cost is far from negligible.

In order to reduce the CPU time dedicated to this stage, the notion of filters within the acceleration structure creation phase was introduced. These filters enable using the existing methodologies with minimum modification of the original algorithms. The basic idea is to include a label on elements/nodes from the source mesh during

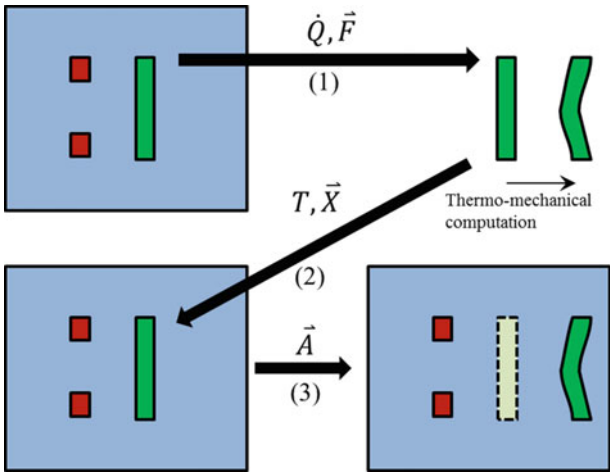


Fig. 9 Main communication stages between the electromagnetic solver and the thermo-mechanical solver. (1) Transfer of Joule heat term and Lorentz forces. (2) Transfer of temperature and displacements. (3) Transfer of magnetic vector potential from the previous time-step, if remeshing of the electromagnetic mesh (Color code: blue = air, red = coil(s), green = billet). (Color figure online)

Table 3 Comparison of CPU time burden of field transport operations (notation: EMAG—electromagnetic module, MECA—thermomechanical module)

	(1) EMAG to MECA	(2) MECA to EMAG	(3) EMAG to EMAG
Without filter	~14 s	~800 ms	~20 s
With filter	~0–150 ms	~800 ms	~2 s

the creation of the search tree in order to skip them. In this particular case, the filter is applied to all elements "labeled" as belonging to the air and the coil.

In the following example, case 1 will be considered as a coupled configuration as in [6]. The electromagnetic model contains 281,265 elements and 58,883 nodes, while the thermo-mechanical model of the aluminum tube contains 66,895 elements and 12,696 nodes. The computation runs until a stop time of $100\mu s$ with a coupling time-step of $1\mu s$. In this case, a single electromagnetic increment requires 9 s.[3] When running the simulation without the filters, the total CPU time amounts to 1 h, while it is reduced to 0.5 h when including the filters. This reduction by a factor of 2 is caused by the optimization of the transport operation in stage (1). As seen in Table 3, stage (1) takes 14 s on average without filters and almost 25 min in total (100 couplings). This communication time is reduced enormously by applying the filter, making it almost negligible. A large reduction is also attained for stage (3) but since remeshing

[3]Computations done on 8 processors of an Intel® Xeon® CPU E5-2630 v3 @ 2.40 GHz on a Windows7 OS.

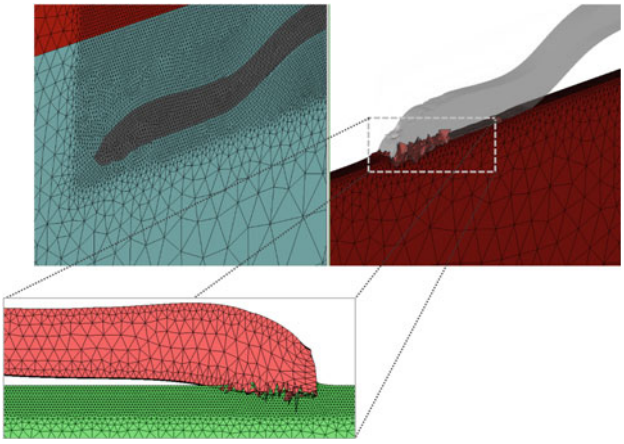


Fig. 10 Numerical defect at impact condition (mesh interpenetration between colliding bodies) if constant mechanical time-step is used [2]. (Color figure online)

of the electromagnetic mesh is done just once[4] it doesn't have a big impact on the overall computing time.

6 Automatic Thermo-Mechanical Time-Stepping

It was reported in [2] that one of the weaknesses of the established simulation strategy was the requirement of using a constant time-step for the mechanical computation, mainly to enable a proper update of the electromagnetic mesh. As a consequence, there was a certain lack of flexibility in dealing with impact conditions (see Fig. 10). This problem could be bypassed by simply restarting the simulation stage just before the impact and then enable automatic time-step adaptation. Such an approach is nonetheless cumbersome to enable ease of use and generality of the numerical approach. In order to fix this issue, the information that is recovered by the electromagnetic solver was modified. The previous approach was based on the transport of the current velocity field. In the new approach, the total cumulated displacements added to the storage of the initial configuration of the system are used instead. While demanding more memory to allocate an additional field information (initial configuration), this cost is totally negligible, and the change of mesh update paradigm allows for a greater flexibility.

The new approach was tested using test case number 2. A constant time-step for communication between the solvers ($0.5\,\mu$s) was established but the thermo-mechanical solver was allowed to automatically adapt the time-step to loading conditions. As seen in Fig. 11, the time-step decreases in order to enable correct conver-

[4] For the other increments a nodal relocation algorithm is used allowing to reuse a given mesh longer.

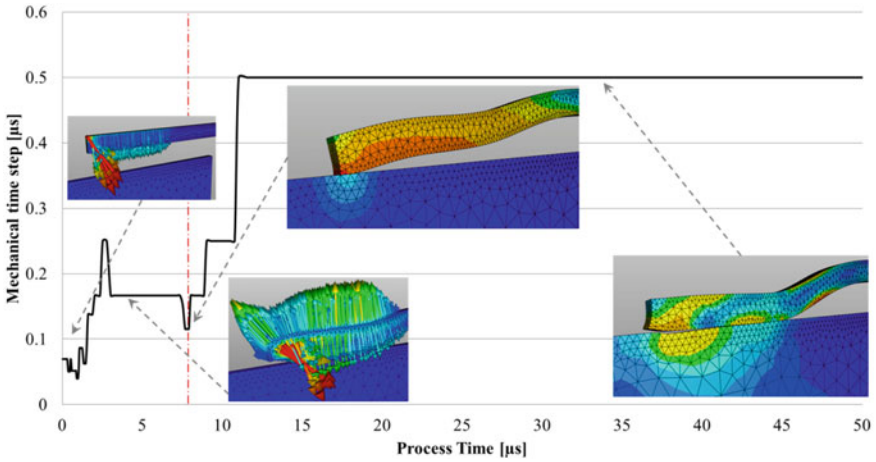


Fig. 11 Automatic adaptation of the mechanical time-step. (Color figure online)

gence of the nonlinear iterative algorithm at the beginning of the mechanical computation. The time-step increases as the simulation advance because a regular evolution path is found. A drop occurs when approaching contact in order to enable proper impact without interpenetration of the meshes. After impact, an almost steady-state is reached allowing for the time-step to reach the maximum value ($0.5\,\mu$s).

7 Conclusions and Perspectives

In this work, the state-of-the-art regarding the simulation of induction-driven processes and particularly for MPF simulations within the FORGE® framework was reviewed. It was presented how to make use of external material databases to define complex material behaviors. All these developments are the result of cross-related needs in different technological domains which have pushed the software forward to enable faster computations with reliable, robust, and easily parallelizable algorithms. A recent development introduced in the software is the possibility of defining experimentally obtained FLDs. This option was also rendered depending on additional fields such as strain rate in order to enable studying processes such as magnetic pulse forming which show increased formability within certain loading conditions.

Models with increasing complexity can be computed, as the simulation software regularly increases its computational capability and enables to reduce computational time.

The definition of material behavior is one important aspect undergoing great advances. Besides describing complex rheological paths, it is also possible to include

metallurgical aspects such as by-phase behavior. Enabling this approach will allow increased accuracy in material behavior modeling.

Another ongoing project devoted to error estimation and adaptive remeshing will enable using mesh adaptation techniques based on error estimator for the electromagnetic computation.

References

1. Balanethiriam V, Daehn GS (1994) Hyperplasticity: increased forming limits at high workpiece velocity. Scr Metall Mater 30:515–520
2. Alves Zapata JR (2016) Magnetic pulse forming processes: computational modelling and experimental validation
3. Li GR, Cheng JF, Wang HM, Li PS, Li CQ (2016) Influence of a high pulsed magnetic field on the tensile properties and phase transition of 7055 Aluminum alloy. Mater Res Express 3(10)
4. Alves Zapata JR, Bay F (2016) Modeling and analysis of electromagnetism in magnetic forming processes. IEEE Trans Magn 52(5): 1–12
5. Nédélec JC (1986) A new family of mixed finite elements in $\mathbb{R}3$. Numer Math 50(1):57–81
6. Bay F, Alves J (2018) A computational model for magnetic pulse forming processes—application to a test case and sensitivity to dynamic material behaviour. Ichsf 2–10
7. Alves JR, Barlier J, Marie S, Beraudo C, Bay F (2015) Modelling of large displacements and large strains in coupled electromagnetic/solid mechanics/heat transfer problems. In: EPM 2015, 8th international conference on electromagnetic processing and materials 2015, Cannes, Fr., no. SIMAP laboratory proceedings-EPM Group, pp 243–246
8. Soyris N (1990) Modelisation Tridimensionnelle du couplage thermique en forgeage a chaud. Ecole Nationale Superieure des Mines de Paris
9. Pelissou C (2005) Discrétisation spatio-temporelle du problème thermique à deux champs. Application au procédé de forgeage à chaud. Ecole Nationale Superieure des Mines de Paris

The High-Speed Deformation Behavior of High-Strength Lightweight Al-Li Alloy Sheets



Ali Abd El-Aty, Shi-Hong Zhang, Xunzhong Guo, Yong Xu, Ma Yan, Dayoung Chen, and Jie Tao

Abstract Since high-strength lightweight Al-Li alloys gained much attention recently, investigating the dynamic behavior of high-strength lightweight AA2060-T8 sheets is crucial because of their outstanding mechanical properties. Thus, uniaxial tensile tests were performed under high strain rate conditions using universal testing machines and split Hopkinson tensile bars. The ductility of AA2060-T8 sheets was improved under HSR deformation because of the adiabatic softening with increasing strain rate and the inertia effect, which may diffuse necking, slow down the necking development, and delay the onset of fracture. The present study results can efficiently develop a new manufacturing route based on impact hydroforming technology (IHF) to manufacture sound thin-walled-complex shape components from high-strength lightweight Al-Li alloy sheets at room temperature.

Keywords Al-Li alloys · AA2060-T8 · High-speed deformation · Impact hydroforming

1 Introduction

In recent years, Al-Li alloys have acquired much attention for their weight and stiffness-critical structures used in aircraft, military, and aerospace because of their superior outstanding properties, such as low density and high specific strength, than

A. Abd El-Aty (✉) · X. Guo · J. Tao
College of Material Science and Technology, Nanjing University of Aeronautics and Astronautics, Nanjing 211100, P.R. China

X. Guo · J. Tao
Jiangsu Key Laboratory of Nuclear Energy Equipment Materials Engineering, Nanjing University of Aeronautics and Astronautics, Nanjing 211100, P.R. China

A. Abd El-Aty · S.-H. Zhang · Y. Xu · M. Yan · D. Chen
Institute of Metal Research, Chinese Academy of Sciences, Shenyang 110016, P. R. China

A. Abd El-Aty
Mechanical Engineering Department, Faculty of Engineering-Helwan, Helwan University, Cairo, Egypt

© The Minerals, Metals & Materials Society 2021

G. Daehn et al. (eds.), *Forming the Future*, The Minerals, Metals & Materials Series,
https://doi.org/10.1007/978-3-030-75381-8_102

those of commercial Al alloys. The exceptional properties of Al-Li alloys are principally attributed to the added Li, which impacts the elastic modulus and weight reduction, where 1 wt.% of Li increases the elastic modulus by approximately 6% and reduces the resultant Al alloy's density by approximately 3% [1–3]. Based on the production date, Al-Li alloys are classified into three generations: first-generation Al-Li alloys such as AA1420, AA1421; second-generation Al-Li alloys such as AA8090, AA2090; and third-generation Al-Li alloys such as AA2050, AA2060 [2, 3].

AA2060-T8 is one of the newest candidates in the family of the third-generation Al-Li alloys launched by Alcoa Inc. in 2011 to replace AA2024-T3 and AA7075-T6 for upper and lower wings and fuselage structures [1, 3, 4]. The challenges associated with using AA2060-T8 sheets with conventional forming technologies are (1) poor formability because of the micro-voids and micro-cracks during processing; (2) anisotropic tensile properties, which caused serious issues during press forming; (3) and wrinkling and springback, which, in turn, adds to the cost of the die and the final products because of the try-out time. The aforementioned issues of AA2060-T8 restrict its broad applications [2, 3].

For the reason that AA2060-T8 was launched a few years ago, few studies on understanding the mechanical behavior, deformation mechanism, and anisotropic response of this alloy, notably at elevated temperatures, have been accomplished. For instance, Abd El-Aty et al. [5] studied the mechanical behavior and the texture evolution of AA2060-T8 during the bending process using PRM. Abd El-Aty et al. [6] learned the dislocation boundary structures of AA2060-T8 during the bending process, and they found that three types of microstructures were formed during bending. Ou et al. [7] revealed the deformation behavior of AA2060-T8 under hot forming conditions. Gao et al. [8] used their outstanding results [7] to investigate the feasibility of manufacturing aircraft components from AA2060-T8 using the HFQ process. Abd El-Aty et al. [4–6] proposed a computational method-based crystal plasticity modeling to link the mechanical response of AA2060-T8 sheets with their microstructural states and predict their deformation behavior at room temperature and different strain rates. Later, Abd El-Aty et al. [3] investigated the mechanical behavior of AA2060-T8 sheets at room temperature and a wide range of strain rates.

From the discussion mentioned above, it is evident that the quasi-static and high-speed deformation behavior of high-strength lightweight AA2060-T8 Al-Li alloy sheets and the constitutive relations which describe the flow behavior of AA2060-T8 sheets under high strain rate conditions are not investigated. The flow behavior of Al-Li and Al alloys under high strain rate deformation is complicated because they depend on several factors, such as the deformation mode, strain, and strain rates [9]. These factors control the strain hardening and dynamic softening, which affects the flow behavior and formability of these alloys [10–12]. Thus, characterizing the quasi-static and high-speed deformation behavior of high-strength lightweight AA2060-T8 Al-Li alloy sheets is meaningful to describe their mechanical response at various deformation conditions.

2 Experimental Procedures

The material used in this study was rolled AA2060-T8 sheet. HSR tensile tests were done using SHTB apparatus at room temperature to investigate the dynamic behavior of AA2060-T8 sheet at RD and strain rates of 1733, 3098, 3651, and 3919 s^{-1}. The sample orientations in HSR tensile tests were not considered since the sample orientations significantly impacted the case of quasi-static strain rates rather than HSR [1, 3]. The experimental setup of the SHTB apparatus and the details of the tensile specimen used in this test are depicted in Fig. 1. The HSR experiment was supposed to be started once the tensile sample was placed between the incident and the transmitter bars. However, the material being studied was rolled sheets with 2 mm thickness. Thus, a novel gripping method (clamp) was designed to integrate it in the SHTB apparatus for providing adequate clamping forces to avoid the tensile specimens from slipping during the experiments and introducing a low mechanical impedance to prevent the distortion of the waves. Once the novel clamp was implemented in the SHTB apparatus, the tensile specimen was placed between the incident and transmitted bars; thereafter, the striker situated on the incident bar impacted the flange, leading to the generation of a tensile wave (incident wave) that propagated along the incident bar, as depicted in Fig. 2. The strain gauge located on the incident bar recorded the incident wave ($\boldsymbol{\varepsilon_I}$) once it passed. Once the incident wave ($\boldsymbol{\varepsilon_I}$) hits the specimen, it is partly reflected ($\boldsymbol{\varepsilon_R}$) through the incident bar and partly transmitted ($\boldsymbol{\varepsilon_T}$) through the tensile specimen and the transmitted bar, as shown in Fig. 2. These reflected and transmitted waves were recorded by the strain gauges (using a high-velocity acquisition system, i.e., an oscilloscope) situated on the incident and transmitted bars, respectively. A schematic and a real set of waves detected during the SHTB experiment are depicted in Figs. 3 and 4. The progress of the HSR tensile

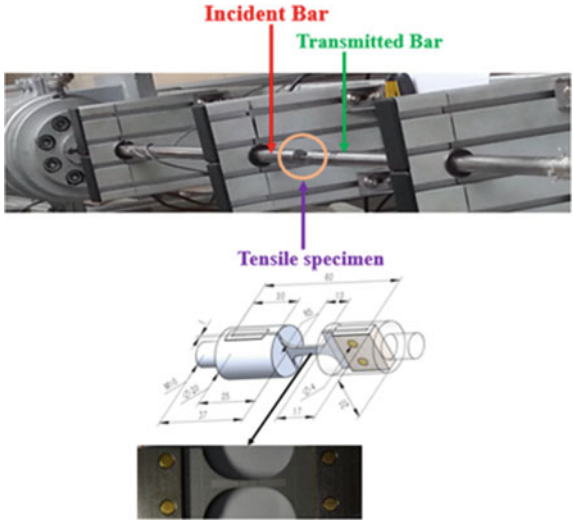


Fig. 1 The actual setup of the SHTB apparatus. (Color figure online)

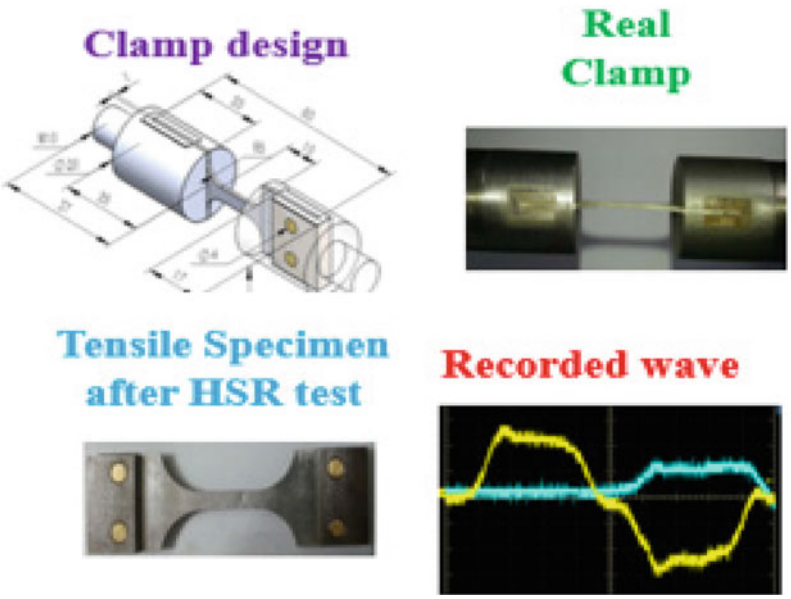


Fig. 2 The final version of the novel clamp used to avert the specimens from slipping during the test. (Color figure online)

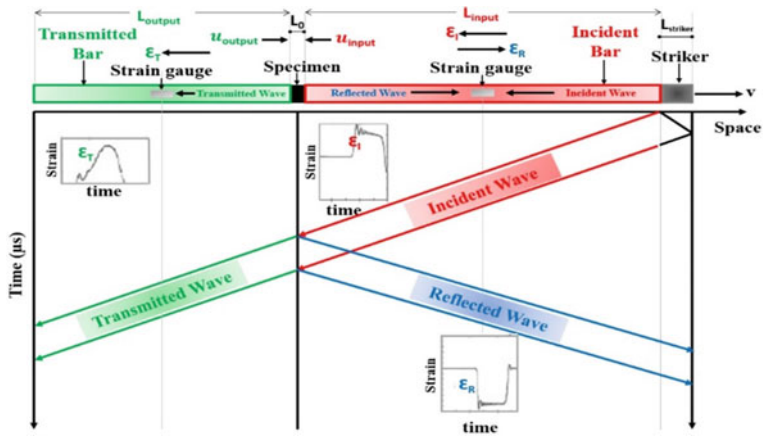


Fig. 3 The schematic representation of stress waves propagation in the bars. (Color figure online)

specimen during HSR tensile testing is illustrated in Fig. 5.

For simplicity, it was assumed that the equilibrium condition was verified during all the test, thus the mean strain and mean stress are generalized as:

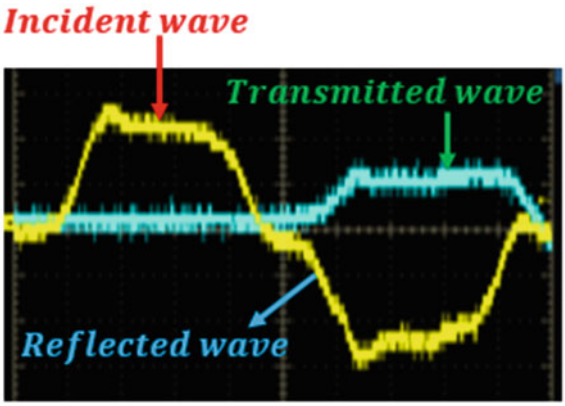


Fig. 4 The waveforms recorded by the oscilloscope during the HSR test. (Color figure online)

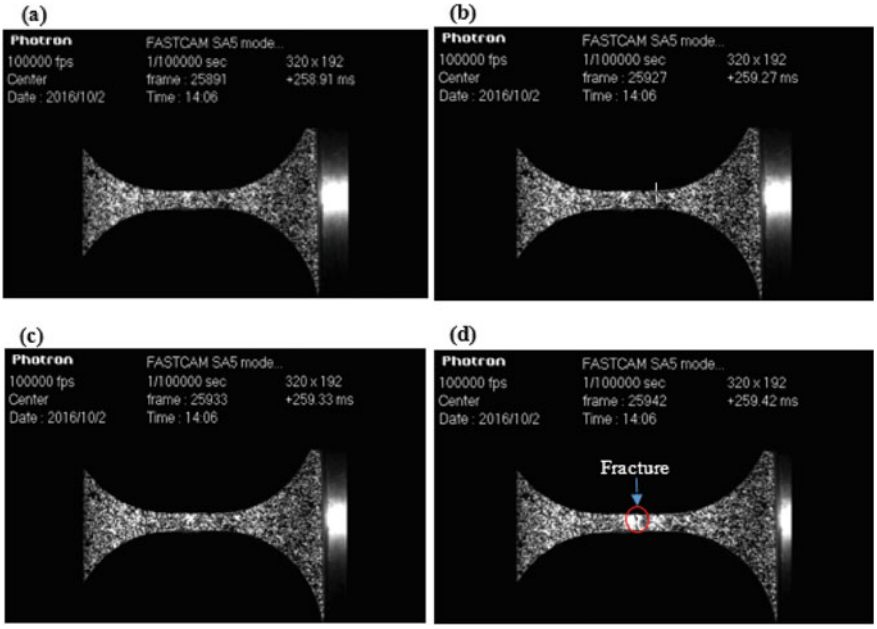


Fig. 5 The HSR tensile specimen **a** at the beginning of HSR tensile testing; **b** after 36 μs; **c** after 41 μs; and **d** after 51 μs from the beginning of HSR testing, in which the tensile specimen was broken. (Color figure online)

$$\varepsilon(t) = -\frac{2C}{L_0}\int_0^t \varepsilon_R(t)dt \tag{1}$$

$$\sigma(t) = E\frac{A}{A_0}\varepsilon_T(t) \tag{2}$$

The promptly axial strain rate ($\dot{\varepsilon}$) in the tensile sample was calculated from the first derivative of Eq. 1, so it can be written as

$$\dot{\varepsilon}(t) = \frac{v_{\text{input}}(t) - v_{\text{output}}(t)}{L_0} = -\frac{2C}{L_0}\varepsilon_R(t) \tag{3}$$

From Eq. 3, it could be perceived that with the SHPB equipment, the tests are not performed precisely at a constant strain rate. Only in the ideal case of the perfectly rectangular reflected wave, i.e., an entirely plastic response of the specimen, the strain rate is constant during the whole specimen deformation. In practice, this is almost impossible to observe and, generally, the nominal strain rate (average value of the effective strain rate) which used to indicate the strain rate of tests performed on the Hopkinson bar apparatus. Thus the HSR experiments were accomplished at strain rates of 1733, 3098, 3651, and 3919 s^{-1}.

3 Results and Discussion

3.1 Stress–Strain Behavior

The (σ_e, e) curves of AA2060-T8 sheets under HSR conditions are shown in Fig. 6. The work hardening behavior observed in HSR testing is more prominent than that

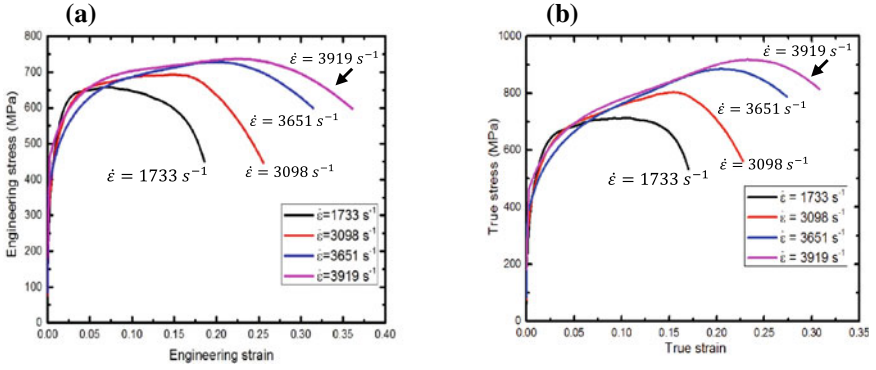


Fig. 6 **a** Engineering, and **b** true stress–strain curves of AA2060-T8 sheets at RD and HSR zone (i.e., $\dot{\varepsilon} = 1733s^{-1}$,$\dot{\varepsilon} = 3098s^{-1}$, $\dot{\varepsilon} = 3651s^{-1}$, and $\dot{\varepsilon} = 3919s^{-1}$). (Color figure online)

detected in QSR and ISR testing [1–3]. Thus, the yield, flow, and ultimate tensile stresses at HSR were higher than their QSR and ISR counterparts, which are generally attributed to the increased strain rates. Notwithstanding, the strain hardening rate observed in HSR testing was lower than that in QSR and ISR testing. This is attributed to the competition between the strain hardening and thermal softening due to adiabatic temperature rise with increasing strain rate. Thus, adiabatic softening influence is significant in HSR deformation and leads to abnormal mechanical behavior [34–37]. The strain rate increased to 1733, 3098, 3651, and 3919 s^{-1} (i.e., strain rate changed from QSR to HSR). The elongation to fracture of AA2060-T8 sheets in the HSR zone was simultaneously improved by increasing the strain rate, which is an appealing feature in HSR deformation. This enhancement is attributed to the adiabatic softening with increasing the strain rate and the inertia effect, which may diffuse necking, slow down the necking development, and delay fracture onset.

3.2 Design and Manufacturing a Novel Machine Based on IHF Technology

Based on the results mentioned above and the results obtained from Ma et al. [13], a new manufacturing route based on HSF was developed and denoted as IHF. Based on this new manufacturing route and principle of IHF, an advanced IHF machine was designed and manufactured, depicted as Fig. 7. There are four zones in this machine. Power zone can provide very high acceleration to the projectile, which is as high as 3200 m/s^2. The acceleration zone supplies the acceleration distance for the projectile and the release rig. The dynamic resistance reduction technology is implemented by controlling the air and adopting a special structure to reach high impact velocity.

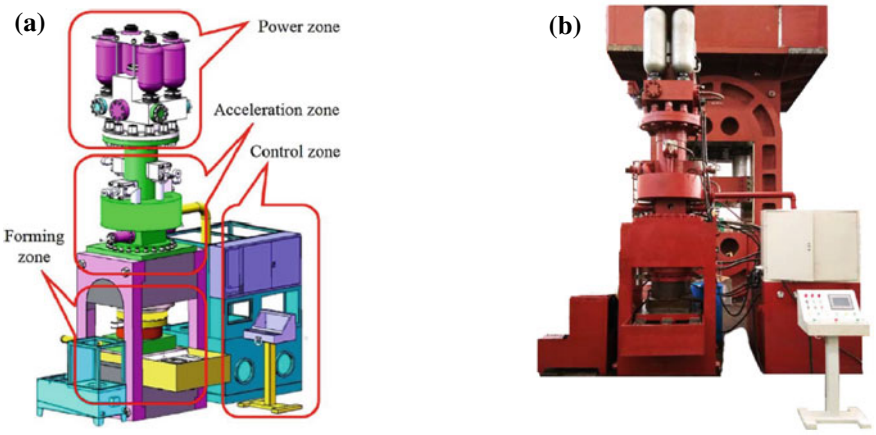


Fig. 7 (**a**) The schematic description, and (**b**) actual setup of IHF machine. (Color figure online)

Forming zone supplies the liquid chamber, binder hydraulic cylinder, and moveable working table. The control zone supplies the control function to all of the hydraulic valves to control the equipment's action. And the machine can run both under manual and automatic mode by inputting the code to the control board. The current research equipment's power source is the hydraulic-driven system, which can provide higher forming energy. For previous works, the power source is a pneumatic or explosive material, and their projectile is a solid cylinder that can freely move in the acceleration tube. The projectile of the current equipment is connected and controlled by a driven rod, capable of realizing more precise control. Furthermore, this equipment is more automatically run, which is suitable for industrial applications. The projectile's mass and the impact velocity and impact energy of the designed IHF machine are 60 kg (changeable), 10–80 m/s, and 3–200 kJ, respectively. The diameter and the volume of the liquid chamber are 250 mm (changeable) and 3–9 L. The dimensions of the working table are 800×800 mm, the max blank holder force is 250 T, and the binder hydraulic cylinder can be opened up to 400 mm.

3.3 Bulging Test

This novel IHF machine was used in this study to conduct a hydro-bulging test to investigate the formability of AA2060-T8 sheets under IHF loads and compare these results obtained from the bulging test under conventional hydroforming (quasi-static loading) loading. The specimens used in the bulging test were machined from AA2060-T8 sheets, and the radius of these samples is 83.6 mm.

Since the IHF machine's impact energy is 3–200 kJ, the impact velocity can be reached up to 80 m/s. As depicted in Fig. 7, the test specimen placed on the lower and upper dies was fixed on the master cylinder of the IHF machine by the fixing ring. The locating ring was used to guide the upper die to the right position along the axial direction. After the upper die contacted the test specimen with suitable clamping pressure, the high-speed hammer accelerated the liquid (Projectile). Thereafter, the test specimen was formed by the liquid with high energy in the shock wave. The velocity sensor was set in the chamber's lateral wall, whose position was near the liquid's upper surface to detect exactly the final velocity of the accelerated hammer. Each test condition was investigated at least three times to ensure consistency and repeatability.

The bulge height (h_B) of each test specimen was measured as depicted in Fig. 8 to assess the IHF loading effect on the formability of AA2060-T8 sheets and build up a window to describe the relationship between the impact energy (E_I) and the corresponding bulge height. This window is denoted as bulge height–impact energy (h_B–E_I) window, as presented in Fig. 9. The impact energy was used in this study instead of the pressure because the projectile's speed and mass mainly decide the impact energy. Furthermore, it is easy to calculate it compared to the pressure, especially under IHF conditions. As shown in the (h_B–E_I) window, under the IHF loading, the bulge heights of the test specimens were increased by increasing the impact energy



Fig. 8 The measurement tool used to measure the bulge height of each test specimen. (Color figure online)

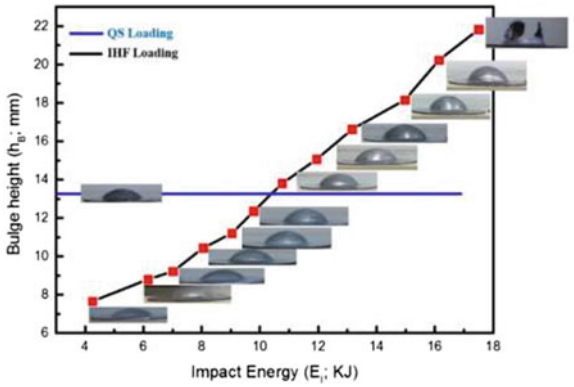


Fig. 9 Bulge height–impact energy (h_B–E_I) window describing the relation between the impact energy (k_J) and the corresponding bulge. (Color figure online)

up to 16.2 kJ; beyond this value, the test specimens were ruptured. The max bulge height obtained from IHF loading before rupture was 20.23 mm; however, the max bulge height obtained from conventional hydroforming loading using max pressure of 28 MPa was 13.3 mm as depicted in (h_B–E_I) window. This means and proves that the developed IHF technology can improve the formability of AA2060-T8 sheets at room temperature.

3.4 Manufacturing Aircraft Frame Part by IHF Technology

To investigate IHF technology's feasibility to fabricate thin-walled complex-shaped components, a complicated aircraft frame part was selected as a case study. The details of the aircraft frame part are depicted in Fig. 13. As shown in Fig. 13a, the aircraft frame part consists of eight convex shapes, outer surfaces, two concaves (concave 1 and concave 2), with drawing ratios (DR) of 3.88 and 3.52, respectively.

The ***DR*** in this study was calculated from Eq. 4 as:

$$DR = \frac{\textbf{blankarea}}{\textbf{concavearea}} \tag{4}$$

Because of the complexity of the shape of the aircraft frame and high ***DR*** compared to the common DR limit of steel sheets, 2 or many redrawing steps were required to reduce the DR for each step. The convex zones between the two concave zones are relatively easy to crack, as depicted in Fig. 10b since the strain is easy to exceed the forming limits. Furthermore, there are many small fillets (2 mm) at the outer surfaces and the concaves' bottoms. These small fillets increase the difficulties of forming this component. According to the theories of hydroforming, the smaller the radius, the higher the pressure, since it is challenging to supply the material to the radius zone because of the frictions under the high pressure, and form the material which already contacted the surface of the die and supply the material to the radius zone because of the friction under this increased pressure.

In the beginning, actual trials were performed to investigate the feasibility of forming the aircraft frame part using a quasi-static sheet hydroforming process (QS-SHF). As depicted in Fig. 11a, b large crack has appeared, and the outer surface of the frame part has a wrinkling tendency. This is because there is not enough material flowing to the fillet area to achieve the feeding effect. The rounded material's plastic deformation ability cannot meet the forming requirements, thus causing large area cracking. Therefore, the IHF technology was used to address the issues mentioned

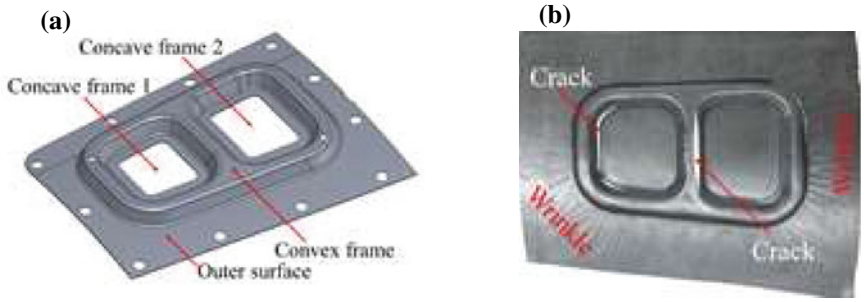


Fig. 10 **a** The aircraft frame part's details, **b** The actual aircraft frame part with wrinkle and crack formed by sheet hydroforming process (SHF). (Color figure online)

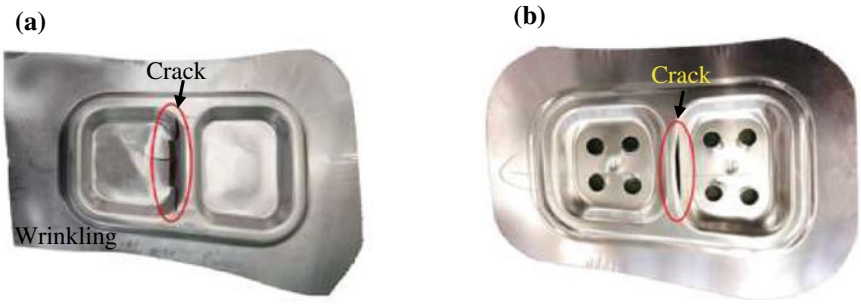


Fig. 11 Actual trials to produce the frame part by one step **a** QS-SHF, **b** IHF. (Color figure online)

above of QS-SHF. It is observed that the formability of the AA2060-T8 sheets was improved under the HSR condition. Furthermore, the cracking tendency and wrinkling were reduced compared to QS-SHF. However, the final product still has a small crack, as depicted in Fig. 11b. By analyzing the results obtained from both one-step QS-SHF and IHF, as shown in Fig. 11, it is challenging to manufacture the frame part by the one-step forming process. This is attributed to the high ***DR*** of concave 1 and concave 2. Thus, multi-step forming processes were used to overcome the limitations of the one-step forming process.

First, the pre-forming stage was accomplished using QS-SHF. The pre-forming stage improved and controlled the flow and the distribution of the material during the deformation. After that, to investigate and compare the effect of forming process on the formability and the crack tendency, the second forming stage was performed using either QS-SHF or IHF. Based on the original design of the frame part, the pre-formed parts were proposed as depicted in Fig. 12, since the rounded part of the inner side of the two cavities was increased from 2 to 20 mm. Furthermore, the width of the eight convex shapes is also increased.

After successfully carrying out the pre-forming stage, many trials were performed using both QS-SHF and IHF as a second forming stage. It is observed that the cracks still exist in the frame part produced by QS-SHF. However, no cracks were detected,

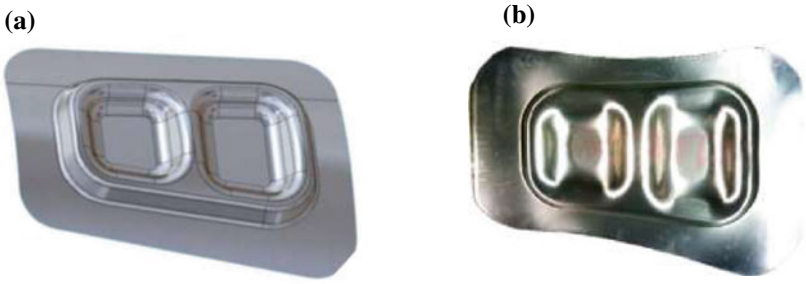


Fig. 12 **a** The CAD model, and **b** the actual trial of the pre-formed frame part. (Color figure online)

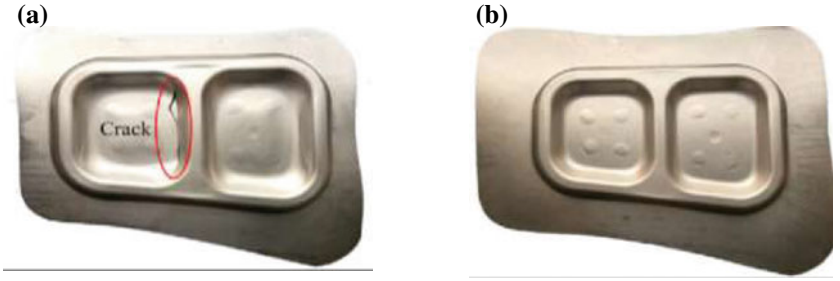


Fig. 13 The frame part was produced by **a** QS-SHF, **b** IHF after pre-forming. (Color figure online)

and the wrinkling was reduced in the frame part produced by IHF, as depicted in Fig. 13.

4 Conclusions

The main conclusions of this investigation can be deduced based on the achieved results as follows:

1. The work hardening behavior observed in HSR deformation is more prominent than that detected in QSR deformation. Thus, the YS, flow stress, and UTS at HSR were higher than their QSR counterparts. The strain hardening rate observed in HSR deformation was lower than that in QSR deformation, which was attributed to the competition between the strain hardening and thermal softening due to increasing the adiabatic temperature with increasing strain rate. The ductility of AA2060-T8 sheets was improved under HSR deformation because of the adiabatic softening with increasing strain rate and the inertia effect, which may diffuse necking, slow down the necking development, and delay the onset of fracture.
2. These results obtained from this study were efficiently used to develop a new manufacturing route called impact hydroforming technology (IHF). The IHF technology can improve the formability of lightweight metals and manufacture thin-walled complex-shaped components from Al-Li and Al alloys.

Acknowledgments The authors greatly acknowledge the financial support from the National Natural Science Foundation of China—International (Regional) Cooperation and Exchange Program (No. 5201101342), Jiangsu Province Science and Technology Project (No. BK20200453), and the National Natural Science Foundation of China (Grant No. 51875548).

References

1. Abd El-Aty A, Xu Y, Guo X, Zhang S, Ma Y, Chen D (2018) Strengthening mechanisms, deformation behavior, and anisotropic mechanical properties of Al-Li alloys: a review. J Adv Res 10:49–67
2. Rioja R, Liu J (2012) The evolution of Al-Li base products for aerospace and space applications. Metall Mater Trans A 43A:3325–3337
3. Abd El-Aty A, Xu Y, Zhang S, Ma Y, Chen D (2017) Experimental investigation of tensile properties and anisotropy of 1420, 8090 and 2060 Al-Li alloys sheet undergoing different strain rates and fibre orientation: a comparative study. Procedia Eng 207:13–18
4. Abd El-Aty A, Xu Y, Ha S, Zhang S (2018) Computational homogenization of tensile deformation behaviors of a third generation Al-Li alloy 2060–T8 using crystal plasticity finite element method. Mater Sci Eng A 731:583–594
5. Abd El-Aty A, Ha S, Zhang S, Xu Y (2018) Prediction of tensile deformation behavior of Al-Li alloy 2060–T8 by computational homogenization-based crystal plasticity finite element method. J Phys Conf Ser 1063:12058
6. Abd El-Aty A, Zhang S, Xu Y, Ha S, Deformation behavior and anisotropic response of 2060 Al-Cu-Li alloy: experimental investigation and computational homogenization-based crystal plasticity modelling. J Mater Res Technol
7. Ou L, Zheng Z, Nie Y, Jian H (2015) Hot deformation behavior of 2060 alloy. J Alloys Compd 648:681–689
8. Gao H, Weng T, Liu J, Li C, Li Z, Wang L (2016) Hot stamping of an Al-Li alloy: a feasibility study. Manufacturing Rev 9:9–15
9. Lin Y, Chen X (2011) A critical review of experimental results and constitutive descriptions for metals and alloys in hot working. Mater Des 32:1733–1759
10. Liang H, Nan Y, Ning Y, Li H, Zhang J, Shi Z, Guo H (2013) Correlation between strain-rate sensitivity and dynamic softening behavior during hot processing. J Alloy Compd 632(25):478–485
11. Babu B, Lindgren L (2013) Dislocation density based model for plastic deformation and globularization of Ti-6Al-4V. Int J Plast 50(8):94–108
12. Derogar A, Djavanroodi F (2011) Artificial neural network modeling of forming limit diagram. Mater Manuf Process 26(11):1415–1422
13. Ma Y, Xu Y, Zhang SH, Banabic D, Abd E-A, Chen D et al (2018) Investigation on formability enhancement of 5A06 aluminium sheet by impact hydroforming. CIRP Ann 67(1):281–284

The Effects of the High-Velocity Shearing Speed on the Sheared Edge Quality and Edge Cracking



J. Gu, F. Alamos, D. Schoch, J. Bornhorst, and H. Kim

Abstract High-speed shearing was studied to potentially improve the sheared edge quality of advanced high-strength steels. The AIRAM pneumatic press can provide significantly higher speed than a conventional press, up to 1.5 m/s depending on equipment setup at a low energy cost. The study evaluated the pneumatic press that could increase the slide speed up to 1.5 m/s. Various grades of AHSS steel, DP780 and GEN3-980, were sheared using the pneumatic press with two different operating pressure levels as well as using a conventional press with 0.2 m/s with the same tooling. The edge quality of the sheared blanks was evaluated using half-specimen dome test (HSDT) and microhardness tests. The effects of high-speed shearing are discussed in this paper.

Keywords Edge cracking · Pneumatic press · Advanced high-strength steel (AHSS) · High-velocity shearing

1 Introduction

As the lightweight steel demand has been increasing in the automotive industry, more advanced high-strength steel (AHSS) has been considered for the automotive body structure. However, the edge cracking issue of the AHSS has been a challenge. Many research programs have been conducted to evaluate and improve the sheared edge quality.

(a) The effect of shear die clearances on the edge formability has been reported by Konieczny and Henderson [1] and Lee et al. [2].
(b) The critical parameters that influence the edge local formability were investigated by Pathak et al. [3].

J. Gu (✉) · F. Alamos · H. Kim
EWI - Forming Center (EWI-FC), Columbus, OH, USA
e-mail: jgu@ewi.org

D. Schoch · J. Bornhorst
AIRAM, Covington, OH, USA

© The Minerals, Metals & Materials Society 2021

G. Daehn et al. (eds.), *Forming the Future*, The Minerals, Metals & Materials Series,
https://doi.org/10.1007/978-3-030-75381-8_103

(c) Shearing with different punch configurations was conducted by Shih et al. [4], to improve the sheared edge quality.
(d) Interestingly, a recent study on the high-speed impact cutting process by Fraunhofer IWU has shown that the adiabatic softening effect creates a smooth edge finish [5].
(e) However, little research has been done to investigate the effect of speed on the edge local formability.

Therefore, a study to evaluate edge formability by the effect of shearing speed was conducted by EWI. This study also considered the effect of different shear clearances on edge quality. The edge local formability was evaluated by the failure strain from the half-specimen dome test (HSDT).

2 Approach

Two AHSS materials, DP780 and GEN3-980, were selected for this study. The material properties are given in Table 1. Shear testing with different speeds and clearances was conducted on both materials. The edge quality created by different speeds and clearances was evaluated by the HSDT, microhardness testing, and optical microscopy.

2.1 Shear Test

Both materials were sheared with four different speeds from an AIDA 300-ton servo-press and AIRAM 12-ton pneumatic press as shown in Fig. 1. Two press motions, silent deceleration and crank motion, were used in the servo-press. The crank motion imitates the conventional mechanical press motion, while the silent deceleration motion slows the ram down to one-tenth of the overall velocity before the tool contacts the blank. The press load and press speed were measured and exported from the servo control module. The pneumatic press was used to create shearing speed up to 1.8 m/s with the shear test tooling, and the speed can be adjusted using different press operating pressure settings. The instantaneous shearing speed was measured using a laser sensor. Thirty psi and 50 psi pneumatic press settings were considered, which provided approximately ten times higher shearing speed than a mechanical press.

Table 1 Material properties of the selected sheet materials

Material	Thickness (mm)	Yield strength (MPa)	Tensile strength (MPa)	Total elongation (%)
DP780	0.9	499	855	18.0
GEN3-980	1.2	609	1022	22.1



Fig. 1 Servo-press (left), pneumatic press (middle), and shear test tooling (right). (Color figure online)

2.2 Die Clearance

The tooling clearance of the shear die was adjusted using shims. At each speed, each material was tested in four different clearances except one condition that corresponds to DP780 material 15% shear clearance with crank motion. The test matrix is shown in Table 2. The sample was cut into 100 by 200 mm, with the interested sheared edge on the 200 mm side.

The shear clearance is calculated with Eq. 1:

$$\text{Shearclearance}\% = \frac{\text{Dieclearance}}{\text{Materialthickness}} * 100\% \tag{1}$$

2.3 Half-Specimen Dome Test (HSDT)

As an alternative test to evaluate the sheared edge stretchability, HSDT was extensively used by Kim et al. [6] and Gu et al. [7]. HSDT can evaluate the straight sheared

Table 2 Test matrix of the shearing test

DP780	GEN3-980		Repetition	
Shear clearance (%)		Shearing speed	Shearing	HSDT
9	9	4	Minimum 5	Minimum 3
12	11			
15	15			
18	18			

[a]Excluded condition in mechanical press crank motion speed

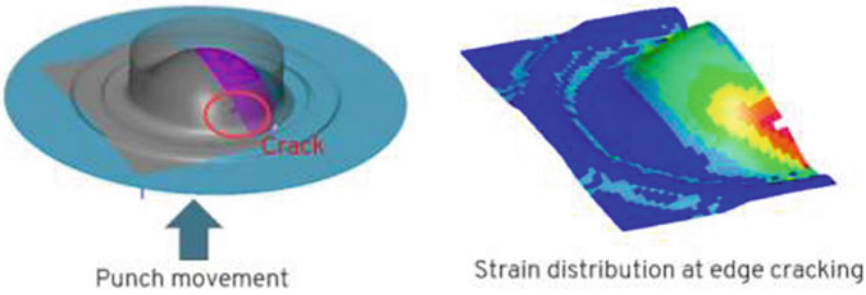


Fig. 2 HSDT experiment setup [7]. (Color figure online)

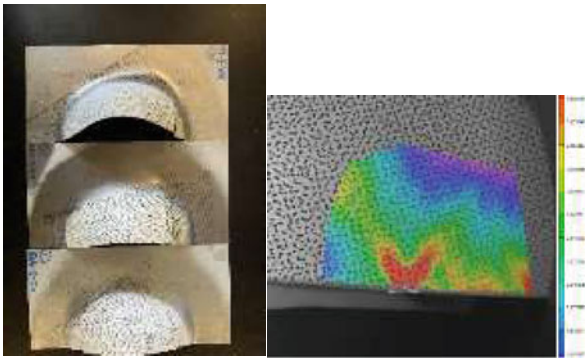


Fig. 3 HSDT sample and strain contour measured by DIC. (Color figure online)

edge, instead of punched holes for hole expansion test. HSDT uses a 100 mm diameter dome punch to stretch the sheared edge, and the die ring has a knurl pattern to prevent any material draw-in in the flange area. The tooling setup is illustrated in Fig. 2. The punch moves up to stretch the sheared edge and creates a uniaxial tension failure in the area between the punch and the die ring. The edge local formability was evaluated using the DIC measured failure strain as close to the edge as possible. The tested sample and digital imaging camera (DIC) post-processing result is shown in Fig. 3. At least three test repetitions were conducted for each sheared edge condition.

2.4 Microhardness and Optical Microscopy

The change of hardness-induced during shearing was measured by microhardness test and the measured hardness on the sheared edge was compared with the base metal hardness. The sheared edge was cut with an abrasive saw, mounted, and polished for the Vickers microhardness measurement. Ten indentations were made starting from the edge horizontally across the shear-affected zone for each shearing condition. The starting point of the indentation at the sheared edge is indicated in Fig. 4. The

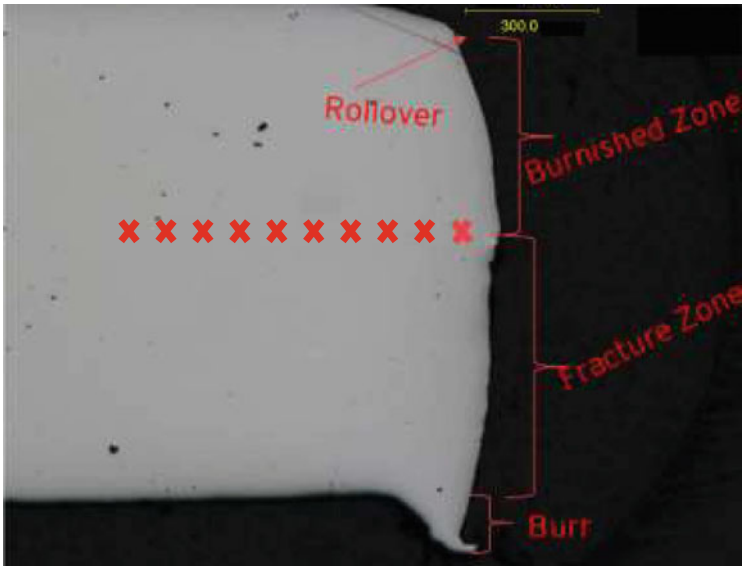


Fig. 4 Starting point selection of hardness test. (Color figure online)

starting point was selected at the transition of the burnished zone to the fracture zone, where the highest hardness value is normally measured along the vertical sheared edge surface.

3 Results

Two different press speeds and position profiles of the servo-press motions created from the servo-press control module are shown in Fig. 5. Instantaneous shearing speed was measured at the initial contact of the shearing die to the blank. The kinetic

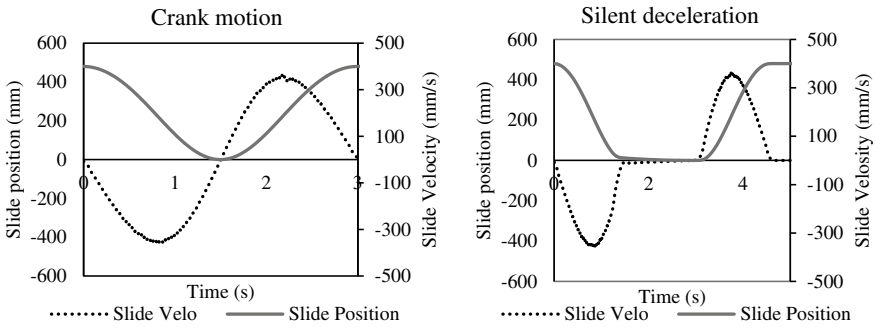


Fig. 5 AIDA servo-press speed and position versus time of crank motion and silent declaration

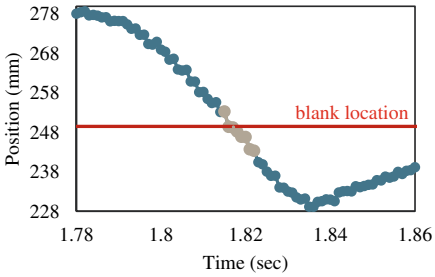


Fig. 6 AIRAM pneumatic press position versus time. (Color figure online)

energy created by the pneumatic press is very high, so the die velocity was high enough that the press speed was not reduced during the shearing operation. The AIRAM pneumatic press displacement–time curve is given in Fig. 6.

3.1 Shearing Speed

The shearing speed from the different types of press motions is summarized in Table 3 and Fig. 7. The four press settings provide four different speeds from 0.012 to 1.8 m/s. Note that the 1.8 m/s velocity conditions of the pneumatic press is over 100 times higher than the silent deceleration speed of the servo-press. Also, the silent deceleration has one-tenth the speed of the crank motion, and the pneumatic press motion has approximately ten times the speed higher than the crank motion. The higher pressure setting of the pneumatic press provides a higher shearing speed. However, the increase in speed is not as significant as in the two servo-press motions.

Table 3 Shearing speed obtained from different press motions

	Press motion	Speed (mm/s)	St. dev
Servo-press	Silent deceleration	12.7	0.3
	Crank motion	144.7	1.6
Pneumatic press	30psi-AIRAM	1283.1	142.2
	50psi-AIRAM	1810.7	245.8

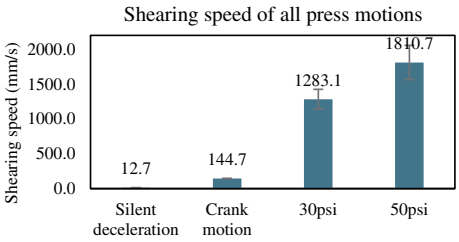


Fig. 7 Shearing speed obtained from different press motions. (Color figure online)

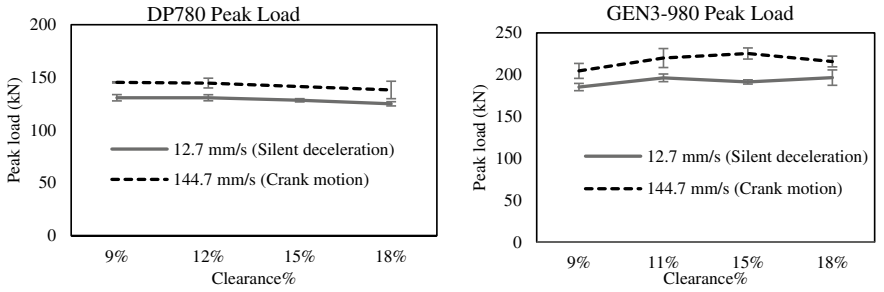


Fig. 8 Press peak load in the different shearing speeds of DP780 and GEN3-980

3.2 Press Peak Load at Shearing

The press load in the servo-press is measured by the servo load analyzer. For both materials, at each clearance, the slower silent deceleration speed (12.8 mm/s) shows a significantly lower shearing peak load than the speed of conventional mechanical press motion (144.7 mm/s), shown in Fig. 8. For DP780, the average peak load between silent deceleration and crank motion shows about 14 kN difference, while for GEN3-980, the average peak load changed about 24 kN between two different press speeds. It appears that the slow speed creates less impact loading the tooling, which can be beneficial to increase tool life.

3.3 Half-specimen Dome Test Result

Half-specimen dome tests were conducted on both materials. The equivalent strain before edge cracking was recorded using a DIC system. The higher failure strain means the larger local formability of the sheared edge. The equivalent failure stain is compared for various conditions in Fig. 9. With the same shear clearance, the higher shearing speeds of the AIRAM pneumatic press, creating velocities of 1283.1 mm/s and 1810.7 mm/s show larger equivalent failure strain compared to the other two relatively lower speeds of the servo-press. Overall, the lowest speed of 12.7 mm/s of the servo-press showed a slightly worse result compared to 144.7 mm/s crank motion that represents conventional mechanical press speed.

3.4 Microhardness Measurements

The microhardness data of DP780 and GEN3-980 are shown in Fig. 10. The other hardness data for different shear clearances and speeds showed similar trends with Fig. 10. The hardness at the sheared edge has the maximum value and as the measurement location approaches the base metal, the hardness decreases and becomes equal

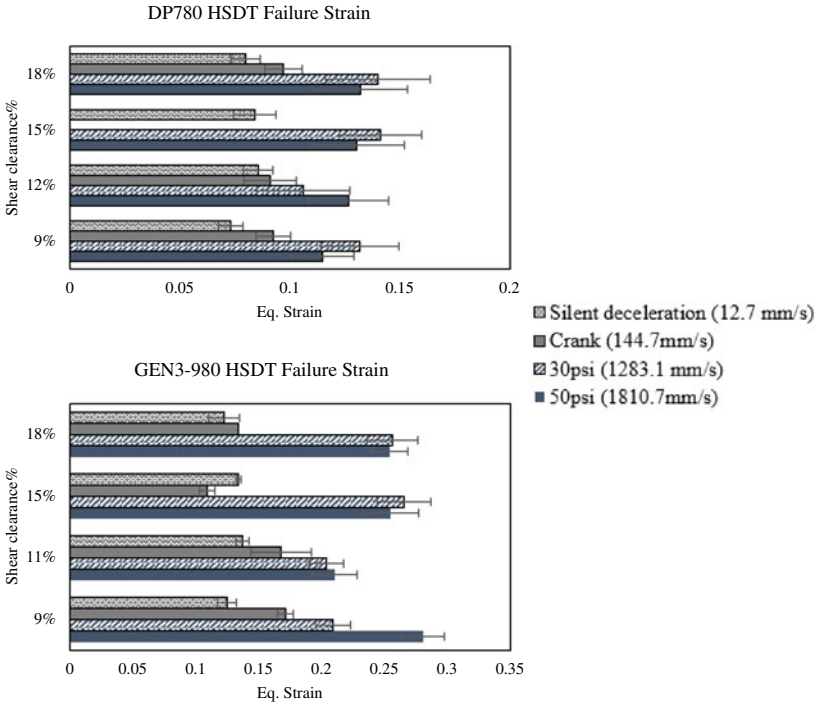


Fig. 9 HSDT equivalent failure strain of each speed with available clearances. (Color figure online)

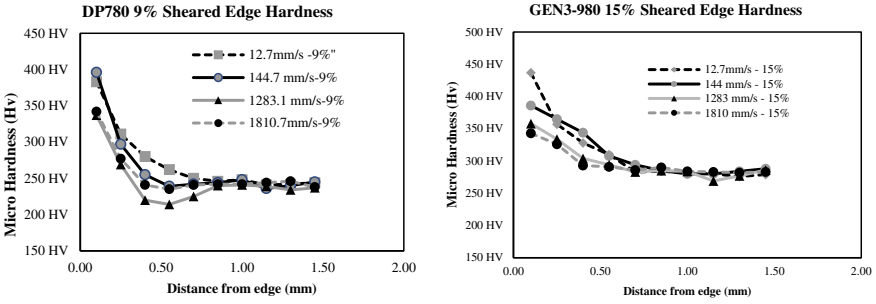


Fig. 10 Hardness measurements result of DP780 sheared with 9% clearance and GEN3-980 with 15% clearance. (Color figure online)

to the hardness value of the base metal. The first hardness measurement which is closest to the sheared edge represents the critical hardness of the sheared edge. The critical normalized hardness is calculated by Eq. 2. The normalized critical hardness closer to 1 indicates less hardness increase and less damage to the edge during shearing.

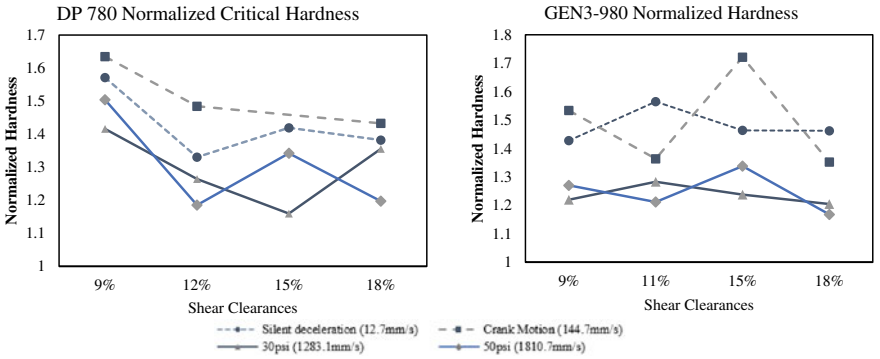


Fig. 11 Summary of the normalized critical hardness of DP780 and GEN3-980. (Color figure online)

$$\text{NormalizedCriticalHardness} = \frac{\text{Criticalhardness}}{\text{Basemetalhardness}} \tag{2}$$

Figure 11 compares the critical normalized hardness for different press speeds. The lower normalized hardness indicates less work-hardening during shearing and a significant preferred edge condition. For both materials, the normalized critical hardness is lower for the two higher speeds produced by the AIRAM pneumatic press (i.e., 1283.1 and 1810.7 mm/s) for each shear clearance. However, the shearing conditions to obtain the lowest normalized hardness (i.e., preferred result) varies with shear clearance and press speed.

3.5 Optical Microscopy

The optical microscopic image of the sheared edge was taken to qualitatively evaluate the edge quality. The lowest speed setting shows the largest burnished zone of all. Most samples from the two high-speed shearing conditions produced with pneumatic press show negligible rollover height, smooth shear zone transition, smooth fracture zone, and negligible burr. Example images of DP780 sheared edges with different shearing speeds and 11% shear clearance are compared in Fig. 12.

4 Conclusions

The following conclusions can be drawn from this study:

- The high-speed shearing velocities produced by the pneumatic press improved local formability.
- The preferred shearing conditions for DP780 and GEN3-980 are:

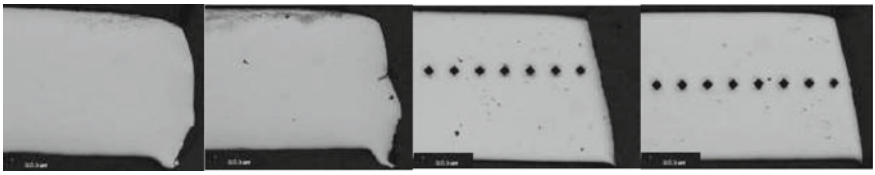


Fig. 12 Sheared edge of DP780 with the different shearing speeds with 11% shear clearance

- DP780: 15% clearance with 1283 mm/s shearing speed, which is 92% higher failure strain than that of crank motion average
- GEN3-980: 9% clearance with 1810 mm/s shear speed, which has 50% higher failure strain than that of crank motion average
- The effect of shear clearance on local formability varies with the press speed. Therefore, at the higher press speeds, the sensitivity of different shear clearances to the sheared edge quality is reduced.
- Regardless of shear clearances, two higher speed sheared samples show the better edge quality compared with the lower speed.
- The better edge conditions produced by the pneumatic press high-velocity shearing should produce less microcrack conditions and thus a higher resulting strength part with higher reliability.

References

1. Konieczny A, Henderson T (eds) (2007) On formability limitations in stamping involving sheared edge stretching. SAE Technical Paper
2. Lee JS, Ko YK, Huh H, Kim HK, Park SH (2007) Evaluation of hole flangeability of steel sheet with respect to the hole processing condition. Key Eng Mater 340:665–670
3. Pathak N, Butcher C, Worswick M (2016) Assessment of the critical parameters influencing the edge stretchability of advanced high strength steel. J Mater Eng Perform 25(11)
4. Shih HC, Shi MF (2012) Robust shearing process for improving ahss sheared edge stretchability. In: Proceedings of the ASME 2012 international manufacturing science and engineering conference collocated with the 40th North American manufacturing research conference and in participation with the international conference on tribology materials and processing. ASME 2012 international manufacturing science and engineering conference, pp 363–369. Notre Dame, Indiana, USA. June 4–8, 2012. https://doi.org/10.1115/MSEC2012-7318
5. Muller R, High speed impact cutting of sheets and tubes. Fraunhofer IWU. www.iwu.fraunhofer.de/content/dam/iwu/en/documents/Infosheet/Infosheet-High-Speed-Impact-Cutting-Of-Sheets-And-Tubes.pdf
6. Kim H, Shang J, Dykeman J, Samant A, Hoschouer C (2017) Practical evaluation and prediction of edge cracking in forming advanced high strength steels (AHSS). SAE Technical Paper. No. 2017-01-0308
7. Gu JC, Kim H, Dykeman J, Shih H (2018) A practical methodology to evaluate and predict edge cracking for advanced high-strength steel. IOP Conf Ser: Mater Sci Eng 418:012072. https://doi.org/10.1088/1757-899x/418/1/012072

Local Microscopic and Integral Macroscopic Analysis of Magnetic Pulse Welds and Deformations for Dissimilar Metal Joints



Frank Huberth, Balaji Ragupathi, Christian Scheffler, Verena Psyk, and Johannes Preußner

Abstract Magnetic pulse technology is used for high-speed forming as well as for joining. Joining by magnetic pulse welding (MPW) is the combination of high-speed forming, impact, and a resulting weld in the collision zone of the accelerated flyer and the impacted target. This MPW process allows the welding of dissimilar metals, like aluminum and steel for lightweight construction or aluminum and copper for E-mobility applications. Investigations showed up scattering in binding strength and failure for comparable welds. The effects leading to the bond formation and the reasons for the quality variation are not fully understood until now. For further understanding, a combined experimental investigation of integral and local mechanical weld properties supported by simulations and microstructure analysis was performed considering dissimilar metal joints of aluminum EN AW1050 H14/24 and copper Cu DHP R240 for different configurations and impact energies. Lap shear tests served for quantifying integral mechanical properties, while local mechanical properties were determined by microtensile tests on samples prepared in the thickness direction of the welded metal sheets and microstructural analysis. These local microscopic testing and analysis results provide information about the weld strength distribution. These investigations give new hints on the bond-forming mechanisms and local process depending on material effects.

Keywords Lightweight construction · Local joint strength · Process effects

F. Huberth (✉) · J. Preußner
Fraunhofer Institute for Mechanics of Materials IWM, Woehlerstrasse 11, 79108 Freiburg, Germany
e-mail: frank.huberth@iwm.fraunhofer.de

B. Ragupathi
Department of Sustainable Systems Engineering, EFM University of Freiburg, Faculty of Engineering, Emmy-Noether-Str. 2, Solar Info Center, 4, 79110 Freiburg, Germany
e-mail: balaji.ragupathi@inatech.uni-freiburg.de
URL: https://www.inatech.uni-freiburg.de/efm

C. Scheffler · V. Psyk
Fraunhofer Institute for Machine Tools and Forming Technology IWU, Reichenhainer Strasse 88, 09126 Chemnitz, Germany

© The Minerals, Metals & Materials Society 2021

G. Daehn et al. (eds.), *Forming the Future*, The Minerals, Metals & Materials Series,
https://doi.org/10.1007/978-3-030-75381-8_104

1 Introduction

Magnetic pulse welding (MPW) is a technology providing high potential for the metallic bonding of dissimilar metal materials without largely heating and melting them [1]. The connection of multi-material joints has been a key technology for different applications for multiple years. Joining aluminum and steel for hybrid lightweight constructions [2] or electromobility is essential for further developments in hybrid lightweight construction [3]. This concerns structural applications as well as the electric connections for the power supply [4].

Many joining technologies reduce the performance of the components beneath the level of the weakest part in the load path. This is well investigated in the literature [5]. The authors resumed that the combination of EN AW 1050/ Cu-ETP R240 MPW "provided joints with the highest mechanical properties" [5]. Combining the advantages of distributed force transmission, which is characteristic for adhesive bonding with the processing speed of the dynamic welding process, the magnetic pulse welding (MPW) process provides both good load-bearing capacity and short processing interval. MPW is a solid-state metal joining process. This means that it can join metallic materials generating a true metallurgical weld. The main advantage of these processes is that no heat affects the components and materials with very different melting temperatures can be welded. The most extended current overview for these processes is given in [6].

During the investigation presented in this paper, a combination of aluminum EN AW1050 H14/24 and copper Cu DHP R240 was welded by MPW and analyzed by mechanical test at different scales. Numerical simulations using FEM were performed for the process to derive supporting information. The simulations were used to determine the local conditions for the impact angle and velocity.

Detailed microstructure investigations were performed. The correlation of local microstructural investigations and micro test is discussed in detail here and a first hypothesis is developed for the strength distribution.

2 Methods

This paragraph describes the MPW process and explains the integral macroscopic analysis via lap shear tests. Furthermore, information about the sample preparation and the test execution of the local microscopic analysis via microtensile is given.

3 Process and Process Parameters

For the welding process the flyer and target blank must be positioned with a small gap (approx. 0.5–2.0 mm) in-between them and close to a so-called tool coil as

illustrated in Fig. 1. The coil is electrically connected to a pulsed power generator, which is the forming machine of this process that provides the energy for the process as capacitatively stored electrical energy. A sudden discharge of a capacitor battery via the tool coil causes electromagnetic forces in the flyer, which accelerate it toward the target and cause an impact of flyer and target with impact velocities in the range of several hundred meters per second and varying impact angle α_{impact}. If the collision properties are within a material-specific parameter window, the impact results in a partial weld in the impact zone. MPW is welding in the cold, solid phase with large local deformations at extremely high strain rates. A detailed description of the process is given in [7].

Together with other important parameters such as the capacitor charging energy or geometrical parameters of the tool coil and the joining partners, the gap significantly influences the collision parameters and thus the resulting weld properties [8]. Fraunhofer IWU developed a trident-shaped working coil described in [9], which is used for the welding experiments in this study. Two different setups indicated in the start configuration of the setup shown in Fig. 1 are regarded. The first setup is a symmetric one with a completely overlapping flyer and target and the weld seam positioned in the middle of the sheets. Exemplary welded parts are shown in Fig. 2 on the right side. The second setup is asymmetric. This means that the flyer and

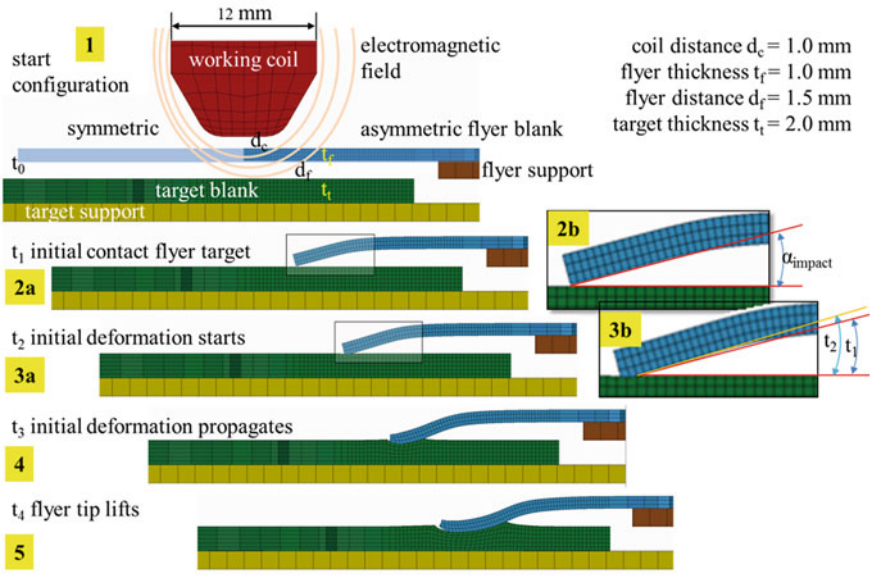


Fig. 1 Schematic MPW process for different time steps 1 to 5 based on a FE simulation using LS-DYNA and modeled with solid elements (0.3 mm), material model *MAT_PIECEWISE_LINEAR_PLASTICITY, and contact type *CONTACT_AUTOMATIC_SURFACE_TO_SURFACE. For the process the FEM–BEM electromagnetic solver of LS-Dyna is used coupled to the mechanical domain [14]. The detailed illustrations 2a and 2b show the definition of the impact angle α_{impact} at two time steps t_1 and t_2. (Color figure online)

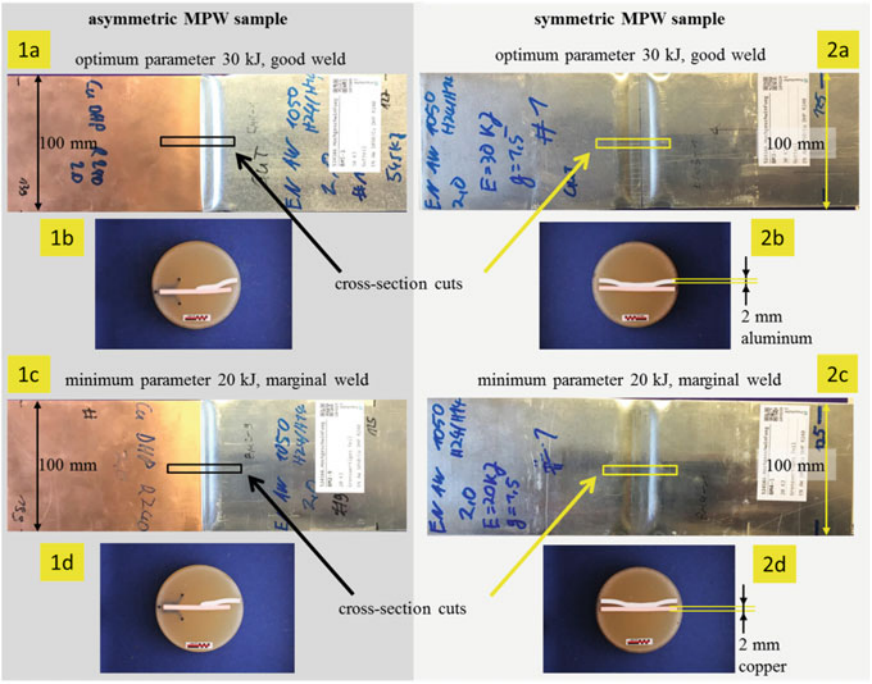


Fig. 2 MP welded samples, symmetric (1 a–d) and asymmetric variant (2 a–d), with optimum parameters (a, b) and minimum parameters (c, d); cross-section cuts for each variant (b, d). For the MP weld 1, the used parameters were 30 kJ, 544kA, and 22.2 kHz; for weld 2 reduced to 20 kJ (Pulsar MPW 50/25). (Color figure online)

target overlap each other only partially and the edge of the flyer sheet is welded to the target as shown in the different forming stages presented in Fig. 1.

An exemplary welded part with the asymmetric setup is presented in Fig. 2 on the left side. In order to achieve similar collision parameters for the transient impact velocity and consequently similar weld quality, the symmetric setup required slightly higher capacitor charging energy, when keeping all other process parameters, the coil and flyer distance, constant. The reason is that the deformation process is completely different. In the case of the asymmetric setup, the flyer edge is bent toward the target (see Fig. 1) resulting in a one double-bent deformation zone between the contact area of the flyer and target and the undeformed area (see Fig. 2 left). In the case of the symmetric setup, the middle section of the flyer moves toward the target resulting in two double-bent deformation zones between the contact area of the flyer and the target and the undeformed areas (see Fig. 2 right). Additionally, in the case of the symmetric setup, the true length of the flyer slightly increases due to the deformation leading to very different strain states in the sheet. Therefore, depending on the setup different energies were applied leading to similar weld quality. Precisely, two different energies were regarded for each setup. The first one was chosen just high enough to lead to

welding. In the following, this is referred to as "marginal weld". The second one was chosen significantly higher so that high-quality welds characterized by failure in the base material when being tested in macroscopic lap shear tests are expected. In the following, this is referred to as "good weld". Exemplary samples and cross-section cut for each variant are shown in Fig. 2.

During the process the local conditions in the contact zone change continuously. This is illustrated in Fig. 1 by the zoomed parts for t_1 and t_2. Different local conditions result in different local weld properties ranging from high weld strength over low weld strength up to no established weld at all. Figure 3 shows an exemplary process window for welding the specific material combination considered here. This means that it indicates the combinations of normal impact velocity v_{normal} and the impact angle α_{impact} leading to welding as green dots and the collision conditions leading to no weld as red crosses. This process window corresponds to the one determined in [8] but it is extended by some more detailed data. In the boundary area between the separation of the green region from the red one, the weld conditions are critical. This means that the process is not robust and already slight changes in the process parameters, e.g., due to material or positioning tolerances can lead to non-welded specimens. Additionally, the welds manufactured with these critical weld parameters typically show minor weld quality characterized by early failure in mechanical tests such as lap shear tests.

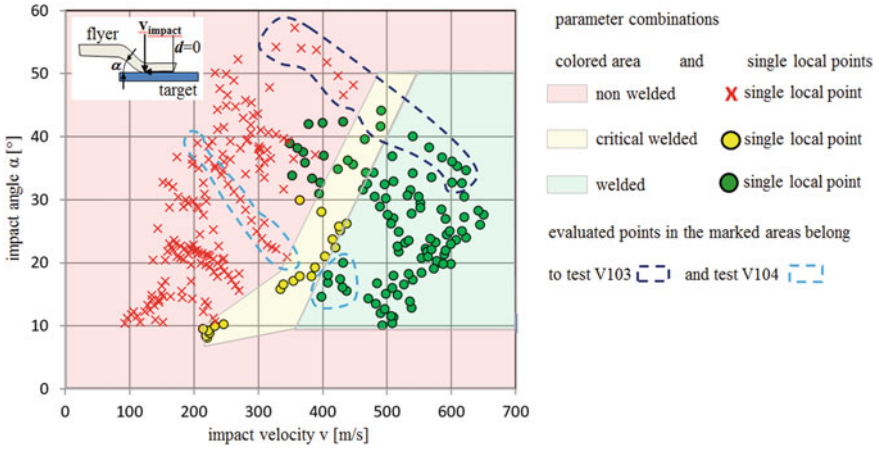


Fig. 3 Process parameters impact velocity v and impact angle α for established weld (green), transition area with critical conditions (yellow), and no weld (red) based on a combined approach of experimental and numerical results. Experimental results are compared with the simulation by the resulting MPW connection at the process conditions for two samples shown here, V103 and V104 in the marked area, as well as for simulation of each test [14]. (Color figure online)

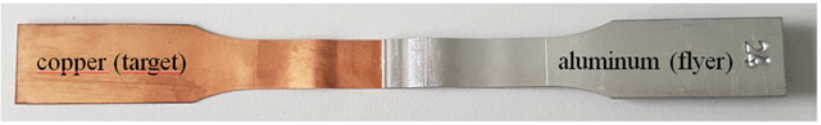


Fig. 4 MPW-lap shear sample, machined from the asymmetric variant of the weld samples (Fig. 2, left). (Color figure online)

4 Integral Macroscopic Analysis

The welded samples were machined to dumbbell-shaped lap shear samples as exemplarily shown in Fig. 4. For the machining process, the samples are clamped in a way that a load on the weld is prevented and during the milling process the sample is cooled. By this process, the end parts of the welding zone were eliminated and the results represent pure weld strength without edge effects. Typical edge effects and this approach with machined samples to avoid them are described in [10]. Edge effects are initiated by the run-out zones of the MPW process in lateral directions. Lap shear tests were performed on samples prepared from good and marginal asymmetric welded samples (Fig. 2, left). The tests were performed analog to tensile tests in a universal testing machine. The integral axial force was measured via the integrated load cell, while the total sample elongations were recorded via the traverse path sensor during the tests. This elongation measurement features only limited accuracy, but as the main intention of the lap shear tests is to characterize the weld quality by quantifying the maximum transferable force of the hybrid sheet and to identify the failure type (failure in the weld vs. failure in the base material), this limitation of the very simple test setup is accepted here.

5 Local Microscopic Analysis

To get access to the local strength distribution of the weld, local microtensile tests were performed at small dumbbell-shaped samples with the interface region in the waisted sample center. The segmentation of the weld zone by stripes and the sample contours were machined in a specifically developed process by wire-electro discharge machining, polishing, and micro water jet cutting in different steps. A similar approach to sample extraction is described in [10]. There, different cutting techniques were used. The welding zone is identified via light microscopy. For each variant of the welded samples, a separate extraction plan was prepared to extract the stripes as shown in Fig. 5 for the good asymmetric sample. As the welded region for the marginal samples is smaller, fewer stripes are extracted. The positions of the stripes are shown in the results paragraph by micrographs.

The tests are performed at the IWM using the DynMicro testing machine (Fig. 6). This machine allows testing at different tensile speeds. The concept of dynamic

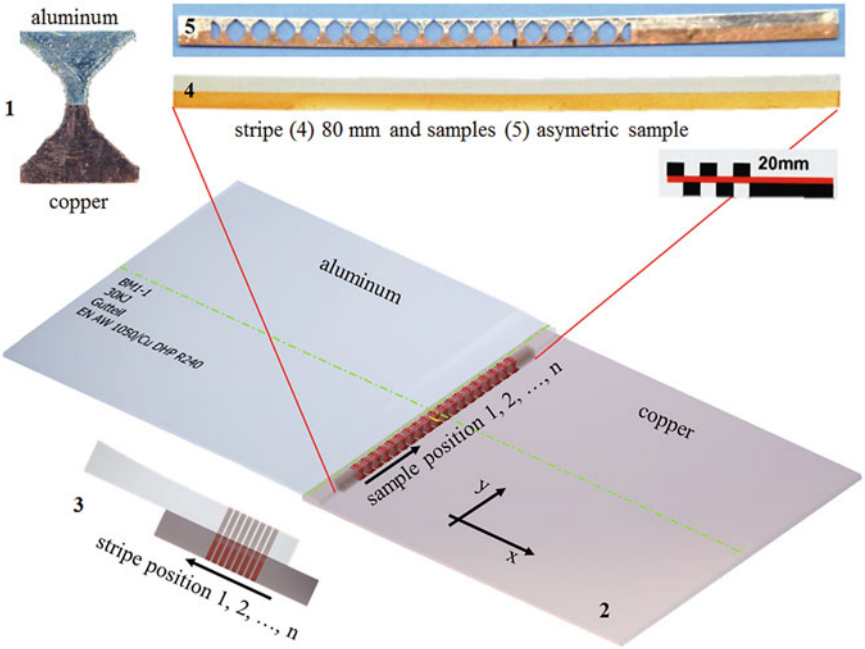


Fig. 5 Sketched microsample extraction process: Aluminum–copper sample with central weld zone (1, top left) extracted by stripes in thickness direction all through the two welded blanks, overview (2), side view (3), prepared stripe (4), and stripe with samples (5). (Color figure online)

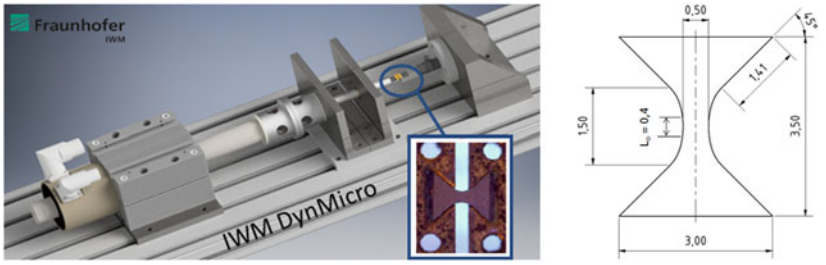


Fig. 6 Sketch of the micro testing machine IWM DynMicro with a detailed view of the sample in the clamps and a technical drawing with the sample geometry (right). (Color figure online)

microtesting is described in general in [12] and [13]. Force measurement is realized by a fixed 5 kN piezo sensor scaled down to the calibrated range of 500 N. Displacement analysis is done by digital image correlation (DIC) on the sample. To get the images for DIC with a high time resolution high-speed camera Photron SA5 with microoptics is applied to the setup. The natural surface texture of the prepared samples is sufficient for DIC. Two image series of the tests are shown in Figs. 9 and 11.

6 Results and Discussion

The results of the different test series with samples from different process conditions are shown and discussed for the integral macroscopic and local microscopic approaches.

6.1 Integral Testing for Different Process Parameters

The lap shear tests on samples with good and marginal asymmetric welds are discussed in this paragraph. The results of the lap shear tests are shown for these two variants in Fig. 7. As the samples showed a mixed deformation of bending and tension, it is not possible to calculate reliable stress–strain curves or flow curves. Therefore, only the measured force over total sample elongation is shown. However, the width and initial sheet thickness of the samples were equal, and the results are absolutely comparable with each other. As expected, the marginal welded samples reached a lower maximum load compared to the good welded samples. Moreover, the variation in the maximum transferable load measured for the three individual specimens shown in Fig. 7 is higher, which confirms the expected lower robustness of the process in the case of critical weld parameters. Regarding the elongation, the comparison of the curves shows that similar values can be achieved for marginal and good welds, and also this parameter can vary remarkably due to unstable conditions in the case of marginal welds. To evaluate the results tensile tests were performed on the weaker base material (i.e., EN AW1050 H14/24) using comparable sample size in order to allow direct comparison of the force–elongation curves for the lap shear

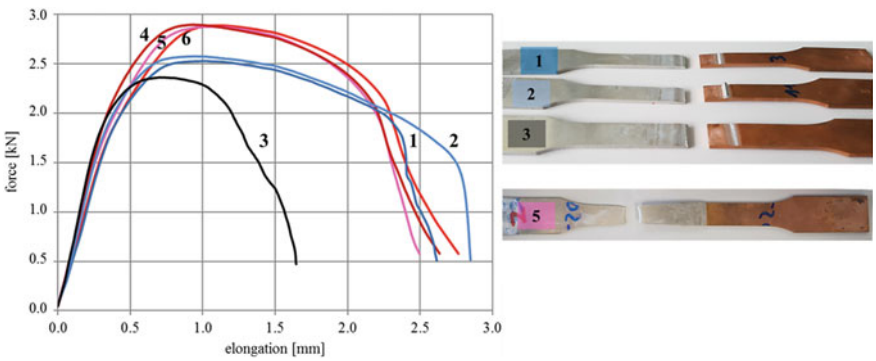


Fig. 7 Force and sample elongation diagram on the left side for MPW-lap shear tests for good (red curves 4–6) and marginal (1, 2—blue and 3—black curves) welded samples. The black curve (3) represents the minimum loading capacity tested. Different failure modes for the corresponding samples 1–3 and a representative failure of sample 5 with tensile failure in the aluminum section at the right side. (Color figure online)

tests and the tensile tests. Figure 8 clearly demonstrates that the maximum transferable force is similar for both specimens. This proves that the weld can transfer the same forces as the weaker base material. Even the weakest MPW-lap shear sample (sample 3) reached a maximum force comparable to that of the tensile sample (Fig. 8). For the other marginal and good MPW samples, the measurements suggest an even higher load-bearing capacity than the base material, which is surprising at first glance. However, these measured higher forces in the lap shear tests compared to the forces measured during tensile tests on the pure aluminum can be explained by the different stress state in the shorter and bended aluminum section of the welded sample compared to the uniaxial stress state in the tensile sample. The elongation measured during the lap shear and tensile tests is not comparable here as the MPW samples were bended during the tests.

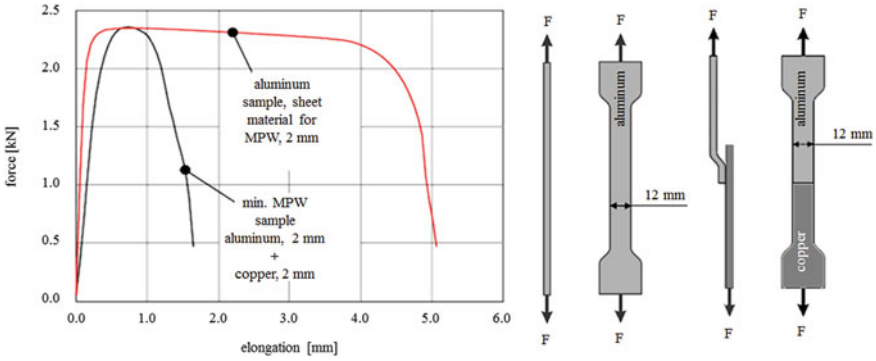


Fig. 8 Diagram of force and sample elongation comparing an aluminum tensile sample (red curve) and an MPW-lap shear sample (min. curve from diagram Fig. 5, black) and the two sketched sample variants at the right. (Color figure online)

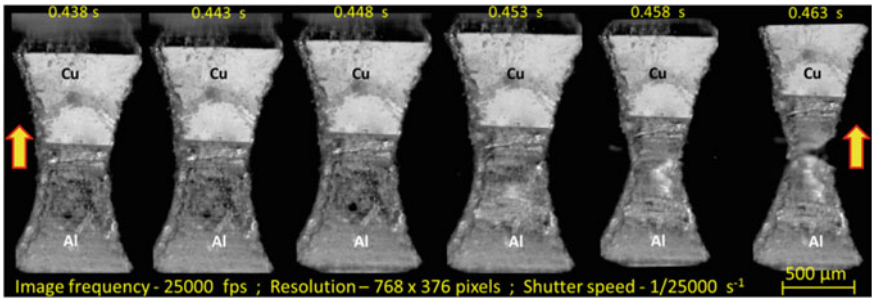


Fig. 9 Deformation states of the sample (diagram code AOH-BM3-1S-L1-M09), showing a pure aluminum failure, tested at 0.02 ms^{-1} with the arrow marks indicating the tensile direction. The microsample was extracted from a good symmetric welded sample in stripe 1 at position 9. (Color figure online)

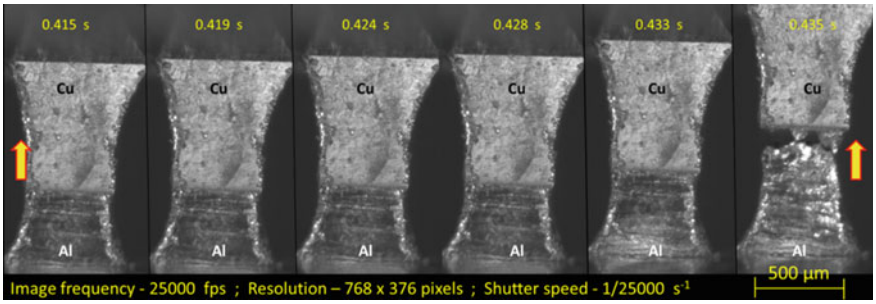


Fig. 10 Deformation states of the sample (diagram code AOH-BM3-1S-L3-M09), showing a failure at the weld interphase tested at 0.02 ms^{-1} with the arrow marks indicating the tensile direction. The microsample was extracted from a good symmetric welded sample in stripe 3 at position 9. (Color figure online)

6.2 Local Strength Distribution and Process Correlation

The micro tests for different samples showed two different failure types. The first one is characterized by deformation and failure in the aluminum section. The development of this failure type is shown in the image series in Fig. 9. The second failure type is characterized by failure in the bonding zone. The corresponding deformation states are illustrated in the image series shown in Fig. 10. The samples were taken for the same sample position in the lateral direction (position 9) at different distances to the initial impact (stripe 1, Fig. 9 and stripe 3, Fig. 10).

As shown in the image series in Figs. 9 and 11, the different failure modes occurred in the symmetric welded samples. In the following, the results for the asymmetric welded samples are discussed and compared to the macroscopic tests. For the samples extracted from the good and marginal welded samples, the same two failure types were observed, depending on the position of the stripe along with the propagation of the contact point during the joining process (longitudinal sample direction). As only the good welded samples allow more than one stripe to be extracted, the influence of the position was investigated for this variant only. Figure 11 shows a typical micrograph of a good weld. Here the positions 1 and 3 are marked and the diagram in Fig. 11 shows stress–strain curves determined in micro tests on samples taken from these positions. Precisely, the samples were taken at positions 5, 7, and 9 in the lateral direction from these two stripes. At position 1, next to the initial impact position, the samples show a reproducible stress–strain curve for all positions. For samples extracted from the stripe position 3, the results are significantly different. The stress level and the strain show a significantly larger scatter. Sample 9 reached maximum stress of 150 MPa. Samples 5 and 7 didn't reach the average stress of 130 MPa for position 1.

These two samples failed in the bonding zone as shown in Fig. 13. All samples related to position 1 failed in the aluminum. For the marginal weld, tests were performed only at position 1. The results are shown in Fig. 12. The micrograph

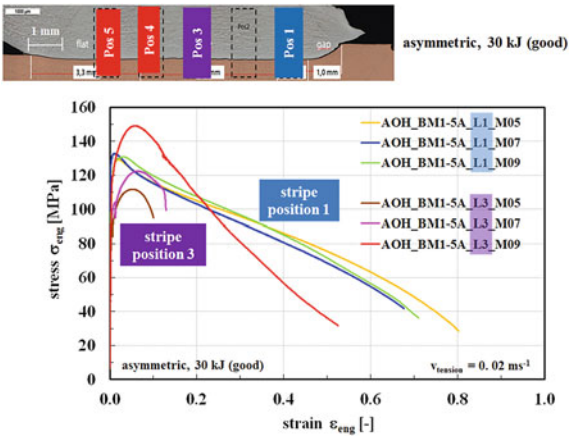


Fig. 11 Illustrated micrograph of the weld cross-section of an asymmetric good weld with marked positions for stripe positions 1 to 5 and diagram of the stress–strain curves for the microtensile tests with samples. (Color figure online) taken from stripe L1 at position 1 and L3 at position 3. Stripes at positions 4 and 5 (red) failed during processing or had no connection; at position 2 the stripes are not cut to sample shape. The complex sample code gives full information on the sample extraction position. (Color figure online)

shows the positions of the stripes. The stripe at position 2 had such a weak bond between the two sheets that it failed after extraction (Fig. 13).

The samples tested from this marginal asymmetric variant for position 1 failed in the aluminum comparable to the good one. But the stress level shown in the diagram of Fig. 12 is lower for the marginal weld. The maximum stress for these tests is 105 MPa on average compared to 130 MPa for the good weld. This different stress level must be influenced by the different deformation histories and the correspondingly different strain hardening effects leading to variations in the resulting strength of the aluminum

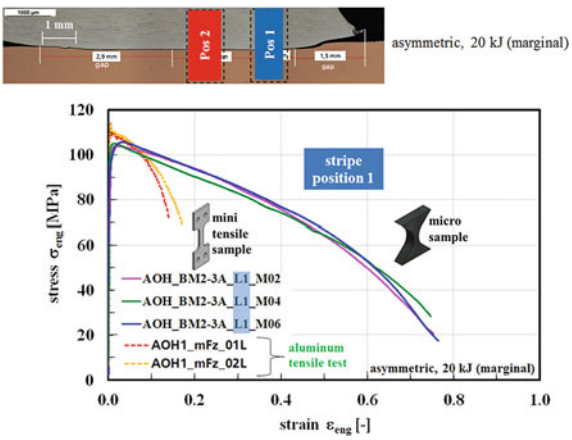


Fig. 12 Illustrated micrograph of the weld cross-section of an asymmetric marginal weld with marked positions for stripe positions 1 and 2 (red, failed) and diagram of the stress–strain curves for the micro tensile tests ($L_0 =$ 0.4 mm) with samples taken from stripe $L1$ at position 1 and the stress–strain curves of tested mini tensile samples ($L_0 = 14$ mm) taken from the base material (dotted curves). (Color figure online)

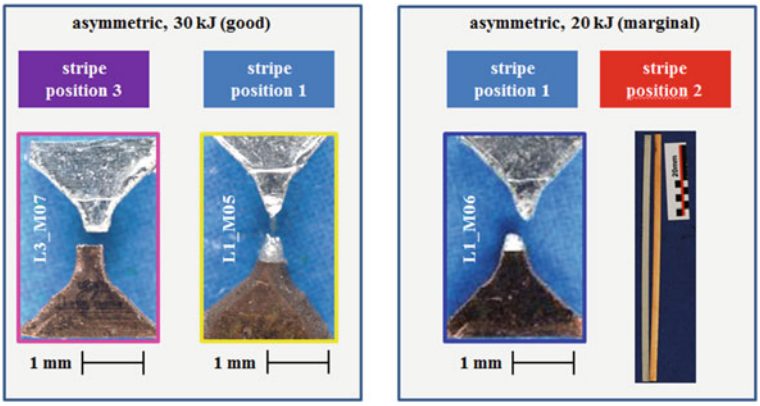


Fig. 13 Different failure modes for the stripe positions taken from a good weld (left) and a marginal weld (right). For the marginal weld at position 2 the failed stripe is shown. The box colors are the graph colors in the diagrams. (Color figure online)

for the two process variants. In the region of the initial impact high deformation rates occur, and for the good weld at 30 kJ higher velocities are applied compared to 20 kJ. This is supported by the results for the mini tensile test on larger samples taken from the sheet material shown in the diagram in Fig. 12. The maximum stress for the two tests is 110 MPa. Considering the different sample geometries, potential damage in the microsample, and other potential effects, this is a comparable stress level for the marginal weld and the aluminum base material. A high stress level of 130 MPa for the good weld with failure in the aluminum indicates a local strain hardening of the material. This observation is supported by microhardness measurements in the aluminum next to the bonding zone with an average value of 58 ± 4 HV0.001 compared to a reference value of 51 ± 4 HV0.001 in the uninfluenced base material.

The observation that the samples at position 1 failed all in the aluminum indicates high local weld quality for the region next to the initial impact. This finding is supported by the process window shown in Fig. 3, where it is shown that smaller joining velocities lead to weaker bonding. As the lower impact energy for the 20 kJ process is exhausted after a short distance from the initial impact, the stripe at position 2 already showed a critical weld with very weak bonding. At higher impact energies of 30 kJ, the welding area is increased, but the strength and thus the quality of the connection decreases with increasing distance to the initial impact zone. As both the impact angle (see Fig. 1 for t_1 and t_2) and the impact velocity decrease during the process, the actual process parameters are shifted to the yellow and finally toward the red zone of Fig. 3. This is illustrated by the single points in the boxes for V103 and V104 in Fig. 3.

7 Summary and Conclusions

The combined approach of process variation, macroscopic integral characterization, and local micro characterization lead to a better understanding of the MPW performance and mechanisms. The principal method shows a high potential for characterization of other welding or bonding processes.

The micro tests support the process window initially developed on the basis of macroscopic lap shear tests and the inhomogeneous failure observed for the marginal welded samples. The good samples showed an improved load-bearing capacity based on combined mechanisms of the larger welded zone and local strain hardening. Further investigations in combination with microsimulations based on smoothed particle hydrodynamics (SPH) and high-resolution microstructure analyses are ongoing and will promote a deeper understanding of the joining mechanisms on small length scales. The test results discussed in this paper enable the local and global calibration of the simulation models.

Acknowledgments The authors would like to thank all of the colleagues who contributed to the project that made the results possible for the publication, especially Dr. Sommer as project manager Fraunhofer IWM and the members of the authors' groups from Fraunhofer IWM and IWU, Dr. Bierwisch and his group from Fraunhofer IWM, Dr. Riedel and co-workers from Fraunhofer IWU and on behalf of the colleagues from the Chemnitz University of Technology Dr. Drehmann and his colleagues.

Special thanks go to Prof. Dr. Neugebauer, Fraunhofer-Gesellschaft for funding the project "Binding Mechanisms EMW".

References

1. Psyk V, Risch D, Kinsey BL, Tekkaya AE, Kleiner M (2011) Electromagnetic forming—a review. J Mater Process Technol 211:787–829
2. Daimler AG (2011) Bodyshell and passive safety: maximum stability and high-quality lightweight design. Global Media Site, Press Release 15.03.2011. https://media.daimler.com/marsMediaSite/en/instance/ko.xhtml?oid=9904243
3. Interview mit Bundeswirtschaftsminister Peter Altmaier, Leichtbau sichert Wettbewerbsfähigkeit des Industriestandorts Deutschland, VDI Nachrichten Ausgabe 11 vom 15.03.2019, VDI Verlag GmbH, Düsseldorf 2019
4. Marsch U (2011) Aluminum to replace copper as a conductor in on-board power systems. Press Release Technische Universitaet Muenchen 07.02.2011. https://portal.mytum.de/pressestelle/pressemitteilungen/NewArticle_20110207_090316/110207_eKart_PW_EN.pdf
5. Schmal C, Broda T, Fenzel R, Faes K, Kwee I, Van Rymenant P, Hendrickx P (2016) Final Report for the research project "Development and evaluation of advanced welding technologies for lightweight multi-material design with dissimilar sheet metals" (01/2014–06/2016), DVS-Nb.: 05.056 / IGF-Nb.: 00.108 E
6. Cai W, Daehn G, Vivek A, Li J, Khan H, Mishra RS, Ko-marasamy M (2019) A state-of-the-art review on solid-state metal joining. J Manuf Sci Eng 141(3): 031012 (35 pages) Paper No: MANU-18-1431

7. Schäfer R, Pasquale P, Material hybrid joining of sheet metals by electromagnetic pulse technology. Key Eng Mater 473: 61–68. https://doi.org/10.4028/www.scientific.net/KEM.473.61
8. Psyk V, Scheffler C, Linnemann M, Landgrebe D (2017) Process analysis for magnetic pulse welding of similar and dissimilar material sheet metal joints. Procedia Eng 7(2017):353–358
9. Psyk V, Scheffler C, Linnemann M, Landgrebe D (2017) 2017, Manufacturing of hybrid Aluminum copper joints by electromagnetic pulse welding—identification of quantitative process windows. AIP Conf Proc 1896:110001
10. Huberth F, Klitschke S, Gall M, Sommer S, Schnabel K, Baumgartner J (2018) Crash and durability of aluminum and mixed steel aluminum joints made by electro-magnetic pulse welding. In: International conference on high speed welding (ICHSF) 2018. Columbus, Ohio
11. Beckmann C, Kennerknecht T, Preußner J, Farajian M, Luke M, Hohe J (2018) Micromechanical investigation and numerical simulation of fatigue crack formation in welded joints. Eng Fract Mech 198:142–157
12. Huberth F, Lienhard J, Klitschke S, Ragupathi B, Bimi P, Stadtmüller P (2018) Ratenеffekte und Skaleneffekte bei der Werkstoffprüfung auf der Mikroskala. In: Tagungsband Tagung Werkstoffprüfung 2018, S. 261–266, 2018 Stahlinstitut VDEh. Düsseldorf. ISBN 978-3-941269-99-6
13. Huberth F, Lienhard J, Ragupathi B, Hauber M (2019) Dynamic micro-testing over a large range of strain rates for homogenous and heterogeneous local material characterization. WIT Trans Eng Sci, Mater Contact Characterisation IX 124: 143–150. Open Access.https://doi.org/10.2495/MC190141
14. Psyk V, Scheffler C, Linnemann M, Landgrebe D (2017) Manufacturing of hybrid aluminum copper joints by electromagnetic pulse welding—an analysis of important process parameters. In: 20th international ESAFORM conference on material forming, 26th–28th April 2017. Dublin. https://doi.org/10.1063/1.5112574

Computational Modeling of Magnetic Pulse Dissimilar Alloys Welding: Aluminum Alloy 6082-T6 and HC420LA Steel



N. Rodriguez-Barrio, E. Iriondo, D. Jouaffre, and F. A. Girot

Abstract The use of lightweight materials such as high-strength steel, aluminum alloys, and composites is increasing. The joints of dissimilar alloys as the aluminum alloy 6082-T6 and the HC420LA steel are studied in this work. The selected joining process is the magnetic pulse welding (MPW) which enables welding of these two alloys, being non-joinable by other traditional welding technologies. The technology involves a strong electromagnetic–mechanical–thermal interaction. The investigation will be developed mostly on computational modeling by means of using LS-DYNA software, taking into account the key process parameters and their influence. The work includes experimental results for validating the numerical analysis. All the analyzed cases showed welding of the blanks, which was confirmed by metallographic characterization. The simulations show the same deformation behavior as experiments.

Keywords Impulse joining · Dissimilar materials welding · Magnetic pulse welding (MPW) · MPW simulation

1 Introduction

Reducing the weight of structures for transport, whether for the aeronautical, automotive, naval, or railway sectors, has been a strategic objective for product and component manufacturers. The ability to design and manufacture light, durable, and economically profitable structures is essential to maintain competitiveness and advance in minimizing energy consumption and emissions into the atmosphere. An

N. Rodriguez-Barrio · E. Iriondo (✉) · F. A. Girot
Escuela de Ingeniería de Bilbao, UPV/EHU, Plaza Ingeniero Torres Quevedo 1, 48013 Bilbao, Spain
e-mail: edurne.iriondo@ehu.eus

D. Jouaffre
Plateforme INNOVALTECH, 17 rue Henri Hertz, 02100 Saint-Quentin, France

F. A. Girot
Basque Foundation for Science, IKERBASQUE, María Díaz de Haro 3, 48013 Bilbao, Spain

© The Minerals, Metals & Materials Society 2021

G. Daehn et al. (eds.), *Forming the Future*, The Minerals, Metals & Materials Series,
https://doi.org/10.1007/978-3-030-75381-8_105

advanced strategy for achieving this is the use of different materials based on the specifications to be met by each component.

The assembly of the subsystems whose components have been manufactured in dissimilar materials can become a limiting aspect due to the fact that conventional joining technologies are not capable of welding certain combinations of materials. The joining of dissimilar materials by means of conventional fusion welding processes is not possible in certain cases, due to the differences existing between both materials in terms of melting point, thermal conductivity, specific volumetric heat, and coefficient of thermal expansion. Electromagnetic joining, also called magnetic pulse welding (MPW), offers the possibility of welding dissimilar materials, allowing manufacturers and designers to improve their designs and productive results. This will permit the integration of components manufactured by light and resistant combined materials.

The use of electromagnetic driving forces is one of the variants that characterize MPW with respect to other impact welding technologies, where the welding of two different materials occurs through the high-speed impact of both alloys, by means of a controlled acceleration. The magnetic forces, produced between the electromagnetic coil and the moving element to be joined, provide the acceleration force to the moving work element and are the reason for the formation of a solid-state cold weld [1–3].

2 Magnetic Pulse Welding (MPW) of AA 6082-T6 and HC420LA Alloys

Solid-state welding depends on the pressure between the elements to be welded and this pressure can be applied in different ways. The present study focuses on the application of pressure through a high-speed impact. In the particular case of MPW, the impact is created by an electromagnetic pulse (see Fig. 1) and could be applied to both flat and cylindrical parts [4].

Figure 1 shows schematically the three stages that occur in a magnetic pulse welding operation. In the lower part of the system, the electromagnetic coil will be located through which a high amount of current of tens of kiloamperes will be discharged in a short period of time—approximately 100 μs. This discharged primary

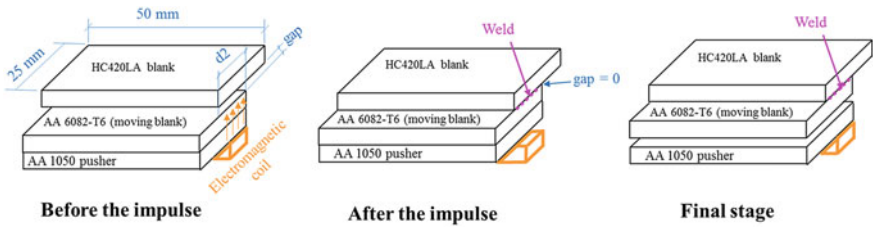


Fig. 1 Stages of the experimental magnetic pulse welding tests. (Color figure online)

current will induce an electromagnetic field in the sheet adjacent to the coil. In this case, a pusher plate made of AA 1050 aluminum alloy of the same dimensions as the moving plate is introduced, due to its lower electrical resistivity, 0.028×10^{-6} Ωm compared to 0.038×10^{-6} of the AA 6082-T6 alloy. The use of the pusher improves the energy efficiency of the pulses. The moving elements of this study will be the pusher and the moving plate of AA 6082-T6.

The two moving blanks are placed on the electromagnetic coil. On the top of the AA 6082-T6 plate, some positioning gauges made of G10 material are set. This is a laminated material made with fiberglass and epoxy resin, whose most outstanding properties for the present application are its high mechanical resistance and good electrical insulation. The gauges, in addition to maintaining the clearance or necessary distance between the HC 420 LA steel plate and the mobile AA 6082-T6, fix the overlap distance (d2) of the pusher and moving plate above the coil. The clearance between the two plates is what allows the moving plate to accelerate and reach a higher impact velocity, which is transformed into a higher mechanical impact pressure.

The second stage of Fig. 1 presents the state after the discharge of the capacitor bank through the coil. This discharge creates an oscillating electromagnetic field that induces currents in the nearby conductive material (pusher plate in the case of the present study). The currents in the piece or moving material are those that react with the oscillating electromagnetic field generating the Lorentz forces, which are the ones that create the deformation of the piece. In the same way that Lorentz forces are generated, the material is also heated instantly by the Joule effect, but the sheet as a whole does not, at any time, approach the melting temperature or undergo any metallurgical transformation [5, 6].

The pusher blank is repulsed with respect to the coil and pushes the AA 6082-T6 plate, accelerating it until it impacts the HC 420 LA steel blank. This impact is what generates significant pressure and the solid-state union.

The third stage, or final situation, reproduces the state of the system after the impact. The two plates that have impacted have been permanently joined and the pusher remains in its deformed shape, but it is not joined to the AA 6082-T6 blank.

3 Finite Element Modeling of the Process

The operations carried out by means of magnetic pulses require a multiphysics solution with electro-magneto-thermo-mechanical interactions [7]. Most of the studies carried out in the field of modeling magnetic pulse operations have assumed that most of the material deformation occurs after the first electromagnetic pulse [8]. This assumption results in the separation of the physical phenomena that are part of the process, to the electromagnetic and mechanical response of the problem, and they are proposed to be solved sequentially.

LS-DYNA [9] is an advanced nonlinear finite element multiphysics software capable of simulating highly complex real problems. It is useful for analyzing

phenomena with large deformations, models of sophisticated materials, or complex contact conditions. Forming and metal welding is one of the most important applications of LS-DYNA because it is capable of simulating many of the phenomena that occur in these processes. This software integrates an electromagnetic module that is very useful for electromagnetic impact welding since mechanical/thermal/electromagnetic simulations can be coupled [7]. This module allows introducing the source of electric current in solid conductors and to compute the resulting electromagnetic field and the induced currents. The generated fields are solved with Maxwell's equations. These equations are solved in turn using the finite element method and the boundary element method. This module allows the coupling of different solutions of both electromagnetic and thermo-mechanical simulations.

3.1 Model Specifications

The present research work aims to model the welding of dissimilar materials using magnetic pulses: the aluminum alloy AA 6082-T6 and the steel alloy HC 420 LA. The materials used are widely applied in the automotive industry. Table 1 shows the main mechanical properties, in addition to the electrical resistivity of both materials.

Once the materials with those which validate the MPW method have been selected, the experimental setup is defined. The aluminum alloy is chosen as the mobile element of the system, due to its lower electrical resistivity. The lower the electrical resistivity, the less discharge energy will be required to generate the same induced current, or what is the same, to generate the same level of acceleration in the moving material or sheet.

The size of the blanks is 50 × 25 × 1 mm and they are completely overlapped longitudinally at a certain distance between them and it is in this overlapping area that the weld will be generated. The distance between the plates is a process variable.

The finite element (FE) model consists of a coil, a tool, the HC420LA steel blank, the AA6082-T6 blank as the moving part, and finally, an AA 1050 aluminum alloy plate that acts as a pusher for the moving plate. The pusher is placed in the closest position to the coil.

The mesh used in both materials has been the same. The total number of cells of each blank is 8000 and it has been made with cells in the form of 1 × 0.5 × 0.25 mm hexahedrons. The duration of the calculations for each simulation has been approximately 2 h.

Figure 2 shows the configuration of the model including all the elements that

Table 1 Mechanical properties and electrical resistivity of the studied materials

Properties	AA 6082-T6	HC 420 LA
Yield strength (MPa)	289	475
Ultimate strength (MPa)	331	547
Electrical resistivity (Ωm)	0.038×10^{-6}	1.585×10^{-7}

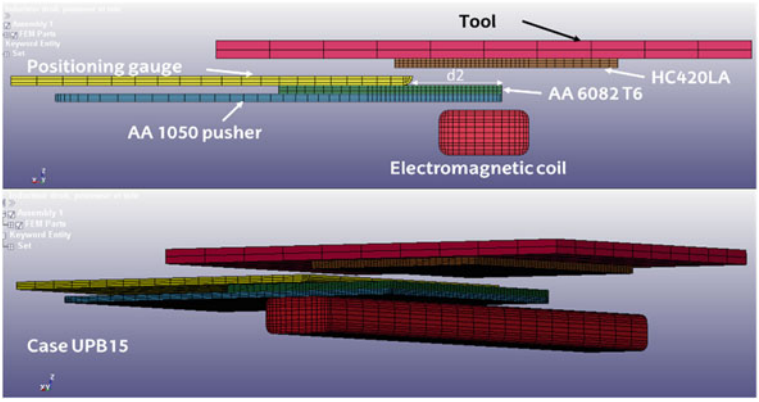


Fig. 2 LS-DYNA model. (Color figure online)

take part in the simulation. The elements that will be used during the experimental validation are simplified in the case of simulations, for example, limiting the geometry of the coil to its active zone.

To describe briefly the configuration of the elements of the models, four elements are observed in each of the models. The electromagnetic coil is the element that is in the lower position and on it is positioned the AA 1050 aluminum alloy pusher used to improve the efficiency of each impulse. On the pusher is the moving plate that impacts and will be welded with the plate positioned on it. The element positioned at the top is the tool that stops the movement of the two sheets: AA6082-T6 and HC420LA. The angle of impact, see Fig. 3, is the angle formed by the materials at the point of contact. At the first point of contact, or impact point, a shock wave is created between the two materials in the radial direction due to the high value of the generated impact velocity. This shock wave creates the jet of air that cleans the surface to be welded of oxides and other particles, favoring the joint.

Four different cases have been simulated: UPB15, UPB17, UPB28, and UPB41. The energy conditions and the design distances are shown in Table 2. The parameters

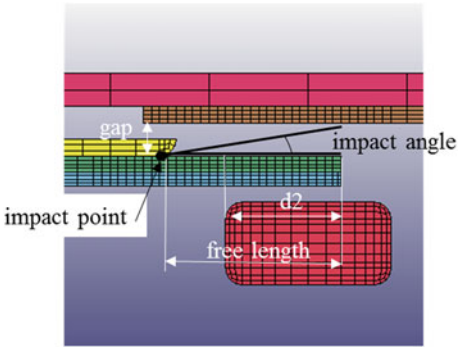


Fig. 3 LS-DYNA model detail: impact angle and impact point. (Color figure online)

Table 2 Model conditions

Case	Energy (kJ)	Gap (mm)	d2 (mm)	Impact angle (°)
UPB15	22	2	7	11
UPB17	19.4	2	7	11
UPB28	25	2	6	13
UPB41	25	1	8	5

that have been calculated are: plastic deformation, previous speed at the instant of impact, and impact pressure.

3.2 Computational Modeling Results

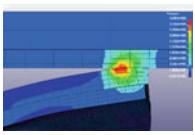
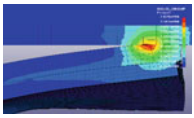
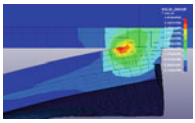
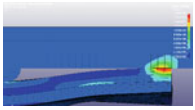
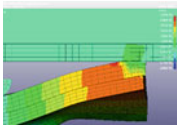
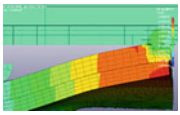
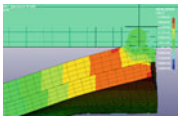
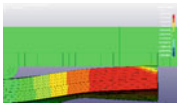
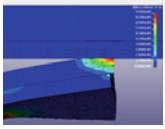
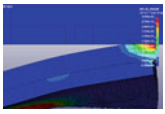
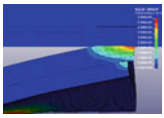
The results obtained from the simulations carried out are shown in Table 3, where the maximum values of impact pressure developed between the blanks to be welded, the velocity at the previous instant to the impact, and the plastic deformation suffered after the welding are displayed. The analysis to carry out will be done based on the maximum values obtained from these parameters due to their inherent relevance for MPW technology.

The maximum impact pressure values are within the range of 1–15 GPa, and this range being considered valid for mechanical welds [10]. The maximum values of the impact pressure appear at the point where the impact occurs (see Table 4). The highest pressure level is achieved at the UPB15 case. On the other hand, it is observed that with the same arrangement of the blanks and when the value of the applied energy decreases, the value of the maximum pressure also decreases. However, when the blank configuration changes, the increase in the applied energy does not lead to an increase in the pressure achieved. The last-mentioned case occurs in the UPB41 test, as can be seen in Table 3. In this case, the discharge energy level has been the maximum (25 kJ); however, by drastically reducing the impact angle to 5°, the maximum pressure reached has decreased by 41% compared to UPB 15 (22 kJ and 11°).

Table 3 Maximum values obtained from the four modeled cases

Case	Energy (kJ)	Impact angle (°)	Pressure (GPa)	Velocity (m/s)	Plastic deformation
UPB15	22	11	3.09	537.6	0.35
UPB17	19.4	11	2.63	504.9	0.3
UPB28	25	15	2.91	576.8	0.5
UPB41	25	5	1.85	329	0.06

Table 4 Images of maximum values of simulation parameters. (Color figure online)

CASE	Pressure (GPa)	Velocity (m/s)	Plastic deformation
UPB15			
UPB17			
UPB28			
UPB41			

The velocity of the moving plate, at the previous instant to the impact, behaves in a similar way to the maximum pressure achieved. The most remarkable thing is that the higher the energy applied for the same arrangement, the higher the speed is. Using the same configuration, when lowering the energy value the velocity of the blank also decreases. However, when using another arrangement, such as UPB41, the increase in energy does not translate into a rise in velocity.

The maximum velocity obtained in the UPB41 case simulation is 39% lower than the UPB15 case, with the energy discharged being practically the same.

With regard to plastic deformation, this parameter continues the same trend as the previous two.

4 Experimental Validation

The experimental tests were carried out on the Innovaltech platform (Saint-Quentin, France). The equipment used to develop the tests consists of a capacitors bank, a circuit in which there will be an electromagnetic coil specifically designed to carry out these experiments, and the blanks to be welded. The capacitor bank used is a PULSAR, with a maximum capacity of 25 kJ/9 kV (690 μF) and the pulse frequency was 17 kHz.

The used electromagnetic coil is flat (see Fig. 4) due to the nature of the joint to be

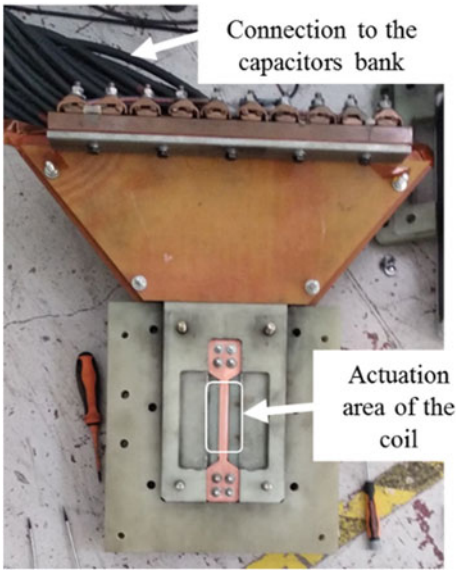


Fig. 4 Flat electromagnetic coil and the connections to the capacitors bank. (Color figure online)

made. To isolate the current discharged through the coil, with respect to the metallic elements of the system (joining elements, blocks to stop the impact, and the press used to contain the different components), the electromagnetic coil is embedded in a block of G10 as shown in Fig. 4. This figure also shows the connections required by the coil for its coupling to the capacitor bank and the actuating area of the coil: the area where the coil induces currents on the pusher and the Lorentz forces are generated. The mobile plates are placed on the actuation area of the coil, where the magnetic pulse will be generated.

In Fig. 5 the pusher blank is not shown, which would be located on the coil and this is covered with Kapton tape. This wrap is also called polyamide tape with silicone

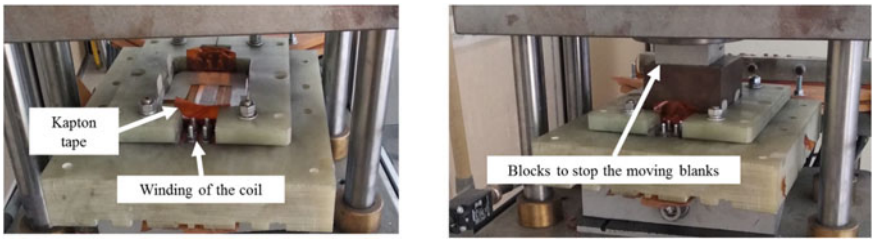


Fig. 5 Experimental setup. Left: after positioning the blanks to be welded on the coil. Right: final position of the setup elements before the electric discharge of the capacitors bank. (Color figure online)

adhesive, being an electrically insulating adhesive tape that is highly resistant to high temperatures, up to 250 °C.

Figure 5-Left shows the Kapton tape placed on the coil. The main function is to protect the coil from electrical arcs that may be created during the electrical discharge: between the coil and the other metallic elements of the system, such as the blanks to be welded or the joining elements such as screws. If the elements that configure the experimental setup are not electrically isolated, currents can be derived and electric arcs could be generated with catastrophic results for the coil and other elements of the test [11].

The tests have been carried out with a voltage between 7 and 8.5 kV. The distance between the moving and the fixed blanks has varied, increasing from 1 to 3 mm. The third parameter to evaluate was the superposition of the moving blank (AA 6082-T6) in regard to the coil, varying between 6 and 8 mm.

4.1 Experimental Validation Results

After welding, the joint is generally 20 mm long and 2 mm wide, as shown in Fig. 6.

The UPB15 and UPB17 tests were carried out with the same geometry, but applying different energy levels, 22 kJ and 19.4 kJ, respectively. In both cases, the welding is achieved.

In the UPB28 test, the overlap distance between the moving blank and the coil changes from 7 to 6 mm, the impact angle goes from 11 to 13° and the energy is set at 25 kJ. In this case, the welding is also considered acceptable. Finally, to carry out the UPB41 test, the energy used is 25 kJ, the distance between the two blanks changes from 2 to 1 mm, and the overlapping distance between the moving plates and the coil is increased to 8 mm, obtaining an impact angle of 5°. In this last-mentioned case, the weld is considered correct.

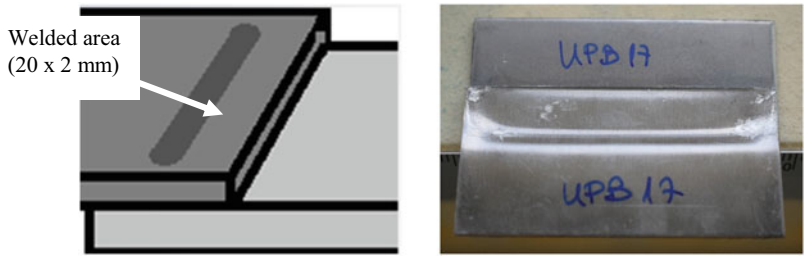


Fig. 6 Left: Rendering of the weld area. Right: Image of the experimental sample UPB17. (Color figure online)

5 Metallurgical Characterization

Hereunder, the results of the metallurgical characterization performed on the four welded specimens by magnetic pulses are shown. The cross-sections of the specimens have been analyzed. The specimens have been polished and etched following a standard procedure and the images were captured using a Leica confocal microscope. Figure 7 shows the images obtained for UPB cases 15, 17, 28, and 41. In the upper part is the steel blank and in the lower part the aluminum base. The bond between them is distinguished in the central area of the image.

It has been observed that the morphology of the joint varies by means of the modification of the parameters of the magnetic welding process. For example, Fig. 7d shows the influence of the impact angle on the morphology. The UPB41 case has an impact angle of 5° compared to 11° for the UPB15 and UPB17. Continuing with the analysis of this case, UPB41, it is observed that the bonding has a lower continuity than the other cases studied, and the start of the weld does not start at the point of the impact and shows a slight curvature in this area, while in the other cases the start of the welds is closer to the point of the impact.

It is observed that the higher is the angle of impact of the experimental setup, the higher levels of plastic deformation are reached.

Regarding the microstructure of the bonding, the characteristic sinusoidal or wavy shape of MPW [12] has been observed (see Fig. 8). However, the joints do not show homogeneity in their cross-section.

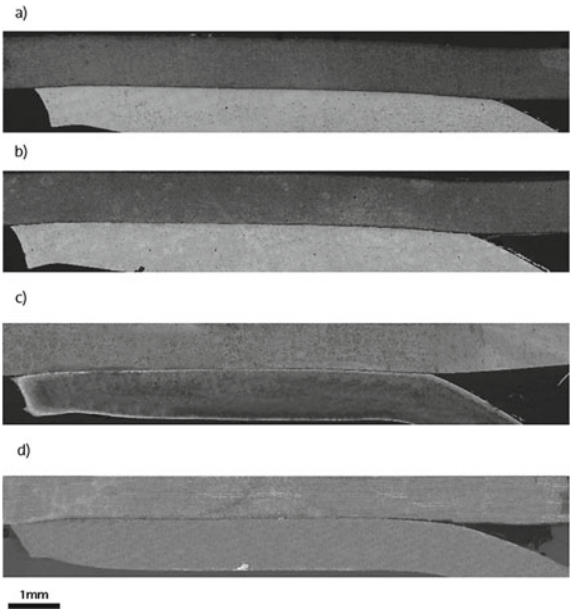


Fig. 7 Optical images of the cross-section of **a** UPB15, **b** UPB17, **c** UPB28, **d** UPB41 specimens

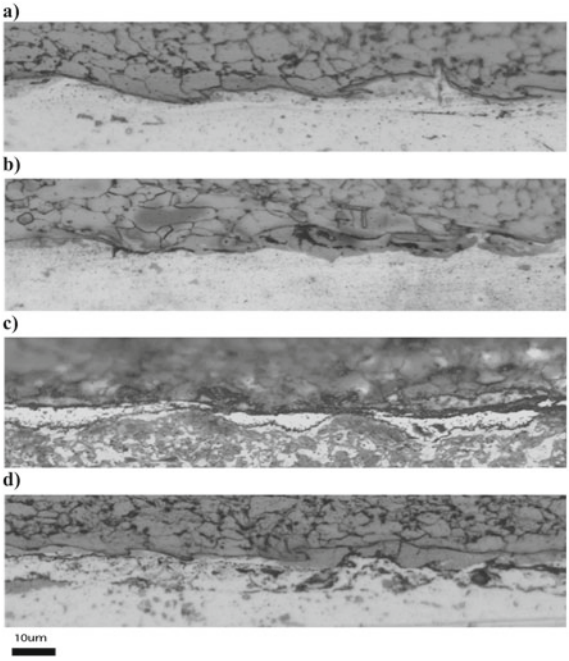


Fig. 8 Micrographs of the weld interfaces **a** UPB15, **b** UPB17, **c** UPB28, **d** UPB41

In the metallurgical analysis carried out, it has been observed that the microstructure varies with the process parameters tested. An increase in the angle of impact has a direct influence on the deformation of the material, being this higher, as bigger is the angle. The welds do not have a uniform morphology and show a characteristic wavy-interface configuration of MPW.

6 Concluding Remarks

After developing the present research work, whose main hypothesis was the determination of the feasibility of welding dissimilar materials, the main conclusion reached confirms that MPW is capable of joining dissimilar materials, such as steel and aluminum alloys. In the experimental validation carried out, using different test conditions, it was possible to bond the two blanks of HC420LA and AA 6082-T6.

LS-DYNA software has been capable to simulate processes like those analyzed in this study. The simulations carried out reveal approximate information on the process parameters, such as pressures, speeds, and maximum plastic deformations. From the impact pressures obtained from the simulations, it can be concluded that a greater amount of experimentally tested case modeling is required to conclude that a simulation is a valid tool to accurately predict the behavior of the joint.

Metallurgical characterization has been performed to verify that the joints made through this process produce good welds. The morphology of the transverse bond of the tested specimens has been studied and the four cases studied have presented favorable results that confirm the existence of the weld. The micrographs have shown the deformations generated, as well as the influence that the process variables exert on them.

References

1. Shribman V, Tomer Y (2006) Magnetic pulse technology for improved tube joining and forming. Tube Pipe Technol 91–95
2. Aizawa T, Matsuzawa K, Okogawa K, Ishibashi M (2014) Parallel seam welding of aluminum sheets by magnetic pulse welding method with collision between metal jets. Mater Sci Forum 767:171–176
3. Zhang P (2009) Joining enabled by high velocity deformation. Ph.D. thesis. The Ohio State University
4. Kapil A, Sharm A (2015) Magnetic pulse welding: an efficient and environmentally friendly multi-material joining technique. J Clean Prod 100:35–58
5. Sapanathan T, Raoelison RN, Buiron N, Rachik M (2016) Magnetic pulse welding: an innovative joining. INTECH. https://doi.org/10.5772/63525
6. Psyk V, Risch D, Kinsey BL, Tekkaya AE, Kleiner M (2011) Electromagnetic forming: a review. J Mater Process Technol 211:787–829
7. Dirksen U (2016) Fully coupled multiphysics finite element simulation of magnetic pulse welding of flat parts. MetalMorphosis Final Seminar Presentation. 2016. Ghent, Belgium. https://www.metalmorphosis.eu/images/News/Content_Files/Final_Event_PPT/3_Fully%20coupled%20multiphysics%20finite%20element%20simulation%20of%20magnetic%20pulse%20welding%20of%20flat%20parts.pdf
8. El-Azab A, Garnich M, Kapoor A (2003) Modeling of the electromagnetic forming of sheet metals: state-of-the-art and future needs. J Mater Process Technol 142:744–754
9. L'Eplattenier P, Cook G, Ashcraft C, Burger M, Imbert J, Worawick M (2009) Introduction of an electromagnetism module in LS-DYNA for coupled mechanical-thermal-electromagnetic simulations. Steel Res Int 80(5):351–358
10. Liu BC, Palazotto AN, Nassiri A (2019) Experimental and numerical investigation of interfacial microstructure in fully age-hardened 15–5 PH stainless steel during impact welding. J Mater Sci 54:9824–9842
11. Iriondo E (2007) Electromagnetically Impulsed Springback Calibration. Ph.D. Thesis. University of the Basque Country, Bilbao
12. Lee KJ, Kumai S, Arai T, Aizawa T (2007) Interfacial microstructure and strength of Steel/Aluminum alloy lap joint fabricated by magnetic pressure seam welding. Mater Sci Eng 471:95–101

Influence of Ultrasonic Assistance on the Forming Limits of Steel



Manuel Jäckisch and Marion Merklein

Abstract Since Blaha discovered the beneficial effect of superimposing high-frequency oscillations to the metal forming process, the occurring force and stress reduction are well-known phenomena. Leading to an immediate flow stress reduction, the so-called ultrasonic assistance is a promising approach to enable forming with reduced process forces. While the achievable force reduction has been investigated intensively, only a few analyses have been conducted in the context of the impact of ultrasonic superposition on the forming limits. The latest investigations state earlier material failure due to localized forming with recurrent high strain rates. Within this paper, the influence of superimposed vibrations on the forming limits of C35E is investigated with regard to distinct oscillation amplitudes and press velocities. It was found that superimposed 20 kHz oscillations of 10 and 20 μm cause considerable earlier material failure. In comparison to conventional testing, the crack initiation, as well as the shear zone formation, is alternated due to the ultrasonic assistance.

Keywords Ultrasonic · Forming · Failure · Steel

1 Introduction

The global goal to reduce CO_2 emissions affects almost every industrial sector. In the European Union (EU) 21% of the overall CO_2 emissions are caused by road transport [1]. Consequently, lightweight construction offers a high potential to reduce emissions and comply with critical limits. A common measure is the use of high-strength steels, which allow a significant reduction of wall thicknesses, and therefore lead to a decrease of component weight. High flow stresses as well as limited formability limit the application of conventional manufacturing processes for these materials. Therefore, there is a demand for innovative production methods. One approach is the superposition of high-frequency oscillations to the forming process. In this way, the so-called ultrasonic assistance enables a substantial reduction of the forming

M. Jäckisch (✉) · M. Merklein
Friedrich-Alexander-Universität Erlangen-Nürnberg, Institute of Manufacturing Technology (LFT), Egerlandstr. 13, 91058 Erlangen, Germany
e-mail: manuel.jaeckisch@fau.de

© The Minerals, Metals & Materials Society 2021

G. Daehn et al. (eds.), *Forming the Future*, The Minerals, Metals & Materials Series,
https://doi.org/10.1007/978-3-030-75381-8_106

forces. The ultrasonic-based softening, which is also known as the Blaha effect [2], has already been confirmed for several processes such as deep drawing, wire drawing, and forging, as well as for various materials like copper [3], aluminum [4], and mild and high-strength steel [5]. However, most investigations focused on the achievable force reduction and the process characteristics. Only a few analyses dealt with the influence of high-frequency oscillations on the forming limits of metallic materials.

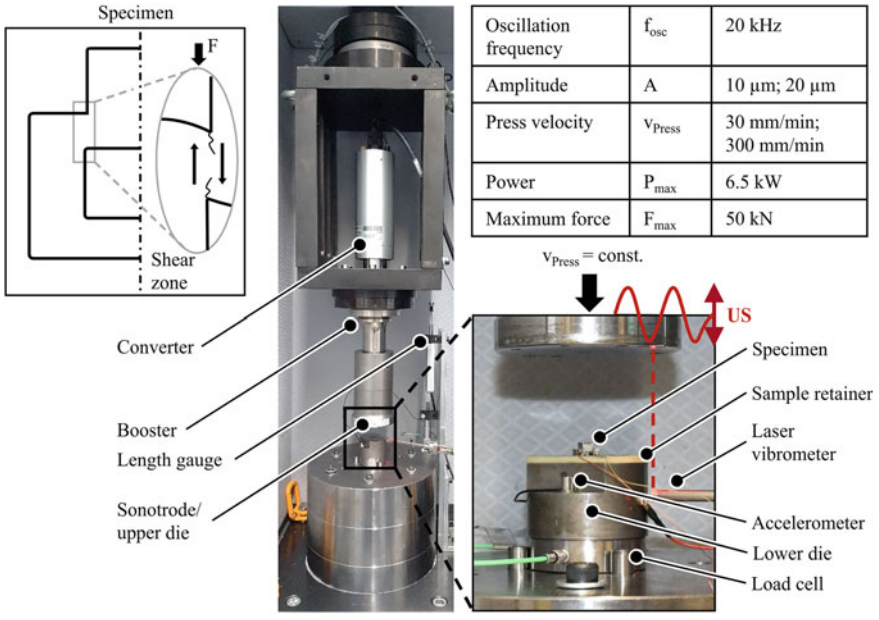
In order to investigate the ultrasonic-based influence on material failure under shear loading, Michalski et al. [6] superimposed hat-shaped specimens with a 20 kHz oscillation and amplitudes of 10 and 20 μm. In comparison to conventional shear tests without vibrational influence, they found earlier material failure due to crack initiation as well as reduced maximum shearing loads because of the superimposed oscillations. These findings were confirmed for cast aluminum, mild steel and high-strength steel. Moreover, the superimposed oscillation caused transversal cracks. Schmauder et al. [7] investigated ultrasonic-induced effects on the forming limits under torsional loading. Therefore, torsion tests were superimposed with 22 kHz oscillations in the axial direction. It was found that the forming limits of mild steel and nickel silver were extended, whereas a reduction occurred for aluminum. Independent of the material, the vibrational effects were weakened with increasing strain rates. Wittauer et al. [8] conducted ultrasonic-assisted blanking tests with aluminum. They presumed enhanced material plasticity due to the high-frequency vibration since increasing oscillation amplitudes caused decreasing fracture zones. In contrast, analyses of oscillation-induced effects with compression and tension testing indicate a material-dependent reduction of the formability for high-strength steels and titanium alloys [9]. Nerubai ascribed this behavior to damaged crystal structures. Wen et al. [10] also conducted tension testing with superimposed vibration. For an oscillation frequency of 15 kHz and amplitudes up to 1.5 μm, an enhanced material formability was found for AZ-31. Greater amplitudes of 2.7 μm resulted in earlier material failure. They assumed different predominant dislocation movement mechanisms for the contrary findings.

Regarding the influence of ultrasonic assistance on material failure, the present studies indicate varying findings as well as material dependencies. Moreover, for mild steel both reduced [6] and enhanced [7] material formability was determined. Therefore, this experimental analysis aims for a systematic investigation of vibrational induced effects on the forming limit of steel and a more in-depth analysis of characteristic process states in comparison to previous investigations. For this, a common bulk-forming steel C35E is used, which has a well examinable microstructure. Based on the methodology in [6], hat-shaped specimens are formed by two distinct press velocities of $v_{Press} = 30$ mm/min and $v_{Press} = 300$ mm/min with superimposed longitudinal 20 kHz oscillations of 10 and 20 μm oscillation amplitude A. As a reference, conventional testing without superimposed vibration, equivalent to 0 μm oscillation amplitude, is carried out. On the basis of the force–displacement curves, substantial process influences are investigated and material failure is determined. The shear zones are evaluated by means of qualitative and quantitative metallographic analyses. Moreover, stepwise shear testing is conducted and the crack initiation and propagation is investigated by microsections.

2 Experimental Setup

The specimen geometry for ultrasonic-assisted shear testing is derived from high-speed shear testing [11]. The hat-shape enables a predominantly homogenous stress state in the shear plane and has already been successfully applied for ultrasonic-assisted shear tests [6]. The C35E specimens are precisely cut by electrical discharge machining with an AgieCharmilles CUT2000. As depicted in Fig. 1 the samples are mirror-symmetric with two identical 10.0 mm long, 1.0 mm high, and 0.1 mm wide shear zones.

The experimental investigations on the impact of ultrasonic assistance on the forming limits of steel are carried out on a universal testing machine Walter + Bai LFEM 300. An individual tool that enables the superposition of high-frequency oscillations to the constant feeding rate is mounted to the testing machine. The testing rig for ultrasonic-assisted forming, introduced in [12], consists of a fixed lower and a moveable upper tool and is depicted in Fig. 1. The moveable upper tool is mounted to the traverse of the testing machine and comprises a converter, a booster, and a sonotrode, which also functions as the upper die. To superimpose ultrasonic oscillations to the forming process, the converter is fed with a high-frequency AC voltage. Based on the inverse piezoelectric effect, the converter transforms the electrical voltage into a mechanical oscillation of the same frequency. Due to the booster's geometry and the interaction with the sonotrode, the oscillation amplitude is amplified by a specific ratio. This way, the constant feed of the testing machine is



Oscillation frequency	f_{osc}	20 kHz
Amplitude	A	10 µm; 20 µm
Press velocity	v_{Press}	30 mm/min; 300 mm/min
Power	P_{max}	6.5 kW
Maximum force	F_{max}	50 kN

Fig. 1 Specimen geometry and experimental setup. (Color figure online)

superimposed with a high-frequency oscillation of 20 kHz and amplitudes of 10 and 20 µm. A length gauge is used for measuring the tool displacement and controlling the ultrasonic system. Moreover, the lower tool is shown in detail in Fig. 1. Besides the lower flat die, where the samples are positioned in a retainer, measurement instrumentation for process control is included. A piezoelectric force transducer directly underneath the die gauges the dynamic forces. Since the dynamic behavior of the load cell and the whole lower tool is frequency-dependent, the transfer function is determined by means of the approach proposed in [13]. This way, oscillating forces are assessed correctly and the true maximum oscillatory forces are identified. A laser vibrometer and an accelerometer are utilized to monitor the oscillation of the upper and lower tool, respectively. All signals are sampled with 1 MHz.

3 Results

Material failure is determined based on the force–displacement curves. As proposed in [6] the displacement at failure initiation is analyzed by the gradient of the mean process force. Therefore, the derivative of the mean process force with respect to the displacement is calculated. Since the derivative's zero-crossing indicates the decline of the process forces, this position marks the material failure. The respective maximum oscillatory process force is the force at failure. In Fig. 2 the force–displacement curves are depicted for conventional and ultrasonic-assisted shear testing with 20 kHz oscillation frequency and 10 and 20 µm amplitude. For each parameter combination, three valid repetitions are conducted. The results for the press velocity of 30 and 300 mm/min are separated in two diagrams. Essentially, the force–displacement curves are similar for the distinct press velocities. After the initial steep rise, which indicates the elastic range, the process forces increase moderately until material failure occurs. With continuing plastic shear deformation the process forces decrease. For 30 mm/min press velocity the respective process forces are lower and the ultrasonic-based force reduction is more pronounced than for 300 mm/min. These findings are in accordance with the investigation of the ultrasonic-based force

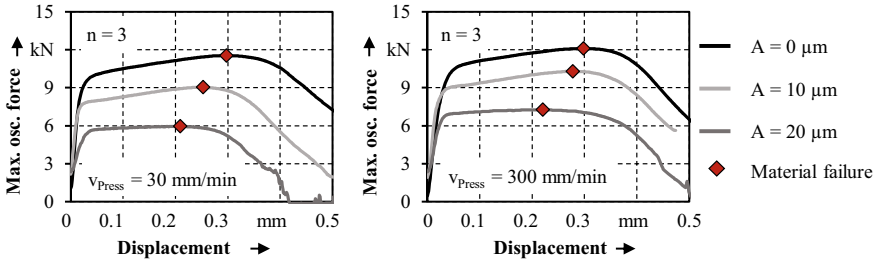


Fig. 2 Force–displacement curves for conventional and ultrasonic-assisted shear testing with 30 and 300 mm/min press velocity. (Color figure online)

reduction in compression tests with the identical material [14]. The increased force reduction is explained by the enhanced vibrational energy input due to the greater oscillation amplitude. Additionally, the lower press velocity, leading to an extended process duration, further increases the energy input.

For a quantitative analysis of the displacement and force at failure, the respective results are plotted in Fig. 3. Without superimposed oscillation failure occurs for 30 and 300 mm/min press velocity at a displacement of 0.30 mm. Thus, the evaluated strain rate range has no influence on the displacement at failure. A press velocity of 30 mm/min and ultrasonic assistance with 10 and 20 µm amplitude lead to considerable earlier failure at 0.25 and 0.21 mm displacement, respectively. For higher press velocity, the points of crack initiation under oscillation superposition are determined later; however, the deviations in comparison to 30 mm/min press velocity are insignificant. Regarding the force at material failure, similar behavior is detected. Maximum shear forces are 11.54 and 12.11 kN for conventional forming with 30 and 300 mm/min, respectively. Superimposed oscillations of 20 µm amplitude lead to a maximum force reduction of 5.59 and 4.85 kN for the respective process velocities. The force reductions due to the lower forming velocity and the higher oscillation amplitudes are consistently significant. In conclusion, the oscillation amplitude has the most prominent influence on the ultrasonic-based force reduction and therefore on the force at failure. Since these outcomes are in accordance with investigations on the ultrasonic-based force reduction under compressive stress [14], it can be assumed that the findings are applicable to a shear stress state.

In order to evaluate the crack initiation and propagation precisely, for each parameter combination at the lower press velocity, six characteristic microsections of stepwise shear tests are illustrated in Fig. 4. The upper row depicts the process states for conventional shear testing, equivalent to A = 0 µm. Up to 0.25 mm feed plastic forming leads predominantly to a rollover. As initial cracks occur, the rollover formation is interrupted at 0.26 mm displacement. This behavior is similar to conventional shear cutting. During the following process stages the cracks grow smoothly in the axial direction and a defined shear zone is formed. Superimposing a 20 kHz oscillation of 10 µm amplitude results in the crack formation presented in the middle

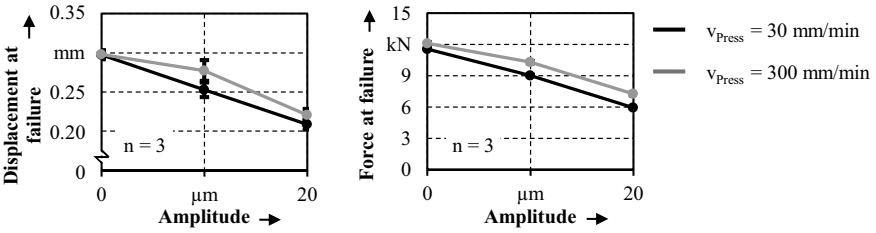


Fig. 3 Material failure displacement and force for conventional and ultrasonic-assisted shear testing. (Color figure online)

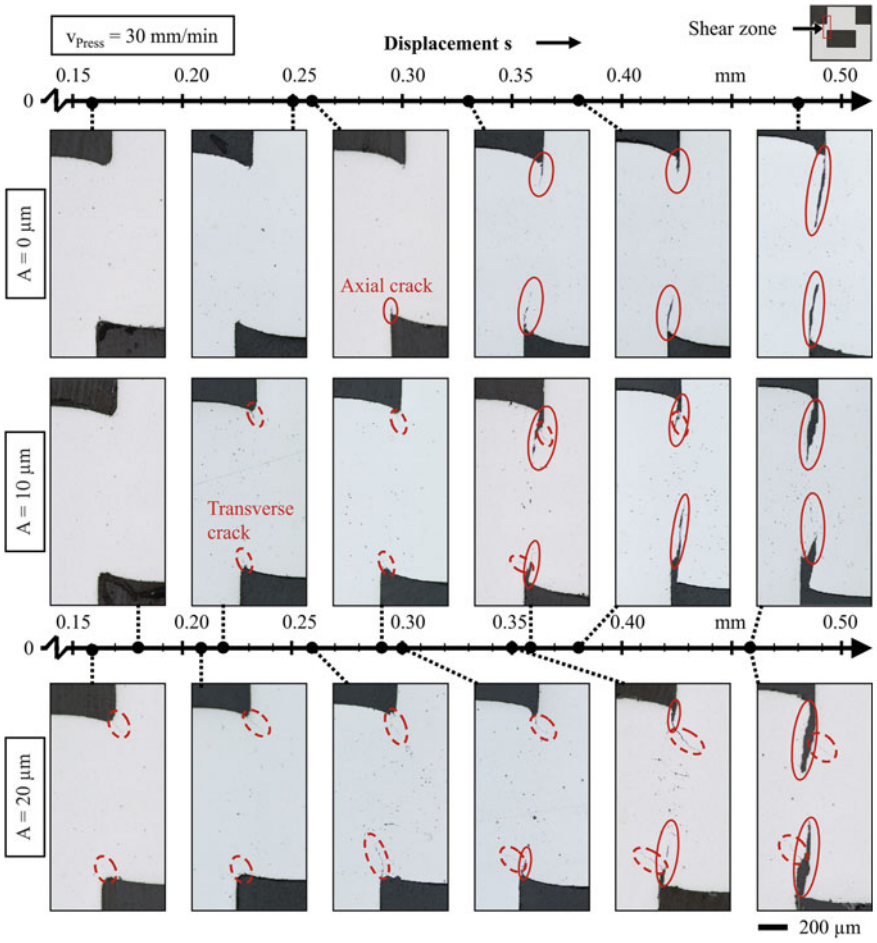


Fig. 4 Crack initiation and propagation at characteristic process states for shear testing with v_{Press} = 30 mm/min and oscillations amplitudes of 0, 10, and 20 µm. (Color figure online)

row. First cracks are identified at 0.22 mm displacement. In contrast to conventional forming, the cracks are also transverse-orientated. According to [6], this transverse crack formation is caused by cyclic high frequent stress alternation as well as stress concentration at the edges. Further deformation results in the formation of a pronounced upper and lower axial crack with smaller transverse cracks. Consequently, the final shear fracture is more rugged. As indicated by the microsections in the last row, superimposed vibration with 20 µm amplitude results in a similar crack propagation as oscillations of 10 µm amplitude. Nevertheless, the effects are more severe. Initial transverse cracks are detected at 0.16 mm stroke. At first, crack growth is predominantly orientated transversal before the axial crack propagation

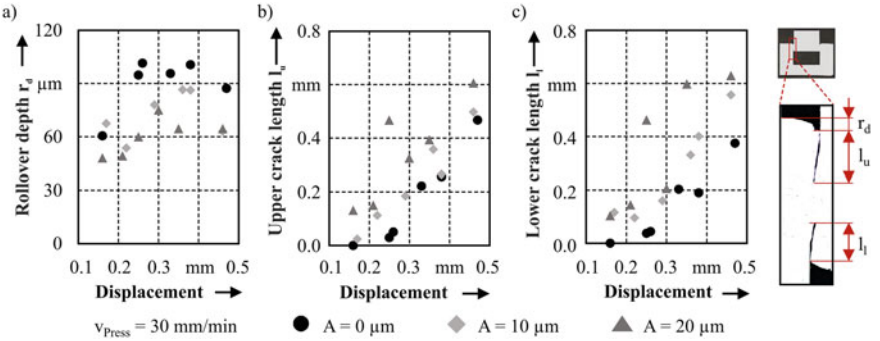


Fig. 5 Quantitative analysis of **a** rollover depth as well as **b** upper and **c** lower crack propagation for shear testing with $v_{Press} = 30$ mm/min and superimposed oscillations of 0,10, and 20 µm amplitude. (Color figure online)

becomes dominant. In conclusion, ultrasonic assistance causes both earlier and transverse crack growth. Moreover, fine microcracks occur for all evaluated parameter combinations in earlier process states than previously determined on the basis of the force–displacement curves.

In addition to the qualitative mircosections, a quantitative evaluation of the rollover depth and the crack growth from the upper and lower edge of the shearing zone is carried out for the respective process states. Each data point in Fig. 5 represents the mean of the left and right shear zone of a single sample. Figure 5a presents the rollover depths r_d for conventional and ultrasonic-assisted shear testing with 30 mm/min press velocity. The most considerable rollover occurs for conventional shearing. The maximum rollover depth is already reached at a process state of 0.25 mm stroke. Since the continuing stroke leads to substantial crack propagation, further rollover is inhibited. Similar behavior is identified for vibration superimposed shearing tests with 10 and 20 µm amplitude. The maximum rollover depth develops until the deformation results predominantly in axial crack propagation. This process state is attained at about 0.3 mm displacement for both amplitudes. Furthermore, the maximum occurring rollover depth reduces with greater oscillation amplitudes. These findings indicate reduced plasticity due to ultrasonic assistance. Moreover, the effect is promoted by greater amplitudes. The analysis of crack lengths growth is plotted in Fig. 5b, c. Regarding the upper crack l_u, the largest cracks occur due to high-frequency oscillations with 20 µm amplitude. Additionally, cracks are formed at earlier process states. Reducing the oscillation amplitude to 10 µm results in both later crack initiation and shorter cracks. This trend is enhanced for conventional shear testing with 0 µm amplitude. Essentially, mainly steady crack growth is measured for all the analyzed parameter combinations, which correlates with the linear increasing displacement. Similar behavior is detected with respect to the crack propagation emerging from the lower edge. However, superimposed oscillations of 20 µm amplitude appear to lead to unsteady crack formation. The results indicate an interruption of the rollover formation due to the axial crack initiation. Regarding ultrasonic-assisted shear testing,

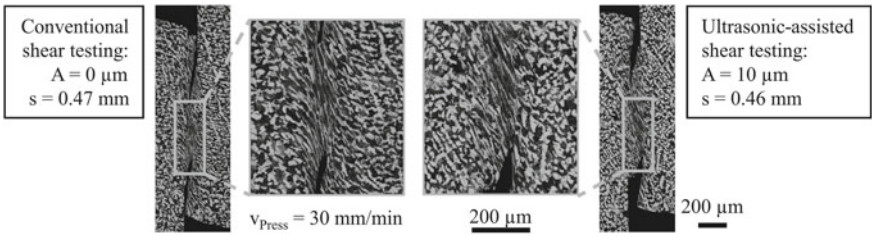


Fig. 6 Comparison of the microstructure due to conventional and ultrasonic-assisted shear testing

axial cracks develop from the initial transverse cracks. Hence, these initial cracks are crucial to the early material failure under the ultrasonic influence.

Considering the identified points of material failure based on the force–displacement curves and the qualitative and quantitative evaluation of the microsections, slight deviations are present. Even though initial fine cracks occur prior to the calculated point of crack initiation, the deviations are similar for the various process parameters. Thus, the methodology is appropriate to determine the influence of ultrasonic assistance on the material failure. Since these fine cracks are apparently insignificant to the process force, the formation cannot be directly measured. Nevertheless, qualitative and quantitative results verify reduced material formability due to superimposed oscillations. Michalski et al. [6] explained this effect by the formation of adiabatic shear bands. Therefore, Fig. 6 compares the microstructures of deformed specimens after conventional and ultrasonic-assisted shear testing with 10 µm amplitude. The etched microsections of both parameter combinations reveal narrow shear bands with highly deformed grains close to mainly undeformed microstructure. Even though this formation is characteristic to adiabatic shear bands [15], in this case, it is addressed to specimen geometry, which promotes a narrow shear zone. Moreover, the precondition of very high strain rates due to the high-frequency oscillation is not fulfilled for the conventional shear tests. Considering the similar microstructures of conventional and ultrasonic-assisted shear tested specimens, adiabatic shear bands are unlikely for the steel C35E. Consequently, other causes for the reduced shear formability are present. The experimental findings prove a promoted crack initiation at early process stages due to the superimposed oscillations. Thus, the instantaneous cross-section in the shear zone is decreased and stress concentration at the crack tips occurs. Hence, it can be assumed that the initial material failure is a crucial cause for the reduced shear formability.

4 Summary

Within this investigation, the influence of ultrasonic assistance on the material failure was analyzed. Conventional and ultrasonic-assisted shear testing with 20 kHz oscillations and 10 and 20 µm oscillation amplitude was carried out for C35E. Based

on the force–displacement curves material failure was determined by means of the mean forming force derivative with respect to the stroke. It was found that the forming forces are considerably reduced by superimposed oscillations. This behavior accords with the usual influence of ultrasonic assistance on forming processes. Moreover, material failure occurred earlier and at lower process forces. The oscillation amplitude predominantly influenced this behavior, while distinct press velocities and thus the process duration had minor effects. Conducting stepwise shear tests, the formation and propagation of the shear zone were investigated. Mircosections at characteristic process states revealed smooth crack formation for conventional forming and transverse crack growth as well as rugged shear zones due to ultrasonic assistance. Quantitative analyses of the shear zone geometry confirmed the findings. Crack initiation and size were promoted by superimposed oscillations and correlated with the amplitude's magnitude.

Acknowledgments This research project is funded by the DFG. The authors gratefully thank the German Research Foundation (DFG) for funding the project ME 2043/69-2 with the title "Fundamental investigation of ultrasonic-assisted metal forming by compressive and shear stress". The authors are responsible for the contents of this publication.

References

1. European Commission: Road transport: reducing CO_2 emissions from vehicles, http://ec.europa.eu/clima/policies/transport/vehicles_en. Accessed 25 Nov 2020
2. Langenecker B (1966) Effects of ultrasound on deformation characteristics of metals. IEEE Trans Sonics Ultrason 13:1–8. https://doi.org/10.1109/T-SU.1966.29367
3. Jäckisch M, Merklein M (2019) Residual effects of ultrasonic-assisted compression testing on pure copper. AIP Conf Proc 2113:110001–1-110001–6. https://doi.org/10.1063/1.5112644
4. Yao Z, Kim GY, Faidley L, Zou Q, Mei D, Chen Z (2012) Effects of superimposed high-frequency vibration on deformation of Aluminum in micro/meso-scale upsetting. J Mater Process Tech 212:640–646. https://doi.org/10.1016/j.jmatprotec.2011.10.017
5. Michalski M, Piott F, Merklein M (2017) Compression testing of martensitic stainless steel with superimposed ultrasonic vibration. Procedia Eng 207:1970–1975. https://doi.org/10.1016/j.proeng.2017.10.1100
6. Michalski M, Lechner M, Gruber M, Merklein M (2018) Influence of ultrasonic vibration on the shear formability of metallic materials. CIRP Ann—Manuf Technol 67: 277–280. https://doi.org/10.1016/j.cirp.2018.04.108
7. Schmauder S, Siegert K (2000) Experimentelle und theoretische Beschreibung des Verformungsverhaltens bei überlagerter Schwingungsbeanspruchung. In Abschlussbericht SFB 543 Ultraschallbeeinflusstes Umformen metallischer Werkstoffe—Teilprojekt A1, Stuttgart, Germany
8. Witthauer AT, Kim GY, Faidley L, Zou QZ, Wang Z (2014) Effects of acoustic softening and hardening in high-frequency vibration-assisted punching of Aluminum. Mater Manuf Processes 29:1184–1189. https://doi.org/10.1080/10426914.2014.921704
9. Nerubai MS (1987) Effect of ultrasonic vibrations on the mechanical properties of difficult-to-deform materials. Met Sci Heat Treat 29:254–258. https://doi.org/10.1007/BF00769422
10. Wen T, Wei L, Chen X, Pei C-l (2011) Effects of ultrasonic vibration on plastic deformation of AZ31 during the tensile process. Int J Miner Metall Mater 18:70–76. https://doi.org/10.1007/s12613-011-0402-4

11. Meyer LW, Kruger L (2000) Shear testing with hat-shaped specimen. In: Kuhn H, Medlin D (eds) ASM handbook Vol. 8—mechanical testing and evaluation, 10th edn, ASM International, p 451–452
12. Michalski M, Leicht U, Engler S, Merklein M (2015) Tool system for ultrasonicassisted forming and material characterisation with 15 kHz oscillation frequency. Appl Mech Mater 794:427–434. https://doi.org/10.4028/www.scientific.net/AMM.794.427
13. Michalski M, Leicht U, Heath A, Merklein M (2017) Dynamic correction of oscillatory forces during ultrasonic-assisted metal forming. Prod Eng Res Devel 11:455–465. https://doi.org/10.1007/s11740-017-0762-3
14. Jäckisch M, Merklein M (2020) Investigation of thermal effects during ultrasonic-assisted upsetting. Procedia Manuf 50:220–225. https://doi.org/10.1016/j.promfg.2020.08.041
15. Dodd B, Bai Y (2012) Adiabatic shear localization. Elsevier, Oxford

Design and Fabrication of a High-Performance Magnetic Actuator for Magnetic Pulse Welding of Metal Tubes with Large Diameters



Xiaoxiang Li, Quanliang Cao, Zhipeng Lai, Yiliang Lv, Siyuan Chen, Yi zhang, Xiaotao Han, and Liang Li

Abstract Magnetic pulse welding (MPW) is a high-speed joining process that uses pulse electromagnetic force to achieve welding. It is a clean welding process and it can be applied to dissimilar metals welding, which has a wide range of application prospects. However, this technology is currently mainly used for welding small-diameter thin-walled tubes. This is because the energy and electromagnetic force required for welding increase significantly as the tube size increases, which consequently places strict requirements on welding tools, including pulsed power and coil. To solve this issue, this work developed a two-dimensional (2D) axial-symmetry finite element model to optimize the tube welding process and designed a high-performance magnetic actuator with a high-strength coil to generate a strong enough electromagnetic force. On this basis, both numerical and experimental studies were performed to investigate the welding behavior of a 6061 aluminum alloy tube and a 304 stainless steel tube with 110 mm diameter and 3 mm thickness. Finally, a mechanical test and scanning electron microscope (SEM) were used to verify the joining quality, and the results show that the metallurgical bonding occurred between the two tubes. The presented optimization method and tool design could be of significance to the practical applications of MPW technology.

Keywords Magnetic pulse welding · Tube welding · Dissimilar metals welding · Large diameter tube

X. Li · Q. Cao · Z. Lai · Y. Lv · S. Chen · Y. zhang · X. Han · L. Li (✉)
Wuhan National High Magnetic Field Center, Huazhong University of Science and Technology, Wuhan 430074, China
e-mail: liangli44@hust.edu.cn

State Key Laboratory of Advanced Electromagnetic Engineering and Technology, Huazhong University of Science and Technology, Wuhan 430074, China

© The Minerals, Metals & Materials Society 2021

G. Daehn et al. (eds.), *Forming the Future*, The Minerals, Metals & Materials Series,
https://doi.org/10.1007/978-3-030-75381-8_107

1 Introduction

Magnetic pulse welding (MPW) is an advanced and clean technology, which can translate electric power into kinetic energy of metallic tubes or sheets and achieve welding by high-speed impact. Compared with traditional fusion welding, MPW is a kind of solid-state welding process. Without an obvious welding seam, the shortcoming of a heat-affected area can be avoided. In addition, the joining of dissimilar materials is impossible for the conventional fusion welding process due to huge differences in melting point, thermal conductivity, volumetric specific heat, and coefficient of thermal expansion [1]. As MPW can achieve atomic diffusion of two materials by high-speed impact, this method can be used to join dissimilar materials and achieve lighter and stronger material combinations. Other high-speed welding technologies, like explosive welding, laser impact welding, and vaporizing foil actuator welding are mainly applied to sheet welding. MPW has significant advantages in tube welding because of the axisymmetric structure of the coil actuator.

At present, MPW technology is mainly used for tubes with a diameter of less than 50 mm and thickness thinner than 1 mm, like automotive space frame and cable connector, as in [2]. To the best of our knowledge, the largest diameter of magnetic tube welding research latest reported is 80 mm [3]. Welding large and thick tubes needs more input energy to generate high driving pressures between magnetic actuator and tubes in a short acceleration time. The lack of high-energy power supplies or the low efficiency of welding actuators makes the energy input unsatisfactory. Furthermore, high driving pressures can also lead to shorten the longevity of the actuator or even damage the equipment which makes it difficult to weld large diameter tubes [4]. To solve these problems, a necessary task is to optimize the welding system via an effective simulation model, which can be used to improve the utilization of magnetic energy. As the MPW system is not a perfect two-dimensional axial-symmetry system, the existing simulation models are mainly based on the 3D model [5, 6]. Although these models can analyze the whole MPW process accurately, it is complex and low efficiency to achieve optimization work. Yu et al. 2005 established a 2D model by ANSYS to explore the effect of field shaper on magnetic pressure distribution in electromagnetic modules [7]. But the MPW is a multi-physics coupling process and the optimization of detailed parameters of magnetic actuators is rarely mentioned. In addition to optimization work, how to increase the structural strength of the coils used in the MPW process is also critical, which is the key to ensuring that a sufficiently strong electromagnetic force can be generated. In this regard, our group has done some related research. For example, the high-field pulsed magnet manufacturing technology has been introduced to increase the coil strength in the field of electromagnetic forming [8]. A new discharge circuit configuration with a crowbar circuit was proposed to reduce the Joule heating of the coil [9]. A dual-coil system was developed to improve the forming ability of sheet and tube processing [10, 11].

This paper provides an effective two-dimensional model for the optimization of design of the MPW process by simplifying the boundary conditions in COMSOL.

Aiming at welding aluminum tubes with 110 mm diameter and 3 mm thickness, the effects of actuator parameters such as the coil turns and the structural parameters of the field shaper on the magnetic pressure are analyzed in detail, and a high-strength coil has been designed and fabricated. Furthermore, a variable-size, multi-function MPW experimental platform is developed and a series of experiments are carried out to achieve the high-quality welding between the AA6061 and SS304 tubes. Finally, some mechanical and metallography tests are performed to evaluate the welding quality.

2 Simulation

For tube welding, a magnetic actuator is placed outside the two tubes and energized with a capacitor bank. The interaction between the generated magnetic field and the induced eddy current in the outer metal tube will trigger a strong Lorentz force that induces the high-speed impact of two tubes, as shown in Fig. 1a. Field shaper (FS) is an important part that has an effect on the distribution of the magnetic field. The magnetic actuator is not a perfect two-dimensional axial symmetry model and a slot exists in the FS. Through this slot structure, the magnetic field generated by the coil can access the area near the outer tube, as shown in Fig. 1b. In the FS region, the slot cuts off the current in the hoop direction, and the FS can be regarded as a single-turn secondary coil [12]. In COMSOL software, the model can be treated as a 2D axial symmetry model by defining the FS region as a coil characteristic and making its total current to zero all the time.

A 2D axial symmetry finite element simulation model has been built by the COMSOL Multiphysics software package. In the time domain, five physical modules are solved by the unity coupling mode: (1) the "global ordinary differential equations (ODEs) and differential algebraic equations (DAEs)" module; (2) the "magnetic fields" module; (3) the "solid mechanics" module; (4) the "Heat transfer in solid"

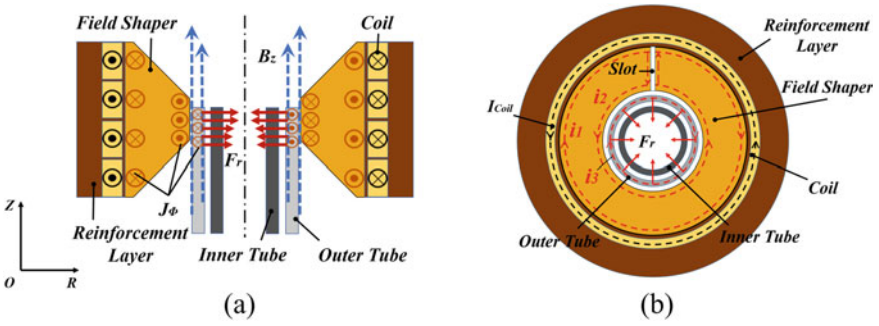


Fig. 1 Schematic diagram of the MPW process: **a** The front view and **b** the top view. (Color figure online)

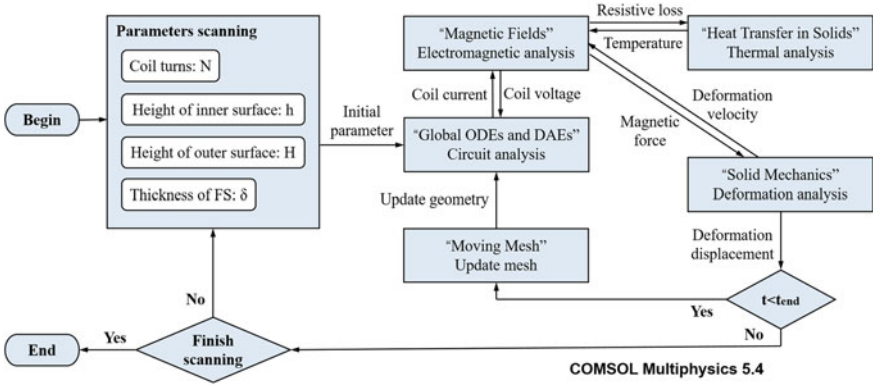


Fig. 2 Flowchart of the implemented algorithm. (Color figure online)

module; and (5) the "moving mesh" module. A flowchart of the simulation process is shown in Fig. 2.

Higher impact velocity means more likely to achieve welding in MPW. The maximization of impact velocity of the outer tube is regarded as an optimization objective. COMSOL has an outstanding ability to solve multi-physics coupling problems and very convenient to use its built-in optimized model. As the simulation model is based on the finite element method (FEM), the air region is required to calculate the electromagnetic field and to define the boundary of the whole area. Considering the air mesh will be distorted when solving the above coupling physical fields, the "Moving Mesh" model is applied to update and redraw the air mesh to ensure high-precision simulation. Note that the air resistance was not considered in this optimization design model. To get the optimized parameters, combining the results of magnetic pressure calculated by "magnetic fields" model and the velocity which is calculated by "solid mechanics" model can be more convincing. The diagram of mesh subdivision is shown in Fig. 3. The magnetic pressure represents the magnetic field energy density, which can be calculated by Eq. (1) based on the magnetic field intensity near the tube:

$$p_m(t) = \frac{1}{2}\mu\left(H_o^2(t) - H_i^2(t)\right) \tag{1}$$

where H_o represents the magnetic field intensity between FS and tube, and H_i represents the field intensity inside the tube [13]. The second method is to take the line integral of the Lorentz force on the wall thickness of the workpiece, as shown in Eq. (2):

$$p_m(t) = \int_{r_{in}}^{r_{out}} f_m(r,t)dr \tag{2}$$

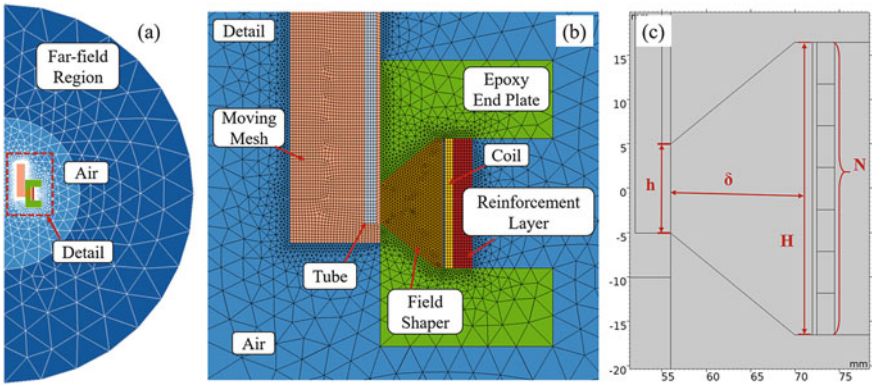


Fig. 3 Finite element mesh for the MPW system and a schematic diagram of the simulation model. (Color figure online)

where f_m represents the Lorentz force, r_{in} and r_{out} are the inner and outer diameter of the tube, respectively. The two methods mentioned above are both feasible. As this paper mainly analyzes the velocity of the tube end, the second method was adopted.

3 Experiment

3.1 Experimental Configuration

The actuator with optimized parameters is made according to the simulation results. Figure 4 shows the experimental configuration. An aluminum alloy tube (AA6061) with a diameter of 110 mm and thickness of 3 mm was welded to steel tubes with

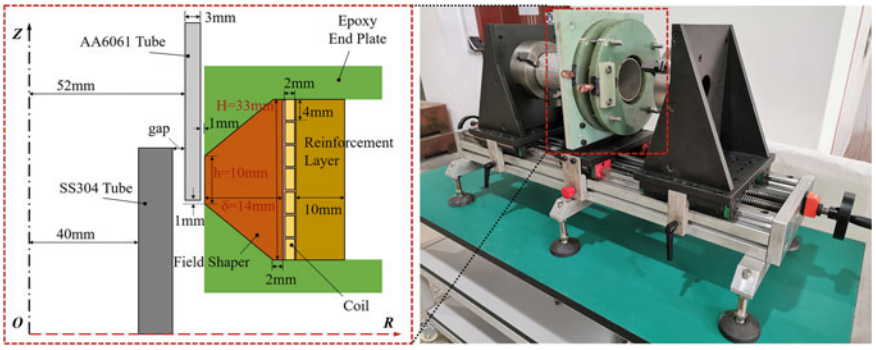


Fig. 4 Geometric model of the experimental configuration and experimental platform. (Color figure online)

different diameters. In order to improve the magnetic energy utilization, the multi-turn coil structure was chosen and the field shaper was wound by copper wires with rectangular cross-section directly. The copper wires were covered with polyimide film to ensure a high degree of insulation between turns. This design makes the distance between the coil and the field shaper only 0.5 mm, and reduces the stray losses significantly. In addition, decreasing the length of the overlap between the tube and the FS working area can reduce the non-effective connection [14]. In the experiment and optimization design, there is an uncovered distance between the end of the tube and the inner surface edge of the FS along the axial direction to enhance the electromagnetic force, and the distance is set to 1 mm. The reinforcement layers are very important for improving the strength of the coil. High-tensile strength material (Zylon) was used to increase the strength of the reinforcement. The detailed system parameters are shown in Table 1.

To adapt to tubes with different diameters, two three-jaw chucks were used to fix the outer and inner tubes. And the actuator was coaxially placed with two three-jaw chucks. The horizontal position of chucks is controlled by two screw rods with a position indicator. This design makes the repetitive experiment of different-sized tubes become realizable. Our laboratory, the Wuhan National High Magnetic Field Center, has developed several sets of pulse capacitance supplies for MPW, and the parameters of the discharge circuit are shown in Table 2.

Table 1 System parameters used in this experiment

Parameters	Description	Value
Coil (Copper conductor)		
ρ_c	Mass density	8.9×10^3 kg/m^3
E_c	Young's modulus	110 GPa
v_c	Poisson's radio	0.34
σ_{y0c}	Initial yield stress	135 MPa
E_c^T	Tangent modulus	0.4 GPa
Reinforcement (Zylon fiber)		
ρ_z	Mass density	1.56×10^3 kg/m^3
E_z	Young's modulus	3/230/3 GPa
v_z	Poisson's radio	0.34/0.0148/0.0148
Coil frame (Epoxy resin board)		
ρ_e	Mass density	2.6×10^3 kg/m^3
v_e	Young's modulus	22 GPa
E_e	Poisson's radio	0.34
Stycast W19		
ρ_s	Mass density	2.4×10^3 kg/m^3
E_s	Young's modulus	22 GPa
v_s	Poisson's radio	0.34

Table 2 System parameters used in this experiment

Parameter	Description	Value/category
C	Capacitance	150 μF
L_l	Line inductance	2.6 μH
R_l	Line resistance	18 mΩ
U_c	Charging voltage	0–20 kV
S	Switch	Self-breaking spark gap switch

3.2 Experimental Design

First, a series of discharge experiments were performed to explore how the discharge voltage and accelerate gap influence the welding quality. The discharge voltages range from 8 to 17 kV for the interval 1 kV. The gap distances between the two tubes range from 2 to 6.5 mm, and the interval is 1.5 mm. Since the surface treatment of the two tubes has a significant impact on the mechanical properties of weldments [15], the roughness of the outer surface of the steel tube was controlled at 0.65 ± 0.15 μm. During the welding process, the discharge voltages and currents were measured by a high-voltage probe and a Rogowski coil. After discharge experiments, the weldment was processed to mechanical testing samples by wire-electrode cutting. Peel tests and tensile tests were used to evaluate the quality of joining. Finally, scanning electron microscopy (SEM) is used to observe the distribution of elements. The results can be used to judge whether the metallurgical bonding occurs between the two dissimilar materials tubes.

4 Results and Discussion

4.1 Distribution of Magnetic Pressure and Stress

Figure 5a shows the current and voltage curves of the coil from discharge voltage to be 15 kV. The experimental curves are consistent with simulation results, demonstrating that the simulations accurately reflected the experimental process. The distribution of magnetic field and pressure is shown in Fig. 5b. FS can concentrate the pressure on the tube surface effectively and the distribution of pressure is the same as the results calculated by Yu et al. [7]. As the maximum discharge capacity of our equipment is 20 kV, the von Mises stress in the radial direction of the coil and reinforce parts were calculated at 20 kV situation. The results are shown in Fig. 5c. The coil is reinforced by Zylon fiber composite, whose ultimate tensile strength is about 3.5 GPa. When the thickness of the reinforcement is 10 mm, the maximum von Mises stress in the Zylon is 3.5 GPa. In practice, the maximum discharge voltage of our experiments is 17 kV, lower than the maximum discharge voltage. So, the 10 mm thickness of the reinforcing layer to ensure safety is enough.

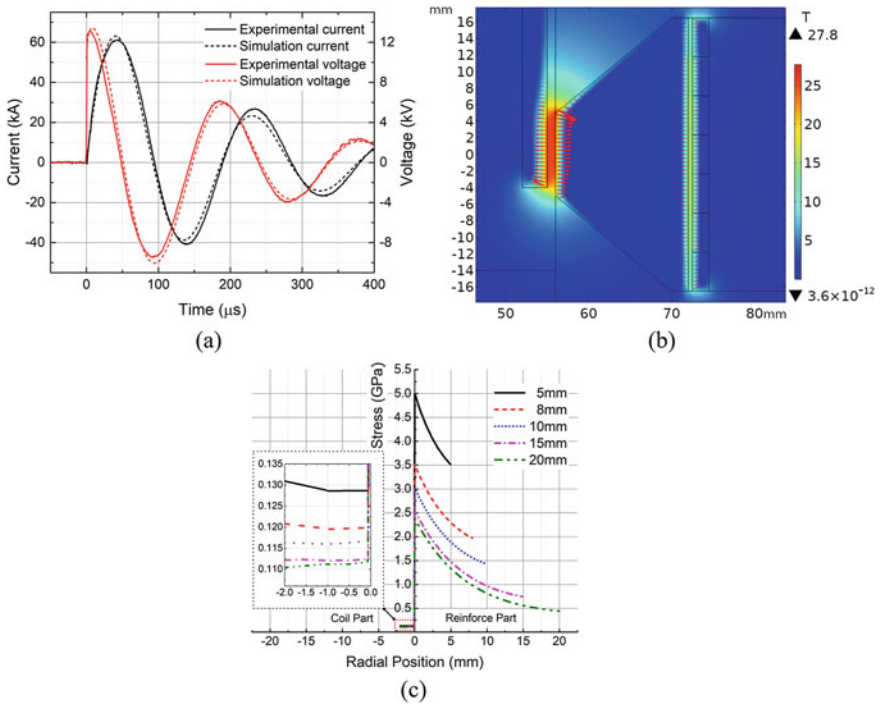


Fig. 5 Simulation results: **a** current and voltage curves compared with experimental results, **b** the distributions of magnetic field and pressure, and **c** the von Mises stress of coil and reinforce parts. (Color figure online)

4.2 Optimization Results of Coil and FS

The optimal results of coil turns N, height of FS inner surface h, height of FS outer surface H, and FS thickness δ are presented in Fig. 6. The velocity and pressure increase first and then decreases with increasing coil turns N can be found in Fig. 6a. According to Biot-Savart law, it can be derived that the magnetic flux density B is proportional to ampere-turns NI. As coil current I decreased with N increasing, there is a maximum value of NI and B. Figure 6b presents that magnetic pressure and velocity are monotonically decreasing with the height of inner surface h. It can be explained that the smaller the inner surface is, the magnetic field can be more concentrated. However, the welding area should not be too small for comprehensive consideration, and $h = 10$ mm was selected.

To explore the universal laws of the size effect, the ratios of FS thickness and outer surface height to inner surface height are defined as two coefficients to reflect the relative dimension. The influence of the coefficient of the thickness ($k_\delta = \delta/h$) and the outer surface height ($k_H = H/h$) both have the same variation trend, which is increased first and then decreased, as shown in Fig. 6c, d. It is speculated that this

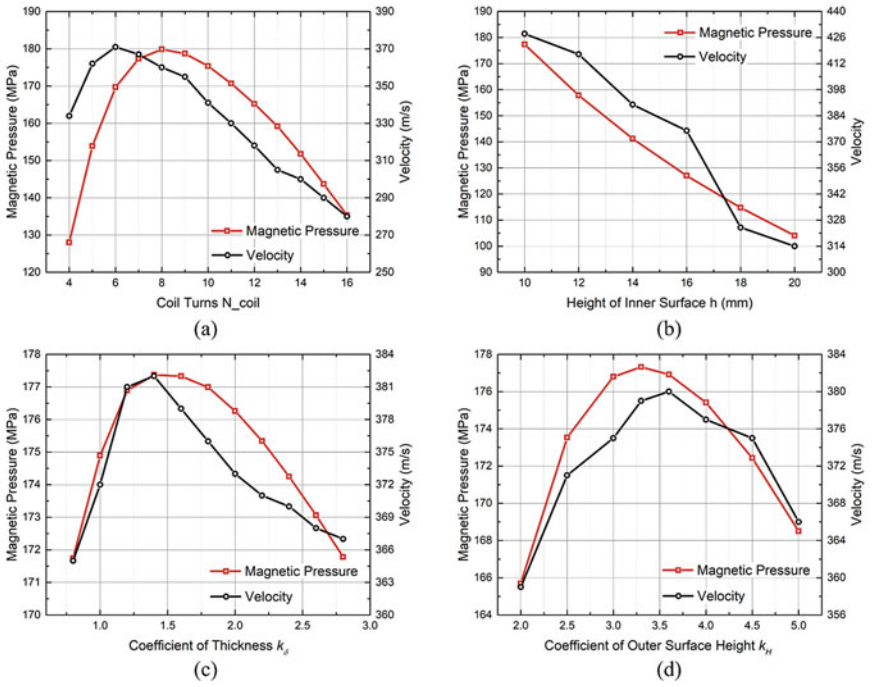


Fig. 6 Magnetic pressure and velocity variation curves with **a** coil turns, **b** height of inner surface, **c** coefficient of thickness, and **d** coefficient of outer surface height. (Color figure online)

change in trend is related to the energy utilization rate. The change of FS thickness and outer surface height leads to variety of impedance and inductive reactance of the load. As the energy is consumed in the circuit part and load part, this variety will affect the energy transformation ratio eventually.

For synthesis, considering the optimal results of magnetic pressure and velocity, the parameters of coil and FS were chosen finally. The details are shown in Fig. 4.

4.3 Mechanical Testing and Welding Windows

The results of welding characteristics and quality were obtained by peel testing and tensile test. According to the tensile test methods on the weld and deposited metal (GB/T 2652-2008), the tensile samples were designed and processed by wire-electrode cutting. As the welding joint is thick and long (both more than 10 mm), it is difficult to keep the direction of tensile force on a fixed line, and therefore two improvement measures were carried out. First, a metal block with a thickness of steel tube was placed on the aluminum side, while another metal block with a thickness of aluminum tube was placed on the steel side. Second, an epoxy splint was used

to avoid the bending of samples' working areas. Considering the influence of the FS slot, two positions of weldment of each tube were tested: the positions near or opposite the slot of the FS. And the results of characteristics can be classified into three types: (1) No falling off at two positions, the situation was regarded as **fully weld**, (2) only one position bonding, the situation was regarded as **part weld**, (3) both two positions falling off, this situation was regarded as **no weld**.

Further, the tensile test was done on fully weld samples to evaluate the welding quality. If a sample fracture at the base material or the tensile force is greater than 3200 N (corresponding to 90 MPa stress), it can be regarded that the strength of the weldment is stronger than the aluminum base material, and it can be defined as a high-strength combination. If the fracture occurs at the weld joint and the tensile force is less than 3200 N, it means that the strength of the weldment failed to obtain promotion.

Considering the results of the two positions as mentioned above, the welding quality can be divided into three categories: (1) when high-strength combination occurs at two positions, the situation is regarded as **high-quality weld**, (2) when high-strength combination occurs at only one position, this situation is regarded as **medium-quality weld**, (3) when no high-strength combination occurs at these two positions, the situation is regarded as **low-quality weld**. The welding window of a large diameter metal tube was obtained and drawn in Fig. 7. The results show that there are some differences and correlations between welding boundary and high-quality welding boundary.

For each fixed gap, an increasing voltage can improve the welding quality. As the radial deformation is fixed, the energy lost to overcome the deformation of the material is the same. So, more energy input from the actuator means more kinetic energy can be translated into the outer tube. Higher impact velocity makes it easier to achieve welding and improve the welding quality. Moreover, both welding boundary and high-quality welding boundary have optimal welding gap and lowest discharge

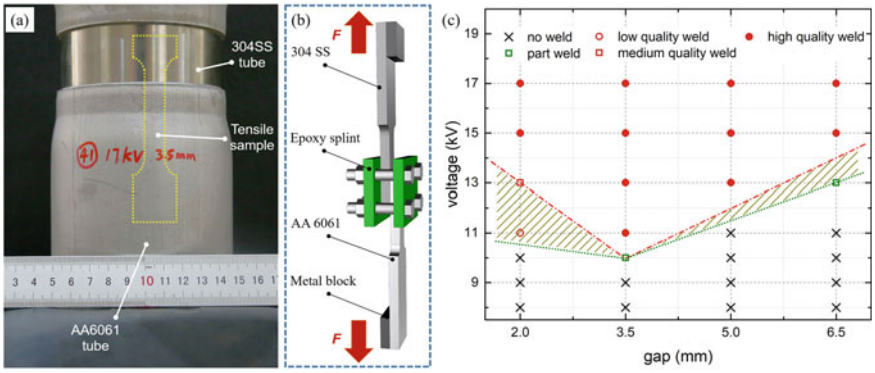


Fig. 7 The welding window of large diameter metal tubes: **a** The result of 17 kV voltage and 3.5 mm gap discharge conditions, **b** schematic diagram of tensile test, and **c** welding window. (Color figure online)

voltage. It is supposed that when the gap distance is small, increasing the gap can increase the acceleration space so that more kinetic energy can be loaded on the metal tube. As the gap continues to increase, more energy is needed to overcome the plastic deformation of the tube, resulting in the reduction of kinetic energy.

4.4 Metallographic Analysis

The test results of the welding sample using SEM and energy dispersive spectrum (EDS) under the conditions of 17 kV discharge voltage and 3.5 mm gap distance are shown in Fig. 8. It can be clearly found that the diffusion process occurred between Al and Fe. As a result, an obvious element transition layer is formed at the weldment area. Also, the dimension of the transition layer is about 10 μm. Considering the SEM image of the interlayer characteristics, the temperature was enough to melt the whole interface due to the high collision velocity under this discharge condition [16]. A large volume of mixtures of Al and Fe were formed at the interface under the high-pressure condition. These results demonstrate the metallurgical bonding occurring between the two dissimilar materials tubes.

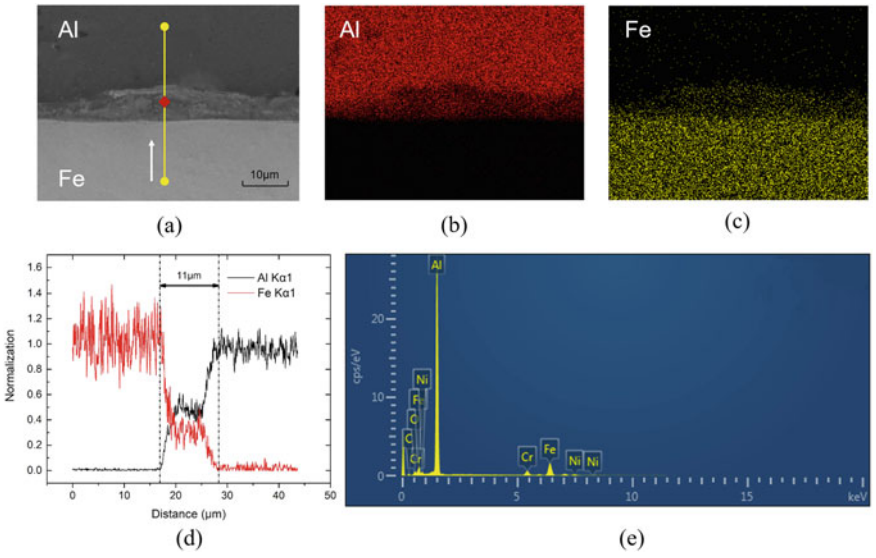


Fig. 8 Pictures of **a** SEM photo, **b** distribution of Al atoms, **c** distribution of Fe atoms, **d** EDS line results, and **e** EDS spot results. (Color figure online)

5 Conclusions

In this paper, the optimal design and experimental study for magnetic pulse welding of dissimilar metal tubes with large diameters were analyzed in detail. Some conclusions can be summarized as follows:

(1) An effective two-dimensional simulation model for the optimization of the design of MPW was built by COMSOL, and the results obtained from the simulations are consistent with the experimental observations, providing an efficient approach for MPW system design.
(2) Some optimization parameters were analyzed how to influence the magnetic pressure and tube velocity. These principles are helpful to understand the operating principles of the magnetic actuator and provide a practical basis for further numerical model building.
(3) By the experimental method, the welding windows of gaps and discharge voltages were built up. The experimental results also prove that the magnetic welding of tubes with 110 mm diameters and 3 mm thickness became reality, and the strength of the welding area can be stronger than the basic material.
(4) By using SEM, the element diffusion phenomenon was observed between Al and Fe. This result also demonstrates the metallurgical bonding occurring between the two dissimilar materials tubes.

Acknowledgments This work was supported by the National Key Research and Development Program of China (Grant No. 2016YFA0401701), the National Basic Research Program of China (Grant No. 2011CB012801), and Young Elite Scientists Sponsorship Program by CAST (YESS, 2018QNRC001).

References

1. Kapil A, Sharma A (2015) Magnetic pulse welding: an efficient and environmentally friendly multi-material joining technique. J Clean Prod 100:35–58
2. Weddeling C, Walter V, Haupt P, Tekkaya AE (2015) Joining zone design for electromagnetically crimped connections. J Mater Process Technol 225:240–261
3. Bellmann J, Schettler S, Dittrich S, Lueg-Althoff J, Schulze S, Hahn M, Beyer E, Tekkaya AE (2019) Experimental study on the magnetic pulse welding process of large aluminum tubes on steel rods. In: IOP conference. Materials science and engineering, vol 480, 012033
4. Vivek A, Hansen SR, Liu BC, Daehn GS (2013) Vaporizing foil actuator: a tool for collision welding. J Mater Process Technol 215:2304–2311
5. Sapanathan T, Yang K, Chernikov D, Raoelison RN, Gluschenkov V, Buiron N, Rachik M (2017) Thermal effect during electromagnetic pulse welding process. Trans Tech Publ 879:1662–1667
6. Rajak AK, Kumar R, Basumatary H, Kore SD (2018) Numerical and experimental study on effect of different types of field-shaper on electromagnetic terminal-wire crimping process. Int J Precis Eng Man 19(3):453–459
7. Yu HP, Li CF, Zhao ZH, Li Z (2005) Effect of field shaper on magnetic pressure in electromagnetic forming. J Mater Process Technol 168(2):245–249

8. Qiu L, Han XT, Peng T, Ding HF, Xiong Q, Zhou ZY, Jiang CX, Lv YL, Li L (2012) Design and experiments of a high field electromagnetic forming system. IEEE Trans Appl Supercon 22(3):3700504
9. Cao QL, Han XT, Lai ZP, Xiong Q, Zhang X, Chen Q, Xiao HX, Li L (2015) Analysis and reduction of coil temperature rise in electromagnetic forming. J Mater Process Technol 225:185–194
10. Lai ZP, Cao QL, Han XT, Huang YJ, Deng FX, Chen Q, Li L (2017) Investigation on plastic deformation behavior of sheet workpiece during radial Lorentz force augmented deep drawing process. J Mater Process Technol 245:193–206
11. Li XX, Cao QL, Lai ZP, Ouyang SW, Liu N, Li M, Han XT, Li L (2020) Bulging behavior of metallic tubes during the electromagnetic forming process in the presence of a background magnetic field. J Mater Process Technol 276:116–411
12. Kim YB, Platner ED (1959) Flux concentrator for high-intensity pulsed magnetic fields. Rev Sci Instrum 30(7)
13. Welddeling C, Demir OK, Haupt P, Tekkaya AE (2015) Analytical methodology for the process design of electromagnetic crimping. J Mater Process Technol 222:163–180
14. Lu ZY, Gong WT, Chen SJ, Yuan T, Kan CL, Jiang XQ (2019) Interfacial microstructure and local bonding strength of magnetic pulse welding joint between commercially pure aluminum 1060 and AISI 304 stainless steel. J Manuf Process 46:59–66
15. Cui JJ, Sun T, Geng HH, Yuan W, Li GY, Zhang X (2018) Effect of surface treatment on the mechanical properties and macrostructures of Al-Fe single-lap joint by magnetic pulse welding. Int J Adv Manuf Tech 98:1081–1092
16. Cui JJ, Ye L, Zhu CC, Geng HH, Li GY (2020) Mechanical and microstructure investigations on magnetic pulse welded dissimilar AA3003-TC4 joints. J Mater Eng Perform 29:712–722

Deformation Behavior in Magnetic Pressure Parallel Seam Welding



Takashi Ichimura, Yusuke Ito, Makoto Miyazaki, and Akira Hatta

Abstract Magnetic pressure seam welding has attracted attention as a new joining method for aluminum sheets. Magnetic pressure seam welding is a collision welding process for producing metallic bonds of similar and dissimilar materials, utilizing electromagnetic force as the acceleration mechanism. Pressure seam welding is a method of abruptly adding a high-density magnetic flux around a metal material and utilizing the generated electromagnetic force to deform the sheet at high speed and pressure welding. This paper deals with the deformation behavior of aluminum sheet with single and parallel coils. The sample used for this analysis is assumed to be a sheet made of aluminum and composed of quadrilateral elements of plane strain. Numerical analysis of the dynamic deformation process of the metal plate is performed by the finite element method. As a result, it was shown that the collision point velocity is very fast at the initial collision point, but decreases continuously during welding. In addition, the thinner the sheet, the wider the gap length for obtaining higher equivalent stress and frictional stress. The initial collision point velocity, equivalent stress, and friction stress at the time of collision in the parallel coils showed the same tendency as in the single coil.

Keywords Magnetic pressure seam welding · Deformation behavior · Numerical analysis · Aluminum sheet

1 Introduction

The development of a new welding method for dissimilar materials is strongly required for the weight reduction of automobiles. Several joining methods, such as diffusion bonding, explosive bonding, and rolling welding have been attempted so far. However, it is known that a sound welding with acceptable strength cannot be obtained mainly because a brittle layer is formed at the bonding interface [1].

T. Ichimura · Y. Ito · M. Miyazaki (✉) · A. Hatta
National Institute of Technology, Nagano College, 716 Tokuma, Nagano-City 381-8550, Nagano, Japan
e-mail: miyazaki@nagano-nct.ac.jp

© The Minerals, Metals & Materials Society 2021

G. Daehn et al. (eds.), *Forming the Future*, The Minerals, Metals & Materials Series,
https://doi.org/10.1007/978-3-030-75381-8_108

Aluminum has higher electrical conductivity and thermal conductivity than iron, so welding is difficult due to low heating efficiency. In previous studies, there is a report on the magnetic pressure seam welding method [2–12]. Magnetic pressure seam welding is a collision welding process similar to explosive welding and utilizes electromagnetic force as an acceleration mechanism. In magnetic pressure seam welding, the central area of the lower sheet (flyer sheet) bulges radially and collides with the upper sheet (parent sheet).

When the impulse current from the capacitor bank passes through the single coil, a magnetic flux is instantly generated under the flyer sheet. When this magnetic flux intersects the flyer sheet, an eddy current is induced in the flyer sheet. Due to the eddy current, the flyer sheet receives a large upward electromagnetic force. This electromagnetic force causes the flyer sheet to deform toward the parent sheet. In addition, the surface oxide of the metal interfaces is disrupted due to the jet action, and metallurgical bonding is achieved between clean surfaces.

The purpose of this paper is to discuss the dynamic deformation behavior of magnetic pressure seam welding of aluminum sheets.

2 Welding Principle

The welding principle is shown in Fig. 1. Magnetic pressure seam welding uses electromagnetic force to accelerate aluminum sheet (flyer sheet) against another stationary aluminum sheet (parent sheet). When a large current flows through the coil, a high magnetic field $\boldsymbol{B}$ is suddenly generated. Then, the magnetic field intersects the flyer sheet, and an eddy current (current density $\boldsymbol{i}$) is generated. The current density $\boldsymbol{i}$ and magnetic flux density (high magnetic field) $\boldsymbol{B}$ are given, as shown in Eq. 1. As

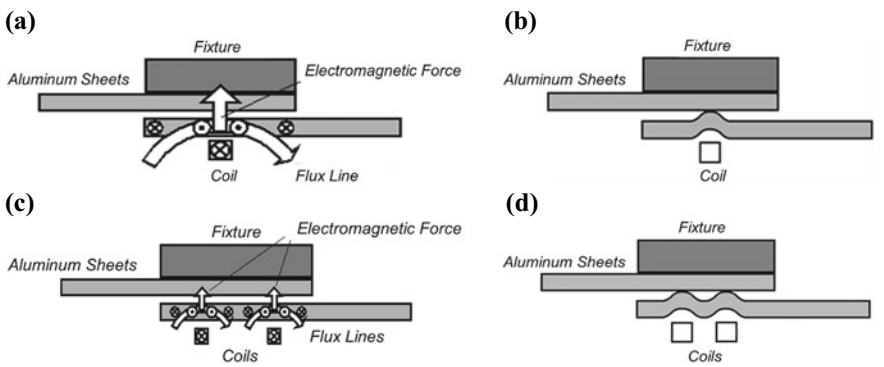


Fig. 1 Schematic illustrations of welding principle (cross-sectional view). **a** Single coil (before welding), **b** single coil (after welding), **c** parallel coils (before welding), **d** parallel coils (after welding)

a result, the electromagnetic force $\boldsymbol{f}$ given by Eq. 2 mainly acts on the flyer sheet, accelerates away from the coil, and rapidly collides with the parent sheet [13].

The eddy $\boldsymbol{i}$ and joule heat Q are calculated by the following Eq. 3. κ and $\boldsymbol{B}$ are electric conductivity and magnetic flux density of aluminum sheet.

$$\mathrm{rot}\, \boldsymbol{i} = -\kappa \frac{\partial \boldsymbol{B}}{\partial t} \tag{1}$$

$$\boldsymbol{f} = \boldsymbol{i} \times \boldsymbol{B} \tag{2}$$

$$Q = \frac{\boldsymbol{i}^2}{\kappa} \tag{3}$$

3 Numerical Analysis

The analysis was made by nonlinear structure–analysis program (MARC 2018). An element division model and boundary condition are shown in Fig. 2. The sample used for this analysis is assumed to be a sheet made of aluminum (A1050-H24, 100 mm length, 0.5 and 1 mm thickness) and composed of quadrilateral elements of plane strain. The gap length between the flyer sheet and the parent sheet varied from 0.5 to 1.5 mm. The relationship between true stress σ and true strain ε is given by the following Eq. 4. Since the effect of the strain rate of aluminum is smaller than that of other materials such as iron, the experimental results are almost in agreement with the FEM analysis [14, 15].

$$\sigma = F\varepsilon^n \tag{4}$$

Material properties obtained by a static tension test are shown in Table 1 [15]. The deformation of the aluminum sheet is reported to end with the first discharge waveform [16].

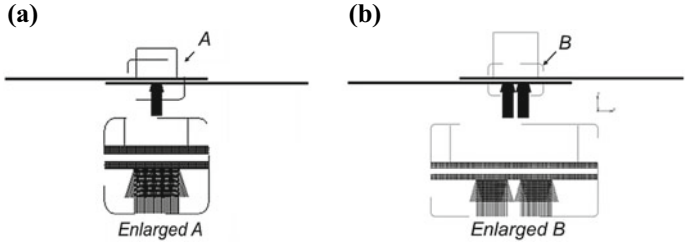


Fig. 2 Finite element model of magnetic pressure seam welding. **a** single coil, **b** parallel coils

Table 1 Material properties of A1050H24 sheets

Young's modulus	E (GPa)	69
Poisson's ratio	N	0.33
Density	ρ (kg/m^3)	2.71×10^3
Strength coefficient	F (MPa)	118
Strain hardening exponent	N	0.0623

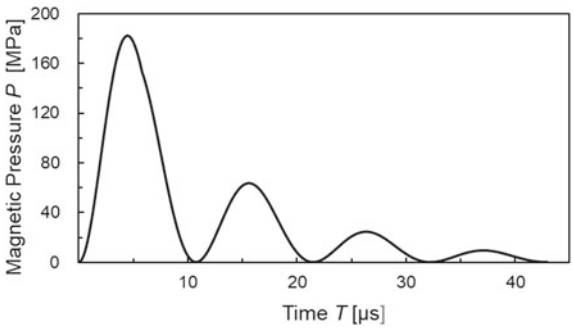


Fig. 3 Relationship between time T and magnetic pressure P (discharge energy 1.0 kJ)

In the analysis, the calculation time was 10.8 μs, and the calculation step was 5000. The time integration method was a single-step method of the implicit solution method. The relationship between the magnetic pressure P and the measured magnetic flux density B is given by Eq. 5. The parameters t, μ, and δ are the thickness of aluminum sheet, magnetic permeability, and surface depth, respectively. The surface depth is calculated by the following Eq. 6. At this time, ω represents the frequency at which the magnetic flux changes periodically.

Figure 3 shows the relationship between time T and magnetic pressure P. In the analysis, the discharge energy was set to 1.0 kJ.

$$P = \frac{B}{2\mu}\left\{1 - \exp\left(-\frac{2t}{\delta}\right)\right\} \tag{5}$$

$$\delta = \sqrt{\frac{2}{\omega\kappa\mu}} \tag{6}$$

4 Results and Considerations

The analysis in this study was examined from the initial collision point to the outside (directions +x). The collision angle and collision point velocity relations are given as follows [17]:

$$\upsilon_p = 2\upsilon_c \sin\frac{\beta}{2} \tag{7}$$

$$\upsilon_p = \sqrt{\upsilon_x{}^2 + \upsilon_y{}^2} \tag{8}$$

where β, v_c, v_p, v_x, and v_y are collision angle, welding velocity (collision point velocity), collision velocity, x-direction element of v_p, and y-direction element of v_p, respectively. Spatial relationships of v_p, v_c, and β are shown in Fig. 4.

Figure 5 shows the schematic diagram of the collision behavior between the flyer sheet and the parent sheet. The point where the flyer sheet and the parent sheet first collide is called the initial collision point. The collision point moves outward (directions +x) at the same time as the pressure welding. The speed at which this collision point moves is called the collision point velocity. The distance from the initial collision point is defined as shown in Fig. 6.

It has been reported that the joint start of electromagnetic magnetic pressure seam welding is affected by the collision angle and the joint end is affected by the collision point velocity [18]. In addition, above the speed of sound that can be transmitted through aluminum, metal jets are generated. The velocity of the metal jet is 1000–2000 m/s [19]. When the surface layer of the aluminum sheet is released as a metal jet, a strong metal bond is established [20]. Since the emission of the metal jet changes depending on the collision point velocity and the collision angle, it is considered to be related to the collision friction stress.

Therefore, in this study, in addition to the collision point velocity, the collision frictional stress and the equivalent von Mises stress after the completion of deformation are examined.

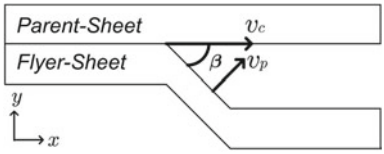


Fig. 4 Definition of collision angle β, collision velocity v_p, and collision point velocity v_c

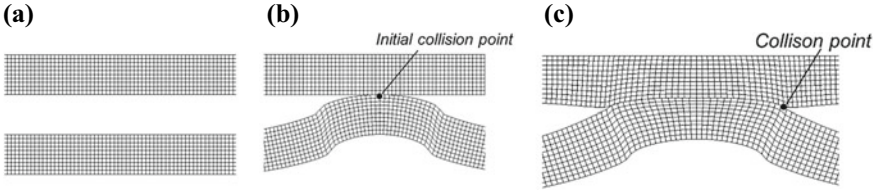


Fig. 5 Schematic diagram of the collision behavior between the flyer sheet and the parent sheet. **a** Before deformation, **b** initial collision, **c** after deformation

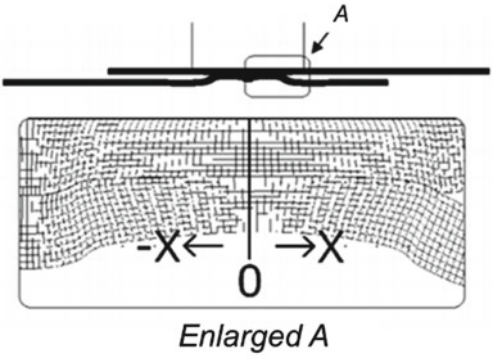


Fig. 6 A model of magnetic pressure parallel seam welding

4.1 Collision Point Velocity

Figure 7 shows the relationship between the distance from the initial collision point and the collision point velocity. The velocity of the collision point is very fast near the initial collision point but decreases continuously during welding. There was no difference in these trends even if the sheet thickness changed. When the thickness is

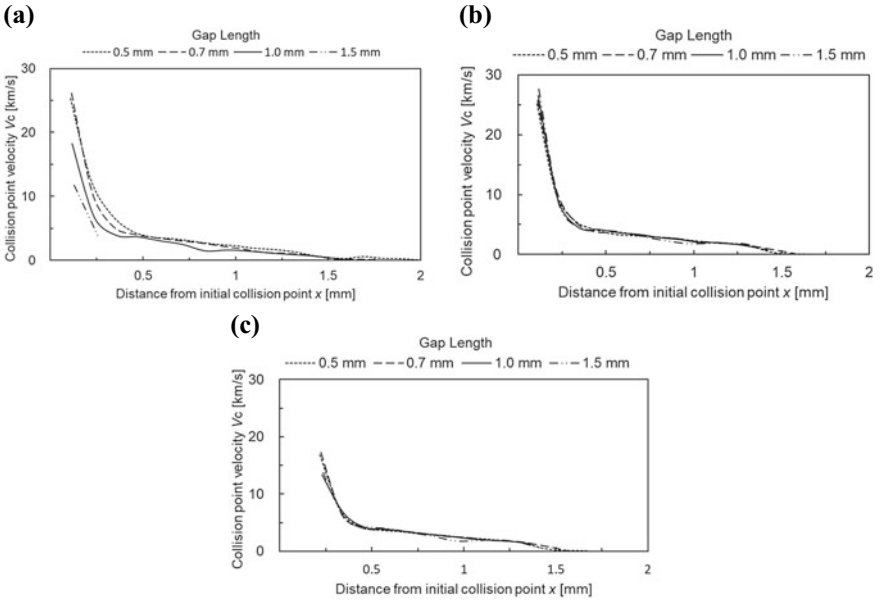


Fig. 7 Relationship between distance from initial collision point x and collision point velocity v_c **a** 1.0 mm thickness (single coil), **b** 0.5 mm thickness (single coil), **c** 0.5 mm thickness (parallel coils)

1.0 mm, the collision point velocity largely depends on the gap length. However, by reducing the thickness, the influence of the gap length on the collision point velocity is reduced.

The tendency of the analysis results of the parallel coils from the initial collision point to the outside was the same as that of the single coil. However, the collision point velocity of the parallel coils was slower than that of the single coil.

4.2 Collision Frictional Stress

Figure 8 shows the relationship between the distance from the initial collision point and the collision frictional stress. The collision frictional stress was very small at the initial collision point and increased during welding. It also reached its maximum at a certain distance from the initial collision point and slowed down from there. When the sheet thickness was 1.0 mm and if the gap was increased, sufficient collision could not be obtained, and the deformation behavior was close to that of stretch forming. Therefore, the experimental data with a gap length of 1.5 mm is unsuitable and is excluded. The frictional stress at the time of collision between the single coil

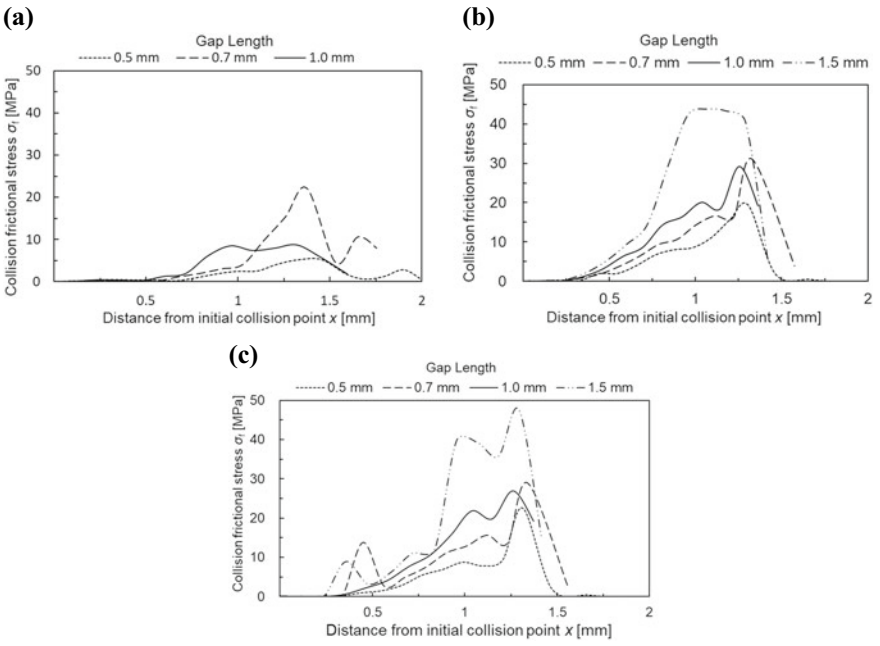


Fig. 8 Relationship between distance from initial collision point x and collision frictional stress σ_f **a** 1.0 mm thickness (single coil), **b** 0.5 mm thickness (single coil), **c** 0.5 mm thickness (parallel coils)

and the parallel coils was maximum when the position was 0.75–1.5 mm. It is known that these are determined by the collision point velocity and the collision angle. The collision point velocity and collision angle are determined by the influence of the sheet thickness and the gap length [18].

From the analysis results, it is considered that a larger collision frictional stress can be obtained by reducing the sheet thickness. There is no definite value for the optimum value of the gap length, and there is a local optimum value. In other words, the optimum gap length for obtaining high collision frictional stress depends on the thickness of the sheets. In addition, the thinner the sheet, the wider the optimal gap length. It is known that the optimum gap length is about 1.0 mm when the sheet thickness is 1.0 mm. However, the optimal gap length has only been empirically clarified. In this study, it was found that the optimum gap length for a sheet thickness of 0.5 mm is about 1.5 mm.

The collision frictional stress of the parallel coil was not much different from that of the single coil in the analysis result from the initial collision point to the outside (directions +x).

4.3 Equivalent von Mises Stress

Figure 9 shows the relationship between the distance from the initial collision point and the equivalent von Mises stress. By reducing the sheet thickness, the equivalent von Mises stress near the initial collision point was reduced. The collision point velocity near the initial collision point is faster than the speed of the metal jet. Therefore, the equivalent von Mises stress became unstable due to the non-coupling region near the initial collision point. In other words, if the initial collision point velocity exceeds the metal jet generation speed, it indicates that the metal jet is confined.

In the position where the collision point velocity is slower than the speed of the metal jet, the collision frictional stress and equivalent von Mises stress begin to increase in the range of 0.5–1.0 mm. Therefore, it can be said that the collision frictional stress and equivalent von Mises stress are important parameters related to the joint state.

5 Conclusions

(1) In the parallel coil, the tendency of the analysis result from the initial collision point to the outside was the same as that of the single coil.
(2) In the case of parallel coils, collision point velocity near the initial collision point tends to be slow.

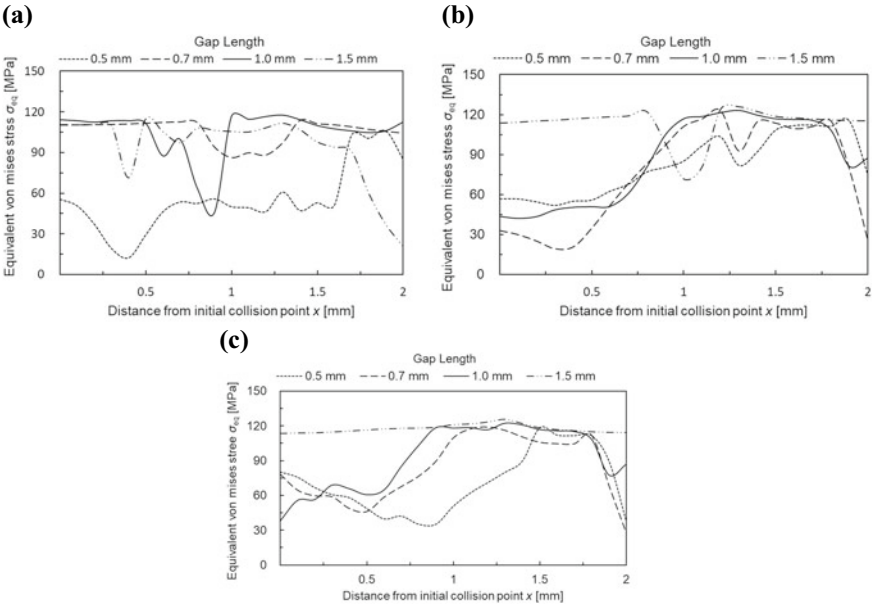


Fig. 9 Relationship between distance from initial collision point x and equivalent Von mises stress σ_{eq} **a** 1.0 mm thickness (single coil), **b** 0.5 mm thickness (single coil), **c** 0.5 mm thickness (parallel coils)

(3) The optimum gap length for obtaining high collision frictional stress depends on the thickness of the plate. Also, the thinner the plate, the wider the optimum gap length.
(4) Collision frictional stress and equivalent von Mises stress are important parameters related to the joint state.
(5) Knowledge of the effects of certain parameters such as plate thickness and gap length is essential to obtain high equivalent von Mises stress.

References

1. Lee KJ, Kumai S, Arai T, Aizawa T (2007) Interfacial microstructure and strength of steel/aluminum alloy lap joint fabricated by magnetic pressure seam welding. Mater Sci Eng A 471(1–2):95–101
2. Okagawa K, Aizawa T (2007) Effect of gap and characteristics on seam welding by applying magnetic pressure. J Jpn Soc Technol Plast 48(555):323–327
3. Aizawa T, Kashani M, Okagawa K (2007) Application of magnetic pulse welding for a aluminum alloys and SPCC steel sheet joints. Weld J 86:119–124
4. Kore SD, Date PP, Kulkarni SV (2007) Effect of process parameters on electromagnetic impact welding of aluminum sheets. Int J Impact Eng 34(8):1327–1341

5. Miyazaki M, Okagawa K, Aizawa T, Kunagai M (2007) Magnetic pressure seam welding for aluminum and various metal foils. J Jpn Inst Light Metals 57(2):47–51
6. Watanabe M, Kumai S (2009) High-speed deformation and collision behavior of pure aluminum plates in magnetic pulse welding. J Jpn Inst Light Metals 50(8):2035–2042
7. Serizawa H, Shibaharaa I, Rashed S, Murakawa H (2010) FEM analysis of joint interface formation in magnetic pressure seam welding. Mater Sci Forum 638–624:2166–2171
8. Stern A, Becher O, Nahmany M, Ashkenazi D, Shribman V (2015) Jet composition in magnetic pulse welding: Al-Al and Al-Mg couples: Weld J 94:257–264
9. Miyazaki M, Sasaki K, Okada M (2014) Influence of gap length on collision angle and collision point velocity of magnetic pressure seam welding. Mater Sci Forum 767:166–170
10. Aizawa T, Matsuzawa K (2015) Interfacial observation of parallel seam welded-aluminum sheets by magnetic pulse welding method with collision between metal jets. J Jpn Weld Soc 33(2):130–134
11. Yamagishi H, Okazawa K (2019) Analysis of magnetic pulse welding from the wave equation. Trans Jpn Soc Ind Appl Math 29(2):165–186
12. Hatta A, Miyazaki M, Kajiro Y (2019) Collision behavior in various magnetic pressure seam welding of aluminum sheets. Int J Multiphys 13(3):295–306
13. Aizawa T, Okagawa K, Kashani M (2013) Application of magnetic pulse welding technique for flexible printed circuit boards (FPCB) lap joints. J Mater Process Technol 213(7):1095–1102
14. Tanimura S, Hayashi H, Yamamoto T, Mimura K (2009) Dynamic tensile properties of steels and aluminum alloys for a wide range of strain rates and strain. J Solid Mech Mater Eng 12(3):1263–1273
15. Miyazaki M, Sasaki K, Okada M (2011) Simulation of collision behavior on magnetic pressure seam welding of aluminum sheets. J Jpn Inst Light Metals 61(1):20–23
16. Okagawa K, Aizawa T (2006) Effect of gap on seam weding by applying magnetic pressure. J Jpn Soc Technol Plast 47(546):632–636
17. Hokamoto K, Fujita M, Ohtsuka M (2017) Impact forming (high-energy rate forming). CORONA Publishing Inc., Tokyo, pp 66–74
18. Okagawa K, Ishibashi M, Kabasawa E, Yamagishi H (2015) Proceedings of the 66th Japanese joint conference for the technology of plasticity influence of velocity with moved sheet on joining position in weld sheet obtained by magnetic pulse welding, pp 389–390
19. Kakizaki S, Watanabe M, Kumai S (2011) Simulation and experimental analysis of metal jet emission and weld interface morphology in impact welding. Mater Trans 52(5):1003–1008
20. Watanabe M, Kumai S (2009) Interfacial morphology of magnetic pulse welded aluminum/aluminum and copper/copper lap joints. J Jpn Inst Light Metals 50(2):286–292

Shaping of Sharp-Edged Design Elements by Electromagnetic Forming



Verena Psyk, Christian Scheffler, Albrecht Stalmann, and Martin Goede

Abstract Modern car body design includes parts with sharp-edged elements, which are challenging for conventional sheet metal forming technologies. This is especially critical when implementing aluminum parts in order to consider lightweight design requirements. Applying high strain rates allows increasing formability for numerous materials, including typical aluminum alloys used in the automotive industry. Therefore, integrating high-speed forming into a conventional process can help to extend forming limits. The feasibility of locally sharpening a deep-drawn radius by integrated electromagnetic forming was proved in the literature, but up to now, the investigated target radii were much larger compared to the sheet thickness. The presented paper shows that target radii in and below the size of the sheet thickness are possible by this process combination. Based on a simplified 2D component geometry, complementary experimental and numerical investigations served for developing different variants of a modular test tool and analyzing the influence of important process and tool parameters on the forming result.

Keywords Electromagnetic forming · Tool design · Design edge

1 Introduction

Statistics show that, in addition to the price or price-performance ratio, safety, and comfort, the design of an automobile is one of the most important decision criteria when buying a car. In an online survey conducted by IFA Marktforschung Bremer + Partner GmbH by order of the Aral AG in March 2019, 37% of respondents

V. Psyk (✉) · C. Scheffler
Fraunhofer Institute for Machine Tools and Forming Technology, Chemnitz, Germany
e-mail: verena.psyk@iwu.fraunhofer.de

C. Scheffler
e-mail: christian.scheffler@iwu.fraunhofer.de

A. Stalmann · M. Goede
Volkswagen AG, Wolfsburg, Germany
e-mail: Martin.goede@volkswagen.de

© The Minerals, Metals & Materials Society 2021

G. Daehn et al. (eds.), *Forming the Future*, The Minerals, Metals & Materials Series,
https://doi.org/10.1007/978-3-030-75381-8_109

who were planning to buy a new car or a year-old car stated that the vehicle design was a reason for their choice. Environmental friendliness, on the other hand, is an essential criterion for only 25% of these interviewees [1]. In another survey conducted between 2015 and 2018 by several market research institutes in Germany, the most important criteria are safety, reliability, and value for money, but for more than 70% of those surveyed, design is an important criterion when buying a car, too. Here, this criterion is almost on par with environmental friendliness and low CO_2 emissions. This prioritization has remained constant over the last few years [2]. According to these trends, the automotive industry may not neglect design-oriented developments, although current political initiatives set a focus on promoting and funding developments related to resource efficiency and environmental friendliness for a good reason.

Over the years, automotive design has changed dramatically. While the early car bodies in the 1930s and 1940s had a more round (e.g. Adlerwerke Type 10) or shell-shaped design (e.g. Porsche 356), later on, the favored designs comprised clear lines, trapezoidal (e.g. DKW F12) and box shapes (e.g. Peugeot 604), or wedge shapes (e.g. Lamborghini Countach). In modern design, aerodynamically modeled edges such as the so-called Tornado line shall lend the car elegance and make it look longer. Here, the aim is to achieve edges as sharp as possible. However, the limited formability in conventional forming processes, e.g. deep drawing, restricts the possible geometries, which is especially true for modern body-in-white materials such as aluminum alloys. The radii achievable via deep drawing of aluminum parts typically lie in the range of 2 mm, while radii of 0.5 mm are mostly desired. Therefore, new technologies are required for enabling extended forming limits in order to increase the freedom of design. One principle approach to extend forming limits lies in adapting the strain rate and/or the forming temperature. Either very low or very high values of these parameters can be beneficial, depending on the material. For typical automotive aluminum alloys, e.g. EN AW-6111, high-speed forming processes such as electromagnetic forming (EMF) are suited to extend the formability significantly [3].

EMF uses the energy density of pulsed electromagnetic fields to exert forces on electrically conductive workpieces, thus forming them. In contrast to deep drawing processes, a so-called tool coil or inductor replaces one active element of the tool set (usually the punch), while the counterpart (the die) is retained and serves as a form definition for the process. Depending on the geometry and arrangement of the workpiece and the tool coil, it is possible to compress or expand tubes and hollow profiles and form flat or curved sheet metal [4]. The setup for EMF consists of the forming machine (pulsed power generator), the tool coil (possibly including a field shaper), the workpiece, and application-dependent tool components such as cutting tools, forming dies, or joining partners. Charging and then discharging the capacitor of the pulsed power generator starts the process. As a result, a damped sinusoidal current pulse flows through the coil with maximum values of up to several hundred kiloamperes and typical rise times between 10 and 100 μs. This time-dependent current induces a corresponding magnetic field with local field strengths of up to several 10 T. Moreover, if an electrically conductive workpiece is located in the direct vicinity of the inductor, a second current in the opposite direction to the

inductor current results in this workpiece. Due to the interactions of the currents and magnetic fields, Lorentz forces arise, which accelerate and deform the workpiece. It is possible to transform these volume forces mathematically in an equivalent surface load, the so-called magnetic pressure. In EMF, the motion of the workpiece is always directed away from the tool coil. Depending on the other tool components and their interaction with the workpiece, it is possible to execute forming, cutting, and joining operations [5].

In addition to its use as a single solution, EMF has special potential for extending forming limits in combination with conventional forming processes. Ideally, the respective process-specific advantages complement each other so that process-specific limits can be extended. The technological feasibility and the benefits have already been demonstrated for the following process combinations:

- Deep drawing with integrated EMF (e.g. [6])
- Combined bending, EMF, and hydroforming [7]
- Combined joining by EMF and hydroforming [8]
- Combined extrusion and EMF [9]
- Combined bending and EMF [10]
- Combined roll forming and EMF [11].

The process of deep drawing with integrated EMF is most relevant with regard to the calibration of sharp-edged design elements in automotive body-in-white components. In this context, Vohnout showed in fundamental tests that combined quasi-static pre-straining and subsequent EMF can extend the overall forming limit of EN AW-6061. The gain is greater if the forming capacity is already exhausted as far as possible after deep drawing. Vohnout also demonstrated the applicability of the process combination of deep drawing and EMF for car body components. In particular, he sharpened the corner radius of an inner door panel from approx. 50 mm after deep drawing to approx. 10 mm [6]. Similarly, Imbert and Worswick sharpened a preformed 20 mm radius in a v-shaped part to 5 mm by EMF [12]. Burden et al. investigated the EMF of a door handle cavity in deep-drawing parts and showed that homogeneous pressure distribution has a positive effect on the forming result [13]. Psyk et al. and Risch et al. integrated an EMF step into a conventional deep-drawing process by incorporating the tool coil into the punch [14] and into the die [15], respectively. In another variant of the process combination, Vohnout et al. use numerous small pulses during the deep-drawing process to achieve a more homogeneous strain distribution, thus extending the forming limits and reducing the number of forming steps [16]. Studies that are more recent deal with the numerical simulation and mathematical optimization of the process combination. For these basic investigations, simple geometries are used such as cylindrical cups [17] or cross-shaped cups [18].

This clearly shows that deep drawing with integrated EMF offers technological advantages regarding formability and corner filling with small target edge radii. However, the implemented radii always amount to a multiple of the sheet metal thickness (i.e. approx. 5–10 times the sheet thickness or more), while so far there have been no reports aiming at forming of sharp-edged design elements such as the Tornado line with radii in or even below the magnitude of the sheet thickness.

From the point of view of forming technology, this is an important change because the process can no longer be considered a conventional sheet metal forming process. However, it is a process of so-called "sheet-bulk metal forming" or "solid sheet metal forming". According to [19], this class of processes comprises forming technologies with three-dimensional stress and strain states within the sheet metal. The aim of the presented studies was to prove that electromagnetic forming is applicable for calibrating sharp-edged design elements with radii, which are smaller than the sheet thickness. Moreover, recommendations for the design of tool coils suitable for this kind of manufacturing task are given.

2 Regarded Forming Task

In a cooperative project, the Fraunhofer Institute of Machine Tools and Forming Technology IWU and Volkswagen AG investigated the potential of mechanical preforming with integrated EMF for manufacturing components with sharp design edges for outer body parts. The focus of the investigation was on processing EN AW-6016 material with a thickness of 1.2 mm, an aluminum alloy typically used for body-in-white components. However, some tests were performed on other semi-finished parts in order to prove the transferability of the results and to analyze the influence of workpiece-dependent properties.

The investigations considered a 2D geometry (see Fig. 1b), which was based on an industrial fender geometry featuring two distinct design edges (see Fig. 1a). In order to generate the 2D shape, the middle cross-section of the fender was geometrically extruded to a length of 280 mm. Due to this simplification, strictly speaking, the preforming is no longer a deep-drawing operation but a bending process. However, the advantage of this approach is that it allows comparative tests on different material thicknesses without elaborate adaptation of the tooling, e.g. in order to adjust the

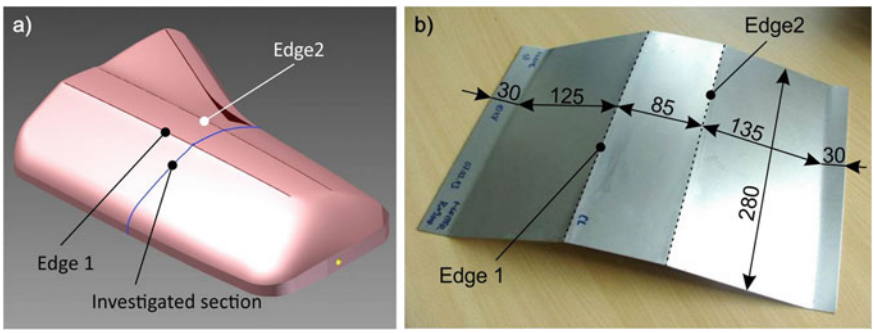


Fig. 1 **a** Basic punch geometry of 3D-fender; **b** simplified 2D part geometry for laboratory tests. (Color figure online)

drawing gap. Thus, the transferability of the results can be easily verified and principal correlations can be identified.

3 Tool Design

The tooling for the combined process includes the punch incorporating the tool coil and the forming die. Manufacturing sharp-edged concave geometries is a challenge for milling processes due to the tool radius. In a conventional deep-drawing process, this is usually solved by a cut out in the die, since the resulting radius of the formed part is determined by the convex radius of the deep-drawing punch and the thickness of the material, while the local die geometry is of minor influence. Contrary, in the investigated case, the die radius limits the minimum radius achievable in the electromagnetic calibration process. In order to work around the problem, the die geometry was separated at the two edges; the three segments of the die were manufactured individually and mounted onto a base plate. Thus, manufacturing a sharp-edged concave geometry was possible.

The punch features a modular setup, which allows implementing different coil variants and analyzing the respective influence on the forming result. The coil design concerns the conductor winding as well as the housing. The major function of the coil winding is to conduct the current, thus shaping the magnetic field and the corresponding magnetic pressure required for the forming process. Here a highly efficient energy transfer is desired in order to realize the forming task with minimum energy input, consequently operating at minimum equipment load. Therefore, different conductor variants were drafted based on a numerically assisted design using a harmonic 2D magnetic field simulation by David Meeker [20]. This simulation provides the magnetic field in the gap between the tool coil and sheet metal workpiece H_{gap} and the penetrated magnetic field at the workpiece surface facing away from the tool coil H_{pen}. These field distributions and the magnetic permeability μ make up the input data for analytically estimating the magnetic pressure according to Eq. 1.

$$p = \frac{1}{2} \cdot \mu \cdot \left(H_{\mathrm{gap}}^2 - H_{\mathrm{pen}}^2 \right) \tag{1}$$

Figure 2 shows the calculated maximum of the magnetic pressure course (i.e. the magnetic pressure as a function of time) as a function of the coil current for different frequencies of the discharging current and for different coil conductor variants. It compares conductor variants with one single turn, three parallel turns, and five parallel turns. As indicated via the sketched cross-sections, the turns are concentrated on the two calibration areas beneath edges one and two. The current direction in each bundle of turns is uniform but opposed to the current direction in the other bundle. For the five-turn variant, the turns are arranged in two layers in order to find a compromise between the limited extension of the calibration area and the required

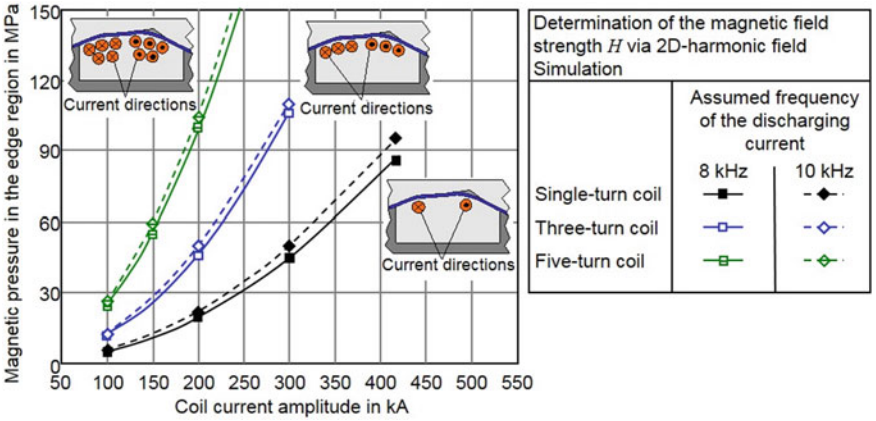


Fig. 2 Magnetic pressure as a function of coil current amplitude and discharging frequency for different coil conductors. (Color figure online)

space for dimensioning reasonable conductor cross-sections and insulation distances between the individual turns. As expected, the pressure maximum increases squarely with the coil current for all coil variants. Furthermore, it is obvious that for a higher number of turns, a significantly lower coil current is required in order to reach a defined pressure.

This simple calculation approach suggests that the five-turn coil is the most promising one. However, it neglects the influence of the number of turns on the electrical parameters of the oscillating circuit, especially on the resistance R and the inductance L. These influences are described via fundamental electrotechnical equations, which are summarized in [5]. Amalgamating these equations leads to Eq. 2, which describes how these parameters affect the course of the discharging current $I(t)$. This means that in order to have the same current course in different coil variants, these influences must be compensated by varying the other electrical parameters of the oscillating circuit, i.e. the capacitor, the charging voltage U, and the capacitance C. However, the latter is a property of the pulsed power generator and can only be adjusted in discrete steps, if possible at all. Therefore, adjusting the same current course for different conductor variants is hardly possible in practice so that a more sophisticated evaluation of the different coil types is necessary, taking into consideration the described correlations.

$$I(t) = \frac{U}{\sqrt{\frac{1}{LC} - \frac{R^2}{4 \cdot L^2}} \cdot L} e^{-\frac{R}{2L}t} \cdot \sin \sqrt{\frac{1}{LC} - \frac{R^2}{4 \cdot L^2}} t \tag{2}$$

The detailed design of the setup, including aspects of the housing, is relevant when considering the influences of all relevant components of the structure, i.e. the pulsed power generator and the consumer unit consisting of tool coil and workpiece, on the parameters of the oscillating circuit. The major functions of this housing are

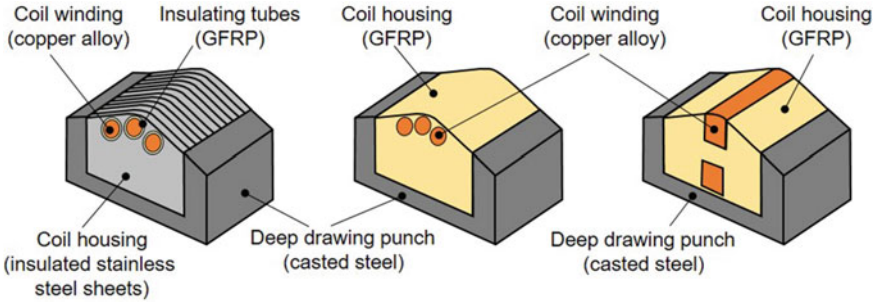


Fig. 3 Design concepts for the coil insert. (Color figure online)

the electrical insulation and mechanical stabilization of the conductor winding. In the investigated process combination, the housing must also be suitable for applying the load during the mechanical preforming operation. This study compares three different housing concepts (see Fig. 3).

The first one consists of a metallic coil body with integrated insulation tubes. The motivation for this approach was the desire to manufacture the tool insert for the integrated electromagnetic forming as far as possible from steel materials in order to guarantee high pressure and wear resistance. Furthermore, the goal comprised achieving good compatibility with the material of the surrounding deep-drawing tool, e.g. in terms of thermal expansion. However, it must be considered that this metallic body can influence the magnetic field distribution possibly, even to the extent that no more workpiece deformation is possible. To reduce this influence as far as possible, a non-ferromagnetic material can be applied and the formation of eddy currents in the coil body can be suppressed by building this body from individual layers, which are oriented perpendicular to the expected current direction and electrically insulated from each other by a suitable coating or foil. The total induced voltage is distributed among the individual layers so that the requirements on this insulation are relatively low with small layer thicknesses and a correspondingly high number of layers. In contrast, the requirements for the insulation of the coil winding itself are considerably higher so that additional continuous insulation tubes are necessary, e.g. tubes made of glass fiber-reinforced plastic (GFRP).

The second housing concept consists of an insulation coil body made of GFRP, which combines high insulation capability and acceptable mechanical strength for tensile and compression loads. Furthermore, this material does not influence the distribution of the magnetic field and the resulting pressure. The coil body completely encloses and insulates the individual turns so that no additional insulation tubes are required here. Thus, in comparison to the metallic coil body, the conductors can be arranged closer to each other and to the workpiece. This allows better focusing of the magnetic pressure on the very small calibration zone. However, when dimensioning the minimum insulation distance, the anisotropic insulation properties of GFRP must be taken into consideration.

In the third housing concept, the conductor is embedded in a similar GFRP coil body, but here the channels incorporating the conductor are open toward the workpiece. Here, an additional thin polyimide film provides the necessary insulation. This insulation material features excellent insulation capabilities, but due to its very limited strength and wear resistance, special design measurements such as a slight local recess must be taken to avoid mechanical loads. Nevertheless, this approach allows for much smaller insulation gaps between conductor and workpiece, which significantly improves the process efficiency [21].

In order to draw a substantiated comparison and to evaluate the different coil variants, it is much more meaningful to consider the estimated resulting pressure for the same capacitor charging energy and voltage, respectively, than the equal coil current postulated in Fig. 2. This means that different coil currents must be considered depending on the different electrical properties of the setup. However, neither the current course nor the electrical parameters of the oscillating circuit are known during the design phase. In the case of complex structures, in particular, the calculation is complicated by the circular dependency between these parameters. To solve this conflict [22], suggests a simple iterative approach. Still assuming a harmonic oscillation of the coil current, and consequently disregarding the damping effects caused by the resistance of the electrical circuit, the calculation strategy approximates the frequency and amplitude of the coil current as well as the frequency-dependent inductance of the electrical circuit.

Table 1 lists the parameters identified via this iterative approach for three investigated coil variants with five turns, three turns, and one single turn. These coil variants also served for testing the different design concepts for the coil inserts. Specifically, in the case of five-turn coil, the metallic coil housing (see Fig. 3 left) was chosen; for the three-turn coil the GFRP housing with closed conductor channels (see Fig. 3 middle) was selected; and for the single-turn coil, the GFRP housing with open conductor channels and additional polyimide film (see Fig. 3 right) was applied. Figure 4 shows the corresponding local pressure distributions acting at the moment of maximum current. The calculations were performed via the free special-purpose program of finite element simulation femm 4.2 by David Meeker [20]. As this program is limited to 2D harmonic field simulations, only the parallel sections

Table 1 Current course parameters and important characteristics of the oscillating circuit for different coil variants

Tool coil	Capacitor charging		Inductance of oscillating circuit (μH)	Discharging current	
	Voltage (kV)	Energy (kJ)		Amplitude (kA)	Frequency (kHz)
Five-turn coil	10	16.5	3.4	79	4.7
Three-turn coil	10	16.5	1.9	132	6.4
Single-turn coil	10	16.5	0.33	319	15.4

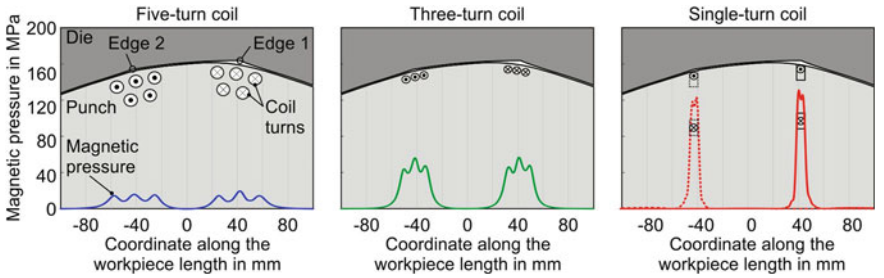


Fig. 4 Estimated pressure distribution for different coil variants assuming a capacitor charging voltage of 10 kV. (Color figure online)

of the coil can be modeled. In order to consider the additional inductance caused by the coil ends (variable depending on the specific coil design) and the pulsed power generator (determined as 85 nH by measurements without any load inductance), an additional inductance is added to the calculated value. This additional inductance is estimated as 1500 nH for the five-turn coil, 900 nH for the three-turn coil, and 100 nH for the single-turn coil. All calculations are based on a capacitor charging voltage of 10 kV. An efficiency of 65% was assumed for the transfer of capacitor charging energy to inductive energy of the tool coil according to the calculations of Risch [23].

As expected, a decreasing number of turns leads to a decrease of the inductance, therefore causing a higher and faster current pulse. The smaller insulation distances between the individual turns and between coil winding and workpiece, which were enabled via the different housing concepts, enhance this effect. At the same time, the geometric modification leads to better focusing of the magnetic pressure. This means that especially in the case of the single-turn coil, a very high-pressure pulse acts directly below edge 1.

Important differences between the investigated single-turn coil variant and the two multi-turn coil variants (i.e. the three-turn coil and the five-turn coil) comprise the non-rotationally symmetric cross-section and the arrangement of the return conductor. The change in the cross-section geometry results from the attempt to keep the distance between the tool coil and workpiece as small as possible. In order to reach this aim, the coil surface was adjusted to the shape of the preformed sheet. Realizing this cross-section requires changing the manufacturing strategy of the coil winding. In the case of the multi-turn coils for the round conductors, round copper rods served as input material so that only marginal subsequent processing was required here. The connection of the different linear conductors to one complete coil turn was realized via insulated clamps at the ends of the coil. On the contrary, the more complex cross-section shape of the single-turn coil was manufactured by milling. In order to facilitate the milling of the complete turn from a copper plate, the return conductor was arranged in one vertical plane with the forward conductor far away from the workpiece. Compared to a similar single-turn coil with the same cross-section but with the return conductor arranged close to the workpiece below the

second calibration edge, this layout increases the load inductance. However, since the absolute inductance of the single-turn coil is very low, this phenomenon was accepted here. In order to calibrate edge 2, a second coil winding was inserted in this area (without electrical connection to the first one). Figure 4 (dashed lines) indicates this second winding and the corresponding pressure. After calibrating edge 1, the second coil turn is connected to the pulsed power generator and edge 2 is calibrated in a second discharging process.

4 Experimental Results

First tests of the developed tools were carried out with steel workpieces (DC04; thickness 0.6 mm) and aluminum workpieces (EN AW-3103; thickness 0.6 mm). Figure 5 shows the experimental setup on the example of the five-turn coil and compares the measured coil current with the numerically predicted one. Although the simulation slightly overestimates the current, the accuracy of the simulation approach is good, considering all simplifications.

Figure 6 compares the preformed reference components and exemplary calibrated parts. In this example, a capacitor charging voltage of 12 kV was used, which corresponds to a capacitor charging energy of 23.8 kJ. After solely preforming the sheet metal workpiece by closing the tool halves, the parts show strong springback. Permanent deformation is hardly noticeable, especially in the case of aluminum workpieces. On the contrary, the calibrated part features much better geometric accuracy.

The tests have also proved to be qualitatively successful regarding the intended sharpening of the radii of edge 1 and edge 2. In order to quantify this effect, the obtained edge radius was determined in the cross-section. For this purpose, samples were taken from the components in the area of the formed edges, which were then embedded and measured with an optical microscope as shown in Fig. 7.

The figure also shows a comparative overview of the edge radii achievable with the regarded coil variants. It is obvious that in all cases increasing the capacitor

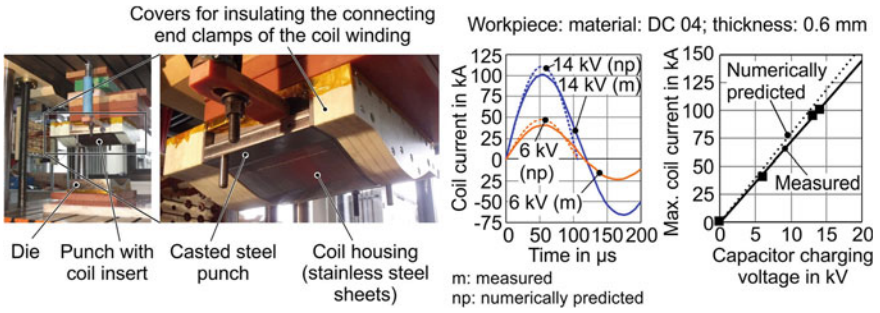


Fig. 5 Experimental setup for the electromagnetic calibration of sharp-edged design elements and verification of numerically predicted coil current. (Color figure online)

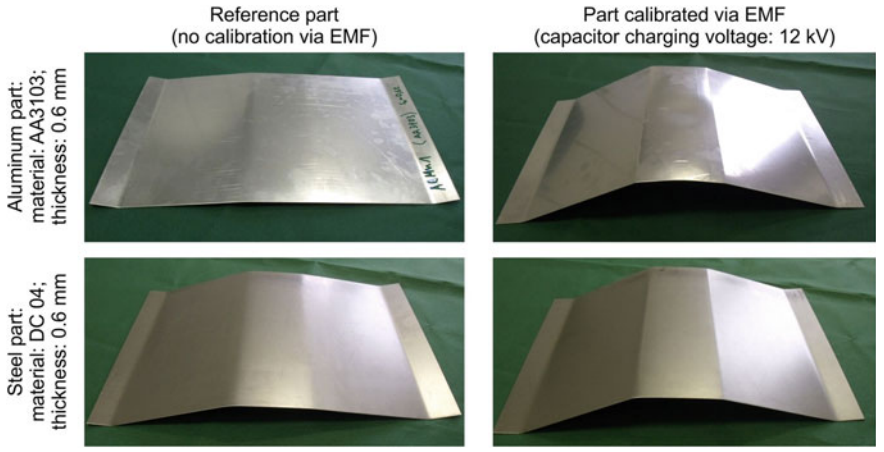


Fig. 6 Exemplary preforms and calibrated aluminum and steel parts. (Color figure online)

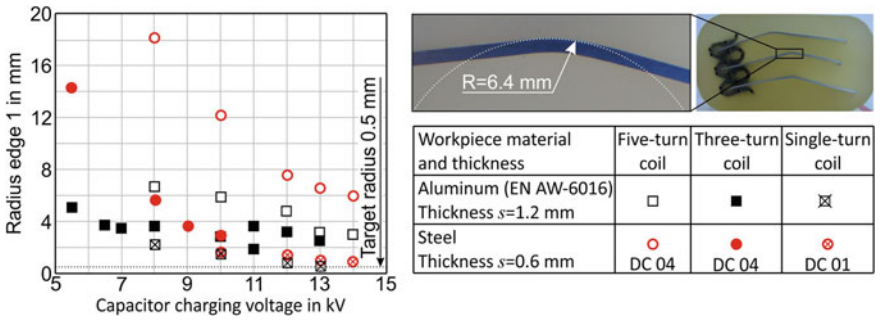


Fig. 7 Edge radii achievable by electromagnetic calibration. (Color figure online)

charging energy leads to a decreasing edge radius. This trend is strong at first and eases off later. This fundamental relationship is independent of the respective coil variant and the workpiece material (steel or aluminum). In addition, the investigations on all coil variants confirm that, with otherwise identical parameters, significantly sharper edges are achieved for aluminum semi-finished products than for steel sheets. These results were expected since the higher electrical conductivity and the lower strength and density aluminum in general are considered to be more suitable for being processed by EMF.

A comparison of the different inductor variants with each other shows that, compared to the five-turn coil, sharp edges result at significantly lower capacitor charging voltages if the three-turn coil is applied with otherwise identical process parameters. Similarly, the achievable edge radius is lower again if the single-turn coil is used. This trend correlates well with the magnetic pressures calculated for the coil variants (see Fig. 4) and confirms that the single-turn coil leads to the highest process

efficiency compared to the other investigated coil types. Using EMF to calibrate the part with this coil made it possible for the first time to achieve the target edge radius of 0.5 mm for semi-finished aluminum products.

5 Summary and Conclusions

Innovative forming technologies and process combinations are essential in order to increase freedom of design and enable manufacturing of technologically challenging sharp-edged details in body-in-white components even from difficult-to-form materials such as aluminum alloys. Deep drawing with integrated electromagnetic calibration is a suitable approach for extending forming limits, although up to now all examples of this process combination for corner filling or edge sharpening have focused on forming radii equal to or greater than five times the sheet thickness. In contrast, the goal of the project "Sharp Design Edge" was to use electromagnetic forming for calibrating sharp-edged design elements with an edge radius of 0.5 mm.

In order to demonstrate the feasibility of this forming task, a modular prototype tool was designed, implemented, and tested for the electromagnetic calibration of sharp two-dimensional edges. The influence of essential parameters on the resulting component edge radius was investigated in a combined numerical-experimental process analysis considering process-specific, component-specific, and tool-specific aspects. In this study, the best solution proved to be a coil variant consisting of two individual windings for shaping the edges 1 and 2 with the return conductor being arranged far away from the sheet metal. An insulation insert made of glass fiber reinforced epoxy provides the insulation between the conductors and the surrounding metallic deep-drawing punch, while polyimide foil (Kapton) serves as insulation between the conductor and the sheet metal workpiece. The achieved edge radii show the great potential of the process, especially for aluminum workpieces. Here, the target radius of 0.5 mm was achieved, which is significantly smaller than the investigated sheet thickness of 1.2 mm. Therefore, this process must be considered a process of "bulk sheet metal forming".

References

1. https://de.statista.com/statistik/daten/studie/73970/umfrage/wichtigste-kriterien-beim-pkw-kauf/. Accessed 23 October 2019
2. https://de.statista.com/statistik/daten/studie/171605/umfrage/wichtige-kriterien-beim-autokauf/. Accessed 23 October 2019
3. Golovashchenko SF (2007) Material formability and coil design in electromagnetic forming. J Mater Eng Perform 314–320
4. Harvey GW, Brower DF (1962) DE Patent 1122188
5. Psyk V, Risch D, Kinsey BL, Tekkaya AE, Kleiner M (2011) Electromagnetic forming: a review. J Mater Process Technol 211:787–829

6. Vohnout V (1998) A hybrid quasi-static/dynamic process for forming large sheet metal parts from aluminum alloys. PhD thesis, Ohio State University
7. Psyk V (2010) Prozesskette Krümmen - Elektromagnetisch Komprimieren - Innenhochdruckumformen für Rohre und profilförmige Bauteile. PhD thesis, Technische Universität Dortmund
8. Psyk V, Lieber T, Kurka P, Drossel WG (2014) Electromagnetic joining of hybrid tubes for hydroforming. Procedia CIRP 23:1–6
9. Jäger A, Risch D, Tekkaya AE (2009) DE Patent 10 2009 039 759.0
10. Golovashchenko SF (2005) Springback calibration using pulsed electromagnetic field. In: AIP conference proceedings, p 778
11. Eguia I, Zhang P, Daehn GS (2004) Crimped-joining of aluminium tubes onto mandrels with undulating surfaces. In: 1st international conference on high speed forming ICHSF 2004, Dortmund
12. Imbert J, Worswick M (2011) Electromagnetic reduction of a pre-formed radius on AA5754 sheet. J Mater Process Technol 211:896–908
13. Burden R, Snowden L, Hasegawa K, Newman D, Bauer D (2000) Elektromagnetisches Umformen (EMF). In: Neuere Entwicklungen in der Blechumformung, pp 331–343
14. Psyk V, Beerwald C, Henselek A, Homberg W, Brosius A, Kleiner M (2007) Integration of electromagnetic calibration into the deep drawing process of an industrial demonstrator part. Key Eng Mater 344:435–442
15. Risch D, Psyk V, Tekkaya AE (2009) Investigation on a deep drawing and in-process electromagnetic calibration. Steel research 80:329–334
16. Vohnout V, Shang J, Daehn GS (2004) Improved formability by control of strain distribution in sheet stamping using electromagnetic pulses. In: 1st international conference on high speed forming, Dortmund
17. Taebi F, Demir OK, Stiemer M, Psyk V, Kwiatkowski L, Brosius A, Blum H, Tekkaya AE (2012) Dynamic forming limits and numerical optimization of combined quasi-static and impulse metal forming. Comput Mater Sci 54:293–302
18. Kiliclar Y, Demir OK, Vladimirov IN, Kwiatkowski L, Brosius A, Reese S, Tekkaya AE (2012) Combined simulation of quasi-static drawing and electromagnetic forming by means of a coupled damage-viscoplasticity model at finite strains. In: 5th international conference on high speed forming, Dortmund
19. Merklein M, Allwood JM, Behrens BA, Brosius A, Hagenah H, Kuzman K, Mori K, Tekkaya AE, Weckenmann A (2012) Bulk forming of sheet metal. CIRP Ann 61:725–745
20. Meeker D. Finite element method magnetics. http://www.femm.info/wiki/HomePage. Accessed 04 December 2019
21. Beerwald C (2005) Grundlagen der Prozessauslegung und -gestaltung bei der elektromagnetischen Umformung. PhD thesis, Technische Universität Dortmund
22. Neugebauer R, Psyk V, Scheffler C (2014) A novel tool design strategy for electromagnetic forming. Adv Mater Res 1018:330–340
23. Risch D (2009) Energietransfer und Analyse der Einflussparameter bei der formgebundenen elektromagnetischen Blechumformung. PhD thesis, Technische Universität Dortmund

Augmentation of Plasma-Based Impulse Generation with Rapid Chemical Reactions



Brian Thurston, Yu Mao, Troy Lewis, Anupam Vivek, and Glenn Daehn

Abstract The use of a chemical explosive mixture to augment the vaporizing foil actuator (VFA) and laser impact welding (LIW) processes is introduced in this study. A liquid explosive known as Picatinny liquid explosive (PLX) was used to augment the capabilities of both the VFA and LIW processes. The 304 stainless steel flyers 3 mm thick driven by PLX augmented VFA and unaugmented VFA are compared. Similarly, 0.442 mm thick Al3003 flyers driven by laser impact and PLX augmented laser impact are compared. In all cases, a photon Doppler velocimetry (PDV) system was used to collect the velocity–time profiles of the flyers. All PLX augmented experiments showed increases in both flyer acceleration and peak velocity over the same time scales as the unaugmented experiments. This indicates that the PLX-provided impulse occurs at the same time as the VFA/laser impulse. The augmented VFA experiments showed a 28% velocity increase over the unaugmented experiments at 10 kJ input energy. The augmented laser impact process exhibited peak flyer velocities 236% higher than laser impact using only the laser. Here we demonstrate that chemical augmentation is capable of significantly increasing flyer velocities for both VFA and LIW at the same input energies and under similar conditions. This development should expand the repertoire of flyer materials and thicknesses that can be impact welded by VFA and LIW.

Keywords Impulse forming · Explosive forming · Laser impulse · Vaporizing foil method

1 Introduction

Impulse forming techniques have various uses, including embossing, shearing, and welding. Safely producing a sufficient impulse to accomplish a given task presents some challenges. Safety, reliability, equipment design, etc. are all concerns. Here we demonstrate a hybrid approach for driving metal sheets for use in impact processes,

B. Thurston (✉) · Y. Mao · T. Lewis · A. Vivek · G. Daehn
Department of Materials Science and Engineering, The Ohio State University, Columbus, OH 43210, USA
e-mail: thurston.56@osu.edu; thurston.56@buckeyemail.osu.edu

© The Minerals, Metals & Materials Society 2021

G. Daehn et al. (eds.), *Forming the Future*, The Minerals, Metals & Materials Series,
https://doi.org/10.1007/978-3-030-75381-8_110

chiefly for impact welding. For the purposes of impact welding, the impact velocity is of crucial importance. Several approaches, as discussed in the next section, have been developed to drive flyer sheets to high enough velocity at impact, known as the critical velocity. As discovered, impact welding occurs with impact velocities ranging from 150 to 1500 m/s [1]. However, in general, to obtain a successful impact weld, an impact velocity of higher than 300 m/s is required [2–5]. Several techniques for driving flyer sheets to such high speeds have been developed, a subset of which can be used in a laboratory setting. In this document, we first briefly discuss the existing impact welding tools used in the industry, and then we do the same for two alternative impact welding technologies: vaporizing foil actuator (VFA) welding and laser impact welding (LIW). We then present hybrid approaches for VFA welding and LIW where a chemical explosive is added to the process. Experiments were performed to assess the feasibility of this hybrid approach for both the VFA and LIW techniques. The experimental process and results for the hybrid VFA approach are presented, followed by the same for a hybrid LIW process. The ramifications of the success of these two approaches are then discussed.

2 Industrial Impact Welding Tools

Two common tools for driving metals to high speed and causing them to impact weld are chemical explosives [6] and electromagnetic actuators [7], both of which present certain hurdles to widespread industrial application. A schematic of these processes is shown in Fig. 1. Besides the obvious safety concerns related to handling, storage, and application, explosives have a critical volume or diameter [8] below which they are difficult to detonate reproducibly. Therefore, while they are ideal for impact welding of very large workpieces, they do not scale down well for welding small areas. Electromagnetic forming or welding utilizes the principles of electromagnetic induction and forces between current-carrying conductors to launch a workpiece away from a stationary electromagnetic solenoid actuator [9]. As the process needs the workpiece as well as the actuator to carry the current, a low conductivity workpiece material is difficult or impossible to push directly. Therefore, launching titanium or austenitic stainless steel will require a driver made from a conductive material like, for instance, copper [10]. An excellent review of electromagnetic forming is provided by Psyk et al. [9] and they estimate the electrical to mechanical energy conversion efficiency of electromagnetic forming to range from 1 to 20%. However, to get the best efficiency in the conditions of coupling, conductivity, and discharge current, the characteristics have to be ideal. Additionally, process inefficiencies are difficult to overcome in electromagnetic welding due to limitations in current and resulting pressures that the solenoid actuator itself can experience before catastrophic failure [11].

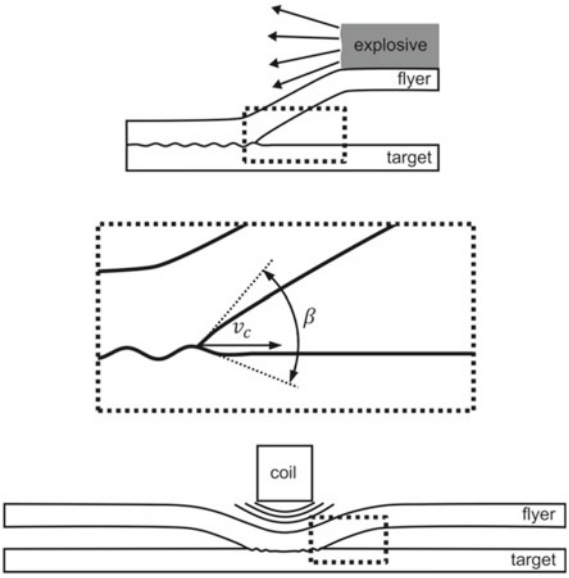


Fig. 1 Schematic of explosive welding (top) and magnetic pulse welding (bottom). From Groche et al. [2]

3 Alternate Indoor Impact Welding Tools

The VFA metalworking process is a novel technique developed at the Impulse Manufacturing Laboratory (iml.osu.edu) at the Ohio State University. Using the impulse generated by rapid electrically driven vaporization of an aluminum foil actuator, a metal sheet as a flyer can be accelerated to velocities of several hundreds of meters per second in a few microseconds, followed by a high-speed impact [12]. Various VFA applications have been developed, including welding, forming, shearing, embossing, etc. [13]. Depending on the flyer properties and processing parameters, the impact velocity can be as high as around 1000 m/s [13] and the pulse pressure magnitude is in the range of gigapascals [14]. Aluminum alloys as thick as 6.35 mm have been successfully joined to steel by VFA welding [15]. Compared to electromagnetic and explosively driven impulses, VFA can be safely performed in an indoor laboratory environment and can achieve higher energy efficiency [16]. However, the applications are limited to flyers with thickness in the magnitude of millimeters. Scaling to large sizes, thicker, or stronger flyers can be problematic because of a diminishing return for increasing input energy, and the maximum impact velocity tends to be capped by the capacity of the equipment [13]. The cost of upgrading a VFA system, including using capacitors with higher capacitance and a power supply with a higher maximum charging voltage, is high and marginally increasing.

It is possible to launch flyer sheets to velocities suitable for impact welding with a high-energy laser pulse. This technique, first proposed by Daehn and Lippold [17], has been given the name laser impact welding (LIW). The basic setup for this technique requires a high-energy pulsed laser system capable of providing several

joules of energy over a time period normally measured in the tens to hundreds of nanoseconds [18, 19]. This laser pulse can be used to propel flyers on its own, or more commonly the pulse can be directed to an absorbing or backing material applied to the flyer to convert the laser energy more efficiently to kinetic energy. Here, a backing material should be understood to be an optically transparent material used to confine the expanding plasma generated by a laser pulse. Black paint is a common absorbing material used along with water, glass, or polycarbonate as a backing material for inertial constraint [20]. This technique has been used to propel 25 μm thick 1100 aluminum flyers to speeds in excess of 900 m/s with a laser pulse energy of 3 J [20]. However, this technique is limited to flyers of relatively small thicknesses, measured in the low hundreds of micrometers or less. As the flyer thickness increases, the maximum achievable speed decreases for a laser pulse of a fixed power [18]. Increasing the power density of the laser beam, either by reducing the focal size and/or increasing the output power, can produce greater flyer speeds. However, there are limitations to the power density that can be delivered to a flyer sheet. Using an ND:YAG laser with a pulse length of 8 ns and pulse energy of 3 J, Wang et al. found that beam energy densities greater than 1.19×10^{14} W/m^2 can cause a breakdown of the air, resulting in a plasma spark that absorbs the pulse energy [20]. This puts a limit on the power density of a beam traveling through air. Backing materials also have their limits, Berthe et al. found that power densities beyond 10^{14} W/m^2 caused the formation of parasitic plasmas at the surface of water layers used as backing materials [21]. Similar limitations are also likely to exist for other backing materials.

4 Hybrid Concept

Here a hybrid concept is described where VFA and laser impulses can be augmented with an explosive chemical mixture applied at the site of the impulse. For the purposes of safety, an explosive mixture having relatively low sensitivity and fast detonation velocity is desired. Safe chemical byproducts are also desirable. For the purposes of VFA welding where larger energy deposition into a foil is impractical, either because of cost or available capacitor storage energy, additional energy may be provided by augmentation via a chemical explosive. This chemical explosive would be placed near the vaporizing foil in quantities that add useful energy to the foil explosion. In the case of LIW, where energy is greatly constrained by the cost of pulsed laser systems and the fundamental limitations of pulsed power density in air, any additional energy could be of great utility in driving foil sheets.

It has been found that an explosive mixture based on nitromethane (CH_3NO_2) is well suited for the purpose of augmenting the VFA and LIW processes. The nitromethane-based explosive used here is referred to as Picatinny liquid explosive (PLX). The mixture used here is based on a recipe described in a YouTube video on the Tech Ingredients channel, “DON’T TRY THIS AT HOME!”, [22], and US patent 3,713,915 [23]. The tested recipe consists of the following ingredients which can be

freely purchased: 30 ml of nitromethane 99+%, 1.5 ml of ethylenediamine 98+%, 2.1 cm^3 loose spherical 3.0–4.5 micron aluminum powder, and 1.18 g of PMMA (acrylic) chips. The purposes of the ingredients are as follows: nitromethane as an explosive material, ethylenediamine as a sensitizer, and fine aluminum powder as a sensitizer and fuel [22, 23]. The PMMA is added as a gelling agent to prevent the aluminum powder from falling out of suspension [22], although we have found stirring is still necessary prior to use. All of these components can be easily purchased. While the detonation velocity of this exact mixture has not been measured, the literature reports the detonation velocity for PLX (nitromethane 95% with ethylene diamine 5% only) to be around 6200 m/s [24], and the detonated nitromethane will decompose into CO_2, CO, NO_2, and NO [25]. The critical diameter for the propagation of a detonation in PLX at 20 °C is estimated to be 18 mm, when tested in a long glass tube [26]. In this work, we demonstrate that useful detonations of very small volumes of PLX can be created via the VFA method and by laser impulse.

Nitromethane is reported to be a high explosive material, although an insensitive one. Nitromethane has been found to be unaffected by drops of 1.95 m [26] and in ten out of ten shots to be unaffected by rifle fire [27]. U.S. Army Material Command reports an explosion temperature of 430 °C for nitromethane alone and for nitromethane sensitized with 5% ethylenediamine, both for confined samples [27]. Nitromethane is known to be a skin, eye, and lung irritant and is harmful if swallowed [28]. Once sensitized with ethylenediamine, nitromethane becomes more sensitive to shock; however, it is still relatively difficult to detonate. In tests by U.S. Army Material Command nitromethane sensitized with 5% ethylenediamine was unaffected in five out of five rifle bullet impacts [27]. With the addition of aluminum powder, the PLX will become relatively more sensitive to shock [22].

5 Enhancement of the VFA Technique via Chemical Augmentation

Here, a technique for chemically augmenting the VFA process is presented. A schematic of the setup is shown in Fig. 2a, b. A 3.175 mm thick 304 stainless steel sheet was used as a flyer. A 6.35 mm thick Al5052 block with a central hole of 30 mm diameter was used as the standoff. A capacitor bank system with a capacitance of 426 μF, a maximum charging voltage of 8.66 kV, a maximum charging energy of 16 kJ, and a current rise time of 12 μs was used. Two layers of 0.762 mm thick foils with 10.16 mm wide effective area were applied as the original actuator, the geometry of which is shown in Fig. 2c. For augmentation, 0.4 mL of the PLX mixture was soaked into eight layers of paper towel material. The eight layers of PLX-soaked paper towel were placed with three layers above and below the foils and with the remaining two layers placed between the foils. At discharge, the effective area of the actuator was vaporized to plasma, deforming the flyer into the standoff hole area. A photon Doppler velocimetry (PDV) probe was set above to measure the velocity

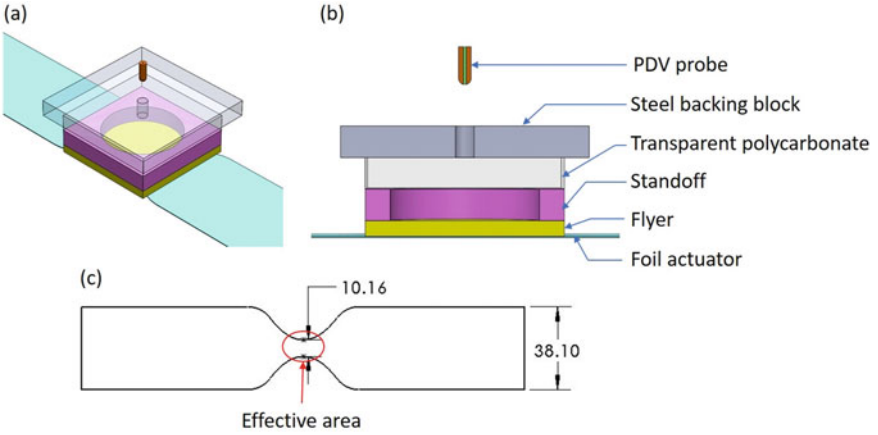


Fig. 2 Isometric (**a**) and front cross-section, (**b**) schematic of experiment setup, and foil actuator geometry (**c**). Units are in mm. (Color figure online)

Table 1 Processing parameters for the three tests

Test #	Actuator	Input energy (kJ)
1	Original	10
2	Augmented	10
3	Original	16

of the center of the flyer. A transparent polycarbonate block was used to protect the probe. The whole stack-ups were fixed by a pair of S7 steel backing blocks which were bolted together. The top S7 block had a central hole for the PDV laser. For comparison, three different inputs were tested, and the processing parameters are shown in Table 1.

Flyers were deformed by VFA and impacted with the polycarbonate block for all three tests. The sound of the augmented test at 10 kJ was not easily distinguished from that of the unaugmented 10 kJ test. The shapes of the deformed steel sheets are similar for each test and a representative example is shown in Fig. 3. Velocity traces of the three tests are also shown in Fig. 3. The peak velocity is maximum with the augmented actuator at 10 kJ reaching 457 m/s, followed by 419 m/s with the unaugmented actuator at 16 kJ and 357 m/s with the unaugmented actuator at 10 kJ.

As shown by the velocity curves in Fig. 3, instead of extending the time of the acceleration period, the PLX increases the acceleration (slope of the curve) of the flyer, which reaches a higher peak velocity at a similar time or even earlier than the flyer driven by the unaugmented actuator at 10 kJ. This indicates that the reaction for chemical shock is fast enough compared to the plasma driving process to add useful work. As shown by the data, in terms of peak velocity of the flyer, the impulse generated by the augmented actuator is not only increased by 28% compared to that by the same amount of input energy (10 kJ) without augment but is also 9%

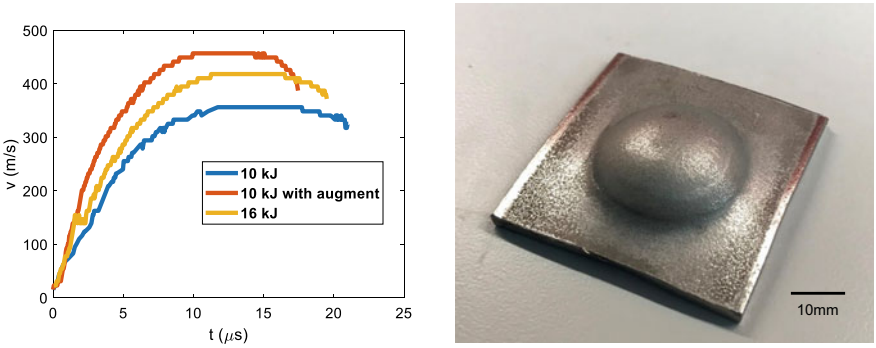


Fig. 3 Left—velocity versus time curves for the three test conditions. Right—a steel flyer after VFA test 1 (see Table 1). (Color figure online)

higher than the impulse generated by the unaugmented actuator at an input energy of 16 kJ, which itself had a 17% higher velocity than with an input energy of 10 kJ. The data also proves the mentioned diminishing return of increasing input energy, and that from input energy of 10–16 kJ without augmentation, the peak velocity only increased 17% with a 60% increase in the input energy. With augmentation, the energy efficiency is dramatically enhanced and the capability limit of the VFA system is therefore significantly boosted with a minimal increase in cost.

6 Augmentation of Laser-Driven Flyers

A technique for augmenting a laser pulse for propelling flyers is illustrated in Fig. 4. For comparison, a similar setup as in Fig. 4 was used where the PLX layer was replaced with water to show the difference in effectiveness with and without the addition of PLX. The flyer sheets were prepared from Al3003 shim stock. The shim stock came with yellow paint which was removed with a fiber laser engraver. The

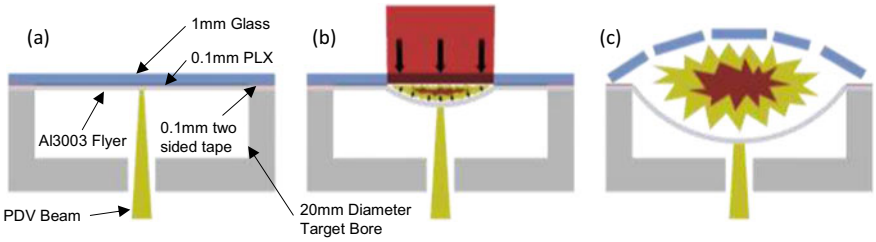


Fig. 4 Experimental setup and sequence of events. **a** Setup with PDV probe. **b** Laser pulse arrives and detonates PLX through glass. **c** Explosion drives the flyer and ejects the glass microscope slide. Images are to scale. (Color figure online)

thickness of the flyer sheets was then measured to be 0.442 mm. One side of each flyer was painted black with a black Sharpie marker to better absorb laser light. The flyers were then placed over a 20 mm diameter bore with the black painted side facing outward. The bore contained an access hole at the bottom for a PDV beam which was used to measure the flyer velocity. The surface of the flyer was covered with clear packing tape. This tape was used to prevent components of the PLX from interacting with the Sharpie ink. Double-sided tape of 0.1 mm thickness was used as a spacer to create a cavity in which a PLX film would sit. This tape was added to the flyer outside the cavity area of the bore (see Fig. 4a). A bead of PLX was placed onto the packing tape in the center of the flyer and pressed flat with a 1 mm thick glass microscope slide. The microscope slide was adhered to the flyer by means of the double-sided tape spacers. This resulted in a PLX film of 0.1 mm thickness which was semi-transparent and gray in color. The PLX was detonated by an 8.1 ns laser pulse with a total energy of 3.15 J focused to a diameter of 10 mm at the flyer surface. The laser system used has a flat-top beam profile [20]. This resulted in an average light intensity of 4.95×10^{12} W/m^2 being absorbed by the PLX film and the painted flyer surface. The total volume of PLX impinged upon by the laser beam amounted to 7.85 mm^3. Flyer velocities were captured using a PDV system, and the placement of the beam can be seen in Fig. 4.

In total, ten flyers were driven with the laser system. Five of the flyers were driven with the laser impulse and PLX. When detonated by the laser the PLX added to the sound of the laser impact, resulting in a pop similar in volume to a loud clap. The remaining five flyers were driven by laser energy only; in this case, the PLX was replaced with water. The velocity profiles of these flyers are shown in Fig. 5. The peak velocities of the flyers with PLX occur at approximately 7 μs. With water, only the peak velocity occurs at 5 μs. It is clear from this data that PLX augmentation provides a significant boost to the flyer velocity and that the impulse from the PLX occurs simultaneously with the impulse from the laser. The average velocity of the PLX flyers was 353 ± 25 m/s. The average velocity of the flyers with water only was

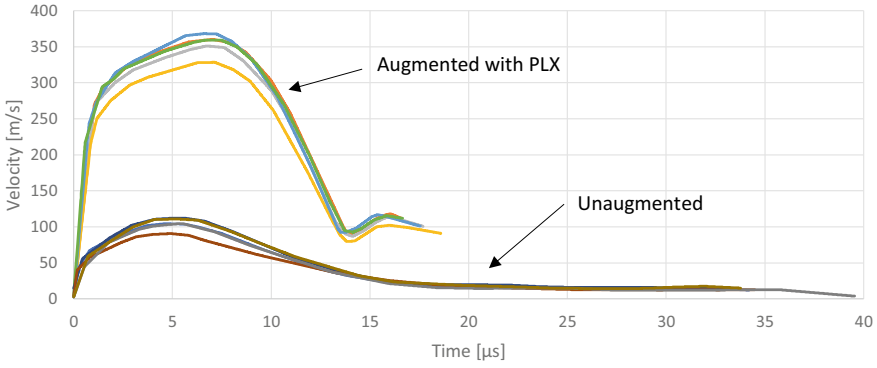


Fig. 5 The velocity profiles of augmented and unaugmented laser impulses to flyer sheets. (Color figure online)

105 ± 13 m/s. On average the flyers driven by the laser and PLX had peak velocities 236% higher than the flyers driven by the laser energy alone.

In Fig. 6a–c, a representative result of the shots without PLX can be seen. In Fig. 6b, a mark left by the laser beam can be seen in the center of the flyer. Figure 6c shows a side profile of a flyer backed with glass and water. The average displacement of such flyers was 1.2 mm. In Fig. 6d–f, a flyer deformed by the laser and PLX can be seen. From Fig. 6d, f, one can make out a conical profile. This cone shape is believed to result from the difference in area between the PLX detonated by the laser beam and the area of the bore into which the flyer was driven. Because of this conical shape, we believe that only the PLX illuminated by the laser light was detonated and that this detonation failed to propagate (the total area of the PLX was a 20 × 20 mm^2). Additionally, in several tests, remnants of PLX were found at the periphery of the flyer. The estimated volume of PLX detonated is 7.85 mm^3 below the 10 mm diameter laser spot. This diameter/volume is significantly smaller than the diameters/volumes for which detonation was possible in PLX without aluminum powder according to Makovky and Lenji [26]. The exact energy contributed by the PLX and the efficiency by which it propelled the flyer is unknown, but the effect is significant. In Fig. 6e the side of the flyer upon which the PLX and laser light acted is shown. From this image, it can be seen that the damage to the Sharpie mark is minimal and there is no aesthetic damage to the flyer base material from the PLX explosion.

The effect of chemical augmentation on the laser impact process is similar to the effect on the VFA process. Just as before, augmentation by PLX increases both the maximum flyer velocity and the rate of acceleration, all within the same time period over which these processes normally occur. The implications for LIW of this

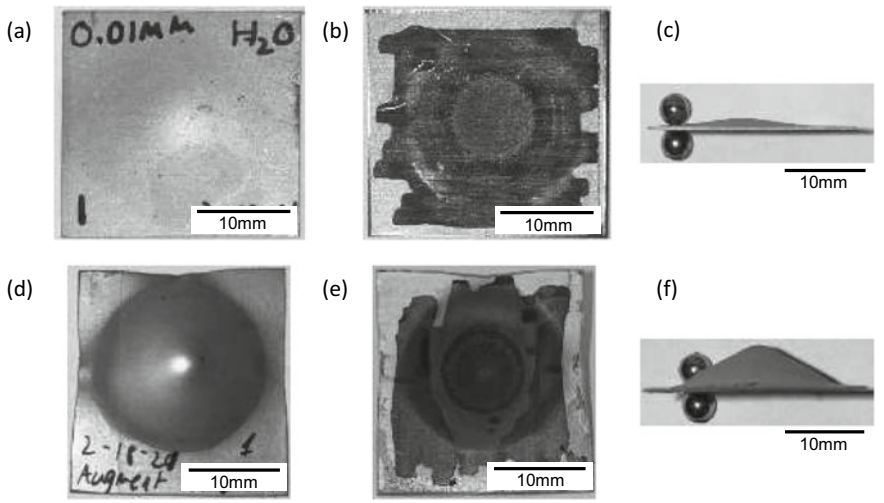


Fig. 6 Comparison between the flyer deformation induced by the laser with water (**a**, **b**, **c**) and the deformation produced with the use of PLX with the laser (**d**, **e**, **f**)

chemical augmentation process are significant. Here we have demonstrated that with a layer of only 0.1 mm of chemical explosive the 3 J laser pulse of an existing LIW welding system can be used to drive a flyer of 0.442 mm thickness to a velocity beyond 300 m/s, which is considered a safe minimum necessary for impact welding. Whereas by itself such a laser was only able to attain speeds of around 100 m/s under similar conditions. In addition, the surface finish of the flyer was relatively unaffected by the blast of the chemical explosive.

7 Conclusions and Open Questions

In this work, we have shown that it is possible to chemically augment both the VFA and LIW processes via a nitromethane-based chemical explosive. The detonation period of the explosive is sufficiently fast to add meaningful amounts of energy to the velocities of flyers driven by VFA and laser impact. For the VFA process, a 28% velocity increase in a 3 mm steel flyer was observed when using a PLX-augmented double-foil actuator through which 10 kJ of energy was discharged. When augmented, a double-foil driven with 10 kJ outperformed an unaugmented double-foil driven by 16 kJ of energy by 9%. For the purposes of laser impact welding, the use of chemical augmentation by PLX has been shown to be of great significance. A 0.1 mm thick, 10 mm diameter volume (7.85 mm^3) of PLX detonated by a 3.15 J laser pulse focused to a 10 mm diameter produced a 236% velocity increase compared to flyers driven by the laser impulse alone for 0.442 mm thick Al3003 flyers. Augmentation by PLX or other mixtures shows promise for improving the process efficiency of both VFA and LIW.

There is much work left to be done to optimize this technique. The minimum energy density for VFA foils necessary to detonate the PLX is unknown. Similarly, the energy density of a laser beam required for detonation has not been measured. The optimal PLX recipe for these processes still needs to be determined. The amount of aluminum powder in the PLX may have a significant impact on the size of impulse necessary for detonation and on the amount of energy that can be produced. The effect of flake versus spherical aluminum powder is unknown. Other chemical explosives may perform better than PLX for these processes. For laser impact purposes the backing material can play a significant role. It is hypothesized that the use of thicker glass backing materials could lead to higher flyer velocities. An ideal backing material for laser impact welding would survive the explosions and would also be massive enough to direct most of the energy of the chemical augment into the flyer. As it stands, a significant amount of the PLX energy is wasted in shattering and scattering the glass microscope slide used as a backing material for laser impact purposes. Additionally, it should be noted that the PLX recipe used here degrades within 24 h when exposed to air, and when sealed the mixture slowly degrades over a period of weeks. The recipe used in this work was one week old at the time of the experiments and had been stored in a sealed glass bottle after production. The degradation of the

sealed mixture is hypothesized to be due to chemical reactions between the aluminum powder and the other ingredients in the mixture.

Acknowledgments The authors gratefully acknowledge the support of the National Science Foundation for MRI Award 1531785, *Development of a Dynamic Material Processing and Testing Instrument*, and the Ohio Development Services Administration for supporting *Supply Chain and Market Development for Lightweight Multi-Materials Manufacture with Vaporizing Foil Actuator Welding*.

References

1. Zhang Y et al (2011) Application of high velocity impact welding at varied different length scales. J Mater Process Technol 211(5):944–952
2. Groche P, Becker M, Pabst C (2017) Process window acquisition for impact welding processes. Mater Des 118:286–293
3. Grignon F et al (2004) Explosive welding of aluminum to aluminum: analysis, computations and experiments. Int J Impact Eng 30(10):1333–1351
4. Zhang Y, Babu S, Daehn GS (2009) Impact welding in a variety of geometric configurations. https://doi.org/10.17877/DE290R-8635
5. Vivek A et al (2014) Accessing collision welding process window for titanium/copper welds with vaporizing foil actuators and grooved targets. J Mater Process Technol 214(8):1583–1589
6. Crossland B, Williams JD (1970) Explosive welding. Metall Rev 15(1):79–100. https://doi.org/10.1179/mtlr.1970.15.1.79
7. Lueg-Althoff J, Bellmann J, Hahn M, Schulze S, Gies S, Tekkaya AE, Beyer E (2020) Joining dissimilar thin-walled tubes by magnetic pulse welding. J Mater Process Tech 279
8. Petel OE, Mack D, Higgins AJ, Turcotte R, Chan SK (2007) Minimum propagation diameter and thickness of high explosives. J Loss Prev Process Ind 20(4):578–583
9. Psyk V, Risch D, Kinsey BL, Tekkaya AE, Kleiner M (2011) Electromagnetic forming—a review. J Mater Process Tech 211(5):787–829
10. Weimar G (1963) Hochgeschwindigkeitsbearbeitung III-Umformung von Blechen und Rohren durch magnetische Krafte. Werkstatt und Betrieb 96(12):893–900
11. Golovashchenko SF (2007) Material formability and coil design in electromagnetic forming. J Mater Eng Perform 16(3):314
12. Vivek A et al (2013) Vaporizing foil actuator: a tool for collision welding. J Mater Process Technol 213(12):2304–2311
13. Vivek A, Hansen SR, Daehn GS (2014) High strain rate metalworking with vaporizing foil actuator: control of flyer velocity by varying input energy and foil thickness. Rev Sci Instrum 85(7):075101
14. Grigoriev AN, Pavlenko AV (2009) Pressure generated by the electric explosion of metal foils. Tech Phys Lett 35(9):865–868
15. Lee T et al (2018) Civilized explosive welding: impact welding of thick aluminum to steel plates without explosives. J Manuf Process 36:550–556
16. Hahn M et al (2009) Vaporizing foil actuator welding as a competing technology to magnetic pulse welding. J Mater Process Technol 230:8–20
17. Daehn GS, Lippold JC (2009) Low temperature spot impact welding driven without contact. US Patent PCT/US2009/036499. 9 March 2009
18. Swift DC, Niemczura JG, Paisley DL, Johnson RP, Luo SN, Tierney TE (2005) Laser-launched flyer plates for shock physics experiments. Rev Sci Instrum 76(9)
19. Wang H, Liu D, Taber G, Lippold JC, Daehn GS (2012) Laser impact welding-process introduction and key variables. ICHSF 2012:255

20. Wang H, Taber G, Liu D, Hansen S, Chowdhury E, Terry S, Lippold JC, Daehn GS (2015) Laser impact welding: design of apparatus and parametric optimization. J Manuf Process 19:118–124
21. Berthe L, Fabbro R, Peyre P, Tollier L, Bartnicki E (1997) Waves from a water-confined laser-generated plasma. J Appl Phys 82(6):2826
22. Tech Ingredients (7/2/2020) Don't try this at home [Video]. YouTube. https://youtu.be/24Dz5THmfrw
23. Fast CR (1973) Thickened nitromethane explosive containing encapsulated sensitizer. US Patent 3713915. 30 January 1973
24. Kunzel M, Selesovsky J, Pachman J (2017) First attempts in cylinder expansion testing. New Trends Res Energ Mater 736–742
25. Liu W, Bai C, Liu Q, Yao J, Zhang C (2020) Effect of metal dust fuel at a low concentration on explosive/air explosion characteristics. Combust Flame 221:41–49
26. Makovky A, Lenji L (1958) Nitromethane physical properties, thermodynamics, kinetics of decomposition, and utilization as fuel. Scientific Department, Ministry of Defence, Tel-Aviv, Israel, pp 627–644
27. Engineering Design Handbook, Explosives series properties of explosives of military interest (1971). U.S. Army Materiel Command, pp 298–301
28. SIGMA-ALDRICH. Nitromethane material safety data sheet. V0.5 3/19/2014. sigma-aldrich.com

Recent Developments of Vaporizing Foil Actuator Technique for Manufacturing Applications



K. Sajun Prasad, Jianxiong Li, Blake Barnett, Yu Mao, Glenn S. Daehn, and Anupam Vivek

Abstract Vaporizing foil actuator (VFA) is an impulse or high-speed manufacturing technology using electrically driven rapid vaporization of thin conductors to produce short-duration pressure pulses of high magnitude. This impulse technique has been implemented for various applications such as high strain rate forming, shearing, collision welding, and springback calibration. VFA technology for manufacturing processes potentially offers improved accuracy, reliability, and environmental safety and creates opportunities to design new products by joining similar and dissimilar material combinations. The paper includes the results of industrially relevant "work-in-progress" research with the VFA tool. The applications of the process, mainly regarding advanced manufacturing such as metal-matrix composite (MMC) welding, axisymmetric welding, and impact-mediated additive manufacturing processes, are presented and discussed. The applications of the method characterize adequate responses to support the manufacturing process.

Keywords Vaporizing foil actuator · Impulse manufacturing · Metal-matrix composite joining · Axisymmetric welding · Ballistic additive manufacturing

1 Introduction

Vaporizing foil actuator (VFA) is an innovative manufacturing technology that utilizes high-pressure impulse created by sudden vaporization of thin metallic foils and wires, activated by the passage of a high current for a minute fraction of time. For the past few decades, explosives [1], magnetic pulse (MP) [2], and hydraulic discharge [3] are a few tools that are prevalently applied for impulse metalworking processes. Each of these impulse manufacturing process variants has some advantages over the others. Explosives are challenging to automate in a production line due to the limitations to scale the process to thin sheets or small weld zones; moreover, increasingly stringent safety regulations inhibit their use. However, processes

K. Sajun Prasad · J. Li · B. Barnett · Y. Mao · G. S. Daehn · A. Vivek (✉)
Department of Materials Science and Engineering, The Ohio State University, Columbus, OH 43210, USA
e-mail: vivek.4@osu.edu

© The Minerals, Metals & Materials Society 2021

G. Daehn et al. (eds.), *Forming the Future*, The Minerals, Metals & Materials Series,
https://doi.org/10.1007/978-3-030-75381-8_111

like magnetic pulse (MP), VFA, and laser-induced processes (LI) can be automated and integrated into the conventional production environment. Both MP and LI are environmentally friendly processes with limited to no emission of gas or smoke, radiation, heat, or shielding gas during the process [4]. MP operation is limited to specific energy and pressure levels due to coil longevity issues. VFA allows for the mitigation of these issues as the actuator employed is a consumable. The group at The Ohio State University (https://iml.osu.edu/) implemented the VFA tool successfully for low-cost collision welding at characteristic scales comparable to magnetic pulse welding (MPW) [5], and it is often referred to as vaporizing foil actuator welding (VFAW) . VFAW has been successfully utilized to produce strong joints for various similar and dissimilar combinations such as Al-Steel [6], Al-Cu [7], Al-Ti [8], Ti-SS [9], Ti-Cu [10], steel-steel [11], NiTi-SS [12], and many other exotic and hard to join material combinations. The technique also provides the ability to weld in several geometries, viz., sheet to sheet, sheet to castings, sheet to extruded parts, sheet to tube, and tube to tube under different geometries, i.e., patch, spot, butt, flange, and line configurations. The ability to weld a wide range of material pairs allows manufacturers to improve product designs and manufacturability substantially.

The group also used the concept VFA for various manufacturing processes, including shearing [13], tube compression [14], joining [14], forming, and embossing [15]. Recently, Prasad et al. [16] demonstrated an innovative facility using the VFA technique to utilize different high-speed impact processes such as powder compaction, spallation, and impact collision bonding of dissimilar material. Stress relief is another VFA application, which could find use when forming high-yield-strength material that exhibits significant springback. Vivek [17] described springback calibration technique, where the VFA would allow the part with retained elastic strains (causing severe springback) to be formed, then shocked with pressure from the vaporizing foil. This shock would relieve the elastic strains and stresses in the sheet and, in effect, lock the metal into its desired shape. Here we present VFA as a complementary driving mechanism to existing technologies in the specific cases of metal-matrix composites (MMCs) , axisymmetric welding, and impact-mediated additive manufacturing.

Metal-matrix composites can present challenges to deformation-mediated processing due to their high strengths and the abrasive nature of reinforcement phases. Solid-state processing of MMCs is currently accomplished via friction stir welding (FSW) and ultrasonic welding (USW) and has demonstrated success in several applications [18, 19]. In USW, MMC material candidates are confined to those with relatively soft metal phases, such as aluminum and copper, which are natively compatible with the welding process. USW also has the unique advantage of preserving the integrity of continuous fiber-reinforced composite phases due to the minor strains induced during welding [20]. In contrast, FSW introduces large shear strains into the weld zone, disrupting and even breaking reinforcement phases into smaller fragments [18]. This intimate contact between ceramic reinforcement phases and the FSW stir tool can lead to rapid tool wear, increasing FSW costs [21]. Recently, VFA has been demonstrated to successfully weld a variety of flyer plate materials to thick steel MMC targets with nugget pullout failures in mechanical

testing. This complements the strength, thickness, and tool wear challenges observed in the current state-of-the-art of MMC solid-state joining.

In axisymmetric joining, there are two significant modes of consolidation: tube expansion and tube contraction. Tube expansion, in particular, faces challenges across length scales due to accessibility to the internal diameters of the expanding donor tube and the durability of driving mechanisms and fixtures. Tube expansion axisymmetric joining is most often accomplished via MPW or explosive welding (EXW) [22]. MPW is most effective when the donor tube has high magnetic permeability and a moderate size range of tubes. Small donor tubes require MPW coils that can fit into the tube interior, and the combination of small wire gauge in the coil and the high impulse loads generated by reaction forces can create challenges for MPW coil longevity [23]. EXW has a long history of axisymmetric joining [24] and is insensitive to the electromagnetic properties of the donor tube. However, procurement, handling, and process control for EXW can present challenges in cost and repeatability. VFA and exploding conductor techniques have recently been demonstrated to achieve axisymmetric joining in their own right and can also provide an accessible testbed to rapidly optimize process parameters before committing to the infrastructure required by EXW trials.

Deformation-mediated processing techniques provide desirable advantages when applied to additive manufacturing, where traditional melt-based methods often require post-processing to rehabilitate microstructural porosity, phase segregation, and solidification texturing [25, 26]. While dimensional control in deformation-mediated additive manufacturing is not as refined as traditional methods, they can bring advantages in build rate, build envelope size, and as-built microstructures and material properties. Gas dynamic cold spray (CS) and additive friction stir (AFS) deposition are both deformation-based additive manufacturing techniques that have been successfully developed for applications across a wide range of materials [27, 28]. Ballistic additive manufacturing (BAM) has been demonstrated, wherein a succession of disks sheared from continuous feedstock sheets are deposited via impact for near-net-shape manufacturing and repairs [29]. While cold spray uses inert process gas such as nitrogen or helium to accelerate powdered feedstock, BAM uses VFA or laser shock ablation to shear its feedstock from sheet stock and reduce consumables costs. BAM also serves as a tool to explore the effects of varying the surface area to volume ratio of highly strained zones in deformation-based consolidation; AFS completely recrystallizes its deposited material [30], while cold spray deposits are characterized by a mosaic of recrystallized feedstock particle boundaries with largely retained particle core crystallography on the length scale of the particles themselves (typically 10s of microns) [31, 32]. BAM creates similar variation but on the order of millimeters and offers new opportunities to explore the effects of engineered microstructures on as-built additively manufactured component performance.

2 Recent Developments Using the VFA Technique

2.1 MMC Welding

SiC-reinforced 8009 aluminum (8009/SiC/11$_p$) of 10 mm thick plate was welded to Al7075-T6 sheet of 1 mm thick using VFA spot welding technique. MMC has superior high-temperature mechanical properties compared to conventional aluminum alloys [33]. In the present work, a maximum capacitor bank energy of 16 kJ and a current rise time of 12 μs was applied for successful MMC welding. A 0.0762 mm thick actuator with the foil dimension as per Fig. 1a was used. The VFA experimental setup sequence for the welding is shown in Fig. 1b. Before welding, a circular pocket of 12.7 mm diameter and 0.6 mm depth was machined on the MMC block using a CNC mill. Al7075 flyer driven by the plasma from the actuator vaporization accelerated through the pocket and impacted with MMC, resulting in impact welding as depicted in Fig. 1c.

Further, a peel test was performed on the welded sample, during which the MMC side was fixed and Al7075 was being pried, which resulted in a nugget failure (Fig. 1c). This indicates the stronger weld than the parent Al7075 material, which is desirable for a successful joint. The welded sample was sectioned across the red dash line (Fig. 1c), and the corresponding microstructure shows no evidence of melting, heat-affected zone, or cracking (Fig. 1d). Additionally, a clear wave profile signifying

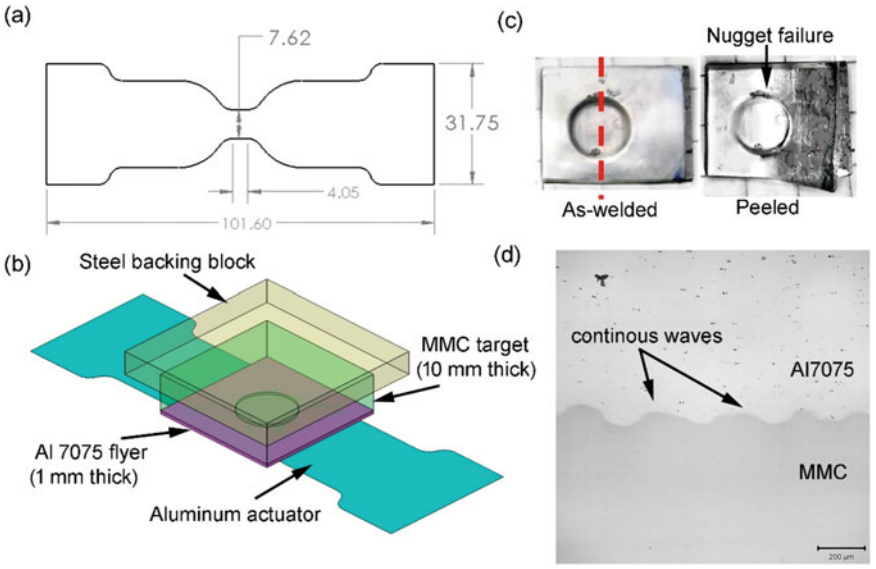


Fig.1 Schematic of **a** actuator geometry, **b** experiment setup, **c** sample as-welded and after peel test, and **d** cross-section of Al7075-MMC weld. (Color figure online)

solid-state metallic bonding was formed between the MMC and Al7075, indicating good weld strength.

2.2 *Axisymmetric Welding by Tube Expansion*

For the first time, axisymmetric welding of aluminum tubes has been achieved through vaporizing foil actuator (VFA). Figure 2 shows the schematic of the tube welding fixture and welded tube. Two plastic tubes were used as the standoffs to provide an acceleration distance for the flyer tube. The dimensions of the flyer tube, standoff tubes, and target tube are shown in Table 1. The central mandril used to withstand high-velocity impact was not purely metallic but insulated by two urethane rods. The tubular foil was composed of five parallel-connected 0.002″ spot-type foils

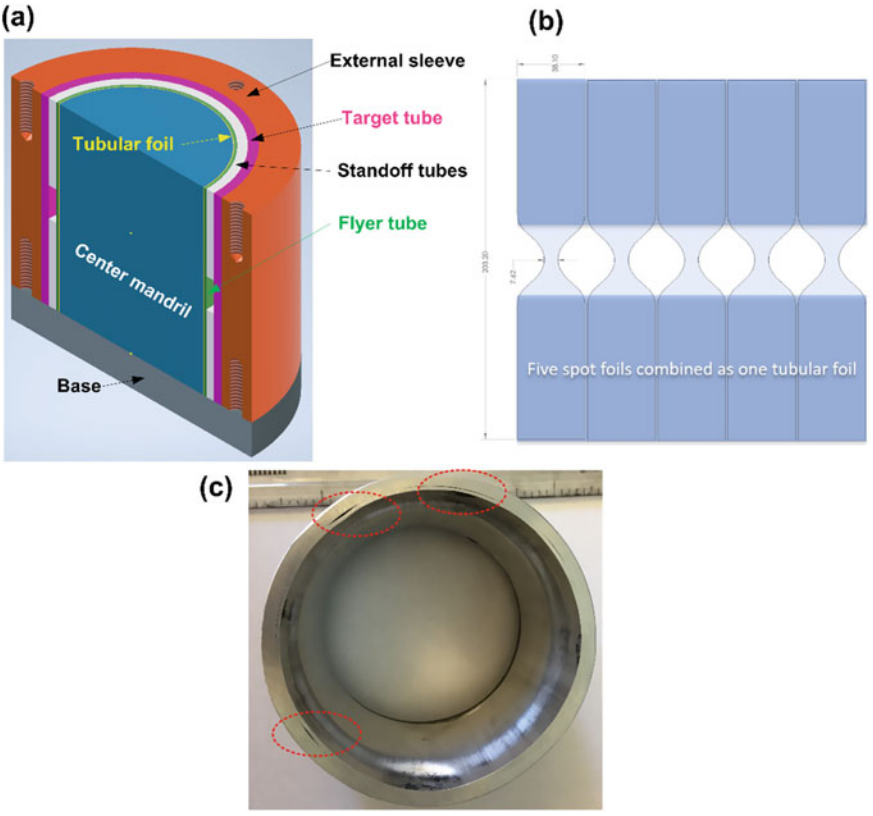


Fig. 2 **a** Schematic of axisymmetric welding of aluminum tubes using vaporizing foil actuators, **b** configuration of tubular foil composed of five spot-type foils, and **c** cross-section of welded aluminum tubes. (Color figure online)

Table 1 Dimensions of flyer tube, standoff tubes, and target tube used in tube welding trials

	Outer diameter (mm)	Inner diameter (mm)	Thickness (mm)
Flyer tube	63.5	61.7	0.89
Standoff tubes	69. 3	64	2.65
Target tube	76.2	69.85	3.175

(Fig. 2b). All the other conductors were insulated to avoid shunt electrical surges away from the tubular foils. The outer backing block was made of high-strength steel to prevent further deformation after the tube welds formed. The standoff separation distance is 24 mm and the standoff distance is 3.15 mm. The energy source was a capacitor bank entailing maximum energy of 16 kJ and a current rise time of 12 us. Input energy of 15.8 kJ was used to vaporize the tubular foil in several microseconds. After welding, the cross-section of the aluminum tube weld was prepared and observed in the optical microscope. The cross-section image of the tube weld in Fig. 2c shows a clean axisymmetric weld with some unwelded zones, which was caused by incomplete sublimation of foils due to insufficient input energy.

The key aspect in tube welding using VFAs are the confinement between the inner backing block, tubular VFAs, and flyer tube; the confinement between standoff tube, flyer tube, target tube, and outer backing block; and the complete vaporization of all foil actuators at the same time under proper input energy. VFA tube welding advantages over magnetic pulse welding are the irrelevancy of material conductivity and no tube size limitation if the input energy is enough. Theoretically, using tubular VFAs, tubes of any size can be welded under vaporization of corresponding numbers and shapes of VFAs. In the future, axisymmetric welding using VFAs can be applied to join dissimilar metal tubes since VFA welding of dissimilar metals has been proven effective [34, 35]. This strong adaptability provides high potential in automobiles and other engineering sectors that need different-sized tube welds.

2.3 Ballistic Additive Manufacturing

A novel additive manufacturing method based on vaporizing foil actuator has been demonstrated, referred to as ballistic additive manufacturing (BAM) . There are two ways to achieve BAM parts using VFA. One is to directly weld thin flyer sheets to a pre-machined part that generally exhibits a V-shape groove with an inclined angle around 10–25°. The second is to use a combined shearing and welding method to deposit multiple sheared parts through a die block to a pre-machined part. After deposition, the BAM part can be machined to the desired shape.

BAM can be applied to conduct a crack repair on parts. As shown in Fig. 3a–d, three 2 mm thick 1100 aluminum sheets were welded to a target sheet (6061 Al) with a pre-machined hole. After machining and cross-sectioning, the repaired part

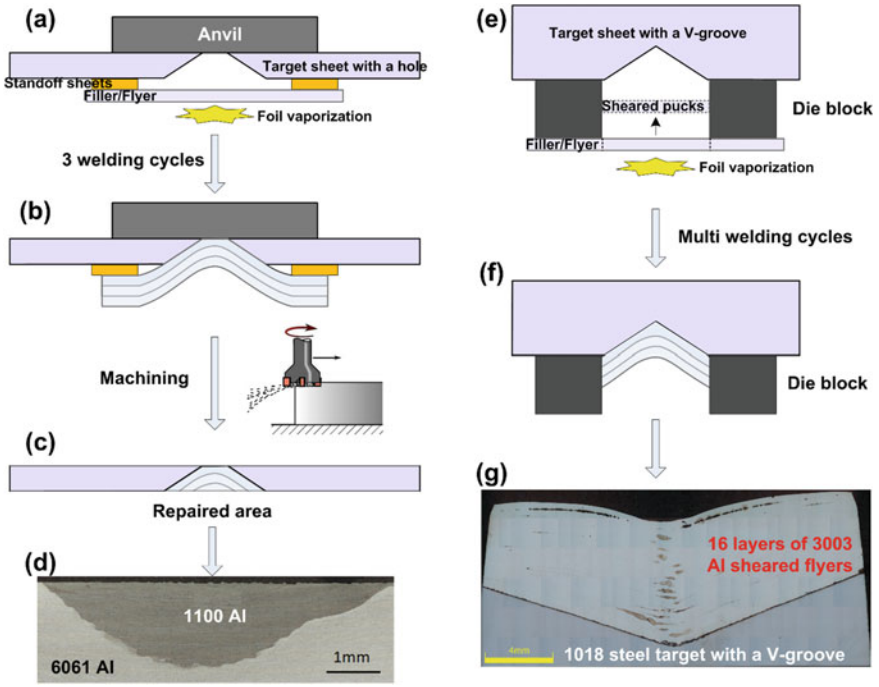


Fig. 3 **a**–**d** Ballistic additive manufacturing achieved by directly welding flyer sheets to a pre-machined part and **e**–**g** shearing metal pucks into the pre-machined part. (Color figure online)

exhibits defect-free microstructures. Wavy interfaces were exhibited between the matrix and the first additive layer, which is typical of impact welding. Figure 3e–g depicts the crack repair process using a combined shearing and welding method. Sixteen 0.5 mm thick 3003 Al flyer sheets were sheared into oval-shaped pucks. These sheared aluminum pucks travel through the die block and are welded to a 1018 steel target with a V-groove. The cross-section image shows that these aluminum sheared parts are connected well except for some jetting segregations in the middle and voids in the top layer interface. These two trials proved that BAM could be achieved reliably through VFA while more process optimization, design, and property examinations are needed.

Future interests lie in several aspects. First, the development of an automatic launch system including a separate shooting gun and a robot arm holding the target will play a vital role in the BAM process. The robot arm could change the impact angle and standoff distance of the flying metal pucks coming out from the gun. In this way, the impact angle and flyer velocity could be in situ controlled, and thus optimal parts could be potentially achieved. Second, a holistic comparison between BAM and traditional metal AM technologies should be carried out in terms of energy efficiency, deposition rate, resolution, and dimension limitations. BAM plus conventional subtractive manufacturing process will show great potential in

fabricating components with complex structures and repairing cracks in automotive and aerospace components.

3 Conclusions

In the present paper, recent trends and developments of vaporizing foil actuator for manufacturing applications are reviewed. Recent advances in component manufacturing processes such as high strain rate forming, shearing, collision welding, and springback calibration processes face increasing demands to achieve low cost, material versatility, high dimensional accuracy, high strength, and environmental safety. VFA-assisted applications are an increasingly helpful solution for meeting these requirements. The paper includes niche research applications such as joining metal-matrix composite, axisymmetric welding, and additive manufacturing processes using the VFA tool. The practical applications of the method resulted in good responses to support manufacturing process definition. The VFA process needs more development to compete with traditional mass-production methods because of its lower production rate.

Acknowledgments The authors gratefully acknowledge the support of the National Science Foundation for MRI Award 1531785, *Development of a Dynamic Material Processing and Testing Instrument*, and the Ohio Development Services Administration for supporting *Supply Chain and Market Development for Lightweight Multi-Materials Manufacture with Vaporizing Foil Actuator Welding*.

References

1. Holtzman AH (1964) Sulla balso
2. Psyk V, Risch D, Kinsey BL, Tekkaya AE, Kleiner M (2011) Electromagnetic forming: a review. J Mater Process Technol 211:787–829. https://doi.org/10.1016/j.jmatprotec.2010.12.012
3. Daehn GS, Fenton G, Vohnout VJ (2010) Pressure heterogeneity in small displacement electrohydraulic forming processes. In: 4th international conference on high speed form 2010, pp 65–74
4. Kapil A, Sharma A (2015) Magnetic pulse welding: an efficient and environmentally friendly multi-material joining technique. J Clean Prod 100:35–58. https://doi.org/10.1016/j.jclepro.2015.03.042
5. Hahn M, Weddeling C, Taber G, Vivek A, Daehn GS, Tekkaya AE (2016) Vaporizing foil actuator welding as a competing technology to magnetic pulse welding. J Mater Process Technol 230:8–20
6. Sridharan N, Poplawsky J, Vivek A, Bhattacharya A, Guo W, Meyer H et al (2019) Cascading microstructures in aluminum-steel interfaces created by impact welding. Mater Charact 151:119–128. https://doi.org/10.1016/j.matchar.2019.02.019
7. Benzing JT, He M, Vivek A, Taber GA, Mills MJ, Daehn GS (2017) A microsample tensile test application: local strength of impact welds between sheet metals. J Mater Eng Perform 26:1229–1235. https://doi.org/10.1007/s11665-017-2514-0

8. Chen S, Huo X, Guo C, Wei X, Huang J, Yang J et al (2019) Interfacial characteristics of Ti/Al joint by vaporizing foil actuator welding. J Mater Process Technol 263:73–81. https://doi.org/10.1016/j.jmatprotec.2018.08.004
9. Li J, Schneiderman B, Song S, Gilbert SM, Vivek A, Yu Z et al (2020) High strength welding of Ti to stainless steel by spot impact: microstructure and weld performance. Int J Adv Manuf Technol 108:1447–1461. https://doi.org/10.1007/s00170-020-05506-4
10. Lee T, Zhang S, Vivek A, Daehn G, Kinsey B (2019) Wave formation in impact welding: study of the Cu–Ti system. CIRP Ann 68:261–264. https://doi.org/10.1016/j.cirp.2019.04.058
11. Kapil A, Lee T, Vivek A, Daehn G, Bockbrader J, Abke T (2018) Benchmarking strength and fatigue properties of spot impact welds. J Mater Process Tech 255:219–233. https://doi.org/10.1016/j.jmatprotec.2017.12.012
12. Li J, Panton B, Liang S, Vivek A, Daehn G (2020) High strength welding of NiTi and stainless steel by impact: process, structure and properties. Mater Today Commun 25:101306. https://doi.org/10.1016/j.mtcomm.2020.101306
13. Tekkaya AE, Homberg W, Brosius A (2015) 60 Excellent inventions in metal forming. https://doi.org/10.1007/978-3-662-46312-3
14. Vivek A, Weeldeling C, Hahn M, Daehn GS, Tekkaya AE (2014) Electrically driven plasma via vaporization of metallic conductors: a novel tool for joining tubular workpieces. Procedia CIRP 18:62–67. https://doi.org/10.1016/j.procir.2014.06.108
15. Vivek A, Brune RC, Hansen SR, Daehn GS (2014) Vaporizing foil actuator used for impulse forming and embossing of titanium and aluminum alloys. J Mater Process Technol 214:865–875. https://doi.org/10.1016/j.jmatprotec.2013.12.003
16. Prasad KS, Mao Y, Vivek A, Niezgoda SR, Daehn GS (2020) A rapid throughput system for shock and impact characterization: design and examples in compaction, spallation, and impact welding. J Manuf Mater Process 4:116
17. Vivek A (2012) Rapid vaporization of thin conductors used for impulse metalworking. The Ohio State University
18. Wert JA (2003) Microstructures of friction stir weld joints between an aluminium-base metal matrix composite and a monolithic aluminium alloy. Scr Mater 49:607–612. https://doi.org/10.1016/S1359-6462(03)00215-X
19. Li J, Monaghan T, Nguyen TT, Kay RW, Friel RJ, Harris RA (2017) Multifunctional metal matrix composites with embedded printed electrical materials fabricated by ultrasonic additive manufacturing. Compos Part B Eng 113:342–354. https://doi.org/10.1016/j.compositesb.2017.01.013
20. Clews JD (2009) Ultrasonic consolidation of continuous fiber metal matrix composite tape. Univ Delaware
21. Fernandez GJ, Murr LE (2004) Characterization of tool wear and weld optimization in the friction-stir welding of cast aluminum 359+20% SiC metal-matrix composite. Mater Charact 52:65–75. https://doi.org/10.1016/j.matchar.2004.03.004
22. De Rosset WS (2006) Analysis of explosive bonding parameters. Mater Manuf Process 21:634–638. https://doi.org/10.1080/10426910600611136
23. Kore SD (2018) Magnetic pulse welding. Weld Fundam Process 6:704–710. https://doi.org/10.31399/asm.hb.v06a.a0005595
24. Didyk RP, Krasnovskii SS, Teslenko AG (1968) Approximate calculation of the axisymmetric motions of a pipe wall in explosive welding. Combust Explos Shock Waves 4:260–265
25. Frazier WE (2014) Metal additive manufacturing: a review. J Mater Eng Perform 23:1917–1928. https://doi.org/10.1007/s11665-014-0958-z
26. Sames WJ, List FA, Pannala S, Dehoff RR, Babu SS (2016) The metallurgy and processing science of metal additive manufacturing. Int Mater Rev 61:315–360. https://doi.org/10.1080/09506608.2015.1116649
27. Pattison J, Celotto S, Morgan R, Bray M, O'Neill W (2007) Cold gas dynamic manufacturing: a non-thermal approach to freeform fabrication. Int J Mach Tools Manuf 47:627–634. https://doi.org/10.1016/j.ijmachtools.2006.05.001

28. Yu HZ, Mishra RS (2021) Additive friction stir deposition: a deformation processing route to metal additive manufacturing. Mater Res Lett 9:71–83. https://doi.org/10.1080/21663831.2020.1847211
29. Nault IM, Ferguson GD, Nardi AT (2021) Multi-axis tool path optimization and deposition modeling for cold spray additive manufacturing. Addit Manuf 38:101779. https://doi.org/10.1016/j.addma.2020.101779
30. Yu HZ, Jones ME, Brady GW, Griffiths RJ, Garcia D, Rauch HA et al (2018) Non-beam-based metal additive manufacturing enabled by additive friction stir deposition. Scr Mater 153:122–130. https://doi.org/10.1016/j.scriptamat.2018.03.025
31. Xie W, Alizadeh-Dehkharghani A, Chen Q, Champagne VK, Wang X, Nardi AT et al (2017) Dynamics and extreme plasticity of metallic microparticles in supersonic collisions. Sci Rep 7:1–9. https://doi.org/10.1038/s41598-017-05104-7
32. Rokni MR, Nardi AT, Champagne VK, Nutt SR (2018) Effects of preprocessing on multi-direction properties of aluminum alloy cold-spray deposits. J Therm Spray Technol 27:818–826. https://doi.org/10.1007/s11666-018-0723-1
33. Lienert TJ, Nagy PB, Baeslack WA (1998) Ultrasonic characterization of microstructures in inertia friction welds on SiC-reinforced 8009 aluminum. Weld J New York 77:14-s
34. Vivek A, Hansen SR, Liu BC, Daehn GS (2013) Vaporizing foil actuator: a tool for collision welding. J Mater Process Technol 213:2304–2311. https://doi.org/10.1016/j.jmatprotec.2013.07.006
35. Cai W, Daehn G, Vivek A, Li J, Khan H, Mishra RS et al (2019) A state-of-the-art review on solid-state metal joining. J Manuf Sci Eng Trans ASME 141:1–35. https://doi.org/10.1115/1.4041182

Grain Size Effect on Formability in Electromagnetically Assisted Micro-Bulging of Pure Titanium Sheet



Chengxi Zhu, Jie Xu, Haiping Yu, Debin Shan, and Bin Guo

Abstract It has been revealed that the grain size effect has a great effect on the formability of metal foils during quasi-static forming processes. However, there is little research on how size effects influence the formability of metal foils during the high-speed forming process, e.g., electromagnetically-assisted forming. To characterize the grain size effect in electromagnetically assisted micro-bulging, a miniaturized Nakazima test was conducted using a specially designed device. Pure titanium foils of thickness 103 μm and different grain sizes were utilized in the experiment. In addition, SEM and TEM methods were used to clarify how grain size influences the fracture surface and microstructure in electromagnetic forming.

Keywords Size effect · Formability · Electromagnetic micro-bulging · Micro-forming · Pure titanium

1 Introduction

Due to the requirement of product miniaturization in many industry clusters, many technologies for micro-manufacturing received a wide study and were well developed recently. Among them, micro-forming is the most attractive approach to fabricate micro-parts because of its numerous advantages, such as low cost, high production efficiency, and the good mechanical properties of the micro-formed parts [1, 2]. However, there exists a key issue which is called size effect during micro-forming which affects the deformation behaviors, especially in sheet metal forming [3, 4]. The size effect is mainly caused by the significant reduction of grain number in deforming zone. It is necessary to study how the size effect affects the deformation behaviors of sheet metals. Fu et al. [5] conducted a tensile test with annealed pure copper foils with different thicknesses and grain sizes to study the size effects on fracture behavior. It is found that flow stress, fracture stress and strain, and the number of micro-voids on the fracture surface decrease with the decreasing ratio of specimen size to grain size.

C. Zhu · J. Xu (✉) · H. Yu · D. Shan · B. Guo
School of Materials Science and Engineering, Harbin Institute of Technology, 92 West Dazhi Street, Harbin 150001, PR China
e-mail: xjhit@hit.edu.cn

© The Minerals, Metals & Materials Society 2021

G. Daehn et al. (eds.), *Forming the Future*, The Minerals, Metals & Materials Series,
https://doi.org/10.1007/978-3-030-75381-8_112

Meng et al. [6] performed forming limit experiments of SUS304 foils with different thicknesses and grain sizes and found that the micro-formability of metal foils was shifted down with a reduction in the ratio of specimen size to grain size, and the severe scatter in the forming limit curve (FLC) of 20 μm thick foil was observed.

Electromagnetic forming technology (EMF) was developed in the early 1960s. It is a high-energy, high-speed forming method that uses electromagnetic force to deform the sheet metal. It is suitable for forming complex shapes of workpieces because it needs no punch. Due to the precise control of the power supply, the controllability and accuracy of electromagnetic forming are very high [7]. Furthermore, the output displacement of the micro-forming system driven by electromagnetic force can reach the order of millimeters, which can fully meet the micro-forming displacement requirements. Because of the advantages of electromagnetic forming technology, it has received great attention from the industry and has been widely used in automotive, instrumentation, electronics, and military industries. Choi et al. [8] employed electromagnetic sharp edge forming in order to form a sharp edge with a corner radius of 10 mm which was not successful in conventional square cup drawing. In addition, the electromagnetic tool coil was designed with the aid of topology optimization to enhance the efficiency of the electromagnetic sharp edge forming process. Su et al. [9] proposed a new two-step electromagnetic forming that combines electromagnetic forming with electromagnetic calibration for local features of large-size sheet metal parts, such as an oblique hole-flanging. Simulation results showed that during EM calibration, the stress distribution of the workpiece was improved, the bending moment was reduced which is responsible for the shape and size errors, then the rebound was restricted. Consequently, the fitting ability and the forming accuracy were significantly enhanced.

Kamala et al. [10–12] from Ohio State University developed a driving device capable of generating uniform magnetic pressure. The device was used for the rapid manufacturing of micro-boxes and for the research on electromagnetic micro-forming of foils. The results show that the electromagnetic forming technology effectively suppresses wrinkling and the material surface has high accuracy and has greater flexibility than traditional sheet forming. Cheng and Lee [13] from Taiwan Cheng Kung University carried out research on electromagnetically assisted high-speed bulging of A5052 aluminum alloy to study the grain size and forming speed on the forming limit of the spherical cap. The results show that regardless of the microstructure of the sample, the formability of the electromagnetically formed aluminum plate is better than that of quasi-static forming. And when the t/d presenting the ratio of specimen thickness to average grain diameter increased from 6.99 to 27.17, the limit dome height (LDH) value showed an initial increasing trend, then decreased, and the maximum LDH value appeared in the case of t/d of 9.45. However, there is still little research on how the size effect affects the deformation behavior of titanium sheets in electromagnetic bulging.

2 Experiments

2.1 Sample Preparation

Commercially pure titanium foils of thickness 103 μm were used as the testing material in this research. To obtain different strain paths, specimens with three different shapes were designed in this study for the forming limit tests. The dimensions of the test samples of three strain paths are presented in Fig. 1a.

After cutting, the samples were ready for the bulging test, which is termed as the "as-received" in this paper. Meanwhile, some machined samples were heat-treated to explore the effect of material microstructure on deformation behavior. The annealing temperatures and dwelling times are 670 °C and 0.5 h, 700 °C and 1 h, and 720 °C and 5 h in the vacuum environment, respectively. To attain the microstructure of the specimens, the specimens were etched with a solution of 2 ml HF, 1 ml HNO_3, and 17 ml H_2O for 30 s. The metallographic observation was conducted on the microscope, and Fig. 2 shows the metallographic structure. The average grain size and the ratio of specimen thickness to average grain size (t/d) under different heat treatment conditions are shown in Table 1, respectively. It is observed that the grain size increases with the annealing temperature. To calculate the strain after bulging,

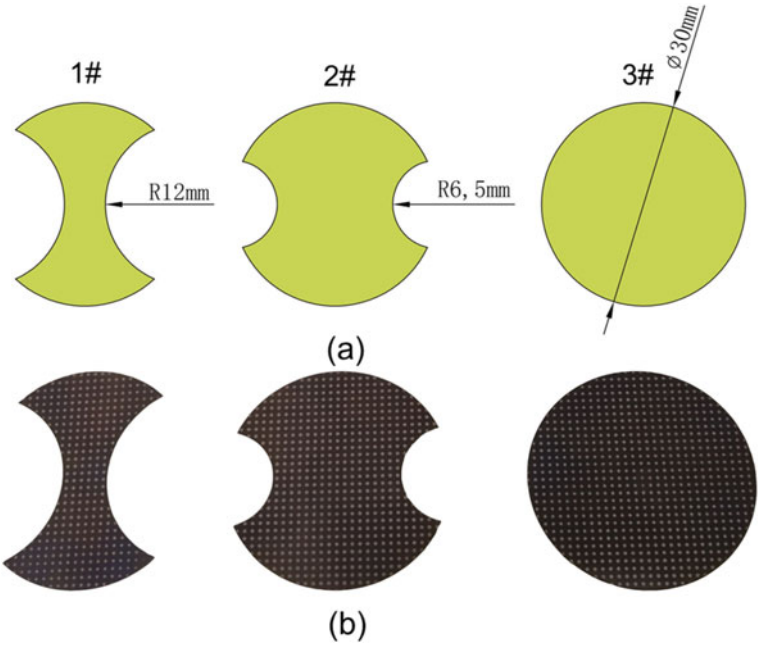


Fig. 1 The test samples of three strain paths. **a** Dimension of the samples; **b** the dotted samples. (Color figure online)

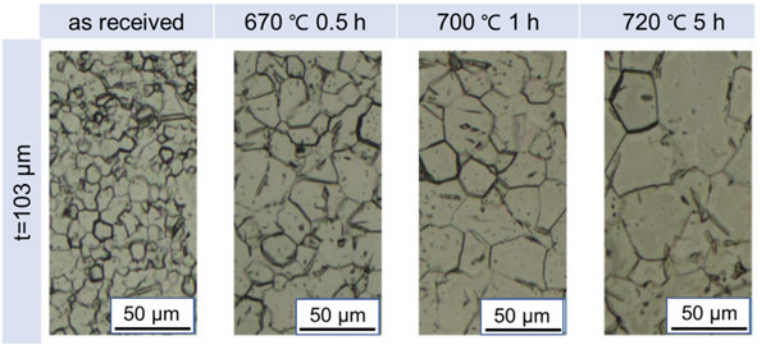


Fig. 2 Microstructure of specimens with different heat treatments. (Color figure online)

Table 1 Grain size and t/d value of different heat treatment condition

	As received		670 °C 0.5 h		700 °C 1 h		720 °C 5 h	
t = 103 μm	d/μm	t/d	d/μm	t/d	d/μm	t/d	d/μm	t/d
	7.5	13.7	15.5	6.6	27.4	3.8	38.2	2.7

all the samples were etched before bulging to produce white dots that are 0.5 mm in diameter and spaced 0.5 mm from each other. Figure 1b shows the dotted samples.

2.2 Electromagnetic Bulging Test

The equipment used in this experiment is a 25 kJ electromagnetic pulse system. To increase the punch speed during forming, we designed a set of electromagnetic bulging device, including the coil, driving plate, punch, blank holder, and the bottom die (Fig. 3). The diameter of the semi-spherical punch used in this experiment was 15 mm. To ensure that all the specimens would be bulged at the same speed, all the bulging tests were conducted at the voltage of 5 kV and the electric capacity of 100 μF. The strong electromagnetic force generated by the coil expelled the driving plate and punch to impact the specimen at high speed. After bulging, the strain distributions of the bulged specimens were measured by ARGUS system, which is a 3D strain measurement system of high accuracy. The strains near the fracture were selected as the forming limit of the different specimens.

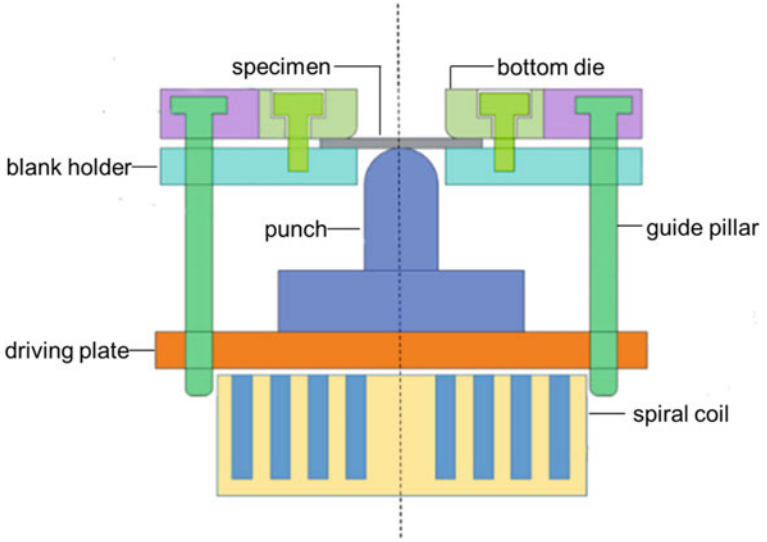


Fig. 3 Specially designed electromagnetic bulging device. (Color figure online)

3 Results and Discussion

3.1 Effect of Size Effect on Forming Limit

Figure 4 shows the strain distribution of the specimens with t/d = 13.7 after electromagnetic bulging. The strain of the dot beside the fracture zone is selected as the forming limit strain. Figure 5 illustrates the forming limit strain of different strain paths and different t/d. It is found that the forming limit shifts down with the decrease of t/d from 13.7 to 2.7, especially for the bi-stretching condition. On the one hand, the uniform strain will decrease with t/d resulting in a decreasing forming limit strain.

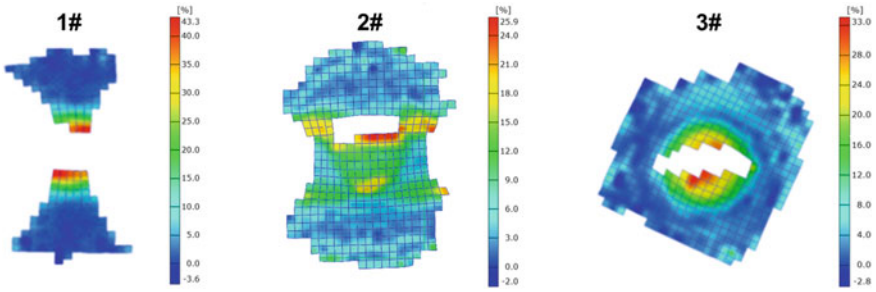


Fig. 4 Strain distribution of the specimens with t/d = 13.7 after electromagnetic bulging. (Color figure online)

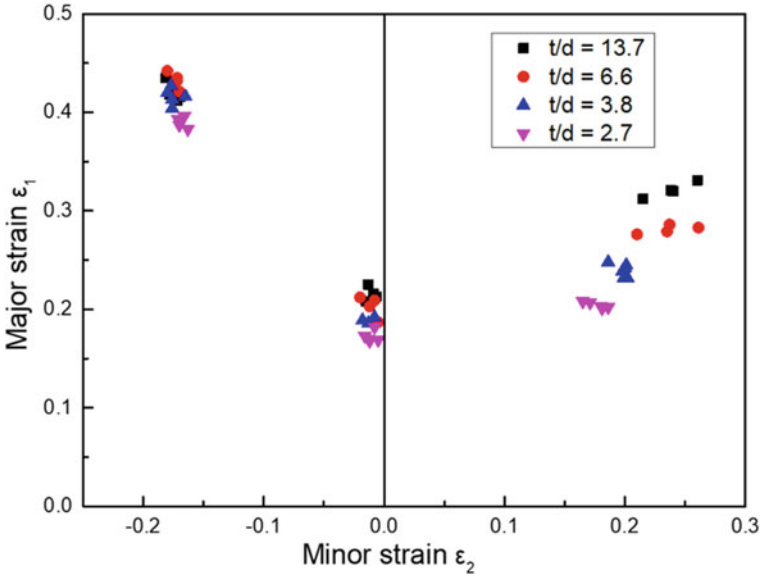


Fig. 5 Forming limit diagram of pure titanium sheet with different t/d. (Color figure online)

On the other hand, according to the surface layer model, the internal layer of the specimen can be treated as polycrystalline material and the thickness of it decreases with t/d. As a result of a decrease of t/d and the internal layer, it becomes easier for micro-voids and micro-cracks to coalesce and grow over the sheet thickness in such a way to form macroscopic fracture.

3.2 Effect of Size Effect on Fracture Surface

To study the size effect on the fracture surface of titanium sheet in electromagnetic bulging, the SEM method was adopted. Figure 6 shows the fracture surface of the 1# specimens with different t/d. As can be seen, there are many dimples on the fracture surface that are well distributed when t/d is 13.7, which indicates a ductile fracture of the specimen. However, the dimples on the fracture surface distribute more and more inhomogeneously with the decrease of t/d and there are dimples much bigger than others when t/d reaches 2.7. It can be considered that when t/d is high, the small dimples which take place during deformation endures many restrictions. But when t/d decreases, the restriction becomes smaller and smaller, leading to abnormal growth of the small dimples. This coordinates with the analysis about forming limit above.

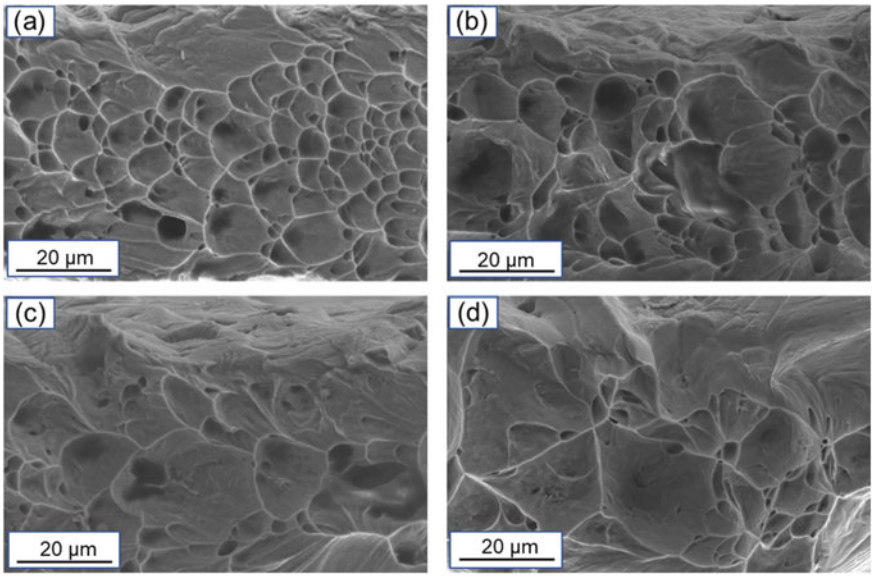


Fig. 6 SEM of fracture surfaces of specimens with different t/d. **a** t/d = 13.7; **b** t/d = 6.6; **c** t/d = 3.8; **d** t/d = 2.7. (Color figure online)

3.3 Effect of Size Effect on Microstructure

The microstructures of the 1# specimen near the fracture surface were characterized by TEM, and the results are displayed in Fig. 7. It shows that numerous dislocations were piled up at the grain boundaries twin boundaries or phase boundaries as marked

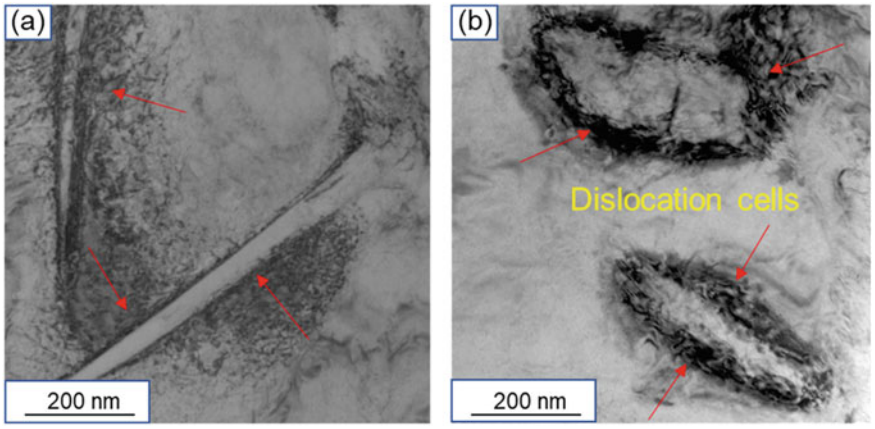


Fig. 7 TEM of specimens with different t/d. **a** t/d = 13.7; **b** t/d = 2.7. (Color figure online)

by red lines in Fig. 7a and there are few dislocation cells when t/d is 13.7. Meanwhile, when t/d is 2.7, some tangled dislocation configurations marked by the red lines can be observed in Fig. 7b. The grains are fine when t/d is 13.7, so there is no sufficient slipping distance for dislocations to tangle together and dislocations prefer to pile up at grain boundaries. Meanwhile, dislocations tend to tangle together and form dislocation cells when grains are coarse.

4 Conclusion

In this study, grain size effect on forming limit, fracture, and microstructure evolution of pure titanium foils in electromagnetic micro-bulging was explored using a specially designed device.

(1) The forming limit of titanium foils in electromagnetic forming shifts down with the decrease of t/d from 13.7 to 2.7 especially for the bi-stretching condition. This is mainly because of the decrease of an internal layer with a decrease of t/d according to the surface layer model.
(2) The dimples on the fracture surface distribute more and more inhomogeneously with the decrease of t/d. And there are dimples much bigger than others when t/d reaches 2.7. The root cause is that the small dimples which take place during deformation endure fewer restrictions with a decrease of t/d, leading to abnormal growth of the small dimples and earlier fracture of the specimen.
(3) Dislocations prefer to pile up at grain boundaries when grains are fine because of lack of slipping distance while dislocations tend to tangle together and form dislocation cells when grains are coarse.

Acknowledgments This work was financed and supported by the National Science Foundation of China (No. 51635005).

References

1. Geiger M, Kleiner M, Eckstein R, Tiesler N, Engel U (2001) Microforming. CIRP Ann 50:445–462
2. Vollertsen F, Hu Z, Niehoff HS, Theiler C (2004) State of the art in micro forming and investigations into micro deep drawing. J Mater Process Tech 151:70–79
3. Engel U, Eckstein R (2002) Microforming—from basic research to its realization. J Mater Process Tech 125–126:35–44
4. Vollertsen F, Schulze Niehoff H, Hu Z (2006) State of the art in micro forming. Int J Mach Tool Manu 46:1172–1179
5. Fu MW, Chan WL (2011) Geometry and grain size effects on the fracture behavior of sheet metal in micro-scale plastic deformation. Mater Des 32(10):4738–4746
6. Meng B, Zhang YY, Cheng C, Han JQ, Wan M (2018) Effect of plastic anisotropy on microscale ductile fracture and microformability of stainless steel foil. Int J Mech Sci 148:620–635

7. Psyk V, Risch D, Kinsey BL, Tekkaya AE, Kleiner M (2011) Electromagnetic forming—a review. J Mater Process Technol 211(5):787–829
8. Choi MK, Huh H, Park N (2017) Process design of combined deep drawing and electromagnetic sharp edge forming of DP980 steel sheet. J Mater Process Technol 244:331–343
9. Su H, Huang L, Li J, Ma F, Huang P, Feng F (2018) Two-step electromagnetic forming: a new forming approach to local features of large-size sheet metal parts. Int J Mach Tools Manuf 124:99–116
10. Kamal M, Shang J, Cheng V, Hatkevich S, Daehn GS (2007) Agile manufacturing of a micro-embossed case by a two-step electromagnetic forming process. J Mater Process Technol 190(1–3):41–50
11. Golowin S, Kamal M, Shang J, Portier J, Din A, Daehn GS, Hatkevich S (2007) Application of a uniform pressure actuator for electromagnetic processing of sheet metal. J Mater Eng Perform 16(4):455–460
12. Kamal M, Daehn GS (2007) A uniform pressure electromagnetic actuator for forming flat sheets. J Manuf Sci Eng 129(2):369–379
13. Cheng TC, Lee RS (2018) The influence of grain size and strain rate effects on formability of aluminium alloy sheet at high-speed forming. J Mater Process Technol 253:134–159

Mathematical Model and Quantitative Analysis of Residual Stress Hole During Laser Shock Peening



Xiuquan Cheng, Junhao Zhang, Sizhu Cheng, Chang Yan, and Qinxiang Xia

Abstract Laser shock peening (LSP) can induce residual compressive stress on the component surface, thus improving the fatigue life of the component. Therefore, LSP has been extensively employed in aerospace, vehicle engineering, and other industrial fields. To research the influence factors of residual stress hole (RSH) which often occurred in LSP, a "volcano shape" mathematical model was conducted. Indexes for quantitatively describing RSH were proposed, such as relative crater depth, relative crater width, and stress loss ratio. Preliminary analysis based on the experimental study was carried out. The results showed that the relative crater depth is the main impact factor to RSH. Overlapping LSP is suggested to be adopted when the relative crater depth is more than 10%. In addition, the spacing of the adjacent spot centers should be equal to the "crater" radius of RSH so as to get the uniform residual stress under the premise of higher LSP efficiency.

Keywords Laser shock peening · Surface strengthening · Residual stress hole · Stress loss ratio · Quantitative analysis

X. Cheng · S. Cheng
School of Aircraft Maintenance Engineering, Guangzhou Civil Aviation College, Guangzhou 510403, China
e-mail: 591404558@qq.com

S. Cheng
e-mail: chengsizhu@caac.net

J. Zhang (✉) · C. Yan · Q. Xia
School of Mechanical and Automotive Engineering, South China University of Technology, Guangzhou 510640, China
e-mail: 415709826@qq.com

C. Yan
e-mail: 626025822@qq.com

Q. Xia
e-mail: meqxxia@scut.edu.cn

© The Minerals, Metals & Materials Society 2021

G. Daehn et al. (eds.), *Forming the Future*, The Minerals, Metals & Materials Series,
https://doi.org/10.1007/978-3-030-75381-8_113

1 Introduction

Shot peening has been widely used in aviation, vehicle, construction, and other fields. In recent years, laser shock peening (LSP), which can more effectively improve the strength and fatigue life of the treated components [1, 2], has gradually been applied.

Many reported researches of LSP focused on the residual stress distribution and the fatigue performance [2–5]. Some researchers found that the residual compressive stress at the laser projection center is smaller than the surrounding area [6–8]. This phenomenon is called residual stress hole (RSH) or loss of residual compressive stress [9]. According to the research of Wang et al. [10], sparse wave generates in the laser projection area and propagates. Then, part of the sparse wave reflects back when it propagates to the spot edge. The reflected sparse wave will encounter in the laser projection center and causes secondary plastic deformation. The secondary plastic deformation with severe shear plastic strain reduces the axial and radial strain generated in the shock wave loading stage. Then, an RSH occurred in the laser projection center.

The existence of RSH not only reduces the residual compressive stress value but also deteriorates the uniformity of stress distribution. Both of them reduce the strengthening effect of LSP.

2 Establishment of Mathematical Model of RSH

Figure 1 shows the typical distribution of surface residual stress after single-point

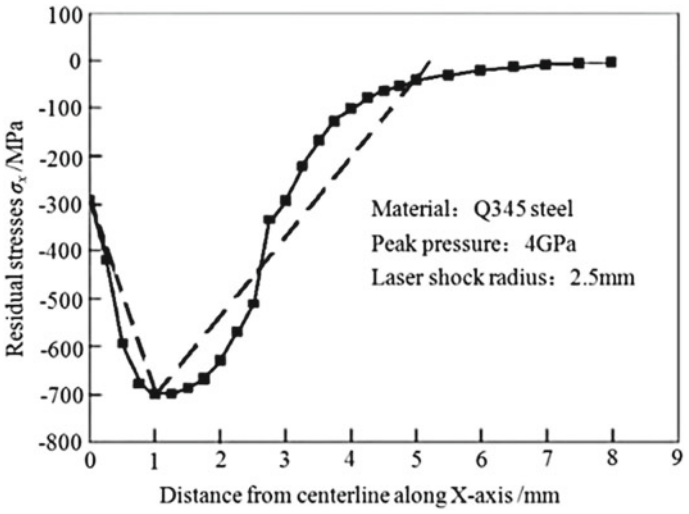


Fig. 1 The typical distribution of the residual stress after single point LSP

LSP [11]. The solid line corresponds to actual residual stress distribution, and the dotted line corresponds to simplified residual stress distribution. Circular spot laser is widely used in the LSP process, which can induce residual stress in the form of axisymmetric distribution. The research of this paper is based on the LSP with circular spot. The simplified residual stress dotted line in Fig. 1 is similar to a half-inverted volcano. By flipping the simplified residual stress dotted line, "volcano model" can be established and as shown in Fig. 2. In this "volcano model", the crater region (inverted cone region) represents the region of RSH, D_0 is the diameter of the residual compressive stress region induced by single point LSP, and D_c is the crater diameter of the RSH. σ_0 is the maximum residual compressive stress on the peened surface, and σ_c is the residual stress loss at the bottom of the crater, where it is located in the laser projection center.

According to the "volcano model" in Fig. 2, the larger the volume of the inverted cone, the more serious is the RSH. The volume of the inverted cone is determined by the crater diameter D_c and crater depth σ_0. Therefore, the stress loss ratio k was defined as the ratio of the volume of the inverted cone V_c to the total volume V_0, as shown in Eq. (1):

$$k = \frac{V_c}{V_0} = \frac{D_c^2 \sigma_c}{(D_0^2 + D_0 D_c + D_c^2)\sigma_0} \tag{1}$$

The larger the stress loss ratio, the more severe is the RSH. k_1 is defined as the relative crater depth and k_2 is defined as the relative crater width:

$$k_1 = \sigma_c / \sigma_0 \tag{2}$$

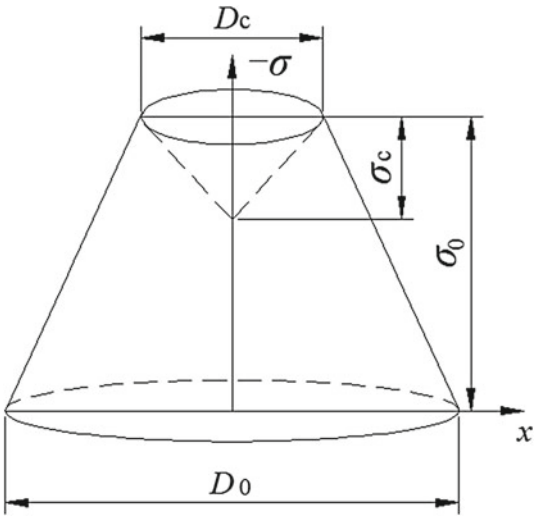


Fig. 2 The volcano model of surface RSH

$$k_2 = D_c/D_0 \tag{3}$$

Substituting Eqs. (2) and (3) into Eq. (1):

$$k = k_1 k_2^2/(1 + k_2 + k_2^2) \tag{4}$$

3 Effect of Main LSP Parameters on RSH

According to Eqs. (2)–(4) and residual stress data of LSP test, the effect of the main LSP parameters on RSH was quantitatively analyzed. The target material is 7075-T6 aluminum alloy covered with a transparent flexible energy confinement layer and an energy-absorbing layer. The confinement layer was cured by bisphenol A-epichlorohydrin epoxy resin and cycloaliphatic amine curing agent [12]. The energy-absorbing layer is obtained by laminating black electrical tape and black double-sided tape. The equipment used in the LSP test is Nimma-Extra type solid-state laser. The residual stress was measured by an X-ray diffractometer. The parameters adopt in the LSP test were presented in Table 1. The number of test specimens in each group was 5, and the average value of five specimens was regarded as the final result.

3.1 Effect of Laser Shock Energy E *on RSH*

Figure 3 shows the residual stress loss ratio k, relative crater depth k_1, and relative crater width k_2 of the specimens after LSP with different laser energy value. It can be seen that with the increase of laser energy, the stress loss ratio k, relative crater depth k_1, and relative crater width k_2 show a large increase. This shows that the intensity of the secondary plastic deformation in the laser projection center is positively related to the laser energy. The influence of laser energy on the relative crater depth k_1 is

Table 1 The parameters of laser shock

Spot condition	Parameters	Parameter value	Constant parameters
Single-point LSP	Laser energy E/J	1.0, 1.5, 2.0, 2.5, 3.0	$T = 1, D = 2$
	Repeated shock times T	1, 2, 3, 4, 5	$E = 2, D = 2$
	Diameter of spot D/mm	1.0, 1.5, 2.0, 2.5, 3.0	$E = 2, T = 1$
Overlapping LSP	Overlap ratio η/%	30, 40, 50, 60, 70	$E = 2, T = 1, D = 2$

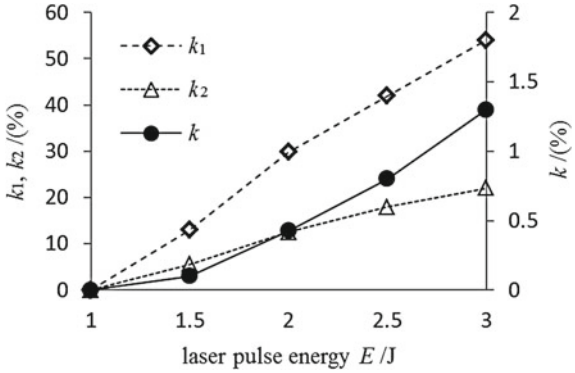


Fig. 3 Influence of laser pulse energy E

significantly greater than that on the relative crater width k_2. In addition, the value of stress loss ratio k is always less than 2% among the energy range of Fig. 3. But it cannot be considered that the residual stress on the surface is uniform because when the laser energy is 3 J, the relative crater depth k_1 has exceeded 50%.

3.2 Effect of Laser Spot Diameter D *on RSH*

Figure 4 shows the residual stress loss ratio k, relative crater depth k_1, and relative crater width k_2 of the specimens after LSP with different spot diameter. It can be seen that with the increase of the spot diameter, the stress loss ratio k and the relative crater depth k_1 are obviously decreased, while the relative crater width k_2 is relatively stable, which shows that the hole size changes synchronously with the spot size. In addition, when the spot diameter increase from 1 to 3 mm, the relative crater depth k_1 decreases from 68% to about 13%, which indicates that the loss of residual compressive stress is significantly reduced.

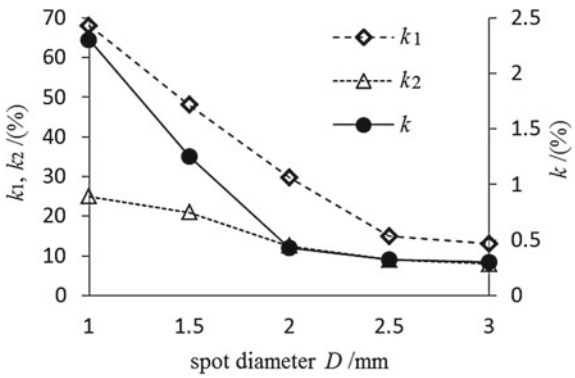


Fig. 4 Influence of spot diameter D

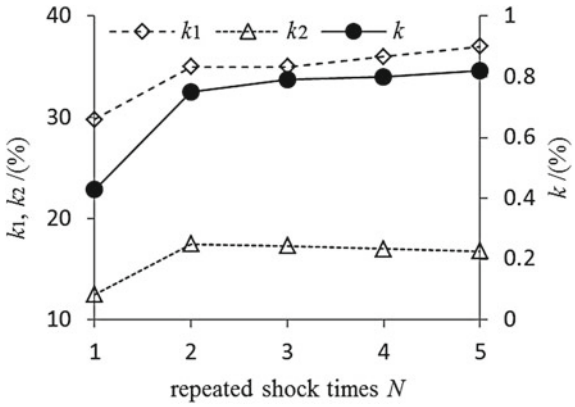


Fig. 5 Influence of shock times *N*

3.3 Effect of Repeated Shock Times N *on RSH*

Figure 5 shows the residual stress loss ratio k, relative crater depth k_1, and relative crater width k_2 of the specimens after LSP with different repeated shock times. It can be seen that with the increase of repeated shock times, the stress loss ratio k and relative crater depth k_1 increased. And the most obvious increase occurs in the second shock. After the second shock, k_1 and k_2 tend to be stable. The impact mechanism of increasing repeated shock times on RSH is similar to that of increasing laser energy. The material undergoes work hardening during the first shocking, which makes it more difficult for secondary plastic deformation during subsequent shocking. Therefore, starting from the second shocking, the stress loss ratio k and the relative crater depth k_1 tend to stabilize. The stress loss ratio k increases from 0.4 to 0.8% when the number of repeated shock times increases from 1 to 5. It shows that increasing the number of repeated shock times can improve the level of residual compressive stress, but the loss of residual stresses is still serious.

3.4 Effect of Overlap Ratio H *on RSH*

The overlap ratio η refers to the overlapping ratio of adjacent light spots in the direction of the centerline, which can be calculated according to Fig. 6, that is:

$$\eta = L/D \times 100\% \tag{5}$$

Figure 7 shows the residual stress loss ratio k, relative crater depth k_1, and relative crater width k_2 of the specimens after LSP with different overlap ratio values. It can be seen that with the increase of overlap ratio, the stress loss ratio k, relative crater depth k_1, and relative crater width k_2 all decrease significantly. When the overlap ratio increases from 30 to 70%, the relative crater depth k_1 decreases from 14 to

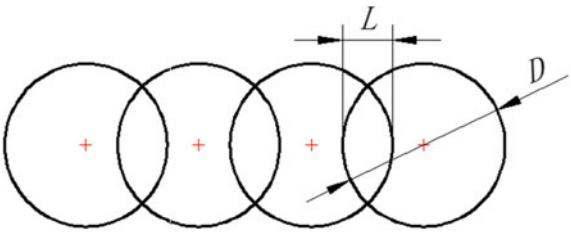


Fig. 6 The calculation of overlap ratio. (Color figure online)

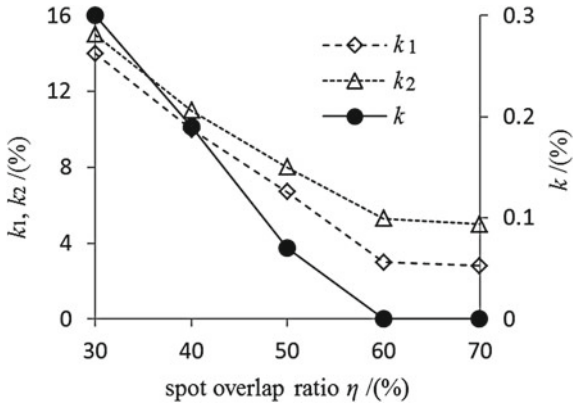


Fig. 7 Influence of overlap ratio η

2.8%, and the stress loss ratio k decreases from 0.3 to 0%. This is because when the overlap ratio increased, the light spots overlap with each other, and the position where the surface residual stress generated by a spot may superpose with an adjacent spot. Thereby, a complementary effect formed, and the uniformity of the residual stress on the surface is improved.

In addition, the residual stress loss does not decrease linearly with the increase of the overlap ratio, and it does not change much when the overlap ratio is larger than 60%. The spot diameter used in this group of tests is 2 mm, and the RSH radius of single point and one-time LSP is about 0.6 mm. If the distance between the adjacent spot centers is set to 0.6 mm, the spot overlap rate $\eta = 60\%$. According to the experimental data, when the center distance between the adjacent spots is equal to the radius of the RSH, the uniformity of residual stress was improved obviously. However, if the overlap ratio of the spot is further increased, the uniformity of the residual stress will not be significantly improved, and the work efficiency will be reduced.

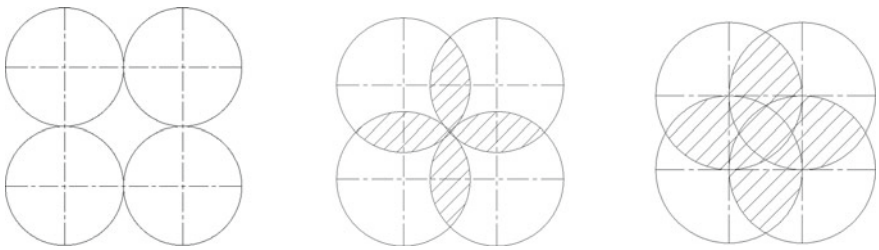
4 Results Analysis and Discussion

According to Sect. 3, the stress loss ratio k caused by the RSH is not large and, basically, less than 2.5%. The influence of LSP parameters on relative crater width k_2 is relatively small and, basically, less than 25%. The relative crater depth k_1 is very sensitive to changes of LSP parameters, and the variation range of k_1 is 0–68%. Therefore, the main impact factor on the stress loss ratio k is relative crater depth k_1, which will seriously affect the uniformity of residual stress distribution on the surface.

It can be obtained from Sect. 3 that when the laser energy E increase from 1 to 5 J, or the repeated shock times N increase from 1 to 2 times, the stress loss ratio k increase significantly. When the spot diameter D increase from 1 to 2.5 mm, or the overlap ratio η increase from 30 to 60%, the stress loss ratio k is reduced greatly.

The surface residual compressive stress level can be increased by increasing the repeated shock times or the overlap ratio. In terms of improving the uniformity of the residual stress, a large overlap ratio has obvious effects. The overlap ratio is easy to implement in practice and is an effective way to improve the uniformity of residual stress.

The overlap ratio in engineering is generally selected based on the overlapping features of the spot geometry, such as the typical overlap ratio of 0, 29.3, and 50%, as shown in Fig. 8. However, the existence of RSH was not taken into consideration when trying to improve the uniformity of the residual stress on the surface. Therefore, the uneven distribution of surface residual stress cannot be effectively suppressed. If the center distance between the adjacent spot is equal to the radius of RSH, the loss of the residual stress can be compensated to the greatest extent so as to obtain a better distribution uniformity of the surface residual stress with higher efficiency of LSP.



(a) η=0% (b) η=29.3% (c)η=50%

Fig. 8 The common overlap ratio

5 Conclusions

(1) Quantitative analysis indexes for residual stress hole were proposed, such as relative crater depth k_1, relative crater width k_2, and residual stress loss ratio k. It is found that k is not large (<2.5%), but it will seriously affect the uniformity of the residual stress on the surface of the component, and the degree of unevenness may even reach 68%. Relative crater depth k_1 is the main factor that causes uneven distribution of residual stress.
(2) As the laser shock energy or shock times increases, the degree of residual stress loss becomes more severe. Conversely, as the spot diameter or spot overlap ratio increases, the degree of residual stress loss decrease.
(3) In the case of constant laser shock energy, in order to increase the residual compressive stress on the surface and improve the uniformity of its distribution, it is recommended to use the spot overlap LSP instead of increasing the shock times at the same location.
(4) The spot overlap ratio should be selected to ensure that the distance between adjacent spot centers is equal to the crater radius of RSH.

Acknowledgments The authors are grateful for the financial support provided by the National Natural Science Foundation of China (NSFC) (No. 51575117) and the R & D projects in key areas of Guangdong Province (2019B090918004).

References

1. Peyre P, Fabbro R, Merrien P, Lieurade HP (1996) Laser shock processing of aluminium alloys. Application to high cycle fatigue behavior. Mater Sci Eng A 210(1–2):102–113
2. Achintha M, Nowell D, Fufari D, Sackett EE, Bache MR (2014) Fatigue behavior of geometric features subjected to laser shock peening: experiments and modelling. Int J Fatigue 62:171–179
3. Ma Z, Li YH, Ren XD, Zhou L (2007) Strengthening of aerial aluminum alloy with laser shock peening. Mater Mech Eng 31(8):P32–34 (In Chinese)
4. Trdan U, Skarba M, Grum J (2014) Laser shock peening effect on the dislocation transitions and grain refinement of Al–Mg–Si alloy. Mater Charact 97:57–68
5. Bhamare S, Ramakrishnan G, Mannava SR, Langer K, Vasudevan VK, Qian D (2013) Simulation-based optimization of laser shock peening process for improved bending fatigue life of Ti–6Al–2Sn–4Zr–2Mo alloy. Surf Coat Technol 232:464–474
6. Jia KX, Zhang CW, Nie XF (2014) Sensitivity analysis of "residual stress hole" induced by laser shock peening. Fire Control Command Control 39(8):1384–1388 (In Chinese)
7. Wang XD, Zhou X, Wang LC, Yang L, Chu F (2012) Surface residual stress of GH742 alloy after laser shock processing. Mater Mech Eng 36(3):79–80, 88 (In Chinese)
8. Jiang YF, Lai YL, Zhang L, Tang ZZ (2010) Li ZF (2010) Investigation of residual stress hole on a metal surface by laser shock. Chin J Lasers 37(8):2073–2079 (In Chinese)
9. Wang B, Chen DL, Zhou LC, He WF (2014) Central residual compressive stress drop on metal materials after laser induced shock wave. Infrared Laser Eng. 43(11):3521–3526 (In Chinese)
10. Wang XD, Nie XF, Zang SL, He WF, Li QP (2014) Formation mechanism of "residual stress hole" induced by laser shock peening. High Power Laser Part Beams. 26(11):1–5 (In Chinese)

11. Liu GJ, Yang SR (2015) Finite element simulation of residual stress hole induced by laser shock processing. T Mater Heat Treat 36(10) (In Chinese)
12. Cheng XQ, Xia QX, Wu J, Shuai GP, Xu X (2019) A flexible constraint layer and its fabrication method for on-line repair of laser shock strengthening. Patent, China

Part XIV
Joining by Forming and Deformation

Simulation and Experimental Analysis of Electromagnetic Pulse Spot Welding of Sheet Metal with a Field Shaper



Hang Zhang, Ning Liu, Qingjian Wang, and Hongfa Ding

Abstract The magnetic pulse spot welding studied in this paper can achieve the connection of sheet metal with the aid of a field shaper. The magnetic field shaper which is placed between the metal components and an electromagnetic coil has the function of concentrating the magnetic field, enhancing the electromagnetic force around the weld zone; meanwhile, it can protect the electromagnetic coil. This paper carried out a numerical simulation of the principle of the field shaper for magnetic pulse welding of sheet metal by means of the FEA software COMSOL. The electromagnetic and structural parameters of the high-strength coil and field shaper have been designed, and an electromagnetic welding platform is built, the welding experiments of 304 stainless steel sheet and 1060 aluminum sheet both with a thickness of 1 mm are carried out, respectively. The experimental results show that the method can achieve the connection of sheet metal very well.

Keywords Magnetic pulse spot welding · Field shaper · Electromagnetic force · Welding platform · COMSOL

1 Introduction

Resistance welding is a commonly used spot welding method, which started in the 1850s and is widely used in the field of industrial manufacturing [1]. Spot welding is a resistance welding method, which is to assemble the weldment into a lap joint and press it between the two columnar electrodes to melt the base metal with resistance heat to form the welding spot. When welding, there is no need for filler metal, high productivity, small deformation of weldment, and easy to realize automation. However, resistance welding needs to meet the condition that the melting point of the metal to be welded is close, which makes resistance welding limited on some occasions. Aluminum and its alloy are widely used on many occasions because of their good mechanical properties and low density. However, when an aluminum

H. Zhang · N. Liu · Q. Wang · H. Ding (✉)
Wuhan National High Magnetic Field Center, Huazhong University of Science and Technology, Wuhan 430074, China
e-mail: dhf@hust.edu.cn

© The Minerals, Metals & Materials Society 2021

G. Daehn et al. (eds.), *Forming the Future*, The Minerals, Metals & Materials Series,
https://doi.org/10.1007/978-3-030-75381-8_114

alloy is connected with stainless steel, it is difficult to realize it by traditional resistance welding because of its large melting point difference. Magnetic pulse welding (MPSW) is a solid-state welding technology, which can well weld the same and different metals, and there is no requirement for the melting point of metals [2].

At present, the commonly used electromagnetic pulse welding methods are mainly divided into plate welding and pipe welding [3]. Pipe welding usually uses the combination of the solenoid coil and field shaper [4], which is placed inside or outside the pipe, and the high-speed movement of pipe driven by electromagnetic force collides to complete the welding process. Because of the unique ring shape of pipe fitting, which is conducive to the formation of eddy current and ensures the quality of welding, and the research of electromagnetic pulse welding technology in pipe fitting is also relatively sufficient, so it has been widely used in industry [5].

However, the research on the magnetic pulse welding of plates is relatively less. Among them, Aizawa et al. first designed a method for electromagnetic pulse welding of plates [6]. In this way, the coil made of a single wire drives the plates to accelerate, and the plates move relative to each other and collide with each other at high speed to complete the welding process. However, this method has high requirements for welding equipment. Weddeling et al. designed a new electromagnetic welding method for plates [7], which uses a uniform pressure coil to drive the plate movement, and completed the welding and analysis of aluminum joints. For the first time, Deng used a flat structure field shaper in the magnetic welding of plates, and successfully realized the welding of aluminum and stainless steel [8].

Through the simulation analysis and summarizing of the rules, this paper design a set of welding equipment. The welding equipment is designed to realize the connection between aluminum plate and stainless steel plate. In the following chapters, the basic principles, finite element simulation, and experimental research are introduced, respectively.

2 Basic Principle and Design

2.1 Basic Principle

The MPSW system mainly comprises a charging system, capacitor bank, discharge switch, drive coil, field shaper and plates, as shown in the schematic diagram of Fig. 1. A strong magnetic field is generated by the discharge of the capacitor to the coil, and the field shaper placed between the coil and the plate converges to the magnetic field so that the powerful Lorentz force in the welding area drives the flyer plate to impact the parent plate with high-speed movement to realize the welding. As shown in Fig. 2a, the traditional flat field shaper is a circular platform structure with a straight hole in the center, and there is a slit along the radial direction so that the induced current on the upper surface can flow to the lower surface, and the current density through the lower surface is greater due to the area difference between the

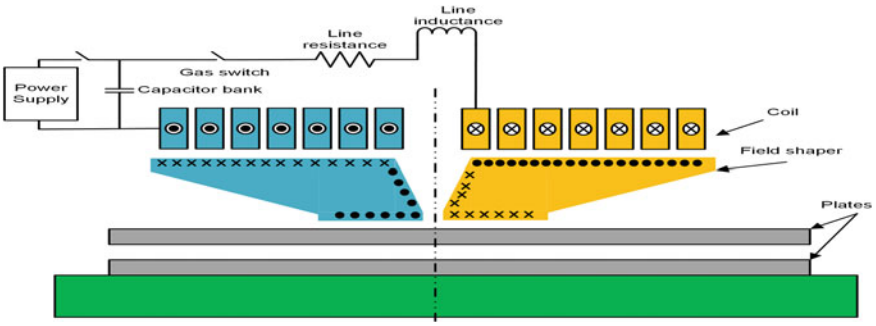


Fig. 1 Schematic diagram of the welding system. (Color figure online)



Fig. 2 **a** Traditional field shaper, **b** optimized field shaper. (Color figure online)

upper and lower surfaces. The instantaneous current in the field shaper induces eddy current in the plate, and the magnetic field generated by the eddy current and the coil current overlaps linearly, resulting in a local strengthened magnetic field, so a huge Lorentz force is generated under the action of the induced current in the plate.

The Lorentz force generated by the field shaper is pulse-shaped. The area with a large Lorentz force deforms and moves first, thereby driving the deformation of other areas. The pulsed electromagnetic force will have the problem that the deformation of some areas is not enough to achieve the welding. In order to overcome this problem, this paper optimizes the structure of the field shaper as shown in Fig. 2b, thus increasing the area of the welding area.

The equivalent circuit model of the MPSW device based on field shaper is shown in Fig. 3. It can be seen that the coil, field shaper and plate are all equivalent to a series connection of resistance and inductance. The field shaper is coupled by the electromagnetic field with the coil and the plate, respectively. The equivalent circuit of magnetic pulse welding satisfies the following equations:

$$i_c = -C\frac{du_c}{dt} \tag{1}$$

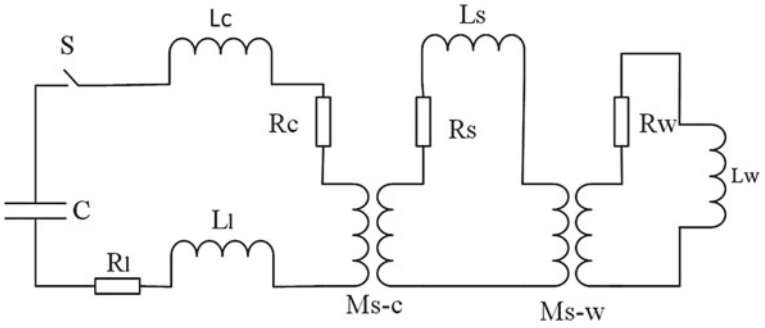


Fig. 3 Equivalent circuit model of EMPW device

$$i_c R_l + L_l \frac{di_c}{dt} + u_{coil} = u_c \tag{2}$$

$$i_c R_c + L_c \frac{di_c}{dt} + M_{s-c} \frac{di_s}{dt} = u_{coil} \tag{3}$$

$$i_s R_s + L_s \frac{di_s}{dt} + M_{s-c} \frac{di_c}{dt} + M_{s-w} \frac{di_w}{dt} = 0 \tag{4}$$

$$i_w R_w + L_w \frac{di_w}{dt} + M_{s-w} \frac{di_s}{dt} = 0 \tag{5}$$

where R_l, R_c, R_s, and R_w represent the equivalent resistance of circuits, coils, collectors, and workpiece, respectively. L_l, L_c, L_s, and L_w represent the equivalent inductance of circuits, coils, collectors, and workpiece, respectively. M_{s-c} and M_{s-w} represent the equivalent mutual inductance.

The essence of the electromagnetic effect of MPSW can be well understood by the equivalent circuit treatment of the system. The equivalent circuit model considers the electromagnetic coupling between components, which can improve the calculation accuracy. The calculation of the equivalent circuit model is less, which can reduce the calculation time and improve the processing efficiency.

2.2 Numerical Model

There is a strong coupling relation between the electromagnetic and structure fields in the electromagnetic pulse welding process. Finite element modeling is a reliable simulation tool to solve the problem of complete coupling in MPSW calculation. Compared with the advantages and disadvantages of many finite element software, COMSOL is used to simulate the process of electromagnetic welding in this paper. The software can couple the circuit, electromagnetic field, and structure field in order,

and get more accurate results. In order to facilitate the simulation analysis, this paper decided to adopt the 2-D model, but the existence of the gap in the field shaper led to the non-axisymmetric structure of the device. In order to simplify the device into the 2-D axisymmetric model, the area of field shaper is set as a single turn coil, and the cross-section current is set as zero in COMSOL.

A 2-D axial symmetry finite element model is developed using COMSOL for the welding system in Fig. 4. The simulation includes three physical models: "Circuit analysis model" to calculate Eqs. (1)–(5) for the discharge current, "Magnetic analysis model" to calculate flux density and electromagnetic, and "Solid mechanics" to simulate the plate deformation behavior caused by the electromagnetic force. The system parameters used in the simulation analysis are listed in Tables 1 and 2. For a discharging voltage of 10 kV, the current waveform obtained through simulation and experimental measurements, respectively, are in good agreement with each other as shown in Fig. 5. Since the first pulse of current is the main function of welding, only the first pulse waveform is taken. The distribution of electromagnetic force and deformation behavior are numerically analyzed, and the nephogram of the electromagnetic force and the deformation behavior of the plates are shown in Fig. 6.

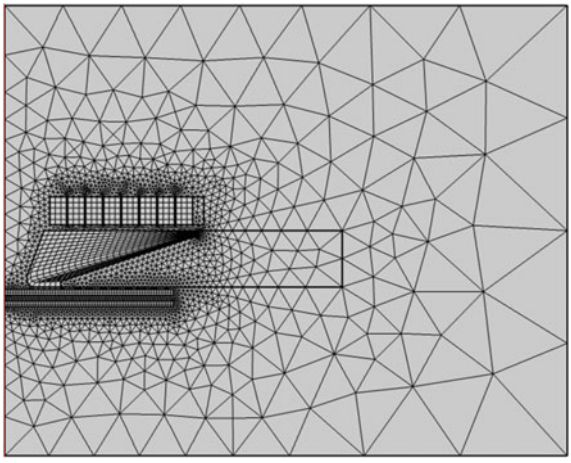


Fig. 4 2-D axial symmetry finite element model. (Color figure online)

Table 1 Line parameters

Symbol	Description	Value
C	Capacitance	100 μF
R_l	Line resistance	50 mΩ
L_l	Line inductance	1.5 μH
U	Discharge voltage	10 kV

Table 2 The basic parameters of each material

Material	Parameter	Value
A1060	Conductivity	3.53e7 S/m
	Permeability	4πe-7 H/m
	Density	2.7e3 kg/m^3
	Young's modulus	80.7 GPa
	Poisson ratio	0.34
SS304	Conductivity	1.35e6 S/m
	Permeability	4πe-7 H/m
	Density	7.93e3 kg/m^3
	Young's modulus	220 GPa
	Poisson ratio	0.25
	Initial yield stress	280 MPa
Coil	Conductivity	5.71e7 S/m
	Permeability	4πe-7 H/m
Field shaper	Conductivity	4.52e7 S/m
	Permeability	4πe-7 H/m

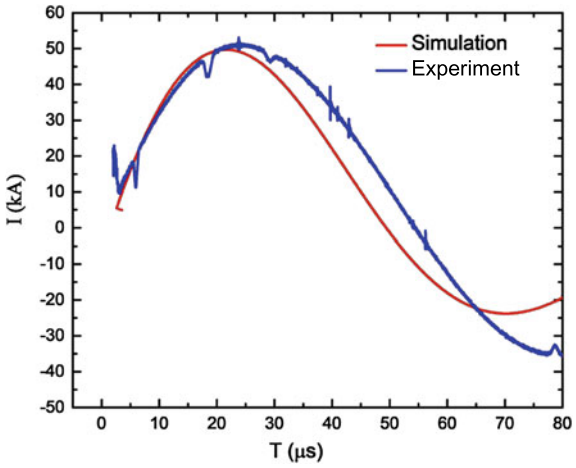


Fig. 5 Current waveform. (Color figure online)

2.3 Welding Device Design

The schematic of the designed welding device is shown in Fig. 7. Two epoxy plates are fixed under the support of the bolt to resist the huge reaction force produced in the welding process. The upper oxygen plate is also used as the coil framework, as shown in Fig. 8a, and the copper conductor with a section of 3×5 mm^2 is wound on

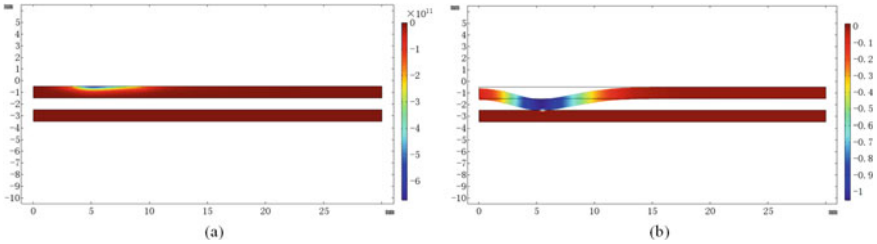


Fig. 6 **a** Nephogram of the electromagnetic force, **b** Nephogram of the deformation behavior. (Color figure online)

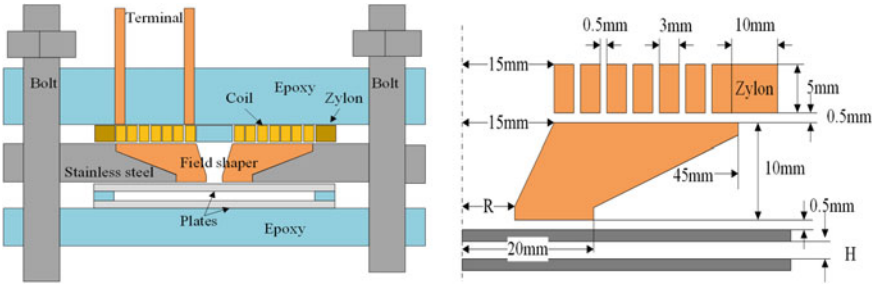


Fig. 7 Schematic of the designed welding device. (Color figure online)

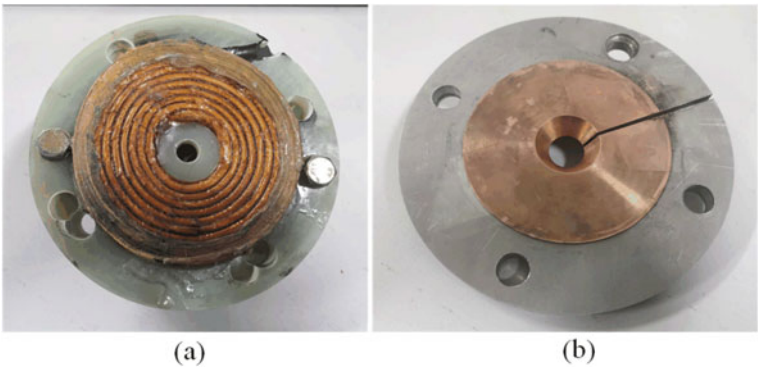


Fig. 8 **a** Coil, **b** stainless steel tray. (Color figure online)

the framework by the winding machine. In order to avoid the local gap of the coil in the winding process, special glue is needed to be used for filling during the winding process. The outermost layer is reinforced by Zylon fibers to prevent the wire from being damaged due to the huge stress and deformation during the discharge process. As the core part of the device, the field shaper will be repelled by both coils and plates during the welding process, so it is urgent to ensure its reliability. By comparing the

properties of various materials, Cu-Cr-Zr can meet the needs. In order to fix and protect the field shaper, it is embedded in a stainless steel tray with a thickness of 10 mm as shown in Fig. 8b. Opening a gap on the stainless steel bracket in the same direction with the gap of the field shaper can cut off the conductive circuit, avoid the short circuit at the gap of the field shaper, and also reduce the eddy current in the stainless steel bracket. All parts are fixed by bolts, and the plate is placed between the epoxy plate and the stainless steel bracket during the welding process.

3 Experiment and Discussion

The equipment used in the experiment is presented in Fig. 9, including a power supply of 200 kJ, a capacitor bank of 100 μF with a peak voltage of 15 kV, the welding device, and the plates.

The welding experiments are carried out under different voltage and different pre-welding gap. Considering the insulation strength of the coil, the maximum discharge voltage is set as 12 kV, and the welding experiments are carried out under the voltage of 7–12 kV by an increase of 0.5 kV and the pre-welding gap of 1–2.5 mm by an increase of 0.25 mm. The welding window was obtained according to welding results, which show the effects of the discharge voltage and pre-welding gap on the welding performance as shown in Fig. 10. It can be seen that effective coordination between the welding voltage and gap is needed for obtaining a good welding performance in the MPSW process. From the results, it can be concluded that the welding of the two sheet metals can be realized when the voltage was over 8 kV.

The following sections analyze the welding samples, which were welded by the optimized field shaper with the discharge voltage of 10 kV and the pre-welding gap of 1.5 mm. The appearance of the welding sample is shown in Fig. 11a. It can be seen that the deformation area of the plate exactly coincides with the lower contour of the field shaper. The bulge area corresponds to the central hole of the field shaper.



Fig. 9 **a** Power supply, **b** capacitor bank, **c** welding device. (Color figure online)

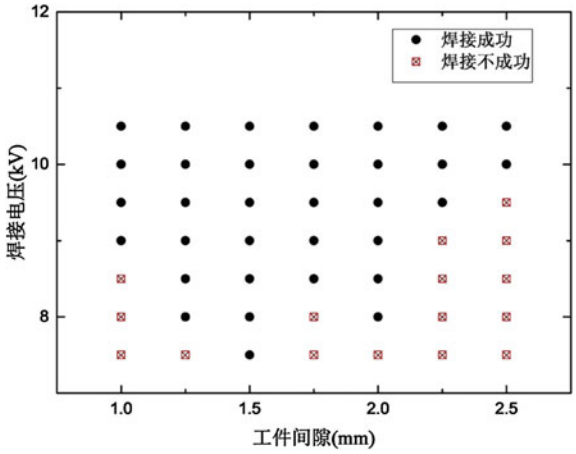


Fig. 10 Schematic of the designed welding device. (Color figure online)

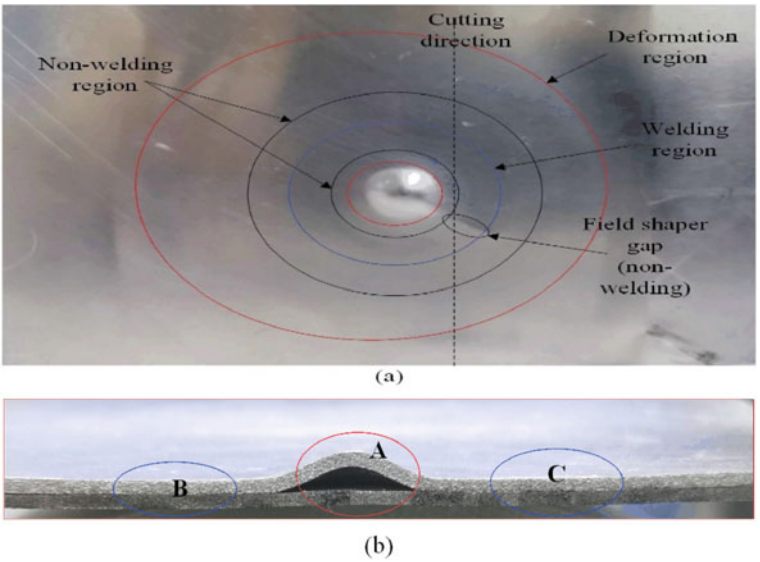


Fig. 11 **a** Appearance of the welding sample, **b** section of the welding sample. (Color figure online)

The welding area is located at the periphery of the bulge area. The non-welding area is mainly divided into two parts, one part is between the bulge area and the welding area and the outermost area, the other part corresponds to the gap of the field shaper. The welding device completes the local welding of the plates.

In order to study the detailed characteristics of welding, the section analysis of the welding sample is carried out in this paper. The cutting direction of the interface

is shown in Fig. 11a. In Fig. 11b, we can clearly see the bulge part in the center of the deformation area in region A, and both regions B and C are well welded.

4 Conclusion

In this paper, the welding device for the plate welding is designed, which is verified by simulation and experiment. A 1060 aluminum alloy sheet of thickness 1 mm can be effectively actuated by the use of the high-strength coil system with a field shaper and welded to a 304 stainless steel sheet with the same thickness at a capacitor discharge voltage of 7.5 kV. Also, an effective coordination between the welding voltage and gap is needed for obtaining a good welding performance in the MPSW process.

References

1. Wang N, Yamaguchi T, Nishio K (1895) Interface microstructure and weld strength of steel/aluminum alloy joints by resistance spot welding. Appl Mech Mater 117–119
2. Raoelison RN, Buiron N, Rachik M, Haye D, Franz G (2012) Efficient welding conditions in magnetic pulse welding process. J Manuf Process 14:372
3. Oliveira IV, Cavaleiro AJ, Taber GA, Reis A (2017) Magnetic pulse welding of dissimilar materials: aluminum-copper. In: Silva LFMD (ed) Materials design and applications. Springer International Publishing, Cham
4. Lueg-Althoff J, Bellmann J, Gies S, Schulze S, Tekkaya AE, Beyer E (2018) Influence of the flyer kinetics on magnetic pulse welding of tubes. J Mater Process Technol 262:189
5. Chen S, Jiang X (2015) Microstructure evolution during magnetic pulse welding of dissimilar aluminium and magnesium alloys. J Manuf Process 19:14
6. Aizawa T (2003) Magnetic pressure seam welding method for aluminium sheets. Weld Int 17:929
7. Weddeling C, Hahn M, Daehn GS, Tekkaya AE (2014) Uniform pressure electromagnetic actuator—an innovative tool for magnetic pulse welding. Procedia CIRP 18:156
8. Deng F, Cao Q, Han X, Li L (2018) Electromagnetic pulse spot welding of aluminum to stainless steel sheets with a field shaper. Int J Adv Manuf Technol 98:1903

Mechanical Properties of Aluminium/Stainless Steel Bimetal Composite Fabricated by Extrusion Process



Kai Soon Fong, Danno Atsushi, Dharmesh Kumar, Wee Kiat Ong, and Suwat Jirathearanat

Abstract In this work, an indirect extrusion process was designed to manufacture a stainless steel reinforced aluminium composite. The design utilized a feeding mandrel to prevent the deformation of the stainless steel wire and to facilitate the embedding of the wire within the aluminium alloy during extrusion. By using this method, a 12 mm diameter 6061 aluminium alloy embedded with a 2 mm diameter 304 stainless steel wire was successfully fabricated. Energy-dispersive X-ray spectroscopy revealed that aluminium and iron elements had diffused into the interfacial layer between the aluminium/stainless steel to induce some degree of metallurgical bonding. The yield strength, tensile strength, and elongation to failure of the extruded composite after solution and ageing heat treatment were 343.8 ± 5.5 MPa, 405.3 ± 5.1 MPa, and 18.0 ± 1.3%, respectively. As compared to extruded aluminium, yield strength, ultimate tensile strength, and elongation to failure were improved by 41.8%, 31.6%, and 6.3%, respectively. This result suggests that the composite material has better strength and toughness as compared to aluminium alone.

Keywords Metallic composite · Backward extrusion · Indirect extrusion · Aluminium fastener · Aluminium alloy · Stainless steel

1 Introduction

A metallic composite structure consisting of two or more metals was developed to achieve unique and better mechanical performances by combining the advantages of the different metals [1–5]. Kleiner et al. [5] demonstrated a method to produce aluminium and steel composite by the extrusion process. In this process, a modified extrusion tooling with supply channels was designed to continuously or selectively feed steel wires or steel wire ropes into the aluminium to improve its strength. The aim was to make the extrusion process more economical for manufacturing high-strength metallic composite structures by overcoming the current disadvantages seen in metal

K. S. Fong (✉) · D. Atsushi · D. Kumar · W. K. Ong · S. Jirathearanat
Singapore Institute of Manufacturing Technology, 73 Nanyang Drive, Singapore 637662, Singapore
e-mail: ksfong@SIMTech.a-star.edu.sg

© The Minerals, Metals & Materials Society 2021

G. Daehn et al. (eds.), *Forming the Future*, The Minerals, Metals & Materials Series,
https://doi.org/10.1007/978-3-030-75381-8_115

matrix composites (MMC) extrusion. MMC extrusion, such as particle or short fibre reinforced aluminium profiles, is manufactured by extrusion of a reinforced billet prepared from powder metallurgy. This method leads to a significantly higher extrusion force, increases tool wear, and imposes a limitation on the minimum wall thickness that can be extruded. However, by feeding the reinforcement wires during the extrusion process, the extrusion force can be significantly reduced which reduces tool wear. Also, the manufacturing cost will be lower since a normal aluminium billet can be used. Based on this work, other studies were conducted to expand the process capabilities such as open die hot forging process for post-shaping the aluminium composite [6], a method for achieving functionally graded properties along with the extruded profiles [7], method of embedding of non-metallic material [7], die design optimization for embedding lower strength materials [8], and fabrication of a "nervous" structure by the embedding of shape memory alloy [9].

In this study, a simplified indirect extrusion tooling was designed for the manufacturing stainless steel wire reinforced aluminium composite, suitable for low-volume manufacturing of small composite components. To reduce the cost and productivity, a general-purpose 100 ton vertical hydraulic forming press was used instead of a horizontal extrusion press typically used for continuous extrusion for aluminium profiles. To examine the quality of the composite extrusion, the joining interface was investigated by scanning electron microscope (SEM) and energy-dispersive X-ray spectroscopy (EDX), the mechanical properties were examined by tensile tests, and the fracture morphology was examined by SEM.

2 Experimental Procedure

2.1 Materials and Experimental Setup

The materials used in the extrusion tests were 6061 aluminium and 304 stainless steel (spring temper). Figure 1a shows a schematic of the indirect extrusion process to illustrate the configuration of the workpieces before the start of extrusion. In this study, the aluminium preform has a height of 50 mm, an outer diameter of 38 mm in diameter, a centre hole diameter of 2.2 mm, and a machined profile at the base of the preform for inserting over the mandrel. The diameter of the stainless steel wire was 2 mm with a total length of 280 mm. The outer surface of the wire was prepared with silicon carbide grinding paper and cleaned with isopropyl alcohol. The inner surface of the centre hole diameter in the aluminium preform was prepared by wire brushing and rinsed with isopropyl alcohol. The extrusion tests were performed using a 100 ton hydraulic press and the extrusion speed was 5 mm/s. The container die was preheated to 420/450 °C and allowed to dwell for 15 min before the start of the extrusion tests.

The aluminium preform was first dropped into the container die. After which, the wire was manually inserted into the centre hole of the aluminium preform from

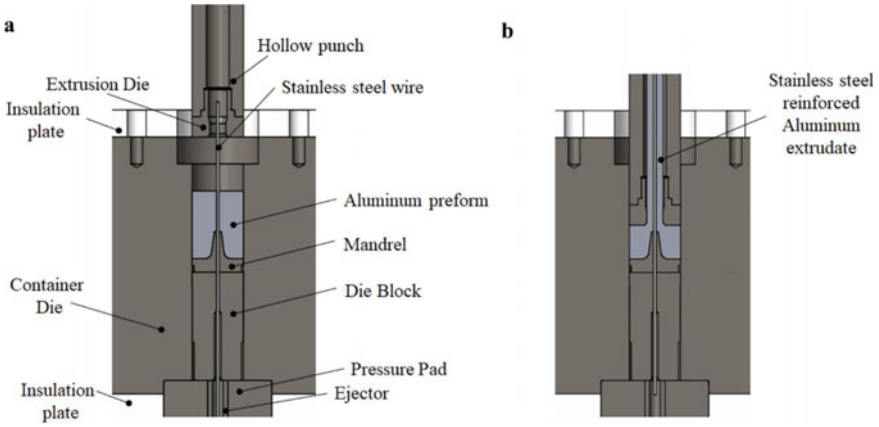


Fig. 1 **a** Schematic diagram of the indirect extrusion tooling and forming process before extrusion, **b** after extrusion. (Color figure online)

the top, and into the centre holes of the mandrel and die block. Both the aluminium preform and stainless steel wire were heated within the container for 15 min before extrusion.

Figure 1b shows a schematic of the aluminium and stainless steel composite after extrusion. By using the mandrel, the wire can be continuously embedded and drawn into the aluminium alloy without fracture or significant deformation. The extrusion die hole diameter, bearing length, and extrusion ratio was 12 mm, 10 mm, and 10, respectively. The aluminium/stainless steel composite was ejected from the container die after extrusion and allowed to cool in air.

Figure 2a, b show the images of the tooling and the extruded aluminium/stainless steel composite, respectively. For benchmarking purpose, an aluminium alloy without

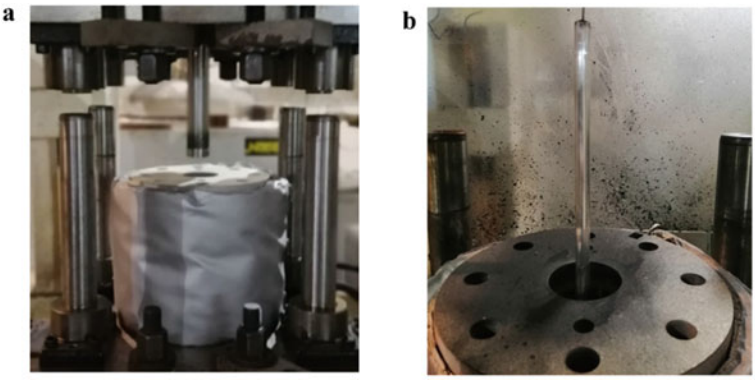


Fig. 2 **a** Experimental tooling, **b** image of the extruded aluminium/stainless steel composite. (Color figure online)

wire was also extruded. For the tensile tests, all the extruded samples were subjected to T6 heat treatment which consists of a solution treatment at 545 °C for 60 min and artificial ageing at 177 °C for 8 h.

The aluminium/stainless steel interface was examined using a scanning electron microscope (SEM) and energy-dispersive X-ray spectroscopy (EDX). Tensile tests were performed on Instron 5982 testing machine at room temperature with a nominal strain rate of 10^{-3} s^{-1}. Cylindrical tensile samples with a gauge length of 24 mm and a diameter of 6 mm were machined from the extrusion. A minimum of three tensile specimens was tested to ensure repeatable stress–strain curves and for obtaining an average yield strength, tensile strength, and total elongation. Computed tomography (CT) of the extruded samples were performed using GE Phoenix v|tome|x m 3D CT metrology system (GE sensing and Inspection Technologies GMBH) equipped with a 180 kV Nanofocus X-ray tube. The CT scanning parameters were 160 kV tube voltage, 200 μA tube current, 15 μm voxel size, 14 μm focal spot size, and 100 μm detector pixel size.

2.2 Simulation Procedures

The extrusion of 6061 aluminium and 304 stainless steel wire was simulated using the commercial FE software DEFORM 3D. A 1/4 section model was carried out to reduce computation time. Rigid-visco-plastic deformation and thermal effects were incorporated in this simulation. The friction between the die and the specimen interface was expressed by using the friction model defined as follows:

$$\tau = mk = m\frac{\tilde{\sigma}}{\sqrt{3}} \tag{1}$$

where τ is the shear stress, m is the friction factor, k is the shear strength, and $\tilde{\sigma}$ is the flow stress of the specimen material. The exact friction coefficient between the materials depends on the temperature and pressure and is not fully understood or can be mathematically expressed. For the current study, high friction between the aluminium and stainless steel materials were utilized which appropriately represent the extruded samples observed in the experiments. The friction factor of 0.8 was assumed at the billet-container and die interface and 0.4 was assumed at the die bearing interface [10]. The friction between stainless steel interface heat transfer coefficients is generally a complex function determined by the interface pressure, amount of sliding, and interface temperature. In the current study, the interface friction was assumed to be 1.0 to represent bonding of the two materials. The details of the simulation parameters are shown in Table 1.

Table 1 FE simulation parameters

Parameters	Description/values
Billet material	6061 aluminium
Wire material	AISI 304
Die material	H13
Friction factor between aluminium and tool	0.8
Friction factor at die bearing	0.4
Friction factor at aluminium/stainless steel	1.0
Heat transfer coefficient between tooling and air (N s^{-1} mm^{-1} $°C^{-1}$)	0.02
Heat transfer coefficient between tooling and aluminium material (N s^{-1} mm^{-1} $°C^{-1}$)	20
Heat transfer coefficient between aluminium and stainless steel material (N s^{-1} mm^{-1} $°C^{-1}$)	11
6061 thermal conductivity (N s^{-1} $°C^{-1}$)	180.175
6061 heat capacity (N mm^{-2} $°C^{-1}$)	2.43
304 thermal conductivity (N s^{-1} $°C^{-1}$)	20.0
304 heat capacity (N mm^{-2} $°C^{-1}$)	3.7

3 Results and Discussion

3.1 Optimization of the Mandrel to Extrusion Die Distance by Simulation

The simulation results of the indirect extrusion process without and with mandrels are shown in Fig. 3a–c. As shown in Fig. 3a, when mandrel was not used, the wire was subjected to deformation together with the aluminium which led to deformation and subsequent fracture near the start of the extrusion process. This was because of the excessive pressure built up at the bottom of the wire-aluminium interface which tightly constraint the wire from sliding and prevent it from moving together with the aluminium material. Figure 3b–c shows the initial distance, d, between the extrusion die and mandrel that has to be optimized to prevent wire deformation. From this simulation study, d had to be not more than 20 mm for the wire to be successfully drawn into the aluminium extrudate without failure. It was demonstrated that the mandrel is effective in reducing the pressure and friction at the aluminium/wire interface and thus help to facilitate the drawn-in of the wire into the aluminium extrudate during the extrusion process. The use of a feeding mandrel inevitably limits how much material can be extruded without the mandrel colliding or being too close to extrusion die. However, depending on the extrusion ratio, a small amount of billet height reduction can result in a sufficiently long extrusion. In this case, an extrusion die exit diameter of 12 mm and an initial billet diameter of 38 mm can

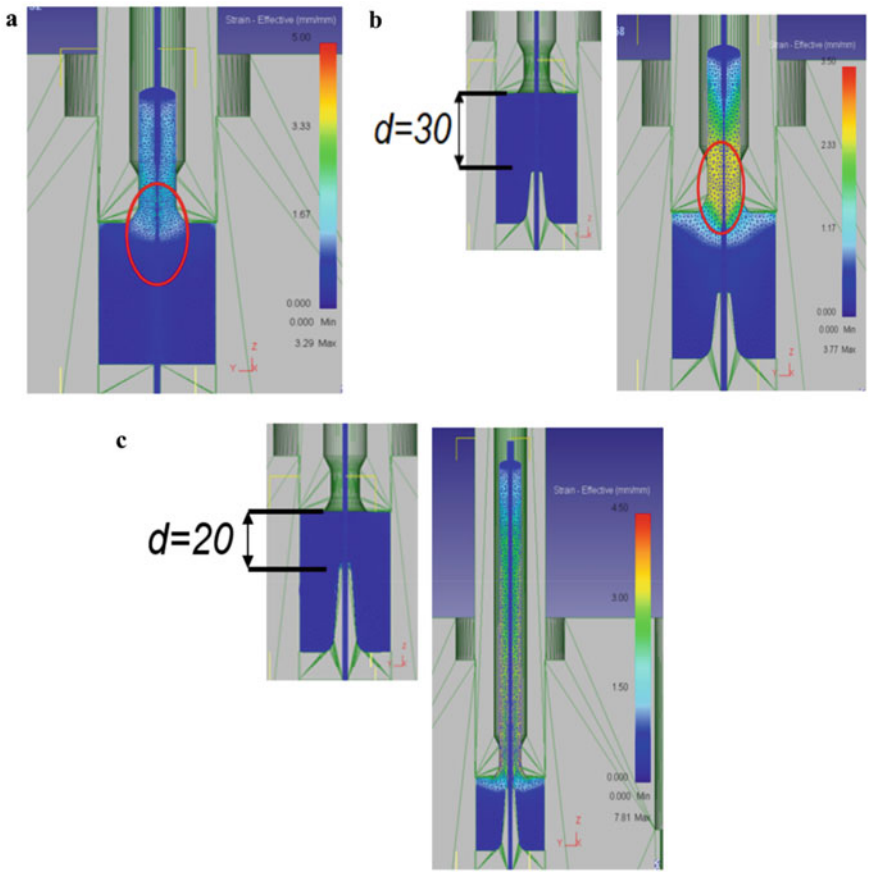


Fig. 3 **a** Wire fractured without mandrel, **b** wire fractured with mandrel d = 30 mm, **c** wire intact with mandrel d = 20 mm. (Color figure online)

result in around 200 mm extruded length with just 20 mm reduction in the billet height.

3.2 Observation of Extruded Composite

Figure 4a shows a sample of the composite extruded with feeding mandrel of d = 30 mm. In this case, the wire was fractured within the extrudate and this was determined simply by measuring the total length of the wire before and after extrusion. When there is a fracture, the wire length will be much longer than the initial length and a significant portion of the wire can be observed to remain below the billet (on the left in the picture) and not drawn into the extrusion. Figure 4b shows the samples



Fig. 4 **a** Extruded sample (wire fractured) without mandrel, **b** extrude samples (wire intact) with mandrel, d = 20 mm. (Color figure online)

extruded using the feeding mandrel with d = 20 mm. The wires were not broken based on the length measurements and the wires were observed to have drawn into the aluminium extrusion with little length remaining below the billet.

CT scanning measurements were also performed on the samples extruded with mandrel d = 20 and 30 mm, as shown in Fig. 5a–d. As shown in the 2D overview scanned results, the wire was not fractured during extrusion when mandrel d = 20 mm was used. These measurements show good agreement with the simulation results. As shown in the detailed cross-sectional CT scan results in Fig. 5c–d, the process is well capable of embedding the stainless steel wire in the middle of the extrudate without any observable delamination or defects.

3.3 SEM Examination of the Aluminium and Steel Interface

Figure 6a, b displayed the SEM image of the aluminium/stainless steel composite and the interfacial morphology between the aluminium and stainless steel after extrusion, respectively. As shown in Fig. 6b, a slightly wavy aluminium/stainless steel interface was created after extrusion without any gap. Furthermore, a thin interface was observed between the two materials. The interface was further analyzed by EDX and the elemental mapping is shown in Fig. 6b. It was revealed that this was a diffusion interface layer of ~500 nm in thickness, and a gradient of Al and Fe atom content distribution was formed at this interface. This suggests that the extrusion process was able to induce a certain extent of metallurgical bonding between the aluminium/stainless steel composite. The extrusion pressure and high extrusion temperature may have promoted the diffusion of Al and Fe atoms from the aluminium and stainless steel material, respectively, to create a diffusion layer. This distribution

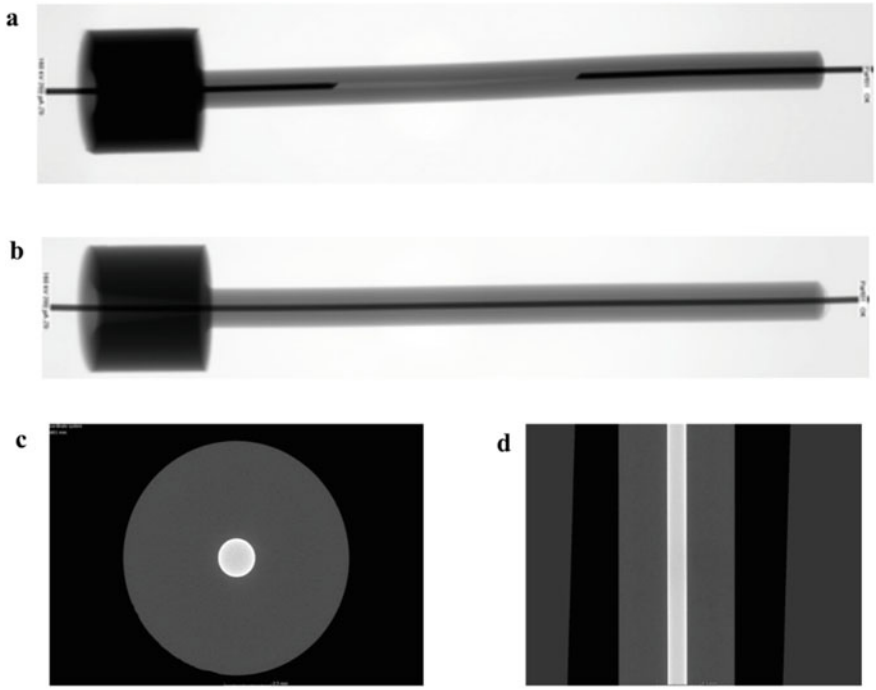


Fig. 5 **a** 2D overview CT scan results of the composite extruded with mandrel d = 30 (**a**), **b** composite extruded with mandrel d = 20, **c** cross-sectional CT analysis of the composite extruded (mandrel d = 20) at the plane perpendicular to the extrusion direction, **d** cross-sectional CT analysis of the composite extruded (mandrel d = 20) at the plane parallel to the extrusion direction. (Color figure online)

of elements was similar to what was observed in the interface layer between 6061 aluminium alloy and 304 stainless steel prepared by laser-metal inert-gas welding [11].

3.4 Mechanical Properties

Figure 7a shows the engineering stress–strain curves of the different extruded samples. A comparison of the values of the yield strength, ultimate tensile strength, and elongation to failure of the different samples are shown in Fig. 7b. From Fig. 7a–b, it can be clearly seen that aluminium/stainless steel composite resulted in a significant improvement in mechanical strength without scarifying ductility. The results of the composites extruded at 420 and 450 °C were quite similar with the latter having slightly better properties. The yield strength, ultimate tensile strength, and elongation to failure of aluminium alloy after extrusion were 242.5 ± 2.5 MPa, 308 ± 7.1 MPa,

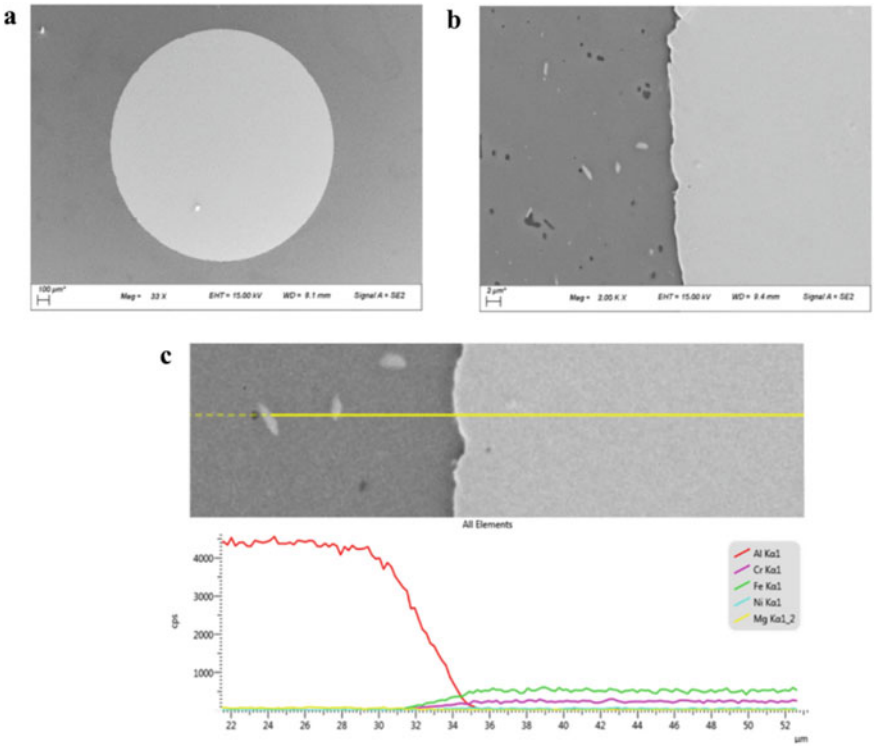


Fig. 6 **a** SEM image of aluminium/stainless steel composite, **b** SEM image of the aluminium/stainless steel interface, **c** EDX analysis of the chemical composition in the aluminium/stainless steel interface. (Color figure online)

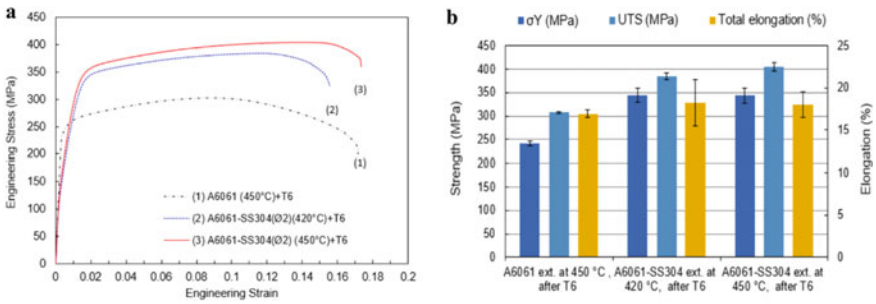


Fig. 7 **a** Engineering stress–strain curves of the aluminium/stainless steel composite, **b** yield strength, ultimate tensile strength, and elongation to failure of the aluminium/stainless steel composite. (Color figure online)

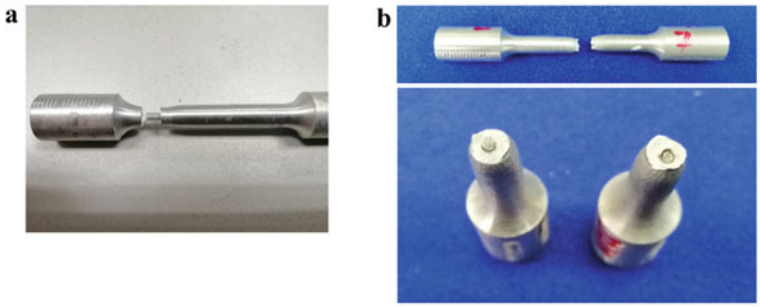


Fig. 8 **a** Failure of the tensile specimen in non-metallurgical bonded condition, **b** failure of the tensile specimen in the metallurgically bonded condition. (Color figure online)

and 16.95 ± 1.2%, respectively. The yield strength, ultimate tensile strength, and elongation to failure of aluminium/stainless steel composite extruded at 450 °C were 343.8 ± 5.5 MPa, 405.3 ± 5.1 MPa, and 18.0 ± 1.3%, respectively. This translated into an overall improvement of yield strength, ultimate tensile strength, and elongation to failure by 41.8%, 31.6%, and 6.3%, respectively. This result suggests that the composite material has better strength and toughness as compared to aluminium alone.

Figure 8 shows the images of the failures of the aluminium/steel composite tensile specimens. The tensile failure in the case of insufficient metallurgical bonding at the aluminium/stainless steel interface is shown in Fig. 8a. In this case, delamination of the wire/aluminium interface occurred early in the tensile test and resulted in the wire slipping from the aluminium alloy. Insufficient bonding can happen when surface contamination and oxide layers were not properly removed during the surface preparation and cleaning steps. If sufficient metallurgical bonding had occurred, the failure will appear like what was observed in Fig. 8b. Here, it can be seen that both materials fractured together. This was only possible because the interface bonding strength was high enough to prevent the wire from slipping.

3.5 Fracture Morphology

The fracture morphology was examined under SEM and the results are shown in Fig. 9a–b. The fracture surfaces of the stainless steel wire are shown in Fig. 9b location 1 and 2. The fracture surface at the middle (location 1) of the wire contained dimples of varied size and depth. The outer area (location 2) of the wire displayed more cleavage facets which was an indication of shear fracture mode. From Fig. 9a, it can be seen that necking of the wire occurred before fracture. These observations suggest that the wire failed by ductile–brittle fracture mode.

The fracture surfaces of aluminium are shown in locations 3 and 4 that contained a high fraction of dimples and were more uniform as compared to that of the wire

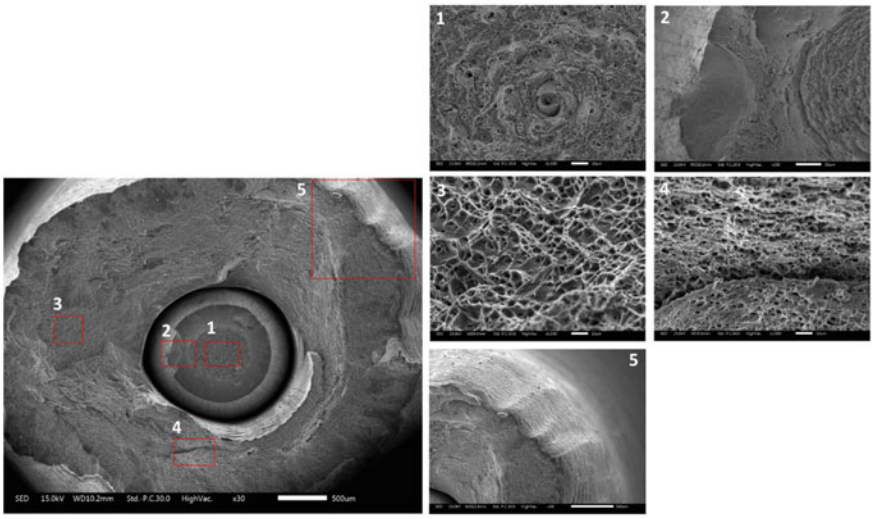


Fig. 9 **a** Fracture morphology of the aluminium/stainless steel tensile specimen, **b** enlarge images of the fracture surface at different areas of the tensile specimen. (Color figure online)

fracture surface. These fibrous appearances and the cup-and-cone fracture appearance of the tensile specimens (in Fig. 8b) were indicative of a ductile fracture mode. Location 4 shows one of the typical appearances of a discontinuity of the fracture surface that were observed in the aluminium material. This occurred due to the sudden dislodged of the material caused by the constraint imposed by the secondary wire material. Location 5 shows the image of the outer edge of the aluminium material which appeared wrinkled and supposedly caused by the constraint imposed by the wire. This observation suggests that the wire was metallurgically bonded to the aluminium material which agrees well with EDX analysis shown in Fig. 6.

4 Conclusions

A bimetal 6061 aluminium alloy and 304 stainless steel cylindrical extrusion rod of 12 mm diameter and 200 mm length were successfully manufactured by indirect extrusion process. From this study, the following conclusions can be made:

(1) FEM simulation and experiment confirmed that an initial distance of not more than 20 mm between the feeding mandrel and extrusion die was necessary to ensure that wire deformation can be avoided and for it to be drawn into the aluminium extradite.

(2) A diffusion interface layer, containing both Al and Fe atoms, of 500 nm in thickness was observed between the aluminium and stainless steel materials. This suggests that the extrusion pressure and temperature were high enough

to promote the diffusion of Al and Fe atoms from the aluminium and stainless steel material to create a metallurgical bonding.

(3) After solution and ageing heat treatment, the yield strength, ultimate tensile strength, and elongation to failure of the bimetal composite were 343.8 ± 5.5 MPa, 405.3 ± 5.1 MPa, and 18.0 ± 1.3%, respectively. When compared to the extruded aluminium alloy without wire, the yield strength, ultimate tensile strength, and elongation to failure were improved by 41.8%, 31.6%, and 6.3%, respectively. This result suggests that the composite material has better strength and toughness as compared to aluminium alone.

(4) The fracture surface of stainless steel wire contained dimples and cleavage facets which are indicative of a ductile–brittle fracture mode. The aluminium fracture surface appeared more fibrous with a high fraction of dimples. Furthermore, the presence of discontinuity of fracture surface and wrinkled appearances in the aluminium was indicative of good bonding between the aluminium and stainless steel material.

References

1. Binotsch C, Nickel D, Feuerhack A, Awiszus B (2014) Forging of Al-Mg compounds and characterization of interface. In: 11th international conference on technology of plasticity, Elsevier, Nagoya Congress Center, Nagoya, Japan, pp 540–545
2. Berski S, Dyja H, Maranda A, Nowaczewski J, Banaszek G (2006) Analysis of quality of bimetallic rod after extrusion process. J Mater Process Technol 177:582–586
3. Feng B, Xin Y, Sun Z, Yu H, Wang J, Liu Q (2017) On the rule of mixtures for bimetal composites. Mater Sci Eng A 704:173–180
4. Marko K, Mohammad J, Yannis PK, Irene JB (2014) Material-based design of the extrusion of bimetallic tubes. Comput Mater Sci 95(1):63–73
5. Kleiner M, Klaus A, Schomäcker M (2006) Composite extrusion—determination of the influencing factors on the positioning of the reinforcing elements. Adv Mater Res 10:13–22
6. Foydl A, Pfeiffer I, Kammler M, Pietzka D, Matthias T, Jäger A, Tekkaya AE, Behrens BA (2012) Manufacturing of steel-reinforced aluminum products by combining hot extrusion and closed-die forging. Key Eng Mater 504–506:481–486
7. Dahnke C, Pietzka D, Haase M, Tekkaya AE (2014) Extending the flexibility in the composite extrusion process. Procedia CIRP 18:33–38
8. Dahnke C, Hilbring J, Kloppenborg T, Haase M, Tekkaya AE (2015) Investigations for the embedding of functional elements in the composite extrusion process. Mater Today Proc 2(10):4763–4770
9. Dahnke C, Shapovalov A, Tekkaya AE (2017) Thermally activated lightweight actuator based on hot extruded shape memory metal matrix composites. Proedia Eng 1511–1516
10. He YF, Xie SS, Cheng L, Huang GJ, Fu Y (2010) FEM simulation of aluminum extrusion process in porthole die with pockets. Trans Nonferrous Met Soc China 20:1067–1071
11. Xue J-Y, Li Y-X, Chen H, Zhu Z-T (2018) Wettability, microstructure and properties of 6061 aluminum alloy/304 stainless steel butt joint achieved by laser−metal inert-gas hybrid welding−brazing. Trans Nonferrous Met Soc China 28:1938–1946

From Bridge to Bumper: Utilization of Pre-stressing During Manufacturing of Hybrid Sheet Metal Structures



Henning Husmann and Peter Groche

Abstract Pre-stressing is often used in civil engineering to increase the load-bearing capacity of bridges and buildings. In order to exploit this potential in sheet metal structures as well, efficient processes for joining and pre-stressing of tendons are required. Therefore, an approach to join and pre-stress fiber-reinforced plastic (FRP) straps and sheet metals during a forming process is proposed. The FRP strap is placed around two collars drawn into the sheet. A punch plastically expands the collar, while the FRP strap is elastically elongated, resulting in beneficial pre-stresses after unloading due to the different spring-back. In this paper, the predominant mechanism is verified and parameters influencing the pre-stress are identified by experimental and numerical investigations. The hypothesis is investigated that a customized pre-stress and thus a higher strength during the structure's usage can be controlled by varying the collar's expansion. Possible applications include bumpers and side-impact beams.

Keywords Pre-stress · Joining · Forming

1 Introduction

The principle of pre-stressing has been used for hundreds of years to increase the load-bearing capacity and performance of products and structures. Barrels, for example, receive their tightness by a purposeful compression of the individual wooden staves by means of tensioned hoops [1]. But also modern structures are pre-stressed in order to fulfill their function [2]. This is due to the fact that pre-stressing allows versatile possibilities of influencing the properties of functional structures. In addition to increased stiffness and strength [3, 4], the vibration behavior [5], as well as the fatigue strength [6], can be influenced. Applications can be found in a variety of industries. In most cases, compressive stresses are applied to structures at failure-critical locations in order to compensate for tensile stresses that occur during use. Cold forging dies, for example, which are usually made of brittle, high-strength materials,

H. Husmann · P. Groche (✉)
Institute for Production Engineering and Forming Machines, Technische Universität Darmstadt, Otto-Berndt-Str. 2, 64287 Darmstadt, Germany
e-mail: groche@ptu.tu-darmstadt.de

© The Minerals, Metals & Materials Society 2021

G. Daehn et al. (eds.), *Forming the Future*, The Minerals, Metals & Materials Series,
https://doi.org/10.1007/978-3-030-75381-8_116

are pre-stressed by containers so that their inner wall is set under compressive stresses counteracting the tangential tensile stresses occurring during forming. Thus, higher strength materials can be processed and the number of endurable load cycles can be increased [7]. Further examples are pre-stressing of piezo crystals to bear tensile forces [8], tempering of safety glass in order to increase the bending strength [9], as well as autofrettage of tubes and vessels to bear higher pressures and more load cycles [10].

In structures like bridges, which are mainly submitted to bending loads, a compressive pre-stress at the bottom of the girder can be used to compensate for the tensile stresses arising from external bending loads and thus significantly increase the load-bearing capacity while decreasing the total deflection. This makes it possible to considerably reduce dead loads and to achieve leaner structures. The compressive pre-stress is created by high-strength tendons, which are set under tension and subsequently connected to the structure. After the external tensile load is removed from the tendon, the girder is compressed until the system is in equilibrium. The positive effects of pre-stressing are used in both concrete and steel structures. For concrete constructions, a distinction is made between pre-tensioned and post-tensioned structures. In pre-tensioned structures, the tendons are pre-stressed before the concrete is casted and then molded in the pre-stressed state. In steel construction and in post-tensioned concrete structures, on the other hand, the tendons are attached to a girder after its shape is given [11].

High-strength steels and, more recently, fiber-reinforced plastics (FRP) are used as the material for the tendons. Due to corrosion and in some cases fatigue failure of steel tendons, FRP are increasingly gaining in interest and significance in construction [12]. Here, FRPs are mainly used in the form of strips and laminates made of carbon fiber-reinforced plastics [13]. Numerous research projects dealt with the influence of such pre-stressing systems on the load-bearing behavior of structures. Deuring [3] describes the beneficial effects of pre-stressed carbon fiber-reinforced plastics adhered to the bottom side of concrete beams. By means of four-point bending tests, it was shown that the load carried by the FRP as well as the stiffness and strength of the girder were significantly increased with increasing pre-stress of the tendon [3]. Ghafoori and Motavalli investigated the influence of pre-stressed carbon fiber-reinforced plastic plates attached to steel beams on the flexural behavior. Their investigations showed that the geometric and mechanical properties of the FRP can increase the stiffness and the yield load capacity of the beam, whereas the pre-stress does not affect the stiffness of the beam until cracks occur. Nevertheless, it is possible to both increase the yield and the ultimate load capacity by applying a pre-stress to the FRP [14].

The attachment of the FRP has a considerable influence on the failure behavior of such reinforced structures since very high shear stresses can lead to a premature failure of the FRP or the structure to be reinforced [15]. For this reason, manifold investigations are focused on the development of suitable anchorage systems for FRP tendons in the form of rods, lamellae, straps, and strands. The most common systems are based on bonding or a frictional connection. An extensive overview of the proposed systems can be found in the reviews of Erki and Rizkalla [16], Schlaich

et al. [17] as well as Schmidt et al. [18]. According to Zwingmann [19], bonded and friction-locked connections are usually less suitable for lightweight construction solutions, as they require complex massive metallic anchor bodies to be attached to. Here, pin-loaded straps can be an alternative, since the connection geometry is created out of the lightweight FRP strap itself. For this reason, pin-loaded straps are also used in applications with a high demand for lightweight designs like sailing rigs [19].

Even though the principle of pre-stressing is already used on a large scale in the construction industry and also occasionally in many other areas of technology, it is far from being established in all load-bearing structures. If, for example, sheet metal structures used in cars, trucks, airplanes, and trains are considered, it can be seen that high efforts are being made to increase the performance of the structures at low weight. The approaches range from new materials, complex component geometries, energy-intensive heat treatment processes to hybrid designs employing different materials to decrease the mass of the structures. However, the principle of pre-stressing is not represented. This can be explained by the necessity for complex systems for tensioning and anchoring the tendons. While the effort required for pre-stressing and the weight of the anchor systems have a negligible influence on a structure like a bridge with significant dead loads, mass-produced sheet metal structures, such as those found in cars, are subject to fundamentally different requirements. In addition to an enormous cost pressure prohibiting complex assembly and pre-stressing processes, there are hardly any anchoring systems available that are suitable from a lightweight point of view, as the anchors can easily exceed the weight of the tendon itself.

At the same time, established forming processes for sheet metals offer suitable possibilities to solve these issues, as they allow creating attachment points in an integral form. In addition, spring-back differences after a conjoint forming can be utilized to generate a frictional connection. Marré et al. [20] illustrated this mechanism in the context of joining by hydroforming. As shown in Fig. 1, tube A is placed inside of the joining partner B leaving an initial gap between them. By applying an increasing pressure p on the inside of tube A, the tube is expanded until the gap is closed and the

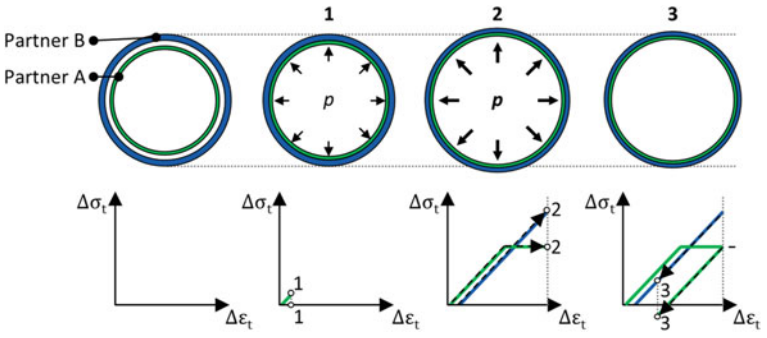


Fig. 1 Mechanism for joining by hydroforming according to Marré et al. [20]. (Color figure online)

two parts are in contact (state 1). A further increase of the pressure leads to a conjoint expansion of both parts. Here the inner part is deformed elastically and plastically, while the outer part only experiences elastic deformations (state 2). After the pressure p has been relieved, the elastic spring-back of the outer part is stopped by the plastically deformed inner part leaving residual stress, which results in a frictional connection. Afterward, the inner part is loaded by compressive tangential stresses σ_t resulting from the outer part which is submitted to tensile stresses (state 3) [20].

2 Joining and Pre-stressing by Widening of an FRP-Wrapped Metal Collar

A novel joining and pre-stressing technique is proposed, which enables the reinforcement of sheet metal structures using continuous fiber-reinforced thermoplastic tapes. The proposed process is shown in Fig. 2. Here, an FRP strap is loosely wound around two collars previously drawn into the sheet metal. Subsequently, one of the collars is widened elastic-plastically using a conical-shaped punch, while the FRP strap is elongated purely elastically. After the punch is retracted, both components spring-back. Here, the FRP strap is prevented from returning to its initial shape by the plastically widened collar. The resulting stresses are used to join the components and to counteract external bending loads submitted to the hybrid structure during its usage.

While the bending stiffness of the resulting structure is to be influenced to a large extent by the geometric shape of the sheet metal and the FRP strap arranged orthogonally to it, the generated pretension shall, in particular, increase the yield and failure strength of the metallic component under bending loads. By varying the expansion ratio of the collar, the pre-stress is to be varied in a targeted manner in order to enable an application-optimized adjustment of the strength against bending. Internal sheet metal components in cars, buses, trains, and airplanes that are subjected to one-sided loads are seen as a promising field of application for the structural components that can be produced with this technology since the structural properties can be influenced, both in terms of design and process technology. This is of particular

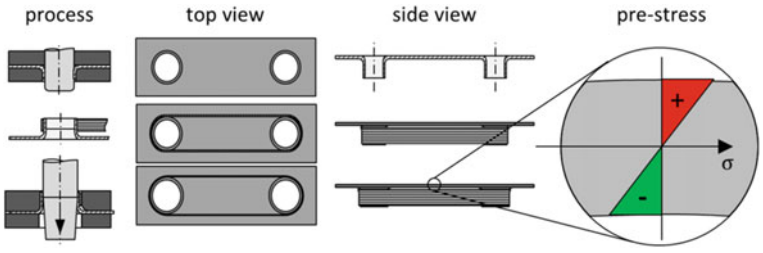


Fig. 2 Proposed joining and pre-stressing process. (Color figure online)

interest for crash structures, as these are subject to strict requirements regarding stiffness, strength, and energy absorption capacity. The possibility of setting different pre-stress values could be used to influence the load-deformation behavior without significantly changing the geometry of the structures.

The assumed structural behavior described shall be investigated and confirmed in the paper at hand. Here, the following hypotheses are to be investigated:

- By means of a plastic expansion of at least one of the two wrapped collars, an FRP strap can be joined to a sheet metal structure and to create a beneficial bending pre-stress
- The generated pre-stress can be significantly influenced, both in terms of design and process technology, thus enabling a targeted influence on the mechanical behavior of the hybrid structure
- A targeted pre-stress counteracting the stresses resulting from an external bending load can increase the maximum failure load of a hybrid structure.

Numerical and experimental investigations are carried out to test these hypotheses. The mechanism for joining and pre-stressing of the hybrid structures as well as the resulting pre-stresses for different process and design parameters are analyzed by means of a finite element simulation. An experimental setup serves for the qualitative validation of the model. Finally, bending tests are performed, to prove the stiffening and reinforcing effect against bending loads.

3 Materials and Methods

3.1 Specimen Geometry and Preparation

The specimens geometry used for the experimental investigations is shown in Fig. 3. The sheet metal structure to be reinforced is represented by a rectangular, laser-cut sheet metal blank made of 1 mm thick steel (DC04, 1.0338) with a width of 50 mm, and a length of 150 mm. Two drilled holes with a diameter of 8 mm are placed in the sheet's center axis with a distance of 100 mm center to center. In a combined

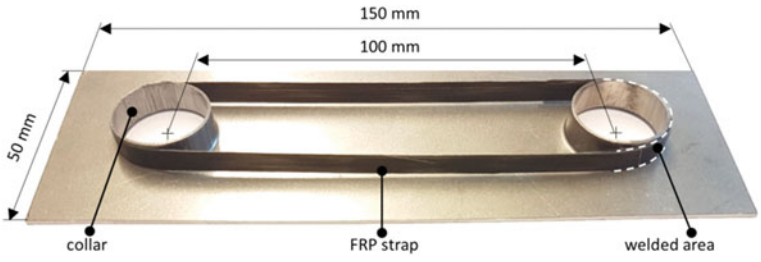


Fig. 3 Specimen geometry. (Color figure online)

collar drawing and wall-ironing process using a die with a diameter of 21.24 mm and a tractrix-shaped punch with a diameter of 20 mm, two collars are produced. Afterward, they are ground to a collar height of 7.5 mm measured from the blank top surface. The collars produced in this way have an inner diameter of 20.00 mm and an outer diameter of approx. 21.27 mm. Finally, an FRP strap with unidirectional fiber orientation and a thickness of 0.25 mm is manually wound around the two collars. In the bending tests performed, the width of the strap is set to 5.5 mm, while a width of 6.5 mm is used for comparison with the numerical results. The glass-fiber-reinforced polyamide tape (*BASF Ultratape B3WG12 UD01*, glass content: 60 wt.%) is locally melted by hot air and welded to itself within the area of the right side collar by applying a slight tension at the tape's free end. For the bending tests, also sheet metal blanks with two collars but without an FRP strap are used as a reference structure.

3.2 Setup for Joining and Pre-stressing of the Hybrid Structures

The experimental setup for widening the collar of the hybrid structures is based on the tool shown in Fig. 4. It consists of a cylindrical punch with a conical tip, a blank holder, a die, and two 3D printed support structures. The diameter of the punch increases from 19.5 mm at the smallest point to 21.5 mm at its maximum. The tapered section has an axial length of 25 mm. It is followed by a cylindrical shaft. The blank holder has a larger inner diameter of 25.5 mm to avoid contact with the collar and two grooves to take in the strap. Thus, it is only contacting the blank on its top planar surface. The die serves to support the sheet during the widening process. It has a hole with a diameter of 21.7 mm so that there is only a small gap between the punch and the die during the widening process, thus preventing the sheet from bending downwards. Two additional sheet supports are arranged next to the blank holder and the die to prevent curvature of the sheet metal due to the increasing pre-stresses. As they are only subjected to minor loads, they are 3D printed using PLA (polylactide), whereas all other tool components are made of steel (1.2379). The upper sheet support has a groove for the strap, while the lower sheet support is flat.

The single-acting tool is used on a 2,500 kN servo press. Figure 5 depicts the

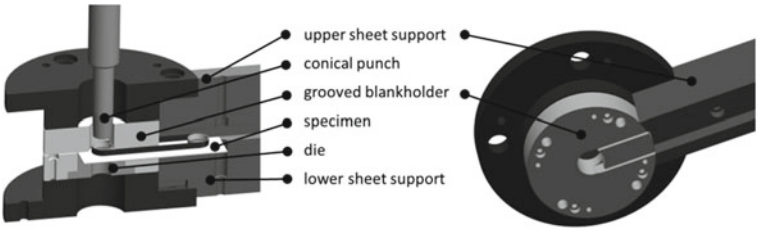


Fig. 4 Sectional view of the tool system (left) and blank holder components (right)

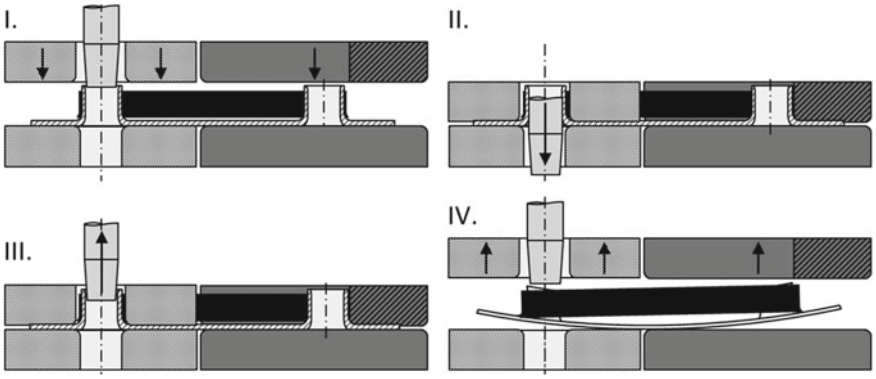


Fig. 5 Experimental process procedure

process steps of the experimental investigations, in which only the collar opposing the welded zone of the FRP strap is expanded. As a lubricant, a non-water-miscible, highly alloyed drawing, and punching oil (*Multidraw CF 4 by Zeller + Gmelin GmbH & Co. KG*) is applied with a cloth to the punch and inner collar surface. Then, the specimen is placed on the die, and the lower sheet support with the collar concentrically aligned to the punch. Afterward, the blank holder loaded by eight compression springs with a spring rate of 66.03 N/mm is moved down until it is in contact with the blank (phase I.). The collar is then widened by moving the punch downwards until the cylindrical area is fully inserted into the collar. During the downward movement of the punch, the springs are compressed providing an increased blank holder force. The total force increases from approx. 2.64 kN at the beginning of the widening process to a maximum of approximately 15.85 kN at its end (phase II). After fully retracting the punch (phase III), the blank holder is moved upwards so that the hybrid structure can completely spring-back (phase IV).

3.3 Setup for the Numerical Investigations

The numerical investigations are used to carry out the majority of the parameter studies. For the FEM analyses, the software *Dassault Systèmes Abaqus 6.14* is used. Since the model is primarily designed to identify influencing parameters and qualitative phenomena, the model complexity is reduced in comparison with the experimental setup. The blank holder, the die, as well as the sheet supports are considered in the form of two fixed analytical rigid planes arranged parallel to each other at a distance of 1 mm while contacting solely the sheet metal blank's planar surfaces. The punch is also designed as an analytical rigid with the already described geometry. Furthermore, the strap consists of one to three layers, each modeled as a seamless loop with a constant thickness. The sheet metal and the FRP strap are meshed with

deformable continuum hexahedral elements with reduced integration and hourglass control (C3D8I) with at least three elements over the component's thickness. The element edge lengths in the area of the collars are set to a maximum of 0.5 mm and increase to a maximum of 2 mm in the middle of the specimen. All contacts are modeled using the option "hard contact" in the normal direction and a penalty algorithm with a constant coefficient of friction in the tangential direction. By means of a numerically performed parameter variation during the widening of a non-wrapped collar and comparison with experimental results, a frictional coefficient between the planar sheet metal areas and the blank holder planes as well as between the inner collar wall and the punch of 0.1 was determined. Between the outer collar wall and the FRP strap, on the other hand, it is varied between 0.1 and 0.5 within the conducted parameter study, representing a span of coefficients stated in the literature and manufacturer's data for the contact between PA6 and steel [21, 22] as well as FRP tapes and steel [23, 24]. For the contact between the individual layers of the FRP strap, finally, the frictional coefficient is set to 0.4, which corresponds to a mean value the manufacturer's data suggests for a contact of PA6 with itself and glass-fiber-reinforced PA6 with itself [22] since micrographs show a fiber agglomeration in the tape's core and only a few fibers near the tape's surface. For the metallic component, an isotropic elastic–plastic material model is used, allowing for plastic deformation of the structure. The necessary flow curves are determined by tensile tests and extrapolated using the "Ludwik" equation [25]. It should be noted that the pre-hardening of the material in the collar area by the previously performed collar drawing process is not considered in the model. Due to the low plasticity of FRPs in the fiber direction, the CFRTP strap is modeled as fully elastic. Its anisotropy is taken into account by a material model based on engineering constants, calculated from manufacturer's specifications and data from literature. A material orientation tangent to the edge of the strap accounts for the fiber direction. Table 1 lists the most relevant material properties.

The whole pre-stressing process is divided into three steps, each lasting one second. The model is shown in Fig. 6. In the first step, the punch is moved downwards until the cylindrical part of the punch is completely inserted in the collar. Subsequently, the punch is moved back to its initial position. In the last step, the contacts to the two blank holder planes are released so that the sheet can spring back completely. During the spring-back phase, the sheet's edge near the expanded collar is fixed. While the first two steps use an explicit solver with a mass scaling of 10,000,

Table 1 Material properties of sheet metal and FRP tape

Material	Young's modulus (N/mm^2)	Density (g/cm^3)	Strain at break (%)	Yield strength (N/mm^2)	Tensile strength (N/mm^2)
DC04 (1.0338)	210,000	7.85	27.5	195	330
FRP tape 0° (PA6-GF)	33,000	1.72	3.4	–	770

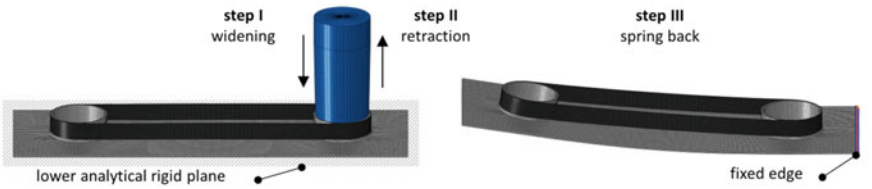


Fig. 6 Model and procedure of the numerical investigations (upper analytical rigid plane not depicted). (Color figure online)

Table 2 Parameter variations for the numerical investigations (reference configuration highlighted in bold)

Parameter for variation	Variant 1	Variant 2	Variant 3
Number of layers (-)	**1**	2	3
FRP layer thickness (mm)	**0.25**	0.30	0.35
FRP strap width (mm)	5.5	6.0	**6.5**
Frictional coefficient FRP-collar (-)	**0.5**	0.3	0.1
Maximum punch diameter (mm)	20.5	**21.0**	21.5
Distance between the collars (mm)	**100**	150	200

the last step is solved using a static implicit solver to avoid extensive oscillations due to the release of the energy elastically stored in the deformed specimen.

Six parameters are investigated in the numerical studies. To determine the dependence of the pre-stress on the stiffness of the tendon, straps with 1–3 layers are modeled. In addition, the thickness, as well as the width of the straps, is varied to three different values. Different coefficients of friction between metal and FRP, maximum punch diameters, and collar distances are also part of the variation. Based on the reference configuration highlighted in bold in Table 2, the individual parameters are changed according to the listed values.

3.4 Setup for the Bending Test

For the evaluation of the reinforcing and stiffening influence, three-point bending tests are performed. The test setup shown in Fig. 7 is used for this purpose. It consists of two supports with a 90° edge on which the specimen is placed with the collar facing downwards and a cylindrical punch with a horizontally oriented axis and a diameter of 10 mm. The support edges are spaced 127 mm apart so that the wrapped collars have enough distance to the supports so that they do not collide with them during bending. The influence of the non-reinforced sheet sections is minimized by keeping the gap as small as possible. The position-controlled tests are carried out using a tensile/compression testing machine (*Zwick Allround-Line 100 kN*) with a punch

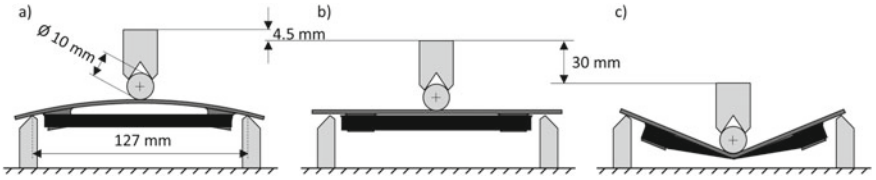


Fig. 7 Test setup for three-point bending

speed of 0.10 mm/s. At the start of the test (Fig. 7a), the punch is located 5.5 mm above the supports (4.5 mm above a flat sheet's top surface) so that the specimens curved by the pre-stressing can be inserted free of force. Afterward, the punch is moved down by 34.5 mm. In addition to the pre-stressed specimens, two types of comparison geometries are investigated. One type consists of a sheet metal blank with two collars and an almost tension-free wound strap. The other sample geometry consists of a sheet with two collars and without a strap. In order to take the stiffening effect of a collar with a larger diameter into account, one of the collars is widened in these samples as well. Since these specimens are almost flat at the beginning of the test, the punch comes into contact with the sheet after a distance of about 4.5 mm has been covered (Fig. 7b). Three samples are examined for each variant.

4 Results

4.1 Validation and Evaluation of the Results After the Collar Widening Process

Figure 8 shows a first overview of the results of the experimental and numerical investigations after the widening and spring-back of the specimen with the geometry described in Sect. 3.1 of this paper and a 6.5 mm wide FRP strap. It can be seen from both results that the sample has a distinct curvature due to the pre-stressing force generated by the collar's expansion. Although the collars' axes are, due to this curvature, no longer parallel to each other, the strap is securely held in its position and

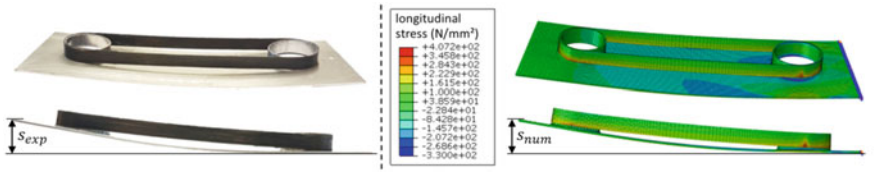


Fig. 8 Experimentally pre-stressed specimen (left) and numerical result (right). (Color figure online)

does not slip off the structure. To estimate the quantitative agreement of the numerical and experimental results, the extent of the curvature is examined. For this purpose, the specimens end with the widened collar is clamped flat on a surface, while the vertical deflection s_{exp} (cf. Fig. 8) of the other end of the upper edge is measured using a dial gauge. Three samples are measured. For the experimentally produced structures, the average displacement of the edge is 11.78 mm. The deviations are −0.71 mm to the minimum and 0.80 mm to the maximum. In the numerical representation of the process, the edge shifts by a distance of $s_{num} = 11.46$ mm in the vertical direction. Although the experimentally pre-stressed specimens are subject to comparatively high fluctuations, both investigations show comparable results so that both can be regarded as valid.

In order to evaluate if a frictional connection between collar and strap was created, the contact normal stresses between the components after completion of the collar widening process but before spring-back are analyzed. Here, the numerical results show that contact stresses of between 5 and 15 N/mm^2 occur at over 95% of the wrapped area. The numerical model is also used to examine the amount of pre-stressing more closely. For this purpose, the stresses in the longitudinal direction of the specimen are evaluated along a path that lies centrally in the transverse direction of the sheet on the concave surface (cf. left side of Fig. 9). After complete spring-back, pronounced compressive stresses appear on this collar-side surface. These amount to 142.85 N/mm^2 on an arithmetic average. While the compressive stresses increase to up to 148.21 N/mm^2 at a distance of about 6 mm to the edges, the center of the sheet has lower stress of about 137.00 N/mm^2. The non-uniform distribution of the stresses is due to the onset of plastic deformation of the base sheet around the collar. The inhomogeneous plastic compression of the sheet in the longitudinal direction leads to an inhomogeneous planar stress state after spring-back, in which the highly compressed areas in the middle of the sheet are set under tensile stresses by the less plastically compressed areas at the sheet edges. This non-uniform deformation is also evident in a local increase of the sheets width in the area of the collars to about 50.75 mm. While the pre-stress in the sheet metal is manifested as a bending load, the strap is loaded by tension.

The diagram on the right side of Fig. 9 shows the development of the tensile force F_s transmitted by the strap during the pre-stressing process. When the punch

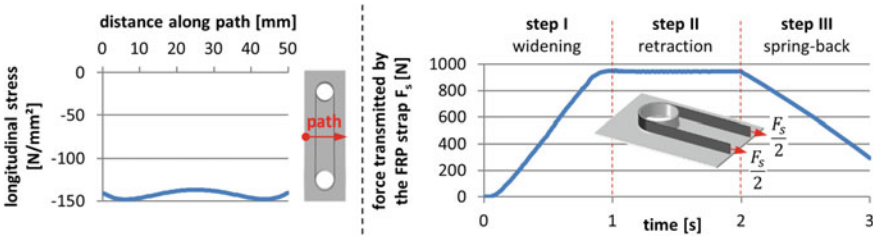


Fig. 9 Longitudinal stresses at the sheets collar-side surface (left) and force transmitted by the FRP strap during the pre-stressing process (right). (Color figure online)

is inserted into the collar, the strap force increases nonlinearly until the collar wall is completely in contact with the conical punch. Afterward, the force increases in an almost linear manner until the cylindrical section of the punch gets in contact with the collar. After one second, the punch has reached its bottom dead center with the maximum strap force of approx. 953.94 N. This force decreases when the punch is pulled out, leaving a strap force of approx. 943.20 N at the end of step two. Particularly noteworthy is the low level of collar spring-back. In the third and final simulation step, the sample can spring back completely, whereby the force decreases considerably to a value of about 293.37 N due to the bending of the sheet metal blank. However, this strong reduction of the strap's tension due to the spring-back is highly dependent on the bending stiffness of the sheet metal structure. An equally strong decrease is not to be expected for stiffer structures.

In summary, both the experimental and numerical results confirm the hypothesis presented at the beginning, that a hybrid FRP sheet structure can be joined and simultaneously pre-stressed by widening one of two FRP-wrapped collars.

4.2 Determination of Parameters Influencing the Pre-stress

In the following, the influence of various parameters on the pre-stress will be examined. The previously presented strap force F_s will serve as a comparative value. Figure 10 shows the numerically determined strap forces depending on the varied parameters. Since the curve described in Fig. 9 (right) is qualitatively identical for all variations, only the forces at the end of the respective steps are shown.

Overall it can be stated that almost all parameters have a significant influence on the pre-stressing strap force that can be generated. It is also shown that even if there is a greater effect on the pre-load after the first step, only minor changes occur after the punch is withdrawn, i.e., at the end of step 2. In the following, the individual variation results will be briefly presented and discussed.

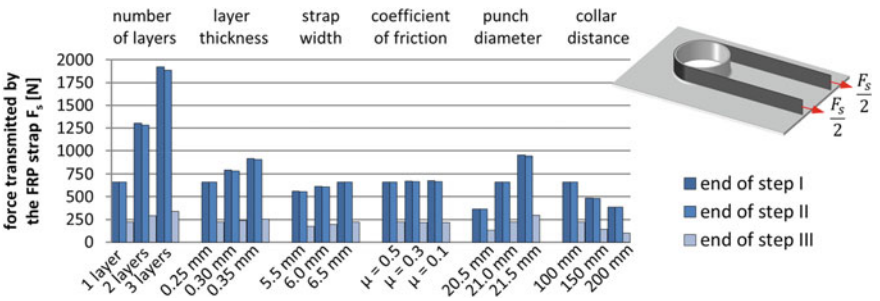


Fig. 10 Results of the numerical parameter study—forces transmitted by the FRP strap. (Color figure online)

If the **number of the straps layers** is increased, the total transmitted force increases almost proportionally with the increased total cross-section area of the strap. This can be explained by the fact that the absolute elongation is imposed geometrically by the ideally stiffly modeled punch. As the cross-section of the strap increases, its stiffness increases by the same factor. Correspondingly, the tensile force, which is linearly dependent on the stiffness, is increased equally. The same behavior can be observed when increasing the **layer thickness** or the **strap width**. As the cross-section and thus the stiffness of the tendon is increased here as well, a greater tension force is created. At first sight unexpected is the almost completely negligible influence of the **frictional coefficient** between the collar and FRP-strap. In order to explain this, the development mechanism of the strap's tension force must be examined more closely. It results from the change in length of the strap as a reaction to the widening of the collar. Since this change in length mainly depends on the expansion ratio, the absolute strains do not change by varying the frictional coefficient. The strain distributions and therefore the stresses occurring in the strap, however, are significantly influenced by the apparent friction. As described above, the elongation of the strap is mainly caused by the expansion of the collar. If the **punch diameter** is increased, the force transmitted by the strap increases accordingly. A larger **collar distance** finally leads to a reduction of the strap force. This is due to the fact that a constant expansion ratio leads to a constant absolute elongation of the strap. If the initial strap length is increased, its stiffness is reduced so that lower forces occur.

4.3 Mechanical Properties of the Pre-stressed Hybrid Structures Under Bending Loads

The results of the bending tests are shown in Fig. 11. The diagram on the left side shows the force–displacement curves of one representative specimen per tested variant. The deviating values of the other samples of the same type are shown as

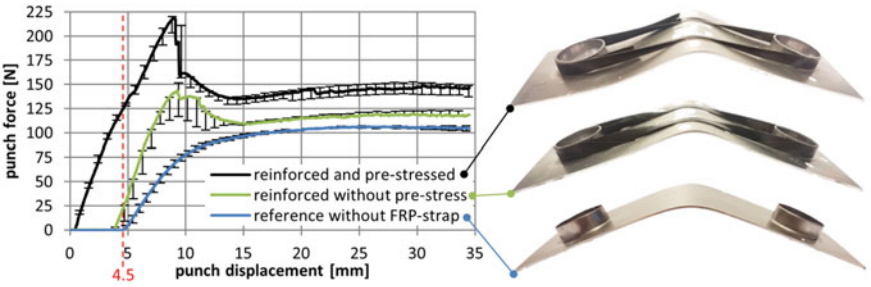


Fig. 11 Results of the bending tests: force–displacement-curves (left) and specimens after the bending tests (right). (Color figure online)

error bars in the diagram. Since the sudden drop in force does not occur at the same punch displacement for all samples, the deviations increase around this area. The specimens after bending are shown on the right side of Fig. 11. Their order from top to bottom corresponds to that of the graphs in the diagram.

First, the **reference sample without a reinforcing strap** shall be examined. As described in Sect. 3.4 of this paper, the punch in the test setup starts 4.5 mm above the sheet surface. As soon as this distance has been covered and the punch comes into contact with the plate, the forces increase linearly with stiffness of about 18.0 N/mm. Above approx. 55 N, the sample starts to yield, and the slope decreases. The maximum force of 106.4 N is reached after a punch stroke of about 27.1 mm. In comparison, the **specimen provided with a non-pre-stressed strap** shows a distinctly different curve. As the wrapped strap already applies a very small preload to the sheet, the sheet is slightly curved so that the punch comes into contact with the sample shortly before reaching a distance of 4.5 mm. The force then increases almost linearly with stiffness of approximately 35.6 N/mm. The maximum force of 143.6 N is reached at a punch displacement of about 9.3 mm. Here the force drops spontaneously due to the tilting of one side of the FRP strap. Afterward, the force rises again until the other side of the strap tilts as well and another drop occurs. Subsequently, the curve approaches a path running parallel to that of the reference curve. The **reinforced and pre-stressed specimen**, finally, comes into contact shortly after the start of the test due to the initial curvature resulting from the pre-stress. While a qualitatively similar behavior like that of the loosely reinforced specimen can be seen, the forces are considerably higher for the pre-stressed sample. The maximum force is about 220.96 N. The stiffness in the elastic area, however, is very similar and amounts to approx. 37.0 N/mm.

In summary, the test results show that joining a sheet metal structure with an FRP strap can significantly increase the stiffness and strength compared to a metallic reference structure. In addition, it can be concluded, that the introduction of a targeted pre-stress can significantly increase the failure loads under bending stresses, even if the individual components are not changed in their cross-section. The pre-stress, however, has no significant influence on the stiffness of the respective structure.

5 Conclusion and Outlook

In the paper at hand, a novel joining method was presented, which allows for strengthening and purposefully pre-stressing of sheet metal structures by widening of an FRP-wrapped collar. Based on the results of experimental and numerical investigations regarding the joining and pre-stressing process as well as characterizing bending tests on the structures produced this way, the following conclusions can be made:

- By means of a plastic expansion of at least one of two wrapped collars, an FRP-strap can be joined to a sheet metal structure and a beneficial bending pre-stress in the metallic component can be generated.

- The generated pre-stress can be significantly influenced both in terms of design and process technology, thus enabling a targeted influence on the mechanical behavior of the hybrid structure. Here, an increase of the FRP strap's stiffness or the expansion ratio of the collar leads to an increase of the generated pre-stress, whereas it is decreased by a larger distance of the collars.
- A targeted pre-stress counteracting the stresses resulting from an external bending load can increase the maximum load before failure of a hybrid structure by more than 50% without changing the cross-sectional geometry of its components.

Due to the manifold influencing parameters and their impact on the generated pre-stress, it is expected that fluctuations in process parameters and properties of semi-finished products can have significant effects causing deviations from a targeted mechanical behavior. In further investigations, the process control is to be improved by enabling an in-situ measurement of the pre-stresses. It is also planned to transfer the new process technology to more complex sheet metal structures such as bumpers and side-impact beams, in which the influence of a defined pre-stress on the mechanical properties can be used to create structures with a desirable failure behavior.

Acknowledgments Funded by the Deutsche Forschungsgemeinschaft (DFG, German Research Foundation)—Project Number 453074727.

References

1. Tamerl I (2010) Das Holzfass in der römischen Antike. Studien-Verlag, Innsbruck
2. Ploch J (2004) Zur Definition und zum Sicherheitskonzept der Vorspannung. PhD thesis, Universität Stuttgart
3. Deuring M (1993) Verstärkung von Stahlbeton mit gespannten Faserverbundwerkstoffen. PhD thesis, ETH Zürich
4. Ghafoori E, Motavalli M (2015) Normal, high and ultra-high modulus carbon fiber-reinforced polymer laminates for bonded and un-bonded strengthening of steel beams. Mater Design 67:232–243
5. Ampatzidis T, Chronopoulos D (2016) Acoustic transmission properties of pressurised and pre-stressed composite structures. Compos Struct 152:900–912
6. El-Saikaly G, Chaallal O (2015) Fatigue behavior of RC T-beams strengthened in shear with EB CFRP L-shaped laminates. Compos B Eng 68:100–112
7. Merklein M, Allwood JM, Behrens BA, Brosius A, Hagenah H, Kuzman K, Mori K, Tekkaya AE, Weckenmann A (2012) Bulk forming of sheet metal. CIRP Ann 61(2):725–745
8. Wolf F, Sutor A, Rupitsch SJ, Lerch R (2011) Modeling and measurement of influence of mechanical prestress on hysteresis of ferroelectric actuators. Procedia Eng 25:1613–1616
9. Veer F, Bos F, Zuidema J, Romein T (2005) Strength and fracture behaviour of annealed and tempered float glass. In: Associates C (ed) 11th international conference on fracture (ICF11), pp 3055–3060
10. Alegre JM, Bravo P, Preciado M (2007) Fatigue behaviour of an autofrettaged high-pressure vessel for the food industry. Eng Fail Anal 14(2):396–407
11. Hurst MK (1998) Prestressed concrete design, 2nd edn. Spon Press, London

12. Meier U, Brönnimann R, Anderegg P (2015) Long term reliability of CFRPs in bridge engineering. In: Paper presented at the 20th international conference on composite materials, Copenhagen, 19–24 July 2015
13. Michels J, Barros J, Costa I, Sena-Cruz J, Czaderski C, Giacomin G, Kotynia R, Lees JM, Pellegrino C, Zile E (2016) Prestressed FRP systems. In: Pellegrino C, Sena-Cruz J (eds) Design procedures for the use of composites in strengthening of reinforced concrete structures. Springer, Netherlands, pp 263–301
14. Ghafoori E, Motavalli M (2013) Flexural and interfacial behavior of metallic beams strengthened by prestressed bonded plates. Compos Struct 101:22–34
15. Kotynia R, Walendziak R, Stoecklin I, Meier U (2011) RC slabs strengthened with prestressed and gradually anchored CFRP strips under monotonic and cyclic loading. J Compos Constr 15(2):168–180
16. Erki MA, Rizkalla SH (1993) Anchorages for FRP reinforcements. Concr Int 15(6):54–59
17. Schlaich M, Zwingmann B, Liu Y, Goller R (2012) Zugelemente aus CFK und ihre Verankerungen. Bautechnik 89(12):841–850
18. Schmidt JW, Bennitz A, Täljsten B, Goltermann P, Pedersen H (2012) Mechanical anchorage of FRP tendons: a literature review. Constr Build Mater 32:110–121
19. Zwingmann B, Liu Y, Schlaich M, Janetzko S (2017) The sling anchorage: approach to anchor the full load bearing capacity of pin-loaded straps. Compos Struct 178:110–118
20. Marré M, Brosius A, Tekkaya AE (2008) New aspects of joining by compression and expansion of tubular workpieces. Int J Mater Form 1:1295–1298
21. Voyer J, Klien S, Velkavrh I, Ausserer F, Diem A (2019) Static and dynamic friction of pure and friction-modified PA6 polymers in contact with steel surfaces: influence of surface roughness and environmental conditions. Lubricants 7(2):17
22. BASF SE (2014) Technical Information - Reibung und Verschleiß bei Polymerwerkstoffen
23. Winistörfer A, Mottram JT (2001) Finite element analysis of non-laminated composite pin-loaded straps for civil engineering. J Compos Mater 35(7):577–602
24. Fan H, Vassilopoulos AP, Keller T (2018) Numerical and analytical investigation of tensile behavior of non-laminated and laminated CFRP straps. Compos Struct 200:79–87
25. Ludwik P (1909) Elemente der technologischen Mechanik. Springer-Verlag, Berlin

Computer-Aided Modeling of the Hot Forming Staking Process Based on Experimental Data



Sebastian Härtel, Eric Brückner, Birgit Awiszus, and Michael Gehde

Abstract As a non-detachable and point-acting joint, thermoplastic staking is primarily used for the production of electronic and sensor elements as well as for the joining of components in the automotive interior and exterior. Commonly, the advantages of staking processes are its cost-efficient and seemingly simple process control. Regarding the industrial application, staking is principally a well-established forming process. However, despite the high number of applications, the joint design and the process settings are mainly based on extensive empirical tests. At present, the FE simulation of these thermoplastic staking processes is not state-of-the-art. Due to these facts, within the frame of the paper, these gaps are to be closed by the computer-aided modeling of the hot forming staking to map the heating and forming behavior of this process close to reality. This procedure demands the associated experimental validation of the simulation. In summary, the numerical model shows high conformity to the experimental data and allows a simulative mapping of the morphological characteristics of the riveted joint as well as indicative statements to the process parameters, which means in particular the minimal heating time for forming and the optimized post-heating time for a morphological homogenization.

Keywords Staking · Riveting · Plastic · FE simulation · Forming behavior · Process optimization

S. Härtel (✉) · B. Awiszus
Virtual Production Engineering, TU Chemnitz, Reichenhainer Str. 70, 09126 Chemnitz, Germany
e-mail: haseb@hrz.tu-chemnitz.de; sebastian.haertel@mb.tu-chemnitz.de

B. Awiszus
e-mail: birgit.awiszus@mb.tu-chemnitz.de

E. Brückner · M. Gehde
Professorship of Plastics Engineering, Reichenhainer Str. 70, 09126 Chemnitz, Germany
e-mail: eric.brueckner@mb.tu-chemnitz.de

M. Gehde
e-mail: michael.gehde@mb.tu-chemnitz.de

© The Minerals, Metals & Materials Society 2021

G. Daehn et al. (eds.), *Forming the Future*, The Minerals, Metals & Materials Series,
https://doi.org/10.1007/978-3-030-75381-8_117

1 Introduction

Conventionally, the staking processes are differentiated according to their type of heat input. Referring to this, it has to be distinguished in heat conduction (hot forming staking), convection (hot air staking), intermolecular friction (ultrasonic staking), and radiation (infrared and laser staking). However, the fundamental forming procedure of all staking processes is basically equivalent. Figure 1 schematically shows the associated processes sequence. In this regard, the rivet pin is formed by a forming tool (punch), starting at its end face and continuing to the end position, until the punch touches down on the upper part. The characteristic design of the rivet head is introduced into the forming punch in its negative style.

As a significant advantage, the staking processes ensure the joining of different material types. While one of the joining partners, which means the lower part with the mostly constructively integrated rivet pin, has to be a thermoplastic one, there are nearly no limitations for the material selection of the upper part. This fact predestines the staking processes for their application in the field of mixed-material compounds.

Due to the high diversity of applications and materials, the plastic staking process is subjected to complex requirements that must be compensated by a sufficient understanding of the process and targeted quality assurance in order to ensure safe process application. In this context, the knowledge of the interactions between process setting, material properties, and joint quality is an essential prerequisite. However, these issues have not yet been adequately covered by the scientific community. In fact, the dimensioning of the rivet design as well as the process optimization is mainly based on empirical tests and special expert knowledge.

While plastic staking has been increasingly investigated in depth in recent years using experimental studies to increase process understanding [2, 3, 5, 6], the numerical analysis and simulative representation of the staking processes are not the common state-of-the-art. Regarding simulation, the basic challenge is the change of the plastic material from solid to a molten state and back during staking. Furthermore, the thermal condition has a very high influence on the material's structure and must be considered very precisely.

For manufacturing processes, in which solids interact with fluids, various calculation approaches currently exist. By using a coupled-fluid structure calculation, the

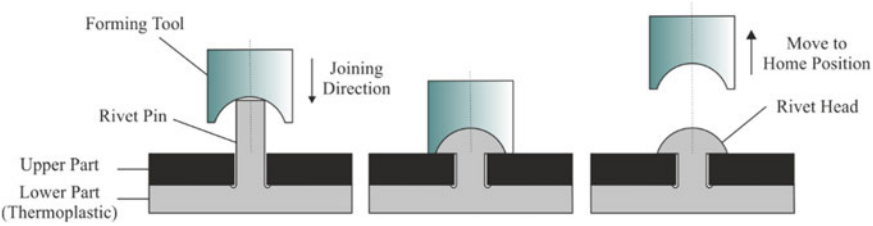


Fig. 1 Principle of a staking process, **a** before staking, **b** rivet joint after staking [1]. (Color figure online)

polymer injection forming (PIF) was simulated in [4]. However, this kind of simulation could not be applied because of the continuously changing of the material state during the staking process. Additionally, calculations in [7, 8] were already done, which use pure structure code and the rate-power-law. Nevertheless, by using even this type of process simulation, the definition of the melt range was carried out in advance and not continuously during forming. The literature also provides some numerical simulation results of the infrared staking process. However, in [9, 10] the viscous flow behavior of the plastic melt was neglected and the elastic–plastic material behavior was only considered in the temperature range of 15–100 °C.

The first and so far only scientific analysis and numerical mapping of a real staking process, by considering material and process conditions close to reality, was carried out by [1]. Härtel et al. has successfully simulated the double-stage process of hot air staking. In this regard, the Hensel-Spittel approach was used to describe the material behavior for the elastic–plastic state. Additionally, the Lagrange approach was applied to describe the flow behavior of the molten thermoplastic material. In detail, it was done with the Ostwald-de Waele power-law model. In contrast to [9, 10], the numerical model also considers the viscous material behavior of the melt during the staking process. Finally, the model shows high qualitative conformity to the experimental data, allows the evaluation of the minimum heating time, and provides information about the material's structure based on the hot air staking process.

However, the simulation of [1] still has the limitation that the melt formation and forming are carried out in separate process steps and thus represent the double-stage process of hot air staking. In contrast, for single-stage staking processes the melt formation and forming alternate continuously. This kind of staking process has not yet been numerically modeled.

2 Research Objectives

In comparison between simulation and experiment, the single-stage process hot forming staking should be numerically modeled for the first time. In this context, the influence of the process parameters, in particular the joining force and heating time, was the focus of the present experimental and numerical investigations.

In this regard, the heating and forming behavior during staking was analyzed in depth. It was the aim to create a simulation model close to reality, to predict the melt formation, the forming behavior, as well as the morphology of the riveted joint. The simulation should give some information about the minimal heating time of the rivet pin to form the rivet head and should predict potentially the weak points of the joint. Additionally, the numerical simulation should increase the process transparency in regard to the influence of the rivet design as well as the influence of the thermoplastic material. Based on these information, in the future, it should be possible to predict the joint properties by numerical simulation close to reality.

3 Experimental Process Analysis—Reference Test

The following experimental investigations were carried out using a hot staking machine (type B2000-H) of the company bdtronic GmbH (Weikersheim, Germany). The advantages of the machine concept are a precise temperature control to a maximum of 400 °C, a pneumatic joining force application up to a maximum of 120 N, and the existing configuration of the cooling system. Figure 2 shows a schematic illustration of the hot forming staking procedure. It can be described as a single-stage process, which means the heating and forming of the rivet pin take place simultaneously.

In the first process step, the forming punch is heated in its home position to the operating temperature without coming into contact with the rivet pin. Once this temperature is reached, the forming punch is moved toward the rivet pin with a constant joining force. As a result of the applied temperature and force, the rivet pin is continuously shaped by the forming punch. In this regard, the heat transfer is based on thermal conduction. After reaching the end position of the punch, which means a perfect joint, the punch is actively cooled by having a cool airflow to the top of the punch (step 3). After the end of the cooling period, the punch moves back to its home position (step 4). The joined components can then be removed.

The following results in the present paper are based on the material polypropylene (PP), type Moplen HP501 H (manufacturer LyondellBasell, Rotterdam, the Netherlands). Polypropylene is a semi-crystalline thermoplastic material that tends to crystallize strongly, exhibits ductile material behavior, and has excellent properties for structural analysis by microscopy to investigate the heating and forming behavior. The rivet pin has a diameter of 3.0 mm and a length of 10.8 mm. By using an upper mating part of steel X5CrNi18-10 (1.4301) its properties are not changed by the staking process. The thickness of the mating part is 3.0 mm, which leads to a constant protruding length of the rivet pin of 7.8 mm. The rivet head had the common industrial design of a hemisphere with a diameter of 6.0 mm and was adapted to the protruding volume of the rivet pin. Regarding the experimental investigation of the heating and forming behavior, transmitted-light microscopy was used. Therefore,

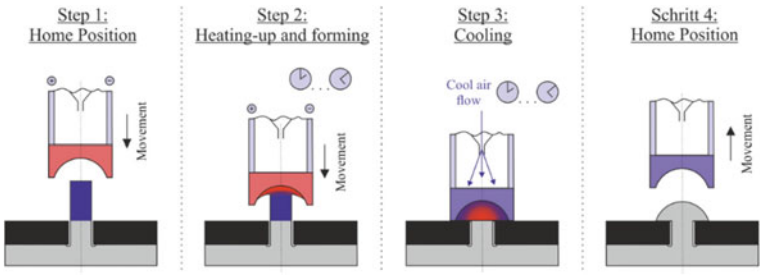


Fig. 2 Schematic illustration of the hot forming staking consisting of four process steps. (Color figure online)

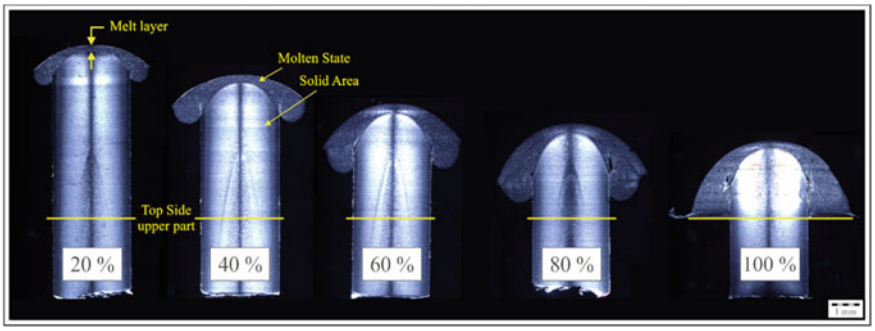


Fig. 3 Melt formation and forming behavior shown by thin sections of the rivet pin/rivet head for different steps of forming (transmitted-light microscopy). Process parameters: material polypropylene (PP), joining force 30 N, and punch temperature 300 °C. (Color figure online)

the rivet pin and rivet joint were prepared as an extracted thin cut (thickness 10 μm) in the center plane of the rivet pin. By using a polarization microscope (Olympus BX51, Olympus Corporation, Shinjuku City, Tokyo, Japan), the melted and recrystallized area was measured (software Imagej, National Institutes of Health, Bethesda, Rockville, MD, USA) characterized by the melt formation during staking.

Based on the experimental tests, Fig. 3 shows the time-dependent melt formation and forming behavior by means of a stepwise sequence during hot forming staking. Resulting from the thermal energy input of the punch, a thin melt layer could be detected on the upper side of the rivet pin during the entire staking procedure. As a consequence of the joining pressure, the punch displaces the melt into its side areas and thus continuously shapes the rivet pin. As forming progresses, the free volume of the punch fills up increasingly and the displaced plastic melt goes into contact with the non-plasticized rivet pin. However, when the punch has reached its end position, a geometrically complete rivet head is shaped.

However, a closer examination of the rivet joint (see Fig. 4) shows that the rivet head is not intrinsically tied to the rivet pin. Consequently, the theoretical "maximum load-bearing head height" must be divided into the two components of the "reduced load-bearing head height" and the "weld line height". It can be noted that this kind of weld line seems to be very similar to a cold weld line in injection molding. Due to the unequal thermal levels of the generated plastic melt (high temperature) and the not plasticized rivet pin (low temperature), the melt cannot tie to the rivet pin during the encounter.

4 Numerical Process Simulation

In regard to the numerical process simulation, the software simufact.forming (Simufact Engineering GmbH, Hamburg, Germany) was used to build a numerical model

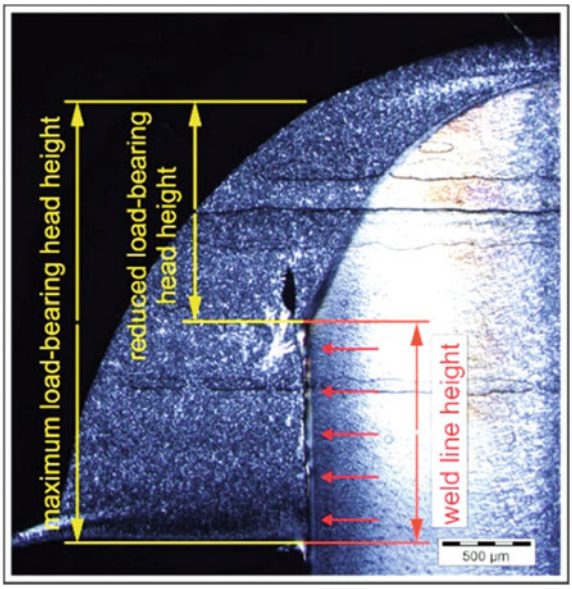


Fig. 4 Resultant materials morphology in the rivet joint based on Fig. 3 shown by a thin section (transmitted-light microscopy). An incomplete joint of the rivet head and the rivet pin by having a characteristic weld line. Derivation of the important design parameters of the joint material polypropylene (PP). (Color figure online)

of the hot forming staking process. The process simulation was carried out with a 2D rotationally symmetrical model by using the real tool geometry. However, the punch is constantly force-controlled in accordance with the experimental investigations. Additionally, the punch has a temperature of 300 °C and the upper part (joining partner) has a temperature of 20 °C. The heat transfer coefficient of the tools to the workpiece is set to 10.000 W/m^{2}K. To be able to reproduce the material flow close to reality, the rivet pin was meshed very finely with an element edge length of 0.1 mm (quad elements). Figure 5a shows the basic simulation setup of the hot forming staking process.

Regarding numerical simulation, one of the biggest challenges is the definition of material behavior. The material is partially melted by contact with the hot punch and is consequently displaced in the molten state. Thus, during the entire staking process, the PP material is present in both the solid and the molten material state. In order to be able to reproduce this within a contact body, a suitable subroutine must be used. This subroutine has been already developed by Härtel et al. for hot air staking and is presented in [1]. Furthermore, Härtel et al. describe in detail how the necessary material data are determined and mathematically considered by the subroutine in the simulation [1].

However, as presented in Fig. 5b, the core elements of the material determination and description are summarized for both the solid and the molten state. The simulation setup allows the simulation of the hot forming staking process for the first time and thus a deeper process analysis than it is possible through purely experimental work. To ensure that the simulation gives realistic results, a comparison with the experimental results was necessary. Afterward, the verified simulation can be used for deeper

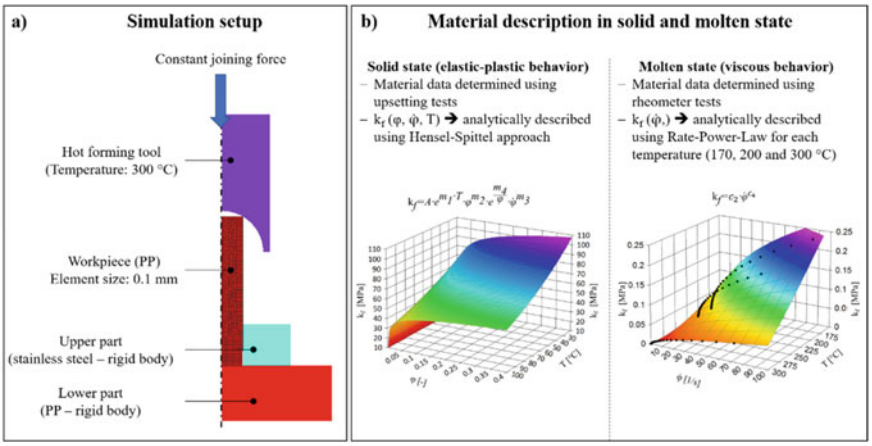


Fig. 5 **a** Simulation setup for the hot forming staking process; **b** material properties for the solid and molten state concerning [1]. (Color figure online)

process analysis. The following process parameters were used for the verification of the numerical simulation:

- Temperature of the punch: 300 °C
- Joining force: 30 N/120 N
- Variation of the post-heating time: $t_A = 0$ s/5 s/10 s/20 s.

At the beginning of the numerical analysis, the calculated process duration was compared with the experimentally determined heating time which is necessary to shape the rivet pin completely and form out the rivet head. Table 1 shows that the calculated process duration correlates very well with the experimentally measured duration. The deviation is less than 10%.

Additionally, based on the experimental data in Fig. 3, Fig. 6 shows the results of the simulated melt formation and melt flow in comparison to the experiment for different steps of forming (stroke of 40 and 80%) by having a joining force of 30 N. In this context, a high-level agreement could be detected between the calculated and the real conditions. In both cases, the material is successively melted and displaced.

Furthermore, in Fig. 6 the numerically calculated temperature distribution is displayed. From this, the melt layer thickness formed can be derived indirectly, insofar as the temperature is above the melting temperature of approx. 160 °C. The experimentally determined melt layer thickness of 0.26 mm, by having a stroke of 80%, is very close to the calculated melt layer thickness of 0.22 mm.

Table 1 Comparison of the experimentally measured and numerically calculated process duration

Process duration—experiment	Process duration—simulation	Deviation
5.0 s	5.35 s	7%

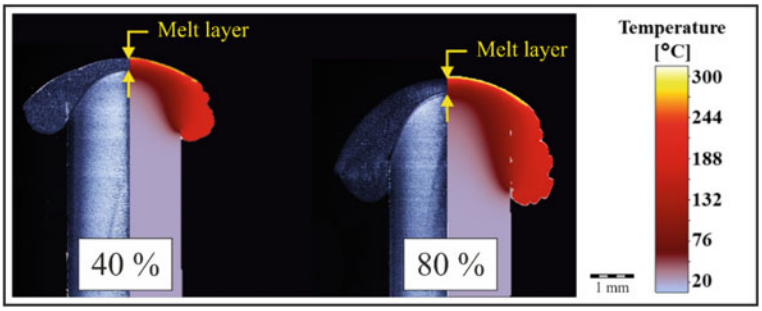


Fig. 6 Comparison of the experimental data according to Fig. 3 (thin sections) and the calculated melt formation (simulation) during forming for different steps of forming (exemplary stroke of 40 and 80%). Process parameters: material polypropylene (PP), joining force 30 N, and punch temperature 300 °C. (Color figure online)

Due to the high agreement between the numerical and the experimental data, the created model can subsequently be used for this kind of process simulation. Consequently, in the next step, the influence of the joining force was analyzed. For this purpose, a further simulation was carried out with a constant joining force of 120 N. Additionally, the rivet joint was analyzed focusing on the formation of weld lines. Concerning this matter, self-contacting areas at the end of the process were evaluated in the simulation, analogous to the approach in [1]. As shown in Fig. 7, a higher joining force of 120 N leads to an increasing in the weld line height. By using a joining force of 30 N, the weld line height is only 1.20 mm, which means a percentage of 65% compared to the weld line by using a joining force of 120 N. Consequently, based on the numerical results and the assumption that a weld line weakens the

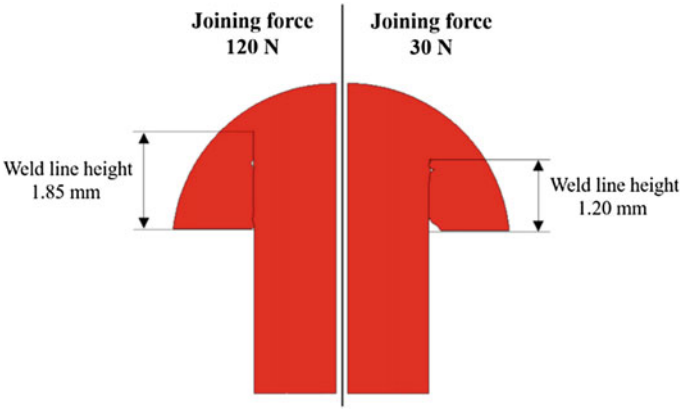


Fig. 7 Emerging weld lines for a joining force of 120 N in comparison to a joining force of 30 N. (Color figure online)

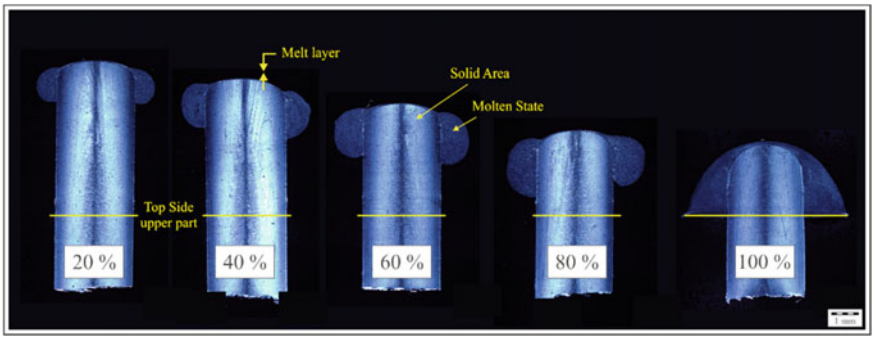


Fig. 8 Melt formation and forming behavior shown by thin sections of the rivet pin/rivet joint for different steps of forming (transmitted-light microscopy). Process parameters: material polypropylene (PP), joining force 120 N, and punch temperature 300 °C. (Color figure online)

Table 2 Comparison of the experimentally measured and numerically calculated weld line height for different joining forces of 30 and 120 N

Joining force (N)	Calculated weld line height (mm)	Experimental weld line height (mm)
30	1.20	1.20
120	1.85	1.90

seam properties, a low joining force should be preferred to have maximized joint properties.

In order to prove the influence of the joining force experimentally, the melt formation and forming behavior was also carried out by using a joining force of 120 N. The time-dependent melt formation and forming steps are shown in Fig. 8. It could be demonstrated that the melt formation, and in particular the weld line height, could be influenced by the joining force of the punch significantly. In contrast to Fig. 3, an increased joining force of 120 N leads to a smaller melt layer between punch and rivet pin. At the end of the forming process also, increased weld line height could be detected. The real measured weld line height was very close to the calculated values as shown in Table 2. Regarding the strength of the joint, by using a high joining force lower mechanical properties are expected, which was already shown in [2] for several thermoplastic materials.

5 Experimental and Numerical Analysis of the Post-heating

The experimental investigations revealed that the joint quality can be significantly improved by additional energy input. In this case, additional heating follows directly after the forming process. Here, thermal energy is introduced into the rivet head without any further punch movement. This procedure leads to an increasingly melt formation of the rivet head and is so-called “post-heating”. However, the post-heating

is mainly described by the post-heating time t_A. The numerical simulation was now used to determine the minimum reheating time in order to minimize the weld line height. In this regard, Fig. 9 shows the results of simulation and experiment in comparison. It can be seen that the distribution of molten areas (red-colored) and still solid areas (blue-colored) significantly depends on the post-heating time. However, the weld line height only decreases disproportionately with an increasing post-heating time. A complete bond between the rivet pin and the rivet head, which means no weld line would appear, does not seem to be possible. The simulation model clearly shows that the reason for this effect is the heat dissipation of the joining partner because of the high thermal conductivity of stainless steel. It can thus be stated that a post-heating time of 10 s leads to a significant reduction of the weld line height. A further increase in the post-heating procedure must be rated as inefficient.

These findings can be confirmed by tests regarding the mechanical properties of the rivet joint (tensile load). Nevertheless, in order to detect this effect precisely, the material-specific as well as design-specific properties of the joint must be taken into account. As shown in Fig. 10, no determinable increase of the breaking force could be detected for the material PP. This fact could be explained by the failure behavior of the joint and the pronounced ductile material behavior in combination with the present rivet design. In this case, the combination of the boundary conditions resulted in the failure occurring predominantly in the rivet pin. Consequently, the principally improved joint quality is not reflected in the breaking forces of the joint.

In contrast, the material PA66-GF30, reinforced with 30% of short glass fibers, reveals a significant increase of the breaking force by having a rising post-heating time in the range of 5–20 s (see Fig. 10) and thus confirms the results of the numerical model clearly. Consequently, the post-heating process enables the systematical optimization of the joint properties regarding specific requirements in terms of mechanical properties.

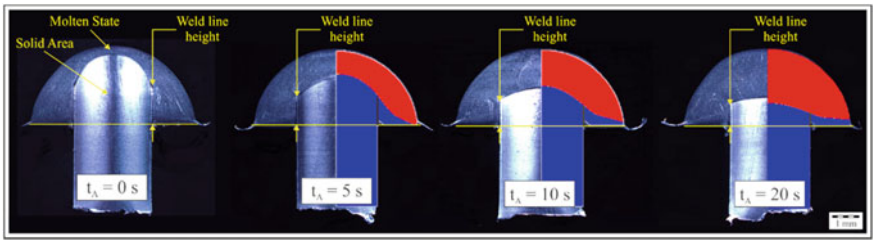


Fig. 9 Comparison of the experimental data (transmitted-light microscopy) and numerically calculated melt formation by using a post-heating time t_A. Distribution of molten (red-colored) and solid (blue-colored) areas in order to analyze the resulting weld line height (black-colored line). Process parameters: material polypropylene (PP), joining force 30 N, punch temperature 300 °C, and variation of the additional heating time t_A. (Color figure online)

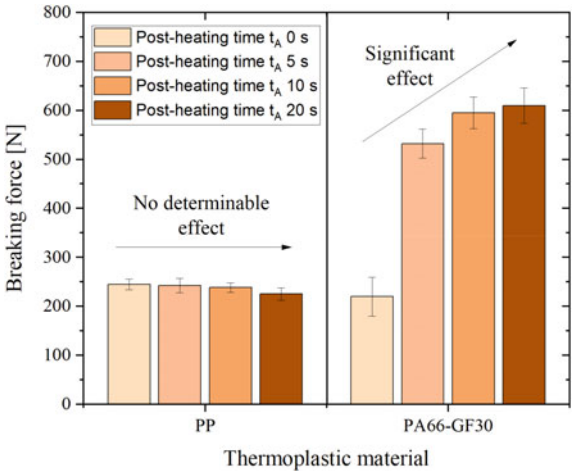


Fig. 10 Influence of the post-heating time t_A on the breaking force under head tensile loading for PP and PA-GF30. (Color figure online)

6 Conclusion

The present paper demonstrates the computer-aided modeling of the hot forming staking process based on experimental data. Hereby, the numerical model shows high qualitative conformity to the experimental data, which means that the simulation represents the material behavior very realistically with a high degree of accuracy. As shown by the experimental data, the melt formation and the forming alternate continuously during the staking process, which leads to a constant shaping of the rivet pin. As a consequence of these boundary conditions, the rivet joint has some process-related weak points in form of weld lines between the rivet pin and the side areas of the rivet head. This fact can significantly decrease the joint quality. By adapting the process procedure, by using a so-called post-heating, the joint quality can be improved. Nevertheless, the required cycle time increased as well. However, the presented numerical model of the hot forming staking process is able to build up the joint formation close to reality. As a consequence, it is possible to simulate the staking process by using different process parameters and consequently analyze the final properties of the joint. Additionally, the numerical model allows the simulation of the additional heat input (post-heating). It showed that the weld line height can be predicted with high accuracy. Regarding an industrial application of the hot forming staking process, a low joining force leads to an improved joint quality without a post-heating. A post-heating leads to improved joint quality as well. Finally, it should be positively noted that the experimental investigations of Brückner [2] completely support the presented numerical results and findings.

However, an outstanding topic is to validate the numerical model by using different material types and to link the heating and forming properties with the mechanical properties of the joint (strength and failure behavior).

Acknowledgments This study is promoted from budgetary fund of the German Research Foundation (DFG - Project number 413515815). The authors would like to record our appreciation for this support. Furthermore, they would also like to thank the company bdtronic GmbH for their technical and advisory support.

References

1. Härtel S, Brueckner E, Awiszus B, Gehde M (2020) Development of a Numerical Model of the Hot Air Staking Process Based on Experimental Data. Appl Sci 10:7115
2. Brueckner E (2021) Thermisches Kunststoffnieten – Verfahrensablauf, mechanische Eigenschaften, Versagensverhalten. PhD thesis, Technische Universität Chemnitz. https://nbn-resolving.org/urn:nbn:de:bsz:ch1-qucosa2-735102
3. Brückner E, Gehde M, Jahnke T et al (2015) Konstruktions- und Prozessoptimierung von Kunststoffnietverbindungen, gemeinsamer Schlussbericht der Forschungsstellen zu dem IGF-Vorhaben, Technische Universität Chemnitz - Professur Kunststoffe, Reportnr. IAIF17997BR, Förderkennzeichen AIF17997, Technische Informationsbibliothek (TIB). https://www.tib.eu/de/suchen/id/TIBKAT%3A866664661
4. Behrens BA, Bouguecha A, Götze T (2010) Simulation eines wirkmedienbasierten Blechumformprozesses. www.utfscience.de II
5. Brückner E, Gehde M. Analyse des Prozessablaufs beim thermischen Kunststoffnieten am Beispiel von Polypropylen. In: Technomer 2017–25. Fachtagung über Verarbeitung und Anwendung von
6. Hahn O, Finkeldey C (2004) Warmluftnieten von langglasfaserverstärkten Thermoplasten mit beschichteten metallischen Werkstoffen, Berichte aus dem Laboratorium für Werkstoff- und Fügetechnik, vol 63. Shaker Verlag, Aachen
7. Etemadi S (2012) Entwicklung einer praxisnahen Methodik für die Simulation des Clinchklebeprozesses. PhD thesis, Universität Paderborn
8. Gerstmann T, Awiszus B (2020) Hybrid joining: numerical process development of flat-clinch bonding. J Mater Process Technol 277:116421
9. Park H-S, Nguyen TT (2015) Development of infrared staking process for an automotive part. Mater Sci Eng 95:012019
10. Park H-S, Nguyen TT (2017) Development of a new staking process for an automotive part. Int J Adv Manuf Technol 89:1053. https://doi.org/10.1007/s00170-016-9132-0. Polymeren, Chemnitz. ISBN: 978-3-939382-13-3

Fatigue Characteristics and Failure Mechanism of Self-piercing Riveted Joints of DP590 and AA6061 Plates



Zhichao Huang, Yinglian Jia, and Jiamei Lai

Abstract Duplex steel, aluminum alloy, carbon fiber-reinforced composites, and other materials have become the preferred lightweight materials for automobiles. The self-piercing riveted joints of dual-phase steel DP590 and aluminum alloy AA6061 were selected for fatigue tests, and the fatigue properties of the joints were analyzed. The typical fatigue failure fractures were observed by scanning electron microscopy (SEM), and the microfailure mechanism of the joints was analyzed. The results show that the fatigue properties of self-piercing riveted joints are different with different upper substrates. The failure modes of the AA35 joints are all fractures of the lower substrates. When the upper substrate is DP590 plate under high fatigue load, the cracks are easy to initiate in the rivet area. The cracks of the other self-piercing riveted joints originate on the side of the lower plate and extend along the riveted area to the width of the substrate.

Keywords Self-piercing riveting · DP590 · AA6061 · SEM · Fatigue characteristics · Failure mechanism

1 Introduction

In response to the increasingly stringent requirements of the country for automobile exhaust emissions, major automobile manufacturers have increased the research and development of automobile lightweight design technology. From the point of view of reducing the weight of the whole vehicle, the designers can reduce fuel consumption during the use of the vehicle and achieve the purpose of reducing CO_2 emissions. Under the premise of ensuring the strength and safety performance of the vehicle, the vehicle lightweight must take comprehensive measures from the material of

Z. Huang (✉) · Y. Jia
Key Laboratory of Conveyance and Equipment, Ministry of Education, East China Jiaotong University, Nanchang 330013, China
e-mail: hzcosu@163.com

J. Lai
School of Mechanical and Electrical Engineering, Nanchang University, Nanchang 330031, China

© The Minerals, Metals & Materials Society 2021

G. Daehn et al. (eds.), *Forming the Future*, The Minerals, Metals & Materials Series,
https://doi.org/10.1007/978-3-030-75381-8_118

parts, the connection mode, and the structural design of the whole vehicle. The test shows that the application of new materials (such as carbon fiber composite board) and light materials (such as aluminum alloy) is an effective way to realize the lightweight of the automobile body and improve the driving economy. At this time, the connection between parts of different materials becomes an urgent problem. Because the melting point temperature of different materials, such as dual-phase steel, aluminum alloy, and carbon fiber composite, is quite different, resistance spot welding is not suitable for the connection of these heterogeneous materials. In recent years, the self-piercing riveting technology has become a research hot spot of different material connection modes, which is through the plastic deformation of rivets and plates to form a mechanical internal lock to complete the connection of parts. The technology has the advantages of no heat generated in the process of connecting parts, no need for pre-drilling, no damage to the anti-corrosion ability to connect parts, simple operation, and easy to realize automation. It is very suitable for connecting parts of different materials [1–3].

Some scholars have analyzed the mechanical properties of the self-piercing riveted joints structure of parts with different materials, such as Rao, Hirsch, and Ding Wenyou [4–6], and pointed out that the interaction between the specimen shape and the fatigue properties of the self-piercing riveted aluminum carbon fiber composite. Abe et al. [7] obtained that the flow stress of high-strength steel plates and the combination of plates have an effect on the connection performance of plates by using conventional rivets and dies for self-piercing riveting of high-strength steel and aluminum alloy plates. Jin Wenhao et al. [8] studied the corrosion mechanism of steel aluminum dissimilar metal self-piercing riveting joint, which is of great significance to improve the corrosion resistance of metal material self-piercing riveting joint. Mori et al. [1] studied the process optimization of aluminum alloy high-strength steel dissimilar metal self-piercing riveting and proposed that the length of rivet is the most important factor affecting the undercut and bottom thickness. Chung et al. [9] used aluminum alloy 5052 with a thickness of 1.5 mm and high-strength steel SPCC as a base plate for the self-piercing riveting test. The results showed that the static strength of U.S-L.A joint was higher than that of U.A-L.S joint, but the fatigue strength of the two joints was higher than that of the former.

At present, the research on self-piercing riveting of parts with different materials mainly focuses on the connection between composite materials, high-strength steel, and aluminum alloy, while the research on dual-phase steel and high-strength aluminum is rare. In this study, DP590 and AA6061 plates were tested by self-piercing riveting. The influence of the upper substrate on the fatigue life of the riveted joints was analyzed by a fatigue test. The typical fatigue failure fracture was observed by SEM. The microfailure mechanism of DP590 and AA6061 joints was explored.

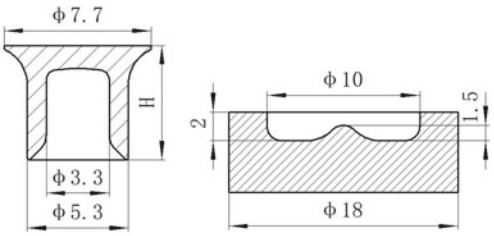


Fig. 1 Dimensions of the rivets and the die

Table 1 Mechanical properties of the rivet

Young's modulus (GPa)	Poisson's ratio	Yield strength (MPa)	Compressive strength (MPa)	Rockwell hardness (HRC)
206	0.3	1719.7	1595.6	44

2 Experimental Procedure

2.1 Self-piercing Riveting Test

2.1.1 Rivet and Die

The self-piercing riveting test was carried out on RV300023 self-piercing riveting machine of Henrob Company in the UK. Figure 1a shows the dimensions of the semi-hollow rivets. The rivet is made of 36MnB4 high-strength steel and is coated with zinc-tin alloy. The rivet head is Φ 7.7 mm, the rivet leg is Φ 5.3 mm, and the length of the leg is different. The mechanical behavior of the rivets is listed in Table 1 [10]. The concave die is shown in Fig. 1b.

2.1.2 Materials and Experimental Setup

The self-piercing riveting test connecting materials of base plates are, respectively, DP590 and AA6061. The mechanical properties of these materials are listed in Table 2. In this study, the dissimilar SPR joint was made of 1.2 mm thick DP590 plate and 2.0 mm thick AA6061 plate. In addition, 1.5 mm thick AA6061 plate and 2.0 mm thick AA6061 plate were made up of similar SPR joint. The thicker plates in each

Table 2 Mechanical properties of DP590 and AA6061 plate

Materials	Ultimate tensile strength (MPa)	Yield strength (MPa)	Young's modulus (GPa)	Elongation (%)
DP590	520	275	200	25
AA6061	315	205	68.6	12

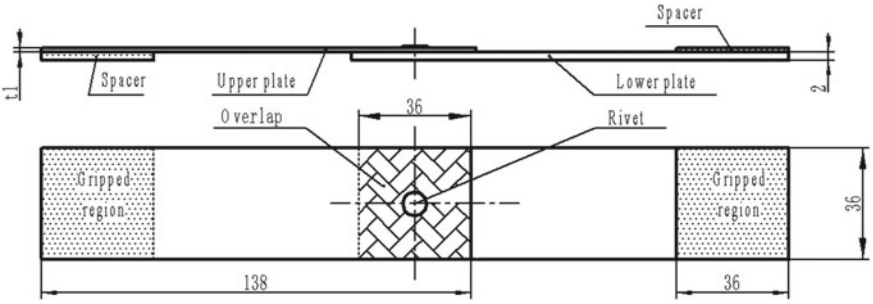


Fig. 2 Dimensions of plates and connection mode

Table 3 Rivet length of each group of joints and joint ID

Joint ID	Upper thickness (mm)		Lower thickness (mm)		Joint stack (mm)	Rivet length (mm)
DA32	DP590	1.2	AA6061	2.0	3.2	6
AA35	Al6061	1.5	AA6061	2.0	3.5	6

group were in the lower layer. The materials were sheared into 138 mm × 36 mm samples. All are connected by a lap joint. Also, details of plate assemblies and joining parameters were shown in Fig. 2.

The hardness of rivets in this test is the H4 series. Table 3 listed the rivet length of each group of SPR joints.

2.2 Mechanical Property Test

According to the test method shown in Fig. 2 and Table 3, the riveting pressure is about 190 MPa. The 14 test samples are prepared for each group, five of which are used for the tensile test and others for the fatigue strength test.

2.2.1 Tensile Test

The strength of all self-piercing riveting joints was evaluated by the tensile test. RGM-4030 microcomputer-controlled electronic universal material testing machine is used for the tensile test. Figure 2 showed an overlap area of 36 mm × 36 mm. In order to avoid the deviation between the load axis and the centerline of the test samples loaded, a spacer shall be placed at each gripping end of the test sample. The size of the spacer was 36 mm × 36 mm. For each group of joints prepared, five test samples are randomly selected for the tensile test. And the tensile test was set at a constant speed of 2 mm/min on the universal material testing machine.

Table 4 Statistics of the mean values of the maximum static loads of two groups of joints

Joint ID	Statistical parameters			
	Mean value of maximum static load F_{MAX}/kN		Coefficient of variation	Confidence interval
DA32	F_{1MAX}	9.18	0.01692	8.9842–9.3698
AA35	F_{2MAX}	6.87	0.03521	6.5737–7.1749

The maximum static loads of DA32 and AA35 joints are obtained by the tensile test, and the validity of the data is verified by Origin software. At the level of 5%, the two groups of tensile test data are significantly from the normal distribution population. According to the statistical theory, random samples are extracted from the normal population, and the validity of data can be tested by t-distribution when the sample size n value is small (generally $2 \leq n \leq 30$). Interval estimation was carried out by using the pivot variable method, and the mean values of the maximum static loads of the joints in each group were tested within the 95% confidence interval. The mean values of maximum static loads of DA32 and AA35 joints were 9.18 kN and 6.87 kN, respectively, as shown in Table 4.

2.2.2 Fatigue Test

The fatigue test equipment is a QBG-50 microcomputer-controlled high-frequency fatigue test machine produced by Changchun Qian bang Test Equipment Co., Ltd. The samples DA32 and AA35 used for the fatigue test are the same batches as those used for the tensile test. The mean values of the maximum static loads of the two groups of samples in the tensile test are taken as the limit values of the maximum static loads and dynamic loads set in the fatigue test. The clamping method of samples is the same as that of the tensile test, and the spacer should be added at the clamping end. It is required that the same sample test cannot be stopped from the beginning to the end of the test during the fatigue test. If the test must be stopped in the middle of the test due to the failure of the testing machine or other reasons, the number of cycles and downtime shall be recorded. And the data of the test sample can only be used as reference data.

The fatigue test was conducted in the pull–pull mode. The excitation applied to the fatigue test was the cyclic load of a sine wave with the frequency f of 80 Hz, and the stress ratio was set as $R = 0.1$. First, 1–2 specimens were extracted, respectively, for the pre-fatigue test at selected load levels to estimate the fatigue life of samples at each stress load level. Subsequently, three stress levels of the maximum static load mean value of the joints in each group were selected as corresponding fatigue load levels in the fatigue test, and three specimens were tested at each load level. In the process of the fatigue test, the failure judgment of the samples is based on when the fatigue cycle of the specimen exceeds 2 million times or obvious cracks appear in the specimen. Statistical data such as the mean life of each specimen of the two

Table 5 Fatigue life statistics of two groups of SPR joints

Joints ID	DA32			AA35		
Load level	70%	50%	30%	70%	50%	40%
Life mean	17,600	50,500	427,667	43,167	151,567	400,500
AD	0.586	0.294	0.402	0.477	0.468	0.323
Shape parameter	12.22	7.661	8.694	10.93	12.17	2.386
Scale parameter	18,466	53,978	455,099	45,115	157,764	454,814

groups of joints obtained in the fatigue test are shown in Table 5. The AD in Table 5 is Anderson darling statistics, indicating the degree to which the measured data obey a specific distribution. The smaller the statistic is, the better the distribution fits the data. The shape parameters describe the distribution of data and determine the shape of the distribution function. The scale parameter defines the position of the Weibull curve relative to the threshold.

3 Results and Discussion

3.1 Analysis of the Fatigue Test Results

Weibull distribution is the most commonly used distribution for reliability data modeling, so this test data is processed by Weibull distribution. The principle of Weibull distribution data processing is to model the life distribution of multiple identical and independent processes that lead to failure based on the weakest link model, in which the failure time is determined by the first process that reaches the critical stage. Since the Weibull distribution is theoretically derived from the minimum extreme distribution, an effective model can be provided for the application of the weakest link, such as the failure of material strength. In this test, two-parameter Weibull distribution was used to analyze and test the fatigue life of all joints [11], and the distribution density function was

$$f(x) = \frac{\alpha}{\beta}\left(\frac{x}{\beta}\right)^{\alpha-1} \exp\left(-\left(\frac{x}{\beta}\right)^{\alpha}\right)$$

where α and β are the shape parameters and scale parameters of the Weibull distribution.

Since the fatigue test data has the characteristics of small samples and large dispersion, it is difficult to directly solve the Weibull parameters. Therefore, Minitab can be used to process the fatigue test data. It can be seen from Table 5 that the scale parameter β calculated at a 95% confidence interval is greater than the life mean value, which can verify that the data obtained from the fatigue test is effective.

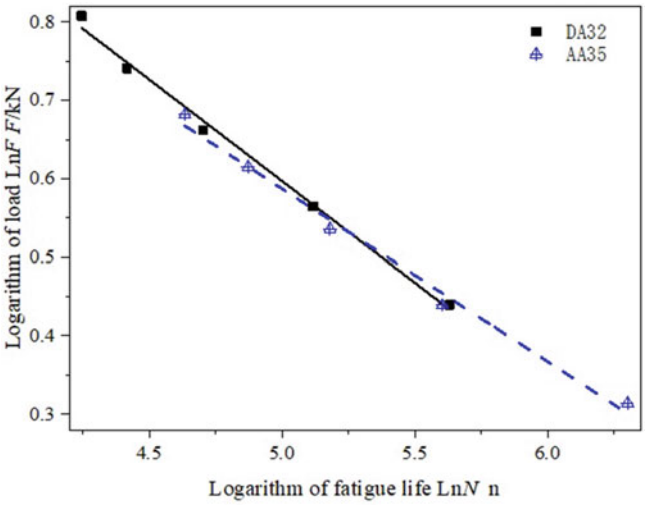


Fig. 3 *F–N* curves of two sets of joints. (Color figure online)

According to the test data obtained from the fatigue test, the least square method was used to fit the fatigue test data of each group of joints, and the two-parameter logarithmic *F–N* curve was obtained [3, 12]. The fatigue load–life (*F–N*) curves of DA32 and AA35 joints were obtained by calculation, as shown in Fig. 3. The fitting equations are $\ln N = 0.26\ln F + 1.89$ and $\ln N = 0.22 \ln F + 1.69$. The fitting goodness $R2$ of the two groups of fitting curves is 0.9943 and 0.9911, respectively. It can be seen that the fatigue load life curve fitted by the test data is effective.

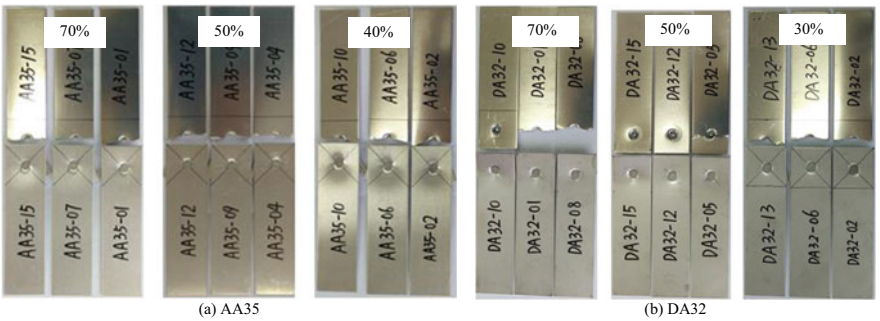
Figure 3 shows that the two fatigue load–life curves of $\ln N = 0.26 \ln F + 1.89$ and $\ln N = 0.22 \ln F + 1.69$ fitted from the fatigue test data intersect at the point (5.26, 0.53). And the fatigue life at this junction is 181,970 cycles, which is between 30 and 50% of DA32 joints load level or between 40 and 50% of AA35 joints load level, respectively. It can be seen that at a higher load level, the fatigue life of DA32 joints is longer than that of AA35 joints under the same load. However, at a lower load level, the fatigue life of AA35 joints is longer than that of DA32 joints under the same load. It means that the upper plate of different materials will affect the fatigue life of the self-piercing riveted joints.

3.2 The Influence of the Upper Plate on Fatigue Failure Mode

In DA32 and AA35 self-piercing riveted joints, only the upper plate is different. The upper plate of DA32 joints is duplex steel with a thickness of 1.2 mm DP590, and the upper plate of AA35 joints is AA6061 aluminum alloy with a thickness of

1.5 mm. It can be seen from Fig. 4a that the fatigue failure mode of AA35 joints is all lower plate fracture. The fracture position of the lower plate is extending along the riveting area of the lower plate to the width of the plate and running through the middle of the riveting area. Since the upper and lower plates of AA35 are all made of aluminum alloy AA6061, the fretting wear of the self-locking structure formed by the rivet leg and the lower plate in the locking area becomes the stress-sensitive area during the fatigue test. So the fatigue failure of AA35 joints is due to the fatigue wear and fracture of the lower plate.

It can be seen from Fig. 4b that the fatigue failure modes of self-piercing riveted joints DA32 are different under different load levels. When the load level is 30%, the fatigue failure is lower plate failure. With the increase of the applied load, when the load level reaches 50%, the fatigue failure mode is transferred from the fracture failure of the lower plate to the rivet fracture failure of all the rivets. However, one specimen is a mixture of a rivet and a lower plate fracture. When the load level continues to increase to 70%, the main fatigue failure mode of DA32 joints is lower plate failure and one sample is rivet fracture failure. In addition, the fracture failure of the lower plate gradually expands from the middle part of the rivet to the direction of plate width and plate thickness in the form of fatigue failure of DA32 joints, and finally, the joint connection fails. At the lower load level, the rivet leg and the lower plate of DA32 joints produce fretting wear under the action of a small variable load. In the self-locking area, the fatigue resistance of the lower plate aluminum alloy AA6061 is the weakest. And the weak part of the DA32 joints is the lower plate aluminum alloy AA6061, so the fatigue failure mode under this load level is the lower plate fracture failure. The alternating force of rivets in DA32 joints increases gradually with the increase of load level, and the fretting wear between the rivet leg and the base plate is not the main contradiction of connection failure. The impact resistance of the rivets connecting the upper and lower plates is the key to the failure of the connection. Therefore, the main fatigue failure mode of the DA32 joint under the medium load level is rivet fracture. When the fatigue load increases to a certain value, the fatigue life of DA32 joints is obviously reduced under the action of a large variable load. At this time, the rivet and upper plate in the riveting lock area have



(a) AA35 (b) DA32

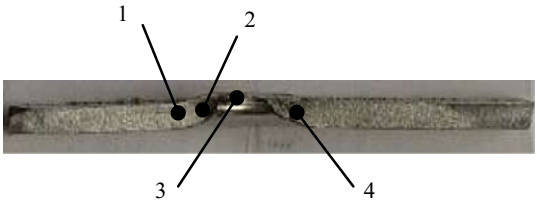
Fig. 4 Two sets of fatigue failure samples for SPR joints. (Color figure online)

good tensile strength. And the lower plate becomes the weakest position in the lock, so the main fatigue failure form becomes the fracture failure of the lower plate.

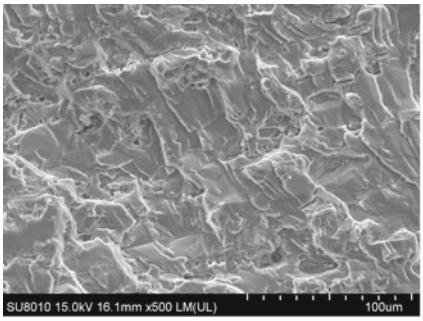
3.3 Failure Mechanism of Joints

3.3.1 Failure Mechanism of AA35 Joints

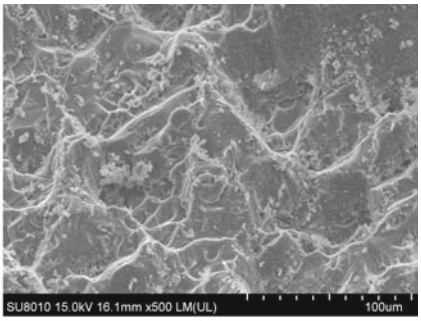
The fracture morphology of the lower plate of the No. 4 sample AA35 joint is shown in Fig. 5. In Fig. 5c, e, micropores, a large number of particles, tearing edges, and secondary cracks can be observed, which is the remarkable feature of the fatigue



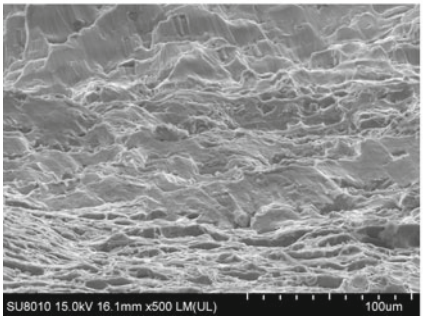
(a) Macroscopic morphology of fatigue fracture



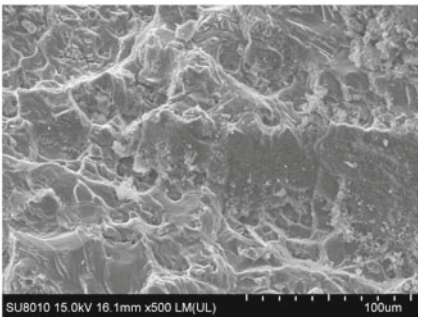
(b) 1 # Regional microstructure



(c) 2 # Regional microstructure



(d) 3 #Regional microstructure



(e) 4 # Regional microstructure

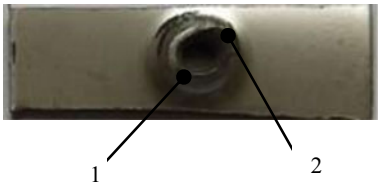
Fig. 5 Fracture surface of the lower plate for group AA35 No. 4. (Color figure online)

source area. According to the macroscopic morphology of the 2# and 4# regions in Fig. 5a, there are a large number of black abrasive particles in this part, indicating that the microcrack growth of this part is slow and there is no obvious fatigue striation. Under the action of alternating stress, the crack will open and close repeatedly on the surface of the crack when it is expanding, which will cause the fracture surface to experience many times severe "rubbing" and "abrasion" process so that a large number of black oxide particles appear on the fracture surface.

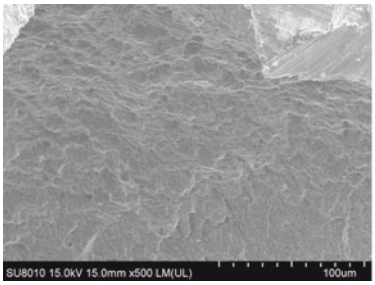
There are obvious fatigue striations, microcracks, and "beach marks" in Fig. 5d. With the passage of time, under the action of alternating tensile stress, the cracks sometimes expand and sometimes stop, and the separated parts of the cracks sometimes close and sometimes open, so the fracture produces the so-called "beach mark". Corresponding to each stress cycle, there will be a striation pattern on the fatigue fracture surface, which is a significant feature of the fatigue fracture surface. In Fig. 5b, there are dense fatigue fringes and small hole-like secondary crack sources. Here is the stable crack growth area. Under the stress cycle, the crack propagates to the direction of plate thickness and width, and finally, the lower plate fracture connection fails.

3.3.2 Failure Mechanism of DA32 Joints

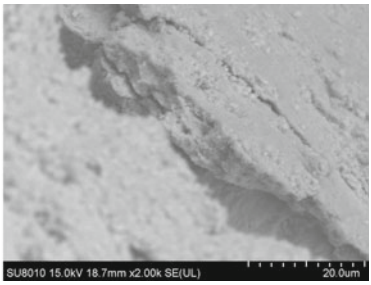
The results of SEM of the rivet fracture of DA32 group 5 are shown in Fig. 6. Select an area of rivet fracture as shown in Fig. 6a, and the observation results are shown in Fig. 6b. It can be found that the morphology of this region shows the characteristics



(a) Macroscopic morphology of fatigue fracture



(b) 1 # Regional microstructure

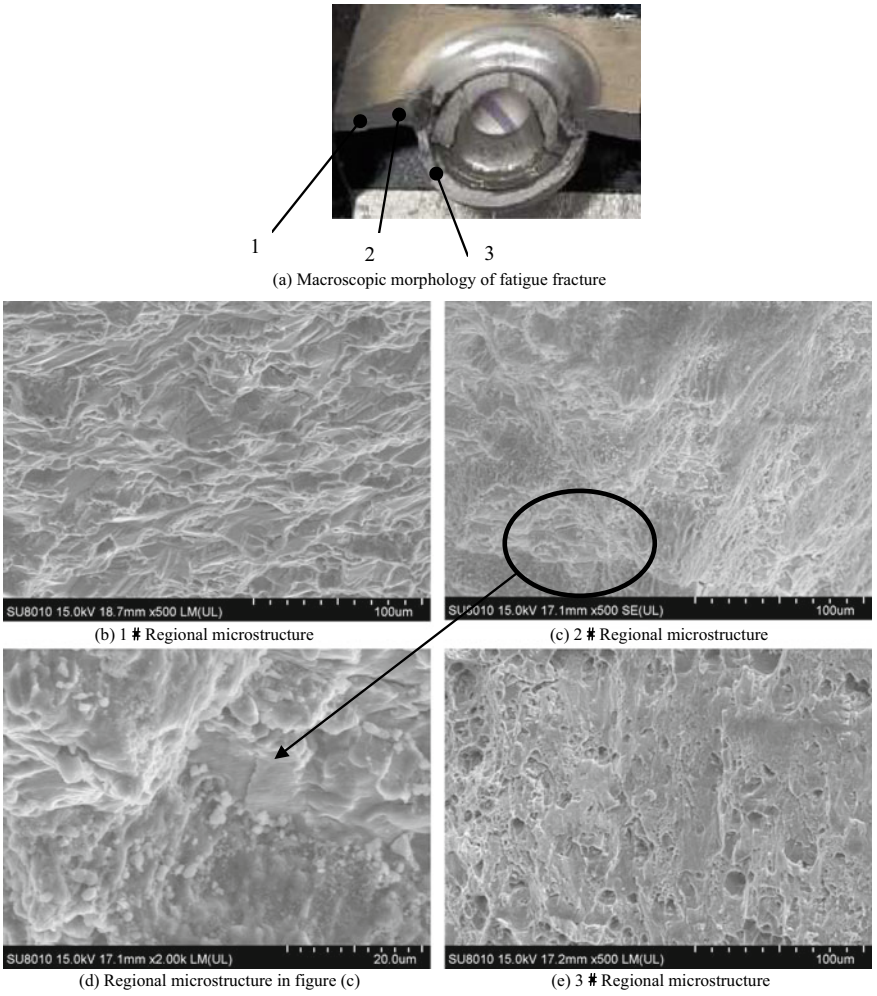


(c) 2 # Regional microstructure

Fig. 6 Fracture surface of rivet for group DA32 No. 5. (Color figure online)

of fatigue stripe and river pattern, which belongs to the fatigue quasi-brittle fracture feature. In Fig. 6c, a large number of microfatigue cracks and particles are observed on the rivet leg, and it can be seen that the rivet also has plastic deformation in the fatigue test of the DA32 sample.

The lower plate fracture of DA32 Group No. 5 sample was observed by SEM, as shown in Fig. 7. From Fig. 7a of the actual failure sample, it can be seen that there are a large number of black particles in 2#. It can be seen from the microstructure of Fig. 7c, d that there are micropores and a large number of particles in this part. These particles are the wear debris formed by strong microvibration at the contact between rivet foot and lower plate under the action of alternating load. In the local position



(a) Macroscopic morphology of fatigue fracture

(b) 1 # Regional microstructure

(c) 2 # Regional microstructure

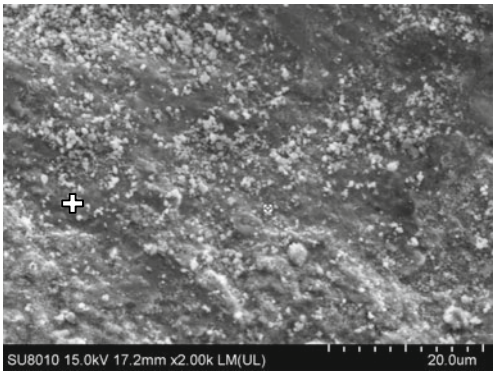
(d) Regional microstructure in figure (c)

(e) 3 # Regional microstructure

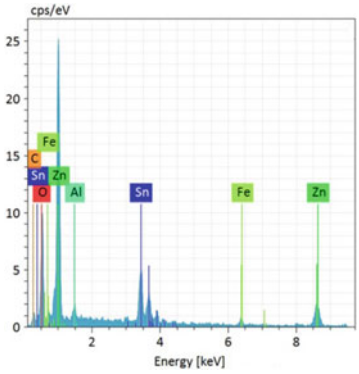
Fig. 7 Fracture surface of the lower plate for group DA32 No. 5. (Color figure online)

of the contact surface, the wear debris gathers here to produce stress concentration, which leads to the damage of the interface of the base metal and the formation of tiny cavities. Under the action of alternating load, these micro-holes connect and expand gradually, the stress at the crack tip will increase continuously, and new microholes will be generated at the same time. And finally, the joint connection fails, so this part is the fatigue source area. In Fig. 7b, obvious fatigue strip tearing edge, a large number of microcracks, and wider cracks are seen, which are obvious microscopic characteristics of the fatigue growth zone. In Fig. 7e, a large number of torn dimples and microcracks can be seen, which is the transition area from the fatigue growth zone to the transient fracture zone. In the process of forming local microcracks, the joint between dimples is stretched or broken, which makes the fracture crack expand. With the increase of the number of cycles, the crack propagates to the thickness and width of the plate, which eventually leads to the instantaneous fracture of the joint. The high hardness of rivets in DA32 group joints leads to a quasi-brittle fracture of rivets under moderate fatigue load. At the same time, the rivet leg and the lower plate, and the upper plate and the lower plate produce severe vibration wear in this process, which makes the lower plate break and leads to connection failure.

According to the energy spectrum analysis of the black particles in the contact between the rivet foot and the lower plate in Fig. 7, the main components are Zn, O, Sn, C, Fe, and Al, and the atomic mass percentages are, respectively, 38.75%, 26.42%, 23.05%, 7.61%, 2.92%, and 1.48% in Fig. 8. Among them, Zn and Sn elements are the coating elements on the rivet surface, respectively. C and Fe elements are from the worn rivets or the upper plate, and the Al element is from the substrate. It can be speculated that the rivets in the fatigue test of DA32 joints have severe microvibration wear, which leads to the steel rivets falling off. The friction heat produced in the process of vibration intensifies the speed of forming black oxide particles by chemical changes with oxygen elements in the air, which is the source of the initiation and propagation of fatigue cracks. It is also confirmed that under the action of alternation, contact wear will occur and eventually lead to the failure of the connection.



(a) Microstructure of the lower plate surface



(b) Energy spectrum of fatigue wear debris

Fig. 8 Fracture surface of the lower plate for group DA32 No. 5. (Color figure online)

4 Conclusions

(1) At a higher load level, the fatigue life of DA32 joints is higher than that of AA35 joints under the same load. At a lower load level, the fatigue life of the AA35 joints is higher than that of the DA32 joints under the same load.
(2) The failure mode will change obviously if the upper substrates are different. When the upper plate of the joint is replaced by DP590, the fatigue failure is changed from one form to many forms. When the DA32 joint is at a medium load level, the joint is rivet fracture failure. At high load level and low load level, the failure mode of the joint tends to be the fracture failure of the lower plate. The fracture zone is located in the rivet fastening area and extends to the width and thickness of the plate. AA35 joints all have lower plate fracture failure, and the fracture zone is under the rivet region, which transfers from the middle part of the rivet to the direction of plate thickness and plate width.
(3) Rivet fracture is characterized by fatigue stripe and river pattern, which belongs to fatigue quasi-brittle fracture. There are a lot of particles, micropores, and tearing edges in the source area of fatigue crack of the lower plate fracture, and a lot of fatigue stripes and beach marks in the crack propagation area.
(4) The energy spectrum analysis of the black particles in the contact area between the rivet foot and lower plate indicates that the rivet suffers from severe fretting wear in the joint fatigue test, which results in the peeling of the surface coating on the rivet foot and aggravates the failure rate. Therefore, the fatigue life of the joint can be effectively increased by slowing down the friction and wear of the joint.

Acknowledgments This research is supported by the National Natural Science Foundation of China (51875201) and Key Research and Development Plan of Jiangxi Province (20192BBEL50013).

References

1. Mori K-I, Abe Y (2018) A review on mechanical joining of aluminium and high strength steel sheets by plastic deformation. Int J Lightweight Mater Manuf 1(1):1–11
2. Huang ZC (2006) Progress in sheet metal joining technology. Forg Stamp Technol 4:119–122
3. Liu Y, He XC, Xing BY et al (2018) Fatigue properties and failure mechanisms of self-piercing riveted joints in metal form sandwich structures. Mater Rev 32(7):2431–2436
4. Rao HM, Kang J, Huff G et al (2018) Impact of specimen configuration on fatigue properties of self-piercing riveted aluminum to carbon fiber reinforced polymer composite. Int J Fatigue 113:11–22
5. Hirsch F, Müller S, Machens M et al (2017) Simulation of self-piercing rivetting processes in fibre reinforced polymers: material modelling and parameter identification. J Mater Process Tech 241:164–177
6. Ding WY, He XC, Liu JM et al (2018) Performance of self-pierce riveting based on carbon fiber reinforced polymer-AA5052 aluminum alloy three-layer sheets. Sci Technol Eng 18(25):143–147

7. Abe Y, Kato T, Mori K (2009) Self-piercing riveting of high tensile strength steel and aluminium alloy sheets using conventional rivet and die. J Mater Process Technol 209(8):3914–3922
8. Jin WH, Xing BY, He XC et al (2019) Failure behavior analysis of self-piercing riveted joints in steel-aluminum dissimilar metal under acid environment. Ordnance Mater Sci Eng 42(01):123–126
9. Chung CS, Kim HK (2016) Fatigue strength of self-piercing riveted joints in lap-shear specimens of aluminium and steel sheets. Fatigue Fract Eng Mater Struct 00:1–10
10. Zhao L, He X, Xing B et al (2017) Fretting behavior of self-piercing riveted joints in titanium sheet materials. J Mater Process Tech 249:246–254
11. Xing B, He X, Wang Y et al (2016) Fatigue properties and failure mechanisms of self-piercing riveted joints in aluminium alloy. Trans China Weld Inst (06):50–54 + 131
12. Gao ZT, Fu HM, Liang MX (1987) A method for fitting S-N curve. J Beijing Inst Aeronaut Astronaut 1(1):115–119

Fretting Damage and Fatigue Property Analysis of Self-piercing Riveted Joints of AA5052 Aluminium Alloy



Zhichao Huang, Yongchao Zhang, and Jiamei Lai

Abstract The fatigue tests of self-piercing riveted joints of AA5052 aluminium alloy were carried out by axial tension-tension loading mode. The microfracture characteristics of the specimen were analyzed by a scanning electron microscope. The fatigue property as well as the fretting damage failure mechanism of SPR joints with different parameters (distance, stress ratio, load level and riveting direction) were studied. The results show that the fatigue cracks occur in the fretting damage area where stress concentration exists. The form and the distribution of the fretting debris are important factors that affect the fatigue property of the joint. Within the value range, fatigue life increases with the increase of stress ratio, however, decreases with the increase of loading level adopted. The fatigue property of joints differs between different riveting directions. Better strength property could be obtained when the riveting direction reverses.

Keywords Self-piercing riveting · Fretting damage · Fatigue strength · Riveting direction · Stress ratio

1 Introduction

With the promotion of energy-saving and emission reduction as well as the popularization of environmental protection awareness, the increasing application of the lightweight concept in the design and manufacturing phase of a vehicle has become an inevitable trend. The light metal materials such as aluminium alloy, magnesium alloy, and titanium alloy are widely used. The emergence of all-aluminium car bodies could achieve effective weight reduction on the basis of ensuring the basic functions. However, questions such as oxidation and deformation arise when

Z. Huang (✉) · Y. Zhang
Key Laboratory of Conveyance and Equipment, Ministry of Education, East China Jiaotong University, Nanchang 330013, China
e-mail: hzcosu@163.com

J. Lai
School of Mechanical and Electrical Engineering, Nanchang University, Nanchang 330031, China

© The Minerals, Metals & Materials Society 2021

G. Daehn et al. (eds.), *Forming the Future*, The Minerals, Metals & Materials Series,
https://doi.org/10.1007/978-3-030-75381-8_119

the lightweight materials are connected by the traditional resistance spot welding process. As a cold forming technology, self-piercing riveting (SPR) technology has advantages of simple process, low energy consumption, low pollution, stable and controllable forming quality, all of which could effectively connect homogeneous and heterogeneous light material and is widely used in manufacturing industry [1–4].

The fatigue fracture destruction in mechanical structure accounts for about 50–90% of the total mechanical failure, so it is of great importance to study the fatigue property and failure mechanism of the SPR joints. Xing et al. conducted static and fatigue tests of SPR joints with different numbers and distribution patterns of rivets. The results show that the mechanical properties are influenced by not only the rivet number but also the rivet distribution pattern [5]. Han et al. studied the effect of specimen configuration on the mechanical behaviour of multi-layer SPR joints. The effect of configuration on the strength and the failure mechanism is significant. Secondary bending plays an important role in the static shear failure of the specimen [6]. Liu et al. generalized the process parameters which influence the fatigue property of the SPR joint and summarized the methods to improve the fatigue performance of SPR joint [7]. Li et al. conducted the fatigue characteristic study of 6111T4 aluminium alloy and HSLA340 steel SPR joints. It is found that rivet shank fracture is prone to occur under high-load level and frictional wear generates on the interface between substrates, as well as substrate and rivet [8]. Han et al. investigated the fretting behaviour of aluminium alloy SPR joints with different interfacial conditions. The results show that the use of wax-based solid surface lubricant and PTFE tape could prolong fatigue life [9]. Huang et al. found that the fatigue strength of SPR joints increases with the increase of stress ratio, and the fatigue strength decreases with the increase of the maximum load through the TA1 titanium alloy SPR joint fatigue test and fracture wear analysis. In addition, the influence of riveting position on the fatigue strength of shear specimens was studied [10, 11]. Zhao et al. systematically studied the influence factors of the fatigue life and failure modes of SPR joints. The results show that the increase of the substrate thickness and strength can effectively improve the fatigue life of SPR joints [12]. Moraes et al. discovered that interface contact force exists in the initial area of fretting wear from a high-accuracy finite element analysis of SPR forming process. They also found that the fatigue cycle failure prediction model based on linear elastic fracture mechanics indicates that initial wear fatigue occurs in the high interface contact force area [13].

At present, the research of the influence factors on fatigue property and failure mechanism of light metal material SPR joint is not thorough enough. On the basis of the single-factor experiment method, the influence of riveting position, load level, stress ratio, and riveting direction on the fatigue property and failure mode of the AA5052 aluminium alloy SPR joints were analyzed. The scanning electron microscope was adopted to analyze the microstructure of fatigue fracture, and the joint fatigue failure mechanism was generalized. Through the fatigue test and mechanism analysis of the AA5052 aluminium alloy SPR joints, the fatigue behaviour characteristics were discussed, which can provide a certain reference for the extended application of SPR technology of aluminium alloy and other light metal materials in automobile manufacturing and other industries.

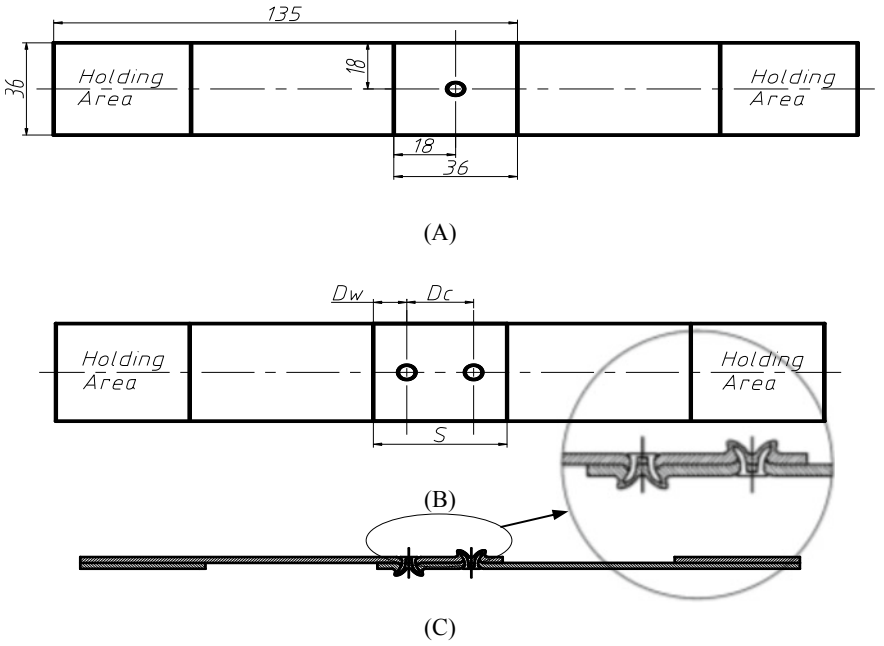


Fig. 1 Schematic diagram of lap specimen

2 Experiment Preparation

2.1 Specimen Preparation

In this experiment, the AA5052 aluminium alloy substrate was used to prepare the specimen for the static tensile test and the fatigue test. The geometry dimension of aluminium alloy was 135.0 * 36.0 * 2.0 mm, and the geometric size of the lap specimen was shown in Fig. 1. Figure 1a, b is schematic diagrams of a specimen with one and two rivets, respectively. Dw represents the distance between the centre of the nail hole and the short edge, while Dc represents the distance between the centres of the two nail holes longitudinally, and S represents the lap length. The rivet adopted is the semi-tubular rivet produced by Henrob company, and the size of which is ϕ 5.3 * 6.0 mm.

2.2 Experiment Scheme

Firstly, the static tensile tests of a single-rivet specimen and a two-rivet specimen with different Dc and riveting directions were conducted. Their failure maximum loads

Table 1 Maximum load in static tensile test

Specimen	Single-rivet	Two-rivet					
		Same direction			Opposite direction		
		15.0	25.0	35.0	15.0	25.0	35.0
Load/KN	4.76	9.53	9.75	9.67	9.25	9.90	9.26

Table 2 Fatigue test scheme

Rivet number	*Dc*/mm	Stress ratio (*R*)	Load level (*L*)	Riveting direction
Single	–	0.1	50%	–
Two	15.0	0.1	30%	Same direction (*T*) Opposite direction (*F*)
	25.0	0.2	50%	
	35.0	0.3	70%	

were obtained. A different percentage of the load was taken as the maximum load in the tension-tension fatigue test. The RGM4030 universal tensile testing machine was adopted and the displacement control speed was 2.0 mm/min. Five specimens were tested in a static tensile test for each parameter, and 3 specimens with similar results were selected for analysis. The *Dc* adopted in the test was 15.0 mm, 25.0 mm, and 35.0 mm, respectively. The failure maximum load obtained was listed in Table 1.

The fatigue tests of SPR specimens were carried out on the basis of the data in Table 1. The experiment scheme was shown in Table 2. The symbol *R* represents stress ratio; *L* represents load level; *T* represents same direction and *F* represents opposite direction.

The QBG-50 high frequency fatigue testing machine was adopted in the fatigue test. The sinusoidal wave was selected for tension-tension loading with a loading frequency of about 85 Hz. The fatigue test was carried out 5 times for each parameter, and 3 specimens with similar results were selected for analysis, so as to avoid inaccurate results caused by data dispersion.

3 Fatigue Test and Analysis

3.1 Fatigue Test of Single-Rivet Specimen

The fatigue test of a single semi-tubular rivet SPR joint was conducted. The lap length was 36.0 mm, and the stress ratio *R* was 0.1. 70% of the maximum load (4.76 KN) obtained in the tensile test was taken as the maximum load in the fatigue test. The static load was 1.83 KN and the dynamic load was 1.49 KN from the formula. The mean number of load cycles of the specimen is about 180.3 * 103 times. If the

maximum load adopted was 9.75 KN obtained in the two-rivet SPR joint static tensile test, then the fatigue life was shorter and the failure of the joint occurred sooner.

3.2 *Influence of Dc on Fatigue Property*

The influence of parameter *Dc* on the fatigue property of specimen was analyzed, and the *Dc* was 15.0 mm, 25.0 mm, 35.0 mm, respectively. 50% of the maximum load value (9.75KN) obtained in the tensile test of the specimen with better static strength was taken as the maximum fatigue cyclic load, and the stress ratio *R* was 0.1. The fatigue life of the specimen with different *Dc* was shown in Fig. 2.

It can be seen from Fig. 2 that the fatigue life of the specimen increases with the increase of *Dc*. While the base material is connected by self-piercing riveting technology, the riveting point is the location of main material failure and flow moulding, and stress concentration easily generates under the action of cyclic load, which inevitably promotes the damage and destruction of SPR joints. The smaller the distance between the centres of the rivet holes, the less material that can bear the impact of the cyclic load. And the two moulded riveting points are more likely to interact with each other, resulting in the accelerated failure of the specimen.

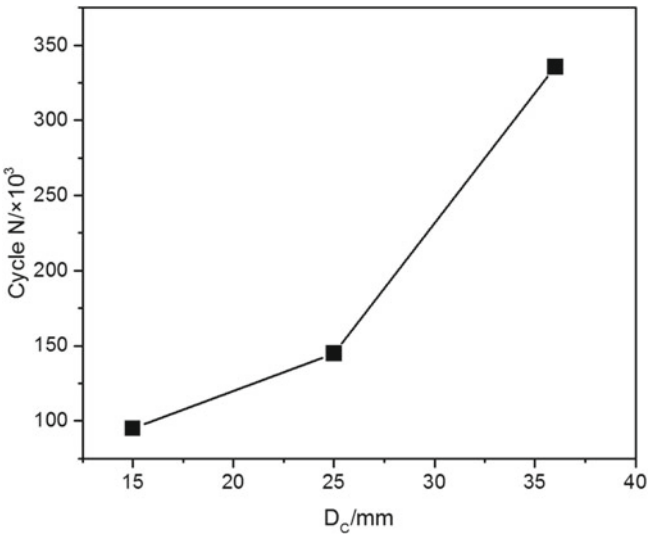


Fig. 2 Fatigue life with different *Dc*

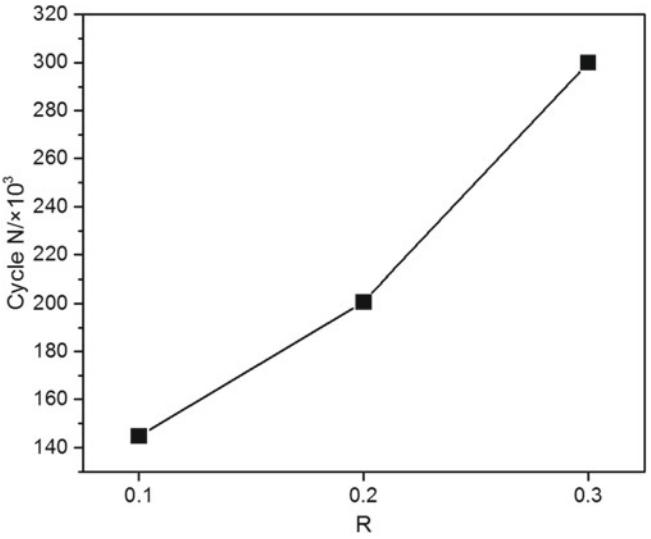


Fig. 3 Fatigue life with different *R*

3.3 Influence of Stress Ratio on Fatigue Property

The stress ratio adopted was 0.1, 0.2, 0.3, respectively. 50% of the maximum load value (9.75 KN) obtained in the static tensile test was taken in the fatigue test and the *Dc* was 25.0 mm. In the fatigue test the static load was 2.68 KN and the dynamic load was 2.19 KN. The influence of stress ratio on fatigue property of the specimen was analyzed and the relationship of cycle fatigue life and stress ratio was shown in Fig. 3.

As can be seen from Fig. 3, the higher the stress ratio, the higher the cycle fatigue life. The stress ratio is the ratio of the minimum load to the maximum load under cyclic loading. The stress amplitudes corresponding to the three stress ratios were 2.19 KN, 1.95 KN, and 1.70 KN, respectively. It can be seen that as the stress ratio increases, the stress amplitude decreases gradually, then the driving force of dislocation motion under cyclic load decreases likewise. The destruction rate of the material flow moulding decreases and the fatigue life increases accordingly. The result indicates that the value of stress amplitude adopted in the fatigue test has a great influence on the fatigue life of the SPR joints.

3.4 Influence of Load Level on Fatigue Property

30%, 50%, and 70% of the maximum load value (9.75 KN) obtained in the static tensile test were taken, respectively, as fatigue load for fatigue property analysis.

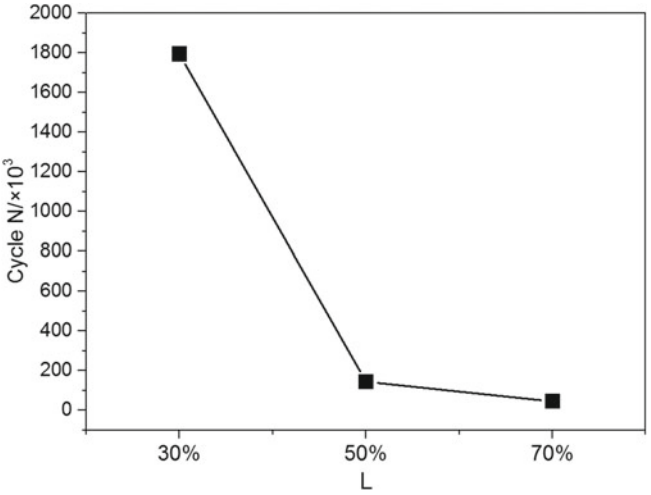


Fig. 4 Fatigue life with different load

The stress ratio adopted was 0.1. The relationship of cycle times and load level was obtained, as shown in Fig. 4.

When the static load was 3.75 KN and the dynamic load was 3.07 KN, the number of load cycles is 45.1 * 103. When the static load was 1.61 KN and the dynamic load was 1.32 KN, the number of load cycles is 1796.2 * 103. As seen in Fig. 4, the fatigue life of the specimen decreases significantly with the increase of the load level. When the riveting point is subjected to cyclic loading, the joint damage gradually accumulates and the substrate gets broken at the last stage of fatigue test. While the load value decreases, the static load and dynamic load decrease accordingly. The linear change rate of rigidity of the SPR joint gradually tends to be gentle, then the surface wear, crack initiation and propagation slow down, and the fatigue life of the joint increases.

3.5 Influence of Riveting Direction on Fatigue Property

The fatigue property of a two-rivet SPR joint with two kinds of riveting directions was analyzed. The opposite riveting direction was shown in Fig. 1c, and the comparison of the specimen can be seen from Fig. 5.

Compared with the specimen connected from the same riveting direction, the fatigue life could be increased by about 14.8% by changing the riveting direction. Self-locking structures are moulded on both the upper and the lower surface of the substrates by opposite direction riveting. Under cyclic loading, the relative micro-amplitude motion of the substrates could be better suppressed. In addition, the premature occurrence of buckling could be prevented and the lateral force of substrates on

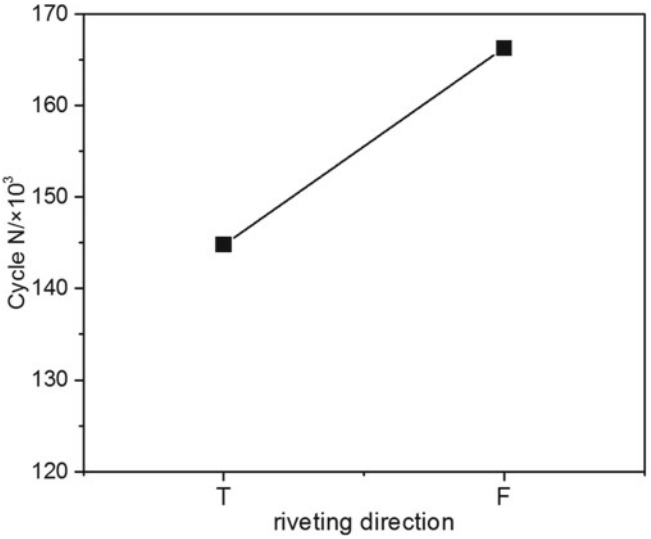


Fig. 5 Fatigue life with different riveting direction

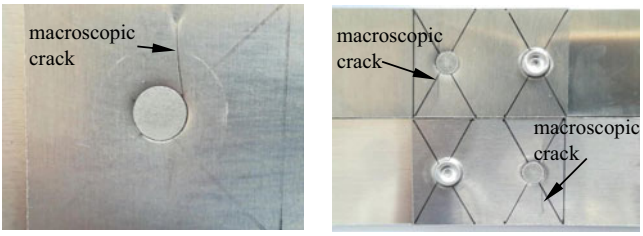
the rivet could also be reduced, thus damage of self-piercing riveting structure can be delayed to some extent.

4 Failure Mode and Fracture Analysis

4.1 Macroscopic Failure

The fatigue failure mode of specimens with different parameters is the substrate material fracture, while the rivets are not broken. The failure mode of a single-rivet SPR joint is the fatigue fracture of substrate at the moulding structure. The crack direction is about 90°from the loading direction, showing a symmetrical distribution along the direction of the substrate width. The failure mode of the two-rivet SPR joint with the same riveting direction is the fatigue fracture of the substrate at the moulding structure close to the piercing end near the upper fixture while no macroscopic crack occurs at the other riveting point. Macroscopic fatigue cracks occur both at the riveting holes when riveting direction reverses and are distributed at the end of the piercing substrate. Once the crack emerges around the riveting hole, it would expand rapidly along the substrate width to both ends under cyclic loading. The overall crack length is about 20.0 mm, accounting for half the width of the substrate. The failure modes of various riveting specimens were shown in Fig. 6.

The Dino microscope was adopted for preliminary analysis of the upper substrate section, as shown in Table 3. It can be seen that there are obvious material groove



(A) Single-rivet joint (B) Two-rivet joint

Fig. 6 Macroscopic crack and fracture. (Color figure online)

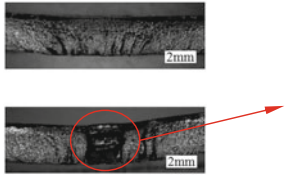
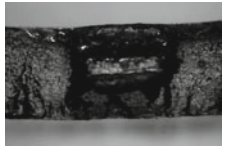
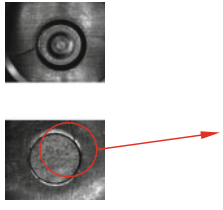
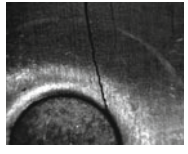
faults around the riveting hole along the direction of substrate thickness. This kind of morphology radiates upward from the contact surface between the substrates, and the length is about two-thirds of the substrate thickness, which does not extend to the upper surface of the upper substrate. The substrate profile around the hole is relatively rough and that away from the hole is smoother.

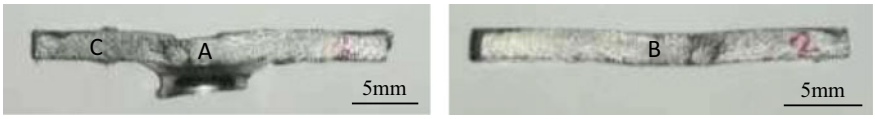
4.2 Microscopic Morphology Analysis of Substrate Fracture

The fatigue fracture specimens were naturally pulled off on the tensile testing machine, and then the scanning electron microscope samples of the section were prepared for observation. The macroscopic fracture section was shown in Fig. 7.

SEM microstructures of the fatigue failure fracture were shown in Fig. 8. Obvious macroscopic cracks can be observed in Fig. 8a and the cracks extend along the direction of substrate thickness. Figure 8b is the microscopic morphology of area A in Fig. 7a with a magnification of 1000 times, and under cyclic loading the micro-cracks initiate in this area. Obvious micro-cracks could be observed. Figure 8c is obtained by magnifying 5000 times of the same area. It can be found that micro-cracks exist along the direction of substrate thickness, and fatigue striation characteristics are dispersed on the micro-morphology. Figure 8d shows the microscopic morphology of area B in Fig. 7b with a magnification of 10,000 times. From the graph evident fatigue striation characteristics can also be discovered. Figure 8e is obtained by magnifying 2000 times of area near the surface of the upper substrate. Figure 8f shows the microscopic morphology of area C in Fig. 7a with a magnification of 500 times. Both figures present evident brittle fracture characteristics and it is consistent with the phenomenon of rapid fracture in the later stage of fatigue test. In addition, evident accumulation of powdery substance can be observed on the contact surface between the substrates, and the area is highly coincident with the crack initiation area. Therefore, during the fatigue fracture failure process of the AA5052 aluminium alloy SPR joint, material fretting wear occurs violently on the contact surface between upper and lower substrates. The generation and nucleation of fretting debris which is torn off from the substrates promote the initiation of fatigue micro-cracks, and the

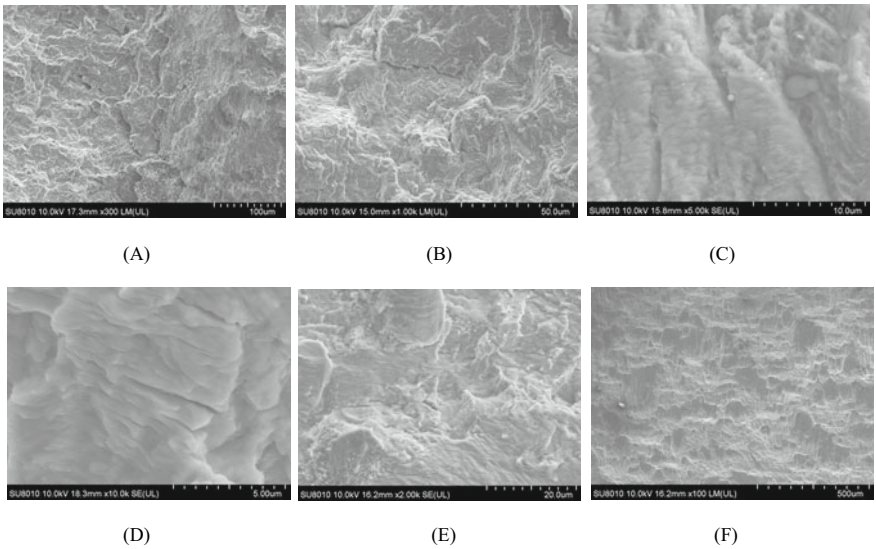
Table 3 Dino micro-graph. (Color figure online)

Fatigue fracture macroscopic section	Section around hole	Macroscopic fracture	Local amplification
			



(A) (B)

Fig. 7 Macroscopic fracture morphology of fatigue failure. (Color figure online)



(A) (B) (C)

(D) (E) (F)

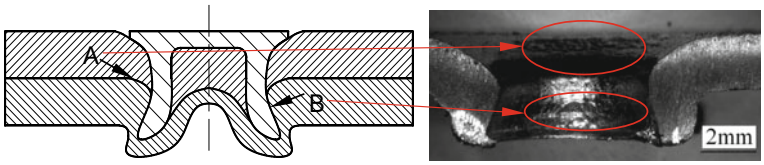
Fig. 8 Microscopic morphology of different fracture region

cracks extend to a certain depth below the surface of the substrate. Simultaneously the cracks extend along the direction of substrate width till the macroscopic fatigue fracture failure finally.

4.3 Wear Analysis

The SPR specimens with macroscopic fatigue cracks after the fatigue test were pulled off on the tensile testing machine to prepare for the wear analysis test sample. Observation shows that there are black wear areas on the surface between the substrates as well as rivet shank and the lower substrate, as shown in Fig. 9 (A area: contact surface between substrates; B area: contact surface between rivet shank and lower substrate).

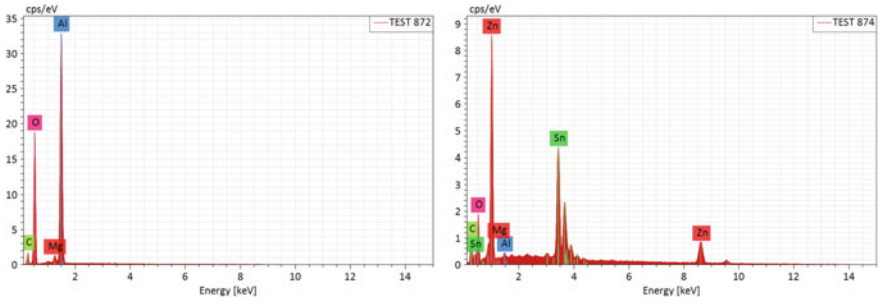
By the combination of scanning electron microscope observation and energy spectrum analysis, it can be seen that there exist more aluminium and oxygen elements in



(A) (B)

Fig. 9 Wear area diagram of SPR joint. (Color figure online)

the fretting debris on the contact surface between substrates. It can be inferred that the composition of the black fretting debris is mainly Al_2O_3, that is the *Al* element torn off from the substrate is oxidized into fretting debris. In the fretting debris on the surface between the rivet and the lower substrate, there exist more *Zn*, *Sn*, *Mg*, and other elements. This is because the rivet surface has anti-oxidation coating containing Zn, Sn, and other elements. The result indicates that small relative motion and contact force exist in the area under cyclic loading. Therefore, it can be seen that the fretting wear of the SPR joints under cyclic loading mainly exists on the contact surface between substrates and rivet shank. Exfoliation, oxidation as well as nucleation occur during the fatigue test till final failure. The formation of fretting debris in the wear area is related to material property and the environment. At the initial stage of wear, the substrate material falls off under the action of shear force and then becomes fretting debris, which moves on the surface of the material and produces cold welding points under the action of extrusion. With the increase of cold welding points, the mutual adhesion and tear increase. The oxidation would be enhanced and the wear rate would be accelerated, resulting in the increase of abrasive particles that promote the initiation and propagation of micro-cracks. Under continuous cyclic loading, the micro-cracks unite into macro-crack and lead to the fatigue failure of the riveting structure (Fig. 10).



(A) Contact surface between substrates (B) Contact surface between rivet and substrate

Fig. 10 Energy spectrum analysis of fretting debris. (Color figure online)

5 Conclusions

(1) Within the distance value range of two riveting centres, the fatigue life of the SPR joint increases with the increase of the distance. Compared with the two-rivet SPR specimen with the same riveting direction, the fatigue life could be increased by about 14.8% when the riveting direction is opposite.
(2) With the increase of stress ratio or the decrease of load level, the relative fretting and damage of the riveting structure decrease, consequently the fatigue fracture failure would be delayed and the fatigue life of the SPR joint can be significantly improved.
(3) The fatigue failure of the specimen is the fracture of the upper substrate, and it can be known that the fatigue micro-cracks initiate on the contact surface between the substrates through SEM analysis. The micro-cracks unite into the macroscopic crack and extend along the direction of substrate thickness and width. The area far away from the rivet hole represents brittle fracture and has typical fatigue failure characteristics.
(4) On the contact surface between substrates as well as the rivet and the lower substrate, there exist obvious fretting wear areas. Fretting debris and accumulation exist in these areas, and the black debris is mainly Al_2O_3 mixed with Mg, C, Zn, Sn, and other elements. The debris accelerates the initiation and propagation of fatigue crack and finally results in the fatigue fracture failure of the SPR joints.

Acknowledgments This research is supported by the National Natural Science Foundation of China (51875201) and Key Research and Development Plan of Jiangxi Province (20192BBEL50013).

References

1. Zheng H, Zhao XY (2016) Lightweight automobile and application of Aluminum alloys in modern automobile production. Forging Stamping Technol 41(2):1–6
2. Zhang Q, Ye PC, Yang ZY et al (2019) Application and development of connecting technique in automobile lightweight. Nonferrous Met Process 48(1):1–9
3. Wu XD, Wang M, Kong L et al (2016) Research status and application prospect of SPR self-riveting technology. Electric Weld Mach 46(4):31–36
4. Li DZ, Chrysanthou A, Patel I et al (2017) Self-piercing riveting-a review. Int J Adv Manuf Technol 92:1777–1824
5. Xing BY, He XC, Zeng K et al (2014) Mechanical properties of self-piercing riveted joints in Aluminum alloy 5052. Int J Adv Manuf Technol 75:351–361
6. Han L, Chrysanthou A, Young KW (2006) Mechanical behaviour of self-piercing riveted multi-layer joints under different specimen configurations. Mater Des 28(7):2024–2033
7. Liu Y, Zhuang WM, Shi HD (2019) Influencing factors on fatigue performance of self-piercing riveted joints: a review. Mater Rep 33(6):1825–1830
8. Li H, Bonnen J, Lasecki J et al (2016) Fatigue and fretting of mixed metal self-piercing riveted joint. Int J Fatigue 83:230–239

9. Han L, Chrysanthou A, O'Sullivan JM (2006) Fretting behaviour of self-piercing riveted aluminium alloy joints under different interfacial conditions. Mater Des 27(3):200–208
10. Huang ZC, Song TC, Lai JM (2019) Fatigue property and failure mechanism of self-piercing riveted joints of TA1 titanium alloy. Trans China Welding Inst 40(3):41–46
11. Huang ZC, Huang QW, Li SJ et al (2017) Influence of the self-piercing riveting position of dissimilar metal on fatigue strength. Forging Stamping Technol 42(9):150–156
12. Zhao L, He XC, Zhang XL et al (2017) Fretting wear and fatigue behavior of self-piercing riveting of lightweight alloys. Mater Rev 31(6):72–75
13. Moraes JFC, Rao HM, Jordon JB et al (2017) High cycle fatigue mechanisms of Aluminum self-piercing riveted joints. Fatigue Fracture Eng Mater Struct 1–14

Elastoplastic Finite-Element Analysis of Multi-Body Processes for Joining Mechanical Parts



SukHwan Chung, Jaedong Yoo, and ManSoo Joun

Abstract Fabricating lightweight assembly of auto parts is of great importance and joining technology using plastic deformation is very attractive because of high strength and structural reliability. In developing such assembling processes, prediction technology with high accuracy is essential to optimize the structural system and minimize the manufacturing cost. However, the related technologies are still insufficiently developed for the sake of application because of complexity of the problem. In this paper, an improved methodology of conducting elastoplastic finite-element analysis of multi-body metal forming processes is given with emphasis on the contact condition treatment. The presented approach is applied to simulate a rotary forging process of assembling a third-generation hub bearing unit. The inner races of the duplex pair taper roller bearings are considered elastic materials. Prestresses imposed on them are predicted.

Keywords Elastoplastic finite-element method · Multi-body metal forming · Rotary forging · Penalty method

1 Introduction

Finite-element predictions have become prevailing in the related industries because they can contribute to constructing an acceptable scientific platform for process design and technical management. The simulation technology has played key roles in innovating especially the forging industry [1, 2]. Our experiences [3–5] make us say that most predictions are reliable and that the costly trial-and-errors can be excluded from the process development procedure of common forgings including bearing parts, gear parts, fasteners, etc.

S. Chung
MFRC, Jinju, South Korea

J. Yoo · M. Joun (✉)
School of Mechanical Engineering, Gyeongsang National University, Jinju, South Korea
e-mail: msjoun@afdex.com

© The Minerals, Metals & Materials Society 2021

G. Daehn et al. (eds.), *Forming the Future*, The Minerals, Metals & Materials Series,
https://doi.org/10.1007/978-3-030-75381-8_120

To the contrary, there are still some topics in metal forming simulation which should be improved, theoretically and practically, which include finite-element predictions of forging processes for hard-to-form materials such as magnesium and titanium and predictions of multi-body forming processes. These topics belong to major interests of metal forming researchers owing to strong request to save global environments. The trend of global automobile market can be characterized by steadily increasing use of light materials and/or high strength materials with high structural reliability. To cope with this trend, researchers are focusing their efforts on expanding the applications of lightweight material and integrating several parts into a single part and thus joining technology relying on plastic deformation has increasingly become one of the core technologies.

Even though metal forming simulation technique already became indispensable in the field of metal forming, engineers, or researchers are not still supported by appropriate CAE technologies for solving some practical problems and related mechanics occurring in various joining processes because of their mechanical and geometric complexity. Recently, several predictions of multi-body metal forming or joining processes [6] were introduced, which are based on some improved numerical schemes including contact condition treatment scheme of the singular nodal points which meet over two objects or planes of symmetry.

In this study, theoretical backgrounds of joining process simulation or multi-body metal forming simulation based on the elastoplastic finite-element analysis are given and its application to a rotary forging process of assembling a third-generation hub bearing unit are presented, which is one of extreme applications of multi-body problems in metal forming, showing the versatility of the approach.

2 Elastoplastic Finite-Element Formulation

Because elastoplastic deformation is path-dependent, total process should be analyzed by a series of solution steps with sufficiently small step sizes. In dealing with large deformation, large rotation as well as large strain should be considered. For this purpose, deformation gradient tensor **F** for each solution step is calculated, which is polar decomposed into the rotation tensor **R** and the right stretch tensor **U** as follows:

$$\mathbf{F} = \mathbf{RU} \tag{1}$$

From the right stretch tensor defined in the above equation, the strain increment $\Delta\boldsymbol{\varepsilon}_{ij}$ is defined by

$$\Delta\boldsymbol{\varepsilon}_{ij} = \ln(\mathrm{U}_{ij}) \tag{2}$$

Stress increment from solution step n to solution step $n + 1$, denoted as $\Delta\boldsymbol{\sigma} = [\Delta\sigma_{xx}, \Delta\sigma_{yy}, \Delta\sigma_{zz}, \Delta\sigma_{xy}, \Delta\sigma_{yz}, \Delta\sigma_{zx}]^T$, is calculated by the radial return method

using strain increment $\Delta\boldsymbol{\varepsilon} = [\Delta\varepsilon_{xx}, \Delta\varepsilon_{yy}, \Delta\varepsilon_{zz}, \Delta\varepsilon_{xy}, \Delta\varepsilon_{yz}, \Delta\varepsilon_{zx}]^T$ as follows:

$$\boldsymbol{\sigma}^*_{n+1} = \boldsymbol{\sigma}_n + \Delta\boldsymbol{\sigma} = \boldsymbol{\sigma}_n + \mathbf{C}\left(\Delta\boldsymbol{\varepsilon} - \Delta\boldsymbol{\varepsilon}^p\right) = \boldsymbol{\sigma}_n + \mathbf{C}^{ep}\Delta\boldsymbol{\varepsilon} \tag{3}$$

where $\boldsymbol{\sigma}^*_{n+1}$ is stress calculated without considering the rotation from the solution step n to solution step $n+1$. $\boldsymbol{\sigma}_n$ expresses the stress at the solution step n which was already calculated in the previous solution step. $\mathbf{C}$ is elastic stiffness matrix and $\Delta\boldsymbol{\varepsilon}^P$ is the plastic strain increment. During iteration to obtain converged solution of Eq. (3), the elastoplastic consistent tangent stiffness $\mathbf{C}^{ep}$ is applied for better convergence. The process of calculating the elastoplastic consistent tangent stiffness and stress increment. $\Delta\boldsymbol{\sigma}$ depends on yield criterion and the way of calculating $\Delta\boldsymbol{\varepsilon}^P$. In this study, von Mises yield criterion is applied.

Stress at the solution step $n+1$, denoted as $\boldsymbol{\sigma}_{n+1}$, is calculated by transforming the stress $\boldsymbol{\sigma}^*_{n+1}$ calculated from Eq. (3) using the rotation tensor R as follows:

$$\boldsymbol{\sigma}_{n+1} = \mathbf{R}\boldsymbol{\sigma}^*_{n+1}\mathbf{R}^T \tag{4}$$

It has been well known that hexahedral elements are better of tetrahedral elements in terms of numerical stability and solution accuracy. However, it is very difficult to generate automatically hexahedral finite-element mesh system for metal forming simulation. To the contrary, tetrahedral finite-element mesh system can be generated in any situation for such purpose. However, they are exposed to numerical locking phenomena due to excessively constrained incompressibility, which can be solved by adding a degree-of-freedom of hydrostatic pressure onto a node.

In general, metal forming simulation problem is conceptually defined by a deformable body V with displacement (or velocity) prescribed boundary S_u and traction prescribed boundary S_t to find out the unknowns of displacement (or velocity) $\mathbf{u}$ and hydrostatic pressure p. The above boundary value problem can be formulated by the following weak form:

$$\int_V \delta\boldsymbol{\varepsilon}^T\boldsymbol{\sigma}dV - \int_V \delta\boldsymbol{\omega}^T\mathbf{b}dV - \int_{S_t} \delta\boldsymbol{\omega}^T\mathbf{t}dS = 0 \tag{5}$$

$$\int_V \delta q\left(\varepsilon_v + pK^{-1}\right)dV = 0 \tag{6}$$

where $\delta\boldsymbol{\omega}$ is arbitrary except that $\delta\boldsymbol{\omega} = 0$ on S_u and δq is arbitrary. In the above equations, $\boldsymbol{\sigma}$ and $\boldsymbol{\varepsilon}$ are stress tensor and strain tensor, respectively, and $\mathbf{b}$ and $\mathbf{t}$ are body force and traction, respectively. In addition, $\boldsymbol{\varepsilon}_v$ means volumetric strain and K is the bulk modulus of elasticity. The volumetric strain can be expressed as

$$\boldsymbol{\varepsilon}_v = \mathbf{m}^T\boldsymbol{\varepsilon} \tag{7}$$

where $\mathbf{m}^T = [1\ 1\ 1\ 0\ 0\ 0]$.

If the solution at the solution step n was calculated, the solution at the solution step $n+1$ can be calculated by substituting Eqs. (3) and (7) into Eqs. (5) and (6) as follows:

$$\int_V \mathbf{B}^T\left(\boldsymbol{\sigma}_n' + \mathbf{D}_d\mathbf{B}\Delta\mathbf{U}\right)dV - \int_V \mathbf{B}^T\mathbf{m}\mathbf{N}_p\, p dV - \int_V \mathbf{N}_u^T\mathbf{b}dV - \int_{S_t} \mathbf{N}_u^T\mathbf{t}dS = 0 \tag{8}$$

$$-\int_V \mathbf{N}_p^T\mathbf{m}^T\varepsilon_v dV - \int_V \mathbf{N}_p^T\mathbf{m}^T\mathbf{B}\Delta\mathbf{U}dV - \int_V \mathbf{N}_p^T K^{-1}\mathbf{N}_p p dV = 0 \tag{9}$$

where $\boldsymbol{\sigma}'$ is the deviatoric stress, $\mathbf{D}_d$ the deviatoric stress–strain relationship and $\mathbf{B}$ the strain–displacement matrix.

When the interpolation function of displacement, denoted as $\mathbf{N}_u$ and that of hydrostatic pressure, denoted as $\mathbf{N}_p$ are of the same order in the tetrahedral finite-element mesh system, numerical vibration of hydrostatic pressure occurs. To cope with this problem, tetrahedral MINI-element is applied [7]. In this scheme, the bubble interpolation function $\mathbf{N}_b$ with bubble displacement $\Delta\mathbf{U}_b$ is additionally employed to increase the order of displacement and to solve the numerical problem.

Applying Newton–Raphson method to Eqs. (8) and (9), the following finite-element equations can be derived.

$$\begin{bmatrix} \mathbf{K}_0 & \mathbf{H}_{ub} & \mathbf{H}_{up} \\ \mathbf{H}_{ub}^T & \mathbf{H}_{bb} & \mathbf{H}_{bp} \\ \mathbf{H}_{up}^T & \mathbf{H}_{bp}^T & \mathbf{V} \end{bmatrix} \begin{bmatrix} \Delta\mathbf{U} \\ \Delta\mathbf{U}_b \\ \Delta\mathbf{P} \end{bmatrix} = \begin{bmatrix} \mathbf{f}_{ext} \\ 0 \\ 0 \end{bmatrix} - \begin{bmatrix} \mathbf{f}_{int} \\ 0 \\ \mathbf{f}_p{}^p \end{bmatrix} \tag{10}$$

where $\mathbf{f}_{ext}$, $\mathbf{f}_{int,}$ and $\mathbf{f}_p$ are external force vector, internal force vector and internal force vector concerned with hydrostatic pressure, respectively. The subscript 0 represents the term concerned with standard interpolation function, the subscript b expresses the term concerned with bubble interpolation function, and the subscript p represents the term concerned with hydrostatic pressure. The submatrices of total stiffness matrix are defined as

$$\begin{aligned} &\mathbf{K}_0 = \int_V \mathbf{B}_0^T\mathbf{D}_d\mathbf{B}_0 dV,\ \mathbf{H}_{ub} = \int_V \mathbf{B}_0^T\mathbf{D}_d\mathbf{B}_b dV,\ \mathbf{H}_{bb} = \int_V \mathbf{B}_b^T\mathbf{D}_d\mathbf{B}_b dV \\ &\mathbf{H}_{up} = -\int_V \mathbf{B}_0^T\mathbf{m}\mathbf{N}_p dV,\ \mathbf{H}_{bp} = -\int_V \mathbf{B}_b^T\mathbf{m}\mathbf{N}_p dV,\ \mathbf{V} = -\int_V \mathbf{N}_\mathrm{u}^\mathrm{T} K^{-1}\mathbf{N}_u dV \end{aligned} \tag{11}$$

$\mathbf{f}_{ext} = \int_V \mathbf{N}_u^T\mathbf{B}_0 dV + \int_{S_t} \mathbf{N}_u^T\mathbf{t}dS$, $\mathbf{f}_{int} = \int_V \mathbf{B}_0^T\left(\boldsymbol{\sigma}_n' + \mathbf{m}\mathbf{N}_p\mathbf{P}\right)dV$, $\mathbf{f}_p = -\int_V \mathbf{N}_p^T\left(\mathbf{m}^T\varepsilon_v + K^{-1}\mathbf{N}_p\mathbf{P}\right)dV$

Deleting the bubble displacement $\mathbf{U}_b$ from Eq. (10), the following finite-element equations can be derived:

$$\begin{bmatrix} \mathbf{K}_0 - \mathbf{H}_{ub}\mathbf{H}_{bb}^{-1}\mathbf{H}_{ub}^T & \mathbf{H}_{up} - \mathbf{H}_{ub}\mathbf{H}_{bb}^{-1}\mathbf{H}_{bp} \\ \mathbf{H}_{up}^T - \mathbf{H}_{bp}^T\mathbf{H}_{bb}^{-1}\mathbf{H}_{ub}^T & \mathbf{V} - \mathbf{H}_{bp}^T\mathbf{H}_{bb}^{-1}\mathbf{H}_{bp} \end{bmatrix} \begin{bmatrix} \Delta\mathbf{U} \\ \Delta\mathbf{P} \end{bmatrix} = \begin{bmatrix} \mathbf{f}_{ext} \\ 0 \end{bmatrix} - \begin{bmatrix} \mathbf{f}_{int} \\ \mathbf{f}_p \end{bmatrix} \tag{12}$$

3 Treatment of Multi-Body Boundary Conditions

Considering that two materials are contacting each other during joining process as shown in Fig. 1, it should be satisfied that the normal velocity component of material 2 at *j*-th node should be the same with that at the same position of material 1. The normal velocity of material 1 at the same position of *j*-th node of material 2 can be calculated from Eq. 13, where the normal velocity at the contacting node of material 2, denoted by $\mathbf{n}_i^1$, is defined by the surface normal direction of material 1 and r is the relevant ratio of position of *j*-th node of material 2 at the corresponding segment of material 1.

$$\mathbf{v}_j^{1n} = \mathbf{v}_j^{2n} \rightarrow \left((1-r)\mathbf{v}_{i-1}^1 + r\mathbf{v}_i^1\right) \bullet \mathbf{n}_i^1 = \mathbf{v}_j^2 \bullet \mathbf{n}_i^1 \tag{13}$$

The constraint can be numerically treated by using penalty method, where the term shown in Eq. (14) is added to the weak form for the elastoplastic finite-element equations shown in Eq. (5), where ξ is the penalty constant.

$$\xi\left(\left((1-r)\mathbf{v}_{i-1}^1 + r\mathbf{v}_i^1\right) \bullet \mathbf{n}_i^1 - \mathbf{v}_j^1 \bullet \mathbf{n}_i^1\right)\left(\left((1-r)\delta\mathbf{v}_{i-1}^1 + r\delta\mathbf{v}_i^1\right) \bullet \mathbf{n}_i^1 - \delta\mathbf{v}_j^1 \bullet \mathbf{n}_i^1\right) \tag{14}$$

If two materials are perfectly bonded, the additional constraint that the tangential velocity at the contacting points should be satisfied likely to the normal directional velocity constraint as shown in Eq. (15), where $\mathbf{t}_i^1$ is the tangential direction defined by the contacting surface of material 1. Otherwise, the frictional force acts on the contacting area as shown in Eq. (16), where $\boldsymbol{F}_n$ is the normal directional nodal force

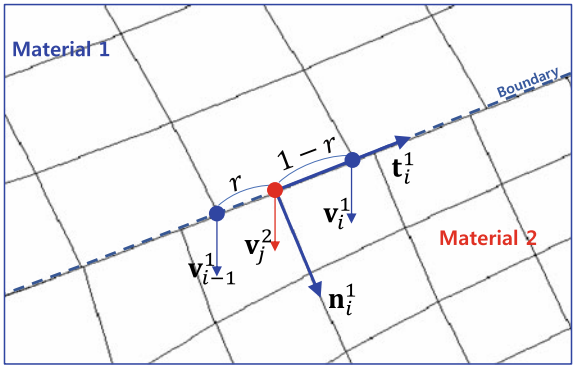


Fig. 1 Schematic description of the relation between the velocities at the contacting surface of multi-body. (Color figure online)

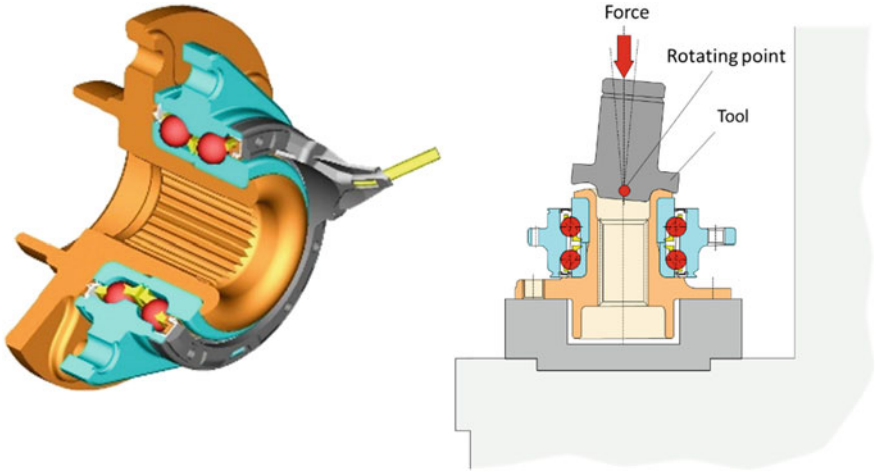
of given node.

$$\xi\left(\left((1-r)\mathbf{v}_{i-1}^{1}+r\mathbf{v}_{i}^{1}\right)\bullet\mathbf{t}_{i}^{1}-\mathbf{v}_{j}^{1}\bullet\mathbf{t}_{i}^{1}\right)\left(\left((1-r)\delta\mathbf{v}_{i-1}^{1}+r\delta\mathbf{v}_{i}^{1}\right)\bullet\mathbf{t}_{i}^{1}-\delta\mathbf{v}_{j}^{1}\bullet\mathbf{t}_{i}^{1}\right) \tag{15}$$

$$\boldsymbol{F}_{t}=\mu\boldsymbol{F}_{n}\mathrm{g}(\Delta\mathbf{v}_{t}),\ \mathrm{g}(\Delta\mathbf{v}_{\mathrm{t}})=\frac{\pi}{2}tan^{-1}\left(\frac{|\Delta\mathbf{v}_{t}|}{\mathrm{a}}\right) \tag{16}$$

4 Simulation of a Rotary Forging Process of Assembling a Third-Generation Hub Bearing Unit

With the development of automobile fabrication technology, a third-generation hub bearing assembled with ABS sensor becomes generalized through the consistent integration with surrounding parts as shown in Fig. 2a. It is usual that an orbital forming or rotary forging process [8–10] has been applied to assemble hub with bearing units as shown in Fig. 2b. In designing the orbital forming process, proper residual stress after assembly is one of the major concerns not only because excessive stress during orbital forming can cause damage in bearing unit [11] but also because insufficient stress can cause the clamping force to be much reduced. Nonstandard prestresses can thus cause premature fracture of bearing parts. However, most studies on these topics [12–15] have focused on revealing plastic deformation of material



(a) Third-generation hub bearing unit (b) Rotary forging process

Fig. 2 Third-generation hub bearing unit and its rotary forging process to assemble hub and bearing units. (Color figure online)

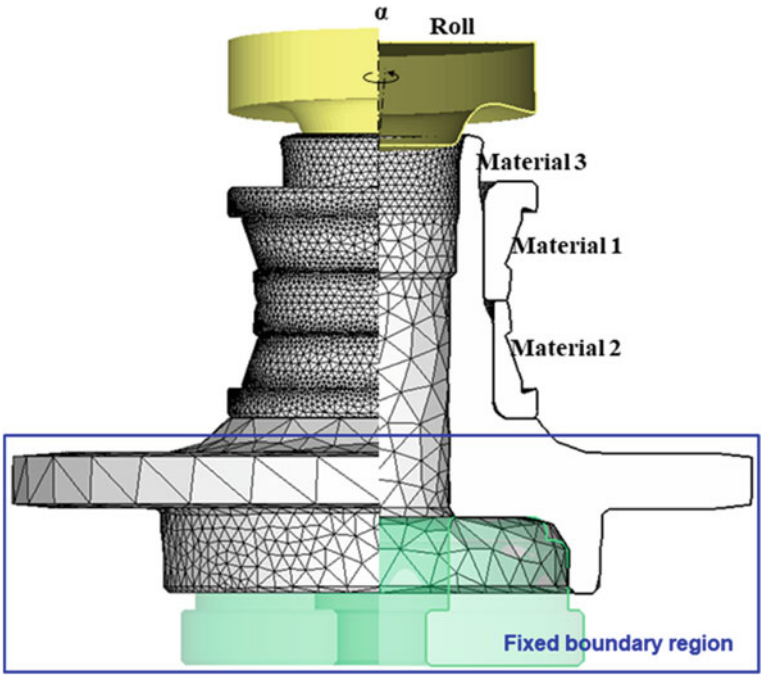


Fig. 3 Finite-element analysis model. (Color figure online)

during assembling the unit. As far as we know, there is no research work published with keywords of both hub bearing and residual stress. Most research works have thus seemed to stay outside of main issues of this subject.

Figure 3 shows an elastoplastic finite-element analysis model of the multi-body flow analysis problem, composed of three materials including hub (S50C) and two inner races (STB2) of a duplex pair taper roller bearing, an upper die, that is, a forming tool in the upper side and a clamping tool to assign essential boundary conditions. The forming tool was assumed rigid while all the materials were assumed to behave elastoplastically. The clamping tool at the lower side is employed to impose zero-velocity boundary conditions onto all the nodes which are inside the clamping tool. Young's moduli of all the materials are assumed 210 GPa and flow stresses are shown in Fig. 4 [4]. The frictional stresses between the rotating tool and the hub material were formulated by hybrid law of Coulomb friction and constant shear friction and coefficient of Coulomb friction and friction factor were assumed 0.1 and 0.2 [5, 16], respectively. The interfaces between materials were assumed frictionless because sliding motions between them are negligible. It was assumed that the hub material is fixed and that the forming tool evolves while moving downwards and it rotates with respect to its own idling axis. Note that the above tool motion in the analysis model is mechanically the same with its original motion, that is, the forming tool moves down only while idling with respect to its central axis, implying that the relative

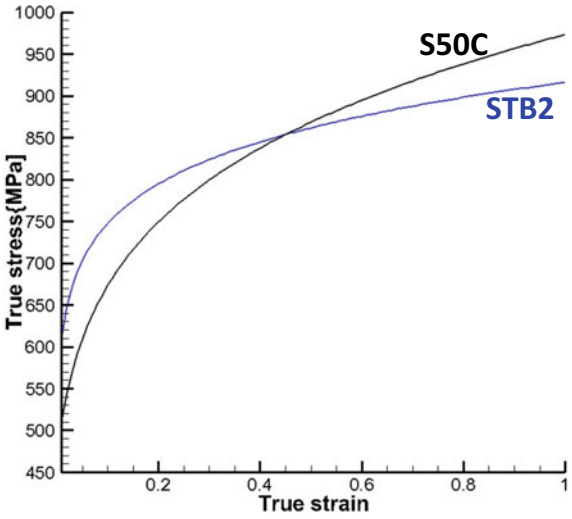
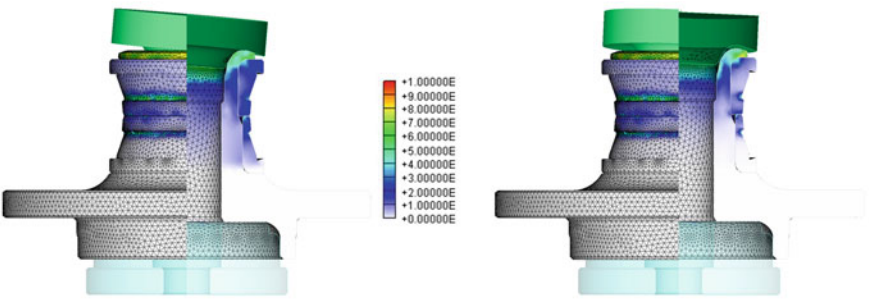


Fig. 4 Flow stresses of the materials. (Color figure online)

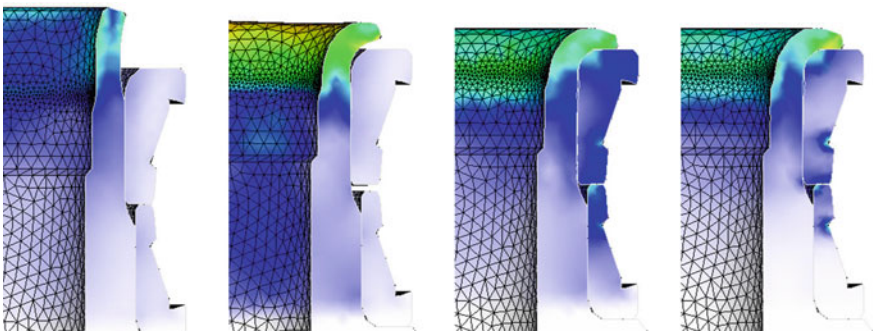
velocity is the same with each other. The evolving velocity was assumed 200 rpm and the moving-down velocity 1.6 mm/s. The forming tool moves down for 8.2 s, stays for 0.8 s, and returns for 1.5 s to its original position. Total number of tetrahedral elements amounts to 33,000 and that of solution steps 8400. The penalty constant ξ was assumed 10,000,000.

Figure 5a shows the effective stress at the instant when the forming tool touches its lowest position and Fig. 5b shows the residual after the forming tool returns. It should be noted that the difference between the effective stress at the final contact of the forming tool with the material (see Fig. 5a) and the final residual stress is not remarkable because the forming tool always contacts very partially with the material to be formed. Of course, the stress distribution of the material during being formed varies quite much with the location of the forming tool. Figure 6 shows the



(a) At the end of forming (b) After unloading

Fig. 5 Effective stresses at the end of forming and after unloading. (Color figure online)



(a) t = 1.459s (b) t = 6.667s (c) t = 9.018s (d) t = 9.073s

Fig. 6 Variation of effective stress (**a**–**c**) and residual stress (**d**). (Color figure online)

variation of effective stress at a cross-section with the elapsed time. Because we exerted purposely a little greater forming load on the forming tool (180 kN) than its limit (120 kN), so much greater stress can be observed at the round corners of the inner races. Of course, we can simulate the process with limit forming load assigned to avoid the excessive prestresses at the fatal corners.

5 Concluding Remarks

In this paper, multi-body metal forming simulation technology was presented, which is based on elastoplastic finite-element method with tetrahedral finite-elements and contact treatment scheme based on penalty method. To check the rigidity of the approach and some numerical schemes employed, an extremely complicated multi-body forming process of a rotary forging process of assembling a third-generation hub bearing unit was simulated. It was verified from this application that the approach with various numerical schemes is stable and general.

The finite-element predictions were discussed with emphasis on the residual stresses, which are greatly important in conducting the assembling process design. From the application, it was shown that the proposed multi-body metal forming simulation technology can provide process engineers with meaningful information about prestresses and interfacial stresses for optimizing an assembly process of mechanical parts as well as their joining process and that it will contribute to advances in plastic deformation based assembling technology in terms of increased strength with reduced weight.

References

1. Joun MS (2020) Recent advances in metal forming simulation technology for automobile parts by AFDEX. IOP Conf Ser Mater Sci Eng 834:012016
2. FAG-HanHwa Bearing (2003) The history of Korean bearing industry of 50 years
3. Joun MS (1996–2019) MFCAE (Conference on Metal Forming CAE Technology)
4. Joun MS, Eom JG, Lee MC (2008) A new method of acquiring true stress-strain curves over a large range of strains using a tensile test and finite element method. Mech Mater 40:586–593
5. Lee SW, Lee JM, Joun MS (2020) On critical surface strain during hot forging of lubricated Aluminium alloy. Tri Int 141:105855
6. Chung SH, Jeong SW, Chung WJ, Joun MS (2018) Finite element analysis of three-dimensional multi-body forming processes. In: Proceedings of the Korean society for technology of plasticity conference spring meeting 42–43
7. Chung WJ, Kim BS, Lee SW, Ryu HY, Joun MS (2014) Finite element simulation of plate or sheet metal forming processes using tetrahedral MINI-elements. J Mech Sci Technol 28(1):237–243
8. Han XH, Hua L (2009) Comparison between cold rotary forging and conventional forging. J Mech Sci Technol 23:2668–2678
9. Sivam SPSS, UmaSekar VG, Shubham M, Avishek M, Mondal A (2016) Orbital cold forming technology—combining high quality forming with cost effectiveness—a review. Indian J Sci Technol 9(38):1–7
10. Nowak J, Madej L, Ziolkiewicz S, Plewinski A, Grosman F, Pietrzyk M (2008) Recent development in orbital forging technology. Int J Mater Form 1(1):387–390
11. Moon HK, Jeong JH, Joun MS (2003) Development of analysis technology for rotary forging process. In: Proceedings of the Korean society for technology of plasticity conference on 8th forging symposium 63–76
12. Moon HK, Lee MC, Joun MS (2007) An approximate efficient finite element approach to simulating a rotary forming process and its application to a wheel-bearing assembly. Finite Elem Anal Des 44:17–23
13. Cho HJ, Koo JS, Bae WR, Lim JS (2008) A study on orbital forming analysis of automotive hub bearing using the explicit finite element method. Trans KSAE 16:29–36
14. Moon HK, Lee MC, Chung JH, Joun MS (2005) Finite element analysis of orbital forming process in bearing manufacturing. Trans Mater Process 14(1):29–36
15. Nam CH, Lee MC, Eom JG, Choi MH, Joun MS (2014) Finite element analysis model of rotary forging for assembling wheel hub bearing assembly. Procedia Eng 81:2475–2480
16. Joun MS, Moon HG, Choi IS, Lee MC, Jun BY (2009) Effects of friction laws on metal forming processes. Tri Int 42:311–319

A New Non-destructive Testing Method Applied to Clinching



Rémi Lafarge, Alexander Wolf, Christina Guilleaume, and Alexander Brosius

Abstract To pursue better quality, there is a strong need for efficient and robust non-destructive testing methods for joining processes. A new approach has been proposed to detect loose bolted joints using acoustic waves. This method measures the dissipation of energy by recording the propagated waves on the surfaces of the joining partners next to the joint. The authors show a link between the torque moments applied to the bolt and the ability of the joint to transfer acoustic energy using both simulations and experiments. In this article, the method's ability to detect variations of certain process parameters of the clinching process was investigated numerically. To this extent, results of FEM calculations of the joining process are used to simulate the non-destructive testing method. By varying parameters of the clinching model, their influence on the transmission of energy within the joint is studied.

1 Introduction

Clinching is a joining by forming process without the application of additional components. Using specific tools, an interlock between two or more sheets is formed. This joining process has numerous advantages from an industrial perspective including the ability to join different materials and a great cost-effectiveness. However, the main testing solutions employed to assess the quality of a joint are currently destructive: mechanical testing like the peel test or measuring geometric properties like the undercut, neck thickness, or the final bottom thickness in cross-sections.

R. Lafarge (✉) · A. Wolf · C. Guilleaume · A. Brosius
Technische Universität Dresden, 01069 Dresden, Germany
e-mail: remi.lafarge@tu-dresden.de

A. Wolf
e-mail: alexander.wolf3@tu-dresden.de

C. Guilleaume
e-mail: christina.guilleaume@tu-dresden.de

A. Brosius
e-mail: alexander.brosius@tu-dresden.de

© The Minerals, Metals & Materials Society 2021

G. Daehn et al. (eds.), *Forming the Future*, The Minerals, Metals & Materials Series,
https://doi.org/10.1007/978-3-030-75381-8_121

For a given tool geometry and corresponding parameter set, the general quality of the clinching process can be validated before the beginning of mass production using conventional destructive testing methods. Non-destructive testing (NDT) is mainly aimed at a fast quality assessment during production to detect defective joints resulting from process disturbances like tool wear, punch displacement or material variations like sheet thickness, surface roughness, or yield strength.

The article numerically investigates the sensitivity of a new NDT method to changes in different input parameters that could be evolving during the process: friction forces, punch displacement and die punch relative positioning.

2 State of the Art

The aim for a lightweight design concept, especially in the area of transportation demands a flexible usage of different materials to best utilise their respective properties. Therefore, various joining techniques exist for applying form-locking as well as material or frictional bonds between two or more materials [1].

The focus of this paper is the clinching process, where two overlapping sheets of metal are formed plastically to create an interlock without an additional functional element like a rivet or bolt. The load capacity of the form-locking and frictional bond is primarily defined by the undercut and the neck thickness, see Fig. 1. In the process, the two sheets are fixed in position on the die and the punch presses the material into the die, thereby creating the undercut and form-lock. The geometry of the resulting joint regarding undercut, neck thickness and bottom thickness can be varied by using different die and punch geometry combinations, adjusting the process to different materials and sheet thicknesses. Neugebauer et al. [2] improved the process for the joining of magnesium alloys and presented a die-less clinching process. Due to this easy and variable setup and high flexibility of joinable materials, clinching is one of the most applied processes in the automotive industry [3].

A number of or non-destructive evaluation techniques exist for different kinds of joints. The selection of the particular method in each case depends on, e.g. the

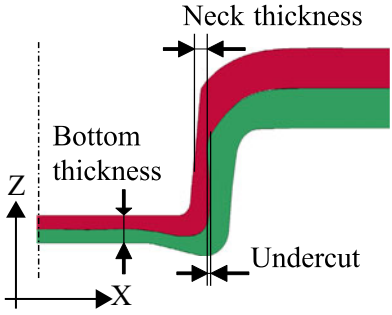


Fig. 1 Geometrical properties of a joint. (Color figure online)

material combination, the safety requirements and regulations, or the accessibility of the connection. A well-known procedure is the pulsed thermography testing that analyses the heat propagation in and around the joint [4]. It is suitable for all kinds of materials and can also be used on large structures like wind turbines for condition monitoring [5]. Another option is the ultrasonic sound testing which is mainly used for welded joints [6]. Other lesser known testing solutions for joints next to the expensive CT-scan or radiography testing are measurements of the electrical profile [7] or Terahertz imaging [8]. All the mentioned options are limited in their applicability to clinched joints. Sometimes the dimensions of the connection are too large or too small, sometimes the material properties are incompatible with the process parameters. Most importantly, the costs often exceed the usefulness of the procedure when having hundreds of joints on large structures consisting of 10000–30000 parts in a car up to several million part in an aircraft [9].

Different NDT are available for the clinching process. Optical tests using crack detection lack safety and are not suited for industrial application [10]. Measuring bottom thickness is possible but lacks reliability [11]. Finally, the condition monitoring of process parameters by pre-defined hull curves is currently the best and most reliable method to ensure a safe connection and is also used with regard to quality management norms [12]. However, this method does not verify the geometrical forming of a proper cross section of the joint.

Wolf et al. [13] proposed a new NDT for evaluating joint quality. A elastic stress wave is generated and travels through the joint. Part of the energy is transmitted through the link while another part is reflected, so three waves are present: one emitted, one reflected and one transmitted. By measuring the transmitted and reflected stress waves, it is possible to evaluate the bolted connection, in this case determining whether the bolt is loose or tightened. This proposed method has the advantages of being non-destructive, very fast, and theoretically applicable to many different materials including composites. In Wolf et al. [14] the ability of this method to detect loose joint was studied numerically and experimentally. In this paper, the possibility of extending this method to clinched joint will be studied.

3 Modelling

The sensitivity of the testing method will be investigated numerically. For this purpose, a complete model of the evaluation process must be implemented. The sequence of the analysis starts with the forming process of the clinching point. Then, as the tools are removed, springback occurs and will be simulated. Finally, the measurement process itself will be simulated. Post-processing is then done using a user routine implemented in Python. LS-DYNA (R11) is used to compute the model, using Massively Parallel Processing (MPP) and double precision. Between every simulation of the analysis sequence, a dynain file is created, containing the current deformed mesh

coordinates and stress information for every element. These values are then used to initialise the next simulation step. Every simulation is performed in three dimensions using a single symmetry plane.

3.1 Forming Simulation

The forming process is simulated first. The geometry of the tools used is represented Fig. 1. The simulation is run using implicit mode of LS-DYNA, with dynamic analysis activated and adaptive timesteps. Implicit integration scheme is here used due to the quite slow process, compared to the critical timestep (following Courant's stability criteria) associated with the mesh. Using explicit scheme would therefore lead to a very high number of timestep and therefore a very high computation time. The mesh is created using Hypermesh, using a variably sized hexahedral mesh for the sheet and shell elements for the tools. The deformable parts contain around 691000 elements. A fully integrated element formulation is used to prevent hourglassing issues. The material model is implemented as an elastic–plastic model with von Mises criteria and associated flow rule and isotropic strain hardening parametrised with a power law. No strain rate effect is taken into account. The material parameters correspond to a DC04 (1.0338) steel. The contact is simulated using a penalty function. The friction model implemented is a simple Coulomb law. Default friction coefficient is 0.1 and the punch displacement is set to 5.1 mm. The simulation time is about 7 h using 16 cores on Intel Xeon CPU E5-2680 v3 @ 2.50GHz.

3.2 Springback Simulation

Simulation of springback is also performed using an implicit scheme. The simulation is initialised using the dynain file written at the end of the preceding forming simulation. The same material and contact models are used as in the forming simulation. All additional degrees of freedom are removed by fixing an adequate number of nodes. A dynain file is generated as output at the end of the simulation. Running time is about 1 h using 8 cores.

3.3 Stress Wave Simulation

The measurement process consists of an analysis of a stress wave propagation through the joint. It is, therefore, done using the explicit mode of the solver, as the explicit integration scheme is much more adapted to short time simulation and stress wave propagation studies. The simulation is initialised using the dynain file output of the previous springback simulation. The same contact model is employed, but a purely

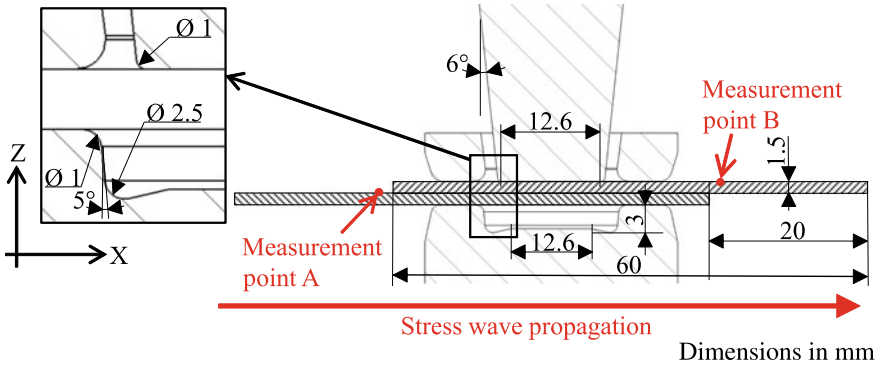


Fig. 2 Tool's geometry and measurement points. (Color figure online)

elastic material model is used. The load consists in nodal force in x-direction (see Fig. 2) applied on the surface of the lower sheet. The amplitude and length are chosen such that the resulting stress wave peak at given stress value of 25 MPa and with length of 20 ms. For post-processing, a user routing implemented in Python is employed, which enables calculations on node and element values. Two measurement points are created by selecting elements on the blank and averaging their stress level for the component colinear to wave propagation (σ_{xx}), see Fig. 2.

4 Results and Conclusions

The parameters of the numerical analysis are presented in Table 1. For each simulation, only one parameter is changed. The goal is to validate the idea that the parameters can influence stress wave propagation through the joint. If there is a detectable difference between resulting stress waves, this method can theoretically be used to test clinched joints.

Table 1 Parameter change for every simulations

Simulation	Parameter change
#1	All parameters are nominal
#2	Friction is increased to 0.3
#3	Punch displacement is decreased to 4.1 mm
#4	Punch is displaced 0.2 mm in the X direction
#5	Die is rotated 1° around Y axis

Table 2 Properties of simulated clinched joint

Simulation	Neck thickness in µm				Undercut in µm				Bottom thickness in mm			
	Left		Right		Left		Right		Left		Right	
#1	490		490		106		106		1.04		1.04	
#2	493	0.6%	493	0.6%	119	12%	119	12%	1.05	1%	1.05	1.0%
#3	488	0.4%	488	0.4%	80	24%	80	24%	1.78	71%	1.78	71%
#4	406	17%	578	17%	9	90%	170	60%	1.04	0%	1.04	0.0%
#5	487	0.6%	496	1.2%	160	22%	82	22%	1.1	5%	1.19	14%

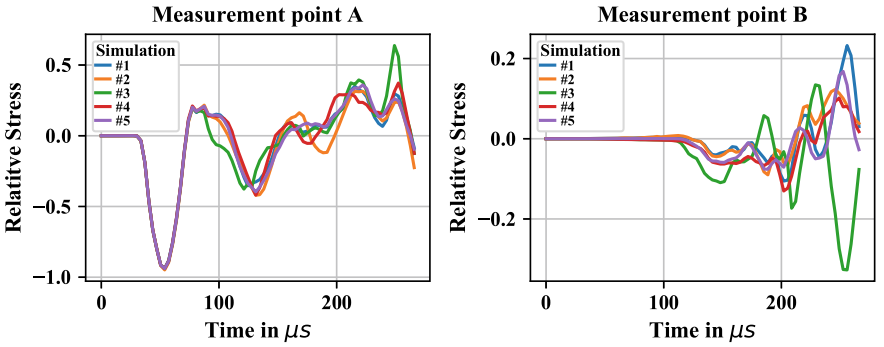


Fig. 3 Stress values at point A and B. (Color figure online)

Table 2 presents the results of the forming and spring back simulation. Neck thickness, bottom thickness, and undercut have been measured using mesh information. The percentages represent the relative deviation to the first simulation.

Figure 3 presents the measurement at the two measuring points for all simulations. The relative stress is the average stress value divided by the peak of the stress wave. From the results of the five simulations, it can be derived that both reflected and transmitted waves are affected by changes to the different input parameters analysed here. Table 3 present characteristic values of the first transmitted wave and the first reflected wave. The percentages represent the relative deviation to the first simulation. By comparing this information with the results of the forming simulation presented in Fig. 2, it appears that changes to the friction coefficient have very little influence on the geometric properties of the joint and consequently on the transmitted and reflected first wave. Unlike the bolted connection investigated in [14], where friction forces transmitted most of the energy, it seems that in clinching point, the energy transmission is more dependent on the geometrical parameters of the joint.

The results of the simulation show that the transmission of the energy is affected by the process parameter variation. Therefore, this method is generally suitable to detect deviations in clinched joints. At this point, the method does not yet link a specific property change to a certain characteristic of the transmitted and reflected

Table 3 Properties of transmitted and reflected waves

Simulation	Reflected wave				Transmitted wave			
	Length in μs		Peak		Length in μs		Peak	
#1	37.5		0.2		103		−0.105	
#2	34.1	9%	0.216	8%	102	1%	−0.09	14%
#3	19.5	48%	0.199	1%	70	32%	−0.11	5%
#4	39.1	4%	0.21	5%	107	4%	−0.131	25%
#5	36.9	2%	0.208	4%	100	3%	−0.07	33%

stress waves, but a general sensitivity is demonstrated. This issue might be circumvented with a frequency domain analysis, where the exiting signal is sinusoidal. Some variation might be linked to specific frequencies, which then would be visible on a spectral diagram.

Acknowledgments This research has been funded by the Deutsche Forschungsgemeinschaft (DFG, German research foundation)—Project-ID 418701707-TRR 285, subproject C04. We thank the Centre for Information Services and High Performance computing (ZIH) at TU Dresden for generous allocations of computer time.

References

1. Groche P, Türk M (2011) Smart structures assembly through incremental forming. CIRP Ann 60(1):21–24. https://doi.org/10.1016/j.cirp.2011.03.003
2. Neugebauer R, Mauermann R, Dietrich S, Kraus C (2007) A new technology for the joining by forming of magnesium alloys. Prod Eng 1(1):65–70. https://doi.org/10.1007/s11740-007-0045-5
3. Mucha J (2017) Clinching technology in the automotive industry. Arch Motoryz 76(2)
4. Meola C, Carlomagno GM, Squillace A, Giorleo G (2004) The use of infrared thermography for nondestructive evaluation of joints. Infrared Phys Technol 46(1–2):93–99. https://doi.org/10.1016/j.infrared.2004.03.013
5. García Márquez FP, Tobias AM, Pinar Pérez JM, Papaelias M (2012) Condition monitoring of wind turbines: techniques and methods. Renew Energy 46:169–178. https://doi.org/10.1016/j.renene.2012.03.003
6. Chassignole B, El Guerjouma R, Ploix M-A, Fouquet T (2010) Ultrasonic and structural characterization of anisotropic austenitic stainless steel welds: towards a higher reliability in ultrasonic non-destructive testing. NDT E Int 43(4):273–282. https://doi.org/10.1016/j.ndteint.2009.12.005
7. Füssel U, Kalich J, Großmann S et al (2014) Elektrisches Eigenschaftsprofil Umformtechnischer Fügeverbindungen vol 389(1), Aufl. Hannover: Europäische Forschungsgesellschaft für Blechverarbeitung e.V. (EFB)
8. Jansen C, Wietzke S, Peters O et al (2010) Terahertz imaging: applications and perspectives. Appl Opt 49(19):E48-57. https://doi.org/10.1364/AO.49.000E48
9. Mori K, Bay N, Fratini L, Micari F, Tekkaya AE (2013) Joining by plastic deformation. CIRP Ann 62(2):673–694. https://doi.org/10.1016/j.cirp.2013.05.004

10. Merkblatt DVS-EFB 3420, Clinchen—Überblick. DVS (2012) https://www.dvs-regelwerk.de/inhalt/430/3420
11. GmbH E (1999) Eckold-Clinchen: Informationen und Entscheidungshilfen. Ein Leitfaden zur Anwendung Der Eckold-Clinchtechnik, Eckold GmbH
12. Khrebtov P (2011) Neuartiges Verfahren zur Online-Prozessüberwachung und—Fehlerklassifizierung beim Durchsetzfügeverbinden von Blechen, Universitätsbibliothek Clausthal
13. Wolf A, Brosius A (2017) Concept for a fast analysis method of the energy dissipation at mechanical joints. In: AIP Conference Proceedings 1896(1). https://doi.org/10.1063/1.5008133
14. Wolf A, Lafarge R, Brosius A (2019) A non-destructive testing method for joints by the measurement of the energy dissipation. Prod Eng. 13(1):99–106. https://doi.org/10.1007/s11740-018-0860-x

Investigation on the Strain Induced Oxide Layer Fracture and Bonding During Cold Rolling of Aluminum Alloys



Mahsa Navidirad, Wojciech J. Stepniowski, Elijah Cartier, Tyler Christ, Masashi Watanabe, and Wojciech Z. Misiolek

Abstract Physical bond rolling experiments of aluminum sheets have been investigated in this study. In addition to native oxides on surface of aluminum, a thick oxide layer was deliberately added to AA3xxx aluminum sheets by anodization. For better monitoring of evolution of the oxide layer during roll bonding, the anodized layer was colored with Indigo Carmine in the anodization process. A progressive reduction per pass ranging from 2 to 70% has been performed in consecutive experiments at a constant rolling speed to develop different degrees of oxide surface expansion leading to its fracture and leaving disparate oxide fragments. The evolution of the oxide fragmentation and bonding of aluminum sheets were systematically characterized as a function of deformation by electron microscopy. It was revealed that the crack width between fragmented oxides increases exponentially while the oxide fragment size decreases exponentially as a function of the reduction ratio.

Keywords Roll bonding · Direct recycling · Aluminum recycling · Coated strips · Metal expansion · Coating fracture

1 Introduction

Aluminum recycling process, which mainly involves re-melting of aluminum scraps and casting, is far less expensive and energy intensive than creating prime aluminum through the electrolysis of aluminum oxide mined as bauxite [1]. However, material loss during re-melting cannot be avoided due to contamination with oxides, oil, and plastic coatings of the scraps [2]. To overcome this problem associated with the re-melting, an alternative solid-state recycling, which is a process of converting metal chips to final or semifinal product through hot deformation techniques, has been proposed [3]. Until now, several attempts have been made regarding solid-state recycling of aluminum alloys by using machining chips of different shape and chemical compositions in combination with various severe plastic deformation methods

M. Navidirad · W. J. Stepniowski · E. Cartier · T. Christ · M. Watanabe · W. Z. Misiolek (✉)
Loewy Institute, Lehigh University, Bethlehem, PA 18015, USA
e-mail: wzm2@lehigh.edu

© The Minerals, Metals & Materials Society 2021

G. Daehn et al. (eds.), *Forming the Future*, The Minerals, Metals & Materials Series,
https://doi.org/10.1007/978-3-030-75381-8_122

including hot extrusion [4–6]. One of the main challenges of this process is yielding a product with optimum mechanical properties by fulfilling the best condition for solid-state welding of aluminum chips. In fact, the natural oxide layer on the surface of the chips acts as a barrier in bonding a virgin metal to metal [7].

In this regard, studies of the cold-welding process a.k.a. solid-state welding would provide fundamental mechanism of chips welding [8]. Bay correlated the weld strength to the contact surface area and normal pressure and found that the bonding between chips is not achieved until a certain critical surface expansion has occurred [7]. According to Guley et al. [8] the sound welding of chips would be ensured when two criteria are fulfilled: (1) the oxide layer has to break down by imposing shear stress greater than a criterial shear stress level to cause the breaking of the oxide layer, and (2) the cumulative value of the ratio of the mean stress to the flow stress must be greater than a defined constant value for a given alloy and specific extrusion process conditions. Cooper et al. [9] also indicated that an aluminum interface must be stretched by a threshold strain to cause welding. The required strain would be decreased by increasing the normal contact stress, temperature, or shear stress. Moreover, increases in the strain rate have little influence on the bond strength at low temperatures, but significantly decreases the bond strength at temperatures above 423 K. In contrast, solid-state welding of aluminum strips at different temperatures and over different process paths revealed that diffusion is an important mechanism in bonding aluminum at high temperatures [10]. Le et al. [11] studied the crack propagation behavior in the oxide layer of a single aluminum sheet and showed that the spacing between cracks increases as the oxide film thickness increases. The oxide layer was fragmented into far smaller pieces when the oxide film was below a critical thickness. They concluded that metal will not penetrate through the broken oxide layer until a critical reduction of about 13% is reached.

All the mentioned theories above are in agreement that the main phenomena yielding a sound bonding are fracture of the surface oxide layer and exposure of fresh metal surface. It seems obvious that the fracture process of the oxide layer and the extrusion of metal through the oxide cracks is a topic requiring much more attention. In this work, the fragmentation of the surface oxide layer and metal deformation behavior of the aluminum sandwiches are systematically studied as a function of the reduction ratio during cold rolling. To obtain a comprehensive assessment on the fragmentation of oxide layer, aluminum strips were deliberately covered with anodically grown colored oxide film. The oxide fragmentation behaviors were carefully characterized by electron microscopy.

2 Experimental Procedures

Commercial purity Aluminum alloy (AA3003) strips with initial dimensions of 80 $\times$ 20 $\times$ 2 mm^3 were used as starting material. Samples were chemically polished by immersing them in 20% HNO_3 for 3 min followed by rinsing in 10% NaOH for 30 s. In order to anodize only one surface of the strips, backs, and edges of the samples

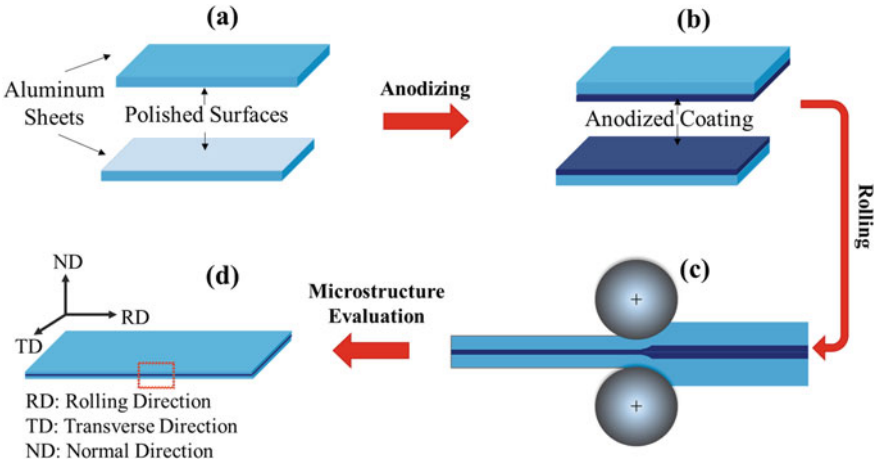


Fig. 1 Summary of roll bonding process of anodized aluminum sheets: **a** chemical polishing and painting, **b** anodizing, **c** roll bonding and **d** definitions of sample geometry for observation. (Color figure online)

were coated with acid-resistant paint. The strips were finally anodized in electrolyte of 20% H_2SO_4 at 1 °C under applied voltage of 23 V for 4 h to fabricate the oxide film with a thickness of ~40 μm. For better observation of evolution of the oxide layer, the electrolyte was dyed with Indigo Carmine, the organic dye-containing nitrogen and sulfur and providing a strong color. Several sandwich samples were made by clamping the coated surfaces of two sheets as internal sides of the bonded sandwich.

Roll bonding of the sandwiches was carried out using a laboratory 4-high rolling mill with a 40 mm working roll and rolling speed of 26 rpm. Each sandwich was rolled at specific reduction ratio between 2 and 70%. Finally, the Scanning Electron Microscope (SEM) with an X-ray energy dispersive spectrometer (XEDS) (Hitachi 4300SE/N) was used to observe evolution of oxide layer fragmentation, crack formation, and extrusion of metal through broken oxide layer as function of the reduction ratio. The schematic procedures of roll bonding process of anodized aluminum sheets are summarized in Fig. 1.

3 Results

A cross-sectional SEM image of a single coated Aluminum strip as well as XEDS spectra from the metal and coating layer are shown in Fig. 2. A uniform, smooth, and almost defect-free coating with a thickness of ~40 μm can be observed (Fig. 2a). The coating layer also seems to have a good adhesion to the substrate. By comparing XEDS spectra between the substrate and coating layer, Nitrogen and Sulfur, which

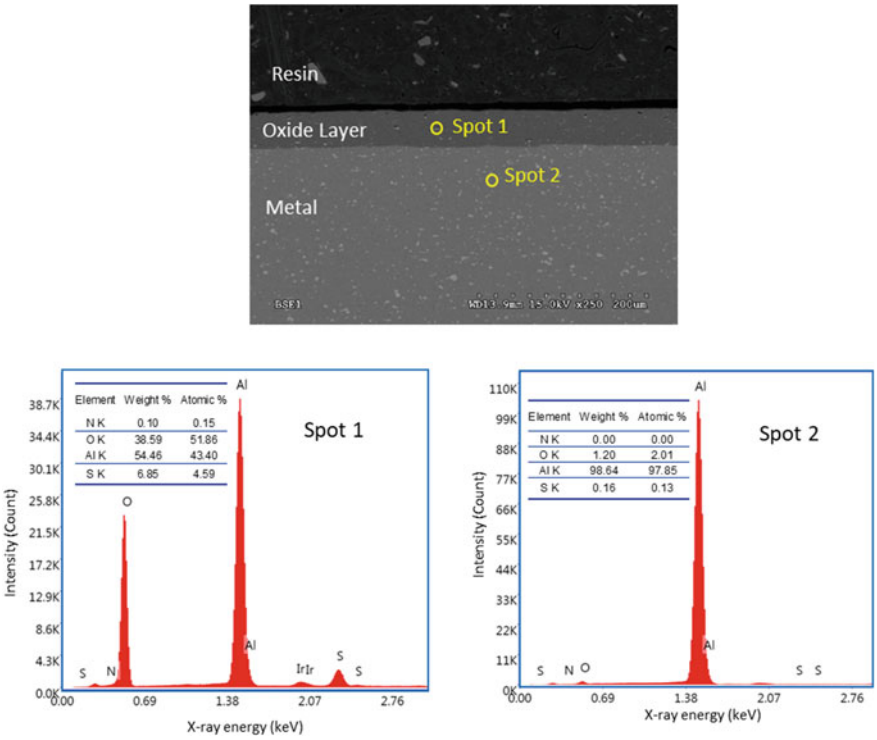


Fig. 2 A cross-sectional SEM micrograph of coated aluminum strip before rolling and XEDS spectra taken from regions indicated as spots 1 and 2 in the SEM image. (Color figure online)

are the main constituents of Indigo Carmine, are found in the coating layer as well as Oxygen.

None of these sandwich sheets were bonded by rolling below 70% reduction. There is even no sign of initial bonding at all at lower strains. In contrast, tight bonding between the strips was achieved in the sandwich rolled at 70% and the strips were hardly pulled away using hand force.

The oxide layers of unsuccessful bonded sandwich samples were observed by the SEM. Figure 3a–f shows a series of SEM images of oxide layer from the samples rolled at reduction ratios between 2 and 70%. Cracks are seen in the oxide layer of all the samples even at lowest reduction (2%) and the formed cracks in all the samples are running perpendicular to the rolling direction. At 10% reduction or higher reduction, oxides are clearly fragmented and almost uniformly stretched from one side of the sample toward the other side (Fig. 3c, d) and it seems that as the reduction ratio increases the density of cracks increases 3. This phenomenon is much more pronounced in the sample rolled at reduction ratios of 35 and 45% (Fig. 3e, f) in which some cracks even started to grow parallel to the rolling direction and leave small equal-sized fragments behind. Moreover, by increasing the reduction per pass,

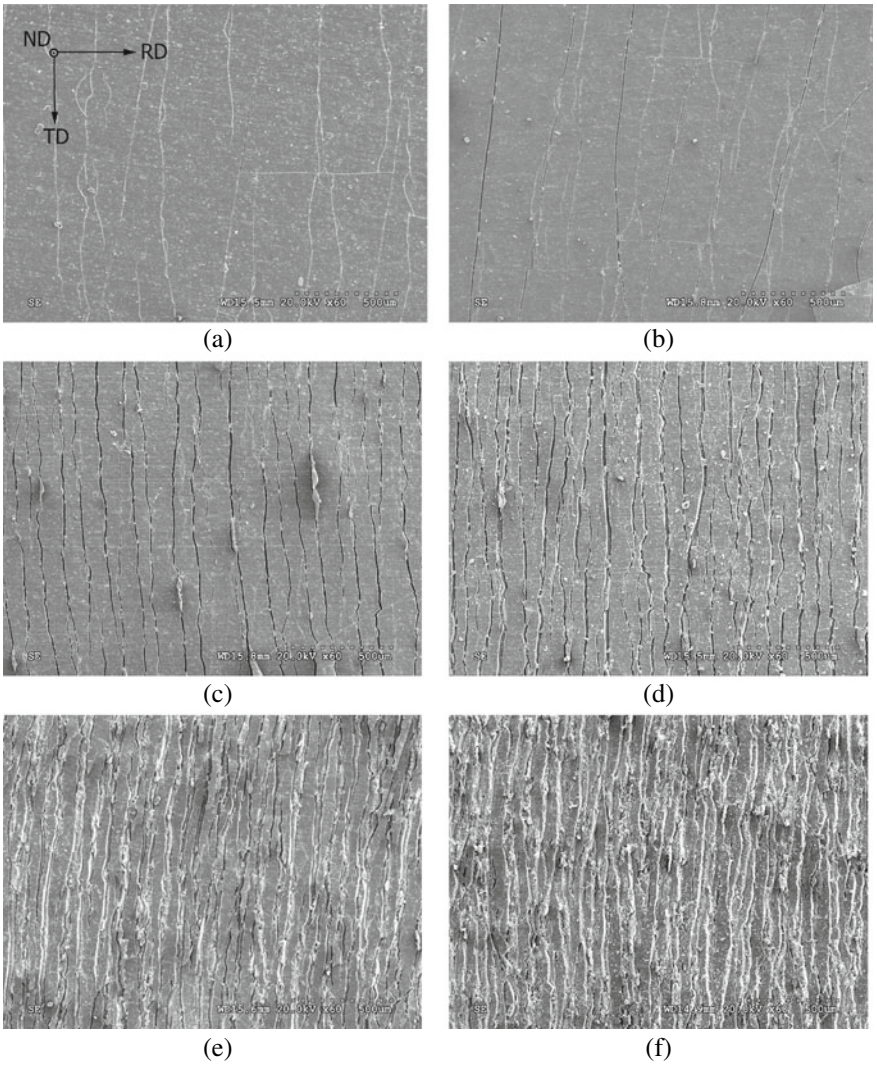


Fig. 3 A series of SEM images of the strip surface rolled at different reduction ratios: **a** 2%, **b** 5%, **c** 10%, **d** 18%, **e** 35%, and **f** 45%. RD, TD and ND represent rolling direction, transverse direction, and normal direction, respectively

the oxide layer is no longer flat, which indicates that some oxide fragments are raised and others are lowered during rolling. For better evaluation of oxide fragmentation as well as degree of oxide topography, cross section of the samples in the rolling direction was observed by the SEM (Fig. 4).

Figure 4 shows a series of cross-sectional images of the rolled sandwiches parallel to rolling direction at the different reduction ratios. It is seen that for samples rolled at

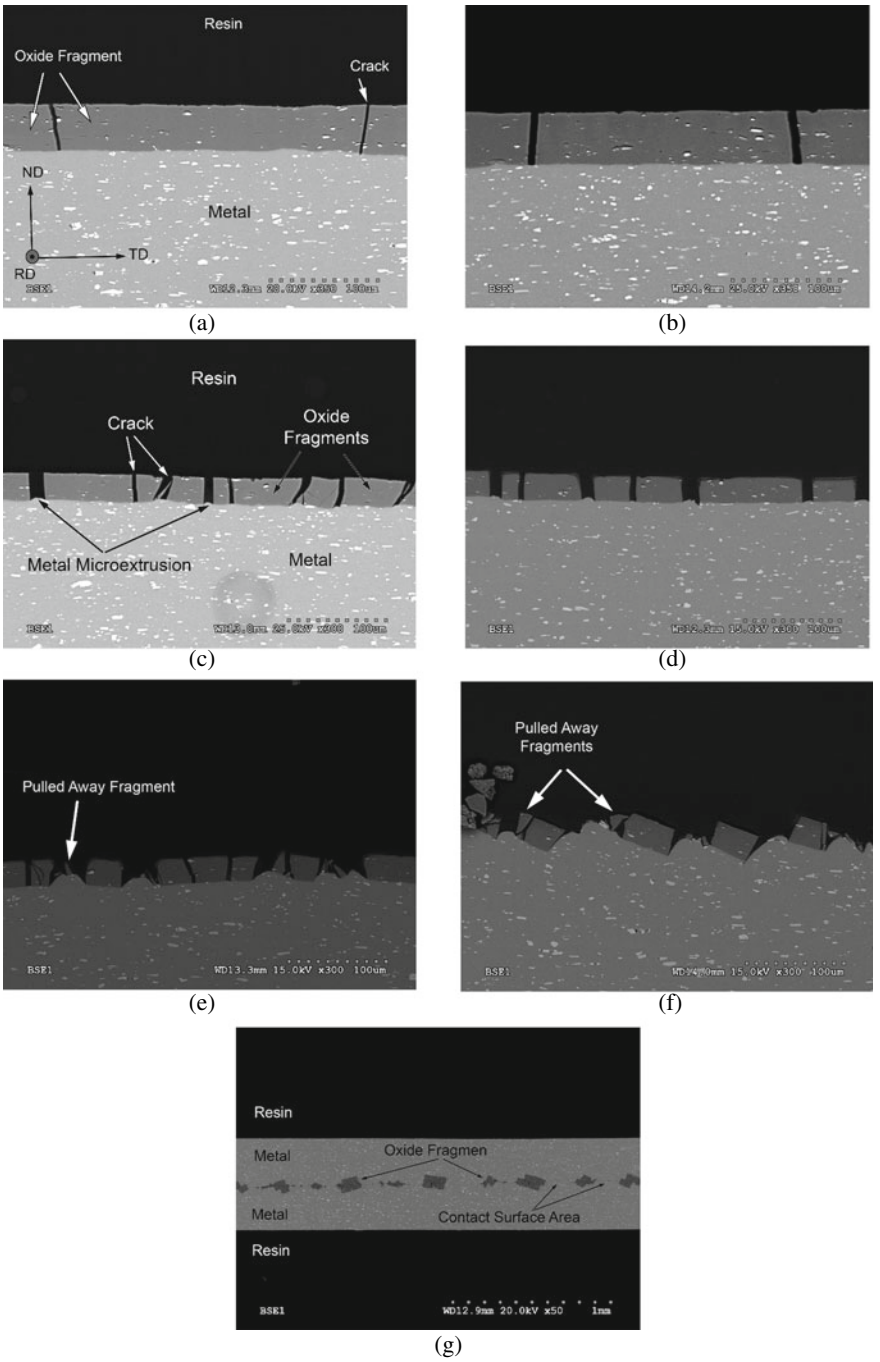


Fig. 4 A series of cross-sectional SEM images of strip rolled at the different reduction ratios: **a** 2%, **b** 5%, **c** 10%, **d** 18%, **e** 35%, **f** 45%, and **g** 70%

all reduction ratios cracks propagated through the entire oxide layer and the width of cracks increases by increasing the reduction ratio. At small reductions of 2 and 5% no metal micro extrusion was observed to happen through the cracks indicating that the applied strain at these ratios was not high enough for metal flow to happen through the crack channels. At 10% and 18% metal has only extruded partially through the cracks (Fig. 4a, b). However, it is seen that the chance of metal extrusion for 18% reduction is somehow higher than for 10% which could be due to the presence of wider cracks and higher amount of applied strain.

By increasing the reduction ratio, metal extrusion becomes more significant in the analyzed samples. For instance, in the cases of 35 and 45% reduction metal flow is high enough to extrude between fragmented oxides (Fig. 4e, f). It is seen that such high strains not only lead to higher degrees of metal micro extrusion through the cracks but also result in larger metal deformations. It means that deformation of metal substrate is in a way that rearranges the fragments and pulls some small fragments toward the contact surface area. This phenomenon seems to be a justifying reason for the observed topography in Fig. 3e, f. The metal extrusion between the fragmented oxides becomes more significant in the sample rolled at 70% reduction, which means that metal penetrated through the oxide layer and reached metal of another strip. This is why two strips were strongly bonded even with existence of enhanced oxide layers. In fact, equal or even higher fraction of metal area is connected than the presence of oxide fragments at the interface of both strips.

To find out the relationships between the crack spacing including the local extrusion of metal through fragmented oxides and the reduction ratio, the oxide fragment width and crack width are plotted as a function of reduction ratio in Fig. 5a, b.

The size of oxide fragments decreases with increasing the reduction ratio, which indicates more cracks are formed at higher reduction ratios. The decrease of the oxide fragmentation size is not linear, but rather exponential, i.e., the fragmentation size is abruptly reduced especially between the 2 and 10% reduction per pass conditions. On the other hand, increasing of the reduction ratio results in wider cracks as shown in Fig. 5b.

4 Summary

Cold rolling of aluminum sandwiches comprising of two anodized strips was carried out at different amount of reductions ranging from 2 to 70%. Expect the sample rolled at 70%, no bonding between the strips of the sandwiches rolled at different reduction ratios has occurred. Microstructure imaging of the surface and cross sections of the rolled strips revealed that by increasing the reduction ratio, the cracks tended to widen and the size of the oxide fragments had a decreasing trend which both behaviors were exponential. Decreasing pattern of fragment size could be explained as a result of increasing density of cracks as a function of the increasing reduction ratio. Increasing trend of crack width could also be due to the higher expansion of base metal under higher strains.

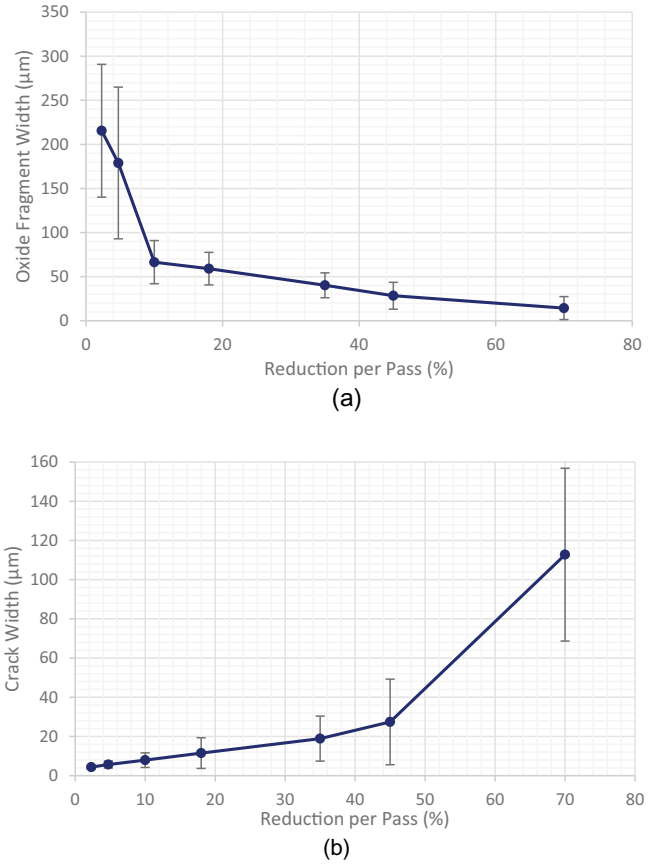


Fig. 5 The plots of **a** spacing between cracks and **b** width of cracks as a function of the reduction ratio. (Color figure online)

References

1. Ab Rahim SN, Lajis MA, Ariffin S (2015) A review on recycling aluminum chips by hot extrusion process. Procedia CIRP 26:761–766
2. Schmitz Ch (2006) Handbook of aluminium recycling. Vulkan-Verlag GmbH
3. Wan B, Chen W, Lu T, Liu F, Jiang Z, Mao M (2017) Review of solid state recycling of aluminum chips. Resour Conserv Recycl 125:37–47
4. Tekkaya AE, Schikorra M, Becker D, Biermann D, Hammer N, Pantke K (2009) Hot profile extrusion of AA-6060 aluminum chips. J Mater Process Technol 209:3343–3350
5. Lela B, Krolo J, Jozić S (2016) Mathematical modeling of solid-state recycling of aluminium chips. Int J Adv Manuf Technol 87:1125–1133
6. Chiba R, Yoshimura M (2015) Solid-state recycling of aluminium alloy swarf into c-channel by hot extrusion. J Manuf Process 17:1–8
7. Bay N (1979) Cold pressure welding—the mechanisms governing bonding. J Manuf Sci Eng 101:121–127

8. Güley V, Güzel A, Jäger A, Ben Khalifa N, Tekkaya AE, Misiolek WZ (2013) Effect of die design on the welding quality during solid state recycling of AA6060 chips by hot extrusion. Mater Sci Eng A 574:163–175
9. Cooper DR, Allwood JM (2014) The influence of deformation conditions in solid-state aluminium welding processes on the resulting weld strength. J Mater Process Technol 214:2576–2592
10. Cooper DR, Allwood JM (2014) Influence of diffusion mechanisms in aluminium solid-state welding processes. Procedia Eng 81:2147–2152
11. Le HR, Sutcliffe MPF, Wang PZ, Burstein GT (2004) Surface oxide fracture in cold aluminium rolling. Acta Mater 52:911–920

Ultrasonic Forming—Alternative to Orbital Riveting for Small Bimetallic Components



Wojciech Presz

Abstract The development of electrical equipment has resulted in an increase in the demand for electrical switches whose key element is contact. The orbital riveting technology has been successfully applied in assembling silver contacts. With the increase in production, attention has been paid to the possibility of obtaining significant savings by replacing part of the rivet with copper. As a result, bimetallic contacts have been created. It has also been proved that the direct transfer of orbital riveting technology from monometallic to bimetallic contacts narrows the technological window that the cost-effectiveness of the whole process is debatable. One of the factors behind the use of orbital forming is the decisive reduction in friction. A similar effect is given by ultrasonic assistance in microforming processes. Within this work, based on the laboratory experiment results, it was suggested to replace the orbital riveting with ultrasonic riveting in relation to the miniature bimetallic contacts.

Keywords Ultrasonic riveting · Orbital riveting · Bimetallic contacts

1 Introduction

In recent years, there has been a clear shift toward replacing heat engines with electric motors and, in general, replacing equipment using different types of energy with electrical equipment. The vast majority of electrical devices have a different type of construction that is simpler than other devices. This feature in particular predisposes them to miniaturisation, which is ubiquitous in the twenty-first century. Micro-electromechanical, micro-electro-electromechanical systems, micro-sensors, micro-machines, and micro-robots are no longer futuristic, but a reality. These advanced systems require parts and a large extent, metal parts. Parts that must meet high requirements for dimensional accuracy and surface quality. These requirements can

W. Presz (✉)
Warsaw University of Technology, Narbutta 85, 02-524 Warsaw, Poland
e-mail: wojciech.presz@pw.edu.pl

© The Minerals, Metals & Materials Society 2021

G. Daehn et al. (eds.), *Forming the Future*, The Minerals, Metals & Materials Series,
https://doi.org/10.1007/978-3-030-75381-8_123

be met by parts made using metal forming technology [1, 2], specifically microforming technology [3]. Microforming mainly due to so-called "scale effects" [4] has been isolated from the metal forming area and is now a separate field. In this technology, special emphasis is placed on precise control of the structure of the material [5] and the structure of the surface layer [6]. This has a large impact on processes and the broadly understood quality of products [7]. Namely, surface layer and contact phenomena, affecting friction [8], lubrication [9], and galling [10], increasing the role of methods for preparing surfaces [11]. They also refer to the internal structure [12], which affects the surface quality and cracking mechanisms [13]. The scale effect even applies to machine construction [14], instrumentation [15, 16], tools [17] and to the design of the technological process plan [18]. Materials and friction tests using micro-samples are also done as their results differ from those obtained in macro tests [19]. Reducing the size of manufactured parts on one hand is a major challenge for traditional technologies, but on the other hand, mainly by removing the energy barrier the possibility of using other unconventional techniques like electrical assistance, magnetic waves [20], laser processing [21], and mechanical vibrations at different frequencies [22]. In the last few of these methods, ultrasonic vibrations are particularly of interest [23–25]. Ultrasonic vibrations can reduce ECAP forces [26] and micro-extrusion when friction is almost eliminated [27]. The use of ultrasonic vibrations may also cause phase changes [28], grains rotation [29], and specific macroscopic consequences in terms of cracking [30]. Under certain conditions of upsetting supported with ultrasonic vibrations, a specific shape of the side surface of the sample is formed to a phenomenon leading to antibarreling [31]. The name to a phenomenon called "barreling". This relates to the formation of the convex side surface of an upset cylinder. It is formed as a result of friction forces occurring on contact surfaces with the help of tools. Anti-barreling is the creation of a concave lateral surface. This effect is not observed in any upsetting processes involving ultrasonic vibrations [32]. The causes and consequences of this phenomenon are not fully explained and are currently being investigated. One of the hypotheses is that the punch "nose" temporarily detaches from the same surface [33]. The construction of micro-mechanisms requires appropriate joining technologies. Attention was paid to technologies that do not affect the precisely controlled material structure of micro-products—mechanical joining technologies. In the area of these technologies, a similar tendency is observed as in the case of metal forming. That is the tendency to separate mechanical micro-joining technologies [34] out of macro-solutions. In structural optimization, solid structures have long been replaced by structures made of materials with different properties. This concept is observed on a larger scale in the field of metal forming [35], and interest in methods of forming objects composed of various materials is growing. Such objects pose a particular technological challenge in the field of microforming [36]. Another area of metal forming technology that is undergoing rapid development is incremental forming [37]. It is an interesting alternative to material forming of the whole volume of the material. It consists of plasticizing only part of the volume of the element and successively moving the deformation zone to finally deform the entire object [38]. The main positive features of such methods are the most common reduction in maximum process force, and

local reduction in pressure and frictional forces. The presented subject of the analysis, is the technology of making bimetallic electric microcontact under ultrasonic assisted forging. It is in line with the latest trends in technology development and refers to relatively unknown issues.

2 Problem Statement and Method of Solution

2.1 Development of Orbital Riveting

Jeremiash Grant Kingsbury, an engineer employed as a top engineer by Thomas Edison, invented and patented a rotary tool for spin-forming heads on rivets and pins. Introducing his "Noiseless Rivet-spinning Machine". However, the description of the patent included a significant wording of "Improving on existing processes", which would indicate the existence of previous solutions. The company has developed a patented technology. An example of a table machine for the orbital riveting from the year 1950 of the last century is shown in Fig. 1b [39]. The real revolution was the patent of Z. Marciniak from the year 1970 [40], which introduced a method resulting from the construction of a machine—independent drive of two eccentricities. The motion of the matrix is composed of two movements in a circle with possible parameters to change. This means that all movements with the trajectory described by the X- and Y-coordinates resulting from the Eq. (1) are possible.

$$\begin{pmatrix} x \\ y \end{pmatrix} = r \cdot \cos\left(\frac{P}{Q} \cdot \alpha\right) \begin{pmatrix} \cos\alpha \\ \sin\alpha \end{pmatrix} \tag{1}$$

where: R is the radius (range) of the motion, and P and Q are the parameters from which the ratio depends on the type of circular curve.

A similar solution but in the riveting area was patented in 1973 years (c). C. Mink [41] presented the head used in riveting processes capable of executing complex punch movements. Currently, there are many planetary and radial riveting machines in the market (d) [42]. In the work it is suggested to use ultrasonic support (e) to form forming miniature rivets (e).

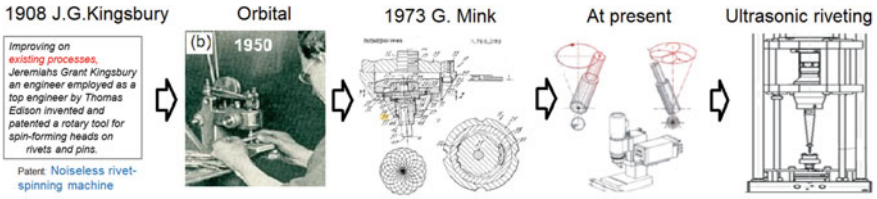


Fig. 1 Development of small/miniature component riveting—description in text. (Color figure online)



Fig. 2 Replacing the monolithic "rivet" in the production of double-sided contacts with a bimetallic rivet (b) causes delamination of the upper layer in some products. (Color figure online)

2.2 Orbital Riveting of Electric Contacts

The standard technological process for the production of small electrical contacts provides for the use of semi-finished products that are on the market in a wide range of dimensions in the form of silver rivets, Fig. 2. These rivets are connected to the frames most often by means of the planetary riveting process. This technology is well controlled and widely used. Riveting machines are also available in a wide range of size. Recently, in order to reduce material costs, a significant part of silver is replaced with copper and bimetallic rivets consisting of a copper shaft and silver contact part, Fig. 1b. In the analysed case, Fig. 2, the direct replacement of solid rivet with bimetallic rivet in the production process carried out by planetary riveting has encountered serious difficulties. In some parts of the products, delamination of the silver part from the copper part was observed. This phenomenon occurred at various stages of production and operation.

One of the factors in favour of using orbital forging is to significantly reduce friction. A similar effect has the use of ultrasonic assisted forming. Strengthening effect is achieved by the conditions of the so-called "dynamic effect" which is relatively easy to achieve in miniature products [43]. The paper suggests replacing orbital micro-riveting with ultrasonic micro-heading in relation to the assembly of miniature bimetallic contacts. Figure 3 shows successive modifications of the upsetting process to reduce frictional forces.

2.3 Delamination Process

The delamination observed in some products can occur in two stages: during operation and during the riveting process. As established on the basis of previous analyses [44], the distribution of materials in the contact head affects the tendency to delaminate during operation. The distribution shown in Fig. 4a is considered favourable because the lines of possible deformation converge when the contact surface is loaded. The most desirable form is that the outer material is "recessed" into the core material which forms a small coating at the edge of the contact head.

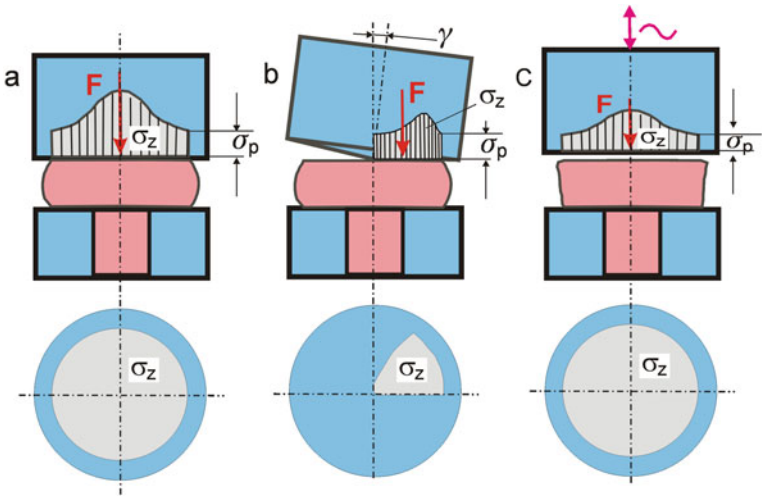


Fig. 3 Heading/riveting methods: **a** conventional heading—high process force, strong friction dependence, **b** orbital/planetary riveting—low process force, low friction, **c** vibration assisted heading/riveting—under development—expected: low friction uniform material flow. (Color figure online)

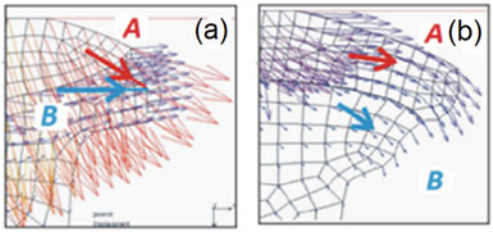


Fig. 4 Material flow in loaded head of contact: **a** concave and **b** convex border surface of materials distribution [44]. (Color figure online)

In general, the distribution of materials in the processes of metal forming of bimetallic billets depends, in addition to, geometrical factors such as the shape of tools, on their mutual interaction in the plastic state. A plastic interaction between two materials described with two-parameter stress–strain curves (2) is determined with the help of the Coefficient of Mutual Interactions of Plastic deformations—H_{MIP}, which is the ratio of their plastic resistance (3). It is decomposed into the product of two H_{C} and H_{n} coefficients according to (4) and (5). The first of the coefficients, H_{C} is a constant value.

$$\sigma_{\mathrm{pA,B}}(\varepsilon) = C_{\mathrm{A,B}} \cdot \varepsilon^{\mathrm{n_{A,B}}} \tag{2}$$

$$H_{\mathrm{MIP}}(\varepsilon) = \frac{\sigma_{\mathrm{pA}}(\varepsilon)}{\sigma_{\mathrm{pB}}(\varepsilon)} = \frac{C_{\mathrm{A}} \cdot \varepsilon^{\mathrm{n_A}}}{C_{\mathrm{B}} \cdot \varepsilon^{\mathrm{n_B}}} = \frac{C_{\mathrm{A}}}{C_{\mathrm{B}}} \cdot \varepsilon^{\mathrm{n_A} - n_{\mathrm{B}}} = H_{\mathrm{C}} \cdot H_{\mathrm{n}}(\varepsilon) \tag{3}$$

$$H_{\mathrm{C}} = \frac{C_{\mathrm{A}}}{C_{\mathrm{B}}} = const \tag{4}$$

$$H_{\mathrm{n}}(\varepsilon) = \varepsilon^{n_{\mathrm{A}} - n_{\mathrm{B}}} \tag{5}$$

where: $\sigma_{\mathrm{pA,B}}$—yield stress of material A and B, ε—equivalent strain, $C_{\mathrm{A,B}}$ (MPa), $n_{\mathrm{A,B}}$ [1]—material constant.

The second one changes according to deformation. Within this work, the role of this coefficient was neglected, limited only to the H_{c} coefficient.

2.4 FEM 3D Modelling

The commercial Simufact.Forming 14.0 package was used in isothermal static conditions with an elasto–plastic material model with deformation hardening. The 3D model shown in Fig. 5 consists of 2 deformable bodies: material A-1 and material B-2, and rigid bodies: matrix-3, base-4, and punch-5. Punch movement is an planetary motion around point P_0 while the end of the axis—P_1 moves along the rosette, Fig. 5c described by Eq. (6). The die has also a constant angular velocity. During the process, the base and frame moves at a velocity directed along the axis. Tilt angle $\gamma = 4°$.

$$\begin{pmatrix} x \\ y \end{pmatrix} = 0.7 \cdot \cos\left(\frac{11}{7} \cdot \alpha\right) \cdot \begin{pmatrix} \cos(\alpha + \varphi \\ \sin\alpha \end{pmatrix} \tag{6}$$

In addition, the other process was carried out in which the planetary movement was turned off and the process was transformed into a 3D upsetting process. Four variants of H_{c} factor (8) were tested. Assuming equal value of the hardening factors

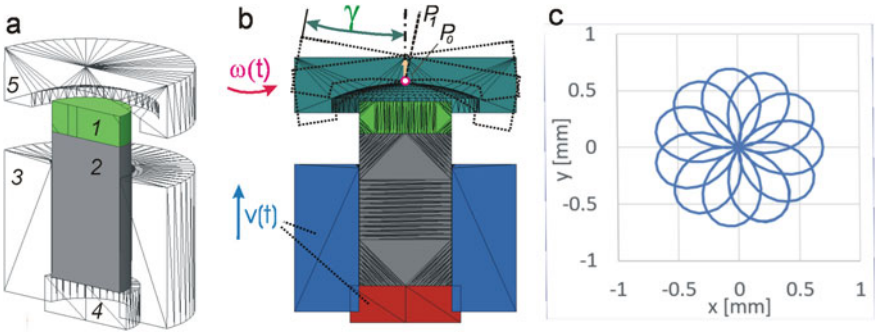


Fig. 5 **a** FEM model—description in text. **b** path of planetary motion, **c** linear velocity of edjector and rotational velocity of die. (Color figure online)

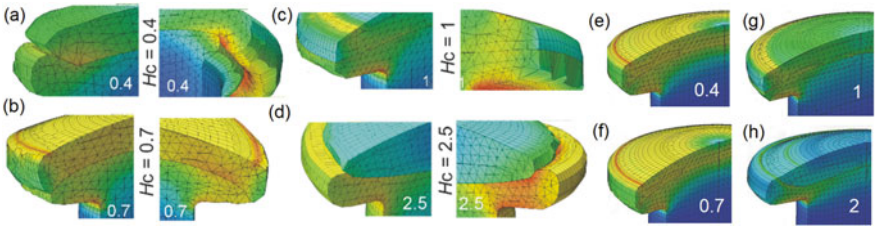


Fig. 6 Equivalent strain distribution after orbital (**a**, **b**, **c**, **d**) and standard (**e**, **f**, **g**, **h**) upsetting of bimetallic contacts consisting of materials of different H_c coefficient. (Color figure online)

for both materials (7).

$$n_A = n_B = 0.2 \tag{7}$$

$$H_C = 0.4, 0.7, 1, 2.5 \tag{8}$$

where H_c complies with (4).

The simulation results are shown in Fig. 6. In all cases, FEM simulations of orbital pressing in which $H_c \neq 1$ was observed to delaminate with a difference in deformation at the contact surface of both materials. Note that $H = 1$ in this case means the "plastic" identity of both materials, which is virtually impossible to achieve. Especially when we also take into account the hardening factors n that are different for different materials. The reason for the weakening of the bond of both materials is the cyclical change in the direction of the material flow, which occurs with each rotation of the swing die. Materials with different plastic properties generate shear stresses at the connection boundary when the direction of stress and strain changes. In classic upsetting this tendency was observed only in the case of (h). In this case, the outer material is much harder and is "pressed" into a much softer material making the process similar to extrusion. Thus, it can be concluded that the classical upsetting process does not entail any risk of delamination of the materials. However, the problem of obstructed flow of material in spherical tool upsetting conditions, which is related to friction, still remains unsolved. The solution to this problem is the main topic of this article and is presented in the next chapter.

2.5 Proposed Method of Solution

Classic upsetting has been replaced with orbital pressing due to riveting processes leads to the drastic reduction in the effect of friction in the process. This reduction increases the tool life and improves the surface quality of the product. As shown for bimetallic contacts, this method is associated with a high risk of delamination. The proposed solution is the use of ultrasonic upsetting. This process maintains a

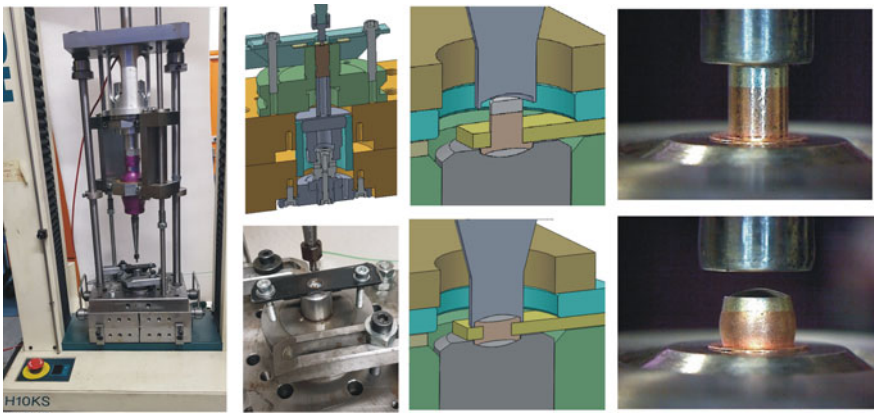


Fig. 7 Experimental setup—description in text. (Color figure online)

constant flow direction of materials as in classic upsetting but at the same time lowers the friction coefficient analogously to orbital forging.

3 Materials and Methods

3.1 Experimental Setup

The experimental stand, Fig. 7, consists of a testing machine and a set of dies placed on it. An ultrasonic system is mounted on the ram of the testing machine. The ultrasonic head consists of a piezoelectric transducer, a booster, and a sonotrode with a punch. An alternating current, oscillating with an ultrasonic frequency, is fed through a power supply to a piezoelectric transducer. The amplifier and sonotrode act as half-wavelength resonators, generating a standing waves at resonant frequency. The frequency used is 20 kHz. It is possible to adjust the amplitude indirectly, that is, by changing the supplied power. Prior to testing, the system characteristics were determined by measuring displacement on the punch face using the Keyence LK-H008 sensor. The results are shown in Fig. 8.

3.2 Specimens and Experimental Procedure

The research concerns bimetallic contacts with dimensions shown in Fig. 9. The hardness measurement showed similar hardness of both materials and thus a probable factor of H_c 1.

The experimental procedure includes several steps as outlined below.

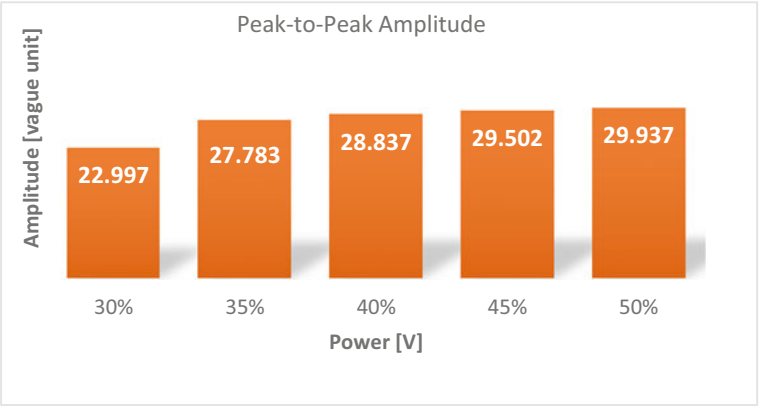


Fig. 8 Results of vibration amplitude testing of the upsetting tool. (Color figure online)

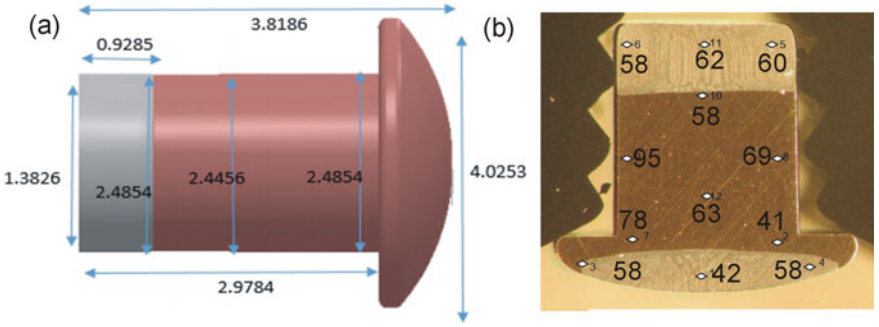


Fig. 9 Bimetallic contact tested: **a** dimensions, **b** structure with HV hardness measurement points marked. (Color figure online)

- Initial rivet height measurement.
- Lubricate the punch and matrix with MoS_2 content.
- Placing the rivet in the frame on the lower die.
- Tightening the frame with the clamp using screws.
- Approaching the punch system to the sample at the initial distance.
- Turning on the ultrasonic assistance system.
- Activation of the data acquisition system from the lower force sensor.
- Activating machine feed.
- Riveting to the assumed machine position at the set speed.
- Unloading at the set speed.
- Turning off the data acquisition system from the bottom sensor.
- Withdrawal of the stamp system.
- Removing the clamp.
- Removal of the frame with the contact highlighted.

- Measurement of final contact height.

  Warning! In the case of free upsetting, no frame or clamp was used.

4 Results

The riveting was performed with and without ultrasonic vibrations. Moreover, free upsetting processes were carried out. Examples are shown in Fig. 10. The contacts were riveted to different heights h_1. The examples selected for the analysis are summarised in Table 1.

Process forces were recorded in two ways.

1. Using the standard equipment of a testing machine. The strain gauge force sensor located on the ram and the built-in displacement sensor allows the registration of the vertical component of the process force as a function of the ram path.
2. By means of an additional piezoelectric sensor placed on the machine table under the lower die. This sensor, in combination with an acquisition system with adjustable sampling rate, enables the registration rapidly changing axial forces as a function of time. The records of the forces of selected riveting processes are shown in Figs. 11 and 12

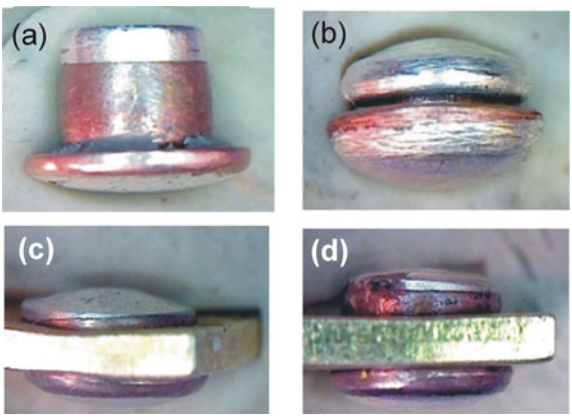


Fig. 10 Selected examples: **a**, **b** free upsetting, **c**, **d** riveting **a**, **c**—no vibrations, **b**, **d**—US vibrations. (Color figure online)

Table 1 Selected examples for analysis

Specimen	S10	S11 (With Vibration)	S13	S12vib	S15	S14vib
h_0 (mm)	3.856	3.857	3.854	3.854	3.852	3.848
h_1 (mm)	3.119	2.979	2.887	2.717	3.690	2.655
$h_0 - h_1$ (mm)	0.737	0.878	0.967	1.137	1.162	1.193
Equation strain [1]	0.212	0.258	0.288	0.349	0.359	0.371

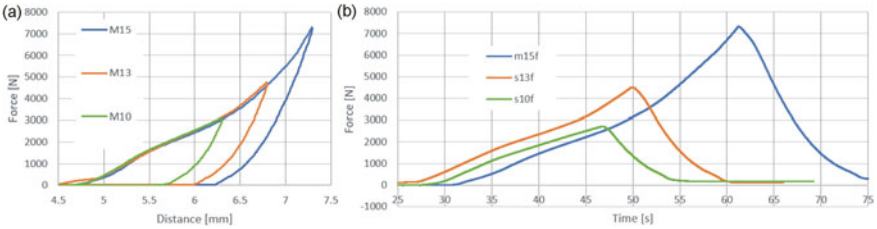


Fig. 11 Riveting without vibrations: **a** testing machine, **b** additional transducer. (Color figure online)

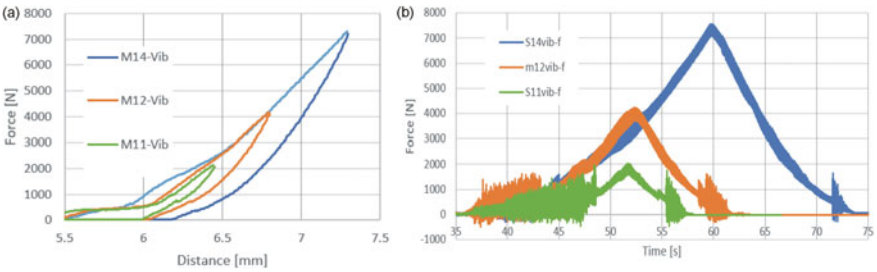


Fig. 12 US vibration assisted riveting: **a** testing machine, **b** additional force transducer. (Color figure online)

Processes with partial ultrasound support were also carried out. A record of the force during the process is shown in Fig. 13. The process begins without the use of vibrations, and after reaching a certain position of the piston, vibrations are periodically activated. They are also switched on periodically during the unloading phase.

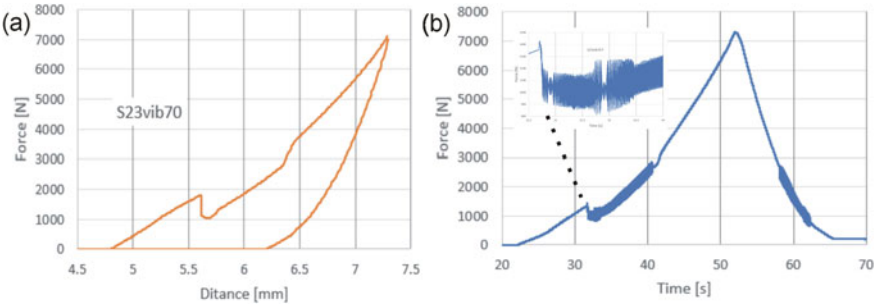


Fig. 13 Temporary vibration assisted riveting process: **a** Testing machine, **b** additional transducer. (Color figure online)

5 Analysis of Results

5.1 Process Force

During upsetting with vibrations, the recording of the process force, Fig. 14a indicates the occurrence of the so-called "dynamic effect". It involves the surface of the punch breaking away from the surface of the workpiece. Each of the processes can be divided into four phases.

Phase 1 is the occurrence of a dynamic effect during the increase of force. This phase ends after reaching a force of about 550 N.

Phase 2 is ultrasonic upsetting with a punch in contact and the increasing process force.

Phase 3 is ultrasonic upsetting during unloading.

Phase 4 begins during unloading when the process load drops to a value (approx. 550 N) that allows the occurrence of a dynamic effect. This phase ends with complete relief.

During upsetting with vibrations, the recording of the process force, Fig. 14a indicates the occurrence of the so-called "dynamic effect". It involves the surface of the punch breaking away from the surface of the deformed object. The use of vibration support provides additional energy which is used to increase the deformation achieved. Figure 14b shows experimental rivet deformation courses as a function of process force. For example, with a given process force of 4000 N, vibration support increases the achieved deformation by approx. 0.1—segment *a* on the graph. As the force increases, this effect gradually decreases—sections *b* and *c*. This effect can also be presented as the occurrence of a decrease in the process strength as shown in Fig. 15. The process force as a function of the height of upset contact is presented there. For example, to reach a contact height of 2.95 mm, a traditional upset force of approx. 4000 N is needed. Vibration assistance reduces this force by a distance of *a*, which means a 40% decrease. For smaller contact heights—the dashed lines in Fig. 14, vibration support reduces the necessary strength successively by 36 and 23%. As the assumed height of the rivet decreases, the vibration efficiency decreases.

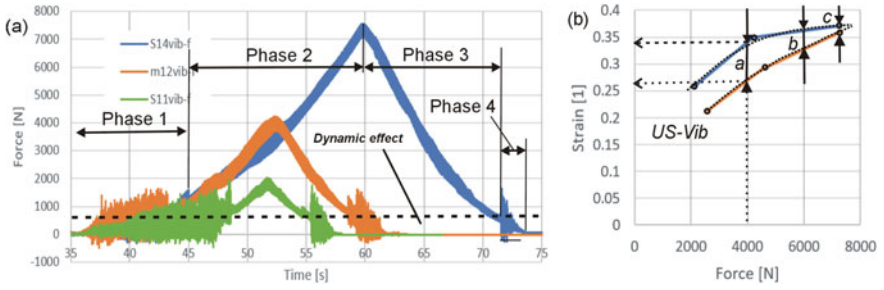


Fig. 14 **a** Analysis of US heading process forces recorded by piezo-transducer. **b** Obtained strain versus process force. (Color figure online)

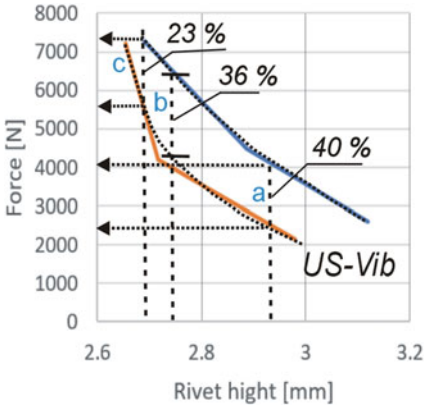


Fig. 15 Process force versus contact height. (Color figure online)

The highest support effectiveness is when there is a dynamic effect throughout the process or as much of it as possible.

5.2 Structure of Bimetallic Micro-contact

In all the processes carried out, there was no tendency of delamination of the silver layer from the copper matrix. A more even flow of material was observed compared to the classic upsetting process. In the example of Fig. 15c, the material flowed unevenly as opposed to example in Fig. 15d. The result of the dynamic effect is the intense deformation of material layers from those in direct contact with the punch and die to the lower layers.

Figure 16b shows the structure of upset contact. It is typical for ultrasonic dynamic upsetting, where so-called antibarrelling effect is present—outline *b*. The outermost layers underwent intensive deformation, while the central part remained practically undeformed. Traditionally upset contact has developed completely differently. Here, Fig. 16a, the outline *a* is convex and the middle part has been most deformed.

6 Conclusions

- The use of orbital forging to rivet the tested contacts may cause delamination.
- The use of the traditional upsetting process, as demonstrated by the FEM model study, does not indicate the risk of delamination; however, it causes an increase in frictional force, which due to the small size of the object, can cause asymmetrical deformations.

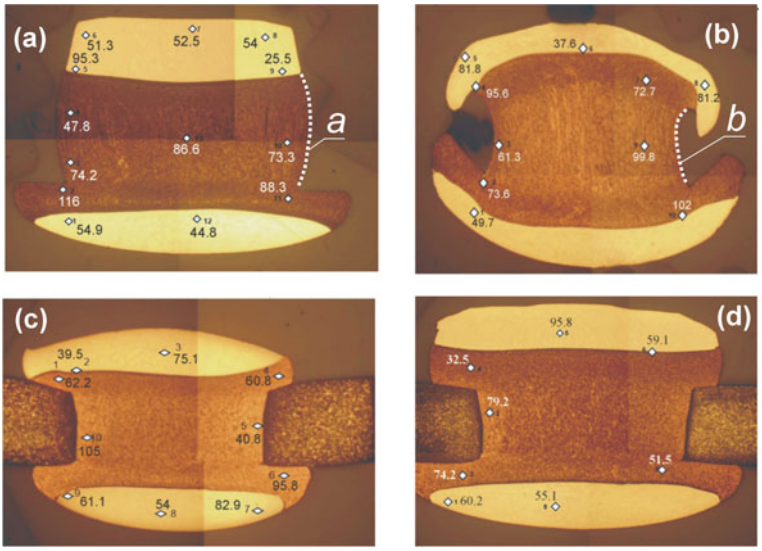


Fig. 16 Cross sections of deformed bimetallic micro-contacts: **a**, **b** free upsetting, **c**, **d** heading, **a**, **c** no vibration, **b**, **d** vibration assisted. (Color figure online)

- The application of the Ultrasonic forming process promotes uniform deformation and reduces the process force in the range of 23–40% compared to the conventional upsetting process.
- In the first and the last phase of all processes dynamic effects were observed, i.e. the surface of the punch was temporarily detaching from the component surface.
- In free upsetting tests, dynamic effect was dominating strongly effecting the shape into "antibarreling" one—concave side surface.
- To take full advantage of the possibilities of ultrasonic vibration support, it is recommended to select the system and shaped system in such a way that during the greatest possible part of the process occurs *dynamic effect*.

References

1. Ma J, Gong F, Yang Z, Zeng W (2016) Microdeep drawing of C1100 microsquare cups using microforming technology. Int J Adv Manuf Technol 82:1363–1369
2. Geißdörfer S, Rosochowski A, Olejnik L, Engel U (2008) Micro extrusion of a can, pp 0–3
3. Geiger M, Kleiner M, Eckstein R, Tiesler N, Engel U (2001) Microforming. CIRP Ann Manuf Technol 50:445–462
4. Zheng JY, Yang HP, Fu MW, Ng C (2019) Study on size effect affected progressive microforming of conical flanged parts directly using sheet metals. J Mater Process Technol 272:72–86
5. Olejnik L, Presz W, Rosochowski A (2009) Backward extrusion using micro-blanked aluminium sheet. Int J Mater Form 2

6. Deng JH, Fu MW, Chan WL (2011) Size effect on material surface deformation behaviour in micro-forming process. Mater Sci Eng A 528:4799–4806
7. Presz W, Rosochowski A (2006) The influence of grain size on surface quality of microformed components. In: 9th international conference on material forming, ESAFORM 2006, pp 587–590
8. Engel U (2006) Tribology in microforming. Wear 260:265–273
9. Wang C, Guo B, Shan D, Zhang M, Bai X (2014) Tribological behaviors in microforming considering microscopically trapped lubricant at contact interface. Int J Adv Manuf Technol 71:2083–2090
10. Muster A, Presz W (1999) Influence of initial surface roughness on galling behavior of a steel-steel couple. Scand J Metall
11. Salacinski T, Chmielewski T et al (2018) Roughness of metal surface after finishing using ceramic brush tools. Adv Mat Sci 18–1:20–27
12. Chan WL, Fu MW, Lu J, Liu JG (2010) Modeling of grain size effect on micro deformation behaviour in micro-forming of pure copper. Mater Sci Eng A 527:6638–6648
13. Wang JL, Fu MW, Shi SQ (2017) Influences of size effect and stress condition on ductile fracture behaviour in micro-scaled plastic deformation. Mater Des 131:69–80
14. Presz W, Andersen B, Wanheim T (2006) Piezoelectric driven micro-press for microforming. J Achiev Mater Manuf Eng 18:411–414
15. Paldan NA, Arentoft M, Eriksen RS, Mangeot C (2008) Piezo driven prestressing of die-system for microforming of metal components. Int J Mater Form 1:467–470
16. Cannella E, Nielsen EK, Stolfi A (2017) Designing a tool system for lowering friction during the ejection of in-die sintered micro gears. Micromachines 8:1–15
17. Presz W, Cakco R (2017) Application of complex micro-die for extrusion of micro-rivets for micro-joining. In: Proceedings of the METAL 2017—26th international conference on metallurgy and materials, conference proceedings, Jan 2017
18. Presz W, Wanheim T, Lagergren J, Jonsson NG (2011) Application of surface load—a new calibration method. In: Proceedings of the proceedings of the 10th international conference on technology of plasticity, ICTP 2011
19. Kang W, Rajagopalan J, Saif MTA (2010) In situ uniaxial mechanical testing of small scale materials—a review. Nanosci Nanotechnol Lett 2:282–287
20. Gayakwad D, Dargar MK, Sharma PK, Purohit R, Rana RS (2014) A review on electromagnetic forming process. Procedia Mater Sci 6:520–527
21. Gao H, Cheng GJ (2010) Laser-induced high-strain-rate superplastic 3-D microforming of metallic thin films. J Microelectromech Syst 19:273–281
22. Presz W (2007) Flexible manufacturing system for vibration assisted microforming. AIP Conf Proc
23. Hung JC, Tsai YC (2013) Investigation of the effects of ultrasonic vibration-assisted micro-upsetting on brass. Mater Sci Eng A
24. Cao M, Li J, Yuan Y, Zhao C (2017) Flexible die drawing of magnesium alloy sheet by superimposing ultrasonic vibration. Trans Nonferrous Met Soc China (English Ed) 27:163–171
25. Culp DR, Gencsoy HT (1973) Metal deformation with ultrasound. In: 1973 ultrasonics symposium, pp 195–198
26. Ahmadi F, Farzin M, Meratian M, Loeian SM, Forouzan MR (2015) Improvement of ECAP process by imposing ultrasonic vibrations. Int J Adv Manuf Technol 79:503–512
27. Bunget C, Ngaile G (2011) Influence of ultrasonic vibration on micro-extrusion. Ultrasonics 51:606–616
28. Presz W, Kulik T (2019) Ultrasonic vibrations as an impulse for glass transition in microforming of bulk metallic glass. Arch Civ Mech Eng 19:100–113
29. Dutta RK, Petrov RH, Hermans MJM, Richardson IM (2015) Accommodation of plastic deformation by ultrasound-induced grain rotation. Metall Mater Trans A Phys Metall Mater Sci 46:3414–3422
30. Presz W, Cacko R (2018) Ultrasonic assisted microforming. In: 26th international conference on metallurgy and materials, METAL 2017, January 2018, pp 521–526

31. Hu J, Shimizu T, Yang M (2018) Investigation on dynamic impact effect of ultrasonic-assisted compression test. Mater Sci Forum 920:102–107
32. Liu Y, Suslov S, Han Q, Hua L, Xu C (2013) Comparison between ultrasonic vibration-assisted upsetting and conventional upsetting. Metall Mater Trans A Phys Metall Mater Sci 44:3232–3244
33. Presz W (2018) Dynamic effect in ultrasonic assisted micro-upsetting. In: Proceedings of the AIP conference proceedings, vol 1960, p 100012
34. Wang X, Li C, Ma Y, Shen Z, Sun X, Sha C, Gao S, Li L, Liu H (2016) An experimental study on micro clinching of metal foils with cutting by laser shock forming. Materials (Basel) 9
35. Politis DJ, Lin J, Dean TA (2012) Investigation of material flow in forging bi-metal components, pp 231–234
36. Presz W (2019) Planetary riveting of electric bimetallic micro-contacts. Procedia Manuf 27:83–90
37. Amini S, Hosseinpour Gollo A, Paktinat H (2017) An investigation of conventional and ultrasonic-assisted incremental forming of annealed AA1050 sheet. Int J Adv Manuf Technol 90
38. Presz W (2018) Ultrasonic orbital microforming—a new possibility in the forming of microparts. Metals 8(11):1–14
39. http://www.grantriveters.com
40. Marciniak Z (1970) Method of producing the metal objects of variable thickness and a device for application of this method. U.S. Patent 3523442, pp 11–14
41. Mink G (1972) Planetary head forming tool. U.S. Patent 3768289
42. https://baltecorporation.com
43. Hu J, Shimizu T, Yoshino T, Shiratori T, Yang M (2018) Ultrasonic dynamic impact effect on deformation of aluminum during micro-compression tests. J Mater Process Technol 258:144–154
44. Presz W, Cacko R (2018) Determination of material distribution in heading process of small bimetallic bar. In: Proceedings of the AIP conference proceedings, vol 1960

Self-Piercing Riveting Using Rivets Made of Stainless Steel with High Strain Hardening



Benedikt Uhe, Clara-Maria Kuball, Marion Merklein, and Gerson Meschut

Abstract Self-piercing riveting is an established technique for joining multi-material structures in car body manufacturing. Rivets for self-piercing riveting differ in their geometry, the material used, the condition of the material and their surface condition. To shorten the manufacturing process by omitting the heat treatment and the coating process, the authors have elaborated a concept for the use of stainless steel with high strain hardening as a rivet material. The focus of the present investigation is on the evaluation of the influences of the rivet's geometry and material on its deformation behaviour. Conventional rivets of types P and HD2, a rivet with an improved geometry made of treatable steel 38B2, and rivets made of the stainless steels 1.3815 and 1.4541 are examined. The analysis is conducted by means of multi-step joining tests for two material combinations comprising high-strength steel HCT780X and aluminium EN AW-5083. The joints are cut to provide a cross section and the deformation behaviour of the different rivets is analysed on the basis of the measured changes in geometry and hardness. In parallel, an examination of the force–stroke curves provides further insights. It can be demonstrated that, besides the geometry, the material strength, in particular, has a significant influence on the deformation behaviour of the rivet. The strength of steel 1.4541 is seen to be too low for the joining task, while the strength of steel 1.3815 is sufficient, and hence the investigation confirms the capability of rivets made of 1.3815 for joining even challenging material combinations.

B. Uhe (✉) · G. Meschut
Laboratory for Material and Joining Technology (LWF), Paderborn University, Pohlweg 47-49, 33098 Paderborn, Germany
e-mail: benedikt.uhe@lwf.upb.de

G. Meschut
e-mail: meschut@lwf.upb.de

C.-M. Kuball · M. Merklein
Institute of Manufacturing Technology (LFT), Friedrich-Alexander-Universität Erlangen-Nürnberg, Egerlandstraße 11-13, 91058 Erlangen, Germany
e-mail: clara-maria.kuball@fau.de

M. Merklein
e-mail: marion.merklein@fau.de

© The Minerals, Metals & Materials Society 2021

G. Daehn et al. (eds.), *Forming the Future*, The Minerals, Metals & Materials Series,
https://doi.org/10.1007/978-3-030-75381-8_124

Keywords Self-piercing riveting · Lightweight design · Deformation behaviour · Stainless steel · High nitrogen steel

1 Introduction

The lightweight design of car bodies offers an opportunity for further reducing fuel consumption and CO_2 emissions in traffic. As consequence of lightweight design, increasing use is being made of high-strength steel and aluminium [1]. Self-piercing riveting (SPR) is a common technique for the joining of these materials [2]. The four stages of the SPR process are demonstrated in Fig. 1. Two or more sheets are clamped between a blank holder and a die. A punch presses a semi-tubular rivet into the sheets. The rivet pierces the sheet on the punch side before flaring in the sheet on the die side. This then creates an interlock [3]. A typical force–stroke curve from the start of the joining process until the end of the return stroke of the punch is shown in Fig. 2. An analysis of the measured process curve permits the joining process to

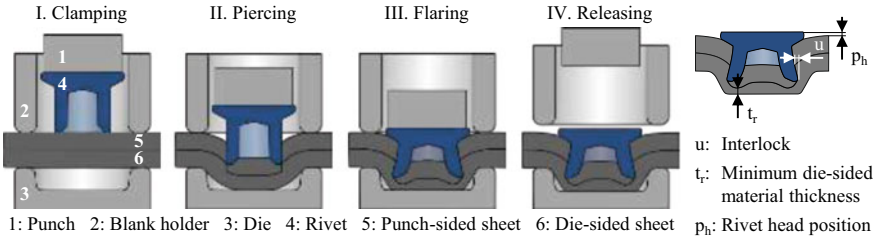


Fig. 1 SPR process stages and characteristic joint parameters in the cross section of a joint according to [4]. (Color figure online)

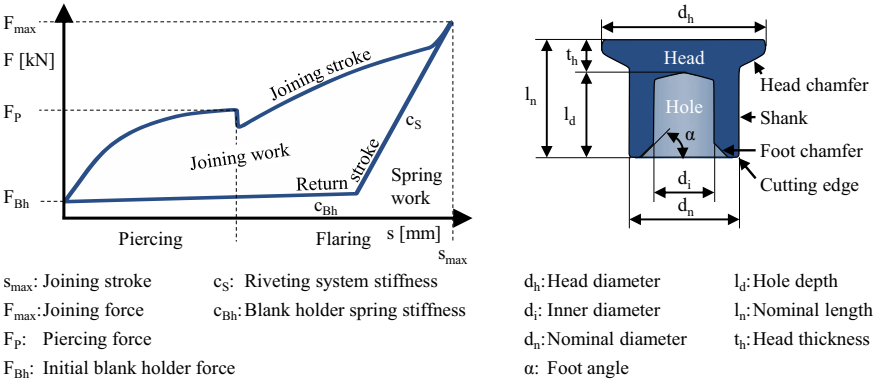


Fig. 2 Typical force–stroke curve and geometry parameters in the cross section of a rivet according to [4]. (Color figure online)

be examined by evaluating parameters like the joining force and the piercing force and is often used for non-destructive process monitoring.

The central components of SPR are the rivet and the die. The die is characterised by its depth and any shape elements like mandrels, while the rivet is characterised by its geometry, the material used, the condition of the material and the surface condition. The geometry parameters in the cross section of a rivet as per [5] are shown in Fig. 2. The rivet and the die are selected individually for each material combination as a function of the sheets to be joined [6].

The riveted joint has to meet certain quality criteria. The required values for the characteristic joint parameters must be reliably achieved. These are an indicator of the joint strength that can be expected. It is primarily the interlock and the minimum die-sided material thickness (see Fig. 1) that are of interest. Freedom from cracks in the joint must also be ensured in general. With brittle materials such as cast aluminium on the die side, cracks on the surface of the closing head are typical [7]. They are acceptable if they run in a radial direction. However, cracks in the tangential direction are never allowed. Cracks and other process faults are known from [8, 9]. These typically occur in the case of unsuitable process configurations or too large variation in the properties of the sheets to be joined. By changing the rivet or the die, it is possible to avoid the faults in the riveted joint. The commonly seen process faults are illustrated schematically in Fig. 3. In general, a distinction must be made between rivet faults and sheet faults.

Rivet overloading and hence a rivet fault occurs when the rivet is not adequately adapted to the strength and the thickness of the sheets to be joined. Not only the rivet geometry, which defines the stiffness of the rivet and the stress and strain conditions within the rivet, but also the rivet material, which determines the deformation resistance and the deformability, are crucial in this respect. Stress peaks, which normally occur in the rivet at the transition from the shank to the head, can cause cracks or fracture of the rivet. The emergence of cracks and fractures is facilitated by the use of brittle rivet materials with a high strength and low deformability. Depending on the individual situation regarding the properties of the sheets to be joined, the rivet can also be bent or compressed. Another type of process fault is the fracture of the

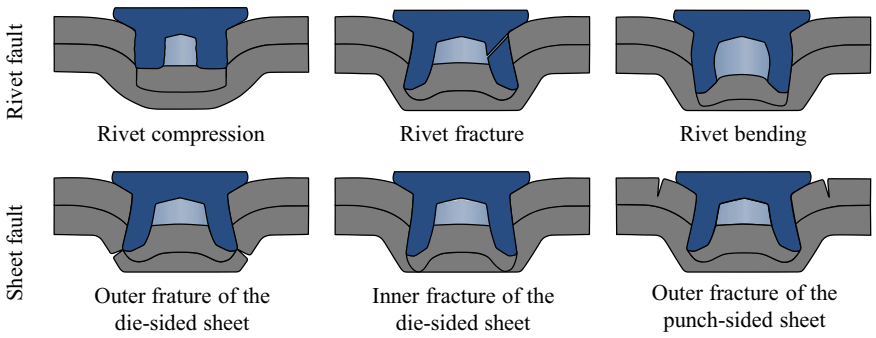


Fig. 3 Typical types of process faults of self-piercing riveted joints. (Color figure online)

sheets to be joined. This is especially the case with brittle die-sided sheet materials with low deformability, such as high-strength steel and cast aluminium. Outer fracture occurs in the case of excessive deformation, such as with deep dies. Inner fracture can occur when the rivet hole is filled with material and inner pressure is evolving or when a rivet is pressed too far. Fracturing of the punch-sided sheet is also possible, especially with thin sheets made of brittle materials. In the past, rivets with different features have been developed as a function of the requirements of the material combinations for car bodies. One promising approach is the use of stainless steel with high strain hardening as a rivet material. As already mentioned in [10], this has certain advantages. Due to the corrosion resistance of stainless steel, it is not necessary to coat the rivets. With stainless steel that has an adequate strength, it is also possible to omit the heat treatment. This shortens the manufacturing process for the rivets. Because the strength of the stainless steel is achieved through cold forming, systematic adjustment of the local strength is also possible. Attempts to use stainless steel as rivet material are known from [11, 12]. However, the strength attained in the rivet materials used for that attempts is not sufficient to meet the requirements for modern sheet materials. The focus of the present investigation is on an analysis of the deformation behaviour of rivets in high nitrogen steel 1.3815 and stainless steel 1.4541 and the evaluation of the joining result by comparison to conventional rivets. A common material used for conventional rivets is the treatable steel 38B2. An overview of the chemical composition of the rivet materials under investigation is given in Table 1. 38B2 contains the typical elements of treatable steel and 1.4541 represents a typical stainless steel. The high nitrogen steel 1.3815 has a special composition, however, with a high proportion of manganese, chromium and nitrogen. As nitrogen is normally undesirable in steels, it has a highly positive effect on the mechanical properties when interacting with the other elements of 1.3815 and is the reason for the high strain hardening [13]. The flow curves of the rivet materials under investigation are shown in Fig. 4. It can be seen that the attainable strength of 1.3815 is comparable to the strength of quenched and tempered 38B2, while the strength of 1.4541 is even lower.

Table 1 Chemical composition of the rivet materials

Material	Mass fraction of the chemical components [m%]						
	C	Mn	Cr	Ni	Ti	B	N
38B2	0.38	0.73	0.22	<0.05	<0.05	0.004	<0.05
1.3815	0.08	18.86	17.07	0.58	<0.05	<0.05	0.76
1.4541	0.02	1.55	17.14	9.19	0.27	<0.05	<0.05

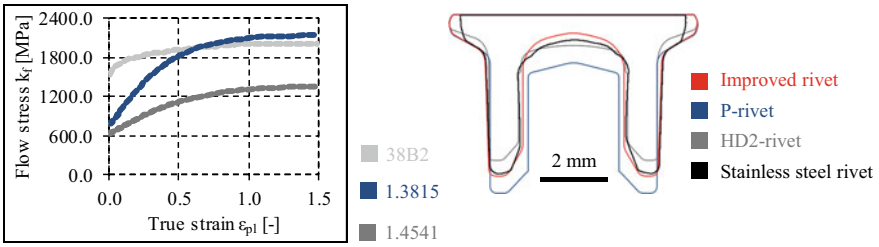


Fig. 4 Comparison of the rivet materials and the rivet geometries according to [10]. (Color figure online)

2 Concept for Rivets Made of Stainless Steel with High Strain Hardening

The investigation is conducted for the same material combinations as in [4]. Material combination 1 consists of high-strength steel HCT780X on both sides. Material combination 2 consists of aluminium EN AW-5083 on the punch side and HCT780X on the die side. All the sheets have a thickness of 1.5 mm. Experimental tests show the yield strength of steel HCT780X to be 565 MPa, with a tensile strength of 861 MPa at an elongation of 12.4%. The yield strength of aluminium EN AW-5083 is 157 MPa and its tensile strength is 292 MPa at an elongation of 18%. The steel sheets are galvanised, while the aluminium sheets are uncoated. These material combinations have different requirements regarding the rivet and the die. They are thus representative for the designing and testing of an innovative rivet. To join material combination 1, the rivet has to have an adequate strength and stiffness to pierce the high-strength steel on the punch side. The probability of cracks in the rivet is higher than for material combination 2. At the same time, the rivet must be able to pierce the punch-sided aluminium and take up the aluminium in the rivet hole in material combination 2. Additionally, the rivet must be able to flare without any fracture of the high-strength steel on the die side. Experimental sampling of both material combinations is carried out in [4]. For joining material combination 1, a rivet of type P and a flat die with a diameter of 8.4 mm and a depth of 2.0 mm are selected, while, for material combination 2, a rivet of type HD2 and a mandrel die with a diameter of 8.5 mm and a depth of 2.0 mm are used. Both the selected rivets, the P-rivet and the HD2-rivet, are coated with Almac®. They are made of steel 38B2, quenched and tempered to a hardness of 480 ± 30 HV10. Working on the basis of the properties of the selected rivets as well as on the simulation-based analysis of the material flow and the stress and strain conditions in the rivet during the joining process, an improved rivet geometry (see Fig. 4) is elaborated. This permits the reliable joining of both material combinations with just a single rivet geometry. The aim pursued by rivet design in [4] is the guaranteed attainment of the required values for the characteristic joint parameters, freedom from cracks in the joint and

Table 2 Rivets under investigation and their properties according to [10]

Rivet	Geometry	Properties
P	5.2 × 5.5 SK	Material: 38B2 Hardness level: 480 ± 30 HV10 Coating: Almac®
HD2	5.3 × 4.5 SK	
Improved	5.3 × 5.0 SK	
Stainless steel	5.3 × 5.0 SK (not fully formed)	Material: 1.3815 and 1.4541 Hardness level: Locally varying Coating: –

the avoidance of any bending and compression of the rivet. In addition, the manufacturability of the rivet by cold forming and the feedability of the rivet to the riveting system using common equipment are ensured. The rivet geometry of [4] is used as the target for the elaboration of a manufacturing concept for rivets in high nitrogen steel 1.3815 and stainless steel 1.4541 in [14].

A two-step concept is used for the cold forming process. The high strain hardening of the high nitrogen steel causes very high tool loads. The foot chamfer is thus increased from 60° to 70° compared to the target in [4] in order to reduce the stress prevailing in the tools. Due to the fact that the stress in the tools cannot be sufficiently reduced and that the tool materials used are already the most capable ones, it proved necessary to reduce the forming stroke. That leads to deviations in the manufactured rivets made of 1.3815 and 1.4541 from the target for the cold forming process, especially in the area of the rivet head. The head diameter is much lower than intended, and the hole depth and the rivet length deviate as well. On top of the systematic deviations, there are also deviations between the single rivets caused by process fluctuations. A comparison of the rivet geometries under investigation is given in Fig. 4. An overview of the properties of the different rivets is given in Table 2. In [15] an investigation concerning the deformation behaviour of rivets in accordance to the rivet's surface condition is conducted. It is seen that a zinc-nickel coating with a friction-reducing topcoat promotes rivet flaring, resulting in larger interlocks. The deformation behaviour of rivets coated with Almac® and uncoated rivets is similar, however. Thus, it can be stated that the joining process can also be performed without a rivet coating. The rivets in 1.3815 and 1.4541 are hence not coated. As the material strength is achieved by strain hardening during the forming process, they are not heat treated, too.

3 Analysis of Experimental Joining Tests

The aim of the investigation is the evaluation of the deformation behaviour of rivets made of stainless steel with high strain hardening by comparison to conventional rivets. For this, experimental joining tests are conducted and the joining results are

analysed. As in [4], riveting tongs of type TOX TE-X 80.250.351 (TOX® PRESSOTECHNIK GmbH & Co. KG, Germany), which can be mounted on industrial robots, are used for joining. The joining velocity is kept at 80 mm/s. Only the joining stroke is adapted depending on the different rivet types. Representative force-stroke curves for each combination of boundary conditions are shown in Fig. 5. With material combination 1, the characteristic force drop, which marks the piercing of the punch-sided high-strength steel sheet, can be seen with all rivets except the rivets made of 1.4541. As explained in detail below, this rivet is not able to pierce the punch-sided sheet and is compressed instead. The joining force with the improved rivet is higher than with the P-rivet. This is despite the fact that the joining stroke of 7.0 mm for the improved rivet is lower than the value of 7.3 mm for the P-rivet. The joining stroke is the distance between the stroke of the punch at first contact between the rivet and the punch-sided sheet and the maximum stroke. But as the length of the improved rivet geometry is reduced by 0.5 mm compared to the P-rivet, the improved rivet is pressed 0.2 mm further into the sheets. Moreover, the higher joining force results from the bevelled shank geometry of the improved rivet. The joining force is lower with rivets made of 1.3815 due to the lower head diameter, which results in a smaller contact area between the rivet head and the punch-sided sheet at the end of the process. With material combination 2, the punch-sided aluminium sheet is pierced continuously and no force drop is evident. On account of the same head diameter, the joining force of the HD2-rivet and the improved rivet are nearly equal. Due to the lower head diameter of the rivet made of 1.3815, the joining force is on a lower level.

For a detailed evaluation of the deformation behaviour, the joining process is interrupted four times, so that five steps, including the final joint, can be examined and the material flow, the mechanisms of material separation, and the interlock creation during the different process stages become visible. The strokes for the different steps are marked in Fig. 5. At each step, the joint is cut to provide a cross section and the Vickers hardness of the rivet is mapped in accordance with [16] using the measuring device KB 30 S (KB Prüftechnik GmbH, Germany). This allows the strain hardening during joining to be evaluated. The deformation of the different rivets when joining

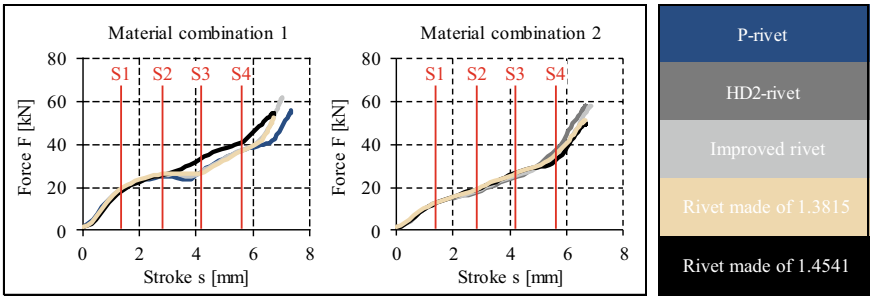


Fig. 5 Measured force–stroke curves with different material combinations and rivets. (Color figure online)

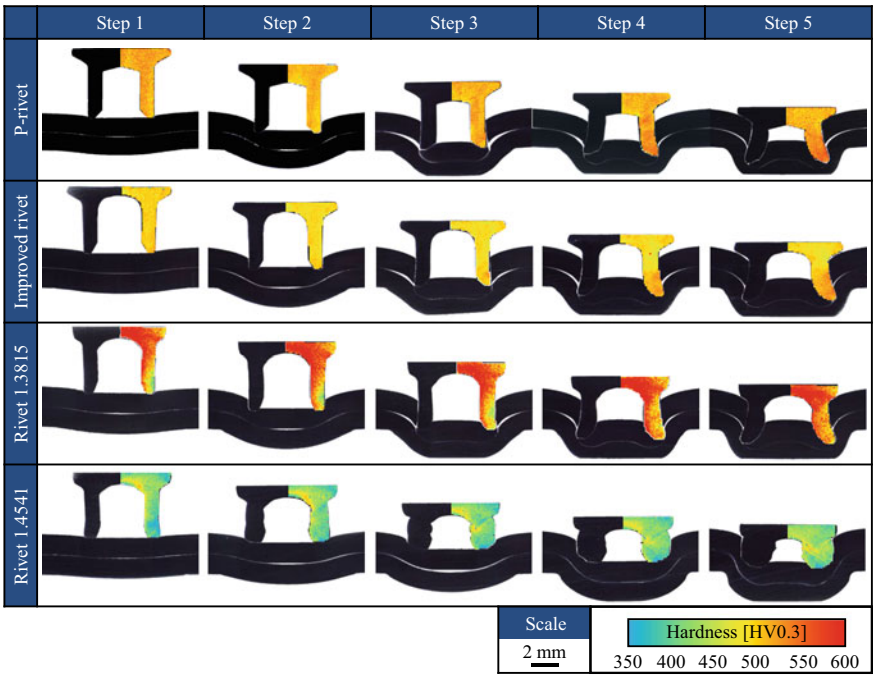


Fig. 6 Deformation of different rivets with material combination 1. (Color figure online)

material combination 1, together with the respective measured hardness, is shown in Fig. 6. In the first stage, the rivets are almost in the initial state. The first differences are evident and the special characteristics of the rivet hardness can be compared. The P-rivet and the improved rivet have a relatively homogenous hardness, which is slightly lower for the improved rivet due to batch variations. For both rivets, the hardness is in the targeted range of 480 ± 30 HV10. The hardness of the rivet made of high nitrogen steel 1.3815 displays local variations and is a function of the plastic strain attained during the forming process. Due to the higher plastic strain in the rivet head, the hardness and strength is higher there than for the conventional rivets, whereas the hardness in the outer rivet foot is lower. Since the forming process is the same, the hardness distribution is very similar in the rivets made of stainless steel 1.4541, but the hardness level is even lower due to the properties of the material. During the joining process, the hardness within the rivets increases as a function of the deformation. The affected areas are mainly the rivet shank and the rivet foot. The hardness within the P-rivet and the improved rivet is approximately 15% higher in the rivet foot at the end of the joining process. The increase in the hardness is limited by the material properties. In the rivets made of high nitrogen steel, the hardness also increases within the foot. At the end of the process, the hardness is no lower than the hardness within the rivets made of treatable steel. The hardness of the rivets in stainless steel 1.4541 does not increase significantly, because the

rivet has already attained its maximum hardness during the forming process. Due to its low hardness, the rivet is not able to pierce the punch-sided sheet. Instead, the rivet is highly compressed, starting at Step 2 already. The deformation of the other rivets, by contrast, starts after the piercing of the punch-sided sheet and is restricted almost exclusively to the flaring, which is needed to create the interlock. Only with the P-rivet can a slight compression and occasional cracks at the transition from the shank to the head be observed. As already mentioned in [4], this is be prevented for the improved rivet through the bevelling of the shank.

The joining results with material combination 2 are shown in Fig. 7. The material flow of the sheets is different from material combination 1, where a slug is created due to the low ductility of the high-strength steel on the punch side. In material combination 2, the punch-sided sheet is continuously pierced and the aluminium is formed into the hole in the rivet. Because of the missing slug, a die with a mandrel is needed to support the rivet flaring. Due to the mandrel, the die-sided sheet thins out a great deal during the joining process. This effect carries the danger of a fracture in the die-sided sheet, especially when using high-strength steel HCT780X as the die-sided sheet material. Because of that, the hole depth of the improved rivet is adjusted to this situation in [4]. The foot chamfer, which also has an impact on the deformation behaviour, is additionally adjusted to the piercing of the aluminium and the rivet flaring during the design of the improved rivet geometry in [4]. In the first

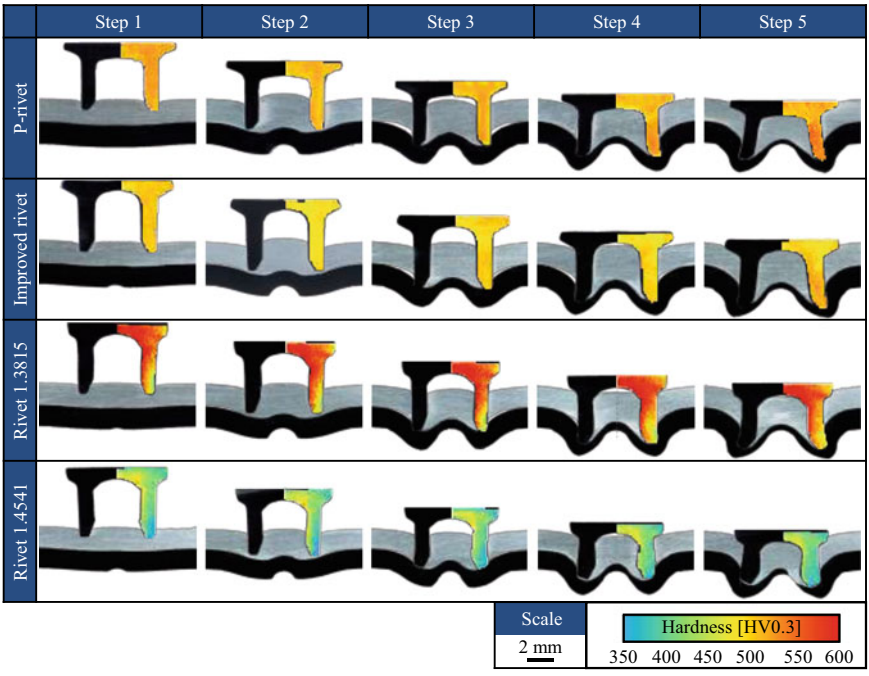


Fig. 7 Deformation of different rivets with material combination 2. (Color figure online)

stage, the same rivet hardness effects as have already been mentioned can be seen. After joining, the hardness within the foot of the HD2-rivet is higher than in the improved rivet due to the greater deformation. For this same reason, the hardness within the rivet made of 1.3815 is lower than the hardness achieved with material combination 1. Despite the deviations in the geometry of the rivet in 1.3815 and the varying hardness distribution, the deformation behaviour is similar to the behaviour of the improved rivet in overall terms, and it can be stated that rivets made of high nitrogen steel 1.3815 are able to join the two challenging material combinations under investigation. As for the HD2-rivet and the improved rivet, no cracks occur within the joint when using the high nitrogen steel rivets. A joint cannot be created for either of the two material combinations using rivets made of stainless steel 1.4541. The strength of the material is too low for its use as rivet material. With material combination 2, the rivet in 1.4541 is able to pierce the low-strength aluminium. However, after piercing, the rivet is unable to flare in the die-sided high-strength steel sheet. The rivet is compressed instead. The compression of the rivet causes a decreasing hole volume and, as a consequence, the fracture of the die-sided sheet.

The characteristic joint parameters with the rivets made of 1.3815 are measured over the cross section of the joints. The values are compared to the values from [4] in Fig. 8. It can be seen that the different lengths of the rivets have a significant influence on the minimum die side material thickness t_r. With material combination 1, in particular, the lower lengths of the improved rivet and the rivet made of 1.3815 cause a higher value for this parameter, while the value for material combination 2 is also slightly higher, despite the higher length of the improved rivet and the high nitrogen steel rivet compared to the HD2-rivet. This effect results from the bigger hole depth in the rivet, which makes for a lower inner pressure by providing more space for the aluminium that is formed into the rivet hole. When it comes to the interlock, the values achieved by the improved rivet are slightly lower than the values achieved with the P- and HD2-rivets. For all the values, a higher scattering is observed with the high nitrogen steel rivets due to deviations in the manufactured rivet geometry. However, the values required for a quality-assured joint are achieved in all cases.

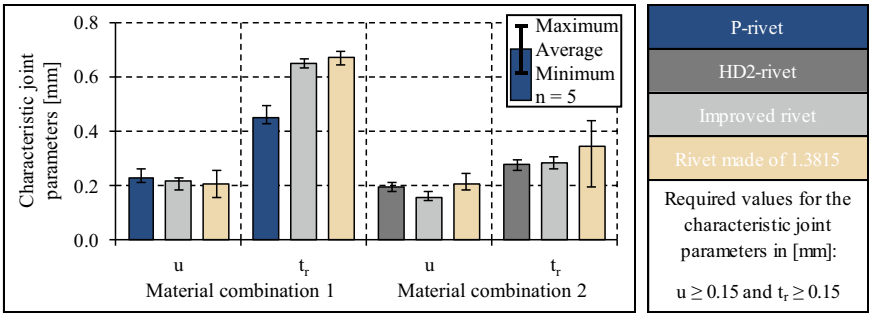


Fig. 8 Characteristic joint parameters achieved with different rivets. (Color figure online)

4 Summary and Outlook

Based on the improved rivet geometry of [4], a forming concept for the manufacture of rivets in stainless steels 1.3815 and 1.4541 was elaborated in [14]. The present investigation focusses on the properties of these rivets and their deformation behaviour during the joining process by comparison to conventional rivets made of treatable steel. Stopping the joining process at several different stages for a detailed analysis of the joint formation contributes to a deeper process understanding regarding the joining with rivets made of stainless steel with high strain hardening. The experimental tests are analysed on the basis of determined geometrical parameters, the measured hardness, and checks for cracks. The results confirm the assumption that the strength of stainless steel 1.4541 is not sufficient for its use as rivet material. Rivets in this material are not able to create an interlock and only facilitate process faults. With rivets made of high nitrogen steel 1.3815, by contrast, it is possible to create joints of the required quality. It can thus be stated that the capability of these rivets is essentially comparable to the capability of conventional rivets made of treatable steel. However, since the characteristic joint parameters are a good indicator of the expected strength of the joint, it must be noted that, despite the equal values achieved by the rivet in 1.3815, the deviations of the rivet caused by the challenging forming process are critical with regard to the attainable joint strength with the punch-sided aluminium in material combination 2. The results of the investigation presented in [10] indicate that especially the smaller rivet head diameter is problematic and leads to a reduction of the joint strength. Based on these insights and the findings of the present investigation, it is planned to further enhance the existing solution for the use of rivets in high nitrogen steel 1.3815. This will focus, in particular, on improving the joint properties through the use of a more accurate rivet geometry and the systematic local adjustment of the material hardness within the rivet during the forming process. In addition, an evaluation of the corrosion resistance of the rivets and the riveted joint with conventional coated rivets and uncoated rivets in stainless steel is to be conducted in future.

Acknowledgments The authors would like to thank the German Research Foundation (DFG) for its support of the research project “Forming and joining of semi-tubular self-piercing rivets made of high-strength steel with adapted mechanical properties and numerical analysis of the process chain” (ME 1840/8-1), on which this paper is based.

References

1. Smith B, Spulber A, Modi S, Fiorelli T (2017) Technology roadmaps: intelligent mobility technology, materials and manufacturing processes, and light duty vehicle propulsion. Center for Automotive Research, Ann Arbor, MI, USA.
2. Michalos G, Makris S, Papakostas N, Mourtzis D, Chryssolouris G (2010) Automotive assembly technologies review: Challenges and outlook for a flexible and adaptive approach. CIRP J Manuf Sci Technol 2(2):81–91. https://doi.org/10.1016/j.cirpj.2009.12.001

3. Li D, Chrysanthou A, Patel I, Williams G (2017) Self-piercing riveting: a review. Int J Adv Manuf Technol 92:1777–1824. https://doi.org/10.1007/s00170-017-0156-x
4. Uhe B, Kuball CM, Merklein M, Meschut G (2020) Improvement of a rivet geometry for the self-piercing riveting of high-strength steel and multi-material joints. Prod Eng Res Devel 14(4):417–423. https://doi.org/10.1007/s11740-020-00973-w
5. DVS/EFB 3410 (2019) Merkblatt Stanznieten - Überblick. DVS Media, Düsseldorf, Germany
6. Mori K, Abe Y (2018) A review on mechanical joining of aluminium and high strength steel sheets by plastic deformation. Int J Lightweight Mater Manuf 1(1):1–11. https://doi.org/10.1016/j.ijlmm.2018.02.002
7. Jäckel M, Grimm T, Niegsch R, Drossel W-G (2018) Overview of current challenges in self-piercing riveting of lightweight materials. Proceedings 2(8):384. https://doi.org/10.3390/ICEM18-05206
8. Mori K, Kato T, Abe Y, Ravshanbek Y (2006) Plastic joining of ultra high strength steel and aluminium alloy sheets by self piercing rivet. CIRP Ann Manuf Technol 55(1):283–286. https://doi.org/10.1016/S0007-8506(07)60417-X
9. Abe Y, Kato T, Mori K (2009) Self-piercing riveting of high tensile strength steel and aluminium alloy sheets using conventional rivet and die. J Mater Process Technol 209(8):3914–3922. https://doi.org/10.1016/j.jmatprotec.2008.09.007
10. Uhe B, Kuball CM, Merklein M, Meschut G (2021) Strength of self-piercing riveted joints with conventional rivets and rivets made of high nitrogen steel. In: 24th international conference on material forming (ESAFORM), Liège, BE. https://doi.org/10.25518/esaform21.1911
11. Schulz-Beenken A, Budde L (2002) Stanzniet aus rostfreiem Stahl. Patent DE4431769C2
12. Hahn O, Flügge W, Schulz-Beenken A, Schulte J, Schuberth S, Heise FJ (2009) Entwicklung von Verfahren zum Stanznieten nichtrostender hochlegierter Stähle mit nichtrostenden Nieten. FOSTA research report P401
13. Gavriljuk VG, Berns H (1999) High nitrogen steels: structure, properties, manufacture, applications. Springer-Verlag, Berlin
14. Kuball CM, Uhe B, Meschut G, Merklein M (2020) Process design for the forming of semi-tubular self-piercing rivets made of high nitrogen steel. Procedia Manuf 50(2020):280–285. https://doi.org/10.1016/j.promfg.2020.08.052
15. Uhe B, Kuball CM, Merklein M, Meschut G (2021) Influence of the rivet coating on the friction during self-piercing riveting. Key Eng Mater 883:11–18. https://doi.org/10.4028/www.scientific.net/KEM.883.11
16. DIN EN ISO 6507–1:2018–07 (2018) Metallic materials - Vickers hardness test - Part 1: Test method. Beuth-Verlag, Berlin

Numerical and Experimental Investigations on Riveting Assembly Processing Parameters of Hub Bearing Unit



You Wang, Wei Xiong, Jia-hua Zhou, and Peng Ren

Abstract Applying the rotary forging process (RFP) to the shaft-end riveting assembly of hub bearing units (HBU) is an important technological innovation with promising application prospect. Due to its advantages of stable pre-tightening, low cost and high integration, shaft-end riveting assembly have become a vital process in assembling the third generation HBU. However, due to the lack of systematic application research on RFP, there are still gaps between the domestic hub bearings and the imported products especially in terms of accuracy and consistency of performance. In the study, a numerical simulation platform (NSP) was adopted to simulate the assembling processes of HBU, in which the interference assembly, loading, and unloading of RFP were simulated with ABAQUS/Standard, ABAQUS/Explicit, and ABAQUS/Standard, respectively. The influence of processing parameters on product quality has been carried out by investigating several levels of feed displacement and feed rate, and relevant experimental research has also been conducted. It is found that the experimental results are in consistence with the numerical simulation results, demonstrating that the NSP adopted could be an alternative in determining and optimizing the processing parameters of RFP.

Keywords Hub bearing unit · Rotary forging · Riveting assembly · Numerical simulation

1 Introduction

Rotary forging process (RFP) has been successfully adopted into shaft-end riveting assembly of hub bearing units (HBU) due to its merits of high efficiency, energy saving, low cost, and low noise [1–4]. In shaft-end riveting process, the shaft end

Y. Wang · W. Xiong (✉)
School of Mechanical Engineering, Hubei University of Arts and Science, Xiangyang 441000, China
e-mail: xwhubei@163.com

J. Zhou · P. Ren
Hubei New Torch Technology Co. Ltd., Xiangyang 441000, China

© The Minerals, Metals & Materials Society 2021

G. Daehn et al. (eds.), *Forming the Future*, The Minerals, Metals & Materials Series,
https://doi.org/10.1007/978-3-030-75381-8_125

of inner flange is flanged gradually and finally pressed against the upper surface of inner ring for the purpose of assembling and axial clamping. In the past decades, with the imperious demands on lightweight, high integration and reliability of automobile parts, researchers and engineers engaged in hub bearing manufacturing have dedicated in exploring systematic application, mainly involving forming apparatus, test equipment, forming principles, design, and optimization of processing parameters through numerical simulation [5].

Yin explored the effects of processing parameters, such as feed speed of riveting head, thickness, and height of shaft end, on pre-tightening force, outside diameter change of inner ring, and geometrical shape of final riveted product [6]. Xiao and his coworkers carried out design of riveting machine tool and theoretical analysis of riveting force, which pointed out that the feed speed of riveting head should be determined in view of impact effect and production efficiency [7]. Qu et al. systematically studied the influence of initial axial distance, friction factor, radius ratio, and maximum inclination angle on pre-tightening force and energy consumption [8, 9]. Similarly, Li et al. explored the influence of inclination angle and feed speed on riveting force and pre-tightening force [10]. Yang et al. systematically studied the effects of riveting head movement trajectory, inclination angle, and dwell time on riveting force, pre-tightening force, inner ring deformation, and product performance [11]. Shu et al. studied the deformation characteristics of shaft end and explored the influence of feed displacement of riveting head and tempering temperature [12].

The research mentioned above has been carried out detailed investigations on the main processing parameters of shaft-end riveting assembly, involving inclination angle and feed speed of riveting head, material, and structure of shaft end and lubrication state between riveting head and shaft end. The results are of great significance for engineering application. However, inevitable deviations in predicting key performance indexes of HBU would be occurred as only dynamic explicit algorithm was employed without considering the interference assembly and the unloading of RFP [13]. Therefore, the study will rely on the basis of the authors' previous research to carry out numerical and experimental investigations on riveting assembly process of HBU, mainly exploring the influence of feed displacement and feed speed of riveting head.

2 Forming Apparatus and Test Platform

The riveting machine comes from SCFA Company (shown in Fig. 1), which is driven by electromagnetic force and its maximum vertical riveting force is 300 kN. The displacement of the riveting head is controlled and detected by a grating sensor during shaft-end riveting assembly. Testing samples are all provided by NTP Company and the main dimensions are denoted as shown in Fig. 2.

The shaft-end riveting process can be concluded into four stages, as shown in Fig. 3. Firstly, the riveting head is rapidly pushed downward to establish contact with the shaft end. Secondly, the riveting head is continuously pushed downward to the

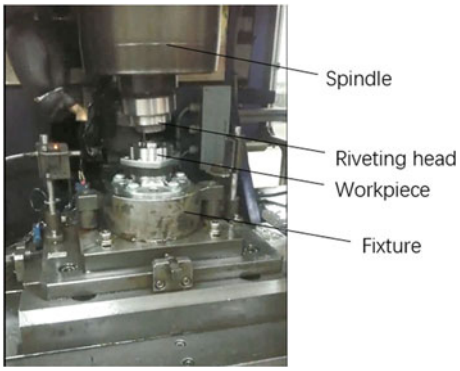


Fig. 1 Riveting machine. (Color figure online)

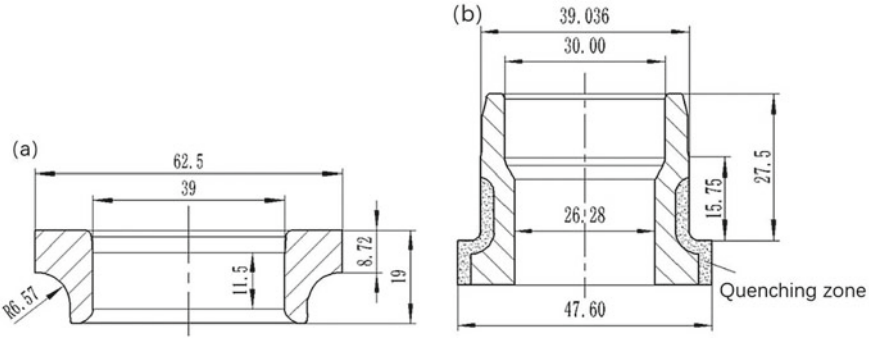


Fig. 2 Main dimensions of testing sample. **a** Inner ring, **b** inner flange

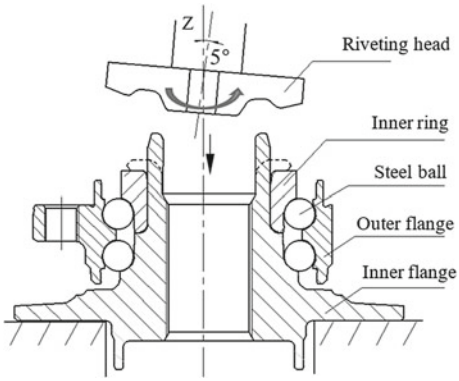


Fig. 3 Schematic of riveting assembly process

pre-set location with a constant lower speed. And then, the third stage is also referred to the smoothing stage, in which the displacement of riveting head remains constant for several rotations to flatten the shaft end. Finally, with the riveting head lifting up quickly to its initial position, the inner ring and the inner flange are undergoing unloading process. In the study, it is noted that the steel balls and the outer flange are excluded as their influence on employed indexes could be ignored. Moreover, it is noted that the riveting force is measured through a built-in pressure sensor, and the other employed indexes are all measured by micrometers.

3 NSP Modeling

The NSP was established based on the general finite element (FE) software ABAQUS. Specific steps concluded are as follows. Firstly, the interference fit between inner ring and inner flange was simulated by utilizing ABAQUS/Standard module. Then, the riveting loading process was conducted with ABAQUS/Explicit, by taking the simulation result of the interference fit as its predefined stress field. Finally, the springback analysis of RFP was conducted in ABAQUS/Standard, by taking the simulation result of the previous step as its predefined stress field. The FE model of HBU is given in Fig. 4, where the linear reduction integration element C3D8R was adopted to mesh the inner flange, inner ring, and riveting head. In order to speed up the simulation process, the riveting head was constrained into rigid. The friction coefficients at the interfaces were set to be 0.15 and assumed to follow the Coulomb friction model.

The materials adopted for the inner ring and inner flange are quenched GCr15 bearing steel and quenched and tempered 65Mn spring steel, respectively. Their mechanical properties are illustrated in Fig. 5 and Table 1. The stroke of riveting

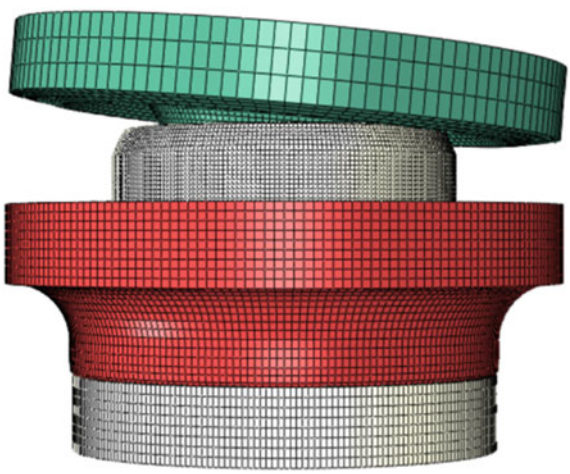


Fig. 4 FE model for NSP. (Color figure online)

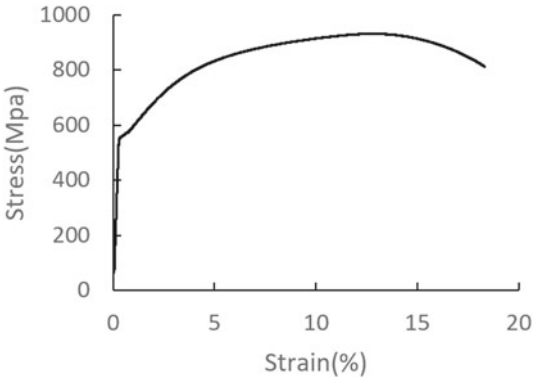


Fig. 5 Real stress–strain curve of quenched and tempered 65Mn

Table 1 Mechanical properties of quenched 65Mn and GCr15 steels

Mechanical property	Density (Kg/m^3)	Young's modulus (GPa)	Poisson's ratio	Yield strength (MPa)
65Mn	7800	212	0.288	1400
GCr15	7800	220	0.3	1700

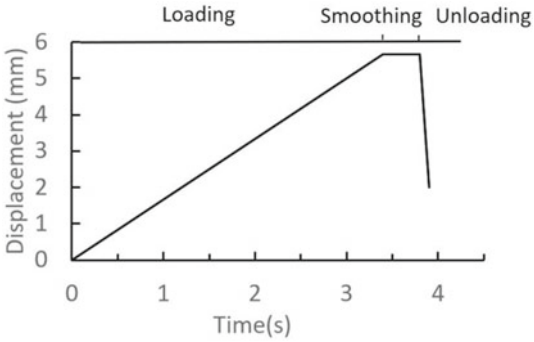


Fig. 6 Stroke of the riveting head

head during the shaft-end riveting assembly is defined as shown in Fig. 6. To save computation time, the mass scaling strategy was also adopted and the reliability of numerical results was evaluated through the ratio of kinetic energy to internal energy.

4 Results and Discussion

In terms of product performance, HBUs are required to have high stiffness, long life, and low noise. Reflecting on the riveting process, it is required that the riveted products have proper clearance and pre-tightening force. However, the two parameters

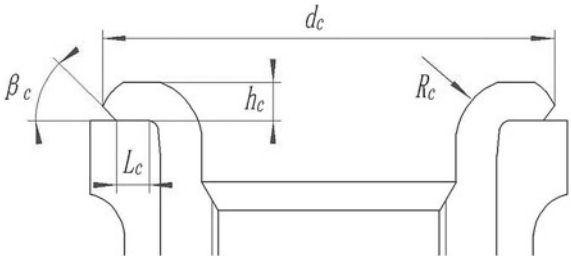
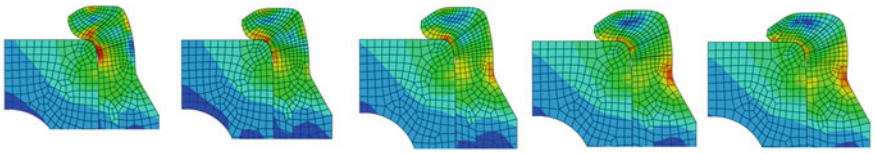


Fig. 7 Main parameters of the shaft end after riveting assembly

could not be easily measured especially for mass production. Therefore, it is of practical significance to establish the relationship between the geometrical dimensions of the riveted products and their performance indexes and to monitor and evaluate the shaft-end riveting process by controlling the geometric parameters. The main parameters are indicated in Fig. 7, where d_c, β_c, h_c, R_c, L_c refers to riveting diameter, throat angle, riveting thickness, riveting filet, and contact length, respectively. In the study, riveting diameter, riveting thickness, radial displacement of inner ring, and riveting force were employed to evaluate the influence of processing parameters. Here, the riveting force refers to the force that the riveting head exerted on the inner flange.

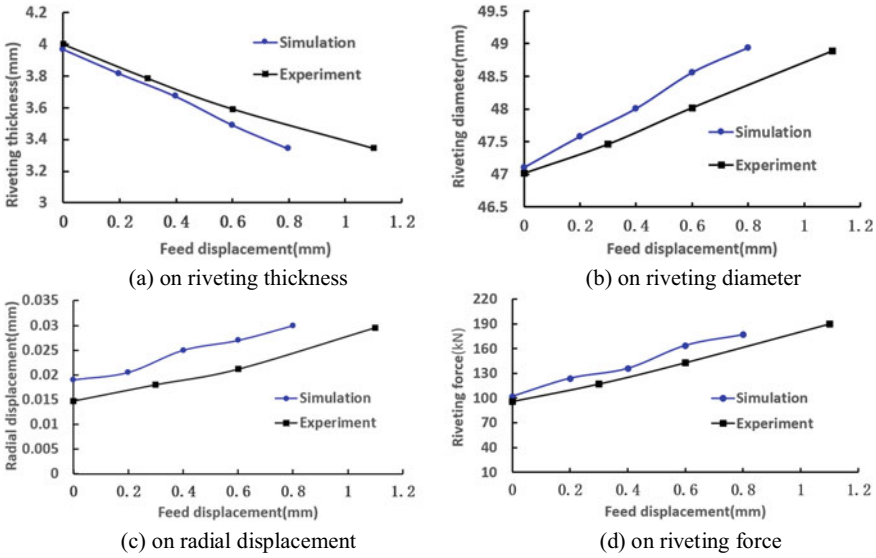
4.1 The Influence of the Feed Displacement

Five levels of feed displacements, i.e., 0, +0.2 mm, +0.4 mm, +0.6 mm, +0.8 mm relative to a reference value, are designed to explore the feed displacement on the riveted products. The configurations of the shaft end after riveting assembly are given in Fig. 8, which indicates that the riveting thickness decreases with the feed displacement increased. In order to investigate the effects of feed displacement quantitatively, the relationships between the employed indexes and the feed displacements are illustrated in Fig. 9. From an overall perspective, the riveting diameter, the radial displacement, and the riveting force are all increased with the increasing of feed displacement. Specifically, it can be seen from Fig. 9a that the ratios of feed displacement change to riveting thickness change approximately stand at 1:0.9 and 1:0.6 for



a) 0 b) +0.2 mm c) +0.4 mm d) +0.6 mm e) +0.8 mm

Fig. 8 Configuration of the shaft end under different feed displacements. (Color figure online)



(a) on riveting thickness (b) on riveting diameter

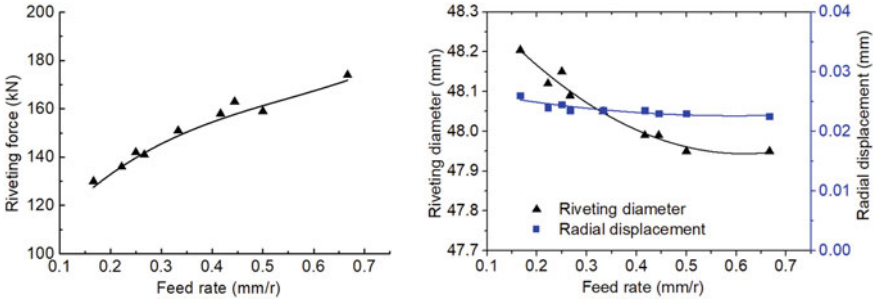
(c) on radial displacement (d) on riveting force

Fig. 9 Effects of feed displacement. (Color figure online)

the simulation result and for the test result, respectively, indicating that deformation recovery occurred after the unloading process. On the other hand, the ratio of feed displacement change to riveting diameter change approximately stands at 1:2.2, indicating that the feed displacement on riveting diameter is more sensitive than that on riveting thickness. Therefore, it is drawn that the riveting diameter would be more suitable as index in view of processing control. Then, it can be seen from Fig. 9c that the radial displacement increases with the feed displacement increased, meaning that the shaft-end riveting assembly not only compresses the inner ring axially but also enlarges the inner ring radially. Moreover, it is seen from Fig. 9d that the riveting force shows an increasing trend, indicating the deformation of shaft end increases with the increase of feed displacement. Finally, experimental tests are performed and the results are in good agreement with their relative numerical results, indicating that NSP is solid in predicting geometrical and performance indexes.

4.2 The Influence of the Feed Rate

Firstly, it should be noted the feed rate of riveting head p refers to the ratio of its axial displacement to its rotational speed per unit time, which can be expressed as $p = 60v/n$. Where v and n refer to feed speed and rotational speed of the riveting head, separately. Figure 10a illustrates the distribution of riveting force under different feed rates. It is clear that the riveting force indicates an increasing trend with the feed rate increased, showing the same trend to the previous studies conducted by



(a) on riveting force (b) on riveting diameter and radial displacement

Fig. 10 Effects of feed rate. (Color figure online)

Zhang, Marcinik, Slater, and Appleton [14]. The reason is that the contact area rate is increased with the increase of feed rate, and the greater the contact area rate is, the greater the riveting force is. At meanwhile, a higher contact area rate would also cause more power consumption for the riveting machine. To quantitatively analyze the feed rate on riveting diameter and radial displacement, Fig. 10b shows their distributions under different feed rates. With the feed rate change from 0.167 to 0.667 mm/r, it is seen that the riveting diameter is fluctuated from 48.20 to 47.95 mm and the radial displacement is varied between 0.02 and 0.03 mm, meaning the effects of feed rate on riveting diameter and radial displacement could be ignored at the same pre-set axial displacement of the riveting head.

5 Conclusions

Based on the NSP of HBU, the study explored the influence of processing parameters on the assembly quality of the riveted product. Five levels of feed displacements and nine levels of feed rates were designed to simulate their influence on key performance indexes of HBU. Moreover, the relevant experimental tests were carried out to consolidate the simulation results. The main conclusions are included as follows:

(1) The experimental results demonstrate that NSP built by the joint use of ABAQUS/Standard and ABAQUS/Explicit is valid and precise in predicting the key performance indexes of HBU, providing an effective way for hub bearing analysis.
(2) Besides riveting thickness, the riveting diameter, radial displacement, and riveting force are all increased with the increase of feed displacement. It is also drawn that the riveting diameter is more suitable in processing control as it is more sensitive to changes in feed displacement.
(3) The riveting force increases with the feed rate increased, but the influence of feed rate on riveting diameter and radial displacement is so small as to be negligible.

Acknowledgments The authors would like to acknowledge the Youth Project of Hubei Province Department of Education (Q20202605).

References

1. Ishida H, Kaneko T (2001) Development of hub unit bearings with swaging. NSK Tech J 670:11–16
2. Numata T (2005) Latest technical trends regarding hub unit bearings. Koyo Eng J 168:8–13
3. Satou H (2003) Latest development of rolling bearing and related products for environmental pretection. Koyo Eng J 162:10–16
4. Morita K (2001) Trends of production engineering for bearings and unit products. Koyo Eng J 159:31–36
5. Wang Y, Xiong W, Mei S et al (2020) Research progress on shaft-end riveting process of automobile wheel hub bearings. J Plast Eng 27(9):1–11 (in Chinese)
6. Yin ZG (2012) CAE analysis of automotive hub unit bearing shaft-end clinching procedure. Master thesis, South China University of Technology (in Chinese)
7. Xiao YY, Zhou ZX, Li W et al (2013) Axial force test and analysis in riveting assembly of automotive hub bearing Unit. Appl Mech Mater 268–270:1058–1062
8. Qu J, Zhang GJ (2016) Determination of motion equation of rivet head during shaft riveting assembly process for wheel hub bearing units. J Manuf Sci E 138(4):1–9
9. Qu J, Zhang GJ (2016) Numerical and experimental investigations of the shaft-clinching assembly process of automobile wheel-hub-bearing units. J Auto Eng 230(13):1741–1757
10. Li XY, Lei LY, Liu B et al (2017) Finite element analysis of rivet head angle in shaft end riveting of automobile hub bearing units. Bearing 3:22–25 (in Chinese)
11. Yang J, Yang YS, Li W et al (2017) Theoretical analysis and experimental studies for riveting and assembly process of automotive hub bearing units. China Mech Eng 28(24):2949–2956 (in Chinese)
12. Shu WC, Yang JG, X LP et al (2019) Stress-strain and mechanical analysis of shaft clinching plastic forming of hub unit. J Plast Eng 26(4):220–227 (in Chinese)
13. Xiong W, Wang Y, Li XP et al (2019) Study on the forming process and deformation behaviour of inner ring in the wheel hub bearing based on riveting assembly. Materials 12(22):3785. https://doi.org/10.3390/ma12223785
14. Zhang M (1984) Calculations of force and energy in rotating forging. Metal Sci Tech 3(2):62–80 (in Chinese)

Part XV
Lubrication and Surface Effects

Evaluation of Lubricant Performance for Thick Sheet Ironing Process by Ball Ironing Test



Nuttakorn Sae-eaw and Yingyot Aue-u-lan

Abstract A thick sheet ironing process is normally used to manufacture a uniform wall thickness of products. To evaluate the performances of lubricants by conventional tests, such as Ring Compression Test (RCT) is not suitable due to the limitation in low levels of contact pressure, surface expansion ratio, and relative velocity. In this research, Ball Ironing Test (BIT) was proposed as a new simulative tribo-test to evaluate the lubricants of the thick sheet ironing process. Finite Element Modeling (FEM) together with statistical analysis was employed to determine a frictional indicator (i.e., maximum load and final height of specimen). According to the results, the maximum load is very sensitive to the friction and used as an indicator to evaluate and approximate the friction coefficient via Frictional Calibration Curve (FCC). Different types of lubricants were tested experimentally and demonstrated different performances by the BIT. In conclusion, the BIT is suitable for evaluating the lubricants of the thick ironing process.

Keywords Ball ironing test · Tribo-test · Friction evaluation

1 Introduction

Nowadays, time and cost savings in production are the main challenges for engineers. For metal forming processes, Flow Control Forming process (FCF) was proposed by combining the advantages of sheet and bulk metal forming processes to reduce the material waste, load, and forming steps [1]. A thick sheet is formed by drawing and, later on, ironing process to produce a controlled thickness cup shape. It is called thick sheet ironing process. Nowadays, most of the pulleys are produced by this process instead of the backward extrusion process. The tribological conditions of the forming processes are the important factors which have effect on the forming results such as forming load, shape, and dimension on the workpiece [2]. For ironing process, if the

N. Sae-eaw · Y. Aue-u-lan (✉)
Materials and Production Engineering, The Sirindhorn International Thai-German Graduate School of Engineering, King Mongkut's University of Technology North Bangkok, Bangkok 10800, Thailand
e-mail: yingyot.a@tggs.kmutnb.ac.th

© The Minerals, Metals & Materials Society 2021

G. Daehn et al. (eds.), *Forming the Future*, The Minerals, Metals & Materials Series,
https://doi.org/10.1007/978-3-030-75381-8_126

friction as a result of the tribological conditions is increased, the forming load and the cup height will increase. The high friction may lead to a thinning problem because of the high tensile stress acting on the workpiece's wall [3]. Therefore, the lubricant is applied for controlling or reducing the friction level in the forming process.

A simulative tribo-test is used as a tool for evaluating the performance of the lubricant or the tribological conditions. The test should provide the same process conditions, i.e., contact pressure, surface expansion ratio and relative velocity, as the actual process [4]. Ring Compression Test (RCT) was accepted as the standard tribo-test for bulk metal forming processes [5]. The change in diameter of the disc-shaped specimen was used as the friction indicator. However, this test provided the low process conditions compared with the conditions of common forged products. Therefore, the new tests are always proposed to design the proper conditions for their products. Spike Forging Test (SFT), T-shape compression test, and Double Cup Extrusion Test (DCET) are the examples of the tests developed for forging processes. The tests for sheet forming processes, Strip ironing and Drawing and ironing tests [6, 7] were similar to the ironing process. For Strip ironing test, the thickness reduction of the specimen was controlled by the constant load. The friction coefficient can be evaluated by the ratio of the pulling force and the applied constant load. However, this test still provided the low contact pressure because it was a thin sheet. Moreover, the uniaxial tension stress was the main stress stage of this test in which was not the same as that of the real ironing process. Therefore, the drawing and ironing test was proposed by considering the condition near the actual ironing process. A cup-shaped specimen was formed by drawing process and the thickness was reduced by ironing process. The difficulty of this test was specimen preparation, because there were 2 steps of forming dies, including machining step. These 2 forming steps are deep drawing and later on ironing process, and they need to perform separately. These tests are not suitable for thick sheet ironing process. The suitable tribo-test should reproduce the same characteristics as the existing process. The process conditions, the stress stage, and the gradient of surface expansion would be considered for determining the suitable tribo-test. For that test, the lubricants can be applied easily for lubricant screening test. The results of the test should provide the good friction sensitivity.

The aim of this research was to propose the new tribo-test named "Ball Ironing Test (BIT)" that can be used to evaluate the performance of the lubricant with the same tribological conditions as the thick sheet ironing process. Finite Element Modeling (FEM) was used as a tool to investigate the friction indicator and to develop the Friction Calibration Curve (FCC). The new test will be validated by the experiment with different types of the lubricants. The friction coefficients of the selected lubricants will be determined.

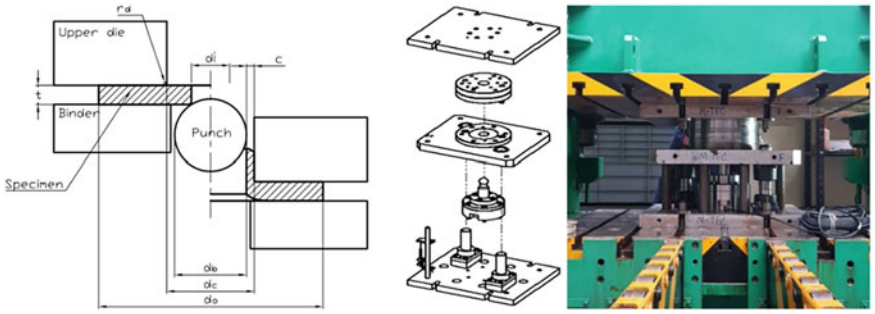


Fig. 1 Ball ironing test; **a** schematic of the BIT and **b** BIT die set. (Color figure online)

2 Ball Ironing Test

To select a suitable simulative tribo-test for the thick sheet ironing process, their process characteristics and process conditions were considered. At the existing process, the contact pressure was around 800-1,400 MPa and the surface expansion ratio was around 3.5–4.5. These conditions were depended on the thickness reduction of the specimen. Moreover, the gradient of new generated surface from the workpiece is demonstrated as the uniform area due to the ironing process. Therefore, the Ball Ironing Test (BIT) was proposed as a suitable test because it can duplicate these specific conditions of the thick sheet ironing process.

The schematic of the BIT is shown in Fig. 1a. The main components consisted of a specimen, a ball-shape punch, an upper die, and a binder. The specimen was a thick disc-shape. It was clamped by the upper die and the binder. The clamped specimen was pushed through the fixed lower punch. The deformation zone was designed only at the inner diameter of the specimen. In the beginning, the material was deformed by drawing process and, later on, ironing process. The clearance between punch and die was used to control the final thickness of the tested specimen.

3 Methodology

3.1 Ball Ironing Test Simulation

The simulation model is shown in Fig. 2a. Due to the symmetrical geometry of the test, 2D model was used for reducing time in calculation. The specimen was assumed as plastic material. The number of mesh were 10,000 elements created on specimen by quadrilateral elements. The SPHC steel with outer diameter at 5 mm and height at 10 mm was compressed to determine the mechanical property. In Fig. 2b,

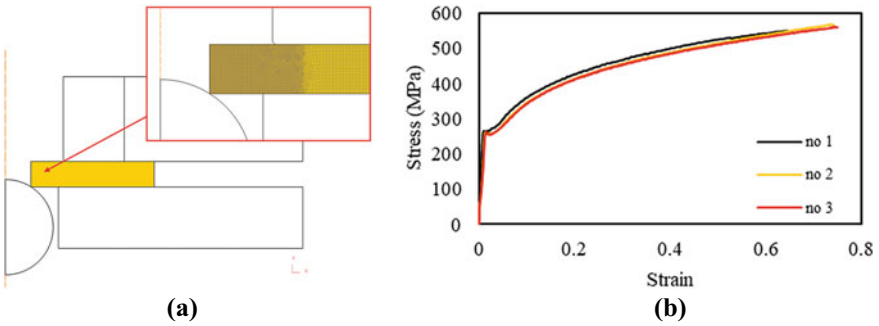


Fig. 2 Finite Element Modeling (FEM) of the BIT; **a** 2D simulation model and **b** stress-strain curve of the SPHC steel. (Color figure online)

these stress–strain curves were input into FEM code, Deform2D version 10.2. The tool components were assumed as a rigid body. Shear friction model was selected because of the high level of normal contact pressure of the thick sheet ironing process as shown in Eq. (1).

$$\tau = mk \tag{1}$$

where shear friction coefficient (m) was a fraction of shear strength of material (k) [8]. In this research, the shear friction coefficients were varied from 0 to 0.4 to evaluate the friction effect on the BIT results.

The flow behavior and strain distribution of the specimen will be illustrated by FEM to confirm the process conditions of the BIT. Moreover, friction indicator of the test will be determined and used to create the Friction Calibration Curve (FCC) for friction evaluation.

3.2 Tooling Setup

In this study, the specimen was the SPHC steel widely used to produce the common automotive parts. For the die set of the BIT as seen in Fig. 1b, most of the tool components are made of the S45C steel. The upper die was made of the SKD11 steel with the hardness value of 58 HRC. The die surface was prepared by grinding and polishing processes controlled the average surface roughness value at 0.15 μm. The ball-shape punch was made of the JU2 bearing steel with the hardness of 60 HRC. This die set was conducted on the single action with cushion hydraulic press machine. The maximum press capacity was at 200 tons. The clamping force was applied by the cushion pins at 13 tons. The testing speed was set at 1 mm/s and the total displacement was at 60 mm. Table 1 shows the tooling geometries of the BIT.

Table 1 Tooling geometries of ball ironing test

Workpiece		
Inner diameter (d_i)	24	mm
Outer diameter (d_o)	140	mm
Thickness (t)	12	mm
Tooling		
Bearing ball diameter (d_b)	45	mm
Die clearance (c)	4.8	mm
Upper die radius (r_d)	1	mm

4 Experiment Procedure

Different types of the lubricants will be tested such as dry, solid, and liquid lubricants. Dry lubricant condition was the metal-to-metal contact at the surfaces of the die and the workpiece. Zn-Ph coating was the solid lubricant normally used in the common cold forging processes. For the experiment, the combined lubrication layer weight of this solid lubricant was more than 8 g/m^2. The oil with EP (Extreme Pressure additives) was selected as liquid lubricant that the viscosity was at 480 cSt@40 °C. At the specimen surfaces, the oil was applied by brushing technique which the oil quantity was controlled at 5 ml per specimen.

The BIT was performed for evaluating the performances at various lubricants. The results, the final height of specimen (h_f) and the maximum load (L_{max}), were measured and used to indicate the friction effect. The comparison of the BIT results will be used to rank their performances.

5 Results and Discussion

5.1 Simulation Results

The flow behavior during the test is shown in Fig. 3. The deformed grids created on the specimen can confirm the location of the deformation that was occurred only at the inner diameter of the specimen. At the first step, it was drawing process, the specimen was bent and drawn by ball-shape punch into the die cavity. Next step,

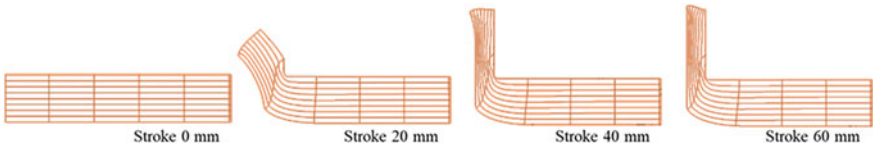


Fig. 3 Flow behavior of the BIT specimen. (Color figure online)

the thickness was reduced by ironing process. Amount of deformed material was used to create the wall of the specimen. When the stroke was increased, the height of specimen was also increased.

Moreover, the effective strain distributions on the BIT specimen are shown in Fig. 4a. It can be seen that the location of the most deformation was at the inner surface of the specimen's wall. The gradient of the strain showed as the uniform area was suitably used to study the surface defects; such as wear and galling. From the FEM calculation, the process conditions of the BIT were determined. The level of the normal contact pressure was around 1,200 MPa at the maximum load and surface expansion ratio was around 4. The uniform surface expansion distributions are shown in Fig. 4b. This test can duplicate the specific conditions of the thick sheet ironing process.

The shear friction coefficients were varied in FEM model. In Fig. 5, the effects of friction were determined on the BIT results. When the friction was increased, the height of specimen and load were increased. However, it was clearly seen that the maximum load was highly sensitive to friction. The wider range of the response,

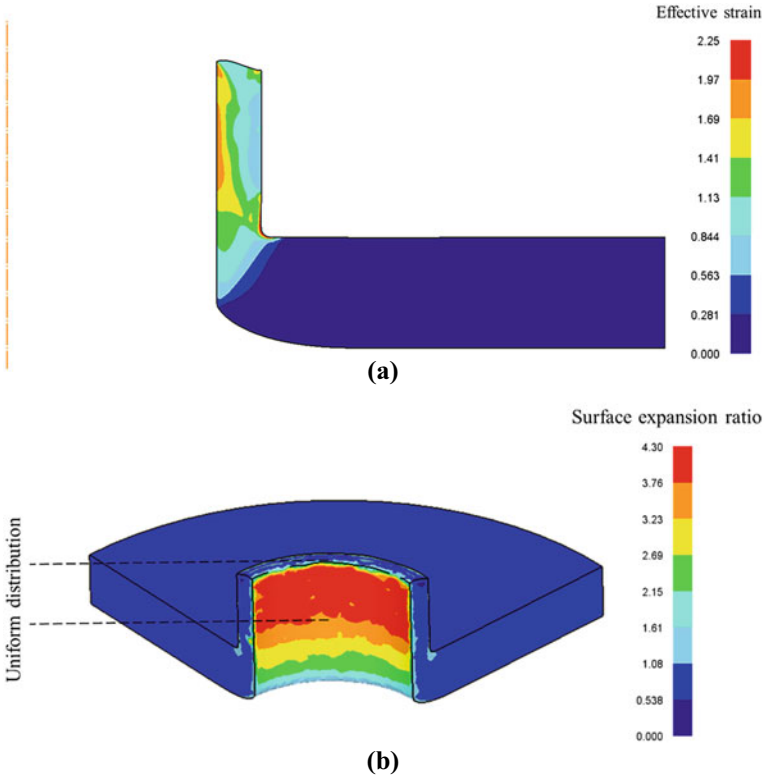


Fig. 4 FEM results; **a** effective strain distribution and **b** surface expansion distribution. (Color figure online)

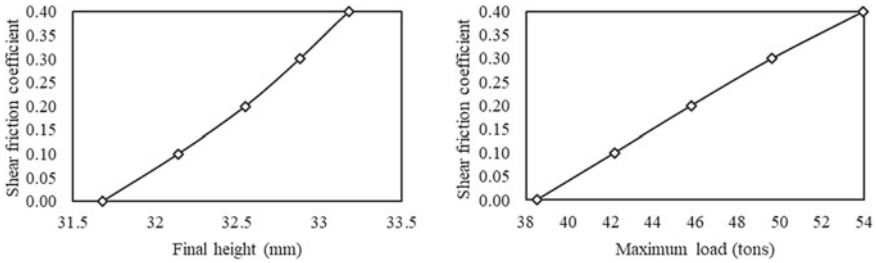


Fig. 5 BIT results with various shear friction coefficients; **a** final height and **b** maximum load

maximum load, can be used to approximate the friction value easily. The linear relationship between shear friction coefficient and maximum load is shown in Fig. 5b. So, the Friction Calibration Curve (FCC) was fit as shown in Eq. (2).

$$m = 0.026(L_{\max}) - 0.9989 \tag{2}$$

5.2 Experimental Results and Validation

The specimens after BIT testing are shown in Fig. 6. Only the dry lubricant cannot be formed successfully. At the wall of specimen, the fracture was found due to the high contact pressure from the metal-to-metal contacting. Solid and liquid lubricants, Zn-Ph coating and oil with EP, showed the excellent performances. The specimen can be formed without any surface defects. In Fig. 7, the maximum load comparison was presented. BIT can use to rank the performances of the lubricants. The lowest testing load was Zn-Ph coating. For friction evaluation, these maximum load values were input to predicted mathematical model, and the results showed that the approximated shear friction coefficients were 0.025 and 0.067 for Zn-Ph coating and oil with EP, respectively.

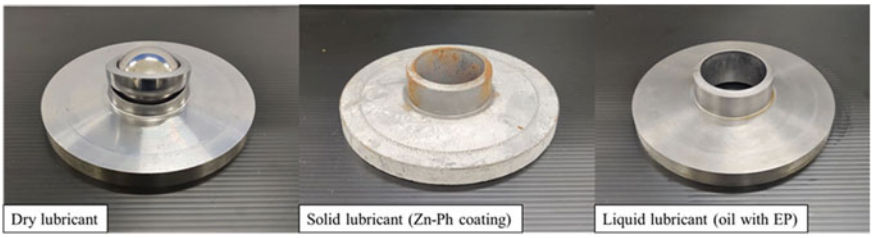


Fig. 6 Specimen after Ball ironing test. (Color figure online)

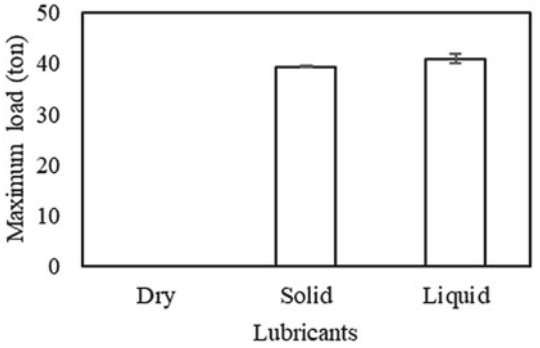


Fig. 7 Maximum load comparison

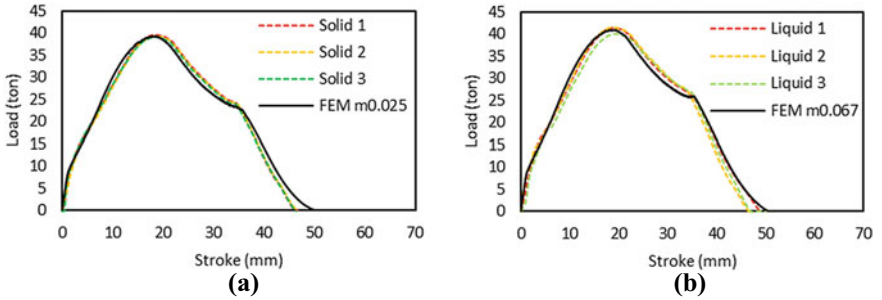


Fig. 8 Load profile compassion; **a** solid lubricant and **b** liquid lubricant. (Color figure online)

To validate the experimental results, these approximated shear friction coefficients were input to FEM code for simulation. The load-stroke curves calculated from FEM were compared with the experiment as seen in Fig. 8. The result comparison between the FEM and the experiment showed the perfect match of the load-stroke profiles.

6 Conclusions

1. Ball Ironing Test (BIT) was proposed for evaluating the tribological conditions of the thick sheet ironing processes. BIT can provide the same tribological conditions as that of the actual process.
2. According to the simulation results, when the friction was increased, the final height of specimen and the maximum load were increased. It was clearly seen that the maximum load had good sensitive to friction, so it was used as friction indicator. For friction evaluation, the shear friction coefficient (m) was determined by using a simplified mathematical model.

3. The performances of various lubricants were determined by the BIT. The fractured specimens were found for dry lubricant, while the solid lubricant (Zn-Ph coating) and liquid lubricant (oil with EP) presented the excellent performances to protect the specimen without any surface defect. The maximum load of Zn-Ph coating was lower than that of the oil with EP. From the maximum load comparison, BIT can obviously rank the performances of each lubricant.
4. The approximated shear friction coefficients were evaluated. There were 0.025 and 0.067 for Zn-Ph coating and oil with EP, respectively.

Acknowledgments This work was partially supported by The Thailand Research Fund (TRF), Research and Researchers for Industries (RRi) [grant number PHD60I0072].

References

1. Nakano T (2009) Introduction of flow control forming (FCF) for sheet forging and new presses. In: Paper presented at the 5th JSTP international seminar on precision forging, Kyoto, 16–17 March 2009
2. Joun MS, Moon HG, Choi IS, Lee MC, Jun BY (2009) Effects of friction laws on metal forming processes. Tribol Int 42:311–319
3. Zein H, El-Sherbiny M, Abd-Rabou M, El Shazly M (2013) Effect of die design parameters on thinning of sheet metal in the deep drawing process. Am J Mech Eng 1(2):20–29
4. Groche P, Kramer P, Bay N, Christiansen P, Dubar L, Hayakawa K, Hu C, Kitamura K, Moreau P (2018) Friction coefficients in cold forging: A global perspective. CIRP Ann Manuf Technol 61(1):261–264
5. Rao KP (1993) A review of ring-compression testing and applicability of the calibration curves. J Mater Process Technol 37:295–318
6. Aleksandrović S, Đorđević M, Stefanović M, Lazić V, Adamović D, Arsić D (2014) Different ways of friction coefficient determination in stripe ironing test. Tribol Ind 36(3):293–299
7. Kim H, Altan T, Yan Q (2009) Evaluation of stamping lubricants in forming advanced high strength steels (AHSS) using deep drawing and ironing tests. J Mater Process Technol 209:4122–4133
8. Altan T, Tekkaya E (2012) Sheet metal forming: fundamentals. ASM International

Development of Oil-Type Lubricants for Cold Forging Using Phase Transition Behavior Under High-Pressure Conditions



Tomoaki Okano, Nobuhide Tanino, and Kazuhiko Kitamura

Abstract In the cold forging process, lubricants are essential because they prolong die life and improve product surface quality. In contrast, it is well known that lubricants are exposed to very severe conditions such as high contact pressure and processing-induced high temperatures. Oil-based cold forging lubricants induce processing defects when the oil film is insufficient. In the search for better alternatives, we explored the possibility of phase transition materials that changeover from liquid to solid under high-pressure conditions. In this study, we developed new oil-type cold forging lubricants with phase transition material additives. Moreover, we found that these hybrid materials show superior lubricating performance in the cold forging process to conventional lubricants. These results indicated that phase transition behavior under high-pressure conditions supports more efficient cold forging process lubrication.

Keywords Lubricants · Cold forge · Phase transition · High-pressure conditions

1 Introduction

From a plastic working process viewpoint, including forge and press work, lubricants assume a very important role in limiting tool wear and seizure prevention. An appropriate lubricant choice contributes to improved final product surface finish, precision, and accuracy [1, 2]. Among them, the cold forging process is especially severe and lubrication is difficult due to exposure to high surface pressure conditions and excessive temperatures caused by work hardening and die friction with the work product [3, 4].

T. Okano (✉) · N. Tanino
Lubricant Research Laboratory, Idemitsu Kosan Co, Ltd, 24-4, Anesakikaigan, Ichihara-Shi, Chiba 299-0107, Japan
e-mail: tomoaki.okano.1000@idemitsu.com

K. Kitamura
Department of Electical and Mechanical Engineering, Nagoya Institute of Technology, Gokiso-Cho, Showa-Ku, Nagoya 466-8555, Japan

© The Minerals, Metals & Materials Society 2021

G. Daehn et al. (eds.), *Forming the Future*, The Minerals, Metals & Materials Series,
https://doi.org/10.1007/978-3-030-75381-8_127

Referring to cold forging process lubricants, those chemical conversion coating-types, such as phosphate film have been in the mainstream since they were developed more than half a century ago [5, 6]. Conversely, chemical conversion coatings have industrial waste problems due to numerous processing steps. So, most new chemical conversion coating-type lubricants that reduce industrial wastes are being developed and practicalized for these reasons [7].

On the other hand, oil-type lubricants for cold forging processes do not lubricate as well as chemical conversion coating-types because oil film is thinner and cannot easily be sustained under severe conditions. However, oil-type lubricants have high potential because they do not need nearly as much processing as chemical conversion coatings and have less industrial waste [8]. So, if we develop new oil-type lubricants with equivalent lubricating properties, they will become more popular.

To solve these problems, we found new materials that phase transition from liquid to solid under high-pressure conditions and infused oil-type lubricants with them. In this work, we evaluate oil-type lubricants containing phase transition materials using a ball penetration test that determines lubrication properties for cold forging processes [9]. As a result, we found that phase transition materials have better lubricity in cold forging processes compared to lubricants without it.

2 Experimental Details

2.1 Phase Transition Behavior Observations of Lubricants

We evaluated phase transition behavior of samples using a plunger-type high-pressure vessel observation system, developed in-house, as shown in Fig. 1 [10]. The observation window inside the cylinder is made of sapphire glass and is built in the middle of a high-pressure vessel. An LED light source was installed on one side of the observation window, and an optical microscope was installed on the other side. Optical micrographs obtained from this device were recorded on a PC and by synchronizing the applied pressure data recorded by a data logger, visualized the phase transition behavior under various pressure conditions and determined the phase transition pressure values.

2.2 Ball Penetration Test

We evaluated the lubricating properties of lubricants for cold forging processes using a ball penetration test, as shown in Fig. 2. High carbon chromium steel balls (hardness, 58 HRC; surface roughness, $R_a < 0.05$ μm) were used with 0.1% C carbon steel workpieces (hardness, 119 HV; surface roughness, $R_{max} = 1$–5 μm). After both the ball and the workpiece were dipped in the prepared sample oils and set up in a

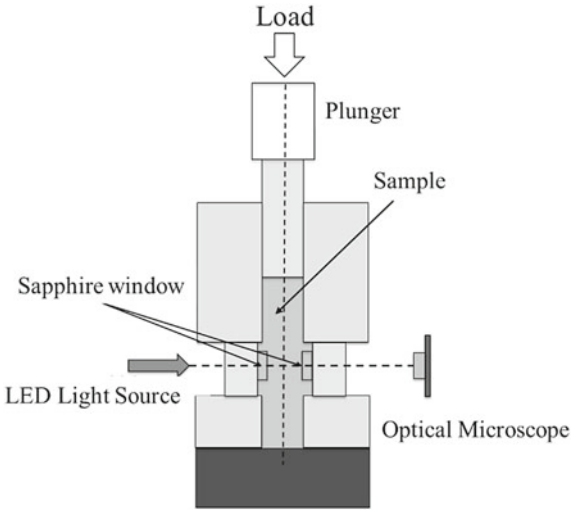


Fig. 1 Schematic drawing of our high-pressure vessel

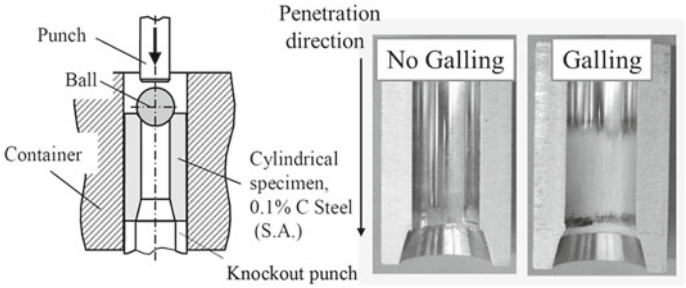


Fig. 2 Schematic drawing of our ball penetration test and result examples about galling

container, the ball was forced to penetrate the cylindrical workpiece. The tests were carried out using a mechanical press and severity is determined by cross-sectional area reduction and ball diameter, as shown in Table 1. A larger reduction in the

Table 1 Reduction by ball penetration test

R (%)	D_b (mm)	D_i (mm)
4	15.88	15
6	15.88	14.5
8	16.67	15
10	16.67	14.5
D_b: Ball diameter		
D_i: Inside diameter of workpiece		

Table 2 Formulation and properties of sample oils

	Oil A	Oil B	Oil C	Oil D
High Viscosity B/O	remain	remain	remain	remain
Low Viscosity B/O	–		–	–
Fatty Acid Type Additive	5.0	5.0	5.0	5.0
Sulfur Type EP Additive	25.4	25.4	25.4	25.4
Other Additives (Ester, etc.)	15.0	15.0	–	–
Phase Transition Material X	–	–	15.0	–
Phase Transition Material Y	–	–	–	15.0
Kinematic Viscosity (40°C), mm^2/s	130.1	61.02	64.05	60.84

workpiece cross-sectional area means a more severe condition. The galling prevention ability of the sample oils was evaluated from the maximum reduction (Max *R*) determined by the workpieces surface after the ball penetration test.

2.3 Lubricants Formulation

We formulated four sample oils for evaluation as described in Table 2 and divided them into the following four types. Oils A and B are the same additive formulation but have different viscosity and do not include phase transition materials. The viscosity of Oils C and D is identical to that of Oil B; however, Oils C and D contain two different types of phase transition materials; that are ester-type lubricant additives. Kinematic viscosity of these lubricants was measured by the procedures determined by ASTM D445.

3 Results and Discussion

3.1 Direct Observations of Phase Transition Behavior

We evaluated the phase transition behavior using phase transition materials diluted with paraffinic base oil. As shown in Fig. 3a, the samples condition before testing was at a liquid state. Figure 3b–d displays the optical photomicrographs of phase transition behaviors of each of the phase transition materials under several pressure conditions. Here, phase transition pressure is determined by measurement pressure when the phase transition behavior occurs on the optical photomicrographs.

It is clear in Fig. 3 that the phase transition behavior from liquid to solid occurred under high-pressure conditions. All of these materials formed needle-like crystals and their shape was different based on the material type and dilution rate.

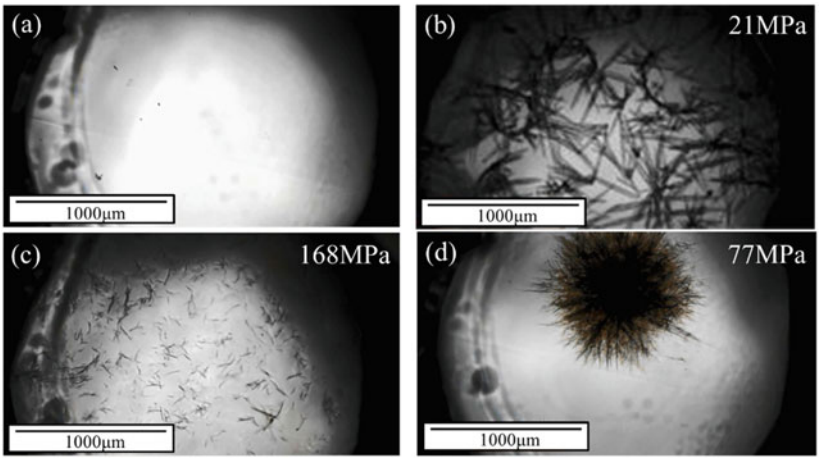


Fig. 3 Optical photomicrographs under optional pressure conditions of **a** Before Testing (No pressure), **b** Phase transition material X 100%, **c** Phase transition material X 20% (Diluted with paraffinic base oil), **d** Phase transition material Y 20% (Diluted with paraffinic base oil). (Color figure online)

Hereafter, we focus on the phase transition materials dilution rate effects based on phase transition pressure. Figure 4 shows the phase transition pressure of phase transition materials as a function of their paraffinic base oil dosage. Here, Phase transition material Y precipitated at just over 40 wt%; indicating the phase transition pressure decreases with an increase of phase transition material dosage. In addition, phase transition pressure of Phase transition material Y is lower than that of Phase

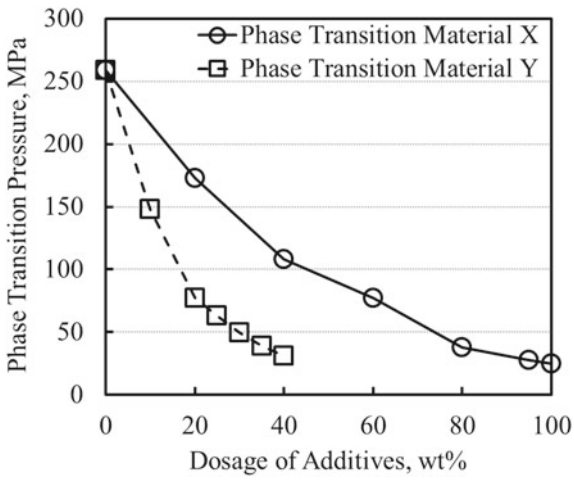


Fig. 4 Effects of dilution rate of phase transition materials on phase transition pressure. (Diluted with paraffinic oil)

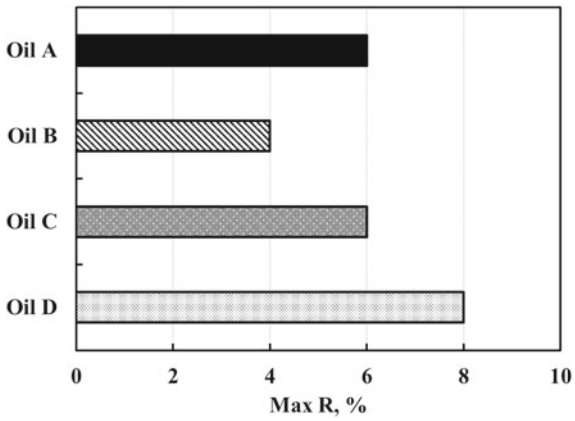


Fig. 5 Lubrication properties of sample oils in ball penetration test

transition material X. These results mean that Phase transition material Y is prone to phase transition from liquid to solid under lower pressure conditions.

3.2 Lubrication Properties of Phase Transition Materials for Cold Forging Processes

Figure 5 shows the ball penetration test results using each sample oil. Comparing Oil A to Oil B, Oil A has better lubricity. It is speculated that the difference between Oils A and B is attributed to its viscosity; because high viscosity lubricant makes a thicker oil film between workpieces and prevents workpiece galling more effectively than lower viscosity oil.

On the other hand, Oils C and D show better lubrication properties compared to Oils A and B even though these lubricants had low viscosity. We suggest that these lubricity improvements are supported by the lubricant phase transition behavior as discussed in Sect. 3.1. In summary, the phase transition pressure of Phase transition material Y is lower than Phase transition material X, and the lubricity of Oil D is better than Oil C.

As shown in Fig. 6, general oil-type lubricant causes oil film shortage between workpieces, but lubricant with applied phase transition materials causes phase transition from liquid to solid under high-pressure conditions and creates a solid film between them. For these reasons, phase transition materials improve lubricity effectiveness for oil-type lubricants.

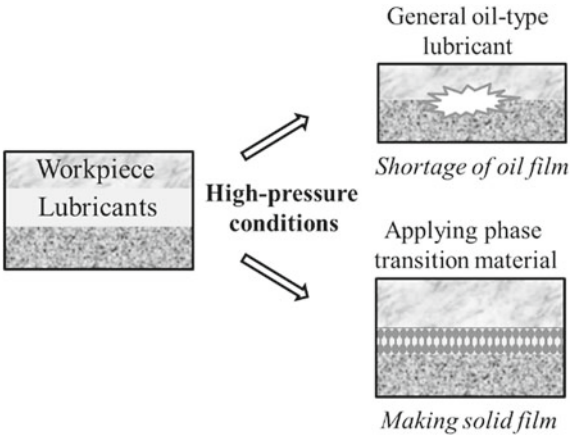


Fig. 6 Schematic drawing of lubrication image by phase transition materials

4 Conclusions

In this study, we investigated the phase transition behavior of lubricants and their possibility for application to cold forging processes. We derived the following findings from this study:

(1) We succeeded in direct observation of lubricant phase transition behavior from liquid to solid under high-pressure conditions.
(2) Oil-type lubricants that include phase transition materials showed improved lubricity for cold forging processes even at low viscosity.
(3) The lubrication properties of phase transition materials for oil-type lubricants depended on their phase transition pressure and a lower pressure at transition is better.

These results led us to deduce that phase transition behaviors under high-pressure conditions enhance lubricity for cold forging processes. In conclusion, we succeeded in development of new oil-type lubricants using phase transition materials.

References

1. Schey JA (1975) Metal deformation process/friction and lubrication. Marcel Dekker, New York, p 664
2. Kawai N, Dohda K, Akao S (1986) A consideration of correlation in friction tests for metal forming processes. Trans JSME C 52:2716
3. Komatsuzaki S, Nakano F, Uematsu T, Narahara T (1985) Antiweld properties of metal-forming lubricants using extreme-pressure agents. Lub. Eng 41:98
4. Kaiser H (1972) Investigation into the possibilities of testing lubricants for cold and warm extraction of steel. In: Proceedings of the 13th International MTDR Conference, 555p
5. James D (1961) Phosphate coating and lubricating steel for cold extraction. Sheet Met Ind 28:171

6. Bay N (1994) The state of the art in cold forging lubrication. J Mater Process Technol 46(1–2):19–40
7. Bay N, Azushima A, Groche P, Ishibashi I, Merklein M, Morishita M, Nakamura T, Schmid S, Yoshida M (2010) CIRP Ann 59–2:760–780
8. Ohmori T, Kitamura K, Kawamura M, Danno A (1990) A new cold forging oil and its galling prevention property. Adv Technol Plast 1:41–46
9. Ohmori T, Kitamura K, Danno A, Kawamura M (1992) Evaluation of galling prevention properties of cold-forging oils by ball penetration test. Wear 155:183–192
10. Ohno N (2007) High-pressure behavior of toroideal CVT fluid for automobile. Tribol Int 40:233–238

Analysis of Work Hardening and Tribological Changes After a Gap Controlled Drawbead Passage



Harald Schmid and Marion Merklein

Abstract In deep drawing processes, drawbeads are frequently used to control the material flow while forming. It is well known that material parameters are changed significantly after a drawbead passage. Also, there are many references that the tribological system after a drawbead is changed and that this has influences on the ongoing forming process. In this study, the connection between work hardening and the tribological system after a drawbead is analyzed with respect to the initial state. Therefore, sheets are drawn through a gap controlled drawbead passage while parameters like the gap between blank holder and die or the materials are varied. Afterwards, hardness measurements will be carried out as well as 3D surface measurements to correlate them. For these investigations, three different sheet metals are used: a conventional deep drawing steel, an advanced high strength steel AHSS, and an aluminum alloy, as they represent the variety of industrial used sheet metal.

Keywords Deep drawing · Drawbead · Work hardening · Surface modification · Friction

1 Introduction

Functional integration of modern deep drawing parts, for example, in the automotive industry, leads to complex design in modern forming processes [1]. As consequence, forming operations of sheet metal face demanding geometries. Failure and defects are possible as well as unwanted thinning. Therefore, material flow control in a deep drawing process is important. In literature [2], different types of material flow control are described: Firstly, the adjustment of the blank holder force to control the flow

H. Schmid (✉) · M. Merklein
Friedrich-Alexander-Universität Erlangen-Nürnberg, Institute of Manufacturing Technology (LFT), Egerlandstraße 13, 91058 Erlangen, Germany
e-mail: harald.schmid@fau.de

M. Merklein
e-mail: marion.merklein@fau.de

© The Minerals, Metals & Materials Society 2021

G. Daehn et al. (eds.), *Forming the Future*, The Minerals, Metals & Materials Series,
https://doi.org/10.1007/978-3-030-75381-8_128

in the flange area. In addition, the sheet metal layout can be changed and double-checked in simulations. Also, a change of the lubrication system, most of the times by changing the oil type or the oil amount is possible. For higher retention forces, drawbeads are used usually. Drawbeads do not only affect the material flow, but also have impact on mechanical properties [3] and tribological characteristics [4]. On the mechanical sector, work hardening and the significance of the Bauschinger effect was investigated and proven before [5]. Also the failure behavior is changed, according to Ke et al. [6], what was examined in tensile tests with material preloaded in a drawbead. This was also investigated by the authors in [7], and it was demonstrated that important material parameters are changed significantly. Next to that, there are also indications for tribological changes. For example, Staeves [8] showed an effect by drawbeads on the topography and Green [9] demonstrates that every contact of the drawbead has influences on the material itself. Trzepiecinski and Lemu [10] are analyzing a 5xxx-series of Aluminum and parameters like the rolling direction (R.D.) or the lubrication. Trzepieciński et al. [11] show various topographies of material in the initial state and after a drawbead passage and also differences compared to the bounder area. In addition, significant differences in the smoothening can be seen by the preloading direction. Azushima et al. [12] analyze the behavior of aluminum in bending tests and investigate a combination of roughening and smoothing effects. [13], a roughening effect on the outside of free bending is observed. According to the authors, smoothing takes place especially under high loads, and the differences on the surface of both sides of the sheet are also described. In [14], a change of friction coefficients after a drawbead is proven. By the authors, it was shown in [15] that an effect of the drawbead is evident for S_a and V_{cl} and it needs to be distinguished between the in- and outside of the sheet metal after a drawbead passage. The abrasive behavior of aluminum and the oil distribution after the drawbead is discussed. It is determined that steel materials are smoothened significantly while aluminum is roughened on the outside. Also, the coefficient of friction is influenced by pre-stretching in the forming area. To summarize this, a change of the mechanical and the tribological system is stated in many scientific publications. Until now, there is no cause-dependent correlation and therefore no physical explanations of these effects. Therefore, strip drawing tests with drawbead geometry are analyzed on the mechanical and tribological side. As a result, retention forces are evaluated as well as the surface topography on the in- and outside as a characteristic value for the tribological behavior. Variation is done for the tool distance of the drawbead and the material itself. Hardness measurements are performed for one tool distance variation. Analysis and discussion is done to find or determine if there is any direct connection between the parameters and the effect variables that can influence the tribological behavior.

2 Materials and Experimental Setup

In this chapter, the used materials and the experimental setup as well as the applied methodology are named. One material investigated is the aluminum alloy EN AW AA6014-T4 according to EN 573-1:2005-02, which was aged to a stable condition for six months. These sheets are mostly used in body shell or structural components as a lightweight material because of the low density and high strength compared to other materials. Also a deep drawing steel CR 3 GI 50/50-U [16] with 50 g/m^2 of hot-dip zinc coating is analyzed and will be called DC04. In addition, the material AHSS CR 440Y780T-DP GI40/40 [16] as a representative for a high strength steel is analyzed and will be called DP800. All sheet metals are delivered in the initial thickness $t_0 = 1.0$ mm. In Table 1, the material parameters derived, from uniaxial tensile tests A_{50} and from results of confocal microscopy, are presented.

As expected, DP800 has the highest yield strength YS and tensile strength TS. In comparison, the uniform elongation ε_u of DP800 is smaller compared to AA6014 and DC04. The confocal microscopy was used to describe the surface topography of the applied materials. Therefore, similar to the methodology in [15], the parameter S_a of the analyzed area as the mean arithmetic height is chosen to quantify the surface globally. S_a as the arithmetic mean height is able to describe the overall roughness and is, for example, also applied in commercial tribological software like TriboForm [17]. It can be seen that the surface of aluminum before forming is smoother compared to the steel. With these initial values, different behavior in mechanical and tribological changes can be expected. The drawbead geometry and the tool are shown in Fig. 1.

The nominal thickness of the material is $t_0 = 1.0$ mm; in reality, the materials AA6014 and DC04 are slightly thicker (~1.02 mm) while DP800 is a little bit thinner (0.96 mm). As mentioned before, strip drawing tests with drawbead geometry and a constant tool distance d between die and blank holder are used in the setup. The drawbead chosen has a height of h = 5.0 mm. The tool distance d is varied between 1.05, 1.10 and 1.15 mm as these are common values. The gap is defined by an adaptive system with two rails to fulfill an exact distance when closing with forces up to 100 kN. The gap to be set is double-checked with gauge-blocks and repeatable adjusted with a tolerance of +0.01 mm. All drawbead tests are performed with a drawing velocity of v = 50 mm/s and a lubrication of 2.0 g/m^2 KTL N 16, the oil amount was controlled with an optical system INFRALYTIC NG 2 (Infralytic GmbH), that was

Table 1 Material and topography parameters for AA6014, DC04 and DP800 in initial thickness of $t_0 = 1.0$ mm from uniaxial tensile tests A_{50} and confocal microscopy by Nanofocus µsurf

	Tensile strength TS [MPa]	Uniform elongation ε_u [%]	Mean arithmetical height S_a [µm]
AA6014	249.6 ± 1.7	20.0 ± 0.2	0.72 ± 0.01
DC04	303.7 ± 0.3	25.7 ± 0.6	1.31 ± 0.03
DP800	808.2 ± 3.4	12.9 ± 0.3	1.28 ± 0.02

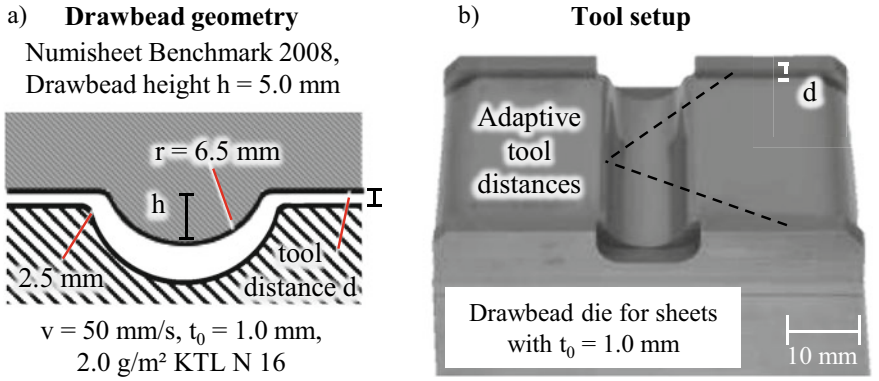


Fig. 1 **a** Details of drawbead geometry and **b** drawbead die with applied tool distancing. (Color figure online)

calibrated before. For every variation, n = 5 repetitions are drawn through the drawbead. Before and after the drawbead preloading, Brinell hardness measurements are performed. In pretesting, it was found that Vickers measurements are not suitable as the imprint was not evaluable after preloading due to the springback and deformation of the strips. So, Brinell hardness with circular imprints is determined by using the so-called Testor (Instron-Wolpert GmbH) with a loading of HBW 2.5/62.5 according to DIN EN ISO 6506-1:2014 with a ball diameter of 2.5 mm and a measuring force of 62.5 kP corresponding to 612.9 N. This evaluation is used to determine the surface hardness and was found to work suitable on the in- and outside and differentiate the hardening. The hardness is measured on every specimen on the in- and outside. Due to the deformed specimen after a drawbead, the sheet metal was clamped. In Fig. 2, the Brinell hardness measurements and the 3D-surface measurement by using Nanofocus µsurf are shown.

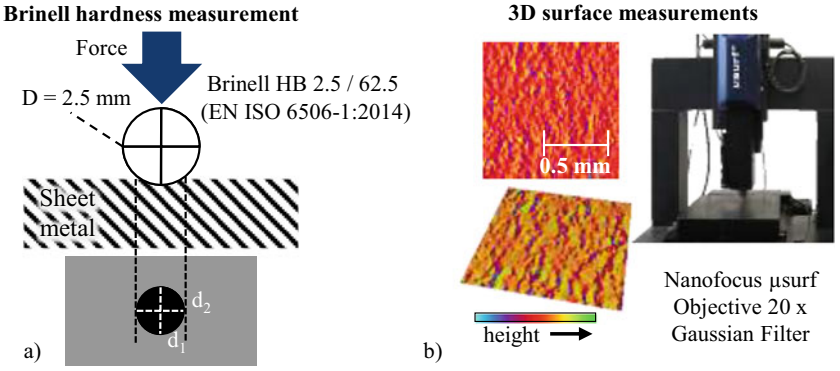


Fig. 2 **a** Process of hardness measurements Brinell HBW2.5/62.5 and **b** process for confocal microcopy of sheet metal after a drawbead preloading. (Color figure online)

For the confocal measurements, an objective with 20× magnification and a measuring size larger than 2 × 2 mm^2 was used and a Gaussian filter is applied. Every specimen was measured on the in- and outside after a drawbead passage for three times: left side, middle, right side. This is to guarantee repeatable values and to prevent any deviations between right and left sides. This means, every single specimen was measured by confocal microscopy six times, one variation is measured 30 times in total. In the following chapter, the results of the different measurements are presented.

3 Results of Drawbead Preloading

In this chapter, the results of the mentioned experimental setups are shown: the specific retention forces for different drawbead and material variations, confocal microscopy results and the corresponding Brinell hardness measurements.

3.1 Strip Drawing Tests and Retention Forces

In Fig. 3, the specific retention force, defined as the retention force related to the strip width, is shown as subject to the material and the applied tool distance d. The standard deviations are varying about maximum of 3.5% around the average and are therefore reasonable. A first observation is that AA6014 has specific retention forces up to 100 N/mm, DC04 up top 150 N/mm and DP800 up to nearly 300 N/mm. This is also due to the varying material strength as can be seen in Table 1. It is also obvious that the specific retention force is maximum for a tool distance of 1.05 mm. The rise of the retention force is between 5 and 7.5% for a step of 0.05 mm in the tool distance. The highest changes can be seen for AA6014, as also having the lowest

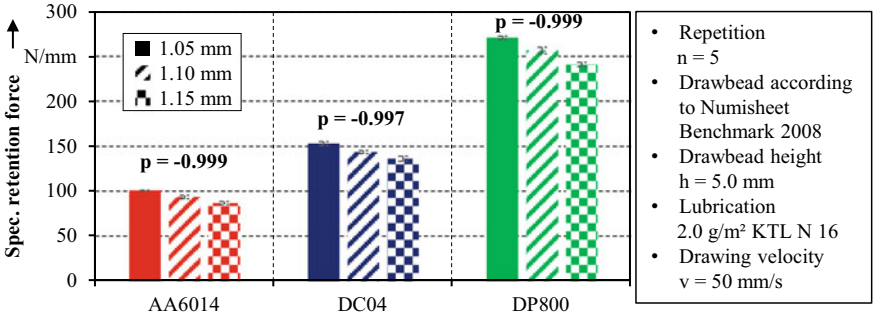


Fig. 3 Specific retention forces for AA6014, DC04 and DP800 when varying the tool distance d between 1.05, 1.10 and 1.15 mm. (Color figure online)

yield strength YS. When correlating the tool distances with the specific retention forces, Pearson's correlation coefficient can be evaluated to $p_{AA,DP} = -0.999$ for AA6014 and DP800 and $p_{DC} = -0.997$ for DC04. This means a nearly perfect negative linear relationship between the tool distance and the specific retention force. This relationship is expected to be valid in a defined range of d, as the geometrical conditions might change otherwise.

With the tool, various tool distances d can be realized by changing the rails. The tool distance d was set to match all materials. After the investigation of the retention forces as a specific value for the drawbead, the surface topography will now be considered.

3.2 *Confocal Microscopy After a Drawbead Passage*

Figure 4 shows the results for the arithmetic mean height S_a by confocal microscopy that was explained in chapter "A Vision of Numerically Controlled, Autonomous Manufacturing and Metal Forming". All of the different variations of Fig. 4 were tested on the in- and outside as well as the initial state.

Each bar represents the average of five specimen with each three measurements on the in- and outside. First of all, the initial arithmetic mean height S_a is lowest for AA6014 with 0.8 µm followed by DP800 with 1.2 µm and DC04 with about 1.3 µm. This could be also a result of the zinc coating on the steel materials. For AA6014, changes can be seen after a drawbead passage compared to the initial state, which was already stated in [14, 15]. On the outside, a roughening is apparent after the drawbead, which becomes more noticeable with higher tool distancing to a rise of nearly 20%

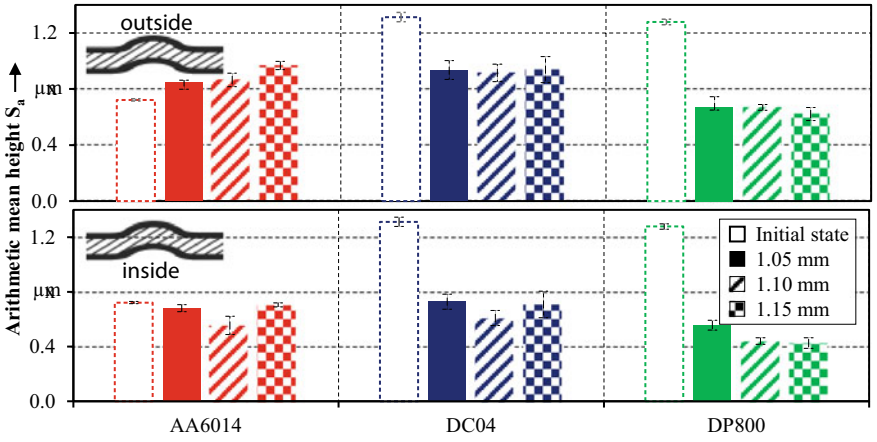


Fig. 4 Arithmetic mean height S_a for the initial state and after a drawbead passage for different variations of the tool distance d, the materials and the in- and outside for n = 5 specimen for each variation. (Color figure online)

at 1.15 mm. On the inside of AA6014, a smoothening is visible and S_a is reduced about 30%. Interestingly, smoothing is not maximum for the smallest tool distance. This could indicate different stress states according to the changed geometry. For DC04, the changes for S_a are even higher. The smoothing on the outside leads to a value of $S_a = 0.9\ \mu m$ and results in a reduction of 30% which is constant in between the standard deviation. The arithmetic mean height on the inside of DC04 is reduced between 44 and 53%. Also here, the reduction is maximum for the tool distance of d = 1.10 mm what was also seen for the inside of DC04. The material DP800 shows the highest reduction of S_a in general. The inside value is reduced up to 40%, the outside even to 64%. For the smoothing behavior, higher S_a values for smaller tool distances are the outcome. Regarding retention forces, expectation would have been also the other way round. In general it can be stated, that surface parameters after a drawbead passage are not clearly predictable by the geometrical value tool distance but a smoothing is expected for steel materials.

3.3 Hardness Measurements After Drawbead Preloading

For a better understanding of the work hardening effects on the sheet metal surface, Brinell hardness measurements were done on the in- and outside. Brinell's hardness was chosen to measure directly on the surface. This is also due to spring back effects when evaluating the imprint optically. The specimen were clamped on a metal plate. To measure the inside of the specimen, a formed tool with a smaller radius than the strip was used to ensure the planar measurement without any suspensions. In Fig. 5, the results for the Brinell hardness measurements are shown.

First of all, the initial hardness of the three materials varies: the hardness of AA6014 values is located around 60 HB in the beginning while DC04 locates around

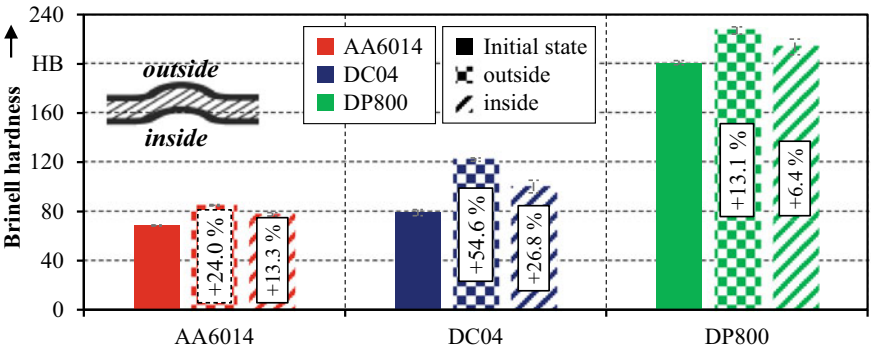


Fig. 5 Brinell hardness measurements for AA6014, DC04 and DP800 before and after a drawbead passage at d = 1.10 mm and grouped by in- and outside with n = 3 specimen measured. (Color figure online)

80 HB, DP800 has more than the doubled initial hardness with nearly 200 HB before the forming process. After the geometrically identical drawbead passage, a rise of the hardness between 6% up to 55% can be observed. In addition, on the outside the hardness is higher, what was also investigated for a another drawbead geometry by microhardness measurements in [3]. For AA6014 a rise of 24.0% on the outside and of 13.3% on the inside are visible. The final hardness locates around 80 HB. The initial hardness of DC04 is also located at 80 HB, the outside is hardened to 120 HB and the inside to 100 HB. For the deep drawing material DC04, the work hardening effects are the highest compared to the others. DP800 rises its hardness between 6 and 13%. In the following chapter, results will be correlated and discussed by giving possible explanations.

4 Discussion

First of all, a correlation between the specific retention force and the surface parameter S_a as a characteristic value for the tribological changes is discussed. Therefore, in Fig. 6, the forces and the surface parameters on the in- and outside after a drawbead preloading are shown normalized.

The retention forces were normalized to the value of the variation d = 1.15 mm, and the surface values were normalized to its initial state. The retention forces follow a linear correlation with the tool distance d, what could be possible due to a linear rise of friction and bending forces in this range of d what was also shown in Fig. 3. On the other hand, the surface parameter S_a does not behave the same way. Depending on the material, the smoothing on the inside is most significant for d = 1.10 mm and the inside is smoothened higher compared to the outside. DP800 has the highest retention forces but also has the lowest values for S_a compared to its initial state. Considering the materials only, a negative correlation between the smoothing and the forces can be drawn. Higher retention forces for each material are followed by more

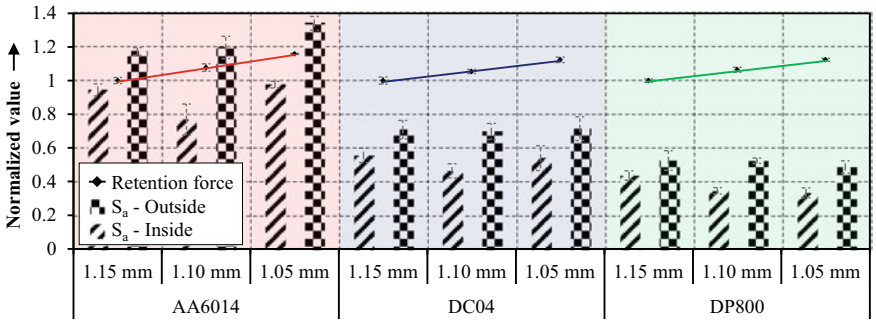


Fig. 6 Retention forces correlated and normalized with the arithmetic mean height S_a on the inside and outside. (Color figure online)

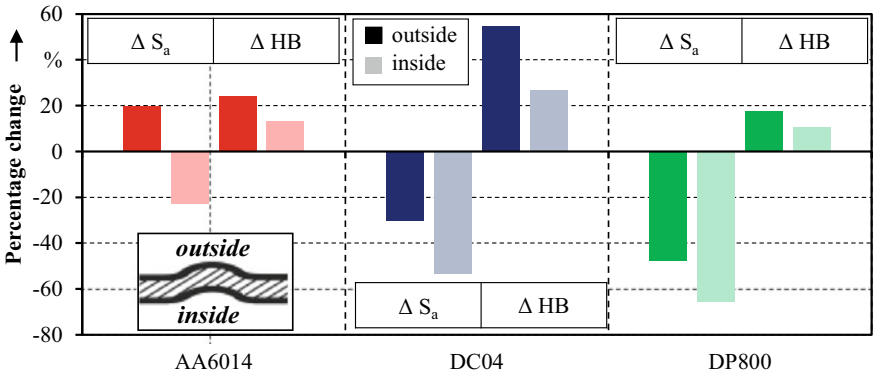


Fig. 7 Percentage change of the arithmetic mean height S_a and the Brinell hardness HB for the tool distance variation of d = 1.10 mm and the materials AA6014, D0C4 and DP800. (Color figure online)

significant smoothing, what could also be said in connection to the yield strength YS. After considering the surface and the retention forces for all the variations, a connection between the Brinell hardness results for the tool distance d = 1.10 mm and the surface parameter S_a will be drawn. Therefore, the percentage change of both values compared to the initial material value is shown in Fig. 7.

For all materials, except for the outside of AA6014, a smoothing simultaneously with a hardness increase is certifiable. The smoothing is also higher on the inside while the rise of hardness is higher on the outside. For aluminum, a statement is hard to make. The outside of AA6014 is the only area to roughen in a drawbead passage while the hardness is increased. In general, for AA6014, the arithmetic mean height S_a and the hardness are changed with a maximum of about 20–30%. The roughening effect for AA6014 compared to the steel seems to be interesting for further investigations. For DC04, the percentage change is located between 50 and 60% considering maximum values. In opposite, the material DP800 has only a rise lower than 20% looking at the hardness but a reduction of S_a of over 60% for the inside. That means, the material with the smallest rise in hardness has the highest reduction in its surface parameter S_a. Correlating these results to DC04, the changes seem to be more balanced there. A geometrical explanation of the correlation of hardness and smoothing behavior can not be drawn directly. Here, different approaches for an explanation are possible: The contact on the inside in a drawbead passage seems to provoke a higher smoothing effect for every material. Otherwise, on the outside the hardness is increased higher compared to the inside after a drawbead passage. An idea could be that the contact conditions are playing a key role for the behavior. A longer contact area with lower values on the inside could lead to higher smoothing effects while higher contact pressure located in a smaller area follow in a more significant increase of hardness. This would also be dependent on the geometrical circumstances of the alternating bending the location of contact areas. Also, the used aluminum and steel materials having different coating and therefore most possible

different friction and smoothing behavior. Next to the contact pressure, the effect of topography changes due to tension, compression, or bending effects needs to be considered. According to Wechsuwanmanee et al. [18], the surface roughness plays an important role on the bending behavior and a difference to an ideal smooth surface is existent. For example, Muhamad et al. [13] show the increase of roughness during a wrap-bending process on the outside for a extruded aluminum and analyze material related reasons. For an integrated understanding of the topography changes in a drawbead, the combination of alternating bending processes with overlying tension needs to be investigated in detail step by step, also differentiating between the in- and outside. As an example, in investigations from Jonasson et al. [19] a direct correlation between the friction coefficient and common surface parameters was not found and can also not expected. As only the tool distance d is varied in a range of $\Delta d = 0.1$ mm, the variation of surface parameters in between one material is expected to be most likely a reason top different contact pressure effects. Also the yield strength YS and the hardening coefficient n could also influence the hardness behavior, which was also described in [7]. While YS and the work hardening coefficient n are quite similar for AA6014 and DC04, these two values are differing significantly for DP800. The influence of an oil reduction after a drawbead passage was also varying [15]. It seems that the oil reduction is high on the outside, where also the highest hardness increase takes place. This could also indicate a connection between the applied contact pressure, the oil reduction, and the final hardness. Unfortunately, this effect is very difficult to investigate in an experimental setup in a drawbead geometry although experimental setups like Filzek's [20] with respect to the Hertzian stress seem as a good start for further investigations.

5 Summary and Outlook

In this publication, the specific retention force, the surface parameter S_a as a value representing the tribological condition of sheet metal and the Brinell hardness were investigated before and after a drawbead passage and correlated. Therefore, the Numisheet Benchmark 2008 drawbead geometry was used with a drawbead height of $h = 5.0$ mm and tool distancing d was varied in three steps from 1.05 to 1.15 mm for the materials AA6014, DC04, and DP800. The most distinctive findings are

- There is a clear linear correlation evidenced by Pearson with $p = -0.99$ between the specific retention forces and the tool distance d for all investigated materials. This is expected to be valid in a specific range only.
- A correlation between the tool distance d and the surface parameter S_a could not be drawn clearly.
- Smoothing is visible for all materials and preloaded surfaces except for the outside of AA6014. This could be explained by the aluminum oxide layer and its special

reaction to alternating bending with overlying tensions. Next to the contact pressure variation, the influence of alternating bending and tensions on the surface roughness needs to be mentioned.

- Smoothing effects are more significant on the inside than on the outside after a drawbead passage. The reduction of the arithmetic mean height are up to - 60% for DP800.
- Hardness is increased on the in- but more significantly on the outside of sheet metal after a drawbead. While the outside hardness increased, the smoothing effect is more significant on the inside. An interesting observation is that low hardness changes are corresponding with high reductions of S_a for DP800. This could be due to higher contact pressure in combination with a higher yield strength of DP800.
- A significant influence on the tribological behavior is expected for every material deriving from the changes in hardness and surface values. Regarding the value S_a, the highest change is expected for DP800. Also considering the surface hardness, a tribological transition is probable for the mild steel DC04, too. After the results for the same blank holder force in [15], an integrated approach of the mechanical and tribological behavior taking in account all parameters is indicated.

In general, a geometric correlation between the hardness and the mean arithmetic height by varying the tool distance d could not be proved, a direct relationship could not be drawn. The influence of the same tool distancing on the materials was shown. As an outlook, the findings need to be connected in detail using other methodologies in further investigations. The connection between surface changes by contact pressure and forming effects by tension, compression and bending need to be separated in detailed investigations and step by step. This would also help to improve simulations and also to identify the contact pressure height and its distribution. On the experimental side, an idea would be to preload materials with a specific tool radius only and calculate the Hertzian stresses and the final surface parameters. The following hardness and surface changes could be combined with the results above. Comparing the materials, higher specific retention forces seem to lead to higher surface changes, what might be due to the contact pressure. The interaction between the mechanical and tribological system represented by the surface values seems to interact in a complex way that needs to be investigated furthermore.

Acknowledgments For the support in the research project EFB 05/217 (AiF 20015 N) “Analysis of the influence of tribological properties on the deep drawing process of sheet metals after passing a drawbead”, the authors would like to thank the European Research Association for Sheet Metal Working e.V. (EFB) as well as the German Federation of Industrial Research Associations “Otto von Guericke” e.V. (AiF).

References

1. Barthau M, Liewald M, Christian H (2017) Improved process robustness by using closed loop control in deep drawing applications. Journal of physics: conference series, vol 896, p 12040
2. Doege E, Behrens BA (2010) Handbuch umformtechnik: grundlagen, technologien, maschinen, vdi-buch. Springer-Verlag
3. Schmid H, Suttner S, Merklein M (2017) An incremental analysis of a deep drawing steel's material behaviour undergoing the predeformation using drawbeads. In: Journal of physics: conference series, vol 896, no 1, p 012010
4. Trzepiecinski T, Fejkiel R, Lemu HG (2017) Experimental investigation of frictional resistances in the drawbead region of the sheet metal forming processes. In: IOP conference series: materials science and engineering, vol 269, p 12042
5. Larsson M (2009) Computational characterization of drawbeads. J Mater Process Technol 209 (1):376–386
6. Ke J, Liu Y, Zhu H et al (2018) Formability of sheet metal flowing through drawbead – an experimental investigation. J Mater Process Technol 254:283–293
7. Schmid H, Merklein M (2019) Study of the mechanical properties of sheet metals drawn through drawbeads. Manuf Rev 6:14
8. Staeves J (1998) Beurteilung der Topografie von Blechen im Hinblick auf die Reibung bei der Umformung. Darmstadt, TU, Dissertation
9. Green L (2003) Effect of bending over a radius on the North American forming limit curve. In: IDDRG 2003, pp 69–78
10. Trzepiecinski T, Lemu HG (2014) Frictional conditions of AA5251 aluminium alloy sheets using drawbead simulator tests and numerical methods
11. Trzepiecinski T, Kubit A, Slota J et al (2019) An experimental study of the frictional properties of steel sheets using the drawbead simulator test. Materials (Basel, Switzerland) 12(24)
12. Azushima A, Sakuramoto M (2006) Effects of plastic strain on surface roughness and coefficient of friction in tension-bending test. CIRP Ann Manuf Technol 55(1):303–306
13. Muhammad W, Ali U, Brahme AP et al (2019) Experimental analyses and numerical modeling of texture evolution and the development of surface roughness during bending of an extruded aluminum alloy using a multiscale modeling framework. Int J Plast 117:93–121
14. Leocata S, Senner T, Reith H et al (2020) Experimental analysis and modeling of friction in sheet metal forming considering the influence of drawbeads. Int J Adv Manuf Technol 286–287(4):66
15. Schmid H, Merklein M (2020) Influence of a drawbead passage in deep drawing processes on surface values and the tribological system. In: IOP conference series: materials science and engineering 967:12008
16. VDA 239-100: Flacherzeugnisse aus Stahl zur Kaltumformung. Ausgabe May 2016
17. Hol J, Wiebenga JH, Carleer B (2017) Friction and lubrication modelling in sheet metal forming–Influence of lubrication amount, tool roughness and sheet coating on product quality. In: Journal of physics: conference series, vol 896, 12026 p
18. Wechsuwanmanee P, Lian J, Shen F et al (2020) Influence of surface roughness on cold formability in bending processes: a multiscale modelling approach with the hybrid damage mechanics model. Int J Mater Form 103(6):755
19. Jonasson M, Wihlborg A, Gunnarsson L (1998) Analysis of surface topography changes in steel sheet strips during bending under tension friction test. Int J Mach Tools Manuf 38(5–6):459–467
20. Filzek J (2004) Kombinierte Prüfmethode für das Reib-, Verschleiß- und Abriebverhalten beim Tief-und Streckziehen. Darmstadt, Techno Univ Diss., Zugl, Berichte aus Produktion und Umformtechnik Heft 62. Shaker, Aachen

Investigations on Dynamic Characteristics of a Mechanical Press Considering Both Translational Clearance Joint and Lubrication Effect

Xuze Wu and Yu Sun

Abstract The existence of clearance in the joints of multibody systems can significantly influence the system behaviors. The introduction of joint clearance in the dynamic analysis of the mechanical press can generally lead to a higher analysis precision. In this paper, a lubricant revolute joint and a translational clearance joint are conducted in the dynamic model of a mechanical press, to identify their combined influence on the system dynamics. The Pinkus and Sternlicht approach is employed to obtain the hydrodynamic forces, while the IMPACT function is used to evaluate the contact forces. Simulations are carried out in the cases where the translational joint is assumed to be ideal or with clearance. The results show that the lubricated revolute joint presents practically similar to an ideal one in the global responses while the existence of the translational joint will lead the slider trajectory into chaos. Moreover, the translational clearance joint seems to have little influence on the local dynamics of the lubricated joint, due to the limited amount of contacts resulted from a low input crank speed. This observation indicates that in the dynamic analysis of heavy-load mechanical presses with a low operation speed, the effects of these two joints can be analyzed separately.

Keywords Clearance joint · Lubrication · Mechanical press · ADAMS

Nomenclature

FN, FT (N)	Normal and tangential force vectors at the contact points
K (N/m)	Generalized contact stiffness
δ(m)	Penetration depth
$C(\delta)$ (Ns/m)	Instantaneous damping coefficient
c_t (m)	Normal clearance in the translational joint
E_k (Pa)	Elastic module of body k

X. Wu · Y. Sun (✉)
School of Mechanical Engineering, Nanjing University of Science and Technology, Nanjing 210094, China
e-mail: sunyu@njust.edu.cn

© The Minerals, Metals & Materials Society 2021

G. Daehn et al. (eds.), *Forming the Future*, The Minerals, Metals & Materials Series,
https://doi.org/10.1007/978-3-030-75381-8_129

υ_k	Poisson's ratio of body k
S_c (m^2)	Area of the contact region
l_a, l_b (m)	Length and width of the rectangular surface
v_0, v_1 (m/s)	Tolerances for the tangential velocity
$\mathbf{v}_T$ (m/s)	Tangential velocity vector
c_f	Friction coefficient
$c_{\max}$ (Ns/m)	Normal maximum damping coefficient
$d_{\max}$ (m)	Maximum normal boundary penetration
F_r, F_t (N)	Radial and tangential component of the hydrodynamic forces
F_r, F_t (N)	Components of the hydrodynamic forces projected onto the X- and Y-directions
μ (Pa)	Fluid viscosity
L_b (m)	Length of the bearing
ω(rad)	Relative angular velocity between the journal and bearing
c (m)	Radial clearance in the revolute joint
ε	Eccentric ratio
γ (rad)	Eccentric angle
e_x, e_y, e_l (m)	Eccentric length along the X-, Y-, and radial directions
$\dot{u}$	Time derivative of variable u

1 Introduction

The effects of clearance joint on the dynamics of multibody systems have received much attention over the decades. In the literature, the contact model and the lubrication model are widely applied to describe the clearance joint [1]. The nonlinear damping spring model, which was proposed by Lankarani [2] and comprehensively analyzed by Flores et al. [3], has been proved to be consistent with the experiments. In engineering applications, the clearance joint is extensively described by hydrodynamic forces, due to the existence of lubricating oil. Moreover, one of the key points in the present work focuses on the influence of multiple clearance joints. Erkaya et al. [4] analyzed the vibrations and noise in the slider-crank mechanism with both revolute and translational clearance joints. In the same mechanism, Ma et al. [5] conducted three revolute clearance joints by dry contact models and suggested that the interactions of the joints with clearance should be carefully studied. A slider-crank mechanism with one and two clearance joints was studied by Megahed and Haroun [6]. They pointed out that when the mechanism works in the horizontal plane, the rate of impacts at each clearance joint increase, compared with the vertical plane operation condition. The presented research shows that the existence of multiple clearances will tend to complicate the system responses.

The mechanical press, which could be regarded as a practical application of the slider-crank mechanism, has been analyzed in numerous studies, considering the effects of clearance. A high-speed press system with flexible bodies and revolute

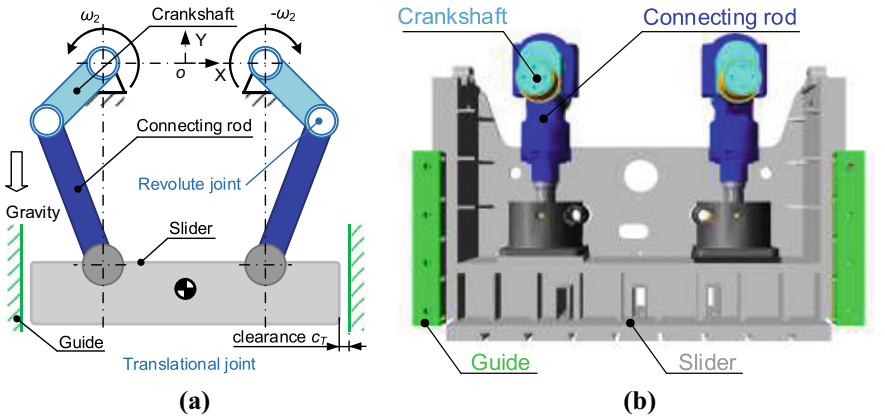


Fig. 1 Configuration of the mechanical press: **a** the kinematic sketch; **b** dynamic model of the press with clearance joints conducted in MSC.ADAMS package. (Color figure online)

joints was modeled in Zheng et al.'s work, where the lubrication forces and dry contact forces were considered in the model [7]. Chen et al. [8] proposed planar analysis models for a heavy-load press with a revolute clearance. Numerical and experimental methods are both employed to describe the effects of clearance on the system performance.

As far as the authors are concerned, there are few studies concerning the effect of translational clearance joint on the dynamics of the mechanical press. In addition, the combined influence of translational clearance joint and the lubricated revolute joint is virtually unknown in the literature. Thus, the presented work is aimed at the combined action and interaction of the two clearance joints. Figure 1a illustrates the configuration of the planar motion mechanism of the press, where the two symmetrical cranks possess the opposite constant rotational speed. The mechanism is regarded to be over-constraint when all the joints of the mechanism are perfect. The introduction of planar joint clearance will remove two degrees of freedom in every joint. However, we assume that the cranks rotate strictly synchronously and no external distribution is applied on the slider, thus the rotational degree of the slider is supposed to be constrained. Figure 1b depicts the dynamic model of the press conducted in MSC.ADAMS package. The model is first built in the software SolidWorks and then transferred to ADAMS for dynamic simulations. The mass centers of the parts are all located in the XOY plane. The revolute clearance joint between the crankshaft and connecting rod is conducted as a lubricated joint. The simulations are carried out in the cases with translational clearance joint or ideal translational joint. Additionally, motion trajectories and Poincaré portraits are employed to characterize the joint dynamics and global responses.

2 Dynamics of Joints with Clearance

2.1 Dry Contact Model for the Translational Clearance Joint

The existence of clearance in a planar translational joint will introduce two extra degrees of freedom to the slider and remove two kinematic constraints in the dynamic formulations. Hence, instead of kinematic constraints, the dynamic responses of the joint are governed by the developed contact-impact forces. In this paper, it is assumed that when the collision occurs, the colliding bodies penetrate with each other in a dry contact manner.

Considering the energy loss and the nonlinear nature of contact forces, the normal component of the generalized impact force can be represented by [7].

$$F_N = K\delta^{1.5} + C(\delta)\dot{\delta} \quad (\delta > 0) \tag{1}$$

The contact stiffness K is determined by the geometric shape of the contact region. When the inclination angle of the slider is rather small (minor than 0.1 degree), the influence of the slider's rotation on the system response might be negligible. Therefore, when the contact region is characterized by a rectangular surface with length l_a and width l_b, the area of contact region can be predetermined and the stiffness is obtained from [9],

$$K \approx \frac{\sqrt{S_c}}{(\sigma_i + \sigma_j)} \frac{1}{11.15(l_a/l_b + 15.72)^{-1} + 0.2854} \tag{2}$$

where and denote the material parameters of the colliding bodies i and j, respectively.

$$\sigma_k = \frac{1 - \upsilon_k^2}{E_k} \quad (k = i, j) \tag{3}$$

In Eq. (1), the instantaneous damping coefficient $C(\delta)$ is presented by a cubic step function of the penetration [7, 8],

$$\begin{aligned} C(\delta) =& STEP(\delta,\ 0,\ 0,\ d_{\max},\ c_{\max}) \\ =& \begin{cases} 0 & if\ \delta \le 0 \\ c_{\max}(\delta/d_{\max})^2(3 - 2\delta/d_{\max}) & if\ 0 < \delta \le d_{\max} \\ c_{\max} & if\ \delta \ge d_{\max} \end{cases} \end{aligned} \tag{4}$$

where $c_{\max}$ is the damping coefficient when δ reaches the maximum depth $d_{\max}$.

In the clearance joints, the friction force is likely to play a vital role in system responses. To avoid some integral difficulties caused by the sudden transformation of the direction in friction forces, the modified Coulomb method is adopted in this paper [10],

$$\mathrm{F}_T = -c_f c_d \|\mathrm{F}_N\| \mathrm{v}_T \big/ \|\mathrm{v}_T\| \tag{5}$$

where $\mathbf{F}_N$ is the normal contact force vector, $\mathbf{v}_\mathrm{T}$ represents the tangential velocity vector, and c_f is the friction coefficient. The dynamic correction coefficient c_d is obtained from,

$$c_d = \begin{cases} 0 & if \ \|v_T\| \le v_0 \\ \frac{\|v_T\| - v_0}{v_1 - v_0} & if \ v_0 \le \|v_T\| \le v_1 \\ 0 & if \ \|v_T\| \ge v_1 \end{cases} \tag{6}$$

where v_0 and v_1 represent the given tolerances for the tangential velocity.

Generally, the conduction of contact model is based on the kinematic analysis of the clearance joint. In the previous studies, Flores had proposed a comprehensive formulation to describe the kinematics of planar translational clearance joints [11]. Hence, the kinematics of the joints will not be presented here in detail. To embed the normal contact forces and friction forces estimated by Eq. (1) and Eq. (5), respectively, the IMPACT function is acted between the colliding bodies in the model established in MSC.ADAMS.

2.2 *Lubricated Model for the Revolute Joint*

This section briefly describes the hydrodynamic force model adopted in the revolute clearance joint, which connects the crank and connecting rod. The revolute joint with clearance is generally modeled by contact models or lubricated models. The engineering application of the revolute joint in the mechanical press requires the lubricant to cool down the joint and reduce friction. When the space between the journal and bearing is filled with lubricant, hydrodynamic forces originated from both the wedge and squeeze actions will dominate the dynamic response of the joint. During the running of the mechanism, the dynamic load applied to the journal will vary in both magnitude and directions, which leads to the fluctuation of the film thickness.

Figure 2 shows a generalized smooth dynamically loaded journal-bearing. The hydrodynamic force components, which consist of the tangential component F_t and the radial force F_r along the direction of the eccentricity, are illustrated in the schematic representation. Margarida [12] analyzed the effect of three classical hydrodynamic force models in the system responses of the slider-crank mechanism. He emphasized that the film evolutions vary from the selections of the models. The Pinkus and Sternlicht approach for long journal-beading is employed here to obtain the generalized forces in the revolute joint, due to its regular and steady behaviors in the system response, i.e., this model features higher stability. The hydrodynamic forces are obtained from [13],

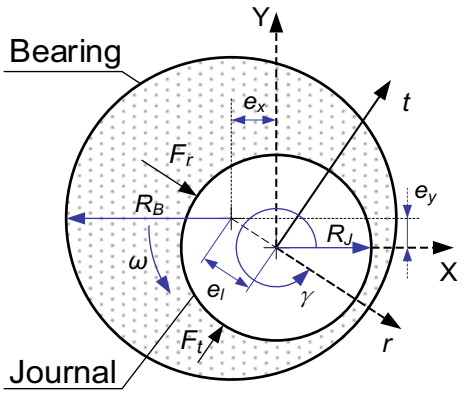


Fig. 2 Cross section of a smooth dynamically loaded journal-bearing. (Color figure online)

$$
\begin{aligned}
F_r &= -\frac{\mu L R_J^3}{c^2}\frac{6}{\left(2+\varepsilon^2\right)\left(1-\varepsilon^2\right)^{1.5}}\left[4k\varepsilon^2+\left(2+\varepsilon^2\right)\pi\left(sign(\dot{\varepsilon})+\frac{3}{2k+3}\right)\right]\\
F_t &= \frac{\mu L R_J^3}{c^2}\frac{6\pi\varepsilon(\omega-2\dot{\gamma})}{\left(2+\varepsilon^2\right)\left(1-\varepsilon^2\right)^{0.5}}\left(sign(\dot{\varepsilon})-\frac{3}{2k+3}\right)\\
\varepsilon &= e_l/c
\end{aligned}
\tag{7}
$$

where c presents the radial clearance between the journal and bearing. The parameter k and the sign function are, respectively, defined as

$$
k^2=\left(1-\varepsilon^2\right)\left[\left(\frac{\omega-2\dot{\gamma}}{2\dot{\varepsilon}}\right)^2+\frac{1}{\varepsilon^2}\right] \tag{8}
$$

$$
sign(\dot{\varepsilon})=\begin{cases}\dot{\varepsilon}/|\dot{\varepsilon}| & if\ \dot{\varepsilon}\neq 0\\ 0 & if\ \dot{\varepsilon}=0\end{cases} \tag{9}
$$

The time derivation of angle γ is calculated by

$$
\dot{\gamma}=\frac{d\left(\tan^{-1}\left(e_y/e_x\right)\right)}{dt}=\frac{e_x\dot{e}_y-\dot{e}_x e_y}{e_l^2} \tag{10}
$$

Finally, to employ the hydrodynamic forces obtained from Eq. (7) to the dynamic model of the mechanism, the radial and tangential force components should be projected onto the X- and Y-directions, and are given by

$$
\begin{bmatrix}F_x\\F_y\end{bmatrix}=\begin{bmatrix}\cos\gamma & -\sin\gamma\\ \sin\gamma & \cos\gamma\end{bmatrix}\begin{bmatrix}F_r\\F_t\end{bmatrix} \tag{11}
$$

The minimum film thickness, which can indicate the load-bearing capacity of oil film, is defined as

$$h_{\min} = c(1 - \varepsilon) \tag{12}$$

Within the application of hydrodynamic bearings in engineering, it is suggested that the safe minimum film thickness should be greater than 1.5×10^{-4} mm/mm of the bearing diameter to ensure good operation conditions [12].

3 Simulation and Discussions

The dynamic simulations of the mechanical press are carried out and analyzed in this section. Considering the influence of clearances and lubrication effect, the dynamic model with imperfect joints is constructed in MSC.ADAMS package, as presented in Fig. 1b. The simulation characteristics and properties of the components in the system are listed in Table 1. With the consideration to achieve higher simulation precision, the integration formulation (SI1) is chosen, which takes the constraint derivatives into account [14].

During the simulations, the translational joint is first assumed to be ideal, while the hydrodynamic forces are always applied in the revolute joint. Simulations are carried out with different crank speeds. The motion trajectories of the journal center with respect to the bearing are shown in Fig. 3a to c, where the geometrical limits defined by the clearance are plotted by dashed lines. And the results are obtained from the four full crank rotations after the steady states have been reached. It indicates that the shapes of the trajectories vary with the crank speed, and the journal basically approaches the bearing boundary as the speed increases. As the crank speeds up, the inertia forces of the bodies are intensified, which develops the greater dynamic loads on the revolute joint. Consequently, the lubricant film becomes thinner to achieve a greater load-bearing capacity. Meanwhile, we chose the time delay equal to the

Table 1 Simulation characteristics of the mechanical press

Nominal radius of journal R_J	0.12 m	Clearance size c_t	0.2 mm
Width of the bearing L_b	0.21 m	Friction coefficient c_f	0.02
Fluid viscosity μ	320 cP	Mass of crankshaft	447.55 kg
Clearance size c	0.1 mm	Mass of connecting rod	390.27 kg
Generalized stiffness K	3.66×10^{10} Nm	Mass of slider	5589.80 kg
Maximum damping coefficients $c_{\max}$	3.66×10^{8} Nm^{-1}	Length of crank	0.14 m
Elastic module of guide	103 GPa	Length of connecting rod	0.97 m
Elastic module of slider	207 GPa	Length of guide	1050 mm
Poisson's ratio	0.3	Width of guide	80 mm

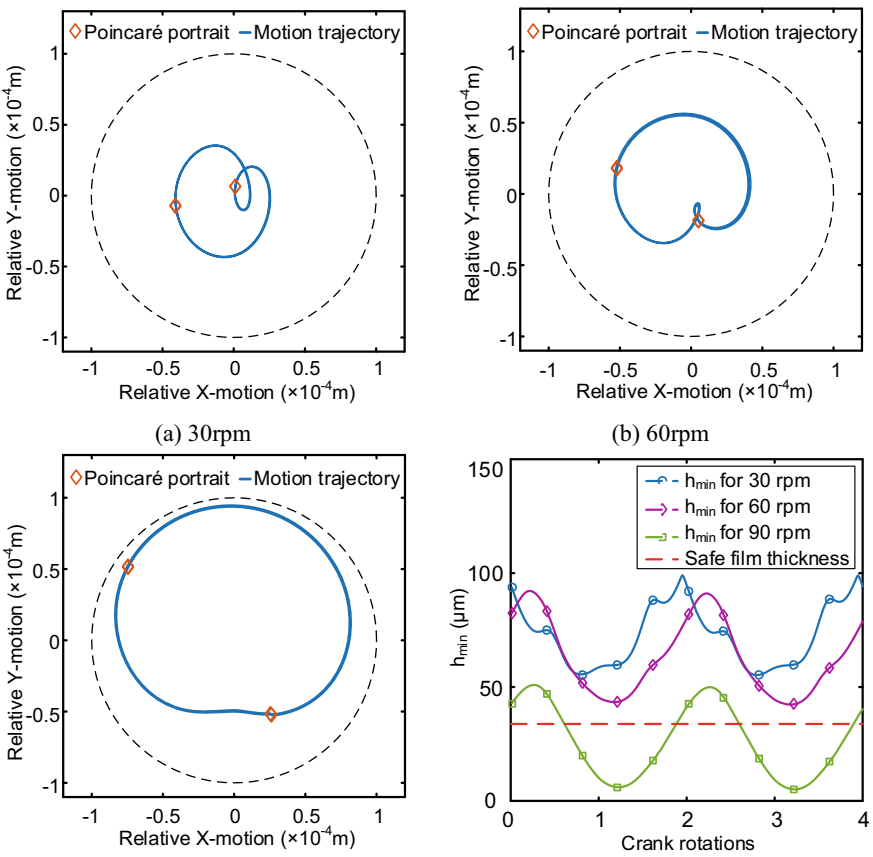


Fig. 3 Dynamic characteristics of the lubricated joint: **a**, **b**, and **c** motion trajectories and Poincaré portrait for different crank speeds; **d** minimum film thickness. (Color figure online)

period of crank speed to conduct the Poincaré portrait of the trajectory. It appears that the journal position varies twice the cycle times of the crank rotation. However, the hydrodynamic forces in the joint share the same period time with the crank. In the work proposed by Machado et al. [12] and Zheng et al. [7], where the lubricant joint between the slider and connecting rod was investigated, such an unusual phenomenon was not observed.

The minimum film thickness for different crank speeds is displayed in Fig. 3d. It is demonstrated that the increase in speed can cause less fluctuation in the film thickness. For the maximum value of the speed, the minimum film thickness is even below the recommended safe value. Moreover, during the post-processing of the simulations, the global system responses of the mechanism, including the driving torque applied on the crankshaft, the acceleration and displacement of the slider, are observed no obvious difference with those obtained from ideal joints only. The

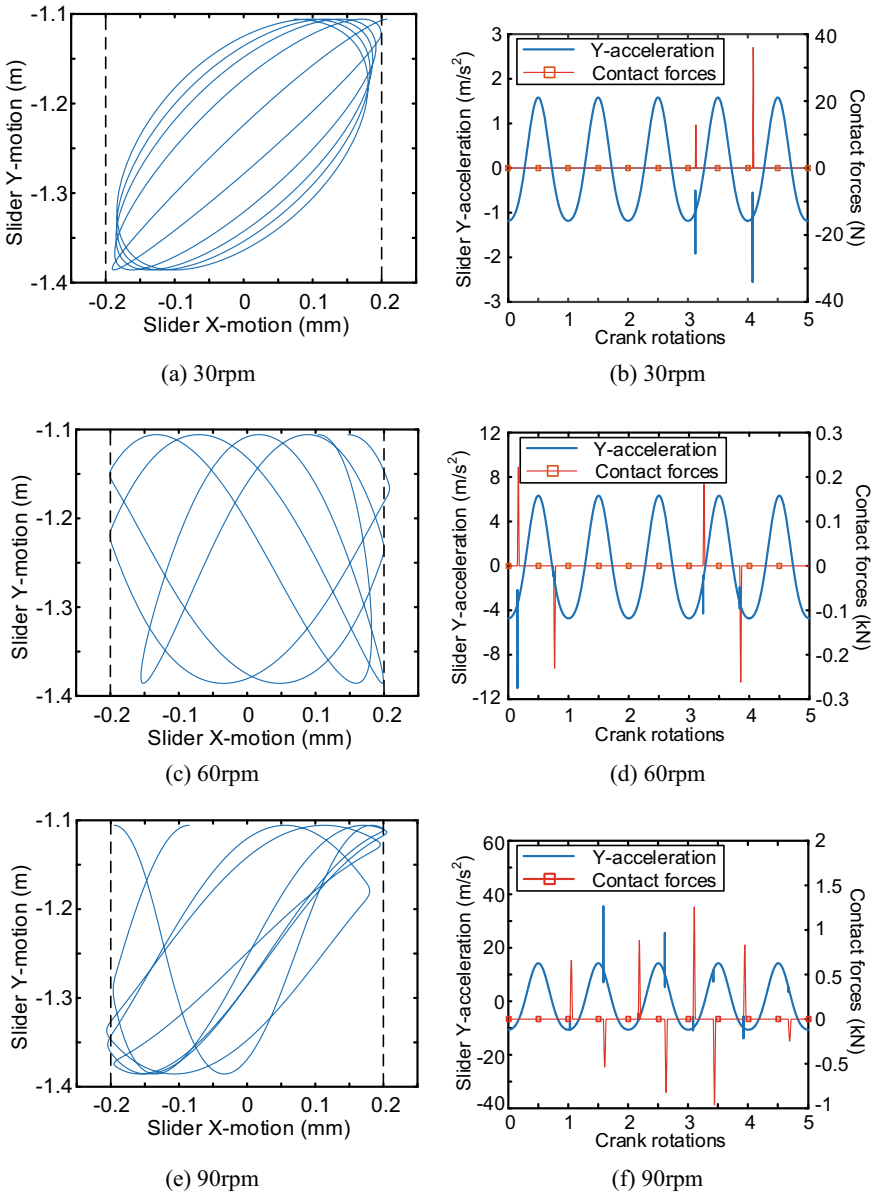
lubricated joint performs similarly to the ideal joint when investigating the local performance of the slider. The subsequence is also affirmed by the previous studies according to the reference [1].

Considering the combined effect of the lubricated joint and translational clearance joint, the system responses of the mechanical press are then investigated. The motion trajectories of the slider for different crank speeds are depicted in Fig. 4a, c, and e, which indicate irregular or chaotic behaviors of the system. As the crank speeds up, the motion trajectories become rather irregular and the maximum penetration depth magnifies. Moreover, high peaks in the slider acceleration along the Y-direction are observed. It shows that there is a direct connection between these peaks and the contact forces developed in the translation joint, as shown in Fig. 4b, d, and f. The growth of crank speed leads to the increase of slider acceleration spikes both in quantity and magnitude. It has been proofed by Flore et al. that the existence of clearance can disturb the slider acceleration with high peaks [15], which is also observed in this work.

However, the relative motion trajectories in the journal-bearing joint are found no significant differences when the translational joint is assumed to be ideal or a clearance one. This may result from the weak effects of short-term and small quantities of collisions on the slider displacement and velocity along the Y-direction. Therefore, according to Eq. (7), the hydrodynamic forces that dominate the dynamic responses of the lubricant revolute joint are almost unaffected.

4 Conclusions

The consideration of joint clearance in the dynamic analysis of the mechanical press can generally lead to a higher simulation precision. In this paper, a lubricant revolute joint and a translational clearance joint are simultaneously conducted in the model to identify their combined influence. The results show that the lubricated revolute joint presents practically as an ideal one in the global responses, with the parameters chosen in this paper. The minimum lubricant film thickness decreases as the crank speeds up, which indicates a strict control to the crank speed. The combined effect of the two clearance joints shows that the translational clearance joint could influence the system response significantly, leading to undesirable peaks in slider accelerations. However, it seems that the translational clearance joint has little influence on the dynamics of the lubricated joint, due to the limited amount of contacts under a low input crank speed. This observation implies that the effects of the two joints can be analyzed separately, for the dynamic analysis of heavy-load mechanical press with a low operation speed.



(a) 30rpm (b) 30rpm

(c) 60rpm (d) 60rpm

(e) 90rpm (f) 90rpm

Fig. 4 System responses of the press considering two clearance joints: **a**, **c**, and **e** motion trajectory of the slider with various crank speeds; **b**, **d**, and **f** acceleration of the slider and contact forces of the guides for various crank speeds. (Color figure online)

References

1. Tian Q, Flores P, Lankarani HM (2018) A comprehensive survey of the analytical, numerical and experimental methodologies for dynamics of multibody mechanical systems with clearance or imperfect joints. Mech Mach Theory 122:1–57
2. Lankarani HM (1988) Canonical equations of motion and estimation of parameters in the analysis of impact problems. Ph.D. thesis, University of Arizona
3. Flores P, Ambrósio J, Claro JCP, Lankarani HM (2008) Kinematics and dynamics of multibody systems with imperfect joints: models and case studies. Lecture Notes in Applied and Computational Mechanics, vol 34. Springer, Berlin
4. Erkaya S, Uzmay ˙I (2010) Experimental investigation of joint clearance effects on the dynamics of a slider-crank mechanism. Multibody Syst Dyn 24(1):81–102
5. Ma J, Qian L (2017) Modeling and simulation of planar multibody systems considering multiple revolute clearance joints. Nonlinear Dyn 90(3):1907–1940
6. Megahed SM, Haroun AF (2012) Analysis of the dynamic behavioral performance of mechanical systems with multi-clearance joints. J Comput Nonlinear Dyn 7(1):
7. Zheng E, Zhu R, Zhu S, Lu X (2016) A study on dynamics of flexible multi-link mechanism including joints with clearance and lubrication for ultra-precision presses. Nonlinear Dyn 83(1–2):137–159
8. Chen Y, Sun Y, Peng B, Cao C (2016) A comparative study of joint clearance effects on dynamic behavior of planar multibody mechanical systems. Lat Am J Solids Struct 13(15):2815–2833
9. Wu X, Sun Y, Wang Y et al (2020) Dynamic analysis of the double crank mechanism with a 3D translational clearance joint employing a variable stiffness contact force model. Nonlinear Dyn 99:1937–1958
10. Ambrósio JAC (2003) Impact of rigid and flexible multibody systems: deformation description and contact models. In: Schiehlen W, Valášek M (eds) Virtual nonlinear multibody systems. Springer, Dordrecht, pp 57–81
11. Flores P, Leine R, Glocker C (2010) Modeling and analysis of planar rigid multibody systems with translational clearance joints based on the non-smooth dynamics approach. Multibody Syst Dyn 23(2):165–190
12. Machado M, Costa J, Seabra E, Flores P (2012) The effect of the lubricated revolute joint parameters and hydrodynamic force models on the dynamic response of planar multibody systems. Nonlinear Dyn 69(1–2):635–654
13. Pinkus O, Sternlicht SA (1961) Theory of hydrodynamic lubrication. McGraw-Hill, New York
14. Khemili I, Romdhane L (2008) Dynamic analysis of a flexible slider–crank mechanism with clearance. Eur J Mech 27(5):882–898
15. Flores P, Ambrósio J, Claro JCP, Lankarani HM (2008) Translational joints with clearance in rigid multibody systems. J Comput Nonlinear Dyn 3(1):11007

Part XVI
Microstructure and Damage Development and Characterization

Temperature-Dependent Fracture Loci of AZ31 Magnesium Alloy Sheets



R. Bertolini, Q. Wang, A. Ghiotti, and S. Bruschi

Abstract Magnesium alloys have been used in the automotive and aerospace industry for several years, thanks to their high strength-to-density ratio. Their mechanical characteristics at room and even at elevated temperature have been well studied, whereas, when it comes to temperatures lower than room one, only a few studies are available in the literature. To this aim, the present paper investigates the mechanical behavior of AZ31 magnesium alloy sheets deformed at different temperature regimes. Tensile tests till fracture were carried out at room temperature, −100, −50, 100, and 300 °C using different specimen geometries in order to vary the stress triaxiality. The fracture strain values were identified making use of a combined numerical–experimental approach, whereas the fracture surfaces were qualitatively characterized by means of stereoscopy and scanning electron microscopy. Finally, the AZ31 fracture locus as a function of the stress state and temperature was constructed.

Keywords Magnesium alloys · Cryogenic · Fracture locus · Fracture surface

1 Introduction

Magnesium alloys can be used in many structural and non-structural applications thanks to their high specific strength, high specific stiffness, and good damping capacity [1]. Nevertheless, the major limitation to their widespread application is represented by the poor formability characteristics of their hexagonal close packed (HPC) crystalline structure. In fact, in magnesium alloys, non-basal slip planes are hardly operative at room temperature since their critical resolved shear stress (CRSS) is much higher compared with one of the basal planes [2]. In addition, in case of sheets, the rolling process generally introduces a strong basal texture, aligning the hexagonal structure mostly normal to the rolling plane [3]. This confers a high anisotropy to the sheet and increases the difficulty in deformation accompanied with thickness reduction and consequently leads to very limited formability at room

R. Bertolini (✉) · Q. Wang · A. Ghiotti · S. Bruschi
Department of Industrial Engineering, University of Padova, Via Venezia 1, 35131 Padova, Italy
e-mail: rachele.bertolini@unipd.it

© The Minerals, Metals & Materials Society 2021

G. Daehn et al. (eds.), *Forming the Future*, The Minerals, Metals & Materials Series,
https://doi.org/10.1007/978-3-030-75381-8_130

temperature [4]. For these reasons, magnesium alloy sheets are generally formed within the warm/hot temperature regime and a lot of research works are available on this topic [5].

Magnesium alloys can be exposed to very low temperatures when used for aerospace, satellite parts, or tanks for liquefied gases. Some studies are available in the literature addressing their mechanical behavior at cryogenic temperatures, which may also useful to evaluate if an increase of ductility can be obtained at those temperatures, with the aim of proving the feasibility of cryogenic forming.

Bussiba et al. [6] studied the uniaxial mechanical response of round specimens made of ZK60 and AZ31 magnesium alloys at temperatures of 123 and 296 K. A completely different behavior was found for the two materials, namely ductile in the case of ZK60 and semi-brittle for the AZ31. This was attributed to the presence of different second phases, which were found to be responsible for controlling both the non-basal and basal plane slip activities. Jiang et al. [7] evaluated the strategy of applying a cryogenic treatment (CT), namely cooling the material to 77 K at a rate of 2 K per minute, as a strategy to increase both the tensile strength and ductility of the AZ31 magnesium alloy. Different soaking times were applied. The obtained results showed that the highest increase in mechanical performance (+42%) was found for the sample soaked for 2 h. The contribution of CT was identified on two levels: (i) the formation of a frame-like twinning due to the movement of grains as a consequence of thermal contraction at low temperatures and (ii) the development of a compressive residual stress state. Different conclusions were achieved by Wang et al. [8], who studied the tensile deformation behavior of the Mg–3Al–1Zn alloy at low temperatures ranging from 300 to 77 K at different strain rates. By reducing the temperature, the yield stress and ultimate tensile stress increased while the strain to failure was found to decrease. It was argued that the dislocation motion changed with temperature. Specifically, above 173 K, the interaction between dislocations and forest dislocations was dominant, whereas at temperature below 173 K, the dislocation motion was governed by the interaction with local lattice friction.

It is worth noting that in all these studies, the mechanical performances of magnesium alloys were evaluated in a wide range of temperatures, including that below room temperature, but solely under uniaxial loading conditions, without considering different stress states. In this framework, the present paper investigates the mechanical behavior of the AZ31 magnesium alloy at different temperatures and stress triaxiality conditions. For each experimental condition, the strain at fracture was identified by means of a combined experimental–numerical approach, whereas the fractured surfaces were inspected using a scanning electron microscope (SEM) at different magnifications.

Table 1 Chemical composition (% mass) of the AZ31 magnesium alloy sheets

Element	Aluminum	Zinc	Manganese	Magnesium
Content	3	1	0.2	Bal

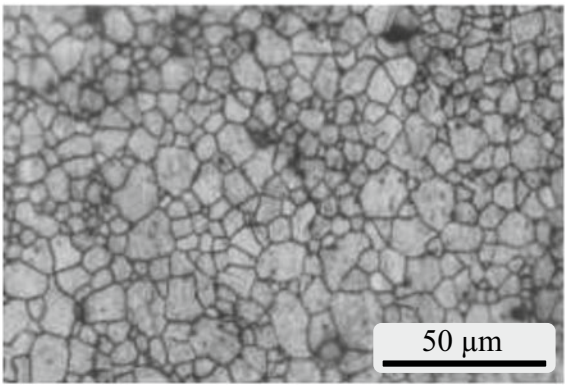


Fig. 1 Microstructure of the AZ31 magnesium alloy sheets in the as-delivered condition

2 Experimental

2.1 Material

The material under investigation is the AZ31 magnesium alloy provided in form of 1 mm thick sheets. The chemical composition of the alloy in the as-delivered condition is reported in Table 1, whereas its microstructure is shown in Fig. 1. The latter was obtained by cutting the sheet along with its thickness, then polishing, etching, and inspecting the sample through a Leica DMRE™ optical microscope equipped with a high-definition digital camera. The microstructural analysis revealed that the as-delivered material was characterized by a dual grain size distribution, a possible consequence of the dynamic recrystallization phenomenon during hot rolling. The resulted average grain size was calculated to be equal to 9 ± 4.8 μm. The AZ31 sheets were laser-cut along the rolling direction to provide specimens for the mechanical tests. Afterward, a finishing milling step was carried out to avoid any influence of the laser heat-affected zone on the experimental results.

2.2 Mechanical Testing

Tensile tests were carried out on the MTS™-322 hydraulic wedge shown in Fig. 2a, equipped with an environmental chamber that allowed setting the testing temperature in a range from –130 (±2) to 315 (±2) °C. To control the temperature during testing, a k-thermocouple was spot-welded on each specimen, as can be seen in Fig. 2b. Each

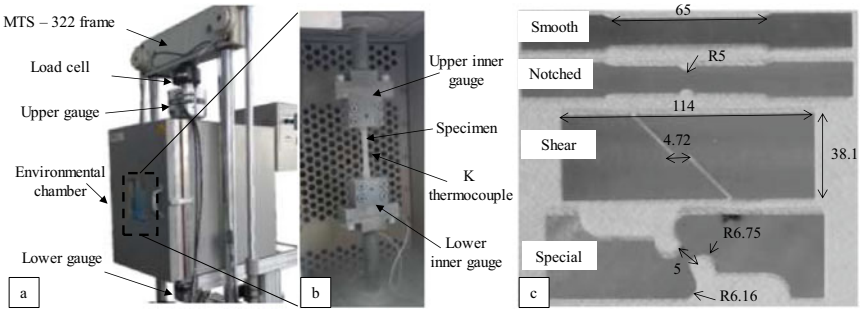


Fig. 2 **a** MTS™-322 hydraulic wedge equipment, **b** experimental setup configuration for testing smooth specimens, and **c** geometry of samples used in this study (measures are given in mm). (Color figure online)

test was carried out at a fixed strain rate of 0.1 s^{-1} and repeated three times to assure reproducibility of the results.

The effect of the testing temperature and stress triaxiality was investigated. To this aim, five different temperatures, namely −100, −50, 25, 200, and 300 °C, as well as four different stress triaxiality states were adopted. The latter was achieved by changing the specimen geometry: besides the classical dog bone sample, a 5 mm notched sample, a shear sample, and a special one, which accounts for a shear–tension state according to [9], were selected. The nominal stress triaxiality values are 0.1, 0.17, 0.33, and 0.47 for shear, special, smooth, and notched, respectively [10]. Figure 2c shows the specimen geometries considered in this paper and highlights their main geometrical features.

2.3 Procedure to Identify the Fracture Strain

The determination of the fracture strain is always a challenging issue in mechanical testing. It is generally recognized that its evaluation by measuring the specimen cross-section area through a microscope leads to some uncertainties due to the high level of strain attainable especially in hot conditions [11]. Nevertheless, the presence of the environmental chamber makes impossible the use of any kind of optical technique for its direct measure. For these reasons, in the present study, a hybrid experimental–numerical method was used to assess the strain at fracture.

The numerical simulations were performed as implicit analysis using the Ls_Dyna™ code version R9.1.0 (Ls_Prepost V4.7) with shell elements. The results of the tensile tests in terms of flow stress as a function of the temperature were used to calibrate the hardening law. The developed FEM model was validated using experimental data other than the ones used for its calibration.

Figure 3 illustrates the procedure used in this paper in the case of a shear specimen tested at −100 °C, as a reference example. The experimental and simulated force

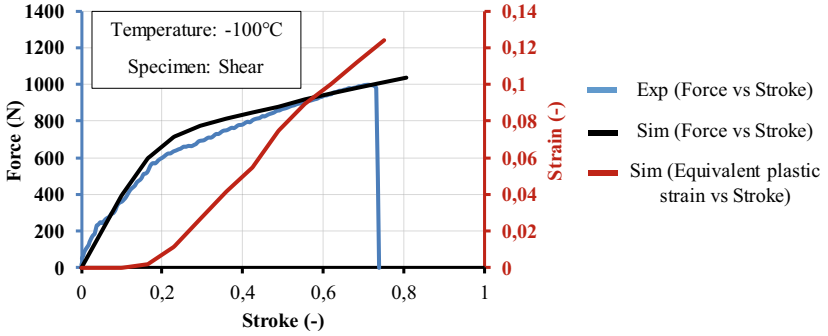


Fig. 3 Calculation of the equivalent plastic strain at fracture using the hybrid experimental–numerical method (case of a shear specimen deformed at −100 C). (Color figure online)

versus stroke curve is represented in the same figure, as well as the equivalent plastic strain versus stroke curve. It can be observed that the simulated force–stroke curve agrees with the experimental one with a good level of accuracy. The strain at fracture was assumed to be the maximum equivalent plastic strain at the experimental fracture stroke.

2.4 Characterization After Mechanical Testing

After mechanical testing, the specimen fracture surfaces were analyzed using the FEI™ QUANTA 450 scanning electron microscope (SEM) equipped with the Everhart–Thornley Detector (ETD). Images at 2000X and 5000X magnifications were acquired in different zones of the samples for each testing condition.

3 Results and Discussion

3.1 Mechanical Behavior

The force versus stroke curves for the investigated experimental conditions are reported in Fig. 4. Both the temperature and specimen configuration played a significant role in affecting the alloy mechanical behavior.

For a given stress triaxiality, the force increased as the testing temperature was reduced. On the contrary, the stroke at fracture diminished by deforming the specimen at temperatures lower than room one compared to tests conducted at higher temperatures. It is worth noting that for the special and shear samples, no sensible differences were seen between tests performed at 25, −50, and −100 °C. The smooth

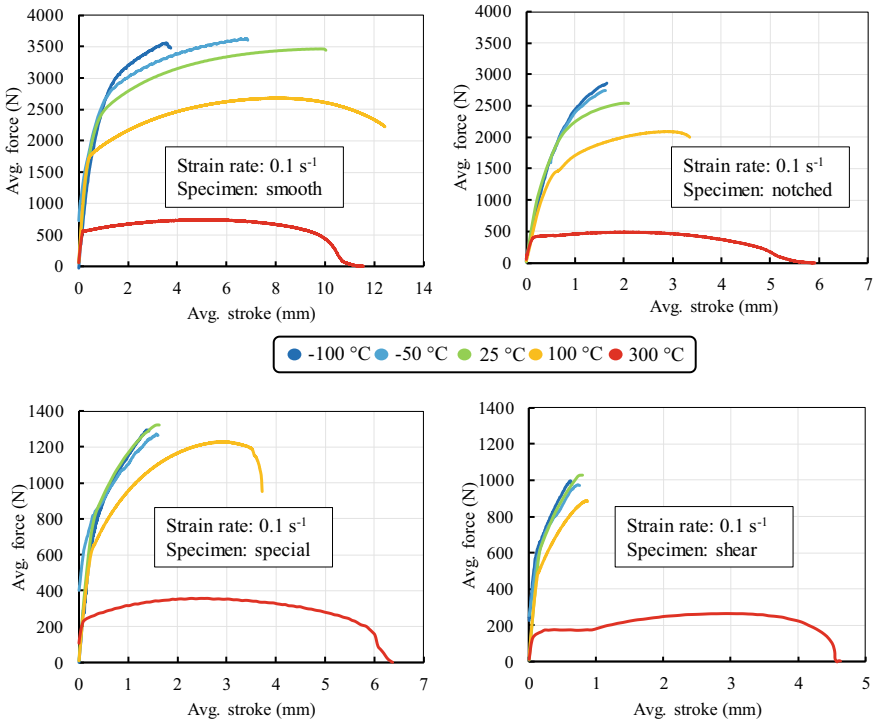


Fig. 4 Force versus stroke curves at varying testing temperature and stress triaxiality. (Color figure online)

specimen was characterized by the highest recorded forces, whereas the shear specimen by the lowest ones. Similarly, the stroke at fracture gradually decreased from smooth, notched, special to shear specimens.

Similar results in terms of force sensitivity to temperature can be found in Jiao et al. [12], where the AZ31B magnesium alloy was tested at −230, −196, −73, and 27 °C, but under uniaxial testing conditions. The specimen deformed at the lowest temperature showed an increase in the ultimate tensile strength and yield strength over 60% compared with the one deformed at room temperature. This was attributed to the reduced solubility of aluminum and zinc atoms at low temperatures, which are the main strengthening elements of the AZ31 alloy, inducing the formation of a fine distributed second phase in the matrix, which reinforced the alloy.

The AZ31 fracture loci as a function of the temperature and stress triaxiality are reported in Fig. 5. As an example, in case of smooth specimens, the maximum fracture strain value (identified on the basis of the procedure described in Section 2.3) was exhibited by the specimen deformed at the highest testing temperature, with an increase up to 1000% compared with the specimen deformed at the lowest temperature. This indicates the activation of additional deformation mechanisms above 200 °C. The fracture strain gradually decreases from 300, 100, 25 to −50 °C.

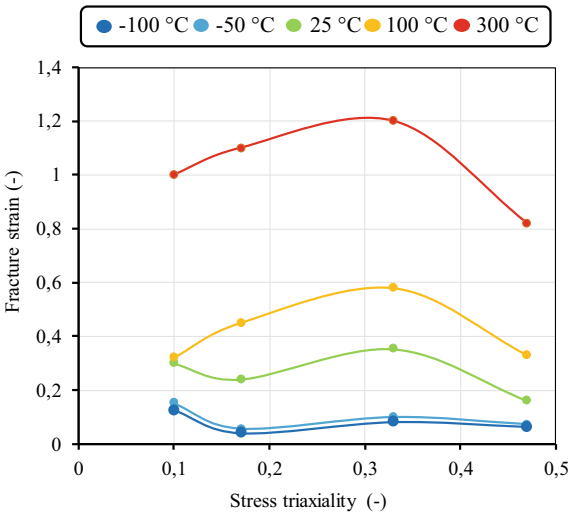


Fig. 5 AZ31 fracture loci at varying testing temperature and stress triaxiality. (Color figure online)

However, the fracture strain at −50 °C nearly overlapped the one at −100 °C, regardless of the stress triaxiality indicating the presence of a threshold temperature value below which the alloy ductility is no more sensitive to the testing temperature.

It is worth noting that the fracture strains of the shear and special specimens tested at room temperature are 50 and 81% higher compared with the ones obtained at low temperature, even if the same maximum load was reached during mechanical testing.

3.2 Fracture Surfaces

Figures 6 and 7 show the SEM images of the AZ31 specimens fractured at 300, 25, and −100 °C at magnifications of 2000X and 5000X, respectively. In Fig. 6i–l, wide and deep dimples structures, indicative of a ductile fracture mode, can be seen in the specimens deformed at 300 °C. On the contrary, at the lowest testing temperature, no ductile fracture features can be seen, since the dimples disappeared in favor of elongated fluted that are known to be symptomatic of a brittle fracture [10] (see Fig. 6a–d). In addition, on the fracture surfaces of Fig. 6(c and d), cracks along the grain boundaries can be observed, which is another typical brittle fracture structure. The fracture surfaces of the specimens deformed at room temperature have features in the middle, being a mixture of ductile and brittle type of fracture. Even if not here reported, the fracture surfaces of the specimens deformed at −50 °C are similar to those obtained at −100 °C, thereby confirming a fragile rupture when testing below the room temperature.

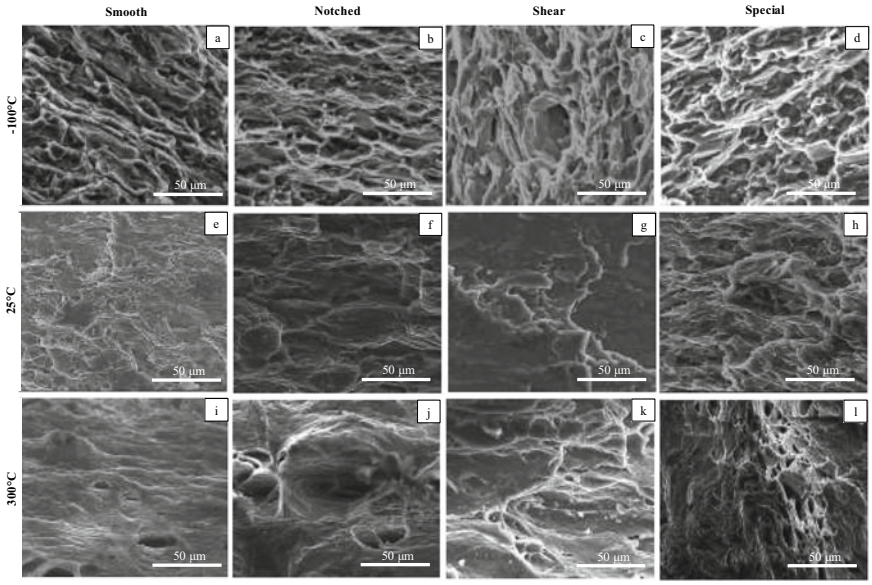


Fig. 6. 2000X SEM magnification of the AZ31 fractured surfaces as a function of the temperature and stress triaxiality

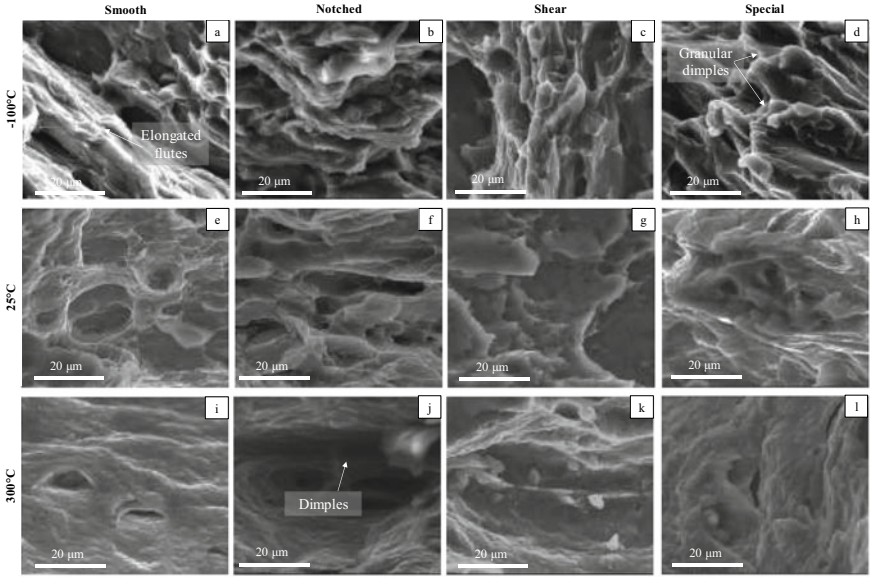


Fig. 7 5000X SEM magnification of the AZ31 fractured surfaces as a function of the temperature and stress triaxiality

4 Conclusions

In this work, tensile tests till fracture and SEM observations of the fracture surfaces were employed to characterize the mechanical properties and fracture morphology of the AZ31 magnesium alloy deformed in a wide range of temperature and stress triaxiality.

The main conclusions can be summarized as follows:

- The force increased monotonically by decreasing the temperature for the smooth and 5 mm notched samples. In the case of shear and special samples, at temperatures below than room one, the force was no longer sensitive to the testing temperature.
- Higher fracture strains were obtained at elevated temperatures, whereas no sensible differences were shown between tests carried out at −50 and −100 C.
- The reduction of temperature favored a brittle mode of fracture. The fractured surfaces of the specimens deformed at −50 and −100 C were in fact characterized by the presence of elongated flutes and intergranular cracks.

References

1. Liu Z, Dong Y, Mao P, Yu J (2019) Dynamic tensile and compressive properties of vacuum and ordinary die-casting AT72 magnesium alloy at high strain rates. J Magnes Alloy 1:150–162. https://doi.org/10.1016/j.jma.2013.07.004
2. Yoo MH (1981) Slip, twinning, and fracture in hexagonal close-packed metals. Metall Trans A 12:409–418
3. Sambasiva Rao G, Prasad YVRK (1982) Grain boundary strengthening in strongly textured magnesium produced by hot rolling. Metall Trans A 13(12):2219–2226
4. Huang X, Suzuki K, Watazu A, Shigematsu I, Saito N (2009) Improvement of formability of Mg–Al–Zn alloy sheet at low temperatures using differential speed rolling. J Alloy Compd 470(1–2):263–268
5. Doege E, Dröder K (2001) Sheet metal forming of magnesium wrought alloys-formability and process technology. J Mater Process Technol 115(1):14–19
6. Bussiba A (2003) Fracture and deformation potential of magnesium alloys at low temperatures 84:84–91. https://doi.org/10.1063/1.1472529
7. Jiang Y, Chen D, Chen Z, Liu J (2010) Effect of cryogenic treatment on the microstructure and mechanical properties of AZ31 magnesium alloy. Mater Manuf Process 25:837–841. https://doi.org/10.1080/10426910903496862
8. Wang H, Dong S, Lv G (2016) Plastic deformation characteristics of an Mg–3Al–1Zn alloy at low temperatures. Mater Des 92:143–150. https://doi.org/10.1016/j.matdes.2015.12.027
9. Bao Y, Wierzbicki T (2004) On fracture locus in the equivalent strain and stress triaxiality space. Int J Mech Sci 46:81–98. https://doi.org/10.1016/j.ijmecsci.2004.02.006
10. Wang Q, Bertolini R, Bruschi S, Ghiotti A (2019) Anisotropic fracture behavior of AZ31 magnesium alloy sheets as a function of the stress state and temperature. Int J Mech Sci 163. https://doi.org/10.1016/j.ijmecsci.2019.105146

11. Valoppi B, Brushi S, Ghiotti A, Shivpuri R (2017) Johnson–Cook based criterion incorporating stress triaxiality and deviatoric effect for predicting elevated temperature ductility of titanium alloy sheets. Int J Mech Sci 123:94–105. https://doi.org/10.1016/j.ijmecsci.2017.02.005
12. Jiao XD, Li LF, Liu HJ, Yang K (2006) Mechanical properties of low density alloys at cryogenic temperatures. AIP Conf Proc 824(1):69–76. https://doi.org/10.1063/1.2192335

Influence of Specimen Preparation Methods on the Mechanical Properties and Superplastic Behavior of AA5083 Sheets



Mohammad S. Dastgiri, Leo Kiawi, Iman S. Sarraf, Eugene Ryzer, and Daniel E. Green

Abstract The process used to fabricate tensile specimens inevitably introduces imperfections at their edges, which can affect the resulting experimental mechanical properties. It has been reported that, for ambient temperature testing, tensile specimens prepared by less aggressive machining methods yield more accurate data due to the absence of plastic deformation at the edges. However, for superplastic forming (SPF) where forming is performed at elevated temperatures, the results are different. In this study, AA5083 sheet specimens were prepared using different machining methods: wire-electro-discharge machining, waterjet cutting, and conventional milling. Mechanical properties were determined from tensile tests carried out at 450 °C and at a quasi-static strain rate. The edges of tensile specimens were observed under optical and scanning electron microscopes (SEM) both before and after testing. It was found that milled specimens resulted in greater values of total elongation. The microscopic investigation revealed that specimens whose edges have a lower arithmetic mean roughness (Ra) have greater values of elongation. The SEM investigation also revealed that micro-cracks are more prevalent at the edges of specimens that have a greater surface roughness. Therefore, tensile specimens used to characterize sheet mechanical properties in view of SPF applications should be fabricated by a process that yields a lower surface roughness, such as conventional milling.

M. S. Dastgiri (✉) · L. Kiawi · I. S. Sarraf · D. E. Green
University of Windsor, 401 Sunset Ave., Windsor, ON, Canada
e-mail: shirinz@uwindsor.ca

L. Kiawi
e-mail: kiawi@uwindsor.ca

I. S. Sarraf
e-mail: sarisa@uwindsor.ca

D. E. Green
e-mail: dgreen@uwindsor.ca

E. Ryzer
AEM Power Systems Inc., Windsor, ON, Canada
e-mail: eryzer@aempowersystems.com

© The Minerals, Metals & Materials Society 2021

G. Daehn et al. (eds.), *Forming the Future*, The Minerals, Metals & Materials Series,
https://doi.org/10.1007/978-3-030-75381-8_131

Keywords SPF · Superplastic forming · Surface roughness · Tensile testing · Aluminum AA5083

1 Introduction

Aluminum AA5083 is a non-heat-treatable aluminum alloy with excellent cold formability and can reach moderate levels of superplasticity [1]. This alloy is affordable and has reasonable environmental resistance and good mechanical properties, which make it ideal for aerospace, marine, and automotive applications [2].

Tensile testing is the most common way to determine mechanical properties. Experimental mechanical characteristics can be used to compare different batches and for input in numerical simulations of forming or post-forming operations. It has been reported that specimen preparation methods can affect the specimen edge quality and consequently affect reported mechanical properties for steels at ambient temperature [3, 4]. Although the mechanical properties of aluminum AA5083 have been investigated by many researchers [5–7], there is a striking lack of information regarding the specimen preparation methods in most of these publications. Since the machining method can affect the results of tensile testing makes it difficult to use these published results. Computer numerical controlled (CNC) waterjet cutting (WJet), wire-electro-discharge machining (WEDM), and milling are among the most common machining methods used to prepare tensile specimens. Therefore, this research focuses on investigating the effects of these specimen preparation methods on the results of tensile tests carried out on AA5083 aluminum sheet specimens at 450 °C in view of superplastic forming applications.

2 Experimental Procedures

2.1 Specimen Preparation

In this research, three types of preparation methods were used to cut tensile specimens, namely milling, WEDM, and WJet. Specimen dimensions were selected according to the ASTM E2448 standard, which does not provide any recommendations as to the machining method that should be used. However, ASTM E2448 requires that the gauge width and thickness be measured at a minimum of four locations within the gauge area, and the measurement tolerance should not exceed 1% or 12 μm. AA5083 sheets with a thickness of 1.42 mm were cut in such a way that there was no thickness reduction at the edge. In order to reach this tolerance, process parameters were selected as follows: for milled specimens, machining was carried out with a 1/8-inch diameter tool rotating at 7500 rpm with a feeding rate of 30 mm/min. The full sheet thickness was machined in two successive passes. For WEDM, a 0.0254-inch diameter wire was tensioned at 17 N and fed at a rate of

8.1 mm/min. The cutting rate was 0.01 Versus and the electrical current was AC 28 Hz, 17Amp. For WJet, the nozzle diameter was 0.030 inch, distant at 0.080 inch and the average cutting rate was 1200 mm/min.

2.2 Roughness Evaluation

Before performing the tensile tests, all the specimens underwent a surface roughness evaluation. The ISO 4287:1997 standard was employed to determine the arithmetic mean surface roughness (R_a), the maximum height of the assessed profile (R_z), the maximum peak height (R_p), and the maximum valley depth (R_v) [8]. The surface that was evaluated was the edge of the specimens where each machining method left a different surface roughness. In this research, two-dimensional and three-dimensional arithmetic mean roughness (R_a) was measured. Two-dimensional data were extracted from perpendicular to cutting edge optical images taken with an Olympus GX51 at 50X magnification, and each profile covered 1760 ± 3 μm. For each tensile specimen, three profiles were measured and analyzed. For three-dimensional surface roughness measurements, back-scattered electron (BSE) images of the specimen edge were calibrated with BSE image of the reference specimen.

2.3 Scanning Electron Microscopy

Test specimens were investigated for surface morphology using scanning electron microscopy, and this was carried out with a FEI Quanta 200 FEG scanning electron microscope (SEM).

2.4 Tensile Tests

Quasi-static tensile testing was conducted using an MTS Criterion® model 45. For better accuracy, an additional "Strainsert FL1U(C)-2SGKT" load cell with a maximum capacity of 1Kip was employed. Strains were recorded using an MTS integrated video extensometer. The high-temperature environment was generated using a tubular radiant furnace with an additional controlled conductive heater located at lower specimen holder. Two contacting thermocouples were used to record the temperature at both ends of the specimen and another thermocouple was located near the middle of the gauge length. The temperature was controlled using a PID controller, which allowed the temperature gradient from one end of the specimen to the other to remain within 2 °C throughout the test.

3 Results and Discussion

3.1 Surface Roughness

The arithmetic mean surface roughness (Ra) of the specimen edges prepared with different machining processes is summarized in Table 1 and Fig. 1. The Ra values clearly show that milled specimens had the lowest surface roughness ($R_a = 0.45$ μm, on average). The Ra value increases 18 and 24 times, in WEDM and WJet specimens, respectively, compared to milled specimens. It can be seen that 3D and 2D surface roughness parameters are slightly different; 2D roughness measurements were obtained from profiles taken parallel to the specimen loading direction. However, 3D surface roughness measurements were calculated across selected 1 mm × 1 mm areas. Therefore, the orientation of the 2D surface roughness profiles parallel with the specimen loading direction is no doubt the cause of these minor differences.

3.2 Surface Morphology

Figure 2 presents the surface profile of the edge of the three types of specimens prior to tensile testing, and the scale of *Z*-axis was kept identical for all three machining methods. WJet specimens are characterized by deep markings (Fig. 3) that show the abrasive nature of the waterjet cutting process. These marks are oriented perpendicular to the loading direction of the tensile specimen. These abrasion marks are potential regions for crack nucleation, and in some areas, it appears that microcracks already exist. During a tensile test, the applied load effectively opens any cracks, causing further damage to the edge of the specimen.

In contrast to WJet specimens, the surface morphology of the edges of WEDM specimens is non-directional and is characterized by rounded globules that are a residue of local melting caused by electrical sparking. Figure 4 shows a secondary electron image of the edge of a WEDM specimen prior to testing. The size of the globules appears to be randomly distributed. Furthermore, the local melting and solidification also cause shrinkage of the base metal that leaves a conical dimple under each globule. These shrinkage dimples are susceptible to stress concentrations, which may become crack nucleation sites during tensile testing.

The edges of milled specimens exhibit a uniformly directional pattern, as seen in Fig. 5. This pattern appears as shallow score marks that are oriented parallel to the loading direction of the tensile specimen. According to Table 1, the maximum height of these machining marks ($R_z = 3.2$ μm) is considerably less than those at the edge of WJet specimens ($R_z = 31.1$ μm). In addition, even if these milling marks led to the initiation of edge cracks, these cracks would not be responsible for the final failure and fracture of the specimen because they lie parallel to the loading direction.

Table 1 Arithmetic mean roughness (R_a), maximum height of assessed profile (R_z), maximum peak height (R_p), and maximum valley depth (R_v) at the edges of AA5083 aluminum specimens prepared with different machining methods

		R_a (μm)			R_v (μm)			R_p (μm)			R_z (μm)		
		Mill	WEDM	WJet	Mill	WEDM	WJet	Mill	WEDM	WJet	Mill	WEDM	WJet
Sample1	3D	0.46	8.28	10.85	1.80	10.69	16.11	1.50	11.31	15.34	3.30	22.00	31.45
Sample1	2D1	0.40	8.29	10.35	1.79	11.20	13.58	1.76	10.51	16.00	3.55	21.70	29.58
	2D2	0.57	7.44	11.00	1.70	11.74	18.82	1.56	10.55	18.04	3.26	22.30	36.86
Sample2	2D1	0.42	8.52	11.11	1.56	10.46	13.97	1.21	12.04	15.72	2.77	22.51	29.69
	2D2	0.51	7.88	10.52	1.76	9.84	14.81	1.36	11.48	13.40	3.12	21.32	28.21
Sample3	2D1	0.41	9.41	11.66	1.81	11.65	19.31	1.28	10.27	13.08	3.09	21.92	32.38
	2D2	0.45	8.13	10.47	1.91	11.97	13.37	1.49	10.46	16.53	3.40	22.43	29.89

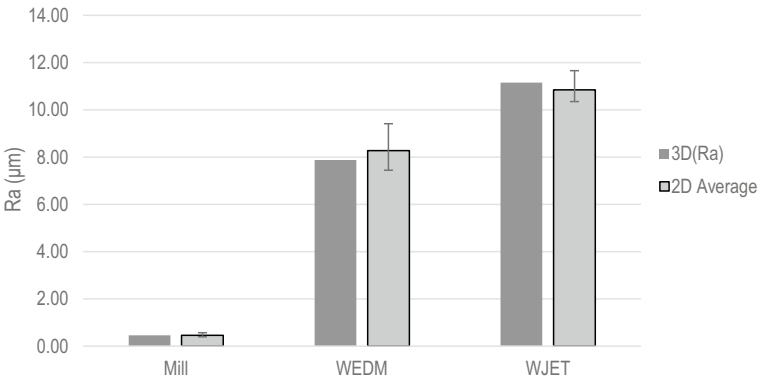


Fig. 1 Arithmetic mean roughness for 3D surface profile and 2D linear profile

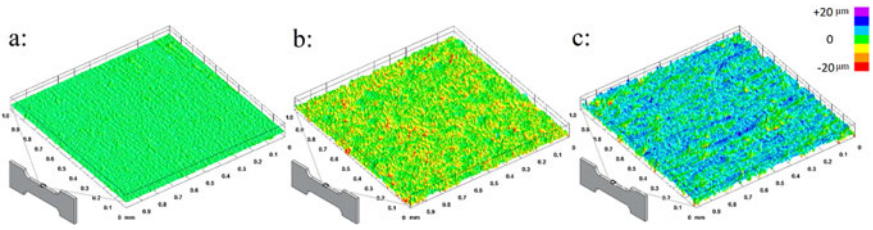


Fig. 2 3D surface profile of (**a**) milled, (**b**) WEDM, and (**c**) WJet specimen edges. Each scan covered 1.0 mm^2 of area. (Color figure online)

3.3 Effect of Preparation Method on the Yield Stress

The effect of the machining process on the yield stress of AA5083 specimens loaded in tension at 450 °C is presented in Fig. 6a. It appears that the yield stress remains virtually unchanged for each machining method. However, the range of measured yield stress values differs for each specimen preparation method. The range of recorded yield stress values is very small (±) for milled specimens whereas the range for WJet samples is greatest. Figure 7 compares the engineering stress–strain curve of the most representative specimens for each type of machining method. During high-temperature superplastic forming, this aluminum alloy exhibits a softening behavior and therefore the yield stress is also the maximum stress before fracture. A comparison of the stress–strain curves in Fig. 7 shows that the machining method only affects the total elongation and practically has no effect on the elastic modulus and flow behavior of AA5083.

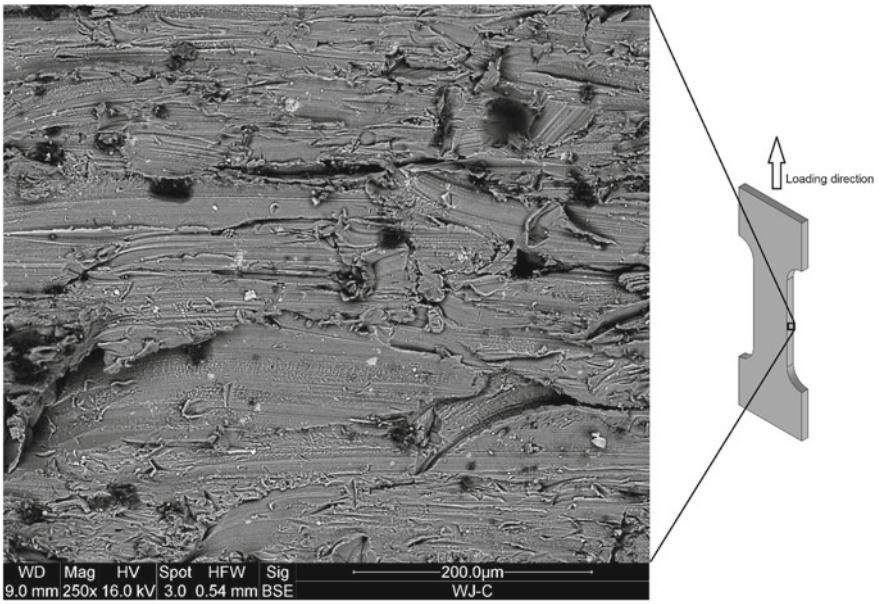


Fig. 3 SEM-BSE image of the edge of a WJet specimen prior to tensile testing

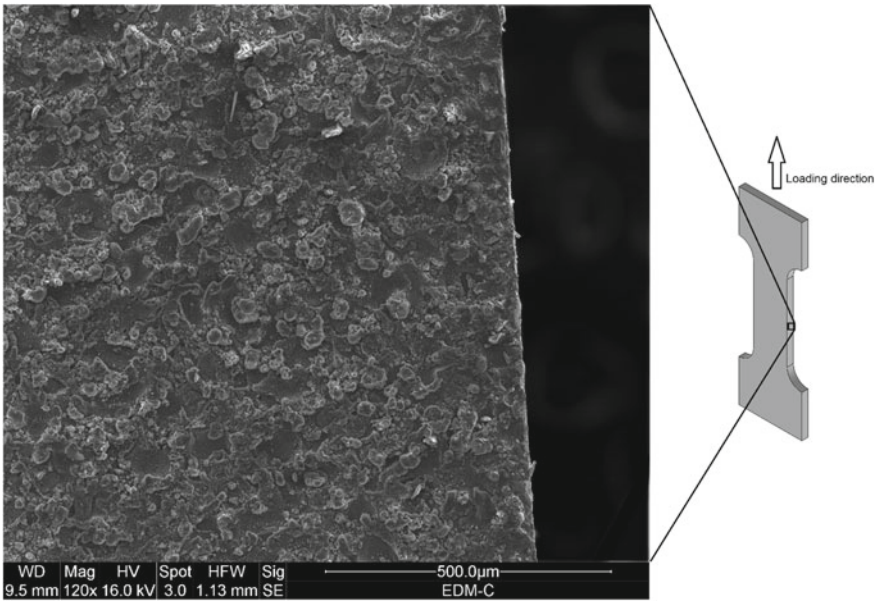


Fig. 4 SEM-BSE image of the edge of a WEDM specimen prior to tensile testing

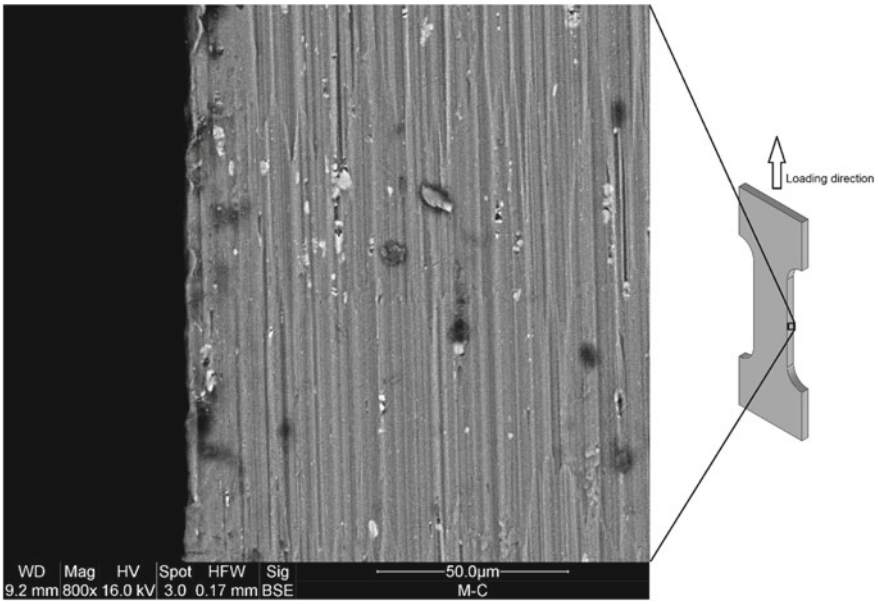


Fig. 5 SEM-BSE image of the edge of a milled specimen prior to tensile testing

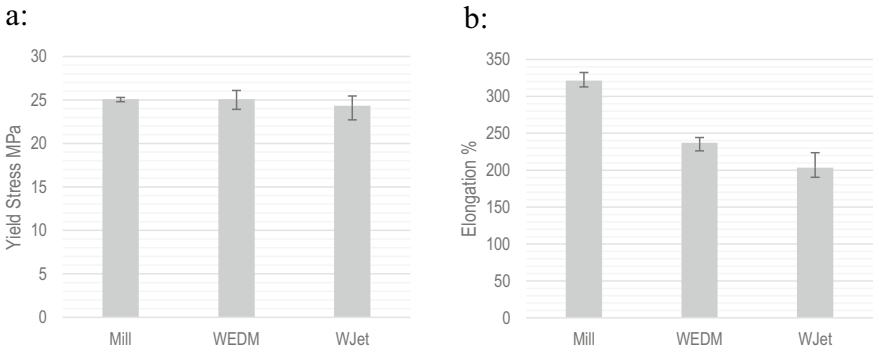


Fig. 6 Effect of machining process on mechanical characteristics of AA5083 at 450 °C

3.4 Effect of Preparation Method on the Total Elongation

Figure 6b shows the sensitivity of the total elongation to the specimen preparation process. Milled specimens deformed in tension at 450 °C exhibit a total elongation of 3.1, which is, on average, 30 and 59% more than that of WEDM and WJet specimens, respectively. The range of measured elongation values is presented in the form of error bars in Fig. 6b, and it is evident that the range is greatest for WJet specimens compared to the other machining processes. In order to better understand the reasons

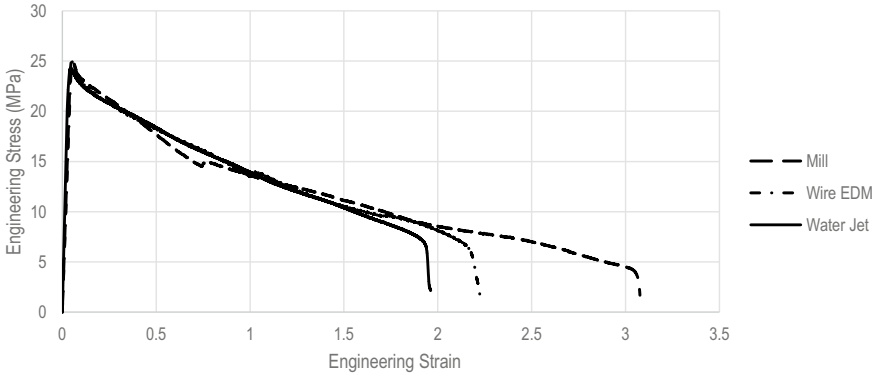


Fig. 7 Engineering stress–strain curve of AA5083 specimens loaded in tension at 450 °C and prepared with different machining methods

for the differences in the ranges of measured elongation values, the edge of deformed specimens was also observed using macro SEM imaging (see Fig. 8). These images were taken within the gauge length and approximately 5 mm away from the fracture site. Figure 8.a shows that the edges of milled specimens deformed uniformly in high-temperature tensile testing. Due to the decreased surface roughness and the absence of sites of potential crack nucleation, the deformation reached greater values before the onset of fracture. In contrast, Fig. 8b, c shows increased non-uniformity of the through-thickness strain in WEDM and WJet specimens, respectively, compared to the milled specimen. All the specimens that were prepared by waterjet cutting were observed to fracture by the propagation of a crack that started at one of the two edges. This trend was also observed in the case of WEDM specimens. Even though the width strain of WEDM specimens is more uniform than that of WJet specimens, all the WEDM specimens also failed because of a crack that started from the machined edge.

4 Conclusions and Recommendations

The microscopic investigation that was carried out indicated that the three different machining methods used to prepare AA5083 tensile specimens resulted in very different surface roughness parameters. Conventional milling had the lowest surface roughness ($R_a = 0.46\,\mu m$) whereas WEDM and WJet resulted in considerably greater surface roughness ($R_a = 8.28\,\mu m$ and $R_a = 10.85\,\mu m$, respectively). Moreover, three-dimensional surface mapping showed the presence of micro-cracks in undeformed specimens that were prepared using waterjet cutting.

High-temperature tensile test data showed that milled specimens, which had the lowest surface roughness, exhibited the greatest values of total elongation (ε_f = 3.1) compared to specimens machined by wire-EDM and waterjet cutting (ε_f =

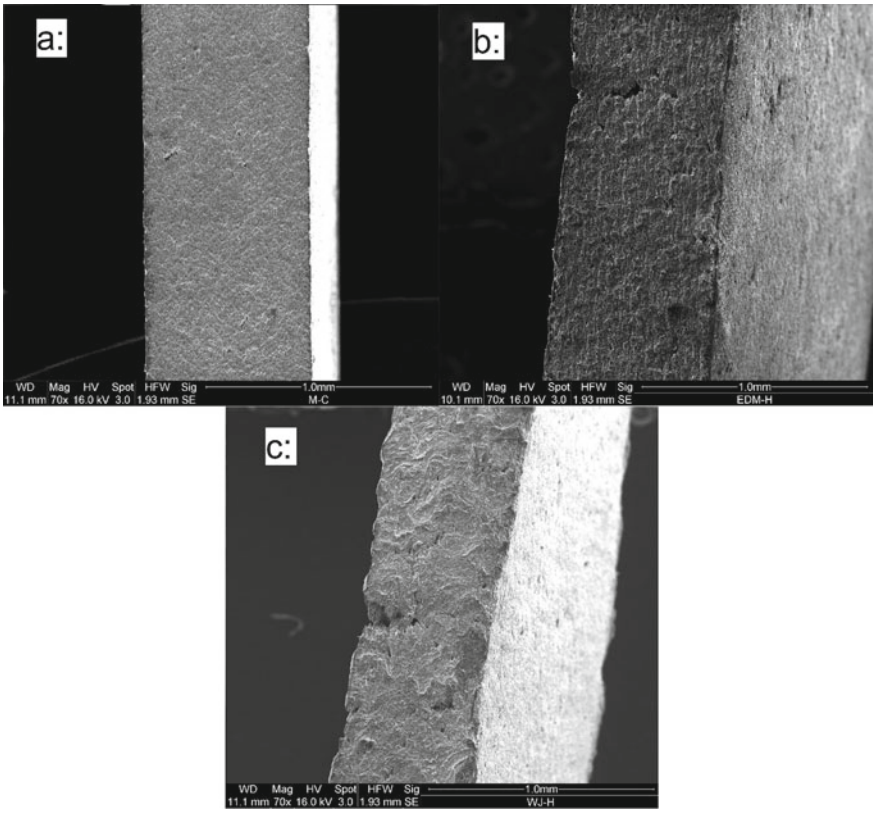


Fig. 8 SEM-SE images of the edge of (**a**) milled, (**b**) WEDM, and (**c**) WJet specimens after tensile testing

2.38 and $\varepsilon_f = 1.95$, respectively). However, the yield stress remained essentially unchanged for each of the machining methods considered. Microscopic investigation also confirmed that milled specimens deformed more uniformly in their gauge length compared to WEDM and WJet specimens.

This work shows that the type of machining method can significantly affect the values of the total elongation, which are measured in high-temperature tensile tests. The following recommendations can be made:

- The recommended method for preparing tensile specimens for the characterization of high-temperature mechanical properties of superplastic aluminum sheets is by conventional milling: this is due to the smoother surfaces imparted to the edges of the specimen.
- If experimental fracture strain data obtained from high-temperature tensile tests are intended to validate the outcome of numerical simulations of a superplastic forming process, it is recommended that the tensile specimen preparation method should be selected in such a way that the resulting surface roughness corresponds

as closely as possible with that of the edge of the sheet metal blank that will be used in the actual forming process.

- Finally, it is recommended that the machining method used for tensile specimen preparation and the corresponding surface roughness measured at the specimen edges be reported in publications, with the high-temperature experimental mechanical properties that are obtained from these specimens: this will avoid inappropriate utilization of experimental tensile data for superplastic aluminum alloys. Similarly, comparisons between high-temperature tensile data obtained from different laboratories should only be done after careful consideration of the surface roughness at the specimen edges prior to tensile testing.

Acknowledgments The authors would like to thank AEM Power Systems Inc. for sponsoring this research, and the Great Lakes Institute for Environmental Research (GLIER) at the University of Windsor is acknowledged for the use of their scanning electron microscope.

References

1. Giuliano G (2011) Superplastic forming of advanced metallic materials. In: Superplastic forming of advanced metallic materials. Woodhead Publishing Limited, p 15
2. Davoodi B, Payganeh GH, Eslami MR (2012) Cutting forces in dry machining of aluminum alloy 5083 with carbide tools. Adv Mater Res, 259–262
3. Dykeman J, Malcolm S, Yan B, Chintamani J, Huang G, Ramisetti N, Zhu H (2011) Characterization of Edge Fracture in Various Types of Advanced High Strength Steel. In: SAE 2011 world congress & exhibition. SAE 2011 World Congress & Exhibition
4. Goshert B, Terrazas OR, Matlock DK, Van Tyne CJ (2018) Sample edge effects on tensile properties and sheet formability. In: IOP Conf Ser Mater Sci Eng 418. https://doi.org/10.1088/1757-899X/418/1/012064
5. Dai Q, Deng Y, Jiang H, Tang J, Chen J (2019) Hot tensile deformation behaviors and a phenomenological AA5083 aluminum alloy fracture damage model. Mater Sci Eng A 766. https://doi.org/10.1016/j.msea.2019.138325
6. Hosseinipour SJ (2009) An investigation into hot deformation of aluminum alloy 5083. Mater Des 30:319–322. https://doi.org/10.1016/j.matdes.2008.04.063
7. Yan H, Zhang K (2009) Superplasticity and fracture behavior of fine grained 5083 Al alloy. J Wuhan Univ Technol Mater Sci Ed 24:800–804 . https://doi.org/10.1007/s11595-009-5800-3
8. Bhushan B (2001) Surface Roughness analysis bharat bhusan. In: Modern Tribology Handbook, pp 49–120

Application of the Nondestructive Evaluation (NDE) Method to Evaluate the Sheared Edge Quality and Edge Cracking



J. Gu, N. Pathak, S. Freed, E. Todorov, and H. Kim

Abstract Evaluating the shear edge quality and edge cracking is important in forming the advanced high-strength steel (AHSS) for automotive structural parts. This paper introduces the eddy current-based NDE method to evaluate the sheared edge quality. Different shear clearances from 5 to 25% of the sheet thickness were used to create different work-hardening levels on the sheared edges, which change the local formability. The NDE sensor scanned the sheared DP780 blanks to obtain the NDE data. The micro-hardness at the sheared edge was measured to compare the NDE data to the work-hardening level of the sheared edge. The edge formability was evaluated using the half specimen dome test (HSDT) with digital image correlation (DIC). The measured HSDT failure strain was correlated with the NDE data. The NDE result showed a good correlation with the DIC measured failure strain and micro-hardness. With further development effort, the eddy current-based NDE method can be implemented to inspect the sheared edge quality in a production environment.

Keywords Edge cracking · Nondestructive evaluation · Eddy current · Advanced high strength steel (AHSS) · Shearing · Stamping

1 Introduction

Eddy current (EC) technology is widely used as one of the nondestructive evaluation (NDE) methods. The EC is the induced current with closed contour patterns generated by alternating the magnetic field in a conductive material by Faraday's law of induction [1]. The contour of the EC signal is affected by sample electromagnetic property, standoff distance of the sensor, and sample geometry [2]. Discontinuity of conductivity from microcracks can distort the eddy current contour [3]. Therefore, EC is often used to detect structural defects that can be used to evaluate the work-hardening level from the shearing process. The effect of structural defects on EC contour is shown in Fig. 1.

J. Gu (✉) · N. Pathak · S. Freed · E. Todorov · H. Kim
EWI - Forming Center (EWI-FC), Columbus, OH, USA

© The Minerals, Metals & Materials Society 2021

G. Daehn et al. (eds.), *Forming the Future*, The Minerals, Metals & Materials Series,
https://doi.org/10.1007/978-3-030-75381-8_132

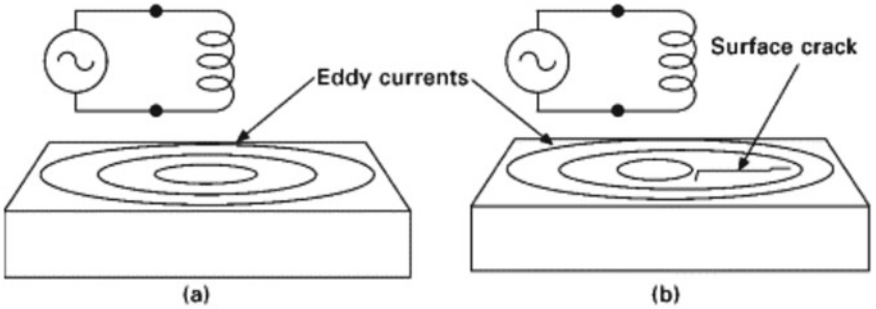


Fig. 1 Schematic of EC (L) and detecting surface crack (R) [1]

A sheared edge stretching operation involves a two-stage, nonproportional loading process that includes through-thickness shearing followed by in-plane stretching under uniaxial tensile loading. Various research has been conducted on evaluating and predicting edge cracking on AHSS. The critical parameters affecting edge local formability were investigated by Pathak et al. [4]. The study concludes that the edge local formability is mainly affected by the work-hardening introduced during the shearing process. To evaluate the edge formability, various destructive tests [4–6] were used to evaluate the edge work-hardening and sheared edge stretchability by measuring grain rotation and micro-hardness testing. However, most lab-scale tests cannot be used for real-time assessment of the edge formability in a production environment.

Following up the previous work on this topic at EWI [8], this study contributed further improvements in using an EC NDE tool to evaluate edge local formability. The previous experimental setup and EC scanning result are shown in Fig. 2 [8]. However, the previous NDE setup was found very sensitive to edge alignment. In this study, the NDE setup was upgraded with a high-resolution EC probe and improved fixture to obtain more accurate NDE data by directly scanning the sheared edge in the thickness direction. Multiple stacked samples with spacers were scanned in one path with the new scanning setup. Other validation tests, HSDT and micro-hardness testing, were conducted to correlate with the NDE result.

2 Objective

The objective of this study was to develop and validate an NDE method to evaluate the sheared edge quality in sheet metal forming.

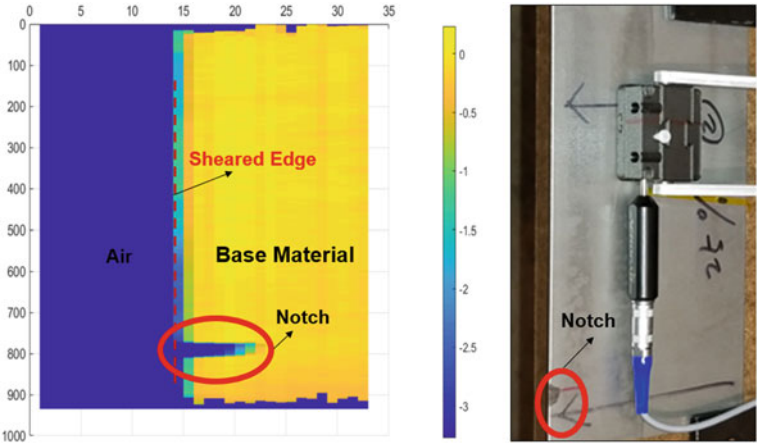


Fig. 2 Eddy current measurement result colormap (L) and setup (R) from the previous study [8]. (Color figure online)

3 Approach

This study was conducted on the basis of previous work published by EWI [8]. DP780 material with 1.2-mm thickness was selected for this study. The following various conditions were used to create different work-hardening levels on the sheared or machined edge:

- 5%: Die shearing at 5% die clearance
- 10%: Die shearing at 10% die clearance
- 15%: Die shearing at 15% die clearance
- 20%: Die shearing at 20% die clearance
- 25%: Die shearing at 25% die clearance
- Milling: machined edge
- Sheared: Sheared using a conventional lab shear machine with unknown shear clearance.

The die clearance is calculated by the percentage of breakage with respect to material thickness (1.2 mm). The shearing with precisely controlled shear clearance was performed by US Steel, and the other edge conditions are prepared by EWI.

a. **NDE Measurement Setup**
A small size surface probe was used to measure the eddy current signals as shown in Fig. 3. The probe is attached to the fixture that has CNC control in *x* and *y* directions horizontally as shown in Fig. 4. The interested edges were aligned facing up vertically and the stacked samples were separated layer by layer with non-conductive material.

b. **NDE Measurement**

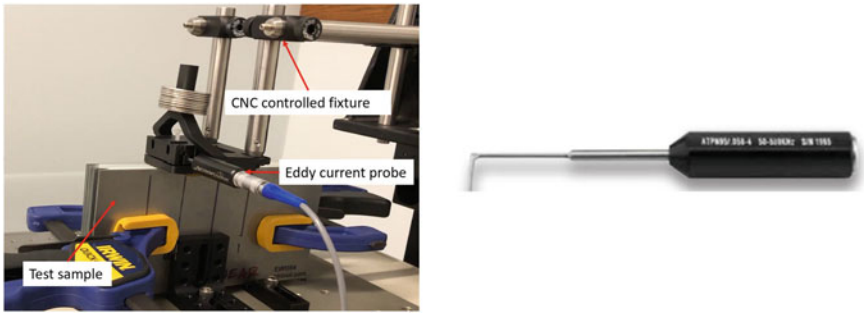


Fig. 3 Eddy current probe setup and the eddy current probe. (Color figure online)

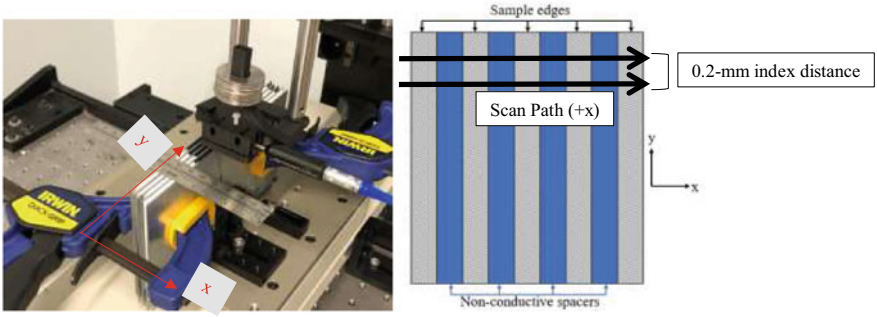


Fig. 4 Measurement setup and schematic of sample layout. (Color figure online)

In this study, the EC measurement frequency was set to be 500 kHz to obtain high-resolution EC data. The NDE measurement system was calibrated for the selected DP780 material. The NDE probe was set to travel 25 mm in *x*-direction using the CNC-controlled fixture as indicated in Fig. 4. 1000 data points were collected in each second. In each scan path, approximately16,000 data points were collected. A total of 200 scan paths in *x*-direction were conducted for each set of the stacked five samples as shown in Fig. 4. The probe position was incrementally changed with 0.2-mm in *y*-direction after finishing each scan path. The three scan data from different scan paths were selected to calculate an average NDE data for each sheared sample. The signal component that is sensitive to work-hardening level is isolated, which is called the vertical component. The NDE scan data reported in this study are referred to as the vertical component.

c. **HSDT and hardness tests**

Two different tests, HSDT and micro-hardness testing, were used to establish a relationship between NDE data and the edge quality. HSDT evaluates the straight sheared edge by stretching the sheared edge with a 100-mm diameter dome punch shown in Fig. 5 [7]. Three samples were repeated in HSDT for each representative edge condition. The local strain distribution of the sheared edge



Fig. 5 HSDT setup, HSDT tested sample, and DIC strain contour. (Color figure online)

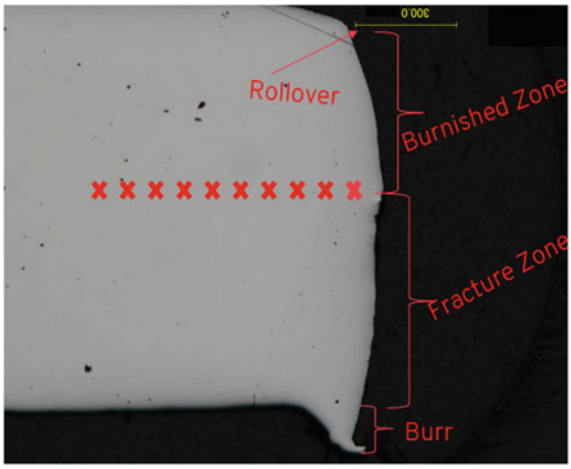


Fig. 6 Schematic of indentation locations of micro-hardness testing. (Color figure online)

was measured using DIC cameras. The equivalent failure strain before initiation of edge cracking was recorded as shown in Fig. 5.

A micro-hardness test was also conducted to evaluate the work-hardening introduced by different edge conditions. Ten indentations were made for each measured sample from the sheared edge to the base metal as shown in Fig. 6. The starting point of indentation was selected at the transition between the burnished zone and fracture zone since the work-hardening was known to be more pronounced in this transition area. The first indentation was 100 μm from the sheared edge, and the subsequent indentations had 150-μm step pitch.

4 Results

4.1 EC results

Figure 7 shows a contour plot of the NDE data distribution of five samples that had different edge conditions from shearing and machining. The red color indicates the

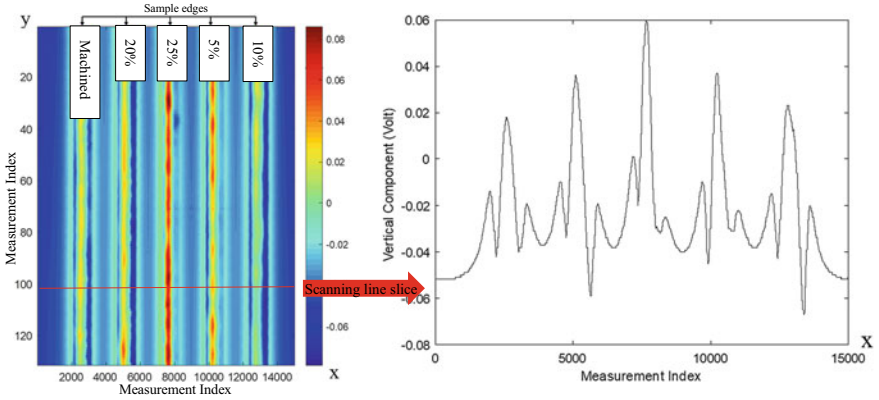
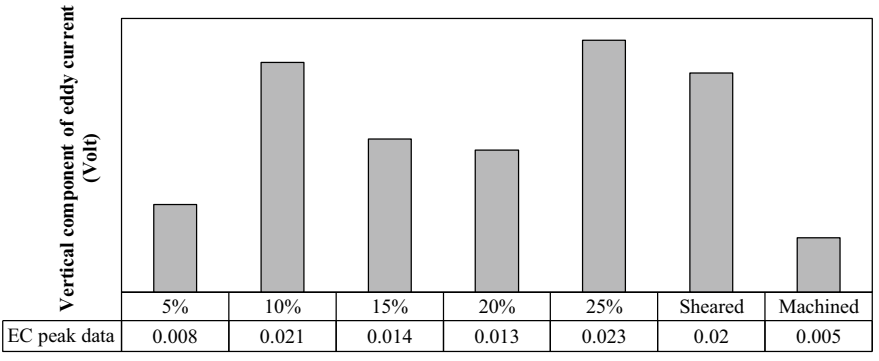


Fig. 7 Colormap and schematic of selection of data slices from EC scanning of machined edge, 20, 25, 5, and 10% sheared clearance (L–R), and example of peak data across the thickness in the same order. (Color figure online)

maximum NDE signal that was measured on the sheared edges. Each sample has different work-hardening levels from shearing at different clearances. The NDE scan data were sliced horizontally as shown in Fig. 7. Due to the limitation of the fixture, only five samples can fit in one scan. The five local peak values of the continuous NDE data correspond to the five stacked samples during scanning. The scanning direction is along the $+x$ direction, which is the same as the thickness direction. Peak value occurs around the middle point of the sample thickness.

The EC peak values of the sample in all edge conditions are compared in Fig. 8.



	5%	10%	15%	20%	25%	Sheared	Machined
EC peak data	0.008	0.021	0.014	0.013	0.023	0.02	0.005

Fig. 8 Summary of EC peak value of different edge conditions

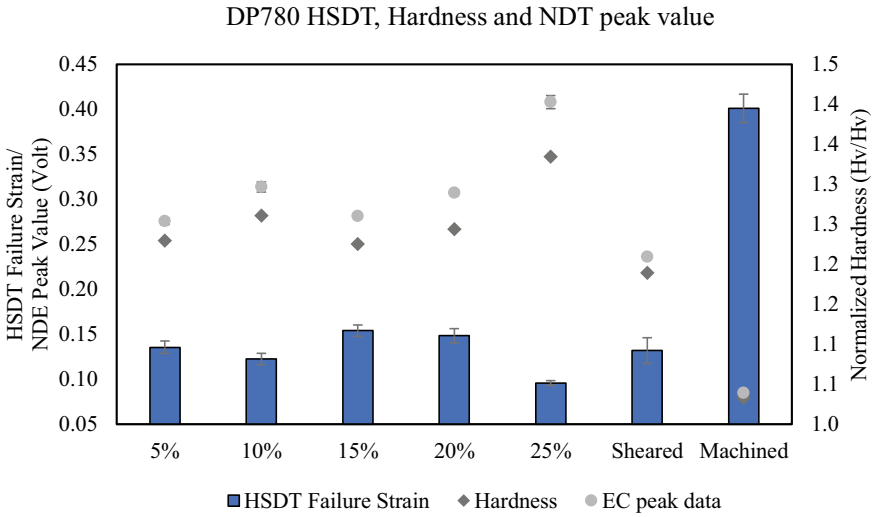


Fig. 9 Comparison of NDE result and destructive evaluations of edge formability. (Color figure online)

4.2 Correlation of NDE result with HSDT and hardness results

The NDE result was compared with the equivalent strain for the onset of edge cracking from HSDT and the normalized edge hardness from Vickers micro-hardness measurement. Figure 9 compares the NDE and destructive evaluation of edge quality. The higher equivalent failure strain in HSDT indicates the more formable edge condition. The lower hardness represents the better edge quality.

The critical hardness value was calculated using Eq. 1. HV_{edge} was obtained from the first indentation at the edge. HV_{base} was the average hardness value of the last four indentations of the measurement array.

$$\text{Normalized Hardness} = HV_{Edge} / HV_{base} \tag{1}$$

A correlation between NDE and destructive tests can be modeled using the power regression method as shown in Fig. 10. The regression model between NDE result and normalized hardness shows R-squared value over 94%, which indicates good reliability of the model. The regression model between NDE result and average HSDT failure strain shows R-squared value around 80%, which indicates relatively less correlation. Therefore, more experiment data should be considered to improve the correlation.

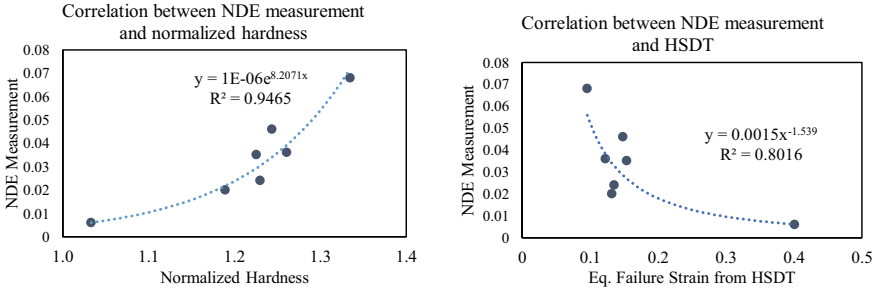


Fig. 10 Potential correlation of NDE measurement with destructive measurements. (Color figure online)

5 Conclusions

The following conclusions can be made from this study:

- The eddy current NDE tool can be used to measure the work-hardening level on sheared edges.
- The NDE data show a strong correlation with the edge quality evaluation results of HSDT and micro-hardness test.
- The NDE value increases as the HSDT strain decreases or hardness increases.
- As future work, NDE data can be attempted for predicting the edge failure by correlating with the formability test results such as hole expansion test and HSDT.

Acknowledgments The authors acknowledge great support from the Ohio Development Service Agency on Edison Advanced Manufacturing Program (Grant number AMP 17-103-2017) and wonderful collaborations with the industry partners: General Motors Company, Fiat Chrysler Automobiles (FCA), Cosma International, POSCO, Novelis, ESI, AutoForm, Diversified Tooling Group, AMEPA, Fuchs Lubricants Co., Selmatec, and GBTP.

References

1. Mouritz AP (2012) Chapter: 23 Nondestructive inspection and structural health monitoring of aerospace materials. Introd Aerosp Mater, Elsevier, 2012, pp. 534–557
2. Innerspec Technologies., Inc., EMAT Technology (2017) Retrieved August 30, 2017, http://www.innerspec.com/knowledge/emat-technology/
3. Fraunhofer IZFP (2014) PHS process monitoring & product quality control with 3MA
4. Pathak N, Butcher C, Worswick M (2016) Assessment of the critical parameters influencing the edge stretchability of advanced high strength steel. J Mater Eng Perform 25(11)
5. Wu X, Bahmanpour H, Schmid K (2012) Characterization of mechanically sheared edges of dual phase steels. J Mater Process Technol 212(6):1209–1224
6. Levy B, Van Tyne C (2012) Review of the shearing process for sheet steels and its effect on sheared-edge stretching. J Mater Eng Perform 21(7):1205–1213

7. Gu J, Kim H, Shih H, Dykeman J (2018) Effects of blanking conditions to edge cracking in stamping of advanced-high strength steels (AHSS). SAE Technical Paper 2018-01-0626. https://doi.org/10.4271/2018-01-0626
8. Pathak N, Gu J, Kim H (2019) A novel method to nondestructively measure the shear edge properties for edge cracking evaluation with advanced high strength steels. SAE Technical Paper 2019-01-1090

An Extended Ductile Fracture Prediction Model Considering Hydrostatic Stress and Maximum Shear Stress



Zhe Jia, Lei Mu, Ben Guan, and Yong Zang

Abstract An uncoupled ductile fracture model, based on Mu–Zang model, is extended by incorporating a hydrostatic stress term. An aluminum alloy material (Al 6016-T6) is selected with a series of static ductile fracture tests performed on four different specimens, which can cover a wide range of stress states. A robust simulation-experiment approach is adopted to characterize the correlation between the material's ductility and distinct stress states. The extended model is then calibrated using least-squares optimization. The resulting 3D fracture surface demonstrates acceptable deviations from the tested data, manifesting a promising capability of the extended model to describe the ductility of the considered material within a wide stress state range. In addition, the comparison against other representative ductile fracture models further confirms a good prediction performance of the model proposed.

Keywords Ductile fracture · Hydrostatic stress · Stress triaxiality · Lode parameter

1 Introduction

Aluminum alloys with a high strength-to-weight ratio are being increasingly used in the automobile industry due to the demand for weight reduction, fuel efficiency, and environmental friendliness. Accordingly, it is an urgent issue to accurately predict the ductile fracture behavior of aluminum alloys during the forming process.

For the last decades, various ductile fracture models have been developed, which have been classified into two major types: coupled models and uncoupled models [1]. In the framework of a coupled model (i.e. GTN model), the ductile damage-induced material strength degradation is elaborately considered, whereas an uncoupled model

Z. Jia · B. Guan (✉) · Y. Zang
School of Mechanical Engineering, University of Science and Technology Beijing, Beijing 100083, China
e-mail: guanben@ustb.edu.cn

L. Mu
Department of Mechanical and Aerospace Engineering, New Mexico State University, Las Cruces, NM 88003, USA

© The Minerals, Metals & Materials Society 2021

G. Daehn et al. (eds.), *Forming the Future*, The Minerals, Metals & Materials Series,
https://doi.org/10.1007/978-3-030-75381-8_133

(i.e. MMC model, Lou–Huh model) ignores the interaction between ductile damage and material constitutive model by empirically or semi-empirically formulating the damage accumulation in a specialized function containing several macroscopic variables (such as equivalent plastic strain, tensile stress, hydrostatic stress, etc.) [2–4]. In the past decade, many extensive efforts have been made in the development of modern uncoupled models, which demonstrate sensitivities to both stress triaxiality and Lode parameter. These novel models have been successfully used to characterize the formability of various materials, including DP590, Al 2024-T351, and 5083-O [4–7]. The prediction accuracy of proposed models on ductile fracture behavior needs to be further improved from the perspective of void evolution. Mu et al. recently proposed a new phenomenological fracture model, considering the two well-known void deformation modes, viz., void dilation and void elongation/rotation [5, 6]. In the Mu–Zang model, the normalized first principal stress ($\sigma_1/\overline{\sigma}$) is used to characterize the void dilation, whereas the normalized maximum shear stress ($\tau_{\max}/\overline{\sigma}$) is used to characterize the void elongation/rotation. However, the void dilation theoretically determines how the volume of voids enlarges due to all-sided (triaxial) tension conditions and is caused by hydrostatic tensile stress [8]. Thus, the current paper has been proposed to modify Mu–Zang model through characterizing the void dilation mode using stress triaxiality, which is defined by the ratio of hydrostatic stress to von Mises stress. A hybrid experimental-simulated method is used to calibrate the model under a large range of stress state. The results show that the proposed model has a good ability of prediction for aluminum alloys.

2 A Modified Ductile Fracture Model

The void dilation part of Mu–Zang model is slightly modified by using a normalized hydrostatic tensile stress term, as shown in Eq. (1). C_1 and C_2 indicate the sensitivities of various materials to the two major void deformation modes, namely, void dilation and void elongation/rotation, respectively; C_3 represents the effect of superposition of two void modes; C_4 expresses the threshold value of ductile fracture; D_n takes a form of $D_n = R_n(\overline{\varepsilon}^p)^m$ according to [6].

$$C_4 = \int_0^{\overline{\varepsilon}^f} \left\langle C_1 \frac{\sigma_m}{\overline{\sigma}} + C_2 \frac{\tau_{\max}}{\overline{\sigma}} \right\rangle^{C_3} D_n d\overline{\varepsilon}^{\mathrm{p}}. \tag{1}$$

When using an uncoupled ductile fracture model to capture the occurrence of ductile fracture during a certain form process, researchers generally reformulate the selected model in the space of stress triaxiality (η), Lode parameter (L), and fracture strain ($\overline{\varepsilon}^f$) based on a linear loading assumption, constructing a 3D fracture surface function [9, 10]. Then the constructed 3D fracture surface function is used in a linear ductile damage indicator framework to define the ductile damage evolution. Likewise, Eq. (1) is reformulated in the space of (η, L, $\overline{\varepsilon}^f$), as follows,

Table 1 Material parameters of hardening model

	A/MPa	ε_0	n	Q_s/MPa	Q_0/MPa	V_0/MPa	h
AA 6016-T6	475.5	0.025	0.126	380.93	299.31	5819.32	0.1

$$\bar{\varepsilon}^f = C_{4N}\left\langle \frac{\sqrt{L^2+3}}{C_1\eta\sqrt{L^2+3}+C_2} \right\rangle^{C_{3N}} \tag{2}$$

where

$$C_{3N} = \frac{C_3}{m+1}, C_{4N} = \left[\frac{C_4(m+1)}{R_m}\right]^{\frac{1}{m+1}}. \tag{3}$$

3 Model Calibration

3.1 The Stress–Strain Curve of AA 6016-T6

In this study, an aluminum alloy sheet (AA 6016-T6) with a thickness of 1.5 mm is selected to verify the predictive ability of the modified model. Its stress–strain curve is obtained by performing several uniaxial tension tests on the dog-bone specimens cut along the rolling direction. The Swift-Voce combined model (Eq. 4) is used to describe the stress–strain curve, with the identified parameters listed in Table 1.

$$Y\left(\bar{\varepsilon}^p\right) = h\left[A\left(\varepsilon_0+\bar{\varepsilon}^p\right)^n\right] + (1-h)\left[Q_s - (Q_s - Q_0)e^{\left(-\frac{V_0}{Q_s}\bar{\varepsilon}^p\right)}\right] \tag{4}$$

where A, ε_0, n, Q_s, Q_0, and V_0 are material constants, h denotes the superposition coefficient of two hardening models.

3.2 Experiments and Simulation of Ductile Fracture

Four different specimen geometries, which can cover a wide range of stress states (from simple shear to balanced biaxial tension), are carefully designed, as illustrated in Fig. 1. Each specimen is extracted from the same sheet along the rolling direction. Tension tests on No. 1, No. 2, and No. 3 are conducted on a universal testing machine with the cross-head traveling at a speed of 1 mm/min. Nakajima tests (on specimen No. 4) are performed on Zwick-BUP 600 testing machine with the punch traveling at

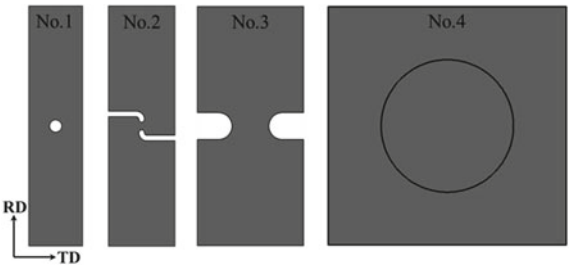


Fig. 1 Specimens with different geometries: (1) specimen with a central hole (No. 1); (2) simple shear specimen (No. 2); (3) plane strain tension specimen (No. 3); (4) specimen for Nakajima test (No. 4, the solid line stands for draw-bead)

a speed of 0.5 mm/s. To capture the surface strain field of each specimen, the Digital Image Correlation (DIC) technique is utilized. Besides, the load–displacement curves of specimens Nos.1–3 are obtained using a DIC-based extensometer. Each test is repeated three times to ensure the reliability of the results.

Parallel simulations are carried out using ABAQUS/Explicit 6.14. All specimens are meshed by C3D8R elements, meanwhile loading condition is achieved by applying displacement control to each loading unit. The duration of each simulation is carefully defined to assure a quasi-static condition. Considering the fact that ductile fracture propagates very quickly after its onset, the fracture moment is identified as the one corresponding to the sudden drop in the measured load–displacement curve for each simulation. The simulated and measured force–displacement curves and surface strain fields are compared to validate the corresponding simulations, as demonstrated in Fig. 2.

3.3 Construction of 3D Ductile Fracture Surface

As postulated by other researchers [11, 12], the element presenting the highest strain is identified as the critical location where the ductile fracture initiates for each simulation. Figure 3 shows the η and L evolutions of each specimen at the critical location before the identified fracture moment. It is obvious that the values of η and L keep changing during the deformation process. Therefore, we average these values by using Eq. (5), and the results are shown in Table 2.

$$\eta_{\text{av}} = \frac{1}{\overline{\varepsilon}^f} \int_0^{\overline{\varepsilon}^f} \eta \mathrm{d}\overline{\varepsilon}^p, \; L_{\text{av}} = \frac{1}{\overline{\varepsilon}^f} \int_0^{\overline{\varepsilon}^f} L \mathrm{d}\overline{\varepsilon}^p. \tag{5}$$

Then the least-square method is used to identify a group of model parameters, which can minimize the accumulation between the targeted 3D fracture surface and the ductile fracture data points shown in Table 2. The resulting 3D surface and the calibrated parameters are shown in Fig. 4. It is clear that the constructed 3D fracture surface can well describe the correlation between material ductility and stress state for AA 6016-T6. Figure 4 shows that fracture strain $\overline{\varepsilon}_f$ is a decreasing function with

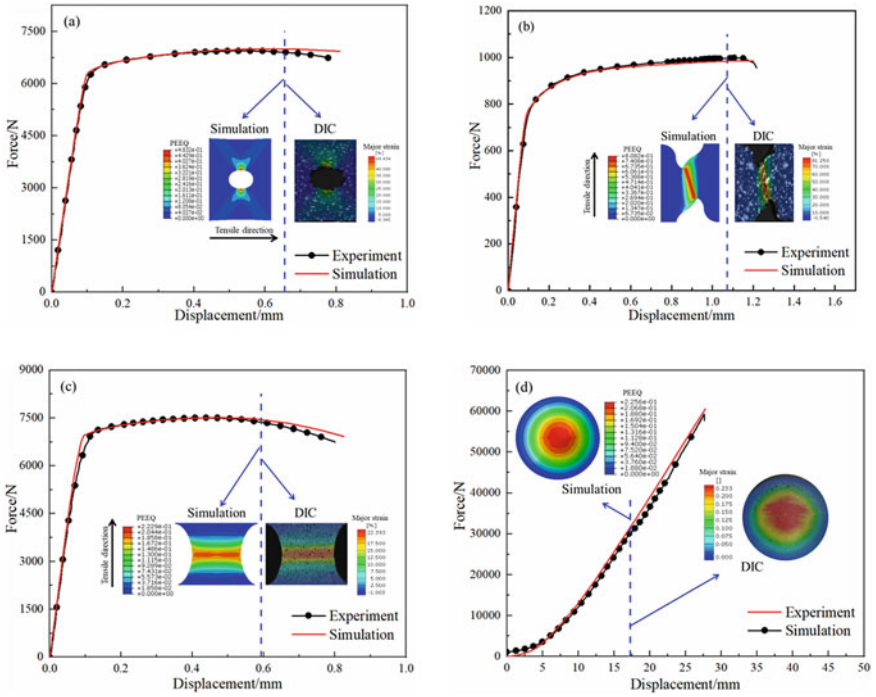


Fig. 2 Comparison between experimental and simulated force–displacement curves and surface strain distributions: **a** specimen No. 1; **b** specimen No. 2; **c** specimen No. 3; **d** specimen No. 4. (Color figure online)

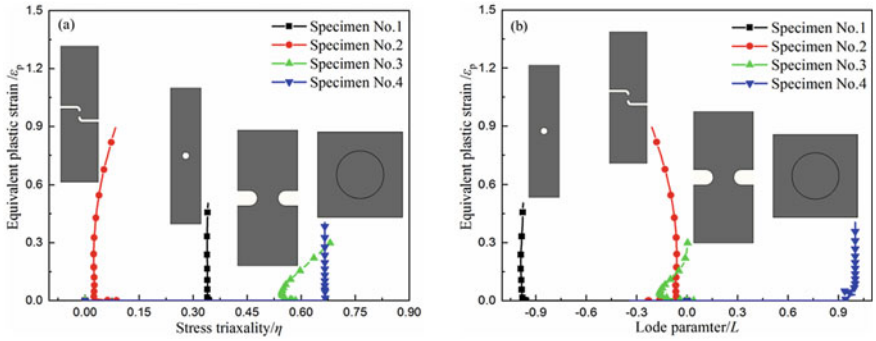


Fig. 3 The η and L evolutions of the critical location before the identified fracture moment: **a** η; **b** L. (Color figure online)

Table 2 Ductile fracture data of four specimens

Specimen	Stress triaxiality/η_{av}	Lode parameter/L_{av}	Equivalent fracture strain $\bar{\varepsilon}_f$
No. 1	0.3396	−0.9827	0.5567
No. 2	0.0401	−0.1006	0.8930
No. 3	0.5999	−0.0652	0.3559
No. 4	0.6654	0.9936	0.3837

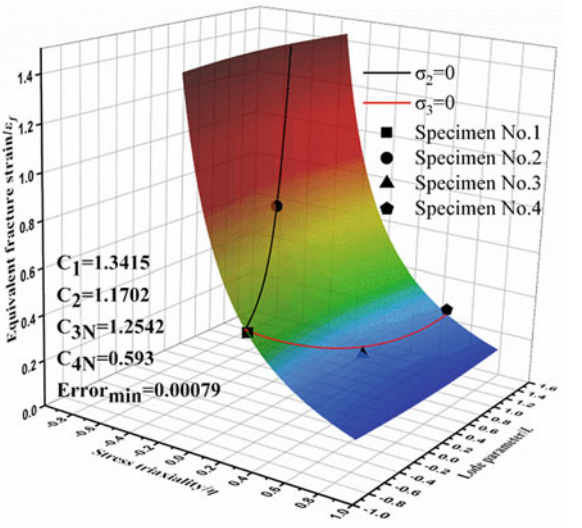


Fig. 4 3D ductile fracture surface of AA 6016-T6 constructed with the calibrated model. (Color figure online)

respect to stress triaxiality for a given Lode parameter. The reason for this trend is that a higher stress triaxiality promotes void dilation, resulting in a poor ductility.

4 Comparison of Three Ductile Fracture Models

MMC model (Eq. 6) and Lou–Huh model (Eq. 7) have been deemed as typical representatives of modern uncoupled ductile fracture models [3, 4].

$$\bar{\varepsilon}_{f-MMC} = \left\{ \begin{array}{l} \dfrac{A}{C_6}\left[C_7 + \left(2+\sqrt{3}\right)(1-C_7)\left(\sqrt{L^2+3}-\sqrt{3}\right)\right] \\ \left[\sqrt{\dfrac{1+C_5^2}{L^2+3}} + C_5\left(\eta - \dfrac{L}{3\sqrt{L^2+3}}\right)\right] \end{array} \right\}^{-\frac{1}{n}} \tag{6}$$

$$\overline{\varepsilon}_{f-Lou} = C_{10}\left(\frac{\sqrt{L^2+3}}{2}\right)^{C_8}\left[\frac{3(1+C_{11})\sqrt{L^2+3}}{3(\eta+C_{11})\sqrt{L^2+3}-L+3}\right]^{C_9}. \quad (7)$$

For the purpose of comparison, these two models and three aluminum alloys (Al 6016-T6 of the current study, 2024-T351 [4], and 5083-O [7]) are selected. Following the same calibration procedure, the results are given in Figs. 5 and 6. It is observed that using the same model, the constructed 3D fracture surfaces of different materials differ from each other in surface height and surface curvature, representing differences in ductility. Also, different models demonstrate varying levels of error from the tested data for the same material: for 6016-T6 and 5083-O, the minimized error by the modified model is the smallest one, followed by Lou–Huh model and MMC model; as for 2024-T351, MMC model yields the smallest minimized error, followed by Lou–Huh model and the modified model. Regardless of the observed differences in the model performance, these three models all can work well for the selected aluminum alloys with acceptable errors (Fig. 7).

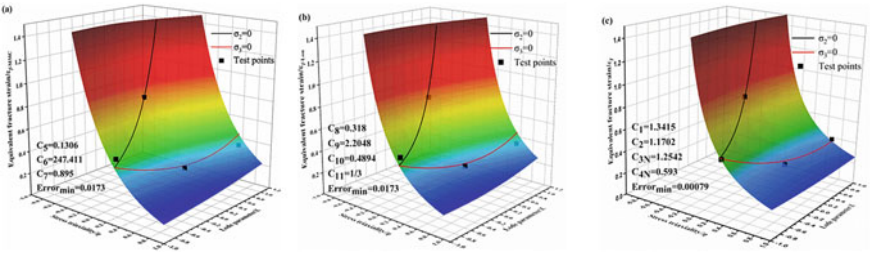


Fig. 5 3D ductile fracture surface of 6016-T6: **a** MMC model; **b** Lou–Huh model; **c** modified model. (Color figure online)

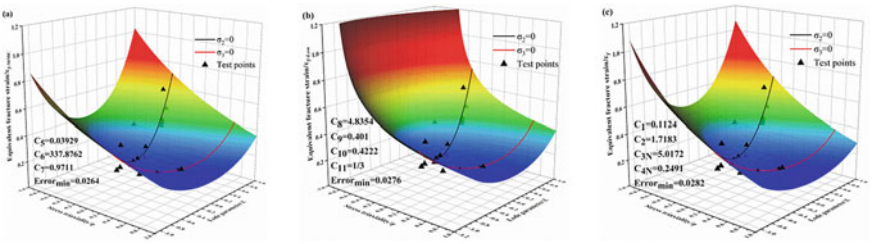


Fig. 6 3D ductile fracture surface of 2024-T351: **a** MMC model; **b** Lou–Huh model; **c** modified model. (Color figure online)

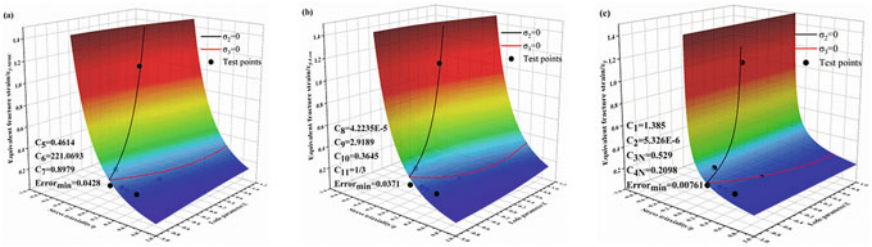


Fig. 7 3D ductile fracture surface of 5083-O: **a** MMC model; **b** Lou-Huh model; **c** modified model. (Color figure online)

5 Conclusion

An extended ductile fracture prediction model is proposed by considering hydrostatic stress that controls the behavior of void dilation. Four specimens with various shapes are employed to achieve different stress states ranging from simple shear to biaxial tension. The comparison between experiments and predicted results shows a good prediction performance of the proposed model. Meanwhile, the proposed model has a good applicability for the aluminum alloys selected.

References

1. Li H, Fu MW, Lu J, Yang H (2011) Ductile fracture: experiments and computations. Int J Plast 27(2):147–180
2. Nahshon K, Hutchinson JW (2008) Modification of the Gurson model for shear failure. Eur J Mech A-Solid 27(1):1–17
3. Lou Y, Yoon JW, Huh H (2014) Modeling of shear ductile fracture considering a changeable cut-off value for stress triaxiality. Int J Plast 54:56–80
4. Bai Y, Wierzbicki T (2010) Application of extended Mohr–Coulomb criterion to ductile fracture. Int J Fract 161(1):1–20
5. Mu L, Jia Z, Ma ZW, Shen FH, Sun YK, Zang Y (2020) A theoretical prediction framework for the construction of a fracture forming limit curve accounting for fracture pattern transition. Int J Plast. https://doi.org/10.1016/j.ijplas.2020.102706
6. Mu L, Zang Y, Wang Y (2018) Phenomenological uncoupled ductile fracture model considering different void deformation modes for sheet metal forming. Int J Mech Sci 141:408–423
7. Qian LY, Fang G, Zeng P, Wang Q (2015) Experimental and numerical investigations into the ductile fracture during the forming of flat-rolled 5083-O aluminum alloy sheet. J Mater Process Technol 220:264–275
8. Hering O, Tekkaya AE (2020) Damage-induced performance variations of cold forged parts. J Mater Process Technol 279:116556
9. Hu Q, Li X, Han X, Chen J (2017) A new shear and tension based ductile fracture criterion: modeling and validation. Eur J Mech A-Solid 66:370–386
10. Quach H, Kim JJ, Nguyen DT, Kim YS (2020) Uncoupled ductile fracture criterion considering secondary void band behaviors for failure prediction in sheet metal forming. Int J Mech Sci 169:105297

11. Roth CC, Mohr D (2016) Ductile fracture experiments with locally proportional loading histories. Int J Plast 79:328–354
12. Erice B, Roth CC, Mohr D (2018) Stress-state and strain-rate dependent ductile fracture of dual and complex phase steel. Mech Mater 116:11–32

Full-Field Strain Measurement in Multi-stage Shear Cutting: High-Speed Camera Setup and Variational Motion Estimation



Christoph Hartmann and Wolfram Volk

Abstract Shear cutting is a prominent process in the chip-less separation of metallic sheet materials. The cut surface characteristics have been the basis for quality assessment but the shear-affected zone becomes increasingly important with regard to the functionality of the produced components, such as further processing or its final application. Multi-stage shear cutting processes may be used to specifically adjust the mechanical and geometrical properties of shear cut edges. Originally, multi-stage shear cutting was aimed at producing smooth and clean-cut surfaces with high-dimensional accuracy and improved load capacity. However, nowadays, it is also used to reduce the sensitivity to edge cracking, for example. In this paper, we present a novel approach for the experimental analysis of multi-stage shear cutting as a basis for advanced process analysis and validation. Moreover, the achieved results may serve for future database process design, modeling, and control. We developed an in-situ test design and measurement setup that preserves the real process boundary conditions of shear cutting. An enhanced high-speed optical full-field evaluation method based on optical flow methods allows local and time-resolved measurement of strain fields and strain rate fields for each shear cutting stage. A mapping of these state variables between the individual cuts enables us to analyze consistently the shear-affected zone throughout the whole multi-stage process and thus to characterize the final state of the shear-affected zone experimentally.

Keywords Multi-stage · Shear cutting · Strain · Strain rate · Deformation measurement · Shear-affected zone

C. Hartmann (✉) · W. Volk
Technical University of Munich, Walther-Meissner-Strasse 4, 85748 Garching, Germany
e-mail: christoph.hartmann@utg.de

© The Minerals, Metals & Materials Society 2021

G. Daehn et al. (eds.), *Forming the Future*, The Minerals, Metals & Materials Series,
https://doi.org/10.1007/978-3-030-75381-8_134

1 Introduction

Shear cutting represents the most prominent, chip-less separation process for sheet metal. Two-stage shear cutting consists of a conventional shear cutting stage and a second stage, which we denote the shaving[1] stage throughout this work. Multi-stage shear cutting extends this concept and applies several shaving stages. The guideline VDI2906-1 defines shaving as trimming of narrow edges of semi-finished sheet metal [1]. As originally stated by Kuhlmann, the process was aimed at producing smooth and clean-cut surfaces that were as free of tears and cracks as possible with high-dimensional accuracy and improved load capacity [2, 3]. However, for example, Pätzold et al. and Feistle et al. also used multi-stage shear cutting to reduce the sensitivity to edge cracking [4, 5]. The use of shaving operations to prevent edge cracking is only one example that emphasizes the rising importance of the shear-affected zone when assessing the quality of shear cutting processes. In general, the shear cutting process strains and damages the material in the shear-affected zone at the component's edge, which impedes further processing or lifetime use and application. Weiss et al. showed the effect of internal stresses in the shear-affected zone on the magnetic loss in electrical sheet metal processing or Hamada et al. its influence on fatigue crack propagation [6, 7]. Hence, and in contrast to typical procedures that entirely rely on the cut surface characteristics, the induced pre-straining and pre-damaging in the shear-affected zone should be taken into account for advanced process design, whether or not shear cutting or multi-stage shear cutting is used.

Today's process design heavily incorporates numerical models to predict part properties and to size the manufacturing equipment. However, the simulation of the shear cutting process alone remains a challenging task for its multiscale characteristics, large deformations, localization, damage, and thermomechanical interactions, as reported exemplarily by Bolka et al. and Sonkamble et al. [8, 9]. Due to error propagation and mapping dependencies, the numerical analysis of the multi-stage shear cutting process presents even more challenging, as shown in the investigations of Wang et al [10]. In essence, the experimental validation of this simulation model faces the same major challenges, especially regarding the development of the shear-affected zone, see for example Wang et al. [11]. To evaluate experimentally the development of the shear-affected zone, highly resolved full-field measurements are necessary. Furthermore, these measurements should be carried out under the natural process boundary conditions that are assumed plane strain in classical shear cutting processes, as for example stated by Aoki and Takahashi as well as Manopulo [12, 13].

In this investigation, we, therefore, propose an experimental setup to observe the shear cutting under plane strain conditions in high spatial and temporal resolution using a tailored precision shear cutting tool equipped with a high-speed camera and a microscope lens, see Fig. 1a. We further present an evaluation procedure for the robust calculation of displacements, strains, and strain rates from the high-speed image sequence. To enable a multi-stage analysis, we incorporated a mapping of the

[1] The term *shaving* commonly is limited to small cutting offsets.

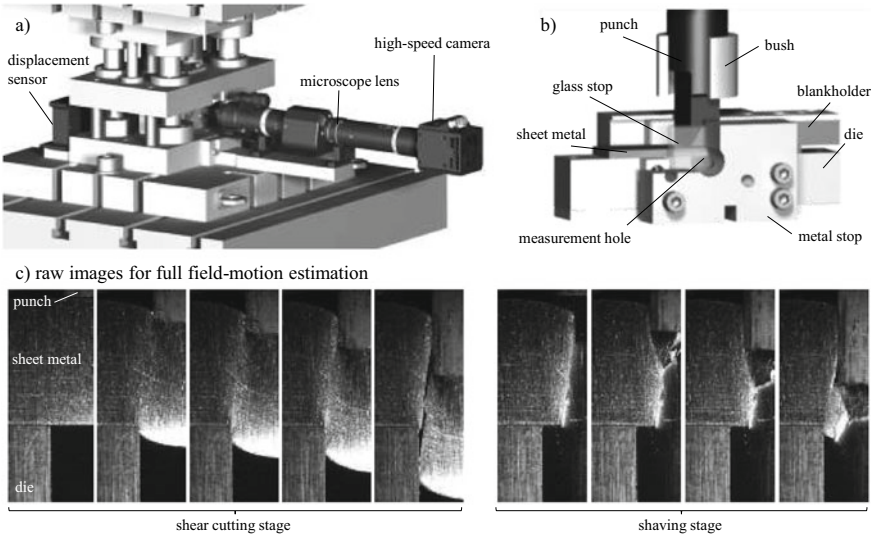


Fig. 1 **a** Precision shear cutting tool equipped with displacement sensor, microscope lens, and high-speed camera. **b** Free-cut view on the sheet metal specimen, the glass stop (supported by a metal stop), and the active elements of the shear cutting tool [16]

measured state fields between the subsequent cutting stages. Finally, two variants of a two-stage shear cutting process are subject to the evaluation.

2 Approach

In order to observe the shear cutting process under its natural boundary condition that is plane strain, we follow the tool setup proposed by Takahashi and Aoki using glass stops at the sheet metal edge [14]. Figure 1b illustrates the arrangement of the active elements, the sheet metal specimen, and the glass stop in the shear cutting tool. In previous work, our coworkers and we validated that the glass stops prevent bulging and thus maintain the plane strain boundary condition present inside the sheet material [15]. Next to the high-speed camera with the microscope lens, the shear cutting tool is also equipped with a laser displacement sensor and a load cell to measure punch travel and cutting force. A single trigger ensures synchronous recording of all measurement signals [16].

We utilized the acquired high-speed camera images, see Fig. 1c, to calculate the deformation fields during the shear cutting process. The classic way to do this motion estimation in engineering practice is digital image correlation (DIC), introduced by Yamaguchi as well as Peters and Ranson [17, 18]. Besides its many advantages, like flexibility, reliability, and simplicity, DIC has some drawbacks, such as, for example, the handling of discontinuities, described by Hassan [19] and Balle et al. [20], density

of the motion field, or the subsequent calculation of derivatives as our coworkers and we showed [16, 21].

3 Full-Field Motion Estimation

We implemented an alternative approach for full-field motion estimation based on optical flow methods, which are popular for object tracking in the field of computer vision but rarely used in experimental mechanics. We did not apply any artificial speckle pattern, as common in DIC analysis, since it would smear in the contact area with the glass stop. However, we achieved to use the material texture from machining specimen preparation for the deformation measurement algorithm. We validated the general usability of the machined specimens in a detailed analysis, where we compared them to polished and etched specimens that provide speckle-like patterns due to the grain structure of the material [22]. In contrast to etched and polished samples, machined specimens are suitable for experimental parameter studies, since they can be produced in large quantities without great effort.

The core of optical flow methods is a variational formulation with respect to the digital image intensity values (8-bit grey values in our case) over the region of interest Ω defined in the image domain. Based on this variational formulation, optical flow methods obtain the motion field[2] $\boldsymbol{u}$, where $\boldsymbol{u} = (u_1, u_2)$ for plane motion, by minimizing the energy functional $E(\boldsymbol{u})$, which is often split into a data term $D(\boldsymbol{u})$ and a regularization term $R(\boldsymbol{u})$. The data term D proposes the interaction of the motion field and the provided image data, while the regularization term R models the structure of the motion field. In general form, the energy functional reads

$$E(\boldsymbol{u}) = D(\boldsymbol{u}) + \alpha R(\boldsymbol{u}) \tag{1}$$

where α is a positive scalar weighting factor. Various approaches exist for modeling the data term D and the regularization term R. For example, Baker et al draw a comparison of different methods [23]. We utilize a combination of spatial and temporal regularization [16, 24]. Therefore, we combined the recursive regularization approach by Hewer et al. [25] and the trajectorial, temporal regularization proposed by Volz et al. [26]. The energy functional in Eq. (1) thus takes the following form

$$E(\boldsymbol{u}) = D(\boldsymbol{u}) + \alpha_t R_t(\boldsymbol{u}) + \alpha_s R_s(\boldsymbol{u}), \tag{2}$$

where R_t and R_s are the temporal and spatial regularization terms with the respective weighting factors α_t and α_s. The data term D contains a combination of the image intensity consistency assumption and the spatial gradient consistency assumption, as

[2] We use the term motion field here for consistency with the computer vision literature, which is known as the displacement field in the engineering discourse.

proposed, for example, in [27]. To couple five consecutive images also in the data term D, it consists of a sum of four respective data terms D_i, where $i = 1, 2, 3, 4$. The target displacement $\boldsymbol{u}$ is the displacement $\boldsymbol{u}_2$ and may be used analogously. The weighting of the penalty between both assumptions is controlled by the positive scalar factor β, and contribution of each data term D_i by the scalar factors γ_i.

$$D(\boldsymbol{u}) = \sum_{1}^{4} D_i(\boldsymbol{u}) = \sum_{1}^{4} \gamma_i \int_{\Omega} \psi\left(|I_{i+1}(\boldsymbol{u}) - I_i|^2 + \beta|\nabla I_{i+1}(\boldsymbol{u}) - \nabla I_i|^2\right)\mathrm{d}\omega. \quad (3)$$

The function $\psi\left(x^2\right) = \sqrt{x^2 + 0.001^2}$ introduces a regularized L_1-norm minimization for convexity of the optimization objective [27]. Applying this generic framework of Hewer et al. [25], the spatial regularization term inherently provides a predetermined n-th order smoothness of the motion field $\boldsymbol{u}$. We applied a regularization term R_s of 3rd order. Again, the total term R_s results from the sum over four consecutive images.

$$R_s(\boldsymbol{u}, \boldsymbol{A}, \boldsymbol{B}) = \sum_{1}^{4} R_{s,i}(\boldsymbol{u}, \boldsymbol{A}, \boldsymbol{B}) = \sum_{1}^{4} \int_{\Omega} \delta_1\left(|\boldsymbol{A}_i - \nabla \boldsymbol{u}_i|^2 + \delta_2\left(|\boldsymbol{B}_i - \nabla \boldsymbol{A}_i|^2 + \delta_3\left(|\nabla \boldsymbol{B}_i|^2\right)\right)\right)\mathrm{d}\omega \quad (4)$$

Here, the factors δ_1, δ_2, and δ_3 weight between the spatial smoothness terms. $\boldsymbol{A}$ and $\boldsymbol{B}$ represent auxiliary variable to introduce the prior information on the smoothness of the displacement field. Furthermore, the formulation in Eq. (4) allows for direct calculation of displacement gradients, hence strains, using the auxiliary variable $\boldsymbol{A}$ also as an output. We implemented a trajectorial regularization term R_t of second order, which results in piecewise linear displacement trajectories. The temporal regularization term reads

$$R_t(\boldsymbol{u}) = |\boldsymbol{u}_1 - 2\boldsymbol{u}_2 + \boldsymbol{u}_3|_1 + |\boldsymbol{u}_2 - 2\boldsymbol{u}_3 + \boldsymbol{u}_4|_1. \quad (5)$$

The temporal regularization enables the robust computation of strain rates and, more important in the present investigation, also stabilizes the calculations of the other deformation fields. To cope with large deformations in the evaluation of the high-speed camera images, we implemented a coarse-to-fine image pyramid framework according to Burt and Adelson [28]. To reduce the data, we furthermore implemented an adaptive selection procedure to evaluate a minimum number of images but accordingly prevent linearization errors using predefined maximum displacement and strain increments. For detailed description of the algorithm implementation, parameter selection, and detailed derivation, we refer to our respective references [16, 24].

In general, we emphasize that spatio-temporal regularization is a promising technique to integrate physical relationships and assumptions in optical full-field evaluation. The presented variational model yields third spatial order smoothness and second-order temporal smoothness of the motion field. Besides the incorporation

of prior knowledge, the full-field measurement results are dense and allow further processing without the use of filters or hole-filling algorithms.

4 Experiments

The shear cutting experiments have been carried out on universal tension–compression testing machine of type 1484/DUPSM by Zwick GmbH & Co.KG, Ulm, Germany. We used specimens of the micro-alloyed fine-grained structural steel S355MC in the dimension 100 mm by 25 mm and 4 mm thickness. A cutting clearance of 10% and a punch velocity of 1 mm/s were set for all tests. The cutting edge geometry was equal at the punch and the die (50 µm radius).

First, the desired contour is pre-cut by conventional shear cutting leaving a narrow strip on the sheet metal component. The narrow strip is removed in the subsequent shaving stage. Shaving has different boundary conditions compared with conventional shear cutting and almost resembles a machining process. The die-side sheet metal represents the component; the punch-side material of both cuts is considered waste. As common in industrial practice, we used a closed cutting line setup on the first stage. After the first cut, tailored stops in the die allow to move the two sheet metal strips by the cutting offset in preparation of the second stage. We analyzed two different cutting offsets. Cutting offset 1 is 2 mm and cutting offset 2 is 1 mm.

5 Results and Discussion

Table 1 summarizes the resulting cut surface characteristics according to the guideline VDI2906-2 [28] for the two-stage processes. It also contains the values for the first shear cutting stage. Both two-stage strategies reduce the edge draw-in height, where offset 2 has a higher impact on this cut surface characteristic. Offset 2 yields an increase in the clean-shear share, where offset 1 leads to earlier fracture.

Table 1 Tactile measurements of the cut surface characteristics for the first shear cutting operation and the subsequent second stage operations. h_i represents the heights of the draw-in (d), the clean-shear (c), the fracture (f), and the burr (b), w_i the respective heights and α_i the respective angles. All values are based on five tests and five measurements for each test along the cutting line

	h_d in %	h_c in %	h_f in %	h_b in µm	w_d in µm	w_b in µm	α_c in °	α_f in °
Pre-cut	12.2 ± 2.1	23.4 ± 1.1	64.4 ± 1.7	51 ± 13	2259 ± 103	49 ± 9	90 ± 0.2	81 ± 1.1
Offset 1	7.3 ± 1.9	20.0 ± 1.7	72.7 ± 1.9	32 ± 16	1877 ± 59	46 ± 15	90 ± 0.1	81 ± 0.2
Offset 2	6.5 ± 2.3	34.0 ± 2.1	59.5 ± 2.1	49 ± 11	1606 ± 36	51 ± 16	90 ± 0.1	80 ± 0.1

In addition to the manipulation of the cut surface geometry, the multiple-stage shear cutting processes increasingly focus on the specific modification of the shear-affected zone, as we briefly explain above. The local analysis of the conducted two-stage shear cutting experiments, therefore, centers on the representation of the accumulated deformation in the shear-affected zone after the second shear cutting operation. For this purpose, we mapped the state variables between the two stages. The mapping represents a straightforward intermediate step in the evaluation algorithm, which carries out a rigid body translation. The rigid body translation describes the displacement of all material points during the sheet metal feed. We computed the displacement fields from the last image of the first cutting operation and the first image of the second cutting operation. The allocation of all information of a tracked material particle is, therefore, preserved and may be seamlessly used in the evaluation.

Figure 2 shows the equivalent strain E_{eq} distribution in the shear-affected zone for the first shear cutting stage, the two-stage shear cutting process using offset 1, and the two-stage shear cutting process using offset 2. We use the classical strain measure E_{eq}, although other possibilities are present, as, for example, the thermodynamic consist measure is derived by Butcher and Abedini [29]. We calculated the equivalent strain fields E_{eq} according to

$$E_{\mathrm{eq}} = \int_0^t \sqrt{\frac{1}{2}\left(\frac{\partial}{\partial t}\boldsymbol{A} + \frac{\partial}{\partial t}\boldsymbol{A}^{\mathrm{T}}\right) \cdot \frac{1}{2}\left(\frac{\partial}{\partial t}\boldsymbol{A} + \frac{\partial}{\partial t}\boldsymbol{A}^{\mathrm{T}}\right)}\,\mathrm{d}t \tag{6}$$

where t represents the shear cutting process time.

We visualized the strain distribution in two different color scales to give a better overall impression of the deformation state. In addition, the diagram of the principle strains E_1 and E_2 is shown next to the shear-affected zone graphs, whereby the color of each single coordinate reflects its probability density. The first-stage experiment, see Fig. 2a, shows a high straining along the clean-shear share and along the fracture surface. A strong gradient in vertical direction exists that starts from the cut surface and leads to smaller pre-deformation inside the sheet metal. Already ~0.8 mm away from the cut surface, the equivalent strain E_{eq} values decrease by at least 80%. The pre-deformation is higher in the edge draw-in region than on the underside of the sheet metal part. The imaginary connecting line from the beginning of the edge draw-in to the burr covers the area of moderate pre-deformation geometrically.

The shear-affected zone of the two-stage shear cutting with offset 1 has a similar strain distribution appearance as the first-stage experiment, when considering the coarser color scale, see Fig. 2b. The offset 1 experiment comes close to shear cutting with an open cutting line, which, however, the sheet metal material processed is already affected. Although the areas near the cut surface experience similar deformation, but with reduced peak values. In total, pre-deformation is reduced, with the change from closed to open cutting line. Especially on the burr side of the sheet metal component, the affected zone becomes thinner. The width of this zone at the edge

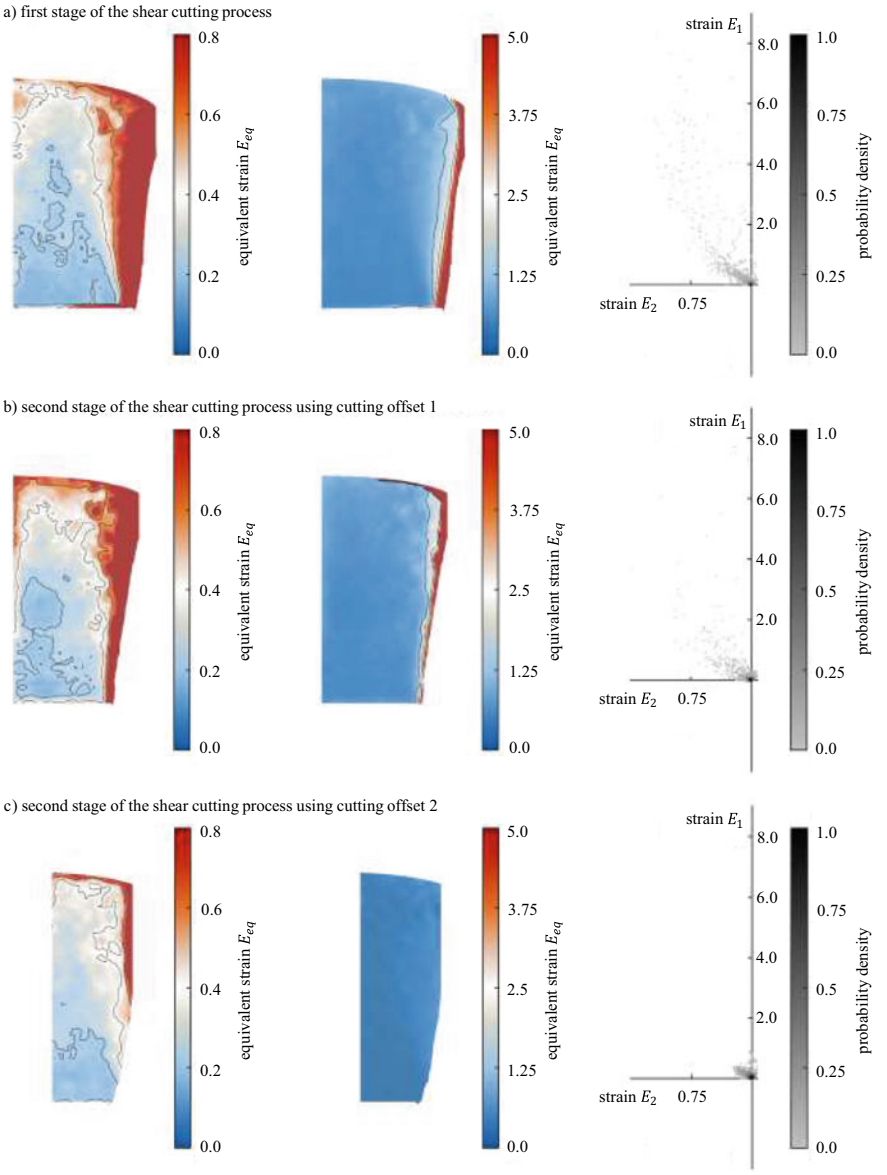


Fig. 2 Experimental measurement results for the conducted shear cutting processes. **a** Shear-affected zone after the first shear cutting operation. **b** Shear-affected zone after the second shear cutting operation using cutting offset 1. **c** Shear-affected zone after the second shear cutting operation using cutting offset 2. Please note that the principle strain diagrams may not be interpreted similar to the well-known pendant from sheet metal forming, the FLD, since deformation boundary conditions are different. (Color figure online)

draw-in is 0.8 mm and decreases to 0.4 mm at the burr. In the diagram of principal strains, this leads to lower probability densities for increased principal strain values compared to the reference experiment. Moderate pre-deformation distributes in a region spanned between the beginnings of the edge draw-in to the die edge.

The two-stage shear cutting with offset 2 results in a different shear-affected zone condition, see Fig. 2c. The deformation processes take place almost exclusively in the waste part of the sheet metal, so that hardly any additional deformation affects the sheet metal component. This becomes particularly clear when looking at the shearing influence zone with the coarse color scale. The pre-deformed areas that are already severely affected are separated from the waste and only regions that suffered moderate deformation remain in the part. The shear-affected zone, therefore, reveals lower equivalent strain values in its final state. The highly pre-deformed edge zone along the cut surface is almost completely eliminated. The shear zone shows only moderate deformation, which is also apparent in the diagram of the principal strains in comparison to the reference experiment and the two-stage shearing with cutting offset 1. The material particles occupied by the shear-affected zone using cutting offset 2 concentrate around the coordinate origin. Here, the principal strain distribution comes closer to that in the origin region of the reference experiment than that of the two-stage shear cutting using offset 1. In this sense, two-stage shear cutting with offset 2 eliminates the large scatter of pre-deformation and expands the diagram by certain portions along the E_1-axis, which mainly originate from shear deformation along with the clean-shear share of the second shearing stage.

6 Conclusion and Outlook

We proposed an experimental setup that is suitable to study multi-stage shear cutting processes under real process conditions. The conducted measurement equipment provides high temporal and spatial resolution data. Our full-field motion estimation approach based on variational methods can handle the raw images from the high-speed camera in a robust way and delivers full-field strain and strain rate information. By mapping the computed fields between the different stages, eventually a combined strain measure field for evaluation, analysis, and comparison of different process variants was possible. Based on the straightforward mapping between different process stages, also other multi-stage processes may be tested in the same way, such as combined shear cutting, forming, and stamping operations.

With the analysis of the two-stage shear cutting process, we have experimentally proven the effectiveness of shaving in reducing pre-deformations and pre-damage introduced in the first stage using full-field information. The choice of the cutting offset controls the process characteristics of the second stage that ranges from open cutting (offset 1) to machining-like boundary conditions (offset 2).

The high-resolution experimental data in the future can be used to validate and enhance numerical models, serve as a basis for inverse analysis and parameter identification, or offer a labeled information for database modeling.

Acknowledgments We gratefully acknowledge the German Research Foundation (Deutsche Forschungsgemeinschaft, DFG) for supporting this work carried out within the research project VO 1487/27.

References

1. VDI2906-1 (1994) Schnittflächenqualität beim Schneiden, Beschneiden und Lochen von Werkstücken aus Metall—Allgemeines, Kenngrößen, Werkstoffe. (in German)
2. Kuhlmann E (1954) Schabebearbeitung für die Fertigbearbeitung von Stanzteilen. Werkstattstechnik und Maschinenbau 44(4):157–162
3. Kuhlmann E (1954) Schabebearbeitung für die Fertigbearbeitung von Stanzteilen. Werkstattstechnik und Maschinenbau 46(2):67–68
4. Pätzold I, Feistle M, Golle R, Volk W, Frehn A, Ilksens R (2018) Determination of the minimum possible damage due to shear cutting using a multi-stage shear cutting process. IOP Conf Ser: Mater Sci Eng 418:012070
5. Feistle M, Pätzold I, Golle R, Volk W, Frehn A, Ilksens R (2018) Maximizing the Expansion Ratio through Multi-stage Shear-cutting Process during Collar Forming. IOP Conf Ser: Mater Sci Eng 418:012071
6. Weiss HA, Leuning N, Steetjes S, Hameyer K, Andorfer T, Jenner S, Volk W (2017) Influence of shear cutting parameters on the electromagnetic properties of non-oriented electrical steel sheets. J MagnMagn Mater 421:250–259
7. Hamada S, Zhang K, Zhang J, Koyama M, Yokoi T, Noguchi H (2018) Effect of shear-affected zone on fatigue crack propagation mode. Int J Fatigue 116:36–47
8. Bolka S, Slavic J, Boltezar M (2015) Identification of out-of-plane material characteristics through sheet-metal blanking. J Mech Eng 61(4):217–226
9. Sonkamble V, Dhondapure P, Narasimhan K, Tewari A (2019) Experimental investigation of shear band and shear strain field evolution during blanking of AA6082 sheet. J Strain Anal Eng Des 54(2):149–158
10. Wang K, Greve L, Wierzbicki T (2015) FE simulation of edge fracture considering pre-damage from blanking process. Int J Solids Struct 71:206–218
11. Wang K, Wierzbicki T (2015) Experimental and numerical study on the plane-strain blanking process on an AHSS sheet. Int J Fract 194(1):19–36
12. Aoki I, Takahashi T (2003) Material flow analysis on shearing process by applying Fourier phase correlation method—analysis of piercing and fine-blanking. J Mater Process Technol 134(1):45–52
13. Manopulo N (2011) An ALE based FE formulation for the 3D simulation of the Fineblanking process, PhD thesis, ETH Zurich
14. Takahashi T, Aoki I (1996) Analysis of shearing by visioplasticity method using image processing: proposal and verification of displacement measurement method usable for large deformations. Trans JpnSoc Mech Eng C(62):3196–3201
15. Hartmann C, Weiss HA, Lechner P, Volk W, Neumayer S, Fitschen JH, Steidl G (2021) Measurement of strain, strain rate and crack evolution in shear cutting. J Mater Process Technol 288:116872
16. Hartmann C (2021) Spatio-temporal optical flow methods for process analysis—robust strain, strain rate, and crack propagation measurement in shear cutting, PhD thesis, Technical University of Munich
17. Yamaguchi I (1981) Speckle displacement and decorrelation in the diffraction and image fields for small object deformation. Int J Opt 28(10):1359–1376
18. Peters WH, Ranson WF (1982) Digital imaging techniques in experimental stress analysis. Opt Eng 21(3):427–431

19. Hassan GM (2021) Deformation measurement in the presence of discontinuities with digital image correlation: a review. Opt Lasers Eng 137:106394
20. Balle F, Beck T, Eifler D, Fitschen JH, Schuff S, Steidl G (2019). Strain analysis by a total generalized variation regularized optical flow model. Inverse Probl Sci Eng 27(4):540–564
21. Hartmann C, Opritescu D, Volk W (2018) Implementation and evaluation of optical flow methods for two-dimensional deformation measurement in comparison to digital image correlation. Opt Lasers Eng 107:127–141
22. Hartmann C, Volk W (2019) Digital image correlation and optical flow analysis based on the material texture with application on high-speed deformation measurement in shear cutting. In: Proceedings of the international conference on digital image & signal processing 2019, pp 1–8
23. Baker S, Scharstein D, Lewis JP, Roth S, Black MJ, Szeliski R (2011) A database and evaluation methodology for optical flow. Int J Comput Vis 92:1–31
24. Hartmann C, Lechner P, Volk W (2021) In-situ measurement of higher-order strain derivatives for advanced analysis of forming processes using spatio-temporal optical flow. CIRP Ann
25. Hewer A, Weickert J, Seibert H, Scheffer T, Diebels S (2013) Lagrangian Strain Tensor Computation with Higher Order Variational Models. In: Proceedings of the British Machine Vision Conference 2013, vol 129, pp 1–129.10
26. Volz S, Bruhn A, Valgaerts A, Zimmer H (2011) Modeling temporal coherence for optical flow. In: Proceedings of the IEEE international conference on computer vision 2011, pp 1116–1123
27. Brox T, Bruhn A, Papenberg N, Weickert J (2004) High accuracy optical flow estimation based on a theory for warping. Lect Notes Comput Sci 3024:25–36
28. VDI2906-2 (1994) Schnittflächenqualität beim Schneiden, Beschneiden und Lochen von Werkstücken aus Metall—Scherschneiden
29. Butcher C, Abedini A (2017) Shear confusion: Identification of the appropriate equivalent strain in simple shear using the logarithmic strain measure. Int J Mech Sci 134:273–283

A Novel Continuum Damage Constitutive Model for Predicting the Formability of AA7075 Alloy at Elevated Temperatures



Hai Rong, Liang Ying, Ping Hu, and Wenbin Hou

Abstract Hot forming has been proposed to improve the formability of high-strength aluminum alloys. The main objective of this paper is to formulate a continuum damage model and to describe the damage evolution features of AA7075 alloy at elevated temperatures. Hot uniaxial tensile tests and hot Nakajima tests were conducted. Subsequently, a novel continuum damage model was proposed and incorporated into a set of multi-axial visco-plastic constitutive equations to describe the thermal flow behaviors and predict the thermal forming limit diagram (TFLD) of AA7075. Material constants were determined based on the experimental data with a genetic algorithm. Moreover, the TFLD of AA7075 was numerically simulated by implementing the multi-axial continuum damage constitutive equations (CDCEs) via the user material subroutine VUMAT in commercial software ABAQUS. Simulation results agree well with experimental results and theoretically predicted results, which indicates the set of multi-axial CDCEs is capable of predicting the formability of AA7075 at elevated temperatures.

Keywords Continuum damage model · Forming limit diagram · Visco-plastic constitutive model · AA7075 aluminum alloy · VUMAT

1 Introduction

Lightweight and high-strength aluminum alloys such as AA7075 are greatly needed in automotive industries to reduce vehicle mass. Forming at elevated temperatures is an effective way to improve the formability of high-strength aluminum alloys [1].

The thermal formability of aluminum alloys is commonly evaluated by thermal forming limit diagram (TFLD), which reflects the maximum deformation capacity of materials before failure appears. Lots of investigations have been conducted on TFLDs of aluminum alloys in experimental, theoretical, and numerical methods [2]. Lin et al. [3] first proposed a set of multi-axial continuum damage constitutive

H. Rong · L. Ying · P. Hu (✉) · W. Hou
School of Automotive Engineering, Dalian University of Technology, Dalian, Liaoning 116024, China
e-mail: pinghu@dlut.edu.cn

© The Minerals, Metals & Materials Society 2021

G. Daehn et al. (eds.), *Forming the Future*, The Minerals, Metals & Materials Series,
https://doi.org/10.1007/978-3-030-75381-8_135

equations (CECEs) to predict the TFLD of AA5754, where the effect of stress states on the damage evolution was discussed in detail. Subsequently, the set of multi-axial CDCEs was formulated for various alloys [4, 5]. The results proved that the multi-axial CDCEs are capable of describing damage evolutions and predict forming limits of aluminum alloys at elevated temperatures.

In this paper, a set of multi-axial CDCEs was established to predict the TFLD of AA7075 at elevated temperatures. Moreover, the thermal forming limits of AA7075 were numerically simulated with commercial software ABAQUS via subroutine VUMAT.

2 Experimental Procedures

The commercial AA7075-T6 alloy sheet produced by Kaiser Aluminum Corporation with a thickness of 1.6 mm was investigated in this paper. The weight fraction of additive chemical compositions is listed as: 5.48%Zn, 2.3%Mg, 1.52%Cu, 0.01%Zr, 0.16%Fe, 0.03%Mn, 0.21%Cr, 0.03%Ti, 0.11%Si. Hot uniaxial tensile tests and Nakajima tests were conducted within the temperature range of 300–400 C at different deformation rates. Specimens were heated to the target temperature and soaked for 10 min and then deformed to fracture. Strain histories were recorded by the ARAMIS™ 4 M optical measuring system.

3 Establishment of Multi-axial Continuum Damage Constitutive Equations

3.1 Continuum Damage Model

A modified continuum damage model was proposed in this paper and formulated as Eq. (1). The first item represents the nucleation and growth rate of micro-voids in the earlier deformation stage, and the second item reveals the growth and coalescence rate of micro-voids in the later and final deformation stages. Macroscopic cracks are considered to appear once ω reaches a critical value of 0.7.

$$\dot{\omega} = D_1(1-\omega)\dot{\varepsilon}_p^d + \frac{D_2\dot{\varepsilon}_p^{D_3}\cosh(D_4\varepsilon_p)}{(1-\omega)^{D_5}}. \tag{1}$$

3.2 Multi-Axial Continuum Damage Constitutive Equations

To describe the visco-plastic flow behaviors and predict fractures of AA7075, a set of multi-axial CDCEs were established [3] and formulated as Eqs. (2)–(7). Traditional power-law formula is chosen to describe the constitutive relation between equivalent plastic strain rate $\dot{\varepsilon}_e^p$ and equivalent stress σ_e, as given in Eq. (2). Equation (3) reveals the associated flow rule based on Mises yield criterion, where $\dot{\varepsilon}_e^p$ is plastic strain rate tensor and S_{ij} is stress deviator. Normalized dislocation density rate $\dot{\overline{\rho}}$ and dislocation-based isotropic hardening rate $\dot{R}$ are given in Eqs. (4) and (5), respectively. In order to correct the damage evolution features in different stress states, a multi-axial correction formula was introduced, as given in Eq. (6), where σ_1 and σ_H are major principle stress and hydrostatic stress, respectively. The flow stress σ_{ij} is calculated by generalized Hooke's law as shown in Eq. (7), where ε_{kl} and ε_{kl}^p are strain tensor and plastic strain tensor.

$$\dot{\varepsilon}_e^p = \left\langle \frac{\sigma_e/(1-\omega) - R - k}{K} \right\rangle^n \tag{2}$$

$$\dot{\varepsilon}_{ij}^p = \frac{3}{2}\frac{S_{ij}}{\sigma_e}\dot{\varepsilon}_e^p \tag{3}$$

$$\dot{\overline{\rho}} = A(1-\overline{\rho})\left|\dot{\varepsilon}_e^p\right| - C\overline{\rho}^{n_2} \tag{4}$$

$$\dot{R} = 0.5B\overline{\rho}^{-0.5}\dot{\overline{\rho}} \tag{5}$$

$$\dot{\omega} = \Delta\left(\frac{a_1\sigma_1 + 3a_2\sigma_H + a_3\sigma_e}{(a_1+a_2+a_3)\sigma_e}\right)^{\varphi}\left(D_1(1-\omega)(\dot{\varepsilon}_e^p)^d + \frac{D_2(\dot{\varepsilon}_e^p)^{D_3}\cosh(D_4\varepsilon_e^p)}{(1-\omega)^{D_5}}\right) \tag{6}$$

$$\sigma_{ij} = D_{ijkl}(1-\omega)(\varepsilon_{ij} - \varepsilon_{ij}^p). \tag{7}$$

In the multi-axial CDCEs, d, n_2, a_1, a_2, and a_3 are material constants, $k, K, n, A, C, B, D_1, D_2, D_3, D_4, D_5, \Delta$, and φ are material variables expressed by the corresponding material constants, as listed in Table 1. R, T, and $\dot{\varepsilon}$ represent gas constant, absolute

Table 1 Material variables in the multi-axial CDCEs

$K = K_0\exp(Q_K/RT)$	$n = n_0\exp(Q_n/RT)$	$A = A_0\exp(Q_A/RT)$
$C = C_0\exp(-Q_C/RT)$	$B = B_0\exp(Q_B/RT)$	$D_1 = D_{10}\exp(-Q_{D1}/RT)$
$D_2 = D_{20}\exp(Q_{D2}/RT)$	$D_3 = D_{30}\exp(Q_{D3}/RT)$	$D_4 = D_{40}\exp(Q_{D4}/RT)$
$D_5 = D_{50}\exp(Q_{D5}/RT)$	$\Delta = \Delta_{11} + \Delta_{21}\exp(\Delta_{22}/\dot{\varepsilon})$	$\varphi = \varphi_{11}\exp(-\varphi_{12}/T)$
$E = E_0\exp(Q_E/RT)$	$k = k_0\exp(Q_k/RT) + k_1\exp(k_2/\dot{\varepsilon})^{k_3}$	

temperature, and strain rate, respectively.

4 Calibration of Multi-axial Continuum Damage Constitutive Equations

All of the material constants were calibrated with the Non-dominated Sorting Genetic Algorithm II (NSGAII) based on the experimental results. The determined material constants have been listed in Table 2.

Good agreement has been found between experimental and predicted results, as shown in Fig. 1. The larger elongation and higher forming limit curves show that the formability of AA7075 is improved with temperature and strain rate increasing.

Table 2 Determined material constants in the multi-axial CDCEs

A_0	6.8	D_{50}	1.51e-6	n_2	4.9	Q_{D5}	7.5e4	φ_{11}	2.05e2
B_0	2.27	E_0	1.21e4	Q_A	1.02e4	Q_E	6.88e3	φ_{12}	2.002e3
C_0	2.2e3	K_0	6.29e–1	Q_B	3.95e3	Q_K	2.09e4	Δ_{11}	49.76
d	1.17	k_0	1.54e2	Q_C	6.1e3	Q_k	3.77e3	Δ_{21}	−49.03
D_{10}	15.2	k_1	−88.16	Q_{D1}	5.05e3	Q_n	1.81e4	Δ_{22}	3.3e–3
D_{20}	2.46e–20	k_2	43.69	Q_{D2}	1.86e5	a_1	13.73		
D_{30}	2.88e–2	k_3	1.5e–2	Q_{D3}	1.56e4	a_2	−1.43		
D_{40}	12.56	n_0	0.35	Q_{D4}	6.57e2	a_3	−9.67		

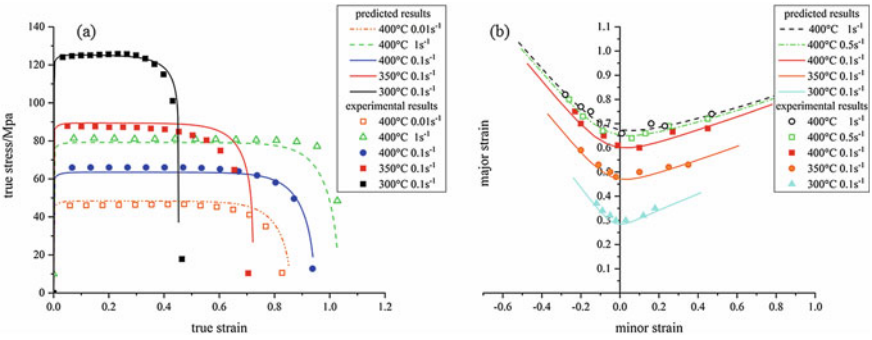


Fig. 1 Comparison of experimental and predicted results by CDCEs. (Color figure online)

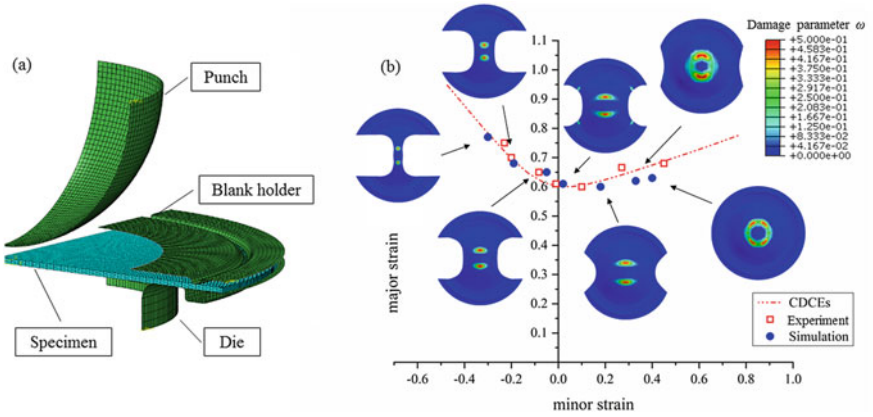


Fig. 2 Numerical simulation model and results of TFLD. (Color figure online)

5 Numerical Simulation for Thermal Forming Limit Prediction of AA7075

Numerical simulations of the hot Nakajima test were carried out using commercial software ABAQUS. The set of multi-axial CDCEs was implemented into ABAQUS/Explicit via the user material subroutine VUMAT. One quarter symmetry simulation model was established based on the experimental Nakajima device and specimens, as shown in Fig. 2a. The C3D8R element type with the size of 0.5 mm was chosen to mesh specimens. The punch, die, and blank holder were modeled as rigid bodies. Figure 2b shows that the forming limits (400 °C, 0.1 s^{-1}) of AA7075 obtained from numerical simulations are in good agreement with the forming limit curve predicted by multi-axial CDCEs and experimental results. Damage parameter ω accelerates rapidly around the center of specimens in the final deformation stages resulting in fractures ultimately.

6 Conclusions

The set of multi-axial CDCEs was established and calibrated based on experimental results. Good formability of AA7075 is found at relatively higher temperatures and strain rates. The calibrated set of CDCEs was implemented in ABAQUS via VUMAT to obtain the TFLD of AA7075. Simulation results show good agreement with experimental results and predicted results by CDCEs, which proves the multi-axial CDCEs can be used to predict the formability of AA7075 at elevated temperatures.

Acknowledgments This work was supported by the National Natural Science Foundation of China (51705065).

References

1. Zheng K, Politis D J, Wang L, Lin J (2018) A review on forming techniques for manufacturing lightweight complex-shaped aluminium panel components. J Light Mater Manuf 1:55–80
2. Ying L, Liu W, Wang D, Hu P, Wang Q (2016) Experimental and simulation of damage evolution behavior for 7075-T6 aluminum alloy in warm forming. Chin J Nonferrous Metals 26(7):1383–1390
3. Lin J, Mohamed M, Balint D, Dean T A (2014) The development of continuum damage mechanics-based theories for predicting forming limit diagrams for hot stamping applications. Int J Damage Mech 23:684–701
4. Xiao W, Wang B, Zheng K (2017) An experimental and numerical investigation on the formability of AA7075 sheet in hot stamping condition. Int J Adv Manuf Tech 92:3299–3309
5. Bai Q, Mohamed M, Shi Z, Lin J (2017) Application of a continuum damage mechanics (CDM)-basedmodel for predicting formability of warm formed aluminum alloy. Int J Adv Manuf Technol 88:3437–3446

The Influence of Temperature and Strain Rate on the Superplastic Deformation Behavior and Microstructure Evolution of TNW700 Alloy



Lixia Ma, Min Wan, Weidong Li, Jie Shao, and Xuepiao Bai

Abstract TNW700 titanium, as a new near-α high-temperature titanium alloy, is designed to work at 700 °C for a short-term service. Superplastic deformation behavior of TNW700 alloy at 900–975 °C and strain rate of 0.0005–0.01 s^{-1} was investigated to identify the optimum deformation temperature and strain rate. The microstructure evolution after high temperature tensile was investigated using scanning electron microscope. The research found that TNW700 alloy has an excellent superplasticity. The elongation exceeds 200% at various deformation conditions except 975 °C with higher strain rate of 0.005 and 0.01 s^{-1}, and the maximum elongation of 613% was obtained at a temperature of 925 °C and strain rate of 0.001 s^{-1}. The flow stress is sensitive to temperature and strain rate, and it increases with decreasing temperature and increasing strain rate. In addition, the flow stress exhibits strong work hardening with increase in true strain, and the instantaneous work hardening exponent n as well as critical hardening strain is accelerated as the strain rate decreases. The strain rate sensitivity exponent (m) is higher than 0.4 when the temperature is lower than 975 °C, which corresponds to dynamic recrystallization and grain boundary sliding mechanisms. The m is 0.229 at temperature of 975 °C, corresponding to dynamic grains growth mechanism. The deformed microstructure of TNW700 alloy consists of β grains and equiaxed α grains. Increasing the temperature is beneficial to the transformation of α phase into the β phase, which resulted in an increase in the volume fraction of the β phase. The β grains grow rapidly at higher temperatures and lower strain rates due to the higher diffusion coefficient.

Keywords TNW700 titanium alloy · Superplasticity · Work hardening · Microstructure evolution · Grain growth

L. Ma · M. Wan · W. Li (✉)
School of Mechanical Engineering and Automation, Beihang University, Beijing 100191, China
e-mail: space@buaa.edu.cn

J. Shao · X. Bai
AVIC Manufacturing Technology Institute, Beijing 100024, China

© The Minerals, Metals & Materials Society 2021

G. Daehn et al. (eds.), *Forming the Future*, The Minerals, Metals & Materials Series,
https://doi.org/10.1007/978-3-030-75381-8_136

1 Introduction

Titanium alloy has been widely utilized in aerospace, chemical, and biomedical engineering industries for its high specific strength, good corrosion resistance and biocompatibility, and excellent high-temperature performance [1–3]. Superplastic forming is a promising process to achieve complex shape parts forming, material saving, part accuracy and quality improvement, and weight reduction. Near-α and α titanium alloy are attractive because of their lightweight, excellent fatigue and creep properties, and appropriate strength; meantime, they are commonly shaped for complex jet engines components by high-temperature superplastic forming due to their low machinability and poor cold formability [4, 5].

Depending on the temperature, strain rate, and strain, titanium alloys display different microstructural evolutions, such as α/β phase transformation, precipitation of the second phase (silicide and Ti_3X), grain coarsening, and grain refinement with dynamic recrystallization (DRX) [6, 7]. However, different microstructures, in turn, affect titanium alloy deformation behavior and formability. The microstructure and texture evolution of a near-α Ti–6Al–1.21Nb–9.04Zr–3.88Sn–1.59W–0.28Si alloy were investigated by Lin et al. at 900 °C and strain rates of 3×10^{-3} and 3×10^{-2} s^{-1} [8]. It was found that work hardening and softening reach a dynamic equilibrium at strain rate of 3×10^{-3} s^{-1}, and DRX is the main softening mechanism accompanied by weakening of the initial texture. Liu et al. [9] systematically studied superplastic behavior and microstructure evolution of the Ti55 alloy, and they showed that work hardening predominates at the initial deformation stage, then the flow stress decreases rapidly and reaches a quasi-steady state before fracture. In addition, grain boundary sliding (GBS) and grain rotation are the primary and auxiliary deformation mechanisms, respectively, and the main softening mechanism is discontinuous dynamic recrystallization (DDRX). Mikhaylovskaya et al. [5] researched the superplastic deformation behavior of Ti–2.5Al–1.8Mn alloy and found that the strain hardening coefficient increases with increase in temperature resulted from dynamic grains growth.

Although the superplastic deformation behavior and microstructure evolution of some near-α titanium alloys have been extensively investigated, however, few literatures have been reported regarding the superplasticity of TNW700 alloy. To accurately and deeply study the superplastic and work hardening behavior, and determine the internal mechanism of TNW700 alloy, high-temperature tensile tests and the microstructure evolution observation were performed in this work.

2 Experimental Description

The TNW700 alloy with the composition shown in Table 1 was produced by Baoji Titanium Industry Co., Ltd. with a thickness of 0.71 mm. Adding α phase stabilizing elemental Al can increase tensile strength, creep resistance, and reduce alloy density.

Table 1 Nominal chemical composition of the TNW700 alloy (wt%)

Element	Al	Sn	Zr	Nb	W	Si	Ti
Wt.%	5.86	3.4	5.56	1.15	1.6	0.19	Balance

The neutral elementals Sn and Zr have large solid solubility and can form high-strength compounds with Al, playing a complementary and strengthening role. Si is an important element to enhance high-temperature strength and creep resistance. The elements Nb and W can improve the oxidation resistance and heat resistance, respectively.

Mechanical tests were conducted using specific electronic uniaxial testing machine (Fig. 1a) with four different temperatures (900, 925, 950, and 975 °C) and four different constant strain rates (0.0005, 0.001, 0.005, and 0.01 s^{-1}). Tensile specimens with gauge length, width, and thickness of 10 × 6 × 0.71 mm were machined from sheets along the rolling direction. The specimen coated with Ti-1 antioxidant was clamped in a tensile testing machine, then was heated to a predefined temperature and maintained under isothermal conditions for 10 min to ensure a heat balance before the tensile test. The specimen deformation distance was accurately recorded with extension poles and grating rulers, and the specimen deformation force was recorded by S-type force sensor. Tensile test scheme and partially deformed specimens are shown in Fig. 1b, c respectively.

After tensile deformation, the specimens were water quenched as quickly as possible, to avoid microstructure modification during slow cooling from the testing temperature. Then, the sections were mechanically ground, polished, and

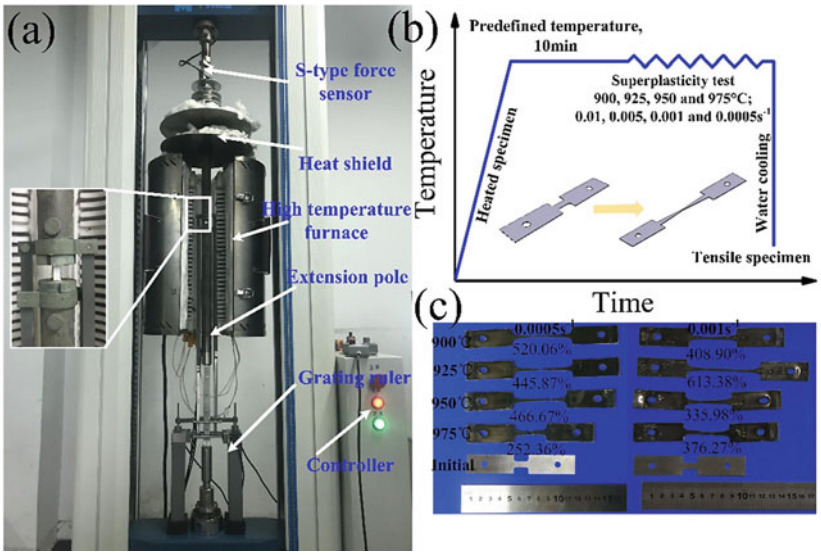


Fig. 1 Scheme of high-temperature tensile test. (Color figure online)

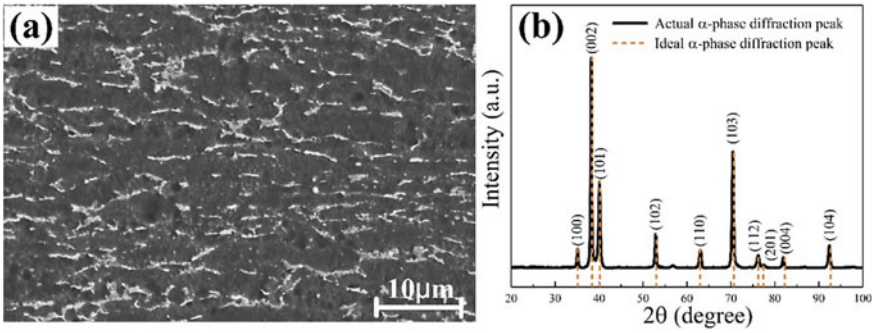


Fig. 2 The microstructure and phase composition of the TNW700 as-received alloy, (**a**) SEM image; (**b**) XRD diffraction pattern. (Color figure online)

etched in a 10%HF:10%HNO_3:80%H_2O mixed solution. The microstructures were characterized by Zeiss Supra55 scanning electron microscope (SEM).

3 Results and Discussion

3.1 Initial Microstructure

The SEM micrograph of the initial microstructure is shown in Fig. 2a. The microstructure mainly composed of dark α phase and small amounts of bright intergranular β phase. Figure 2b is the typical XRD diffraction pattern of as-received materials. Obviously, α phase diffraction peaks, such as (100), (002), (101), (102), (110), (103) etc. were observed, and there are no β phase diffraction peaks. In addition, α-phase diffraction peak deviates from the ideal diffraction peak (as highlighted by brown dashed line). This is related to the dissolution of the alloying element Zr with large atomic radius in α-phase matrix.

3.2 Plasticity Flow Behavior

Figure 3a and b show flow stress–true strain curves at 925 °C with different strain rates and at strain rate of 0.001 s^{-1} with different temperatures, respectively. Obviously, the flow stress of TNW700 alloy is highly dependent on deformation temperature, strain rate, and strain. Higher flow stress is exhibited at higher strain rates and lower temperatures, and it decreases remarkably with increasing temperature and decreasing strain rate. This phenomenon is consistent with the previously reported results of other titanium alloys [1, 5]. Meanwhile, the all flow stress curves manifest remarkable work hardening phenomenon with long period, namely, all curves reach

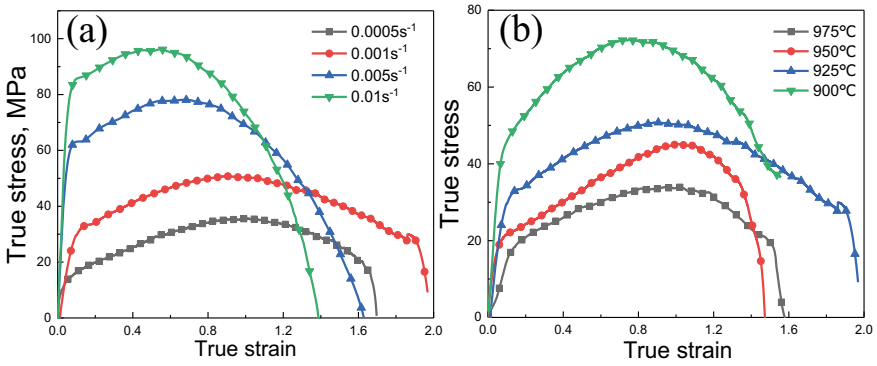


Fig. 3 Flow stress–strain curves obtained at different strain rates and temperatures, (**a**) 925 °C, (**b**) 0.001 s^{-1}. (Color figure online)

a peak stress at higher strain, then followed by the flow softening, which is the result of α grain refinement.

Quantitative data can more intuitively reflect the alloy flowing behavior. Figure 4a and b show- the variation of peak stress and elongation, respectively. Evidently, the peak stress decreases with increasing temperature at a constant strain rate, which is related to the enhancement of the thermal activation effect, the increase in the atomic kinetic energy and the weakening of the critical shear stress at high temperature. Meanwhile, another factor affecting peak stress is the increase of β phase volume fraction, which has more slip systems than α phase. The peak stress increases significantly with increase in strain rate at a constant temperature. This is because the time required for unit strain is shortened, and the dislocation density, motion speed, and the probability of dislocation tangle increase at higher strain rate, all of those leading to an increase in critical shear stress. Undoubtedly, the largest and smallest

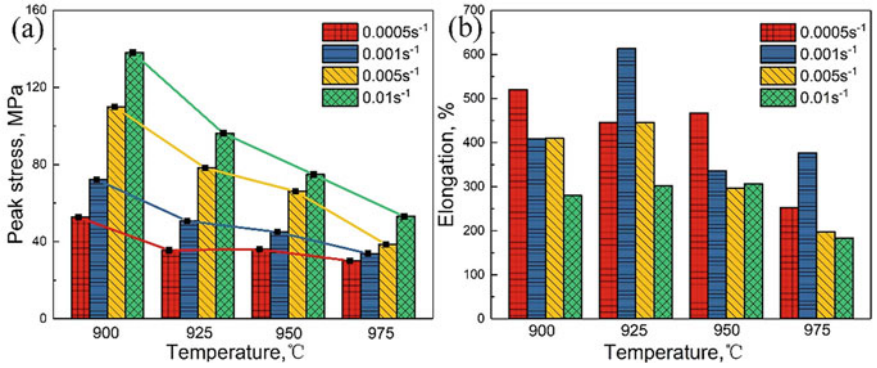


Fig. 4 Peak stress and elongation of the TNW700 alloy at different strain rates and temperatures, (**a**) peak stress, (**b**) elongation. (Color figure online)

peak stresses were observed at 900 °C/0.01 s^{-1} and 975 °C/0.0005 s^{-1}, respectively, with values of 138 MPa and 30 MPa, respectively.

The specimen elongation was calculated according to the following equation

$$\text{Elongation} = 100\left(\frac{\Delta l}{l_0} + 1\right)\% \tag{1}$$

where l_0 and Δl are the specimen initial gauge length and deformation length respectively. This study corresponds to average displacement of grating rulers when the specimen fracture force/stress is zero. The variation of elongation under different conditions is shown in Fig. 4b, demonstrating that most of the specimens exhibited excellent superplasticity. No distinct relationship was found between elongation and temperature or strain rate. The maximum elongation of 613% occurs at 925 °C and 0.001 s^{-1}, and the lower elongation of 183% is acquired at 975 °C and 0.01 s^{-1}. Overall, high temperature of 975 °C and high strain rate of 0.01 s^{-1} are not conducive to obtaining large elongation, which may be related to grain coarsen.

3.3 Work-Hardening and Strain Rate Sensitivity Exponent

To quantify the superplastic deformation behavior of TNW700 alloy, the variation of work hardening and strain rate sensitivity exponent were respectively analyzed, as shown in Fig. 5. The instantaneous work hardening exponent (n) and strain rate sensitivity exponent (m) were calculated from the slope of the $\ln\sigma - \ln\varepsilon$ and $\ln\sigma - \ln\dot{\varepsilon}$ according to the following equations,

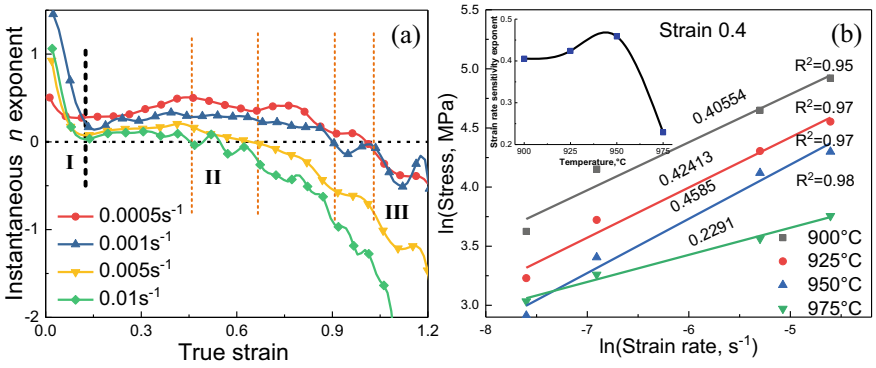


Fig. 5 **a** Instantaneous n exponent of the TNW700 alloy for different strain rates at 925 °C; **b** strain rate sensitivity exponent at a strain of 0.4. (Color figure online)

Table 2 Relationship between average n value in stage II and strain rate at 925 °C

Strain rate	0.01 s^{-1}	0.005 s^{-1}	0.001 s^{-1}	0.0005 s^{-1}
Average n value in stage II	0.096	0.162	0.272	0.379

$$n = \left.\frac{d(\ln \sigma)}{d(\ln \varepsilon)}\right|_{\dot{\varepsilon},T} \tag{2}$$

$$m = \left.\frac{d(\ln \sigma)}{d(\ln \dot{\varepsilon})}\right|_{\varepsilon,T} \tag{3}$$

where σ, ε, $\dot{\varepsilon}$, and T are the true stress, true stain, strain rate, and deformation temperature, respectively. Positive and negative n values represent work hardening and softening, respectively. At low strain condition, the positive n decreases rapidly with increasing true strain, as shown in stage I of Fig. 5a. Then, the n value curves displayed a slight increase, a steady state and a slight decrease in stage II with a relatively long period. In addition, the average n value at the steady stage decreases from 0.379 to 0.096 with the increase in strain rate from 0.0005 to 0.01 s^{-1}, as shown in Table 2. Lager n value and critical hardening strain (marked as short brown lines) are manifested at small strain rate of 0.0005 s^{-1}, and the critical hardening strain decreased from 1 to 0.45 as strain rate increased from 0.0005 to 0.01 s^{-1}. The longer work hardening period may be related to β grain coarsening and silicide precipitation. The n value is lower than 0 in stage III, which corresponds to the flow softening.

The m values are the slopes of the $\ln \sigma - \ln \dot{\varepsilon}$ lines obtained by linear regression method at various temperatures in the plots of Fig. 5b, and the inset exhibits the variation tendency of m value. Obviously, the m values first increase with increasing deformation temperatures, and achieved the maximum value at 950 °C, then decrease. The m values are 0.405, 0.424, 0.458, and 0.229, when the temperature range is 900–975 °C and the interval is 25 °C. Based on Ma et al. [1], the deformation mechanism corresponds to DRX and GBS in the temperature range of 900–950 °C and may correspond to the dynamic grains growth at 975 °C.

3.4 Microstructure Evolution

The microstructure evolution after superplastic deformation at a temperature of 925 °C with different strain rates was analyzed by SEM to determine the causes of work hardening behavior of TNW700 alloy. Obviously, the deformed microstructure contains more β grains than the initial TNW700 alloy, which is related to the transformation of α to β at high temperature. In addition, the volume fraction and average grain size of β phase and α phase are heavily dependent on strain rate, respectively. When the strain rate was reduced from 0.01 to 0.0005 s^{-1}, the average

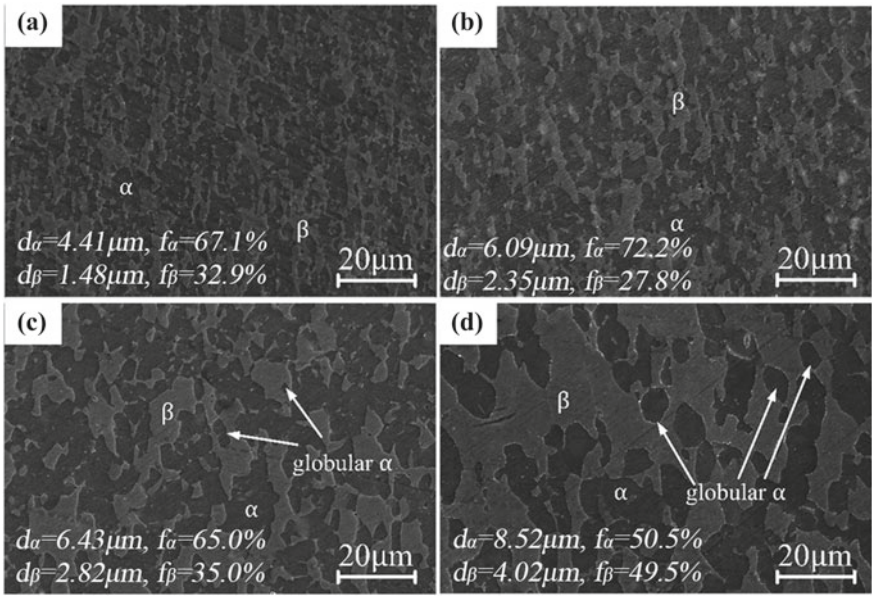


Fig. 6 The microstructure evolution of the TNW700 alloy after tensile deformation for different strain rates at 925 °C. **a** 0.01 s^{-1}, **b** 0.005 s^{-1}, **c** 0.001 s^{-1}, **d** 0.0005 s^{-1}

grain size of α grains increased from 4.41 to 8.52 μm, and the size of β grains increased from 1.48 to 4.02 μm with volume fraction increased from approximately 32.9 to 49.5%. Just as superplastic deformation is a diffusion-controlled hot deformation process, the β grains with higher diffusion coefficient grow up rapidly when deformed at low strain rates and high temperature. Therefore, the instantaneous n coefficient increases with a decrease in the strain rate from 0.01 to 0.0005 s^{-1} is mainly related to the grain growth effect. In addition, although a small amount of α grains spheroidization were observed at low strain rate, the geometric morphology of α grains got less morphological change at various strain rates (Fig. 6).

4 Conclusions

The superplastic deformation behavior and microstructure evolution of TNW700 alloy subjected to high temperature tension deformation were investigated in this study. The main conclusions of this study are as follows:

(1) During the superplastic tension test, the flow stress is sensitive to the deformation temperature and strain rate, and the peak stress increases with decrease in

strain rate and increase in temperature. The maximum peak stress and elongation were respectively obtained at 900 °C/0.01 s^{-1} and 925 °C/0.001 $s^{-1}$with the value of 138 MPa and 613%.

(2) The TNW700 alloy has a longer work hardening period due to second phase and grain growth. The positive n value and critical hardening strain increase with decrease in strain rate. A negative n value corresponds to flow softening caused by grain refinement.

(3) The microstructure of the TNW700 alloy is consisted of β and equiaxed α phase after deformation at high temperature, and the β grain size and volume fraction increase with decreasing strain rate. The α grain spheroidizes at lower strain rate.

References

1. Ma L, Wan M, Li W, Shao J, Bai X (2019) Constitutive modeling and processing map for hot deformation of Ti–15Mo–3Al-2.7Nb-0.2Si. J Alloy Compd 808:151759
2. Alabort E, Putman D, Reed RC (2015) Superplasticity in Ti–6Al–4V: characterisation, modelling and applications. Acta Mater 95:428–442
3. Zhang W, Liu H, Ding H, Fujii H (2019) Grain refinement and superplastic flow in friction stir processed Ti–15V–3Cr–3Sn–3Al alloy. J Alloy Compd 803:901–911
4. Moiseyev V (2005) Titanium alloys Russian aircraft and aerospace applications. CRC Press, New York, p 206
5. Mikhaylovskaya AV, Mosleh AO, Kotov AD, Kwame JS, Pourcelot T, Golovin IS, Portnoy VK (2017) Superplastic deformation behaviour and microstructure evolution of near-α Ti-Al-Mn alloy. Mater Sci Eng A 708:469–477
6. Guo J, Zhan M, Wang YY, Gao PF (2018). Unified modeling of work hardening and flow softening in two-phase titanium alloys considering microstructure evolution in thermomechanical processes. J Alloy Compd 767:34–45
7. Wang T, Li B, Wang Z, Nie Z (2018) A microstructure with improved thermal stability and creep resistance in a novel near-alpha titanium alloy. Mater Sci Eng A 731:12–20
8. Lin P, Feng A, Yuan S, Li G, Shen J (2013) Microstructure and texture evolution of a near-α titanium alloy during hot deformation. Mater Sci Eng A 563:16–20
9. Liu Z, Li P, Xiong L, Liu T, He L (2017) High-temperature tensile deformation behavior and microstructure evolution of Ti55 titanium alloy. Mater Sci Eng A 680:259–269

Finite Element Simulation of Edge Fracture by Mapping the Shear-Induced Ductile Damage into Hole-Expansion Simulation



Lei Mu, Zhe Jia, Ben Guan, and Yong Zang

Abstract A ductile fracture criterion (uncoupled type, originally presented at ICTP2017), which is endowed with both stress triaxiality (T) and Lode parameter (L) dependence, is selected to define the ductile damage accumulation from hole-blanking simulation to the subsequent hole-expansion simulation for a DP780 sheet. The calibrated ductile fracture criterion yields an asymmetric 3D fracture surface, which can well describe the material's ductility within a wide range of stress states from simple shear to balanced biaxial tension. With the help of a fully integrated simulation framework, the ductile damage induced by the hole-blanking is completely mapped into the hole-expansion simulation to incorporate the pre-damage field for the sheared edge. We find that after considering the pre-damage field, the accuracy of edge fracture simulation is significantly improved in terms of both hole-expansion ratio and fracture propagation path.

Keywords Ductile fracture · Uncoupled model · Edge fracture · Hole expansion

1 Introduction

Advanced high-strength steels (AHSS) have been deemed as promising materials to fabricate modern vehicles, which are aimed at a reasonable balance between light weight, cost efficiency, durability, and good looks. Mechanical shearing (such as blanking and trimming) is an important process to prepare sheet metal blanks that are subsequently formed to fabricate a variety of vehicle body components through various stamping processes. However, the mechanically sheared edges of AHSS sheets have been reported to exhibit a strong tendency to rupture at the strains, which are lower than the predictions given by the traditional forming limit approach [1].

L. Mu (✉)
Department of Mechanical and Aerospace Engineering, New Mexico State University, Las Cruces, NM 88003, USA

Z. Jia · B. Guan · Y. Zang
School of Mechanical Engineering, University of Science and Technology Beijing, 30 Xueyuan Road, Beijing 100083, China

© The Minerals, Metals & Materials Society 2021

G. Daehn et al. (eds.), *Forming the Future*, The Minerals, Metals & Materials Series,
https://doi.org/10.1007/978-3-030-75381-8_137

One of the important indicators characterizing the edge formability of a certain sheet metal is the hole-expansion ratio (HER), which can be obtained through performing a standard hole-expansion test, as detailed by ISO/TS16630. Wang et al. [2] tested HERs of different edge conditions for a dual phase (DP) steel sheet. They found that the HER of a milled edge was much higher than that of the sheared edge prepared by hole-blanking. Taylor et al. [3] successfully improved the edge formability of DP980 steels by hardening the ferrite microstructure and meanwhile softening the martensite microstructure. The experimental study performed by Teng et al. [4] pointed out that the edge fracture of a DP980 sheet indeed originates from the pre-existing micro-crack induced by the prior mechanical shearing. This study indicates that the pre-existing ductile damage caused by shearing process should be carefully considered when trying to accurately predict edge fracture behavior for DP steel sheets.

Thanks to the relatively simple forms and comparatively fewer number of parameters to be calibrated, uncoupled ductile fracture (DF) criteria have been widely adopted in various sheet metal forming applications, including fracture forming limit curve [5–8] and edge fracture phenomenon of AHSS steels [9, 10]. Through mapping, the simulated ductile damage field from a 2D hole-blanking simulation to the subsequent 3D hole-expansion simulation, Wang et al. [9] successfully predicted HERs of a DP780 sheet using the famous MMC criterion [11]. It should be mentioned that the edge fracture phenomenon involves a non-linear loading path from shear state to tensile state. Therefore, it is crucial to select a reasonable DF criterion for a reliable edge fracture prediction, as discussed in our previous work [10], in which various uncoupled DF criteria (Lou-Huh [12], Oh [13], and Brozzo [14]) are selected. It was found that Lou–Huh criterion [12] yielded the best HER prediction. Accordingly, it was concluded that a preferred model should be the one, which is capable of capturing DF in a wide range of stress states.

The current work has been proposed to test the performance of a novel uncoupled DF criterion in edge fracture prediction, serving as a follow-up study of the criterion presented at ICTP 2017 [15]. To consider the effects of the pre-existing ductile damage, a fully integrated simulation framework is used, through which the pre-damage fields from 3D hole-blanking simulations are completely mapped to the following hole-expansion simulations. Meanwhile, a user-defined material subroutine of Abaqus-Explicit is coded with the considered DF criterion integrated. It should be mentioned that the material considered in this study is a DP steel (DP780) sheet with a thickness of 1.6 mm. For the detailed information concerning the ductile fracture and hole-expansion tests of this DP780 sheet, readers are referred to Wang et al. [2, 9].

2 Ductile Fracture Criterion and Calibration

2.1 Ductile Fracture Criterion

The DF criterion used in this study is a micromechanically motivated uncoupled model, which was first developed by considering two major void deformation modes (void dilation and elongation/rotation) [15] and further improved by integrating with a void nucleation term [16], as follows,

$$C_3 = \int_0^{\bar{\varepsilon}^f} \left\langle C_1 \frac{\sigma_1}{\sigma_{\text{eq}}} + (1 - C_1) \frac{\tau_{\max}}{\sigma_{\text{eq}}} \right\rangle^{C_2} D_n \mathrm{d}\bar{\varepsilon}^p, \text{ with } D_n = R_n \left(\bar{\varepsilon}^p\right)^m. \tag{1}$$

In Eq. (1), $\sigma_1 / \sigma_{\text{eq}}$ is the normalized first principal stress (σ_1) by equivalent stress (σ_{eq}), characterizing the void dilation mode; $\tau_{\max} / \sigma_{\text{eq}}$ is the normalized maximum shear stress ($\tau_{\max}$) by σ_{eq}, characterizing the void elongation/rotation mode; C_1 modulates material's sensitivity to different void deformation modes, ranging from 0 to 1; C_2 controls the effect of the linear combination of the two void deformation modes; D_n is a power function quantifying the number of the nucleated voids with respect to equivalent plastic strain ($\bar{\varepsilon}^p$). Equation (1) originally assumes that DF occurs when C_3 is reached by Eq. (1). Researchers in the DF community usually make the use of the so-called linear ductile damage indicator framework to define ductile damage evolution during a certain plastic deformation process, as follows,

$$\mathrm{d}D = \frac{\mathrm{d}\bar{\varepsilon}^p}{\bar{\varepsilon}^f(T, L)}. \tag{2}$$

In Eq. (2), dD stands for the increment in damage indicator (D). To simulate DF initiation and propagation in a sheet metal forming simulation, the element deletion approach is frequently implemented to remove the critical element whose D value reaches at 1. The term, $\bar{\varepsilon}^f(T, L)$ in Eq. (2), is a 3D fracture surface function defined in the space of stress triaxiality (T), Lode parameter (L), and fracture strain ($\bar{\varepsilon}^f$). The form of $\bar{\varepsilon}^f(T, L)$ varies with the selection of DF criterion. Generally speaking, $\bar{\varepsilon}^f(T, L)$ can be derived from a certain DF criterion using a linear loading path assumption. The specific $\bar{\varepsilon}^f(T, L)$ corresponding to Eq. (1) is as follows,

$$\bar{\varepsilon}^f(T, L) = a \left[\frac{3\sqrt{L^2 + 3}}{C_1 \left(3T\sqrt{L^2 + 3} - L\right) + 3} \right]^b, \; a = \left[\frac{C_3(m + 1)}{R_n} \right]^{\frac{1}{m+1}}, \; b = \frac{C_2}{m + 1}. \tag{3}$$

2.2 Model Calibration

According to Eqs. (2) and (3), a, b, and C_1 are the three parameters to be calibrated (C_3, R_n, and m merge into a; C_2 and m merge into b). To this end, the least-squares optimization is performed to identify a pair of (a, b, and C_1), which can minimize the accumulated error of the targeted 3D fracture surface as compared to each DF data point, as listed in Table 1. It should be mentioned that the DF data of the DP780 sheet considered were initially obtained by Wang et al. [2, 9] and later converted into the space of (T, L, $\overline{\varepsilon}^f$) by Mu et al.[10]. The optimized pair of (a, b, and C_1) is (0.1115, 3.2186, 0.1273) with the resultant 3D fracture surface given in Fig. 1. It is observed that the constructed 3D fracture surface can well demonstrate the distribution of the DF data points in the space of (T, L, $\overline{\varepsilon}^f$) with acceptable deviations. Moreover, the 3D fracture surface exhibits two special features: (a) the surface is asymmetric with respect to the plane of $L = 0$; (b) the L sensitivity of the surface increases with a decrease in T. These two features have been confirmed from the results yielded by the well-established unit cell approach, as reported by Dunand and Mohr [17] and Luo and Gao [18].

Table 1 DF data points in the space of (T, L, $\overline{\varepsilon}^f$)[10]

Specimen no.	Specimen type	T (averaged)	L (averaged)	$\overline{\varepsilon}^f$
1	1# butterfly	−0.035	0.090	0.717
2	2# butterfly	0.234	−0.649	0.473
3	Specimen with a center hole	0.330	−0.974	0.628
4	3# butterfly	0.546	−0.133	0.402
5	Balanced biaxial tension specimen	0.659	0.718	0.718

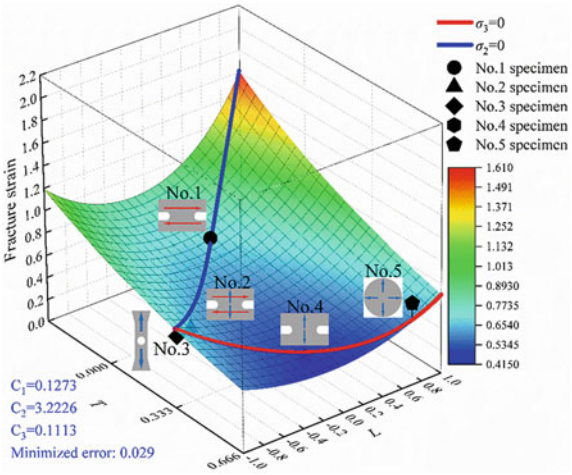


Fig. 1 3D fracture surface of the DP780 sheet. (Color figure online)

3 Simulation Framework

To predict the edge fracture behavior of a blanked circle hole during the subsequent hole-expansion test, the simulation framework of the current study is proposed to comprise two sub-simulations, namely, hole-blanking simulation and hole-expansion simulation. For the purpose of enabling the hole-expansion simulation to consider the shear-induced ductile damage field, three Python scripts are coded to process the results from the hole-blanking simulation: (a) the first Python script is specialized to remove all the nodes, whose displacements (in the blanking direction) are larger than the sheet thickness (1.6 mm), thereby removing the circular sheet cut out from the original material; (b) the second Python script rebuilds the elements based on the remained nodes, thereby constructing the geometry model for the hole-expansion simulation with the morphology of the sheared edge inherited; (c) the third Python script extracts $\overline{\varepsilon}^p$ and D fields from the hole-blanking simulation, which are further prescribed as the initial state variable fields for the hole-expansion simulation.

$$Y_{\text{Swift}}\left(\overline{\varepsilon}^p\right) = A\left(\overline{\varepsilon}^p + \varepsilon_0\right)^n \tag{4}$$

$$Y_{\text{Voce}}\left(\overline{\varepsilon}^p\right) = Y_s - (Y_s - Y_0)e^{\left(-\frac{H_0}{Y_s}\overline{\varepsilon}^p\right)} \tag{5}$$

$$Y_{\text{Swift - Voce - combined}}\left(\overline{\varepsilon}^p\right) = \alpha Y_{\text{Swift}}\left(\overline{\varepsilon}^p\right) - (1-\alpha)Y_{\text{Voce}}\left(\overline{\varepsilon}^p\right) \tag{6}$$

$$f\left(\sigma_{ij}\right) = \sqrt{F\left(\sigma_{yy}-\sigma_{zz}\right)^2 + F\left(\sigma_{zz}-\sigma_{xx}\right)^2 + H\left(\sigma_{xx}-\sigma_{yy}\right)^2 + 2\left(L\sigma_{zy}^2 + M\sigma_{zx}^2 + N\sigma_{xy}^2\right)} \tag{7}$$

The plastic properties of the DP780 sheet are characterized using Swift-Voce-combined hardening law (Eqs. 4–6) and Hill's 1948 quadratic yield function (Eq. 7), with the relevant parameters given in Table 2 and Table 3, respectively. The Young's modulus and Poisson's ratio of the DP780 are set to be 200 GPa and 0.3, respectively.

Table 2 Strain hardening parameters [2, 9]

Swift law			Voce law			Weight factor α(–)
A (MPa)	ε_0 (–)	n (–)	Y_s (MPa)	Y_0 (MPa)	H_0 (MPa)	
1460.3	0.0024	0.1943	1020	507.9	19,321	0.7

Table 3 Parameters of the Hill's 1948 quadratic yield function [2, 9]

F	G	H	L	M	N
0.6619	0.5872	0.4128	1.5	1.5	1.8029

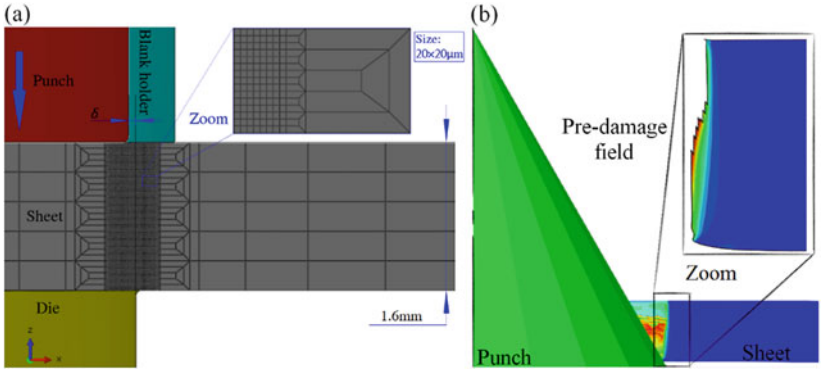


Fig. 2 Simulation configurations: **a** hole-blanking simulation; **b** hole-expansion simulation. (Color figure online)

A user-defined material subroutine (VUMAT) compatible with Abaqus/Explicit is coded to describe the abovementioned elastic–plastic characteristics with the ductile damage evolution law defined by Eq. (2) embedded. In addition, C3D8R elements are used to discretize the DP780 sheet with the shear zone assigned fine elements; tools are all assumed to be rigid bodies; a quarter of the sheet is modeled to make use of the symmetric nature of the problem; Coulomb friction model is used to describe the friction of each contact pair with the friction coefficient set to be 0.1. Simulation configurations of the hole-blanking and hole-expansion processes are illustrated in Fig. 2a, b, respectively. Note that in Fig. 2b, the pre-damage (denoted by D value) field, which is defined by Eq. (2) and inherited from the prior hole-blanking simulation, is prescribed as an initial state variable field. Also, the clearance ratio (δ) in Fig. 2a is defined as the blanking clearance divided by the sheet thickness.

4 Results and Discussion

The hole-expansion simulation results corresponding to a δ value of 5% are given in Fig. 3. Figure 3a shows the case where the shear-induced pre-damage is considered, whereas Fig. 3b shows the case without considering the pre-damage. It is observed from Fig. 3a that the predicted cracks initiate from the middle of the sheared edge, where there are relatively higher values of D. As the punch further travels upward, the initial cracks primarily propagate at 45° with respect to the sheet thickness direction. This is in accordance with the experimental observation, as shown in Fig. 4a. When the occurrence of the first through-thickness fracture is captured, the corresponding HER value is identified to be 0.13, which is slightly larger than the experimental value (0.12). However, when the pre-damage field is ignored (Fig. 3b), the prediction yields unacceptable errors: (a) the propagation direction of the through-thickness fracture is not 45° with respect to the thickness direction; (b) only one crack initiates and

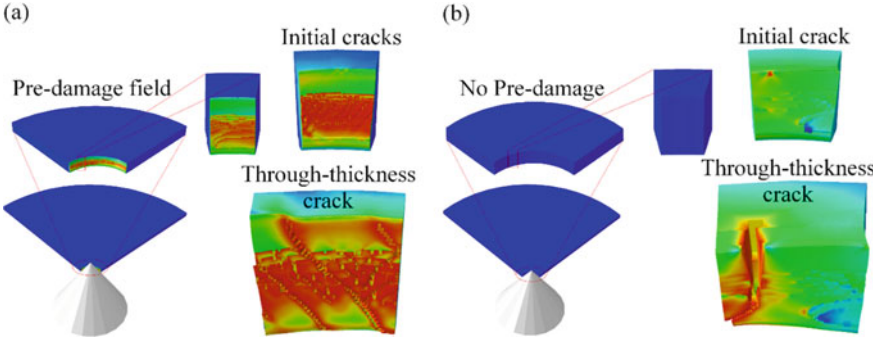


Fig. 3 Simulated evolution of macroscopic cracks: **a** with pre-damage; **b** without pre-damage. (Color figure online)

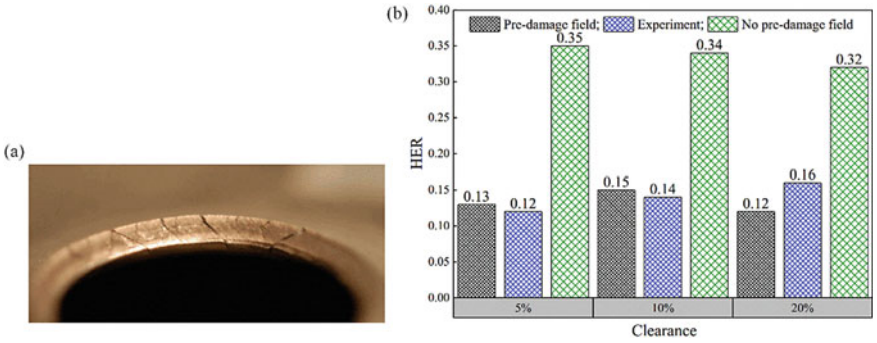


Fig. 4 Experimental observations: **a** observed crack initiation and propagation (δ: 5%) [9]; **b** HERs. (Color figure online)

grows; (c) the predicted HER is 0.35, which is much larger than the tested value (0.12).

It should be mentioned that the predicted crack initiations and propagations of other δ values (10% and 20%) are similar to those shown in Fig. 3. Meanwhile, the predicted HERs of different δ values are compared with experimental ones in Fig. 4b. Obviously, a careful consideration of the pre-damage field can significantly improve the HER predictions of different blanking clearances for the DP780 sheet. Also, the used DF criterion is able to give reliable predictions in terms of not only the HER values but also the crack initiations and propagations.

In addition, the performance of various DF criteria is compared as shown in Fig. 5. Here, only the case of 5% δ is considered because the experimental HER shows minor changes with a varying δ from 5 to 20% as shown in Fig. 4b. For the detailed prediction results by Lou–Huh criterion [12], Oh criterion [13], and Brozzo criterion [14], readers are referred to one of our previous works [10], in which an identical simulation framework was used except for the DF criterion. It is

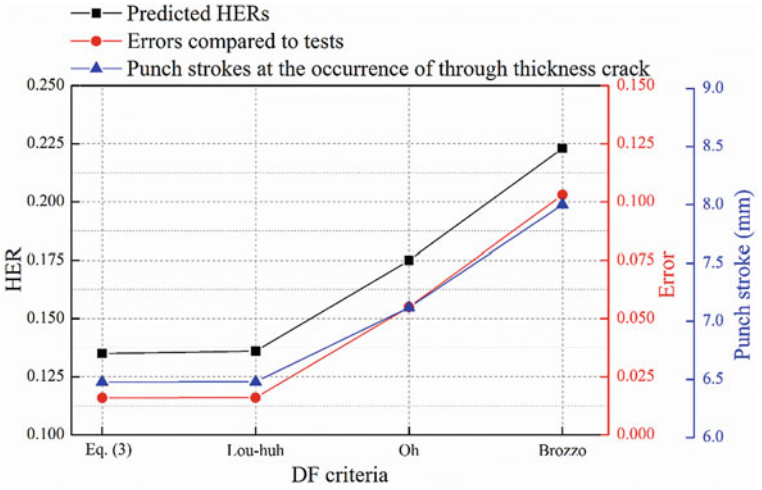


Fig. 5 Comparison of HER predictions between various DF criteria (the predictions by Lou–Huh, Oh, and Brozzo criteria are cited from Ref. [10]). (Color figure online)

found that Lou–Huh criterion and the one described in Section 2.1 produce the best predictions as compared with the experimental data. This could be contributed to the fact that these two criteria are able to accurately characterize the ductility of the DP780 sheet in a wide range of stress states from simple shear to balanced biaxial tension. This lines up with the conclusion made in [10]. Also, we find that the HER predictions by these two criteria are almost the identical, which could be explained by the following aspects: (a) The crack initiation and propagation are simulated based on the element deletion operation, which is executed according to the ductile damage accumulation defined by a 3D fracture surface through Eq. (2); (b) Since the 3D fracture surfaces defined by the currently selected criterion (Eq. 3) and Lou–Huh criterion only demonstrated minor deviations, the resultant crack initiation and propagation predictions are similar between these two criteria, contributing to the identical HER predictions. (c) It should be also mentioned that the crack initiation and propagation simulations are also sensitive to the mesh size in a FE simulation. The identical HERs predicted could also imply that the mesh size used in this study cannot distinguish the minor deviations between these two criteria.

5 Conclusion

In the current study, a newly proposed DF criterion is selected to define the ductile damage evolution from hole-blanking simulation to the following hole-expansion simulation. The shear-induced pre-damage is elaborately considered through a fully integrated simulation framework. The model calibration result points out that this

criterion can well describe the ductility of the DP780 in a wide range of stress states. It is also confirmed by the comparison between the simulation and experimental observation that the shear-induced pre-damage plays an important role in an accurate HER prediction for the DP780 sheet considered. Again, after considering the pre-damage, the selected DF criterion can well predict the edge fracture behavior of the DP780 sheet.

References

1. Sartkulvanich P, et al (2010) Finite element analysis of the effect of blanked edge quality upon stretch flanging of AHSS. CIRP Ann Manuf Technol 59:279–282
2. Wang K, Luo M, Wierzbicki T (2014) Experiments and modeling of edge fracture for an AHSS sheet. Int J Fract 187:245–268
3. Taylor MD, et al. (2014) Correlations between nanoindentation hardness and macroscopic mechanical properties in DP980 steels. Mater Sci Eng A 597:431–439
4. Teng ZK, Chen XM (2014) Edge cracking mechanism in two dual-phase advanced high strength steels. Mater Sci Eng A 618:645–653
5. Li YN, et al. (2010) Prediction of shear-induced fracture in sheet metal forming. J Mater Process Technol 210:1858–1869
6. Lou YS, Yoon JW (2017) Anisotropic ductile fracture criterion based on linear transformation. Int J Plast 93:3–25
7. Park N, Stoughton TB, Yoon JW (2020) A new approach for fracture prediction considering general anisotropy of metal sheets. Int J Plast 124:199–225
8. Mu L, et al (2020) A theoretical prediction framework for the construction of a fracture forming limit curve accounting for fracture pattern transition. Int J Plast. https://doi.org/10.1016/j.ijplas.2020.102706
9. Wang K, Greve L, Wierzbicki T (2015) FE simulation of edge fracture considering pre-damage from blanking process. Int J Solids Struct 71:206–218
10. Mu L, et al. (2017) Edge fracture prediction using uncoupled ductile fracture models for DP780 sheet. J Fail Anal Prev 17(2):321–329
11. Bai YL, Wierzbicki T (2010), Application of extended Mohr–Coulomb criterion to ductile fracture. Int J Fract 161:1–20
12. Lou YS, et al. (2012) New ductile fracture criterion for prediction of fracture forming limit diagrams of sheet metals. Int J Solids Struct 49(25):3605–3615
13. Oh SI, Chen CC, Kobayashi S (1979) Ductile fracture in axisymmetric extrusion and drawing: Part 2: workability in extrusion and drawing. ASME J Eng Ind 101:36–44
14. Brozzo P, DeLuca B, Rendina R (1972) A new method for the prediction of the formability limits of metal sheets. Paper presented at the 7th Biennial Conference of IDDRG on Sheet Metal Forming and Formability, Amsterdam, Netherlands, 9–13 October 1972
15. Mu L, et al (2017) A Micromechanically-motivated Phenomenological Model for Predicting Ductile Fracture Initiation. Procedia Eng 207:2054–2059
16. Mu L, et al (2018) Phenomenological uncoupled ductile fracture model considering different void deformation modes for sheet metal forming. Int J Mech Sci 141:408–423
17. Dunand M, Mohr D (2014) Effect of Lode parameter on plastic flow localization after proportional loading at low stress triaxialities. J Mech Phys Solids 66:133–153
18. Luo T, Gao XS (2018) On the prediction of ductile fracture by void coalescence and strain localization. J Mech Phys Solids 113:82–104

Relaxation Characteristics of Creasing Process of Scored Paperboard for Liquid Container



Shigeru Nagasawa, Takaomi Nagumo, Azusa Sakamoto, and Kazuki Umemoto

Abstract In this work, dynamic creasing characteristics of liquid-container-purpose paperboard of basis weight 313 g/m^2 (a thickness of $t = 0.47$ mm) were investigated, when varying the holding time of two creasing knives (a round edge and/or a flat edge) at an indentation depth of $d = 0.8$ mm. In a scoring process, the relationship between the time-dependent behavior of reaction force f and the permanent scored depth d_{as} was approximately linearized with a logarithmic function of the elapsed holding time $t_{ep} =$ 0-60 s. When using the paperboard scored with the specified indentation depth and varying the tracking holding time T_{ep}, the relationship of the bending moment M and the rotation angle θ was investigated. The effects of the tracking holding time at the scoring process on the bending moment resistance (as the maximum strength) $M_{90}(0)$ at $\theta =$ 90° and the initial gradient $C_1 = \partial M/\partial\theta(\theta = 0–5°)$ were characterized with a logarithmic function of T_{ep}, and also an explicit expression of C_1 with $M_{90}(0)$ was revealed. Namely, a time-dependent relaxation of scoring reactional force f and the time-dependent relaxation of C_1 (and/or $M_{90}(0)$) in a folding process has occurred with a logarithmic term of the holding time.

Keywords Folding · Shear · Bending moment · Creasing · Relaxation · Creep · Paperboard

1 Introduction

Coated paperboard is a fundamental raw material for various printed-decorated packaging and transport packaging industries due to its advantages such as high strength-to-weight ratio, high surface smoothness, printability, sustainability, and recyclability [5]. If any cracks occur on the outside of the folded parts of paperboard, which is used for making a cabinet, the mechanical strength of the cabinet is weakened, and also folded parts are inferior in decorative aspects. The actual creasing range was investigated based on the relationship between the crease depth and crease width

S. Nagasawa (✉) · T. Nagumo · A. Sakamoto · K. Umemoto
Mechanical Engineering Department, Nagaoka University of Technology, 1603-1 Kamitomioka, Nagaoka 940-2188, Japan
e-mail: snaga@mech.nagaokaut.ac.jp

© The Minerals, Metals & Materials Society 2021

G. Daehn et al. (eds.), *Forming the Future*, The Minerals, Metals & Materials Series,
https://doi.org/10.1007/978-3-030-75381-8_138

[3]. Carey [1] and Carlsson [2] explained about the bending behavior of the creased part as composed of two parallel beams. There are several reports for estimating the anisotropic properties of the paperboard and the delamination-based folding resistance in the creasing process [15]. Nagasawa et al. [6–10] reported about the quasi-static folding stiffness and bulging profile with respect to the indentation depth of the creaser and also discussed about a fundamental crease deviation effect on the folding deformation characteristics, by the use of a creasing strength tester CST-J-1, which was based on a cantilever type [4], namely a single-point method (TAPPI, T-556 om-11). Empirically, the folding performance of the creased part is estimated using the relative creasing strength (*RCS*, a ratio of bending peak maximum resistance of the creased sheet by that of uncreased sheet) or the folding factor *F* (decrease rate of bending moment resistance) defined as 1-*RCS.* The bending strength of creased part was generally based on the quasi-static solid mechanics, while a real scoring of the paperboard was processed under various dynamic conditions: a high velocity for making a high productivity, a trial low velocity in a laboratory. Since the paperboard has time-dependent behaviors (e.g., visco-elasticity), the velocity effect on the folding factor seems to be changed. Sakamoto et al. [14] reported the stress relaxation response of liquid container board during a scoring process. However, the effects of stress relaxation on the bending stiffness (as the bending moment resistance) were not sufficiently pursued. The relationship between the dynamic scoring of creasing knife against the paperboard and the quasi-static folding factor (the bending moment resistance acting on a hinge) is important in order to adjust mechanical conditions for boxing a paperboard. In this work, therefore, in order to reveal the dynamic creasing characteristic of a liquid container board, when the holding time of a creasing knife was changed at each pushed position, the reaction force of scoring at the specified indentation depth was observed and its effect on the bending moment resistance was investigated.

2 Experimental Condition and Method

2.1 Pre-processing of Specimen

The chosen paperboard was popular for making a milk carton box, which had a thickness of 0.47 mm and a basis weight of 313 g/m^2. In-plane tensile test properties in the Machine Direction (MD) and Cross machine Direction (CD) are shown in Table 1. As for the pulp combination ratio of the paperboard, a broad-leaved lumber of 60.3% and a needle-leaved lumber of 39.3% were measured by a fiber analyzer Kajaani-FS300. From this fiber analysis, it was confirmed that the paperboard was made from virgin softwood and hardwood fibers. Figure 1 shows a sectional view of the liquid container sheet across the fiber grain machine direction. The wetted (inside) surface of the liquid container sheet had a thickness 28–29 μm of polyethylene, and the printed (outside) surface had a thickness 16–17 μm of polyethylene, respectively.

Table 1 In-plane tensile properties of liquid container sheet. Humidity: 50%RH, temperature: 296 K

Breaking true stress σ_B (MD/CD) MPa	40.72/18.77
At feed velocity 0.33 mm/s	
Breaking true strain ε_B (MD/ CD) %	1.96/4.55
Young modulus E (MD/ CD) GPa	4.40/1.86
0.2% proof stress (MD/ CD) MPa	26.64/11.75

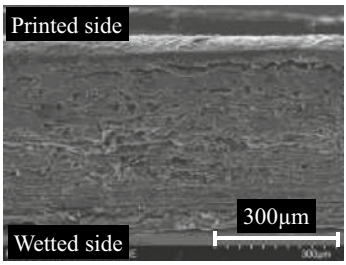


Fig. 1 SEM photograph of sectional view across the fiber grain machine direction of liquid container sheet of 313 g/m^2

The specimens were kept in a room, which had a temperature of 296 K and a humidity of 50% RH. The scoring test pieces were prepared as eight pieces of the rectangle formed liquid container sheet, which had a width of $W_S = 15$ mm, a length of 60 mm, and a thickness of $t = 0.47$ mm for each mechanical condition: (1) two kinds of creasing knives (flat-edge and round-edge) and (2) the holding time of scoring from 1 to 60 s at the specified bottom position. Chosen three pieces from these specimens were examined in the bending resistance test with respect to the mechanical condition. The specimens were scored on the printed surface with an indentation velocity of 0.0167 mm/s using rubber blocks and a creasing knife (flat-edge or round-edge) against a grooved counter face plate as shown in Fig. 2. The creasing knife was set across MD of the specimen. When the knife was indented to the specimen with the indentation depth d, the normalized indentation depth $2d/B = \gamma$, a kind of average shearing strain, was chosen as a certain range (Nagasawa

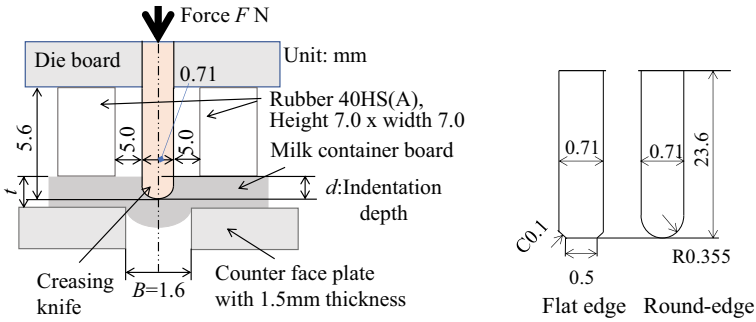


Fig. 2 Layout of out-of-plane scoring by creasing knife, and profile of knife edges. (Color figure online)

2001). The groove width B was empirically chosen as 1.6 mm ($\approx 2t + b$). Here, a thickness of knife body $b = 0.71$ mm and a thickness of specimen $t = 0.47$ mm were considered.

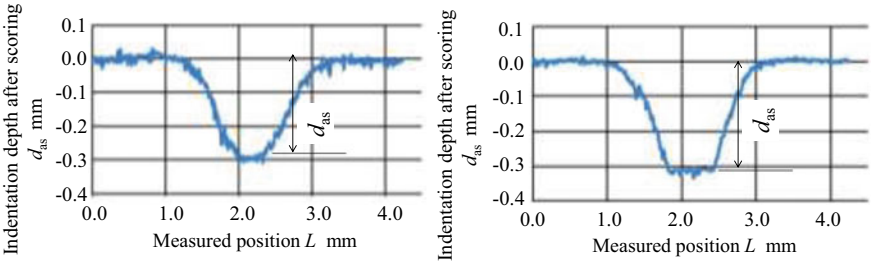
In the previous report [14], a range of $\gamma = 0.4$–2.0 ($d/t = 0.68$–3.4) was used for investigating the spring back effect when the holding time of scoring was zero. The permanent depth after scoring d_{as} was experimentally approximated as Eqs. (1) and (2) for the round-edge and the flat-edge knife, respectively. Defining the spring back $SP = 1 - d_{as}/d$ when choosing $\gamma = 1.0$ ($d/t = 1.7$), that of round-edge and flat-edge was 0.58 and 0.56, respectively. Namely, the spring back of flat-edge scoring seemed to be a little smaller than that of round-edge scoring. Figure 3 shows a representative two-dimensional profile, which was measured at the middle zone of the specimen by a laser microscope, on the printed surface of the specimen scored (at a holding time of zero) by the round-edge and the flat-edge knife, respectively.

$$d_{as}/t = 0.699(d/t) - 0.474 \tag{1}$$

$$d_{as}/t = 0.704(d/t) - 0.451. \tag{2}$$

Obviously, since the minimum distance (clearance) of flat-edge type between the edge of creasing knife and the groove edge of counter face plate was the smaller than that of round-edge type against the specified indentation depth d, the strain state of the flat-edge type is severer than that of the round-edge type. In this work, the holding time of scoring at the bottom end position ($\gamma = 2d/B = 1.0$, $d/t = 1.7$) was chosen as $T_{ep} = 1, 2, 5, 10, 20$ and 60 s. According to a preliminary experiment, seeing both sides of the printed surface and wetted surface of scored part by the flat-edge type, a permanent depth d_{as} of wetted surface was almost equal to that of printed surface, although distributed profiles of scored zone were different with each other.

Figure 4 illustrated a response of scoring line force $f = F/W_S$ with the elapsed time t_{ep}. The creasing knife was initially indented to the specimen until reaching



(a) In case of round-edge knife (b) In case of flat-edge knife

Fig. 3 Representative 2 dimensional profile of permanent depth on printed surface when choosing $\gamma = 1.0$ ($d = 0.8$ mm), scanned by a laser microscope. Here, the holding time of scoring was zero. (Color figure online)

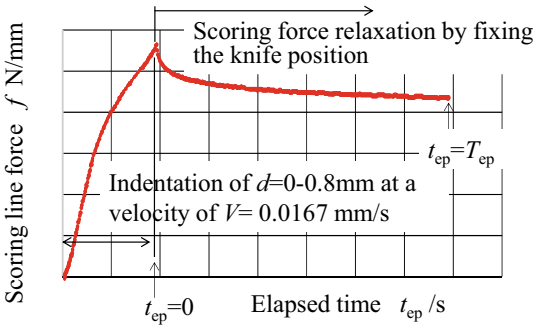


Fig. 4 Scoring load response model and holding time zone. (Color figure online)

the position of $d = 0.8$ mm ($\gamma = 1.0$) at a velocity of $V = 0.0167$ mm/s. At that position, the creasing knife was locked and the reaction line force f was recorded with the elapsed time $t_{ep} = 0 - T_{ep}$. After releasing the knife from the specimen, the permanent depth d_{as} was measured with the specified T_{ep}, using the laser microscope.

2.2 *Measurement of Bending Moment Resistance*

Figure 5 shows a schematic diagram and a general view of the experimental apparatus [4] used for the folding motion test. A clamped specimen on the right side as a cantilever beam (sheet) was rotated at the hinge (the center of rotation) while the left side of specimen was fastened by the load cell edge. The fixture (right side) rotated from $\theta = 0$ up to $\theta = 90°$ at a rotation velocity of $\omega = 0.2$ rps. Figure 6 shows the examples of the relationship between the folding angle θ and the bending moment resistance M per unit width Nm/m. As for characteristic parameters of the bending moment resistance, the initial gradient $C_1 = \partial M/\partial\theta$ ($\theta = 0$–$5°$), the bending moment $M_{90}(0)$ at the tracking position of $\theta = 90°$, and the initial release angle $\theta_{2,1}(0)$ were experimentally collected when varying the holding time of scoring T_{ep}. Here, $M_{90}(0)$ denotes a moment resistance when the stopping time was zero at the tracking position of 90° [11, 12]. Since the maximum peak bending moment resistance of non-scored specimen was $M_{p1,0} = 1.61$ Nm/m in across MD, the ratio of $M_{90}(0)/M_{p1,\gamma=0}$ as *RCS*

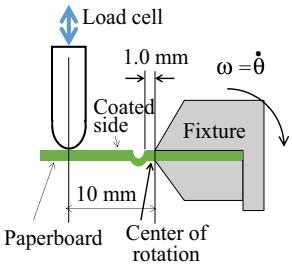


Fig. 5 Bending test apparatus. (Color figure online)

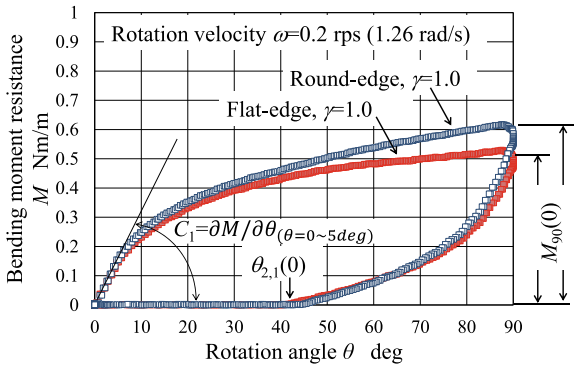


Fig. 6 Analysis parameters on folding resistance diagram. (Color figure online)

was estimated as 0.37, 0.31 for the round-edge and flat-edge, respectively when $T_{ep} = 0$. The initial gradient of non-scored $C_{1,\gamma=0}$ was 0.123 Nm/m/degree.

3 Results and Discussion

3.1 *Relaxation of Scoring Line Force and Permanent Indentation Depth*

Figure 7 shows the line force of scoring $f = F/W_S$ with the elapsed time $t_{ep} =$ 0–60 s after fixing the creasing knife at a specified indentation of $d/t = 1.7$ ($\gamma =$ 1.0). Here, two dashed lines were linear approximations with a logarithmic term $\ln(t_{ep})$ expressed by Eq. (3). Two relaxation coefficients a_1, a_0 were experimentally determined for the round-edge and flat-edge knife, respectively.

$$f = -a_1 \ln(t_{ep}) + a_0 = a_0\left(1 + \ln(t_{ep})^{-a1/a0}\right). \tag{3}$$

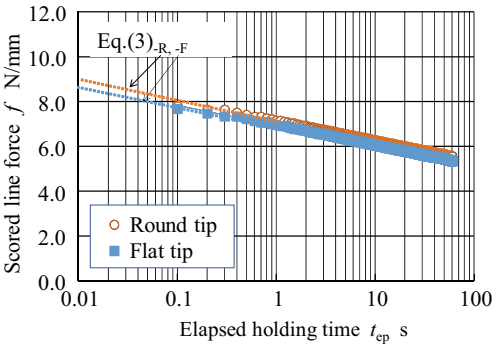


Fig. 7 Relationship between scored line force and elapsed holding time when $\gamma = 1.0$ across MD. (Color figure online)

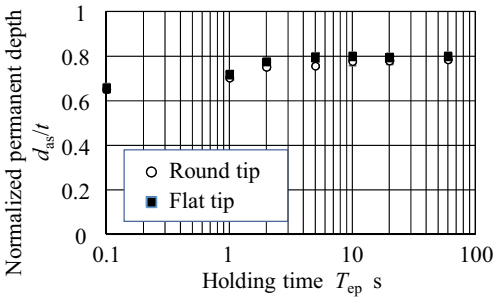


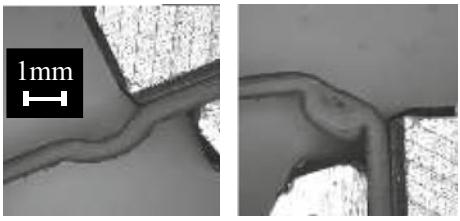
Fig. 8 Effect of holding time on permanent indentation depth when $\gamma = 1.0$ across MD. (Color figure online)

Seeing $t_{ep} = 0.1$–60 s, the index ratio a_1/a_0 and the coefficient a_0 (=f at $t_{ep} = 1$ s) were 0.054, 7.2 for the round-edge, and 0.056, 6.9 for the flat-edge, respectively. According to Sakamoto's report [13], the relaxation index ratio of a_1/a_0 with in-plane MD tensile test was 0.046 (for 0.1–60 s). Hence, the relaxation of scoring reaction force appeared to be larger than that of in-plane simple tensile stress.

Figure 8 shows the permanent indentation depth d_{as} with respect to the holding time $T_{ep} = 1$, 2, 5, 10, 20 and 60 s. Here, dots at $T_{ep} = 0.1$ s were referenced data when the scoring was executed without any holding time. The value of d_{as} transiently increased and appeared to be saturated for $T_{ep} > 5$ s. Assuming that the time-dependent response of d_{as} was described as the first-order delay model, the time constant was roughly estimated as 2 s (up to 63.2% of total variance).

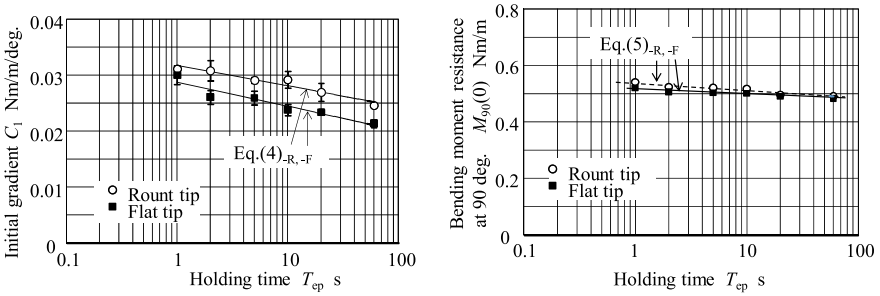
3.2 *Effects of Holding Time on Bending Relaxation Characteristics*

Figure 9 shows an example of photographs of side views of scored zone of the specimen at $\theta = 0$, 90°. Here, the state of the paperboard at $\theta = 0°$ was the same as that of Fig. 5. The relationship between the bending moment resistance per unit width M and the rotation angle θ, as shown in Fig. 6, was measured when T_{ep} was chosen as 1, 2, 5, 10, 20, and 60 s, using two creasing knives. Figure 10a shows the



(a) θ=0° (b) θ=90°

Fig. 9 Photographs of bending process after flat-edge scoring across MD at $\gamma = 1.0$, $T_{ep} = 0$



(a) Initial gradient C_1=$\partial M/\partial\theta$ (θ=0-5°) (b) Bending moment resistance at θ=90°.

Fig. 10 Effect of holding time on folding factors in the bending moment response. (Color figure online)

initial gradient $C_1 = \partial M/\partial\theta$ ($\theta = 0$–5°), while Fig. 10b shows the bending moment resistance at the tracking position $\theta = 90°$ with respect to T_{ep}. In these graphs, lines described approximations with a logarithmic term $\ln(T_{ep})$ as expressed in Eqs. (4) and (5).

$$C_1 = -c_{11}\ln(T_{ep}) + c_{10} = c_{10}\left(1 + \ln(T_{ep})^{-c11/c10}\right) \tag{4}$$

$$M_{90}(0) = -m_{90.1}\ln(T_{ep}) + m_{90.0} = m_{90.0}\left(1 + \ln(T_{ep})^{-m90.1/m90.0}\right) \tag{5}$$

here, the coefficient $c_{10} = C_1(T_{ep} = 1\text{ s})$ was 0.032, 0.029 Nm/m/deg. for the round-edge and the flat-edge, while the index ratio c_{11}/c_{10} was 0.063, 0.069 for the round-edge and the flat-edge, respectively. The RCS factor (at $\gamma = 1.0$) $c_{10}/C_{1,g=0}$ was 0.26, 0.24 for the round-edge and the flat-edge knife, respectively. Similarly, the coefficient $m_{90.0}$ was 0.54, 0.52 Nm/m for the round-edge and the flat-edge, while the index ratio $m_{90.1}/m_{90.0}$ was 0.022, 0.015 for the round-edge and the flat-edge, respectively. The time-dependent response of C_1 was fairly sensitive, because the ratio c_{11}/c_{10} was larger than a_1/a_0. On the other hand, the value of $M_{90}(0)$ was relatively insensitive with T_{ep} owing that a large deformation of $\theta = 90°$ reduces the residual strain state with the holding time, although there was a small effect of T_{ep} on the bending stiffness at $\theta = 90°$. The RCS factor (at $\gamma = 1.0$) $m_{90.0}/M_{p1,0}$ was 0.34, 0.32 for the round-edge and the flat-edge knife, respectively. Seeing C_1 and $M_{90}(0)$, they were similarly varied with T_{ep}. Figure 11 shows a scatter plot of C_1 and $M_{90}(0)$ when changing the parametric T_{ep}. Also, a monotonous, static relationship Eq. (6) was derived from Eqs. (4) and (5).

$$C_1 = \frac{c_{11}}{m_{90.1}}M_{90}(0) + c_{10} - \frac{c_{11}}{m_{90.1}}m_{90.0}. \tag{6}$$

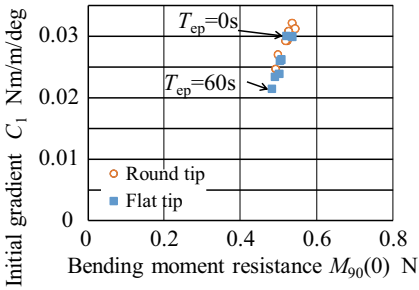


Fig. 11 Variation of folding parameters C_1, $M_{90}(0)$ in the bending moment response when increasing the holding time. (Color figure online)

It was found that C_1 decreased with 30% (23%) and $M_{90}(0)$ decreased with 10% (8%) when changing $T_{ep} = 0$–60 s with respect to the flat-edge (round-edge) knife. Namely, a positive holding time of scoring at the bottom end position promotes an additional indentation depth equivalently.

As for a spring back deformation of folded hinge, the initial release angle $\theta_{2,1}(0)$ was measured and about 42–44° when changing T_{ep}. Any monotonous correlation was not detected between $\theta_{2,1}(0)$ and T_{ep}. Dependencies of the rotational velocity of ω and the stopping time at a folded angle of $\theta = 90°$ on $\theta_{2,1}(0)$ were already reported using a white-coated paperboard [12]. Since this work was carried out under keeping $\omega = 0.2$ rps and the stopping time of folded angle as zero, the effect of T_{ep} on $\theta_{2,1}(0)$ seemed to be sufficiently negligible.

4 Conclusions

In a scoring process using two kinds of creasing knives (round-edge and flat-edge), when increasing the holding time T_{ep} of the creasing knife up to 60 s, at a specified indentation depth of $\gamma = 2d/B = 1.0$, one-loop bending characteristics of a creased liquid container sheet of 0.47 mm thickness were investigated by using a crease stress tester. Obtained results were as follows.

(1) Considering the holding time T_{ep}, the permanent depth increases in the scoring process. As the result, the bending characteristics (as the relative creasing strength) such as the initial gradient $C_1 = \partial M/\partial\theta$ ($\theta = 0$–5°) and the bending moment resistance at the right angle $M_{90}(0)$ decrease in a certain level.

(2) The difference between a round-edge and a flat-edge knife almost does not affect the relaxation coefficient (the index ratio of scoring force: a_1/a_0, that of initial gradient: c_{11}/c_{10}), but the difference affects the permanent depth and the intercept values a_0, c_{10}.

(3) The permanent depth against the specified indentation depth or the spring back of scored depth apt to be saturated when setting the holding time larger than 5 s. The estimated time constant of first-order delay model was 2 s. However, the time-dependent relaxation of scoring reaction force and the time-dependent

relaxation of the initial gradient of the folding process occurred with a logarithmic term of the holding time T_{ep} = 1–60 s. Namely, the relaxation of bending moment resistance does not disappear for T_{ep} = 1–60 s.

Abbreviations: t: a thickness of paperboard 0.47(mm); W_S: a width of paperboard 15(mm); B: a width of groove on a counter (mm); b: a thickness of body of creasing knife 0.71 (mm); F: a force applied to a creasing knife (N); $f = F/W_S$: a line force (N/mm); d: a displacement of creasing knife (= an indentation depth to a paperboard) (mm); d/t: a normalized indentation depth of creasing knife against the specified thickness (–); $\gamma = 2d/B$: a normalized indentation depth of creasing knife as an average shear strain (–); d_{as}: a permanent indentation depth of a paperboard after releasing the creasing knife, a scored depth on a paperboard (mm); t_{ep}: an elapsed holding time at the bottom end position $0 - T_{ep}$ (s); T_{ep}: a (tracking) holding time (s); V: a velocity of a creasing knife (mm/s); θ: a rotation angle of fixture arm (degrees); $\omega = \partial q/\partial t/360$: a rotation velocity of fixture arm (in this work, $\omega = 0.2$rps = 72°/s/360); M: a bending moment resistance per unit width (N mm/mm = N m/m = N); $C_1 = \partial M/\partial q$: an initial gradient of the bending moment M with θ (for θ = 0–5°) (N/deg.); $M_{90}(0)$: a bending moment at the tracking position of $\theta = 90°$ when the elapsed time of folded state was zero at θ = 90°. $\theta_{2,1}(0)$: an initial release angle after releasing the fixture arm (degrees); $M_{p1,0}$: the maximum peak of bending moment during a folding process when choosing $\gamma = 0$; $SP = 1 - d_{as}/d$: a spring back of indentation depth in a scoring process; $RCS_{(90)} = M_{90}(0)/M_{p1,0}$: a relative creasing strength at $\theta = 90°$; A classical/original RCS is defined as $M_{p1}/M_{p1,0}$ (a ratio of the peak maximum bending moment of creased sheet by that of uncreased sheet); $F_{(90)} = 1 - RCS_{(90)} = 1 - M_{90}(0)/M_{p1,0}$: a folding factor at $\theta = 90°$. MD: a Machine (transferred) Direction for papermaking, a fiber grain making direction; CD: a Cross machine Direction; a_0, a_1: Coefficients of Eq. (3) ; c_{10}, c_{11}, $m_{90,0}$, $m_{90,1}$: Coefficients of Eqs. (4) and (5).

References

1. Carey KB (1992) Creasing: turning failure into success. Packag Prod 1(1):1–20
2. Carlsson L, de Ruvo A, Fellers C (1983) Bending properties of creased zones of paperboard related to inter laminar defects. J Mater Sci 18(5):1365–1373
3. Hine DJ (1959) Testing boxboard creasing. Mod Packag 8:122–128
4. Katayama Steel Rule Die Inc., Crease Stress Tester CST J-1, http://diemex.com/sale/cst_e.html. Accessed 20 May 2013
5. Kirwan MJ (ed) (2013) Folding cartons in: handbook of paper and paperboard packaging technology. Wily-Blackwell, pp 265–312
6. Nagasawa S, Fukuzawa Y, Yamaguchi T, Tsukatani S, Katayama I (2003) Effect of crease depth and crease deviation on folding deformation characteristics of coated paperboard. J Mater Process Technol 140:157–162
7. Nagasawa S, Fukushima Y, Sudo A, Fukuzawa Y, Katayama I (2004a) Effect of tip shape of creasing rule on creasing deformation characteristics of paperboard. J Jpn Soc Technol Plast 45(518):178–182 (in Japanese)

8. Nagasawa S, Murayama M, Sudo A, Yamaguchi T, Fukuzawa Y, Katayama I (2004b) Effect of creaser deviation on folding deformation characteristics of creased paperboard. J Jpn Soc Technol Plast 45(519):239–243 (in Japanese)
9. Nagasawa S, Endo R, Fukuzawa Y, Uchino S, Katayama I (2008) Creasing characteristic of aluminum foil coated paperboard. J Mater Process Technol 201(1–3):401–407
10. Nagasawa S, Nasuruddin M, Shiga Y (2011) Bending moment characteristics on repeated folding motion of coated paperboard scored by round-edge knife. J Adv Mech Des, Syst, Manuf 5(4):385–394
11. Nagasawa S, Shiga Y, Fukuzawa Y (2014) Effects of scoring depth, tracking angle, rubbering on bending moment relaxation of creased paperboard. Adv Mater Res 939:53–59
12. Nagasawa S, Kaneko S, Adachi D (2019) Effects of rotational velocity and hold time at folding posture on time-dependent release behavior of creased white-coated paperboard. J Adv Mech Des, Syst, Manuf 13(1):18-00230, 1–10
13. Sakamoto A, Nagasawa S (2017) Stress relaxation response of paperboard for liquid container under in-plane tensile testing. In: Proc. of the 68th Japanese Joint Conf. for the Technology of Plasticity, pp 623–624
14. Sakamoto A, Nagasawa S (2018) Spring back and relaxation in scoring process of paperboard for liquid container. In: Proc. of the 69th Japanese Joint Conf. for the Technology of Plasticity, pp. 99–100
15. Stenberg N, Fellers C, Östlund S (2001) Measuring the stress-strain of paperboard in the thickness direction. J Pulp Pap Sci 27:213–221

Hot Cutting of Press-Hardened Parts in Different Heat Treatment Regimes



R. Schmidt, A. Rautenstrauch, and V. Kräusel

Abstract Parts made of press-hardened steel are cut in general by laser cutting. Shear cutting at room temperature of materials with a tensile strength above 1,500 MPa is not an alternative due to insufficient tool life quantity. The presented investigation relates to the hot cutting of press-hardenable materials such as 22MnB5 and 34MnB5 and includes the determination of the cutting parameters (measuring rate of 100,000 Hz), the temperature, the formation of the microstructure, and the dimensional accuracy of the cut parts during different heat treatments. The results of this investigation show that, when comparing two process routes, the maximum cutting force was reduced to approximately 70 % when cutting in the austenitic range, the acceleration during the cutting impact was close to zero and the deviations from the target geometry were very small. With regard to the measurement results, hot cutting can be an alternative to laser cutting.

Keywords Hot cutting · Press-hardened steels · Thermal treatment

1 Introduction

In recent years, the use of high-strength press-hardened steel has increased, especially for structural parts of the car body. This is due to the increasing need for weight savings while maintaining the same safety requirements in the automobile. The use of press-hardenable boron–manganese steels offers a promising approach to further optimize the lightweight design of structural components. If a critical cooling rate is taken into account during the hot forming of these steels and the targeted quenching in the cooled forming tool, a martensitic structure with strengths >1,200 MPa is obtained [1].

Due to the high tensile strength, press-hardened parts are difficult to cut with mechanical cutting tools due to high abrasive tool wear and even complete tool breakage. Mechanical cutting represents a conventional shear cutting operation. The

R. Schmidt (✉) · A. Rautenstrauch · V. Kräusel
TU Chemnitz, Chemnitz, Germany
e-mail: rainer.schmidt@mb.tu-chemnitz.de

© The Minerals, Metals & Materials Society 2021

G. Daehn et al. (eds.), *Forming the Future*, The Minerals, Metals & Materials Series,
https://doi.org/10.1007/978-3-030-75381-8_139

greatest challenge in the processing of press-hardened sheet metal parts is the very high cutting force and the resulting cutting impact. This results in a high alternating load on the cutting tools, which is manifested as heavy wear on the active cutting elements. As a result, the cutting tools require frequent maintenance, which is associated with high operating and maintenance costs. Laser cutting is currently the most widely used method for cutting press-hardened steel parts. However, laser cutting as a flexible thermal cutting process is very cost-intensive as well as time and energy-consuming [2–4].

The following optimization potentials for the processing of press-hardened steels can be derived from these facts: One approach that is examined in this article is the substitution of the complex laser cutting after press hardening by hot cutting the component in the austenitic state. Currently, only limited experience is available regarding the hot cutting of sheet metal parts made of boron–manganese steels and the corresponding process parameters. Hot cutting offers the possibility to reduce time and operating costs by simultaneously cutting and quenching during forming after previous heating above the austenitizing temperature. Direct quenching in the tool leads to an increase in the tensile strength of the heat-treated and sheared sheet metal part. At the same time, however, the ductility also decreases [5, 6].

In this paper, the influence of the thermal treatment and carbon content of the press-hardenable material on cutting force, cutting impact, part quality, and mechanical properties of hot cut boron–manganese steels is examined. The approach of this work is to punch the sheet metal part in a ductile state to avoid the high dynamic stress on the cutting punch and thus achieve a longer tool life quantity. Of course, the tool heats up with the number of cuts with a consequent change in its strength properties, but this will be initially neglected in this study.

2 Experimental Details

2.1 Selection of Alloys

In this work, a selected group of steel alloys were investigated based on their similarities, e.g. their similar chemical compositions, which are summarized in Table 1. Strip samples with dimensions of 400 × 30 × 1.5 mm were used for all experiments. The manganese–boron steel alloys 22MnB5 and 34MnB5 in supply condition, i.e. cold-rolled, show a ferritic–pearlitic microstructure with the presence of some carbides.

Table 1 Nominal composition of the studied alloys (wt%)

Steel alloy	C	Si	Mn	P	S	Cr	Mo	B	Ti
22MnB5	**0.17**	0.22	1.19	0.01	0.008	0.12	0.01	0.001	0.03
34MnB5	**0.35**	0.29	1.28	0.01	0.01	0.17	0.01	0.004	0.03

The 22MnB5 has a carbon content of about 0.17 % and the material 34MnB5 of about 0.35 % (Table 1).

2.2 Punching Tool and Measurement Concept

The tool has two tool halves, which are guided with four columns and dimensioned primary for cutting of ultra-high-strength steels. The tool material Böhler K890 was used for the punch and the selected material for the die was a Böhler S600. The tool has an integrated cutting shock absorption, which was in tests always enabled. The stripes were 5 mm above the cutting die and the distance to the next support surface was 60 mm. Therefore, the cooling of the strips on contact with the tool is negligible. The manual transport of the stripes from the oven to the cutting process needs around about 2 seconds. The diameter of the punch is 10 mm and the constant cutting clearance is 0.2 mm. A constant blank holder force of 90 kN was set and the punch velocity was adjusted with an industry-relevant value of 50 mm/s. The tool was moved path-controlled by a servo-driven spindle press of the company Dunkes [7] (Fig. 1).

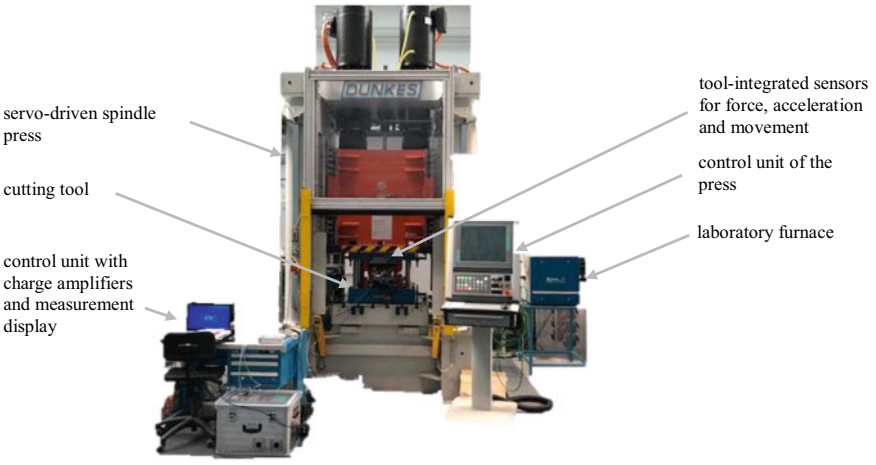


Fig. 1 Experimental setup with the position of measurement sensors. (Color figure online)

Tool-integrated sensors measure the cutting force, acceleration, and movement. The force sensor is positioned directly above the punch in a special construction to measure the pure cutting force without force shunt and other influencing factors. The position of the sensors for acceleration and movement is near the cutting zone. The controlling and saving of the measurement values implement with a control unit of National Instrument. The selected measurement frequency of 100,000 Hz is necessary to obtain a sufficient resolution of the measurement values, especially in

the area of the cutting impact, and to be able to execute a frequency filtration of the measurement values.

2.3 Thermal Treatments

Two different heat treatments were carried out in this work. The first heat treatment route (HTR 1) starts with an austenitization of the test samples at a temperature of 1,000 °C during 10 min and quenched in water by a cooling rate of approximately 10,000 K/s. The hardened strips are then tempered in a furnace in a temperature range between 600 °C and 400 °C for 6 min. The next step is the transfer of the sheet metal strips from the furnace to the cutting tool for punching in the temperature range between 540 °C and 320 °C. After the hot cutting, the tool is opened and the punched sheets are removed for subsequent air cooling to room temperature (Fig. 2).

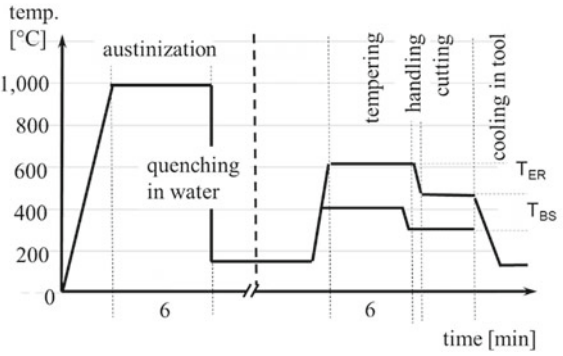


Fig. 2 Heat treatment route 1—HTR 1

In the second heat treatment route HTR 2, the samples are heated at a temperature of 1,000 °C for 10 min. Afterward, the austenized samples are transferred from the furnace to the cutting tool and cut between 800 °C and 600 °C. During handling, the samples cool down from the furnace temperature to the cutting temperature at a cooling rate of approximately 14 K/s (Fig. 3).

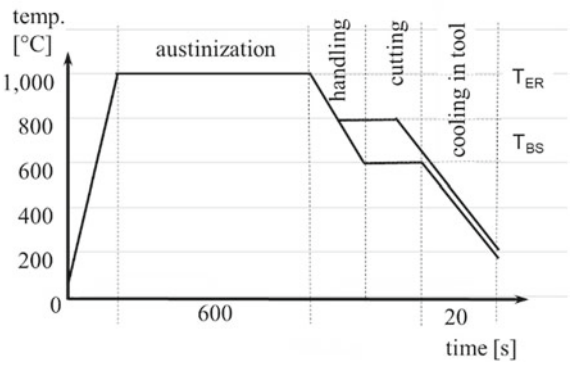


Fig. 3 Heat treatment route 2—HTR 2

3 Results

3.1 Determination of Cutting Performance

The measurement values were evaluated with a self-developed algorithm in the software MATLAB R2019b and filtered against the noisy frequency with a standard MATLAB filter function. To prepare a comparison of different force–displacement curves, the beginning of the curves with the first increase in cutting force is determined for further investigation. In Fig. 4, three typical force–displacement curves

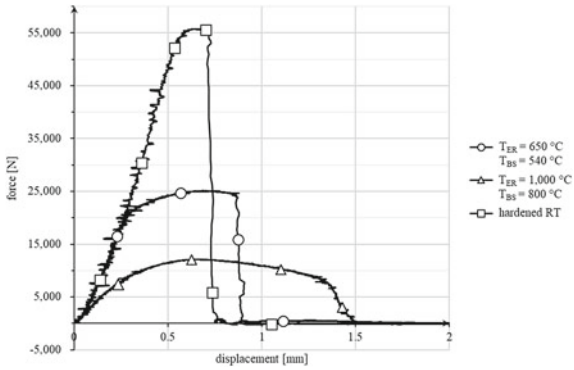


Fig. 4 Typical force–displacement curves for punching of strips made of 34MnB5

are shown as an example of the tested material 34MnB5 with three different heat treatment routes.

The highest cutting force and the shortest flush-cut amount can be determined when cutting from the hardened strip. The abrupt dropdown of the force by approximately 0.7 mm punch penetration results in the highest measured cutting impact in this study. In comparison, a much more pronounced shear zone can be seen on the hot cut sample due to the better forming capacity and thus material flow. Especially, the

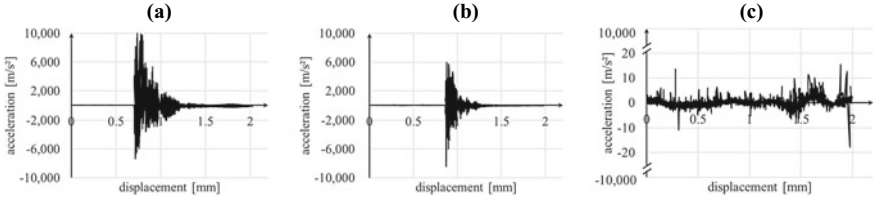


Fig. 5 Acceleration–displacement curves for punching of strips made of 34MnB5 of (**a**) hardened RT; (**b**) $T_{ER} = 650$ °C; $T_{BS} = 540$ °C; (**c**) $T_{ER} = 1{,}000$ °C; $T_{BS} = 800$ °C

material 34MnB5 shows an elastic behavior at 800 °C up to a displacement of 0.2 mm. Afterward, the plastic deformation proceeds until the end of the cutting process with a smooth run-out of the force–displacement curve without any recognizable cutting influence (Fig. 5).

As shown in Fig. 6, after punching a hole with a diameter of 10 mm, the punch enters the die 1 mm and remains at the bottom dead center for one second. Then the punch moves out of the die and the sheet strip while the blank holder continues to press the workpiece onto the die. At this point, the material cools to martensite start temperature and hardening occurs. This is followed by the opening of the tool and the sheet strip is removed. For both the HTR 2 and the uncured material, an increase in retraction force was noticeable after cutting. This suggests that at the time of cutting, no hardening of the material took place during the process route HTR 2 because the martensite start temperature has not yet been reached.

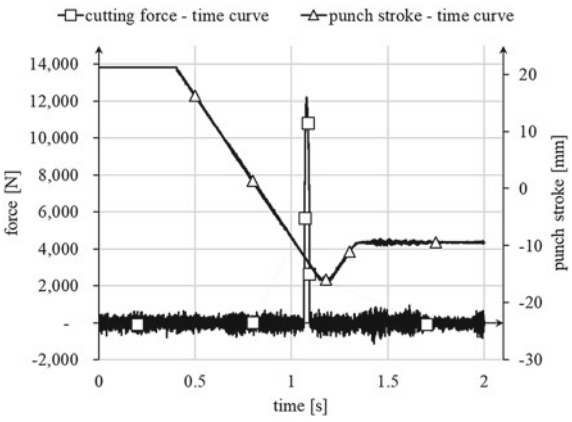


Fig. 6 Development of cutting force for cutting of 34MnB5 at HTR 2

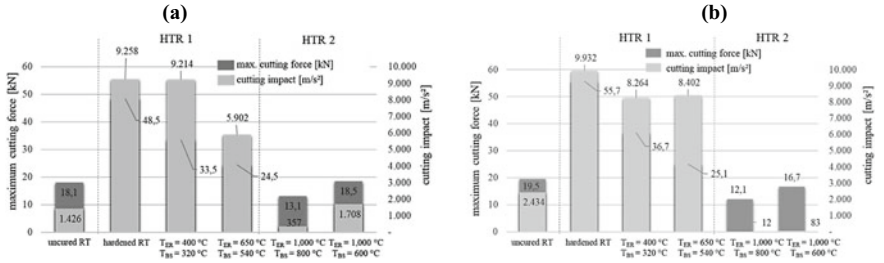


Fig. 7 Maximum cutting force and cutting impact of **a** 22MnB5; **b** 34MnB5

3.2 Determination of the Maximum Cutting Force and Cutting Impact

To determine the maximum cutting force and the cutting impact, the interference signals are filtered with the MATLAB filter function. The cutting impact values after the break are included in the evaluation. The results in Fig. 7 show that the highest maximum cutting forces correlate with the highest measured cutting impact values. Furthermore, it is found that the lowest cutting forces show a correlation with the lowest measured cutting impact values. The results were found to be independent of the material. When cutting hardened steels according to heat treatment route 1, higher cutting forces and higher cutting impact values are recorded compared with heat treatment route 2. In contrast, the lowest maximum force of 12.1 kN was obtained during hot cutting of the material 34MnB5 along HTR 2 at a cutting temperature of 800 °C. The cutting impact could not be measured for this low cutting force.

3.3 Determination of Cutting Quality

In addition to the investigation of Neumayer et al. [6] and So et al. [8], the diameters of the round holes are measured optically with a Keyence microscope VHX-600 with a deviation of about 0.02 mm. The following Fig. 8 shows the diameter of the hole from the punch side compared to the punch diameter.

For both investigated materials, a similar diameter of the perforated stripe on the side of the punch could be measured for the respective heat treatment routes. The hole in the hardened stripe increased significantly after cutting, which is why no retraction forces were measured. In contrast, the hole in the hardened stripe, which was reheated to 650 °C and cut at 340 °C, was reduced to 9.94 and 9.97 mm respectively. As a result of HTR 1, a retraction force of approximately 500 N could be measured during cutting for both materials examined. In particular, the diameters determined according to HTR 2 scarcely changed compared to the punch diameter, taking into account the measurement inaccuracy. Since no retraction forces greater

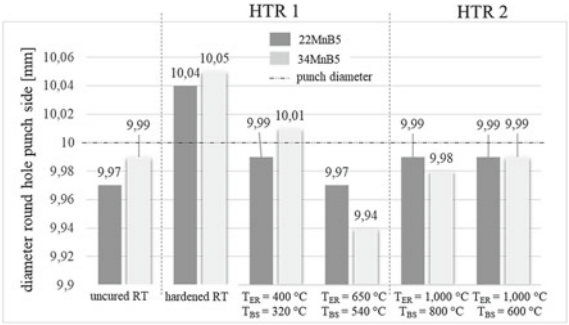


Fig. 8 Round hole diameter versus punch diameter

than 100 N were measured, no abrasive wear at higher stroke rates is likely to be detected.

3.4 Determination of the Mechanical Properties

To investigate the influence of the heat treatment routes on the mechanical properties, the cut specimens were embedded, subjected to a hardness test and metallographic examination. Vickers Hardness tests were performed using the load range HV 1. The experimentally determined Vickers hardness of the heat-treated sheets is shown in Fig. 9. The samples were prepared for micrographs. Microstructural analysis was performed using optical microscopy from ZEISS.

Samples were chemically etched using 3 % Nital solution. In heat treatment route 1 after austenitization followed by quenching in water, both materials show a clear hardening, for the 22MnB5 of 640 HV1 and for the 34MnB5 of 738 HV1. The microstructure of both hardened materials shows martensite (Figs. 10 and 11). Because of reheating to 650 and 400 °C, the material relaxes and after cooling, it has a reduced hardness. The material 22MnB5 shows 365 HV1 at 650 °C and 484 HV1 at 400 °C. In addition, a hardness of 332 HV1 for the material 34MnB5 after heat treatment at 650 °C and 528 HV1 after 400 °C (Fig. 9) was measured. The

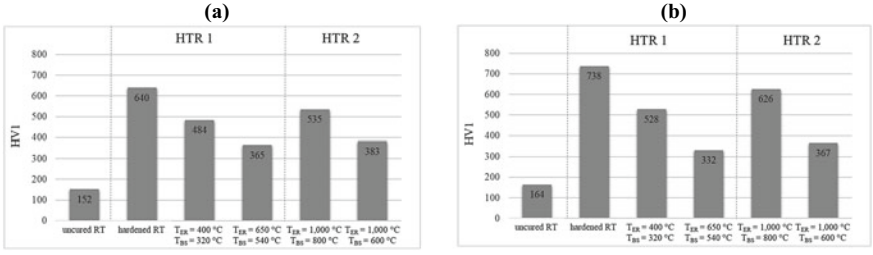


Fig. 9 Hardness values HV1 for **a** 22MnB5; **b** 34MnB5

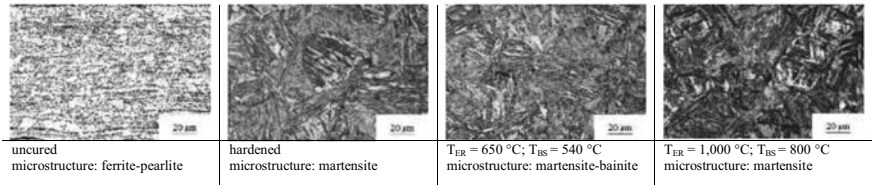


Fig. 10 Microstructure development for 22MnB5

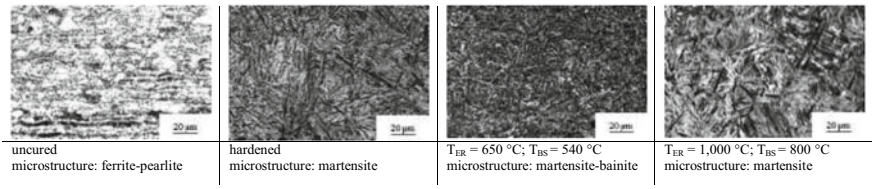


Fig. 11 Microstructure development for 34MnB5

microstructure showed a martensitic–bainitic structure in both materials due to the subsequent tempering (Figs. 10 and 11).

Along heat treatment route 2, the materials 22MnB5 and 34MnB5 are heated to 1,000 °C in the furnace, hot cutting in the tool, and cooled to room temperature. After heat treatment and cutting, the material 22MnB5 has a hardness of 535 HV1 at 800 °C and 383 HV1 at a cutting temperature of 600 °C. Because of the heat treatment, the material has a martensitic structure after treatment. The material 34MnB5 shows, after austenitization and hot cutting a hardness of 626 HV1 at 800 °C and a hardness of 367 HV1 at a cutting temperature of 600 °C. The microstructure shows also here a martensitic structure due to the heat treatment (Figs. 9, 10, and 11).

4 Conclusions and Outlook

The presented results show that the maximum cutting force as well as the cutting impact are considerably reduced due to the hot cutting of boron–manganese steels. Along heat treatment route 1, an improvement in mechanical cutting for press-hardened materials could be achieved. For example, for the press-hardened 22MnB5, a reduction of the cutting force by up to 50 % was achieved by cutting at a cutting temperature of 650 °C.

The measured cutting impact close to zero has no influence on the tool life quantity. With regard to tool production, it can be deduced for hot cutting to use a tool material with higher heat resistance. Small deviations in the cutting clearance are negligible in route 2 and allow a greater margin with regard to the tool tolerances.

With the heat treatment route 2, proof could be provided that in a direct heat treatment process, the process heat can be used for hot cutting and a martensitic microstructure can be set. For this purpose, approaches are being pursued to combine the hot cutting with the press-hardening process in one step and to integrate the hot cutting in a press-hardening tool.

Acknowledgments The authors acknowledge Salzgitter Flachstahl GmbH, especially Dr. Stefan Mütze, for providing the 34MnB5 material and acknowledge AWEBA Werkzeugbau GmbH Aue, especially Dipl.-Ing Thomas Aurich, for providing the cutting tool.

References

1. Neugebauer R, Schieck F, Rautenstrauch A and Bach M (2011) Hot sheet metal forming: the formulation of graded component characteristics based om strategic temperature management for tool-based and incremental forming operations. CIRP J Man Sci Technol 4:180–188
2. Krönauer B, Hirsch M, Golle R, Hoffmann H, Golle M and Jesner G (2010) Beschneiden von pressgehärteten Blechen: Ultrahochfestes 22MnB5-Blech im Scherschneidprozess. ZWF Zeitschrift für wirtschaftlichen Fachbetrieb, 26–31
3. Mori K, Maeno T, and Fuzisaka S (2012) Punching of ultra-high strength steel sheets using local resistance heating of shearing zone. J Mater Process Technol 212:534–540
4. Mori K, Saito S and Maki S (2008) Warm and hot punching of ultra high strength steel sheet. CIRP Ann - Manuf Technol 57:321–324
5. Hoffmann H, So H and Steinbeiss H (2007) Design of hot stamping tools with cooling system. CIRP Ann 56:269–72
6. Neumayer FF, Vogt S, Gueffroy M, Jesner G, Kelsch R, Sommer A, Golle R, Volk W (2019) Proc Man 29:345–352
7. Nestler M, Galiev E, Schmidt R, Psyk V, Winter S and Kräusel V (2020) Scherschneiden höchstfester Stähle mit fluidischem Gegenhalter. ZWF Zeitschrift für wirtschaftlichen Fachbetrieb Jahrg 115:7–8
8. So H, Faßmann D, Hoffmann H, Golle R and Schaper M (2012) An investigation of the blanking process of the quenchable boron alloyed steel 22MnB5 before and after hot stamping process. J Mat Process Technol 212:437–449

High-temperature Properties of Hot-Work Tool Steel (AISI H13) Deposited via Direct Energy Deposition



Jongyoun Son, Gwangyong Shin, Kiyong Lee, Chang-hwan Choi, and Dosik Shim

Abstract Conventionally, a defected tool steel is repaired by welding; however, that repairing does not guarantee homogeneous quality. Hence, this study focused on developing an alternative repairing technique using direct energy deposition (DED) to minimize thermal effects. To investigate a repair using powder-fed DED, AISI H13 powder was deposited onto heat-treated JIS SKD61. The deposited material was observed through scanning electron microscopy and its hardness and tensile properties were determined at 25, 200, 400, 600, and 800 °C. The deposited material showed different hardness distributions in its cross-section, revealing four representative features. The deposited region and dilution showed a hardness of 620 HV with a dendrite structure. The hardness decreased to 490 HV in the heat-affected zone, revealing a tempered martensite structure; however, it increased to 550 HV in the substrate and revealed a typical martensite structure. At all temperatures, the deposited material showed higher hardness than heat-treated SKD61. Moreover, it showed higher ultimate tensile strength and lower elongation in the deposited region. Therefore, this result indicates that without pre- or post-heat treatment, a part repaired using powder-fed DED can have better mechanical properties than heat-treated SKD61.

Keywords Direct energy deposition · AISI H13 · Tensile properties · Elevated temperature · Repair

J. Son · C. Choi
Department of Mechanical Engineering, Stevens Institute of Technology, Hoboken, NJ, USA

G. Shin · K. Lee
Smart Manufacturing Process Group, Korea Institute of Industrial Technology, Goryeong-gun, Republic of Korea

D. Shim (✉)
Division of Mechanical Engineering, Korea Maritime and Ocean University, Busan, Republic of Korea
e-mail: think@kmou.ac.kr

© The Minerals, Metals & Materials Society 2021

G. Daehn et al. (eds.), *Forming the Future*, The Minerals, Metals & Materials Series,
https://doi.org/10.1007/978-3-030-75381-8_140

1 Introduction

AISI H13 and JIS SKD61 steels have been typically used as hot-work tool steels, and they are heat-treated with quenching and tempering to improve their mechanical properties at high temperatures [1]. In hot-working processes, such as die-casting and forging, tool steels are exposed to severe working conditions at high temperatures; they are partially heated by molten or heated metals and cooled using lubricants or coolants repeatedly. These partial heating and cooling processes generate thermal stresses inside of these hot-work tool steels, and repeated thermal stresses eventually cause fatigue cracks and fractures on the inside and outside of the tool steels [2–4].

Defective tool steels with cracks and fractures resulting from thermal fatigue are typically repaired by welding; the repairing processes involve pre-machining, buildup welding, post-machining, and finishing [5]. However, this conventional repairing method with welding causes excessive thermal effects, which partially anneal the heat-treated tool steel; these repairing techniques are performed manually by skilled craftsmen based on their individual experiences. Therefore, repairing tool steels using these conventional methods cannot guarantee a homogeneous quality in the repaired part.

Therefore, this study focused on developing an alternative repairing technique using direct energy deposition (DED). DED is a three-dimensional (3D) printing technique; it deposits metal powder or wire using a laser heat source. DED can minimize the thermal effects on metal depositions, and it enables the fabrication of various shapes with precise control. To investigate repairing with DED, AISI H13 powder was deposited onto heat-treated JIS SKD61, and the deposited material was observed via scanning electron microscopy (SEM); its hardness and tensile properties were examined at 25, 200, 400, 600, and 800 °C.

2 Materials and Methods

2.1 Description of the Powder-Fed DED Process

The DED process is typically used with metals and metal-based hybrids in the form of either wire or powder [6]. Figure 1 shows a schematic of the powder-fed DED process. In this process, a substrate is irradiated by a laser beam, and a pool of molten material forms on the substrate. Then, a metal powder is simultaneously fed into the melting pool, and a single bead is deposited onto the substrate. Another bead is deposited right next to the deposited single bead; these two deposited beads overlap one another. In this way, a single layer is formed with depositions of multiple beads and is then built upon additively, layer-by-layer, to deposit multiple layers.

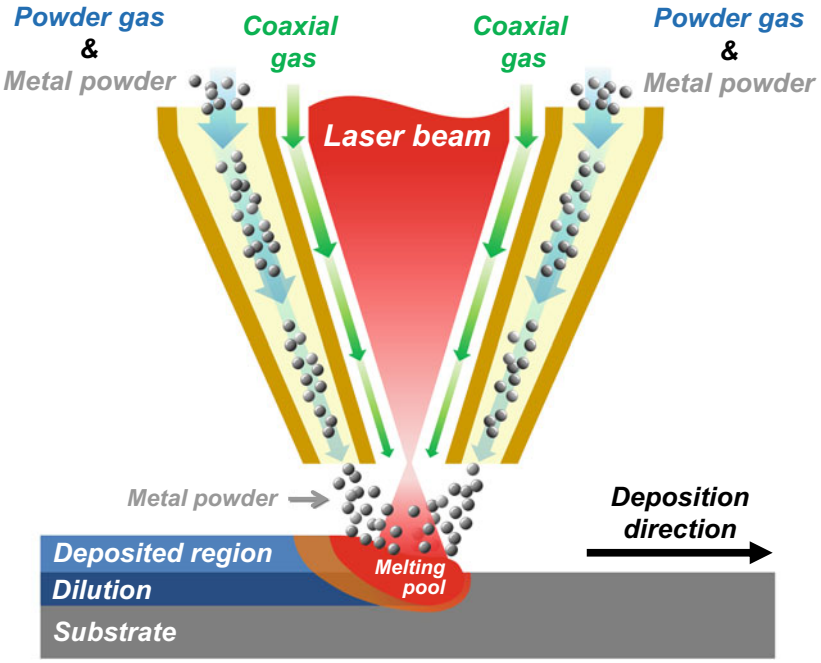


Fig. 1 Schematic of metal deposition in the DED process. (Color figure online)

2.2 Powder-Fed DED Equipment

Figure 2 shows the direct metal tooling (DMT) MX3 laser-assisted metal deposition device. This device is mainly composed of a 4 kW CO_2 laser, metal powder feeder, and computer numerical controller, and it uses argon (Ar) as the carrier gas for injecting the metal powder and as the shielding gas to protect the workpiece from oxidation. The processing head of this device is equipped with a laser beam nozzle, powder feeding nozzles, and charge-coupled device cameras. During depositions, the working distance between the processing head and the workpiece is set at 9 mm to focus the laser spot having a diameter of 1 mm on the workpiece.

2.3 Deposition Process and Experimental Specimen Preparation

Table 1 presents the chemical composition of the AISI H13 powder and the JIS SKD61 material. The H13 powder comprises spherical particles with diameters of 50–160 μm, as shown in Fig. 3. This H13 powder was used as the deposition material, and heat-treated SKD61 was used as the substrate with dimensions of 100

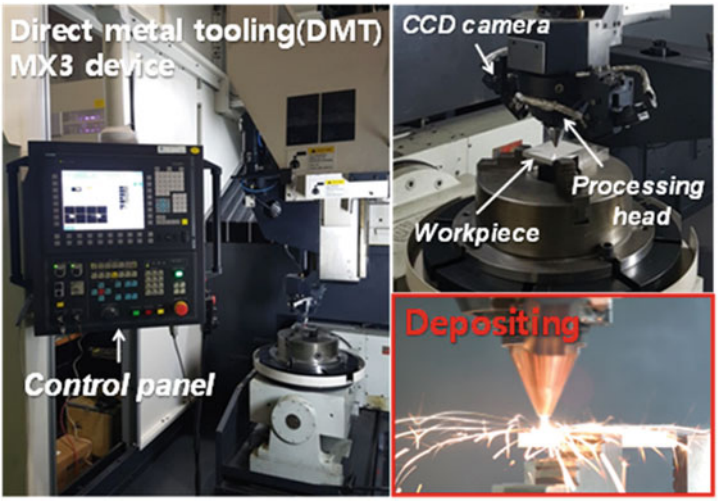


Fig. 2 Direct metal tooling (DMT) MX3 device. (Color figure online)

Table 1 Chemical composition of the JIS SKD61 and AISI H13 materials [wt%]

Material	C	Si	Mn	P	S	Mo	Cr	Ni	N	V	O
AISI H13	0.4	0.98	0.45	<0.015	0.005	1.53	5.33	0.25	0.03	1.05	0.02
JIS SKD61	0.32	0.8	<0.5	<0.03	0.03	1.00	4.5	<0.25	0.03	0.8	–

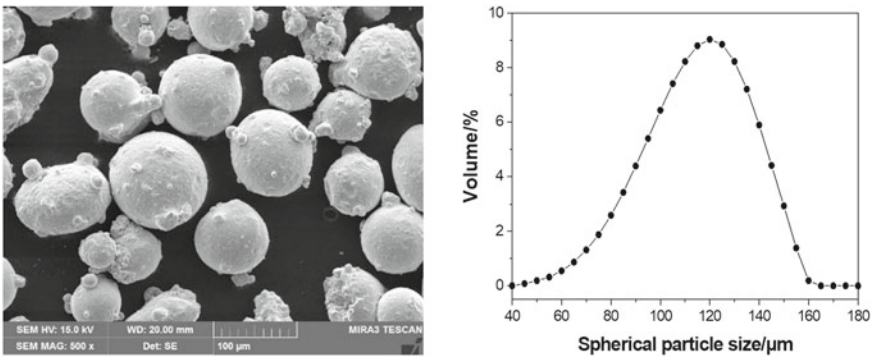


Fig. 3 A SEM image of the AISI H13 powder and the distribution curve of the spherical particles

× 50 × 15 mm^3. Every single bead was deposited and overlapped in a width of 0.5 mm with the adjacent bead. Multiple layers were deposited through back-and-forth motion in a fixed direction following a "zigzag" path, and the final heights of the deposited layers were 2 mm (0.25 mm for each layer) for tensile test specimens and 3.25 mm for hardness test specimens. The specimens for the tensile tests were cut such that they included the substrate and deposited region using wire electrical discharge machining, as shown in Fig. 4a; the tensile test specimens were cut to have equal thicknesses of the substrate and deposited regions, as shown in Fig. 3b. Table 2 lists the main parameters used in the powder-fed DED process for the deposition of the H13 material; these parameters were established through preliminary experiments.

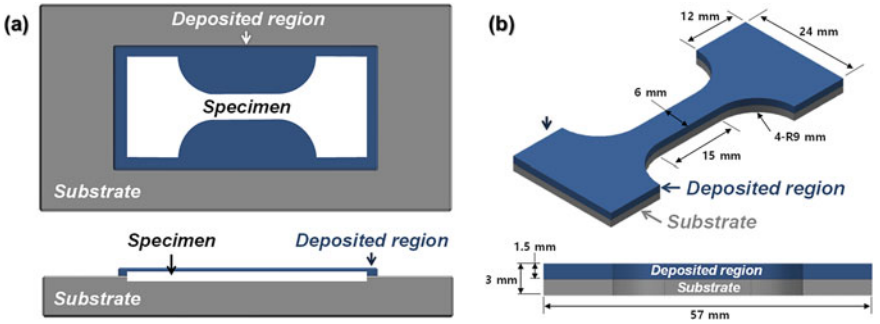


Fig. 4 Schematics of (**a**) a tensile test specimen cut from the deposited region and (**b**) dimensions of a tensile test specimen. (Color figure online)

Table 2 Process parameters of the powder-fed DED and controlled ranges of the main parameters

Process parameters	Value
Power of laser beam	800 W
Powder feeding rate	3.0 g/min
Overlap width between beads	0.5 mm
Laser scanning speed	800 mm/min
Laser beam diameter (fixed)	1 mm
Powder gas (fixed)	2.5 L/min
Coaxial gas (fixed)	8.0 L/min

3 Results and Discussion

3.1 Microstructures of the Deposited Material

To observe the microstructure of the deposited material, it was cut perpendicular to the substrate and the deposited region. The cut samples were etched using Nital etchant (nitric acid 5% + ethyl alcohol 95%) and then observed via field emission SEM (FE-SEM; JEOL Ltd., 7100f).

Figure 5 shows SEM micrographs of the cross-section of the deposited material. The deposited material reveals four different features; these features are identified in the deposited region, dilution, heat-affected zone (HAZ), and substrate. Figures 5a and b show the microstructures of the deposited region and dilution, and these revealed typical dendrite structures. During laser irradiation, the H13 powder, having a ferrite phase in its microstructure, reaches the homogeneous austenite temperature (1020 °C) in a short time. Then, if the metal at its austenite temperature cools

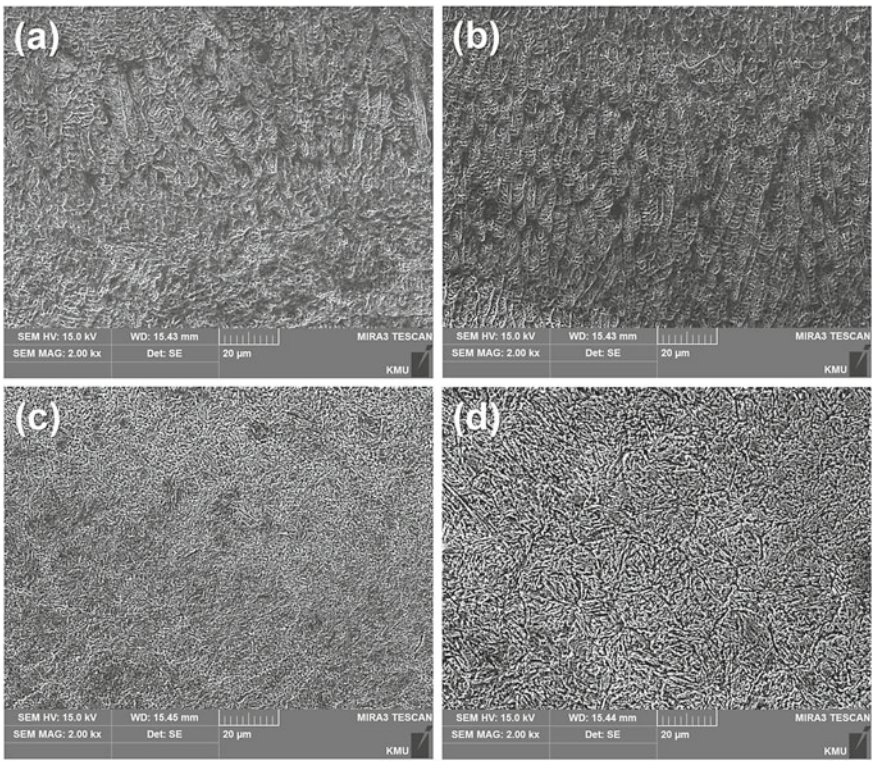


Fig. 5 SEM micrographs showing the microstructures of **a** deposited region, **b** dilution, **c** HAZ, and **d** substrate

rapidly, a martensite phase is formed, and the deposited metal is further strengthened. However, deposited beads or layers overlap previously deposited layers/beads during powder-fed DED, and the temperature in the deposited region remains below the austenite temperature during deposition. Therefore, the deposited region and dilution cannot cool as rapidly as required for full transformation to the martensite phase; this assumes to be the reason for the formation of dendrite structures, partially including martensite phases and retained austenite phases [7–10]. Figures 5c and d, respectively, shows the microstructure of the HAZ and the substrate. The substrate, heat-treated SKD61, shows martensitic phases in its microstructure, typical of a quenched material. However, the HAZ reveals a tempered martensite phase, also called the troostite phase. During metal deposition, the part of the substrate adjacent to the dilution was heated by the deposited metal, instantly molten and solidified, and the temperature of this heated area was just below the molten temperature. Then, the heated area in the substrate with martensitic phases was tempered; these martensitic phases were assumed to be transformed to troostite phases.

3.2 Hardness Tests

Depth-sensing microindentation tests were performed using AAV-502 tester to examine the hardness distribution of the deposited material and Nikon QM-2 tester to evaluate its hardness at elevated temperatures. In the hardness tests, a load of 1.9 N was applied to each indentation for 15 s, in accordance with the ASTM E384 test method.

To examine the hardness distribution of the deposited H13 on heat-treated SKD61, the deposited specimens were linearly indented in a 4 mm length along the deposition direction on the substrate; the indentations were evenly spaced at 100 μm intervals from the center of the previous indentation. This test was repeated thrice. Figure 6 shows the hardness distribution on the cross-section of the deposited material. The hardness of the substrate, typically quenched and tempered SKD61, was around 550 HV. The hardness decreased to around 490 HV in the HAZ, but it increased to around 620 HV in the deposited region and dilution. These results indicate that different microstructures of the deposited material led to different hardness values. The substrate revealed a typical martensite structure with fine carbides, but The HAZ had tempered martensite structures. From this result, it is assumed that the martensite structure in the substrate was partially tempered by the thermal effect from the laser irradiation, and this partial tempering resulted in slightly decreased hardness in the HAZ. The deposited region and the dilution, rapidly molten and solidified by the laser, had a dendrite structure with extremely fine carbides [5]; this structure and finer carbides than in the other areas were considered to lead to the highest hardness. Figure 7 shows the hardness graphs of the heat-treated SKD61 and the deposited H13 on heat-treated SKD61 at 25, 200, 400, 600, and 800 °C. The hardness of the deposited H13 was identical to that of the heat-treated SKD61 at 25 and 200 °C. The deposited H13 revealed slightly lower hardness than that of the heat-treated SKD61

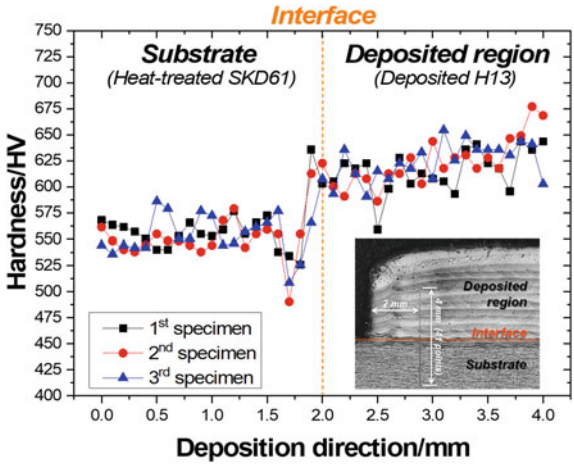


Fig. 6 Hardness distributions on the cross-section of deposited H13 on heat-treated SKD61. (Color figure online)

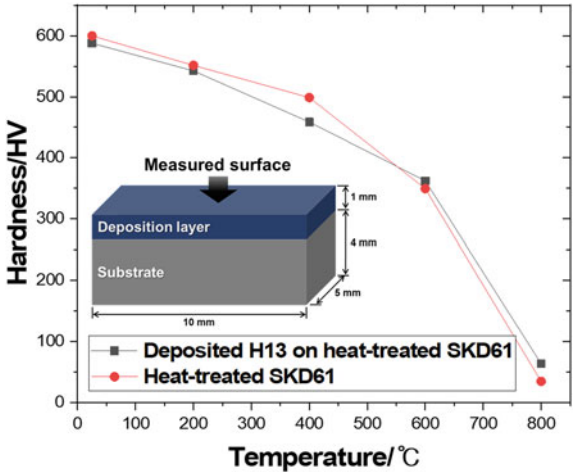


Fig. 7 Hardness of deposited H13 on heat-treated SKD61 and heat-treated SKD61 at 25, 200, 400, 600, and 800 °C. (Color figure online)

at 400 °C; however, the deposited H13 showed a higher hardness at 600 and 800 °C. These results reveal that the hardness of the deposited H13 had an identical tendency as the heat-treated SKD61 at elevated temperatures.

3.3 Tensile Tests

The tensile tests at elevated temperatures were performed using MTS 810 material testing machine and a heating furnace, as shown in Fig. 8. Tensile specimens were placed in the heating furnace at the tested temperatures for 20 min to stabilize their

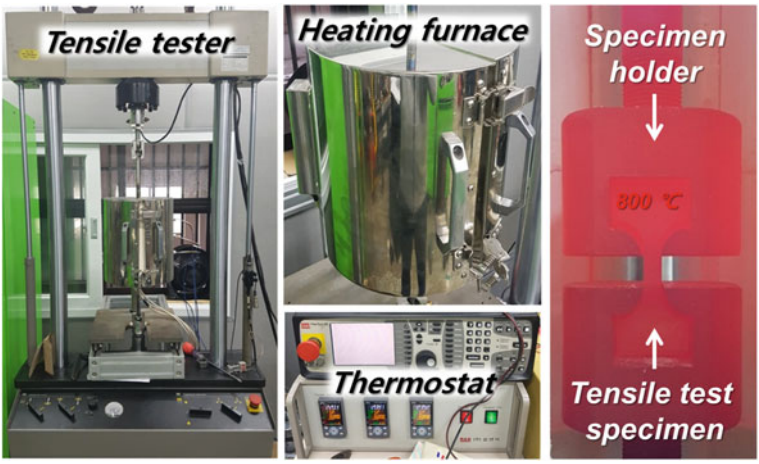


Fig. 8 Tensile testing machine and heating furnace. (Color figure online)

thermal expansion. The tests were conducted with a cross-head speed of 2 mm/min at 25, 200, 400, 600, and 800 °C and repeated thrice.

Figures 9 and 10 represent the true stress and true strain curves for the deposited H13 on heat-treated SKD61 and the heat-treated SKD61 at various temperatures. At 25 °C, the heat-treated SKD61 showed ultimate tensile strength (UTS) of 1798 MPa and elongation of 0.175, and the deposited H13 showed UTS of 1807 MPa and elongation of 0.085. These UTS values of both specimens were very close; however, the deposited H13 had two times lower elongation than that of the heat-treated SKD61. At 200, 400, 600, and 800 °C, the deposited H13 shows higher UTS values than the heat-treated SKD61. However, elongations of the deposited H13 were all lower than those observed on heat-treated SKD61 at elevated temperatures; these differences of

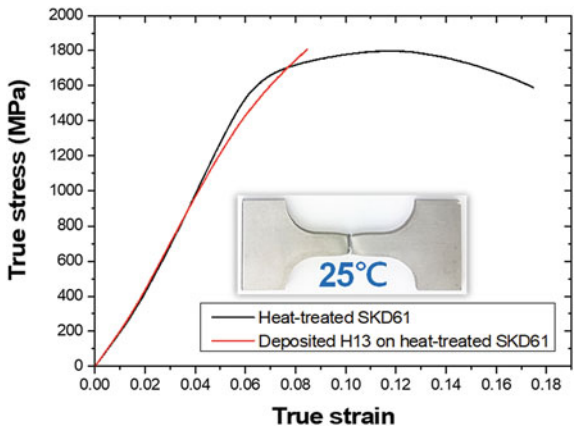


Fig. 9 True stress and true strain curves for deposited H13 on heat-treated SKD61 and heat-treated SKD61 at 25 °C. (Color figure online)

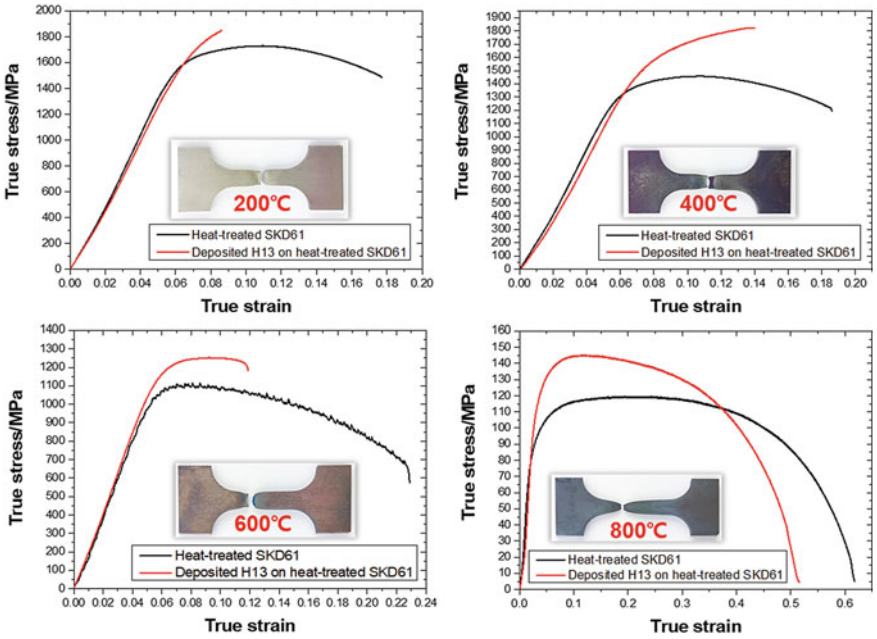


Fig. 10 True stress and true strain curves for deposited H13 on heat-treated SKD61 and heat-treated SKD61 at 200, 400, 600, and 800 °C. (Color figure online)

the elongations between the deposited H13 and the heat-treated SKD61 decreased with an increase in temperature.

In addition, fractured surfaces of the tensile tested specimens were observed via FE-SEM to examine the failure modes of the specimens. Figure 11 shows SEM images of fractured planes at 600 °C. The heat-treated SKD61 showed a dimple-like appearance typical of ductile fractures. In contrast, the deposited H13 on heat-treated SKD61 showed a flat-fractured surface, indicating a brittle fracture, in the deposited region and a dimple-like appearance on the substrate area. Moreover, the fractured area of the heat-treated SKD61 was smaller than that of the deposited H13 on heat-treated SKD61. This result indicates that the deposited H13 had not shrunk much in the plastic deformation by tensile loading, and then it was suddenly fractured. Thus, it is assumed that the brittleness of the deposited materials led to the lower elongations of the deposited H13 as compared with the heat-treated SKD61, as shown in Fig. 10.

4 Conclusions

In this study, H13 powder was deposited onto heat-treated SKD61, and the microstructures of the deposited material were observed via FE-SEM; its mechanical properties were evaluated by performing hardness and tensile tests at elevated

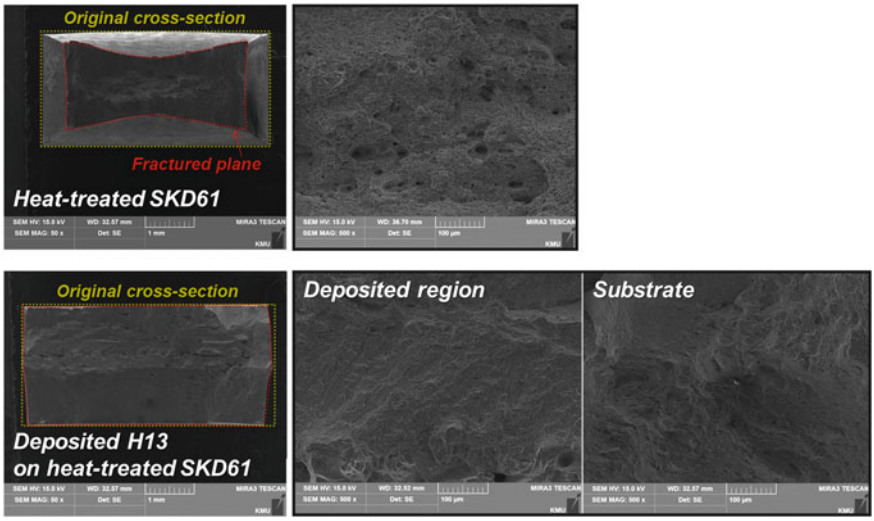


Fig. 11 SEM micrographs of fracture planes of tensile tested specimens at 600 °C. (Color figure online)

temperatures to demonstrate the effectiveness of powder-fed DED as an alternative repairing method.

The deposited material exhibited four representative features with different microstructures, and these different microstructures led to different hardness values. The deposited region and the dilution had the highest hardness; their hardness was higher than that of the heat-treated SKD61, a conventional hot-working tool steel. However, the hardness of HAZ was lower than the heat-treated SKD61, but the substrate showed identical hardness as compared with that of the heat-treated SKD61. The deposited H13 on heat-treated SKD61 had similar hardness as compared to the heat-treated SKD61 at high temperatures. Tensile test results showed that the deposited H13 on heat-treated SKD61 and the heat-treated SKD61 had similar UTS values at 25 °C, whereas the elongation of the deposited H13 was two times lower. At 200, 400, 600, and 800 °C, the deposited H13 on heat-treated SKD61 showed higher UTS values than the heat-treated SKD61. The elongations of the deposited H13 were lower than those of the heat-treated SKD61 at all temperatures; however, differences in the elongations between the deposited H13 and the heat-treated SKD61 rather decreased with an increase in temperature. Therefore, the heat-treated SKD61 can be repaired using powder-fed DED without pre- or post-heat treatments, and moreover, the repaired parts could have improved mechanical properties compared with typical hot-work tool steels. This study only examined fundamental properties of the deposited H13; however, there are other crucial properties, such as wear and thermal fatigue life. In the future, further crucial properties of deposited materials will be investigated.

Acknowledgments This work was supported by the Korea Institute of S&T Evaluation and Planning (KISTEP) under grant number 20008753.

References

1. Park GJ, Kang MW, Jung JG, Lee YK, Kim BH (2013) The effects of homogenization, hot-forging, and annealing condition on microstructure and hardness of a modified STD61 hot-work tool Steel. J. Korean Soc. Heat Treat. 26: 72–79
2. Mellouli D, Haddar N, Köster A, Ayedi HF (2013) Thermal fatigue failure of brass die-casting dies. Eng. Fail. Anal. 20:137–146
3. Skumavc A, Tušek J, Nagode A, Klobčar D (2016) Thermal fatigue study of tungsten alloy WNi28Fe15 cladded on AISI H13 hot work tool steel. Surf Coat Tech 285:304–311
4. Kundalkar D, Mavalankar M, Tewari A (2016) Effect of gas nitriding on the thermal fatigue behavior of martensitic chromium hot-work tool steel. Mater Sci Eng A 651:391–398
5. Kim SH (2003) lengthening of hot forging die life for flange yoke forming. Korea Acad Ind Coop Soc 4:36
6. Shahrubudin N, Lee TC, Ramlan R (2019) An overview on 3D printing technology: technological, materials, and applications. Procedia Manuf 35:1286–1296
7. Son JY, Yoon HS, Lee KY, Park SH, Shim DS (2019) Investigation into high-temperature interfacial strength of heat-resisting alloy deposited by laser melting process. Met. Mater. Int. https://doi.org/10.1007/s12540-019-00335-x (2019)
8. Chiang KA, Chen YC (2005) Laser surface hardening of H13 steel in the melt case. Mater Lett 59:1919–1923
9. Yan JJ, Zheng DL, Li1 HX, Jia1 X, Sun JF, Li YL, Qian M, Yan M (2017) Selective laser melting of H13: microstructure and residual stress. J Mater Sci 52:12476–1248
10. Tong X, Dai MJ, Zhang JH (2013) Thermal fatigue resistance of H13 steel treated by selective laser surface melting and CrNi alloying. Appl Surf Sci 271:373–380

The Study of Energy Absorption of Dual-Material Tailored Plane Strain Sheet



Pengfei Ying, Yulong Ge, and Yong Xia

Abstract In this paper, new tailored structure design has come forward based on ultra-high-strength steel (UHSS) material properties. The analytical model and finite element model are established in this study for the investigation of the energy absorption properties of the plane strain sheet. Via analytical calculation, the mechanical characters of the tailored sheet are deeply investigated before fracture initiation under extreme conditions. An optimized structure geometry configuration is obtained according to the quantity of structural energy absorption. The promotion of energy absorption of the tailored structure before fracture initiation is not obvious comparing with the pure material ones. In the FE model, the properties of the energy absorption of the tailored sheet after fracture initiation are investigated. Under a designed geometry setting, the energy absorption of the tailored sheet can provide 135% and 77% promotion, respectively, compared with the pure material ones. Besides, the designed configuration can also provide a good effect of crack inhibition, which shows great potential for further engineer applications.

Keywords Tailored sheet · Plane strain structure · Energy absorption · Analytical model · Finite element model

1 Introduction

The high strength steel is widely applied in the automotive industry [1]. The tensile strength of the UHSS sheet has reached more than 1500 MPa now [2]. The outstanding properties of UHSS have spawned a lot of new design of engineering structures. However, this material has some non-negligible defects compared with conventional steel such as low ductility, brittle failure, etc. [3, 4]. As to fully utilize the UHSS and avoid the defects, the concept of tailored properties structure is becoming more and more popular as different material area function differently in structure [5, 6]. Laser quenching is a technology that is applied for structure manufacturing with

P. Ying · Y. Ge · Y. Xia (✉)
State Key Laboratory of Automotive Safety and Energy, School of Vehicle and Mobility, Tsinghua University, Haidian District, Beijing 100084, P. R. China
e-mail: xiayong@tsinghua.edu.cn

© The Minerals, Metals & Materials Society 2021

G. Daehn et al. (eds.), *Forming the Future*, The Minerals, Metals & Materials Series,
https://doi.org/10.1007/978-3-030-75381-8_141

tailor properties [7]. Creating a selected quenched area structure with a homogeneous material distribution originally, the structure performance is decided by the configuration of the quenched area and the mechanical properties of the material before and after processing.

In the study of structure mechanics, the energy absorption structures are widely investigated. As the macro structure is an integration of material elements, each element is under a uniform loading state approximately [6]. It is reasonable to improve the structural performance by adjusting the performance of each material element delicately, and this is also the fundamental idea of the tailored structure. As the plane strain condition is one of the basic loading conditions for functional structure [8], this study is focusing on a plane strain sheet with a combination of different material properties. The material properties are based on the simplified ideal elasto-plastic model obtained from tension tests of 22MnB5 [7]. The maximum effective plastic strain criterion for fracture is applied. An analytical model is established to analyze material behavior before the fracture initiation. An FE model is also established to provide more analysis of the fracture characters of the structure.

2 The Analytical Modeling of Tailored Sheet

We will focus on the energy absorption ability of the sheet with different geometry configurations under certain material properties. The analytical model will be used for the optimization of the energy absorption of the tailored plane strain sheet and the investigation of the mechanical properties of the sheet. With the help of this model, some interesting numerical phenomena are revealed under several cases for the understanding of the structural response. Besides, the basic configuration of the sheet is a stripy distribution along the loading direction.

2.1 Hypotheses and Methodology

Considering a simple configuration of tailored dual-material sheet with manufacture possible, Figure 1a shows the stripy distribution of the conceptual design. As to fully understand the mechanical performance of this structure, more constraints are required, and mechanical hypotheses are also required for the analytical modeling.

Three hypotheses and two boundary conditions are made for the analytical model:

Hypotheses:

1. The material follows the ideal elasto-plastic material behavior hypothesis
2. The material follows the maximum effective plastic strain fracture criterion
3. The structure is a thin wall structure: no stress distribution in the out-of-plane direction

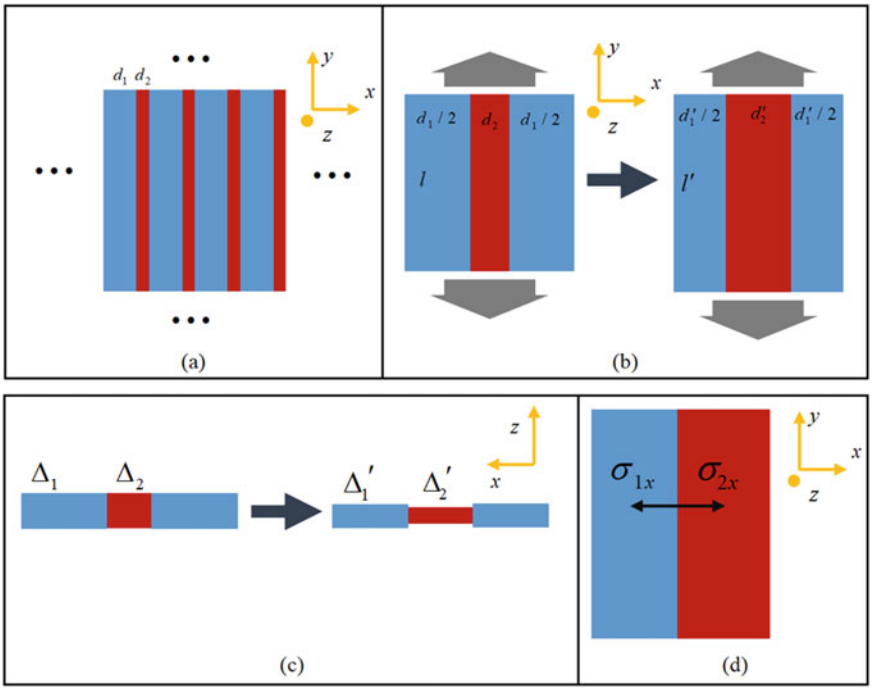


Fig. 1 The schematic of (**a**) the infinite periodic condition sheet, (**b**) the extracted analysis area and the deformation process, (**c**) the cross-section, and (**d**) the interface balance condition. (Color figure online)

Boundary conditions:

1. The sheet is under an infinite periodic boundary condition
2. Longitudinal quasi-static loading only

Figure 1a demonstrates the structure configuration. The materials are distributed in a stripy arrangement. According to the infinite boundary condition, we can use the area showed in Fig. 1b as a representative element of the plane strain sheet. The blue color blocks represent the soft material (low yield stress), the red blocks represent the strong material (high yield stress). Assuming the initial width of soft material and strong material is d_1, d_2 separately, the initial length of the representative element is l.

Because of the length limitation of this paper, some mathematical derivation of the iteration process and the energy accumulation process are omitted. Here only provides the basic functions for the calculation and the flow chart is shown for explanation.

As to interpret the possibility of the mathematical operation of this model, all the unknowns and the numbers of the equations are listed below. Necessary explanations are provided.

According to the structural symmetry, we may assume each material bar has the uniform distribution of stress and strain, which provide 24 unknowns for stress and strain during the loading process. However, the boundary condition 2 eliminates the shear stress and the shear strain, which reduced the unknowns to 12.

The relations between geometry and strain can be established as follow:

$$\varepsilon_{1x} = \ln\left(d_1'/d_1\right) \tag{1}$$

$$\varepsilon_{2x} = \ln\left(d_2'/d_2\right) \tag{2}$$

$$d_1 + d_2 = d_1' + d_2' \tag{3}$$

$$\varepsilon_{1y} = \varepsilon_{2y} = \ln\left(l'/l\right). \tag{4}$$

The strain along the out-of-plane direction of the two materials is different during the deformation as shown in Fig. 1c, which will influence the consistency of the material near the interface. However, hypothesis 3 provides two more equations for the deformation incompatibility.

$$\sigma_{1z} = 0 \tag{5}$$

$$\sigma_{2z} = 0. \tag{6}$$

Besides, the balance condition requires the stress along the x-direction should be the same for both materials as shown in Fig. 1d:

$$\sigma_{1x} = \sigma_{2x}. \tag{7}$$

For constitutive relations, the ideal elasto-plastic model is applied. The fracture criterion is based on the maximum effective plastic strain theory. Thus, there are three strain unknowns and three stress unknowns for two materials separately, and the material widths are also unknowns. Thus, 14 unknowns are included in this problem. Equations 1–7 provide eight independent equations. The constitutive relations always provide three independent equations for each material. Thus, 14 independent equations will be provided for the 14 unknowns theoretically.

According to the previous studies [5, 7], the yield stress of the original material of 22MnB5 is approximate to 500 MPa, and the yield stress of the material after laser quenching is approximate to 1500 MPa. The fracture strain is close to 0.3 for the original material, but the fracture strain of 22MnB5 after processing is approximate 0.1.

Thus, a simplified stress–strain curve is obtained as shown in Fig. 2. As materials perform differently in elastic stage and plastic stage, we divide the loading into three stages for ease of calculation:

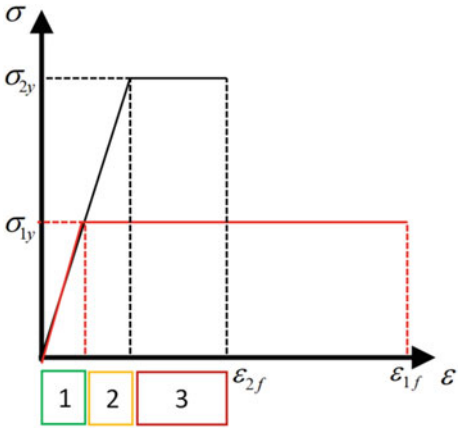


Fig. 2 The schematic of materials response and the loading stage classification. (Color figure online)

Stage 1: Both materials stay in the elastic state.

Stage 2: The soft material yields and the strong material stays in the elastic state.

Stage 3: Both materials yield.

Stage 1 provides explicit expressions for materials response, but the numerical iteration calculation is required for stage 2 and stage 3. The mathematical process of the derivation is omitted for stage 1 and all the calculation processes of stage 2 and stage 3 are omitted.

Here provides the expression of the final states of the materials at stage 1:

$$\ln\left(\frac{l_{ter}}{l}\right) = \frac{1-\upsilon^2}{E}\sqrt{\frac{1}{\upsilon^2-\upsilon+1}}\sigma_{1y} \tag{8}$$

where *lter* is the terminal length of the sheet of stage 1, σ_{1y} is the yield stress of soft material under uniaxial tension test. Besides, the energy absorption of stage 1 can be written as follow:

$$E_{Stageone} = e^{-\frac{\upsilon}{1-\upsilon}}\Delta\frac{E}{1-\upsilon^2}(d_1+d_2)l^2\left[\frac{1}{2}\left(\frac{l_{ter}}{l}\right)^2\ln\left(\frac{l_{ter}}{l}\right)-\frac{1}{4}\left(\frac{l_{ter}}{l}\right)^2+\frac{1}{4}\right]. \tag{9}$$

For stage 2 and stage 3, as the explicit form is unobtainable, a system of numerical explicit iteration equations is derived for the calculation. Figure 3 shows the flow chart of the subroutine of all the calculations included in this model.

Besides, the energy accumulation of stage 2 and stage 3 is based on the increments of input energy:

$$dE_{stagetwo\&three} = \left(\Delta_1'\sigma_{1y}d_1' + \Delta_2'\sigma_{2y}d_2'\right)dl'. \tag{10}$$

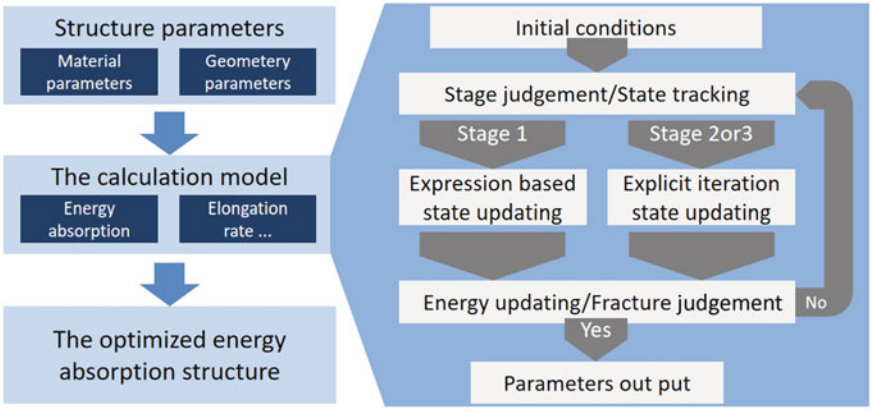


Fig. 3 The flow charts of the analytical model. (Color figure online)

2.2 Results Analysis and Discussion

2.2.1 The Description of Analytical Model

Three groups of system input parameters are variable for the initial conditions: the calculation-related parameters, the geometry-related parameters, and the material property-related parameters. As the influence of the geometry configuration is discussed in this paper, the geometry-related parameter is the default. The calculation-related parameter is also default as the convergence test will be conducted later.

All the parameters contained in this model are shown in Table 1. Some values of parameters are also provided. The unit is ignored as the analytical model is a

Table 1 The initial value and the name for all the parameters contained in this calculation mode

Calculation related	Material properties related	Geometry related
Step length: $dl' = default$	Young's modulus: $E = 210$	The length of the structure: $l = 1$
	Poisson ratio: $\upsilon = 0.3$	Thickness of the structure: $\Delta = 0.01$
	Yield stress of soft material: $\sigma_{1y} = 0.5$	Width of the soft material: $d_1 =$ default
	Yield stress of strong material: $\sigma_{2y} = 1.5$	Width of the strong material: $d_2 = 1 - d_1$
	Fracture strain of soft material: $\varepsilon_{1fra} = 0.3$	
	Fracture strain of strong material: $\varepsilon_{2fra} = 0.1$	

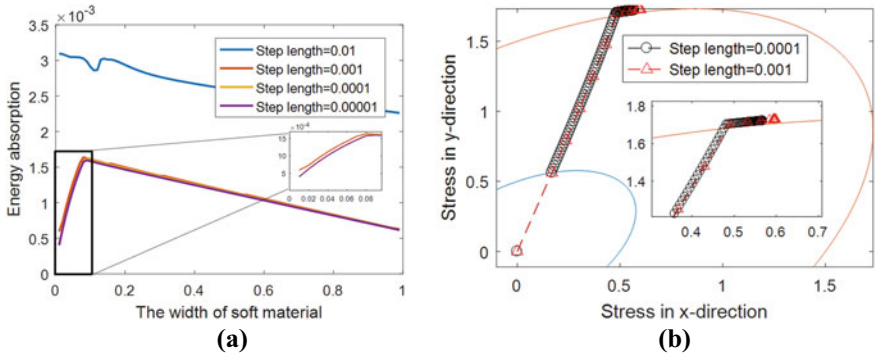


Fig. 4 **a** The convergence results with different calculation step length (**b**) the trace of the stress of strong material with different calculation step length ($d_1 = 0.05$). (Color figure online)

normalized system. The calculation results contained below are a direct calculation output from the parameters inputted as shown in Table 1.

To decide a proper step length for the calculation, a convergence test was conducted. The curve of energy absorption versus width of soft material is shown in Fig. 4a and the curve of y strain vs x strain for strong materials is shown in Fig. 4b, in which the fine lines represent the yield surface of materials.

For explanation, Fig. 4b is the state tracking of the calculation process with certain structure geometry, $d_1 = 0.05$.

The commercial software MATLAB is applied for the establishment of this model. According to the results in Fig. 4a, the energy absorption curve can reach convergence with step length lower than 0.001. The results of time length lower than 0.0001 are overlapped with each other. However, this step length may cause a sparse calculation point distribution of material stress in stage 2 and stage 3. Thus, the step length of 0.0001 is chosen for calculation step length for the balance of computational accuracy and computational economy.

2.2.2 The Results of the Analytical Model

Figure 5a shows the calculation results. The dashed line (fracture index) represents the fracture type. The upper platform represents the fracture initiation of strong material, and the lower platform represents the fracture initiation of soft material.

According to the results shown in Fig. 5a, an optimized geometry configuration is obtained to maximize energy absorption. The width ratio of d_1:d_2 is approximate to 1:9. Under this setting, the tailored plane strain sheet can provide the highest energy absorption before the fracture initiation.

As to deeply understand the material behavior, the extreme conditions (extreme material distribution) are calculated and their state tracking results are shown in Fig. 6. The extreme conditions are defined as follow:

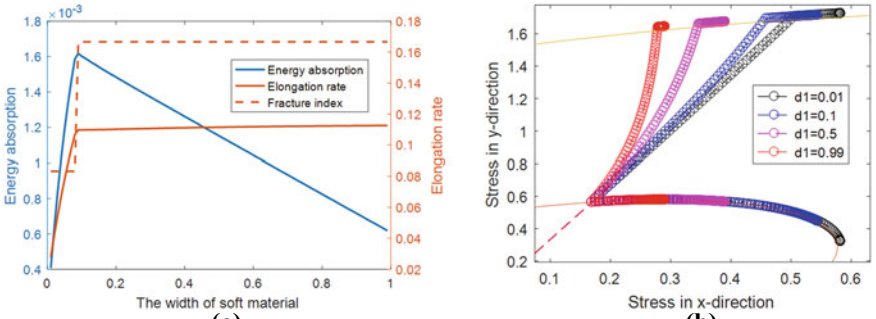


Fig. 5 (**a**) The structural properties of different structure geometry (**b**) the stress states of two materials under different structure geometry. (Color figure online)

Limit on the left: $d_1$close to 0.
Limit on the right: $d_1$close to 1.

The energy absorption and elongation of the pure material sheet and the optimized sheet are shown in Table 2. The effective stiffness is defined as the ratio of energy absorption and elongation. The unit is ignored too.

2.2.3 Results Analysis and Discussion

Under plane strain condition, as the transverse deformation of sheet is limited, the summation of transverse deformation for each periodic structural unit is equal to zero.

Figure 5a is an exhibition of the final calculation results. According to the fracture index, the fracture transformation decides the local maximum of the energy absorption. Figure 5b shows the stress in the *x*-direction is gradually released with the increase of the width of the soft material. As the response of the sheet is influenced by many parameters, it is necessary to fully analyze the material behavior during the deformation process. The extreme conditions are very helpful for the understanding of material behavior. Here provide results' analysis:

Considering the limit on the left. In Fig. 6a, b, the strong material shows a stable stress response under tension. However, the fracture strain of structure is positively correlated with the width of soft material. According to Fig. 6c, d, the first principle strain is in the transverse direction, which contributes to the effective plastic strain significantly and leads to the earlier fracture. If the width of soft material is close to zero, the limit of elongation is close to 0.01, where the strong material just steps into stage 3. It means that within the decrease of the width of soft material, the plastic stage of strong material will be shortened. What is more, the plane strain loading condition for pure material sheet provides a stress ratio (Stress-*y* vs. stress-*x*) of 2. But for the tailored sheet at the limit on the left, the soft boundary can release the transverse constraint a lot and the stress ratio is decreased to 3.

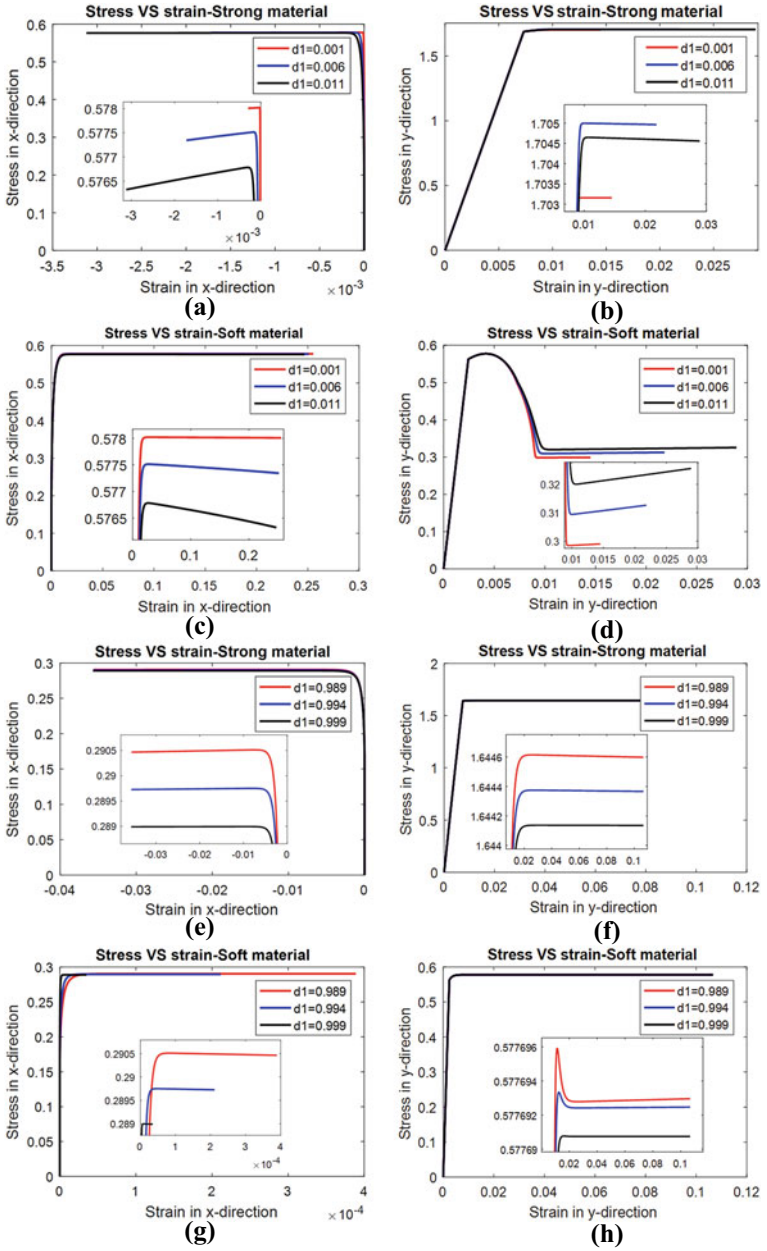


Fig. 6 The stress–strain state tracking of the material under extreme geometry setting. (Color figure online)

Table 2 The energy absorption of sheet with different combination of materials

Type of sheet	Strong material	Soft material	Tailored
Energy absorption	1.57e−3	1.55e−3	1.62e−3
Elongation	0.10	0.30	0.11
Effective stiffness	1.57e−2	5.17e−3	1.47e−2

Considering the limit on the right. At this condition, the fracture is dominated by strong material. Figure 6e, f, h shows the stable stress and strain response of both materials. It means that the strong material cannot be stretched by the soft material transversely, the fracture is mainly caused by the longitudinal deformation. Besides, as the strain of strong material in the x-direction has no correlation with the material width, and the strain of soft material in the x-direction is approximate to 0, it provides a plane strain condition for soft material and the stress ratio is equal to 2.

The analysis of extreme conditions not only provides a deeper understanding of the mechanical behavior of the tailored sheet but also represents engineering practices. For example, if an area for plane strain loading is expected for quenching strengthening, but a narrow area is left without quenching because of the machining precision, the sheet strength may become much lower than expected. The strong doping material could also influence the elongation of the sheet then cause performance reduction.

As shown in Table 2, the increment of energy absorption of the tailored sheet is not significant. However, two advantages are expected. First, comparing with the soft sheet, the stiffness of the tailored sheet is higher, which is good for the resistance of constant loading. Second, the high-strength steel has a bad fracture character as the fracture process is very brittle. However, the design of the striped structure can inhibit the propagation of brittle crack and improve energy absorption after fracture initiation. This phenomenon will be discussed later in detail.

3 The FE Model of Tailored Sheet

3.1 Description of FE Model

The previous model investigated the energy absorption of the tailored sheet before fracture and the material performance inside the sheet. The results show that the energy absorption for this optimized tailored sheet has not been promoted obviously comparing with the pure material ones. The energy absorption after fracture initiation was also ignored.

As the structure behavior after fracture initiation is too complex to establish an analytical model, the commercial software is used for the investigation of the crack propagation and the energy absorption after fracture initiation.

The software LS-DYNA was applied for this study. The keyword *MAT_PIECESISE_LINEAR_PLASTICITY is used for the ideal elasto-plastic

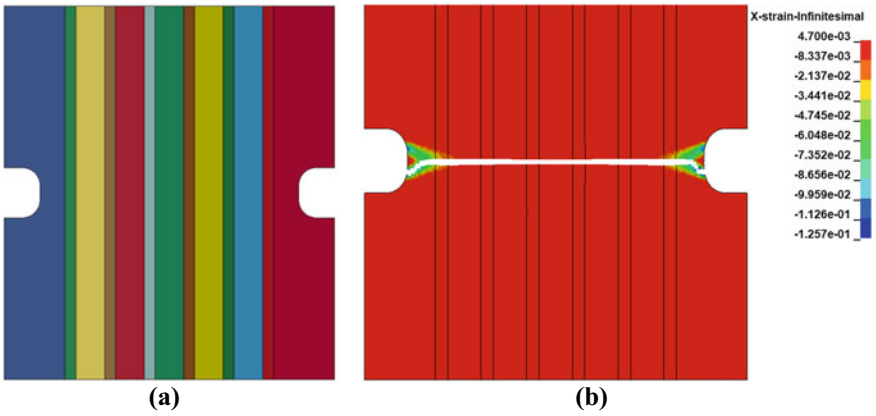


Fig. 7 **a** The FE model of the plane strain sheet **b** the transverse strain contour of soft material sheet. (Color figure online)

material model. The effective plastic strain at failure is 0.1 and 0.3 respectively. The yield stresses are 500 MPa and 1500 MPa separately. The thickness of this model is 1 mm. The soft material is 3 mm wide and the strong material is 8 mm wide. The geometry of the structure is shown in Fig. 7a. The element size is 0.5 mm.

As to verify the plane strain loading condition, the post-fracture contour for the transverse strain of soft material is shown in Fig. 7b. A similar distribution can be observed in the strong material sheet. Those simulations are quasi-static simulations as scarcely kinematic energy was observed in the data of energy output.

3.2 Results and Discussion

Fig. 8a–c represents the fracture morphology and the effective plastic strain contour of the different sheet.

Considering the pure material sheets, according to Fig. 8a, b, the fracture is a highly localized behavior. With the crack propagation, the geometry near the crack may experience a large distortion. What is worse, the strong material has a high yield stress and low failure plastic strain. Once if the fracture is initiated, the crack propagates at a very fast speed and the structure just lost all the ability of force maintenance.

For the tailored sheet shown in Fig. 8c, a much better energy absorption form is observed. First, according to the contour, the distribution of plastic strain is relatively uniform for most of the material, which is good for the improvement of the structural ability to absorb energy. Second, according to Fig. 8d, the crack propagates in a very limited way in this structure. The crack still propagates very quickly in strong material, but the soft material will stop the crack propagation, which provides a

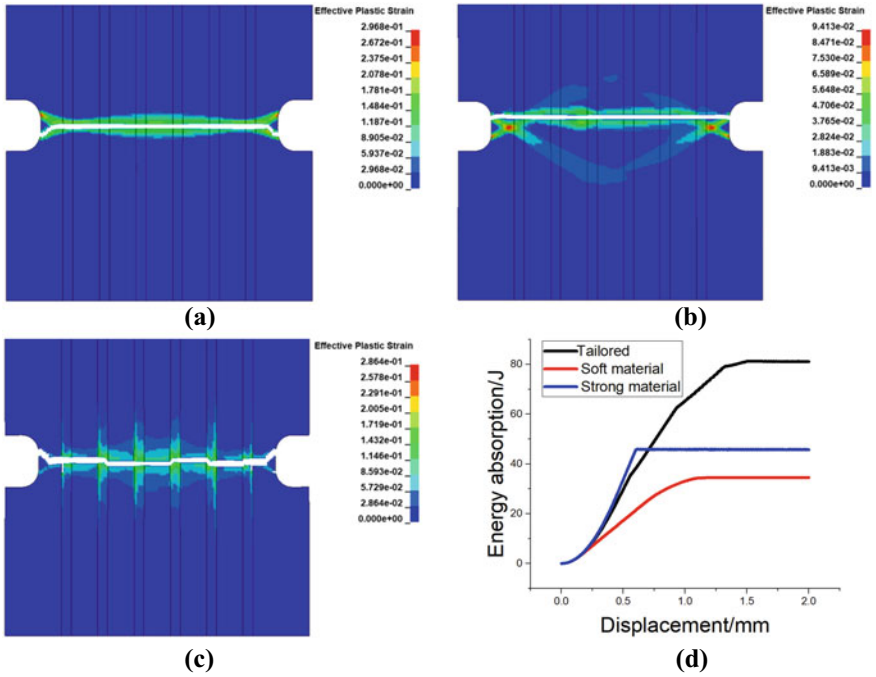


Fig. 8 The fracture morphology and effective plastic strain contour of (**a**) soft material sheet, (**b**) strong material sheet, (**c**) tailored sheet and (**d**) the curves of energy absorption versus displacement of different sheets. (Color figure online)

continuous energy absorption mode. Third, the crack shape of the tailored sheet is not a straight line but a z shape curve. This is also good for energy absorption as the crack length is prolonged.

According to the previous study and the fracture behavior of pure material sheets, two main reasons are provided for the promotion of the tailored sheet.

Firstly, the combination of heterogeneous materials can release the transverse constraint of the strong material from plane strain condition and fully utilize the elongation of the soft material by stretch the soft material in the transverse direction. If the constraints of the local structure were weakened, the far-field deformation is allowed to contribute to the energy absorption process. As the soft material cannot provide enough stress to resist the deformation of strong material, it has to deform transversely. Combining with the character of high failure plastic strain, the soft material can also provide a great deal of energy absorption.

Second, the local crack energy liberation will be absorbed by the soft material. As the failure of elements will cause a local energy liberation (elastic energy stored in local structure), and this energy liberation will cause a shack loading to the elements nearby and cause structure vibration for a short time. For soft material, this energy shock is not high enough to destroy the near crack field elements during this short

moment. Thus, a ductile fracture mode is observed. For strong material, the elastic energy stored in the element is high enough to destroy those near field elements and cause a continuous fracture mode. Thus, a brittle fracture mode is observed. For the tailored sheet, the local energy shock of the crack tip is not high enough to break the layer of soft material. Thus, crack propagation is inhibited.

To summarize, the designed tailored plane strain sheet performs much better than pure material sheets for energy absorption and provides a better ability to crack inhibition. FE results show great potential for the further application of this tailored structure. What is more, the laser quenching technology makes the manufacture of tailored sheets possible.

4 Conclusions

This study focuses on the energy absorption of tailored plane strain sheets before fracture initiation and after fracture initiation. Here shows the main conclusions of this study:

An analytical model is established to analyze the characters of the tailored plane strain sheet before the fracture initiation, and the extreme conditions were discussed. According to the material performance under extreme conditions, the soft material is under a biaxial tension loading condition and the constraints of the strong material are released.

For a certain material combination, an optimized geometry configuration is obtained before the fracture initiation. The width ratio of soft material vs strong material equal to 1:9 is suggested for the maximization of the energy absorption of the tailored sheet. But the optimized tailored sheet has similar energy absorption ability with the pure material ones.

The FE analysis is conducted based on a certain sheet geometry. Under this arrangement, the tailored sheet performs a promotion at the ability of energy absorption compared with the pure material sheets, the promotions are approximate to 135% for soft material sheet and 77% for strong material sheet, and a good form of crack inhibition is obtained according to this design.

Acknowledgments This study is sponsored by the Program of High-end CNC Machine Tools and Basic Manufacturing Equipment (Number 2019ZX04002030)

References

1. Kuziak R, Kawalla R, Waengler S (2008) Advanced high strength steels for automotive industry. Arch Civ Mech Eng 8(2):103–117
2. Wei D (2004) Fatigue behavior of 1500 MPa bainite/martensite duplex-phase high strength steel. Int J Fatigue 26(4):437–442

3. The software LS-DYNA was applied for this study. The keyword *MAT_PIECESISE_LINEAR_PLASTICITY is used for the ideal elasto-plastic material modeling
4. Kim H-S (2002) New extruded multi-cell aluminum profile for maximum crash energy absorption and weight efficiency. Thin-Walled Struct 40(4):311–327
5. Eller TK, Greve L, Andres MT, Medricky M, Hatscher A, Meinders VT, van den Boogaard AH (2014) Plasticity and fracture modeling of quench-hardenable boron steel with tailored properties. J Mater Process Technol 214(6):1211–1227
6. Lin Y, Min J, Li Y, Lin J (2019) A thin-walled structure with tailored properties for axial crushing. Int J Mech Sci
7. Pervez T, Qamar SZ, Al-Abri OS, Khan R (2012) Experimental and numerical simulation of in-situ tube expansion for deep gas wells. Mater Manuf Process 27(7):727–732
8. Ladevèze P (2012) Nonlinear computational structural mechanics: new approaches and non-incremental methods of calculation. Springer Science & Business Media

Cyclic Hardening/Softening of a TRIP Duplex Stainless Steel



Miao Jin, Lei Chen, Zongyuan Zou, Shuo Hao, Qun Li, and Shiyan Zhao

Abstract Recently, a series of duplex stainless steels (DSSs) have been developed by replacing Ni–Mo with Mn–N, which makes DSS more economical and produces TRIP effect with higher strength and plasticity. In this work, the mechanical properties of a TRIP-assisted DSS under monotonic and cyclic loading conditions were studied and the micro-structure under cyclic loading was analyzed by transmission electron microscopy (TEM). The test steel exhibits enhanced mechanical properties and a typical "three-stages" hardening characteristic due to TRIP effect under monotonic loading conditions. Cyclic hardening/softening characteristics of the test steel are affected by strain amplitude and the number of cycles. With smaller strain amplitude, cyclic hardening occurs first, and then shifts to cyclic softening and gradually trends to stabilization. With larger strain amplitude, after initial rapidly cyclic hardening, the test steel still changes to cyclic softening, however, no stabilization occurs until failure. The dislocation walls in ferrite during cyclic deformation are responsible for the overall cyclic softening of the test steel; While austenite produces ε martensite transformation at larger strain amplitude, which suppresses the cyclic softening, so that with an increase in strain amplitude the cyclic softening rate increases rapidly, followed by a slow increase and a final decrease.

Keywords Duplex stainless steel · TRIP effect · Cyclic loading · Hysteresis loop · Cyclic hardening/softening · Martensite transformation

M. Jin · Z. Zou (✉) · Q. Li · S. Zhao
Key Laboratory of Advanced Forging & Stamping Technology and Science of Ministry of Education, Yanshan University, Qinhuangdao 066004, China
e-mail: zzy@ysu.edu.cn

L. Chen · S. Hao
National Engineering Research Center for Equipment and Technology of Cold Strip Rolling, Yanshan University, Qinhuangdao 066004, China

© The Minerals, Metals & Materials Society 2021

G. Daehn et al. (eds.), *Forming the Future*, The Minerals, Metals & Materials Series,
https://doi.org/10.1007/978-3-030-75381-8_142

1 Introduction

Duplex stainless steels have a ferrite–austenite duplex structure. In recent years, in order to further reduce the cost of raw materials, researchers developed high-performance, economical duplex stainless steel with transformation induced plasticity (TRIP) effect [1, 2] through Mn–N alloying instead of expensive Ni, to replace the traditional Ni–Mo duplex stainless steel and Cr–Ni austenitic stainless steel to manufacture structural parts in petrochemical, marine, and other engineering fields. The mechanical properties of material under cyclic loading are different from that under monotonic loading. Existing research [3–5] shows that in duplex stainless steel the mechanical properties of the two phases are different, so that the deformation is not harmonious, which causes the cyclic deformation of the mechanical response to be in multiple stages, and the dominant deformation mechanism is obviously different in different stages; however, the study object is traditional Ni–Mo type duplex stainless steel. For duplex steel with metastable austenite, most studies focused on its mechanical properties under monotonic loading [6, 7], and corresponding TRIP microscopic mechanism [8, 9]. However, deformation-induced martensite transformation also occurs during cyclic loading in metastable austenite [10, 11], thus may affect cyclic hardening and softening. However, the cyclic deformation behavior of this TRIP duplex stainless steel has been reported rarely, and its mechanical response characteristics under cyclic loading conditions are still unclear. Therefore, this work takes a kind of duplex stainless steel with metastable austenite as the research object and focuses on analyzing and discussing its mechanical properties and microscopic mechanism during cyclic loading.

2 Materials and Experimental Methods

In this paper, the test duplex stainless steel was smelted by 20 kg vacuum induction furnace. After vacuum extraction, nitrogen with high purity was added to refine the ingot. The main chemical components are shown in Table 1. After casting, the ingot was then heated at 1150 °C and kept warm before forging, then was forged into a square billet of 20 mm × 20 mm. The forged billet was heated at 1050 °C and kept warm for 30 min, then cooled with oil. The original microstructure of the test steel is shown in Fig. 1, it can be seen that the two phases along the forging direction show a strip uniform distribution(the light color is austenitic γ, the dark color is ferritic α), and the ratio of the two phases is V_γ:$V_\alpha \approx 47$:53. The austenite is the hard phase

Table 1 Chemical composition of test steel (mass fraction wt%)

C	Si	Mn	Cr	Ni	N	Mo	Fe
0.04	1.6	2.9	19.6	2.0	0.2	0.1	bal

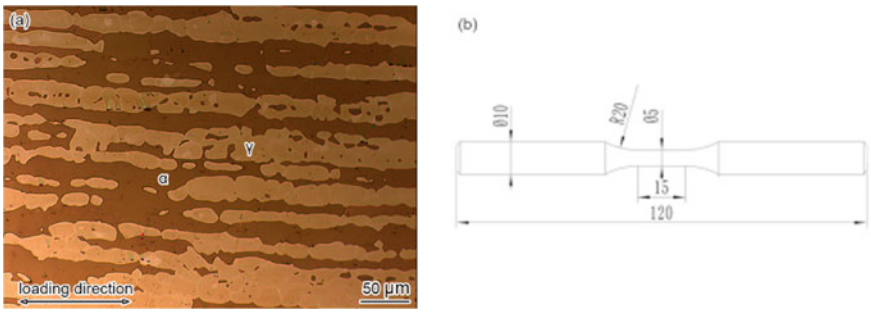


Fig. 1 Metallographic microscopic image (**a**) and sample schematic (**b**). (Color figure online)

with a hardness of about 272Hv, and the ferrite is the soft phase with a hardness of about 260Hv.

The tensile test and cyclic loading test were conducted on Instron 8801 hydraulic servo fatigue test machine at room temperature, with a strain rate of 0.002 S^{-1}, and the loading direction is parallel to forging direction. The samples meet the requirements of ISO 26077-2010 international standard, and the sample size is shown in Fig. 1b. The strain amplitudes of cyclic loading tests are 0.3%, 0.7%, 0.8%, and 1.0%, respectively.

Transmission electron microscopy (TEM) was used to observe the microscopic characteristics of the samples after cyclic loading. The samples were cut along the axis of the round rod in the gage section, polished to 30 um, and then be thinned with the TenuPol-5 electro polisher at room temperature. The electrolyte is perchlorate alcohol solution with 7% volume fraction and the voltage was 20 V. TEM analysis was performed on JEM-2010 transmission electron microscopy, and the operating voltage was 20 kV.

3 Results and Discussion

3.1 Mechanical Properties of Monotonic Loading

Figure 2 shows the engineering stress–strain curve (Fig. 2a) and the true stress–true strain and work-hardening curve (Fig. 2b) for the monotonic loading of the test steel. As can be seen from Fig. 2a, the steel has good mechanical properties, with yield strength of 517 MPa, tensile strength of 883 MPa, fracture elongation rate of 87.2%, and the product of strength and ductility of 77GPa%. When the engineering strain exceeds 20% (the true strain is about 0.18), the engineering stress increases rapidly again, and the engineering stress–strain curve is rough "S" shape. With the progress of deformation, work hardening rate first decreases, then increases to the peak, and finally decreases until fracture, showing the "three-stages" hardening characteristic,

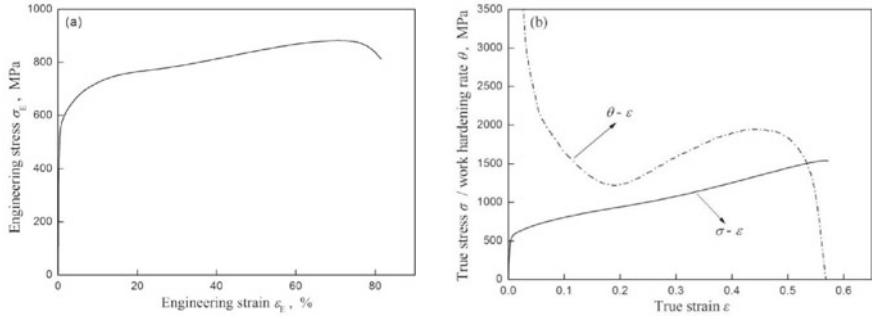


Fig. 2 Engineering stress–strain curve (**a**) and true stress–true strain and work hardening curve (**b**) of the test steel during monotonic loading

as shown in Fig. 2b. Therefore, it can be inferred that the austenitic phase in the duplex stainless steel produces deformation-induced martensitic phase transformation during the deformation process, resulting in the TRIP effect, which significantly improved the strength and plasticity [6].

3.2 Hysteresis Loops Under Cyclic Loading

Figure 3 shows the variation of hysteresis loop with cycles (N) of the cyclic loading tests. As can be seen, at the initial stage of cycles ($N < 5$) under different strain amplitudes, the loop becomes sharper from flat, meanwhile, the peak stress $\sigma_{\max}$ and the valley stress $\sigma_{\min}$ both increase rapidly with the increase of cycles, which shows the characteristics of initial cyclic hardening, however, with the continued increase of cycles, the loop flattens again from sharp, and the $\sigma_{\max}$ and $\sigma_{\min}$ begin to decrease slowly, the test steel shows the characteristics of subsequent cyclic softening. For the cyclic softening, with a smaller strain amplitude ($\varepsilon_a = 0.3\%$), the softening characteristic gradually slows down with cycles until stabilization and $\sigma_{\max}$ and $\sigma_{\min}$ remain unchanged, and the loop shape does not change significantly. However, when the strain amplitude is larger ($\varepsilon_a = 1.0\%$), the peak stress and the valley stress continue to decrease until failure.

3.3 Cyclic Hardening/softening

The cyclic stress response curve can show the variation of the stress amplitude with cycles under certain strain amplitudes, which is commonly used to describe the cyclic deformation of the material, the cyclic stress response curve of the tested steel is shown in Fig. 4. The cyclic hardening/softening characteristics of the test steel are affected by the amplitudes and cycles. With smaller strain amplitudes, the test steel

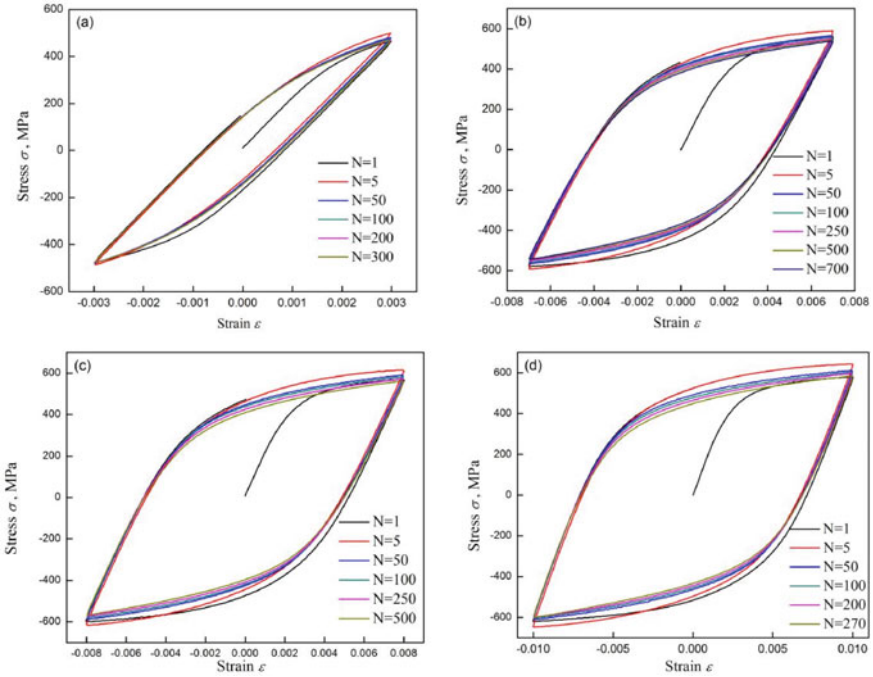


Fig. 3 Hysteresis loops with the number of cycles (**a**) $\varepsilon_a = 0.3\%$ (**b**) $\varepsilon_a = 0.7\%$ (**c**) $\varepsilon_a = 0.8\%$ (**d**) $\varepsilon_a = 1.0\%$. (Color figure online)

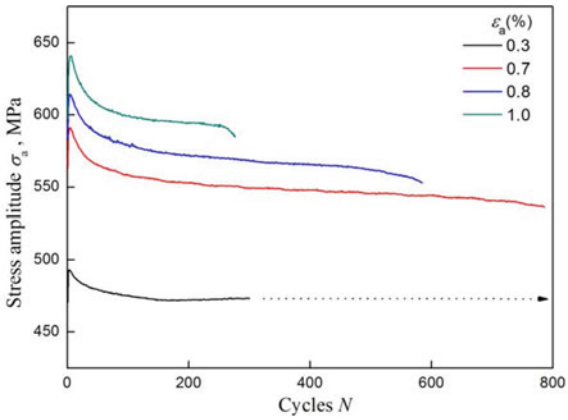


Fig. 4 Cyclic stress response curves. (Color figure online)

is cyclic hardening with initial cycles ($N < 5$), then turns to be cyclic softening and gradually stabilization, however, under larger strain amplitudes, after rapid initial cyclic hardening ($N < 5$), the test steel turns to be cyclic softening, and fails to reach cyclic stabilization until failure.

In order to further evaluate the influence of strain amplitude on the cyclic softening of the test steel, the cyclic softening rate parameter is introduced, and its expression is:

$$\delta = \frac{\sigma_{\max} - \sigma_s}{\sigma_{\max}}. \tag{1}$$

In the formula, δ is the cyclic softening rate, $\sigma_{\max}$ and σ_s are the maximum stress amplitude and stable stress amplitude (or half-life stress amplitude) in the cyclic loadings respectively.

The cyclic softening rate of the test steel under different plastic strain amplitudes is shown in Fig. 5, the corresponding relationship between strain amplitudes and plastic strain amplitudes is shown in Table 2. As can be seen from Fig. 5, the cyclic softening rate of the test steel increases rapidly with the increase in the plastic strain amplitude under smaller strain amplitude ($\varepsilon_{ap} < 0.42\%$), then within a certain range of plastic strain amplitude ($\varepsilon_{ap} = 0.42$–0.51%), the softening rate increases at a slower rate, and after exceeding a certain strain amplitude ($\varepsilon_{ap} > 0.51\%$), the softening rate decreases. The comparative analysis shows that the plastic strain amplitude is within the range of 0–0.6%, with an increase in plastic strain amplitude, the cyclic softening rate of duplex stainless steel increases first and then decreases. Figure 6 is the TEM image of the test steel after more than 700 cycles with strain amplitude

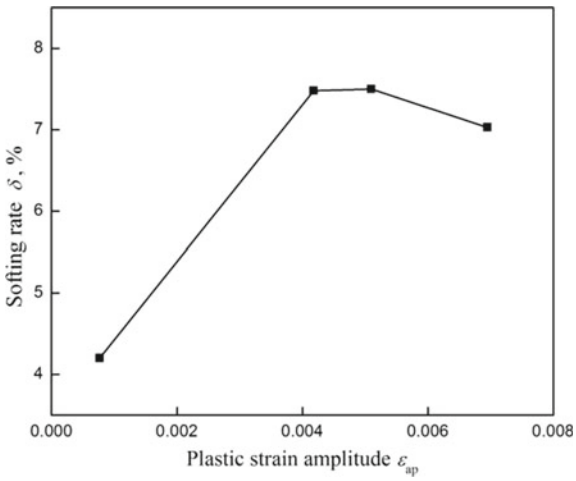


Fig. 5 Cyclic softening parameter δ as a function of the plastic strain amplitude

Table 2 Correspondence between strain amplitude and plastic strain amplitude

ε_a/%	0.3	0.7	0.8	1.0
ε_{ap}/%	0.08	0.42	0.51	0.70

Note ε_a—strain amplitude, ε_{ap}—plastic strain amplitude

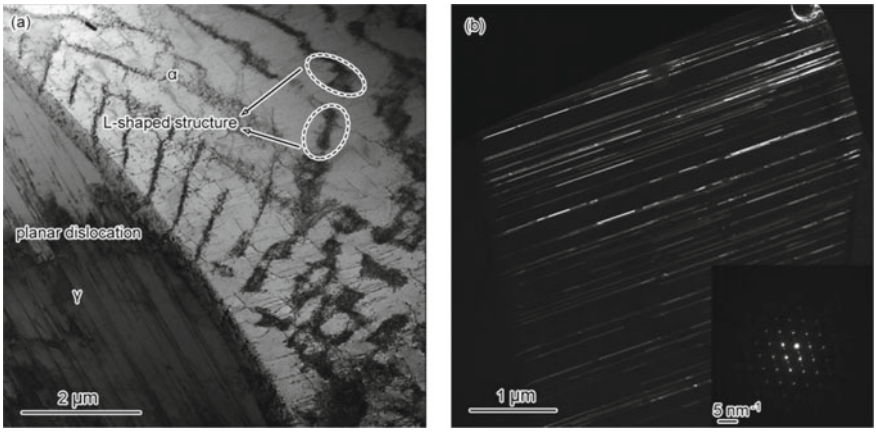


Fig. 6 Typical microstructure observed by transmission electron microscopy after more than 700 cycles ($\varepsilon_a = 0.7\%$). **a** Spatial dislocation structure in ferrite phase and planar dislocation structure in austenite phase (bright field), **b** ε martensite phase in austenite phase (dark field)

$\varepsilon_a = 0.7\%(\varepsilon_{ap} = 0.42\%)$. According to Fig. 6a, the ferrite phase is a spatial dislocation structure with high dislocation density. There are not only long dislocation walls that are nearly parallel to each other but also short dislocation walls that are perpendicular to each other, locally formed "L" structure or maze structure. The microscopic characteristics indicate the ferrite slips along two slip systems during cyclic deformation, which is the embodiment of cyclic plastic strain localization. The formation of such low energy dislocation structures as dislocation wall and dislocation cell in ferrite phase is the main reason for cyclic softening of duplex stainless steel [4]. Compared with ferrite, the cyclic deformation mechanism of austenitic phase is mainly planar dislocation structure [12]. It is worth noting that in the austenitic phase, the deformation band structure across the whole austenitic grain is distributed in parallel. Combined with the dark field image of Fig. 6b, it can be seen that the deformation bandwidth is between 30 and 60 nm, and the diffraction pattern indicates that it is an ε martensite with dense hexagonal structure, which indicates that the austenite in the test steel has cyclic deformation inducing martensite transformation under this deformation condition. Research has shown that the ε martensite during the deformation of metastable austenite could hinder the dislocation movement and strengthen it [11]. Therefore, although the deformation mechanism of austenitic phase is still dominated by plane dislocation slip, the occurrence of ε martensite would result in hardening of austenitic phase in some extent, although it is not enough to cause the overall cyclic hardening, it inhibits the cyclic softening, then slows down and even reduce the cyclic softening rate with an increase in strain amplitude (as shown in Fig. 5).

4 Conclusion

Under monotonic loading, the test steel shows the characteristics of three-stages hardening with obvious TRIP effect, which makes its mechanical properties excellent, the fracture elongation rate is up to 87.2%, the tensile strength is up to 883 MPa, and the product of strength and ductility is up to 77GPa%.

The cyclic hardening/softening characteristics of the test steel are sensitive to strain amplitude and cycles. Under the smaller strain amplitude, it shows cyclic hardening by initial circles ($N < 5$), then severely cyclic softening and gradually stabilization. However, in the case of larger strain amplitude, after the initial rapid cyclic hardening ($N < 5$), continuous cyclic softening is followed, and cyclic stabilization is not reached until failure.

Different forms of dislocation wall forming in ferrite phase during cyclic deformation are the main reasons for the overall cyclic softening. The austenite undergoes deformation-induced martensite transformation, which inhibits the macroscopic cyclic softening rate of the material, so that the cyclic softening rate of the test steel increased first and then gradually decreased with an increase in plastic strain amplitude.

Acknowledgments The authors gratefully acknowledge support provided by National Natural Science Foundation of China (Number 51905467, 51675467), and Natural Science Foundation of Hebei Province (Number E2019203560) and State Key Laboratory of Materials Processing and Die & Mould Technology, Huazhong University of Science and Technology, China (P2019-018).

References

1. Zhao Y, Zhang W, Liu X, et al (2016) Development of TRIP-aided lean duplex stainless steel by twin-roll strip casting and its deformation mechanism. Metall Mater Trans A 47(12):6292–6303
2. Herrera C, Ponge D, Raabe D (2011) Design of a novel Mn-based 1GPa duplex stainless TRIP steel with 60% ductility by a reduction of austenite stability. Acta Mater 59:4653–4664
3. Magnin T, Lardon JM, Coudreus L (1988) A new approach to low cycle fatigue behavior of a duplex stainless steel based on the deformation mechanisms of the individual phases. Am Soc Test Mater (Philadelphia), 12–823
4. Mateo A, Llanes L, Iturgoyen L, et al (1996) Cyclic stress-strain response and dislocation substructure evolution of a ferrite-austenite stainless steel. Acta Mater 44:1143–1153
5. Polák J, Petrenec M, Kruml T (2010) Cyclic plastic response and fatigue life in superduplex 2507 stainless steel. Int J Fatigue 32:279–287
6. Guo BF, Zhang QF, Chen L, et al (2018) Influence of annealing temperature on the strain-hardening behavior of a lean duplex stainless steel. Mater Sci Eng A 722:216–224
7. Kang JY, Kim H, Kim K, et al (2017) Effect of austenitic texture on tensile behavior of lean duplex stainless steel with transformation induced plasticity (TRIP). Mater Sci Eng A 681:114–120
8. Glage A, Weidner A, Biermann H (2010) Effect of austenite stability on the low cycle fatigue behavior and microstructure of high alloyed metastable austenitic cast TRIP steels. Procedia Eng 2:2085–2094

9. Mateo A, Girones A, Keichel J, et al (2001) Cyclic deformation behaviour of superduplex stainless steels. Mater Sci Eng 314:176–185
10. Alvarez-Armas I, Marinelli MC, Hereñú S, et al (2006) On the cyclic softening behavior of SAF 2507 duplex stainless steel. Acta Mater 54:5041–5049
11. Nikulina I, Sawaguchi T, Ogawa K (2016) Effect of γ to ε martensitic transformation on low-cycle fatigue behaviour and fatigue microstructure of Fe-15Mn-10Cr-8Ni-xSi austenitic alloys. Acta Mater 105:207–218
12. Cai ZH, Ding H, Misra, RDK, et al (2015) Austenite stability and deformation behavior in a cold-rolled transformation-induced plasticity steel with medium manganese content. Acta Mater 84:229–236

The Local Strain Evolution for Structured Sheet Metals During Uniaxial Deformation



Evgenia Ermilova, Alexander Nikitin, and Sabine Weiß

Abstract Structured materials can be progressive alternatives to commonly used flat sheets because of their higher bending stiffness and stability compared to flat sheet metals, made of the same alloy. The application of sheet metals requires accurate information regarding their strength and deformation behavior. Such data are not commonly available and have to be measured by specific test setups and implementation of tests. The aim of this work is to obtain new knowledge about deformation mechanisms of structured sheet metals. Structured sheet metals (SSM) made of conventional deep-drawing steel DC04 were investigated by means of tensile tests. The influence of the structure type arrangement on the deformation behavior was analyzed. The evolution of local strains was analyzed by means of strain gauge measurements as well as 3D-displacement measurements with an ARAMIS high-resolution camera system. Local orientation changes in different structural elements were measured using the electron backscatter diffraction technique.

Keywords Structured sheet metals · SSM · Tensile test · ARAMIS · Strain gauge · EBSD · REM · Electron microscopy · DC04 steel

1 Introduction

Weight reduction without loss of carrying capacity is the primary purpose of using lightweight materials. In comparison with traditional flat materials, structured sheet metals have improved mechanical characteristics. Application of structured sheet metals enables to reduce the thickness as well as the weight of the sheet metals and

E. Ermilova (✉) · A. Nikitin · S. Weiß
Department of Physical Metallurgy and Materials Technology, Brandenburg Technical University, 03046 Cottbus, Germany
e-mail: evgeniia.ermilova@b-tu.de

A. Nikitin
e-mail: nikitale@b-tu.de

S. Weiß
e-mail: weiss@b-tu.de

© The Minerals, Metals & Materials Society 2021

G. Daehn et al. (eds.), *Forming the Future*, The Minerals, Metals & Materials Series,
https://doi.org/10.1007/978-3-030-75381-8_143

thus the weight of the entire construction. Structured materials could be a progressive option for construction compared to widely used non-structured sheet metals, where the price depends directly on the amount of material used [1–5].

In the present work, the material characteristics were determined using a modified tensile test. Usually, sheet metals are tested according to DIN 6892-1 (N), which describes the test procedure as well as the specimen dimensions. However, this standard is deficient for the structural sheet investigation as the width of a single structured element is larger than the recommended specimen width. In addition, it is necessary to reduce the stress during placing of the sample into the test machine and the construction of special clamping systems, adapted to the structure of the respective sheet. The geometric dimensions of the test specimens have to be determined to evaluate the structured sheet metals (SSM) with regard to the single structured elements size.

The main interest of this study is to obtain new knowledge about deformation mechanisms of SSMs by means of an optical system ARAMIS [6], strain gauge measurements, and microstructure analysis of the material.

2 Materials and Methods

In the present work, structured steel sheets made of cold-rolled low carbon steel DC04 (EN steel number 1.0338) [7] were tested in tensile tests. The chemical composition of steel is according to EN 10130: 2006 (N) (Cold rolled low carbon steel flat products for cold forming. Technical delivery conditions) is presented in the Table 1. The sheet metals were structured by means of a hydraulic press. The thickness of the structured sheet metals was 0.5 mm. The depth of the honeycomb structure elements was $s = 3.1$ mm. The microstructure of the base material was fully recrystallized and isotropic. The rolling direction was not noticeable and the tensile strength in longitudinal and transverse direction was similar.

The structure consists of three elements: honeycomb, bridge, and triple point (Fig. 1). Wrench size and other important geometric parameters of each honeycomb are given in Fig. 1 as well.

Since the force is applied in one direction, the direction of the structural elements can have an influence on the mechanical behavior. Thus, sheets with the main structure directions will be investigated in this work with respect to their mechanical properties.

The direction of the structure is determined by the position of the structural element in the center of the specimen. There are three different types of specimen configuration (Fig. 2).

Table 1 Chemical composition of DC04 Steel

Grade	Number	Classification	C (%)	Mn (%)	P (%)	S (%)
DC04	1.0338	Non-alloy quality steel	≥0.08	≥0.40	≥0.03	≥0.03

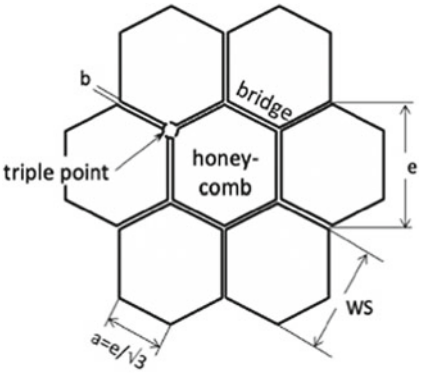


Fig. 1 Structured sheet metal (detail) with three structural elements: honeycomb, bridge, and triple point. Geometric parameters of a honeycomb—wrench size WS = 33 mm, across corners dimension e = 38 mm, edge length a = e/$\sqrt{3} \approx 22$ mm, width of the bridge b = 2 mm, diameter of the triple point = 3.8 mm

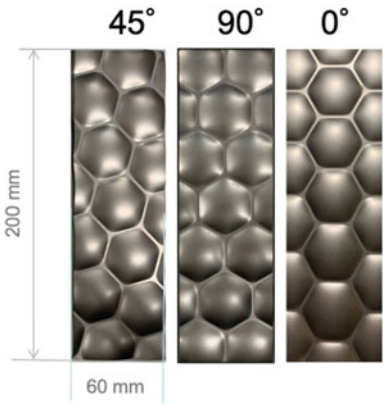


Fig. 2 Tensile test specimens: arrangement of the honeycomb structure. (Color figure online)

In order to study the influence of the structure arrangement on the mechanical properties of the sheet, it is necessary to have at least one entire structural element in the center of the specimen.

Rectangular specimens with a width of 60 mm were tested. The total length of the specimens was 200 mm. All specimens were laser-beam cut.

3 Test Setup Measuring System

The tensile tests were carried out using a universal material testing machine of the company "Walter + Bai ag". Five measurements were performed for each type to ensure reproducibility. By installing the test samples into the tensile test machine, the ends of the samples may be smoothened by the clamps, which can cause unwanted effects on the deformation. To eliminate this influence, existing methods can be adapted by developing special clamping jaws that perfectly fit to each variant of

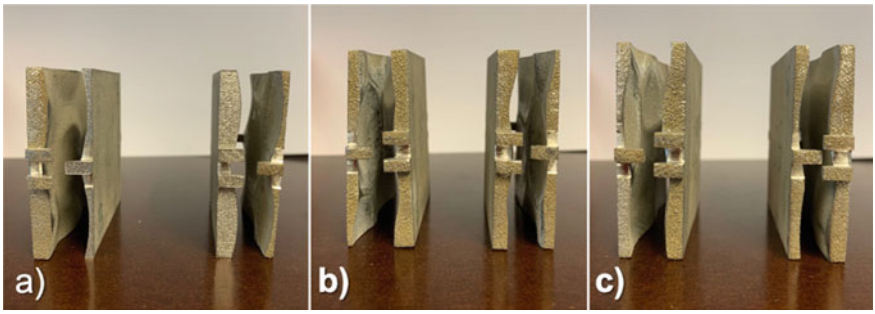


Fig. 3 Clamping jaws: structure directions: **a** 0°, **b** 45°, **c** 90°. (Color figure online)

the structure orientation. These clamping jaws were produced using the 3D Print Technology Selective Laser melting. In Fig. 3, photos of these clamping jaws for different structure directions are presented.

The inner surfaces of the clamping jaws perfectly fit the surfaces of the respective structural elements in this area of the samples. Thus, the honeycomb structure is not smoothened during mounting and further impact on the strain distribution in the gauge length during the test is avoided.

Specimen deformation and elongation were recorded by three different methods: measurement of the global position of the test machine (traverse position) and measurement of the local displacement by the optical ARAMIS system as well as strain gauge measurement.

The ARAMIS system allows to fully define the material and component behavior and to track experiments with high temporal and local resolution. ARAMIS is a non-contact and material independent optical measuring system. A dot pattern is applied onto the previously prepared surface of the sample. Each point is recognized by the high-speed camera and tracked during the entire process. From the measurement data material parameters are calculated, numerical simulations are validated and component motion as well as information are analyzed using the digital image correlation and evaluation software GOM Correlate.

A Strain gauge (SG) is a sensor, whose resistance varies with the applied force. It converts force, pressure, tension, weight, etc., into differences in electrical resistance, which can be measured.

In Fig. 4, the structure of the SG is shown schematically.

Stress and strain are the results if external forces are applied to a stationary object. Stress is defined as the internal resisting forces of the object, and strain is defined as the occurrence of displacement and deformation. SGs are used for the measurement of strain. Strain is referred to as positive if a material is stretched and negative if it is compressed. When a SG is compressed, its electrical resistance decreases and increases when it is stretched, respectively [8].

Linear SGs were used because of the uniaxial load application. For each structure direction, local stress was estimated in three structural elements: honeycomb (HB), triple point (TP), and bridge (B). Regarding the investigated structural element, two

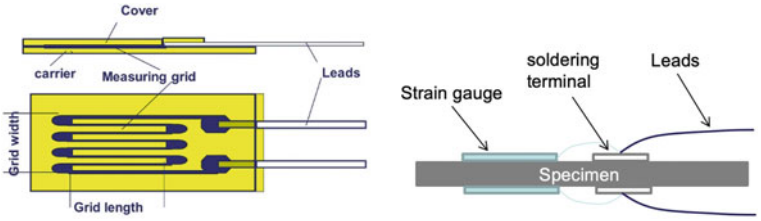


Fig. 4 Schematic illustration of the SG structure [8]. (Color figure online)

types of SGs of suitable length and width were selected. The SG type FLGB-1-11 with gauge length 1 mm and gauge width 1,1 mm was used for HB and SG type FLGB-2-11 with gauge length 2 mm and gauge width 1,5 mm for TP and Bridge element, respectively.

In total six strain gauges are installed on each structural element on both, the upper and the lower side of the structure sheet metals surface (Fig. 5).

For a better understanding of the development of stresses during deformation and the influence of the structure direction, the microstructure was investigated at different phases of the tensile test in different structural elements. The microstructure in the different processed conditions was characterized by ZEISS DSM962 scanning electron microscopy (SEM) using back-scattered electrons. For SEM, a Tescan Mira II XMH microscope and the above-mentioned Zeiss microscope were

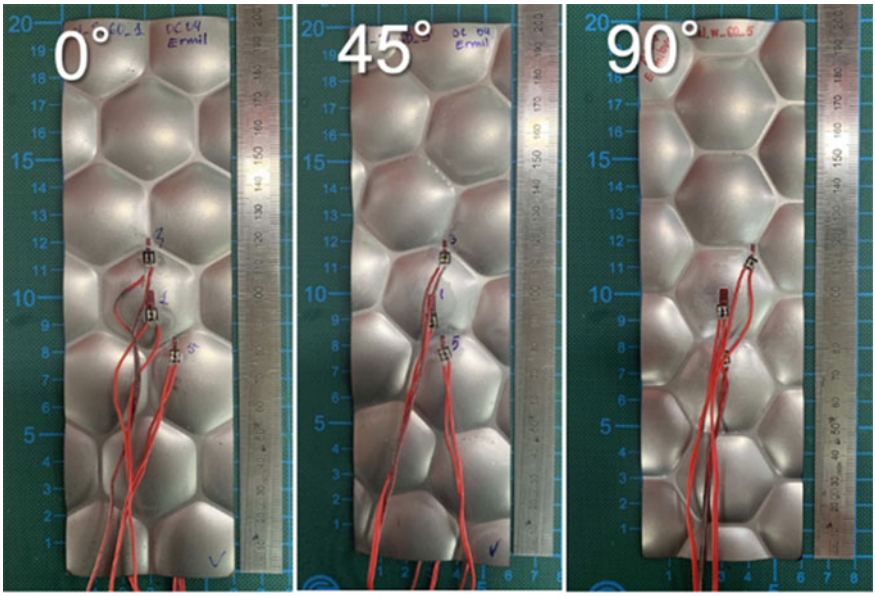


Fig. 5 Samples with strain gauges. (Color figure online)

used. Microstructural samples were taken with an image plane perpendicular to the long axis of the cast piece and parallel to the deformation axis of forged specimens, respectively.

4 Results and Discussion

All tested variations of samples show repeatable deformation behavior. The variance of the stress–strain curve is low. Figure 6 shows representative stress–strain curves for different structure directions: 0°, 45°, and 90°.

The tensile test data are presented in Table 2.

According to Table 2, structure 45° has the highest tensile strength.

Figure 6 shows that the structural direction 90° has significantly lower elongation values. Also as shown in Table 2, this structure has mean values. In structures structural direction 0° and 45° the uniaxial load is distributed more optimally for strength-elongation relationship.

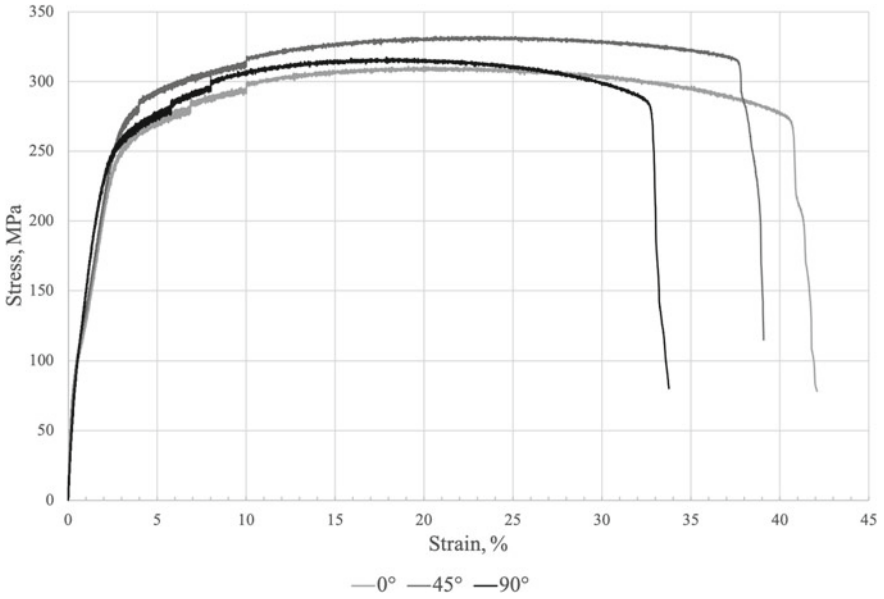


Fig. 6 Stress–strain curves for structure direction: 0°, 45°, and 90°

Table 2 Material properties of SSM

Structure direction	0°	45°	90°
Tensile strength (MPa)	310	332	316
Elongation (%)	38	35	30

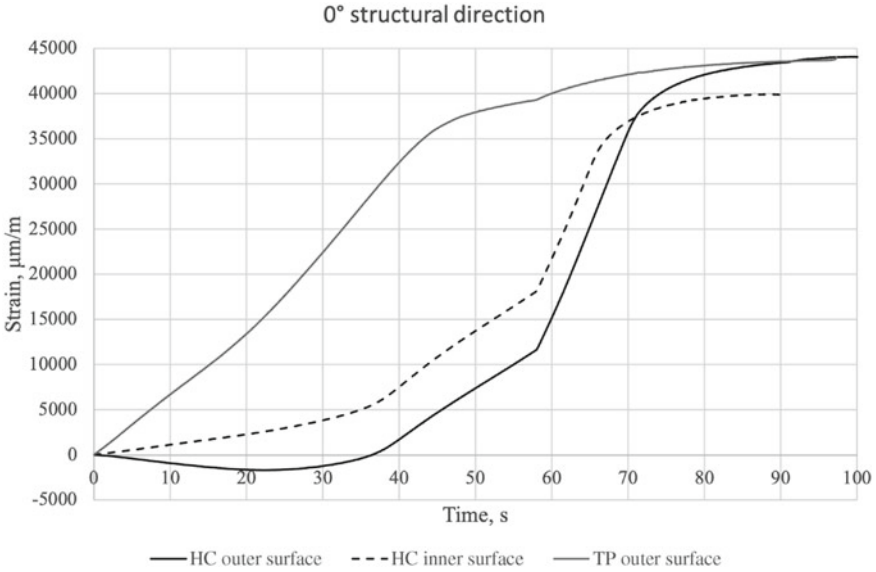


Fig. 7 Strain time histories for structural direction 0°

Strain gauges are very delicate to handle and can be damaged during the experiment, thus, measured values are not available for all structural elements in the following figures (Figs. 7, 8, and 9).

The curves of all three structure variants show that deformation starts in the structural element type bridge. Subsequently, strains arise in structural element type triple point and last, strains increase in the centers of the honeycombs. The differences between the stresses on the upper and lower surface are most pronounced in the centers of the honeycombs for all cases.

Similar results were obtained by the optical measuring system ARAMIS. Representative strain distributions are presented in Fig. 10.

At the beginning of the tensile tests, the deformation distributing over the sample is not evenly but localized in the structural element type bridge. Deformations in horizontal (or partially perpendicular to the direction of load application) bridges are higher than in vertical or inclined ones. Subsequently the structure begins to flatten and finally, maximum deformations are distributed over the entire honeycomb surface. Fracture is observed for all specimens to be parallel to the direction of maximum shear stress across the center of the HC.

The fractures of the samples with structure type 0 degree exclusively have zigzag form. Samples of structure type 45° always show a linear fracture line parallel to the direction of maximum shear stress. In samples with structure type 90° both types of fracture occur.

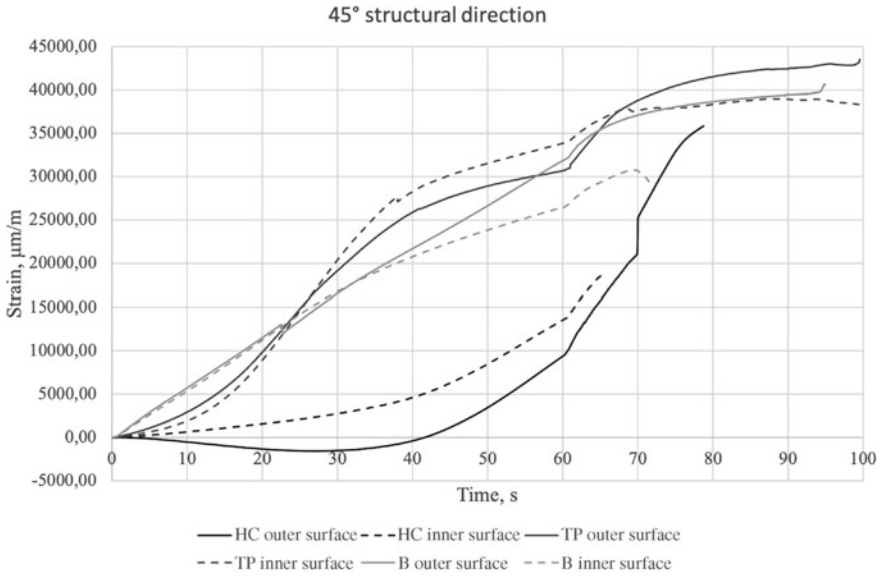


Fig. 8 Strain time histories for structural direction 45°

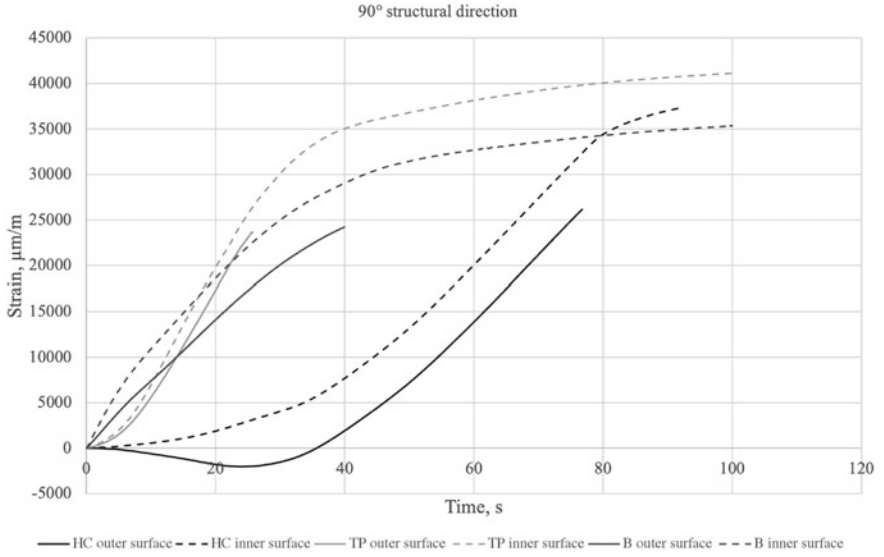


Fig. 9 Strain time histories for structural direction 90°

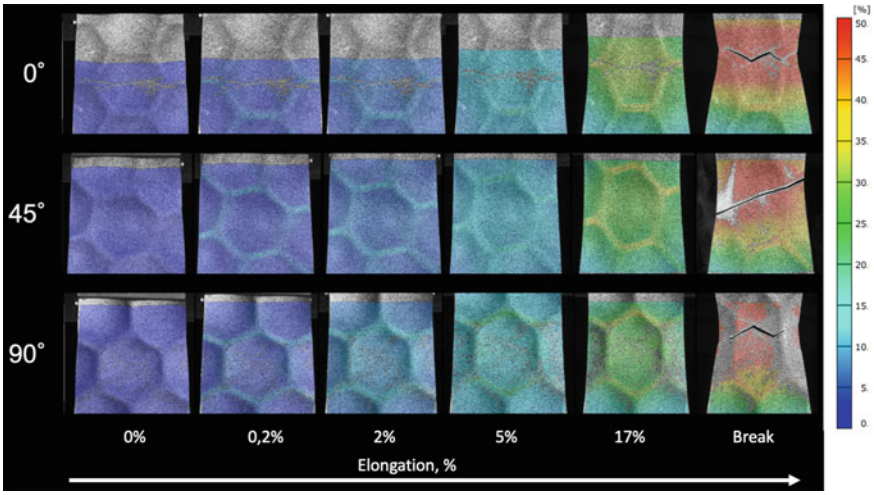


Fig. 10 ARAMIS data during tensile test. (Color figure online)

In order to fully understand the development of strains and the effect of the structure direction during deformation, the initial microstructure in different structural elements was analyzed.

Microstructure analysis in different phases of the tensile test for all three structural elements (honeycomb, triple point and bridge) and each structure direction is planned for future work.

Representative EBSD-mappings (Image Quality, Inverse Pole Figure, and Kernel Average Misorientation) of the respective structural elements are given in Fig. 11.

According to the Image quality mappings, the honeycomb structure seems to be fewest deformed, in the bridges the degree of deformation is slightly higher and the highest degree of deformation with obviously elongated grains was found for the triple points.

The inverse Pole Figure column shows the crystallographic orientation of each grain with respect to the rolling direction. In all cases, no preferred orientation is visible.

The local misorientation with regard to a central measuring point and a number of surrounding neighboring measuring points is determined for the Kernel Average Misorientation Mappings. Local misorientations, as indicators for local deformations, are colored according to the color code in Fig. 11. The blue color for the honeycomb documents very low deformation in this region. Green color coding in the surrounding of the grain boundaries in the structure element bridge indicates that the deformations are located close to the grain boundaries and inside some of the grains.

These grains are marked in pink, turquoise, white, and lilac colors in the IPF mapping corresponding to grains, oriented for single slip. For the structural element triple point highest misorientations become obvious, apparent by a large number

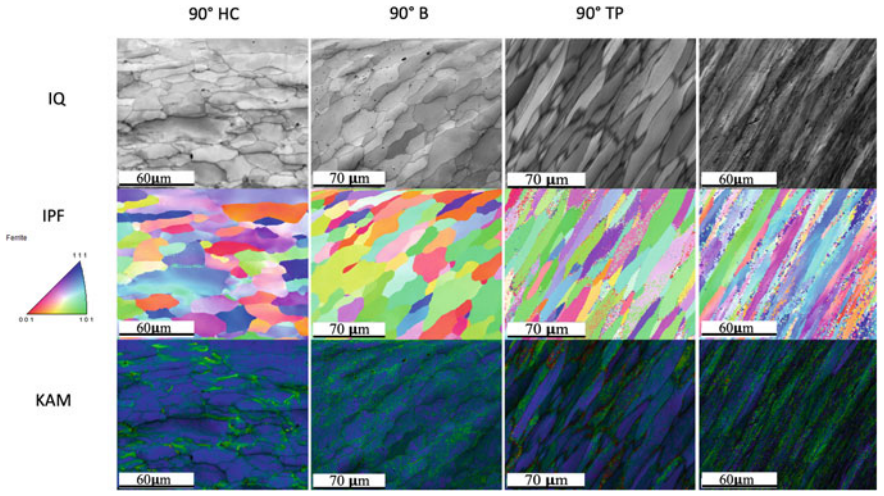


Fig. 11 EBSD-mappings (**I**mage **Q**uality, **I**nverse **P**ole **F**igure and **K**ernel **A**verage **M**isorientation) of honeycomb, bridge and triple point for 90° and triple point for 45° structural orientation. (Color figure online)

of light green colored grains. From these results it can be expected that the initial deformation, induced by the structuring of the samples, will influence the subsequent deformation during the tensile tests. It can be assumed that the earlier increase in strain in the bridges than in the triple points may be due to the lower strain hardening in the bridges during structuring. The deformation behavior of structured sheet metal can be identified as an interaction between local initial deformation and local subsequent deformation, depending on the structure direction.

5 Conclusion

In the present study, the influence of the structure direction on the deformation behavior of structured sheet metals was analyzed using tensile tests. Specimen deformation and elongation were recorded by three different methods: measurement of the global position of the test machine (traverse position) and measurement of the local displacement by the optical measurement system ARAMIS as well as by strain gauge measurements. The ARAMIS system enables visualization of the deformation distribution during the tensile test and numerical models of the deformation process. According to test data, the most optimal structure for strength/elongation relationships for uniaxial load is structural direction 45°. This estimation shows the localization of deformation in bridges perpendicular to the direction of load application. The fracture occurs nearly parallel to the direction of maximum shear and sometimes a zigzag shape of the fracture surface is obtained.

Electron microscopy results reveal initial deformation of the samples due to structuring, strongest within the structural element TP. An influence of this initial deformation on the further deformation behavior could be identified.

Acknowledgments The present work was carried out at the Brandenburg University of Technology (Cottbus). The authors are grateful to the German Federal Ministry of Education and Research (BMBF) for financial support of the project (Grant No. 03IP707).

References

1. Mütze S (2002) Beurteilung des Einsatzes von Teilstrukturierten Stahlfeinblechen im Kfz-Karrosseriebau zur Gewichtreduzierung, Schriftenreihe der Forschungsvereinigung Automobiltechnik e.V. 171, 82. Frankfurt a. M., Germany: s.n.
2. Sterzing A (2005) Bewertung von Leichtbaupotential und Einsatzfächigkeit wölbstrukturierter Feinbleche, Zwickau, Verl. Wiss. Scripten; Zugl.: chemnitz, Techn. Univ., Diss., 2005
3. Hoppe M (2003) Viehweger, als Ms.gedr. "Umformverhalten strukturierter Feinbleche". Berlin: dissertation.de - Verlag im Internet GmbH
4. Mirtsch F, Weinert N, Pech M, Selinger G (2006) Vault structures enabling sustainable products. In: Proceedings of 13th CIRP international conference on life cycle engineering, Leuven, Belgium, pp 629–633
5. Simon S, gedr., Viehweger Als Ms B (2008) "Werkstoffgerechtes Konstruieren und Gestalten mit metallischen Werkstoffen" Hrsg:. Verlag im Internet GmbH, Berlin, dissertation.de
6. Behrung D, Gometcic G, Michailov VG, Ritter R, Wohlfahrt H (2000) Advances in mechanical behaviour, plasticity and damage. In: Proceedings of EUROMAT 2000, 7–9 November TOURS, vol 2. France, pp 905–910
7. Norm DIN ISO 6892, Metallic materials—Tensile testing – part 1, December 2009
8. Hoffmann K (1987) Eine Einführung in die Technik des Messens mit Dehnungsmessstreifen. Hottinger Baldwin Messtechnik GmbH, Berlin

Part XVII
Microstructure Development by Forming

Development and Implementation of Static Recrystallization Model of 6XXX Aluminum Alloy Using Industrial Experiments



Artem Alimov, Ivan Kniazkin, and Nikolay Biba

Abstract The paper focuses on the development of a static recrystallization model of 6XXX aluminum alloy based on industrial profiles extrusion analysis. 6XXX aluminum alloys are widely used for complex shapes with smooth surfaces suitable for visible architectural applications. Mechanical properties and surface defects, for example, streaking lines, are dependent on the microstructure. Static recrystallization occurs in alloys such as 6XXX due to high stacking fault energy. At the moment, there is no reliable static recrystallization model of 6XXX aluminum alloys found in the literature. In the presented paper, a new approach has been proposed to determine the parameters of Johnson–Mehl–Avrami–Kolmogorov equation. It is based on using strain and temperature history during extrusion of industrial profiles and examining the microstructure in their cross-sections and implementing the inverse analysis approach. The developed model has been verified and used for simulation of the microstructure evolution in industrial extrusion cases and has shown sufficient accuracy.

Keywords Microstructure · Static recrystallization · Aluminum alloy · Qform · Simulation

A. Alimov (✉)
Brandenburg University of Technology Cottbus-Senftenberg, Konrad-Wachsmann-Allee 17, Cottbus 03046, Germany
e-mail: art.alimov@gmail.com

I. Kniazkin
Bauman Moscow State Technical University, 5 Vtoraya Baumanskaya Str., Bldg. 1, 105005 Moscow, Russian Federation

A. Alimov · I. Kniazkin
QuantorForm Ltd, 16 2nd Yuzhnoportoviy Pass., Bldg. 2, 115088 Moscow, Russian Federation

N. Biba
Micas Simulation Ltd., 107 Oxford Road, Oxford OX4 2ER, UK

© The Minerals, Metals & Materials Society 2021

G. Daehn et al. (eds.), *Forming the Future*, The Minerals, Metals & Materials Series,
https://doi.org/10.1007/978-3-030-75381-8_144

1 Introduction

Extrusion of aluminum alloys is widely used in the production of bars, tubes, wires as well as for the manufacture of profiles. The cross-section of profiles could be solid, semihollow or hollow and rather complex. Acceptable mechanical properties, low density, good corrosion resistance, and high processability are the reasons for the predominance of aluminum profiles in extrusion [1]. The moderate level of working temperatures of aluminum alloys that is lower than tempering temperature of tool steels allows producing the largely unrestricted shape of the cross-sectional geometry profiles with good precision and high surface quality.

Thermomechanical processing during extrusion and subsequent cooling led to the microstructure evolution of the material. It can involve static recrystallization, dynamic recrystallization (geometric or continuous), grain growth (normal or abnormal), and particle precipitation [2]. The occurrence of each metallurgical process depends on the mode of thermomechanical processing and the chemical composition of the alloy [3, 4]. In materials with high stacking fault energy, such as pure aluminum, low-alloyed aluminum alloys such as 6005, 6060, 6063, etc. dynamic recrystallization does not occur [5]. Static recrystallization occurs in such materials after deformation. In high-alloyed aluminum alloys, such as 7020, 7050, and 7075 that have a lower stacking fault energy, the dynamic recrystallization can occur [6, 7]. The division into two groups of alloys is conditional and a number of alloys are recrystallized both dynamically and statically. Simulation of microstructure evolution is essential for control of mechanical properties and to get high-quality extruded profiles.

The usual way to develop a model of microstructure evolution is to perform a series of laboratory experiments. The most widespread technique is to use a thermomechanical simulator. For example, Yi et al. [7] used Gleblee 1500 to develop a dynamic recrystallization model for 7050 aluminum alloy. Some researchers adopted real processes to perform them in the laboratory. For example, Donati et al. [8] used backward cup extrusion to study the microstructure evolution of 6060 and 6082 aluminum alloys. Segatori et al. [9], Bandini et al. [10], Güzel et al. [11] used laboratory forward extrusion setup to investigate the microstructure evolution during extrusion. Laboratory experiments have some restrictions because, for example, it is impossible to reach the same high strain and strain-rate levels as a real extrusion process. Moreover, it is necessary to make special samples use special testing equipment and so on. Another way is to use industrial experiments. For suppliers of aluminum profiles, it is much easier to use sections of the profiles for the study of microstructure evolution and development of the models. Different models were developed for the simulation of microstructure evolution in metals during thermomechanical processing [12–15].

The aim of the present research is to study a microstructure evolution in extrusion process and to develop a static recrystallization model for 6XXX aluminum alloys where the model parameters can be derived from industrial experients.

Table 1 Chemical composition of the studied 6XXX aluminum alloy (wt.%)

Mn	Fe	Mg	Si	Zn	Ti	Cu	Al
0.03	0026	0.56	0.67	0.04	0.03	0.03	Bal

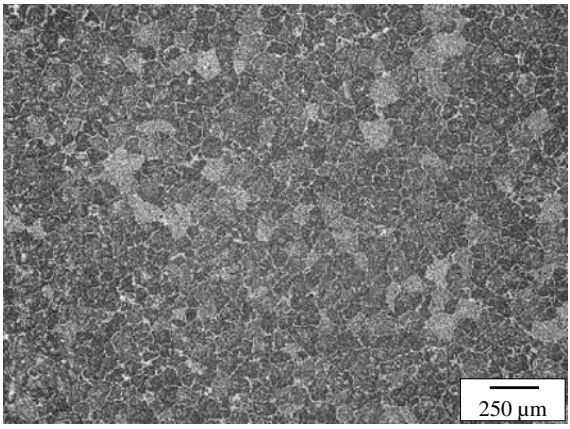


Fig. 1 The initial microstructure of the studied aluminum alloy

2 Materials and Methods

2.1 Materials

The study has been performed using the industrially extruded profile. The chemical composition of studied 6XXX aluminum alloy is presented in Table 1, and it corresponds to the alloy 6005.

The initial microstructure of the billet is presented in Fig. 1. The measured average grain size was 80.7 ± 9.2 µm. During the heating and extrusion grains were grown and the average grain size of non-deformed butt-end was 122.2 ± 24.9 µm.

2.2 Industrial Trials and Finite Element Simulation of the Extrusion Process

Studied profile was produced in industrial conditions. The extrusion trials were performed on 8 inch 20 MN direct single action horizontal hydraulic extrusion press. After extrusion, the profile was cooled by air. The parameters of the industrial extrusion trial are summarized in Table 2.

Extrusion process was simulated in QForm Extrusion FEM commercial code with the same parameters as in the industrial experiment. QForm Extrusion is the software

Table 2 The parameters of industrial extrusion trial

Parameter	Value
Velocity or ram, mm/s	4
Billet temperature, °C	480
Billet diameter, mm	185
Billet length, mm	650
Die set temperature, °C	450
Bolster and sub-bolster temperature, °C	25
Dummy block temperature, °C	450
Container temperature, °C	450



Fig. 2 Workpiece during extrusion simulation with strain field shown (the die set and container are not shown). (Color figure online)

which is able to simulate extrusion processes using the combined Lagrangian–Eulerian approach. Eulerian domain (Fig. 2) represents the stationary mesh created in a container and cavities of the die set including short part of the profile. Lagrangian domain is used to follow the profile flow. The combination of coupled mechanical task, namely the consideration of the influence of tool deformation on profile flow, and precise solve of the thermal task allows the software to achieve proper temperature, velocity and consequently strain distribution in the profile that finally defines the accuracy of the microstructural calculation. After simulation of the extrusion process, the profile geometry and calculated workpiece fields were then exported from QForm Extrusion to QForm General Forming finite element commercial code in.csv2d format for further simulation of cooling and static recrystallization that was carried out by means of the Heating–Cooling module.

Static recrystallized volume fraction was calculated by Johnson–Mehl–Avrami–Kolmogorov equation:

$$X_s = 1 - \exp\left[-0.693\left(\frac{t}{A_s \bullet \varepsilon^{N_s} \bullet \exp\left(\frac{Q_s}{RT}\right)}\right)^{k_s}\right], \quad (1)$$

where t is the time (s); ε is the retained strain; T is the temperature, °K; A_s, N_s, Q_s, k_s are the coefficients.

Average grain size in each node was calculated according to the mixture rule:

$$d_{\text{avg}} = d_s \bullet X_s + d_0(1 - X_s), \tag{2}$$

where d_s is the static recrystallized average grain size, μm; d_0 is the initial average grain size, μm.

2.3 Microstructure Characterization

The optical microscopy was used to characterize the microstructure. The samples were cut from the profile by a band saw and then were mounted in phenolic resin by mounting press Struers CitoPress-20. Samples were ground on abrasive clothes with successively finer grades of silicon carbide papers from 320 to 1200 grit and then polished with 0.1 μm diamond suspension. Olympus GX51 optical microscope was used to obtain images. Kellers etchant was used to reveal the microstructure. The average grain size has been evaluated by the planimetric procedure according to ASTM E1181-02 in certain areas of the samples followed by statistical processing with a significance level of 0.05. The software ImageJ (imagej.nih.gov/ij) was used for image analysis.

3 Results and Discussion

3.1 Static Recrystallization Model of 6XXX Aluminum Alloy Based on Industrial Experiments

Approach for development of static recrystallization model using industrial experiments is based on the inverse analysis. Profile section for investigation was cut out from the steady-state extrudate. To get an experimental average grain size distribution, it is necessary to choose a number of points on the profile and measure an average grain size in these points. QForm Extrusion simulation gives us such the process parameters in each point of the profile as strain, average deformation temperature, and strain-rate after extrusion. Using the assumption that static recrystallization is the only microstructure evolution process taking place according to Eqs. (1) and (2), it is possible to calculate an average grain size in every location after cooling. After that, the least square method could be used for obtaining the unknown coefficients A_s, N_s, Q_s, k_s. For this purpose, it is necessary to minimize the following target function:

Table 3 Parameters of 6XXX aluminum alloy static recrystallization model

A_s	N_s	Q_s	k_s
2.453E-5	−1.76	37,500	1.2

$$\Phi = \sum_{i=1}^{n} \left(d_{\exp_i} - d_{\mathrm{sim_i}}\right)^2, \tag{3}$$

where $d_{\exp}$ is the measured grain size, μm; d_{sim} is the simulated grain size, μm; n is the number of studied points.

Mathcad software was used for minimization of the target function by Levenberg–Marquardt algorithm. Obtained parameters of 6XXX aluminum alloy static recrystallization model are presented in Table 3.

3.2 Numerical and Experimental Study of Microstructure Evolution of 6XXX Aluminum Alloy

Obtained parameters of 6XXX aluminum alloy static recrystallization model were used to simulate average grain size distribution after cooling the profile.

The simulated average grain size in the profile cross-section is shown in Fig. 3. As we can see, grain size distribution is highly non-uniform and average grain size is within the range from 50 to 150 μm. Further study was focused on two regions of the profile cross-section, which are also shown in Fig. 3.

Grain size distribution in extruded profiles is highly dependent on the strain. Strain field in the profile is shown in Fig. 4.

We can see that strain values in the cross-section of the profile is in the range from 4.0 to 50.0. In general, the higher strain is in point, the lower average grain size. But there is a danger of secondary recrystallization occurrence, which may lead to abnormal grain growth. In the studied case, the profile has thin walls and cooling speed is sufficient to avoid the secondary recrystallization.



Fig. 3 Simulated average grain size distribution in the profile. (Color figure online)

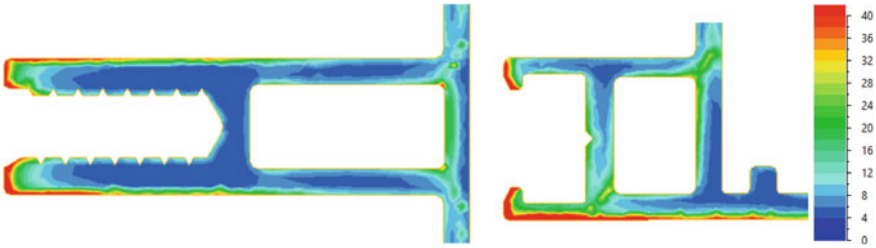


Fig. 4 The strain distribution in samples #1 and #2. (Color figure online)

Another feature of hollow profile aluminum extrusion technology is dividing the metal flow to a several streams and consequent welding due to high temperature and high pressure. Material streams in samples #1 and #2 are shown in Fig. 5.

Temperature in the studied part of the profile is highly uniform and equals 510 ± 10 °C (Fig. 6).

The simulated average grain size distribution and experimental microstructure in samples #1 and #2 are shown in Figs. 7 and 8, respectively.

As we can see, in most points correspondence is quite good, while in some points the difference is up to 1.5 times. Grain refinement in the welding seams can be seen on the simulated average grain size field. The correlation coefficient between experimental and simulated data is 0.89.



Fig. 5 Material streams in samples #1 and #2. The material from different streams is shown by different colors. (Color figure online)



Fig. 6 The temperature distribution in samples #1 and #2. (Color figure online)

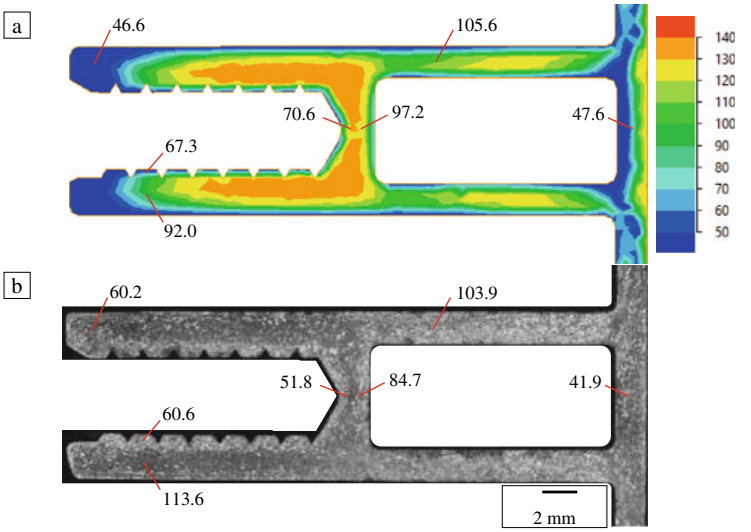
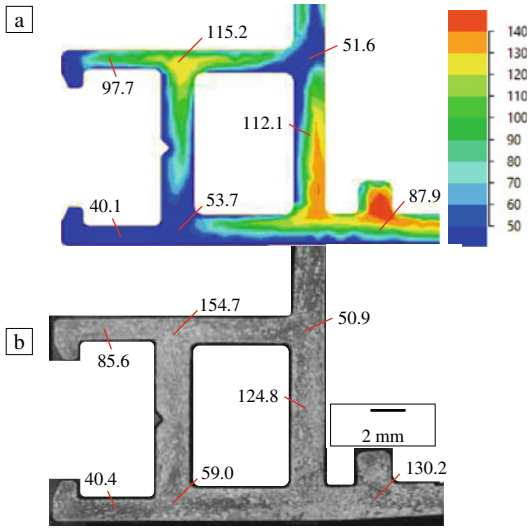


Fig. 7 The simulated average grain size **a** and experimental microstructure **b** of sample #1. (Color figure online)

Fig. 8 The simulated average grain size **a** and experimental microstructure **b** of sample #2. (Color figure online)



3.3 *Validation of the 6XXX Aluminum Alloy Static Recrystallization Model*

Experimental data for validation of the model is provided by ASAŞ Alüminyum Sanayi ve Ticaret A.Ş., Istanbul, Turkey (https://www.asastr.com/home).

The developed model of the static recrystallization was validated on another industrially extruded profile. This time the used aluminum alloy was 6063, which is in the same group of alloys as one used in the study.

The studied extruded profile has a complex shape and presented in Fig. 9. This is a solid profile with some detailed areas for assembling purposes.

The studied part of the extruded profile, macrograph, and microstructure is shown in Fig. 10. The zone for measurement of the average grain size is shown by the red square. The measured average grain size in this zone was 62.2 ± 4.8 μm.

Extrusion of the profile and consequent cooling was simulated. The simulated average grain size of the part of the extruded profile is shown in Fig. 11.

The studied area is shown by the red square on the profile. As we can see, the simulation predicts a high gradient of average grain size in the studied area. Average grain size varies approximately from 45 to 87 μm in the studied zone. Meanwhile, there is no such high gradient of the grain size in the extruded profile as can be seen in Fig. 10b. The simulated average grain size throughout the region was approximately 66 μm, which has good correspondence with experimental data.



Fig. 9 The studied extruded profile

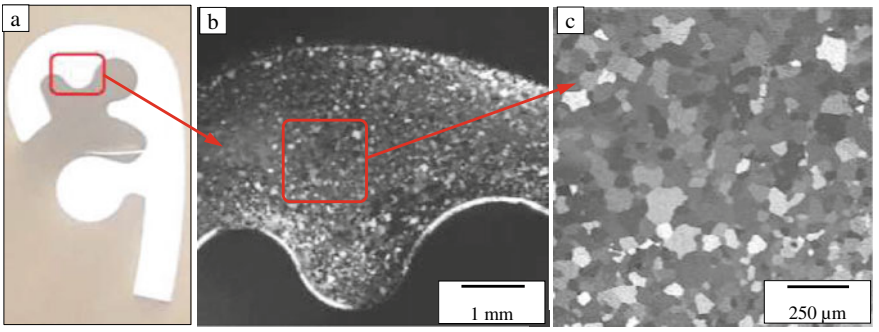


Fig. 10 The studied part of the extruded profile (**a**), macrograph (**b**), and microstructure (**c**). (Color figure online)

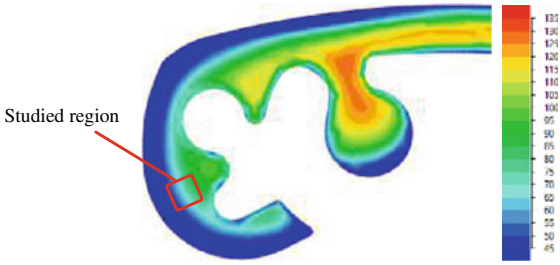


Fig. 11 The simulated average grain size of the part of the extruded profile. (Color figure online)

4 Conclusions

1. The microstructure of 6XXX aluminum the profiles after industrial extrusion process has been investigated and characterized.
2. The model of static recrystallization of 6XXX aluminum alloy based on industrial profiles extrusion analysis was developed and implemented in QForm finite element simulation code.
3. The new method of developing a microstructure evolution model using industrial experiments is quite simple and gives satisfactory results for preliminary analysis of profile microstructure.
4. The developed model was validated on 6063 aluminum alloy industrial extruded profile and shown satisfactory correspondence while further improvement is required.
5. Related processes of microstructure evolution should be taken into account to improve the accuracy of the average grain size calculation.

References

1. Bauser M, Sauer G, Siegert K (2006) Extrusion second edition. ASM international
2. Doherty RD, Hughes DA, Humphreys FJ, Jonas JJ, Jensen DJ, Kassner ME et al (1998) Current issues in recrystallization: a review. Mater Today 1(2):14–15
3. McQueen HJ (1980) The experimental roots of thermomechanical treatments for Aluminum alloys. JOM 32(2):17–26
4. Komura S, Horita Z, Nemoto M, Langdon TG (1999) Influence of stacking fault energy on microstructural development in equal-channel angular pressing. J Mater Res 14(10):7
5. Gardner KJ, Grimes R (1979) Recrystallization during hot deformation of Aluminium alloys. Met Sci 13(3–4):216–222
6. Yi Y, Fu X, Cui J, Chen H (2008) Prediction of grain size for large-sized aluminium alloy 7050 forging during hot forming. J Cent South Univ Technol 15(1):1–5
7. Yi Y, Shi Y, Yang J, Lin Y (2007) Effects of forging process parameters on microstructure evolution of Aluminum alloy 7050. In: AIP conference proceedings. AIP, p 481–486
8. Donati L, Dzwonczyk JS, Zhou J, Tomesani L (2008) Microstructure prediction of hot-deformed aluminium alloys. Key Eng Mater 367:107–116
9. Segatori A, Reggiani B, Donati L, Tomesani L, El Mehtedi M (2013) Prediction of fibrous and recrystallized structures in 6xxx alloy extruded profiles. Key Eng Mater 585:123–130

10. Bandini C, Reggiani B, Donati L, Tomesani L (2015) Code validation and development of user routines for microstructural prediction with qform. Mater Today Proc 2(10):4904–4914
11. Güzel A, Jäger A, Parvizian F, Lambers H-G, Tekkaya AE, Svendsen B et al (2012) A new method for determining dynamic grain structure evolution during hot aluminum extrusion. J Mater Process Technol 212(1):323–330
12. Miodownik MA (2002) A review of microstructural computer models used to simulate grain growth and recrystallisation in aluminium alloys. J Light Met 2(3):125–135
13. Biba N, Alimov A, Shitikov A, Stebunov S (2018) The implementation of microstructural and heat treatment models to development of forming technology of critical aluminum-alloy parts. AIP Conf Proc 1960:040004
14. Alimov A, Stebunov S, Biba N (2018) Simulation of microstructure evolution during forging and heat treatment of Ti-6Al-3.5Mo-1.5Zr-0.3Si titanium alloy. Comput Methods Mater Sci 18:90–97
15. Alimov A, Zabelyan D, Burlakov I, Korotkov I, Gladkov Y (2018) Simulation of deformation behavior and microstructure evolution during hot forging of TC11 titanium alloy. Defect Diffus Forum 385:449–454

The Effect of T8 Heat Treatment on Wear Behaviour and Microstructure of 6063 Aluminium Alloy Deformed by Cryo and RT ECAP



Srinivasulu Arnuri and Swami Naidu Gurugubelli

Abstract The effect of T8 heat treatment on wear behaviour of AA6063 was studied and precipitation kinetics was evaluated by SEM and XRD studies. AA6063 square rods of 9.5 mm X 9.5 mm X 100 mm were solution treated at 520 °C for 2 h and quenched in water. One set of samples was processed by ECAP at room temperature and the other set was processed by Cryogenic ECAP after soaking in liquid nitrogen for 20 min. A die of 108° channel intersection angle and 36° outer curvature angle was used and each sample was given four passes in route A and aged at 180 °C for different timings and results compared. Hardness measurements were obtained at regular intervals and peak hardness was observed after 90 min of ageing for both Cryo-ECAPed and RT-ECAPed alloys. The solution treated alloy ECAPed at cryogenic temperature has shown maximum wear rate during the initial stages of ageing and reached the minimum after 90 min and nearly same wear rate was maintained until the overaged condition. The solution treated alloy ECAPed at room temperature has shown minimum wear rate during the initial stages of ageing and reached the maximum at about 50 min and it was not consistent during the later stages. SEM studies were performed on worn-out samples at different time intervals during ageing and the wear behaviour of the alloy was correlated with the microstructures. The wear results obtained were in good agreement with the microscopic analysis.

Keywords Ageing · 6063 aluminium alloy · Wear · Hardness · Cryo ECAP

1 Introduction

Equal Channel pressing of Aluminium 6063 was carried out by two different routes named RT ECAP and CRYO ECAP following by ageing treatment done. These two types of speciments were subjected to wear test to study wear beaviour difference.

Severe Plastic Deformation (SPD) has received enormous interest over the last two decades as a method capable of producing fully dense and bulk sub microcrystalline and nanocrystalline materials. It has shown a major impact on the field of material

S. Arnuri (✉) · S. N. Gurugubelli
Department of Metallurgical Engineering, JNTUK-UCEV, Vizianagaram, Andhra Pradesh, India

© The Minerals, Metals & Materials Society 2021

G. Daehn et al. (eds.), *Forming the Future*, The Minerals, Metals & Materials Series,
https://doi.org/10.1007/978-3-030-75381-8_145

science [1, 2]. Equal Channel Angular Extrusion (ECAE) is one of the prominent procedures among the various severe plastic deformation techniques and has emerged as a widely known procedure for the fabrication of ultrafine-grained metals and alloys. Significant progress has been taking place in the development of ECAP in recent years, thereby suggesting there are excellent prospects for the future successful incorporation of the ECAP process into commercial manufacturing operations [3]. This technique allows obtaining ultra-fine grain in larger volumes; moreover, without change of its original cross-sectional area. The materials thus obtained can be used in automotive, military, and aerospace industries.

The 6063 aluminium alloy is a medium strength alloy commonly referred to as an architectural alloy. Its wide applicability is due to its good surface finish; high corrosion resistance, good weldability, and anodizing ability. Most commonly available as T6 temper and in the T4 condition, it exhibits good formability. The 6063 aluminium alloy is age-hardnable and it contains Mg and Si, which forms Mg_2Si during artificial or natural ageing. Several researchers worked on ageing and forming processes of these alloys and observed significant increase in hardness, strength, and other mechanical properties [4–12].

Post-ECAP ageing gives good strength along with ultrafine-grain size. Emanuela Cerri. Et al studied the influence of severe plastic deformation induced by post-ECAP ageing on the microstructure hardness and electrical conductivity [13]. Pre-ECAP solid solution treatment combined with post-ECAP ageing treatment has been found to be more effective than pre-ECAP peak-ageing treatment in enhancing the strength of a 6061 Al alloy [14]. Nicolae Serban et al. studied the die angle influence on ultimate compressive strength, yield strength, compression modulus, and microhardness and reported their observations [15]. Kameswari Bolem and Anandababu Varadala et al. said that microstructure and mechanical properties were highly improved after the third pass when the billets were pressed in route B_C through the dies having channel angle of 105° when Aluminium 5083 subjected to different passes and different die angle ECAP processes. [16]. Martin Fujda et al. studied the application of the optimal artificial-ageing regimes and observed that ageing after severe plastic deformation improved only the tensile ductility of the alloys. While their strength was slightly decreased because the softening effect caused by the solid solution recovery and the relaxation of the internal stress dominated over the hardening effect caused by the expected metastable β”- and β’-Mg_2Si phase precipitation during artificial ageing treatment [17].

Sushanta Kumar Panigrahi et al. worked with cryorolled and room temperature-rolled Al 6063 alloys and compared their mechanical properties. The ageing treatment of the severely deformed Al 6063 alloy has improved its strength and ductility significantly due to the precipitation hardening and grain coarsening mechanisms, respectively [18]. The work on the effect of cryogenic temperature on ECAP states that cryogenic temperature is supposed to suppress grain dynamic recovery in the cryogenic ECAP process, which provides gain in strength, tensile ductility, as well as a particularly uniform strain [19–21], This suppression of dynamic recovery is likely to preserve the high-density of defects, which could act as potential recrystallisation sites for the production of fine grain structures. Hence, ECAP at cryogenic

temperature has a promising role in the achievement of enhanced mechanical properties. However, literature on precipitation-hardenable alloys, especially on 6000 series alloys, is scarce. The improvement in the mechanical behaviour of AA2219, and AA6061, subjected to cryorolling followed by annealing and ageing treatment has been reported in literature [22, 23]. One of the known ways to improve the wear resistance of the heat treatable aluminium alloys is by using the artificial ageing [24]. YanboChen et al. studied and observed that high density dislocations can be observed inside some grains after eight cryoECAP passes, which obviously differs from the microstructure produced by ECAP at room temperature (RT-ECAP) for commercial pure Aluminium 1050.[25].

K. Sivaprasada et al. investigated the wear characteristics of the composite in the as-cast conditions by conducting abrasive wear test and slurry erosive test. Studies on abrasive wear behaviour of the metal matrix composites (MMCs) were also performed by varying parameters like wt% of TiB2 particles and load [26]. V. Daniel Jebin et al. studied the wear behaviour of Al6063 and observed that the wear rate decreased with weight percent of aluminium oxide [27]. S. Natarajan et al. worked on the sliding wear behaviour of Al 6063/TiB2 in situ composites at elevated temperatures [28]. The effect of humidity on the erosive wear of 6063 Al alloy was studied, by C. K. Fang and T. H. Chuang. They found that the humidity had a minor effect on the peak attack angle for target volume 7 loss, while its effects on the amount of volume loss and worn depth were significant and complex in most of the environmental conditions [29]. A. Karthikeyan and S. Nallusamy studied experimental analysis on Sliding Wear Behaviour of Aluminium-6063 with SiC Particulate Composites. They found from the experimental results that the sliding velocity greatly affects the wear rate, and on increasing the sliding velocity, the wear loss increases. It was also found that the wear loss decreases by increasing the amount of reinforcement element [30]. The effect of artificial ageing on wear properties of AA 6063 alloy was studied by M. Gavgali, Y. Totik, and R. Sadeler [31]. Wear studies on nano red mud particle aluminium matrix composites were performed by Satyanarayana G et al. and reported that the wear resistance significantly increases with reinforcement fraction up to some extent and then decreases [32].

The effect of T8 heat treatment on wear behaviour and microstructure of Cryogenic and room temperature Equi Chanel Angular Processed (ECAPed) 6063 aluminium alloy is studied in the present investigations. The wear behaviour of the alloy is correlated with the microstructures.

2 Materials and Method

Commercial Aluminium 6063 T6 graded with the chemical composition of 0.63 Mg, 0.43 Si, 0.15 Fe, 0.049 Cu, 0.03 Zn, 0.054 Mn, 0.005 P, and 98.6 Al considered as work material in this study. The square cross-sectional samples with the dimensions 9.5 mm X 9.5 mm size and 100 mm length were solution treated at 520 °C for 120 min and then water quenched for attaining a supersaturated solid solution. The treated

samples were divided into two sets. The first set of samples were processed for Cryo-ECAP after soaking for 20 min in liquid nitrogen(-196 °C) and another set of samples were processed for ECAP at room temperature directly after water quenching. All the samples were then severely deformed by pressing through a die having channel intersection angle of 108^0 and outer curvature angle of 36° for four passes in route A (no rotation of billet). The Molybdenum disulfide (MoS_2) lubricant was applied to all the faces of the billets and the square channels of the die before pressing. The computer-assisted universal testing machine (UTM) is used to perform the ECAP, as shown in Fig. 1a. The deformed billet in the exit channel of ECAP die is shown in Fig. 1b. Solution treated and CRYO treated after solution treatment samples shown in Fig. 1c and ECAPed samples were shown in Fig. 1d.

The billets deformed after dipping in liquid nitrogen required more pressing force than the other case and shiny surfaces were observed on the Cryo-ECAPed samples. Samples of 1:1 aspect ratio were obtained from the ECAPed alloys and aged at 180 °C for 500 min. Hardness measurements were obtained at the intervals of 15 min using Vickers hardness tester at an applied load of 300 gm and the average of three readings was noted after every 15 min. Wear tests were conducted using Pin-on-disc wear testing machine over a few samples of under aged, peak aged, and over aged. The specimens remain fixed and disc rotates during wear tests and the load was applied through a deadweight loading system to press the pin against the disc. The speed of the disc or motor rpm can be varied through the controller. The pin and the disc surfaces were polished with emery papers before conducting the test and tests were conducted as per ASTM G-99 standard under the unlubricated condition in a normal laboratory atmosphere at 50–60% relative humidity and a temperature of 28–32 °C.

3 Results and Discussion

The strength of the material increases tremendously due to the grain refinement and strain hardening the occurred by severe plastic deformation during ECAP. In addition, the increase in dislocation density during severe plastic deformation forms dislocation tangles, which, results in further strengthening of the alloy. The age hardening and wear behaviour of the alloy after four passes of ECAP at Cryogenic and RT are evaluated. SEM structures were obtained and the wear behaviour of the alloy is correlated with the microstructures.

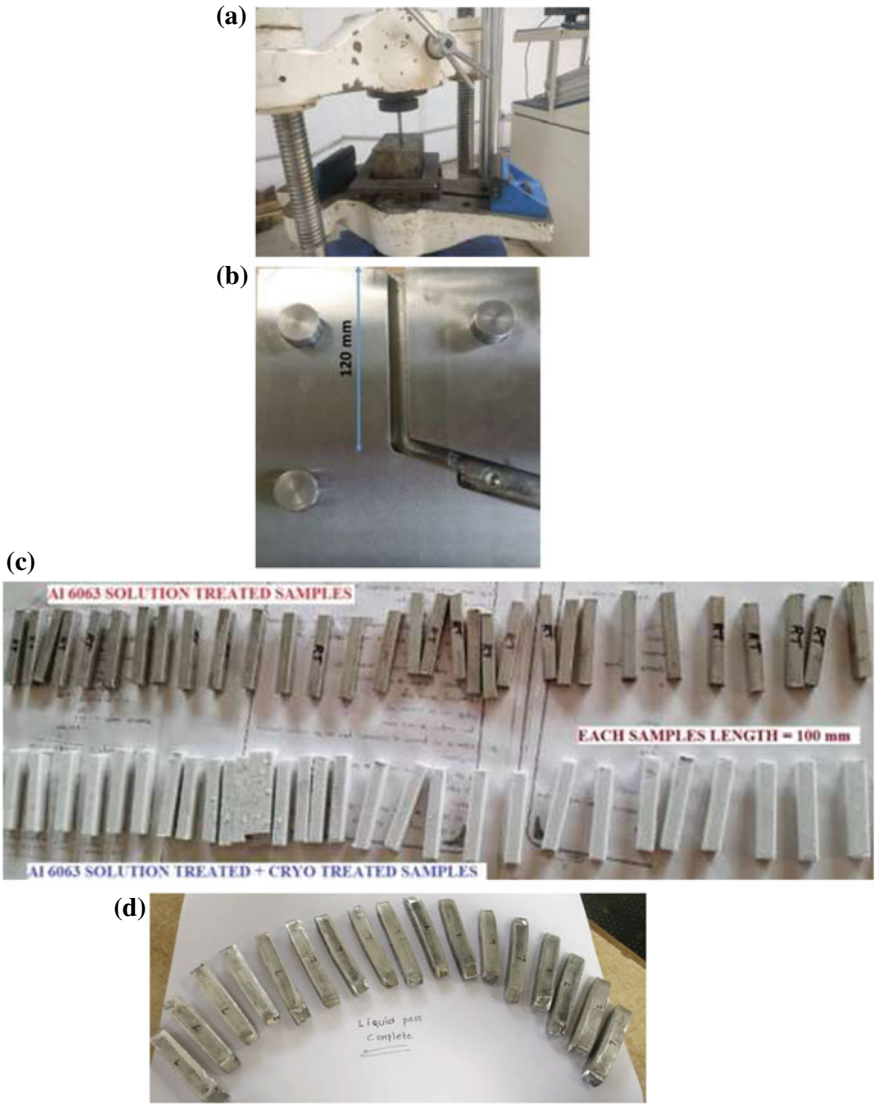


Fig. 1 **a** Experimental set-up of UTM for pressing. **b** ECAP die with deformed billet. **c** Al 6063 Solution-treated and Solution-treated + CRYO-treated samples. **d** ECAPed samples each 100 mm length. (Color figure online)

3.1 *Age Hardening Behaviour of Cryo-ECAPed and RT-ECAPed Alloys*

The T6 hardness curves of undeformed, room temperature ECAPed, and Cryogenic ECAPed alloys are shown in Fig. 2. The solution-treated alloy directly aged without ECAP at 180 °C has shown the peak hardness of 75 VHN after 400 min. The solution treated alloys ECAPed at cryogenic and room temperature have shown peak hardness at 90 min of ageing. Two microstructural phenomena including precipitation and restoration take place by performing ageing after ECAP. The precipitates formed during ageing will pin dislocations and obstruct the glide motion of dislocations. The restoration processes are a direct result of the loss via recovery and recrystallization, of the dislocations introduced by ECAP. Nucleation and growth of dislocation-free grains occur during recrystallization within the deformed structure. Thus, the T8 hardness of the ECAPed alloy is more compared to that of the undeformed alloy. The increase in dislocation density due to severe plastic deformation enhances the diffusion rate of Mg and Si through dislocation pipes and hence the peak hardness point was reached much earlier during ageing of ECAPed alloy than that of the alloy aged without ECAP. Further, the dislocations, act as nucleation sites and promotes the precipitation of β″ and β′ finely dispersed phases in the microstructure. The T8 hardness of cryogenic ECAPed alloy was observed as 120 VHN and that of the alloy ECAPed at room temperature was 112 VHN. ECAP at subzero temperatures, leads to the formation of ultrafine-grain structures and dislocation pinning by precipitates formed during ageing will be higher and hence, higher T8 hardness was observed for the cryogenic ECAPed alloy.

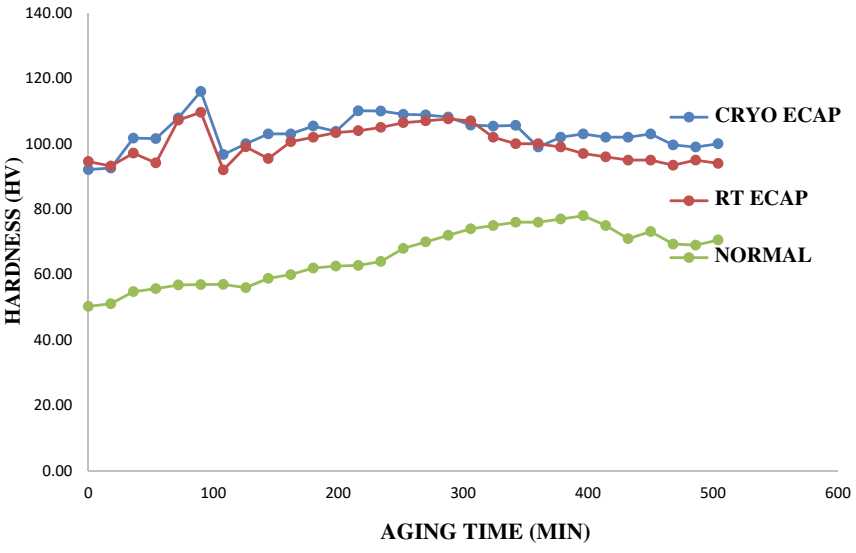


Fig. 2 Ageing curves for Cryo-ECAP and RT-ECAP conditions. (Color figure online)

3.1.1 SEM and EDX Analysis of the Alloy During Age Hardening

The scanning electron microscope (SEM) with Energy-Dispersive X-ray (EDX) spectroscopy attachment is used to perform the structural and elemental analysis on the precipitates formed in Cryo and RT-ECAPed Al6063 billets during ageing at 180 °C. The SEM images were obtained at 0 min, 90 min, 360 min of ageing and are shown in Fig. 3. At 0 min of ageing, ultrafine-grain structure is observed in the cryo-ECAPed alloy. With ageing, precipitates are formed and the coherency of precipitates is more for the cro-ECAPed alloy than RT-ECAPed alloy at 90 min of ageing. This is in agreement with the higher hardness obtained for the cryo-ECAPed alloy than the other(Fig. 4). Due to over ageing, the precipitates were grown and their coherency was also deviated in both the cases and the deviation is more for the

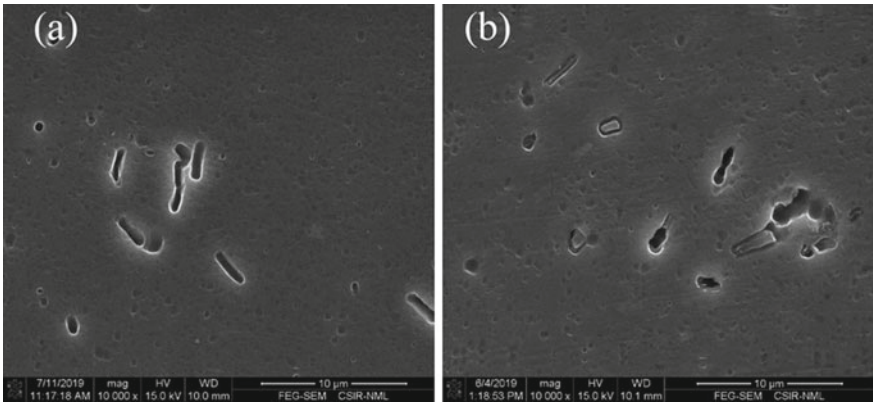


Fig. 3 SEM images of Al6063 at ageing time T = 0 min **a** Cryo ECAP **b** RT-ECAP

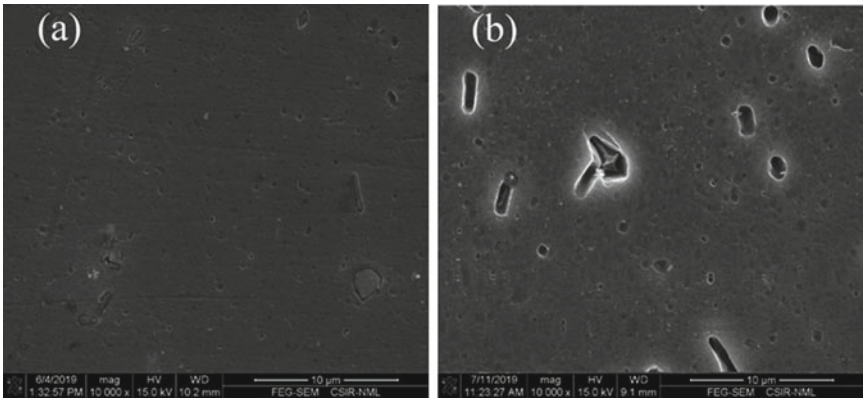


Fig. 4 SEM images of Al6063 at ageing time T = 90 min after **a** Cryo ECAP **b** RT-ECAP

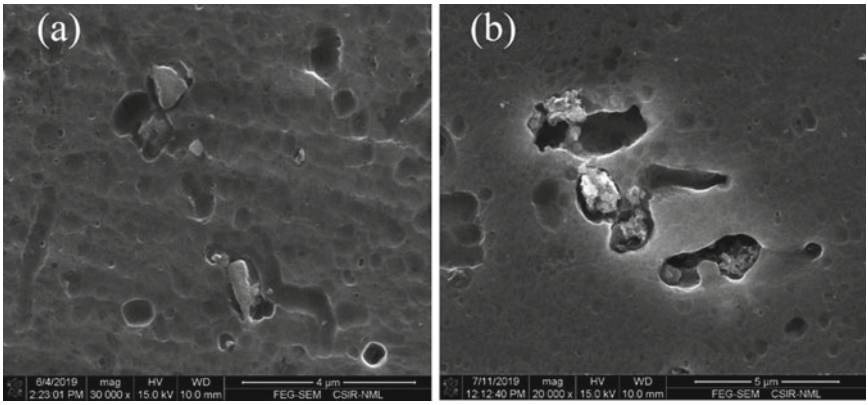


Fig. 5 SEM analysis of Al6063 at ageing time T = 360 min after **a** Cryo ECAP **b** RT-ECAP

RT-ECAPed alloy. Further, after 360 min of ageing, it has been observed tremendous growth of the precipitates in RT-ECAPed alloy and hence the hardness is not maintained consistently (Fig. 5).

The SEM and EDX analysis obtained for cryo-ECAPed and RT-ECAPed alloy at 90 min of ageing is depicted in Fig. 6a, b. From Fig. 6c, d it can be observed that a fraction of nitrogen is shown in the EDX of cryo-ECAPed alloy, which is due to the immersion in liquid nitrogen. A fraction of Ti is also observed and the formation of nitrides might be the reason for the higher hardness of cryo-ECAPed alloy compared to the RT-ECAPed alloy.

3.2 Effect of Ageing on Wear Behaviour of Cryo-ECAPed and RT-ECAPed Alloys

Wear rate was estimated by measuring the mass loss in the specimen after each test. The wear rate which relates to the mass loss to sliding distance (L) is calculated using the expression $W_r = \Delta m/L$. The curves showing wear rate of cryogenic and room temperature processed alloys aged at 180^0 C are shown in Fig. 7. The solution treated alloy ECAPed at cryogenic temperature has shown maximum wear rate during the initial stages of ageing and reached the minimum after 90 min and nearly same wear rate was maintained until the overaged condition. The solution treated alloy ECAPed at room temperature has shown minimum wear rate during the initial stages of ageing and reached to the maximum within 50 min and it was not consistent during the later stages. The strength of both the alloys was increased due to grain refinement and strain hardening that occurred by severe plastic deformation by ECAP. On the other hand, the deformation at subzero temperatures increases the brittleness of the alloy. Further, the liquid nitrogen immersion may lead to the formation of delaminated

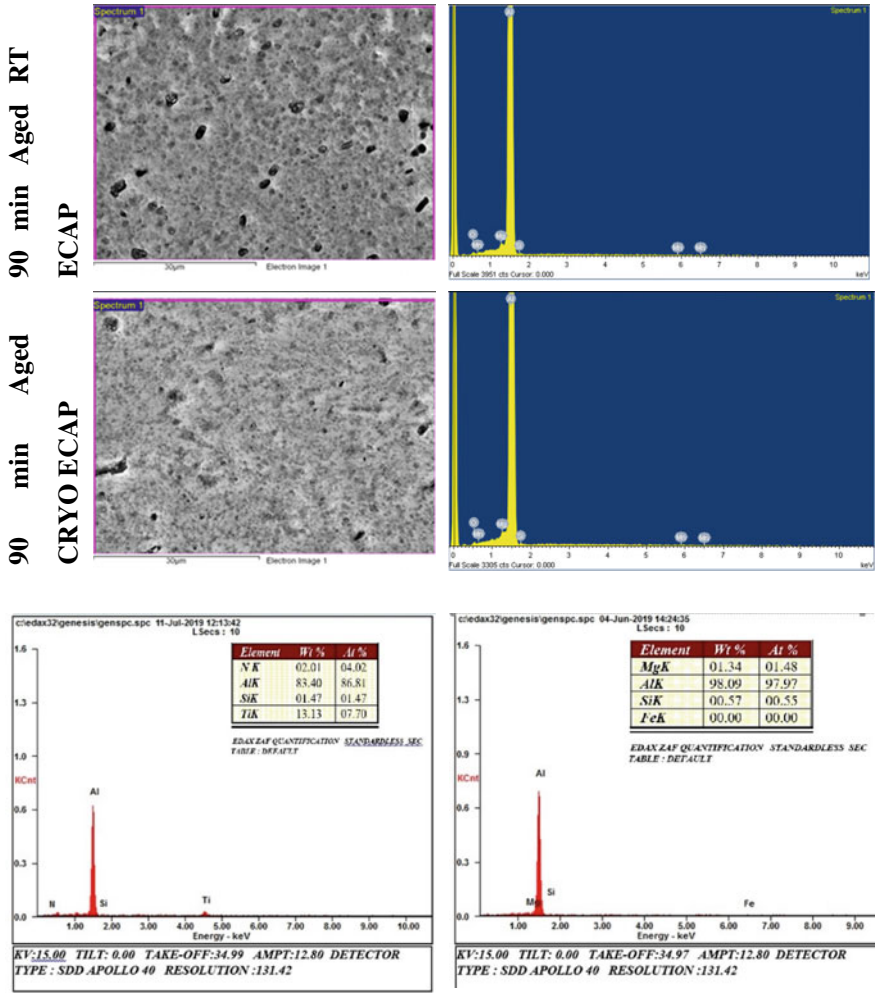


Fig. 6 **a** SEM and EDX images of 90 min hours aged RT ECAP. **b** CRYO ECAP. **c** EDX analysis of Al6063 at ageing time T = 90 min after Cryo ECAP. **d** EDX analysis of Al6063 at ageing time T = 90 min after RT-ECAP. (Color figure online)

layers and pits in case of cryo-ECAPed alloy. Hence, the alloy ECAPed at cryogenic temperatures has shown maximum wear rate during the initial stages of ageing.

3.2.1 SEM Analysis and Correlation with Hardness Behaviour

The wear test samples were observed under Scanning Electron Microscope and the SEM images of the cryogenic and room temperature ECAPed worn-out samples at 0 min of ageing are shown in Figs. 8 and 9 respectively. The Cryo-ECAPed fractograh

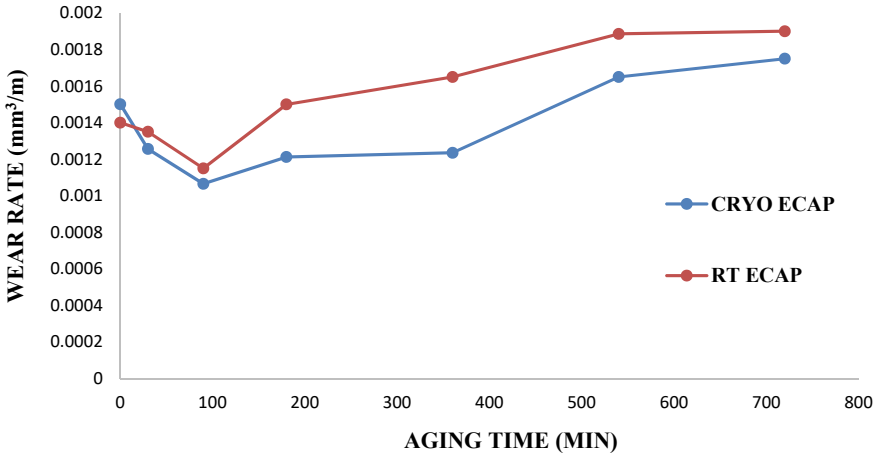


Fig. 7 Variation of wear rate with respect to the ageing time of Cryo and RT ECAPed specimens. (Color figure online)

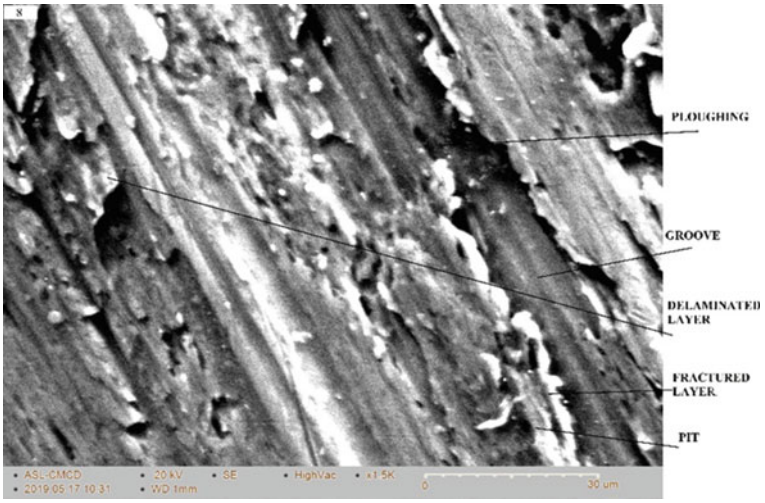


Fig. 8 Wear SEM analysis of Al6063 at ageing time T = 0 min after Cryo ECAP. (Color figure online)

shows groves, delaminated layers, ploughing places, and pits. This is due to the liquid nitrogen immersion effect. Grooves and small delaminated layers were also observed in the fractograph of room temperature ECAPed alloy but to a lesser extent as it is free from liquid nitrogen immersion. Therefore, the cryo-ECAPed alloy has shown a significantly higher wear rate at 0 min of ageing than that of room temperature

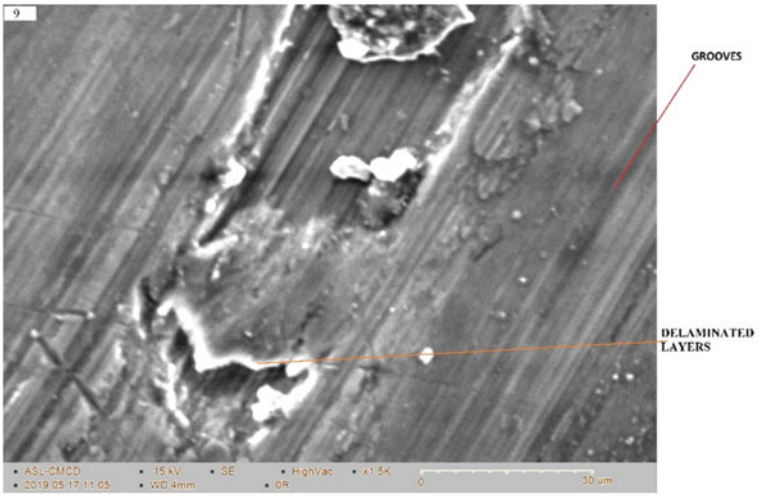


Fig. 9 Wear SEM analysis of Al6063 at ageing time T = 0 min after RT- ECAP. (Color figure online)

ECAPed alloy. Therefore, the SEM images are in consistent with the wear behaviour of the alloy.

The SEM images of the cryogenic and room temperature ECAPed worn-out samples at 90 min of ageing are shown in Figs. 10 and 11, respectively. The groves, delaminated layers, ploughing places, and pits are minimized in the Cryo-ECAPed

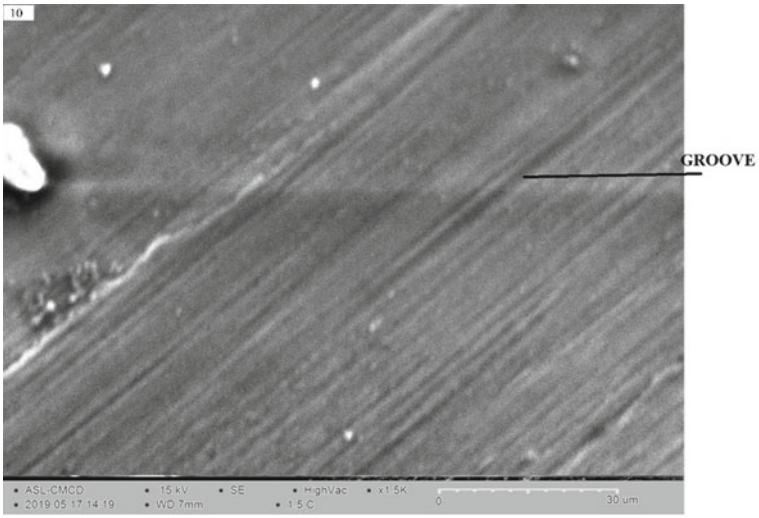


Fig. 10 Wear SEM analysis of Al6063 at ageing time T = 90 min after Cryo ECAP

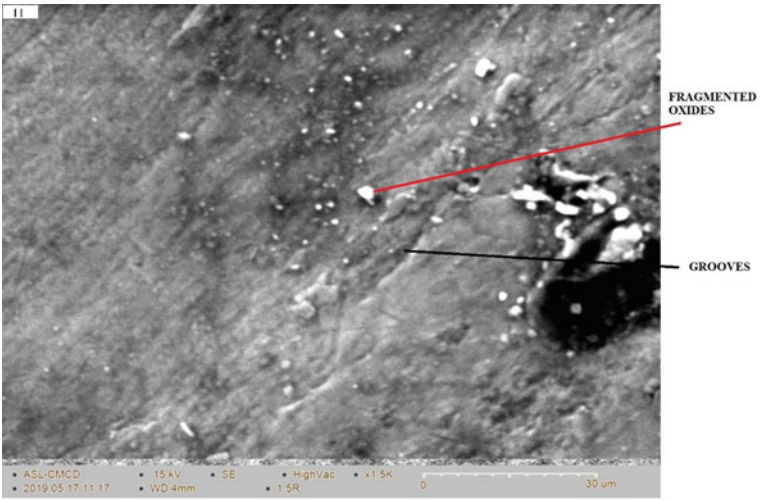


Fig. 11 Wear SEM analysis of Al6063 at ageing time T = 90 min after RT-ECAP. (Color figure online)

alloy after 90 min of ageing and are lowered even below that observed in the RT-ECAPed alloy. This might be the reason for the significantly decreased wear rate of Cryo-ECAPed alloy aged for 90 min. The SEM images are well in agreement with the wear behaviour of the alloys.

The SEM images of the cryogenic and room temperature ECAPed worn out samples at 360 min of ageing are shown in Figs. 12 and 13 respectively. Ageing

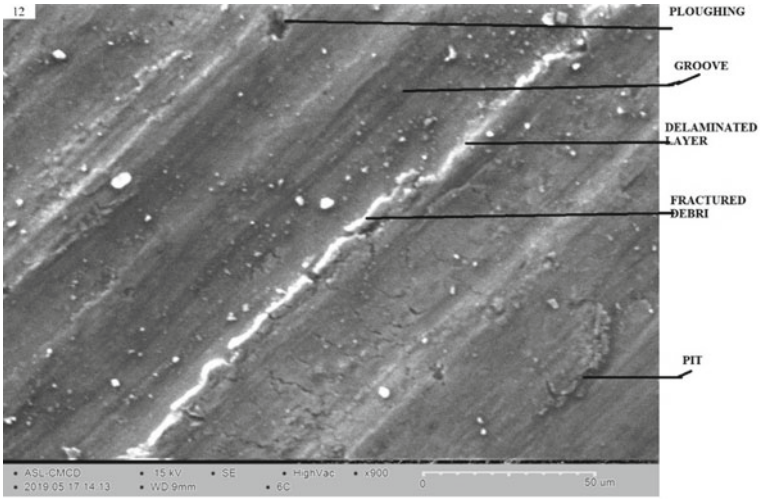


Fig. 12 Wear SEM analysis of Al6063 at ageing time T = 360 min after Cryo ECAP

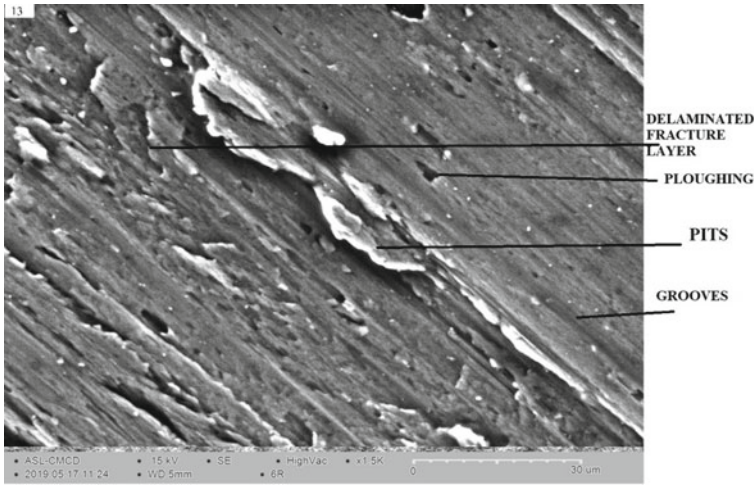


Fig. 13 Wear SEM analysis of Al6063 at ageing time T = 360 min after RT- ECAP

beyond 90 min, has caused a further increase in the formation of grooves, pits, and delaminated layers in the RT-ECAPed alloy and no such development was observed in Cryo-ECAPed alloy. Therefore, the wear rate was almost consistent at the minimum level for the Cryo-ECAPed alloy even during over ageing conditions. The observed SEM images are well correlated with the wear behaviour of the alloys.

4 Conclusions

The effect of T8 heat treatment on wear behaviour and microstructure of 6063 aluminium alloy is studied and the results are correlated. The following conclusions are drawn from the present experimental investigations.

1. The increase in dislocation density due to severe plastic deformation enhances the diffusion rate of Mg and Si through dislocation pipes and hence the peak hardness point was reached much earlier, i.e. at 90 min of ageing in case of ECAPed alloy, rather than that occurred at 480 min for the undeformed alloy.
2. The T8 hardness of cryogenic ECAPed alloy was observed as 120 VHN and that of the alloy ECAPed at room temperature was 112 VHN. ECAP at subzero temperatures, leads to the formation of ultrafine-grain structures and dislocation pinning by precipitates formed during ageing will be higher and hence, higher T8 hardness was observed for the cryogenic ECAPed alloy compared to the RT-ECAPed alloy.
3. The solution treated alloy ECAPed at cryogenic temperature has shown maximum wear rate during the initial stages of ageing and reached to the minimum after 90 min and nearly same wear rate was maintained until the

overaged condition. The liquid nitrogen immersion has led to the formation of delaminated layers and pits which was observed from the SEM images. This might be the reason for the higher wear rate.

4. The solution treated alloy ECAPed at room temperature has shown minimum wear rate during the initial stages of ageing and reached the maximum within 50 min and it was not consistent during the later stages.
5. Excellent agreement between the wear behaviour and microstructures is observed from the present investigations.

References

1. Estrin Y, Vinogradov A (2013) Extreme grain refinement by severe plastic deformation: A wealth of challenging science. Acta Mater 61(3):782–817
2. Langdon TG (2011) Processing by severe plastic deformation: Historical developments and current impact. In: Materials Science Forum, vol 667. Trans Tech Publications Ltd., pp 9–14
3. Valiev RZ, Langdon TG (2006) Principles of equal-channel angular pressing as a processing tool for grain refinement. Prog Mater Sci 51(7):881–981
4. Edwards GA, Stiller K, Dunlop GL, Couper MJ (1998) Acta Mater 46(11):3893
5. Matsuda K, Sakaguchi Y, Miyata Y, Uteni Y, Sato T, Kamio A, Ikeno S (2000) J Mater Sci 35 179
6. Matsuda K, Gamada H, Fuji K, Uteni Y, Sato T, Kamis A, Ikeno S (1998) Metall Mater Trans 29A:1161
7. Perovic A, Perovic DD, Weatherly GC, Lloyd DJ (1999) Scripta Mater 41(7):703
8. Gupta AK, Lloyd DJ (1999) Met Trans 30A:879
9. Miao MF, Laughlin DE (1999) Scripta Mater 40(7):873
10. Gupta AK, Lloyd DJ (1995) Proceedings of 34th annual conference on recent metallurgical advances in light metal industries. In: MacEwen S, Galardeau J-P (eds) The metallurgical society of the canadian institute of mining, metallurgy and petroleum, Vancouver, British Columbia, August 20–24, p 243
11. Muruyama N, Uemori R, Hashimoto N, Saga M, Kikuchi M (1997) Scripta Mater 36(1):89
12. Lynch JP, Brown LM, Jacobs MH (1982) Acta Metall 30:1389
13. Cerri E, Leo P (2005) Influence of severe plastic deformation on aging of Al–Mg–Si alloys. Mater Sci Eng A 410–411:226–229
14. Kim JK, Jeong HG, Hong SI, Kim YS, Kima WJ (2001) Effect of aging treatment on heavily deformed microstructure of a 6061 aluminum alloy after equal channel angular pressing Author links open overlay panel. Scripta Materialia 45(8):901–907
15. Serban N, Ghiban N, Cojocaru V-D Mechanical behavior and microstructural development of 6063-T1 aluminum alloy processed by equal-channel angular pressing (ECAP): die channel angle influence
16. Bolem K, Varadala S, Swaminaidu G Equal channel angular pressing of aluminium alloy 5083 using different die geometries
17. Fujda M, Matvija M, Kva T, Milkovi O, Zubko P, Nagyová K STRUKTURA IN LASTNOSTI ZLITIN AlMgSi, STARANIH PRED ECAP IN PO NJEM, UDK 669.715:621.785.7:620.17 ISSN 1580-2949 Original scientific article/Izvirni znanstveni ~ lanek
18. Panigrahi SK, Jayaganthan R, Pancholi V (2009) Effect of plastic deformation conditions on microstructural characteristics and mechanical properties of Al 6063 alloy. Mater Des 30(6):1894–1901
19. Baldissera P, Delprete C (2008) Open Mech Eng J 2:1
20. Schiradelly R, Diekman FJ (2001) Heat Treat Prog: 43

21. Kalia S (2010) J Low Temp Phys 158:934
22. Chen YB, Li YL, He LZ, Lu C, Ding H, Li Q.Y (2008) The influence of cryoECAP on microstructure and property of commercial pure aluminum. Mater Lett 62:2821–2824
23. Shanmugasundaram T, Murty BS, Sarma VS (2006) Development of ultrafine grained high strength Al–Cu alloy by cryorolling. Scr Mater 54:2013–2017
24. Suresh S, Vasudevam AK, Bretz PE (1984) Metall Trans A 15:369–372
25. Chen Y, Li [Y,] He L, Lu C, Ding H, Li Q The influence of cryoECAP on microstructure and property of commercial pure aluminum
26. Sivaprasad K, Babu SK, Natarajan S, Narayanasamy R, Kumar BA, Dinesh G (2008) Study on abrasive and erosive wear behaviour of Al 6063/TiB2 in situ composites. Mater Sci Eng A 498(1–2):495–500
27. Jebin VD, Shivalingappa D, Rino JJ (2013) Wear behavior of AL6063-alumina metal matrix composite. Wear 3(92):8
28. Natarajan S, Narayanasamy R, Babu SK, Dinesh G, Kumar BA, Sivaprasad K (2009) Sliding wear behaviour of Al 6063/TiB2 in situ composites at elevated temperatures. Mater Des 30(7):2521–2531
29. Fang CK, Chuang TH (1999) The effect of humidity on the erosive wear of 6063 Al alloy. Wear 236(1–2):144–152
30. Karthikeyan A, Nallusamy S (2017) Experimental analysis on sliding wear behaviour of aluminium-6063 with SiC particulate composites. JERA 31:36-43.
31. Gavgali M, Totik Y, Sadeler R (2003) The effects of artificial aging on wear properties of AA 6063 alloy. Mater Lett 57(24–25):3713–3721
32. Satyanarayanaa G, Swami Naidub G, Hari Babu N (2018) Artificial neural network and regression modelling to study the effect of reinforcement and deformation on volumetric wear of red mud nano particle reinforced aluminium matrix composites synthesized by stir casting. Boletín de la Sociedad Española de Cerámica y Vidrio 57(3):91–100

Metal Foils for Bipolar Plates—Correlation of Initial Grain Size and Forming Behavior of 316L



Alexander Bauer, Thomas Mehner, Birgit Awiszus, and Thomas Lampke

Abstract As the forming of metallic bipolar plates is mostly still in the state of research, the underlying forming mechanisms are not fully understood. This study deals with the topic of different grain sizes in the initial metal sheets and their influence on the forming results. Therefore, a work-hardened 316L-foil (0.1 mm) was processed with different heat treatment strategies resulting in three different grain sizes with average grain diameters of 47.4, 19.3, and 7.9 μm. Afterward, all heat-treated blanks were cut and deep-drawn between two rigid dies to form a bipolar plate flow field. Besides force and geometrical factors like thinning and springback, the microstructure was analyzed by XRD and EBSD. Using these characterization methods, the mechanisms of twinning and preferred deformation of specific grain orientations during the forming process can be identified. Therefore, the impact of size effects on the forming behavior of metallic bipolar plates is shown. It can be concluded that a fine-grained initial state is preferable.

Keywords Bipolar plates · Microstructure · Forming · 316L

1 Introduction

Metallic bipolar plates for Proton-Exchange Membrane (PEM) fuel cells are a promising component in the context of relevant topics like resource efficiency and the reduction of emissions in the mobility sector. An application of metallic bipolar plates can significantly reduce manufacturing costs and therefore help the PEM fuel cell to achieve a widespread market penetration in general. Nevertheless, the mass

A. Bauer (✉) · B. Awiszus
Faculty of Mechanical Engineering, Virtual Production Engineering, Chemnitz University of Technology, Institute of Machine Tools and Production Processes, Reichenhainer Straße 70, 09126 Chemnitz, Germany
e-mail: a.bauer@mb.tu-chemnitz.de

T. Mehner · T. Lampke
Materials and Surface Engineering, Faculty of Mechanical Engineering, Chemnitz University of Technology, Institute of Materials Science and Engineering, Erfenschlager Straße 73, 09125 Chemnitz, Germany

© The Minerals, Metals & Materials Society 2021

G. Daehn et al. (eds.), *Forming the Future*, The Minerals, Metals & Materials Series,
https://doi.org/10.1007/978-3-030-75381-8_146

production of metallic bipolar plates is still being researched. One reason for that is the underlying forming mechanisms of metal foils, which are not easily scaled down from conventional thicknesses to thicknesses of of 0.5 mm. The related size effects, which cause these kinds of differences, were analyzed in several publications. *Tiesler* et al. provide a good overview about the size effects that occur in deep-drawing processes, for instance, the increasing influence of single grains [1]. For a comparison of metal sheets (thicknesses > 1 mm) with the corresponding metal foils (<25 µm) of aluminum and unalloyed steel, it was found that the friction values increased during the forming of the metal foils, while the limited drawing ratio decreased [2]. Other scientists found out that the anisotropy values decreased and the yield strength as well as the tensile strength increased with a rising number of grains over the sheet thickness of 0.1 mm in 1.4301 stainless steel foils [3, 4]. Several other publications also dealt with the appearance of size effects during the forming of copper foils [5, 6] or aluminum [7, 8]. In general, it can be seen that the particular forming mechanisms of metal foils are mostly analyzed separately and without a special focus such as the use as a bipolar plate. In this article, the relevant effects are analyzed concerning the requirements for bipolar plates. Therefore, three different grain sizes, which were generated from the initial metal foils and which were subsequently formed to bipolar plate-shaped test samples, were analyzed. Besides general methods for the analysis of the macro- and microscopical geometry development, X-ray diffraction (XRD), and electron backscatter diffraction (EBSD) were used to achieve an in-depth understanding of the microstructural phenomena, which appear during the forming process. On the one hand, this leads to better insights into the forming process and the parameters that affect it. On the other hand, the knowledge gained from this research results in a recommendation of an initial state of the metal foils which differs from those currently used for the majority of semi-finished products for metallic bipolar plates.

2 Materials and Methods

The initial material was a conventional 316L (1.4404) stainless steel foil with a thickness of 0.1 mm in a work-hardened state. The chemical composition (mass fraction) is specified as follows: C: 0.02%; Si: 0.41%; Mn: 1.34%; P: 0.03%; S: 0.004%; Cr: 16.64%; Ni: 10.01%; Mo: 2.00%. The tensile strength was 1274 MPa, which is an increase of about 85% compared to the annealed material state. In preparation for the heat treatments, the samples were cut from the coil with a stationary precision cutting machine to a size of 80 mm × 50 mm. Afterward, the cut samples were heat-treated in a *Torvac 12 Mark IV* vacuum furnace. The required temperatures in order to achieve three significantly different grain sizes were obtained from preliminary investigations (Table 1).

Subsequent to the holding times from Table 1, the samples were slowly cooled down to room temperature within the furnace, under vacuum condition, and without additional coolants.

Table 1 Different grain sizes with associated heat treatment parameters

Requested grain size	Nomenclature	Temperature (°C)	Duration (h)
Coarse (≈50 µm)	316L-CG	1100	0.5
Medium (≈25 µm)	316L-MG	970	1
Fine (≈7.5 µm)	316L-FG	850	1

After the heat treatment, four specimens of each material state (316L-CG, -MG, -FG) were formed within a four-column servo press (*Hegewald & Peschke Meß- und Prüftechnik GmbH*) (Fig. 1a). This forming machine, which is specialized in performing microforming operations with high accuracy, enabled a precise forming process with an identical start at a pre-force of 150 N, a velocity of 1 mm/s, and a defined stop at a drawing gap of 0.12 mm. This gap was combined from the sheet thickness (0.1 mm) and an additional offset (0.02 mm). No additional lubrication was used. The geometry was defined by a rigid punch and a rigid die with the shape of relevant bipolar plate channel geometries and a circumferential outer structure (Fig. 1b, c). Figure 1c shows the relevant channel dimensions: RE: entry radius, RG: ground radius, BW: bottom width, FA: flank angle, and h: channel height.

Subsequent to the forming operation, a variety of evaluation methods was used to examine the results. First of all, the geometry evolution was analyzed on the macro- and microscale. The macroscale investigations were carried out with a photogrammetric *GOM ATOS Core* system, which digitized the formed 3D geometry and enabled a separate evaluation with a direct comparison of the CAD or FEM geometry in the software tool *GOM* Inspect (Fig. 2 left, middle). For this comparison, four spots on the edge of the flow field were defined at first. In the second step, the perpendicular distance between the experimental GOM geometry and the CAD or FEM result was measured to determine the differences in the geometrical development.

The channel thinning was analyzed with micrographs from the channel cross sections under an optical microscope. Therefore, the samples were prepared with a

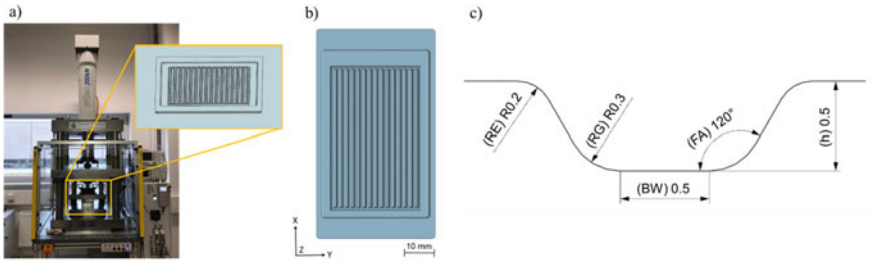


Fig. 1 Left: Servo press with enlarged CAD-surface of die [9]; middle: top view of a test sample [9]; right: channel cross section of a test sample [according to 10]. (Color figure online)

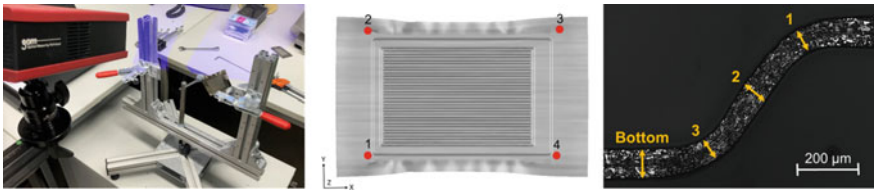


Fig. 2 Left: GOM measurement; middle: arrangement of measurement positions for comparison of the macroscopic geometry; right: arrangement of measurement positions for thinning. (Color figure online)

Discotom cutting machine transversal to the channels, embedded in epoxy resin, and subsequently polished and etched to show microstructural features. Afterward, the specimens were analyzed and measured under an *Axiovert 200* microscope with the corresponding software *AxioVison*, both from the *Carl Zeiss AG*. The results were averaged from three different channels in the middle of the flow fields. Furthermore, four different spots were measured for each channel: upper radius, flank, lower radius, and bottom (Fig. 2 right).

Furthermore, the roughness was evaluated with a *VK-X1000* confocal microscope from the *Keyence Corporation*. The measurements by focus variation were implemented at an area of 5.5 mm × 4.5 mm and consecutively examined within the *Keyence Multi-File-Analyzer* software. Therefore, multiple measuring sections were defined at the channel top, the flank, and the channel bottom and afterwards combined to a mean value.

To achieve a deeper understanding of the microstructural phenomena like twinning and grain orientation dependent deformation, EBSD was used. The experiments were conducted in a *Neon 40EsB* scanning electron microscope of the *Carl Zeiss AG* using a voltage of 15 kV and a sample tilt of 70°. The step size was 0.1 µm. For the evaluation, the software *TEAM EBSD Analysis System* (*EDAX Inc.*) was used. A cleanup has been performed using Grain Confidence Index Standardization (tolerance angle 15°) and Neighbor Confidence Index Correlation (minimum confidence index of 0.2). All of the EBSD images were taken from the upper radius area as one of the spots, which is affected the most by the forming process (Fig. 3).

Further investigations of the microstructure were done by XRD using a diffractometer *D8 Discover* (*Bruker AXS*) with Co Kα radiation (tube parameters: 40 kV,

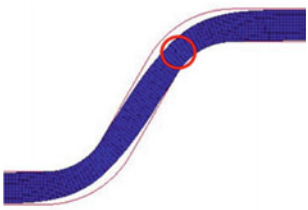


Fig. 3 Position of the EBSD measurements (red mark). (Color figure online)

40 mA), polycap optics for beam focusing, a pinhole aperture with a diameter of 0.5 mm, and an energy-filtered 1D detector Lynxexe XE. A step size of 0.02° with a measurement time of 7.2 s/step. Microstrains (peak broadening caused by lattice defects) and crystallite sizes were evaluated using the program *TOPAS* (*Bruker AXS*).

3 Results and Discussion

3.1 Heat Treatments of the Metal Foils

The 316L stainless steel foil was used in a work-hardened state to enable recrystallization with a broad spectrum of possible grain sizes (Fig. 4). Besides the average grain diameter (316L-CG: 47.4 µm; 316L-MG: 19.3 µm; 316L-FG: 7.9 µm), the micro-sections of all different grain sizes show the presence of crystal twins. One reason for the occurrence of the crystal twins in face-centered cubic materials is the tendency to develop twins during annealing processes [11]. On the one hand, a higher amount of annealing twins can be seen in the fine-grained specimen (316L-FG) due to its smaller grain sizes. On the other hand, the ratio of the total length of the boundaries of crystal twins to the total length of grain boundaries in general is lower in the fine-grained specimen (316L-FG) than in the coarse-grained specimen (316L-CG). This implies that the impact of the twins on the forming behavior, as a possible boundary for the accumulation of dislocations, has to be analyzed based on forming experiments. All forming-relevant mechanical properties, like flow and forming limit curves, were affected by the heat treatments. This has previously been discussed by the authors [9].

For comparison, a work-hardened and an annealed state of 316L foil were measured by XRD to analyze the amount of dislocations (i.e., microstrains, which are directly connected to the presence of dislocations). The measured microstrain of the work-hardened state was 0.47, in contrast to the annealed state, for which the microstrain is below the detection limit. According to the measured values, the investigated samples showed a complete recrystallization after the heat treatments with the temperatures given in Table 1.

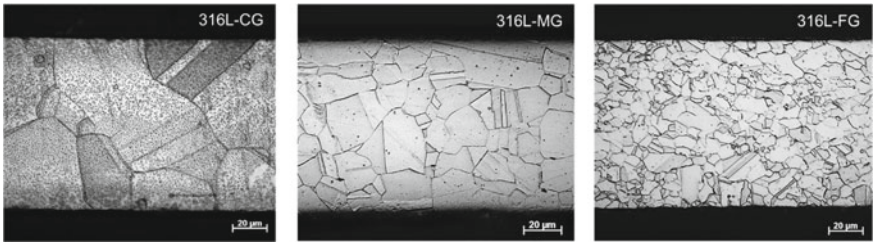


Fig. 4 Microsections of 316L with different heat treatment temperatures

3.2 Forming Experiments

All specimens were intentionally formed without a binder (blank holder) to show the impact on the forming results more clearly and unaffected by additional material flow controlling technologies (Fig. 5). A comparison of the required forming forces between the samples of different grain sizes showed no significant differences. Therefore, it is not discussed in more detail within this publication. In general, the sheets of all grain sizes reached the final shape at approximately 90 kN.

At first sight, it can be directly seen that the three grain sizes show different values for the distortion caused by the springback of the samples. The springback of the coarse-grained specimens (316L-CG) is the lowest, whereas for 316L-MG and 316L-FG, it is almost identical. This classification can be confirmed in the photogrammetric analyses. The coarse-grained specimens show the lowest perpendicular deviation between the experimental geometry and the CAD construction (Fig. 6). The wrinkles in all specimens appear as the reason for the stresses connected with the material flow into the die.

The corresponding values of all samples can be found in Table 2.

Regarding the detected springback effect and the related accuracy of the forming result, the coarse-grained specimens show the best values for a forming process without binder. As the macrostructural development of the geometry is just one factor which has to be considered for a comparison of initial material states. Further aspects have to be examined for a reliable statement.

The thinning behavior of the three grain sizes is shown in Table 3. The fine-grained and the middle-grained specimens look almost identical in regards to the thinning.

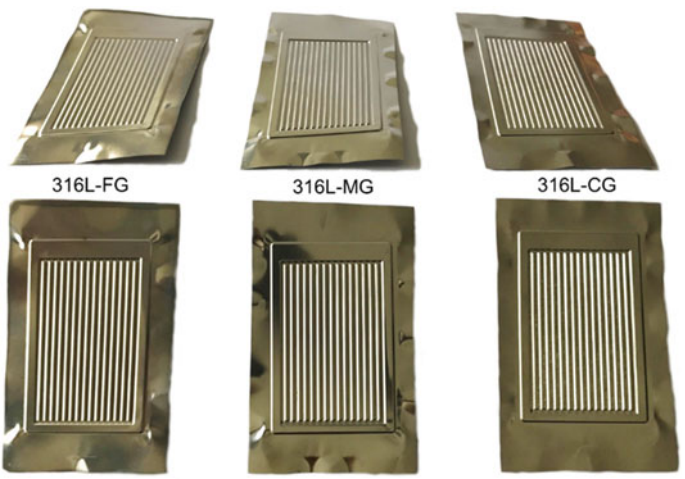


Fig. 5 Forming results for different heat-treatment temperatures and without binder. (Color figure online)

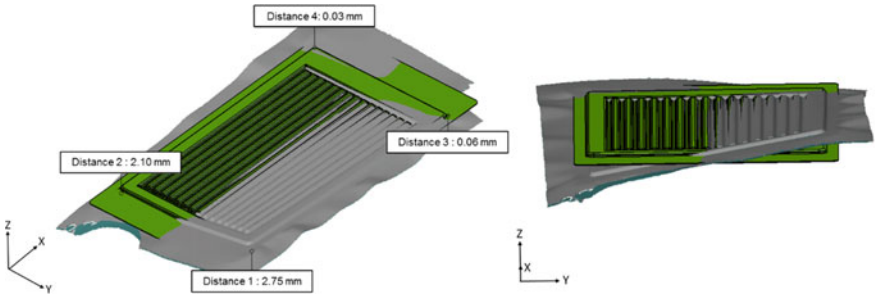


Fig. 6 Differences of 316L-MG between CAD geometry (green) and experimental forming results (gray). (Color figure online)

Table 2 Comparison of the distances between experiments and CAD construction

	Deviations forming versus CAD (mm)		
Measuring point	316L-CG	316L-MG	316L-FG
Distance 1	+1.75	+2.75	+3.20
Distance 2	−1.32	−2.10	−2.10
Distance 3	−0.02	−0.06	−0.04
Distance 4	+0.06	+0.03	+0.07

Table 3 Comparison of the thinning in the formed specimens with different gain sizes

Measuring point	316L-CG	316L-MG	316L-FG
Bottom, reference value (μm)	98.9	96.1	98.2
	Thinning (%)		
1. Channel top radius	23.5	23.0	25.4
2. Flank	20.0	13.4	14.6
3. Channel bottom radius	23.1	19.0	21.8

The greatest difference can be seen in the coarse-grained specimen, which shows a more uniform thinning, even in the channel flanks.

The coarse-grained specimens show excess thinning effects in a few channel flanks over the whole specimen, which is not considered in the mean values of Table 3. An example is shown in Fig. 7.

For comparability, these exceptional cases were not considered for the values in Table 3 as only just a few channels were affected by this exaggerated thinning, but in terms of the microstructural effects, these cases are of special interest. The otherwise similar values of the thinning require an in-depth investigation in order to understand the additional effects caused by the forming and their influence on the future application in fuel cells. Thus, the measurements of the thinning were directly correlated to the results from the EBSD. The differences in the material-flow behavior

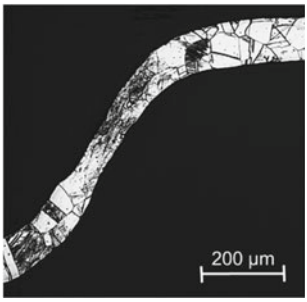


Fig. 7 Example for excess thinning in the channel flanks of 316L-CG

and the grain structure result from the specific microstructure of the specimens with different grain sizes.

During the analysis of the medium grain sizes, the annealing twins, which were caused by the heat treatment, were still clearly visible (Fig. 8, left). Most of them can be seen for orientations close to {111} (blue, violet) or {001} (red, orange). The right image of Fig. 8 shows the forming twins as well as the annealing twins with red lines. The formation of forming twins is related to energetic reasons. While crystallographic slipping is the main forming mechanism, which appears in ductile materials, plastic deformation can also be enabled by twinning [12]. In the length measurements of the grain and twin boundaries in all measured grains, almost identical values can be measured for both boundary types (total length grain boundaries: 4.40 mm; total length twin boundaries: 4.47 mm). However, not all of the twin boundaries could be

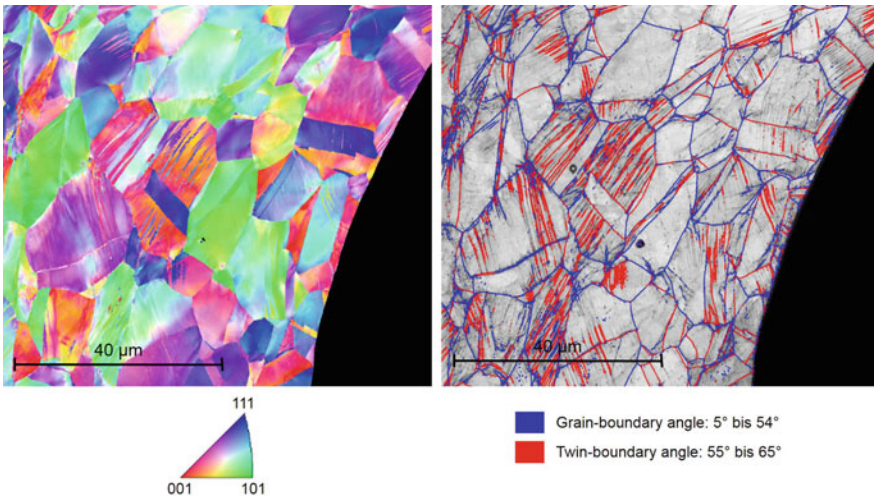


Fig. 8 EBSD micrographs of formed 316L-MG, left: grain orientation (inverse pole figure), right: grain (blue), and twin (red) boundaries. (Color figure online)

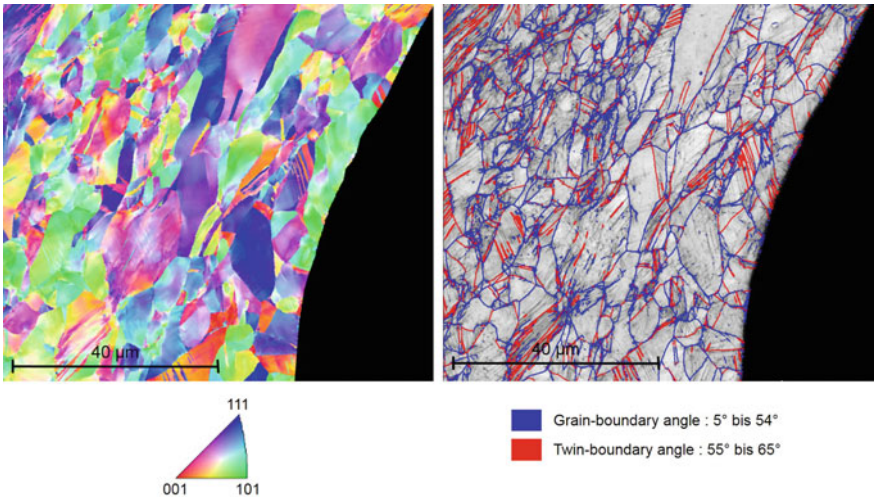


Fig. 9 EBSD micrographs of formed 316L-FG, left: grain orientation (inverse pole figure), right: grain (blue), and twin (red) boundaries. (Color figure online)

analyzed due to their small width and the limited resolution of EBSD. With a closer analysis of Fig. 8, the annealing twins can still be observed by their characteristic straight boundaries. In the left image, the forming twins can be identified as sharp, wide bands within the grains.

The evaluation of the EBSD image of a 316L-FG specimen showed a similar deformation as seen in 316L-MG, as there exists a variety of grain boundaries (Fig. 9). Therefore, a homogenous deformation is possible for the medium as well as for the fine-grained sizes (Table 3). Further refinement of the grain size would not change the thinning significantly.

In a direct comparison between 316L-FG and 316L-MG, it can be seen that the fine-grained specimen developed less forming twins. The total length of all grain boundaries comes to 6.55 mm, whereas the twin-boundary length just reached a total of 3.85 mm. This means that the summed-up length of grain boundaries is nearly twice as large as for the twin boundaries, while the ratio within the medium grain sizes was almost equivalent. The reason is the higher number of possible slip planes in the fine-grained specimen, which is more favorable for the forming mechanisms from the energetic point of view. This means that the size effects have a higher impact on the forming mechanisms with a decreasing amount of grains over the thickness of the specimen. In particular, this can be seen most clearly for the coarse-grained specimen 316L-CG (Fig. 10).

The microsections in Fig. 7 already showed that some of the flanks within the 316L-CG samples underwent an excess thinning. One reason for this material behavior is that some areas of the 316L-CG samples are only one or two grains thick. This means that in parts of the sample there is no possibility for crystallographic slipping, which results in a significant stretching of single grains and thus

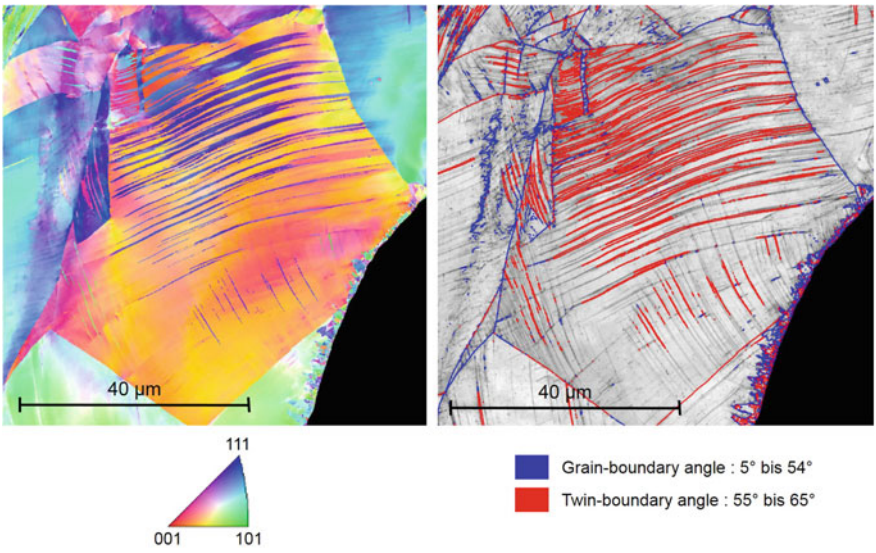


Fig. 10 EBSD micrographs of formed 316L-CG, left: grain orientation (inverse pole figure), right: grain (blue), and twin (red) boundaries. (Color figure online)

unwanted thinning in formed areas. Such a material behavior can also be referred to as a size effect, which means that there are changes in the plasticity between highly fine-grained materials and local areas with fewer grains over the specimen's thickness. This can also be concluded from the EBSD analysis in Fig. 10. The total amount of crystal twins, which occur during the forming process, are more than double the length as the grain boundaries (total length of grain boundaries: 2.34 mm; total length of twin boundaries: 5.07 mm; some very thin twin boundaries are not included). This implies that the samples lack slipping planes and therefore crystal twinning became the major forming mechanism. In combination with the presence of only one or two single grains across the thickness, this leads to increased thinning effects.

Concluding the analyses of the thinning behavior and the crystallographic effects, the fine-grained specimens show the best attributes for the use as a bipolar plate. A clearly polycrystalline microstructure enables good forming behavior and the highest forming capacity without unpredictable thinning or damage. The total length of 10.40 mm for grain and twin boundaries is the highest value of the investigated specimens, which indicates that 316L-FG contains the longest boundaries to accumulate dislocations. This means that the fine-grained structures have a higher stability against external deformation.

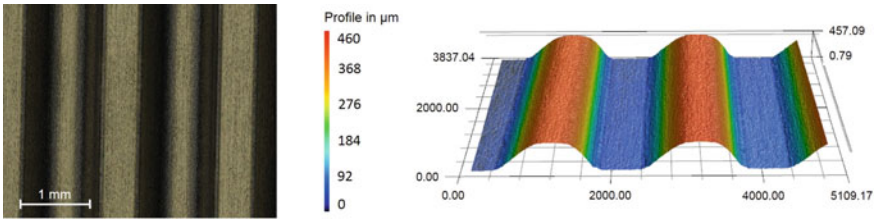


Fig. 11 Confocal measurements of a formed specimen (316L-FG), left: scanned area, right: sample profile. (Color figure online)

Table 4 Arithmetical mean deviation (R_a) values of formed samples with different initial grain sizes

Measuring position	Arithmetical mean deviation R_a (µm)		
	316L-CG	316L-MG	316L-FG
Channel top	3.69	3.25	3.21
Flank	6.25	4.10	3.68
Channel bottom	3.64	2.89	2.03

3.3 Roughness

For metallic bipolar plates, roughness is an important factor during the operational cycles with a flowing medium and the corrosive environment. Therefore, the evolution of the roughness that results from the forming processes with different initial grain sizes is important. The roughness of the initial metal foils prior to the heat treatments was measured with $R_a = 3.2$ µm. With a focus on the roughness, of the heat-treated and formed specimen, at the channel top, the flank, and the channel bottom, distinct differences can be observed between the three sample types. Figure 11 shows the measured area from the fine-grained formed specimen and the corresponding profile.

All measured values are summarized in Table 4.

From the measured values in Table 4, different conclusions can be drawn. Firstly, it is visible that all specimens reached the highest roughness values in the flank areas, which also include the radii. From the forming point of view, this is an expected behavior because in areas with free strain, the surface is enlarged, which in turn causes an increase in roughness [13]. The highest loads for the forming of these bipolar plate channel structures can be found in the radii and flank areas. Additionally, the different initial grain sizes can be seen to have an effect. The highest roughness values can clearly be observed in the coarse-grained material and the lowest ones were measured in the fine-grained samples. For that reason, it can be concluded that the initial grain size has a major impact on the development of the surface roughness after the forming process. This is of special interest for future use as a bipolar plate. A higher roughness provides a bigger surface for corrosion while the accumulation of produced water in pits or gaps is supported by bigger grains. This can lead to the formation of local elements where the corrosive attack starts. With respect to the

durability of the bipolar plates, fine-grained specimens would be preferable due to the lower roughness after forming.

4 Conclusions

In summary, it can be clearly seen that different grain sizes in the semi-finished products lead to considerable differences in the forming results, which occur due to size effects. For the definition of an ideal initial material state, the results are contrary. The coarse-grained specimens showed the lowest springback for a forming without binder, which would be preferable. However, the fine-grained specimens showed the best microstructural properties with regard to the application as a bipolar plate in PEM fuel cells. With a view on the roughness evolution, the best results were achieved by the fine-grained material, which could reduce corrosion during the operation of the fuel cell.

Another argument, which supports the use of fine-grained specimens, can be found in the production technology. In the specific case of deep drawing of metallic bipolar plates, a binder can be added to the tool design. An optimization of this process, which was used in the experiments presented, showed that the springback effect, which occurred in different intensities depending on the grain size, was almost eliminated (Fig. 12).

Within Fig. 12, it is clearly visible that, when compared to Fig. 5, no springback and no differences between the different grain sizes can be observed. This means

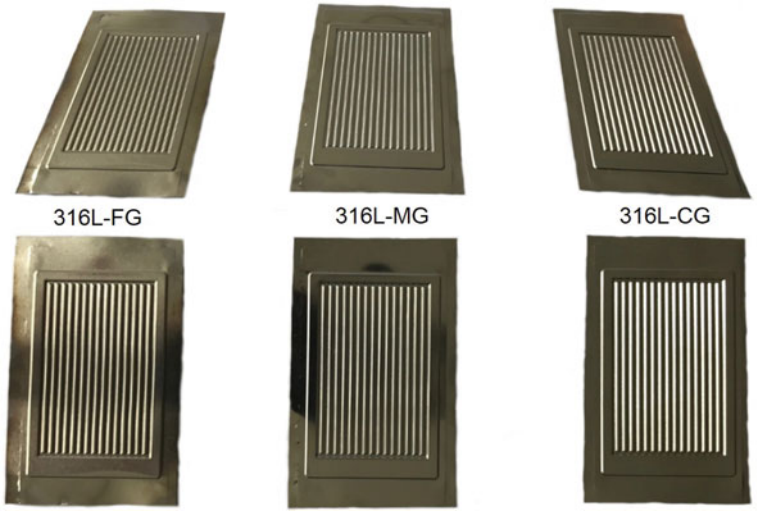


Fig. 12 Optimized forming results for different heat treatment temperatures and with binder. (Color figure online)

that the fine-grained specimen, which led to the highest springback effect without a binder, also gave flat results without wrinkles. Thus, it can be seen that even the worst springback effect of the fine-grained specimen was successfully compensated by technological adaption.

Furthermore, considering the production costs, a fine-grained microstructure could be produced with a low annealing temperature after the last rolling pass. In the present case, the fine-grained specimens were annealed at a temperature of 850 °C, whereas conventional heat treatments were done at around 1000 °C for medium grain sizes. The production of coils of fine-grained material is more resource- and cost-efficient. Overall, based on the results of this investigation, the fine-grained initial state (grain diameter < 10 μm) can be recommended for the production of metallic bipolar plates.

Within modern engineering product or process developments, the use of numerical simulations like FEM is a conventional strategy to predict requested results. The FEM simulation of metal foil forming processes is challenging because of the appearance of size effects like mentioned in this paper. Nevertheless, numerical simulations were done to predict the forming results even with different initial material states and grain sizes. The results with the specific material data like flow curve, anisotropy values, and forming limit curve showed a very good agreement with the experiments, especially compared with conventional 316-L database materials. An associated research project will be described in more detail in upcoming publications.

Acknowledgments The authors gratefully acknowledge the support by the colleagues at Chemnitz University of Technology from the Micromanufacturing Technology group for providing access to the servo press as well as from the Forming and Joining group for providing access to the GOM ARGUS system. The authors thank Steffen Clauß for performing the EBSD measurements and Morgan Uland for English proofreading.

References

1. Tiesler N, Engel U, Geiger M (1999) Forming of microparts—effects of miniaturization on friction. In: Proceedings of the 6th ICTP, 19–24 September, S 889–894
2. Vollertsen F, Hu Z, Schulze Niehoff H, Theiler C (2004) State of the art in micro forming and investigations into micro deep drawing. J Mater Process Technol 151:70–79
3. Chen C-H, Gau J-T, Lee R-S (2009) An experimental and analytical study on the limit drawing ratio of stainless steel 304 foils for microsheet forming. Mater Manuf Process 24:1256–1265
4. Lee RS, Chen CH, Gau JT (2008) Effect of thickness to grain size ratio on drawability for micro deep drawing of AISI 304 stainless steel. In: Conference presentation: 9th international conference on technology of plasticity, ICTP, S 183–188
5. Chan WL, Fu MW (2012) Experimental and simulation based study on mirco-scaled sheet metal deformation behavior in microembossing process. Mater Sci Eng A 556:60–67
6. Fu MW, Yang B, Chan WL (2013) Experimental and simulation studies of micro blanking and deep drawing compound process using copper sheet. J Mater Process Technol 213:101–110
7. Hu Z, Wielage H, Vollertsen F (2011) Forming behavior of thin foils. Key Eng Mater 473:1008–1015

8. Brabie G, Costache EM, Nanu N, Chirita B (2013) Prediction of minimization of sheet thickness variation during deep drawing of micro/milli parts. Int J Mech Sci 68:277–290
9. Bauer A, Graf M, Härtel S, Awiszus B (2018) Investigations on the optimization of the initial state for the forming process of metallic bipolar plates. In: Conference presentation: 21st international conference on advances in materials & processing technologies, Dublin City University, Ireland
10. Bauer A, Härtel S, Awiszus B (2019) Manufacturing of metallic bipolar plate channels by rolling. Jo Manuf Mater Process 3:48
11. Kauffmann A (2014) Gefügeverfeinerung durch mechanische Zwillingsbildung in Kupfer und Kupfermischkristalllegierungen. PhD thesis, Technische Universität Dresden
12. Choi WS (2018) Deformation mechanisms and the role of interfaces in face-centered cubic Fe-Mn-C micro-pillars. RWTH Aachen University, PhD thesis
13. Lötsch K, Jendras P, Härtel S, von Unwerth T (2017) Gestaltanforderungen bei metallischen Bipolarplatten in PEM-Brennstoffzellen. In: XIV. international colloquium on surfaces—proceedings, S 41–51

Study of the Influence of the Mixed-Grain Structure on the Microscopic Deformation Behavior of 316LN Steel



Y. Q. Li, H. M. Zhang, M. X. Liu, and Z. S. Cui

Abstract Mixed grains are often encountered in heavy forgings. Taking 316LN austenitic stainless steel as an investigated material, two kinds of grain structures were tested for observation of microscopic deformation heterogeneity: uniform fine grains and mixed structures with millimeter-grade coarse grains (MCGs). Tensile tests, optical microscope (OM) observations, EBSD tests as well as crystal plasticity (CP) simulations were performed. Results showed that obvious slip bands were observed in the MCGs. During the deformation, the MCGs exhibited single slip bands if they were with soft orientation, and cross slip bands if they were with hard orientation. The fine grains were seen easily rotated in the deformation, forming distinguished bumpy grain boundaries, while the MCGs displayed smooth and collapsed grain morphology. The interior MCGs undertook severer deformation than the fine grains, which showed the strain partitioning ability of MCGs was limited. This deformation behavior is possible to lead the crack initiation in the interface among MCGs and surrounding fine grains.

Keywords 316LN austenitic stainless steel · Millimeter-Grade Coarse Grains (MCGs)

1 Introduction

ASTM-TP316LN (316LN) austenitic stainless steel, which contains extra low carbon grade and strictly controlled nitrogen content, is widely used in the nuclear power station equipment (NPSE) for its excellent combination of high strength, good corrosion resistance, and adequate weldability [1]. Owing to the inhomogeneous distributions of the temperature and deformation during the forging, the coarse and fine grains, i.e., the mixed-grain structures, usually coexist in the forged pipes, resulting in the heterogeneous microstructure and anisotropic performance. Figure 1a presents the relationships between ductility and grain size of this steel. Figure 1b shows the

Y. Q. Li · H. M. Zhang · M. X. Liu · Z. S. Cui (✉)
School of Materials Science and Engineering, Institute of Forming Technology and Equipment, Shanghai Jiao Tong University, Shanghai 200030, China
e-mail: cuizs@sjtu.edu.cn

© The Minerals, Metals & Materials Society 2021

G. Daehn et al. (eds.), *Forming the Future*, The Minerals, Metals & Materials Series,
https://doi.org/10.1007/978-3-030-75381-8_147

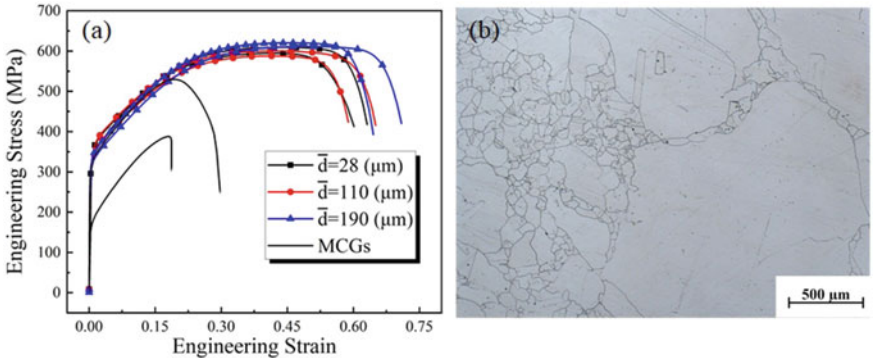


Fig. 1 Experimental results of the relation between ductility and grain size. **a** Engineering stress–strain curves for the samples with different grain sizes and **b** undeformed metallography showing the MCGs [4]. (Color figure online)

typical feature of MCGs. One can see that the elongation of the sample with the mixed-grain structure is about 20% which is much smaller than that with uniform grains. Since the testing material does not show phase transformation and multi-phase-induced heterogeneous deformation, the phenomenon above is mainly due to grain structure. In general, it is significant to refine the austenitic grains for its better material property. Recrystallization is an effective way to refine the grains, and there are many studies about recrystallization [2, 3]. In the research of recrystallization, two key factors that are most concerned about are the temperature and the corresponding deformation. This study takes the sample with the mixed-grain structure as the main research object and investigates the influence of the MCGs on the deformation by ex-situ tensile tests, scanning electron microscope (SEM), and other test methods in order to provide the guidance for the future refinement process.

2 Material Preparation and CP Modeling

2.1 Experiment

The material selected for this study is an as-forged 316LN stainless steel with major element compositions shown in Table 1. Two as-received samples were prepared to probe the influence of the mixed-grain structure on the deformation behavior.

Table 1 Major element composition of studied material in wt%

Element	Cr	Ni	Mo	Mn	Si	Fe	Others
wt%	17.46	11.33	2.11	1.62	0.47	66.82	0.19

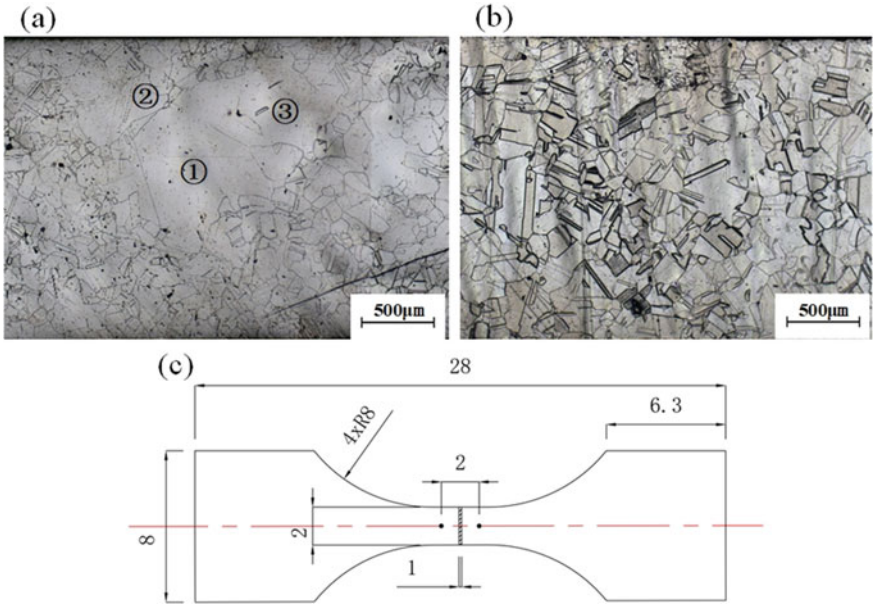


Fig. 2 The microstructures and dimensions of the tensile testing samples. **a** With mixed-grain structure, **b** with uniform grain structure, and **c** the dimensions of the micro tensile testing sample. (Color figure online)

One possesses the mixture of MCGs and fine grains, and as a contrast, the grain of the other is uniform. After standard grinding and polishing, two samples were still prepared by electrochemical polishing for the convenience of optical observation and EBSD observation. The electrolyte for electrochemical polishing is 4% oxalic acid solution. Figure 2 shows the dimension of the non-standard tensile testing sample and the optical micrographs of the gauge part. The grains (marked as 1, 2, and 3) in the center of the sample are the typical microstructure of MCGs.

The ex-situ micro uniaxial tensile tests were carried out at room temperature in a microtester machine (MTest5000, China Mechanical Testing Equipment Co., Ltd) with a load cell of 5000 N (CHcontech) at a strain rate of 0.001 s^{-1}. The tensile specimen was deformed to different strain levels by interrupted tensile testing. After every interruption, the microstructure was observed under an optical microscope (OM; Zeiss Axio Imager M2m), and the specimen was analyzed using a scanning electron microscope NanoSEM 230 equipped with an EBSD detector.

Table 2 Material parameters of the studied 316LN steel for the CP simulations

C_{11}	C_{12}	C_{44}	g_0	g_s
262.5 GPa	112.5 GPa	75.0 GPa	95.0 MPa	395.0 MPa
h_0	$\dot{\gamma}_0$	m	a	
1050.0 MPa	0.001 s^{-1}	0.02	2.95	

2.2 Modeling Methodology and Simulation Setup

The CP using a spectral numerical solver [5] was adopted based on DAMASK [6]. The CP model of the representative volume element (RVE), as well as the corresponding parameter and the boundary conditions setup, is introduced as follows.

2.2.1 Crystal Plasticity-Based Constitutive Model

A phenomenological rate-dependent flow law is adopted to describe the slip rate of the α-th slip system.

$$\dot{\gamma}^{\alpha} = \dot{\gamma}_0 \left(\frac{|\tau^{\alpha}|}{\mathrm{g}^{\alpha}} \right)^{1/m} \mathrm{sign}(\tau^{\alpha}) \tag{1}$$

With $\dot{\gamma}_0$ the reference strain rate, τ^{α} the resolved shear stress, g^{α} the resistance to shear, and m the strain rate sensitivity exponent. g^{α} is generally given by

$$\dot{\mathrm{g}}^{\alpha} = \sum_{\beta} h_{\alpha\beta} \dot{\gamma}^{\beta} \tag{2}$$

where $h_{\alpha\beta}$ is the matrix of slip hardening moduli, and can be expressed as

$$h_{\alpha\beta} = h_0 \left[q + (1-q)\delta^{\alpha\beta} \right] \left| 1 - \frac{\mathrm{g}^{\beta}}{\mathrm{g}_s} \right|^{a} \mathrm{sign}\left(1 - \frac{\mathrm{g}^{\beta}}{\mathrm{g}_s} \right) \tag{3}$$

In which h_0, g_s, and a are the reference self-hardening moduli, saturation shear resistance, and hardening exponent, respectively. q is the ratio of self-hardening to latent hardening, and here q is set to 1 for self-hardening and 1.4 for latent hardening as proposed by Pierce et al. [7]. The determined parameters for the studied material are listed in Table 2 [4].

2.2.2 RVEs and Representative Microstructures

In this research, considering the computational cost, the 2D RVEs were generated through the EBSD data for the CP simulation. The periodic boundary was imposed

in the length and thickness direction. The surfaces along the width direction were defined as free surface by adding an air layer to the surface. During the uniaxial tensile simulation, each RVE underwent the prescribed total deformation gradient $\bar{\mathbf{F}}$ and the first P–K stress $\bar{\mathbf{P}}$ along the length direction under a strain rate of 0.001 s^{-1}. Two tensors are expressed as Eq. (4):

$$\bar{\mathbf{F}} = \begin{bmatrix} 1.349 & 0 & 0 \\ 0 & * & 0 \\ 0 & 0 & * \end{bmatrix} \text{ and } \bar{\mathbf{P}} = \begin{bmatrix} * & * & * \\ * & 0 & * \\ * & * & 0 \end{bmatrix} \tag{4}$$

where the asterisk "*" denotes the undefined component. 1.349 means a maximum nominal strain of 0.349, which is equivalent to a true strain of about 0.3.

Fig. 3a1, b1 presents the representative microstructures used in simulation, and the distribution of the Taylor factor is shown in Fig. 3a2, b2. Owing to the characteristic of single phase, the Taylor factor of the studied material can be used to represent the ability of initial slip or initial deformation. The smaller the value of the Taylor factor, the easier the initial slip. From Fig. 3a2, it was clear that one of the MCGs in the center of the gauge showed soft orientation.

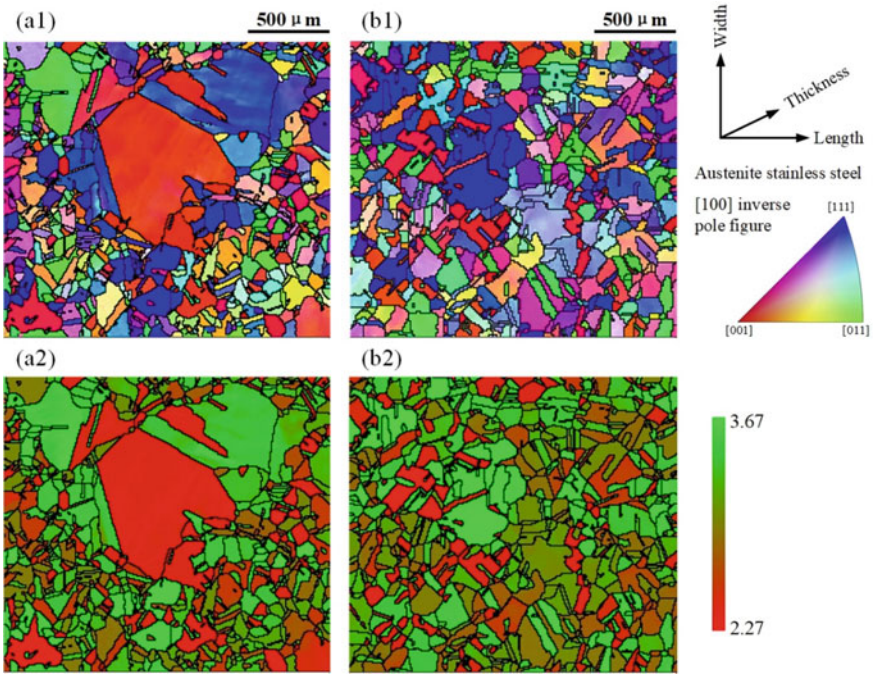


Fig. 3 OIM images obtained from EBSD used for CP simulation of micro-tensile tests and the initial distribution of Taylor factor. **a** With mixed-grain structure, and **b** with uniform grain structure. (Color figure online)

3 Results and Discussion

Figure 4 presents the change of the microstructure for two samples in each interruption. The levels of the true strain were 0.5%, 3%, and 10%, respectively. The selections of the interruptions of true strain have different meanings. The strain level of 0.5% represents the stage that the yielding of the material starts and the strain level of 3% means a stable deformation state. The strain level of 10% signifies a relatively large deformation state. One can see in Fig. 4a1–a3 that the microstructural change of the sample with uniform fine grains is consistent in every strain level. It implies that the deformation or the strain distribution is homogeneous. The typical characteristics contain slip bands and uniform bumpy surfaces which indicates the occurrence of both crystal slip and rotation. By contrast, when the specimen is initially strained to 0.5%, distinct slip bands appear in the MCGs (marked as 1 and 2) as shown in Fig. 4b1. However, this phenomenon is not obvious in other grains containing the coarse grain (marked as 3) and fine grains. It indicates that, in the beginning of the deformation, the deformation takes place mainly in the grains (marked as 1 and 2) because of their soft orientation and large grain size. It is also concluded that for the same phase of similar orientations, the larger the grain size, the smaller the yield strength. The aforementioned conclusions agree well with the Hall–Patch relationship [8, 9]. The result of 3% true strain is shown in Fig. 4b2. One can see that the single slip bands of MCGs (marked as 1 and 2) deepen and inconspicuous cross slip bands appear in the MCG (marked as 3). The surface of MCGs is smooth while the surface of the region of fine grains is bumpy. It elucidates that the MCGs in soft orientations undertake the primary deformation in the form of the single slip.

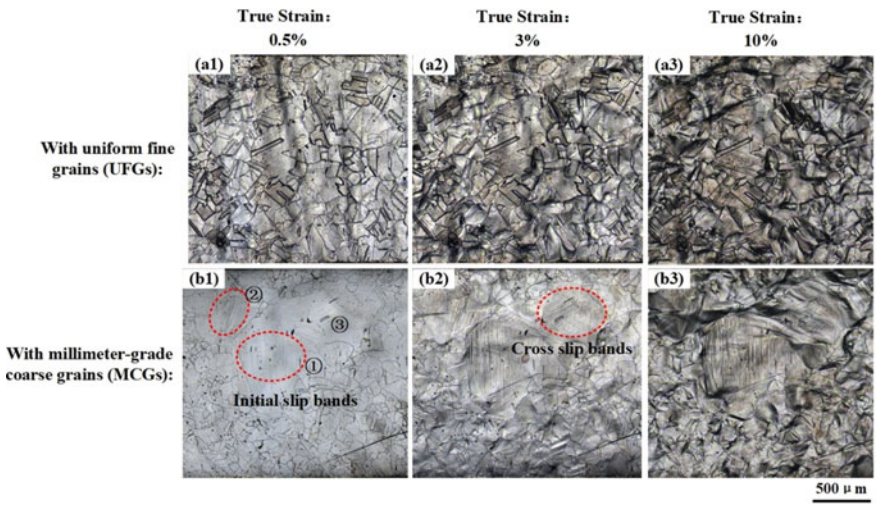


Fig. 4 The microstructure of two samples after deformation is characterized by optical microscopy. **a** The sample with uniform fine grains and **b** the sample with MCGs. (Color figure online)

However, although the MCG in hard orientations bears no much plastic deformation at the beginning of the tensile test, it has no choice but to undertake some plastic deformation in the subsequent deformation process because the crystal rotation is not easy to happen due to its large grain size. It is noted that the plastic deformation of hard-oriented grains is achieved in a way of multi-slip system. As shown in Fig. 4b3, the surface of MCGs collapses when the true strain reaches 10%. But the surrounding fine grains also show a bumpy surface as the sample with uniform fine grains. It once again verifies the conclusion that the crystal rotation is hard to occur for MCGs and the plastic deformation is performed in the form of crystal slip which is reflected in the tensile sample as the smooth and collapsed surface caused by the material flow of MCGs. It can be deduced that the stress in the collapsed MCGs is bigger and the interface among the MCGs and the surrounding fine grains is the region of stress concentration.

The simulation results are shown in Fig. 5. One can see that in Fig. 5b1, the strain distribution of the sample with MCGs agrees well with the experimental results that: (i) the MCGs with soft orientations undertake the main plastic deformation and (ii) even though the hard-oriented MCG is difficult to undertake plastic deformation at the initial stage of tensile tests, it has to bear some plastic deformation to make the overall deformation coordinate due to its large grain size and difficult crystal rotation. The results of the stress distribution shown in the Fig. 5b2 indicates that the stress of the MCG in hard orientation is bigger than other grains, and the stress concentration (marked by the dashed ellipse) is also observed in the interface among the MCGs

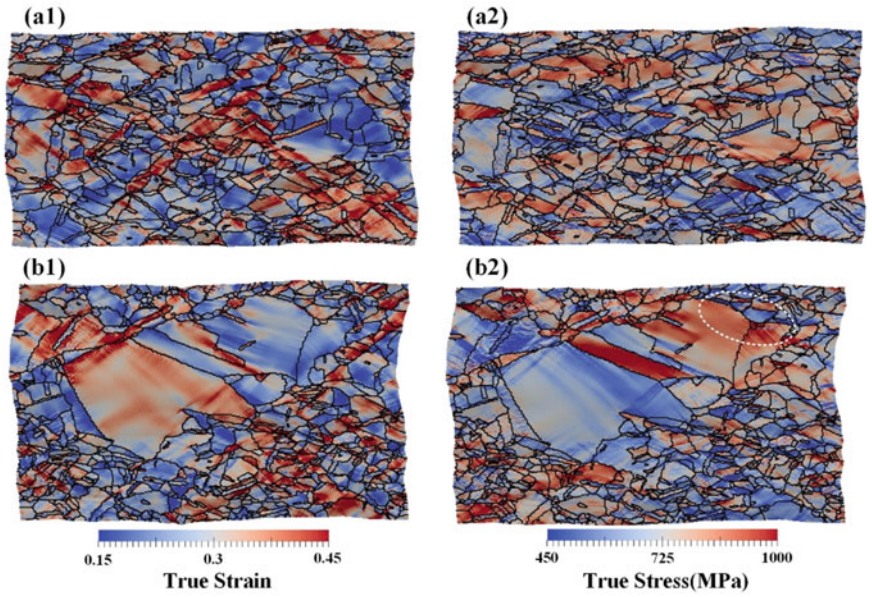


Fig. 5 The simulated von Mises stress and von Mises strain to 30% true strain. **a** The sample with uniform fine grains and **b** the sample with MCGs. (Color figure online)

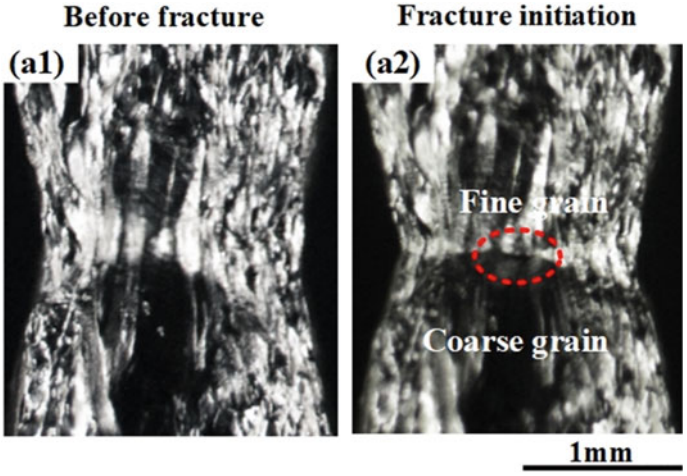


Fig. 6 The fracture initiation of the sample with MCGs obtained by the optical microscopy. (Color figure online)

and the surrounding fine grains. But the stress in the region of soft-oriented MCGs is small. It is noted that the stress concentration is not distinct in the interface among the soft-oriented MCGs and the surrounding fine grains. The reason is that soft-oriented grains bear main plastic deformation, which leads to less deformation of fine grains around them. Therefore, the stress in these fine grains is low and the stress concentration is not obvious. As for the sample with uniform fine grains, the stress distribution is more uniform. The fracture initiation of the sample with MCGs was captured by the optical microscope, and the results are given by Fig. 6. The collapsed area at the bottom of the figure is the region containing the MCGs. One can see that the crack initiated in the interface among the MCGs and fine grains. Thus, the results of the macroscopic mechanical curves shown in Fig. 1 can be explained as follows that the deformation of the MCGs is mainly conducted by the crystal slip due to their coarse grain size. As the deformation continues, the surface of the MCGs collapses because of the sharp flow of the material which reducing the thickness of this part, thus leading to the increase of stress. More importantly, the stress concentration existing in the interface among the MCGs and the surrounding fine grains accelerates the nucleation of the crack. That is why the elongation is greatly reduced.

Figure 7 shows the SEM results of the fracture morphologies for both samples. One can see that the fracture of the sample with uniform fine grains shows the typical microstructure of the dimples as well as the big holes caused by the initial hole of the material and the inclusion. By contrast, for the sample with MCGs, the region corresponding to the fracture initiation shown in Fig. 7b3 is characterized by the mixture of shear and dimples. The differences also exist in fracture propagation. As shown in Fig. 7b1, in the region of the MCGs, the fracture propagation is in the form of transgranular fracture, and the surface shows smooth morphology caused by shear deformation. It indicates that the crystal slip in the MCGs and their big grain size

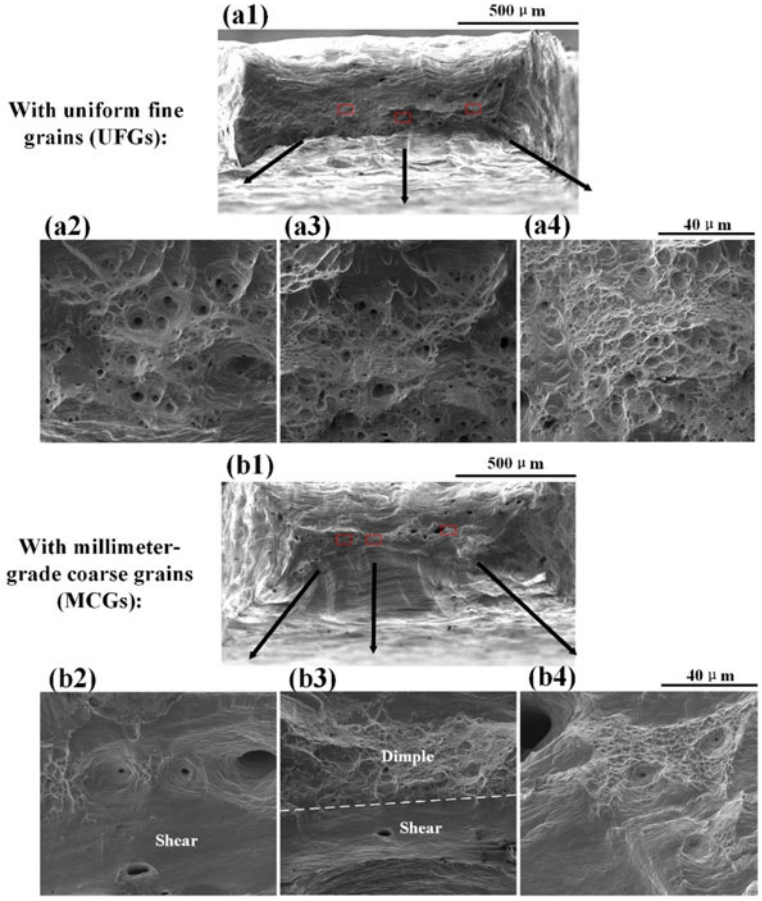


Fig. 7 The SEM results of the fracture morphologies. **a** The sample with uniform fine grains, and **b** the sample with MCGs. (Color figure online)

have a great influence on fracture propagation. While in the region of the fine grains, the ductile fracture with typical dimple morphologies is the main mode for fracture propagation.

4 Conclusion

This study applied the ex-situ tensile tests as well as SEM and other methods to probe the effect of the mixed-grain structure existing in 316LN stainless steel on the deformation. It can be concluded as follows:

1. The yielding strength of the MCGs is smaller than fine grains which is manifested by the occurrence of the initial slip band on their surface. As the deformation continues, the plastic deformation of the MCGs in soft orientation is mainly achieved in the way of single slip, while the MCGs in hard orientation bear the deformation in the mode of multi slip system.
2. When the deformation reaches some degree, the surface of the MCGs collapses seriously which increases the stress of this part and the stress concentration in the interface among the MCGs and surrounding fine grains. The severe stress concentration leads to the early crack initiation. In addition, the fracture propagation is also affected by the MCGs which is characterized by the morphology of shear.

Acknowledgments The authors gratefully acknowledge the funding support from the National Natural Science Foundation of China with the project of Nos. 51675335 and Nos. 51705317, as well as the support from the Program of Shanghai Academic Research Leader (Grant No. 19XD1401900).

References

1. Zinkle SJ, Was GS (2013) Materials challenges in nuclear energy. Acta Mater 61:735–758
2. McQueen HJ (2004) Development of dynamic recrystallization theory. Mater Sci Eng A 387–389(15):203–208
3. Chen F, Cui ZS, Chen SJ (2011) Recrystallization of 30Cr2Ni4MoV ultra-super-critical rotor steel during hot deformation. Part I: dynamic recrystallization. Mater Sci Eng A 528:5073–5080
4. Shang XQ, Zhang HM, Cui ZS, Fu MW, Shao JB (2019) A multiscale investigation into the effect of grain size on void evolution and ductile fracture: experiments and crystal plasticity modeling. Int J Plasticity 125:133–149
5. Zhang HM, Liu J, Sui DS, Cui ZS, Fu MW (2018) Study of microstructural grain and geometric size effects on plastic heterogeneities at grain-level by using crystal plasticity modeling with high-fidelity representative microstructures. Int J Plasticity 100:69–89
6. Roters F, Diehl M, Shanthraj P, Eisenlohr P, Reuber C, Wong SL, Maiti T, Ebrahimi A, Hochrainer T, Fabritius HO, Nikolov S, Friák M, Fujita N, Grilli N, Janssens KGF, Jia N, Kok PJJ, Ma D, Meier F, Werner E, Stricker M, Weygand D, Raabe D (2019) DAMASK—The Düsseldorf Advanced Material Simulation Kit for modeling multi-physics crystal plasticity, thermal, and damage phenomena from the single crystal up to the component scale. Comp Mater Sci 158:420–478
7. Peirce D, Asaro RJ, Needleman A (1982) An analysis of nonuniform and localized deformation in ductile single crystals. Acta Metall 30(6):1087–1119
8. Hall EO (1951) The deformation and ageing of mild steel: III discussion of results. Proc Phys Soc Sect B 64:747–753
9. Petch NJ (1953) The cleavage strength of polyscrystals. J Iron Steel Inst 174:25–28

Dependence of Mesoscale Structure of Drawn High-Carbon Steel Wire on Wire Diameter



Shiori Gondo, Rena Tanemura, Ryuki Mitsui, Satoshi Kajino, Motoo Asakawa, Kosuke Takemoto, Kenichi Tashima, and Shinsuke Suzuki

Abstract This study aims to clarify the transition of mesoscale structure of a drawn wire versus drawing strain. High-carbon steel wires 0.276, 0.444, and 0.936 mm in diameter were drawn until wires could be drawn without rupture. Two results were obtained from a crystal orientation analysis of the electron backscatter diffraction pattern. First, the mesoscale structure in the wire consisted only of a subprimary fiber texture {100}<110>-{111}<110> at the drawing limit, that is the largest drawing strain when the wire could be drawn without rupture. Second, it is predicted that the transition of the mesoscale structure versus the drawing strain will occur as follows

S. Gondo (✉) · S. Kajino
Materials Processing Group, Advanced Manufacturing Research Institute, Department of Electronics and Manufacturing, National Institute of Advanced Industrial Science and Technology (AIST), 1-2-1, Namiki, Tsukuba, Ibaraki 305-8564, Japan
e-mail: shiori-gondo@aist.go.jp

S. Gondo
(previous affiliation) Department of Applied Mechanics, Graduate School of Fundamental Science and Engineering, Waseda University, 3-4-1 Okubo, Shinjuku, Tokyo 169-8555, Japan

R. Tanemura
Department of Applied Mechanics, Graduate School of Fundamental Science and Engineering, Waseda University, 3-4-1 Okubo, Shinjuku, Tokyo 169-8555, Japan

R. Mitsui
Department of Applied Mechanics and Aerospace Engineering, School of Fundamental Science and Engineering, Waseda University, 3-4-1 Okubo, Shinjuku, Tokyo 169-8555, Japan

M. Asakawa · S. Suzuki
Department of Applied Mechanics and Aerospace Engineering, Faculty of Science and Engineering, Waseda University, 3-4-1 Okubo, Shinjuku, Tokyo 169-8555, Japan

K. Takemoto · K. Tashima
Factory-Automation Electronics Inc, 1-6-14 Higashi-Nakajima, Higashi-Yodogawa, Osaka, Osaka 533-0033, Japan

S. Suzuki
Department of Materials Science, Faculty of Science and Engineering, Waseda University, 3-4-1 Okubo, Shinjuku, Tokyo 169-8555, Japan

Kagami Memorial Research Institute of Materials Science and Technology, Waseda University, 2-8-26 Nishi-Waseda, Shinjuku, Tokyo 169-0051, Japan

© The Minerals, Metals & Materials Society 2021

G. Daehn et al. (eds.), *Forming the Future*, The Minerals, Metals & Materials Series,
https://doi.org/10.1007/978-3-030-75381-8_148

regardless of the initial wire diameter: In the beginning of wire drawing, the wire will have only a primary fiber texture {100}<110>-{111}<110>. After a slight increase in the drawing strain, the wire will have the primary fiber texture at its outer side and a secondary fiber texture {111}<110>-{110}<110> at the inner side. After a further increase in the drawing strain, the wire will have a subprimary fiber texture at the outer side and a secondary fiber texture at the inner side. Moreover, increase in the drawing strain, the wire will have only a subprimary fiber texture.

Keywords High-carbon steel wire · Wire drawing · Crystal orientation · Fiber texture · EBSD analysis

1 Introduction

An increase in the strength of metallic materials through the wire drawing process is required for reduction of the load on the environment. Recently, high-carbon steel wire with a tensile strength of 7000 MPa was fabricated by a wire drawing process at the laboratory scale [1]. However, in general, the ductility of the wire significantly decreases with increasing its strength which follows on an increase in drawing strain. Thus, the clarification of an effective microstructure is necessary in order to maintain the balance between strength and ductility.

Some existing literatures have focused on vacancies [2], dislocations [2], the lamellar angle in the longitudinal direction of the wire [3, 4], lamellar spacing [5], and the fragmentation and decomposition of cementite [6–9]. However, no previous report has mentioned the relationship between microstructures and a decrease in ductility of the drawn wire.

On the contrary, we established the tensile testing method and the measurement method for ductility of the fine metal wire [10], and clarify the effect of back stress which applied to the wire at entrance side of the die during wire drawing on mechanical properties of drawn fine high-carbon steel wire [11]. Although the ductility of the wire significantly decreased on 1st pass, after that, the ductility of the wire slightly decreased and then increased with increasing drawing strain. Furthermore, a decrease in back stress improved the ductility of the drawn wire. To clarify the mechanism, we have focused on crystal orientation distribution in the radial direction of the wire as one of the microstructures that had not yet been analyzed detailly [12]. For a high-carbon steel wire with an initial diameter of 0.444 mm, the transition of the crystal orientation distribution, “mesoscale structure” characterized by the fiber textures, versus the drawing strain was clarified as follows. In the beginning of wire drawing, the wire had only a primary fiber texture {100}<110>-{111}<110>. After a slight increase in the drawing strain, the wire had a primary fiber texture at the outer side and secondary fiber texture {111}<110>-{110}<110> at the inner side. After a further increase in drawing strain, the wire had a subprimary fiber texture {100}<110>-{111}<110> at the outer side and secondary fiber texture at the inner side. Although the tendency that a decrease in thickness of subprimary fiber texture

via decreasing back stress improves ductility has been obtained, it is not clarified whether this tendency is universal or not. Because the mesoscale structure at the drawing limit, i.e., the largest drawing strain at which the wire can be drawn without rupture, and the dependence of mesoscale structure on wire diameter are not clarified well. Two approaches are adopted for obtaining a more beneficial understanding of the relationship between mesoscale structure and the mechanical properties. The first is clarifying the mesoscale structure at the wire drawing limit. The second is clarifying the effect of the initial diameter of the wire on the mesoscale structure, because it is expected that crystal orientation distribution in the radial direction of the wires with a small diameter would be uniformized following a decrease in the stress gradient. The theoretical analysis has reported that the strain gradient in the radial direction of the wire decreases with decreasing wire diameter [13]. Therefore, the objective of this study is to clarify the transition of the mesoscale structure of the wires with different initial diameters with respect to the drawing strain up to the wire drawing limits.

2 Experimental Procedures

The starting materials were patented pearlitic steel wires 0.276, 0.444, and 0.936 mm in diameter. They were provided by Nippon Steel SG Wire Co., Ltd. Table 1 shows the chemical composition of the wires. The composition was measured according to the Japanese Industrial Standards (JIS) G1211 [14], G1212 [15] and G1258 [16] for C, Si, and other relevant elements, respectively.

The wires were drawn under areal reduction for one pass of 7% and a back stress ratio less than 5% using non-slip type drawing machines (Factory-Automation Electronics Inc., D3UlTM-5D/D3UlTM-10D). The definitions of the areal reduction for one pass, the back stress ratio and the drawing strain ε_n were the same as definitions in our previous works [10–12, 17]. The subscript n indicates the pass number. Figure 1 shows the relationship between the drawing direction and direction of back stress. The wire with an initial diameter of 0.444 mm, which had already been drawn

Table 1 Chemical composition of high-carbon steel wires (mass%)

C	Si	Mn	P	S	Cr	Fe
0.98	0.20	0.30	0.004	0.006	0.20	Bal.

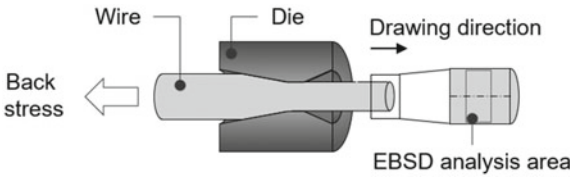


Fig. 1 Schematic figure of the wire drawing process and electron backscatter diffraction analysis area

to 0.063 mm in our previous work [12], was drawn in this study. After the wires were drawn, the diameters of the wires were measured using a laser interferometer (Zumbach Electronics AG, DU600-RO-OL). The surface of the wires was observed through a field emission scanning electron microscope (FE-SEM) (Carl Zeiss AG, Ultra Plus).

The preparation methods for the samples of transmission electron microscope (TEM) observation and crystal orientation analysis were similar to that of our previous work [12]. The sample for TEM was prepared by focused ion beam (FIB) (JEOL Ltd., JIB-4000). The lamellar structure of starting materials was observed through TEM (JEOL Ltd., JEM-2100F). The samples for electron backscatter diffraction (EBSD) analysis were polished by Ites Co., Ltd. The width of the polished plane was larger than 90% of the diameter of the wire. Kikuchi patterns of the drawn wires were obtained by FE-SEM with EBSD (Bruker Co., XFlash 6130) at the magnification the observation field was full with the polished plane. Then, pole figures of divided analysis areas in several were drawn by using software (Bruker Co., Esprit 2.1). The width of the separated areas was approximately one tenth of the width of the polished plane. After analysis, the mesoscale structure was decided based on the fiber textures: primary, secondary, and subprimary fiber textures [12].

3 Results

Figure 2 shows TEM image of lamellar structure in a starting wire with an initial diameter of 0.444 mm [12]. The obvious difference of lamellar spacing was not observed because the average of lamellar spacings of the starting wires with diameters of 0.276, 0.444, and 0.396 mm were approximately 58 nm, 58 nm, and 61 nm, respectively.

Figure 3 shows the relationship among the initial diameter of wires, the smallest diameter of drawn wires, and drawing strain, and the SEM images of the drawn wires with the smallest diameter. The wires with the initial diameters of 0.276 and 0.936 mm were able to be drawn to 0.021 mm ($\varepsilon = 5.12$) and 0.093 mm ($\varepsilon = 4.62$) without rupture, respectively. The wire with an initial diameter of 0.063 mm ($d_0 = 0.\ 444$ mm) could be drawn to 0.029 mm ($\varepsilon = 5.42$) without rupture. The wire with a diameter of 0.093 mm ($d_0 = 0.936$ mm) fractured as soon as the drawing

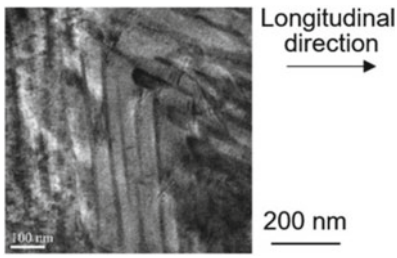


Fig. 2 Transmission electron microscope image of lamellar structure in starting wire with an initial diameter of 0.444 mm [12]

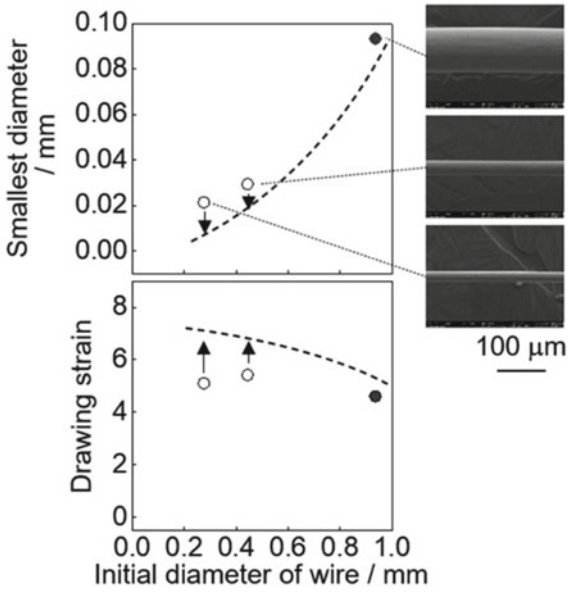


Fig. 3 Relationships among the initial diameter of wires, the smallest diameter of drawn wires and their drawing strain, and the scanning electron microscope images of the most finely drawn wires. The wires with the initial diameters of 0.276, 0.444, and 0.936 mm could be drawn to 0.021 mm ($\varepsilon = 5.12$), 0.029 mm ($\varepsilon = 5.42$), and 0.093 mm ($\varepsilon = 4.62$) without rupture, respectively. At the next drawing step, the wire with a diameter of 0.936 mm (indicated by gray-colored plot) could be put through the die hole but was fractured as soon as the drawing commenced. The wires indicated by white-colored plots could not be put through the die hole. The dashed curves are rough estimation of the wire drawing limit, i.e., the largest drawing strain at which the wire can be drawn without rupture

commenced. The wires with diameters of 0.021 mm ($d_0 = 0.276$ mm) and 0.029 mm ($d_0 = 0.444$ mm) were too fine to be put through the die hole.

Figure 4 shows the mesoscale structure of the drawn wires with initial diameters of 0.276, 0.444, and 0.936 mm. Regardless of the initial diameter, the wires with a drawing strain of approximately 1.5 had a primary fiber texture and secondary fiber texture at outer and inner sides of the wire, respectively. The wires with diameters of 0.029 mm ($d_0 = 0.276$ mm, $\varepsilon = 4.48$), 0.029 mm ($d_0 = 0.444$ mm, $\varepsilon = 5.42$) and 0.093 mm ($d_0 = 0.936$ mm, $\varepsilon = 4.62$) had only a subprimary fiber texture throughout the entire wire.

4 Discussion

Although the wires with initial diameters of 0.276 and 0.444 mm were too fine to be put through the die hole after drawing to 0.029 and 0.021 mm, respectively and could

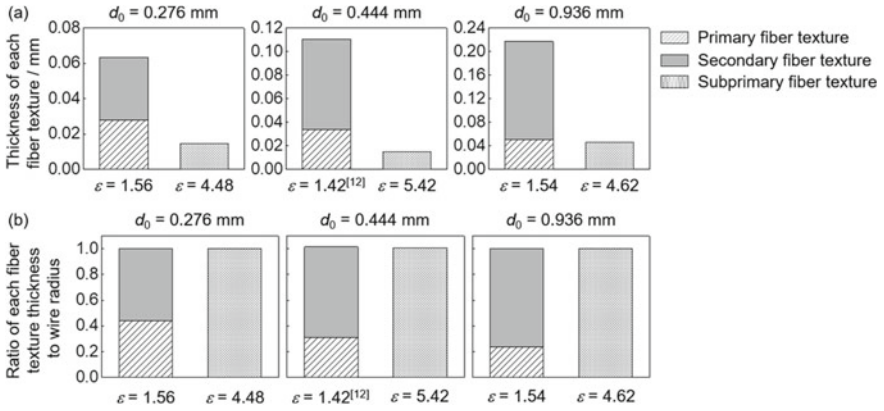


Fig. 4 Mesoscale structure of the wires with $d_0 = 0.276$ mm ($\varepsilon = 1.56$, $\varepsilon = 4.48$), $d_0 = 0.444$ mm ($\varepsilon = 1.42$ [12] and $\varepsilon = 5.42$), and $d_0 = 0.936$ mm ($\varepsilon = 1.54$, $\varepsilon = 4.62$): **a** the thickness of each fiber texture and **b** its ratio to the wire radius

not be drawn to their drawing limits by using the drawing machine, it was implied that wires with a smaller diameter can be drawn to a higher drawing strain.

The drawn wire with a diameter of 0.093 mm ($d_0 = 0.936$ mm, $\varepsilon = 4.62$) had only a subprimary fiber texture. For the wires with initial diameters of 0.276 and 0.444 mm, the wire with the drawing strain less than the limit strain had only subprimary fiber texture. Thus, the wire with the greatest drawing strain had mesoscale structure that consisted only of a subprimary fiber texture

In wires with a drawing strain of approximately 1.5, the mesoscale structure consisted of a primary fiber texture and secondary fiber texture regardless of the initial diameter, as shown in Fig. 5. In contrast, wires with a drawing strain around approximately 5 had a mesoscale structure that consisted only of a subprimary fiber

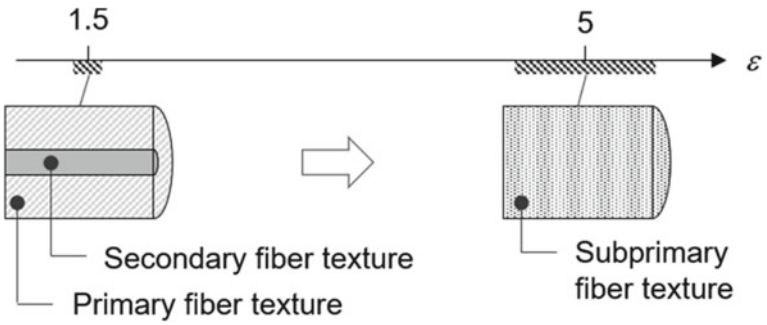


Fig. 5 Schematic figure of mesoscale structure transition versus the drawing strain of the wires with initial diameters of 0.276, 0.444, and 0.936 mm. Regardless of the initial diameter, the wires with drawing strains of approximately 1.5 had primary and secondary fiber textures. The wires with drawing strains around 5 had only a subprimary fiber texture

texture. Therefore, it is predicted that the transition order of mesoscale structure versus drawing strain is not dependent on the initial diameter as follows: In the beginning of wire drawing, the wire has only a primary fiber texture. After a slight increase in the drawing strain, the wire has the primary fiber texture at its the outer side and a secondary fiber texture at the inner side. After a further increase in the drawing strain, the wire has a subprimary fiber texture at the outer side and a secondary fiber texture at the inner side. Moreover at a large the drawing strain, the wire has only a subprimary fiber texture.

At a drawing strain of approximately 1.5, the ratio of the thickness of the secondary fiber texture to the radius of the wire increased when the initial diameter decreased. In addition, our previous work indicated that the transition of the ratio of the secondary fiber texture thickness to wire radius could be fit with a quadratic function [12]. The study also clarified the tendency that an increase in the back stress ratio shifted the transition to a lower drawing strain. Assuming that the transition can be accurately fitted by the quadratic function regardless of the initial diameter of the wires, it is predicted that one of the following patterns occurs when the initial diameter decreases. First, the drawing strain at the formation of fiber textures decreases and disappearance of secondary fiber texture increases; furthermore, the maximum value of the fitting curve increases. Second, the transition of mesoscale structure versus drawing strain shifts to a higher drawing strain. Third, both patterns happen at the same time. These guesses differ from the prediction based on the strain gradient mentioned in the introduction; this would be due to the small variation in strain gradients for the different initial diameter wires used in this study. The authors predict that obtaining a large variation of strain gradients required comparing the mesoscale structure of the wire on a scale of several micrometers to that on a scale of several millimeters.

5 Conclusion

The following conclusions were obtained by clarifying the mesoscale structure, which is characterized by the fiber textures of the drawn high-carbon steel wire, versus the drawing strain for the wires with initial diameters of 0.276, 0.444, and 0.936 mm.

(1) The mesoscale structure of the drawn wire consists only of subprimary fiber texture at the largest drawing strain when the wire can be drawn without rupture.
(2) It is predicted that the transition order of the mesoscale structure versus the drawing strain is independent of the initial wire diameter.

Acknowledgments This work was supported by Japan Society for the Promotion of Science (JSPS) Grant-in-Aid for JSPS Research Fellow Grant Number 16J11098 and was partly executed under the cooperation of the organization between Waseda University and JXTG Nippon Oil & Energy Corporation. The previous affiliation of the author, Dr. Shiori Gondo, was Waseda University. This

work was performed while the author belonged to Waseda University. We also express our gratitude to Nippon Steel SG Wire Co., Ltd. for providing materials.

References

1. Li Y, Raabe D, Herbig M, Choi PP, Goto S, Kostka A, Yarita H (2014) Segregation stabilizes nanocrystalline bulk steel with near theoretical strength. Phys Rev Lett 113:
2. Daitoh Y, Hamada T (2000) Microstructures of heavily-deformed high carbon steel wires. Tetsu-to-Hagané 86(2):105–110
3. Zelin M (2002) Microstructure evolution in pearlitic steels during wire drawing. Acta Mater 50:4431–4447
4. Lamontagne A, Massardier V, Kléber X, Sauvage X, Mari D (2015) Comparative study and quantification of cementite decomposition in heavily drawn pearlitic steel wires. Mater Sci Eng A 644:105–113
5. Guo N, Luan BF, Wang BS, Liu Q (2013) Microstructure and texture evolution in fully pearlitic steel during wire drawing. Sci China Technol Sci 56(5):1139–1146
6. Hong MH, Reynolds WT, Tarui T, Hono K (1999) Atom probe and transmission electron microscopy investigations of heavily drawn pearlitic steel wire. Metall Mater Trans A 30:717–727
7. Fang F, Zhao Y, Liu P, Zhou L, Hu XJ, Zhou X, Xie ZH (2014) Deformation of cementite in cold drawn pearlitic steel wire. Mater Sci Eng A 608:11–15
8. Tarui T, Maruyama N, Tashiro H (2005) Cementite decomposition in high carbon steel wires. Tetsu-to-Hagané 91(2):265–271
9. Li YJ, Choi P, Goto S, Borchers C, Raabe D, Kirchheim R (2012) Evolution of strength and microstructure during annealing of heavily cold-drawn 6.3 GPa hypereutectoid pearlitic steel wire. Acta Mater 60:4005–4016
10. Gondo S, Suzuki S, Asakawa M, Takemoto K, Tashima K, Kajino S (2018) Establishing a simple and reliable method of measuring ductility of fine metal wire. Int J Mech Mater Eng 13(5). https://doi.org/10.1186/s40712-018-0091-0
11. Gondo S, Suzuki S, Asakawa M, Takemoto K, Tashima K, Kajino S (2015) Improvement of the limit of drawing a fine high-carbon steel wire by decreasing back tension. In: Proceedings of the 85th Annual Convention WAI, Atlanta, USA, 27–29 April
12. Gondo S, Tanemura R, Suzuki S, Kajino S, Asakawa M, Takemoto K, Tashima K (2019) Microstructures and mechanical properties of fiber textures forming mesoscale structure of drawn fine high carbon steel wire. Mater Sci Eng A 747:255–264
13. Juul KJ, Nielsen KL, Niordson CF (2017) Steady-state numerical modeling of size effects in micron scale wire drawing. J Manuf Process 25:163–171
14. JIS G1211-3 (2011) Iron and steel—determination of carbon content—part 3: infrared absorption method after combustion
15. JIS G1212 (1997) Iron and steel—methods for determination of silicon content
16. JIS G1258-3 (2014) Iron and steel—ICP atomic emission spectrometric method—part 3; determination of various elements—decomposition with acids and fusion with sodium carbonate
17. Gondo S, Suzuki S, Asakawa M, Takemoto K, Tashima K, Kajino S (2016) Improvement of ductility with maintaining strength of drawn high carbon steel wire. Key Eng Mater 716:32–38

Thermomechanical Analysis and Experimental Validation of ECAP for Aluminum Sheet Metal



Maximilian Gruber, Yiheng Yang, Christian Illgen, Philipp Frint, Martin F.-X. Wagner, and Wolfram Volk

Abstract Equal-channel angular pressing (ECAP) is an established method for the improvement of mechanical properties by grain refinement through shear strains. While there is a profound knowledge about ECAP of bulk materials, there is only a little information on the effect of ECAP on sheet metals. Therefore, a tool was developed that is able to perform ECAP tests for metals with a thickness of 1.8 mm. In this contribution, a thermomechanical simulation model is used to examine the novel process. The simulation is performed to investigate the dissipated forming heat and the heat due to friction. To validate the numerical results, experiments with the ECAP tool for sheet metal are performed. By drilling holes in the sheet material, the forming temperature can be measured with thermocouples and friction parameters used in the simulation can be calibrated inversely. Since a detailed material model is essential for the inverse determination of individual parameters, a special focus of this article is on the determination of the thermomechanical parameters. For example, the plastic flow behavior or thermomechanical conversion, expressed as the Taylor–Quinney coefficient, is examined under a stress state similar to ECAP by means of a Miyauchi test. In this way, fundamental correlations between the heat development in the ECAP process for aluminum sheet metal and the shear strain introduced into the material can be obtained.

Keywords Equal-Channel Angular Pressing (ECAP) · Aluminum AA5083 · Thermomechanical analysis · Miyauchi test · Taylor–Quinney coefficient

M. Gruber (✉) · Y. Yang · W. Volk
Metal Forming and Casting, Technical University of Munich, Walther-Meissner-Str. 4, Garching 85748, Germany
e-mail: Maximilian.gruber@utg.de

C. Illgen · P. Frint · M. F.-X. Wagner
Institute of Materials Science and Engineering, Chemnitz University of Technology, Erfenschlager Str. 73, Chemnitz 09125, Germany

© The Minerals, Metals & Materials Society 2021

G. Daehn et al. (eds.), *Forming the Future*, The Minerals, Metals & Materials Series,
https://doi.org/10.1007/978-3-030-75381-8_149

1 Introduction

In recent years, Equal-channel Angular Pressing (ECAP) , which was already introduced in the 1980s by Segal [1], has been attracting increasing scientific and technological interest [2]. In particular, ECAP offers the possibility of introducing high shear deformations into semi-finished products, which makes it possible to produce (ultra-)fine-grained microstructures. During ECAP, a typically square or circular cross-sectioned billet is pressed through a rigid and angled channel. Both channels (entrance and exit channels) are intersected by a shear plane, where shear deformation is introduced into the material. To impose higher strains, processing by ECAP can be performed repeatedly in several consecutive passes and also in different processing routes.

While there are already scientifically valuable, fundamental parameter studies on the effects of channel geometry, processing temperature and processing route on the resulting microstructure and mechanical properties [3, 4], an important and still unresolved problem is the viability of ECAP processing for use in industrial environment. Different approaches were already pursued to solve industrial suitability: On the one hand, the ECAP process has been modified. This has resulted in processes such as *Conshearing* or the *ECAP-Conform* process [5–7]. Another approach, on the other hand, deals with adapting the geometry of the semi-finished product to conventional ECAP. Some studies already investigated the influence of up-scaling on the refinement of the grains, since conventional ECAP processing is typically performed on a laboratory scale [7]. In addition, investigations on plate samples with a thickness of 5 mm have already been conducted successfully [8].

The tool used in the present study was developed by Suh et al. [9]. Its unconventional design allows processing of sheet materials with sheet thicknesses of 1.8 mm. Initial numerical investigations have already shown the influence of different channel geometries (r, R, w, h, and Φ) on the processes for sheet metal [10], see Fig. 1. In addition, it has already been shown that this ECAP-tool can be used to carry out various process routes. Using these process routes, different deformations and thus textures can be generated in the material [11]. Initial successes with regard to an industrial use of ECAP have already been achieved. However, especially with regard to the homogeneity of the microstructure over the sheet thickness, the process still needs to be further improved. This inhomogeneity is mainly influenced by the friction in the channel [12]. Figure 1b exemplarily shows a small region at the upper surface of the sheet where the material is severely sheared in a direction opposite to the ECAP direction, followed by a second region with a large number of grains showing a distinct orientation toward the direction of induced shear strain.

Temperature-related effects also have a major influence on the characteristics of the microstructure and the design of the process. The energy terms investigated in this study include plastic strain energy, frictional sliding energy, and heat transfer energy. Especially the thermomechanical conversion, well known as the Taylor–Quinney coefficient (TQC), has a strong influence on the heat development in the process [13]. Nonetheless, the TQC is often generally assumed to be equal to 0.9 in numerical

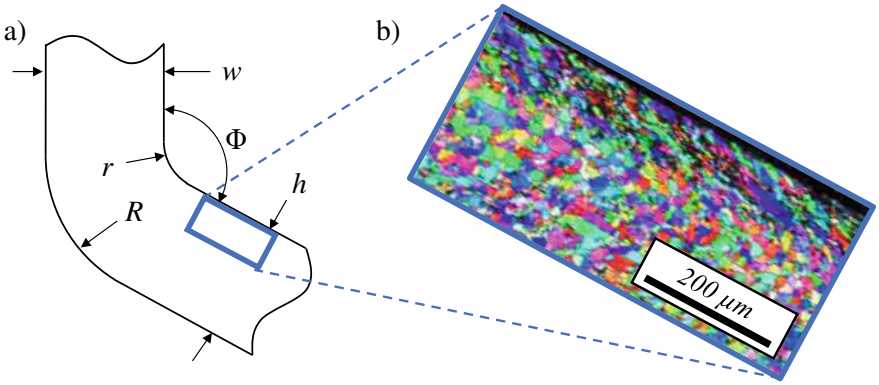


Fig. 1 **a** Schematic sketch of the channel parameters; **b** orientation maps determined by electron backscatter diffraction of the severely deformed microstructure, indicating inhomogeneity especially at the sheet metal surface (top of the box). (Color figure online)

investigations. However, several studies already show that the TQC depends on the material or alloy, the stress mode, and the strain rate [14]. For aluminum, one can find some literature values for the TQC, but they vary greatly between 0.25 and 1.0 [14, 15]. In addition, when determining the TQC, it should be noted that temperature losses must be taken into account at slow forming speeds. For example, Behrens et al. show that heat losses and thermal conduction depend on the forming time for the determination of the TQC of high-strength steels [16]. Thus, an increasing forming speed leads to a temperature increase.

In order to get a detailed basic understanding of the ECAP process for aluminum sheets, numerical investigations are carried out within the scope of this work. A particular focus is placed on the consideration of frictional and thermomechanical effects with the aim of reducing the inhomogeneity of the microstructure. The material parameters for the numerical model are determined for this purpose. Friction, which is essential for the understanding and optimization of the process, can then be inversely determined by experimental validation and calibration. Using this simulation, the introduced strains that cause the desired grain refinement during ECAP can be examined. This provides the basis for a subsequent optimization of process parameters.

2 Experimental Investigations

This section explains the experimental investigations and the temperature measurement during the ECAP test. Conventionally cold-rolled AA5083 sheets with a thickness of 1.8 mm were used in this work. To provide a homogenous microstructure, a recrystallization annealing heat treatment was performed at 500 °C for 1 h. In the initial position of the ECAP test tool (see Fig. 2a), a sheet with a dimension of 200 ×

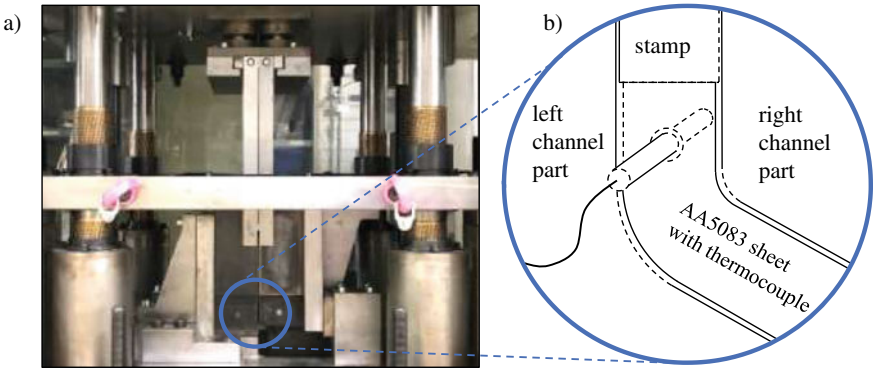


Fig. 2 **a** ECAP tool for sheet metals with 1.8 mm thickness; **b** schematic sketch of the temperature measurement in the experiment. Holes with a diameter of 0.55 mm were drilled 10-mm-deep in the middle of the sheet metal thickness to place thermocouples inside the sheet metal. (Color figure online)

$200 \times 1.8\ \text{mm}^3$ is laterally inserted between the channel parts. The sheet was pressed through the channel, consisting of the left and the right channel parts (see Fig. 2b), with a constant stamp speed of 5 mm/s with a channel angle of $\Phi = 120°$. The inner radius r is 0.5 mm and the outer radius R is 2.5 mm. For the present study, a width w of 2.22 mm and a height h of 1.8 mm were used. The pressing direction during ECAP was parallel to the rolling direction of the AA5083 sheet. The experiments were performed at room temperature.

In order to measure the temperature in the sheet metal during the ECAP process, 10 mm deep holes with a diameter of 0.55 mm for thermocouples were placed in the middle of the sides of the tested sheets, see Fig. 2b. The holes were positioned in the middle of the length of the specimens (100 mm from the edge of the sheet). Type K thermocouples with a thickness of 0.5 mm were used to measure the temperature. Thermal copper paste was used to fill the holes with the thermocouples to ensure a good heat transfer between the thermocouple and the aluminum sheet. The experiments were conducted with (f_{low}) and without (f_{high}) lubrication, to investigate the temperature development due to frictional effects. To reduce friction, the lubricant Bechem Beruforge 150D was used for the f_{low} tests [17].

Figure 3a shows the results of the temperature measurements during ECAP. The maximum temperatures develop when the position of the thermocouple (position = 100 mm) is in the shear zone of the ECAP channel. A maximum temperature increase of 15.2 K was observed in the lubricated tests (f_{low}). An increase of 18.6 K was measured without lubrication (f_{high}). Even before the maximum one can determine an increased temperature in the f_{high} sample compared to f_{low}. Due to the high thermal conductivity of the aluminum material, it is assumed that the increased friction in the channel causes higher temperatures even after passing through the shear zone. This also affects the following sheet metal sections. In addition, frictional effects at the channel walls already occur with the non-lubricated sample before it enters the

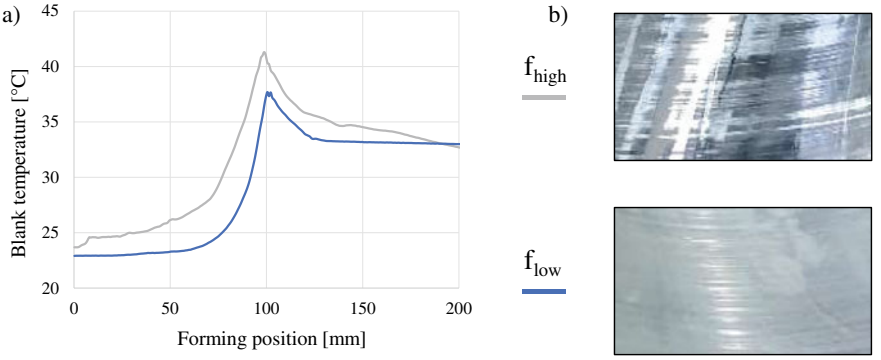


Fig. 3 **a** Absolute temperatures measured in the middle of the sheet in the experiment with (f_{low}) and without (f_{high}) lubrication; **b** surfaces of the ECAP processed sheets with high and low friction. (Color figure online)

shear zone. After the temperature maximum, localized in the shear zone at position 100 mm, the ECAP-processed material is still in contact with the tool surfaces. This produces heat conduction into the channel parts of the tool and thus leads to faster cooling for a distance of 20 mm (100–120 mm), which corresponds to the length of the channel exit after the shear zone. After the sheet metal leaves the tool, heat radiation and convection to the environment occur. Compared to the heat transfer into the active elements, the temperature therefore sinks more slowly. In the area without tool contact, it is noticeable that the temperature of the sample drops faster with increased friction. This can be attributed to damage to the sheet metal surface and the associated changes in radiation and convection behavior. Figure 3b shows the surfaces of the tested samples. The damage caused by low lubrication (f_{high}) can be seen clearly. These assumptions will be examined in more detail in the numerical part. In the area of the thermocouples, cracks form more easily in the aluminum. After the thermocouple has passed through the ECAP channel, however, the process stabilizes again immediately and proceeds as before the thermocouple passed through. The thermocouple cannot be pulled out of the sheet after the test, the shear deformation of the aluminum thus clamps the thermocouple and there is still continuous contact between the thermocouple and the material.

To determine the strains in the experiment, the approach according to Iwahashi is followed [18]. In the following formula, other symbols are used than in the original reference, since the symbols are necessary for the description of the thermomechanical characteristics. The formula describes the analytical calculation of the true plastic strain φ. The angle Φ' describes the angle of the specimen at the channel inner radius, ψ describes the angle at the channel outer radius. The angles are shown in Fig. 4.

$$\varphi = \frac{2\cot\left(\frac{\Phi'}{2} + \frac{\psi}{2}\right) + \psi cosec\left(\frac{\Phi'}{2} + \frac{\psi}{2}\right)}{\sqrt{3}} \tag{1}$$

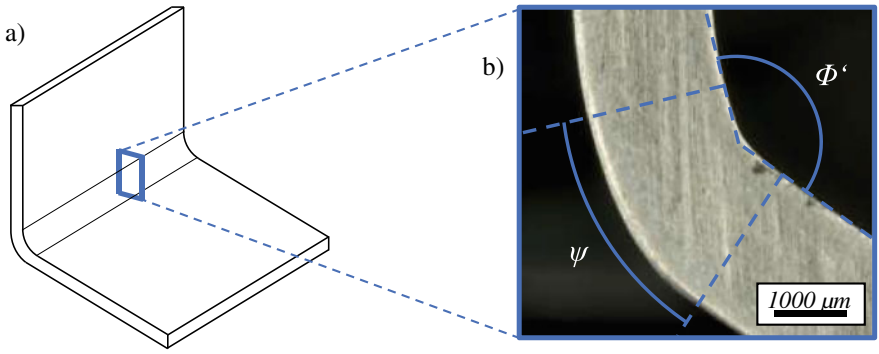


Fig. 4 **a** schematic sketch of the ECAP-deformed sheet metal. The specimen is cut out in the middle of the channel section; **b** Cross section of the specimen for determining the deformation angles Φ’ and ψ. (Color figure online)

To determine the geometric parameters for this approach, a sample is taken parallel to the ECAP direction in the center of the sheet. The specimen cross section is shown in Fig. 4b. Due to the fact that the sheet thickness is smaller than the channel width, the angle Φ' increases compared to the channel angle Φ. For the inner angle Φ', the value is 139°. The outer angle is 45°. Thus, according to Iwahashi's formula, a plastic strain φ of 0.413 is obtained.

3 Material Modeling

As a basis for the numerical investigations, first the used material model is described. To describe quasi-static hardening and elastic behavior, tensile tests according to ISO 6892 [19] were carried out at 0° with respect to the rolling direction (RD). Hydraulic bulge tests according to ISO 16808 [20] were performed to determine the equi-biaxial flow curve and to extrapolate the uniaxial flow curve. Since shear stress predominates in the ECAP process, quasi-static Miyauchi tests as described in Yin et al. were also performed [21]. These were used as a second extrapolation approach to investigate the influence of hardening behavior on the thermomechanical conversion. For the Miyauchi test a tool (Fig. 5a) was implemented in a ZwickRoell 150 kN machine. The specimen geometry is shown in Fig. 5b). To keep the shear strain homogeneous within a certain area, grooves were milled into the shear deformation area of the samples, see Fig. 5c). The load direction (LD) was parallel to the rolling direction (0°). 3D strain measurements were performed with the Aramis system (GOM GmbH) on the left shear zone of the symmetric specimen, see Fig. 5b). A constant crosshead speed of 0.0025 mm/s was used to obtain a quasi-static strain rate. The hardening curve with the bulge extrapolation approach was modeled using a combined Gosh and Hockett–Sherby approximation with a combination factor $\alpha = 0.265$ for the strains up to a value of 2 [22, 23]. The hardening curve of the

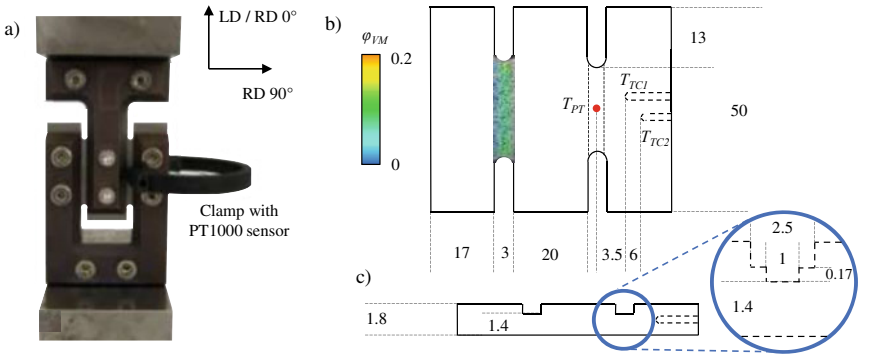


Fig. 5 **a** Miyauchi test tool with a clamp for the PT1000 sensor; **b** geometry [mm] of the Miyauchi specimen (top view). On the left side, the strains are detected; on the right side, temperature is measured with a PT1000 sensor (T_{PT}) and two thermocouples Typ K (T_{TC1}, T_{TC2}); **c** geometry [mm] of the Miyauchi specimen (side view). (Color figure online)

Miyauchi approach was modeled with an approximation according to Voce [24]. All experiments were mainly evaluated by the freely available Material Modeler tool [25]. The parameters defining the mechanical characteristics are summarized in Table 1 and the underlying mechanical data as well as the extrapolated curves are shown in Fig. 6.

In addition, intensive studies were carried out on the thermomechanical parameters, with a particular focus on an exact determination of the TQC. In order to generate a stress state comparable to the ECAP test, Miyauchi tests with LD oriented at 90° to RD were performed for the measurements. The temperature T_{PT} was detected

Table 1 Mechanical properties used for numerical investigations

Parameter	Value	References
Young's Modulus E	71.5 GPa	Measured
Poisson's ratio ν	0.33	[26]
Density ρ	2,670 kg/m^3	[26]

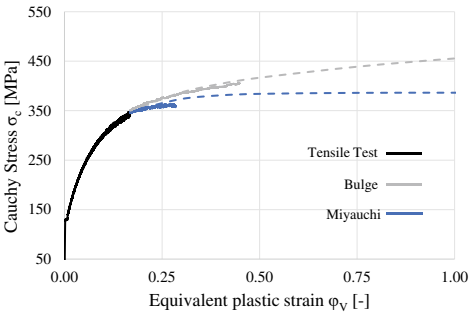


Fig. 6 Flow curve with the extrapolation strategies for bulge und Miyauchi tests. (Color figure online)

inline by a method based on a PT1000 sensor [27]. The sensor was applied to the sample with a clamp, see Fig. 5a, measuring the absolute temperature on the right shear zone of the specimen, see Fig. 5b. In order to draw conclusions about the heat conduction in the material, holes were also drilled into the side of the sample, see Fig. 5b). In these holes, the temperatures were measured with type K thermocouples (T_{TC1}, T_{TC2}). The distances between measuring points T_{PT} and T_{TC1} and between T_{PT} and T_{TC2} were 3.5 mm and 9.5 mm, respectively. The symmetry of the specimen allows the measured strain and temperature to be correlated. A crosshead speed of 2.5 mm/s was used in order to achieve a strain rate of 1/s, which approximately corresponds to the test conditions in the ECAP process. To validate the Miyauchi method, measurements were also carried out at a strain rate of 4/s with a crosshead speed of 10 mm/s.

In the Miyauchi test, no adiabatic condition can be assumed to evaluate the TQC since the tool is located very close to the forming zone and the forming motion of the testing machine is too slow for an adiabatic process. The following formulas therefore describe the individual terms that are assumed for the calculation of the TQC under consideration of the dissipated heat. In forming processes, heat is generated by energy dissipation. The sources of this are plastic deformation and friction:

$$\dot{W}_{Dissipation} = \dot{W}_{p,diss} + \dot{W}_{f,diss} \tag{2}$$

In the Miyauchi tests, the specimen is screwed on the test tool. This avoids relative movement between specimen and tool and the test is frictionless. Therefore, $\dot{W}_{f,diss}$ can be assumed to be 0. The TQC $\beta(t)$ is then introduced as the ratio of dissipated heat $\int_0^t \dot{W}_{p,diss} \cdot dt$ to plastic work $\int_0^t \dot{W}_p \cdot dt$.

$$\beta(t) = \frac{\int_0^t \dot{W}_{p,diss} \cdot dt}{\int_0^t \dot{W}_p \cdot dt} \tag{3}$$

The plastic power $\dot{W}_p$ is then calculated based on the plastic flow curve as follows:

$$\dot{W}_p = V \cdot \sigma_s \cdot \dot{\varphi} \tag{4}$$

where σ_s is the shear stress and $\dot{\varphi}$ is the plastic strain rate. For volume V, a homogenously deformed area in the milled section is assumed ($2.5 \times 24 \times 1.57$ mm^3). For the calculation of the dissipated heat rate $\dot{W}_{diss}$ several terms have to be considered:

$$\dot{W}_{p,diss} = \dot{W}_{heat} + \dot{W}_{cond} + \dot{W}_{conv} + \dot{W}_{rad} \tag{5}$$

where $\dot{W}_{heat}$ is the rate of thermal energy that is stored in the deformation area, $\dot{W}_{cond}$ represents the heat conduction from the deformation area into another part of the sample, $\dot{W}_{conv}$ is the heat loss rate across the surface into air, and $\dot{W}_{rad}$ is the heat loss rate related to radiation into the environment:

$$\dot{W}_{heat} = \rho \cdot c_p \cdot \dot{T}_{PT} \tag{6}$$

$$\dot{W}_{cond} = k \cdot A_{ref} \cdot \frac{T_{PT} - T_{ref}}{l_{ref}} \tag{7}$$

$$\dot{W}_{conv} = h \cdot A_{surf} \cdot (T_{PT} - T_{\infty}) \tag{8}$$

$$\dot{W}_{rad} = \varepsilon \cdot \sigma \cdot A_{surf} \cdot \left(T_{PT}^4 - T_{\infty}^4\right) \tag{9}$$

where T_{PT} is the temperature in the middle of the plastic deformation area and T_{∞} is the room temperature. The heat conduction $\dot{W}_{cond}$ plays an important role due to the non-adiabatic state. The term l_{ref} is calculated as follows:

$$l_{ref} = l_{12} \cdot \frac{A_{ref}}{A_{12}} \cdot \frac{T_{PT} - T_{ref}}{T_{TC1} - T_{TC2}} \tag{10}$$

where l_{ref} is a virtual quantity used to describe the length required in the observed metal from the measured temperature T_{PT} to the reference temperature T_{ref}, which is selected as the room temperature. l_{12} is the distance between T_{TC1} and T_{TC2}. A_{ref} is the area connecting the deformation area and the reference area ($2 \times (24 \times 1.57$ mm^2)). A_{12} is the cross section between the measuring points T_{TC1} and T_{TC2} (50×1.8 mm^2)). A_{surf} is the radiation surface of the homogenous deformed area ($2 \times (24 \times 1.57) \times 2.5$ mm^2). The associated values and references can be found in Table 2. The thermal conductance h_c 40,000 W/(m^2 K) depending on the clearance to the tool surface is based on the results of Cooper et al. and varied in the numerical investigations, see Table 3 [28].

The flow curve of the Miyauchi test and the measured temperature ΔT_{PT} are shown in Fig. 7a. The curves are representative of four tests with the strain rate 1/s (SR1). The tests showed a mean value for the ultimate strength of 192.75 MPa (standard deviation ± 0.9). In addition, two tests were carried out at a strain rate of 4/s (SR4), resulting in an average ultimate strength of 185.2 MPa (standard deviation ± 0.1). The evolution of the calculated TQC values (Eqs. (2)–(10)) with increasing true plastic strain is shown in Fig. 7b). The calculation with Iwahashi's formula (1) has shown that an averaged equivalent plastic strain of ~0.41 is achieved with the

Table 2 Thermomechanical properties used for the numerical investigations

Parameter	Value	References
Specific heat capacity c_p	960 J/(kg K)	[29]
Thermal conductivity k	116.6 W/(m K)	[29]
Heat transfer coefficient h	10 W/(m^2 K)	[30]
Emissivity ε	0.09	[31]
Boltzmann constant σ	5.67e−08 W/(m^2 * K^4)	[29]

Table 3 Thermal conductances h_{c1} and h_{c2} depending on the clearance used for the numerical investigations

Clearance (μm)	h_{c1} (W/(m^2 * K))	h_{c2} (W/(m^2*K))
0	40,000	4,000
1	7,900	3,450
10	2,000	1,500
30	700	700
100	0	0

present ECAP-setup. Therefore, the TQC value was also determined at this strain (average of SR1 and SR4) as 0.47 and used for further simulations.

4 Numerical Investigations and Discussion

The ECAP test is about introducing high shear strains as homogeneously as possible into the material. Therefore, 2D plane strain simulations were conducted using the explicit FE code Abaqus (Version 2020). The channel and the stamp were modeled as discrete rigid. The sheet was meshed with rhomboid-shaped CPE4R-elements. An element size of $e = 0.12$ mm and a minimum mass-scale time increment of 1e−005 s were used. These values were adapted from the numerical setup of [10]. Since it is a continuous process without large accelerated masses, no dynamic effects or erroneous mesh distortions could be detected and an acceptable simulation time could be achieved. The material parameters as described above were used for the model. The friction was modeled as isotropic penalty. For the contact, the "hard contact" implemented in Abaqus was selected. The temperature was analyzed at the same position as in the experiment on an element in the center of the sheet. Simulations with a low friction $f = 0.02$ were first performed to investigate the influence of a variation in material parameters. These variations were carried out in order to investigate the influences on the temperature profiles. The effect of a change of the thermal conductivity h_c value is shown in Fig. 8a. When the literature value of 40,000 W/(m^2 K) is reduced to 4,000 W/(m^2 K), the temperature in the sheet metal is increased by ~4 K. Less heat, therefore, is transferred to the tool. Since this value has a great effect on the result of the simulation, it should not be referred to literature values but to experimental investigations for further studies, based on the ECAP setup and materials. A variation of the heat transfer coefficient h, which represents the convection of the process, is considered in Fig. 8b. For the heat transfer coefficient $h = 10$ W/(m^2 K), the temperature curve behaves like in the experiment with good lubrication and good workpiece surface (f_{low}). If the value of h is decreased, no difference is obtained. If the value of h is increased, the temperature of the sheet decreases more strongly after leaving the channel. This behavior corresponds to the experiment with increased friction and poor surface (f_{high}). The assumption that the poor surface effectively causes a higher amount of convective heat transfer is thus confirmed. Moreover, since there are no differences in the temperature maximum

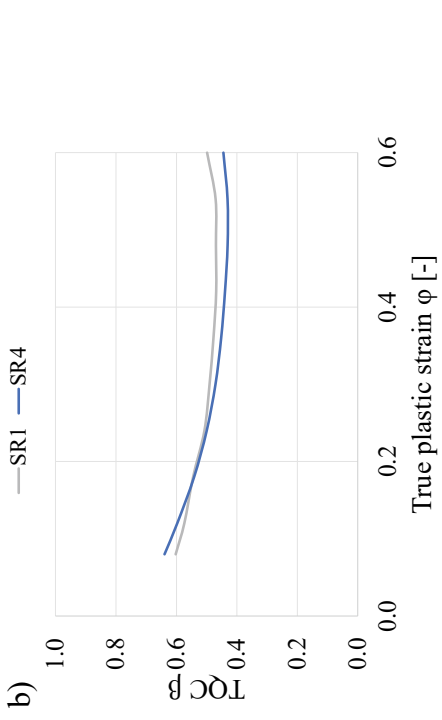


Fig. 7 **a** Shear Stress–True strain curve of the Miyauchi test and temperature differences ΔT_{PT}, ΔT_{TC1} and ΔT_{TC2} at a strain rate of 1/s; **b** TQC—True strain curves for strain rate 1/s (SR1) and 4/s (SR4). (Color figure online)

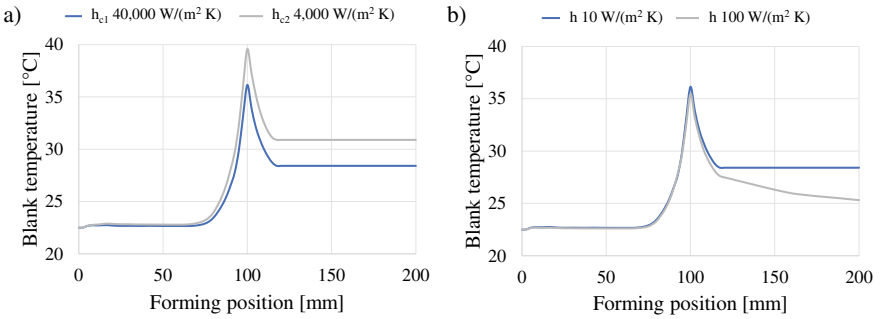


Fig. 8 **a** temperature depending on the position of the ECAP sheet for different thermal conductivities; **b** sheet metal temperature depending on the position of the ECAP sheet for different heat transfer coefficients. (Color figure online)

for the two relevant values 10 and 100 W/(m^2 K), the value 10 W/(m^2 K) was used in all further numerical investigations discussed below. Radiation has a negligible influence at the relatively low temperatures observed during sheet metal ECAP and was therefore not examined in more detail.

In the next step, the difference in the extrapolation strategies (bulge and Miyauchi) and the influence of the TQC are discussed, see Fig. 9. The maximum temperature difference of the bulge extrapolation is 14.1 K, whereas the maximum temperature difference of the Miyauchi extrapolation is 13.6 K (Fig. 9a). This shows that the experimental determination of flow behavior has an influence on the accuracy of the simulation of SPD processes, but does not play an important role in the consideration of thermomechanical effects. In order to map the stress state in the ECAP process as precisely as possible, even for high deformations, extrapolation using the Miyauchi test is used for the following numerical testing. Figure 9b shows the considerable influence of the TQC. The measured value of 0.47 is compared with the frequently used default value of 0.9. A difference of 11.4 K can be seen between the maxima

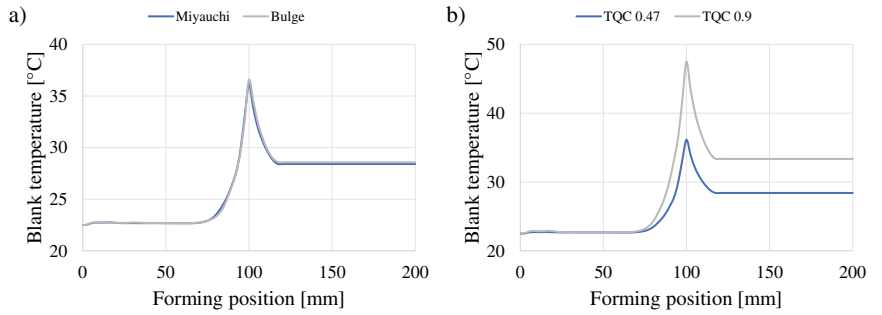


Fig. 9 **a** temperature depending on the position of the ECAP sheet for different flow curve extrapolations (Miyauchi and Bulge); **b** blank temperature depending on the position of the ECAP sheet for different TQC values. (Color figure online)

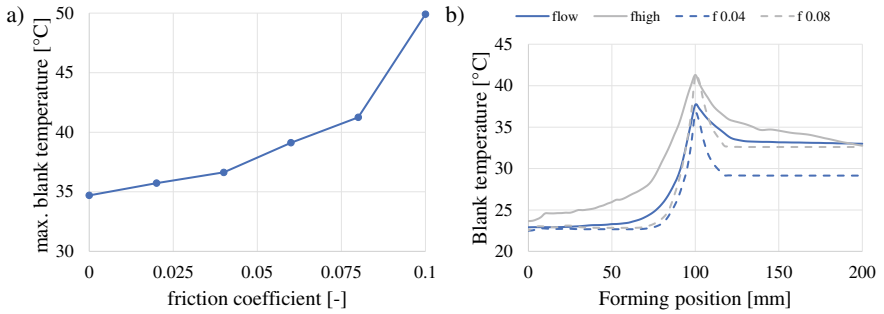


Fig. 10 **a** maximum blank temperature depending on different friction coefficients determined in the numerical investigation; **b** Comparison between simulation and experiment. A friction coefficient of 0.04 fits well for the lubricated experiment (f_{low}) whereas a friction coefficient of 0.08 matches the unlubricated experiment (f_{high}). (Color figure online)

of the curves. This demonstrates that the material parameters must be considered in detail and adapted carefully for numerical investigations, especially if they concern friction. Since the strain rate and also the stress state also have an influence on the TQC, the determination of this parameter should also be adapted to the present process, as in this study.

In the following, the influence of friction on the process is examined. For this purpose, the simulation was conducted with different coefficients of friction in a range from 0.0 to 0.1. Figure 10a shows the temperature maxima with the associated friction coefficients. An almost linear rise in temperature can be seen between 0.0 and 0.04 with increasing friction. The temperature increases more strongly after this initial linear region. Figure 10b shows the curves for the coefficients 0.04 and 0.08 (dashed lines) and, for comparison, the two experimental curves. For the selected parameter setup, the friction values can therefore be determined for a lubricated and not lubricated surface. These findings agree well with the results of Frint et al., who determined a friction coefficient of 0.06 for the (bulk) ECAP process also using the lubricant Bechem Beruforge 150D [17].

5 Conclusion and Outlook

In the present study, ECAP experiments were carried out with two different friction states (f_{high} = not lubricated and f_{low} = lubricated). In order to determine this friction, Miyauchi tests were carried out and three temperatures were measured at several positions in order to determine the TQC during the shear deformation. With this parameter setup, numerical investigations were carried out in order to predict the friction inversely. Temperatures were measured in the experiments and used for the

validation of the numerical model. By comparing the temperatures between simulation and experiment, it was possible to determine coefficients of friction for the ECAP process. The following findings were obtained in this way:

- An increase in temperature of 18.6 K can be measured in the ECAP process for sheet metals. With lubrication, the temperate is lower by 3.4 K.
- In the numerical investigations, the hardening curve, and thus the selected extrapolation approach, have an influence on thermal conversion in the process. Nevertheless, this difference is comparatively small and it is not necessary to resort to extrapolation using shear tests (Miyauchi) for an accurate ECAP simulation.
- It turns out that, in addition to the TQC, the thermal conductance h_c also has an influence on the simulation. For further studies, this parameter should also be determined experimentally.
- It was shown that a default TQC of 0.9 is clearly too high for the present material and process. A TQC of 0.47 was determined for the AA5083 material using the Miyauchi test. The testing parameters (strain, strain rate, stress state) were adapted to the ECAP process. The tests also showed that fluctuations occur primarily in the temperature measurement. In order to estimate the TQC even more accurately, further strain rates should be tested. In addition, a validation by means of a Miyauchi simulation can produce a more detailed result of the parameter l_{ref}. In further studies it can be investigated whether this method can also be used for other materials.
- A second validation method for the ECAP-simulation could be the determination of the process forces. In further studies, this approach could provide additional confirmation of the TQC value
- A friction coefficient of 0.04 was determined by the new method within the lubricated process. Without the use of the lubricant, the component surface was poor and the coefficient increased to 0.08.

Acknowledgments The authors gratefully acknowledge the German Research Foundation (Deutsche Forschungsgemeinschaft, DFG) for supporting this work carried out within the framework of the collaborative research projects VO 1487/32-2 and WA 2602/13-2.

References

1. Segal V, Reznikov V, Dobryshevshiy A, Kopylov V (1981) Plastic working of metals by simple shear. Russ Metall (Metally) 1:99–105
2. Lowe TC, Valiev RZ (2004) The use of severe plastic deformation techniques in grain refinement. J Miner Metals Mater Soc (TMS) V 56/10:64–68
3. Furukawa M, Horita Z, Langdon TG (2002) Factors influencing the shearing patterns in equal channel angular pressing. Mater Sci Eng A 332:97–109
4. Jufu J, Ying W, Zhiming D, Jianjun Q, Yi S, Shouhing L (2010) Enhancing room temperature mechanical properties of Mg-9Al-Zn alloy by multi-pass equal channel angular extrusion. J Mater Proc Tech 210:751–758

5. Utsunomiya H, Saito Y, Suzuki H, Sakai T (2001) Development of the continuous shear deformation process. Proc Inst Mech Eng Part B J Eng Manuf 215(7):947–957
6. Shahab AR, Akbari Mousavi SAA, Ranjbar Bahadori S, Ebrahimi SM (2012) The comparison between continuous confined strip shearing (C2S2) and ECAP Conform In Regard To Equivalent Plastic Strain Distribution for Al 1100. Int J Mod Physi Conf Series 05:400–409
7. Horita Z, Fujinami T, Langdon TG (2001) The potential for scaling ECAP: effect of sample size on grain refinement and mechanical properties. Mater Sci Eng A 318(1–2):34–41
8. Kamachi M, Furukawa M, Horita Z, Langdon TG (2003) Equal-channel angular pressing using plate samples. Mat Sci Eng A361:258–266
9. Suh J, Victoria-Hernandez J, Letzig D, Golle R, Yi S, Bohlen J, Volk W (2015) Improvement in cold formability of AZ31 magnesium alloy sheets processed by equal channel angular pressing. J Mater Process Technol 217:286–293
10. Gruber M, Illgen C, Frint P, Wagner MFX, Volk W (2019) Numerical and Experimental Study on ECAP-Processing Parameters for Efficient Grain Refinement of AA5083 Sheet Metal. Key Eng Mater 794:315–323
11. Illgen C, Frint P, Gruber M, Volk W, Wagner MFX (2019) Evolution of grain refinement in AA5083 sheet metal processed by ECAP; Light Metals 2020. The minerals, metals & materials series
12. Segal VM (2003) Slip line solutions, deformation mode and loading history during equal channel angular extrusion. Mater Sci Eng A 345(1–2):36–46
13. Taylor GI, Quinney H (1934) The latent energy remaining in a metal after cold working. Proc R Soc Lond 143:307–326
14. Rittel D, Zhang LH, Osovski S (2017) The dependence of the Taylor-Quinney coefficient on the dynamic loading mode. J Mech Phys Solids 107:96–114. https://doi.org/10.1016/j.jmps.2017.06.016
15. Macdougall D (2000) Determination of the plastic work converted to heat using radiometry. Exp Mech 40:298–306. https://doi.org/10.1007/BF02327503
16. Behrens BA, Chugreev A, Bohne F, Lorenz R (2019) Approach for modelling the Taylor-Quinney coefficient of high strength steels. In: 18th international conference on sheet metal, SHEMET, pp 464–471
17. Frint P, Wagner MFX, Weber S, Seipp S, Frint S, Lampke T (2017) An experimental study on optimum lubrication for large-scale severe plastic deformation of aluminum-based alloys. J Mat Proc Tech 239:222–229
18. Iwahashi Y, Wang J, Horita Z, Nemoto M, Langdon TG (1996) Principle of equal-channel angular pressing for the processing of ultra-fine grained materials. Scr Mater 35:143–146
19. ISO 6892-1:2016-06 (2016) Metallic materials—tensile testing—part 1: method of test at room temperature
20. ISO 16808:2014 (2014) Metallic materials—sheet and strip—determination of biaxial stress-strain curve by means of bulge test with optical measuring systems
21. Yin Q, Zillmann B, Suttner S, Gerstein G, Biasutti M, Tekkaya AE, Wagner MFX, Merklein M, Schaper M, Halle T, Brosius A (2014) An experimental and numerical investigation of different shear test configurations for sheet metal characterization. Int J Solids Struct 51:1066–1074
22. Ghosh AK (1977) Tensile instability and necking in materials with strain hardening and strain-rate hardening. Acta Metall 12:14131424. https://doi.org/10.1016/0001-6160(77)90072-4
23. Hockett JE, Sherby OD (1975) Large strain deformation of polycrystalline metals at low homologous temperatures. J Mech Phys Solids 23:87–98. https://doi.org/10.1016/0022-5096(75)90018-6
24. Voce E (1948) The relation between the stress and strain for homogeneous deformation. J Inst Metals 74:537–562
25. Benkert T, Hartmann C, Eder M, Speckmaier F, Volk W (2019) MaterialModeler—from experimental raw data to a material model. SoftwareX 10: https://doi.org/10.1016/j.softx.2019.100249
26. Boyer HE, Gall TL (1985) Metals Handbook. American Society for Metals, Materials Park, OH

27. Vitzthum S, Hartmann C, Eder M, Volk W (2019) Temperature-based determination of the onset of yielding using a new clip-on device for tensile tests. In: 18th international conference on sheet metal, SHEMET, pp 490–497
28. Cooper MG, Mikic BB, Yovanovich MM (1968) Thermal contact conductance. Int J Heat Mass Transf 12:279–300
29. Mm El-Sayed, Shash AY, Abd-Rabou M (2017) Finite element modeling of aluminum alloy AA5083-O friction stir welding process. J Mat Proc Tech 252:13–24. https://doi.org/10.1016/j.jmatprotec.2017.09.008
30. Khalif AJN, Al Mousawi IRA (2016) Comparison of heat transfer coefficients in free and forced convection using circular annular finned tubes. Int J Appl Innov Eng Manag IJAIEM 5:194–204
31. Wen CD, Mudawar I (2005) Emissivity characteristics of polished aluminum alloy surfaces and assessment of multispectral radiation thermometry (MRT) emissivity models. Int J Heat Mass Transf 48:1316–1329

Transformation of α→β During Hot Deformation in the Two-Phase Region of Ti–6Al–2Zr–1Mo–1V Alloy



Lei Chen, Qifei Zhang, Qun Li, Miao Jin, Shiyan Zhao, and Baofeng Guo

Abstract Isothermal compressive tests were performed on a Ti–6Al–2Zr–1Mo–1V alloy below the beta-transus. The results showed that straining caused a decrease in the primary α phase, indicating that a strain-induced phase transformation of α→β occurred, whereby an additional dynamic softening was shown. This transformation was sensitive to temperature and strain rate. The higher the temperature was, the more the primary α phase transformed. The extent of α→β increased as the strain rate decreased. The α phase even transformed to β phase completely so long as the deformation duration was enough. Besides deformation, the overall heat duration which included the reheating before deformation and the absolute duration during deformation caused the additional dissolution of primary α phase. In this work, a quantitative model for dissolution kinetics of the primary α phase was established considering the strain-induced phase transformation and the overall heat duration.

Keywords Ti–6Al–2Zr–1Mo–1V alloy · Isothermal compressive tests · Dynamic transformation

1 Introduction

Dynamic transformation of steels was first reported by Yada in the 1980s. When conventional steels had been compressed or/and rolled at a temperature above the Ae3, transformation of austenite into ferrite occurred in the samples [1]. Similarly, this phenomenon was found in titanium alloys. However, the dynamic transformation of titanium alloy is different from that in steels. Generally, the dynamic transformation of titanium alloy was thermally deformed below the β-transus temperature, and the phenomenon of α phase transforming into β phase occurred [2–9]. The superplastic deformation of Ti–5.5Al–1Fe titanium alloy in the two-phase region was tested by Koike and co-workers [2]. Their results showed the stress of the α phase increased during the superplastic deformation and caused the stress-induced

L. Chen · Q. Zhang · Q. Li · M. Jin · S. Zhao · B. Guo (✉)
School of Mechanical Engineering, Yanshan University, Qinhuangdao 066004, People's Republic of China
e-mail: baofengysu@163.com

© The Minerals, Metals & Materials Society 2021

G. Daehn et al. (eds.), *Forming the Future*, The Minerals, Metals & Materials Series,
https://doi.org/10.1007/978-3-030-75381-8_150

phase transformation of α→β that further resulted in a large superplastic elongation. Although Koike showed that the primary α phase changed with strain, they didn't report changes in β phase caused by dynamic transformation. Similar results were reported by Matsumoto [3], Zhang [4], Sun [5], etc. But they also ignored the effects of changes in β phase on the mechanical behavior. Recently, Guo et al. [6] reported the dynamic transformation of Ti–6Al–4V alloy during hot torsion tests and proposed that the critical stress required to initiate dynamic transformation was less than the peak stress [7]. They expressed the change of β phase produced by dynamic transformation, but they did not propose a systematic model to describe the special microstructural change and, meanwhile, the effect of static heat duration before deformation on the β phase was not considered. Aranas [8] and Foul et al. [9] showed that the dynamic transformation took place during hot compression of pure titanium depended on the total energy obstacle and driving force. Similarly, the heat duration effect during reheating was not be involved.

In the current work, the static heat treatment of Ti–6Al–2Zr–1Mo–1V titanium alloy was carried out at the temperature from 940 to 970 °C. It was found that the primary α phase fraction is sensitive to holding time. Dynamic transformation was observed during hot compression under various conditions. On this basis, the predicted model of the primary α phase fraction was proposed in order to understand the dynamic transformation better.

2 Experimental Procedure

2.1 Experimental Material

The studied material, commercial Ti–6Al–2Zr–1Mo–1V titanium alloy, was forged into a bar with a diameter of 300 mm. The β-transus temperature of the alloy was 995 °C by means of metallographic method. Figure 1 shows the initial microstructure of the test alloy. It can be seen that the initial microstructure is mainly composed of primary equiaxed α phase with a fraction of 55%, β-transformed structure consists of lamellar α and residual β. The average size of primary α phase is about 18 μm and the thickness of lamellar α phase is about 2.2 μm.

2.2 Compression Deformation Tests

Cylindrical specimens with 10 mm in diameter and 15 mm in length were machined along the forging direction. Hot compression tests were carried out on the Gleeble-3800 thermal–mechanical simulator. Samples were carried out to deformation of 50% at a strain rate 0.01 s^{-1} and at the temperatures of 940, 950, 960, and 970 °C, respectively. The deformation of 5–70% was carried out at a strain rate of 0.001 s^{-1}

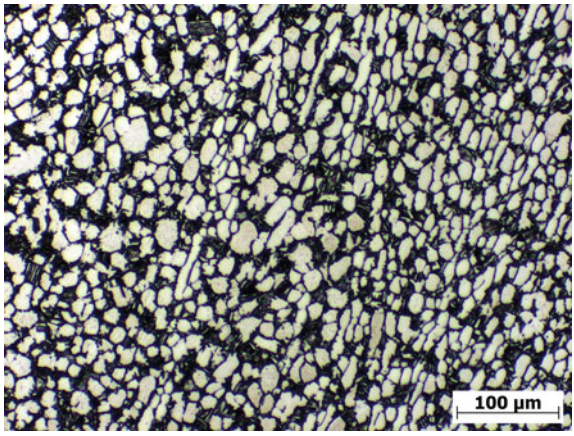


Fig. 1 Initial microstructure of Ti–6Al–2Zr–1Mo–1V titanium alloy. (Color figure online)

and at 960 °C in order to determine the effect of strain on the transformation. Strain rates of 1, 0.1, 0.01, and 0.001 s^{-1} were applied for analyzing the effect of strain rate on the transformation when the deformation is 30% and the temperature is 960 °C. Heating rate for all compression is 10 °C/s. Specimens were held at deformation temperature for 10 min and then deformed. Subsequently, deformed samples were cooled to room temperature in air.

2.3 Heat Treatment

In order to compare the microstructural differences during hot compression and heat treatment, the quantitatively microstructural analysis was done. The size of specimens for heat treatment tests was the same as that for heat compression to eliminated the size effect. The specimens were heated at 960 °C for 0, 3, 5, 10, 30, and 60 min, respectively. Then, reheated specimens also were cooled to room temperature in air.

2.4 Microstructural Characterization

Deformed microstructures were investigated using optical microscopy (OM). They were sectioned along their symmetry axes and ground on silicon carbide papers with particle sizes from 120 to 2500 mesh by an automatic polishing machine. Subsequently, the mechanochemical method was carried out to polish samples. Final polishing was carried out by using the 80–100 nm alkaline colloidal silica solution with mash fraction and followed by etching with a mixed etchant solution of 2 ml HF+12 ml HNO_3+14 ml H_2O for 5–15 s. The metallographic analysis was performed the Image-Pro Plus software to quantify the fraction of equiaxed primary α grains.

The average α and β phase fractions were evaluated on the basis of five graphs for each sample.

3 Experimental Results

3.1 Flow Curves

The flow curves for Ti–6Al–2Zr–1Mo–1V alloy, at a strain rate of 0.01 s^{-1} are displayed in Fig. 2. As can be seen in the figure, the stress decreases with the increasing temperature. At each temperature, the stress rapidly increases to the peak stress with increasing strain at the deformed temperature, and gradually decreases and then reaches the steady-state stress when the work hardening and the flow softening tend to a balance. Here, the stress at the strain of 0.2% is taken as the initial yield stress. It is worth mentioning that the steady-state stress is lower than the initial yield stress at each deformation temperature. Generally, the flow softening occurs during hot deformation of most metal materials due to the DRX, because the dislocation density decreases rapidly once the DRX starts [10, 11]. However, it is well known that work hardening cannot be completely eliminated by dynamic recrystallization whereby a part of deformed microstructure (unrecrystallized microstructure) remains, so the steady-state stress is always higher than the initial yield stress [12, 13]. Obviously, an additional flow softening mechanism exists during hot deformation of the test alloy.

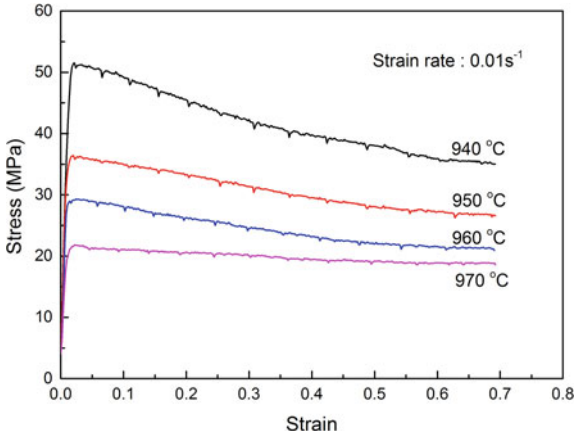


Fig. 2 Stress–strain curves at a strain rate of 0.01 s^{-1}. (Color figure online)

3.2 Microstructure Analysis

Figure 3 shows the microstructures of undeformed and deformed specimens tested at different temperatures in the two-phase region. Obviously, the primary α phase fraction decreases with increasing temperature. The relationship between deformation temperature and primary α phase fraction is displayed in Fig. 6a. The α phase fraction changes from 0.371 to 0.293 during the deformation of 940 °C. Particularly, the α phase almost disappears after deformation of 50% at 960 °C and 970 °C. The primary α phase in the undeformed samples decreases is due to the gradual dissolution of primary α phase into β during static reheating [6, 14, 15]. However, the decrease of the primary α phase during deformation indicates that the dynamic phase transformation of α→β occurs. The decreasing of harder α phase during deformation is the important cause for the aforementioned additional flow softening.

The effects of strain and strain rate on the microstructures are depicted in Figs. 4 and 5, respectively. Meanwhile, the changes of the primary α phase fraction after deformation at 960 °C and 0.001 s^{-1} are displayed in Fig. 6b. It can be seen that the α phase fraction and grain size decrease as the strain increases. Compared with the undeformed sample, when the strain is 0.051, the primary α phase fraction reduces to 0.133. When the strain was increased to 0.693, the α fraction was close to zero (0.0003). With further increase in the strain to 1.204, the primary α phase completely disappeared.

The effect of strain rate on such dynamic transformation of α→β is depicted in Fig. 6c. It is evident that the primary α phase fraction and grain size decrease with the decreasing strain rate. At the same strain, the primary α fraction is 0.157 at the strain rate of 1 s^{-1} while it was reduced to 0.006 at the strain rate of 0.001 s^{-1}.

3.3 Static Transformation During Heat Treatment

The microstructures during static heat treatment at 960 °C display in Fig. 7. And the change in the α phase fraction is illustrated in Fig. 8. It can be seen that the α phase fraction decreases with increasing holding time. It gradually trends to the equilibrium state where the α phase fraction does not change with holding time. For the test alloy, the α volume fraction changes from 0.317 to 0.161 when the holding time is from 3 to 30 min. With further increase in the holding time to 60 min, the α phase fraction still remains 0.159 indicating the α volume fraction is stable after a heat duration of 30 min.

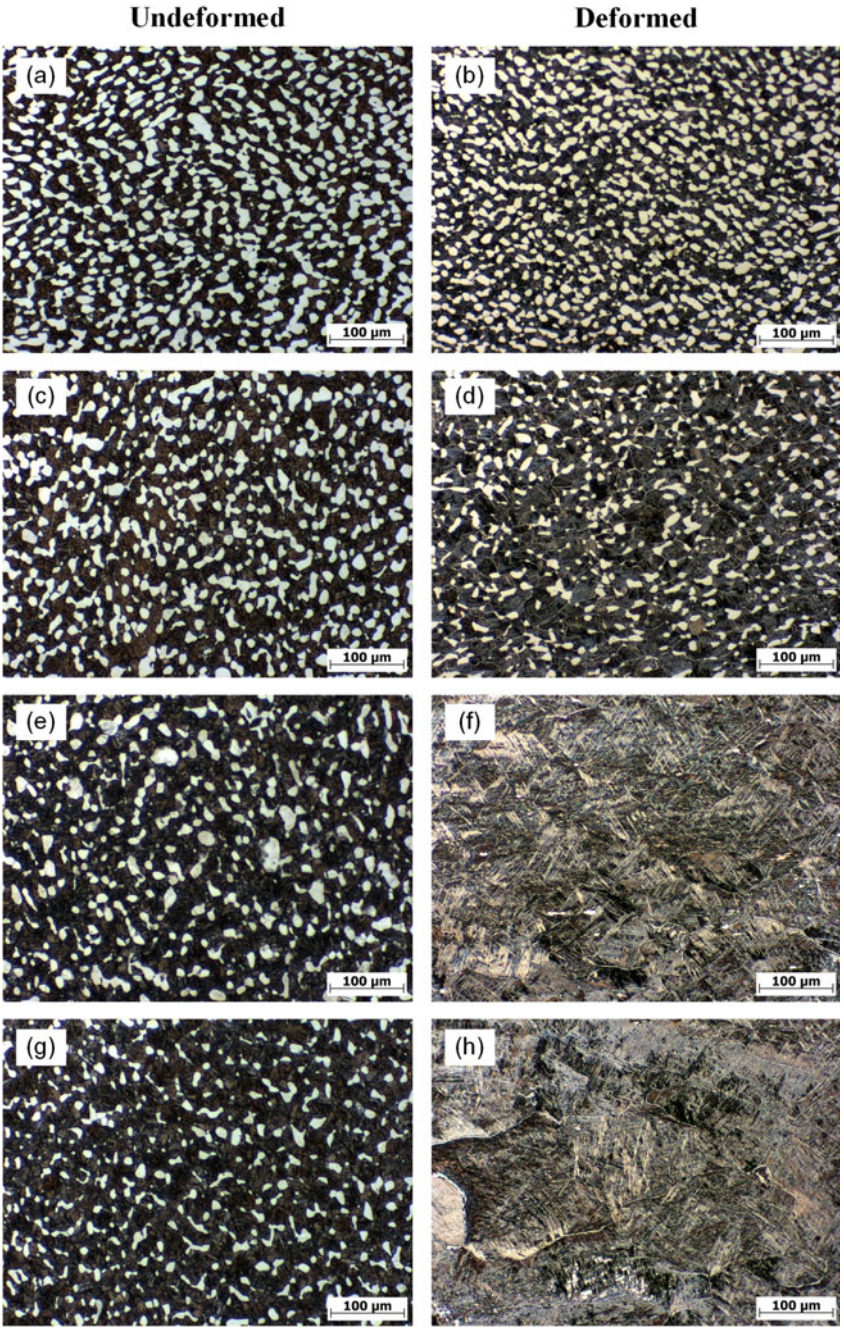


Fig. 3 Undeformed (left) and deformed (right) microstructures at the strain of 0.693 and the strain rate of 0.01 s^{-1}, 940 °C: (**a**) and (**b**), 950 °C: (**c**) and (**d**), 960 °C: (**e**) and (**f**), 970 °C: (**g**) and (**h**). (Color figure online)

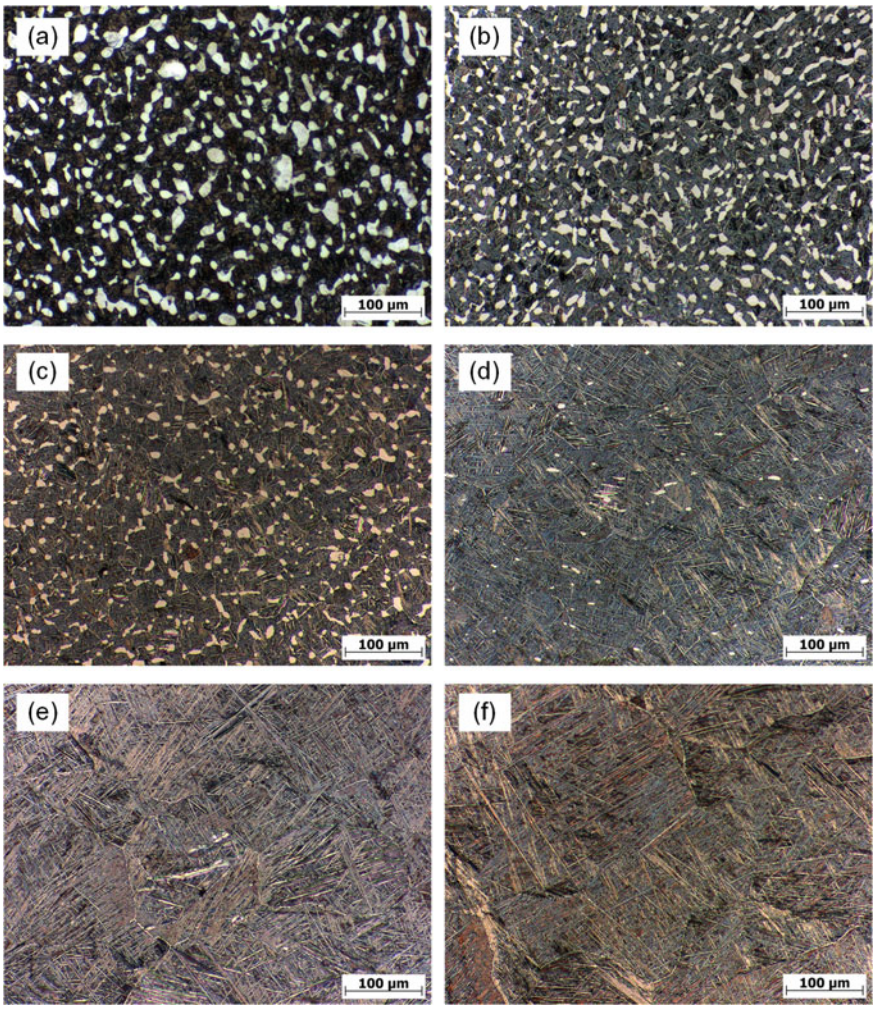


Fig. 4 Microstructures of samples deformed to different strain at a strain rate of 0.001 s^{-1} at 960 °C: **a** 0%, **b** 5%, **c** 10%, **d** 30%, **e** 50%, and **f** 70%. (Color figure online)

4 Discussion

4.1 The Effect of Deformation Heat

The effect of the deformation heat on the alloy cannot be ignored during hot deformation [16, 17] because the material properties will change due to this increasing temperature, especially for the titanium alloy that has poor thermal conductivity [18, 19]. The change in temperature attributable to deformation is given by

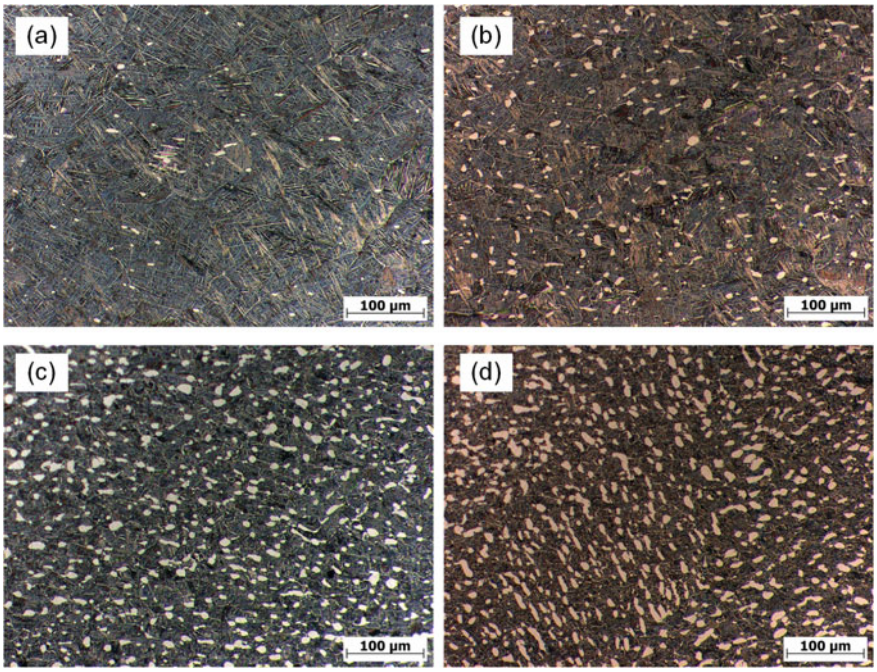


Fig. 5 Microstructures of samples deformed to a strain of 0.357 with different strain rates at 960 °C: **a** 0.001 s^{-1}, **b** 0.01 s^{-1}, **c** 0.1 s^{-1} and **d** 1 s^{-1}. (Color figure online)

$$\Delta T = \frac{0.95\eta \int_0^{\varepsilon} \sigma d\varepsilon}{\rho C_{\mathrm{p}}} \tag{1}$$

where ΔT refers to the temperature increase, η is the adiabatic correction factor, σ is the stress, ε is the strain, ρ is the density of test alloy, C_{p} is the specific heat [20]. The adiabatic correction factor employed here is 0.25 when the strain rate is 0.01 s^{-1} [20]. At the same strain (0.693) and strain rate (0.01 s^{-1}), the temperature increase caused by deformation heating at different conditions is listed in Table 1. The temperature increase decreases slightly as the deformation temperature increases. Compared with the deformation temperature, the deformation heating at the condition of 0.01 s^{-1} is too small to be neglected [6].

4.2 Model of Dynamic Transformation of α→β

The primary α phase fraction changes during heat treatment when the holding time is not enough to reach equilibrium state [21]. In present compression tests, samples reheated for 10 min have no nonequilibrium α phase fraction. Therefore, during deformation, especially at a lower strain rate, the transformed α phase fraction includes

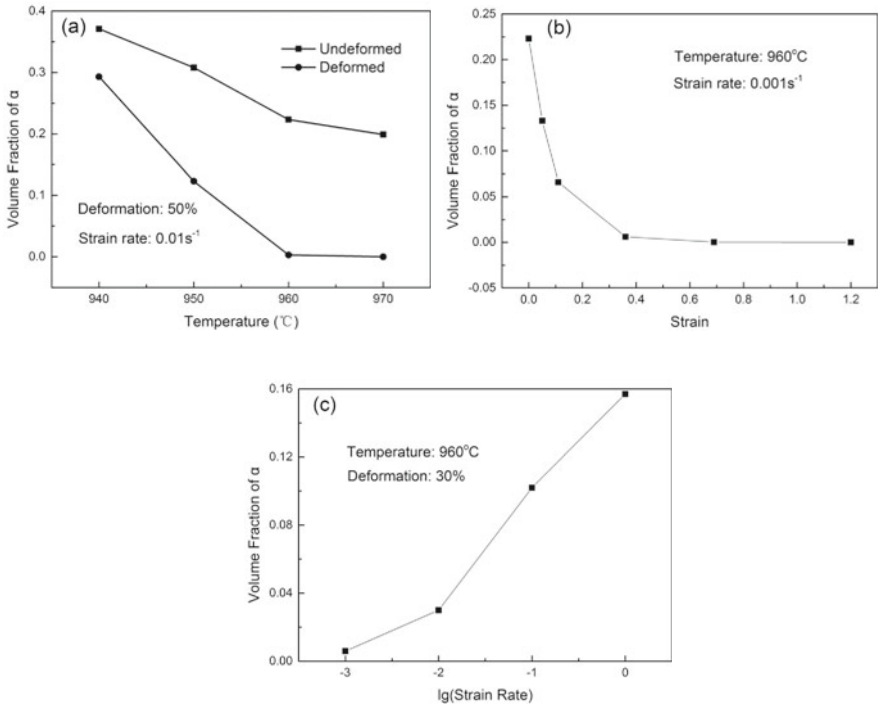


Fig. 6 The primary α phase fraction at different conditions. **a** temperature effect; **b** strain effect; **c** strain rate effect

two parts. The first part is due to dynamic transformation induced by deformation and the second part comes from static transformation due to longer heat duration during deformation with lower strain rate. So the true change in the primary α phase fraction caused by dynamic deformation can be expressed:

$$\omega_{\mathrm{DT}}(\alpha) = \omega_{\mathrm{HT}}(\alpha) - \omega_{\mathrm{D}}(\alpha) \tag{2}$$

where $\omega_{\mathrm{DT}}(\alpha)$ is the transformed fraction of the α phase caused by dynamic transformation, $\omega_{\mathrm{HT}}(\alpha)$ is the primary α phase fraction after the overall heat duration (including the holding time before deformation and deformation time), and $\omega_{\mathrm{D}}(\alpha)$ is the remaining primary α phase fraction after deformation.

Based on the results in Figs. 6b and 8, the variation of the primary α phase during overall deformation at 960 °C is obtained, as shown in Fig. 9. The shadow region represents the true change in primary α phase fraction caused by dynamic deformation. It can be seen that the values of aforementioned $\omega_{\mathrm{HT}}(\alpha)$ at a certain strain actually correspond to the spot on the black line, but always not to the spot at 600 s (10 min) which represents the value before the deformation.

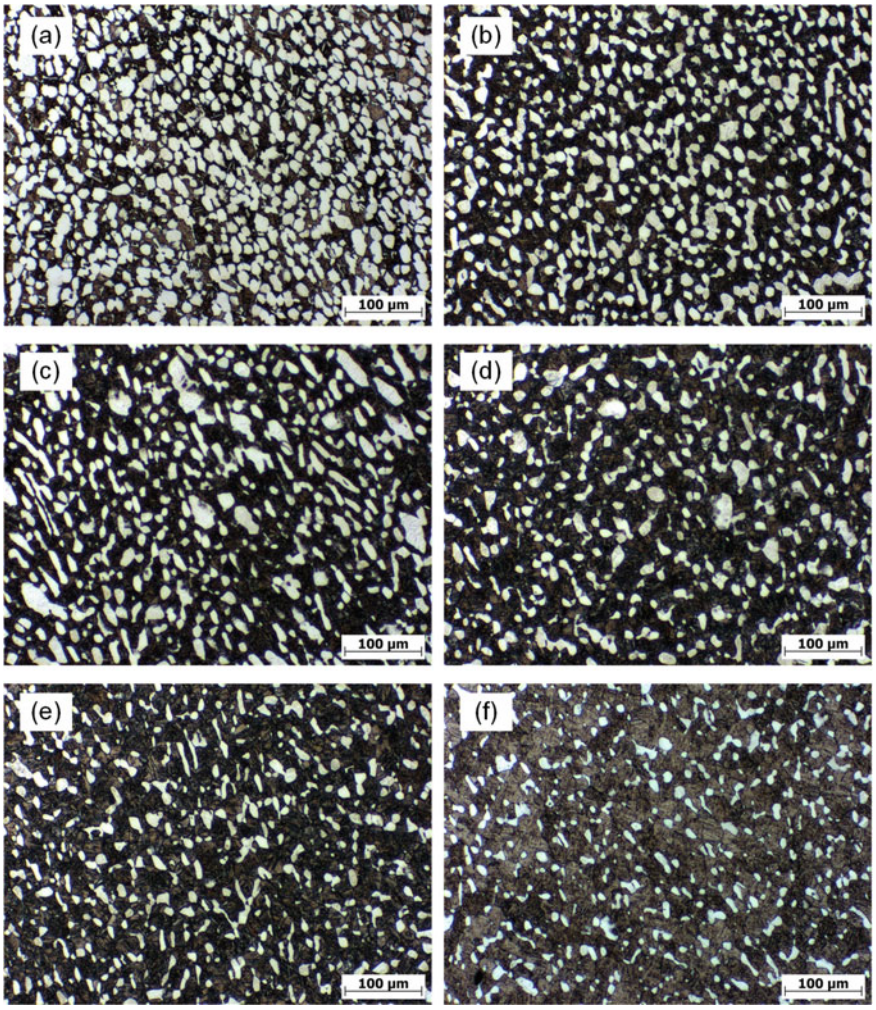


Fig. 7 Microstructures after reheating at 960 °C for different holding time. **a** 0 min, **b** 3 min, **c** 5 min, **d** 10 min, **e** 30 min and **f** 60 min. (Color figure online)

The model of classical Johnson–Mehl–Avrami (JMA) is widely used to describe the models of phase transformation in titanium alloy [22, 23]. In this paper, the model for dissolution kinetics of the primary α phase at 960 °C can be represented:

$$\omega_{\alpha}(t) = 1 - \exp\left[-(kt)^{n}\right] \tag{3}$$

where $\omega_{\alpha}(t)$ is the extent of the transformation at a given time t, n is the JMA exponent, k is a rate constant which depends on the temperature.

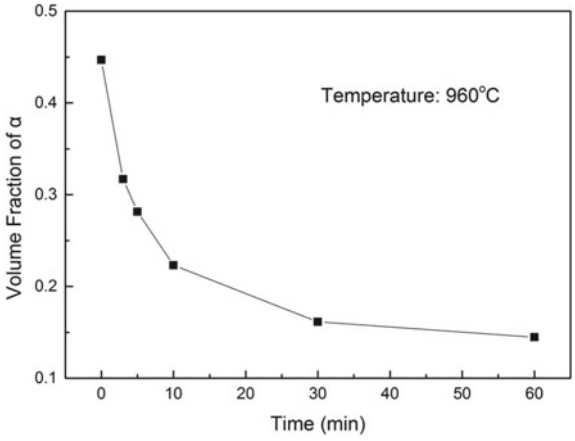


Fig. 8 Volume fraction of primary α phase at different holding time and the same holding temperature

Table 1 The deformation heating at different conditions

Deformation temperature (°C)	940	950	960	970
Temperature increase (°C)	1.72	1.27	1.0	0.82

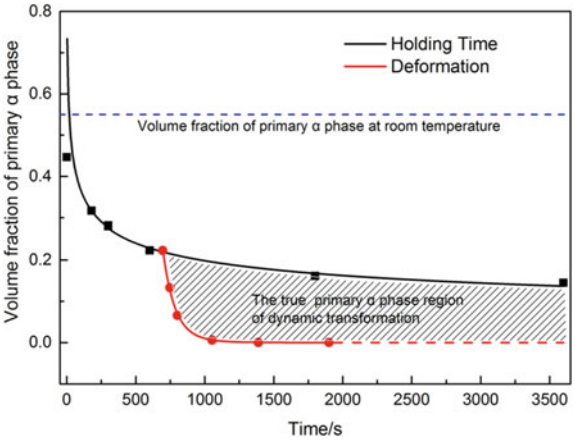


Fig. 9 The variation of primary α phase during overall deformation at 960 °C. (Color figure online)

The parameters k and n are calculated by regression analysis based on Fig. 9, and then the transformed kinetic of the primary α phase during the overall heat duration at 960 °C is given by Eq. (4) and the transformed model for the remaining primary α phase after deformation is expressed as Eq. (5), respectively, as follows:

$$\omega_{HT-\alpha}(t) = 1 - \exp\left[-(0.116t)^{-0.318}\right] \tag{4}$$

$$\omega_{D-\alpha}(t) = 1 - \exp\left[-(0.002t)^{-8.815}\right] \tag{5}$$

Therefore, the model of dissolution kinetics for the primary α phase during dynamic transformation is given by

$$\omega_{DT-\alpha}(t) = \exp\left[-(0.002t)^{-8.815}\right] - \exp\left[-(0.116t)^{-0.318}\right] \quad (6)$$

On basis of these models, the primary α phase fraction can be accurately predicted for overall hot working process in order to tailor the microstructure and mechanical properties.

5 Conclusion

The dynamic transformation behavior of Ti–6Al–2Zr–1Mo–1V titanium alloy was studied by means of hot compression deformation tests. The current results can be summarized as follows:

1. Dynamic transformation of α→β took place during hot forging which caused an additional dynamic softening.
2. Dynamic transformation depended on the deformed temperature and strain rate. It can be facilitated by increasing temperature and/or decreasing strain rate. The primary α phase even completely disappeared at some conditions.
3. A predicted model of the primary α phase during overall hot working was proposed.

Acknowledgments The authors are grateful for the financial support by the National Natural Science Foundation of China (Grant Nos. 51675467,51675465), the Natural Science Foundation of Hebei province, China (Grant No. E2019203560), and the Project funded by China Postdoctoral Science Foundation (Grant Nos. 2016M600194, 2017T100712)

References

1. Yada H, Matsumura Y, Senuma T (1986) Massive type transformation induced by hot deformation in low carbon steels. In: Proceedings of the international conference on martensitic transformation, JIM, pp 515–520
2. Koike J, Shimoyama Y, Ohnuma I et al (2000) Stress-induced phase transformation during superplastic deformation in two-phase Ti–Al–Fe alloy. Acta Mater 48(9):2059–2069
3. Matsumoto H, Yoshida K, Lee SH et al (2013) Ti-6A1-4V alloy with an ultrafine-grained microstructure exhibiting low-temperature-high-strain-rate superplasticity. Mater Lett 98:209–212
4. Zhang T, Liu Y, Sanders DG et al (2014) Development of fine-grain size titanium 6Al–4V alloy sheet material for low temperature superplastic forming. Mater Sci Eng A 608:265–272
5. Sun QJ, Wang GC (2014) Microstructure and superplasticity of TA15 alloy. Mater Sci Eng A 606:401–408

6. Guo B, Semiatin SL, Jonas JJ, et al (2018) Dynamic transformation of Ti–6Al–4V during torsion in the two-phase region. J Mater Sci: 1–11
7. Ghosh C, Basabe VV, Jonas JJ et al (2013) The dynamic transformation of deformed austenite at temperatures above the Ae3. Acta Mater 61(7):2348–2362
8. Aranas C, Foul A, Guo B et al (2017) Determination of the critical stress for the initiation of dynamic transformation in commercially pure titanium. Scripta Mater 133:83–85
9. Foul A, Aranas C, Guo B, et al (2018) Dynamic transformation of α → β titanium at temperatures below the β-transus in commercially pure titanium. Mater Sci Eng A 722:156–159
10. Chun XU, Zhu WF (2010) Transformation mechanism and mechanical properties of commercially pure titanium. Trans Nonferrous Metals Soc China 20(11):0–2167
11. Mao WM (1994) Metal recrystallization and grain growth. Metallurgical Induety Press
12. Favre J, Koizumi Y, Chiba A et al (2013) Deformation behavior and dynamic recrystallization of biomedical Co-Cr-W-Ni (L-605) alloy. Metall Mater Trans A 44(6):2819–2830
13. Jonas JJ, Aranas C, Fall A et al (2017) Transformation softening in three titanium alloys. Mater Des 113:305–310
14. Zhou YG, Zeng WD, Yu HQ (2005) An investigation of a new near-beta forging process for titanium alloys and its application in aviation components. Mater Sci Eng A 393(1–2):204–212
15. Mikhaylovskaya AV, Mosleh AO, Kotov AD et al (2017) Superplastic deformation behaviour and microstructure evolution of near-α Ti-Al-Mn alloy. Mater Sci Eng A 708:469–477
16. Wang M, Wang W, Liu Z, et al (2018) Hot workability integrating processing and activation energy maps of Inconel 740 superalloy
17. Tan L, Li Y, Liu F, et al (2019) Microstructure evolutions of a powder metallurgy superalloy during high-strain-rate deformation. J Alloys Comp
18. Xu YB, Bai YL, Meyers MA (2006) Deformation, phase transformation and recrystallization in the shear bands induced by high-strain rate loading in titanium and its alloys. J Mater Sci Technol 22(6):737–746
19. Pramanik A, Littlefair G (2015) Machining of titanium alloy (Ti-6Al-4V)—theory to application. Mach Sci Technol 19(1):1–49
20. Goetz RL, Semiatin SL (2001) The adiabatic correction factor for deformation heating during the uniaxial compression test. J Mater Eng Perform 10(6):710–717
21. Jones NG, Dashwood RJ, Dye D, et al (2008) Thermomechanical processing of Ti–5Al–5Mo–5V–3Cr. Mater Sci Eng A 490(1–2):369–377
22. Christian JW, Otte HM (1965) The theory of transformations in metals and alloys. In: The theory of transformations in metals and alloys. Pergamon Press
23. Elmer JW (2004) Phase transformation dynamics during welding of Ti–6Al–4V. J Appl Phys 95(12):8327

Formability Improvements of AA5754-H32 at Room Temperature via Continuous Bending Under Tension (CBT) and Pre-forming Heat Treatment



Jinjin Ha, Antonio Piccininni, Yannis P. Korkolis, Gianfranco Palumbo, Marko Knezevic, and Brad L. Kinsey

Abstract Aluminum (Al) alloys play a critical role for the transportation applications where weight reduction is a key aspect; however, the poor formability at room temperature limits their application for complex components. An innovative methodology to overcome this limitation is based on subjecting the material to a local, short-term heat treatment before stamping, to obtain a tailored distribution of properties. In addition, Continuous-Bending-under-Tension uses the action of three rollers to remarkably increase the total elongation to failure. In the present work, the combination of the two approaches is investigated to improve the formability at room temperature of a strain-hardenable 5xxx Al alloy, AA5754-H32. Specimens were subjected to both CBT and pre-forming heat treatments, and force-displacement curves were compared to evaluate the formability improvements.

Keywords Al alloys · Formability · Continuous-bending-under-tension · Heat treatment · Material characterization

1 Introduction

As an interest in stronger and lighter automotive materials continuously increases, so does the need to discover new forming processes to improve limited ductility of these materials. One such process is continuous-bending-under-tension (CBT) [1–4], in which, as explicitly described in the name, bending is superimposed on tension by several rollers throughout loading. The beneficial effect of bending with tension is enhancing elongation-to-fracture (ETF), as a result, a higher strain than the conventional forming limit can be achieved. Zecevic et al. [4] reported that large plastic

J. Ha (✉) · M. Knezevic · B. L. Kinsey
Mechanical Engineering, University of New Hampshire, Durham, NH 03824, USA
e-mail: Jinjin.ha@unh.edu

A. Piccininni · G. Palumbo
Mechanical Engineering, Polytechnic University of Bari, Bari 70125, Italy

Y. P. Korkolis
Integrated Systems Engineering, The Ohio State University, Columbus 43210, USA

© The Minerals, Metals & Materials Society 2021

G. Daehn et al. (eds.), *Forming the Future*, The Minerals, Metals & Materials Series,
https://doi.org/10.1007/978-3-030-75381-8_151

strain in the CBT processed specimen resulted in formation of a strong <111> fiber texture throughout the material. This observation indicates that an adequate amount of CBT processing prior to forming can be promising to enhance a certain texture like <111> fiber which improves formability in the subsequent forming operation. On the other hand, the manipulation of microstructure by an appropriate heat treatment [5–7] is also an important aspect on formability, especially for aluminum alloys. Moreover, it has been reported that the local modification of the material properties prior to the forming operations is considered a promising approach to improve the formability of Al alloys at room temperature: in the case of the deep drawing of a 6xxx age-hardenable Al alloys, it has been demonstrated that if the peripheral region of the circular specimen is locally brought from an initial T6 state to a fully solutioned one, a remarkable improvement of the limit drawing ratio (LDR) can be achieved [8]. This suggests a possibility that the CBT processing integrated with local heat treatment can further improve LDR in the cup drawing arose from both <111> texture and strength variation in the material. In this paper, a preliminary study of local heat treatment (LHT) effect on the CBT process is performed for AA5754-H32. Bending depth and crosshead velocity which changes strain rate of tension are controlled to maximize ETF. The experimental procedure and results are presented in the following sections.

2 Continuous-Bending-Under-Tension (CBT) and Local Heat Treatment (LHT)

The custom CBT machine built at the University of New Hampshire [9–11], which includes three rollers, is used for the experiments. The schematic and details are described in Fig. 1. The machine consists of a moving carriage, two stationary stands assembled with three rollers, a base, and control systems. The bending depth, δ, can be varied by adjusting the top roller in the vertical direction. The machine is equipped with two load cells, which are located at the actuator and the carriage, respectively. The signal used for this work is from the load cell on the carriage. The bending depth

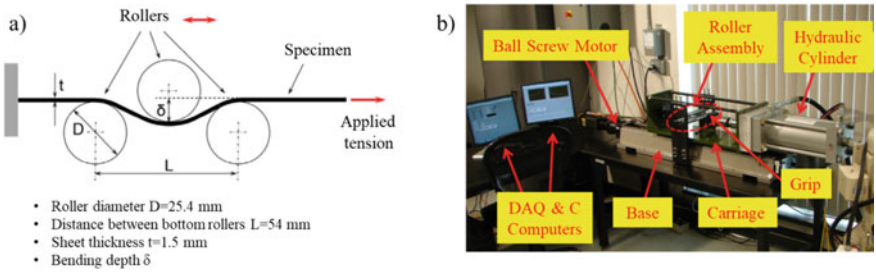


Fig. 1 **a** Schematic of the CBT process and **b** a photograph of the machine at the University of New Hampshire [8]. (Color figure online)

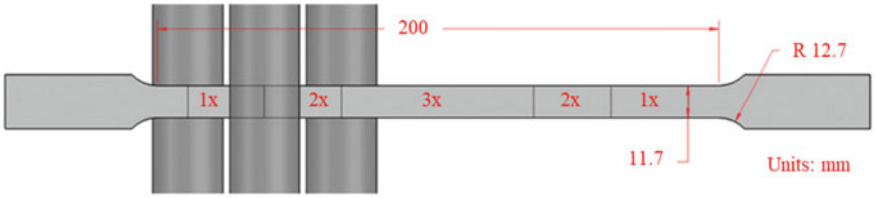


Fig. 2 Initial CBT specimen with three rollers and the 1x, 2x, and 3x deformation regions [8]. (Color figure online)

and crosshead velocity, which is calculated by a cylinder position, are test variables, while the carriage moving velocity is kept constant at 66 mm/s. Figure 2 represents a sample deformed specimen for the CBT with different bending cycles, i.e., x1, x2, and x3, in the gage section: the material at both ends is subjected to only one bending-unbending cycle per stroke, while three cycles per stroke in the center. A stroke is defined as the carriage moving from one end of the machine to the other and back again.

In order to investigate the heat treatment effect on the formability, the experiments are performed using two different types of specimens, as shown in Fig. 3a and b. One is the as-received condition (AA5754-H32 of 1.5 mm thickness) and the other is the locally heat treated. Laser treatment is designed by means of preliminary thermal FE simulations (Abaqus CAE 6.17) with the aim of locally bringing the material to the annealed state: the heating strategy is based on five consecutive linear tracks (length equal to the specimen width) setting the spot dimension at 10 mm and considering a top-hat energy distribution (the sequence of the laser track is also reported in Fig. 3b).

One of the key aspects in the laser treatment design is the evaluation of its effectiveness, i.e., properly calculating the distribution of the material properties at the end of the heat treatment. To accomplish such an ambitious goal, an experimental study is carried out exploiting the potentialities of the Gleeble 3180 system (shown in Fig. 4a): striped specimens in wrought conditions (AA5754-H32) are heated up by Joule effect modulating the current flow according to the acquisition of the "pilot" thermocouple, indicated as TC2 in Fig. 4b. Being the two ends of the specimen

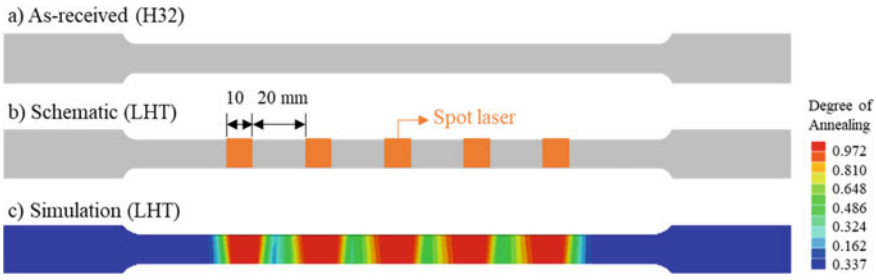


Fig. 3 Specimen preparation for the CBT test: **a** as-received (AA5754-H32), **b** locally heat treated (AA5754-LHT), and **c** simulation result of degree of annealing. (Color figure online)

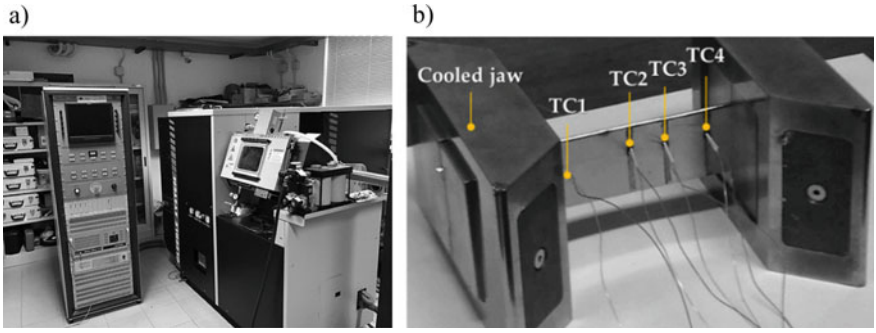


Fig. 4 Experimental setup for the annealing tests: **a** Gleeble 3180 physical simulator, **b** thermocouples arrangement for the temperature monitoring. (Color figure online)

clamped between cooled jaws, a parabolic distribution of temperature is obtained thus subjecting the material simultaneously to several heating treatments within the same test.

At the end of each test, the treated specimens are subjected to hardness tests at room temperature (Qness micro hardness tester Q10 A+, setting a load of 200 g and a dwell time of 15 s) thus relating the hardness value with a specific combination of heating temperature and holding time. Results from the annealing tests are expressed in terms of an output variable—the Degree of Annealing (DoA)—defined according to Eq. (1).

$$\mathrm{DoA} = \frac{\mathrm{HV}_{\mathrm{H32}} - \mathrm{HV}_{\mathrm{meas}}}{\mathrm{HV}_{\mathrm{H32}} - \mathrm{HV}_{\mathrm{H111}}} \tag{1}$$

where $\mathrm{HV}_{\mathrm{H32}}$, $\mathrm{HV}_{\mathrm{H111}}$, and $\mathrm{HV}_{\mathrm{meas}}$ are, respectively, the reference hardness of the material in the as-received conditions, the hardness in the annealed state, and the one measured at the end of each physically simulated annealing test; in such a way, a value of the DoA variable equal to 1 means a fully annealed material, whereas small value of the DoA means the material maintaining the purchasing conditions. All the results from the annealing tests are arranged and implemented within a Python-based post-processing script able to associate a single DoA value to each node of the specimen according to its thermal history: the final DoA distribution (thus providing also a distribution of the material properties at the end of the laser heating) relative to the heating at a temperature of 500 °C and setting a material/radiation interaction time equal to 2 s is reported in Fig. 3c. The laser heat treatment, according to what is defined by the FE numerical runs, is then experimentally replicated on a 1 kW diode laser (specimens are previously painted with graphite spray to increase the radiation absorption during the heating).

3 Results and Discussion

Figures 5 and 6 present the force–displacement curve with different bending depths and crosshead velocities for AA5754-H32 and -LHT. In general, the CBT force–displacement curve includes repetitive peaks during the process, which indicates the moment when the rollers are locating at each end of the gage section and the overall deformation is approaching to the simple tension without the bending effect. It is not noise or anything like that, but directly tied to the kinematics of the CBT process, as detailed in one of our earlier works [11]. The tested bending depths are $\delta = 1.5$, 2.5, and 3.5 mm with a constant crosshead velocity at $v = 0.8$ mm/s (Fig. 5a), and crosshead velocities are $v = 0.18$, 0.8, and 1.6 mm/s with a constant bending depth at $\delta = 2.5$ mm (Fig. 5b). Monotonic tension without bending (-H32, gray line in figures) is plotted as a reference. As the bending depth increases, the overall force level decreases, and can be even lower than the initial yield stress of the monotonic

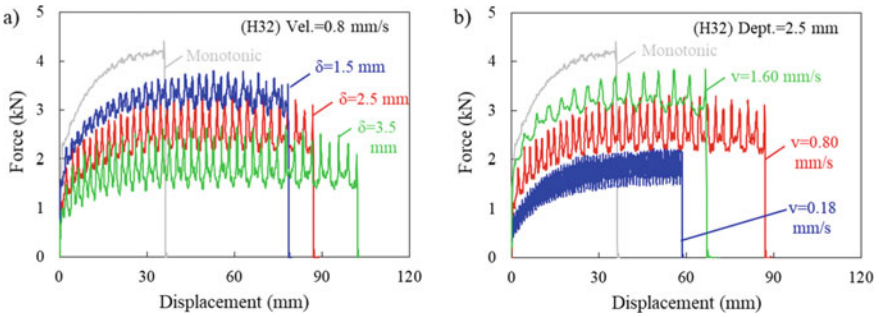


Fig. 5 Sensitivity test on AA5754-H32 (as-received) for **a** the bending depth with a constant crosshead velocity $v = 0.8$ mm/s and **b** the crosshead velocity with a constant bending depth $\delta = 2.5$ mm. (Color figure online)

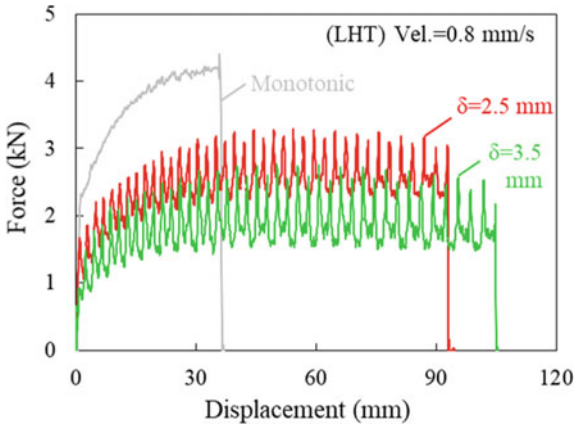


Fig. 6 Sensitivity test on AA5754-LHT for the bending depth (locally heat treated) with crosshead velocity $v = 0.8$ mm/s. (Color figure online)

curve when the bending depth is δ = 3.5 mm (Figs. 5a and 6). This indicates that the plastic flow produced by the bending–unbending cycles becomes dominant over the one by the tension force. In contrast, the higher crosshead velocity increases the force level and reduces the number of cycles at the same displacement level (Fig. 5b). This represents that the plastic flow produced by the tension force is more significant than the bending–unbending effect at the higher crosshead velocity. As is evident from Figs. 5 and 6, the optimal condition is the bending depth δ = 3.5 mm with the crosshead velocity v = 0.8 mm/s for both AA5754-H32 and -LHT samples.

Figure 7 shows the comparison of AA5754-H32 and -LHT at the bending depth δ = 2.5 (Fig. 7a) and 3.5 mm (Fig. 7b) with the crosshead velocity v = 0.8 mm/s. At both bending depths, ETF, represented by the total displacement to failure, is slightly improved in AA5754-LHT. This may result from the microstructural change related to the heat treatment, which is the objective of the authors' ongoing study. Tested specimens are compared in Fig. 8, along with an undeformed and a deformed ones under uniaxial tension without bending. It is seen that the CBT process enhances

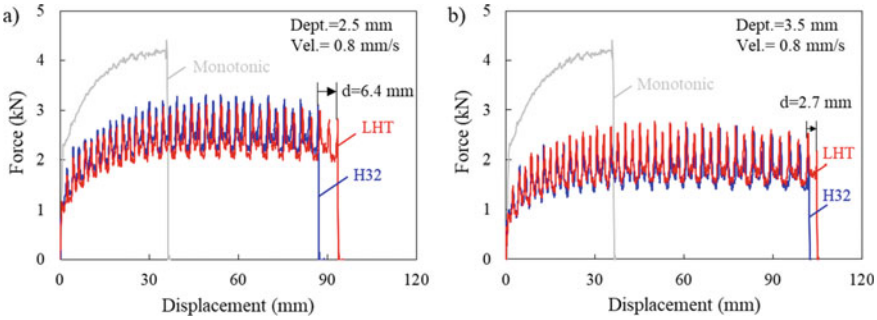


Fig. 7 Comparison of force–displacement for AA5754-H32 and -LHT: **a** bending depth δ = 2.5 mm and **b** bending depth δ = 3.5 mm with crosshead velocity v = 0.8 mm/s. (Color figure online)

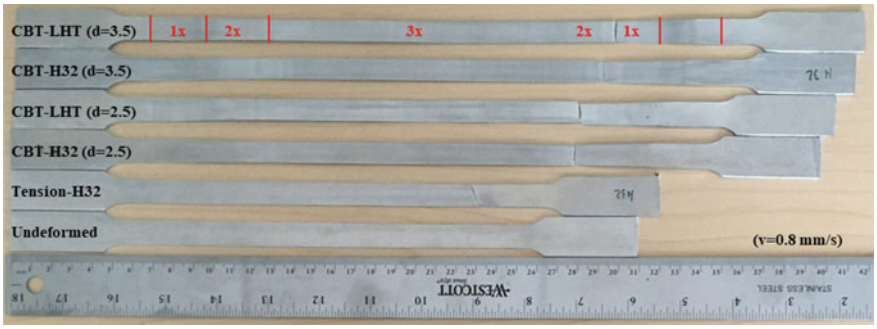


Fig. 8 Comparison of the failed specimens with bending depths δ = 2.5 and δ = 3.5 mm with a crosshead velocity v = 0.8 mm/s along RD. Undeformed and deformed specimens under uniaxial tension are included as references. (Color figure online)

the formability more than twice compared to uniaxial tension. The orientation of the fracture is also changed from an angle to the loading direction for localized necking (uniaxial tension specimen) to perpendicular to the tensile loading direction (CBT specimen).

4 Conclusion

In this work, CBT processing of AA5754-H32 and -LHT conditions is investigated through a parametric study on the bending depth and crosshead velocity. The force–displacement curves show a high sensitivity on these process parameters, from which the optimal condition is found as the bending depth $\delta = 3.5$ mm and crosshead velocity $v = 0.8$ mm/s. Under this condition, the formability of the material is improved more than twice compared to the uniaxial tension. The ductility is further improved by the local heat treatment (LHT) compared to the as-received condition (H32), even though not as drastically as in comparison to uniaxial tension.

References

1. Swift H (1948) Plastic bending under tension. Engineering 166:333–359
2. Emmens WC, van den Boogaard AH (2009) Incremental forming by continuous bending under tension—an experimental investigation. J Mater Process Technol 209:5456–5463
3. Benedyk J, Parikh N, Stawarz D (1971) A method for increasing elongation values for ferrous and nonferrous sheet metals (Ferrous and nonferrous sheet metals neck formation prevention for increasing elongation in tensile tests, using continuous plastic bending method). J Mater 6:16–29
4. Zecevic M, Roemer TJ, Knezevic M, Korkolis YP, Kinsey BL (2016) Residual ductility and microstructural evolution in continuous-bending-under-tension of AA-6022-T4. Materials. https://doi.org/10.3390/ma9030130
5. Wells MA, Lloyd DJ, Samarasekera IV, Brimacombe JK, Hawbolt EB (1998) Modeling the microstructural changes during hot tandem rolling of AA5XXX aluminum alloys: part I. Microstruct Evol 29B:611–620
6. Ha J, Choi Y, Dunn C, Lee MG, Korkolis YP (2019) Formability prediction in hole-expansion test for AA7075 sheet in—W temper. SAE, Detroit, MI, USA
7. Lee J, Bong HJ, Kim D, Lee YS, Choi Y, Lee MG (2019) Mechanical properties and formability of heat-treated 7000-series high-strength aluminum alloy: experiments and finite element modeling. Metals Mater Int: 1–13
8. Piccininni A, Palumbo G (2020) Design and optimization of the local laser treatment to improve the formability of age hardenable aluminium alloys. Materials 13(7):1576. https://doi.org/10.3390/ma13071576
9. Poulin CM, Vogel SC, Korkolis YP, Kinsey BL, Knezevic M (2020) Experimental studies into the role of cyclic bending during stretching. Int J Mater Form Int. https://doi.org/10.1007/s12289-019-01530-2

10. Poulin CM, Korkolis YP, Kinsey BL, Knezevic M (2019) Over five-times improved elongation-to-fracture of dual-phase 1180 steel by continuous-bending-under-tension. Mater Des. https://doi.org/10.1016/j.matdes.2018.11.022
11. Roemer TJ, Barrett TJ, Knezevic M, Kinsey BL, Korkolis YP (2019) Experimental study of continuous-bending-under-tension of AA6022-T4. J Mater Proc Tech. https://doi.org/10.1016/j.jmatprotec.2018.11.046

Microstructure Evolution During Isothermal Forging of 7A85 Aluminum Aviation Component



Jian-Liang Hu, You-Ping Yi, Miao Jin, and Hong Bo

Abstract A 7A85 aluminum aviation component with high ribs and thin webs was successfully formed by the isothermal forging process, and its microstructure was investigated by optical microscope (OM), transmission electron microscope (TEM), and cellular automaton simulation. Metallographic images show the recrystallization phenomenon takes place all over the aviation forging, and a uniform grain size is obtained. The cellular automaton model of 7A85 aluminum alloy, including dislocation density model, nucleation rate equation as well as grain growth model was established, and the parameters of the cellular automaton models were determined by the hot compression experiment on the thermal-mechanical simulator Gleeble-1500. The cellular automaton simulation results agree well with the optical micrographs of the aviation forging, showing good homogeneity in both the size and the distribution of grain structure. The TEM images show that a homogeneous distributed dislocations and precipitates of the forging formed by the isothermal forging process can be attained, which can inhibit the migration of the grain boundaries, resulting in the small and uniform grains of the aviation forging.

Keywords Isothermal forging · Cellular automaton simulation · Dislocation density · Dynamic recrystallization · Aviation component

J.-L. Hu · M. Jin
College of Mechanical Engineering, Yanshan University, Qinhuangdao 066004, China

Y.-P. Yi
State Key Laboratory of High Performance Complex Manufacturing, Central South University, Changsha 410083, China

H. Bo (✉)
State Key Laboratory of Metastable Materials Science and Technology, Yanshan University, Qinhuangdao 066004, China
e-mail: bohong@csu.edu.cn

© The Minerals, Metals & Materials Society 2021

G. Daehn et al. (eds.), *Forming the Future*, The Minerals, Metals & Materials Series,
https://doi.org/10.1007/978-3-030-75381-8_152

1 Introduction

The weight reduction of the aviation component plays a very important role in the aerospace field [1–3]. Thus, aviation components are usually designed into thin webs and high ribs to reduce the weight. However, this causes some problems, which are the forming difficulty and non-uniform properties of complex aviation component. In fact, the temperature of dies and the billet are the same during the isothermal forging process, thus the deformation resistance of material significantly reduced. Therefore, it is a suitable way for the deformation of complex aviation components.

In order to obtain an appropriate forming process for aviation components with irregular shape, massive works have been done on isothermal forging process in the past few years [4–7]. In the work by Shan et al. [8], a bracket of magnesium alloy with irregular shapes was forged by isothermal forging process, and the dimensional precision of the forging met the requirement well. An aluminum alloy component with complex shape was obtained by isothermal forging process, and the optimum conditions of the forging process were determined [9]. The simulation of AZ31B magnesium alloy was carried out by Rao et al. to optimize the parameters of forging process [10].

Dynamic recrystallization, which affects the microstructure and mechanical properties of forging, is a common phenomenon during the isothermal forging process. Therefore, in order to numerically simulate the dynamic recrystallization processes by cellular automaton method, numerous attempts have been made in the past decade. A multi-scale model of 1050 aluminum alloy was proposed to analyze the softening kinetics and microstructure revolution during the isothermal annealing process by Shabaniverki et al. [11], and the predicted results agree well with the experimental data. A three-dimensional cellular automaton model of Al–Si-Mg alloy was established to investigate the grain growth of different crystallographic orientations during the polycrystalline solidification by Chen et al. [12]. Li et al. [13] and Huang et al. [14] both developed a cellular automaton program of 7050 aluminum alloy to simulate the influence of the forging process on the dynamic recrystallization phenomenon and the size of grains. Whereas little work was reported to predict the dynamic recrystallization phenomenon of aviation components in the isothermal forging process using the cellular automaton method. In this work, the isothermal forging process of complex aviation component with thin webs and high ribs is carried out, and the microstructure evolution of the aviation forging is studied by optical microscope, transmission electron microscope, and cellular automaton simulation.

Table 1 Chemical composition of 7A85 aluminum (mass fraction, %)

Element	Zn	Mg	Cu	Fe	Si	Zr	Al
Content	7.0–8.0	1.2–1.8	1.3–2.0	≤0.08	<0.06	0.08–0.15	Bal.

2 Experimental

2.1 The Hot Compression Experiments of 7A85 Aluminum Alloy

The hot compression experiments of 7A85 aluminum alloy were performed on the thermal-mechanical simulator Gleeble-1500. The chemical composition of 7A85 aluminum alloy is given in Table 1. The deformation temperature of the hot compression experiments ranges from 300 to 450 °C in the strain rate interval 0.001–1 s^{-1}. The total strain of the samples is 0.9. Before compression, the samples were heated to set temperature at a rate of 10 °C/s and heat preservation time was 5 min. After compression, the samples were quenched immediately. A graphite lubricant was applied to reduce the friction of specimens during the hot compression experiments.

2.2 The Isothermal Forging Experiment of Aviation Component

The isothermal forging experiment of the aviation forging was conducted on the 40 MN hydraulic machine. The deformation temperature of the forging was 450°, and the dies along with billet were holding at the set temperature for 4 h. In order to reduce the friction of the billet during deformation, a water-based lubricant was used. Figure 1 shows the load and velocity curve of the isothermal forging experiment, the maximum load is up to 32.7 MN. To shorten the process time, the loading velocity was set into four levels of 1, 0.1, 0.01, and 0.002 mm/s.

The aviation forging with a maximum web thickness of 42 mm and maximum lib height of 125 mm is successfully obtained in this work, shown in Fig. 2. It can be seen that during the isothermal forging process, the metal flows smoothly and thus it is very likely to cause underfill, crack, and other defects. The aviation forging was cut along the cross section, which is shown in Fig. 2. And the specimens of microstructure analysis were taken from the cross section. Microstructures of the aviation forging were studied by means of optical microscope.

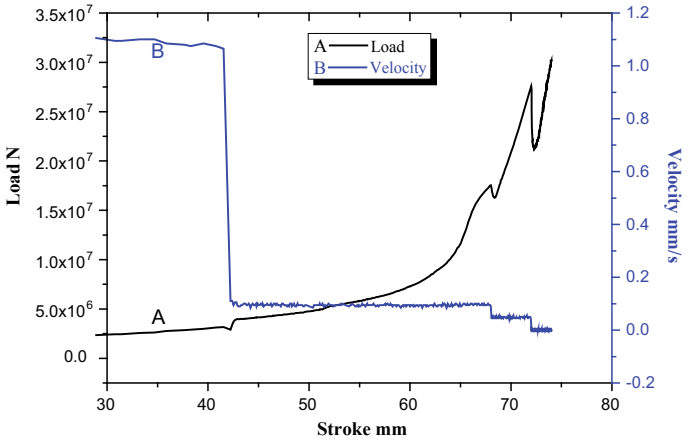


Fig. 1 Plot of load and velocity versus stroke during isothermal forging process. (Color figure online)

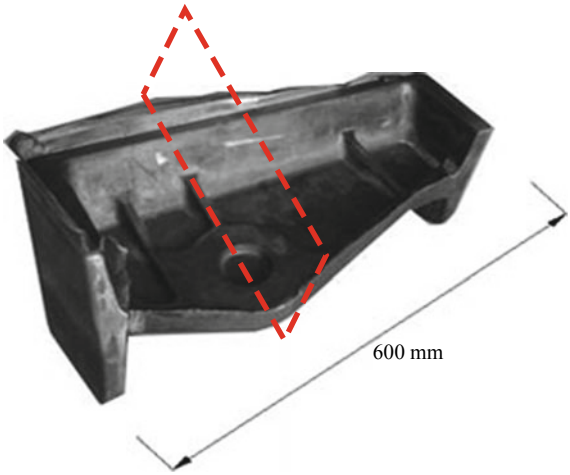


Fig. 2 The aviation forging formed by isothermal forging process. (Color figure online)

3 Results and Discussion

3.1 Flow Behavior of 7A85 Aluminum Alloy

The stress-strain curves were obtained by hot compression experiments under different deformation conditions as shown in Fig. 3. The flow behavior of 7A85 aluminum alloy is significantly influenced by deformation conditions. While the deformation temperature grows, the flow stress decreases. And with the decrease of strain rate, the flow stress decreases as well. In general, work hardening, dynamic

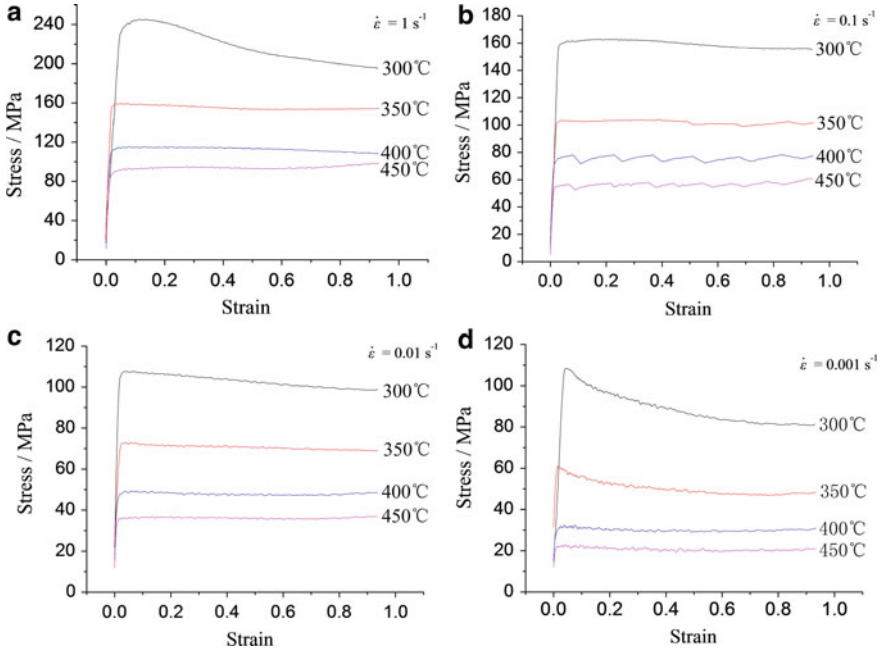


Fig. 3 The stress-strain curves of 7A85 aluminum alloy at different strain rates. (Color figure online)

recovery as well as dynamic recrystallization are metallurgical phenomena during the hot deformation process of 7A85 aluminum alloy [15, 16].

3.2 Microstructure Simulation

In general, the dislocation density is influenced by work hardening, dynamic recovery, and dynamic recrystallization. Both the dynamic recovery and dynamic recrystallization have softening effects on the dislocation density. The dislocation density equation can be established as [17].

$$\frac{d\rho}{d\varepsilon} = k_1\sqrt{\rho} - k_2\rho \tag{1}$$

where ρ stands for the dislocation density. ε is the strain. k_1 and k_2 are the work hardening parameter and the softening parameter, respectively, which can be expressed as the following formulas:

$$k_1 = 2\theta_0/(\alpha\mu b) \tag{2}$$

$$k_2 = 2\theta_0/(\sigma_s) \tag{3}$$

where α stands for the dislocation interaction term. For 7A85 aluminum alloy, $\alpha = 0.5$. μ stands for the shear modulus. b is the Burgers vector. σ_s is the peak stress. $\theta_0 = \mathrm{d}\sigma/\mathrm{d}\varepsilon$ is the work hardening rate. The relationship of work hardening rate and deformation temperature, strain rate is as follows:

$$\theta_0 = A_1 \dot{\varepsilon}^{B_1} \exp(C_1/T) \tag{4}$$

where A_1, B_1, C_1 are constants.

The natural logarithm of both sides of the formula (4) is obtained.

$$\mathrm{In}\,\theta_0 = \mathrm{In}\,A_1 + B_1\,\mathrm{In}\,\dot{\varepsilon} + C_1/T \tag{5}$$

According to the results of hot compression experiments, the relationships of ln θ_0 and In $\dot{\varepsilon}$, T^{-1} are obtained, shown in Figs. 4 and 5, the linear regression fitting analysis of the data is carried out to obtain the value of A_1, B_1, and C_1. And the work hardening rate is formed.

$$\theta_0 = 583.013\dot{\varepsilon}^{0.182725} \exp(1539.608/T) \tag{6}$$

Thus, the dislocation density model of 7A85 aluminum alloy during hot forming can be generated as follows:

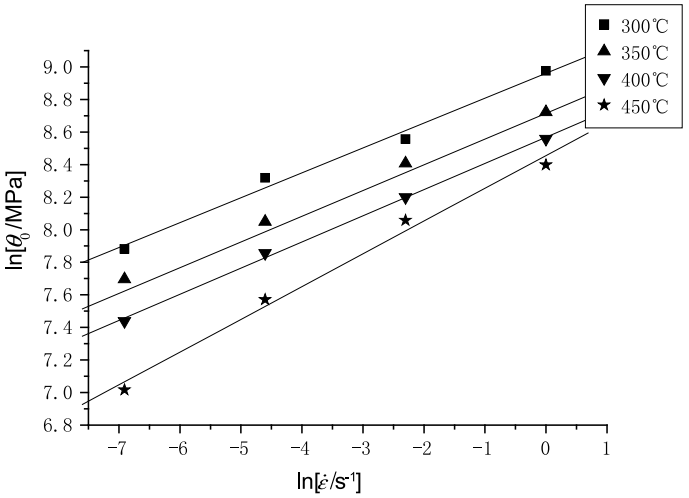


Fig. 4 The relationship of ln θ_0 to In $\dot{\varepsilon}$

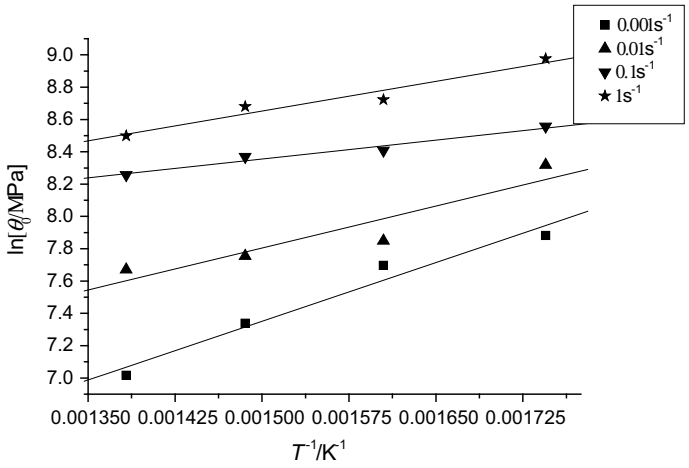


Fig. 5 The relationship of ln θ_0 to T^{-1}

$$\frac{\mathrm{d}\rho}{\mathrm{d}\varepsilon} = \frac{1166.026\dot{\varepsilon}^{0.182725}\exp(1539.608/T)}{\alpha u b}\sqrt{\rho} - \frac{1166.026\dot{\varepsilon}^{0.182725}\exp(1539.608/T)}{\sigma_s}\rho \tag{7}$$

Nucleation is assumed to occur when the dislocation density reached up to the critical value ρ_c. The nucleation rate ($\dot{n}$) can be considered as a function of the deformation temperature and the strain rate [18].

$$\dot{n} = C \cdot \dot{\varepsilon} \cdot \exp\left(-\frac{Q_{act}}{RT}\right) \tag{8}$$

where C is nucleation coefficient. For 7A85 aluminum alloy, $C = 200$. Q_{act} is activation energy. R is the universal gas constant.

Grain boundary migrates from low dislocation density area to high dislocation density area [19]. The migrating velocity mainly depends on the mobility of grain boundary, and the difference in dislocation densities inside and outside of grain boundaries. So the growth velocity of grain can be expressed as the following formula:

$$v_i = Mp_i \tag{9}$$

where v_i is the migrating velocity of grain boundary. M stands for the grain boundary mobility. p_i is the driving force of dynamic recrystallization grain.

$$M = \frac{b^2}{kT} D_0 \exp\left(-\frac{Q_b}{RT}\right) \tag{10}$$

$$p_i = \tau \Delta\rho - \frac{2\gamma_i}{r_i} \tag{11}$$

where b is the Burgers vector. k stands for the Boltzmann constant. D_0 is the self-diffusion coefficient of grain boundary. R is the universal gas constant. Q_b is the activation energy of grain boundary self-diffusion. $\Delta\rho$ is the difference of dislocation density between the growing and the non-growing grains. r is the radius of the growing grain. $\tau = 0.5\mu b^2$ is the dislocation line energy. γ_i stands for the grain boundary energy which can be calculated by

$$\gamma_i = \begin{cases} \gamma_m \frac{\theta_i}{\theta_m}\left(1 - \mathrm{In}\frac{\theta_i}{\theta_m}\right) & \theta_i \le \theta_i \\ \gamma_m & \theta_i > \theta_m \end{cases} \tag{12}$$

where θ_i is the misorientation between grains. And θ_m, γ_m stand for critical misorientation and critical grain boundary energy, respectively.

The cellular automaton model is employed to investigate the dynamic recrystallization phenomenon of the aviation forging by isothermal forging process. The material parameters of 7A85 aluminum alloy in the simulation are as shown in Table 2. The area of aviation forging for the simulation is 1 mm × 1 mm, which can be divided into 500 × 500 simulation meshes. The primary grain orientation was randomly set at the range of 0º–180º.

Figure 6 is the cross section of aviation forging for metallographic observation and the metallographic images of the isothermal forging are shown in Fig. 7. Large deformation takes place at Point 2 of the intersecting surface of the forging. Thus, the line shape distribution of grains is obvious. On the contrary, the metal flew gently

Table 2 Material parameters of 7A85 aluminum alloy

Material parameter	Value
b (m)	2.0×10^{-10}
μ (MPa)	2.69×10^{4}
Q_act (KJ/mol)	313.386
Q_b (KJ/mol)	117.2
D_0 ($\mathrm{m^2/s}$)	3.8×10^{-4}
γ_m ($\mathrm{J/m^2}$)	0.76

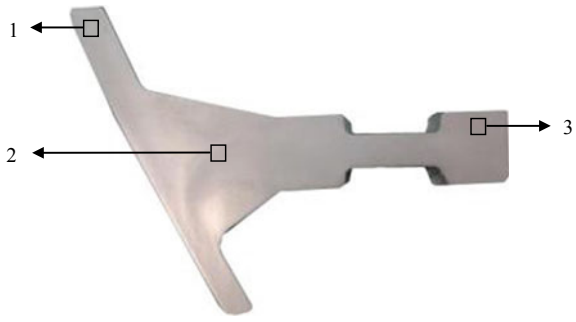


Fig. 6 The cross section of aviation forging for metallographic observation. (Color figure online)

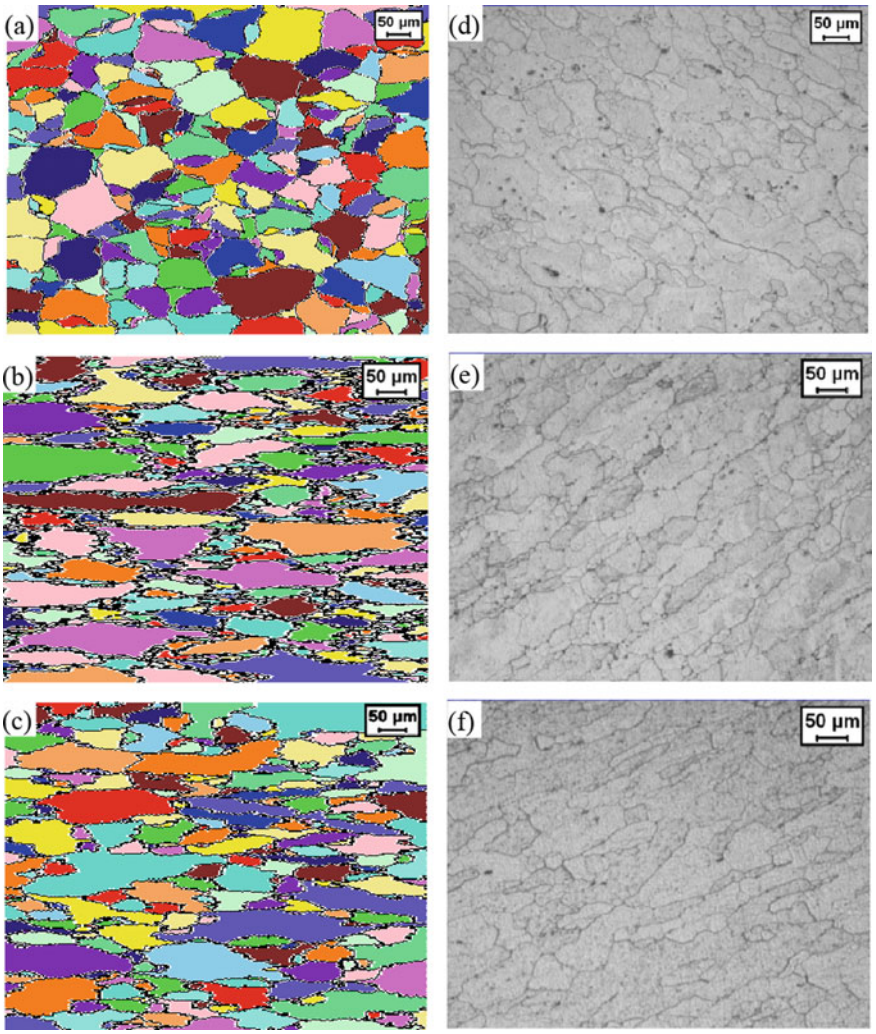


Fig. 7 Grain structure of simulation and experimental results **a**, **d** Point 1; **b**, **e** Point 2; **c**, **f** Point 3. (Color figure online)

at Point 1 and Point 3 of the forging. So the line shape distribution of grains is inconspicuous. What is more, uniform recrystallization grains can be seen all over the intersecting surface of the joint forging. The average grain sizes of Point 1 to Point 3 are 62 μm, 48 μm, and 73 μm, respectively. Besides, the average grain sizes of the cellular automaton simulation are 72, 45, and 62 μm, which agree well with the optical micrographs of the aviation forging, showing good homogeneity in both the size and the distribution of grain structure.

3.3 Microstructure Evolution Analysis

In order to seek the reason why the aviation forging has a uniform microstructure, the dislocation and precipitate of the forging were studied as shown in Fig. 8. During the isothermal forging process, the dynamic recrystallization occurs all over the aviation forging, leading to the reduction of dislocation density. As the deformation continued, due to different grain orientation, some grains with favorable orientation are likely to slip along the grain boundary as shown in Fig. 8a. While the movement of those grains with unfavorable orientation is restrained, resulting in the increase of dislocation density, as shown in Fig. 8b. Under extremely slow speed and isothermal conditions, dislocations slide and climb around the grain boundary, and the sliding fraction

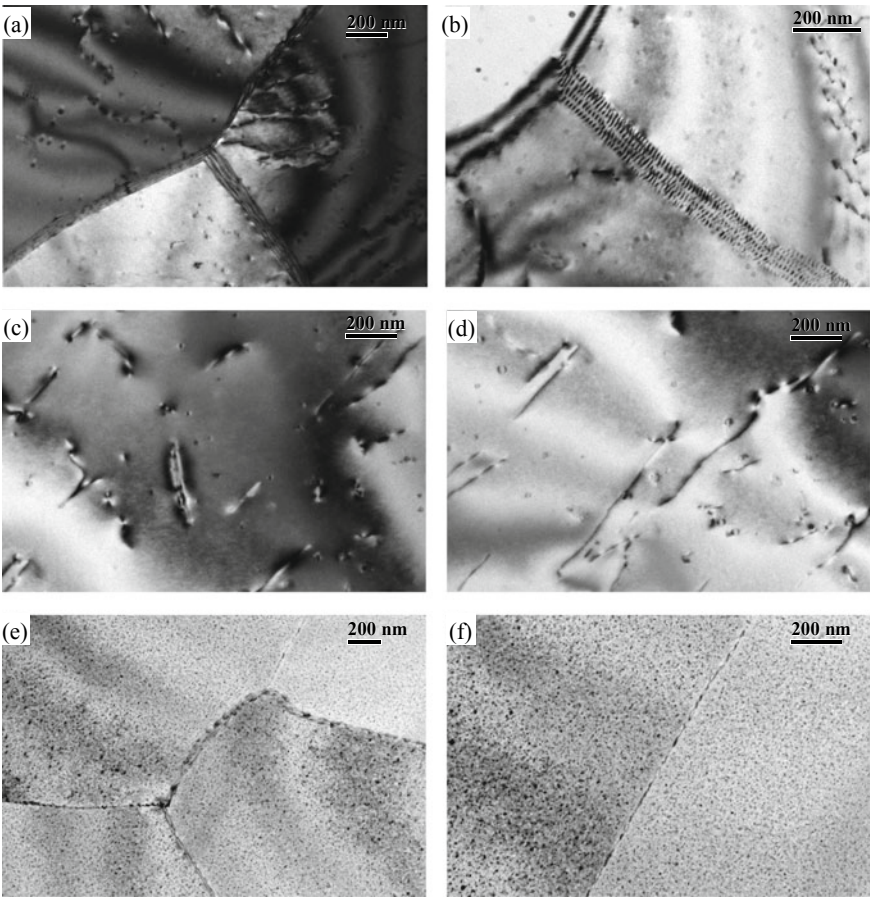


Fig. 8 TEM images of aviation forging: **a** grain boundary sliding; **b** dislocation wall; **c** dislocations at the surface; **d** dislocations at the core; **e** precipitates at the surface; **f** precipitates at the core. (Color figure online)

causes the grain boundary sliding, while the climbing fraction causes diffusion creep [20]. So, during the isothermal forging process, the grain boundary sliding is the main mechanism of deformation, and the diffusion creep is the principal factor of improving grain boundary sliding.

As can be seen from Fig. 8c, d, there is a relatively homogeneous distribution of dislocations at both the surface and the core of the forging. And the precipitates are more prone to form around dislocations of high strain energy and interface energy [16, 21, 22]. As a consequence, the morphology of the precipitates is homogeneous both in the matrix and at the grain boundary of the aviation forging formed by the isothermal forging process as shown in Fig. 8e, f.

From what has been mentioned above, it can be known that the reasons why such a homogenous microstructure was obtained by isothermal forging process are as shown below. Firstly, the billet during the isothermal forging process is at a nearly constant temperature, and the loading speed is extremely slow, so grain boundary sliding is the main mechanism of deformation, and the diffusion creep is the principal factor of improving grain boundary sliding. Thus, the dislocations have enough time to move into the grain boundary or annihilate each other, resulting in the homogeneous distribution of dislocations. Secondly, the precipitates are more prone to form around the homogeneous distributed dislocations, so that uniform precipitates can be attained. Eventually, the grain boundaries can be pinned by the dispersed precipitates so that the small and uniform grain is obtained by the isothermal forging process.

4 Conclusions

(1) The 7A85 aluminum aviation component with high ribs and thin webs was successfully forged by the isothermal forging process. And there are little defects such as underfill or crack of the aviation forging.

(2) The cellular automaton models of 7A85 aluminum alloy, including dislocation density model, nucleation rate equation as well as grain growth model, were established to investigate the dynamic recrystallization phenomenon of the aviation forging by isothermal forging process. The cellular automaton simulation results agree well with the optical micrographs of the aviation forging, showing good homogeneity in both the size and the distribution of grain structure.

(3) During the isothermal forging process, the grain boundary sliding is the main mechanism of deformation, and the diffusion creep is the principal factor of improving grain boundary sliding. Because of the homogeneous distributed dislocations and precipitates, which inhibit the migration of the grain boundaries, the grains of the aviation forging are small and uniform.

Acknowledgments Foundation item: Project (Grant No. 51401179 and No. 51675465) supported by National Natural Science Foundation of China; Project (Grant No. E2015203116 and No. E2019203075) supported by Natural Science Foundation of Hebei Province; Project (Grant

No. BJ2019001) supported by Top Young Talents Project of the Education Department of Hebei Province; Project (Kfkt2017-07) supported by the State Key Laboratory Program of High Performance Complex Manufacturing.

References

1. Dursun T, Soutis C (2014) Recent developments in advanced aircraft aluminum alloys. Mater Design 56:862−871
2. Williams JC, Starke EA (2003) Progress in structural materials for aerospace systems. Acta Materialia 51: 5775−5799
3. Huda Z, Edi P (2013) Materials selection in design of structures and engines of supersonic aircrafts: a review. Mater Design 46:552–560
4. Shi Z-F, Guo H-Z, Liu R, Wang X-C, Yao Z-K (2015) Microstructure and mechanical properties of TC21 titanium alloy by near-isothermal forging. Transa Nonferrous Metals Soc China 25(6):72–79
5. Huang S-H, Zong Y-Y, Shan D-B (2013) Application of thermohydrogen processing to Ti6Al4V alloy blade isothermal forging. Mater Sci Eng A 561:17–25
6. He H-L, Huang S-Q, Yi Y-P, Guo W-F (2017) Simulation and experimental research on isothermal forging with semi-closed die and multi-stage-change speed of large AZ80 magnesium alloy support beam. J Mater Process Technol 246:198–204
7. Luri R, Luis CJ, Salcedo D, Leon J, Fuertes JP, Puertas I (2013) FEM analysis of the isothermal forging of a connecting rod from material previously deformed by ECAE. Procedia Eng 63:540–546
8. De-bin SHAN, Wen-chen XU, Xiu-zhu HAN, Xiao-lei HUANG (2012) Study on isothermal precision forging process of rare earth intensifying magnesium alloy. Mater Sci Eng B 177(4):1689–1702
9. Petrov P, Perfilov V, Stebunov S (2006) Prevention of lap formation in near net shape isothermal forging technology of part of irregular shape made of aluminum alloy A92618. J Mater Process Technol 177:218–223
10. Rao KP, Prasad YVRK, Suresh K (2011) Materials modeling and simulation of isothermal forging of rolled AZ31B magnesium alloy: anisotropy of flow. Mater Design 32:2545–2553
11. Shabaniverki S, Serajzadeh S (2016) Simulation of softening kinetics and microstructural events in aluminum alloy subjected to single and multi-pass rolling operations. Appl Math Modell 40:7571–7582
12. Chen R, Xu Q-Y, Liu B-C (2015) Cellular automaton simulation of three-dimensional dendrite growth in Al–7Si–Mg ternary aluminum alloys. Comput Mater Sci 105:90–100
13. Li J-C, Xie Z-Y, Li S-P, Yan-yan ZANG (2016) Modeling on dynamic recrystallization of aluminium alloy 7050 during hot compression based on cellular automaton. J Cent South Univ 23:497–507
14. Huang S-Q, Yi Y-P, Liu C (2009) Simulation of dynamic recrystallization for aluminium alloy 7050 using cellular automaton. J Cent South Univ 16:19–24
15. Wang G-S, Zhao Z-H, Cui J-Z, Guo Q (2013) Microstructure and RRA treatment of LFEC 7075 aluminum alloy extruded bars. J Wuhan Univ Technol-Mater Sci Ed 28(1):184–191
16. Liu W-Y, Zhao H, Li D, Zhang Z-Q, Huang G-J, Liu Q (2014) Hot deformation behavior of AA7085 aluminum alloy during isothermal compression at elevated temperature. Mater Sci Eng A 596:176–182
17. Estrin Y (1996) Unified constitutive laws of plastic deformation. Academic Press, London
18. Ding R, Guo ZX (2001) Coupled quantitative simulation of microstructural evolution and plastic flow during dynamic recrystallization. Acta Mater 49(16):3163–3175

19. Liu Y-X, Lin Y-C, Zhou T (2017) 2D cellular automaton simulation of hot deformation behavior in a Ni-based superalloy under varying thermal-mechanical conditions. Mater Sci Eng A 691:88–99
20. Li DF, Zhang DZ, Liu SD et al (2016) Dynamic recrystallization behavior of 7085 aluminum alloy during hot deformation. Trans Nonferrous Metals Soc China 26(6):1491–1497
21. Mohsen MB, Saeed F, Noordin MY et al (2013) The influence of bismuth, antimony, and strontium on microstructure, thermal, and machinability of aluminum-silicon alloy. Mater Manuf Process 28(11):1184–1190
22. Wang GS, Zhao ZH, Cui JZ, et al (2013) Microstructure and RRA treatment of LFEC 7075 aluminum alloy extruded bars. J Wuhan Univ Technol-Mater Sci Ed 28(1):184–191

The Deformation and Microstructure Analysis of Medium Carbon Steel During Die Forging Process and the Effect of Microalloying Elements



Bo Jiang, Guoning He, Chengcheng Zhang, Xiaolei Ma, Chaolei Zhang, and Yazheng Liu

Abstract The deformation and microstructure of medium carbon steel during die forging process was analyzed by using thermo-simulation test in this paper. The effect of microalloying elements V, Ti, and Nb on the microstructures after deformation was also analyzed. The results showed that there are a critical deformation amount of 6% which increases the grain size of steel in die forging process. The deformation amount during die forging process should reach 20% in order to refine the microstructures. The addition of Ti can largely reduce the grain size of the final product while the further addition of Nb doesn't have significant effect on the grain size. The addition of Ti can significantly increase the ferrite and intra-granular ferrite in the steel by refining the microstructure and offering the precipitates (V, Ti)(C, N) as the nuclei of intra-granular ferrite. The further addition of Nb in the V-Ti-N steel can further increase the size of the precipitates (V, Ti, Nb)(C, N) but suppress the formation of ferrite by improving the hardenability of steel. Thus, there are few ferrite and intra-granular ferrite in the V-Ti-Nb-N steel than that in the V-Ti-N steel.

B. Jiang (✉) · C. Zhang · X. Ma · C. Zhang · Y. Liu
School of Materials Science and Engineering, University of Science and Technology Beijing, 30 Xueyuan Road, Haidian District, Beijing, People's Republic of China
e-mail: jiangbo@ustb.edu.cn

C. Zhang
e-mail: chengchengzhangvip@163.com

X. Ma
e-mail: maxiaoleicl@163.com

C. Zhang
e-mail: zhangchaolei@ustb.edu.cn

Y. Liu
e-mail: lyzh@ustb.edu.cn

G. He
Institute for Advanced Materials and Technology, University of Science and Technology Beijing, 30 Xueyuan Road, Haidian District, Beijing, People's Republic of China
e-mail: heguoyouxiang@163.com

© The Minerals, Metals & Materials Society 2021

G. Daehn et al. (eds.), *Forming the Future*, The Minerals, Metals & Materials Series,
https://doi.org/10.1007/978-3-030-75381-8_153

Keywords Microalloying elements · Die forging · Intra-granular ferrite · Grain size

1 Introduction

Low toughness of medium carbon steel products produced by die forging process has been continuously limiting its application in the high-performance automobile engine. Previous results showed that coarser grain in some parts of the products had resulted in the deterioration of toughness. However, the reason why the coarser grain was formed in the forged steel was not clear and there is no theory basis for the optimization of the manufacturing process. Up to now, microalloying elements have been widely used for the refinement of microstructures by preventing the grain growth in the reheating process [1–3]. However, the microalloying precipitates are very complex in different steels and the effect of microalloying elements on the grain size of different steels is different.

In recent years, many people have focused on the intra-granular ferrite in the forged steel because the pearlite can be divided and thus the microstructures can be refined [4–6]. The intra-granular ferrite often nucleates at microalloying nitrides which precipitated at manganese sulfide particles because the intra-granular ferrite had the Baker–Nutting orientation relationship with the precipitates [7, 8]. Thus, there is an important influence of the microalloying elements on the formation of intra-granular ferrite because the composition, size, and distribution of the precipitates can vary a lot with the microalloying elements. Reports showed that the addition of Ti into V-N steel could increase the size of the precipitates (Ti, V)(C, N) and promote the formation of intra-granular ferrite [9, 10]. For the given medium carbon steel, the effect of microalloying elements was only focused on the rolled billet by my previous work [11]. No reports about the effect of microalloying elements on the microstructures after die forging process have been found.

In this paper, the effect of deformation amount on the microstructure during die forging process was investigated. Based on the results, the reason of the formation of coarser grain was analyzed and the optimization of process parameters was suggested. In addition, the effects of microalloying elements on the grain size, the ferrite, and the intra-granular ferrite were analyzed.

2 Experimental Section

2.1 Materials and Processes

The investigated steel was produced as a 39 kg ingot in a vacuum melting furnace. The diameter of the ingot was around 100 mm. It was then reheated at 1200 °C and soaked for nearly 3 h. After that, the experimental ingot was forged into a round billet with

Table 1 Chemical compositions of steels (wt%)

Steel	C	Si	Mn	S	Cr	N	V	Ti	Nb
No. 1	0.37	0.53	1.34	0.056	0.27	0.019	–	–	–
No. 2, V-N steel	0.36	0.55	1.35	0.061	0.26	0.018	0.10	–	–
No. 3, V-Ti-N steel	0.35	0.54	1.37	0.058	0.27	0.019	0.10	0.018	–
No. 4, V-Ti-Nb-N steel	0.37	0.55	1.37	0.057	0.26	0.017	0.10	0.017	0.025

the diameter of 60 mm in a steel mill. The starting and finish forging temperatures were 1150 and 900 °C, separately. The cooling process was conducted in a furnace with the starting furnace temperature of 700 °C. The chemical compositions of the investigated steels were listed in Table 1. The difference of the chemical composition was designed in order to analyze the effect of microalloying elements V, Ti, and Nb. The reference steel is the medium carbon steel No. 1 which was determined as 0.37C-0.53Si-1.34Mn-0.056S-0.27Cr and was Fe balanced. This steel has been mostly used in the market until now. The microstructures of different steels have been analyzed in the previous study [11]. The grain sizes of steels No. 3 and No. 4 were the finest while that of steel No. 1 was the largest. Although there exists an effect of the starting microstructure on the grain size of the steel after thermo-simulation experiment. However, there was no difference of the grain size for a given steel while the reheating temperature was 1200 °C and the soaking time was 3 min.

A Gleeble thermo-simulation machine was employed to analyze the deformation behavior and microstructure of the experimental steel during die forging process. Figure 1a schematically shows the process routes in the experiments on the Gleeble thermo-simulation machine. The parameters were set based on the manufacturing process in the factory. The specimens for the experiments were all cut from 1/2 diameter of the billets and then were machined into cylinders of 8 mm in diameter and 20 mm in length. Then the specimens were firstly heated up at the heating rate of 15 ℃/s to a peak temperature of 1200 ℃, held for 3 min and then cooled to the deformation temperature of 1100 ℃ with the cooling rate of 15 ℃/s. After that, the specimens were soaked for 10 s for temperature homogenization and then were

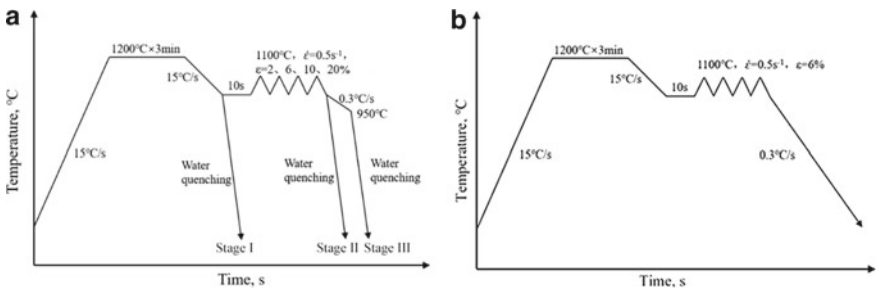


Fig. 1 The schematic process route of the thermo-simulation experiment: **a** water quenching; **b** slow cooling

deformed at the rate of 0.5 s^{-1} with different deformation amounts 2, 6, 10, and 20%. After deformation, the specimens were cooled to 950 ºC with the cooling rate of 0.3 ºC/s and then water quenched. The cooling rate was set based on the real condition. Argon is used in this experiment for protection in order to prevent the surface of the sample from oxidation. Three specimens were prepared for the experiments because the quenched microstructures at different stages I, II, and III as shown in Fig. 1a were all needed to analyze the microstructure evolution. In addition, another thermo-simulation experiment was also conducted to analyze the microstructure cooled with the rate of 0.3 ºC/s to room temperature after deformation. The schematic route can be seen in Fig. 1b.

2.2 Microstructural Investigation

Quenched specimens were polished by conventional metallographic techniques and then etched in a saturated picric acid buffer aqueous solution at 50–60 °C to reveal the prior austenite grain boundary. Metallographic examination was observed by means of optical microscope (OM, model: Zeiss Scope A1). The average grain sizes were measured by a quantitative image analyzer. The samples after the experiment with the route shown in Fig. 1b were mechanically ground, polished, and then etched in 4% nital. Micrographs were obtained by OM and field emission scanning electron microscopy (FESEM, model: FEI quanta FEG 450). Transmission electron microscopy (TEM, model: JEM-2100(HR)) analysis was also performed to investigate the microalloying precipitates on carbon extraction replicas. The energy dispersive X-ray spectrum (EDS) in the FESEM and TEM was used to identify the chemical composition of the precipitates. The extraction replicas were prepared by evaporating carbon film on the samples which were pre-polished and pre-etched in 4% nital. Then the specimens were immersed in 4% nital to strip the carbon film from the surface.

3 Results and Discussion

3.1 Quenched Microstructure Investigation

3.1.1 Effect of Deformation Amount on the Grain Size

Firstly, the prior austenite grains of steel at the final stage III with different deformation amounts were observed in order to analyze the effect of deformation amount. The optical microstructures and the grain size distribution can be seen in Fig. 2. The grain size firstly increased with the deformation amount from 2 to 6% and then decreased with the deformation amount from 6 to 20%. When the deformation amount reached

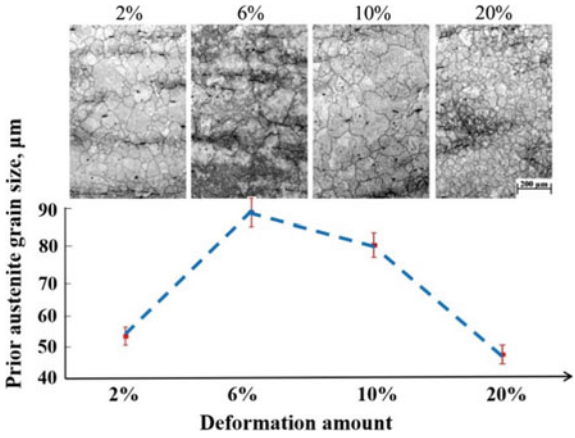


Fig. 2 The optical microstructures of prior austenite grain of steel No. 4 at stage III with different deformation amounts. (Color figure online)

20%, the grain size was almost the same as the size of the microstructure at the stage I without deformation which can be seen in Fig. 4d. Thus, there existed a critical deformation amount zone at which the grain size increased dramatically. In this steel, the critical deformation amount at which the grain size was the largest was 6%. A question is arisen now here whether this big increase in grain size should be attributed to the small deformation amount or the following slow cooling process. Another experiment can be used for verification. The process parameters were totally the same as the route as shown in Fig. 1a except that no deformation was conducted in this route. The prior austenite grain was shown in Fig. 3. The grain size was 52.3 μm which meant that there was no big increase in the process without deformation. It has been known to us that the recrystallization after deformation is an energy-driven process and can promote the nucleation of new grain and thus refine the grain [12, 13]. However, nucleation of grain cannot proceed if the deformation amount is small

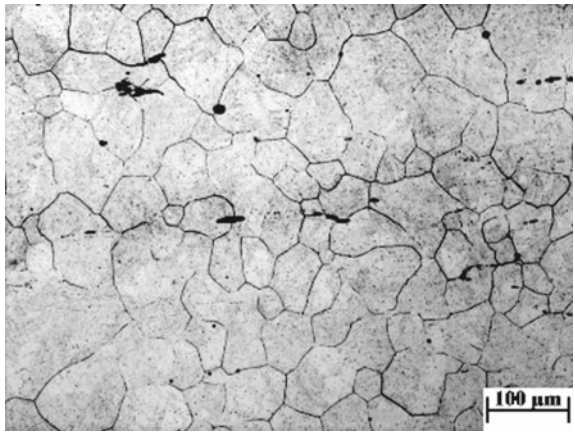


Fig. 3 The optical microstructures of prior austenite grain of steel No. 4 after the thermo-simulation experiment without deformation

[14]. In this case, only recovery can occur and then the grain grows in the following slow cooling process with the energy driving.

According to our previous research, the microstructures in die forging products were very inhomogeneous and the toughness of the steel was very low because there always existed coarser grains in the microstructures [15]. Besides the deformation amounts across the section of forged products varied a lot thus there were some places with deformation amount which should be as low as less than 10%. In that sense, the appearance of coarser microstructure should be attributed to the low deformation amount during die forging. Also, the deformation amount should be higher than 20% in order to avoid the coarsening of grain according to the results in this work.

3.1.2 Effect of Microalloying Elements on the Grain Size

The quenched microstructures of different steels at different thermo-simulation stages with the deformation amount 6% were shown in Fig. 4. The prior austenite grain sizes were also measured and the results were shown in Fig. 5. It can be seen in the figure that the prior austenite grain sizes of steel No. 1 and No. 2 are very close and much larger than that of steel No. 3 and steel No. 4 at stage I. These results are unanimous to the previous study which showed that the existence of precipitates Ti (C,N) and (Nb, Ti)(C,N) in steel No. 3 and steel No. 4 had reduced the austenite grain size [16]. The precipitates V(C, N) were dissolved at 1200 °C and thus the grain size in steel No. 2 was nearly the same as in steel No. 1. In Figs. 2 and 3, the prior austenite grains of different steels at the stages II and III were also shown. As can be seen, there are only small increase in grain size from stage I to stage II. However,

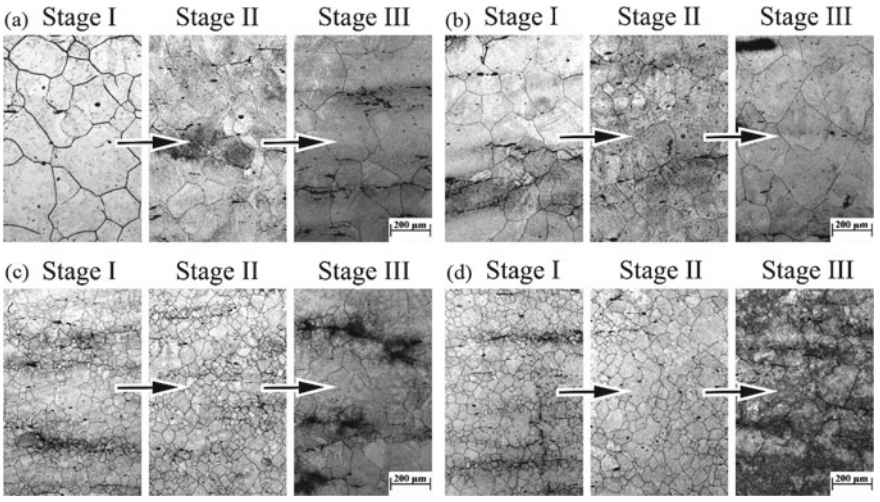


Fig. 4 The optical microstructures of prior austenite grain of different steels at different thermo-simulation stages: **a** steel No. 1; **b** steel No. 2; **c** steel No. 3; **d** steel No. 4

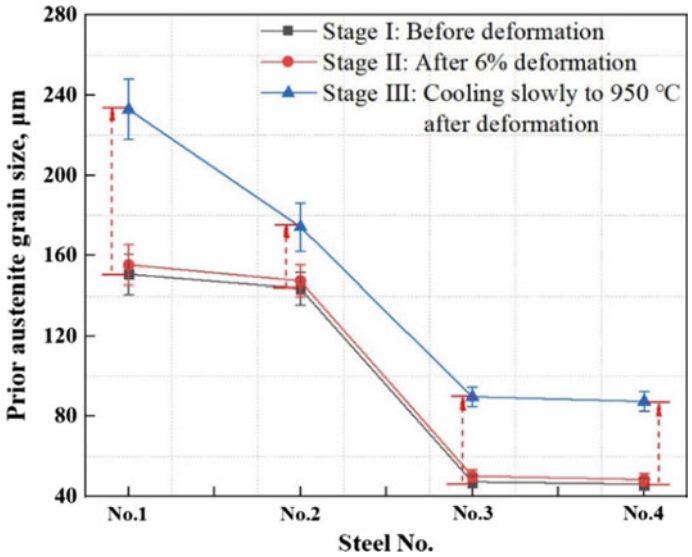


Fig. 5 The prior austenite grain size of different steels at different thermo-simulation stages. (Color figure online)

a big increase in grain size occurred from stage II to stage III when the deformed specimen was cooled to 950 °C. This result was also unanimous to part 3.1.1 which showed that the grain growth occurred in the slow cooling process while was driven by the energy offered by deformation with small amount.

For different steels, effects of the microalloying elements on the grain size at different stages were almost the same. The grain size of steel No. 1 was almost the same as that of steel No. 2 at all stages. The grain sizes of steel No. 3 and steel No. 4 were also nearly the same. However, the grain sizes of steel No. 3 and steel No. 4 were much smaller than that of steel No. 1 and steel No. 2. In addition, there was no much difference in grain size of steel No. 3 and steel No. 4. The addition of Nb cannot obviously prevent the growth of grain in the steel with the given chemical composition.

3.2 Slow Cooled Microstructure Investigation

3.2.1 OM Analysis

The optical microstructures of different steels after the experiment with the route in Fig. 1b can be seen in Fig. 6. As seen in the figure, the microstructures in different steels mainly consisted of pearlite, grain boundary ferrite, and intra-granular ferrite.

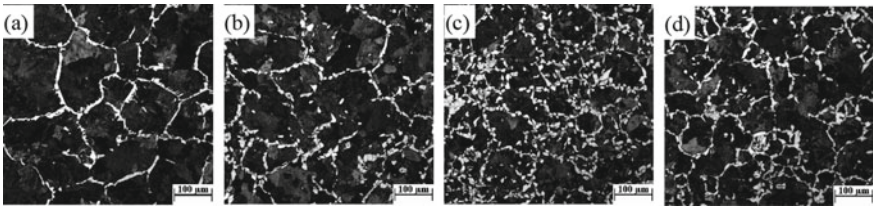


Fig. 6 The optical microstructures of different steels after the experiment with the route in Fig. 1b: **a** steel No. 1; **b** steel No. 2; **c** steel No. 3; **d** steel No. 4

Table 2 The grain size and the volume fractions of ferrite and intra-granular ferrite in different steels

Steel	Size of grain boundary ferrite network (μm)	Volume fraction of ferrite (%)	Volume fraction of intra-granular ferrite (%)
No. 1	159.3	6.9	0.07
No. 2	142.8	8.8	0.84
No. 3	62.3	14.4	1.38
No. 4	61.9	12.4	0.86

The effect of microalloying elements on the grain size in the slow cooled microstructure as shown in Table 2 was almost the same as that in the quenched microstructure. The grain sizes in steel No. 3 and steel No. 4 were the smallest while that of steel No. 1 and steel No. 2 were relatively larger. However, the difference in microstructures of different steels was also obvious. As can be seen, there existed more intra-granular ferrite in steel No. 2, steel No. 3, and steel No. 4. The volume fractions of ferrite and intra-granular ferrite were shown in Table 2. The volume fractions of ferrite and intra-granular ferrite in steel No. 1 were the smallest while that in steel No. 3 were the highest. As we know, the refinement of austenite can promote the formation of ferrite by offering more boundaries for nucleation. Thus, steel No. 1 had the lowest volume fraction of ferrite because of its larger grain size. However, the grain size of steel No. 4 was nearly the same as that of steel No. 3 but had the smaller volume fractions of ferrite and intra-granular ferrite. The volume fraction of intra-granular ferrite in steel No. 4 was even approximately half that of steel No. 3.

3.2.2 FESEM and TEM Analysis

The FESEM microstructures of different steels were shown in Fig. 7 to analyze the intra-granular ferrite and the microalloying precipitates. It can be seen in the figure that most intra-granular ferrites were formed on the particles. To further analyze the particles, the EDS results showed that the nuclei of the intra-granular ferrite were microalloying particle on MnS inclusions. The nuclei of the intra-granular ferrites in steel No. 2, steel No. 3, and steel No. 3 were V(C, N), (V, Ti)(C, N), and (V, Ti,

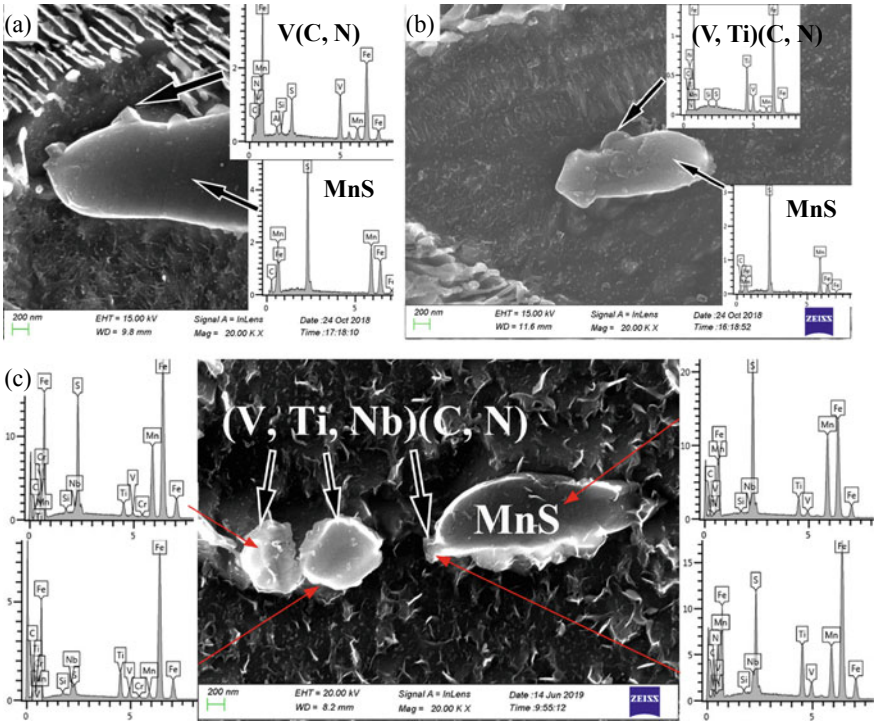


Fig. 7 The FESEM microstructures of different steels after the experiment with the route in Fig. 1b: **a** steel No. 2; **b** steel No. 3; **c** steel No. 4. (Color figure online)

Nb)(C, N) particles, respectively. The results were unanimous to the many previous studies which showed that the intra-granular ferrite had the Baker–Nutting orientation relationship with microalloying nitride [7, 8]. Thus, the microalloying nitrides in the steel played an important in the formation of intra-granular ferrite.

TEM morphologies of the precipitates in steel No. 3 and steel No. 4 are shown in Figs. 8 and 9 by means of observing the carbon extraction replicas evaporated on the samples. Results showed that there existed three kinds of precipitates in steel No. 3: clustered precipitates V(C, N) with the diameter less than 50 nm, ellipsoidal precipitates (V, Ti)(C, N) with the diameter nearly 50 nm in Fig. 8b, and quadrate precipitates (V, Ti)(C, N) with the diameter larger than 100 nm in Fig. 8c. In Fig. 9, the distribution of precipitates in steel No .4 was nearly the same as in steel No. 3. However, the precipitates in steel No. 4 were (V, Ti, Nb)(C, N) and there were Nb-rich and Ti-rich precipitates as shown in Fig. 9b, c. The Nb-rich precipitate could be formed on the Ti-rich precipitate and thus increase the size of the composite precipitate. Further quantitative analysis on the number and size of the precipitates showed that the average sizes of the precipitates in steel No. 3 and steel No. 4 were 55 nm and 72 nm, respectively. The numbers of the precipitates per μm^2 in steel No.

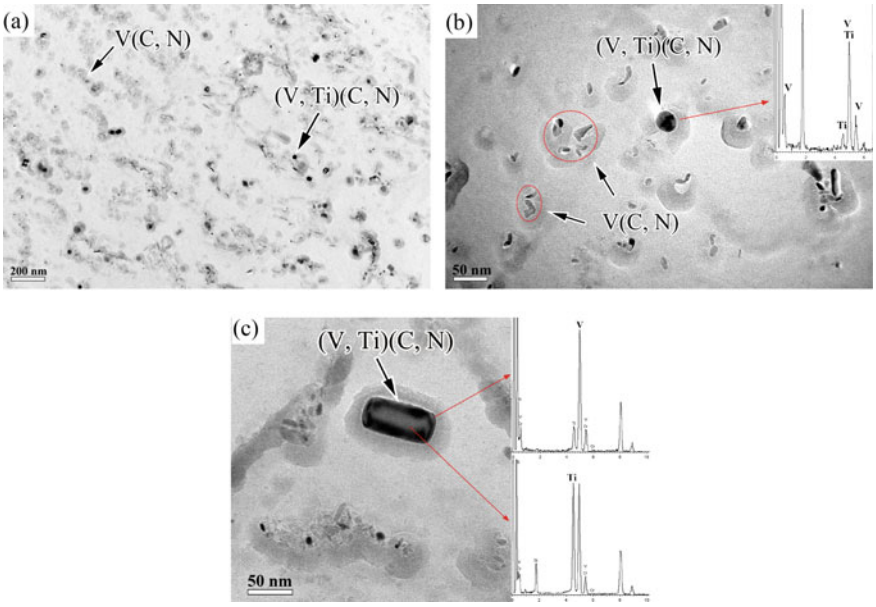


Fig. 8 TEM morphology and EDS results of the precipitates in steel No. 3: **a** low magnification; **b** elliptical precipitates (V, Ti)(C, N) with high magnification; **c** quadrate precipitates (V, Ti)(C, N) with high magnification. (Color figure online)

3 and steel No. 4 were approximately 9.1 and 8.3, respectively. The addition of Nb in the investigated steel can obviously increase the size of the precipitates.

3.2.3 Effect of Microalloying Elements on the Formation of Intra-granular Ferrite

Many researches showed that the size of the precipitates should reach a critical size which may be a few hundred nanometers in order to induce the nuclei of intra-granular ferrite [9, 10, 17–19]. Based on the results in part 3.2.2, the addition of Nb can increase the size of the precipitates and thus should promote the formation of intra-granular ferrite. However, the volume fraction of intra-granular ferrite in steel No. 4 was much lower than that in steel No. 3. Also, the addition of Nb reduced the volume fraction of ferrite. To further analyze the effect of Nb on the formation of ferrite, the linear expansion amount versus temperature in the cooling process is shown in Fig. 10. The phase transformation temperatures can be obtained as shown in the figure according to the curve slope changes. The transformation temperature range of ferrite and pearlite in steel No. 4 was obviously delayed to lower range compared with that in steel No. 3. Previous studies showed that Nb can improve the hardenability of steel and thus promote the pearlite formation and suppress the ferrite formation [20, 21]. It can be concluded the effect of Nb on the hardenability of steel

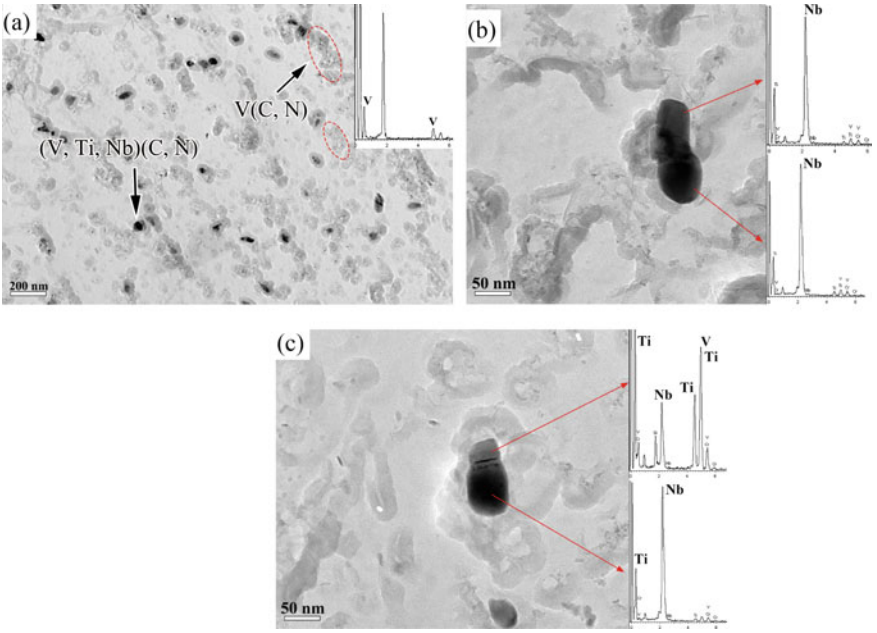


Fig. 9 TEM morphology and EDS results of the precipitates in steel No. 4: **a** low magnification; **b** Nb-rich precipitates (V, Ti, Nb)(C, N) with high magnification; **c** Nb and Ti composite precipitates (V, Ti, Nb)(C, N) with high magnification. (Color figure online)

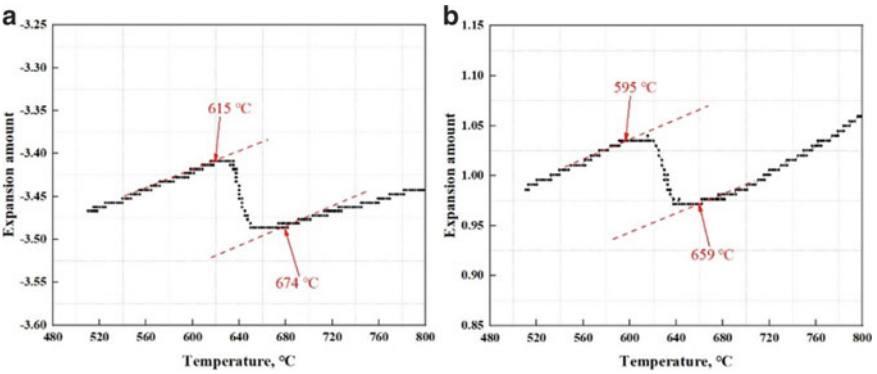


Fig. 10 The linear expansion amount versus temperature in cooling process: **a** steel No. 3; **b** steel No. 4. (Color figure online)

was higher than that on the formation of intra-granular ferrite. Thus, there were few ferrite and intra-granular ferrite in steel No. 4 than that in steel No. 3 in the process with the cooling rate of 0.3 °C/s.

4 Conclusions

(1) There is a critical deformation amount 6% which increases the grain size of steel in die forging process. The grain growth occurred at the cooling process after deformation and was driven by the energy offered by the deformation with small amount. The deformation amount during die forging process should reach 20% in order to refine the microstructures.
(2) The addition of V in the investigated steel can only reduce the grain size of the final product by 16.5 μm. The addition of Ti can largely reduce the grain size from 142.8 to 62.3 μm while the further addition of Nb doesn't have significant effect on the grain size.
(3) The addition of Ti can significantly increase the ferrite and intra-granular ferrite in the steel by refining the microstructure and offering the precipitates (V, Ti)(C, N) as the nuclei of intra-granular ferrite. The further addition of Nb in the V-Ti-N steel can further increase the size of the precipitates but suppress the formation of ferrite by improving the hardenability of steel. Thus, there are few ferrite and intra-granular ferrite in the V-Ti-Nb-N steel than that in the V-Ti-N steel.

Acknowledgments The authors appreciate the financial support by the National Natural Science Foundation of China (No. 51701015) and Fundamental Research Funds for the Central Universities of China (No. FRF-TP-19-006A2).

References

1. Yang HL, Xu G, Wang L et al (2017) A study of growth of austenite grains in a steel microalloyed with Ti and Nb. Met Sci Heat Treat 59(1–2):8–13
2. Zhang C, Fang W, Cai B et al (2019) Austenite grain growth and its effect on splitting fracture property of a V-N microalloyed medium carbon steel connecting rod. J Iron Steel Res Inter 26(8):875–881
3. Ji G, Gao X, Liu Z et al (2019) In situ observation and modeling of austenite grain growth in a Nb–Ti-bearing high carbon steel. J Iron Steel Res Inter 26(3):292–300
4. Ishikawa F, Takahashi T, Ochi T (1994) Intragranular ferrite nucleation in medium-carbon vanadium steels. Metall Mater Trans A 25(5):929–936
5. Miyamoto G, Shinyoshi T, Yamaguchi J et al (2003) Crystallography of intragranular ferrite formed on (MnS+ V (C, N)) complex precipitate in austenite. Scr Mater 48(4):371–377
6. Zhao F, Wu M, Jiang B et al (2018) Effect of nitrogen contents on the microstructure and mechanical properties of V-Ti microalloyed steels for the forging of crankshafts. Mater Sci Eng, A 731:360–368
7. Furuhara T, Shinyoshi T, Miyamoto G et al (2003) Multiphase crystallography in the nucleation of intragranular ferrite on MnS + V(C, N) complex precipitate in austenite. ISIJ Inter 43(12):2028–2037
8. Zhao F, Zhou N, Wu M et al (2017) Intragranular Ferrite Formed in a V-Ti–N medium-carbon steel containing MnS inclusions. Steel Res Inter 88(12):1700133
9. Hu J, Du LX, Wang JJ. Effect of V on intragranular ferrite nucleation of high Ti bearing steel. Scr Mater 68(12):953–956

10. Shi Z, Chai X, Chai F et al (2016) The mechanism of intragranular ferrite formed on Ti-rich (Ti, V)(C, N) precipitates in the coarse heat affected zone of a V-N–Ti microalloyed steel. Mater Lett 175:266–270
11. Jiang B, Fang W, Chen R et al (2019) Mechanical properties and microstructural characterization of medium carbon non-quenched and tempered steel: microalloying behavior. Mater Sci Eng A 748:180–188
12. Cho SH, Kang KB, Jonas JJ (2001) The dynamic, static and metadynamic recrystallization of a Nb-microalloyed steel. ISIJ Inter 41(1):63–69
13. Chen MS, Lin YC, Ma XS (2012) The kinetics of dynamic recrystallization of 42CrMo steel. Mater Sci Eng A 556:260–266
14. Oyarzábal M, Martínez-de-Guerenu A, Gutiérrez I (2008) Effect of stored energy and recovery on the overall recrystallization kinetics of a cold rolled low carbon steel. Mater Sci Eng A 485(1–2):200–209
15. Wu M, He G, Zheng X et al (2018) The bainite transformation behavior, the influencing factors and control strategy in ferritic-pearlitic forged crankshafts with coarse grains. Maters Sci Eng Tech 49(7):843–850
16. Fang W, Zhang CC, Jiang B, et al (2019) The effect of microalloying elements (V, Ti) additions on the austenite grain growth behavior in medium carbon steel containing N. Mater Sci Eng Tech. https://doi.org/10.1002/mawe.201900053
17. Shim JH, Oh YJ, Shu JY et al (2001) Ferrite nucleation potency of non-metallic inclusions in medium carbon steels. Acta Mater 49(12):2115–2122
18. Lee TK, Kim HJ, Kang BY et al (2000) Effect of inclusion size on the nucleation of acicular ferrite in welds. ISIJ Inter 40(12):1260–1268
19. Madariaga M, Gutiérrez I (1999) Role of the particle-matrix interface on the nucleation of acicular ferrite in a medium carbon microalloyed steel. Acta Mater 47(3):951–960
20. PA M, Chandra T, CR K (1996) Continuous cooling transformation behaviour of microalloyed steels containing Ti, Nb, Mn and Mo. ISIJ Inter 36(12):1486–1493
21. Yan P, Bhadeshia H (2015) Austenite–ferrite transformation in enhanced niobium, low carbon steel. Mater Sci Tech 31(9):1066–1076

Effect of Ferrite Rolling Temperature on the Microstructure and Properties of an Ultra-Low Carbon Steel Produced by CSP Process



Guoning He, Xuewen Hu, Bo Jiang, Chaolei Zhang, Haibo Wang, and Yazheng Liu

Abstract The higher strength of hot rolled steel sheet by compact strip production (CSP) process has been restricting its application in higher formability and thinner steel sheet because of higher cold rolling load. Ferrite rolling process has been widely researched since it has successfully reduced the strength of cold rolling feeds. In this paper, the microstructures and properties of a hot rolled ultra-low carbon steel SPHE by CSP process with different rolling temperatures were investigated. Strengthening mechanism was discussed by EBSD and TEM analysis. Results showed the mechanisms why the strength of the steel deformed with the finishing rolling temperature at single ferrite zone was increased while the elongation was decreased. The deformation resistance and microstructure versus temperature and the transformation behavior were analyzed. It was found that deformation at dual phase zone near to Ac1 can further increase the grain size and thus decrease the strength and meantime keep the elongation.

Keywords CSP · SPHE · Ferrite rolling · Yield strength

G. He
Institute for Advanced Materials and Technology, University of Science and Technology Beijing, 30 Xueyuan Road, Beijing, People's Republic of China
e-mail: heguoyouxiang@163.com

X. Hu · B. Jiang · C. Zhang · H. Wang · Y. Liu (✉)
School of Materials Science and Engineering, University of Science and Technology Beijing, 30 Xueyuan Road, Beijing, People's Republic of China
e-mail: lyzh@ustb.edu.cn

X. Hu
e-mail: hxw_mg@sina.com

B. Jiang
e-mail: jiangbo@ustb.edu.cn

C. Zhang
e-mail: zhangchaolei@ustb.edu.cn

H. Wang
e-mail: wanghaibo@ustb.edu.cn

© The Minerals, Metals & Materials Society 2021

G. Daehn et al. (eds.), *Forming the Future*, The Minerals, Metals & Materials Series,
https://doi.org/10.1007/978-3-030-75381-8_154

1 Introduction

Compact strip production (CSP) process is one of the main thin slab continuous casting and rolling production lines, which produces hot strips using a brief production line combining science, technology, and engineering [1, 2]. CSP appeared in 1989 and has developed rapidly because of its low cost and high efficiency. China has the largest thin slab continuous casting and rolling production line and output. By the end of 2018, China has built 17 thin slab continuous casting and rolling production lines, 15 of which are still in operation, with a total capacity of more than 35 million tons/year. Compared with traditional technology, CSP products have finer microstructure and higher strength with the same composition [3, 4]. Therefore, it has obvious advantages to develop high-strength steel by CSP process. CSP manufacturers all over the world are developing to fine grain ultra-high-strength steel, including multi-phase steel, pipeline steel, and other high value-added products [5–7].

The sheet thickness can be reduced while adopting high-strength steel, which is an important way to realize a vehicle is lightweight [8, 9]. This requires sheets that should not only maintain higher mechanical properties, but also should be thinner and lighter. For the CSP process, the unique funnel-shaped crystallizer and high casting speed can easily result in slag entrapment. In addition, after continuous casting, soaking and rolling are carried out directly, and surface defects cannot be removed. It is difficult to produce ultrathin hot rolled sheet by CSP process because of its poor surface quality [10].

Due to the poor quality of hot rolled sheet, CSP process often provides base material of cold rolling. However, when taking the CSP hot rolled sheet as base material to produce the cold rolling sheet, it has higher yield strength, lower elongation ratio, and poorer stamping performance. The high yield strength has adverse effects on cold rolling. Several studies suggest that boron added in low carbon steel can make grain coarsening, leading to reduction of yield strength but brings little effect. Recent years, study on hot rolled in ferrite region based on CSP line achieved good results in reduction of yield strength [11].

In this paper, the microstructures and properties of a hot rolled ultra-low carbon steel SPHE by CSP process with different ferrite region rolling temperatures were investigated. The results can provide a reference for study and application of ferrite region rolling on CSP line.

2 Experimental Procedure

2.1 Materials

The chemical composition of the experimental ultra-low carbon steel sheet SPHE by CSP process is shown in Table 1. The phase transition point Ar1 and Ar3 at this composition are 881 °C and 915 °C. The production process flow diagram of the

Table 1 The chemical composition of SPHE sheet

Elements	C	Si	Mn	P	S	Als	Ti
Mass fraction (%)	0.002	0.012	0.11	0.014	0.004	0.053	0.060

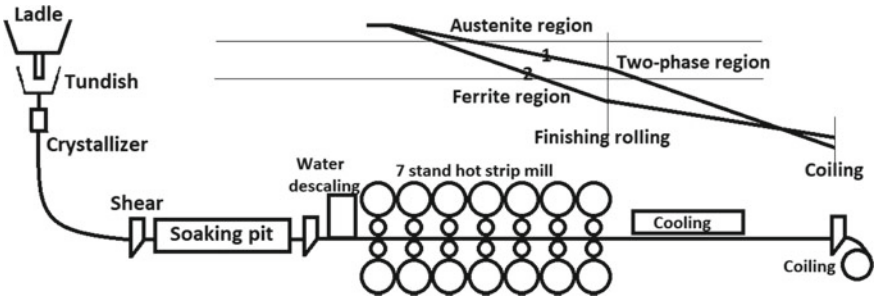


Fig. 1 The production process flow diagram of CSP process

experimental sheet is shown in Fig. 1. Hot rolled sheets of 3 mm thickness were produced by two different rolling processes named 1 and 2, one with the finishing rolling temperature about 890 °C and the other with about 807 °C. Process 1 represents a kind of two-phase region rolling or high-temperature ferrite rolling, and process 2 represents a kind of low-temperature ferrite rolling. Both sheets were coiled at the temperature of 660 ± 30 °C after rolling.

2.2 Microstructural Characterization

The optical microscope (OM) microstructures were observed in normal direction (ND), rolling direction (RD), and transverse direction (TD) at the 1/2 width of the hot rolled sheet, and the surface of sample was etched by 4% nitric acid in alcohol. Electron backscatter diffraction (EBSD) measurements were made in TD of the sample in a scanning electron microscope (SEM), operated at 20 kV. The surface of sample was electropolished in 15% perchloric acid in alcohol. The precipitates and dislocation were observed by transmission electron microscope (TEM) analysis and energy dispersive spectrometer (EDS).

2.3 Mechanical Properties

The standard samples were cut to test the mechanical properties at the 1/2 width of the hot rolled sheet. The transversal, longitudinal, and diagonal of sheets were all analyzed, and the sampling method is shown in Fig. 2. The average plastic strain

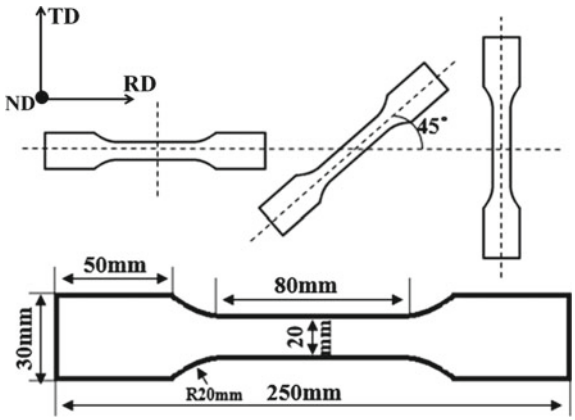


Fig. 2 The sampling method of mechanical properties

ratio r value and the anisotropic coefficient Δr value were also calculated. Mechanical properties tests were carried out according to the Chinese national standard GB/T228-2010 and GB/T5028-2008.

The deformation resistances and microstructures under different deformation temperatures were investigated by Gleeble 3800 thermal–mechanical simulation. The deformation temperature was set as 930, 900, 885, 870, 835, 800, and 700 °C after austenitizing at 1000 °C for 1 min. The deformation true strain was 0.92 and deformation rate was 40 s^{-1}.

3 Results and Discussion

3.1 OM Microstructure

The OM microstructures of two hot rolled sheets in different observation directions were shown in Fig. 3. The microstructure of the sheet in process 1 was equiaxed ferrite and the grain boundary of ferrite was clear. There is no significant difference among the ferrite morphology in ND, RD, and TD. Because of the low finishing temperature in process 2, more work hardening exists at the strip. And yet the grain boundary was not etched by nitric acid in process 2, only ferrite grains with different etching degrees could be seen indistinctly. It can be surmised that the energy in grains was higher than that in grain boundaries.

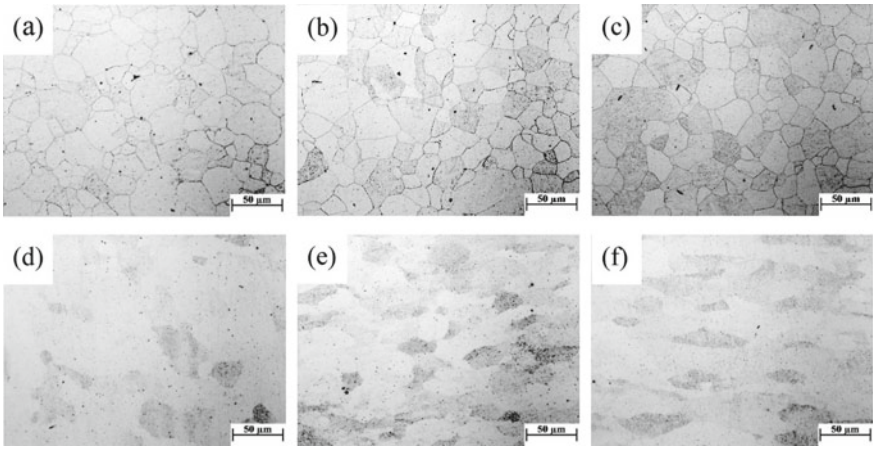


Fig. 3 OM microstructure of two sheets in different observation directions: **a**, **b**, **c** process 1, **d**, **e**, **f** process 2, **a**, **d** ND, **b**, **e** RD, **c, f** TD

3.2 EBSD Analysis

The grain boundaries analyzed by EBSD of two hot rolled sheets were shown in Fig. 4. The grain boundaries of ferrite in process 1 were mainly high-angle grain boundaries (>15°), the average grain size was 25.3 μm. But there were many low-angle grain boundaries (<15°) in process 2, the ferrite was deformed and irregular.

The grain orientations referenced to the sheet plane (the rolling surface) and rolling direction were obtained by EBSD, as shown in Fig. 5. EBSD result showed that there was a good agreement with the grain orientations of the two hot rolled sheets. The grains referenced to the sheet plane were mainly in blue and red, and the grains referenced to the rolling direction were mainly in green. This represented

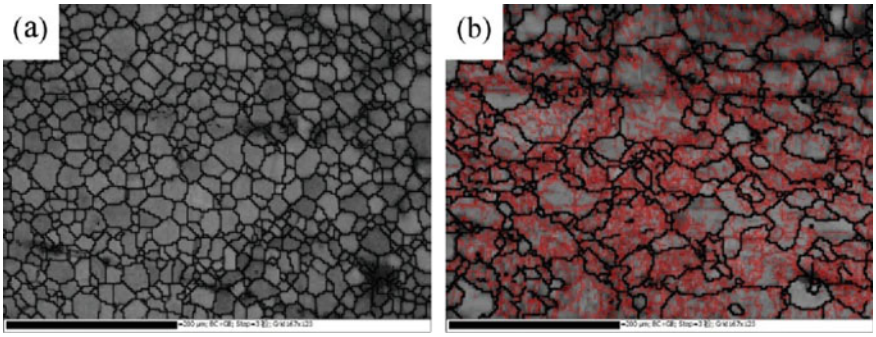


Fig. 4 Grain boundaries morphology in TD observed by EBSD: **a** process 1, **b** process 2. (Color figure online)

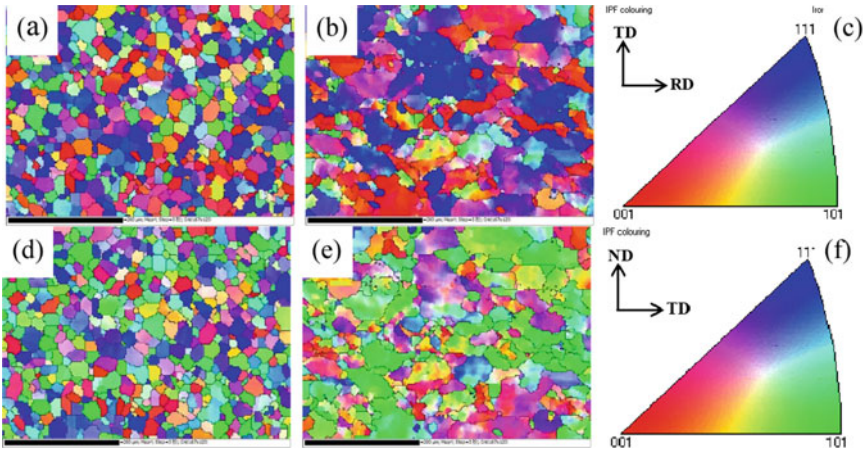


Fig. 5 The grain orientations referenced to the sheet plane and rolling direction: **a**, **c** process 1, **b**, **d** process 2, **a**, **b**, **c** the sheet plane, **d**, **e**, **f** rolling direction. (Color figure online)

that both of the grain orientations in process 1 and process 2 were {111}<110> and {001}<110>. The grain orientation in process 1 was more disordered.

3.3 TEM Analysis

The dislocation morphologies of two hot rolled sheets were observed by TEM, and the results were shown in Fig. 6. The number of dislocation lines observed in process 1 were quite lower than that in process 2. There were no or little single dislocation line observed in most field of view in process 1, and dislocation tangle existed in the rare case. But the observation in process 2 showed a lot of dislocation pile up and nets, as well as subgrain boundaries.

The precipitates in two hot rolled sheets were investigated by carbon extraction replica method, as shown in Fig. 7. A large number of small round-shaped precipitates were found in process 1, with size of 20–30 nm, which could be identified as $Ti_4C_2S_2$ by EDS [12]. The number of $Ti_4C_2S_2$ precipitates increased in process 2, while the size and shape have almost no change. It was speculated that the low finishing temperature deformation induced the $Ti_4C_2S_2$ precipitation.

3.4 Mechanical Property

The mechanical properties in different sampling directions of the two hot rolled sheets were shown in Table 2. The mechanical properties of process 1 in different

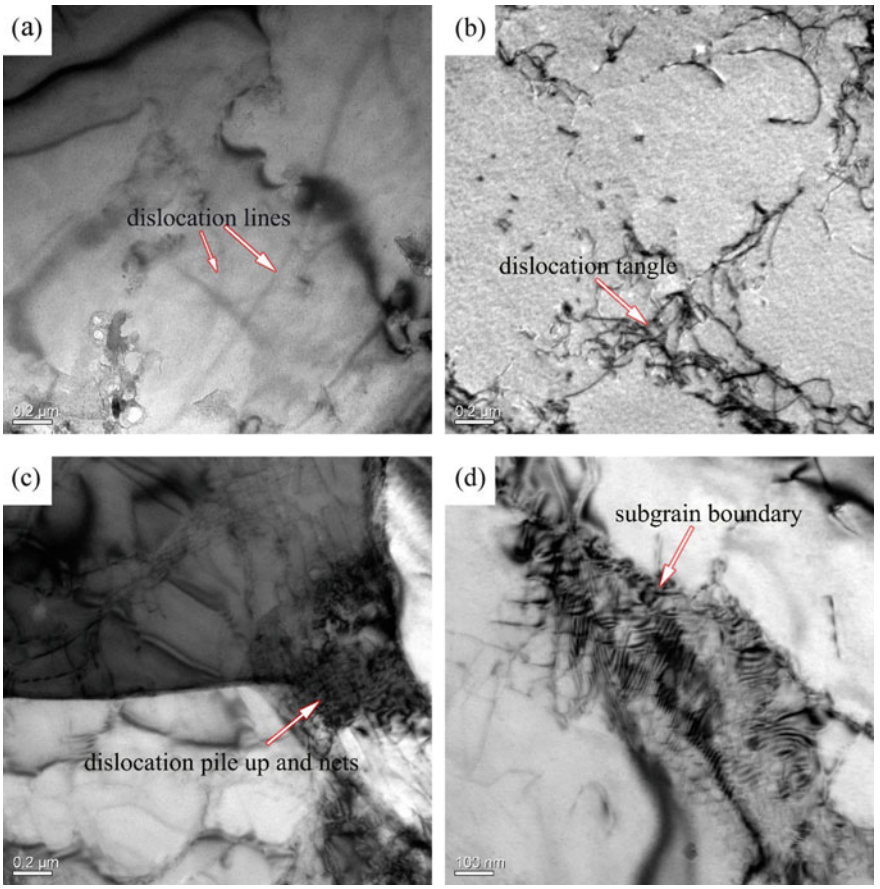


Fig. 6 The dislocation morphologies observed by TEM: **a**, **b** process 1, **c**, **d** process 2. (Color figure online)

directions had no obvious difference, whereas the mechanical properties of process 2 in longitudinal direction were relatively low. Comparing the mechanical properties of the two hot rolled sheets, the average yield strength and tensile strength of process 2 were increased by 61 MPa and 45 MPa, respectively, while the average elongation was decreased by 22%. The average n value of process 2 was also decreased 0.11, but the Δr and $\bar{r}$ changed little.

The average deformation resistances and microstructures of experimental SPHE steel under different deformation temperatures were shown in Fig. 8 and Fig. 9, respectively. With the increase of deformation temperature, the average deformation resistance of SPHE steel decreased firstly, then increased, and reached a minimum value in the vicinity of 870 °C. Moreover, the decrease of deformation temperature from 930 to 870 °C led to an obvious increase of grain size. But with the deformation temperature continuing to decrease, the grains were elongated along the direction of deformation and the amount of crystal defects increased.

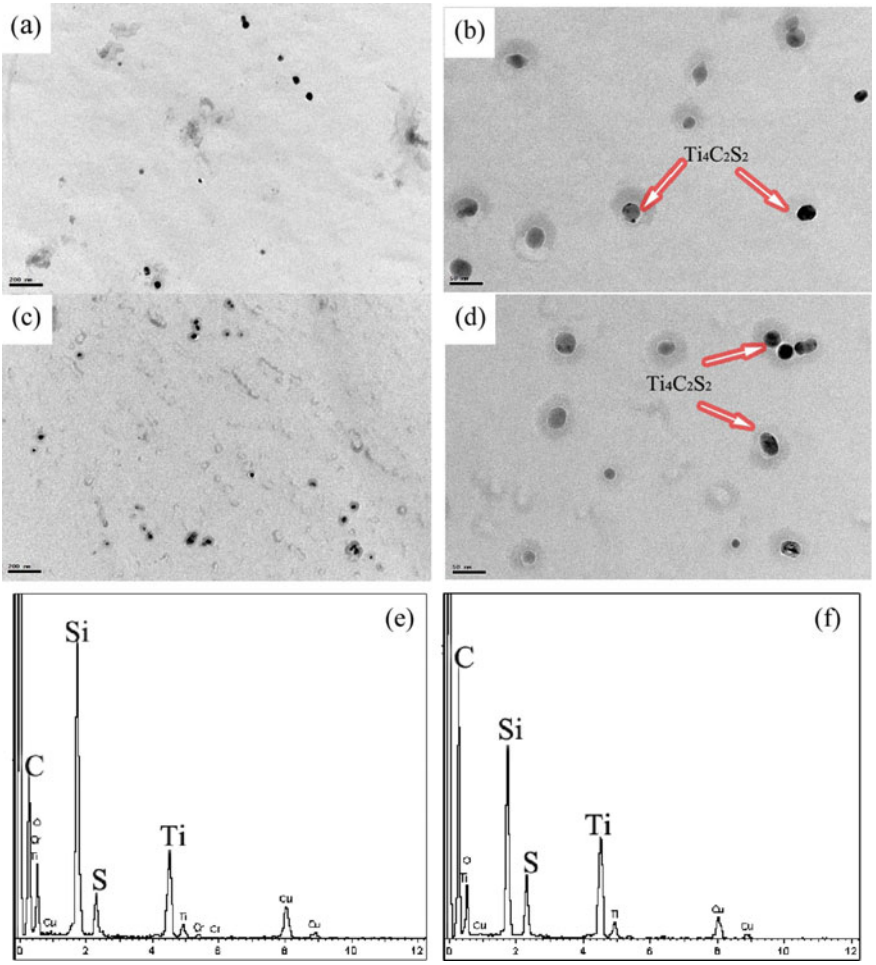


Fig. 7 $Ti_4C_2S_2$ precipitate observed by TEM with corresponding EDS analysis: **a**, **b**, **e** process 1, **c**, **d**, **f** process 2. (Color figure online)

At the same temperature, the yield strength of ferrite was lower than that of austenite, while the slip systems of ferrite with BCC structure were less than austenite with FCC structure, so the plasticity of austenite is better than ferrite [13]. When the deformation temperature got into the two-phase region, the appearance of low strength ferrite led to the significant reduction of deformation resistance. Meanwhile, austenite dynamic recrystallization and phase transformation consumed the deformation energy, and large size grains with little crystal defects were formed. With the deformation temperature continued to decline, single phase ferrite with BCC structure was hard to dynamic recrystallize and recover, a large number of deformation

Table 2 Mechanical properties in different sampling directions of hot rolled sheets

Process	Direction	Yield strength (MPa)	Tensile strength (MPa)	Elongation (%)	n	r	Δr	$\bar{r}$
Process 1	Transversal	205	289	44.8	0.24	1.07	−0.05	1.08
	45°	204	286	44.3	0.23	1.13		
	Longitudinal	204	292	43.4	0.23	0.99		
	Average	204	289	44.2	0.23			
Process 2	Transversal	271	333	21.6	0.13	0.96	−0.02	0.96
	45°	280	335	26.0	0.12	0.98		
	Longitudinal	250	335	18.9	0.12	0.91		
	Average	265	334	22.2	0.12			

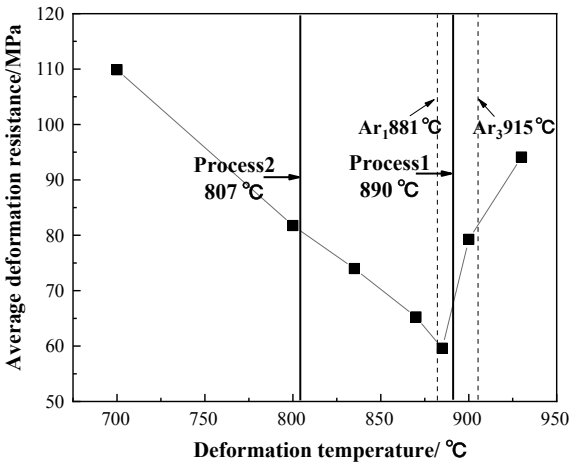


Fig. 8 The average deformation resistances of experimental SPHE steel under different deformation temperatures

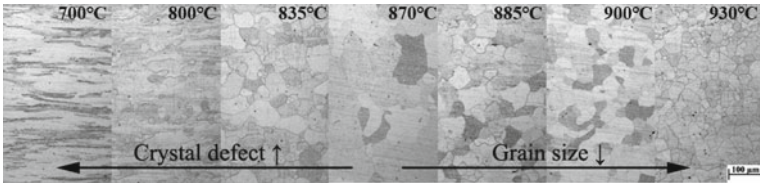


Fig. 9 The microstructures of experimental SPHE steel under different deformation temperatures

energy and crystal defects will be introduced, and the deformation resistance will substantially increase.

Table 3 The comparison of influence parameters of each strengthening factor of hot rolled sheets

Strengthening factor	Influence parameter	Process 1	Process 2
σFe	Microstructure	Ferrite	
σss	Chemical composition	The same SPHE sheet	
σd	Dislocation	Lower density	Higher density
σsg	Substructure	Less	More
σt	Texture	Negligible	
σp	Precipitation	Less	More
σg	Grain size	Bigger	Smaller
σs	All	Lower	Higher

3.5 Strengthening Mechanism

The yield strength of ferrite steel can be regarded as a combination of several strengthening factors, such as the strength of ferrite matrix σFe, the solid solution strengthening σss, the dislocation strengthening σd, the substructure strengthening σsg, the texture strengthening σt, the precipitation strengthening σp, and the fine grain strengthening σg. Therefore, the yield strength can be factorized as follows in Eq. (1) [14].

$$\sigma s = \sigma Fe + \sigma ss + \sigma d + \sigma sg + \sigma t + \sigma p + \sigma g \quad (1)$$

The influence parameters of each strengthening factor were compared and analyzed for the two sheets. Each influence parameter was shown in Table 3. For the two hot rolled SPHE sheets in process 1 and 2, σFe and σss were the same because of the same ferrite single phase and chemical composition. The dislocation density in process 2 was much higher than that in process 1, so the dislocation strengthening σd was also higher. In addition, the subgrain boundaries and larger number of $Ti_4C_2S_2$ precipitates meant that σsg and σp in process 2 will be higher than that in process 1. The variation of grain orientation of the two sheets was relatively small, thus σt was negligible. Due to the bigger grain size in process 1, the σg was quite smaller than that in process 2. Superposition of all factors resulted in the difference of yield strength in the two processes.

4 Conclusions

(1) Ultra-low carbon steel SPHE hot rolled sheet with the finishing rolling temperature about 890 °C mainly had high-angle grain boundaries, and the average

grain size of ferrite was 25.3 μm. But there were many low-angle grain boundaries in the steel sheet with the finishing rolling temperature about 807 °C, and the ferrite was deformed and irregular.

(2) Compared with low finishing rolling temperature sheet, the steel sheet with the finishing rolling temperature about 890 °C had lower dislocation density, less number of subgrain boundaries and $Ti_4C_2S_2$ precipitates, and larger grain size, the comprehensive action of these effects brought the obvious decrease of yield strength and increase of elongation.

(3) With the increase of deformation temperature, the average deformation resistance of SPHE steel decreased firstly and then increased. The decrease of deformation temperature from 930 to 870 °C led to an obvious increase of grain size and with the deformation temperature continuing to decrease, the grains were elongated along the direction of deformation and the amount of crystal defects increased.

Acknowledgments The authors appreciate the financial support by Fundamental Research Funds for the Central Universities of China (No. FRF-TP-19-006A2) and the National Natural Science Foundation of China (No. 51701015).

References

1. Yu H, Kang YL, Fu J (2002) Analysis on microstructure and misorientation of ultrathin hot strip of low carbon steel produced by compact strip production. J Mater Sci Technol 18(6):501–503. https://doi.org/10.3321/j.issn:1005-0302.2002.06.006
2. Yu H, Kang YL, Dong HB (2006) Comparison and analysis of dislocation density, morphology and evolution in microstructure of low-carbon steel produced using different technologies. J Univ Sci Technol Beijing 13(5):406–410. https://doi.org/10.1016/s1005-8850(06)60082-0
3. Mao XP, Huo XD, Sun XJ et al (2010) Strengthening mechanisms of a new 700 MPa hot rolled Ti-microalloyed steel produced by compact strip production. J Mater Process Technol 210(12):1660–1666. https://doi.org/10.1016/j.jmatprotec.2010.05.018
4. Xu G, Yang Y, Zhang XQ (2008) Study of aging behavior of CSP hot bands for cold sheets. Mater Charact 59(9):1355–1358. https://doi.org/10.1016/j.matchar.2007.09.007
5. Reip CP, Klinkenberg C, Tong L, et al (2012) Potential of hot rolled dualphase steel from compact strip production CSP(R) in automotive applications. In: 7th international conference on processing and manufacturing of advanced. Trans Tech Publications. https://doi.org/10.4028/www.scientific.ne/MSF.706–709.2278
6. Gao JX, Li LJ, Wei SJ (2014) Microstructure and properties of Niobium microalloyed pipeline steel in CSP and steel pipe produced by ERW. Adv Mater Res 1061–1062:23–29. https://doi.org/10.4028/www.scientific.net/AMR.1061-1062.23
7. Mao XP, Huo XD, Sun XJ, et al (2009) Study on the Ti micro-alloyed ultra-high strength steel produced by thin slab casting and direct rolling. Paper presented at the international symposium on thin slab casting and rolling meeting, Nanjing, China 13–15 May 2009
8. Song H, Yoo J, Kim SH et al (2017) Novel ultra-high-strength Cu-containing medium-Mn duplex lightweight steels. Acta Mater 135:215–225. https://doi.org/10.1016/J.ACTAMAT.2017.06.035
9. Ma MT, Yi HL (2011) Lightweight car body and application of high strength steels. Advanced steels. Springer, Berlin, Heidelberg, pp 187–198

10. Liu XJ, Cao GM, Nie DM et al (2013) Mechanism of black strips generated on surface of CSP hot-rolled silicon steel. J Iron Steel Res Int 20(8):54–59. https://doi.org/10.1016/S1006-706X(13)60141-7
11. Hu XW, He GN, Peng H et al (2019) Microstructures and mechanical properties of low carbon steel hot rolled in ferrite region based on CSP line. Steel Res Int 90(7):1800643. https://doi.org/10.1002/srin.201800643
12. Dong FT, Fei X, Du LX et al (2015) Promoting $Ti_4C_2S_2$ strain induced precipitation during asymmetrical hot rolling to improve r value and advantaged texture in Ti stabilized IF steel. J Alloy Compd 620:240–248. https://doi.org/10.1016/j.jallcom.2014.09.136
13. Ma FJ, Wen GH, Tang P et al (2010) Causes of transverse corner cracks in microalloyed steel in vertical bending continuous slab casters. Ironmaking Steelmaking 37(1):73–79. https://doi.org/10.1179/030192309X12506804200465
14. Yu H, Chen QX, Kang YL et al (2005) Microstructural research on hot strips of low carbon steel produced by a compact strip production line under different thermal histories. Mater Charact 54(4–5):347–353. https://doi.org/10.1016/j.matchar.2004.12.012

The Effect of Temperature on the Strain-Induced Austenite to Martensite Transformation in SS 316L During Uniaxial Tension



Elizabeth M. Mamros, M. Bram Kuijer, Mohammad Ali Davarpanah, Ian Baker, and Brad L. Kinsey

Abstract Controlling the microstructure of components is of interest to achieve optimal final part properties, i.e., materials by design. The manufacturing process itself can affect a material's characteristics by changing the microstructure. For example, past research has shown that austenite to martensite phase transformation in stainless steel occurs during deformation. Temperature is known to have a significant influence on this phenomenon. In this paper, the effect of temperature on the austenitic to martensite phase transformation in SS 316L under uniaxial tension is investigated. Both a cooling system and a heat exchanger were employed in a uniaxial tension experimental setup to control the temperature. Tensile specimens were strained to fracture at four temperatures of −15, 0, 10, and 20 °C. Digital imaging correlation (DIC) and a thermal imaging camera were used for tests at 0 °C and above to capture strain and temperature data, respectively. Strain and temperature data could not be obtained at −15 °C due to the DIC paint flaking during testing. X-ray diffraction was used to measure the volume fraction of martensite in both the as-received and the tensile-tested materials.

Keywords Forming · Uniaxial tension · Martensitic transformation · Stainless steel

1 Introduction

One means to achieve optimal final part properties during forming is by controlling the microstructure of materials. However, this objective is extremely complex due to the number of variables involved, including temperature, strain rate, stress–strain state, and deformation path, and their interdependence [1].

E. M. Mamros (✉) · M. A. Davarpanah · B. L. Kinsey
University of New Hampshire, Durham, NH 03824, USA
e-mail: emm1109@wildcats.unh.edu

M. Bram Kuijer · I. Baker
Dartmouth College, Hanover, NH 03755, USA

© The Minerals, Metals & Materials Society 2021

G. Daehn et al. (eds.), *Forming the Future*, The Minerals, Metals & Materials Series,
https://doi.org/10.1007/978-3-030-75381-8_155

A microstructural phase transformation to martensite occurs during forming in austenitic stainless steels (SS) at room temperature. This effect is increased at temperatures below zero Centigrade and at high strains [2]. Hecker et al. found that at strains <0.25, high strain rates produced more martensite, while the converse occurred at larger strains [1]. Thus, for uniaxial tensile tests of ductile materials, low strain rates and low temperatures are preferred to obtain a larger volume fraction of martensite.

As is typical for all metals and alloys, austenitic SS exhibits plasticity-induced heating. Nonhomogeneous deformation along the gauge length and heat conduction from the center toward the ends of the specimen lead to temperature gradients which affect the amount of martensitic transformation. The volume fraction of martensite increases from the end of the gauge length toward the center in deformed specimens [3]. Huang et al. [4] found that at temperatures >50 °C, martensite is not present. At −70 °C, the martensitic transformation rate reaches a maximum at approximately 0.15 strain. As the temperature increases toward room temperature, the maximum martensitic transformation rate decreases and occurs at higher strains.

At low temperatures between approximately −80 and −50 °C, the strength increases rapidly due to the high rate of martensitic transformation at low strains. Due to the large amount of martensite near the beginning of the forming process, the strain hardening rate suddenly decreases at higher strains. If the temperature is approximately 25 °C, then the rate of martensitic transformation is lower at low strains but occurs over a larger range of strains. This leads to a lower rate of increase in flow stress due to martensitic transformation and a more gradual decrease in the strain hardening rate at high strains. Consequently, maximum uniform elongation occurs around 0 °C [4].

Moser et al. [5] conducted isothermal uniaxial tension tests for SS 304 specimens at temperatures ranging from 0 to 100 °C and found the largest weight percent of martensite in the 0 °C specimens. Therefore, additional experiments are required at subzero temperatures to verify that the volume fraction of martensite continues to increase with decreasing temperature.

In this paper, results from “isothermal” uniaxial tensile tests on SS 316L specimens are presented for temperatures ranging from −15 to 20 °C (room temperature). (Note that a temperature gradient exists just prior to fracture, so the test is not truly isothermal.) To investigate the temperature effect on martensitic phase transformation, X-ray diffraction (XRD) was used, and the resulting volume fractions in the gauge section were compared for the formed specimens. Digital image correlation (DIC) and thermal imaging were used to measure strain and temperature, respectively, for tests with a temperature above 0 °C. The required speckle pattern was not able to withstand the subzero temperature conditions due to paint flaking. Based on previous work, the hypothesis is that the volume fraction of martensite will increase with decreasing temperature.

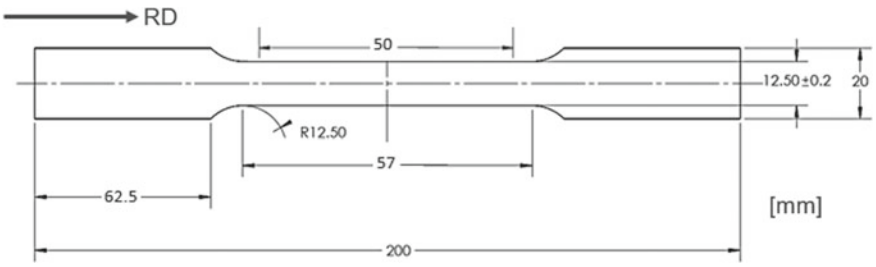


Fig. 1 ASTM E8 specimens obtained from 1.2 mm thick SS 316L

2 Experimental Setup and Methods

2.1 Material and Specimen Preparation

Dogbone specimens, dimensioned according to the ASTM E8 standard, were waterjet cut from SS 316L, 1.2 mm thick sheets with the 57 mm gauge length oriented along the rolling direction (Fig. 1). Due to the rough surfaces created by waterjet cutting, the edges were sanded, and the initial width and thickness were measured with a caliper and micrometer, respectively, prior to testing.

2.2 Cooling System

A cooling system, which consisted of a compressor (Thermo Fisher), pump (Thermo Fisher), and cold plate (AAVID), was used with a 60% ethylene glycol/40% water mixture to create "isothermal" testing conditions. The cooling system temperature range is −50 to 200 °C, but the lower threshold for the ethylene glycol/water coolant is −30 °C. The temperature range of the cold plate is −65 to 155 °C. To account for heat transfer, the temperature setting for the cooling system was adjusted accordingly to ensure that the specimen reached the desired steady-state temperature prior to each experiment. The specimen temperature was verified with a thermocouple.

2.3 Experimental Setup

A MTS Landmark machine with a 250 kN load cell was utilized to perform the uniaxial tension tests. A pulling speed of 0.1 mm/s was used, which produced an initial strain rate of ~1×10^{-3} s^{-1}. The cold plate was clamped to the bottom half of each specimen in the grip area and remained stationary during the experiment (Fig. 2). A small force was applied out-of-plane behind the cold plate to create

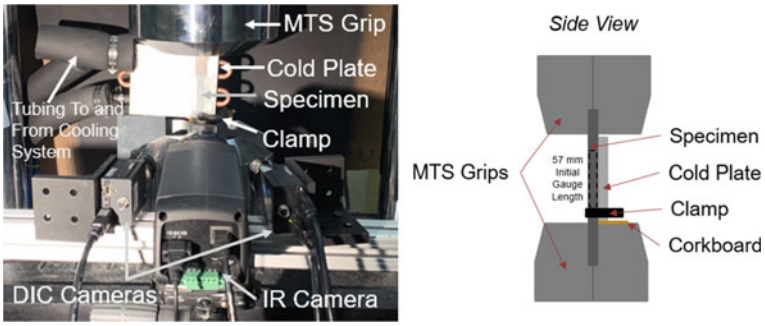


Fig. 2 Experimental setup with DIC, IR camera, cooling system, and MTS grips. (Color figure online)

uniform contact across the entire specimen gauge area for the duration of the test. A piece of corkboard was used to ensure that no contact occurred between the MTS grips and the cold plate.

2.4 Digital Image Correlation and Thermal Camera

To capture local strains *in situ*, two FLIR 5.0-megapixel cameras with 17 mm Schneider Xenoplan compact lenses were set up for three-dimensional DIC (Fig. 2). To create the contrast required for this technique, white background with a black speckle pattern in the foreground was created with spray paint.

Coupled with the DIC cameras in VIC Snap, the image capturing software (Correlated Solutions Inc.), a FLIR SC-645 infrared (IR) camera was used to measure the temperature during the tests. The infrared camera has a temperature range of −20 to 650 °C with a temperature resolution of 0.05 °C. The spatial resolution is 640 × 480 pixels. The emissivity was set to 0.98 based on the specimen speckle pattern. This value was determined by calibrating the infrared camera to thermocouple readings on painted specimens. All images, i.e., strain and thermal, were captured synchronously every 500 ms.

All images were post-processed with subset and step sizes of 17 and 4, respectively, in VIC-3D (Correlated Solutions Inc.). An area slightly larger than the 57 mm gauge length was selected for the analyses along with an inspect rectangle surrounding the fracture location and an inspect point at the fracture location to extract strain and temperature data.

2.5 Martensitic Transformation Measurements

A Bruker GADDS AXS XRD with a cobalt X-ray source was utilized to measure the volume fraction of the BCC phase or martensite. Two scans were performed, centered at 55 and 85° two-theta, using a voltage and current of 40 kV and 20 mA, respectively. The goniometer radius was set to 123.3 mm. DIFFRAC.EVA was used to convert the captured Debye rings into peak data. Additional post-processing was completed in MAUD [6] to determine the volume fraction of the FCC (austenite) and the BCC (martensite) phases in each specimen. Each specimen was ground using a polishing wheel with 600-grit SiC paper to create a flat surface as required for the XRD. A large water flow was used to eliminate a heat-induced phase change and damage during polishing.

3 Results and Discussion

3.1 Temperature

Figure 3 shows the strain and temperature distributions from the last image captured by the DIC and IR camera prior to fracture for the 0, 10, and 20 °C specimens. Table 1 shows the corresponding true strain and temperature values at a point located in the center of the fracture location. Neither DIC nor IR data could be captured from the −15 °C specimens as the paint used to provide the speckle pattern lost adhesion at subzero temperatures.

From Fig. 3, it is evident that the cold plate is able to maintain nearly isothermal conditions near the ends of the specimen throughout the duration of the test. However, the gauge section still undergoes plasticity-induced heating and reaches gradients up to approximately 35 °C across the 57 mm gauge length for the room temperature experiments. This heating occurs rapidly as the specimen approaches fracture (Fig. 4) because the cold plate is no longer sufficient to maintain an isothermal temperature. The sequential frame numbers and strain values are provided in Fig. 4 to show that the temperature increase is primarily at the end of the test as the strain localization occurs.

As is evident in Table 1, the 10 and 20 °C specimens experienced a maximum increase in temperature of approximately 35 °C, but the 0 °C specimen's temperature increased nearly 43 °C. The 0 and 20 °C specimens showed nearly the same true strain just before fracture, but the 10 °C specimen exhibited a slightly higher true strain around 80% just before fracture. This difference in strain is due to specimen to specimen variations in material and the sampling rate of the DIC.

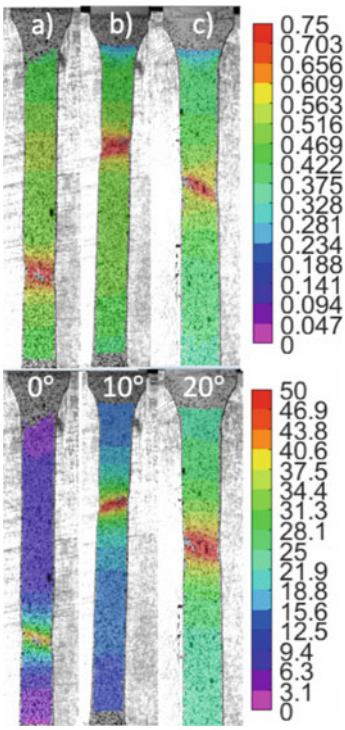


Fig. 3 True strain (top) and temperature (bottom) distributions prior to fracture for **a** 0 °C, **b** 10 °C, and **c** 20 °C specimens. (Color figure online)

Table 1 DIC and IR results from uniaxial tests

Specimen (°C)	True strain just before fracture	Temperature just before fracture (°C)
0	0.721	42.74
10	0.805	45.90
20	0.733	56.05

3.2 Stress–Strain Curves

Since DIC data is not available for −15 °C experiments, engineering stress versus plastic strain curves were created using the MTS cylinder location data for the strain calculation (Fig. 5). A general trend of increased engineering flow stress as the temperature decreases occurs from 20 to −15 °C, which is consistent with results in Huang et al. [4]. This strain data represents the deformation over the entire gauge area with the engineering stress calculated from the initial specimen cross-section. As shown in Fig. 3 though, the strain localizes in the necked region of the specimen during the tests.

DIC allows the strain in the fracture region to be assessed and the stress to be calculated based on the instantaneous gauge area, i.e., the true stress, up to localized

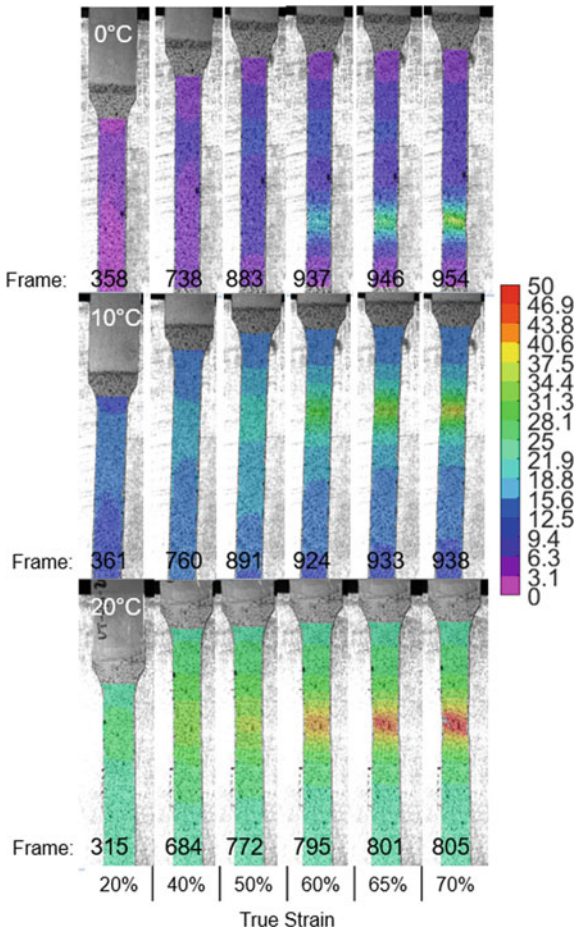


Fig. 4 Temperature distribution (°C) over time (represented by frame number) for 0 °C (top), 10 °C (middle), and 20 °C (bottom) specimens. (Color figure online)

necking. Figure 6 shows the true stress–true strain curves for specimens tested at 0, 10, and 20 °C. As is evident, the temperature effect of Fig. 5 is also present when probing data in the fracture location. While at least three specimens have already been tested at each temperature, additional trials will be conducted to assure the consistency of this data.

3.3 Martensitic Transformations

An additional set of experiments were conducted, stopping at 60% engineering strain for consistency, to obtain samples for XRD measurements. Table 2 shows the volume fractions of martensite for these specimens measured in the gauge area 15 mm above

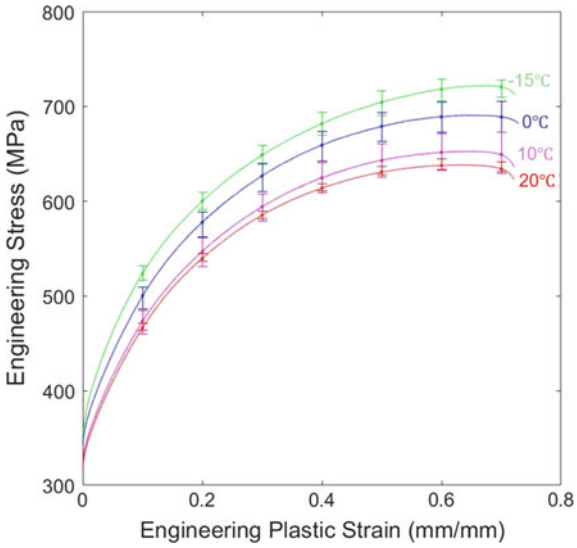


Fig. 5 Engineering stress–engineering plastic strain for −15, 0, 10, and 20 °C tests. (Color figure online)

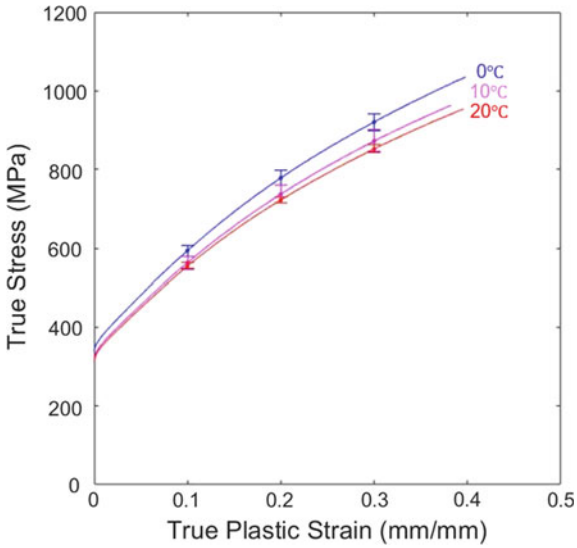


Fig. 6 True stress–true plastic strain curves for 0, 10, and 20 °C tests. (Color figure online)

Table 2 Martensite volume fractions from XRD in the gauge section

Temperature (°C)	Volume fraction
−15	0.135
0	0.115
10	0.089
20	0.100

the bottom grip section. This nearly follows the expected trend that the volume fraction of martensite increases with decreasing temperature. The increased martensite causes the higher stress values as seen in Fig. 5. As anticipated, the as-received material shows no martensite present so the plasticity-induced austenite to martensite transformation occurs at all temperatures investigated. Note that higher values of martensite that followed the expected trend were measured in the failure location of the specimen, but the localized deformation in this region was not uniaxial tension. Therefore, only martensite measurements in the gauge section away from the failure location are reported.

4 Conclusion and Future Work

SS 316L specimens were loaded in uniaxial tension until fracture under nearly isothermal conditions at −15, 0, 10, and 20 °C. XRD measurements showed that reducing the temperature generally increases the volume fraction of martensite in the tested specimens at the fracture location and in the gauge section. Future experiments could include a different method of creating isothermal conditions, e.g., an enclosed cooling system, to further reduce the observed plasticity-induced heating effects. Alternatively, a different coolant could be used with the current cooling system to perform additional experiments at even lower temperatures. Electron backscatter diffraction (EBSD) will be used to verify the martensite volume fractions. In the future, crystal plasticity modeling will be implemented to provide a fundamental understanding of the phase transformation mechanisms and determine optimal deformation paths to intentionally manipulate final material properties.

Acknowledgments Support for the NH BioMade Project is provided by the National Science Foundation through the EPSCoR Research Infrastructure Improvement Award #1757371. Special appreciation to Marguerite Kennish for her assistance with uniaxial tension testing and processing the data.

References

1. Hecker SS, Stout MG, Staudhammer KP, Smith JL (1982) Effects of strain state and strain rate on deformation-induced transformation in 304 stainless steel: part I. Magnetic measurements and mechanical behavior. Metall Trans A 13A:619–626
2. Lichtenfeld JA, Van Tyne CJ, Mataya MC (2006) Effect of strain rate on stress–strain behavior of alloy 309 and 304L austenitic stainless steel. Metall Mater Trans A 37:147. https://doi.org/10.1007/s11661-006-0160-5
3. Kumar A, Singhal LK (1989) Effects of strain state and strain rate on deformation-induced transformation in 304 stainless steel: part I. Magnetic measurements and mechanical behavior. Metall Mater Trans A 20:2857. https://doi.org/10.1007/BF02670178

4. Huang GL, Matlock D, Krauss G (1989) Martensite formation, strain rate sensitivity, and deformation behavior of type 304 stainless steel sheet. Metall Mater Trans A 20:1239. https://doi.org/10.1007/BF02647406
5. Moser NH, Gross TS, Korkolis YP (2014) Martensite formation in conventional and isothermal tension of 304 austenitic stainless steel measured by X-ray diffraction. Metall Mater Trans A 45:4891. https://doi.org/10.1007/s11661-014-2422-y
6. Lutterotti L, Chateigner D, Ferrari S, Ricote J (2004) Texture, residual stress and structural analysis of thin films using a combined X-ray analysis. Thin Solid Films 450:34–41

Energy-Dependent Surface Integrity of Stainless Steel AISI 304 After Robot-Based Machine Hammer Peening



Robby Mannens, Lars Uhlmann, Andreas Feuerhack, and Thomas Bergs

Abstract Machine hammer peening (MHP) is a high-frequency, incremental surface treatment with a spherical plunger which enables reproducible local plastic forming of metallic surface layers. The elasto-plastic deformation leads to a targeted smoothing or structuring of the surface as well as to the induction of compressive residual stresses and strain hardening. However, since MHP is still a relatively new process, there are still considerably knowledge deficits with regard to the cause–effect relationships of the energy inputs set by the MHP process parameters and the resulting surface integrity of technically relevant alloys. Therefore, the objective of this work is to investigate the influence of the peening strategies and the resulting contact energies on the surface roughness, the surface hardness, the residual stresses, and the microstructure of AISI 304. The results show that MHP leads to smoother and harder surfaces resulting from deformation-induced martensite formation accompanied by high compressive residual stresses and subgrain refinement resulting from higher dislocation densities.

Keywords Machine hammer peening · Stainless steel · Surface integrity

1 Introduction and State of the Art

1.1 Initial Situation and Motivation

In the course of current efforts such as lightweight construction and resource efficiency, forming technology plays a key role [1]. By means of forming, components with outstanding mechanical properties can be manufactured while retaining the initial volume. Since the component or tool surface layer is often the most heavily loaded area, even a targeted local forming of the surface layer leads to a significant improvement in fatigue strength and wear resistance [2]. In addition to established

R. Mannens (✉) · L. Uhlmann · A. Feuerhack · T. Bergs
Laboratory for Machine Tools and Production Engineering WZL at RWTH Aachen University, Campus-Boulevard 30, 52074 Aachen, Germany
e-mail: r.mannens@wzl.rwth-aachen.de

© The Minerals, Metals & Materials Society 2021

G. Daehn et al. (eds.), *Forming the Future*, The Minerals, Metals & Materials Series,
https://doi.org/10.1007/978-3-030-75381-8_156

manufacturing processes such as shot peening [3], deep rolling [4], and laser shock peening [5], machine hammer peening (MHP) has been used and researched for several years.

In MHP, a plunger with a mostly spherical hammer head is accelerated at high frequency toward a workpiece surface to be machined [6]. The periodic oscillation movement can be realized according to the pneumatic, mechanical, piezoelectric, or electrodynamic active principle. The hammer tools are mainly guided by machining centers, in some cases also by industrial robots with high rigidity [7]. The contact conditions for highly dynamic MHP are described using energy-based approaches [8]. Due to the impact velocities of the hammer head and the resulting contact energies, the MHP smoothes or structures metallic surfaces, introduces compressive residual stresses and strain hardening [9]. Recent investigations on the influence of MHP on the microstructure [7] as well as the MHP of hard material particles into the surface layer [10] were also carried out.

Due to its technology-related kinematics, MHP enables defined local machining of the workpiece surface layer [6] in contrast to shot peening, which usually leads to lower roughness. By using the MHP in machining centers, the workpiece can be machined in one clamping to the preceding machining process, which allows high reproducibility and short secondary processing times. The surface smoothing, compressive residual stress maxima, and work hardening achievable with MHP are comparable to deep rolling [11]. On the other hand, surface cracks can form during deep rolling if unsuitable process parameters are selected [12].

However, since electrodynamic MHP is still a relatively new manufacturing technology, there are still considerable knowledge deficits with regard to the contact energy applied and the resulting surface integrity, especially in the area of subgrain size and dislocation density modification of technically relevant alloys. Due to the interesting hardening properties of austenitic stainless steels during mechanical forming at room temperature [13], the surface integrity of an AISI 304 stainless steel influenced by the electrodynamic MHP is investigated in this paper.

1.2 Objective

The aim of this work is the experimental analysis of the cause–effect relationships between the energy input resulting from different process settings during electrodynamic machine hammer peening (MHP) and the surface integrity of an AISI 304 stainless steel. Based on this knowledge, an energy-based design of the electrodynamic MHP as a consequence of process parameters can be carried out to achieve advantageous surface integrities of AISI 304 stainless steel.

1.3 Approach

In the first step, the existing electrodynamic MHP system will be extended by implementing a fiber-optic distance sensor for in-process measurement of the plunger stroke. In the second step, point hammer tests will be performed to determine the hammer kinematics and impact energy. By knowing the impact velocities and thus contact energies, further cause–effect relationships to the resulting surface integrity are to be determined in comparison to earlier work on MHP of stainless steels [14]. In the third step, experimental MHP tests will be performed on flat AISI 304 stainless steel samples and the surface layer will then be characterized with respect to roughness, surface hardness, residual stresses, and subgrain size. The experimental results will be synthesized and an energy–based recommendation for the adjustment of the MHP process parameters to achieve defined AISI 304 surface layer states will be formulated.

2 Experimental Work

2.1 Further Development of an Electrodynamic MHP System

Before the experimental MHP tests were carried out, the hammer tool of the used electrodynamic hammer system type 2002 from accurapuls was upgraded, see Fig. 1a. For this purpose, a fiber-optic distance sensor RC20 from PHILTEC was integrated into the hammer tool. This sensor works according to the principle of reflected intensity. Since the oscillating mass in the hammer tool can be regarded as a coherent unit, the stroke exerted on the workpiece can be determined by means of a back-sided sensor placement, see Fig. 1b.

For the best possible reflection conditions, a thin stainless steel plate polished to $Sa = 0.3$ µm was cast into an epoxy resin matrix at the upper end of the oscillating body, see Fig. 1c. The additional mass added is $m_{er} = 4$ g and, compared to the mass of the oscillating body $m_{ob} = 363$ g together with the plunger mass $m_{p12} = 67.1$ g (hammer head diameter $d = 12$ mm) or $m_{p6} = 77.2$ g ($d = 6$ mm), has a negligible influence on the MHP process kinematics. The sensor was calibrated by means of programmed vertical movement of an ABB IRB6660-205/1.9 robot with the aid of a compensation curve and a high-speed camera Phantom v7.3 with the lens AF NIKKOR 24-85 MM 1:2, 8-4D. After calibration, the stroke h could be determined with an accuracy $\Delta h = \pm$ 10 µm in the operational range $h = 0.25 \ldots 1.7$ mm. Furthermore, based on the results of HABERSOHN, the influence of axial elastic strains in the hammer tool during MHP processing and thus a distortion of the stroke measurement could be excluded [15]. The software LABVIEW and DIADEM from National Instruments were used for data acquisition, visualization, and evaluation.

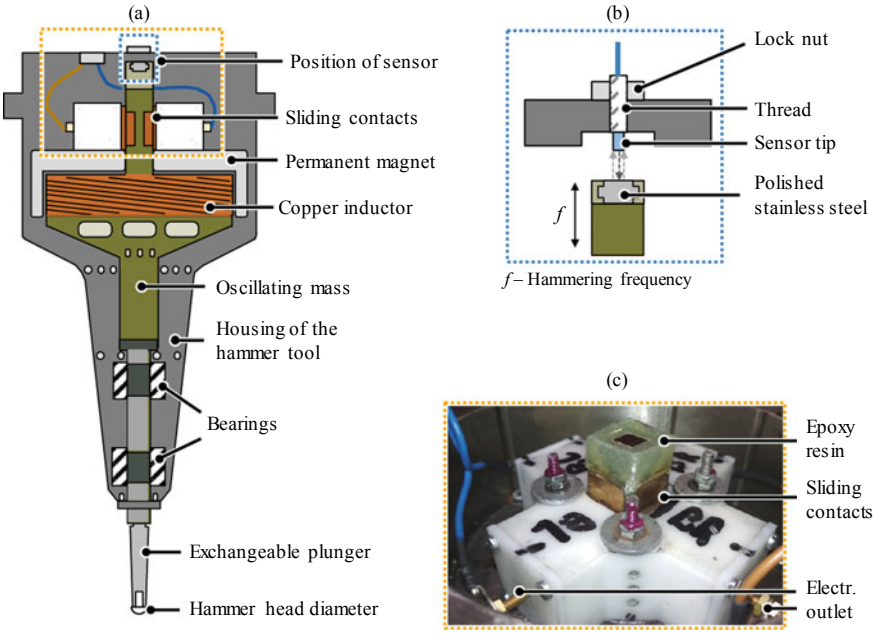


Fig. 1 **a** Structure of the electrodynamic accurapuls hammer tool, **b** scheme of sensor implementation, and **c** stainless steel plate embedded in epoxy resin. (Color figure online)

2.2 MHP Setup for Determination of Process Kinematics

To determine the kinematics of the electrodynamic MHP system, hammering tests were carried out on a pre-strengthened point on a AISI 4140 specimen, varying the process parameters hammering frequency $f = 20 \ldots 400$ Hz in 20 Hz steps, electrical power stage $P_{el} = 40 \ldots 80\%$ in 10% steps, stroke $h = 0.1 \ldots 1.0$ mm in 0.1 mm steps, and hammer head diameter $d = 6$, 12 mm. The corresponding electrical power P in the specified range was calculated from the voltage and current values measured with a multimeter at $P = 22 \ldots 713$ W. A parallelepiped specimen with the dimensions $40 \times 40 \times 100$ mm (W × H × L) was clamped centrally on a machine table using a vice and hammered in the center of the specimen. Using the LABVIEW software, the stroke measurement data recorded with a sampling frequency of $f_s = 50$ kHz were visualized and then evaluated using the DIADEM software. By means of the first test series, the general process kinematics of the accurapuls hammer system type 2002 used at the WZL were determined.

Table 1 Chemical composition of the used AISI 304 stainless steel

Elements	C	Si	Mn	P	S	Cr	Ni	N
Weight (%)	0.014	0.357	1.943	0.024	0.002	18.32	8.607	0.058

2.3 Materials and Sample Preparation

For the MHP tests, milled AISI 304 specimens (1.4301) with the dimensions 100 × 40 × 30 mm (L × W × H) were used. The specimens were ground plane-parallel on a surface grinding machine Blohm Planomat HP 620 CNC using a ceramic bonded grinding wheel Elbe S2704, a cutting speed $v_{cu} = 30$ m/s, and an infeed $a_p = 0.01$ mm to achieve an average roughness $Sa < 1$ µm. The mean value of the chemical composition determined by spark spectroscopy out of three measurements meets the requirements of DIN EN 10088-3, see Table 1.

2.4 MHP Parameter Study

The MHP tests were carried out using an electrodynamic hammer system type 2002 from accurapuls on a robot ABB IRB6660-205/1.9, see Fig. 2a.

For the analysis of the effects of selected MHP process parameters on the surface integrity, a full factorial experimental design was chosen according to the rules of statistical experimental methodology with triple repetition. The hammering frequency $f = 120, 180$ Hz, the stroke $h = 0.3, 0.5$ mm, the hammer head diameter $d = 6, 12$ mm, and the indentation distance $a =$ path distance $b = 0.05, 0.2$ mm were varied in two steps, see Table 2. All tests were carried out with an impact angle

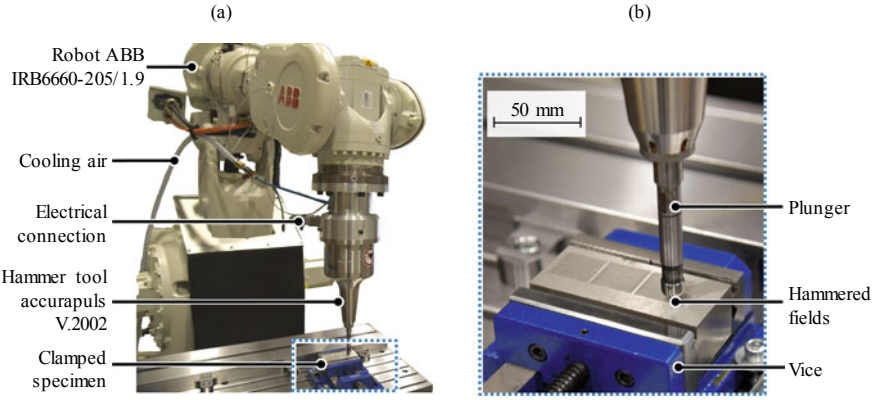


Fig. 2 **a** Hammer tool accurapuls type 2002 adapted to a robot ABB IRB 6660-205/1.9 and **b** specimen clamped in vice. (Color figure online)

Table 2 Parameter setups for MHP processing

No.	1	2	3	4	5	6	7	8	9	10	11	12	13	14	15	16
a	0.05								0.2							
h	0.3				0.5				0.3				0.5			
d	6		12		6		12		6		12		6		12	
f	120	180	120	180	120	180	120	180	120	180	120	180	120	180	120	180

$\beta_i = 0°$, which corresponds to an orthogonal alignment of the hammer tool to the specimen surface, and a meander-shaped machining strategy on a field size of 25 × 25 mm. The high-temperature lubricant Castrol Viscogen KL3 was used as lubricant because of industrial recommendations and one overrun was chosen. This second series of experiments investigated the cause–effect relationships between selected MHP parameters and the resulting surface integrity of AISI 304 stainless steel.

2.5 Analysis Methods

The roughness of the specimens was determined by means of a measuring system Hommel Etamic T8000 RC according to ISO 25178 on 1.6 × 1.6 mm measuring fields. The surface macrohardness according to Vickers was determined by five-fold repeated measurement and subsequent averaging using a Zwick Roell Indentec ZHU250 hardness tester according to DIN EN ISO 6507-1. The depth profiles of the residual stresses were measured with the PRISM hole drilling system from Stresstech according to the principle of electronic speckle pattern interferometry (ESPI) and calculated according to the SCHAJER integral method and TIKHONOV regularization [16]. The grain size distribution was determined by the Central Facility for Electron Microscopy (GFE) of RWTH Aachen University using the scanning electron microscope JEOL JSM7000F and an integrated EBSD/EDX system EDAX Pegasus.

3 Results

3.1 Process Kinematics and Impact Energies

Figure 3a shows selected stroke characteristics with a set power stage $P_{el} = 70\%$ and a hammer head diameter $d = 12$ mm as a function of frequency f with a defined stroke $h = 0.5$ mm. Figure 3b compares different stroke characteristics $h = 0.3, 0.5, 0.7$ mm for a set hammering frequency $f = 120$ Hz.

Figure 3a shows that the set stroke $h = 0.5$ mm is maintained very precisely. Before the actual stroke cycle is executed, the oscillating mass undergoes a first slight

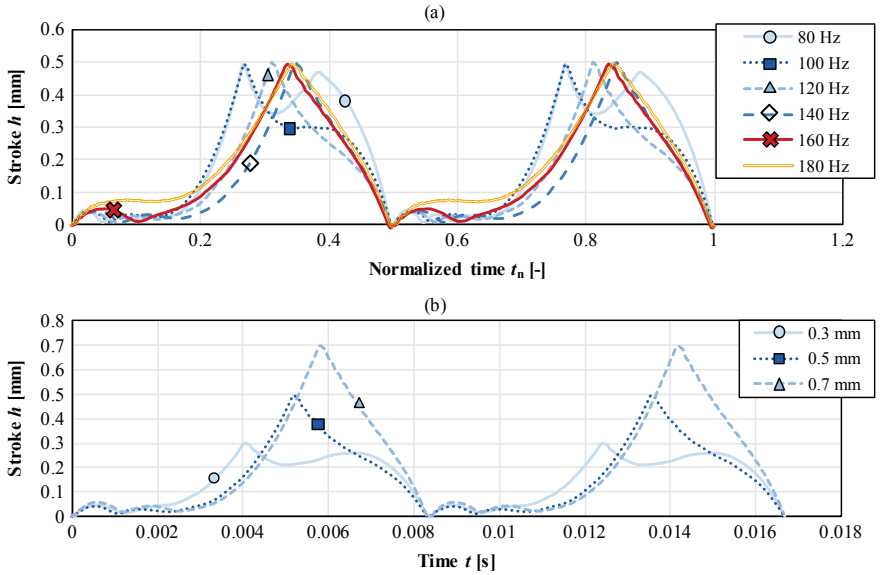


Fig. 3 Stroke characteristics of electrodynamic hammer system for **a** different hammering frequencies and **b** for different strokes. (Color figure online)

oscillation movement, with the exception of the hammer frequency $f = 180$ Hz. At a low frequency $f = 80$ Hz, a second contact occurs after the first contact of the hammer head with the workpiece surface. With increasing frequency, this effect decreases further and a symmetrical stroke before and after the workpiece contact occurs. As the frequency increases, the hammer head comes into contact with the workpiece with a delay. In addition, it can be seen that the acceleration of the hammer head between the frequencies $f = 80 \ldots 140$ Hz is similar (comparable gradient) and decreases for the frequencies $f = 160 \ldots 180$ Hz.

DIADEM was used to determine the impact velocity curve by deriving the stroke characteristics. Within these curves, three sections with 10 stroke cycles each were selected. From the thirty stroke cycles, the maximum impact velocity was determined each per stroke and the mean value was then calculated. Figure 4a shows the impact velocities for the hammer head diameter $d = 12$ mm at the electrical power stage $P_{el} = 70\%$ for various stroke–frequency combinations. It can be seen that as the stroke increases, the impact velocity increases along the hammer frequency band. A maximum impact velocity $v_{c,max} = 620$ mm/s is achieved with a stroke $h = 1.0$ mm and a frequency $f = 180$ Hz. As the stroke increases, the maximum impact velocity shifts toward lower hammering frequencies. The range of impact velocities relevant for the parameter setups selected for the MHP tests lies between $v_c = 300 \ldots 420$ mm/s. By knowing the weight of the oscillating mass and the masses of the plunger, the contact energy E_c was calculated using the following equation:

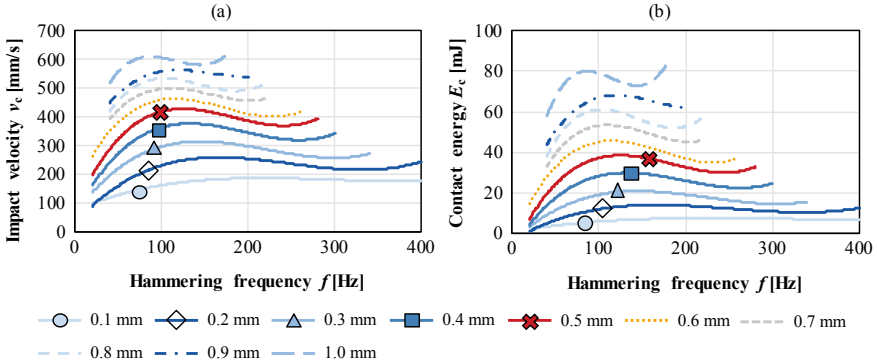


Fig. 4 **a** Experimentally determined impact velocities and **b** calculated contact energies. (Color figure online)

$$E_{\text{kin}} = E_{\text{c}} = \frac{1}{2} \cdot \left(m_{\text{ob}} + m_{\text{p}}\right) \cdot v_{\text{c}}^2 \tag{1}$$

with m_{ob}—mass of the oscillating body, m_{p}—mass of the plunger, and v_{c}—impact velocity. The calculated contact energies are shown in Fig. 4b. Similar to the impact velocities, the maximum contact energy shifts to lower hammer frequencies as the stroke increases. The maximum contact energy in the investigated parameter range and electrical power level $P_{\text{el}} = 70\%$ is $E_{\text{c,max}} = 84$ mJ. Due to the increasing stroke, the acceleration path of the plunger and thus also the contact energy increase. The deviations between the contact energies at $d = 6$ mm and $d = 12$ mm are in the range $\Delta E_{\text{c}} = \pm 5\%$.

3.2 Surface Roughness and Hardness

Figure 5a shows the roughness values *Sa* and *Sz* as a function of the MHP setups. It can be seen that the electrodynamic MHP can lead both to an increase and to a reduction of the roughness of the ground initial surface. However, the already very low roughness of the ground surface must be taken into account. The greatest influence in the parameter range considered is the indentation distance *a*. Contrary to expectations, an increased indentation distance tends to lead to a reduction of roughness parameters. Thus, it is assumed that an indentation distance $a = 0.05$ mm was selected too small. The increased energy density associated with a smaller indentation *a* and stepover distance *b* could therefore be too high for the strength of the AISI 304 stainless steel. This leads to the formation of pronounced surface structures with material build-up. The next largest effect on the roughness values results from the stroke *h* and the interaction of the hammer head diameter *d* with the stroke *h*, see Fig. 5b. The lowest

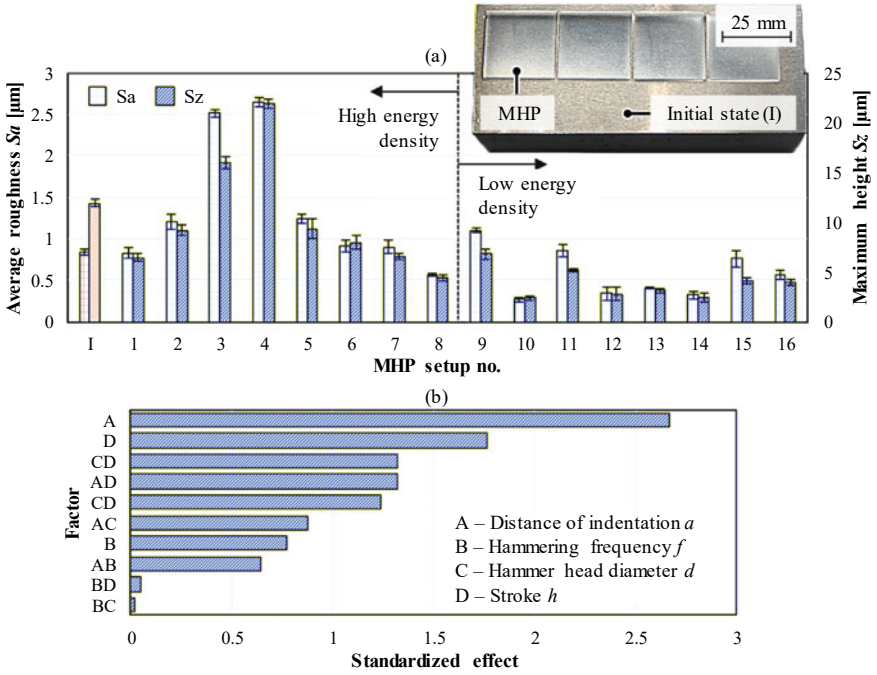


Fig. 5 **a** Surface roughness *Sa* and *Sz* as a function of the selected MHP setups compared to the initial state (I) and **b** DOE results of the analysis of significance in terms of average roughness *Sa* – Pareto chart of effects. (Color figure online)

roughness values $Sa = 0.264$ µm and $Sz = 2.35$ µm due to the MHP setup 10 are even higher than a polish quality.

The surface hardness is shown in Fig. 6. It can be seen that the surface hardness for all MHP setups could be increased significantly compared to the initial ground

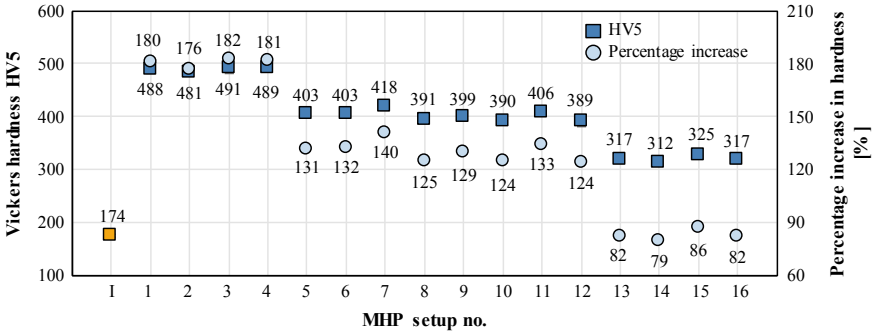


Fig. 6 Resulting surface hardness HV5 for the used MHP setups compared to the initial ground state (I). (Color figure online)

state (I). For the MHP setup 3, a maximum hardness of 491 HV5 could be achieved, which corresponds to a percentage increase in hardness of 182%. In addition to the indentation distance a, the stroke h and the hammer frequency f also have a significant influence on the surface hardness. A smaller indentation distance a and thus a higher energy density leads to higher surface hardness. A lower hammer frequency f also leads to an increase in surface hardness. Contrary to expectations that a higher stroke and thus a higher contact energy results in greater surface hardness, a higher stroke h tends to result in lower surface hardness.

3.3 Residual Stresses

For the sake of clarity, only two different MHP setups of the largest and lowest compressive residual stress maxima were compared to the ground sample initial state in Fig. 7a. The characteristic curve of the residual stresses introduced by the MHP could be determined for all MHP setups. All other residual stress curves of the other MHP setups lie between the curves shown here.

The residual stresses were measured in the middle of the hammered sample fields (white field, Fig. 7a). According to the stored coordinate system, the y-coordinate

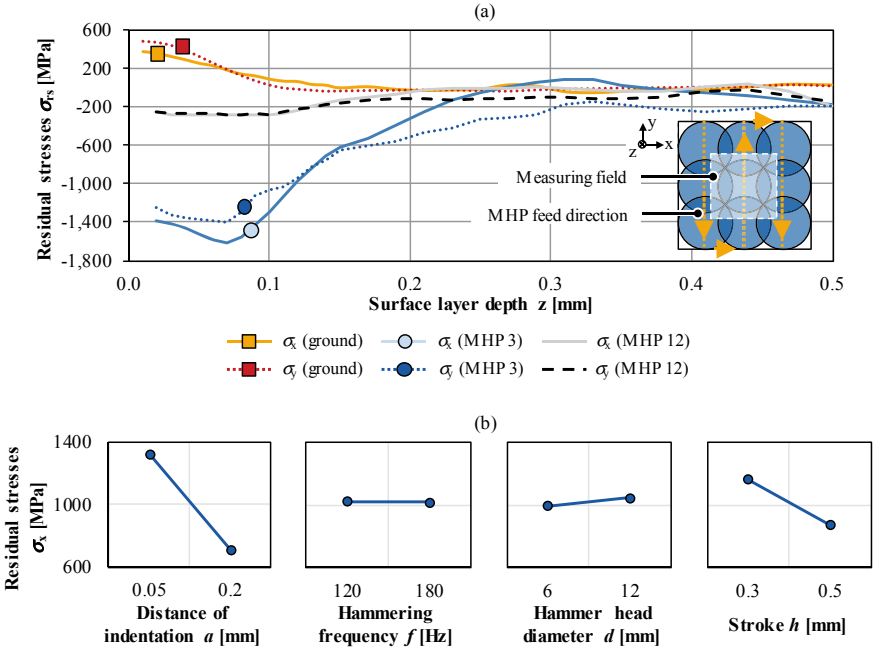


Fig. 7 **a** Comparison of residual stress depth distributions and **b** main effect diagrams. (Color figure online)

describes the path feed direction of the MHP tool and the x-coordinate the orthogonal direction. For all MHP setups, the maximum of the compressive residual stresses in the x-direction, i.e., orthogonal to the MHP feed direction, was applied directly below the sample surface in a surface layer depth $z = 0.04 \ldots 0.1$ mm. The generated compressive residual stress maxima were in a large range $\sigma_x = 330 \ldots 1700$ MPa. The indentation distance a and the stroke h had the greatest influence and by reducing them, the maximum residual stresses can be significantly increased, see Fig. 7b. In addition, it was found that the zero crossing of the residual stresses was already achieved at a surface layer depth $z = 0.25 \ldots 0.41$ mm.

3.4 Microstructure

In addition to IPF maps (Inverse Pole Figure Maps), see Fig. 8a, KAM maps (Kernel Average Misorientation), see Fig. 8b, of the hammered specimen no. 3 (highest contact energy) were also produced. KAM maps indicate the misorientations between adjacent measuring points and can provide a suitable quantitative estimate of the internal distortions since the total distortions are displayed independently of their dislocations or subgranular origin. In order to enable a direct comparison of the unhammered initial surface layer with the hammered surface layer, initial surfaces adjacent to a hammered area were analyzed. For the material AISI 304, a significant subgrain refinement of the surface layer to a depth $z = 200$ µm could be demonstrated. The initial grain size of $l_{g,i} = 22 \ldots 80$ µm could be reduced by MHP to

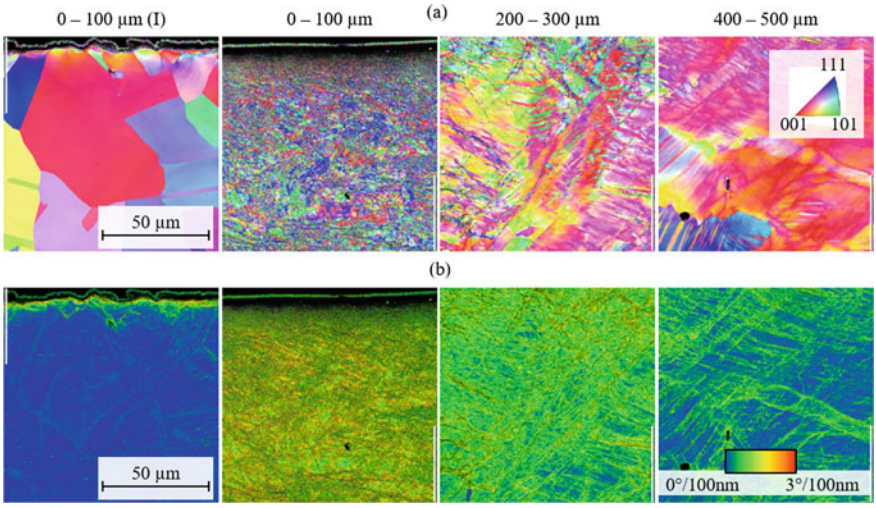


Fig. 8 **a** IPF maps of ground initial surface (A) compared with MHP treated specimen and **b** corresponding KAM maps. (Color figure online)

$l_{g,MHP} = 0.5 \ldots 5$ µm in the first 100 µm surface layer depth. In a surface layer depth of $z = 200 \ldots 500$ µm, pronounced cubic face-centered twin grain boundaries were generated. Based on the KAM maps, it is assumed that there has been a significant increase in dislocation density in the near-surface layers. Only at a depth $z \approx 1{,}000$ µm was a structure similar to the initial state detected.

4 Discussion

The presented results showed a significant impact of the electrodynamic MHP on the resulting surface integrity of AISI 304 stainless steel. The effects can be explained by means of the applied contact energy depending on the selected MHP process parameters. The implementation of a fiber-optic reflection-compensating distance sensor made it possible for the first time to permanently measure the stroke of the electrodynamic MHP inline and thus to calculate the contact energy. It could be shown that the hammering frequency f has a significant impact on the MHP process kinematics. If a low hammer frequency was selected, the phenomenon of multiple impacts of the hammer head on the workpiece surface was observed. The results correspond to the findings of [17]. The phenomenon of repeated workpiece contact during a peening cycle can be described in such a way that, due to the very short contact time resulting from the hard workpiece contact, the hammer head rebounds from the surface before the voltage pulse is over. At low frequencies, the intensity of the voltage pulse is still sufficient to accelerate the hammer head again in the direction of the workpiece. This assumption was confirmed by analysis of the hammer forces using a Kistler 9257B force measuring platform. The hammer system follows the excitation frequency with a small phase shift, which is due to induction.

Furthermore, it could be shown that by means of electrodynamic MHP, the surface roughness can nearly reach a polished quality. Nonetheless, the result that a higher indentation distance a leads to lower roughness values is new. Due to the characteristics of AISI 304 with a low yield strength $R_{p0.2} = 516 \ldots 560$ MPa determined in compression tests in the strain rate range relevant for electrodynamic MHP $\dot{\varphi} = 10 \ldots 100\ s^{-1}$, the selected indentation and path distance $a = b = 0.05$ mm and the associated high energy density w are possibly responsible for the increase in roughness. While the energy density for an indentation distance $a = 0.05$ mm lies between $w \approx 11{,}300 \ldots 26{,}200$ mJ/mm^2, for an indentation distance $a = 0.2$ mm, the energy density $w \approx 700 \ldots 1{,}600$ mJ/mm^2 is lower by a factor of 16. Since the diameter of an indentation is in the range $d_i = 1$ mm, a sufficient overlapping of the single indentations and thus complete machining of the workpiece surface with larger indentation distances can be achieved. Another positive side effect is the shorter machining time. Since the test series presented here was carried out with plungers with a high surface quality ($Sa < 0.1$ µm), the quality of the hammer head surface must also be taken into account in the machining result of the surface roughness, as described in [18].

The evaluation of the surface hardness shows a significant increase in hardness. By selecting a small test force, a deformation-induced martensite transformation could be avoided by the hardness impression. In preliminary tests, it was found that the hardness values determined hardly fluctuate between HV1 and HV5 and that the mean indentation depth of the hardness indentation is $z_i = 35$ µm. Regarding the observed effect of reduced hardness values using higher stroke values, one possible explanation is the exceeding of a critical energy value above which first annihilation processes of the dislocations occur in the surface layer due to a very high dislocation density. The dislocation density thus decreases again a little and the strength of the material thereby is lower compared to the machined surface layer with a lower stroke.

The residual stress characteristic typical for surface layer machining processes was obtained for all selected MHP parameter setups. Due to inhomogeneous elastic–plastic deformation, compressive residual stresses are induced in the near-surface area. The interaction between plastic elongation and Hertzian pressure leads to the development of the characteristic residual stress curves. Plastic elongation describes the deformation of surface layer areas near the surface by a superposition of normal and tangential forces. This results in the compressive residual stress maxima at the surface. For the comparatively soft stainless steel, this mechanism dominates, which is why the compressive residual stress maximum of the AISI 304 lies directly below the surface. Hertzian pressure due to orthogonal forces to the workpiece surface causes shear and residual stresses to develop below the surface. With harder materials, this mechanism is dominant and causes a displacement of the residual compressive stress maxima to greater surface layer depths.

According to SHAKOVA ET AL., it is possible to quantitatively determine the dislocation density using KAM-Maps with comparable values as in a TEM measurement for materials formed at low strains [19]. The AISI 304 with its low stacking fault energy favors the formation of planar lattice defects such as stacking faults, deformation twins, or martensite during forming with sufficient forming work. It is observed that the metastable austenitic initial structure (cubic face-centered, fcc, γ-austenite) is strongly crossed by cubic body-centered (bcc) α′-martensite after MHP at a surface layer depth z <100 µm due to the deformation-induced structural transformation. It has been shown that martensite formation has increased at intersection points of shear bands. This is consistent with the findings of [20].

5 Conclusion and Outlook

It could be shown that an inline stroke tracking of the electrodynamic MHP is possible by means of a fiber-optic distance sensor, which guarantees a high resolution of a few µm in the small stroke range. By deriving the stroke characteristics, impact velocity and contact energies can be calculated by knowing the oscillating mass and thus the deformation work used. Despite the low contact energies available for the electrodynamic MHP for forming the surface layer, significantly different properties can be set. Although a ground starting surface with already low roughness

values was available, the roughness could be improved to a level similar to that of a polished surface by selecting suitable MHP parameters. However, it is important to note the high energy density associated with a small indentation and path distance, which can lead to a deterioration of the roughness values and macroscopic waviness. The analysis of the surface hardness showed that the MHP can generally increase the surface hardness. However, the use of increased contact energies can limit this effect. Due to the low strength of the investigated ASIS 304, the maximum residual compressive stress was very close to the surface. Furthermore, the zero crossing of the residual stress was at low depths. For the first time, a subgrain refinement could be determined due to a significant increase of the dislocation density for the stainless steel ASIS 304 according to the electrodynamic MHP. In addition to this strengthening mechanism, further effects such as twin and shear band formation as well as deformation-induced martensite formation in different surface layer depths were observed.

In future work, the influence of individual MHP impacts on the resulting indentation volume and the influence of different contact energies on the deformation-induced martensite transformation in near-surface areas for the austenitic stainless steel AISI 304 can be investigated. In addition, analyses of the microhardness in the surface layer depth should be carried out in order to describe further cause–effect correlations, especially in connection with subgrain refinement. If necessary, the different mechanisms must be separated and their effects on friction wear and fatigue properties investigated.

Acknowledgments The authors would like to thank the German Research Foundation (Deutsche Forschungsgemeinschaft, DFG) for the proportionate funding of the research work (KL 500/170-1) and (KL 500/192-1).

References

1. Marré M, Beihofer D, Haggenmueller W, Grupp P (2015) Forming for resource-efficient Industry 4.0. Paper presented at the 5th international conference on accuracy in forming technology, Chemnitz, Germany, 10–11 Nov 2015
2. Schulze V, Bleicher F, Groche P, Guo YB, Pyun YS (2016) Surface modification by machine hammer peening. CIRP Ann Manuf Technol 65(2):809–832
3. Luo P, Wang Z, Wu G, Wang Y, Cheng M (2017) Literature review on state of the art in shot peening in the last decade (2006–2015). Paper presented at the 2nd international conference on advanced high strength steel and press hardening, Changsha, China, 15–18 Oct 2015
4. Delgado P, Cuesta II, Alegre JM, Díaz A (2016) State of the art of deep rolling. Precis Eng 46:1–10
5. Ding K, Ye L (2006) Laser shock peening—performance and process simulation. Woodhead, Cambridge
6. Bleicher F, Lechner C, Habersohn C, Kozeschnik E, Adjassoho B, Kaminski H (2012) Mechanism of surface modification using machine hammer peening technology. CIRP Ann Manuf Technol 61(1):375–378
7. Krall S (2019) Beeinflussung der Randschicht durch diskrete Mikroumformung. PhD thesis, TU Wien

8. Sticht P, Steitz M, Groche P (2016) Prediction and experimental validation of an impact energy threshold for mechanical surface smoothing. Paper presented at the 3rd CIRP Conference on Surface Integrity (CSI), Charlotte (N.C.), USA, 8–10 June 2016
9. Trauth D (2016) Tribology of machine hammer peened tool surfaces for deep drawing. PhD thesis, RWTH Aachen University
10. Rodríguez Ripoll M, Heindl F, Lechner C, Totolin V, Jech M, Bleicher F (2016) Enhanced sliding wear resistance of technical alloys by hard particle reinforcement using machine hammer peening. Tribol Trans 60(3):479–489
11. Klocke F, Trauth D, Schongen F, Terhorst, M (2013) Zeiteffiziente Prozessauslegung beim Festklopfen. wt Werkstattstechnik online 103(10):758–763
12. Groche P, Engels M, Steitz M, Müller C, Scheil J, Heilmaier M (2012) Potential of mechanical surface treatment for mould and die production. Int J Mater Res 103(6):783–789
13. Nikitin I (2007) Zur Verbesserung des Ermüdungsverhaltens des austenitischen Stahls X5CrNi18-10 im Temperaturbereich 25–600 °C durch mechanische Randschichtverfestigungsverfahren. PhD thesis, Kassel University
14. Mannens R, Trauth D, Mattfeld P, Klocke F (2018) Influence of impact force, impact angle, and stroke length in machine hammer peening on the surface integrity of the stainless steel X3CrNiMo13-4. Procedia CIRP 71:166–171
15. Habersohn C (2015) Analytische und simulative Betrachtung eines Oberflächenhämmerprozesses. PhD thesis, TU Wien
16. Schajer GS, Rickert TJ (2011) Incremental computation technique for residual stress calculations using the integral method. Exp Mech 51(7):1217–1222
17. Trauth D, Klocke F, Schongen F, Shirobokov A (2013) Analyse und Modellierung der Schlagkraft beim elektro-dynamischen Festklopfen zur kraftbasierten Prozessauslegung. UTFScience III:1–8
18. Lechner C (2014) Oberflächenmodifikation unter Einsatz der Technologie des Schlagverdichtens (machine hammer peenings). PhD thesis, TU Wien
19. Shakhova I, Belyakov A, Yanushkevich Z, Tsuzaki K, Kaibyshev R (2016) On strengthening of austenitic stainless steel by large strain cold working. ISIJ Int 56(7):1289–1296
20. Müller-Bollenhagen C (2011) Verformungsinduzierte Martensitbildung bei mehrstufiger Umformung und deren Nutzung zur Optimierung der HCF- und VHCF-Eigenschaften von austenitischem Edelstahlblech. PhD thesis, University of Siegen

Non-isothermal Modeling of Static Recrystallization in Hydroformed Steel Tube Using a Coupled Cellular Automata and Finite Element Model



Amir Asgharzadeh, Sobhan Alah Nazari Tiji, Taejoon Park, and Farhang Pourboghrat

Abstract A thermo-microstructural modeling setup was developed to model the progress of static recrystallization (SRX) during annealing of hydroformed steel tube under non-isothermal annealing condition. In this model, a coupled Cellular Automata and Finite Element thermal model was implemented to predict the kinetics of SRX, which accounts for the impact of multiaxial deformation and annealing temperature regime. First, an analytical solution was developed to calculate the flow behavior of the steel tube during hydroforming experiment based on the data extracted from digital image correlation (DIC) measurements. Second, the actual microstructure and texture of the as-deformed material was obtained with EBSD test. Third, the calculated deformation characteristics as well as the obtained crystallographic and microstructural data were imported to the developed Finite Element-Cellular Automata model to predict the progress of SRX and temperature changes during annealing. The results show a reasonable agreement between the experimental data and predictions, confirming the accuracy of the developed modeling setup in the prediction of the kinetics of SRX within hydroformed steel tubes.

Keywords Tube hydroforming · Finite element method · Cellular automata · Static recrystallization

1 Introduction

The final microstructure of heavily deformed metallic materials significantly depends on the behavior of static recrystallization (SRX) taking place during post-deformation annealing process [1]. The deformation and annealing parameters including the amount of imposed strain as well as the annealing temperature and duration are

A. Asgharzadeh · S. A. Nazari Tiji · T. Park · F. Pourboghrat (✉)
Department of Integrated Systems Engineering, The Ohio State University, 210 Baker Systems, 1971 Neil Avenue, Columbus, OH 43210, USA
e-mail: pourboghrat.2@osu.edu

F. Pourboghrat
Department of Mechanical and Aerospace Engineering, The Ohio State University, 201 W 19th Ave, Columbus, OH 43210, USA

© The Minerals, Metals & Materials Society 2021

G. Daehn et al. (eds.), *Forming the Future*, The Minerals, Metals & Materials Series,
https://doi.org/10.1007/978-3-030-75381-8_157

the most influential parameters on the kinetics of SRX [2]. To obtain a desired final microstructure, several attempts have been performed to effectively predict the influence of the aforementioned parameters on the SRX behavior for different materials [3–7]. Among all the proposed empirical and numerical models, Cellular Automata (CA) model has been extensively utilized to model the SRX kinetics, since it is based on a powerful algorithm to predict the morphological features of annealing microstructure with high prediction accuracy and computational efficiency [8].

The basics of CA model for modeling of SRX kinetics were developed by Hesselbarth and Göbel [9], where the simultaneous operation of nucleation and grain growth phenomena was assumed to control the progress of SRX. Based on the proposed CA algorithm, different CA models have been developed to model the kinetics of SRX under complex deformation and annealing conditions. For instance, Lin et al. [10] have simulated the SRX kinetics within Ni-based superalloy during annealing after hot compression test using a 2D CA model. Using a similar model, Huang et al. [11] have predicted the SRX behavior of an aluminum alloy after double-pass hot compression tests. In other studies, a coupled Finite Element (FE) and CA model has been developed to model the SRX kinetics within single- and multi-pass cold-rolled Al alloys [6, 12].

Since the temperature regime during annealing process is greatly influential on the SRX behavior, a few researchers have incorporated the thermal model into the CA model to predict the SRX kinetics under non-isothermal annealing condition. In this regard, Salehi and Serajzadeh [13] have developed a coupled FE thermal model and CA model to predict the SRX features of cold-rolled steel. In another study, a FE-CA model has been utilized to model the SRX kinetics during non-isothermal annealing of cold-rolled carbon steels [14]. In addition, Schäfer et al. [15] have simulated the progress of SRX in a cold-rolled Al alloy using a non-isothermal CA model, in which the complex effects of recovery and precipitation on the kinetics of SRX have been considered.

In this study, a modeling setup based on the coupled FE-CA model has been developed to predict the kinetics of SRX in the bulged steel tube under non-isothermal annealing condition. The impact of process parameters including deformation characteristics as well as the subsequent annealing condition on the SRX features has been investigated. In many of earlier research, variety of assumptions have been made to model the kinetics of SRX, which significantly affected the modeling results. Examples of such assumptions are adopting constitutive models for deformation characterization, approximation of initial grain topology, considering a random orientation, and assuming isothermal annealing condition. To improve the accuracy of the predictions, all the mentioned assumptions have been removed from the modeling setup employed in the present study. To that end, first, an analytical solution based on membrane theory has been utilized to calculate the principal stress components during tube hydroforming (THF) process using the strain field data obtained experimentally from DIC measurements and the internal pressure and axial load applied during the bulging experiment. Second, the initial state of CA model including grain topology and crystallographic data has been defined based on the EBSD data, collected from the as-deformed tubes. Third, a thermal FE model has

been incorporated into the 2D CA model to predict the temperature variations, SRX kinetics, and final grain topology. Finally, the predicted features of the recrystallized microstructure have been compared with the experimental data.

2 Experimental Procedure

In the present study, a low carbon steel tube with outer diameter and thickness of 38 mm and 1.24 mm, respectively, and chemical composition of Fe—0.13 wt% C—0.3 wt% Mn—0.02 wt% P—0.15 wt% Si—0.3 wt% S was investigated. The as-received tubes were annealed at 900 °C for 75 min followed by air cooling to obtain a single phase ferritic initial microstructure. The mechanical properties of these tubes were assessed through tensile test based on E8-E8M-09 ASTM standard. For the tensile tests, the dog-bone specimens with the gauge length and width of 32 mm and 6 mm, respectively, were cut along the longitudinal direction of the tubes. Furthermore, the tube hydroforming tests were carried out with a combination of axial feed and internal pressure, which were applied by the actuators and intensifier, respectively. The prescribed boundary conditions (the pressure and axial feed profiles) were precisely followed by the THF machine by means of a controlling station. Note that the internal pressure was applied through a water pressurization medium. The deformation characteristics of the bulging tube was recorded using a Digital Image Correlation (DIC) machine throughout the hydroforming process. Finally, the crystallographic texture of the as-deformed tube was measured by means of a ThermoScientic^{TM}ApreoLoVacfield emission EBSD microscope equipped with EDAX Hikari XP camera.

Afterward, the as-deformed tubes were annealed in a furnace that was preheated to the temperature of 700 °C. The temperature change within the bulged specimen during the annealing process was recorded using a K-type thermocouple, which was attached to the specimen through a hole drilled in the thickness of the specimen. After the annealing process, each specimen was quenched in cold water to preserve the final microstructure. Then, the hardness measurements were performed on all specimens to assess the changes in mechanical properties of the specimen during annealing treatment. Because of the curvature of the bulged tube, the convex surface of the specimen was placed on a flat holder, and the concave side of the sample was penetrated by the spherical indenter of the Rockwell hardness machine [16]. Moreover, the annealed specimen was cut along the hoop and axial direction, followed by sample preparation to observe the annealed microstructure through optical microscopy. To that end, all the samples were mounted, polished up to 0.05 μm roughness, and etched by Nital detergent containing 100 ml ethanol and 5 ml nitric acid.

3 Modeling Methodology

3.1 Analytical Modeling of THF

The multiaxial flow behavior of the bulged tube can be determined using the displacement data obtained from DIC measurement and the internal pressure and axial load applied during the hydroforming test. In this regard, an analytical solution is employed to determine the principal strain and stress components at the pole of the bulged tube based on membrane theory. After calculation of the strain components along the hoop and axial directions based on the DIC measurement, and assuming plastic incompressibility and neglecting elastic strains, the instantaneous thickness (t) at the pole of the bulged tube can be calculated as below

$$t = t_0 \exp(-(\varepsilon_h + \varepsilon_A)) \tag{1}$$

where t_0 is the initial tube thickness, and ε_h and ε_A are the hoop and axial strain components at the pole of the bulging tube, respectively. Besides, the force applied to the tube in axial direction can be calculated as below

$$F_A = -F_R + \pi R_0^2 P_i \tag{2}$$

where F_A is the axial force applied to the mid-cross section of the tube, F_R is the measured reaction force at the end of the tube, P_i is the internal pressure, and R_0 is the initial inside radius of the tube. Then, the calculated tube thickness, axial force, and internal pressure are used to calculate the stress components in axial and hoop directions at the pole of the bulging tube, as follows

$$\sigma_A = \frac{F_A}{2\pi R_h t} \tag{3}$$

$$\sigma_h = \frac{\left(R_A - \frac{t}{2}\right)\left(R_h - \frac{t}{2}\right)P_i - \sigma_A R_h t}{R_A t} \tag{4}$$

where σ_A and σ_h are the axial and hoop stress components, respectively. In addition, R_A and R_h are the radius of the bulging tube in the axial and hoop directions at the pole of the bulging tube, respectively, which are determined based on the displacement data obtained from DIC measurement throughout the THF process. To do so, the equation of circle is fitted to the multiple points' coordinate using the least mean square fitting algorithm [17]. The detailed description of the utilized approach can be found in Ref. [17, 18]. The texture analysis performed on the EBSD images taken from the as-received tube (it will be discussed in the next section) confirmed that the investigated material is isotropic. Therefore, the equivalent stress ($\bar{\sigma}$) and equivalent strain ($\bar{\varepsilon}$) at the pole of the bulged tube can be determined based on the isotropic von-Mises function, as below

$$\bar{\sigma} = \sqrt{\sigma_A^2 - \sigma_A \sigma_h + \sigma_h^2} \tag{5}$$

$$\bar{\varepsilon} = \frac{2}{\sqrt{3}} \sqrt{\left(\varepsilon_A^2 + \varepsilon_A \varepsilon_h + \varepsilon_h^2\right)} \tag{6}$$

In order to connect the deformation characteristics of THF process to the microstructural events happening during subsequent annealing process, the equivalent stress at the last time increment of THF is used to estimate the amount of dislocation density generated during deformation. Therefore, the local dislocation density (ρ_d) is calculated through the following relationship [19]:

$$\rho_d = \left(\frac{\Delta\sigma}{\alpha M_\alpha G b}\right)^2 \tag{7}$$

where $\Delta\sigma$ is the difference between the yield stress of fully recrystallized specimen and the final equivalent stress at the pole of the bulged tube, M_α is the Taylor factor, α is a constant, b is the burgers vector, and G is the shear modulus.

3.2 Microstructural Model

The progress of static recrystallization is identified by two simultaneous phenomena: nucleation of defect free nuclei and growth of these grains toward the deformed context. Both mechanisms are controlled by the internal energy stored during deformation as well as the temperature regime during subsequent annealing process. In CA model, the growth mechanism can be interpreted by the term of local velocity of grain boundary (V), which can be defined as below based on the Turnbull's rate equation [20],

$$V = M \cdot P \tag{8}$$

where P is the local driving pressure, and M is the local mobility of grain boundary that can be calculated for low carbon steel as follows [21],

$$M = \frac{5.4 \times 10^{-8} b}{kT} \exp\left(-\frac{Q_m + Q_{gb}^\alpha}{RT}\right) \tag{9}$$

where k is the Boltzmann constant, T is temperature, Q_m is the activation energy of grain boundary motion, Q_{gb}^α is the activation energy for the grain boundary diffusion, and R is the universal gas constant. On the other hand, the local driving pressure (P) acting on the grain boundary can be calculated by

$$P = \alpha G b^2 \Delta\rho_d + \kappa\gamma \tag{10}$$

where $\Delta\rho_d$ is the difference between the dislocation density of two sides of the moving grain boundary, κ is the grain boundary curvature, which is calculated through the kink template method [22], and γ is the grain boundary energy. In the developed CA model, the total annealing time is discretized into multiple time steps, in which the growth phenomenon is assumed to occur in a stable manner. Therefore, the simulation time step (Δt) can be calculated using the following relationship:

$$\Delta t = \frac{\lambda}{V_{\max}} \tag{11}$$

where λ is the cell length, and $V_{\max}$ is the maximum velocity of the GB obtained from Eq. (8).

The kinetics of nucleation phenomenon during the progress of static recrystallization is a function of temperature and the change in system's energy due to the formation of defect free nuclei. Therefore, the nucleation rate ($\dot{n}$) can be defined through the following equation [23],

$$\dot{n} = c_0 \Delta E \exp\left(\frac{-Q_N}{RT}\right) \tag{12}$$

where c_0 is a positive fitting factor, Q_N is the nucleation activation energy, and ΔE is the energy change due to the change in dislocation density and surface energy of grain boundaries during nucleation. Therefore, based on the calculated time step for the time increment i, the local nucleation probability is calculated using the following equation:

$$P^i_{\text{nucleation}} = \dot{n}^i \lambda^3 \Delta t_i \tag{13}$$

where $\dot{n}$ is obtained from Eq. (12), and Δt is obtained from Eq. (11) for the time increment i. Then, the calculated nucleation probability is compared to a pseudorandom number, generated through Mersenne-Twister algorithm [24], as a probabilistic transformation rule to decide whether the transformation from deformed site into a fresh nucleus can occur. The detailed description of the developed CA model can be found in Ref. [18].

3.3 Thermal Model

As explained in the previous section, temperature is one of the most important parameters that controls the kinetics of static recrystallization and progress of softening mechanisms. In this regard, a thermal finite element model has been developed to precisely asses the temperature changes in the bulged specimen during annealing process. Accordingly, a 2D transient thermal model in Cartesian coordinate has been utilized to determine the temperature distribution within the anneal specimen as

below [13],

$$\frac{\partial}{\partial x}\left(\Lambda\frac{\partial T}{\partial x}\right)+\frac{\partial}{\partial y}\left(\Lambda\frac{\partial T}{\partial y}\right)=\rho_m c\frac{\partial T}{\partial t} \tag{14}$$

where ρ_m, c, and Λ are the material density, specific heat, and coefficient of heat conduction, respectively. In addition, the following boundary condition was applied to all material sides that are exposed to the environment with different temperature [25]

$$\Lambda\left(\frac{\partial T}{\partial \xi}\right)_{\Gamma}+h(T-T_{\text{furnace}})=0 \tag{15}$$

where h is the heat transfer coefficient, T_{furnace} is the stabilized temperature of the furnace, and ξ is the normal direction to every surface boundary Γ. To solve Eq. (14), the FE formulation based on the standard Bubnov-Galerkin technique considering 4-node isoperimetric elements has been developed [26].

3.4 Modeling Scheme and Model Parameters

A coupled Cellular Automata-Finite Element model is implemented to predict the SRX behavior of a hydroformed steel tube during non-isothermal annealing process. The initial state for the modeling of SRX is created based on the data from prior deformation characteristics (dislocation density), as well as the tube's as-deformed microstructure data (grain topology and texture). The microstructural data are extracted from EBSD maps using MATLAB toolbox MTEX, and directly imported into the spatial region designed for CA model. In addition, the real-time temperature during annealing is imported from the thermal FE model. The solution algorithm for modeling the SRX at each time increment follows these steps:

(I) Compute the time step (Δt) based on the data from previous time increment,

(II) Update the temperature field based on the time step Δt,
*If the maximum temperature change in the solution domain ($\Delta T_{\max}$) is larger than a predefined critical value ($\Delta T_{\text{cr}} = 0.5\,^{\circ}\text{C}$), then update the time step as follows:

$$\Delta t_{\text{new}}=\frac{\Delta T_{\text{cr}}}{\Delta T_{\max}}\Delta t \tag{16}$$

(III) Calculate $\dot{n}$ and $P_{\text{nucleation}}$ for each cell located on the grain boundaries and triple junctions,

(IV) Calculate local velocity of the grain boundary (V) and probability of grain growth for each recrystallized cell surrounded by unrecrystallized cells,

(V) Compare a pseudorandom number to the calculated probability of nucleation and grain growth to decide whether the transformation can take place,
(VI) Update the recrystallization state of cells based on the decisions made in previous step.

4 Results and Discussion

The THF experiment was carried out on the investigated low carbon steel tube using a combination of axial feed and internal pressure as depicted in Fig. 1a. The corresponding distribution of the von-Mises equivalent strain in the bulged tube measured through DIC technique is shown in Fig. 1b. The DIC measurement shows a non-uniform distribution of equivalent strain in longitudinal direction with the highest strain value localized at the pole of the bulged tube. Because of the highest amount of the equivalent strain at the pole of the bulged tube, this region is chosen for calculating the flow characteristic of the tube under deformation, which consequently provides the maximum driving force for the occurrence of SRX in the tube. The equivalent flow curve calculated using Eqs. (1)–(6) is shown in Fig. 2, which is based on the

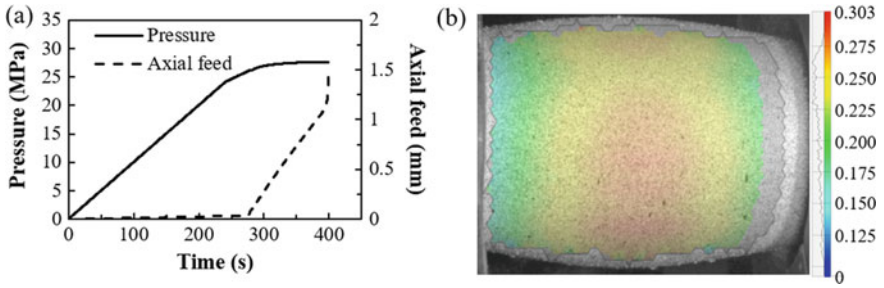


Fig. 1 **a** The applied boundary condition during THF process, and **b** the corresponding distribution of von-Mises equivalent strain obtained from DIC. (Color figure online)

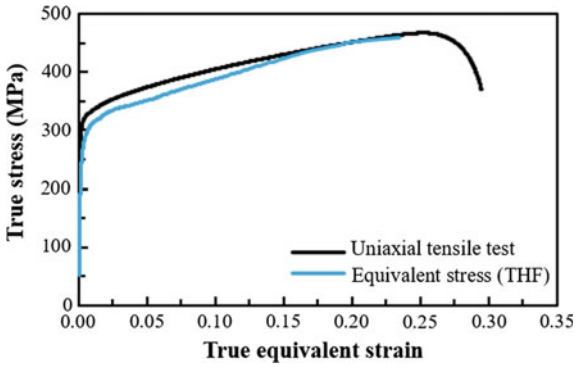


Fig. 2 The von-Mises equivalent flow stress of the bulged tube shown in Fig. 1b, compared to the uniaxial flow curve of low carbon steel. (Color figure online)

strain data obtained from DIC measurements at the pole of the tube. As seen, the flow properties of the bulged tube are different from the uniaxial flow curve of as-received steel tube, so that the tube under THF process yields at lower stress level followed by higher strain hardening coefficient in comparison to uniaxial flow curve.

As explained in the previous section, the progress of SRX within hydroformed steel tube under non-isothermal annealing condition was simulated through a thermo-microstructural model. The material properties as well as the CA model coefficients for the investigated low carbon steel are listed in Table 1 [18, 21]. Among the parameters given in Table 1, the CA model parameters (Q_m, Q_N, and Q_{gb}^{α}) were defined based on the multiple simulations performed to calibrate the model coefficients against the experimental results, while the rest of the parameters are material properties. The calibration approach employed in this study was similar to the approach proposed in references [27, 28]. Furthermore, to solve the thermal model used in this work, the thermal model coefficients in the form of temperature-dependent functions were required to improve the accuracy of predictions. These functions for low carbon steel are listed in Table 2 [13]. Note that, although the material properties given in Tables 1 and 2 can be slightly different for various low carbon steel products, the difference is very negligible to significantly influence the simulation results. Therefore, these parameters were assumed the same for every low carbon steel.

As temperature is the most important factor controlling the kinetics of SRX, it is crucial to account for the temperature variation within the specimen during

Table 1 The properties of low carbon steel required for CA model [18, 21]

Parameters	Value
α	0.5
M	3
G (GPa)	69.3
b (m)	2.48×10^{-10}
γ_{HAGB} (J/m^2)	0.56
$\Delta\theta_{HAGB}$ (°)	15
Q_m (kJ/mole)	149
Q_N (kJ/mole)	144
Q_{gb}^{α} (kJ/mole)	124

Table 2 The properties of low carbon steel required for thermal model [13]

Parameters	Temperature-dependent function (in K)
Material density (kg m^{-3})	7800
Specific heat (J kg^{-1} K^{-1})	$284.7217 + 0.5051 \times T$
Thermal conductivity (W m^{-1} K^{-1})	$114.6667 - 0.0917 \times T$; if T <900 33; if $T \geq$900

annealing process. Assuming isothermal annealing condition imposes an extra error to the predictions, since part of SRX can take place during heating up stage. In order to evaluate the accuracy of the developed thermal model, the predicted temperature history is compared to the experimentally recorder data, as shown in Fig. 3. As seen, a good agreement between the experimental and the predicted temperature history within specimen under annealing is obtained. It should be noted that the heating rate within specimen is very high at the beginning of annealing process, while it decreases when getting close to the stabilized temperature of the furnace. In addition, a significant difference between the actual temperature history with the isothermal assumption is seen, which may lead to an increased amount of error in the modeling results.

Figure 4 depicts the EBSD map collected from the hoop cross section of the as-deformed steel tube. As seen, the microstructure consists of a very fine grain

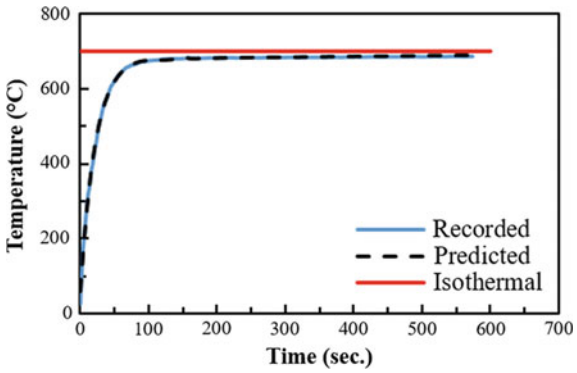


Fig. 3 The recorded and predicted temperature history under non-isothermal annealing condition, as well as the isothermal temperature regime assumption. (Color figure online)

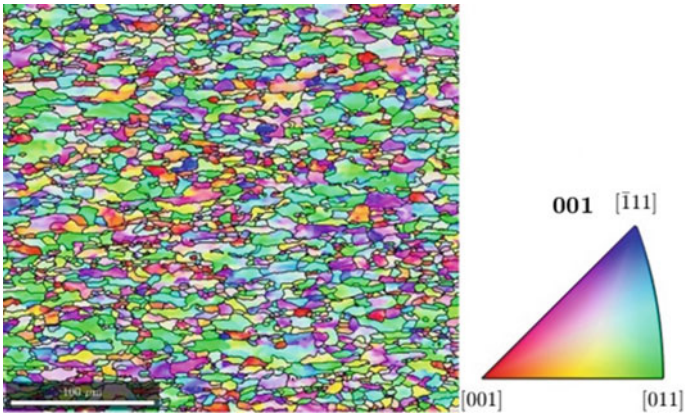


Fig. 4 The EBSD image collected from the hoop cross section of the as-deformed steel tube [18]. (Color figure online)

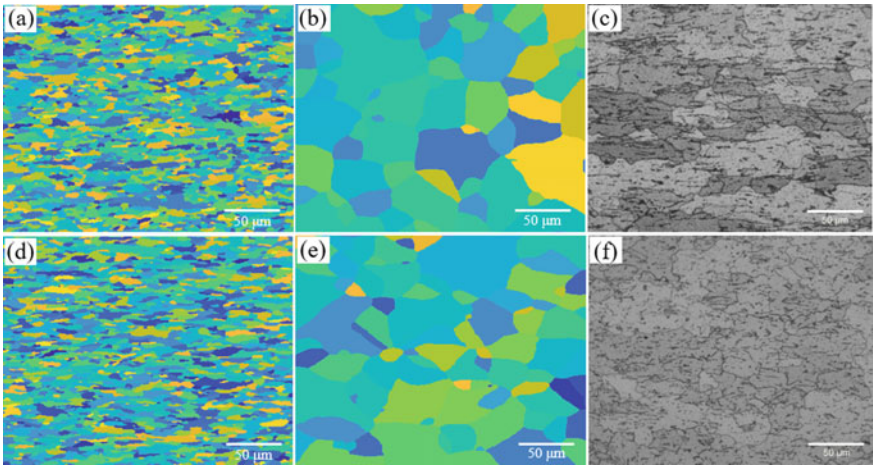


Fig. 5 **a**, **d** The initial grain topology of the annealing specimens, as well as **b**, **e** the predicted microstrure, and **c**, **f** the experimental OM image of fully recrystallized specimen under annealing condition of $T = 700$ °C and $t = 5$ min in the hoop and axial directions, respectively. (Color figure online)

structure, which are slightly elongated toward the longitudinal direction of the tube. In this study, the microstructure changes during annealing process are investigated on the hoop and axial cross sections of the pole of the bulged tube. Figure 5 shows the comparison between the predicted microstructure through FE-CA modeling with the experimental OM images on the two hoop and axial cross sections. The initial microstructures of the annealing specimen in hoop and axial directions are shown in Fig. 5a and d, respectively. These microstructures are generated based on the imported grain topology and orientation data from EBSD maps collected from each cross section. For instance, the initial microstructure of the hoop cross section (Fig. 5a) is generated based on the EBSD data provided in Fig. 4. For this cross section, the predicted fully recrystallized microstructure after annealing time of 5 min is shown in Fig. 5b, while the corresponding OM image is illustrated in Fig. 5c. Similarly, the final predicted and experimental microstructures of the annealed specimen for axial cross section are shown in Fig. 5e and f, respectively. As seen in both cross sections, a close agreement exists between the predicted and the experimental microstructures. The final grain topology of the annealed specimen is more equiaxed in comparison to the as-deformed microstructure. Furthermore, a significantly coarse grain structure in the final microstructure of annealed specimen is seen when compared to the as-deformed microstructure, inferring the faster kinetics of grain growth in comparison to the nucleation.

In order to quantify the comparison between the experimental data and CA predictions, the kinetics of SRX in terms of the fraction of recrystallization obtained using both approaches were compared together. The experimental fraction of recrystallization (X_{SRX}) as a function of time can be computed based on the measured hardness values of the specimens annealed under different durations, as follows

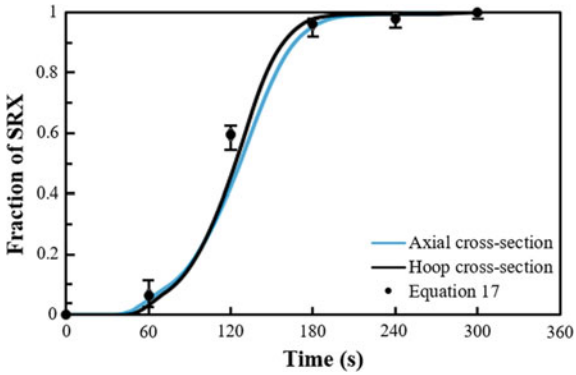


Fig. 6 The fraction of recrystallization obtained from the developed CA model and calculated through Eq. (17). (Color figure online)

$$X_{SRX} = \frac{H_0 - H}{H_0 - H_f} \tag{17}$$

where H_0,H and H_f are the hardness values for the as-received, partially recrystallized, and fully recrystallized specimens, respectively. The fraction of recrystallization obtained from the developed CA model for both hoop and axial cross sections of the bulged tube and calculated through Eq. (17) are shown in Fig. 6. As seen, the predicted rate of SRX in the axial and hoop cross sections are very similar. The minor difference in the kinetics of SRX in axial and hoop cross sections can be due to the difference in their initial grain topologies. In addition, a good agreement between the numerically predicted and the experimentally obtained fraction of recrystallization is seen.

5 Conclusions

In this study, the microstructural changes within bulged steel tube during annealing after THF process were investigated. To that end, a modeling setup based on the Finite Element thermal model and CA model was developed to account for the impact of multiaxial deformation mode as well as the temperature regime during annealing process on the kinetics of SRX. The actual microstructure and texture of the as-deformed specimen were obtained through EBSD test, which were directly imported to the CA model to create the initial state for the simulations. In addition, an analytical solution was developed to characterize the flow behavior of steel tube during THF process. The results showed that the predictions through the developed FE-CA model matches the experimental data in terms of the rate of recrystallization and final grain topology, confirming the accuracy of the developed modeling setup in the prediction of the progress of static recrystallization within hydroformed steel tubes. In addition, the final microstructure of the annealed specimens showed a

significantly coarse grain structure in comparison to the as-deformed microstrure, inferring the faster kinetics of the grain growth in comparison to the nucleation.

Acknowledgments The authors wish to thank the U.S. Department of Energy for the support of this project through the DOE award DE-FG02-13ER41974 and DOE DE-EE000597, with United States Automotive Materials Partnership LLC (USAMP).

References

1. Shen G, Hu B, Zheng C, Gu J, Li D (2018) Coupled simulation of ferrite recrystallization in a dual-phase steel considering deformation heterogeneity at mesoscale. Comput Mater Sci 149:191–201
2. Wu C, Jia B, Han S (2019) Coupling a cellular automaton model with a finite element model for simulating deformation and recrystallization of a low-carbon micro-alloyed steel during hot compression. J Mater Eng Perform 28:938–955
3. Kalu PN, Waryoba DR (2007) A JMAK-microhardness model for quantifying the kinetics of restoration mechanisms in inhomogeneous microstructure. Mater Sci Eng A 464:68–75
4. Zhang J, Zheng CW, Li DZ (2018) A multi-phase field model for static recrystallization of hot deformed austenite in a C–Mn steel. Acta Metall Sin 31:208–215
5. Vafaeenezhad H, Seyedein SH, Aboutalebi MR, Eivani AR (2019) Hybrid Monte Carlo—finite element simulation of microstructural evolution during annealing of severely deformed Sn-5Sb alloy. Comput Mater Sci 163:196–208
6. Shabaniverki S, Serajzadeh S (2016) Simulation of softening kinetics and microstructural events in aluminum alloy subjected to single and multi-pass rolling operations. Appl Math Model 40:7571–7582
7. Asgharzadeh A, Aval HJ, Serajzadeh S (2016) A study on flow behavior of AA5086 over a wide range of temperatures. J Mater Eng Perform 25:1076–1084
8. Sieradzki L, Madej L (2013) A perceptive comparison of the cellular automata and Monte Carlo techniques in application to static recrystallization modeling in polycrystalline materials. Comput Mater Sci 67:156–173
9. Hesselbarth HW, Göbel IR (1991) Simulation of recrystallization by cellular automata. Acta Metall Mater 39:2135–2143
10. Lin YC, Liu YX, Chen MS, Huang MH, Ma X, Long ZL (2016) Study of static recrystallization behavior in hot deformed Ni-based superalloy using cellular automaton model. Mater Des 99:107–114
11. Huang C, Jia X, Zhang Z (2018) Modeling and simulation of the static recrystallization of 5754 aluminium alloy by cellular automaton. Metals 8:585–591
12. Salehi MS, Serajzadeh S (2013) Simulation of static softening behavior of an aluminum alloy after cold strip rolling. Comput Mater Sci 69:53–61
13. Salehi MS, Serajzadeh S (2012) Simulation of static recrystallization in non-isothermal annealing using a coupled cellular automata and finite element model. Comput Mater Sci 53:145–152
14. Mortazavi SNS, Serajzadeh S (2019) Simulation of non-isothermal recrystallization kinetics in cold-rolled steel. Multiscale Multidiscip Model Exp Des 2:23–33
15. Schäfer C, Mohles V, Gottstein G (2011) Modeling of non-isothermal annealing: interaction of recrystallization, recovery, and precipitation. Acta Mater 59:6574–6587
16. Asgharzadeh A, Nazari Tiji SA, Esmaeilpour R, Park T, Pourboghrat F (2020) Determination of hardness-strength and -flow behavior relationships in bulged aluminum alloys and verification by FE analysis on Rockwell hardness test. Int J Adv Manuf Technol 106:315–331

17. Nazari Tiji SA, Park T, Asgharzadeh A, Kim H, Athale M, Kim JH, Pourboghrat F (2020) Characterization of yield stress surface and strain-rate potential for tubular materials using multiaxial tube expansion test method. Int J Plast 133:
18. Asgharzadeh A, Nazari Tiji SA, Park T, Kim JH, Pourboghrat F (2020) Cellular automata modeling of the kinetics of static recrystallization during the post-hydroforming annealing of steel tube. J Mater Sci 55:7938–7957
19. Verdier M, Brechet Y, Guyot P (1998) Recovery of AlMg alloys: flow stress and strain-hardening properties. Acta Mater 47:127–134
20. Humphreys FJ, Hatherly M (2012) Recrystallization and related annealing phenomena. Elsevier
21. Nm SVS, Torizuka S, Nagai K (2005) Ferrite grain size formed by large strain-high Z deformation in a 0.15 C steel. Mater Trans 46:2454–2460
22. Janssens KG, Raabe D, Kozeschnik E, Miodownik MA, Nestler B (2010) Computational materials engineering: an introduction to microstructure evolutions. Academic Press
23. Kim DK, Woo W, Park WW, Im YT, Rollett A (2017) Mesoscopic coupled modeling of texture formation during recrystallization considering stored energy decomposition. Comput Mater Sci 129:55–65
24. Matsumoto M, Nishimura T (1998) Mersenne twister: a 623-dimensionally equidistributed uniform pseudo-random number generator. ACM Trans Model Comput Simul 8:3–30
25. Asgharzadeh A, Serajzadeh S (2016) Development of a stream function-upper bound analysis applicable to the process of plate rolling. Multidiscip Model Mater Struct 12:254–274
26. Stasa FL (1985) Applied finite element method. CBS Publishing Ltd., Japan
27. Afsharhasani R, Karakouzian M, Farhangi V (2020) Effect of competent caliche layers on measuring the capacity of axially loaded drilled shafts using the Osterberg test. Appl Sci 10:6169
28. Farhangi V, Karakouzian M (2020) Effect of fiber reinforced polymer tubes filled with recycled materials and concrete on structural capacity of pile foundations. Appl Sci 10:1554

Fast Development of New Alloys for Metal Forming Using Additive Manufacturing



Alexander Sviridov, Irina Sizova, and Markus Bambach

Abstract The industrial development of new materials in metal forming is a time consuming, iterative process. Although it is already being attempted to predict the properties of new materials using computational methods, experimental production and characterization must always be carried out. This typically involves casting of larger blocks of material, which are then processed to specimens. Particularly in the case of high-alloyed materials (e.g., nickel-base superalloys) pronounced macrosegregations occur, which must be removed by time-consuming homogenization. In this paper, additive manufacturing of small specimens is investigated as an alternative to traditional ways for developing new alloys for metal forming. The microstructure and thermomechanical transformation behavior of as-built material are analyzed and it is shown that thermomechanical treatment of the as-built state allows for transforming the microstructure in such a way that processing parameters for forming and final product properties can be identified.

Keywords Additive manufacturing · Hot rolling · Microstructure · Alloy development

1 Introduction

Currently, a wide range of sheet materials with excellent mechanical properties and specific features is available for various applications. However, the development of new materials remains an important task that draws upon different scientific fields. Increasing demands on the properties of components set new standards and development trends with high requirements on materials. For instance, in automotive engineering, new materials are developed to achieve higher hardness and better crash properties [1]. The properties, which are relevant for the manufacturing processes, such as formability, are also of great importance. The number of alloying elements in modern sheet metal and various post-processes such as heat treatment makes the

A. Sviridov (✉) · I. Sizova · M. Bambach
Brandenburg University of Technology Cottbus-Senftenberg, 03046 Cottbus, Germany
e-mail: sviridov@b-tu.de

© The Minerals, Metals & Materials Society 2021

G. Daehn et al. (eds.), *Forming the Future*, The Minerals, Metals & Materials Series,
https://doi.org/10.1007/978-3-030-75381-8_158

development of new alloys or the modification of already available alloys difficult and time consuming. Consequently, the success of new materials can only be guaranteed if material development is realized in a short time and with minimum effort.

The typical way of testing new alloys begins with the casting of larger blocks of material. This requires a large volume of alloying elements and is often expensive especially in the case of high-performance alloys. For some materials (e.g. high-manganese steels), heat treatment should be applied to remove the pronounced macrosegregations [2]. This process can also be very time consuming. For the development of materials for sheet metal, the new alloy should first be cast in blocks, homogenized and hot rolled. Finally, the hot-rolled strip is cold rolled to the appropriate thickness in many rolling passes and eventually annealed. Only after this long process chain, the final microstructure and the mechanical properties of the sheet metal can be analyzed. In an iterative process, the alloy can be improved by the casting of the new trials alloy compositions, and the whole process is repeated until a suitable sheet metal alloy is identified.

Currently, there are trends for faster alloy development based on digital approaches, which allow to develop real material solutions for industrial applications [3]. Vecchio and Cheney [4] applied high-performance analysis software for big data to develop new alloys, which enables revolutionary material compositions. By using the software and digital analysis tools, the development time can be reduced from several years to a few months. However, the probability of success of these methods is difficult to estimate without physical tests. Finally, experimental tests are needed to verify the developed alloys.

In recent years, the development of additive manufacturing processes has progressed significantly. Additive manufacturing is not only used to produce prototypes and components but also has great potential as a method for material development. There are wire and powder-based additive manufacturing techniques. Especially the powder-based processes have great potential for alloy development since the samples can be produced from various powder mixtures in a relatively short time. In the case of wire-based processes, mixing materials by supplying several wires made of different materials is possible by means of laser [5] and plasma [6] metal deposition. The wire feed speed of each material determines the mixing ratio. Welding technologies using flux-cored wire could be also an alternative for mixing materials. The conventional material development process can be significantly shortened by the additive manufacturing of smaller samples with different compositions in the first stage of the alloy development (Fig. 1).

Selective laser melting (SLM) uses a powder bed and is suitable for the production of complex components with a relatively small volume. Some studies are already known to implement the SLM process with various powder mixtures in order to operate the alloy development more efficiently—the so-called Rapid Alloy Development. In work of Ewald et al. [7], systematic variation of the mechanical properties was possible by preparing different powder mixtures. The mechanical properties of the investigated Al0.26CoFeMnNi system were significantly improved by the addition of 0.6 wt. % C, resulting in both increased strength and ductility. However, a large amount of powder comparable to the sample volume is required for the SLM

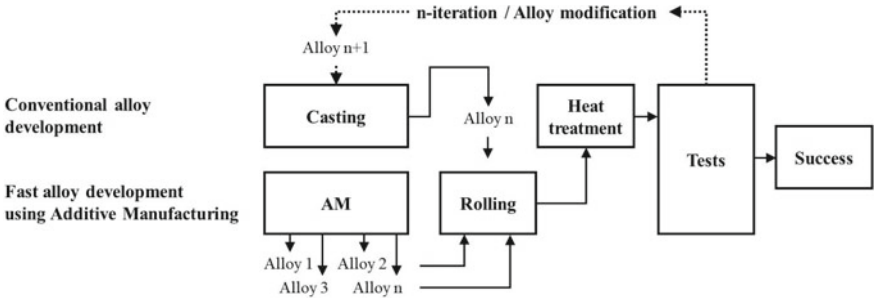


Fig. 1 Optimization of the iterative development process by using additive manufacturing

process, since the entire build chamber has to be filled with powder. In the most cases this causes high costs during development, because the powder blends cannot be separated again after powder mixing [7].

In the laser metal deposition (LMD) process, the powder is fed directly into the process via two or more powder containers [8]. This enables high flexibility of the alloy mixture. Moreover, it is possible to build a component with areas of different alloy mixtures in order to investigate the material more efficiently. The LMD process also enables a higher deposition rate in comparison to SLM and is, therefore, more suitable for productive material development.

The properties and microstructure of the additively manufactured material generally differ from the material which was conventionally produced by casting. The reasons for this are very different and depend on the material, for example, the layer structure of the material, higher cooling rates, phase transformation processes, etc. One of the most important scientific questions is whether the additively manufactured material is comparable to the conventional material in terms of microstructure and properties before and after forming and heat treatment.

In the present work, the stainless steel 316L was used to compare the microstructure and the mechanical properties of the conventional and additively (LMD) produced sheet metal. Materials in both states (conventional and as-build) were processed into sheets by hot rolling, followed by heat treatment under the same conditions and analyzed by means of optical metallography. The main aim was to compare the mechanical properties of the heat-treated sheets to demonstrate the transferability of the additively manufactured materials to the conventional sheets.

2 Material and Methods

2.1 Samples Manufacturing by Laser Metal Deposition

Stainless steel 316L material was used in the present investigation. The 316L stainless steel powder was provided by TLS Technik GmbH & Co. Spezialpulver KG

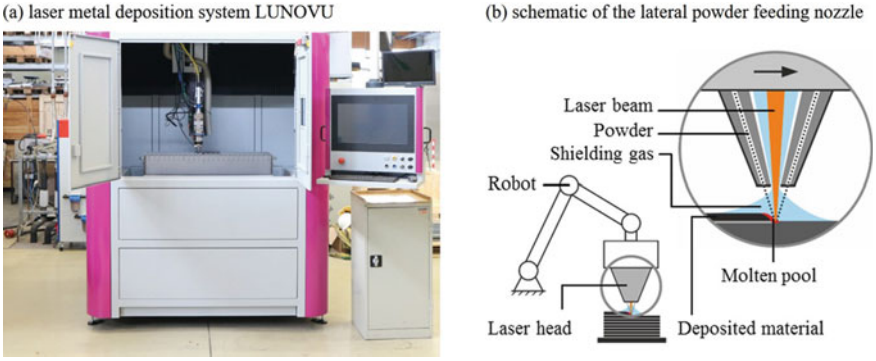


Fig. 2 **a** LUNOVU laser metal deposition system and **b** schematic of the lateral laser beam and feeding lance arrangement. (Color figure online)

with a particle size range of 45–100 μm. The specimens were fabricated using a LUNOVU laser metal deposition system equipped with a 2.5 kW diode laser with a lateral powder feeding nozzle (Fig. 2). Standard good quality build settings for 316L stainless steel were used (laser power 800 W, scan speed 800 mm/s, feed rate 10 g/min). To prevent the melt pool from oxidizing, a flow rate of protecting gas (argon) was set as 8 l/min during the experiment. A bidirectional scanning strategy with a rotation of 90° was chosen for manufacturing. The powder was deposited on 316L stainless steel plates with a thickness of 12 mm. All substrate surfaces were cleaned prior to the deposition process using acetone. Cuboid samples were produced with the dimensions of approximately $50 \times 50 \times 20$ mm^3 (Fig. 6a).

2.2 Rolling Experiments and Heat Treatment

From the deposited cuboids samples with the dimensions of $50 \times 40 \times 10$ mm^3 were cut and used for the rolling process. The LMD samples were joined with conventional wrought plates with a length of 100 mm and the same thickness by means of arc welding to provide samples of suitable dimension for the rolling process. Moreover, welding of LMD specimens to conventional wrought plates allows for the analysis of microstructure evolution and mechanical properties under identical heating and rolling conditions. The schematic of specimens used for the rolling is given in Fig. 3.

The rolling experiments were performed in an instrumented laboratory rolling mill (Carl Wezel KG model No. BW 850/330, Fig. 4). The rolling mill is equipped with a duo roll set, the rolls being 800 mm in width and 330 mm in diameter. Both the rolls and the support table were preheated to a temperature of 300 °C. Tests were carried out at a rolling speed of 1 m/min without lubrication. A true strain of approximately 0.8 was achieved in a single rolling pass. Samples were heated to 1250 °C for 10 min. prior to rolling in a batch-type furnace. The temperature

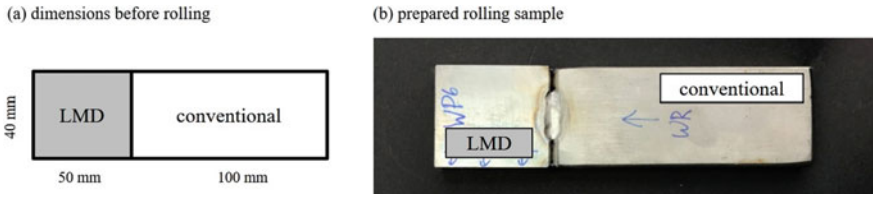


Fig. 3 **a** Schematic representation of rolling sample combining LMD and conventional wrought materials used in the present study and **b** illustration of the prepared rolling sample. (Color figure online)

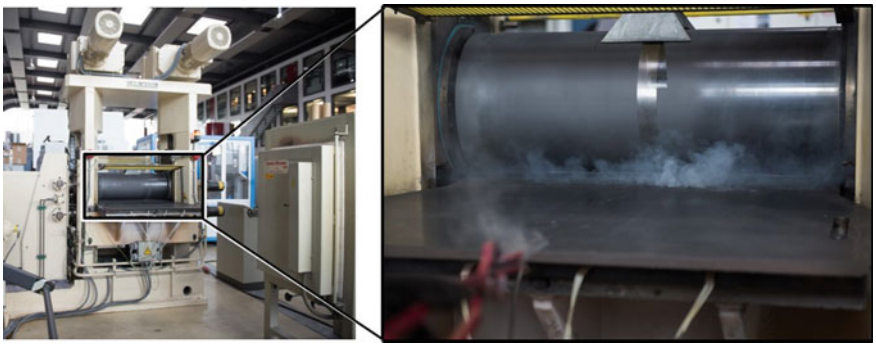


Fig. 4 Hot rolling mill Carl Wezel KG model BW 850/330. (Color figure online)

of the specimens was monitored with an appropriate thermocouple (type K). The transfer time between the furnace and the rolls was less than 5 s. After the rolling process, the samples were cooled in air. To generate the appropriate microstructure and mechanical properties the samples after rolling were subjected to annealing at a temperature of 1050 °C for 10 min followed by air cooling.

2.3 Microstructure Characterization

In order to investigate the microstructure after the processing, the specimens were sectioned in the middle parallel to rolling direction and mounted with the cut cross sections on top. The sections were ground flat on SiC papers with grit sizes from 320 to 1200. The specimens were then polished using two steps diamond suspension (6 and 3 μm) and finally, oxide polish (0.05 μm silica solution, Struers OP-S Suspension) was used. The polished samples were etched at a temperature of 60° C for 40 s in a mixture of (100 ml H_2O, 100 ml HCl, 10 ml HNO_3) and then analyzed by optical light microscopy (Carl Zeiss Microscopy, Jena, Germany).

2.4 Tensile Testing

For the mechanical testing, flat tensile samples were extracted from hot-rolled and heat-treated LMD and conventional wrought materials parallel to the rolling direction. The flat tensile specimen had a gauge length of 26 mm and a thickness of 2 mm. The dimensions of the samples are presented in Fig. 5. The tensile properties, including ultimate tensile strength, yield strength, and elongation, were measured utilizing a tensile testing machine from Hegewald und Peschke 100 INSPEKT with a 100 kN load cell. The specimens were tested at a constant loading rate with a velocity of 0.02 mm/s. The tensile tests were carried out at room temperature according to the DIN EN ISO 6892-1:2016 standard.

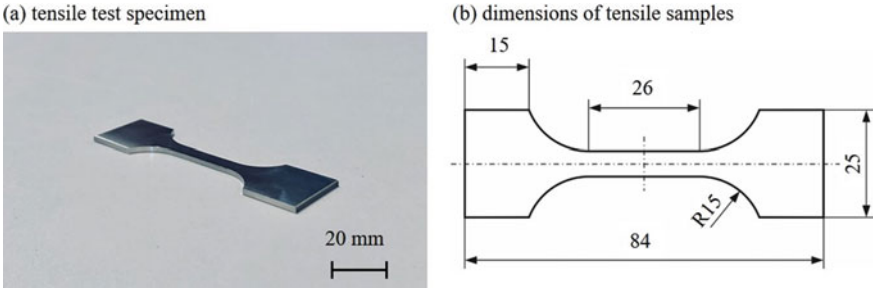


Fig. 5 **a** Image of the flat tensile sample used in the present study and **b** dimensions of tensile samples. (Color figure online)

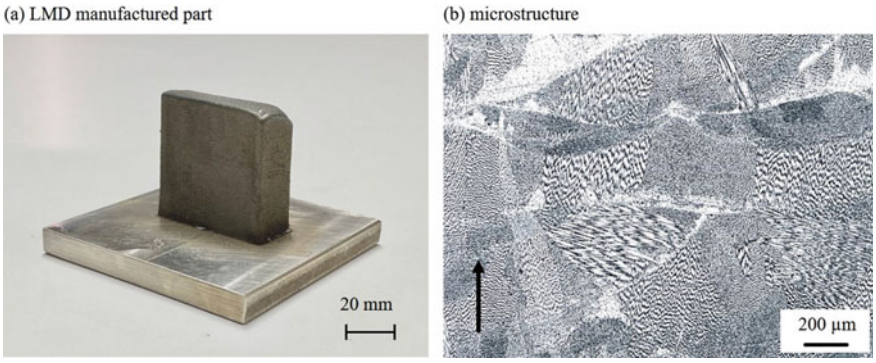


Fig. 6 **a** Cuboid samples manufactured by means of LMD and **b** optical images of etched microstructure of the manufactured LMD material in the cross-section. The build direction is shown with an arrow. (Color figure online)

3 Results and Discussion

3.1 Laser Metal Deposited Material

As was mentioned above, cuboid samples with the dimensions of approximately 50 × 50 × 20 mm^3 were manufactured using LMD. A sample is shown in Fig. 6a. A relatively smooth surface (with no obvious defects like humps or pits) is observed. The optical microstructure images are presented in Fig. 6b. The LMD material shows a good metallurgical bonding between the deposited layers. Dense samples without gaps or lacks of fusion are observed. Only small single pores can be found in the microstructure. A dendritic microstructure with partial cellular and columnar geometries is found in the samples, which is in good agreement with the literature [9, 10]. The total growth direction was perpendicular to the deposition direction because of the effect of temperature gradients opposite to the direction of heat flow.

3.2 Rolling Experiments: Microstructure Evolution and Mechanical Properties

Figure 7 illustrates the hot-rolled samples with indications of LMD and conventional wrought materials. The samples with dimensions 150 × 40 × 10 mm^3 were hot rolled in a single rolling pass. The rolling time was around 10 s. The rolling process was performed at a temperature of approximately 850 °C. The maximum experimental rolling force reached was around 900 kN. Hot rolling was performed to a strain of 0.8 (based on the initial thickness of 10 mm), i.e. to the thickness of 4.5 mm.

An overview of the microstructure evolution of LMD and conventional wrought materials during processing is presented in Fig. 8. The morphology of the conventional wrought material in the initial state (as-delivered condition) is shown in Fig. 8a. It consists of an austenite grain structure, which is the typical microstructure of 316L stainless steel. The microstructure of material manufactured by LMD is presented as well to provide a direct comparison of different microstructures, Fig. 8d. As can be seen in Fig. 8b, e, after hot rolling, the grains of both materials are elongated to such an extent that a fibrous microstructure results that indicate extensive

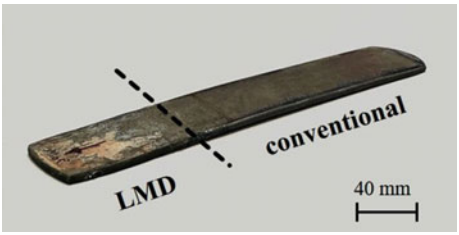


Fig. 7 Illustration of the final hot-rolled sample. (Color figure online)

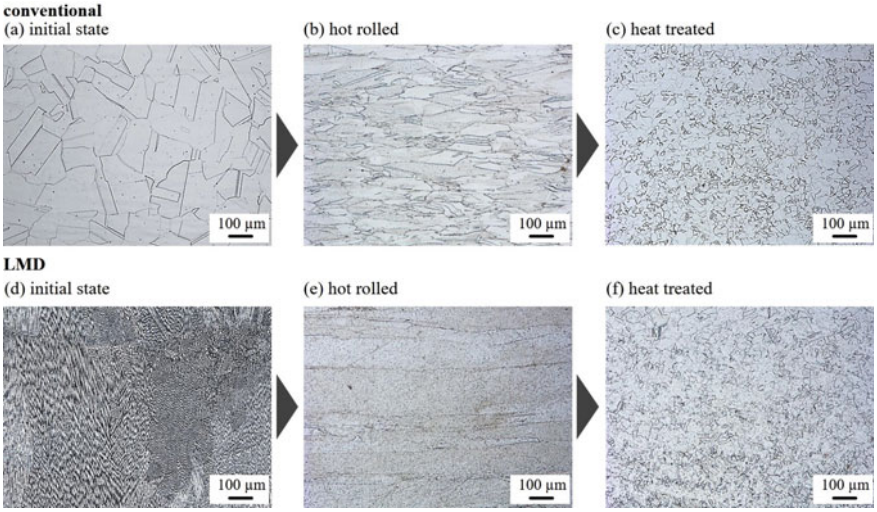


Fig. 8 Microstructure evolution of LMD and conventional wrought material during processing: **a**, **d** initial state, **b**, **e** after hot rolling and **c**, **f** after hot rolling followed heat treatment (1050 °C/10 min/AC). (Color figure online)

deformation. The observed microstructural evolution is comparable to that reported during the hot rolling of conventionally produced 316L stainless steel [11]. However, the microstructure of conventional wrought material after hot rolling appears much finer compared to LMD material. This can be attributed to the differences in the initial microstructure, and the remarkable influence of starting dendritic microstructure on hot rolling behavior. However, after applying a subsequent heat treatment (1050 °C/10 min/AC) both materials become similar and represent a fine homogeneous austenitic microstructure, with similar average grain sizes in both types of materials, i.e. in conventional wrought material about 28 µm, and in LMD material about 30 µm. The grain refinement is due to static recrystallization, which takes place when high temperature is applied to material priorly subjected to intense plastic deformation.

Tensile tests were carried out with hot-rolled and heat-treated materials. As was mentioned above, the tensile samples were extracted parallel to the rolling direction. The resulting yield strength, the ultimate tensile strength, and the total elongation to failure are compared in Table 1.

As can be seen, both materials yield almost the same value of ultimate tensile strength. LMD material shows a slightly lower elongation value of approximately 40.1%, compared to 43.1% in conventional wrought material, which could be a consequence of the residual porosity that appears during LMD. Hence, thermomechanical treatment of LMD material provides microstructures and mechanical properties very similar to conventional wrought material and appears to be a good alternative to conventional development of new materials for sheet metal production.

Table 1 Comparison of yield strength, tensile strength, and elongation at failure for samples produced by LMD and hot rolling followed by heat treatment and of conventional wrought samples treated in the same way

	YS (MPa)	UTS (MPa)	A_5 (%)
LMD	323	633	40.1
Conventional wrought	338	635	43.1
Datasheet 821 for hot-rolled sheet [12]	220	530	40

4 Conclusion

In the present study, the microstructure and thermomechanical transformation behavior of conventional and additively manufactured stainless steel 316L during rolling and heat treatment were analyzed. The following conclusions can be drawn:

- Stainless steel 316L produced by LMD shows a fine dendritic microstructure without defects with only small single pores. The produced microstructure differs significantly from the microstructure of conventional wrought material,
- Hot rolling leads to similar microstructures in both types of materials, i.e. both materials exhibit elongated grains after rolling indicating extensive deformation. However, the microstructure of LMD material exhibits larger grain sizes, probably due to dendritic initial microstructure,
- Applying heat treatment after rolling enables the full transformation of highly deformed grains. A fine homogeneous austenitic microstructure was found in both types of materials after hot rolling and subsequent heat treatment. The average grain sizes were almost identical in both types of materials,
- The results of tensile tests show that both types of materials represent comparable mechanical properties after the presented thermomechanical processing. This confirms that LMD could be a sound alternative to traditional ways of developing new materials for sheet metal production.

Hence, this research represents the viability of the process chain LMD—rolling—heat treatment for alloy development using the example of stainless steel 316L. Future work will focus on studying whether the effect of alloying elements on the mechanical properties can be revealed by the proposed process chain, such that the methods can indeed be used to assist the development of new steel compositions.

Acknowledgments The authors are grateful to the colleagues A. Neumann and I. Ünsal from the Chair of Mechanical Design and Manufacturing of BTU Cottbus-Senftenberg for performing the rolling experiments and to B. Kunze from the Chair of Physical Metallurgy and Materials Technology for the preparation of the metallographic images used in this study.

References

1. Ghassemieh E (2011) Materials in automotive application, state of the art and prospects. In: Chiaberge M (ed) New trends and developments in automotive industry. InTech Croatia, Rijeka, pp 365–394
2. Wietbrock B, Bambach M, Seuren S, Hirt G (2010) Homogenization strategy and material characterization of high-manganese TRIP and TWIP steels. Mater Sci Forum 638:3134–3139
3. Oerlikon Rapid Alloy Development (2020) The benefits of computationally designed alloys. https://www.oerlikon.com/metco/en/products-services/coating-materials/rapid-alloy-development/. Accessed 16 Jan 2020
4. Vecchio J, Cheney J (2019) Developing corrosion resistant alloys using big data. In: Paper presented at the annual event of the European Federation of corrosion (EUROCORR), Seville (Spain), 9–13 Sept 2019
5. Syed WUH, Pinkerton AJ, Li L (2006) Simultaneous wire-and powder-feed direct metal deposition: an investigation of the process characteristics and comparison with single-feed methods. J Laser Appl 18:65–72
6. Reisgen U, Sharma R, Oster L (2019) Plasma multiwire technology with alternating wire feed for tailor-made material properties in wire and arc additive manufacturing. Metals 9:745–756
7. Ewald S, Kies F, Hermsen S, Voshage M, Haase C, Schleifenbaum JH (2019) Rapid alloy development of extremely high-alloyed metals using powder blends in laser powder bed fusion. Materials 12:1706–1720
8. Brueckner F, Riede M, Müller M, Marquardt F, Willner R, Seidel A, Lopez E, Leyens C, Beyer E (2018) Enhanced manufacturing possibilities using multi-materials in laser metal deposition. J Laser Appl 30:032308
9. Guo P, Zou B, Huang C, Gao H (2017) Study on microstructure, mechanical properties and machinability of efficiently additive manufactured AISI 316L stainless steel by high-power direct laser deposition. J Mater Process Technol 240:12–22
10. Yadollahi A, Shamsaei N, Thompson SM, Seely DW (2015) Effects of process time interval and heat treatment on the mechanical and microstructural properties of direct laser deposited 316L stainless steel. Mater Sci Eng A 644:171–183
11. Venugopal S, Vasudevan M, Venugopal S, Sivaprasad PV, Jha SK, Pandey P, Mannan SL, Prasad YVRK (1996) Industrial validation of processing maps of 316L stainless steel using hot forging, rolling, and extrusion. Mater Sci Technol 12:955–962
12. Merkblatt 821: Edelstahl Rostfrei – Eigenschaften, Informationsstelle Edelstahl Rostfrei, 5. Auflage 2014

Effects of Residual Strain on Grain Growth of Extruded Aluminum Micro-channel Tubes During Heat Treatment



Wenli Fang, Xiaole Chen, Ding Tang, Huamiao Wang, Dayong Li, and Yinghong Peng

Abstract Post-extrusion cold deformation followed by brazing has a significant effect on mechanical properties of micro-channel tubes used in heat exchangers. To understand this relationship, cold rolling with different thickness reductions (0–15%) and a following brazing are conducted on extruded tubes, and the microstructure and strength are examined. The results show that with increasing rolling reduction, tensile strength and burst strength of the as-rolled tubes increase monotonously. While after brazing, both strengths decline obviously, and them decrease first and then increase with increasing rolling reduction. The change is attributed to recrystallization and grain growth observed in the post-braze tubes. Driven by different levels of strain from the rolling, recrystallized grain size increases first and then decreases. At 5% thickness reduction, abnormal large grains form in the web and result in the minimum post-braze strength. Finally, the ductile fraction mode is observed in the web, which shear strength determines the burst strength.

Keywords Cold rolling · Brazing · Grain growth · Mechanical strength

1 Introduction

Micro-channel tubes, also known as multi-port extruded (MPE) tubes, are widely used in the heat exchangers of air conditioning systems. The tube, typically made of 1xxx or 3xxx aluminum alloys, is a flat body with a row of side-by-side channels, which allow the refrigerant to flow through and transfer the heat. Apart from the heat transfer requirement, the tube must withstand internal pressure from the pressurized refrigerant, particularly of those for eco-friendly refrigerant systems that operate at higher pressures [1]. Therefore, to maximize the mechanical strength of the final product, especially its pressure bearing capacity, is an important goal of the production.

W. Fang · X. Chen · D. Tang (✉) · H. Wang · D. Li · Y. Peng
School of Mechanical Engineering, Shanghai Jiao Tong University, 800 Dongchuan Road, Shanghai 200240, China
e-mail: tangding@sjtu.edu.cn

© The Minerals, Metals & Materials Society 2021

G. Daehn et al. (eds.), *Forming the Future*, The Minerals, Metals & Materials Series,
https://doi.org/10.1007/978-3-030-75381-8_159

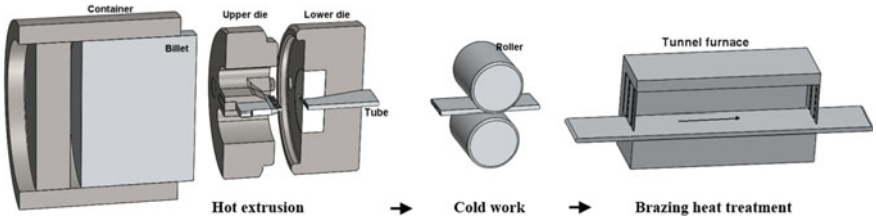


Fig. 1 Schematic of the process chain for the producing the micro-channel tube. (Color figure online)

In general, the process of producing MPE tubes for heat exchanger applications involves multiple manufacturing steps, as shown in Fig. 1. Firstly, the primary forming process of MPE tubes is performed by hot forward extrusion, where a heated aluminum billet is forced through a porthole die. After extrusion, to achieve precise external dimensions required for assembly of heat exchangers, the extruded tubes are straightened, roll-sized, and cut into final lengths. In this process, a small amount of cold work (plastic strain) is imposed on the tubes. Finally, after assembled into heat exchangers, the tubes undergo a brazing (or annealing) heat treatment to join the individual components. The brazing process is generally done at 600–605 °C (about 91% of the melting point for the alloy) inside a tunnel furnace with a nitrogen atmosphere. In this whole process chain, material microstructure and thus mechanical properties will change from step to step [2]. Therefore, it is necessary to understand how process conditions, microstructure, and final properties interact for metal production. Güzel et al. [3] investigated the grain structure evolution in the hot extrusion process of aluminum rods. Fan et al. [4] observed the evolution of the microstructure along the forming path and analyzed the geometrical dynamic recrystallization within the die during extrusion. Murai et al. [5] investigated the effects of billet homogenization and extrusion conditions on microstructure and mechanical properties of AZ31B magnesium alloy.

However, most of the previous studies on mechanical behaviors of the extruded profile are focusing on the process of the hot extrusion. In fact, these subsequent processes following the extrusion sometimes have a significant influence on the mechanical behaviors of extruded profiles, which has been rarely investigated. Taking the MPE tube as an example, the combination of the cold work and the brazing heat treatment induce recrystallization and grain growth, and this greatly influences mechanical properties of the final tubes.

In this study, a post-processing experiment (including cold work and brazing) of MPE tubes after extrusion is carried out. Through imposing thickness reduction with different levels on the tubes, the effect of residential strain on grain growth of the tube during brazing heat treatment is investigated. In addition, the mechanical strength of the tubes is examined by uniaxial tensile and burst pressure tests. The relationship between cold work, microstructure, and strength for the brazed tube is established.

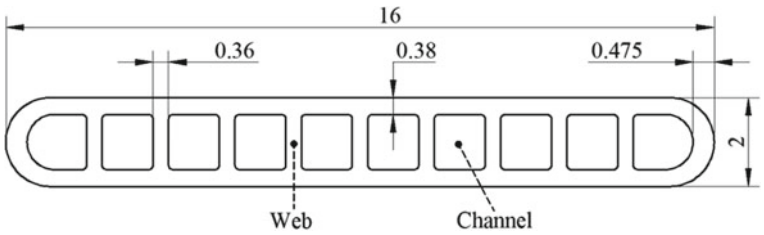


Fig. 2 Cross section of the MPE tube (unit: mm)

Table 1 Chemical composition of the AA1100 alloy (wt%)

Si	Fe	Cu	Mn	Zn	Al	Others
0.09	0.23	0.18	0.0005	0.0035	99.39	0.106

2 Experimental Procedure

2.1 Material

The specimens used in this study are AA1100 extruded micro-channel tubes, which are produced by hot extrusion using homogenized billet. The cross section and main dimensions of the tube are shown in Fig. 2. The chemical composition of the alloy is listed in Table 1. The experimental specimens with 300 mm in length are prepared for the cold rolling and brazing heat treatment.

2.2 Rolling Experiments

Rolling process is designed to simulate the practical straightening and sizing operation. The rolling equipment is shown in Fig. 3. In the experiment, different amount of thickness reductions are imposed on the tube specimens, and thus different residential strains will be left. The tubes after rolling are denoted as x% E–R tubes, where x% is the amount of the reduction ratio. In this work, x% is chosen as 0% (without rolling), 0.7, 3, 5, 9, 12, and 15%, respectively.

2.3 Brazing Experiments

After rolling, the specimens with different residual strains are put into a brazing furnace which simulates the actual heat treatment process. Figure 4 shows the tubes

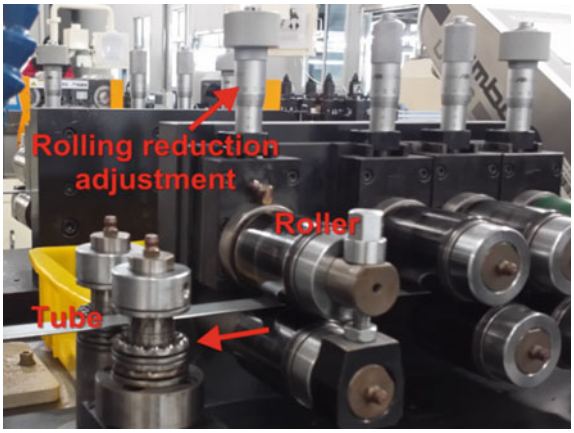


Fig. 3 Rolling of the MPE tube. (Color figure online)

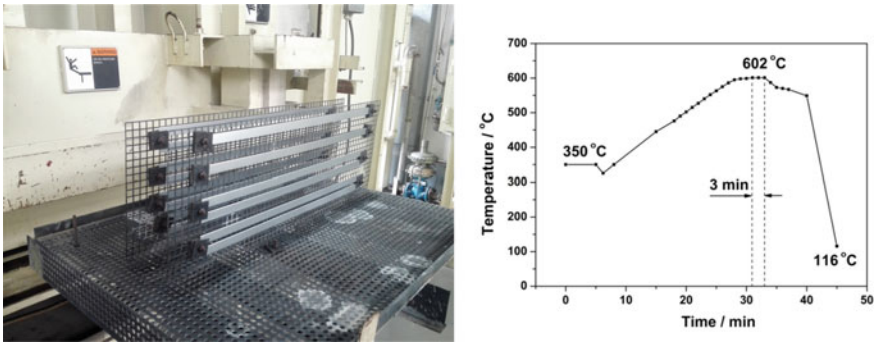


Fig. 4 The tubes to be brazed and temperature curve of the brazing process. (Color figure online)

to be brazed and temperature curve of the heat treatment, respectively. These tubes are hold at temperature of 602 °C for 3 min.

2.4 Mechanical Tests

The mechanical properties of the tubes are examined by uniaxial tensile and burst pressure tests, respectively. Strength along the extrusion direction is measured using an INSTRON EM3367 testing machine (Fig. 5a), while pressure bearing capacity of the tubes is measured with pressure bearing testing machine that is specially designed for this application. The testing equipment is shown in Fig. 5b and the testing procedure is described in detail in the work of Tang et al. [6].

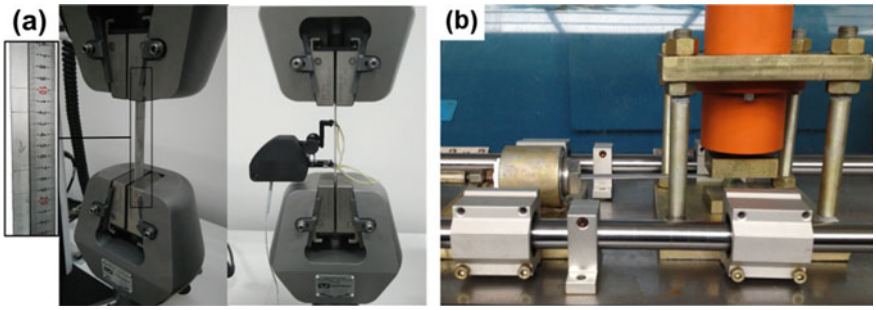


Fig. 5 Equipments for mechanical tests: **a** INSTRON EM3367 for uniaxial tension; **b** pressure bearing capacity testing machine for burst pressure. (Color figure online)

2.5 Microstructure Observation

Optical microscopy (OM) and electron backscattered diffraction (EBSD) techniques are used to characterize the microstructure of the tubes. Samples for OM are ground and polished using alumina suspension and 0.02 μm colloidal silica suspension, then etched with modified Keller's etchant. For EBSD mapping, they are ground with SiC paper up to 2000, and then electro-polished by LectroPol 5 with electrolyte A2. EBSD examination is carried out by NOVANanoSEM 230 with AZtec HKL Max System.

3 Results and Discussion

3.1 Mechanical Properties of the Tubes

The tensile strength of the tubes as a function of rolling reduction ratios are shown in Fig. 6a. It is found that, for the as-rolled tube before brazing, the strength increases gradually with increasing of the rolling reduction ratio. This can be due to the strain hardening effect and a slight increase in the thickness of internal walls. However, after brazing, the tensile strength is lower than that of the tubes before brazing. Moreover, the trend becomes different. The strength first drops sharply, then rises. At the reduction ratio of about 5%, the tensile strength of the brazed tube reaches the minimum.

Figure 6b compared the equivalent internal web strength of the tubes before and after brazing obtained by pressure bearing tests. From the results, the strength of the as-rolled and heat-treated tubes shows the same trend as that of tensile tests. Similarly, at the reduction ratio of about 5%, the strength of the brazed tube reaches the minimum, which decreases about 40%.

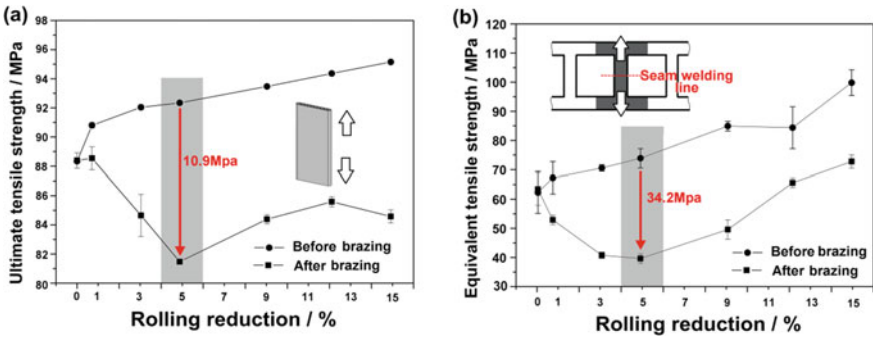


Fig. 6 Measured strengths: **a** tensile strength; **b** equivalent internal web strength. (Color figure online)

These mechanical behaviors are relevant to the change in the microstructure of the tubes during rolling and brazing process, which are discussed later.

3.2 Microstructure of the Tubes

Figure 7 shows the microstructure in the cross section of the brazed tubes with different rolling reduction ratios. It can be seen that the grain size in the web varies significantly with different amount of rolling reduction. There is little difference in the grain size between the as-extruded and brazed tubes without rolling (Fig. 7a, b). However, individual grain growth is observed when 0.7% of rolling reduction is

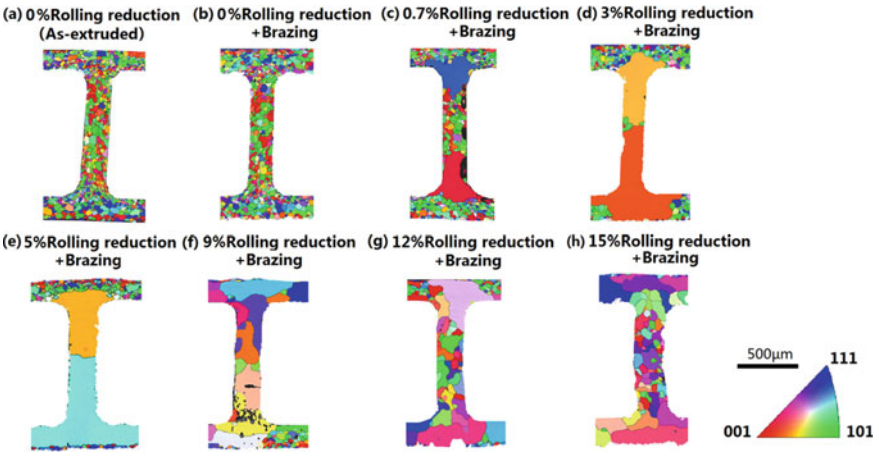


Fig. 7 Effect of rolling reduction ratio on the microstructure of the tubes after brazing. (Color figure online)

applied (Fig. 7a). With increasing of the rolling reduction ratio, the grains continue to grow until the grain size increases to a maximum at reduction ratio of 5%, where abnormal large grains envelop the entire web. After that, the grain size decreases gradually. Clearly, variation of the grain size is due to the recrystallization and grain growth during the brazing process, which is induced by the residual strain from the cold rolling. Note that a certain amount of cold work (critical strain) is required to initiate recrystallization during heat treatment. At this point, few nuclei are formed in the material and the growth of relatively few recrystallized grains is allowed to proceed with minimum resistance. However, as the amount of cold work increases, more nuclei are produced and the recrystallized grain size decreased.

In the rolling process, strain distribution in the cross section of the tube is uneven. Because of the "I" shaped structure, the deformation mainly concentrates at the web and the maximum residual strain locates in the zone close to the intersections of internal webs and out walls. The deformation feature gives rise to the inhomogeneous distributions of recrystallization nuclei and stored energy (dislocation density), which are responsible for inhomogeneous growth rates of the recrystallizing grains. As the rolling reduction increases, the levels of strain vary in both webs and out walls, as well as the amount of stored energy and the number of nuclei. A small strain only activates a very low number of nuclei. These nuclei then consume the remainder of the structure resulting in local grain structure where only a few large grains are left. While a high strain provides more nuclei per unit volume and growth of the grains will be restricted by impingement with their neighbors, resulting in relatively small grains. Consequently, the microstructure in the cross section of the tube will change with the amount of rolling reduction. At 0% rolling reduction, without the introduction of strain, the microstructure of the brazed tube is almost unchanged compared to that of as-extruded tube. At the rolling reduction of 0.7, 3, and 5%, with the extension of low level of strain (critical strain) from the intersection to the web, large grains first appear in the intersection and gradually spread along the web. With the further increase in the rolling reduction (9, 12, and 15%), the strain in the web is high enough to form relatively small grains, while the strain in out walls reaches critical strain and induces the formation of large grains.

Figure 8a–h shows polarized optical micrographs of the tube along the longitudinal section of the web with different rolling reduction ratios. The variation of the grain size is consistent with that in the cross section in Fig. 7. Without the limitation of the wall size, the grains grow to be as large as 10 mm at 3 and 5% of rolling reduction.

According to the Hall–Petch relationship [7], the changes in grain size of the brazed tubes are responsible for the different strengths of tubes with different rolling reduction ratios shown in Fig. 6. The 5% of rolling reduction that the biggest decrease in the tensile strength and the pressure bearing capacity of the tube after brazing occurs is exactly the one where the largest grains appear. The pressure bearing capacity decreases by ~40%, while the tensile strength decreases by ~10%. It is suggested, from current study, that certain range of residual strain which degrades the strength of the seam welding zone should be avoided in the process chain during manufacturing.

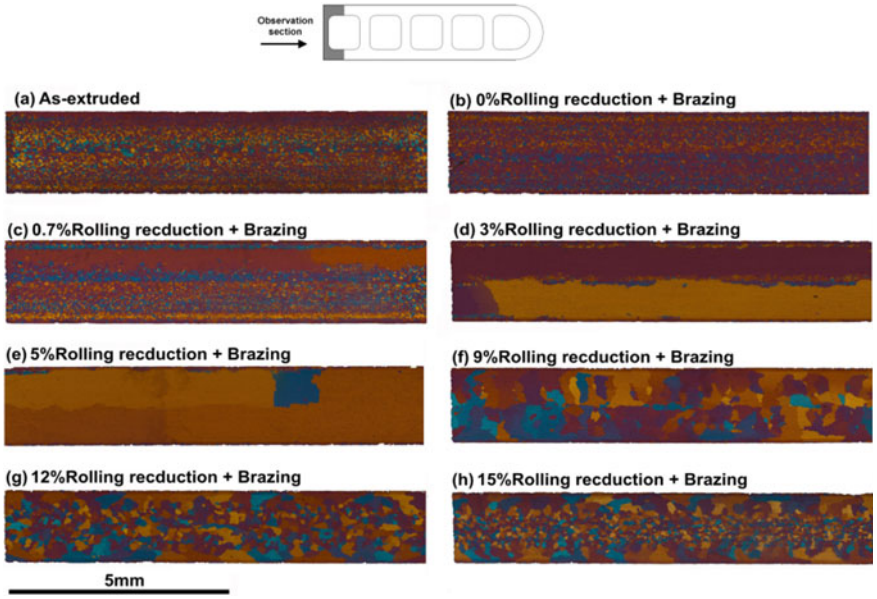


Fig. 8 Polarized optical micrographs in the longitudinal section. (Color figure online)

3.3 Fracture Mode of the Tubes

Figure 9 exhibits the polarized microscopic graphs of the internal webs after burst pressure tests. The profile of all the breaking interfaces shows a typical ductile fracture mode, which is governed by the maximum shear stress. This finding is consistent with the previous experimental observations by Yu et al. [8]. The failure happens mainly within the webs, whose shear strength determines the pressure bearing strength of the tube. In other words, the pressure bearing strength of a tube can be estimated in terms of the material's property of shear strength. Therefore, either increasing the thickness of the webs or reducing the area of the channels can enhance the pressure bearing strength of the tube.

4 Conclusion

The mechanical behaviors of MPE tubes through cold rolling and brazing operation are investigated. Through imposing thickness reduction with different levels on the tubes, the relationship between cold work, microstructure, and strength for the brazed tube is discussed. The following conclusions can be drawn:

(1) Before brazing, the mechanical strength of the MPE tube increases monotonically with the increasing of the rolling reduction ratio, which is due to strain

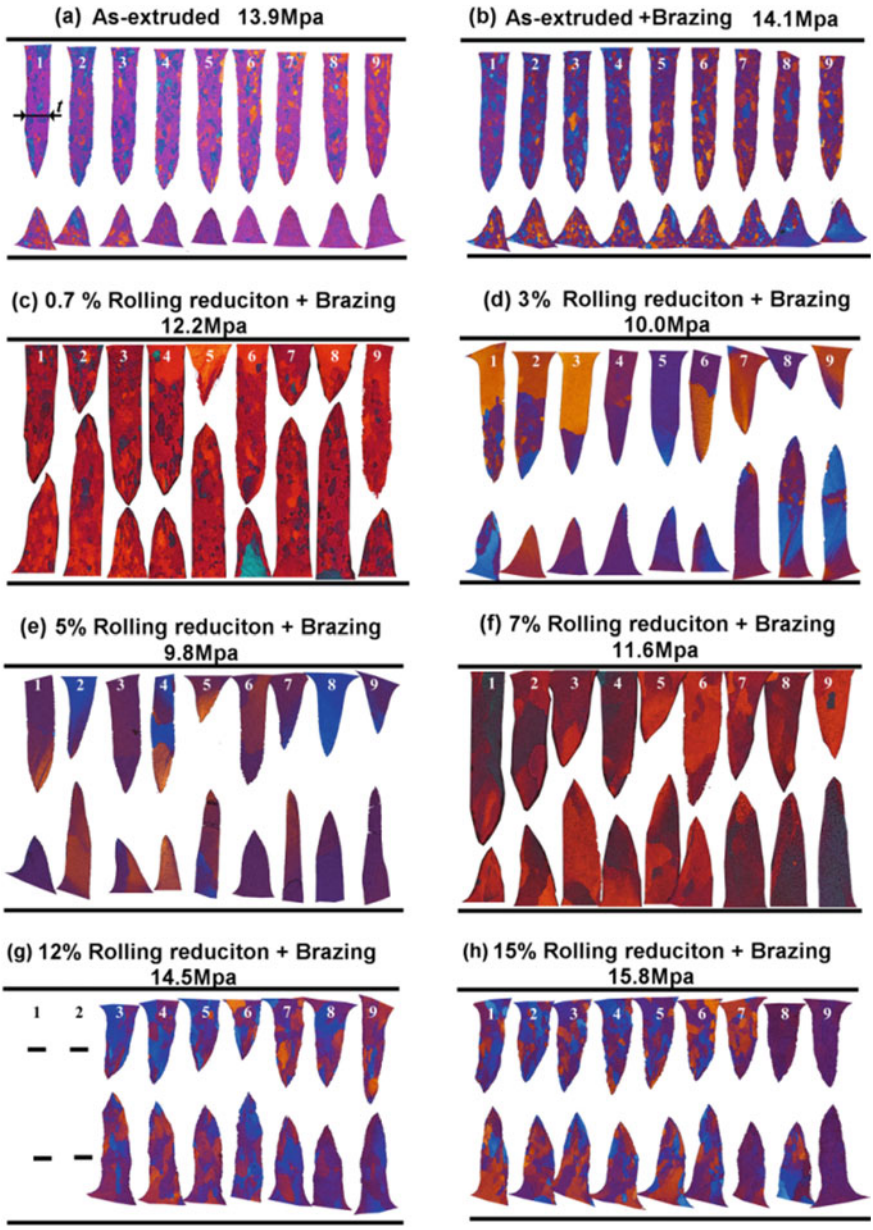


Fig. 9 Polarized optical micrography in the cross section of micro-walls after burst testing. (Color figure online)

hardening from the cold rolling. After brazing, the overall strength of the tube decreased significantly. The strength of the tube reaches its minimum at 5% rolling reduction.

(2) Due to the recrystallization and grain growth during the brazing process, the grain size in the tube web varies significantly with different amount of rolling reduction. The largest grains that form at rolling reduction of 5% result in a minimum strength of the tube.

(3) The fracture surface observed by OM shows ductile fracture mode. The lowest strength (largest grain size) induced by 5% pre-rolling reduction and brazing should be avoided in real manufacturing.

References

1. Kraft FF (2001) Method for predicting and optimizing the strength of extruded multi-void aluminum heat exchanger tube. SAE Technical Paper Series
2. Poole WJ et al (2012) A through process model for extruded AA3xxx aluminum alloys. In: Paper presented at 13th international conference on aluminum alloys, Pittsburgh, Pennsylvania, pp 293–298
3. Güzel A, Jäger A, Parvizian F, Lambers HG, Tekkaya AE, Svendsen B, Maier H (2012) A new method for determining dynamic grain structure evolution during hot aluminum extrusion. J Mater Process Technol 212(1):323–330
4. Fan X, Tang D, Fang W, Li D, Peng Y (2016) Microstructure development and texture evolution of aluminum multi-port extrusion tube during the porthole die extrusion. Mater Charact 118:468–480
5. Murai T, Matsuoka SI, Miyamoto S, Oki Y (2003) Effects of extrusion conditions on microstructure and mechanical properties of AZ31B magnesium alloy extrusions. J Mater Process Technol 141(2):207–212
6. Tang D, Fan X, Fang W, Li D, Peng Y, Wang H (2018) Microstructure and mechanical properties development of micro channel tubes in extrusion, rolling and brazing. Mater Charact 142:449–457
7. Hall EO (1951) The deformation and ageing of mild steel: III. Discussion of results. Proc Phys Soc B64:747–753
8. Yu J, Zhao G, Chen L (2016) Analysis of longitudinal weld seam defects and investigation of solid-state bonding criteria in porthole die extrusion process of aluminum alloy profiles. J Mater Process Technol 237:31–47

Forming of Parts with Locally Defined Mechanical and Ferromagnetic Properties by Flow-Forming



Eugen Wiens, Werner Homberg, Bahman Arian, Kerstin Möhring, and Frank Walther

Abstract To generate the highly efficient use of material resources for formed parts, local adaptation of the required strength and integrated functions is advised. When using austenitic steel, the volume fraction of deformation-induced α'-martensite, which has an influence on the strength and the magnetic permeability of the material, is highly dependent on the degree of deformation and the workpiece temperature in the deformation zone. Through selective adjustment of the process parameters of wall thickness reduction Δs and deformation temperature T_d it proved possible to produce locally restricted areas with an α'-martensite volume from almost negligible to 80% at an identical stage of deformation, using a spinning or flow-forming process. In this way, axially graded and locally varying mechanical and sensory properties can be produced, such as for a magnetic displacement sensor. The aim of this ongoing work is the closed-loop control of properties through the use of micro-magnetic sensors during spinning processes.

Keywords Spinning process · Property control · Strain hardening · Martensite content · TRIP-effect · Micro-magnetic measurement · Actuators and soft sensors

1 Introduction

Today, the responsible handling of resources is more important than ever before. It is thus necessary to adapt the characteristics of the part to the requirements placed on it. First of all, the mechanical properties can be adapted to the expected loads and, secondly, a specific functionality can be integrated in the part. By using austenitic steel, it is possible to achieve a locally varying strength and hardness within an individual part through work hardening while forming the part. In addition, a further

E. Wiens (✉) · W. Homberg · B. Arian
University of Paderborn, Warburger Straße 100, 33098 Paderborn, Germany
e-mail: ew@luf.uni-paderborn.de

K. Möhring · F. Walther
Department of Materials Test Engineering, TU Dortmund University, Baroper Str. 303, 44227 Dortmund, Germany

© The Minerals, Metals & Materials Society 2021

G. Daehn et al. (eds.), *Forming the Future*, The Minerals, Metals & Materials Series,
https://doi.org/10.1007/978-3-030-75381-8_160

increase in strength and hardness can be generated by using deformation-induced α′-martensite formation, which is highly dependent on the degree of deformation and the workpiece temperature in the deformation zone. The α′-martensite is ferromagnetic, contrary to the case for austenite, and can be used for sensory properties, such as for a magnetic displacement sensor or to produce invisible labeling on a product. This paper examines the influence of the process parameters of wall thickness reduction Δs and deformation temperature T_d of a flow-forming process on the mechanical properties and the α′-martensite volume of the austenitic steel 1.4301(AISI 304, X5CrNi18-10).

2 Process Principles

2.1 Deformation-induced α′-martensite

The austenitic phase of a metastable austenitic steel is not in the equilibrium state and can be converted by a thermally or mechanically induced energy input [1]. In an austenitic chrome-nickel steel, mechanical energy input through deformation results in a diffusion-free phase transformation in which deformation-induced martensite is formed by crystal shearing within the austenite grains. The austenite and martensite phases have the same chemical composition but differ in their lattice structure. The main impact factors for martensite formation in metastable austenites are the degree of deformation, the forming temperature, and the chemical composition. In addition, the grain size, sample size, and type of deformation can have a quantitative impact on the result. Above an alloy-dependent temperature limit, no martensite is formed even with the highest degrees of deformation [2]. The phase formation of α′-martensite occurs directly from austenite, via deformation-induced ε-martensite as intermediate stage. While ε-martensite and austenite are paramagnetic, α′-martensite is ferromagnetic and can therefore easily be detected in volume terms by using magnetic measurement methods [3, 4]. The strong dependence of the α′-martensite formation on the forming temperature and the degree of deformation is shown in the diagram on the left of Fig. 1a as an example for the material 1.4301 (AISI 304, X5CrNi18-10). The data were determined by Angel [5] in a uniaxial tensile test. The additional increase in strength of a Cr–Ni steel due to martensite formation, over and above the other work hardening mechanisms, is shown schematically in the yield stress curves of the diagram on the right in Fig. 1b. Most of the investigations into α′-martensite formation have been carried out in tensile tests, whereby it is assumed that tensile stresses favor phase transition and pressure loads hinder it on account of the volume increase that takes place during α′-martensite transformation. Knigge [1] has used compression tests to demonstrate that local deformation-induced α′-martensite formation is also possible under compressive stresses.

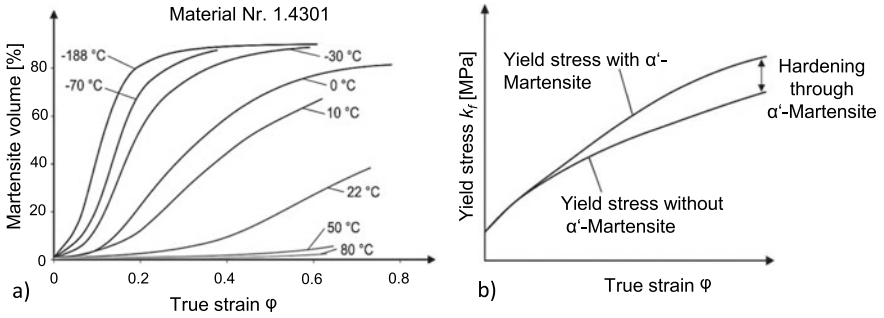


Fig. 1 **a** Martensitic phase volume fraction in tensile specimens as a function of the degree of deformation and the temperature [5]; **b** theoretical hardening of a Cr–Ni steel through deformation-induced martensite formation [6]

2.2 Flow-Forming

The manifold advantages of spinning processes, e.g., in terms of flexibility and efficiency, are countered by what is frequently a highly complex process characteristic with a multitude of process parameters [7]. The flow-forming of workpieces is employed for machining mostly prefabricated tubular or cup-shaped tubular parts with a defined reduction in wall thickness. The forming process is often carried out with a multi-roller arrangement in a single or multiple overrun. Flow-forming can be used to produce hollow bodies with a very good shape and dimensional accuracy as well as very good surface qualities [8]. In addition, the multi-axial compressive stress state in the forming zone also permits the forming of less ductile and high-strength materials. The material flow during flow-forming has axial, radial, and tangential components. The ratio of each component is decisively determined by the roller attack angle, the transition radius, and the exit angle. The ratio of the axial to the radial contact area of the roller and the workpiece determines the ratio of the axial to the radial material flow. This dependence has already been investigated experimentally on several occasions, among others by Tsivoulas et al. [9] and Jahazi and Ebrahimi [10]. Roy et al. [11] have developed an analytical model for calculating the contact surface between the roller and the workpiece for different roller geometry elements. In addition, the related feed rate has an influence on the contact area ratio of the axial to circumferential tool/workpiece contact in the forming zone [10]. The hardness devolution over the wall thickness, which is important for many components, can be influenced by the wall thickness reduction [12] and by the roller attack angle, which also influences the direction of the hardness distribution (axial/circumferential) [9]. Kleditzsch developed an analytical approach to the calculation of the equivalent plastic strain [13]. No investigations into the strain hardening and phase transformation of metastable austenites by flow-forming are known at present.

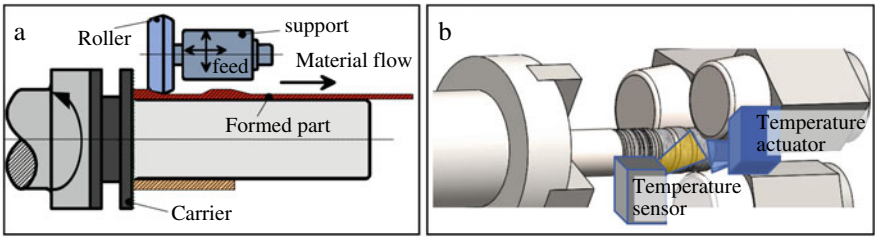


Fig. 2 Setup of the flow-forming (**a**) and the temperature devices (**b**). (Color figure online)

3 Experimental Methods

3.1 Forming Process

The investigation was carried out on the flow-forming machine BD 40 from Bohner-Köhle. The roller used in the experiments have an attack angle of $\alpha = 12°$, a rolling diameter of 158.4 mm and were arranged as a triple configuration in a 120° formation. Figure 2 shows a pictogram of the setup. On the left, a diagram of the reverse flow-forming employed is shown (a). The tube samples are of an austenitic chrome–nickel stainless steel (EN 1.4301) and have an (outer) diameter of 80 mm and a wall thickness of 4 mm in the initial state. Figure 2b illustrates the tool setup as well as the temperature sensor and actuator (cooling and heating device). The samples as well as the mandrel were warmed up or cooled down to the desired start temperature T_d right before the forming process. During the process the sample temperature was kept by cooling with liquid nitrogen (tests under room temperature (RT)), with a cooling lubricant (RT) or heating with a hot-air blower (above RT). All presented tests were conducted with a rotation speed of 400 rev/min and a feed of 50 mm/min.

3.2 Testing Methods and Instruments

The α'-martensite volume fraction was measured with a Fischerscope MMS. The measurements of each state are mean values of six measuring points over the tube circumference and were taken on the outer surface of the deformed tube. The logging of the specimen temperature was performed with the thermographic camera VarioCam hr head 600 of the company InfraTec with a measuring frequency of 50 Hz. The samples for the tensile test were eroded from the tube in axial direction. The shape of the sample is illustrated in Fig. 6. For each parameter combination 4 tensile samples were tested with the universal testing machine Z020. The sample heads were flattened by clamping jaws and the eroded flanks in the area of the free forming length were ground to a surface roughness of at least Rz 6.3. The hardness tests were carried out on the INNOVATEST Nexus 4303 with hardness testing methods

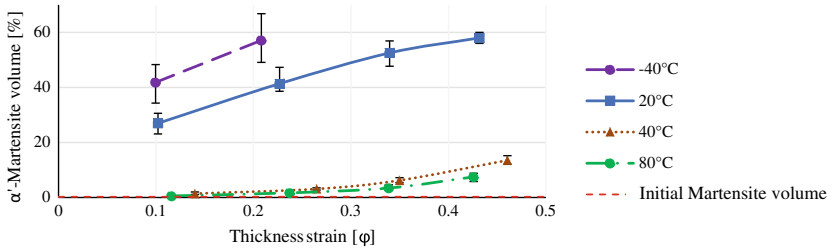
to Vickers with a testing force of 9,807 N and a holding time of 10 s which is equal to hardness unit HV1. Each hardness value is a mean value of three measurements with an equal distance to the rolling surface.

4 Experimental Results and Discussion—Influence of the Process Parameters on the Material Properties

4.1 Degree of Deformation and Forming Temperature

In Fig. 3, the evolution of the α′-martensite volume by deformation through flow-forming in a metastable austenite (1.4301) reveals the same characteristic development as a tensile test [5] or compression test [1]. The wall thickness reduction in this diagram is generated by 0.25 mm in each overrun step, so that each point in a curve from left to right means an additional overrun. The results show that the deformation-induced α′-martensite volume increases with a declining forming temperature and an increasing degree of deformation. The curve characteristics for higher temperatures reveal a progressive growing trend while the lower temperatures show a degressive growing trend. Though the overall trend is comparable with the curves of the tensile test, the $T_d = 20$ °C curve here already has a degressive progression, while the $T_d = 22$ °C curve in the tensile test displays a progressive trend. By comparison to the tensile test, the high temperature curves ($T_d = 20$ to $T_d = 80$ °C) tend to have a higher α′-martensite volume, with the values of the $T_d = -40$ °C curve being comparable to the ones of the tensile test. The α′-martensite volume for room temperature and elevated temperatures in the flow-formed specimens compared to the values of compression-formed specimens by Knigge [1] tends to reveal a higher α′-martensite volume.

Which forming method leads to a higher α′-martensite volume can be differentiated by the wall thickness reduction steps of the flow-forming deformation. For small



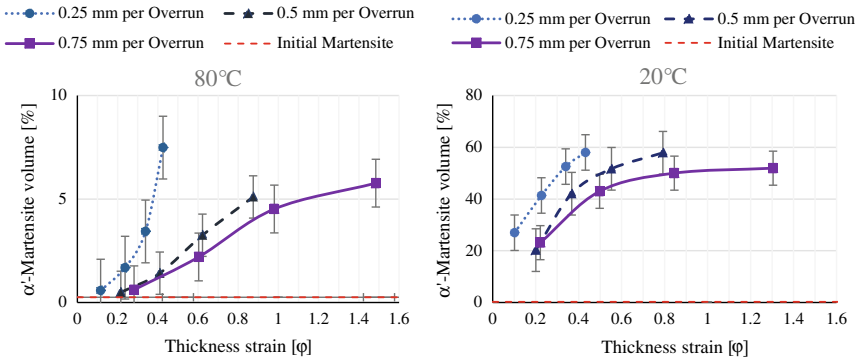
Material:	EN 1.4301	Initial tube wall thickness	4 mm
Outer tube diameter:	80 mm	Number of overruns (left to right):	1 – 4
Wall thickness reduction per overrun:	0.25 mm	Initial martensite vol. :	0.25 %
Average value calculated of 6 measurements in tube circumference			

Fig. 3 α′-Martensitic volume percentage in flow-formed tube depending on the degree of deformation and the temperature. (Color figure online)

overrun steps (0.25 mm) the flow-forming process leads to a higher α′-martensite volume than the Knigge compression tests. Figure 4 shows the influence of the forming history. The study revealed that the smaller the forming steps of the commutated deformation are (here the thickness strain φ), the higher the α′-martensite volume will be for an equal total wall thickness reduction. These findings agree with the findings of Müller-Bollenhagen et al. [14] which revealed the martensite formation to be strongly dependent on the strain rate. This tendency is independent of the forming temperature. In Fig. 4, the diagrams show the trend for $T_d = 20$ °C and $T_d = 80$ °C in overrun steps of 0.25, 0.5, and 0.75 mm. For small overrun steps the curve progression does not show an asymptotic pattern toward a limit value of α′-martensite like it shows for bigger overrun steps.

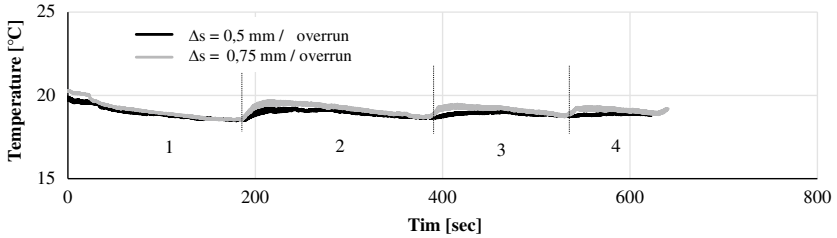
The specimen temperature, which is proven to influence the α′-martensite volume, does not remain constant during a forming operation of several overruns when using a liquid-cooling system with a constant volume flow. The higher the wall thickness reduction in a single overrun, the higher the temperature scatter will be. This is shown, for example, by the comparison in Fig. 5 of the temperature profile during flow-forming in four overrun steps for a set value of 0.5 and 0.75 mm per overrun.

Besides the wall thickness reduction, a higher feed also leads to an increased scatter due to the higher energy input over the same period of time. Among other mechanisms, the higher energy input of a bigger wall thickness reduction, leading to a local increase in the deformed material temperature, can be the reason for a lower α′-martensite volume by comparison with an identical degree of deformation in smaller deformation steps. This correlation is still part of the ongoing investigations, however, and requires further research.



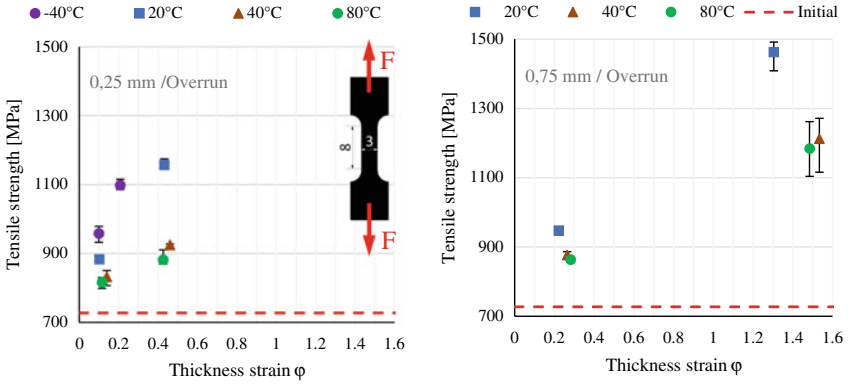
Material:	EN 1.4301	Initial tube wallthickness:	4 mm
Outer tube diameter :	80 mm	Number of overruns (left to right):	1 – 4
Wall thickness reduction per overrun :	0.25 - 0.75 mm	Initial martensite vol.:	0.25 %
Process temperature:	ca. 80/20 °C	Averageof 6 measurements in circumference	

Fig. 4 α′-Martensitic volume percentage in flow-formed tube as a function of the degree of deformation and the temperature as a function of the wall thickness reduction in a single overrun. (Color figure online)



Material:	EN 1.4301	Initial tube wallthickness:	4 mm
Outer tube diameter :	80 mm	Number of overruns (left to right):	1 – 4
Wall thickness reduction / overrun:	0.5 / 0.75 mm	Rotational speed:	400 rev/min

Fig. 5 Temperature profile of flow-formed specimen in a four-step forming operation with a 0.5 mm and 0.75 mm wall thickness reduction in a single overrun with a constant liquid-cooling volume flow



Material:	EN 1.4301	Initial tube wall thickness	4 mm
Outer tube diameter:	80 mm	Number of overruns:	1 & 4 (2 at -40°C)
Wall thickness reduction per overrun:	0.25 / 0.75 mm	Process temperature:	-40 to 80 °C

Fig. 6 Tensile strength of flow-formed tubes as a function of the degree of deformation, the temperature, and the wall thickness reduction step per overrun; Left: one and four steps with 0.25 mm overruns; Right: one and four steps with 0.75 mm overruns. (Color figure online)

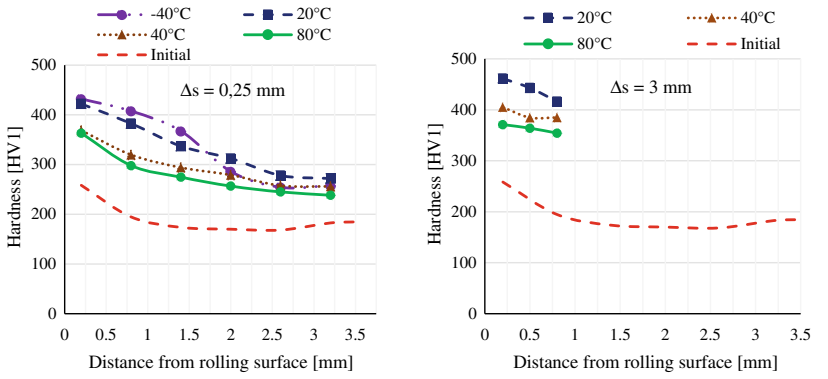
4.2 Mechanical Properties

The mechanical properties of the flow-formed specimens at different degrees of deformation and forming temperatures show the expected correlation with the α′-martensite volume. The higher the α′-martensite volume, the higher the tensile strength and hardness of the deformed material will be. By way of an example, Fig. 6 demonstrates the tensile strength of flow-formed tubes with a single and four-overrun wall thickness reduction in steps of 0.25 and 0.75 mm per overrun. The higher α′-martensite volume with a decreasing deformation temperature leads to a

higher tensile strength for similar wall thickness reductions. The spread in the thickness strain at different temperatures for identical reduction steps is caused by the varying material behavior at different temperatures, the machine stiffness, and the thickness scatter of the initial tube. The gradient of tensile strength with an increasing wall thickness reduction is greater with smaller overrun steps. For a predictable curve progression, the amount of the difference in thickness-strain values has to be extended by a long way, which is part of the ongoing research project. The yield stress shows the assumed behavior of Fig. 1b. The gap of yield stress between samples with small and higher martensite volume fraction gets bigger with increasing true strain.

By way of an example, Fig. 7 shows the hardness development of two tube cross sections with a wall thickness reduction of $\Delta s = 0.25$ mm in a single-step (left) and $\Delta s = 3$ mm in four steps of 0.75 mm (right) at different deformation temperatures. The increase in the α'-martensite volume with a decreasing deformation temperature leads, in the same way as the tensile strength, to an increasing hardness. With a small deformation, it is obvious that the hardness increase mainly takes place in the area of the tube's outer surface, where the rolling surface is located and where the local deformation is higher. As of 2 mm rolling distance, there is only a slight increase in hardness and this does not really depend on the deformation temperature (Fig. 7, left).

With a high deformation, the hardness gradient across the tube wall is far smaller. In addition, the increase in hardness over the degree of deformation is far less significant than the increase in tensile strength. For example, the tensile strength shows an increase of about 35% when the wall thickness reduction is increased from $\Delta s = 0.25$ mm to $\Delta s = 3$ mm at a deformation temperature of $T_d = 80$ °C. The hardness increase near the rolling surface for this same condition is only 2%. But the increase



Material:	EN 1.4301	Initial tube wall thickness	4 mm
Outer tube diameter:	80 mm	Number of overruns (left / right):	1 – 4
Wall thickness reduction per overrun:	0.25 / 0.75 mm	Process temperature:	-40 to 80°C

Fig. 7 Vickers hardness development across the tube wall of flow-formed tubes for a wall thickness reduction of $\Delta s = 0.25$ mm (left) and $\Delta s = 3$ mm (right) at different deformation temperatures. (Color figure online)

in the average hardness across the wall thickness of these two conditions is then again 30%, which is similar to the increase in the tensile strength.

4.3 Microstructure

As shown in Fig. 8a, b, a comparable martensite volume partition of 40% measured using the Fischerscope, corresponds additionally to the different hardness degrees shown in Fig. 7, with a different elongation of grains and a different radial gradient of the martensite volume partition distribution. This is shown for a deformation of 0.5 mm, respectively, 0.25 mm, achieved through two deformation steps of 0.25 mm wall thickness reduction per overrun, together with a forming temperature of T_d = 20 °C (material state A), respectively, by one step with 0.25 mm thickness reduction per overrun with a forming temperature of $T_d = -40$ °C (material state B). As can be seen in Fig. 8(I–III), in qualitative terms, the grain size in the radial direction is reduced, while the grain size in the tangential direction is increased. The measurement

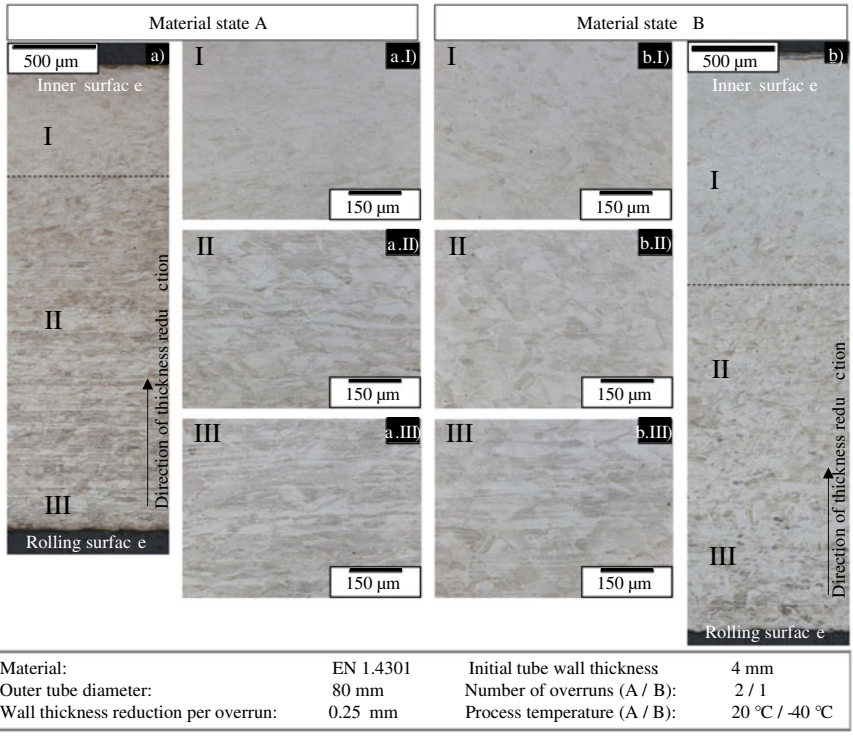


Fig. 8 Radial gradient of microstructure for material state **a** A and **b** B (overview) and detailed information (I–III). (Color figure online)

value used, which is detected with the Fischerscope (compare Fig. 3), is based, ceteris paribus, on an increased number of grains. The measured value relating to the martensite volume partition is influenced by the grain orientation due to deformation, the real martensite volume partition, the hardness (compare Fig. 7), and also the penetration depth of the measurement technique. Segregation of these parameters needs to be achieved in further investigations.

4.4 Measurement Technique and Local, Non-destructive Measurement of Martensite Content

For the non-destructive detection of the martensite volume partition on each sample, use was made of different measurement techniques. The Fischerscope measures a ferrite equivalent based on the magnetic-inductive-created voltage signal of the material compared to a reference voltage signal and is thus appropriate for detecting the content of the ferromagnetic phase. In the case of the investigated 1.4301 material, this measurement value corresponds to the partition of α'-martensite after deformation. The measurement depth is fixed and material-specific. Both the 3MA-II (Fraunhofer IZFP) and the μ-magnetic (Qass) measurement principle are based on the accelerating-current-supported induction of magnetic fields in the material investigated. The measurement depth depends on the frequency of the applied current and can be adapted to the material prior to testing by means of the quality/height of the output signal or the measurement depth, ceteris paribus. The change in the output signal for different volume partitions of the material is dependent on the microstructure of the material investigated, as is the type of material, the grain size and orientation, the hardness, and the residual stresses. The change in the output signal is transformed with the 3MA-II per Fourier transformation and can be analyzed using different analysis methods (harmonic analysis of the tangential-magnetic field strength, the Barkhausen noise, the incremental permeability signal, and multi-frequency eddy-current technique) and different key parameters. The selection of the key parameters is made as a function of the material and microstructural feature investigated. The Qass system is also based on the induction of magnetic fields. The change in these fields is detected by means of an energy level parameter.

A comparison of the gradient and the results of the integrally measured martensite volume partition of the Fischerscope indicates a correlation between the martensite volume partition detected by the measurement technique and the microscopically characterized partition up to a depth of non-definable distance from the surface. It was thus possible to detect the martensite volume partition independently of the deformation state. Nevertheless, the different microstructure can be discussed as an explanation for the different tensile strengths. Further information regarding a more detailed detection of material properties might be obtained by frequency-dependent measurement techniques for ferromagnetic material behavior, like the Fraunhofer IZFP 3MA-II or the Qass μ-magnetic technique. Due to the variation of the frequency,

different depths of the material volume and hence different volume partitions of martensite will be characterized.

5 Conclusions

The study is carried out to analyze the influence and adjustability of deformation-induced α′-martensite volume in a flow-forming process for a metastable austenite. It shows that the incremental forming character of the process leads to a higher α′-martensite volume for identical deformation degrees than the known values for single-step forming processes, such as compression or tensile tests. The study revealed that, besides the overall degree of deformation and the deformation temperature, the forming history also has an impact on the amount of the plasticity-induced α′-martensite volume. The division of the overall deformation into smaller forming steps leads to a higher α′-martensite volume than with big wall thickness reduction steps. Mechanical properties, like tensile strength and hardness, show an increase that correlates with the α′-martensite volume for an equal deformation degree, whereby the hardness of the near-rolling-surface areas tends to depend more on the α′-martensite volume than on the degree of deformation. The scatter of the temperature profile and the influence of the wall thickness reduction and the feed on this scatter shows the need for closed-loop control of the temperature actuator and the flow-forming process for the precise induction of a specifically α′-martensite volume in a predefined area.

The results presented indicate that further investigations are necessary in order to quantify the martensite volume partition in a depth that is deterministic for the material properties, thus making stable dynamic control of material properties feasible. In addition, the integration and application of measurement techniques and sensors in the machine, the identification, and reduction of forming-induced effects on signal detection during the forming process will be a matter of research. Additionally, the just-in-time valuation of measurement signals based on deformation-state-dependent thresholds remains topic for further investigations.

Acknowledgments The authors would like to thank the German Research Foundation (Deutsche Forschungsgemeinschaft, DFG) for supporting this project number 424335026 “Property control during spinning of metastable austenites” within Priority Programme SPP2183 “Property controlled deformation processes”.

References

1. Knigge J (2015) Lokale Martensitbildung in metastabilen austenitischen Stählen durch Verfahren der Massivumformung. Dissertation, Berichte aus dem IFUM Band
2. Heller HJ, Herbsleb G, Kleinfeld F, Pfeiffer B (1981) Der Einfluss von Martensit auf das Korrosionsverhalten von 18Cr-10 Ni-Stahl. Werkst Korros 32:157–167

3. Talonen J (2007) Effect of strain-induced α′-martensite transformation on mechanical properties of metastable austenitic stainless steels. Doctoral dissertation, Helsinki University of Technology
4. Weilandt K (2011) Experimentelle und numerische Untersuchungen zur Martensitbildung unter quasistatischer und zyklischer Belastung. Dissertation, Berichte aus dem IFUM Band 5/2011
5. Angel T (1954) Formation of martensite in austenitic stainless steels. J Iron Steel Inst
6. Springup B (2005) Semi-analytische Betrachtung des Tiefziehens rotationssymmetrischer Bauteile unter Berücksichtigung der Martensitevolution. Dissertation, Universität Hannover
7. Runge M (1993) Drücken und Drückwalzen. Verlag Moderne Industrie AG. Landsberg/Lech
8. Sivanandini M, Dhami SS, Pabla BS (2012) Flow forming of tubes—a review. Int J Sci Eng Res 3(5)
9. Tsivoulas D, Timar G, Tuffs M, da Fonseca JQ, Preuss M (2014) Texture formation in flow formed ferritic steel and the influence of the process parameters. Mater Sci Forum 783–786:2602–2607
10. Jahazi M, Ebrahimi G (2000) The influence of flow-forming parameters and microstructure on the quality of a D6ac steel. J Mater Process Technol 103:362–366
11. Roy MJ, Maijer DM, Klassen RJ, Wood JT, Schost E (2010) Analytical solution of the tooling/workpiece contact interface shape during a flow forming operation. J Mater Process Technol 210:1976–1985
12. Roy MJ, Klassen RJ, Wood JT (2009) Evolution of plastic strain during a flow forming process. J Mater Process Technol 209:1018–1025
13. Kleditzsch S (2013) Beitrag zur Modellierung und Simulation von Zylinderdrückwalzprozessen mit elementaren Methoden. Dissertation, TU Chemnitz
14. Muller-Bollenhagenll C, Zlrnmermann M, Christl HJ, Schroder X, EngeI B, Große-Wöhrmann A, Suttmeier FT (2008) Modelling and closed-loop control of complex tube forming based on an optimized application of martensite formation in austenitic stainless steels. Steel Res Int 79(10):745–752

Constitutive Modeling and Processing Map of Ti–5Al–5Mo–5V–3Cr–1Zr Alloy During Hot Deformation



Yuting Zhou, Jie Zhou, and Peng Wang

Abstract To investigate the hot deformation behavior of Ti–5Al–5Mo–5V–3Cr–1Zr (Ti55531) alloy, a series of compression tests were performed within the temperature range of 1033–1153 K at constant strain rates 0.001–1 s^{-1} on a Gleeble-3500 isothermal simulator. The results show that the flow stress decreases with an increase in temperature and a decrease in strain rate. At high strain rate, the flow curves are characterized by obvious discontinuous yielding, followed by slight strain hardening before flow softening and/or steady-state flow. The magnitude of the discontinuous yield drop increases with an increase in temperature. The flow behaviors were described by the Arrhenius equation in $\alpha + \beta$ phase region and in β phase region respectively. The processing maps considering strains of 0.05, 0.4, 0.6, and 0.9 were drawn. In combination with microstructural observations, it is found that this alloy represents typical instability of flow localization and flow rotation in an unstable flow region. The optimum conditions for hot deformation were found at 0.001–0.1 s^{-1} and 1003–1153 K.

Keywords Compression tests · Ti–5Al–5Mo–5V–3Cr–1Zr alloy · Arrhenius equation · Processing map · Microstructural observation

1 Introduction

Near-β titanium alloys show good corrosion resistance and workability, together with a superior combination of strength and ductility as well as excellent fatigue strength as compared to α/β alloys. Due to these characteristics, these alloys have been widely used in the production of critical components for aerospace, automotive, and offshore industry by hot working processes [1, 2]. The hot deformation of near-β titanium alloys has been studied in many previous works. For example, Ti-7333 has been found weaker deformation resistance compared to Ti5553, and its main instability mechanism is the bands of flow localization [3]. Qu et al. [4] investigated the

Y. Zhou (✉) · J. Zhou · P. Wang
School of Material Science and Engineering, Chongqing University, Chongqing 400044, China
e-mail: 1262434838@qq.com

© The Minerals, Metals & Materials Society 2021

G. Daehn et al. (eds.), *Forming the Future*, The Minerals, Metals & Materials Series,
https://doi.org/10.1007/978-3-030-75381-8_161

effects of different thermomechanical parameters on the deformation behavior and microstructure characteristics of Ti–4Al–2.5V–1.5Fe. Jackson et al. [5] investigated the effect of initial microstructure on plastic flow behavior during the isothermal forging of Ti–10V–2Fe–3Al and found that the flow behavior was highly dependent on the initial morphology of α phase.

Usually, near-β titanium alloys are sensitive to initial microstructures and working parameters (like temperature, strain, and strain rate) during hot working process. Therefore, to optimize the processing procedure and obtain desired microstructure characteristics of a near-β titanium alloy, it is essential to investigate the relationship between initial microstructure, processing conditions, and final microstructure. In this regard, Prasad [6] proposed the dynamic material model (DMM) to conduct these studies for metallic material. In this approach, parameters to describe the formability are developed as a function of temperature, strain, and strain rate using the true stress–true strain curves; and processing map is constructed to provide the distinct stable/unstable region for manufacture. The simplicity of DMM model has resulted in its widespread use. Bao et al. [7] constructed the processing maps of Ti1023 alloy based on its deformation behavior and mechanisms. Seshacharyulu et al. [8] developed a process map of Ti–6Al–4V titanium alloy on the basis of flow stress data and calculated the apparent activation energy of Ti–6Al–4V when the deformation is performed in the $\alpha + \beta$ region and β region. Hao et al. [9] determined the hot deformation characteristics of the new near-β titanium alloy Ti-1300 by constructing the processing maps within the temperature range of 920–1010 °C and strain rate range of 0.01–10 s^{-1}.

These studies provide a broad perspective on the microstructural evolution, constitutive model, processing map and deformation mechanism of β alloys during hot deformation. However, few studies have been reported regarding the hot deformation behavior and microstructure evolution of Ti–5Al–5Mo–5V–3Cr–1Zr. The objective of this work is to investigate the high-temperature deformation behavior of the Ti55531 alloy using hot compression test. Thus, the processing map is constructed to acquire the optimum processing conditions and the flow instability regions by using the experimental flow stress curves. Also, the Arrhenius constitutive equation is established to correlate the relationships among the stress, strain rate, temperature. Finally, the microstructural observation is used to determine the effect of deformation temperature and strain rate on the microstructure characteristics.

2 Experimental Procedure

The material used in this research was an as-forged block of Ti55531 alloy machined with a diameter of 360 mm. Figure 1 shows the initial microstructure image of the as-received material. It consists of a large number of globular α phase surrounded by soft β matrix. The β transus temperature (T_β) previously reported [10] for this alloy is 1076 K.

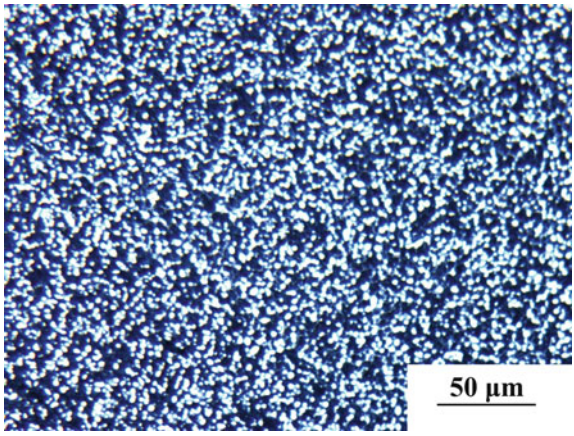


Fig. 1 The as-received material of Ti55531 where α phase is bright and β phase is dark. (Color figure online)

The hot deformation tests were conducted on a Gleeble-3500 machine using cylindrical specimens of 12 mm diameter and 8 mm length machined. Graphite lubricant was used between sample and anvil to reduce the temperature gradient and the interface friction. The compression tests were carried out at temperatures between 1003 and 1153 K with 30 K increment and at four strain rates from 0.001 to 1 s^{-1}, then up to true strain of 0.9. During the process, the samples were heated at 10 K/s to deformation temperature, held for 180 s, deformed, finally water quenched. All specimens were compressed in an isothermal environment and the deformation reduction was 60%. Finally, the processed specimens were cut along the load axis. The longitudinal section was mechanically polished under the standard metallographic procedure and etched in Kroll's reagent. Optical microscopy (OM) and scanning electron microscope (SEM) were carried out to characterize the microstructures.

3 Results and Discussion

3.1 Flow Behavior

The true stress–true strain curves of the Ti55531 alloy after hot deformation are shown in Fig. 2. It is apparent that the flow stress decreases with an increase in temperature and a decrease in strain rate. From Fig. 2a–d, it can be seen that the $\alpha + \beta$ field (1003–1063 K) stress–strain curves show larger degrees of flow softening than β field stress–strain curves. Following the peak stress, evident drops of flow stress curves are observed. When the hot deformation was carried out near or above β-transus, the curves exhibit almost constant flow, which suggests dynamic restoration processes (dynamic recrystallization or dynamic recovery) in operation. At the low-temperature cases of 1003 K, except for the high strain rate examined (1 s^{-1}), the flow curves exhibit strain hardening at low strains from 0.05 to 0.3. Moreover, at

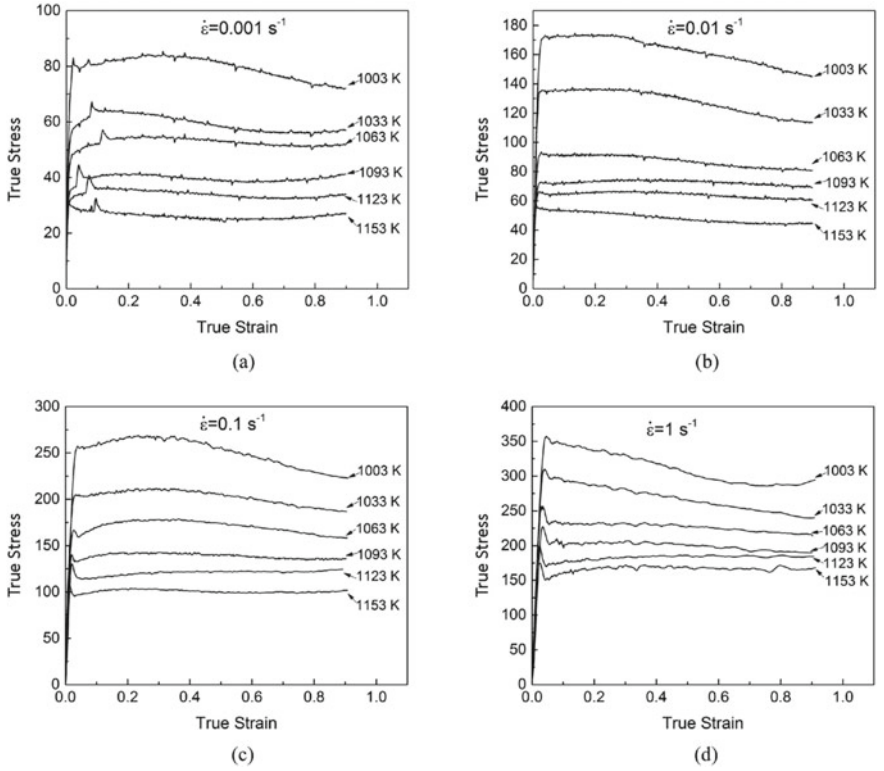


Fig. 2 True stress–true strain curves for the Ti55531 alloy deformed at strain rates of **a** 0.001 s^{-1}; **b** 0.01 s^{-1}; **c** 0.1 s^{-1} and **d** 1 s^{-1} at temperatures from 1003 to 1153 K

strain rates of 0.001 s^{-1} (Fig. 2a) and 1 s^{-1} (Fig. 2d), some curves also exhibit strain hardening at high strains. In addition, discontinuous yielding (a sharp initial peak stress) in the stress–strain curves is observed when the material was deformed at strain rates of 0.1 s^{-1} (Fig. 2c) and 1 s^{-1} (Fig. 2d). The discontinuous yielding phenomenon is consistent with the dynamic yield theory where the discontinuous yield behavior is related to sudden multiplication of mobile dislocations in grain boundaries [11]. As shown in Fig. 2c, d, the amplitude of yield drop increases with an increase in temperature, and this phenomenon is more distinct for deformation in β-phase field.

3.2 Constitutive Model

In this study, Arrhenius-type equations were used to depict the constitutive relationship among flow stress, temperature, and strain rate during hot deformation of the Ti55531 alloy, which can be expressed as follows [12, 13]:

$$\dot{\varepsilon} = A\sigma^{n'} \exp(-Q/RT), \alpha\sigma < 0.8 \tag{1}$$

$$\dot{\varepsilon} = A \exp(\beta\sigma) \exp(-Q/RT), \alpha\sigma > 1.2 \tag{2}$$

$$\dot{\varepsilon} = A[\sinh(\alpha\sigma)]^n \exp(-Q/RT), \text{ full all } \sigma \tag{3}$$

where, σ is the flow stress (MPa) for a given strain, $\dot{\varepsilon}$ is the strain rate (s^{-1}), T is the deformation temperature (K), Q is the apparent activation energy (kJ/mol), R is the gas constant (8.314 J/mol/K), n' and n are the stress exponent, A, α and β are the material constants.

Taking natural algorithms on both sides of Eqs. (1–3) respectively, then β, n', n, and α can be calculated at a constant temperature by following Eqs. (4–7), generally, the average slope values of the linear plots of $\ln\dot{\varepsilon}$ versus $\ln\sigma$ and $\ln\dot{\varepsilon}$ versus σ, n' and β respectively.

$$n' = \left.\frac{\partial \ln\dot{\varepsilon}}{\partial \ln\sigma}\right|_T \tag{4}$$

$$\beta = \left.\frac{\partial \ln\dot{\varepsilon}}{\partial \sigma}\right|_T \tag{5}$$

$$n = \left.\frac{\partial \ln\dot{\varepsilon}}{\partial \ln[\sinh(\alpha\sigma)]}\right|_T \tag{6}$$

$$\alpha = \beta/n'. \tag{7}$$

When the strain rate is a constant, the activation energy of the deformation process can be estimated by the average slope of the plot $\ln[\sinh(\alpha\sigma)]$ versus $1/T$ within the linear range, as shown in Eq. (8):

$$Q = nR \left.\frac{\partial \ln[\sinh(\alpha\sigma)]}{\partial(1/T)}\right|_{\dot{\varepsilon}}. \tag{8}$$

In addition, the coupling effect of temperature and strain rate on the hot deformation behavior is expressed by Zenere–Hollomon (Z) parameter as:

$$Z = \dot{\varepsilon}\exp(-Q/RT) \tag{9}$$

According to Eqs. (3) and (9),

$$Z = A[\sinh(\alpha\sigma)]^n \tag{10}$$

Then the Eq. (10) can be written as:

$$\ln Z = \ln A + n\ln[\sinh(\alpha\sigma)] \tag{11}$$

where ln$A$ is the intercept of the linear plots ln[sin$h(\alpha\sigma)$] versus ln$Z$.

To apply the Arrhenius constitutive model at different strains, a series of six-order polynomial regression functions (as shown in Eq. (12)) were employed to fit the relationship between material constants and strain [13].

$$\begin{cases} \alpha = B_6\varepsilon^6 + B_5\varepsilon^5 + B_4\varepsilon^4 + B_3\varepsilon^3 + B_2\varepsilon^2 + B_1\varepsilon + B_0 \\ Q = C_6\varepsilon^6 + C_5\varepsilon^5 + C_4\varepsilon^4 + C_3\varepsilon^3 + C_2\varepsilon^2 + C_1\varepsilon + C_0 \\ n = D_6\varepsilon^6 + D_5\varepsilon^5 + D_4\varepsilon^4 + D_3\varepsilon^3 + D_2\varepsilon^2 + D_1\varepsilon + D_0 \\ lnA = E_6\varepsilon^6 + E_5\varepsilon^5 + E_4\varepsilon^4 + E_3\varepsilon^3 + E_2\varepsilon^2 + E_1\varepsilon + E_0 \end{cases} \tag{12}$$

Finally, the Arrhenius-type equation can be expressed as:

$$\sigma = \frac{1}{g(\varepsilon)} \ln \left\{ \left(\frac{\dot{\varepsilon} \exp[j(\varepsilon)/8.314T]}{f(\varepsilon)} \right)^{1/h(\varepsilon)} + \left[\left(\frac{\dot{\varepsilon} \exp[j(\varepsilon)/8.314T]}{f(\varepsilon)} \right)^{2/h(\varepsilon)} + 1 \right]^{1/2} \right\}. \tag{13}$$

where $g(\varepsilon)$, $f(\varepsilon)$, $h(\varepsilon)$, $j(\varepsilon)$ are polynomial functions of strain for α, Q, n, ln$A$.

Figures 3 and 4 show the comparison between the predicted values using the above Arrhenius equation (Eq. (13)) and experimental values for the strain range of 0.05–0.9. These plots illustrate good correlations and the regression coefficients R2 were 0.99159 and 0.99801 for $\alpha + \beta$ and β field respectively. The absolute average relative errors (AARE, as defined in Eq. (14), calculated to quantitatively describe the accuracy of the Arrhenius equations, are 6.6571% and 3.7691%, respectively, meaning that this constitutive equation has a good predictive ability for this alloy.

$$\text{AARE} = \frac{1}{N} \sum_{i=1}^{N} \left| \frac{P_i - E_i}{E_i} \right| \tag{14}$$

where E_i is the experimental value and P_i is the predicted value, N is the number of data employed in present work.

3.3 Processing Maps

In last few decades, many researchers have studied the hot formability of titanium alloys by using processing maps based on the dynamic material model (DMM) developed by Prasad et al. [14, 15]. In that procedure, a visual map of formability

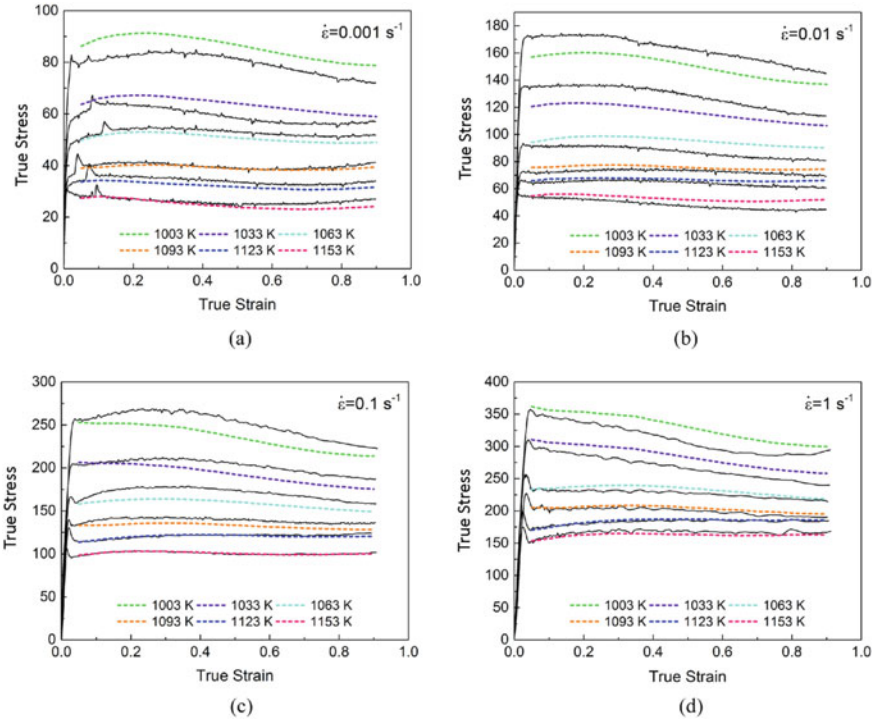


Fig. 3 The comparison between the values predicted by the Arrhenius equation and experimental values at different temperatures (1003–1153 K) and strain rates **a** 0.001 s^{-1}; **b** 0.01 s^{-1}; **c** 0.1 s^{-1}; **d** 1 s^{-1}. (Color figure online)

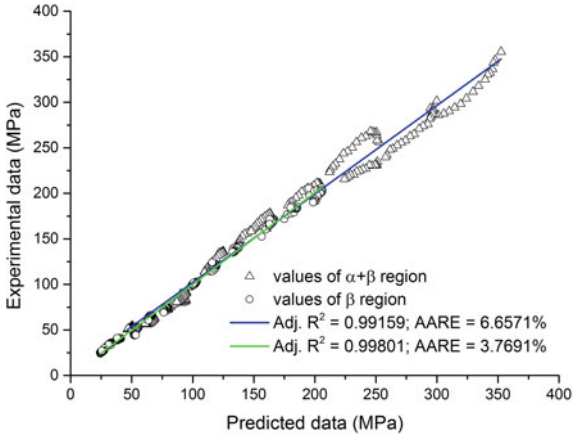


Fig. 4 The linear correlation relationships between predicted and experimental stress values. (Color figure online)

is developed to give an idea of deformation mechanism and processing window of a metallic material by using experimental flow stress. More details about DMM model are given by Refs. [6, 16, 17].

In general, the DMM model derives from the separation of the total power of dissipation P to two complementary parts, G associated with the plastic deformation and J related to microstructural changes [15]. The relation among them is shown as follows:

$$P = \sigma\dot{\varepsilon} = G + J = \int_0^{\dot{\varepsilon}} \sigma d\dot{\varepsilon} + \int_0^{\sigma} \dot{\varepsilon} d\sigma. \tag{15}$$

Furthermore, Eq. (16) defined the power positioning between G and J for the given temperature and strain, where m is the strain rate sensitivity.

$$\left.\frac{\partial J}{\partial G}\right|_{T,\varepsilon} = \left.\frac{\partial \ln\sigma}{\partial \ln\dot{\varepsilon}}\right|_{T,\varepsilon} \approx \left.\frac{\Delta \ln\sigma}{\Delta \ln\dot{\varepsilon}}\right|_{T,\varepsilon} = m. \tag{16}$$

The DMM processing map consists of two parameters, identified by the efficiency of power dissipation (η) and the instability parameter (ξ) [14, 18]. First, the efficiency of power dissipation (η) can be calculated by:

$$\eta = \frac{2m}{1+m}. \tag{17}$$

The flow instabilities can be predicted by the following equation:

$$\xi(\dot{\varepsilon}) = \frac{\partial \ln[m/(1+m)]}{\partial \ln\dot{\varepsilon}} + m < 0. \tag{18}$$

Then the variation of power dissipation efficiency (η) with strain rate and temperature constitutes a power dissipation map and the variation of instability parameter (ξ) constitutes an instability map. As a result, the DMM processing map is constructed by superimposing the instability map over the power dissipation map, where good hot formability is given by high η values and no instabilities.

The efficiency of power dissipation map with the superimposed instability values for different strains (0.05, 0.4, 0.6, 0.9) is plotted in Fig. 5. The values of η as a function of temperature and strain rate are given by Eq. (17), which is associated with the strain rate sensitivity $\left(m = \frac{\partial \log(\sigma)}{\partial \log(\dot{\varepsilon})}\right)$. As shown as the contour lines in Fig. 5, the highest η values (>0.5) are mostly observed at low temperature, T <1033 K, and low strain rate, $\dot{\varepsilon}$ <0.01 s^{-1}. As the deformation strain increases, there is no significant change in η values. Generally, high η values (0.35–0.55) indicate much less thermal dissipation during hot processing and more significant microstructural changes such as DRX, corresponding to good formability [19–22]. Thus, the power dissipation map in the present work can be divided into two areas: (I) the area with η <0.35, mostly at high strain rates (0.1–1 s^{-1}) over all test temperatures, which is

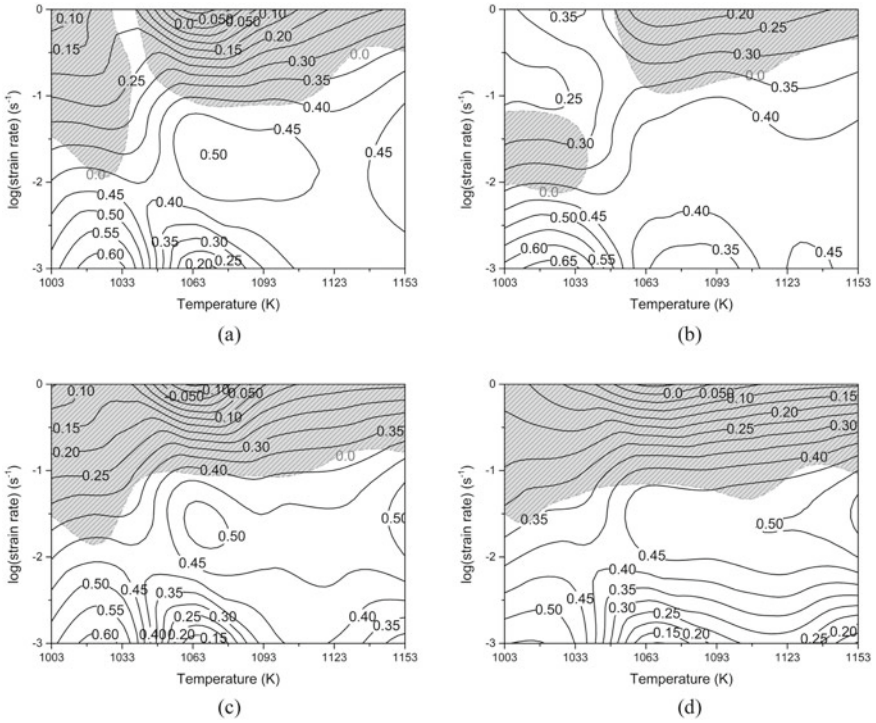


Fig. 5 The DMM processing maps of the Ti55531 alloy at strain of **a** 0.05, **b** 0.4, **c** 0.6 and **d** 0.9

consistent with the gray-shaded area in Fig. 5; (II) a relatively wide area of $0.35 < \eta < 0.55$, occurring at low to intermediate strain rates for all temperatures. Further microstructural verification is summarized in the next section.

3.4 Microstructure Observation

As depicted in Fig. 5, application of the DMM flow instability criteria ($\xi < 0$) results in two distinct regions with unstable/stable processing window for the hot deformation of the Ti55531 alloy. The flow stability region for this alloy was found at 0.001–0.1 s^{-1} and 1003–1153 K as well as the unstable flow regions are both shown as the gray-shaded areas in Fig. 5.

Figure 6 shows representative micrographs of the Ti55531 alloy under different deformation conditions. From Fig. 6a, it appears the serial growth of α grains along the direction of flow and somewhere a series with more than five grains. This phenomenon may be associated with persistent grain growth and annexation of α grains in the hot deformation process that is the typical dynamic recrystallization

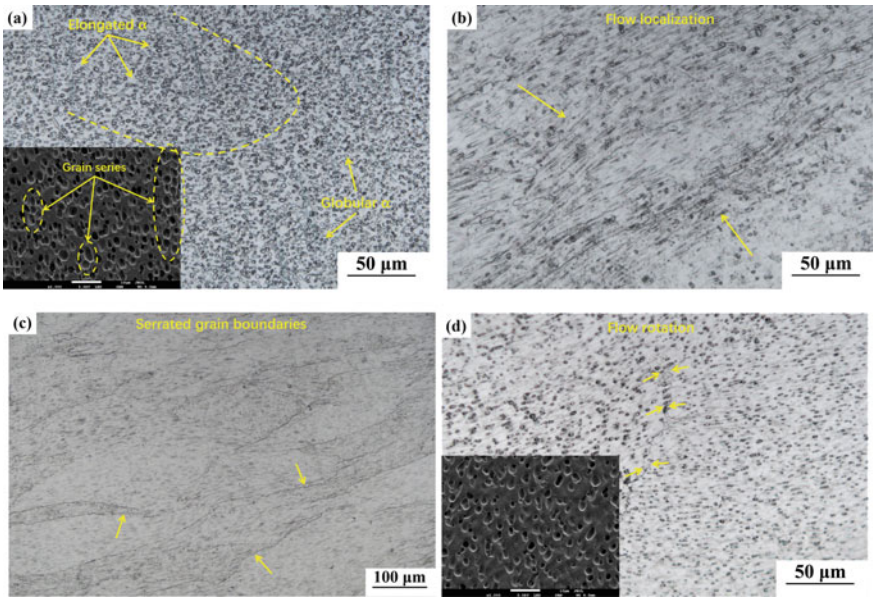


Fig. 6 The typical microstructures of the Ti55531 alloy in the flow instability region for **a** 1003 K, 1 s^{-1}; **b** 1123 K, 1 s^{-1}; **c** 1153 K, 1 s^{-1}; **d** 1093 K, 1 s^{-1}. (Color figure online)

feature. Moreover, it is noted from Fig. 6c that β grains are elongated and deformation bands are formed vertically to the compression direction. β grain boundaries become serrated as some small recrystallized β grains formed in the vicinity of grain boundaries. Generally, all of these processes are beneficial steps in producing the desired fine equiaxed grains for stable plastic flow [18, 23].

The efficiency of power dissipation under the flow instability region is relatively small (η <0.35). Catastrophic flow localization is observed at the temperature of 1123 K and the strain rate of 1 s^{-1} (Fig. 6b). From Fig. 6a, inhomogeneous distribution of α grains is observed, where elongated prior α grains are surrounded by globular α, which indicates slightly localized flow under this condition (1003 K, 0.1 s^{-1}). When the working temperature reached 1153 K (Fig. 6c), there are significantly flow localization zones in the samples, only elongated β with serrated grain boundaries are observed. In general, the flow localization occurs at relatively low temperatures or/and high strain rates due to a combination of microstructure changes and adiabatic heating below T_β. Flow localization is mainly caused by the lack of restoration processes as observed from the instability parameter φ values, which reached values between 5 and 35 [15, 24]. In addition, the other type of flow instability is also found in the microstructure. As shown in Fig. 6d, the sample deformed at 1093 K and 1 s^{-1} developed an evident change in the misorientation toward the grain boundaries during deformation, which represents the typical flow rotation feature. Obviously, these microstructure characteristics observed are consistent with that predicted from the processing maps (Fig. 5) and flow curves (Fig. 2). The flow instability caused by

flow localization or flow rotation is not beneficial for the workability and mechanical properties of materials. It needs to be avoided in the processing of the Ti55531 alloy.

4 Conclusions

The hot deformation behavior of the Ti55531 alloy in the $\alpha + \beta$ and single-β phase field was investigated to optimize the processing window and microstructure characterization. The following conclusions can be drawn:

(1) The flow stress of the Ti55531 alloy decreases with increase in temperature and a decrease in strain rate. Discontinuous yielding phenomenon is observed in the stress–strain curves when the material was deformed at strain rates of 0.1 and 1 s^{-1}. The amplitude of yield drop increases with an increase in temperature.

(2) Arrhenius equations were used to depict the constitutive relationship among flow stress, temperature, and strain rate during hot deformation of the Ti55531 alloy and were proved a good predictive ability.

(3) The DMM processing maps were constructed by superimposing the instability map over the power dissipation map for strains of 0.05, 0.4, 0.6, and 0.9. The efficiency of power dissipation (η) changes slightly with strain rates.

(4) The instability region according to DMM processing map appears at high strain rates ($\dot{\varepsilon}$ >0.1 s^{-1}) but for all test temperatures (1003–1153 K). The efficiency of power dissipation under these deformation conditions is relatively small (η <0.35), which represents the typical instability of flow localization and flow rotation. The optimum conditions for hot deformation were found to 0.001–0.1 s^{-1} and 1003–1153 K.

Acknowledgments The authors gratefully appreciate the financial support from the National Key Research and Development Program of China (Number 2018YFB1106504), Graduate Scientific Research and Innovation Foundation of Chongqing, China (Number CYB19005).

References

1. Weiss I, Semiatin SL (1998) Thermomechanical processing of beta titanium alloys—an overview. Mater Sci Eng A 243(1):46–65
2. Boyer RR, Briggs RD (2013) The use of beta titanium alloys in the aerospace industry. J Mater Eng Perform 22(10):2916–2920
3. Fan JK, Kou HC, Lai MJ, Tang B, Chang H, Li JS (2013) Characterization of hot deformation behavior of a new near beta titanium alloy: Ti-7333. Mater Des 49:945–952
4. Meng Q, Bai C, Xu D (2018) Flow behavior and processing map for hot deformation of ATI425 titanium alloy. J Mater Sci Technol 34(4):679–688
5. Jackson M, Jones NG, Dye D, Dashwood RJ (2009) Effect of initial microstructure on plastic flow behaviour during isothermal forging of Ti–10V–2Fe–3Al. Mater Sci Eng A 501(1–2):248–254

6. Prasad Y, Gegel HL, Doraivelu SM, Malas JC, Morgan JT, Lark KA, Barker DR (1984) Modeling of dynamic material behavior in hot deformation—forging of TI-6242. Metall Trans A 15(10):188
7. Bao RQ, Huang X, Cao CX (2006) Deformation behavior and mechanisms of Ti-1023 alloy. Trans Nonferrous Met Soc China 16(2):274–280
8. Seshacharyulu T, Medeiros SC, Frazier WG, Prasad Y (2000) Hot working of commercial Ti–6Al–4V with an equiaxed alpha-beta microstructure: materials modeling considerations. Mater Sci Eng A 284(1–2):184–194
9. Zhao Y, Ge P, Yang G, Zhao Y, Mao X (2009) Forging simulation of Ti-1300 alloy by hot compressing testing. Rare Met Mater Eng 38(3):550–553
10. Warchomicka F, Poletti C, Stockinger M (2011) Study of the hot deformation behaviour in Ti–5Al–5Mo–5V–3Cr–1Zr. Mater Sci Eng A 528(28):8277–8285
11. Philippart I, Rack HJ (1998) High temperature dynamic yielding in metastable Ti–6.8Mo–4.5Fe–1.5Al. Mater Sci Eng A 243(1–2):196–200
12. Long S, Xia YF, Hu JC, Zhang JS, Zhou J, Zhang P, Cui ML (2019) Hot deformation behavior and microstructure evolution of Ti–6Cr–5Mo–5V–4Al alloy during hot compression. Vacuum 160:171–180
13. Quan Gz, Pan J, Wang X (2016) Prediction of the hot compressive deformation behavior for superalloy nimonic 80A by BP-ANN model. Appl Sci Basel 6(3)
14. Ma LX, Wan M, Li WD, Shao J, Bai XP (2019) Constitutive modeling and processing map for hot deformation of Ti–15Mo–3Al–2.7Nb–0.2Si. J Alloy Compd 80:13
15. Dikovits M, Poletti C, Warchomicka F (2014) Deformation mechanisms in the near-β titanium alloy Ti-55531. Metall Mater Trans A 45(3):1586–1596
16. Long S, Xia Y, Wang P, Zhou Y, Gong-ye F, Zhou J, Zhang J, Cui M (2019) Constitutive modelling, dynamic globularization behavior and processing map for Ti–6Cr–5Mo–5V–4Al alloy during hot deformation. J Alloy Compd 796:65–76
17. Murty SVS, Rao BN, Kashyap BP (2000) Development of a processing map for the hot working of Ti–25Al–15Nb. Z Metallk 91(9):769–774
18. Tan YB, Duan JL, Yang LH, Liu WC, Zhang JW, Liu RP (2014) Hot deformation behavior of Ti–20Zr–6.5Al–4V alloy in the α+β and single β phase field 609:226–234
19. Peng X, Guo H, Shi Z, Qin C, Zhao Z, Yao Z (2014) Study on the hot deformation behavior of TC4-DT alloy with equiaxed α+β starting structure based on processing map. Mater Sci Eng A 605:80–88
20. Liang HQ, Nan Y, Ning YQ, Li H, Zhang JL, Shi ZF, Guo HZ (2015) Correlation between strain-rate sensitivity and dynamic softening behavior during hot processing. J Alloy Compd 632:478–485
21. Quan Gz, Wang Y, Yu Ct, Zhou J (2013) Hot workability characteristics of as-cast titanium alloy Ti–6Al–2Zr–1Mo–1V: a study using processing map. Mater Sci Eng A 564:46–56
22. Quan GZ, Lv WQ, Liang JT, Pu SA, Luo GC, Liu Q (2015) Evaluation of the hot workability corresponding to complex deformation mechanism evolution for Ti–10V–2Fe–3Al alloy in a wide condition range. J Mater Process Technol 221:66–79
23. Li X, Lu SQ, Fu MW, Wang KL, Dong XJ (2010) The optimal determination of forging process parameters for Ti–6.5Al–3.5Mo–1.5Zr–0.3Si alloy with thick lamellar microstructure in two phase field based on P-map. J Mater Process Technol 210(2):370
24. Ma X, Zeng W, Xu B, Sun Y, Xue C, Han Y (2012) Characterization of the hot deformation behavior of a Ti–22Al–25Nb alloy using processing maps based on the Murty criterion. Intermetallics 20(1):1–7

Part XVIII
Mini-Symposia Characterization of Plasticity and Ductile Fracture of Metals under Proportional and Non-proportional Loading

Establishment of Sheet Plastic Wrinkling Instability WLD and Study on Strain Distribution Characteristics in Instability Region



Bing Du, Han Li, Jun Xie, Pengfei Song, and Changcai Zhao

Abstract In the field of thin-plate plastic forming, the efficient and accurate prediction and control of wrinkles are the basis for product and mold design and process flow formulation. In this paper, a diagonal tensile test of a square plate is taken as an example, and a numerical simulation model for plastic wrinkle analysis of a thin plate is established by using ABAQUS. On this basis, the morphology and characteristics of the critical wrinkle main strain diagram (WLD) under the condition of nonuniform tension are investigated. The distribution position relationship between the strain value at different positions in the deformation region of the specimen and the critical wrinkle main strain curve (WLD) is discussed. The research content of this paper provides ideas for determining the wrinkle instability and establishing the wrinkle critical line under other various bearing conditions.

Keywords Sheet forming · Wrinkle instability · Square plate diagonal stretching · Numerical simulation · Wrinkle instability threshold

1 Introduction

For the design of products and molds, the establishment of technological processes, improving the forming quality and production efficiency of parts, it is very important to how to efficiently and accurately predict and control the wrinkle instability and clarify the relationship between wrinkling instability and forming process parameters. The extensive use of the forming limit diagram (FLD) for the determination of fracture instability has provided ideas for the study of the wrinkle limit diagram (WLD) and stimulated the academic community to study the critical wrinkling curve of sheet forming. Jasion et al. [1] performed analytical, numerical, and experimental studies of the global and local buckling/wrinkling of the face sheets of sandwich beams and sandwich circular plates and developed a mathematical model for displacements that included a shear effect. Jasion's work also derived governing

B. Du (✉) · H. Li · J. Xie · P. Song · C. Zhao
Key Laboratory of Advanced Forging Stamping Technology and Science, Yanshan University, Ministry of Education of China, Qinhuangdao City 066004, China
e-mail: pangpang115@ysu.edu.cn

© The Minerals, Metals & Materials Society 2021

G. Daehn et al. (eds.), *Forming the Future*, The Minerals, Metals & Materials Series,
https://doi.org/10.1007/978-3-030-75381-8_162

differential equations for sandwich plates and solved these equations analytically to obtain critical loads. Liewald et al. [2] obtained wrinkle limit curves experimentally using the improved YBT as well as the cone cup drawing test and found some differences between the results. Wang et al. [3] used Hill's general theory of uniqueness and bifurcation to model local wrinkling phenomena and proposed wrinkling criteria for plastic anisotropic shells with compound curvatures. Triantafyllidis [4] developed a suitable bifurcation criterion and a phenomenological corner theory to investigate wrinkling instability during the cup convex test. Based on this bifurcation theory, Kim et al. [5] generated WLDs for anisotropic sheet metals subjected to plane stress and determined the effects of the strain hardening coefficient, yield stress, anisotropy coefficient, and sample thickness on critical wrinkling stress in two-dimensional stress space. Similar to an FLD, the main use of a WLD is to predict wrinkling instability through analyzing the in-plane critical principal strain index of a thin shell and to establish a curve that defines the safety, critical, and instability intervals. This conversion of the internal mechanism of thin shell material wrinkling into the apparent numerical relationship of principal strains is more convenient for engineering applications.

In the present work, the YBT (Yoshida Buckling Test) was used during comparative verification experiments to establish a dynamic explicit numerical analysis model for shell elements incorporating initial defects. Based on the above, real-time visual monitoring of the deformation of test specimens was employed to investigate the morphology and characteristics of critical wrinkle principal strain curves (that is, WLDs) generated during the application of nonuniform tension. The simulated WLD is compared with the experimental WLD. The WLD obtained by the two methods is basically the same. This shows that WLD has very good reliability. Moreover, the wrinkle on the test piece can be determined by the strain distribution, and the strain located below the WLD is considered to be the wrinkled zone. The innovation of this method is that it is inspired by FLD, and analogizes the problem of wrinkling instability to the problem of rupture instability, and establishes WLD (i.e. critical wrinkle main strain curve). The determination method of wrinkle instability was explored, that is, the state at different times in the forming process was judged according to the principal strain value curve.

2 Research Process and Methods

In this work, we used the buckling mode in conjunction with eigenvalue buckling analysis as the disturbance source, to perturb a so-called ideal calculation model in the Explicit algorithm. A nonlinear buckling analysis was then employed to investigate the reliability of the buckling analysis results obtained using this method. Figure 1 summarizes the specific analysis process. In this section, we will use the wrinkling instability numerical analysis model established in reference [6] to explore the existence of WLD under uneven tensile load properties, the morphology, and the relative

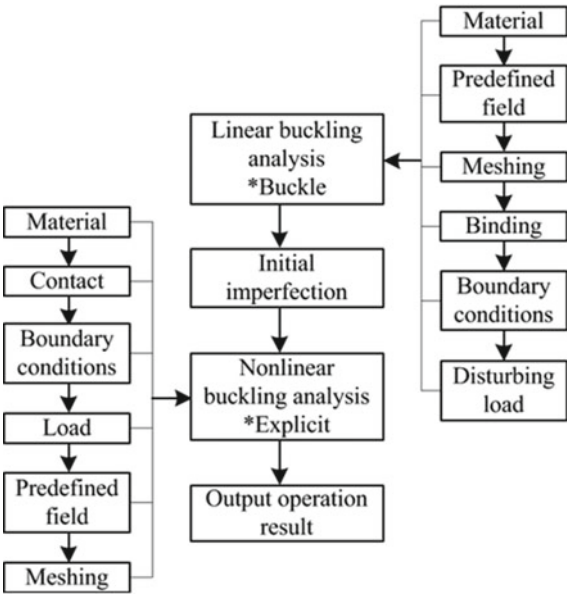


Fig. 1 A flow chart summarizing the nonlinear buckling analysis of sheet metal forming

relationship between the strain value at different locations of wrinkle and WLD And other issues.

WLD is similar to an FLD, a WLD is a curve composed of critical wrinkling strains at the initial positions of wrinkling instability for various stress paths. However, unlike an FLD, the combination of in-plane principal stress states leading to wrinkling instability must include at least one principal compressive stress. Therefore, the critical instability strains will only be distributed in the second principal strain space quadrant. Five models, with plate thicknesses t of 1 mm and side lengths l of 95, 100, 105, 110, and 115 mm, were created, as shown in Fig. 2, and the wrinkling simulation was performed using dynamic numerical simulations of buckling.

On the definition of critical instability in numerical simulation, this paper uniformly defines the vertical distance between the highest point of the wrinkle center and the lowest point of the plate boundary as the wrinkle height. In addition,

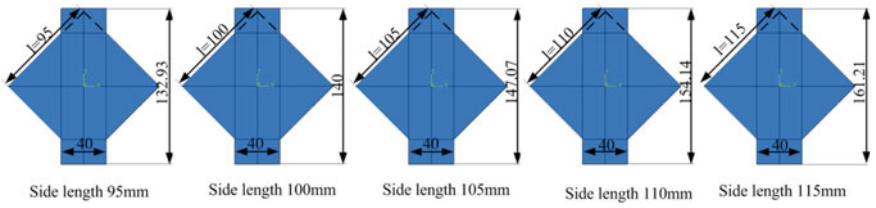


Fig. 2 Buckle-explicit simulation analysis model under different geometric sizes. (Color figure online)

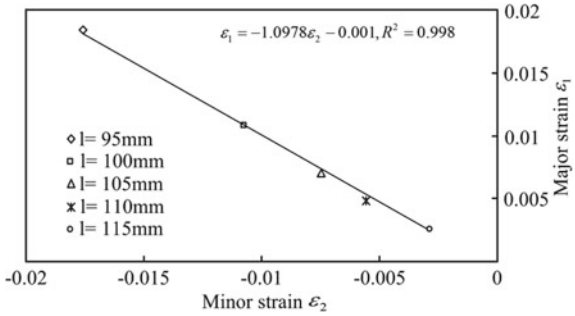


Fig. 3 The WLD generated for 304 stainless steel

the moment at which the wrinkle height equals 10% of the sheet thickness (having a value of 0.1 mm) is considered to indicate the critical wrinkling moment for the specimen. The in-plane critical wrinkle strain of the five model specimens in Fig. 2 at this moment was extracted and plotted in the main strain space for curve fitting, as shown in Fig. 3.

Figure 3 confirms that a critical strain curve for the wrinkling instability of the sheet under uneven tension conditions can be constructed. It is also evident from the equation of the curve that this plot describes a straight line located in the second quadrant and approximately passing through the origin (0, 0), with a slope of approximately −1.

3 Results and Discussion

In order to verify the validity of the WLD obtained by the numerical analysis above, the true plastic wrinkling and instability mechanism of the sheet was obtained through the test strain data of the test piece. The VIC-3D non-contact full-field strain measurement system is used to measure and process the strain data of the 304 stainless steel test specimens of typical size and thickness during the tensile process, as shown in Fig. 4a–c. The strain development trajectories at instability point A for each specimen under the three different combinations of side lengths and thicknesses were extracted during the tensile testing of the square plates (as shown in Fig. 4d). It should be noted that, when the test piece entered the post-buckling stage, the strain trajectory at point A on the upper and lower surfaces of the specimen is bifurcated. This occurred because buckling caused the surface on the side associated with the warping direction of the test piece to be compressed in the horizontal direction at point A, while the tension at the same point on the opposite side was gradually increased. Therefore, the strain trajectories on the upper and lower surfaces at point A gradually deviated. Consequently, the bifurcation point of the strain trajectories at point A on the upper and lower surfaces corresponded to the critical wrinkling strain point for the specimen. Based on the order of the three sets of strain trajectory bifurcation points, the critical buckling order for the three operating conditions can be

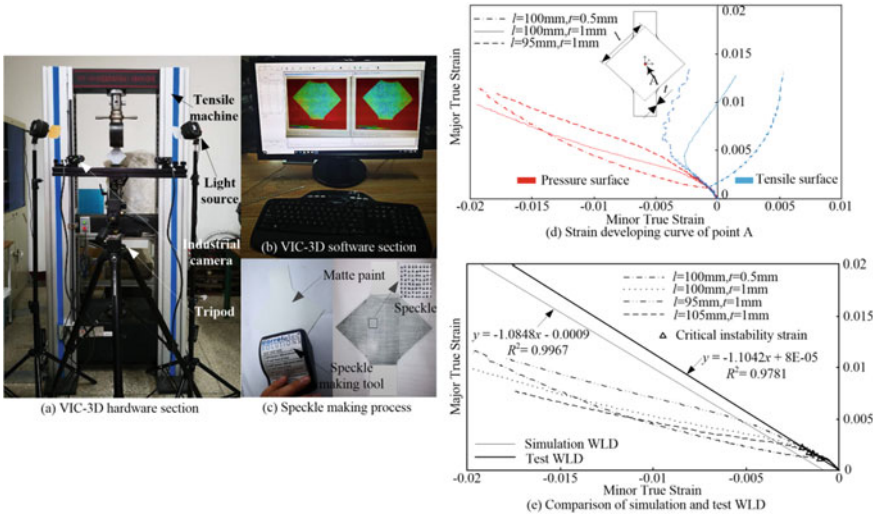


Fig. 4 Test methods and data extraction. (Color figure online)

determined. It can be seen that a smaller side length and greater thickness postpones the onset of instability, which is in complete agreement with the numerical analysis results.

The strain trajectories of point A on the compression surface and their bifurcation points with the tension surface trajectory were extracted under four geometric conditions, and these bifurcation points were used to fit the test WLD, after which the simulated and experimental WLD plots were compared (The results are shown in Fig. 4e). This comparison established that the discrepancy between the simulated and experimental WLDs was only approximately 0.58%, indicating that the WLD obtained by numerical simulations was sufficiently reliable.

When the wrinkle height of the square plate specimen with a side length of 100 mm and a thickness of 0.5 mm reached 9.5 mm, 10 typical positions of the wrinkle area were selected to examine the strain distribution characteristics, as shown in Fig. 5. The 10 observation points on the compressive surface were labeled 1–10 while the relative positions on the tensile surface were identified as 1′ to 10′. The primary and secondary strains at the observation points at the unbuckling and buckling moments (shown in Fig. 5a, b) were all extracted and drawn in the principal strain space, after which they were compared with the simulated WLD (see Fig. 5c). This figure confirms that the strains in the wrinkling areas on the upper and lower surfaces of the specimen overlapped when the test piece was not buckling, and were located near the zero point above the WLD. With the development of buckling, the strain values at different locations were gradually dispersed and exhibited highly regular distributions. The strains on the compressive surface were located below the WLD and along the longitudinal section of the wrinkle, while the absolute values of the

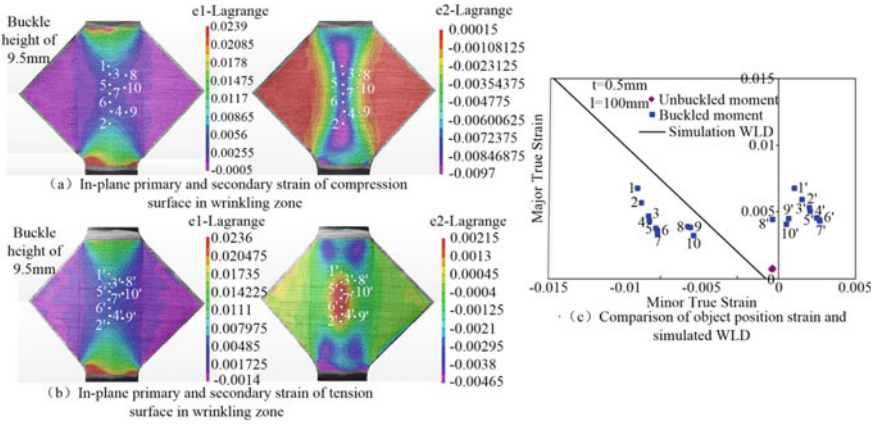


Fig. 5 Strain characteristics of sheet wrinkled zone. (Color figure online)

direction 2 strains at both ends of the wrinkling area were higher than in the central zone.

These results are attributed to differences in cross-sectional areas at the monitoring points. A smaller cross-sectional area at the monitoring point will increase the longitudinal tensile stress. Consequently, the lateral shrinkage of the material will be greater and the corresponding horizontal compressive stress will increase so that the absolute values of the direction 2 strains will also be larger. In contrast, the strains on the tensile surface of the specimen were distributed over the WLD but primarily located in the first quadrant of the double tensile strain space. The numerical distribution trend, in this case, was the same as on the pressure surface. It is also noteworthy that the above rule appears to be less consistent in the case of the transverse compressive strains for the three points 8′, 9′, and 10′ located in the longitudinal wrinkle edge region. This may have resulted from blockage of the transmission of in-plane compressive stress by the wrinkle.

The above figure demonstrates that the strains in the wrinkling area on the compressive surface of the specimen were located below the WLD after buckling, which may be significant with regard to predicting the wrinkling state of the piece. To clarify the meaning of this finding, it is necessary to further analyze the distribution characteristics of strains in the remaining areas on the compressive surface in the principal strain space. As well, to ensure the universality of the analysis results, the strain data on the compressive surface of the specimen under four geometric conditions were extracted for analysis. The test strain cloud map was divided into three zones according to color: the buckled, critical, and unbuckled zones. Some points distributed across the three regions were randomly chosen and the primary and secondary strains associated with these points were output in principal strain space and then compared with the simulated WLD, as shown in Fig. 6.

It can be seen from Fig. 6 that the strain distribution characteristics of the specimen under different geometric conditions after entering the buckling state were the same.

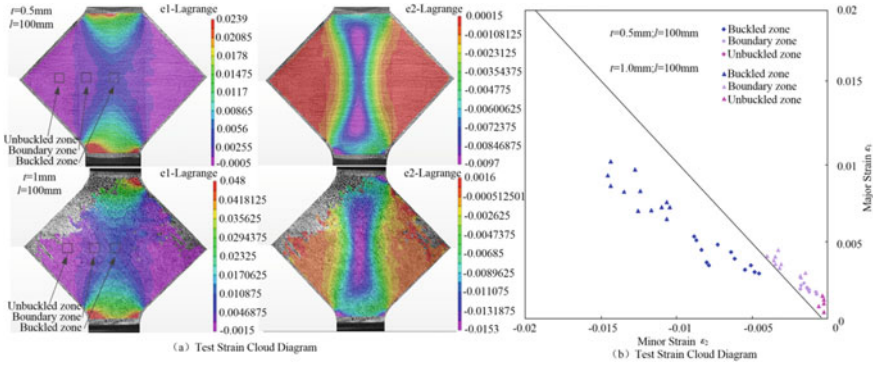


Fig. 6 Strain cloud diagrams for the buckling compression surfaces and the strain of varying zone distributions in principal strain space for specimens. (Color figure online)

The strains in the buckled zone were all below the WLD, while the strains in the critical zone were greater than the strains in the unbuckled zone and both were above the WLD. Increasing the wall thickness gradually moved the strains in the buckled zone away from the ordinate origin such that they spread out. This outcome indicates that changes in the geometrical conditions enhance the uniform deformation of the specimen, such that the occurrence of wrinkling instability is delayed. A change in the shape of the central purple region representing the buckled zone can be clearly observed by comparing the secondary strain clouds. The data show that decreasing the side length and increasing the wall thickness gradually moves the wrinkle away from the clamping end of the specimen in the longitudinal direction. The cross-sectional shape of the wrinkle also became more uniform in the lateral direction.

It is determined from the above analysis that the strain distribution on the buckling compression surface of the test piece can be used to ascertain the wrinkle position on the test piece. Specifically, the region over which the strain is located below the WLD corresponds to the wrinkling instability zone.

4 Conclusions

1. A comparison of simulated and experimental WLDs shows that the disagreement between the two is approximately 2%, indicating that the WLD obtained by the numerical simulation method is sufficiently reliable.
2. The position at which wrinkles appear on a specimen can be determined from the strain distribution on the buckling compression surface of the test piece. The corresponding area where the strains are located below the WLD represents the wrinkling instability zone.

References

1. Jasion P, Magnucka-Blandzi E, Szyc W, Magnucki K (2012) Global and local buckling of sandwich circular and beam-rectangular plates with metal foam core. Thin Walled Struct 61:154–161
2. Liewald M, Han F, Radonjic R (2015) New criterion for prediction of the wrinkle formation in deep drawing process. Key Eng Mater 651–653:71–76
3. Wang CT, Kinzel G, Altan T (1994) Wrinkling criterion for an anisotropic shell with compound curvatures in sheet forming. Int J Mech Sci 36(10):945–960. https://doi.org/10.1016/0020-7403(94)90056-6
4. Triantafyllidis N (1985) Puckering instability phenomena in the hemispherical cup test. J Mech Phys Solids 33(2):117–139. https://doi.org/10.1016/0022-5096(85)90026-2
5. Kim Y, Son Y (2000) Study on wrinkling limit diagram of anisotropic sheet metals. J Mater Process Technol 97(1):88–94
6. Bing D, Fenglong G, Pengfei S, Zhaojian H, Xin Z, Changcai Z (2018) Numerical simulation methods of sheet metal wrinkling instability problem. J Mech Eng 54(24):42–50

Plasticity and Fracture Characterization of Advanced High-Strength Steel: Experiments and Modeling



Fei Han, Changwei Lian, Jichao Zhang, and Haomin Jiang

Abstract As one of the means of lightweight, more and more ultra-high-strength steel (UHSS) has been applied to the car body. Plasticity and fracture behavior of UHSS under a complex stress state is the key to accurate simulation of forming process and crash. In order to describe the various hardening exponent that lies with the advanced high strength steels, a new hardening law of Modified Power Law (MPL) was proposed and validated for the newly developed high elongation quench & partition steel (QP1180-EL) by Baosteel. Different loading conditions, including shear, uniaxial tension, plane strain tension, and biaxial tension were conducted with the help of digital image correlation technology to test the fracture limit of QP1180-EL under various stress states. Based on testing results and numerical simulation, Modified Mohr–Coulomb (MMC) fracture model and Generalized Incremental Stress State Dependent Model (GISSMO) were calibrated and validated. The research results will provide guidance for parts design and structural performance evaluation in the application of ultra-high-strength steel.

Keywords Ultra-High-Strength Steel · Hardening · Fracture · Damage · Digital Image Correlation

1 Introduction

Advanced high-strength steel materials have been widely used in the automotive industry in recent years due to the advantage of improved crash energy absorption. With the increase in strength, ductility of traditional high-strength steel materials decreases, posing challenges to the forming process and the crash safety of the vehicle. In order to accurately predict the failure behavior of advanced high-strength

F. Han (✉) · C. Lian · J. Zhang · H. Jiang
Baoshan Iron & Steel Co., Ltd, 655 Fujin Road, Shanghai 201900, China
e-mail: hanfei@baosteel.com

State Key Laboratory of Development and Application Technology of Automotive (Baosteel), Shanghai, China

© The Minerals, Metals & Materials Society 2021

G. Daehn et al. (eds.), *Forming the Future*, The Minerals, Metals & Materials Series,
https://doi.org/10.1007/978-3-030-75381-8_163

steel materials, an accurate hardening, failure criteria and damage accumulation model need to be established.

The hardening model is the most important factor for accurate simulation of forming and crash process. Uniaxial tensile test is widely used to generate experimental stress–strain data due to its convenience. Because of the edge effect, strain data from uniaxial tensile tests are limited to a certain level, which is much lower than the maximum equivalent plastic strain appearing in metal forming and under crash testing. There are two kinds of hardening models widely used for steel. One is power law like Hollomon [1] and Swift [2]. The other is saturation models like Voce and Hockett–Sherby [3]. There is a significant difference by extrapolating the experimentally stress–strain curve to larger strain values with assuming constitutive equations [4]. To overcome the limitation of uniaxial tensile test, other test methods used to obtain stress–strain curve under larger strain were proposed, including hydraulic bulge test [5, 6] and in-plan torsion test [7]. Combinations of models such as the Swift–Voce or Swift/Hockett–Sherby models were used to yield better fitting result [5], but more parameters need to be calibrated.

Fracture criteria can be divided into two types: one is the micro-cavity development theory based on the continuum mechanics, and the other is the semi-empirical failure criterion based on the fracture strain. The second failure criterion is widely embedded in general commercial software since its failure parameters can be more easily determined through tests [8]. Johnson and Cook fracture proposed the Johnson–Cook fracture criteria where fracture strain is function of triaxiality [9]. Recently, modified Mohr–Coulomb model was proposed by Bai and Wierzbicki [10]. Dependence of triaxiality and lode angle for the fracture strain is considered and good fracture prediction results have been achieved for various metal materials. The Generalized Incremental Stress State Dependent Model (GISSMO) was developed by Neukamm et al. [11, 12], which takes into account the damage evolution and fracture dependence on triaxiality and Lode parameter. GISSMO damage model is implemented in the LS-DYNA solver and widely used in the automotive industry to predict material failure in crash simulation.

In this paper, the hardening behavior of QP1180-EL steel was studied and a new modified power law hardening model was proposed to improve extrapolation accuracy. DIC method was used to measure fracture strain under different stress state and MMC fracture criteria as well as GISSMO damage model were calibrated based on experiment results. Three-point bending test was conducted to validate MPL hardening model and GISSMO damage model.

2 Hardening Behavior Under Large Strain

2.1 Modified Power Law Hardening Model

Table 1 lists common hardening model equations with true stress σ, true plastic strain ε, and corresponding parameters. The strain hardening exponent n, which represents material's hardening rate, was used in different models.

There is often a large deviation between experimental hardening data and predicted results. One of the key reasons is the difference in the hardening characteristics of the material. DC56D+ZF (mild steel), HC220B (bake-hardening steel), QP1180-EL (quench & partition steel) were chosen to calculate n value within uniform deformation range respectively using Hollomon respectively. As shown in Fig. 1, instantaneous n value varies with plastic strain developing, especially for high strength steels, indicating that it cannot be well described when extrapolating to larger strain using constant n value.

To improve the modeling accuracy of high strength steels with non-constant n value, modified power law model with adjustable parameter is provided based on power law, where λ_H is a new parameter, expressed as follows:

$$\sigma = k(\varepsilon_0 + \lambda_H \varepsilon)^n. \tag{1}$$

Table 1 Equations of different hardening models

Model	Equation	No. of Parameters
Hollomon	$\sigma = k_H(\varepsilon)^{n_H}$	2 (k_H, n_H)
Swift	$\sigma_{\text{Swift}} = k_s(\varepsilon_0 + \varepsilon)^{n_s}$	3 $(k_s, \varepsilon_0, n_s)$
Hockett–Sherby	$\sigma_{H-S} = \sigma_{\text{sat}} - (\sigma_{\text{sat}} - \sigma_0)\exp(-m\varepsilon^n)$	4 $(\sigma_{\text{sat}}, \sigma_0, m, n)$
Combine Swift/H–S	$\sigma = (1-\alpha)\sigma_{\text{Swift}} - \alpha\sigma_{H-S}$	8 $(\alpha, k_s, \varepsilon_0, n_s, \sigma_{\text{sat}}, \sigma_0, m, n)$

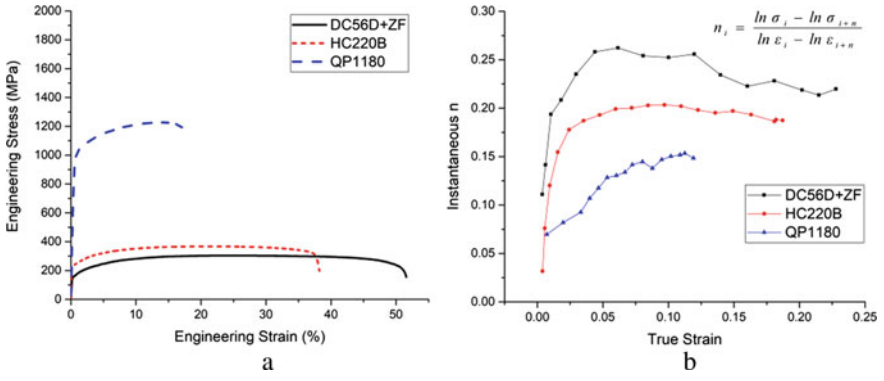


Fig. 1 Engineering stress–strain curve (left) and instantaneous n versus true strain (right). (Color figure online)

Considering the strain hardening trend of high-strength steels, λ_H is defined as Eq. (2). When $\alpha = 0$, it is equivalent to the Swift equation. When $\alpha > 0$, it can well correct the decrease of instantaneous n value at larger plastic strains by varying a value.

$$\lambda_H = \frac{1}{1 + \alpha\varepsilon}. \tag{2}$$

2.2 Test and Calibration of QP1180-EL

QP steel is a typical third-generation advanced high-strength steel. With both high strength and high plasticity, it can meet the needs of automotive users for high-performance ultra-high-strength steel and provide support for the lightweight development of the automotive industry. Baosteel has become the first steel company in the world capable of producing first, second, and third generation advanced high-strength steels in batches. Table 2 shows the tensile properties of QP1180-EL steel at the thickness of 1.2 mm. The valid range of stress–strain curve obtained from uniaxial tensile test is up to the uniform elongation 0.11 (true strain), while the rest need to be extrapolated.

Based on the uniaxial tensile test data, Swift, Hockett–Sherby, and MPL models were used to fit and extrapolate the stress–strain curve. All three models give a relative good fit result but have large differences under large strain, which are shown in Fig. 2.

Table 2 Tensile properties of QP1180-EL steel

Steel grade	Yield strength (MPa)	Tensile strength (MPa)	Uniform elongation (%)	Total elongation (%)
QP1180-EL	896	1179	11.5	16.3

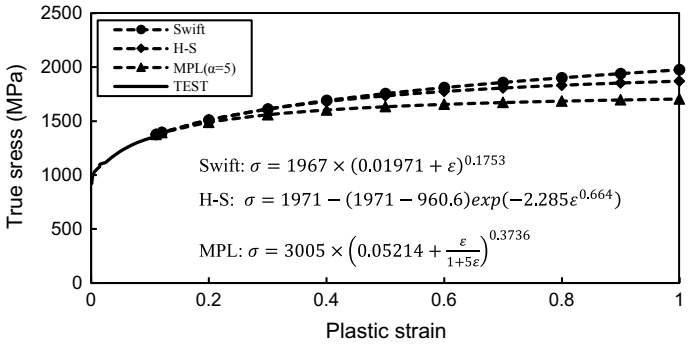


Fig. 2 Extrapolation result of different hardening models

According to the experimental conditions, uniaxial tensile simulation model is established, using the three hardening curve stated above. The results of the experimental and simulated force–displacement curves are shown in Fig. 3. The results show that the MPL model can improve the prediction results of the hardening behavior under large strain.

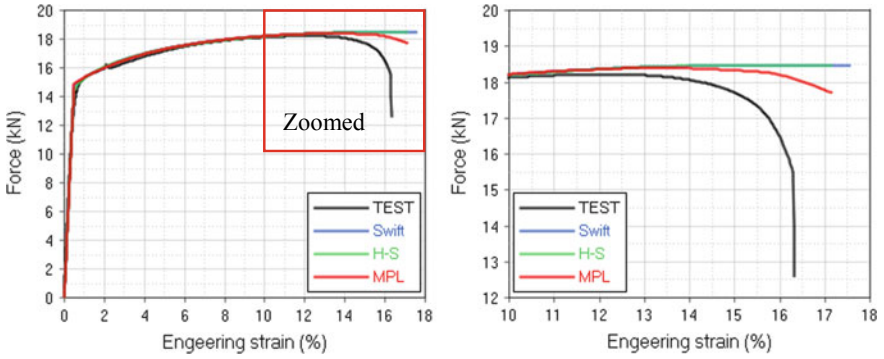


Fig. 3 Force–displacement simulation result of different hardening models. (Color figure online)

3 Damage Behavior Under Complex Stress States

3.1 Damage Accumulation and Fracture Limit Characterization

Most of the ductile fracture models are based on the idea of damage. According to whether the accumulation of damage during the deformation process affects the mechanical response of the material, common ductile fracture models can be divided into two types: coupled damage models and uncoupled fracture models. These two types of ductile fracture models have been widely used in academia and industry [8]. Uncoupled ductile fracture models usually use failure strain as a weight function to integrate equivalent plastic strain and define it as a damage factor:

$$D = \int_0^{\overline{\varepsilon}_f} \frac{d\varepsilon_p}{\overline{\varepsilon}_f(\sigma, \varepsilon, \dot{\varepsilon}, \ldots)} \tag{3}$$

where $d\varepsilon_{\mathrm{p}}$ is equivalent plastic strain increment, and ε_f is the equivalent plastic strain at fracture, which is function of stress tensor σ, strain tensor ε, and strain rate tensor $\dot{\varepsilon}$.

In recent years, research on the fracture behavior of ductile materials shows that stress triaxiality and lode angle are considered to be the key parameters affecting ductile fracture limit. The most influential research work comes from Wierzbicki T (Modified Mohr–Coulomb model). Bai Y. and Wierzbicki T. converted the Mohr–Coulomb model from stress space to equivalent plastic strain, stress triaxiality, and lode angle parameters $\{\varepsilon_f, \eta, \theta\}$, and established a Modified Mohr–Coulomb (MMC) model [10]. The basic formula is as follows:

$$\overline{\varepsilon}_f = \left\{ \frac{A}{c_2}\left[c_3 + \frac{\sqrt{3}}{2-\sqrt{3}}(1-c_3)\left(\sec\frac{\pi\overline{\theta}}{6} - 1\right)\right] \times \left[\sqrt{\frac{1+c_1^2}{3}}\cos\frac{\pi\overline{\theta}}{6} + c_1\left(\eta + \frac{1}{3}\sin\frac{\pi\overline{\theta}}{6}\right)\right]\right\}^{-\frac{1}{n}} \tag{4}$$

where η is stress triaxiality and $\overline{\theta}$ is normalized Lode angle, A, n are parameters related to material hardening rule and c_1, c_2, c_3 are parameters that need to be determined from fracture test.

The Generalized Incremental Stress State Dependent Model (GISSMO) was and developed by Neukamm et al. [11] and later formally presented in more detail by Andrade et al. [13]. Damage accumulation ΔD is calculated at every time step, given by:

$$\Delta D = \frac{DMGEXP}{\mathrm{reg}(L_e, \eta) \times \overline{\varepsilon}_f(\eta, \theta)} D^{\left(\frac{DMGEXP-1}{DMGEXP}\right)} \Delta\varepsilon_p \tag{5}$$

where *DMGEXP* is the damage accumulation exponent. In crash simulation application, element size is usually limited to 2–5 mm in order to reach a balance between reasonable prediction results and overall calculation time. To deal with the influence of mesh size on fracture behavior, a regularization function reg(L_e, η) is introduced, which defines the fracture limit reduction coefficient between element size L_e and stress triaxiality η. Another index instability, which describes the onset of diffuse necking, is also considered in GISSMO model and is calculated similar to the damage accumulation:

$$\Delta F = \frac{DMGEXP}{\overline{\varepsilon}_{\text{ins}}(\eta, \theta)} F^{\left(\frac{DMGEXP-1}{DMGEXP}\right)} \Delta\varepsilon_p. \tag{6}$$

As soon as the instability F reaches unity, the current value of damage D_{crit} in the respective element is stored and damage will from this point on be coupled to the flow stress using the following relation:

$$\sigma = \tilde{\sigma}\left(1 - \left(\frac{D - D_{\text{crit}}}{1 - D_{\text{crit}}}\right)^{FADEXP}\right). \tag{7}$$

The GISSMO damage/failure model is implemented in LS-DYNA solver and can be activated by setting IDAM = 1 and DMGTYP = 1 in keyword *MAT_ADD_EROSION [14]. The modular nature of *MAT_ADD_EROSION allows GISSMO to be combined with any other plasticity model and fracture limit model.

3.2 Fracture Limit Test and Calibration

In order to achieve fracture limit of QP1180-EL under different stress states and calibrate parameters of MMC fracture model, fuve different loading cases and testing coupon were designed. These tests covered the stress state of shear, uniaxial tension, stretching, plane strain, and equi-biaxial stretching. Schematic of these five individual tests is shown in Fig. 4.

Digital Image Correlation (DIC) was used for strain measurement in the five calibration test. Load speed of each test was limit to 0.6 mm/min and DIC image acquisition rate was set to 2 frame per second to get the critical fracture moment as close as possible. DIC strain fields were recorded at both 1 and 2 mm virtual gauge length (VGL) to determine the mesh size regularization curve directly. Figure 5 shows DIC and CAE model strain results at different VGL of the plane strain state.

During calibration of MMC model parameters, in order to represent deformation and damage accumulation history, average triaxiality should be used instead of the triaxiality at fracture moment [15]. Average triaxiality of each loading case is first calculated by following equation, assuming damage accumulation exponent

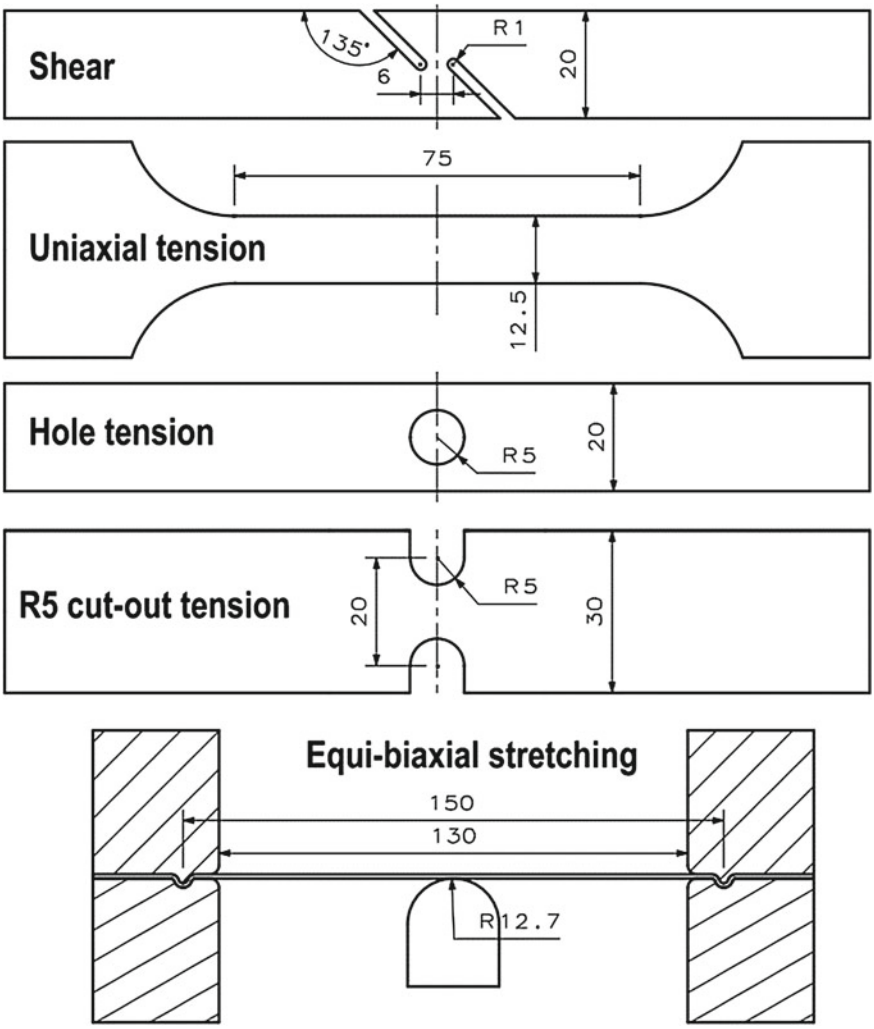


Fig. 4 Fracture limit test specimen. **a** Shear tensile, **b** uniaxial tensile, **c** hole tensile, **d** R5 cut-out tensile, **e** equibiaxial stretching

DMGEXP equals to 2. Fracture strain and average triaxiality of each loading case are shown in Table 3. The final calibrated MMC model and loading path result of the five different tests are shown in Fig. 6, this was used in the following GISSM model calibration.

$$\eta_{\text{avg}} = \frac{1}{D}\int \frac{2}{\varepsilon_f(\eta)} D^{\frac{1}{2}} \eta d\varepsilon_p. \tag{8}$$

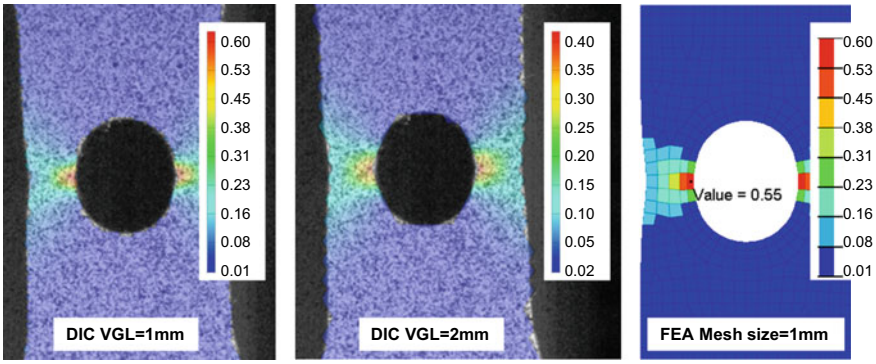


Fig. 5 Strain result of DIC and simulation at different VGL/mesh size. (Color figure online)

Table 3 Fracture limit stain test result

Load case	Average triaxiality	Fracture strain
Shear	0.06	0.476
Uniaxial	0.46	0.440
Hole	0.48	0.553
R5	0.57	0.390
Equi-biaxial	0.66	0.810

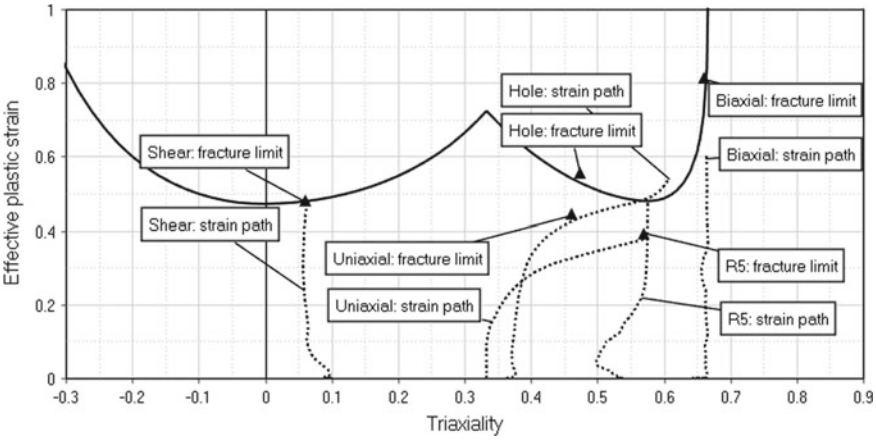


Fig. 6 Calibrated MMC fracture limit and loading path result of different tests

3.3 GISSMO Damage Model Calibration and Validation

As stated above, calibration of GISSMO damage model requires identification of several key parameters besides fracture limit, including instability limit, damage

accumulation exponent, stress fadeout exponent as well as regularization curve that depends on element mesh size and stress state.

Instability limit curve is first set with reference to uniform elongation value tested from uniaxial tension and iteratively identified until a good agreement between simulation and experiment Force–displacement curve was achieved for all five loading conditions. *DMGEXP* and *FADEXP* were set to 2 and 2.5 respectively. *MAT_024 material formulation is used in the calibration process. Finite element mesh size was set between 1, 2, and 4 mm allowed by the specimen geometry, in accordance with the mesh size requirement in vehicle crash simulation.

The experimental as well as simulation results for the force versus gauge point displacement curve in the five loading conditions are shown in Fig. 7. All force and displacement results were regularized to 1 by the maximum force and fracture displacement from the corresponding test. The result shows that GISSMO damage simulation model delivers good agreement with experiments for uniaxial tensile, hole tensile, R5 cut-out tensile, and biaxial stretching, while force simulation result is higher than in experiment, indicating that hardening behavior of QP1180-EL is not correctly described using *MAT_024 material formulation. This should be improved later on by implementing more comprehensive material model that can describe material's yield behavior more precisely. A relatively good convergence between different mesh sizes is also achieved.

Three-point quasi-static bending test was performed in order to validate the calibrated GISSMO damage model. The hat profile used in the bending test was produced using roll-forming process, which can minimize the effects of work hardening and corresponding damage. Figure 8 shows the predicted fracture location and test result. Figure 9 compares the force–displacement result between tests and simulation. In order to obtain relatively accurate simulation results, average mesh size needs to be refined to 2 mm. The simulation results with the calibrated GISSMO fracture model match the test results well.

4 Summary

- A new Modified Power Law (MPL) hardening law was proposed to better describe the phenomenon that hardening index of advanced high-strength steel materials changes with an increase in strain. Simple tensile test shows that MPL model gives better prediction result for QP1180-EL steel.
- MMC fracture model and GISSMO damage model were calibrated to describe the ductile fracture behavior of QP1180-EL and show a good correlation between simulation and experiment. Advance material constitutive model needs to be used to describe yield behavior more precisely.

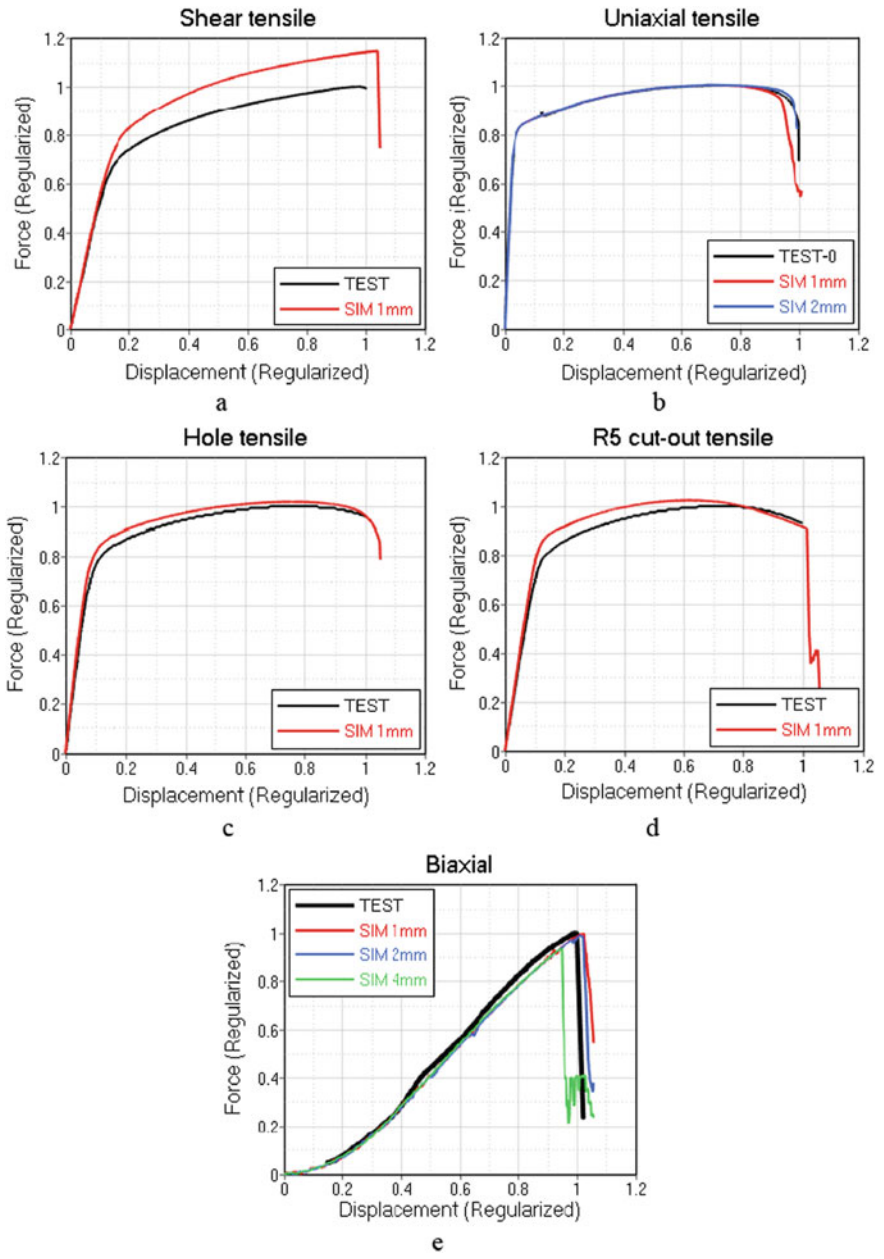


Fig. 7 Comparison of experimental and simulation force–displacement results. (Color figure online)

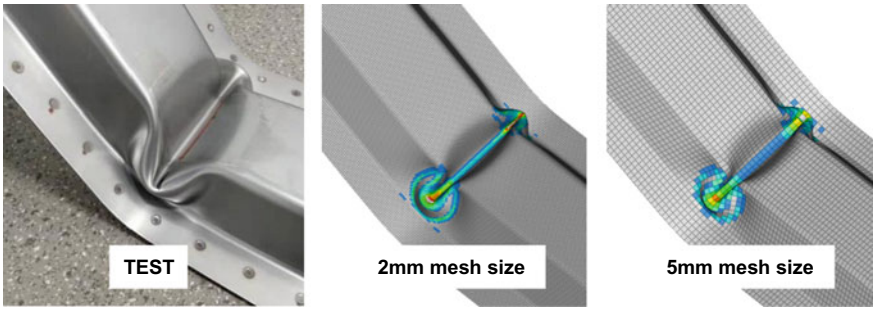


Fig. 8 Experiment and simulation result of three-point bending test. (Color figure online)

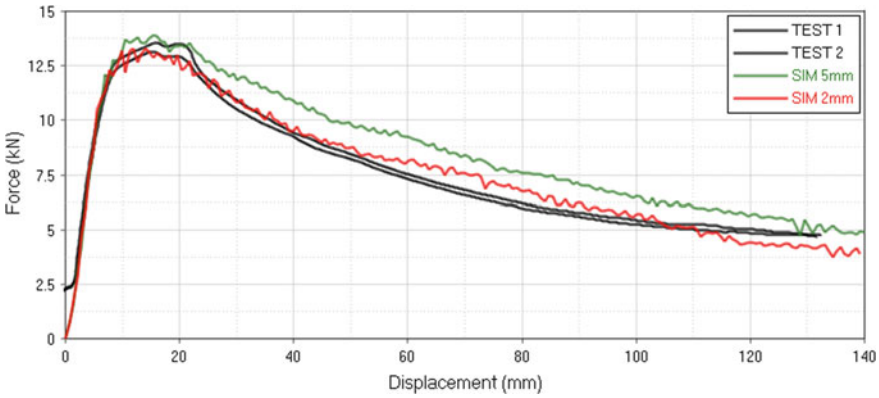


Fig. 9 Comparison of three-point bending test force–displacement result. (Color figure online)

Acknowledgments The author would like to thank Nation Key Research and Development Plan (2017YFB0304403) for the support to this research work.

References

1. Hollomon JH, Member J (1945) Tensile deformation. Met Technol 12:268–290
2. Swift HW (1952) Plastic instability under plane stress. J Mech Phys Solids 1:1–18
3. Hockett JE, Sherby OD (1975) Large strain deformation of polycrystalline metals at low homologous temperatures. J Mech Phys Solids 23:87–98
4. Chen JJ, Lian CW, Lin JP (2019) Validation of constitutive models for experimental stress-strain relationship of high-strength steel sheets under uniaxial tension. IOP Conf Mater Sci Eng 668
5. Kessler L, Gerlach J (2006) The impact of materials testing strategies on the determination and calibration of different FEM material models. Conf Proc IDDRG 113–120
6. Mulder J, Vegter H, Aretz H et al (2015) Accurate determination of flow curves using the bulge test with optical measuring systems. J Mater Process Technol 226:169–187

7. Traphöner H, Heibel S, Clausmeyer T et al (2018) Influence of manufacturing processes on material characterization with the grooved in-plane torsion test. Int J Mech Sci 146–147:544–555
8. B Gu, J He, S Li et al (2019) Research progress on anisotropic fracture models and fracture tests for sheet metals. J Plast Eng 29(1):01–14
9. Johnson GR, Cook WH (1985) Fracture characteristics of three metals subjected to various strains, strain rates, temperature and pressures. Eng Fract Mech 21(1):31–38
10. Bai Y, Wierzbicki T (2008) A new model of metal plasticity and fracture with pressure and lode dependence. Int J Plast 24(6):1071–1096
11. Neukamm F, Feucht M, Haufe A (2009) Considering damage history in crashworthiness simulations. In: 7th European LS-DYNA conference
12. Neukamm F, Feucht M, Haufe A, Roll K (2008) On closing the constitutive gap between forming and crash simulation. In: 10th international LS-DYNA users conference, Detroit
13. Andrade FX, Feucht M, Haufe A, Neukamm F (2016) An incremental stress state dependent damage model for ductile failure prediction. Int J Fract 200:127
14. LSTC (2016) LS-DYNA keyword user's manual—volume II: material models, Livermore
15. Huang G, Zhu H, Sriram S et al (2014) Fracture prediction and correlation of AlSi hot stamped steels with different models in LS-DYNA. In: 13th international LS-DYNA users conference, Detroit

Design of a New Cruciform-Like Specimen for Combined Tension and Shear of Metal Sheets



Minki Kim, Jinjin Ha, Samantha Bonica, and Yannis P. Korkolis

Abstract This paper is concerned with the design of a new cruciform-like specimen to measure plastic flow under combined tension and shear loading conditions. An AA6013-T4 aluminum sheet is used as example material. The specimen design borrows from the "smiley" shear specimen, which is commonly used for the simple shear experiment, but has four arms, as a cruciform specimen: two arms are used to induce shearing, while the other two induce tension. The details of the geometry are determined by FEA to promote stress uniformity in the gage-section under combined loading conditions with the force ratio of 1 to 1. Parametric studies are conducted to determine the final design in terms of notch shape, gage-length, gage-width and offset of the notch. The dimensions of the final design are suggested with good uniformity in stress distribution along the gage-length.

Keywords Cruciform specimen · Biaxial test · Combined tension–shear · Multi-axial property · Specimen design

1 Introduction

As the design of structures is becoming complicated, material properties in complex stress states are becoming of interest in the automotive industry. Characterization of multi-axial properties must be established with various stress states to predict the deformation of a complicated structure accurately by finite element (FE) simulation. Combined loading conditions, such as tension–torsion or tension–shear, have been

M. Kim (✉) · J. Ha · Y. P. Korkolis
Integrated Systems Engineering, The Ohio State University, Columbus, OH 43210, USA
e-mail: kim.7834@osu.edu

J. Ha
Mechanical Engineering, University of New Hampshire, Durham, NH 03824, USA

S. Bonica
Mechanical Engineering, University of Massachusetts Amherst, Amherst, MA 01003, USA

Weapons and Mechanical Systems, General Dynamics Electric Boat, New London, CT 06320, USA

© The Minerals, Metals & Materials Society 2021

G. Daehn et al. (eds.), *Forming the Future*, The Minerals, Metals & Materials Series,
https://doi.org/10.1007/978-3-030-75381-8_164

implemented to identify the effect of complex stress state on material properties in terms of flow and fracture behavior [1–5]. Especially for metal sheets, biaxial testing machines are utilized to apply the combined loading to butterfly [2, 3], notch [4], and cruciform-like specimens [5]. A conventional biaxial tension machine [6] is useful to realize various combined loading conditions by control of force ratios, so that the multi-axial flow behavior can be measured in a straightforward way. In this paper, a new cruciform-like specimen is suggested to obtain multi-axial flow behavior under combined tension and shear, including cyclic effects and multiple path changes. The dimensions of the final design are determined by parametric studies with FE simulations.

2 A New Cruciform-Like Specimen

The main idea of the new cruciform-like specimen is the combination of commonly used cruciform specimen [6–8] and the smiley shear specimen [9] for biaxial tension and simple shear tests, respectively. The new design has four arms: two arms for inducing tension while the other two arms for inducing shear in the gage-section as shown in Fig. 1a. The symmetric design with respect to the 22-axis allows the study to be performed on the half model depicted in Fig. 1b. The design parameters are the gage-length L, the gage-width W, and the parallel length G, which are determined by FEA in the next section. Not shown in Fig. 1b is an additional parameter, i.e., the offset along the 11-axis between the two notches is shown.

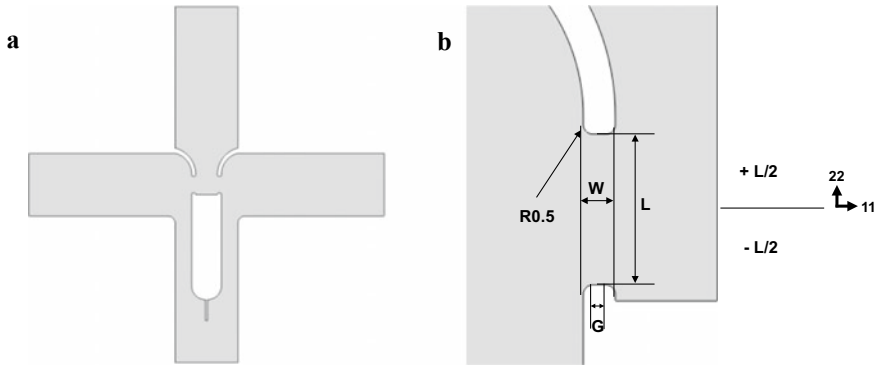


Fig. 1 Schematics of: **a** new cruciform-like specimen, **b** design parameters in gage-section

3 Determination of Specimen Dimensions

To determine the details of the new cruciform-like specimen, specimen geometries are examined by FEA with various notch shapes, gage-lengths, gage-widths, and offsets of notch. The main purpose of the FEA is to find out a proper dimension set with good uniformity of stress distribution in the gage-section under combined tension and shear. Furthermore, it is intended to establish the viability of using the forces measured at the four arms using load cells, to determine the stresses in the gage-sections [8]. For the parametric studies, all FEAs are conducted with the ABAQUS 2019 implicit and reduced integration, quadratic, plane-stress elements (CPS8R). Figure 2 shows the FEA conditions including applied material property and boundary conditions. The stress–strain curve of AA6013-T4 was obtained from uniaxial tension test along the RD [10] as shown in Fig. 2a and the material behavior is assumed to be isotropic hardening. Figure 2b, c represents boundary conditions for the half model of the cruciform-like specimen so the force ratio for the full model is set as 1 to 1.

For the determination of the design parameters, parametric study on the notch shape is performed with various geometries as shown in Fig. 3. All candidates with various notch shapes have a gage-length (L) of 8 mm and a gage-width (W) of 1.7 mm. The radius of the circular notch is 0.85 mm and the parallel length (G) of the flat notch is 0.7 mm to match the gage-width of 1.7 mm. The PST (Plane Strain

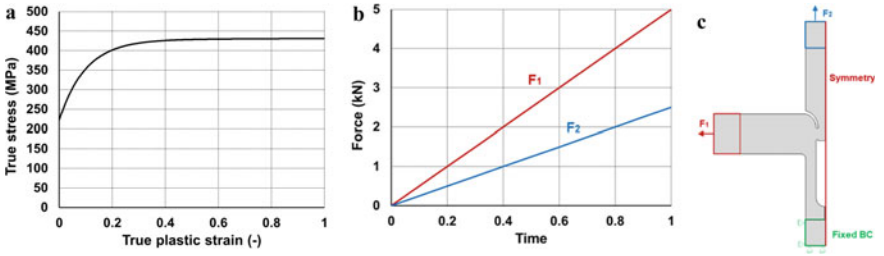


Fig. 2 FEA condition: **a** applied material property, **b** applied load, **c** schematics of boundary conditions. (Color figure online)

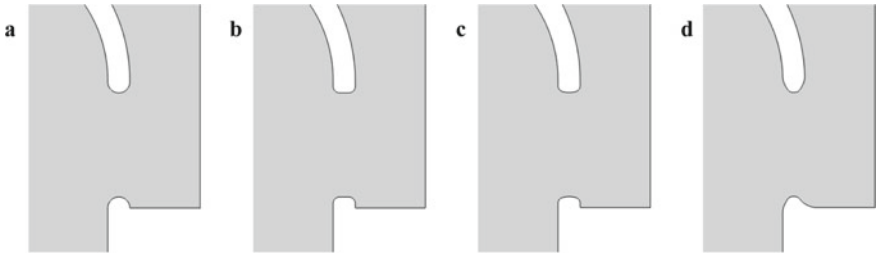


Fig. 3 Notch shapes: **a** circular notch, **b** flat notch, **c** PST notch, **d** groove notch

Tension) [11, 12] notch has two radii of 0.45 and 1.8 mm while the groove notch has the radius of 0.5 mm and the parallel length of 0.1 mm.

In order to evaluate the performance of each geometry, the uniformity of the axial and the shear stresses are investigated along the gage-length at the center of the gage-section. Figure 4 shows the distribution of axial and shear stresses along the gage-length with respect to the displacement in 22-direction, U2 (shear loading direction). The dashed line corresponding to each U2 is the average engineering stress, calculated by the force in each direction divided by the initial area of the gage-section. In the case of the flat notch, the axial stress along 11-direction (tensile direction) and the shear stress are quite uniform compared with other candidates when the deformation amount is high. The axial stress along 22-direction (shear

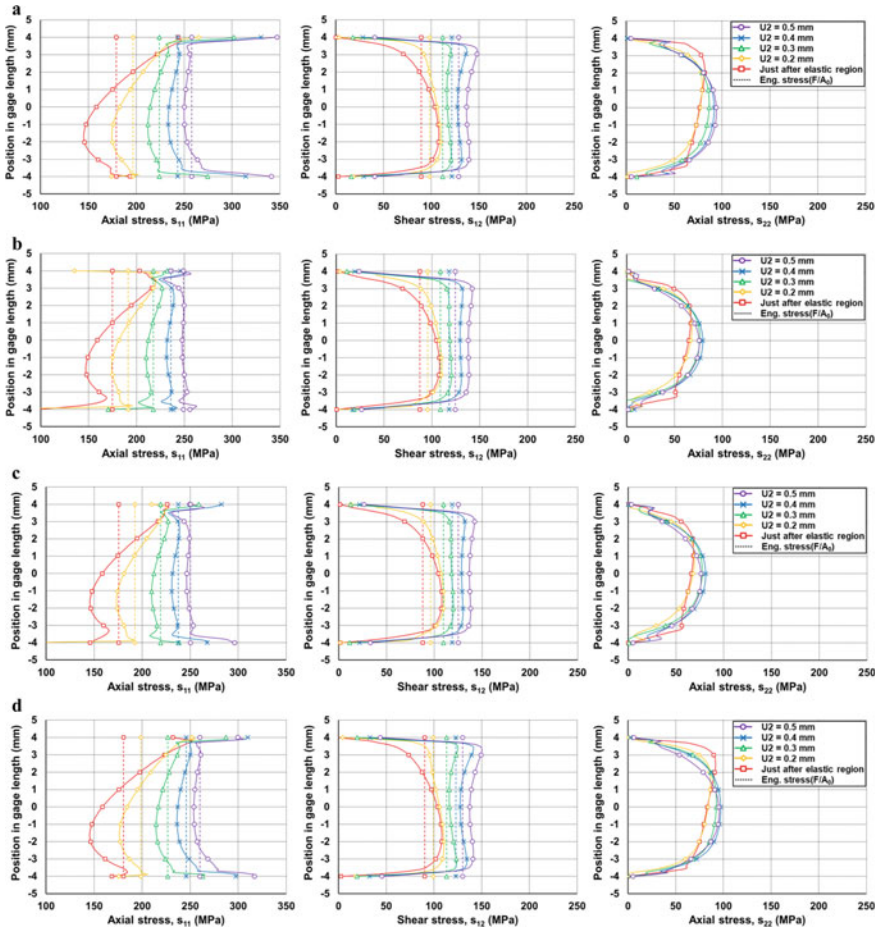


Fig. 4 Axial and shear stress distribution in deformation: **a** circular notch, **b** flat notch, **c** PST notch, **d** groove notch. (Color figure online)

direction) is smaller for the flat notch. This means that most of the shear loading contributes to shear deformation rather than the elongation in 22-direction. The flat notch shape is, therefore, selected for the parametric studies to determine specimen dimensions.

For parametric studies to decide the design parameters, specimen geometries with different gage-length, gage-width, and offset of notch are prepared as illustrated in Fig. 5, Fig. 6, and Fig. 7, respectively. The performance of each geometry is examined with the same method in the case study on the notch shape. As the gage-length becomes smaller, the amount of axial stress along 22-direction becomes smaller while the distribution becomes irregular. For other stress components, the uniformity of the distribution is not sensitive to change of the length from 8 to 6 mm. In case of the gage-width, the distribution of all stress components becomes more uniform when the gage-width increases from 1.5 to 1.9 mm. The offset of upper notch in the gage-section can affect the stress uniformity during the deformation in general [13]. The geometries with ±0.35 mm offset of the upper notch along 11-direction are evaluated to identify the effect of offset on the stress uniformity under combined tension and shear. When the (+) offset exists, the shear stress becomes uniform. The

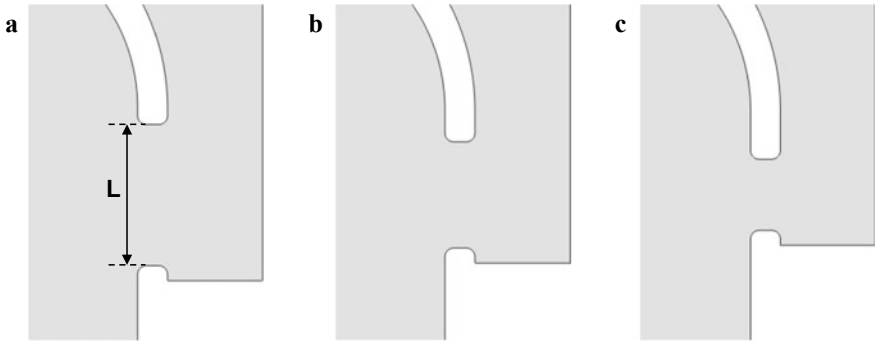


Fig. 5 Geometries of gage-section with the length (L) of: **a** 8 mm, **b** 6 mm, **c** 4 mm

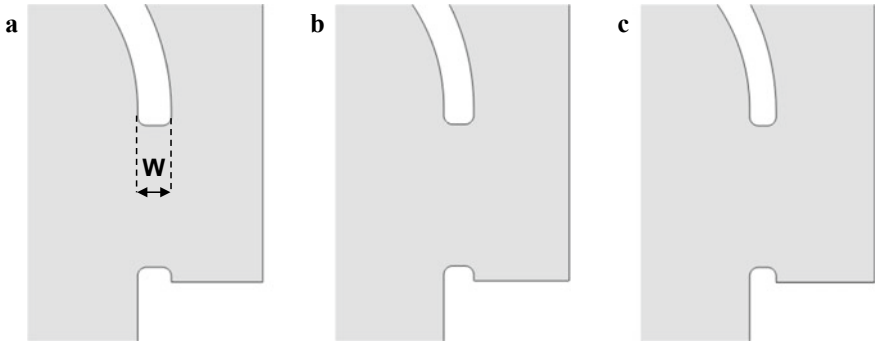


Fig. 6 Geometries of gage-section with the width (W) of: **a** 1.9 mm, **b** 1.7 mm, **c** 1.5 mm

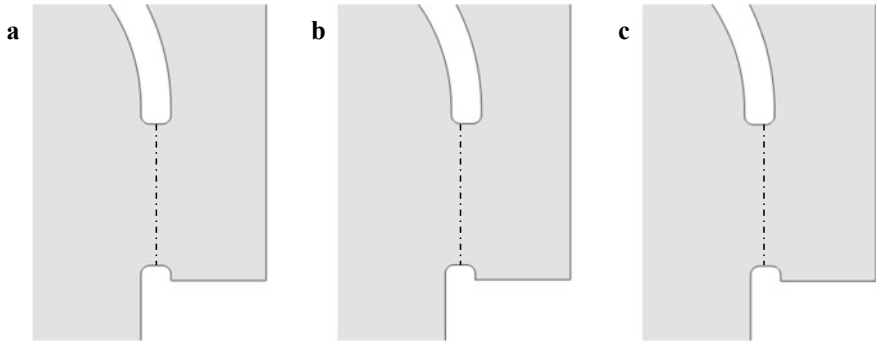


Fig. 7 Geometries of gage-section with the offset of: **a** 0 mm, **b** 0.35 mm, **c** −0.35 mm

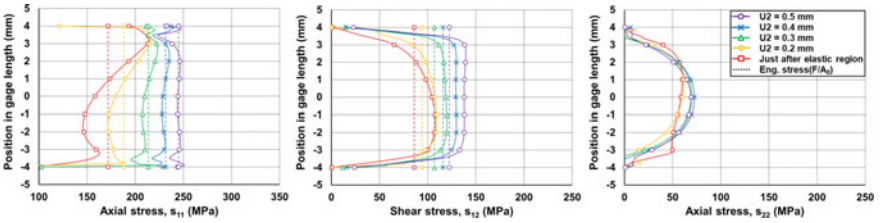


Fig. 8 Stress distributions of the final design. (Color figure online)

tensile stress, however, becomes non-uniform. For the (–) offset case, both tensile and shear stress distributions become irregular. It is noted from the results that the (+) offset is good for the design of a simple shear specimen while the case of without offset is proper to specimen design under combined tension and shear.

According to the parametric studies, the dimensions of the gage-section are determined with the gage-length of 8 mm and the gage-width of 1.9 mm. Figure 8 depicts the axial and shear stress distribution of the final design of the cruciform-like specimen during the deformation. The stress distributions are uniform except early part of the deformation so that the material property could be measured from the gage-section under the combined tension and shear.

4 Conclusion and Future Works

In this work, a new cruciform-like specimen with four arms and two gage-sections is proposed, to obtain multi-axial flow behavior of metal sheets under combined tension and shear, including cyclic loading. Based on the stress uniformity along the gage-length, the dimensions of the final design are determined by parametric studies with FEA. For future works, the final design will be examined for various force ratios. Experiments will be then performed using an in-plane biaxial testing machine, with

different force ratios between tension and shear, so that combined stress states in (σ_{11}, σ_{22}, σ_{12}) 3D-stress space are probed. An anisotropic yield function, such as Yld2000-2D, will be calibrated with multi-axial data, and the influence of shear stress on the yield function parameter calibration will be evaluated by comparing yield surfaces identified by different calibration approaches. Similarly, material models suitable for load-reversals will be examined based on cyclic data obtained with these specimens.

Acknowledgments The support of NSF under the CMMI-1563216 and -1929873 awards, which also provided a Research Experience for Undergraduates supplemental award for SM, is acknowledged with thanks. We also recognize the contributions of Jacqueline McNally in earlier stages of this work.

References

1. Korkolis YP, Kyriakides S (2009) Path-dependent failure of inflated aluminum tubes. Int J Plast 25(11):2059–2080
2. Dunand M, Mohr D (2011) On the predictive capabilities of the shear modified Gurson and the modified Mohr-Coulomb fracture models over a wide range of stress triaxialities and Lode angles. J Mech Phys Solids 59(11):1374–1394
3. Abedini A, Butcher C, Worswick MJ (2017) Fracture characterization of rolled sheet alloys in shear loading: studies of specimen geometry, anisotropy, and rate sensitivity. Exp Mech 57(1):75–88
4. Mohr D, Dunand M, Kim KH (2010) Evaluation of associated and non-associated quadratic plasticity models for advanced high strength steel sheets under multi-axial loading. Int J Plast 26(7):939–956
5. Gerke S, Adulyasak P, Brünig M (2017) New biaxially loaded specimens for the analysis of damage and fracture in sheet metals. Int J Solids Struct 110–111:209–218
6. Kuwabara T (2007) Advances in experiments on metal sheets and tubes in support of constitutive modeling and forming simulations. Int J Plast 23(3):385–419
7. Korkolis YP, Deng N, Kuwabara T (2013) Biaxial unloading and springback behavior of dual-phase DP590 steel using cruciform specimens. AIP Conf Proc 1567:700–704. https://doi.org/10.1063/1.4850068
8. Deng N, Kuwabara T, Korkolis YP (2015) Cruciform specimen design and verification for constitutive identification of anisotropic sheets. Exp Mech 55:1005–1022
9. Roth CC, Mohr D (2016) Ductile fracture experiments with locally proportional loading histories. Int J Plast 79:328–354
10. Ha J, Baral M, Korkolis YP (2018) Plastic anisotropy and ductile fracture of bake-hardened AA6013 aluminum sheet. Int J Solids Struct 155:123–139
11. Tardif N, Kyriakides S (2012) Determination of anisotropy and material hardening for aluminum sheet metal. Int J Solids Struct 49(25):3496–3506
12. Tian H, Brownell B, Baral M, Korkolis YP (2017) Earing in cup-drawing of anisotropic Al-6022-T4 sheets. Int J Mater Form 10(3):329–343
13. Roth CC, Mohr D (2018) Determining the strain to fracture for simple shear for a wide range of sheet metals. Int J Mech Sci 149:224–240

A Study of Anisotropic Yield Function Based on J_2 and J_3 Invariants



YoungSuk Kim, PhuVan Nguyen, and JinJae Kim

Abstract In this paper a new anisotropic yield function that describes the elasto-plastic behavior of sheet metals depends not only on the second stress invariant J2 for the yield, but also on the third stress invariant J3, both may affect the shape of the yield surface. The new anisotropic yield function is general and applicable to three-dimensional stress states. The proposed model is identified by calibration parameters from experimental data of material including uniaxial and biaxial tests. In this study, the predictive capabilities of the new anisotropic yield function are demonstrated by comparison between the predictions and experimental data for yield locus, normalized yield stress, and r-value. The result indicates that the new anisotropic model is reasonable to predict not only the symmetric shape but also the asymmetric shape of yield surface of the sheet metals.

Keywords Invariant J_2 · Invariant J_3 · Stress deviator · Isotropic yield function · Anisotropic yield function and asymmetric yield function

1 Introduction

In industry, sheet metal forming is one of the most important technologies, the metal forming process is an irreversible plastic deformation to form a product. These mechanisms of plastic deformation are slip, twin, creep, diffusion, etc. From the continuum mechanics, the plastic deformation is described mainly by yield condition, plastic flow rule, and hardening behavior. Among these components, the yield condition is one of the important things because it describes the elastoplastic behavior of sheet metals.

Y. Kim (✉)
School of Mechanical Engineering, Kyungpook National University, 80 Daehakro, Daegu 41566, South Korea
e-mail: caekim@knu.ac.kr

P. Nguyen · J. Kim
Graduate School, Kyungpook National University, 80 Daehakro, Daegu 41566, South Korea

© The Minerals, Metals & Materials Society 2021

G. Daehn et al. (eds.), *Forming the Future*, The Minerals, Metals & Materials Series,
https://doi.org/10.1007/978-3-030-75381-8_165

Many yield criteria have been proposed in previous studies, for anisotropic material, the yield function ought to be invariant with respect to any orthogonal transformation and it depends on the stress deviator s only through its invariants J_2 and J_3 [1], defined as

$$\begin{aligned} &\mathrm{J}_2 = \frac{1}{2}\left(\mathrm{s}_1^2 + \mathrm{s}_2^2 + \mathrm{s}_3^2\right);\ \mathrm{J}_3 = \mathrm{s}_1\mathrm{s}_2\mathrm{s}_3 \\ &\mathrm{s}_1 = \frac{2}{3}\sigma_1 - \frac{1}{3}(\sigma_2 + \sigma_3);\ \mathrm{s}_2 = \frac{2}{3}\sigma_2 - \frac{1}{3}(\sigma_1 + \sigma_3);\ \mathrm{s}_3 = \frac{2}{3}\sigma_3 - \frac{1}{3}(\sigma_1 + \sigma_2) \end{aligned} \tag{1}$$

where s_k and σ_k, $k = 1.0.3$ denote the principal values of s and σ.

The first isotropic yield function for sheet metals was proposed by Tresca (1864). In Tresca's yield function, the maximum shear stress must have a constant value. Von Mises (1913) proposed the isotropic yield function as below [1]:

$$\mathrm{J}_2 = \mathrm{k}^2 \tag{2}$$

where k is the yield stress in pure shear, which has a relationship of $k = \sigma_\mathrm{T}/\sqrt{3}$, σ_T is the yield stress in uniaxial tension.

Another yield function that involves both invariants J_2 and J_3 was proposed by Drucker. The results indicated Drucker's yield function predicted more accurate than either Tresca or von Mises's yield function on aluminum sheets. To account for anisotropic sheet metals, many anisotropic yield functions have been proposed [2, 3], for example, Hill-48 (1948), Hill-79 (1979), Hosford (1979), Yld2000-2d (2000), Cazacu and Barlat (2001), Yld2004-18p (2004), Banabic (2010), etc.

For the Hexagonal Closed Pack (HCP) metals such as titanium and magnesium alloys, the deformation phenomenon of twinning ultimately leads to distinct strengths in tension and compression loading conditions, which is referred to as the strength differential (SD) effect. In these kinds of material, texture evolution and twinning are important factors that affect specific flow behavior. However, uniaxial tension and compression are utilized for deformation modes in most studies. One of the challenges for these kinds of material that is mechanical behavior in biaxial compressive stress conditions is limited due to experimental difficulties. In the previous study, biaxial compressions were carried out using a unique device developed by Shimizu and Tada [4]. For the prediction of yield surface of these kinds of material, Cazacu and Barlat [5] proposed anisotropic yield criterion that is capable of describing the SD effect with the employment of an odd function of the second and third invariants of the stress deviator is shown as below:

$$f = J_2^{3/2} - \mathrm{c}J_3 \tag{3}$$

Cazacu et al. [6] also developed another yield function by using a fourth-order linear transformation on the stress deviator, referred to as CPB'06, to take into account both anisotropy and tension/compression asymmetry for pressure-insensitive metals.

Gao [7] developed a yield function coupling effect of all three stress invariants as below:

$$f = a(bI_1^6 + 27J_2^3 + \mathrm{c}J_3^2)^{1/6};\ I_1 = \sigma_1 + \sigma_2 + \sigma_3 \tag{4}$$

Another approach, Khan et al. [8] developed a criterion considering the effects of temperature and strain rate based on the experimental investigation of Ti-6Al-4 V alloy in both tension and compression considering the anisotropic effect. In their approach, the normalized third stress invariant was employed to describe the SD effect. Yoon [9] proposed a yield function with three invariants as below:

$$f = a\left[bI_1 + (J_2^{3/2} - \mathrm{c}J_3)^{1/3}\right] \tag{5}$$

In this paper, a new isotropic yield function is proposed. Using the generalized invariants approach, an anisotropic yield function of this criterion is developed. The theoretical prediction of anisotropy in tensile properties for uniaxial tension for arbitrary orientation of the loading axis is presented. In particular, the comparison between the predictions and experimental data for yield locus, the normalized yield stresses and r-values on AA6016-T4 is discussed. Besides that, in this study, the strength differential (SD) effect for hcp crystal structure materials such as titanium, magnesium are also considered in the proposed yield function.

2 New Proposed Model

2.1 New Yield Function

From early discussions, we propose a new isotropic yield function named as Kim-Van 6 (KV6) yield function as expressed below:

$$f \equiv J_2^3 + \alpha J_3^2 + \beta(J_2^{\frac{3}{2}} \times J_3) = \mathrm{k}^6 \tag{6}$$

where J_2 and J_3 are expressed as the above section, k denotes the yield stress in pure shear, α and β are material constants.

If $\beta = 0$, the proposed yield function becomes the Cazacu–Barlat (2001) which is applied for symmetric materials such as aluminum and steel and the proposed yield function as expressed below:

$$\mathrm{f} \equiv J_2^3 + \alpha J_3^2 = \mathrm{k}^6 \tag{7}$$

If $\beta \neq 0$, the proposed yield function represents for asymmetric yield function which is applied for hcp crystal structure materials such as titanium and magnesium

and the proposed yield function as expressed below:

$$f \equiv J_2^3 + \alpha J_3^2 + \beta(J_2^{\frac{3}{2}} \times J_3) = \mathrm{k}^6 \tag{8}$$

In the above expressions a_i (i = 1…6) and b_k (k = 1…11) are coefficients that describe anisotropic property. If $a_i = b_k = 1$, the below Eqs. (12) and (13) return to isotropic yield function.

Using these anisotropic invariants, the anisotropic yield function for asymmetry is developed as below:

$$f\left(J_2^0, J_3^0\right) \equiv \left(J_2^0\right)^3 + \alpha\left(J_3^0\right)^2 + \beta\left(J_2^0\right)^{3/2} \times J_3^0 = \mathrm{k}^6 \tag{9}$$

The anisotropic generalizations of the second and third invariant of the stress deviator should be expressed as follows [10, 11]:

$$J_2^0 = \frac{a_1}{6}(\sigma_{xx} - \sigma_{yy})^2 + \frac{a_2}{6}(\sigma_{yy} - \sigma_{zz})^2 + \frac{a_3}{6}(\sigma_{xx} - \sigma_{zz})^2 + a_4\sigma_{xy}^2 + a_5\sigma_{xz}^2 + a_6\sigma_{yz}^2$$

$$\begin{aligned} J_3^0 = {} & \frac{1}{27}(b_1 + b_2)\sigma_{xx}^3 + \frac{1}{27}(b_3 + b_4)\sigma_{yy}^3 + \frac{1}{27}[2(b_1 + b_4) - b_2 - b_3]\sigma_{zz}^3 \\ & - \frac{1}{9}\left(b_1\sigma_{yy} + b_2\sigma_{zz}\right)\sigma_{xx}^2 - \frac{1}{9}(b_3\sigma_{zz} + b_4\sigma_{xx})\sigma_{yy}^2 \\ & - \frac{1}{9}\left[(b_1 - b_2 + b_4)\sigma_{xx} + (b_1 - b_3 + b_4)\sigma_{yy}\right]\sigma_{zz}^2 + \frac{2}{9}(b_1 + b_4)\sigma_{xx}\sigma_{yy}\sigma_{zz} \\ & - \frac{\sigma_{xz}^2}{3}\left[2b_9\sigma_{yy} - b_8\sigma_{zz} - (2b_9 - b_8)\sigma_{xx}\right] \\ & - \frac{\sigma_{xy}^2}{3}\left[2b_{10}\sigma_{zz} - b_5\sigma_{yy} - (2b_{10} - b_5)\sigma_{xx}\right] \\ & - \frac{\sigma_{yz}^2}{3}\left[2b_7\sigma_{xx} - b_6\sigma_{yy} - (2b_7 - b_6)\sigma_{zz}\right] + 2b_{11}\sigma_{xy}\sigma_{xz}\sigma_{yz} \end{aligned} \tag{10}$$

The effective stress, $\tilde{\sigma}$ is expressed as below:

$$\tilde{\sigma} = V\left[\left(J_2^0\right)^3 + \alpha\left(J_3^0\right)^2 + \beta\left(J_2^0\right)^{3/2} \times J_3^0\right]^{1/6} \tag{11}$$

In the above expressions, V is a constant value which defined for uniaxial tension in one of the orthotropic axes (e.g., for a sheet, in the rolling direction (RD)) the effective stress reduces to the yield stress,

$$V = \frac{1}{\left[\left(\frac{a_1+a_3}{6}\right)^3 + \alpha\left(\frac{b_1+b_2}{27}\right)^2 + \beta\left(\frac{a_1+a_3}{6}\right)^{\frac{3}{2}}\left(\frac{b_1+b_2}{27}\right)\right]^{1/6}} \tag{12}$$

In plane stress $\sigma_3 = 0$, the yielding under equi-biaxial tension in the plane (x–y) occurs when $\sigma_{xx} = \sigma_{yy} = \sigma_b$ with:

$$\sigma_b/\sigma_0 = \frac{1}{\sqrt{3}}\left\{\left(\frac{a_2+a_3}{6}\right)^3 + \alpha\left(\frac{2b_1-b_2-b_3+2b_4}{27}\right)^2 + \beta\left(\frac{a_2+a_3}{6}\right)^{3/2} \times \left(\frac{2b_1-b_2-b_3+2b_4}{27}\right)\right\}^{-1/6} \tag{13}$$

The biaxial coefficient r_b is calculated in the form [12]:

$$r_b = \frac{\frac{\partial f}{\partial \sigma_{yy}}}{\frac{\partial f}{\partial \sigma_{xx}}} \tag{14}$$

The Lankford coefficients r_θ are calculated based on the formula:

$$r_\theta = -\frac{\frac{\partial f}{\partial \sigma_{xx}}\left(\sin^2\theta\right) - (\sin 2\theta)\frac{\partial f}{\partial \sigma_{xy}} + \frac{\partial f}{\partial \sigma_{yy}}\left(\cos^2\theta\right)}{\frac{\partial f}{\partial \sigma_{xx}} + \frac{\partial f}{\partial \sigma_{yy}}} \tag{15}$$

The new anisotropic yield function predicts the following dependence of the normalized uniaxial yield stress σ_θ/σ_0 on the angle θ between the direction of loading and the rolling direction by using the relationship of $\sigma_x = \sigma_\theta cos\theta$, $\sigma_y = \sigma_\theta sin\theta$, $\sigma_{xy} = \sigma_\theta sin\theta\ cos\theta$:

$$\begin{aligned}
&\sigma_\theta/\sigma_0 = \\
&\frac{1}{\sqrt{3}}\left\{\left[\left(\frac{a_1}{6}+\frac{a_3}{6}\right)\cos^4\theta + \left(a_4 - \frac{a_1}{3}\right)\cos^2\theta\sin^2\theta + \left(\frac{a_1}{6}+\frac{a_2}{6}\right)\sin^4\theta\right]^3\right. \\
&+\alpha\left[\cos^6\theta\frac{b_1+b_2}{27} + \sin^6\theta\frac{b_3+b_4}{27} - \cos^4\theta\sin^2\theta\frac{b_1+3b_5-6b_{10}}{9} - \cos^2\theta\sin^4\theta\frac{b_4-3b_5}{9}\right]^2 \\
&+\beta\left[\left(\frac{a_1}{6}+\frac{a_3}{6}\right)\cos^4\theta + \left(a_4 - \frac{a_1}{3}\right)\cos^2\theta\sin^2\theta + \left(\frac{a_1}{6}+\frac{a_2}{6}\right)\sin^4\theta\right]^{3/2} \\
&\left.\times\left[\cos^6\theta\frac{b_1+b_2}{27} + \sin^6\theta\frac{b_3+b_4}{27} - \cos^4\theta\sin^2\theta\frac{b_1+3b_5-6b_{10}}{9} - \cos^2\theta\sin^4\theta\frac{b_4-3b_5}{9}\right]\right\}^{-1/6}
\end{aligned} \tag{16}$$

2.2 *Convexity Condition of Yield Function*

The proposed yield function is convex if $f(\sigma_{xx}, \sigma_{yy})$, $f(\sigma_{xx}, \sigma_{xy})$, and $f(\sigma_{yy}, \sigma_{xy})$ are convex. In order to each $f(\sigma_i, \sigma_j)$ is convex, its Hessian matrix H defined as below is positive semi-definite [13–15]:

$$H_1(\sigma_{xx}, \sigma_{yy}) = \frac{\partial^2 f}{\partial \sigma_i \partial \sigma_j} = \begin{bmatrix} \frac{\partial^2 f}{\partial \sigma_{xx}^2} & \frac{\partial^2 f}{\partial \sigma_{yy}\partial \sigma_{xx}} \\ \frac{\partial^2 f}{\partial \sigma_{xx}\partial \sigma_{yy}} & \frac{\partial^2 f}{\partial \sigma_{yy}^2} \end{bmatrix}; H_2(\sigma_{xx}, \sigma_{xy}) = \frac{\partial^2 f}{\partial \sigma_i \partial \sigma_j} = \begin{bmatrix} \frac{\partial^2 f}{\partial \sigma_{xx}^2} & \frac{\partial^2 f}{\partial \sigma_{xy}\partial \sigma_{xx}} \\ \frac{\partial^2 f}{\partial \sigma_{xx}\partial \sigma_{xy}} & \frac{\partial^2 f}{\partial \sigma_{xy}^2} \end{bmatrix}$$

$$H_3(\sigma_{yy}, \sigma_{xy}) = \frac{\partial^2 f}{\partial \sigma_i \partial \sigma_j} = \begin{bmatrix} \frac{\partial^2 f}{\partial \sigma_{yy}^2} & \frac{\partial^2 f}{\partial \sigma_{xy} \partial \sigma_{yy}} \\ \frac{\partial^2 f}{\partial \sigma_{yy} \partial \sigma_{xy}} & \frac{\partial^2 f}{\partial \sigma_{xy}^2} \end{bmatrix} \tag{17}$$

The property of the positive semi-definite can be proved by showing that the eigenvalues of the Hessian matrix H are non-negative. Based on this analysis, it is easy to check the convexity condition of the proposed yield function. In this study, the results indicated that the proposed yield function satisfies the convexity condition.

2.3 *Effect of A and B on Yield Surface for the Case of Plane Stress*

From the results are shown in Fig. 1, this new isotropic yield function involves the parameters α and β, which affect on the shape of the yield surface. If the parameter β is zero, the yield locus shapes become the symmetric yield locus. If parameter β is positive, the yield locus shapes become the asymmetric yield locus. In this case, the compression region is larger than the tension region as shown in Fig. 1a. If parameter β is negative, the yield locus shapes are also changed to asymmetric yield locus. However, the tension region is larger than the compression region as shown in Fig. 1b. The results indicated that the arbitrary coefficients α and β give a greater degree of flexibility to these shapes of the yield locus.

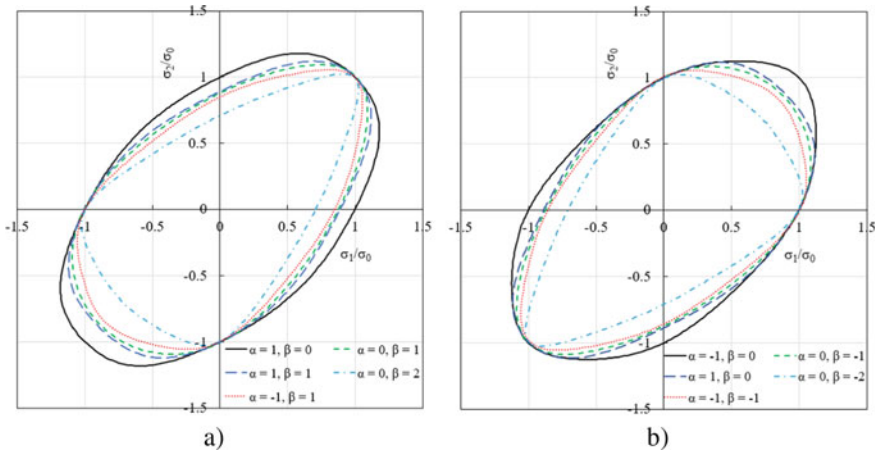


Fig. 1 The yield locus according to the proposed isotropic yield function for different values of the parameters α and β: **a** β is positive **b** β is negative. (Color figure online)

3 Applications of the Proposed Model

3.1 Application of the Proposed Yield Function to AA6016-T4 Sheet

Uniaxial tension and bulge data for the AA6016-T4 sheet were reported in Cazacu-Barlat et al. [10, 16, 17]. To identify the coefficients by fitting the experimental data with predicted ones, we adopt the following error function to be minimized:

$$F = \sum_{i}^{n} \eta_i \left(1 - \frac{(\sigma_\theta)_i^{\text{th}}}{(\sigma_\theta)_i^{\text{data}}}\right)^2 + \sum_{j}^{m} \gamma_j \left(1 - \frac{(r_\theta)_i^{\text{th}}}{(r_\theta)_i^{\text{data}}}\right)^2 + \delta\left(1 - \frac{(\sigma_b)_i^{\text{th}}}{(\sigma_b)_i^{\text{data}}}\right)^2 + \upsilon\left(1 - \frac{(r_b)_i^{\text{th}}}{(r_b)_i^{\text{data}}}\right)^2 + \sum_{k}^{t} \chi_k \left(1 - \frac{(r')_k^{\text{th}}}{(r)_k^{\text{data}}}\right)^2 \tag{18}$$

In the above equation, n and m represent the number of experimental yield stresses and r-values, respectively, for uniaxial tensile tests, corresponding to different orientations θ are available, σ_b and r_b are equi-biaxial tensile yield stress and biaxial coefficient, respectively, t represents the number of experimental biaxial tension and compression at different load ratios, the superscript indicates whether the respective value is experimental or calculated data while η_i, γ_j, δ, υ, and χ_k are weight factors, φ_k is the loading angle of the i^{th} stress point from the x-axis in the principal stress space, r is the distance between the origin of the principal stress space and the ith measured stress point and r' is the distance between the origin of the principal stress space and the calculated yield locus along the loading direction φ_k as shown in Fig. 2 [18].

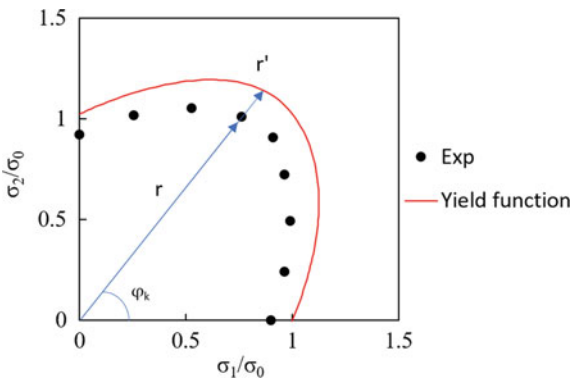


Fig. 2 Schematics for the calculation of the error distance of a calculated yield locus from the measured work contour. (Color figure online)

The yield locus and the predicted variation of the normalized uniaxial yield stress σ_θ/σ_0, r-values r_θ according to the KV6 yield function are shown in Fig. 3a, c, d, respectively, in comparison with the measured yield locus, yield stresses, and r-values for AA6016-T4 sheet [16]. The AA6016-T4 material is one of the FCC crystal structure materials. In previous studies, the yield locus shape of the AA6016-T4 was symmetric shape. Therefore, the parameter $\beta = 0$ is taken in this case. The numerical values of the coefficients involved in the KV6 yield function in plane stress $\sigma_3 = 0$ were determined by minimizing the error function (18) from the experimental yield stresses and r-values for $\theta = 0°$, 15°, 45°, 75°, 90°, the equi-biaxial tensile yield stress $\sigma_b/\sigma_o = 1.0$. These coefficients are shown in Table 1. Figure 3b shows 3D yield surface of the KV6 yield function considering the influence of the shear stress.

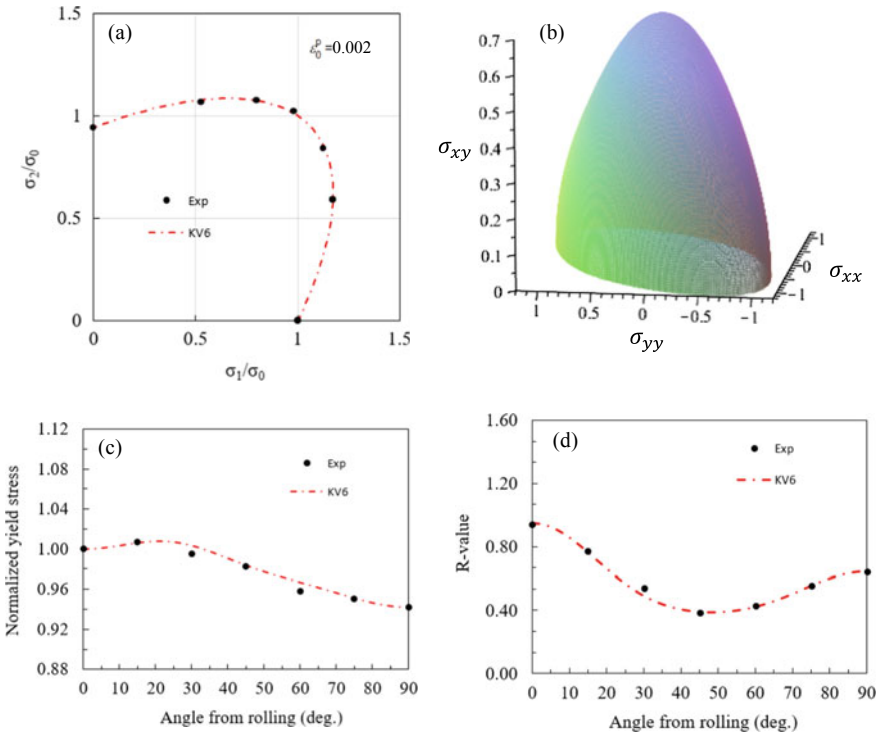


Fig. 3 Predicted anisotropy according to the KV6 yield function for AA6016-T4 sheet: **a** Yield locus, **b** 3D yield surface **c** Uniaxial yield stresses, **d** R-values. (Color figure online)

Table 1 Anisotropic coefficients of the KV6 yield function

Parameters	a_1	a_2	a_3	a_4	b_1	b_2	b_3	b_4	b_5	b_{10}	α	β
KV6	1.085	0.846	0.696	0.697	0.384	1.616	2.408	0.271	1.315	1.257	1.986	0

From the results are shown in Fig. 3, the yield locus shape and the following dependence of the predicted r-values on the angle θ between the direction of loading and the rolling direction in the KV6 model are in good agreement with experimental data.

3.2 *Application of the Proposed Yield Function to the Magnesium Sheet*

The yield locus for the magnesium sheet is shown in Fig. 4. The numerical values of the coefficients involved in the KV6 yield function were determined by minimizing the error function (18) from the experimental biaxial stresses including 7 load ratios of biaxial tensions data (1:0; 4:1; 2:1; 4:3; 1:1; 1:2; 0:1) and 2 load ratios of biaxial compressions data (1:0; 0:1) are shown in Fig. 4 [19]. These coefficients are shown in Table 2.

The yield locus shape in the KV6 model is in good agreement with experimental data [19] as shown in Fig. 4. The comparison between the KV6 yield function and

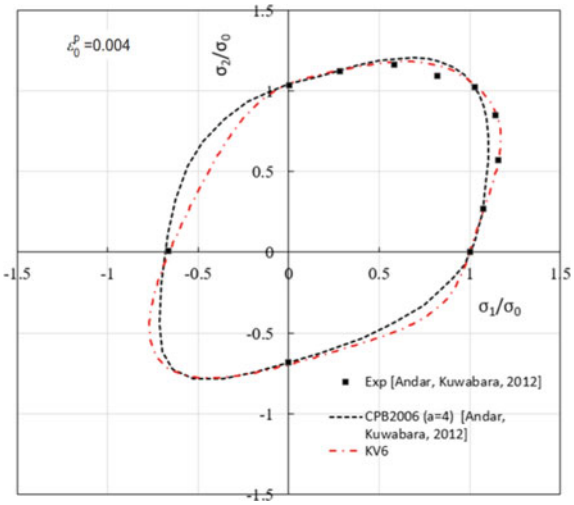


Fig. 4 Predicted yield locus according to the KV6 yield function and CPB2006's yield function for magnesium sheet. (Color figure online)

Table 2 Anisotropic coefficients of the KV6 yield function for Mg AZ31 sheet

Parameters	a_1	a_2	a_3	a_4	b_1	b_2	b_3	b_4	b_5	b_{10}	α	β
KV6	1.385	1.439	1.441	0	1.526	3.932	3.810	0.316	0	0	3.324	−3.105

CPB2006's yield function shows that both predicted yield loci are fitted well with experimental data.

3.3 *Application of the Proposed Yield Function to the Pure Titanium Sheet*

The yield locus for the pure titanium sheet is shown in Fig. 5. The numerical values of the coefficients involved in the KV6 yield function were determined by minimizing the error function (18) from the experimental biaxial stresses including 6 load ratios of biaxial tensions data (1:0; 2:1; 1:1; 3:4; 1:2; 0:1) and 3 load ratios of biaxial compressions data (1:0; 1:1; 0:1) are shown in Fig. 5 [20]. These coefficients are shown in Table 3.

The yield locus shape in the KV6 model is in good agreement with experimental data [20] as shown in Fig. 5. The comparison between the KV6 yield function and Yoon2014' yield function of Eq. (5) shows that both predicted yield loci are fitted well with experimental data. It is clear that the proposed yield function can predict with accuracy for the asymmetric materials as hcp crystal structure materials.

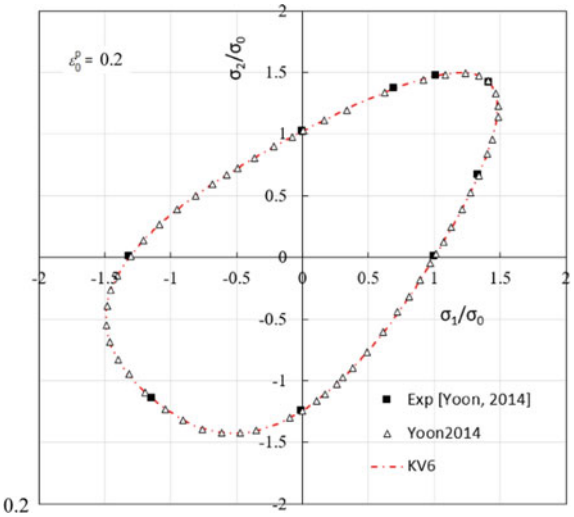


Fig. 5 Predicted yield locus according to the KV6 yield function and Yoon2014 yield function for high-purity α-titanium sheet. (Color figure online)

Table 3 Anisotropic coefficients of the KV6 yield function for high-purity α-titanium sheet

Parameters	a_1	a_2	a_3	a_4	b_1	b_2	b_3	b_4	b_5	b_{10}	α	β
KV6	0.976	0.645	0.634	0	0.964	1.112	0.906	0.634	0	0	0.473	1.397

4 Conclusions

In this paper, a new isotropic yield function expressed in terms of both invariants J_2 and J_3 was proposed. This new isotropic yield function involves the parameters α and β, which affect on the shape of the yield surface. If both parameters are zero, the von Mises yield function is recovered. The extension of the new isotropic yield function to anisotropic yield function has been developed. In this study, the result indicates that the proposed anisotropic model is reasonable to predict the yield locus, the normalized yield stresses and r-values of the sheet metals with the strong anisotropy. It was emphasized that the combination of two terms including α and β parameters in the KV6 yield function generates a new yield function that is able to describe the strong anisotropic material with high flexibility. In further work, the application of the new proposed yield function to predict the forming limit curve should be considered and discussed in more detail.

Acknowledgments This work was supported by the Ministry of Education of the Republic of Korea and the National Research Foundation of Korea (NRF-2019R1A2C1011224).

References

1. Fah CW, Han DJ (1987) Plasticity for structural engineering. Springer, New York, pp 46–84
2. Ram NW, Lee MG (2016) Yield functions for sheet metal forming applications. Trans Mater Process 25:275–282
3. Banabic D (2010) Sheet metal forming processes, Constitutive modelling and numerical simulation. Springer, Heidelberg
4. Shimizu I, Tada N (2007) Plastic behavior of polycrystalline aluminum during biaxial compression with strain path change. Key Eng Mater 340–341:883–888
5. Cazacu O, Barlat F (2004) A criterion for description of anisotropy and yield differential effects in pressure-insensitive metals. Int J Plast 20:2027–2045
6. Cazacu O (2006) Orthotropic yield criterion for hexagonal closed packed metals. Int J Plast 22:1171–1194
7. Gao X, Zhang T (2011) On stress-state dependent plasticity modeling: significance of the hydrostatic stress, the third invariant of stress deviator and the non-associated flow rule. Int J Plast 27:217–231
8. Khan AS (2012) Deformation induced anisotropic responses of Ti-6Al-4V alloy Part II: a strain rate and temperature dependent anisotropic yield criterion. Int J Plast 38:14–26
9. Yoon JW, Lou YS (2014) Asymmetric yield function based on the stress invariants for pressure sensitive metals. Int J Plast 56:184–202
10. Cazacu O, Barlat F (2001) Generalization of Drucker's yield criterion to orthotropy. Math Mech Solids 6:613–630
11. Cazacu O (2018) New yield criteria for isotropic and textured metallic materials. Int J Solids Struct 200–210
12. Zhang S, Zang SL (2014) Calibration of anisotropic yield criterion with conventional tests or biaxial test. Int J Mech Sci 85:142–151
13. Cardoso RPR, Adetoro OB (2017) A generalization of the Hill's quadratic yield function for planar plastic anisotropy to consider loading direction. Int J Mech Sci 253–268

14. Barlat F (2003) Plane stress yield function for aluminum alloy sheets – part 1: theory. Int J Plast 19:1297–1319
15. Laydi MR (2010) Yield criteria for shape memory materials: Convexity conditions and surface transport. Math Mech Solids 15:165–208
16. Lazarescu L (2013) Determination of material parameters of sheet metals using the hydraulic bulge test. Acta Metallurgica Slovaca 19:4–12
17. Tamura S, Yoshida F (2011) Experimental observation of Elasto Plasticity behavior of type 5000 and 6000 Aluminum alloy sheets. Mater Trans 52(5):868–875
18. Hakoyama T, Kuwabara T (2015) Effect of biaxial work hardening modeling for sheet metals on the accuracy of forming limit analyses using the Marciniak—Kuczynski approach. Springer International Publishing Switzerland
19. Andar MO, Kuwabara T, Steglich D (2012) Material modeling of AZ31 Mg sheet considering variation of r-values and asymmetry of the yield locus. Mater Sci Eng A 549:82–92
20. Yoon JW, Lou YS, Glazoff MV (2014) Asymmetric yield function based on the stress invariants for pressure sensitive metals. Int J Plast 56:184–202

Experimental Implementation of SS 316L Cruciform Testing to Achieve Various Deformation Paths



Elizabeth M. Mamros, Sarah M. Mayer, Jinjin Ha, and Brad L. Kinsey

Abstract By following varying deformation paths, e.g., a linear path to equibiaxial loading versus a bilinear path of uniaxial loading followed by biaxial loading, the same final strain state can be achieved. However, the stress state that the material is subjected to is considerably different due to the varying deformation. This is of interest in a growing field of stress superposition to improve formability and manipulate final part properties in metal forming applications. One potential application is forming patient-specific, trauma fixation hardware with differing strength and weight reduction requirements in various regions. In this paper, experiments were performed on a custom fabricated cruciform machine with the goal of subjecting stainless steel 316L to various deformation paths. A novel cruciform specimen geometry was designed in collaboration with the US National Institute of Standards and Technology to achieve large strain values in the gauge region. Digital Image Correlation was utilized to measure surface strain fields in real time.

Keywords Forming · Deformation path · Biaxial loading · Stainless steel · Cruciform

1 Introduction

Due to both work hardening and possible phase transformations during forming, the initial material properties are not necessarily representative of the properties in the processed part. Conventional experiments for the material characterization, including uniaxial tension, and basic constitutive laws do not capture the material behavior correctly under complex and varying loading paths that are often intrinsic to forming processes [1].

E. M. Mamros · S. M. Mayer · J. Ha · B. L. Kinsey (✉)
University of New Hampshire, Durham, NH 03824, USA
e-mail: bkinsey@unh.edu

E. M. Mamros
e-mail: emm1109@wildcats.unh.edu

© The Minerals, Metals & Materials Society 2021

G. Daehn et al. (eds.), *Forming the Future*, The Minerals, Metals & Materials Series,
https://doi.org/10.1007/978-3-030-75381-8_166

In order to capture such complex loading experimentally, Shiratori and Ikegami proposed the cruciform biaxial tension experimental procedure in 1967 [2]. In contrast to hemispherical dome tests (another technique for biaxial loading experimentation), cruciform tests do not involve a pressurization effect, allow the same specimen geometry to be used for all experiments, and enable the deformation path to be varied during a test [3]. In recent decades, several biaxial cruciform machines have been developed, some of which are summarized in [3], but, thus far, an ASTM standard for the cruciform specimen geometry does not exist. Common problems that arise when designing cruciform specimens include early failure in the arms, low strain values at failure, and a non-homogeneous strain distribution in the gauge area.

Austenitic stainless steels (SS) undergo stress-induced phase transformation to martensite during forming, particularly at low temperatures and high strains [4]. Hecker et al. found that for the case of balanced biaxial tension of SS 304L, the degree of martensitic transformation is more than twice the amount observed, per maximum principal strain value, during uniaxial tension [5]. Thus, characterization of the transformation kinetics at various proportional loading paths is required to determine the deformation path most beneficial in terms of stress superposition.

In this paper, SS 316L specimens were loaded on a custom cruciform frame [7] designed to implement non-linear deformation paths. A custom cruciform specimen able to achieve large strain values in the gauge area was created in collaboration with the US National Institute of Standards and Technology (NIST) via a previously used methodology [1, 6]. The three loading paths investigated, 4:4 (equibiaxial), 4:2, and 4:0, were applied as constant displacement ratios between the perpendicular axes ($\Delta Y : \Delta X$). The area of interest on the specimen, i.e., the flat surface within the pocket in the gauge area, was chosen to capture a region containing relatively uniform deformation. Digital Image Correlation (DIC) was used to measure the strains *in-situ.* The martensitic transformations of SS 316L will be measured using electron backscatter diffraction (EBSD) with the scanning electron microscope, but this is outside of the scope of this paper.

2 Experimental Setup and Methods

2.1 Material and Specimen Preparation

SS 316L, a biocompatible material, with a thickness of 1.2 mm was used in this study. In collaboration with NIST, a cruciform specimen geometry was designed based on past research [1, 6]. The slightly modified design objectives were to create a specimen that could be manufactured in-house, i.e., with waterjet cutting and milling operations, and achieve both a high equivalent plastic strain and a homogeneous strain distribution in the gauge area. The high equivalent plastic strain threshold was targeted to enhance the amount of martensitic phase transformations, a microstructural change that is common in austenitic stainless steels, including 316L, with large

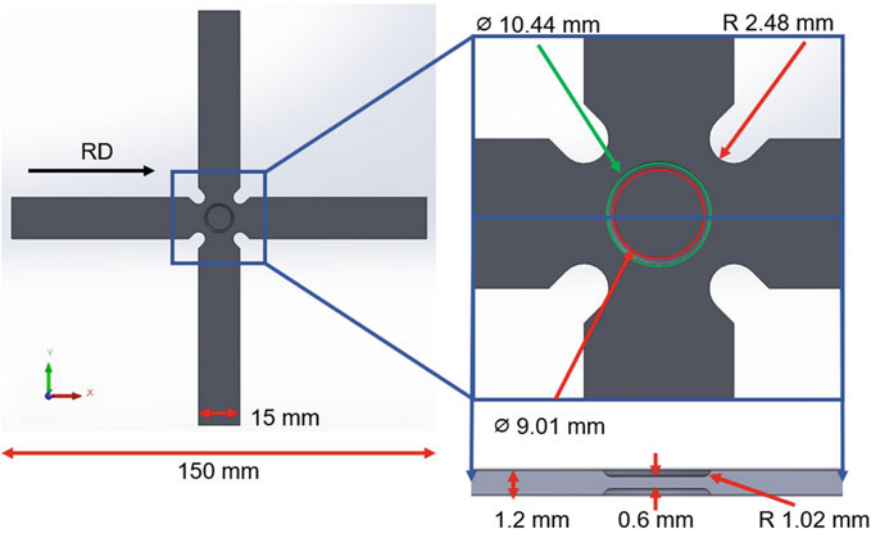


Fig. 1 Overall cruciform specimen geometry obtained from 1.2 mm thick SS 316L [8]. (Color figure online)

deformations. The homogeneous strain distribution in the gauge area will be critical for accurate martensitic transformation measurements. The specimens were oriented with arms parallel to the rolling and transverse directions, and the profile was waterjet cut (see Fig. 1). The edges were sanded prior to testing. A 4 mm diameter end mill was used on each side of the specimen to machine the pocket in the gauge section. The fabricated specimen dimensions were measured using a confocal microscope (Olympus OLS5000-SAF) to confirm that all desired tolerances were achieved.

NIST has investigated this specimen geometry during previous research [1, 6], but in order to use this geometry in conjunction with the cruciform machine at UNH, modifications were required. Two key factors necessitating this geometry study were accounting for the size difference between the testing equipment and meeting the desired minimum equivalent plastic strain threshold of 30% in the center pocket. Table 1 lists the dimensions used to fabricate the specimens at UNH. Figure 2 shows a schematic of the cruciform specimen geometry with dimensions that correspond to the values in Table 1.

2.2 Cruciform Machine

A cruciform machine capable of applying biaxial tension along perpendicular axes was constructed at UNH in collaboration with Prof. Kuwabara at the Tokyo University of Agriculture and Technology [9] (see Fig. 3). The loading is applied via four Parker 3LX Series hydraulic cylinders (see Table 2 for key specifications).

Table 1 Cruciform geometry dimensions

Dimension	Value (mm)
Gauge thickness, T_{pocket}	0.60
Sheet thickness, T_{sample}	1.20
Fillet, F_{pocket}	1.02
Flat area radius, R_{gauge}	4.51
Pocket diameter, D_{pocket}	10.44
Arm width, W_{arm}	15.00
Notch radius, R_{notch}	2.48
Notch diameter, D_{notch}	4.96
Diagonal	21.21

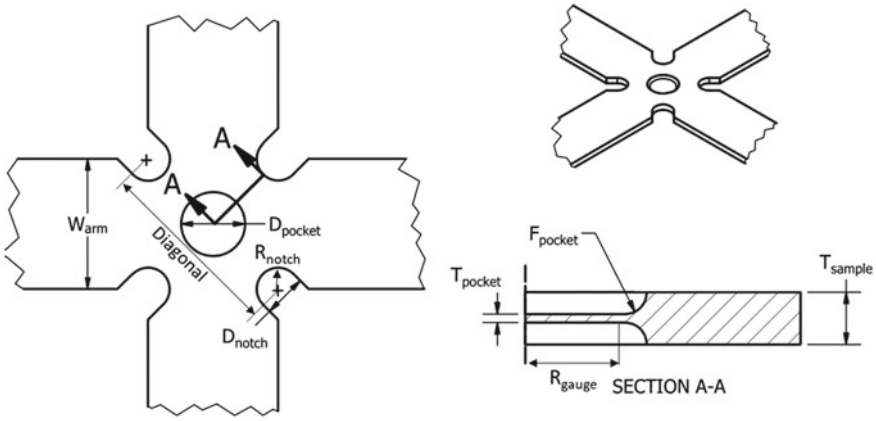


Fig. 2 Schematic of final cruciform specimen geometry (modified from [6])

Greenerd Press and Machine Co. designed and built the hydraulic system and control circuitry. The machine can displace the opposing cylinders equally within 0.1 mm of the programmed value at a maximum velocity of 80 mm/min. A human–machine interface was programmed in LabVIEW software to control the machine.

2.3 Digital Image Correlation

To capture strain measurements in-situ, two FLIR 8.9 megapixel cameras with 50 mm Schneider Xenoplan compact lens were used (see Fig. 3) for 3D DIC analyses. The specimens were prepared with a white background and overlaid black speckle pattern using spray paint. The images were post-processed in VIC-3D from Correlated Solutions, Inc. with subset, step, and filter sizes of 21, 5, and 5 pixels, respectively. The area of interest selected was the ~ 9 mm diameter flat region in the gauge section.

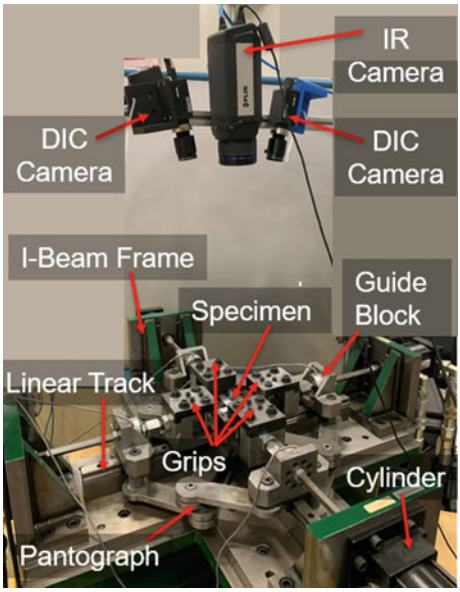


Fig. 3 UNH cruciform machine. (Color figure online)

Table 2 Parker 3LX Series hydraulic cylinder specifications [7]

Parameter	Value
Maximum pressure	9.65 MPa
Bore diameter	63.5 mm
Stroke	12.7 mm
Maximum tensile force	25.8 kN
Maximum compressive force	30.7 kN

The temperature increase during these experiments, captured by the FLIR SC-645 infrared camera, was < 15 °C, and thus, further temperature data is not presented in this work.

2.4 Biaxial Experiments

The biaxial experiments were conducted on the cruciform machine by programming displacements and pulling speeds in each axis. A removable fixture to ensure consistent specimen placement and proper alignment in the grips was designed and 3D-printed (see Fig. 4). For consistency, the arms oriented along the rolling direction (RD) were positioned parallel to the x-axis for each experiment. For equibiaxial conditions, a total displacement of 10 mm, i.e., 5 mm along each arm, and pulling speed of 0.1 mm/s were prescribed to each axis. For the other loading conditions,

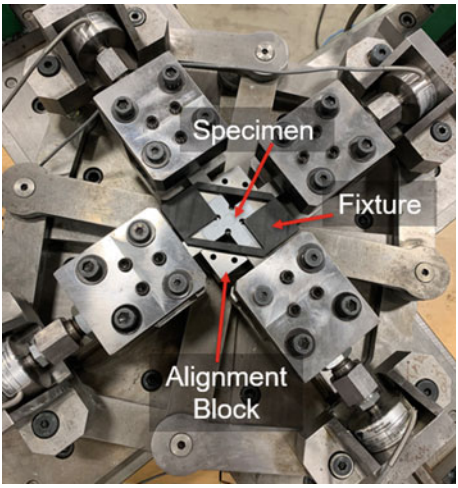


Fig. 4 Specimen alignment fixture on cruciform machine. (Color figure online)

the pulling speed of the x-axis was decreased according to the desired displacement to ensure that the displacement ramps would terminate at the same time. The strain rate along each axis for all experiments was approximately 10^{-3} – 10^{-4} s^{-1}. Three experiments were completed for each displacement case of interest to verify repeatability.

3 Results and Discussion

3.1 Force Versus Displacement Results

During each experiment, the biaxial cruciform machine recorded force and displacement data for each axis from the load cells and embedded linear variable displacement transducers, respectively. The displacement values presented represent the displacement along the positive axes, i.e., the total displacement for each axis is twice the stated value. Figure 5 summarizes these results for all displacement paths. Comparing the maximum displacements along the y-axis (TD), the 4:0 path had the largest value, followed by the 4:2 path, and the 4:4 path had the smallest value as expected. With respect to the y-axis (TD), the maximum force values follow the same trend for the three displacement paths presented.

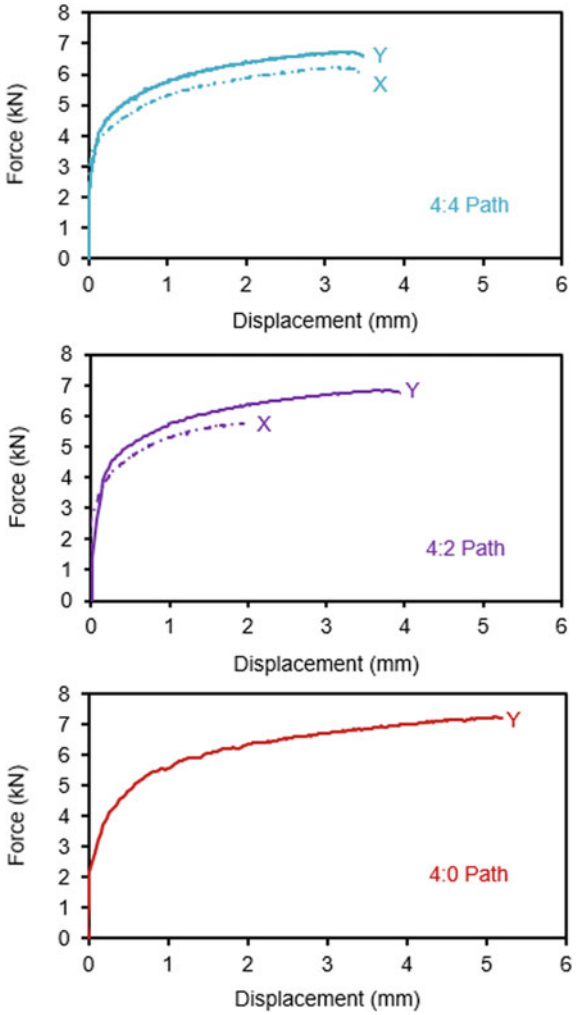


Fig. 5 Force–displacement curves for all 4:4, 4:2, and 4:0 displacement paths. (Color figure online)

Table 3 DIC true strain results from the image prior to fracture for 4:4, 4:2, and 4:0 displacement paths

	Value at center point (mm/mm)		
True strain	4:4 path	4:2 path	4:0 path
ε_{xx}	0.188	0.127	−0.136
ε_{yy}	0.185	0.249	0.233
ε_{VM}	0.189	0.218	0.323

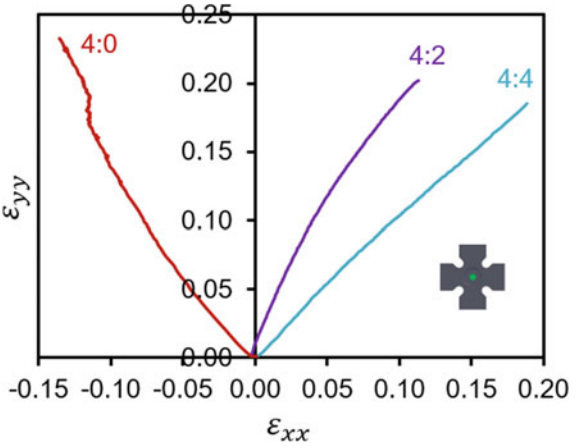


Fig. 6 True strain paths extracted from DIC analyses at the center of the specimen for 4:0, 4:2, and 4:0 displacement paths. (Color figure online)

3.2 Strain Results

Table 3 shows the true strain values onset of fracture at the center point of the specimen geometry. The corresponding strain paths, ε_{yy} versus ε_{xx}, are shown in Fig. 6. The strain contours and values at the center point for the x-direction and y-direction are nearly equivalent as expected for the equibiaxial case, with variations being due to the anisotropy of the material. The 4:2 path had a slightly larger true strain along the y-direction than the 4:0 path, but the 4:0 path exhibited a much larger equivalent von Mises strain than the 4:2 path.

The strain distributions in the gauge area are shown in Fig. 7. The strain contours show that the equivalent von Mises strain is >30% within the gauge region, not necessarily at the center point, for all displacement paths. This indicates that significant martensitic transformation is expected in the corresponding locations.

4 Conclusion and Future Work

Initial experimental results from SS 316L cruciform specimens deformed with 4:4, 4:2, and 4:0 displacement paths have been presented. The resulting strain values were determined with 3D DIC and indicate the propensity for martensitic transformation. Future experiments will be conducted to investigate varying deformation paths and to determine the relationship between a specific non-linear deformation path and the induced martensitic transformations measured by EBSD. An analytical model will also be developed to determine multiple non-linear deformation paths that will result in the same final strain state but hypothesized differing martensite volume fractions.

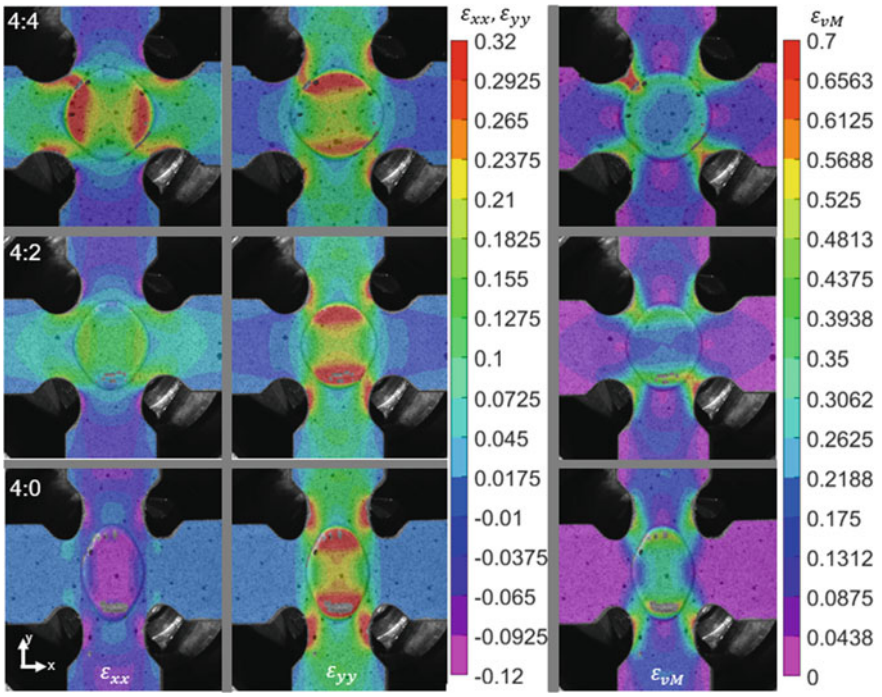


Fig. 7 True strain distribution immediately prior to fracture: x-direction, y-direction, and von Mises for 4:4, 4:2, and 4:0 displacement paths. (Color figure online)

Acknowledgments The authors would like to thank Mark Iadicola and Dilip Banerjee from NIST for their assistance in designing this cruciform specimen. The Olympus confocal microscope used is managed by the University Instrumentation Center (UIC) at the University of New Hampshire (UNH). Support for the NH BioMade Project is provided by the US National Science Foundation EPSCoR award (#1757371).

References

1. Creuziger A, Iadicola MA, Foecke T, Rust E, Banerjee D (2017) Insights into Cruciform Sample Design. JOM (1989) 69(5): 902–906. https://doi.org/10.1007/s11837-017-2261-6
2. Shiratori E, Ikegami K (1967) A new biaxial tensile testing machine with flat specimen. Bull Tokyo Instit Technol 82:105–118
3. Xiao R (2019) A review of cruciform biaxial tensile testing of sheet metals. Exp Tech 43:501. https://doi.org/10.1007/s40799-018-00297-6
4. Lichtenfeld JA, Van Tyne CJ, Mataya MC (2006) Effect of strain rate on stress-strain behavior of alloy 309 and 304L austenitic stainless steel. Metall Mater Trans A 37:147. https://doi.org/10.1007/s11661-006-0160-5

5. Hecker SS, Stout MG, Staudhammer KP, Smith JL (1982) Effects of strain state and strain rate on deformation-induced transformation in 304 stainless steel: part I. magnetic measurements and mechanical behavior. Metall Trans A 13A: 619–26.
6. Iadicola MA, Creuziger AA, Foecke T (2014) Advanced biaxial cruciform testing at the NIST Center for Automotive lightweighting. In: Rossi M, Sasso M, Connesson N, Singh R, DeWald A, Backman D et al. (eds) Residual stress, thermomechanics and infrared imaging, hybrid techniques and inverse problems, vol 8, Springer International Publishing, pp 277–285
7. Wilson JF (2015) Development of a biaxial loading frame for thin sheet cruciform specimens. Master's Theses and Capstones, University of New Hampshire, 1027. scholars.unh.edu/thesis/1027
8. Mamros EM, Eaton MC, Ha J, Kinsey BL (2021) Numerical analysis of SS316L biaxial cruciform specimens under proportional loading paths. In: Proceedings of ASME manufacturing science and engineering conference
9. Deng N, Kuwabara T, Korkolis YP (2015) Cruciform specimen design and verification for constitutive identification of anisotropic sheets. Exp Mech 55:1005. https://doi.org/10.1007/s11340-015-9999-y

An Application of Homogeneous Anisotropic Hardening Model to the Prestrained Hole-Expansion Experiment



Jinjin Ha and Yannis P. Korkolis

Abstract In this work, the plastic anisotropy of AA6022-T4 in hole-expansion is investigated focusing on prestraining effect, and its numerical solution is predicted by Homogeneous Anisotropic Hardening (HAH) model combined with an anisotropic yield function. For the prestraining, the material is subjected to a prestrain of 8% in uniaxial tension in the RD. Then, hole-expansion is conducted in a fully instrumented hydraulic press with a flat-headed punch. In both experiments, Digital Image Correlation (DIC) is used, to confirm the prevalence of uniaxial loading in the prestraining step and to measure thickness strain in the hole-expansion. The results show that the plastic anisotropy is manifested as a non-axisymmetric strain distribution around the hole. The prestraining, leading to non-proportional loading, changes the location of failure from ~45° to RD. The simulation shows the current version of HAH model is limited in capturing the thickness contours and the failure location.

Keywords Non-proportional loading · Anisotropy · Hole-expansion · Aluminum alloy

1 Introduction

Stretch flange formability is a particular interest in sheet metal forming, where holes can be an initiator of edge cracking during a subsequent forming operation, such as wheels and suspensions of automotive parts [1]. The edge is deformed under uniaxial tension because of the free surface, but the forming limit is often much higher than that of standard uniaxial tension due to the delayed geometrical instability. In this regard, the flange formability has been evaluated using other kinds of experiments like hole-expansion instead of the standard uniaxial tension. As an approximated solution for the hole-expansion, Parmar and Mellor [2] derived an analytical solution to predict

J. Ha
Mechanical Engineering, University of New Hampshire, Durham, NH 03824, USA

Y. P. Korkolis (✉)
Integrated System Engineering, The Ohio State University, Columbus, OH 43210, USA
e-mail: korkolis.1@osu.edu

© The Minerals, Metals & Materials Society 2021

G. Daehn et al. (eds.), *Forming the Future*, The Minerals, Metals & Materials Series,
https://doi.org/10.1007/978-3-030-75381-8_167

stress and strain variations in the hole periphery and showed that the prediction highly depended on the yield function used for the analytical model and r-value of the material. More recently, numerous studies used the hole-expansion experiment to validate the ability of the yield function to capture the plastic anisotropy manifested as strain variation around the hole using finite element simulation [3–5].

In this regard, the current study also adopts the hole-expansion experiment but with the accent on the evaluation of the prestraining effect on the evolution of plastic anisotropy [6–9]. Because it is a very simple example of a non-linear strain path, which are prevalent in stamping of complex components. The experiment is performed in 2 steps: (1) uniaxial prestraining in the rolling direction (RD) and 2) hole-expansion with a flat-headed round-punch. Test material is AA6022-T4 sheet of 1 mm thickness [10] which is one of the common automotive aluminum materials. The process is simulated using the Yld2000-2d yield function [11] combined with the Homogeneous Anisotropic Hardening (HAH) model [12–14]. The yield function chosen has been widely used to capture the plastic anisotropy of various aluminum sheets; the strain hardening model, i.e., HAH, is a recent proposal with improved performance in predicting non-linear path behavior, such as the Bauschinger effect, albeit its full potential is not yet known.

2 Material Characterization and Parameter Identification of Constitutive Models

The plastic anisotropy and strain hardening behavior of the material are characterized by uniaxial tension and tension–compression experiments. Uniaxial tension is conducted in every 15° from the RD, from which the plastic anisotropy is presented by normalized flow stress and r-value ($d\varepsilon_w/d\varepsilon_t$) as seen in Fig. 1a. The result represents

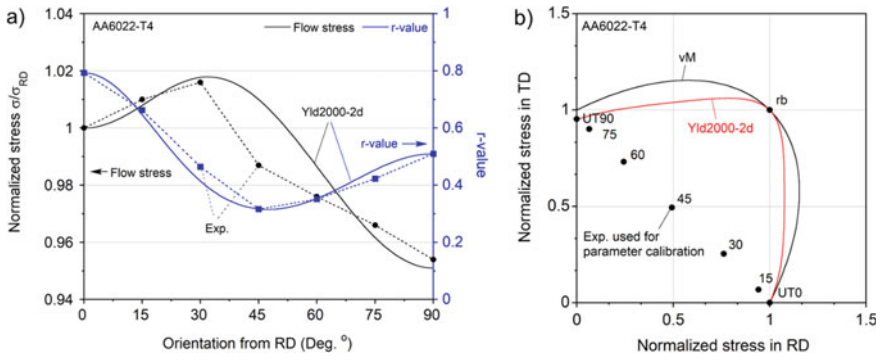


Fig. 1 The experiment of uniaxial tension in every 15° from the RD and the calibration of Yld2000-2d: **a** plastic anisotropy for normalized flow stress and r-value and **b** yield loci of Yld2000-2d and von-Mises (vM). (Color figure online)

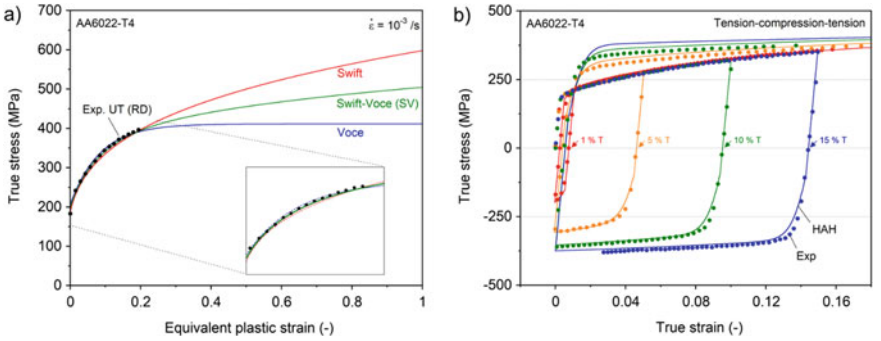


Fig. 2 Hardening parameter identification for **a** Swift-Voce combined model for the uniaxial tension in the RD and **b** HAH model for tension–compression in the RD. (Color figure online)

that higher anisotropy in the strain field is expected than that in the stress field, especially at 45°, which has the lowest resistance to thinning. The data is used to calibrate a non-quadratic anisotropic yield function, i.e., Yld2000-2d (Fig. 1a) using Newton–Raphson method, and the corresponding yield locus in the 1st quadrant is described in Fig. 1b with a quadratic isotropic yield function, i.e., von-Mises, as a reference. Isotropic strain hardening behavior is also identified by the stress–strain curve from uniaxial tension in the RD (Fig. 2a), which is extrapolated by Swift-Voce combined model. In addition, anisotropic strain hardening behavior under a non-proportional loading path is characterized by a tension–compression experiment with different amounts of prestraining in tension (symbol in Fig. 2b), from which HAH model is calibrated (solid line) like in Fig. 2b. The model captures anisotropic strain hardening behavior very well such as Bauschinger effect, i.e., early re-yielding on load reversal, and following transient behavior, i.e., subsequent high strain hardening rate region. The calibrated model parameters are summarized in Tables 1, 2, and 3.

Table 1 Parameters for Swift-Voce combined model

w_a	K_s	ε_0	n	K_v	q	p
0.5	576.17	0.012	0.263	381.4	190.6	11.96

Table 2 Parameters for Yld2000-2d

m	α_1	α_2	α_3	α_4	α_5	α_6	α_7	α_8
8	1.0125	0.9397	0.8643	1.0458	1.0121	1.0158	0.8844	1.0997

Table 3 Parameters for HAH model (q = 2)

k	k_1	k_2	k_3	k_4	k_5	k_L	L	k_s	S
30	230	75	0.4	0.8	2	0	1	5	0.8

3 Hole-Expansion Experiment with Prestraining

In order to impose the prestraining effect on the hole-expansion, the material is first subjected to 8% true uniaxial tension in the RD using a large specimen (Step 1 in Fig. 3), and then the hole-expansion experiment (Step 2 in Fig. 3) is conducted using a specimen extracted from step 1. The prestraining specimen is designed to induce uniform strain only in the major deformation region for the hole-expansion experiment, i.e., from the hole to the punch radius. The uniform true strain, approximately 8% of uniaxial tension, in this area is confirmed by the digital image correlation (2D-DIC) system. After the prestraining, the large specimen is unloaded from the testing machine, and the hole-expansion specimen is prepared by end-milling for a fine surface quality, to prevent early failure. The hole-expansion experiment is conducted in a double action hydraulic press of 260 kN load capacity, and the real-time strain field during the experiment is acquired by the 3D-DIC system.

In Fig. 4, thickness strain spatial distributions at the onset of fracture are presented for the as-received hole-expansion (HE) and uniaxial tension followed by hole-expansion (UT-HE) in the RD. The profiles measured at 40 mm dia. hoop are compared in the graph as well. As expected from the r-value evaluation, the highest thickness reduction is observed near at 45° from the RD in the HE, while it changes to the RD in the UT-HE. All locations of highest thickness reduction lead to the first rupture that ends the HE experiment. This comparison reveals that the current non-proportional loading path has a strong influence on the evolution of plastic anisotropy, which alters the failure behavior in HE and even reduces the overall formability, i.e., lower level of thickness strain in average for UT-HE (solid line in red) compared to that for HE (dashed line in blank).

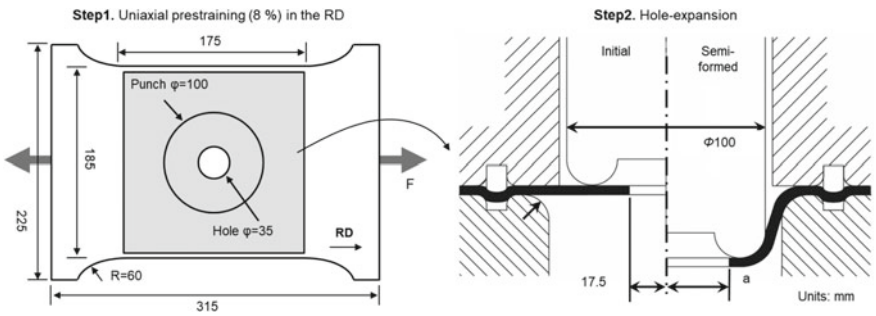


Fig. 3 Illustration of 2-step experiment: the uniaxial prestraining followed by hole-expansion experiment

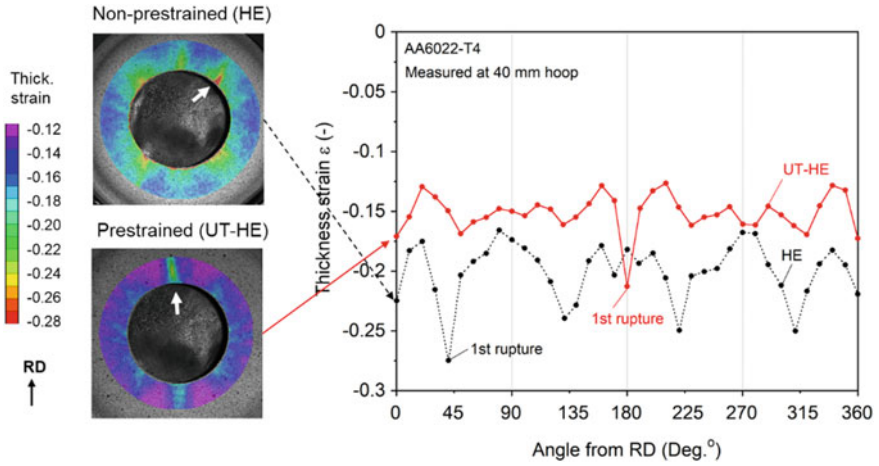


Fig. 4 Thickness strain distribution on the surface and the profiles along 40 mm dia. hoop for the hole-expansion (HE) and the 8% uniaxial tension followed by the hole-expansion (UT-HE). (Color figure online)

4 FE Simulation

The experiment is used to evaluate the adopted constitutive models through the FE simulation using the Abaqus 2019 implicit solver. The constitutive models, i.e., Yld2000-2d and HAH are implemented in a user subroutine. As with the experiment, the simulation is carried out in 2 steps: the uniaxial prestraining around 8% in the RD and the subsequent hole-expansion (Fig. 5). The specimen is modeled in a quarter size considering plane-symmetry and composed of shell elements with reduced thickness (S4R). The necessary initial conditions for Step 2 such as stress, strain, state variables,

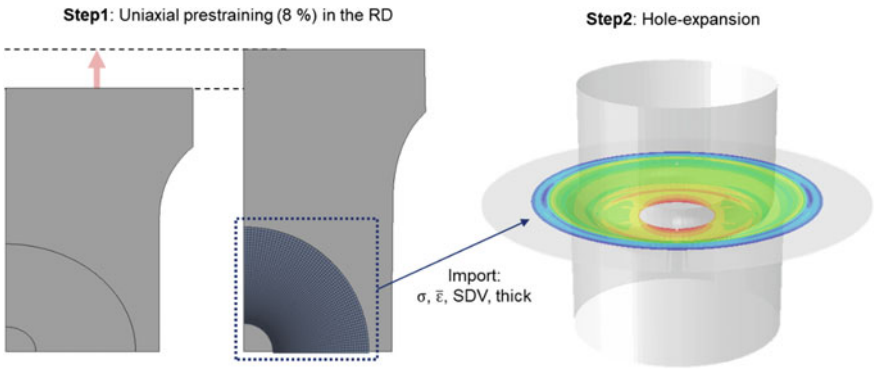


Fig. 5 Schematic of FE simulation for the uniaxial prestraining followed by the hole-expansion. (Color figure online)

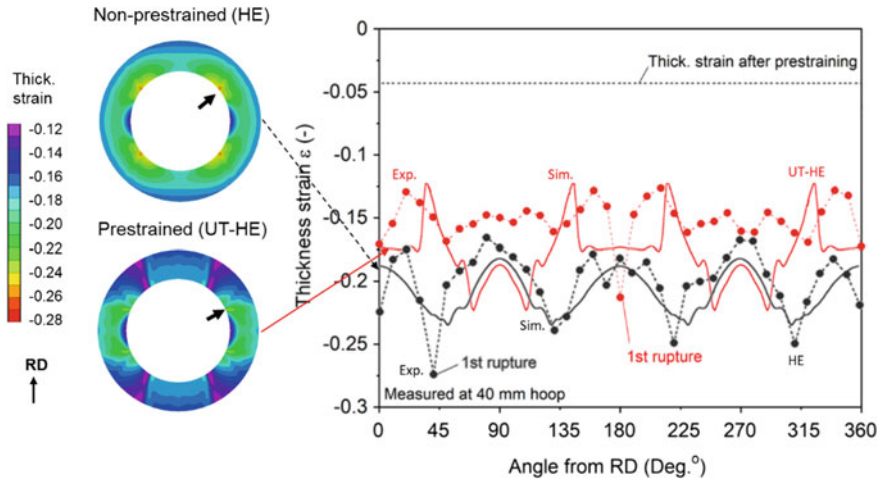


Fig. 6 Prediction of thickness strain variation along the circumference for the hole-expansion (HE) and 8% uniaxial tension followed by hole-expansion (UT-HE). (Color figure online)

thickness, and the geometry are imported from Step 1. Coulomb friction law is assumed with a constant friction coefficient $\mu = 0.17$. This was determined by optimal matching of the punch force–displacement curve by the FE model.

Figure 6 shows the prediction result with the experiment. The same colors correspond to the same experiment and simulation, i.e., blank for HE and red for UT-HE, in which the experiment is in the dashed line with symbol and the simulation in the solid line. Overall, the average strain variation in HE is well captured by the models and, in an average sense, in a good agreement with the experiments. In the as-received HE, the point-to-point, circumferential distribution is also very close between experiments and predictions. However, in the prestraining one, i.e., UT-HE, the predicted distribution is quite off from the experiments, with extreme values appearing at 40° and 70° from the RD.

The prediction difference in HE and UT-HE is caused by the amplitude of non-proportionality of loading path: throughout the hole-expansion deformation, each material point is exposed to light non-proportionality in HE while it is more significant in UT-HE. Especially, the irregular strain variation at 34.6° from the RD, in which the stress state is uniaxial tension in 55.6° from the RD, coincides with the discontinuity in the fluctuation component F, i.e., $F = (\phi_h/\tilde{\sigma})^q$, where $\phi_h = f_1^q \left|\widehat{\mathbf{h}} : \mathbf{s} - \left|\widehat{\mathbf{h}} : \mathbf{s}\right|\right| + f_2^q \left|\widehat{\mathbf{h}} : \mathbf{s} + \left|\widehat{\mathbf{h}} : \mathbf{s}\right|\right|$ with state variables $f_{i,i=1,2}^q$, deviatoric stress $\mathbf{s}$, and normalized microstructure deviator tensor $\widehat{\mathbf{h}}$, which controls the distortional shape of the yield locus as seen in Fig. 7. It should be noted that a solid line presents the yield locus predicted by HAH model with a distortion while a dashed line is a reference yield locus with an isotropic hardening assumption. Dots indicate uniaxial tension in every 15° from the RD, and empty dots represent projected states

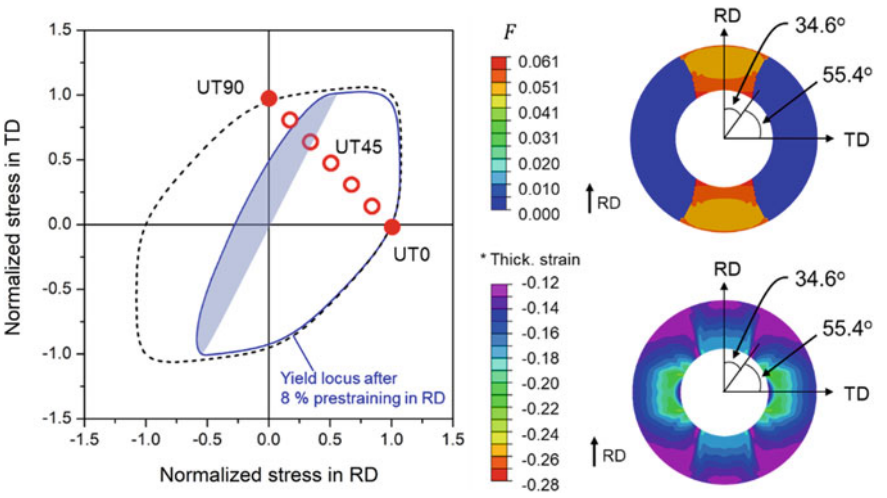


Fig. 7 Discontinuity near distortion affected area. (Color figure online)

on x–y plane, i.e., $\sigma_{12} = 0$. Further analysis for the limited prediction of HAH model related to this discontinuity is necessary in the future to improve the model.

5 Conclusion

The effect of the non-proportional loading path on the evolution of plastic anisotropy is clearly demonstrated through the hole-expansion experiment with uniaxial prestraining, for AA6022-T4. The experiment exhibits that the plastic anisotropy is interrupted by the prior deformation and the overall material formability can be reduced for the particular non-proportional loading paths. The constitutive models adopted for the FE simulation show prediction limitations for the strain variation in the non-proportional loading path case. Thus, further analysis will be necessary with a focus on the observed discontinuity of the fluctuating component and distortional shape in the future.

References

1. Lee J-Y, Lee K-J, Lee M-G, Kuwabara T, Barlat F (2019) Numerical modeling for accurate prediction of strain localization in hole expansion of a steel sheet. Int J Solids Struct 156–157:107–118
2. Parmar A, Mellor PB (1978) Plastic expansion of a circular hole in sheet metal subjected to biaxial tensile stress. Int J Mech Sci 20(10):707–720

3. Kuwabara T, Hashimoto K, Iizuka E, Yoon JW (2011) Effect of anisotropic yield functions on the accuracy of hole expansion simulations. J Mat Proc Tech 211(3):475–481
4. Korkolis YP, Brownell B, Coppieters S, Tian H (2016) Modeling of hole-expansion of AA6022-T4 aluminum sheets with anisotropic non-quadratic yield functions. J Phys: Conf Ser NUMISHEET 734
5. Ha J, Coppieters S, Korkolis YP (2020) On the expansion of a circular hole in an orthotropic elastoplastic thin sheet. Int J Mech Sci 182:105706
6. Ha J, Lee M-G, Barlat F (2013) Strain hardening response and modeling of EDDQ and DP780 steel sheet under non-linear strain path. Mech Mat 64:11–26
7. Ha J, Kim JH, Barlat F, Lee M-G (2014) Continuous strain path change simulations for sheet metal. Comp Mat Sci 82:286–292
8. Lee J, Ha J, Bong JH, Kim D, Lee M-G (2013) Evolutionary anisotropy and flow stress in advanced high strength steels under loading path changes. Mat Sci Eng: A 672: 65–77
9. Ha J, Lee J, Kim JH, Lee M-G, Barlat F (2017) Investigation of plastic strain rate under strain path changes in dual-phase steel using microstructure-based modeling. Int J Plast 93:89–111
10. Tian H, Brownell B, Baral M, Korkolis YP (2017) Earing in cup-drawing of anisotropic Al-6022-T4 sheets. Int J Mater Form 10(3):329–343
11. Barlat F, Brem JC, Yoon JW, Chung K, Dick RE, Lege DJ, Pourboghrat F, Choi S-H, Chu E (2003) Plane stress yield function for aluminum alloy sheets-part 1: theory. Int J Plast 19(9):1297–1319
12. Barlat F, Grácio JJ, Lee M-G, Rauch EF, Vincze G (2011) An alternative to kinematic hardening in classical plasticity. Int J Plast 27:1309–1327
13. Barlat F, Ha J, Grácio JJ, Lee MG, Rauch EF, Vincze G (2013) Extension of homogeneous anisotropic hardening model to cross-loading with latent effects. Int J Plast 46:130–142
14. Barlat F, Vincze G, Grácio JJ, Lee MG, Rauch EF, Tomé CN (2014) Enhancements of homogenous anisotropic hardening model and application to mild and dual-phase steels. Int J Plast 58:201–218

Work Hardening and Fracture Strain Evaluation of Hardened SKD11 Steel Using Shear Punching Test



Takashi Matsuno, Kouta Nakagiri, Hiroto Shoji, and Mitsuru Ohata

Abstract This study identified the work-hardening parameters and fracture strain of a hardened die-steel (SKD11). Herein, a shear punching test was used as the low stress-triaxiality suppresses material fracture due to the brittle behavior of SKD11 in tensile tests. Furthermore, a minute punch-die clearance was used to increase the compression stress due to the material deformation. SKD11 steel sheets of 1.0 mm thickness were successfully deformed, and the punching force as well as stroke were recorded for inverse analysis using the finite element analysis (FEA). Subsequently, FEA of the shear punching test was repeated to optimize the parameters of Swift's work-hardening law. Consequently, the Swift parameters were derived to ensure that the measured values of the punching force and stroke correspond with the numerically simulated curve. The fracture strain was identified as the maximum equivalent plastic strain at the punch stroke of specimen rupture.

Keywords Tool material · Shear punching test · Ductile fracture · Inverse analysis

1 Introduction

In recent years, ultra-high strength steel sheets have been used in automobiles. Thin ultra-high strength steel sheets can be substituted for thick and mild steel sheets in order to reduce the weight of automobiles without adversely affecting their crash-worthiness. Recent ultra-high strength steels exhibit both high elongation and good tensile strength [1–3] and consequently, a high crash absorption energy.

However, the strengthening of steels for automobiles has introduced difficulties in press-forming. Spring-back and material fracture are well-known phenomena, which are associated with the use of ultra-high strength steel sheets. Further, die failures

T. Matsuno (✉) · K. Nakagiri
Faculty of Engineering, Tottori University, 4-101 Koyama-cho-minami, Tottori 680-8552, Tottori, Japan
e-mail: matsu@tottori-u.ac.jp

H. Shoji · M. Ohata
Division of Materials and Manufacturing Science, Osaka University, 1-1 Yamadaoka, Suita 565-0871, Osaka, Japan

© The Minerals, Metals & Materials Society 2021

G. Daehn et al. (eds.), *Forming the Future*, The Minerals, Metals & Materials Series,
https://doi.org/10.1007/978-3-030-75381-8_168

during press-forming have particularly become a problem in the shearing process, in addition to conventional die wear. As reported by Yasutomi et al. [4], the edges of the shearing punch are plastically deformed in the piercing process for the 1180 MPa class cold-rolled steel sheets with 1.4 mm thickness. After such an edge deformation, the punch edges are chipped; however, shearing of the 590 MPa class cold-rolled steel sheets did not exhibit punch edge deformation and chipping. Tool materials for shearing punch are extremely hard and brittle, but these undergo ductile fracture in the shearing process of ultra-high strength steel sheets.

To solve this problem, some studies proposed improving the shape of the punch edge, e.g., punch edge chamfer [5, 6] and obtuse punch edge [7]. Finite element (FE) analysis accelerates the design process of the punch edge shapes when the punch edge deformation and fracture are simulated precisely. However, the analysis requires input parameters, work-hardening, and a fracture criterion.

The objective of this study is to identify these parameters for the fabrication of a tool material by using a shear punching test [8–10]. Herein, hardened die steel, SKD11, which was standardized by Japanese Industrial Standards (JIS) G 4404:2015, was studied. In this method, punching force and stroke were measured when the SKD11 plate with 1.0 mm thickness was pierced; further, FE analyses were recursively performed with different work-hardening parameters. These were to ensure that the punching force–stroke simulation corresponded with the measurement. A compression state around the punch edge suppressed the material fracture, which caused even the brittle SKD11 to plastically deform. The fracture strain was evaluated as the equivalent plastic strain numerically simulated at the punch displacement when the abrupt force release was measured.

The following sections present the method and result of this parameter identification for hardened SKD11.

2 Method

2.1 Material

A commercial hardened SKD 11 die steel, produced by Hitachi Metals Ltd. under the trade name of SLD, was used for this study. Table 1 presents the chemical composition of this steel. The steel was quenched from 1000 °C by air cooling and tempered at 150 °C for 60 min, which resulted in a hardness of 62.6 HRC on the Rockwell scale. The steel was shaped by wire cutting it into thin sheets with thicknesses of 1.0 mm for the shear punching test. The surfaces of the sheets were polished by emery paper.

Table 1 Chemical composition of SKD11 (mass %)

C	Si	Mn	P	S	Cr	Mo	V
1.47	0.25	0.41	0.021	< 0.001	11.82	0.83	0.24

Table 2 Mechanical property of 590 MPa steel with 1.2 mm thickness. The steel was used in validating punching force and stroke simulation through FE analysis

Tensile strength	Yield stress	Uniform elongation	Total elongation
621 MPa	493 MPa	13%	23%

For validation of FE analysis, 590 MPa class of cold-rolled steel sheets with 1.2 mm thickness was evaluated through the shear punching test. The mechanical properties were already measured for this steel, and they are shown in Table 2. The measurement and simulation of the punching force and stroke curves was compared to estimate the validity of FE analysis.

2.2 Shear Punching Test

The shear punching test consisted of fabricating holes with 10.0 mm diameter through the specimens. An image of the experimental setup is shown in Fig. 1. The piercing punch and die were composed of cemented carbide coated with TiCN. They are harder than SKD11 steels. The specimen was clamped using a cylindrical holder to avoid the inflection accompanying punch penetration. The holder was bolt-locked to the base for the specimen. A hydraulic tension/compression testing machine, whose maximum force is 294.2 kN, pressed the punch with a measured punching force and ram displacement until the punch passed through the sheet thickness.

The punching speed was set to 0.1 mm/s.

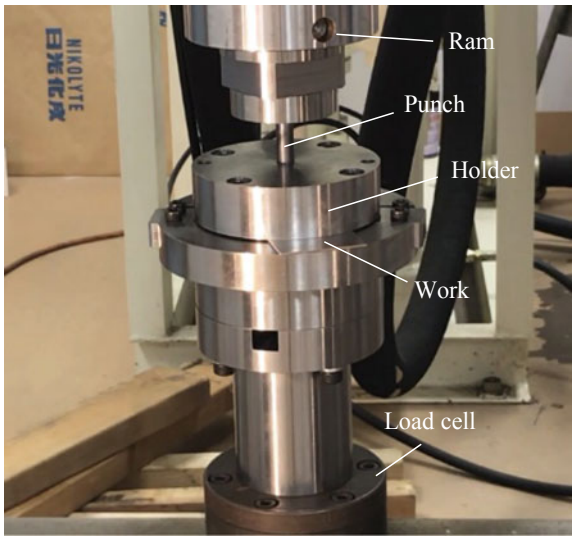


Fig. 1 Experimental set up of the shear punch test. (Color figure online)

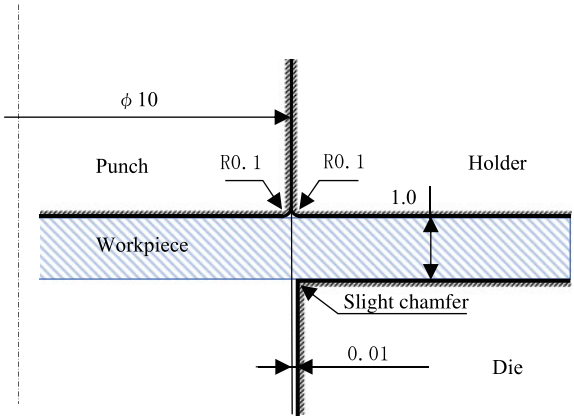


Fig. 2 Schematic figure of tool setting for the shear punching test. (Color figure online)

The condition for the shear punching tools is schematically presented in Fig. 2. As shown in Fig. 2, the tests were done with 0.01 mm clearance between punch and die edges. Such a minute clearance is for imposing compression state around the tool edges, where the brittle material plastically deforms under a compression state. A large clearance would generate a state of tension and result in an earlier material fracture during shear punching. Indeed, the SKD 11 sheets were irregularly fractured at separate sites from the contact zone with punch and die edges; this was observed when the clearance was 0.05 mm, which is conventionally used in the actual shearing processes.

Additionally, a punch edge was rounded with a 0.1 mm radius. This was to achieve the suppression of edge chipping, and such a dull edge induces more plastic deformation than a sharp edge. Furthermore, the edge roundness avoids the contact problem in FE analysis. The sharp edge frequently causes a singularity problem, which can adversely affect the corner contact with the specimen surface.

As mentioned above, the punching stroke was measured as the ram displacement of the tension/compression machine. For accurate evaluation of the punching stroke, we had to remove the tool deformation factors caused by the low stiffness of the assembled tools. The ram displacement is much larger than the actual punching stroke. For this correction from the ram displacement to the punching stroke, we referred to the FE-simulated punching force and stroke curves. Assuming that the linear parts of the curves were accurately simulated when the material was elastically deformed, we concluded that the difference between the ram displacement measurement and the punching stroke simulation at the same punching force was caused by tool deformation. The relationship between the punching force and this difference was the tool stiffness; further, the ram displacement was corrected to the punching stroke by subtracting the tool deformation calculated from the punching force.

2.3 *Finite Element Simulation*

The conditions of the shear punching test are schematically presented in Fig. 2; these parameters were numerically simulated by the commercial FE solver TP-Mform. Axisymmetric two-dimensional solid elements were used for this simulation. Figure 3 shows the simulation.

The mechanical behaviors of the materials were characterized based on their isotropic elasticity, von Mises plasticity, associated flow rule, and isotropic hardening as governed by the Swift law shown in the following equation:

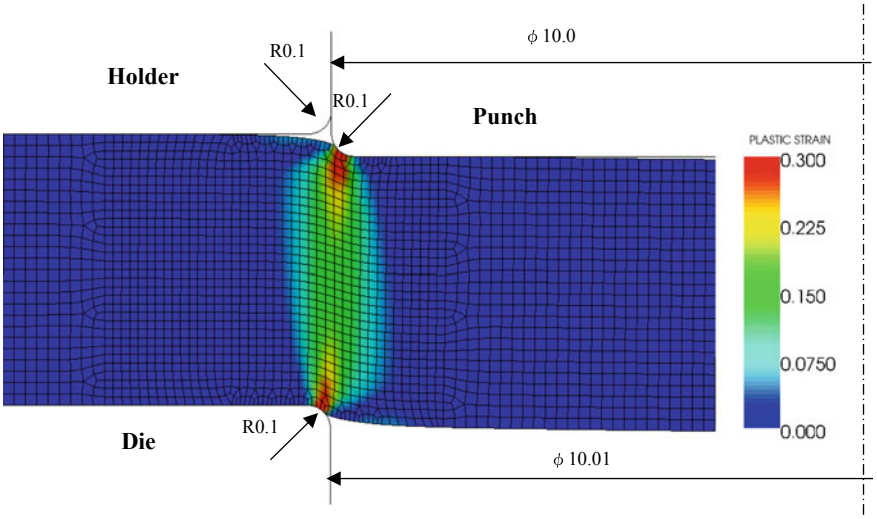


Fig. 3 Finite element simulation of shear punching test under axisymmetric two-dimensional condition. The figure exemplifies contour map of equivalent plastic strain for the shear punching of JSC590R. The punch stroke is approximately 0.1 mm. (Color figure online)

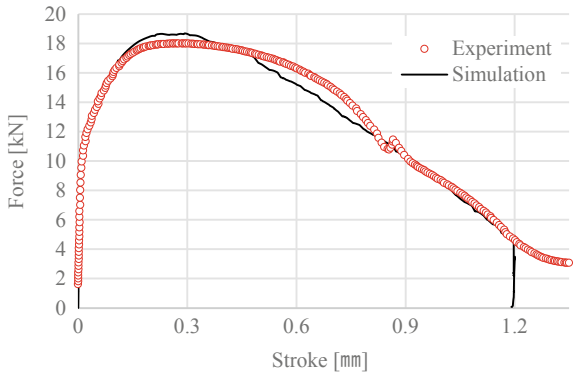


Fig. 4 Measurement and simulation of punching force–stroke curves for JSC590R. (Color figure online)

$$Y = F\left(\varepsilon_0 + \bar{\varepsilon}_p\right)^n, \tag{1}$$

where Y is yield stress, $\bar{\varepsilon}_p$ is equivalent plastic strain, and F, ε_0, n are material parameters.

The fracture was not included in this FE simulation. Fracture strain was evaluated as the equivalent plastic strain around the punch edge at the point of the material fracture in the experiments.

2.4 Fitting Scheme for the Swift Law's Parameters

The Swift law parameters F, ε_0, n for the SKD 11 steel were identified so that the punching force–stroke curve measured in the shear punching test corresponds to the numerically simulated curve.

The scheme for this identification is as follows: Firstly, the temporal values of F and n were set as F_t and n_t. The remaining ε_0 was derived from the initial yield stress, which is expressed as $F_t\varepsilon_0^{n_t}$ from Eq. (1), where the elasticity limit in the punching force–stroke curve provided the actual initial yield stress for the SKD11 steel. The FE simulation was done with the parameters F_t and n_t, and error sum of squares between measurement and simulation was evaluated. Then, the simulated punching force was scaled by r so that the error sum of squares is minimized. Because the punching force is proportional to the parameter F, the scaled punching force is in the case with $F = rF_t$. This sequence was repeated with a slight increase (or decrease) in n to find the parameter sets that minimize the error sum of squares. In this study, the initial n was 0.01 and it increased by 0.01 for each sequence.

3 Results and Discussion

3.1 Validation of FE Simulation

Figure 3 presents the measurement and simulation of the punching force–stroke curves for JSC590R with the mechanical properties shown in Table 2. The simulation agrees with the measurement up to the punching stroke of 0.15 mm.

Taking the large strain in shear punching into account, which exceeds 200% at the punching stroke of 40% of material thickness [11], the simulation is valid. The mechanical properties were measured through the tensile test. The tensile test can measure stress–strain curves in the region of uniform elongation, where uniform elongation of the JSC590R is 13%. Thus, the measurement and simulation have to be compared in the short punching stroke, where the strain is not so large. As shown in Fig. 3, the plastic strain around the punch and die edge definitely exceeded the 13% at the punching stroke of 0.1 mm.

3.2 *Flow Stress and Fracture Strain of SKD11*

The parameter identification of the Swift law for the SKD11 steel resulted in $F = 3203, n = 0.04, \varepsilon_0 = 7.68 \times 10^{-6}$. The measurement and simulation of the punching force–stroke curves are shown in Fig. 5 and the two curves are shown be in accordance, except for the load range between 10 and 18 kN. In the load range from 10 to 18 kN, mechanical slipping of the ram was observed, which probably caused the disagreement between the measurement and the FE simulation.

These parameters correspond to values of 2706 MPa for tensile strength and 2000 MPa for initial yield stress. The validity of these values has to be proven using other mechanical tests, which we will conduct as future work.

The contour map of equivalent plastic strain at the punch stroke of approximately 0.05 mm is shown in Fig. 6. The load measurement presented a sudden decrease

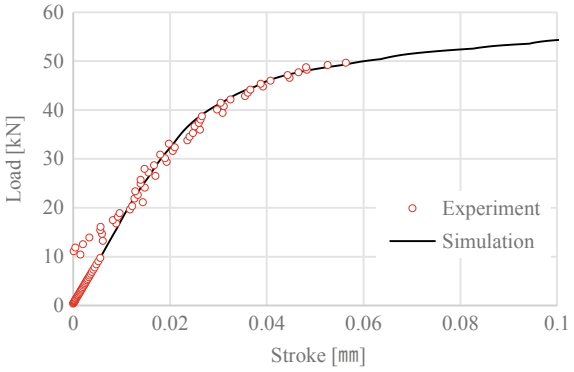


Fig. 5 Measurement and simulation of punching force–stroke curves for SKD11 steel. (Color figure online)

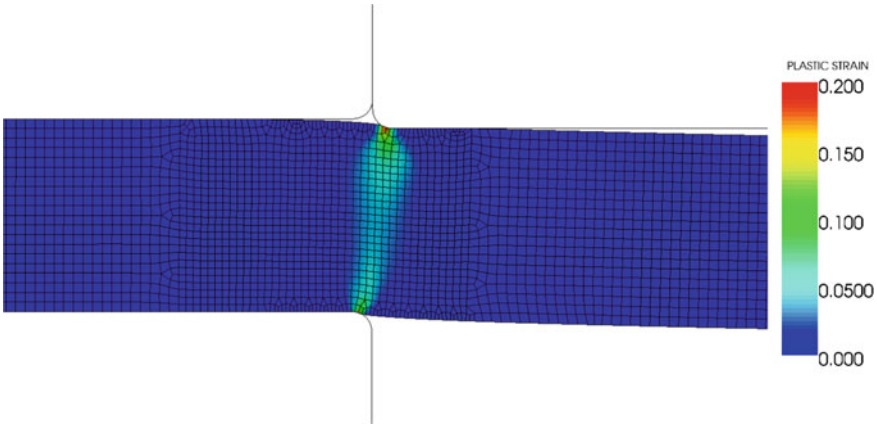


Fig. 6 Contour map of the equivalent plastic strain for SKD11 steel. (Color figure online)

at this punch stroke by material fracture. From this figure, the fracture strain was evaluated approximately 20%.

4 Summary

The study identified the stress–strain curve for the hardened JIS SKD11 steel. Shear punching test was used for this identification, wherein the Swift law's parameters were optimized; this was aimed at minimizing the error sum of squares between the measurement and the FE simulation of the punching force–stroke curves. Further, fracture strain was evaluated as the equivalent plastic strain at the punch penetration, when the material fracture had occurred. For preliminary validation of the FE simulation, the shear punching test was performed using the 590 MPa class steel(JSC590R), whose mechanical properties were measured using the tensile test. The results were as follows:

(1) The FE simulation was validated in the case of the shear punching test for JSC 590R. The simulation resulted in a good agreement with the measurement of the punching force–stroke curve.
(2) The parameters of the Swift law for the SKD11 steel were identified as $F = 3203, n = 0.04, \varepsilon_0 = 7.68 \times 10^{-6}$ in $Y = F\left(\varepsilon_0 + \overline{\varepsilon}_p\right)^n$, where Y and $\overline{\varepsilon}_p$ denote flow stress and equivalent plastic strain, respectively. These parameters produced the values of 2706 MPa and 2000 MPa for tensile strength and initial yield stress, respectively.
(3) The fracture strain was evaluated as approximately 20% for the SKD11 steel.

References

1. Takahasi M(2003) Development of high strength steels for automobiles. Nippon Steel Tech Rep 88: 2–7. https://www.nipponsteel.com/en/tech/report/nsc/pdf/n8802.pdf
2. Lee J, Lee S, Cooman BCD (2012) Effect of micro-alloying elements on the stretch-flangeability of dual phase steel. Mater Sci Eng A 536:231–238. https://doi.org/10.1016/j.msea.2012.01.003
3. Khan AS, Baig M, Choi S-H, Yang H-S, Sun X (2012) Quasi-static and dynamic responses of advanced high strength steels: Experiments and modeling. Int J Plast 30–31:1–17. https://doi.org/10.1016/j.ijplas.2011.08.004
4. Yasutomi T, Nishimura R, Yonemura S, Nakata M, Yoshida T, Mizumura M (2019) Shearing Technology for High-tensile-strength Steel. Nippon Steel Tech Rep 122: 28–34. https://www.nipponsteel.com/en/tech/report/pdf/122-06.pdf
5. Matsuno T, Kuriyama Y, Murakami H, Yonezawa S, Kanamaru H (2010) Effects of punch shape and clearance on hole expansion ratio and fatigue properties in punching of high strength steel sheets. Steel Res Int 81:853–856
6. Luo SY (1999) Effect of the geometry and the surface treatment of punching tools on the tool life and wear conditions in the piercing of thick steel plate. J Mat Proc Tech 88:122–133. https://doi.org/10.1016/S0924-0136(98)00375-6

7. Golovashchenko SF (2008) Quality of trimming and its effect on stretch flanging of automotive panels. J Mat Eng Perf 17(3):316–325. https://doi.org/10.1007/s11665-008-9220-x
8. Guduru RK, Darling KA, Kishore R, Scattergood RO, Koch CC, Murty KL (2005) Evaluation of mechanical properties using shear–punch testing. Mat Sci Eng A395:307–314. https://doi.org/10.1016/j.msea.2004.12.048
9. Guduru RK, Darling KA, Scattergood RO, Koch CC, Murty KL, Bakkal M, Shih AJ (2006) Shear punch tests for a bulk metallic glass. Intermetallics 14:1411–1416. https://doi.org/10.1016/j.intermet.2006.01.052
10. Karthik V, Visweswaran P, Vijayraghavan A, Kasiviswanathan KV, Raj B (2009) Tensile–shear correlations obtained from shear punch test technique using a modified experimental approach. J Nuc Mat 393:425–432. https://doi.org/10.1016/j.jnucmat.2009.06.027
11. Matsuno T, Seto A, Suehiro M, Kuriyama Y, Murakami H (2012) FEM Analysis of high strength steel sheets up to fracture and its application to piercing process. In: Proceedings of IDDRG2012, pp 134–140

Deformation of Metals Under Complex Loading



R. A. Abirov

Abstract The purpose of the issue is to present the approaches of complex loading for the possible reduction of energy consumption at metal processing. When forces are applied to isotropic material, there is always an active process of complex loading at which the work of external forces is less than the one under simple loading upon reaching the same strained state. Experiments on complex loading and approaches of the mathematical theory of plasticity are used in this article. Empirical results on complex loading were mathematically explained based on the Il'yushin's theory of elastic–plastic processes.

Keywords Stress · Strain · Plasticity · Complex loading

1 Introduction

At some complex loading processes at a constant strain rate, the value of equivalent stress drops [1]. These experimental data provide a base for assuming that the effect of complex loading on the amount of work under plastic strain can be substantially lower than that at simple loading.

In processing metals by pressure like cold-drawing reduction, face broaching, extrusion forging, cold rolling, etc., it is observed that the work of external forces at various ways of complex strain is less than at simple loading. These effects were established in experimental studies. This can be clearly traced on the strain process with breakpoint. This effect can be explained on the basis of Il'yushin's theory of elastoplastic processes and the so-called "damping memory" principle or the principle of delay of vector and scalar properties of the material (confirmed in numerous experiments). On the basis of this, the following lemma is proposed, which will be useful in what follows. Here, we will specify the positions and hypotheses on which we will base:

R. A. Abirov (✉)
Institute of Mechanics, 33, Dormon Yoli Str., AkademgorodokTashkent 700125, Uzbekistan
e-mail: rustam_abirov@mail.ru

© The Minerals, Metals & Materials Society 2021

G. Daehn et al. (eds.), *Forming the Future*, The Minerals, Metals & Materials Series,
https://doi.org/10.1007/978-3-030-75381-8_169

– we assume that the total strain consists of the sum of elastic and plastic parts, independent of each other;
– the work of forces on elastic strains is conservative;
– the principle of delay is a clearly manifested property of material.

Lemma The minimum work of external forces to achieve a given form under plastic strain of the body is achieved only with the implementation of strain processes with breakpoint.

Proof Based on the generalized Clapeyron theorem, which states that the work of external forces on the corresponding displacements is equal to the accumulated potential energy of the deformable body, we have:

$$A = \int_V \int_0^s \sigma_{ij} d\varepsilon_{ij} \mathrm{d}V = \int_V 3 \int_0^s \sigma_0 \mathrm{d}\varepsilon_0 \mathrm{d}V + \int_V \int_0^s s_{ij} de_{ij} \mathrm{d}V,$$

here s—is a magnitude of strain path, de_{ij}—are the components of strain deviation increment, σ_{ij}—are components of stresses, s_{ij}—are components of stress deviator, σ_0—is the modulus of spherical stress tensor, and $\mathrm{d}\varepsilon_0$—is the increment in mean tensile strain, V—is the volume of considered continua.

Follow Il'yushin, let us consider vector space in stress and strain representation. Relations between vector components and tensors ones in our case as:

$$\sigma_1 = \sqrt{\frac{2}{3}}\sigma_{11}, \quad \sigma_3 = \sqrt{2}\sigma_{12}, \quad \vartheta_1 = \sqrt{\frac{3}{2}}\varepsilon_{11}, \quad \vartheta_3 = \sqrt{2}\varepsilon_{12}.$$

Since the work of forces on elastic strains does not depend on the loading path, the created field of stress vector on strains prior to the onset of flow is conservative. The work of hydrostatic pressure on strains of volume compression is also conservative. This is based on the fact that material is taken as plastically incompressible.

Further, we have:

$$\int_0^s s_{ij} \mathrm{d}e_{ij} = \int_0^s \bar{\sigma} \mathrm{d}\bar{\vartheta} = \int_0^s \sigma \cos\vartheta \mathrm{d}s = \int_0^{e_s} \sigma \mathrm{d}s + \int_{e_s}^s \sigma \cos\vartheta \mathrm{d}s$$

where ϑ—is an angle of approach of stress vector and the increment of vector of strain.

Under active loading process, a minimum of the functional of work is achieved when the approach angle is $\pm\ \pi/2$. This is possible only if the stress vector σ is normal to the Frenet basis vector $\overline{p}_1$ (tangent to strain path), i.e. at path breakpoint. ⊗

Maintaining the angle of approach at that value is not possible over the whole process of strain, according to the principle of delay. This means that when loading up to the exhaustion of delay trace of vector properties of material, it is necessary to produce a bend point of strain path. Such breakpoint in strain path, generally speaking, realizes multi-link strain processes. In [2], the problem of optimal control of strain path under complex loading of metals is posed and solved. The solution to the optimization problem is obtained using dynamic programming method. Strain process of a homogeneous cylindrical sample is considered. It is shown that the Il'yushin theory of elastic–plastic processes describes the effect of reducing the work of plastic forming of metals under complex loading.

This effect finds application in the optimization of technological processes of metal working with pressure [3]**.** The disadvantage is that the problem of optimal control is not solved with a fixed right end, i.e. the given point in strain space is not reached.

In manufacturing steel hollow cylinder by the method of reverse extrusion (pressing-out), the application of zigzag strain paths leads to a significant decrease in extrusion force.

Conclusion: To attach a certain shape to material in metal working with pressure, by punching, etc., the possibility of optimal control of loading process is important. Thus, to achieve the goal, it is necessary to put as a term the optimal number of links of the path. With this term, it is possible to determine at what stage to produce a breakpoint. Here, in addition to classical physical parameters of material, one should also know its delay trace $\overline{\lambda}$.

Note: When implementing loading processes with breakpoint (stress space), a situation arises when the scalar product of the stress vector $\overline{\sigma}$ and the vector of strain increments $\overline{p}_1$ is at a minimum. But the difference in the breakpoint in strain space and in stress space is that, in addition to the change in vector properties of material, the stress "leaps" occur in the former case, which gives the minimum work precisely under the strain processes with a breakpoint.

The possibility of using the effect of reducing the external force in the development of new technologies for plastic processing of metals and controlling the strain paths of these processes is considered in [2]. Strain processes of a specified length are also studied in the paper with minimization of the energy expended. Thus, the consideration of complex loading and identification of the effects arising in this case, besides revealing the reserves of bearing capacity of materials, allows to minimize the work of external forces (to reduce energy costs) in technological processes.

For further discussion, we need to accept the following statements: the Il'yushin isotropy postulate, the delay principle, universality of the loading diagram $\sigma = \sigma(s)$.

The universality of the function ϑ for material at the same angles at breakpoint was observed experimentally. Based on this, empirical formulas (1–2) for the approximations of function ϑ were proposed. The delay trace of vector material properties is assumed as equal to $\overline{\lambda} = 5\varepsilon_s$.

$$\vartheta = \theta / \exp\left(k\left(1 + \frac{1}{\bar{\lambda}}\right)\Delta s\right), \text{ here} k = \ln 16/(1 + \bar{\lambda}) \tag{1}$$

$$\vartheta = Carcctg\left(\frac{r}{\bar{\lambda}}\Delta s\right), \text{ here } C = \frac{2\theta}{\pi}, \quad r = ctg\left(\frac{\pi}{32}\right) \tag{2}$$

Δs is a magnitude of strain path after break point, ε_s is yield strain.

2 To Optimal Control of Metal Forming Under Complex Loading

Consider the following optimal control problem: to find the minimum of functional:

$$J = \min \int_{S_{in}}^{S_{ult}} \sigma \cos\vartheta \, ds \tag{3}$$

subject to restrictions: $S_{in} \le s \le S_{ult}$, $\vartheta \le \pm\frac{\pi}{2}$.

Since, according to the lemma, we have chosen a multi-link broken line as an optimal one, the strain path can be represented as a piecewise continuous curve and the initial problem can be represented as a quadrature sum

$$J = \min \sum_{k=1}^{n} \int_{s_k}^{s_{k+1}} \sigma \cos\vartheta \, ds \tag{4}$$

with initial conditions $\gamma_{(1)} = 0$, $\beta^{(1)} = 0$ with a control function β and restrictions in the form $\vartheta_1^l = \vartheta_1^{l-1} + \Delta s^{(l)} \cos\alpha^{(l)}$, $\vartheta_2^l = \vartheta_2^{l-1} + \Delta s^{(l)} \sin\alpha^{(l)}$, $s_l = s_{l-1} + \Delta s^{(l)}$.

Functional $B_w = \inf \sum_{k=w}^{n} \int_{s_k}^{s_{k+1}} \sigma \cos\vartheta \, ds$ at k = 1, n is the Bellman function of the basic problem (3), which satisfies the recurrence relations (5)**.**

$$B_w = \inf \int_{s_w}^{s_{w+1}} \sigma \cos\vartheta \, ds + B_{w+1}. \tag{5}$$

When choosing the approach angle in the form (2), the minimum of the Bellman function is achieved at:

$$\vartheta = \left\{\left[\gamma_{(l-2)} + \beta^{(l-1)}\right]\frac{2}{\pi} arcctg\left(\frac{r}{\bar{\lambda}}\Delta s^{(l-1)}\right) + \beta^{(l)}\right\}\frac{2}{\pi} arcctg\left(\frac{r}{\bar{\lambda}}(y - s_l)\right). \tag{6}$$

The recurrence relation for the control function β, in this case, has the form:

$$\beta^{(l)} = \pm\frac{\pi^2}{4} - \left\{\beta^{(l-1)} + \gamma_{(l-2)}\right\}\frac{2}{\pi} arcctg\left(\frac{r}{=}\Delta s^{(l-1)}\right). \tag{7}$$

The general solution to problem (4) for the control function β at equal lengths Δs of path links is:

$$\beta^{(l)} = \pm\frac{\pi}{2}\left(\frac{\pi}{2} - arcctg\left(\frac{r}{=}\Delta s\right)\right). \tag{8}$$

When choosing an approximation for the approach angle in the form (1), we get:

$$\vartheta = \left\{\left[\gamma_{(l-2)} + \beta^{(l-1)}\right]/\exp(k(1+\frac{1}{=})\Delta s^{(l-1)}) + \beta^{(l)}\right\}/\exp(k(1+\frac{1}{=})(y - s_l)).$$

The recurrence relation for the control function β and the general solution to problem (3) are, respectively:

$$\beta^{(l)} = \pm\frac{\pi}{2} - \left\{\beta^{(l-1)} + \gamma_{(l-2)}\right\}/\exp(k(1+\frac{1}{=})\Delta s^{(l-1)})$$

$$\beta^{(l)} = \pm\frac{\pi}{2}\left(1 - 1/\exp(k(1+\frac{1}{=})\Delta s)\right). \tag{9}$$

As can be seen, the minimum of functional (3) is achieved for a multi-link strain path at kink angles depending on the link length of the broken line. At a link length $\Delta s = \overline{\lambda}$, the breakpoint angle is ± π/2, at a link length $\Delta s = \overline{\lambda}/2$, the breakpoint angle is β = 3π/8, provided that the loading (strain) process activity is maintained.

Introducing additional restrictions into the main problem (4) in the form of $\left(\vartheta_1^l\right) + \left(\vartheta_2^l\right) \geq \left(\vartheta_2^{l-1}\right)^2 + \left(\vartheta_1^{l-1}\right)^2$, instead of (8) and (9), we get the solutions:

$$\beta^{(l)} = (-1)^{l-1}\frac{\pi}{2}\left(1 - 1/\exp\left(k\left(1+\frac{1}{=}\right)\right)\Delta s)\right),$$

$$\beta^{(l)} = (-1)^{l-1}\frac{\pi}{2}\left(\frac{\pi}{2} - arcctg\left(\frac{r}{=}\Delta s\right)\right).$$

Under other initial conditions, it is possible to obtain similar conditions for the minimum of functional (3).

According to the isotropy postulate, the loading process image does not depend on the rotation and reflection procedures. Any deformed state in the five-dimensional vector space of strains can be achieved in the form of a plane multi-link trajectory. All plane trajectories out of their entire set are isomorphic ones.

Based on this, we make the following statements:

When a force is applied to an isotropic material, there will always be an active process of complex loading in which the work of external forces is less than under simple loading in the same deformed state.

Note: It should be noted that there is no universal function for the approach angle ϑ under spatial loading processes. This does not give us the right to state that the minimum of functional of work in the general case of the spatial process of strain is achieved precisely under plane processes of complex loading. We also note that the behaviour σ is assumed to be strengthening under complex loading (without local softening – "drops").

3 The Effect of Work Reducing Under Complex Loading in Technological Problems.

Let consider the technological problems where it is possible to apply the effect of work reducing plastic forming under complex loading. Various studies are being carried out in this field and proposed in some issues [4–6].

Consider the cold-drawing process of brass pipe through a conical matrix where dimensions are: $y = C - ax$, here: C = 113.75, a = 5.67, the angle at the top of the matrix is 100, 0.2 m ≤ x ≤ 0.25 m. The narrowing is 0.8, which meets the condition of the maximum possible narrowing of the pipe. Pipe's wall thickness is h = 0.002 m, at an external axial force $P_0 = 26948$ Pa. The friction coefficient is taken equal to f = 0.3. The pipe pressure on the walls of the matrix depends on the friction forces with the parameter k = 0.15.

The stress and strain diagram in vector space is taken in the form:

$$\bar{\sigma} = Ath(\beta\ \ni), \quad \bar{\ni} = {}^{1}\!/_{\beta} arth\left({}^{\bar{\sigma}}\!/_{A}\right), \quad A = \sigma_\infty, \quad \beta = 2G/\sigma_\infty, \quad \sigma_\infty = {}^{5}\!/_{3}\bar{\sigma}_s$$

$$\sigma_s = 117MPa, \quad E = 113796MPa, \quad \mu = 0.348.$$

We have here the equilibrium equations as:

$$(T_1 \sin\theta - Q\cos\theta) \cdot 2\pi r = F(s)$$

$$F(s) = P_0 + \int_{s_0}^{s} (q_n \cos\theta - q_1 \sin\theta) 2\pi r ds.$$

At axisymmetric deformation of shell of revolution, we have:

$$-\frac{T_1}{R_1} - \frac{T_2}{R_2} + q_n = 0, T_1 = \frac{F}{2\pi r \sin\theta}$$

here T_1, T_2—tension forces in normal cross section, θ—angel between perpendicular to shell surface and + OY axis, R_i—curvature radiuses, P_0—tensile force.

Taking in the relations: $R_1 = \infty$; $\cos\theta = \frac{1}{\sqrt{1+a^2}}$; $\sin\theta = \frac{a}{\sqrt{1+a^2}}$; $R_2 = -\frac{r}{\sin\theta}$; $F(x) = \pi q_n\left(x^2 - x_0^2\right) - \pi q_1 a\left(x^2 - x_0^2\right)$.

So, external forces are:

$$q_1 = \frac{F}{f\,\pi L(r_0 + r_n)}, q_n = -q_1 k.$$

At simple loading, we apply forces at the same time, at complex loading apply forces sequentially.

Calculate the work of forming $\int_{s_0}^{s} \overline{\sigma} d$, since precisely this part of the work gives us the opportunity to reduce the costs of the forming process. When calculating the work, the strains in equidistant layer were taken equal to the middle surface strains. To analyse the qualitative pattern, this can be taken as a first approximation. As can be seen (Fig. 1), work under complex loading is less than under simple loading.

Figure 2 shows the work process depending on the degree of loading. At the initial stage, under complex loading, work is greater. This can be explained by the very process of complex loading. First, the internal pressure was set, and then surface friction. The effect of internal pressure on work (as this is the main load) dominates compared with other loads.

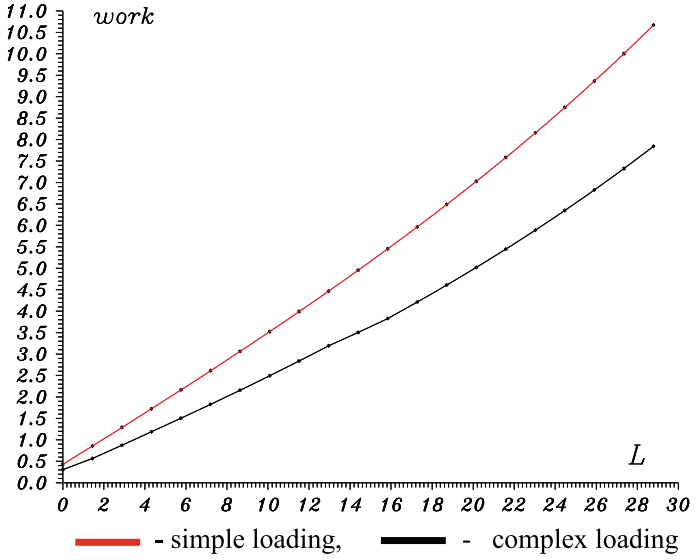


Fig. 1 Work on forming. (Color figure online)

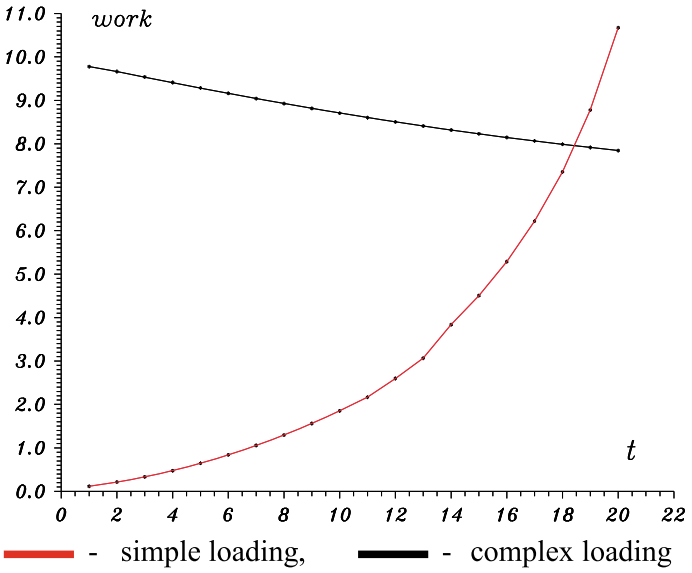


Fig. 2 Work vs loading process. (Color figure online)

4 Conclusion

The minimum of work of external forces at metal processing is achieving only at strain processes with breakpoint. This statement was used during analytical derivation of conditions for minimization of work of external forces.

On the picture, we can see the conditions for work of plastic deformation at complex loading comparing with simple loading. These data can be used in metal processing in different stages of manufacturing.

References

1. Babamuratov KSh, Abirov RA (2001) On physical reliability in the theory of plasticity. Strength Mater 33(1):1–7
2. Stolbov VYu, Trusov PV (1999) Optimal control of the deformation path of a metal under complex loading. J Appl Math Mech 63(2):299–303
3. Sadok L, Urbansky S (1989) Theoretical and practical aspects of tube sinking by a rotary die. Steel Res 60(6):263–268
4. Stolbov VYu, Trusov PV (1999) Coupled problems of the optimization of the elasto-plastic deformation of metals. J Appl Math Mech 63(4):657–664
5. Gitman MB, Trusov PV, Fedoseev SA (2000) On optimization of metal forming with adaptable characteristics. Korean J Comput Appl Math 7(2):387–396
6. Gitman MB, Stolbov VYu, Nadymov AN (2013) Strengthening of pump rods with regard for the stochastic distribution of plastic properties of the material. Strength Mater 45(2):242–247

Part XIX
Novel Processes

Numerical Simulation of Tube Bending Supported by Hydraulic Pressure for Manufacturing Butt-Welding Fittings



Josef Domitner, Peter Auer, and Christof Sommitsch

Abstract An innovative tube bending process supported by hydraulic pressure was patented in 1995. This process was designed for producing butt-welding fittings which particularly fulfil the dimensional specifications of the ASME B16.9, MSS SP-75, and MSS SP-43 standards. Since the patent has meanwhile expired, the bending process is now available for common use. This work presents a novel finite element (FE) model build using the software package LS-DYNA, which enables determining the process window for bending defect-free butt-welding fittings. This model was exemplarily applied for investigating the bending process of a 90° stainless steel elbow based on a straight tube of nominal pipe size (NPS) 6. Comparing the calculated geometry of the elbow with the actual geometry of an industrially produced elbow revealed very good dimensional agreement. This confirms that the presented model can be utilized for determining suitable process conditions, which allow for producing defect-free components.

Keywords Piping system · Stainless steel pipe · Butt-welding fitting · Tube bending · Tube forming · Hydroforming · Hydraulic pressure · Buckling · Finite element simulation

1 Introduction

1.1 Butt-Welding Fittings

Butt-welding fittings are important components of industrial piping systems. They join straight pipe sections, connect pipes of different sizes or shapes, change the flow direction, branch off or join the flow, integrate equipment such as measuring or regulating devices, etc. [1]. The size of fittings is classified based on the nominal pipe size (NPS). The dimensions and tolerances are defined in the ASME B16.9 standard

J. Domitner (✉) · P. Auer · C. Sommitsch
Institute of Materials Science, Joining and Forming, Research Group of Tools & Forming, Graz University of Technology, Inffeldgasse 11/I, 8010 Graz, Austria
e-mail: josef.domitner@tugraz.at

© The Minerals, Metals & Materials Society 2021

G. Daehn et al. (eds.), *Forming the Future*, The Minerals, Metals & Materials Series,
https://doi.org/10.1007/978-3-030-75381-8_170

"*Factory-Made Wrought Buttwelding Fittings*" (NPS ½-48) [2] and in the MSS SP-75 standard practice "*High-Strength, Wrought, Butt-Welding Fittings*" (NPS 16–60) [3] for carbon steel, and in the MSS SP-43 standard practice "*Wrought and Fabricated Butt-Welding Fittings for Low Pressure, Corrosion Resistant Applications*" [4] for stainless steel.

Large quantities of pipe fittings are produced using rotary-draw bending (mainly 45° and 90° elbows) or compression bending (mainly 180° returns) [5]. These processes are fast and efficient, however, in particular bending of materials possessing marked springback tendency, e.g. high-strength stainless steels or aluminium alloys [6, 7], and bending of components possessing strong wrinkling tendency, e.g. elbows of large diameter, low wall thickness, and small bending radius [8–10], is challenging. In order to improve the dimensional accuracy of the bends, mechanical [11] or usually hydraulic [12] pressure is often applied to stabilize the inner surface of the tube during the bending process. In addition to the pressure support, axial forces can be applied in rotary-draw bending [12, 13] or double-layer support tubes can be used in ram bending [14, 15]. In push bending, deformable polyurethane rods [16, 17] or granular media [18] are used instead of hydraulic fluids for stabilizing the inner surface of the tube. Though these measures may generally improve the bendability, the active control of the material flow during the bending processes and, therefore, the influence on the final shape of the bends are limited.

1.2 Tube Bending Process

An innovative cold push bending process patented in 1995 [19] was designed with the aim to fulfil, in particular, the dimensional specifications of the fore-mentioned butt-welding fitting standards by active adjustment of the internal hydraulic pressure. Since the patent has meanwhile expired, this process is now available for common use. As the bending process is applicable to materials that are basically difficult to bend, its two major advantages are: (i) elbows or returns can be produced from the same material as the straight sections in the piping system and (ii) both outer diameter as well as shape of the tube stay constant during bending, i.e. the diameter of the final elbow or return is de facto identical with the original diameter of the straight tube. The industrial practice has shown that these two features—same material and same outer diameter—are highly favourable for butt-welding of fittings and pipes.

The tube bending process investigated in this study works as follows [19]: A massive steel die is used for guiding the tube at its outer surface and for determining the movement directions of the mandrel and of both punches. The die is divided horizontally into the lower half and the upper half, which separate after bending has completed. Before inserting the straight tube into the die, it must be well lubricated for reducing friction. The tube endings are sealed with two hemispherical caps for obtaining the closed internal volume, which is mandatory for supporting the inner surface of the tube by high hydraulic pressure. The pressure prevents buckling of the tube during the bending process. For adapting the internal pressure, a valve controls

filling and releasing the hydraulic fluid through a hole inside the working punch. In order to ensure sealing, the working punch presses one sealing cap against the front-ending of the tube, and the counterpunch presses the other sealing cap via flexible mandrel against the rear-ending of the tube. The working punch pushes the tube into the die while the counterpunch controls the position of the multi-segment mandrel. The mandrel consists of five hemispherical segments, which can tilt and rotate relative to each other.

Due to the complex interactions between the working punch force, F_W, the counterpunch force, F_C, the die closing force, F_D, and the internal hydraulic pressure, p, controlling the bending process is the key challenge. Therefore, this work presents a novel three-dimensional finite element (FE) model build using the software package LS-DYNA [20] for determining the suitable process window.

2 Numerical Model

2.1 Geometry and Mesh

The three-dimensional model of the 90° bending process is shown in Fig. 1. The model includes the tube of ND 6 (Ø 168.3 mm × 11 mm × 520 mm); both tube endings are tapered with 15°. The working punch is only able to move axially in y-direction and the counterpunch is only able to move axially in x-direction, but the five segments enable the mandrel to follow the 90° bend of the die. The die and the punches are modelled as rigid and meshed with triangular shell (2D) elements. Elastic deformation of the sealing caps and of the mandrel segments, as well as elastoplastic deformation of the tube are considered. The mandrel segments and the caps are meshed with tetrahedral solid (3D) elements. The tube is meshed with five layers of

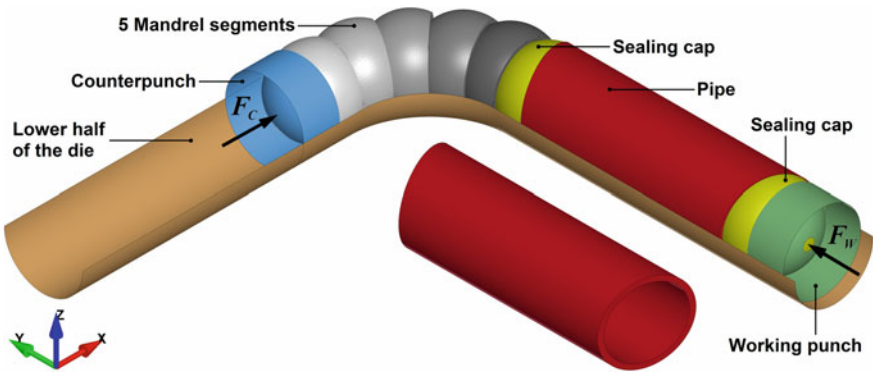


Fig. 1 Initial tube geometry and model of the bending process (for visualization reasons, the upper half of the die is hidden). (Color figure online)

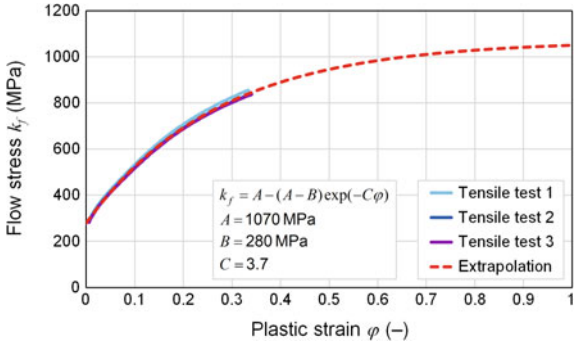


Fig. 2 Extrapolated flow curve of steel TP316/316L (the curves of tensile tests 1, 2, and 3 overlap). (Color figure online)

hexahedral solid (3D) elements arranged along the wall thickness direction. In total, the model consists of approximately 127,000 shell elements and of approximately 562,000 solid elements.

2.2 Material Properties

The 90° elbow was produced using a straight tube of stainless steel TP316/316L. The elastoplastic properties of this steel were determined using a Zwick/Roell Z100 uniaxial testing machine, which was combined with a GOM ARAMIS camera system for optical strain measurement. The testing speed was 5 mm/min. Three cylindrical tensile samples (type A 8 × 40 according to DIN 50,125) were extracted from different sections of the straight tube. Based on the results of the tensile tests, the flow curve shown in Fig. 2 was extrapolated using the Voce model [21]. For the elastic components, the Young's modulus was 207 GPa, the Poisson's number was 0.28, and the density was 7,850 kg/m^3.

2.3 Process Conditions

The main conditions of the investigated bending process are summarized in Table 1. In order to reduce the required calculation time, the actual velocity of the working punch, v_W, was scaled up by the factor of 100 in the present model. This scaling method is feasible, because the kinetic energy is significantly smaller than the internal energy of the system. Both, kinetic and internal energy of the modelled system, were directly calculated using the LS-DYNA software. Note that the force applied by the counterpunch, F_C, must be sufficient to ensure sealing at both endings of the tube when applying the internal hydraulic pressure, p. Insufficient counterpunch force would cause leakage between the sealing caps and the tube. Graphite is used for lubricating the tube surface, which is in contact with the die during the bending

Table 1 Process conditions

Velocity of the working punch, v_W (unscaled)	25 mm/s
Force at the counterpunch, F_C	1.55 MN
Internal hydraulic pressure, p	800 bar
Total time of the process, t_t (unscaled)	20 s
Coefficient of friction between die and components, μ_1	0.08
Coefficient of friction between tube endings and sealing caps, μ_2	0.20

process. To consider the effect of lubrication in the model, a comparatively low and uniform coefficient of friction, μ_1, was defined at the contact faces between the die and the components contacting the die. Since the tube is bent in the as-cut condition with rough faces at both endings and in order to model the interlocking effect of the sealing cap edges, the coefficient of friction, at the tube endings μ_2, was comparatively high. In addition, a rigid plane was introduced at each of these two contact faces for preventing local distortion of the mesh and, therefore, for improving the numerical stability of the model.

The total time of the bending process, t_t, was 20 s. The time increment predefined to run the explicit LS-DYNA solver was 0.275×10^{-6} s. In order to avoid the actual time increment to decrease below this value, automated global mass scaling was enabled for all components of the model.

3 Results and Discussion

3.1 Design of the Process

Figure 3 illustrates the geometry of the elbow calculated using the numerical model. Since neither buckling nor severe local thinning occurred, the bending process can obviously be considered as stable under the conditions listed in Table 1.

The numerical model provides important information, which is mandatory for designing the basic equipment of the bending process. In this context, the minimum die closing force, F_D, which acts against the internal pressure and which is perpendicular to the partition plane of the die, is of central interest. F_D is the minimum force required to keep the die closed during the process, i.e. to prevent both halves of the die to separate from each other. As shown in Fig. 4, F_D varies with process time t. From the practical point of view, the closing force required for producing the particular elbow geometry should be about 10 MN, which includes a safety margin of 15–20%. Figure 4 also illustrates that for bending the tube, the force applied by the working punch, F_W, should be about 5 MN. Note that the force of the counterpunch, F_C, was almost constant over time in the industrial bending process and, therefore, the force was also predefined as constant in the numerical model.

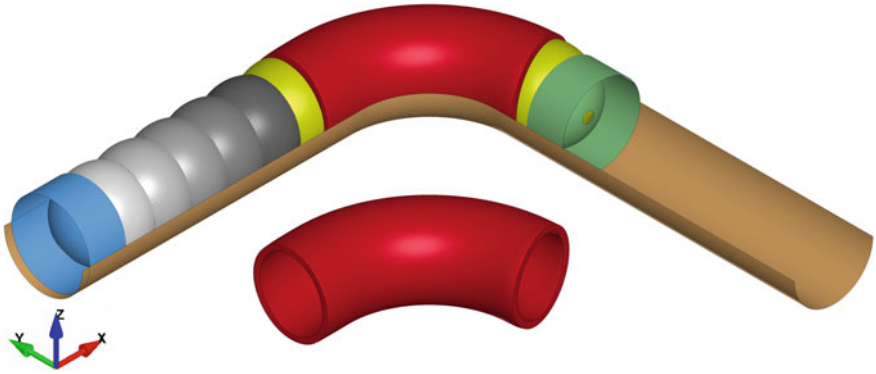


Fig. 3 Elbow geometry calculated with the numerical model (the upper die half was opened after completing the bending process). (Color figure online)

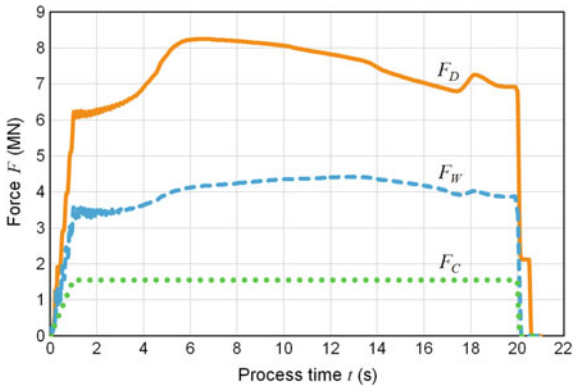


Fig. 4 Minimum die closing force, F_D, working punch force, F_W, and counterpunch force, F_C. (Color figure online)

As shown in Fig. 3, a defect-free elbow is obtained when using the counterpunch force of $F_C = 1.55$ MN and the internal pressure of $p = 800$ bar. Figure 5 illustrates typical problems that may occur in the bending process, if either F_C or p, or even both, are chosen inappropriately. As example, Fig. 5a shows the leakage between the sealing cap and the elbow, whereas Fig. 5b shows buckling at the inner bending radius of the elbow. Leakage would be initiated at $t = 16.8$ s, if F_C decreases just slightly from 1.55 MN to 1.40 MN, but p remains 800 bar. Buckling would start at $t = 13.4$ s, if F_C remains 1.55 MN, but no internal pressure is applied.

3.2 Geometry of the Elbow

As shown in Fig. 6, comparatively high effective plastic strain of about 0.5 resulting in unfavourable plastic deformation was observed only at the ending of the elbow

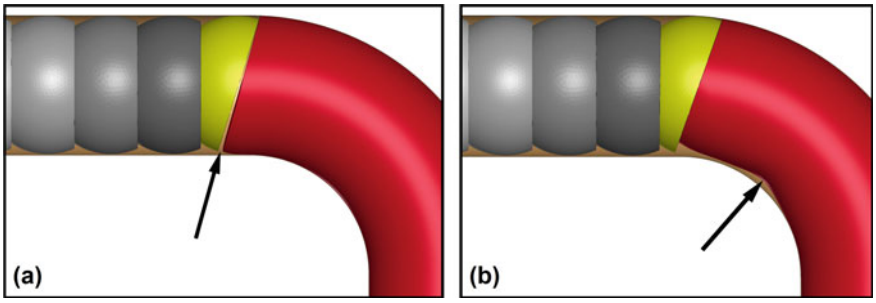


Fig. 5 Typical problems due to inappropriate process conditions: **a** leakage between sealing cap and elbow and **b** buckling of the elbow. (Color figure online)

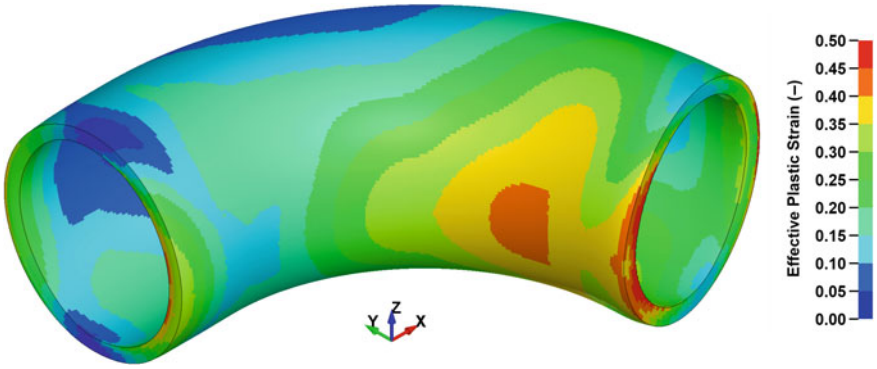


Fig. 6 Effective plastic strain at the elbow. (Color figure online)

where the working punch had pushed the sealing cap against the tube. However, from the practical point of view, this local deformation is negligible, because after bending both endings are usually machined for obtaining the final geometry of the 90° elbow.

The results illustrated in Figs. 3 and 6 demonstrate that the presented numerical model can be applied successfully for predicting the outcome of the bending process. In order to validate the prediction quality of the model, the calculated geometry was compared with the geometry of the elbow shown in Fig. 7, which was produced in the industrial bending process. The full 3D geometry of this elbow was captured using the GOM ATOS III Triple Scan measuring system. Measured and calculated elbow geometries were then superimposed using the GOM Inspect 2019 [22] software for quantifying dimensional differences. Note that the geometries and nominal process parameters of both, industrial bending process and numerical model, were de facto identical. Due to lack of monitoring in the industrial process, however, the time-dependent variation of the parameters is actually unknown.



Fig. 7 Elbow produced in the industrial bending process and machined to obtain final dimensions (the circular black/white reference markers on the surface are required to capture the 3D geometry; the measuring tape is scaled in cm). (Color figure online)

As illustrated in Fig. 8, good dimensional agreement is generally achieved between the calculated geometry and the actual geometry of the industrially produced elbow. The colour scale represents the dimensional difference between both geometries. It is obvious that the biggest difference of more than −1 mm occurs near the front-ending of the elbow, as marked with the dark blue area. This area is located where the most serious die wear occurred in the industrial bending process which, however, is not considered in the numerical process model. Note that the circumferential dark blue

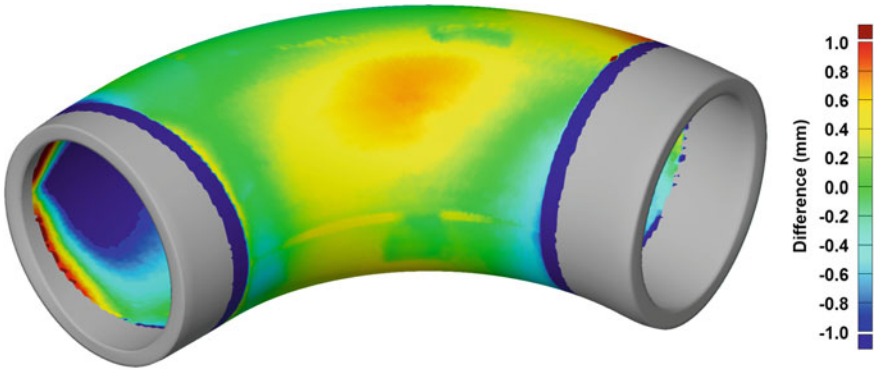


Fig. 8 Comparison between calculated geometry of the elbow and geometry of the industrially produced elbow. (Color figure online)

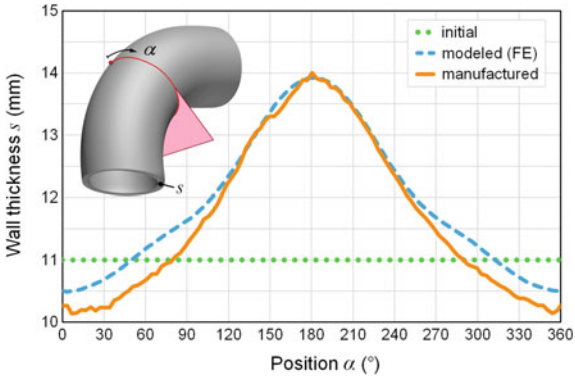


Fig. 9 Variation of the local wall thickness, s, of the elbow. (Color figure online)

bands shown in Fig. 8 origin from the chamfers, which are machined after removing the grey endings of the elbow. These chamfers are also shown in Fig. 7.

Figure 9 illustrates the variation of the wall thickness along the circumference of both the modelled elbow and the manufactured elbow. The thickness of the manufactured elbow was calculated from the 3D data captured at the central cross-section. It is obvious that the wall thicknesses of both elbows was de facto identical at the inner bending radius ($\alpha = 180°$), whereas the maximum difference of approximately 0.4–0.5 mm was observed close to the outer bending radius ($\alpha = 0°/360°$). This difference could be due to local variations of the friction conditions during the bending process, which were not included in the present model. However, from the practical point of view, this comparatively small difference is negligible, since the initial wall thickness of the straight pipe was 11 mm.

4 Summary and Conclusions

In this work, a novel three-dimensional finite element model of a tube bending process supported by hydraulic pressure for manufacturing butt-welding fittings according to ASME B16.9, MSS SP-75, and MSS SP-43 standards was presented. The model build in LS-DYNA was exemplarily applied for investigating the bending of a 90° stainless steel elbow from a straight tube of NPS 6. The results of the simulations were compared with an elbow produced in the industrial bending process. Based on the results, the following conclusions are drawn:

- The numerical model can be used for predicting the required pushing force of the working punch and the closing force of the die. In order to manufacture the elbow geometry presented exemplarily, the force of the working punch is about 5 MN and the closing force of the die is about 10 MN.
- The relationship between the force of the counterpunch and the internal pressure was identified as critical process parameter influencing the stability of the

bending process and, therefore, influencing the geometry of the elbow. In order to avoid leakage during the bending process, the counterpunch force must match the hydraulic pressure acting on the internal surface of the pipe.

- Comparing the calculated geometry with the actual geometry of the elbow revealed very good dimensional agreement. Therefore, (i) the experimentally validated model enables predicting the geometry of the elbow for a given set of process conditions or (ii) the particular process window for bending defect-free butt-welding fittings in accordance with the specifications of the standards can be determined for a given nominal pipe size.

References

1. Geiger EL (2000) Chapter A2: Piping Components. In: Nayyar ML (ed) Piping Handbook 7th ed, McGraw-Hill, New York, NY, A.53–A.123
2. ASME B16.9–2018: Factory-Made Wrought Buttwelding Fittings (2018) American Society of Mechanical Engineers, New York, NY
3. MSS SP-75–2019: High-Strength, Wrought, Butt-Welding Fittings (2019) Manufacturers Standardization Society, Vienna, VA
4. MSS SP-43–2019: Wrought and fabricated butt-welding fittings for low pressure. Corrosion Resistant Applications. Manufacturers Standardization Society, Vienna, VA, 2019
5. Miller G (2003) Tube forming processes: a comprehensive guide. Society of Manufacturing Engineers (SME), Dearborn, MI, pp 129–130
6. Dx E, He HH, Liu XY, Ning RX (2009) Springback deformation in tube bending. Int J Miner Metall Mater 16(2):177–183
7. Fang J, Lu S, Wang K, Yao Z (2017) Springback law of high-strength 21-6-9 stainless steel tube in numerical control bending under different process parameters. Proceedings of IMechE Part B: J Eng Manuf 231(10):1783–1792
8. Wang X, Cao J (2001) Wrinkling Limit in Tube Bending. Transactions of the ASME: J Eng Mater Technol 123:430–435
9. Li H, Yang H, Zhang ZY, Li GJ, Liu N, Welo T (2014) Multiple instability-constrained tube bending limits. J Mater Process Technol 214:445–455
10. Kong D, Lang L, Ruan S, Sun Z, Zhang C (2017) A novel hydroforming approach in manufacturing thin-walled elbow parts with small bending radius. Int J Adv Manuf Technol 90:1579–1591
11. Shi SC, Yang LF, Guo C (2011) Deformation behaviors of tube rotary-draw bending filled with steel balls. Adv Mater Res 328–330:1403–1407
12. Wang J, Agarwal R (2006) Tube Bending Under Axial Force. Transactions of the ASME: J Manuf Sci Eng 128:598–605
13. Li H, Yang H, Zhan M, Kou YL (2010) Deformation behaviors of thin-walled tube in rotary draw bending under push assistant loading conditions. J Mater Process Technol 210:143–158
14. Wang X, Li F (2015) Analysis of wall thickness variation in the hydro-bending of a double-layered tube. Int J Adv Manuf Technol 81:67–72
15. Xie W, Teng B, Yuan S (2015) Deformation analysis of hydro-bending of bi-layered metal tubes. Int J AdvManuf Technol 79:211–219
16. Baudin S, Ray P, Mac Donald BJ, Hashmi MSJ (2004) Development of a novel method of tube bending using finite element simulation. J Mater Process Technol 153–154:128–133
17. Zheng Y, Li Z (2002) Experimental research on the tube push-bending process. J Mater Process Technol 122:237–240

18. Liu H, Zhang S-H, Song H-W, Shi G-L, Cheng M (2019) 3D FEM-DEM coupling analysis for granular-media-based thin-wall elbow tube push-bending process. Int J Mater Form 12:985–994
19. Auer G, Bitsche E, Pötsch A, Renner A (1995) Verfahren und Vorrichtung zum Biegen von Hohlprofil-Werkstücken. European Patent 0677342A2
20. Livermore Software Technology Corporation (LSTC) (2019) Livermore, CA, https://www.lstc.com/products/ls-dyna
21. Voce E (1955) A practical strain-hardening function. Metallurgia 51:219–226
22. GOM GmbH (2019) Braunschweig, Germany, https://www.gom.com/de/3d-software/gom-inspect.html

Fluidity of Wood Composite Combined with Natural Binder on Injection Molding



Shohei Kajikawa, Masaya Horikoshi, Takashi Kuboki, Soichi Tanaka, Kenji Umemura, and Kozo Kanayama

Abstract This paper describes injection molding of a new wood composite with a natural binder composed of sucrose and citric acid. The wood composite was plasticized to be deformable when heated, making molding possible. In this study, the effects of the natural binder content and mixture ratio of the sucrose and the citric acid on the fluidity of the wood composite on injection molding were investigated. At first, the appropriate molding temperature for plasticizing the wood composite was determined to be 180 °C by thermal analysis. In the injection molding test, products were obtained successfully when the fluidity of the wood composite was high. The fluidity was improved by increasing the binder content, and the optimum mixture ratio of the sucrose and the citric acid was 75:25.

Keywords Injection molding · Thermal flow · Wood · Composite · Cedar · Natural binder · Sucrose · Citric acid

S. Kajikawa (✉) · M. Horikoshi · T. Kuboki
Department of Mechanical and Intelligent Systems Engineering, The University of Electro-Communications, 1-5-1 Chofu-Gaoka, Chofu, Tokyo 182-8585, Japan
e-mail: s.kajikawa@uec.ac.jp

T. Kuboki
e-mail: kuboki@mce.uec.ac.jp

S. Tanaka · K. Umemura · K. Kanayama
Research Institute for Sustainable Humanosphere, Kyoto University, Gokasho, Uji, Kyoto 611-0011, Japan
e-mail: soichi_tanaka@rish.kyoto-u.ac.jp

K. Umemura
e-mail: umemura@rish.kyoto-u.ac.jp

K. Kanayama
e-mail: kozo-kanayama@rish.kyoto-u.ac.jp

© The Minerals, Metals & Materials Society 2021

G. Daehn et al. (eds.), *Forming the Future*, The Minerals, Metals & Materials Series,
https://doi.org/10.1007/978-3-030-75381-8_171

1 Introduction

Research and development for processing technology for naturally derived materials are needed for preventing mass disposal of petroleum-derived plastics. In particular, wood is an appropriate alternative to plastics because it has high strength and is sustainable and biodegradable. However, mass production techniques have not been established for processing wood into various shapes, because the deformability of wood is low. Therefore, wood products are manufactured mainly by cutting, which makes their cost higher than that of plastics.

Wood material development studies have been conducted. For example, wood-plastic composites (WPC), composed of wood powder and plastics, are used for automotive components, architectural materials, and household electronics [1]. The production of WPC is easier than that of wood, because mass production techniques, which include press molding, extrusion, and injection molding, are available for the production of WPC. However, petroleum-derived plastics, which act as the binder, must be combined with wood, and the binder content is generally at least 40–50% to maintain good moldability and product properties [2–4]. Therefore, problems related to the disposal of petroleum-derived plastics remain.

The use of a natural binder for wood is proposed. In a previous study, sucrose was used as a natural binder, which allowed fabrication of the product by injection molding of wood powder with the sucrose [5]. In this method, the binder plasticizes upon heating at first. When the wood powder is pressed with the binder, the wood powder flows with the binder during the deformation of the binder. The fluidity of the binder is important, and the moldability of the wood composite is improved by using a highly flowable binder.

In this study, the use of a mixture of sucrose and citric acid, called SC (sucrose:citric acid) binder here, is proposed. The sucrose is hydrolyzed by citric acid to low-molecular-weight sugars [6]. Therefore, the fluidity of SC binder should be higher than that of sucrose alone. To verify the effectiveness of the SC binder, the fluidity of the wood composite with SC binder in injection molding was investigated, and appropriate molding conditions, binder content B and binder mixture ratio of the sucrose and the citric acid S:C, were clarified. At first, thermal analysis of sucrose, citric acid, and SC binder was carried out to understand the thermal properties of the SC binder and determine the appropriate molding temperature. After that, an injection molding test of the wood composite with SC binder was conducted, and the effects of the molding conditions on fluidity were investigated.

2 Material and Methods

2.1 Material Preparation

Japanese cedar powder, after passing through a 500 μm sieve, was used as a wood filler, and sucrose and citric acid (anhydrous), produced by Nacalai Tesque, Inc. (Kyoto, Japan), were used as the materials for the SC binder. The wood powder, sucrose, and citric acid were dehydrated in a drying oven at 80 °C for 24 h to equalize the moisture conditions of the materials before mixing the wood powder with the binder.

Figure 1 shows a schematic diagram of the material preparation for the experiment. First, the sucrose powder was mixed with the citric acid powder at a prescribed *S*:*C* mixture ratio (Fig. 1i), and the mixture was dissolved in distilled water (Fig. 1ii). For preparing a sample for thermal analysis, the aqueous solution of the binder was dehydrated in a drying oven at 80 °C for 48 h, and the dried binder, composed of the sucrose and citric acid, was the sample used for thermal analysis. For preparing a sample for the molding test, the wood powder was added to the aqueous solution of the binder and mixed (Fig. 1iii). The aqueous solution with the wood powder was dehydrated in a drying oven, and the dried composite powder was used in the molding test. The moisture content of the dried composite powder was less than 3%. The binder content *B* in the composite powder was fixed at 20, 30, 40, and 50 wt%

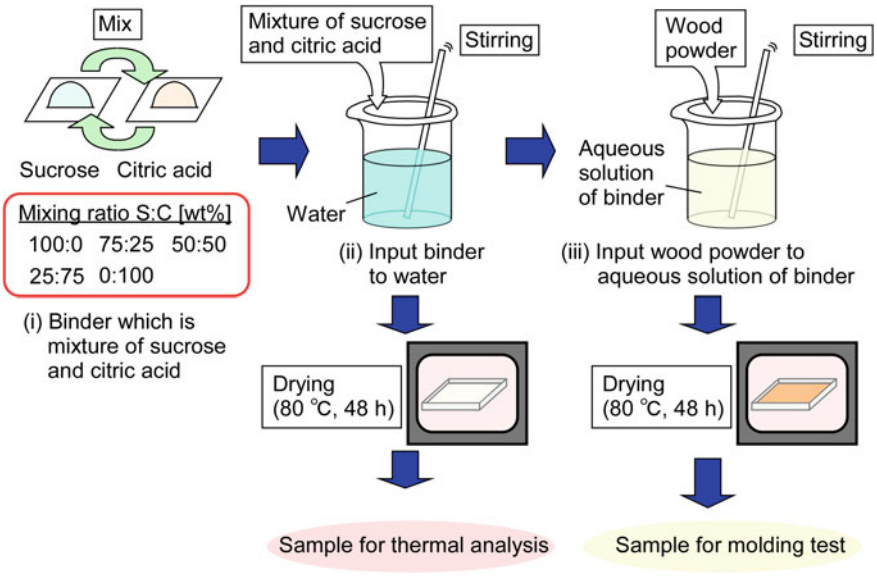


Fig. 1 Schematic diagram of material preparation. (Color figure online)

by controlling the concentration of the aqueous binder solution during the process of Fig. 1ii.

2.2 Differential Thermal Analysis and Thermogravimetry

Differential thermal analysis (DTA) and thermogravimetry (TG) analysis of the binder of various *S*:*C* mixture ratios were carried out to determine the appropriate molding temperature by clarifying the thermal properties of the binder. A differential thermogravimetric analyzer (TG8120), produced by Rigaku Corporation, was used for DTA and TG. The binder was placed in an aluminum pan, and aluminum oxide was used as a reference. For the analysis, the temperature was increased at a constant rate of 10 °C/min with purging nitrogen gas.

2.3 Injection Molding Test

Figure 2 and Table 1 show a schematic diagram and conditions for the injection molding test, respectively. Various composite powders with different binder content *B* and mixture ratios *S*:*C* were used in this test. The equipment included the container, nozzle, and cavity, and the container and the nozzle had axial symmetry. The composite powder flowed from the container to the cavity via the nozzle in

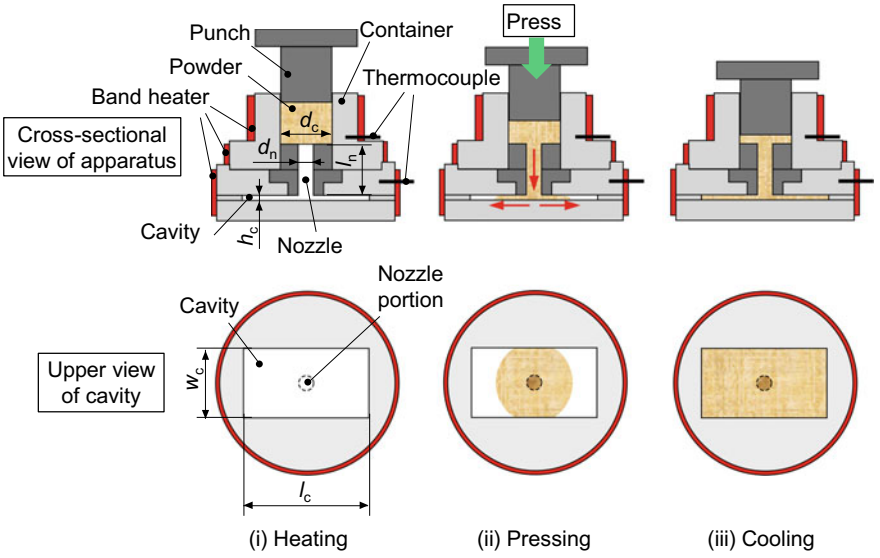


Fig. 2 Schematic diagram of injection molding test. (Color figure online)

Table 1 Molding Conditions

Container inner diameter d_c [mm]	30
Nozzle diameter d_n [mm]	10
Nozzle length l_n [mm]	25
Length of cavity l_c [mm]	90
Width of cavity w_c [mm]	50
Height of cavity h_c [mm]	4
Press velocity v_p [mm/s]	0.1
Punch surface pressure limit P_{lim} [MPa]	200
Temperature T_m [°C]	180
Pre-heating time t_h [min]	5
Mass of composite powder m [g]	30
Sucrose and citric acid mixture ratio S:C [wt%]	75:25, 50:50, 25:75
Binder content B [wt%]	20, 30, 40, 50

the molding. The band heaters heated the equipment from the outer periphery for preventing temperature variation in the equipment. The temperatures at two positions on the outer surface were measured by two thermocouples as shown in Fig. 2i, and these temperatures were kept constant by controlling the power of the band heaters during the experiment. The temperature inside the equipment was the same as that of the outer surface before inputting the powder. The target temperature T_m was set to 180 °C based on the thermal analysis results. First, the composite powder was added to the heated container and heated in the container for 5 min (heating time, t_h) as shown in Fig. 2i. After heating, the composite powder was pressed at a constant velocity of 0.1 mm/s (press velocity, v_p) in the container, and then the composite flowed into the cavity via the nozzle (Fig. 2ii). When the punch surface pressure P reached 200 MPa (pressure limit, P_{lim}), the punch movement was stopped. The equipment was cooled to 80 °C (Fig. 2iii), and the molded product was removed from the cavity. If the composite completely filled the cavity, a plate with dimensions of 90 × 50 × 4 mm was obtained. Fluidity was evaluated by observing the appearance of the plate and the punch surface pressure P variation during the molding.

3 Results and Discussion

3.1 Thermal Reaction of Binder During Heating-Up

Figure 3 shows the thermal analysis results. The DTA results (Fig. 3a) show two endothermic peaks for each S:C mixture ratio. For sucrose (S:C = 100:0) and citric acid (S:C = 0:100), the first endothermic peak indicates melting, because the melting temperatures of sucrose and citric acid are 185–192 °C and 153 °C, respectively [7].

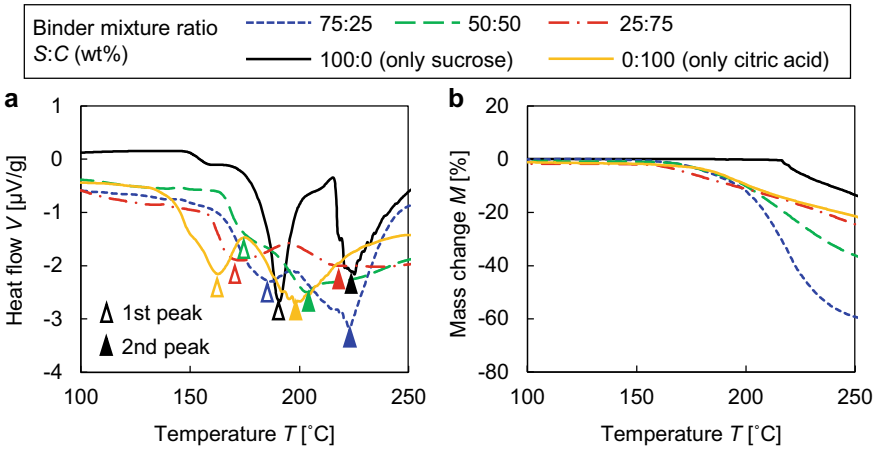


Fig. 3 Thermal analysis results: **a** Differential thermal analysis, **b** Thermogravimetry. (Color figure online)

The first peak of the SC binder for each *S*:*C* (75:25, 50:50, and 25:75) also was to be considered due to melting. The first peak of the SC binder occurred between that of citric acid and sucrose, and the first peak temperature increased with sucrose amount in the SC binder ratio. Results of TG (Fig. 3b) indicated that mass decreased with an increase in temperature *T*. The mass reduction occurred because some components in the binder volatilized due to thermal decomposition. In particular, the mass reduction rate of *S*:*C* = 75:25 increased dramatically above 200 C compared with that of other *S*:*C*, and the mass reduction increased with sucrose ratio in the SC binder when *T* reached 250 °C. Sucrose is hydrolyzed to low-molecular-weight components with acid at high temperatures [6]. Therefore, the large mass reduction was thought to occur due to thermal decomposition of the low-molecular-weight sugars, glucose and fructose.

Thus, the appropriate heating temperature for injection molding, T_m, should be near or above the melting temperature of the binder to provide good fluidity of the composite powder. However, large gas generation from the binder adversely affects molding, which can cause gas blowout from the mold. In addition, high temperatures, such as those over 200 °C, could decrease the strength of the molded product due to the thermal decomposition of the wood component [8]. Therefore, 180 °C was applied as the molding temperature T_m in this study.

3.2 Relation Between Moldability and Fluidity

Figure 4 shows the typical appearance of the molded plates, and Table 2 shows the effect of binder content *B* and mixture ratio *S*:*C* on the moldability of the plate. The

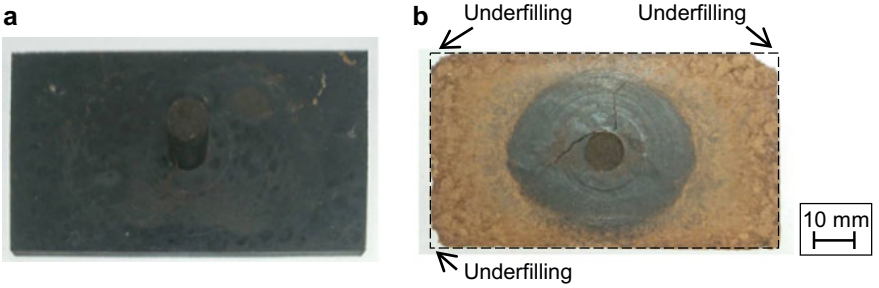


Fig. 4 Typical appearance of plates (binder mixture ratio S:C = 50:50): **a** successfully molded plate (binder content B = 50 wt%), **b** plate molded with defects (binder content B = 30 wt%). (Color figure online)

Table 2 Effect of binder content and mixture ratio on moldability

Mixture ratio S:C [wt%]	Binder content B (wt%)			
	20	30	40	50
75:25	D	D	S	S
50:50	F	D	S	S
25:75	F	F	S	S

S: Success (completely filled)
D: With defects (filled except edge portion)
F: Failure (not molded)

moldability was evaluated by a degree of the composite material filling in the cavity. When B was 40 and 50 wt%, the composite was completely filled in the cavity, and plates with a uniform dark brown color (Fig. 4a) were obtained at all S:C values; this state is defined as "success" in Table 2. However, an underfilling molding defect occurred when B was decreased to 30 wt%. For S:C = 75:25 and 50:50, plates were obtained, but the composite was not filled at the plate edge as shown in Fig. 4(b); this state is defined as "with defects" in Table 2. For S:C = 25:75, plates were not obtained because the composite powder did not flow into the cavity upon pressing the composite powder at 200 MPa, or the molded plate was too brittle for removal from the cavity; this state is defined as "failure" in Table 2. When B was decreased to 20 wt%, S:C for obtaining the plate was only 75:25. To summarize, moldability improved with an increase in B and the sucrose ratio of the SC binder; appropriate B and S:C were 40–50 wt% and 75:25, respectively, in this experiment.

Figure 5 shows the punch surface pressure P-stroke S curve during injection molding. In these graphs, the P–S curve had two bending points for each condition. These bending points generally appear when the material is extruded from a nozzle, or the flow direction changes during wood powder molding [9]. Therefore, the composite powder flow behavior was estimated from the P–S curve, as shown in Fig. 5c. Before the first small bending point, the composite powder was

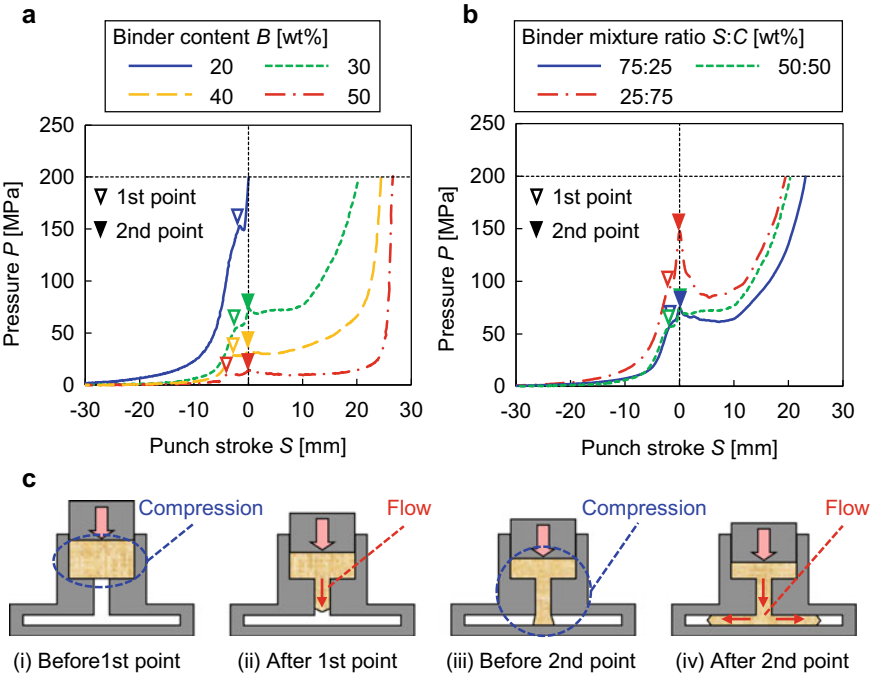


Fig. 5 Punch surface pressure variations during injection molding: **a** Effect of binder content B (binder mixture ratio S:C = 50:50), **b** Effect of binder mixture ratio S:C (binder content B = 30 wt%), **c** Schematic of composite powder flow. (Color figure online)

compressed in the container without flow (Fig. 5c(i)). At the first small bending point, the composite powder started to flow into the nozzle from the container, and the increase in P stopped (Fig. 5c(ii)). When the composite powder reached the bottom of the cavity, P increased again (Fig. 5c(iii)). The composite powder started to flow in a direction perpendicular to the pressing direction at the second bending point (Fig. 5c(iv)). In Fig. 5a, b, P variations are summarized by punch stroke s from the second bending point to consider the fluidity during composite powder flow into the cavity.

Figure 5a shows the effect of the binder content B on the P–S curve. A large binder content B decreased the punch surface pressure P. For B = 20 wt%, P reached the pressure limit of 200 MPa before the second bending point. Therefore, the composite powder did not flow into the cavity. Except for B = 20 wt%, the composite powder flowed into the cavity, and P decreased with an increase in B. Thus, the fluidity of the composite powder improved by increasing B. The maximum punch stroke S became small when P was large, indicating that the composite powder did not completely fill the cavity, as shown in Fig. 4b, due to low fluidity of the powder. Therefore, the moldability, shown in Table 2, improved by increasing B.

Figure 5b shows the effect of the binder mixture ratio *S*:*C* on the *P*–*S* curve. The punch surface pressure *P* decreased with an increase in the sucrose ratio of SC binder, i.e., the fluidity of the composite powder improved by increasing the sucrose ratio of the SC binder. Many low-molecular-weight components, apparently, were generated by hydrolysis of the sucrose by acid in the SC binder with a high sucrose ratio. Many low-molecular-weight components could have had a positive effect on the fluidity of the composite powder. Therefore, the moldability, shown in Table 2, improved by increasing the sucrose ratio in the SC binder.

Based on the above results, the fluidity of the composite powder was correlated with moldability. The fluidity could be activated by low-molecular-weight components generated from the sucrose in the SC binder. The binder content *B*, or the sucrose ratio in the SC binder, should be increased by increasing the low-molecular-weight components. However, too large a value of *B* could have a negative effect on the strength of the molded product, based on a previous study of sugarcane bagasse particleboard that was bonded with sucrose and citric acid [10]. Therefore, the optimum *S*:*C* was 75:25, and *B* should be controlled depending on the cavity shape and size.

4 Conclusions

The use of a natural binder, composed of sucrose and citric acid, was proposed for fabricating a naturally derived wood composite, and the fluidity of the wood composite with the natural binder on injection molding was examined. At first, differential thermal analysis and thermogravimetry of the binder were carried out to clarify the thermal properties of the binder. Endothermic reactions, which indicate melting, appeared between the melting temperature of sucrose and the citric acid. In contrast, some components of the binder volatilized at temperatures over 200 °C due to thermal decomposition, and this volatilization could have negative effects on the molding process. Therefore, molding should be conducted at a temperature between melting and volatilization. In the injection molding test of the composite powder, wood composite plates were successfully molded under appropriate molding conditions of binder content *B* and binder mixture ratio of sucrose and citric acid *S*:*C*. Moldability was improved with fluidity of the composite powder by increasing the binder content *B* and the sucrose ratio in the binder. However, when the fluidity of the composite powder was low, molding defects, such as cracks and chipped edges, occurred because the composite powder could not reach the cavity end. In this experiment, the appropriate binder mixture ratio *S*:*C* was 75:25 for successfully fabricating products.

Acknowledgments This work was supported by a KAKENHI grant (number 16K18265) from the Japan Society for the Promotion of Science and by Grants-in-Aid for Humanosphere Mission Research in 2016 (number 11) from the Research Institute for Sustainable Humanosphere at Kyoto University.

References

1. Eder A, Carus M (2013) Global trends in wood-plastic composites. Bioplastic Mag 8:16–17
2. Stark NM, Matuana LM, Clemons CM (2004) Effect of processing method on surface and weathering characteristics wood-flour/HDPE composites. J Appl Polym Sci 93:1021–1030
3. Nagaya T (2014) Mass production of automobile interior material using kenaf fiber which is one of the biomass. J Jpn Soc Technol Plast 55(637):108–111 (in Japanese)
4. Ansari F, Granda LA, Joffe R, Berglund LA, Vilaseca F (2017) Experimental evaluation of anisotropy in injection molded polypropylene/wood fiber biocomposites. Compos A 96:147–154
5. Kajikawa S, Horikoshi M, Tanaka S, Umemura K, Kanayama K (2017) Molding of wood powder with a natural binder. Procedia Eng 207:113–118
6. Bailey PS, Bailey CA (eds) (1989) Organic chemistry—a brief survey of concepts and applications, 4th edn. Allyn and Bacon, Boston
7. Roos Y (1993) Melting and glass transitions of low molecular weight carbohydrates. Carbohydr Res 238:39–48
8. Kajikawa S, Iizuka T (2015) Effect of molding temperature on fluidity and injection moldability of oven-dry steam-treated bamboo powder. J Mater Process Technol 225:433–438
9. Kajikawa S, Iizuka T (2014) Injection molding using only 200 °C steamed bamboo powder by controlling metal mold temperature. Procedia Eng 81:1186–1191
10. Liao R, Xu J, Umemura K (2016) Low density sugarcane bagasse particleboard bonded with citric acid and sucrose: effect of board density and additive content. BioResources 11(1):2174–2185

Accurate Mapping of Thermal Camera Measurements on Planar Deformations



Celalettin Karadogan and Mathias Liewald

Abstract Synchronous measurement of temperature distribution with infrared cameras has been increasingly used in the thermomechanical analysis of sheet material behavior. Measured temperatures are used, however, only qualitatively due to the absence of well-developed coordinate mapping methods applicable to thermographic measurements. The study introduces a primitive, easy to use, yet effective approach for accurate coordinate mapping from real to image coordinates, and inverse, applicable to even highly oblique thermographic and photographic measurements of planar deformations. The method is not limited to any camera model and precisely counteracts inhomogeneous image distortion. It can be used as a standalone optical measurement approach, but at the same time, it allows flawless correlation with available digital image correlation systems by enabling accurate mapping between thermographic and photographic measurements of planar deformation in real and image coordinates.

Keywords Temperature · Sheet metal · Full-field · Optical

1 Introduction

Thermomechanical full-field measurements have a growing and promising potential in thermomechanical analysis of material behavior [1–3]. Deformation measurement by digital image correlation (DIC) is well developed in mechanical testing [4], whereas the accurate integration of infrared thermography (IRT) is still under development [5, 6]. A major necessity addressed in these studies is the mapping of measured temperature fields, i.e. temperature images, in real space defined on the specimen surface. There are two requirements for such a mapping: a mapping function and a calibration plate for the parameter fitting. The features on the calibration plate must be visible to the infrared camera. Some researchers have approached this issue by using geometric shapes [6], infrared visible led-lighted plates [7], paintings

C. Karadogan (✉) · M. Liewald
Institute for Metal Forming Technology, University of Stuttgart, Holzgartenstraße 17, D70174 Stuttgart, Germany
e-mail: celalettin.karadogan@ifu.uni-stuttgart.de

© The Minerals, Metals & Materials Society 2021

G. Daehn et al. (eds.), *Forming the Future*, The Minerals, Metals & Materials Series,
https://doi.org/10.1007/978-3-030-75381-8_172

[8], or test fields made of reflective patterns [9]. The control points defined on these calibration plates are then used to determine the parameters of camera models. Due to difficulties in the application, some researchers have ignored the camera models and performed mapping by uniform scaling, relying on the closer and perpendicular positioning of the infrared camera [3, 4]. Simple and invertible polynomials were also used for mapping between IRT and DIC images [6]. Decoupling linear exterior (affine transformation) and interior (combination of focal length factor and pixel ratio) mappings and combining these with a polynomial distortion function considered as a classical camera model parameters of which are usually computed by optimizing the linear least-squares of the error function [10, 11].

The use of a 45°-positioned dichroic mirror [8, 12] allowed the splitting of infrared and visual radiations, which virtually positions both measurement systems to the same location in space. This advantage, along with the introduced difficulties, cannot eliminate the necessity of an accurate coordinate mapping due to the difference in camera and lens structures and resolutions.

The "infrared image correlation" was alternatively proposed [13], where only the infrared image measurements of a speckle pattern clearly distinguished due to the emissivity difference is also used for image correlation and displacement measurement. Temperature measurement is done on a single pixel value. This is, however, not possible for DIC, since the displacement tracking of a single material point requires a bunch of pixels around this point. Hence, the accuracy of the displacement measurement is drastically reduced especially when done by an infrared camera, which usually has low resolution compared with digital cameras.

To gain the state-of-the art accuracy also for the IRT camera, available DIC camera models can also be used as mapping functions for IRT [4, 7]. Image distortion can be corrected by using a calibration grid and the parameterized Bezier patches fitting on the distorted image to compute the new corrected pixel coordinates from the original pixels [14]. Higher order radial lens-distortion functions are proposed to counteract the local image distortion being variably dependent on physical depth [15]. These approaches, however, do not offer a complete solution for real coordinate mapping. It is not always possible or correct to perform DIC and IRT measurements at the opposing faces of the specimen. Therefore, the oblique positioning of cameras pointing at the same side becomes inevitable and the use of higher order lens-distortion models is necessary. In such applications, the correct determination of the temperatures over a speckle painting with varying emissivity has already been studied [8].

Referring to Zhang [16] and covering the recent advancements, MathWorks has recently introduced a comprehensive single-camera calibration application in MATLAB. As explained in [17], this can be used "*to estimate the camera parameters which can be used for removing the effects of lens distortion from an image, measuring planar objects, or reconstructing 3D scenes from multiple cameras.*" However, the number of calibration snapshots and the number of points on the calibration plates increase drastically with complicated camera models. A single-image linear calibration method is introduced recently by using a calibration gadget having two perpendicular faces with checkerboard pattern [18]. These attempts concentrate on finding the best-fitting model parameters of camera models.

The extraction accuracy of the control points from the calibration targets is also influential in the overall accuracy of the measurement. It is reported that the checkerboard pattern, for which the intersection of edges are used as control points, may yield inaccurate results due to blurred edges and low-resolution images [10]. On the other hand, control points corresponding to circular patterns are computed as the center of the approximated ellipse, which yields better accuracy [10].

Authors readdress the problem of constructing an experimental setup with separate IRT and DIC systems positioned at either common or opposing faces of the specimen. Accurate mapping of in-plane measurements even for oblique positioning of cameras is intended. This paper develops and demonstrates the successful application of a nonlinear finite-element interpolation-based mapping function, performed on a single snapshot of the calibration object. Hence, the method is independent of any kind of camera models and applicable to any kind of cameras for either thermographic or digital measurements of planar deformations. The method is proven to bring a better accuracy even for the extremely oblique views of cameras making it possible to measure the thermographic and digital images from the same face of the specimen. The procedural application of the proposed method only to thermographic measurements where the digital deformation measurements are done by the available system is also demonstrated. An easy to manufacture calibration plate with accurately drilled holes and a speckle painting is clearly visible for IRT and DIC systems. Beyond constructing a well-defined common coordinate system attached to the specimen surface, such a holed pattern in N-by-N grid layout initiated the idea of using finite element shape functions to define a mapping from real coordinates to image coordinates for the IRT measurements. This novel mapping approach maps real coordinates directly to image coordinates and provides accurate mapping with more parameters despite its theoretical simplicity and practicality. The necessary inverse mapping from image coordinates to real coordinates is performed by a primitive approach by computing all at once, in a relatively short time, the corresponding real coordinates for all the pixels in the relevant measurement area right after the calibration snapshot. This discrete mapping data still allow sub-pixel calculations if desired.

The paper presents the experimental setup consisting of a calibration plate, calibration snapshot, and the mapping approach. The coordination of many simultaneous IRT and DIC measurements for precisely overlapping measurements is also explained. The methodology is then applied to a photographic and thermographic measurement to demonstrate functionality and accuracy.

2 Experimental Setup

This study focuses on experimental setups consisting of a mechanical testing device, optical deformation measurement camera, and a thermographic infrared camera observing either the same or the opposing faces for planar deformations of a specimen. Figure 1 shows two possible configurations where the infrared camera is positioned either at the same side or at the opposing side of the specimen with respect to

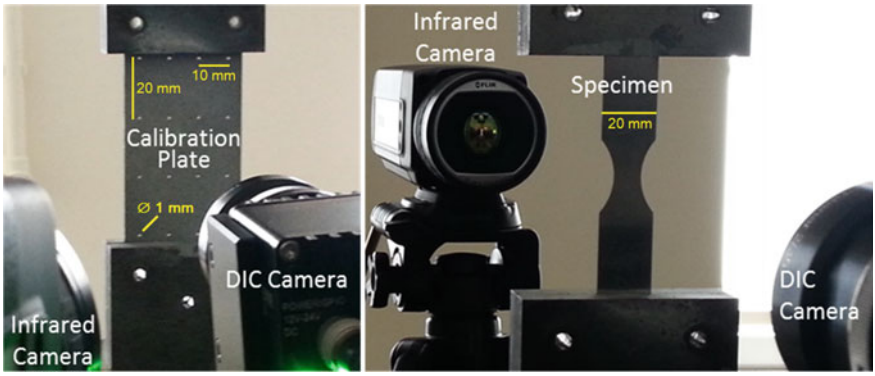


Fig. 1 Possible camera positions for thermomechanical measurements. (Color figure online)

the deformation measurement camera. When both cameras are positioned at the same side at least one of them must be positioned oblique. When cameras are positioned at the opposing sides of the specimen, they can be positioned close and perpendicular to the specimen faces, but camera distortion is still at work even for this configuration. For all cases, precise real-to-image and image-to-real mappings are necessary for accurate evaluation of the measurements. This study develops an accurate and easy to use mapping and matching approach for infrared cameras, and homemade or commercial deformation measurement systems. This is achieved by a new mapping approach, which uses a single calibration snapshot on a simple calibration plate before the experiment begins. These are introduced in the rest of this section.

2.1 Calibration Plate

The recent proposal in [7] for the calibration of thermal cameras using infrared visible light falls short in several aspects. First of all, the light grid cannot be produced with the ordinary milling machine accuracy of 10 microns and the observed edges of the lights are not sharp. Furthermore, the light grid is not a common platform to create a spatial matching between IRT systems and commercial DIC systems. Alternatively, an object with a few geometric features is used in [6] as a means to define easy to invert linear mapping between the DIC and IRT measurements. Such a mapping is unfortunately inaccurate [4].

A planar calibration plate providing a sharp infrared image obtained by accurately drilled 16 holes in the form of a 4×4 Cartesian grid layout is proposed, Fig. 2. This calibration plate defines a common real coordinate system in the plane of the specimen for both IRT and DIC measurements. Grid separation may be different between Cartesian directions but suggested to be common in each direction to create a rectangular measurement region. Such a calibration plate can be manufactured

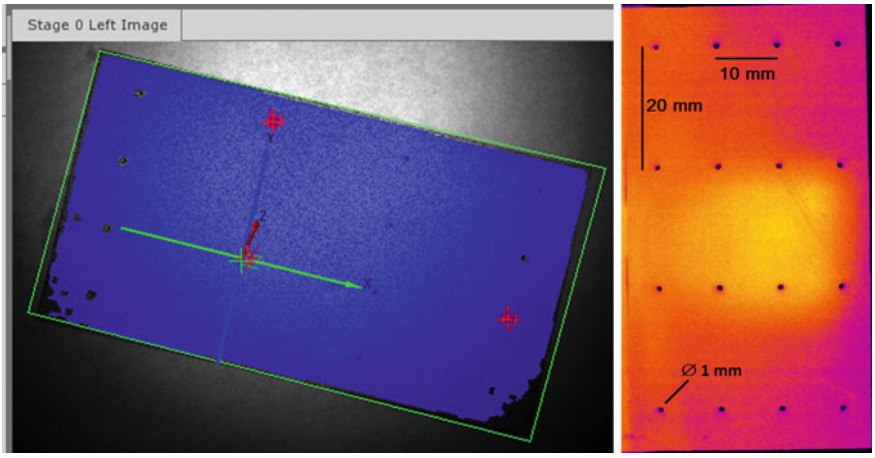


Fig. 2 Calibration snapshot for an IRT measurement (right) and a commercial DIC system (left). (Color figure online)

from a flat sheet material on a milling machine with at worst 10-micron locational accuracy.

2.2 Calibration Snapshot

A calibration snapshot is taken to determine the image (i.e. pixel) coordinates of the calibration plate holes. This is used to build an interpolative mapping function from real coordinates to the corresponding image coordinates. As shown in Fig. 2, a two-dimensional Cartesian coordinate system in real space is centered at any one of the holes and aligned with the grid directions defined by the holes. This is achieved either by using the proposed coordinate mapping strategy for a homemade DIC system or transforming the coordinate system of a commercial system using the holes' locations, e.g. 3-2-1 coordinate system transformation used by GOM-ARAMIS [19]. In this way, all the infrared and digital measurements done during the experiment are set up to use the same real coordinate system defined by the calibration plate. To gain this extensibility, the calibration plate must be painted by a speckle pattern. The visible holes buried in the speckle pattern create a snapshot to be used for the coordinate system transformation in the commercial DIC system as shown in Fig. 2.

Together with the mapping functions constructed for each IRT and DIC measurement device, real-to-image, image-to-real, and image-to-image mappings are then trivial as explained in Sect. 2.3. Furthermore, the holed nature of the calibration plate makes it irrelevant whether different cameras are located to view the same or the opposing faces of the specimen. During the calibration snapshots taken from all measurement devices, the calibration plate must be positioned stationary in the

plane where the deformation of the specimen takes place. Furthermore, the rectangular periphery formed by the holes is defined as the measurement range and must cover the specimen's gauge. After the calibration snapshots from all the devices, the cameras must remain stationary.

The accuracy of the calibration snapshot totally depends on the accurate determination of the holes' pixel locations. Since only 16 locations need to be determined, this could be done precisely by manual work in a short time. The accuracy can be further increased by using sub-pixel location detection approaches as proposed in the literature [20–22]. Calibration snapshot from an infrared camera can always be made further clear and sharp, by placing either hotter or a colder object behind the calibration plate, without changing the temperature of the calibration plate.

2.3 Mapping Algorithm

The common strategy in the available camera models is to compute the extrinsic (position and orientation) and intrinsic (optical and internal geometric characteristics) parameters of the camera model by using calibration snapshots of predefined calibration plates. Since inverse mapping from pixel to real coordinates is necessary, intrinsic and extrinsic characteristics of cameras are expressed preferably by invertible, hence simple, functions of geometry and optics possibly with the least number of parameters. The camera parameters are computed by regression analysis and/or many smaller sub-regions are considered to reduce the possible mapping errors. The proposed approach, however, does not consider the camera as a device with intrinsic and extrinsic characteristics but rather as a mapping function. This approach with an increased number of parameters improves the accuracy of the mapping function and further eliminates the necessity of using excessive number of points on the calibration plates or considering sub-zoning for better accuracy in mapping.

The proposed approach uses the bi-cubic shape functions (1) from the finite element method as the mapping function:

$$\begin{aligned} u &= \alpha_1 + \alpha_2 X + \alpha_3 Y + \alpha_4 XY + \alpha_5 X^2 + \alpha_6 Y^2 + \alpha_7 X^2 Y + \alpha_8 XY^2 + \alpha_9 X^2 Y^2 \\ &\quad + \alpha_{10} X^3 + \alpha_{11} Y^3 + \alpha_{12} XY^3 + \alpha_{13} XY^3 + \alpha_{14} X^3 Y^2 + \alpha_{15} X^2 Y^3 + \alpha_{16} X^3 Y^3 \\ V &= b_1 + b_2 X + b_3 Y + b_4 XY + b_5 X^2 + b_6 Y^2 + b_7 X^2 Y + b_8 XY^2 + b_9 X^2 Y^2 \\ &\quad + b_{10} X^3 + b_{11} Y^3 + b_{12} X^3 Y + b_{13} XY^3 + b_{14} X^3 Y^2 + b_{15} X^2 Y^3 + b_{16} X^3 Y^3 \end{aligned} \tag{1}$$

The mapping function (1) defines the mapping from the real coordinates (X, Y) to image coordinates (u, v). The real coordinates of the 16 holes on the calibration plate are well known as far as a coordinate system is defined on the calibration plate.

As soon as the corresponding image coordinates of holes obtained from the calibration snapshot are determined, (1) can be used to construct two equation systems to determine the coefficients α_i and β_i for which a unique solution always exists.

The major weakness of this extended, nonlinear, and monolithic definition (1) instead of a camera model is the necessity to perform an iterative solution for the inverse (i.e. from image to real) mapping. This is true but practically not a drawback for the proposed approach at all. Knowing the corresponding 16 calibration plate locations in real and image space, inverse mapping from image to real coordinates for these 16 pixels is already known exactly. Starting from these locations and progressing to the neighboring pixels, it takes only a couple of minutes for practical camera resolutions to accurately find the corresponding real coordinates of all the pixels within the measurement range. Newton–Raphson approach applied for this purpose uses the known real coordinates of the neighboring pixels as initial guesses for the iterative solution. This iterative root finding for each pixel generates a correspondence table, which can be stored for later use as a mapping function from image coordinates to real coordinates. Since real-to-image mapping function (1) is more accurate, the inverse mapping from image to real coordinates obtained by its inverse solution is also more accurate as far as sufficiently tight tolerances for the inverse solution are used. Practical examples in Sect. 3 provide the computation times for the inverse mapping, which turns out to be totally reasonable in exchange for improved accuracy. In fact, computation of the corresponding real coordinates and storing them for later use right after the calibration snapshot, once for all, save time in the experimental image analysis phase by eliminating repetitive calculations for the same pixels. For mapping from sub-pixel locations to real coordinates, the computed mapping table still provides an accurate solution by means of interpolation.

The real-to-image mapping function (1) and its inverse for each relevant pixel from image to real coordinates in terms of a stored table provide the complete mapping functionality for a thermographic or a photographic measurement. In case more than one measurement devices are used, real coordinates can be used as an intermediate mapping space, to obtain the image-to-image mapping from one measurement device to another. The discussion above provides the necessary mathematics for the computation of the mapping functions in case all the measurement systems are located to view the same face of the specimen. If infrared and digital cameras are positioned to view the opposing faces of the specimen, the horizontal X-coordinate of one of the systems should be redefined to be $X_{\text{backside}} = -X_{\text{front}}$ to construct a collaborative measurement setup.

3 Results

The proposed mapping strategy between real and image coordinates is applicable to any kind of digital or infrared camera. This section presents the comparative performance of this mapping approach for two camera types with respect to the results computed by the METROVISIONLAB Toolbox [23]. For this purpose, two types

of cameras are considered, namely, an 8 MP digital camera and an infrared camera to investigate the accuracy performance and infrared applicability of the proposed approach, respectively. With a 10 mm spacing, a square grid of 90 mm size was manufactured using a 1 mm thick sheet metal on a CNC milling machine, Fig. 3. This creates a total of 100 grid points. Evenly distributed 16 points, 12 of which are at the corners and edges, are used as the calibration locations for the proposed approach. The comparison is done against the results obtained by the METROVISION Toolbox using all of the 100 grid points for calibration. Locations of the 100 grid points are well defined in real coordinate space. Their pixel locations are precisely determined by applying manual image zooming and ignoring sub-pixel estimation. The precision of reconstruction for the known image and real coordinates is used to evaluate the accuracy of the reconstruction, where image coordinates are expressed using Eq. (1) and real coordinates are reconstructed by inverting and computing the correspondence table from image to real coordinates. Due to convenience, distance and component errors are provided only over mean and maximum values in Tables 1 and 2.

Another measure for the performance of the proposed approach is the time spent on the necessary computations. The bottleneck here is the computation time spent for the construction of the correspondence table from image to real coordinates for all the pixels located within the measurement range. This computation uses the pixel distance residual threshold of 10^{-9} for the iterative Newton–Raphson solution of the Eq. (1). The total number of pixels and the corresponding computation time are also provided below for the studied cases. The platform for the mentioned computations is MathWorks® MATLAB.

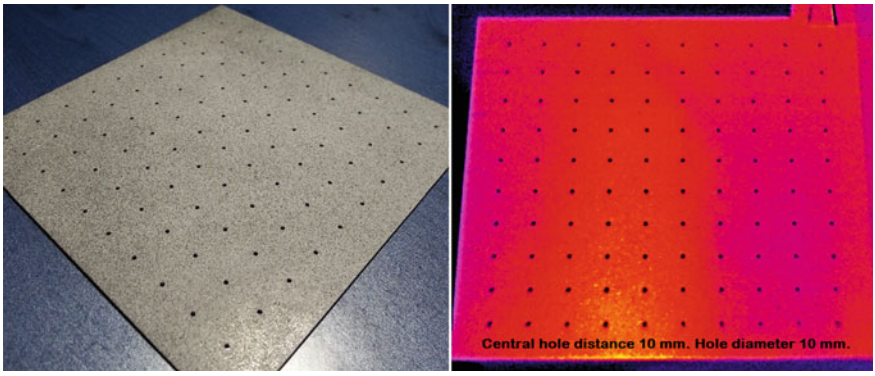


Fig. 3 Photographic and thermographic snapshots of the square holed plate of 90 mm. (Color figure online)

Table 1 Reconstruction performance for photographic camera

Mapping errors from real to image coordinates	Mean (pixel)			Max. (pixel)		
	u	v	dist	u	v	dist
Proposed Mapping Approach	0.569	0.497	0.836	2.057	1.814	2.334
METROVISIONLAB Toolbox	1.174	1.213	1.845	5.736	4.512	6.499
Mapping errors from image to real coordinates	*Mean (mm)*			*Max. (mm)*		
	X	Y	dist	X	Y	dist
Proposed Mapping Approach	0.032	0.041	0.058	0.161	0.180	0.181
METROVISIONLAB Toolbox	0.065	0.088	0.120	0.224	0.331	0.331

Table 2 Reconstruction performance for thermographic camera

Mapping errors from real to image coordinates	Mean (pixel)			Max. (pixel)		
	u	v	dist	u	v	dist
Proposed Mapping Approach	0.341	0.304	0.522	1.235	1.000	1.274
METROVISIONLAB Toolbox	0.556	0.353	0.715	2.596	1.601	2.605
Mapping errors from image to real coordinates	*Mean (mm)*			*Max. (mm)*		
	X	Y	dist	X	Y	dist
Proposed Mapping Approach	0.089	0.115	0.165	0.283	0.398	0.404
METROVISIONLAB Toolbox	0.102	0.189	0.231	0.463	0.806	0.814

3.1 Photographic Performance

The accuracy of the proposed mapping approach is demonstrated on the introduced grid shown in Fig. 3, with a perspective of roughly 20 cm distance, 60° from the vertical and 45° from the *X*-direction using a digital camera with an 8 MP CMOS sensor and F2.6 lens. This perspective can be considered as an extreme situation. The construction of the inverse mapping table from image to real coordinates for all the 2 megapixels lying within the measurement range takes only 397 s on the Intel® i5-3317U@1.7 GHz processor and occupies a storage of 30 MB in MATLAB. The corresponding computation time reduces to 261 s on Intel® Xeon® E5-1620@3.6 GHz.

3.2 Thermographic Performance

The functionality of the proposed approach using a 640 × 480 pixel resolution infrared camera FLIR-A655-sc with F24.6 mm lens is demonstrated next. For this purpose, a perspective of roughly 45 cm distance and 15° from the vertical is used as shown in Fig. 3. This perspective can be considered as a probable orientation for a two-camera measurement on the same specimen face. The construction of the inverse mapping table from image to real coordinates for all the 82,285 pixels lying within the measurement range takes only 9 s on the Intel® i5-3317U@1.7 GHz processor and needs a storage of 1.2 MB.

The reconstruction quality of the proposed approach as shown in Tables 1 and 2 for all the 100 grid locations is significantly better. Despite the fact that the proposed approach uses only 16 points, whereas the compared and similar strategies require all of the 100 points for the calibration.

4 Summary, Discussion, and Outlook

A new real to image mapping approach is introduced for the planar measurements. The approach uses the bi-cubic interpolation functions based only on 4 × 4 grid points identified by a single calibration snapshot. The calibration plate is manufactured by precisely drilling small holes in a 4 × 4 grid pattern on a flat thin rigid sheet. This enables accurate mapping for thermographic measurements. Simultaneous IRT and DIC measurements are also possible by positioning the systems either at the same side or at the opposing sides of the specimen. The gauge of the specimen must be in the same plane and totally covered by the 4 × 4 grid on the calibration plate. The holed calibration plate painted by speckle pattern facilitates a flawless collaboration with commercial DIC systems for deformation measurements. As demonstrated in the paper, the proposed mapping approach is more accurate compared with available digital camera modeling techniques. In this way, highly oblique views are made practicable without losing measurement accuracy. Any available technique used to increase the accuracy by sub-pixel evaluation can also be integrated in the proposed mapping approach. No more than 16 calibration points are required, so that a manual determination of the pixel positions is practically possible and the error-prone automation of control point detection is eliminated. The approach is simple and does not require any expertise in camera modeling approaches.

Having them apparent for both infrared and digital cameras, it is suggested to have the holes' diameters as small as possible to increase the accuracy of mapping. The proposed approach can be extended to use higher order mapping functions with more parameters as a better alternative to (1). Hence, the number of holes on the calibration plate should be increased accordingly. A 5 × 5 grid, for example, will provide a bi-quartic mapping function. The proposed approach is applicable to only planar measurements and provides only a mapping function from real to image

coordinates. Due to its nonlinear nature, the inverse mapping from image to real coordinates is done by inverse numerical solution of the forward mapping functions. Practical time loss due to this drawback, however, is a couple of minutes only once for all of the pixels within the measurement range. This primitive approach of calculating and storing real coordinates corresponding to all relevant pixels once as part of the calibration procedure saves time in the later evaluation phase.

Determination of camera orientation and position, elimination of camera distortion, camera calibration, and modeling are not concerns of this approach and can be considered as a weakness in the perspective of camera modeling. An extension to three-dimensional measurements is possible for photographic measurements with a two-camera system. For this purpose, accurate repositioning of the calibration plate perpendicular to itself to cover the whole volumetric range of measurement is necessary. Hence, a tri-cubic interpolation function, for example, can be obtained using four positions of the calibration plate. A three-dimensional thermographic measurement is only possible over a coupled three-dimensional photographic measurement. A further limitation of the approach could be the change in camera distance due to thickness changes during the testing of the sheet specimen. This is a general concern for all single-camera measurement systems that use a camera model and can be reduced by positioning the cameras as perpendicular as possible to the specimen surface.

The accurate measurement of the thermomechanical full-field opens the way for new characterization methods. Tracking the temperature of a material point during mechanical loading yields a temperature progression as shown in Fig. 4, [24]. This figure shows the measured temperatures at the two marked locations, on a tensile specimen, and on an in-plane shear specimen. The shown measurements start in

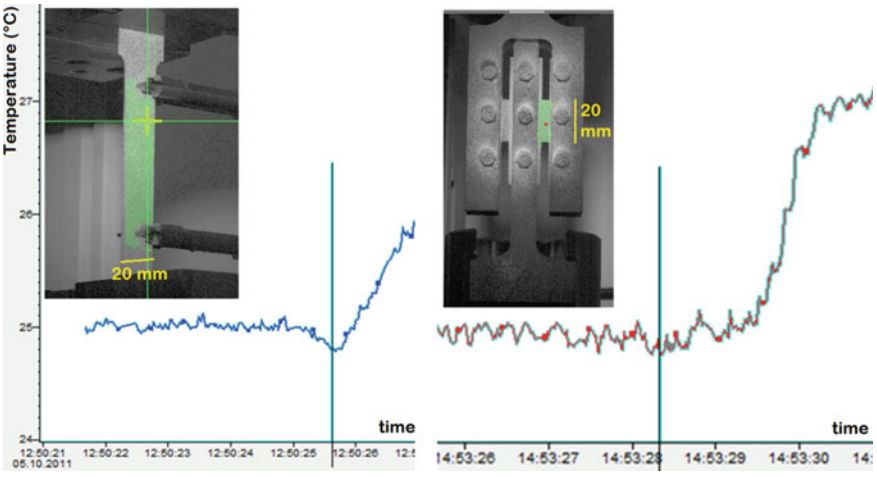


Fig. 4 Temperature development during tensile (left) and in-plane shear test (right) [24]. (Color figure online)

the phase of elastic deformation and go further in the early phase of the plastic deformation. Depending on the stress state causing expansion or contraction of the material, a slight cooling or warming can be observed during elastic deformation. However, the plastic deformation is always associated with a considerable increase in temperature due to generated heat. Using this advantage of thermomechanical full-field observations, stress values on the yield locus of a material can be determined more accurately. For this purpose, specimen geometries that simultaneously exhibit a wider range of practical stress ratios could be useful to reduce the number of experiments required for the characterization of the yield locus [25].

References

1. Banabic D, Huetink J (2006) Determination of the yield locus by means of temperature measurement. In: Paper presented at the 9th ESAFORM conference on Material Forming, Glasgow, U.K
2. Foecke T, Iadicola MA, Lin A, Banovic SW (2007) A method for direct measurement of multiaxial stress-strain curves in sheet metal. Metall Mater Trans A 38(2):306–313
3. Chrysochoos A, Huon V, Jourdan F, Muracciole J-M, Peyroux R, Wattrisse B (2010) Use of full-field digital image correlation and infrared thermography measurements for the thermomechanical analysis of material behaviour. Strain 46:117–130
4. Sutton MA, Schreier HW, Orteu JJ (2009) Image correlation for shape, motion and deformation measurements: basic concepts, theory and applications. Springer, New York
5. Li L, Latourte F, Muracciole JM, Waltz L, Sabatiera L, Wattrisse B (2015) Calorimetric analysis of coarse-grained polycrystalline aluminum by IRT and DIC. Quantitative InfraRed Thermography J 12(1):80–97
6. Moustafa A-R, Berthel B, Fouvry S, Charkaluk E (2015) Experimental study of the stress gradient effect under fretting loading by full field measurement techniques. Wear 330–331:160–169
7. Lagüela S, González-Jorge H, Armesto J, Arias P (2011) Calibration and verification of thermographic cameras for geometric measurements. Infrared Phys Technol 54(2):92–99
8. Cholewa N, Summers PT, Feih S, Mouritz AP, Lattimer BY, Case SW (2015) A technique for coupled thermomechanical response measurement using infrared thermography and digital image correlation. Experimental Mech 1–20
9. Luhmann T, Piechel J, Roelfs T (2013) Geometric calibration of thermographic cameras. Remote Sens Digital Image Process 17:27–42
10. R. Usamentiaga DF, Garcia C, Ibarra-Castanedo X, Maldague, (2017) Highly accurate geometric calibration for infrared cameras using inexpensive calibration targets. Measurement 112:105–116
11. Bodelot L, Sabatier L, Charkaluk E, Dufrénoy P (2009) Experimental setup for fully coupled kinematic and thermal measurements at the microstructure scale of an AISI 316L steel. Mater Sci Eng A 501:52–60
12. Marcin N, Maj M (2018) Determination of coupled mechanical and thermal fields using 2D digital images correlation and infrared thermography: numerical procedures and results. Archives Civil Mech Eng 18:630–644
13. Maynadier A, Poncelet M, Lavernhe-Taillard K, Roux S (2011) One-shot measurement of thermal and kinematic fields: infrared image correlation (IRIC). Exp Mech 52:241
14. Ardeshir G (1989) Correction of image deformation from lens distortion using bezier patches. Comput Vis Graph Image Process 47:385–394
15. Alvarez L, Gomez L, Sendra JR (2011) Accurate depth dependent lens distortion models: an application to planar view scenarios. J Math Imaging Vis 39:75–85

16. Zhang Z (2000) A Flexible New Technique for Camera Calibration. IEEE Trans Pattern Anal Mach Intell 22(11):1330–1334
17. MATLAB R2015b, User Manual for Computer Vision System Toolbox
18. Zhang Z, Zhao R, Liu E, Yan K, Ma Y (2018) A single-image linear calibration method for camera. Measurement 130:298–305
19. GOM ARAMIS (2015) Theory and User Manual, http://www.gom.com
20. Shimizu M, Okutomi M (2003) Significance and attributes of subpixel estimation on area-based matching. Syst Comput Jpn 34(12):1–111
21. Morgan GLK, Liu JG, Yan H (2010) Precise subpixel disparity measurement from very narrow baseline stereo. IEEE Trans Geosci Remote Sens 48(9):3424–3433
22. Xiao Y, Fisher RB (2010) Accurate feature extraction and control point correction for camera calibration with a mono-plane target. In: Paper presented at the Conf. 3D Data Processing, Visualization and Transmission (3DPVT), Paris 2010
23. Samper D, Santolaria J, Aguilar JJ (2019) METROVISIONLAB Toolbox for Camera Calibration and Simulation. http://metrovisionlab.unizar.es
24. Karadogan C et al. (2012) Development of a novel experimental technique based on simultaneous temperature and strain measurements to identify yield locus of sheet metals, Published Report of the TUBITAK Project 110M586, 30.10.2012
25. Karadogan C, Tamer ME (2017) A novel and simple cruciform specimen without slits on legs yet higher plastic strains in gauge. Paper presented at the International Conference on the Technology of Plasticity ICTP 2017, Cambridge UK, 17–22 Sept. 2017, Procedia Engineering 207:1922–1927

Effect of Bending Intensity on Straightness in Spinner Straightener



Keiichiro Kawasaki, Shohei Kajikawa, Hiromichi Matumura, Tetushi Ono, Hikaru Seimiya, and Takashi Kuboki

Abstract This paper presents the optimum processing condition of spinner straightener. Spinner straightener straightens wire rod using several straightening tools by subjecting the rod to repetitive bending and unbending with rotational movement. This research investigated the effect of bending intensity on the straightness of wire by changing the die positions, which determine the bending intensity. Both the experiment and analysis were carried out for the investigation. One of the unique points of this study is the usage of the actual operation line for the experiment instead of laboratory equipment. Another unique point is the combination of the finite element analysis (FEA) and a purpose-built fundamental analysis. The analysis and experiment were in good agreement and showed the existence of the optimum condition. The straightness was improved with the increase in the bending intensity up to the optimum bending intensity. However, the excessive bending intensity deteriorated the straightness.

Keywords Spinner · Straightener · Straightness · Curvature · FEM

1 Introduction

Straightening is located at the end of the manufacturing process for bars and wire rods. Bars and wire rods are used as materials for precision parts such as automobile and printer shafts. Recently, the requirements for the dimensional precision of bars and wire rods are getting stricter due to the recent trend of requirements to the final products, which use the bars and wire rods. So the role of the straightening process is more and more important. Figure 1 shows the process line of bars. The initial bar is unwound from the coils on the supply stand and drawn before the line of

K. Kawasaki (✉) · S. Kajikawa · T. Kuboki
The University of Electro-Communications, 1-5-1 Chofu Gaoka, Chofu-shi, Tokyo 182-8585, Japan
e-mail: kawasaki@mt.mce.uec.ac.jp

H. Matumura · T. Ono · H. Seimiya
Shimomura Tokushu Seiko Co, 668-1 Matsuomachi Kashikehongo, Sammu-shi, Chiba 289-1537, Japan

© The Minerals, Metals & Materials Society 2021

G. Daehn et al. (eds.), *Forming the Future*, The Minerals, Metals & Materials Series,
https://doi.org/10.1007/978-3-030-75381-8_173

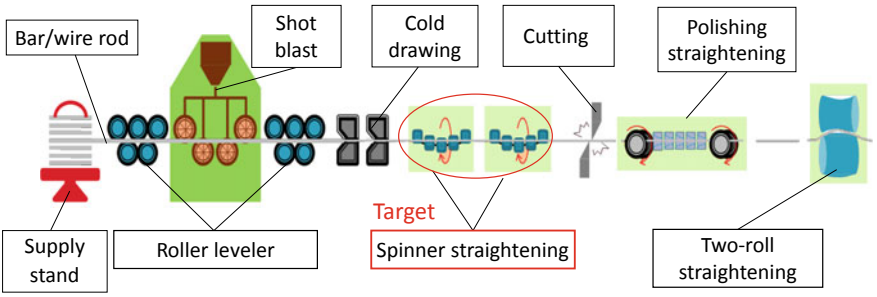


Fig. 1 Process of line for bars and wire rods. (Color figure online)

straitening processes. The straightening line includes spinner, polishing, and two-roll straighteners. These straightening processes would collaboratively determine the quality of the bars, and the spinner is located at the first of the three processes.

There are few research works for the spinner, though there are many for the final process, like two-roll straighter. Yanagihashi et al. [1] and Mutrux et al. [2] tried to apply the FEM to solid-bar straightening by deciding the deformed shape in advance. Kuboki et al. composed a Finite Element Method (FEM) model applying the implicit scheme for three-stand tube straightening [3]. Wu et al. carried out a theoretical approach for analyzing the mechanism of the two-roll straightener [4]. However, all the above works focused upon the final process in the production line without knowing phenomena in the first process, which is spinner straightening. Although Tsurumi et al. conducted a study on a spinner-like machine, the material was a very thin wire and the study is not so general [5].

The present study focuses upon the spinner straightening, which is the first process and may play an important role in the production line. Analysis methods are proposed utilizing the Finite Element Method for clarifying a guideline for optimum conditions. Two types of analysis methods are shown. Model 1, full actual model with explicit scheme [F-Model], considers the rotational movement of dies as the actual process using the explicit scheme. Model 2 is a model carrying out fundamental analysis by approximating the spinner process to three bending processes with bar rotation based on the results of simple bending in FEM, named [B-Model]. B-Model used FEM only for calculation of simple bending without rotation for obtaining the deformed bar shape. A series of experiments were conducted in an actual production line as well as the analyses by Models [F-Model] and [B-Model]. The examination mainly focused upon the effect of straightening intensity by changing the die positions for showing mechanism in spinner straightening and a guideline for the optimum working condition.

2 Condition for Spinner

Figure 2 shows a schematic illustration of the spinner. The die positions h_i(i = 1–5) were defined so that the h_i should be zero when the dies contact with a completely straight bar without any load. The sign (positive/negative) of h_i was defined as shown in the figure. The die positions h_i determine the bending intensity during straightening. The detailed condition on the die positions is shown in Table 1. Condition [A] is intuitively expected to have the strongest straightening effect. Table 2 shows the drawing condition in advance of spinner straightening. Coils of lead-free free-cutting steel were annealed and drawn. Table 3 shows other working conditions.

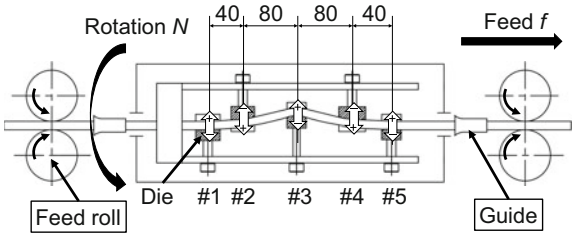


Fig. 2 Composition of spinner straightener

Table 1 Die position for spinner straightening

Condition	Die position h_j (i = 1–5)/mm				
	#1	#2	#3	#4	#5
[A]	0	−2.25	11	−2.25	0
[B]	0	−1.875	10	−1.875	0
[C]	0	−1.55	9	−1.55	0
[D]	0	−1.3	8	−1.3	0
[E]	0	−0.97	6	−0.97	0
[F]	0	−0.92	5.5	−0.92	0

Table 2 Drawing condition before spinner straightening

Initial		Die inside diameter
Diameter d_0/mm	Heat treatment	Last d/mm
6.5	Annealing	6.05

Table 3 Working condition

Feed pitch f/mm.rev^{-1}	9.52
Rotation N/rpm	5250

Material: Lead-free free-cutting steel flow stress: $\sigma = 420(\varepsilon + 0.11)^{0.089}$

3 Analytical Models

3.1 Full Explicit Scheme Model [F-Model]

Two analytical models were composed, and the detailed settings are explained in this section. Figure 3 shows the composition of spinner in the Finite Element Analysis (FEA). Guides and rollers were made as well as the bar and the dies. Residual stresses are assumed to be zero in the analyses in this study.

The first model almost fully reproduced the movement of spinner straightening using the explicit scheme. The analysis was carried out by two steps as shown in Fig. 4. The bar was set through Guide 1 to roller 2 via dies #1−#5, and the front tension T was applied. The dies gradually moved to the target position of h_i(i = 1 ~ 5) at Step 1. At Step 2, the rotational movement was given to the dies, while feeding movement was given to the bar end. Although model [F-Model] would not be as

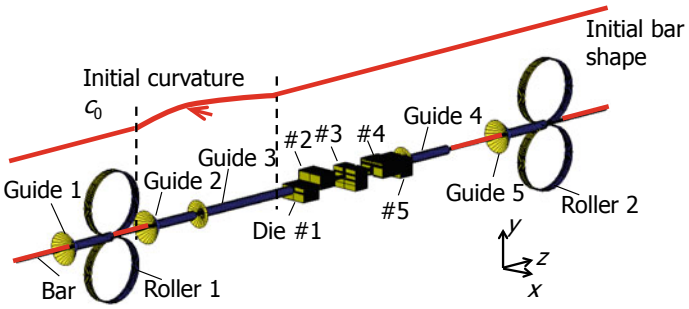


Fig. 3 Analysis steps in [F-Model]. (Color figure online)

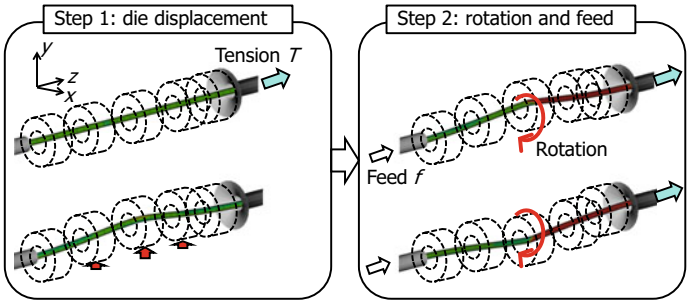


Fig. 4 Analysis steps in the model [F-Model]. (Color figure online)

precise as a model with the implicit scheme, it can consider the centrifugal force and the convergence would be stable. An initial curvature C_0 was given to the bar between the Roller 1 and Die #1, and the curvature was evaluated at the same portion of the bar during and after the spinner straightening.

3.2 *Approximation to Three-Point Bending from FE Bending [B-Model]*

B-Model was also composed of two steps as shown in Fig. 5 and the meanings of symbols are shown in Table 4. This model assumed that the bending deformation of the bar by spinner straightener can be approximated to three-point bending with

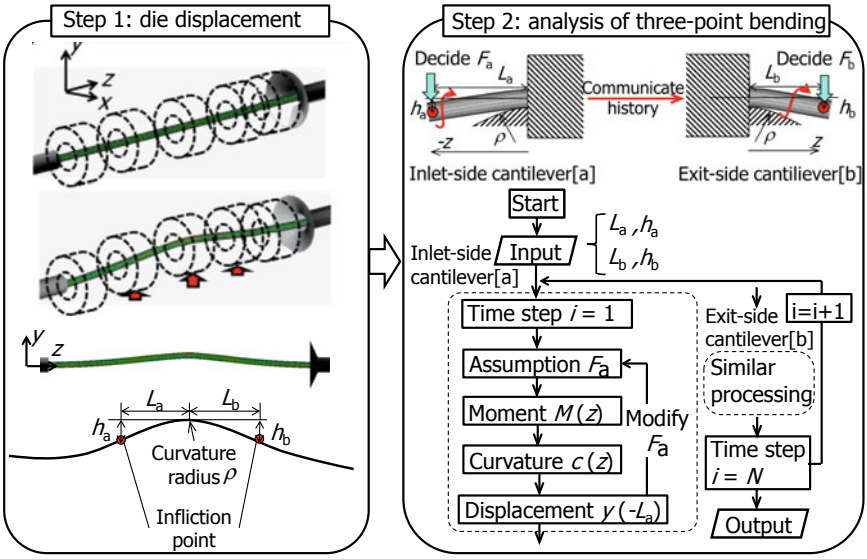


Fig. 5 Analysis steps in model [B-Model]. (Color figure online)

Table 4 Notion

L_a distance between #3 die and inform point in inlet-side cantilever	z axial position
L_b distance between #3 die and inform point in exit-side cantilever	$M_{(z)}$ moment of z
h_a height inflection point in inlet-side cantilever	$C_{(z)}$ curvature of z
h_a height inflection point in exit-side cantilever	$Y_{(z)}$ displacement of z
F_a force in inlet-side cantilever	F_b force in exit-side cantilever

bar rotation. The composition of tools and the work Step 1 is the same as that of model [F-Model]. There is an inflection point for inlet and exit sides. The positions of the inflection points, i.e. L_a, L_b, h_a, and h_b were extracted. The distance between #3 die and inflection point L_a in inlet-side cantilever, the distance between #3 die and inflection point L_b in exit-side cantilever, height of inflection point h_a in inlet-side cantilever, and height of inflection point h_b in exit-side cantilever were extracted and transferred to Step 2. Step 2 calculated moment distribution $M_{(Z)}$, curvature distribution $C_{(Z)}$, displacement distribution $y_{(z)}$ in order. Bauschinger effect was taken into account. The curvature was evaluated at the exit-side inflection point where moment was zero.

3.3 Numerical Representation of the Bauschinger Effect

The Bauschinger effect is a phenomenon in which the yield stress or flow stress decreases during stress reversal. The bar is repeatedly bent by rotating the die and feeding the bar while undergoing repeated plastic deformation in a reciprocating manner. Therefore, it is necessary to consider Bauschinger effect in the analysis of spinner straightening.

Figure 6 shows the numerical representation of the Bauschinger effect, which is proposed in the present paper. The flow stress calculated by isotropic hardening rule is $\sigma_{iso}(\varepsilon_p)$, plastic strain is ε_p, and the coefficient is γ, and γ is assumed as a function of stress σ. The relationship between stress and plastic strain considering the Bauschinger effect is expressed by Eq. (1). The Young's modulus is E, the elastic strain is ε_e, the stress–elastic strain relationship is expressed by Eq. (2). The stress–strain relationship taking the Bauschinger effect is expressed by Eq. (3), As the total strain ε_t is represented by the sum of ε_e and ε_p.

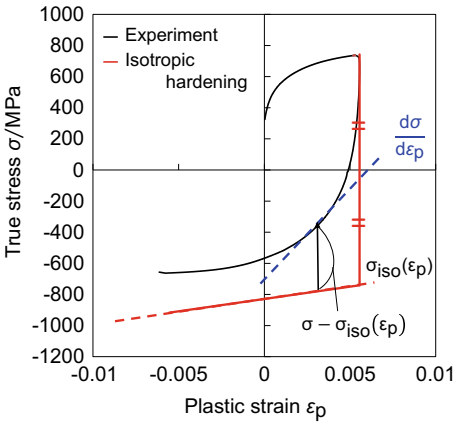


Fig. 6 Numerical representation of Bauschinger effect. (Color figure online)

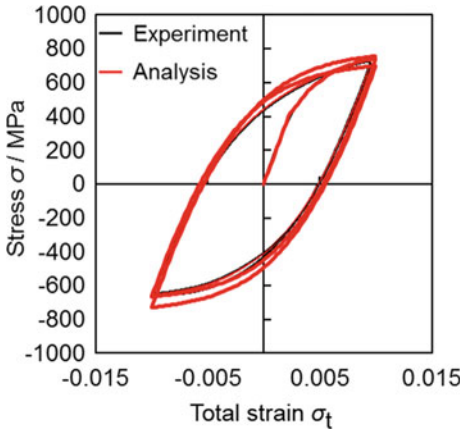


Fig. 7 Comparison stress–strain curve of experiment and analysis. (Color figure online)

$$\frac{\mathrm{d}\sigma}{\mathrm{d}\varepsilon_p} = \gamma\left(\sigma_{iso}\left(\varepsilon_p\right) - \sigma\right) \tag{1}$$

$$\frac{\mathrm{d}\varepsilon_e}{\mathrm{d}\sigma} = \frac{1}{E} \tag{2}$$

$$\frac{\mathrm{d}\sigma}{\mathrm{d}\varepsilon_t} = \frac{1}{\frac{1}{E} + \frac{1}{\gamma\left(\sigma_{iso}\left(\varepsilon_p\right) - \sigma\right)}} \tag{3}$$

The reproducibility of the stress–strain curve of the proposed model was verified. Figure 7 shows the results of a comparison between the experimental and the calculated values of the proposed model at the same strain history. The tension and compression test of the bar was controlled the strain history between −1% and +1%. The proposed model accurately reproduced the Bauschinger effect during compression and the stress during reloading and agreed with the experimental results. [B-Model] analysis adopted the proposed stress–strain relationship and considered the Bauschinger effect.

3.4 Evaluation of Straightness

Curvature was used for the evaluation of straightness and was defined as shown in Fig. 8. Curvature was calculated for each node as shown in Fig. 8a. When the value was positive, the node was placed on the extrados of the bar arc. When it was negative, the node was on the intrados. The chord lengths L_{sp} were set to be 9.52 mm (feed pitch f) and 190.4 mm ($10f$) for the evaluation of short-span curvature C_S and long-span curvature C_L.

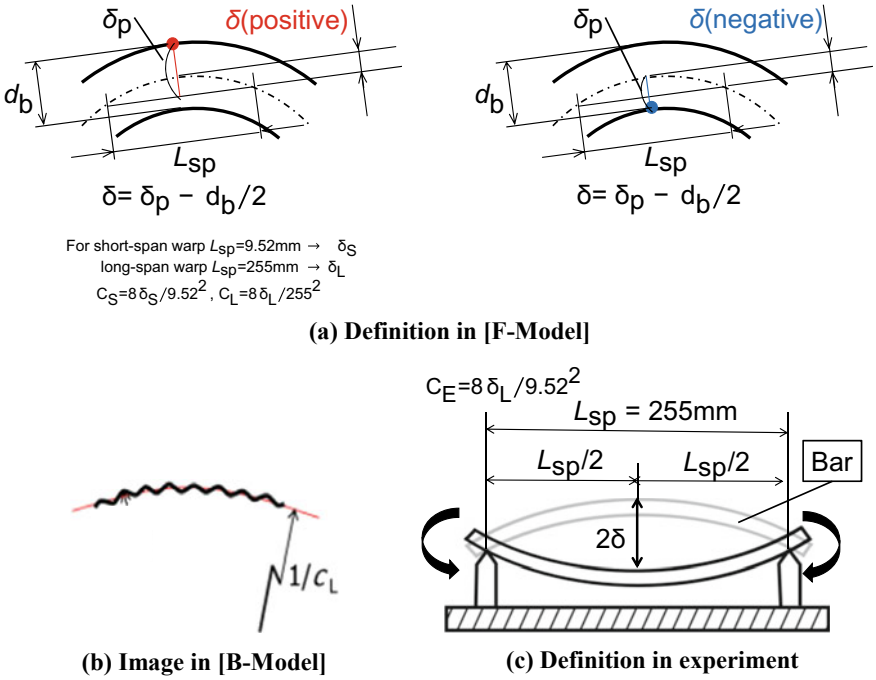


Fig. 8 Curvature. (Color figure online)

In Model [B-Model], the short-span curvatureC_S and long-span curvature C_L were calculated by equations in Fig. 5. The image of C_S and C_L is shown in Fig. 8b. The long span curvature C_E was measured in the experiment as shown in Fig. 8c.

4 Analytical and Experimental Results

4.1 Result in Full Explicit Scheme Model [F-Model]

Figure 9 shows the curvature distribution after spinner straightening under the condition of Table 1[B]. It is noteworthy that the extrados (red part) and the intrados (blue part) are found to be inconsistent before and after spinner straightening by comparing (a) and (c). In other words, the initial curvature was eliminated by spinner straightening. On the other hand, short-span curvatures periodically exist as shown in (b). If these curvatures C_S cancel each other, the long-span curvature C_L should be leveled to zero. However, the C_S did not cancel each other, and then C_L appeared.

Figure 10 shows the effect of Die #3 position h_3 on the curvature after spinner straightening in [F-Model]. 0.1 times of C_L was used for the prediction. The spinner

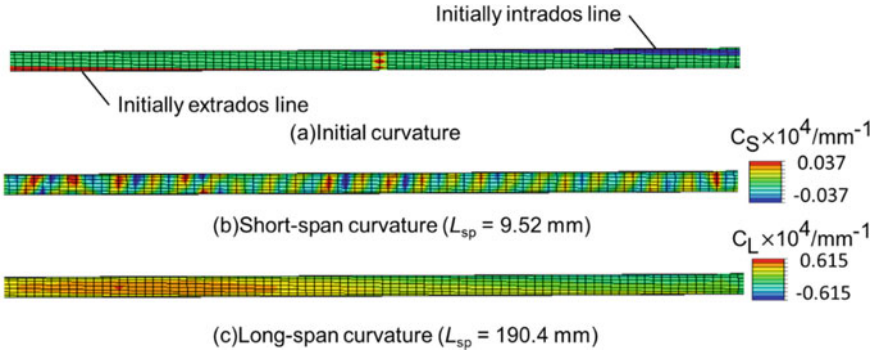


Fig. 9 Spiral and warp after spinner straightening. (Color figure online)

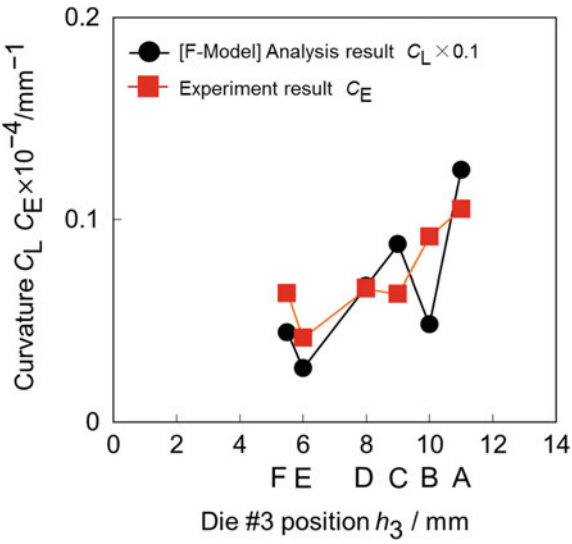


Fig. 10 Effect of die position on curvatures In [F-Model] and experiment. (Color figure online)

conditions in Table 1 might be strong enough for the elimination of the initial curvature. In the conditions [E] –[F] ($h_3 \leq 6$mm), the curvatures C_L and C_E decreased with an increase in h_3. These conditions would be called as "under straightening". The conditions [E]–[A] ($h_3 \geq 6$mm), thecurvatureC_L and C_E increased with an increase in h_3. These conditions would be called "over straightening", which shows optimum condition is [E] ($h_3 = 6$ mm) in this study. The model [F-Model] and experimental results qualitatively show the same tendency. As the result, the large h_3 caused large short-span curvature C_S, resulting in large long-span curvature C_L.

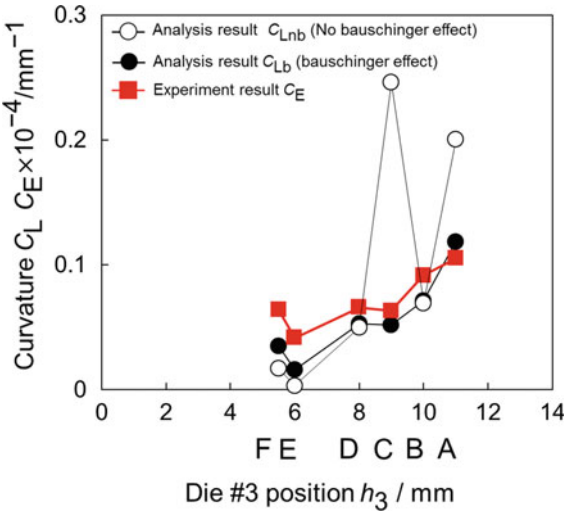


Fig. 11 Effect of die position on curvatures In [B-model] and experiment. (Color figure online)

4.2 Result in Approximation Three-Point Bending from FE Bending [B-Model]

Figure 11 shows the effect of Die #3 position h_3 on the curvature after spinner straightening [B-Model]. The analyses were conducted to obtain the curvatures C_{Lb} with considering Bauschinger effect and C_{Lnb} without Bauschinger effect. The curvatures C_{Lnb} and C_{Lb} were shown the similar tendency to the curvature C_E and C_L in [F-Model]. Curvature C_{Lb} was better agreement with the curvature C_E than curvature C_{Lnb}. Above all, Bauschinger effect needs to be considered in the analysis of spinner straightening. In the spinner conditions in Table 1, the condition for obtaining the most straight bar was [E] ($h_3 = 6$ mm) in both the experimental and analytical results.

5 Conclusion

This paper presents two analytical models. One is model [F-Model] and the other is model [B-Model].

- [F-Model] almost fully reproduced the movement of spinner straightening using the explicit scheme.
- [F-Model] shows the distribution of both short and long-span curvatures in a visual way.
- [F-Model] showed the existence of optimum Die #3 position in this study. Long-span curvature decreased with an increase in the intensity less than 6 mm, and the curvature increased with an increase in the intensity greater than 6 mm. Optimum

intensity is 6 mm in this study. This analytical tendency is qualitatively the same to that in experiment.
- The proposed numerical expression of Baschinger effect could precisely express the same stress–strain relationship as the experimental result.
- [B-Model] was modeled by approximation to three-point bending with bar rotation based on the FEM result of simple bending deformation in straightener without bar rotation.
- [B-Model] showed the effect of die position on curvatures. Analytical result is qualitatively and quantitatively the same to the experimental result. Analysis of spinner straightening needs to consider the Baushinger effect.

References

1. Yanagihashi T, Hama T, Onoda Y, Asakawa M (2005) Effect of plastic ratio and repeat bending on straightness in two-roll straightening - higher straightening and lower residual stress technology of bar products 3 -. J Jpn Soc Technol Plast 46–537:972–976 in Japanese
2. Mutrux A, Berisha B, Weber M, Hora P (2009) Fe simulation of cross roll straightening: COMPLAS X. Barcelona, 23 in Index
3. Kuboki T, Huang H, Murata M, Yamaguchi Y, Kuroda K (2010) Fem analysis of tube straightener adopting implicit scheme. Steel Res Int 81–9:584–587
4. Wu B, Chan L, Lee T, Ao L (2000) A study on the precision modeling of the bars produced in two cross-roll straightening. J Mater Process Technol 99:22–206
5. Tsurumi K, Asakawa M, Kato N, Urabe M, Yoshida M, Sakumoto K, Kanno TJ (2014) Jpn Soc Technol Plast 55–640:435–439 in Japanese

Using Local Heat Treatment for Producing Uniform Profile Hollow Components by Radial Rotation Profile-Forming



Robert Laue, Sebastian Härtel, and Birgit Awiszus

Abstract The incremental forming process Radial Rotation Profile-Forming (RRPF) has been developed at the Professorship Virtual Production Engineering of the Technical University of Chemnitz. The aim is to enable the production of profiled hollow parts with low sheet thinning and high geometrical accuracy. Because of low thinning due to the process, a smaller initial sheet thickness can be used, whereby material and weight can be saved. RRPF is a two-step forming process. The two principal steps are the production of the preform by Rotational Swing-Folding and the subsequent radial profile-forming of the hollow part in one clamping position. During the preform production, wrinkles occur and these wrinkles can be directly formed in the indentation of the mandrel. In the second process step, the wrinkles are used to form the finished profile of the component. However, due to the geometrical stiffness and the material behavior, there is no wrinkle formed in every indentation of the mandrel. An indentation without wrinkle lead to a high sheet thinning, wich occurs due to forming of the final profile. The best component with less sheet thinning and uniform properties is created for a preform with uniform wrinkles in each indentation of the mandrel. Therefore, the approach of a local laser heat treatment is carried out to control the wrinkling for the first time. This extends the original two-step forming process by a further process step. Before forming, local heat treatment creates a tailored blank with locally varying strength. Therefore, wrinkling occurs in the area with the lower strength of the basic material. The approach and experimental basic investigations of the laser heat treatment are shown in this paper.

Keywords Local heat treatment · Laser · Wrinkling · Incremental forming · Rotational Swing-Folding · Radial Rotation Profile-Forming

R. Laue (✉) · S. Härtel · B. Awiszus
Faculty Mechanical Engineering, Institute for Machine Tools and Production Processes, Professorship Virtual Production Engineering, Chemnitz University of Technology, Reichenhainer Str. 70, 09126 Chemnitz, Germany
e-mail: robert.laue@mb.tu-chemnitz.de

© The Minerals, Metals & Materials Society 2021

G. Daehn et al. (eds.), *Forming the Future*, The Minerals, Metals & Materials Series,
https://doi.org/10.1007/978-3-030-75381-8_174

1 Introduction

Tailored Blanks have local adapted properties like material, roughness, or sheet thickness and are used for sheet metal forming processes [1]. Basically, Tailored Blanks are classified according to the production (Fig. 1) in Tailored Rolled Blanks (TRB), Patchwork Blanks (PB), Tailored Welded Blanks (TWB), and Tailor Heat-Treated Blanks (THTB) [2].

Tailored Heat-Treated Blanks have locally adapted material properties due to local heat treatment. The local heat treatment of metallic materials can be carried out by flame hardening, induction hardening, or laser hardening. These processes are often used for surface hardening in order to increase the hardness values on the component surface [4].

Using laser hardening, the surface layer of the workpiece is heated above the austenitizing temperature and then cooled very quickly by the surrounding material (self-quenching). As a result, the metal lattice cannot return to its original shape, and martensite is formed. Typical surface hardening depths are between 0.1 mm and 2.5 mm, for higher surface hardening depths, there must be a corresponding surrounding volume so that the heat can be dissipated quickly enough [5, 6].

The process is mainly used to optimize component properties, such as increasing the surface hardness to reduce wear or increasing the crash stability. Through the targeted introduction of hardening structures by a laser, for example, the deflection of a tube in bending tests could be reduced by 55% [7]. Another possible application is the use of locally adapted material properties in the production process, to extend the procedural limits significantly. Investigations at the Fraunhofer IPT show that laser heat treatment processes can reduce the minimal bending radius without damage by 87%. In addition, the deep drawing depth without damage can be increased by more than 100% [8]. Further investigations show that the influence of anisotropy can be reduced by local heat treatment. In the numerical investigations, the height of lip formation after the deep drawing of a cup from DC04 can be reduced by 85% [9].

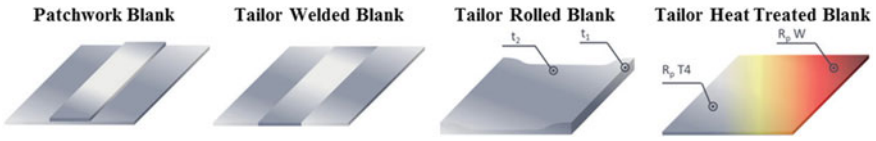


Fig. 1 Different kinds of tailored blanks according to [3]. (Color figure online)

2 Process Analysis of Radial Rotation Profile-Forming

The Radial Rotation Profile-Forming was recently developed based on the idea of reducing the relative movement between the tool and the workpiece [10]. The incremental sheet forming process is used for the production of profiled hollow components, like clutch plate carriers, sensor disks, or synchronous pulleys. The principle of the process is shown in Fig. 2. The two principal tasks are the production of the preform by Rotational Swing-Folding and the afterward profiling of the hollow part. For the preform production, the circular blank is fixed on a rotating profiled mandrel. Due to the swinging of a cylindrical forming tool, the blank is placed on the contour of the mandrel and shaped into the preform. In turn, a minimum relative movement in the axial and radial directions between the tool and the workpiece exists, due to the special position of the swinging axis. As a result, low sheet thinning occurs in the flange of the workpiece In addition, tangential compressive stresses occur because of the reduction of the diameter, which initially leads to a thickening of the edge. Furthermore, wrinkling occurs when the buckling stability is exceeded and the wrinkles are formed in the indentation of the profiled mandrel (Fig. 2: detail Z).

However, in the second process step, the material distribution at the edge and the wrinkles are used to produce a profiled hollow part with low sheet thinning by radial profile-forming. Due to the rotation and continuous radial feed of the forming tool to the profiled mandrel, the axial profiling is formed.

Wrinkle formation during Rotational Swing-Folding depends on the material and geometry. These two parameters influence the buckling stability (stiffness against wrinkling) mainly. Wrinkling occurs when the tangential compressive stress during Rotational Swing-Folding exceeds this stiffness. In previous experimental and numerical investigations, the stress distribution during the forming process was analyzed [11]. The implicit simulation model uses hex-volume elements and experimentally determined elastic/plastic material properties. The tangential stresses during the forming process (Fig. 3) show that the stress distribution is similar to sheet metal spinning and an elastic dent forms under the tool. This disturbs the rotational symmetry of the workpiece and the highest stresses are formed on the underside of

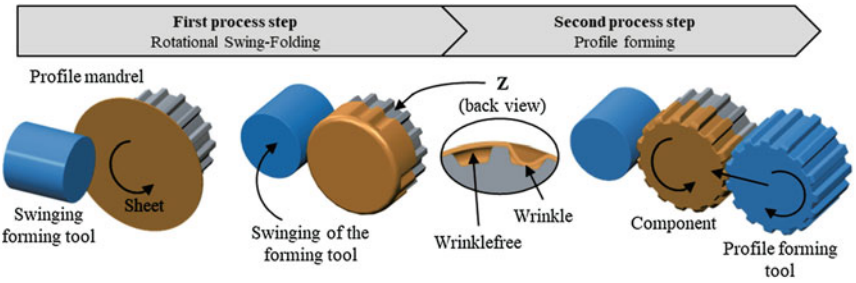


Fig. 2 Process principle of Radial Rotation Profile-Forming. (Color figure online)

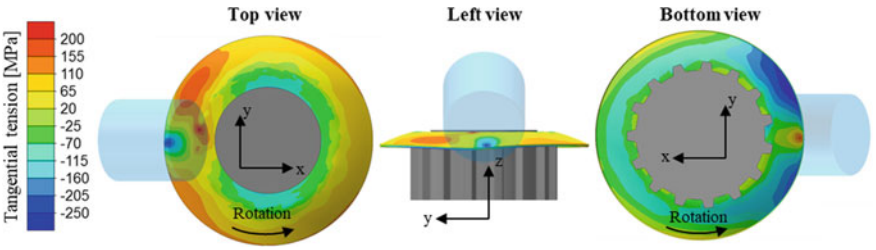


Fig. 3 Tangential stresses during Rotational Swing-Folding. (Color figure online)

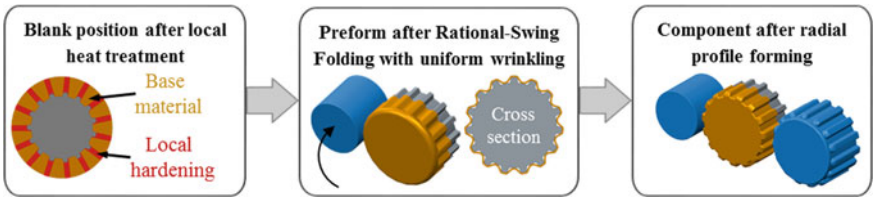


Fig. 4 Solution approach for the production of components with homogeneous properties. (Color figure online)

the blank after contact between tool and workpiece. These tangential compressive stresses are responsible for the formation of wrinkles.

If a wrinkle occurs, depending on the material and sheet geometry, the tangential compressive stresses may be too low for further wrinkling. Therefore, it is possible that a wrinkle will not form in every indentation of the mandrel. Consequently, the formation of wrinkles can only be minimally influenced by process parameters. Investigations show that in this case, a high sheet thinning occurs during the profile forming in the second forming step. The consequences are non-homogeneous component properties or even cracks. However, if a wrinkle forms in the indentation of the mandrel, the profile is formed very well with minimal sheet thinning [12]. Therefore, the aim is to identify an approach that allows controlling the wrinkle formation independent of material and geometry so that forms a wrinkle in each indentation of the mandrel.

3 Local Heat Treatment

3.1 Solution Approach

To control the formation of wrinkles, a local heat treatment with a laser was investigated. This results in the production of a Tailored Blank before the forming steps, which has areas with higher stiffness. These are positioning on the profiled mandrel

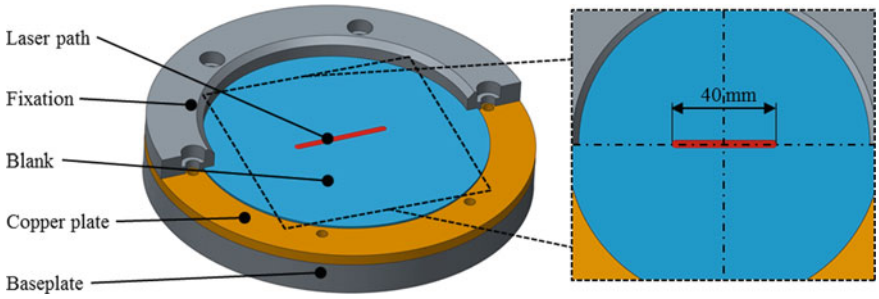


Fig. 5 Clamping device (left) and laser path (right). (Color figure online)

in such a way that the wrinkles do not form in these areas, but in the less hard initial material, as shown in Fig. 5.

Experimental investigations have already shown that wrinkling in deep drawing without a blank holder can be influenced by local heat treatment [13]. Sufficient knowledge about the mechanisms during heat treatment of low-alloy steel has not yet been achieved. Due to the low carbon content, no phase transformation to martensite is assumed. In addition, it is necessary to investigate how the heat treatment must take place in order to bring sufficient heat energy into the circular blank to create a big difference in strength but without melting the material.

The aim of this paper is to obtain a straight uniform track without melting and to investigate the mechanism inside of the blank. First of all, it is to be investigated what happens in the material and how the local heat treatment is deflected. Subsequently, the findings will be used to validate a numerical simulation model, which will be used for the calculation of the Tailored Blank for Radial Rotation Profile-Forming.

3.2 Experimental Setup

For further investigations, a typical cold-forming steel with a very low carbon content is used, as shown in Table 1. Due to the low carbon and manganese content, excessive hardening in the heat-affected zone is not expected. This material was also used for the preceding forming tests since it is well suited for forming and unalloyed steels are usually used for profiled hollow components.

A device as shown in Fig. 5 (left) was manufactured for the experimental investigations. This device can also be used for the local heat treatment of the blanks, which will be used for the afterward forming process steps. The circular blank is

Table 1 Chemical composition DC04 (1.0338) according DIN EN 10130

C	P	S	Mn
0.08%	0.03%	0.03%	0.40%

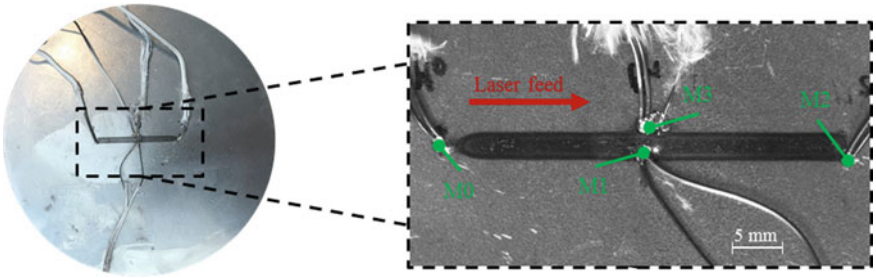


Fig. 6 Laser path after local heat treatment. (Color figure online)

clamped in the middle of a copper plate, which on the one hand leads to a high heat conduction, and on the other hand the position of the blank is exactly defined and the local areas of the heat treatment can be positioned exactly.

For the first investigations, a simple CNC-controlled track with a length of 40 mm is assumed (Fig. 5: right) in the middle of the sheet. Laser parameters are similar to those used in the previous studies were used, in which an influence on wrinkling was experimentally proven. The laser is switched on and off in a ramp of 50 ms and has a power of 1200 W. The constant feed speed of the laser is 2 m/min, resulting in a processing time of 1.2 s. A lens is used for focusing, which should produce a uniform power distribution within the laser beam.

3.3 Experimental Results

Figure 6 (left) shows the round blank after the local heat treatment. The shape of the laser path is very uniform and no melting of the material is visible. This shows that there is enough surrounding material to cool very quickly and that the surface has become hot enough to get tarnish colors. The length of the track is 38.35 mm and the width is 2.65 mm (Fig. 6: right).

For a detailed investigation of the heat input, four thermocouples of type K were mounted on the circular blank, one each at the beginning and end of the laser track and the other two in the middle. The two thermocouples in the middle (M1 and M3) are located behind each other in order to be able to measure the radial heat flow. The measurement frequency was 280 Hz, which is very important because the heat flow is very fast. Figure 7 shows the measured temperatures. At the beginning of the process, the laser power increases evenly, the measuring sensor M0 is located directly next to the starting point of the laser. The temperature increases evenly up to a maximum of about 150 °C and then the uniform cooling begins. The sensor M1 is located nearly to the middle (+0.1 mm) of the laser seam and measures a maximum temperature of 754 °C. However, the temperature in the center of the contact point between the laser and the surface will be much higher. Moreover, the measuring point is at the surface, in deeper areas, the temperature may be higher. The measuring sensor is located in

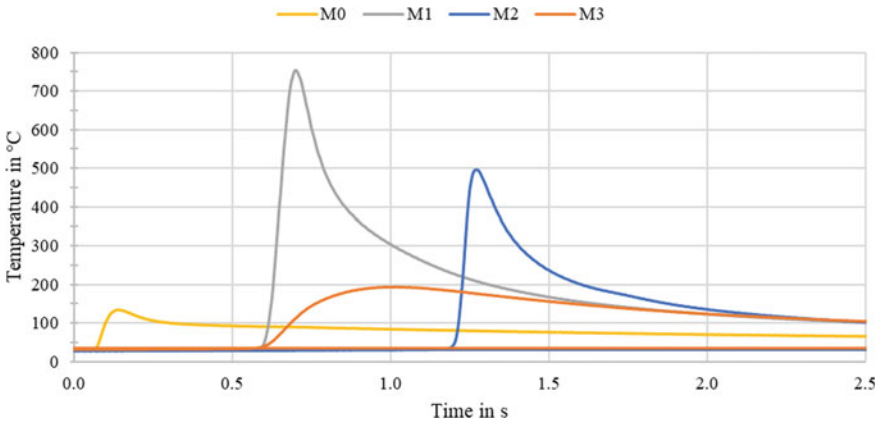


Fig. 7 Temperature during the laser heat treatment. (Color figure online)

the quasi-static area of the heat treatment. A time of 0.146 s is required for heating up to the maximum. Cooling from 750 °C to 450 °C takes about 0.114 s. The sensor M3 is located at a distance of 2.12 mm and has a lower maximum temperature of 550 °C. This makes it clear that a very large temperature gradient occurs. Sensor M2 is located at the end of the laser seam and rises abruptly to 500 °C and then cools down evenly.

To obtain more information about the mechanisms in the blank during the local heat treatment, macro-section samples were prepared. Figure 8 (left) shows a cross-section of the laser feed direction from the middle of the laser path. It can be seen

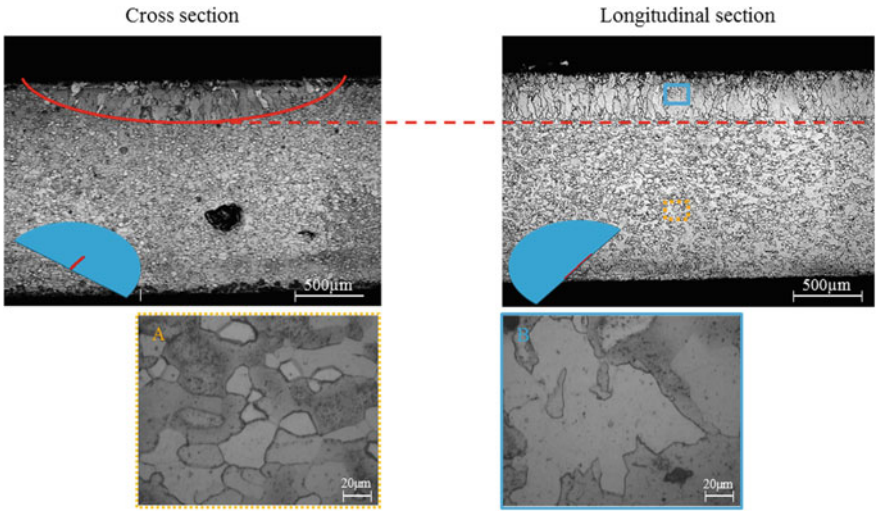


Fig. 8 Grinding pattern. (Color figure online)

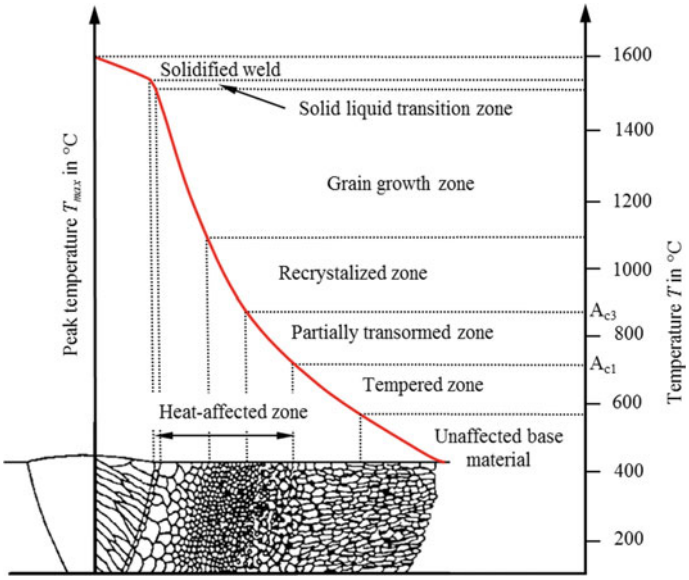


Fig. 9 Heat-affected zone (HAZ) [14]. (Color figure online)

that the heat-affected zone is similar to an ellipse and in a radial direction from the contact between laser and the blank; the grain size is very big and elongated.

Especially, for the comparison from details A (base material) and B (heat-affected zone), the grain growth can be seen. Furthermore, it can be assumed that after the heat treatment, no phase transformation has occurred. The grain growth is also shown in the longitudinal section in Fig. 8 (right). In addition, a uniform depth of the heat influence is achieved and a uniform cross-section can be assumed. The area of influence by heat treatment has a maximum depth of 0.39 mm.

Overall, the grain size distribution is similar to that of the heat-affected zone during welding (Fig. 9). Based on the grain growth, it is indicated that the temperatures in the center of the laser beam were at least above A_3 temperature. However, the measured temperatures are not above the A_3 temperature, which may be due to the fact that the measuring point is not exactly in the center of the laser beam and was on the surface of the sheet. The micrographs clearly show that grain growth has occurred. Afterward, there is a small transition area to the unaffected base material. However, no hot cracks are visible in the middle of the laser beam (temperature under melting temperature), this is very important for afterward forming processes.

To investigate the change in hardness, micro-hardness tests were carried out in accordance with DIN EN ISO 6507–1 (Fig. 10). The results show that the hardness increases about 34% toward compared to the base material. The reason for the different hardness is the different cooling rates in the middle and at the edge of the heat treatment.

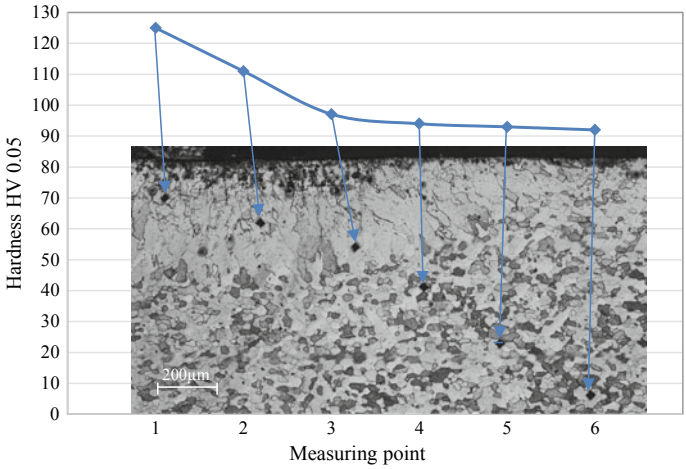


Fig. 10 Measured hardness. (Color figure online)

4 Summary and Outlook

In this paper, the new production technology RRPF is presented, which has the aim to produce profiled hollow components with low sheet thinning and homogeneous component properties. Previous investigations carried out that the wrinkling control is necessary during the preform production to achieve an evenly wrinkled preform. The approach is to change the local material properties by laser heat treatment. This changes the buckling stability and the number, position, and shape of the wrinkle can be influenced. A simplified laser heat treatment is shown and investigations of the laser seam geometry, temperature, microstructure, and hardness were performed. The main findings are:

- There is no material melting with the selected laser parameters.
- Heating and cooling of the material are very fast, about 0.15 s.
- Grain growth occurs radially to the contact point of the laser beam.
- A uniform depth is created in the longitudinal direction.
- The hardness in the heat-affected zone increases up to 34%.

The next step will be to calibrate a simulation model using these data in order to vary numerically individual process parameters. Furthermore, it will be necessary to find out how the laser heat treatment has to be done in order to influence wrinkling during the preform production.

Acknowledgments The authors thank the German Research Foundation (DFG) for its financial support of this work (DFG project number 334894279) and the chair of welding engineering of the TU Chemnitz.

References

1. Merklein M, Lechner M (2013) Manufacturing flexibilisation of metal forming components by tailored blanks. In Proceedings/international conference on competitive manufacturing. COMA '13, pp 165–170
2. Merklein M (2014) Tailored Blanks, 1–5
3. Merklein M, Johannes M, Lechner M, Kuppert A (2014) A review on tailored blanks—Production, applications and evaluation. J Mater Process Technol 214(2):151–164
4. Böge A, Böge W (eds) (2015) Handbuch Maschinenbau. Grundlagen und Anwendungen der Maschinenbau-Technik ; mit 424 Tabellen. Springer Vieweg, Wiesbaden
5. Eichler H, Eichler J (2015) Laser. Springer, Berlin Heidelberg, Berlin, Heidelberg
6. Hügel H, Graf T (2009) Laser in der Fertigung. Vieweg+Teubner, Wiesbaden
7. Wagner M (2013) Laserverfestigte Fahrzeugcrashstrukturen. Wie die Fahrzeugmasse gesenkt und gleichzeitig die Crashsicherheit gesteigert werden kann. Wt Werkstattstechnik online, 6/2013, pp 485–487
8. Brecher C, Emonts M, Eckert M (2013) Laserunterstützte Blechbearbeitung. Umformtechnik, 01/2013
9. Wagner M, Jahn A, Beyer E, Balzani D (2018) Local laser-strengthening. Customizing the forming behavior of car body steel sheets. In: Proceedings of the 21st international ESAFORM conference on material forming. AIP Conference Proceedings. 150016. https://doi.org/10.1063/1.5035023
10. Laue R, Härtel S, Awiszus B (2018) Radial-rotation profile forming. A new processing technology of incremental sheet metal forming. In: Proceedings of the 21st international ESAFORM conference on material forming. AIP Conference Proceedings. 160016. https://doi.org/10.1063/1.5035042
11. Groche P, Schäfer R (2006) Faltenbildung beim Drücken. Numerische Untersuchung des Einflusses gyroskopischer Momente. Wt Werkstattstechnik online, pp 746–750
12. Laue R, Härtel S, Awiszus B (2019) Numerical analysis and experimental validation of radial rotation profile-forming. In: The 22nd international conference on advances in materials & processing technologies (AMPT), Taipei, Taiwan
13. Laue R, Awiszus B (2019) Beeinflussung der Faltenbildung in der Blechumformung durch lokale Wärmebehandlung. 20. Simufact Round Table, Marburg, Germany
14. Easterling K (1992) Introduction to the physical metallurgy of welding

Analysis of Tube Spinning



E. C. Sarıyarlıoğlu, O. Music, and M. Bakkal

Abstract Tube spinning is a bulk deformation process used to produce seamless, cylindrical, conical, and contoured tubes. Over the last six decades, tube spinning process has been applied in a wide range of engineering applications; especially in automotive, aerospace, and nuclear industry. However, the process has seen little change, and despite a large volume of literature investigating the process, understanding of the process mechanics is limited and the key references have been published about 50 years ago. This paper investigates the process mechanics, looking into the mechanism of deformation. The process is investigated using a numerical model using an implicit time integration and Arbitrary Lagrangian–Eulerian scheme (ALE). The numerical model has been developed and validated against physical trials. The maximum difference between tube geometry predicted by the model and measured in the trials is 4%. Model results further show that both equivalent plastic strain and plastic strain rate are concentrated in the region immediately under and ahead of the roller and that the process reaches a steady state early in the process. The stress state is dominated by compressive normal stresses in all three directions.

Keywords Tube spinning · Flow forming · Power spinning

1 Introduction

The term *metal spinning* refers to a group of forming processes used for the production of hollow, axially symmetric sheet, and bulk metal components. The basic spinning technique involves clamping a sheet, plate, or a tube against a mandrel on a spinning plate, and gradually forming this workpiece against a mandrel surface using an idle roller (Fig. 1a). The process can be performed in a single step or a series of steps, depending on the process window for a given material.

E. C. Sarıyarlıoğlu · M. Bakkal
Department of Mechanical Engineering, Istanbul Technical University, Istanbul, Turkey

O. Music (✉)
Department of Mechanical Engineering, TED University, Ankara, Turkey
e-mail: omer.music@tedu.edu.tr

© The Minerals, Metals & Materials Society 2021

G. Daehn et al. (eds.), *Forming the Future*, The Minerals, Metals & Materials Series,
https://doi.org/10.1007/978-3-030-75381-8_175

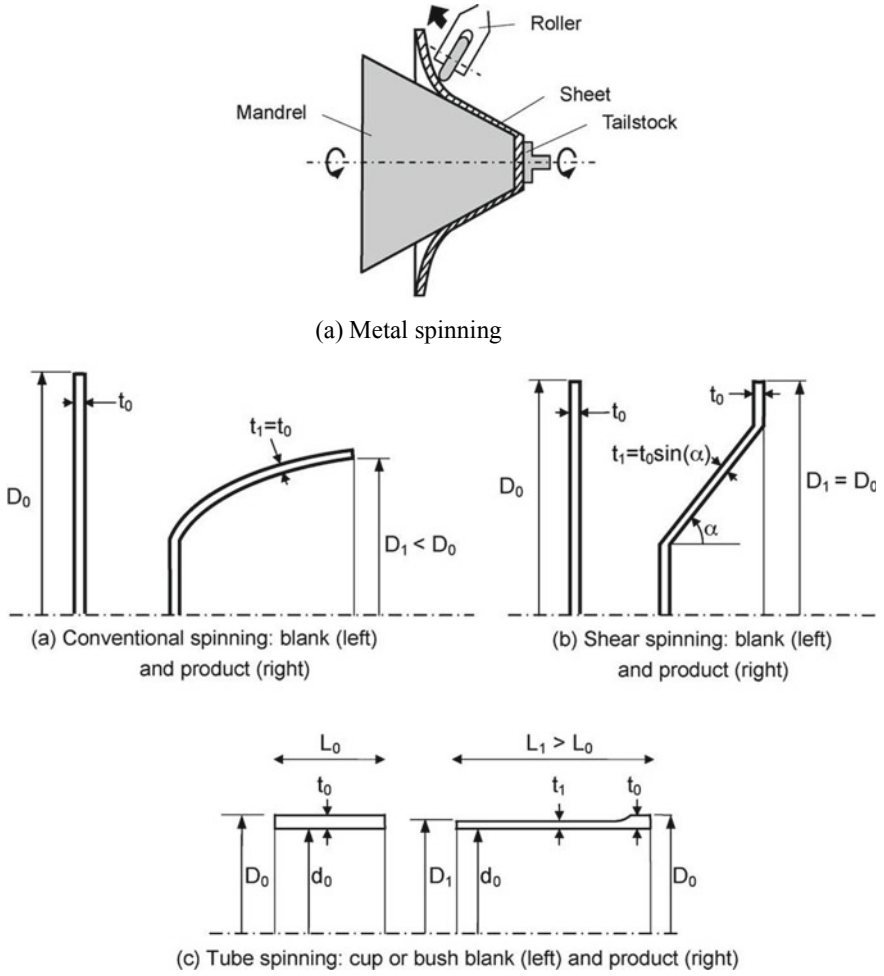


Fig. 1 Metal spinning processes

Three processes that the term metal spinning refers to are conventional spinning, shear spinning, and tube spinning (Fig. 1b). Conventional spinning is used to form a sheet metal blank into a target shape by gradually pushing it onto a mandrel in a single step or multiple steps while largely preserving the sheet thickness. Shear spinning, on the other hand, reduces the blank thickness, and the thickness is determined by the wall angle; the angle between the wall of the component and the axis of rotation. Both processes are classified by [6] as sheet metal forming processes, together with bending, stretching, and drawing [5]. While conventional spinning

involves bending, stretching, and compressive stresses, shear spinning, as the name implies is dominated by shear stresses with some bending.

In tube spinning, a roller pushes the outer wall of the tube against a rotating mandrel while moving along its length. As the roller pushes against the tube and moves forward, wall thickness is reduced, and the tube elongates. The material flows mainly axially (along the mandrel length) and any increase in the internal diameter of the tube is undesirable. Tube spinning process is used in the production of seamless, cylindrical, conical, and contoured tubes (Fig. 3).

There are two approaches to spinning tubes; forward and backward tube spinnings (Fig. 2). In forward tube spinning, the tube elongates in the same direction as the roller movement (Fig. 2a). This method requires a closed-end tube with a base or an internal flange (cup) to allow the tube to be clamped against the mandrel (tailstock). This method is preferred for the production of high-precision tubes but requires a mandrel covering the complete length of the tube. In backward tube spinning, the tube is clamped between the serrated driven part and the rollers in order to transmit the torque (Fig. 2b). The tube elongates in the opposite direction as the roller movement towards the unsupported end of the mandrel. There is no length limit of the final tube. Therefore, this method is preferred for the production of long tubes. Achievable geometries in tube spinning are shown in Fig. 3.

As mentioned before, the mechanics of conventional and shear spinning processes is largely similar. However, the mechanics of tube spinning is different. Reference [2] shows that tube spinning is a combination of extrusion and rolling and treats it as a bulk-forming process in their investigation [2]. This is further supported by Kalpakcioglu [3, 5] who shows that the mode of deformation in tube spinning resembles extrusion [3, 4].

Over the past 60 years, a large volume of research on tube spinning has been published. Reference11 [10] reports on studies on the mechanics of spinning and existing and novel machine configurations [8]. They conclude that the mechanics of the process is complex, and it is clear that it is still largely not understood and as such requires further research.

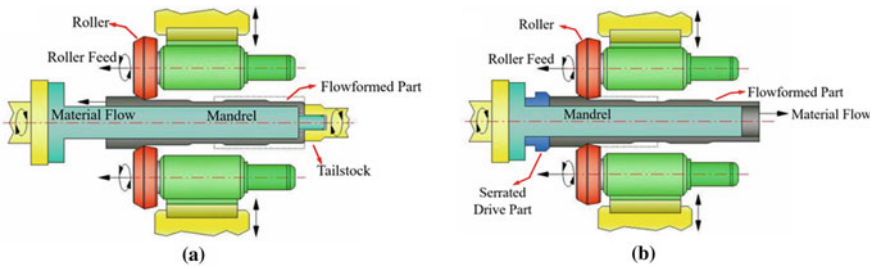


Fig. 2 Forward **a** and backward **b** tube spinning [6]. (Color figure online)

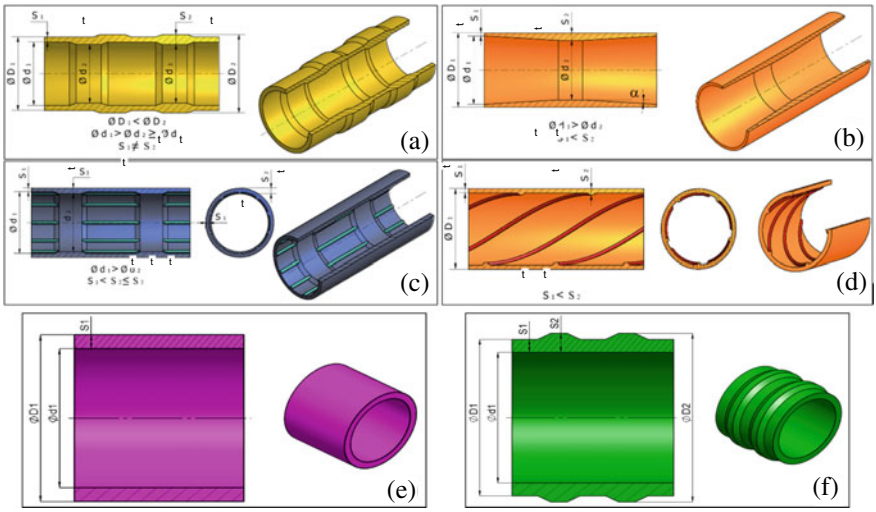


Fig. 3 Feasible geometries in tube spinning: **a**, **b**, **c**, **d** geometries produced by using specialised tube spinning processes and mandrels [9]; **e**, **f** geometries produced using conventional mandrels. (Color figure online)

This paper is aimed at developing a model of the backward tube spinning process and investigating its mechanics; mechanism of deformation. The investigation focuses on backward tube spinning; however, the general principles applied here should be applicable to forward tube spinning as well.

2 Modelling Approach

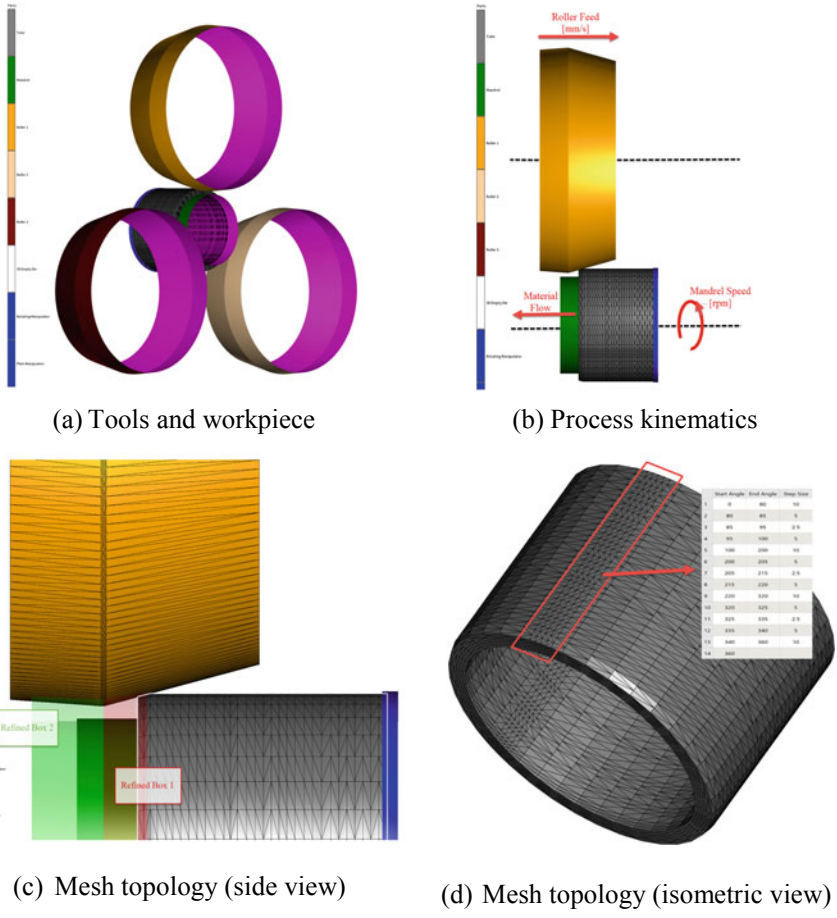
Given the relatively complex nature of deformation in tube spinning, analytical models are limited to estimates of forming forces and power in tube spinning. A detailed analysis of the process mechanics requires the use of numerical models. However, numerical models of tube spinning require long solution times. Two main reasons for this come from the incremental nature of tube spinning: continuously changing contact conditions requiring repetitive iterations between the roller and the tube and the long path traversed by the roller requiring a large number of steps in the numerical solution.

A potential solution to this problem was proposed by Houillon et al. [1] using an Arbitrary Langrangian–Eulerian (ALE) formulation [7]. This formulation allows for a significant reduction in both the number of elements and remeshing attempts. In this study, commercial software package Transvalor Forge is used to model the backward tube spinning process. This software package uses the approach proposed by Houillon et al. [1].

2.1 Numerical Model

Figure 4 shows the main components of the model (Fig. 4a). The model uses an implicit time integration scheme, with an isotropic elastic–plastic material. The tools and mandrel are assumed to be rigid, and the only deformable body is the tube, meshed using tetrahedral elements. To allow the model to accurately capture the behaviour around the high stress and strain gradient areas, elements are concentrated in the region around the nose radius of the roller, both in the radial and axial directions (Fig. 4c) and the circumferential direction. The three rollers forming the tube are located at the same radial and axial position and are idle.

Process parameters, roller, and tube geometry used in the analyses are given in Table 1.



(a) Tools and workpiece

(b) Process kinematics

(c) Mesh topology (side view)

(d) Mesh topology (isometric view)

Fig. 4 Numerical model. (Color figure online)

Table 1 Process parameters, tool, and tube geometry

Process parameters	Roller feed ratio (mm/rev)	Mandrel rotational speed (rpm)	Roller feed (mm/s)	Roller axial offset	Number of rollers	Thickness reduction (%)
	0.5	120	0.25−1	0	3	0.25−0.75
Total geometry	Mandrel diameter (mm)	Roller max. diameter (mm)	Attack angle (degrees)	Roller nose radius (mm)	Exit angle (degrees)	
	96.6	225	15	5	4	
Tube geometry	Inner diameter (mm)	Outer diameter (mm)	Thickness (mm)	Length (mm)		
	96.6	112.6	8	100		

Table 2 Flow curve coefficients for Hänsel–spittel equation

Coefficient	A_1	m_1	m_2	m_3	m_4	m_5	m_6	m_7	m_8	m_9
Value	929.8	−0.00064	0.0089	0.0011	−0.008	0	0	0	0	0

Material behaviour was modelled assuming elastic–plastic isotropic behaviours, and the flow curves for 42CrMo4 were described by the Hänsel–Spittel equation, with material coefficients shown in Table 2, using the material library available in the software. The computational time for the final model used was 13 h on a 12-core Xeon processor using parallel processing.

Even using the ALE approach, a typical tube spinning analysis requires a relatively large number of elements and steps, leading to high computational time. To reduce computational time, only the transient and steady-state stages of the process were simulated. This approach is proposed based on the examination of a force–time graph for a roller in tube spinning (Fig. 5). The figure shows that for the specific configuration used in this study, beyond 25 s (30% of the total roller stroke), the process seems to reach a steady state. Therefore, modelling only a fraction of the process, coupled with a short tube length reduces the computational time significantly, allowing for a detailed three-dimensional mesh to be used, and improving the overall accuracy of the model.

Since this approach does not model the process from the beginning to the end, it does have its disadvantages; however, if the purpose is to study the process and its mechanics, it should be sufficient.

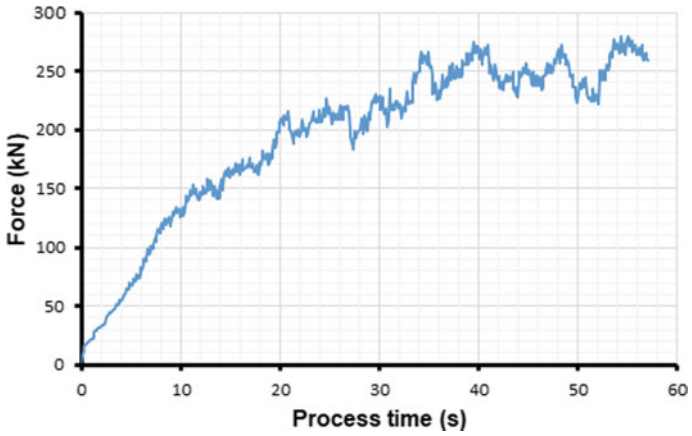


Fig. 5 Roller radial force versus time. (Color figure online)

2.2 Numerical Model Validation

The model is validated by first performing a sensitivity study on numerical parameters, followed by a comparison with physical trials on an industrial high-precision three-roller tube spinning machine.

A sensitivity study was performed on three parameters; element size under the tool, size of the elements through the thickness and along the circumferential direction. For a sensitivity of approximately 5%, element size in the locally refined zone underneath and around the roller should be selected so that there are at least three elements under the roller nose radius in both circumferential and axial direction, and at least six elements through the thickness. The strain distribution was observed to be sensitive to element size, due to its non-linear distribution through the thickness.

Comparison of tube profiles from physical trials and numerical model results shows agreement within ~96% of physical trials. The model captures the geometry and the potential defects well. Both tube geometry and roller radial force were measured, and the comparison is shown in Figs. 6 and 7.

Comparison of tube profiles for physical trials and numerical model results shows that the maximum difference in diameter is just under 2%. The model captures the bulge at the outer diameter and the ridge at the inner diameter accurately. The length of the tube is not predicted as accurately, with the maximum difference of just over 11%. This discrepancy occurs because of the difficulty in accurately adjusting the roller starting axial position in physical trials and the fact that even a small difference in the starting position makes a significant difference in tube length.

Comparison of roller radial force measured in physical trial with numerical model prediction shows a difference of just under 30%. While this is relatively high, both forces show similar trends. This is considered to be acceptable for the purposes of this study. The difference is likely because material property values were extracted

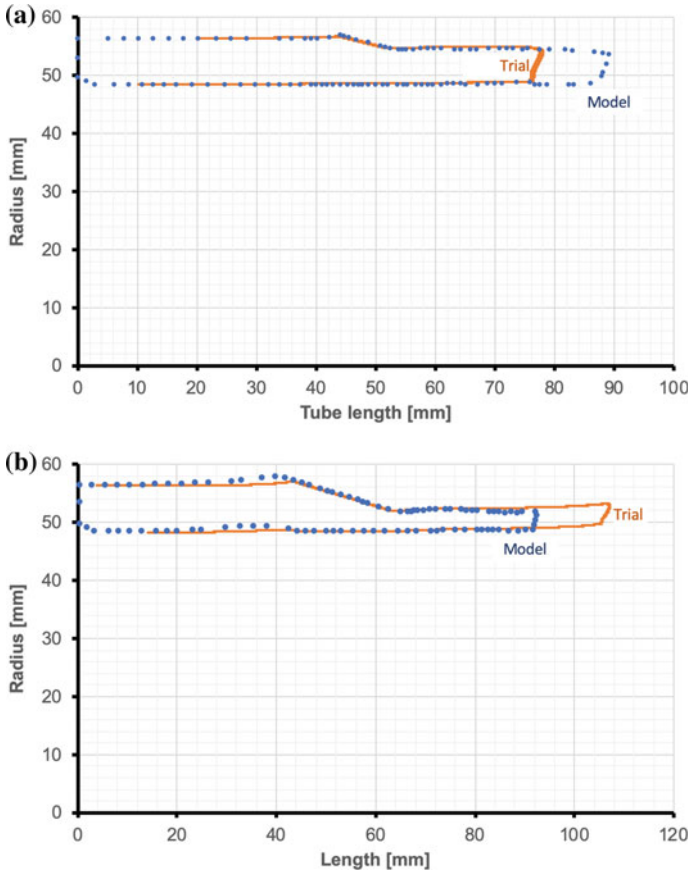


Fig. 6 Tube geometry for **a** 25% thickness reduction and **b** 60% thickness reduction. (Color figure online)

from the literature. A separate set of material tests will be conducted to determine the material properties and re-run the numerical analyses.

3 Process Mechanics

Having described the modelling approach and validated the model, the model can now be used to study the mechanics of the process. There are two main aspects of the mechanics of tube spinning: mechanism of deformation and mechanism of failure, the latter leading to an understanding of the process operating window.

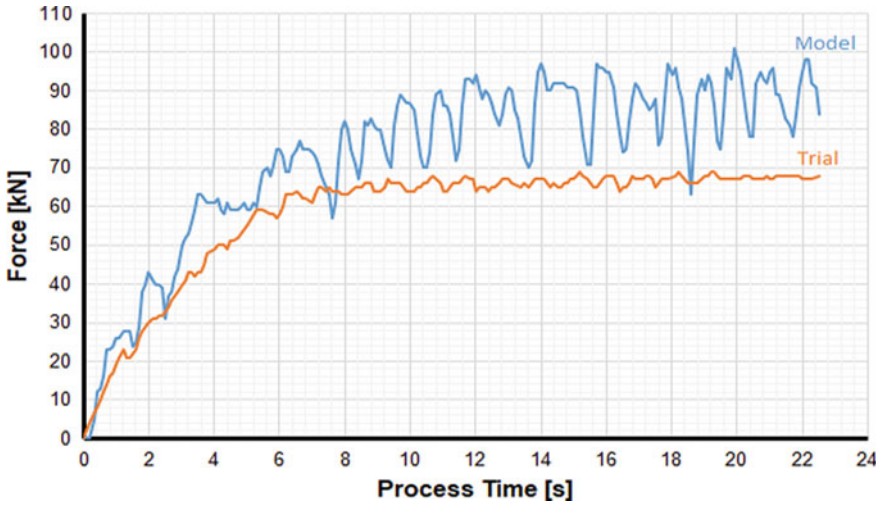


Fig. 7 Roller radial force for 25% thickness reduction. (Color figure online)

3.1 Deformation Mechanism

To examine the effect, the roller has on the tube as it is spun, contour plots of equivalent plastic strain, equivalent plastic strain rate, and stresses generated in the tube are used. All plots show a radial cross-section of the tube along its axis and the distribution of strain, strain rate, or stress in this cross-section.

A plot of equivalent plastic strain and strain rate is shown in Fig. 8. Strain and strain rate are shown for three stages in the process, early-stage, mid-process, and

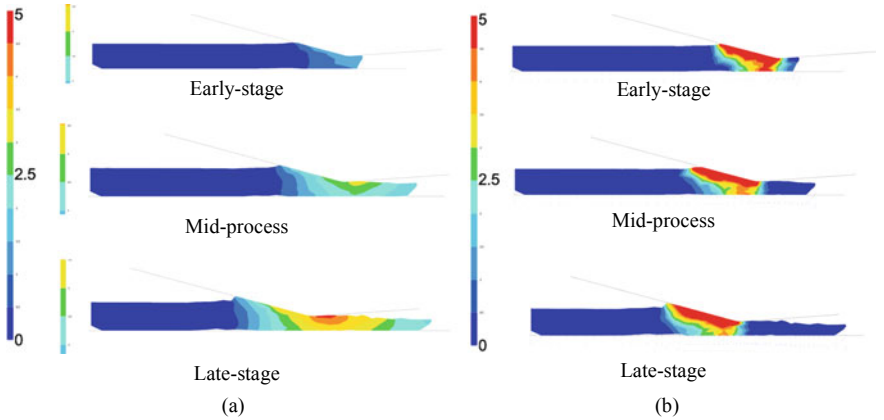


Fig. 8 Equivalent plastic strain **a** and strain rate **b** distribution in tube cross-section at different stages in the process. (Color figure online)

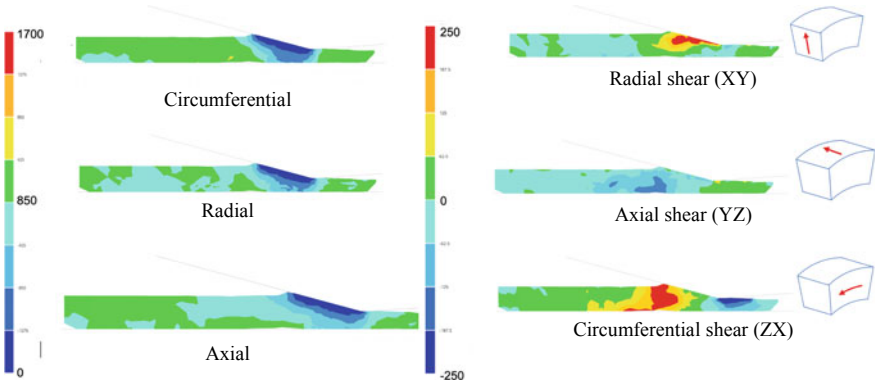
late-stage, corresponding to 30%, 60, and 90% of the roller stroke along the tube. Three main conclusions can be drawn from the results in Fig. 8a, b.

The equivalent plastic strain distribution and therefore deformation through the thickness of the spun section is highly non-uniform, with the strain gradually increasing from the minimum at the inner diameter to the maximum at the outer diameter. This agrees well with measurements and observations by [8, 1]. As the roller moves forward, the strain levels increase, reaching 3.5 at the inner diameter and 5 at the outer diameter.

Equivalent plastic strain rate distribution shows the instantaneous deformation in the tube providing information about the mechanism of deformation. As suggested by the strain results described previously, the tube deformation is concentrated in the region ahead of and immediately under the roller.

Perhaps more importantly, the strain rate distribution does not seem to change as the process progresses from beginning to end. While the plot of roller force vs. time in Fig. 5 shows that the steady state is reached at just over 80% of roller stroke, these strain rate plots suggest that the mechanism of deformation does not change throughout the process; that steady state is reached even at the early stage. The increase in force observed in Fig. 7 is likely caused by an increase in the contact area as the material accumulates in front of the roller, forming a bulge.

Normal and shear stresses in the tube cross-section are shown in Fig. 9 below. Two observations can be made based on these results. All three components of the normal stress are compressive, implying a stress state with high hydrostatic stress reaching up to 1700 MPa. Compared with normal stresses, shear stresses are low, at a maximum value of 250 MPa, suggesting that principal stresses are closely aligned with the tube axes.



(a) Normal stress [MPa] (b) Shear stress [MPa]

Fig. 9 Stresses in tube spinning. (Color figure online)

4 Conclusions

In this paper, to understand the deformation mechanism of the process, a numerical model of tube spinning has been developed using an ALE approach and the results are compared with the physical trials. The comparison shows that the difference between the tube geometry for FE results and physical trials is within 4%. Also, the difference of radial force measurements between FE results and physical trials is just under 30%. However, force shows a similar trend in both the numerical model and the physical trial, which considered to be sufficient for the purposes of this study.

A detailed examination of equivalent plastic strain, equivalent plastic strain rate reveals four key points:

- Equivalent plastic strain increases gradually from the minimum inner diameter to maximum outer diameter. Also, strain levels increase as the roller moves along the tube
- Equivalent plastic strain rate does not change after the process reaches the steady-state conditions. Also, the deformation is concentrated in front of and under the roller.
- In the region under and around the roller, all of three normal stress components are compressive and also, it shows that the stress state is that of high hydrostatic stress. At the maximum value, normal stress it reach values of up to 1700 MPa.
- In comparison with the normal stresses and shear stresses, the normal stresses are higher. At the maximum value, the shear stress reaches up 250 MPa.

Further studies of the process will involve a set of material tests to accurately determine the properties of the material used in physical trials, friction coefficient and most importantly, a set of trials combining the physical trials with the numerical will be done to generate an understanding of the mechanism of failure leading to an estimate of the process operating window.

Acknowledgments The author, E. C. Sarıyarlıoğlu acknowledges funding and technical support by Repkon Machine and Tool Industry and Trade Inc.

References

1. Gur M, Tirosh J (1982) Plastic flow instability under compressive loading during shear spinning process. J Eng Ind Trans ASME 104(1):17–22
2. Hou M, Massoni E, Ramel E, Logé RE (2007) 3D FEM simulation of the flow forming process using Lagrangian and ALE methods. In: Materials processing and design, modeling, simulation and applications; NUMIFORM ’07: 9th international conference on numerical methods in industrial forming processes. Porto, Portugal, pp 257–262
3. Kalpakcioglu S (1961a) On the mechanics of shear spinning. J Eng Ind Trans ASME 83 (Series B) 125–130

4. Kalpakcioglu S (1961b) A study of shear-spinnability of metals. J Eng Ind Trans ASME (Series B) 83:478–484
5. Kalpakcioglu S (1964) Maximum reduction in power spinning of tubes. J Eng Ind Trans ASME (Series B) 86:49–54
6. Kalpakjian S (1989) Manufacturing engineering and technology. McGraw-Hill
7. Kubilay C (2014) Flow forming of aeroengine materials. University of Manchester.
8. Roy MJ, Klassen RJ, Wood JT (2009) Evolution of plastic strain during a flow forming process. J Mater Process Technol 209(2):1018–1025. https://doi.org/10.1016/j.jmatprotec.2008.03.030
9. Sarıyarlıoğlu EC, Aydin G, Simsek AK, Aybüke G (2018) Comparison Between "Core Mandrel" flow forming and conventional flow forming methods. In: Paper presented at the 5th international conference on new forming technology. Bremen, Germany
10. Wong CC, Dean TA, Lin J (2003) A review of spinning, shear forming and flow forming processes. Int J Mach Tools Manuf 43(14):1419–1435

Transcription of Mirror-Finished Surface onto A5083 Aluminum Alloy Plate by Friction Stir Forming

Takahiro Ohashi, Kento Okuda, Hamed Mofidi Tabatabaei, and Tadashi Nishihara

Abstract In this study, the surface smoothing effect of friction stir forming on a JIS A5083 aluminum alloy plate with a mirror-finished die was investigated. A material plate was placed on a mirror-finished die, and friction stirring was conducted on its back surface. The material deformed because of the high pressure and heat caused by the friction stir process, and the surface profile of the die was transferred to the material. The average arithmetical mean height (Ra) and maximum profile height (Rz) of the material plate surface were improved from 2 to 1 μm and 17 to 9 μm, respectively, by using a die with surface roughness and an Ra of 1 μm and Rz of 8 μm. Details of the finished surface, including its surface profile and microstructure, and the transcription mechanism were investigated using spectrum analysis with the maximum entropy method.

Keywords Friction stir forming · Mirror-finished surface · Burnishing · Spectrum analysis

1 Introduction

Friction stir welding (FSW) was developed as a new joining technology at The Welding Institute (TWI) in the UK [1]. Its applications have been extended to joining, material processing, and forming. For example, the authors have attempted to apply friction stirring to metal forming with a die and termed the process "friction stir forming (FSF)" [2–4], (see Fig. 1). Sasahara et al. [5] proposed friction stir burnishing. They utilized a burnishing tool to stir the surface of a product for metallic grain refinement and martensitic transformation for strengthening. It is well known that the conventional burnishing process is employed for not only product surface strengthening but also smoothing rough surface textures. In this study, the utilization of FSF for product surface smoothing is proposed, which can contribute to improving the surface quality of products joined by FSW.

T. Ohashi (✉) · K. Okuda · H. M. Tabatabaei · T. Nishihara
School of Science and Engineering, Kokushikan University, 3-4-1 Setagaya, Setagaya-ku, Tokyo 154-8515, Japan
e-mail: tohashi@kokushikan.ac.jp

© The Minerals, Metals & Materials Society 2021

G. Daehn et al. (eds.), *Forming the Future*, The Minerals, Metals & Materials Series,
https://doi.org/10.1007/978-3-030-75381-8_176

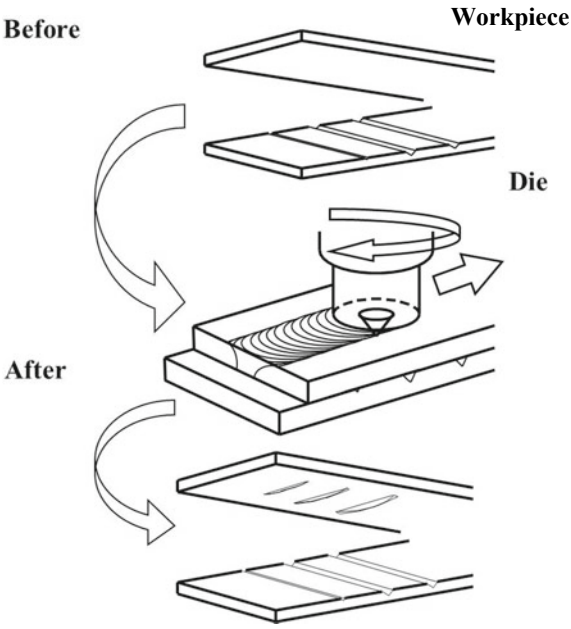


Fig. 1 Schematic of friction-stir forming (FSF) [3]

In the previous study [6], the transcription of the mirror-polished surface of SUS304 stainless steel dies onto the A5083P-O aluminum alloy plate was examined using FSF. In that study, no lubricant was applied to prevent surface deterioration during the plastic deformation of the material. A probe-less tool was utilized in the previous study to control the contact pressure between the material and die, though probe-less tools are not practical options in FSW. The probe-less tool contributed to preventing the excessively high pressure, which causes a reaction between the material and die surface to result in a rough surface of the product. Consequently, the mirror-finished surface was successfully printed on the aluminum alloy plate; however, the experimental results implied that a higher contact pressure may indicate a better surface from view to material deformation.

In the present study, a tool with a probe for higher contact pressure was utilized. Electroformed nickel die was employed to prevent the die from reacting with the material. In addition, details of the finished surface, including its surface profile and microstructure, and the transcript mechanism are discussed using spectrum analysis with the maximum entropy method (MEM).

Spectrum analysis has been utilized to evaluate the characteristics of the surface topographies of metal forming products [7–10]. For example, Kawai et al. [7] investigated the change in wavelength of the spectrum with different strain paths in the bulging process of an aluminum plate with a press. They plotted the primary frequency of the analysis at polar coordinates, revealing that an isotropic structure was created under single and biaxial tensile conditions and observing the array structure at the right angle with the main strain direction under a plane tensile condition.

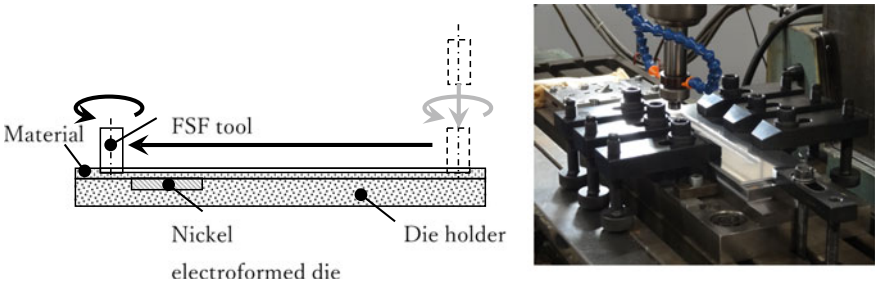


Fig. 2 Experimental setup. (Color figure online)

In addition, they reported that the primary wavelength was 15–20 times the crystal size, which was independent of the strain magnitude. Nagaki et al. [8, 9] conducted tensile and compressive tests to evaluate the surface roughness's wave of their specimens. They reported that there exists a correlation between roughness and strain magnitude; however, the primary wavelength was not found to be correlated to the strain magnitude. Nosho et al. [10] analyzed the plastic deformation behavior on the free surface of copper during plane strain compression using spectrum analysis and found that a microscopically small uneven deformation was averaged over a range longer than 20 times the crystal size. Thus, the spectrum analysis and primary wavelength of a deformed surface can contribute to the understanding of the deformation mechanism through comparison with the lengths of known structures, e.g., grain size. In the transcription of the mirror-finished surface, the surface of the product may contain the roughness's waves owing to the plastic deformation as described above, imprinted structure from the die, and remaining structure from the original material. In this study, spectrum analysis is utilized to classify the causes of the roughness of the product surface.

2 Experiment

2.1 Materials

JIS A5083P-O aluminum plates with thicknesses of 3 mm were utilized as the base metal. The mirror-finished die was fabricated by nickel electroforming. No lubricant was utilized to prevent the surface deterioration of the products.

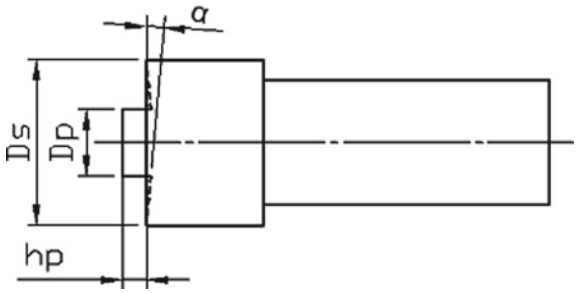


Fig. 3 FSF tool (Ds = 20 mm, Dp = 5 mm, hp = 2.5 mm, α = 5°)

Table 1 Experimental conditions

Lubricant	None
Tilt angle $\boldsymbol{\alpha}$ (°)	3
Tool feed rate $\boldsymbol{v_t}$ mm/min	50
Tool spindle speed $\boldsymbol{n}$ rpm	1,240
Tool plunge depth $\boldsymbol{z_p}$ mm	2.5
Tool rotating direction	Counterclockwise

2.2 Methods

Figures 2 and 3 depict the die and the FSF tool used in the experiment. Table 1 lists the experimental conditions. The die was set in a die holder, and an approach run longer than 150 mm was conducted on the die holder to obtain stable results. A probe was prepared on top of the tool for increased contact pressure between the material and die. No adherence was observed between the material and the electroformed nickel die without lubricant. The tool rotated in a counterclockwise direction, the tilt angle was 3°, and the tool plunge depth was 2.5 mm. Additionally, the spindle speed was 1,240 rpm and the feed rate was 50 mm/min. The non-contact three-dimensional (3D) measurement system Keyence VR-3000/3200 (resolution: 0.0001 mm, repeat accuracy: 0.0005 mm, inspection field 1.9 mm × 1.4 mm) was employed for the evaluation of the surface roughness of the product. The sequence of measured surface points was processed by SPCANA (Ver.4.92) for the analysis of the power spectra of the roughness waves on the base metal surfaces, product, and die.

3 Results and Discussion

3.1 Surface Profiles and Textures

Figure 4 illustrates an image of the product surface near the boundary between the processed and raw parts. The raw part appears brighter than the processed part

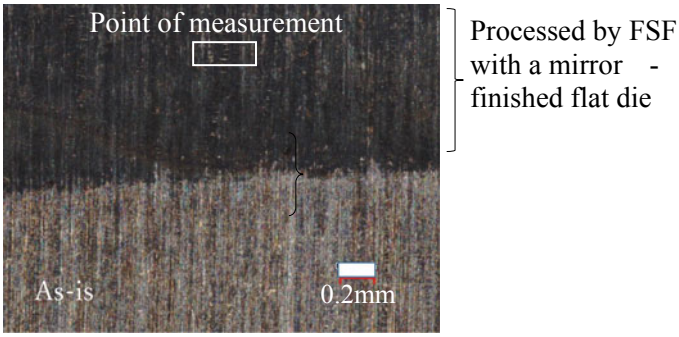
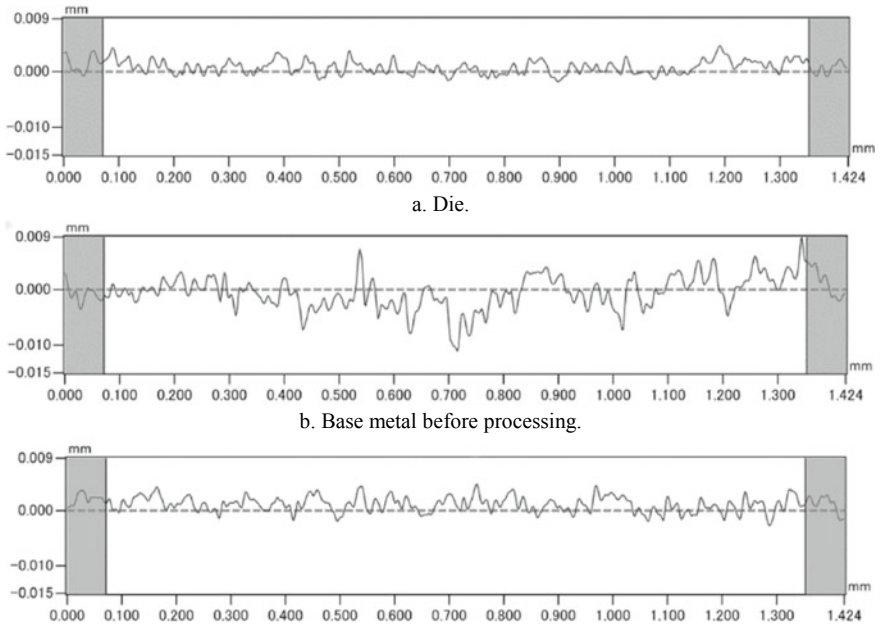


Fig. 4 Surface of product (FSF tool rotating speed: 1,240 rpm; feed rate: 50 mm/min; tool plunge depth 2.7 mm). (Color figure online)

because of its diffused reflection, and the processed part appears mirror-finished to the naked eye.

Figure 5 depicts the primary surface profiles of the die, base metal, and product after processing. The average arithmetical mean height (Ra) and the maximum profile height (Rz) of the surface of the material plate were improved from 2 to 1 μm and 17 to 9 μm, respectively, using a die with surface roughness and an Ra of 1 μm and Rz



a. Die.

b. Base metal before processing.

c. Product after processing.

Fig. 5 Primary surface profile for tool travel direction

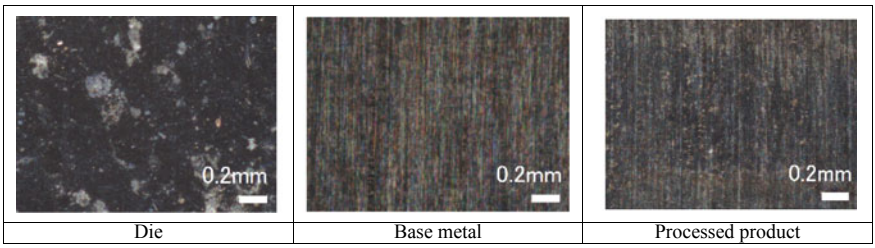


Fig. 6 Texture of the die and product. (Color figure online)

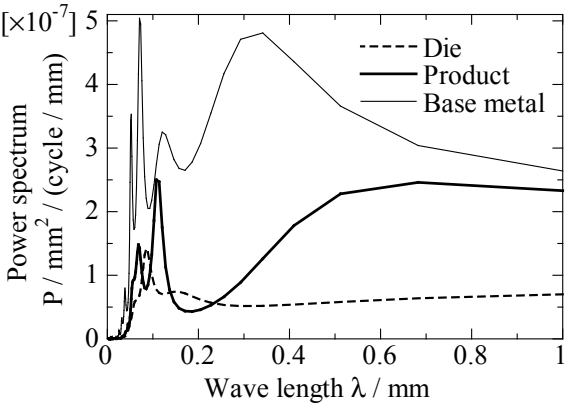
of 8 μm. Figure 6 depicts the textures of the die and product. A faint brushed pattern, which was not observed on the die surface, remained on the surface of the processed product, although the surface appeared mirror-finished to the naked eye. The power spectra of the roughness waves of each surface were evaluated to investigate the causes of this pattern.

3.2 Spectrum Analysis

Figures 7 and 8 illustrate the power spectra of the roughness waves on the surfaces of the die and product compiled using MEM. Only one peak was observed at 0.0853 mm on the die surface; however, no corresponding peak was observed in the processed part. It is thought that this peak corresponded to the surface roughness of the die with an Ra of 1 μm and Rz of 8 μm. Considering the surface roughness of the finished part with an Ra of 1 μm and Rz of 9 μm, the roughness with an Ra of 1 μm and Rz of 8–9 μm was a resolution limit in the pattern transfer of the process.

Multiple peaks were included in the graph of the original base metal, and the peaks at wavelengths longer than 0.2 mm and shorter than 0.06 mm were eliminated after

Fig. 7 Power spectrum



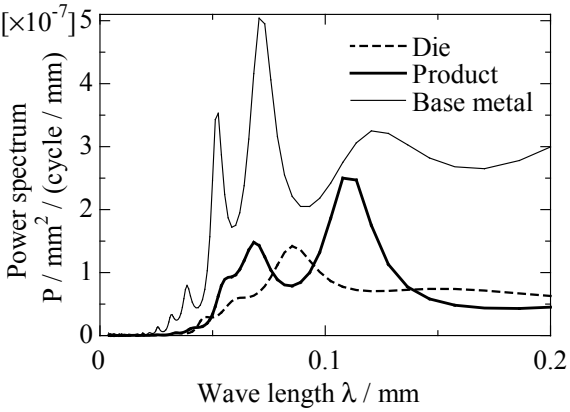


Fig. 8 Detailed power spectrum with 0–0.2 mm wavelength

processing. It is thought that the longer wavelength belonged to the large structures, e.g., surface waviness, which was removed successfully via smoothing. In addition, it is unclear what the shorter wavelength indicated. Nagaki et al. [8] proposed a model in which short roughness waves vanish and long waves are developed with plastic deformation under compression (See Fig. 9). The results of our study appear to support their model.

Only two peaks at wavelengths of approximately 0.101 and 0.0682 mm were observed on the finished part. A peak corresponding to a wavelength of 0.0682 mm appeared to exist on the original base metal. However, the peak at the wavelength of 0.101 mm did not appear to indicate any peaks on the surfaces of the die and base metal.

3.3 Microstructure and 3D Measurement of Surfaces

Figure 10 depicts the microstructure of the base metal surface and the processed product in contact with the die surface. Figure 11 illustrates the contour map compiled from the 3D measurement of the surfaces. Structures associated with the 0.101 mm wavelength were not observed in the microstructure. It has been reported that roughness waves with lengths 15–20 times crystal size are newly created during the plastic deformation on the free surface [6, 8]. Hence, there is a possibility that the above newly created wave can be associated with a peak of approximately 0.101 mm.

Besides, the compression of convex spots on the surface can shorten the concave part, as depicted in Fig. 12. In Fig. 11, the size of the convex spots, that is, red spots, and their intervals appear larger and shorter, respectively, after processing. In addition, the shift in the frequency of the peaks at shorter wavelengths after the processing can be explained by Nagaki's model, as illustrated in Fig. 9. Furthermore, it is thought that the power of the convex pattern can be reduced more easily than that of the concave pattern through compression. From these points of view, the

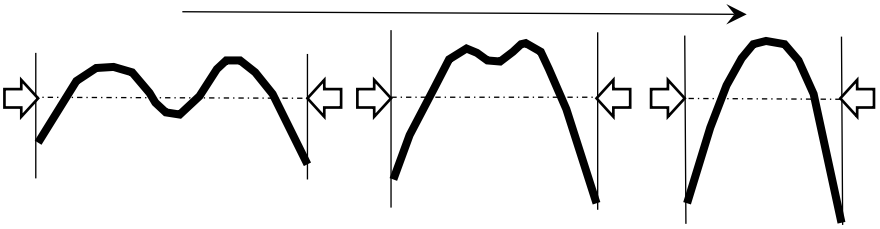


Fig. 9 Model of the change of a surface roughness wave in compression by Nagaki et al. [8]

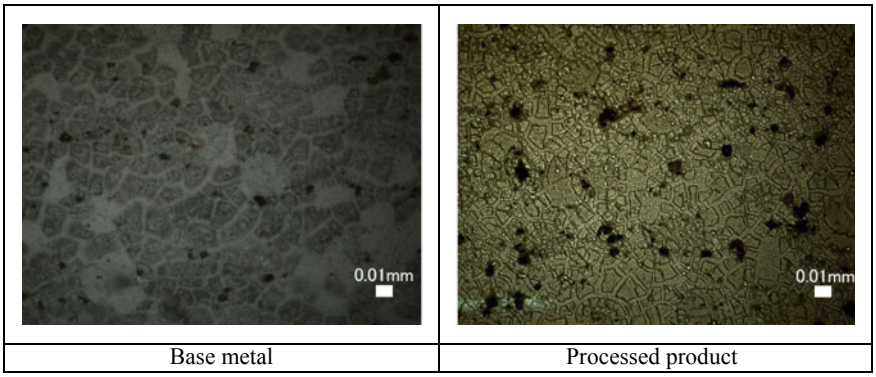


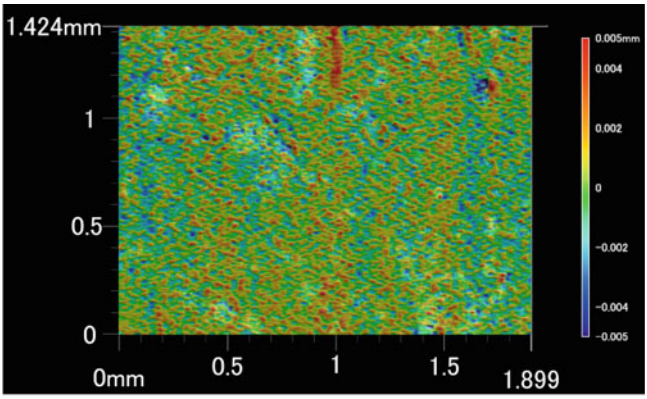
Fig. 10 Microstructure of the material surface. (Color figure online)

third strongest peak of the base metal is found to be associated with concave structures rather than with crystal size and remains after processing at the wavelength of 0.101 mm.

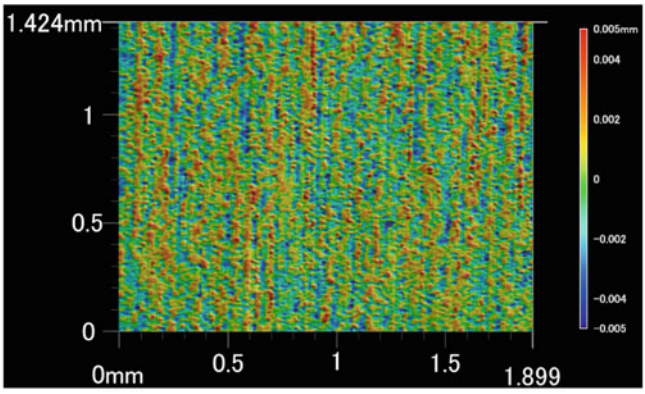
4 Summary

FSF was employed for transcription of the surface of a mirror-finished die onto a metal plate. It was confirmed that a mirror-finished surface of an electroformed nickel die was successfully transferred onto the surface of an A5083 aluminum alloy plate. Next, a non-contact 3D measurement system was used to evaluate the surface roughness of the product. A series of measured surface points was analyzed using MEM to evaluate the power spectra of the roughness waves of the base metal surfaces, product, and die Consequently,

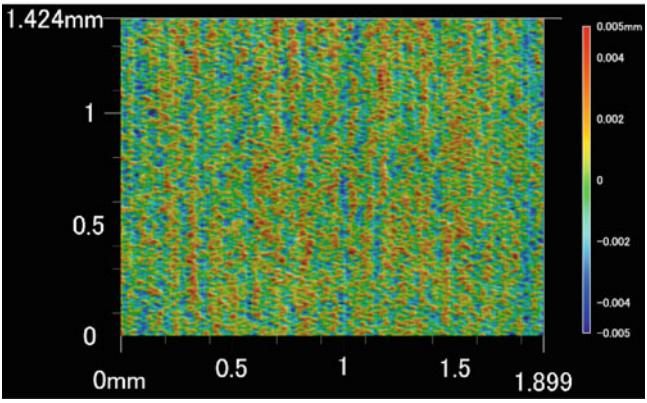
(1) the Ra and Rz of the material plate surface were improved from 2 to 1 μm and 17 to 9 μm, respectively, by using a die with surface roughness and an Ra of 1 μm and Rz of 8 μm.



(1) Die



(2) Base metal



(3) Processed product.

Fig. 11 3D measurement of surfaces (counter map). (Color figure online)

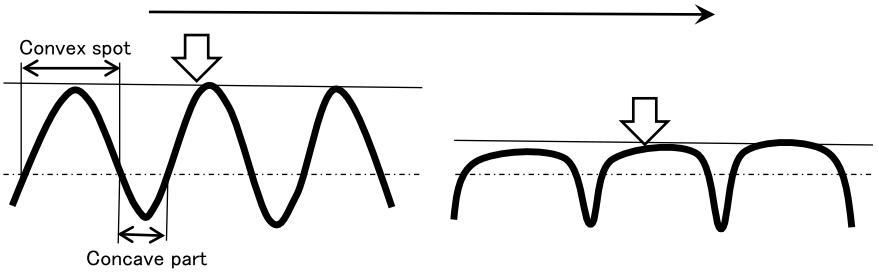


Fig. 12 Compression of convex spots of the surface and shortening of concave parts

(2) In the spectrum analysis, only one peak was observed at 0.0853 mm on the die surface, and multiple peaks were observed in the original base metal. However, the peaks at wavelengths longer than 0.2 mm and shorter than 0.06 mm were eliminated after processing. Only two peaks at wavelengths of approximately 0.10 and 0.0682 mm were observed on the finished product.

In our future work, we intend to utilize mirror-polished base metals to investigate the cause of the remaining peak on the finished product.

References

1. Thomas MW, Nicholas J, Needham JC, Murch MG, Templesmith P, Dawes CJ (1995) Friction welding. US Patent, 5,460,317, 24 Oct 1995
2. Nishihara T (2002) Friction stir forming. Japanese Patent, 4,646,421, 11 Sept 2002
3. Nishihara T (2003) Development of friction stir forming. Mater Sci Forum 426–432:2971–2978. https://doi.org/10.4028/www.scientific.net/MSF.426-432.2971
4. Ohashi T, Mofidi Tabatabaei H, Nishihara T (2017) Cylindrical pin embossment on A5083 aluminum alloy substrate fabricated by friction stir fforming. Key Eng Mater 730:253–258. https://doi.org/10.4028/www.scientific.net/KEM.730.253
5. Takada Y, Sasahara H (2018) Effect of tip shape of frictional stir burnishing tool on processed layer's hardness, residual stress and surface roughness. Coatings 8–1:32. https://doi.org/10.3390/coatings8010032
6. Ohashi T, Okuda K, Mofidi Tabatabaei H, Nishihara T (2018) Surface smoothing of A5083 aluminum alloy plate by friction stir forming. Key Eng Mater 803:50–54. https://doi.org/10.4028/www.scientific.net/KEM.803.50
7. Kawai N, Nakamura T, Ukai Y (1986) Surface Roughness Mechanism of Polycrystalline Metal Sheet during Plastic Deformation. Bull Jpn Soc Mech Eng 29–250:1337–1343
8. Nagaki S, Abe T, Ohta E, Iguchi K (1991) Frequency analysis of surface roughness wave during plastic deformation of iron. Trans Jpn Soc Mech Eng Ser A 57–536:983–988
9. Kakimoto Y, Nagaki S, Itagai S, Abe T (1993) Observation of surface roughness and analysis of wavelength during plastic deformation of iron. Trans Jpn Soc Mech Eng Ser A 59–564:1888–1894
10. Nosho T, Himizu I, Abe T, Wakayama M, Tsutsumi K (1997) Microscopic plastic deformation behavior on free surface of copper during plane strain compression. J Soc Mater Sci 46–8:887–892

Combined Computed Tomography and Numerical Modeling for the Analysis of Bending of Additively Manufactured Cellular Sheets



S. Rosenthal, E. Jost, C. Saldana, T. Clausmeyer, M. Hahn, and A. E. Tekkaya

Abstract Applying additively manufactured (AM) metallic sheets with internal cellular structures are formed in a bending operation. This enables a higher degree of lightweighting potential due to design freedom and strain hardening. Computed tomography (CT) of those structures with wall thicknesses of 0.3 mm reveal manufacturing inaccuracies of the AM process between the nominal CAD and actual geometry. The CT-data shows that the geometric deviation of the unit cells is periodic. A surface model based on CT-data is used to evaluate volume-meshing strategies in a finite element model, benefiting from the periodicity of the core structure. Model simplifications due to a large number of elements within the simulation are presented and used to convert the CT-data into a volume mesh that can be used in a forming simulation. With the CT-based numerical model, the accuracy in predicting force–displacement response can be increased when compared to the ideal CAD-based model. The influence of the geometric deviation and its impact on the deformation behavior in a bending dominated forming operation is evaluated. It is demonstrated that accurate representation of the actual geometry in the numerical model is critical for a correct prediction of the bending behavior and the investigation of localization phenomena during deformation.

Keywords Additive manufacturing · Computed tomography · Numerical simulation · Bending · Sandwich sheets · Lightweight

S. Rosenthal (✉) · T. Clausmeyer · M. Hahn · A. E. Tekkaya
Institute of Forming Technology and Lightweight Components (IUL), TU Dortmund University, Baroper Straße 303, 44227 Dortmund, Germany
e-mail: stephan.rosenthal@iul.tu-dortmund.de

E. Jost · C. Saldana
George W. Woodruff School of Mechanical Engineering, Georgia Institute of Technology, Atlanta, GA 30332, USA

© The Minerals, Metals & Materials Society 2021

G. Daehn et al. (eds.), *Forming the Future*, The Minerals, Metals & Materials Series,
https://doi.org/10.1007/978-3-030-75381-8_177

1 Introduction

Additive manufacturing (AM) as a process to produce semi-finished parts for a subsequent forming operation is a novel field of research. The combination of these two processes enables synergies, such as the production of complex parts with integrated functions and the increased strength by strain hardening through a subsequent forming operation. However, disadvantages such as long production times and small build chamber volumes are problems that have to be addressed. Rosenthal et al. [1] proposed a new process combination of additive manufacturing with a subsequent forming operation of additively manufactured sandwich sheets with internal cellular core structures. The feasibility of forming AM parts has been shown and the influence of anisotropic material properties on the deformation behavior was evaluated to be negligible [2]. The development and prediction of the forming behavior of additively manufactured sandwich sheets is more challenging due to different forming characteristics. The material properties of additively manufactured parts are dependent on the produced geometry [3], the process parameters, and build orientation.

The development of formable core structures requires the help of numerical simulations. To validate those simulations an accurate representation of the nominal geometry is necessary. Thus, computed tomography (CT) inspections were used to assess the as-built geometry and improve the prediction accuracy of the simulations. Due to the very fine, sub-millimeter, internal features of the sandwich sheets, a geometric deviation between the nominal CAD geometry and the AM sheets is present. The AM process suffers from manufacturing deviations of up to 0.088 mm on an EOS M290 machine [4]. On an absolute scale, this deviation may be small, but when dealing with part dimensions of 0.3 mm and smaller, this leads to differences of up to 30% and thus significantly influences local part performance. This geometric deviation leads to an insufficient agreement between the numerical simulation and the bending experiment of the sandwich structures. To investigate the effect of the geometric inaccuracy of the AM-produced parts on the bending response, X-ray CT is conducted.

X-ray CT is a non-destructive inspection technique that utilizes high-energy x-rays to visualize the internal structure and form of a component. CT is used to inspect the complex structures commonly created through AM for both geometric and internal defects [5]. Recently, CT has been leveraged for AM to gain a better understanding of the effects of structural heterogeneities innate to the manufacturing process on deviation from nominal mechanical performance, specifically in lattice or cellular structures [6]. As AM has grown in prominence, the need for non-contact metrological inspection has increased as well [7]. Thus, CT has been used as a common tool to address this need.

CT is increasingly being used to extract quantitative information about the as-built AM geometry and inform finite element models to more accurately predict component behavior, as done in this study. One significant issue in directly using CT volumes for modeling is the large datasets associated with CT and therefore an inability to create efficient models from a computational time perspective, with

many current models requiring super-computer clusters. To address this issue, much current research is using simplified or smoothed CT data to lower computational time. For example, Liu et al. [8] utilized CT to extract statistical data on geometric defects in architected lattice structures, showing the variation of strut characteristics typical of these components. Using this data, FE model geometry was modified to reflect the statistical variability of these characteristics and improve model prediction accuracy. Similarly, Hernández-Nava et al. [9] used computed tomography and image analysis methods to assess the variation of lattice structures and their effect on overall compressive deformation and failure mechanisms. They concluded that lattice defects and slight variations in strut diameters only have a small influence on the deformation behavior under direct compressive loading, but not in a forming operation.

Using this method, an accurate representation of the sandwich structure can be created and used in a numerical simulation. Since the geometry should be closer to the true geometry in the improved simulation, the majority of the remaining deviation between simulation and experiment should derive from the deviation of the material properties due to a different geometry and leave a difference between experiment and simulation. Thus, the focus of this paper is the influence of the manufacturing deviations on the bending response of additively manufactured sandwich sheets with internal core structures and the capability of the numerical simulation to predict the forming behavior based on the CT-data. The influence of geometric deviations between the nominal and real geometry is investigated to assess if further improvements on manufacturing accuracy or the material model lead to a better understanding of the deformation behavior of such sandwich sheets in a bending dominated forming operation.

2 Methods

2.1 Experiments

Bending experiments were done on a Zwick/Roell 2015 universal testing machine. A top die with a tool radius of $R_{\text{tool}} = 5$ mm was used in the experiments. The specimens rested on solid rollers to reduce the influence of the friction between the tool and the specimens. The distance of the rollers was set to $l = 37.3$ mm. The radius of the rollers was $R_{\text{B}} = 15$ mm. The desired tool displacement was set to 8 mm. The bending experiments were conducted with a constant tool velocity of $v_{\text{tool}} = 2$ mm/min (Fig. 1a).

The specimens were produced on an EOS M290 machine with default parameters delivered by EOS for a layer height of 20 µm as sheets with the dimensions 120 mm × 40 mm, from the stainless steel material EOS GP1 (1.4542/17-4PH). Figure 2 shows the geometry of the unit cells which were used in the present study—as unit cells and in the geometry of the full sheet. The sheets were cut down to smaller samples with a diamond saw blade to pieces of approximately 55 mm × 25 mm. Next to

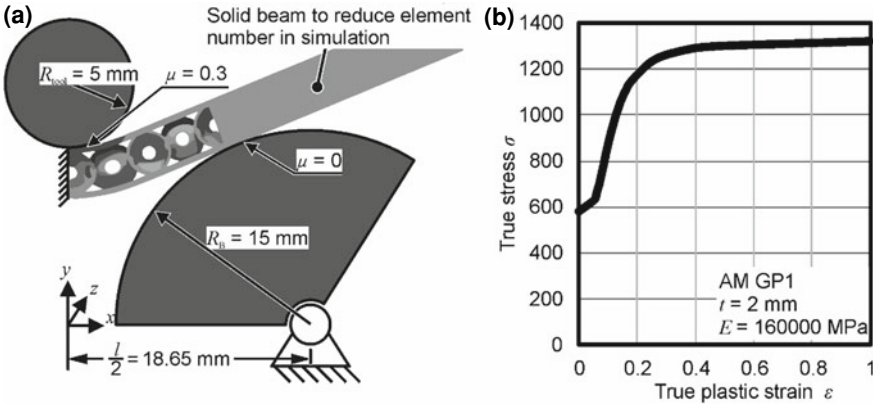


Fig. 1 **a** Bending test setup with the top die $R_{\text{tool}} = 5$ mm, **b** Material behavior for the numerical simulations

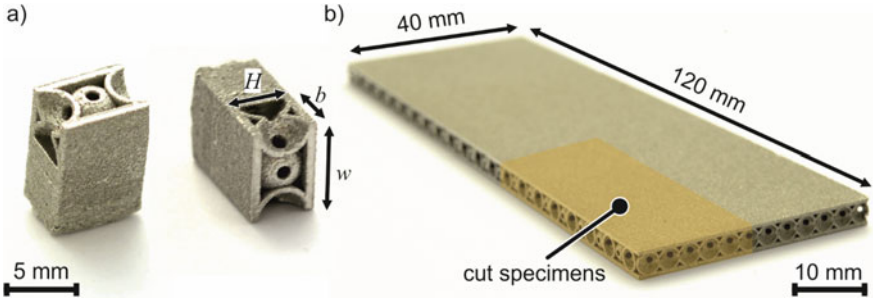


Fig. 2 Additively manufactured specimens. **a** Single unit cells, **b** produced sandwich sheet to cut the bending samples from. (Color figure online)

the bending specimens single unit cells were produced from which the spherical sandwich sheets are designed (Fig. 2a). The unit cells are duplicated in the sheet plane to generate a full sandwich sheet (Fig. 2b). The unit cells are manufactured to enable the generation of high-quality CT-measurements to build a numerical model with the real geometry.

2.2 Computed Tomography

X-ray CT inspections were performed on samples in the as-built and deformed states. To accurately assess geometry, individual unit cells were inspected using a high-resolution, microfocus Zeiss Metrotom 800, which achieved a resolution of approximately 9 μm. Full-size bend samples were inspected using the higher energy

Table 1 CT inspection parameters

	Zeiss metrotom 800	Visiconsult XRH222
Resolution	9 μm	72 μm
Number of projections	1500	300
Inspected geometry (Size)	Unit cell (3.25 × 5.629 × 4 mm)	Bend Sample (50 × 20 × 4 mm)
Accel. Voltage	130 kV	221 kV
Pre-filtering	0.25 mm Cu	1 mm Cu

Visiconsult XRH222 CT in as-built and deformed states at a resolution of 72 μm to confirm the periodicity of geometric print defects, measure wall thickness, and observe global deformation. The high-resolution scan was used to construct simulation geometry and was determined to be representative of overall geometry when patterned due to the periodic nature of lattices geometries. CT Parameters from both inspections are summarized in Table 1.

All CT analyses were performed using Volume Graphics VGStudioMAX 3.2. Surface determination was done by establishing an initial ISO-50 threshold followed by a Volume Graphics advanced refinement technique. Using this determined surface, wall thickness measurements were made using a largest fitting sphere algorithm to quantitatively understand where and by how much the as-built part deviated from nominal geometry. CT volumes were converted to STL meshes using Volume Graphics and patterned for modeling.

Computed tomography was used to measure the real geometry of the additively manufactured specimens. The methodology (Fig. 3) is to prepare CT-scans of the single unit cells (Fig. 3a) and create a high-resolution surface model of the real geometry. Considering the large number of polygons of the CT-scan, the model needs to be simplified without losing or changing the geometry too much. Rosenthal et al. [1] showed that the surface roughness of additively manufactured specimens does not influence the load-bearing capacity significantly. Thus, the unit cells can be modeled without the need to consider the surface roughness, which will reduce the number of polygons drastically. This, in combination with a surface smoothing yields a surface model with approximately 30,000 polygons (Fig. 3b). Based on the surface model, a solid model with roughly 300,000 ten-node tetrahedral elements per unit cell was created (Fig. 3c).

2.3 Numerical Simulations

Numerical simulations were performed with Abaqus/CAE 2018. The mechanical boundary conditions are the same as in the experiment (Fig. 1a) with the difference of the implementation of symmetry boundary conditions for reduced computation

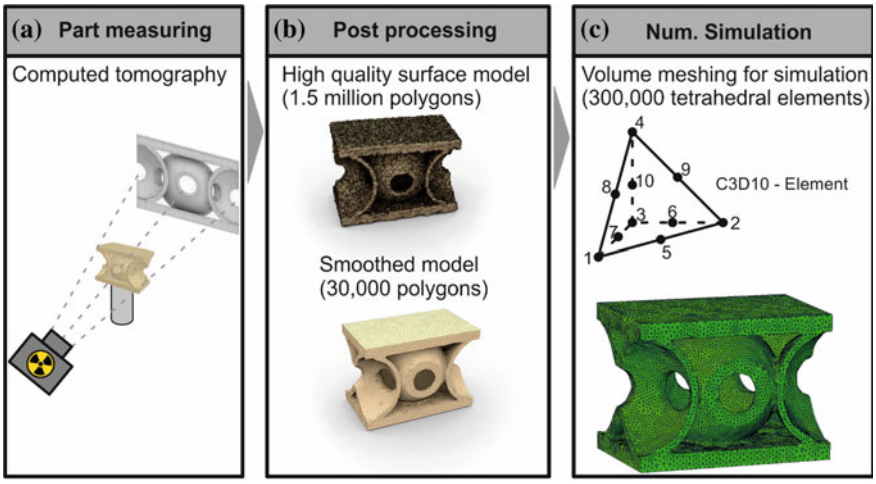


Fig. 3 Methodology for creating a volume mesh for the numerical simulation from the computed tomography scans. (Color figure online)

time. The model was simplified in a way that only two unit cells are used in the bending zone which are attached to a beam with a smaller number of volume elements (Fig. 1). Simulations were performed for:

(i) The nominal CAD-geometry, which was used to produce the specimens for the experiments.
(ii) The CAD-geometry, which was redesigned by the measurements taken from microscopic images of the structure
(iii) The geometry is taken directly from the high-resolution CT-scans of the single unit cells.

Simulations (i) and (ii) were meshed with eight-node hexahedral volume elements and reduced integration (C3D8R-elements). Simulation (iii) was done with the geometry taken from the CT-scans and meshed with ten-node tetrahedral elements (C3D10) since the geometry of the CT-scan necessitates the use of a free mesh generation. The material used in this study was the EOS stainless steel GP1 (17-4PH) and modeled with isotropic von Mises plasticity. The material behavior was characterized through tensile and in-plane torsion tests [10] (Fig. 1b). The stress–strain values were implemented in Abaqus in tabular order.

A convergence study revealed a mesh size of 0.3 mm as sufficient to model the bending operation with only a negligible influence on the load–displacement response (Fig. 4). Larger mesh sizes were not possible since the minimal wall thickness in the part was 0.25 mm and larger meshes led to failed meshing. In addition, the influence of the element formulation—eight-node hexahedral elements with reduced integration formulation (C3D8R-elements) and ten-node tetrahedral elements (C3D10) can also be neglected. The convergence study for the CT-scanned geometry yielded a mean

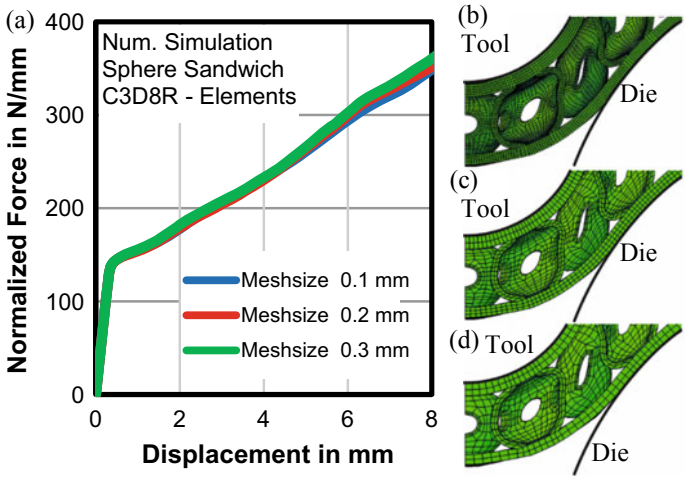


Fig. 4 Mesh convergence study. **a** Force–displacement response in the numerical simulation of the bending experiment with different mesh sizes. **b** Mesh size 0.1 mm, **c** Mesh size 0.2 mm, **d** Mesh size 0.3 mm. (Color figure online)

element size of 0.08 mm for a sufficiently accurate simulation. The mesh of the CT-scanned part needs to be that small to be able to model the small details and graded wall thicknesses of the real part.

3 Results and Discussion

3.1 Bending Experiments

The bending experiments were performed up to a tool displacement of 8 mm and led to a deformed specimen as depicted in Fig. 5. Three specimens were tested. The bending zone is clearly visible in the area where the tool was in contact with the part (Fig. 5a). The bending angle after the release of the tools was 55°. The bent zone under the punch exhibited a pronounced indentation. Clearly visible is the deformed core of the sandwich sheet. Due to the bending loads, shear deformation is introduced into the core as a result of the different strains in the top and bottom face sheet. The relative displacement led to a shearing deformation of the core. The transition from fully elastic deformation to plastic deformation due to bending is marked by the pronounced change of the slope of the force versus displacement curve at a displacement of 0.5 mm. The curve then exhibits a second almost linear, monotonically increasing section. The increase is not only due to the hardening of the material but also due to a kinematic influence.

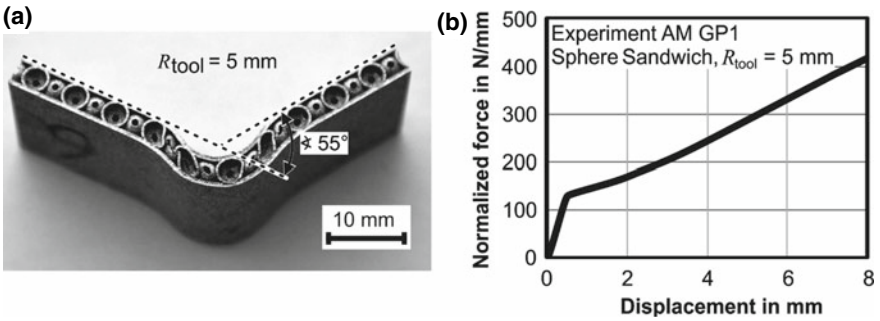


Fig. 5 Additively manufactured bending samples and corresponding load–displacement diagrams. **a** Tool radius $R = 5$ mm, **b** Experimental load–displacement diagram with $R_{tool} = 5$ mm, maximum tool displacement is 8 mm

3.2 Geometric Comparison

The specimens were investigated with CT-scanning methods and with optical microscopy. The aim is to investigate the geometric deviation of the built parts compared to the nominal CAD-geometries. The optical microscopy was done on slices in the mid-plane of a unit cell (Fig. 6a). The plane in which the wall thickness was investigated was estimated to be in the middle of a sphere. The geometric deviations are periodic across the single unit cells, which was revealed during the analysis of the CT-scans as well as during the investigations of the micrographs (Fig. 6b). As described in Sect. 2.2, the segmentation of the CT-scans yielded a surface model with roughly 1.5 million polygons, which was not possible to be transferred into a volume mesh for the numerical simulation. Therefore, the model was smoothed and edited such that a volume mesh could be generated (Fig. 3).

The CT-scans of the unit cells were compared to the nominal CAD-geometry (Fig. 7a), and the model that was used in the simulation (Fig. 7b) was compared against the nominal CAD-geometry (Fig. 7c). In general, the agreement between the CT-scans and the nominal CAD-geometry was good. During the manipulation of the high-quality surface model, the boundaries were flattened to be able to assign the correct boundary conditions at the symmetry planes. This yielded higher deviations at the boundaries of the CT-scanned part but a good approximation of the geometry in the

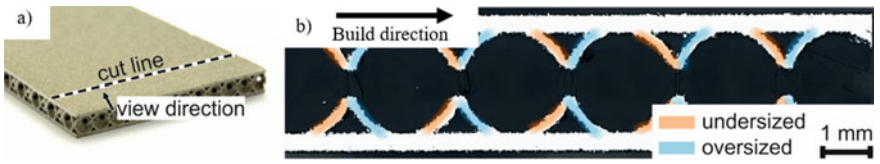


Fig. 6 **a** Area for the wall thickness measurements with optical microscopy, **b** periodic wall thickness deviation of the core wall thicknesses. (Color figure online)

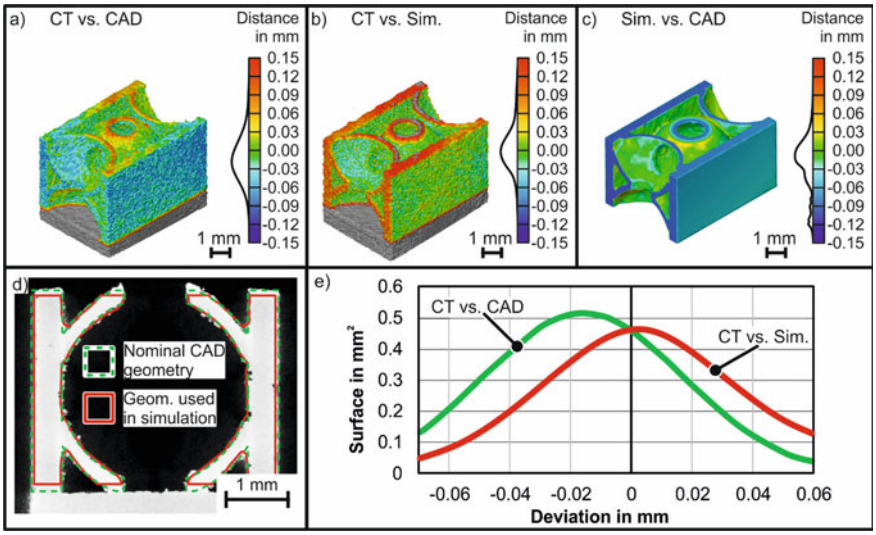


Fig. 7 Comparison of used geometries, **a** CT-scan versus nominal CAD geometry, **b** CT-scan versus model used in simulation, **c** simulation model versus nominal CAD-geometry, **d** Slice through the unit cell and overlayed geometries, **e** surface deviations. (Color figure online)

rest of the part (Fig. 7b). The comparison of the simulation model and the CT-scanned part with the nominal CAD-geometry revealed a slightly undersized real part.

3.3 Wall Thickness Measurement

The specimens were cut with a diamond sawblade and embedded into resin (Fig. 8c). The core wall thickness was measured ($n = 50$ measurements) and the thickness of the face sheet ($n = 10$ measurements) (Fig. 8a). The box plots (Fig. 8a) show the maximum, minimum, median, upper and lower quartiles, and mean values. The wall thickness of the core shows a large deviation of the measured values. The nominal value of the core wall thickness should be 0.25 mm. The mean value of 0.24 mm is close to that value but the scattering is large. The histogram (Fig. 8b) shows the thickness distribution and the absolute and relative frequency of the measured values. The mean value of 0.47 mm is under the nominal face sheet thickness value of 0.5 mm. The global distribution of the measured values shows a periodic deviation of the values. The core wall thicknesses are oversized in areas where the wall of the spheres grows toward the face sheet (Fig. 6) and undersized where the wall thickness grows into an unsupported area.

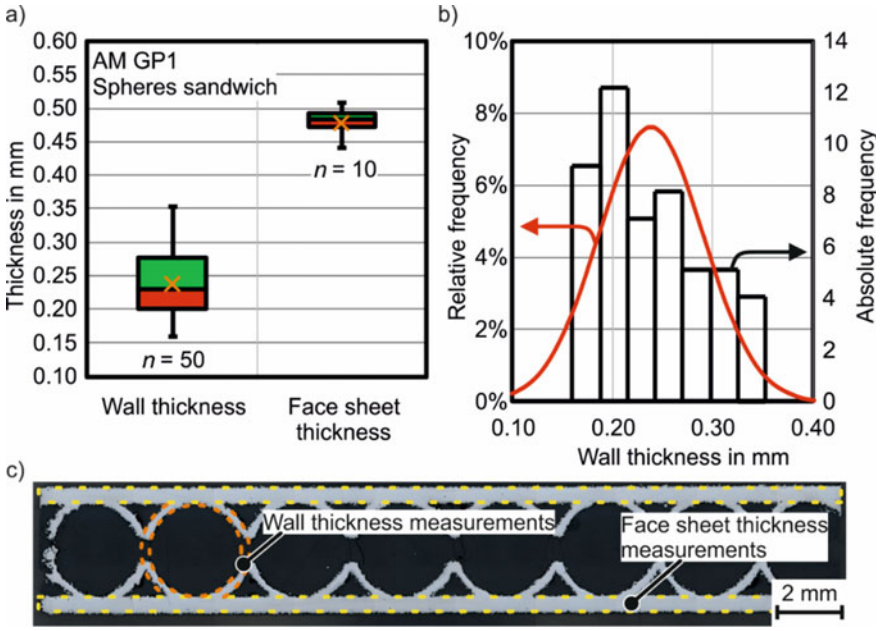


Fig. 8 Thickness measurements of the spherical sandwich structure. **a** Box-plot of the wall thickness and the face sheet thickness, **b** histogram of the wall thickness distribution, **c** picture of the cut sheet with locations of the measurements. (Color figure online)

3.4 Numerical Simulations

Three different simulation setups were done as described in Sect. 2.3. Models resulting from the nominal CAD-geometry, the geometry from the measurements made by optical microscopy, and the geometry resulting from CT-scans. The focus is to obtain the load–displacement response (Fig. 9) and the deformation behavior. The force is normalized to the width of the specimens to ease comparisons. Taking a closer look at the magnifications of the diagram (Fig. 9b) in the beginning of the experiment, the diagrams reveal different stiffnesses in the elastic range. The geometries tested in the experiment have a lower stiffness $^{\Delta F}/_{\Delta x} = 288$ N/(mm · mm) than the simulations predict (Fig. 10), where F is the force in the elastic range and x the corresponding displacement (Fig. 9b). The values for the stiffness calculations were taken from linear regression between 50 N/mm to 100 N/mm. The stiffness of the part simulated with nominal geometry had the highest stiffness with $^{\Delta F}/_{\Delta x} =$ 466 N/(mm · mm). With a stiffness of $^{\Delta F}/_{\Delta x} = 375$ N/(mm · mm) the other geometries were in between the aforementioned. Thus, the geometric deviation influences the stiffness of the geometry during the elastic deformation significantly. Additionally, Young's modulus used in the simulation overestimates the real material tensile

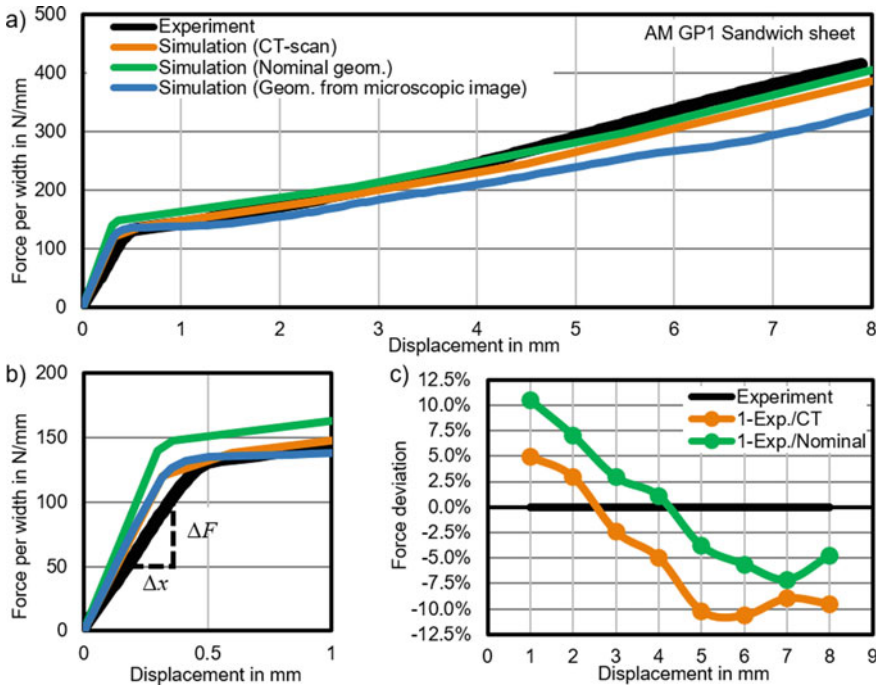


Fig. 9 Load–displacement diagrams of the bent spherical sandwich sheets in three-point bending, $R_{tool} = 5$ mm, maximum tool displacement is 8 mm, **a** experimental and numerical results, **b** magnification: 0 mm–1 mm displacement, **c** deviation between experiment and simulation. (Color figure online)

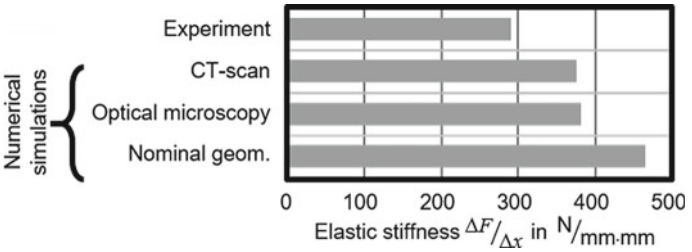


Fig. 10 Elastic stiffness of the spherical sandwich sheet in the experiments and simulations

behavior measured in tensile tests. Since the characterization was done for specimens without a core structure, the thermal history between the specimens with core structure differs from the dogbone specimens. The finer inner structure of the core possibly leads to a lower cooling rate, since the surrounding powder isolates the part and therefore probably yields a softer material behavior, which in return leads to a reduced Young's modulus. Similar results have been discovered during an inverse

parameter identification of the flow curve to compare the material properties of solid tensile tests and tensile tests with internal core structures.

The force at which the specimens started to deform plastically was nearly identical for the simulations with the geometries that were made from the CT-scans and the simulations with the geometries that were constructed based on the measurements done by optical microscopy. The geometry from the optical microscopy measurements showed a horizontal slope until 1.5 mm displacement. The core structure in this case collapsed under the normal loads at the beginning of the bending process since the wall thicknesses were too small to withstand the load from the tool. The simulation of the CT-scanned geometry overestimates the experimental loads at the beginning with a difference of 5% (Fig. 9c). After a tool displacement of 2.5 mm, the forces from the simulation started to underestimate the experimental loads. This is possibly caused by a different hardening behavior of the material in experiment and simulation. It is unlikely that the change in slope is a result of a different geometry, on the one side because the unit cell geometry is based on an accurate CT-scan. On the other side, the slope of the force–displacement from the simulations based on the CAD- and CT-scan geometry are almost parallel until a tool displacement of 6 mm, just shifted by approximately 5% (Fig. 9c). Therefore, further investigations need to be performed on the characterization of the materials flow behavior.

3.5 Deformation Behavior

CT-scans of the deformed bending specimens were performed after the experiments and are compared to the deformation states from the simulations (Fig. 11). Thickness variations of the ct-scan after the bending experiment possibly result from a lower resolution of the projections, therefore also the edges in the projections are not that crisp and sharp which leads to wall thickness overestimations of the resulting part. The influence is negligible, since the comparison is qualitative. The deformation behavior was qualitatively almost identical to each other. The regions right and left to the middle axis were deformed in a shear-dominated state. The initially spherical holes in the core deformed to ellipsoids, independently from the manner of geometry used in the simulation (Fig. 11a–c). The unit cell directly underneath the tool deformed under a compression load (Fig. 11a, c). This behavior cannot be investigated in the simulation based on the CT-scan (Fig. 11b) because the boundaries of the unit cell had to be trimmed to be used in the simulation (see Sect. 3.2). The bending angles and the radii were nearly identical.

Summarizing the evaluation of the deformation behavior, the deformation and mechanics were almost identical and independent of the methodology used to describe the geometry. One main deformation mechanism is shearing due to the relative movement of the face sheets.

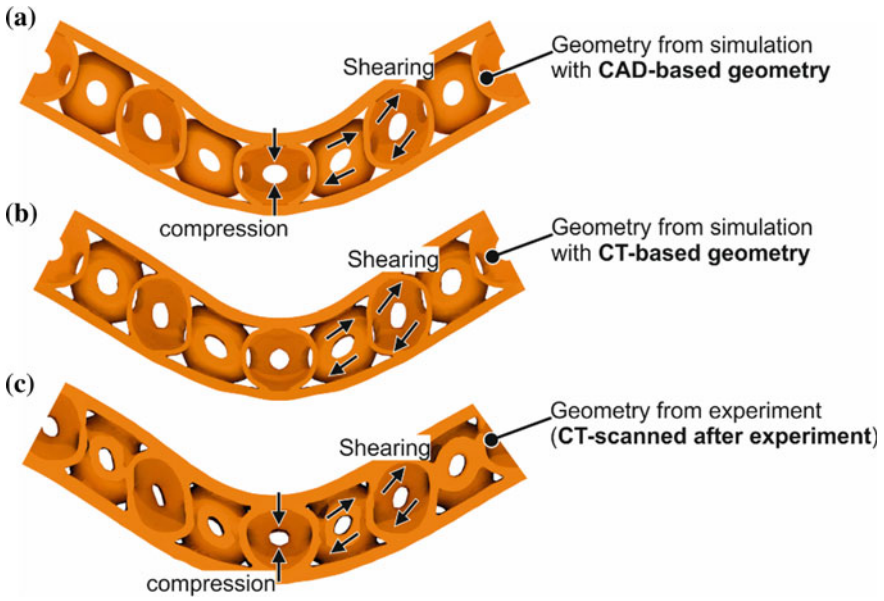


Fig. 11 Deformed bending specimens after a tool displacement of 7.4 mm. **a** Simulation with CAD-based geometry, **b** Simulation with CT-based geometry, **c** Experiment, CT-scan after the bending operation. (Color figure online)

4 Conclusion and Outlook

The investigations in this study dealt with the bending of additively manufactured metallic sandwich sheets and the influence of geometric deviations between the real and nominal CAD-geometry on the prediction accuracy of the bending forces in three-point bending. CT-scans of the 3D-printed specimens were performed to evaluate the additive manufacturing accuracy. It was found that there is a periodic pattern to the geometric deviations between the nominal CAD-geometry and the as-built parts. Numerical simulations using the geometry from the CT-scans showed a higher prediction accuracy of the bending forces, for displacements up to ~4 mm than the simulations that were performed with the nominal CAD-geometry. This is due to the fact, that the simulations were done with the real and correct geometry. Up to a tool displacement of 4 mm. the differences between experiment and simulation are approximately ±5%. The experiments show higher strain hardening values than predicted by the numerical simulations. The material for the simulation was characterized with flat tensile test specimens, and therefore, the material behavior in the fine cellular core of the sandwich sheet is assumed to be the same as a solid additively manufactured part. From the numerical results, it can be seen that the initial yield forces were very similar between the experimental and numerical results, but the forces in the further stages of the bending process were slightly different.

The deformation behavior is independent of the methodology that is used to create the geometry and mainly a result of shearing and relative movement of the face sheets. An important result of this study is that the use of CT-scans to describe additively manufactured geometry is a tedious and time-consuming task. This methodology results in FE-mesh with a high number of tethrahedral elements and therefore a very time-consuming numerical simulation. This results in a better approximation of the bending forces but does not show benefits in describing the deformation behavior of the core structure. It still needs to be investigated if the remaining deviation between experiment and simulation can also be attributed to an inaccurate description of the material behavior.

Future research will deal with the correct description of the material behavior in dependency of the geometry of the core structure, to further increase the prediction accuracy of the bending forces as well as unloading experiments to determine the springback behavior. Due to the different geometry of the sandwich core structure, different thermal gradients emerged inside the parts, which resulted in different cooling rates and therefore slightly different material behavior, which needs to be proofed in further investigations. This probably results in the remaining differences between experiment and simulation. Another field of research is the development of indicators to evaluate the strain to failure values to predict the maximum allowed strains during a bending operation.

Acknowledgments This paper is based on the results of the project TE 508/63-1, which is kindly supported by the German Research Foundation (DFG). The support of Christopher Saldana by the Dortmund Gambrinus-Fellowship to establish the scientific exchange is highly acknowledged. We thank Gerd Witt and Sebastian Platt of the Institute of Product Engineering, Universität Duisburg-Essen for providing the additively manufactured specimens.

References

1. Rosenthal S, Platt S, Hölker-Jäger R, Gies S, Kleszczynski S, Tekkaya AE, Witt G (2019) Forming properties of additively manufactured monolithic Hastelloy X sheets. Mater Sci Eng A 753:300–316. https://doi.org/10.1016/j.msea.2019.03.035
2. Rosenthal S, Hahn M, Tekkaya AE (2019) Simulation approach for three-point plastic bending of additively manufactured Hastelloy X sheets. Procedia Manuf 34:475–481. https://doi.org/10.1016/j.promfg.2019.06.201
3. Kunze K, Etter T, Grässlin J, Shklover V (2015) Texture, anisotropy in microstructure and mechanical properties of IN738LC alloy processed by selective laser melting (SLM). Mater Sci Eng A 620:213–222. https://doi.org/10.1016/j.msea.2014.10.003
4. Mitchel WF, Lang DC, Merdes TA, Reutzel EW, Welsh GS (2016) Dimensional accuracy of titanium direct metal laser sintered parts. In: Proceedings of the 26th annual international solid freeform fabrication symposium
5. Du Plessis A, Yadroitsev I, Yadroitsava I, Le Roux SG (2018) X-ray microcomputed tomography in additive manufacturing: a review of the current technology and applications. 3D Print Addit Manuf 5(3):227–247. https://doi.org/10.1089/3dp.2018.0060

6. Dressler AD, Jost EW, Miers JC, Moore DG, Seepersad CC, Boyce BL (2019) Heterogeneities dominate mechanical performance of additively manufactured metal lattice struts. Addit Manuf 28:692–703. https://doi.org/10.1016/j.addma.2019.06.011
7. Koester L, Taheri H, Bond LJ, Barnard D, Gray J (2016) Additive manufacturing metrology: state of the art and needs assessment. AIP Publishing LLC, S 130001
8. Liu L, Kamm P, García-Moreno F, Banhart J, Pasini D (2017) Elastic and failure response of imperfect three-dimensional metallic lattices: the role of geometric defects induced by selective laser melting. J Mech Phys Solids 107:160–184. https://doi.org/10.1016/j.jmps.2017.07.003
9. Hernández-Nava E, Smith CJ, Derguti F, Tammas-Williams S, Leonard F, Withers PJ, Todd I, Goodall R (2016) The effect of defects on the mechanical response of Ti-6Al-4V cubic lattice structures fabricated by electron beam melting. Acta Mater 108:279–292. https://doi.org/10.1016/j.actamat.2016.02.029
10. Yin Q, Soyarslan C, Isik K, Tekkaya AE (2015) A grooved in-plane torsion test for the investigation of shear fracture in sheet materials. Int J Solids Struct 66:121–132. https://doi.org/10.1016/j.ijsolstr.2015.03.032

Cutting Blades for Food Processing Applications Manufactured Using Innovative Spin Forming



Tim Rostek, Hanna Makeieva, and Werner Homberg

Abstract Cutting blades for various food processing applications are primarily manufactured by standardized grinding processes. This results, on the one hand, in time-consuming and hence expensive production and, on the other hand, in the surface roughness not being optimized in a microbiological manner. This leads to high healthcare costs for foodborne infections. Further, the strength of the cutting blades is additionally less-than-ideal, which causes a high expenditure on wear. Current research work at the Department for Metal Forming Technologies (LUF) is focused on innovative flow-forming processes which have a high potential for manufacturing parts with an excellent surface roughness in short process times. Along with the process-integrated thermal treatment, this is fundamental for the research and development of improved manufacturing technologies for high-performance cutting blades. This paper looks into innovative process strategies for manufacturing parts with locally graded characteristics, improved surface roughness characteristics, and greater strength of the cutting edge.

Keywords Cutting blades · Flow-forming · Incremental forming · High-strength steels · Work hardening

1 Introduction

Knives and cutting tools are used in a wide variety of applications in the food industry. Very different requirements are thus imposed on these knives. They include specific geometries, cutting-edge geometries, wear resistance, corrosion resistance, food safety, and manufacturing costs. For this reason, a large variety of knives exists.

The main focus of the research work carried out is on circular knives and sickle knives for the food industry. From a microbiological point of view, particularly smooth surfaces are required. These reduce the number of bacteria on the cutting

T. Rostek (✉) · H. Makeieva · W. Homberg
Paderborn University, Warburger Str. 100, 33098 Paderborn, Germany
e-mail: tr@luf.upb.de

© The Minerals, Metals & Materials Society 2021

G. Daehn et al. (eds.), *Forming the Future*, The Minerals, Metals & Materials Series,
https://doi.org/10.1007/978-3-030-75381-8_178

tool and the resulting contamination of the food clippings. This reduces the likelihood of food infections due to contamination, which currently also represents an economically significant problem [1]. A smooth surface also prevents clippings from adhering to the knife. This improves process safety. A high level of wear resistance is another requirement for knives. Knives in the food industry are subject to constant wear and have to be replaced as a function of their service life. This leads to downtimes in production and thus to a significant drop in productivity. To sum up, there is thus a need for knives which have a high surface quality and a high wear resistance. At the same time, these knives must be economical to manufacture.

The manufacturing process for knives for the food industry usually consists of several standardized but not adapted process steps. First of all, blanks made from sheet metal are usually thermally sliced. The wall thickness is typically 0.6–5 mm. The diameter of circular knives is typically in the range of 50–220 mm. Subsequently, a near-net-shape pre-deformation can be carried out. This applies in particular to the areas of the cutting edges. The parts are then further produced by grinding. A comparatively large amount of material is removed here. With a typical feed rate of 0.01 mm, the processing time for the production of sickle knives is approx. 1–1.5 h. In addition, heat treatment of the knives is customary in order to adapt the mechanical properties of the knives to their subsequent applications. The hardness of a knife is then in the range of 55–62 HRC. The surface roughness *Ra* is in the range of 1.4–2 µm.

The manufacture of knives for food processing requires a number of forming steps and grinding processes. These are not suitable for ensuring a very good surface quality. Furthermore, the process times are very long. This leads to considerable manufacturing costs, resulting in very high component costs. In addition, a great deal of grinding dust and contaminated cooling water are generated during processing. The appropriate form of cleaning is expensive and pollutes the environment.

The motivation for the research work being carried out is derived from this. The aim is to research a technology kit and associated manufacturing processes for the economical manufacture of industrial knives with a focus on the food industry as shown in Fig. 1.

On the one hand, the central starting point is the use of incremental flow-forming processes. These enable effective shaping, very good surfaces, and the introduction of a high degree of deformation. This is essential for effective work hardening of the material. Formed shapes can also be generated with process control.

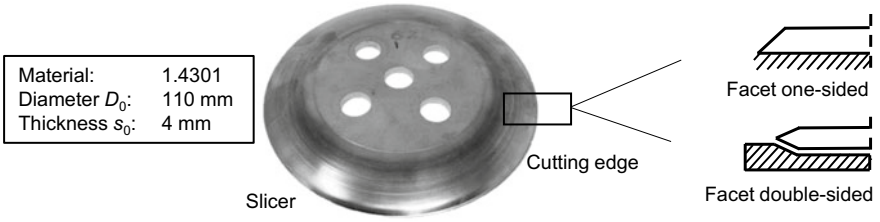


Fig. 1 Knife for the food industries and common facet designs

This enables a high variety of geometries to be generated economically. At the same time, hot forming or heat treatment can also be integrated. This is particularly important against the background of processing innovative steel materials. Furthermore, near-net shapes can be manufactured with good geometrical and dimensional accuracy.

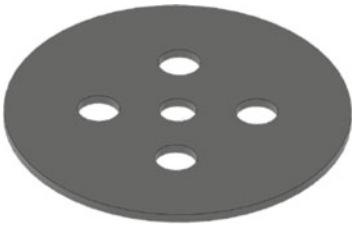
On the other hand, the intention is to use innovative steel materials. Conventionally, primarily martensitic stainless cold work steels have been employed. These are chrome alloyed steels with a high carbon content and secondary hardening properties [2]. They can normally only be formed in the soft annealed condition. Stainless chrome steels with copper as an alloying element are becoming increasingly important for cost reasons [3]. Copper as an alloy element improves formability. Precipitation hardening and work hardening also enable a high strength to be achieved in the corresponding components [4]. This is analogous to maraging steels. The high copper content is particularly advantageous in terms of microbiological aspects (food safety). The high hardness through work hardening and the food safety of these materials are promising for the intended application [5].

A combination of incremental and possibly hot flow-forming processes with the processing of innovative steel materials thus offers a high potential for the cost-efficient production of improved knives. The near-net shaping achieved by means of rollers can reduce the costly machining work. Furthermore, a multitude of geometries can be flexibly produced for a low mechanical outlay through the kinematically controlled generation of the design. In addition, very good surfaces with antibacterial properties can be produced by the flow-forming process. In combination with innovative steel materials, it is possible to increase this potential still further. The high mechanical strength of these steels leads to an increased service life [6, 7]. This produces further cost advantages. Initial research into this is presented in this article.

2 Experimental Setup

The central element of knife production is the flow-forming of sheet blanks to produce a preform for the final grinding process. In this latter process, the cutting edge is sharpened. Round blanks for the experiments were thus cut out of sheet metal by means of laser cutting. Steels 1.4301 and 1.4112 were used as a material., as these materials are common materials for blades for food applications. The round diameter D_0 was 110 mm and the wall thickness s_0 was 4 mm. These are shown in Fig. 2. The corresponding openings are required for mounting on the spindle.

A friction spinning test rig was used for the flow-forming. This is an in-house design by the LUF. It contains a spindle with a holder for sheet blanks with a diameter D_0 of 110 mm. The blanks are centered using dowel pins. In addition, there are two supports that guide the rollers or supporting tool elements. In principle, heating can take the form of inductive heating. Corresponding induction coils can be put in position by industrial robots. In the puncture tests shown below, however, an acetylene–oxygen burner was initially used to heat the blanks shortly before the



Material:	1.4301, 1.4112
Diameter D_0:	110 mm
Thickness s_0:	4 mm

Fig. 2 Round blank sheet for experiments

forming operation. As an alternative, liquid nitrogen was used at a temperature T of −200° C in order to reduce the forming temperature T_f. The friction spinning test rig used is shown in Fig. 3. A spindle speed n of max. 3,000 rpm is set. The feed rate f was in the range of 10–50 mm/min. The spinning rollers had radii R of 1, 2, and 3 mm.

Two process routes were essentially investigated in the research work carried out. On the one hand, this was partial kinematic design generation and full kinematic design generation as shown in Fig. 4. In the former, a sheet metal blank is attached to a holder. The cutting edge is then formed iteratively using a roller. The cutting edge geometry is thus determined by the kinematic movement of the spinning roller and a shape-specific holder. The blank holder must correspond to the desired cutting-edge

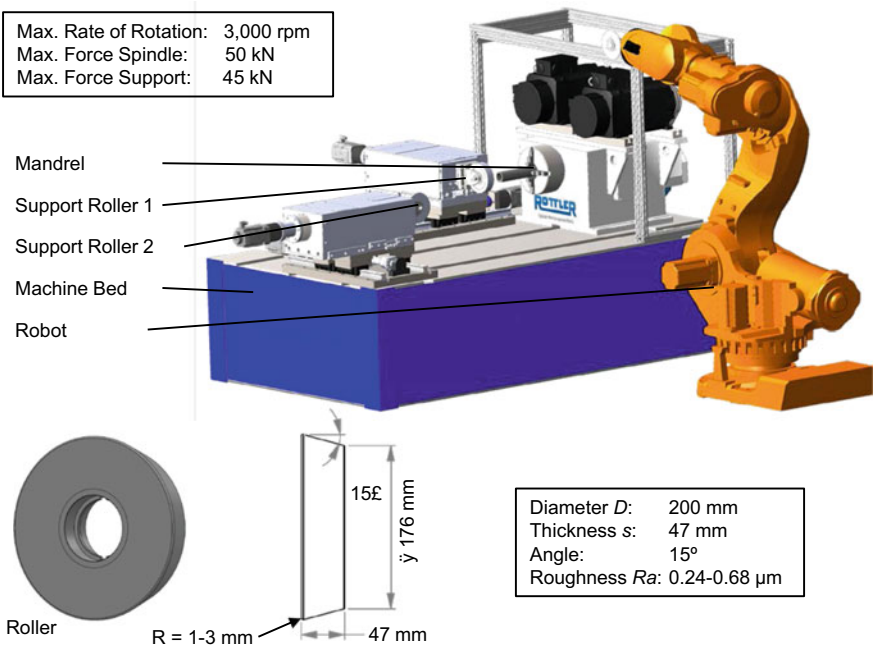


Fig. 3 Friction spinning test rig and roller geometry. (Color figure online)

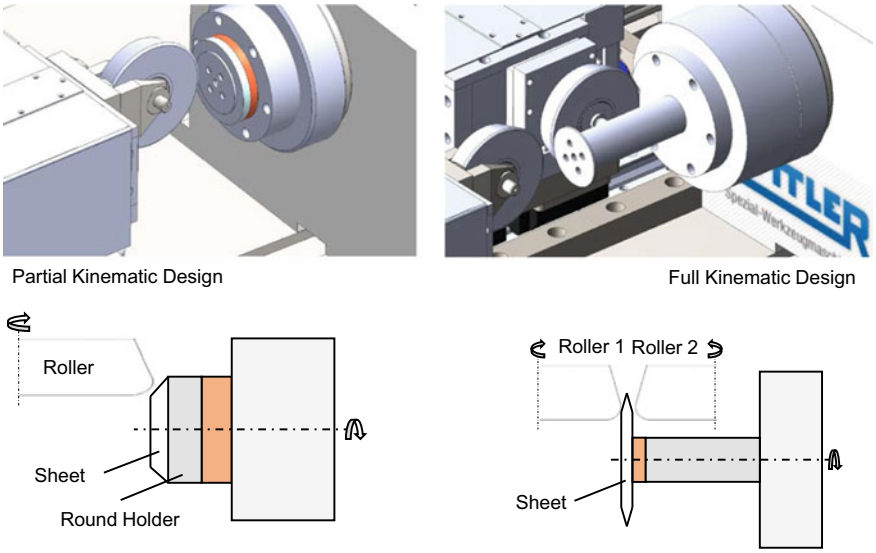


Fig. 4 Partial kinematic design and full kinematic design of flow forming of cutting blades. (Color figure online)

geometry. Different blank holders can thus be used to form different geometries. In the case of fully kinematic design generation, the circular blank is also firmly clamped. The geometry is equally dependent on the kinematic movements of the roller. At the same time, the forming is supported by a kinematically moving counter-roller. Shape-specific blank holders are thus no longer required for the round sheet blank. Nevertheless, an increased outlay results in tooling and adequate machines. At the same time, however, fully kinematic design generation permits significantly greater flexibility with regard to the respective cutting edge geometry without the use of different shape-specific blank holders.

Hardness measurements, metallographic evaluation, and roughness measurements were carried out in order to evaluate corresponding sample components. To this end, samples were taken orthogonally to the cutting edge and examined. Three measurements were carried out for hardness measurements and the arithmetic mean was formed. For the metallographic examinations, the samples were ground, polished, and constricted using Nital. For the roughness measurements, the cutting edge was scanned at three measuring positions for a length l of 5.6 mm. The measurements were carried out all around the circumference at a measuring angle of 10°. The standard deviation is 0.0056 µm. The individual measuring positions are shown in Fig. 5.

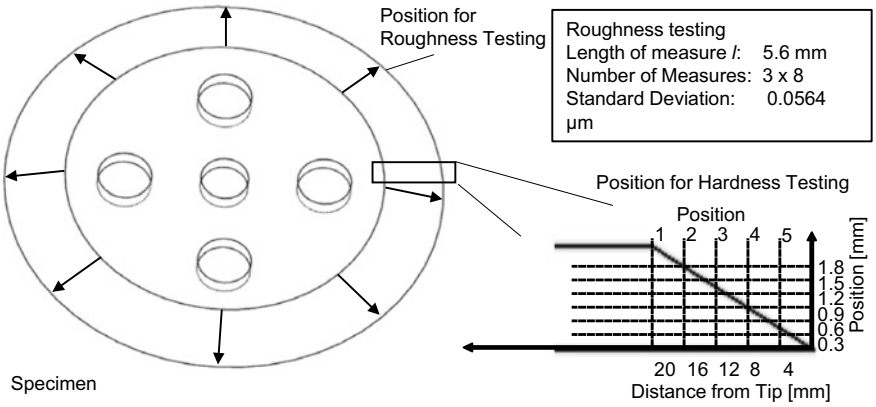


Fig. 5 Positions for roughness testing and hardness testing

3 Results

The results of the experimental investigations are presented below. These include, in particular, the attainable surface quality of the flow-formed surfaces. This is particularly dependent on the feed rate f and the roller geometry or roller dimensions. The microstructure and the resulting mechanical properties are a function, in particular, of the degree of deformation and the forming temperatures T_f. Basically, the cutting edges can be molded in the cold state. This shows that material 1.4112 has an increased springback by comparison to material 1.4301.

3.1 Surface Quality

The roughness *Ra* of the surface is approximately 3.0 µm in the initial state. The cutting edges were processed using various rollers. The spinning rollers have a radius R of 1, 2, and 3 mm. The feed rate f was varied in the range of 10–50 mm / s. The theoretical roughness Ra_{th} can basically be derived from the feed rate f and the tool radius R. Basically, the roughness is reduced with a high feed rate f and an increasing radius R. The relationship between the experimentally determined roughness and the feed rate f and the radius R is shown by way of example in Fig. 6.

The experimental results show that the roughness *Ra* is significantly reduced with an increasing radius R. The feed rate f also has a similar tendency. However, it is noticeable that the influence of the feed rate f decreases as the radius R increases. Furthermore, the processing time for the flow-forming process increases as the feed rate f becomes smaller. With regard to economical production with short process times, high feed rates f with larger radii R are suitable. This leads to a significantly

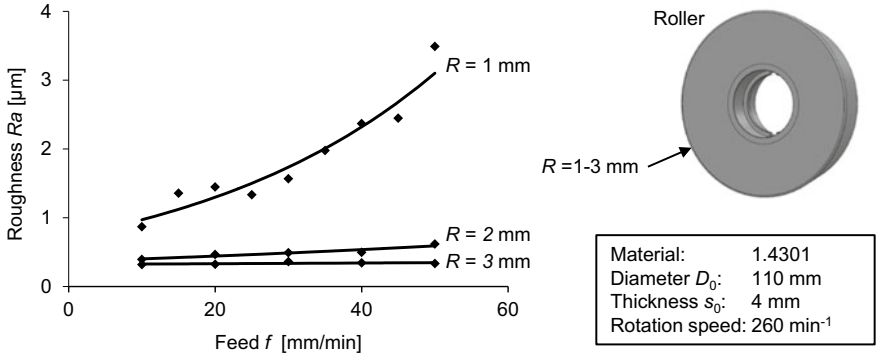


Fig. 6 Influence of feed rate f on the surface roughness *Ra* of a specimen of 1.4301

improved surface quality compared to the initial state. Furthermore, the most economical production possible should be feasible. The speed n has a minor influence on the surface roughness *Ra.* Accordingly, this should be chosen at a high level, aiming for a short process time. The influence of the forming temperature T_f has a minor influence on the resulting roughness *Ra.*

3.2 Mechanical Strength

Metallographic studies have shown that the texture of the structure is significantly influenced by the deformation. The shaping in the area of the cutting edge results in a finer grain structure. This is shown in Fig. 7. This applies, in particular, to material 1.4301.

The mechanical deformation of the material also changes as a result of the forming operation and the microstructure influenced by it. The strengthening increases with increasing deformation. Accordingly, areas that are in contact with the roller have a higher strength. This increases significantly in the direction of the cutting edge. Figure 8 illustrates this. As these areas have to endure the highest mechanical loads and are therefore subject to the highest wear, this is advantageous in terms of service life. Compared to conventionally manufactured knives, this should mean significant added value.

Similarly, the amount of deformation and the forming temperature T_f have a significant influence on the phase transformation from residual austenite to martensite. The higher the deformation, the more residual austenite is converted to martensite. However, this effect decreases significantly with higher forming temperatures T_f. Lower forming temperatures T_f below room temperature intensify this effect. This is shown in Fig. 9. Lower forming temperatures T_f are thus advantageous for

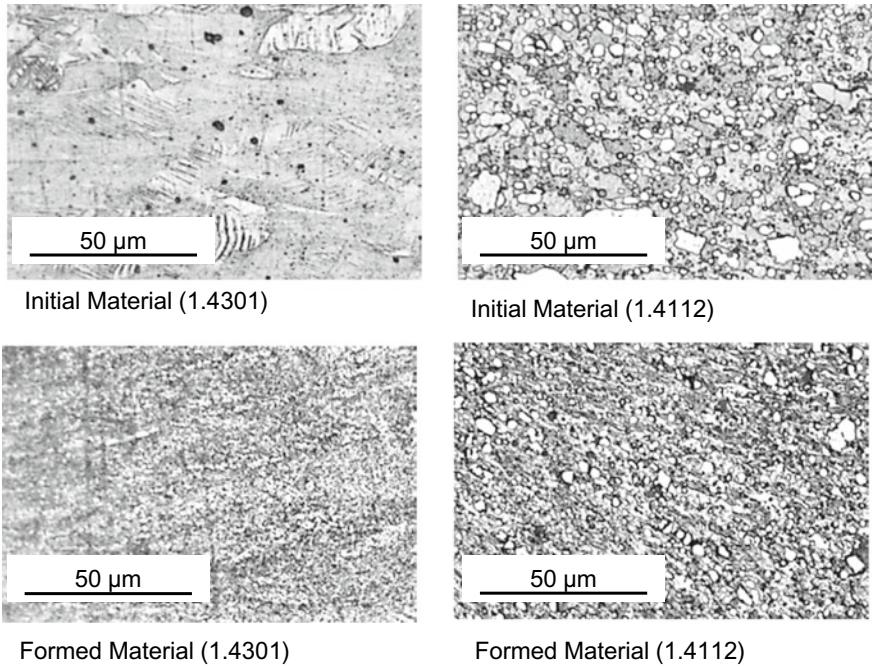


Fig. 7 Influence of deformation on the microstructure of parts made from 1.4301 and 1.4112

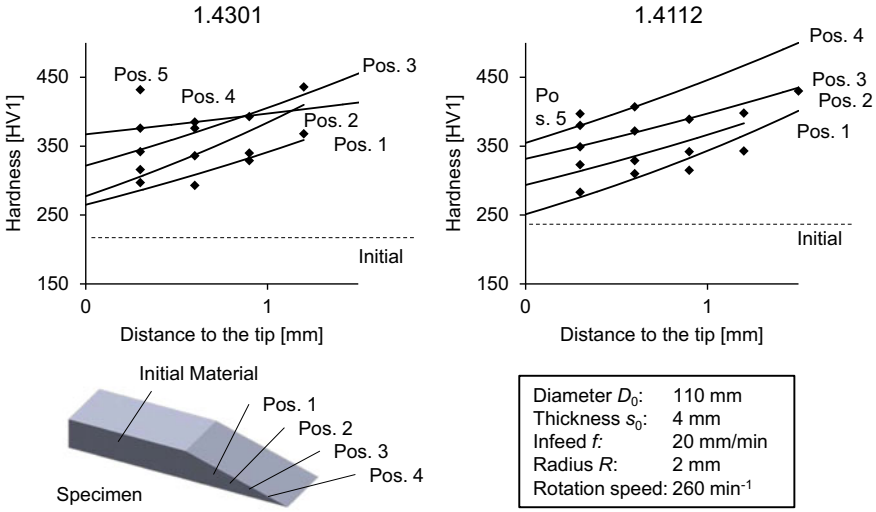


Fig. 8 Influence of deformation on the strength of parts made from 1.4301 and 1.4112. (Color figure online)

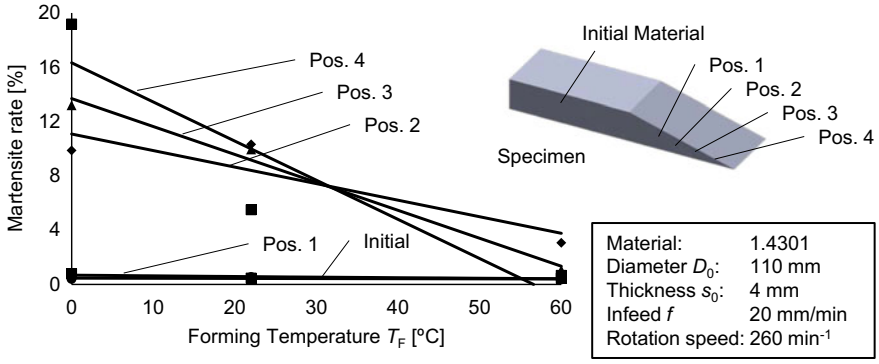


Fig. 9 Influence of forming temperature T_f on the martensite rate of parts made from 1.4301. (Color figure online)

this desired effect.

The above effect is shown in Fig. 10 in relation to the hardness of the material used in accuracy experiments. It becomes clear that the effect requires significantly less deformation, especially at lower temperatures T_f, in order to achieve high strengths. However, this does not change the maximum attainable strength. It can thus be deduced that lower forming temperatures T_F are suitable for high component strengths.

4 Summary

The experiments have shown that the preform for knives can be produced very well by means of flow-forming. On the one hand, very high deformation can be achieved by comparison to conventional processes. This significantly reduces the amount of grinding in subsequent process steps, thus enabling a significant reduction in process times as well as in the cost of material/machining and hence component costs. Furthermore, significantly better surface qualities can be produced. The roughness *Ra* of 0.3 µm is significantly better than that of conventional knives at 1.4–2 µm. This is associated with a better antibacterial effect. With regard to food safety, significantly better product properties are achieved. Greater forming is also achieved by the flow-forming process. In this way, suitable microstructural effects can be exploited. Cold forming opens up significant potential for higher component strengths. The component strength is targeted in the area of the cutting edge, which means it is increased in the area of the highest load in the application. This should reduce wear and improve service life. Further research work also includes the potential for improving product properties and cost-effectiveness. To sum up, however, it can be said that the research

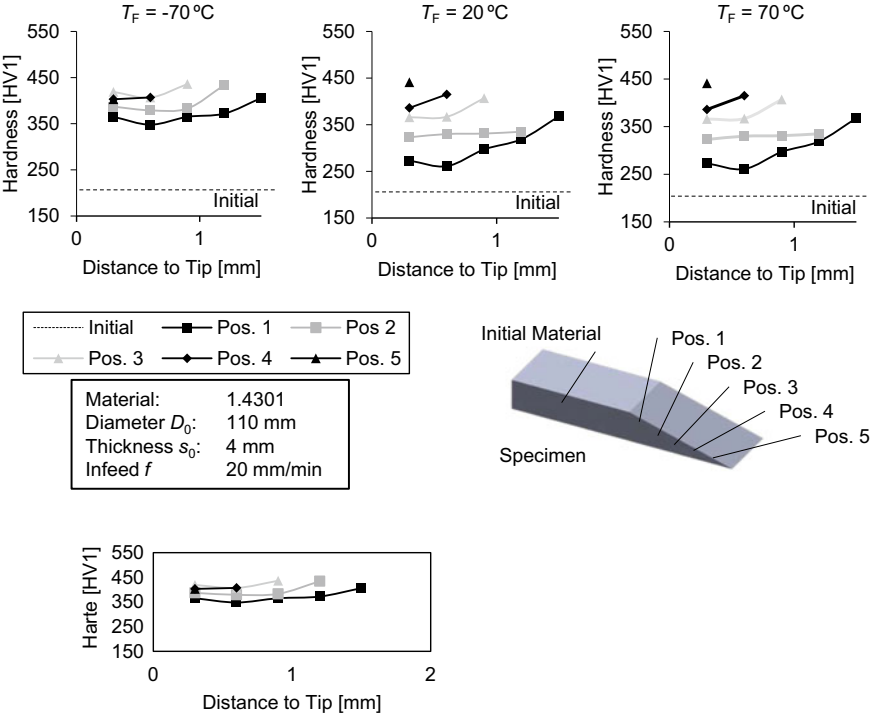


Fig. 10 Influence of forming temperature T_f on the strength of a part made from 1.4301. (Color figure online)

results achieved should make it possible to produce significantly improved knives for the food industry with improved cost-efficiency.

Acknowledgments This research and development project is being funded by the European Union and managed by the Project Management Agency Jülich (PTJ). The authors are responsible for the contents of this publication. The Research project was carried out at the Department for Metal Forming Technology (LUF), Paderborn University, in cooperation with Hermann Jennert GmbH & Co. KG, Wilnsdorf, Matplus GmbH, Wuppertal, DynaWeld GmbH & Co. G, Kamen, Friedr. Lohmann GmbH, Witten-Herbede, Marel Pultry B.V., Boxmeer.

References

1. Scharff RL (2012) Economic burden from health losses due to foodborne illness in the US. J Food Prod 75(1):123–131
2. Ponge D, MiUan J, Raabe D (2011) Design of lean maraging TRIP steels. In: Weng Y, Dong H, Gan Y (eds) Advanced steels. Springer, Berlin, pp 199–208
3. Murthy A (2012) Role of alloy additions on strengthening in 17–4 PH stainless steel. Ph.D. thesis, Missouri University of Science and Technology

4. Panwar S, Goel D, Pandey O (2005) Effect on cold work and aging on mechanical properties of a copper bearing HSLA-100 steel. Bull Mater Sci Bd 28(3):259–265
5. Wang S, Yang C, Shen M, Yang K (2014) Effect of aging on antibacterial performance of cu-bearing martensitic stainless steel. Mater Technol 29(5):257–261
6. Homberg W, Rostek T, Wiens E (2015) Internal flow-turning—an innovative technology for the manufacturing of tailored tubes. Key Eng Mater 639:65–70
7. Wiens E, Homberg W (2017) Internal flow-turning—efficient manufacture of load-adapted tubes with a constant external diameter. In: Paper presented at the 5th international conference on steels in cars and trucks. Amsterdam, Netherlands, pp 18–22

Influence of Axial Feed Rate on Shape and Thickness Changes During Multi-Pass Tube Spinning: Experiments and Modelling



Biplov K. Roy, Yannis P. Korkolis, Yoshio Arai, Wakako Araki, Takafumi Iijima, and Jin Kouyama

Abstract This research investigates the influence of axial feed rate on shape and thickness changes in multi-pass, mandrel-free tube spinning for producing a hemispherical shape at room temperature. The target shape is formed experimentally by 7 spinning passes from annealed, pure aluminium AA1070 tube. The experiments are conducted with two different axial feed rates, i.e. 2 and 7.5 mm/rev. It was found that increasing the axial feed rate generates lower elongation and higher thickness change. In every experiment, the tube wrinkled at some point during the process, due to the high radial feed. A 3D elastic–plastic finite element (FE) model of the multi-pass tube spinning process is described. The influence of the axial feed rate on axial wrinkling, tube elongation, and thickness change is discussed through the comparison between experimental and FE prediction results.

Keywords Tube spinning · Multi-pass · AA1070-O · Hemispherical shape · Axial feed rate

1 Introduction

During the past few years, new demands of the market caused the development of new methods of manufacturing seamless, dimensionally precise axisymmetric products like a pressurized spherical fuel tank. Tube spinning is one of the most popular incremental metal forming processes that satisfy the demanded agility and versatility of the market. The process is capable of using a variety of workpiece sizes

B. K. Roy (✉) · Y. Arai · W. Araki
Saitama University, Saitama, Japan
e-mail: biplov@duet.ac.bd

B. K. Roy
Dhaka University of Engineering & Technology, Gazipur, Bangladesh

Y. P. Korkolis
The Ohio State University, Columbus, USA

T. Iijima · J. Kouyama
Asahi Seisakusho Co. Ltd, Saitama, Japan

© The Minerals, Metals & Materials Society 2021

G. Daehn et al. (eds.), *Forming the Future*, The Minerals, Metals & Materials Series,
https://doi.org/10.1007/978-3-030-75381-8_179

with a wide range of thicknesses [1]. In comparison with an alternative process, e.g. deep drawing, tube spinning exhibits low deformation force, low production cost, simple tooling, and increased process flexibility.

In the spinning process, the final part is obtained by the localized plastic deformation induced by the roller contact. Due to the complex and rotary incremental nature of the manufacturing process, it is essential to predict the effects of process parameters early-on in product development. Among the various process parameters of tube spinning, axial feed rate (mm/rev.) and radial feed rate (mm/pass) play a vital role in the successful manufacturing of the desired product. The axial feed rate (mm/rev.) is defined by the rate of roller movement in the axial direction to the rotational speed of the chuck, and the radial feed rate (mm/pass) is defined by the ratio of roller movement along the radial direction for each spinning pass. Previous researchers [2–5] performed experiments on tube spinning and reported that an optimum feed rate is important for the product quality. Numerous researchers [6–13] have conducted FE simulations of tube spinning to understand the effect of spinning parameters, e.g. feed rates in axial and radial direction, roller path and geometry and contact condition, etc. Process design for tube spinning is inherently difficult due to their complexity in many process control variables; the virtual process makes the use of process models highly attractive as a means of eliminating the need for trial error.

The main aim of this study is to investigate the influence of axial feed rate on shape and thickness changes in multi-pass, mandrel-free tube spinning for producing a target shape at room temperature. A finite element (FE) 3D model is developed for virtual process investigation, and its capabilities as a prediction method of the final shape and thickness of this process are analyzed.

2 Experiments

An annealed AA1070-O tube with outer diameter of 100 mm, average thickness of 3 mm, and overhang of 150 mm was selected to produce a target shape. The roller used had diameter of 158 mm and nose radius of 12.5 mm. The spinning experiments were performed on a computerized numerical control (CNC) spinning machine, at room temperature. A schematic of the experimental setup is shown in Fig. 1a.

The angle of attack angle of the roller with respect to the tube was kept at 45°. The axial and radial movement of the roller was controlled according to linear spinning pass as shown in Fig. 1b. A series of experiments were carried out for two different axial feed (AF) rates: 2 and 7.5 mm/rev. The radial feed rate was constant for each experiment, and equal to 5 mm/pass. The shape and thickness of the tubes after spinning were measured. For shape measurement, a 3D contact gauge (Model: Master3dGage™ with laser scanning marker accuracy of ±40 μm) was used. Thickness was measured by a point micrometre, from the free end.

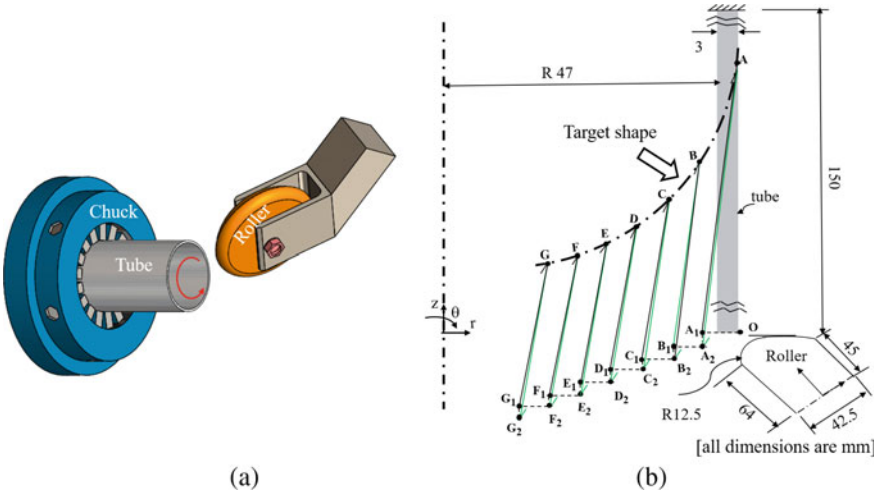


Fig. 1 **a** Schematic of the experimental setup, **b** Spinning pass and roller starting position. (Color figure online)

3 Finite Element Models for Tube Spinning

The explicit commercial FE code Abaqus 6.14 was used to simulate this process. The tube was considered an elastic–plastic deformable solid and the roller was modelled as a rigid analytical surface with the same dimensions and attack angle to the tube as in the experiment. Rate-independent, isotropic hardening using associated flow-rule based on the von Mises yield surface was assumed for the simulation. A Voce-type [14] large-strain hardening curve was fit to the experimental data of Ref. [15]. The fitted curve is shown in Fig. 2a, and the fitted Voce hardening equation parameters are listed in Table 1. The other material properties used in the model are listed in Table 2. Figure 2b shows the detailed arrangement of FE model for spinning. The geometry of the model replicated the geometry of the experiment exactly. For meshing, the C3D8R, continuum, 8-node linear brick element with reduced integration and hourglass control was adopted. The tube was discretized with 34,800 elements, with 104 elements along the circumference and 5 elements through the thickness. The mesh was refined in the contact zone and its nearby region (Fig. 2c).

The boundary conditions for this process were split into three stages as in the experiment: clamping the tube-end, rotating the tube, and performing the multi-pass tube spinning by the displacement of the roller.

The roller axial and radial movements were given according to the design spinning pass as shown in Fig. 1b. The penalty contact algorithm and Coulomb's friction law were adopted in this FE model. The friction between the tube and roller was assumed to be relatively low, so a frictionless status was adopted in this FE model. To reduce the computational cost, the deformable contact surface was divided into many parts,

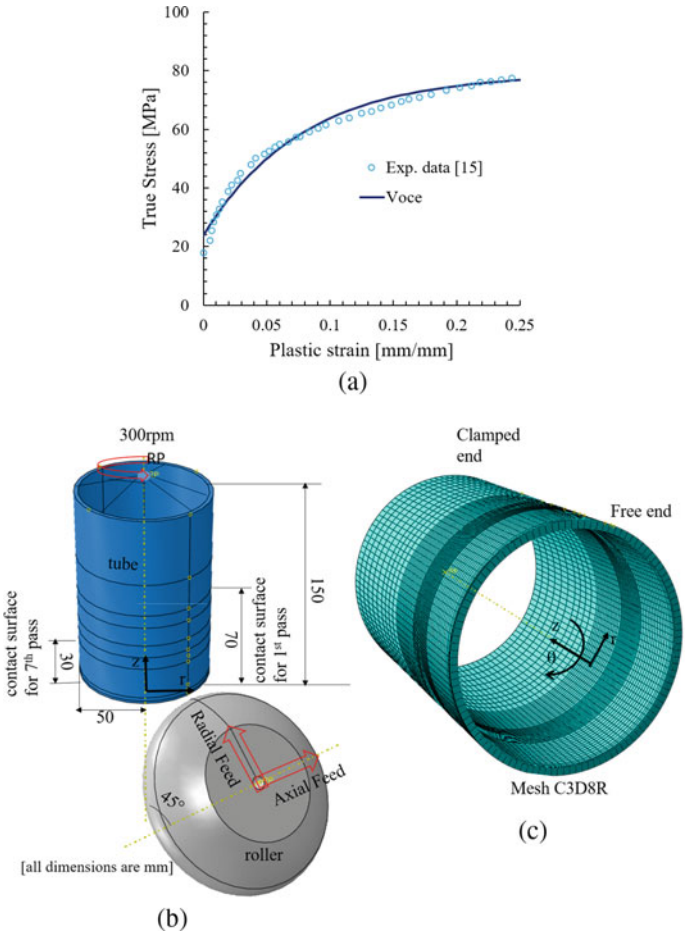


Fig. 2 **a** Voce hardening curve, **b** schematic of the FE model for multi-pass tube spinning simulation, **c** mesh distribution along the tube length. (Color figure online)

Table 1 Voce hardening parameters

$\sigma_{(voce)} = L_0 - q exp\left(-\beta \varepsilon_p^t\right)$		
L_0 (MPa)	β	Q (MPa)
78.9	55.2	12.1

Table 2 Material property

Material: AA1070	
Young's modulus	69 GPa
Poisson's ratio	0.33
Initial yield stress	24 MPa
Density	2700 kg/m^3

each active during a different spinning pass, as shown in Fig. 2a. To speed up the simulation, the mass scaling method was adopted, using a scaling factor of 64.

4 Results and Discussion

4.1 The Influence of Axial Feed Rate on the Deformed Shape

The target shape progressively developed after 7 spinning passes. Figure 3 shows the outer shape of the tubes spun with low and high axial feed rates (AF 2 and 7.5 mm/rev.). The figure demonstrates that the deformed tube is wrinkled at a specific space on the hemispherical shape region, see the top magnified image in Fig. 3.

The figure also shows that the deformed tube in the conical region is elongated in the low axial feed rate case (AF 2 mm/rev.) and shortened at the high one (AF 7.5 mm/rev.), see the lower magnified image in Fig. 3. Therefore, it appears that the toolpaths examined in this study (see Fig. 1b) can provide approximately correct shapes, but still need improvement.

Figure 4 shows a comparison of the sectional view of final shapes in experiments and FE predictions. It confirms that the simulation predicts elongation and shortening with the change of axial feed rates as in the experiments. Furthermore, the FE model also predicts the wrinkled shape during multi-pass spinning. Figure 4 also illustrates that, in the case of high axial feed rate, the sectional view of the deformed tube is of poor quality (see Fig. 4a). In contrast, the surface quality of the deformed tube becomes smooth during low axial feed rate spinning (see Fig. 4b).

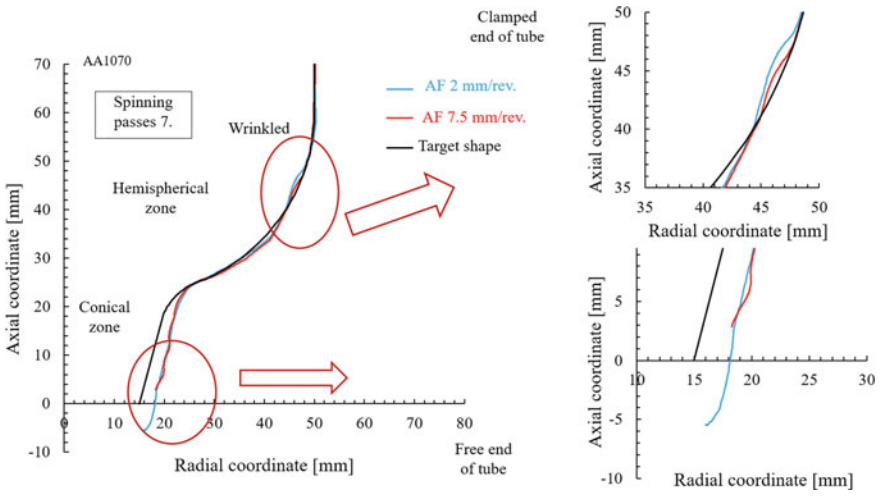


Fig. 3 Comparison of the tube shape at different axial feed rates. (Color figure online)

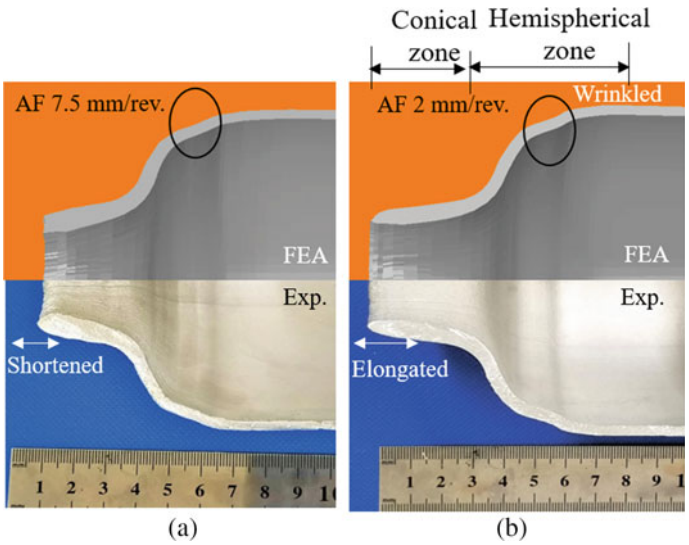


Fig. 4 Comparison of final deformed shape at different axial feed rates experiment and FEA predictions: **a** AF 7.5 mm/rev., **b** AF 2 mm/rev. (Color figure online)

4.2 The Influence of Axial Feed Rate on the Thickness Change

Figure 5 shows the influence of the axial feed rates on the thickness change of the deformed tube. Due to the limitation of the measuring thickness by micrometre, the simulated results are compared with the experiments on the free-end-zone only.

The figure shows that in the conical zone region, the change in thickness is lower during low axial feed rate (2 mm/rev.) than during high (7.5 mm/rev.). Previous researchers [3–7] also observed the same tendency during the spinning process. The FE predicts the thickness increase in the free end-zone quite well, as well as the influence of axial feed rate on the thickness change in the conical shape region. In the hemispherical zone region, the influence of the axial feed rate is quite low. The average deviation between predicted and measured thickness is approximately 5%.

5 Conclusions

This study analysed numerically and experimentally the shape and thickness changes at different axial feed rates for room temperature, mandrel-free, multi-pass spinning of AA1070 tubes. The intent was to develop a realistic virtual method for selecting spinning process parameters. In the future, this model will be used to determine the

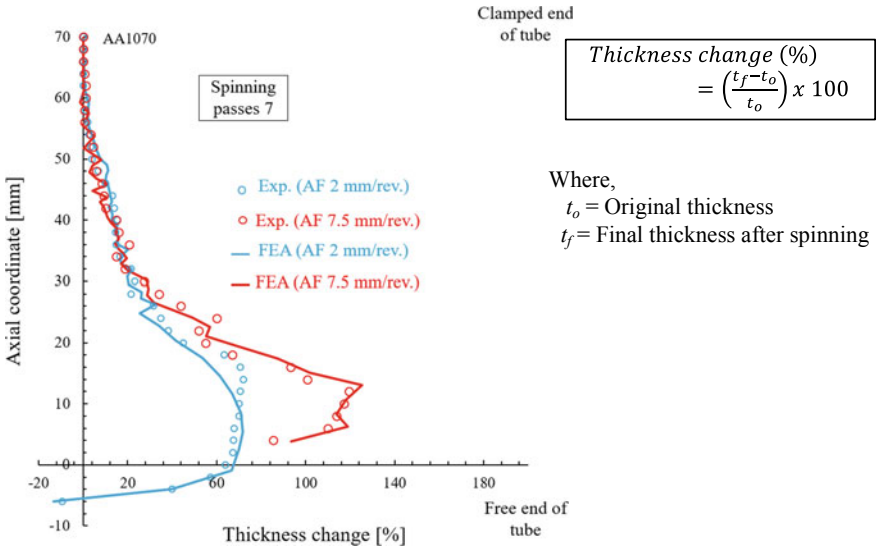


Fig. 5 Comparison of thickness changes experiments and FE prediction at different axial feed rates. (Color figure online)

optimum process parameters for producing a smooth product. The results lead to the following conclusions:

- The axial feed rates play a vital role in the shape and thickness change during tube spinning. A low feed rate produces higher elongation and lower thickness change than a high one.
- The 3D FE modelling of the spinning process can predict the significant plastic deformation of complex shape forming, including the shape and thickness with different axial feed rates.
- The large-scale thickness change occurred in the conical zone region due to significant diametral reduction both in the experiments and FE predictions.
- The FE predictions show that in the hemispherical zone, the thickness is insensitive to the axial feed rate.
- Both experiments and FE predictions show axial wrinkling in the same region due to the high radial feed rate.

Acknowledgments The financial support from the Ministry of Education, Science, Sports, and Culture, of the Government of Japan, is gratefully acknowledged. The authors would also like to thank the Saitama University machine shop for helping with the 3D contact measurements.

References

1. Music O, Allwood JM, Kawai K (2010) A review of the mechanics of metal spinning. J Mater Process Technol 210(1):3–23. https://doi.org/10.1016/j.jmatprotec.2009.08.021
2. Srinivasulu M, Komaraiah M, Rao CKP (2012) Experimental studies on the characteristics of AA6082 flow formed tubes. J Mech Eng Res 4(6):192–198. https://doi.org/10.5897/JMER11.063
3. Yao J, Murata M (2005) An experimental study on spinning of taper shape on tube end. J Mater Process Technol 166(3):405–410. https://doi.org/10.1016/j.jmatprotec.2004.08.025
4. Yao J, Murata M (2002) Effects of indented feed of roller tool on parallel spinning of circular aluminum tube. J Mater Process Technol 128(1–3):274–279. https://doi.org/10.1016/S0924-0136(02)00465-X
5. Akkus N, Kawahara M (2006) An experimental and analytical study on dome forming of seamless Al tube by spinning process. J Mater Process Technol 173(2):145–150. https://doi.org/10.1016/j.jmatprotec.2005.11.011
6. Zoghi H, Fallahi Arezoodar AF, Sayeaftabi M (2012) Effect of feed and roller contact start point on strain and residual stress distribution in dome forming of steel tube by spinning at an elevated temperature. Proc Inst Mech Eng B 226(11):1880–1890. https://doi.org/10.1177/0954405412461325
7. Zoghi H, Arezoodar AF, Sayeaftabi M (2013) Enhanced finite element analysis of material deformation and strain distribution in spinning of 42CrMo steel tubes at elevated temperature. Mater Des 47:234–242. https://doi.org/10.1016/j.matdes.2012.11.049
8. Zhan M, Zhou Q, Yang H, Zhang J (2007) Establishment of 3D FEM model of multi-pass spinning. Chin J Mech Eng-En 20(4):19–23. https://doi.org/10.3901/CJME.2007.04.019
9. Huang CC, Hung JC, Hung C, Lin CR (2011) Finite element analysis on neck-spinning process of tube at elevated temperature. Int J Adv Manuf Tech 56(9–12):1039–1048. https://doi.org/10.1007/s00170-011-3247-0
10. Wong CC, Lin J, Dean TA (2005) Effects of roller path and geometry on the flow forming of solid cylindrical components. J Mater Process Technol 167(2–3):344–353. https://doi.org/10.1016/j.jmatprotec.2005.05.039
11. Roy BK, Korkolis YP, Arai Y, Araki W, Iijima T, Kouyama J (2018) Experiments and simulation of shape and thickness evolution in multi-pass tube spinning. In: IOP Conference Series, No 1, p 012087. https://doi.org/10.1088/1742-6596/1063/1/012087
12. Hua FA, Yang YS, Zhang YN, Guo MH, Guo DY, Tong WH, Hu ZQ (2005) Three-dimensional finite element analysis of tube spinning. J Mater Process Technol 168(1):68–74. https://doi.org/10.1016/j.jmatprotec.2004.10.014
13. Parsa MH, Pazooki AMA, Ahmadabadi MN (2009) Flow-forming and flow formability simulation. Int J Adv Manuf Tech 42(5–6):463–473. https://doi.org/10.1007/s00170-008-1624-0
14. Voce E (1948) The relationship between stress and strain for homogeneous deformation. J Inst Met 74:537–562
15. Takahashi H, Moro J, Tsuchida S (1998) Plastic anisotropy in aluminium drawn tubes. Met Mater Int 4(3):380–385. https://doi.org/10.1007/BF03187796

A Brief Review on Theoretical Aspects of Bar Straightening with Recent Developments in Its Modelling, Simulation, Control System, and Stabilization



Sanjib Roy, Arun Kiran Pal, and N. K. Das Talukder

Abstract This paper presents a brief review of various research done on bar straightening. Bar straightening can be considered as a significant process in the value stream of bar production. The paper dealt briefly on various types of arrangements available in bar straightening process. The theoretical perspectives have been looked into in simplified manner. Residual stresses, curvature, and bending moment thereof due to reverse kinematic bending have been discussed. A system approach has been taken as how development on bar straightening process emerged over the years. The recent developments in bar straightening using modelling / numerical modelling give an insight of reduction in curvature after reverse bending. Simulation/Numerical simulation approaches in bar straightening process have been looked into. Key aspects like positioning of rolls and minimization of straightness errors have been considered. How control system is applied with Multi-Step Straightening Control System (MSSC) in reducing curvature has been discussed. The paper has been intended to present an overall view of bar straightening from inception till modern times.

Keywords Kinematic loading · Residual curvature · Straightness · Bauschinger effect · Cross-roll straighteners · Rollers

1 Introduction

Production of various types of beams and bars including round bars of various sizes and lengths are quite common requirement in industries as these are used many times directly as raw materials in fabrication of structures or sometimes used as a raw material to produce designed product as per specifications. Like many products as they come out from shop floor requires inspection to ascertain quality uprightness so that imperfections are within acceptable quality limits; the bars are of no exception. With the advent of high speed turning, straightness requirement of drawn bars

S. Roy (✉) · A. K. Pal · N. K. Das Talukder
Jadavpur University, Salt Lake Campus, Kolkata 700098, India

© The Minerals, Metals & Materials Society 2021

G. Daehn et al. (eds.), *Forming the Future*, The Minerals, Metals & Materials Series,
https://doi.org/10.1007/978-3-030-75381-8_180

increased due to imperfections of drawing process. The imperfections of such drawn bars through drawing process essentially called for further straightening process.

Long bars as produced through various rolls are sometimes compromised with degree of straightness either at various sectional lengths or as a whole. It is therefore essential to look into the various quality aspects before the products are out of shop floor. Small diameter round bars are often intentionally coiled to save storage and transportation cost. Therefore, straightness of such products is indeed an issue before they are actually employed further into job, batch, or mass production.

The straightness of drawn bars is often compromised due to imperfections of the drawing process; therefore a straightening operation becomes essential. In production of long products, straightening process through rollers is often the terminal step [1]. Cross-roll straightening is quite a common straightening technique in which the bars are cyclically bent with varying amplitude. The round bars to be straightened are bent and simultaneously rotated as they pass between a set of two rolls, i.e. one being a convex while the other is concave or some other arrangements of cross-roll.

Theoretical aspects of bar straightening start with bending, more specifically reverse bending which is actually necessary to mend the already bent item. The concept of application of bending moment and consequent curvature in a beam is quite old [2]. Brazier indicated that bending moment increases as curvature increases initially in Bending moment–Curvature diagram and reaches a maximum value at a point then decreases even with the increase of curvature up to a certain point.

In case of round bars and tubes, on deformation, the circular shape of the cross section undergoes change and takes an elliptical shape. Deformation relationship can be established as done by Ades [3]. Determination of shape of cross section of tube is possible as a function of bending moment and longitudinal curvature by application of principle of least work when subjected to stress in the plastic range. Although both the works were primarily on the shape of tubes and on ovalisation of circular sections, sufficient indication is available on the relationship of application of the bending moment and curvature of bar when subjected not only in elastic range but also in plastic range. The present study is largely on solid bars.

2 Types of Straighteners

There are many different types of rotary straighteners [4] based on number of rollers, arrangements of rollers, types of rollers. In all the rotary straighteners, the rollers are usually of concave hyperbolic contour, but in some special cases, the cylindrical or drum type is used. There has been advancement over years in the design of bar straightening machines [5]. There are several types of cross-roll straightening machines with different roll arrangements. Various types of machines are in use. Each type has superior advantage in specific circumstances. Cross-roll straightening machine or reeling machines are most popular. In cross-roll straighteners, there are several combinations of idle and driven roll arrangements. Beside these machines,

there are section straightening machines and stretch straightening machines which are used for straightening purposes.

2.1 Section Straightening Machines

Section straightening machines are of cantilever design. These machines are based on the process of rotary straightening. Section Straightening Machine is known for its robust construction, high level resistance, and optimum stability. The Section Straightening Machines are used to straighten rolled steel sections like angle, channels, rounds, beams, etc. Straightening Rolls are made according to section. Some manufacturers use Adamite material (a kind of high carbon steel with carbon percentage ranging from 1.35 to 2%) for rolls [6].

2.2 Stretch Straightening Machines

Stretch straightening machines grip both ends of the bar and exert a certain amount of tension to the bar in order to straighten it. Extrusion stretch straightening and forming is a fast, economical, and accurate way to straighten and form large extrusions. This process involves stretching an extrusion to yield, followed by straightening and forming over a tool. Stretching profiles are made between the two heads, fixed and mobile. The movable head is usually set to the length of the expandable profile. The distance between the heads can be controlled through laser system [7].

2.3 Cross-Roll Straightening Machines

Cross-roll straightening machines are designed for straightening of both tubes and bars of circular cross section. The rolls are mounted at an angle to the line of pass. The material or bar rotates as it proceeds through the machine. Although there are several types, generally four basic types of cross-roll machines are in use which may be put as below [5]

1. Two-roll Straighteners or Reeling machines
2. Six-roll types (six rolls which are mounted in a set of three pairs)
3. Multi-staggered roll types having five, seven, or even ten rolls
4. Cluster-roll machines having seven rolls. A set of two-clusters each cluster is made of three-rolls and another roll at centre, i.e. deflecting roll.

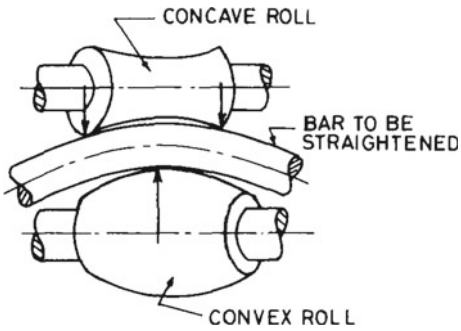


Fig. 1 Straightening of bar in a two-roll 'Air-Bend' machine

2.3.1 Two-Roll Bar Straighteners or Reeling Machines

Two-roll Bar Straighteners or bar straightening machines comprises one convex roll and one concave roll. The ends of concave roll act as horns while the convex roll can exert reverse load at centre of the bar to be straightened. The bending of round bar takes place across horns of the concave roll. Reeling machines are classified again into two types which are as below

(a) Free-bend straighteners or Air-bend straighteners
(b) Line-contact type rolls straighteners.

In free-bend or air-bend straighteners as illustrated in Fig. 1, the application of load is concentrated at a point [8, 9]. This means that loading pattern is actually like simply supported beam with a centralised load. The relevant equations of concentrated load acting on simply supported beam are useful here. The span of the horns may be considered as beam length.

On the other hand, in line contact roll straighteners, the bar happens to be deformed between a set of two rolls. The deformation so occurs can be considered as equivalent to conventional simply supported beam which is loaded uniformly over the length or simply uniformly distributed loading. Loading on the beam is across the span which may be called as 'beam length' of the bar. In this bar straightening machine, angular adjustment of rolls is possible from 5 to 10° for air-bend and 10°–20° for line contact roll straighteners.

2.3.2 Six-Roll Straighteners

As the name suggests, six-roll straighteners are having six rolls. The rolls are mounted in a set of three pairs as shown in Fig. 2. The beam length is more or larger in case of six-roll straighteners in comparison to free-bend or air-bend straighteners. However, loading is distributed but over a span of small length which is in line contact, i.e. near mid-span of the bar [8, 9].

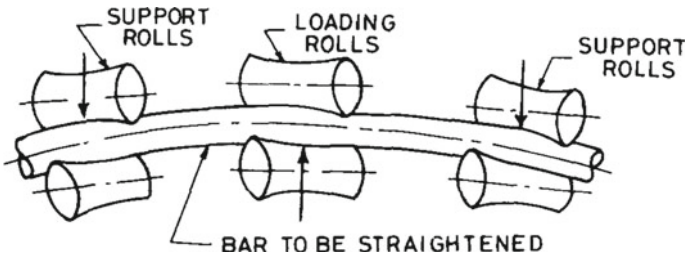


Fig. 2 Straightening of bar in a six-roll straightening machine

In this case, there are support rolls which are at the end and rolls at centre are actually the loading rolls. In this machine, mean value of angular adjustment of rolls is about 30°.

2.3.3 Multi-Staggered Roll Types Having Five, Seven, or Even Ten Rolls

As the name indicates these machines have staggered rolls and number of rolls is five rolls, seven rolls, or even ten rolls. The rolls are so arranged that it functions like practically number of "loading bays" and at each loading bay beam length is subjected to a point load or concentrated load and acting at opposite directions at consecutive bays. In this machine, angular adjustment of rolls is possible up to 35°.

2.3.4 Cluster-Roll Straighteners

In cluster-roll straightening machines, there are seven rolls which are arranged in a set of two-clusters of three-rolls each along with one roll at centre which is for deflecting purpose. The beam length of these machines is considered as simply supported. The concentrated point load is at mid-span. In this case, the beam length is as similar as six-roll straighteners. The beam length is also higher than free-bend straightening machines or air-bend straighteners.

2.4 Spinner Straighteners

Spinner straightening is the first process before cross-roll straightener. Spinner straightening is a process of straightening resistant materials mechanically as cold working. A typical application is in wire production. Wire is pulled through high speed, rotating rollers made of bronze which gives torsional twist resulting in condition of straightness. While feeding movement is given to the bar end but rotational movements are given to the dies. The resultant deformation leads to decrease in yield stress value which makes it strained and also softened. Initial curvature can

be eliminated by spinner straightening. As wire rods are usually available in coiled form, hence spinner straightening is quite helpful to straighten short-span curvatures which periodically exist [10].

2.5 Pulse Straightening

In this straightening system, high tensile wire which is to be straightened is pulsed in special machines which give magnetic pulse treatment taking into account the effect of hyper plasticity. The specific advantage of this machine is that it permits straightening of highest tensile wire. In this process, tensile yield stress is not altered. The process results in smoother surface of wire, hence less friction [11, 12].

There are two kinds of internal straightening methods in straightening machine, the first is rotary hub straightening, the other is parallel roller straightening [13].

2.6 Rotary Hub Straightening

In rotary straightening, the straightening block is usually installed in the straightening mechanism of the hub. Through high speed rotation and staggered arrangement of straightening blocks, the wire rod is bent many times in the process of moving forward, and gradually tends to be straight. This straightening method straightens the steel bar with good straightness and fast speed, but it causes damage to the surface of the steel bar [13].

2.7 Parallel Roller Straightening

The straightening method is parallel-roll type roller straightening CNC steel bar straightening machine. The wire rod steel bar meshes through two rows of staggered multi-wheel press roll groups, which directly deforms the steel bar to be straightened, so as to achieve the purpose of straightening. Although the speed of this straightening method is slightly slower than that of rotary straightening equipment, the straightness of steel bar can meet the construction requirements, and this straightening method does not damage the steel bar [13].

2.8 Skew-Roll Straightening Machine

This straightening machine is designed and built to straighten very small stainless steel medical tubing [14]. Using identical hyperbolic profiles of rolls, accurate tube

can be achieved [15, 16]. These machines are available in 3 × 3 skew roll designs or 5 × 5 skew roll designs. This straightening machine is designed and built to straighten very small stainless steel medical tubing.

These bar straightening machines individually have certain advantages and disadvantages. In order to make right selection of machine, it is necessary to consider the type of material being fed, the degree of straightness required, surface finish, machine capacity, and straightening speeds, etc. Two-roll straighteners are used for improving surface finish. The speed at which the process of straightening can be operated depends upon the degree of control that can be applied to the rotating material. All cross-roll straightening machines cause bar material to rotate during straightening operation. Obviously, a long badly bent bar cannot be rotated as fast as a short and fairly straight bar.

3 Theoretical Aspects

The concept of working on bar in plastic range prevailed well, and Tokunaga [4] reported that certain phenomenon of residual stresses is in place. Tokunaga stated that residual stress distribution in the bar by rotary straighteners represents alternate vortex of tensile and compressive stress zones around the centre of bar, which is not affected by repeated rotary bending. As the entire discussion is on straightening of bars, it is imperative that searches were on how better straightness can be achieved.

3.1 Straightness

Since, it is quite usual that available bars in market are seldom straight and degree of straightness varies. Degrees of straightness (commercial straightness) from 1 in 750 to 1 in 5000 can be achieved. Kemshall [5] indicated that degree of straightness depends on type of machine selected. Residual stress developed during straightening and straightness of finished bar depends on the applied loads in straightening machines [17]. In case, better straightness is to be achieved, then the bar in question has to be bent more severely at the point of application of load so that curvature reduces and consequently straightness improves [4]. These features of improvement of straightness were achieved through rolls, more specifically in cross-roll arrangements. It has been stated that multiple rotary bending helps improving degree of straightness. Rotary straighteners having oblique rollers are preferred to be used for straightening process of round bars.

3.2 Plastic Deformation

In the straightening machine, bars are subjected to elasto–plastic deformations as it undergoes alternate bending under high magnitude of loads [17]. Tokunaga stated that two zones surround the centre of the bar which undergoes no plastic deformation and retains initial deformations. Residual stress distribution of section of the bar and zones left by the compressive residual stress and tensile residual stress, respectively, surround the centre of the bar which do not undergo any plastic deformation. The residual stress of the plastic zone builds up residual moment to the centre of the bar.

The bending moment arising out of residual stresses rotates accordingly as sections change between pitch lengths (the length of bar advanced during revolution) of the bar in straightening. Tokunaga indicated that the bar and tubing straightened by rotary straightener can be considered as spring coil form which has very small coil diameter and pitch length. But the centre of this coil is affected by the core of the bar which is not straightened and retains the initial bend. Tokunaga inferred that bar and tubing are straightened more exactly which have smaller residual stress, when rotary straightener is used by a method which applies more severe bend. This involves more multiple rotary plastic bending at the period of the reducing bending moment.

In case of bar straightening, loads are applied externally. The deformation response of tubular structure or a bar may be analysed to assess structural integrity [17]. Using Ludwik power law equations [18], the effects of creep and plasticity are allowed for as an adjustment to initially elastic conditions. Stress (σ)—strain (ε) relationship can be expressed using Ludwik power law [19]:

$$\sigma = C\varepsilon^n$$

where C is constant stress,

n is an exponent of strain-hardening ($0 \leq n \leq 0.5$).

This can lead to pessimistic or conservative results of the structure [17]. Hence, for the purpose of realistic predictions, it is essential to have good 'constitutive relations' which may reflect true behaviour of material accurately. If the material in question can be considered that as it happens to 'remember' its previous loading history, then its subsequent behaviour can fairly be predicted with the help of related equations. This is indicated to some extent by Bauschinger effect [20].

3.3 Bauschinger Effect

Bauschinger effect is a phenomenon which is defined as reducing the proportional limit or elastic limit (elastic limit is actually slightly above the proportional limit) in compressive load or simply compression after following previous tension or tensile loading and vice versa. If the deformation caused is considered in one direction only,

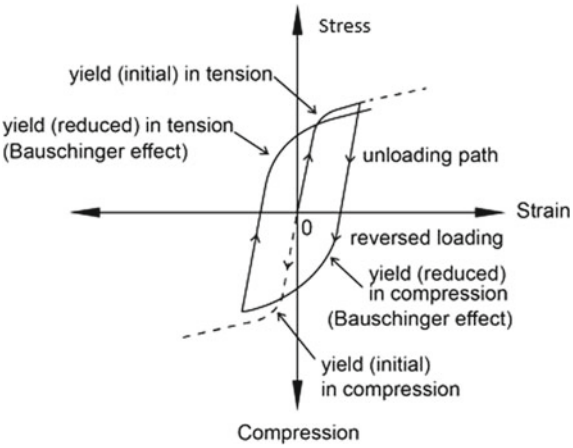


Fig. 3 Illustration of Bauschinger effect

reloading the specimen in simple compression will show the elastic limit appreciably smaller in magnitude than that of the previous yield point. This occurs whenever there is a reversal of stress. The lowering of the yield stress as indicated in reversed loading is primarily caused by the residual stresses. This residual stress is actually left in the specimen on a very small or microscopic scale due to the different stress states in the individual crystals of the material that the specimen is made of [18].

Bauschinger effect can be largely removed and it is generally neglected in the theory of plasticity assuming that the material is having identical yield stresses both in tension and compression, irrespective of cold work involved previously [18]. It is quite significant in bar straightening as bars are subjected to elasto–plastic bending and the process is subjected to cold working (Fig. 3).

4 Mechanics of Bar Straightening

Bar straightening process was in practice and various kinds of straightening machines were in operation at various industries [5]. In the United Kingdom, the Bronx Engineering Company, Lye, Stourbridge (Worcs) and Joshua Bigwood & Sons, Wolverhampton are considered pioneers in the advancement of design of straightening machines. Later on, there have been several manufacturers in various countries. The theoretical aspect initiated by Tokunaga was very much restricted to preliminary stage with measurement of residual stress calculation.

However, the design and development were not much supported by any kind of theoretical approach based on analysis of plasticity or involvement of the plastic deformation processes. Analytical approach of the straightening processes was

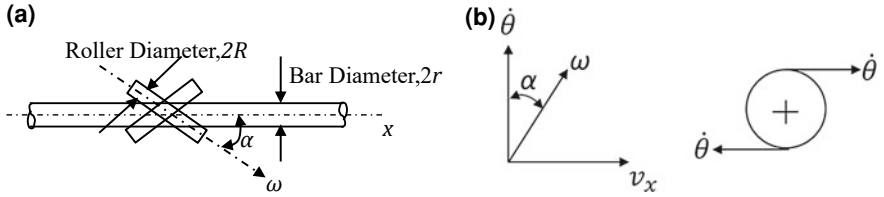


Fig. 4 **a** Sketch of Cross-Roll straightening process showing the angular arrangement of rolls [8, 9], **b** Throughput speed and angular speed of the bar has been shown [8, 9]

further enhanced by Yu and Johnson. Significant contribution was made in estimation of bar curvature after the process of cross-roll straightening [21]. Moment—curvature relationship was established in non-dimensional form. Curvature change by considering residual curvature and final curvature was developed.

4.1 Assumptions

The mathematical treatment of bar straightening proceeded with certain assumptions as below [22]

i. Elastic work hardening is present in the straightened bar.
ii. In pure bending condition, round bar's cross-sectional area is circular and neutral axis passes through the centre.
iii. Outside shapes of bars and tubing are round and tubing have uniform wall thickness.
iv. Cross section remains on a plane at right angles to the axis.
v. Variation of strain is proportional to distance from perpendicular point on neutral axis at any point in bar section.
vi. Material is considered as perfectly elastic–plastic, and its stress–strain relations in uniaxial tension is same as in compression. It has same elastic modulus and yield point both in tension and in compression.
vii. All stress components other than longitudinal direction are zero.

Detailing on motion of the bar through the various rolls has been elaborated by Das Talukder et al. [9] with substantial mathematical treatment [8, 9]. We consider Rollers with radius R, angular speed of bar being $\dot{\theta}$, and throughput speed of bar being v_x and cross-roll straighteners are set at an angle $\pm\alpha$ to the axis of the bar as indicated in Fig. 4a and b. Illustration of bar in motion through cross-rolls in straightening processes is shown in these figures.

Now, as bar's throughput speed, v_x is in the axial direction, and its rotation about its longitudinal axis at an angular speed $\dot{\theta}$, we can state as below [9] $\dot{\theta} = \frac{v_x cot\alpha}{r}$, where r is bar radius.

The bar speed can be expressed as $v_x = \frac{2\pi N R \sin\alpha}{60}$, where N is r.p.m. of rollers [23].

Considering any arbitrary point on outer surface of round bar at distance r from the centre which moves in a helix angle α, pitch length, p can be expressed as below [9].

$$p = 2\pi r \tan\alpha$$

The bars on proceeding through rolls rotate about their own longitudinal axis with the initial curvature plane which makes different angles at various different instants with loading plane and also progresses through the rolls. This is well explained in Fig. 5 [8, 9].

As bar progresses through the rolls, there will be corresponding variations of resisting moment or effective bending moment. In a span of pitch length, bar's osculating plane rotates 360°. Oscillation of effective bending moment or resisting moment will occur through one cycle (Refer Fig. 5). Effective bending moment will have variation. The effective bending moment is maximum at half the pitch length.

For simplicity, we assume the bar of uniform initial curvature. The curvature change-resisting moment of a bar can be drawn as indicated in Fig. 6 [8, 9].

The cross-rolls are so staggered that maximum loading moment M^* is developed while passing through the rolls and corresponding curvature change is κ^*. Residual curvature change, $\Delta\kappa_r$ or $\Delta\overline{\kappa}_r$ (in non-dimensional form) can be expressed as $\overline{\kappa}_r = \frac{\kappa_r}{\kappa_y}$. $\overline{\kappa}_r$ is equal and opposite to initial curvature [9]. The non-dimensional form of bending moment, M may be expressed as $\overline{M} = \frac{M}{M_y}$. Based on above diagram, we can

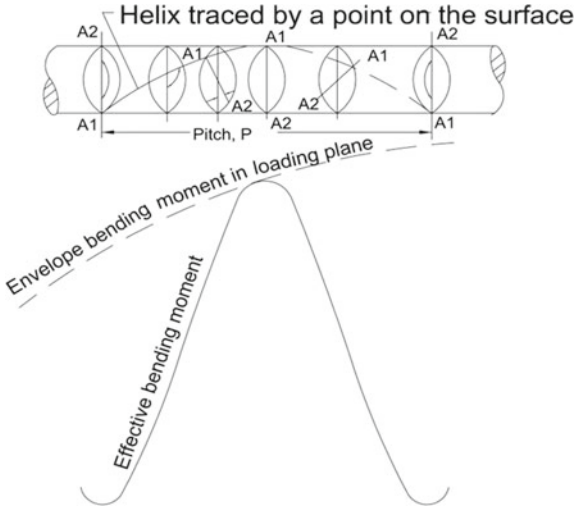


Fig. 5 Illustration of variation of resisting moment or effective bending moment in loading plane [8, 9]

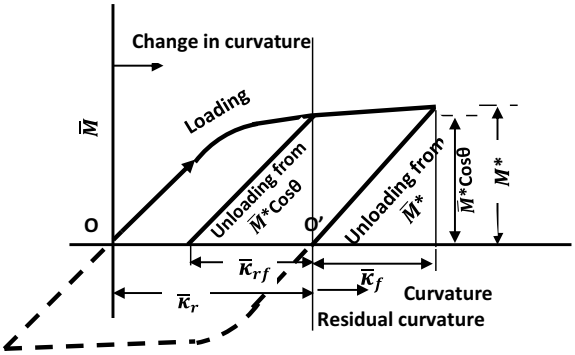


Fig. 6 Simplified relationship between resisting moment or effective bending moment in the bar and change in curvature [8, 9]

say that effective bending moment will be a component of bending moment which is acting in the plane of loading along with osculating plane. Therefore, effective bending moment,$\overline{m}$ can be expressed as $\overline{m} = \overline{M}\cos\theta$. Loading moment is developed at a distance of bar $\left(x - \frac{1}{2}l\right)$.

At the time, when a bar section approaches $x = \frac{l}{2}$, the curvature plane and loading plane may not have any angle or zero angle in between. In that case, effective bending moment in the plane of initial curvature will then not be equal to M^*. The effective bending moment as explained in the diagram will achieve such value only at a few sections. Such sections will be at pitch length distance, p of the bar [9].

Drawing of loading-moment curves repeatedly at pitch length interval over the bar length shall result in an envelope of curves which will give a distribution of effective bending moment over entire bar length as shown in Fig. 7. Considering $\overline{m}$ is the effective resisting moment with the highest value as $\overline{m}_h$ and $\overline{m}_{\,\mathrm{a}}$, $\overline{m}_{\,\mathrm{b}}$ being the largest value on ascending and descending sides, respectively [9]. We can say at a section BB of Fig. 7, $\overline{m}_{\,\mathrm{a}} = \overline{m}(1)$ and $\overline{m}_{\mathrm{d}} = \overline{m}(2)$. Also, $\overline{m}_{\,\mathrm{d}} > \overline{m}_{\,\mathrm{a}}$.

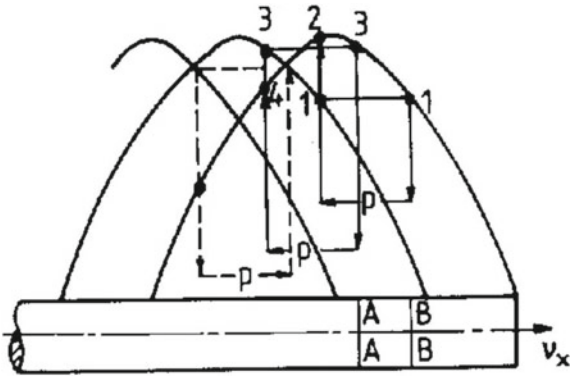


Fig. 7 Illustration of various points where the highest effective resisting moment will be available at various bar sections, viz., AA, BB, etc. [9]

It is to be looked into at section BB which corresponds to point 1 at the curve which is on ascending side. Now let us consider a measure of pitch distance p from point 1 up to corresponding point 2 on the curve which is on descending side. Thus, the highest effective bending moment, $\overline{m}_h = \overline{m}(2)$ [9].

But for section AA of (Refer Fig. 7), effective bending moment on ascending side is $\overline{m}_\mathrm{a} = \overline{m}(3)$ and effective bending moment on descending side, $\overline{m}_\mathrm{d} = \overline{m}(4)$ by taking a measure from pitch distance p, i.e. $\overline{m}_\mathrm{a} > \overline{m}_\mathrm{d}$ and thus $\overline{m}_h = \overline{m}(3)$.

5 Role of Rollers and Straightening Processes

In cross-roll straightening processes, the role of rollers is obviously quite significant. Hence, the profile of rollers is naturally of immense importance. Profile of tube-straightening rollers can be determined simply by application of envelop theory. There is always a requirement of straightening process in order to correct out-of-straightness and out-of-roundness even after accurate industrial process of production of steel tubes or bars [15]. It can therefore be stated that bending and unbending operations depend on rollers. Profile of roller is one of the significant factors. In six-roll type bar straighteners, skew-rolls are deployed. The supporting rollers happen to be driving rollers while loading rollers are actually driven rollers. To suit different tubes or bars, adjustment of skewed angle of rollers can be done. The distance can be adjusted between supporting rollers and loading rollers according to the different tube diameters and straightening force.

Several researchers worked on skew-roll straightening machine. Li et al. have provided a versatile technique and convenient method for the three-dimensional roller contour design and researched much on machining detail, i.e. on cutter path for the purpose of achieving three-dimensional curved surface of rollers.

In cross-roll straightening process, plastic bending will occur naturally. It is assumed that in reverse bending of the bars, for straightening and spring-back, a section having initial curvature shall finally be bent to another curvature. Wu et al. examined the condition of equivalent curvature in order to ease the study of curvature change in bar straightening process. Straightening process essentially involves multiple plastic reverse bending. This covers bars of different initial curvatures to the same final curvature [23].

Straightness improves significantly when bars pass through cross-roll arrangements [24]. Yali et al. considered rotation blocking mechanism of three-roller equal curvature rotation blocking straightening system. Most rods with small diameter less than 12 mm bars are usually supplied in coiled form. These rods of such diameters can be used after uncoiling and thereafter by straightening [24].

Hub-straightening machines, which are traditional, have usually low productivity in the industrial application. Such machines can barely meet the need of production demand. Although straightening speed improves significantly in parallel-roll straightening device, the subjected bar also rotates about its own axis while going through the straightening processes [24]. In such cases, the straightening accuracy is

compromised and becomes low. Therefore, to compensate the same, a roll-layout of equivalent curvature and standstill-locking straightening system is provided. By this way, it improves straightening speed and desired accuracy is reasonably ensured. It is feasible to deploy a mechanism of standstill-locking for large bending system. Yali and Herong deduced formula for standstill-locking torque which provides helpful theoretical backup for development of high speed straightening cutting machine [24].

6 Residual Stresses in the Process and Measurements

Due to straightening process, unfavourable residual stresses mainly occur in the final products; the effects appear in the cross-section during multiple bending [1]. With the introduction of numerical modelling in bar straightening processes, researches extended to the application of FEM. Non-linear analysis of residual stresses was conducted by Biempica in the rails [25]. Study was made for reduction of residual stresses by means of roller straightening. Finite element models can be used to understand the combination of effect of contact stresses and bending stresses under the rollers for changes in roller profile. Biempica [25] explained through application of various one-dimensional, two-dimensional, and three-dimensional finite element models. Application of one-dimensional models is quite simplistic and advantageous with respect to complex models. Computational time and effort is less to solve one-dimensional models [25].

Srimani et al. [30] studied and developed suitable methodology in straightening machine to estimate the straightness of finished product (rail) for a set of loading parameters. Straightness values were examined along the entire length. It has been noticed that both front and rear ends are actually subjected to loading which has different patterns in comparison to middle portion during passing through straightening machine. Straightness differs considerably near ends in comparison to other portions which are quite uniform [30]. The loading pattern and straightness will also be same in case of round bars. In the industrial application, a decision can be taken as to what portion of such long bars is acceptable on quality level. Srimani et.al. provided guidance for the minimum length of the rail at the ends, which need to be cut to achieve the straightness within the acceptable limit.

Prediction of residual stress state of cyclic softening during cross-roll straightening agrees qualitatively with experimental values [26]. Residual stress distribution has a beneficial effect apart from increasing straightness in bars of cross-roll straightening. Tensile residual stresses are induced in straightening process at surface of bar which is reduced considerably by previous drawing operation. The objective was to predict the evolution of the internal stresses qualitatively. On a section, the residual stress distribution is not symmetrical about the axial direction. As a whole, residual stresses are naturally in equilibrium in the bar.

7 Modelling/Numerical Modelling

It is said that a metal is actually no mere rigid or dead body. A material can be considered as endowed with a life of its own. This results in many complex processes which may go on within it. In a simple model produced for the Bauschinger effect during stress reversal, we can say that a metal may be considered as possessing a limited memory of its previous work hardening or past history [17]. Mathematically, the constitutive laws of stress–strain behaviour for engineering assessment depend on the following:

(a) Characteristics of deformation of the material
(b) Structural complexity and
(c) Spectrum of loading.

These constitutive models should take ideally the following into account:

- Non-linear response of stress–strain
- Behaviour of material with repeated cycling, viz., cyclic hardening, cyclic softening, or steady-state response
- Kinematic hardening or softening due to change in plastic slope
- Isotropic hardening or softening due to change in yield stress
- Relaxation of mean stress under strain control, or strain ratchet under stress control
- Bauschinger effect
- Other memory of past deformation.

Numerical modelling in cross-roll straightening emerged with researches by Mutrux et al. [26]. Processes of cross-roll straightening were studied in a simulated situation. There is significance of the research in a simulated form. It indicated that reduction of curvature can be predicted. In straightening processes of the bent rod, the plastic zone is propagated along the helix. Study indicated that bending of the bar can be controlled by changing the angle α between rolls and bar. Bending occurs more with smaller angle, α. Optimal value of angle α will be when degree of straightness is reached at the highest level. However, a realistic transition speed and also economic viability is to be ensured. The similitude between the stress state obtained in three points bending and in cross-roll straightening has been indicated and consequently inferred that by passing through the rolls, the curvature of a bent bar can be significantly reduced [27].

8 Simulation/Numerical Simulation

Simulation approach on rolls is now quite old. Although not directly on bar straightening using cross roller, experimental simulation of pass rolling was undertaken by Macura and Petruska [28]. Researches have been done on simulation of straightening operations. To straighten steel plates or strips, roller levelling is used after

final rolling and heat treatment or cooling operations [29]. An essential requirement for steel manufacturer is that after straightening, the result should show low residual stresses and the product is sufficiently flat in case of flat strips. The concept is applicable on round bars as well. Plate or strips are subjected to multiple forth and back bending sequences with decreasing roll penetration in roller levelling.

Simulated model of straightening process with schematic arrangement of rollers in straightening process was discussed by Srimani et al. [30]. However, in this case also, the bar used was rail. As the rails undergo alternate bending and subjected to elasto–plastic deformations in a straightening machine, it is subjected to high magnitude of loads. Simulated model is therefore immensely useful considering high magnitude of loads.

FE Simulation of cross-roll straightening was done by Mutrux et al. [26]. The deformation of the bar—the strain tensor field—between the rolls was obtained through a FE simulation. Mutrux et al. tried a better understanding of the straightening process through simulation. Strain tensor field approach was taken. Numerical simulation was used to study optimization of straightening regulation in heavy rail compound roll straightening processes. By using FEM software ANSYS/LS-DYNA, numerical simulation calculation was carried out by Song et al. Song et al. used a system of nine horizontal straightening rollers and eight vertical straightening rollers for a 60 kg/m heavy rail [31].

Finite Element Analysis (FEA) model is used often for a quantitative analysis. Huang et al. used sixty nodes on the cross-sectional outline with intervals of 6 degrees. Straightening nodes were selected and polar radius thereof was calculated. The quantitative analysis was for tolerance of roundness of the straightening bar. Model with nine roller straightening process has been used by Kaiser et al. [1]. Variation of curvature has been shown with position in straightening machine. Simulation of the roller straightening process has been discussed with respect to residual stresses and curvature trend [1].

Petruska et al. [32] discussed through a schematic view of typical multi-roller straightening machine and shown the distribution of longitudinal stress at initial state and residual stress after levelling. Computational simulation of cross-roll straightening of bars was done through models of bar-rollers contact at one-point and two-points.

9 Control System and Stabilisation

Geometrical stability of products and its assurance is a significant problem in manufacturing engineering for the success of further assembly work or automation-based assembly. In cold work metal forming, fluctuations of properties like yield stress, hardness, ductility, etc. of the input material contribute significantly to the geometrical shape of final product. Positioning of tools that causes bending can influence forming of material. In wire forming by cold work, appropriate corrections of position of bending tools can influence the process.

In bar straightening process, positioning of rolls plays an important role as bending moment and curvature depends on the same. The only precondition for stabilization system for wire bent products is that straightening machines are required to have sufficient number of rollers [33]. Nastran and Kuzman confirmed that several plastic bending is essential to reduce residual curvature. This has naturally necessitated the requirement of multi-step straightness and so Multi-Step Straightening Control system (MSSC) got importance in the process.

Minimization of straightness error in deflected shafts was studied by Kim and Chung [34]. To meet this purpose, multi-step straightening and three-point bending process for the MSSC was developed. Due to various processes involved, many manufactured shapes of parts are known to get deformed. Because of such deformation, straightness of shafts is degraded. Hence, to control the shaft's straightness, grinding operations become essential. Straightening machines so developed use bending processes for compensation of straightness error before grinding with an increased level of automation [34].

It can be seen that roller levelling took a significant place in bar straightening. Researches have been done on roller levelling process optimization [35]. Roller levellers have been considered as the most desirable elements for elimination of undesirable curvatures. Analytical study of Das Talukder et al. helps to eliminate unevenly distributed residual curvature along the axis or longitudinal direction of a pipe on dynamic load for various kinds of cross-roll levellers. The analysis revealed that to effect on straightness of levelled pipe, the most important factor is pitch [35]. In case of wires, residual stresses as generated in bending, straightening operations play a significant role in their mechanical properties. Measurement of various parameters is often considered important. Neutron strain scanning machines have been found used for this purpose [36].

10 Discussion

The theoretical aspect being the backbone of the process has been brought out with an understandable clarity. Various types of straighteners have been featured in simplified form. Although it is considered that materials will have uniform yield point for bending, in reality the bars may not have well-defined yield point, hence the unloading curves may not be straight lines. Mathematical treatment shows that considerable reduction of curvature is possible through straightening process. The review of bar straightening process concerning various aspects which were dealt by various researchers time to time has been briefly looked into with theoretical analysis. Reduction of residual stress can be done through roller straightening and prediction of residual stress state is possible. Researchers have gone into numerical modelling and created simulated situation and studied the process of straightening. Elasto–plastic deformation of high magnitude is difficult whereby simulated environment made it easier to study the same. Stabilization of geometrical shape is an ultimate necessity in any straightening process where many important parameters of bar straightening

featured. Roundness tolerance of bars in some cases can nearly be eliminated [37]. Positioning of rolls is considered important in the process. Specifically which roller in the process has more effect can now be understood easily. Multi-Step Straightening Control System found a place which is indeed a significant contribution in modernization of bar straightening process. This article may be considered as a consolidated work assimilating variety of areas related to bar straightening till date. This review paper has dealt with bar straightening from its historical concepts to present time contributions with important significance of simulation, measurement, control, and stabilization aspects briefly.

11 Conclusion

There have been consolidations of various key features of bar straightening process. Industrial bending-straightening operations may generate significant residual stresses. Modification of residual stress profile is done through cold working; therefore, theoretical aspects of straightening process play a significant role. Although in earlier times thrust was primarily on theoretical development, in recent time numerical modelling and simulation has helped to assess arrangement of rollers and draw conclusion on heavy-duty application of bar straightening [27]. Qualitative prediction on residual stresses and reduction of curvature is now much easier. Application of control systems in stabilization will improve commercial aspects of bar straightening due to minimization of straightness errors [34]. There has been discussion on most aspects of bar straightening in brief, hence it will now be possible to look into the areas of further work much easily. Researchers can look upon recent areas for further thrust and investigation on bar straightening which may be of immense benefit to the design and production engineers. It is obvious that probabilistic approach and statistical aspects have barely been dealt with although there is actually a lot of scopes.

References

1. Kaiser R, Hatzenbichler T, Buchmayr B, Antretter T (2014) Simulation of the roller straightening process with respect to residual stresses and the curvature trend. Mater Sci Forum 768–769:456–463
2. Brazier LG (1927) On the flexure of thin cylindrical shells and other “Thin” sections. Proc R Soc Lond A 116:104–114
3. Ades CS (1957) Bending strength of tubing in the plastic range. J Aeronaut Sci 605–610
4. Tokunaga H (1961) On the roller straightener. Bull JSME 4(15):605–611
5. Kemshall GE (1974) Bar straightening and bending equipment, light bar and section mill technology. Steel Times 13:243

6. Lotey Heavy Machines Ltd. http://www.rollingmillmachinery.org/section-straightening-machine-angle-straightening-machine-straightening-machine-section-straightener-rolling-mill-straightening-machine-channel-straightening-machine-section-straightening-machine-manufacturer-section-straightening-machine-india.html
7. Aluminium-Guide.com. https://aluminium-guide.com/en/rastyazhnaya-mashina-ekstruzionnogo-pressa-teoriya-i-praktika/
8. Das Talukder NK, Johnson W (1981) On the arrangements of rolls in cross-roll straighteners. Int J Mech Sci 33:213–220
9. Das Talukder NK, Singh AN, Johnson W (1990) Cross-roll straighteners and their performance. J Mater Process Technol 21:101–109
10. Kuboki T, Kawasaki K, Kajikawa S, Matsumura H, Ono T, Seimiya H (2019) Analysis of spinner straightening utilizing the finite element method. In: COMPLAS XV: international conference on computational plasticity, fundamentals and applications
11. Falaleev AP, Meshkov VV, Shymchenko A (2016) Hyperplasticity effect under magnetic pulse straightening of dual phase steel. IOP Conf Ser Mater Sci Eng
12. www.slideshares.net
13. https://www.ukocarbide.com/blog/2-straightening-methods-of-nc-steel-bar-straightening-and-cutting-machine/
14. http://www.shivamengineerings.com/products/3-x-3-skew-roll-design.html
15. Li KY, Yang SC, Chen CK (1999) Profile determination of a tube straightening roller by envelope theory. J Mater Proc Tech 94:157–166
16. Masakileison AM, Moskalev DS, Khotimskii YUL (1989) Machines for accurate tubes straightening. Steel in USSR 19:224–226
17. Frederick CO, Armstrong PJ (1966) A mathematical representation of the multiaxial Bauschinger effect. CEGB Intern Res Rep RD/B/N660 Mater High Temp 24(1):1–26
18. Chakrabarty J (2006) Theory of plasticity, 3rd edn. Butterworth-Heinemann
19. Ludwik P (1909) Elemente der technologischen mechanik. Springer Verlag, Berlin
20. Drucker DC (1951) A more fundamental approach to plastic stress-strain relations. In: 1st US national congress of applied mechanics
21. Yu TX, Johnson W (1982) Estimating the curvature of bars after cross-roll straightening. In: Proceedings of the 22nd international MTDR conference, pp 517–521
22. Roy S, Pal AK, Rawal S (2020) A review on straightening of bars and application of probabilistic approach on Moment-curvature relationship. IOP Conf Ser Mater Sci Eng 810:012080
23. Wu BJ, Chan LC, Lee TC, Ao LW (2000) A study on the precision modeling of the bars produced in two cross-roll straightening. J Mat Proc Tech 99:202–206
24. Yali Y, Herong J (2012) Three roller curvature scotch straightening mechanism study and system design. Energy Procedia 16:38–44
25. Biempica CB, del Coz Diaz JJ, Nieto PG, Sanchez IP (2009) Nonlinear analysis of residual stresses in a rail manufacturing process by FEM. Appl Math Model 33:34–53
26. Mutrux A, Berisha B, Hora P (2011) Prediction of cyclic softening in a medium carbon steel during cross roll straightening. J Mater Proc Tech 211:1448–1456
27. Mutrux A.,Berisha B, Hochholdinger B, Hora P (2008) Numerical modelling of cross roll straightening, metallumformung I. LS-DYNA Anwenderforum, Bamberg, pp C-I-33–40
28. Macura P, Petruska J (1996) Numerical and experimental simulation of pass rolling. J Mater Proc Tech 60:55–60
29. Widmark M, Melander A, Meurling F (2000) Low cycle constant amplitude fully reversed strain controlled testing of low carbon and stainless sheet for simulation of straightening operations. Int J Fatigue 22:307–317
30. Srimani SL, Pankaj AC, Basu J (2005) Analysis of end straightness of rail during manufacturing. Int J Mech Sci 47:1874–1884
31. Song H, Pei LW, Li HF, Chen M, Wang ZQ (2010) Study on the optimization straightening regulation of heavy rail compound roll straightening. Adv Mater Res 102–104:227–231
32. Petruska J, Navrat T, Sebek F (2016) Novel approach to computational simulation of cross roll straightening of bars. J Mater Proc Tech 223:53–67

33. Nastran M, Kuzman K (2002) Stabilisation of mechanical properties of the wire by roller straightening. J Mater Proc Tech 125–126:711–719
34. Kim S-C, Chung S-C (2002) Synthesis of the multi-step straightness control system for shaft straightness process. Mechatronics 12:139–156
35. Huh H, Heo JH, Lee HW (2003) Optimisation of a roller levelling process for Al7001T9 pipes with finite element analysis and Taguchi method. Int J Mach Tool Manuf 43:345–350
36. Martinez-Perez ML, Borlado CR, Mompean FJ, Garcia-Hernandez M, Gil-Sevillano J, Ruiz-Hervias J, Atienza JM, Elices M, Lin PR, Daymond MR (2005) Measurement and modelling of residual stresses in straightened commercial eutectoid steel rods. Acta Mater 53:4415–4425
37. Huang H, Zheng H, Du F, Wang W (2012) Numerical simulation analysis on the ten cross rolls straightening process of the heavy calibre seamless steel tube. Adv Mater Res 421:56–59

Development of Anti-Loosening Bolts Based on Innovative Double Thread Mechanism



Teruie Takemasu, Toshinaka Shinbutsu, Shuichi Amano, and Jyo Shimura

Abstract Anti-loosening bolted joints were developed with an innovative double-thread mechanism composed of coaxial single and multiple coarse threads. The number of coarse threads of the multiple-thread was set to 3 (denoted as 3thread DTB-II), and its thread structure was fundamentally modified as follows: (i) one of the three multiple-thread grooves was removed for 3thread DTB-II specimens and one of the two remaining grooves shifted downwards by a half pitch (denoted 3-1thread DTB-IIB) and (ii) the depth of the multiple-thread grooves was reduced by up to 50% of the thread height (denoted 3-1thread DTB-IIC). FEM thread rolling simulations were performed using a dedicated die. The two kinds of modified DTB-II specimens were rolled precisely and the thread heights reached the target value at all cross sections. The forming states in the thread rolling experiments well matched the FEM simulation states. The performance evaluation tests demonstrated that the 3-1thread DTB-IIC specimens had sufficient tensile strength, and its anti-loosening performance exceeds the reference level given in DIN25201.

Keywords Bolted joint · Double thread mechanism · Thread rolling · FEM · Tensile strength · Loosening test

T. Takemasu (✉)
Happy Science University, 4427-1 Hitotsumatsu-hei, Chosei-mura, Chosei-gun 299-4325, Japan

T. Shinbutsu · S. Amano
Nissei Co. Ltd., 2022 Torisawa, Thomihama-cho, Ohtsuki 409-0502, Japan
e-mail: t_shinbutsu@nisseiweb.co.jp

S. Amano
e-mail: s_amano@nisseiweb.co.jp

J. Shimura
Suwa University of Science, Toyohira 391-0292, Japan
e-mail: jyo@rs.sus.ac.jp

© The Minerals, Metals & Materials Society 2021

G. Daehn et al. (eds.), *Forming the Future*, The Minerals, Metals & Materials Series,
https://doi.org/10.1007/978-3-030-75381-8_181

1 Introduction

It is well known that cyclic stresses or impact loading during service can cause the loosening and fatigue failure of bolted joints, possibly leading to serious accidents [1]. The loosening of bolted joints can be roughly divided into the non-rotational type, in which the axial force decreases without nut rotation, and the rotational type, in which return rotation of the nut occurs [2, 3]. Non-rotational loosening can easily be dealt with by additional tightening of the nut or a design change. In contrast, rotational loosening is an inevitable issue because it occurs suddenly in an environment with cyclic loading, severe vibration, and impact forces. Most commercially available anti-loosening screw parts exhibit macro slip on the nut-bearing surface when subjected to a severe transverse vibration load and cannot completely suppress rotational loosening because most of them only enhance the frictional force between the bolt and the nut or between the nut and the bearing surface [4–7]. In comparison, it has been proven that the double-thread bolted (DTB) joints having two types of coaxial screw thread with different lead angles have an excellent anti-loosening performance [8]. For such joints, a higher lead nut is first fastened, and then a lower lead nut is added to form a double nut structure. The anti-loosening mechanism of DTB is enhanced by a mechanical locking based on the interference effect of two kinds of nut with different loosening speeds.

DTB joints with a very simple structure composed of a single coarse thread and a single fine thread (denoted DTB-I), have been a major research target [9]. However, as DTB-I has become more widely used, various disadvantages associated with the fine screw thread have been pointed out by users, including troublesome torque management for each nut, insufficient strength of the fine thread, high manufacturing cost of rolling dies, and low durability. Bolt fasteners, denoted DTB-II, was then proposed based on an innovative double-thread mechanism composed of a single coarse thread and a multiple coarse thread [10, 11]. Nut fastening and torque management for DTB-II can be performed very easily since the inner multiple-thread nut, mounted first, is also rotated when the outer single-thread nut is tightened, solving most of the problems encountered with the conventional DTB-I. Thread rolling experiments and tensile strength tests were conducted on DTB-II specimens with 2, 3, and 4 threads on the multiple-threads, which were denoted 2, 3 and 4thread DTB-II, respectively, to evaluate the proposed double-thread structure. It is found that 3thread DTB-II formed relatively well, although the height of the screw thread profile of 2 and 4thread DTB-II did not reach the target level. The tensile strength of these DTB-II specimens tended to decrease with increasing number of multiple-threads, and 3 and 4thread DTB-II were damaged by the shear failure of the screw thread even with the double-nut structure. Accordingly, to solve these problems, the authors designed several kinds of modified DTB-II, in which the number of multiple-thread grooves superimposed on the single screw thread was selectively reduced to $m - 1$ (m: number of multiple-threads) or fewer from the m-thread DTB-II, manufactured them by thread-cutting, and carried out tensile strength tests. The shear

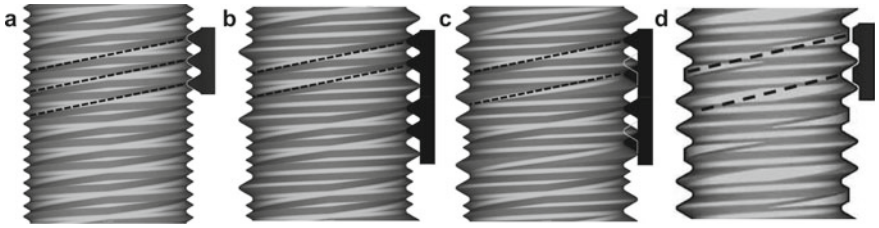


Fig. 1 Diagrams of screw thread structure of **a** 3thread DTB-II, **b** 3-1thread DTB-IIA, **c** 3-1thread DTB-IIB, **d** 3-1thread DTB-IIC

fracture of the screw thread of all DTB-II specimens mounted with double nuts was successfully suppressed by reducing the number of multiple-threads by at least one.

In this study, thread rolling FEM simulations and experiments were conducted on the two types of modified 3thread DTB-II (see below for description) to examine the material deformation state and forming accuracy. Several performance evaluation tests were then performed to determine the effect of the modified screw thread profile on the tensile strength and the anti-loosening performance of those DTB-IIs.

2 Methods

2.1 Screw Thread Structure of Modified DTB-II

Figure 1 shows a comparison of the screw thread structure of 3thread DTB-II [10] and those of the three modified types. Figure 2 shows the changes in the thread cross-sectional area ratio, ξ, of each DTB-II, which was calculated by dividing the thread cross-sectional area of three pitches at each angular position of DTB-II by that of the normal single screw-thread. Figure 1a shows the thread structure of the original 3thread DTB-II, and b shows that of the modified 3-1thread DTB-IIA, in which one thread groove was simply removed from the three thread grooves and the remaining two thread grooves were superimposed onto a single screw thread. With this modification, the minimum value of the thread cross-sectional area ratio, ξ_{min}, increased to approximately 55%, as shown in Fig. 2. However, since there are four consecutive small threads at the groove bottom at the 90° and 270° positions, at which thread shear fracture may initiate, 3-1thread DTB-IIA was excluded from further testing. One of the remaining two thread grooves was shifted downwards by a half pitch to be aligned at an equal pitch, as shown in Fig. 1c; this joint is denoted 3-1thread DTB-IIB or simply DTB-IIB [11]. For 3-1thread DTB-IIA, the complete screw thread appears at only the 0° and 180° positions, whereas 3-1thread DTB-IIB has one or two complete screw threads in three pitches at all cross sections. The ξ value of 3-1thread DTB-IIB changes at the 90° cycle, as shown in Fig. 2, which is half that of 3-1thread DTB-IIA, and ξ_{min} is 70%, which is twice that of 3thread

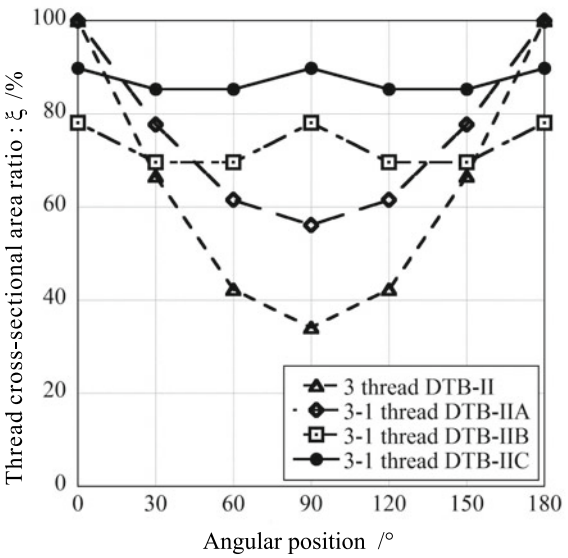


Fig. 2 Comparison of changes in the thread cross-sectional area ratio, ξ, of each DTB-II specimens, which was calculated from the thread cross-sectional area of three pitches at each angular position

DTB-II. However, a small-thread portion remains at the groove bottom for all angular positions, which reduces tensile strength. In order to completely remove these small threads, the depth of the multiple-thread grooves was reduced by up to 50% of the thread height, as shown in Fig. 1d; this joint is denoted 3-1thread DTB-IIC or simply DTB-IIC. With this modification, ξ_{min} increased up to 85% and improvements in tensile strength were expected.

2.2 FEM Simulation Model and Experimental

To reduce cost, DTB-II joints have to be manufactured using a mass production process. Thread rolling is most suitable for this task because of its productivity and widespread use. In the thread-rolling of DTB-II, both the single and multiple coarse threads should be formed simultaneously on a single rod axis through one rolling process. To realize this process, the authors developed a dedicated roller die (denoted DTB-II die) with a special groove profile, which has almost the same outline as that of the thread profile of DTB-II specimens in each corresponding cross section. Thread rolling simulations of M12 DTB-IIB and C were first performed using a 3D FEM model to examine the forming process of the screw thread. The commercial FEM code Simufact.forming ver.15 was used. Figure 3a and b show the FEM simulation model, in which the workpiece is an elasto-plastic cylindrical material and the rolling flat dies are rigid bodies. During processing, the two flat dies were moved synchronously in opposite directions (see arrows in the figure) and simultaneously pushed into the workpiece at the same constant speed. The total amount of indentation of the die,

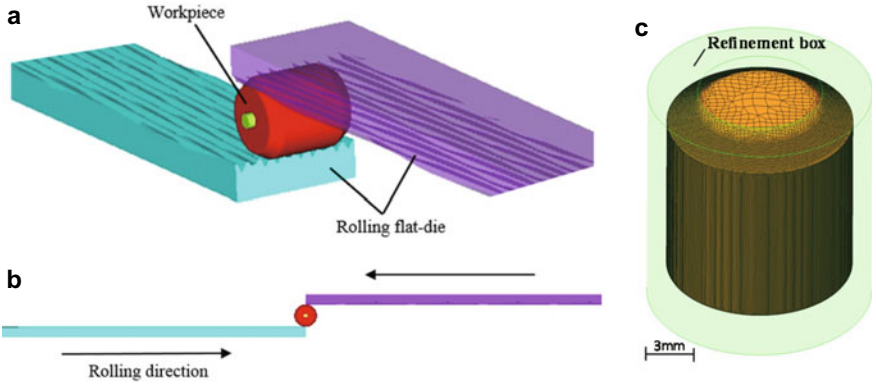


Fig. 3 **a** Perspective view of FEM model. **b** Side view. **c** FEM mesh of workpiece. (Color figure online)

δ_{max}, was set to a prescribed value for each DTB-II ($\delta_{max} = 0.56$ mm for DTB-IIB and $\delta_{max} = 0.62$ mm for DTB-IIC) until the workpiece was rotated 8 times; then, the dwelling process was performed for two rotations. Coulomb's friction law was assumed at the contact interface between the dies and the workpiece, and the coefficient of friction μ was set to 0.2. Figure 3c shows the initial FEM mesh of the workpiece with a diameter of $\phi 10.8$ mm. A semitransparent refinement box was placed in the region from an inner diameter of 8 mm to an outer diameter of 14 mm; this region is divided by hexahedron fine elements with a reference size of 0.4 mm. The height of the cylindrical workpiece was restricted to the 9-pitch length of a single screw-thread bolt to reduce calculation time and to avoid the effect of edge droop on thread forming around the central portion in the axial direction.

The thread rolling experiments of M12 DTB-IIB and C were conducted using a manual rolling machine with a two-roller die plunge feed (FA-16U, Nissei Co., Ltd.) under a die rotational speed of 62 rpm and a net processing time of 4 s, which included a 1 s dwelling time. The initial diameter of the workpiece and the final amount of the die radial feed were decided based on the screw thread forming state. A low-carbon steel bar made of DIN 17100 was used as the bolt material.

The methods and conditions of the several performance tests are described later.

3 Results and Discussion

3.1 Thread Rolling FEM Simulation and Experiments

Figures 4a and 5b show the equivalent plastic strain distribution, $\bar{\varepsilon}$, of thread-rolled DTB-IIB and C obtained from the FEM simulation, and Figs. 4b and 5b show the outer appearance of the samples used in the experiment, respectively. Figure 6a and b

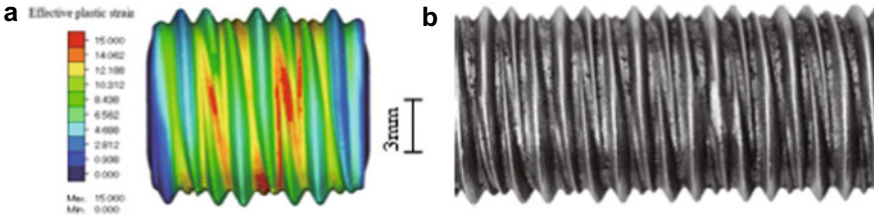


Fig. 4 **a** Equivalent plastic strain distribution of rolled 3-1thread DTB-IIB using FEM. **b** Rolled sample of 3-1thread DTB-IIB used in experiment. (Color figure online)

compare the filling state transition of the material at each representative angular position of the die grooves at each amount of die radial feed δ value obtained from FEM simulation. The final deformation state of each modified DTB-II in the analysis well agrees with that in the experiments, and the target screw thread profiles for both cases are obtained for the entire external surface. The thread forming state during rolling in the FEM simulation also progressed as expected. Therefore, both the multiple- and single-thread nuts were fastened easily and smoothly on the thread-rolled DTB-II specimens. However, the equivalent plastic strain distribution, $\overline{\varepsilon}$, of DTB-IIB is very high at the groove bottom and its maximum value reaches approximately 15. In contrast, that of DTB-IIC is very low and its maximum value is 7, less than half of that for DTB-IIB. Hence, in the thread rolling experiments conducted at room temperature, the material temperature immediately after the processing of DTB-IIB increased to 110 °C, whereas that of DTB-IIC increased to only about 70 °C. The reason is that the material filling of the two shallower die grooves located at the center of the 0° position and at the right of the 90° position of DTB-IIB completed in the early deformation stage of $\delta = 0.28$ mm and (surrounded by enclosed space with no room for overflow) then the material was over-rolled, as shown in Fig. 6a. The material near completely filled grooves flows along the same single screw thread to the unfilled deeper grooves, and this material flow in the circumferential direction causes severe shear deformation, leading to material surface peeling and shortening tool life. Many cutting chips appeared in the thread rolling process of DTB-IIB; considerably fewer chips were observed for DTB-IIC. Since the material deformation of DTB-IIC advances in the same manner as that of the normal single-thread bolt, in which the material mainly rises in the radial direction until 70% of $\delta_{\max}$ (δ0.47 mm), the thread forming state does not depend on angular position. Although material flow in the circumferential direction occurs after the shallow trapezoidal grooves located at the center of the 0° position and at the right of the 90° position of DTB-IIC are filled, as shown in Fig. 6b, its amount is much smaller than that for DTB-IIB, and there is no portion around the groove bottom where is excessively high. These results indicate that the thread rolling formability of DTB-IIC is greatly improved over that of DTB-IIB because of the good thread profile balance in the circumferential direction.

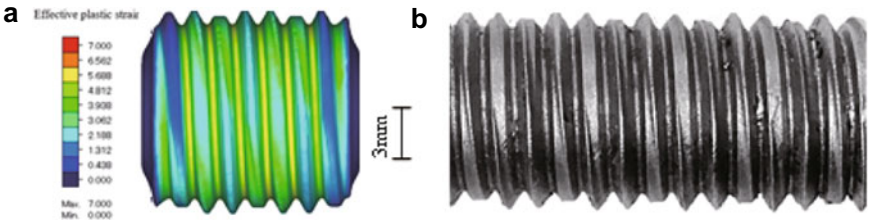


Fig. 5 **a** Equivalent plastic strain distribution of rolled 3-1thread DTB-IIC using FEM. **b** Rolled sample of 3-1thread DTB-IIC used in experiment. (Color figure online)

a

Die radial feed	Angular position		
	0°	45°	90°
0.14 mm			
0.28 mm			
0.42 mm			
0.56 mm			

b

Die radial feed	Angular position		
	0°	45°	90°
0.16 mm			
0.31 mm			
0.47 mm			
0.62 mm			

Fig. 6 Comparison of material filling state in various typical sections of die groove using FEM simulation between **a** 3-1thread DTB-IIB and **b** 3-1thread DTB-IIC

3.2 Tensile Strength Tests

The tensile strength tests of M12 rolled 3-1thread DTB-II specimens (denoted DTB-IIs) and a conventional rolled single-thread bolts were conducted using a hydrolic universal material testing machine (UH-300kN made by Shimadzu Corp.) equipped with a special rig with a self-aligning function in the axial direction. A test specimen mounted with double nuts or a single screw nut was placed in the rig and extended at a constant speed of 2 mm/min. The under-head full length of the bolt specimen was 110 mm and the length of the screw portion was 60 mm. The failure mode of all modified DTB-IIs mounted with double nuts was the breaking of the base material and the maximum loads were almost the same as that for the normal single-thread bolt. Here, the non-shear fracture condition of the screw thread was determined by mounting only a single screw nut with different heights, namely normal height (10 mm), 1.25 times normal height (12.5 mm), and 1.5 times normal height (15 mm). Figure 7a–c show the appearance of the fractured DTB-IIB and C with a single-nut structure, and Fig. 7d compares the load-stroke curves obtained from the tensile tests. All these tests were conducted three times under the same conditions; the same results were obtained in each trial. DTB-IIB was damaged by the shear fracture of the screw thread with the 1.25-times-normal-height single nut, and was fractured via necking of the base material with the 1.5-times-normal-height single nut. For DTB-IIC, breaking of base material with the 1.25-times-normal-height single nut and damage by shear fracture with the normal-height-single nut were observed. The maximum load reached approximately 90% (47 kN) in the case of base material breaking. Since the minimum and maximum values of the axial tension of the JIS M12 standard single-thread bolt are 14 and 25 kN [12], respectively, it is possible to use DTB-IIC even with the normal single-nut structure. Accordingly, DTB-IIB and C have remarkably improved tensile strength compared with that of 3thread DTB-II in the previous study [10]. The axial load of DTB-IIC is almost equal to that of the normal single-thread bolt because of the elimination of the small threads at the groove bottom.

3.3 Vibration Loosening Tests

Comparative vibration loosening tests were conducted using the conventional M12 DTB-I and modified M12 3-1thread DTB-IIB and C with a double-nut structure. A Junker test bench (J120T, Vibrationmaster), shown in Fig. 8a, was employed to analyze the self-loosening behavior of secured bolted joints [13]. This apparatus can specify the state in which a bolted joint loses its axial preload when subjected to shear loading by transverse vibration. The transverse displacement and the oscillation frequency were set to 1 mm and 12.5 Hz, respectively, which are the most extreme conditions for this apparatus. The initial axial preload, P_0, of the modified DTB-IIs was set by adjusting only the tightening torque of the outer single nut to be

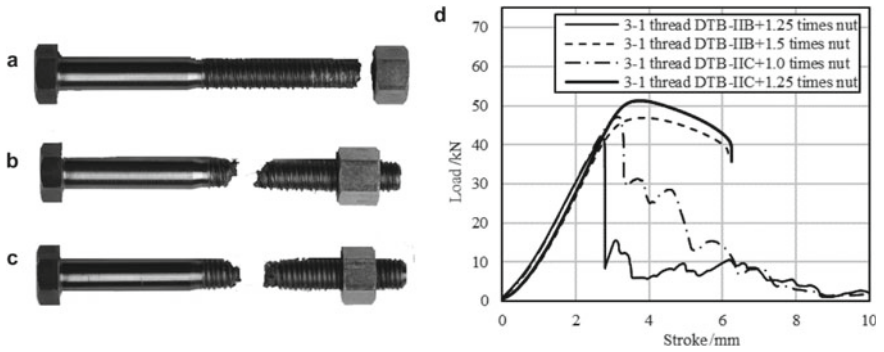


Fig. 7 Tensile strength test results of **a** 3-1thread DTB-IIB with 1.25-times-normal-height sigle nut, **b** 3-1thread DTB-IIB with 1.5-times-normal-height single nut, **c** 3-1thread DTB-IIC with 1.25-times-normal-height single nut. **d** Stroke-load curves obtained from tensile tests

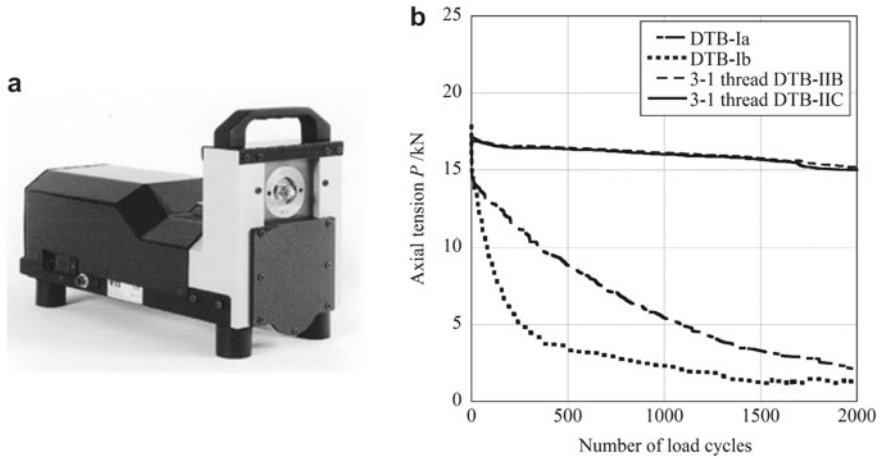


Fig. 8 **a** Junker vibration loosening test bench. **b** Axial tension versus number of load cycles in Junker's vibration loosening tests

fastened later. The proper P_0 for a bolted joint with a nominal size of M12-1.75 is prescribed to be approximately 20 kN in JIS strength class 4.8. However, since the anti-loosening performance of the modified DTB-IIs was so high that the axial force hardly decreased when tightening was conducted with the specific axial load, the bolt head shank exhibited shear fracture during testing. P_0 was thus set to a slightly lower value, within the range of 17–18 kN. A test was considered to have completed when the total number of oscillations exceeded 2000 cycles (about 160 s) or when it became apparent that the bolted joint had loosened. Figure 8b shows the variation in the axial load of the conventional DTB-I and modified DTB-IIs with the number of load cycles in the Junker vibration test. Here, DTB-Ia denotes the case where the inner nut was rotated back according to the regular instruction, and DTB-Ib denotes

the case where that procedure was omitted. The final residual rate of the axial load was approximately 15% for DTB-Ia and 10% for DTB-Ib. In contrast, those for the two DTB-IIs were larger than 85%, which is considerably higher than those for DTB-I and exceeds the reference value of 80% given in DIN25201. A detailed comparison of the changes of the axial load indicates that the rates of both DTB-Ia and DTB-Ib suddenly drop by about 4 kN immediately after the starting point; then, that of DTB-Ia continues to decrease with a nearly constant slope, whereas that of DTB-Ib rapidly decreases for about 300 cycles and then decreases very gradually. The rates of both DTB-IIs are almost constant after an initial decrease of about 1 kN. The reason for this significant difference is as follows. (i) The loosening speed ratio between the inner nut and the outer nut of DTB-IIs is 3:1, which is larger than that of DTB-I (2:1). (ii) The outer nut of DTB-IIs with a single coarse screw thread can hold the axial load of a bolted joint more strongly than can DTB-I with a single fine screw thread.

4 Conclusions

1. The rolling formability of the modified 3-1thread DTB-II specimens was considerably improved. Since the material deformation of DTB-IIC advanced in the same manner as that of the normal single thread bolt up to 70% of the total amount of die radial feed, the over-rolled area was greatly decreased around the thread groove portion and the material temperature immediately after the processing was much lower compared with that for DTB-IIB (70 °C vs. 110 °C).
2. The tensile strengths of DTB-IIB mounted with a 1.25-times-normal-height single-thread nut and DTB-IIC mounted with a normal-height single-thread nut reached the range of 14–25 kN prescribed by JIS.
3. It is found that both DTB-IIB and DTB-IIC have outstanding anti-loosening performance, as determined using Junker vibration loosening test. The final residual axial loads were kept at more than 80% after the prescribed 2000 cycles by adjusting only the tightening torque of the outer single nut to be fastened later.

References

1. Nishida S (1993) Failure analysis in engineering applications. Butterworth Heineman Co., Ltd, pp 68–104
2. Fukuoka T (2015) Threaded fasteners for engineering and design. Corona Publishing Co., Ltd
3. Hongo K (1964) Loosening of bolt and nut fastenings. Trans Jpn Soc Mech Eng Ser 1(30–215):934–939
4. Yamamoto A, Kasei S (1977) Investigation on the self-loosening of threaded fasteners under transverse vibration-A solution for self-loosening mechanism. J Jpn Soc Precision Eng 43–4:470–475

5. Ohashi N, Ishimura M (1985) On thread-loosening test by transversely repeated impact force. JSPE 51(06):1264–1268
6. Kasei S, Ishimura M, Ohashi N (1988) On self-loosening of threaded joints in the case of absence of macroscopic bearing-surface sliding. JSPE 54(07):1381–1386
7. Ishimura M, Yamanaka H, Shoji Y, Kobayashi T, Sawa T (2011) Loosening of bolted joints under transverse repeated displacement. JAR 0341:1444–1452
8. Nagawa M, Noda N, Ichikawa H, Yamada M, Saito K (2003) Study on anti-loosening super lock nuts and super lock bolts (first volume). Mach Des 47(8):35–42
9. Tekemasu T, Miyahara H (2005) Development of thread rolled anti-loosening bolts based on the double thread mechanism and a performance evaluation. https://doi.org/10.1299/jsmea.48.305
10. Shinbutsu T, Amano S, Takemasu T, Kuwabara T (2017) Thread rolling and performance evaluation of new double-thread bolt-study on development of antiloosening bolt fasteners based on coarse-single coarse-multiple double-thread mechanism, 1st report. https://doi.org/10.9773/sosei.58.404
11. Shinbutsu T, Amano S, Takemasu T, Kuwabara T, Shimura J (2017) Thread rolling and performance evaluation of a new anti-loosening double thread bolt combining single thread and multiple thread. https://doi.org/10.1016/j.proeng.2017.10.1028
12. Tonichi Torque Handbook (2014) Tonichi Mfg. Co., Ltd., p 28–39
13. Junker GH (1969) New criteria for self-loosening of fasteners under vibration. https://doi.org/10.4271/690055

Study on Precision Forging Methods of Difficult-to-Knockout Components with Non-parallel Internal Grooves



Luyi Han, Guangchun Wang, Xin Wang, and Zhao Liu

Abstract Due to the difficulty of knock-out and complex metal flow law caused by the non-parallel internal grooves, the manufacturing of the cross groove CVJ (constant velocity universal joints) outer races mainly relied on machining. Taking the VL-type outer race as a case study, this paper made an exploratory study on the precision forging of these difficult-to-knockout components. A retractable forming mandrel was developed based on which the metal flow behavior through different metal forming methods, including the multi-ram forging and closed backward extrusion, had been researched. The effect of billet shape on forgings and metal flow were analyzed for the multi-ram forming process, and the deformation load and press on the mandrel were focus of the closed backward extrusion method. Influenced by the V-shaped cross grooves, the filling conditions and the pressure distribution between adjacent grooves exhibited regional differences.

Keywords Cross groove CVJ · Precision metal forming · Multi-ram forging · Closed backward extrusion · Material flow behavior · Forming pressure

1 Introduction

Due to the problem of knockout, the cross grooves which are not parallel to the axial direction of workpiece are conventionally machined after forging. And the CVJ (constant velocity universal joints) is a component [1] for connecting the wheel part of a car and the drive shaft, and the batch of those components is large. Geometrically, it can be divided into parallel and non-parallel forms through internal grooves. Among them, the products with parallel grooves have achieved to be produced by metal forming [2]. For such products with non-parallel internal grooves, such as VL-type

L. Han · G. Wang (✉)
School of Material Science & Engineering, Shandong University, Jinan 250061, P.R. China
e-mail: wag@sdu.edu.cn; wgc@sdu.edu.cn

X. Wang (✉) · Z. Liu
School of Mechanical Engineering, Shanghai Dianji University, Shanghai 201306, P.R. China
e-mail: wangx31915@sdju.edu.cn

© The Minerals, Metals & Materials Society 2021

G. Daehn et al. (eds.), *Forming the Future*, The Minerals, Metals & Materials Series,
https://doi.org/10.1007/978-3-030-75381-8_182

CVJ, due to the difficulty of knockout caused by their geometric asymmetry, they can only be processed by milling, grinding and finishing methods, but it is still different to achieve the direct production by metal forming which has become a bottleneck restricting the processing efficiency and production quality of such products.

Compared with mechanical production methods such as milling, metal forming has the advantages of high efficiency, reducing material waste, and improving product performance [3]. In recent years, precision forging has been widely used for the production of mechanical parts with complex geometries. This type of near-net forming method has been studied to wider application in actual industrial production since the high efficiency and high precision of its products [4, 5].

For precision forging of hollow cylindrical workpieces, extrusion is generally adopted [6]. And forgings with concave structures on the external structure, multi-ram forging methods [7, 8] or closed extrusion methods [9, 10] are generally used. There are different characteristics of metal flow in whole or in part under multi-directional press for the above-mentioned methods. The forgings have prominent flow line characteristics, good product performance, and good dimensional accuracy. This kind of forging method has higher requirements for equipment due to the large forging load and complicated die structure. For the workpieces with radial geometric features in the cavity, of which the forging load is directly applied in the radial direction to achieve the radial reduction of the billet and then the internal geometric features are radially forged. Compared to the closed extrusion, the forming load of radial multi-ram forging will be significantly reduced, but this radial forging processing method has higher requirements on the relative movement between the dies and the accuracy of mechanical control.

This paper takes the VL-type CVJ outer race as the research object, and carries out researches on the precision forming method of difficult-to-knockout parts with non-parallel internal groove structure. The non-parallel grooves in the cavity make it impossible to achieve a smooth demolding of the inner mandrel after forging. Combining the structural characteristics of these components, a inner mandrel with retractable ribs is designed in this paper, which can shrink the ribs at the end of forming to achieve smooth knockout. Based on this, two corresponding forming methods—closed backward extrusion and multi-ram forging—are proposed. In order to achieve precision forging of VL-type CVJ workpieces, the exploratory simulation study is carried out.

2 The Objective Products and Design of Die

VL-type CVJ currently used in automobiles can be divided into two forms with bottoms and through holes, as shown in Fig. 1. Among them, the CVJ with a bottom as illustrated in Fig. 1a can be connected to the automobile shaft through a sliding pin, and the another type CVJ, shown in Fig. 1b, is generally connected by bolts. Compared with the parallel slide type, the VL-type CVJ has a longer track grooves, which can effectively reduce its axial size. The specific dimensions of these two

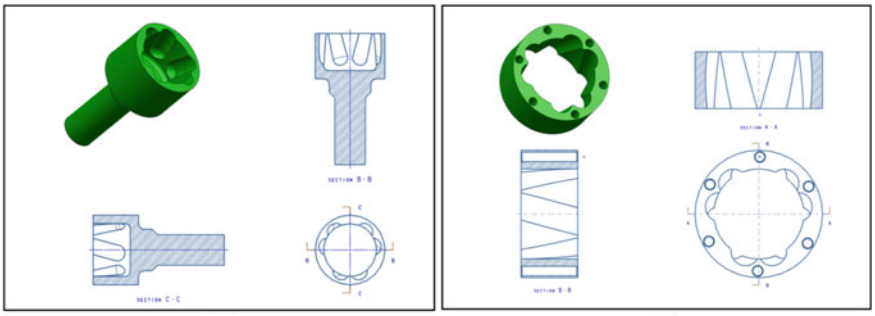


Fig. 1 The objective components, **a** VL outer race with a bottom, **b** VL outer race without a bottom. (Color figure online)

Table 1 The geometric parameters of the CVJs

	Outer diameter	Inner diameter	Axial height	Depth of hole cavity	Corner radius	Volume
CVJ with a bottom	84 mm	63.6 mm	50 mm	45 mm	5 mm	140,539.73 mm^3
CVJ without a bottom	84 mm	63.6 mm	40 mm	40 mm	0 mm	72,796.54 mm^3

objective CVJ are shown in Table 1. Both on the inner walls of these two CVJs, there are 3 pairs of V-shaped symmetrical slide. After forming, the metal will be close to the surface of the die, and the inner mandrel can't be knocked out from the forgings since it will be stuck in these slides.

In order to solve the problem of knockout after the VL-type CVJ is forged, this paper first designs a mandrel die with retractable ribs. As shown in Fig. 2a, this retractable mandrel is mainly composed of four parts, of which the push rod cooperates with the mandrel die, when the push rod is pushed down to the maximum position, the six retractable ribs in the mandrel can be fully expanded. After the forming is completed, the push rod can be reset by the springback device, and the retractable ribs are driven to shrink into the mandrel die by the push rod to achieve smooth knockout.

In this paper, the different forging processes for the above two structures VL-type CVJ are simulated. The simulation of the forging process does not consider the subsequent knockout problems, it means that the scalability of the six ribs on the mandrel does not need to be considered, therefore, the mandrel is simplified into a one-piece structure during the simulation, as shown in Fig. 2b and c. The die shown in Fig. 2b is used for closed backward extrusion of VL-type CVJ with a bottom, and the die illustrated in Fig. 2c is used for multi-ram forging of VL-type CVJ without bottoms.

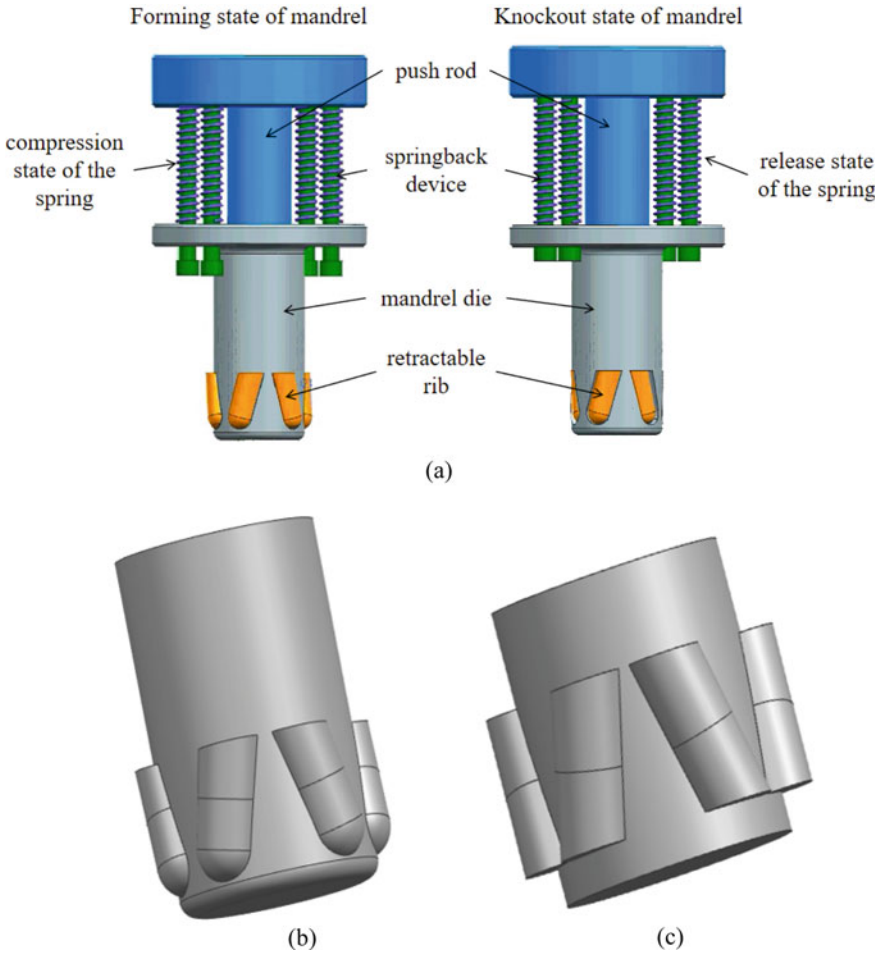


Fig. 2 The design punch for VL outer race. **a** Model of the retractable die. **b** The simplified die model for the VL outer race with a bottom. **c** The simplified die model for the VL outer race without a bottom. (Color figure online)

3 Precision Forging Methods

3.1 Multi-Ram Radial Extrusion Process

The number of punches in the multi-ram radial forging process proposed in this paper depends on the number and pattern of non-parallel grooves in the cavity. For the CVJ with three pairs of V-shaped inner grooves as shown in Fig. 1b, it is suitable to adopt three punches for radial forging, and the die setup is shown in Fig. 3. The axial length of the mandrel rib is 41 mm, which is greater than the effective height of the forging

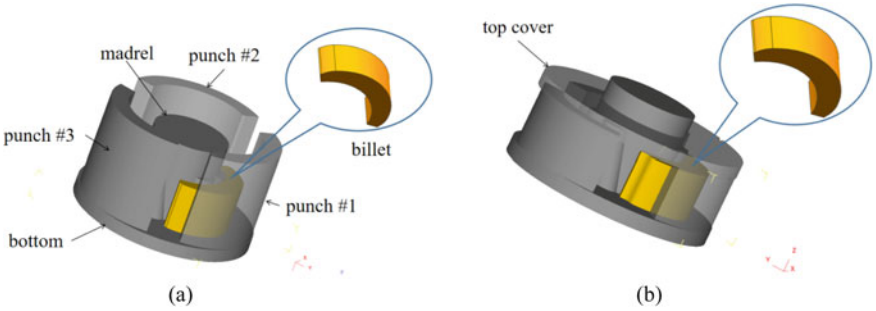


Fig. 3 Layout of dies. **a** Dies assembly without top cover. **b** Die assembly with top lid. (Color figure online)

raceway by 40 mm. The punch is a 118° arc-shaped structure with an inner diameter of 90 mm and corner edges of R2mm. According to the analysis of the geometric relationship, the force of the billet is symmetrical under the action of the punches. In order to improve the efficiency of the simulation calculation, the billet is modeled as one-third according to the 120° equally, and the symmetry plane is set at the cutout.

This three-punch radial forging process has two options. The first is an open top type, which allows the metal to flow in the axial direction at the same time the metal radial flow to fill the grooves during the radial pressure of the punch. As shown in Fig. 3a, the three punches radially feed to compress billet synchronously, and the billet metal radially reduces the diameter while flowing upward to fill the groves. In this way, the axial length of the punches needs to be much higher than the height of the workpiece in order to achieve radial restraint on the material during the forming process. The axial length of the punches in this paper is set to 60 mm.

Another way is to set a top cover on the upper end of the ribs to restrict the axial flow of the metal. In the process of pressurizing the punches, similarly, the metal firstly flows upward in the axial direction while reducing the diameter, and the axial flow of the metal stops when it contacts the cover. So the metal will be forced to flow toward the area that needs to be filled in the radial direction, and a small amount of excess metal will form flashes along the gap between the punches. The corresponding punch height in this way is 44 mm.

In order to prevent the formation of flashes between the punches and reduce the forging pressure by using the divided flow, the billet is designed into a hollow cylinder with unequal thickness, in which the thickness enveloped by the punches is the largest. On the other hand, the thin-walled concave area of the billet should avoid metal folding during the forging process. In order to optimize the outer shape of the final forging, as illustrated in Fig. 4, two types of billet are designed in this paper. The plan A mainly highlights the difference between the material thickness of the enveloping part and the concave area, ensuring that as the punch is pressed down in the radial direction more material can flow into the V-shaped grooves area. As for Plan B, in order to achieve a smoother material flow, the rounded corners between the convex area and the concave area of the blank are greatly increased, and

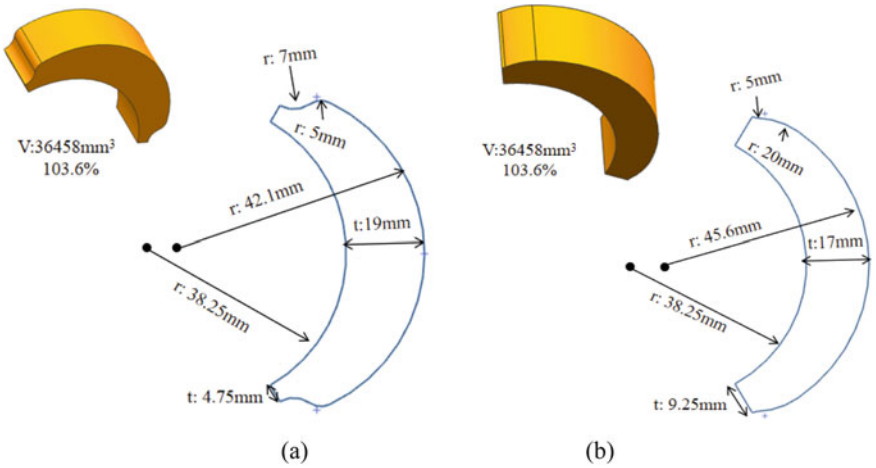


Fig. 4 Geometry design of the billet. **a** Plan A, **b** Plan B. (Color figure online)

the changes in material thickness between the convex area and the concave area of the billet are smoother.

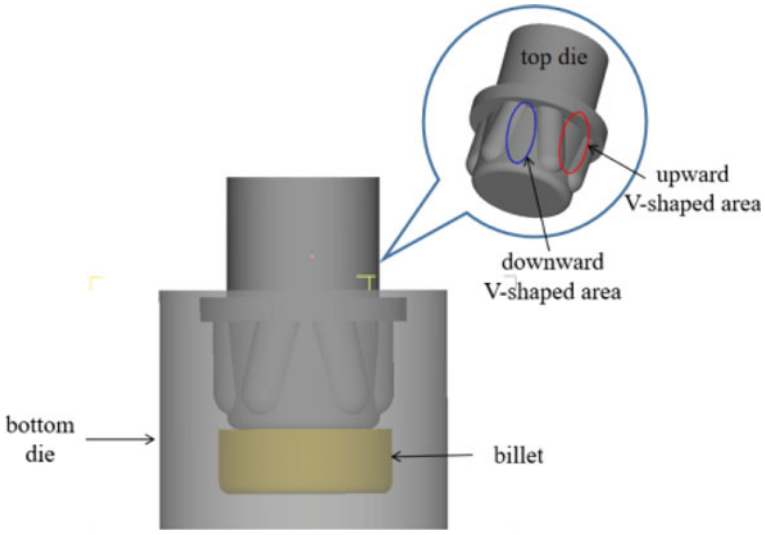


Fig. 5 Setup of the extrusion. (Color figure online)

3.2 Closed Backward Extrusion Process

For the forming of VL-type CVJ with a bottom, this paper proposes a closed backward extrusion method. During the extrusion process, the constraint structure forges the billet in a closed form. And the structure of the simulation dies is shown in Fig. 5. The cylindrical billet has an outer diameter of 83.5 mm, which is convenient for placing in the bottom die with an inner diameter equal to the outer diameter of the forging of 84 mm. According to the principle of constant volume, the height of the cylindrical blank is 26 mm. And the bottom die is designed as an 85 mm deep hole cavity with an inner diameter of 84 mm and a R5 round corner. For the top die used in this method, on the basis of the mandrel structure proposed in the Sect. 2, in order to prevent the underfilling of the up-turned V-shaped area (red area shown in Fig. 5) caused by the upward flow, a fixed cover structure is added on the top of the rib.

4 Simulation Results and Discussion

In this paper, the forging process of VL-type CVJ is simulated by commercial software Deform-3D, AISI-1055 is selected as the material of billet, for dies the material is set to AISI-H-13. The initial temperature of the material is set to 1200 °C and the number of elements of the whole workpiece is set to 150,000, and the corresponding grids of one-third part is 50,000. For the mesh distortion caused by the large deformation of the metal, remesh and target volume techniques are adopted during the forging process. The heat transfer coefficient is set to 11 N/sec/mm/C, and for all contact surfaces of billet and dies the shear friction model is used with the friction factor is set to 0.3. In the backward extrusion process, the pressing speed of the mandrel is 50 mm/s, and the simulation stops when the distance between the bottoms of the mandrel and the deep hole is 5 mm in the Z-direction. In the multi-ram forging simulation, the punch simultaneously presses the blank at a speed of 50 mm/s until it completes the whole stroke.

4.1 Analysis of the Multi-Ram Radial Extrusion Process

First, in order to explore the effect of the billet shape on the forgings, the billets of Plan A and Plan B were used in the simulation of the multi-ram forging method with the top cover. The results are shown in Fig. 6. The volume of the both billets was set to 36458 mm^3. Both forgings formed by the two billet schemes appear flashes in the recess, as highlighted by the red oval in the Figure. The difference is that the metal of Plan A shows a strong tendency to flow radially inward, while the metal of Plan B flows radially outward. Through point tracking analysis at the deepest of the two concave areas, it can be seen that the folds of Plan A are located inside the volume

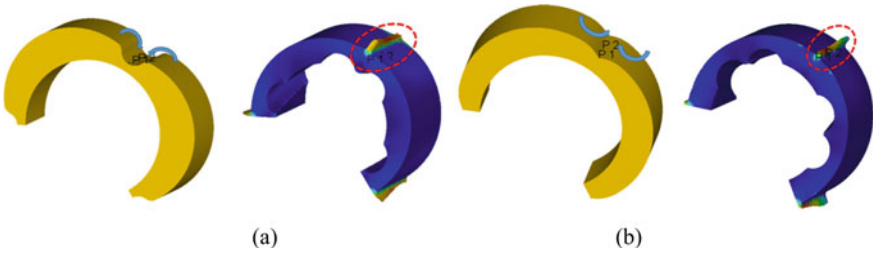


Fig. 6 Folding results of different billet. **a** Plan A, **b** Plan B. (Color figure online)

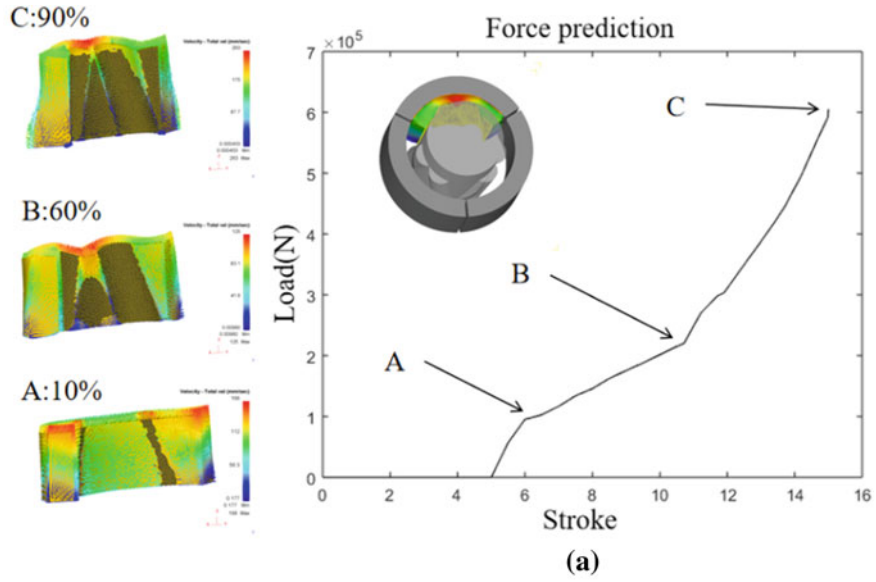
of the forged part, however, the folds of Plan B have been extruded to the flash part, so that the forgings can eliminate the effects of metal folding after machining.

According to the above simulation, it can be seen that the shape of the billets plays a crucial role in the quality of the forgings. The billet in Plan B can effectively eliminate the impact of metal folding and ensure the quality of the forgings. From that point, the billets in plan B are adopted in the following simulations.

Figure 7 shows the results of the two types of multi-ram forging method mentioned in Sect. 3.1. And the billet volume of the type without top cover is set to 37,866 mm^3.

In this paper, the contact rate between the inner wall of the forging and the mandrel is used as a criterion for evaluating the filling condition during the forming process. It can be seen from the simulation results that the filling rate of the final forging is about 90% through the scheme without the top cover, and the metal filling rate reaches 100% when the top cover is added. In the way without the top cover, due to more metal being pressed, the load of the die increases greatly in the initial stage. In this stage, the metal begins to contact the ribs portion of mandrel. With the feed of the punches, the metal slowly flows upward, and the contact rate of the inner wall increases. In this process, the increase in the load of mandrel is slower. At point B, the metal flows to the area near the tip of V-shaped grooves, and the load of the mandrel increases rapidly again. Finally, the metal will flow through the range of the ribs, but the intersecting line areas between the upper part of the grooves and the cylindrical inner wall are still difficult to be filled, which will cause the size defect of the forgings so that it‘s difficult to meet the application requirements.

After the top cover is added, in the initial stage of forging, similarly the metal first contacts the ribs portion of the mandrel, and the load on the punches slowly increases. Until the contact rate of the groove reached about 85%, when the metal began to contact the cover, the load begins to increase sharply. After that, the metal began to flow to the intersecting line areas, this is considered to be the most difficult part to fill the VL-type CVJ. In order to fill in this area, the forging load increases by about 4 times after the cover is added.



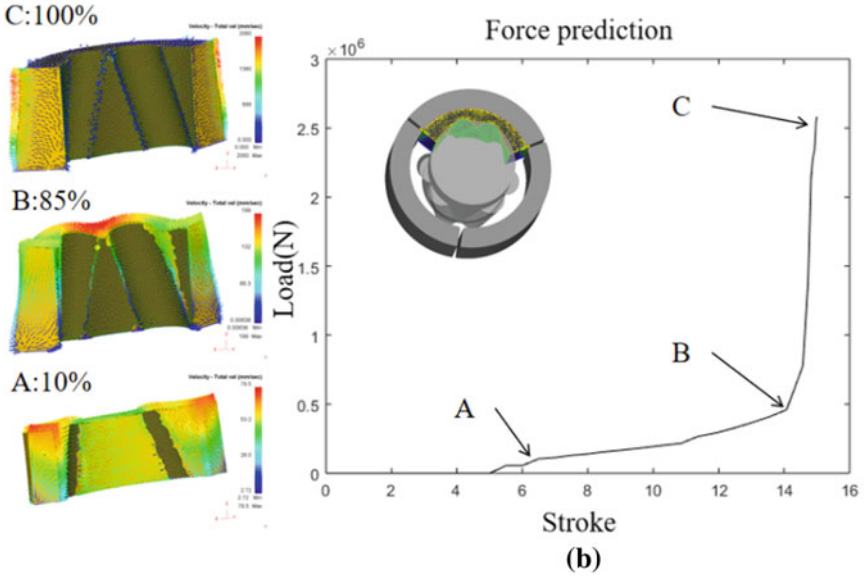


Fig. 7 Forging results of the 3-rams forming. **a** Forging without top cover, **b** Forging with top cover. (Color figure online)

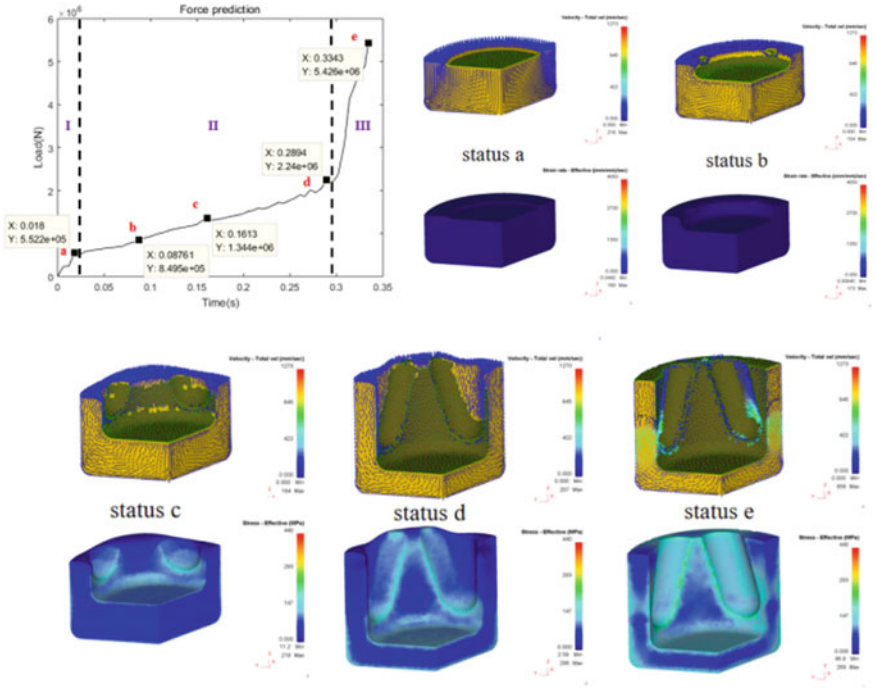


Fig. 8 The forming condition of extrusion. (Color figure online)

4.2 Analysis of the Closed Backward Extrusion

In the closed backward extrusion of the VL-type CVJ with a bottom, the filling process can be divided into 3 stages, as shown in Fig. 8. In the initial stage of extrusion, the bottom surface of the mandrel starts to contact the billet, and the load on the mandrel begins to increase significantly. In this process, the stress value is small and the distribution is relatively uniform. The second stage begins with the metal completely passing through the corner edge of mandrel, at this stage, the material begins to flow upward into the area between the bottom die and mandrel and the forming load rises steadily with the increase of the billet height. Due to the special geometry of the mandrel, the metal flow state is different from that of hollow cylindrical parts, the cavity is divided into 6 regions by the ribs-three upward V-shaped regions and three downward V-shaped regions. From the filling state change of status b to status c, it can be seen that the downward V-shaped area has been in a good contact state during the upward flow of the metal, while the upward V-shaped area is only full at the bottom, and most of the upper area has never been filled. And due to the division of the flow space by the V-shaped ribs, the top end surface of the billet is uneven (status d). At this time, the stress in the area of the intersecting lines of the downward V-shape grooves and cylinder wall is the largest. The third stage

is the closed backward extrusion stage, which starts from the upper end of the billet contacting the cover of the punch to the end of extrusion. When the metal contacts the top cover, the downward V-shaped area is completely filled, but nearly half of upward V-shape area is still not filled. Therefore, as the mandrel continues to press, the metal mainly flows into the area between the upward V-shape area until it is fully formed (status e). The load increased sharply at this stage, its maximum load is about three times that of multi-ram forging. And the stress near the intersecting line is more concentrated than that of its adjacent area.

5 Conclusions

1. In this paper, a simulation study of the three-punch radial forging and backward extrusion processes is performed for the VL-type CVJ. The three-punch radial forging directly affects the metals from the radial direction, and the geometry of the billets plays a crucial role in the quality of the final forgings. The closed backward extrusion mainly relies on the axial flow of the metal to fill the entire forging.
2. In the process of multi-ram forging, it is difficult to fill the area around the intersecting line area of the upward V-shape grooves and cylinder wall without the top end constrained. After adding the cover to restrict the axial flow of the metal, the entire groove area can be filled with a smaller amount of billet, but the corresponding load is increased by about 4 times.
3. For closed backward extrusion, due to the special geometry of the workpiece, the downward V-shaped areas are always formed firstly, and the upward half of the workpiece is not formed until the metal contacts the cover of the mandrel. At the same time, forging load continues to increase as the metal rises, and its value is about three times that of multi-ram forging. The stress is concentrated in the intersecting area of grooves and cylinder. So during the design of the dies, these areas need to be chamfered to facilitate the flow of the metal and reduce the stress concentration.

Acknowledgments The work presented in this paper is supported by the Plateau Disciplines in Shanghai.

References

1. Cardozo WS, Weber HI (2018) A compact formulation for constant velocity joint kinematics. Mech Mach Theory 121:1–14
2. Ku TW, Kim LH, Kang BS (2013) Multi-stage cold forging and experimental investigation for the outer race of constant velocity joints. Mater Des 49:368–385

3. Zhao JH, Deng YL, Zhang J, Tang JG (2019) Effect of forging speed on the formability, microstructure and mechanical properties of isothermal precision forged of Al–Zn–Mg–Cu alloy. Mater Sci Eng A 767:138366
4. Deng L, Ren ZH, Guo P, Jin JS, Wang XY, Li JJ (2019) Precision forming of long-axis forgings with rib-web sections via billet optimization based on flow characteristics. Int J Light Mater Manuf 2(2):97–106
5. Behrens BA, Doege E, Reinsch S, Telkamp K, Daehndel H, Specker A (2007) Precision forging processes for high-duty automotive components. J Mater Process Technol 185(1–3):139–146
6. Yu JQ, Zhao GQ, Cui WC, Chen L, Chen XX (2019) Evaluating the welding quality of longitudinal welds in a hollow profile manufactured by porthole die extrusion: experiments and simulation. J Manuf Process 38:502–515
7. Cheng M, Zhang ZM (2013) Study of metal flow of tee valve body bu multidirectional extrusion and recrystallization. Rev Adv Mater Sci 33:251–256
8. Sun ZC, Cao J, Wu HL, Yin ZK (2018) Inhomogeneous deformation law in forming of multi-cavity parts under complex loading path. J Mater Process Technol 254:179–192
9. Kim YJ, Chitkara NR (2001) Determination of preform shape to improve dimensional accuracy of the forged crown gear form in a closed-die forging process. Int J Mech Sci 43(3):853–870
10. Nayak KC, Sahoo SK (2019) Experimental and finite element analysis of closed-die combined extrusion-forging process: development of socket adopter. Mater Today Proc 18:3482–3491

Incremental Grooving of Thin-Walled Tubes Filled with Discrete Media



Hao-Xing Tang, Tong Wen, and Xia Chen

Abstract To control the undesired deformations like section-distortion and springback during incremental tube wall grooving, we examined the effect of discrete fillers on the deformation of thin-walled tubes during forming. Al6061 tubes with outer diameter of 38 mm and thickness of 1 mm were used in the studies, with silica sands as the fillers. Generalized plastic mechanics was employed to analyze the coupled deformation of the composite structures of discrete media filled tubes; the aggregation of sands was assumed to be compressible continuous body, of which yield behavior was described by the Drucker–Prager criterion. The results proved that compared with hollow tubes, the forming accuracy of incremental tube grooving can be improved under the support of fillers. Specifically, the maximum springback was reduced by more than 3.9%, and the section-distortion also decreased. Moreover, a special deformation mode, the prism-shape distortion, was found to occur when the tool feeding step was large.

Keywords Thin-walled tube · Incremental grooving · Springback · Discrete filler · Defect

1 Introduction

Thin-walled tubular parts are widely used as structural and functional components in the fields of transportation, household appliance, aerospace, etc. In practice, there are large demands of small-batch tubular parts and meanwhile, the geometries become more and more complicated [1].

As a flexible sheet metal forming technology that can satisfy the requirements of efficiency and cost in small lot productions, incremental sheet forming (ISF) has been extended to the manufacturing of tubular parts in recent years [2–4], e.g., to conduct tube end expansion/flaring, reduction, tapering, crimping, bulging, hole flanging on tube wall, etc. Due to the nature of hollow structures and deformation features of

H.-X. Tang · T. Wen (✉) · X. Chen
College of Materials Science and Engineering, Chongqing University, Chongqing 400044, China
e-mail: wentong@cqu.edu.cn

© The Minerals, Metals & Materials Society 2021

G. Daehn et al. (eds.), *Forming the Future*, The Minerals, Metals & Materials Series,
https://doi.org/10.1007/978-3-030-75381-8_183

these processes, the forming accuracy varies with different processing strategies [5, 6]. Main failures, including distortion, unevenness, buckling/wrinkling, and fracture, were investigated from the aspects of force and deformation behavior [7, 8]. Among, springback is the primary factor bringing about geometric deviations from the desired shape. In order to reduce the defects caused by springback, a couple of prediction and compensation models have been proposed [9–11]. However, it is still difficult to obtain a workpiece with acceptable accuracy by conventional incremental sheet forming, especially when the single-point configuration is utilized.

In this paper, we examined the influence of discrete fillers on the deformation of thin-walled tubes during incremental tube grooving. The main aim is to verify the potential of filled media on the control of undesired deformations, such as section-distortion and springback.

2 Analysis Method

To examine the deformation behavior of tube wall under simple and complicated loading, and clarify the effects of filled media on wall deformation during incremental grooving, experiments of dot-denting under lateral pressure and incremental tube grooving, as shown in Fig. 1, were designed. Al 6061 tubes with size of Φ38 mm (outer diameter) × 1 mm (thickness) × 200 mm (length), were used.

Considering the performance, acquirability, recyclability and cost, powdery silica sands with average size of 200 meshes were used as fillers. The silica sands were sealed inside the mother tubes by plugs at both ends before operation. Bar tools with diameter of 10 mm and hemispherical head were used.

Dot-denting tests were conducted on a universal material testing machine (Fig. 2a), where the bar tool moves down at a uniform velocity of 0.1 mm/s to dent the tube wall, with the desired total denting depth of 11 mm. For incremental tube grooving, the mother tubes were horizontally fixed on the lathe chuck (Fig. 2b). The expected depth H of circular groove is from 0.5 mm to 4 mm. During forming, the tubes circumferentially rotate at a speed of 45 rad/min, at the same time the bar tool is radially fed.

Numerical simulations were conducted in ABAQUS®. According to the theory of generalized plastic mechanics, the aggregation of discrete sands is assumed to be

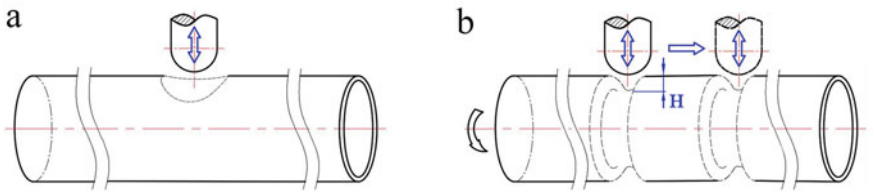


Fig. 1 Schematic of the experiments: **a** lateral dot-denting; **b** circular groove. (Color figure online)

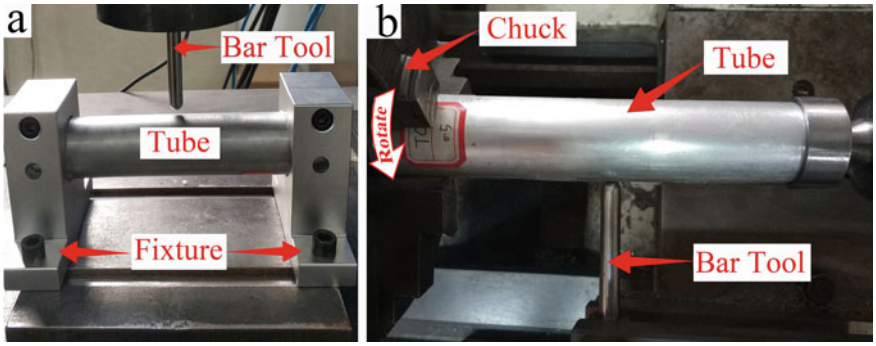


Fig. 2 Experimental sets: **a** lateral dot-denting; **b** incremental tube wall grooving. (Color figure online)

compressible continuous body, and the yield behavior is described by linear Drucker–Prager (D-P) model, which can be written as [12]

$$Fs = t - p\tan\beta - d = 0 \tag{1}$$

where Fs is the function of yield surface, t is the deviatoric stress, p is the equivalent pressure, β is the material's internal friction angle and d is the material's cohesion.

The internal friction angle was tested using a model ZBQ-4 strain-controlled direct shear apparatus [13], and the yield stress can be written as

$$\sigma = d/(1 - \frac{1}{3}\tan\beta) \tag{2}$$

Mechanical parameters as listed in Table 1 were used in the numerical analysis. Coulomb's friction law was applied to the interface between bar tool and tube wall. General machine oil was used as lubricant, and the friction coefficient μ is 0.15.

Table 1 Mechanical parameters of the fillers and Al 6061

Item	Silica sand	Al 6061
Density ρ (kg/m^3)	1500	2900
Elastic modulus E (MPa)	50	68,900
Poisson ratio v	0.33	0.4
Internal friction angle β (°)	28.7	–
Cohesion d (kN)	81.75	–

3 Results and Discussion

3.1 *Deformation Feature of Tube Wall During Dot-Denting*

Figure 3 shows the dot-denting results of hollow and filled tubes. It can be seen that the silica sands do not change the basic wall deformation mode, which can be approximately described by the plastic hinge model [14].

Since the fillers give support to the wall during forming as in a two-point ISF process, the section-distortion can be reduced, as the displacement distributions shown in Fig. 3.

Figure 4 shows the wall thickness distribution of the dented tubes. Under the compressing of bar tool, the discrete silica sands gradually become denser; consequently, the constraint and friction force of the filler increase, resulting in a decreased fluidity of the filler and less uniform distribution of wall thickness.

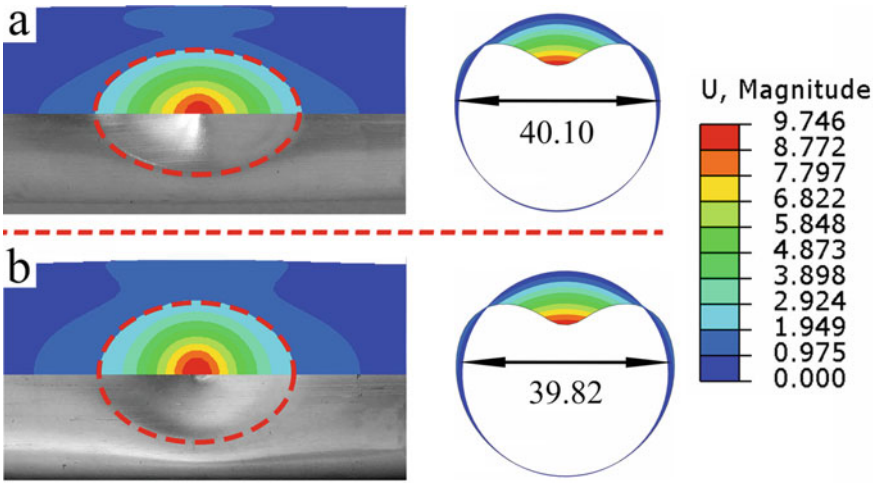


Fig. 3 Experiment and simulation results (displacement) of dot-dented Al 6061 tubes (Denting depth is 11 mm): **a** hollow; **b** filled. (Color figure online)

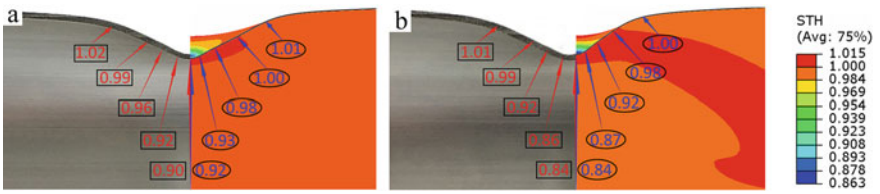


Fig. 4 Comparison of the wall thickness (STH) distribution of dot-dented tubes. **a** hollow; **b** filled. (Color figure online)

3.2 *Deformation Features of Tube Wall During Incremental Grooving*

Figure 5 shows the experiment results of incremental grooving with various denting depths. It can be seen that circular grooves on tube wall were formed under both conditions.

Grooves on filled tubes are relatively more inerratic and smooth, compared with those on hollow tubes. With same feeding distance of the tool, the obtained groove depth on hollow tubes is shorter due to larger springback deformation.

Figure 6 compares the springback amounts of the tube walls grooved with different depths in the experiments. The springback values are calculated by comparing the expected and actually obtained grooving depths. It can be seen that the deeper the groove is, the greater the springback will be. When the filler is employed, the structural stability increases and springback decreases. On average, springback of the filled tubes was reduced by 3.9% compared with that of hollow tubes.

Figure 7 shows the typical defects found in the experiments. When the wall deformation reaches the limit of material, fracture occurs as shown in Fig. 7a. With the filled silica sand, the material flow of tube wall is obstructed and fracture is easier to take place. The nonuniform (or roundness deviation) as shown in Fig. 7b is mainly caused by the bending of mother tubes under the lateral pressure of tool. Figures 7c and 8 show a special failure mode, prism-shape distortion, taking place under certain condition where the formed circular grooves present a section view of polygonal shape,

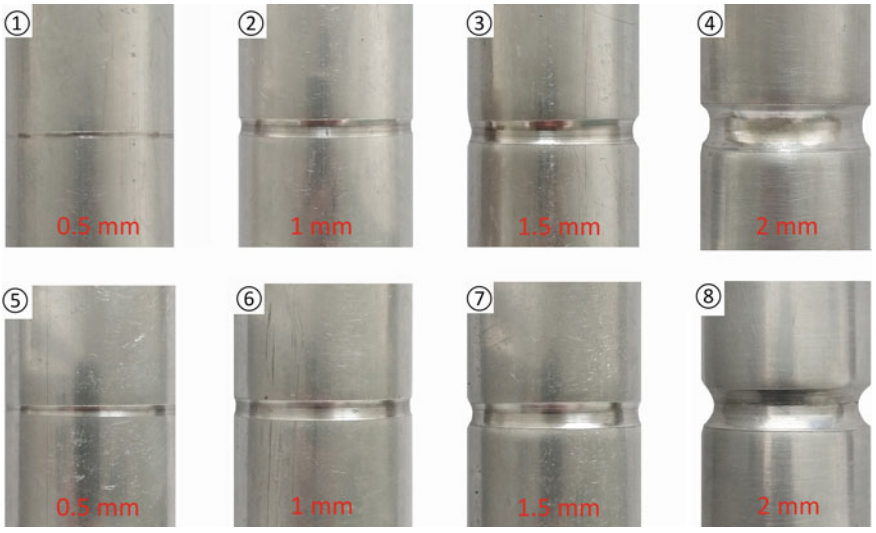


Fig. 5 Tubular samples formed with various groove depths H. (①–④, hollow tubes; ⑤–⑧, filled tubes). (Color figure online)

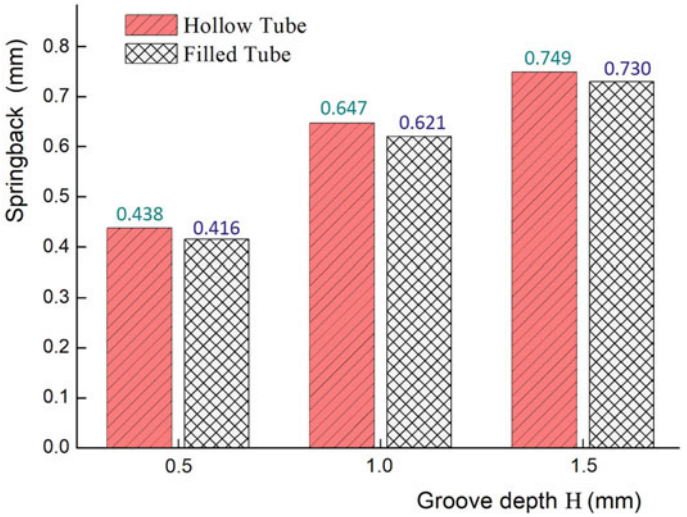


Fig. 6 Amounts of springback with different groove depths. (Color figure online)

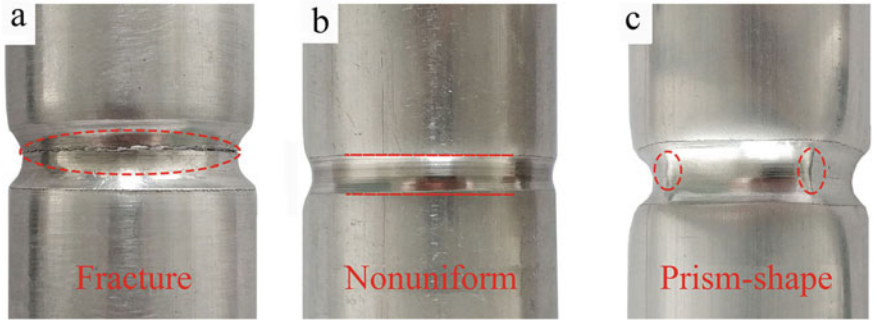


Fig. 7 Typical defects: **a** fracture; **b** nonuniform; **c** prism-shape distortion. (Color figure online)

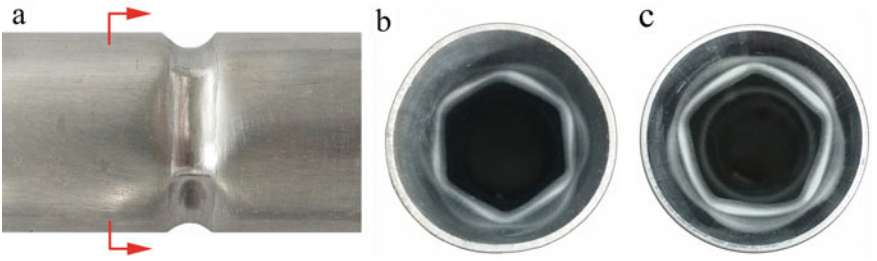


Fig. 8 Appearance of the prism-shape distortion. **a** lateral view; **b** hexagonal section; **c** pentagonal section. (Color figure online)

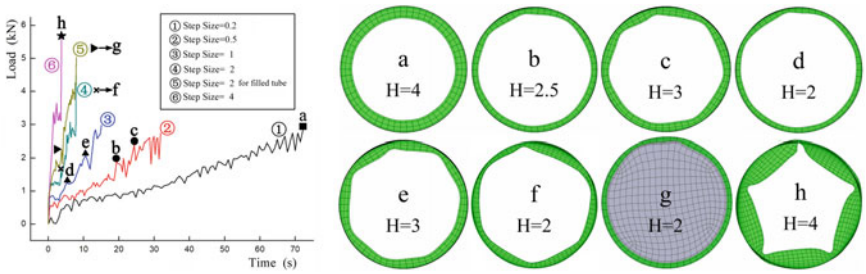


Fig. 9 Forming loads and cross-section shapes of the formed grooves under different conditions. (Color figure online)

especially hexagon or pentagon. In the following, we will discuss the occurrence conditions of such defect.

3.3 Occurrence Conditions of the Prism-Shape Distortion

For thin-walled structures, instability would take place when the load exceeds the limitation of structural stiffness. Instability would lead to unexpected deformation of the wall.

Since the load in incremental sheet forming is directly affected by the feeding velocity of tool, we designed testing groups with the step sizes of 0.2 mm, 0.5 mm, 1 mm, 2 mm, and 4 mm, respectively. The target grooving depth is 4 mm. In the group with step size of 2 mm, hollow and filled tubes were used.

Figure 9 shows the simulated results of the loads and wall deformation under different conditions. It can be seen that the simulation can exactly reflect the phenomenon of prism-shape distortion. For the case with step size of 0.2 mm, no defect occurring throughout the course and the formed groove shape is perfect. When the step size increases, the forming load increases and the critical groove depth without defect decreases, as shown in Fig. 9b and d. In the cases with large step sizes, for example, larger than 1 mm, the cross-section shape becomes more irregular, see Fig. 9c, e, f, and h.

The simulated results in Fig. 9f and h correspond well with the experiment results in Fig. 8b and c. The compressing force on tube wall increases with the step size increases, and then the wall collapses quicker; the cross-section shape evolves toward less number of sides, e.g., from hexagon to pentagon. Compared with the hollow tubes, the composite structure of filled tube has higher integral stiffness, which delays the wall collapse under same conditions (Fig. 9g). Therefore, reducing the step size and using fillers can prevent cross-section distortion during grooving.

4 Conclusions

(1) Tube wall grooving can be performed by the dieless incremental forming with a simple hemispherical bar tool. Typical defects include cross-section distortion, nonuniform, springback , and wall fracture.
(2) Similar to the two-point ISF processes, the accuracy of incremental tube wall grooving can be improved under the support of fillers. In the current study, the maximum springback was reduced by more than 3.9%, and the section-distortion also decreased.
(3) Radial collapse of the tube wall caused by large forming load under large feeding step of the tool is the dominant reason for the occurrence of the special defect mode of prism-shape during tube wall grooving. Reducing the feeding step size and filling discrete media can prevent the defect.

Acknowledgments This project is supported by National Natural Science Foundation of China (Grant No. 51575066).

References

1. Zhang XW, Yu TX (2009) Energy absorption of pressurized thin-walled circular tubes under axial crushing. Int J Mech Sci 51:335–349
2. Behera AK, Verbert J, Lauwers B, Duflou JR (2013) Tool path compensation strategies for single point incremental sheet forming using multivariate adaptive regression splines. Comput Aided Design 45:575–590
3. Movahedinia H, Mirnia MJ, Elyasi M, Baseri H (2018) An investigation on flaring process of thin-walled tubes using multistage single point incremental forming. Int J Adv Manuf Technol 94:867–880
4. Hwang SY, Lee JH, Yang YS, Yoo MJ (2010) Springback adjustment for multi-point forming of thick plates in shipbuilding. Comput Aided Design 42:1001–1012
5. Khan MS, Coenen F, El-Salhi S, Penalva M, Rivero A (2015) An intelligent process model: predicting springback in single point incremental forming. Int J Adv Manuf Technol 76:2071–2082
6. Li ZF, Lu SH, Chen P (2016) Improvement of dimensional accuracy based on multistage single point incremental forming of a straight wall cylinder part. Int J Precis Eng Man 18:1281–1286
7. Wen T, Zheng J, Qing J, Fang JZ (2017) Outwards and inwards crimping of tube ends by single-point incremental forming. Procedia Eng 207:854–859
8. Neto DM, Oliveira MC, Santos AD, Alves JL, Menezes LF (2017) Influence of boundary conditions on the prediction of springback and wrinkling in sheet metal forming. Int J Mech Sci 122:244–254
9. Ambrogio G, Costantino I, De Napoli L, Filice L et al (2004) Influence of some relevant process parameters on the dimensional accuracy in incremental forming: a numerical and experimental investigation. J Mater Process Technol 153–154:501–507
10. Yang C, Wen T, Liu LT, Zhang S, Wang H (2014) Dieless incremental hole-flanging of thin-walled tube for producing branched tubing. J Mater Process Technol 214:2461–2467
11. Wen T, Yang C, Zhang S, Liu LT (2015) Characterization of deformation behavior of thin-walled tubes during incremental forming: a study with selected examples. Int J Adv Manuf Technol 78:1769–1780

12. Hibbitt R, Karlsson D, Sorensen C (2006) ABAQUS user's manual (version 6.3). Pawtucket, RI
13. Wen T, Liu Q, Huang Q, Ou WX, Feng JQ (2016) Deformation and densification behavior of discrete media filled thin-walled tubes during forward extrusion. Trans Nonferrous Met Soc China 26:2162–2169
14. Vasilikis D, Karamanos SA (2009) Stability of confined thin-walled steel cylinders under external pressure. Int J Mech Sci 51:21–32

Vacuum Hot-Roll Bonding of Titanium and Carbon Steel Using Pure Iron Interlayer



Chao Yu, Hong Xiao, and Xiao Liu

Abstract In this paper, the effect of a pure iron interlayer on the properties of the multi-pass hot-roll bonding titanium/carbon steel plate was studied. The mechanical and microstructural properties of the composite plate were investigated by optical microscopy and scanning electron microscopy, as well as tensile-shear, bending, and tensile tests. The results show that when the reduction ratio is below 18%, the shear strength of the interface is higher with the pure iron interlayer than without it. At 35% reduction, the shear strength is similar in both cases. At a reduction ratio of 68%, with the pure iron interlayer, fracture of the bonding interface occurs on the titanium matrix, whereas without the pure iron interlayer, fracture occurs on both the titanium matrix and the compound layer on the interface; the pure iron interlayer improves the bending and tensile properties of the titanium/carbon steel plate appreciably.

Keywords Titanium · Steel · Pure iron interlayer · Hot-roll bonding · Properties

1 Introduction

Titanium clad steel plates not only have the corrosion-resistant of titanium but also have the weldability, formability, and thermal conductivity of carbon steel, and it also saves precious titanium metals [1, 2]. Due to these characteristics, titanium-clad steel plates are widely used in the petrochemical, shipbuilding, marine industries, and nuclear industry, among others [3–5]. Currently, several methods have been used to manufacture titanium-clad steel plates, such as diffusion bonding, explosive welding, and rolling bonding.

Compared with the diffusion bonding and the explosive cladding methods, the rolling bonding method can produce large-sized and thin titanium clad steel plates with high production efficiency, low pollution, and low energy consumption [6, 7]. In the production of titanium clad steel plates, the formation of brittle compounds

C. Yu · H. Xiao (✉) · X. Liu
National Engineering Research Center for Equipment and Technology of Cold Strip Rolling, Yanshan University, Qinhuangdao 066004, Hebei, P.R. China
e-mail: xhh@ysu.edu.cn

© The Minerals, Metals & Materials Society 2021

G. Daehn et al. (eds.), *Forming the Future*, The Minerals, Metals & Materials Series,
https://doi.org/10.1007/978-3-030-75381-8_184

such as TiC, FeTi, and Fe_2Ti on the interface may cause the degradation of mechanical properties [8, 9]. Many studies used Cu, Ni, and Nb interlayers to prevent the formation of TiC, FeTi, and Fe_2Ti compounds and improved the mechanical properties of the titanium-steel plate. Zhao et al. [10] studied the interfacial structure and mechanical properties of hot-roll bonded joints between titanium alloy and stainless steel using copper interlayer. The maximum tensile strength of 343 MPa was obtained at a bonding temperature of 780 °C and the reduction of 20% due to the smaller volume fraction of brittle intermetallics. Yan et al. [11] used a nickel interlayer in hot-roll bonding of titanium alloy and stainless steel. The maximum tensile strength of 440 MPa was obtained at a bonding temperature of 760 C and a reduction of 20%. Ti_2Ni and $TiNi_3$ appear on the fracture surface, and the fracture occurs at the transition layers, which mainly consist of the intermetallic. Zhao et al. [12] carried out a hot-roll bonding between titanium alloy and stainless steel in a vacuum using niobium interlayer. The maximum interface tensile strength of ~417.5 MPa was obtained at a bonding temperature of 900 C and a reduction of 25%. The tensile fracture occurred in the niobium interlayer and had the characteristics of plastic fracture. However, because of high costs, these materials are not widely used in the production of titanium-clad steel plates. Yu et al. [13] used a pure iron as interlayer in the hot-roll bonding of titanium/carbon steel plate with a single pass reduction ratio of 25%, the properties of the plate with and without pure iron interlayer were compared. Yu found that, using the pure iron interlayer and at a bonding temperature of 850 C, the formation of the TiC and FeTi compounds are effectively prevented. The shear strength of the bonding surface reaches a maximum of 237.6 MPa and it is higher with the pure iron than without it (~197.9 MPa) under the same rolling process.

The above studies used a single pass reduction ratio to bond the titanium and steel at different temperatures; however, multi-pass rolling is often required in the industrial production in order to obtain a large and wide composite plate. The properties of the composite plate will also change in the multi-pass rolling process. It is necessary to study the performance of the composite plate after multi-pass rolling. Therefore, in this paper, the effect of the reduction ratio on the properties of the hot-roll bonding titanium/carbon steel plate with pure iron interlayer is studied, and the bending and tensile tests of the composite plate are carried out to study the mechanical and microstructural properties after multi-pass rolling.

2 Experiments

The assembly pattern is shown in Fig. 1, in which the thicknesses from top to bottom are 6 mm (carbon steel), 3.7 mm (titanium), 1 mm (pure iron), and 5 mm (carbon steel). The chemical compositions of these materials are presented in Table 1. Before assembling the billet, the oxides on the surfaces of the metals were removed via grinding machine, and then, the surfaces were repeatedly cleaned with acetone and alcohol and immediately dried. While the exterior of the assembled billet was welded,

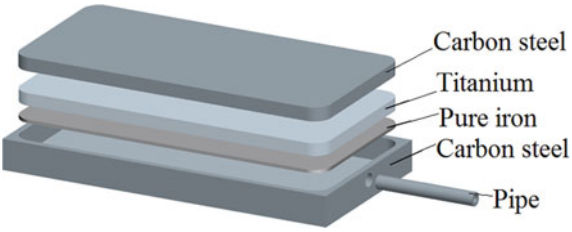


Fig. 1 Assemble pattern. (Color figure online)

Table 1 Chemical composition of the raw materials

Materials	Composition (wt.%)									
	C	Si	Mn	P	S	O	N	H	Ti	Fe
Titanium	0.012	–	–	–	–	0.07	0.01	0.008	Bal.	0.062
Carbon steel	0.127	0.162	0.382	0.015	0.008	–	–	–	0.01	Bal.
Pure iron	0.002	0.02	0.05	0.007	0.003	–	–	–	–	Bal.

argon gas was blown into the billet through a pipe to prevent internal oxidation at high temperatures caused by the welding. Next, the pressure inside of the billet was brought to 0.1 Pa through the pipe using a vacuum pump, at which point, the pipe was sealed. The size of the assembled billet was 100 mm × 50 mm × 15.7 mm. Because the phase transition temperature of titanium is 882°C, the mechanical properties of the titanium change radically near this temperature. Above 882°C, Fe readily dissolves in titanium to form Fe_2Ti and FeTi compounds. Therefore, in order to stabilize the mechanical properties of titanium during rolling, the heating temperature of the billet was chosen to be 850°C to limit both the deformation resistance during rolling and the formation of Fe_2Ti and FeTi compounds. The billets were heated in a furnace for 2 h, rolled at a speed of 50 mm/s, and cooled to room temperature in air. The rolling reduction ratios were 8%, 18%, 35%, 54%, and 68%, among them, the reduction rate of 8%, 18%, and 35% is single-pass rolling, 54% (35% + 30%) and 68% (35% + 30% + 30%) are two passes and three passes rolling respectively. To exclude the influence of air entry and other accidental factors on the experimental results (e.g. the entry of air will cause the formation of oxides at the interface during heating, which will significantly reduce the bonding strength), three billets were rolled at each temperature, and the experiments were repeated to ensure that at least two experimental datasets were reliable.

The tensile-shear, bending, and tensile tests were carried out using an Inspekt Table 100 kN instrument. The speed was 1 mm/min. The tension-shear (6 samples), bending (6 samples) and tensile (6 samples) test samples are shown schematically in Fig. 2.

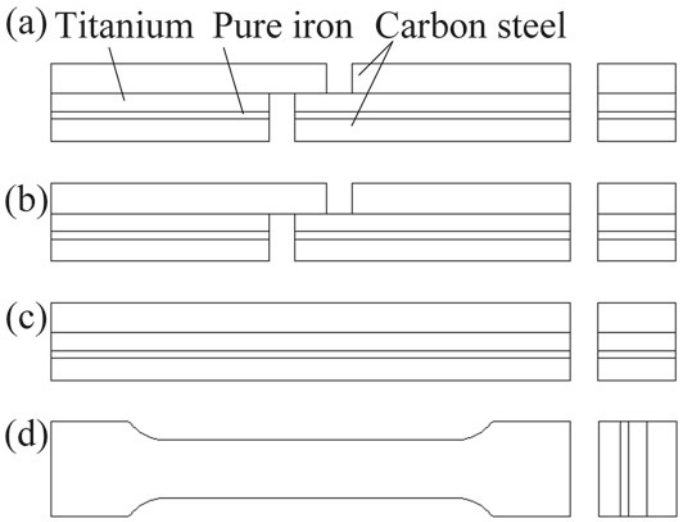


Fig. 2 Schematic of the test samples: **a** measuring the tension-shear strength of the side without the pure iron, **b** measuring the tension-shear strength of the side with the pure iron, **c** bending test sample, **d** tensile test sample

3 Results and Discussion

3.1 Interfacial Structure of Titanium/Carbon Steel Clad Plates

Secondary electron images of the interfaces are shown in Fig. 3. At an 8% reduction ratio and without the pure iron, there are some pores on the interface, as shown in Fig. 3a. On the other hand, with the pure iron, the interface is smooth and has no pores, as shown in Fig. 3b. This indicates that at the 8% reduction ratio, the pure iron combines with titanium better than carbon steel combines with titanium. When the reduction ratios are 35 and 68%, there are no pores on the interface, and grain refinement occurs on both the carbon steel and pure iron sides, as shown in Fig. 3c,d,e, and f. From Fig. 3f, it can be seen that at a reduction ratio of 68%, some pearlites are formed on the pure iron side, indicating that C atoms have diffused from carbon steel to pure iron.

Figure 4 shows the secondary electron images and element surface scanning analysis images of the fracture surface on the pure iron side using the pure iron at a 68% reduction. Fe element is not found by the element surface scanning. As shown in Fig. 4b, with using the pure iron, the fracture surface is full of Ti, and as shown in Fig. 4c, there are a large number of dimples distributed along the fracture surface, which is characteristic of ductile fracture. This indicates that the fracture absolutely occurs on the titanium matrix. This indicates that the strength of the bonding surface

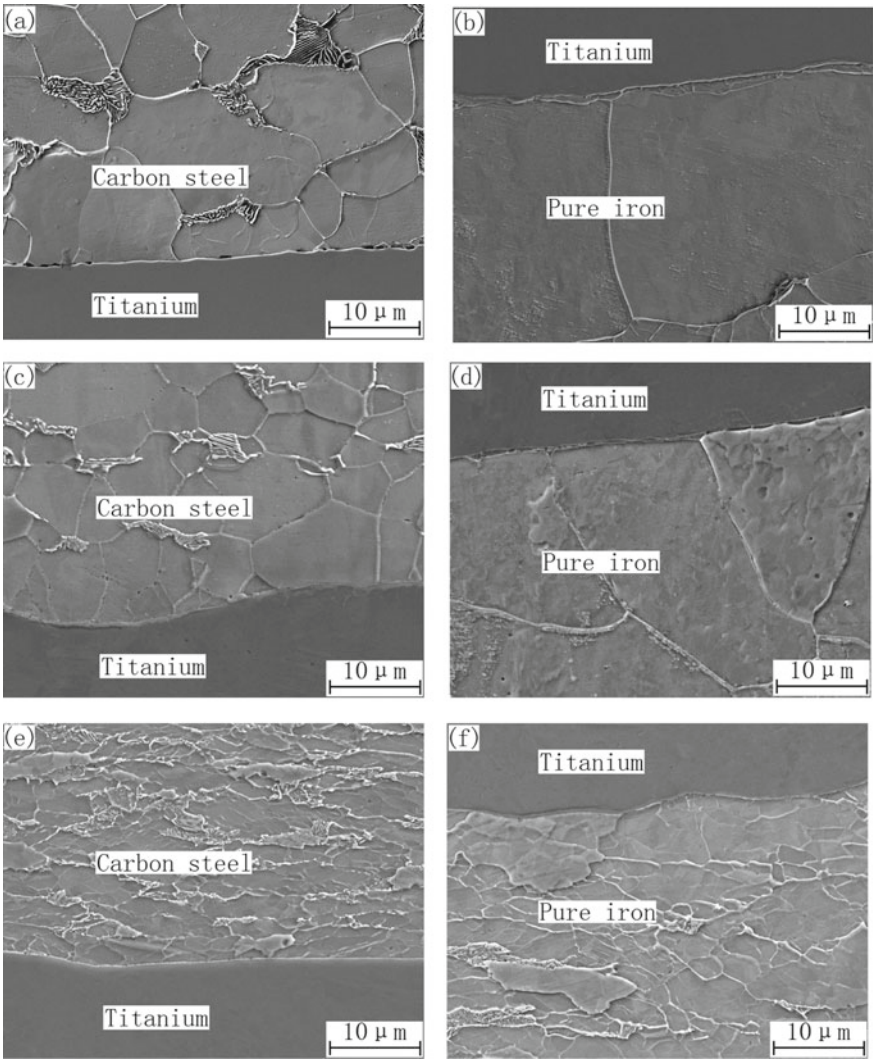


Fig. 3 SEM images of the bonding interface at **a** and **b** 8%, **c** and **d** 35%, **e** and **f** 68%

is high and between the pure iron and the titanium is also high. The strength of the pure iron matrix was intensified for the increase of the pearlite and the grain refinement as shown in Fig. 3f.

Without using the pure iron, the fracture surface on the carbon steel side at 68% is shown in Fig. 5a. The elements' distribution is shown in Fig. 5b and c, there is a large amount of Ti and a smaller amount of Fe distributed on the fracture surface. The microstructures of these two main element distribution regions are, respectively, shown in Fig. 5d and e. Figure 5d reveals brittle fracture characteristics on the surface,

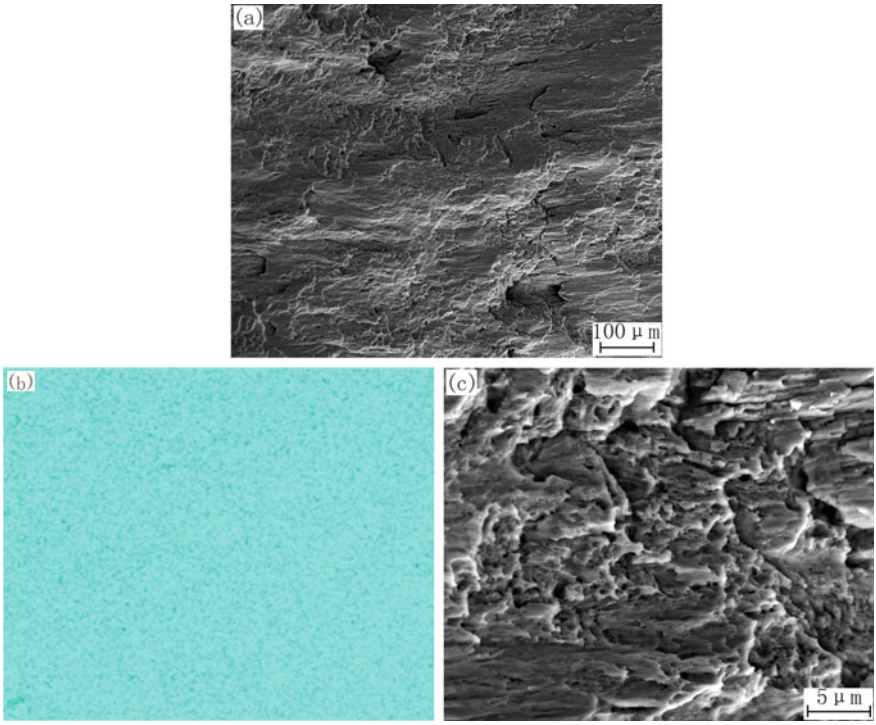


Fig. 4 SEM images of the fracture surface on the pure iron side at 68%: **a** overall morphology, **b** Ti distribution on Fig. 4a, **c** microstructure of the fracture surface. (Color figure online)

indicating that brittle intermetallic compounds have been formed there. Figure 5e presents obvious ductile fracture features with many dimples. The results indicate that fractures occur mainly on the Ti matrix, though some occur in the brittle region at the interface.

Figure 6 shows the element distribution profiles across the interface at a bonding reduction ratio of 68%. The Ti and Fe diffusion distances are similar for both interfaces and are approximately 1.5 μm. Comparing the intensity of C across the interface between Fig. 6a and b, it can be seen that, without the pure iron, the C is concentrated near the interface. Conversely, with the pure iron, such concentration is not as obvious. This shows that adding the pure iron interlayer can effectively reduce C diffusion to the interface from carbon steel, thus reducing the formation of brittle compounds TiC on the interface.

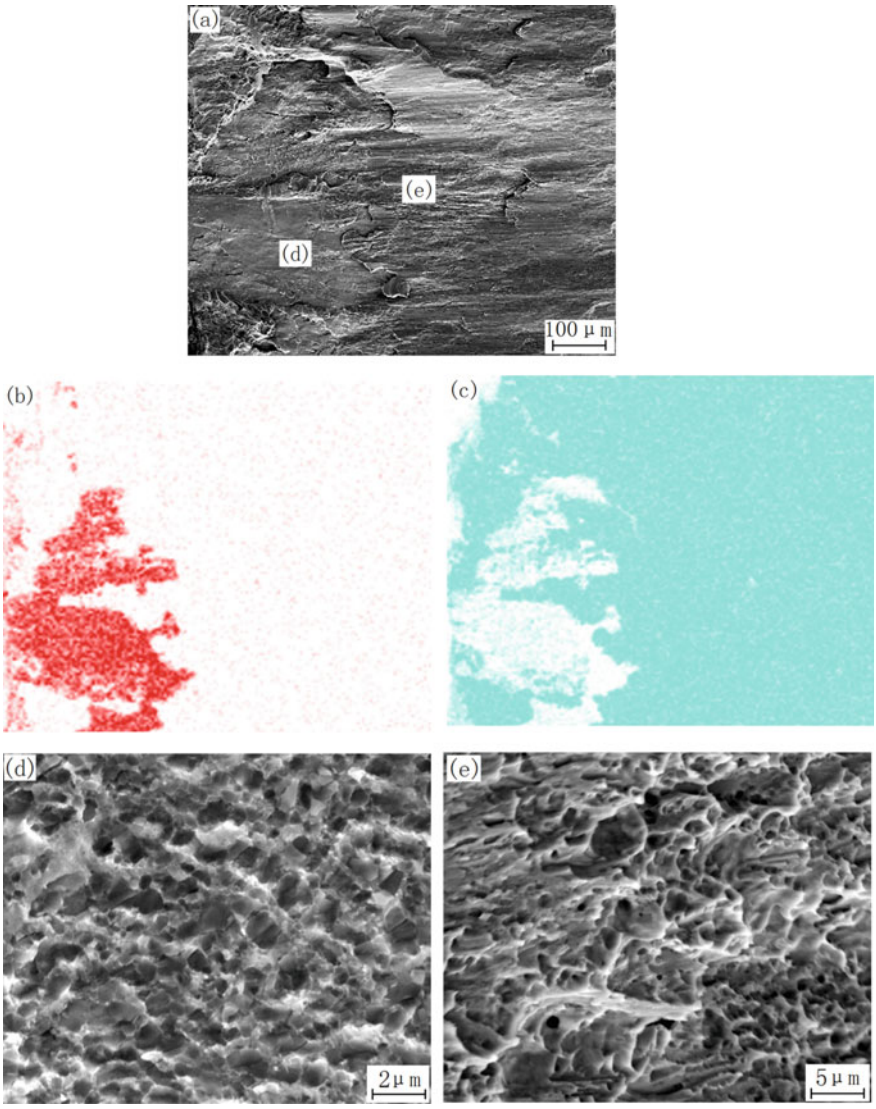


Fig. 5 SEM images of the fracture surface on the carbon steel side at 68%: **a** overall morphology, **b** Fe distribution on Fig. 5a, **c** Ti distribution on Fig. 5a, **d** and **e** microstructure of areas selected from Fig. 5a. (Color figure online)

3.2 Mechanical Properties of Titanium/Carbon Steel Clad Plates

The effect of the rolling reduction ratio on the interfacial shear strength of titanium clad steel plate with and without the pure iron interlayer is shown in Fig. 7. When the

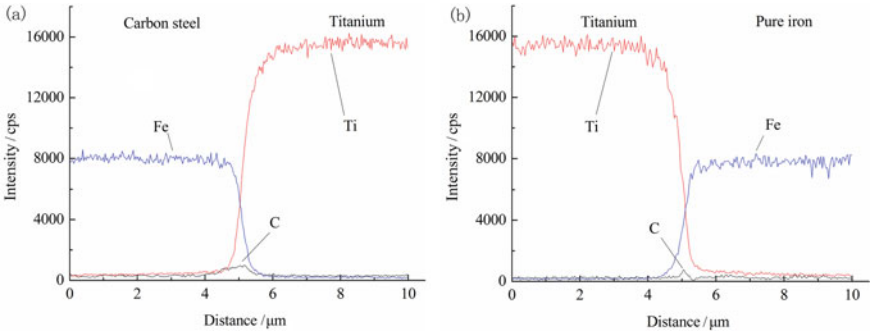


Fig. 6 Element distribution profiles across the interface: **a** between carbon steel and titanium, **b** between titanium and pure iron. (Color figure online)

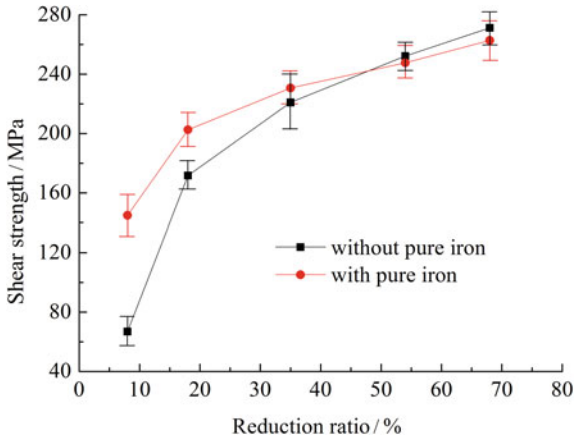


Fig. 7 Effect of reduction ratio on the shear strength of titanium clad steel plates. (Color figure online)

reduction ratio is between 8% and 68%, the shear strength of the interface increases with an increase in reduction ratio: without a pure iron interlayer, the shear strength increased from 66.9 MPa to 271.2 MPa, and with a pure iron interlayer, the shear strength increased from 144.8 MPa to 262.8 MPa. When the reduction ratio is less than 18%, the shear strength is much higher with the pure iron interlayer than without it. When the reduction ratio is greater than 35%, the shear strengths on both sides are similar. The shear strength of the interface reaches the standard value of 140 MPa from the GB/T 8547–2006 type 1 titanium clad steel plate when the reduction ratio is 18% without the pure iron interlayer and 8% with it. The shear strength reaches the standard value of 196 MPa from the type 0 titanium-clad steel plate when the reduction ratio is 35% without the pure iron interlayer and 18% with it. It can be concluded that the addition of the pure iron interlayer improves the shear strength of the composite plate at small reduction ratios. When the reduction ratio is large, the shear strength of the interface on both sides is close to the shear strength of the titanium matrix, meaning the effect of the pure iron interlayer on the shear strength

is not as obvious. This is due to the low deformation resistance and the good metal fluidity of the pure iron interlayer, when the reduction ratio is small, the pure iron can contact the titanium and the steel more closely, making the pores on the interface disappear, as shown in Fig. 3a and b. The close contact can promote the diffusion of elements, so as to improve the bonding strength. When the reduction ratio is large, without the pure iron interlayer, the titanium and the steel can also contact closely, making the pores disappear, as shown in Fig. 3c. The amount of compounds at the interface of both sides is not much, and the shear fractures almost occur on the side of the titanium matrix, so the shear strength of both sides is relatively close.

Figure 8 shows the macro photographs of a bent specimen at a reduction ratio of 68%. Whether the pure iron is on the interior or the exterior, there are no macroscopic cracks after bending. An optical specimen was taken from the bent specimen to observe the microstructure, which is shown in Fig. 9. Without the pure iron, there are some microcracks on the titanium side whether the pure iron is on the interior or the exterior as shown in Fig. 9a and d. Because the amount of deformation is greater on the outside than on the inside, there are more cracks on the outside. With the pure iron, no microcracks were found on the interface as shown in Fig. 9b and c. Therefore, when titanium and carbon steel are composited by hot rolling, brittle compounds are easily formed on the interface. The poor plasticity of such compounds results in the formation of microcracks during bonding. This suggests that the addition of a pure iron interlayer can effectively inhibit the generation of compounds, thereby improving the bending performance of the composite plate.

Tensile specimens were taken along the rolling direction of the composite plate with a 68% reduction ratio. The tensile test results are shown in Fig. 10. Take one of the specimens as an example, without the pure iron, when the strain was 0.185, carbon steel and titanium became divided, resulting in the invalid. With the pure iron, when the strain was 0.192, the pure iron and titanium became divided, and

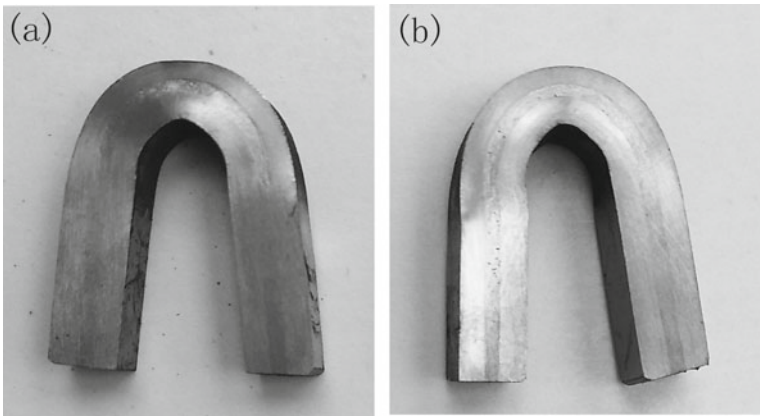


Fig. 8 Macro photographs of bent specimen: **a** pure iron is on the interior, **b** pure iron is on the exterior

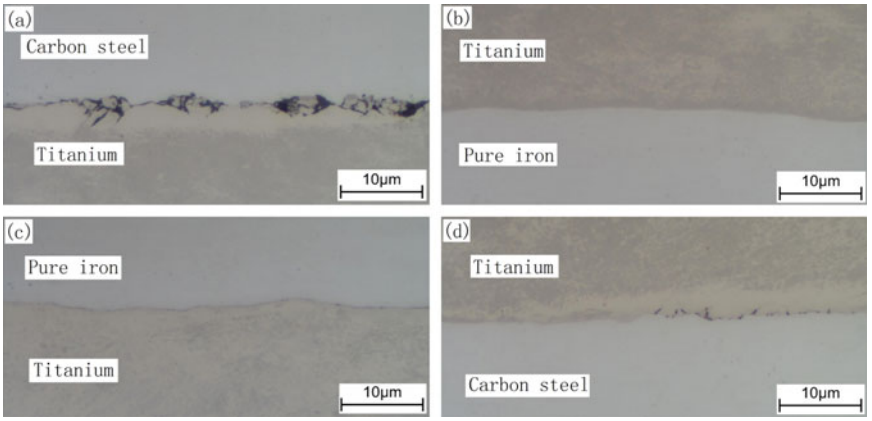
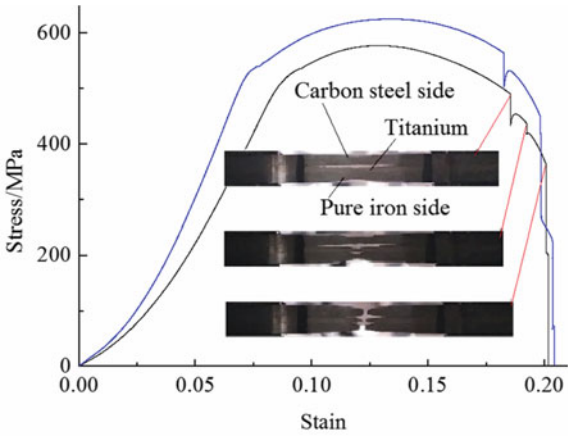


Fig. 9 Optical micrograph of bent specimen: **a** and **b** pure iron is on the interior, **c** and **d** pure iron is on the exterior. (Color figure online)

Fig. 10 Tensile test results. (Color figure online)



the crack length of the side without pure iron is significantly longer than that of the side with pure iron. When the strain was 0.202, the composite plate underwent overall fracture. This indicates that since adding a pure iron interlayer can effectively prevent the formation of brittle compound TiC, crack sources are reduced on the interface during tensile deformation. Therefore, with the pure iron interlayer, the tensile properties are improved, and the divided invalid is relieved.

4 Conclusions

Titanium/carbon steel plates were fabricated by multi-pass hot-rolling to compare the effect of the pure iron interlayer on the microstructures and mechanical properties of the clad plates under different reduction ratios. Based on the results, the following conclusions are drawn:

1. The bonding strength of the interface increases with the reduction ratio on both sides with or without the pure iron interlayer. When the reduction ratios are small, the pure iron interlayer can improve the bonding strength of the composite plate. When the reduction ratio is large, the effect of the pure iron interlayer on the shear strength is not as obvious.
2. The pure iron interlayer can prevent the diffusion of C element in carbon steel to the titanium side, thus reducing the formation of brittle compound TiC at the bonding surface. Therefore, the bending and tensile properties of the composite plates are improved.

References

1. Su H, Luo XB, Chai F, Shen JC, Sun XJ, Lu F (2015) Manufacturing technology and application trends of titanium clad steel plates. J Iron Steel Res Int 22:977–982
2. Dong H, Yu L, Deng D, Zhou W, Dong C (2011) Effect of post-weld heat treatment on properties of friction welded joint between TC4 titanium alloy and 40Cr steel rods. J Mater Sci Technol 31:962–968
3. Ha JS, Hong SI (2016) Deformation and fracture of Ti/439 stainless steel clad composite at intermediate temperatures. Mater Sci Eng A 651:805–809
4. Manikandan P, Hokamoto K, Fujita M, Raghukandan K, Tomoshige R (2008) Control of energetic conditions by employing interlayer of different thickness for explosive welding of titanium/304 stainless steel. J Mater Process Tech 195:232–240
5. Bhola SM, Kundu S, Bhola R, Mishra B, Chatterjee S (2014) Electrochemical study of diffusion bonded joints between micro-duplex stainless steel and ti6a14v alloy. J Mater Sci Technol 30:163–171
6. Hosseini M, Manesh HD (2015) Bond strength optimization of Ti/Cu/Ti clad composites produced by roll-bonding. Mater Des 81:122–132
7. Kim IK, Hong SI (2013) Effect of component layer thickness on the bending behaviors of roll-bonded tri-layered Mg/Al/STS clad composites. Mater Des 49:935–944
8. Kundu S, Chatterjee S (2010) Evolution of interface microstructure and mechanical properties of titanium/304 stainless steel diffusion bonded joint using Nb interlayer. ISIJ Int 50:1460–1465
9. Momono T, Enjo T, Ikeuchi K (1990) Effect of carbon content on the diffusion bonding of iron and steel to titanium. ISIJ Int 30:978–984
10. Zhao DS, Yan JC, Wang CW, Wang Y, Yang SQ (2014) Interfacial structure and mechanical properties of hot roll bonded joints between titanium alloy and stainless steel using copper interlayer. Sci Technol Weld Joi 13:765–768
11. Yan JC, Zhao DS, Wang CW, Yang SQ (2009) Vacuum hot roll bonding of titanium alloy and stainless steel using nickel interlayer. Mater. Sci. Tech-lond. 25:914–918

12. Zhao DS, Yan JC, Liu YJ, Ji ZS (2014) Interfacial structure and mechanical properties of hot-roll bonded joints between titanium alloy and stainless steel using niobium interlayer. T. Nonferr. Metal. Soc. 24:2839–2844
13. Yu C, Xiao H, Yu H, Qi ZC, Xu C (2017) Mechanical properties and interfacial structure of hot-roll bonding titanium/carbon steel plate using DT4 interlayer. Mater Sci Eng A 695:120–125

Investigation on the Whole Forming Process of Super-Large Flat Ring



Dan Xie, Wujiao Xu, Yu Wang, and Rui Chen

Abstract The main concerns of forming a super-large rectangular ring are forming accuracy, rolling stability, uniformity of deformation, and accordingly the distributed microstructure and related mechanical property of the rolled ring. In this paper, a flat ring with a diameter of 9 m is taken as an example, which is the bearing ring of a carrier rocket. To meet the requirements of formation and performance, the whole forming process, including multidirectional forging, punching, reaming and ring rolling is investigated step by step. Due to the poor internal quality of large ingot, three multidirectional forging schemes are compared in order to improve the internal quality of the ring billet. For the reaming process, four different reduction amounts per pass are designed to control the end surface quality of the reaming operation part. To refine grain and minimize the anisotropy of the rolled ring, the ring rolling process is divided into high-temperature rolling and low-temperature rolling, the feeding strategy of which are studied respectively. Based on the FORGE software platform, the simulation results show that the seven upsetting and six stretching process, 30% reduction per pass, and the optimized feed strategy are the optimal multidirectional forging process, reaming process, and ring rolling process.

Keywords The whole forming process of ring · Multidirectional forging · Reaming · Ring rolling

1 Introduction

Super-large ring parts are widely used in the fields of wind energy, nuclear energy, petroleum, and aerospace, and its manufacturing technology has a great impact on the independent development of energy and major mechanical equipment. The whole forming process of a super-large ring is shown in Fig. 1, which is divided into multi-direction upsetting, punching, reaming and ring rolling (e.g. [1]).

D. Xie (✉) · W. Xu · Y. Wang · R. Chen
College of Material Science and Engineering, Chongqing University, Chongqing 400044, China
e-mail: 395627072@qq.com

© The Minerals, Metals & Materials Society 2021

G. Daehn et al. (eds.), *Forming the Future*, The Minerals, Metals & Materials Series,
https://doi.org/10.1007/978-3-030-75381-8_185

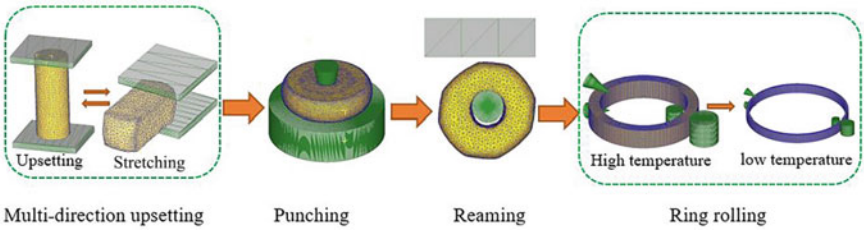


Fig. 1 The whole forming process of super-large ring. (Color figure online)

In the process of casting cooling, the temperature distribution of large diameter ingot is uneven and the cooling rate is greatly reduced, which leads to the phenomena of uneven microstructure, coarse grain, and segregation of chemical composition in large diameter ingot. Therefore, it is necessary to increase the plasticity of ingot by forging billet and improve the uniformity of material microstructure and the grain refinement degree, so as to improve the comprehensive properties of the material. The properties of material are improved due to the flow of material in the multi-direction upsetting process and the reaming process, so the multi-direction upsetting process and the reaming process need to be studied. Yamamoto [2] reported that multidirectional forging can cause continuous static recrystallization. Miura et al. [3] revealed the improvement of AZ61Mg alloy mechanical properties by multidirectional forging.

The ring rolling is a kind of advanced manufacturing technology used for producing all kinds of seamless rings. Through feed and rotation of the rolls, the deformation behavior of the ring is caused by the reduction of wall thickness, the expansion of diameter, and the forming of cross-section (e.g. [4, 5]). The working conditions of super-large ring parts are poor, such as high or low temperature, corrosion, external force impact, radiation, uncertain external force load, and so on, so the requirements of ring internal microstructure and properties are higher. Because the rolling process of a large flat ring is more complex, in order to ensure the forming and properties of a large ring, the following points should be paid attention to: (1) the stability of ring rolling process; (2) the coordination between ring growth speed and ring cross-section forming; (3) the control of ring microstructure and properties (e.g. [6]). Xu KH et al. [7] studied the rolling process of 9 m super-large ring and realized the precise control of roundness and size. He et al. [8] proposed an improved process for grain refinement of large 2219 Al alloy rings, which can improve the mechanical properties of ring. So super-large ring rolling is generally used for high-temperature rolling and low-temperature rolling. The low-temperature rolling is mainly to refine grains and improve the properties of ring.

Although the seven-heading six-stretching process, reaming process, and rolling process of ring have been studied by many researchers, the whole forming process design of super-large ring is not yet comprehensively researched. Therefore, in this paper, the whole process design of super-large 2219 Al alloy ring is studied.

Table 1 The multidirectional forging process and billet parameter

Parameters	Values
Billet parameters (mm)	Ø 1220 × 3110
Punch velocity (mm/S)	15
Friction coefficient	0.3
Billet temperature (°C)	500
Die temperature (°C)	350
Density (kg/m$^{3)}$	2840
Special heat capacity (J/kg K)	864
Heat transfer coefficient (conductivity) (W/(m^2 K))	10,000
Heat transfer coefficient (convection) (W/(m^2 K))	20

2 Design of Multidirectional Forging Process

The billet of the super-large ring is formed by casting. Due to the large size of the ingot, the internal quality of ingot is poor. In order to improve the internal quality of billet, multidirectional forging is used to modify the billet. Three kinds of multidirectional forging processes are designed, including direct upsetting, four upsetting and three stretching, and seven upsetting and six stretching. According to the multidirectional forging process and billet parameter listed in Table 1, the multidirectional forging process was simulated under FORGE software platform. The finite element mesh, considering the simple shape of ingot, is divided by an adaptive meshing technique in FORGE software. To speed up the computation, the rolls are set as steel body. The material of ring is 2219 Al alloy, and its flow stress curve is established by Wang et al. [9].

In order to obtain fine and uniform internal microstructure, the temperature uniformity and strain uniformity of forgings are used as the index to judge the multidirectional forging process, which was reported by Zhou et al. [10]. Figure 2 shows the temperature distribution and equivalent strain distribution of these three multidirectional forging processes. The temperature standard deviation and equivalent strain standard deviation of these three multidirectional forging processes are listed in Table 2. The temperature standard deviation and equivalent strain standard deviation of seven upsetting and six stretching are the lowest, so the seven upsetting and sixth stretching process is the best process.

3 Design of Reaming Process

The outer diameter and wall thickness of the ring billet need to be limited to a certain range because of the limitation of force and energy of ring rolling mill equipment, so it is necessary to obtain reasonable ring billet by reaming. The reaming process is a

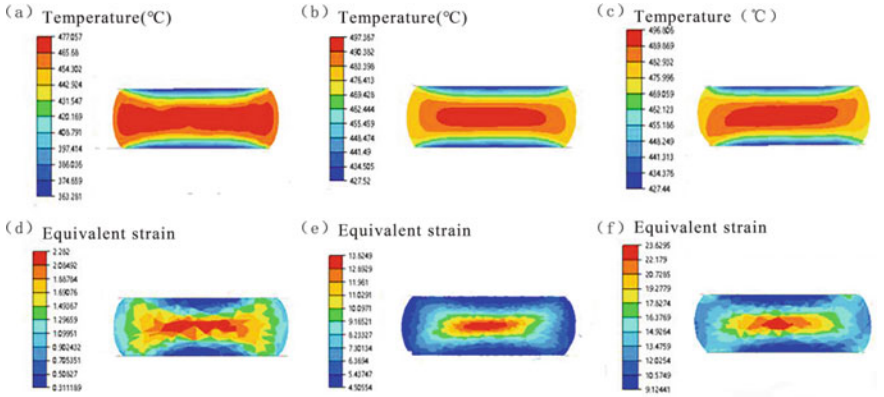


Fig. 2 Temperature distribution of direct upsetting (**a**), four upsetting and three stretching (**b**), seven upsetting and six stretching (**c**); and equivalent strain distribution of direct upsetting (**d**), four upsetting and three stretching (**e**), and seven upsetting and six stretching (**f**). (Color figure online)

Table 2 The temperature standard deviation and equivalent strain standard deviation of these three multidirectional forging processes

Multidirectional forging process	Temperature standard deviation	Equivalent strain standard deviation
Direct upsetting	25.19	2.0744
Four upsetting and three stretching	16.85	0.447
Seven upsetting and six stretching	16.54	0.22326

metal forming process in which the hollow billet is gradually compressed along the circumferential direction by using the mandrel and the upper anvil board to reduce the wall thickness and expand the diameter of the hollow billet. Due to the large deformation of large-scale ring billet in the reaming process, fishtail defects are easy to appear on the end face of ring billet. Therefore, the reasonable wall thickness reduction amount per revolution is the key parameter to control the end surface quality of ring billet.

A reaming model was established under FORGE software platform, which is illustrated in Fig. 1. Due to the heat treatment of billet before the reaming process, the flow stress curve is the same as that of the multi-direction upsetting process. The reaming process and hollow billet parameter are listed in Table 3. Four different wall thickness reduction amounts per revolution are designed, which are 15%, 20%, 25%, and 30% of wall thickness per revolution, respectively. The forming condition of the end surface of the ring billet is shown in Fig. 3. According to the analysis of the fishtail amount (FT) of the end surface of ring billet after reaming with different reduction amounts per revolution, the fishtail amount (FT) with 30% reduction per revolution is the lowest. On the one hand, the increase in the reduction amount per revolution increases the deformation of the material in the axial direction, thus increasing the

Table 3 The reaming process and hollow billet parameter

Parameters	Billet parameters (mm)	Punch velocity (mm/s)	Friction coefficient	Billet temperature (°C)	Die temperature (°C)
Values	Ø 2840 × Ø 900 × 660	15	0.3	500	400

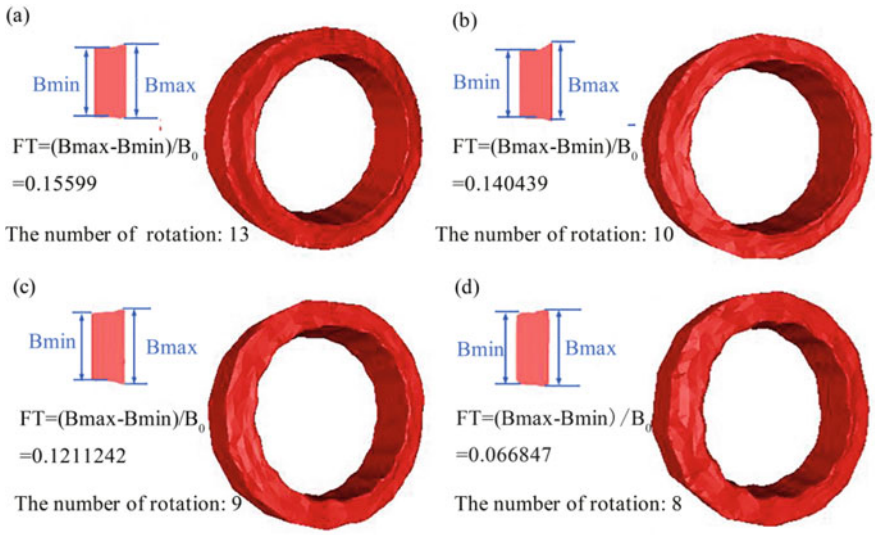


Fig. 3 The end surface of the ring billet under 15% of wall thickness reduction (**a**), 20% of wall thickness reduction (**b**), 25% of wall thickness reduction(**c**), and 30% of wall thickness reduction (**d**). (Color figure online)

fishtail amount (FT) of ring billet; on the other hand, the increase in the reduction amount per revolution reduces the number of reaming revolution, which lead to the decrease in the fishtail amount (FT) of ring billet. The reason why the reduction of the number reaming revolution decreases the fishtail amount is that the accumulative deformation material in the axial direction is decreased.

4 Design of Ring Rolling Process

4.1 Radial Feed Curve

In ring rolling process, the radial feed of the mandrel makes ring wall thickness thinner and material flow circumferentially, which leads to the growth of ring diameter. Therefore, the growth speed of ring outer diameter is related to the feed speed of

mandrel. The growth speed of ring outer diameter is related to the dynamic contacts and collisions between ring and rollers, which affects the properties of ring and the rolling stability of ring. In order to ensure the rolling stability of super-large ring parts, the radial feed speed is controlled to adjust the growth speed of ring outer diameter. According to the principle of ring volume invariance in ring rolling process, the axial width expansion in ring rolling is ignored, Ref. [11] reported the relationship between ring outer diameter growth speed and radial feed speed is deduced, as follows:

$$v_D = \left(\frac{D_0 + d_0}{2} \frac{H_0}{\left(H_0 - \int_0^T v dt\right)^2} - 1 \right) \tag{1}$$

where D_0, d_0, and H_0 are the initial outer diameter, inner diameter, and wall thickness of the ring, respectively. T is the rolling time. v is the feed rate of mandrel, and v_D is the growth speed of ring.

According to the actual production experience, the growth speed of super-large flat ring should be controlled in the range of 6 mm/s, and the limit value of radial feed rate should be calculated by Eq. (1), so that the reasonable radial feed rate range can be obtained. Considering the super-large flat ring rolling instability in the middle and late rolling stage and the increase in rolling instability with an increase in rolling time, the high temperature rolling of ring is divided into the initial stage of ring rolling, the rapid stage of ring rolling, the stable stage of ring rolling, the deceleration stage of ring rolling, and the whole round stage of ring rolling. Rapid rolling stage is to decrease the rolling time, and the stable rolling stage and the deceleration rolling stage are to control ring rolling stability. Due to the decrease in ring temperature in the late rolling stage and the increase in deformation resistance, the ring rolling instability is seriously increased. Because a low radial feed rate can reduce the rolling forces, and the drop of rolling forces can increase the stability of ring rolling, the radial feed rate in the low temperature rolling of ring should be designed to be uniformly decelerated considering the increase in rolling instability in late ring rolling stage.

According to the range of radial feed rate, reasonable rolling time and the characteristics of different rolling stages in the high-temperature rolling and the low-temperature rolling processes, the radial feed curve of ring is designed as shown in Fig. 4a. A 3D-FE model for the super-large ring rolling was established under FORGE software platform, as shown in Fig. 1. Due to the heat treatment of ring billet before ring rolling, the flow stress curve is the same as that of the multi-direction upsetting process. The simulation parameters including the rolling process and ring billet parameters are listed in Table 4. The cross-section forming condition of the high-temperature rolling and the low-temperature rolling is shown in Fig. 5. Because the stability of ring rolling affects the deformation of ring, the ring cross-section can be used as an index to judge ring rolling stability. According to the cross-section forming condition of ring in the high-temperature ring rolling shown in Fig. 5a, the ring end surface has the smaller fishtail amount (FT) and meets the cross-section requirements of forging, and the ring rolling process is basically stable. The ring end

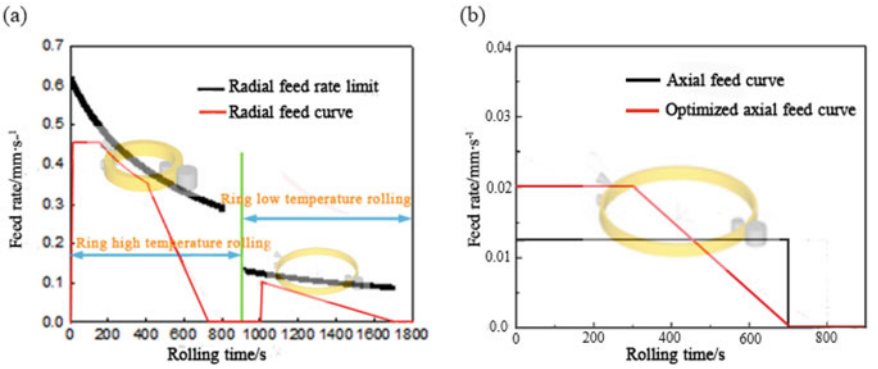


Fig. 4 The radial feeding curve of ring rolling (**a**) and the axial feeding curve of ring rolling (**b**). (Color figure online)

Table 4 The rolling process and ring billet parameter

Parameters	Values
Ring billet parameters in high-temperature rolling (mm)	Ø 3950 × Ø 3120 × 710
Ring billet parameters in low-temperature rolling (mm)	Ø 7630 × Ø 7250 × 690
Drive roll speed (rad/s)	0.75
Friction coefficient	0.3
Billet temperature in high-temperature rolling (°C)	500
Billet temperature in low-temperature rolling (°C)	235
Die temperature (°C)	150
Mesh type	Hexahedron
Mesh size (mm)	60
Mesh number	10,800

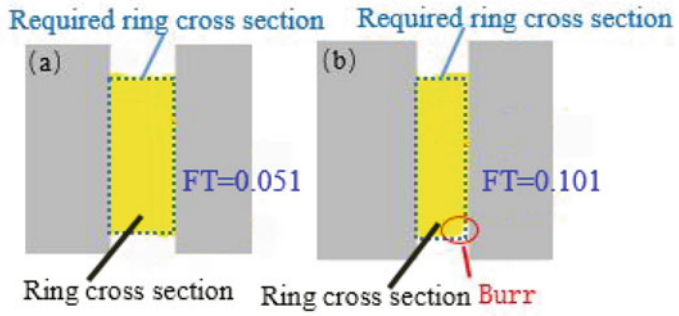


Fig. 5 The cross-section forming condition of ring in the high-temperature ring rolling (**a**) and the low-temperature ring rolling (**b**). (Color figure online)

surface in the low temperature rolling process has a large fishtail amount (FT) and serious burr and does not meet the cross-section requirements of forging, as shown in Fig. 5b.

4.2 Axial Feed Curve

Through analyzing the ring rolling process, the ring has strong up and down movement in ring rolling process, which results in the burr in the ring end surface. The main deformation and growth stage of ring is in the initial stage of ring rolling due to the larger radial feed amount, so the axial feed rate in the early rolling stage is increased to control the axial rolling stability of ring in the early rolling stage. Due to the increase of ring rolling stability with the decrease in rolling time in the late rolling stage, the increase in axial feed rate also can improve the rolling stability and ring end surface condition by reducing the rolling time. Considering the increase in rolling forces in the late rolling stage, the axial feed rate should be decreased with the rolling time. Therefore, the axial feed curve is optimized, as shown in Fig. 4b. Figure 6 shows the cross-section forming condition of ring and the fishtail amount (FT) of ring end surface with different axial feed curves. For the optimized axial feed curve, the fishtail amount is significantly reduced and the ring cross-section meets the cross-sectional requirements of ring. The reason is that the higher axial feed rate in the early stage of low temperature rolling and the shorter rolling time reduce the up and down movement of ring.

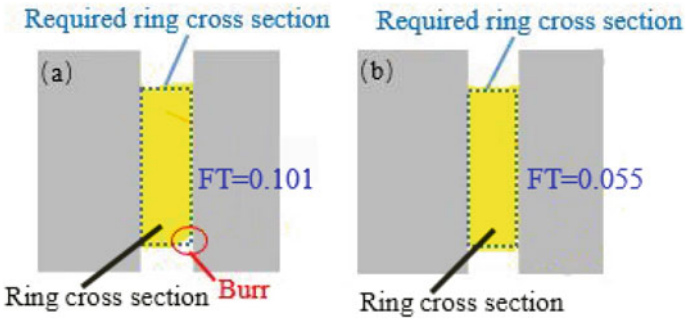


Fig. 6 The cross-section forming condition of low-temperature ring rolling under the axial feed curve (**a**) and the optimized axial feed curve (**b**). (Color figure online)



Fig. 7 The production process of the super-large ring. (Color figure online)

5 Practical Production

Based on the optimized process parameters obtained in Sects. 4.1 and 4.2, the super-large ring was successfully produced, and the technical requirements can be met, which verify the optimum parameters determined in the simulation. The production process of the super-large ring is shown in Fig. 7.

6 Conclusions

In this paper, the design of multidirectional forging, reaming and ring rolling had been researched. Seven upsetting and six stretching is the better multidirectional forging process, which can improve the internal quality of ingot and make the microstructure more uniform. According to the analysis of the fishtail amount of different wall thickness reductions per revolution, 30% wall thickness reduction per revolution is the better reaming process. According to the feed curve of the mandrel that is designed based on the feed rate range of mandrel, the rolling time and the characteristics of different rolling stages in the high-temperature rolling and the low-temperature rolling processes and the optimized axial feed curve, the cross-section of ring meets the requirements.

References

1. Giorleo L, Ceretti E, Giardini C (2013) Energy consumption reduction in Ring Rolling processes: A FEM analysis. Int J Mech Sci 74:55–64
2. Yamamoto M (2008) Continuous static recrystallization in ultrafine-grained copper processed by multi-directional forging. Mater Sci Eng A 478:221–228
3. Miura H, Yu G, Yang X (2011) Multi-directional forging of AZ61Mg alloy under decreasing temperature conditions and improvement of its mechanical properties. Mater Sci Eng A 528:6981–6992
4. Eruc E, Shivpuri R (1992) A summary of ring rolling technology-I. Recent trends in machines, processes and production lines. Int. J. Mach. Tool. Manu. 32(3):379–398
5. Eruc E, Shivpuri R (1992) A summary of ring rolling technology-I. Recent trends in process modeling, simulation, planning and control. Int. J. Mach. Tool. Manu. 32(3):399–413.
6. Yeom JT, Kim JH, Park NK, Choi SS, Lee CS (2007) Ring-rolling design for a large-scale ring product of Ti–6Al–4V alloy. J Mater Process Tech 187:747–751
7. Xu KH, Zhang WX, Yang DK, Zhang GF, Li YJ, Liu D (2016) Manufacture of aluminum alloy 2219 integral ring with 9 m ultra-large diameter. Forg. & Stamp. Tech. 41(10):92–97
8. He HL, Yi YP, Huang SQ, Zhang YX (2019) An improved process for grain refinement of large 2219 Al alloy rings and its influence on mechanical properties. J Mater Sci Technol 35(1):55–63
9. Wang K, Wu YX, Gong H, Liu L (2019) Strain-compensated Constitutive Model for High Temperature Plastic Deformation of 2219 Aluminum Alloy. Hot. Work. Technol. 48(9):120–124
10. Zhou G, Hua L, Qian DS (2013) 3D coupled thermomechanical FE analysis of roll size effects on the radial-axial ring rolling process. Comput Mater Sci 50:911–924
11 Xu WJ, Xie D, Wang Y (2019) Feed strategy design of large rectangular ring. The 16th National Conference on technology of plasticity, TaiYuan, Chian. 683–686

Development of a New Printing Method Using Soft Material Tools



Yasuharu Yoshikawa and Yusuke Masegi

Abstract A new printing method for metal using soft material tools has been developed. This method uses paper or plastic film with a fine pattern produced by the laser printer as a printing tool. The aluminum disc is compressed with a soft material tool between the upper and lower flat dies. In order to print with high accuracy with a uniformed pattern onto a metal surface, the effects of the process conditions on printing have been investigated. Experimental results using the soft material tools showed that the good condition for high accuracy was changed by the combination of the average pressure and the workpiece shape. The new printing method can print patterns easily onto the metal workpiece. The pattern can be observed from each workpiece surface. When using paper, the surface profiles of the workpiece are not clear because the printed pattern is hidden by the surface roughness of the paper. When using the PET film, the surface pattern can be clearly observed. The average pressure is needed to print the pattern clearly and uniformly. When decreasing the diameter and thickness ratio D/t of the workpiece, the required average pressure is decreased.

Keywords Transfer printing · Surface asperity · Soft material

1 Introduction

Coining is used to produce a wide range of parts with high accuracy on coins, medallions, gears, and medical devices. The die of coining has a high accurate cavity formed by fine cutting, electric discharge machining, laser milling, and photolithography. When producing small amounts, the forming process of the die is the cause of high cost.

Nishi and Fujita proposed another printing method where the leaf asperity is printed onto the titanium sheet using shock waves by explosive forming [1]. This printing method can print onto the thin metal workpiece uniformity. Ike reported

Y. Yoshikawa (✉) · Y. Masegi
Department of Mechanical Engineering, Meijo University, Nagoya, Japan
e-mail: yyasu@meijo-u.ac.jp

© The Minerals, Metals & Materials Society 2021

G. Daehn et al. (eds.), *Forming the Future*, The Minerals, Metals & Materials Series,
https://doi.org/10.1007/978-3-030-75381-8_186

the effect of contaminants such as ceramic particles, fiber, and hair between the die and workpiece in coining [2]. The oil between the tool and the workpiece can deform the surface of the metal workpiece when the oil is pooled in the cavity on the surface, which shows that the soft material can be a printing tool in a high-pressure environment.

This report describes a new printing method onto metal using soft materials for the tool. In this method, the fine pattern is printed using soft materials such as paper or a plastic film. The reversed fine pattern produced by the laser printer is used as the printing tool. The toner (A colorant powder for heat transfer printing) is placed on the paper or film surface by laser printing, therefore the controlled asperity is formed. The workpiece of the disc shape and the soft material are compressed using metallic dies. By using this method, small to large amounts of production can be done quickly at low costs. The influence of the parameters (average pressure, disc dimension, and soft tool materials) for printing accuracy and uniformity has been researched.

2 New Printing Method

Figure 1 shows the outline of the newly developed printing method. A disc workpiece and a soft material with fine patterns are set on the lower die. Then the workpiece is compressed between the upper and lower dies with the soft material tool. During the experiment, the compression load was measured by the Amsler Universal Testing Machine. After compression, the soft material tool was released from the workpiece.

The upper and lower dies have a diameter of 60 mm and a height of 25 mm. TiCN is coated on the upper and lower dies, made of the cold working die steel with a roughness of 0.15 μmR_a. The soft material tools are plain paper, kent paper, coated paper (90 and 135 kg of unit weight), and PET (polyethylene terephthalate) film. The fine patterns of concentric circles with a 0.5 and 1.2 mm of pitch, as shown in Fig. 2, are formed by the laser printer on these soft materials. There is toner on the printed area. The toner is composed of styrene/acrylate copolymer, wax, carbon black, and Sirica. Figure 3 shows the surface profile of the laser-printed PET film. The width and the thickness of the circle lines are 295 μm and 4.90 μm, respectively. The workpiece material is a pure aluminum A1050-O (Japanese Industrial Standard). The workpiece sizes are 12, 24, and 36 mm in diameter, 1 mm in thickness with the surface roughness of 0.343 μmS_a. The experiments were carried out in a dry condition with the workpiece ultrasonically cleaned with acetone. The average compression pressure, calculated from the maximum compression load, and the initial contact area were changed. The printing accuracy was analyzed using measured surface profiles.

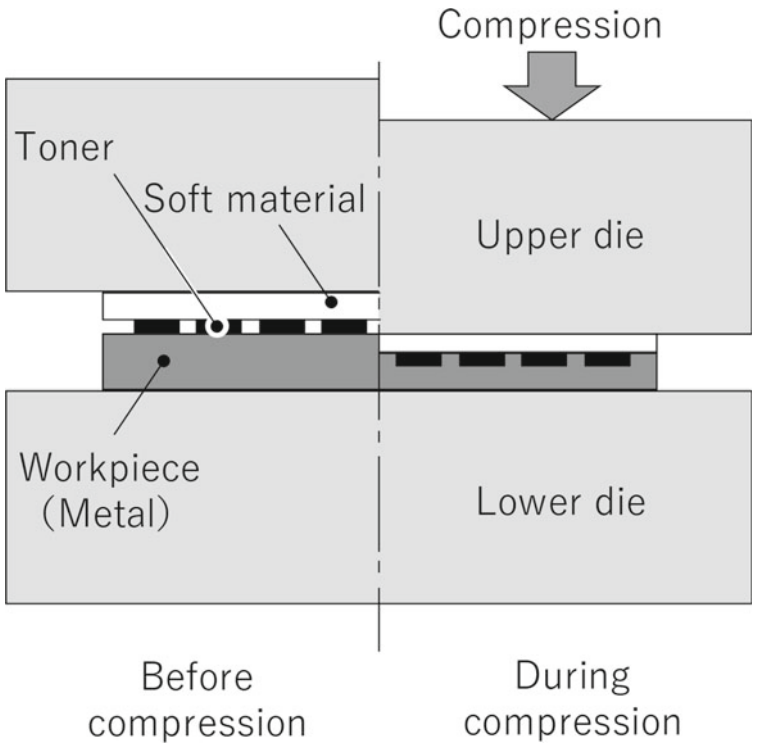


Fig. 1 Schematic diagram of new printing method

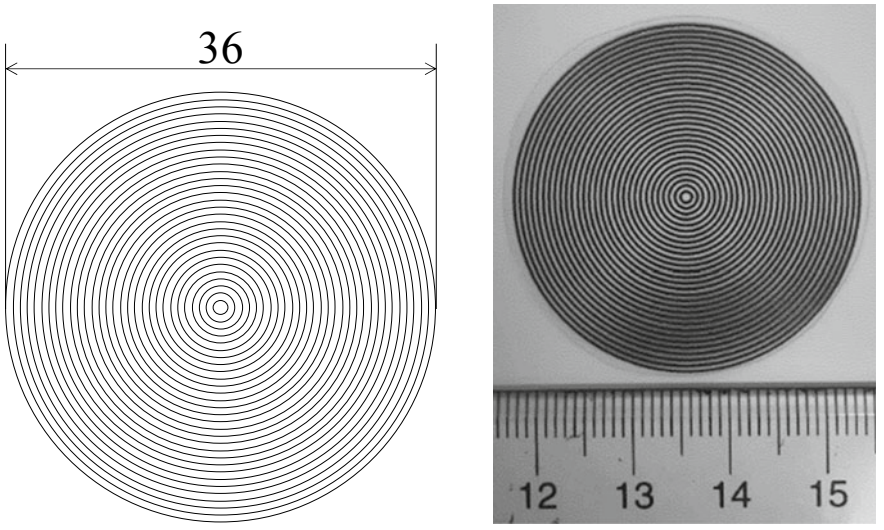


Fig. 2 Pattern printed by laser printer (in case of 36 mm of diameter)

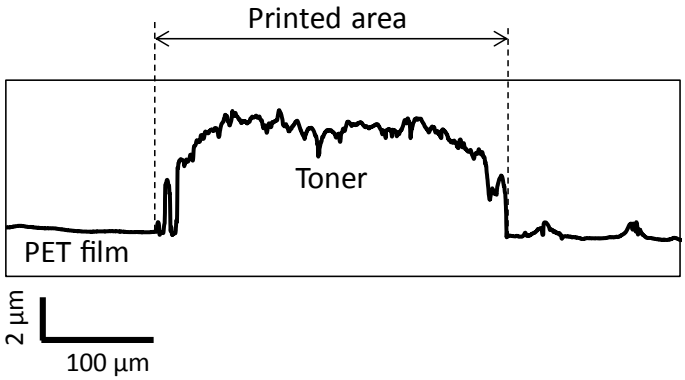


Fig. 3 Surface profile of laser-printed PET film

3 Experimental Results

3.1 Tool Materials

Figure 4 shows the surface image of the workpiece printed by each soft material to 24 of the diameter and thickness ratio D/t with 295 MPa of the average pressure. The left side of this figure is the center of the workpiece and the right side is the outer side of the workpiece. The new printing method can print patterns onto the metal workpiece. The concentric circle pattern can be observed from each surface. Figure 5 shows the surface profiles printed by each soft material. The surface profiles using all four different kinds of paper were not clear because the printed patterns were hidden by the surface roughness of the paper. The surface pattern of using the PET film was clearly observed.

3.2 Average Pressure and Dimension of Work Piece

The surface profiles have measurements of 1.8 mm of the length at each position as shown in Fig. 6. Figure 7 shows the surface profiles of each average pressure at three different positions. From the profile of $p_a = 51.1$ MPa, the printed pattern was changed gradually by the position. The center of the pattern on the workpiece was not shown clearly. The patterns at each position became clearer by increasing the average pressure. The depth of the patterns in the same position seemed to be the same level in more than 197.0 MPa of the average pressure. However, the depth at the edge was marginally deeper than in the center. Figure 8 shows the surface profiles with 24 of D/t in each of the average pressures. The patterns at the edge were deeper than that of the center. It became clearer by increasing the average pressure. When

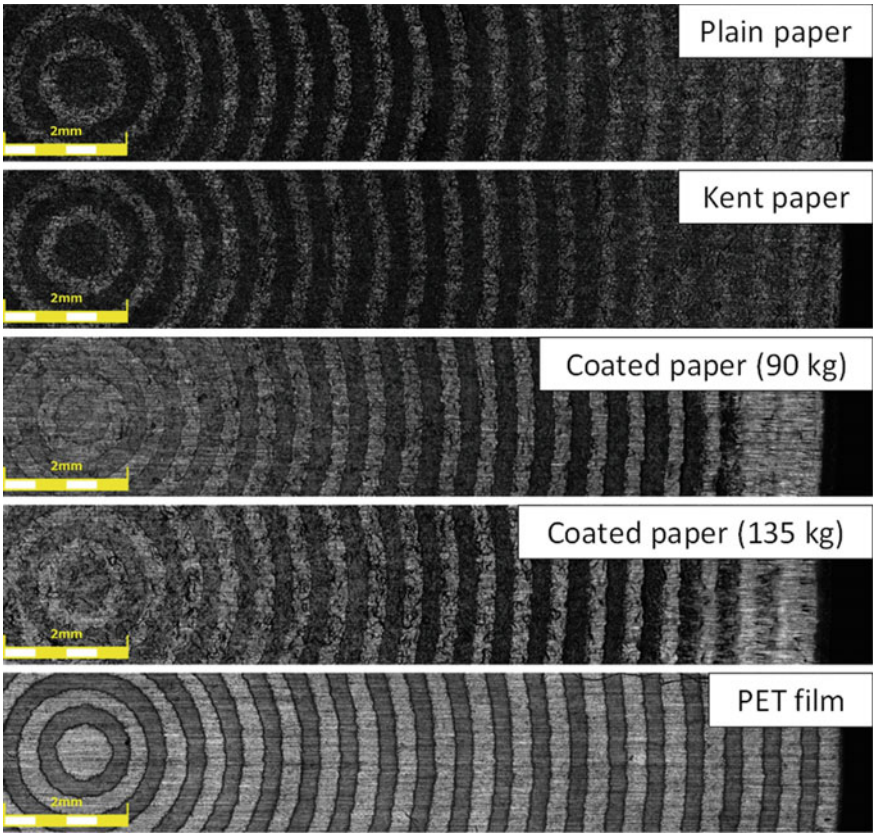


Fig. 4 Optical images of printed surface by each soft material. ($D/t = 24$, average pressure $p_a =$ 295 MPa). (Color figure online)

using more than 221.7 MPa of the average pressure, the depths of the patterns in the center seemed to be of the same level as those at the edge. Figure 9 shows the surface profiles with 12 of D/t in each average pressure. The patterns at the edge were deeper than that of those at the center with the same trend as 24, 36 of D/t. The patterns became clearer by increasing the average pressure. The depth of the patterns was uniform in the case of using more than 106.4 MPa of the average pressure.

From these results, the average pressure was needed to print the pattern clearly and uniformly. The required average pressure was decreased by decreasing the D/t of the workpiece. Ike showed that the transfer accuracy increased if the work material was yielded by compression [3, 4]. The high precision and uniform printing were difficult when using a high D/t because of the high friction condition. The results of this experiment using the new printing method were the same as the performance of the usual coining.

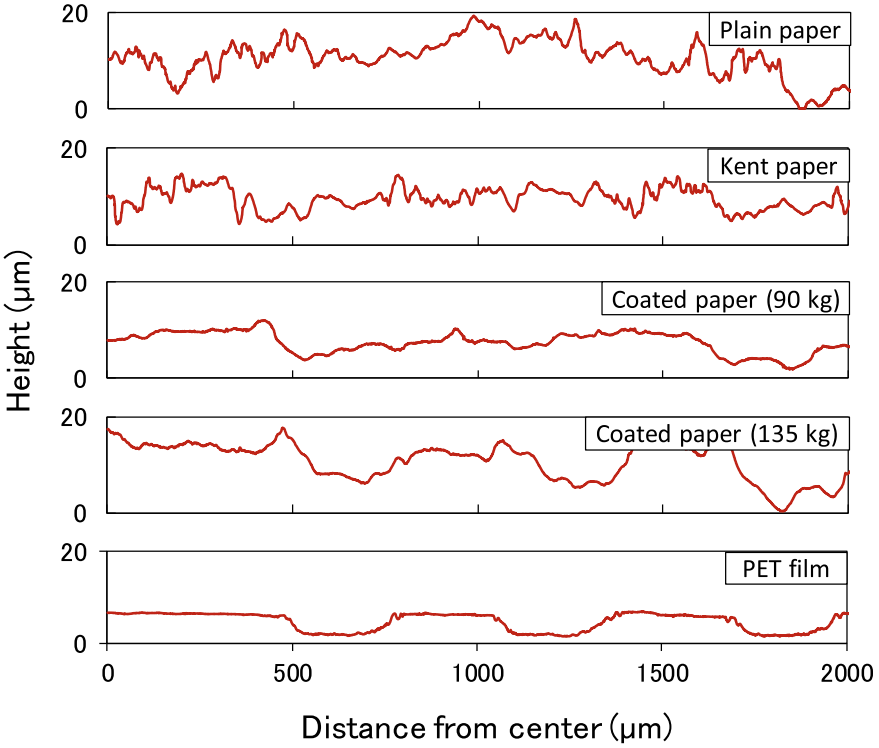


Fig. 5 Surface profiles of printed by each soft material. ($D/t = 24$, average pressure $p_a = 295$ MPa). (Color figure online)

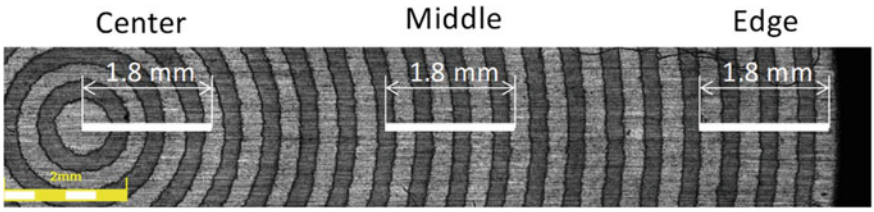


Fig. 6 Measured position of printed workpiece. (Color figure online)

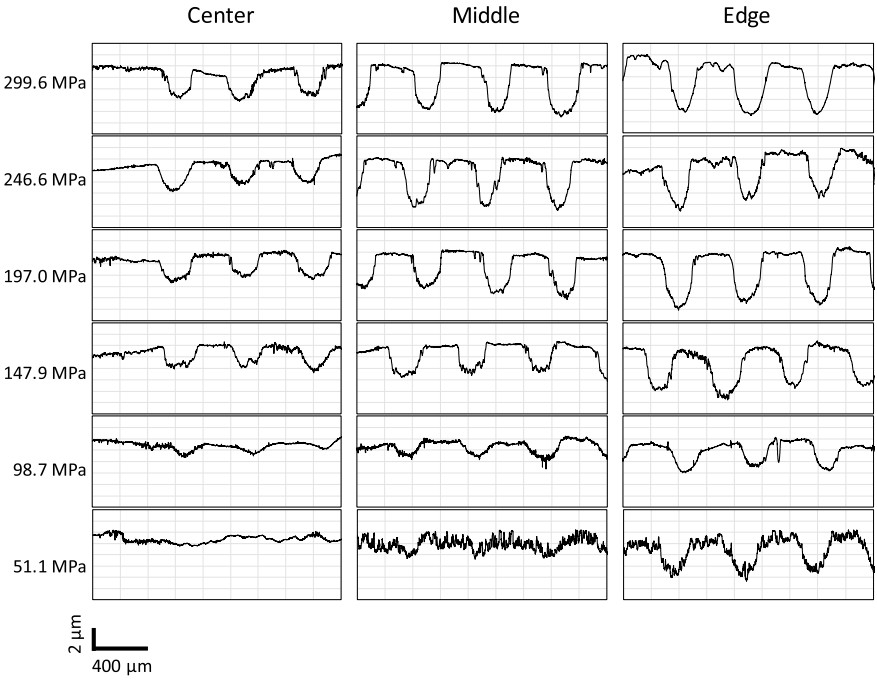


Fig. 7 Surface profiles. ($D/t = 36$, PET film)

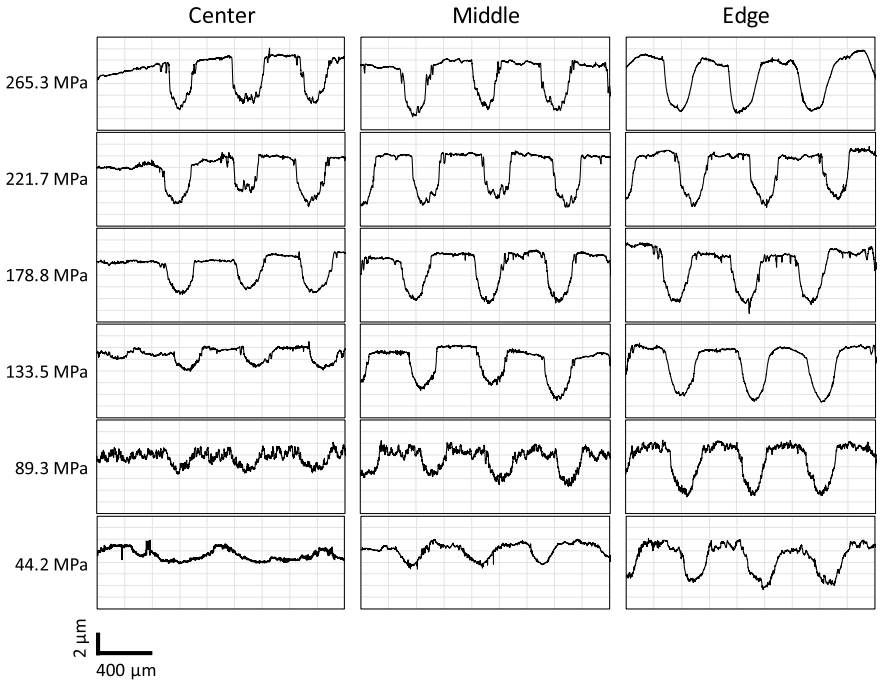


Fig. 8 Surface profiles. ($D/t = 24$, PET film)

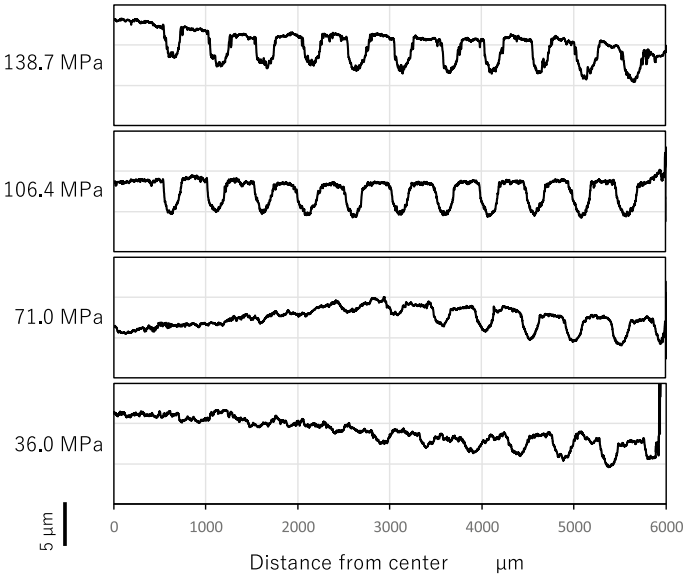


Fig. 9 Surface profiles. ($D/t = 12$, PET film)

4 Conclusion

The new printing method using soft materials as the tool was proposed for forming the pattern on the metal surface. The experiment was performed using paper and PET film to aluminum. The results are as follows.

- The surface geometry of the soft material was printed onto the surface of the aluminum disc. The clear patterns were observed in the case of using the PET film.
- In order to print the clear and uniform patterns, sufficient pressure was needed for each D/t. The required average pressure was decreased by decreasing the D/t of the workpiece.

Acknowledgments This research was supported by JSPS KAKENHI Grant Number JP 19K04131.

References

1. Masatoshi Nishi, Sozo Fujimoto, Masahiro Fujita, Kazuyuki Hokamoto (2013) A simple explosion molding method for art production using vacuum packing. Proceedings of the 64th Japanese Joint Conference for the Technology of Plasticity. 79–78.
2. Hiroshi Ike, Akio Kawano (2002) Factors of microgeometry transfer in coining, Proceedings of the 53th Japanese Joint Conference for the Technology of Plasticity. 445–446.
3. Ike H, Plancak M (1998) Coining process as a means of controlling surface microgeometry. J Mater Process Technol 80–81:101–107
4. Ike H (2003) Surface deformation vs. bulk plastic deformation -a key for microscopic control of surfaces in metal forming. J Mater Process Technol 138:250–255

Plasticity Improvement of CNTs/Mg Nanocomposite Materials Processed by Combining Friction Stir Processing and Ultrasonic-Assisted Extrusion



Qian Zhang, Lehua Qi, Jiming Zhou, Jun Luo, and Junhao Liang

Abstract It is hard to maintain high plasticity for metal matrix composite while increasing their mechanical properties. A new process for preparing carbon nanotubes (CNTs) reinforced magnesium nanocomposites (CNTs/Mg) was developed, which combined friction stir processing (FSP) and ultrasonic-assisted extrusion. It is interesting that the mechanical property of CNTs/Mg nanocomposite materials is improved greatly compared with the supplied Mg alloy at the same time while the plasticity is preserved. The plasticity improvement mechanism is explained from the effect of interface bonding and the liquid–solid extrusion process by different microstructure analyses. HRTEM analysis shows that the Al_2MgC_2 phase at some interfaces between Mg matrix and CNTs is formed, which contributes to good composite interface bonding. Liquid–solid extrusion process can densify the composite and generate severe plastic deformation which is very useful for plasticity improvement.

Keywords Carbon nanotubes · Magnesium composite · Plasticity improve · FSP · Liquid–solid extrusion

1 Introduction

With the development of the automotive and aerospace industries, higher requirements have been placed on magnesium composites in terms of light weight and high strength. Carbon nanotubes [1] have excellent mechanical properties, extremely

Q. Zhang · L. Qi · J. Zhou (✉) · J. Luo
School of Mechanical Engineering, Northwestern Polytechnical University, Xi'an 710072, PR China
e-mail: zhoujm@nwpu.edu.cn

Shaanxi Key Laboratory of Fiber Reinforced Light Composite Materials, Northwestern Polytechnical University, Xi'an 710072, PR China

J. Liang
State Key Laboratory of Solidification Processing, Carbon/Carbon Composites Research Center, Northwestern Polytechnical University, Xi'an 710072, China

© The Minerals, Metals & Materials Society 2021

G. Daehn et al. (eds.), *Forming the Future*, The Minerals, Metals & Materials Series,
https://doi.org/10.1007/978-3-030-75381-8_187

high aspect ratios, and stable chemical properties [2]. It provides a new opportunity for the development of magnesium composite material. The carbon nanotube reinforced Mg matrix composite has both advantages of the Mg alloy matrix and the CNTs, such as lightweight, high specific strength, high specific stiffness, low coefficient of thermal expansion, excellent shock absorption performance, good dimensional stability, etc. So it is a structure–function integrated material and has potential application prospects in aerospace, military vehicles, and electronic packaging.

However, CNTs are easily tangled and agglomerated under the influence of Van der Waals forces due to the small diameter and the large surface energy, which is seriously adverse for the uniform dispersion of the CNTs in the Mg alloy. The agglomerated CNTs also reduce the mechanical properties of the CNTs/Mg composite. Therefore, lots of scholars are seeking an effective method to improve the dispersibility of CNTs in Mg alloys.

Now the processes for dispersing CNTs in Mg alloys mainly include the stirring casting method [3–5], the melt infiltration method [6–8], the powder metallurgy method [9, 10], and the friction stir processing (FSP) method [11, 12]. In our works, a new method is proposed to disperse CNTs in the Mg alloys. First, the CNTs are predispersed in the Mg alloy by FSP. FSP is a good way to disperse the CNTs to small clusters. Then the alloys mixed with CNTs are melted during the ultrasonic process. After that, microscopic defects are reduced in the as-cast composite materials through liquid–solid extrusion process. This work provided a new way to fabricate CNTs/Mg composite with excellent mechanical properties and plasticity.

2 Experimental Details

2.1 Materials

The matrix of the composite is commercial AZ91D alloy. The reinforced material is multi-walled carbon nanotubes (10–20 nm in diameter and approximately 30 μm in length, purity > 95 wt.%, Chengdu Organic Chemicals Co. Ltd., Chinese Academy of Sciences, Chengdu, China).

2.2 Experimental Process

2.2.1 FSP

CNTs need to be pre-dispersed in magnesium alloys. The CNTs/AZ91D predispersed magnesium alloy blocks were fabricated by FSP. The experimental schematic is shown in Fig. 1.

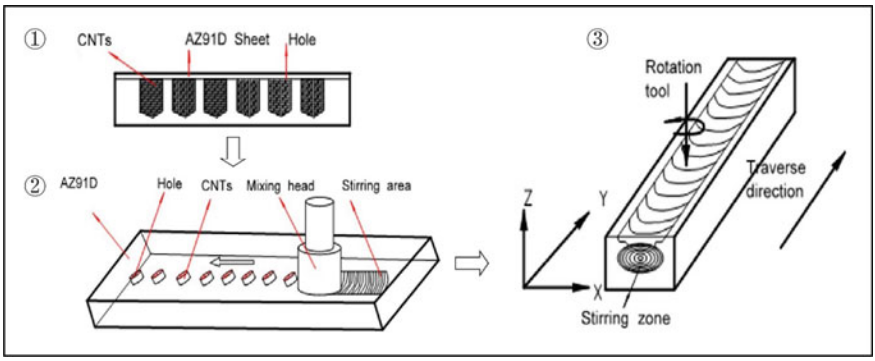


Fig. 1 The experimental schematic of FSP. (Color figure online)

First, blind holes are uniformly drilled on the AZ91D alloy plate, and CNTs are filled in the holes. Then the plate is fixed on the friction stirring device. The stirring head is rotated at a certain speed (800 ~ 1000 rpm) and travel speed (10 ~ 40 mm/min). The CNTs are mixed with AZ91D alloy by rotating friction. The entire operation process is under an argon protective atmosphere. About 4 wt.% of CNTs are added into AZ91D. After FSP processing, the mixed magnesium composite plate is shown in Fig. 2. The region of red circle is the stirring zone.

In order to get more uniformly dispersed CNTs in the stirring area, the stirring area is processed repeatedly for multiple passes. Finally, the FSP area is prepared as a sample by wire cutting, and the samples are used for the next ultrasonic processing step.

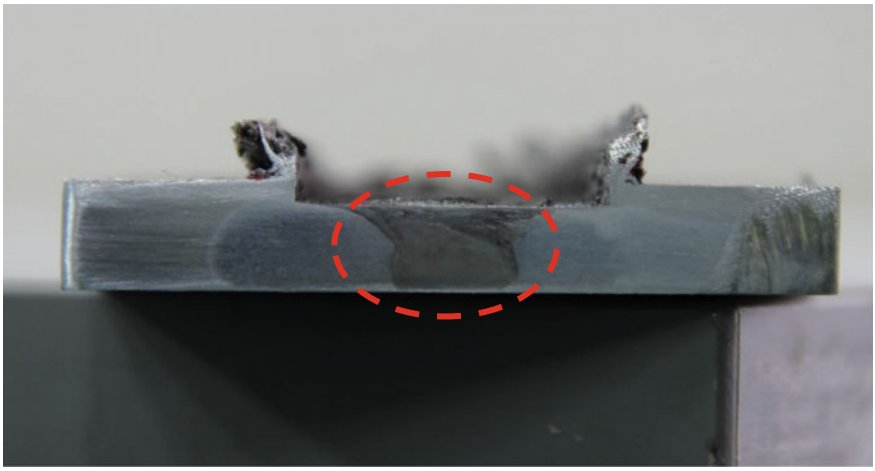


Fig. 2 Cross-section of 4 wt.%CNTs/AZ91D pre-dispersed plate by FSP. (Color figure online)

2.2.2 Ultrasonic Processing

Ultrasonic treatment is an efficient and pollution-free treatment method. The ultrasonic effect on the dispersion of nano-scale reinforcement is obvious [13]. It can produce acoustic cavitation and acoustic flow effects and then remove debris, refine grains and dispersion effects.

After the CNTs are pre-dispersed in magnesium alloy, the mixed block samples are put into the melting magnesium alloy. In order to improve the dispersibility of the CNTs, the ultrasonic treatment is applied.

The schematic diagram of the as-cast CNTs/AZ91D composite material preparation device is shown in Fig. 3. This device is mainly composed of a heating furnace, an ultrasonic amplitude rod, and a crucible. During the melting process, the ultrasonic transducer needs to be water-cooled to prevent damaging the piezoelectric ceramic. The preparation processing steps of the as-cast CNTs/AZ91D composite are as follows:

(1) Pre-heating the iron crucible to the temperature of 200 °C. The AZ91D magnesium alloy is placed in the iron crucible, and argon is introduced to prevent the magnesium alloy from oxidizing, and then continue heating the crucible to 700 °C for 10 min.
(2) The cleaned composite pre-dispersion blocks are put into the molten magnesium alloy and stirred for 3 ~ 10 min. Then the ultrasonic rod is immersed into the melt and removed after the ultrasonic procession. At last, the composite material melt is poured into a steel mold (length: 120 mm, diameter: 45 mm) preheated at 300 °C.

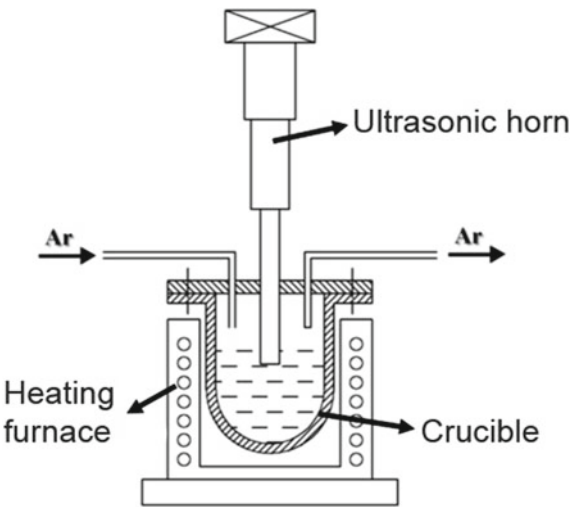


Fig. 3 The preparation device of CNTs/AZ91D composite

2.2.3 Liquid–Solid Extrusion Process

The liquid–solid extrusion process is a new metal matrix composite forming process developed in recent years to fabricate composite tubes and bars. This process integrates solidification, heat conduction, and plastic deformation into one process. It belongs to a non-linear, multi-variable time-varying system, which has fewer processes and a lower cost. Because of these advantages, it is widely applied in fabricating metal matrix composites.

Based on the process and equipment of our previous research, the as-cast CNTs/AZ91D composites are treated through liquid–solid extrusion process. The process is as follows:

(1) The extrusion mold is preheated, and then the as-cast CNTs/AZ91D composite is heated to the extrusion temperature. After that, the as-cast CNTs/AZ91D composite is extruded out at certain extrusion temperatures and speeds;
(2) Finally, T6 heat treatment is performed on the composite extruded bar (400 °C solution treatment 24 h then 168 °C aging treatment 16 h) to improve the mechanical properties such as tensile strength, yield strength, and hardness of the composite.
(3) The AZ91D alloy is also treated in the same extrusion and heat treatment condition for comparison.

The AZ91D alloy and CNTs/AZ91D composite bars are processed into standard cylindrical specimens as the requirements of GB/T228-2002. There are three specimens per group. The tensile test is carried out on the CMT5304-30KN testing machine with a tensile speed of 0.2 mm/min. The specimen specification is shown in Fig. 4.

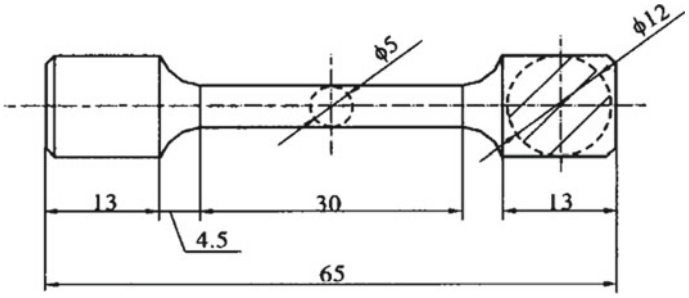


Fig. 4 The specification of tensile specimen

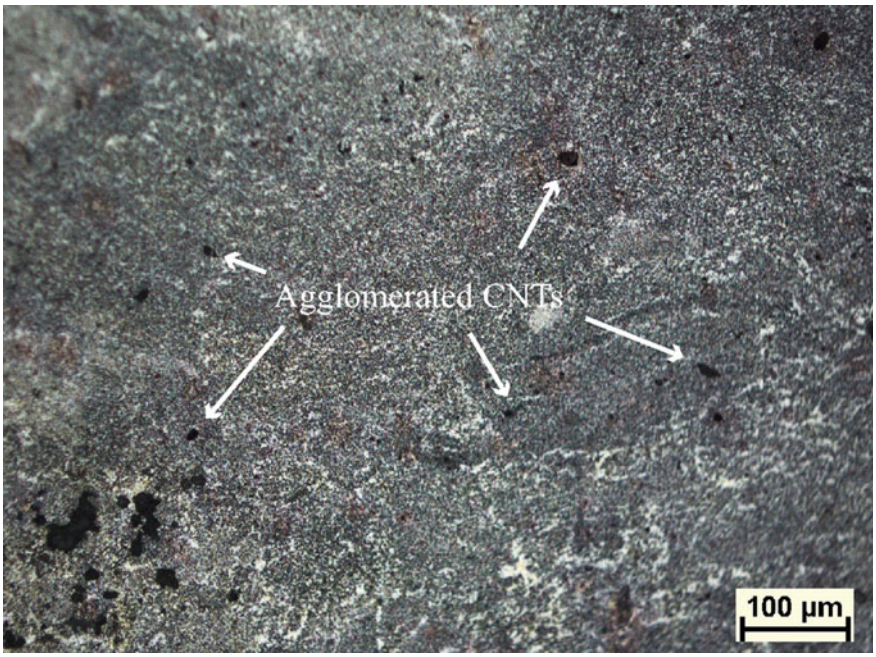


Fig. 5 Microstructure of CNTs/AZ91D pre-dispersed block preform in stir region. (Color figure online)

3 Results and Discussion

3.1 The Effect of FSP on the Dispersion of CNTs

Figure 4 shows the microstructure of the CNTs/AZ91D pre-dispersed block in the stirred region after FSP. The black region in the pre-dispersed block is CNTs and the white region is magnesium matrix. We can observe that the CNTs are well bonded to the magnesium matrix, and black spots of different sizes appear locally in the picture. These black spots are agglomerated CNTs, as shown by the white arrows in Fig. 5. The FSP did not make micro-size CNTs well dispersed because of the high content of CNTs. Therefore, the following process to further disperse the CNTs by ultrasonic processing is necessary.

3.2 Tensile Strength and Plastic Properties of Liquid–Solid Extrusion CNTs/Mg Composites

Figure 6 shows the mechanical properties curve of extruded AZ91D alloy and extruded CNTs/AZ91D composites. We can observe that the tensile strength of

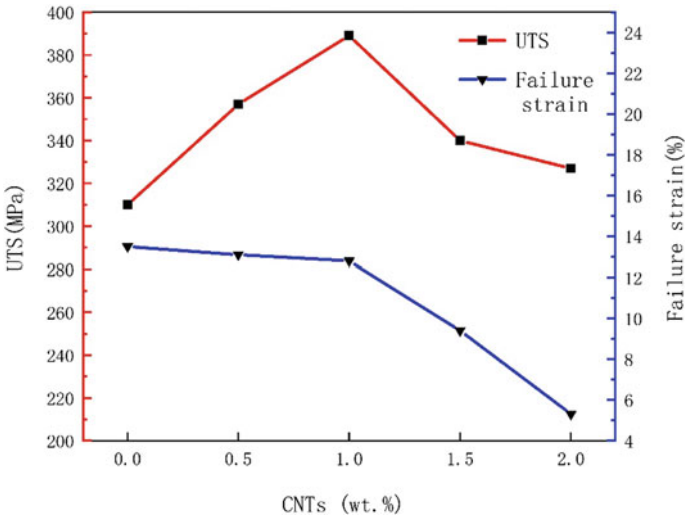


Fig. 6 Mechanical properties curve of extruded AZ91D alloy with and without CNTs. (Color figure online)

extrusion CNTs/AZ91D composites is improved and the plasticity preserves when the CNTs content is less than 1wt.%

When the content of CNTs is 1.0wt.%, the tensile strength of the composite reaches 390 MPa. It is significantly improved compared with the magnesium alloy (310 MPa), about 25.8%. The most important is that the fracture strain of the composite material is almost not reduced compared with the magnesium alloy, which indicates the extrusion CNTs/AZ91D composite still maintains good plasticity.

When the CNTs exceed 1.0 wt.%, the strength and plasticity of the composite decrease. Figure 7 shows the tensile fractograph of AZ91D alloy and 1.0 wt.% CNTs/AZ91D composite. It can observe that a large amount of cleavage planes and

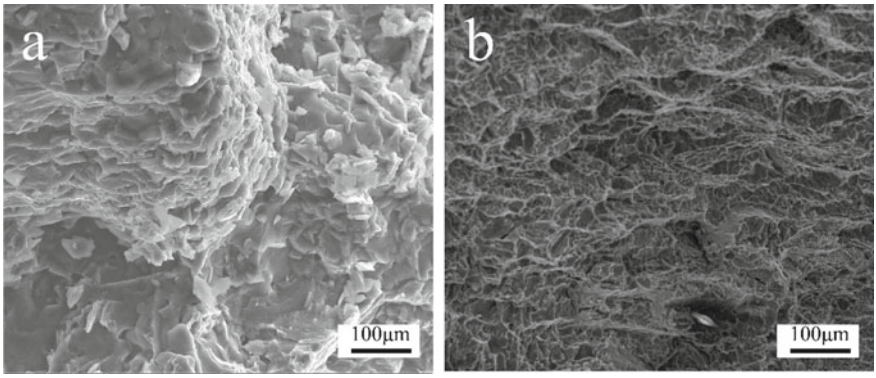


Fig. 7 Fractograph of **a** AZ91D alloy and **b** 1.0 wt.% CNTs / AZ91D composite

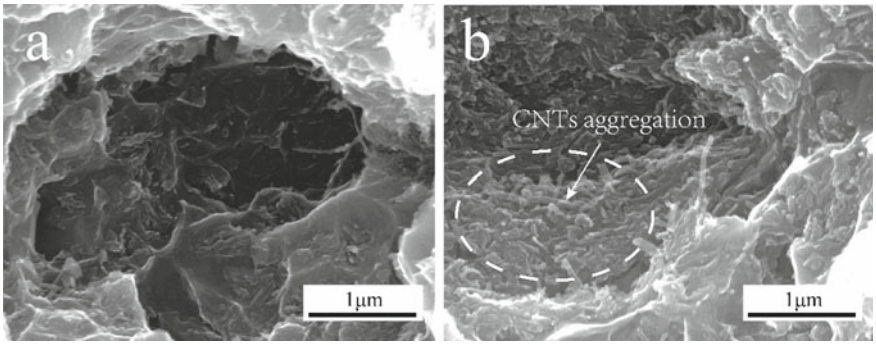


Fig. 8 SEM image of tensile fractograph of **a** 1.0 wt.% and **b** 2.0 wt.% CNTs/AZ91D composites. (Color figure online)

tearing edges appear at the fractograph of AZ91D alloy, which indicate the brittle fracture, as shown in Fig. 7a. On the other hand, 1.0wt.% CNTs/AZ91D composite shows a large amount of dimples and tearing edges at the fractograph, which are the ductile fracture given as in Fig. 7b. Some scholars [14] found that the addition of CNTs in the fabrication of CNTs/Mg composites caused the plastic property decline of composites. This is due to uneven interface bonding. Stress concentration occurs at the interface. Therefore, we can consider that the new fabrication method (especially the liquid–solid extrusion process) improves the interface bonding. It transforms the fracture mechanism from brittle fracture to ductile fracture, which leads to the strength of the composite be improved while the failure strain is maintained.

Figure 8 shows the tensile fractograph of 1.0 wt.% and 2.0 wt.% CNTs/AZ91D composites. CNTs of 1.0 wt.% CNTs/AZ91D composite were pulled out at the fracture region (Fig. 8a). It indicates that the interface between CNTs and magnesium alloy is well bonded. There is no CNTs aggregation found at the fractograph, so that CNTs are well dispersed in magnesium alloy. In the white circle of Fig. 8b, CNT aggregations are observed in the fractograph of 2.0 wt.% CNTs/AZ91D composites. The CNT clusters affected the wettability between magnesium and CNTs. It can introduce porosity and crack defects that should be the main reason for the decline in tensile property of 2.0 wt.% CNTs/AZ91D composites.

3.3 The Interface Between CNTs and AZ91D

Figure 9 shows the HRTEM micrograph of CNTs/AZ91D composites. It can observe that dark areas appear at the interface between CNTs and magnesium alloy. After FFT of the black rectangle area in the figure to obtain a diffraction spectrum, the calibration of IFFT image shows that the crystal plane spacing on the (102) plane is 0.207 nm, and the crystal plane spacing of the (101) plane is 0.260 nm. These results are consistent with Al_2MgC_2 phase. In some scholars' researches [15, 16],

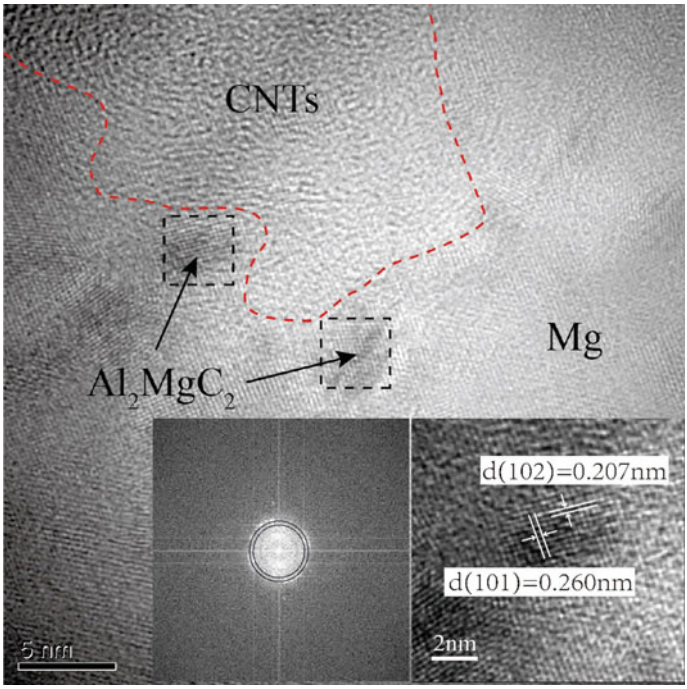


Fig. 9 HRTEM micrograph of CNT/AZ91D composites. (Color figure online)

the Al_2MgC_2 phase helps to produce moderation interfacial adhesion, which can improve the tensile strength and plasticity properties of the composite.

4 Conclusion

(1) CNTs reinforced AZ91D composites were prepared by FSP and ultrasonic treatment assisted with liquid–solid extrusion. Uniform distribution of CNTs in magnesium alloy was achieved.
(2) The extrusion CNTs/AZ91D composite has the highest tensile strength at 1 wt.% CNTs, which can reach 390 MPa, about 25.8% improved compared with AZ91D.
(3) The addition of CNTs can keep good plastic property while improving the tensile strength of composite at proper CNTs content. Al_2MgC_2 was found at the interface between CNTs and Mg. It is beneficial to the formation of good interfacial adhesion.

Acknowledgments This work has been supported by the National Natural Science Foundation of China under Grant Number 51821091 and Number 51972271.

References

1. Iijima S (1991) Helical microtubules of graphitic carbon. Nature 354:56–58
2. Tessonnier J, Rosenthal D, Hansen TW et al (2009) Analysis of the structure and chemical properties of some commercial carbon nanostructures. Carbon 47(7):1779–1798
3. Li Q, Viereckl A, Rottmair CA et al (2009) Improved processing of CNTs/magnesium alloy composites. Compos Sci Technol 69(7–8):1193–1199
4. Li Q, Rottmair CA, Singer RF (2010) CNT reinforced light metal composites produced by melt stirring and by high pressure die casting. Compos Sci Technol 70(16):2242–2247
5. Zeng X, Zhou GH, Xu Q et al (2010) A new technique for dispersion of CNTs in a metal melt. Mater Sci Eng A 527(20):5335–5340
6. Yang J, Schaller R (2004) Mechanical spectroscopy of Mg reinforced with Al2O3 short fibers and C nanotubes. Mater Sci Eng A 370(1):512–515
7. Uozumi H, Kobayashi K, Nakanishi K et al (2008) Fabrication process of CNTs/light metal matrix composites by squeeze casting. Mater Sci Eng A 495(s 1–2):282–287
8. Shimizu Y, Miki S, Soga T et al (2008) Multi-walled CNTs-reinforced magnesium alloy composites. Scripta Mater 58(4):267–270
9. Han G, Wang Z, Liu K et al (2015) Synthesis of CNT-reinforced AZ31 magnesium alloy composites with uniformly distributed CNTs[J]. Mater Sci Eng A 628:350–357
10. Rashad M, Pan F, Asif M et al (2015) Enhanced ductility of Mg-3Al-1Zn alloy reinforced with short length multi-walled CNTs using a powder metallurgy method. Prog Nat Sci Mater Int 25(4):276–281
11. Lu D, Jiang Y, Zhou R (2013) Wear performance of nano-Al 2 O 3, particles and CNTs reinforced magnesium matrix composites by friction stir processing. Wear 305(1–2):286–290
12. Morisada Y, Fujii H, Nagaoka T et al (2006) MWCNTs/AZ31 surface composites fabricated by friction stir processing. Mater Sci Eng A 419(1–2):344–348
13. Chen LY, Xu JQ, Choi H et al (2015) Processing and properties of magnesium containing a dense uniform dispersion of nanoparticles. Nature 528(7583):539
14. Kondoh K, Fukuda H, Umeda J et al (2010) Microstructural and mechanical analysis of carbon nanotube reinforced magnesium alloy powder composites. Mater Sci Eng A 527(16–17):4103–4108
15. Fukuda H, Kondoh K, Umeda J et al (2011) Interfacial analysis between Mg matrix and carbon nanotubes in Mg–6 wt.% Al alloy matrix composites reinforced with carbon nanotubes. Compos Sci Technol 71(5): 705–709
16. Liang J, Li H, Qi L et al (2017) Fabrication and mechanical properties of CNTs/Mg composites prepared by combining friction stir processing and ultrasonic assisted extrusion. J Alloy Compd 728:282–288

Part XX
Residual Stresses in Metal Forming

Complementary Methods for Assessment of Residual Stress Fields Induced by Rotary Swaging of Steel Bars



Dhia Charni, Svetlana Ishkina, Jérémy Epp, Marius Herrmann, Christian Schenck, and Bernd Kuhfuss

Abstract The process investigated in this paper consists of cold rotary swaging of steel bars. In recent work, surface residual stresses were found to be sensitive to process parameters and their fluctuations, leading to variations of residual stresses at different length scales. To properly evaluate the residual stress states in rotary swaged bars, several complementary measurement techniques were applied. Complementary to surface X-ray diffraction measurements, the applicability of micromagnetic methods was evaluated for fast mapping of local residual stress distribution at the surface with a spatial resolution down to 20 μm. Additionally, an evaluation of the full residual stress profile over the cross-section was achieved by neutron diffraction. The combination of the different methods thus allowed a complete characterization of the generated residual stresses at different length scales. Furthermore, a 3D FE-model was developed and process simulation using the Chaboche material model was carried out to investigate the residual stress generation and compare the results with the experimental data. The results show an overall good agreement of the experimental data with the simulation results.

Keywords Incremental forming · Finite element method · X-ray diffraction · Micromagnetic method · Neutron diffraction

D. Charni (✉) · J. Epp
Leibniz Institute for Materials Engineering—IWT, Badgasteiner Str. 3, 28359 Bremen, Germany
e-mail: charni@iwt-uni-bremen.de

S. Ishkina · M. Herrmann · C. Schenck · B. Kuhfuss
Bremen Institute for Mechanical Engineering—Bime, Badgasteiner Str. 1, 28359 Bremen, Germany

University of Bremen, Bremen, Germany

J. Epp · M. Herrmann · C. Schenck · B. Kuhfuss
MAPEX Center for Materials and Processes, University of Bremen, Bremen, Germany

© The Minerals, Metals & Materials Society 2021

G. Daehn et al. (eds.), *Forming the Future*, The Minerals, Metals & Materials Series,
https://doi.org/10.1007/978-3-030-75381-8_188

1 Introduction

For reducing and profiling, the cross-section of bars and tubes, rotary swaging is a common incremental cold forming process. The axisymmetric workpiece is fed into the swaging head. Therefore, the part is incrementally processed by continuously radial strokes of the oscillating dies during their rotation, see Fig. 1. Rotary swaging as manufacturing process is gaining more prevalence, in particular, across the automotive and aerospace industry [16], thanks to its versatility against the increasing demand for lightweight components [15]. Especially, hollow shafts with an advantageous development of the wall thickness enable a cost-effective production of lightweight components with an optimal use of material resources. Besides the advantage of producing near net shape workpieces, rotary swaging leads to products with close tolerances and good surface roughness [13].

Rotary swaging induces complex material flow history depending on the process control, inducing material modifications such as work hardening and residual stress fields [1]. In past studies, surface residual stresses in rotary swaged tubes were found to be sensitive to process parameters [3] as well as their fluctuations, leading to variations of residual stresses at different length scales [10].

In order to evaluate the residual stress fields induced by rotary swaging in a comprehensive way, several complementary measurement techniques can be applied both at the surface and in the volume. Laboratory X-ray diffraction methods are the state of the art for the investigation of residual stress fields [14]. This method is non-destructive but only for residual stress analysis in the first few micrometers beneath the surface, hence, destructive local material layer removal is needed to analyze residual stress depth distribution. On the other hand, non-destructive micromagnetic methods at the microscale have been continuously developed for residual stress analysis [20], offering an important gain of time compared with conventional X-ray diffraction methods. The principle of the micromagnetic method is based on the analysis of Barkhausen noise, crystalline lattice distortion induced by residual stress field with the movement of Bloch walls and with domain rotations during external

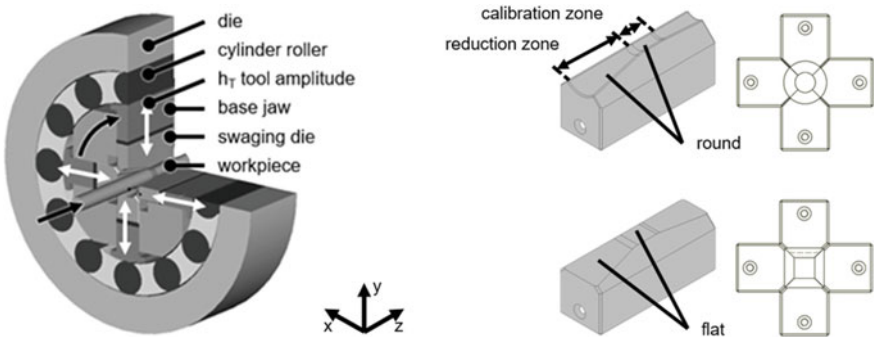


Fig. 1 Illustration of the swaging head for infeed rotary swaging and die geometry features. (Color figure online)

magnetization processes [7]. This method is already well established at macroscopic scale using large probes and has the capability of detecting varying compressive residual stress as for example in shot-peened samples based on Barkhausen noise analysis [11]. However, the application of the micromagnetic method at microscale with the so-called Barkhausen Noise and Eddy Current Microscope (BEMI) still needs to be established for 2D mapping of property variations with high spatial resolution [19]. However, both X-ray diffraction and micromagnetic methods have limitations in terms of penetration depth for non-destructive residual stress analysis. An evaluation of the full residual stress state over the cross-section of steel bars can be achieved via neutron diffraction, which allows the evaluation of different process conditions at global scale [9]. However, the application of this method is limited by the access to neutron sources, which is generally not more than few days per year. Moreover, it can be restricted by the size of the gauge volume leading to low spatial resolution and when scanning thin components due to spurious strain, which affects near surface strain analysis [17].

In this study, the complementary techniques for the residual stress measurement in cold-formed steel bars processed by different parameters are examined and combined for full description of residual stress state generated by the process. In particular, the applicability of non-destructive micromagnetic and neutron scattering methods was investigated and compared. On the other hand, finite element methods were employed to allow a validation of the model by the obtained experimental data.

2 Experimental Methods

The present study has been performed on residual stresses generated by rotary swaging of steel bars. The residual stresses were then analyzed both at the surface and in the entire volume using different measurement methods. For surface stress measurement, XRD and micromagnetic methods were used on rotary swaged bars processed with varying parameters. For the residual stress analysis in the volume, Neutron diffraction was used and compared with the simulation results.

2.1 Process and Material Preparation

The semi-finished part used in the present study was a low carbon low alloy structural steel bars S355, manufactured by cold drawing with a ferritic–perlitic microstructure. To eliminate any pre-existing residual stresses and cold working before rotary swaging, the samples were normalized in a vacuum furnace by gradual slow heating to 890°C and maintaining the temperature for 5 h before slow cooling to room temperature. This also ensures a homogeneous ferrite–pearlite microstructure.

Rotary swaging experiments were performed on bars with an initial length of $L_0 = 300 \pm 0.85$ mm and an initial diameter of $d_0 = 20 \pm 0.30$ mm, under different

Table 1 Experimental setup

Sample	Stroke following angle	Feed per stroke	Die surface shape	Lubrication
BR (standard)	Not controlled	0.46 mm/stroke	Round	Yes
BFd	0°	0.92 mm/stroke	Flat	No
BFl	0°	0.92 mm/stroke	Flat	Yes

process setups, see Table 1. Three different rotary swaging setups were used for the analysis. The first one, which is the standard setup, consists of a reduction of the workpiece diameter to $d_1 = 15$ mm using round swaging dies made of powder metallurgical ASP®2023 steel, which have a round-shaped surface in the calibration as well as in a reduction zone (see Fig. 1), BR in Table 1. An incremental feed of 0.46 mm/stroke was used and the workpiece was lubricated continually during the process using mineral oil Condocut KNR 22. For the second and third process setup, the workpiece was formed with flat swaging dies (flat-shaped calibration and reduction zones) made of 1.2379 steel, see Fig. 1. The combination of these dies with a stroke following angle $\Delta\varphi = 0°$ led to producing a square section workpiece with an edge length of $d_1 = 15$ mm [10]. A higher incremental feed (0.92 mm/stroke) was used to reduce the high back-push stresses that could damage the machine parts. No lubricant was added for the second process setup and a stream of lubricant was used on the workpiece surface for the third process setup. The reduction zone of the round dies is spray-coated by a tungsten carbide layer to increase the effective friction between the swaging dies and the workpiece during the process, reducing the axial reaction force. The samples were fixed using hydraulic clamps before being axially fed into the swaging unit by a distance of $z = 130$ mm. Once the axial feeding is achieved, the rotation of the swaging axle was stopped to prevent additional strokes from affecting the already processed surface while pulling the workpiece out of the swaging unit.

2.2 Process Simulation

For a realistic modeling of complex forming processes, a three-dimensional FEM-Model is required. This representation allows the consideration of all flow directions of the material and influencing variables.

The model for the simulation of infeed rotary swaging was developed with ABAQUS Vers.6.14. To account for the dynamic character of the process, Abaqus/Explicit numerical method was used. Four dies were modeled as rigid bodies and the workpiece as a deformable body. The mesh of the workpiece consisted of linear elements (C3D8R) using distortion control and hourglass control. The length of the edge in an analyzed region was set to 0.5 mm. Figure 2 shows an assembly of the performed simulations with the workpiece and the four dies. The experimental

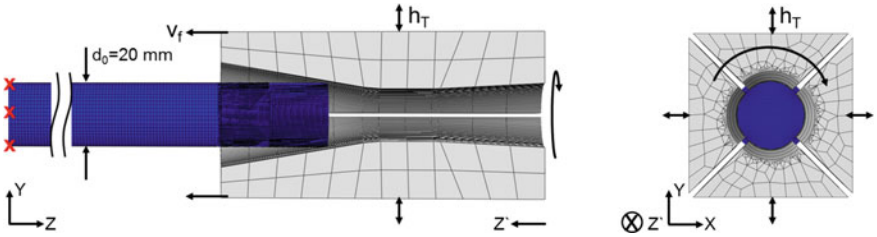


Fig. 2 Design of 3D rotary swaging model. (Color figure online)

process showed low heat generated by the plastic deformation (less than 120 °C) [6]. As a result, the process was considered to be adiabatic.

Similarly to BR process setup, the workpiece was processed from bars with an initial diameter of $d_0 = 20$ mm to a final diameter of $d_1 = 15$ mm. The initial length of the workpiece was $L_0 = 300$ mm. The dies oscillated with a stroke $h_T = 1$ mm with a frequency of 37.5 Hz. For the purpose of simulation time reduction, a feed velocity of $v_f = 2000$ mm/s which is equivalent to the feed per stroke of $l_{st} = 0.92$ mm/stroke was used. Also, contrary to the experimental process, the end of the workpiece was fixed and the dies were rotating and at the same time moving across the workpiece in Z'-direction, assuring the same relative movement as in the real process. The contact conditions between the workpiece and dies were simplified in the simulation by the use of coulomb's law with a constant friction coefficient of the tangential behavior $\mu = 0.1$ in penalty contact method. In order to calculate the residual stresses induced in the process, a static general spring back step with completely removed swaging dies was introduced and realized at the end of the dynamic explicit analysis [18]. To take into account the Bauschinger effect caused by the incremental forming, a non-linear combined hardening material model was chosen in ABAQUS. According to the Chaboche approach [12], a combined kinematic and isotropic hardening model was used. The coefficients of the isotropic hardening were obtained from a cyclic tensile-compression test of an hourglass-shaped annealed sample, which was also simulated with the same parameters for the validation of the obtained material model see Fig. 3a. The samples were cut from the same batch of the semi-finished samples

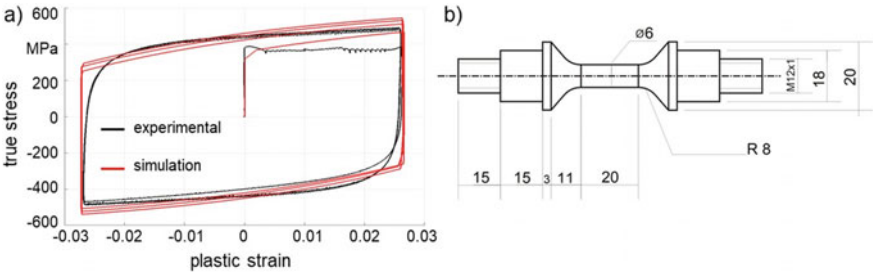


Fig. 3 **a** Validation of the material model, **b** Hourglass sample geometry. (Color figure online)

used for experiments with the dimensions shown in Fig. 3b. The initial yield stress $\sigma_0 = 357.3$ MPa and the parameters used in the isotropic hardening model $Q_\infty = 104.08$ MPa and $b = 2.78$ were determined. For the kinematic hardening by means of "Half Cycle" data type with three back stresses, a yield stress, and plastic strain were carried out using cyclic tension/compression test of annealed samples.

During the cyclic tensile-compression test, bending of the hourglass sample was observed while applying compressive stress, resulting in a progressive shift of the measured stresses with each compression cycle, therefore, only three cycles were taken into account to limit the errors.

2.3 Residual Stress Measurement Methods

2.3.1 X-ray Diffraction

The residual stress measurements were performed with a commercial 8-axis diffractometer Type ETA 3003 from GE inspection technologies, equipped with a position-sensitive detector. A beam of 1 mm diameter of Vanadium filtered Cr-Kα radiation was used. All residual stresses were calculated using the $\sin^2\psi$-method on the {211} diffraction peak of α-iron along 13 χ-angles between $-45°$ and $+45°$ and X-ray elastic constant $½\,S_2 = 5.81\ 10^{-5}$ MPa^{-1} [14]. Surface residual stress measurements were performed by XRD on different bars with different homogeneous residual stress states for the micromagnetic method calibration. Moreover, complementary semi-destructive residual stress measurements were performed by XRD with successive electrochemical layer removal using a solution of H_3PO_4 and H_2SO_4 to determine residual stress depth profile below the surface. No correction of the effect of layer removal was applied. The data were also taken into account for the determination of the stress-free lattice parameter d_0, using the force balance method on a combined X-ray/neutron dataset [21]. Moreover, for the evaluation of surface residual stress homogeneity, the biaxial residual stress state was measured at the surface along a path of 40 mm in axial direction with a step size of 1 mm.

2.3.2 Micromagnetic Method

Measurements of residual stresses were performed using a Barkhausen noise and Eddy current Microscope (BEMI) combined with a 3MA micromagnetic testing system from IZFP Saarbruecken, Germany equipped with a 3-axes positioning system [20]. The sample was fixed on an electromagnetic yoke with a Hall probe underneath the holder see Fig. 4. The magnetization of the sample was applied using a magnetization function generator and an amplifier with a magnetization field strength of 0–125 A/cm and frequencies up to 250 Hz. A spatial resolution of 20 μm could be achieved and the probe position movement had an accuracy of 10 μm in x, y, and z directions. The device was equipped with an Eddy current testing

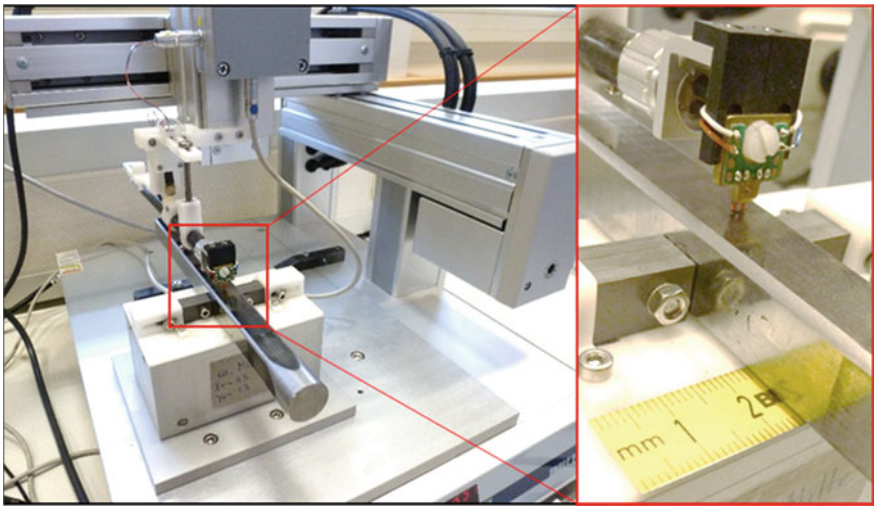


Fig. 4 Barkhausen noise and Eddy current microscope setup. (Color figure online)

unit and a Barkhausen noise measurement unit, which could be used and controlled separately or simultaneously by the computer. The parameters used for the EC and BN analysis are illustrated in Table 2. Since this method aims for fast analysis of property distributions and due to limited space on the BEMI mounting system, only the tangential residual stress component was considered. For this, a calibration of the system was achieved using regression analysis with three reference samples with known homogeneous residual stresses at the surface measured by XRD [4]: annealed state (0 MPa), two rotary swaged bars produced by two different parameters using flat dies and a following stroke angle $\Delta\varphi = 0°$ [10], inducing two different homogeneous compressive tangential residual stress at the surface (−200 MPa and −320 MPa). The magnetic Barkhausen noise parameters and Eddy current parameters were measured along a grid at the surface of the reference samples of 2×10 mm^2 dimensions with a step size of 50 µm in x-direction and 250 µm in y-direction

Table 2 Barkhausen noise and Eddy current analysis parameter setup

Parameter	Setting
Global magnetization frequency	100 Hz
Eddy magnetization amplitude	15 A/cm
Eddy current analysis frequency	500 kHz, 1 MHz, 2 MHz, 4 MHz
Barkhausen magnetization amplitude	30 A/cm
Low and high pass for the Barkhausen noise analysis	100 kHz, 1 MHz

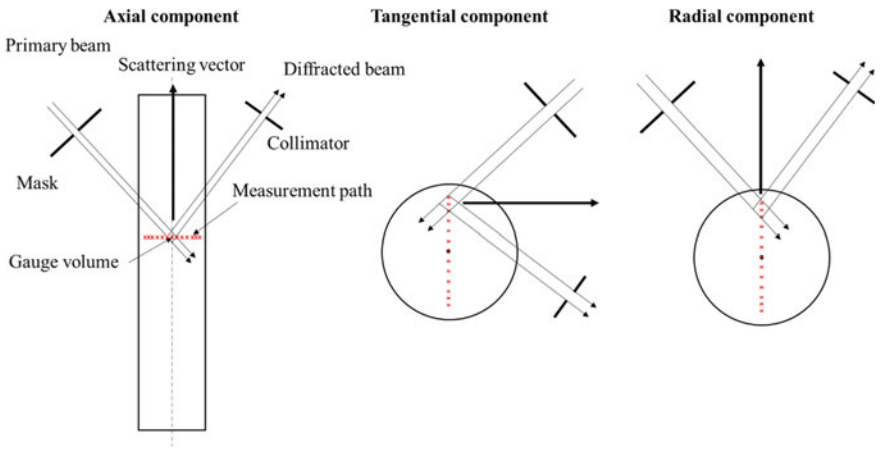


Fig. 5 Neutron diffraction experimental setups in all three stress measurement directions, together with the measured profile line along the cross-section. (Color figure online)

resulting in a dataset averaging 1800 points for each reference sample. For every point, 10 successive measurements were taken and averaged. The measurement time of this magnetic method was less than 1.5 s per point leading to a total of 45 min for one full 2D map.

2.3.3 Neutron Diffraction

Residual stress distributions have been measured by neutron diffraction using the instrument E3 at the reactor BER II (Helmholtz-Zentrum Berlin) using $2 \times 2 \times 2$ mm^3 gauge volume. The {211} diffraction peak of α-iron at 78° with a wavelength of 0.1486 nm was analyzed to determine the lattice spacing $d_{\{211\}}$. Measurements were performed in three principal stress directions, axial, radial, and tangential, see Fig. 5. The measured depth profile was located at an axial position 20 mm away from the last stroke and consists of 17 points along a centered path of 14 mm with step sizes ranging between 0.5 mm and 1.5 mm. The measurement time for a single measurement was between 300 and 2200 s. To control the size of the gauge volume, a mask with a square cross-section was used at the primary beam and an oscillating collimator of 2 mm in width with no height limitation was used in front of the detector. The stress-free lattice parameter d_0^{hkl} was measured at small cubes of the same material ($2 \times 2 \times 2$ mm^3) prepared by electro-discharge-machining. Complementary destructive residual stress measurements were performed by XRD to calculate the residual stress depth profile near the surface. These data took also into account the determination of the stress-free lattice parameter d_0 using the force balance method on a combined X-ray/neutron stress dataset [5]. The analysis of the diffraction pattern was performed using the Software Stresstex developed by C.

Randau of FRMII/TUM. The diffraction peak was obtained by integrating the two-dimensional diffraction frames. The fitting of the diffraction pattern was performed using pseudo-Voigt function after background subtraction. After the fitting, the strain ε_i^{hkl} was calculated using Eq. 1 from the measured diffraction peak position resulting into the d_i^{hkl} through Bragg's Law Eq. 2.

$$\varepsilon_i^{hkl} = \frac{d_i^{hkl} - d_0^{hkl}}{d_0^{hkl}} \tag{1}$$

$$n * \lambda = 2d_{hkl} * \sin\theta \tag{2}$$

Based on the three determined strain components, the residual stresses could be calculated through Eq. 3 in the considered direction where ε_r^{hkl}, ε_θ^{hkl}, and ε_z^{hkl} are the strain in the radial, tangential, and axial direction respectively. The residual stresses were obtained by using the elastic constants $1/2S_2^{hkl} = 5.8181 * 10^{-6}\text{GPa}^{-1}$ and $S_1^{hkl} = -1.2727 * 10^{-3} GPa^{-1}$.

$$\sigma_r = \frac{1}{1/2S_2^{hkl}} \left[\varepsilon_r^{hkl} - \frac{S_1^{hkl}}{1/2S_2^{hkl} + 3S_1^{hkl}} (\varepsilon_r^{hkl} + \varepsilon_\theta^{hkl} + \varepsilon_z^{hkl}) \right] \tag{3}$$

3 Results and Discussion

3.1 Surface/Surface-near Residual Stress Distribution

The biaxial residual stress state measured by X-ray diffraction at the surface along the axial direction of the round and flat rotary swaged samples are presented in Fig. 6a.

On the sample Br, both residual stress distributions are fluctuating along the surface between −250 MPa and −620 MPa in the axial direction and between −280 MPa and −450 MPa in the tangential direction. These fluctuations seem to have a periodic shape along the axial direction of the sample. These rotary swaging signature fluctuations are also reported in previous works on surface residual stress state of rotary swaged tubes and bars of the same steel grade [10]. In contrast, the surface residual stress measurements on sample BFd show homogeneous distribution of both residual stress components. The surface axial residual stress is around −400 MPa and the tangential surface residual stress is at −350 MPa. Previous work has shown congruent surface residual stress homogeneity properties examined on rotary swaged tubes by both process setups [10]. Similarly to tubes, it was also found that these surface residual stress fluctuations disappear under 300 μm below the outer surface of rotary swaged bars. Additionally, it was shown that the feed per stroke parameter has no influence on the residual stress generation below 300 μm from the surface

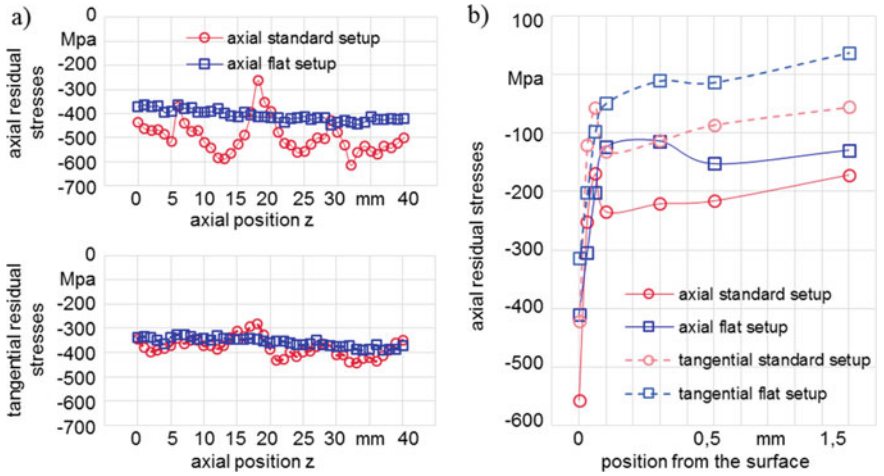


Fig. 6 **a** axial and tangential residual stress distribution at the surface of rotary swaged bars along the axial direction for different process setups (BR: standard setup, BFd: flat setup). **b** axial and tangential residual stress depth profile for different process setups. (Color figure online)

for process standard setup. Complementary to the surface residual stresses, residual stress depth profiles by destructive XRD are shown in Fig. 6b. The residual stresses in both directions for both process setups changed drastically in the first 50 μm under the surface before stabilizing at low compression for deeper positions.

The results of micromagnetic measurements are compared with X-ray diffraction data as a reference. Two different calibration functions were determined, one using Barkhausen noise analysis and Eddy current and one using only the Barkhausen analysis. Figure 7 shows the tangential residual stress distribution measured by micromagnetic analysis at the surface of a rotary swaged rod using flat dies setup featuring high fluctuating back-push loads (BFl).

The calculated tangential residual stress distributions measured by both calibration setups have similar shape and values as shown by the XRD data with the residual

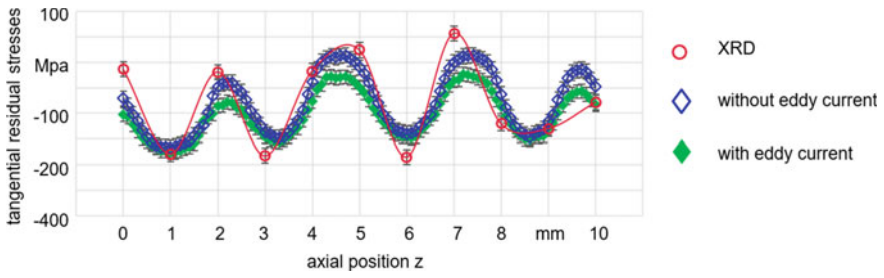


Fig. 7 Surface tangential residual stress measured by XRD and micromagnetic methods on sample BFl. (Color figure online)

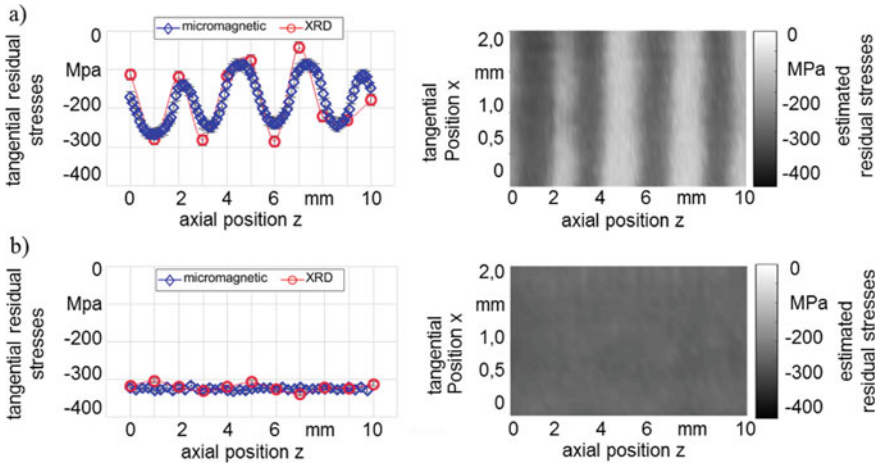


Fig. 8 Surface tangential residual stress measured by XRD and micromagnetic method without Eddy current. **a** sample BFl, **b** sample BFd. (Color figure online)

stresses calculated with only Barkhausen noise analysis having a better agreement, with discrepancies generally below 50 MPa. Scan of the surface of the sample BFl using Barkhausen analysis is shown in Fig. 8.

Due to the high spatial resolution, the micromagnetic results show much clearer periodic fluctuating tangential residual stress distribution shaped like sinusoidal curve. The micromagnetic method seems to have a good accuracy when it comes to measuring low compressive residual stresses with small differences. Similar to the results of BFl sample, surface residual stress at BFd sample shows good concordance between the XRD results and the Barkhausen noise analysis results, highlighting the potential of the micromagnetic method for fast homogeneity examination. However, it has to be kept in mind that the measured signal could also be influenced by variations of the local material properties such as microstructure, dislocation density, and chemical composition, as well as surface topography. Therefore, a prior careful calibration to the target property is still essential. This method remains very accurate while considering the significant reduction of measurement time gain in comparison with the XRD method, while at the same time, offering the benefits of high spatial resolution. On the other hand, it was not possible to analyze surface residual stress distribution using the present setup on round rotary swaged bars. This could be explained by a possible geometry effect taking part in the measured Barkhausen signal [2].

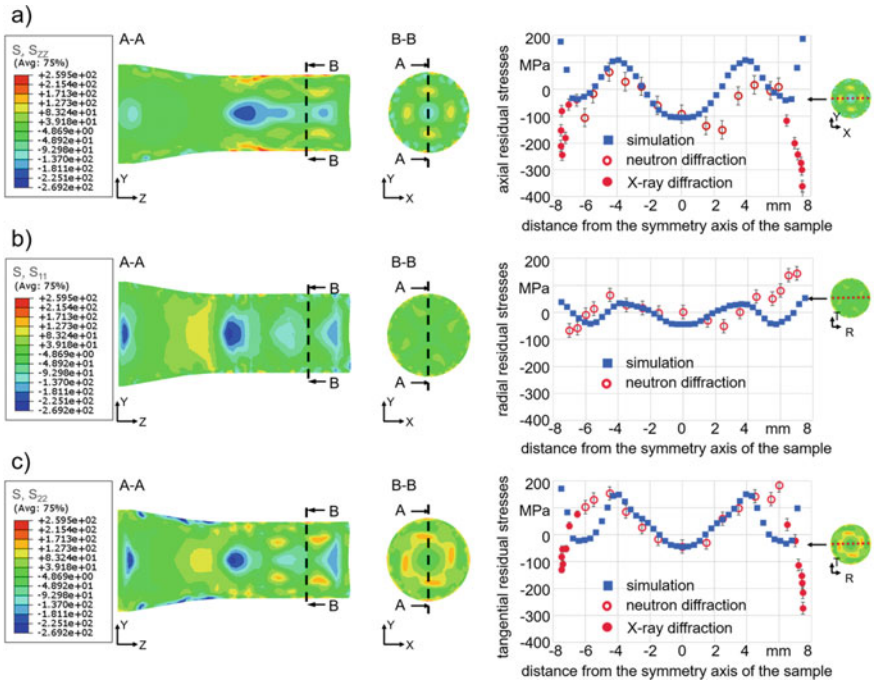


Fig. 9 FEM results of residual stress field and depth profile in a cross-section B-B of a rotary swaged bar using standard parameters (BR), compared with neutron and XRD data; **a** axial residual stresses, **b** tangential residual stresses, **c** radial residual stresses. (Color figure online)

3.2 Residual Stress Distribution in the Volume

The FEM results of residual stresses distribution were determined in the longitudinal section A-A as well as in the cross-section B-B of the bar, as shown in Fig. 9. The axial residual stress component was analyzed by means of the axial stress component S_{ZZ}. These values were obtained for each element node along the cross-section. Radial and tangential residual stresses were obtained in a cylindrical coordinate system. Thus, the values of the stress component S_{11} and S_{22} in the simulation were analyzed as the radial and tangential components of residual stresses respectively.

The through-thickness residual stress neutron data in a standard rotary swaged bar are presented in Fig. 9, combined with near-surface XRD data and compared with simulated residual stress results. Both experimental and simulation results show a compression concave shape around the center of the sample, surrounded by two symmetrical tensile residual stress peaks below the surface in all three principal directions. As expected, the neutron data show low residual stress field in normal direction (mostly between 80 MPa and −50 MPa), which confirms the reliability of the measurements and of the subsequent evaluation procedure, including the stress-free lattice parameter d_0 determination. Additionally, the simulated residual stress

distribution in the whole cross-section shows axial and tangential residual stress tensile peaks, which corresponds to the areas under the center of the die strokes. At the surface, eight tensile peaks can be spotted around the surface, which correspond to the die imprints between two successive strokes. This effect could be attributed to the causes of residual stresses fluctuation at the surface during standard rotary swaging setup. This stroke effect could be eliminated during the flat rotary swaging setup by controlling the stroke following angle ($\Delta\varphi = 0°$), resulting into homogenous surface residual stresses. By comparing simulation and neutron diffraction results, it can be seen for all three principal residual stresses that the simulation gave similar trends and values below 1.0 mm from the surface. In contrast, axial and tangential residual stresses obtained by XRD strongly differ from the simulation results near the surface. These discrepancies can be attributed to several factors influencing the simulation results. First of all, it may be associated with the highly simplified model of friction conditions. In real process, round dies with WC–Co (tungsten carbide-cobalt) layer [8] in the reduction zone were used, which can influence the material flow at the surface of the workpiece. Furthermore, particle abrasion and lubricant as well as microstructure inhomogeneity were also not considered in the simulation. Another aspect is that the material flow differs between simulation and experiment. In the simulation, the axial stiffness in z'-direction is given by the (static) stiffness of the workpiece, which is significantly higher than in the experimental setup. The material flow in this direction causes upsetting of the workpiece (diameter increase of about 19 μm in the simulation). In the machine, the clamping and the feed devices provide (dynamic) stiffness that is low enough to prevent any upsetting. Consequently, the material flow differs between simulation and experiment with a higher difference at the surface than in the core of the workpiece. Finally, the employed mesh size for the considered process was optimized regarding the simulation time and therefore the mesh size was too large to achieve reliable simulation results at the very surface. Nevertheless, simulation results and measurements are in the good agreement below the surface.

4 Conclusion

In this study, complementary residual stress measuring techniques were used and compared with FEM simulation, namely XRD, neutron diffraction and micromagnetic method, allowing the experimental analysis of residual stress fields at different length scales. Rotary swaged components processed with two different geometries were investigated and the obtained experimental data were then compared with FEM simulations in order to validate the model. The following conclusions can be drawn:

- The micromagnetic method proved to be successful at measuring surface residual stresses, offering both shorter measurement time compared with X-ray diffraction method as well as higher spatial resolution.

- The micromagnetic method can be a good replacement or at least complementary method for X-ray diffraction method for fast surface residual stress homogeneity.
- The simulated residual stress analysis using the Chaboche material model showed good agreement with experimental data in the volume below 1.0 mm from the surface. Through the validated model for bulk residual stress development, modified process conditions for residual stress optimization can be analyzed.
- The discrepancies between the simulated and measured residual stresses by means of X-ray diffractions near the surface could be mainly attributed to the simplification of the friction condition and of the process model. Further investigations are needed to study the corresponding effects.

Acknowledgments This project is funded by the Deutsche Forschungsgemeinschaft (German Research Foundation)—374789876 within the sub-project (EP 128/5-2 and KU 1389/16-1) "Control of component properties in rotary swaging process" of the priority program SPP 2013 "The utilization of residual stresses induced by metal forming". The authors thank the institute Helmholtz-Zentrum Berlin and Dr. Robert Wimpory as well as Dr. Mirko Boin for the use of the instrument E3 at the reactor BER II and for the assistance during the scientific research.

References

1. ASM Committee on Rotary Swaging (1988) Rotary swaging of bars and tubes. In: Metals handbook vol 14 forming and forging, 9th edn. Metals Park, Ohio, American Society for Metals, pp 268–309
2. Bobrov I, Epp J (2019) High throughput material state analysis via Barkhausen Noise-Eddy current microscope. In: Proceedings of the 13th International Conference on Barkhausen Noise and Micromagnetic Testing, ICBM13, Prag, Czech Republic
3. Charni D, Ishkina S, Epp J, Herrmann M, Schenck C, Zoch HW, Kuhfuss B (2018) Residual stress generation in rotary swaging. MATEC Web Conf 190:04001
4. Epp J, Hirsch T (2010) Residual stress state characterization of machined components by X-ray diffraction and multiparameter micromagnetic methods. Exp Mech 50:195–204
5. Epp J, Hirsch T, Hunkel M, Wimpory R (2010) Combined neutron and X-ray diffraction analysis for the characterization of a case hardened disc. Mater Sci Forum 652:37–43
6. Gärtner RR (2012) Entwicklung einer optimierten Fertigungsstrategie für das Kaltrundkneten. Ph.D. thesis, Darmstadt University
7. Grum J, Zerovnik P (2000) Use of the Barkhausen effect in the measurement of residual stresses in steel. Insight (Northamp.) 4212:796–800
8. Heislitz F (2000) Kraftbedarf beim Kaltrundkneten. Vorhaben Nr. 224. Vergleichende Untersuchungen des Kraftbedarfs beim Kaltrundkneten mit unterschiedlichen Maschinenkonzepten. Abschlussbericht. In Forschungshefte. Forschungskurato-rium Maschinenbau e. V. (FKM), 254
9. Huchtings MT, Withers PJ, Holden, Lorentzen T (2005) Characterization of residual stress by neutron diffraction. Taylor & Francis, Boca Raton, FL
10. Ishkina S, Charni D, Herrrmann M, Liu Y, Epp J, Schenck C, Kuhfuss B, Zoch H-W (2019) Influence of process fluctuations on residual stress evolution in rotary swaging of steel tubes, Materials
11. Jiles DC, Suominen L (1994) Effects of surface stress on barkhausen effect emissions: model predictions and comparison with x-ray diffraction studies. IEEE Trans 30(6)
12. Kalnins A, Rudolph J, Willuweit A (2015) Using the nonlinear kinematic hardening material model of Chaboche for elastic–plastic ratcheting analysis. J Pressure Vessel Technol 137(3)

13. Lim S-J, Choi H-J, Lee C-H (2009) Forming characteristics of tubular product through the rotary swaging process. J Mater Process Technol 209(1):283–288
14. Noyan IC, Cohen JB (1987) Residual stress measurements by diffraction and interpretation. Springer, New York
15. Piwek V, Kuhfuss B, Moumi E, Hork M (2010) Light weight design of rotary swaged components and optimization of the swaging process. Int J Mater Form 3:845–848
16. Rauschnabel E, Schmidt V (1992) Modern applications of radial forging and swaging in the automotive industry. J Mater Process Technol 35:371–383
17. Šaroun J, Rebelo Kornmeier J, Gibmeier J, Hofmann M (2018) Treatment of spatial resolution effects in neutron residual strain scanning, Phys B: Phys Condens Matter
18. Song F, Yang H, Li H, Zhan M, Li G (2013) Springback prediction of thick-walled high-strength titanium tube bending. Chin J Aeronaut 26:1336–1345
19. Szielasko K, Kopp M, Tschunky R, Lugin S, Altpeter I (2004) Barkhausenrausch- und Wirbelsstrom-Mikroskopie zur ortaufgelösten Charakterisierung von dünnen Schichten, DGZfP-Jahrestagung
20. Szielasko K, Rabung M, Kopp M, Tschuncky R, Hans M, Weber F, Sheikh Amiri M, Richert H, Schmidt H, Kreller M, Fischer C, Eigenmann B (2014) Ortsauflösende Charakterisierung ferro- und ferrimagnetischer Schichten für magneto-resistive und magnetooptische Sensoren, DGZfP-Jahrestagung – Di.1.B.4.
21. Winholtz RA (2003) Analysis of residual stress by diffraction using neutron and synchrotron radiation. In: Fritzpatrick ME, Lodini A (eds) Taylor & Francis, London

Investigations and Improvements in 3D-DIC Optical Residual Stress Analysis—A New Temperature Compensation Method



Frederik Dahms and Werner Homberg

Abstract Highly accurate in-situ measurement of geometric and mechanical quantities is now a requirement for the production of complex and, in particular, incrementally manufactured components. A current research project at the Chair of Forming and Machining Technology (LUF) is thus investigating the application of a 3D digital image correlation measuring system for in-situ residual stress measurements based on the hole-drilling method. The corresponding investigations have initially proven the basic feasibility of the system. It is also shown that the measurement result is affected by thermal influences, unintentionally introduced vibrations, and air flow. These influences can be compensated to a high degree through the appropriate countermeasures. A compensation method is thus presented, taking the example of thermal loads.

Keywords Residual stress measurement · Hole-drilling method · 3D digital image correlation · Friction spinning · Thermal strain

1 Introduction

Economic and ecological constraints are necessitating the development and production of complex and multifunctional components. Against the background of an equally widespread desire for flexibility, incremental manufacturing processes are increasingly becoming the focus of interest. A good example of this is the friction-spinning process [1]. The friction-spinning process is an incremental forming technology based on the principles of metal-spinning, flow-forming, and friction welding [2]. Friction-induced heat leads to an increase in the ductility of the workpiece. This can be used to produce complex workpiece geometries and also to improve their mechanical properties [1–3]. Complex thermomechanical conditions can, however, lead to non-uniform residual stress distributions. Preliminary investigations indicated these non-uniform residual stress distributions

F. Dahms (✉) · W. Homberg
Forming and Machining Technology, Paderborn University, Warburger Straße 100, 33098 Paderborn, Germany
e-mail: fd@luf.upb.de

© The Minerals, Metals & Materials Society 2021

G. Daehn et al. (eds.), *Forming the Future*, The Minerals, Metals & Materials Series,
https://doi.org/10.1007/978-3-030-75381-8_189

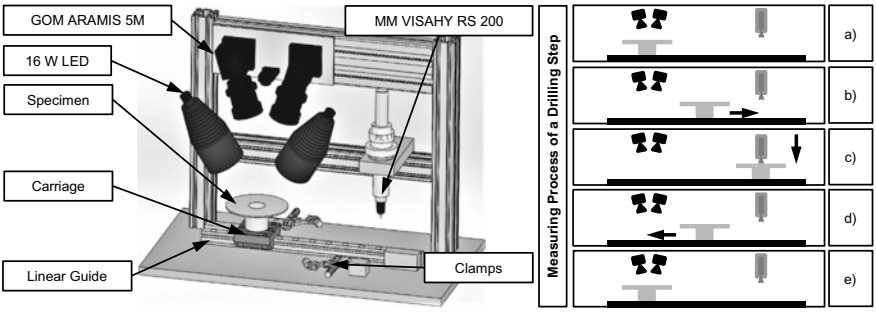


Fig. 1 CAD model of the 3D-DIC optical residual stress measuring system (l). Measuring process of a hole-drilling step (r). (Color figure online)

in the tangential and radial direction of tubular workpieces with a radial flange from AW 6060 through X-ray diffraction (XRD) measurements. For procedural reasons, the XRD method is unable to evaluate non-uniform residual stress distributions that vary over the depth [4]. Metallographic investigations, however, show that these workpieces have a non-uniform degree of deformation distribution over the wall thickness [2]. A depth evaluation of the residual stress distribution would thus make sense. One means of achieving this is through the incremental hole-drilling method, in which the residual stress distributions inside the workpiece can be deduced by strains close to the surface that are released by hole-drilling [5–7]. The drawbacks of this method include the major outlay on apparatus and the time required for the preparation and evaluation of strain-gauge measurements. Another promising approach is the use of optical measuring methods, such as electronic speckle pattern interferometry [8]. One less investigated approach is the utilisation of relatively widespread 3D-DIC systems for residual stress analysis [9, 10]. A possible experimental setup is presented in Fig. 1. The multi-camera system with the lighting unit and the 3D-DIC system is mounted on a frame-shaped device to this end, together with a high-speed drilling turbine (approximately 300,000 rpm). In a future setup, this device, with the hole-drilling and 3D-DIC unit, is to be positioned at the respective measuring or hole-drilling point using an industrial robot. In this case, the measuring points will usually be located in an area of no relevance for the function of the measured component. For fundamental investigations, the measuring device described in Fig. 1 has been configured differently, with the workpiece being moved to the measuring and drilling position with the aid of a linear axis.

2 3D-DIC Optical Residual Stress Measuring System

In the existing approaches, the hole-drilling device is either positioned between two fixed cameras with a fixed specimen [11] or the hole drill is retracted from the field of view after each depth increment before the image is taken [12]. In this new approach,

however, the hole-drilling device and the cameras are fixed. Either the specimen or the complete measuring device thus has to be moved for the incremental measurement procedure. The procedural benefit derived from this setup is the use of ideal camera calibration, respectively, the angle between the cameras and the specimen, leading to an optimal depth of field with a wide-range measuring surface around the drill hole. The use of a 3D-DIC camera setup, in particular, makes it possible to measure tubular specimens, for example.

The design of the optical residual stress measuring system is illustrated in Fig. 1 (*l*). The measuring device is designed as solid as possible to provide high stiffness and avoid vibrations. The linear guide's carriage is fixed with clamps at the outer end to achieve high-repeat accuracy. It is made of a GOM ARAMIS 5 M to capture the images. This is calibrated to an area of 15 mm × 13 mm. The workpiece is illuminated by two 16 W LED lamps. The captured images are processed by GOM ARAMIS 2017 software. For the hole-drilling process, the high-speed air turbine of the Vishay RS 200 is mounted on the measuring system. Inverted-cone drills of 1.6 mm diameter are used as described in ASTM E837-13a [5].

The measuring process is illustrated in Fig. 1 (*r*). Starting in the image acquisition position, the reference stage images are taken (a), then the specimen is moved on the linear guide (b) to the hole-drilling position (c), where a hole increment is drilled, and afterwards, the specimen is moved back (d) to the initial position where the residual strains of the hole-drilling step are measured (e). For further increments, the process restarts with step (b). The strain measurements can be processed full-field or over a defined area like a strain-gauge grid geometry.

The accuracy of the measuring procedure described is proved by solely moving the specimen between the image processing position and the drilling position without drilling. The procedure is completed after a repetition of eight times after capturing the reference stage images. The strains are expected to be zero. The mean deviation of the measured strains ε_1 is 0 µm/m, and ε_3 is 2 µm/m (*cf.* Fig. 2). The average measured displacement of the specimen u is 1 µm. The standard deviations are indicated in the columns of Fig. 2. These results confirm that it is possible to conduct measurements with this new approach for 3D-DIC optical residual stress analysis.

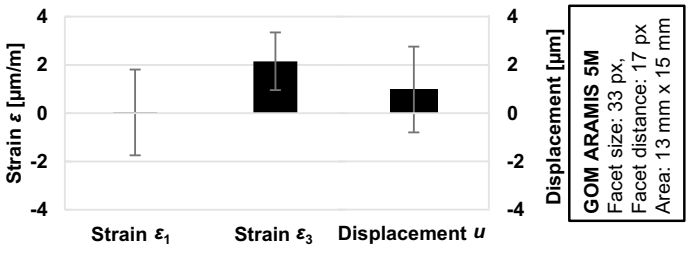


Fig. 2 Averaged deviation of the measured strains ε and displacement u of the specimen

3 Experimental Investigations

This chapter describes the experimental investigations on the accuracy of the 3D-DIC optical residual stress measuring system. Based on these investigations, adjustments are made to the measuring system. The workpieces (the tubular part with a flange) are manufactured using EN AW 6060 (3.3206) tubular profiles with a friction-spinning machine based on Leifeld Metal Spinning GmbH PLB400. Specimens for optical measurements are coated with a speckle pattern by spraying a white acryl-based spray coating layer and black speckles with an airbrush system, leading to better adhesion of the speckles, even when compressed air and fine wipers are used to remove chips and dust. To validate the 3D-DIC optical residual stress measurements, use is made of CEA-13-062UM-120 strain-gauge rosettes and CEA-13-062UW-120 strain gauges, which are soldered to a three-wire half-bridge circuit with a 120-Ω precision resistor and processed with a universal measuring amplifier HBM MX 440. This is also used for processing the type k thermocouple temperature measurements. The strains of the 3D-DIC optical residual stress measurements are always averaged over the same geometry (area, direction, and distances) as those of the used strain gauges. As the measuring area is 0.77 mm distant from the borehole, its speckle pattern is not influenced by the hole drilling operation.

3.1 Optical Micro-Strain Measurements

Initially, the accuracy of the 3D-DIC GOM ARAMIS 5 M system used is investigated by measuring micro strains. Small loads are applied to an aluminium EN AW 6060 (3.3206) specimen of $t = 2$ mm thickness by a Zwick Z100 testing machine. For the optical strain measurements, 15 images are taken for each stage with a frequency of 2 Hz. Preliminary investigations have shown that an optimum facet size and distance can be determined for each application, depending on various factors. These include the size of the calibrated area in relation to the characteristics of the speckle pattern and the character of the strain to be measured, for example, its potential variation within one facet. The resulting computing time must also be considered in the process of selection. Alternatively, a good approximate solution can be determined iteratively based on the manufacturer's specifications, starting with a facet size of 19 px and a facet distance of 15 px. In this case, the facet size is set to 21 px and the facet distance to 11 px. The influence on accuracy is negligible if a minimum facet size is achieved, which in this case means that the facets must be larger than 9 px. The two 16 W LED lamps were only turned on during the 7 s of image acquisition for an individual stage. This reduces the heat induction to the specimen. Figure 3 shows a comparison of the measured 3D-DIC strains with the strains calculated by Hooke's law. The applied load stages are 0 N, 100 N, 0 N, 200 N, 0 N, and 300 N. The strains of the 3D-DIC optical strain measurements are averaged over the same geometry (area, direction, and distances) as those of the used CEA-13-062UM-120

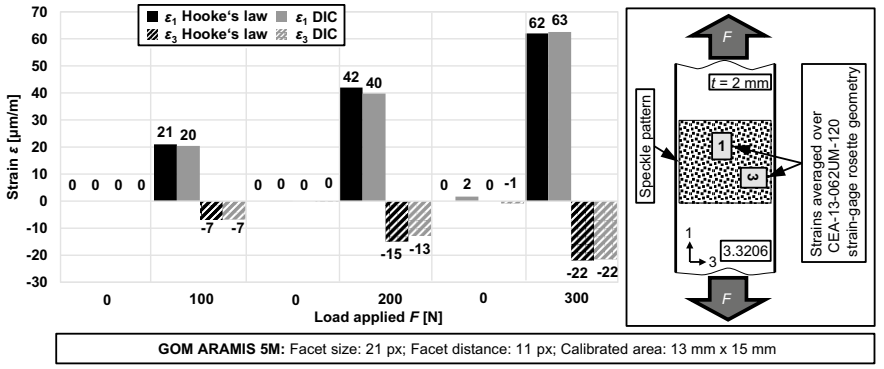


Fig. 3 Comparison of the calculated strains (Hooke's law) with the measured 3D-DIC strain values. Loads applied by Zwick Z100

strain-gauge rosette. The measured strains are averaged over two measurement procedures. The highest deviation of the measured DIC strains from the calculated strains is 2 µm/m. The deviation is not a function of the value of the strain, hence zero can be reliably measured. These results prove that this method meets the required accuracy for the measurement of micro strains and that it is possible to apply 3D-DIC optical residual stress analysis.

In the next step, the accuracy of the 3D-DIC method is investigated concerning the hole-drilling method. The same specimen as described above is set up with a CEA-13-062UM-120 strain-gauge rosette on the front and a speckle pattern on the back. A 1 mm deep hole is drilled on both sides with an RS-200 and a 1.6 mm diameter inverted cone driller (*cf.* Figure 4, left side). The distance between the two holes is 30 mm. The specimen is set up for the Zwick Z100 after a resting time of four hours following the hole drilling. Thus, all the thermal influence of the hole-drilling process can be excluded. The applied loads are 100 N, 200 N, and

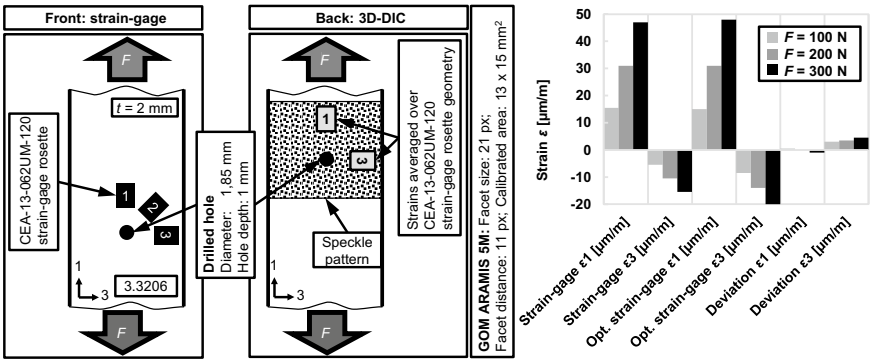


Fig. 4 Comparison of strain-gauge and 3D-DIC strain measurements with drilled holes. Loads applied by Zwick Z100

300 N. The strains of the 3D-DIC optical residual stress measurements are averaged over the same geometry (area, direction, and distances) as those of the used CEA-13-062UM-120 strain-gauge rosette. The measured strains are averaged over two measurement procedures. The 3D-DIC measurement is performed as described above. In Fig. 4 (right side) it is shown that the deviation of the two strain measurement methods has a magnitude of 5 μm/m, and the deviation is higher in direction 3 (ε_3), in particular. The deviation in direction 3 can be explained by the lower depth of field in the marginal area, which is compensated with a closed aperture ($f/16$). The results show that this 3D-DIC method has an acceptable level of accuracy for the application of the hole-drilling method.

3.2 Influence of Air Flow and Vibrations

For the 3D-DIC system, air flow and vibrations can be critical in measuring micro-scale strains. The measurement is affected, for example, by air flow and vibrations due to people talking or moving close to the measuring system so that a shattering live-view image can be observed. This is caused by the oscillation of the air between the cameras and the specimen. Air flow can also be caused by unadapted mounted blowers in the workshop, for example. Even a person speaking at a distance of 500 mm from the cameras can cause shattering live-view images. The air flow initiated by a talking person is considered to have a flow rate of approx. 2 l/s [13]. This reveals a high sensitivity to external influences. In the worst case, it leads to the speckle pattern not being recognised at all or only in part, with the result that a measurement cannot be performed. Consequently, any air flow and vibrations must be prevented during the measuring process. Therefore, the measuring system is designed to be very stiff to avoid vibrations, and a cover is mounted to prevent air flow.

3.3 Influence of the Speckle Pattern Coating

When it comes to incremental hole-drilling measurements, it can be observed that the measured strains vary with the time after a drilling step is performed, which has also been investigated by other scholars [14]. Figure 5 shows the time-dependence of a 3D-DIC optical hole-drilling measurement. The strains of the 3D-DIC optical residual stress measurements are averaged over the geometry (area, direction, and distances) of a CEA-13-062UM-120 strain-gauge rosette. This phenomenon was observed in measurement at a hole depth of 0.7 mm. The first drilling steps were operated continuously. Then the 0.7 mm depth stage is set as a reference stage for illustration purposes. The next 0.1 mm hole-drilling step to 0.8 mm is performed, and strains are measured after 4, 40, and 80 min. The results indicate that the measured absolute value of the residual strain increases with the time after hole

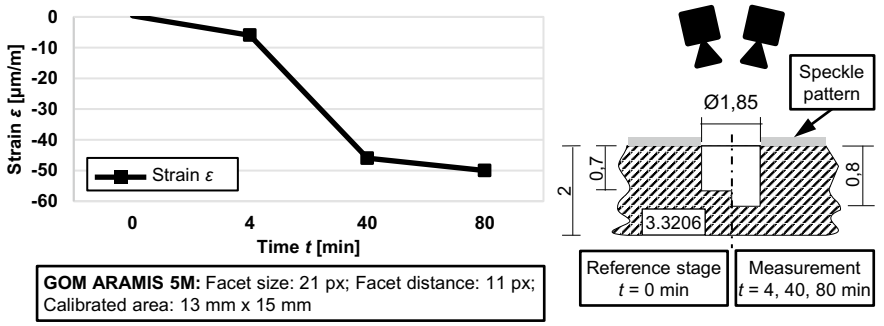


Fig. 5 Time-dependence of a 3D-DIC optical hole-drilling-method measurement

drilling. In this way, it was deduced that the release of the residual strains takes up to 80 min, contradicting the strain-gauge measurements. A different interpretation is that heat is emitted, leading to a decreasing thermal strain until thermal equilibrium is reached. Furthermore, the influence of the speckle pattern layer could influence the heat conduction. Therefore, the phenomenon described must be investigated further, especially regarding the unknown influence of the speckle pattern coating.

4 Temperature Compensation of Optical Residual Stress Measurements

The need for a temperature compensation method for optical residual stress measurements results from the fact that optical residual stress measurements are not temperature-compensated like strain-gauge measurements. Thermal strains induced by the illumination of the specimen or room temperature changes cannot be distinguished from load-induced strains. Additionally, with the high thermal expansion coefficient α_T of aluminium ($23.1 \cdot 10^{-6} \cdot K^{-1}$), for example, small temperature changes lead to significant errors in optical residual stress measurements. Temperature compensation should work as intrinsically as the self-temperature compensation in strain gauges. Numerous possibilities for measuring temperatures on surfaces exist, but there are also limitations to keeping the financial and time deficit as low as possible while retaining high accuracy. It is also desirable to process the temperature measurement values directly with the DIC system. Temperature measurements can be performed with a type k or PT1000 thermocouple, which can be clamped onto the surface. To eliminate the influence of thermal strains on the optical residual stress measurement, use is made of the formula for total strain ε consisting of the elastic strain ε_E and the thermal strain ε_T:

$$\varepsilon = \varepsilon_E + \varepsilon_{T.} \tag{1}$$

This formula is adapted to calculate the thermally corrected residual strains $\varepsilon_{\mathrm{RS}}$ consisting of the strain measured by the DIC method $\varepsilon_{\mathrm{DIC}}$ and the thermal strain ε_{T} by:

$$\varepsilon_{\mathrm{RS}} = \varepsilon_{\mathrm{DIC}} - \varepsilon_{\mathrm{T}} = \varepsilon_{\mathrm{DIC}} - \Delta T * \alpha_{\mathrm{T.}} \tag{2}$$

It is sensible to implement a correction factor k when the measured temperature cannot fully reproduce the thermal strain deviation:

$$\varepsilon_{\mathrm{RS}} = \varepsilon_{\mathrm{DIC}} - \varepsilon_{\mathrm{T}} = \varepsilon_{\mathrm{DIC}} - k(\Delta T) - \Delta T * \alpha_{\mathrm{T.}} \tag{3}$$

The correction factor k can be described by a linear or a polynomial function depending on the remaining thermal strain difference after dividing the calculated thermal strain measured by a thermocouple.

4.1 Validation of the Temperature Compensation Method

The temperature compensation method described above is investigated by comparing the temperature compensated 3D-DIC optical measurements with self-temperature-compensated strain-gauge (CEA-13-062UW-120) measurements in a single test setup on one specimen. Only the illumination heat affects the specimen, where the strain gauge is expected to measure zero strain and the optical strain measurement is expected to measure a strain equal to the temperature delta multiplied by the thermal expansion coefficient α_{T} ($23{,}1 \cdot 10^{-6} \cdot \mathrm{K}^{-1}$) of the aluminium specimen (3.3206). The heat is induced by two 16 W LED lamps on the 3D-DIC system, as in an ordinary. 3D-DIC measurement means that the lamps are not switched off between two measurements. The temperature is measured by a type k thermocouple on the specimen surface. The thermocouple braids are clamped on the specimen, as illustrated in Fig. 6. The optical strain measurements are performed in eight stages in the manner described in Chap. 3. The strains of the 3D-DIC optical strain measurements are averaged over the same geometry (area, direction, and distances) as those of the used CEA-13-062UW-120 strain gauges. The temperature and the strain-gauge measurements are linked to and averaged out over the period of the optical strain measurements. No correction factor is used. Figure 6 shows the averaged optical strain measurement error $\varepsilon_{\mathrm{DIC,err}}$, the averaged compensated optical strain measurement $\varepsilon_{\mathrm{comp}}$, the averaged strain-gauge measurement error, and$\varepsilon_{\mathrm{strain\text{-}gauge}}$ with their standard deviations. The optical strain measurements are described as optical strain measurement errors because the measured strains are induced by the measuring system itself, and the strains to be measured are zero. The compensated optical strains $\varepsilon_{\mathrm{comp}}$ are calculated by:

$$\varepsilon_{comp} = \varepsilon_{\mathrm{DIC,err}} - \varepsilon_{T} = \varepsilon_{\mathrm{DIC,err}} - \Delta T_{therm} * \alpha_{\mathrm{T}}, \tag{4}$$

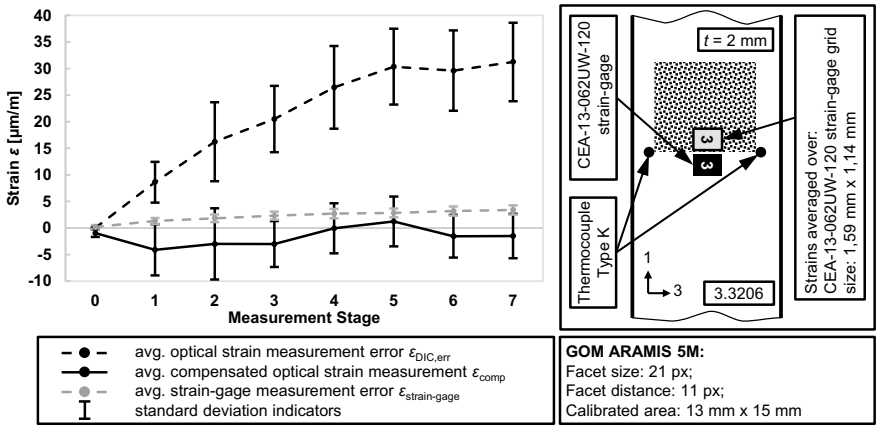


Fig. 6 Temperature compensation of 3D-DIC measurements compared with self-temperature-compensated strain-gauge measurements. Heat is induced by the illumination of the specimen. Loads are not applied

with the temperature difference ΔT_{therm} measured by a type k thermocouple and the thermal expansion coefficient α_T of aluminium ($23{,}1 \cdot 10^{-6} \cdot K^{-1}$). The averaged strain-gauge measurement error $\varepsilon_{\text{strain-gauge}}$ increases continuously to a maximum deviation of 3.4 µm/m from zero. This is due to the fact that the self-temperature compensation for materials with a thermal expansion coefficient of 20 to $23.4 \cdot 10^{-6} \cdot K^{-1}$ is used. The averaged optical strain measurement error $\varepsilon_{\text{DIC,err,}}$ increases significantly more steeply than the strain-gauge measurement to a maximum of 31 µm/m. The averaged compensated optical strain measurement $\varepsilon_{\text{comp}}$ tends towards zero between −4 µm/m and 1 µm/m. This shows that the influence of temperature changes on 3D-DIC optical strain measurements can be reduced
significantly by this method. Finally, the influence and measurability of the hole-drilling heat still have to be investigated and considered in this temperature compensation method. The thermal influence of the coating layer will also have to be investigated in this context.

5 Conclusion

In this paper, a new approach to optical residual stress measurements was proposed and investigated. Systematic errors are identified, and countermeasures are outlined. In particular, a new temperature compensation method for reducing the thermally induced errors is investigated and validated. The experimental investigations prove the required accuracy of the proposed method regarding the measurement of micro strains and, therefore, the possibility of its application in 3D-DIC residual stress

analysis. It is shown that 3D-DIC residual stress measurements (in terms of micro-scale strain measurements) are inaccurate if the specimen temperature is not monitored or if a constant specimen temperature is not ensured through laboratory conditions that maintain a constant room temperature and eliminate air flow and vibrations. In future investigations, the influence of the time-dependent behaviour of the speckle pattern coating must be considered.

Acknowledgments The authors would like to thank the German Research Foundation (DFG) for funding the research project "HO 2356/14-1", "Manufacture of defined residual stress in friction assisted spinning and flow forming". The research work conducted in this project is the basis of the paper.

References

1. Homberg W, Hornjak D, Beerwald C (2010) Manufacturing of complex functional graded workpieces with the friction-spinning process. Int J Mater Form 3(1):943–946. https://doi.org/10.1007/s12289-010-0924-8
2. Lossen B, Andreiev A, Stolbchenko M, Homberg W, Schaper M (2018) Friction-spinning—grain structure modification and the impact on stress/strain behaviour. J Mater Process Technol 261:242–250. https://doi.org/10.1016/j.jmatprotec.2018.06.015
3. Lossen B, Homberg W (2014) Friction-spinning—interesting approach to manufacture of complex sheet metal parts and tubes. Procedia Eng 81:2379–2384. https://doi.org/10.1016/j.proeng.2014.10.337
4. Fitzpatrick ME, Fry AT, Holdway P, Kandil FA, Shackleton J, Suominen L (2005) Determination of residual stresses by X-ray diffraction: Issue 2, Measurement Good Practice Guide. National Physical Laboratory
5. ASTM E837–13a (2013) Standard test method for determining residual stresses by the hole-drilling strain-gage method. https://doi.org/10.1520/E0837-13A
6. Rendler NJ, Vigness I (1966) Hole-drilling strain-gage method of measuring residual stresses. Exp Mech 6(12):577–586. https://doi.org/10.1007/BF02326825
7. Schajer GS (1988) Measurement of non-uniform residual stresses using the hole-drilling method. Part I—stress calculation procedures. J Eng Mater Technol 110(4):338–343. https://doi.org/10.1115/1.3226059.
8. Schajer GS, Steinzig M (2005) Full-field calculation of hole drilling residual stresses from electronic speckle pattern interferometry data. Exp Mech 45(6):526–532. https://doi.org/10.1007/BF02427906
9. Nelson DV, Makino A, Schmidt T (2006) Residual stress determination using hole drilling and 3D image correlation. Exp Mech 46(1):31–38. https://doi.org/10.1007/s11340-006-5859-0
10. McGinnis MJ, Pessiki S, Turker H (2005) Application of three-dimensional digital image correlation to the core-drilling method. Exp Mech 45(4):359–367. https://doi.org/10.1007/BF02428166
11. Rief T, Hausmann J, Motsch N (2017) Development of a new method for residual stress analysis on fiber reinforced plastics with use of digital image correlation. Key Eng Mater 742:660–665. https://doi.org/10.4028/www.scientific.net/KEM.742.660
12. Lord JD, Penn D, Whitehead P (2008) The application of digital image correlation for measuring residual stress by incremental hole drilling. Appl Mech Mater 13–14:65–73. https://doi.org/10.4028/www.scientific.net/AMM.13-14.65
13. Gupta JK, Lin C-H, Chen Q (2010) Characterizing exhaled airflow from breathing and talking. Indoor Air 20(1):31–39. https://doi.org/10.1111/j.1600-0668.2009.00623.x

14. Babaeeian M, Mohammadimehr M (2020) Investigation of the time elapsed effect on residual stress measurement in a composite plate by DIC method. Opt Lasers Eng 128:106002. https://doi.org/10.1016/j.optlaseng.2020.106002

Formation of Residual Stresses in Austenitic Stainless Steels by Infeed and Recess Rotary Swaging



Holger Hoche, Fabian Jaeger, Alessandro Franceschi, Matthias Oechsner, and Peter Groche

Abstract The austenitic stainless steels 1.4307 and 1.4404 significantly benefit from cold forming, due to their high work hardening capability. Great potential to improve the component's fatigue properties is expected by optimizing the forming process chain such that specific residual stresses are induced in critical component areas. In this work, an analysis of the formation of residual stresses during rotary swaging is carried out. Through this incremental forming process, high strain hardening and a complex material flow history are induced in the workpieces. Therefore, measuring strategies for the residual stress measurement of cold deformed austenitic steels by X-ray diffraction, using the $\sin^2\Psi$-method, were developed. Here, especially the 1.4307 is a challenging material due to cold forming-induced martensite formation. Despite phase changes, both cold-formed materials exhibit anisotropic microstructures as well as coarse-grained areas. Moreover, particular notched geometries are produced on the workpieces by rotary swaging. The measuring techniques are further developed for these complex geometries and the residual stresses are investigated.

Keywords 1.4404 · 1.4307 · Austenitic stainless steel · Residual stresses · Rotary swaging · X-ray diffraction · $\mathrm{Sin}^2\ \Psi$

1 Introduction

Rotary swaging is a well-established forming technology in the automotive and aerospace manufacturing industries for the forming of axial symmetric bars and tubes [1]. According to the German standard DIN 8583, it belongs to the open die forming processes [2]. The advantages of this incremental process lie, in particular, in its high flexibility combined with low investment and tooling cost, due to the

H. Hoche (✉) · F. Jaeger · M. Oechsner
Center for Structural Materials, Technische Universität Darmstadt, MPA-IfW, Grafenstr. 2, 6283 Darmstadt, Germany
e-mail: hoche@mpa-ifw.tu-darmstadt.de

A. Franceschi · P. Groche
Institute for Production Engineering and Forming Machines, Technische Universität Darmstadt, Otto-Berndt-Straße 2, 64287 Darmstadt, Germany

© The Minerals, Metals & Materials Society 2021

G. Daehn et al. (eds.), *Forming the Future*, The Minerals, Metals & Materials Series,
https://doi.org/10.1007/978-3-030-75381-8_190

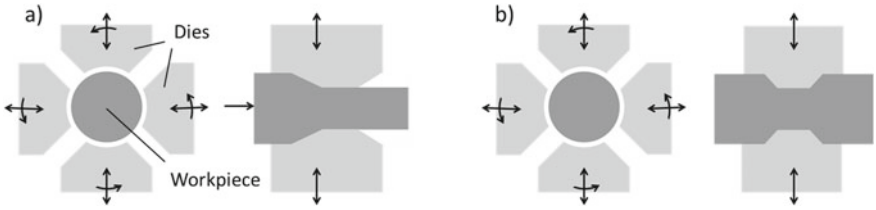


Fig. 1 Schematic representation of infeed (**a**) and recess (**b**) rotary swaging. (Color figure online)

relatively low forming forces needed [3]. Moreover, rotary swaging offers some important advantages on the product side. Very hard materials can be worked and the final parts exhibit high static and cyclic strength due to strain hardening [4]. Two main process variations can be distinguished: the infeed and the recess rotary swaging. These variants differ for the direction of the feed motion, as schematically represented in Fig. 1. The infeed rotary swaging process feeds the workpiece with an axial motion into the machine. The working tools oscillate radially and reduce the diameter of the workpiece along the whole feed length. By recess rotary swaging, the workpiece has no axial motion. In this process, the forming is performed by the radial movement of the working tools, which is superposed to their oscillation. In this way, a localized reduction of the workpiece occurs according to the tool geometry. Infeed and recess rotary swaging can also be combined to obtain geometries that are more complex.

Decisive product qualities for cold-formed components are the residual stresses, especially in the near-surface area. However, in the literature, incremental processes are not analysed to the same extent as conventional continuous technologies. Investigations of residual stresses in rotary swaged products are mainly related to the forming of tubes [1, 5].

The researched materials are the austenitic stainless steels 1.4404 (X2CrNiMo17-12–2, AISI 316L) and 1.4307 (X2CrNi18-9, AISI 304L). Due to their high chrome and nickel content, the materials exhibit good resistance against both oxidation and electrochemical corrosion [6]. Stainless austenitic steels have a great flow behaviour, which makes them extremely suitable for cold working processes [7]. The high deformability is coupled with strain hardening during the deformation, leading to localized enhanced mechanical properties. The challenge with strain hardening is the formation of residual stresses, which have not been extensively researched yet. Especially, the targeted employment of compressive stresses by cold forming could be beneficial for the component lifetime and safety. Both 1.4404 and 1.4307 are used in the food industry due to their great corrosion resistance.

There exist several challenging factors when performing residual stress measurements of austenitic stainless steels. Due to the cold forming process, they reveal a texture, which depends on the local degree of deformation. Moreover, coarse grains make it difficult to measure a sufficient number of grains to achieve results with good statistics. The texture complicates the measurement further since it leads to a shift of the reflex width based on orientation as well as the interference lines. Therefore,

$d(\sin^2\psi)$ plots are not linear, if the sample is textured [8], making the analysis more elaborate. Another challenge is the sample geometry. Since rotary swaging usually produces cylindrical workpieces, there are no flat surfaces, where X-ray diffractometry can be performed easily. Additionally, recess rotary swaging forms notches, which are difficult to examine due to shadowing effects.

The present paper investigates the formation of residual stresses in rotary swaged parts of the materials 1.4307 and 1.4404. Measurements of residual stresses in these rotary swaged parts are challenging due to local non-isotropic strain hardening and texture formation. Especially the 1.4307 makes the matter more complex due to cold forming induced martensite formation. Moreover, the literature provides sparely information about the stress state of rotary swaged components. The task is to provide a better description of the residual stress generation in rotary swaged parts.

2 Materials and Methods

Samples of the materials 1.4307 (0.024 C, 0.275 Si, 2.01 Mn, 0.033 P, 0.034 S, 18.16 Cr, 0.295 Mo 8.00 Ni, 0.07 N) and 1.4404 (0.022 C, 0.413 Si, 1.35 Mn, 0.031 P, 0.027 S, 17.72 Cr, 2.01 Mo, 9.90 Ni, 0.04 N) were milled from billets belonging to the same batch of raw material, to ensure identical material properties. Cylinders, respectively, 14.5 mm and 10.78 mm in diameter, were realized for infeed and recess rotary swaging. These parts were then solution annealed in a preheated vacuum oven for 15 min at 1050 C and cooled in air. Prior to the cold deformation, a lubricant was applied to the samples surfaces. The parameters used for infeed and recess rotary swaging are summarized in Table 1.

In Fig. 2, the tools used for the experiments are shown. For infeed rotary swaging, the diameter of the workpiece is reduced with an entry angle of 4°. The length of the forming and calibrating zones is 50 mm each. With the second tool (Fig. 2b), two

Table 1 Parameters used during the rotary swaging

Parameter	Infeed rotary swaging	Recess rotary swaging
Rotational speed [rot/min]	50	
Feeding velocity [mm/min]	100	–
Hub [mm]	0.7	
Frequency of hub [Hz]	29	
Radial velocity [mm/min]	–	50
Final diameter [mm]	10.9	10.38

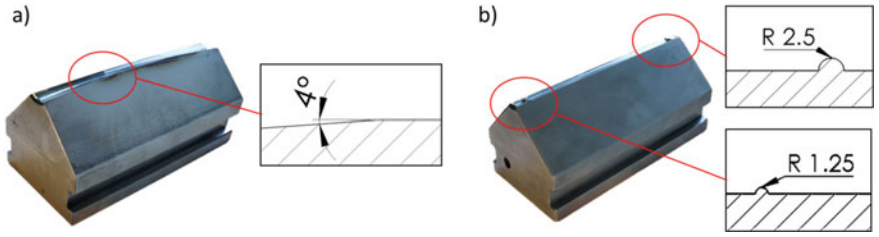


Fig. 2 Forming tools used for infeed (**a**) and recess (**b**) rotary swaging. (Color figure online)

different notched geometries can be manufactured on the samples through recess rotary swaging. The radii of these notches are 1.25 and 2.5 mm, respectively.

The residual stresses were determined by X-ray diffraction (XRD) according to DIN EN 15,305 using the $\sin^2\Psi$-method. Therefore, a diffractometer made by Stresstech, model XStress G3R in a modified Ψ-arrangement was used. The residual stresses were calculated from 7 equidistant Ψ angles from 0° to +45° and from 0° to −45°, respectively. Mn Kα radiation was used for the measurement of the austenitic residual stresses since it yields better results for austenitic steels than Cr Kα. With Mn Kα radiation the reflex (311) can be measured, which exhibits double the multiplicity of the (220) reflex, which is measured with Cr Kα radiation [8]. The measurements in the martensitic phase as well as the determination of the martensite content were performed with Cr Kα radiation. The cylindrical samples produced by the rotary swaging process have a diameter of approximately 1 cm. Since the maximum aperture for this kind of measurement should not exceed a tenth of the diameter of curvature of the sample, according to DIN EN 15,305, the aperture was set to a diameter of 1 mm. The X-ray elastic constant used to calculate the residual stress values was $½S2\,\{311\} = 7.57 \times 10^{-6}$ mm^2/N for austenite and $½S2\,\{211\} = 5.82 \times 10^{-6}$ mm^2/N for martensite [9].

To measure residual stress depth profiles of the material 1.4404, an electropolishing machine type Struers Movipol-3 was employed. The polishing process was stopped at 0.125, 0.25, 0.5, and 1.0 mm to perform residual stress measurements.

In addition, microspecimens were prepared and examined by optical microscopy to reveal the influence of the rotary swaging process on the material microstructures. Also, microhardness depth profiles were conducted at the microspecimens. In addition, hardness measurements were also performed on the surfaces of the specimens.

3 Results

The analysis of the initial state of the samples was already performed in [7]. After the solution annealing of the machined samples, the metallographic examinations of both materials showed a purely austenitic microstructure without deformation-induced defects. With a Vickers hardness of 151.4 HV 0.3 for 1.4307 and 143.3 HV 0.3 for 1.4404, the hardness values are in the characteristic range of solution annealed microstructures of the respective materials. Significant differences between the two materials were observed in the grain sizes. The grain size of 1.4307 was determined to G = 4, which, according to Table C1 of DIN EN ISO 643, corresponds to an average of about 128 grains/mm^2. With a grain size of G = 5.5, the microstructure of 1.4404 is significantly finer, revealing an average of 384 grains/mm^2. The X-ray measurements showed for both materials these samples are close to a residual stress-free state.

The residual stresses on the samples manufactured through infeed rotary swaging were analysed along the path shown in Fig. 3. Along this path, three regions can be distinguished:

- Section 1 goes from 0 to 50 mm. Here the sample has been fully deformed and calibrated by the working tools.
- Section 2, from 50 to 100 mm, the sample has been reduced to its final geometry, but it is still inside the calibration zone at the end of the process
- From 100 to 120 mm, the sample is still in the forming zone and has not reached its final diameter, which can be inferred from its curvature.

Measurements through X-ray diffraction were performed both in axial and tangential direction on the components' surface (Fig. 4). The results of the surface residual stress measurements after the infeed rotary swaging are displayed in Fig. 5.

In all the measured points, these samples are characterized by compressive residual stresses on the surface. In general, the quality of the $\sin^2\Psi$ plots is very good and complies with the criteria to assess the measurement quality of cold deformed parts in [7]. The axial compressive stresses are both, in Sects. 1 and 2, significantly higher than the tangential stresses. In particular in Sect. 1, the axial as well as the tangential stresses of both materials are in good compliance with each other, showing a quite constant behaviour. This means that the calibration process had the desired effect of producing a defined residual stress state. Some differences can be observed

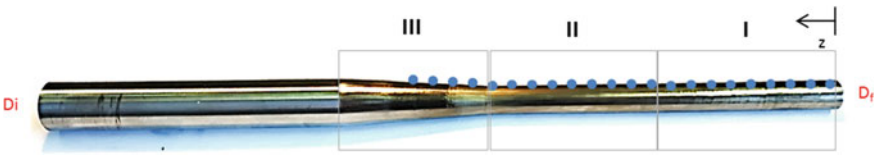


Fig. 3 Position of the measurements of the residual stresses through X-rays on the samples produced by infeed rotary swaging. (Color figure online)

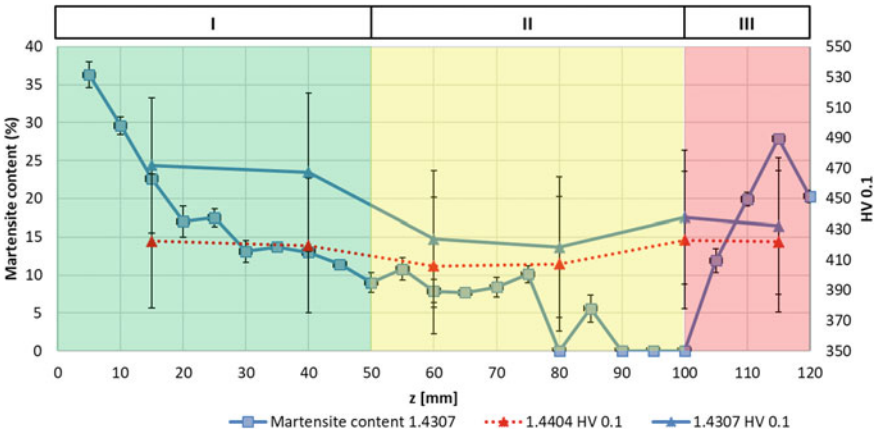


Fig. 4 Martensite content of 1.4307 and result of the hardness measurements on the samples manufactured through infeed rotary swaging. The Martensite content of 1.4404 was measured as well but was not present in a detectable quantity. For this reason, it is not reported in the diagram. (Color figure online)

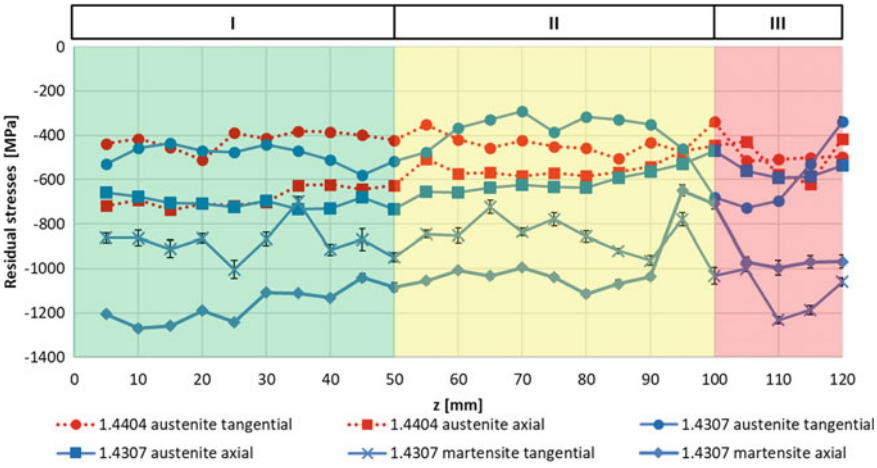


Fig. 5 X-ray residual stress measurements on the samples manufactured through infeed rotary swaging. The martensite phases of 1.4404 were not measured, since the percentage of it is below the detection limit. (Color figure online)

between the behaviour of the axial and tangential stresses in the second section. In the axial direction, the compressive residual stresses tend to increase along the formed section. In the tangential direction instead, the residual stresses fluctuate stronger than in Sect. 1, but there is no definite trend identifiable. In Sect. 2, the axial compressive residual stresses of 1.4404 exhibit higher values than 1.4307, which is interesting it signifies a change to the behaviour in Sect. 1. Nevertheless, the measured residual stresses of Sects. 1 and 2 do not show significant differences, which could be

correlated with the material microstructure, in particular, the martensite formation in 1.4307. In Sect. 3, the size of the fluctuations in residual stresses is very pronounced in 1.4404 for the tangential stresses. At the beginning of Sect. 3, there is a sudden increase in the compressive residual stresses in comparison with the previous section. The material 1.4307, on the other hand, does not show this effect. The martensite content of 1.4307 can be seen in Fig. 4. In Sect. 1, it is higher the closer the measured point, which is to the tip of the sample. Between the middle of Sect. 1 and the middle of Sect. 2, the martensite content does not change. At the end of Sect. 2, the martensite content is zero. However, in Sect. 3, the martensite content is again relevant. The martensite content of 1.4404 was measured as well, but was under the detection limit.

In Sect. 1, the hardness exhibits the highest values for 1.4307 due to the highest degree of deformation achieved by forming as well as calibration. This correlates with the evolution of the compressive residual stresses, which exhibit higher values in Sect. 1 due to the calibration process. Additionally, 1.4307 exhibits higher hardness values than 1.4404, which could be an effect caused by martensite formation. In Sect. 2, the hardness of 1.4307 slightly drops. The decrease in hardness of 1.4307 is approximately 50 HV 0.1. In Sect. 3, the surface hardness of 1.4307 increases again, which could be an effect of the high degree of cold deformation even in this section. The hardness of 1.4404, however, is homogeneous over the length of the sample. The higher hardness of 1.4307 can be explained by the formation of deformation martensite. The reason for the deviating hardness values appears to be that the different points of this section have undergone different stages of calibration.

For the material 1.4404, the tangential residual stresses are nearly identical in Sects. 1 and 2 and only slightly differ in Sect. 3. For material 1.4307 instead, there is a sudden decrease of the austenitic compressive residual stresses in comparison with the previous section. In Sect. 3, the data show even bigger fluctuations, which could be due to inhomogeneous deformation in the section. In the martensitic phase, the axial stresses are bigger than the tangential ones, mirroring the austenitic behaviour. The martensitic compressive stresses are higher than the austenitic ones. Since the forming of martensite is caused by deformations, it is plausible that zones with higher deformation would both have greater stresses and more martensite formation. The relatively low stresses at 905 and 100 mm are measurement artefacts caused by the low martensite content in those points leading to a bad signal to noise ratio.

In Fig. 6, the different microstructures in the infeed rotary swaged samples are exemplarily shown for Sects. 1 and 3. In comparison to the annealed state, the grains are refined by the rotary swaging process. Unfortunately, due to the texture, the grain size according to DIN EN 643–1 cannot be assessed. In general, the microstructure of 1.4404 is finer than of 1.4307, which also corresponds to the differences in grain sizes in the solution annealed state. In both, Sects. 1 and 3, the microstructures are uniform up to a depth of approximately 4 mm from the surface. 1.4404 exhibits deformation structures like slip bands, which are more pronounced in Sect. 1 due to the higher degree of cold deformation. The microstructure of 1.4307 also indicated the formation of deformation-induced martensite, which could be proved by a noticeable magnetism of this material. In the case of 1.4404, the magnetism is negligible.

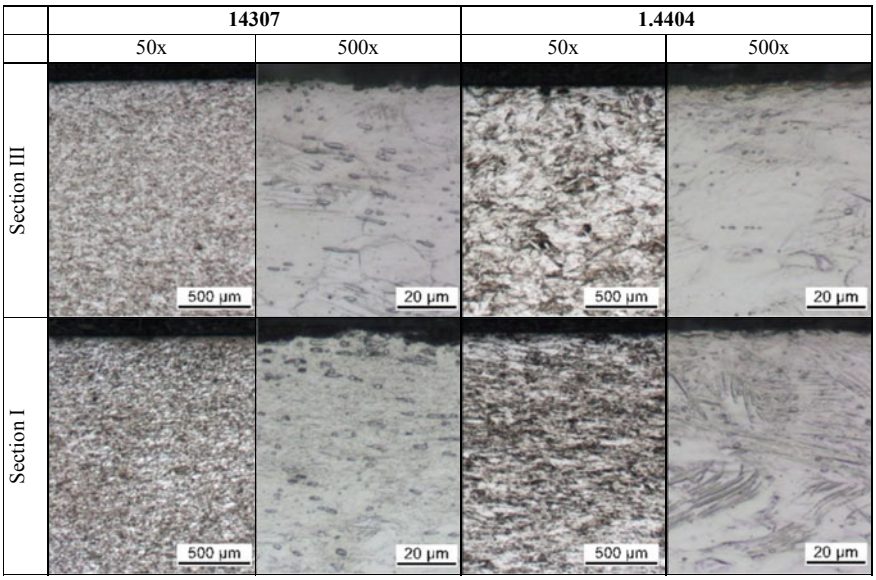


Fig. 6 Microstructure analysis by optical microscopy of Sects. 1 and 3, V2A-etchant. The initial micrographs can be seen in [7]. (Color figure online)

Figure 7 shows an axial cross-section of Sect. 3 of 1.4404. It is visible that the surface of the sample has cracked, which released residual stresses. Processes like this are one of the reasons for the unsteadiness of residual stress measurements.

Through recess rotary swaging, notches with radius 1.25 and 2.5 mm, respectively, were produced on the solution-annealed samples. A distance of 15 mm was maintained among the notches to avoid mutual influence on the stress state. The process was performed with the parameters shown in Table 1. After reaching the final radial position, the tools were kept oscillating in position for 2 seconds for calibrating the

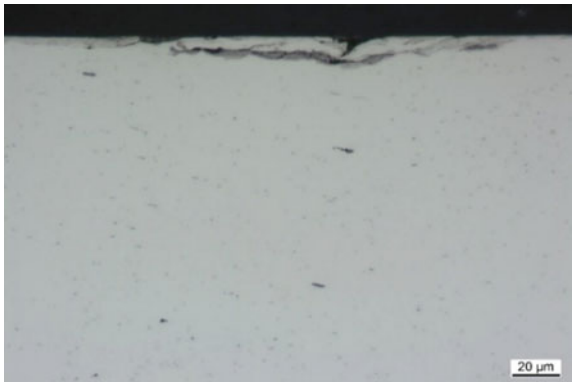


Fig. 7 Exemplary figure of a material overlap due to rotary swaging. 1.4404, Sect. 3, unetched. (Color figure online)



Fig. 8 Position of the X-ray residual stress measurements on the samples produced by recess rotary swaging. (Color figure online)

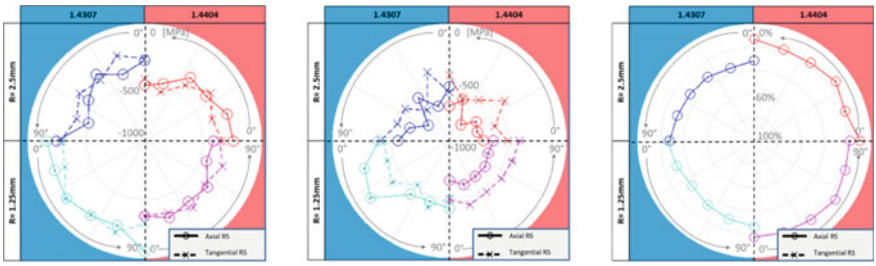


Fig. 9 Residual stresses and martensite content of the notched samples. The angles are between 0 and 90° counter clockwise. The leftmost subfigure shows the residual stress in the austenitic phase, the one in the centre that in the martensitic phase and the rightmost shows the martensite content in percent. (Color figure online)

samples. Then the residual stresses were measured on the bottom of each cavity in eight different points. In Fig. 8, the position of these X-ray measurements along the circumference of the samples is clarified.

Figure 9 shows the residual stresses measured on both 1.4307 and 1.4044 in the 1.25 mm and 2.5 mm notches for the austenitic (left) and martensitic (middle) phases as well as the martensite content (right). Although the notches complicate the measurements, there are only small errors and the criteria of [7] are fulfilled. Although the measurements scatter within the six measurements in the 90° section, some trends are still identifiable. In the 2.5 mm notches of 1.4307, the highest axial austenitic compressive stresses can be observed. Depending on the angle, the stress values fluctuate between −260 MPa and −500 MPa without any dependency on their circumferential position. The compressive stresses inside the 1.25 mm notch of 1.4307 are systematically on a lower level and vary from −160 MPa at 0° to −250 MPa. Only at the 90° position, a value of only −60 MPa was measured, which may be caused by microstructural artefacts, e.g. by material overlapping.

The axial stresses in the 2.5 mm notch of 1.4404 exhibit a graded increase from −240 MPa at 0° to −530 MPa at 90°. While the residual stresses for the materials 1.4404 and 1.4307 show a quite good agreement for the 2.5 mm notch, the behaviour

of the 1.25 mm notch is different. Unlike the 1.4307 sample, the 1.25 mm notch of 1.4404 reveals considerably higher compressive stresses with values between −190 MPa and −450 MPa. In general, it can be stated that the axial stress values for the 2.5 mm notches fluctuate more than for the 1.25 mm ones.

In general, the tangential residual stresses comply with the axial stresses. The compliance is more pronounced for the 1.25 mm notch, while the scatter of the values is again significantly higher for the 2.5 mm notch. In particular, the 2.5 mm notch of 1.4404 has the most notable scatter in residual stresses. For all orientations and materials, the largest compressive stress is bigger for the notch produced with the 2.5 mm tool. The reason for this is the higher deformed area when using a bigger tool, which results in a greater degree of deformation. This is concurrent with the results of the samples produced through infeed rotary swaging, where the stresses were highest in the zone with the most deformation as well (see Fig. 5).

The stresses of the martensitic phases show greater compressive stresses and a bigger isotropic effect. For the 1.4404 sample, the axial stresses of the 2.5 mm notch (between −500 and −830 MPa) and the 1.25 notch (between −470 and −660 MPa) are bigger than the tangential stresses, which range from −380 to −630 MPa and from −270 to −520 MPa respectively. The 1.4307 sample exhibits a larger difference between the notches. In the 2.5 mm notch, the axial stresses from −280 to −780 MPa are generally larger than the tangential ones from −390 to −680 MPa. This behaviour is reversed in the 1.25 notch with smaller stresses in the axial direction from −170 to −460 MPa compared with tangential stresses from −390 to −530 MPa. However, all martensitic graphs fluctuate stronger than the austenitic ones. This can be explained by the stronger deformation processes in the martensitic phases leading to a bigger spread in compressive stresses. The martensite content itself does not change much with the position at which it is measured. It can be seen that 1.4307 is more disposed towards forming martensite than 1.4404.

For better understanding, Fig. 10 shows the different microstructures of the notches produced by recess rotary swaging. In all of them, the notch area itself exhibits deformation structures due to strain hardening that happened during the recess rotary swaging process. Here, 1.4307 and 1.4404 reveal a nearly similar degree of highly deformed microstructures. For 1.4307, there is also evidence for the presence of cold deformation-induced martensite. An interesting outcome is that the degree of deformation of the microstructure is lower for the 2.5 mm notch. The smaller 1.25 mm tool is causing a higher degree of deformation than the broader 2.5 mm tool. For the material 1.4404, this observation is in accordance with the results on the residual stress measurements. For 1.4307, the 1.25 mm notch reveals lower stresses than the less deformed 2.5 mm notch. A reason, therefore, could not be stated yet, but it is likely, that the formation of deformation-induced martensite could change the residual stress state.

Figure 11 shows the comparison of residual stress measurements on the same notch at angles of 0, 90, 180, and 270°, respectively. The goal is to verify the theory that the residual stress state follows the fourfold symmetry of the tools for the recess rotary swaging. For the 2.5 mm notch in 1.4307, the residual stresses in axial as well as tangential direction are clustered between −250 and −350 MPa with the

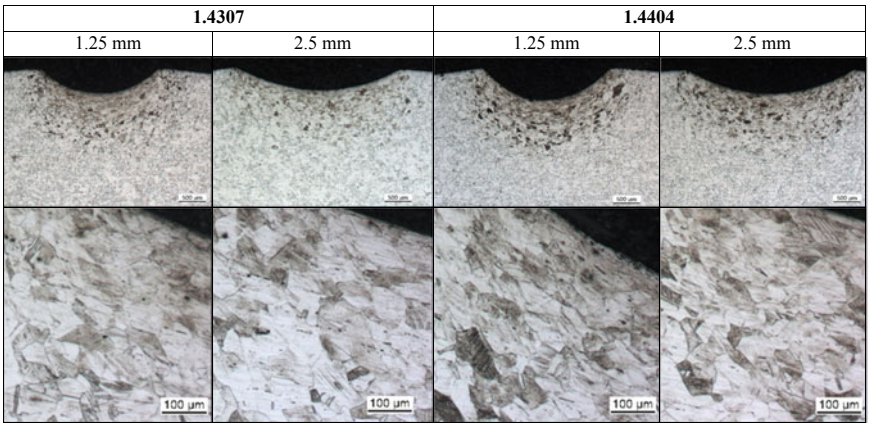


Fig. 10 Microstructure of the notches, produced by recess rotary swaging, V2A-etchant. (Color figure online)

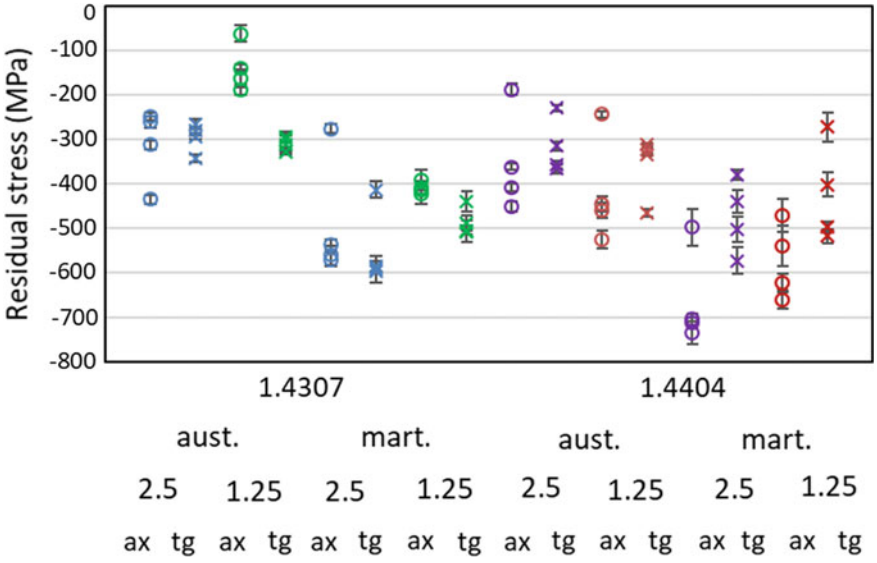


Fig. 11 Comparison of residual stresses for 0, 90, 180, and 270° in all notches. (Color figure online)

exception of a single value of −440 MPa. The residual stresses in axial direction for the 1.25 mm notch of 1.4307 are lowest in comparison to all other parameters, which complies with the circumferential measurements shown in Fig. 8. For the tangential direction of both notches in 1.4307, all the residual stresses are in great accordance with each other and show a low scatter. The martensitic stresses in 1.4307 are generally higher. Similar to the austenitic phase, the stresses in the 1.25 mm notch are clustered closer together. For 1.4404, both, the axial and the tangential notches

reveal a remarkable scatter between the angles. This is especially the case for the axial direction. The 2.5 mm notch shows values between −240 and −530 MPa and the 1.25 mm one between −190 and −450 MPa. Meanwhile, the tangential stresses are in good accordance with each other for three out of four data points, while the fourth point diverges. The martensitic stresses are higher in 1.4404 as well. The spread of the stresses is comparable to the austenitic case.

When looking at all the data points, it can be seen that the tangential stresses are generally closer to each other than the axial stresses. This is plausible, since, for the recess swaged specimens, the stresses in tangential are pointing in the direction of the material flow. The same effect can be seen in Fig. 5, where the material flow is in the axial direction and axial stresses fluctuate less than the tangential ones. However, the theory of the existence of a fourfold symmetry of the stress state caused by the fourfold symmetry of the forming process could not be proven due to large scatter at the measured points.

By examination of the microspecimens, some material overlaps due to the rotary swaging process are present at each specimen (Fig. 12). The length of these overlaps could be up to several 100 μm, while their depth is maximum, some 10 μm. At these sites, there is no homogenous residual stress state, since the stresses are relaxed in the overlap. The overlaps are most pronounced in the bottom of the notches, where the material flow is highest. This also complies with the XRD measurement positions. From the $\sin^2\Psi$-plot, the overlaps cannot be assessed definitely. The overlaps cause non-isotropic stress states and, therefore, contribute to the scatter in the measurements. Moreover, these overlaps affect the cyclic properties, thus compensating for the beneficial effect of the compressive residual stresses.

To further comprehend the changes going on in the material upon deformation, hardness depth profiles were recorded (Fig. 13). Although an influence of the notch

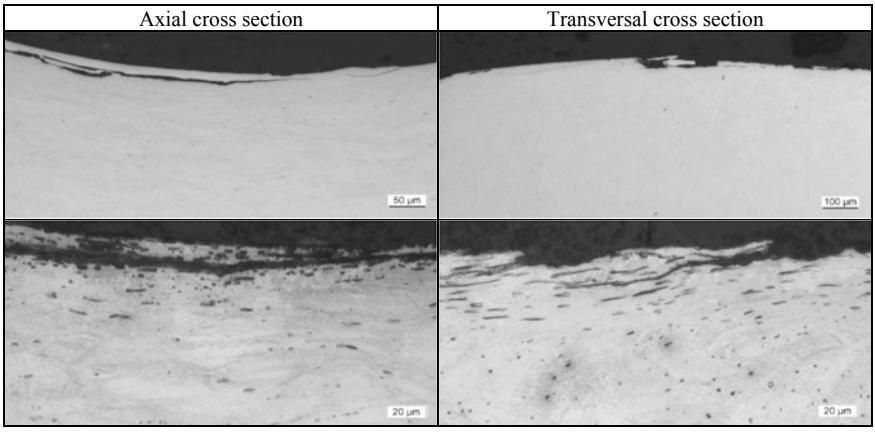


Fig. 12 Microscopic pictures of the 1.25 mm notch of 1.4404 with material overlaps. The microsections are oriented axially (left-hand side) as well as transversal (right-hand side). (Color figure online)

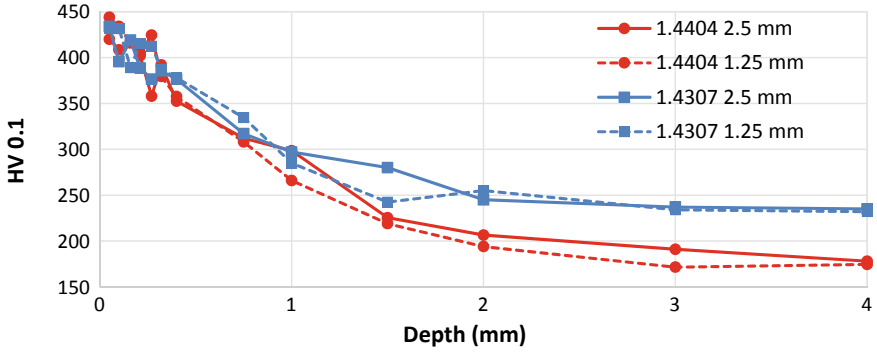


Fig. 13 Result of the hardness measurements (HV 0.1) on both materials in two notches per sample. The hardness values are connected to achieve better visualisation of the results. (Color figure online)

size on the compressive residual stresses was proven, no significant influence, neither of the notch nor the material, could be validated from the hardness depth profiles. In particular, at the surface all values scatter in a narrow range, thus indicating an identical degree of the strain hardening. With progressing depth, the hardness decreases as the effect of strain hardening lessen. Up to a depth of 0.3 mm, the hardness only slightly decreases. Even at a surface distance of more than 2.5 mm, the hardness of the solution annealed state is not reached. However, 1.4404 exhibits lower values of approximately 180 HV0.1 than 1.4307 with approximately 230 HV 0.1. This coincides with the literature values of 151.4 HV 0.3 for 1.4307 and 143.3 HV 0.3 for 1.4404 in the annealed state [7]. It is of note that the decay of the hardness is roughly exponential.

This behaviour can be compared with the depth profiles of the residual stresses of 1.4404 of the 2.5 mm notch, shown in Fig. 14. There, the residual stress is −200 and

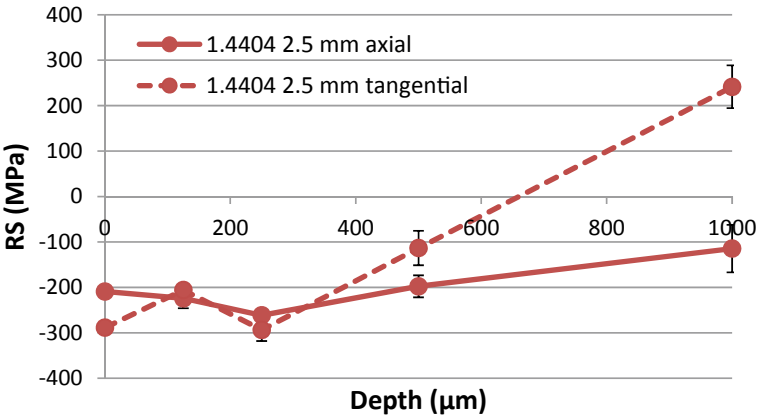


Fig. 14 Depth profile of the residual stresses in austenite for 1.4404. (Color figure online)

−390 MPa at the surface, respectively. The maximum of the compressive residual stresses is in a depth of about 0.25 mm. Exceeding this depth, both, the axial and the tangential compressive stresses decrease, where the tangential ones become tensile stresses in approximately 0.7 mm depth and the axial stresses remain compressive even at 1 mm distance from the surface. The residual stress depth profile complies with the hardness measurements, where the drop in hardness is only slightly up to 0.3 mm, which corresponds to the maximum of the compressive residual stresses.

4 Conclusions

The effect of infeed and recess rotary swaging techniques on the austenitic stainless steels 1.4307 and 1.4404 on the formation of the residual stresses, the changes in microstructure and the work deformation hardening were analysed. Due to rotary swaging, a grain refinement of the initially coarse-grained austenitic microstructure was achieved. Both processes could induce compressive residual stresses at the surface in both, axial and tangential direction. In general, the distribution of the residual stresses exhibits less scattering in the direction of the maximum material flow, i.e. the axial direction for infeed and the tangential direction for recess rotary swaging. It was shown that rotary swaging techniques induced strain hardening and the formation of deformation structures, with both effects being more pronounced on the surface. Overall, the residual stresses comply with the degree of deformation of the microstructures. Additionally, in 1.4307 also, cold deformation martensite has been formed.

Unfortunately, the rotary swaging produced several material overlaps at the surface, which could be some 100 μm in length. At these sites, the residual stresses are inhomogeneous, since the stresses are relaxed by the overlap. Therefore, these surface artefacts are likely to contribute to the scatter in the measured residual stresses. Moreover, these overlaps affect the cyclic properties, thus compensating for the beneficial effect of compressive residual stresses.

Acknowledgments The authors acknowledge the funding by the Deutsche Forschungsgemeinschaft (DFG, German Research Foundation)—OE 558/16-1, GR1818/63-1.

References

1. Rauschnabel E, Schmidt V (1992) Modern applications of radial forging and swaging in the automotive industry. J Mater Process Technol 35:371–383
2. DIN 8583–5:2003–09: Manufacturing processes forming under compressive conditions
3. Groche P, Fritsche D, Tekkaya EA et al (2007) Incremental bulk metal forming. CIRP Annals. https://doi.org/10.1016/j.cirp.2007.10.006

4. Ishkina S, Charni D, Herrmann M et al (2019) Influence of process fluctuations on residual stress evolution in rotary swaging of steel tubes. Mater (Basel, Switzerland) https://doi.org/10.3390/ma12060855
5. Charni D, Ishkina S, Epp J et al (2018) Generation of residual stresses in rotary swaging process. MATEC Web Conf https://doi.org/10.1051/matecconf/201819004001
6. Biehler J, Hoche H, Oechsner M, Kaestner P, Bunk K, Bräuer G (2014) Influence of the microstructure on the corrosion resistance of plasma nitrided austenitic stainless steel 304L and 316L. Mat Sci Eng Tech 45(10):930–946. https://doi.org/10.1002/mawe.201400329
7. Hoche H, Balser A, Oechsner M et al (2019) Enhancement of the residual stresses of cold full-forward extruded parts by application of an active counter punch. Mat Sci Eng Tech 50(6):669–681. https://doi.org/10.1002/mawe.201900050
8. Spieß L, Teichert G, Schwarzer R, Behnken H, Genzel C (2009) Moderne Röntgenbeugung: Röntgendiffrak-tometrie für Materialwissenschaftler, Physiker und Chemiker, 2nd edn Vie-weg+Teubner Verlag; Springer International Publishing AG, Wiesbaden, Cham
9. Eigenmann B, Macherauch E (1995) Röntgenographische Untersuchung von Spannungszuständen in Werkstoffen. Teil II. Fortsetzung von Matwiss. und Werktoffechn. 3:148–160. https://doi.org/10.1002/mawe.19950260410

Influence of Material Delivery Condition on Residual Stresses and Part Properties During Forward Rod Extrusion



Andreas Jobst and Marion Merklein

Abstract During the manufacturing of semi-finished products, the material is subjected to various forming steps to achieve the final geometry. In order to reduce the work hardening introduced and to ensure a good formability, it is annealed before component manufacturing. Forming technologies like forward rod extrusion are well-established methods for the efficient production of resilient components. In this process, however, an inhomogeneous pre-strengthening of the material influences the stress distribution during forming and therefore the mechanical properties and the residual stresses in the component. Since they affect the parts' operating behaviour, knowledge of the influence of the delivery condition of the material is necessary. The aim of this paper is to derive dependencies between material properties and the resulting residual stresses and work hardening in the component. Due to the increasing application, ferritic stainless steel *X6Cr17* in the skin passed (+LC) and soft annealed (+A) states are used. Residual stresses, microstructure, and microhardness distribution of both material states are compared regarding the rods and extruded parts. The effects of the delivery condition are evaluated by comparing process and component properties.

Keywords Forward extrusion · Material condition · Stainless steel · Residual stress · Work hardening

1 Introduction

Cold extrusion is an established process for the fabrication of components in large series. It offers high material and energy efficiency and the production of dimensionally accurate components, which exhibit high strength due to process-related

A. Jobst (✉) · M. Merklein
Institute of Manufacturing Technology (LFT), Friedrich-Alexander-University Erlangen-Nuernberg, 91058 Egerlandstraße 13Erlangen, Germany
e-mail: andreas.aj.jobst@fau.de

M. Merklein
e-mail: marion.merklein@fau.de

© The Minerals, Metals & Materials Society 2021

G. Daehn et al. (eds.), *Forming the Future*, The Minerals, Metals & Materials Series,
https://doi.org/10.1007/978-3-030-75381-8_191

work hardening [1]. However, in the manufactured components, residual stresses are generated due to inhomogeneous forming, which influence the parts' operating behaviour. Tensile residual stresses generally have negative effects as they inhibit crack initiation and propagation and thus reduce fatigue strength [2]. To ensure a long part service life, they must either be relieved by energy-intensive annealing after component manufacturing or taken into account when designing the part. For the prediction of the component properties after forming, knowledge of influencing variables on the component residual stresses is, therefore, necessary. So far, only little data are available about the use of pre-strengthened material. Therefore, in this paper, the influences of the material delivery condition on the properties of the forming process and the produced part are researched.

Since ferritic stainless steels are usually used in the annealed condition [3], the soft annealed state serves as a reference. The skin passed state is used to represent an insufficiently annealed material in which single areas still show a strengthening. The objectives pursued and the approach are shown schematically in Fig. 1.

To characterize the initial state, the material parameters of the non-deformed material are identified in the two investigated states "annealed" (+A) and "skin passed" (+LC). The influence of the material condition on the resulting part properties is determined by the comparison of the initial material and the manufactured components. In addition to near-surface residual stresses, microhardness and grain size distributions are investigated, since they influence the cyclic strength [4] and a depth-dependent residual stress measurement is difficult due to the corrosion resistance of the material. The effects of the material delivery condition on the forming process are identified by the determination of the process forces necessary for forming and ejection. In order to check for thermal effects on the residual stresses, the temperature in the formed part section is also measured after ejection. By comparing billets and components, correlations between material condition and the resulting process and component

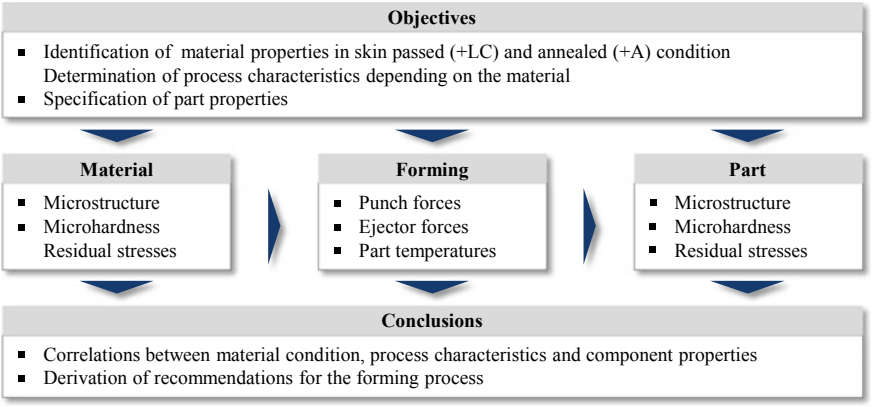


Fig. 1 Objectives and approach. (Color figure online)

properties are determined. On this basis, recommendations for the forming process are derived in order to ensure efficient component production.

2 State of the Art

During the production of steel rods, various rolling steps are carried out after the casting of the slabs in order to achieve the target geometry of the semi-finished product. This involves either rolling in the hot state in order to keep the process forces low or in the cold state, which results in a finer structure and a better surface, but a strong hardening. In forward rod extrusion, stainless steels are usually used in the annealed condition to ensure a good formability. Before part production, the semi-finished product is annealed and pickled in order to remove the scale layer [5]. Ferritic stainless steels usually are soft annealed [3], where the respective delivery condition of the semi-finished product is designated as $+A$ according to [6]. If a high geometric accuracy of the semi-finished product is required, a final drawing operation with low diameter reduction will be performed. This not only achieves a high accuracy of the nominal diameter but also introduces residual stresses and a slight hardening on the surface [7]. This condition is defined as *skin passed* and is abbreviated as $+LC$ according to [6].

In forward rod extrusion, the billet is pressed into the die and formed in the die shoulder area. The inhomogeneous deformation results in residual stresses in the component. After forming, tensile residual stresses are present at the surface [8], which are in equilibrium with compressive residual stresses in the core [9]. After achieving the specified geometry, the component is ejected in reverse to the punch direction. In this step, a change of the residual stress state in the formed section may occur due to the elastic springback of the die [10]. For the chosen component material and process configuration, a reduction of the near-surface tensile residual stresses by the ejection step is shown in [11].

For the determination of the residual stresses, several methods exist. One of the most common techniques is the hole-drilling method, where a change of the stress state is measured, while a small hole is being drilled into the part's surface. It allows depth-dependent residual stress profiles to be determined with little effort, but it is destructive, which means that residual stress mapping with smaller point distances is not possible [12]. As a non-destructive method, radiation diffraction is used. X-ray or neutron radiation is emitted onto the material area to be analysed and the angle and intensity of the beam reflected at the material lattice are determined. The measured angle of reflection is used to calculate the lattice spacing, which changes when residual or load stresses are present [13]. In addition to the residual stresses, the full width at half maximum (FWHM) of the recorded intensity curves can be determined and used as an indicator for the deformation introduced [14].

3 Experimental Setup

The single-phase ferritic stainless steel *X6Cr17* (DIN *1.4016*, AISI *430*) is used as the component material. Due to its classification in corrosion protection class I according to [15], it is used for components in food industry and in medical technology. The soft annealed condition (+A) is selected as reference, since it ensures good formability. The skin passed state (+LC), which is often chosen due to the higher surface quality, is examined as a comparison case. A forward rod extrusion process is used for the forming of the billets. The process for component manufacturing is shown in Fig. 2.

The billets (a) are manufactured from bar-shaped material by cutting and plane-parallel grinding of the end faces. They are coated with a lubrication system consisting of iron-III-oxalate as a carrier layer and a MoS_2-based lubricant. The forming of the components takes place on a hydraulic press *Lasco TZP 400* with the tool system shown in (b). In a one-step process, the components are formed and then ejected in opposite direction to the punch movement. The die (c) is designed and manufactured according to usual design guidelines with a shoulder opening angle of $2\alpha = 90°$. The formed part (d) consists of a non-deformed area, the transition area, which represents the shoulder geometry, and a deformed shaft. The deformation from diameter 25 mm to 15 mm results in an equivalent plastic strain of $\overline{\varepsilon} = 1.02$.

The influences of the material condition on the component properties are determined by material characterization before and after forming. For this purpose, the near-surface residual stresses in the axial and tangential directions in both the non-deformed and the formed section of the component are determined by X-ray diffractometry. The measurements are performed with the 8-axis *Seifert XRD 3003* X-ray diffractometer. Cr-Kα radiation with a wavelength of $\lambda = 0.2291$ nm is used for the measurement since it is within the range of the lattice constant of 0.286 nm of unstressed α-iron. The measuring spot diameter is approximately 0.8 mm with a maximum penetration depth of 5.8 µm. The measurement is carried out on the {2 1 1} lattice plane using the χ-method according to [16] with 13 ψ-tilts from $-50°$ to $+50°$, subdivided for constant $\sin^2\psi$. The reflected beam is detected with a line detector. The angle positions of the recorded intensity curves are determined by fitting with a pseudo-Voigt function. For the evaluation, the $K\alpha_1$ peak is used, which is gained by subtracting the $K\alpha_2$ peak from the measured intensity distributions. The calculation of the present stress state is done by the software *Rayflex Analyze*

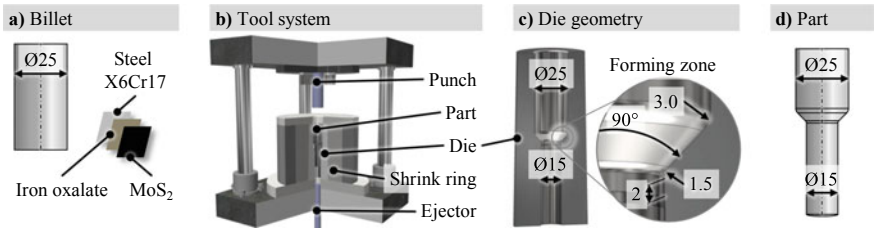


Fig. 2 Experimental setup for part production. (Color figure online)

with the $\sin^2\psi$ method. In addition to the residual stresses, the FWHM values of the recorded peaks are determined, allowing conclusions to be drawn about the induced deformation [17].

The determination of depth-dependent residual stress profiles is difficult due to the corrosion resistance of the material. In order to determine the properties in the interior of the component, the microstructure and the microhardness are, therefore, investigated in the longitudinal section. The samples are embedded and severed by sawing. The preparation of the surface to be examined is carried out by grinding up to a grit size of 15 µm and final polishing with diamond paste with 6, 3, and 1 µm grain size. The grain structure of the material is made visible by etching with an etchant consisting of water, hydrochloric acid, and nitric acid. The aim of the microstructural investigations is to determine the changes in the grain structure during the forming process, depending on the condition of the material used.

To quantify the mechanical properties of the material, the indentation hardness in the initial and formed state is measured. For this purpose, microhardness measurements according to [18] are carried out on longitudinal sections. The Vickers hardness is determined with the *Fischerscope HM2000* microhardness tester in an air-conditioned measuring room. During this test, a tungsten carbide pyramid penetrates the material. The time required to apply and relieve the testing force on the component is 20 s. When the test load of 1 N is reached, a creep time of 5 s is maintained. The hardness is determined from the measured penetration depth. To reduce the required measuring time, the spot distances in the component areas are varied. In the non-deformed area, measurements are taken in lines with a distance of approximately 5 mm and a radial spot distance of approximately 0.8 mm. In the area of the shoulder, a spot distance of 0.3 mm in axial and radial direction is used to achieve a high resolution. In the formed shaft and the tip, the point spacings are 0.8 mm radially and 1.2 mm axially.

4 Results and Discussion

In order to determine the influence of the initial material state, material, process, and part properties are determined. The results are shown and discussed in the following section. Regarding the process properties, maximum forces and part temperatures are taken into account, since these allow drawing conclusions about the die load. As part properties, residual stresses, microstructure, and microhardness distribution are considered, which influence the operational behaviour of the produced component.

4.1 Forming Process Properties

During the extrusion of the components, the process forces required for forming and ejection were determined. Their maxima are shown in Fig. 3. Additionally, the

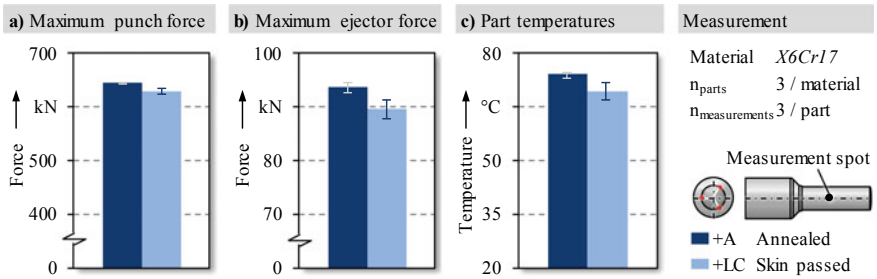


Fig. 3 Process forces and part temperatures. (Color figure online)

component temperatures—measured after ejection and removal from the tool—are displayed.

If annealed material (+A) is used, a punch force of 644 ± 2 kN and an ejector force of 94 ± 1 kN are required for the production of the parts. Due to the deformation of the material and friction between the part and the die, the component heats up to a temperature of 74 ± 1 °C. Using skin passed (+LC) material, however, slightly lower process forces of 628 ± 5 kN are measured at the punch and 90 ± 2 kN at the ejector. This is also mirrored in the part temperature, where only 69 ± 2 °C is reached. Tribology provides an explanation for these differences. Since the skin passed material has a smoother surface than the annealed one, influences on the resulting friction forces are possible here, which correlates with the resulting component temperatures.

4.2 Residual Stresses

To determine the influence of the material condition on the component residual stresses, X-ray stress measurements were performed on the surface of the manufactured components. Since only around 50% of the billet volume is deformed during component manufacture, measurements were carried out both on the non-deformed and on the deformed area of the specimens. In the non-deformed area, an oscillation in the axial direction was necessary during the measurement due to the small measuring point size, resulting in a linear measuring range. In addition to the residual stresses, the FWHM values of the peaks were determined in order to derive qualitative information on the forming history. The results are shown in Fig. 4.

In the non-deformed section, the residual stresses shown in Fig. 4a are present. The surface of the annealed material (+A) shows compressive residual stresses of −49 ± 5 MPa in the axial and −61 ± 14 MPa in the tangential direction. These stresses result from the cooling of the material after soft annealing, since the core will cool after the surface. Thus, thermal shrinkage induces compressive residual stresses in the surface tensile stresses in the core [19]. In the skin passed material (+LC), there are low tensile residual stresses of +44 ± 18 MPa in the axial direction, which are

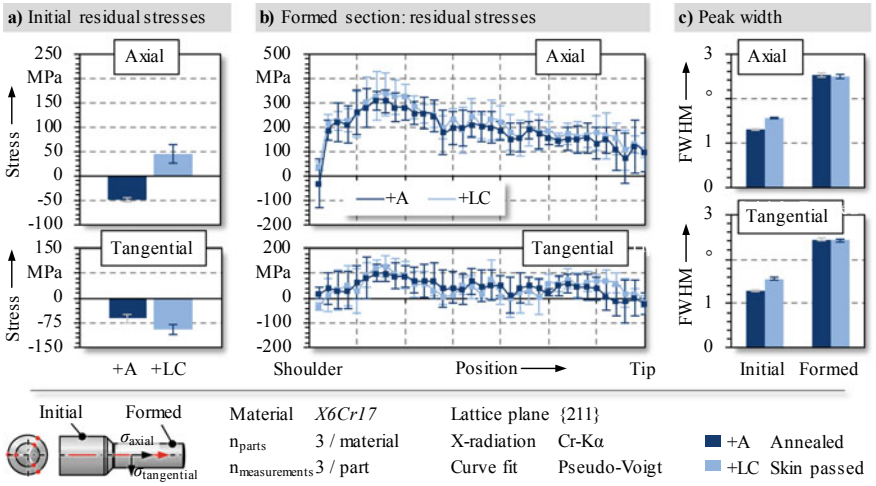


Fig. 4 Residual stresses in formed parts and full width at half maximum (FWHM) values of the measured peaks. (Color figure online)

caused by the cold drawing process [20]. In circumferential direction, compressive stresses with a value of -96 ± 15 MPa are higher than in the annealed material. This residual stress condition is due to the surface load during the cold drawing [21].

The residual stresses on the formed shaft of the components are shown in Fig. 4b. In both main stress directions—axial and tangential—similar curves are present. There are small residual stresses near the shoulder, which change into distinct tensile stresses with increasing distance. Maximum residual stresses are present at a distance of 8 mm from the shoulder with about +310 MPa in axial and about +100 MPa in tangential direction. The residual stresses decrease towards the tip. This stress state can be explained by the inhomogeneous deformation during the flow through the forming zone [9]. It coincides with results from the literature [22]. Despite the different initial conditions, no significant differences can be identified in the formed state between the annealed and the drawn material. One explanation for this is that during the forming of the components, a much higher degree of deformation occurs than during cold drawing of the material. This is backed up by the FWHM values as shown in Fig. 4c. While significant differences can be seen in the initial state due to the different deformation history, the FWHM values in the manufactured components are at the same level.

4.3 Microstructure

However, X-ray diffractometer measurements only map the residual stress state on the component's surface. Since a depth-dependent stress measurement is difficult

to perform due to the corrosion resistance, the hardness and the microstructure are investigated to depict the component properties inside the part. In these investigations, the comparison between the original state and the formed material properties is performed on a longitudinal section. Figure 5 shows the material flow and the microstructure of the manufactured components.

With regard to the material flow, different areas can be identified in the formed specimens in Fig. 5a. The material is not deformed during part production in the area of the initial material. Here, the linear structure of the material with parallel lines in the axial direction may be recognized. The forming takes place in the transition zone in the area of the die shoulder. In this region, the material flows to the centre and in the axial direction. This results in a structure with increasingly elongated grains. In the approximately 36 mm long area "formed material", there is a homogeneous structure in axial direction with strongly elongated parallel grains. In the "tip" area, inhomogeneous flow lines can be seen, which end in the edge area, since this is the place, where the end face of the billet and its edge area is located.

A detailed view of the grains in the core and the edge is shown in Fig. 5b for the component areas "initial material" and "formed material". The initial material has a linear structure with slightly elongated grains. In the annealed condition (+A), the core and edge areas show a homogeneous grain distribution with grain sizes of about 24 µm in the radial direction. In the skin passed condition (+LC), a similar structure is present in the core. In the edge area, however, slightly narrower and longer grains with grain sizes of 20 µm are present, which can be explained by the forming of the material during cold drawing of the semi-finished product.

In the deformed area, there are strongly elongated grains in both material states. In the edge area, with a size of 9 µm, there are thinner grains than with 12 µm in the core, which can be explained by the deformation when passing the die shoulder. While the core area is only axially stretched, the edge area is stretched in axial direction and additionally compressed in the radial direction. There are no significant differences between the annealed and skin passed material. This shows that the deformation during extrusion is so high that the influence on the surface caused by the cold drawing of the bars is negligible.

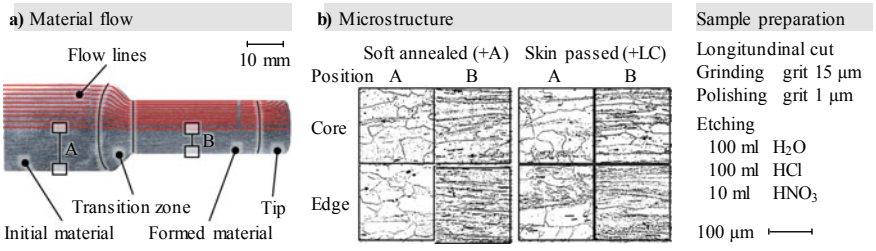


Fig. 5 Material flow and microstructure of formed parts. (Color figure online)

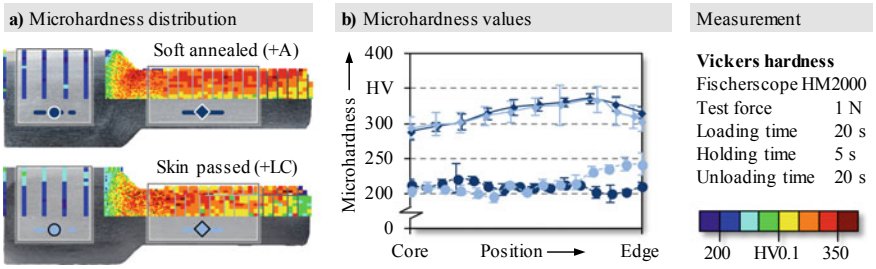


Fig. 6 Microhardness distribution of formed parts. (Color figure online)

4.4 Microhardness

To analyse the mechanical properties of the parts, the microhardness is used, as it provides a measure of the work hardening induced to the material. The hardness distribution in the longitudinal section of the extruded components is shown in Fig. 6.

In the initial state, the annealed material (+A) shows a homogeneous hardness distribution in the axial and radial directions with values of about 210 HV0.1. In the forming zone in the shoulder area, the material hardness increases due to work hardening. In the formed area, there is a homogeneous hardness distribution in the axial direction. In the radial direction, the lowest hardness values of about 290 HV0.1 are located in the area of the symmetry axis. The hardness increases in the direction of the component surface, with the maximum of 335 HV0.1 being approximately 1.5 mm below the surface. The hardness at the tip of the component is lower due to the lower deformation-induced.

In the skin passed (+LC) material, however, there is a hardness gradient in the radial direction in the initial state. With a value of 208 HV0.1, the hardness in the core is similar to that in the annealed material. The surface is strengthened to a depth of approximately 3 mm and has a significantly higher hardness of 230…240 HV0.1. In the transition area, the formed area and the component tip, similar hardness distributions can be found compared with the soft annealed material.

In the formed components, there are comparable microhardness distributions for both material states. Since there is no significant change in the microhardness despite the different levels of pre-hardening in the surface layer, it can be assumed that the low level of deformation during the cold drawing of the semi-finished product has no influence on the forming result.

5 Conclusions and Recommendations

A forward rod extrusion process was performed with a ferritic stainless steel in the delivery conditions “soft annealed” (+A) and “skin passed” (+LC). For the determination of the influence of the material delivery condition, the properties of the

forming process and the initial and the formed material were identified. With the findings shown in this paper, the following conclusions can be drawn.

- The delivery condition affects the material properties
  The cold drawing during the production of skin passed (+LC) material does not only change the appearance of the surface of the material. On the surface, residual stresses are induced. In the near-surface material volume, the microhardness is increased due to work hardening. The microstructure is affected only slightly.
- The material condition slightly affects the process properties
  When skin passed material is used, slightly lower maximum forces are required for forming and ejection. This reduces the tool load, which may result in higher tool life. As a side effect, slightly lower component temperatures are achieved, which improves component handling.
- Skin passing does not affect the parts' microhardness and residual stresses

During the forming of the material with a comparatively high degree of deformation carried out within the scope of this article, no influences of the material condition on the target variables "residual stresses", "grain size" and "work hardening" are detectable. The induced residual stresses and the hardening of the material due to the skin pass process do not cause any significant difference in the target values in the formed component.

For this reason, the following recommendations for process design are derived. The use of skin passed material is recommended if a high accuracy of the billet diameter is required in the process. Furthermore, it is recommended when cost-intensive forming dies are used, as the lower maximum process forces can be expected to increase the tool life. However, if there is, for example due to previous process steps, a certain hardening in the material, which is comparable to the "skin passed" state, it can be tolerated, if the deformation during component production is much higher. In this case, it is advisable from an economic and ecological point of view to avoid heat treatment, as this eliminates the need for a cost-intensive and energy-intensive annealing step. In addition, there is no necessity for pickling with hazardous acids to remove scale after annealing.

6 Summary and Outlook

Semi-finished products for cold extrusion are produced by various rolling, annealing and drawing operations. At the end of this process chain, ferritic stainless steels are soft annealed with final pickling to remove scale and an optional drawing step to achieve a small diameter tolerance. The aim of the paper was to investigate the influence of the material condition on the resulting process properties and component residual stresses and material properties for forward rod extrusion. To determine the process properties, billets made of ferritic stainless steel *X6Cr17* (DIN *1.4016*, AISI *430*) in the soft annealed (+A) and skin passed (+LC) condition were extruded and maximum process forces and part temperatures were determined. The residual

stresses were determined both in the initial and in the formed state on manufactured components. To analyse the material properties inside the component, grain sizes and microhardness distribution in the longitudinal section were identified. The results showed that slightly lower process forces are required for forming and ejection when using skin passed material. Due to the lower part temperatures, tribological influences were identified as the cause. Despite different residual stresses in the initial material, a similar near-surface residual stress condition was measured in the formed components. Differences in grain size and microhardness distribution in the initial material also did not cause any significant change in the formed components. This was attributed to the comparatively large deformation during forming compared to the cold drawing (skin pass) during the manufacturing of semi-finished products. These results led to the conclusion that a low pre-strengthening in the material does not cause any changes in the process and component properties, if the deformation in the forming process is comparatively high. The recommendation was derived from this, that soft annealing can be omitted for semi-finished products with low hardening if a significantly larger forming operation is carried out in the main forming operation.

These findings form the basis for further investigations to ensure reliable handling of residual stresses during cold extrusion. Due to increasing demands on corrosion resistance, the applicability of the findings to materials with a more complex structure, such as duplex steels, will have to be investigated. In order to include the residual stresses in the calculation of the component operating behaviour, the stability of the residual stresses under typical operating loads is to be researched.

Acknowledgments The research activities are funded by the Deutsche Forschungsgemeinschaft (DFG, German Research Foundation) within the scope of the priority programme SPP2013—Targeted Use of Forming Induced Residual Stresses in Metal Components in the subproject P10 (project number: 374688875).

References

1. Semiatin SL (2005) ASM handbook, volume 14A: metalworking: bulk Forming. ASM International, Materials Park, Ohio
2. Almer JD, Cohen JB, Winholtz RA (1998) The effects of residual macrostresses and microstresses on fatigue crack propagation. Metall Mater Trans A 29A:2127–2136. https://doi.org/10.1007/s11661-998-0038-9
3. Maki T (1997) Stainless steel: progress in thermomechanical treatment. Curr Opin Solid St M 2:290–295. https://doi.org/10.1016/S1359-0286(97)80117-9
4. Gerin B, Pessard E, Morel F, Verdu C, Mary A (2016) Beneficial effect of a prestrain due to cold extrusion on the multiaxial fatigue strength of a 27MnCr5 steel. Int J Fatigue 92:345–359. https://doi.org/10.1016/j.ijfatigue.2016.07.012
5. Cardarelli F (2018) Materials handbook—a concise desktop reference. Springer International Publishing, Cham, Switzerland
6. EN 10027–1 (2017) Designation systems for steels—part 1: steel names
7. Lin HS, Hsu YC, Keh CC (2008) Inhomogeneous deformation and residual stress in skin-pass axisymmetric drawing. J Mater Process Tech 201:128–132. https://doi.org/10.1016/j.jmatprotec.2001.11.126

8. Landkammer P, Jobst A, Kiener C, Steinmann P, Merklein M (2019) Investigations on residual stress generation in full-forward-extrusion. Prod Engineer 13:169–180. https://doi.org/10.1007/s11740-019-00892-5
9. Pyzalla A, Reimers W (1999) Residual stress and texture due to cold and hot extrusion processes. Texture Microstruct 33:291–301. https://doi.org/10.1155/TSM.33.291
10. Tekkaya AE (1986) Ermittlung von Eigenspannungen in der Kaltmassivumformung. Springer, Berlin, Germany
11. Jobst A, Kiener C, Merklein M (2019) Investigations on residual stress generation in extruded steel components. In: Wulfsberg JP, Hintze W, Behrens BA (eds) Production at the leading edge of technology. Proceedings of the 9th Congress of the German Academic Association for Production Technology (WGP), Hamburg, Springer, Berlin, Germany, pp 83–92
12. Schajer GS (2010) Advances in hole-drilling residual stress measurements. Exp Mech 50:159–168. https://doi.org/10.1007/s11340-009-9228-7
13. Gustafson J, Shipilin M, Zhang C, Stierle A, Hejral U, Ruett U, Gutowski O, Carlsson PA, Skoglundh M, Lundgren E (2014) High-energy surface X-ray diffraction for fast surface structure determination. Sci 343:758–761. https://doi.org/10.1126/science.1246834
14. Fu P, Chu R, Xu Z, Ding G, Jiang C (2017) Relation of hardness with FWHM and residual stress of GCr15 steel after shot peening. Appl Surf Sci 431:165–169. https://doi.org/10.1016/j.apsusc.2017.09.136
15. EN 1993–1–4 (2015) Eurocode 3: design of steel structures—part 1–4: general rules—supplementary rules for stainless steels
16. EN 15305 (2008) Non-destructive testing—test method for residual stress analysis by X-ray diffraction
17. Spieß L, Teichert G, Schwarzer R, Behnken H, Genzel C (2019) Moderne Röntgenbeugung – Röntgendiffraktometrie für Materialwissenschaftler, Physiker und Chemiker. Springer Nature, Wiesbaden, Germany
18. ISO 14577–1 (2015) Metallic materials—instrumented indentation test for hardness and materials parameters—part 1: test method
19. Sen S, Akal B, Ozel A (2000) Transient and residual thermal stresses in quenched cylindrical bodies. Int J Mech Sci 42:2013–2029. https://doi.org/10.1016/S0020-7403(99)00063-6
20. Kuboki T, Kawamaki I, Neishi Y, Kuroda K, Akiyama M (2001) A study on the influence of mechanical properties on the distribution of axial residual stress after cold drawing of metallic bars. Mater Sci Res Int 7:41–46. https://doi.org/10.2472/jsms.50.3Appendix_41
21. Ruiz-Hervias J, Luzin V, Prask H, Gnaeupel-Herold T, Elices M (2006) Effect of thermo-mechanical treatments on residual stresses measured by neutron diffraction in cold-drawn steel rods. Mat Sci Eng A-Struct 435–436:725–735. https://doi.org/10.1016/j.msea.2006.07.123
22. Atienza J, Martinez-Perez M, Ruiz-Hervias J, Mompean F, Garcia-Hernandez M, Elices M (2005) Residual stresses in cold drawn ferritic rods. Scripta Mater 52:305–309. https://doi.org/10.1016/j.scriptamat.2004.10.010

Experimental and Numerical Investigations on the Development and Stability of Residual Stresses Arising from Hot Forming Processes



Bernd-Arno Behrens, Jörg Schröder, Hendrik Wester, Dominik Brands, Sonja Uebing, and Christoph Kock

Abstract Residual stresses are an important issue as they affect both the manufacturing process as well as the performance of the final parts. Taking the whole process chain of hot forming into account, the integrated heat treatment provided by a defined temperature profile during cooling of the parts offers a great potential for the targeted adjustment of the desired residual stress state. The aim of this work is the investigation of technological reproducibility and stability of residual stresses arising from the thermomechanical forming process. For this purpose, a long-term study of residual stresses on hot-formed components is conducted. In order to develop finite element models for hot forming, a comprehensive thermomechanical material characterisation with special focus on phase transformation effects is performed. The numerical model is validated by means of a comparison between residual stress states determined with X-ray diffraction on experimentally processed components and predicted residual stresses from the simulations.

Keywords Forming process · Finite element analysis · Residual stress stability · X-ray diffraction

1 Introduction

In metal forming, the arising residual stresses influence the material behaviour during manufacturing as well as the performance of the final component [1]. In the past, the focus of forming process design was on minimising or eliminating residual stresses. However, residual stresses can also serve to improve the properties of the components through targeted use, for example with regard to distortions or wear behaviour

B.-A. Behrens · H. Wester · C. Kock (✉)
Institut Fuer Umformtechnik Und Umformmaschinen, Leibniz Universität Hannover, An der Universität 2, 30823 Garbsen, Germany
e-mail: kock@ifum.uni-hannover.de

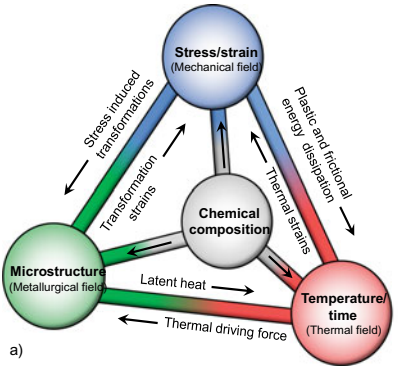
J. Schröder · D. Brands · S. Uebing
Institute of Mechanics, Department of Civil Engineering, University Duisburg-Essen, Universitätsstraße 15, 45141 Essen, Germany

© The Minerals, Metals & Materials Society 2021

G. Daehn et al. (eds.), *Forming the Future*, The Minerals, Metals & Materials Series,
https://doi.org/10.1007/978-3-030-75381-8_192

[2]. This requires the residual stresses to be applied technologically in a reproducible manner and to remain stable over longer periods of time. In this context, reproducibility and stability of residual stresses particularly resulting from the four process types “peening and related surface treatments”, “cold expansion of holes”, “welding”, and “machining” have been investigated by many authors, such as [3]. It is noticeable that most authors examine the development and stability of residual stresses in a strictly defined manner for a specific application. Depending on the type of process and the choice of material, which is linked to the process type, characteristic residual stress profiles are generated. For example, a typical feature of the surface treatment “shot peening” is a highly negative residual stress on the components surface, which decreases significantly towards the inside of the component [4]. Furthermore, it is known that relaxation and redistribution of residual stresses occur due to static or dynamic mechanical loads and thermal exposure. Static relaxation of residual stresses was for example investigated by [5] and [6] on components treated by shot peening. It should be noted that relaxation and redistribution of the local residual stresses occur when the accumulated residual stresses and the applied stresses due to subsequent mechanical loading exceed the yield state of the material. An important issue for many mechanical components is the potential effect of cyclic mechanical loads on the relaxation and redistribution of residual stress, even if the individual mechanical load cycles do not cause macroscopic plastic deformation. For example [5] and [7] investigated the stability of the peening residual stresses. It turned out that the residual stress relaxation is more significant for larger cyclic stress or strain. Little or no relaxation of peening residual stresses occurs, especially for small fatigue stress amplitudes [8]. Furthermore, e.g., in [9], the hole expansion process has shown that thermal exposure also leads to stress relaxation. In this case, the stress relaxation in aluminium samples was investigated at temperatures around 100 °C. After 250 h of thermal exposure they noticed a low relaxation (5 to 15%) and relatively small changes in fatigue life.

Until now, little attention has been paid to the stability as well as the calculation of residual stresses resulting from hot forming processes. The cost-efficient virtual process design of individual process steps or even an entire process chain is gaining in importance due to economic globalisation, continuously rising energy costs and growing competition in the manufacturing industry. Especially in the field of hot forming, process design in trial and error approaches represents a substantial cost and time expenditure [10]. At the same time, hot forming offers great potential for energy-efficient production of components by integrated heat treatment in the cooling phase after forming. Due to the numerous process parameters during forming, such as forming speed, and plastic strains as well as the temperature profile in the subsequent cooling process, there are numerous control parameters influencing the residual stresses. Nevertheless, the finite element (FE) simulation-supported design of hot forming processes using polymorphic steels is very challenging. As shown in Fig. 1a, numerous influencing parameters from thermal, metallurgical, and mechanical fields exist, which affect each other in complex interactions [11, 12]. For realistic process simulation, an appropriate mathematical model capable of consistently describing the polymorphic material behaviour is required. For this purpose, fully



b)

$$d\varepsilon_{ij}^{total} = \underbrace{d\varepsilon_{ij}^{el} + d\varepsilon_{ij}^{pl}}_{\text{Mechanical field}} + \underbrace{d\varepsilon_{ij}^{th}}_{\text{Thermal field}} + \underbrace{d\varepsilon_{ij}^{tr} + d\varepsilon_{ij}^{tp}}_{\text{Metallurgical field}}$$

$d\varepsilon_{ij}^{el}$: elastic strain increment

$d\varepsilon_{ij}^{pl}$: plastic strain increment

$d\varepsilon_{ij}^{th}$: thermal strain increment

$d\varepsilon_{ij}^{tr}$: transformation related strain increment

$d\varepsilon_{ij}^{tp}$: transformation plasticity strain increment

Fig. 1 Interrelated thermomechanical-metallurgical material phenomena during thermomechanical processing of steel [6] (**a**) and basic principles of the additive strain decomposition method (**b**) [15]. (Color figure online)

coupled thermomechanical-metallurgical FE simulations based on the theory of additive strain decomposition method are often used in literature [13, 14]. The resulting strain components are structured in Fig. 1b according to their physical origin.

This article presents the material modelling of two typical hot forming steels with the aim of calculating the residual stresses arising from the thermomechanical process. An experimental hot forming process is carried out and the resulting residual stresses are investigated in a long-term study with respect to their stability. Furthermore, an FE model is created and validated on the basis of the comprehensive experimental data. The FE-model validated in this work is intended to serve in future work as a virtual tool, enabling the determination of process parameters for inducing favourable residual stresses in hot-formed components. As an example, with the help of FE-based process design residual compressive stresses should be generated in components such as crankshafts or gears to increase the product lifetime.

2 Material Characterisation of Hot Forming Steels

For the investigations in this work, the typical hot forming steels with the material numbers 1.3505 (AISI 52,100) and 1.7225 (AISI 4140) according to German standards were used. The chemical composition of the two materials is listed in Table 1.

Table 1 Chemical composition of steel alloys 1.7225 and 1.3505 according to international standards [16] and [17]

[wt%]	C	Si	Mn	P	S	Cr	Mo	Fe
1.3505	0.99	0.25	0.35	0.025	0.015	1.475	0.10	Balance
1.7225	0.42	0.25	0.75	0.025	0.035	1.10	0.22	Balance

As outlined in the introduction, a comprehensive material characterisation is required to model the numerous thermal, metallurgical, and mechanical material phenomena arising from the thermomechanical process. To simulate the plastic deformation behaviour during hot forming, compression tests were performed on the Gleeble 3800-GTC physical forming simulator with cylindrical samples of 10 mm diameter and 15 mm length. The flow curves were determined in the relevant temperature range (T = 900, 1000, 1100, and 1200 °C). In addition, the tests were carried out at the corresponding temperatures with the equivalent plastic strain rates of $\dot{\varepsilon}_{eq}$ = 10 s^{-1} and 50 s^{-1}. Figure 2 shows the experimentally determined flow curves exemplarily for material 1.3505 at different temperatures and the strain rate $\dot{\varepsilon}_{eq}$ = 1 s^{-1} as well as for T = 1000 °C and different strain rates. A strict temperature and strain rate dependence of the strain hardening behaviour could be observed for both materials.

In order to ensure a continuous description of the flow behaviour for the process simulation as a function of the equivalent plastic strain, the equivalent plastic strain rate and the temperature, the analytical approach of the so-called GMT model [19] for calculating the yield stress was calibrated. Equation 1 shows the calculation approach whereas the determined coefficients c_1, c_2, n_1, n_2, l_1, l_2, m_1, and m_2 of the analytical approach for both materials are listed in Table 2.

$$k_f = c_1 e^{c_2 T} \varphi^{n_1 T + n_2} e^{\frac{l_1 T + l_2}{\varphi}} \dot{\varphi}^{m_1 T + m_2} \tag{1}$$

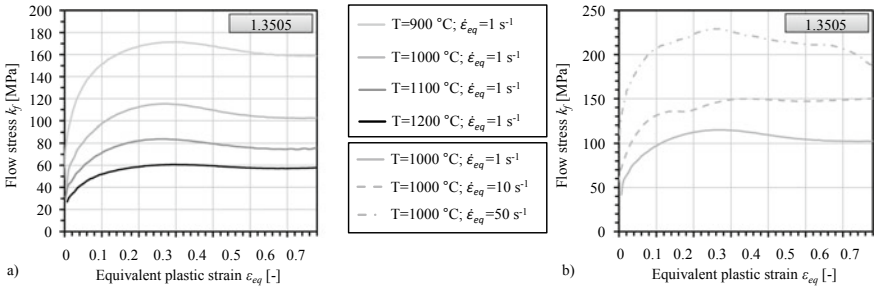


Fig. 2 Flow curves of 1.3505 for different temperatures T (**a**) and different strain rates $\dot{\varepsilon}_{eq}$ (**b**) determined in upsetting tests at the Gleeble 3800-GTC [18]

Table 2 Fitted GMT model parameters for 1.3505 and 1.7225

Material	c_1 [MPa s]	c_2 [°C^{-1}]	n_1 [°C^{-1}]	n_2 [−]	l_1 [°C^{-1}]	l_2 [−]	m_1 [°C^{-1}]	m_2 [−]
1.3505	3113.02	−0.0033	5.0507 * 10^{-5}	−0.1090	−2.0135 * 10^{-5}	0.0024	6.6491 * 10^{-4}	−0.5000
1.7225	6054.21	−0.0039	−3.0846 * 10^{-5}	0.3000	1.8926 * 10^{-5}	−0.03548	−9.4422 * 10^{-5}	0.2484

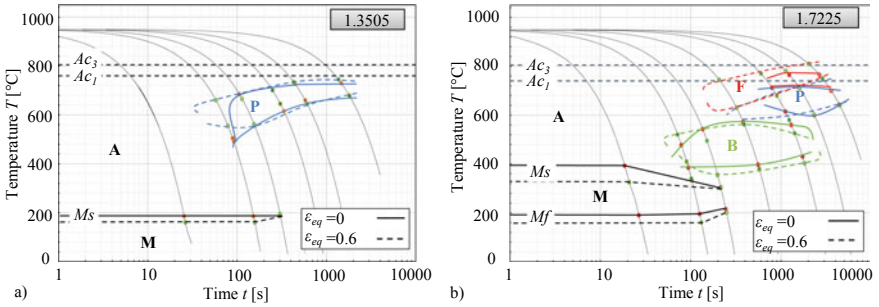


Fig. 3 Continuous cooling transformation diagrams for the materials 1.3505 (**a**) and 1.7225 (**b**) [20]. (Color figure online)

In order to model the phase transformation behaviour during cooling after the forming process, continuous cooling transformation diagrams (cct diagrams) have been determined in experimental studies. Thereby, the phase transformation behaviour was investigated both without and with a previous deformation of the fully austenitised material. These diagrams are shown in Fig. 3.

It can be clearly seen that a previous deformation influences the microstructural transformation behaviour of both materials investigated significantly. For example, a reduction in the martensite start temperature Ms was found in each case. From these cct diagrams, time temperature transformation diagrams (ttt diagrams) were determined and implemented in the Simufact.forming software. Further information on the investigation of phase transformation has already been published in [20] by the authors.

Besides the strains due to phase transformation, the transformation plastic strains (TRIP strains) were investigated by the authors in [21]. For this purpose, the phase transformation behaviour of the materials at a superimposed stress was investigated. The phase-specific TRIP coefficients listed in Table 3 were determined as characteristic material parameters.

In addition to the austenite flow curves, the ttt diagrams and the transformation plasticity coefficients, further phase-specific data are required for the correct modelling of the thermomechanical forming process. This comprises, for instance, characteristic data on specific heat capacity, latent heat, or phase-specific flow curves. In most cases, it is difficult to generate experimental material data for pure microstructural phases [22]. For this reason, supplementary material data have been generated with the thermodynamic simulation software JMatPro [23]. With the help of this

Table 3 The phase-specific coefficients of transformation plasticity for 1.3505 and 1.7225 [21]

	1.7225		1.3505
Phase	TRIP coefficient K_n [MPa^{-1}]	Phase	TRIP coefficient K_n [MPa^{-1}]
Martensite	1.54 * 10^{-4}	Martensite	4.85 * 10^{-5}
Bainite	1.01 * 10^{-4}	Pearlite	6.17 * 10^{-5}

software, it is possible to generate mechanical and thermal material data by means of thermo dynamic calculation approaches from [24] to [25] based on the chemical composition of the steel alloys. Further details on the material data used for simulation of the hot forming process can be found in [18].

3 Experimental and Numerical Procedure for Thermomechanical Processing of Cylindrical Specimen With Eccentric Holes

An experimental reference process was carried out to investigate the residual stress development in hot forming and to validate the material models created. The specimens were provided with thermocouples for a temperature-controlled process management. Subsequently, as shown in Fig. 4a, the specimens were placed in a thermobox to ensure a quasi-isothermal test procedure during the forming phase. Within the thermobox the specimens were heated up to 1000 °C in a furnace. A ten-minute holding time was applied to ensure complete austenitisation. Afterwards, the thermobox with the specimen was transferred from the furnace to the servo hydraulic forming simulator VHS8800 (Instron GmbH). The specimens were upset at a punch speed of 200 mm/s to a final height of 28 mm from the initial height of 50 mm. The untreated specimen is shown schematically in Fig. 5a whereas the deformed specimen is shown in Fig. 5b in the cross-sectional view. Immediately after the forming process, the specimen was removed from the thermobox and cooled down to room temperature either in ambient air or in water. Due to the different cooling routes, different phase transformation phenomena are expected in the material, which lead to different residual stress profiles. In these tests cylindrical specimens with eccentric holes as shown in Fig. 4b were used. Due to the asymmetrical hole, an inhomogeneous development of the residual stresses is expected in the material. For a statistical verification of the residual stress measurements, five identical tests were performed for each cooling medium and material. The experimental test procedure is described in detail in [18].

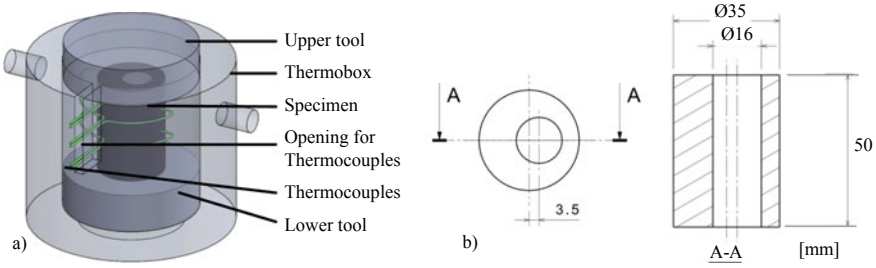
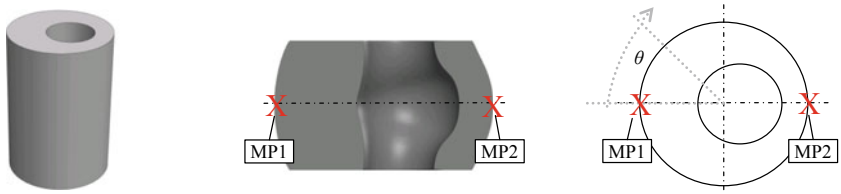


Fig. 4 Schematic representation of the specimen prepared with thermocouples in a thermobox (**a**) and shape of the investigated specimen with dimensions in mm (**b**). (Color figure online)



a) Untreated specimen

b) Measuring points (MP) on the mid-height of the specimen

c) MP on the circumferential surface indicated by the angle θ

Fig. 5 Illustration of the untreated specimen (**a**), the measuring points MP1 and MP2 at the mid-height of the specimen (**b**) as well as the angle θ on the circumference of the specimen. (Color figure online)

X-ray diffraction is used for residual stress analysis. The respective measuring point was initially polished electrolytically in order to avoid influences on the analyses from the scale layer of scale arising in the hot forming process. Subsequently, the tangential residual stresses were determined with the X-ray diffractometer X3000G2 (Stresstech GmbH) employing Cr-Kα radiation according to the corresponding DIN standard [26]. The measuring point was defined by a collimator with a diameter of 2 mm. Nine tilting positions of the measuring device were used per measuring point for stress evaluation. Afterwards, the measurements were evaluated with the software XTronic (Stresstech GmbH) by means of the $\sin^2$ method. The values for the X-ray elasticity constant $½s_2 = 5.81 * 10^{-6}$ mm^{2}N^{-1} and the reference values for the unstressed material ($d_{211} = 1.1703$ Å, $2\theta_{Cr} = 156.084°$) were taken from the tabular data collection of [27]. These data of X-ray elasticity constants were calculated as mean values from the so-called Voigt [28] and Reuß [29] approaches for the pure alpha iron lattice.

The measuring points were placed at the mid-height of the specimen (cf. Fig. 5b). Comprehensive residual stress measurements were carried out the following days after the thermomechanical treatment. The tangential residual stresses on the surfaces of the specimen were determined as shown in Fig. 5b on the thick-walled side, measuring point 1 (MP1) and on the thin-walled side (MP2) of the specimen. In addition, further measurements along the circumference of the specimen were taken at angles $\theta = 45°, 90°, 135°$ according to Fig. 5c. The X-ray measurement was additionally repeated several times per measuring point, to minimise the instrumental error, adjustment of the measurement system, and effect of specimen curvature on the results. The investigation of the specimen, which has undergone the same experimental procedure each, is intended to make a statement about the technological reproducibility of the residual stresses. Additionally, subsequent to the immediate X-ray measurements, the measurements on MP1 and MP2 were repeated after six months and twelve months. In the meantime, the specimens were stored in a laboratory cabinet at a constant temperature of 20 °C. Thus, a statement on the stability of the residual stresses generated by the thermomechanical treatment can be made.

The experimental reference process described above was modelled with the commercial FE software Simufact.forming based on MSC.Marc solver. For this purpose, the comprehensive material data presented in Sect. 2 were implemented

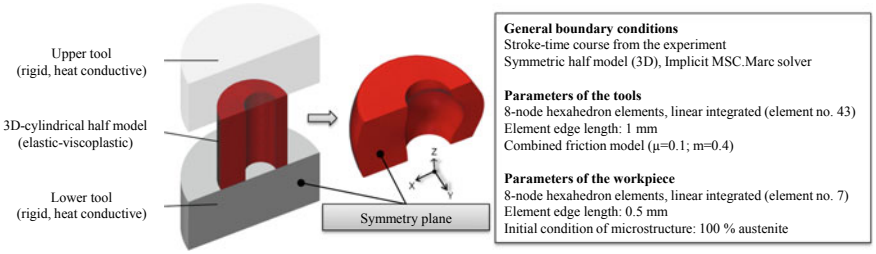


Fig. 6 Design of the investigated FE simulation model with the boundary conditions. (Color figure online)

in the software. In the simulation the heating process was modelled by a volume expansion of the specimen due to the austenitic phase transformation as well as the thermal expansion of the material.

At the beginning of the forming process a stress-free state in the specimen consisting of 100% austenitic sample is assumed. A schematic representation of the FE model and the boundary conditions is shown in Fig. 6.

The tools are considered as heat conducting rigid bodies and provided with a mesh of 1 mm element edge length. For the tools of the material 2.4668 (AISI: Inconel-718) constant values of the specific heat capacity $c_p = 435$ Jkg^{-1} K^{-1} and heat conductivity $\lambda = 11.4$ Wm^{-1} K^{-1} were taken from the data of the supplier [30]. The workpiece is assigned with an adaptive hexagonal mesh with the minimum element edge length of 0.5 mm, determined in a mesh sensitivity analysis.

4 Results of Long-term X-ray Analysis and FE Model Validation

The tangential residual stresses calculated in the simulations and the results of the experimental long-term X-ray analyses are shown in Fig. 7. Considering the results of the residual stress measurements immediately after the hot forming tests, it is noticeable that the residual stresses due to rapid cooling in water are higher than those after cooling in air. After cooling in water, for the material 1.3505 residual stresses of $\sigma_t = 216$ MPa at MP1 and $\sigma_t = 138$ MPa at MP2 are determined, for the material 1.7225 $\sigma_t = 212$ MPa at MP1 and $\sigma_t = 192$ MPa at MP2. After cooling in air, however, significantly lower stresses of $\sigma_t = -83$ MPa at MP1, $\sigma_t = -52$ MPa at MP2 for 1.3505 and $\sigma_t = 27$ MPa at MP1, $\sigma_t = 19$ MPa at MP2 for 1.7225 are measured. At high cooling rates, a diffusion-free transformation of the austenitic into the martensitic phase takes place in the material, which leads to severe stresses in the crystal lattice. During diffusion-controlled phase transformation, which occurs while cooling in air, comparatively lower residual stresses in the range of zero can be observed.

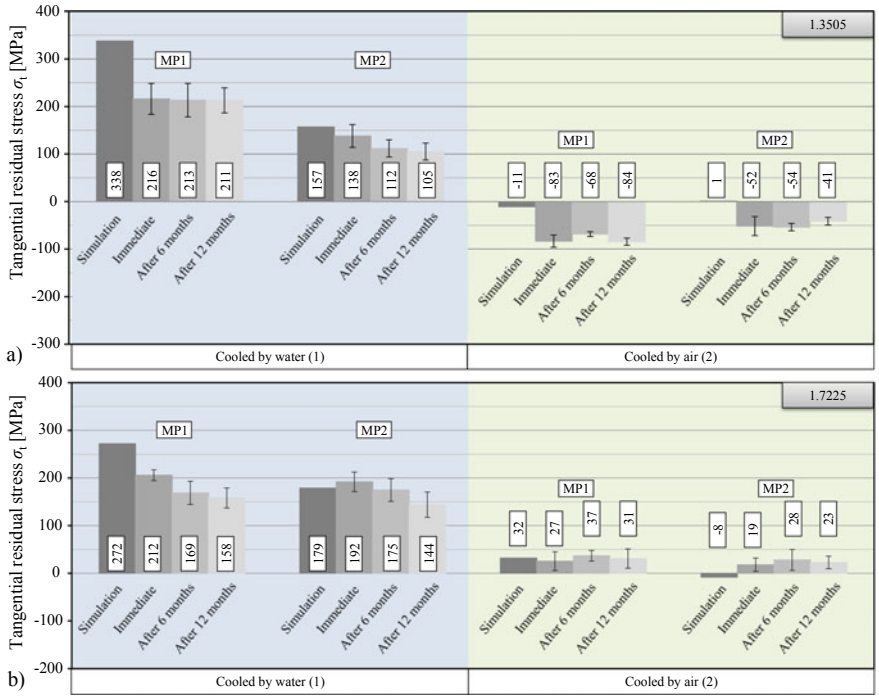


Fig. 7 Calculated tangential residual stresses σ_t in comparison with the results of the experimental long-term residual stress analyses. (Color figure online)

It is noted that cooling of the specimens in water causes positive residual stresses in both materials. Furthermore, cooling of the specimens made of 1.7225 in air lead to positive residual stresses as well. Negative residual stresses are only measured for the air-cooled specimens of material 1.3505. This is primarily due to the changed phase transformation behaviour of 1.3505 during slow cooling. At rapid cooling in water, a martensitic phase transformation occurs for both materials first in the specimen surface and afterwards in the specimen core. Each time this phase transformation is associated with volume expansion due to the larger lattice constants of the martensitic phase compared to the austenitic phase. Since the volume expansion occurs last in the specimen core, a strain gradient is created in the material, which leads to positive stresses at the specimen surface and negative residual stresses in the specimen core. When the specimens from 1.3505 are cooled in air, the volume expansion during the transformation of the austenitic to the pearlitic phase is significantly smaller. In addition, the transformation already takes place at high temperatures between 700 °C and 600 °C (cf. Fig. 3a). Following the pearlitic phase transformation, the specimen is further cooled down from about 600 °C to room temperature. Due to free convection, the specimen surface cools down faster than the specimen core. Once the surface temperature of the sample reaches room temperature, thermal shrinkage of the core continues. In contrast to the water-quenched specimens, where a volume

expansion due to the martensitic transformation occurs in the end of cooling in the core, a thermal shrinkage of the core appears here. This leads to a strain gradient between the specimen surface and the specimen core, which results in negative residual stresses on the specimen surface and positive residual stresses in the core. The effect of the bainitic phase transformation in the material 1.7225 compared to the pearlitic phase transformation in the material 1.3505 starts much later in the temperature range from 400 °C to 600 °C (cf. Fig. 3b). The volume expansion as a result of the bainitic phase transformation and the thermal shrinkage compensate each other so that only low positive stresses up to a maximum of 37 MPa are measured.

Furthermore, it is observed that the amount of residual stresses on the thick-walled side (MP1) of the specimen cooled by water are always higher than on the thin-walled side (MP2). According to the asymmetrical geometry of the specimen, an inhomogeneous residual stress profile is generated on the circumference of the specimen.

The residual stresses were applied reproducibly in each case with an absolute standard deviation of less than 30 MPa by the experimental setup described in Sect. 3. Accordingly, it can be assumed that technologically reproducible residual stresses can also be generated targeted to components in further hot forming processes.

The comparison of the experimentally measured residual stresses and the values obtained from simulations shows that the developed FE model is suitable for a good prediction accuracy of the residual stresses. In particular, the differences in the amount of residual stresses during cooling in water between the thick-walled side (MP1) and the thin-walled side (MP2) of the specimen are calculated properly in the simulations.

Repeating measurements after six months and twelve months shows that the residual stresses generated remain essentially stable in the material. In particular, at MP1 on the specimen of the material 1.3505 which were cooled in water, hardly show any changes in residual stresses with respect to time. In contrast, at the measuring points on the specimens of the material 1.7225 cooled by water, a slight decrease in the tangential residual stresses is observed over time. Despite storage at the constantly low temperature of 20 °C, stress relaxation has occurred. In contrast, the measured values of the stresses on the specimen cooled in air show generally lower initial residual stresses and barely changes in the stresses during the long-term investigations.

It should be noted that the residual stresses arising from the thermomechanical process are significantly influenced by the phase transformations. These transformations take place on the atomic level. With the X-ray method, the residual stresses on a macroscopic level can be measured exclusively. The complex interrelations between the residual stresses of the second and third type on the microscopic scale and their influence on the stability of the residual stresses of the first type on the macroscopic scale can therefore not be measured experimentally. For this reason, a working group of the authors is simultaneously engaged in modelling the effects of the microscopic processes using FE^2 simulations based on the macroscopic calculations from this work [31]. With such multiphase approaches, an improved numerically supported statement on the stability of the residual stresses should be possible in the future.

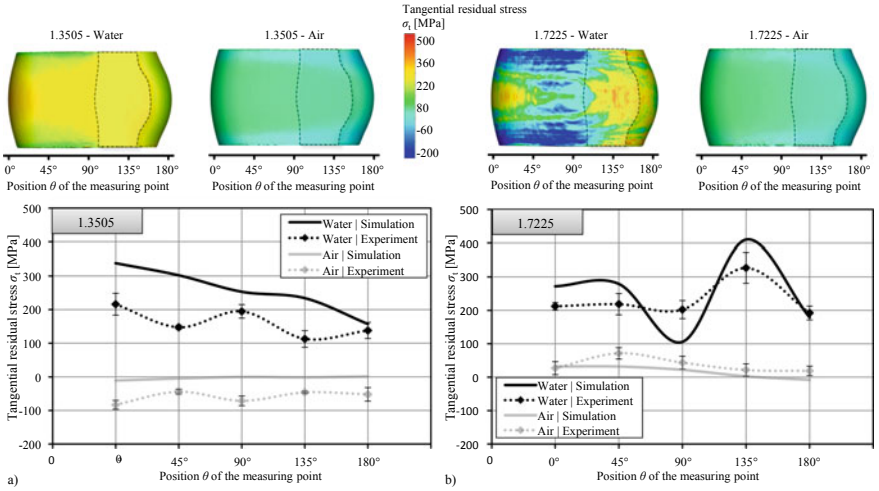


Fig. 8 Contour plots of the tangential residual stress σ_t from the simulations (top) as well as comparison with experimental results on the specimens' circumferential surface (bottom) with respect to the measuring position θ for the materials 1.3505 (**a**) and 1.7225 (**b**). (Color figure online)

For an advanced model validation, the measurements of residual stresses on the circumference of the specimen surface at different angles θ corresponding to Fig. 5c were also evaluated. Figure 8 shows a comparison of the calculated and experimentally determined residual stress values.

In addition, the contour plots for the distribution of the tangential residual stresses on the specimen surface of each case are shown in the top of Fig. 8. The simulations reveal that a homogeneous distribution of the equivalent plastic strain occurs on the surface of the specimens. Equivalent plastic strain values of $\varepsilon_{eq} = 0.46$ at MP1 and $\varepsilon_{eq} = 0.47$ at MP2 for the material 1.3505 as well as $\varepsilon_{eq} = 0.52$ at MP1 and $\varepsilon_{eq} = 0.5$ at MP2 for the material 1.7225 are calculated. The comparison of results for both materials in Fig. 8 shows that the residual stress profile can also be predicted with good quality over the course of the circumference. On the specimens out of 1.3505 cooled in water, a slightly decreasing stress curve can be observed from MP1 ($\theta = 0°$) to MP2 ($\theta = 180°$). In contrast, the stress profile of the specimens made of 1.7225 shows slight oscillations with a minimum at $\theta = 90°$ and a maximum at $\theta = 135°$. The residual stresses of specimens cooled in air are constantly low for both materials. In this way, the developed FE simulation model could be validated for different cooling conditions at different measuring points of the specimen with eccentric hole.

5 Summary and Outlook

In the scope of this work, a material model for the simulation of the interrelated thermal, metallurgical, and mechanical interactions during hot forming was created with the aim of residual stress prediction for the materials 1.3505 and 1.7225. Furthermore, a reference process of hot forming was investigated using cylindrical specimen with eccentric holes regarding the residual stresses resulting from two different cooling procedures (cooling medium water or air) by X-ray diffraction. It was found that the residual stresses can be generated by the hot forming process in a technologically replicable manner. A long-term study showed that the residual stresses are mostly stable over time, whereby slight stress relaxation was observed. Based on the extensive experimental results, the developed FE model of the hot forming process could finally be validated.

In a next step, the stability of the residual stresses resulting from the hot forming processes should be investigated under cyclic mechanical and thermal loads. Besides, the validated numerical model can be used to predict residual stresses in complex industrial processes. The overall objective of the work is the FE-based process design for targeted application of residual stresses to improve the properties of hot-formed components.

Acknowledgments Funded by the German Research Foundation (DFG, Deutsche Forschungsgemeinschaft)—374871564 (BE 1691/223-2, BR 5278/3-2, SCHR 570/33-2) within the priority program SPP 2013.

References

1. Verlinden B, Driver J, Samajdar J, Doherty R (2007) Thermo-mechanical processing of metallic materials. Elsevier Science 11
2. Brands D, Chugreev A, Kock C, Niekamp R, Scheunemann L, Uebing S, Behrens BA, Schröder J (2018) On the analysis of microstructural residual stresses in hot bulk forming parts under specific cooling. In: Proceedings in applied mathematics and mechanics
3. McClung RC (2007) A literature survey on the stability and significance of residual stresses during fatigue. Fatigue Fract Eng Mater Struct Nr 30:173–205
4. Zhuang W, Wicks B (2003) Mechanical surface treatment technologies for gas turbine engine components. J Eng Gas Turbines Power
5. Eigenmann B, Schulze V, Vöhringer O (1994) Surface residual stress relaxation in steels by thermal or mechanical treatment. In: Proceedings of the Fourth international conference on residual stresses, society of experimental mechanics, pp 598–607
6. Cammett JT, Sauer CA, Arnold TE (1993) Observations of shot peening residual stresses in 17 Cr - 7 Ni Austenitic stainless steel and their redistribution via mechan. In: The Fifth international conference on shot peening: ICSP5, pp 282–289
7. Wick A, Schulze V, Vöhringer O (2000) Effects of warm peening on fatigue life and relaxation behaviour of residual stresses in AISI 4140 steel. Mater Sci Eng B 191–197
8. Iida K, Hirose Y (1999) The residual stress distribution in shot peened carburized steel under fatigue. In: Proceedings of the 7th international conference on shot peening, pp 96–101

9. Clark DA, Johnson WS (2003) Temperature effects on fatigue performance of cold expanded holes in 7050-T7451 aluminum alloy. Int. J. Fatigue 159–165
10. Behrens BA, Bouguecha A, Vucetic M, Chugreev A (2016) Advanced wear simulation for bulk metal forming processes. MATEC Web of Conferences
11. Behrens BA, Bouguecha A, Bonk C, Chugreev A (2017) Experimental investigations on the transformation induced plasticity in a high tensile steel under varying thermo-mechanical loading. Comput. Methods Mater Sci 36–43
12. Behrens BA, Olle P (2007) Consideration of phase transformations in numerical simulation of press hardening. Steel Res Int 784–790
13. Denis S, Gautier E, Simon A, Beck G (1985) Stress-phase-transformation interactions—basic principles, modelling and calculation of internal stresses. Mater Sci Technol 805–814
14. Mitter W (1987) Umwandlungsplastizität und ihre Berücksichtigung bei der Berechnung von Eigenspannungen *Materialkundlich-Technische Reihe*
15. Behrens BA, Chugreeva A, Chugreev A (2018) FE-simulation of hot forging with an integrated heat treatment with the objective of residual stress prediction. AIP Conf Proc
16. DIN EN ISO 683–17 (2014) Heat-treated steels, alloy steels and free-cutting steels—Part 17: ball and roller bearing steels, Berlin: Beuth-Verlag
17. DIN EN 10,083–3 (2007) Steels for quenching and tempering—Part 3: Technical delivery conditions for alloy steels, Berlin: Beuth-Verlag
18. Behrens BA, Schröder J, Brands D, Scheunemann L, Niekamp R, Chugreev A, Sarhil M, Uebing S, Kock C (2019) Experimental and numerical investigations on the development of residual stresses in thermo-mechanically processed Cr-alloyed steel 1.3505. Metals Nr. 9(4)
19. Gesellschaft für metallurgische Technologie- und Softwareentwicklung mbH, MatILDa, [Online]. Available: https://www.gmt-stahl.de/en/matilda-2/. [Zugriff am 08 01 2020]
20. Behrens BA, Chugreev A, Kock C (2018) Experimental–numerical approach to efficient TTT-generation for simulation of phase transformations in thermomechanical forming processes. IOP Conference Series, Materials Science and Engineering, Nr. 461
21. Behrens BA, Chugreev A, Kock C, Macroscopic FE-simulation of residual stresses in thermo-mechanically processed steels considering phase transformation effects. In: XIV International conference on computational plasticity: fundamentals and applications. 211–222
22. Acht C, Dalgic M, Frerichs F, Hunkel H, Irretier A, Lübben T, Surm H (2008) Ermittlung der Materialdaten zur Simulation des Durchhärtens von Komponenten aus 100Cr6. J Heat Treat Mater Nr 63:234–244
23. JMatPro (2020) Practical software for materials propertie Sente Software Ldt., [Online]. Available: https://www.sentesoftware.co.uk/jmatpro. [Zugriff am 08 01 2020]
24. Saunders N, Guo U, Li X (2003) Using JMatPro to Model Materials Properties and Behavior. J Miner Met Mater Soc Nr 55:60–65
25. Guo Z, Saunders N, Schillé J, Miodownik AP (2009) Material properties for process simulation. Mater Sci Eng: A Nr 1–2:7–13
26. DIN EN 15,305:2009–1 (2008) Non-destructive testing—test method for residual stress analysis by X-ray diffraction, Berlin: Beuth Verlag
27. Eigenmann B, Macherauch E (1996) Röntgenographische Untersuchung von Spannungszuständen in Werkstoffen—Teil 3. Materialwissenschaften Und Werkstofftechnik, Nr 27:426–437
28. Voigt W (1928) Lehrbuch der Kristallphysik. BG Teubner, Wiesbaden
29. Reuss A (1929) Berechnung der Fließgrenzen von Mischkristallen auf Grund der Plastizitätsbedingung für Einkristalle. Zeitschrift der angewandten Mathematik und Mechanik, Nr 9:49–58
30. Special Metals Co (2020) New Hartford, New York, USA, [Online]. Available: http://www.specialmetals.com/assets/smc/540 documents/pcc-8064-sm-alloy-handbook-v04.pdf. [Zugriff am 08 01 2020]
31. Uebing S, Scheunemann L, Brands D, Schröder J (2019) Numerical thermo-elasto-plastic analysis of residual stresses on different scales during cooling of hot forming parts. In: XIV International Conference on computational plasticity: fundamentals and applications. pp 223–234

Analysis of Cylindrically and Spherically Embossed Flux Barriers in Non-oriented Electrical Steel

Ines Gilch, Simon Vogt, Tobias Neuwirth, Benedikt Schauerte, Kay Hameyer, Michael Schulz, Alex Gustschin, Wolfram Volk, and Hannes Alois Weiss

Abstract In reluctance and permanent magnet synchronous machines, flux barriers are crucial for magnetic flux guidance. Designed as cutouts, flux barriers reduce the mechanical strength of the rotor construction. To operate these electric drives at higher rotational speed, an alternative flux barrier design is required. Since residual stress influences the magnetic properties of soft magnetic materials, this paper deals with embossing induced residual stress as flux barriers in non-oriented electrical steel with 2.4 wt% silicon and a sheet thickness of 0.35 mm. The investigated flux

I. Gilch (✉) · S. Vogt · W. Volk · H. A. Weiss
Technical University of Munich, Walther-Meißner-Str. 4, 85748 Garching, Germany
e-mail: ines.gilch@utg.de

S. Vogt
e-mail: simon.vogt@utg.de

W. Volk
e-mail: wolfram.volk@utg.de

H. A. Weiss
e-mail: hannes.weiss@utg.de

T. Neuwirth · M. Schulz
Heinz Maier-Leibnitz Zentrum (MLZ), Technical University of Munich, Lichtenbergstr. 1, 85748 Garching, Germany
e-mail: tobias.neuwirth@frm2.tum.de

M. Schulz
e-mail: michael.schulz@frm2.tum.de

B. Schauerte · K. Hameyer
Institute of Electrical Machines (IEM), RWTH Aachen University, Schinkelstr. 4, 52062 Aachen, Germany
e-mail: benedikt.schauerte@iem.rwth-aachen.de

K. Hameyer
e-mail: hameyer@iem.rwth-aachen.de

A. Gustschin
Technical University of Munich, James-Franck-Str. 1, 85748 Garching, Germany
e-mail: alex.gustschin@ph.tum.de

© The Minerals, Metals & Materials Society 2021

G. Daehn et al. (eds.), *Forming the Future*, The Minerals, Metals & Materials Series,
https://doi.org/10.1007/978-3-030-75381-8_193

barriers were fabricated with a cylindrical or spherical punch at two different penetration depths and were compared to a flux barrier fabricated as cutout. A residual stress analysis using finite element analysis helps understanding the mechanism of embossed flux barriers. Additionally, the influence of induced residual stress on the magnetic material behavior is measured using standardized single sheet tests and neutron grating interferometry measurements. This investigation aimed at a better understanding of the flux barrier design by local induction of residual stress.

Keywords Electric drive · Electrical steel · Magnetic flux barrier · Embossing · Imprint · Residual stress

1 Introduction

With politics emphasizing energy change, the significance of energy efficiency is increasing. One factor to enhance the energy efficiency of electric drives, especially of reluctance and permanent magnet synchronous machines, is optimizing the magnetic flux guidance in the electrical steel that form the motor core. Conventionally, cutouts are inserted in electrical steel sheets for magnetic flux guidance. Coincidentally, they deteriorate the mechanical strength of the rotor construction. Hence, the maximum rotational speed of the motor is limited. The following investigation focuses on an alternative strategy of magnetic flux guidance in electrical steel to enable higher rotational speed and to increase the power density of electric drives.

Prior studies revealed that mechanical stress has a negative effect on the magnetic properties of non-oriented electrical steel [1]. The inverse magnetostrictive effect describes the correlation between mechanical stress and magnetic material behavior. These studies focused on the effect of mechanical stress caused by dynamic loads, like centrifugal forces [2], or of processing induced residual stress, e.g., by blanking [3], on the magnetic properties of non-oriented electrical steel. Their target was the decrease of the magnetic deterioration by reduction of mechanical stress. It is determined that compressive residual stress has a higher impact on the magnetic material behavior than tensile residual stress [1, 4].

In contrast, the following work aims to enhance the properties of electric drives by focused application of the inverse magnetostrictive effect. As residual stress deteriorates the magnetic material behavior, the local induction of residual stress reduces the magnetic permeability in the affected volume, hence the magnetic flux. As shown in [5] this phenomenon allows a magnetic flux guidance.

Different to [5], the relation between residual stress distribution and magnetic material behavior is analyzed in detail. Furthermore, the influence of cylindrical and spherical embossing geometries and of different penetration depths is examined. To evaluate the relation of embossing and magnetic properties, it is crucial to quantify the distribution of residual stress with a Finite Element Analysis (FEA) of the embossing process. The magnetic material behavior of the specimen is analyzed with

neutron grating interferometry (nGI) [6] and single sheet tests [7]. Additionally, the functionality of the embossed flux barrier is demonstrated by comparing it to a flux barrier fabricated as cutout. This investigation is necessary to show the applicability of the new flux barrier design for electric drives.

2 Methods

2.1 Specimen Manufacturing Process

The specimens were fabricated from a non-oriented electrical steel with a silicon content of 2.4 wt% and a sheet thickness of 0.35 mm, comparable to [5]. The size of 10 mm × 60 mm has been maintained, because it is suitable for both magnetic measurement methods. The strategy of specimen manufacturing is illustrated in Fig. 1. In the first step, locating holes are cut in the specimen and the flux barrier is embossed. Secondly, the final specimen geometry is wire-cut. To finish the specimen manufacturing, the final specimen geometry is measured optically.

To begin, two locating holes are cut in the specimen with the same punching tool used for embossing (Fig. 1b). The locating holes are mandatory to ensure a reproducible position of the embossing in the specimen's center.

Subsequent, the specimens are positioned with the locating holes and the magnetic flux barriers are embossed with a cylindrical or spherical punch (Fig. 1c). The two exemplary punch geometries were selected, because of strongly varying deformations and residual stress distributions. The tool, which is schematically shown in Fig. 2, is designed like a shear cutting tool. The main components are embossing punch, die, and blank holder. The blank holder ensures that the blank keeps its position during embossing. For the embossing, two different punches were selected. One embossing

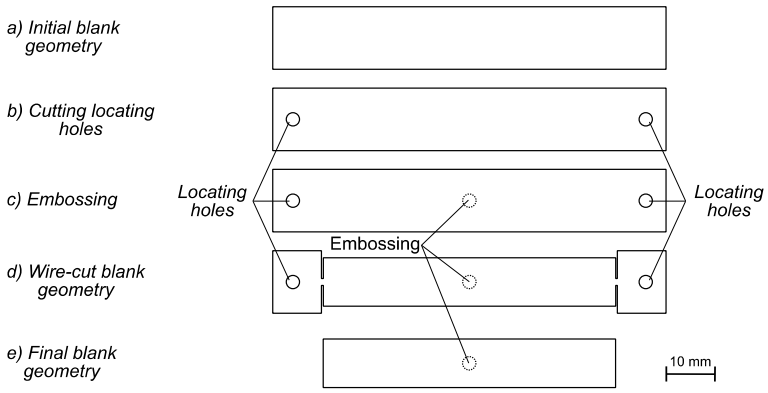


Fig. 1 Schematic illustration of specimen manufacturing: **a** initial blank geometry, **b** cutting of locating holes, **c** embossing of flux barrier, **d** wire-cutting and **e** final blank geometry

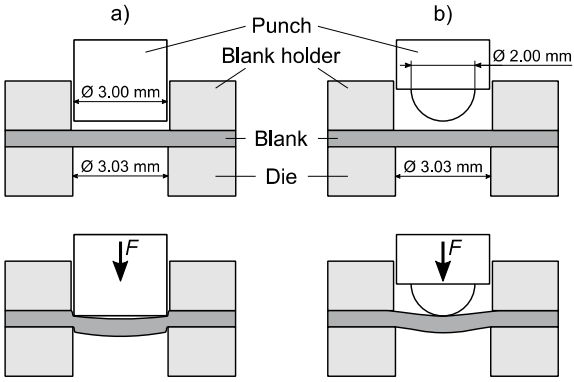


Fig. 2 Schematic illustration of the embossing tool and the embossing of the blank with **a** cylindrical punch and **b** spherical punch

punch has a spherical tip with a diameter of 2.00 mm, while the second embossing punch has a cylindrical tip similar to a punch used for shear cutting with a diameter of 3.00 mm. The cylindrical die remains unchanged for all experiments and has a diameter of 3.03 mm. The tool was utilized on a servo press with a velocity of 30 strokes per minute. The tool concept and the deformation of the blank caused by the punch force F is illustrated in Fig. 2.

The embossing depth, i.e. the way the punch penetrates below the initial upper surface of the blank, is adjustable. This allows a variation of the deformation grade between different embossings, which is for the executed experiments between 36 µm and 240 µm. With the cylindrical embossing punch and a sufficient penetration depth, the electrical steel sheet can be shear cut to produce a specimen with cutout as flux barrier.

Succeeding, the final specimen geometry is produced (Fig. 1d). The contour, shown in Fig. 1, is wire-cut. This cutting method ensures a negligible influence of the cut edges on the magnetic properties of the specimen [8]. Hence the cutting of the specimen doesn't need to be considered for the simulation of residual stress. During the wire-cutting, the specimens are positioned and fixed over the locating holes. Finally, the additional parts on both sides of the specimens are removed (Fig. 1e).

To finish the specimen production, the obtained embossing geometry is analyzed. A 3D-scan of the specimen's surface was executed with a confocal laser scanning microscope to analyze the final deformation and the penetration depth.

The specimen names are combined of the used punch, *Cyl* for cylindrical and *Sph* for spherical punch, and the penetration depth, *PD 1* for a small penetration depth and *PD 2* for a higher penetration depth. The sample names and the resulting depth of embossing are listed in Table 1.

Table 1 Measured final depth of deformation between initial blank surface and center of deformation as well as corresponding simulated penetration depths

Specimen	Punch	Resulting embossing depth (mm)	Simulated penetration depth (mm)
Cyl—PD 1	Cylindrical	0.031	0.036
Cyl—PD 2	Cylindrical	0.235	0.240
Sph—PD 1	Spherical	0.073	0.079
Sph—PD 2	Spherical	0.225	0.230

2.2 Finite Element Analysis

The embossing process is computed to analyze the relation between residual stress distribution in the specimen and its magnetic material behavior. The flux barrier caused by a cutout is not accounted in the Finite Element Analysis (FEA) as Weiss et al. [9] analyzed the effect of cutting in greater depth. With the FEA, a three-dimensional numerical model calculates the embossing related deformation and mechanical stress in the specimen. The embossing process is structured in three steps: clamping the blank with blank holder, embossing with cylindrical or spherical punch and removing external forces on the specimen to allow a springback movement.

To clamp the blank, a blank holder force of 25.5 kN is applied. Next, the punch penetrated the electrical steel. The depth varies because of different final depths of the specimens' embossings, which are listed in Table 1. Completing the numerical analysis, the springback of the blank is simulated: all external forces on the specimen are removed concurrent with punch, blank holder and die. The final geometry after step three is compared to the optically measured specimen profile to iteratively adapt the penetration depth. Thus obtaining a model close to reality. The computed stress without influence of external mechanical forces results in the required residual stress distribution.

The geometric parameters of the numerical model are approximately the same as in the experimental setup, see Chap. 2. The edge radius of the die and the cylindrical punch are set to 0.05 mm.

The non-oriented electrical steel is an approximately homogenous material with slightly different properties in and transverse to rolling direction. Considering the small anisotropy and the symmetry of the embossing process, calculating a quarter of the model is sufficient and reduces the computation time. The deformation of the tools is neglected due to modeling them as rigid bodies.

The material model is built on the measurement of material properties in [9]. The edge lengths of the elements, which are used for the discretization of the blank, are between 0.0017 mm in areas with high deformations and 2.58 mm in areas with small deformations. The mesh consists of 37,870 8-node linear brick C3D8R elements for the embossing simulation with cylindrical punch and 46,823 elements for the model with spherical embossing geometry.

As tensile and compressive residual stress have a different influence on the magnetic properties of electrical steel, von Mises equivalent stress criterion is not applicable for the analysis. A distinction of tensile and compressive residual stress is realized by the analysis of local maximum absolute principle stress $\sigma_{\mathrm{max,principle,abs}}$.

The stress values are evaluated along lines intersecting the specimen perpendicular to the blank surface. For each line 350 stress values are analyzed over the sheet thickness and separated in tensile and compressive stress. Subsequent, the mean tensile and compressive stress is computed for the line. The evaluation lines are arranged in a distance of 5 µm along five cross sections intersecting the center of embossing. Each cross section is rotated in an angle of 22.5°. The residual stress distributions of the cross sections were averaged to a single residual stress distribution plotted to the distance x from the center of embossing. Because of symmetry constraints, the residual stress distribution in and transverse to rolling direction are included with weighting factor 0.5 to the mean residual stress distribution.

2.3 Experimental Methods

2.3.1 Neutron Grating Interferometry

The imaging method neutron grating interferometry (nGI) analyzes the absorption, phase shift and ultra-small-angle neutron scattering (USANS) of a neutron beam passing through the specimen. [10] Neutrons do not interact with the electron hull, but the atomic core. This allows for a high penetration in most metals, i.e. electrical steel. Due to their spin, neutrons also interact with magnetic fields. In the case of a magnetic domain structure, as found in electrical steels, the scattering of the neutrons is in the USANS regime. These two factors cause nGI to be the prime technique to analyze local magnetic properties in bulk samples.

The image containing information about USANS is called the dark field image (DFI). Encoded in the DFI is information about the local magnetic domain structure, which in turn is linked to the residual stress distribution in the evaluated volume [6].

The neutron grating interferometer used for this study is a Talbot-Lau interferometer for neutrons [11]. A detailed explanation of the components and principle of a neutron grating interferometer may be found in [11, 12].

The measurements were performed at the neutron imaging beamline ANTARES at the FRM II [13, 14]. As experimental setting, a correlation length of 1.865 µm was selected. The exposure time of 10 s and an amount of 30 images per sample resulted in a total exposure time of 300 s per nGI-scan. The used detector has a field of view of 70.3 mm × 83.3 mm. The pixel size is 32.5 µm × 32.5 µm and the achieved resolution is roughly 90 µm.

The measurement of the specimens was conducted under the influence of different magnetic fields to analyze the effect of magnetization on the behavior of magnetic flux barriers. The yoke, described in [15] induces the magnetic field in the specimens,

Table 2 Magnetization of specimen in nGI-measurements: applied electric currents I and resulting magnetic field strength H

Applied current I (A)	0.00	0.47	1.34	2.00	3.00	4.00	5.00	6.67
Magnetic field strength H (A/m)	0.00	780	2230	3330	4955	6660	8325	11,105

which is generated by an electric current in the coils. In Table 2, the applied electrical currents I and resulting magnetic field strengths H are listed.

For evaluation of the DFI-signal, the measurement results were normalized to the DFI-signal of a virgin reference specimen. A scaled DFI-signal lower than 1 signifies a higher magnetic domain density and a value higher than 1 a lower magnetic domain density, compared to the reference. To analyze the progression of the magnetic domain structure, the scaled DFI-signal of all pixels at discrete distances of the embossing's center was radially averaged.

The magnetic domain structure of a specimen is highly affected by the residual stress. Additionally, the local magnetic domain structure gives an idea of the movement of magnetic domains under magnetization. The movability and magnetizability of magnetic domains are fundamental for the global magnetic properties.

2.3.2 Single Sheet Tests

Single sheet measurements are used for magnetic property characterization of electrical steel averaged across the entire volume of specimens. The measurement system utilized for this work is a double yoke 60 mm × 60 mm single sheet tester (SST). The specimen is clamped in between two yokes which close the magnetic circuit. The influence of the reluctance return path for the flux in the yokes can be neglected because of the considerably larger cross section of the yoke when compared to the specimen. The specimen is surrounded by two windings. The primary winding applies the magnetic field strength. The secondary winding induces the measurement voltage and thus the magnetic flux density in the specimen. The electrical currents in the primary windings are controlled in such a way, to cause sinusoidal magnetic flux density waveforms with a predefined amplitude B_m at a magnetization frequency f. In this way, the specimen can be compared in terms of characteristic properties such as iron loss, magnetic permeability and hysteresis loop shape [16].

For the selected measurement system, a specimen's geometry of 60 mm × 60 mm is optimal. Its size is reduced to 60 mm × 10 mm for this study, to measure the identical specimen as analyzed in the nGI. The specimen is clamped centrally between the yokes. The magnetic field and the resulting flux density are measured simultaneously and recorded, when a sinusoidal magnetic flux density waveform is set up in the investigated volume. For the measurements, a magnetization frequency f of 50 Hz was selected. The magnetic flux density is the average of the measured magnetic flux across the specimen's cross section. The magnetic field can be calculated by

the known magnetic path length, number of turns of the primary winding and the electrical current in the excitation coil.

A magnetic flux density exists between the yokes even without specimen due to the permeability of the vacuum μ_0, the so-called air flux. It is considered by air flux compensation to solely measure the magnetic flux in the specimen.

By principle, the single sheet tests only enable a conclusion on the global magnetic material behavior without insights on the local distribution of the magnetic flux. The combination of nGI and SST is necessary to analyze the magnetic material behavior of the embossed flux barriers. The connection of global magnetic properties and numerically analyzed local residual stress is shown in [17] by analyzing electrical steel in a tensile test.

3 Results

3.1 Numerical Analysis of Residual Stress

The following part depicts and discusses the FEA results of the embossing process. In Fig. 3, the simulated residual stress distributions distinguished into tensile and compressive stress are displayed. The vertical line at distance $x = 1.5$ mm represents the position of die diameter equal to the edge of embossing.

For the cylindrically embossed flux barriers, the maximal tensile and compressive residual stress values appear at a distance close to 1.5 mm. A higher penetration depth

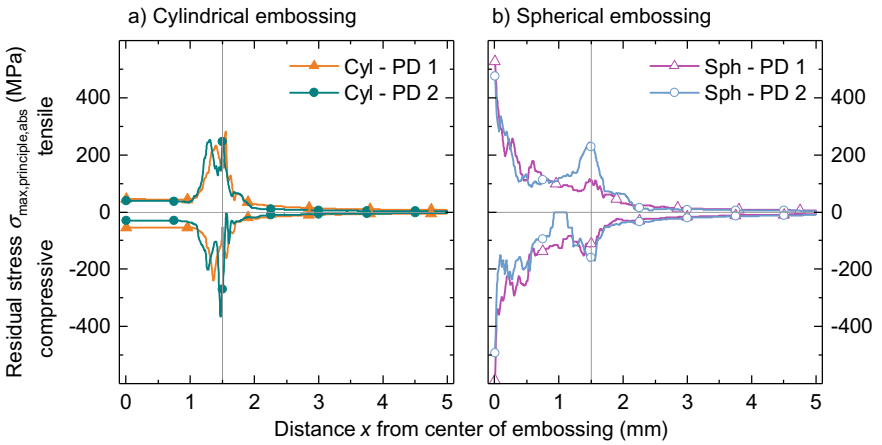


Fig. 3 Numerically analyzed distribution of tensile and compressive residual stress $\sigma_{max,principle,abs}$ plotted to the distance x from center of embossing for **a** the cylindrically embossed specimens and **b** the spherically embossed specimens. (Color figure online)

leads to a larger maximum of compressive residual stress at punch and die diameter and to a lower tensile and compressive stress level in- and outside of the embossing.

The simulated residual stress distributions of the spherically embossed flux barriers show global tensile and compressive stress maxima in the center of the embossing and local maxima at distance $x = 1.5$ mm. The local compressive stress maxima are significantly smaller than the global ones of the cylindrically embossed specimen. For Sph—PD 2, the local maximum of the tensile stress is two times the one of Sph—PD 1 and has a similar magnitude as the global tensile stress maxima of the cylindrical embossings. The residual stress outside the spherical embossings are increased in relation to the cylindrical embossings.

In summary, a higher total residual stress amount is induced using the spherical punch. The maxima of the spherical embossing are higher than the ones of the cylindrically embossed specimens. Additionally, the residual stress outside and inside the spherical embossing is more increased compared to the cylindrically embossed flux barrier.

3.2 Local Magnetic Material Behavior

The effect of residual stress on the local magnetic domain structure of the specimens was determined using neutron grating interferometry. The scaled DFI of the cylindrically and spherically embossed specimens are displayed in Fig. 4. They were fabricated with high penetration depth and measured with an applied magnetic field strength H of 780 A/m. The results of the embossed flux barriers are compared to the specimen with a flux barrier fabricated as cutout (Fig. 4c). The lowest scaled DFI-signals are measured at the edge of the cylindrical, in the center of the spherical embossing and on the right and left side of the cutout. The scaled DFI-signal is strongly increased above and below the cylindrical embossing and the cutout. This effect slightly occurs in the spherically embossed specimen.

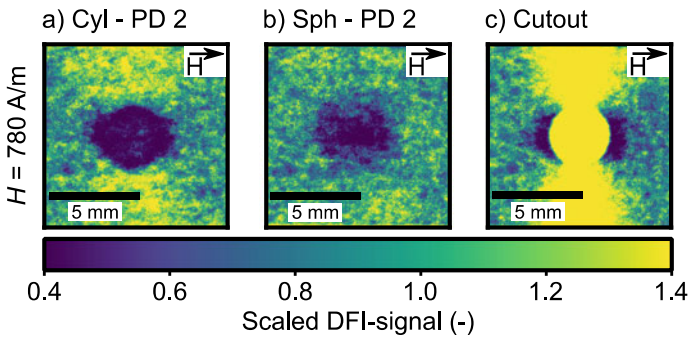


Fig. 4 Scaled DFI of **a** Cyl—PD 2 and **b** Sph—PD 2, with applied magnetic field strength H of 780 A/m. (Color figure online)

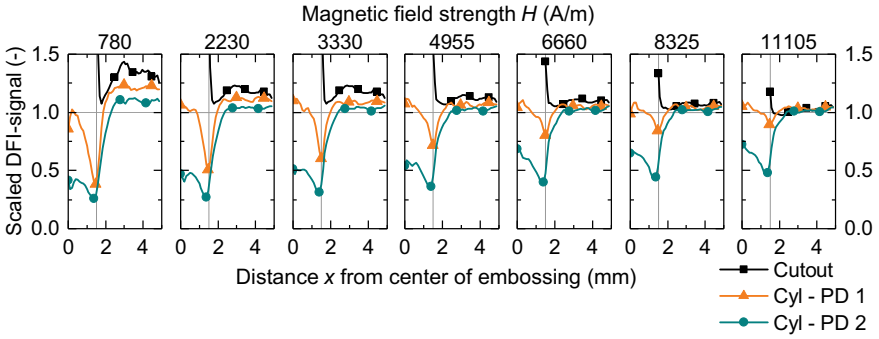


Fig. 5 Scaled DFI-signal of the cylindrically embossed specimens at two different penetration depths compared to a specimen with a cutout (diameter 3.00 mm) as flux barrier measured at different magnetic field strengths H. (Color figure online)

For further evaluation, the scaled DFI-signal progression of the cylindrically embossed specimen is compared to the specimen with cutout (Fig. 5). Close to the cutting line, the magnetic material behavior of this specimen is affected by shear cutting [15]. This causes an increased amount of magnetic domains close to the cutout. For the cutout flux barrier, the magnetic domain density in the remaining material is slightly decreased when compared to the reference material because the same magnetic flux is concentrated to a smaller cross section. Hence, the applied magnetic field strength has a higher impact on the remaining material.

The cylindrically embossed flux barriers show a scaled DFI-signal slightly higher than 1 outside of the embossing, similar to the cutout. At the edge of the embossing, the scaled DFI-signal is characterized by a minimum, which is lower for higher penetration depths. Embossing Cyl—PD 1 has a scaled DFI-signal above 1 in the center of embossing. In contrast, the scaled DFI-signal of embossing Cyl—PD 2 is only slightly increased from the edge to the center of embossing. The difference of minimal value of the scaled DFI-signal from small to high magnetization is approximately 0.5 for Cyl—PD 1 and lower than 0.25 for embossing Cyl—PD 2. Thus, the embossed flux barrier Cyl—PD 2 is more stable and has still an effect of flux guidance at high magnetic field strengths. Deductively, the cylindrically embossed flux barrier has a higher impact on the magnetic domain density in the center of the embossing, if the grade of deformation is sufficient. This is achieved with embossing Cyl—PD 2.

The minimal scaled DFI-signal of the spherically embossed specimen is located in the embossing's center and increases up to a distance of 3 mm, see Fig. 6. The scaled DFI-signals for the whole distance from the center of embossing is lower than 1, consequently more magnetic domains are measured in the evaluated volume than in the reference specimen, except of the measurement results at a magnetic field strength of 780 A/m. Therefore, the magnetic material behavior of the spherically embossed specimen is degraded in the full evaluated volume. The scaled DFI-signal is slightly lower for the specimen fabricated with higher penetration depth. The minimal

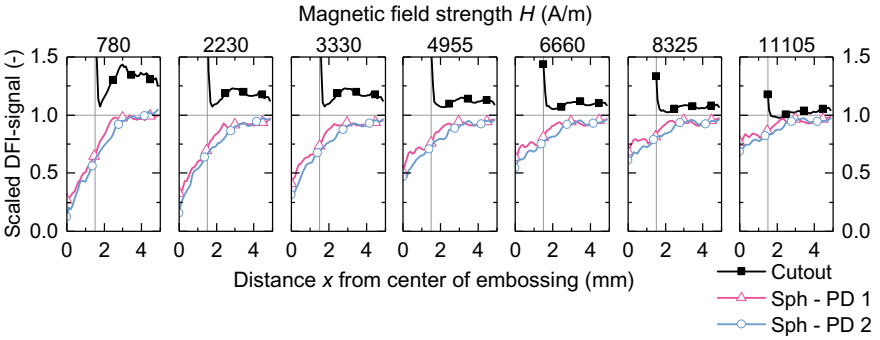


Fig. 6 Scaled DFI-signal of the spherically embossed specimens at two different penetration depths compared to a specimen with a cutout (diameter 3.00 mm) as flux barrier measured at different magnetic field strengths H. (Color figure online)

scaled DFI-signal at the highest magnetization compared to the lowest magnetization increases by 0.5. Due to that, the influence of spherical embossings on the magnetic domain structure is more dependent on the magnetization compared to Cyl—PD 2.

In summary, the difference between Sph—PD 1 and Sph—PD 2 is far smaller than between the cylindrical embossings. The spherically embossed specimens have the highest amount of magnetic domains in the embossing's center. For cylindrical embossings the minimal scaled DFI-signal is located at distance 1.5 mm. The magnetic material behavior of the spherically embossed specimens is additively deteriorated outside the embossed part. The effect on the magnetic domain structure decreases for higher magnetizations. For the two penetration depths, the difference of the scaled DFI-signal progression is small. A concentrated effect on the magnetic material behavior in the area of embossing is detected for the cylindrically embossed flux barriers. Outside the embossing less magnetic domains are measured compared to the reference. At increased magnetic field strength, the effect of the embossing Cyl—PD 2 on the magnetic domain structure is still considerably high in contrast to the other specimens.

3.3 Global Magnetic Material Behavior

The global magnetic properties, iron loss, magnetic permeability and hysteresis loop shape, of the embossed specimen and the reference material were analyzed with single sheet tests. Because the embossing has the highest impact on the permeability, this is the eligible parameter to illustrate the effect of embossed magnetic flux barriers. The comparison to the reference material shows the deterioration of the magnetic properties by the embossings.

In Fig. 7, the magnetic permeabilities of the embossed specimens fabricated with small penetration depth are compared to a higher penetration depth. The embossing

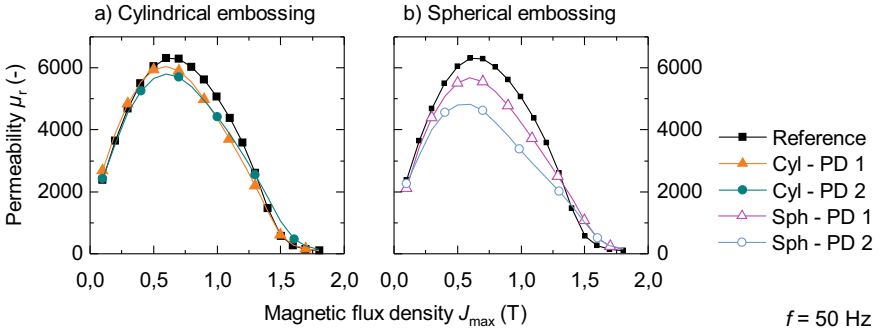


Fig. 7 Magnetic permeability μ_r for **a** cylindrically embossed and **b** spherically embossed specimen, fabricated with two different penetration depths compared to a reference material. (Color figure online)

of flux barriers reduces the permeability of electrical steel compared to the reference material. A cylindrical embossing with a penetration depth of 36 µm has a slightly smaller magnetic material deterioration compared to the penetration depth of 240 µm for magnetic flux densities lower than 1 T. For a magnetic flux density above 1.3 T, the permeability of Cyl—PD 2 is higher than the one of the reference material. Above 1.4 T, the permeability of Cyl—PD 1 and the reference material are approximately the same.

The permeability of spherically embossed specimens is further reduced for higher penetration depth. For magnetic flux densities above 1.3 T, the magnetic permeability of the spherically embossed electrical steel results in values higher than the ones of the reference. This effect only occurs in a comparatively small scope of magnetic flux densities but has to be analyzed in further studies.

The permeabilities of spherically and cylindrically embossed specimen are compared in Fig. 8a and Fig. 8b. For small penetration depths and low magnetization, the permeability of the spherical embossing is further reduced. At high magnetic flux densities, the cylindrically embossed specimen shows weakly increased magnetic deterioration. Figure 8b distinguishes the permeability of the different embossing geometries at penetration depth 2. Sph—PD 2 has a reduced permeability compared to the cylindrically embossed specimen.

To show the effect of embossed flux barriers, the results of Cyl—PD 2 and Sph—PD 2 are compared to a flux barrier fabricated as cutout (Fig. 8c). The permeability of Sph—PD 2 is up to 1.3 T strongly reduced compared to the specimen with cutout. Up to a magnetic flux density of 0.7 T, the permeability of the specimen with the cutout is slightly higher than the one of Cyl—PD 2. As shown in Fig. 5, the magnetic domain density of Cyl—PD 2 at the edge of embossing is higher than the one of the specimens with cutout. Hence, the embossing magnetically deteriorates an enlarged volume. For magnetic flux densities above 0.7 T, the permeability of Cyl—PD 2 is increased compared to the specimen with cutout, because the magnetic flux can partially pass the embossed flux barrier and has therefore a larger cross section. In summary, the cylindrically embossed flux barrier Cyl—PD 2 has almost the same

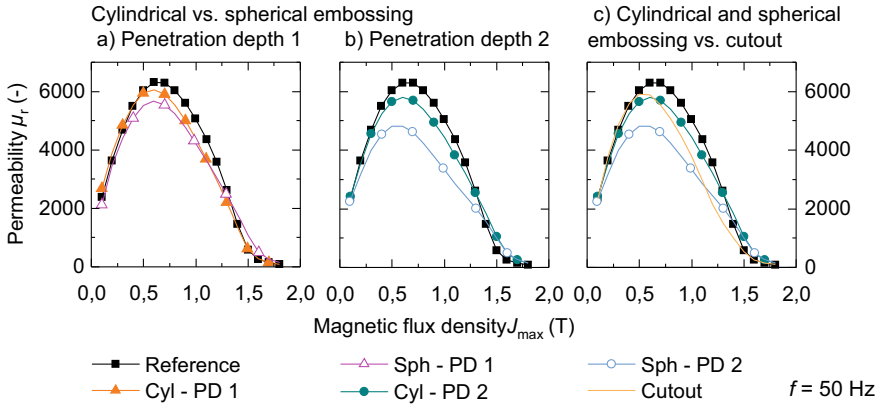


Fig. 8 Magnetic permeability μ_r of cylindrically and spherically embossed specimen fabricated with **a** penetration depth 1 and **b** with penetration depth 2 compared to reference material and **c** comparison of reference material, cylindrically embossed specimen with a penetration depth of 240 μm, spherically embossed specimen with a penetration depth of 230 μm and flux barrier manufactured as cutout. (Color figure online)

influence on the permeability of the specimen like a cutout with similar geometry, if the magnetic flux density is lower than 0.7 T.

4 Discussion

Connecting the numerical analysis with the magnetic measurements, a causal relationship between residual stress distribution and magnetic properties is apparent. For the interpretation of the averaged residual stress distribution, the knowledge of an higher impact on the magnetic material deterioration of compressive stress compared to tensile stress is essential [1]. To illustrate the relation of residual stress distribution and magnetic domain structure, the results are combined in Fig. 9. The diagrams of the nGI were measured with a magnetic field strength of 4955 A/m.

The stress peaks at distance 1.5 mm of the cylindrical embossings lead to an increased magnetic domain density (Fig. 9a). Despite small residual stress inside the embossings, the magnetic domain density is still at an increased level. The cylindrical flux barrier design results in a flux barrier shaped as circle, which adds up to a reduced magnetic flux inside the embossed circle. Inducing lower tensile residual stress (Cyl—PD 1) weakly affects the magnetic domain structure inside the embossing, especially at high magnetic flux densities. As the residual stress in- and outside of Cyl—PD 1 are a bit higher than the stress values of Cyl—PD 2, the magnetic permeability is further reduced (Fig. 7a). To conclude, strongly increased compressive residual stress in a restricted material volume has a higher impact on the magnetic

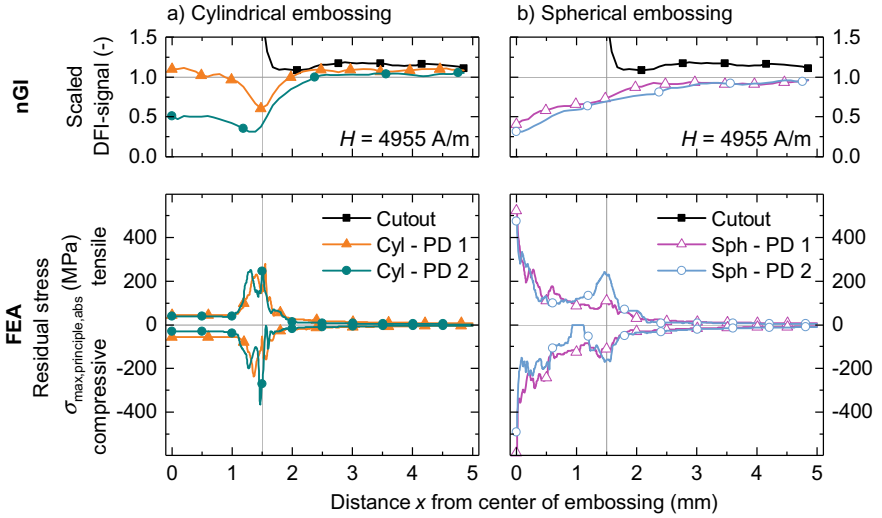


Fig. 9 Comparison of scaled DFI-signal at a magnetic field strength H of 4955 A/m and numerically analyzed residual stress distributions $\sigma_{max,principle,abs}$ of **a** cylindrical and **b** spherical embossings. (Color figure online)

flux guidance than peaks of tensile residual stress, even on the material volume in the embossing, which only has slightly increased residual stress.

In the center of the spherical embossing, the highest stress values and a maximum amount of magnetic domains arise (Fig. 9b). The residual stress outside the embossing as well as the amount of magnetic domains is increased in relation to the cylindrically embossed specimens. Hence, a larger volume is mechanically and magnetically deteriorated. Comparing both spherical embossings, the mean stress is similar (Fig. 3). The slightly increased magnetic domain density approves the reduced permeability of Sph—PD 2 (Figs. 6 and 7).

To compare the cylindrical and spherical embossings, the focus is set on penetration depth 2, because the embossings Cyl—PD 1 and Sph—PD 1 are fabricated with strongly deviating penetration depths. The residual stress and the magnetic domain density outside of the embossed geometry are increased for Sph—PD 2 (Fig. 9). The magnetic domain density in embossing Cyl—PD 2 is slightly smaller than the maximal density of Sph—PD 2 but affects a larger volume and has a stronger effect at higher magnetic field strength. Thus the embossing Sph—PD 2 has locally a higher impact on the magnetic properties but weakly influences the material outside the center of embossing. The spherical embossing deteriorates the magnetic properties up to a distance of 5 mm. These results substantiate the decreased permeability of Sph—PD 2 (Fig. 8).

Finally, Cyl—PD 2 and Sph—PD 2 are compared to a specimen with a cutout (diameter 3 mm) to analyze its effect as flux barrier Fig. 8c. The spherically embossed specimen has a considerably reduced permeability compared to the specimen with

cutout. At low magnetizations, the permeability of the cylindrically embossed specimen is slightly smaller than the permeability of the specimen with cutout. At higher magnetic flux densities, the permeability is above the one of the specimen with cutout (Fig. 8). High magnetizations allow the magnetic flux to partially pass the embossed flux barrier, which is not possible for the cutout, and the permeability is increased. In summary, focused induced residual stress has the potential to guide magnetic flux, especially at magnetic flux densities below 0.7 T for the investigated embossed specimen.

5 Conclusions

This work studied the effect of focused induced residual stress by cylindrical and spherical embossing on the magnetic flux guidance in electrical steel. With the FEA, the residual stress distribution in the specimen was numerically computed. The magnetic properties were evaluated locally by neutron grating interferometry and globally by single sheet tests. The magnetic domain structure and the resulting magnetic permeabilities were approved by the computed residual stress distribution. A large amount of compressive residual stress (Cyl—PD 2) has a sustainable effect on the magnetic domain structure in the embossed geometry. This is achieved by cylindrical embossing. The spherical embossing led to a stress maximum in the embossing's center and higher residual stress up to a distance of 5 mm. The spherical flux barrier has no determined boundaries like the cylindrical embossing. Hence, the global magnetic properties of the spherically embossed specimen are more deteriorated than the ones of the cylindrical embossing.

Summarizing, the magnetic flux guidance by locally induced residual stress was approved, especially by the comparison to a flux barrier fabricated as cutout. Further investigations have to define optimal residual stress distributions and suitable embossing geometries for the application of focused induced residual stress as flux barrier. Furthermore, the increased permeabilities of the embossed specimen compared to the virgin reference material measured at magnetic flux densities above 1.3 T have to be analyzed.

Acknowledgments This work was supported by the Deutsche Forschungsgemeinschaft (DFG) in the DFG priority program "SPP2013—Focused Local Stress Imprint in Electrical Steel as Means of Improving the Energy Efficiency" - HA 4395/22-1; SCHU 3227/2-1; VO 1487/31-1. The results of this work are based upon experiments performed at the ANTARES instrument at Heinz Maier-Leibnitz Zentrum (MLZ), Garching, Germany.

References

1. Naumoski H, Maucher A, Herr U (2015) Investigation of the influence of global stresses and strains on the magnetic properties of electrical steels with varying alloying content and grain size. https://doi.org/10.1109/EDPC.2015.7323206
2. Cao H, Huang S, Shi W (2019) Influence of core stress on performance of permanent magnet synchronous motor. J Magn 24(1):24–31. https://doi.org/10.4283/JMAG.2019.24.1.024
3. Weiss HA, Trober P, Golle R, Steentjes S, Leuning N, Elfgen S, Hameyer K, Volk W (2018) Impact of punching parameter variations on magnetic properties of nongrain-oriented electrical steel. IEEE Trans Ind Appl 54(6):5869–5878. https://doi.org/10.1109/TIA.2018.2853133
4. Kai Y, Tsuchida Y, Todaka T, Enokizono M (2014) Influence of biaxial stress on vector magnetic properties and 2-D magnetostriction of a nonoriented electrical steel sheet under alternating magnetic flux conditions. IEEE Trans Magn 50(4). https://doi.org/10.1109/TMAG.2013.2287875
5. Vogt S, Neuwirth T, Schauerte B, Weiss HA, Falger PM, Gustschin A, Schulz M, Hameyer K, Volk W (2019) Extent of embossing-related residual stress on the magnetic properties evaluated using neutron grating interferometry and single sheet test. Prod Eng Res Devel 13(2):211–217. https://doi.org/10.1007/s11740-018-0863-7
6. Grünzweig C, David C, Bunk O, Dierolf M, Frei G, Kühne G, Kohlbrecher J, Schäfer R, Lejcek P, Rønnow HMR, Pfeiffer F (2008) Neutron decoherence imaging for visualizing bulk magnetic domain structures. Phys Rev Lett 101(2). https://doi.org/10.1103/PhysRevLett.101.025504
7. British Standards Institution (1992) Magnetic materials. Methods of measurement of the magnetic properties of magnetic sheet and strip by means of a single sheet tester (6404–3). Brit Stan Inst https://doi.org/10.3403/00279002. Zugegriffen: 10. January 2020
8. Kurosaki Y, Mogi H, Fujii H, Kubota T, Shiozaki M (2008) Importance of punching and workability in non-oriented electrical steel sheets. J Magn Magn Mater 320(20):2474–2480. https://doi.org/10.1016/j.jmmm.2008.04.073
9. Weiss HA, Leuning N, Steentjes S, Hameyer K, Andorfer T, Jenner S, Volk W (2017) Influence of shear cutting parameters on the electromagnetic properties of non-oriented electrical steel sheets. J Magn Magn Mater 421:250–259. https://doi.org/10.1016/j.jmmm.2016.08.002
10. Strobl M, Grünzweig C, Hilger A, Manke I, Kardjilov N, David C, Pfeiffer F (2008) Neutron dark-field tomography. Phys Rev Lett 101(12). https://doi.org/10.1103/PhysRevLett.101.123902
11. Neuwirth T, Backs A, Gustschin A, Vogt S, Pfeiffer F, Böni P, Schulz M (2020) A high visibility Talbot-Lau neutron grating interferometer to investigate stress-induced magnetic degradation in electrical steel. Sci Rep
12. Reimann T, Mühlbauer S, Horisberger M, Betz B, Böni P, Schulz M (2016) The new neutron grating interferometer at the ANTARES beamline: Design, principles and applications. J Appl Crystallogr 49(5):1488–1500. https://doi.org/10.1107/S1600576716011080
13. Calzada E, Gruenauer F, Mühlbauer M, Schillinger B, Schulz M (2009) New design for the ANTARES-II facility for neutron imaging at FRM II. Nucl Instrum Methods Phys Res, Sect A 605(1–2):50–53. https://doi.org/10.1016/j.nima.2009.01.192
14. Schulz M, Schillinger B (2015) ANTARES: Cold neutron radiography and tomography facility. JLSRF 1. https://doi.org/10.17815/jlsrf-1-42
15. Weiss HA, Steentjes S, Tröber P, Leuning N, Neuwirth T, Schulz M, Hameyer K, Golle R, Volk W (2019) Neutron grating interferometry investigation of punching-related local magnetic property deteriorations in electrical steels. J Magn Magn Mater 474:643–653. https://doi.org/10.1016/j.jmmm.2018.10.098
16. Fiorillo F (2004) Measurement and characterization of magnetic materials, 1. Aufl. Elsevier series in electromagnetism. Elsevier Academic Press, San Diego, Calif
17. Leuning N, Steentjes S, Weiss HA, Volk W, Hameyer K (2018) Magnetic material deterioration of non-oriented electrical steels as a result of plastic deformation considering residual stress distribution. IEEE Trans Magn 54(11). https://doi.org/10.1109/TMAG.2018.2848365

Analysis of Influencing Factors on the Achievability of Bistable Fully Closed Shells by Semi-Analytical Modeling



Pavlo Pavliuchenko, Marco Teller, and Gerhard Hirt

Abstract Bistable fully closed shells can serve as long supporting structures that can be folded into a compact transport geometry and unfolded at the construction place. Bistability is achieved by introducing a specific distribution of residual stresses through the thickness of the shell, e.g., by incremental die-bending. In order to find a suitable bending radii combination a semi-analytical model was developed and experimentally validated for the steel 1.1274 in previous research. Nevertheless, minor deviations have occurred in the prediction of final curvatures of the different stable geometries and it is still unclear to what extent other influencing variables such as shell thickness or material properties influence the achievability of fully closed bistable shells. Therefore, in this paper, an enhancement and generalization of the existing semi-analytical model for different steels is described and the extended model is used for a comprehensive analysis of the influence of different variables on bistability and final shell geometries.

Keywords Bistability · Residual stress · Sheet metal

1 Introduction

Deployable structures can be defined as structures that have two main stable states, namely, a compact and a deployed geometry [1]. The compact state is mainly used for transportation and therefore should occupy the smallest possible volume. Additionally, a housing is necessary to keep the structure in the compact state. In contrast, bistable structures are deployable structures that have stable geometries in both states [1]. Such structures could be produced from metallic thin shells with high yield strength by introducing a specific residual stress distribution over the shell thickness [2]. The general production route of bistable metallic shells was described in [3] and consists of two sequential plastic bending steps in opposite directions, along two orthogonal axes (see Fig. 1). The particular residual stress distribution over the

P. Pavliuchenko (✉) · M. Teller · G. Hirt
Institute of Metal Forming (IBF), RWTH Aachen University, 52072 Aachen, Germany
e-mail: pavlo.pavliuchenko@ibf.rwth-aachen.de

© The Minerals, Metals & Materials Society 2021

G. Daehn et al. (eds.), *Forming the Future*, The Minerals, Metals & Materials Series,
https://doi.org/10.1007/978-3-030-75381-8_194

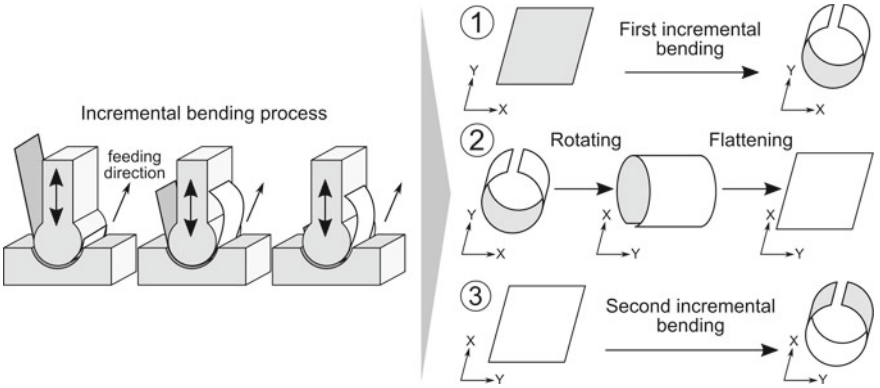


Fig. 1 Scheme of the production process of bistable shells [3]

shell thickness, introduced during the bending process, provides two stable states, as shown in Fig. 2, where X- and Y-axis represent the longitudinal and transverse directions. The Z-axis represents the thickness of the shell and is not shown in the figure, since due to the small thickness the stresses in this direction are not considered.

The analytical models for determining the effect of bistability of such structures are given by Galletly and Guest using beam [4] and shell [5] models and He [6], respectively. In [7], a semi-analytical model for the rapid determination of possible bending radius combinations was developed. This model works with some simplifications and assumptions, which are only valid for the steel 1.1274 used in [7]. In order to enable the investigation of various influencing factors and to allow for a general investigation on the influences on bistability, the model is firstly extended in this paper. Afterward, a comprehensive study of a wide range of parameters is presented. This large number of simulations can only be performed due to the fast computing time (less than 3 s per simulation) of the semi-analytical model.

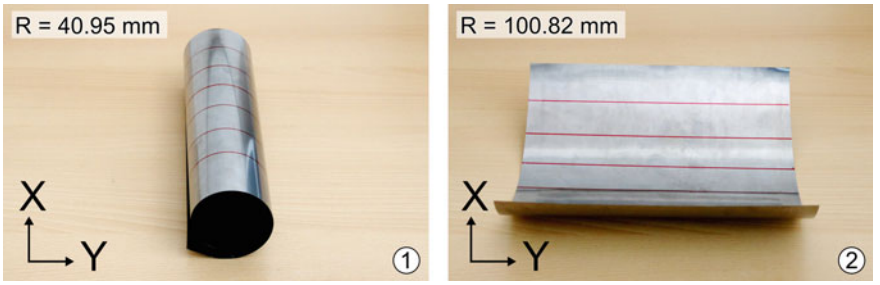


Fig. 2 Bistable tube produced by incremental bending (1: deployed state as the first stable state, 2: (partially) folded configuration as the second stable state) [3]. (Color figure online)

2 Semi-Analytical Model

2.1 Model Extension and Generalization

The semi-analytical model for investigation of the influence of production process parameters on bistable shells for the steel 1.1274 was introduced in [3]. The production process described by this model could be represented by the sequence of following steps: first bending of the shell along X-axis; flattening of the shell; second bending of the shell along Y-axis in opposite direction; springback to the first stable state; flattening of the shell and slight bending of it along X-axis in order to check second stable state.

As already mentioned, some assumptions were made specifically for the material 1.1274 used. A main assumption is that during the first bending process only kinematic hardening and during the second bending only isotropic hardening occurs, respectively. A general combined hardening approach, where both, kinematic and isotropic hardening, contribute to the plastic behavior of the material, seems to be suitable. Hence, a combined isotropic/kinematic hardening behavior during first and second bending was introduced into the new model.

In the original model, the thickness of the shell was divided into an elastic part, where only elastic deformation occurs, and a plastic part, where plastic hardening takes place. Both parts were afterward divided into an equal number of layers. This approach could lead to different layer thickness in elastic and plastic parts of shell, which may affect the accuracy of calculations. Also, the initial division of the shell on elastic and plastic regions leads to difficulties in calculation the second bending step, where the ratio of these regions may differ in comparison with the first bending. To avoid complications, in the new model the shell thickness is initially dived into 100 layers with equal thickness and then stresses are calculated for each layer. An initial splitting into elastic and plastic areas no longer takes place.

2.2 Extended Semi-Analytical Model

Based on the semi-analytical model described in [7] several changes were made. A combined isotropic/kinematic hardening model was introduced. During plastic deformation the yield locus translates (kinematic part) as well as increases in size (isotropic part). The ratio of kinematic and isotropic hardening on the total hardening of the shell is assumed to be 0.5 [8]. Also, the shell thickness is divided by 100 layers with equal size.

In order to avoid unnecessary repetition of the work in [7], here only the most important equations and changes compared to the former model will be described.

The strain along the bending direction is described by the multiplication of shell curvature k and layer thickness z and provided in Eq. (1):

$$\varepsilon = k \cdot z \tag{1}$$

The elastic stress calculation is presented in Eq. (2):

$$\sigma = E\varepsilon_e = E\big(\varepsilon - \varepsilon_p\big), \tag{2}$$

where E is the Young's modulus of the material.

The elastic stress increment is shown in Eq. (3):

$$d\sigma = Cd\varepsilon_e, \tag{3}$$

where C is the stiffness matrix defined as

$$C = \frac{E}{1-v^2}\begin{bmatrix} 1 & v \\ v & 1 \end{bmatrix}, \tag{4}$$

where v is Poisson's ratio.

The equivalent stress is presented in Eq. (5):

$$\sigma_e = \frac{1}{\sqrt{2}}\sqrt{(\sigma - X)^T A(\sigma - X)}, \tag{5}$$

where X is the so-called back stress, and its increment could be calculated by Eq. (6):

$$dX = \frac{c}{\sigma_{y0}}(\sigma - X)dp - \gamma X dp. \tag{6}$$

The isotropic hardening plastic stress increment is calculated via Eq. (7):

$$d\sigma = C\left(I - \frac{a \cdot Ca}{a \cdot Ca + bQe^{-bp}}\right)d\varepsilon \tag{7}$$

and the kinematic hardening plastic stress increment is presented in Eq. (8):

$$d\sigma = C\left(I - \frac{a \cdot Ca}{a \cdot Ca - \left(\gamma + \frac{c}{\sigma_{y0}}\right)a \cdot X + \frac{c}{\sigma_{y0}}\sigma \cdot a}\right)d\varepsilon, \tag{8}$$

where a is the normal to the yield locus, I is identity matrix and γ, c, b, Q are material flow curve constants. The weighting of the two hardening mechanisms is determined by the parameter m. The combined strain rate is presented in Eq. (9) [8]:

$$\dot{\varepsilon}_p = \dot{\varepsilon}_{pi} + \dot{\varepsilon}_{pk} = m\dot{\varepsilon}_p + (1-m)\dot{\varepsilon}_p \tag{9}$$

Combining Eqs. (7) and (8) the plastic stress increment for the combined hardening model is given by Eq. (10):

$$d\sigma = C\left(I - \frac{a \cdot Ca}{a \cdot Ca - (1-m)\left(\left(\gamma + \frac{c}{\sigma_e}\right)a \cdot X - \frac{c}{\sigma_e}\sigma \cdot a\right) + mbQe^{-mbp}}\right)d\varepsilon, \tag{10}$$

where at parameter $m = 0$ pure kinematic hardening and at $m = 1$ pure isotropic hardening occurs during the plastic deformation of the material.

When considering the stability of shell geometry after springback, it is assumed that the resulting bending moment inside the shell is equal to zero. Due to the symmetry about the mid-surface, the integrated, applied bending moment through the thickness can be calculated as

$$M = 2\int_0^{T/2} \sigma(z) z dz, \tag{11}$$

where T is the thickness of shell.

The shell geometry is considered stable if the resulting bending moment per unit length for the required axis is close to zero. Based on the study [9], the applied bending moment per unit length (M) and curvature (k) has a linear relationship during elastic unloading. The slope of this elastic recovery is given by Eq. (12):

$$\frac{M}{k} = \frac{2}{3}\frac{E(T/2)^3}{(1-\nu^2)} \tag{12}$$

As the bending moment after spring back should be zero, then the curvature after spring back, k_{sp}, can be derived from Eq. (12) as

$$k_{sp} = k_x - \frac{3(1-\nu^2)M}{2E(T/2)^3} \tag{13}$$

where k_x is the first bending curvature.

3 Materials

For the parameter studies the steels 1.1274 and 1.4310 were used. The main difference between these materials is the yield strength. The stress–strain curves and material constants are provided in Fig. 3 and Table 1, respectively. The shell thickness is 0.2 mm for both materials.

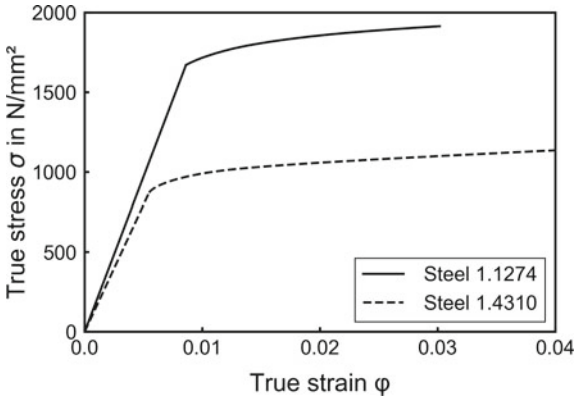


Fig. 3 Stress–strain curves of steels 1.1274 and 1.4310

Table 1 Material property constants

Steel	σ	E	c	γ	b	Q
1.1274	1690 MPa	189,450 MPa	33,933	152.576	152.576	222.403
1.4310	918 MPa	158,920 MPa	30,520	194.284	194.284	157.089

3.1 Choosing Appropriate m-value

In order to find the appropriate ratio between kinematic and isotropic parts of combined hardening the evaluation of experimental data was done. For this reason, the comparison between experimentally obtained springback shell radii after first second bending for the steel 1.1274 was carried out and the results are given in Fig. 4. It can be seen from the graph, that, for all bending radii R_{bend}, shell radius after elastic springback after second bending (bending of pre-bent shell) is always smaller than shell radius after first bending of the flat shell.

To determine which *m*-value should be used during parameter study, the comparison of springback shell radii for different *m*-value after first and second bending using semi-analytical model was carried out. The results are presented in Fig. 5. For a bend radius R_{bend} of 10 mm, the results are not presented, because a stable geometry after the second bending was not achieved. As can be seen, with increasing the isotropic part in the combined hardening (*m* approaches 1), the calculated shell radius after second springback became greater than after first bending. This difference is minimal when the pure kinematic hardening is considered during plastic deformation. It should be mentioned that even for the pure kinematic hardening the calculated shell radius after second springback is not always greater than after first bending. Therefore, the pure kinematic hardening ($m = 0$) was chosen to perform the parameter study with the help of semi-analytical model.

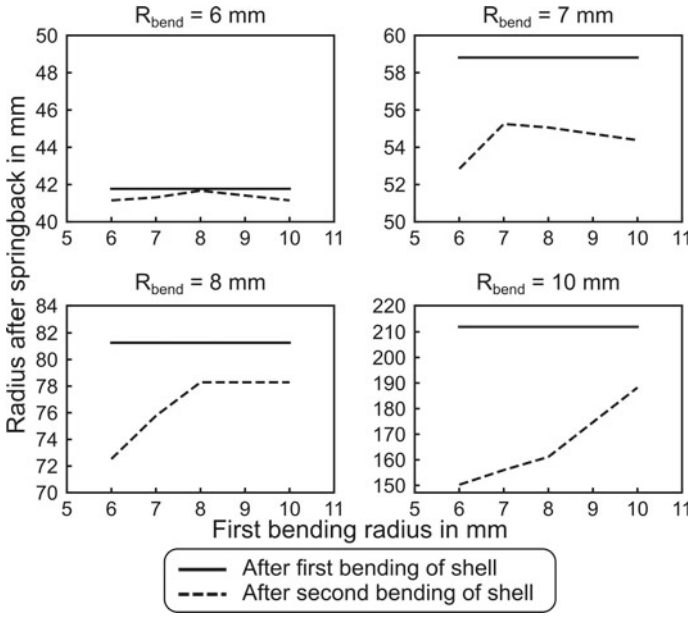


Fig. 4 Experimentally obtained shell radii after elastic springback after first and second bending of the shell

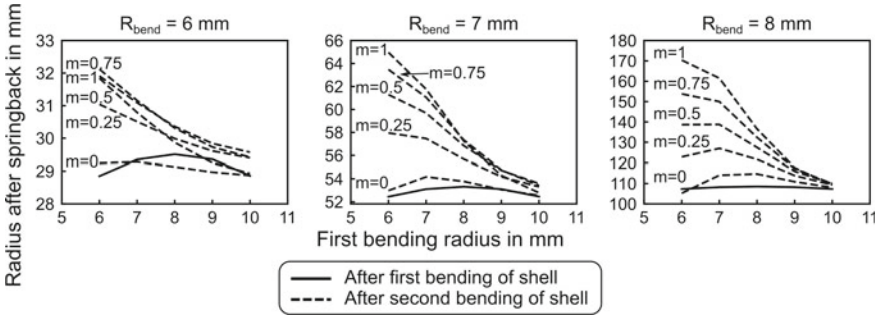


Fig. 5 Shell radii after elastic springback after first and second bending of the shell for the different *m*-values calculated using semi-analytical model

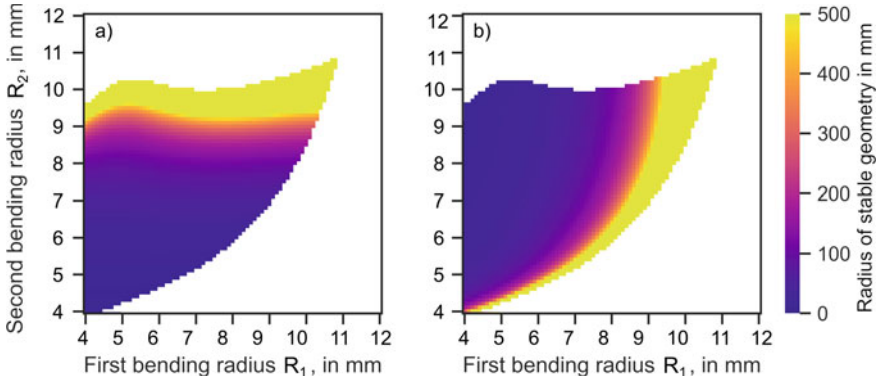


Fig. 6 Bistability and radii of **a** first and **b** second stable geometry for steel 1.1274 depending on different bending radii combinations. (Color figure online)

4 Investigation of Bistability Using the Extended Semi-Analytical Model

4.1 Influence of Bending Radii Combinations for Measured Material Properties

The influence of bending radii combination on the bistability of metallic shells is investigated for the different materials presented in Chap. 3. The shell thickness is equal to 0.2 mm. For steel 1.1274 the study was done using bending radii from 4 to 12 mm with a step size of 0.1 mm. The results are depicted in Fig. 6. For steel 1.4310 the study was done using bending radii from 4 to 17 mm with a step size of 0.1 mm. The results are depicted in Fig. 7. As can be seen, with decreasing yield strength of the material, the range of radii combinations that lead to bistability increases.

4.2 Influence of Yield Stress Disturbances on Bistability

In addition to the calculations with the material values actually measured, parameter studies were also carried out for individually varied characteristic values.

The dependency of stable geometry radii regarding fluctuations of yield strength ($\pm$ 200 MPa) of the shell is presented in Figs. 8 and 9 for the materials 1.1274 and 1.4310, respectively. The analysis was done for the bending radii combinations 6–6 mm, 7–7 mm, 8–8 mm, 9–9 mm, and 10–10 mm for steel 1.1274 and 8–8 mm, 9–9 mm, 10–10 mm, 11–11 mm, 12–12 mm for steel 1.4310, respectively.

It can be seen for both materials that with increasing bending radii the influence of yield strength fluctuation increases rapidly. This can be explained by the fact that

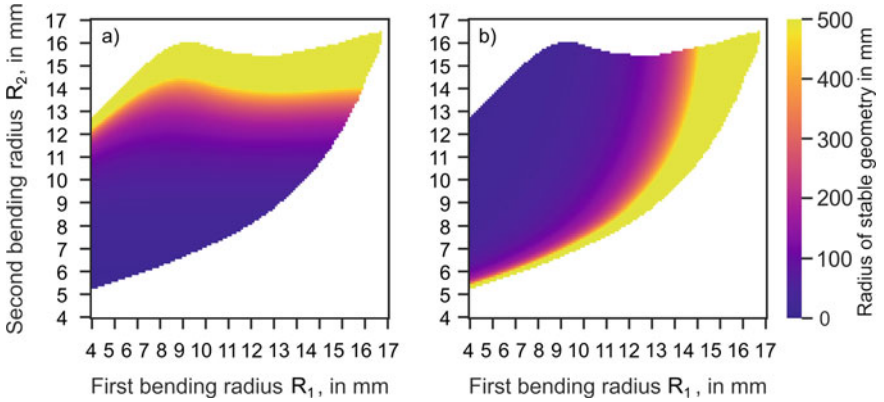


Fig. 7 Bistability and radii of **a** first and **b** second stable geometry for steel 1.4310 depending on different bending radii combinations. (Color figure online)

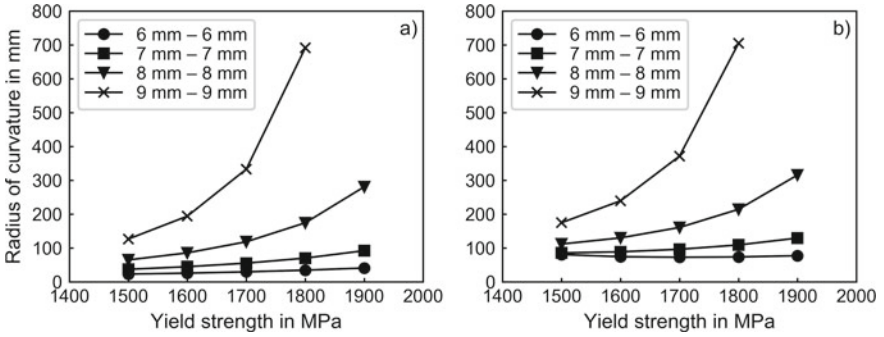


Fig. 8 Dependence of **a** first and **b** second stable state geometries on yield strength fluctuations for steel 1.1274

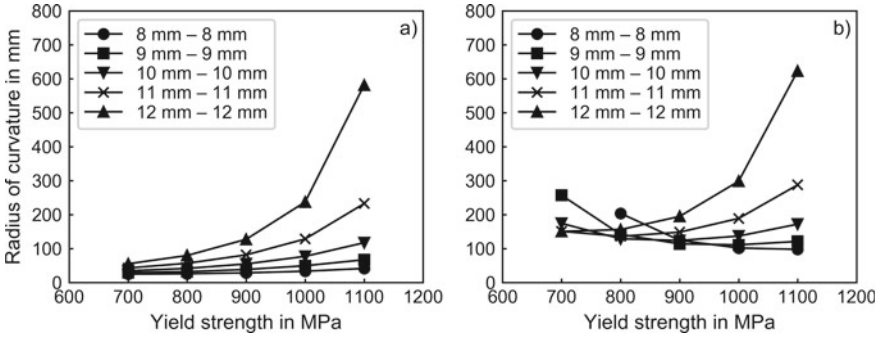


Fig. 9 Dependence of **a** first and **b** second stable state geometries on yield strength fluctuations for steel 1.4310

larger bending radius introduces smaller residual stresses in the shell, and even small changes of the yield strength lead to high deviations of stable geometry radii.

4.3 Influence of Shell Thickness Disturbances on Bistability

The dependency of stable geometry radii regarding fluctuations of the shell thickness (± 0.01 mm) is presented in Figs. 10 and 11 for the materials 1.1274 and 1.4310, respectively. The analysis was done for the same bending radii as in Chap. 4.2. The properties of the materials were taken from Table 1.

As in Chap. 4.2 it can be stated for both materials that with increasing bending radii the influence of shell thickness fluctuations increases significantly. The shell thickness has influence on the residual stress distribution as well as on the global stiffness of the shell and by that on the springback behavior.

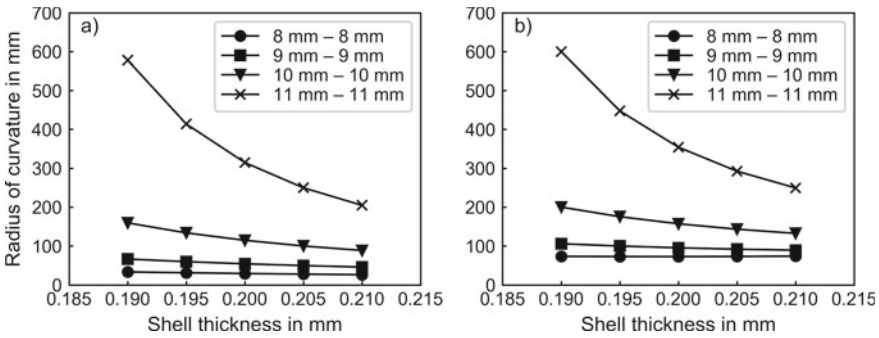


Fig. 10 Dependence of **a** first and **b** second stable state geometries on shell thickness fluctuations for steel 1.1274

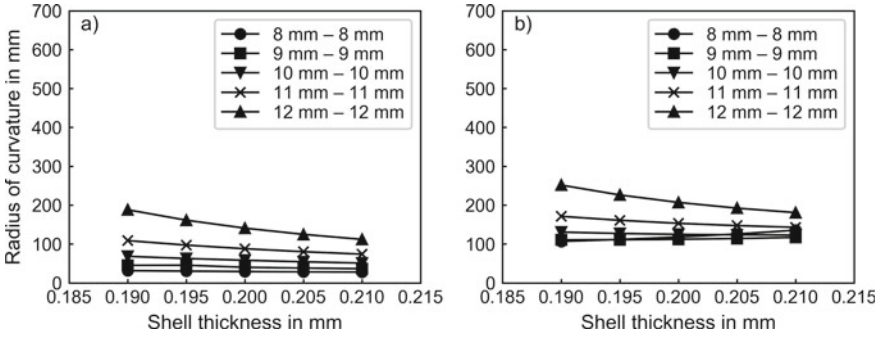


Fig. 11 Dependence of **a** first and **b** second stable state geometries on shell thickness fluctuations for steel 1.4310

5 Conclusions

The analysis of influences of production parameters as well as fluctuation of material properties on bistability of metallic shells was performed via a combined isotropic/kinematic hardening model.

The following conclusions can be made for the variation of the bending radii combination:

- Increasing of the first bending radius at a constant second bending radius leads to an increasing first stable geometry radius as well as a decreasing second stable geometry radius.
- Increasing of the second bending radius at constant first one has the opposite effect.
- Reducing the yield strength of the material increases the number of possible bending radii combinations that lead to bistability.
- Also smaller yield strength of the material allows for obtaining the bistable properties of the metallic shell by bending around higher bending radii, which reduces the number of required incremental bending operations.

  The analysis of the influence of the yield strength fluctuations provides the following conclusions:
- Increasing of the yield stress of the shell while keeping other parameters constant (Young's modulus, shell thickness, bending radii combination) leads to an increase of the radii of both stable geometries for steel 1.1274.
- Nevertheless, the influence of the yield strength fluctuation on the second stable geometry is not so pronounced for steel 1.4310. For small bending radii (8 mm – 8 mm and 9 mm – 9 mm) the second stable geometry decreases with increase of yield strength. For higher bending radii combinations the radius of second stable geometry increases with an increase of the yield strength.
- Nonetheless, the influence of yield strength fluctuation is significantly higher with increase of the bending radii value. The larger the bending radius, the greater the deviation of the stable geometry.

  From the investigation of the shell thickness fluctuations the following conclusions are made:
- The increase of the shell thickness while keeping constant other parameters (Young's modulus, yield strength, bending radii combination) leads to a decrease of the radii of the first and second stable geometry for steel 1.1274.
- Nevertheless, for steel 1.4310 the effect of thickness fluctuations on the radius of second stable geometry is not so straightforward. For the small bending radii (8 mm – 8 mm and 9 mm – 9 mm) the second stable geometry increases with higher thickness. For higher bending radii combinations, the second stable geometry radius starts to decrease with increase of the shell thickness.
- The fluctuation of the shell thickness has much more noticeable effect on the stable state geometries at higher bending radii combinations.

Overall, the new model allows the estimation and calculation of the influence of different sheel and material properties. This allows even tighter requirements to be placed on the semi-finished product used and deviations between experiments (as shown in [3, 4]) and the simulations can be better isolated. This enables the reliable production of bistable shells.

Acknowledgments The authors thank the Deutsche Forschungsgemeinschaft (DFG, German Research Foundation) for funding within the priority program SPP 2013 “The utilization of residual stresses induced by metal forming” (project HI 790/57-1, № 374688658). Moreover, the authors like to thank Mrs. Shaoni Li for her support.

References

1. Pellegrino S (2001) Deployable structures. Springer, Wien, Austria
2. Kebadze, E, Guest, S, Pellegrino, S (2004) Bistable prestressed shell structures. Int J Solids Struct https://doi.org/10.1016/j.ijsolstr.2004.01.028
3. Pavliuchenko, P, Teller, M, Grüber, M, Bremen, T, Hirt, G (2019) Production of bistable fully closed metallic shells by introducing residual stresses during bending processes. Prod Eng Res Devel https://doi.org/10.1007/s11740-019-00875-6
4. Galletly D, Guest S (2004) Bistable composite slit tubes. I A beam model Int J Solids Struct https://doi.org/10.1016/j.ijsolstr.2004.02.036
5. Galletly D, Guest S (2004) Bistable composite slit tubes. II. A shell model Int J Solids Struct https://doi.org/10.1016/j.ijsolstr.2004.02.037
6. He X (2011) Bi-stable character of laminated cylindrical shells. Proc Eng https://doi.org/10.1016/j.proeng.2011.07.077
7. Pavliuchenko P, Teller M, Grüber M, Hirt G (2019) A semianalytical model for the determination of bistability and curvature of metallic cylindrical shells. J Manuf Mater Process https://doi.org/10.3390/jmmp3010022
8. Crisfield M (1997) Non-linear finite element analysis of solids and structures, Volume 2: Advanced Topics; Wiley: Hoboken, NJ, USA
9. Patel S, Lal R, Dwivedi J, Singh V (2013) Springback analysis in shell metal forming using modified Ludwik stress-strain relation. ISRN Mech Eng 2013:1–11

Influence of Shear Cutting Process Parameters on the Residual Stress State and the Fatigue Strength of Gears



Daniel Müller, Jens Stahl, Isabella Pätzold, Roland Golle, Thomas Tobie, Wolfram Volk, and Karsten Stahl

Abstract Shear cutting is used for manufacturing various parts ranging from, e.g. simple washers to complex gears. The latter are typically subjected to cyclic loading and fail foremost due to fatigue damages. Hereby, the part's lifetime is mainly determined by the geometry, the applied load, the material, the hardness, the roughness, and the residual stress state. While numerous research works deal with the influence of the process parameters on the hardness and the part's geometry, the influence of the process parameters on the residual stress state and on the resulting fatigue strength has not been investigated in detail, yet. In an earlier publication, suitable shear cutting techniques, which allow achieving a high amount of clean cut and a favorable residual stress state were compared. In this paper, the influence of the process parameters on the residual stress state and the resulting bending fatigue strength are addressed. To simulate the bending stress occurring in the tooth root, C-shaped specimens were manufactured by different blanking techniques. The die clearance and punch and die edge radii were varied with these blanking techniques. After measuring the cut-surface geometry, the hardness distribution, and the surface roughness, the fatigue strength was determined in a pulsating test rig. By carrying out residual stress measurements using X-ray diffraction and simulating the material flow behavior using the Finite-Element Method, basic mechanisms, which are influencing the residual stress state and the resulting bending fatigue strength, were identified and will be presented and discussed in the paper.

Keywords Shear cutting · Fineblanking · Near-net-shape blanking · Residual stresses · Fatigue · Gears

D. Müller · T. Tobie · K. Stahl
Institute of Machine Elements (FZG), Department of Mechanical Engineering, Technical University of Munich, Munich, Germany
e-mail: mueller@fzg.mw.tum.de

J. Stahl (✉) · I. Pätzold · R. Golle · W. Volk
Department of Mechanical Engineering, Technical University of Munich, Munich, Germany
e-mail: jens.stahl@utg.de

© The Minerals, Metals & Materials Society 2021

G. Daehn et al. (eds.), *Forming the Future*, The Minerals, Metals & Materials Series,
https://doi.org/10.1007/978-3-030-75381-8_195

1 Introduction

Shear cutting is one of the most important manufacturing techniques in sheet metal processing [5]. Due to this high industrial relevance, shear cutting is also an active topic in the research community. Especially, the geometry of the shear cut edge has been of interest [12]. According to [16], the die clearance, the clearance between punch and die, is an important process parameter affecting the cut-surface geometry. It is often given as the relative die clearance u_r which can be calculated by dividing the size of the clearance by the sheet metal thickness [2]. As shown by [16], a smaller die clearance leads to a higher amount of clean cut. The preparation of the punch and die edge significantly affects the cut-surface geometry. An increased burr height and a decreased clean-cut height were observed for simultaneously increased punch and die edge radii in [15]. According to [6], either the punch or the die edge should be rounded when a high amount of clean cut is desired.

In many applications where the manufactured part is subjected to cyclic loading, the fatigue strength of the shear-cut edge is of importance. The investigations by Meuerling et al. showed that edges manufactured by shear cutting with a die clearance of 6 % show a lower fatigue strength than laser-cut edges [10]. Lara et al. found that specimens manufactured with a die clearance of 6 % and sharp cutting edges show a higher fatigue strength than specimens manufactured with a bigger die clearance of 10 % with rounded cutting edges [7]. Maronne et al. found that a too big die clearance significantly reduces the fatigue strength of the shear cut edge [9]. Here, a die clearance range from 5 to 30 % was examined. A similar tendency for small die clearances can be found in [6]. Again, a smaller die clearance increased the fatigue strength of the parts manufactured of thick sheets (thickness 14mm). A beneficial effect of a v-ring was found in this publication as well.

Factors that are known to affect the fatigue strength are, among others, the material and its microstructure, the hardness [11], the part's geometry [1], the roughness [8], and the residual stresses [17]. Thus, the fatigue strength can be increased by a higher hardness, a lower roughness, and compressive residual stresses. Compressive residual stresses are utilized to improve the fatigue strength in many applications, for example, in shot-peened gears [4]. Still, the targeted use of residual stresses is scarce in shear cutting, although it has been published for additional process steps like coining [18].

With Near-Net-Shape Blanking processes (NNSBPs), a high amount of clean cut and thus a large load-bearing surface can be achieved. With these different blanking processes, different residual stresses can be induced, which was addressed in [14]. It was discovered that the sheet metal strip is commonly subjected to a compressive stress state while the blank shows a tensile stress state for most NNSBPs. This work was extended by the effect of the residual stresses on the fatigue behavior of parts manufactured by NNSBPs in [13]. Besides the beneficial effect of compressive residual stresses, the part bending during the cutting process was identified as a major influence parameter on the bending fatigue strength. While the influence of the chosen NNSBP on the residual stress state and the fatigue behavior has been discussed in these earlier works, this research focuses on the influence of the process

parameters such as punch and die edge radius as well as die clearance on the residual stress state and the resulting fatigue behavior.

The aim of this research is to increase the fatigue strength of shear cut edges by using the effect of the residual stresses induced by NNSBPs. The correlation of the part's residual stress state and the chosen NNSBP with its process parameters is investigated and discussed.

2 Experimental Setup and Test Equipment

2.1 Shear Cutting Setup

Five different Near-Net-Shape Blanking Processes are investigated: Fineblanking (FB), blanking with small die clearance and v-ring (BV), precision blanking without blank holder (PBwBH), precision blanking with blank holder (PB), and blanking with small die clearance (B). They are illustrated in Fig. 1. When changing from one NNSBP to another, only one active element is changed which allows drawing conclusions on the effect of this active element on the residual stress state of the manufactured part.

For FB and B, three different relative die clearances u_r were investigated. A die clearance of 0.5 % (30 µm) was used for all NNSBPs, as it allows to produce cut surfaces without a fracture zone. Thus, the effect of the process-induced residual stresses can be investigated without major geometry changes of the shear cut edge. Clearances smaller than 30 µm are challenging to manufacture, especially for complex industry-relevant cutting line geometries, and are therefore not investigated. To examine the influence of the formation of a fracture zone, two additional bigger die clearances of 1 % (60 µm), and 3 % (180 µm) were chosen. Two different cutting edge strategies were chosen: One with a punch edge radius of $r_S = 200\,\mu m$ and a sharp die edge $r_M < 20\,\mu m$ and one with a sharp punch edge $r_S < 20\,\mu m$ and a rounded die edge $r_M = 200\,\mu m$. The cutting edge radii were measured with a tactile surface measurement device (see Sect. 2.3) on at least four positions of each punch and die. The results are listed in Table 1.

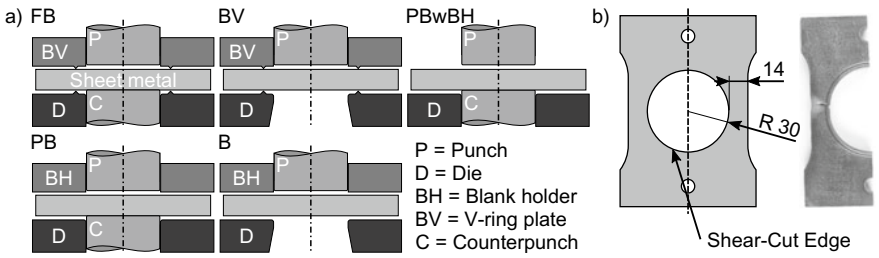


Fig. 1 Schematic of the five investigated NNSBPs (**a**) and the specimen geometry (**b**)

Table 1 Measured punch and die edge radii

Nominal radius	Punch u_r =0.5 %	u_r =1 %	u_r =3 %	Die with v-ring	Without v-ring
200 µm	196 ± 2	200 ± 2	199 ± 4	201 ± 4	204 ± 3
< 20 µm	9 ± 3	12 ± 2	9 ± 1	11 ± 5	11 ± 2

The punch velocity was set to 50 mm s^{-1}, as this is a velocity typically used in industrial fineblanking and as it allows to compare the results to previous publications. A detailed description of the used tool can be found in [14]. The experiments were carried out on a Feintool HFA 3200 plus fineblanking press with a nominal press force of 3200 kN. Here, the v-ring force of 450 kN was set for the NNSBPs involving a v-ring, otherwise a blank holder force of 200 kN was chosen. The counter punch force was set to 200 kN.

2.2 Materials and Specimen Geometry

The fine-grain, hot rolled, microalloyed structural steel S355MC with a thickness of 6 mm was chosen as it is a typical steel used in fineblanking. Its chemical composition, measured with an optical emission spectrometer, is listed in Table 2.

Microsections of the investigated steel after the heat treatment are displayed in Fig. 2. Measured mechanical properties can be found in [14]. A flow curve for specimen taking out of the sheet in 0° and 90° to the rolling direction can be found together with the used extrapolation in Fig. 3a. After milling the contour illustrated

Table 2 Measured chemical composition of the sheet metal material S355MC in percentage by mass.

Alloying element	C	Mn	Si	P	S	Al_{Ges}	Nb	V	Ti
wt%	0.06	0.503	< 0.01	0.014	0.007	0.019	0.023	< 0.002	< 0.001

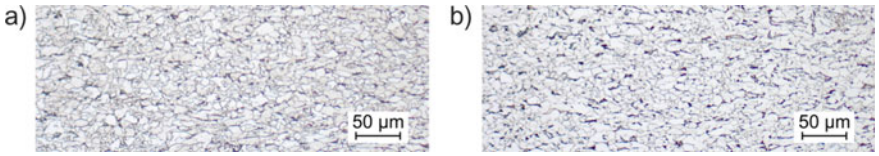


Fig. 2 Microsections of the investigated structural steel S355MC after the stress relief heat treatment taken out in (**a**) and perpendicular to the rolling direction (**b**). (Color figure online)

in Fig. 3c), the specimens were subjected to a stress relief heat treatment. This heat treatment was performed by heating up the specimens with 150 °C h^{-1}, holding the temperature at 540 °C for 15 min according to [3], followed by cooling with less than 50 °C h^{-1}. Afterwards, a hole with a diameter of 60 mm was cut by the different NNSBPs, followed by abrasive cutting to get the final geometry used for fatigue testing as shown in Fig. 1.

2.3 Measurement Techniques

Factors that are known to affect the fatigue strength are the geometry and roughness of the manufactured edge [1, 8]. Additionally, the part bending was identified as a major factor influencing the fatigue behavior in [13]. Accordingly, these part properties were measured. Finally, the fatigue testing setup is explained.

The cut surface characteristics were measured with a tactile surface measurement device with a resolution of 0.5 µm for the used arm length. The part bending was measured optically on the burr side of the part and is given as the deviation from a mean plane. Further information on the measurement methods and devices can be found in [13, 14].

The roughness of the clean cut and the fracture zone was measured using a laser scanning microscope VHK-150 manufactured by Keyence Corporation, Osaka (Japan). The part bending measurement procedure is explained in [13]. The HV 0.2 hardness distribution was examined using a LECO AMH-43 microhardness testing device. The Residual stresses were measured by X-ray diffraction with a Seifert XRD 3003 PTS System and evaluated with the $sin^2\psi$-method. A 1 mm collimator was used and is positioned in the middle of the sheet thickness with a 10 mm distance between collimator and specimen surface. For parts that show a significant fracture zone, three positions were evaluated: in the middle of the sheet thickness and additionally in the middle of the clean cut and in the middle of the fracture zone. Further information on the setup and method can be found in [14].

For the fatigue testing, a servo-hydraulic pulsating test rig was used with a special specimen holder. The C-profiles were loaded with tensile swelling loads at a test frequency of 50 Hz. The fatigue strength was determined on two different load stages, 19 kN and 16 kN, in the limited lifetime range. The lower load limit of the pulsating load is always zero (R = 0).

2.4 Finite-Element Model

A finite-element (FE) model of the NNSBPs was built in Simulia Abaqus 2018 as illustrated in Fig. 3b. This explicit, rotationally symmetric model uses CAX4R elements for all the deformable bodies (punch, die, sheet metal) while the counter punch and the blank holder were modeled as rigid bodies. The mesh in the shearing

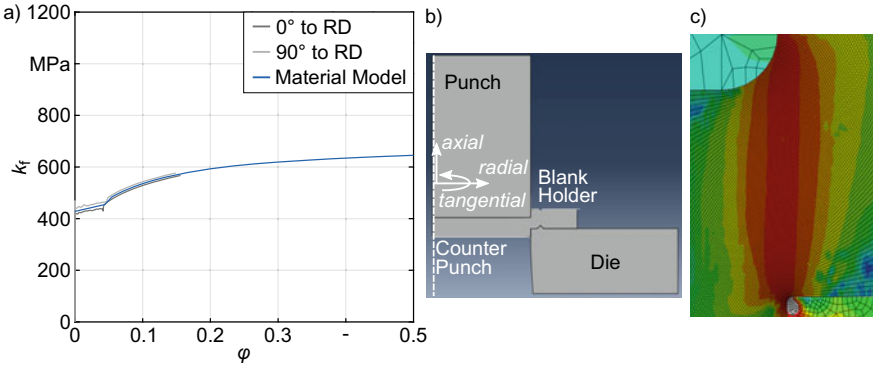


Fig. 3 Stress strain curves of the material together with the flow curve extrapolation (**a**), the simulation setup of the fineblanking process (**b**), and the mesh in the shearing zone shortly before fracture (**c**). (Color figure online)

zone shows elements with a width of 5 µm and a height of 55 µm. This high initial aspect ratio leads to almost quadratic elements shortly before fracture, as illustrated in Fig. 3. Together with the use of ALE, this helps to cope with the severe mesh distortion during the shear cutting process. Mass scaling is used to reduce the long calculation time.

3 Results and Discussion

3.1 Cut-Surface Characteristics and Part Bending

The clean-cut height and the fracture zone height are given in percent of the sheet metal thickness in Table 3. For $u_r = 0.5\,\%$ and $1\,\%$, the configuration with the sharp punch leads to a slightly higher amount of clean cut, except for FB where similar values were measured. For $u_r = 3\,\%$ this tendency changes and a much lower clean-cut height is observed for this configuration. While the specimens show no fracture zone for the small die clearance, a small amount of fracture can be observed for $u_r = 1\,\%$, and a significant amount of fracture of up to 42.3 % of the sheet thickness is observed for $u_r = 3\,\%$.

The roughness of the clean cut ranges from $Ra = 0.61\,\mu m$ to $2.1\,\mu m$. The fracture zone shows a significantly higher roughness ranging from $Ra = 6.3\,\mu m$ to $8.7\,\mu m$. As stated in [13], no correlation between roughness and the used NNSBPs with its process parameters was found.

An overview of the influence of the chosen NNSBP on the microhardness distribution was given in [13]. Thus, the influence of the die clearance and the active element edge radii on the microhardness distribution is investigated on the example

Table 3 Clean-cut height and fracture zone height (in brackets) in percent of the sheet metal thickness together with the values published in [14]

NNSBP	FB	FB	FB	BV	PBwBH	PB	B	B	B
u_r	3 %	1 %	0.5 %	0.5 %	0.5 %	0.5 %	0.5 %	1 %	3 %
$r_S =$ 200 µm; $r_M <$ 20 µm	81.3 (14.8)	93.7 (3.2)	97.6	97.0	90.3	93.2	93.7	87.7 (5.7)	63.8 (29.2)
$r_S <$ 20 µm; $r_M =$ 200 µm	67.7 (29.5)	95.2 (2.3)	97.5	97.9	91.6	94.6	94.2	90.9 (3.7)	51.9 (42.3)

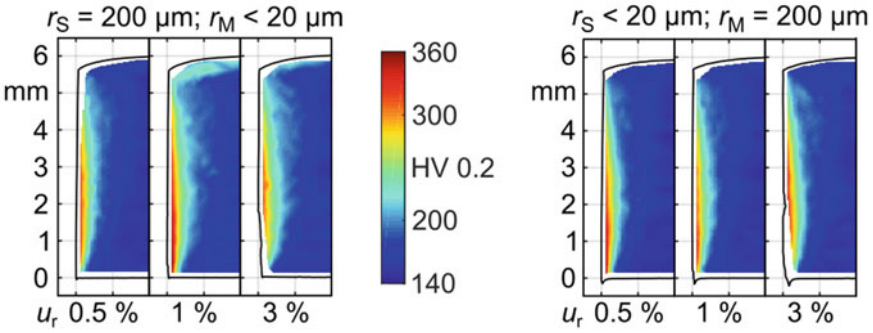


Fig. 4 Microhardness distribution of the specimens manufactured by B together with the result published in [14]. (Color figure online)

of blanking in the following. These results are displayed in Fig. 4. For all variants, a significant hardness increase toward the clean cut can be observed. This is interrupted by the fracture zone for the variants manufactured with $u_r = 3\,\%$.

The part bending is displayed in Fig. 6b. It can be observed that the parts manufactured by PBwBH show the biggest bending, followed by those manufactured by PB and B. A higher deviation is visible for the parts manufactured with $r_S = 200\,\mu m$, especially for PBwBH although this tendency can be observed for PB and B as well. For B, a bigger die clearance leads to a smaller bending. For the processes with a v-ring, i.e. FB and BV, is it so small that a comparison is not possible.

3.2 Residual Stresses

The axial and tangential residual stresses were measured at the shear cut surface of the specimen geometry respective to the coordinate system shown in Fig. 3b. The measured residual stresses for the five NNSBPs, the two different active element edge

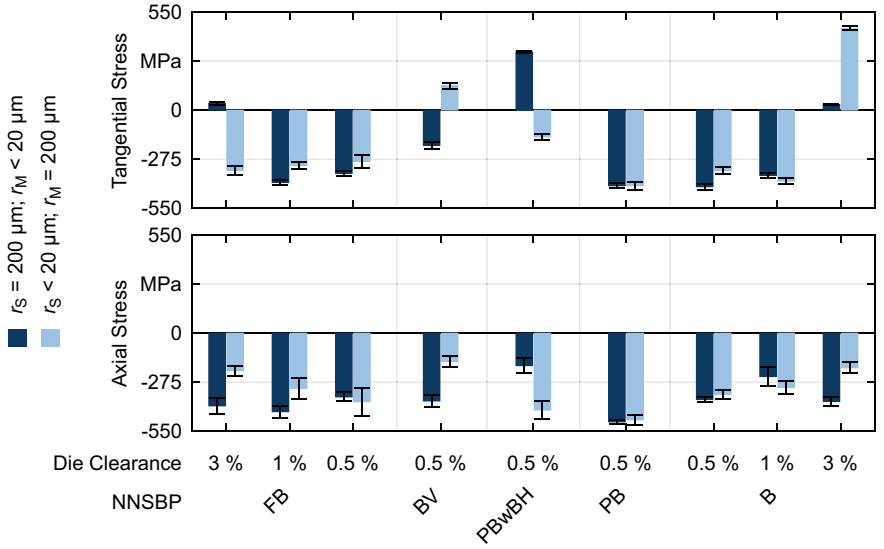


Fig. 5 Residual stresses in tangential and axial directions measured in the middle of the sheet thickness for the five NNSBPs with different die clearances and active element edge radii together with the results published in [14]. (Color figure online)

preparations, and the three die clearances are displayed in Fig. 5. For $u_r = 0.5\,\%$ and $1\,\%$, the parts manufactured by FB, PB, and B show compressive residual stresses in a tangential direction independent of the used active element edge preparation. Only BV and PBwBH show tensile stresses at $u_r = 0.5\,\%$, in the case of BV for the configuration with the sharp punch edge and for PBwBH for the configuration with the rounded punch edge. For the small die clearance of $0.5\,\%$, the configuration with the rounded punch leads to higher compressive residual stresses in the tangential direction compared to the configuration with the sharp punch edge for all the parts except those manufactured by PBwBH. For FB, $u_r = 1\,\%$ leads to higher compressive stresses for both edge preparations. For a die clearance of $3\,\%$, only the configuration with the sharp punch edge leads the even higher compressive residual stresses while the rounded punch edge leads to tensile stresses. When changing u_r from $0.5\,\%$ to $1\,\%$ for B, only the sharp punch edge leads to increased compressive residual stresses. For $u_r = 3\,\%$, the parts manufactured by B show tensile stresses in the tangential direction which are not as high for the configuration with the rounded punch.

All the produced parts show compressive residual stresses in the axial direction. These are higher for the configuration with the rounded punch edge, except for those manufactured by FB and PB with $u_r = 0.5\,\%$ where similar values were measured and for those manufactured by PBwBH and B with $u_r = 1\,\%$. For FB and the configuration with the rounded punch edge, a bigger die clearance leads to increased compressive stresses compared to the configuration with $u_r = 0.5\,\%$ while an opposing trend is observed for the configuration with the sharp punch edge. For B with a sharp punch

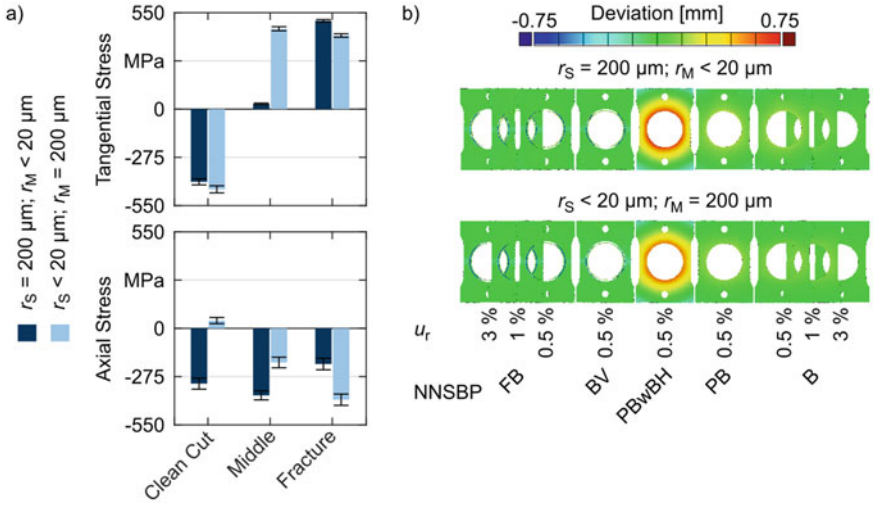


Fig. 6 Residual stresses in tangential and axial directions measured on three positions of specimen manufactured by Blanking (B) with a die clearance of 3 % with two different active element edge radii (**a**), and the surface deviation of the produced sheet metal strips together with the result published in [13] (**b**). (Color figure online)

edge, the same tendency can be observed while the configuration with the rounded punch edge shows no clear trend.

To address the influence of a fracture zone on the residual stress state, additional measurements were carried out on the strips produced by B with a die clearance of 3 % for both active element edge preparations. The first measurement position is in the middle of the clean cut, the second in the middle of the sheet thickness, and the third in the fracture zone. The results are displayed in Fig. 6a. It is visible that the fracture zone is subjected to significant tensile residual stresses. As the fracture zone reaches till the middle of the sheet thickness for the variant with the sharp punch, high tensile stresses are measured there as well.

3.3 Finite-Element Analysis

A comparison of the stresses in the tangential direction after the cutting operation but before springback calculated with the FE model is illustrated for FB in Fig. 7. It can be observed that the variant with the rounded punch edge leads to higher stresses in the sheet metal strip.

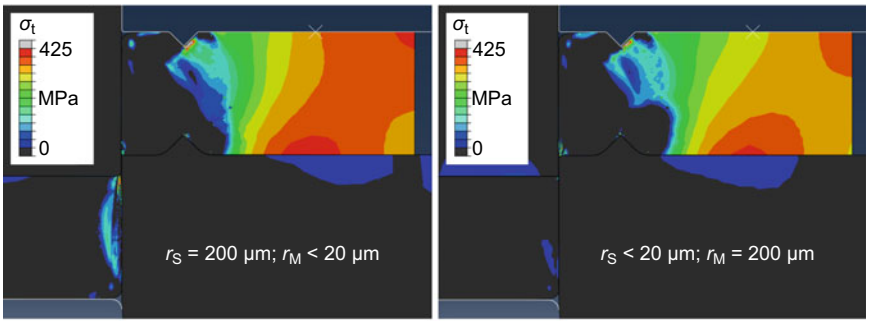


Fig. 7 Tangential stress after the fineblanking operation (but before springback) with a die clearance of 0.5 % for $r_S = 200\,\mu m$ and $r_M < 20\,\mu m$ on the left, and $r_S < 20\,\mu m$ and $r_M = 200\,\mu m$ on the right. (Color figure online)

3.4 Fatigue Behavior

The fatigue behavior of the parts is illustrated in Fig. 8. The fatigue tests are described in [13]. In Fig. 8a, a decreased number of cycles to failure is observed for all the parts manufactured with $r_S < 20\,\mu m$ compared to those manufactured with $r_S = 200\,\mu m$. Only those manufactured by PBwBH stand out. The results for the bigger die clearance of 1 %, illustrated in Fig. 8b, also show this tendency. Figure 8c shows the influence of the die clearance on the fatigue strength. Here, a bigger die clearance causes a lower number of cycles to failure. To further identify the effect of the residual stress, state parts manufactured by BV and FB were subjected to a stress relief heat treatment after the blanking operation. A comparison of those with specimens manufactured by BV without this additional stress relief heat treatment is given in Fig. 8d). This heat treatment causes a significantly lower number of cycles to failure for the high test load for the specimens manufactured by BV. It can be observed that the specimens manufactured by BV+SR and FB+SR show an almost identical fatigue strength.

3.5 Discussion of Parameters Influencing the Residual Stress State and Effect on the Fatigue Strength

3.5.1 Influence of Punch and Die Edge Radius

A rounded punch leads to material flow toward sheet metal strip which leads to higher stresses in the strip in the tangential direction, as shown by the FE model. After springback, these result in higher compressive residual stresses. This is not strictly true for variants with a fracture zone as the earlier fracture changes the material flow behavior. Also, this effect cannot be observed for PBwBH. Due to the

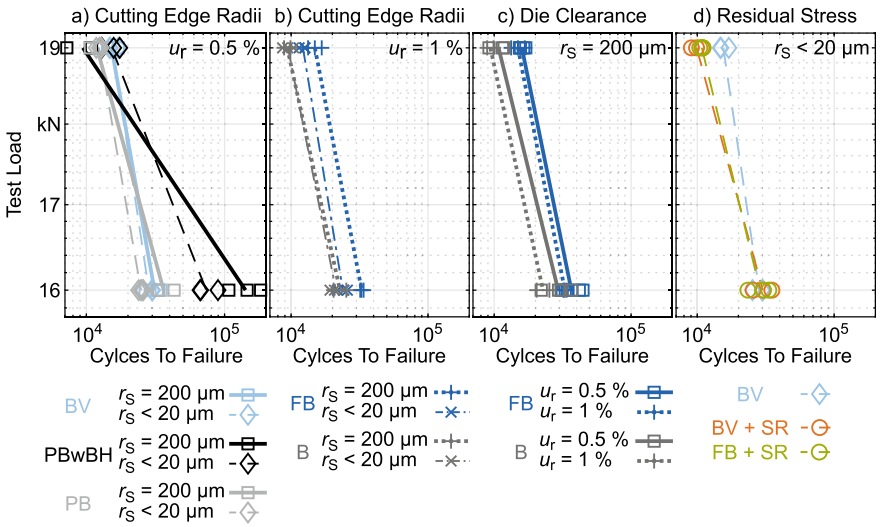


Fig. 8 Influence of the two different active element edge radii combinations ($r_S = 200\,\mu m$; $r_M < 20\,\mu m$ and $r_S < 20\,\mu m$; $r_M = 200\,\mu m$) on the fatigue strength for $u_r = 0.5\,\%$ (**a**), and $u_r = 1\,\%$ (**b**). Influence of the die clearance on the fatigue strength (**c**), and influence of a subsequent stress relief heat treatment (SR) together with the data published in [13]. (Color figure online)

heavy bending of the part, the tangential stress is overlayed by an additional stress from the bending springback. As the bending springback is opposed to the parts' initial bending direction, this leads to tensile stresses on the die-roll side of the sheet metal strip and to compressive stresses on the burr side. As the bending of the part manufactured with a sharp punch is lower compared to the part manufactured with the rounded punch, this effect is most likely responsible for the tensile tangential residual stresses of the PBwBH configuration with the rounded punch.

Axial compressive residual stresses are measured for all the configurations in the middle of the sheet independent of the process parameters. As the material is drawn in the axial direction, which is necessary for the formation of a die roll, axial tensile stresses occur during blanking. After springback, these lead to compressive residual stresses. For $u_r = 0.5\,\%$, the axial stresses are not very sensitive regarding the active element edge preparation for FB, PB, and B. Only BV and PBwBH show different values for different edge preparations. For PBwBH, this is most likely caused by the early fracture of the blank (see [14]) which reduces axial stresses and causes smaller residual stresses after springback. The same behavior may be responsible for the differences between the parts manufactured with a rounded punch and a sharp punch for the die clearances bigger than 0.5 %.

For $u_r = 0.5\,\%$, the fatigue behavior shows the expected result: As the parts manufactured with a sharp die edge show smaller compressive residual stresses, these show a lower number of cycles to failure. The effect is also visible for the specimens subjected to a stress relief heat treatment after the blanking operation even though

the overall stress state (mean from tangential and axial stresses) is comparably low. Again, the parts manufactured by PBwBH stand out. Their behavior confirms the theory on the influence of the part bending on the fatigue behavior given in [13], which is the dominant mechanism in this case.

For u_r =1 % and 3 %, the effect of residual stresses is overlayed by the additional notch caused by the fracture zone. It should be noted that for FB with u_r = 1 % the configuration with the round punch edge still shows a higher number of cycles to failure than the one manufactured with a sharp punch edge although the fracture zone is bigger. This is caused by the significant higher residual stresses in both directions for the rounded punch edge.

3.5.2 Influence of the Die Clearance

For FB, when u_r is changed from 0.5 % to 1 %, higher compressive residual stresses are observed in tangential direction for both active element edge preparations. For B, this effect can only be observed for the configuration with the sharp punch edge while an opposing trend is observed for the rounded variant. Again, the stresses caused by the radial springback are overlayed by those caused by the bending springback. As the bending is small for the parts manufactured by FB, the radial springback mode dominates in this case. For B, the parts show a visible bending accompanied by differences in bending regarding the die clearance and the active element edge preparation. This bending seems to be responsible for this behavior of the residual stress state. Due to the occurrence of a significant amount of fracture zone, the results for a die clearance of 3 % are challenging to interpret. Still, the results from FB with u_r = 3 % show that the fracture zone is subjected to significant tensile residual stresses in the tangential direction.

Even for the bigger die clearances, the axial residual stresses are negative in the middle of the sheet. For the variant with the sharp punch edge, the residual stresses get smaller when a bigger die clearance is chosen. However, the variant with the round punch edge does not strictly show that behavior. This is most likely caused by a different material flow behavior caused by the combination die clearance and active element edge condition in the middle of the sheet. Again, the results for u_r = 3 % are challenging to interpret due to the big fracture zone.

The comparison between the parts manufactured with a u_r = 0.5 % and 1 % show the effect of the residual stresses on the fatigue strength: While the difference is small for FB, the negative effect of the fracture zone can be partly compensated by the higher compressive stresses, the parts manufactured by B show a significantly lower number of cycles to failure for u_r = 1 % as a fracture zone, and a smaller compressive stress state reduces the fatigue strength.

4 Conclusion

A rounded punch edge in combination with a sharp die edge leads to higher compressive residual stresses in the tangential direction compared to parts manufactured with a sharp punch edge and a rounded die edge. Due to the rounded punch, material flow is more likely toward the sheet metal strip, which leads to higher elastic stresses that cause higher residual stresses after springback. This is only valid for configurations without a fracture zone, i.e. for the small die clearance of 0.5 %, and without a significant part bending, i.e. all the processes except PBwBH. The influence of the active element edge radii on the residual stress state is small compared to the influence of the chosen NNSBP.

A fracture zone should be avoided as the rough fracture does not only lead to stress concentrations but also shows significant tensile residual stresses. These effects significantly reduce the parts' fatigue strength. Therefore, a die clearance of 0.5 % should be chosen instead of a die clearance of 1 % or 3 %.

The results lead to the conclusion that the residual stress state of the manufactured parts can be explained by a bending springback, a radial springback, and an axial springback. Furthermore, the residual stresses can be adjusted by the process parameters and may be used for an improved fatigue behavior. As the fatigue strength is caused by a combination of the material properties, the surface geometry and the residual stress state, all of these factors should be considered to achieve a long part life under cyclic loading.

Acknowledgments This work is funded by the Deutsche Forschungsgemeinschaft (DFG, German Research Foundation)—VO 1487/30-1; VO 1487/30-2; STA 1198/13-1; STA 1198/13-2, and is part of the DFG-priority program https://www.utg.mw.tum.de/spp-2013/

References

1. Alam M, Barsoum Z, Jonsn P, Kaplan A, Hggblad H (2010) The influence of surface geometry and topography on the fatigue cracking behaviour of laser hybrid welded eccentric fillet joints. Appl Surf Sci 256(6):1936–1945
2. Boljanovic V (2004) Sheet Metal Forming Processes and Die Design. Industrial Press
3. Flachstahl S (2011) S355MC - high-strength steels for cold-forming, thermomechanically-rolled
4. Güntner C, Tobie T, Stahl K (2017) AGMA 2017 Fall Technical Meeting, chap. Influences of the residual stress condition on the load carrying capacity of case hardened gears. Columbus, Ohio, USA, pp 328–344
5. Hinduja S (2004) Proceedings of the 34th International MATADOR Conference: Formerly The International Machine Tool Design and Research Conferences. Proceedings of the International Matador Conference. Springer
6. Klocke, F (2013) Sheet Metal Separation. Springer Berlin Heidelberg, Berlin, Heidelberg, pp 407–456
7. Lara A, Picas I, Casellas, D (2013) Effect of the cutting process on the fatigue behaviour of press hardened and high strength dual phase steels. J Mater Process Technol 213(11):1908–1919

8. Maiya P, Busch D (1975) Effect of surface roughness on low-cycle fatigue behavior of type 304 stainless steel. Metall Trans A 6(9):1761
9. Maronne E, Galtier A, Robert JL, Ishikawa T (2003) Cutting process influence on fatigue steel sheets properties. WIT Trans on Eng Sci. 40
10. Meurling F, Melander A, Linder J, Larsson M (2001) The influence of mechanical and laser cutting on the fatigue strengths of carbon and stainless sheet steels. Scand J Metall. 30:309–319
11. Pang J, Li S, Wang Z, Zhang Z (2014) Relations between fatigue strength and other mechanical properties of metallic materials. Fatigue Fract Eng Mater Struct. 37(9):958–976
12. Senn S, Liewald M (2019) Investigation of a new sheet metal shear cutting tool design to increase the part quality by superposed compression stress. IOP Conf Ser: Mat Sci Eng. 651
13. Stahl J, Müller D, Pätzold I, Golle R, Tobie T, Volk W, Stahl K (2019) The influence of residual stresses induced by near-net-shape blanking processes on the fatigue behavior under bending loads. IDDRG Conference Proceedings
14. Stahl J, Müller D, Tobie T, Golle R, Volk W, Stahl K (2018) Production Engineering, chap. Residual stresses in parts manufactured by near-net-shape-blanking. Springer. https://doi.org/10.1007/s11740-018-0865-5
15. Taupin E, Breitling J, tsu Wu W, Altan T (1996) Material fracture and burr formation in blanking results of fem simulations and comparison with experiments. Selected Papers on Metal Forming and Machining. J Mater Process Technol. 59(1):68–78
16. Tekiner Z, Nalbant M, Grn H (2006) An experimental study for the effect of different clearances on burr, smooth-sheared and blanking force on aluminium sheet metal. Mater Des. 27(10):1134–1138
17. Townsend DP, Zaretsky EV (1988) Effect of shot peening on surface fatigue life of carburized and hardened aisi 9310 spur gears. Tech. rep, SAE Technical Paper
18. Yasutomi T, Yonemura S, Yoshida T, Mizumura M, Hiwatashi S (2017) Blanking Method with Aid of Scrap to Reduce Tensile Residual Stress on Sheared Edge, vol 896. IOP Publishing

Residual Stresses in Hot Bulk Formed Parts—A Phenomenological Approach for the Austenite-to-Martensite Phase Transformation



S. Uebing, D. Brands, L. Scheunemann, C. Kock, H. Wester, B.-A. Behrens, and J. Schröder

Abstract In production engineering, current research focuses on the induction of targeted residual stress states in components in order to improve their properties rather than follow the usual path of minimizing residual stresses to prevent failure. In this contribution, a focus is laid on the investigation of the subsequent cooling process of hot bulk formed parts. Such cooling of a component leads to a microscopic phase transformation, which has to be considered in order to compute residual stresses inside the material. A numerical approach based on a phenomenological macroscopic material model is presented to depict the related stress evolution.

Keywords Residual stresses · FE-Simulation · Constitutive modeling · Austenite-to-martensite phase transformation

S. Uebing (✉) · D. Brands · L. Scheunemann · J. Schröder
Institute of Mechanics, Faculty of Engineering, University of Duisburg-Essen, Universitätsstraße. 15, 45141 Essen, Germany
e-mail: sonja.uebing@uni-due.de

D. Brands
e-mail: dominik.brands@uni-due.de

L. Scheunemann
e-mail: lisa.scheunemann@uni-due.de

J. Schröder
e-mail: j.schroeder@uni-due.de

C. Kock · H. Wester · B.-A. Behrens
Institute of Forming Technology and Machines, Hannover Centre for Production Technology, An der Universität 2, 30823 Garbsen, Germany
e-mail: kock@ifum.uni-hannover.de

H. Wester
e-mail: wester@ifum.uni-hannover.de

B.-A. Behrens
e-mail: behrens@ifum.uni-hannover.de

© The Minerals, Metals & Materials Society 2021

G. Daehn et al. (eds.), *Forming the Future*, The Minerals, Metals & Materials Series,
https://doi.org/10.1007/978-3-030-75381-8_196

1 Introduction

The adjustment of targeted residual stress states in component production has become more and more the focus of research in recent years. After being considered unfavorable for a long time, residual stresses shall now be used to positively influence component properties such as wear resistance or strength. In general, residual stresses are defined as stresses, which exist in closed systems in the absence of outer forces or moments and fulfill mechanical equilibrium. Often a classification is made following [1–4], i.e., residual stresses are differentiated according to the scale on which they act. Residual stress of the first type, which are also called macroscopic, refer to a certain macroscopic section of the component as average over some grains. They are most important with respect to the final component properties. Residual stresses of the second and third types, respectively, which are also called microscopic, refer to residual stresses in a grain or a number of atoms. Thus, they influence residual stresses of first type.

Residual stresses can be caused by, e.g., phase transformation due to cooling. Considering austenite-to-martensite phase transformation, transformation induced plasticity (TRIP) has a decisive influence on the material response. It describes the occurrence of irreversible plastic deformation although the yield stress is not exceeded. Instead, these deformations are caused by changes in the atomic lattice, which may be associated with a change in volume, which was first observed by [5]. The classical numerical approach to model TRIP in steels is presented in [6], which has been extended to more than one product phase by [7].

Phenomenological material models are one possibility of numerical representation of TRIP, which directly describe the observed phenomena without taking into account their point of origin, e.g., effects occurring at a lower scale. The scientific works [8–14] deal with the interaction of TRIP with microstructural phase transformations considering mechanical, chemical, and/or thermal aspects. Thermomechanical models with a more differentiated view of different contributions, e.g., thermal, metallurgical, and applications to further inelastic simulations are presented in [15–17]. For instance, considerations on lower scales are shown in [18, 19]. Examples for experiments concerning TRIP are given in [20–22].

In this contribution, previous models, which concern the cooling of a cylindrical specimen with eccentric hole, see [23, 24], are extended by the TRIP effect based on the phenomenological material model in [8]. Therefore, this work is organized as follows. In Sect. 2, the underlying experimental process is explained and important parameters for the numerical simulation are derived. The numerical material model including TRIP effects is presented in Sect. 3. It is used to compute the residual stresses inside the component which are then compared to a previously published multiscale simulation done with a two-scale approach without TRIP [24]; see Sect. 4. A conclusion is given in Sect. 5.

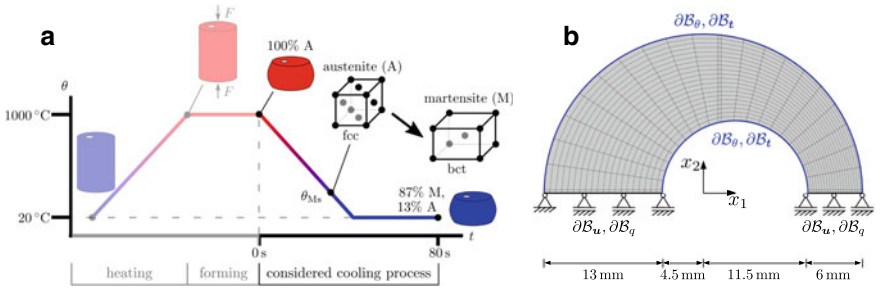


Fig. 1 **a** Schematic representation of the considered cooling process after heating and forming with austenite-to-martensite phase transformation. The considered austenite-to-martensite phase transformation goes along with a lattice shearing. **b** Geometry of 2D horizontal cross section of the cylindrical specimen with boundary definitions for finite element simulation, adopted from [23]. (Color figure online)

2 Setup of Boundary Value Problem

The cooling process of a 2D horizontal cross section taken from a cylindrical specimen with eccentric hole made from Cr-alloyed steel 100Cr6 is analyzed. Details on the experimental setup and macroscopic material simulations, which are carried out at the Institute of Forming Technology and Machines (IFUM), Leibniz University Hannover, are given in [23–26] and the process is illustrated in Fig. 1a.

The specimen is heated to above 1000 °C, then upset, and subsequently cooled in water down to room temperature. Due to the choice of material, it is purely austenitic after heating. The cooling in water results in a diffusionless phase transformation from austenite to martensite (martensitic start temperature $\theta_{\mathrm{Ms}} = 185\,^{\circ}\mathrm{C}$). At the end of the cooling process, the final volume fractions obtained from macroscopic simulations are 87% martensite and 13% austenite.

A 2D horizontal cross section of the experimentally investigated cylindrical specimen is taken into account for numerical modeling, where plane strain condition is assumed. Due to the symmetry with respect to the x_1-axis, we consider only a half of the cylindrical section; see Fig. 1b. Thus, it holds for the displacement $u_{x_2} = 0$ on $\partial\mathcal{B}_{\boldsymbol{u}}$ and for the heat flux $q_0 = 0$ on $\partial\mathcal{B}_{\boldsymbol{q}}$. Furthermore, for the traction vector $\boldsymbol{t}$, it holds $\boldsymbol{t} = \boldsymbol{0}$ on $\partial\mathcal{B}_{\boldsymbol{t}}$. On the lateral surface of the considered geometry, the temperature profile during cooling is applied as boundary condition θ on $\partial\mathcal{B}_{\theta}$. The cooling route is taken from the macroscopic simulations and is illustrated as a function of the process time in Fig. 2. There, the austenitic and martensitic volume fractions are plotted in dependence of the temperature, respectively. The actual volume fraction of martensite c^{M} is computed with the temperature-dependent Koistinen-Marburger equation $c^{\mathrm{M}}(\theta) = 1 - \exp\left(-(\theta_{\mathrm{Ms}} - \theta)/\theta_{\mathrm{M0}}\right)$ with θ_{M0} as temperature-independent material parameter; see [27–29].

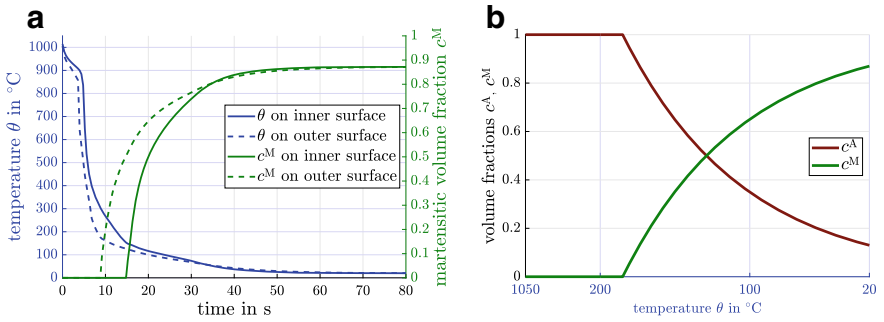


Fig. 2 **a** Temperature θ of outer and inner lateral surfaces of the cylinder over cooling time t, adopted from [24] and **b** related increase of martensitic volume fraction c^{M} and decrease of austenitc volume fraction c^{A} in consequence of the cooling, adopted from [23]. (Color figure online)

3 Phenomenological Material Modeling

In order to depict the microscopic phase transformation, in this section, a phenomenological material model is presented which bases on the work of [8]. Therein, a macroscopic model for the representation of the austenite-to-martensite phase transformation is proposed, which incorporates classical as well as transformation induced plastic effects.

3.1 Constitutive Equations

Following [8], the proposed phenomenological material model for austenite-to-martensite phase transformation bases on an additive decomposition of the total strains $\boldsymbol{\varepsilon}$ into five parts. It takes into account thermal strains $\boldsymbol{\varepsilon}^{\theta}$ and elastic strains $\boldsymbol{\varepsilon}^{\mathrm{e}}$. They are combined together with the plastic strains $\boldsymbol{\varepsilon}^{\mathrm{p}}$, transformation induced plasticity strains $\boldsymbol{\varepsilon}^{\mathrm{trip}}$, and transformation volumetric strains $\boldsymbol{\varepsilon}^{\mathrm{tv}}$, i.e., $\boldsymbol{\varepsilon} = \boldsymbol{\varepsilon}^{\mathrm{e}} + \boldsymbol{\varepsilon}^{\theta} + \boldsymbol{\varepsilon}^{\mathrm{p}} + \boldsymbol{\varepsilon}^{\mathrm{trip}} + \boldsymbol{\varepsilon}^{\mathrm{tv}}$. With material parameter K_{tv}, which describes the volumetric expansion of the atomic lattice during austenite-to-martensite phase transformation, initial and actual temperatures θ_0 and θ, respectively, and heat expansion coefficient α_{T}, the transformation volumetric strains, and thermal strains are defined as

$$\boldsymbol{\varepsilon}^{\mathrm{tv}} = \frac{1}{3} K_{\mathrm{tv}} \mathbf{1}\,, \quad \boldsymbol{\varepsilon}^{\theta} = \alpha_{\mathrm{T}}(\theta - \theta_0)\mathbf{1}\,, \tag{1}$$

respectively. Considering thermo-elasto-plasticity, the free energy function ψ is defined in dependence of the thermal-elastic strains $\boldsymbol{\varepsilon}^{\mathrm{te}} = \boldsymbol{\varepsilon}^{\mathrm{e}} + \boldsymbol{\varepsilon}^{\theta}$, the temperature θ and the strain-like internal variable e as

$$\psi(\boldsymbol{\varepsilon}^{\mathrm{te}}, \theta, e) = \frac{1}{2}\kappa\,(\mathrm{tr}\,\boldsymbol{\varepsilon}^{\mathrm{te}})^2 + \mu\|\,\mathrm{dev}\,\boldsymbol{\varepsilon}^{\mathrm{te}}\|^2 - c_\rho(\theta\ln\frac{\theta}{\theta_0} - \theta + \theta_0) - 3\alpha_{\mathrm{T}}\kappa(\theta-\theta_0)\,\mathrm{tr}\,\boldsymbol{\varepsilon}^{\mathrm{te}} + \frac{1}{2}h\,e^2 \tag{2}$$

with bulk modulus κ, shear modulus μ, and linear hardening parameter h. The abbreviation c_ρ describes the product of specific heat capacity and density. Finally, the differential equations to be solved, neglecting body forces and heat sources, are the balance of momentum $\mathrm{div}\,\boldsymbol{\sigma} = \mathbf{0}$ and the balance of energy $\rho(\dot{\psi} + \dot{\theta}\eta + \theta\dot{\eta}) - \boldsymbol{\sigma} : \dot{\boldsymbol{\varepsilon}} + \mathrm{div}\,\boldsymbol{q} = 0$. Therein, η denotes the entropy and $\boldsymbol{q}$ is the heat flux vector. Evaluating the entropy inequality $-\rho\dot{\theta} + \rho\theta\dot{\eta} + \boldsymbol{\sigma} : \dot{\boldsymbol{\varepsilon}} - \frac{1}{\theta}\,\boldsymbol{q}\cdot\mathrm{grad}\,\theta \geq 0$ yields the well-known constitutive relation for the stresses $\boldsymbol{\sigma} = \frac{\partial\psi}{\partial\boldsymbol{\varepsilon}^{\mathrm{te}}}$. With $k > 0$ as heat conduction coefficient, we assume $\boldsymbol{q} = -k\,\mathrm{grad}\,\theta$. The yield criterion following [30] is given as $\phi = \sqrt{\frac{3}{2}}\|\,\mathrm{dev}\,\boldsymbol{\sigma}\| - h\,e - Q_0(1-\exp(-\delta e)) - Y$. Therein, Q_0, δ, and Y denote a material parameter, the exponential hardening parameter, and the yield strength, respectively. The flow rules for the plastic strains and the strain-like internal variable are derived, and the flow rule for the transformation induced plasticity strains are given according to [6]

$$\dot{\boldsymbol{\varepsilon}}^{\mathrm{p}} = \sqrt{\frac{3}{2}}\,\dot{\lambda}\,\boldsymbol{n}\,, \quad \dot{e} = \dot{\lambda}\,, \quad \dot{\boldsymbol{\varepsilon}}^{\mathrm{trip}} = \frac{3}{2}K_{\mathrm{tp}}\,\mathrm{dev}\,\boldsymbol{\sigma}\,f'(c^{\mathrm{M}})\dot{c^{\mathrm{M}}} \tag{3}$$

with plastic multiplier λ, outer normal $\boldsymbol{n}$, TRIP coefficient K_{tp}, the deviatorical part of the stresses $\mathrm{dev}\,\boldsymbol{\sigma} = \boldsymbol{\sigma} - \frac{1}{3}\,\mathrm{tr}\,\boldsymbol{\sigma}\,\mathbf{1}$, and saturation function $f(c^{\mathrm{M}}) = (2-c^{\mathrm{M}})c^{\mathrm{M}}$ with $f'(c^{\mathrm{M}}) = 2(1-c^{\mathrm{M}})$.

3.2 Material Parameters and Numerical Implementation

To solve the balance laws, thermal and mechanical material parameters have to be determined. Therefore, experimental and simulative data is provided by the Institute of Forming Technologies and Machines (IFUM) at Leibniz University Hannover. A first data set gives information regarding thermal and elastic parameters, namely κ, μ, k, c_ρ, α_{T}, for each phase at certain temperatures. For the numerical simulation, a linear interpolation scheme is applied based on the actual temperature; see [23, 24]. For the plastic regime, the material parameters Y, Q_0, δ, and h are fitted to another data set. This set contains data of isothermal yield functions of each considered phase. Based on these sample points, a least-square fit using Mathematica (version 12.0), see [31], has been performed.

For the numerical simulation, the Finite Element Analysis Program (FEAP) in version 8.2, see [32], in combination with the Pardiso Solver, see [33], provided by the Intel Math Kernel Library in version 10.1.3.027 is used. The required numerical implementation of the material model bases on an integration scheme, which solves the plastic evolution equations given in Eq. (3). The quantities $\boldsymbol{\varepsilon}^{\mathrm{p}}_{n+1}$ and α_{n+1} as well as

Table 1 Material modeling at time step t_{n+1}, based on [8].

(I) Get temperature θ_n and total strains $\boldsymbol{\varepsilon}_{n+1}$

(II) Compute martensitic volume fraction

$$c^{\mathrm{M}}_{n+1}(\theta_n) = \begin{cases} 1 - \exp\left(-\frac{\theta_{\mathrm{Ms}} - \theta_n}{\theta_{\mathrm{M0}}}\right) & \text{for } \theta_n \leq \theta_{\mathrm{Ms}} \\ 0 & \text{else} \end{cases}$$

and saturation function $f_{n+1}(c^{\mathrm{M}}_{n+1}) = (2 - c^{\mathrm{M}}_{n+1})c^{\mathrm{M}}_{n+1}$ with $f'_{n+1}(c^{\mathrm{M}}_{n+1}) = 2(1 - c^{\mathrm{M}}_{n+1})$.

For all phases, here austenite and martensite, do:

(III) Get history variable e_n, $\boldsymbol{\varepsilon}^{\mathrm{p}}_n$ and $\boldsymbol{\varepsilon}^{\mathrm{trip}}_n$

(IV) Interpolate material parameters κ, μ, k, c_ρ, α_{T}, h, δ, Y, Q_0, K_{tp}, K_{tv}, see Sec. 3.2

(V) Compute $\boldsymbol{\varepsilon}^{\mathrm{tv}}_{n+1} = \frac{1}{3}K_{\mathrm{tv}}\mathbf{1}$, $\quad \boldsymbol{\varepsilon}^{\theta}_n = \alpha_{\mathrm{T}}(\theta_n - \theta_0)\mathbf{1}$

(VI) Compute elastic trial strains $\boldsymbol{\varepsilon}^{\mathrm{e,trial}}_{n+1} = \boldsymbol{\varepsilon}_{n+1} - \boldsymbol{\varepsilon}^{\theta}_n - \boldsymbol{\varepsilon}^{\mathrm{p}}_n - \boldsymbol{\varepsilon}^{\mathrm{trip}}_n - \boldsymbol{\varepsilon}^{\mathrm{tv}}_{n+1}$
and deviatorical trial stresses $\operatorname{dev}\boldsymbol{\sigma}^{\mathrm{trial}}_{n+1} = 2\mu \operatorname{dev}\boldsymbol{\varepsilon}^{\mathrm{e,trial}}_{n+1}$
and deviatorical trial tangent $\mathbb{C}^{\mathrm{iso,trial}}_{n+1} = \frac{2\mu}{\beta}\mathbb{P}$ with $\mathbb{P} = \mathbb{I} - \frac{1}{3}\mathbf{1}\otimes\mathbf{1}$
with $\beta = 1 + 3\mu\, K_{\mathrm{tp}} f'(c^{\mathrm{M}}_{n+1})\Delta c^{\mathrm{M}}_{n+1}$

(VII) Compute yield criterion $\phi^{\mathrm{trial}}_{n+1} = \sqrt{\frac{3}{2}}\,\|\operatorname{dev}\boldsymbol{\sigma}^{\mathrm{trial}}_{n+1}\| - h\, e_n - Q_0(1 - \exp(-\delta e_n)) - Y$
if $\phi^{\mathrm{trial}}_{n+1} \leq 0$ then
$e_{n+1} = e_n$, $\boldsymbol{\varepsilon}^{\mathrm{p}}_{n+1} = \boldsymbol{\varepsilon}^{\mathrm{p}}_n$, $\boldsymbol{\varepsilon}^{\mathrm{p}}_{n+1} = \boldsymbol{\varepsilon}^{\mathrm{p}}_n$
$\operatorname{dev}\boldsymbol{\sigma}_{n+1} = \operatorname{dev}\boldsymbol{\sigma}^{\mathrm{trial}}_{n+1}$, $\mathbb{C}^{\mathrm{iso}}_{n+1} = \mathbb{C}^{\mathrm{iso,trial}}_{n+1}$, go to (VIII)
else Radial Return Algorithm

(i) Solve residuum function

$$r(\Delta\lambda) = \sqrt{\tfrac{3}{2}}\,\frac{\|\operatorname{dev}\boldsymbol{\sigma}^{\mathrm{trial}}_{n+1}\| - 2\mu\sqrt{\frac{3}{2}}\Delta\lambda}{\beta} = 0$$

(ii) Update $e_{n+1} = e_n + \Delta\lambda_{n+1}$, $\boldsymbol{\varepsilon}^{\mathrm{p}}_{n+1} = \boldsymbol{\varepsilon}^{\mathrm{p}}_n + \sqrt{\frac{3}{2}}\Delta\lambda_{n+1}\boldsymbol{n}_{n+1}$

(iii) Update stresses $\operatorname{dev}\boldsymbol{\sigma}_{n+1} = \frac{1}{\beta}\left(\operatorname{dev}\boldsymbol{\sigma}^{\mathrm{trial}}_{n+1} - 2\mu\sqrt{\frac{3}{2}}\Delta\lambda_{n+1}\boldsymbol{n}_{n+1}\right)$

(iv) Compute moduli $\mathbb{C}^{\mathrm{iso}}_{n+1} = \frac{2\mu}{\beta}\mathbb{P} - \sqrt{\frac{3}{2}}\Delta\lambda\frac{(2\mu)^2}{\beta}\frac{1}{\|\operatorname{dev}\boldsymbol{\sigma}^{\mathrm{trial}}_{n+1}\|}(\mathbb{P} - \boldsymbol{n}_{n+1}\otimes\boldsymbol{n}_{n+1})$
$+\frac{3}{2}\left(\frac{2\mu}{\beta}\right)^2\frac{1}{f}\boldsymbol{n}_{n+1}\otimes\boldsymbol{n}_{n+1}$ with Jacobian $J(\Delta\lambda) = \partial r(\Delta\lambda)/\partial\Delta\lambda$

(VIII) Update TRIP strains $\boldsymbol{\varepsilon}^{\mathrm{trip}}_{n+1} = \boldsymbol{\varepsilon}^{\mathrm{trip}}_n + \frac{3}{2}K_{\mathrm{tp}}\operatorname{dev}\boldsymbol{\sigma}_{n+1}f'_{n+1}(c^{\mathrm{M}}_{n+1})\Delta c^{\mathrm{M}}_{n+1}$

(IX) Add volumetric stresses $\boldsymbol{\sigma}_{n+1} = \operatorname{dev}\boldsymbol{\sigma}_{n+1} + \kappa\,\mathrm{tr}\,\boldsymbol{\varepsilon}^{\mathrm{e}}_{n+1}\mathbf{1}$
and volumetric tangent $\mathbb{C}_{n+1} = \mathbb{C}^{\mathrm{iso}}_{n+1} + \kappa\mathbf{1}\otimes\mathbf{1}$

(X) Average stresses, tangent moduli and material parameter
$\bullet_{n+1} = (1 - c^{\mathrm{M}}_{n+1})\,\bullet^{\mathrm{A}}_{n+1} + c^{\mathrm{M}}_{n+1}\,\bullet^{\mathrm{M}}_{n+1}$ for $\bullet \in \{\boldsymbol{\sigma}, \mathbb{C}, \kappa, k, c_\rho, \alpha_{\mathrm{T}}\}$

a consistent tangent moduli $\mathbb{C}_{n+1}$ and the stresses $\boldsymbol{\sigma}_{n+1}$ are computed using a classical radial return mapping algorithm; see [30]. The individual steps are summarized in Table 1. This procedure is done for each phase, i.e., austenite and martensite, in each finite element integration point and, afterwards, the volume average of necessary quantities is computed based on the martensite volume fraction; see Equation (X) in Table 1.

4 Comparison of Tangential Stress Distribution

Macroscopic tangential residual stresses σ_{tang} with respect to the outer lateral surface are most important with respect to wear resistance or lifetime. Due to the absence of outer forces during cooling of the investigated section of the cylindrical specimen, see Fig. 1b, the occurring stresses are interpreted as residual stresses. In addition to the overall tangential stresses, phase-specific stresses can be analyzed, which are computed implicitly in the material model. Moreover, the results from the above-proposed material model are compared to the two-scale finite element simulations presented in [24]. Therein, on the microscale a randomized representation of the microstructure consisting of austenite and martensite is used. The resulting total and phase specific tangential residual stresses of both simulation models are shown in Fig. 3. In each upper row the phenomenological material model is evaluated, and in the lower rows results of the FE^2 calculation are shown. Regions in which martensite has not yet formed are not taken into account in the illustration of martensitic stresses.

Here, three prominent points of the phase transformation during cooling are investigated. After nine seconds, the phase transformation has just started on the outer lateral surface; see Fig. 3a. After 15 seconds, martensite is also formed on the inner lateral surface and in the bulk of the thin side, cf. Fig. 3b. In the bulk of the thick side, martensite is initiated last. The final state is reached after 80 seconds; see Fig. 3c.

One can see that both models yield qualitatively similar total tangential stress distributions. At first, the total tangential stresses show tensile stresses σ_{tang} due to thermal contraction. With the onset of phase transformation, these stresses are superimposed with compressive stresses due to lattice shearing from austenite to martensite. Only when the phase transformation occurs in the bulk, this changes. The evoked compressive stresses in the bulk cause tensile stresses at the outer and inner lateral surfaces. Quantitatively, it can be said that the phenomenological material model generally calculates slightly higher stress values.

The results of the phase-specific residual stresses of both models also show qualitative agreement, but differ considerably quantitatively. First, we want to consider the martensitic stresses $\sigma^{\text{M}}_{\text{tang}}$ over time. Compared to the austenitic atomic lattice, martensite exhibits a volumetric expansion of 2%. Thus, compressive stresses form in martensite with the onset of phase transformation. The largest absolute values occur in the region of the component where the phase transformation begins. After phase transformation, at the end of the cooling process, the stress distribution is almost homogeneous; see Fig. 3c. The absolute stress values of the phenomenological model presented here are several times higher than the ones computed with the two-scale approach. In the austenitic phase, after $t = 9\,\text{s}$, compressive stresses near the outer lateral surface result in the austenitic phase-specific tangential stresses $\sigma^{\text{A}}_{\text{tang}}$. This is caused by the heat flux into the bulk of the component and the associated thermal contraction. Thus, with ongoing cooling, more and more of the body shows increasing tensile stresses. Finally, the stress distribution is nearly homogeneous, whereas the values of the two-scale computation are lower, as observed in martensite.

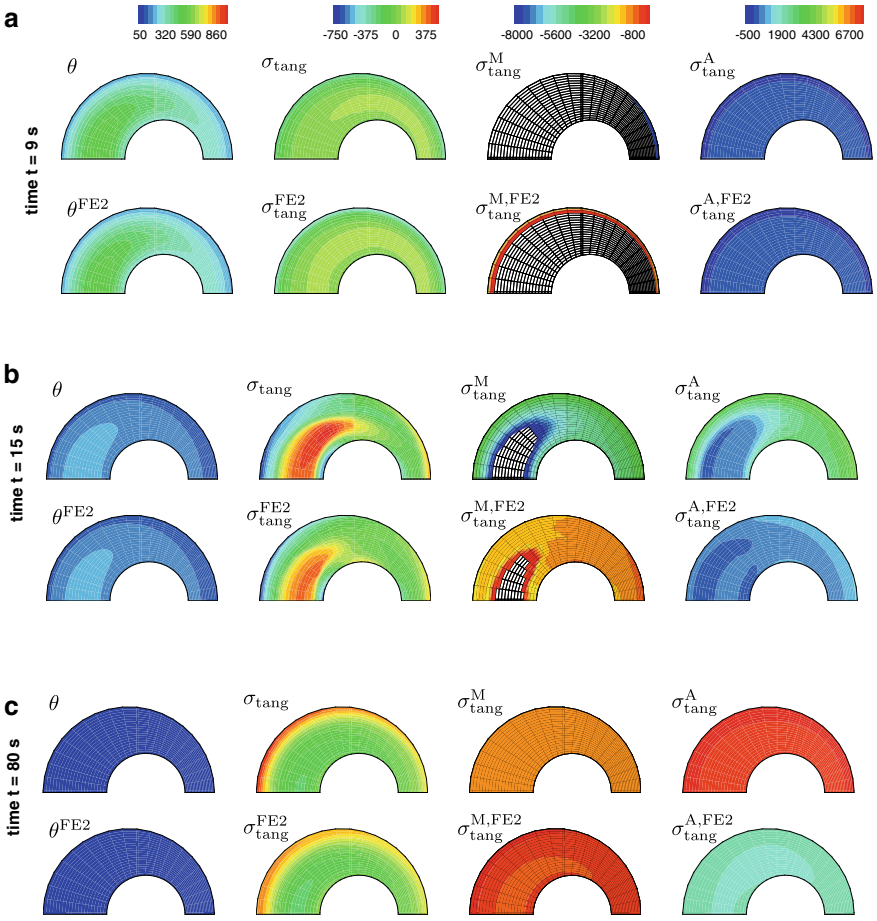


Fig. 3 Temperature distribution θ and tangential stress distribution σ_{tang} and phase-specific tangential stresses in austenite and martensite $\sigma^{\text{A}}_{\text{tang}}$, $\sigma^{\text{M}}_{\text{tang}}$, in MPa, for both computational approaches, after a) $t = 9$ s, b) $t = 15$ s, and c) $t = 80$ s. (Color figure online)

The comparison shows that the phenomenological material model is well suited to qualitatively as well as quantitatively determine the total tangential residual stress as a result of phase transformation. However, this model is not suitable for making statements about phase-specific stress distributions, which seem strongly overestimated.

By setting $K_{\text{tp}} = 0$ in the phenomenological model, one does not consider TRIP effects, as is the case in the two-scale approach. Figure 4 shows the total tangential stresses at time $t = 12$ s with and without TRIP in comparison to the FE^2 computation. It can be seen that the resulting stress values without TRIP are larger than that with TRIP, which exceed the stresses computed with the two-scale approach. In the future, validation with experiments must be done in order to assess the results.

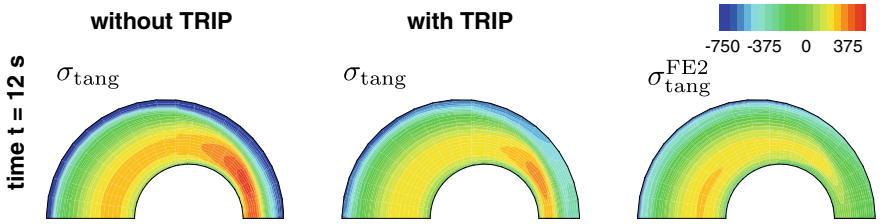


Fig. 4 Tangential stress distribution σ_{tang} computed with the phenomenological model with and without TRIP effects and tangential stresses computed with the two-scale approach $\sigma_{\mathrm{tang}}^{\mathrm{FE2}}$ in MPa after $t = 12\,\mathrm{s}$. (Color figure online)

5 Summary and Outlook

In this contribution, a phenomenological material model has been presented to numerically analyze the cooling process of a cylindrical specimen. Several physical effects such as plasticity or TRIP have been considered in order to illustrate the occurring austenite-to-martensite phase transformation which is associated with the cooling process. The results have been compared to a two-scale finite element simulation of a previous publication, see [24], which does not take into account transformation induced plasticity. It has been observed that the phenomenological approach without TRIP effects yields higher stresses than when TRIP is taken into account. However, these stresses are also higher than the tangential stresses calculated by the FE^2 approach. It is seen that microscopic stresses are strongly overestimated with the phenomenological model, such that it is inevitable to incorporate the TRIP effect in the two-scale approach to make a statement about the influence of TRIP on the phase-specific stresses. Thus, as a next step, a combination of both models should be aimed at, i.e., a two-scale finite element simulation considering also the TRIP effect.

Acknowledgments This project is funded by the Deutsche Forschungsgemeinschaft (DFG, German Research Foundation)—374871564 (BE 1691/223-2, BR 5278/3-2, SCHR 570/33-2) within the priority program SPP 2013. The authors gratefully acknowledge the computing time granted by the Center for Computational Sciences and Simulations (CCSS) of the University of Duisburg-Essen and provided on the supercomputer magnitUDE (DFG grants INST 20876/209-1 FUGG, INST 20876/243-1 FUGG) at the Zentrum für Informations- und Mediendienste (ZIM).

References

1. Macherauch E, Wohlfahrt H, Wolfstied U (1973) Härterei-Technische Mittelungen - Zeitschrift für Werkstoffe. Wärmebehandlung, Fertigung. 28:201–211
2. Kloos KH (1979) Eigenspannungen. Definition und Entstehungsursachen. Zeitschrift für Werkstofftechnik. 10:293–302
3. Withers PJ, Bhadeshia HKDH (2001) Residual stress Part 1 - Measurement techniques. Mater Sci Technol 17:355–365

4. Withers PJ, Bhadeshia HKDH (2001) Residual stress Part 2 - Nature and origins. Mater Sci Technol 17:366–375
5. Greenwood GW, Johnson RH (1965) The Deformation of Metals Under Small Stresses During Phase Transformations. Proceedings of the Royal Society of London A 183:403–422
6. Leblond JB (1989) Mathematical Modelling of Transformation Plasticity in Steels II: Coupling with Strain Hardening Phenomena. Int J Plast 5:573–591
7. Weisz-Patrault D (2017) Multiphase model for transformation induced plasticity. Extended Leblond's model. J Mech Phys Solids **106**:152–175
8. Mahnken R, Schneidt A, Antretter T (2009) Macro modelling and homogenization for transformation induced plasticity of a low-alloy steel. Int J Plast 25:183–204
9. Hallberg H, Håkansson P, Ristinmaa M (2010) Thermo-mechanically coupled model of diffusionless phase transformation in austenitic steel. Int J Solids Struct 47:1580–1591
10. Inoue T (2011) Mechanics and Characteristics of Transformation Plasticity and Metallo-thermo-mechanical Process Simulation. Procedia Eng 10:3793–3798
11. Zaera R, Rodríguez-Martínez JA, Casado A, Fernández-Sáez J, Rusinek A, Pesci R (2012) A constitutive model for analyzing martensite formation in austenitic steels deforming at high strain rates. Int J Plast 29:77–101
12. Ostwald R, Bartel T, Menzel A (2015) An energy-barrier-based computational micro-sphere model for phase-transformations interacting with plasticity. Comp Methods Appl Mech Eng 293:232–265
13. Tahimi A, Barbe F, Taleb L, Quey R, Guillet A (2012) Evaluation of microstructure-based transformation plasticity models from experiments on 100C6 steel. Comput Mater Sci 52:55–60
14. Ni J, Wang X, Gong J, Wahab MA (2018) A multi-phase model for transformation plasticity using thermodynamics-based metallurgical algorithm. Int J Mech Sci 148:135–148
15. Zhang D, Liang Y, Du Z, Mao X (2013) A Material Model for Steel Plates during the Cooling Process. Adv Technol Solut Ind 710:329–333
16. Connolly DS, Kohar CP, Mishra RK, Inal K (2018) A new coupled thermomechanical framework for modeling formability in transformation induced plasticity steels. Int J Plast 103:39–66
17. Seupel A, Burgold A, Prüger S, Budnitzki M, Kuna M (2020) Modeling of the thermomechanical behavior, damage, and fracture of high alloy TRIP-steel. In: Biermann H, Aneziris CG (eds) Austenitic TRIP/TWIP steels and steel-zirconia composites: design of tough, transformation-strengthened composites and structures. 723–769
18. Prüger S, Kiefer B (2020) Towards the crystal plasticity based modeling of TRIP-steels - from material point to structural simulations. In Biermann H, Aneziris CG (eds) Austenitic TRIP/TWIP steels and steel-zirconia composites: design of tough, transformation-strengthened composites and structures. 793–823
19. Prüger S, Gandhi A, Balzani D (2016) Modeling of low-alloyed TRIP-steels based on direct micro-macro simulations. ECCOMAS Congress 2016:2280–2291
20. Soliman M, Palkowski H (2008) On factors affecting the phase transformation and mechanical properties of cold-rolled transformation-induced-plasticity-aided steel. Metall Mater Trans A 39:2513
21. Behrens B-A, Bouguecha A, Bonk C, Chugreev A (2017) Experimental investigations on the transformation-induced plasticity in a high tensile steel under varying thermo-mechanical loading. Comput Methods Mat Sci 17:36–43
22. Liu J, Li M, Zhang P, Zhu Y, Li S (2020) Experiment research on the transformation plasticity by tensile/compressive stress and transformation kinetics during the martensitic transformation of 30Cr2Ni4MoV steel. Mater Res Express 6:1265g8
23. Uebing S, Brands D, Scheunemann L, Schröder J (2021) Residual stresses in hot bulk formed parts - two-scale approach for austenite-to-martensite phase transformation. Archive Appl Mech. https://doi.org/10.1007/s00419-020-01836-7
24. Uebing S, Brands D, Scheunemann L, Schröder J (2021) Residual stresses in hot bulk formed parts - Microscopic stress analysis for austenite-to-martensite phase transformation. Archive Appl Mech. https://doi.org/10.1007/s00419-021-01921-5

25. Behrens B-A, Chugreev A, Kock C (2019) Macroscopic FE-simulation of residual stresses in thermo-mechanically processed steels considering phase transformation effects. XV. Int Conf Comput Plast. Fundam Appl 211–222
26. Behrens B-A, Schröder J, Brands D, Scheunemann L, Niekamp R, Chugreev A, Sarhil M, Uebing S, Kock C (2019) Experimental and numerical investigations on the development of residual stresses in thermo-mechanically processed Cr-alloyed steel 1.3505. Metals 9:28
27. Koistinen DP, Marburger RE (1959) A general equation prescribing the extent of the austenite-martensite transformation in pure iron-carbon and plain carbon steels. Acta Metall 7:59–60
28. Lemaitre J (2001) Handbook of materials behavior models. Academic Press
29. Wolff M, Boettcher S, Böhm M (2007) Phase transformations in steels in the multi-phase case-general modelling and parameter identification. Universität Bremen, Zentum für Technomathematik
30. Simo JC, Hughes TJR (1998) Computational Inelasticity. Springer
31. Wolfram Research, Inc.: Mathematica, Version 12.0. Champaign, IL (2019)
32. Taylor RL (2020) FEAP - Finite element analysis program. http://projects.ce.berkeley.edu/feap
33. Schenk O, Gärtner K (2004) Solving unsymmetric sparse systems of linear equations with PARDISO. Future Gener Comput Syst 20:475–487

Local Creation of Uniform Residual Stresses Into Sheet Metal Components by Means of Multiple One-Side Embossing



Stefan Walzer, Nicola Simon, Mathias Liewald, and Jens Gibmeier

Abstract In sheet metal forming, embossing provides a process for targeted improvement of the mechanical properties of sheet metal materials. The local property modification is thereby achieved by uniform residual stresses induced as a result of the one-side embossing process. For example, such a targeted induction of the residual stresses can significantly increase the fatigue strength of sheet metal components. In order to ensure this kind of component optimization in continuous operation, the induced stresses have to be uniform. In the study presented in this paper, duplex stainless steel (X2CrNiN23—4) specimens having a thickness of 1.5 mm were unilaterally embossed in order to investigate the effects of the embossing process on the component properties. The primary objective of this investigation was to find a suitable embossing strategy for generating preferably uniform stress distributions into sheet metal blanks.

Keywords Residual stresses · Sheet metal · Embossing

1 Introduction

In recent years, both industry and institutional research have been endeavoring to reduce weight and thus material demand of sheet metal products in order to save energy and resources on the one hand and to meet increasing lightweight construction requirements on the other hand. As a consequence, a huge amount of sheet metal materials conventionally used in automotive engineering nowadays

S. Walzer (✉) · M. Liewald
Institute for Metal Forming Technology (IFU), University of Stuttgart, Holzgartenstraße 17, 70174 Stuttgart, Germany
e-mail: Stefan.Walzer@ifu.uni-stuttgart.de

M. Liewald
e-mail: Mathias.Liewald@ifu.uni-stuttgart.de

N. Simon · J. Gibmeier
Institute for Applied Materials (IAM–WK), Karlsruhe Institute of Technology (KIT), Karlsruhe, Germany

© The Minerals, Metals & Materials Society 2021

G. Daehn et al. (eds.), *Forming the Future*, The Minerals, Metals & Materials Series,
https://doi.org/10.1007/978-3-030-75381-8_197

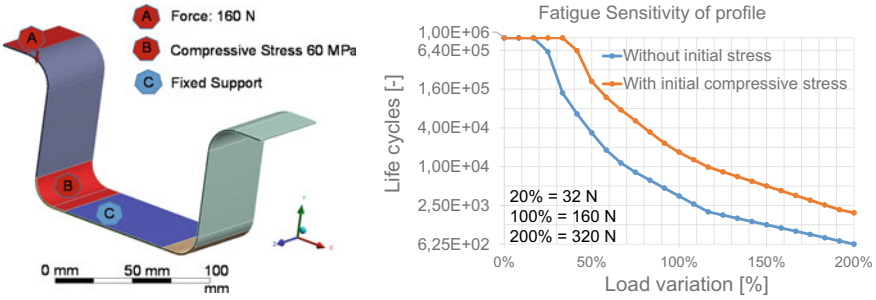


Fig. 1 Fatigue sensitivity analyses performed by using ANSYS Workbench for a u-shaped stripe of sheet metal (left), Investigation of the fatigue sensitivity of the specimen under different load variations (right). (Color figure online)

are replaced by high strength steel materials having comparatively thin sheet thicknesses [7]. However, a reduction in sheet metal thickness also leads to a reduction in fatigue strength and stiffness of the sheet metal components [1]. A common approach for extending the fatigue life of technical components is a post processing surface treatment, such as shot peening or deep rolling. It was found that in most cases, thereby induced compressive residual stresses (RS) in the surface layer counteract with external applied tensile loads in service and therefore are found beneficial with regard to the fatigue performance [2]. Regarding metal sheet components, local embossing enables an alternative approach for targeted induction of residual stresses. The embossing structure can be considered, e.g., in the shape of the deep drawing punch or die geometry, which allows for an integrated manufacturing process regarding both, the components shape and the local RS development. In this case, application of time consuming post surface treatments can be omitted.

For this reason, specific induction of RS into sheet metal components during manufacturing is the declared objective of various current research projects. The surface layer represents the most highly stressed component area for varying stress conditions. This especially applies to quasi-static inhomogeneous stresses due to torsion, bending, or notching as well as to homogeneous or inhomogeneous oscillating stresses [2].

Liewald et al. [8] investigated the effects of strain and stress dependent material properties on the formability of sheet metals and showed that most of the mechanical sheet metal properties are not constant values but should be rather considered as process parameters with dependency on effective strain or strain rate, for example. Thus, sheet metal components can be locally reinforced by inducing residual compressive stresses and hardening conditions via mechanical surface treatment processes such as shot peening or deep rolling [9]. This local increase in strength by RS offers great potential for lightweight construction in order to realize weight-optimized overall structures with simultaneously increased local load-bearing capacity.

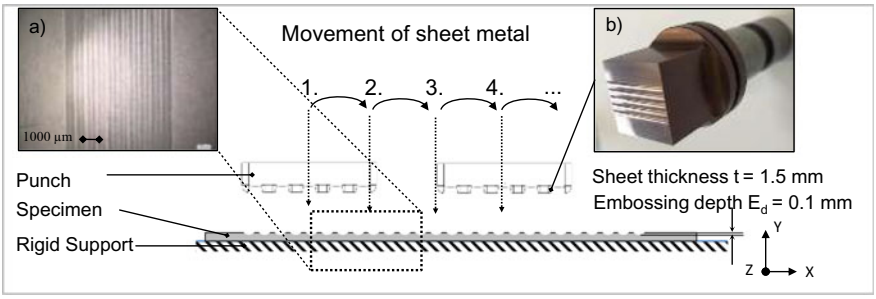


Fig. 2 Schematic embossing process showing repeated relative movement of the sheet metal stripe after each embossing step of 0.1 mm in x-direction; **a** surface structure after multiple one-side-embossing, **b** embossing punch. (Color figure online)

Sheet metal profiles as shown in Fig. 1 (left) are used in many technical applications in order to absorb forces and torques. In electro-driven vehicles, for example, such profiles are responsible for carrying and securing heavy battery packs and are constantly exposed to static and dynamic loads [3]. These superimposed static and dynamic loads may lead to reduced fatigue life of the sheet metal component. One approach to this problem consists in local embossing of the components and thus in the induction of compressive residual stresses into those areas where tensile loading stresses dominate during operation. Thereby, the tensile stresses counteract with compressive residual stresses and delay premature failure of the component. In this respect, finite-element (FE) simulations of the fatigue life of the sheet metal specimen depicted in Fig. 1 have shown that the fatigue life of the component can be extended by inducing residual compressive stresses. Figure 1 (right) shows extended fatigue life of the specimen without and with acting residual compressive stresses in the failure-critical zone of the punch radius B (see Fig. 1, left).

In the study presented in this paper, one-side embossing technology (see Fig. 2) was put forward as an alternative sheet forming manufacturing method with integrated surface treatment with respect of inducing favorable residual stresses. In order to gain more deeper knowledge of the effect and interaction of induced residual stresses, their homogeneity as well as amount of stresses, simulative, and experimental investigations were carried out on a flat sheet metal specimen.

2 Material and Experimental Embossing Method

The embossing experiments presented in this paper were performed with cold rolled duplex stainless steel sheets X2CrNiN23—4 having a sheet thickness of 1.5 mm. This duplex steel consists of ferritic (α) and austenititc phases (γ) in equal volume fraction. The materials' chemical composition is given in Table 1.

Table 1 Chemical composition of X2CrNiN23—4 in weight—% [10]

C	Cr	Ni	Mn	Co	Si	Mo	N	Fe
0.034	23.91	4.74	1.326	0.104	0.38	0.37	0.13	Balance

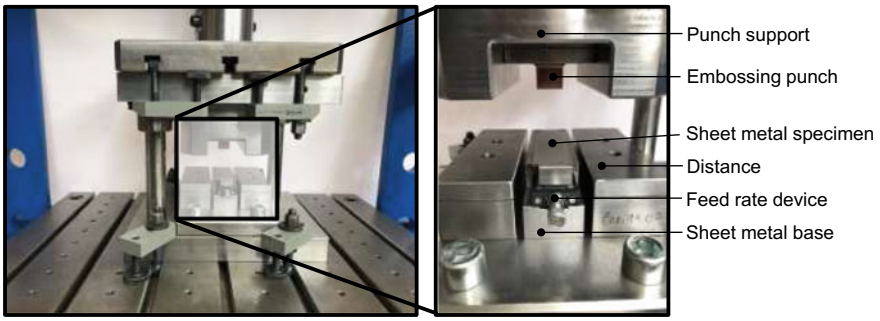


Fig. 3 Embossing tool with detailed components. (Color figure online)

The embossing experiments were carried out using a conventional hydraulic press "Metallkraft WPP 60 MVZ" and a manufactured embossing tool (see Fig. 3) under dry condition, i.e., without lubricant. The sheet metal specimens used were cut from stainless steel blanks and had a size of 100 × 30 × 1.5 mm. The punch force was set to $P_f = 25$ kN to ensure a uniform embossing depth of 0.1 mm even with multiple embossing and thus partially strain-hardened material states. The embossing depth was verified by topography measurements of the embossed structure using the confocal surface microscope "μsurf" subsequent after the embossing process.

For embossing, the sheet metal specimen is placed on the laser hardened (62 HRC) rigid sheet metal base (see Fig. 3). Afterward, the first indentation of the embossing process was performed by indenting the punch geometry (see Fig. 2b) into the sheet metal specimen via vertical movement of ram. The maximum embossing depth of 0.1 mm is limited by the punch geometry and by flat-grinded distances on both sides of the specimen support. After the first stroke, the sheet metal specimen was moved forward horizontally by a defined distance (e.g., 0.25 mm) using a precision linear feed rate device. Subsequently, the embossing process was repeated. After 8 consecutive indentations and equidistant unidirectional specimen movements, a characteristic embossed structure (see Fig. 2a) was created.

3 Experimental Residual Stress Analysis

The residual stress distribution, which was induced into the specimen's surface by the embossing process described above, has subsequently been analyzed by means of X-ray diffraction (XRD) according to the well-known $sin^2\psi$-method. Thereby,

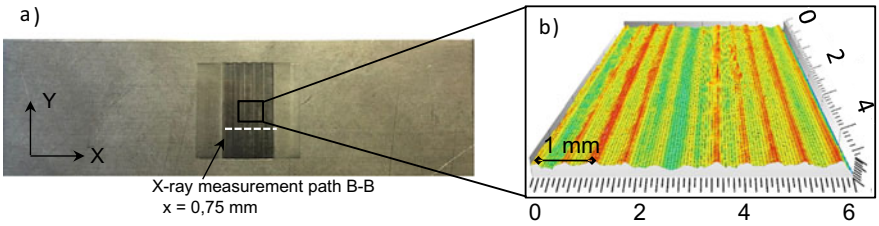


Fig. 4 **a** Measurement path B-B for X-ray residual stress analysis; **b** resulting surface roughness of the embossed area. (Color figure online)

Table 2 X-ray elastic constants for austenite {220} and ferrite {211}, based on single crystal and Eshelby-Kröner model [6]

	$s_1\{hkl\}$	$1/2s_2\{hkl\}$
Austenite {220}	−1.46 E-6 MPa^{-1}	6.16 E-6 MPa^{-1}
Ferrite {211}	−1.27 E-6 MPa^{-1}	5.82 E-6 MPa^{-1}

phase-specific residual stress components in direction X and Y have been determined for both the austenite and the ferrite phase at 12 overlapping measurement points along the measurement path given in Fig. 4.

Measurements were performed using an X-ray diffractometer with vanadium filtered Cr-Kα radiation, which allowed the analysis of {211}-ferrite and {220}-austenite diffraction lines. The spot size was defined by a pinhole collimator having a nominal diameter of 1 mm as primary aperture. On the secondary side, a 2 mm single slit and a 4 mm symmetrization slit were used for analysis of the austenite phase and the ferrite phase, respectively.

An increased number of 21 ψ-tilts from −60° to 60° was used for considering non-linear 2θ-$sin^2\psi$ distributions, as recommended for slightly textured materials. The interference lines 2θ were then determined from the measurement data using Pearson VII peak-fitting after backround subtraction. For residual stress evaluation, X-ray elastic constants have been used for austenite and ferrite, as given in Table 2.

Subsequently, the macro-residual stresses σ^I were calculated according to [4] for each measurement point, assuming a ferrite phase fraction q of 50 vol.%. In addition, the phase-specific micro-residual stresses $<\sigma^{II}>_{\alpha,\gamma}$ were determined, as given in the following equations.

$$\sigma^I = q < \sigma >_\alpha + (1-q) < \sigma >_\gamma \tag{1}$$

$$< \sigma^{II} >_{\alpha,\gamma} = < \sigma >_{\alpha,\gamma} - \sigma^I \tag{2}$$

4 Numerical Method

As already shown in Fig. 1, the embossing process examined consists of several indentions, while the sheet specimen is moved continuously below the embossing punch. These multiple and partly overlapping indentations lead to a homogeneous compressive residual stress distribution in the embossed area. In both the numerical and experimental investigations, the stress distributions after one punch indentation and after 7 steps of movements by 0.25 mm, i.e., after 8 indentations, were investigated (Table 3).

The numerical simulation of the embossing process was performed by using finite-element method. The model surfaces and the tool were designed in the CAD-System CATIA and subsequently imported into the commercial FE-software STAMPACK V7.2.2 (Fig. 5). For simulation objectives, an element number of 5 along the blank thickness of $s_0 = 1.5$ mm was chosen. The simulation model was set up with hexahedral fully integrated solid elements with size of 0.2 mm × 0.2 mm and a height of 0.3 mm to discretize the blank. In contrast, rigid shell elements were used to discretize the tools. No mass scaling was used in simulation. The anisotropic behavior of the material was taken into account according to Hill yield criterion [5] by the implementation of r-values estimated by uniaxial tensile tests. The contact modeling between the blank and tool surfaces was implemented with the Coulomb friction coefficient of $\mu = 0.12$. Explicit dynamic algorithm was used to emboss the blanks and implicit algorithm to simulate springback. Especially for the calculation of stress and strain conditions during the process and after springback, flow curves had to be specified up to the maximum strain occurring. The macroscopic flow resistance of the sheet metal material was modeled by using a stress—strain model that was analytically

Table 3 Parameter of investigated embossing configurations

Configuration	No. of indentations	Distance of indentions	Indention depth	Indention force
1	1	–	0.100 mm	250 kN
2	7	0.25 mm	0.100 mm	250 kN

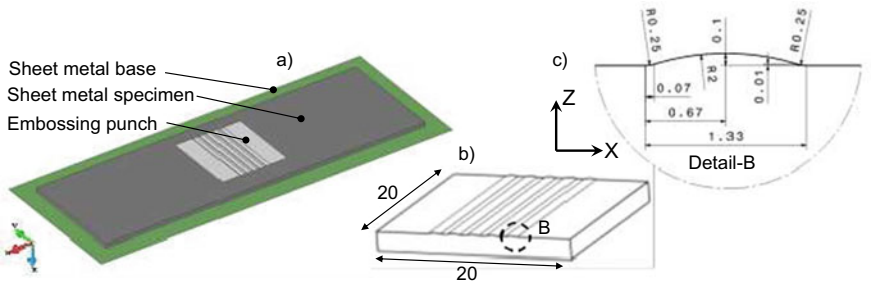


Fig. 5 **a** Fe-model, **b** geometry of embossing punch, **c** enlarged geometry of the indentation beads manufactured onto punch surface. (Color figure online)

approximated using the extrapolation method according to Ludwik-Hollomon. The material parameters used in the model were as follows: Young's modulus of 196 GPa, Poisson's ratio of 0.33, mass density of 7.850 kg/m^3, yield stress of 568 MPa, and tensile stress of 732 MPa. The stress–strain curve determined by tensile test was implemented into the model point by point without using a curve fit equation.

5 Results and Discussion

Figure 6a, b is showing the plastic strain distribution in the direction of sheet metal thickness for the configuration 1 and configuration 2. It can be seen that the plastic deformation due to the embossing process takes place in the upper half of the sheet metal blank and is almost zero on the opposite, unembossed side.

The numerically calculated surface residual stress distribution after a single indentation (see configuration 1 in Table 2) is shown in Fig. 7 on the left-hand side. Here, the upper figure presents the residual stress component σ_{xx} transverse to the orientation of the indentation lines. The lower figure illustrates the stress component σ_{yy} in direction along the indentation lines. For both stress components, negative residual stresses can be observed in the embossed area, whereas compensating tensile stresses are located in the surrounding area. For evaluation of the local surface residual stress states, σ_{xx}- and σ_{yy} are shown in increased depiction in detail for the given section A-A across the embossed area on the right-hand side of Fig. 7.

The calculated residual stress distribution shown in Fig. 7 indicates a periodic lateral RS gradient across the 5 indentation lines having maximum and minimum peaks in compressive residual stress. RS component σ_{xx} contains maxima of approx. −460 MPa, which are located in between the embossed lines. The minima within the

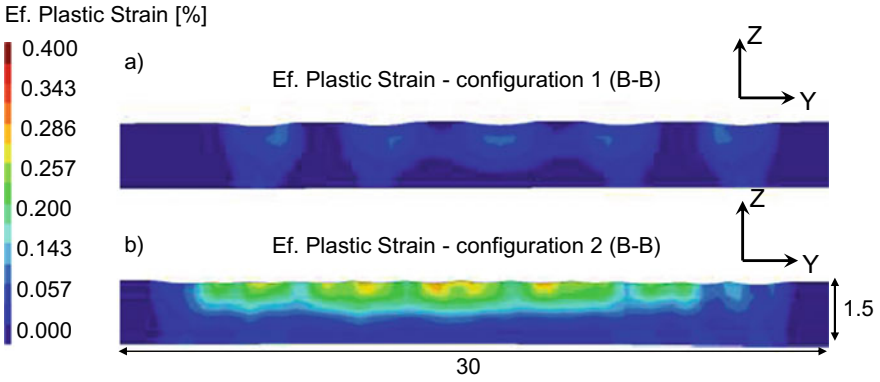


Fig. 6 **a** Effective plastic strain distribution in direction of sheet thickness of configuration 1, **b** Effective plastic strain distribution in direction of sheet thickness of configuration 2. (Color figure online)

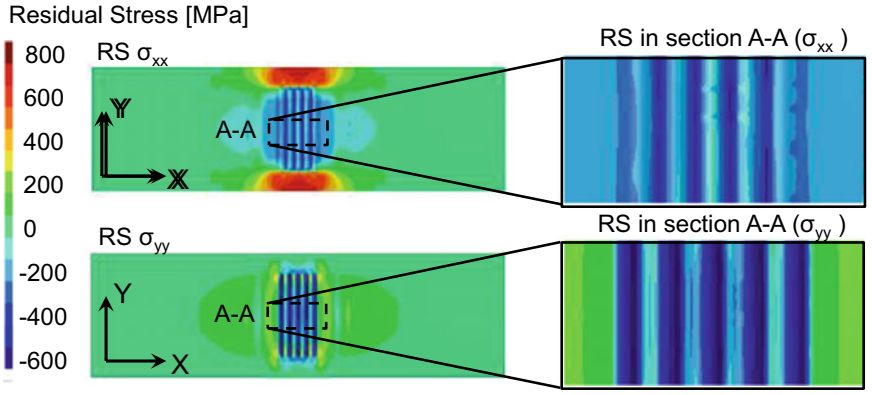


Fig. 7 Residual stresses in section A-A with embossing configuration 1 (Table 2) in σ_{xx}- and σ_{yy}-direction. (Color figure online)

embossed area of approx. −170 MPa are located at the maximum depths of the five-line indentations. This periodic residual stress distribution is even more pronounced for the stress component σ_{yy}, with maximum and minimum compressive residual stresses of −680 MPa and 0 MPa, respectively. For this stress component, however, it should be noted that the periodic residual stress distribution is inverted, since the maximum values are located at the indented lines and the minimum values at the positions in between. Hence, the simulation results obtained for configuration 1 reveal that the used embossing geometry with five linear rounded structures enables plastic material flow in direction X and hinders plastic flow in direction Y. This indicates a complex multiaxial stress state during embossing, which induces the above shown residual stress distribution after unloading.

Figure 8 shows the residual stress distribution in σ_{xx}- and σ_{yy}-direction after 7 subsequent punch indentations and equidistant, linear specimen movements (see configuration 2 in Table 2). Again, the surface residual stresses are depicted in stress mappings on the left-hand side of the Fig. 8, and its distribution in section A-A on the right hand.

After multiple embossing, an asymmetrical surface residual stress gradient has formed along path A-A in contrast to the periodic and symmetrical residual stress distribution in σ_{xx}-direction of the single indentation. In sheet movement direction, the maximum compressive residual stress values increase from approx. −460 MPa to about −550 MPa, whereas the minimum compressive residual stresses remain at about −80 MPa. Although the mean compressive residual stress value in section A-A decreases and a lateral gradient is caused by the unidirectional specimen movements, a more homogenous residual stress distribution can be achieved by the multiple embossing technique for the stress component σ_{xx} than by single embossing. This applies almost equally to the stress component σ_{yy}. Here, the highest values of compressive residual stresses in σ_{yy}-direction remain nearly unchanged at about −680 MPa. But in contrast, the minimum compressive

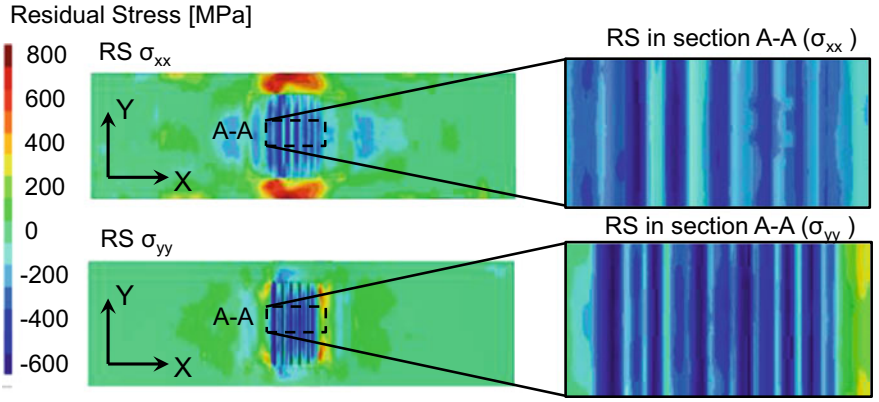


Fig. 8 Residual stresses in section A-A with embossing configuration 2 (Table 2) in σ_{xx}- and σ_{yy}-direction. (Color figure online)

residual stress values predominantly increase to −25 MPa. Consequently, in this case, multiple embossing leads to a more homogenous residual stress distribution and to higher mean compressive residual stresses compared to single embossing. Outside the embossed areas, however, concentrated tensile stresses can be seen which establish a stress balance with regard to the induced residual compressive stresses. Since such concentrated tensile stresses can impair the fatigue strength of the embossed sheet metal components, current research work is concerned with relocating these stresses to non-critical component areas.

After the numerical investigations, the simulation results of the multiple embossing were compared to the results of the experimental residual stress analysis performed by XRD. Here, phase-specific residual stresses were determined for 14 measurement points along a surface path (Fig. 4, B-B) for ferrite and austenite phase. The measuring results for residual stress component in σ_{xx}-direction and σ_{yy}-direction compared to the numerical results are shown in Fig. 9. A comparison of the numerical and experimental results requires the consideration of the measurement volume that contributes to the measured data in the diffraction experiment. Therefore, the numerically determined residual stress distribution is integrated according to size, geometry, and position of the experimental measurement points.

Figure 9 show that the XRD-measurements confirm the induction of predominantly compressive residual stresses in the embossed area for both stress directions. The phase-specific residual stresses in Fig. 10, measured for ferrite and austenite only differ of about 80 MPa in the center of the embossed area. Due to the equal volume fraction of both phases, the macro-residual stress is given by the mean value of both phase-specific stresses in each measurement point. The integrated simulation results show good conformity with the XRD results in σ_{xx}-direction and σ_{yy}-direction. The slightly decreasing trend (Fig. 9, left) of σ_{xx} in sheet movement direction already discussed above is reflected by the experimental results, as can be seen in Fig. 8 (from right to left). Nevertheless, the experimental results reveal that the numerical

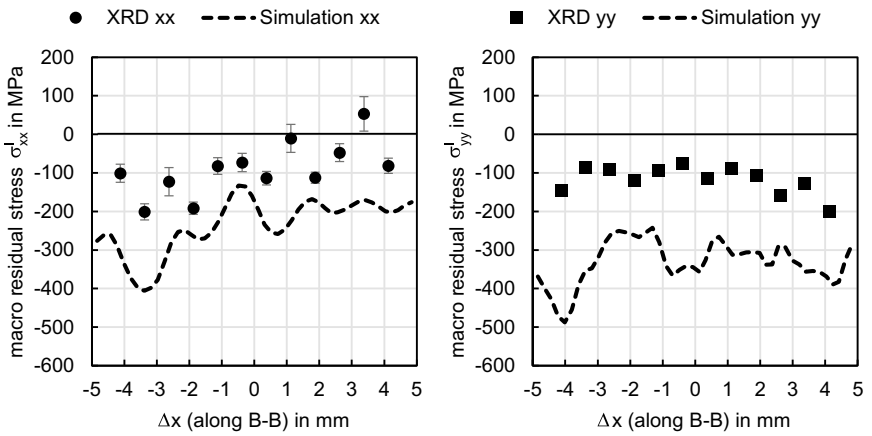


Fig. 9 Left: numerical results of macro-residual stress component σ_{xx} compared to XRD, right: numerical results of macro-residual stress component σ_{yy} compared to XRD

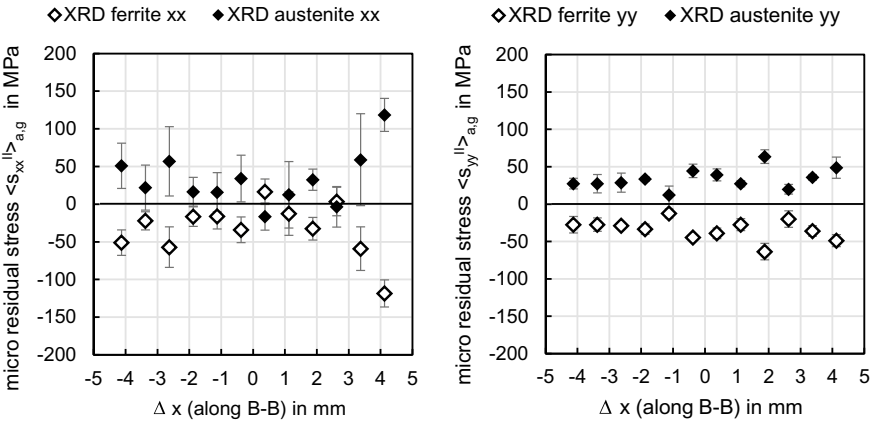


Fig. 10 Experimentally determined phase-specific micro-residual stresses along path B-B for ferrite $<\sigma^{II}>_{\alpha}$ and austenite $<\sigma^{II}>_{\gamma}$ left: micro-residual stresses $<\sigma^{II}{}_{yy}>_{\alpha,\gamma}$ in direction xx, right: micro-residual stresses $<\sigma^{II}{}_{yy}>_{\alpha,\gamma}$ in direction yy

simulation overestimates the true compressive residual stress state for σ_{xx}-direction and σ_{yy}-direction up to 200 MPa and 300 MPa, respectively. The quantitative deviation between numerical and experimental results can be explained by the used material model, since the strain rate of the real embossing process is 5 times lower compared to the tensile tests from which the plastic material behavior is approximated for the simulation. This leads to significantly higher strain hardening effects in the simulation, presumably resulting in the overestimation of the residual stresses after unloading.

In Fig. 10, the phase-specific micro-residual stresses are depicted for ferrite and austenite along the measurement path B-B. Direction xx can be referred to the rolling direction of the initial blank, which is for the given crystal structures commonly more sensitive to residual stress measurement errors in application of the $\sin^2\psi$-method. Apart from one measurement point, which is located close to the border of the embossed area, only small phase-specific micro-residual stresses of less than 60 MPa have been evaluated for both directions, xx and yy. The impact of induced micro-residual stresses on the mechanical behavior of a likewise manufactured sheet component requires further investigation.

6 Conclusion

In the study presented in this paper, the effects of a multiple one-sided embossing process on the local creation of residual stresses in stainless steel sheet material (X2CrNiN23—4) with a thickness of 1.5 mm were investigated. Therefore, a flat embossing punch having five parallel convex line structures of 0.1 mm height was used. Numerical simulation has been shown that by a single indentation, residual compressive stress maxima of up 460 MPa in σ_{xx}- and around 680 MPa in σ_{yy}-direction occur. The areas between the 5 indentation lines of the punch that have not been plastically deformed create areas in which the residual stresses remain at amounts of 0 MPa, which results in an inhomogeneous periodic stress distribution. For this reason, the strategy was pursued to move the sheet unidirectional under the punch in order to generate a high degree of overlap and homogenize the stress distribution.

After 7 subsequent indentations with step wise unidirectional movements of the specimen transverse to the line axis, an overlapping of the indentation lines was achieved. According to the numerical results, the multiple indentations lead to a reduction in the amplitude of the lateral periodic residual stress gradient and a more homogenous compressive residual stress distribution compared to the single indentation. Furthermore, it was found that the unidirectional movement results in a slightly asymmetric residual stress distribution with a decrease of the maximum compressive residual stress in sheet movement direction.

Finally, experimental residual stress analysis was performed for several measurement points along a measurement path within the embossed area by means of XRD. The experimental results not only confirmed the qualitative course of the numerical results, but also revealed that the compressive residual stress values are overestimated by the simulation. Numerical simulation has been shown that after 7 subsequent indentations, residual compressive stress maxima of up to 400 MPa in σ_{xx}- and around 500 MPa in σ_{yy}-direction occur. For this reason, future research work on the simulation of the embossing process will particularly take into account the strain rate dependency of the duplex stainless steel considered.

References

1. Behnken H, Hauk V (1993) On the influence of microresidual stresses during cyclic loading (Oberursel), 733–742
2. De los Rios E, Walley A, Milan M, Hammersley G (1995) Fatigue crack initiation and propagation on shot-peened surfaces in A316 stainless steel, Int J Fatigue, 17(7):493–499
3. Friedrich HE (2013) "Leichtbau in der Fahrzeugtechnik" Springer Fachmedien, Wiesebaden
4. Hauk V, Nikolin HJ (1988) The evaluation of the distribution of residual stresses of the I. kind (RS I) and of the II. kind (RS II) in textured materials. Texture Stress Microstruct 8. Jg., S. 693–716
5. Hill R (1948) A theory of the yielding and plastic flow of anisotropic metals. Proc R Soc Lond A: Math, Phys Eng Sci 193(1033):281
6. Kröner E (1958) Berechnung der elastischen Konstanten des Vielkristalls aus den Konstanten des Einkristalls. Z Phys 151(4):504
7. Liewald M, Weiß A (2018) Szenarische Volumenbetrachtung von Kaltmassivprodukten zwischen Verbrenner und Elektromobilität, Umformtechnisches Kolloqium Darmstadt
8. Liewald M, Schleich R, Vlahovic D, Sindel M (2007) Einfluss dehnungsabhängiger Werkstoffeigenschaften auf die Umformbarkeit von Blechwerkstoffen, Mat.-wiss. und Werkstofftechnik 38, No. 10
9. Seddik R, Bahloul A, Atig A, Fathalla R (2017) A simple methodology to optimize shot-peening process parameters using finite element simulations. Int J Adv Manuf Technol 90:2345–2361
10. Simon N, Erdle H, Walzer S et al (2019) Phase-specific residual stresses induced by deep drawing of lean duplex steel: measurement vs simulation, Prod Eng Res Devel 13: 227

Part XXI
Rolling

Hot Ring Rolling and Cold Expanding Strengthening of Mn18Cr18N Thick-Wall Hollow Ingots



Huiqin Chen, Huihua Wen, Jinliang Wang, Fei Li, and Wenwu He

Abstract A short route manufacturing process of retaining rings was put forward, which was composed of hollow ingots manufacturing by Electro-Slag Re-melting (ESR), hot ring rolling and cold expanding strengthening. And microstructure mechanisms, deformation characteristics, and process parameters during both of hot ring rolling and cold hydraulic expanding strengthening were investigated. The results show that the multi-pass flow stresses decreased with increase of interval time. During multi-pass compression, grain refined at lower temperature of 1050 °C by static recrystallization, then grain refined at higher temperature of 1150 °C by both of dynamic and static recrystallization. Based on the influence of the contact arc length ratio on strain penetration in the wall deformation zone, the driving roller radius of 500 mm and the pressure roller radius of 130 mm were determined for the ring rolling process of φ712 mm/308 mm × 902 mm thick-wall hollow ingot. The optimum rotate velocity of the driving roller should be 0.8 rad/s. And the feeding velocity of the pressure roller should to be 1 mm/s for matching. During cold deformation, planar slip and twinning predominated at small and large deformation, respectively, to increase strength. For the hydraulic expanding process of ϕ937/672 × 1034 mm hollow forging, the optimum matching of 60° punch angle and 5 mm contact seal height can be adopted for obtaining well-shaped strengthening forgings.

H. Chen (✉) · H. Wen · J. Wang · F. Li · W. He
School of Materials Science and Engineering, Taiyuan University of Science and Technology, Taiyuan 030024, People's Republic of China
e-mail: chenhuiqin@tyust.edu.cn

H. Wen
e-mail: m18335100418@163.com

J. Wang
e-mail: wang_Jinliang55@163.com

F. Li
e-mail: 170723191@qq.com

W. He
e-mail: hwwssl@126.com

© The Minerals, Metals & Materials Society 2021

G. Daehn et al. (eds.), *Forming the Future*, The Minerals, Metals & Materials Series,
https://doi.org/10.1007/978-3-030-75381-8_198

Keywords Mn18Cr18N steel · Microstructure evolution · Hot ring rolling · Strain penetration · Cold expanding strengthening

1 Introduction

Mn18Cr18N, a high-nitrogen austenitic stainless steel, is widely used to manufacture retaining rings of generators due to its distinctive advantages such as high strength and toughness, non-magnetic property and excellent stress corrosion resistance [1]. The retaining ring of generators is a thick-wall heavy cylindrical forging. Its traditional manufacturing process is a typical free forging process followed by solid-solution and cold deformation strengthening [2]. The free forging process of the ring forgings consists of ingots logging, upsetting and punching, drawing and expanding with mandrels, which is a complex multiple heating deformation process for controlling. And hot cracking often occurs during the free forging process, size mixed grains often appear in forgings. A short process consisting of ESR hollow ingot manufacturing, expanding and extruding combined forming, cold expanding strengthening has been reported and investigated [3]. However, it was found that the process needs large forming loads due to extrusion deformation manner in the final forming stage. And it was also found that it is not convenient to de-mould after forming. In this paper, a simple manufacturing process of retaining rings was put forward, which is composed of hollow ingot manufacturing, hot ring rolling, and cold deformation strengthening. High-quality hollow ingots can be made by a special metallurgical technique of Electro-Slag Remelting (ESR) [4, 5], which are pure, compact, and coarse column grain structure dominated. Therefore, the hot ring rolling of ESR hollow ingots has to transfer coarse column grains into uniform refined grains by dynamic and static recrystallizaion during hot deformation [6, 7], which is followed by cold deformation for strengthening [8].

2 The Hot Ring Rolling Process of Hollow Ingots

2.1 Flow Stresses and Microstructures During Multi-pass Hot Compression of Mn18Cr18N

The multi- pass hot compression experiments with $\phi 8 \times 12$ mm samples at different pass-reduction rates and holding time were carried out on a Gleeble-1500D thermal modelling simulator for modelling the microstructure evolution during hot ring rolling of Mn18Cr18N. Figures 1 and 2 show the stress–strain curves and microstructures of single-pass and six-pass compressed samples with 60% total reduction rates at the initial heating temperature of 1150 °C and the final rolling temperature of 1050 °C and 1 s^{-1} strain rate. In the six-pass hot deformation experiments, 10, 11.1,

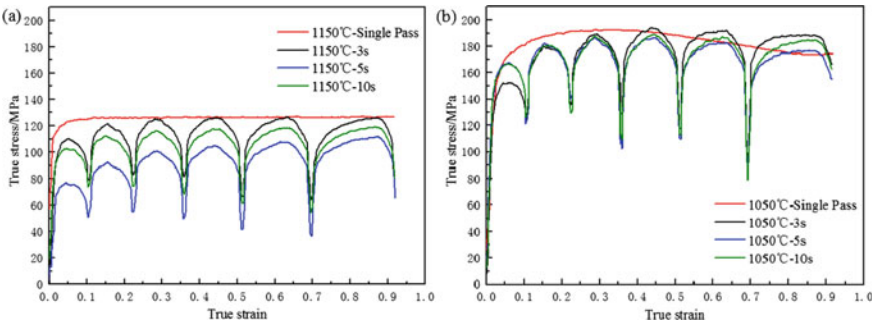


Fig. 1 The single-pass and six-pass compressive stress–strain curves at 1 s^{-1} **a** 1150 °C **b** 1050 °C. (Color figure online)

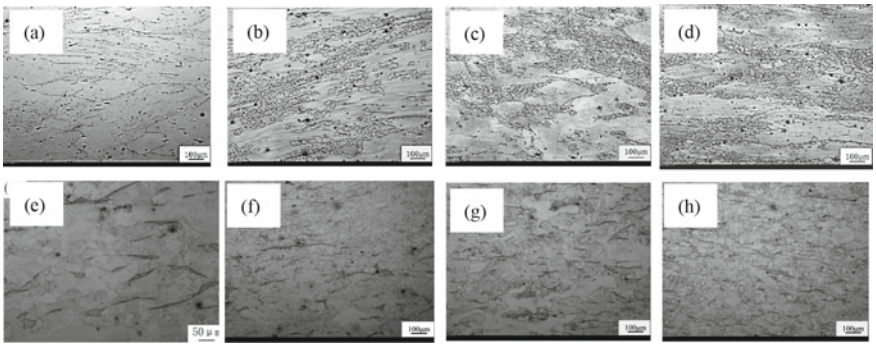


Fig. 2 Microstructures in the six-pass compressed samples at 1 s^{-1} **a** 1050 °C, 0 s **b** 1050 °C, 3 s **c** 1050 °C, 5 s **d** 1050 °C, 10 s **e** 1150 °C, 0 s **f** 1150 °C, 3 s **g** 1150 °C, 5 s **h** 1150 °C, 10 s. (Color figure online)

12.5, 14.3, 16.7, and 20% pass-reduction rates was designed to modelling the gradually increasing radial deformation at constant radial feeding velocity during ring rolling. It can be seen that the multi-pass compression flow stresses increased from 120 MPa of 1150 °C (Fig. 1a) to 180 MPa of 1050 °C (Fig. 1b) at the strain rate of 1 s^{-1}. The multi-pass compression flow stresses of Mn18Cr18N ESR ingot sample coincide with that of the single-pass flow stresses at short interval time of 3 s. It also can be seen that the multi-pass flow stresses decreased with increase of interval time. However, the lowest multi-pass flow stresses were arrived at the 5 s interval time, which may be the result of grain refinement and coarsening competition.

The corresponding microstructures of Fig. 1 were shown in Fig. 2. It can be seen that recrystallization occurred during six-pass compression. It was hardly to observe dynamic recrystallized grains in the sample compressed up to 60% total reduction rate at 1050 °C by single-pass compression (Fig. 2a). However, as shown in Fig. 2b–d, recrystallised grains can be observed, and recrystallized fraction increased slightly with increase of interval time. It suggests that static recrystallization occurred at

1050 °C during six-pass compression. On the contrary, dynamic recrystallization occurred at 1150 °C in the sample compressed up to 60% total reduction rate by single-pass compression (Fig. 2e). And that recrystallized fraction increased with increase of interval time (Fig. 2f–h). Also Grain boundary high temperature ferrite δ disappeared and dispersed distributed gradually with increase of interval time. Therefore, both of dynamic and static recrystallization occurred at 1150 °C during six-pass compression. The above microstructure evolution suggests that the rolling velocity should be slower for the thick-wall rings than that of conventional rings for obtaining the refined and uniform recrystallised grain structure.

2.2 *Strain Penetration During Ring Rolling Forming*

Strain penetration is an important issue for thick-wall ring rolling process design. When the radial reduction is too small, strain could not penetrate the ring wall, the pressure roller could be slip, which could cause that the hollow ingot could not bite into the rollers at the beginning of rolling, or the non-uniform deformation defect of fish tail occurs. The conventional strain penetration model of ring rolling is based on the finite height block drawing theory (Fig. 3a), which can be expressed as follows deduced by slip line field theory [9].

$$\frac{L}{h_a} \geq \frac{1}{8.74} \tag{1}$$

where L is the contact arc length; h_a is the average wall thickness of rings.

Figure 3b was the simulation result of Fig. 3a with the contact arc length ratio of 1, in which the symmetrical distribution of strain in the wall thickness of the ring is clearly shown as shown in the finite height block drawing model (Fig. 3a). However, the contact arc lengths of driving rollers and pressure rollers during ring rolling

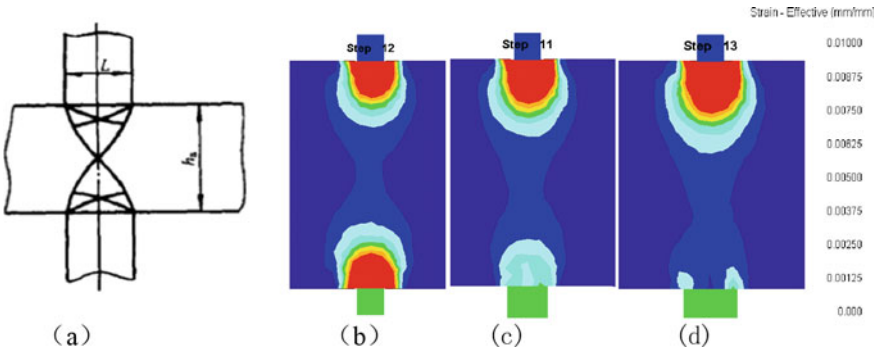


Fig. 3 Strain distribution in the rolled ring wall with different contact arc length ratio **a**, **b** the finite height block drawing model with the contact arc length ratio of 1 **c** the contact arc length ratio of 1.5 **d** the contact arc length ratio of 2. (Color figure online)

process with thick-wall hollow ingot are usually asymmetrical, in which the contact arc length ratio usually does not equal to 1. Figure 3c–d shows strain distributions in the ring wall with different contact arc length ratios. It can be seen that strain distributions are asymmetrical. And the simulation results also show that the strain penetration reduction with different contact arc lengths should be greater than that with the same contact arc length.

2.3 The Ring Rolling Forming Process with Mn18Cr18N Thick-Wall Hollow Ingot

Based on the above analysis, the ring rolling process of φ712 mm/308 mm × 902 mm thick-wall hollow ingot was analysed by numerical simulation method. First, the influence of the driving roller size and the pressure roller size on strain distribution in the deformation zone was analysed. The results show that the pressure roller size has a remarkable influence on strain distribution rather than that of the driving roller size. As shown in Fig. 4, the symmetry centre of strain distributions in the deformation zone along wall thickness varied with the pressure roller size for the constant driving roller with 500 mm radius. The symmetry centre of strain distribution coincided with that of the wall thickness only when the pressure roller radius was 130 mm. The symmetry centre of strain distribution moved towards the pressure roller with increase or decrease of the pressure roller size. The minimum contact arc length ratio also can be reached when the pressure roller radius is 130 mm, as shown in Fig. 4c. The corresponding minimum radial reduction should be 3 mm.

The rotate velocity of driving rollers and the feeding velocity of the pressure rollers also have an important impact on rolling stability and ring forgings. The greater both of the rotate velocity of driving rollers and the feeding velocity of the pressure rollers are, the greater the radial reduction of each pass is. The ring could be deformed to distort. Considering both of rolling efficiency and microstructure improvement of hollow forgings according to microstructure evolution during multi-pass compression as stated in 2.1, the optimum rotate velocity of the driving roller should be 0.8 rad/s, which corresponding the interval time was 7.85 s during rolling

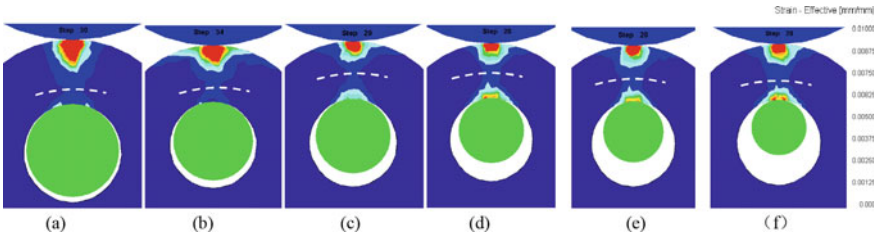


Fig. 4 Strain distributions in the strain penetration region under different radius of pressure rollers **a** 145 mm **b** 140 mm **c** 130 mm **d** 120 mm **e** 110 mm **f** 100 mm. (Color figure online)

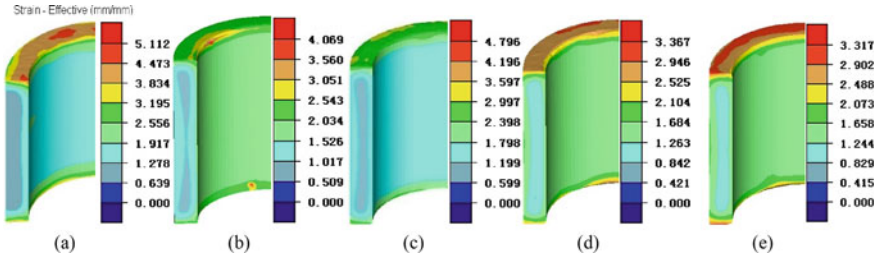


Fig. 5 Strain distribution after rolling at different feeding velocities of the pressure roll (rotation speed = 0.8 rad/s) **a** 0.5 mm/s **b** 0.7 mm/s **c** 1 mm/s **d** 1.3 mm/s **e** 1.5 mm/s. (Color figure online)

of the hollow ingot. And the feeding velocity of the pressure roller had to be 1 mm/s for matching the driving roller (Fig. 5c). Then ring forgings could be has refined uniform microstructure and well shaped.

3 The Cold Hydraulic Expanding Strengthening of Thick-Wall Hollow Forgings

3.1 The Cold Deformation Characteristics of Mn18Cr18N with High Nitrogen

Mn18Cr18N is an austenitic stainless steel without phase transformation during cooling. Strain strengthening becomes the only way to increase its strength. The steel is an f.c.c crystal structure with low stacking fault energy [10]. The deformation mechanisms at room temperature is slipping and twinning mainly. In the early stage of deformation near the yield strain of 0.04 (Fig. 6a), planar slip was predominate. With further deformation, slip is hindered by dislocation tangles, pile-ups and stacking faults, deformation resistance increases, and slip at other directions occur

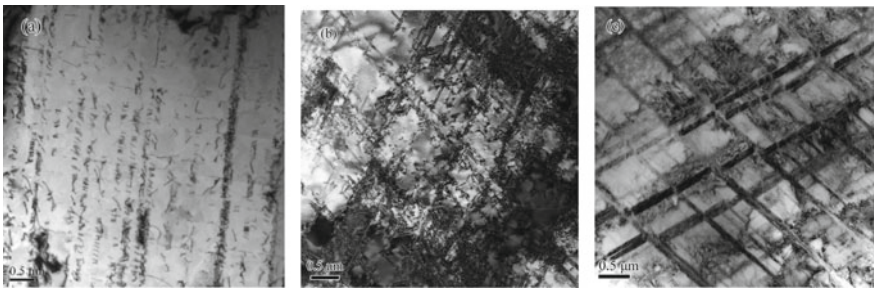


Fig. 6 TEM micrographs of samples compressed up to different reduction rates **a** 4% **b** 15% **c** 35%

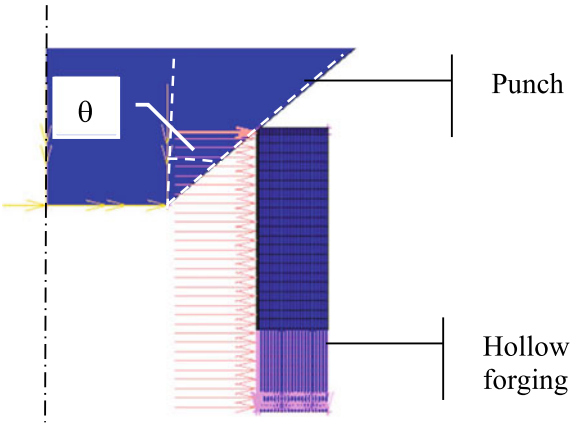


Fig. 7 The hydro-expanding FEM model. (Color figure online)

(Fig. 6b). At large deformation, twinning is activated (Fig. 6c). Although the appearance of deformation twins played an important role in deformation coordination, twin boundary was still a great hindrance for dislocation movement. Therefore, the strength of the steel could be increased with increase of deformation.

3.2 The Hydraulic Expanding Strengthening Process of Mn18Cr18N Hollow Forgings

As shown in Fig. 7, Mn18Cr18N hollow forgings can be strengthened by ultra-high pressure hydraulic expanding process, in which the hollow forgings expand along the radial direction gradually under the action of ultra-high hydraulic pressure. The punch serves only as a seal by contacting the ends of the hollow forgings. During hydraulic expanding process, the punch angle of θ and the contact state between the punch and the hollow forging have a great influence on the expanding manner.

The hydraulic expanding process of ϕ937/672 × 1034 mm hollow forging was analysed. Figure 8 shows the influence of punch angles on expanding manner at constant contact state (the contact seal height of 5 mm) between the punch and the hollow forging with mechanical seal coefficient of 1.2. It can be seen that there was an optimum punch angle in the vicinity of 60° for obtaining well-shaped strengthened forgings (Fig. 8c). When the punch angle is less than 60°, the ends of expanded forgings will be funnel shaped. On the contrary, the expanded forging will be drum-shaped, when the punch angle is greater than 60°.

Figure 9 shows that the influence of the contact seal height (h in Fig. 7a) on expanding manner at constant punch angle of 60° with mechanical seal coefficient of 1.2. It can be found that there was also an optimum contact seal height of 5 mm for obtaining well-shaped strengthened forgings (Fig. 9b). When the contact seal height is less than 5 mm, the ends of expanded forgings will be funnel shaped. On

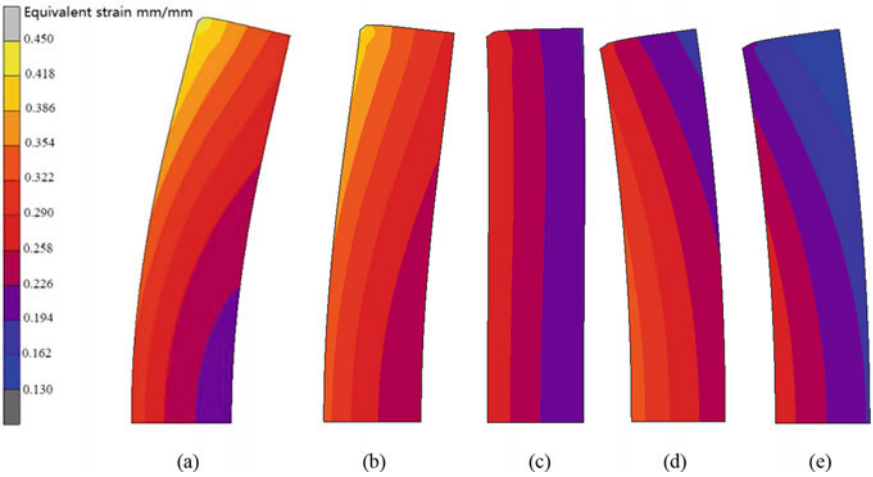


Fig. 8 The influence of punch angles on expanding manner with mechanical seal coefficient of 1.2 **a** 50° **b** 55° **c** 60° **d** 65° **e** 70°. (Color figure online)

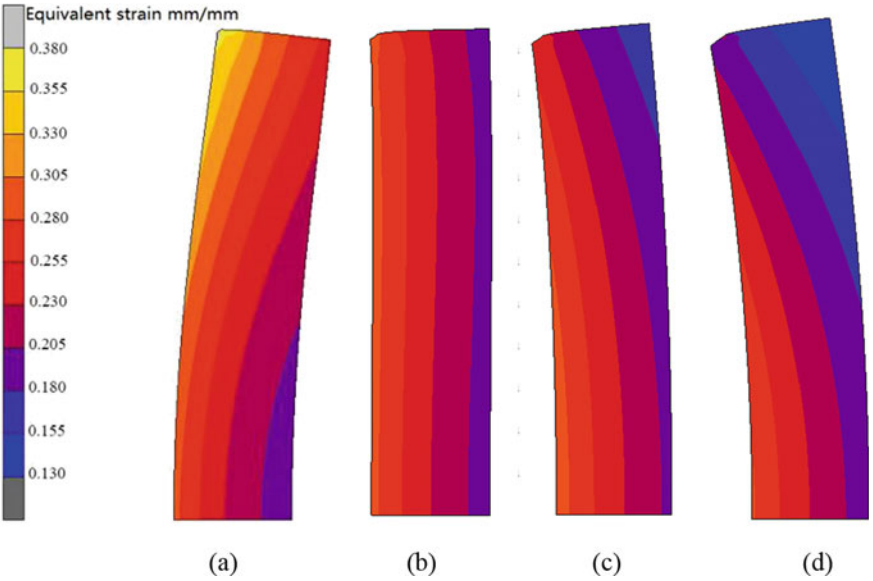


Fig. 9 The influence of the contact seal height on expanding manner with mechanical seal coefficient of 1.2 **a** 2.5 mm **b** 5 mm **c** 7.5 mm **d** 10 mm. (Color figure online)

the contrary, the expanded forging will be drum shaped, when the contact seal height is greater than 5 mm. Therefore, the contact seal height and the punch angle have to be matched to an optimum state for obtaining well-shaped hollow forgings.

4 Conclusions

In this paper, a short route manufacturing process of retaining rings was put forward, which was composed of hollow ingots manufacturing by ESR, hot ring rolling, and cold expanding strengthening. And microstructure mechanisms, deformation characteristics and process parameters during both of hot ring rolling and cold expanding strengthening were investigated. The conclusions can be drawn as follows:

(1) The multi-pass compression flow stresses of Mn18Cr18N ESR ingot sample coincide with that of the single-pass flow stresses at short interval time of 3 s. However, the multi-pass flow stresses decreased with increase of interval time. Grain was refined at lower temperature of 1050 °C by static recrystallization during multi-pass compression. Then, grain was refined at higher temperature of 1150 °C by both of dynamic and static recrystallization during multi-pass compression.

(2) For the thick-wall hollow ingots, strain penetration in the deformation zone must be considered the contact arc length ratio based on the conventional strain penetration model of ring rolling. Based on this, the driving roller radius of 500 mm and the pressure roller radius of 130 mm were determined for the ring rolling process ofφ712 mm/308 mm $\times$ 902 mm thick-wall hollow ingot. The optimum rotate velocity of the driving roller should be 0.8 rad/s. And the feeding velocity of the pressure roller had to be 1 mm/s for matching the driving roller.

(3) During cold deformation, planar slipping and twinning predominated at small and large deformation, respectively, which induce dislocation arrangement and grain boundaries as hindrance for dislocation movement to increase strength. For the hydraulic expanding process of ϕ937/672 $\times$ 1034 mm hollow forging, the optimum matching of 60° punch angle and 5 mm contact seal height can be adopted for obtaining well-shaped strengthened forgings.

Acknowledgments This work was financially supported by the National Natural Science Foundation of China (No. 51575372) Science and Technology Research Plan (Industrial) Project of Shanxi Province, China (No.201603D121006-2) and the Fund for Shanxi Key Subjects Construction.

References

1. Wang Z, Ning X, Meng Q et al (2016) A new insight into manufacturing fine-grained heavy retaining rings. Mater Des 103:152–159
2. Guo HG, Liu JS, Yang CC et al (2005) Development of a new hot forming technology for heavy retaining rings. J Mech Eng 41(11):171–173
3. An HP, Liu JS, Yang CC et al (2006) Research on the numerical simulation and the experimentation of the punching extrusion process with an outer ring for Mn18Cr18N retaining ring. Forg Stamp Technol 6:378–387
4. Scholz H, Biebricher U, Briickmann Esser GD (2013) ESR meets the requirements for big forgings. Iron Steel 48(10):82–87
5. Duan JC, Chen X, Liu FB, Jiang ZH (2013) Quality research of electroslag remelting 35CrMo hollow ingot. J Mater Metall 12(4):260–264
6. Chen HQ, He WW, Zhao XD et al (2017) Hot deformation behavior and dynamic recrystallization of Mn18Cr18N steel with as-cast versus wrought starting structures. Proc Eng 207:1779–1784
7. Qin FM, Zhu H, Wang ZX et al (2017) Dislocation and twinning mechanisms for dynamic recrystallization of as-cast Mn18Cr18N steel. Mater Sci Eng A 684:634–644
8. He WW, Li F, Zhang HY et al (2019) The influence of cold rolling deformation on tensile properties and microstructures of Mn18Cr18 N austenitic stainless steel. Mater Sci Eng A 764:
9. Hua L, Pan LB, Lan J (2009) Researches on the ring stiffness condition in radial–axial ring rolling. J Mater Process Technol 209(5):2570–2575
10. Sun G, Zhang Y, Sun S et al (2016) Plastic flow behavior and its relationship to tensile mechanical properties of high nitrogen nickel-free austenitic stainless steel. Mater Sci Eng A 662:432–442

Achieving an Interference Fit Between Two Rings During Composite Ring Rolling



Christopher J. Cleaver and Julian M. Allwood

Abstract Composite ring rolling could bring substantial material, cost, and energy savings and allow for lighter weight components, by joining concentric rings with different material properties. For there to be any possibility of achieving a material bond, an interference fit between the rings must be maintained. In this paper, a force equilibrium-based model is introduced to predict when such a fit is possible. This model, for radial composite rolling, predicts a limit to the flow stress of the inner ring relative to the outer ring, suggesting a maximum ratio of about 160%. It also shows that the inner tool's diameter must often be significantly smaller than the outer tool's. The model is tested in four composite ring rolling experiments with two grades of Aluminium alloy, 1050 and 6063, and different tool sizes. An interference fit was achieved in two cases: (1) when the inner ring is Al 1050 (flow stress 52% of the outer ring); and (2) when the two rings are both Al 6063 and the inner tool diameter was 39% of the outer tool. It was not achieved when (1) the materials were reversed nor when (2) the inner tool increased to 59% of the outer tool diameter. These outcomes were all predicted by the model, a potentially valuable new guide to designing composite ring rolling processes.

Keywords Ring rolling · Curvature · Joining

1 Introduction

Joining two rings together by ring rolling is an attractive proposition since it might be possible to tailor the material properties so that the ring is strong where it is needed, but expensive or heavy material is not wasted where it is not needed. Applications for such a process could include bearings, whose raceways are most heavily loaded—see Fig. 1a, and therefore increased hardness might be demanded on the outer and inner surfaces for the inner and outer raceways, respectively, regions I.

C. J. Cleaver (✉) · J. M. Allwood
Department of Engineering, University of Cambridge, Trumpington Street, Cambridge CB2 1PZ, UK
e-mail: cjc82@cam.ac.uk

© The Minerals, Metals & Materials Society 2021

G. Daehn et al. (eds.), *Forming the Future*, The Minerals, Metals & Materials Series,
https://doi.org/10.1007/978-3-030-75381-8_199

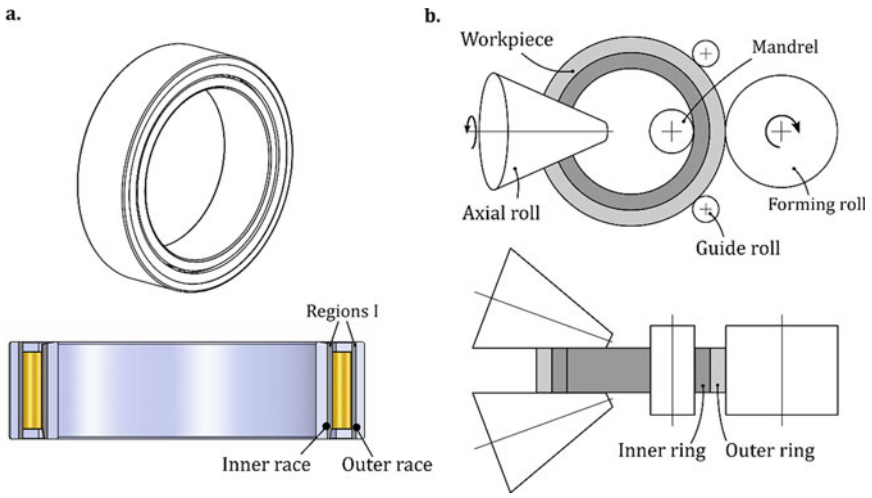


Fig. 1 **a** Possible application of composite ring rolling. **1b** Composite ring rolling machine setup. (Color figure online)

Rather than welding, or mechanically joining two rings of the correct 'final' size, better mechanical properties could be achieved by cold welding the workpieces in the process of expanding the stock material. Several previous studies have suggested this could be achieved by ring rolling two concentric blanks, as shown in Fig. 1b, a process labelled 'composite ring rolling'. Two rings of matching outer and inner radii are loaded together into a conventional radial-axial ring rolling machine. The radial and/or the axial roll gaps are closed as the workpiece rotates and the two rings ideally grow in diameter in tandem, maintaining an interference fit. Bonding occurs due to 'cold welding' in the solid state due to contact between the true surfaces of the metals in the exclusion of oxygen.

Achieving the interference fit throughout the composite ring rolling process is not trivial, and is the subject of this paper. As Fig. 2 demonstrates, a key hindrance is simply the fact that the outer ring is bigger than the inner one to start with; so if it experiences an equal strain, either in the radial or axial direction, it will 'naturally' get bigger by the same proportion, but by a larger *absolute* amount and so lose contact.

In radial rolling, there are two main ways to overcome this problem, i.e. to make it so that the inner ring 'wants' to grow faster than the outer ring. Firstly, the inner ring will want to grow faster if it is made from a softer material than the outer ring. By analogy to compressing two springs in series, the thickness reduction—and hence circumferential length increase—would tend to be larger for the softer inner ring than the harder outer ring. Alternatively, it might also be possible to achieve a faster growth rate by using a very small mandrel tool, even if the inner ring had an equal, or slightly larger, flow stress. By analogy to indentation with unequal indenters, the smallest indenter will tend to penetrate further, and so the inner ring deforms more.

Rather than rely on analogies or rules of thumb, it would be valuable to have a prediction for when an interference fit is possible: the topic of this paper.

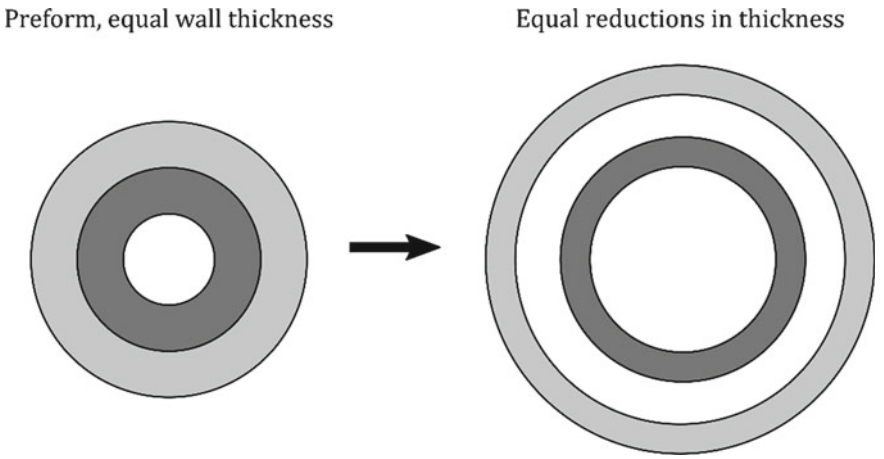


Fig. 2 **a** Tendency for outer ring to get bigger by a larger absolute amount

2 Literature Review

Previous efforts to achieve a 'composite ring rolling process' (Table 1) and past work on curvature change in ring rolling are briefly reviewed. The latter—the authors' recent model for curvature change in open-ended rings—is relevant to the interference fit prediction. Composite ring rolling is in some respects analogous to roll-bonding, which is a relatively well-established technique, both industrially and as a topic of scientific research (e.g. [1, 2]).

Table 1 Studies on joining two rings by ring rolling

Study	Inner ring material	Outer ring material	Flow stress ratio (Inner/Outer)	Description of study
Kluge et al. [3]	Duplex steel: X2CrNiMoN 22-5-3	Construction steel: StE 460	120%	Demonstration of feasibility
Seitz et al. [5]	Tempering steel: 13CrMo4-5	Stainless steel: X5CrNiMo17-12-2	50%	Achieving interference fit: effect of tool size
Kusters et al. [4]	Brass	Steel	Unknown	Cold composite rolling: working principle
Guenther et al. [6]	Tempering steel: 13CrMo4-5	Stainless steel: X5CrNiMo17-12-2	50%	Bonding: preform preparation, oxidation
Guenther et al. [7]	Tempering steel: 13CrMo4-5	Stainless steel: X5CrNiMo17-12-2	50%	Bonding: axial rolling strategies

One of the first studies on joining two rings by ring rolling was carried out in the 1990s by Kuesters et al. [3]. In this, a construction steel outer ring was bonded to a duplex steel inner ring. The two preforms were initially welded together in a conventional way, and then rolled at high temperature. In this case—unlike all other examples that follow—the inner ring was said to have a slightly larger flow stress (620 MPa vs. 520 MPa). The authors discuss the importance of ensuring the inner ring 'wants' to grow faster than the outer ring, however, they do not detail how this might be achieved more generally.

Guenther et al. [4] studied cold composite rolling, and showed that a softer material should be used for the inner ring to achieve an interference fit during the process, and enable bonding. Guenther et al. [5] investigated hot composite ring rolling of an inner ring of tempering steel, and an outer ring of stainless steel. The inner ring had a flow stress about 50% of the outer ring, and so 'wants' to grow at a faster rate. The study showed that in fact unless the mandrel size was increased to almost the same size as the inner diameter, the inner ring 'escaped' from the outer ring out of plane. Despite achieving an interference fit, there was no material bonding. Seitz et al. proposed the rule of thumb that to ensure process stability, the predicted contact length at the forming roll should be larger than that at the mandrel.

Li et al. [6, 7] studied bond formation in radial-axial composite ring rolling, using a tempering steel inner ring, and stainless steel outer ring. They highlighted two key measures to ensure material bonding. Firstly, care should be taken to ensure that no scale develops on the joint surfaces during heating—not trivial due to differing coefficients of thermal expansion. Secondly, that axial rolling tends to lead to debonding (possibly for the reasons given above), and therefore should be avoided early in the process.

The current study returns to the question of when an interference fit can be achieved, in light of the authors' recent work predicting curvature changes in ring rolling. In this, Cleaver and Allwood [8] studied curvature change in open-ended arcs in conditions analogous to ring rolling—a powered outer radial tool and idle inner radial tool, and no entry or exit tension. They developed an analytical model to predict how the roll size ratio—and reduction—influences curvature change. Predicted curvature changes from this model matched experimentally observations and numerical simulations, to within 7%. Could a similar approach be applied to predict when an interference fit is possible in composite ring rolling?

3 Prediction for When an Interference Fit Is Possible

This paper develops Cleaver and Allwood's model for free curvature change [8] to predict if an interference fit can be achieved in composite radial ring rolling. This requires a modification to account for materials of different flow stresses, and the criteria for achieving an interference fit. These are introduced in Sect. 3.1 and an exemplar prediction is then given in Sect. 3.2.

3.1 Force Equilibrium Model to Predict Radius Changes in Composite Radial Rolling

An interference fit requires the inner ring to extend proportionally more than the outer ring, which by volume conservation requires a greater reduction in thickness in the inner ring. Therefore, the first aim of the model is to predict—given a known total reduction in thickness ΔT—the notional reductions in thicknesses ΔT_1^* and ΔT_2^* for the inner and outer rings, respectively. These are notional in the sense that they assume each ring's radius growth is completely independent, i.e. they allow the inner ring to interfere with the outer ring. In reality, despite potentially having a greater 'tendency' to grow, the inner ring is of course constrained by the outer ring.

To predict ΔT_1^* and ΔT_2^*, two simplifications are made—firstly, that the composite rolling process is for two rings of equal thickness, secondly that the reductions ΔT_1^* and ΔT_2^* are exactly equal to the reductions in thickness at each roll ΔT_M and ΔT_F—see Fig. 3. As each reduction increases, the contact length and hence force on each roll will increase; and there will be one value of ΔT_M relative to ΔT_F that achieves force equilibrium in the y-direction.

The force in the y-direction at each roll is found by the well-established model introduced by Hawkyard et al. [9]:

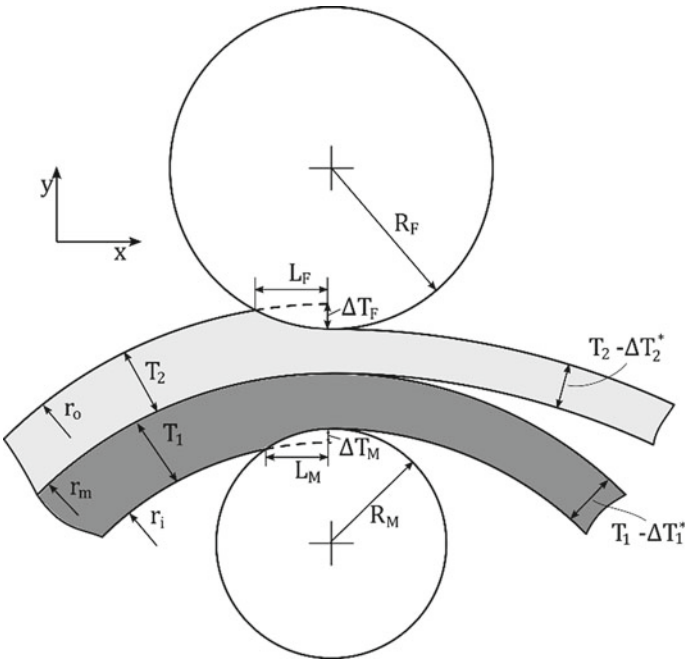


Fig. 3 Setup for composite rolling of two rings that are notionally free to interfere

$$F_M = \gamma_1 \overline{\sigma}_1 L_M \tag{1}$$

$$F_F = \gamma_2 \overline{\sigma}_2 L_F \tag{2}$$

where γ is the pressure factor, $\overline{\sigma}$ is the flow stress, and L is the projected contact length in the x-direction, and the subscripts denote inner and outer rings or rolling tools.

Since ΔT_1^* and ΔT_2^* are assumed to be equal to the equivalent reductions at the rolls ΔT_M and ΔT_F, then standard geometrical results give

$$L_M = \sqrt{\frac{\Delta T_1}{1/2R_M - 1/2r_i} - \Delta T_1^2} \tag{3}$$

$$L_F = \sqrt{\frac{\Delta T_2}{1/2R_F + 1/2r_o} - \Delta T_2^2} \tag{4}$$

where R_M and R_F are the mandrel and forming roll radii, respectively, and r_i and r_o are the composite ring's inner and outer radii.

The pressure factor approach introduced by Hawkyard et al. [9] is approximately

$$\gamma_1 \cong 0.8 + 0.2 * T/2L_M \text{ for } T > 2L_M \tag{5}$$

$$\gamma_2 \cong 0.8 + 0.2 * T/2L_F \text{ for } T > 2L_F \tag{6}$$

Finally, the flow stresses in each material are assumed to be given by

$$\overline{\sigma}_i = K_i \overline{\varepsilon}_i^{n_i} \tag{7}$$

Combining (3)–(7), the forces in Eqs. (1) and (2) are then balanced by a unique value of $\Delta T_1^*/\Delta T_2^*$ which can be found by numerical interpolation through the range $0 < \Delta T_1^*/\Delta T_2^* < 1$. If the effect of hardening can be ignored, then a closed form solution for this is possible, and is provided in Appendix.

Having found ΔT_1^* and ΔT_2^*, then the following condition is used to determine whether an interference fit is feasible. As illustrated in Fig. 2, the inner radius must 'want' to grow by more than the outer radius to account for it being initially smaller, and so we require

$$\Delta r_1^* > \Delta r_2^* + \Delta T/2 \tag{8}$$

where Δr_1^* and Δr_2^* are the notional increases in the inner and outer rings' mean radii, assuming that the rings are completely independent.

By volume conservation, assuming no axial spread we have

$$\Delta r_i^* = r_i \frac{\Delta T_i^*}{T_i} \tag{9}$$

So, the condition on ΔT_1^* to achieve an interference fit in composite ring rolling is

$$\Delta T_1^* > \frac{r_2 \Delta T_2^* + T\Delta T/2}{r_1} \tag{10}$$

3.2 *Predicted Operating Window for Composite Rolling*

Figure 4 sets out an operating window for the range of tool size ratios and ratio of flow stresses for which an interference fit is possible, as predicted by Eq. (10). The coloured lines represent the boundary between feasible and non-feasible operation, for different values of the ratio between the mean ring radius, r_m (of the composite ring) and the forming roll radius.

The model predicts that if the inner ring is softer than the outer ring, then it is always possible to achieve an interference fit. However, this also depends on having the right tool size ratio and the size of the ring relative to the forming tools. The smaller the mandrel is—or via effect 2 'appears' to be—the more likely an interference fit is predicted. Indeed, provided the mandrel is small enough an interference fit is predicted even if the flow stress is moderately higher in the outer ring.

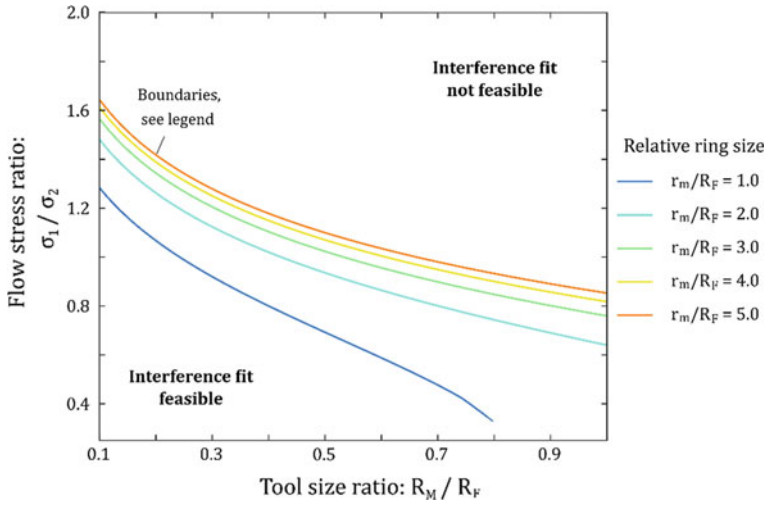


Fig. 4 Prediction for the range of ring size ratios and strength ratios for which an interference fit is possible for different relative ring radii. For $T/R_F = 0.17$, $\Delta T/T = 0.04$, $n = 0.14$. (Color figure online)

Although particular to the parameters listed in the caption, the prediction illustrated in Fig. 4 varies only by a small amount as these change within ranges reasonable to ring rolling.

4 Methodology: Composite Rolling Experiments

A set of four experimental trials was carried out to indicate whether the model could successfully predict if an interference fit is achievable in composite radial ring rolling. Tables 2 and 3 set out the experimental parameters used in the trials. There are four scenarios, labelled in Table 2. In the Soft inner ring trial and Soft outer ring trial, two different grades of aluminium were used with a large difference in flow stress at room temperature. In the Small and Big mandrel trials, the inner and outer ring are of the same material, and the mandrel varies by +30% and –13% from the mandrel size used in the first two trials, chosen because they lie on either side of the predicted feasibility boundary.

Flow stress curves for the two aluminium grades are given in Fig. 5, determined by compression tests on cylinders of diameter 15 mm and height 20 mm, carried out at room temperature. Teflon sheets were used as a lubricating medium. Three tests for each material were carried out and the dotted line represents an average fit to the Holloman model in Eq. (7).

Table 2 Four scenarios for composite radial ring rolling

Trial	Inner ring material	Outer ring material	Flow stress ratio $\overline{\sigma}_1 / \overline{\sigma}_2$	Mandrel size, R_M (mm)	Predicted outcome
Soft inner ring	Al-1050	Al-6063	0.52	45.0	Interference fit
Soft outer ring	Al-6063	Al-1050	1.89	45.0	No interference fit
Small mandrel	Al-6063	Al-6063	0.99	39.0	Interference fit
Big mandrel	Al-6063	Al-6063	0.99	58.9	No interference fit

Table 3 Constants

Variable	Value
Forming roll radius, R_F	100 mm
Ring average radius, r_m	200 mm
Inner ring wall thickness, $T1$	8.5 mm
Outer ring wall thickness, $T2$	8.5 mm
Height, H	18 mm
Nominal reduction in thickness per pass	4%

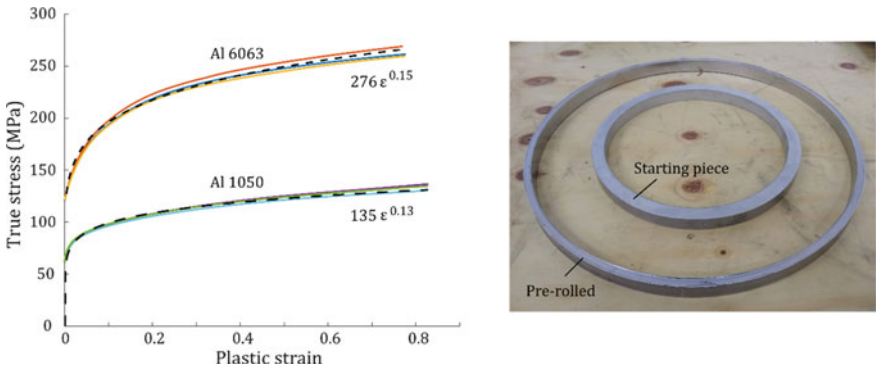


Fig. 5 **a** Flow stress curves for Al-6063 and Al-1050. **b** Pre-rolling. (Color figure online)

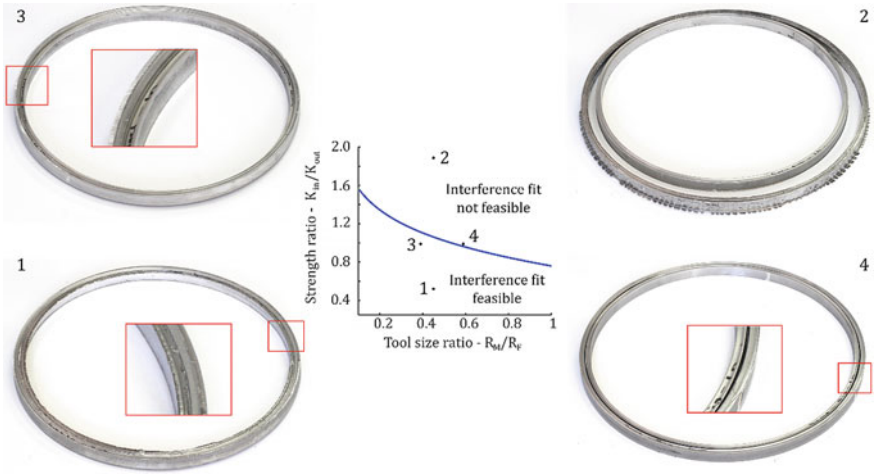


Fig. 6 Results of the four trials, compared to the prediction of Sect. 3. (Color figure online)

In order to prepare the rings for the test, the rings were first pre-rolled to the sizes specified in Table 3; the flow stress ratio quoted in Table 2 accounts for the work hardening due to pre-rolling. The composite rolling trials were carried out until it was clear whether an interference fit was achieved, for at least four revolutions in each case. Radial-only rolling was used, and the guide rolls—six in this case—applied a light force to stabilise the ring and prevent it from climbing out of plane.

5 Results

Figure 6 shows the results of the composite ring rolling trials and locates each on the axes used in Fig. 4. Figure 7 shows a series of images taken during the process.

An interference fit was achieved very rapidly in the Soft inner ring trial, and it was not in the Soft outer ring trial. This agrees with the prediction set out in Sect. 3, although intuition alone would probably also suggest that with such a large difference in flow stress the rings would behave as they did.

The Small mandrel and Big mandrel trials are a better test of the model, since it is *not* obvious a priori what mandrel size will and won't lead to an interference fit. An interference fit is achieved for the Small mandrel and not for the Big mandrel trial, in line with the prediction. It is notable that the clearance is much smaller for

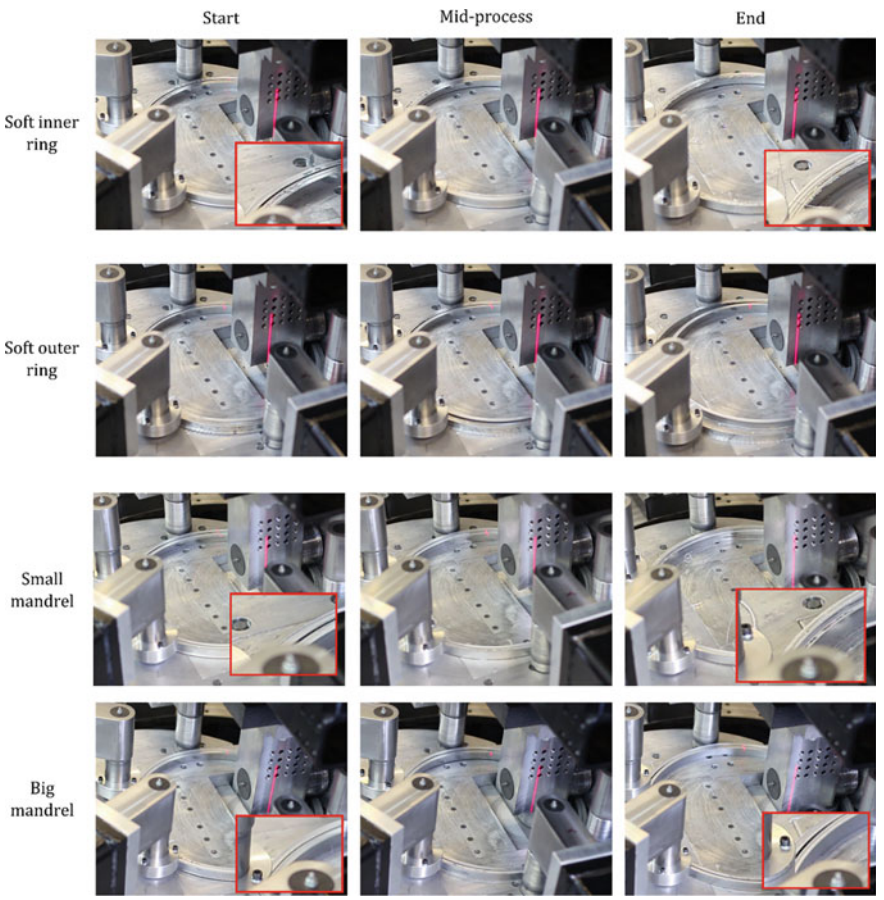


Fig. 7 Experiments on achieving an interference fit in composite ring rolling. (Color figure online)

the big mandrel trial compared to the Soft outer ring trial, which can be inferred by how close the experimental point is to the boundary on Fig. 7.

6 Discussion

This paper set out a way to predict if an interference fit is possible in composite radial ring rolling: a necessary but not sufficient condition for achieving a material bond. The prediction was successful in the four cases tested. Some caution is needed—for instance, the trials on the same material did not precisely establish the mandrel size where the feasibility line lies, simply that it is between 39.0 and 58.9 mm. The model could be anything from 0 to 20% wrong on this measure. Nevertheless, it does seem that Fig. 4 will provide a helpful guide to establishing whether a given composite rolling process is feasible.

A key finding from the operating window in Fig. 4 is the implied limit to the strength of the inner ring relative to the outer ring, at a ratio of somewhere between 125 and 160%. Composite rings with a much higher ratio are probably wanted; yet without further innovation, it seems impossible to produce them by composite radial ring rolling.

7 Conclusions

The following main conclusions are drawn from this work:

- The feasibility of achieving an interference fit in composite ring rolling primarily depends on the flow stress ratio, and on the tool sizes relative to each other and the ring.
- A model to predict if an interference fit is possible suggests the flow stress of the inner ring must be below about 1.6 times the flow stress of the outer ring.
- The model, based on force equilibrium, was tested under four different conditions and correctly predicted if an interference fit was possible in each, suggesting it is sufficiently accurate to *guide* process design
- For moderate values of the flow stress ratio in the region 0.8–1.4, the mandrel size can be adjusted to ensure an interference fit is achieved.

Appendix

Combining Eqs. (1)–(10), we have

$$(0.8 + 0.2T/L_1)K_1\left(\frac{2}{\sqrt{3}}\frac{\Delta T_1}{T/2}\right)^{n_1} L_1 = (0.8 + 0.2T/L_2)K_2\left(\frac{2}{\sqrt{3}}\frac{\Delta T_2}{T/2}\right)^{n_2} L_2 \tag{11}$$

Assuming ΔT_i^2 is small:

$$L_i = \sqrt{\frac{\Delta T_i}{A_i}} \text{ where } A_1 = \frac{1}{2R_M} - \frac{1}{2IR} \text{ and } A_2 = \frac{1}{2R_F} + \frac{1}{2OR} \tag{12}$$

Equation 11 can be rearranged in terms of L_1:

$$\widetilde{B}K_1(4L_1 + T)L_1^{2n_1} = \widetilde{C}K_2\left(4\sqrt{\frac{\Delta T - L_1^2 A_1}{A_2}} + T\right)\left(\Delta T - L_1^2 A_1\right)^{n_2} \tag{13}$$

Assuming no hardening ($n_1 = n_2 = 0$), then the force balance can be rearranged as follows:

$$4\left(K_1 L_1 - K_2\sqrt{\frac{\Delta T - L_1^2 A_1}{A_2}}\right) = T(K_2 - K_1) \tag{14}$$

The solution for L_1 is then

$$L_1 = \frac{\sqrt{16ab + 16ac^2 + bT^2\left(2c - 1 - c^2\right)} + cT(1 - c)}{4\left(b + c^2\right)} \tag{15}$$

where

$a = \frac{\Delta T}{A_2}$ $b = \frac{A_1}{A_2}$ $c = \frac{K_1}{K_2}$

The resulting prediction is compared to the numerically obtained predictions in Fig. 8.

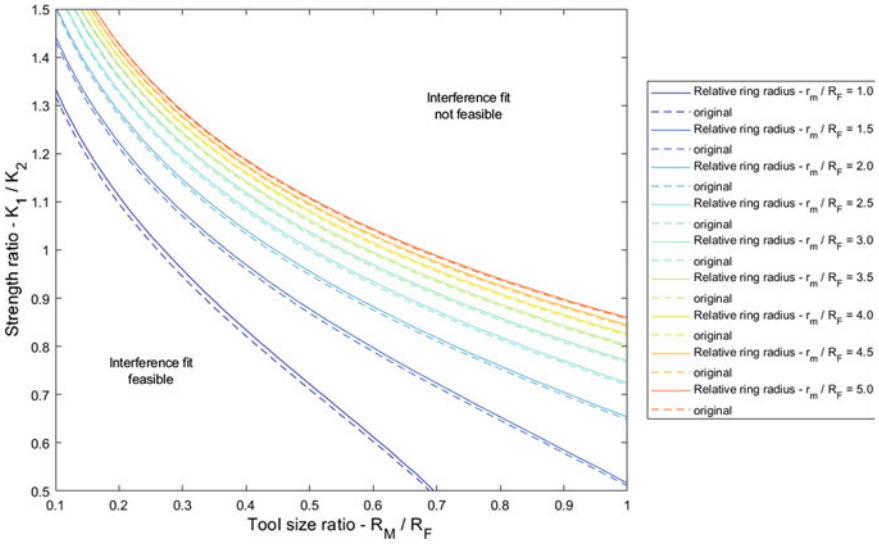


Fig. 8 Simplified closed form solution for the feasibility of composite ring rolling compared to the original numerically obtained solution. (Color figure online)

References

1. Kluge A, Wiegels H, Kopp R (1995) Ringwalzen von werkstoffverbunden. Stahl Eisen 115:37–38
2. Seitz J, Schwich G, Guenther S, Hirt G (2016) Investigation of a composite ring rolling process by FEM and experiment. In: MATEC web of conferences, vol 80, p 15011
3. Kuesters N, Schomaecker M, Brosius A, Kawalla R (2017) Herstellung Kraftschlussiger Messing Stahl Verbindungen Durch Verbundkaltringwalzen – Verfahrensprinzip und Einflussfaktoren
4. Guenther S, Seitz J, Schwich G, Hirt G (2017) Investigation of a composite ring rolling process considering bonding behaviour in FEM and experiment. Proc Eng 207:1236–1241
5. Guenther S, Schwich G, Hirt G (2020) Investigation of bond formation behaviour in composite ring rolling. J Mater Process Technol 275:116364
6. Li L, Nagai K, Yin F (2008) Progress in cold roll bonding of metals. Sci Technol Adv Mater 9:023001
7. Mori K, Bay N, Fratini L, Micari F, Tekkaya AE (2013) Joining by plastic deformation. CIRP Ann – Manuf Technol 62:673–694
8. Cleaver CJ, Allwood JM (2019) Curvature development in ring rolling. J Mater Process Technol 267:316–337
9. Hawkyard JB, Johnson W, Kirkland J, Appleton E (1973) Analyses for roll force and torque in ring rolling, with some supporting experiments. Int J Mech Sci 15:873–893

Advanced Design of Work Roll Contours for Different Roll Mill Types



Xiawei Feng, Xiaochen Wang, Quan Yang, and Zedong Wu

Abstract Steel producers are competing to roll non-grain oriented silicon (NGOS) strip with 1.25 m in width, 0.5–0.35 mm in thickness, and a profile deviation that is less than 5 micron-meters. Mathematical Models are indispensable tools to study the mechanism of work roll contours during rolling, but they require industrial tryouts to validate their effects on strip profile. Thus, this paper presents the effects of various work roll contours designed for (1) the 6th and 7th stand of a 4-high hot tandem rolling mill; (2) single stand 6-high reversing cold mill; (3) 1st to 3rd stands of a 6-high tandem cold mill. Results show that the NGOS strip profile hit rate of 5 micron-meters is increased by the implementations of advanced work roll contours.

Keywords Mathematical model · Edge drop control · Work roll contour

1 Introduction

Non-grain-oriented (NGO) silicon steel strip is an important soft magnetic material. In order to reduce eddy current loss, it is necessary to use hot and cold rolled laminates that are below 0.5 mm in thickness, and then stack them together. The phenomenon of edge drop (ED) defined in Eq. (1) is particularly detrimental to the lamination or stacking coefficient [1], shown in Fig. 1. Edge drop is the fundamental phenomenon during hot and cold rolling process resulting from wear and elastic deformation of work roll, the lateral flow of metal near the edge [2].

$$ED = \frac{1}{2}(h_{\text{eo1}} + h_{\text{ed1}} - h_{\text{ed2}} - h_{\text{eo1}}) \tag{1}$$

NGO strips are first hot rolled shown in Fig. 2, then if the thickness of the hot rolled strip is thicker than 2.2 mm thickness, it will be cold rolled by cold tandem

X. Feng (✉)
Instrumentation Technology and Economy Institute, Beijing, People's Republic of China
e-mail: fengxiawei@qq.com

X. Wang · Q. Yang · Z. Wu
University of Science and Technology Beijing, Beijing, People's Republic of China

© The Minerals, Metals & Materials Society 2021

G. Daehn et al. (eds.), *Forming the Future*, The Minerals, Metals & Materials Series,
https://doi.org/10.1007/978-3-030-75381-8_200

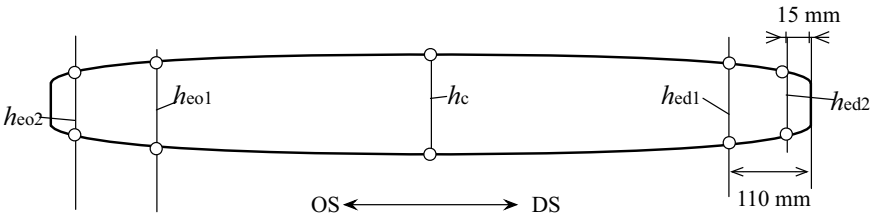


Fig. 1 Definition of strip edge drop

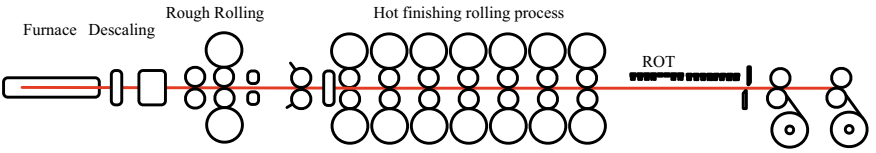


Fig. 2 Schematic illustration of hot rolling process. (Color figure online)

mills shown in Fig. 3, otherwise it will be cold rolled by cold reversing mills shown in Fig. 4. The reversing mill's work roll diameter is 240 mm, which is significantly smaller than cold tandem mills' 420 mm. Previous studies treat them separately: Ma et al. found that the implementation of work roll contours during reversal rolling process leads to flatness problem [3]. They further pointed out that for six-high reversible rolling process, the hot rolled profile has strong relationship with the cold rolled profile [4]. Wang et al. [5] proposed a concept of rectangular section control strategy for hot and cold tandem rolling process, experiments showed that a hot rolled strip with a stable crown and limited wedge, local spot, and single wave is

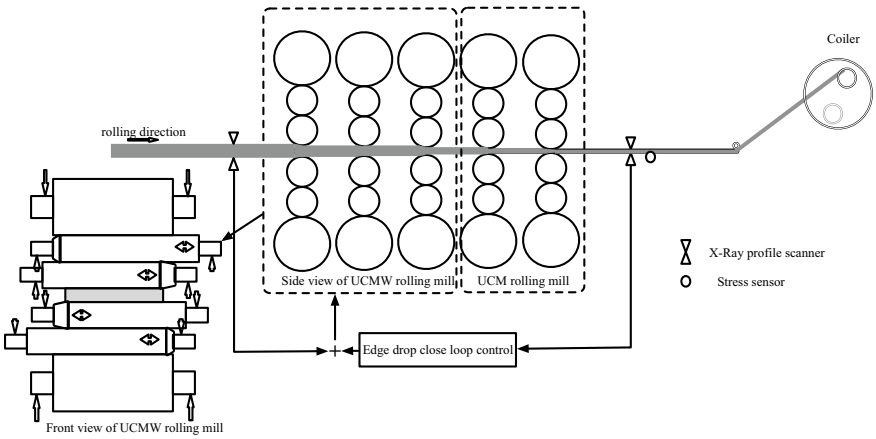


Fig. 3 Schematic illustration of 5-stand six-high cold rolling process

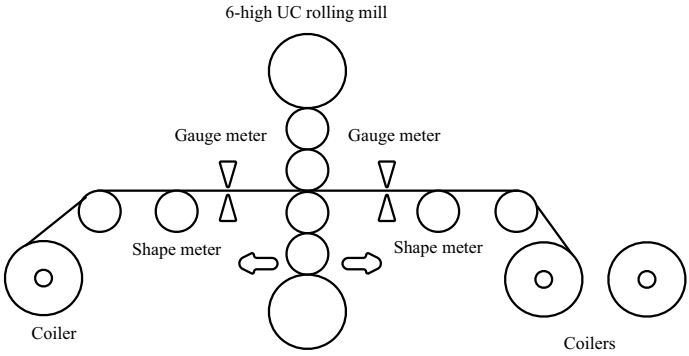


Fig. 4 Schematic illustration of six-high reversing cold rolling process

Table 1 Rolling parameters for 5-stand 6-high cold rolling mill

Stand No.	Back and front tension/MPa	Friction coefficient	Entry/exit thickness/mm
1st stand	15/135	0.085	2.5/1.8
2nd stand	135/140	0.075	1.8/1.18
3rd stand	140/145	0.06	1.18/0.8
4th stand	145/145	0.05	0.8/0.578
5th stand	145/55	0.045	0.578/0.5

recommended, and work roll contour is only needed at first and second stands of 5-stand cold tandem rolling process. The question is why is the work roll contour so different for these two mill types.

2 Industrial Setups of Hot and Cold Strip Rolling

One major difference between six-high reversing mill and cold tandem mill is that the front and back tensions of reversing mill at each pass can be separately set up, but the front tension of previous stand is the back tension for the next stand. The other is the diameter of work roll, as stated above. The rolling parameters of tandem cold rolling process are shown in Table 1 that of reversing mill are shown in Table 2.

3 Analytical Lateral Flow Model Based on FEM

Previous studies show that even though the majority part of strip width undergoes plain strain deformation, but the edge of strip deforms in 3D, that is to say the material of strip lateral flows to the edge. Lateral metal flow is one of the main contributions

Table 2 Rolling parameters for reversing cold mill

Pass No.	Back and front tension/MPa	Friction coefficient	Entry/exit thickness/mm
1st pass	20/118	0.075	2.2/1.36
2nd pass	87/150	0.06	1.36/0.87
3rd pass	88/150	0.05	0.87/0.566
4th pass	107/130	0.047	0.566/0.43
5th pass	100/100	0.045	0.43/0.35

to edge drop, and a lateral flow model has been built to study the effects of rolling parameters on the width of lateral flow zone, and on the maximum value of lateral flow. Given the fact that the lateral flow during strip rolling is complicated, some simplification has to be made. In the previous study [6], the lateral flow G is defined as

$$G = -(1 + d\varepsilon_z/d\varepsilon_x) \tag{2}$$

where x, y, z is rolling, width and thickness direction respectively. Its distribution is simplified as

$$G(y) = \frac{G_{\max}}{(0.5B - y_0)^2}(y - y_0)^2, |y| \in [y_0, 0.5B] \tag{3}$$

where $G_{\max}$ is the maximum value of lateral flow, y_0 is the starting location of lateral flow, B is the strip width. They can be calculated as [6]

$$G_{\max} = 0.05 k_S k_\mu^{\max} k_\sigma^{\max} \tag{4}$$

where

$$\begin{cases} k_S = 0.009(Y_S - 100) + 1 \\ k_\mu^{\max} = 6(\mu - 0.05) + 1 \\ k_\sigma^{\max} = \left[0.0037\left(70 - \sigma_f\right) + 1\right][0.0051(50 - \sigma_b) + 1] \end{cases} \tag{5}$$

where Y_S is the yield limit of strip, μ the friction coefficient, σ_b and σ_f is the back and front tension stress. y_0 can be calculated as

$$y_0 = 0.5B - 30 k_h k_r k_\mu^{y0} \tag{6}$$

where

$$\begin{cases} k_h = 0.21\left(h_{\text{entry}} - 1.2\right) + 1 \\ k_r = 2(re - 5) + 1 \\ k_\mu^{y0} = 5.13(0.18 - \mu) + 1 \end{cases} \tag{7}$$

where h_{entry} is the entry thickness of strip, *re* is the reduction rate of the current pass. Considering the different work roll diameter and tension setups in reversing and tandem rolling process, the above lateral flow model has to include the effects of these parameters by FEM simulations.

As a general mathematic tool, FEM has been widely used to study the fundamentals of rolling process [7], it showed great precision in geometry calculation [8], and it has been used to study the mechanism in rolling process [9]. A 3D FEM model by Abaqus has been built to study the effects of different work roll diameter, back and front tension stress on the lateral flow factor *G,* i.e., $G_{\max}$ and y_0.

Figure 5 shows the effect of different back and front tension on the lateral flow factor. It can be seen that adding front tension has no significant effect on $G_{\max}$, but has some effect on y_0. On the other hand, back tension has great influence on both $G_{\max}$ and y_0. So that k_σ^{max} has to be revised and a k_σ^{y0} term has to be added to y_0:

$$k_\sigma^{\max} = 0.0051(80 - \sigma_b) + 1 \tag{8}$$

$$k_\sigma^{y0} = [0.00068(80 - \sigma_b) + 1]\left[0.00068\left(80 - \sigma_f\right) + 1\right] \tag{9}$$

Figure 6 shows the effect of different work roll diameter on the lateral flow factor. It can be seen that reducing work roll diameter significantly reduced $G_{\max}$ and the width of lateral flow area. So that a $k_D^{\max}$ has to be added to $G_{\max}$ and a k_D^{y0} term has to be added to y_0:

$$k_D^{\max} = -0.05(425 - D)/100 + 1 \tag{10}$$

$$k_D^{y0} = -0.1(425 - D)/100 + 1 \tag{11}$$

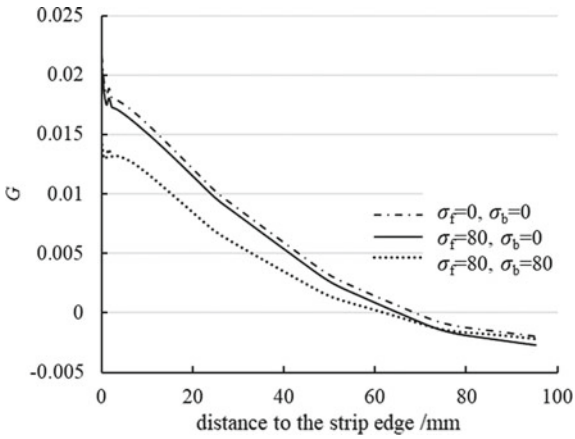


Fig. 5 Lateral flow factor *G* with different front and back tensions

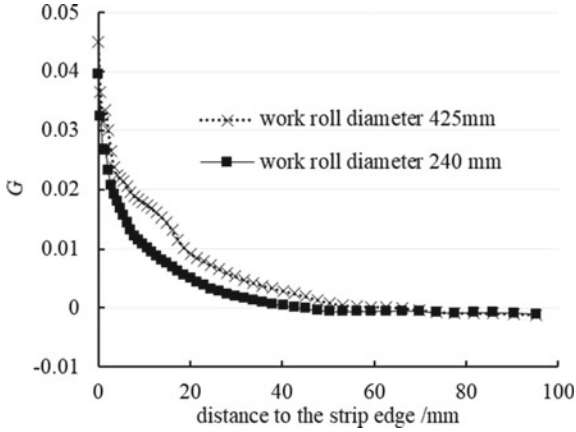


Fig. 6 Lateral flow factor G with different work roll diameters

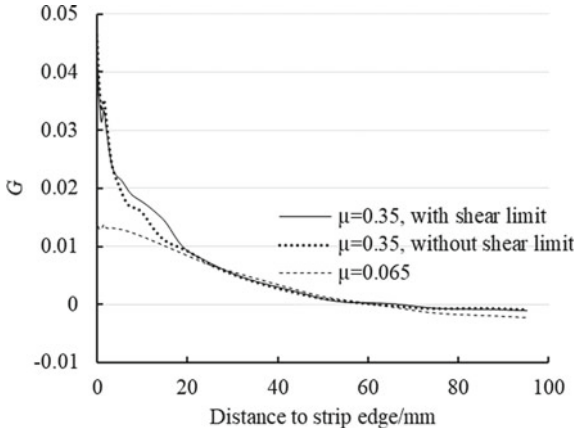


Fig. 7 Lateral flow factor G with different friction conditions

Figure 7 shows the effect of different friction conditions on the lateral flow factor. It can be seen that reducing friction coefficient greatly decreases the lateral flow factor $G_{\max}$, but has no effect on the lateral flow width y_0. So that the term k_{μ}^{y0} has to be taken out.

4 Model Results and Industrial Data

By using the analytical lateral flow model above, the calculated lateral flow factors are shown in Tables 3 and 4 for tandem and reversing cold mills, respectively. It can be seen that for the 1st pass of tandem rolling process, the maximum lateral flow factor $G_{\max}$ is significantly larger than the other 4 passes and also larger than that of reversing mill. It suggests that the taper of work roll contour for tandem mill has to

Table 3 Results of lateral flow model for tandem mill

Stand No.	G_{max}	$0.5B - y_0$
1st stand	0.32	60
2nd stand	0.17	48
3rd stand	0.16	42
4th stand	0.15	38
5th stand	0.15	30

Table 4 Results of lateral flow model for reversing mill

Pass No.	G_{max}	$0.5B - y_0$
1st pass	0.28	49
2nd pass	0.21	38
3rd pass	0.20	34
4th pass	0.19	27
5th pass	0.19	25

be larger than that of reversing mill. The G_{max} of the last 4 passes of tandem rolling process is smaller than that of 4-pass reversing mill; it suggests that there is no need of work roll contour on the last passes of tandem rolling process, and that the cold rolled profile of reversing mill has stronger similarity with hot rolled profile than tandem rolling mill. It also can be seen that the lateral flow width of reversing mill is smaller than tandem rolling. It suggests that in order to avoid flatness problem during reversing mill rolling it is necessary to reduce hot rolled strip edge drop.

A work roll contour has been grounded on the 6–7 stand of a 4-high hot tandem rolling process, shown in Fig. 8. The effect of work roll contour of hot rolling on the cold rolled product is shown in Table 5. It can be seen that the implementation of work roll contour on hot rolling mill makes a larger impact on the reversing mill. It is consistent with lateral flow model prediction.

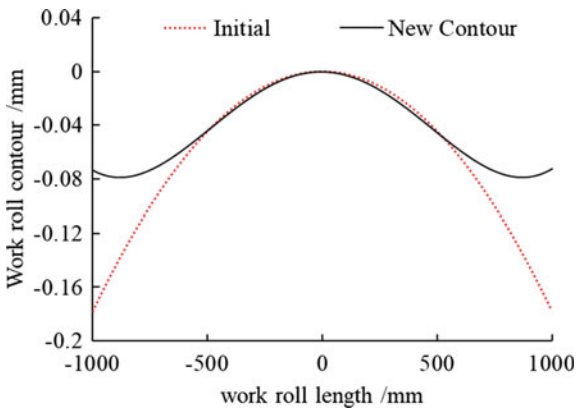


Fig. 8 Work roll contours for the last 2 stands of hot tandem rolling. (Color figure online)

Table 5 Effects of hot rolling work roll contour on cold rolled strip

Mill type	Edge drop (μm)	
	Before	After
Reversing mill	1.91	1.17
Tandem mill	2.61	2.32

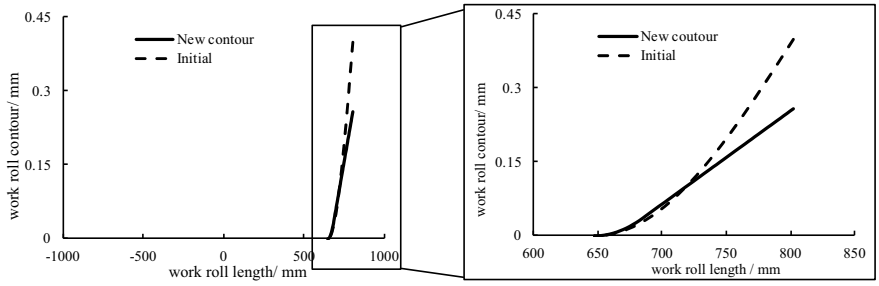


Fig. 9 Work roll contours for the first stand of hot tandem rolling

Table 6 Effects of cold tandem rolling work roll contour on cold rolled strip

	Before (%)	After (%)
Hit rate < 5 μm	19.5	35

A work roll contour has been grounded on the first stand of cold tandem rolling process, shown in Fig. 9. The effect of work roll contour on the cold rolled product is shown in Table 6. It can be seen that the cold rolled product hit rate can be improved by the work roll contour.

5 Conclusion

Finite element model reveals that work roll diameter has a significant effect on lateral flow during strip rolling process, back and front tension setups are different between tandem and reversing mill, and result in a significant difference in lateral flow model results. The results of lateral flow model and the industrial data are in good agreement. Improvement of hot rolled edge drop has larger effect on reversing mill than tandem rolling.

References

1. Li H, Zhao Z, Dong D et al (2018) Edge drop control behavior for silicon strip cold rolling with a sendzimir mill. Metals. https://doi.org/10.3390/met8100783
2. Cao J, Chai X, Li Y et al (2018) Integrated design of roll contours for strip edge drop and crown control in tandem cold rolling mills. J Mater Process Technol 252:432–439
3. Ma X, Wang D, Liu H et al (2018) Influence of profile indicators of hot-rolled strip on transverse thickness difference of cold-rolled silicon steel. Metall Res Technol. https://doi.org/10.1051/metal/2018044
4. Ma X, Wang D, Liu H (2017) Coupling mechanism of control on strip profile and flatness in single stand universal crown reversible rolling mill. Steel Res Int 88:1600495
5. Wang X, Yang Q, Sun Y (2015) Rectangular section control technology for silicon steel rolling. J Iron Steel Res Int 22:185–191
6. Feng X, Wang X, Sun J et al (2019) Analysis of tapered work roll shifting technique in 5-stand UCMW tandem cold rolling process. Aust J Mech Eng. https://doi.org/10.1080/14484846.2019.1606762
7. Montmitonnet P (2006) Hot and cold strip rolling processes. Comput Methods Appl Mech Eng 195:6604–6625
8. Kim TH, Lee WH, Hwang SM (2003) An integrated FE process model for the prediction of strip profile in flat rolling. ISIJ Int 43:1947–1965
9. Feng X, Montmitonnet P, Yang Q et al (2017) An advanced 3d mathematical model for a 6-high tandem cold rolling process. Proc Eng 207:1379–1384

Study on the Transferability of Rolling with Ordered Texturing Roll



Yasuyuki Fujii, Yasushi Maeda, and Hiroshi Utsunomiya

Abstract Surface textured rolling is designed to transfer roughness onto the sheet from the surface of textured rolls. The authors investigated the influence of rolling conditions on transferability using an ordered texture roll experimentally. To understand such influence, we compared the rolled surface profiles during the experiments with those during Finite Element Analysis (FEA). However, at reductions greater than 5%, there is a discrepancy, which is believed to be caused by unknown restraint force. As it is difficult to estimate the restraint force with a 3D profile roll, we carried out experimental transformability tests with 3 simpler kinds of ordered texture rolls, namely, (1) RD, (2) TD, and (3) 45-degree groove rolls. In this paper, the apparent friction coefficients were evaluated experimentally with these rolls. The friction coefficients were found to be affected by several metal flows in the roll bite. In conclusion, it is still difficult to estimate the apparent friction coefficient because these metal flows affect each other.

Keywords Texture rolling · Surface roughness · Friction coefficient · Rolling experiment

Y. Fujii (✉)
Mechanical Working Research Section Materials Research Laboratory, KOBE STEEL, LTD., 1 5-5, Takatsukadai, Nishi-ku, Kobe 651-2271, Japan
e-mail: fujii.yasuyuki@kobelco.com

Y. Maeda
Materials Research Laboratory, KOBE STEEL, LTD., 1 5-5, Takatsukadai, Nishi-ku, Kobe 651-2271, Japan
e-mail: maeda.yasushi@kobelco.com

H. Utsunomiya
Division of Materials and Manufacturing Science, Osaka University, 2-1 Yamadaoka, Suita, Osaka 565-0871, Japan
e-mail: uts@mat.eng.osaka-u.ac.jp

© The Minerals, Metals & Materials Society 2021

G. Daehn et al. (eds.), *Forming the Future*, The Minerals, Metals & Materials Series,
https://doi.org/10.1007/978-3-030-75381-8_201

1 Introduction

The surface property of rolled strip is one of its most important characteristics. In texture rolling, the profile on the textured roll is transferred to that on the strip. In many previous studies, the character of the surface has employed the average roughness such as Ra [1]. Furthermore, numerous studies of skin-pass rolling with dull rolls have mainly discussed this under conditions where there was less than a 5% reduction. For example, Aoki et al. carried out rolling transcription experiments by changing the reduction, roll roughness, and inlet thickness. They reported that the transcribed average roughness on the sheet is dependent on the reduction, the surface pressure, and the shape factor. However, their results only looked at a low reduction region (<5%), and did not examine behavior at a higher reduction region [2]. Some studies have reported on numerical predictions of surface texture. For example, a rolling 2D-FEM simulation using a zooming method was studied by Yukawa et al. [3]. They showed the results of 2D-FEM at a relatively higher reduction region. However, there was no quantitative comparison with experimental results in their report. A simple compression simulation with a solid die using 2D-elastic-plastic FEM was studied by Ike [4]. In his conclusion, the frictional force and the angle of the die wedge were important for the surface profile. However, this model was a simple compression process. In the rolling process, there are relative vertical and horizontal velocities between the die and the material. In our previous research, we took into account the effect of both relative velocities in the rolling process, using the microscopic 3D deformation mode. In our present research, an ordered textured roll was used experimentally, and the profile of the rolled surface was measured as individual transcribed 3D profiles. To predict each individual profile, a 2-step FEA was established. In the first step, the relative velocity between the roll and the material in the roll bite was decided each time using 2D FEM for macroscopic analysis. In the second step, microscopic 3D FEA of the solid die and elastic–plastic material was applied, giving the relative velocity from macroscopic 2D FEA as the time step boundary conditions. Our results showed that, under lower reduction conditions, there was a high degree of agreement between the numerical predictions and the experimental results [5]. However, there was a discrepancy between them at higher reduction region (Fig. 1) [6]. We discovered that it was difficult to estimate the exact value of the material velocity on the microscopic 3D model from the results of 2D-FEM). It is believed that this affects an accurate estimation of the friction coefficient due to the formation of projections and the pattern itself on the roll.

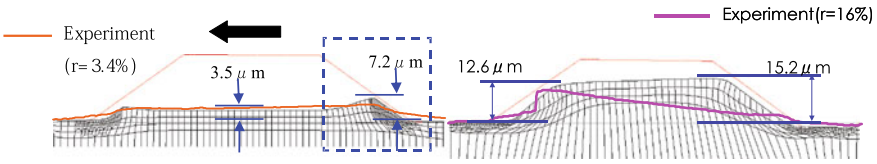


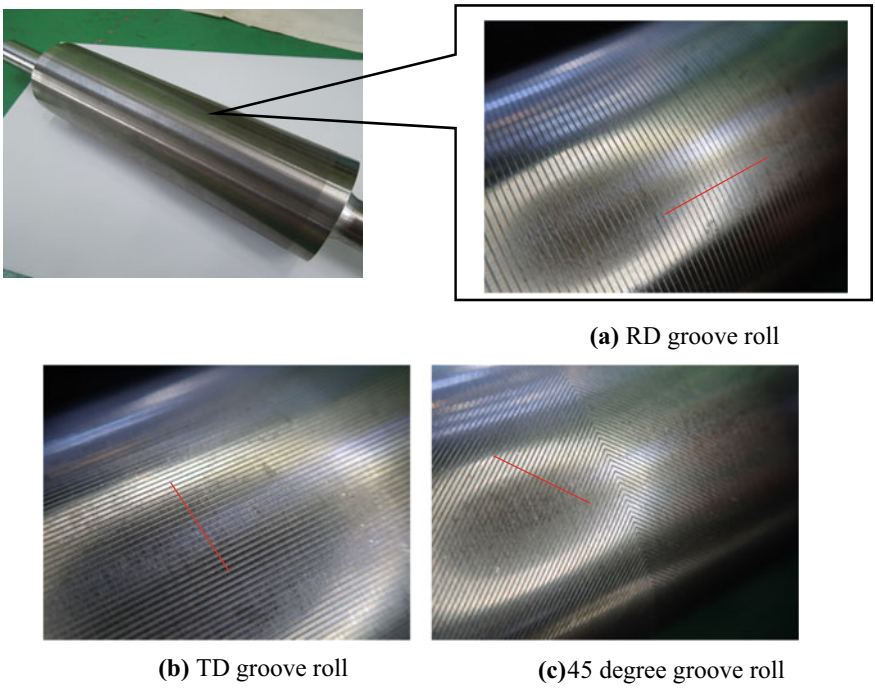
Fig. 1 3D-FEM simulation result (left: r = 3.4%, right: r = 16.0%). (Color figure online)

In this paper, we carried out experiments on transformability with 3 kinds of ordered texture rolls where: (1) the RD groove roll has the groove along the radial direction of the roll, (2) the TD groove roll has the groove along the axial direction of the roll, and (3) the 45-degree groove roll has the groove at an angle of 45° to the roll. We expected that an ordered 3D texture roll might be a mixture of these. These experiments showed that different rolls have different restraint force and friction coefficients.

2 Experimental Conditions

To simplify the discussion, three kinds of work roll with different ordered patterned surfaces were used, as shown in Fig. 2a–c. In Fig. 2a, the RD groove roll has the groove along the cylindrical direction of the roll surface. In Fig. 2b, the TD groove roll has the groove along the axial direction. In Fig. 2c, the 45-degree groove roll has the groove along different 45-degree directions against the center.

These grooves have the same profile as shown in Fig. 3. A 4-high rolling mill was used in the rolling test with these rolls as the work rolls. The back-up roll was 300 mm in diameter, and the work roll 55 mm. The patterned rolls were used as



(a) RD groove roll

(b) TD groove roll

(c)45 degree groove roll

Fig. 2 Roll appearance. (Color figure online)

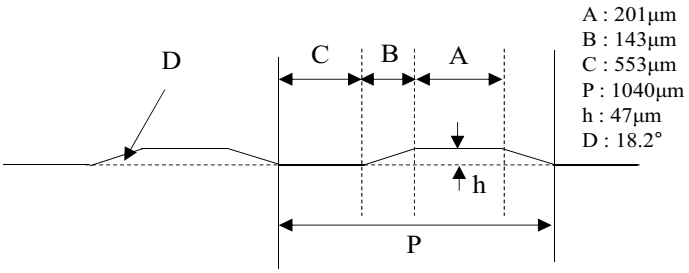


Fig. 3 Roll surface cross section

only the top work roll, and the bottom work roll was set to be a bright roll. The rolled material was pure titanium, 0.61 mm in thickness, 50 mm in width, and about 200 mm in length. The rolling reductions were changed from 5 to 25%. In addition, the 45-degree groove roll was asymmetrical with regard to the direction of rotation. We identified normal rotation and reverse rotation as shown in Fig. 4. A summary of the experimental conditions is shown in Table 1. After the rolling tests, the profiles transcribed onto the surface were measured using a laser microscope.

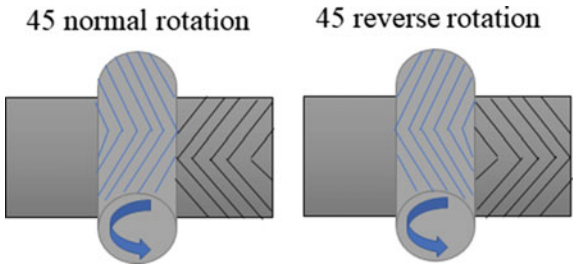


Fig. 4 45-degree groove roll rolling direction. (Color figure online)

Table 1 Experimental conditions

Mill	4Hi
Roll	Upper:groove roll (φ55 mm × L265 mm) (a) RD groove roll (b) TD groove roll (c) 45 degree groove roll Lower:bright (φ55 mm × L265 mm)
Material	Purity titanium (ASME:Gr1) h0.61 mm × w50 mm × L200 mm
Lubricant	Dry
Reduction	5–25%
Tension	0 Mpa
Roll speed	1.0 mpm

3 Experimental Results

3.1 Height of Transcribed Profile

In Fig. 5, the heights of the transcribed profile on the rolled sheets are shown as the relationship of the reductions from the experimental results. The height was strongly dependent on reduction under about 15% with any type of roll. On the other hand, at over 15%, it seems that the height is almost constant, and the values depend on the type of roll. Further, the height of the transcribed profile for each type of roll increases at higher reductions in the following order: TD groove roll, reverse rotation of 45-degree roll, normal rotation of 45-degree roll, RD groove roll. This order is understandable if the following mechanism is assumed, namely, that the height of the profile is formed by compressive metal flow on the surface of the roll bite. In general, material elongates along the rolling direction in the rolling process. In these experiments, surface elongation in the roll bite is resisted by the groove on the roll. The magnitude of such resistance depends on the direction of groove. The RD groove has the smallest resistance. Conversely, the TD grove has the largest one. The resistance of the 45-degree roll lies between the two. Imagining the surface resistance is useful in expecting the order of the type of roll.

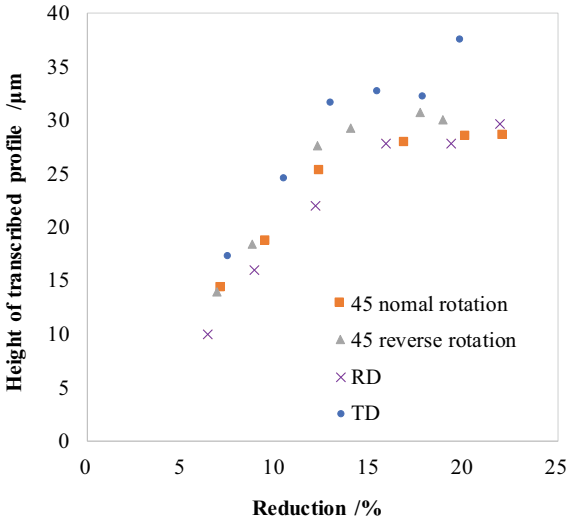


Fig. 5 Relation between rolling conditions and height of transcribed profile. (Color figure online)

3.2 *Estimation of Friction Coefficient*

The influence of the restraint force in the roll bite to be formed the projection height was suggested. To confirm the effect qualitatively, we estimated the friction coefficient during rolling on each roll as a macroscopic parameter. The method used to estimate the friction coefficient is described below. The sheet thickness on both the entry side and delivery side were measured under each condition.

Using the inverse equation of Hill's rolling load model, the estimated friction coefficient is shown in Eq. (1). However, flow stress k was estimated using Eq. (2). R' was calculated with Hitchcock's model using measured rolling load. Here, parameters A and n in Eq. (2) were determined using the fitting method taken from a great deal of experimental rolling data. As shown in Fig. 6, the estimated friction coefficients have strong dependency not only on reduction, but also on the type of roll. In general, the estimated friction coefficients increase as reduction increases. It is believed that there are two reasons for this increase. One is the new active surface, which is mainly formed by higher reduction. The other is the geometrical profile, which is shown in Fig. 3. It is difficult to explain these effects simply. We discuss this in detail in the following section.

$$\mu = \frac{\frac{P}{w\cdot\sqrt{R'\cdot(h1-h2)}\cdot(k-0.5\cdot(S1+S2))} + 1.02\cdot r - 1.08}{1.79\cdot r\cdot\sqrt{R'/h2}\cdot\sqrt{1-r}} \tag{1}$$

μ: friction coefficient P: rolling load w: width

R': flattening roll diameter $h1$: thickness of entry side $h2$: thickness of delivery side

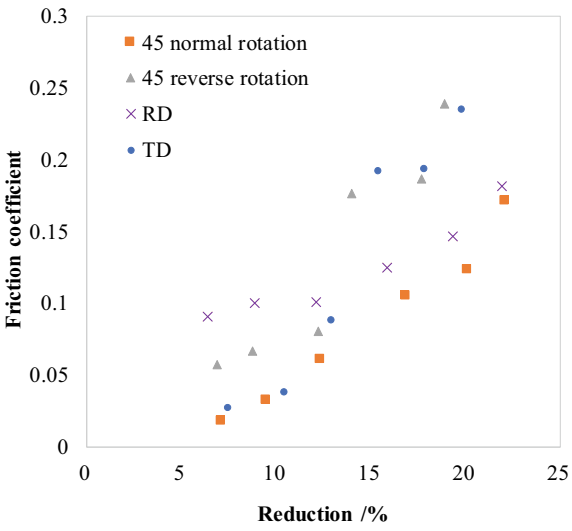


Fig. 6 Relation between reduction and friction coefficient. (Color figure online)

$S1$: tension of entry side $S2$: tension of delivery side
r: reduction k: flow stress

$$k = A \cdot \varepsilon^n \tag{2}$$

A: statical flow stress (112.7 kgf/mm^2) ε: strain n: work-hardening exponent (0.122).

4 Estimated Friction Coefficient at Each Roll

4.1 Friction of TD Groove Roll

A significant characteristic of the TD groove roll is that the friction coefficient shows an increased jump at around 15% reduction. In the TD groove roll, the geometrical distance between neighboring grooves is shorter along the rolling direction. If there is only one groove in the roll bite, the effect of the groove is limited. However, if there is more than one groove, the forward groove is highly resistant to the 2nd one. In evaluating this phenomenon, the contact length between the roll and the sheet was compared with the geometrical groove pitch. The relation between the friction coefficient and the ratio of these is shown in Fig. 7. In this figure, a jump in the friction coefficient exists around 2.0. This means that the number of grooves in the roll bite is important, and more than 2 grooves in the roll bite induce increasing resistance.

Previously, we examined the effect of the number of grooves in a roll bite on the friction coefficient and the height of transcribed profile by using 2D-FEA. The

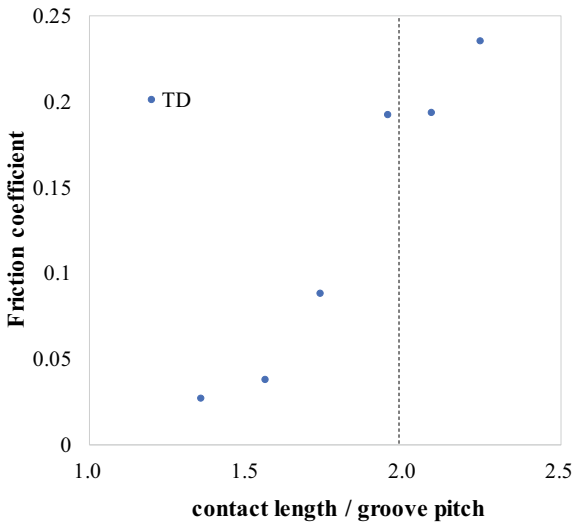


Fig. 7 Relation between rolling conditions and height of transcribed profile. (Color figure online)

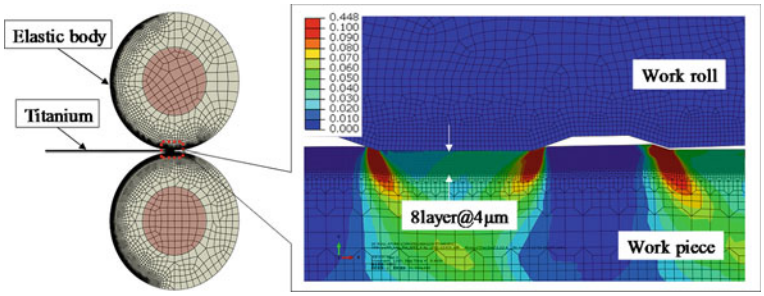
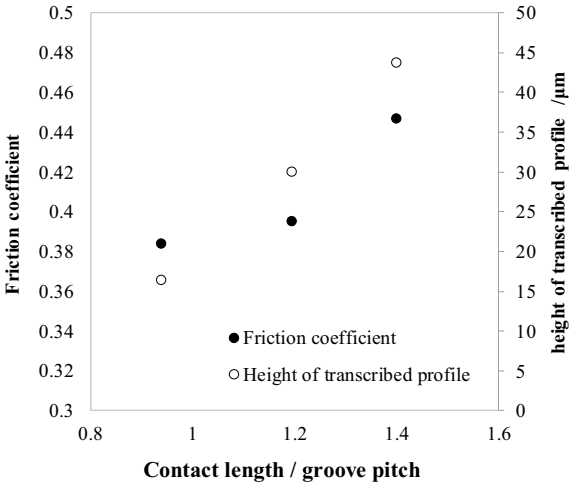


Fig. 8 2D-FEA model of rolling. (Color figure online)

Fig. 9 Relation between rolling conditions and friction coefficient and height of transcribed profile



"ABAQUS-standard" in 2D-FEA was used for the simulations of the rolling test. The rolling model of the 2D-FEA is shown in Fig. 8 [7]. Figure 9 shows the relation between number of contact grooves and the friction coefficient from the 2D-FEA. The friction coefficient in the figure was estimated from Eq. (1) using the rolling load obtained from the 2D-FEA. As a result, it was confirmed that the apparent friction coefficient (restraint force) increased as the number of grooves in the roll bite increased. Also, it was clarified that the height of transcribed profile increased with the increase in the friction coefficient.

4.2 Friction Coefficient of 45-Degree Groove Roll

In the case of a 45-degree groove roll, there is a difference in estimated friction coefficients between normal and reverse rotation. The friction coefficient of reverse

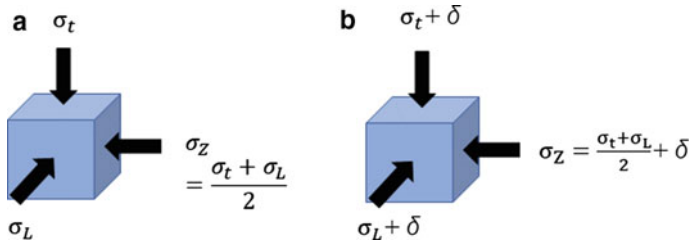


Fig. 10 Yield condition. **a** Plain strain. **b** Plain strain with additional stress δ. (Color figure online)

rotation is higher than in the case of normal rotation (Fig. 6). This difference is considered to be influenced by the lateral metal flow in the roll bite. In normal rotation, the metal flow along the rolling direction must be pushed outward from the center of the strip by the groove. On the other hand, in reverse rotation, the metal flow must be pushed toward the center from outside the groove.

These lateral metal flows along the width cause a compression stress along the width that is higher than in the case of normal rotation. Assuming Mises's yield criteria and associated flow rule, on the plane strain condition, yield condition is Eq. (3). σ_t is stress along the thickness, σ_L is stress along the rolling direction, σ_W is stress along the width direction and σ_{eq} is equivalent stress, as shown in Fig. 10a.

$$(\sigma_t - \sigma_L)^2 = \frac{2}{3}\sigma_{eq}^2 \tag{3}$$

If additional stress by constraint force along the width direction is assumed, the stress along the thickness is increased with compressive additional stress, and is decreased with stretch one as shown in Fig. 10b. As a result, the rolling load in reverse rotation is higher than in normal rotation. This is the reason why the estimated friction coefficient of reverse rotation is higher than in the other cases.

In addition, there is a jump phenomenon around 15%, as in the case of the TD groove roll. This jump might be the same phenomena as the TD groove roll. However, there is no jump in the case of a 45-degree normal rotation roll. This difference might come from the different axial metal flow between each other. In the case of reverse rotation, compressive flow along the width causes compressive stress along the rolling direction, too. On the other hand, in the case of normal rotation, the stretch flow along the width causes tensile stress along the rolling direction. This difference causes significant effect of the 2nd groove on the roll bit. In the case of normal rotation, the effect of the 2nd groove on the roll bite is very important, as it is in the case of the TD roll. However, in the case of normal rotation, the 2nd groove does not cause a strong compressive force, because of the axial metal flow from the center to the edge of the sheet. In Fig. 11, we show the heights of the transcribed projection at the center of the sheet and at the edge of the sheet with the 45-degree roll in both normal and reversed rotation. The height of the transcribed projections is higher in reverse than in normal rotation. Furthermore, this difference is quite large at the



Fig. 11 The height of the transcribed profile at the center of the sheet width and the edge. (Color figure online)

width edge portions in both normal and the reverse rotation. Since the free surface is formed at the width edge, the influence of the metal flow is large. It is presumed that the difference in compressive stress between normal rotation and reverse rotation appears in the height of the transcribed projection.

4.3 Relationship Between RD and TD Groove Roll

Figure 6 shows the estimated friction coefficients of the RD and the TD groove rolls with the reductions. As described above, the rapid increase in the friction coefficient at 15% or more with the TD groove roll is due to the resistance of the metal flow along the rolling direction. It is believed that the friction coefficient of the RD groove roll increases with higher reduction due to the formation of the new surface, which is in contact with the groove. Figure 12 shows the relationship between the friction coefficient and the contact area ratio of the protrusion and the roll bite length on the TD/RD rolls. In the RD roll, the contact area ratio is constant at any reduction. On the other hand, in the case of the TD roll, the contact area ratio increases with an increase in rolling reduction. The estimated friction coefficients are a kind of index of the resistance force along the rolling direction. Microscopic friction depends on the contact area ratio. If the microscopic friction is constant, the estimated friction is shown to relate to the contact area ratio in this figure. In particular, when more than two protrusions exist on the roll bite, it is believed that the restraining force in the rolling direction sharply increases and the friction coefficient jumps, as explained before.

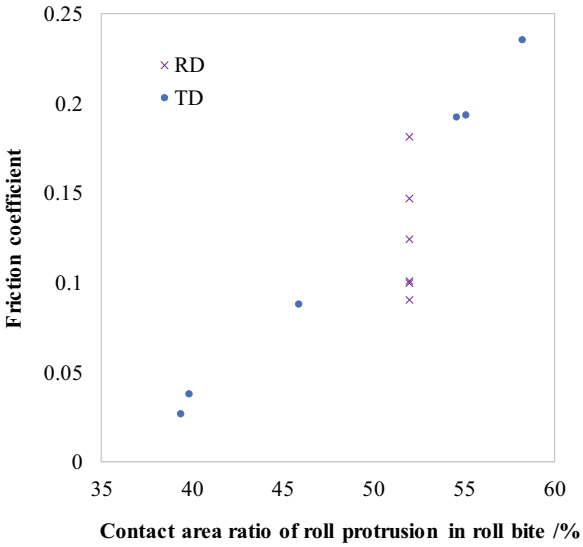


Fig. 12 Relationship between friction coefficient and contact ratio of roll protrusion. (Color figure online)

5 Relation Between Estimated Friction and Transcribed Profile

Figure 13 shows the relationship between the friction coefficient and the height of the projection for each roll.

In lower friction coefficients under 0.15, where the reduction is lower, it is difficult to understand the behavior of the friction coefficient because of the projection

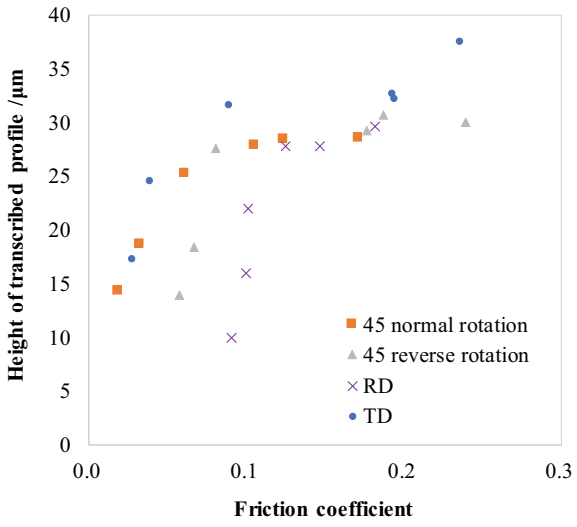


Fig. 13 Relationship between Height of transcribed profile and friction coefficient. (Color figure online)

formation process. In higher friction coefficients over 0.15, where the reduction is higher, higher friction causes higher projections with any of the rolls other than the 45-groove roll in reverse rotation. The compressive stress in the roll bite from the resistant force is helpful in forming the projection, as suggested other Refs. [8, 9]. In the case of the 45-degree groove roll in reverse rotation, an additional compressive stress along the width from the metal flow forces the formation of stronger flow stress on plan strain condition. This effect does not directly affect the resistant force. This might be the reason why a low projection height on the roll has a high friction coefficient.

6 Conclusion

To predict transferability on textured rolling, we have to decide on the adaptive boundary conditions, namely, the microscopic relative velocity between the material and the roll in the roll bite. Based on this idea, experimentally, we estimated the apparent friction coefficients of each roll (1) RD, (2) TD, and (3) the 45-degree groove roll. Based on our experiments, we confirmed that the influence of the following resistant forces exist in textured rolling.

1. Restraint force in the rolling direction due to the formation of protrusions
2. Restraint force in the rolling direction due to the presence of multiple roll grooves in the roll bite
3. Influence of flow stress due to metal flow in the width direction
4. Contact ratio of roll convex in the roll bite.

There is a relationship between the resistant force as the estimated friction coefficients and the projection height in the higher reduction area. However, the theoretical prediction itself of apparent friction coefficients is still difficult as there is an interaction between micro transferability and the resistant force. We conclude that it is important to estimate the apparent friction coefficient in predicting transferability.

References

1. Ataka M, Ueno Y, Watanuki K, Iino Y (2008) Tetsu-to-Hagané 94:63–69
2. Aoki I (1979) J Jpn Soc Technol Plast 20:1121–1125
3. Yukawa N, Akiyama T, Yoshida Y, Ishikawa T (2008) Analysis of surface roughness transcription in skin-pass rolling using zooming method. Iron Steel Inst Jpn 94(10):17–22
4. Ike H (2007) 3D Finite element analysis of surface roughness evolution of steel sheets by micro-indentation of surface asperities. Dev Micro-Deform Anal Pract Technol Temper Rolling Cold Rolled Steel Sheet 10:99–110
5. Fujii Y, Maeda Y (2006) Research of mechanism for surface texture by sheet rolling. In: The Proceedings of the 57th joint conference for the technology of plasticity, vol 215, pp 213–214
6. Fujii Y, Maeda Y (2007) Research of mechanism for surface texture by sheet rolling. In: IX international conference computational plasticity COMPLASIX, pp 787–790

7. Fujii Y, Maeda Y (2014) Proceedings of the international conference on the technology of plasticity, ICTP2014, pp 161–165
8. Akashi T, Shiraishi T, Ogawa S, Matsuse Y (2014) J Jpn Soc Technol Plast 55(639):324–330
9. Akashi T, Shiraishi T, Ogawa S, Matsuse Y, Morihara H (2015) J Jpn Soc Technol Plast 56(648):53–59

Fundamentals of Continuous Helicoid Auger Flighting Rolling—Deformation Mechanics, Kinematics, and Applications



Ming He

Abstract An auger flighting is a helical-shaped circular product used to transfer bulk materials in broad applications. Continuous auger flightings are formed from straight steel strips by a specialty rolling mill. Because of the geometry and configuration of auger flightings, the rolling process is more complex than the ordinary longitudinal rolling. However, there is little published literature on the theoretical features of auger flighting rolling. In this article, the fundamental kinematics and mechanics of auger flighting rolling are mathematically developed. From these mathematical models, the contact area, rolling force, and torque are calculated and the affecting factors are evaluated. The slip characteristics between the strip and forming rolls and the effects of roll offset are studied. The article also provides design considerations, primarily for the main roll shafts and required rolling mill power. Finally, the application results are compared to the actual rolling readings and satisfactory agreement is obtained.

Keywords Auger flighting · Strip steel · Rolling · Plastic deformation · Mechanics · Kinematics · Mill design

1 Introduction

The helicoid auger flighting is the centerpiece of a helicoid auger or continuous screw conveyor, which is commonly used to transfer or propel loose materials in broad applications in the agriculture, food, mining, and construction industries. An auger assembly is composed of a helicoid flighting, outer pipe (container), and inner pipe (central shaft), as shown in Fig. 1. A continuous flighting is formed at room temperature from a straight carbon, alloy or stainless steel strip by a specialty rolling mill. Figure 2a shows the strip being uncoiled, straightened, and fed into the rolling mill. Figure 2b shows the rolled continuous auger flighting that is produced by the rolling mill.

M. He (✉)
The Timken Company, 4500 Mount Pleasant Street NW, North Canton, OH 44720, USA
e-mail: ming.he@timken.com

© The Minerals, Metals & Materials Society 2021

G. Daehn et al. (eds.), *Forming the Future*, The Minerals, Metals & Materials Series,
https://doi.org/10.1007/978-3-030-75381-8_202

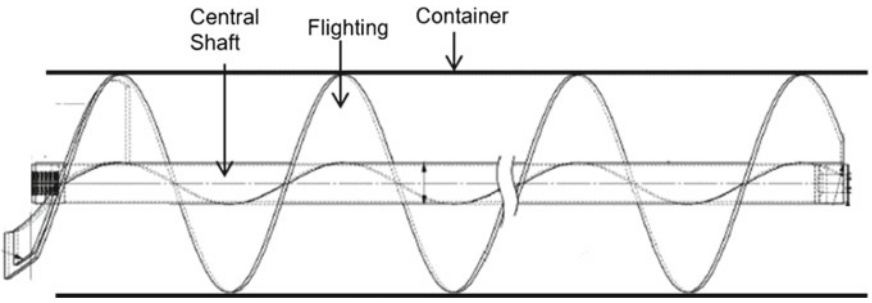


Fig. 1 Schematic of a helicoid auger assembly. (Color figure online)



(a) Feeding straightened strip into the rolling mill



(b) Rolled continuous auger flighting

Fig. 2 Continuous auger flighting rolling. (Color figure online)

Auger flighting rolling is a type of plastic deformation involving complex kinematics, elasticity, and plasticity, along with other important factors that extend from raw material properties to rolling mill operations. Flighting design and manufacturing, however, are mainly based on experience and trial and error because of the unavailability of systematic theories regarding the auger flighting rolling process. This article describes a few key auger flighting rolling features and common practices through theoretical and empirical equations.

2 Geometrical Features of Helicoid Auger Flighting

A rolled auger flighting has the following primary dimensions (Fig. 3): inner diameter d, outer diameter D, pitch P, inner edge thickness T_0, outer edge thickness T_1, and blade or strip width W. The selection of the inner diameter depends on a number of factors, including the size of the central shaft, outer diameter, pitch, and strip thickness. The geometrical relationships derived from a helix are applicable to flightings that are rolled under normal mill settings where the rolls are aligned without any skew, offset or misalignment. When the rolls are set up skewed (the roll axes are not parallel but cross at a small angle), offset (one roll is ahead of the other

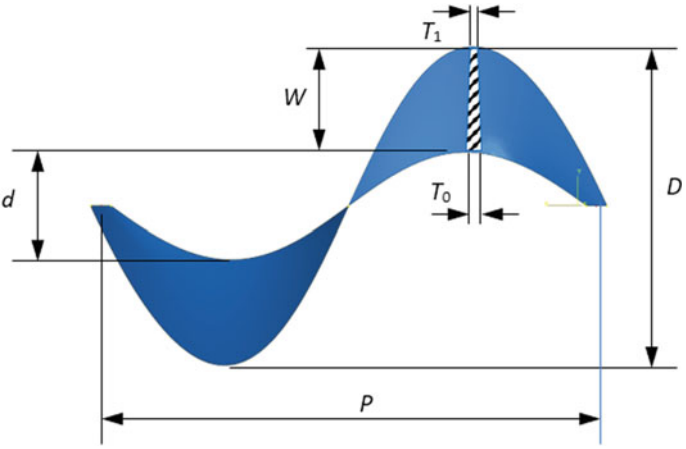


Fig. 3 Nomenclature of helicoid auger flighting. (Color figure online)

one) or misaligned (one roll is lower than the other one) or a combination of those conditions, the flighting's geometry becomes much more complex.

The inner length L_{in} and outer length L_{out} of one revolution of the flighting are calculated from

$$L_{\text{in}} = \sqrt{(\pi d)^2 + P^2} \text{ and } L_{\text{out}} = \sqrt{(\pi D)^2 + P^2} \tag{1}$$

If the initial thickness of the strip steel is T_0, based on the volume conservation rule, the theoretical outer edge thickness T_1 of the rolled flighting is

$$T_1 = \frac{L_{\text{in}}}{L_{\text{out}}} T_0 \tag{2}$$

When substituting Eq. (1) for L_{in} and L_{out} in Eq. (2), the relationship of the outer and inner edge thicknesses expressed by the pitch-to-outer diameter ratio P/D and inner diameter-to-outer diameter ratio d/D, shown in Fig. 4, is:

$$\frac{T_1}{T_0} = \sqrt{\frac{\left(\frac{d}{D}\right)^2 + \left(\frac{1}{\pi}\frac{P}{D}\right)^2}{1 + \left(\frac{1}{\pi}\frac{P}{D}\right)^2}} \tag{3}$$

The relationship in Eq. (3) indicates that the smaller these ratios, the more severe the thickness reduction at the outer diameter will be. Often this is driven by a demand for higher propelling productivity. Figure 4 shows that the thickness of the outer edge can be reduced to 20% of that of the initial strip when small ratios are selected. This requires good workability of the material to prevent the outer edge from cracking during rolling. When the thickness at the outer edge is significantly reduced, the

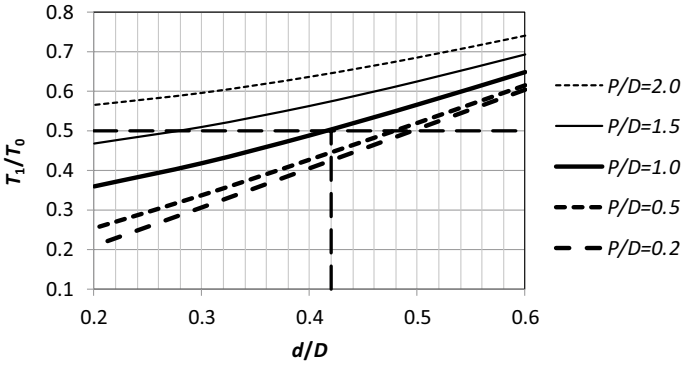


Fig. 4 The outer blade thickness affected by P/D and d/D ratios

service life of the flighting is compromised, since the outer edge is subject to greater wear as the result of its higher linear velocity relative to the inner edge.

To help maintain the minimum outer edge thickness, one can reduce the forming width to narrow the difference between the inner and outer diameters, or increase the pitch while keeping the outer diameter unchanged (Fig. 4). These two methods, however, are not always practical, since they are restricted by the auger flighting dimensional requirements specified by the customer. One might consider preventing a portion of the strip from undergoing any deformation at all by using a so-called "low-strip rolling" technique. Other options are to increase the outer edge thickness via a hard facing technique or to introduce a profile to the forming roll surface, as described in a number of patents [1–4].

"Low-strip rolling" means that a portion of the strip on the inner side is hanging outside the rolls, and therefore, is not rolled. Assume that the width of the hanging portion, or non-deformed zone, is Δ and the diameter at the location where the non-deformed zone ends and the deformed zone begins is d' (Fig. 5). The length of the one-revolution flighting at the diameter d' is:

$$L_{d'} = \sqrt{(\pi d')^2 + P^2}, \text{ where } d' = d + 2\Delta = D - 2(W - \Delta) \tag{4}$$

The outer thickness of the flighting will be

$$T_1^{'} = \frac{L_{d'}}{L_{\text{out}}} T_{d'} = \frac{L_{d'}}{L_{\text{out}}} T_0 \tag{5}$$

where T_0 is the initial thickness at the non-deformed zone.

To calculate how much the thickness of the outer edge increases as a result of this hanging portion, or "hangout," substituting Eq. (2) for T_0 in Eq. (5) leads to

$$\frac{T_1^{'}}{T_1} = \frac{L_{d'}}{L_{\text{in}}} \tag{6}$$

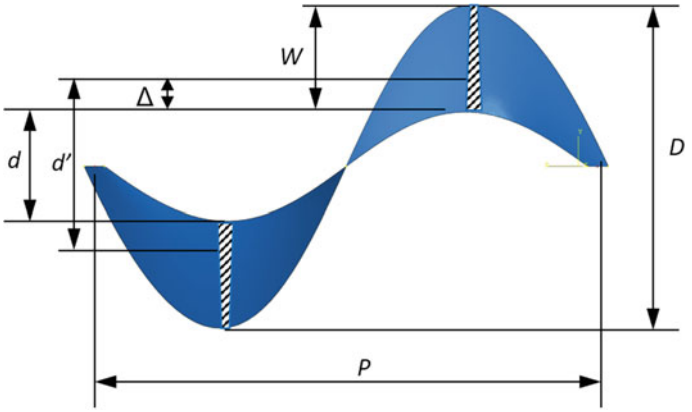


Fig. 5 Nomenclature of helicoid auger flighting in low-strip rolling. (Color figure online)

where T_1 is the thickness of the outer edge after regular rolling without the hangout.

By substituting Eq. (1) for L_{in}, Eq. (4) for $L_{d'}$ and d' in Eq. (6), the ratio between the outer edge thickness with hangout and thickness without hangout is

$$\frac{T_1'}{T_1} = \sqrt{1 + 4\pi^2 \frac{\frac{\Delta}{W}\left(\frac{d}{W} + \frac{\Delta}{W}\right)}{\pi^2\left(\frac{d}{W}\right)^2 + \left(\frac{P}{W}\right)^2}} \tag{7}$$

Because the right side of Eq. (7) is greater than 1 (see Fig. 6), the thickness of the outer edge of the flighting after low-strip rolling is larger than the thickness created by regular rolling. Thus, the flighting's wear life can be increased. The results show

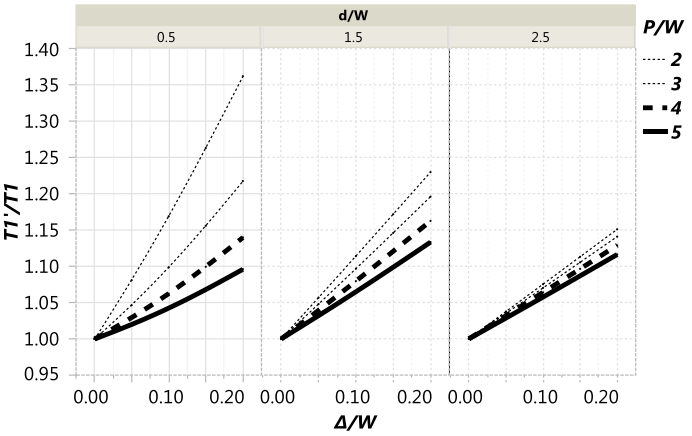


Fig. 6 Outer edge thickening resulting from the hangout after low-strip rolling. (Color figure online)

that the thickness of the outer edge increases with increasing hangout Δ in low-strip rolling. The influence of the hangout on the outer edge thickening is more significant when the d/W and P/W ratios are smaller.

It should be mentioned that applying low-strip rolling is not without potential risk. Notably, assuming that the length of the inner edge is the same as that of the strip with no hangout, the non-deformed hangout zone also causes thickening at the inner edge to occur. Based on the volume conservation rule, the inner edge thickness $T_0^{'}$ of the flighting after low-strip rolling now is

$$T_0^{'} = \frac{L_{d'}}{L_{\text{in}}} T_{d'} = \frac{L_{d'}}{L_{\text{in}}} T_0 \text{ or } \frac{T_0^{'}}{T_0} = \sqrt{1 + 4\pi^2 \frac{\Delta(d+\Delta)}{(\pi d)^2 + P^2}} \tag{8}$$

If the numerator and denominator of the second term on the right side of Eq. (8) are both divided by D^2, the equation becomes

$$\frac{T_0^{'}}{T_0} = \sqrt{1 + 4\pi^2 \frac{\frac{\Delta}{D}\left(\frac{d}{D} + \frac{\Delta}{D}\right)}{\pi^2 \left(\frac{d}{D}\right)^2 + \left(\frac{P}{D}\right)^2}} \tag{9}$$

Since the right side of the equation is greater than 1, $T_0^{'}$ will be larger than T_0 unless $\Delta = 0$. The relationship of Eq. (9) is also expressed in Fig. 7a. It is logical that the smaller the d/D and P/D ratios are, the more thickening will occur at the inner edge. Interestingly, if the numerator and denominator of the second term on the right side of Eq. (8) are both divided by P^2, the equation becomes Eq. (10), where it can be observed that maximum thickening happens when d/P is in the range of 0.2 to 0.3 (see Fig. 7b). Beyond this range, thickening actually decreases gradually.

$$\frac{T_0^{'}}{T_0} = \sqrt{1 + 4\pi^2 \frac{\frac{\Delta}{P}\left(\frac{d}{P} + \frac{\Delta}{P}\right)}{\pi^2 \left(\frac{d}{P}\right)^2 + 1}} \tag{10}$$

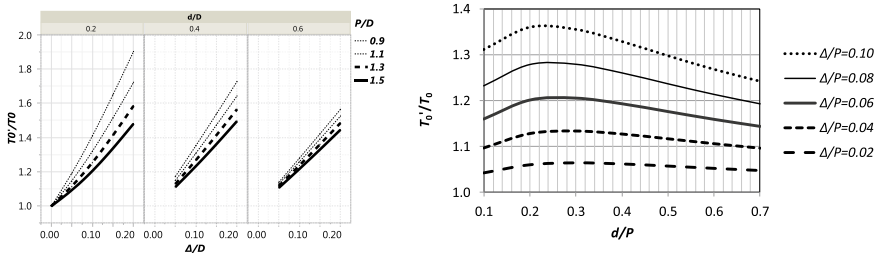


Fig. 7 Thickening of the inner edge after low-strip rolling. (Color figure online)

However, the amount of thickening in the non-deformed portion of the hangout is controlled not only by its geometry, but also by the strip's mechanical properties and the rolled flighting's dimensions. Even if the strip is very ductile, the thickening could be limited because the hangout region can buckle—an instability triggered by the slenderness ratio of the length of the hangout region to its thickness. The buckling pushes the material sideways to form a wavy or wrinkled inner edge, which can adversely affect product quality. That is why correctly selecting the ratios to achieve a balance between productivity and service life is of great importance in auger flighting design.

3 Mechanics of Auger Flighting Rolling

3.1 Stress-Strain Relationship of Auger Flighting Rolling

Auger flighting rolling can be categorized as a type of special longitudinal cold rolling. For this process, when elastic deformation is negligible compared to plastic deformation and the strip is assumed to be a *work-hardening* material with little strain rate sensitivity, the flow stress after yielding, expressed by the Johnson–Cook equation, is simplified into a power-law equation

$$\overline{\sigma} = K\overline{\varepsilon}^{n} \tag{11}$$

The material parameters K (the strength coefficient) and n (the strain-hardening exponent) are calculated from the true stress and true strain data points of a simple uniaxial tensile test of the subject strip. In auger flighting rolling, which is a plane-strain operation of a *work-hardening* strip steel, the von Mises yield criterion is

$$\sigma_1 - \sigma_3 = \frac{2}{\sqrt{3}}\overline{\sigma} = 1.155\overline{\sigma} = \overline{\sigma}_m \tag{12}$$

where $\overline{\sigma}_m = 1.155\overline{\sigma}$ is the effective plane-strain flow stress.

Substituting Eq. (11) for the flow stress $\overline{\sigma}$ in Eq. (12) results in a general effective stress–strain relationship for the work-hardening steel strip

$$\overline{\sigma}_m = 1.155\overline{\sigma} = 1.155K\overline{\varepsilon}^{n} \tag{13}$$

The effective strain in the plane-strain operation is expressed by

$$\overline{\varepsilon} = \left[\frac{2}{3}\left(\varepsilon_1^2 + \varepsilon_3^2\right)\right]^{\frac{1}{2}} \tag{14}$$

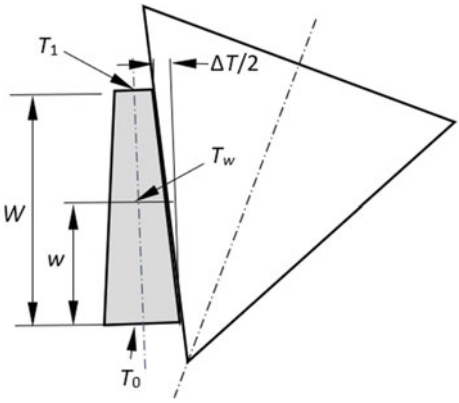


Fig. 8 Cross-section of a deformed flighting. (Color figure online)

In auger flighting rolling, the thickness along the width W of the strip varies (Fig. 8). If the total thickness reduction is $\Delta T = T_0 - T_1$, the strip thickness at the width w is:

$$T_w = T_0 - \frac{w}{W}\Delta T \tag{15}$$

The thickness strain at the width w is

$$\varepsilon_{1_w} = \varepsilon_{t_w} = \ln\left(\frac{T_0}{T_w}\right) = \ln\left(\frac{T_0}{T_0 - \frac{w}{W}\Delta T}\right) \tag{16}$$

where w is the strip width at the strip thickness T_w, measured from the inner edge of the strip, at which the strip has its initial thickness T_0. The longitudinal strain at the width w is

$$\varepsilon_{3_w} = -\varepsilon_{1_w} \tag{17}$$

Substitute Eqs. (16) and (17) for ε_1 and ε_3 in Eq. (14). The effective strain under the plane-strain condition at the width w becomes

$$\bar{\varepsilon}_w = \frac{2}{\sqrt{3}} \ln\left(\frac{T_0}{T_0 - \frac{w}{W}\Delta T}\right) \tag{18}$$

Equation (18) demonstrates that the effective strain increases with increasing strip thickness reduction. When the reduction is large, attention should be paid to ensure that the strip does not exceed its ultimate strength limit.

Substituting Eq. (18) for $\bar{\varepsilon}$ in Eq. (13), the effective plane-strain flow stress at the width w is

$$\overline{\sigma}_{m_w} = \frac{2}{\sqrt{3}} K \left[\frac{2}{\sqrt{3}} \ln\left(\frac{T_0}{T_0 - \frac{w}{W}\Delta T} \right) \right]^n \tag{19}$$

Equations (18) and (19) are closed-form equations that calculate the effective stress and strain at any width of a work-hardening steel strip at any moment during auger flighting rolling.

3.2 Rolling Contact Area

Because of the cone-shaped forming rolls and gradual thickness reduction in the strip from the inner edge to the outer edge, the contact area between a forming roll and the strip during plastic deformation has an irregular profile, as shown in Fig. 9. The following parameters are assigned for calculating the rolling contact area: A is the contact area, α is the included angle of a roll, c is the length of the truncated roll tip (the forming roll does not have a sharp tip), θ is the contact angle at the strip width w, s is the length of the contact arc at the strip width w, x is one-half of the thickness reduction at the strip width w, and r is the radius of the roll at the strip width w. From Fig. 9, the following relationships are established:

$$x = \frac{w}{W}\frac{\Delta T}{2}, r = (c + w)\sin\frac{\alpha}{2}$$

$$\cos\theta = 1 - \frac{x}{r} \text{and } s = r\theta \tag{20}$$

which lead to the extended formula expressed by Eq. (21).

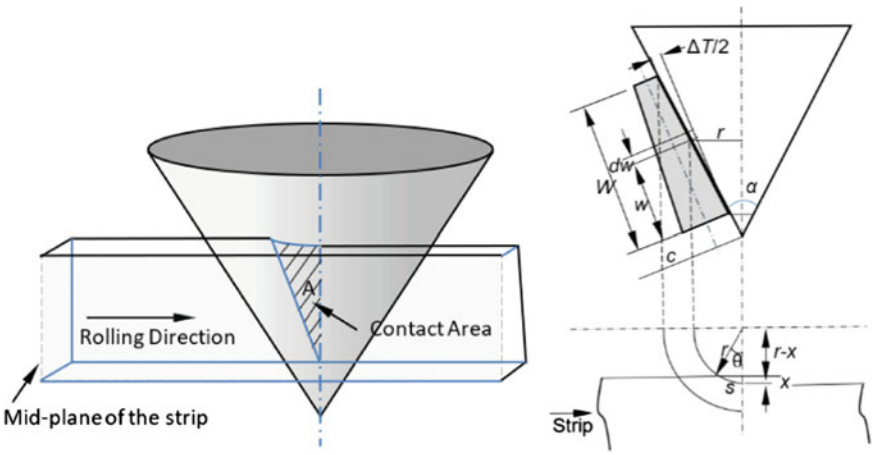


Fig. 9 Definition of the rolling contact area. (Color figure online)

$$\theta = \cos^{-1}\left[1 - \frac{x}{r}\right] = \cos^{-1}\left[1 - \frac{w\Delta T}{2(c+w)W\sin\frac{\alpha}{2}}\right] \tag{21}$$

The length of the contact arc s at the width w is

$$s = (c+w)\sin\frac{\alpha}{2}\cos^{-1}\left[1 - \frac{w\Delta T}{2(c+w)W\sin\frac{\alpha}{2}}\right] \tag{22}$$

The infinitesimal contact area at the width w is

$$dA = sdw|_W \tag{23}$$

where dA is an infinitesimal difference in the area and dw is an infinitesimal difference in the strip width.

After applying the definite integral to Eq. (23), the total contact area is

$$A = \int_0^W sdw = \int_0^W (c+w)\sin\frac{\alpha}{2}\cos^{-1}\left[1 - \frac{w\Delta T}{2(c+w)W\sin\frac{\alpha}{2}}\right]dw \tag{24}$$

3.3 Roll Separating Force

In its simplest form, the roll separating force or rolling force is a product of the rolling pressure from the rolls exerted to the workpiece (and vice versa) in the contact area:

$$F = \int_A pdA \tag{25}$$

where p is the rolling pressure in the roll-workpiece contact area. Because of the existent effect of the friction between the rolls and workpiece, the so-called *friction hill*, the calculation of the roll separating force historically has been very difficult and laborious. Many researchers in the last century presented experimental diagrams and various equations, either theoretical or empirical, to predict the roll separating force (primarily for longitudinal flat slab or plate rolling). All of these equations were proposed with assumptions and simplifications so that they could be used in practice.

3.3.1 Tselikov's Method [5]

Tselikov's method is one of the most famous and influential equations. Because the thickness reduction along the strip width varies, the calculation of the roll separation force is in the following form:

$$F = \int_0^W f(\overline{\sigma}, \overline{\varepsilon}) s dw = \int_0^W \frac{\overline{\sigma}_m (2 - \varepsilon_t)}{\varepsilon_t \delta} \left[\left(\frac{1}{1 - \varepsilon_t} \right)^{\frac{\delta}{2}} - 1 \right] s dw \tag{26}$$

The effective plane-strain flow stress $\overline{\sigma}_m$ is from Eq. (19) and the length of the contact arc s is from Eq. (22). The relative thickness reduction ε_t can be obtained by referring to Eq. (15).

$$\varepsilon_t = \frac{T_w}{T_0} = 1 - \frac{w \Delta T}{W T_0} \tag{27}$$

In addition, coefficient

$$\delta = \mu \sqrt{\frac{4r}{T_0 - T_w}} \tag{28}$$

Substituting Eq. (15) for T_w and Eq. (20) for r in Eq. (28) leads to an extended expression of δ:

$$\delta = 2\mu \sqrt{\frac{W(c + w) \sin \frac{\alpha}{2}}{w \Delta T}} \tag{29}$$

where μ is the coefficient of friction.

Substituting Eq. (19) for $\overline{\sigma}_m$ in Eq. (26), combining Eq. (24) with Eq. (26), and assuming that the total roll separating force acts at two-thirds of the total width W ($w = \frac{2}{3} W$) in the exponent δ, the total roll separating force is

$$F = \int_0^W (c + w) \sin \frac{\alpha}{2} \cos^{-1} \left[1 - \frac{w \Delta T}{2(c + w) W \sin \frac{\alpha}{2}} \right] \frac{2}{\sqrt{3}} K \left[\frac{2}{\sqrt{3}} \ln \left(\frac{T_0}{T_0 - \frac{w}{W} \Delta T} \right) \right]^n \frac{\left(1 + \frac{w \Delta T}{W T_0} \right)}{\left(1 - \frac{w \Delta T}{W T_0} \right) 2\mu \sqrt{\frac{W(c+w) \sin \frac{\alpha}{2}}{w \Delta T}}} \left[\left(\frac{1}{\frac{w \Delta T}{W T_0}} \right)^{\mu \sqrt{\frac{(3c+2W) \sin \frac{\alpha}{2}}{2 \Delta T}}} - 1 \right] dw \tag{30}$$

If the assumption that the total roll separating force acts at two-thirds of the total width W ($w = \frac{2}{3} W$) is applied to the entire Eq. (30), the calculation of the total roll separating force can be further simplified as

$$F = \frac{2}{\sqrt{3}} A \left[K \frac{2}{\sqrt{3}} \ln \left(\frac{T_0}{T_0 - \frac{2}{3} \Delta T} \right) \right]^n \frac{(3T_0 + 2\Delta T)}{(3T_0 - 2\Delta T) 2\mu \sqrt{\frac{(3c+2W) \sin \frac{\alpha}{2}}{2 \Delta T}}} \left[\left(\frac{1}{\frac{2 \Delta T}{3 T_0}} \right)^{\mu \sqrt{\frac{(3c+2W) \sin \frac{\alpha}{2}}{2 \Delta T}}} - 1 \right] \tag{31}$$

3.3.2 Homogeneous Plane-Strain Upsetting Method [6]

By assuming that the deformed zone can be approximated in the same way as homogeneous plane-strain upsetting, the roll separating force per unit width of the strip is given by

$$F = \int_0^W \frac{2\overline{\sigma}_m}{\sqrt{3}} \left(1 + \frac{ms}{4T_w}\right) s\,dw \tag{32}$$

where m is the shear coefficient of friction.

Substituting Eqs. (15), (19), and (22) in Eq. (32) for T_w, $\overline{\sigma}_m$ and s, respectively, gives

$$F = \int_0^W (c + w) \sin\frac{\alpha}{2} \cos^{-1}\left[1 - \frac{w\Delta T}{2(c + w)W \sin\frac{\alpha}{2}}\right] \frac{2}{\sqrt{3}} K \left[\frac{2}{\sqrt{3}} \ln\left(\frac{T_0}{T_0 - \frac{w}{W}\Delta T}\right)\right]^n \left[1 + \frac{mw}{4\left(T_0 - \frac{w}{W}\Delta T\right)}\right] dw \tag{33}$$

If the assumption that the total roll separating force acts at two-thirds of the total width W ($w = \frac{2}{3}W$) is applied to the entire Eq. (33), the calculation of the total roll separating force can be simplified as

$$F = \frac{2}{\sqrt{3}} A \left[K \frac{2}{\sqrt{3}} \ln\left(\frac{T_0}{T_0 - \frac{2}{3}\Delta T}\right)\right]^n \left[1 + \frac{mW}{6\left(T_0 - \frac{2}{3}\Delta T\right)}\right] \tag{34}$$

3.3.3 Example Calculations of Roll Separating Forces

Example calculations of the roll separating forces of an auger flighting using the closed-form equations described in Sects. 3.3.1 and 3.3.2 are shown below. The calculations are also compared with the results from finite element modeling performed with ABAQUS Unified FEA software. The following parameters were used. Strip dimensions: $T_0 = 5.08$ mm, $W = 152.4$ mm. Flighting dimensions: $D = 457.2$ mm, $d = 152.4$ mm, and $P = 660.0$ mm. Strip steel grade: $K = 551.6$ MPa and $n = 0.145$. Roll included angle: $\alpha = 90°$ or 65°. Coefficient of friction: μ or $m = 0.08$, 0.10 or 0.12 (Table 1).

Table 1 Calculated parameters varying with changing roll included angle

α, °	T_1, mm, Eq. (3)	c, mm	s, mm, Eq. (22)	A, mm^2, Eq. (24)
90	2.6232	10.3237	16.8284	1,320.6
65	2.6204	8.6555	14.6065	1,140.8

Table 2 Roll separating forces F in kN, with 90° roll included angle

μ or m	The Tselikov method, Eq. (30)	The simplified Tselikov method, Eq. (31)	The upsetting method, Eq. (33)	The simplified upsetting method, Eq. (34)	Average (Δ, % of average)	FEA
0.08	1,210	1,152	1,221	1,191	1,194 (5.8%)	1,218
0.10	1,351	1,257	1,342	1,301	1,313 (7.2%)	1,204
0.12	1,521	1,376	1,463	1,412	1,443 (10.0%)	1,260

Table 3 Roll separating forces F in kN, with 65° roll included angle

μ or m	The Tselikov method, Eq. (30)	The simplified Tselikov method, Eq. (31)	The upsetting method, Eq. (33)	The simplified upsetting method, Eq. (34)	Average (Δ, % of average)	FEA
0.08	990	949	1,056	1,028	1,006 (10.6%)	1,056
0.10	1,085	1,023	1,161	1,124	1,098 (12.6%)	1,045
0.12	1,195	1,105	1,265	1,219	1,196 (13.4%)	1,103

The roll separating forces F with 90° and 65° roll included angles are given in Tables 2 and 3.

The simplified equations yield smaller forces than those produced by the initial equations. All four equations give similar force values. The difference Δ among all results is smaller in low-friction and larger in roll included angle conditions. The results from the closed-form equations are closer to the finite element results when the friction is low.

3.3.4 Factors Affecting the Roll Separating Force

The roll separating force in flighting rolling is affected by the dimensions of the flighting, roll included angle, lubrication conditions (frictions), skewed rolling (non-parallel roll axes), offset rolling (rolls misaligned in the rolling direction), misaligned rolling (rolls misaligned in the strip width direction), and strip hangout, as well as the carbon content of the steel.

The roll separating force increases with increased friction between the strip and rolls, as shown in Fig. 10. A larger roll included angle results in a higher rolling force, as shown in Fig. 11. The influence of the friction condition and the roll included angle on the roll separating force is more profound as the strip's width, outer diameter, and thickness increase. For simplicity, in these examples, the flighting's inner diameter and pitch are fixed.

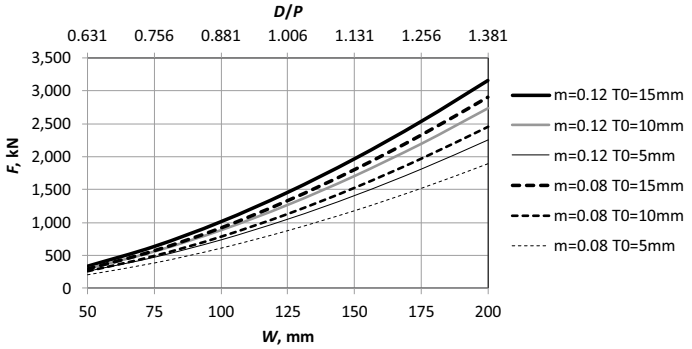


Fig. 10 Influence of friction condition, strip width and D/P ratio on the roll separating forces (90° roll included angle)

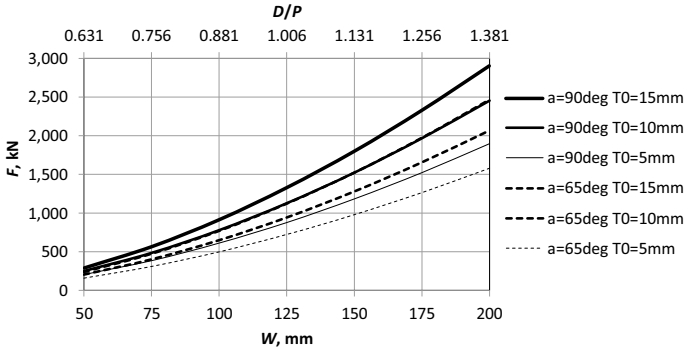


Fig. 11 Influence of roll included angle, strip width and D/P ratio on the roll separating forces ($\mu = 0.08$)

3.4 Rolling Torque on Main Roll Shafts

Because of the roll included angle α, the rolling torque acting on the two main roll shafts results solely from the component F_y of the roll separating force that is in the direction perpendicular to the axes of the main roll shafts (see Fig. 12). The component F_x of the roll separating force that is in the direction parallel to the axes of the main roll shafts will, however, exert a bending moment on the shafts.

The rolling torque T acting on one main roll shaft can be calculated by the following formula after applying the relationships described in Sect. 3.2.

$$T = F_y a = F \cos\frac{\alpha}{2} a = \cos\frac{\alpha}{2} \int_0^W f(\overline{\sigma}, \overline{\varepsilon}) s a d w \tag{35}$$

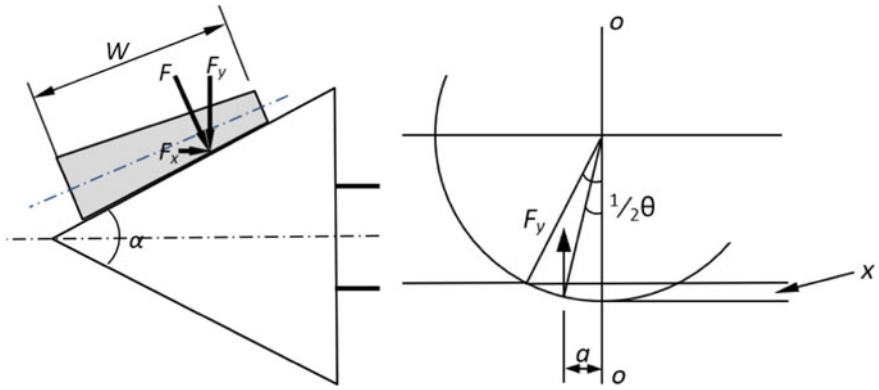


Fig. 12 Resultant torque from roll separating force and torque arm. (Color figure online)

where the torque arm a, assuming that the roll separating force is acting at one-half of the contact arc and is parallel to the rolling plane o-o, is expressed as

$$a = (c+w)\sin\frac{\alpha}{2}\sin\frac{\theta}{2} = (c+w)\sin\frac{\alpha}{2}\sin\left[\frac{1}{2}\cos^{-1}\left[1-\frac{w\Delta T}{2(c+w)W\sin\frac{\alpha}{2}}\right]\right] \tag{36}$$

When adopting Tselikov's method, the regular and simplified one-roll torques on the main shaft, respectively, are

$$T = \int_0^W (c+w)^2 \sin\left[\frac{1}{2}\cos^{-1}\left[1-\frac{w\Delta T}{2(c+w)W\sin\frac{\alpha}{2}}\right]\right]\cos^{-1}\left[1-\frac{w\Delta T}{2(c+w)W\sin\frac{\alpha}{2}}\right]$$
$$\frac{2}{\sqrt{3}}K\left[\frac{2}{\sqrt{3}}\ln\left(\frac{T_0}{T_0-\frac{w}{W}\Delta T}\right)\right]^n \frac{\left(1+\frac{w\Delta T}{WT_0}\right)}{\left(1-\frac{w\Delta T}{WT_0}\right)2\mu\sqrt{\frac{W(c+w)\sin\frac{\alpha}{2}}{w\Delta T}}}$$
$$\left[\left(\frac{1}{\frac{w\Delta T}{WT_0}}\right)^{\mu\sqrt{\frac{(3c+2W)\sin\frac{\alpha}{2}}{2\Delta T}}} - 1\right] dw\left(\sin\frac{\alpha}{2}\right)^2\cos\frac{\alpha}{2} \text{ and} \tag{37}$$

$$T = \left(c+\frac{2}{3}W\right)\sin\frac{\alpha}{2}\cos\frac{\alpha}{2}\sin\left[\frac{1}{2}\cos^{-1}\left[1-\frac{\Delta T}{(3c+2W)\sin\frac{\alpha}{2}}\right]\right]$$
$$\frac{2}{\sqrt{3}}KA\left[\frac{2}{\sqrt{3}}\ln\left(\frac{T_0}{T_0-\frac{2}{3}\Delta T}\right)\right]^n \frac{\left(1+\frac{2\Delta T}{3T_0}\right)}{\left(1-\frac{2\Delta T}{3T_0}\right)2\mu\sqrt{\frac{(3c+2W)\sin\frac{\alpha}{2}}{2\Delta T}}}\left[\left(\frac{1}{\frac{2\Delta T}{3T_0}}\right)^{\mu\sqrt{\frac{(3c+2W)\sin\frac{\alpha}{2}}{2\Delta T}}} - 1\right] \tag{38}$$

By following the same procedures, the regular and simplified one-roll torques calculated by the homogeneous plane-strain upsetting method, respectively, are

$$T = \int_0^W (c+w)^2 \sin\left[\frac{1}{2}\cos^{-1}\left[1-\frac{w\Delta T}{2(c+w)W\sin\frac{\alpha}{2}}\right]\right]\cos^{-1}\left[1-\frac{w\Delta T}{2(c+w)W\sin\frac{\alpha}{2}}\right]$$
$$\frac{2}{\sqrt{3}}K\left[\frac{2}{\sqrt{3}}\ln\left(\frac{T_0}{T_0-\frac{w}{W}\Delta T}\right)\right]^n\left[1+\frac{mw}{4\left(T_0-\frac{w}{W}\Delta T\right)}\right]dw\left(\sin\frac{\alpha}{2}\right)^2\cos\frac{\alpha}{2} \text{ and} \quad (39)$$

$$T = \left(c+\frac{2}{3}W\right)\sin\frac{\alpha}{2}\cos\frac{\alpha}{2}\sin\left[\frac{1}{2}\cos^{-1}\left[1-\frac{\Delta T}{(3c+2W)\sin\frac{\alpha}{2}}\right]\right]$$
$$\frac{2}{\sqrt{3}}KA\left[\frac{2}{\sqrt{3}}\ln\left(\frac{T_0}{T_0-\frac{2}{3}\Delta T}\right)\right]^n\left[1+\frac{mW}{2(3T_0-2\Delta T)}\right] \quad (40)$$

The two roll or total torque is $T_t = 2T$.

Calculations for the one-roll torques of one auger flighting using the above closed-form equations and the rolling parameters in Sect. 3.3.3 are given in Tables 4 and 5, respectively. The calculations are also compared to the results of finite element modeling using ABAQUS Unified FEA software. With influencing factors similar to those of the rolling force, the roll torque is affected more by the reduction ratio or larger *D/P* ratio, as shown in Figs. 13 and 14.

Table 4 One-roll torque T in kN-m, with 90° roll included angle

μ or m	The Tselikov method, Eq. (37)	The simplified Tselikov method, Eq. (38)	The upsetting method, Eq. (39)	The simplified upsetting method, Eq. (40)	Average (Δ, % of average)	FEA
0.08	4.562	4.635	5.280	4.792	4.817 (14.9%)	4.971
0.10	4.981	5.061	5.846	5.237	5.281 (16.4%)	5.289
0.12	5.459	5.537	6.412	5.682	5.772 (16.5%)	5.866

Table 5 One-roll torque T in kN-m, with 65° roll included angle

μ or m	The Tselikov method, Eq. (37)	The simplified Tselikov method, Eq. (38)	The upsetting method, Eq. (39)	The simplified upsetting method, Eq. (40)	Average (Δ, % of average)	FEA
0.08	3.890	3.944	4.721	4.272	4.207 (19.8%)	3.571
0.10	4.189	4.251	5.227	4.668	4.584 (22.6%)	3.990
0.12	4.523	4.589	5.734	5.065	4.978 (24.3%)	4.522

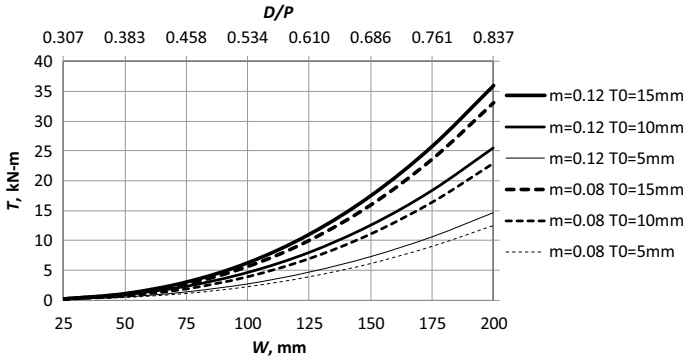


Fig. 13 Influence of friction condition, strip width and *D*/*P* ratio on roll torques (90° roll included angle)

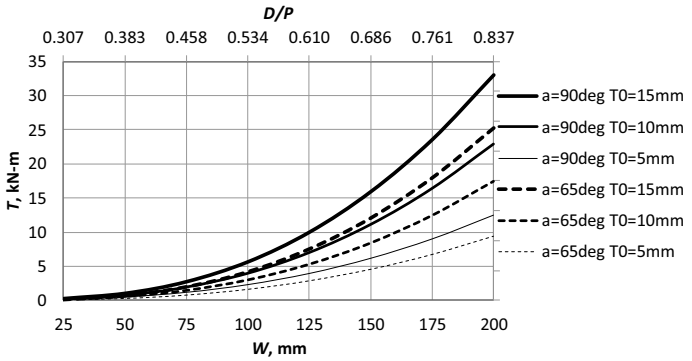


Fig. 14 Influence of roll included angle, strip width and *D*/*P* ratio on roll torques ($\mu = 0.08$)

4 Kinematics of Auger Flighting Rolling

4.1 Strip Velocity in Forming Zone

When the strip enters the forming zone between the two rolls under the conditions that the two rolls have exactly the same rotational speed and the strip is deformed into an annular shape before it is bent into a helicoid auger flighting, the velocity of the strip along the width is not always the same as the tangential surface velocity of the rolls. From Fig. 15, it can be seen that the velocity at the inner edge of the rolled strip is higher than that of the rolls, while the velocity at the outer edge of the rolled strip is lower than that of the rolls because the strip and the rolls have different rotational centers. As a result, there must be a point, *e*, at which the velocities of the rolled strip and the roll surfaces are equal. This point *e* can be referred to as the neutral point.

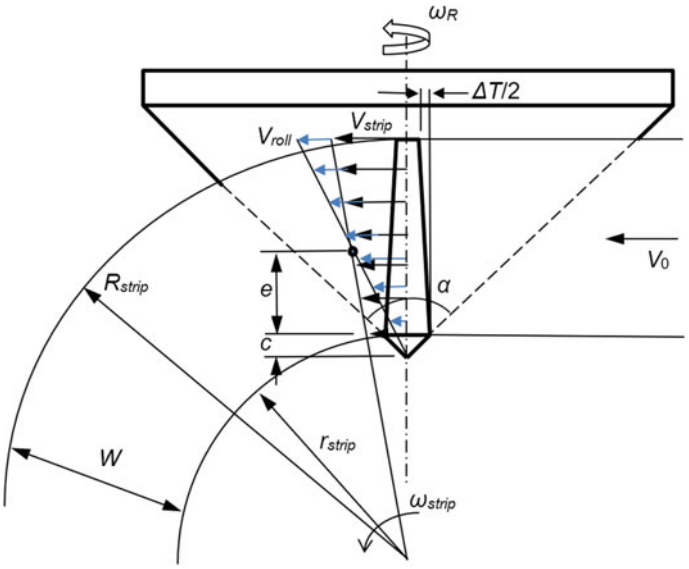


Fig. 15 Schematic of the velocity field in the forming zone. (Color figure online)

From the geometrical relationship, the tangential surface velocity of the rolls and the velocity of the rolled strip at point e are, respectively,

$$V_e = V_{\text{roll_}e} = (c+e)\sin\frac{\alpha}{2}\omega_R = V_{\text{strip_}e} = \left(r_{\text{strip}} + e\right)\omega_{\text{strip}} \tag{41}$$

By assuming that there is no thickening or thinning at the inner edge of the rolled strip in the forming zone, Eq. (2) holds and the following relationships $T_e L_e = T_{\text{inner}} L_{\text{inner}}$and $T_{\text{inner}} = T_0$ are obtained. Differentiating the L values with respect to time on both sides yields

$$T_e V_e = T_0 V_{\text{inner}} \text{or } V_{\text{inner}} = \frac{T_e}{T_0}(c+e)\sin\frac{\alpha}{2}\omega_R \tag{42}$$

where $T_e = T_0 - \frac{e}{W}\Delta T$, $\omega_R = \frac{\pi}{30} n_R$ and $V_{\text{inner}} = r_{\text{strip}}\omega_{\text{strip}} = r_{\text{strip}}\frac{V_e}{(r_{\text{strip}}+e)}$.

To solve for point e and other unknown parameters, the frictional forces from the velocity differential between the rolls and the rolled strip that act on both sides of the neutral point e must be in equilibrium about the point e (Fig. 16),

$$M_L = \int_0^e \mu f(\overline{\sigma}, \overline{\varepsilon}) s dw (e-w) \text{and } M_U = \int_e^W \mu f(\overline{\sigma}, \overline{\varepsilon}) s dw (w-e) \tag{43}$$

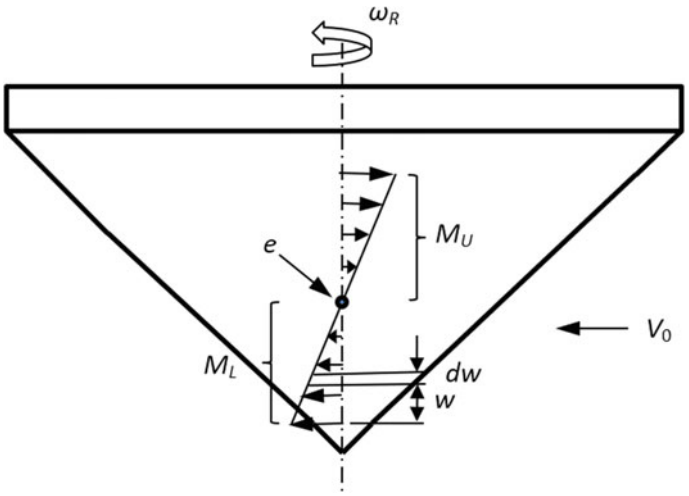


Fig. 16 Rotational frictional moment on roll surface. (Color figure online)

where μ is the coefficient of friction between the roll and strip, $f(\overline{\sigma}, \overline{\varepsilon})sdw$ are the infinitesimal friction forces in dw (Sect. 3.3.1), and $(e - w)$ or $(w - e)$ are moment arms.

Letting $M_L = M_U$ and solving the integration on both sides, the location of the neutral point e can be found, followed by obtaining other unknown kinematical parameters of the rolled strip and the rolls in Eqs. (41) and (42). Using the same dimensions of the example auger flighting shown in Sect. 3.3..3 and assuming that the given rotational speed of the rolls n_R is 9.355 rpm, the parameters calculated from the above closed-form equations are listed in Table 6.

The reason that point e locates more than 50% of the rolled strip width from the inner edge of the rolled strip is because there is more deformation and higher force toward the outer edge. With increasing friction between the rolls and strip, the

Table 6 Rolling velocity-related parameters

Parameters	90° roll angle			65° roll angle		
	$\mu = 0.08$	$\mu = 0.10$	$\mu = 0.12$	$\mu = 0.08$	$\mu = 0.10$	$\mu = 0.12$
Point e (% of the total width) from the inner edge of the rolled strip (mm)	94.89 (62.3%)	92.69 (60.8%)	90.15 (59.2%)	95.96 (63.0%)	94.21 (61.8%)	92.23 (60.5%)
V_e (mm/s)	72.88	71.36	69.60	55.06	54.14	53.11
V_{inner} (mm/s)	50.91	50.35	49.67	38.28	37.94	37.54
V_{outer} (mm/s)	98.70	97.60	96.28	74.21	73.55	72.78
r_{strip} (mm)	219.87	222.07	224.61	218.80	220.55	222.53

distance from the inner strip edge to point e slightly decreases and the velocities of the strip slightly decrease as well. The radius of the rolled strip r_{strip} increases because the upper moment M_U is larger when point e is closer to the inner strip edge. The rolls with a 65° angle, when compared to those with a 90° angle, result in a considerable decrease in the strip velocities owing to a much reduced roll surface linear speed.

The above calculations are based on assumption that sliding friction occurs in all contact zone between the strip and the rolls. In actual rolling, sticking zones can appear if the shear stress caused by the friction force is greater than the shear strength of the strip material. The higher the friction, the larger the sticking zone could be. If this happens, the surface of the rolled strip usually shows sticking marks, such as scratches, peeling, galling, or even some build-up.

With the setting depicted in Fig. 15, the rotational friction moment on the roll surface is in the clockwise direction, as shown in Fig. 16. The strip is, therefore, subject to a counter-clockwise rotational friction moment opposite to that on the roll surface. As a result, the section of the strip immediately prior to entering the rolling zone tends to be lifted upward. The lifting is larger when the rolling friction is higher. The lifting force is sometimes so high that the strip can come out of the lower row of guiding rollers, as shown in Fig. 17. Therefore, it is very important that the guiding mechanism be well designed to (1) provide sufficient retention of the strip to counter the lifting force acting on the strip, as well as maintaining the strip's position, and (2) protect the strip from any damage before it enters the rolling zone.



Fig. 17 Rotational friction moment causing the strip to derail from the guiding rollers. (Color figure online)

Table 7 Auger flighting rolling throughput and rate

Parameters	90° roll angle			65° roll angle		
	$\mu = 0.08$	$\mu = 0.10$	$\mu = 0.12$	$\mu = 0.08$	$\mu = 0.10$	$\mu = 0.12$
V_{auger} (m/min.)	2.473	2.445	2.412	1.859	1.843	1.823
$t_{\text{one-pitch}}$ (s)	16.02	16.20	16.42	21.30	21.49	21.72

4.2 Auger Flighting Forwarding Velocity and Throughput

By assuming that the velocity V_{inner} is equivalent to the total auger flighting velocity V, the forwarding velocity or the throughput of the auger flighting V_Z or V_{auger} in its axial direction during rolling is

$$V_{\text{auger}} = V_Z = \frac{V_{\text{inner}}}{L_{in}} P = \frac{P}{\sqrt{(\pi d)^2 + P^2}} \left(1 - \frac{e}{W} \frac{\Delta T}{T_{\text{inner}}}\right)(c + e) \sin\left(\frac{\alpha}{2}\right) \frac{\pi}{30} n_R \tag{44}$$

The time to roll the auger flighting in one revolution or one pitch is

$$t_{\text{one-pitch}} = \frac{L_{\text{in}}}{V_{\text{inner}}} = \frac{P}{V_{\text{auger}}} \tag{45}$$

If an auger flighting has n pitches, the time spent to roll that auger is

$$T_{n-\text{pitch}} = n t_{\text{one-pitch}} \tag{46}$$

Using the same auger flighting example, the throughput and rate calculated from Eqs. (44) and (45) are given in Table 7.

Auger flighting rolling throughput is slightly affected by rolling friction conditions, but it is considerably affected by the roll angle. As shown in this example, when the roll angle changes from 90° to 65°, under the same friction conditions the throughput of rolling the same auger flighting can decrease by more than 32%.

4.3 Strip Feeding (Bite) Condition

The strip feeding or "bite" condition describes the maximum thickness of a strip that the two rolls can pull into the roll gap under the specified friction and rolling conditions to initiate the rolling process. When the strip thickness exceeds the specified maximum value, the strip will slip over the roll surface and normal rolling cannot be established. The strip thickness that fails in one situation might be satisfactory in another situation once the friction or other rolling conditions are changed.

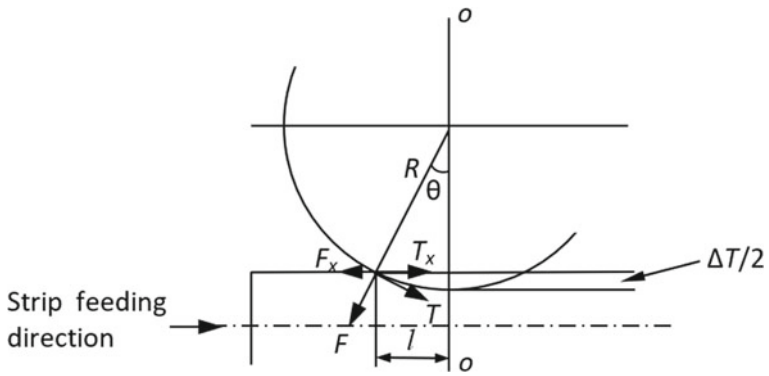


Fig. 18 The outmost edge of a strip during feeding

In auger flighting rolling, the strip's inner edge is deformed very slightly or not deformed at all. The area at the outermost edge of the strip where the largest thickness reduction occurs determines the strip feeding condition.

When the outer edge of the strip contacts the roll surface during feeding (Fig. 18), the relationship of the unit friction force T and unit normal contact force F that a roll gives to the strip at the contact point is $T = \mu F$, where μ is the coefficient of friction at the contact point between the roll surface and strip. When the critical bite condition occurs and the coefficient of friction equals the tangent of the angle of friction $\theta_{\max}$, the two horizontal force components must be in equilibrium, which is $T_x + F_x = 0$ or $\mu F \cos\theta_{\max} - F \sin\theta_{\max} = 0$. Therefore, $\mu = \tan\theta_{\max}$.

For the rolls to "bite" the strip, the condition in which the angle of contact is less than or equal to the angle of friction must be satisfied

$$\tan\theta \le \tan\theta_{\max} \text{or } \tan\theta \le \mu \tag{47}$$

From Fig. 18, it is seen that $\cos\theta = 1 - \frac{\Delta T}{2R}$ and $\sin\theta = \frac{l}{R} = \frac{\sqrt{R^2 - \left(R - \frac{\Delta T}{2}\right)^2}}{R} = \frac{\sqrt{4R\Delta T - \Delta T^2}}{2R}$. Then $\tan\theta = \frac{\sqrt{4R\Delta T - \Delta T^2}}{2R - \Delta T} \le \mu$. By squaring both sides and neglecting the second order of the thickness reduction ΔT, the maximum strip thickness reduction to ensure the strip will be gripped by the rolls is obtained.

$$\Delta T \le \frac{\mu^2}{1 + \mu^2} R \tag{48}$$

Because the radius R of a roll at the outer edge of the strip (also shown in Fig. 9) is

$$R = (c + W) \sin\frac{\alpha}{2} \tag{49}$$

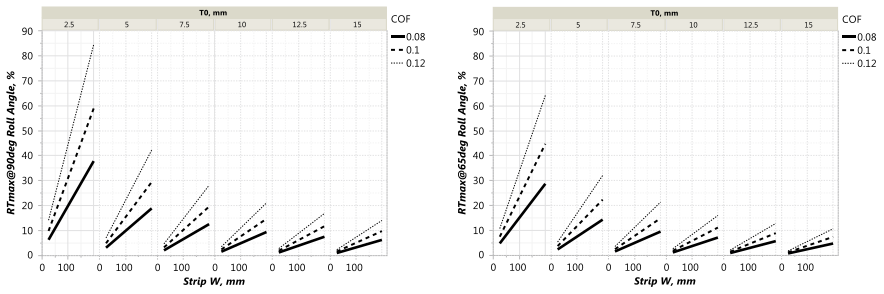
By substituting Eq. (49) for R in Eq. (48), the maximum strip thickness reduction at the outer edge can also be expressed as

$$\Delta T \leq \frac{\mu^2}{1+\mu^2}(c+W)\sin\frac{\alpha}{2} \tag{50}$$

Equation (50) demonstrates that the maximum allowable thickness reduction for secure biting is affected by the coefficient of friction, the roll included angle and the strip width. In production, the biting condition is usually expressed by the maximum thickness reduction ratio $R_T\max = \frac{\Delta T}{T_0} \times 100\% \leq \frac{\mu^2}{1+\mu^2}\frac{c+W}{T_0}\sin\frac{\alpha}{2} \times 100\%$.

The $R_T\max$ (up to 50% of T_0) of the commonly used strips under cold rolling friction conditions ($0.08 \leq \mu \leq 0.12$) with 90° and 65° roll angles are shown in Fig. 19. The selected R_T must be below the curves in the figures. The amount of friction plays a significant role in strip biting. With higher friction, the maximum thickness reduction of the strip necessary to establish biting is considerably larger when the initial strip thickness and width are fixed. The biting condition is improved by increasing the roll included angle and decreasing the initial strip thickness. The thickness reduction at the outer edge of a strip often exceeds the allowable bite condition values. In this situation, the lead of the outer strip should be prepared by either roughing the surfaces to increase the friction, beveling them to reduce the initial thickness or scarfing a portion of the outer strip to let the biting approach to the inner edge.

Over the course of biting, as the strip gradually enters the roll gap, the contact point where the unit contact force and unit frictional force act is moving toward the exit of the roll gap. Once biting is complete and the strip completely fills the roll gap, the total contact force shifts to a location at about half of the contact arc (the angle of contact is reduced by half). Under this circumference, rolling will continue because the bite condition, Eq. (47), is always satisfied. During rolling, at any cross-section along the width of the strip, there always is a neutral plane N where the surfaces of the strip and the rolls have the same linear velocity. At entrance, the surface velocity of the strip is lower than that of the rolls and the friction between the strip and rolls



(a) 90° roll angle (b) 65° roll angle

Fig. 19 Maximum strip thickness reduction ($c = 10.3237$ mm). (Color figure online)

helps draw the material into the roll gap. At exit, the surface velocity of the strip is faster than that of the rolls and the friction between the strip and rolls resists the outflow of the material.

4.4 Roll Offset

The roll offset is a setup adjustment that purposely positions one roll slightly behind the other roll in the rolling direction to achieve the same or similar effect as hangout rolling. When an offset is used, the roll gap changes and the actual rolled strip thickness along the width deviates from the design specification values. Therefore, it is important to understand the relationship between the offset and the rolled strip thickness.

4.4.1 Changes in the Roll Gap Because of the Roll Offset

Assume that the strip always enters the roll gap perpendicular to the roll surfaces and that the elastic recovery in the strip and rolls is not considered. By applying the cosine law, the distance from the roll surface to its centerline R_i at any location along the strip width (see Fig. 20a) is:

$$R_i^2 = \left(\frac{c+w}{\cos\xi}\right)^2 + \left(\frac{c+w}{\cos\beta}\right)^2 - 2\left(\frac{c+w}{\cos\xi}\right)\left(\frac{c+w}{\cos\beta}\right)\cos\frac{\alpha}{2} \tag{51}$$

The relationship of the three angles is $\xi = \frac{\alpha}{2} - \beta$. The geometry of the rolled strip without roll offset is $T_0 = 2W\tan\beta + T_1$. From Fig. 20b, the following relationship can be established

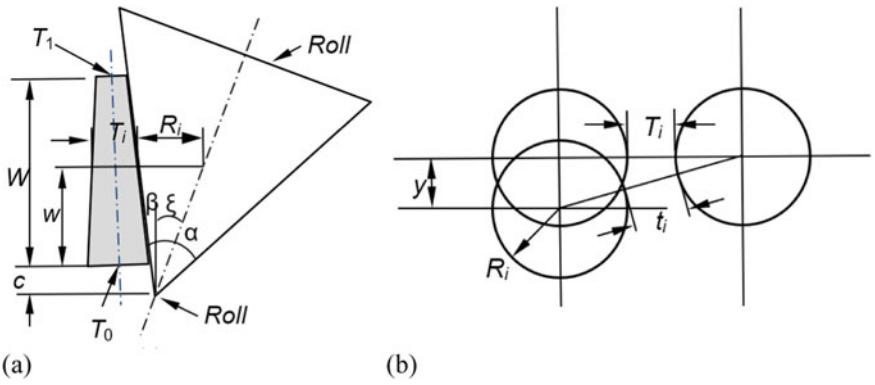


Fig. 20 Schematics of roll offset. (Color figure online)

$$(2R_i + T_i)^2 + y^2 = (2R_i + t_i)^2 \tag{52}$$

where R_i is an arbitrary distance from the roll surface to the roll centerline at the strip width w ($R_i \neq$ the roll radius at location i), T_i is the strip thickness without roll offset at the strip width w, y is the roll offset amount, t_i is the strip thickness with roll offset at the strip width w, and ξ is the roll tilting angle to the vertical mill centerline, which is usually fixed by design.

With a roll offset y, the contact between the strip and rolls is no longer a straight line. The roll gap also changes from a simple trapezoid to a complex configuration. In fact, Eq. (52) expresses a hyperbola relationship of the roll offset and the thickness of the rolled strip along its width. Now, substitute Eq. (51) for R_i in Eq. (52) and select the original strip thickness T_0 and T_1. By running the equation from the roll tip to roll base, the roll gaps under varying roll offsets can be obtained, as shown in Fig. 21.

Figure 21 reveals a number of unique roll gap characteristics that the roll gap lacks when there is no roll offset. These characteristics have a direct impact on the profile of the rolled strip

- First, the roll gap increases as the roll offset increases.
- Second, the larger the roll offset, the greater the thickness reduction at the strip's outer edge.
- Third, because of the hyperbola effect, the roll offset creates a concave profile on the roller strip surfaces. The concave curvature at the roll tip region is much larger

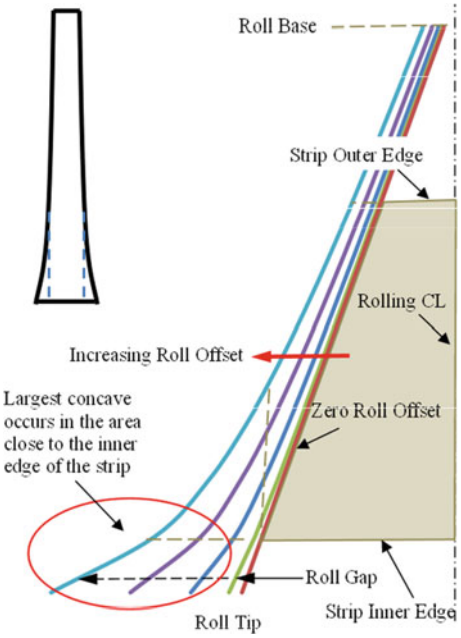


Fig. 21 Influence of roll offset on roll gap. (Color figure online)

than that at the roll base region. When a large roll offset presents, the curvature in the roll tip region is so large that a portion of the inner edge of the strip may not be rolled at all (the dashed lines in the insert in Fig. 21).

This effect is similar to what hangout rolling can achieve. The unrolled or "hang-out" portion increases with the increasing roll offset. The roll offset can also bend the rolled strip naturally to the side of the rear roll, which assists in the formation of a helicoid auger flighting. This bending effect should be considered when determining which roll is set with the forward offset, according to the rotational direction, either the left hand or the right hand, of the rolled auger flighting.

Because of the curved contact zone between the strip and rolls, the strip through the roll gap is twisted from its inner edge to its outer edge. The strip may not always run on a path perpendicular to the connecting line of the two-roll centers, as assumed, which may cause the actual roll gap to be different from the calculated one. As a result, the strip may be rolled to an incorrect thickness, causing the auger flighting to deviate from the required dimensions. To achieve the required thickness in the rolled strip, a new and yet smaller roll gap must be calculated first, from which the amount of roll offset can be determined. The roll offset should be used with caution and the offset amount should be limited if it must be used.

4.4.2 Determination of the Roll Offset Amount for the Required Thickness of the Rolled Strip

Assume R_0 is the distance from the roll surface to roll centerline at the inner edge of the strip T_0 or t_0 ($w = 0$), R_1 is the distance from the roll surface to roll centerline at the inner edge of the strip T_1 or t_1 ($w = W$), T_0 is the initial rolled strip thickness at the inner edge without a roll offset ($w = 0$), t_0 is the targeted rolled strip thickness at the inner edge with a roll offset ($w = 0$), T_1 is the initial rolled strip thickness at the outer edge without a roll offset ($w = W$), and t_1 is the targeted rolled strip thickness at the outer edge with a roll offset ($w = W$).

The following equations are obtained by inserting the above parameters into Eqs. (51) and (52):

$$R_0^2 = c^2\left[\left(\frac{1}{\cos\xi}\right)^2 + \left(\frac{1}{\cos\beta}\right)^2 - 2\left(\frac{1}{\cos\xi}\right)\left(\frac{1}{\cos\beta}\right)\cos\frac{\alpha}{2}\right] \tag{53}$$

$$R_1^2 = (c+W)^2\left[\left(\frac{1}{\cos\xi}\right)^2 + \left(\frac{1}{\cos\beta}\right)^2 - 2\left(\frac{1}{\cos\xi}\right)\left(\frac{1}{\cos\beta}\right)\cos\frac{\alpha}{2}\right] \tag{54}$$

$$R_0 = \frac{c}{c+W}R_1 \tag{55}$$

$$T_0 = \sqrt{(2R_0 + t_0)^2 - y^2} - 2R_0 \tag{56}$$

$$T_1 = \sqrt{(2R_1 + t_1)^2 - y^2} - 2R_1 \tag{57}$$

Then

$$\sqrt{\left(2\frac{c}{c+W}R_1 + t_0\right)^2 - y^2} - 2\frac{c}{c+W}R_1 = 2W\tan\beta + \sqrt{(2R_1 + t_1)^2 - y^2} - 2R_1 \tag{58}$$

The roll offset y, the only unknown in Eq. (58), can be solved by iteration. After obtaining y and inserting it into Eqs. (56) and (57), the initial roll gaps or the strip thicknesses T_0 at the inner edge and T_1 at the outer edge, respectively, are determined. The combination of the required dimensions of the to be rolled strip and the geometry of the rolls may create a situation where the two rolls can come into contact with each other at their bases. In designing an auger flighting rolling, this situation must be checked to prevent the roll bases from contacting.

4.4.3 Strip Deviation Angles

When an offset is created, the strip exits the roll gap at a deviated angle. The deviation angle is an acute angle between the strip feeding direction (perpendicular to the mill front frame face) when it enters the rolling mill and the strip exiting direction when it leaves the roll gap (Fig. 22). The larger the offset, the larger the deviation angle will be. Because the deviation angles at the inner edge and the outer edge are different, the strip also exits the roll gap with a slight twist. This twisting can be expressed by a twisting angle, which is the difference of the deviation angles of the inner and outer

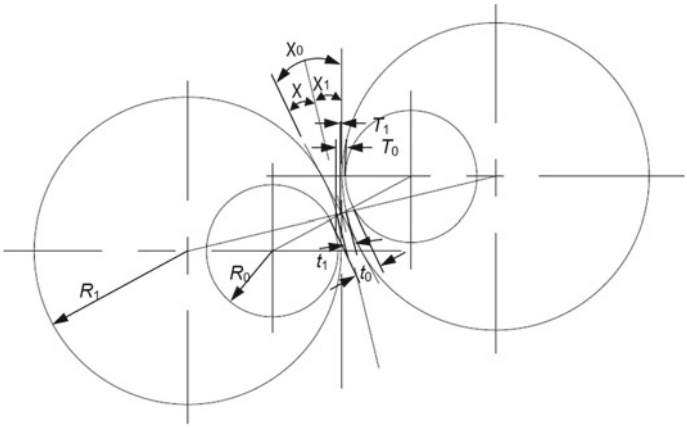


Fig. 22 Calculation of strip deviation and twisting angles. (Color figure online)

edges of the rolled strip. In addition, the roll force component in the rolling direction perpendicular to the mill front frame face increases.

Assume χ_0, χ_1 are the strip deviation angles at the inner edge and outer edge of the rolled strip, respectively, and χ is the strip twisting angle. The strip deviation angles at either the inner or outer edge are, respectively,

$$\chi_0 = \cos^{-1}\left(\frac{R_0 + \frac{T_0}{2}}{R_0 + \frac{t_0}{2}}\right) \text{and } \chi_1 = \cos^{-1}\left(\frac{R_1 + \frac{T_1}{2}}{R_1 + \frac{t_1}{2}}\right) \tag{59}$$

The strip twisting angle is $\chi = \chi_0 - \chi_1$.

5 Design Considerations of the Main Roll Assembly

5.1 Design of Main Roll Shafts

In roll shaft design, the minimum shaft diameter at the location with the highest stresses must have the strength necessary for the shaft to support the loads with a designated life and without premature failure. The shaft is usually subjected to cyclic stresses, which are caused by the combined bending and torsional loads. In this case, the stresses in the main roll shafts are the result of a bending moment originating from the vertical component of the roll separating force F_y, a torsional moment from the torque T, a bending moment from the rotational motion of the strip during rolling and an axial force from the horizontal component of the roll separating force F_x.

Here, only the bending moment from the vertical component of the roll separating force F_y and the torsional moment from the torque T are considered. The other two factors are excluded because: (1) the bending moment from the rotational motion of the strip during rolling is smaller than and in a different phase from the bending moment from the vertical component of the roll separating force F_y, and (2) the axial force is in compressive, which reduces the overall tensile stress at the most critical location in the shaft. The transverse shear also is omitted from this calculation due to its insignificant contribution to the overall stress state when the ratio of the length and diameter of the shaft is sufficiently large. Further, it is assumed that the plane sections remain plane and perpendicular to the neutral axis during bending.

From the mechanics of the materials, the minimum shaft diameter at the critical section A' under combined bending and torsional moments at the critical section is $D_{\min} = \sqrt[3]{\frac{32}{\pi\sigma_{\text{allow}}}\sqrt{M_{\max}^2 + \frac{3}{4}T^2}}$, where σ_{allow} is the allowable working stress of the shaft $\sigma_{\text{allow}} = \frac{\sigma_y}{n_{\text{safe}}}$, σ_y is the yield strength of the shaft material, and n_{safe} is a safety factor. (See Fig. 23.)

It is necessary to note that since the diameters of a main roll shaft vary along its length, the minimum shaft diameter can occur at a location where the bending moment is not at its maximum value. Therefore, the calculation is carried out at

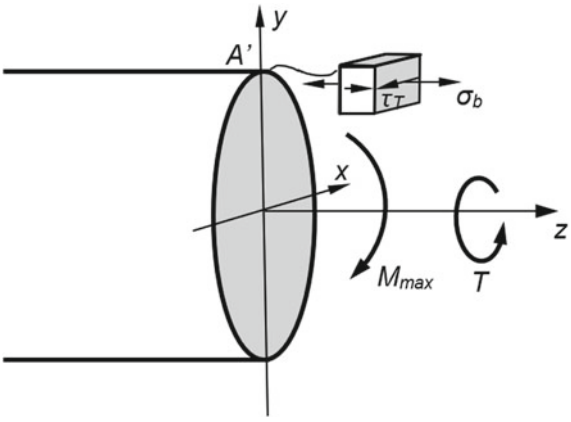


Fig. 23 Stress state at the location A′ of the shaft surface under the combined loads

various locations in addition to the supports (bearing journals) to define the most critical section and the minimum shaft diameter.

5.2 Main Roll Driving Power

The total power provided by the main rolls' driving motor in auger flighting rolling is calculated by considering the following torques: the torques driving the two rolls in rolling P_R, the torques overcoming the frictions in the bearings on the main roll shafts due to the reaction forces P_B, the torques overcoming the frictions in the transmission system (drive chain from the roll-driving motor to the rolls) P_G, the torques during no-load idle running P_M, and the torques coming from the dynamic motion when the rolls change their rotational speed P_D, such as at the start and end of rolling. These powers are

$$P_R = T_t \omega_R = T_t \frac{2\pi n_R}{60} = T_t \frac{\pi}{30} \frac{n_M}{i} \tag{60}$$

where P_R is the power driving the two rolls in kW, T_t is the two roll or total torque in kN-m calculated by using the equations given in Sect. 3.4, ω_R is the angular speed of the rolls in 1/s, n_R is the number of revolutions of rolls per minute (rpm) $= \frac{n_M}{i}$, n_M is the number of revolutions of roll-driving motor per minute (rpm), and i is the gear ratio of the drive chain from roll-driving motor to rolls.

For a two-roll auger rolling mill where the main shafts are laid in an angle approximately equal to one-half of the main roll included angle, the torque to overcome the friction forces in the two main roll bearings and one thrust bearing on each shaft is calculated by the following formula:

$$T_b = 2\left(\mu_{bA} N_A \frac{d_A}{2} + \mu_{bB} N_B \frac{d_B}{2}\right) + 2\mu_{bT} F_x \frac{d_T}{2} \tag{61}$$

The power required for overcoming the friction torque is calculated by

$$P_B = T_b \omega_R = T_b \frac{\pi}{30} \frac{n_M}{i} \tag{62}$$

where P_B is the power overcoming the friction in the four main roll bearings in kW; d_A, d_B, and d_T are the diameters of the main roll shafts at bearings A and B and the thrust bearing, respectively; μ_{bA}, μ_{bB}, and μ_{bT} are the coefficients of friction in bearings A and B and the thrust bearing, respectively; N_A is the reaction force at support A; and N_B is the reaction force at support B.

The torque generated by the frictions in the transmission system of the rolling mill can be determined by the efficiency of the system

$$T_g = \left(\frac{1}{\eta} - 1\right)(T_t + T_b) \tag{63}$$

The power required for overcoming the friction torque in the transmission system is calculated by

$$P_G = T_g \omega_R = T_g \frac{\pi}{30} \frac{n_M}{i}, \tag{64}$$

where η is the efficiency of the main roll power transmission system.

During the no-load idling run, the torque is generated by the friction forces in the bearings, including the main roll bearings and thrust bearing, supporting a proportion of the mass of the main roll assemblies and the components of the transmission system.

$$T_m = \sum_n (mg)_i \mu_{bi} \frac{d_i}{2} \tag{65}$$

where m is the mass of a component in kg, g is acceleration of gravity (=9.81 m/s^2), (mg) is gravity force in N of the component to be supported by a bearing, μ_b is the coefficient of friction of the bearings, and d is the bearing neck diameter of the shaft.

The power in the idling run is

$$P_M = T_m \omega_R = T_m \frac{\pi}{30} \frac{n_M}{i} \tag{66}$$

A dynamic motion happens when the rolling mill starts rotating from an idling condition to full rolling speed, and vice versa. During this period, when a component in the transmission system of mass m and diameter d rotates about its axis in a uniform angular acceleration $d\omega/dt$, the dynamic torque required to generate this acceleration

is

$$T_{d_{\text{comp}}} = F\frac{d}{2} = (ma)\frac{d}{2} = \left(m\frac{d}{2}\frac{d\omega}{dt}\right)\frac{d}{2} = \left(m\frac{d}{2}\right)^2\frac{2\pi}{60}\frac{dn}{dt} = I\frac{2\pi}{60}\left(\frac{n_2 - n_1}{\Delta t}\right) \tag{67}$$

where a is acceleration in m/s^2, I is the torsional moment of inertia of the rotating component $= \left(m\frac{d}{2}\right)^2$, and dn is the rpm change from n_1 to n_2 during the time Δt, which is positive when the rotational speed increases and is negative when the rotational speed decreases.

The total dynamic torque is a summation of the dynamic torques of all of the rotational components in the transmission system

$$T_d = \sum_n T_{d_{\text{comp}}} = \sum_n \left(m_i\frac{d_i}{2}\right)^2\frac{2\pi}{60}\frac{dn_i}{dt} = \sum_n I_i\frac{2\pi}{60}\left(\frac{n_{2i} - n_{1i}}{\Delta t_i}\right) \tag{68}$$

The power required to generate this acceleration is

$$P_D = T_d\omega_R = T_d\frac{\pi}{30}\frac{n_M}{i} \tag{69}$$

The total power that the main rolls' driving motor must provide is as follows, once the different rolling stages or conditions are taken into consideration

(1) Steady auger flighting rolling stage with constant rolling speed

$$P_{\text{Stable}} = P_R + P_B + P_G + P_M \tag{70}$$

(2) Idle running with no load

$$P_{\text{Idle}} = P_G + P_M \tag{71}$$

(3) Dynamic motion during rolling

$$P_{\text{Dynamic Rolling}} = P_R + P_B + P_G + P_M \pm P_D \tag{72}$$

(4) Dynamic motion with no load

$$P_{\text{Dynamic No Load}} = P_G + P_M \pm P_D \tag{73}$$

The above equations were used to calculate the driving powers of the main roll power transmission system in rolling an auger flighting. The results were compared with the actual driving powers of the rolling mill. Since the exact efficiency, friction condition, mass, and dimensions of many components in the overall power transmission system were unavailable or inaccurate, the results from the calculations are

Table 8 Calculated and measured rolling torque (N-m) and power (kW)

	@ $\eta = 85\%$	@ $\eta = 95\%$	Mill reading
Main shaft motor torque T_t, N-m	82.0	73.4	82.3
P_{Stable}, kW	11.56	10.35	11.6
P_{Idle}, kW	1.74	0.53	1.3
$P_{\text{Dynamic Rolling}}$, kW	11.70 (accel.)/11.42 (decel.)	10.49 (accel.)/10.21 (decel.)	n/a
$P_{\text{Dynamic No Load}}$, kW	1.88 (accel.)/1.60 (decel.)	0.67 (accel.)/0.39 (decel.)	n/a

approximate. An important fact is that the calculated values are in the same orders of magnitude as the measured ones.

These equations can be used either to assess a rolling mill's capability when a new product is to be rolled, or to design a new rolling mill when an estimation of the required motor power is needed.

In addition to the driving powers, the total torque was also calculated and compared to the actual torque. The actual and estimated rolling parameters used in the calculations are:

- Bearing neck diameters of the mail roll shafts: $d_A = 266$ mm, $d_B = d_T = 187$ mm
- Mass of one mail roll shaft: $m \approx 800$ kg
- Main motor speed: 1,346 rpm
- Gearbox ratio: 143.8797
- Main roll speed: 9.355 rpm
- Main roll included angle: 90°
- Time from idle to full speed and vice versa: $\Delta t = 0.2$ s
- Coefficient of friction of rolling: $\mu = 0.15$
- Efficiency of the main shaft power transmission system: $\eta = 80\%$ and 90%
- Coefficient of friction of bearings: $\mu_b = 0.003$
- Reaction forces at bearing necks: $N_a = 867.5$ kN, $N_b = 265.2$ kN
- Axial force (thrust from the axial component of the roll separating force): $F_x = 602.3$ kN

The results are given in Table 8.

6 Conclusions

This article describes the mathematical development of the fundamental kinematics and mechanics of auger flighting rolling, from which the contact area, rolling force, and torque are calculated and the affecting factors evaluated. Slip characteristics between the strip and forming rolls and the effects of roll offset are studied. The

design considerations, primarily of the main roll shafts and the required rolling mill power, are also given. The application results were compared to the actual rolling readings with satisfactory agreement.

References

1. Bailey JO (1928) Endless spiral conveyor. US Patent 1,684,254, 11 Sept 1928
2. Barker RP et al (1937) Improvements in or relating to worms or impellers of the Archimedean type. GB Patent 472,254, 17 Sept 1937
3. Hamilton MD (1997) Screw conveyor augers and flighting for use therein. US Patent 5,678,440, 21 Oct 1997
4. Wynnobel R, Wilton A (2011) Flighting for a conveyor and apparatus for producing such flighting. US Patent 8,069,973 B2, 6 Dec 2011
5. Wusatowski Z (1969) Fundamentals of rolling. Pergamon Press, London
6. Dieter GE, Kuhn HA, Semiatin SL (eds) (2003) Handbook of workability and process design. ASM International, Ohio

Evaluating an Automated Avoidance of Ring Climbing in Radial–Axial Ring Rolling



Simon Husmann and Bernd Kuhlenkötter

Abstract The forming process of radial–axial ring rolling involves certain instabilities, causing from the underlying principle of the synchronous and continuous deformation in two opposite rolling gaps. To reduce the occurring consequential errors like climbing of the ring in the radial rolling gap, we installed an image processing system for error detection. Combined with the integration of the camera setting into the control software of the rolling machine, it is possible to test automated rolling strategies to stabilise the forming process in the case of upcoming ring climbing. The paper will illustrate how an intervention limit, in form of limit value, for the control system could be evaluated via statistical process control and evaluates if there is a systematic climbing behaviour of the ring. The combination of an expert interview with an effect analysis of the forming parameters on the stabilising impact leads to the development of an ideal forming strategy. The defined strategy is validated in a final design of experiments.

Keywords Ring rolling · Image processing · Ring climbing

1 Introduction

Radial–axial ring rolling is the most important technology to produce axial symmetrical workpieces. The forming is executed in two opposite arranged rolling gaps, the radial and the axial rolling gap, see Fig. 1. The mandrel is moved in a translational way towards the main roll and therefore defines the ring's wall thickness and its radial contour. Meanwhile, the upper axial roll is also moved linearly towards the lower axial roll to define the height of the ring's cross section. The suppressed material primarily flows into the tangential, respectively, circumferential direction

S. Husmann (✉) · B. Kuhlenkötter
Ruhr-University of Bochum, Chair of Production Systems, Universitätsstr. 150, 44801 Bochum, Germany
e-mail: husmanns@lps.rub.de

B. Kuhlenkötter
e-mail: kuhlenkoetter@lps.rub.de

© The Minerals, Metals & Materials Society 2021

G. Daehn et al. (eds.), *Forming the Future*, The Minerals, Metals & Materials Series,
https://doi.org/10.1007/978-3-030-75381-8_203

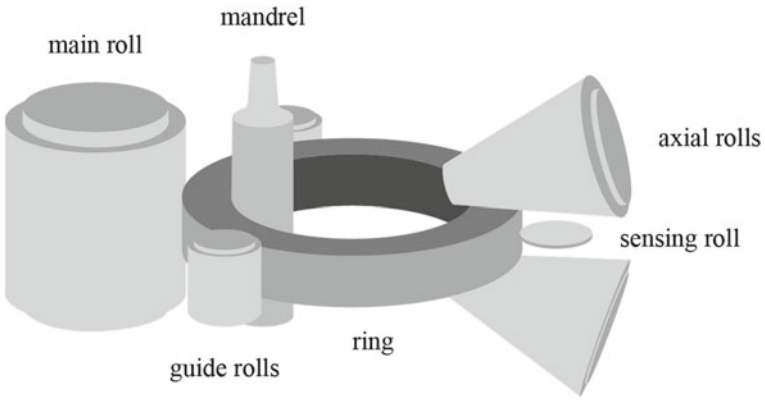


Fig. 1 Schematic structure of a radial–axial ring rolling machine

and therefore increases the diameter of the ring as intended. This way it is possible to form rings with a large diameter as well as a seamless and homogenous structure. The produced components are used because of their huge load capacity in various industries such as the energy and transport sector, the aerospace industry, and in many fields of general mechanical engineering [1, 2].

Due to the fact that the ring is formed continuously and synchronously in two rolling gaps the process itself is unstable and needs to get stabilised through the guide rolls. These also determine the ring's position on the rolling table and could influence it in given boundaries. Because of the unstable process, different process errors can occur. This paper will only focus on the phenomenon of ring climbing, which describes a vertical movement of the ring in the radial gap away from the rolling table. This process error can cause serious deformations of the ring's cross section and could lead to a dish-shaped workpiece and waviness. In this case, the forming process cannot be continued and the ring has to be scrapped.

This work focuses on the evaluation of an automated stabilising control system which should avoid ring climbing and which was developed in recent years. After a short presentation of the corresponding state of the art and the experimental set-up, the evaluation of an intervention limit will be introduced. Based on this intervention limit an ideal stabilising control strategy will be derivated through the combination of an expert interview and an effective study of selected process parameters. Design of experiments will be used for the final evaluation of the stabilising control strategy before the paper closes with brief conclusions.

2 State of the Art

The following state of the art will focus on the avoidance of the phenomenon of ring climbing. While the majority of the research efforts focus on the causal analysis regarding the phenomenon of a climbing ring, only MARCZINSKI, BRISELAT and GOLDBACH mention the thesis, that a climbing ring could be stabilised through different rotational speeds for the axial rolls [3–5]. However, none of the authors has proven the thesis in an experimental or simulative approach or stated the level of speed difference.

Also the displacement of the ring has no proven influence on the climbing behaviour of the ring but has an effect on the ratio of the axial rolls' speed and the radial pass reduction rate [6]. This adjustment of the reduction rate can be used to stabilise the ring [7]. Also, the displacement of the ring is mentioned as a general parameter to stabilise a ring, not specifically in case of a climbing ring [8].

Moreover, different approaches to prevent the climbing of a ring exist. LIEB describes the possibility to observe the axial drive torque to prevent ring climbing, but only deduces this approach in theory without a proof [9]. Furthermore, LIEB mentions a reduction of the chance of ring climbing by tilting the mandrel without explaining if this is mentioned as a preventive or as a reactive measure [10].

Koppers et al. describe that a rolling strategy with high pass reduction rates reduces the evolution of bulges and connect this to the observation of a reduced chance of ring climbing [11]. Also, as a preventive strategy, PENG refers to a geometrical adjustment of the guide rolls [12].

All these publications have in common, that they are either not supported by an experimental or simulative verification if they suggest a reactive rolling strategy or they focus only on preventive measures. Therefore this paper will illustrate how an automated reactive avoidance of a climbing ring could be evaluated.

3 Experimental Set-up

The Chair of Production Systems uses a radial–axial ring rolling machine with a ring's maximum diameter of 1,000 mm, a maximum height of 160 mm, and a unit weight of up to 50 kg. The machine provides rolling forces up to 200 kN in radial and 160 kN in the axial direction. In all presented experiments, the blanks are made of the same alloy, from the same batch, exhibit the same starting geometries as well as the same finishing geometries.

The used camera system consists of an intelligent Matrox Iris GT 1900 camera, which has a resolution of 1600 x 1200 pixels and a maximum frame rate of 15 fps. An intelligent camera has an integrated processor and allows image processing and information extraction without an external PC system. The camera is combined with a 50 mm lens and a Heliopan Digital E27 infrared band-elimination filter. The used algorithm in the image processing set-up was specially developed to detect

the climbing height during radial–axial ring rolling and was presented in a prior publication [13]. A constant airstream in front of the camera lens is realised to reduce the distortion through loose scale particles and heated air.

4 Evaluation of the Intervention Limit

The lower axial roll is always set to a higher level as the rolling table to make sure the roll stays in contact with the workpiece and thereby ensure the forming ability of the roll. Likewise, this disables the friction between the ring and the rolling table. Because of this fact, a process-related gap exists between the ring and the table, which is no sign of a climbing ring, see Fig. 2.

To determine the level of this process-related gap and therefore define a control limit (CL) for the stabilising control system, four rings (R1–R4) are rolled with a standardised configuration of the rolling machine. The rolling processes were captured with an additional video camera to ensure the reliability of the measured data. All recorded data, the video files, the image processing data, and the logged machine data show a non-exemplarily rolling behaviour of ring R4. This ring had an unstable rolling behaviour resulting in a significantly high climbing heights. Therefore, this ring will not be used to define the process-related gap and the correlating control limit. The method of statistical process control (SPC) is used to define the mentioned control limit. The limit is calculated by the process mean $\overline{\overline{x}}$, the process standard deviation $\overline{s}$, and a coefficient A_3:

$$CL = \overline{\overline{x}} + A_3 * \overline{s} \tag{1}$$

For a probability of 99.73% and three rolled rings, the coefficient A_3 could be determined to 1.954. Based on the measured climbing heights of the rings R1–R3 the process mean results to 0.75 mm, the process standard deviation to 0.88, and therefore, the control limit is set to 2.470 mm.

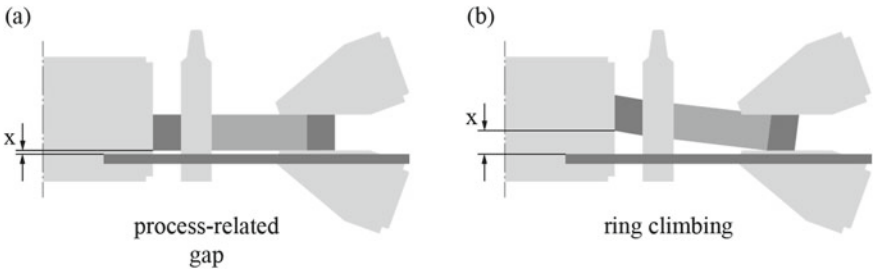


Fig. 2 Schematic difference between **a** the process-related gap and **b** a climbing of the ring

5 Development of an Ideal Stabilising Rolling Strategy

The development of an ideal stabilising control strategy to reduce the climbing of the workpiece during radial–axial ring rolling processes is based on two aspects. On the one hand, the development is influenced by a statistical effect analysis presented in prior publications [14]. These findings show mainly that an adjustment of the rolling table's height has a high impact on the climbing behaviour, especially in correlation with the adjustment of the guide rolls' height difference. On the other hand, the industrial experience is considered through an expert interview.

6 Expert Interview

The interview was held with a rolling-mill worker with over 33 years of experience in forming rings in one of Germany's most important ring manufacturers. According to scientific practice, the interviewee was informed beforehand about the theme procedure of the interview [15]. The most important results of the interview are:

- A definition of a climbing ring, especially of a control limit, is non-existent. At the moment a ring raises significantly from the rolling table, the worker will adjust the control system.
- To stabilise the ring, the worker will set the following adaptions in the listed order
  - Reduction of the main roll speed to gain more time and eventually stabilise the ring in a first step. The amount of reduction is not quantifiable.
  - Increase in the rotational speed of the upper axial roll by 2–3%. This is normally combined with a displacement of the ring of a maximum of 5° towards the radial entrance.
  - Furthermore, it is possible to generate a radial directed force on the workpiece by moving the axial framework. But this method increases the chance of a radial deformation which results in a non-circular ring.
- The above-mentioned measures are implemented in an overlay, respectively, simultaneously, not separated from each other.
- The level of the applied measures is not influenced by the actual duration of the rolling process.
- The measures are held until the ring gets into a stable state near the rolling table. Then the automated rolling procedure is continued.
- If the measures have no effect the worker interrupts the rolling process. The ring is flipped over and a new rolling process starts or the ring needs to be heated again before a new rolling process is started.
- The phenomenon of a climbing ring occurs regularly, often daily.
- A wrong adjustment of the rolling table, high wear of the rolls, and the inhomogeneous temperature of the ring are determined as causes for the phenomenon of a climbing ring.

6.1 Implementation of the Stabilising Control System

Based on the effect study and the expert interview the image processing system is connected to the rolling control to implement the stabilising control system. The implemented stabilising control system is activated automatically, if the rolling process was started, the ring's climbing height exceeds the defined control limit of 2.47 mm and the combined rolling in radial and axial direction is not yet finished. The minimum duration of the stabilising measures is set to 2.0 s. The validation of the implementation is realised in two steps. First, it is tested in the simulation mode of the rolling mill, in which the tools move without rolling an actual ring, with an artificially created and predefined signal to simulate a climbing ring. In the second phase of validation a ring is rolled, while the test signal for a climbing ring is applied in recurring order with durations of 15, 10, and 5 s. The reduction of the main roll speed, the adjustment of the upper axial roll speed in contrast to the lower axial roll speed, and the displacement of the ring are tested.

The first validation shows that the control system reacts as intended but also that especially the engine to accomplish the displacement of the ring has a slow reaction time. The residues of the second validation phase all show a high peak at the beginning of each test signal sequence, marked in the grey areas, with a fast decrease afterwards and a following stable execution of the planned measures, see Fig. 3. Also a high peak occurs at the change back into the automated rolling mode. The residues of the main roll adjustment have an arithmetic mean of 0.393%, the measure of the displacement of the ring of 0.029° and the adjustment of the upper axial roll of 0.274% in the correlating phase. These are significantly lower than the residues during automated control of the rolling mill, especially in the starting phase of the rolling process.

6.2 Derivation of the Stabilising Rolling Strategy

While the measures to stabilise a climbing workpiece during a radial–axial ring rolling process have been derived in their quality before, this chapter focuses on the quantitative validation of the correlating factors. Therefore, a reference has to be set before the design of experiments is conducted. The rolling table has been adjusted with a gap of 1 mm from the upper rolling table edge to the upper edge of the lower axial roll to increase the chance of a climbing ring. To support this chance, the guide rolls have been adjusted with a height difference of 17 mm to each other, while the guide roll on this entrance site of the radial gap has been mounted in the higher position. The reference ring was rolled with the automated control system of the rolling mill. The ring shows a significant increase in its maximum climbing height of 16.06 mm and an average mean of 4.63 mm, see Fig. 4. This equals an increase of about six times the average climbing height, compared to rings rolled with no adjustment of the machinery (R1–R3) which have an average climbing height of

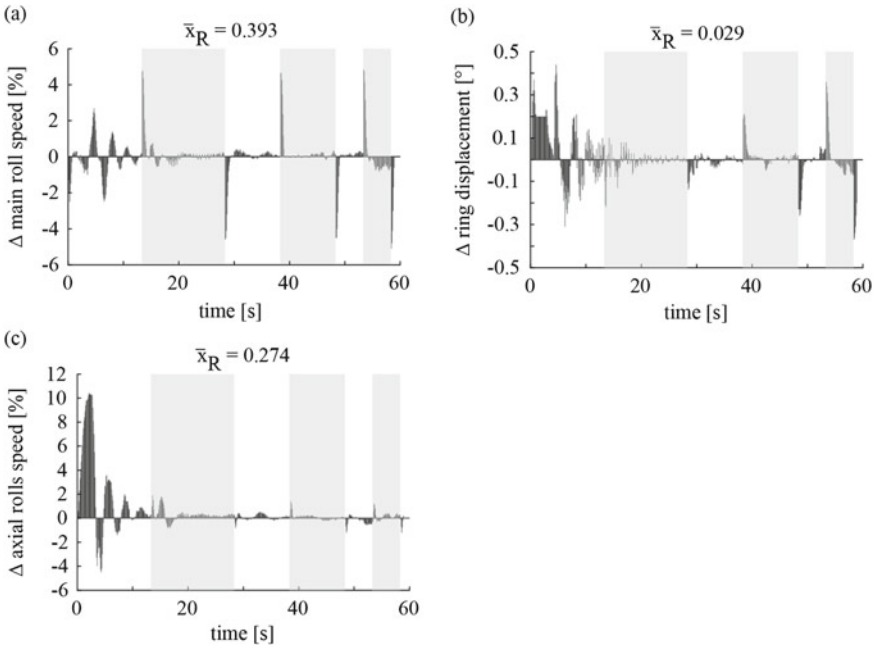


Fig. 3 Residues of **a** the main roll speed, **b** the ring displacement and **c** the axial rolls' speed difference for the evaluation of the implementation of the stabilising control system

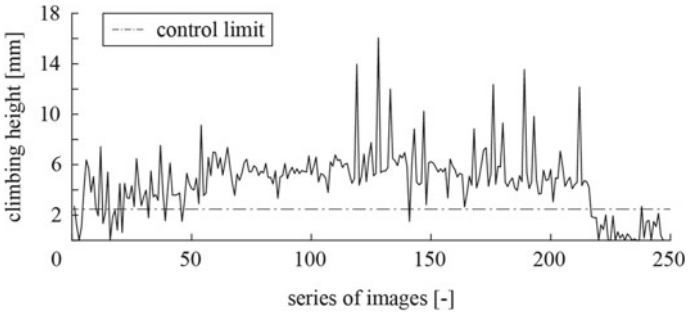


Fig. 4 Climbing heights of the reference ring to evaluate the effectiveness of the stabilising control system

0.75 mm. This is why the reference ring represents a good reference regarding the maximised chance of a climbing ring.

The validation of the process parameters is accomplished via design of experiments with 16 runs (Q1–Q16). The corresponding factors are the rotational speed of the main roll *nMr*, the difference of the axial rolls rotational speed *ΔnAx*, the displacement of the ring *Rd*, and the dynamic of the axial speed difference *axDyn*, see Table 1.

Table 1 Definition of factors and their levels for the design of experiment

Parameter	Unit	Standard	Minimum	Maximum	In short
Main roll speed	(%)	46.5	23.25	41.85	nMr
Axial speed difference	(%)	0	2	5	ΔnAx
Ring displacement	(°)	Automatic	0.74	5	Rd
Dynamic of the axial speed difference	active = 1 inactive = 0	Inactive	0	1	axDyn

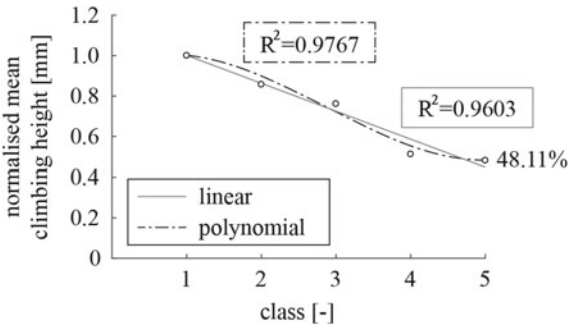


Fig. 5 Classification of the climbing behaviour

Previous ring rolling experiments have shown, that a classification of the normalised single climbing heights over time illustrates a trend of a decreasing average climbing height over the rolling time, see Fig. 5. Because of this effect, the stabilising control system tests a dynamic for the axial rolls' speed difference which decreases the level of intensity linearly over the rolling time. Hereby the effectiveness of this dynamic approach is evaluated in a first step. The intensity is reduced in time steps of 3 mm to the absolute minimum of the normalised data of 48.11% of the initial axial rolls' speed difference.

The reduction of the main roll speed to 41.85% of the maximum potential speed equals a decrease to 90%. The defined minimum of 23.25% which represents a reduction to 50% ensures a large width of variation without slowing down the process excessively. The maximum of the axial rolls' speed difference is defined with 5%, otherwise, the upper roll will lose its forming character and the ring might slip through the axial rolling gap [16]. In this case, the axial roll would also lose the possibility to stabilise the ring and therefore the influence on the climbing height. The minimum of 2% results from the maximum of the process-related variation of the axial rolls' speed difference of the reference ring. This definition is supported by the expert interview which stated an implementation of 2–3% for the axial rolls' speed difference and it also corresponds with the literarily documented industrial level of the axial rolls' speed difference to minimise the chance of a climbing ring [4]. The ring displacement maximum originates from the expert interview and is set to 5°, whereas the minimum of 0.74° is defined by the average maximum of the previously rolled rings (R1–R3).

6.3 Definition of the Dependent Variable

Before the experiments are carried out, it is necessary to define the specific dependent variable. While the amount of repeated transgressions of the control limit may have a higher informative content than the average climbing height, since a low rate indicates a better stabilising control, it lacks in interpreting control interventions without repeated transgressions. Therefore, the authors chose to use the arithmetic mean of the climbing height during the control intervention as the dependent variable. Whereas the median would be more robust, the arithmetic mean is influenced by outliers and therefore better considers repeated transgressions. To maximise the importance of control limit transgressions, a weighted average with a factor of 1.5 is used. The initial transgression of the control limit is not part of the arithmetic mean, respectively, of the dependent variable so that only climbing heights during an active stabilising control system are included.

6.4 Validation via Design of Experiments

Through a plausibility scrutiny with the logged machine data, a screen recorder, and the detected climbing heights ring Q10 had to be excluded from the study. The climbing heights detected via the image processing system could not be reproduced with the screen recorder or the logged data. All the other rings were formed without interruptions to the predefined outer diameter of 800 mm, from a starting diameter of 250 mm.

For all rings, the correlating climbing heights were displayed in contrast to the reference ring, see Fig. 6. While for nearly all rings the reference ring shows a significant higher average climbing height, the ring Q1 tends to climb extensively near the end of the forming. Furthermore, the reference ring shows a longer rolling time, which also indicates an unstable forming process.

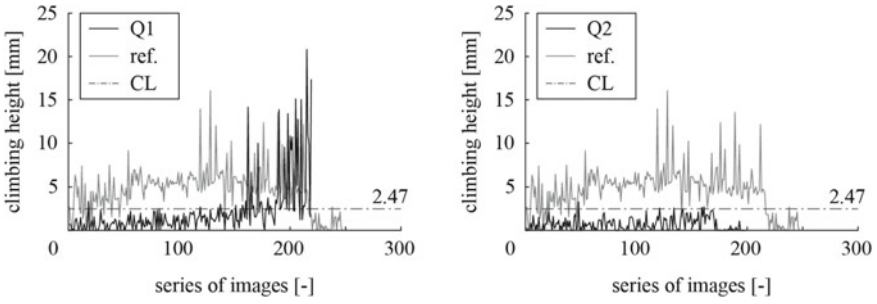


Fig. 6 Excerpt of the measured climbing heights for rings Q1 and Q2

The box plots of all rings including the reference highlight the stable forming of most of the runs, except Q1, and therefore an overall effective stabilising control, see Fig. 7. The median of the reference ring as well as the 75th and 25th percentiles exceed the rings with active stabilising control. The rings with the highest outliers Q1, Q5, and Q7 do not share a parameter with the same factor level for all.

To evaluate basically the indicated difference between the reference ring and all other runs the Wilcoxon signed-rank test is performed, see Table 2. With the assumption H_0 of paired data in each case and a significance level of 0.05, the test could discard this assumption for all rings. Therefore, a significant difference between the reference and all runs is proven which is an additional evidence for an efficient stabilising control system.

The display of the dependent variable y shows a high similarity to the box plots. High peaks for the rings Q1 and the reference ring and low to medium height bars for all other runs of the design of experiments.

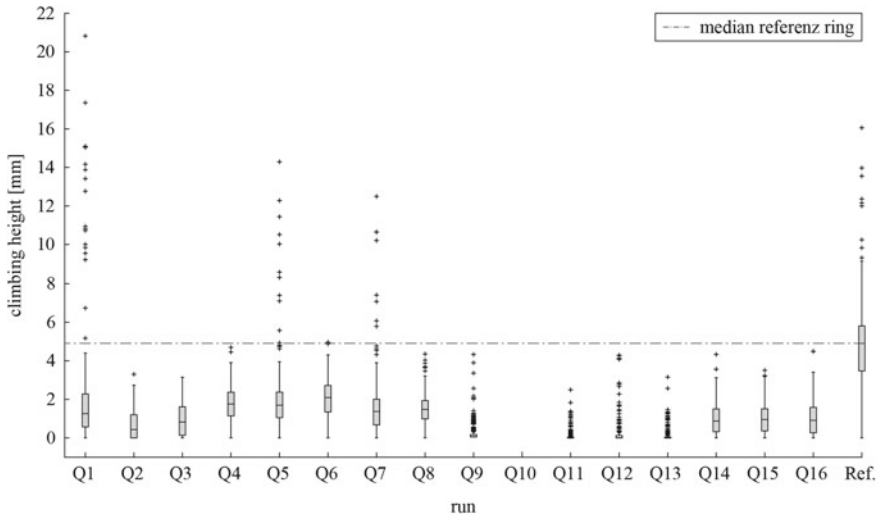


Fig. 7 Boxplot of all measured climbing heights

Table 2 Results of the Wilcoxon signed-rank test for the comparison of each ring to the reference ring

	Q1	Q2	Q3	Q4	Q5	Q6	Q7	Q8
H_0	1	1	1	1	1	1	1	1
p	$1.6*10^{-32}$	$1.1*10^{-53}$	$4.1*10^{-51}$	$1.1*10^{-39}$	$2.0*10^{-40}$	$8.5*10^{-38}$	$9.6*10^{-44}$	$7.2*10^{-46}$
	Q9	Q10	Q11	Q12	Q13	Q14	Q15	Q16
H_0	1	–	1	1	1	1	1	1
p	$3.1*10^{-68}$	–	$1.5*10^{-69}$	$1.6*10^{-63}$	$3{,}7*10^{-69}$	$3.8*10^{-50}$	$4.7*10^{-51}$	$3.9*10^{-48}$

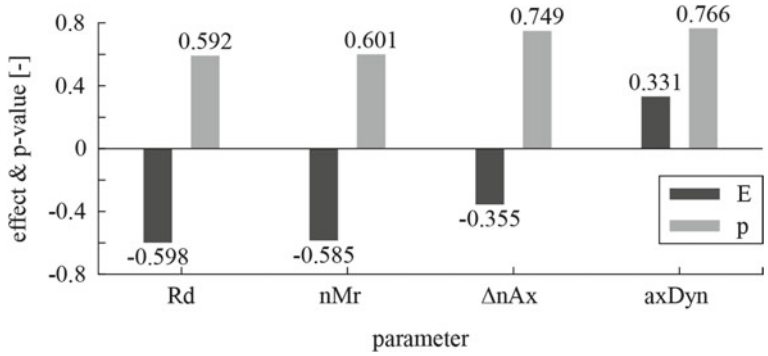


Fig. 8 Effects and p-values for all factors resulting from design of experiments

The computation of the effects E and the correlating significance level p, based on the defined dependent variable, allows a more detailed interpretation, see Fig. 8. Noticeable are the high p-values since they reflect a lack of statistical significance. On the one hand, this is referable to an intrinsic problem of the manipulation of the dependent variable. The intentional influence on the climbing height will resolve in an increased spread and therefore in a higher standard deviation. Since the significance level is influenced by the standard deviation, the p-values will increase too. On the other hand, mass forming processes are underlying higher variations through the high forces and solid workpieces. This adds up through the statically indeterminable system of a radial–axial ring rolling process. This process-related variation combined with a narrow set control limit leads also to an increased spread and therefore to increased significance levels. Furthermore, the amount of runs is comparably low regarding other processes and design of experiments. Due to these facts, the gained results have to be seen as a tendency and correlations, not as causalities or as universal transferable results.

A negative effect, as the ring displacement and the main roll speed show, has to be interpreted as lower ring climbing heights, therefore effects with a negative level have a positive influence on the stabilisation of the rolling process. On the contrary, the dynamic approach of the axial rolls' speed difference has a negative influence on the stabilising behaviour.

The levels of effects are not directly comparable, because they are based on different units. In a normalised comparison the effect of the axial rolls' speed difference with a level of 0.018 mm/min^{-1} is higher than the level of the main roll speed with 0.002 mm/min^{-1}. But this only describes the single effects without paying attention to the correlations between these factors.

For the interpretation of the correlations, a negative gradient also represents a positive stabilisation of the ring and is therefore preferable. All compared pairs interact with each other but with differences in the level of interaction. The correlations between the radial roll speed and the axial dynamic, respectively, the axial dynamic and the axial speed difference are comparatively low. Due to the strong effect of the

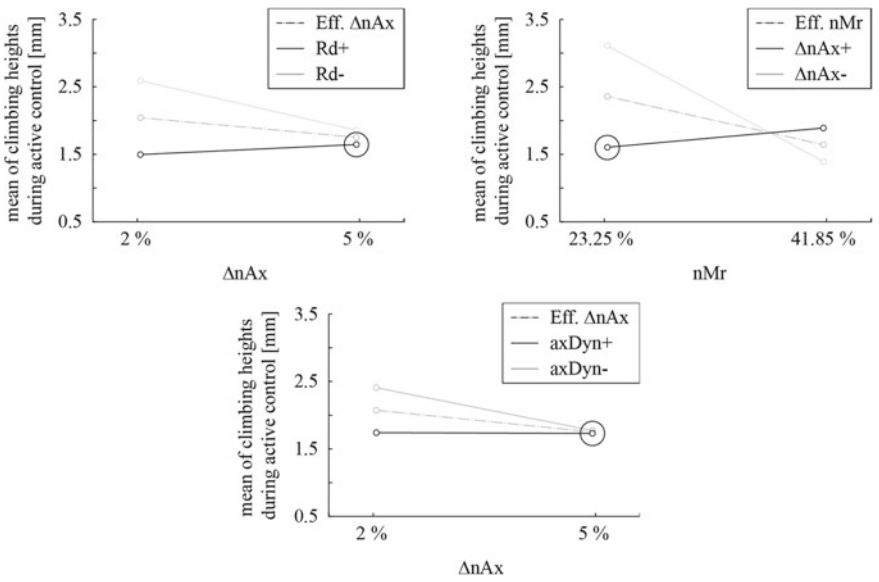


Fig. 9 Different correlations with the marked optimum for the derivation of the stabilising control system

axial speed difference on the climbing height of the ring, this factor is the focus of the derivation of the stabilising control strategy. Through the assumption of the ideal axial speed difference of 5% the interpretation of the corresponding correlations leads to the marked minimum level for the factors of the main roll speed (50%) and the axial dynamic (static) as well as the maximum for the ring displacement (5°) by choosing the optimum of the correlations, respectively, the minimal mean climbing height, see Fig. 9.

This configuration of the factor levels is equivalent to the rolled ring Q14 with a dependent variable y of 1.318 mm. In combination with nine transgressions during the rolling process this run is a valid representation of a rolling process with maximised chance of climbing, see Fig. 10. Compared to the reference ring this combination reduced the arithmetic mean of the climbing heights by about 78.66% and the rolling time is reduced about 11.3%, which is a sign of an effective stabilising control strategy.

7 Conclusions

This paper presents an experimental approach to evaluate an automated stabilising control system to avoid ring climbing during the process of radial–axial ring rolling. To ensure the differentiation between the process-related gap in the radial rolling gap and a climbing ring a control limit was defined. For this purpose, the approach of

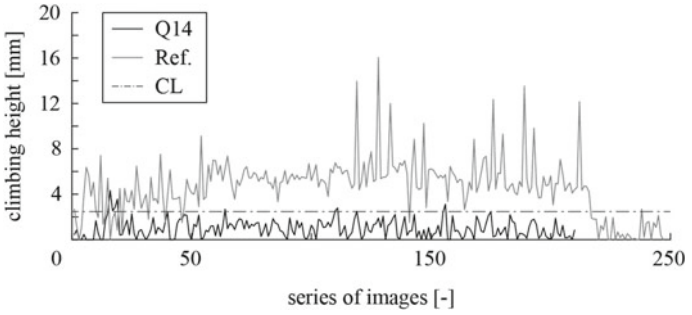


Fig. 10 Measured climbing heights of ring Q14 compared to the reference ring

statistical process control was used and a control limit of 2.47 mm was determined. The definition of the stabilising strategy is based on an expert interview combined with an effect study. The designed stabilising control strategy was implemented on the radial–axial ring rolling machine of the Chair of Production Systems and was successfully tested both in a simulative and experimental way. The final validation of the stabilising control strategy was performed via design of experiments with 16 runs. Therefore a forming reference with a maximised chance of a climbing ring had to be set and a dependent variable, the weighted arithmetic mean of the climbing heights during the control intervention, was defined. The design of experiments and the interpretation of the corresponding effect levels and correlations resulted in an effective stabilising control strategy by adjusting the axial speed difference and the displacement of the ring to the defined maximum of 5% and 5° in the case of a climbing ring. The addressed dynamic of the axial speed difference should not be used because overall it increases the climbing height. The main roll speed should be set to its minimum of 50%. In contrast to the rolled reference ring, this combination of process parameters has reduced the arithmetic mean of the measured climbing heights by about 78.66% and shortened the rolling time by about 11.3%.

References

1. Allwood JM, Tekkaya AE, Stanistreet TF (2005) The development of ring rolling technology - Part 1. Steel Res 76(2/3):111–120
2. Eruc E, Shivpuri R (1992) A summary of ring rolling technology - i. recent trends in machines, processes and production lines. Int J Mach Tools Manuf 32(3):379–398
3. Briselat J (2013) Prozesssynchrone Vermessung der Ringgeometrie durch Bildverarbeitung während des Radial-Axial Ringwalzens. Dissertation Ruhr-Universität Bochum. 1., Aufl. Herzogenrath: Shaker (Schriftenreihe des Lehrstuhls für Produktionssysteme, 2014, 2)
4. Goldbach V (2011) Konzepte zur Erweiterung des walzbaren Geometriespektrums beim Ringwalzen. Dissertation RWTH Aachen. Shaker Verlag (Umformtechnische Schriften, Band 163), Aachen
5. Marczinski H-J (1974) Der Entwicklungsstand neuzeitlicher Ringwalzwerke. Stahl Eisen 94(24):1207–1211

6. Gellhaus, M. (1999) Radial-Axial Ringwalzen. Millenium Edition. Hg. v. Produktbereich Wagner Banning Ringwalzen. SMS Eumuco (Technische Information 2/99)
7. Meier H, Lagao P (2000) Identification of instabilities in radial-axial ring-rolling processes using multivariate detection methods. In: Perryman R, Ellis CD (Hg.) Advances in manufacturing technology - XIV. IEE Inst Mech Engineers. Professional Engineering Publishing ltd., Westminster, England, pp 345–349
8. von Hehl A (2010) Thermomechanische Behandlung beim Ringwalzen. Modelle zur schnellen Simulation der Gefügeevolution. Zugl.: Aachen, Techn. Hochsch., Diss., 2009. Shaker (Umformtechnische Schriften, 152), Aachen
9. Lieb A (1992) Minimierung von Formfehlern beim Ringwalzen. Dissertation RWTH Aachen. Verlag Stahleisen (Umformtechnische Schriften, 35), Düsseldorf
10. Lieb A, Wiegels H, Kopp R (1990) Rundheitsmessung an warmgewalzten Ringen. Stahl u. Eisen 1990:110
11. Koppers U, Wiegels H, Dreinhoff P, Henkel J, Kopp R (1986) Methoden zur Verringerung des Material- und Energieeinsatzes beim Ringwalzen. Stahl Eisen 106(14/15):49–55
12. Peng Y, Song Y, Zeng X, Qian D (2013) Research on mechanism and suppression method of axial climbing in radial-axial ring rolling. Zhongguo Jixie Gongcheng/China Mech Eng 24(12):1665–1670
13. Husmann S, Hohmann M, Kuhlenkötter B (2017) An approach to develop an algorithm to detect the climbing height in radial-axial ring rolling. AIP Conf Proc 1896:1–6
14. Husmann S, Kuhlenkötter B (2016) Determination of influencing factors on ring climbing in radial-axial ring rolling via design of experiments. AMR 1140:19–26. https://doi.org/10.4028/www.scientific.net/AMR.1140.19
15. Brinkmann S, Kvale S (2018) Doing interviews (Flick U (ed)), vol 2, 2nd edn. Sage (The SAGE qualitative research kit), Los Angeles, London, New Delhi, Singapore, Washington, DC, Melbourne
16. Buhl K, Schröder K (2011) Prozeßdatenanzeige Rolltronic. Instructions: Radial-Axial-Ringwalzmaschine RAW 20/16-1000/160

Effect of Delivery Angle on Longitudinal Buckling in Temper Rolling of Thin Steel Strips



Toshiro Okazaki, Yukio Kimura, Hideo Kijima, and Masaru Miyake

Abstract The shape defect called "longitudinal buckling" tends to occur in temper rolling of double reduced thin strips. Although previous research investigated the effects of several rolling conditions on longitudinal buckling, the effect of large delivery angles of over 4° has not been studied experimentally. In this paper, the effect of large delivery angles was investigated in a laboratory rolling experiment. The results showed that the longitudinal buckling pattern becomes more distinct and the number of waves decreases as the delivery angle increases, and buckling disappears when the delivery angle exceeds 24°. At the same delivery angle, the buckling form does not change depending on the distance between the work roll and the auxiliary roll. Following this experimental study, an elementary analysis of the buckling characteristics of a sheet winding around a work roll was carried out, and it was found that the change in the number of waves depending on the delivery angle in the analysis was in good agreement with the experimental results when the delivery angle was larger than 10°. It is estimated that longitudinal buckling is initiated around the roll gap and changes under the influence of the shape of the sheet winding around the work roll.

Keywords Rolling · Temper rolling · Skin pass · Model simulation · Flatness · Buckling · Longitudinal buckle · Cross buckle

T. Okazaki (✉) · Y. Kimura · H. Kijima · M. Miyake
Steel Research Laboratory, JFE Steel Corporation, Kawasaki-Cho 1, Chuo-Ku, Chiba 260-0835, Japan
e-mail: t-okazaki@jfe-steel.co.jp

Y. Kimura
e-mail: yu-kimura@jfe-steel.co.jp

H. Kijima
e-mail: h-kijima@jfe-steel.co.jp

M. Miyake
e-mail: m-miyake@jfe-steel.co.jp

© The Minerals, Metals & Materials Society 2021

G. Daehn et al. (eds.), *Forming the Future*, The Minerals, Metals & Materials Series,
https://doi.org/10.1007/978-3-030-75381-8_204

1 Introduction

A striped surface pattern called cross buckle or longitudinal buckle may occur during temper rolling of thin steel sheets. In particular, longitudinal buckle appears as a wave shape parallel to the longitudinal direction and is generally thought to occur easily in thin sheets that have undergone secondary cold rolling after cold rolling and annealing. Sheets with this type of surface defect often require additional processes such as a correction process.

Longitudinal buckle is considered to be a buckling phenomenon of the steel sheet that occurs at the delivery side of the rolling mill due to the residual stress in the steel sheet caused by rolling [1]. Various studies have been made on buckling phenomenon of thin sheets. Abdelkhalek et al. proposed an FEM model of the flatness defects which appear during rolling of thin sheets [2]. Abdelkhalek et al. also studied the behavior of the flatness that may arise when the rolling tension is released using an FEM model [3]. Fischer et al. and Friedl et al. used analytical buckling calculation to predict the buckling mode of thin sheets related to rolling and leveling [4, 5]. Coman also used analytical buckling model and estimated the critical load and the mode of the buckling with linear distribution of residual stress [6]. Tran et al. carried out an experiment to simulate flatness defects of thin sheets by using thermal stresses, and the behavior was in good agreement with FEM result [7, 8].

On the other hand, there are few studies on longitudinal buckle. Kijima et al. carried out an experimental investigation of the influence of rolling conditions on the occurrence of longitudinal buckle, which revealed the following trends [9].

- When the rolling load is reduced, the wave height decreases.
- Longitudinal buckle occurs regardless of the rolling tension.
- The wave height is reduced by reducing the work roll roughness.
- The wave height increases due to an increase in the delivery angle at the exit side of the rolling mill.

Komori obtained the wavelength of longitudinal buckle by an elementary analysis of buckling, and showed that the wavelength of the longitudinal buckle obtained by the analysis was in good agreement with the trend in the experimental values [10]. The results of that analysis also showed that buckling is less likely when the arithmetic average roughness of the temper rolling rolls is low, which is consistent with the experimental results.

Changing the rolling load and/or work roll roughness is a possible approach for preventing longitudinal buckle. However, in many cases, these changes have a large effect on product properties and are difficult in practice. On the other hand, changing the delivery angle is an important method for preventing longitudinal buckle which has relatively little effect on product properties. In general temper rolling mills, auxiliary rolls are installed on the exit side for purposes such as threading stabilization and tension measurement, and these rolls can also be used to give the strip a delivery angle relative to the horizontal pass line at the exit side.

In a previous study, Kijima et al. investigated the influence of the delivery angle in a laboratory experiment with a delivery angle range of 0°–4° [9]. However, the behavior with larger delivery angles has not been studied experimentally or analytically.

In this report, we conducted a laboratory experiment to examine the effect of larger delivery angles (>4°) on the behavior of longitudinal buckle caused by temper rolling (rolling reduction $\leqq$2%) of a steel sheet that has been cold-rolled and annealed and then subjected to secondary cold rolling (rolling reduction of approximately 40%). There was a possibility that the shape of the part where the steel sheet is wound around the work roll (winding part) on the rolling exit side affects longitudinal buckle generation behavior. In order to investigate this possibility, we also carried out an elementary analysis of the buckling mode of the winding part and compared the analysis results with the results of the laboratory experiment.

Furthermore, when a steel strip is given a delivery angle, it has been shown that the rolled material does not follow the work roll near the roll bite outlet [11]. In other words, a noncontact region exists after exiting from roll bite, and there is also a possibility that this phenomenon may affect buckling behavior. Therefore, we carried out an FEM analysis to investigate the contact state between the roll and the steel sheet near the roll bite outlet in temper rolling of steel sheets subjected to secondary cold rolling.

2 Experiment

A temper rolling experiment using a coil rolling mill was conducted to clarify the occurrence of longitudinal buckle. Figure 1 shows a schematic diagram of the laboratory rolling mill used in the experiment, and Table 1 shows the rolling conditions. The rolling mill was a 2Hi type. The work roll diameter was 330 mm, and the roll surface roughness was set to 1.3 μmRa by cylindrical polishing. An auxiliary roll with a diameter of 200 mm was installed on the exit side of the rolling stand, and

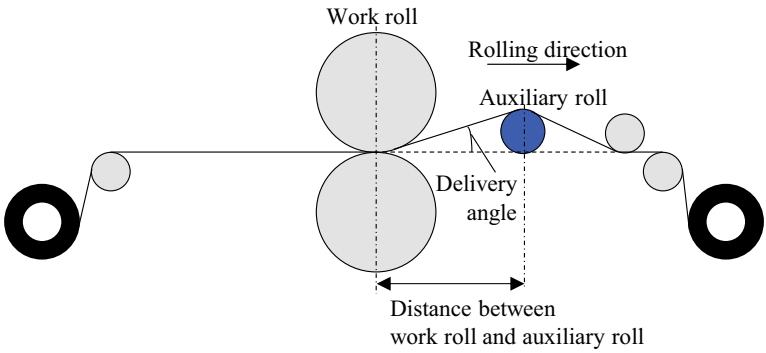


Fig. 1 Schematic illustration of rolling equipment in experiment. (Color figure online)

Table 1 Experiment conditions

Rolling load per width (kN/mm)	5.3
Thickness at entry side (mm)	0.15
Width (mm)	300
Unit tension at entry side (MPa)	100
Unit tension at delivery side (MPa)	100
Work roll diameter (mm)	330
Roughness of work roll surface (μm*Ra*)	1.3
Auxiliary roll diameter (mm)	200
Distance between work roll and auxiliary roll (mm)	225, 375
Delivery angle (°)	0–40
Rolling speed (m/min)	10
Lubrication	Dry

the delivery angle on the exit side of the rolling mill was changed in the range of 0°–40° by changing the height of the auxiliary roll. When the delivery angle was 0°, the auxiliary roll was not placed in contact with the steel sheet. The auxiliary roll was also movable in the rolling direction. In order to investigate the effect of the distance from the winding part to the auxiliary roll, two horizontal distances between the work roll and the center of the auxiliary roll were set: 225 and 375 mm.

The specimen used in this experiment was a cold-rolled steel sheet with a thickness of 0.25 mm and a width of 300 mm that was secondarily cold-rolled to a thickness of 0.15 mm. The yield stress of the specimen was 657 MPa. The rolling conditions were a rolling load of 5.3 kN/mm, an inlet/outlet tension of 100 MPa, and a rolling speed of 10 m/min. The lubrication condition was dry.

After temper rolling, a steel sheet sample taken from the coil was placed on a surface plate with the upper surface during rolling upward, and the surface profile in the width direction was measured with a scanning laser distance meter.

Figure 2 shows the appearance of the sample after rolling when the horizontal distance between the center of the work roll and the auxiliary roll was 225 mm and

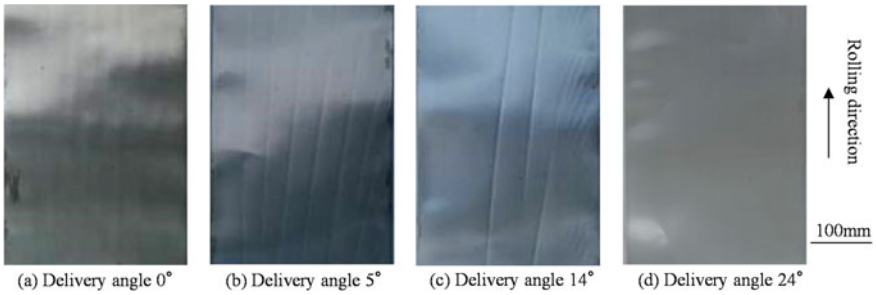


Fig. 2 Appearance of sheet after skin-pass rolling (Distance between work roll and auxiliary roll: 225 mm). (Color figure online)

the delivery angle was changed by changing the height of the auxiliary roll. When the delivery angle is 0°, a number of relatively unclear longitudinal buckles can be observed. When the delivery angle is increased from 5° to 14°, the number of longitudinal buckles (wave number) decreases, and each buckle appears as a clear longitudinal buckle. However, when the delivery angle is increased further to 24°, no longitudinal buckles can be seen. Although not shown in the figure, rolling was also performed with delivery angles larger than 24°, but no longitudinal buckles was observed at these higher delivery angles. In some delivery angle conditions, the longitudinal buckles are not parallel to the rolling direction and not uniformly distributed in width direction. The angle and distribution of longitudinal buckles are considered to be affected by the stress in the longitudinal direction [1], and the difference in elongation in the width direction may have caused the angle and distribution to be not uniform.

Figure 3 shows the measurement results of the surface profile when the horizontal distance between the center of the work roll and the auxiliary roll was 225 mm. The figure shows the profile around the center of the width, where the amount of warpage is small when the steel sheet is left stationary. The measurement location in the longitudinal direction was selected so that longitudinal buckles could be clearly observed visually. At the delivery angle of 14°, the position 175 mm from the left edge of the sheet in Fig. 2 was defined as 0 mm on the horizontal axis in order to show the point where the uneven shape was clear. The surface profile is uneven when the delivery angle is 0°, 5°, or 14°, and this uneven shape becomes increasingly distinct as the delivery angle increases. A clear concavo-convex shape can be confirmed at the delivery angle of 14°, and it has a convex shape toward the bottom surface during rolling. However, the irregular shape is not seen at the delivery angle of 24°.

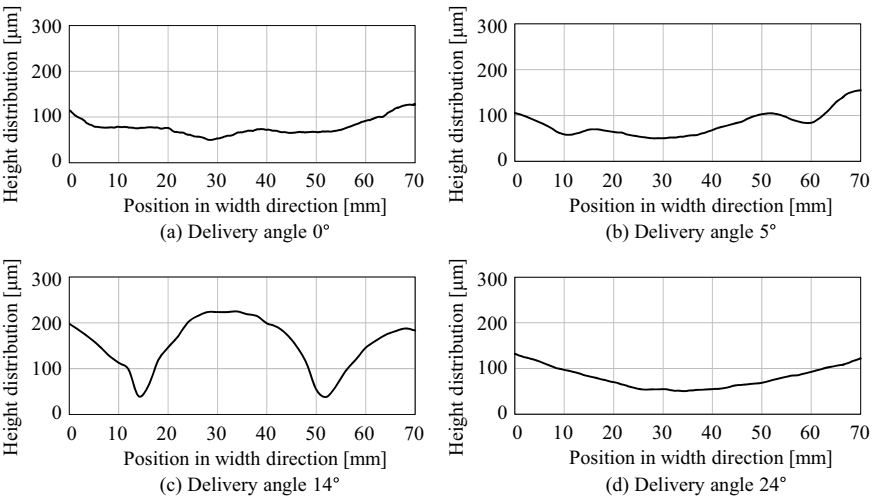


Fig. 3 Wave chart of longitudinal buckling (Distance between work roll and auxiliary roll: 225 mm)

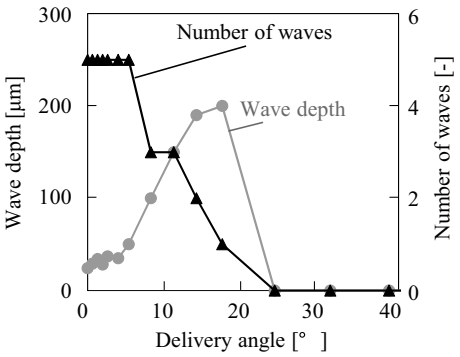


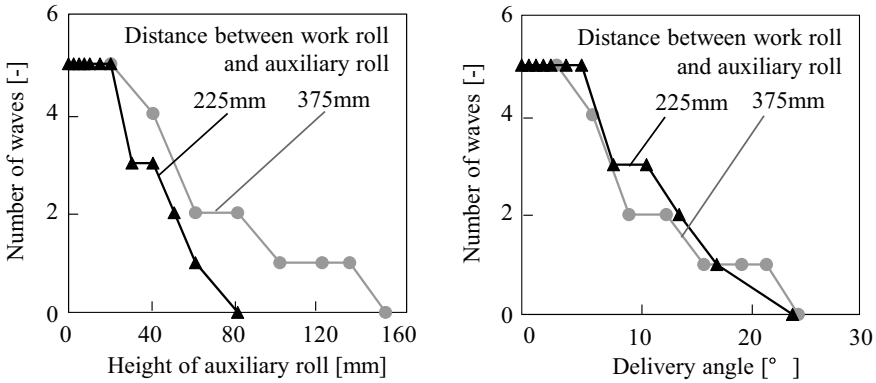
Fig. 4 Effect of delivery angle on buckling behavior (Distance between work roll and auxiliary roll: 225 mm)

From Figs. 2 and 3, in the steel sheet which displays longitudinal buckle, it can be seen that there are some locations where concave and convex portions are locally adjacent on the surface profile. Using the measured surface profile, the height difference between the concave and convex portions was evaluated as the wave depth. At this time, in order to eliminate the influence of the warp shape of the steel sheet, a quadratic approximate curve of the measured surface profile was obtained by the least square method, and the wave depth was evaluated with the difference from the measured surface profile as the evaluation object. The number of longitudinal buckles (wave number) in the entire width was evaluated from the appearance of the steel sheet.

Figure 4 shows the effect of the delivery angle on buckling behavior, i.e., changes in the wave number and wave depth when the horizontal distance between the center of the work roll and the auxiliary roll is 225 mm. The wave number decreases as the delivery angle increases and becomes zero when the delivery angle exceeds 24° and the longitudinal buckle disappears. The wave depth increases as the delivery angle rises and then reaches 0 μm when the delivery angle exceeds 24° and the longitudinal buckle disappears.

Figure 5 compares the change in the wave number of the longitudinal buckle with respect to the delivery angle for the cases where the distance between the work roll center and the auxiliary roll is 225 mm and 375 mm. When compared at the same roll height, the wave number is different depending on the distance between the rolls, but when compared at the same delivery angle, the wave number is very close.

Next, the steel sheet was observed for longitudinal buckle after rolling and passing the auxiliary roll when the distance between the work roll center and the auxiliary roll was 375 mm. When a longitudinal buckle was present after the sheet had passed the auxiliary roll, visual observation of the underside of the sheet between the work roll and the auxiliary roll revealed that the longitudinal buckle was already present before the sheet passed the auxiliary roll.



(a) Influence of height of auxiliary roll (b) Influence of delivery angle

Fig. 5 Effect of the distance between work roll and auxiliary roll on buckling behavior

3 Elementary Analysis

Since the wave number and wave depth of the longitudinal buckle changed depending on the delivery angle, the shape of the part where the steel sheet is wound around the work roll (winding part) may have an effect on the behavior of the longitudinal buckle. For verification, the winding part was modeled as a flat plate with curvature, and the buckling mode was obtained by an elementary analysis and compared with the experimental results.

The model examined in this paper is described in the following. If the elastic strain in the width direction of the plate is assumed to be zero due to restraint by the roll in the vicinity of the exit of the roll bite, Eq. (1) holds. Here, ε_z is the strain in the plate width direction, E is Young's modulus, ν is Poisson's ratio, and σ_x,σ_y,and σ_z are stress in the longitudinal direction, thickness direction, and width direction, respectively. In this paper, tensile stress is denoted as negative and compressive stress as positive.

$$\varepsilon_z = \frac{1}{E}\{\sigma_z - \nu(\sigma_x + \sigma_y)\} = 0 \tag{1}$$

Here, as the stress state at the roll bite outlet, longitudinal stress is assumed to be tension t_f, thickness direction stress is the deformation resistance k_f of the rolled material, and width direction stress σ_z is expressed by Eq. (2) from Eq. (1).

$$\sigma_z = \nu(k_f - t_f) \tag{2}$$

In this model, it is assumed that the stress in the width direction expressed by Eq. (2) acts uniformly on the winding part, and it is considered that a longitudinal buckle occurs if this stress exceeds the elastic buckling limit. Although this is a bold

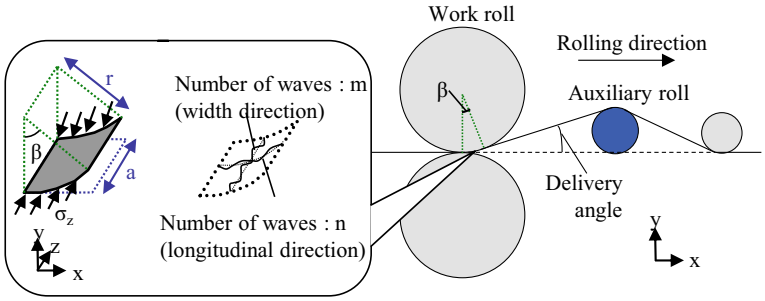


Fig. 6 Buckling model of sheet with curvature. (Color figure online)

assumption, this hypothesis is adopted in this report in order to use the elementary analysis method.

In this report, longitudinal buckle is modeled as an elastic deformation of a flat plate with the same curvature as the work roll in an unloaded state, as shown in Fig. 6, and the buckling limit stress σ_{cr} is calculated by Eqs. (3)–(5) [12]. Here, a is the sheet width, h is the sheet thickness, r is the radius of curvature (work roll radius), β is the winding angle (delivery angle), and m and n are the sheet width direction and longitudinal direction wave number, respectively.

In reality, a steel sheet exists as a continuous strip in the longitudinal direction. However, in this analysis, the part from just below the work roll center to the part wound around the work roll (i.e., the portion of the strip corresponding to β in Fig. 6) is modeled. The longitudinal ends and widthwise edges of this steel sheet are treated as free ends; that is, restraint by the rolling roll and the continuous steel strip existing in the longitudinal direction is not considered, and the tension acting on the sheet is also disregarded. Furthermore, the pressure of the work roll on the steel sheet is ignored. In general, residual stress after rolling is not uniform in the longitudinal direction and sheet width direction [13–15]. Here, however, it is assumed that the stress in the sheet width direction acts uniformly in the flat plate.

$$\sigma_{cr} = \alpha E \frac{\left(\frac{n^2\pi^2}{\beta^2} + \lambda^2\right)^2}{(1-\nu^2)\lambda^2} + E\frac{\lambda^2}{\left(\frac{n^2\pi^2}{\beta^2} + \lambda^2\right)^2} \tag{3}$$

$$\lambda = \frac{m\pi r}{a} \tag{4}$$

$$\alpha = \frac{h^2}{12r^2} \tag{5}$$

Figure 7 shows the theoretical value of the buckling limit stress σ_{cr} calculated by Eq. (3) using the conditions shown in Table 1. Assuming that the steel sheet is bent along the roll, the longitudinal wave number n is 1. Under this condition, the stress

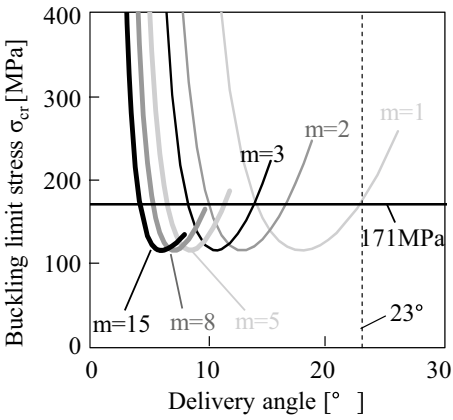


Fig. 7 Calculated buckling limit stress σ_{cr} (Number of waves in longitudinal direction: n = 1)

in the width direction calculated by Eq. (2) is approximately 171 MPa. It may also be noted that Poisson's ratio was set to 0.3.

The results in Fig. 7 show that the buckling limit stress is 171 MPa or more at any wave number *m* in the plate width direction when the delivery angle is 23° or more, which means no buckling occurs. In addition, when the delivery angle is small, the buckling limit stress is small under the condition that the wave number *m* in the sheet width direction is large. Conversely, when the delivery angle is large, the buckling limit stress is small under the condition that the wave number *m* in the sheet width direction is small. In other words, as the delivery angle increases, buckling occurs more easily at a smaller wave number *m*.

Based on the analysis results shown in Figs. 7, 8 shows the wave number *m* in the width direction that minimizes the buckling limit stress at each delivery angle. The figure also shows the change in the wave number of the longitudinal buckle depending on the delivery angle in the experiment, as shown above in Fig. 4. The analysis results and experimental results are in close agreement at high delivery angles (>10°).

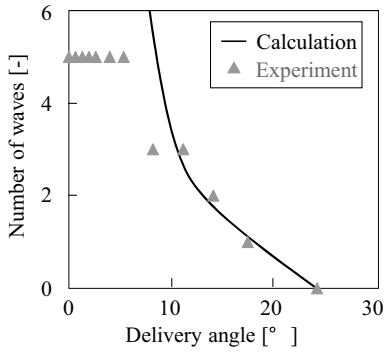


Fig. 8 Effect of delivery angle on buckling behavior (Distance between work roll and auxiliary roll: 225 mm)

Based on the experiments and analysis described above, the influence of the rolling exit delivery angle on the occurrence of longitudinal buckle is discussed.

First, the experimental results are compared with the conventional knowledge. The study by Kijima et al. revealed that the wave height increases and the longitudinal buckle becomes increasingly distinct as the delivery angle increases in the range of 0°–4°, which is similar to the present experimental results [9]. Komori obtained the wavelength of the longitudinal buckle by an elementary analysis of buckling [10]. Assuming deformation near the roll bite, a waveform close to that in the experiment by Kijima et al. was predicted when the delivery angle was 0°, showing that prediction is possible. From the above, it can be understood that the longitudinal buckle wave number is determined by deformation near the roll bite when the delivery angle is 0°.

Next, the experimental results when the delivery angle is larger than the conventional conditions are discussed. The experimental results shown in Figs. 2 and 4 clarified the change in the wave number of the longitudinal buckle when the delivery angle is increased. At this time, the longitudinal buckle already existed before the steel plate passed the auxiliary roll, and when the delivery angle was the same, the longitudinal buckle wave number did not change even if the distance between the work roll and the auxiliary roll was changed. From this, it is considered that the longitudinal buckle wave number is determined by the restraint condition of the steel sheet at the winding part from the vicinity of the roll bite exit.

In addition, the above experimental results are discussed in comparison with the analysis results. The analysis results in Fig. 7 show that buckling in the width direction of a flat plate with curvature becomes more likely at a smaller wave number m as the delivery angle increases, and no buckling occurs beyond a certain delivery angle. This shows good qualitative agreement with the experimental results in Fig. 4. From the comparison of the experimental and analytical results for the longitudinal buckle wave number shown in Fig. 8, it can be seen that the changes in both the experimental and analytical results are very similar at high delivery angles (>10°). Therefore, the longitudinal buckle observed at a high delivery angle is a buckling phenomenon due to compressive stress in the plate width direction on the roll bite exit side, and the plate shape after buckling is assumed to be determined by the shape of the winding part around the work roll. In the analysis, the stress in the plate width direction is assumed to be as shown by Eq. (2). However, even if the actual stress in the width direction is different, a flat sheet with curvature becomes more prone to buckling at a small wave number in the plate width direction as the delivery angle increases. Since there is no change in this characteristic of easy buckling at a small m, the analysis shows good qualitative agreement with the actual phenomenon.

4 FEM Analysis

An FEM analysis simulating the temper rolling experiment described in Chap. 2 was conducted, and the contact condition between the roll and the steel sheet near the roll bite outlet was investigated. Abaqus/Standard Ver. 6.12 was used as the solver, and a two-dimensional plane strain elastoplastic analysis was performed by the implicit method. The rolled material was an elastoplastic material with Young's modulus of 205.8 GPa and Poisson's ratio of 0.3. The yield stress shown in Fig. 9 was used.

The work roll was made of an elastic material with Young's modulus of 205.8 GPa and Poisson's ratio of 0.3. As shown in Fig. 10, a rigid part was provided at the center of the roll, corresponding to half of the roll diameter. A penalty method was used for the surface contact between the rolling roll and the rolled material. The friction model was Amonton-Coulomb friction with a friction coefficient of 0.05 [16–18].

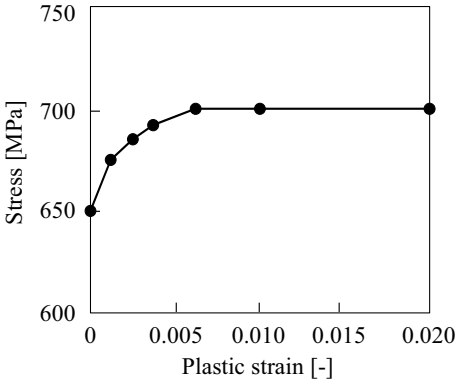


Fig. 9 Stress–strain curve

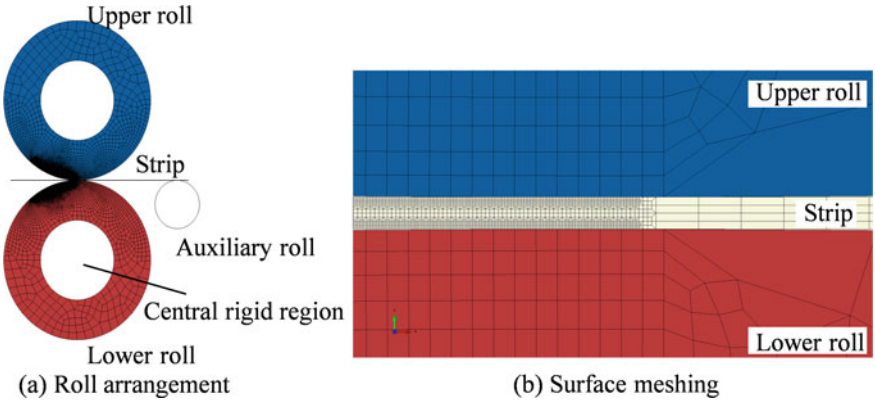


Fig. 10 Rolling model of FEM. (Color figure online)

The exit side auxiliary roll was a rigid body, and friction with the rolled material was ignored. The distance between the center of the work roll and the auxiliary roll was 225 mm. In the element division of the rolling region, the surface of the rolled material was a 10 μm square mesh, the mesh between the rolling roll and the delivery side auxiliary roll was a four-element mesh. The element division of the roll surface was a 100 μm secondary element. Mesh condition is uniform in the rolling region, and rolling distance is 100 mm which is longer than the length of area where the rolled material is in contact with the roll with the delivery angle of 24° (about 70 mm).

The analysis was performed for delivery angle conditions of 4° and 24°. In the analysis, after first determining the roll screw-down position where a rolling load of 5.3 kN/mm was obtained under the condition of a delivery angle of 4°, rolling was performed with that roll position fixed under both delivery angle conditions of 4° and 24°.

Figure 11 shows the curvature distribution of the upper roll surface near the roll bite exit and the center of thickness of the rolled material. The downward convex curvature is positive. The point at which the curvature of the roll surface has a large positive maximum corresponds to the roll bite exit. Immediately after the exit of the roll bite, there is a difference in the curvature between the upper roll surface and the center of thickness of the rolled material, indicating that the rolled material is not following the roll surface; in other words, the rolled material is not in contact with the roll. Further downstream, however, the center of thickness of the rolled material coincides with the curvature of the upper roll surface, which means the rolled material and the roll are in contact. Focusing on the length of the area where the rolled material is not in contact with the roll, the noncontact length is 3.8 mm with both the delivery

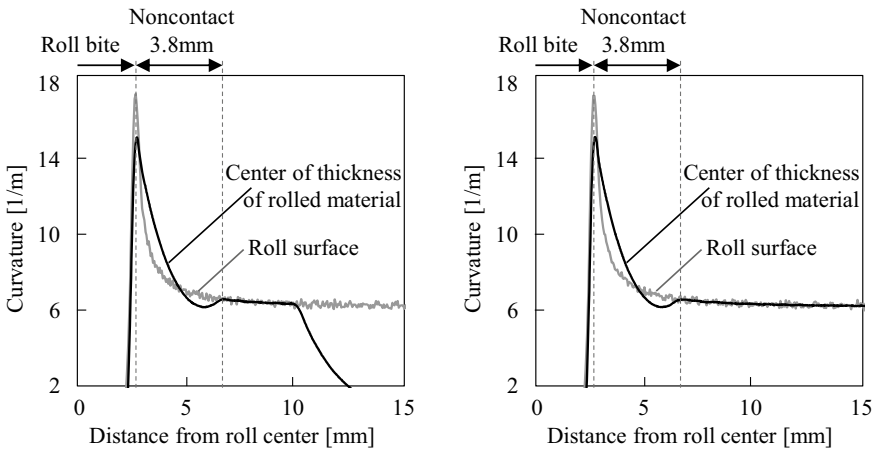


Fig. 11 Curvature distribution of upper roll surface

angles of 4° and 24°; that is, there is no change in this condition even if the delivery angle is increased.

5 Discussion

As shown in the experiments and analysis described above, the elementary analysis shows good qualitative agreement with the actual phenomenon. On the other hand, there are the following differences between the actual phenomenon and the analysis model. First, the analytical model does not consider the fact that a steel sheet exists continuously in the longitudinal direction. If a sheet is actually a continuous strip, compressive stress may have the effect of suppressing buckling. Furthermore, the analysis model assumes that the steel sheet is bent along the roll, and the longitudinal wave number n is 1. If the longitudinal wave number n is assumed to be 1, the analytical results will agree qualitatively with the experimental results, but if higher wave numbers are assumed, buckling may occur even at the delivery angle of 23° or more. Moreover, the FEM analysis results suggest the possibility that there is a region where the rolled material and the roll are not in contact immediately after the roll bite, regardless of the delivery angle.

In addition, the buckling shape assumes a uniform sine curve in the width direction, but the actual shape is not uniform in the width direction, as shown in Figs. 2 and 3, and in some cases, the buckling shape may be convex toward the bottom surface. The surface pressure between the work roll and the steel sheet acts to suppress out-of-plane deformation of the steel sheet, and the surface pressure distribution may be localized, which may be related to the wave shape of the longitudinal buckle. In this model, it is assumed that the stress in the plate width direction due to restraint in the roll bite acts uniformly at the winding part, but as mentioned above, this is a bold assumption. Moreover, it was assumed that the elastic strain in the width direction of the whole winding part is zero, but the validity of this assumption also needs to be examined.

Due to these differences, it is difficult to explain all the experimental results using an analytical model. On the other hand, since the wave numbers at high delivery angles are in good agreement, it can be said that the assumptions made in the analysis model have a great influence on the actual buckling behavior.

From the above discussion, the wave number at the occurrence of a longitudinal buckle can be explained by the mechanism proposed in the past when the delivery angle is 0°. When the delivery angle is increased, the change in the wave number can be explained by the buckling behavior of a flat plate with curvature subjected to compressive stress in the width direction. In addition, the buckling shape observed as a longitudinal buckle is not only determined by the deformation near the roll bite, but the contact state with the downstream work roll has a significant effect. Therefore, it is necessary to understand the longitudinal buckle phenomenon by dividing longitudinal buckling into the generation behavior of buckling, in which

many microwaves are generated, and buckle development behavior, in which the buckling shape grows and disappears.

6 Conclusion

The behavior of longitudinal buckle in temper rolling of steel sheets after secondary cold rolling was investigated in a laboratory experiment using larger delivery angles than in past studies. In addition, the buckling characteristics of the part where the steel sheet is wound around the work roll (winding part) was obtained by an elementary analysis and compared with the experimental results. As a result, the following findings were obtained.

(1) From the experimental results, it was found that the wave number of longitudinal buckle decreased and the individual waves became more distinct as the delivery angle increased. Longitudinal buckle did not occur when the delivery angle exceeded a certain level.
(2) The experimental results also indicated that the distance between the work roll and the auxiliary roll had little effect on longitudinal buckle when the delivery angle was the same.
(3) The analysis of the buckling behavior of the winding part showed that buckling occurs more easily at a small wave number m in the width direction as the delivery angle increase, but buckling does not occur at a certain angle or more. This characteristic is similar to the experimental results under the condition of high delivery angles (more than 10°), suggesting that the generation of longitudinal buckle is related to the shape of the winding part.
(4) From the FEM analysis results, it was found that a region where the rolled material and the roll are not in contact exists immediately after the roll bite exit. The existence of this noncontact region may affect the buckling phenomenon.

References

1. Komori K (1995) Analysis of cross and longitudinal buckle in sheet metal rolling. J Jpn Soc Technol Plast 36(410):211–217
2. Abdelkhalek S, Montmitonnet P, Legrand N, Buessler P (2011) Coupled approach for flatness prediction in cold rolling of thin strip. Int J Mech Sci 53:661–675
3. Abdelkhalek S, Zahrouni H, Legrand N, Potier-Ferry M (2015) Post-buckling modeling for strips under tension and residual stresses using asymptotic numerical method. Int J Mech Sci 104:126–137
4. Fischer FD, Rammerstorfer FG, Friedl N, Wieser W (2000) Buckling phenomena related to rolling and levelling of sheet metal. Int J Mech Sci 42:1887–1910
5. Friedl N, Rammerstorfer FG, Fischer FD (2000) Buckling of stretched strips. Comput Struct 78:185–190

6. Coman CD (2009) The asymptotic limit of an eigenvalue problem related to the buckling of rolled elastic strips. Mech Res Commun 36:826–832
7. Tran DC, Tardif N, Khaloui HE, Limam A (2017) Thermal buckling of thin sheet related to cold rolling: Latent flatness defects modeling. Thin-Walled Struct 113:129–135
8. Tran DC, Tardif N, Limam A (2015) Experimental and numerical modeling of flatness defects in strip cold rolling. Int J Solids Struct 69(70):343–349
9. Kijima H, Kitahama M (2002) Longitudinal buckle in temper rolling of double reduced ultrathin strips. J Jpn Soc Technol Plast 43(493):150–154
10. Komori K (2008) Analysis of longitudinal buckling in temper olling. Tetsu-to-Hagané 94(10):70–77
11. Kijima H (2019) Thin steel strip warping after skin-pass rolling with delivery angle. J Jpn Soc Technol Plast 60(696):13–18
12. Timoshenko SP, Gere JM (1961) Theory of elastic stability. McGraw-Hill, New York, pp 485–487
13. Yukawa N, Ishikawa T, Tozawa Y (1987) Calculation of residual stress in cold rolled strip. J Jpn Soc Technol Plast 28(312):28–33
14. Yukawa N, Ishikawa T, Tozawa Y (1987) Initiation of buckling of strip caused by internal stress: Analytical study on flatness defect of rolled strip I. J Jpn Soc Technol PlastJ Jpn Soc Technol Plast 28(314):251–256
15. Yukawa N, Ishikawa T, Tozawa Y (1987) Shape of strip after buckling caused by internal stress: analytical study on flatness defect of rolled strip II. J Jpn Soc Technol Plast 28(318):726–732
16. Kijima H (2013) Influence of roll radius on contact condition and material deformation in skin-pass rolling of steel strip. J Mater Process Technol 10(213):1764–1771
17. Domanti SA, Edwards WJ, Thomas PJ, Chefneux DIL (1994) Application of foil rolling models to thin steel strip and temper rolling. In: Proceedings of the sixth international rolling conference. Dusseldorf, pp 1764–1771
18. Kijima H, Bay N (2007) Contact conditions in skin-pass rolling. Ann CIRP 57 1(56):301–306

A Fast Computational Model for the Local Stress Distribution and Mechanical and Thermal Work Roll Deformations with Effects on Strip Profile and Flatness During Hot Rolling of Strip in Four-High Mills



Christian Overhagen

Abstract A fast model is presented for the three-dimensional stress distribution in the roll gap. This local data is used to calculate the 3D deformation of the work roll barrel by flattening and deflection using a combined analytical and finite element procedure. Detailed information about the work roll deformation can therefore be obtained because the model does not rely on a constant roll force. The local strip and work roll temperatures are calculated by a numerical solution of the heat equation and the evolution of thermal roll crown is calculated for a given rolling campaign. The strip shape is found by the intersection of the deformed roll with the initial strip shape. An upper-bound technique is applied for the resulting strip flatness. Typical methods of profile and flatness adjustment are discussed with effects on strip profile and flatness. These are static roll crowns as well as work roll bending, zonal roll cooling, and axially shiftable S-shaped grinded rolls (CVC—continuous variable crown).

Keywords Rolling theory · Thickness profile · Flatness · Strip rolling

1 Introduction

Hot strip rolling is one of the most important and commonly applied metal deformation processes. The quality of the rolled product in terms of thickness and flatness distribution is greatly affected by the mechanical and thermal loads which act on the work and backup rolls.

Therefore, a mathematical description of these effects has been a research item for a long time. Most works are based on the slab method or Elementary Plasticity Theory (EPT), assuming plane strain conditions and a constant roll force along the strip width. In the presented research work, these simplified approaches were extended to

C. Overhagen (✉)
Institute for Technology of Metals, University of Duisburg-Essen, Forsthausweg 2, 47057 Duisburg, Germany
e-mail: christian.overhagen@uni-due.de

© The Minerals, Metals & Materials Society 2021

G. Daehn et al. (eds.), *Forming the Future*, The Minerals, Metals & Materials Series,
https://doi.org/10.1007/978-3-030-75381-8_205

gain a more detailed solution to the problem without increasing computation times extremely.

Most of the older approaches are limited to the cold rolling process or disregard flatness effects. Beisemann introduced mechanical models for a variety of rolling mills [1], which are suitable for the calculation of the strip profiles, but disregard roll flattening effects. Rieckmann [2] built a simplified model for the thickness profile and flatness during cold rolling on a six-high mill using a correction factor to account for flatness effects. The flatness calculation was extended by Elsen [3], who introduced an upper bound model to account for the inner lateral material flow. Ren, Tieu et al. have presented a two-dimensional method based on the slab theory for the calculation of the normal stress distribution in cold rolling [4].

The current paper shows a two-dimensional rolling model based on Ren, Tieu et al. [4] to calculate the non-constant rolling force distribution along the lateral strip direction in hot rolling. In the present paper, these roll force and stress distributions are fed into sub-models for roll flattening and roll deflection to calculate the effects on the strip thickness and flatness distributions. The most important of the sub-models are presented and the effects on the strip thickness distribution are discussed.

2 Modelling of the Stress Distribution in Flat Rolling

To enable the calculation of the thickness profile and flatness distribution, a method for calculation of the local stress distribution in the three spatial coordinates must be employed. Different approaches are available for this task. Nowadays, the finite element method (FEM) has reached a highly developed state in metal forming and is used for detailed process simulations in rolling processes [5]. However, for online process control as well as fast design calculations in flat rolling, fast analytical rolling models are more feasible. Simple analytical rolling models have been present for a long time since von Karman introduced the force equilibrium on the strip element in the roll gap and deduced the so-called von Karman's differential equation of the roll gap [6]. The equation in this simple form is limited to a one-dimensional stress distribution. To account for the two-dimensional distribution of stresses, a second differential equation for the lateral direction must be introduced, as to replace the standard strip element with a volume element, that is of infinitesimal width and length and has two inclination angles. These angles are referred to in terms of the spatial derivatives of the two-dimensional height distribution inside the roll gap $h(x, y)$. The two ordinary differential equations for the distribution of the related horizontal and lateral forces are therefore given by Eq. (1), see also [7].

$$\frac{df_x}{dx} = \sigma_N \frac{\partial h}{\partial x} \sqrt{1 + \left(\frac{1}{2}\frac{\partial h}{\partial y}\right)^2} \pm 2\tau_{Fx} \sqrt{1 + \left(\frac{1}{2}\frac{\partial h}{\partial y}\right)^2}$$

$$\frac{df_y}{dy} = \sigma_N \frac{\partial h}{\partial y}\sqrt{1+\left(\frac{1}{2}\frac{\partial h}{\partial x}\right)^2} \pm 2\tau_{Fy}\sqrt{1+\left(\frac{1}{2}\frac{\partial h}{\partial x}\right)^2} \tag{1}$$

In Eq. (1), σ_N is the normal stress acting perpendicular to the roll surface. τ_{Fx} and τ_{Fy} are the frictional shear stress components in the horizontal and lateral directions, respectively.

By simultaneous solution of the differential equations given in Eq. (1), the distribution of the normal stress acting on the work roll–strip interface is calculated in the horizontal and lateral directions. For this purpose, it is important to couple the stresses in the plastic region by using the von Mises yield criterion in 3D [8]:

$$2k_f^2 = \left(\sigma_{xx}-\sigma_{yy}\right)^2 + \left(\sigma_{yy}-\sigma_{zz}\right)^2 + \left(\sigma_{zz}-\sigma_{xx}\right)^2 + 6\left(\tau_{xy}^2+\tau_{yz}^2+\tau_{zx}^2\right) \tag{2}$$

Figure 1 shows a calculated normal stress distribution for a hot flat rolling pass with initial height $h_0 = 4\ mm$ and final height $h_1 = 2\ mm$, work roll barrel diameter of $d_w = 780\ mm$, rolled material C55, and friction coefficient $\mu = 0.3$ at a rolling temperature of $T = 1100°\ C$ and a rolling speed of $2\ m/s$.

The stress distribution as shown in Fig. 1 is valid for the case where the rolls retain their circular shape and there is no roll deformation. In the next sections, the treatment of thermal and mechanical roll deformations is discussed in detail.

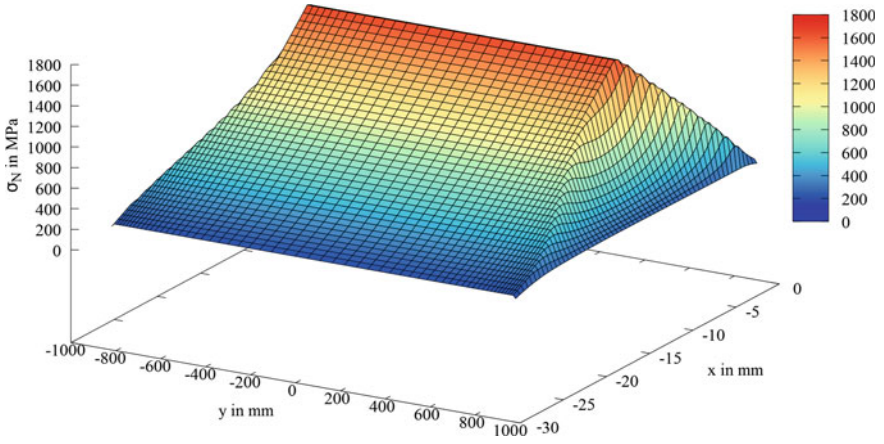


Fig. 1 Calculated two-dimensional stress distribution. (Color figure online)

3 Mechanical Loading of Work and Backup Rolls

To account for the mechanical loading of work and backup rolls, two important effects are regarded, i.e. the work and backup roll deflection as well as the work roll flattening. For the deflection calculation, the one-dimensional finite beam element method is applied, where for the roll flattening, a modified Boussinesq's method is used [3, 8].

3.1 Deflection of Rolls in a Four-High Mill

In a four-high mill, the work rolls are in contact with the strip as well as the backup rolls. The deflection system is modelled using one-dimensional finite beam elements. Instead of using beam elements of a constant area moment of inertia, a beam element thickness that is a linear function of the element length coordinate is used [7]. The contact problem between work and backup rolls is treated analytically. For the radial contact of two cylindrical bodies, the contact elasticity can be written as given in Eq. (3) [7, 9]:

$$\frac{du_r}{df} = \frac{1}{8}\left[C_1 \ln\left(\frac{8R_1}{\sqrt{f\ R_{12}\,(C_1+C_2)}}\right) + C_2 \ln\left(\frac{8R_2}{\sqrt{f\ R_{12}\,(C_1+C_2)}}\right) - (C_1+C_2)\right] \tag{3}$$

In this equation, C_1 and C_2 represent the elastic properties of the roll materials as defined by $C_i = \frac{16}{\pi} \cdot \frac{(1-\nu_i^2)}{E_i}$, R_1 and R_2 are the respective roll radii and f is the contact force per unit barrel length. R_{12} is a mean contact radius defined as $R_{12} = 1/(1/R_1 + 1/R_2)$. u_r is the combined contact displacement in the radial direction of the two cylinders.

Taking Eq. (3) into the reciprocal, the contact stiffness of two meeting nodes of work and backup rolls can be calculated. It should be noted that the contact stiffness in dependent on the contact force. The global finite element equation system of the four-high deflection problem is now written in the following way [7]:

$$\begin{bmatrix} \mathbf{K_W}+\mathbf{K_C} & -\mathbf{K_C} \\ -\mathbf{K_C} & \mathbf{K_B}+\mathbf{K_C} \end{bmatrix} \begin{bmatrix} \mathbf{u_W} \\ \mathbf{u_B} \end{bmatrix} = \begin{bmatrix} \mathbf{f_W}+\mathbf{u_0}\mathbf{K_C} \\ \mathbf{f_B}-\mathbf{u_0}\mathbf{K_C} \end{bmatrix} \tag{4}$$

$\mathbf{K_W}$ and $\mathbf{K_B}$ are the per-roll stiffness matrices for the work and backup rolls, respectively, and $\mathbf{K_C}$ is the contact stiffness matrix. $\mathbf{f_W}$ and $\mathbf{f_B}$ are the load vectors for the work and backup rolls. $\mathbf{u_0}$ is the initial distance vector of the work and backup roll surfaces and is of interest when special grinded roll contours are used, especially for CVC grinded rolls. $\mathbf{u_W}$ and $\mathbf{u_B}$ are the resultant deflection vectors of the work and backup rolls, respectively.

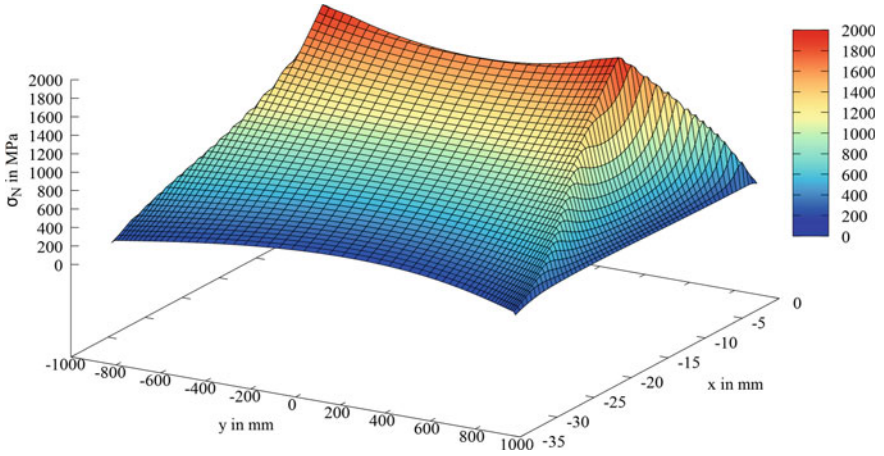


Fig. 2 Calculated stress field influenced by elastic roll deformation (flattening and deflection). (Color figure online)

3.2 Work Roll Flattening

Non-cylindrical work roll flattening is accounted for using a modified Boussinesq approach [7]. With this approach, the local effects of the two-dimensional roll pressure distribution as calculated by the rolling model (see Fig. 1) can be calculated. Therefore, a three-dimensional roll deformation model is obtained.

It is interesting to observe the effect of the roll deflection on the stress distribution in the roll gap. Figure 2 shows the stress distribution that is obtained for the case shown in Fig. 1 if the mechanical roll deformation effects are taken into consideration.

4 Thermal Loading of Work Rolls During a Strip Rolling Campaign

Generally, the heat equation describes the thermal processes which lead to a characteristic temperature profile of the work roll during rolling. The main goal of the present modelling is the calculation of the thermal roll crown contour $V_S(y)$. It is calculated as given in Eq. (5). The roll temperature profile must be integrated over each cross section of the roll to find the thermal crown distribution [10].

$$V_S(y) = \frac{2\alpha}{R} \int_0^R r[T(r, y) - T_0]\, dr \tag{5}$$

In this equation, α is the thermal expansion coefficient of the roll, R is the outer radius of the roll, $T(r, y)$ is the axial–radial temperature field of the roll, and T_0 is the initial or ambient temperature.

It should be noted that small thermal fluctuations in a very thin surface layer can be neglected for the thermal crown. However, the boundary conditions for the heat equations at the roll surface must be formulated so that the temperature profile equals the case where the thermal fluctuations had been considered. Therefore, an azimuthal averaging of the heat fluxes is done as described by Robinson et al. [11]. With this simplification which is well met in practice, the three-dimensional heat transfer problem can be reduced to a two-dimensional problem in axisymmetric coordinates. Therefore, a cylindrical coordinate system (radial and axial) can be used for the work roll barrels. The two-dimensional heat equation to be solved for the work is then given in Eq. (6), where ρ and c_p are the mass density and specific heat of the roll material, respectively.

$$\frac{\partial T}{\partial t}\rho c_p = \frac{1}{r}\frac{\partial}{\partial}\left(r\lambda\frac{\partial T}{\partial r}\right) + \frac{\partial}{\partial y}\left(\lambda\frac{\partial T}{\partial y}\right) \tag{6}$$

Exemplarily, Fig. 3 shows the evolution of the thermal roll crown during a rolling campaign of 20 strips in a hot strip mill.

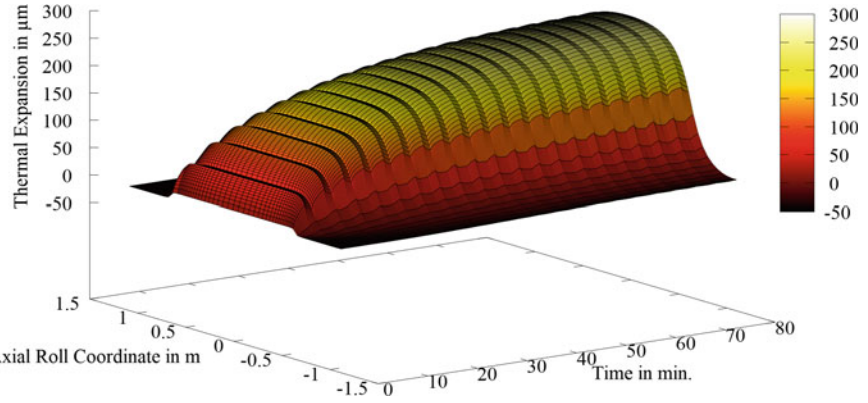


Fig. 3 Evolution of thermal work roll crown during a hot rolling campaign of 20 strips. (Color figure online)

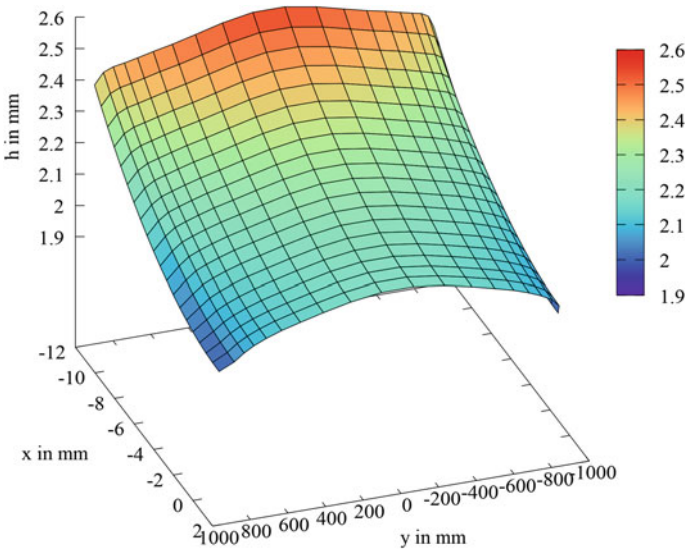


Fig. 4 Calculated example for the two-dimensional strip height distribution in the roll gap for a final pass on a hot strip. (Color figure online)

5 Combining the Mechanical and Thermal Roll Deformations to a Deformed Roll Barrel and Exit Strip Shape

With the mechanically and thermally deformed work roll geometry, the two-dimensional distribution of the strip thickness in the roll gap can be calculated. This height data in the form *h(x,y)* is then used for the next iteration of the rolling model in terms of the spatial derivatives $\frac{\partial h}{\partial x}$ and $\frac{\partial h}{\partial y}$ in Eq. (1). This iteration is repeated, until a converged solution for the stress and strip thickness distributions in the roll gap has been found. Figure 4 shows a result for the strip thickness distribution for a final pass of a hot strip rolling schedule (x: rolling direction, y: lateral direction). This distribution is found by intersecting the deformed roll barrel contours, which are calculated by the sub-models described earlier in the present paper.

6 Methods to Influence the Roll Crown and Strip Shape

During operation of a rolling mill, it is important to control the previously discussed effects which affect strip thickness and flatness to achieve the desired tolerances. The principal effects are now shown with computation examples which were carried out using the complete model that was described above.

We can subdivide the methods that can be used to control the strip shape in different groups. Firstly, the roll crown can be influenced directly by a roll camber. This is shown by an example in Fig. 5. A parabolic camber is grinded into a work roll surface so that the roll shape becomes convex. This reduces the strip convexity as shown in Fig. 5. In extreme cases, as seen for the 0.4 mm camber, it can already cause a concave strip shape under load.

These roll crowns are static, which means that they cannot be changed without changing the rolls. A more dynamic approach is the continuous variable crown approach (CVC), in which work and/or backup rolls are grinded to an S-shape and are axially movable. With this technique, different roll crown profiles can be set up by axial shifting of the rolls.

The principal features of this method are illustrated in Fig. 6. In this example, a third-order polynomial is used for the roll surface contours. When the two work rolls are shifted relative to each other, the roll gap profile can be adjusted very sensitively.

Figure 7 shows the effects of the CVC shifting on the roll surface contour at the effective barrel length (top picture), and on the resulting strip profile (bottom picture).

The adjustment range of the CVC system depends on the polynomial function used; in other words, the polynomial can be designed to achieve a predefined adjustment range of roll gap contours. The roll surface contours are given as a polynomial of third order for the top and bottom work rolls as a function of the axial roll barrel coordinate y:

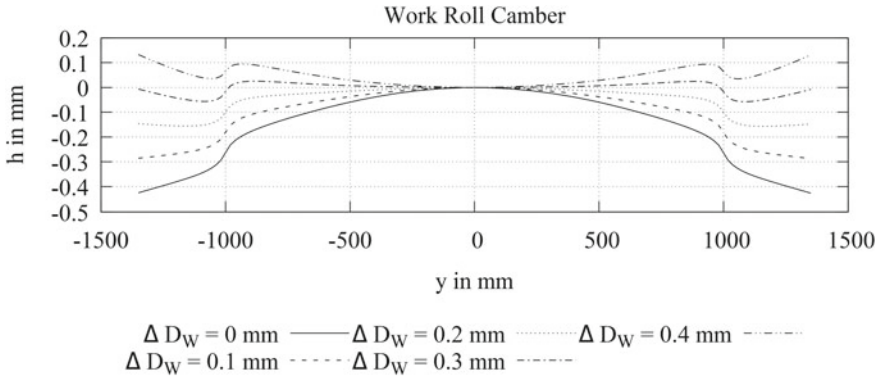


Fig. 5 Effects of work roll camber of the roll gap profiles under load

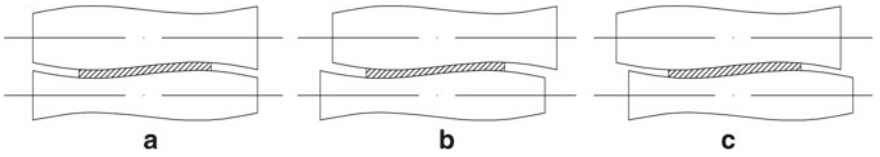


Fig. 6 Methods for influencing the strip thickness distribution with the CVC process: **a** neutral shift; **b** shift for concave strip; **c** shift for convex strip [7]

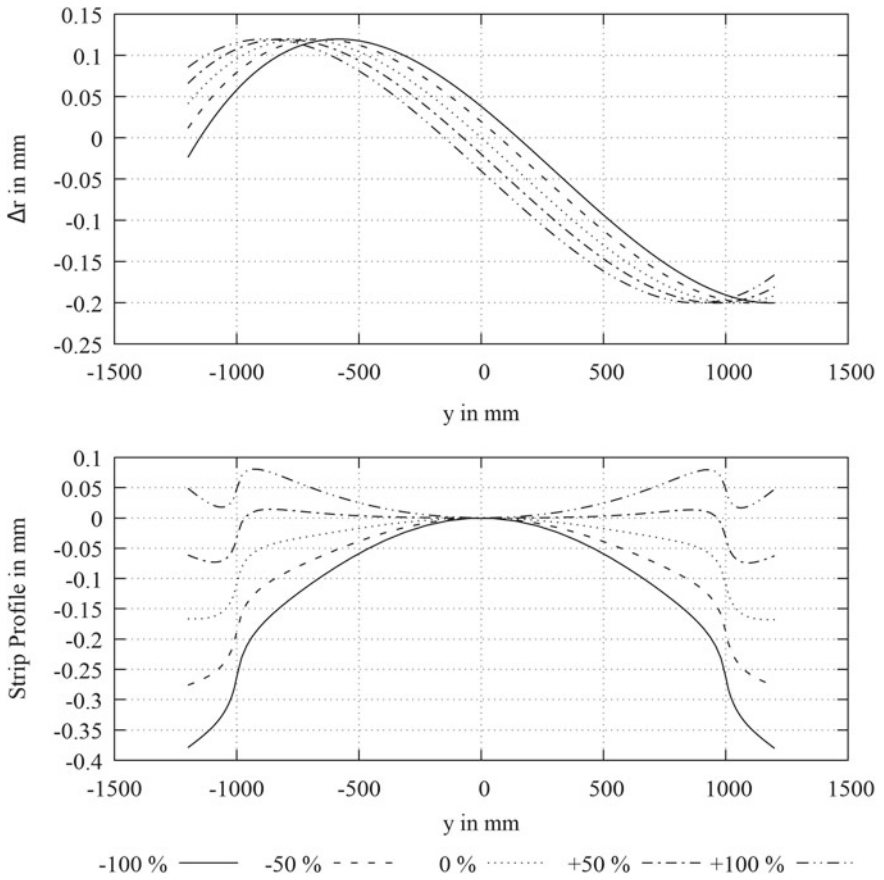


Fig. 7 Roll shapes in the effective barrel region and roll gap profiles for different shifting positions of a CVC system

$$R_{top}(y) = R_0 + Ay^3 + By^2 + Cy$$
$$R_{bot}(y) = R_0 - Ay^3 + By^2 - Cy \tag{7}$$

Apparently, $R_{bot}(y) = R_{top}(-y)$. When the vertical distance of the work roll axes is denoted by a_M, the unloaded roll gap contour (or thickness distribution) $h(y)$ can be worked out under influence of a symmetric axial roll shift c:

$$h(y) = 2Ac^3 - 2Bc^2 + 6Acy^2 + 2Cc - 2By^2 + a_M - 2R_0 \tag{8}$$

From Eq. (8), the adjustable roll crown follows as the difference between the strip thicknesses and strip center and strip edge (l_b: effective barrel length) to Eq. (9):

$$cr(c) = 6Al_b^2c - 2Bl_b^2 \tag{9}$$

Here, it is important to note that cr depends on the roll shift c only linearly, which conveniently simplifies an inverse calculation of the appropriate shift for a given roll crown.

Furthermore, we can calculate the roll contour coefficients A, B, and C from Eq. (8) and therefore design the roll contour for an appreciated adjustment range between a minimum crown $cr_{\min}$ and a maximum crown $cr_{\max}$. The coefficients B and C depend on the adjustment range and follow Eq. (10), where $c_{\max}$ is the maximum axial roll shift.

$$\begin{aligned} A &= -\frac{cr_{\min} - cr_{\max}}{12 l_b^2 c_{\max}} \\ B &= -\frac{cr_{\min} + cr_{\max}}{4 l_b^2} \end{aligned} \tag{10}$$

The so-called wedge factor C is chosen according to a maximum work roll radius difference Δr_m that is desirable acc. to Eq. (11).

$$C = \frac{B^2 - \left(\frac{27 \Delta r_m A^2}{4}\right)^{\frac{2}{3}}}{3A} \tag{11}$$

An in situ control of the strip profile can also be implemented by work and/or backup roll counter bending. The so-called WORB method (work roll bending) uses extra hydraulic cylinders at the work roll journals. This counter bending can be executed against the backup rolls (in-crown bending) or away from the backup rolls (counter-crown bending). The BURB method (backup roll bending) uses a similar technique at the backup roll journals but is not very commonly applied, since much higher forces are necessary compared to the WORB method.

Figure 8 shows the effects of work roll bending (WORB) on the relative roll gap profile and on the contact forces that are present between the work and backup rolls.

A comparison of Figs. 7 and 8 shows, that the effect of WORB concentrates more on the strip edges, where the CVC has a more homogeneous effect throughout the barrel length of the rolls.

It was shown that the thermal profile of the work rolls also has a great significance for the strip thickness distribution. An active intervention in this effect can be carried out by a zonal roll cooling system. The roll cooling system, which is discussed here consists of 37 spray nozzles, which can be controlled independently. Therefore, different roll cooling programmes can be realized. Figure 9 shows three different fundamental cooling programmes (standard cooling, centre cooling, edge cooling) which can be combined with one another. The dimensionless intensity factor is a number between 0 and 1 for each of the spray nozzles. These data have been taken from Degner [12].

Figure 10 shows the effect of the three different work roll cooling programmes on the roll gap shape of the 6th pass of a 7-pass schedule. It is shown by the computation,

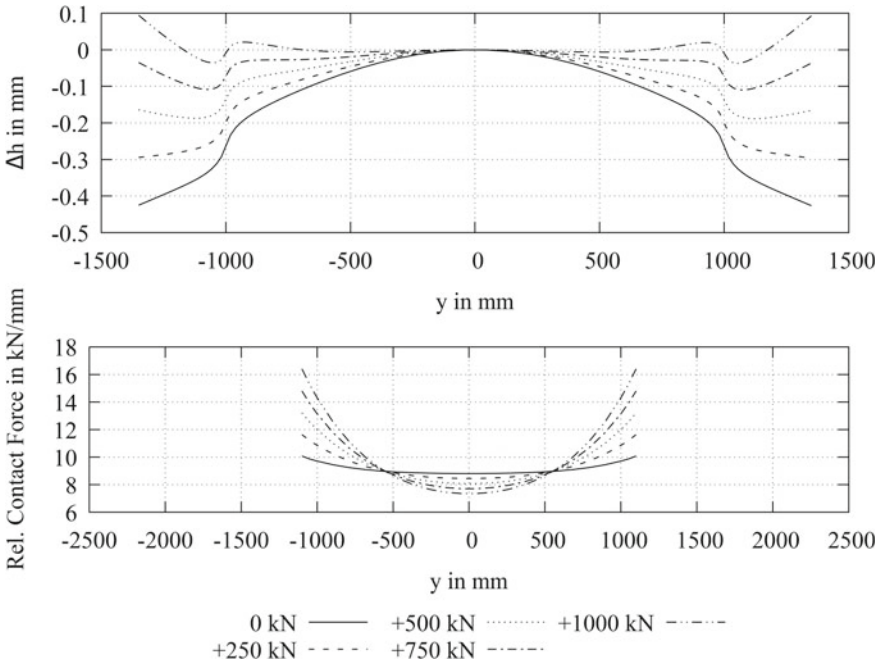


Fig. 8 Effects of work roll bending (WORB) on the roll gap shape (top) and the contact forces at work roll interface

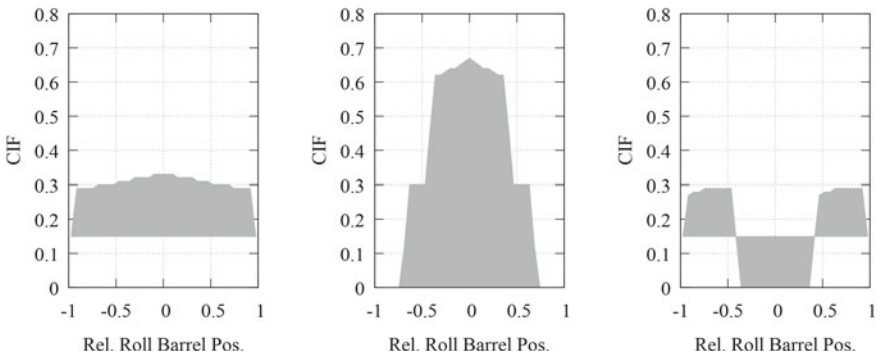


Fig. 9 Distribution of the cooling intensity factor (CIF) for three different cooling programmes (standard cooling, center cooling, edge cooling)

that the edge cooling programme leads to the best improvements of the thickness profile.

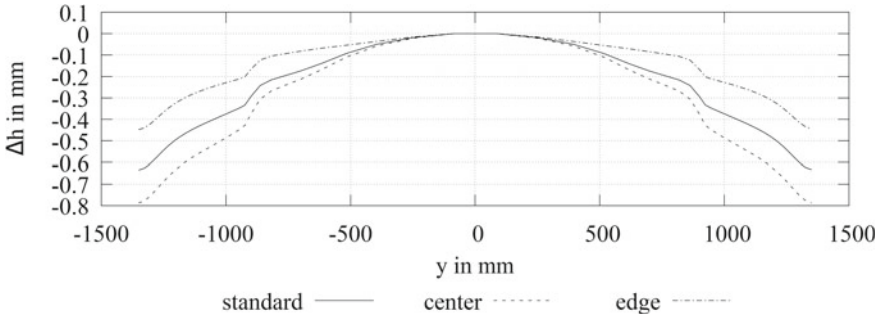


Fig. 10 Effects on a roll gap shape of the three different cooling programmes defined in Fig. 9

7 A Model for Flatness Effects

Apart from the thickness profile, flatness is another important parameter of a flat-rolled product. Flatness defects originate from an inhomogeneous distribution of elongations along the strip width.

If we subdivide the strip width into N narrow elements, the related elongation of each element i with respect to the centre element (index c) is given as in Eq. (12).

$$\left(\frac{\Delta L}{L}\right)_i = \left(\frac{\gamma_c \beta_c}{\gamma_i \beta_i} - 1\right) \tag{12}$$

In this equation, $\gamma_i = h_{1i}/h_{0i}$ is the compression ratio and $\beta_i = b_{1i}/b_{0i}$ is the spread ratio of each strip element.

The initial and final thicknesses of each strip element h_{0i} and h_{1i} is found from the entry and exit strip profiles, where the exit strip profile is calculated as shown in the preceding sections. The local spread ratio β_i is of greater importance, as it resembles the lateral material flow. It can be easily shown that a neglection of the local spread by simply setting $\beta_i = 1$ does not yield practical results and therefore an amount of lateral flow will occur, even in cold rolling of thin strips.

For cold rolling, Rieckmann [2] found that a correction factor in the order of magnitude of $m = 0.01$ can be used to achieve practical results, avoiding the difficult assessment of the inner lateral flow, see Eq. (13).

$$\left(\frac{\Delta L}{L}\right)_i \approx m \cdot \left(\frac{\gamma_c}{\gamma_i} - 1\right) \tag{13}$$

From these circumstances, we can deduce that the local spread plays an important role in the development of flatness faults and cannot be neglected.

To gain a simplified solution which is feasible for a fast analytical model, a method presented by Elsen and Pawelski [3] is employed in the current analysis. This method is based on the upper bound method.

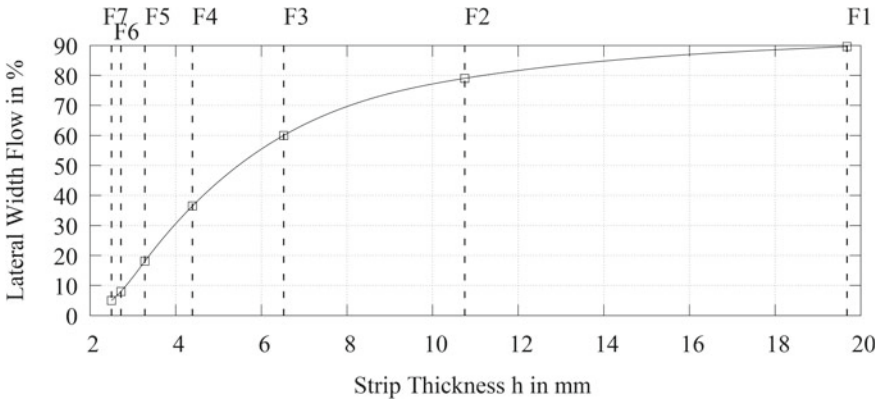


Fig. 11 Lateral flow parameter in seven stands of a hot strip finishing mill in stands F1–F7 and the degradation of the lateral flow with decreasing strip thickness

The model assumes that the strip can be treated a stack of strips having a finite width which are undergoing a compression deformation from an initial height h_0 to a final height of h_1. Each strip element does not spread freely, but the spread is affected by shear deformations occurring at sides where two strip elements meet. According to the upper bound approach, the upper bound on forming power J^* is written out as given by Eq. (14), combining the ideal power P_{id}, the frictional power P_F, the shearing power P_S and the tension power P_T:

$$J^* = P_{id} + P_F + P_S - P_T \tag{14}$$

A free parameter $\omega = -\frac{\dot{\varepsilon}_{lateral}}{\dot{\varepsilon}_{vertical}}$ is a measure for the lateral material flow, resembling the relation of the lateral and vertical strain rates. The velocity field is dependent on this parameter and it is chosen according to a minimum of J^* in Eq. (14) using the golden section search technique (UVMGS of IMSL [13]). With this approach, the dependence of the width flow on the strip thickness could be calculated. Figure 11 shows a plot of the function ω as a function of the strip thickness throughout the hot rolling process of the finishing train of a hot strip mill.

8 Conclusions and Outlook

The present model for rolling processes in four-high mills allows the calculation of the two-dimensional normal stress, and based upon, the mechanical and thermal loading on the rolling tools which lead to a certain thickness and flatness defects. The computation time is in the order of few minutes on an office PC for a seven-pass rolling schedule of a hot strip finishing mill including all mechanical and thermal effects. The effects influencing the strip thickness profile can be shown with the model,

including the interdependence of thermal and mechanical effects. In its current form, the model is set up for two high and four high mills. For the future, an extension to 12-high and 20-high mills is planned to analyse the cold rolling processes for thin strips and foils.

The ongoing digitization of manufacturing processes in the steel industry calls for extremely fast process models to enable prediction and control of thickness profile and flatness during hot and cold rolling. These models will be mostly based on data-driven approaches like neural networks. Because of the low computation times of the present offline optimization model, it is very well suited to generate a big set of data to be fed into these data-driven models.

References

1. Beisemann G (1987) Theoretische Untersuchung der mechanisch einstellbaren Bereiche für die Walzspaltform an unterschiedlichen Walzwerksbauarten, Umformtechnische Schriften Bd. 7. Stahleisen, Düsseldorf
2. Rieckmann J (1989) Berechnung von Bandprofil und Planheit beim Kaltwalzen auf Sechs-Walzen-Walzwerken, Umformtechnische Schriften Bd. 21. Stahleisen, Düsseldorf
3. Elsen S (2004) Beitrag zur lokalen Breitung beim Flachwalzen, Umformtechnische Schriften Bd. 115. Shaker, Aachen
4. Ren H, Tieu A et al (2006) Mater Sci Forum 505–507:1279–1284
5. Bernhardt R, Philipp F-D, Schafstall H (2015) XXXIV. conference on metal forming, Zauchensee, Austria
6. Karman ThV (1925) Z. Ang. Math. Mech. 5:139–141
7. Overhagen Ch (2018) Models for rolling of flat and full sections (in German). PhD Thes., Univ. Duisburg-Essen. https://nbn-resolving.org/urn:nbn:de:hbz:464-20181116-114523-7
8. R. v. Mises, Nachrichten von der Gesellschaft der Wissenschaften zu Göttingen, Mathematisch-Physikalische Klasse (1913), pp. 582–892
9. Johnson KL (2003) Contact mechanics. Cambridge University Press, Cambridge
10. Unger F (1984) Berechnungen zum Temperaturverhalten und zum thermischen Walzprofil von Kaltwalzen, Freiberger Forschungshefte Bd. B 241, Leipzig, VEB Verlag für Grundstoffindustrie
11. Robinson IN et al (1996) Angularly averaged heat transfer for a roller used in strip rolling. Math Eng Ind 5(4):281–304
12. Degner M (2016) Modern hot strip production, Stahleisen
13. Visual Numerics (2010) IMSL fortran numerical library – user's guide: version 7.0, Flatiron: Rogue Wave Software

Investigation of a Novel Constructive Hot Ring Rolling Process for Double Metal Composite Ring



Jiadong Deng, Zhe Cheng, Dongsheng Qian, Jikang Liu, and Rongwen Wu

Abstract Double metal composite ring has the advantages of two materials, and is used in specific fields. The traditional manufacture method is welding. And some scholars try to use ring rolling process to produce a composite ring. However, the interface connection quality is not good. In this paper, a novel constructive hot ring rolling process to manufacture a seamless double metal composite ring is proposed. First, two separate rings with different metals are assembled together. And then the surface interface area on the upper and lower of the assembled ring are welded in an oxygen-free environment, which can suppress the interfacial oxidation during heating process. After that, the surface welded ring is cleaned and heated. Finally, the target double metal composite ring is formed by hot ring rolling. An experiment of constructive hot ring rolling process for double metal composite ring was done. The interface healing effect of the composite ring was studied. The result indicated that the interface healing degree was significantly improved by this method.

Keywords Composite ring · Ring rolling · Constructive · Interface healing

J. Deng · J. Liu · R. Wu
School of Automotive Engineering, Wuhan University of Technology, Wuhan 430070, China

Z. Cheng · D. Qian (✉)
School of Materials Science and Engineering, Wuhan University of Technology, Wuhan 430070, China
e-mail: qiands@whut.edu.cn

J. Deng · D. Qian
Hubei Key Laboratory of Advanced Technology for Automotive Components, Wuhan University of Technology, Wuhan 430070, China

Hubei Engineering Research Center for Green & Precision Material Forming, Wuhan University of Technology, Wuhan 430070, China

© The Minerals, Metals & Materials Society 2021

G. Daehn et al. (eds.), *Forming the Future*, The Minerals, Metals & Materials Series,
https://doi.org/10.1007/978-3-030-75381-8_206

1 Introduction

With the ever-growing demands of material performance, it is difficult for a single metal or alloy to meet the requirements. Multi-material composite component refers to the combination of two or more materials through a certain method, which has the comprehensive properties of different materials, and can greatly save precious metal materials or alloy elements, thus greatly reducing the cost and saving resources [1]. Double metal ring belongs to multi-material composite component, which can be used in the fields of nuclear power, petrochemical and engineering machinery, etc. Such as nuclear pressurized water reactor shell is working in severe condition like high temperature, high pressure, corrosion, etc. for a long time. Therefore, its quality and performance requirements are very high. One method is to use double metal structure, that is, the outer layer is low alloy steel matrix and the inner layer is built up welding with stainless steel [2]. At present, the main manufacturing methods of double metal ring parts are casting [3] and welding [4]. The casting method is mainly used for small- and medium-size double metal rings with a big difference in material melting point, such as casting a layer of copper alloy material on the inner surface of the steel ring. The welding method mainly adopts surfacing welding to add new material layer by layer on the surface of the matrix material. But the production efficiency is low, and prone to produce welding defects.

Ring rolling is an advanced plastic process to manufacture seamless rings. By the feeding and rotating motion of the rolls, the thickness or height of the ring is reduced, the diameter is enlarged and the section profile is formed, as shown in Fig. 1. At present, the process is mainly used in the manufacturing of single metal ring [5–7]. Professor Hirt et al. [8, 9] tried to do ring rolling experiment and simulation of double metal ring. After simple assembling of the inner and outer ring parts with double metals, the hot ring rolling was executed. But the connect effect was not well and the interface was still clear, as shown in the reference [8]. The multi-metal plate rolling process is more mature than double metal ring rolling. Manesh and Taheri [10] and Sheikh [11] studied multi-metal plate rolling connection technology, including the connection of steel and aluminum, aluminum, and magnesium. Bay [12] and Maeda and Teshima [13] discussed the mechanism of interface healing during rolling and emphasized that the key to accomplish rolling connection is to eliminate surface

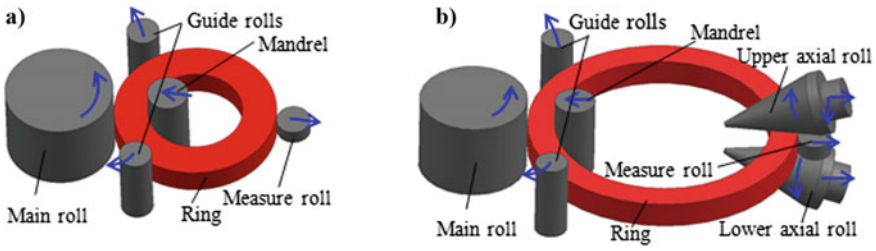


Fig. 1 **a** Radial ring rolling; **b** radial-axial ring rolling. (Color figure online)

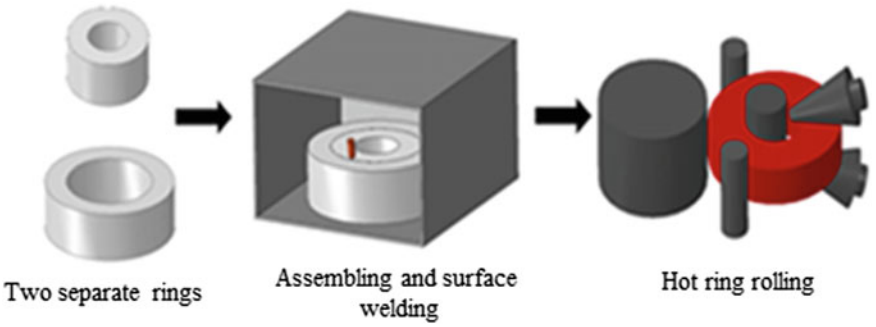


Fig. 2 Main process flow of constructive hot ring rolling process for double metal composite ring. (Color figure online)

oxidation layer and attachments. Xie et al. [14] proposed the use of vacuum rolling method for composite plate rolling of stainless steel and carbon steel. In addition, Sun et al. [15, 16] also obtained a good interface healing effect by thermal compression deformation under high-vacuum conditions.

By the above, it can be inferred that the reason for the poor interfacial healing may be related to the severe interfacial oxidation during the heating process. In this paper, a novel constructive hot ring rolling process for double metal composite ring is proposed, and its basic technical process is shown in Fig. 2. First, two separate rings with different metals are assembled together. And then the surface interface area on the upper and lower of the assembled ring are welded in oxygen-free environment, which can suppress the interfacial oxidation during heating process. After that, the surface welded ring is cleaned and heated. Finally, the target double metal composite ring is formed by hot ring rolling.

2 Experimental Procedure

To verify the feasibility of the above constructive hot ring rolling process, a constructive hot ring rolling experiment of a small-sized double metal ring with 20 steel and 304 stainless steel was tried. Before hot ring rolling, double metal ring blank is constructed based on laboratory conditions. The material of outer ring blank is 20 steel, and the material of inner ring blank is 304 stainless steel. The sizes of the ring blanks are shown in Fig. 3.

The main process of double metal ring blank construction is shown in Fig. 4. The two blank units were machined to the design sizes. Then, the surfaces of the ring blank units were cleaned with acetone. After drying, the inner and outer ring blank units are assembled together to obtain a combined ring blank. The interface of the ring blank is directly in contact with air in this state and easily oxidized during subsequent heating process. Therefore, it is necessary to seal around the upper and

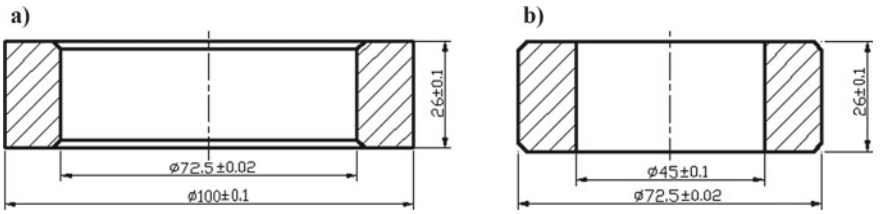


Fig. 3 Size diagram of the ring blanks: **a** outer ring blank; **b** inner ring blank

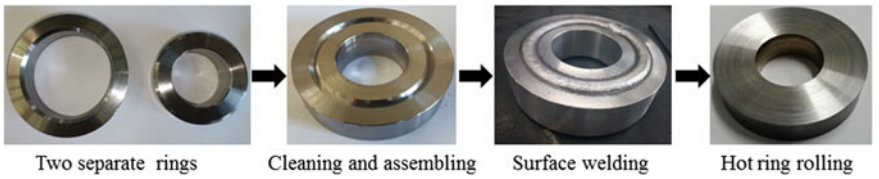


Fig. 4 The main process of double metal ring blank construction. (Color figure online)

lower end faces of the combined ring blank along the interface area in an oxygen-free environment. Thus, the interface is not easy to oxidize during subsequent heating, which can promote interface healing. Finally, the protruding weld material on the end face of the ring billet was removed to ensure the flatness so that the ring blank could be smoothly put into the rolling hole.

The hot ring rolling experiment was performed on a laboratory HHRM160 ring rolling machine (as shown in Fig. 5a). Before ring rolling, the constructed double metal ring blank was heated in a resistance heating furnace to 1150 °C and held for 1 h. Then it was taken out on the ring rolling machine to perform hot ring rolling experiment. The main rolling parameters are shown in Table 1 and the rolling ratio was 2. Figure 5b showed the rolling process, the ring diameter grew normally. Figure 5c showed the rolled ring, and no obvious interface can be seen on the end face of the ring.



Fig. 5 **a** Rolling equipment; **b** rolling process; **c** rolled ring. (Color figure online)

Table 1 Main parameters for hot ring rolling

Parameter	Value
Diameter of main roll (mm)	360
Diameter of mandrel (mm)	40
Rotational speed of the main roll (r/min)	61
Feed rate of the main roll (mm/s)	1
Outer diameter of ring blank (mm)	100
Inner diameter of ring blank (mm)	45
Height of ring blank (mm)	26
Outer diameter of target ring (mm)	140.5
Inner diameter of target ring (mm)	113
Height of target ring (mm)	26

3 Results and Discussion

After hot ring rolling, the rolled ring was cooled in the air. When the temperature of the ring decreased to room temperature, then it was cut along the cross section, as shown in Fig. 6. After grinding and polishing the cross section of the ring sample, it can be found that there is no obvious crack on the ring cross section, which indicates that the ring interface achieved healing in macro-scale.

In order to further observe the behavior of the interface evolution during the hot ring rolling process, the cross-sectional sampling was chosen on the ring blank and the rolled ring. After grinding and polishing, the chemical etching treatment was conducted on the sample surface. Because the sample contained two different materials, the chemical etching treatment should proceed by region. The 20 steel region was etched by alcoholic solution with 3% nitric acid. The 304 stainless steel region was etched by mixed solution with 40 ml hydrochloric acid, 20 ml nitric acid, 40 ml glycerol, 20 ml hydrogen peroxide. Then the sample was observed by metallurgical microscope. The low power (25 magnification times) of the full-scale

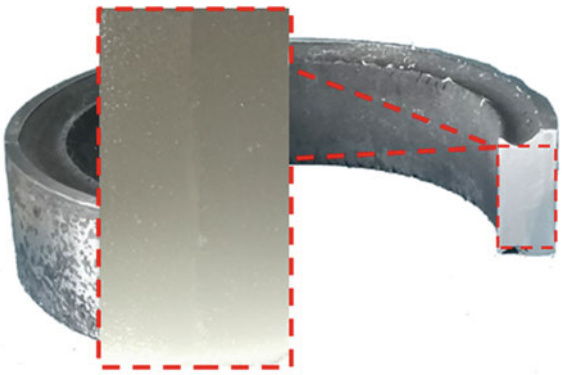


Fig. 6 Macro forming effect of the cross section of the rolled double metal ring. (Color figure online)

metallographic diagram of the ring cross section is obtained, as shown in Fig. 7. It can be found that the cross-sectional sample after corrosion has a limit at the material boundary. The limit of the ring blank is very obvious, and the rolled ring has a fuzzy line.

In order to more clearly observe the healing effect of the interface zone, the center interface areas of the cross section on the above-constructed ring blank and the rolled ring were magnified 500 times on a microscope to observe the high-power morphology, as shown in Fig. 8. The dark seam in the diagram is the interface area. The width of the interface area on the constructed ring blank is larger than 70 μm. The width of the interface area on the rolled ring is smaller than 3 μm. It can be found the interface healing effect is significant.

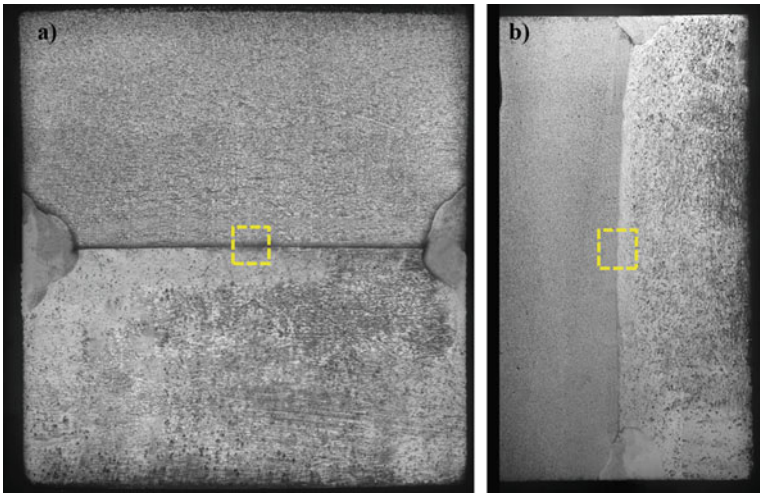


Fig. 7 Low power metallographic diagram of the full cross section: **a** construct ring blank; **b** rolled ring. (Color figure online)

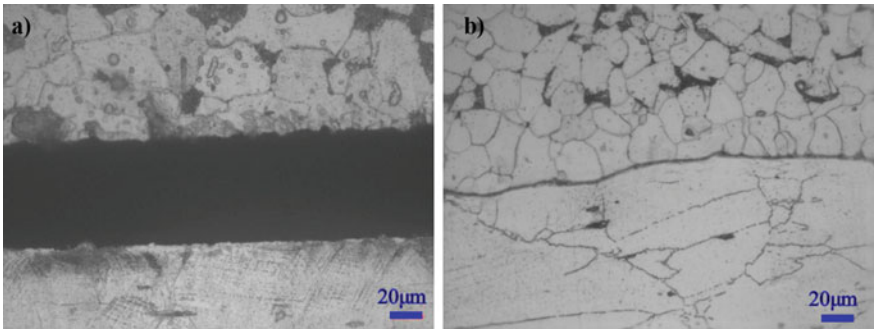


Fig. 8 High-power metallography diagram of the central interface region: **a** construct ring blank; **b** rolled ring. (Color figure online)

Further, small-size tensile test was carried out to evaluate interface bonding strength. From the rolled double metal ring, the tensile samples were taken in the radial direction at three zones A, B, and C. The sampling positions and dimensions of the tensile samples were shown in Fig. 9. The prepared tensile sample was tested on a small size tensile testing machine, as shown in Fig. 10a. The blue part is the marked stainless steel material. It can be found that the geometric position of the tensile sample after fracture is similar and close to the boundary of the two metals.

To measure the interface bonding degree, a comparison of the tensile strength of double metal ring and single metal ring was supplemented. Because the tensile

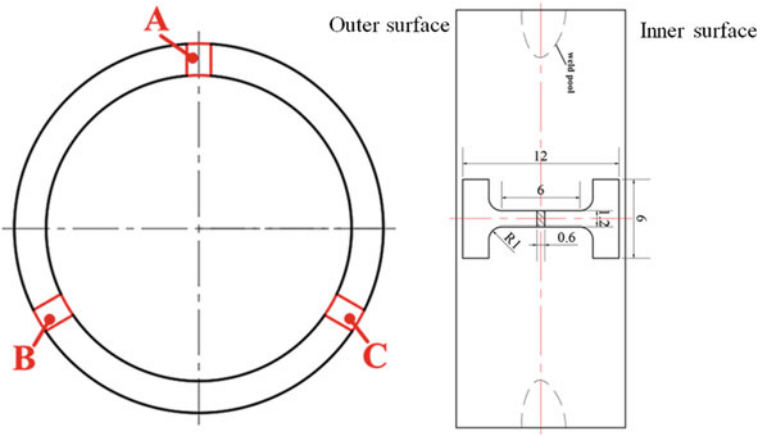


Fig. 9 Sampling method for small size tensile test. (Color figure online)

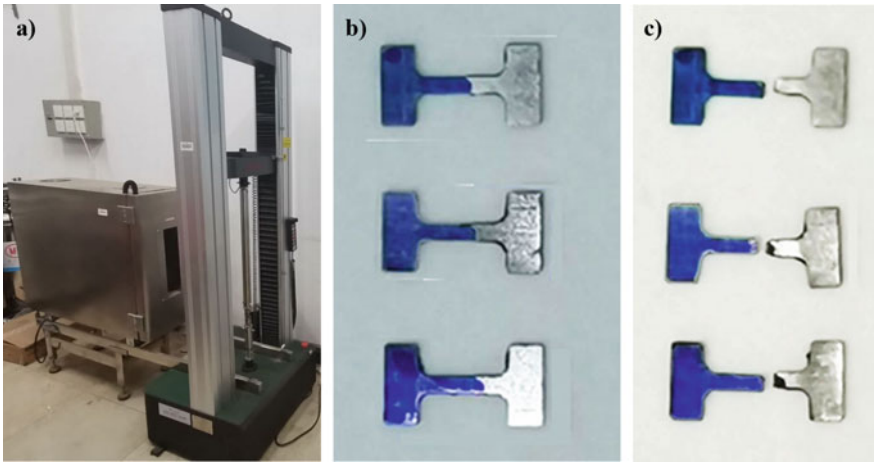


Fig. 10 **a** Tensile testing machine; **b** samples before tensile; **c** samples after tensile. (Color figure online)

Table 2 Tensile strength result

Samples	Tensile strength (MPa)
The rolled 20 steel ring	481.6
Position A on the rolled double metal ring	470.6
Position B on the rolled double metal ring	474.5
Position C on the rolled double metal ring	477.3

strength of the 20 steel is smaller than the 304 stainless steel. So a sample was sampled from a rolled ring with single 20 steel. The tensile strength comparison between the rolled double metal ring and the rolled 20 steel ring was shown in Table 2. The tensile strength of the samples was similar. One side, the interface bonding degree along peripheral direction was uniform. On the other hand, the tensile strength of the rolled double metal ring is close to the rolled 20 steel. That is, the strength can reach the lower strength base material of the two materials. The result further indicates that the interface of the double metal ring by constructive hot ring rolling process is well-healed.

4 Conclusions

In this paper, a novel constructive hot ring rolling process to manufacture a seamless double metal composite ring is proposed. Before hot ring rolling, welding the surface interface area of assembled ring in oxygen-free environment, can suppress the interfacial oxidation during heating process and improve the interface healing degree in hot ring rolling. By the experiment of constructive hot ring rolling process for double metal composite ring, the interface healing degree was significantly improved. Further investigations should focus on the mechanism of the interface healing during hot ring rolling and the influence laws of process conditions on interface healing.

Acknowledgments Financial assistance of the National Key Research and Development Project (2018YFA0702903), National Natural Science Foundation of China (No. 51805391), 111 Project (B17034) and Innovative Research Team Development Program of Ministry of Education of China (IRT_17R83), the Fundamental Research Funds for the Central Universities (WUT: 2019IVB021) are acknowledged.

References

1. Groche P, Wohletz S, Brenneis M et al (2014) Joining by forming—a review on joint mechanisms, applications and future trends. J Mater Process Technol 14(10):972–1994
2. Zheng DH, Wang ZQ, Chen JJ et al (2013) Analysis on SMAW welding procedure qualification and technical practice of corrosion-resistant cladding for primary pressure boundary of pressurized water reactor. Press Vessel Technol 30(3):80–84
3. Wang DL, Wu JH, Cai B et al (2018) Manufacturing defects and control of centrifugal casting double metal composite pipe. Spec Cast & Nonferrous Alloys 38(3):288–290
4. Cai M, Wang SC, Niu LB et al (2008) Preparation of cemented carbide/steel bimetal composite by submerged are automatic welding. Hot Work Technol 37(19):21–24
5. Allwood JM, Erman Tekkaya A, Stanistreet TF (2005) The development of ring rolling technology. Steel Res 76(2):111–120
6. Allwood JM, Erman Tekkaya A, Stanistreet TF (2005) The development of ring rolling technology - part 2: investigation of process behaviour and production equipment. Steel Res 76(7):491–507
7. Hua L, Deng JD, Qian DS (2017) Recent development of ring rolling theory and technique. Int J Mater Prod Technol 54:65–86
8. Guenther S, Seitz J, Schwich G et al (2017) Investigation of a composite ring rolling process considering bonding behaviour in FEM and experiment. Proc Eng 207:1236–1241
9. Seitz J, Schwich G, Guenther S et al (2016) Investigation of a composite ring rolling process by FEM and experiment. In: MATEC web of conferences, vol 80, p15011
10. Manesh HD, Taheri AK (2003) Bond strength and formability of an aluminum-clad steel sheet. J Alloy Compd 361(1):138–143
11. Sheikh H (2011) Role of shear banding on the microtexture of an Al–Mg alloy processed by hot/high strain rate accumulative roll bonding. Scr Mater 64(6):556–559
12. Bay N (1983) Mechanisms producing metallic bonds in cold welding. Bay Niels 62(5):137
13. Maeda M, Teshima S (2016) A study on bonding mechanism of aluminum clad steel by cold rolling. Tetsu-to-Hagane 61:957–962
14. Xie G, Luo Z, Wang G (2011) Effect of rolling parameters on microstructure and property of vacuum rolling clad steel plate. J Iron Steel Res 23(12):27–30
15. Zhang JY, Sun M, Xu B et al (2018) Interfacial microstructural evolution and metallurgical bonding mechanisms for IN718 superalloy joint produced by hot compressive bonding. Metall Mater Trans B 49:2152–2162
16. Zhou LY, Feng SB, Sun MY et al (2019) Interfacial microstructure evolution and bonding mechanisms of 14YWT alloys produced by hot compression bonding. J Mater Sci Technol 35(8):1671–1680

Effect of Feed Rate on Texture Evolution of 42CrMo Casting Blank During Hot Ring Rolling



Huiping Qi, Fangcheng Qin, Yongtang Li, Huiqin Chen, Chongyu Liu, and Haiquan Qi

Abstract The compact casting-rolling technique is an advanced method to produce seamless ring parts. The technique has been paid much attention in recent years. To find out the textual evolution rule of materials in this compact process, hot ring rolling of 42CrMo casting blank was conducted at different mandrel feed rates. The macro-textures of the as-obtained products were studied by X-ray diffraction, and micro-textural associated grain orientations were examined by electron backscattered diffraction techniques. The dominant textures in hot-rolled rings were similar, with γ-fibre consisted of {111}<110> and {111}<112> orientations as the most intense components. The α-fibre and ε-fibre textures in the entire thickness of hot-rolled rings did not show significant change as feed rate increased. Moreover, shear textures, including Copper-type {112}<111> and Goss {110}<001> components were presented in different regions of hot-rolled rings. The grain refinement was found closely related to grain orientation and micro-texture evolution in the entire thickness. The inhomogeneous distribution of grain size in the hot-rolled ring at a higher feed rate resulted in poor plasticity and toughness, which was caused by inhomogeneous γ-fibre orientations, especially in the center layer of the ring. Overall,

H. Qi · Y. Li · H. Chen
Shanxi Key Laboratory of Metallic Materials Forming Theory and Technology, Taiyuan University of Science and Technology, Taiyuan 030024, China
e-mail: qhp9974@tyust.edu.cn

Y. Li
e-mail: liyongtang@tyust.edu.cn

H. Chen
e-mail: chenhuiqin@tyust.edu.cn

F. Qin (✉) · C. Liu · H. Qi
College of Materials Science and Engineering, Guilin University of Technology, Guilin 541004, China
e-mail: qinfangcheng@glut.edu.cn

C. Liu
e-mail: lcy261@glut.edu.cn

H. Qi
e-mail: alexander_qi@163.com

© The Minerals, Metals & Materials Society 2021

G. Daehn et al. (eds.), *Forming the Future*, The Minerals, Metals & Materials Series,
https://doi.org/10.1007/978-3-030-75381-8_207

these findings look promising for future studies dealing with compact hot ring rolling processes.

Keywords Compact casting-rolling forming process · Hot ring rolling · Texture evolution · Grain orientation

1 Introduction

42CrMo ring parts with excellent balance between strength and ductility are widely applied in aerospace, wind power, high-speed rail, and automobile industry. The ring rolling technique is an advanced method to produce the seamless 42CrMo ring parts [1]. During hot ring rolling (HRR), the ring blank driven by friction passes through the gap between the mandrel and driven roll. Consequently, accumulated strain expands from contact area with rollers to the inside of the ring due to the progressively narrowed gap between the mandrel and driven roll. This, in turn, continuously enlarges the diameter and reduces the thickness. So far, numerous studies dealing with deformation behavior and microstructure evolution of as-forged 42CrMo, GCr15 bearing steel, and TA15 titanium alloys have been subjected to HRR [2–7]. In recent years, to save energy, protect environment and reduce cost, a compact casting–rolling forming process was proposed and paid much attention [8–10]. However, in the compact cast-rolling forming process, unforged ring billets are directly used for ring rolling. The geometrical dimensions and microstructural modification must be integrated controlled during HRR. Therefore, hot compression testing was used on as-cast 42CrMo alloys to establish its recrystallization models [11]. Effects of rolling ratio, initial rolling temperature, and feed rate of mandrel on the recrystallization fraction and grain size have been clarified [12–14]. The precise dimensional accuracy and good microstructures were obtained in 42CrMo rings produced by compact casting–rolling process [8, 14].

Many merits such as considerable saved energy, reduced costs, and environmental protection are presented in the compact process when compared with the existing one. However, the texture evolution mechanism and its effect on mechanical properties of 42CrMo casting ring blank during HRR are still unclear [1]. Some studies suggested that improvement in strength and ductility are closely related to grain refinement and texture components of hot-rolled rings in their entire thickness. The shear texture was examined at the top part with a maximum shear strain but the cold rolling texture was operated at the middle and bottom parts of IF steel subjected to differential speed rolling [15]. The formation of shear texture is important for obtaining large grain refinement at the top part when compared to other parts of the specimen. Under the same hot-rolled reduction of grain-oriented silicon steel, much finer microstructures could give rise to higher elongations in fine-grain strips when compared to coarse-grains ones [16]. For fine-grain strips, good ductility could be obtained by a reduction of more than 30%. However, it takes reduction amount of 50% to get good ductility for coarse-grain ones. The increase of rolling reduction will

enhance α and γ fibre textures in hot-rolled strips. Elongation of less than 2% with tensile and yield strength around 1400 MPa has so far been achieved for SAE 1050 steels cold-rolled with a large thickness reduction around 70% [17]. The textures showed no significant changes when thickness reduction amount was less than 50%. Weak γ-fibre with uniform orientation distribution was formed for high strength ultra-low carbon bake hardening steel subjected to hot rolling [18]. The intensities of {111}<110>-{111}<112> for γ-fibre and {111}-{112}<110> for α-fibre were then enhanced by cold rolling. The γ-fibre intensity could be improved by reducing the reduction amount during cold rolling, correspondingly deep drawability of the materials was improved.

Thus, clarification of textural development of 42CrMo rings produced by HRR is important for a better fundamental understanding of the process and possible advanced applications. HRR process of 42CrMo casting blank was conducted at different mandrel feed rates. The influences of mandrel feed rate on the macro- and micro-texture evolution were investigated by XRD and EBSD techniques, respectively. The associated mechanisms of grain refinement were clarified in an effort to fabricate high-performance rings using compact casting–rolling.

2 Experimental

2.1 Preparation of XRD and EBSD Samples

Medium-carbon low alloy 42CrMo steel with chemical compositions of 0.44C, 0.28Si, 0.72Mn, 0.22Mo, 1.13Cr, 0.12Ni, 0.08Cu, 0.012P, 0.007Cu, and balance Fe (in wt%) were used. The casting ring blanks, whose outer diameter, inner diameter, and height were 240, 120, and 45 mm, respectively, were produced according to the previously reported method [1]. HRR tests were performed on a vertical ring rolling equipment [19]. The reduction principle of the entire thickness (three steps: 15-10-5 mm) was adopted in HRR at different feed rates of mandrel. The detailed parameters of HRR process are shown in Table 1 [1]. After HRR, rolled rings were cooled to room temperature in air. The textural samples for XRD and EBSD observations were cut from casting ring blanks and hot-rolled rings. The samples were located in the outer layer (location 1), inner layer (location 3), and center layer (location 2), as shown in Fig. 1. The geometrical dimensions of XRD and EBSD specimens were set to 15 mm × 10 mm × 5 mm and 5 mm × 5 mm × 3 mm, respectively. The XRD specimens were etched by 4% Nital. The EBSD specimens were electrolytic polished in 5% perchloric acid alcoholic solution for 60 s at a voltage of 30 V and electric current of 0.8 A. The corresponding scanning area of 250 μm × 250 μm and step size of 1.5 μm were selected.

Table 1 Parameters used for hot ring rolling

Rolling parameters	Items	Values
Radius of driven roll R1/idle roll R2/guide roll R3/mm	–	340/52.5/52.5
Rotation rate of driven roll n1/(r/min)	–	62
Feed rate of mandrel roll v/(mm/s)	A1	3-2-1.5
	A2	4-3-2
Dimension of casting ring billets/(mm × mm × mm)	–	φ 240 ×φ 120 × 45
Dimension of rolled ring/(mm × mm × mm)	A1	φ 332 ×φ 272 × 51.1
	A2	φ 331 ×φ 271 × 50.5
Rolling ratio λ	–	2.6

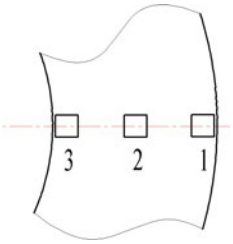


Fig. 1 Sampling location. (Color figure online)

2.2 Textural Characterization

The grain orientations and texture components were studied by means of EBSD system equipped with field emission SEM. EBSD data were analyzed using post-processing TSL-OIM software. After hot rolling, the textural components were quantitatively determined by measuring incomplete pole figures {110}, {200} and {211} at polar angles from 0o to 70o using Schulz back reflection technique on a Panalytical Xpert MRD high-resolution X-Ray diffractometer with Co-kα1 radiation [20]. The orientation distribution functions (ODFs) were obtained by the two-step method [21, 22]. Different textural fibres were then extracted from ODFs and the results were discussed.

3 Results

3.1 Texture of Casting Ring Blank

The initial casting microstructure of 42CrMo with an average grain size of 87 μm can be extracted from the literature [1]. By comparison, Fig. 2 showed initial texture mainly characterized by strong {112}<131> and near {110}<112> components with

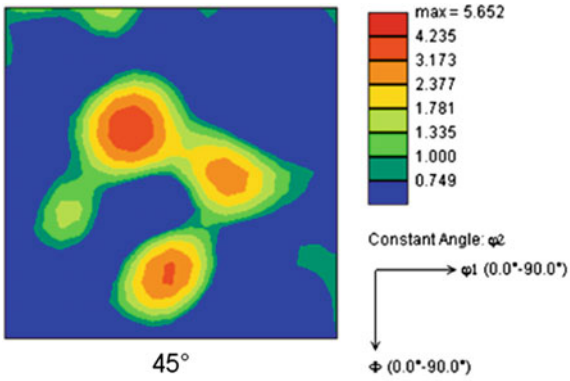


Fig. 2 Orientation distribution function at $\varphi 2 =$ 45o (Bunge notation) of 42CrMo casting ring blank. (Color figure online)

intensities of 4.5 and 3.4, respectively. In addition, {111}<110> with weak intensity of 2.5 and near {111}<110> components were also observed.

3.2 Textures of Casting Blank After HRR

The changes in geometrical dimensions of casting ring blank should follow the development of mechanical properties [1]. At a feed rate of 4-3-2 mm/s, the average ultimate strength of 1160 MPa and yield strength of 961 MPa did not obviously vary but the average total elongation and Charpy impact decreased to 8% and 11.5 J, respectively. These obtained values of hot-rolled rings were superior to reported one [14]. Refined grains with average diameter of 32 μm and homogeneous microstructure can be obtained near the outer layer and inner layer of A1-rolled ring [1]. Inhomogeneous microstructures were observed near the center layer, where small amounts of irregular and coarse grains would play dominant roles. At feed rate of 4-3-2 mm/s, the grain refinement degree decreased slightly with an average diameter around 44 μm. The inhomogeneous grain distribution in the entire thickness of A2 ring was also clearly observed.

After HRR, XRD was used to quantitatively determine the textures of the entire thickness of 42CrMo-rolled rings. Figures 3 and 4 show $\varphi = 45^{o}$ ODF sections (Roe notation) of hot-rolled rings at different feed rates. Compared to the initial condition, the texture showed complete changes (Fig. 2). The textural components of A1 and A2 rings after HRR process were identified as γ-fibre of <111 >//RD, with {111}<110> and {111}<112> shown as dominant components. However, γ-fibre texture looked weak near the outer layer of A2-rolled ring. Both α-fibre and ε-fibre textures did not illustrate significant changes with increased feed rate in the entire thickness of hot-rolled rings. The shear textures consisted of Copper-type {112}<111> and Goss {110}<001> components presented in different regions of hot-rolled rings. During hot rolling, shear deformation was caused by high friction between surface of the rollers and ring, resulting in the formation of Goss texture [16]. Large strains in

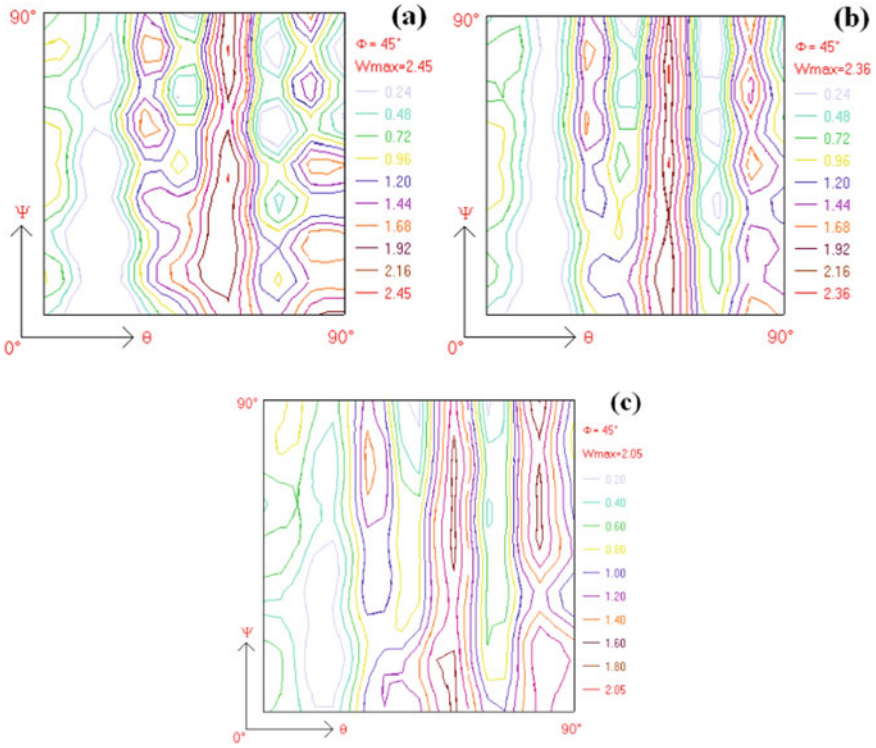


Fig. 3 $\varphi = 45o$ sections (Roe notation) of ODFs in A1-rolled rings at locations: **a** 1, **b** 2, and **c** 3. (Color figure online)

each pass and deformation heat were formed due to increased shear deformation as a function of feed rate. For A1 ring after HRR process, the intensities of Goss texture in surface appeared larger than that in center, but through-thickness texture was mainly dominated by γ-fibre orientation. In Fig. 3, the intensities of Goss texture in outer layer and inner layer increased with feed rate but slightly weakened in the center layer. These features induced inhomogeneous orientation distributions of γ-fibre and shear textures.

4 Discussion

Good mechanical properties are closely connected with refined grains and texture components. The superior ultimate tensile strengths and yield strengths should mainly be attributed to strengthening caused by grain refinement in the entire thickness of hot-rolled rings. Therefore, a better understanding of the analytical strengthening mechanisms would be essential to clarify the effects rules of mandrel feed

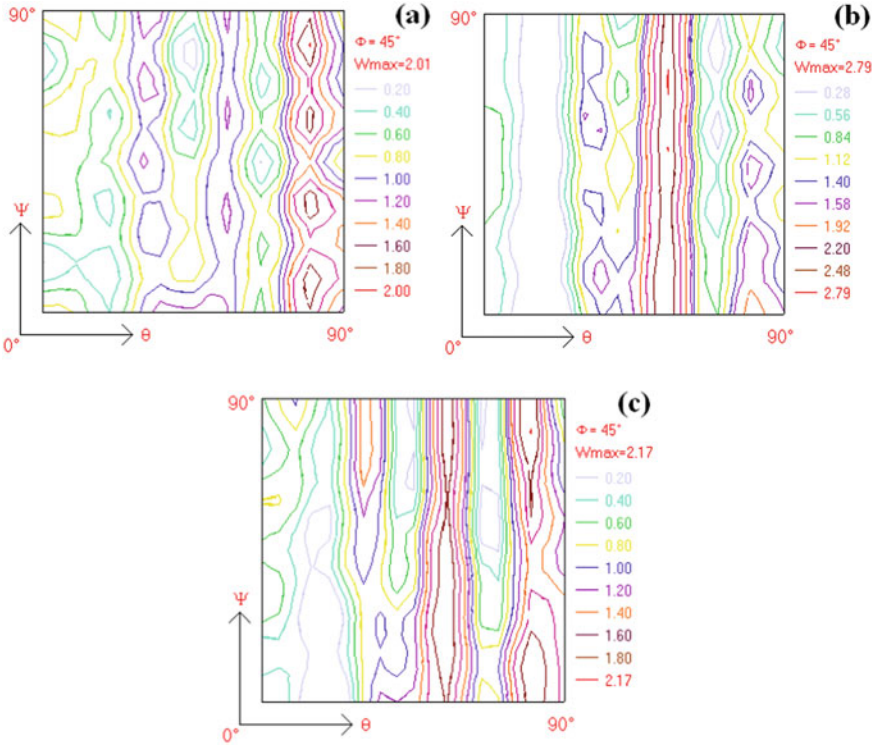


Fig. 4 φ = 45o sections (Roe notation) of ODFs in A2-rolled rings at locations: **a** 1, **b** 2, and **c** 3. (Color figure online)

rate on the microstructure, texture, and mechanical properties of 42CrMo casting blank processed by HRR. [1] The reason for this had to do with microstructure with finer grains, which should have more grain boundary per unit area when compared to initial coarse grains. Therefore, fine grains could provide more obstructions for dislocation motions at grain boundaries during room-temperature tensile deformation [23]. The above results agreed well with the behavior described by Hall–Petch equation for dislocation glide mechanism. In addition, poor plasticity and toughness would strongly depend on inhomogeneous distribution of grain size, which may be associated with shear deformation existing in the entire thickness of the rings. The difference in shear deformation between the surface layer and center layer during HRR was not obvious at low feed rates. However, the additional shear in center layer looked smaller than that in surface layer when feed rate increased.

Figure 5 summarizes the orientation density distribution of textures along the α-fibre, γ-fibre, and ε-fibre. As feed rate rose, significant texture evolution occurred, especially γ-fibre. The inhomogeneous orientation distributions of γ-fibre texture are displayed in Fig. 5c, d. α-fibre texture mainly consisted of {001}<110> and near {112}<110> components (Fig. 5a), implying typical rolling texture. The rolling

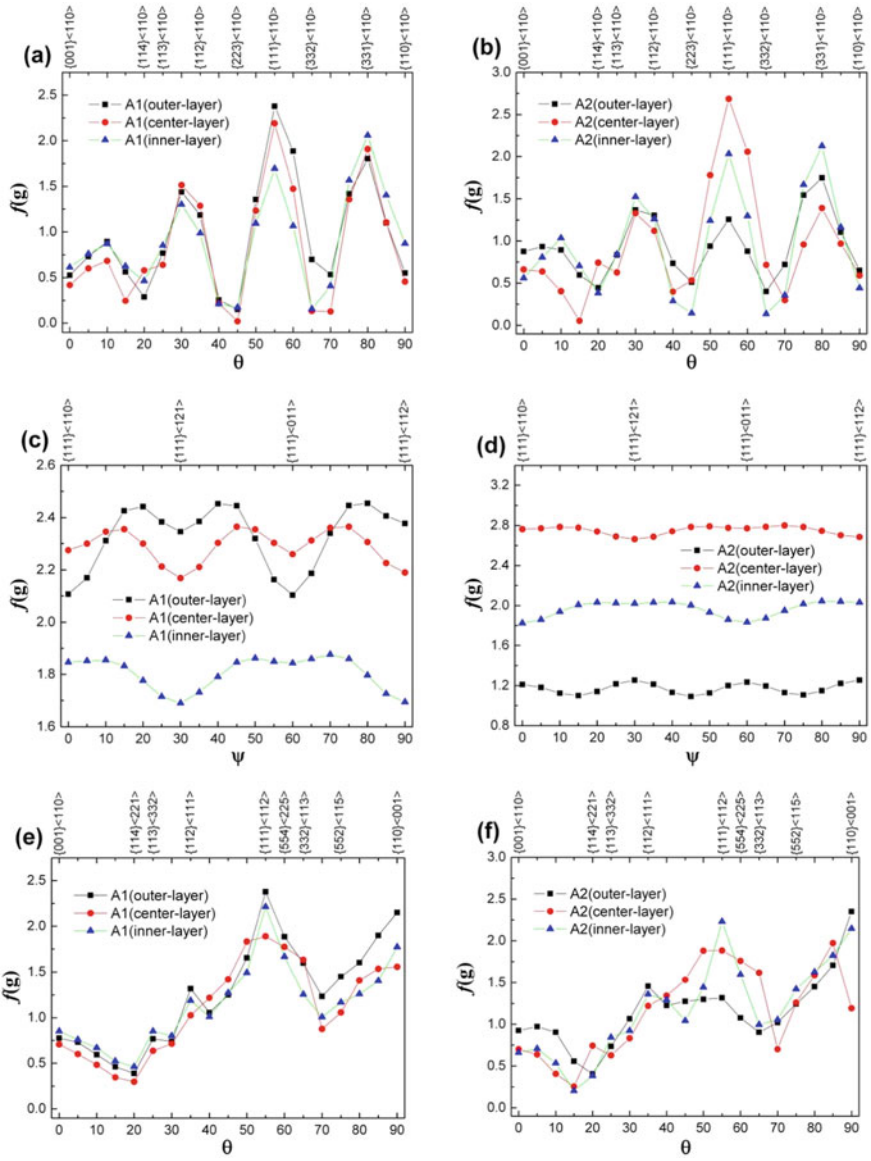


Fig. 5 Orientation density distribution of: **a**, **b** α-fibre, **c**, **d** γ-fibre, and **e**, **f** ε-fibre in the entire thickness of 42CrMo hot-rolled rings. (Color figure online)

texture did not show significant change with the increasing feed rate, but both recrystallization textures {111}<110> and {111}<112> components became stronger. Also, the recrystallization textures with intensities of 2.1–2.5 along γ-fibre dominated the outer layer and center layer. At feed rate from 3-2-1.5 mm/s to 4-3-2 mm/s, recrystallization textures were significant affected (Fig. 5d). Note that textures in the center layer continued strengthening up to approximately 2.8 but the textures in outer layer decreased sharply to 1.2. This induced a rather inhomogeneous distribution of recrystallization texture in the center layer. Thus, variation in recrystallization texture with feed rate obviously influenced the inhomogeneous grain refinement in the entire thickness of 42CrMo hot-rolled rings, especially in center layer [1].

Figure 6 exhibits the grain orientation in the outer-, center- and inner layers of 42CrMo rings after HRR process. Large numbers of sub-grains were recorded in the entire thickness of the rings at different feed rates. The grains were characterized by different orientations. Besides, <111> orientation in A1 hot-rolled ring was significant, and refined sub-grains with <211> orientation was obtained in both outer- and inner layers of A1 ring. The <110> orientation dominated the center layer. The <111> orientation in A2-rolled ring increased with feed rate. Also, transformation from <111> to <001> orientation enhanced, and grains with <110> orientation in both outer- and center layers decreased, leading to inhomogeneous orientation distribution in the entire thickness of hot-rolled rings.

The grain orientation directly reflected the preferred orientation tendency of texture during HRR process. The recrystallization grains with orientations of {111}<110> and {111}<112> were registered in outer- and center layers of A1 hot-rolled ring. However, {111}<112> grains were only found in the outer layer of A2 hot-rolled ring, and the slight preferred orientation was clearly displayed. In Fig. 6f, refined shear grains with {112}<111> were observed, leading to the competition between formation and growth of the grains. On the other hand, recrystallization nuclei were formed in interior of the grain and triangle grain boundaries. The reason for this had to do with large misorientation and high-density nucleation at grain boundaries, which contributed to bow out of the grain nucleation. The nucleation mechanisms of recrystallization grains were dominated by *in situ* recrystallization accompanied by random nucleation. In particular, new grains formed by *in situ* recrystallization had similar orientation in the matrix but those induced by random nucleation displayed different orientation. Moreover, grain orientations were closely related to distribution of grain size at higher feed rates.

Similar to microstructure and texture evolution of bcc metals [24], the texture components would generally develop into two families during rolling process. The γ-fibre contained <111> parallel to normal direction and α-fibre consisted of <110> parallel to rolling direction of the ring surface. Thus, mixed stress state may be induced during rolling process. The dominance of shear stress would induce textures with {110} component. Ryttberg et al. [25] suggested that cold rolling texture components in bcc metals and relative strength of different rolling textures mainly depended on degree of deformation. However, textures were quite independent of other parameters. By comparison, the above results showed slight decrease in tendency of textural

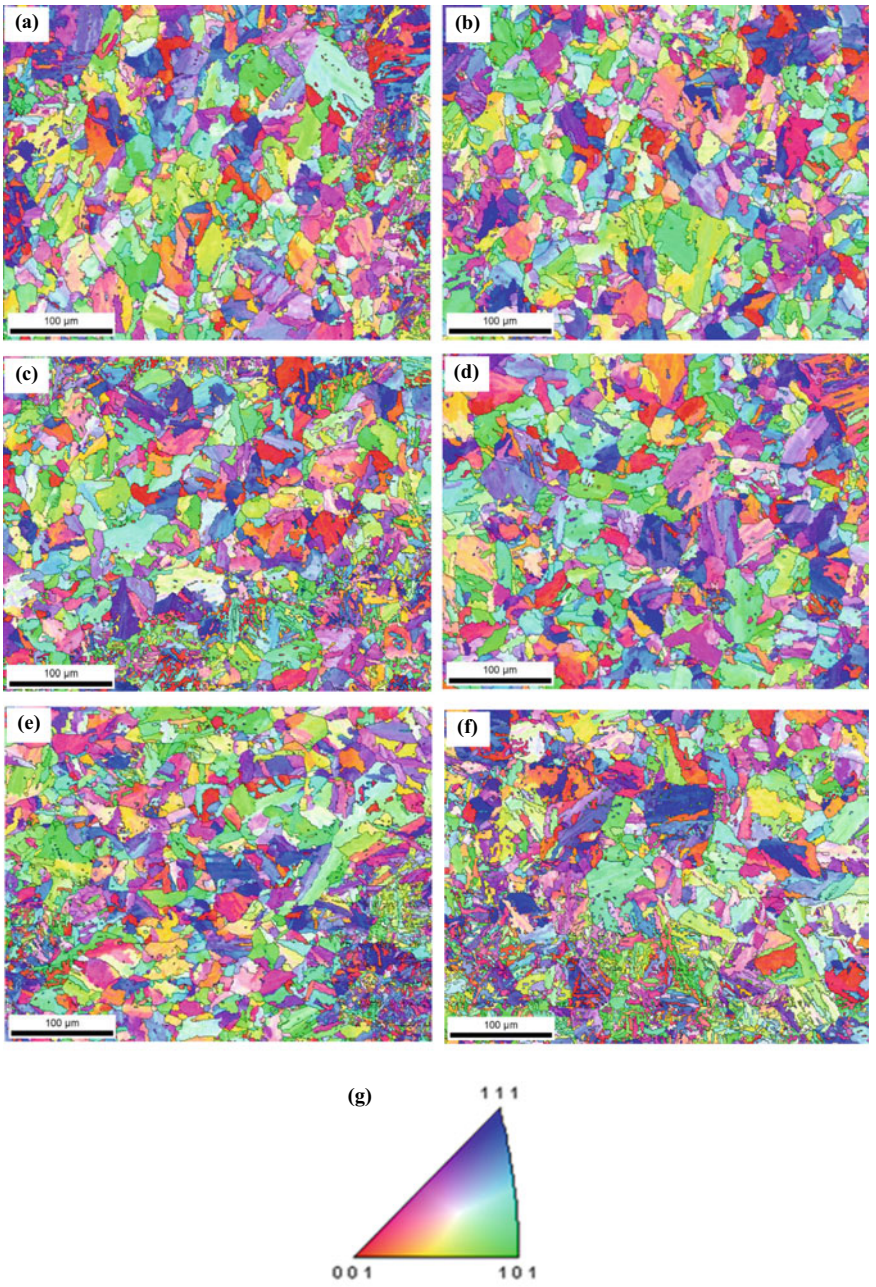


Fig. 6 Grain orientation maps of 42CrMo hot-rolled rings in different areas: **a** 1 of A1, **b** 2 of A1, **c** 3 of A1, **d** 1 of A2, **e** 2 of A2, **f** 3 of A2, and **g** inverse pole figure. (Color figure online)

intensity near the outer layer of hot-rolled ring with the increased feed rate. In addition, γ-fibre components looked more intense in the center layer. These combined textures revealed that HRR process led formation of mixed compression strain with additional shear strain associated with the distance from the surface layer to center layer. Furthermore, such complex texture evolution strongly depended on distribution of additional shear strain caused by non-symmetrical deformation model of HRR process in nature [15, 25]. The high intensity of shear texture, including Copper-type {112}<111> and Goss {110}<001> components showed intense shear strain effectively contributing to the shear texture evolution during HRR. During hot rolling, the shear deformation was caused by high friction between the surface of rollers and the ring, resulting in Goss texture [16]. Large strain in each pass and deformation heat was formed due to the increase in shear deformation with feed rate. Therefore, shear texture would give rise to comparatively higher fractions of refined grains. Previous studies showed that crystallographic orientation of deformed grains would affect the nucleation and following growth of recrystallization nuclei [26]. The nucleation rate and driving force for recrystallized nuclei growth depended on stored energy of various grains and scaled by their Taylor factor M [27]. For example, the Taylor factors were very low for both orientations {110}<001> and {112}<111>, unlikely to form nuclei [26, 28]. Goss texture would form by shear deformation [21]. The textures were characterized by {110}<001> and {112}<111> orientations with very low Taylor factors in the surface layer of 42CrMo rings after HRR process. Besides, stored energy in {110}<001> and {112}<111> grains can only be reduced since no orientation could nucleate easily. On the other hand, Taylor factors for γ-fibre orientations between {111}<110> and {111}<112> looked higher than those of α-fibre orientations between {001}<110> and {112}<110>. The intensities of γ-fibre orientations were also much higher than Goss component (Fig. 5). Consequently, higher stored energy played a dominant role in surface layer when compared to center layer, resulting in preferred nucleation of grains along γ-fibre orientations. Finally, the inhomogeneous distribution of grain size was caused by the distinctly inhomogeneous γ-fibre orientations in the entire thickness of A2 ring after HRR process, especially in the center layer.

As a result, the grain refinement and its uniform distribution in the entire thickness of hot-rolled rings depended heavily on corresponding grain orientation and textural development. This, in turn, should influence the plasticity of the rings, including their elongation and reduction of area. Note that strength and plasticity could be considered as conflicting properties, but elongation increased considerably since fine-grains in a preferential orientation suited better the imposed strain [16, 29]. Here, the texture components and relative strengths of different textures exhibited significant evolution with feed rate. However, the direct effecting mechanism of texture on plasticity was still unclear and should be explored in future studies.

5 Conclusions

The texture evolution of 42CrMo casting blank subjected to HRR process was studied at different feed rates. The mechanisms of grain refinement were examined throughout the entire thickness of hot-rolled rings. The following conclusions could be drawn:

(1) The dominant textures in the hot-rolled rings were similar, with γ-fibre consisting of {111}<110> and {111}<112> orientations as the most intense components. The α-fibre and ε-fibre textures did not significantly change with feed rate in the entire thickness of the hot-rolled rings. Moreover, shear textures, including Copper-type {112}<111> and Goss {110}<001> components were presented in different regions of the rings after HRR process.

(2) Grain refinement was closely related to grain orientation and textural development in the entire thickness of the hot-rolled rings. The inhomogeneous distribution of grain size in the hot-rolled ring at high feed rates induced poor plasticity of 8% and toughness of 11.5 J caused by inhomogeneous γ-fibre orientations, especially in center layer of the ring. Thus, the integrated control of microstructure and mechanical properties could be realized by the application of compact cast-rolling forming process.

Acknowledgments This research was funded by the National Natural Science Foundation of China (Nos. 51875383 and 51575371); the Natural Science Foundation of Guangxi (No. 2018GXNSFBA281056); the Foundation of Guilin University of Technology (No. GUTQDJJ2017140); the Science and Technology Major Project of Guangxi (Nos. GKAA17202007 and 2018AA23004).

References

1. Qin FC, Li YT, Qi HP, Wei XJ (2017) Microstructure and mechanical properties of as-cast 42CrMo ring blank during hot rolling and subsequent quenching and tempering. J Mater Eng Perform 26:1300–1310
2. Lin YC, Chen MS, Zhong J (2009) Study of metadynamic recrystallization behaviors in a low alloy steel. J Mater Process Technol 209:2477–2482
3. Kil TD, Lee JM, Moon YH (2015) Quantitative formability estimation of ring rolling process by using deformation processing map. J Mater Process Technol 220:224–230
4. Wang C, Geijselaers HJM, Omerspahic E, Recina V, van den Boogaard AH (2016) Influence of ring growth rate on damage development in hot ring rolling. J Mater Process Technol 227:268–280
5. Guo LG, Pan X, Yang H et al (2012) Effects of rotational speed of driving roll on microstructure evolution during hot ring rolling of as-cast 42CrMo steel. Heavy Mach 3:59–64
6. Guo J, Qian DS, Deng JD (2016) Grain refinement limit during hot radial ring rolling of as-cast GCr15 steel. J Mater Process Technol 231:151–161
7. Zhu S, Yang H, Guo LG, Gu RJ (2012) Investigation of deformation degree and initial forming temperature dependences of microstructure in hot ring rolling of TA15 titanium alloy by multi-scale simulations. Comput Mater Sci 65:221–229

8. Li YT, Ju L, Qi HP, Zhang F, Cheng GZ, Wang ML (2014) Technology and experiments of 42CrMo bearing ring forming based on casting ring blank. Chin J Mech Eng 27:417–427
9. Qin FC, Li YT, Qi HP, Ju L (2016) Microstructure-texture-mechanical properties in hot rolling of a centrifugal casting ring blank. J Mater Eng Perform 25:1237–1248
10. Qi HP, Li YT (2012) Metadynamic recrystallization of the as-cast 42CrMo steel after normalizing and tempering during hot compression. Chin J Mech Eng 25:853–859
11. Fu J, Li YT, Fu JH, Song JL, Lei BF, Qi HP (2012) Dynamic recrystallization behavior of as-cast 42CrMo steel during hot compression deformation. Mater Mech Eng (in Chinese) 36:91–95
12. Li YT, Qi HP, Fu JH, Cheng GZ, Zhang F, Qin FC (2013) Theoretical and process analyses on the cast-blank rolling forming of 42CrMo bearing rings. J Mech Eng (in Chinese) 49:198–206
13. Zhang F, Li YT, Qi HP, Fu J, Zhao L (2004) Study on rule of microstructure evolution during hot rolling process of annular casting blank. China Metalforming Equip Manuf Technol (in Chinese) 46:96–99
14. Wang ML (2013) Casting-rolling forming process of 42CrMo bearing ring blank. Bearing 12:19–20 (in Chinese)
15. Park JH, Hamad K, Widiantara IP, Ko YG (2015) Strain and crystallographic texture evaluation of interstitial free steel cold deformed by differential speed rolling. Mater Lett 147:38–41
16. Song HY, Liu HT, Lu HH, Li HZ, Liu WQ, Zhang XM, Wang GD (2014) Effect of hot rolling reduction on microstructure, texture and ductility of strip-cast grain-oriented silicon steel with different solidification structures. Mater Sci Eng A 605:260–269
17. Herrera C, Lima NB, Ferreira Filho A, Plaut RL, Padilha AF (2009) Texture and mechanical properties evolution of a deep drawing medium carbon steel during cold rolling and subsequent recrystallization. J Mater Process Technol 209:3518–3524
18. Chen YL, Su L, Zhao AM, Kuai Z, Li BH, Liu GM (2013) Effects of rolling parameters on texture and formability of high strength ultra-low carbon BH steel. J Iron Steel Res Int 20:75–81
19. Han XH, Hua L (2014) Plastic deformation behaviors and mechanical properties of rolled rings of 20CrMnTi alloy in combined radial and axial ring rolling. Mater Des 58:508–517
20. Schulz LG (1949) Determination of preferred orientation in flat transmission samples using a Geiger counter X-ray spectrometer. J Appl Phys 20:1030–1033
21. Ryong JR (1965) Description of crystallite orientation in polycrystalline materials. III. general solution to pole figure inversion. J Appl Phys 36:2024–2030
22. Ray RK, Jonas JJ, Hook RE (1994) Cold rolling and annealing textures in low carbon and extra low carbon steels. Int Mater Rev 39:129–172
23. Yang YB, Zhang ZM, Li XB, Wang Q, Zhang YH (2013) The effects of grain size on the hot deformation and processing map for 7075 aluminum alloy. Mater Des 51:592–597
24. Hutchinson B (1999) Deformation microstructures and textures in steels. Philos Trans R Soc A 357:1471–1485
25. Ryttberg K, Knutson Wedel M, Recina V, Dahlman P, Nyborg L (2010) The effect of cold ring rolling on the evolution of microstructure and texture in 100Cr6 steel. Mater Sci Eng A 527:2431–2436
26. Gao ZL, Liu HT, Wang GD (2013) Evolution of through-thickness texture in ultra purified 17%Cr ferritic stainless steels. J Iron Steel Res Int 20:31–38
27. J Han, Li H, Barbaro F, Zhu ZX, Jiang LZ, Xu HG, Ma L (2014) Effects of processing optimisation on microstructure, texture, grain boundary and mechanical properties of Fe-17Cr ferritic stainless steel thick plates. Mater Sci Eng A 616: 20−28
28. Hu MY, Cho YS, Kim JS (1999) Effect of lubrication on the evolution of through-thickness texture gradients in cold rolled and recrystallization low carbon steel. Z Metallkd 90:124
29. Huo QH, Yang XY, Sun H, Li B, Qin J, Wang J, Ma JJ (2013) Enhancement of tensile ductility and stretch formability of AZ31 magnesium alloy sheet processed by cross-wavy bending. J Alloys Compd 581:230–235

A Novel Flexible Skew Rolling Process for Step Shafts: Feasibility Study



Longfei Lin, Baoyu Wang, and Jinxia Shen

Abstract When the larger-size step shafts with small scale are manufactured, both the forging and rolling method bring about high cost for its need for heavy loading or special dies. This paper develops a novel flexible skew rolling (FSR) process to produce step shafts. The process includes four stages: radial rolling, rollers inclining, skew rolling, and rollers leveling. Each roller has three freedoms (circle rotation, radial rotation, and radial-feeding motion), which can manufacture different axles by programming different rollers' movements that can achieve flexible rolling with the same tools. In order to conduct the experiment and verify the process feasibility, a flexible skew rolling mill with dual-rotatable-shafts (DRM-80) was invented and manufactured, and both rollers have three freedoms that can be dynamically adjusted during the whole rolling process. Feasibility experiments were performed at the DRM-80 mill, a Ø80 × 390 mm C45 steel billet was used to manufacture a single-step shaft. A large and long shaft (total length 605 mm, minimum diameter 50 mm) was formed and has well dimensional accuracy and no serious defects. The main forming defects include knurled pockmarks, helical grooves, side cavity, and diameter tolerance. The experimental FSR part is free from internal cracks by observing the transverse and longitudinal sections. The study results verified that the novel flexible skew rolling process is positive and the new type DRM-80 mill is reliable.

Keywords Flexible skew rolling · DRM-80 mill · Step shafts forming · Feasibility experiment

L. Lin · B. Wang (✉)
School of Mechanical Engineering, University of Science Technology Beijing, Beijing 100083, China
e-mail: bywang@ustb.edu.cn

J. Shen
Beijing Key Laboratory of Metal Lightweight Forming Manufacturing, Beijing, China

© The Minerals, Metals & Materials Society 2021

G. Daehn et al. (eds.), *Forming the Future*, The Minerals, Metals & Materials Series,
https://doi.org/10.1007/978-3-030-75381-8_208

1 Introduction

The near-net-shaped shafts play an important role in axisymmetric profiles manufacturing and die-forging billets preforming which are widely used in machine-building, automotive, and railway industries [1–3]. These shafts are generally formed by forging process (open die forging [4–6], radial forging [7, 8]) or rolling process (cross-wedge rolling [9, 10]). Nevertheless, the forging process can manufacture various shafts by common rollers but needs high forging force (overall deformation) that results in large tonnage of the forging equipment. Conversely, the rolling process can realize lightly foaming by regional deformation but needs large-size special tools. Hence, the cross-wedge rolling process is suitable for rolling in mass quantities because of the lack of flexibility. For manufacturing the small number of products, both the forging and rolling method bring about high cost.

To manufacture shafts flexible the axial feed rolling process was proposed first in Germany (1986) [11]. The schematic diagram of this process is shown in Fig. 1a, the rolling device of this process consists of rollers and chuck, the axial rotation and radial feeding motion are conducted by two rollers, the axial linear movement is conducted by chuck. Two stages are included: the billet deforms radially to the target diameter under the radial movement of rollers and then is stretched axially to the target length under the axial linear movement of truck. Early researchers focused on this flexible process and meaningful research has been conducted, and the relationships

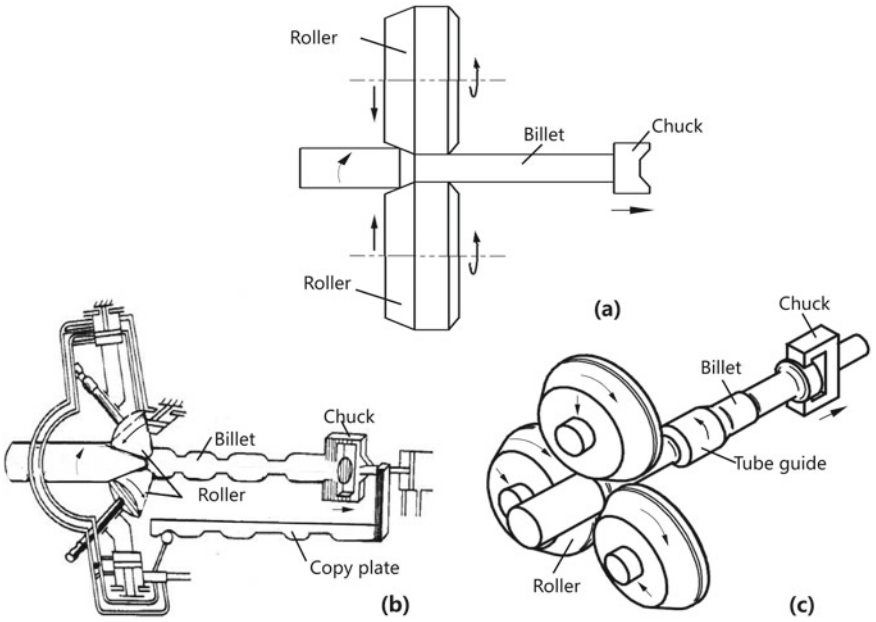


Fig. 1 The flexible rolling process under research phase: **a** axial-feed rolling; **b** copy skew rolling; **c** CNC skew rolling

of the main process parameters and the defects were analyzed by finite element method and engineering experimentation [12]. Whereafter, Chinese researcher Xu [13, 14] conducted series of studies, the contact surface and kinematics analysis of this process are presented. The theoretical analysis, deformation process simulation, and test machine have been investigated. The most striking feature of the process is that a simple-shape die with small size can manufacture various multiple-shaft parts for the formed geometry of the shaft is controlled by the roller's movements. Hence, the main advantage of this process is flexibility.

Another method for flexible producing shaft is skew rolling with three tapered rollers which can be divided into two types. One type of this process is a copy of skew rolling, which is originated in the Soviet Union by Zerikov (1968) [9], as shown in Fig. 1b, this process needs a copy plate to control movements of tapered rollers. The other type is CNC skew rolling which is carried out by Pater Z successfully completed the forming of the rail car axles by a CNC 3-roller mill (2020) [15], and the schematic diagram of CNC skew rolling is shown in Fig. 1c. In CNC skew rolling, apart from axial rotating, these tapered rollers can also move radially toward the axis of the workpiece. By programming the motions of CNC mill, it becomes possible to produce elongated parts with any shape.

Nevertheless, Both axial feed rolling, the copy skew rolling and CNC skew rolling, a chuck is required to draw the forming workpiece for its axis movement, and leads to the following considerations: (1) a considerable amount of chucking allowance that may reduce the material utilization; (2) the maximum rolling length is limited by the chuck stroke that needs an elongated equipment for long axis production. These inevitable limitations limited their applications, until now, all these above flexible forming methods are still under the experiment exploration.

2 Flexible Skew Rolling Process (FSR)

In this paper, a novel flexible skew rolling (FSR) process is presented and the schematic design of two-roller FSR process was shown in Fig. 2a. The rolling device of FSR process mainly consists of two tapered rollers and two tube guides. Two rollers both have three freedoms: the rotation N_0 around its own axis, the radial feed V_0 toward the workspace axis, and the angle adjustment rotation W_0. Two tube guides are fixed on both sides of the rollers for limiting the position of the workplace. The roller motions (N_0, V_0, W_0) are controlled by automatic system, the process is divided into four stages which is shown in Fig. 2b:

I. Radial rolling: two leveled rollers have the motions of N_0 and V_0. The workpiece diameter d_1 is determined by the gap distance between the two rollers, and the front step of the bar is formed at the meantime;
II. Rollers inclining: two rollers have the motion of W_0. The swing angle β is changed and increases to the target value;

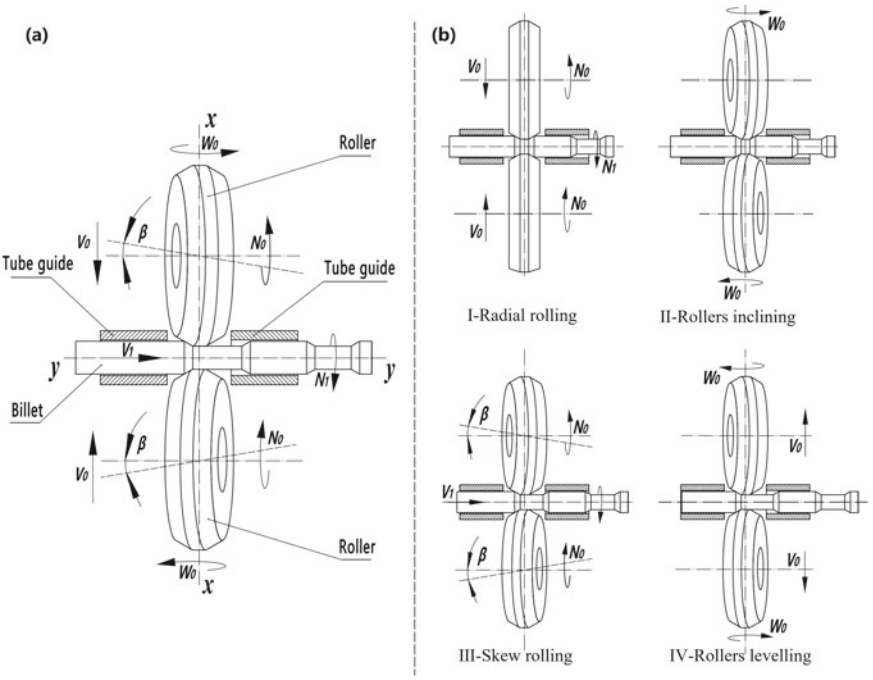


Fig. 2 The flexible skew rolling (FSR): **a** schematic diagram; **b** process stages

III. Skew rolling: two inclined rollers (with invariant angle β) only have the motion of $N_{0.}$ The workpiece rotates circularly and moves axially, then the diameter of workpiece is reduced toward the free end of the bar;
IV. Rollers leveling: two rollers have the motions of V_0 and $W_{0.}$ Two rollers are leveled and backed to the original state.

By controlling the motions of two rollers, FSR process can flexibly form various shafts. According to the above analysis, the FSR process with none-chuck has enormous advantages over low-waste material, unlimited-length of shaft, and compact-structure equipment.

3 Rolling Mill (DRM-80)

To verify the feasibility of the process, a laboratory flexible skew rolling mill is indispensable. Up to now, the skew rolling mill mainly includes skew piercing mill, square-frame rolling mill, power-box rolling mill, and double-arm rolling mill [16]. These mills are widely used in the industrial production of tube piercing, ball rolling, thread rolling, spline rolling, worm rolling, and knurl rolling, which has a great contribution to metal-forming industry. However, all these mills above cannot meet

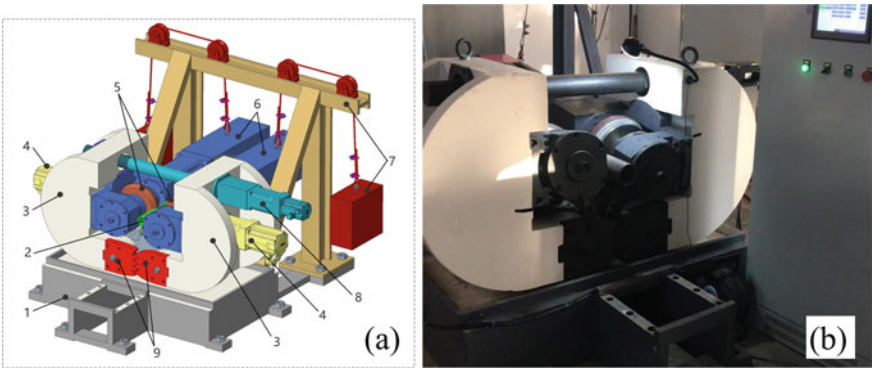


Fig. 3 The DRM-80 mill was designed and constructed: **a** the 3D model; **b** the physical mill. (Color figure online)

the movement requirements of FSR process because the rollers are required three degrees of freedom.

The FSR mill (named as DRM-80, the D stands for dual-rotatable shafts, the R stands for rolling process, the M stands for mill and 80 stands for the maximum diameter of the billet) with dual-rotatable shafts was invented and constructed, and the 3D model of this rolling mill is shown in Fig. 3a. The mill has a segment structure and mainly consists of ten components: a base unit—1, two tube guides—2, two-arm stands—3, two-angle adjusting systems—4, two rollers—5, two main rotating systems—6, a counter-balance unit—7, radial feeding system—8, a radial feeding synchronous unit—9, and a servo control system.

Two main rotating systems of this mill are correspondently mounted under two-arm stands, and drive the two rollers rotating around its own axle. In the same circumstance, two-angle adjusting systems are fixed on the two-arm stands and also inclines the whole main rotating systems to adjust the swing angle. In order to achieve two rollers radial feed together with the same speed at anytime, the radial feeding system and radial feeding synchronous unit are matched, so the radial feeding synchronous unit was proposed. The radial feeding synchronous unit is worked by two matched synchronous gears that ensure two arm stands open or close together. The physical mill is presented in Fig. 3b, and the technical specifications are given in Table 1. What need to pay more attention is that the overall dimension of the mill is only 1.8 m $\times$ 1.7 m $\times$ 1.6 m, the total power is 70 kW and the maximum roller diameter is 350 mm, but the maximum billet diameter can up to 80 mm, the body of the DRM-80 mill has the advantages of compactness and high strength.

Therefore, the designed DRM-80 machine makes it possible to accomplish FSR process test result from the rollers can rotate in the same direction, radial feed toward the workpiece, and adjust the swing angle β dynamically. What's more, this innovative type of mill may have a promising potential in industrial application for the superiority of convenient installation and adjustment, high strength frame, compact structure, and multifunctional rolling and precision control by servosystem.

Table 1 The technical specifications of DRM-80

Parameter	Unit	Value
Main rotating motor power	kW	2 × 30
Main rotating speed	rmp	43
Main rotating torque	Nm	7000
Radial feeding motor power	kW	3
Radial feeding speed	mm/s	5
Radial feeding torque	ton	22
Angle adjusting motor power	kW	2 × 2.3
Angle adjusting speed	°/s	10
Angle adjusting torque	Nm	900
Angle adjusting range	°	±12
Rolling center line range	Mm	±0.15
Maximum roller diameter	mm	350
Maximum billet diameter	mm	80
Overall dimensions	m	1.8 × 1.7 × 1.6
Total weight	ton	5

4 Feasibility Experiment

The purpose of FSR test is to verify the feasibility of the FSR process and equipment, as Fig. 2 shows, rollers inclining and rollers leveling are roller adjustment stages, radial rolling, and skew rolling are billet forming stages.

A single-step shaft foming test was presented, in which a shaft with the minimum diameter 50 mm was formed from a Φ80 × 390 mm C45 steel billet. Because the rolled part only has one step, the rolling process only includes three stages (radial rolling, rollers inclining and skew rolling). However, the FSR process of this shaft doesn't include all these stages but all the billet forming stages were included, so the feasibility experiment is reliable.

4.1 Rollers Design

The FSR roller is radically different from the traditional roller, cross-wedge rolling die, ball rolling roller, or other skew rolling roller. The FSR roller is inspired by the piercing roller but has some development because the center stress state(to avoid center crack) and the four forming stages are taken into account at the same time. Hence, as shown in Fig. 4a, the roller is a symmetrical structure that can be divided into sizing zone in the middle, forming zone on both sides. The roller parameters are diameter D_0= 340 mm, length L_0= 120 mm, forming angle $\alpha = 20°$, and sizing width $L = 25$ mm.

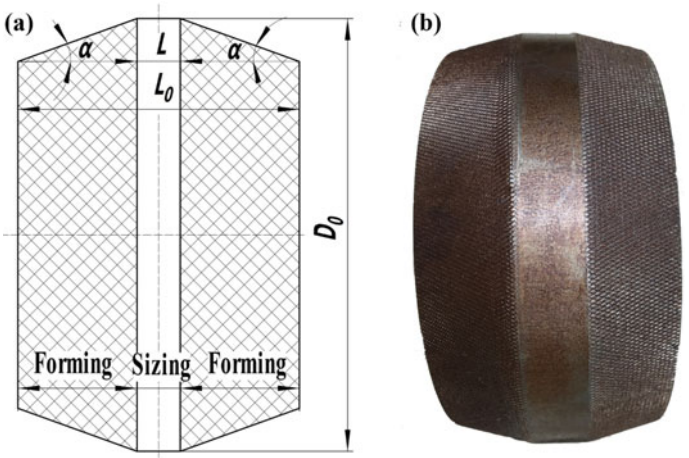


Fig. 4 The FSR roller: **a** geometric model; **b** physical graphics. (Color figure online)

Figure 4b shows the FSR roller used in hot FSR experiments. Because the roller stands high-speed revolution and large rolling force during the hot FSR rolling (temperature is about 1050 °C), so the value of HRC hardness generally needs greater than 50. In consequence, the roller is made by hot-die-material H13 and heat treatment has been done between rough lathing and precise grinding process. Notably, the forming zone surface was knurled by hatching knurling with the size of 2 mm.

4.2 Movements Design

The most significant characteristics of the FSR process is programming different movements to finish each adjusting stage and forming stage. The forming process was designed and the movement parameters were programmed according to Fig. 5. Firstly, at the radial rolling stage, two leveled rollers rotate with a constant speed of N_0= 30 rpm and radial feed speed V_0= 1.5 mm/s. After radial rolling stage (10 s later), the roller reaches the target diameter of 50 mm. Secondly, at the roller inclining stage, two leveled rollers are adjusted into inclined (the swing angle $\beta = 8°$) by the radial rotating movement (W_0= 1 rpm). Thirdly, at the skew rolling stage, two rollers remain the inclined angle $\beta = 8°$ and rotate with speed N_0= 30 rpm. The workpiece rotates and moves axially under the friction action between rollers and workpiece. At the end of this stage, the workpiece is formed into step shaft.

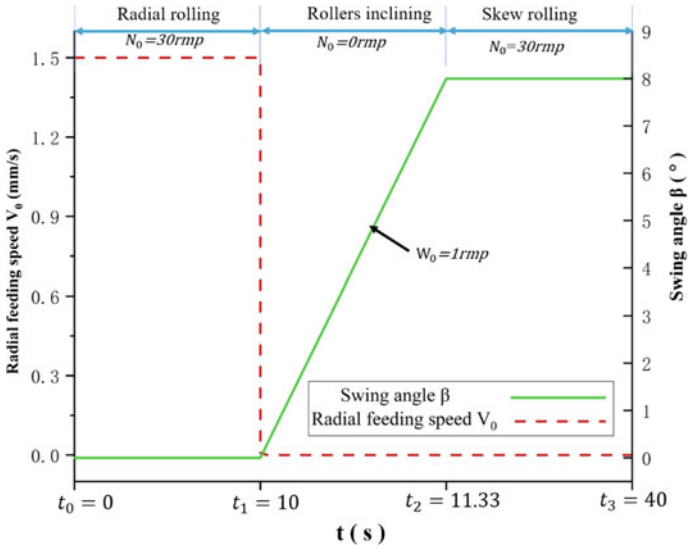


Fig. 5 The FSR rolling stages and process parameters of Φ80 mm single-step shaft. (Color figure online)

4.3 FSR Rolling Test on DRM-80

Feasibility experiments were performed on the DRM-80 mill, and a Φ80 × 390 mm C45 steel billet was used to manufacture a single-step shaft. Prior to rolling, the C45 billet is preheated to 1050 °C in an electric tube furnace, and then immediately transferred into the workspace of the DRM-80 mill.

The test was performed at the University of Science and Technology Beijing, China. The motions of rollers were controlled by the servo program which was preset before. The deformation stages of the shaft were shown in Fig. 6. The workpiece rotated stably under the constraint of tube guides during the whole FSR rolling. After FSR rolling, the mill was stopped and the product was removed from the machine manually. By the feasibility test, the following conclusions are obtained: (1) the novel FSR process is feasible and optimistic; (2) the DRM-80 mill can complete the complex motions regulate dynamically and its technical specifications (shown in Table 1) are sufficient; (3) the temperature of billet is relative stability during the whole rolling process, which is the same as radial forging [7, 8], thus the FSR process can form large and long shafts with one-time heating; (4) the capacity of the DRM-80 mill for hot forming process is that the diameter of the billet can reach 80 mm and its length is unlimited in theory.

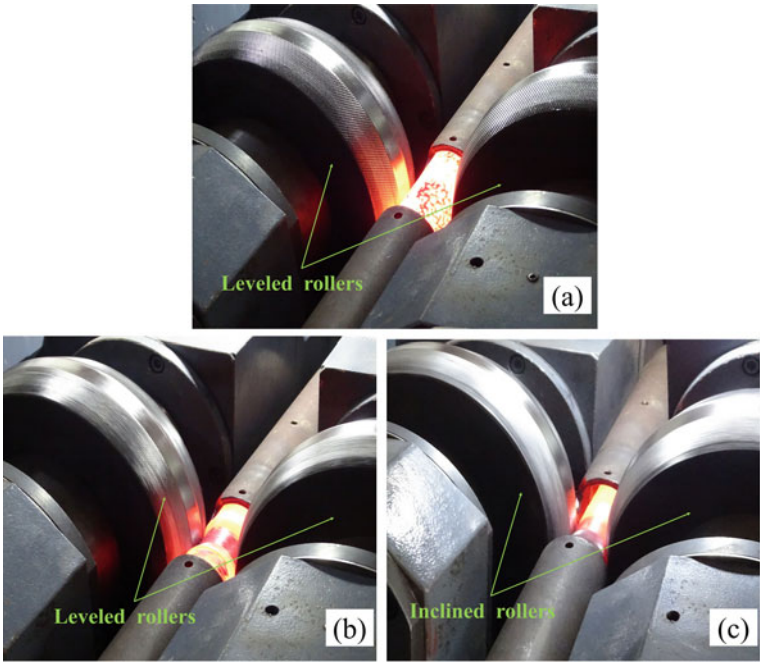


Fig. 6 The laboratory performance of Φ80 mm single-step shaft FSR rolling: **a** beginning; **b** radial rolling; **c** skew rolling. (Color figure online)

5 Results and Discussion

The initial billet is a bar with Ø80 × 390 mm, the diameter of the rolled part is Φ50 mm and the length of the workpiece is 605 mm, which is shown in Fig. 6a, the reduction of this part is up to 60%.

The formed diameter d_1 is measured by the Vernier caliper and the tolerance $\Delta d \approx 1.0$ mm. It turns out that the FSR geometric accuracy is similar to the cross-wedge rolling process (0.8 mm), and better than radial forging process (1.2 mm) [17].

There are forming defects as shown in Fig. 6b, the knurl pockmarks are remained on the step-surface because the rollers were knurled by hatching knurling on the tapered forming zone surface (Fig. 4). In addition, the shallow helical grooves, which are formed by the stage of skew rolling, are obviously presented on the bar surfaces. The helical grooves are the common characteristics of skew rolling and cross-wedge rolling process [18, 19], for which is mainly that the width of the rollers' sizing zone is too short or the chamfering angle between the forming and sizing zone of the rollers is unreasonable, thus the further research is necessary.

The transverse and longitudinal sections of the shaft are observed in Fig. 7c, d. The rolled part are free from any internal defects such as central cracks which frequently occur in skew rolling processes because the stress distribution of FSR is

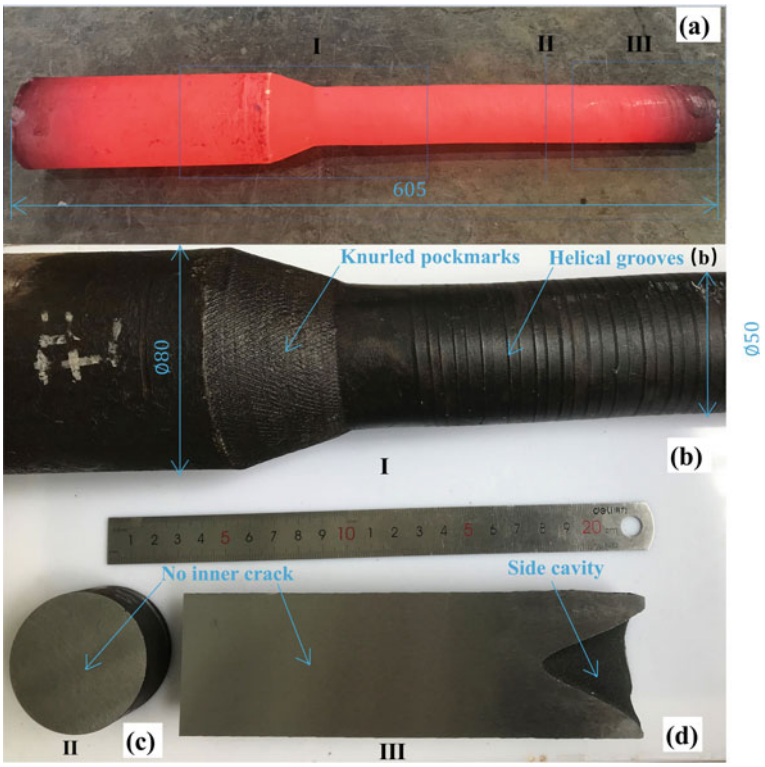


Fig. 7 The manufactured Ø80 mm single-step shaft. (Color figure online)

two orientations tension and one orientation compression [20–22]. Therefore, the relationship between internal defect and inner stress state will be researched in the study of the future.

Another observed defect is the side cavity which is created on the edge of the product as seen in Fig. 7d, which can be explained by the material flow of the outer sphere is rapider than the internal. The side cavity defect leads to the material wastes but does not affect the quality of products.

In conclusion, through hot FSR rolling experiments performed by the DRM-80 mill, it can be proved that both the process and mill are reliable. Although the FSR product has some defects such as knurled pockmarks, helical grooves, and side cavity, the internal metal is free of central cracks. All these observed defects are typical limitations in cross-wedge rolling process [2, 9, 18], which can be removed in later precision machining, so these defects do not affect the quality of produced shaft in any way.

6 Conclusion

- A novel method for forming near-net-shaped shafts, flexible skew rolling process (FSR), has been proposed and verified through a Φ80 mm billet physical experiment. The FSR process is divided into four process stages: radial rolling, rollers inclining, skew rolling and rollers leveling. By coupling the uniform-roller's motions (N_0, V_0, W_0), it can flexible produce elongated-shafts with various sizes.
- A laboratory flexible skew rolling mill (DRM-80) has been invented and constructed to carry out the FSR experiment. The overall dimensions of this mill is 1.8 m × 1.7 m × 1.6 m, the total power is 70 kW, and the maximum diameter of rollers is Φ350 mm, but the maximum billet diameter can up to Φ80 mm. It is worth noting that this type of mill may have a promising potential in industrial application for its convenient installation and adjustment, the frame with high strength, compact structure, and precision rolling by servo control.
- A single-step shaft (length 605 mm, minimum diameter Φ50 mm) was formed and analyzed, the value of diameter tolerance of the shaft is 1.0 mm. Although some forming defects are existed, such as knurled pockmarks, helical grooves, and side cavity, the rolled part is free from internal cracks. The forming defects can be removed by later machining.

Acknowledgments This work was supported by the National Key R&D Program of China (grant number 2018YFB1307900). This work was also supported by the Beijing Laboratory of Modern Transportation Metal Materials and Processing Technology and the Beijing Key Laboratory of Metal Forming Lightweight.

References

1. Zhenghuan HU, Wang B, Zheng Z (2018) Research and industrialization of near-net rolling technology used in shaft parts. Front Mech Eng 13(1):17–24
2. Pater Z (2014) Cross wedge rolling. In: Button ST (ed) Comprehensive materials processing, vol 3. Elsevier Ltd., pp 211–279
3. Zhenghuan HU, Yang C, Baoyu W (2012) Development of part rolling technology in China. J Mech Eng 48(18):7–12
4. Choi SK, Chun MS, Tyne CJV et al (2006) Optimization of open die forging of round shapes using FEM analysis. J Mater Process Technol 172(1):88–95
5. Dyja H, Banaszek G et al (2004) Modelling of shape anvils in free hot forging of long products. J Mater Process Technol 157:131–137
6. Du S, Li Y, Song J (2015) Optimization of forging process parameters and anvil design for railway axle during high-speed forging. In: ASME international mechanical engineering congress & exposition
7. Ghaei A, Movahhedy MR, Taheri AK (2005) Study of the effects of die geometry on deformation in the radial forging process. J Mater Process Technol 170(1–2):156–163
8. Romanenko VP, Stepanov PP, Kriskovich SM (2018) Production of hollow railroad axles by screw piercing and radial forging. Metallurgist 61(9–10):873–877

9. Hu ZH, Zhang KS, Wang BY et al (2004) Technology and simulation of part rolling by cross wedge rolling. Metallurgical Industry Press, Beijing
10. Ji H, Liu J, Xiaobin F et al (2017) Finite element analysis and experiment on multi-wedge cross wedge rolling for asymmetric stepped shaft of C45. J Cent South Univ 04:854–860
11. Ficker T, Hardtmann A (2012) Entwicklung des Axial-Vorschub-Querwalzens an der TU Dresden - ein historischer Überblick von Anfang der 1970-er Jahre bis heute
12. Houska M et al (1999) Experiment and finite-element analysis of axial feed bar rolling (AVQ). In: The 6th international conference on technology of plasticity (ICTP 1999), Nuremberg, pp 1523–1538
13. Xu CG, Liu GH, Ren GS et al (2007) Finite element analysis of axial feed bar rolling. Acta Metall Sin 20(006):463–468
14. Xu CG, Ma CP, Ren GS et al (2004) Thermal coupling finite-element analysis of axial feed bar rolling. J Plast Eng 11(6):80–83
15. Pater Z, Tomczak J, Lis K et al (2020) Forming of rail car axles in a CNC skew rolling mill. Arch Civ Mech Eng 20(3)
16. Hu ZH (2014) Technology of part rolling by skew rolling process. Chemical Industrial Press
17. Li CM, Su XD, Hu ZH (2006) Status and research of axle forming methods for railway shafts. Metall Equip 000(006):5–8
18. Pater Z, Tomczak J, Bulzak T (2020) Problems of forming stepped axles and shafts in a 3-roller skew rolling mill. J Mater Res Technol 9(5):10434–10446
19. Shen J, Wang B, Zhou J et al (2020) Investigation on the inner hole spiral-groove of cross wedge rolling of hollow shafts with mandrel. Int J Adv Manuf Technol 110(5–8)
20. Zhou X, Shao Z et al (2019) A study on central crack formation in cross wedge rolling. J Mater Process Technol 279:
21. Pater Z, Tomczak J, Bulzak T et al (2019) Assessment of ductile fracture criteria with respect to their application in the modeling of cross wedge rolling. J Mater Process Technol 278:
22. Yang C, Dong H, Ku Z (2018) Micro-mechanism of central damage formation during cross wedge rolling. J Mater Process Technol 252:322

A Computational Study on the Producible Rolling Thickness in Ultra-Thin Strip Rolling



Xiao Liu, Chao Yu, and Hong Xiao

Abstract The cold rolling process of a thin strip is difficult to continue when the strip has been thinned to a certain thickness. The Stone formula is the most common approach for predicting this limit, but it was found that the results obtained from this formula are rather inaccurate when applied in experiments or the production of ultra-thin strip rolling. In this paper, a theoretical computational model of producible rolling thickness for an ultra-thin strip based on the Fleck theory was established and the single-pass reduction can be obtained in accordance with the given unit width rolling force, the technical parameters of the rolling mill, the yield strength of the material, and the initial thickness of the strip. The relationship between single-pass reduction and the ratio of the initial thickness of the strip to the theoretical limiting producible thickness under the condition of the maximum allowable rolling force of the rolling mill was discussed. This study provides theoretical guidance for practical production by defining the product specification ranges and rolling regulations for existing rolling mills and determining the roller diameters and force and energy parameters for the design of rolling mills.

Keywords Ultra-thin strip rolling · Producible rolling thickness · Stone formula

1 Introduction

Products with thickness ranging from 0.02 to 0.10 mm are generally called ultra-thin strips, whereas products with a thickness below 0.02 mm are called super-thin strips [1]. The thickness is considered ultra-thin when it approaches the Stone minimum thickness at which point the cold rolling process is difficult to continue. Ultra-thin strips not only provide an important basis for the development of advanced science and technology but are also an embodiment of microforming and micromanufacturing capabilities.

X. Liu · C. Yu · H. Xiao (✉)
National Engineering Research Center for Equipment and Technology of Cold Strip Rolling, Yanshan University, Qinhuangdao 066004, Hebei, China
e-mail: xhh@ysu.edu.cn

© The Minerals, Metals & Materials Society 2021

G. Daehn et al. (eds.), *Forming the Future*, The Minerals, Metals & Materials Series,
https://doi.org/10.1007/978-3-030-75381-8_209

Many researchers have conducted extensive and profound studies using theoretical analysis, finite element simulations, and experimental exploration. Stone [2, 3] treated the profile of the contact deformation zone an arc with increased radius in the studies of the calculation of the average unit pressure for cold strip rolling and this approach considers that the ratio of roller diameter to strip thickness is very large and that the rolling pressure is massive during the cold rolling process. Fleck et al. [4, 5] emphasized that the contact profile of the contact deformation zone of an ultra-thin strip is noncircular, that is, a neutral zone with no obvious reduction in the strip thickness is present, and accurately calculated the contact profile shape and the corresponding contact pressure distribution based on Hertz contact theory. Sutcliffe and Rayner [6] and Ren et al. [7] proved that a neutral zone is present in the contact deformation zone of ultra-thin strip rolling, in agreement with Fleck theory. Limiting producible rolling thickness is a classical problem in the theory of thin strip rolling. When a strip is thinned to a certain thickness in the cold rolling process of a thin strip, the cold rolling process will be difficult to continue. For a given rolling pressure, a small thickness of the strip corresponds to small single-pass reductions, thus requiring high rolling pressure. A minimum thickness referred to as the limiting producible thickness, below which plastic deformation does not occur, exists even if the rolling force and the number of rolling passes are increased. The work of Stone is the most representative among studies on limiting producible thickness. Stone solved the contact profile length of the deformation zone by using the Hitchcock equation and deduced the limiting producible thickness formula by the critical condition of the tangency of two curves. Ford and Alexander [8] considered the elastic recovery of the strip on the basis of Stone theory. Currently, in actual production, the selection of the roller diameter or the determination of product specifications for the existing rolling mills is generally based on the Stone theory formula for the limiting producible thickness. However, when the strip thickness was much smaller than the limiting producible thickness calculated by the Stone formula, a nearly 10% reduction was still obtained by Pawelski and Kading [9] in rolling experiments of deoxidation aluminum. A strip thickness that is smaller than the limiting producible thickness calculated by the Stone formula was achieved in practical production in a thin strip tandem cold rolling mill owned by Baosteel(China). The derivation of the limiting producible thickness by Stone and its improvement by Ford and Alexander was based on the assumption that the work roll remains circular after the contact flattening deformation. Xiao et al. [10] deduced a new formula for the conditional limiting producible thickness considering the restriction of the rolling force and a new formula for the theoretical limiting producible thickness without considering the rolling force restrictions by the rolling pressure distribution in the inlet plastic zone and neutral zone. For the formula of the theoretical limiting producible thickness, tens or even hundreds of roll passes are needed to reach this value, and the single-pass reduction is infinitesimal. In actual production, rolling indefinitely to reach a certain thickness is impossible because of the limitation of productivity. Determine the maximum single-pass reduction for a given foil thickness and technical parameters of the rolling mill, i.e., the limiting producible thickness considers a feasible

rolling force of the rolling mill, which is more practical. The production efficiency is a practical criterion.

In this study, a theoretical calculation model for the producible rolling thickness of ultra-thin strips was established based on Fleck theory. Under the given technical parameters of the rolling mill and the initial thickness of the rolling piece, the single-pass reduction can be calculated in accordance with the given unit width rolling force. The relationship between single-pass reduction and the ratio of the initial thickness of the strips to the theoretical limiting producible thickness under the maximum allowable rolling force of the rolling mill was discussed.

2 Theory of the Producible Rolling Thickness

2.1 Theoretical Model

When the thickness of ultra-thin strips is between the Stone minimum thickness and the theoretical limiting producible thickness, a certain amount of plastic deformation per pass can still be achieved even though a neutral zone is present. Under these conditions, the contact deformation zone was analyzed, and a theoretical description for the contact deformation zone given by Fleck in ultra-thin strip rolling was used, as shown in Fig. 1. The deformation zone is divided into the inlet elastic zone A, the inlet plastic zone B, the neutral zone C, the outlet plastic zone D, and the outlet elastic zone E. Plastic deformation of the metal mainly occurs at the plastic zones B and D, which are separated by the neutral zone C where no significant plastic reduction or slip exists between roll and strip and the roll surfaces are pressed into two horizontal planes by contact elasticity.

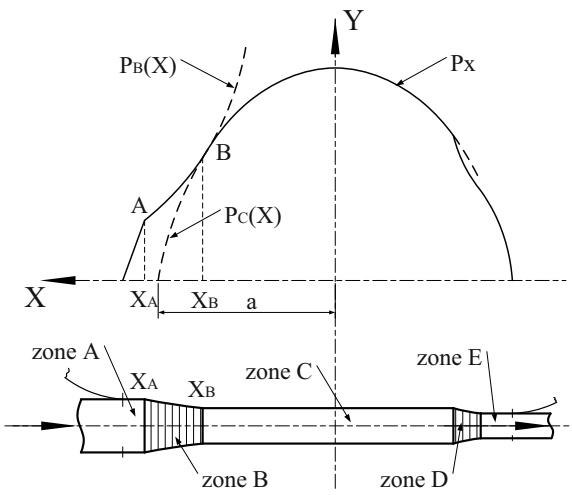


Fig. 1 A schematic of the Fleck model

The centerline of rolls is taken as the Y-axis and the reverse rolling direction as the X-axis. The contact pressure can be expressed by the Tresca plastic yield criterion in the inlet plastic zone [10] as follows:

$$p_B(x) = (1.15\sigma_S - \sigma_T)exp[\frac{2\mu}{h_0}(X_A - x)] \tag{1}$$

where X_A is the initial coordinate of the plastic deformation zone of the strip, σ_S is the yield strength of the strip, σ_T is the mean tensile stress, μ is the Coulomb friction coefficient at the entrance of the contact deformation zone, and h_0 is the initial thickness of the strip.

In the neutral zone C, Hertz theory shows that the contact pressure is a semielliptical distribution given by

$$p_C(x) = p_0[1 - (\frac{x}{a})^2]^{1/2} \tag{2}$$

where p_0 is the maximum unit contact pressure and $2a$ is the length of equivalent contact arc that is expressed as follows:

$$a = \frac{8(1 - \upsilon^2)}{\pi E} R\overline{p} \tag{3}$$

where $\overline{p}$ is the average unit pressure, E and υ are the elastic modulus and the Poisson ratio of the work roll, respectively.

The contact pressure per unit width p_w, a can be expressed as

$$a = \left[\frac{2(1 - \upsilon^2)}{\pi E} Dp_w\right]^{1/2} = \left(\frac{1}{4} C D p_w\right)^{1/2} \tag{4}$$

where $C = \frac{8(1-\upsilon^2)}{\pi E}$ and D is the roller diameter.

The semielliptical distribution is simplified to a parabolic distribution in accordance with Wrinkler elastic theory [11] to obtain the pressure at any point in the flattening zone in a convenient manner. The unit contact pressure observed when the roll surfaces are flattened to become two horizontal planes by the contact elasticity is given by (Figs. 2 and 3)

$$p_C(x) = \frac{3}{CDa}(a^2 - x^2) \tag{5}$$

At the junction ($x = X_B$) of the inlet plastic zone and the neutral zone, $p_B(x)$ and $p_C(x)$ satisfy the condition that the values of the functions and derivatives are equal, as shown in Fig. 4.

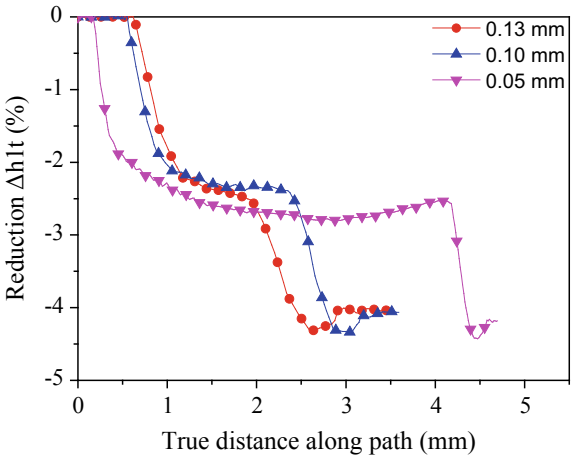


Fig. 2 The contact pressure at 1% reduction. (Color figure online)

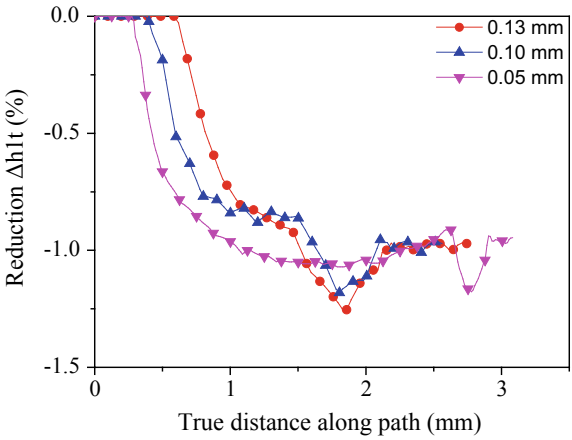


Fig. 3 The roll profile at 1% reduction. (Color figure online)

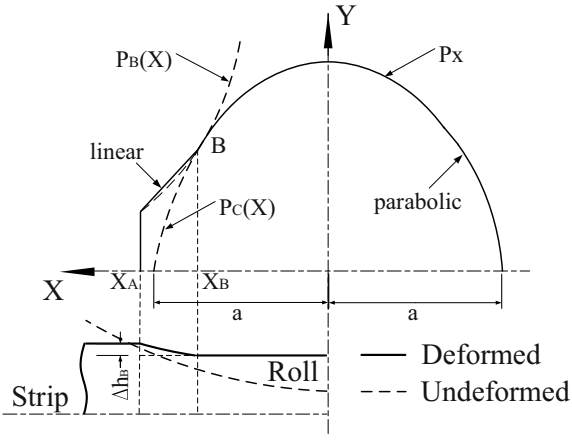


Fig. 4 Deformed and undeformed shapes of the roll under contact pressure

$$p_B(X_B) = p_C(X_B) \tag{6}$$

$$dp_B(X_B)/dx = dp_C(X_B)/dx \tag{7}$$

Equations (1) and (5) are substituted into Eq. (6), and we obtain

$$\frac{3}{CDa}(a^2 - X_B^2) = (1.15\sigma_S - \sigma_T) exp[\frac{2\mu}{h_0}(X_A - X_B)] \tag{8}$$

A derivative of the solution of Eq. (8) is taken, and we obtain

$$-\frac{6}{CDa}X_B = (1.15\sigma_S - \sigma_T)\left(-\frac{2\mu}{h_0}\right) exp[\frac{2\mu}{h_0}(X_A - X_B)] \tag{9}$$

Comparing Eq. (9) with Eq. (8), we can assume that

$$H = (1.15\sigma_S - \sigma_T) exp[\frac{2\mu}{h_0}(X_A - X_B)] \tag{10}$$

and combine Eqs. (8) and (9). Hence, we obtain

$$\begin{cases} \frac{3}{CDa}(a^2 - X_B^2) = H \\ \frac{6}{CDa}X_B = \frac{2\mu}{h_0}H \end{cases} \tag{11}$$

After solving the above equations, we obtain

$$X_B = \frac{CD\mu a}{3h_0}H \tag{12}$$

$$H = \frac{3h_0^2}{2CDa\mu^2}\left(\sqrt{1 + \frac{4a^2\mu^2}{h_0^2}} - 1\right) \tag{13}$$

If the initial thickness h_0 and the contact pressure per unit width p_w are known, then the equivalent contact arc length $2a$ and the value H can be obtained by Eqs. (4) and (13), which can be used to solve $(X_A - X_B)$, i.e., the length of the inlet plastic zone,

$$X_A - X_B = \frac{h_0}{2\mu}\ln\left(\frac{H}{1.15\sigma_S - \sigma_T}\right) \tag{14}$$

with the coordinate values of X_A and X_B.

For ultra-thin strip rolling, the length of the contact deformation zone is much smaller than the roller diameter. The roll is regarded as a semi-infinite body, and the surface displacement of the roll under distributed load can be solved by elastic half-space theory. Figure 4 shows the deformed and undeformed shapes of the roll under contact pressure.

On the basis of the following assumptions,

(1) The distribution of the contact pressure in the inlet elastic zone is neglected, and.
(2) The contact pressure tends to be parabolic except for the inlet plastic zone,

the deformation of the inlet plastic zone can be obtained.

For the distributed load P_x shown in the figure, the normal displacement of any point on the roller surface can be expressed as follows:

$$U_y = -\frac{2\left(1-\upsilon^2\right)}{\pi E}\left[\int_{-a}^{X_a} P_x \ln|\xi - x|dx + \left(\frac{1}{2(1-\upsilon)} - \ln R\right)\int_{-a}^{Xa} P_x dx\right] \tag{15}$$

where R is the roller radius.

P_x is simplified into a linear distribution in the interval $[X_B, X_A]$ and a parabolic distribution in the interval $[-a, X_B]$, and we obtain

$$P_x = \begin{cases} \dfrac{3}{CDa}\left(a^2 - x^2\right), x \in [-a, X_B] \\ P_{X_A} + \dfrac{P_{X_B} - P_{X_A}}{X_A - X_B}(X_A - x), x \in (X_B, X_A] \end{cases} \tag{16}$$

where $P_{X_A} = 1.15\sigma_S - \sigma_T$, $P_{X_B} = \frac{3}{CDa}\left(a^2 - X_B^2\right)$.

Then, the deformation of the inlet plastic zone can be calculated by the following formula:

$$\Delta h_B = 2\left[\frac{(X_A + X_B)(X_A - X_B)}{2R} - \Delta u\right] \tag{17}$$

where Δu is the difference in the normal displacement between points A and B on the roller circumferential surface.

From the Lagrange mean value theorem,

$$\Delta u = \frac{dU_y}{d\xi}(X_A - X_B) \tag{18}$$

and $\xi = \frac{X_A + X_B}{2}$, in other words, the derivative is solved at the midpoint in the interval $[X_B, X_A]$.

When substituting Eq. (16) into Eq. (18) and taking the derivative, we obtain

$$\frac{dU_y}{d\xi}=\frac{2\left(1-\upsilon^2\right)}{\pi E}\left[\int_{-a}^{X_B}\frac{3}{CDa}\left(a^2-x^2\right)\frac{1}{\xi-x}dx+\int_{X_B}^{X_A}\left(P_{X_A}+\frac{P_{X_B}-P_{X_A}}{X_A-X_B}\left(X_A-x\right)\right)\frac{1}{\xi-x}dx\right] \tag{19}$$

Given the similarity in the numerical values of X_A, X_B, and a, the integral of Eq. (19) is solved and simplified as follows:

$$\frac{dU_y}{d\xi}=-\frac{2\left(1-\upsilon^2\right)}{\pi E}\left\{\frac{3}{2CDa}(a+x)^2\Big|_{-a}^{X_B}+\left[-P_{X_A}\ln(\xi-x)+\frac{P_{X_B}-P_{X_A}}{X_A-X_B}x\right]\Big|_{X_B}^{X_A}\right\} \tag{20}$$

After substituting into Eq. (18), we obtain

$$\Delta u=-(X_A-X_B)\left\{\frac{3(X_A+X_B+2a)}{16R}+\frac{2\left(1-\upsilon^2\right)}{\pi E}\left[\frac{3}{CDa}\left(a^2-X_B^2\right)-(1.15\sigma_S-\sigma_T)\right]\right\} \tag{21}$$

The initial form of the formula for the theoretical limiting producible thickness is given by

$$h_{\min}^{X}=\frac{1}{3}CD\mu(1.15\sigma_S-\sigma_T) \tag{22}$$

After substituting Eq. (22) into Eq. (21) and simplifying, we obtain

$$\Delta u=-\left[\frac{3(X_A+X_B+2a)}{16R}+\frac{3(a-X_B)}{4R}-\frac{3h_{\min}^{X}}{8R\mu}\right](X_A-X_B) \tag{23}$$

Equation (23) is substituted into Eq. (17), and we obtain

$$\Delta h_B=\left[\frac{(5X_A+8X_B-9a)}{8R}+\frac{3h_{\min}^{X}}{4R\mu}\right](X_A-X_B) \tag{24}$$

In the contact deformation zone of ultra-thin strip rolling, the plastic deformation occurs mainly in the plastic zone at the entrance and the exit. If no plastic deformation occurs at the entrance, i.e., no plastic deformation occurs under the maximum contact pressure from the entry point to the lowest point of the roll surface, then the same conditions are found in the plastic zone at the exit. Currently, the contact deformation zone includes only the inlet elastic zone, the neutral zone, and the outlet elastic zone within which the upper and lower roller surfaces are pressed into two horizontal planes by contact elasticity. The contact pressure between the roll and the ultra-thin strip and the elastic deformation of the strip are symmetrically distributed on both

sides of the central line of the rolls in accordance with Eq. (5), and the length of the contact profile at the entry side is equal to that at the exit side.

When a minimal plastic deformation occurs at the entrance side of the contact deformation zone, on the basis of Fig. 1, the length of the plastic deformation zone at the entrance is minimal relative to the length of the contact profile at the entrance side. Similarly, the plastic deformation at the exit is minimal relative to the length of the contact contour at the exit side. The length of the contact profile and the plastic deformation at the exit side of the contact deformation zone are smaller than but approximately equal to those at the entrance side. If the exit thickness is approximately equal to the entrance thickness and metalwork hardening is not considered, then the length of the entrance side contact profile is assumed to be approximately equal to that of the exit side. On the basis of Eqs. (1) and (5), the distribution of the contact pressure at the exit side is symmetrical to that at the entrance side, i.e., the length and plastic deformation of the inlet plastic zone are equal to those of the outlet plastic zone. Thus, the total plastic reduction can be calculated as follows:

$$\Delta h{=}2\Delta h_B = \left[\frac{(5X_A + 8X_B - 9a)}{4R} + \frac{3h_{\min}^X}{2R\mu}\right](X_A - X_B) \tag{25}$$

When the thickness of the strip is close to the theoretical limiting producible thickness, the elastic flattening of the roll is considerable, and the length of the neutral zone is large. As a result, the lengths of the plastic zones at the entrance and exit are relatively small. If the unit width contact pressure is assumed to be approximately equal to the unit width rolling force, then the single-pass reduction can be accurately computed by the comprehensive Eqs. (12), (13), (14) and (25) when the technical parameters of rolling mill and unit width rolling force provided by the rolling mill are known.

From Eqs. (3) and (4), we obtain

$$a = CR\overline{p},\ p_w = CD\overline{p}^2 \tag{26}$$

where $C = \frac{8(1-\upsilon^2)}{\pi E}$, if $p_r = C\overline{p}$, $\sigma_r = C\sigma_e$, $h_r = h_0/h_{\min}^X$, where $\sigma_e = 1.15\sigma_S - \sigma_p$,

Equation (13) can be rewritten as

$$H = \frac{h_r^2\sigma_r\sigma_e}{3p_r}\left(\sqrt{1 + \left(\frac{3p_r}{h_r\sigma_r}\right)^2} - 1\right) \tag{27}$$

Equations (12) and (14) are rewriting, and we obtain

$$X_B = \frac{h_0}{2\mu}\left(\sqrt{1 + \left(\frac{3p_r}{h_r\sigma_r}\right)^2} - 1\right) \tag{28}$$

$$X_A - X_B = \frac{h_0}{2\mu} \ln \left[\frac{h_r^2 \sigma_r}{3p_r} \left(\sqrt{1 + \left(\frac{3p_r}{h_r \sigma_r} \right)^2} - 1 \right) \right] \tag{29}$$

After substituting Eqs. (22), (28), and (29) into Eq. (25) and simplifying, we obtain

$$\frac{\Delta h}{h_0} = \frac{1}{24\mu} \left\{ 5h_r \sigma_r \ln \left[\frac{h_r^2 \sigma_r}{3p_r} \left(\sqrt{1 + \left(\frac{3p_r}{h_r \sigma_r} \right)^2} - 1 \right) \right] + 13h_r \sigma_r \left(\sqrt{1 + \left(\frac{3p_r}{h_r \sigma_r} \right)^2} - 1 \right) - 27p_r + 12\sigma_r \right\} \ln \left[\frac{h_r^2 \sigma_r}{3p_r} \left(\sqrt{1 + \left(\frac{3p_r}{h_r \sigma_r} \right)^2} - 1 \right) \right] \tag{30}$$

Steel rolls and oil lubrication are commonly used in cold strip rolling, and the numerical fluctuations of elastic modulus, Poisson's ratio, and friction coefficient are negligible. Thus, these parameters can be treated as constants. Without considering work hardening, a single-pass reduction is essentially a function of the average unit pressure, the equivalent yield strength, and the ratio of the initial thickness to the theoretical limiting producible thickness of the strip obtained from Eq. (30) that can be expressed by

$$\Delta h / h_0 = f(p_r, \sigma_r, h_r) = f\left(C\overline{p}, C\sigma_e, h_0 / h_{\min}^X\right) \tag{31}$$

2.2 The Producible Rolling Thickness

In fact, the unit width rolling force provided by the rolling mill is not infinite in ultra-thin strip rolling. Ensuring that the rolls can operate normally and that no surface peeling or fatigue damage will occur is necessary [12]. From Fig. 1, the distribution of the contact pressure within the contact deformation zone is semielliptical as shown by Eq. (2). The failure strength of rolls is given by

$$p_0 = \frac{4\overline{p}}{\pi} = \frac{4}{\pi} \sqrt{\frac{p_w}{CD}} \leq [\sigma_H] \tag{32}$$

where $[\sigma_H]$ is the allowable contact stress of the roll.

Equation (32) is simplified to present the restrictive conditions for $\overline{p}$ and p_w, and we obtain

$$\overline{p} \leq \frac{\pi [\sigma_H]}{4}, \quad p_w \leq \frac{CD\pi^2 [\sigma_H]^2}{16} \tag{33}$$

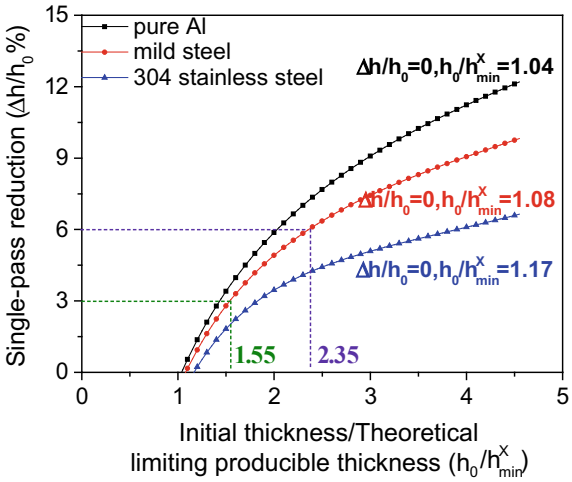


Fig. 5 The relationship between single-pass reduction and the ratio of the initial thickness of the strip to the theoretical limiting producible thickness. (Color figure online)

The surface hardness of steel rolls is higher after quenching. Hence, the allowable contact stress of the roll is 2400 MPa, i.e., the maximum allowable unit width rolling force of the mill corresponds to the average unit pressure value. Given the calculation parameters for steel rolls of elastic modulus of 216 GPa, roller diameter of 210 mm, friction coefficient of 0.1, and mean tension stress of 0. Equation (30) is used to compute the single-pass reductions of three types of different ultra-thin strips, namely, pure Al, mild steel, and 304 stainless steel, which have yield strengths of 180, 350, and 650 MPa, respectively.

The Stone minimum thickness is given by

$$h_{\min}^{S} = 3.58\frac{D\mu(1.15\sigma_S - \sigma_T)}{E} \tag{34}$$

Figure 5 demonstrates the relationship between the single-pass reduction and the ratio of the initial thickness of the strip to the theoretical limiting producible thickness in the rolling process of three different materials under the maximum allowable average unit pressure, and the initial thickness of the strip ranges from the Stone minimum thickness to the theoretical limiting producible thickness. As can be seen from Fig. 5, for a certain strip yield strength, the single-pass reduction increases with the increase in the ratio of the initial thickness to the theoretical limiting producible thickness, but the growth rate decreases. When the ratio of the initial thickness to the theoretical limiting producible thickness is the same, a smaller single-pass reduction is obtained if the yield strength of the strip is larger. The note of the curve such as $\Delta h/h_0 = 0, h_0/h_{\min}^{X} = 1.04$ means that when there is no plastic deformation, the initial thickness of the strip is equal to the conditional limiting producible thickness and it is 1.04 times the theoretical limiting producible thickness. For a given unit width rolling force provided by the rolling mill, the relationship between the single-pass reduction and the ratio of the initial thickness of strip to the theoretical

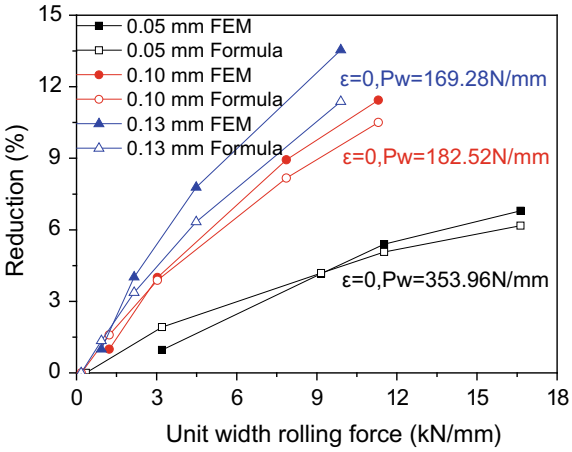


Fig. 6 Comparison between analytical and simulation results for different thickness specifications. (Color figure online)

limiting producible thickness can be obtained by the theoretical calculation model. Furthermore, the relationship can be used to measure the rolling difficulty for the producible rolling thickness.

Actual production gives rise to high productivity requirements, i.e., to ensure a certain single-pass reduction. The red curve of Mild steel with a yield strength of 350 MPa in Fig. 5 is taken as an example. When $h_0/h^X_{\min} \geq 2.35$, i.e., $h_0/h^S_{\min} \geq 0.51$, the rolling process is difficult to some extent, and a certain proportion of the neutral zone exists in the contact deformation zone at this time. However, a significant single-pass reduction can be obtained, and this steel can still be produced in the necessary amounts. When $1.55 < h_0/h^X_{\min} \leq 2.35$, i.e., $0.34 < h_0/h^S_{\min} \leq 0.51$, the obtained single-pass reduction ranges from 3 to 6%, and the length of the neutral zone in the contact deformation zone is larger than that of the plastic zone. In case of a special need, a small amount of the product can be produced, but the process is difficult. For $h_0/h^X_{\min} \leq 1.55$, i.e., $h_0/h^S_{\min} \leq 0.34$, the maximum single-pass reduction is only 3%, and the length of the neutral zone is much higher than the length of the plastic zone. This material is difficult to roll, and the number of rolling passes must be increased to obtain qualified products. If the yield strength of the rolled piece is high and single-pass reduction is small, then the rolling difficulty will increase but can be improved by annealing the strip to reduce the yield strength.

3 Results and Discussion

To validate the theoretical model, the finite element model was used to calculate the contact pressure per unit width corresponding to four different single-pass reductions for ultra-thin strips with a yield strength of 339.4 MPa and thicknesses of 0.13, 0.10, and 0.05 mm. A half rolling model of thin strips was established in commercial software ABAQUS based on rolling symmetry and the assumption of plane strain. The roll and strip were set as elastic and elastic–plastic, respectively. The contact between the roll and strip obeyed the Coulomb friction model, for which the friction coefficient was 0.1. The CPE4R (four nodes) bilinear plane strain reduction integral elements were adopted. The roll mesh was refined at the contact zone between roll and strip to balance the requirements of low calculation time and high accuracy.

There is good agreement between the contact pressure and the strip profiles obtained from the FEM model and those given by Fleck. This approach substituted the material parameters into the theoretical model to solve for the single-pass reduction and compare with the results of the finite element simulations. The minimum values of the maximum allowable rolling force required for the rolling ultra-thin strips with different thicknesses are shown in Fig. 6 where ε means the reduction of the strip. As the initial thickness approaches the theoretical limiting producible thickness, the results of the theoretical computation become closer to the results of the finite element simulations.

The rolling force is obtained from the contact pressure expressed by Eq. (5) on the basis of the assumption of parabolic distribution. The length of the neutral zone in the contact deformation zone accounts for a large proportion of the 0.05-mm-thick strip near the theoretical limiting producible thickness, whereas the length of the plastic deformation zone is small. Here, the rolling force follows the parabolic distribution approximately. Thus, the accuracy of the solution is high. For the 0.13-mm-thick strip, i.e., close to the Stone minimum thickness, a certain length of the plastic zone is still observed in the contact deformation zone and the contact pressure distribution has an obvious peak value. The actual distribution of the contact pressure is different from the parabolic distribution. Consequently, the error is relatively large.

The deformation of the exit plastic zone was assumed to be equal to that of the entrance plastic zone to compute the total deformation. When the thickness and the reduction are small, the plastic deformation of the exit is smaller than that of the entrance and the total deformation is smaller at this time. The error is within the allowable range.

As the thickness of the ultra-thin strip decreases from the Stone minimum thickness to the theoretical limiting producible thickness, the proportion of the length of the neutral zone in the contact deformation zone increases continuously, and the rolling force tends to assume a parabolic distribution. Although the maximum single-pass reduction that can be achieved is small, it can still be reduced, bringing the sample within the range of producible rolling thickness. The closer the thickness of the ultra-thin strip is to the theoretical minimum rolling thickness, the higher the computation accuracy of the theoretical model is. Generally, when the unit width

rolling force is given, the theoretical computation value is smaller than the simulation value, showing that the theoretical model is more conservative and that a large single-pass plastic reduction can be obtained in actual production.

4 Conclusions

(1) Under the condition of the maximum allowable rolling force of rolling mill, single-pass reduction is a function of the equivalent yield strength of strip, and the ratio of the initial thickness to the theoretical limiting producible thickness. For given technical parameters of a rolling mill, a high ratio corresponds to a high single-pass reduction that can be obtained. Under the same ratio, great yield strength leads to a small single-pass reduction rate, and the corresponding conditional limiting producible thickness increases.

(2) A mild steel with a yield strength of 350 MPa is taken as an example, first, for $h_0/h^X_{\min} \geq 2.35$, i.e., $h_0/h^S_{\min} \geq 0.51$, the rolling process is somewhat difficult, but the desired thickness can be produced in the necessary amount. For $1.55 < h_0/h^X_{\min} \leq 2.35$, i.e., $0.34 < h_0/h^S_{\min} \leq 0.51$, the rolling process is more difficult, but if special needs arise, then the desired thickness can be produced in a small amount. For $h_0/h^X_{\min} \leq 1.55$, i.e., $h_0/h^S_{\min} \leq 0.34$, the rolling process is difficult and uneconomical, thus requiring that the number of rolling passes is increased to obtain qualified products.

References

1. Liu X, Song M, Sun XK (2016) Advances in research and application of foil rolling. J Mech Eng 52(18):89–97
2. Stone M (1953) Rolling of thin strip part I. Iron Steel Eng 30(2):61–74
3. Stone M (1956) Rolling of thin strip part II. Iron Steel Eng 33(12):55–76
4. Fleck N, Johnson K (1987) Towards a new theory of cold rolling thin foil. Int J Mech Sci 29(7):507–524
5. Fleck N, Johnson K, Mear M (1992) Cold rolling of foil. J Eng Manuf 206(2):119–131
6. Sutcliffe M, Rayner P (1998) Experimental measurements of load and strip profile in thin strip rolling. Int J Mech Sci 40(9):887–899
7. Ren Z, Xiao H, Liu X, Wang G (2018) Experimental and theoretical analysis of roll flattening in the deformation zone for ultra-thin strip rolling. Ironmak Steelmak 45(9):805–812
8. Ford H, Alexander J (1960) Rolling hard materials in thin gauges basic consideration. J Ins Metal 88(5):193–199
9. Pawelski O, Kading G (1970) Causes of the limiting degree of deformations in the cold rolling of thin strip. Steel Res 41(3):249–254
10. Xiao H, Ren Z, Liu X (2017) New mechanism describing the limiting producible thickness in ultra-thin strip rolling. Int J Mech Sci 133(11):788–793
11. Zhu Q, Yu J, Qi K (1988) Problem of reducibility in sheet cold-rolling and gauge suitable to roll. J Northeast Univ Technol 57(4):420–426
12. Jiang Y, Sehitoglu H (1999) A model for rolling contact failure. Wear 224(1):38–49

Forming Surface Texture on Copper Sheets by Electrically Assisted Micro-Rolling



Zhenhai Xu, Shaoxi Xue, Chunju Wang, Rui Xi, Debin Shan, Guo Bin, and Baosheng Liu

Abstract Electrically assisted (EA) forming is a promising process due to its advantages, such as reducing forming load, increasing formability, and decreasing springback. In order to reduce material waste and environmental pollution in the manufacturing process of surface texture, the EA micro-rolling process was used to form surface texture on T2 copper sheets. The EA micro-rolling system consisted of a micro-rolling device and a power supply. Effects of the voltage, frequency, and pulse duration on feature height were investigated. Compared with conventional micro-rolling, the EA micro-rolling process increased the feature height significantly, improved the flatness of the sheet with surface texture, and decreased the surface roughness remarkably. The influences of electric current for different grain sizes were not identical. The rise of feature height was more significant for rolled sheets than that for annealed sheets. Moreover, the feature height has little variations under voltage magnitude of this study when the grain size was greater. This study proves that forming quality of surface textured sheets can be improved under appropriate electric parameters and the EA micro-rolling process would be a promising surface texturing method.

Keywords Electrically assisted · Rolling · Surface texture · Forming quality

Z. Xu (✉) · S. Xue · R. Xi · D. Shan · G. Bin
National Key Laboratory for Precision Hot Processing of Metals, Harbin Institute of Technology, Harbin 150001, P.R. China
e-mail: xzhenhai@163.com

C. Wang
Robotics and Microsystems Center, Soochow University, Suzhou 215131, P.R. China

B. Liu
AVIC Manufacturing Technology Institute, Beijing 100024, P.R. China

© The Minerals, Metals & Materials Society 2021

G. Daehn et al. (eds.), *Forming the Future*, The Minerals, Metals & Materials Series,
https://doi.org/10.1007/978-3-030-75381-8_210

1 Introduction

Recently, surface texturing has been attracting increasing attention from researchers due to its special functions in hydrophobicity, biocompatibility, tribology, and drag reduction [1]. Various types of texture produce different functions. Two levels of surface roughness such as micro- and nanostructures are a necessity to produce surfaces with a super-hydrophobic property, for example, the surface of lotus leaf is composed of the micro-pillars of 5–10 μm and nano hairs. In Cassie state, nano hairs can produce liquid–air interface to enhance the contact angle, which produces the super-hydrophobic property, but not in Wenzel state [1, 2]. The special types of grooves in aircrafts and vehicles can limit the generation of turbulent flow and related Reynolds stress, which reduce the skin friction. It is reported that compared with semicircular, trapezoid, and blade with an aspect ratio of 0.5, surfaces with equilateral triangle have the best drag reduction effect, and the optimum nondimensional riblet width $s^+ = \frac{s\sqrt{\tau_{0/\rho}}}{v}$ (s is the width of the riblet grooves, τ_0 is the wall shear stress at a smooth surface, ρ is the density, and v is the dynamic viscosity) is between 15 and 20 when the drag reduction achieves maximal [3, 4]. Yang et al. [5] calculated the width $s \leq 0.047$ mm and height $h \leq 0.039$ mm of the V-type groove on the surface of the underwater vehicle, and found that the drag reduction effect can reach 1.77%.

The surface texture is mainly fabricated by electrochemical micromachining, chemical texturing, and micromachining. These manufacturing methods allow for fine shape precision, but pose material waste and environmental concerns. The rolling process as one of many micro-forming methods has the advantages of high efficiency, low cost, and low forming load [6]. Romans and Hirt [7] proposed the riblet rolling process, and the roll was wound with a small high-strength steel wire. They found that the riblet height and rolling force were affected by thickness reduction. Zhou et al. [8] developed a desktop surface texturing rolling system. The flatness of the textured sheet was improved and the channel depth became uniform by asymmetric rolling speed. Gao et al. [9] developed the roll-to-plate (R2P) imprinting process. They studied the effects of grain and geometry size on rolling load and feature height by experiments and numerical simulations.

To further improve the forming quality of surface texture and weaken the size effect, an electric current was introduced into the forming process. Ross et al. [10] found the forming force was significantly decreased and the formability was enhanced by the EA compression test. Perkins et al. [11] carried out a series of EA compression tests of different metals. The threshold current density was identified, beyond which the effect of the electricity on the forming was obvious. Siopis et al. [12] found that if the samples underwent pre-plastic deformation, the flow stress drop was more significant. The electric current could decrease the residual stress in the EA embossing process [13]. Based on the promising advantage of EA forming, the EA rolling processes were also investigated. Compared with conventional micro-rolling, channel depth of the surface texturing on AA3003-H14 and Ti-6Al-4V were improved by the EA micro-rolling [14].

Although it has been indicated that EA micro-rolling is a promising method for surface texturing, the effect of electricity on the forming quality of surface texturing has not been made clear. Therefore, EA micro-rolling was performed on copper sheets to study the effect of electric parameters on feature height, flatness of sheets, and surface roughness of surface texture.

2 Experimental

A commercial T2 copper sheet with a thickness of 1 mm in the rolled state was chosen as the experimental material. To investigate the grain size effect, the rolled T2 copper sheets were annealed at 350 °C and 850 °C for 1 h, respectively. The samples were ground, polished, etched, and examined using an optical microscope (OM). The microstructures and grain size d are shown in Fig. 1 and Table 1, respectively. The sheet was sheared into slices with a size of 10 mm in length and 5 mm in width for rolling.

The EA micro-rolling system consisted of a micro-rolling device and the power supply, as shown in Fig. 2. The parameters of the power supply were shown in Table 2. The micro-rolling device and power supply were connected by a brush. The insulation blocks were inserted between the micro-rolling system and the two rolls. The geometry of surface texturing on the upper roll is shown in Fig. 2a and the surface of the lower roll had no texture.

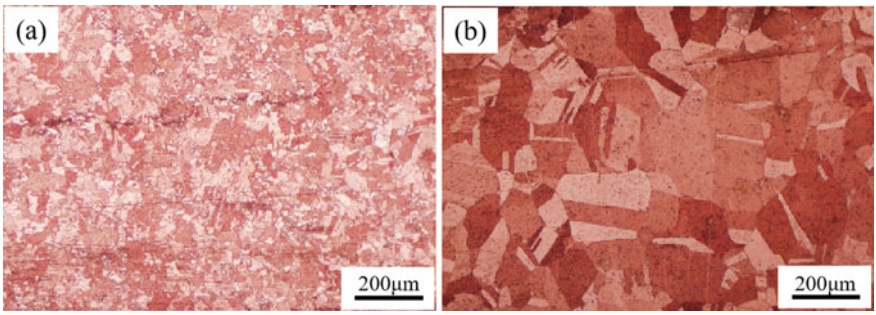


Fig. 1 Microstructure of T2 copper sheet along the thickness direction after annealing treatment at **a** 350 °C and **b** 850 °C. (Color figure online)

Table 1 Grain sizes under different temperatures

Temperature (°C)	Grain size d (μm)
350	30.24
850	194.98

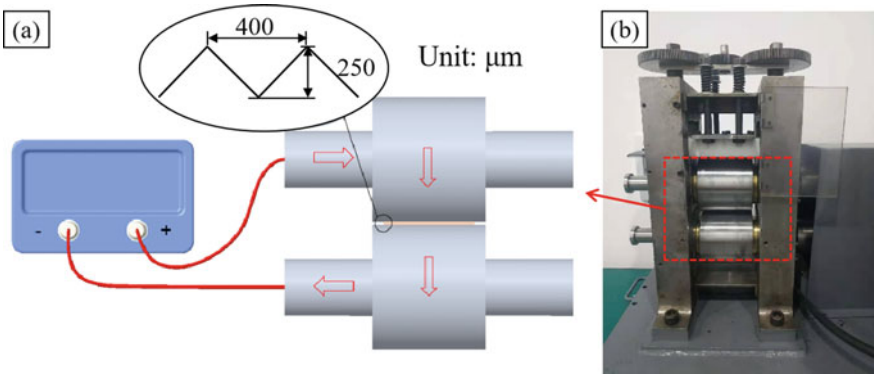


Fig. 2 EA micro-rolling system: **a** schematic of EA micro-rolling **b** micro-rolling device. (Color figure online)

Table 2 DC power parameters

Voltage (V)	Frequency (Hz)	Pulse duration (μs)
0 –30	10–1000	3–500

3 Results and Discussion

3.1 Feature Height

The EA micro-rolling tests were carried out at a clearance of 0.2 mm and a roll speed of 0.76 r/min at room temperature. The feature heights of surface texture at different voltages, frequencies, and pulse durations by the EA micro-rolling test are shown in Fig. 3. The black line in Fig. 3a shows that feature height has a significant improvement at 10 V. Compared with the result at 0 V, the feature heights arise by 5.84% at 5 V and 24.32% at 10 V, respectively. However, there is little variation in the feature height when the voltage is changed from 10 to 30 V. It has been proved by Cao et al. [10] that joule heating plays the main role in increasing the feature height. Due to rapid roll speed and deformation process, the effect of different temperatures is weak on the feature height when voltage increases from 10 to 30 V. The cross sections of surface texture at 0 and 30 V for rolled samples are shown in Fig. 4. The grains in the grooves are obviously elongated and fibered at each voltage level, while other grains have little deformation. The microstructures show little difference at the different voltage levels. However, the feature height at 30 V is significantly greater than that at 0 V, and the symmetry of the texture is greater at 30 V. It is also found from Table 3 that as the thickness of the sheet decreases, the spread slightly increases and the length increases when the electric current is present, however, the variation is little with the increase in voltage.

The feature height increases with the frequency increase. Variable frequencies significantly affect the feature height. With an increase in pulse duration, the feature

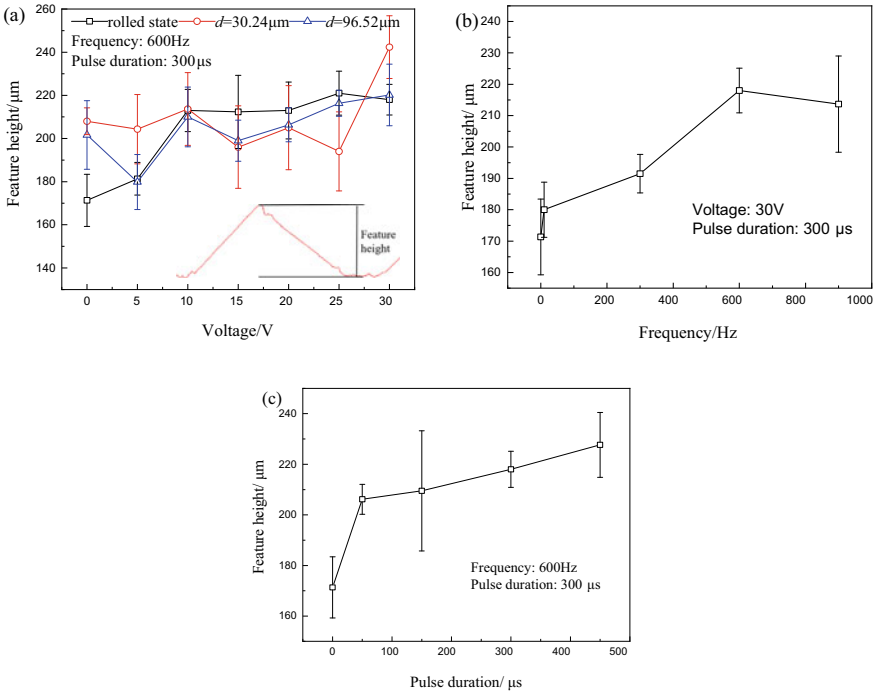


Fig. 3 Feature height under different electrical parameters: **a** voltage, **b** frequency, **c** pulse duration. (Color figure online)

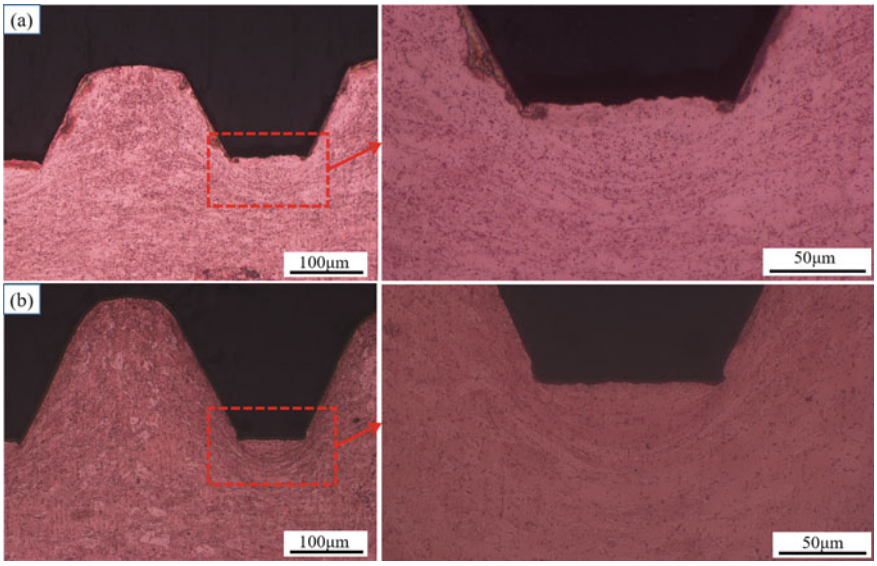


Fig. 4 Cross section of surface texture at different voltages **a** 0 V, **b** 30 V. (Color figure online)

Table 3 Variation of the shape of rolled sheets

Voltage (V)	Thickness (mm)	Spread (mm)	Length (mm)
Initial	1	10	50
0	0.837	10.133	66
10	0.877	10.15	63.4
20	0.847	10.19	65.6
30	0.85	10.13	66

height becomes larger. The feature height increases by 20.26% at 50 μs and 32.92% at 450 μs compared with that at 0 μs. Frequency and pulse duration are also related to the increase in joule heating.

The experimental results of different grain sizes treated by the EA micro-rolling process are shown in Fig. 3a. Compared with the rolled state, feature height has a significant increase in the annealed state, however, feature height is greater for $d = 30.24$ μm than that for $d = 96.52$ μm. The reason is that the feature size restricts the deformation, meanwhile, the number of the grains participating in the plastic deformation reduces due to the big grain size, resulting in the greater deformation resistance. When the electric current is present, the feature height for $d = 30.24$ μm has little variation below 25 V. However, height increases by 16.51% at 30 V and above that at 0 V. For $d = 96.52$ μm, the heights slightly increase when voltages range from 0 to 30 V. These results are different from that for the rolled state. The reason for the above phenomena is that the threshold current density increases with increase of grain sizes [15]. Compared with the annealing state, a higher dislocation density is present in the rolled state. The dislocation movement is improved under the action of electrical current. Therefore, the EA micro-rolling process has a significant effect on feature height for a rolled state at lower voltage. We will explore the threshold current density for $d = 96.52$ μm in future research.

3.2 Flatness of Sheet

The rolled T2 copper sheets at different voltage levels are shown in Fig. 5. The flatness of sheets is improved because the voltage increases. The sheets tend to bend at 0 and 5 V. When the voltage is above 10 V, the bending deformation of sheets is greatly reduced. The bending deformation on one side is mainly because power is turned off in advance in order to avoid electrical discharge. In the micro-rolling process of surface texturing, the bending is caused by asymmetric deformation behavior between the top surface and the bottom surface due to the texture being only on the top surface. As shown in Ref. [4], the sheets bent downward when the deformation on the top surface was larger than that on the bottom surface. Later on, they balanced the deformation through asymmetric roll speed. However, in this study, the bending deformation is reduced by the introduction of electricity. It is indicated that the electrical current can reduce the difference in contact pressure and

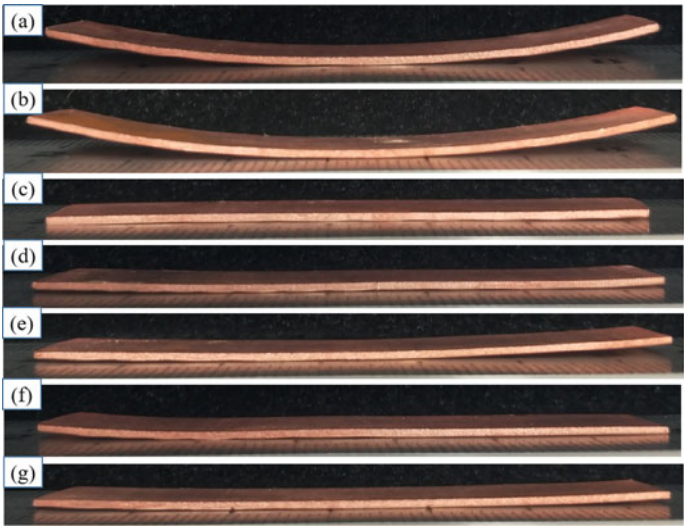


Fig. 5 T2 copper sheets at different voltage levels: **a** 0 V, **b** 5 V, **c** 10 V, **d**)15 V, **e** 20 V, **f** 25 V, **g** 30 V. (Color figure online)

deformation between the top surface and the bottom surface, and then improve the flatness of the sheets.

3.3 Surface Quality

Figure 6 shows the line roughness on the top surface at different voltage levels. The measured position is marked by the red dash in the inset on the right corner of Fig. 6. The line roughness sharply increases after rolling. However, a decrease is significant in EA micro-rolling process, especially at 10 V. At the same time, line roughness slightly increases with the voltage increase. The surface quality is directly affected by the plastic deformation. In the micro-rolling process, dislocations are generated and slide off the surface of the sheets to form steps, at the same time as the coordinated deformation between the different grains, both resulting in a worse surface at 0 V. Electric current can promote the dislocation slide off and overcome obstacles, resulting in a decrease in the slip band generation and grain rotation. The surface in the groove is smoother, as shown in Fig. 4, which indicates that electric current can improve the deformation uniformity. Therefore, the EA micro-rolling process is conducive to the surface quality of sheets.

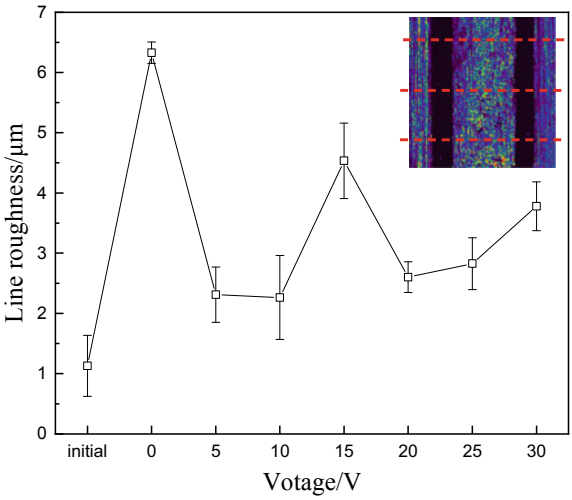


Fig. 6 Line roughness on top surface at different voltage levels. (Color figure online)

4 Conclusions

The effects of the electric current on forming the quality of surface texture were investigated. The feature height shows a significant increase in the EA micro-rolling process. Feature height is firstly increased and then almost unchanged when the voltage increases. The application of electric current in the micro-rolling process can improve the flatness of sheets and reduce the bending deformation. Compared with conventional micro-rolling, line roughness is significantly decreased in the EA micro-rolling process. The grains in the grooves are elongated at both 0 and 30 V, and the difference of microstructures is little. Effects of the electric current on samples with different grain sizes are different due to the threshold current density relating to the grain size. The feature height is significantly improved at 10 V for rolled sheets and 30 V for annealed sheets with a grain size d of 30.24 μm. Nevertheless the voltage at which the feature height for $d = 96.52$ μm will be remarkably increased is above 30 V.

Acknowledgments The authors would like to acknowledge the funding support from the National Natural Science Foundation of China (Grant No.: 51635005).

References

1. Patel D, Jain VK, Ramkumar J (2016) Micro texturing on metallic surfaces: State of the art. P I Mech Eng B-J Eng 232(6):941–964
2. Koch K, Bhushan B, Barthlott W (2009) Multifunctional surface structures of plants: an inspiration for biomimetics. Prog Mater Sci 54(2):137–178

3. Bruse M (1998) Zur Strömungsmechanik Wandreibungsvermindernder Riblet Oberflächen[D]. TU Berlin, Dr.-Ing. Dissertation
4. Denkena B, Köhler J, Wang B (2010) Manufacturing of functional riblet structures by profile grinding. Cirp J Manuf Sci Technol 3(1):14–26
5. Yang Z, Chang YY, Li DL, Wang HC (2020) Underwater micro-structure functional surface design and drag reduction characteristics. Ship Eng 42(1):141–146
6. Fu MW, Wang JL, Korsunsky AM (2016) A review of geometrical and microstructural size effects in micro-scale deformation processing of metallic alloy components. Int J Mach Tool Manuf 109:94–125
7. Romans T, Hirt G (2010) Rolling of drag reducing riblet-surfaces. In: Paper presented at the 51st AIAA/ASME/ASCE/AHS/ASC structures, structural dynamics, and materials conference, Orlando, Florida, 12–15 April 2010
8. Zhou R, Cao J, Ehmann K, Xu C (2011) An investigation on deformation-based surface texturing. J Manuf Sci E-T ASME 133(6):061017
9. Gao ZY, Peng LF, Yi PY, Lai XM (2015) Grain and geometry size effects on plastic deformation in roll-to-plate micro/meso-imprinting process. J Mater Process Technol 219:28–41
10. Ross CD, Kronenberger TJ, Roth JT (2009) Effect of dc on the formability of Ti–6Al–4V. J Eng Mater-T ASME 131(3):031004
11. Perkins TA, Kronenberger TJ, Roth JT (2007) Metallic forging using electrical flow as an alternative to warm/hot working. J Manuf Sci E-T ASME 129(1):84–94
12. Siopis MS, Kinsey BL, Kota N, Ozdoganlar OB (2011) Effect of severe prior deformation on electrical-assisted compression of copper specimens. J Manuf Sci E-T ASME 133(6):064502
13. Mai JM, Peng LF, Lai XM, Lin ZQ (2013) Electrical-assisted embossing process for fabrication of micro-channels on 316L stainless steel plate. J Mater Process Technol 213(2):314–321
14. Ng MK, Fan ZY, Gao RX, Smith EF, Cao J (2014) Characterization of electrically-assisted micro-rolling for surface texturing using embedded sensor. CIRP Ann Manuf Technol 63(1):269–272
15. Siopis MS, Kinsey BL (2010) Experimental investigation of grain and specimen size effects during electrical-assisted forming. J Manuf Sci E-T ASME 132(2):021004

Decoupling of Adverse Effect of Inter-Roll Thrust Force on Steering Control During Strip Rolling



Kazuma Yamaguchi and Atsushi Ishii

Abstract Inter-roll thrust force due to roll misalignment in a 4-high strip rolling mill affects the difference in roll forces measured by load cell on the work side and that on the drive side. Since the roll force difference is utilized for strip steering control, in which roll gap tilting control is done assuming the roll force difference reflects strip off-centering behavior, the inter-roll thrust force gives a serious disturbance to the steering control and may cause troubles like tail crash. In this paper, an inter-roll thrust force decoupling method for the steering control is proposed. The method utilizes measured thrust counter forces acting against work roll chocks to obtain effective roll force difference for the steering control. Validity of the decoupling method is confirmed using a laboratory 4-high mill which can control cross angles between rolls and measure the work roll thrust counter forces.

Keywords Thrust force · Off-centering · Hot strip mill · Steering control · Decoupling method

1 Introduction

In a 4-high strip rolling mill, misalignment between work roll (WR) and backup roll (BUR) causes inter-roll thrust forces which act in the opposite direction to each other (Fig. 1) [1]. The inter-roll thrust forces may cause rolling asymmetry in the widthwise direction [2] as well as shorten fatigue life of roll bearings [3]. Liu et al. proposed a theoretical model to calculate the inter-roll thrust forces, and it was shown that the inter-roll thrust forces depend on the friction coefficient and the cross angle between the rolls [4]. In addition, effects of a roll shifting [5] and a dynamic cross [6] on the inter-roll thrust forces were analyzed.

The inter-roll thrust forces should be balanced by thrust counter forces acting from mill housing through roll chocks, but undesirable moments remain on rolls due to the vertical distance between acting positions of the inter-roll thrust forces

K. Yamaguchi (✉) · A. Ishii
Process Research Laboratories, Nippon Steel Corporation, 20-1 Shintomi, Futtsu 293-8511, Chiba, Japan
e-mail: yamaguchi.8ge.kazuma@jp.nipponsteel.com

© The Minerals, Metals & Materials Society 2021

G. Daehn et al. (eds.), *Forming the Future*, The Minerals, Metals & Materials Series,
https://doi.org/10.1007/978-3-030-75381-8_211

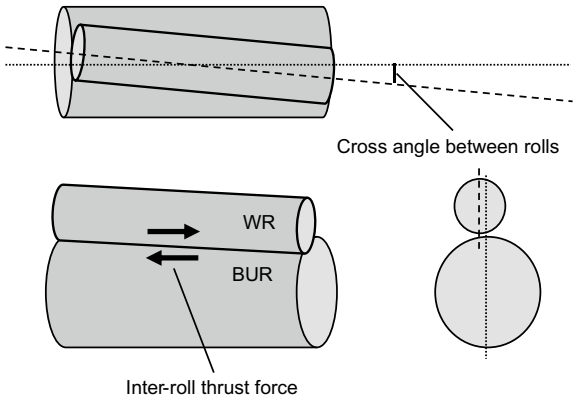


Fig. 1 Cross angle between rolls and inter-roll thrust force

and the thrust counter forces. A difference in roll forces measured by a load cell on the work side (WS) and that on the drive side (DS) is changed such that moment balance of BUR can be maintained even with the moment due to the inter-roll thrust force (Fig. 2) [7, 8]. The change in the roll force difference resulting from the thrust force causes rolling asymmetry in the widthwise direction, and consequently may cause problems such as tail crash due to strip off-centering. Therefore, obtaining the change in the roll force difference is important in a rolling operation.

The change in roll force difference adversely affects strip off-centering in two ways. The first is its influence as a direct factor. Asymmetric vertical deformation of a rolling mill due to the roll force difference causes an unintentional roll gap difference in the widthwise direction which causes strip off-centering. Furumoto et al. carried out a coupled analysis of elastic deformation of rolls and plastic deformation of a rolled strip considering this influence [9]. In addition, they indicated that a Mill Stabilizing Device (MSD) [10] which eliminates the clearance between WR chock or BUR chock and mill housing can reduce the strip off-centering due to

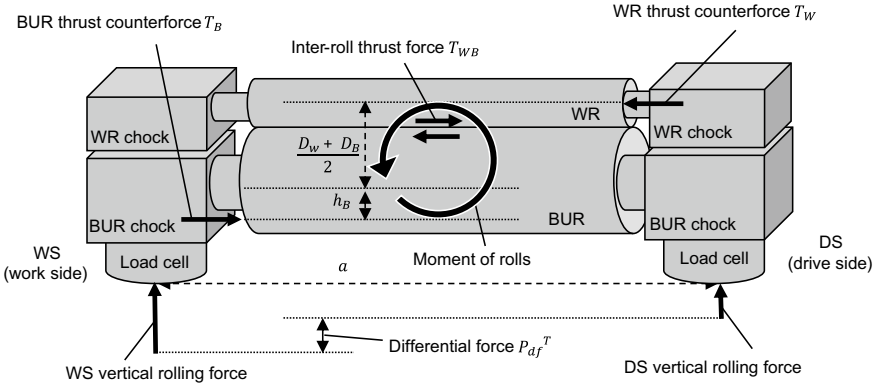


Fig. 2 Effect of thrust force on differential force

inter-roll thrust forces. However, the results also show that MSD cannot perfectly eliminate the inter-roll thrust forces due to wear status of WR chocks and BUR chocks. The second is its influence as an indirect factor. The roll force difference may be utilized for strip steering control, in which roll gap tilting control, namely leveling, is done during rolling by assuming the roll force difference reflects strip off-centering behavior. The inter-roll thrust forces act as a serious disturbance to this steering control. Nakajima et al. firstly developed this steering control method [11] and recent studies made an attempt at improving control model [12–17]. However, there are few studies that have examined the influence of the inter-roll thrust forces on this steering control or proposed improvement method. In this study, confining our attention to this steering control, an inter-roll thrust force decoupling method which can acquire the effective roll force difference without any adverse effect of the inter-roll thrust forces is proposed. The validity of this decoupling method is confirmed using a laboratory 4-high mill which can control cross angles between rolls and measure the WR thrust counter forces.

2 Experiment

2.1 Characteristics of Laboratory 4-High Rolling Mill

A 4-high cold rolling mill of about one-tenth the size of an actual hot strip mill was used for the experiment. Table 1 lists the mill specifications. This rolling mill can control roll gap, roll cross, roll offset, and WR shift with hydraulic servo devices. In addition, it can measure the top and bottom roll forces, and the thrust counter forces of each roll. Figure 3 shows the measurement system used for measuring the thrust counter force. The measurement system was installed at the axial roll edge. Figure 3 shows the measurement system from an overhead perspective, with the rolls being located on the left side of the image. It can track various types of roll movement such as leveling, roll cross, and roll offset using a linear motion guide, so that it can accurately measure the thrust counter forces by means of load cells.

Table 1 Mill specifications

WR diameter (mm)	BUR diameter (mm)	WR barrel length (mm)	BUR barrel length (mm)	WR chock span (mm)	BUR chock span (mm)	Mill motor power (kW)	Max rolling torque (kN·m/roll)	Max rotational speed (rpm)
80	160	220	200	320	320	3.4 (AC)	±490.3	±40

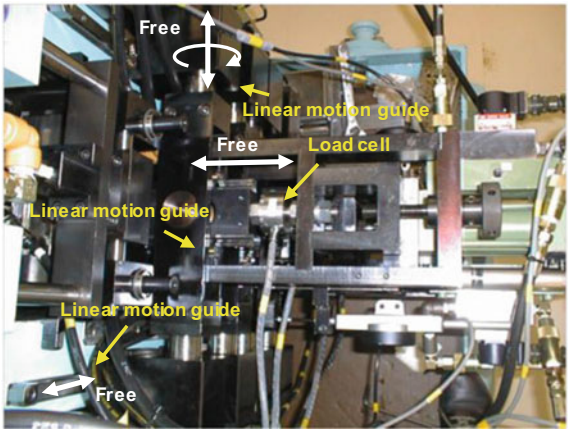


Fig. 3 Measuring equipment of thrust counter force. (Color figure online)

2.2 *Conditions and Procedure of Experiment*

The adverse effects of the inter-roll thrust forces on automatic steering control based on the change in the roll force difference was investigated by means of an aluminum cold rolling experiment. Furthermore, the validity of the decoupling method was also tested. Strip off-centering can become a problem, particularly in the tail end part of the hot strip rolling when the entry side tension is released. Therefore, this experiment tried to simulate the tail end rolling. Initially, a cross angle was given to the top and bottom BUR to generate inter-roll thrust forces, and initial leveling was fixed as a disturbance to create strip off-centering. Second, an aluminum coil was rolled until it converged to steady state. Third, rolling was temporarily stopped and the aluminum coil at the entry side was cut. Finally, tail end rolling was simulated by restarting the rolling, while activating the steering control (Fig. 4). Table 2 shows the experimental conditions. When the steering control is carried out using a lock-on method, a transient change of the roll force difference due to inter-roll thrust forces

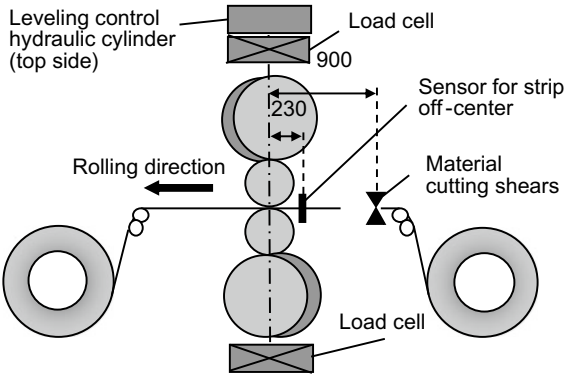


Fig. 4 Arrangements of the experiment. (Color figure online)

Table 2 Experimental conditions

Material (–)	Dimensions (mm)	Roll speed (mpm)	Rolling reduction (%)	WR offset (mm)	Cross angle[a] (°)	Leveling* (mm)
Aluminum coil	$1^{t} \times 100^{W}$	1.5	10–30	1	Top BUR: -0.08 Bottom BUR: + 0.08	±0.02

[a]Define the direction to move the WS of a roll moves to delivery side as plu
*Initial value (WS-DS)

can become a problem. For example, this change is caused by an increase of the roll force due to the temperature drop of the tail end region. In this experiment, to simulate this influence, the rolling reduction was changed from 10 to 30% in the tail end rolling. The cross angle was −0.08° for the top BUR and +0.08° for the bottom BUR. Regarding the 'sign' of the cross angle, the direction to move the WS of the rolls to the delivery side is defined as 'plus'. Initial leveling was ±0.02 mm, and the direction to open the gap of the WS was defined as 'plus'. For the protection of equipment, rolling was terminated when the quantity of off-centering value exceeded 40 mm.

The steering control was done in three ways: without control, conventional control, and improved control. Without control means a condition without any leveling control. Conventional control means a leveling control method that is used conventionally, which directly refers to the roll force difference signal as an indicator of strip off-centering, and calculates a command value of the leveling $S_{\mathrm{df}}{}^{*}$ by PD control. Improved control means a proposed leveling control method in which the roll force difference due to the inter-roll thrust forces is estimated using measured thrust counter forces, and is decoupled from the roll force difference signal (Fig. 5). f in Fig. 5 denotes the influence coefficient of the inter-roll thrust force on the roll force difference. f can be calculated using Eq. (1) which is derived from the equilibrium condition of the axial direction forces and the moment in the vertical plane of the rolls.

$$f = -\frac{(D_W + D_B + 2h_B)}{a} \tag{1}$$

D_W is a WR diameter, D_B is a BUR diameter, a is a BUR chock span—distance between BUR bearing centers on WS and on DS, and h_B is the vertical distance between the BUR axis and the point of application of the BUR thrust counter forces. BUR thrust forces are supported by thrust counter forces acting from reduction devices as well as mill housing through BUR chocks; thus, h_B does not necessarily agree with the roll axis [8]. Therefore, it is important to obtain h_B accurately when Eq. (1) is applied to steering control. In this experiment, f was identified by observing variation of the thrust counter force and that of the roll force difference before and

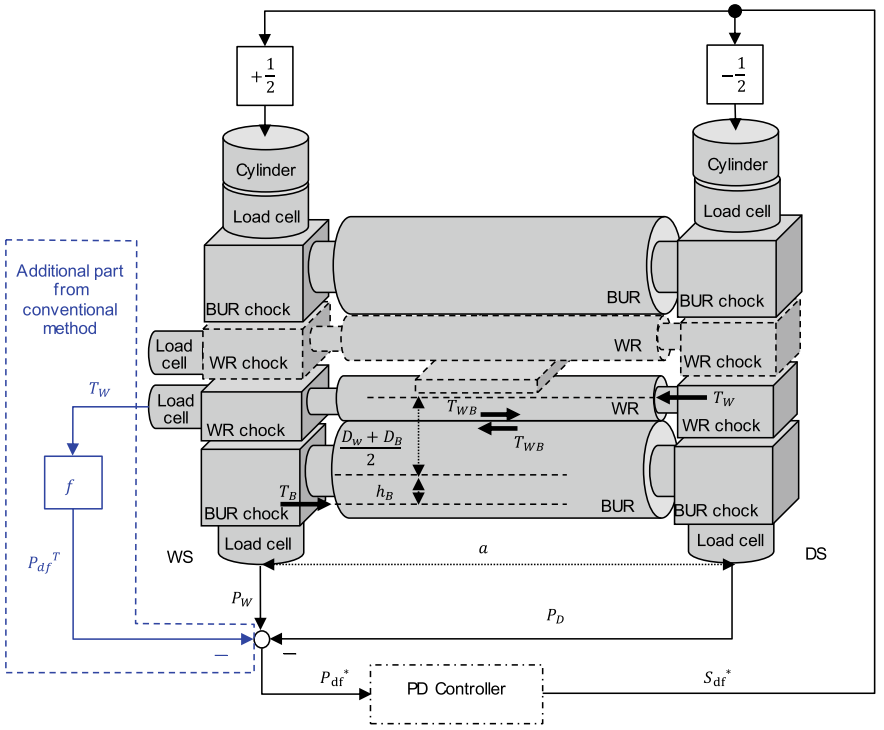


Fig. 5 New improved method for steering control based on differential force considering effect of thrust force. (Color figure online)

after the cross angle was given. Figure 5 shows a steering control model using load cells located on the bottom side, though this rolling mill also has load cells on the top side. Experiments were performed for both cases: using load cells on the bottom side, and those on the top side being used as a reference for steering control. Including the direction of the initial leveling, four cases were tested in total (Table 3).

The control system depicted in Fig. 5 was constructed using LabVIEW which is a system design software application developed by National Instruments Corporation. Proportional gain $K_P = 0.28$ and differential gain $K_d = 0.03$ were set, which happens

Table 3 Experiment list

	BUR cross angle (upper, lower) (°)	Initial leveling[a] (mm)	Reference
Case 1	−0.08, +0.08	+0.02	Bottom load cells
Case 2			Top load cells
Case 3		−0.02	Bottom load cells
Case 4			Top load cells

[a]Initial value (WS-DS)

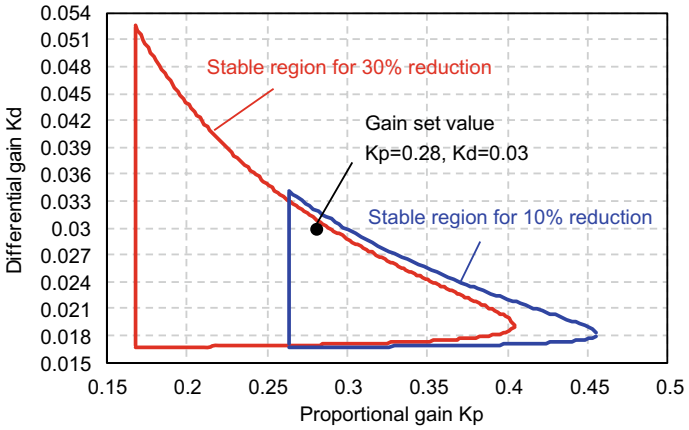


Fig. 6 Calculated stable region in steering control and gain set value. (Color figure online)

to be within a stable control region calculated using the equation of Nakajima et al. [11] when the reduction rate was 10–30% (Fig. 6). Tail end rolling started, and four seconds later steering control began. The control cycle time was two seconds.

2.3 *Results of Experiment*

Figure 7 shows an example of variation of the roll force and the WR thrust counter forces in the tail end rolling. The initial leveling is −0.02 mm and it is without steering control (equivalent to Case 3 or Case 4). Because the reduction rate was changed

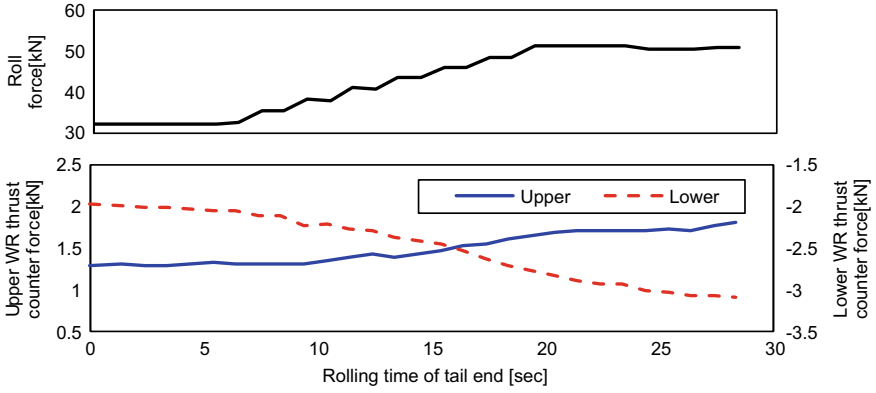


Fig. 7 Example of time series data (leveling −0.02 mm). (Color figure online)

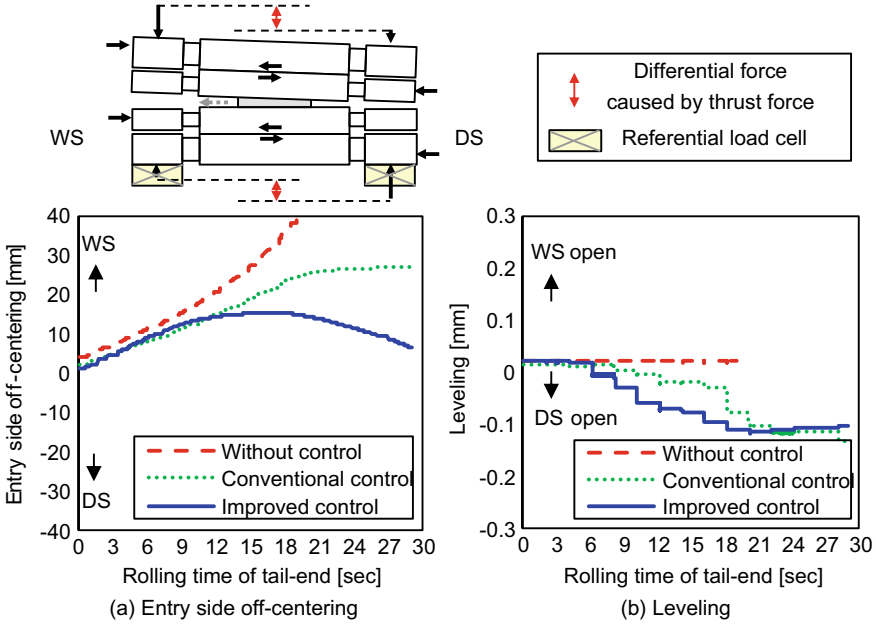


Fig. 8 Results of Case 1. (Color figure online)

from 10 to 30% in 5–20 s, the roll force increased. Consequently, the absolute value of the thrust counter forces increased.

Figures 8, 9, 10, and 11 show the experimental results of the tail end rolling using the three methods (without control, with the conventional control, and with the improved control) in Cases 1–4 as shown in Table 3. Figures 8a, 9a, 10a, and 11a show the entry side off-centering of the strip and Figs. 8b, 9b, 10b, and 11b show the leveling value.

In Case 1 (Fig. 8) where initial leveling is +0.02 mm and bottom load cells are utilized by the leveling controls, strip tail walked toward WS divergently without leveling control. With the conventional control, strip tail behavior was mitigated owing to negative leveling action observed in Fig. 8b. However, comparing the case with the improved control, leveling action was somewhat delayed and strip off-centering was larger in the case with the conventional control.

In Case 2 (Fig. 9) where initial leveling is +0.02 mm and top load cells are utilized by the leveling controls, strip tail also walked toward WS divergently without leveling control. With the conventional control, strip off-centering toward WS was suppressed quickly within 10 s, but due to large negative leveling control action, strip tail overshot the mill center and then walked toward DS. Observing strip tail behavior with leveling action, it seems that strip off-centering would show oscillating behavior in the case with the conventional control. On the other hand, in the case with the improved control, leveling action was rather moderate and strip tail showed more stable behavior than that with the conventional control.

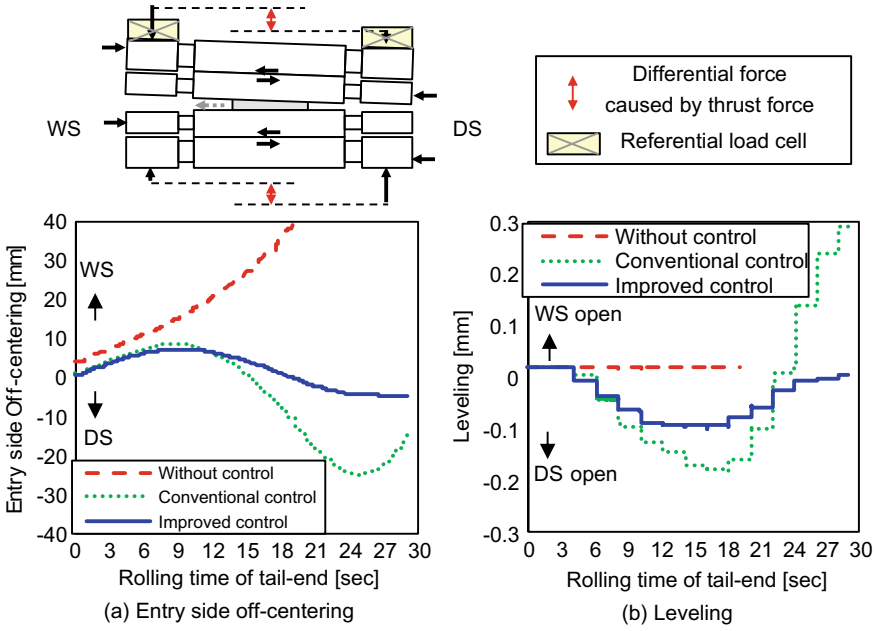


Fig. 9 Results of Case 2. (Color figure online)

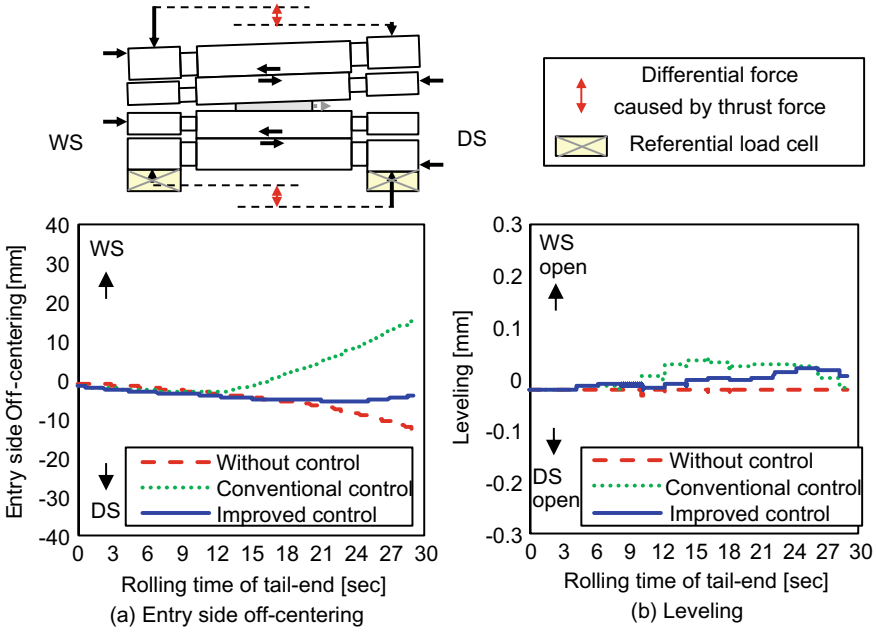


Fig. 10 Results of Case 3. (Color figure online)

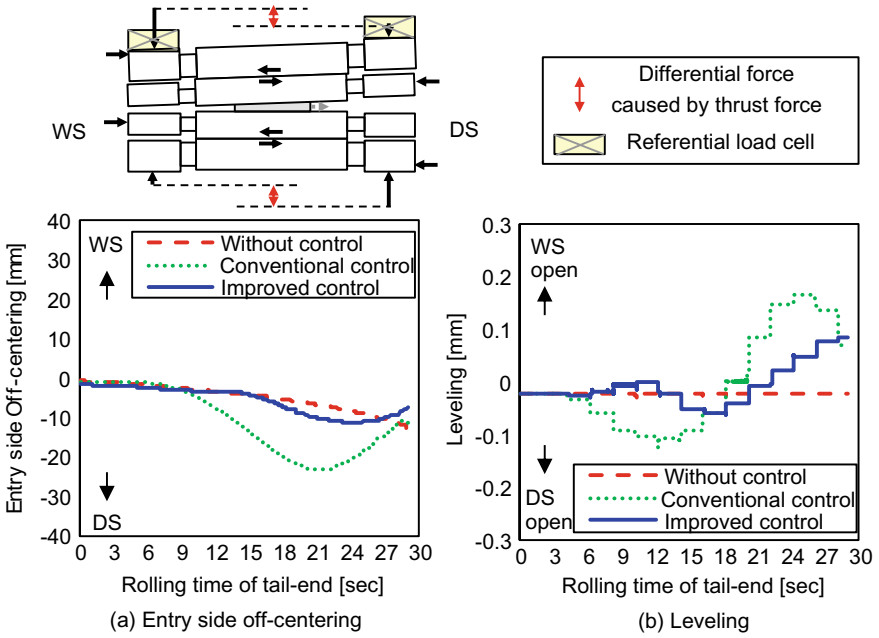


Fig. 11 Results of Case 4. (Color figure online)

In Case 3 (Fig. 10) where initial leveling is −0.02 mm and bottom load cells are utilized by the leveling controls, strip tail gradually but divergently walked toward DS without leveling control. With the conventional control, strip off-centering toward DS was suppressed, but due to large positive leveling control action, strip tail overshot the mill center and then walked toward WS divergently. On the other hand, in the case with the improved control, leveling action was rather moderate and strip tail showed more stable behavior than that with the conventional control.

In Case 4 (Fig. 11) where initial leveling is −0.02 mm and top load cells are utilized by the leveling controls, strip tail also walked toward DS without leveling control. With the conventional control, strip off-centering toward DS was enhanced owing to negative leveling control action. Observing strip tail behavior with leveling action, it seems that strip off-centering would show oscillating behavior in the case with the conventional control in the same way as Case 2. On the other hand, in the case with the improved control, leveling action was rather moderate and strip tail showed more stable behavior than that with the conventional control.

Figure 12 summarizes the maximum value of the entry side off-centering of Case 1–Case 4. In Case 1 and Case 2, results using the conventional control became better than that without control, but in Case 3–Case 4, results using the conventional control got worse than that without control. On the other hand, results of all of the cases using the improved control became better than that without control or the conventional

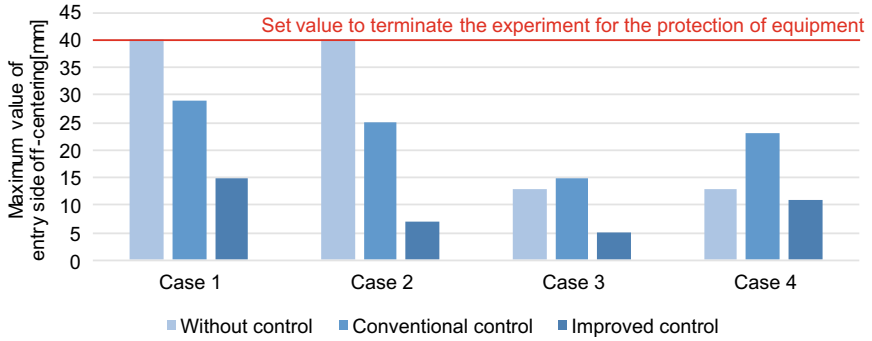


Fig. 12 Maximum value of entry side off-centering of Cases 1–4. (Color figure online)

control. In comparison with the conventional control, the improved control reduced the maximum value of entry side off-centering by half or more.

2.4 Discussion

In Case 1 where initial leveling is +0.02 mm and bottom load cells are utilized by the leveling controls, leveling action with the conventional control is too slow and insufficient. This can be explained by the disturbing effect of the inter-roll thrust force on the roll force difference between WS and DS. Referring to Table 3, bottom BUR cross angle is +0.08°, which causes the inter-roll thrust force on the BUR toward DS, and hence the disturbance of the inter-roll thrust force is larger DS bottom load cell force (negative roll force difference). On the other hand, since strip off-centering toward WS causes larger WS load cell force (positive roll force difference), the disturbance tends to attenuate sensitivity of strip off-centering with the bottom load cells, and hence the leveling control action becomes too slow and insufficient.

In Case 2 where initial leveling is +0.02 mm and top load cells are utilized by the leveling controls, leveling action with the conventional control is too much and oversensitive. This can be explained by the disturbing effect of the inter-roll thrust force on the roll force difference between WS and DS. Referring to Table 3, top BUR cross angle is −0.08°, which causes the inter-roll thrust force on the BUR toward WS, and hence the disturbance of the inter-roll thrust force is larger WS top load cell force (positive roll force difference). Since strip off-centering toward WS causes larger WS load cell force (positive roll force difference), this disturbance tends to enhance sensitivity of strip off-centering with the top load cells, and hence the leveling control action becomes too much and oversensitive.

In Case 3 where initial leveling is −0.02 mm and bottom load cells are utilized by the leveling controls, the conventional control rendered excessive positive leveling control action which led the strip tail to walk divergently toward WS. This can be explained by the disturbing effect of the inter-roll thrust force on the roll force

difference between WS and DS. Referring to Table 3, bottom BUR cross angle is 0.08°, which causes the inter-roll thrust force on the BUR toward DS, and hence the disturbance of the inter-roll thrust force is larger DS bottom load cell force (negative roll force difference). This disturbance is considered to be the main reason for the excessive positive leveling control action.

In Case 4 where initial leveling is −0.02 mm and top load cells are utilized by the leveling controls, the conventional control rendered negative leveling control action in the beginning of the rolling which was false action in view of the strip off-centering toward DS at that time. This false action can be also explained by the disturbing effect of the inter-roll thrust force on the roll force difference between WS and DS. Referring to Table 3, top BUR cross angle is -0.08°, which causes the inter-roll thrust force on the BUR toward WS, and hence the disturbance of the inter-roll thrust force is larger WS top load cell force (positive roll force difference), which causes negative leveling control action. Although the strip off-centering was toward DS and this causes negative roll force difference, the off-centering amount is relatively small at the beginning of the rolling and hence positive roll force difference due to the inter-roll thrust force dominated.

3 Conclusion

This study aimed at automatic steering control based on the effective roll force difference without any adverse effect of the inter-roll thrust forces. To this end, an inter-roll thrust force decoupling method for the steering control has been proposed. Experiments were carried out to investigate the adverse effects of the inter-roll thrust forces on the steering control and to confirm the validity of the decoupling method.

As a result, it has been clarified that the disturbing effect of the inter-roll thrust forces on the roll force difference between WS and DS may seriously damage the performance of the conventional steering control, and that the improved steering control based on the inter-roll thrust force decoupling method exhibits excellent performance. Thus, it has been confirmed that stable steering control, which does not suffer the adverse effects of the inter-roll thrust force, is possible by applying the proposed method.

References

1. Ogawa S, Ishii A, Yamada K, Ohta S, Koumoto K (1999) Sheet rolling method and sheet rolling mill: WO1999/043452, 1999–09–02
2. Ishikawa T, Tozawa Y, Nishizawa J (1988) Fundamental study on snaking in strip rolling. Trans ISIJ 28(6):485–490
3. Vlcek BL, Hendricks RC, Zaretsky EV (2003) Determination of rolling-element fatigue life from computer generated bearing tests. Tribol Trans 46(4):479–493

4. Liu Y, Levick M, Adair D, Liu S (2015) Investigation into roll thrust bearing damage and modeling of roll thrust forces for the 4-high reversing rougher of a hot strip mill. Iron Steel Technol 12(1):267–275
5. Wang JS, Jiang ZY, Tieu AK, Liu XH, Wang GD (2006) Analysis of thrust force in a work roll shifting mill. Int J Mech Sci 48(10):1095–1102
6. Shen G, Zheng Y, Li M (2013) Development of statically determinate plate rolling mills that maintain the rolls parallel. J Manuf Sci Eng Trans ASME 135(3)
7. Ma X, Liu H, Sun J, Zhang Z (2016) Screwdown load deviation model of 5 m heavy plate mill based on influence of back-up roll axial force. Ironmak Steelmak 43(2):112–120
8. Ishii A, Ogawa S (2017) Proceedings of the 2017 Japanese spring conference for the technology of plasticity, pp311–312 (in Japanese)
9. Furumoto H, Kanemori S, Takeguchi T (2017) Reduction of off-centering at tail end caused by unstable work roll position with mill stabilizing device in hot rolling. Proc Eng 207:1373–1378
10. Furumoto H, Nishizaki J, Higashio A, Hayashi K, Kim J (2004) Reducing of impact force at threading of strip head end and mill vibration. MHI Technol Rev 41(3):174–177 (in Japanese)
11. Nakajima K, Kajiwara T, Kikuma T, Kimura T, Matsumoto H, Tagawa M, Shirai Y, Yoshimoto K (1981) Proceedings of the 1981 Japanese spring conference for the technology of plasticity, pp 147–150 (in Japanese)
12. Kiyota T, Matsumoto H (2003) Tail crash control in hot strip mill by LQR. Am Control Conf 4:3049–3054
13. Okada M, Murayama K, Anabuki Y, Hayashi Y (2005) VSS control of strip steering for hot rolling mills. In: IFAC world congress, pp19–24
14. Choi YJ, Lee MC (2009) PID sliding mode control for steering of lateral moving strip in hot strip rolling. Int J Control Autom Syst 7(3):399–407
15. Malloci I, Daafouz J, Iung C, Bonidal R, Szczepan-ski P (2010) Robust steering control of hot strip mill. IEEE Trans Control Syst Technol 18(4):908–917
16. Kim K, Won S (2013) Observer-based guaranteed cost control for lateral motion of a strip in hot rolling process. In: Control and automation(ICCA), 2013 10th IEEE international conference, pp1479–1484
17. Kwon W, Kim S (2015) Active disturbance rejection control for strip steering control in hot strip finishing mill. IFAC 48(17):42–47

Part XXII
Sheet Forming

Evaluating the Reliability of a Nondestructive Evaluation (NDE) Tool to Measure the Incoming Sheet Mechanical Properties



Fernando J. Alamos, Jiahui C. Gu, and Hyunok Kim

Abstract Today, the automotive OEMs and part suppliers are increasing their material suppliers globally. Therefore, the same grade steels are supplied by different steel mills and batch conditions to meet this requirement. However, the variation of the incoming mechanical properties can significantly influence the stamping quality associated with necking, wrinkling, and cracking. This increases the overall manufacturing costs and lowers productivity. Nondestructive evaluation (NDE) tools have become useful to reduce this uncertainty by measuring incoming mechanical properties. The measured data can be used during production in a feed-forward control to select the optimal process parameters or as forming process parameter optimization using simulations. A detailed evaluation of a 3MA (micromagnetic, multiparametric microstructure, and stress analysis) Fraunhofer IZFP's device and its viability of implementations in a production environment is introduced. The 3MA equipment was incorporated into an industrial flexible robot and a practical calibration procedure was developed and validated for Bake-Hardening (BH) 340 steel.

Keywords Nondestructive evaluation tool · 3MA · Mechanical properties · Sheet metal forming

F. J. Alamos (✉)
Department of Aerospace and Mechanical Engineering, University of Notre Dame, Notre Dame, IN 46556, USA
e-mail: falamosd@nd.edu

J. C. Gu · H. Kim
EWI Forming Center, 1250 Arthur E. Adams Drive, Columbus, OH 43221, USA
e-mail: jgu@ewi.org

H. Kim
e-mail: hkim@ewi.org

© The Minerals, Metals & Materials Society 2021

G. Daehn et al. (eds.), *Forming the Future*, The Minerals, Metals & Materials Series,
https://doi.org/10.1007/978-3-030-75381-8_212

1 Introduction

The manufacturing industry is recently experiencing a global scale transformation. This new industrial revolution, often called Industry 4.0, is driven by connectivity, intelligence, and automation [1]. In sheet metal forming, the increased part complexity and emerging high-strength light sheet materials often increase technical challenges associated with the variation of formability and process robustness. To overcome these challenges, smart machines, intelligent systems, and the use of big data have become essential for factories to become more efficient and productive.

Today, the automotive OEMs and part suppliers are globally resourcing various sheet materials from different suppliers considering the geographical distribution of the plants. The same grade steels are supplied by different steel mills and batch conditions to meet this requirement. However, there is significant uncertainty in the incoming material properties of the sheet materials. These uncertainties affect the part quality associated with necking, wrinkling, and cracking, increasing drastically the production cost [2–4]. Nondestructive evaluation (NDE) tools have become useful to reduce this uncertainty by inspecting the incoming coil material properties in production. In several sheet metal forming applications, NDE tools were used to measure incoming mechanical properties, which allows adjusting forming process parameters based on the measured data.

NDE tools have been used in deep drawing of kitchen sink production [5–8]. An eddy current NDE sensor was used to measure the yield strength, tensile strength, uniform elongation, total elongation, and grain size of the incoming material, and a laser triangulation sensor was used to measure the sheet thickness. The measured data was used in simulations to generate the metamodels to determine the process window and as input for a feed-forward control to select the optimal process parameters during production, improving part quality and reducing failure during small-batch productions.

Other studies have used a commercial NDE equipment 3MA (micromagnetic, multiparametric microstructure, and stress analysis), developed by Fraunhofer IZFP to determine the material properties, grain size, and residual stress of strip coils, reporting an important variation in the material properties across same coils [4, 9, 10]. Increased variation in the yield strength, from 160 to 200 MPa, has been reported for an interstitial-free steel-string coil by Wolter et al. [4]. Kim et al. [3] used the 3MA equipment to determine the mechanical properties of the incoming blanks for a sheet forming process to determine the effective servo press parameters to improve part quality and minimize failure. The study showed a good correlation between the measurements from the sensor and the tensile testing results and proposed to use a Machine Learning algorithm instead of a feed-forward control to predict the most effective parameters during the drawing process.

The application of NDE tools has a huge potential in production for the metal forming industry. 3MA has been used to measure mechanical properties in many applications; however, this tool needs to be further improved for practical applications. For example, the calibration procedure recommended by the manufacturer does

not guarantee accurate measurement data of 3MA. Therefore, in this study, a practical calibration procedure was developed and validated for Bake-Hardening (BH) 340 steel. The viability of implementations of 3MA equipment was demonstrated with an automated flexible robot to emulate the production conditions.

2 Approach

In this study, the performance of the automation of a commercial NDE tool, 3MA, integrated with an industrial robot was evaluated. 3MA can measure different properties of ferromagnetic materials by correlating the measured magnetic properties, which are related to the microstructure of the material. Figure 1 illustrates the relationship among microstructure, magnetic properties, and mechanical properties. The batch-to-batch production variation in steel mills varies the microstructure which results in variation of both magnetic and mechanical properties.

The 3MA equipment uses a combination of a field harmonics, eddy current, Barkhausen noise, and incremental permeability analysis [11]. Figure 2 shows how the 3MA probe was mounted to a FANUC LR Mate 200iD/4S industrial robot with a fixture. A batch of BH340 steel with 0.75 mm thickness was used throughout this study. The BH340 steel samples were obtained from two different coils (labeled as HA and HB) of the same mill, to consider variations of the sheet mechanical properties. All blanks were cut to the same size of 508 × 508 mm. Ultimate tensile strength (UTS), yield strength (S_y), and total elongation (e_{tot}) were the measured material properties throughout this study. The automated 3MA equipment integrated with a FANUC flexible robot was first calibrated and then validated for both HA and HB materials individually.

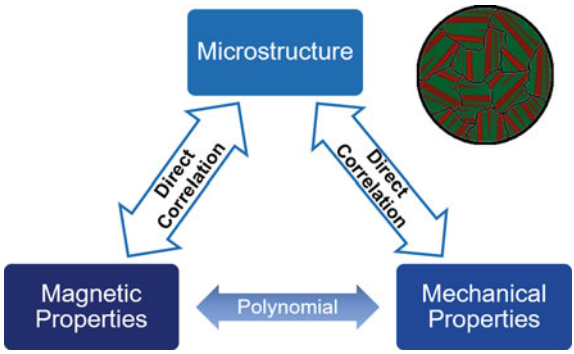


Fig. 1 Principal of 3MA measurement of magnetic properties and its correlations with mechanical properties. (Color figure online)

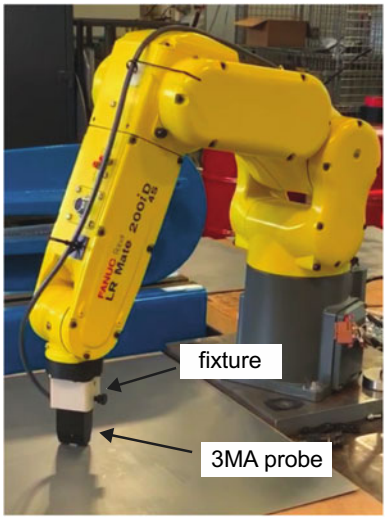


Fig. 2: 3MA probe attached to a FANUC industrial robot. (Color figure online)

2.1 Calibration Procedure

The 3MA equipment is calibrated with tensile test data. The magnetic parameters measured with the 3MA equipment and the tensile testing results of the specimens (UTS, S_y, and e_{tot}) are stored in the same database. Then calibration functions are determined using regression analysis to correlate the magnetic properties to each tensile property. The calibration functions for each tensile property have the following form:

$$y = a_0 + a_1 x_1 + a_2 x_2 + \cdots + a_n x_n \tag{1}$$

where y is the target property, a_i $(i = 0 \ldots n)$ are the computed regression coefficient, and x_i are the 3MA-measured magnetic parameters.

For the calibration of the system, first, 50 tensile specimens for BH340 were drawn on different blanks. The blanks were randomly selected from different batches and different locations to have a representative and broad sampling size. Two sets of tensile specimens were marked at 0°, 45°, and 90° with respect to the rolling direction of the coil, as showed in Fig. 3a, to account for the anisotropic properties of the blank. The gauge area of the specimens was 12.5 mm wide and 50 mm long. The length of area reduction was 57 mm. Second, the automated 3MA-robot system was used to take 40 measurements in four different locations of the specimen (Fig. 3b). The following precautions should be carefully executed for measurement:

- The contacting surface of the 3MA probe needs to be parallel with respect to the blank surface because the measurement is sensitive to contacting angle variation.

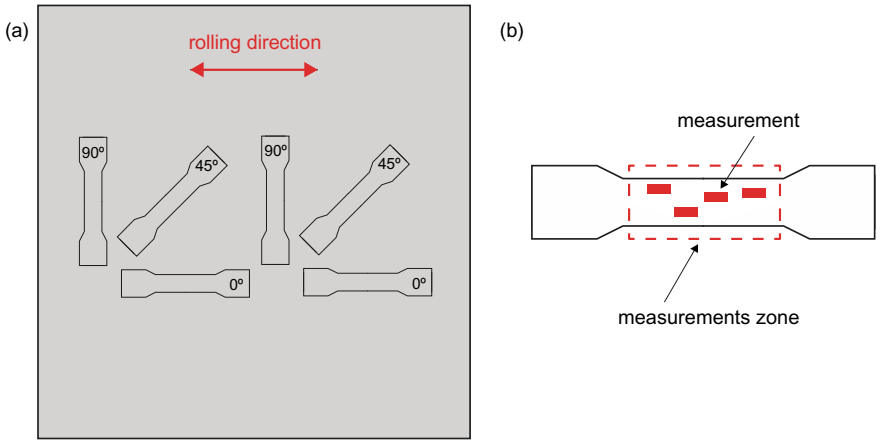


Fig. 3 **a** Layout of the tensile specimens on a blank. **b** Randomly selected four locations with the tensile gauge range for 3MA measurements. (Color figure online)

- The contact force on the probe with the sample should not exceed 15 N; therefore, the robot can be programmed to apply the same contact.
- To avoid edge effects, the 3MA measurement location should have at least 50 mm offset distance from the blank edges.

Third, the specimens were cut and tensile tested following the ASTM E-8 standard. UTS, S_y, and e_{tot} were the measured tensile properties. Finally, calibration functions were used to correlate the 3MA NDE measurements and the tensile testing data. The coefficient of determination (R^2) and the root mean square error (RMSE) values were minimized to find the most reliable regression coefficients a_i in the calibration functions.

2.2 *Validation of the Calibration Function*

To validate the effectiveness of the automated 3MA-robot system after calibration, multiple blanks were randomly selected for the BH340-HA and BH340-HB steel. For each blank, nine measurements were taken at three different positions with the automated 3MA-robot system and direction with respect to the rolling direction (0°, 45°, and 90°). Figure 4 shows the measurement locations for a blank. In addition, all the measurements were repeated by manually holding the 3MA probe to compare the manually measured 3MA data with the automatically measured data and evaluate the effectiveness of the automated system.

An analysis of variance (ANOVA) and a Tukey test were performed to statistically quantify the difference between the mechanical properties measured using the automated 3MA-robot system, the manually handled 3MA equipment, and the

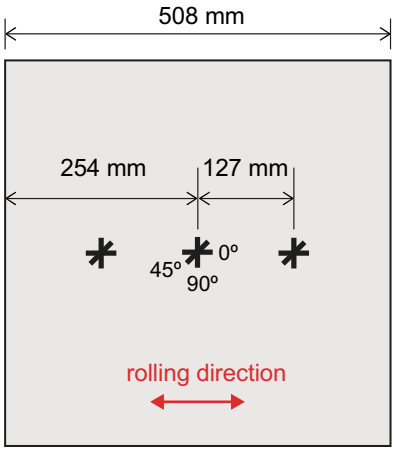


Fig. 4 Nine measurements on each blank for validation at three different locations, 0°, 45°, and 90° with respect to the rolling direction. (Color figure online)

tensile testing results. The results were analyzed with a 95% confidence interval. The ANOVA test compares the similarity of two data sets. Two data sets are significantly different if p-values are lower or equal to 0.05. The assumptions of independence of cases, homoscedasticity, and normality of the residuals were checked. The Anderson–Darling test was used to verify the normality of the residuals. For the cases where the assumption of normality of the residual was invalid, a Kruskal–Wallis nonparametric test was performed, and the p-values were compared with the results from the ANOVA test. The results using both tests gave similar p-values; consequently, the assumptions are satisfied and the standard ANOVA analysis was considered satisfactory [12].

3 Results

3.1 Tensile Testing Results

The detailed tensile testing results are summarized in Table 1. The results show an important variation in the mechanical properties between BH340-HA and -HB batch materials. The BH340-HB steel is stronger and less ductile than the BH340-HA steel. The average UTS is at least 10 MPa higher and the yield strength (S_y) is at least 12 MPa higher for BH340-HB than BH340-HA for all three orientations with respect to the rolling direction. The average total elongation (e_{tot}) is around 2% less ductile for BH340-HB than BH340-HA. The tensile testing results also showed a significant variation in the mechanical properties within the same coil. For example, for BH340-HA, the $S_{y_90^o}$ standard deviation (SD) is 8.83 MPa and the range is 27 MPa, which is 17.2% of the measured value. For $e_{tot\ 90^o}$, the SD is 9.3% and the range is 27.3% of the measured value. Moreover, for some cases, a large variation

Table 1 Tensile testing results for BH340-HA and BH340-HB steels for 0°, 45°, and 90° orientations

Material variation	Property	UTS (MPa)			S_y (MPa)			e_{tot} (%)		
	Angle (°)	0	90	45	0	90	45	0	90	45
BH340-HA	Mean	340.8	341.4	344.1	227.2	233.5	233.5	39.98	39.26	38.95
	St. dev.	9.1	9.0	9.3	8.8	8.4	7.0	2.88	3.64	3.26
	Range	32.0	33.0	34.0	39.0	27.0	28.0	8.60	10.70	10.40
BH340-HB	Mean	350.9	354.6	355.1	241.2	246.2	245.3	37.29	35.71	36.06
	St. dev.	4.6	7.2	7.2	3.7	9.4	4.9	2.48	3.34	3.23
	Range	16.0	20.0	21.0	16.0	38.0	16.0	8.20	9.60	10.10

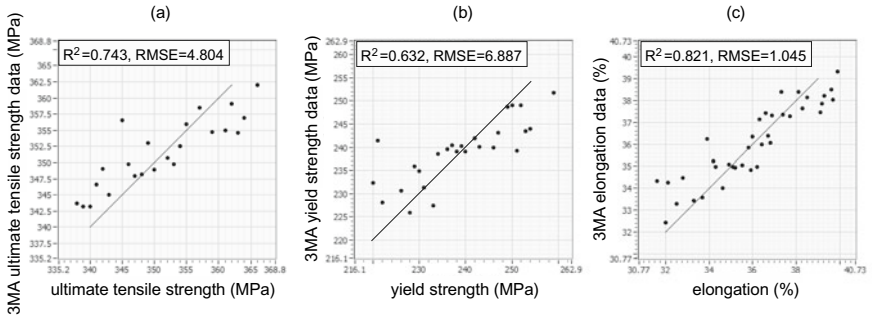


Fig. 5 Calibration correlation plots for UTS **a**, S_y **b**, and e_{tot} **c**

on the material properties was found in the same blank. For example, for a single BH340-HA blank, the values of two different specimens in the rolling direction were 354 and 340 MPa for UTS, 243 and 222 MPa for S_y, and 39.2 and 37.7% for e_{tot}.

3.2 Calibration Model Results

The correlation plots between the 3MA-measured data and the tensile testing properties (ultimate tensile and yield strength, and elongation) are shown in Fig. 5. The manufacturer suggests a model correlation higher than 80%; however, the R^2 values for S_y and UTS were lower than 80%. The correlation was 63.2% for S_y but the RMSE was 6.89 MPa, which is only 2% of the mean value and within the coil specification (6–40 MPa). The UTS model shows a correlation of 74.3%, although the RMSE was 4.8 MPa, which is lower than the 3MA manufacturer specifications (8–40 MPa) [11]. For e_{tot} the correlation is 82%. Therefore, the regression polynomial equations used for the calibration are considered acceptable for the tensile properties. Nevertheless, further tests with 3MA and subsequent statistical analysis were conducted to increase the accuracy of the calibration and the system.

3.3 Validation of the Calibration Function

To prove the repeatability of the automated 3MA-robot system, the same point of the blank, in the same direction, was measured three times. The results showed a consistent value for the same location of the blank. The higher percent deviation (PD) was 1.2% for UTS, 1.4% for S_y, and 3.7% for e_{tot}. All of the results showed a lower PD than specified by the manufacturer [11].

An ANOVA test was performed to quantify the accuracy of the calibration model of the 3MA measurements. The ANOVA test evaluates how similar two different

Table 2 ANOVA p-value results between the 3MA-measured data from the sheet blanks concerning the tensile testing results

Property		UTS			S_y			e_{tot}		
Angle (°)		0	90	45	0	90	45	0	90	45
Material variation	BH340-HA	0.447	0.408	0.002	0.620	0.994	0.155	0.120	0.854	0.173
	BH340-HB	1.000	0.997	0.174	0.074	0.028	0.618	0.797	0.792	0.561

data sets are. From Table 2, it is observed that 89% of the 3MA-measured properties of the new blanks randomly selected from the coil were similar to the tensile testing data (p-values > 0.05). The $UTS_{45°}$ for BH340-HA and $S_{y_90°}$ for BH340-HB showed a small mismatch (p-values $\leq$ 0.05) between the new 3MA measurements and tensile data. Figure 6 shows the box plots for these two cases. The box plot describes groups data based on a five-number summary: minimum, maximum, median, and standard deviation above and below the data mean. Outliers are excluded in the analysis and are represented with a star (*). From the plots, it is observed that the 3MA-measured values for the $UTS_{45°}$ of BH340-HA are slightly higher than the tensile testing results; however, they are within the maximum and minimum values. For $S_{y_90°}$ for BH340-HB, the 3MA-measured values are also within the tensile test data range; however, the 3MA data mean value is lower than the tensile test data mean value. Therefore, the calibration was considered reasonably accurate and robust.

A further analysis used a new calibration model with only 26 random tensile samples from the original 50 samples. The correlation of the calibration (R^2 values) improved over 90% for all the properties. The same blanks were measured again using the new calibration model; however, for this case, the ANOVA test results showed that only 17% of the 3MA-measured data of the new blanks were similar

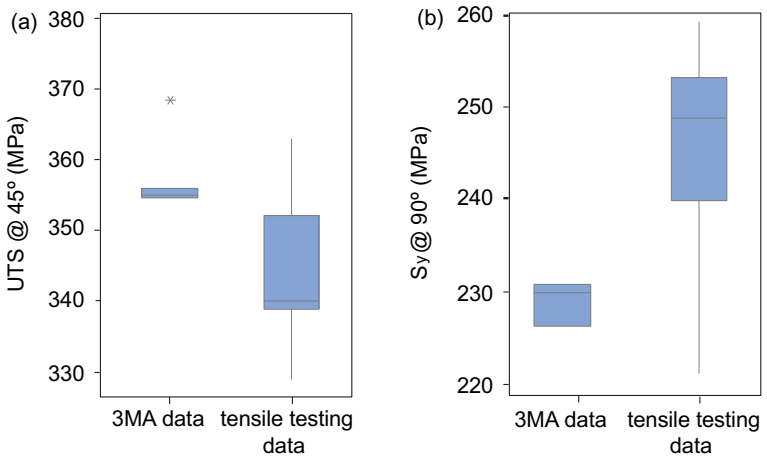


Fig. 6 Box plots for: **a** UTS at 45° for BH340-HA and **b** at 90° for BH340-HB. (Color figure online)

to the tensile testing data. The robustness of 3MA measurements improves significantly with increasing the number of tensile tests; therefore, proper and representative sample size is critical for reliable calibration.

Also, a similar ANOVA test was performed to access the consistency of the 3MA measurement; most measurement variations were made by manually holding the 3MA equipment and then holding it with the flexible robot. An ANOVA test was performed, and the results showed negligible differences of the measured data between both methods.

4 Discussion

In this study, both 3MA data and tensile test data showed a significant variation of the BH340 mechanical properties. Important variations on the material properties (ultimate tensile and yield strength, and elongation) were found even for the same coil. In addition, the automated 3MA-robot system provided accurate, consistent, and repeatable measurements for BH340 steel. Therefore, after a reliable calibration process, automated NDE tools can be practically used in tracking the incoming coil material variations by taking real-time measurements in production to reduce the uncertainties of the process and potentially improve part qualities and reduce costs by adjusting the forming process parameters or machine control.

One of the limitations of 3MA equipment is that different grade or different gauge materials require new calibrations. Different calibration functions need to be used for different coil thickness, or thickness needs to be incorporated as a variable of the calibration function. It is recognized that calibration can be expensive; however, the well-calibrated 3MA tool has great potential for cost-saving by inspecting the incoming coil properties and adjusting forming process in production. Additionally, this study leads to develop generalized material calibration databases and use advanced simulations and machine learning to minimize calibration efforts [4].

The calibration procedures for 3MA recommended by the manufacturer do not fully guarantee a robust calibration. Therefore, from this study, the following calibration procedure for ultimate tensile and yield strength, and elongation is recommended for steel strip coils:

1. Choose at least 24 randomly selected blanks from different parts of the coil for each material variation.
2. Draw two sets of tensile test specimens for each direction (0°, 45°, and 90° with respect to the rolling direction) as shown in Fig. 3a.
3. Record 40 3MA measurements at four random points (10 per each point) for each specimen (Fig. 3b).
4. Conduct tensile testing of the drawn specimens from step 2.
5. Store the 40 3MA measurements and the tensile testing data in the same database and find the calibration functions using regression analysis. The correlation

coefficient of the calibration model should be: R^2 (adjusted) > 0.7 and %RMSE < 10%. If 0.6 < R^2 (adjusted) < 0.7, then %RMSE < 3%.

6. Choose ten randomly selected blanks from different parts of the coil for each material variation and take nine 3MA measurements (three for each direction) for each material as shown in Fig. 4.
7. Run a one-way ANOVA test (significant level = 0.05) for each mechanical property independently, comparing the tensile testing data with respect to the 3MA measurements of step 6. If more than or equal to 75% of the p-values are higher than 0.05 (no significant differences), the calibration is successful. If less than 75% of the p-values are higher than 0.05, the calibration is not successful and more tensile testing data should be included in the ANOVA test.

The 3MA NDE tool is sensitive to the operating conditions and the proper cautions are needed to avoid significant measurement errors. The precautions that need to be considered while taking measurements were discussed in Sect. 2.1.

It was observed that the robustness of the 3MA calibration is significantly improved by increasing the number of tensile testing samples. New advanced high-strength steels typically have a large variation of the material properties because they have multiphase microstructures, which makes them more challenging to obtain consistent mechanical properties [3, 4]; therefore, calibration specimens should be chosen carefully to include the entire range of material properties. Since a coil strip can be kilometers long, it is crucial to select multiple blanks across different parts. Moreover, the 3MA-measured tensile properties are found by computing the calibration functions, which are based on empirical data; therefore, extrapolation outside of the calibration range can lead to significant fault data. For this reason, a wide range of value needs to be used for the calibration to minimize calibration errors.

5 Conclusion

The following conclusions can be made based on this study:

- A significant variation on the incoming mechanical properties was observed for the same batch coil of BH340 steel.
- The automated 3MA equipment integrated with the flexible robot measurements consistently obtains the repeatable results.
- A BH340 steel calibration model for yield and ultimate tensile strength, and total elongation was obtained and validated successfully.
- A new robust calibration procedure was established for industrial applications.
- NDE tools can effectively detect mechanical property variation of the incoming material.
- NDE automated tools used as an input to adjust forming process parameters have a great potential in reducing costs and time for sheet metal forming production environment.

Acknowledgments The authors acknowledge great support from the industry partners: General Motors Company, Fiat Chrysler Automobiles (FCA), Cosma International, POSCO, Novelis, ESI, AutoForm, Diversified Tooling Group, AMEPA, Fuchs, Selmatec, and GBTP.

References

1. Yang DY, Bambach M, Cao J, Duflou JR, Groche P, Kuboki T, Sterzing A, Tekkaya AE, Lee CW (2018) Flexibility in metal forming. CIRP Ann 67:743–765. https://doi.org/10.1016/J.CIRP.2018.05.004
2. Allwood JM, Duncan SR, Cao J, Groche P, Hirt G, Kinsey B, Kuboki T, Liewald M, Sterzing A, Tekkaya AE (2016) Closed-loop control of product properties in metal forming. CIRP Ann 65:573–596. https://doi.org/10.1016/J.CIRP.2016.06.002
3. Kim H, Gu JC, Zoller L (2019) Control of the servo-press in stamping considering the variation of the incoming material properties. IOP Conf Ser Mater Sci Eng 651. https://doi.org/10.1088/1757-899X/651/1/012062
4. Wolter B, Gabi Y, Conrad C (2019) Nondestructive testing with 3MA-an overview of principles and applications. Appl Sci 9. https://doi.org/10.3390/app9061068
5. Fischer P, Harsch D, Heingärtner J, Renkci Y, Hora P (2016) Inline feedback control for deep drawing applications. IOP Conf Ser Mater Sci Eng 159. https://doi.org/10.1088/1757-899X/159/1/012006
6. Fischer P, Harsch D, Heingärtner J, Renkci Y, Hora P (2017) A knowledge-based control system for the robust manufacturing of deep drawn parts. Proc Eng. 207:42–47. https://doi.org/10.1016/J.PROENG.2017.10.735
7. Heingärtner J, Fischer P, Harsch D, Renkci Y, Hora P (2017) Q-Guard—an intelligent process control system. IOP Conf Ser J Phys Conf Ser 896. https://doi.org/10.1088/1742-6596/896/1/012032
8. Fischer P, Heingärtner J, Renkci Y, Hora P (2018) Experiences with inline feedback control and data acquisition in deep drawing. Proc Manuf 15:949–954. https://doi.org/10.1016/j.promfg.2018.07.401
9. Borsutzki M, Dobmann G, Theiner WA (1999) On-line ND-characterization and mechanical property determination of cold rolled steel strips. In: Brusey BW, Bussière JF, Dubois M, Moreau A (eds) Advanced sensors for metals processing. Canadian Institute of Mining, Montreal, pp 77–84
10. Wolter B, Dobmann G (2006) Micromagnetic testing for rolled steel. In: Paper presented at the 9th European conference on nondestructive testing, Berlin, Germany, 25–29 September 2006
11. Fraunhofer IZFP (2016) 3MA testing system: technical Description
12. Montgomery DC (2013) Design and analysis of experiments, 8th edn. Wiley, New Jersey

Study on the Effect of Embossing on the Bending Properties of High-Strength Sheet Metals



David Briesenick, Stefan Walzer, and Mathias Liewald

Abstract Selective embossing of sheet metal blanks, prior to processing, offers the possibility of locally modifying material properties. Small indentations applied on the sheet metal surface by a punch lead to increased material strength due to the induced strain hardening. Moreover, such locally embossed sheet metals show an enhanced process window with regard to forming processes and an improved performance under different loading conditions. The experimental study presented in this paper investigates the bending properties of high-strength steel sheets embossed on the tension or the compression surface of the bent blank. The effect of embossing on the bending resistance of two different materials (DP500 and TRIP780) was analyzed by varying the embossing patterns by density and depth. As a result, bending forces required in the tests rise when increasing the proportion of the embossed surface. Therefore, the paper reveals potentials of local embossing with regard to a specific modification of bending properties of sheet metal components, thus enabling their use in lightweight constructions.

Keywords Embossing · High-strength steel · Bending

1 Introduction

For the last decades, the mobility sector has been exposed to a growing demand for sustainable and efficient vehicle concepts, leading to an increased focus on lightweight construction issues in science and industry. In this context, one lightweight approach consists in replacing conventional steel grades in structural

D. Briesenick (✉) · S. Walzer · M. Liewald
Institute for Metal Forming Technology (IFU), University of Stuttgart, Holzgartenstraße 17, 70174 Stuttgart, Germany
e-mail: david.briesenick@ifu.uni-stuttgart.de

S. Walzer
e-mail: stefan.walzer@ifu.uni-stuttgart.de

M. Liewald
e-mail: mathias.liewald@ifu.uni-stuttgart.de

© The Minerals, Metals & Materials Society 2021

G. Daehn et al. (eds.), *Forming the Future*, The Minerals, Metals & Materials Series,
https://doi.org/10.1007/978-3-030-75381-8_213

components of car bodies with high-strength sheet metals in order to fulfill new requirements in crash safety, vehicle rigidity, recycling rates, and production cost [1]. However, certain disadvantages arise when processing advanced high-strength steel (AHSS) sheet metals by conventional forming technologies. Especially, cost-beneficial cold forming methods are accompanied with limited formability of material and enormous springback phenomena. But since the full potential of high-strength steel alloys may only be exploited via work hardening mechanisms, such cold forming processes are of particular interest [2].

Locally different component properties adapted to the component´s functionality enable the production of lightweight and efficient car body structures. Here, a common approach for locally reinforcing such components represents the use of tailored blanks. Merklein et al. [3], for example, suggested a classification in patchwork, tailor welded, tailor rolled, and tailor heat treated blanks and elaborated advantages and disadvantages in terms of formability and processing capabilities. On the contrary, Namoco et al. focused on an approach of local work hardening of aluminum sheets by an embossing and smooth reforming process and investigated its impact on mechanical properties and formability [4, 5]. These findings are supported by Abe et al. [6], having carried out investigations on punch indentations in areas of excessive thinning during deep drawing of aluminum parts. Furthermore, crash-relevant structural sheet metal parts can show a reproducible increase in energy absorption when local material hardening is applied by forming structuring or laser hardening [7]. A new embossing method for near-surface indentations is presented by Walzer and Liewald [8], demonstrating a pattern and indentation depth-related impact on mechanical properties of high-strength sheet metal DP600. Based on these findings, the study presented in this paper investigates sensitivities of embossing parameters such as the depth, location, and density of indentations on the bending properties of high-strength sheet metal specimens. In view of the increase in strength, this method offers a new approach for a local and load compatible reinforcing of sheet metal parts with simultaneous advantages in lightweight design of corresponding sheet metal components. Additionally, proposed tailor embossed blanks may overcome current challenges regarding joining and forming technology of conventional tailored blanks.

2 Experimental Method

Sheet metal components of modern car body structures are often made of multi-phase steels having high mechanical strengths and limited formability. Therefore, two representative high-strength steels with identical sheet thickness t but different mechanical properties were selected for the investigations described below (see Table 1). Dual-phase steel DP500 exhibits a Yield Strength of 340 MPa, a Uniform Tensile Strength (UTS) of 560 MPa, and shows certain formability of 19% for uniform elongation (U.E.). Applied multi-phase Steel TRIP780 enhances crash worthiness of parts by a strain rate and temperature-dependent phase transformation effect and combines high mechanical strength (UTS = 820 MPa) with acceptable formability (U.E. = 14%).

Table 1 Mechanical properties of investigated high-strength steel DP500 and TRIP780

Material	t (mm)	E (GPa)	Yield strength (MPa)	UTS (MPa)	U.E (%)	n	r_m
DP500	1.2	210	340	560	19	0.18	0.88
TRIP780	1.2	210	470	820	14	0.23	0.93

2.1 Embossing Process

For the investigations, sheet metal specimens were initially processed from the selected materials using a CNC-controlled punching machine (TRUPunch 5000R). For this, the semi-finished sheet metal products were first clamped horizontally and then incrementally embossed in the Z-direction with a spherical punch (Ø = 4 mm). Afterwards, the final specimen contours were produced by nibbling with a rectangle punch (Fig. 1). This procedure enables a flexible production of embossed specimens with different patterns and indentation depths for different types of material properties or sheet thicknesses. The punching machine used provides an operating performance of up to 1400 strokes per minute and thus enables an efficient and flexible structuring method for research and small batch industrial applications.

By using the flexibly controlled punching machine, the high-strength steel sheets (DP500, TRIP780) were embossed with different patterns. Here, the distances between indentations were changed in the X- and Y-direction in order to obtain embossing patterns of varying densities. Likewise, embossing depths T were changed (see Table 2). Subsequently, the embossed and separated specimens were ejected from the punching machine, and measurements of the specimen surfaces were performed via confocal microscope (μsurf nanofocus). The measurements revealed that due to the elasticity of the machine frame and tools, small variations of embossed depth T occurred, although machine settings such as dead bottom center were kept constant. Thereby, the depth variation was mainly affected by the material and density of the pattern. For further evaluation, measured diameters of the surface indentations were

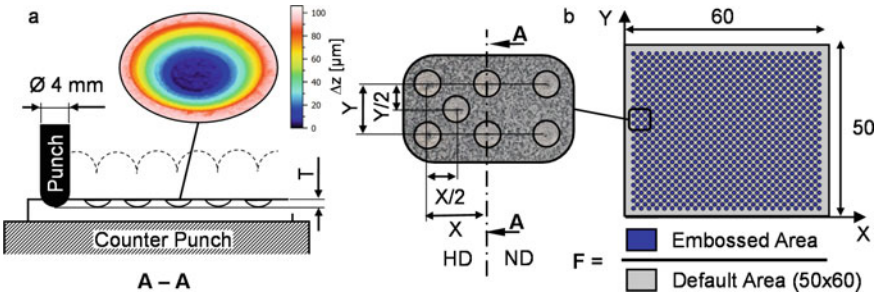


Fig. 1 Schematic representation of **a** embossing process with afterward performed surface measurements and **b** specimen size and variation parameter of embossing patterns with high (HD) and normal density (ND). (Color figure online)

Table 2 Experimental setup with investigated parameters on material, embossing depth T, distance between embossings in X-, Y-direction, embossed area F, nesting density, and amount of embossings

Specimen	Material	T (μm)	X (mm)	Y (mm)	F (%)	Density	∑ Embossings
DP500_F0_T0	DP500	–	–	–	–	–	–
DP500_F85_T170	DP500	170	2,26	2,26	85	HD	1265
DP500_F65_T130	DP500	130	2,26	2,26	65	HD	1265
DP500_F43_T180	DP500	180	2	2	43	ND	644
DP500_F33_T140	DP500	140	2	2	33	ND	644
DP500_F20_T190	DP500	190	3	3	20	ND	304
DP500_F16_T98	DP500	98	3	3	16	ND	304
TRIP780_F0_T0	TRIP780	–	–	–	–	–	–
TRIP780_F43_T160	TRIP780	160	2	2	43	ND	644
TRIP780_F33_T130	TRIP780	130	2	2	33	ND	644
TRIP780_F20_T140	TRIP780	140	3	3	20	ND	304
TRIP780_F16_T106	TRIP780	106	3	3	16	ND	304

used to calculate a percentage value of embossed area (F) on the specimens (see Fig. 1b).

2.2 Three-Point Bending Test

Properties of the differently embossed specimens were examined using three-point bending tests carried out on a tensile and compression testing machine (Roell + Korthaus RKM100). The testing device was equipped with exchangeable punch having different radii as well as a fixture according to testing standard DIN EN ISO 7438 [9]. The different specimens (see Table 2) were placed between the fixture and the bending sword. In addition, the orientation of surface indentations was varied between top- and downside as depicted in Fig. 2a. The main purpose of these tests was to investigate geometrical and work hardening effects of indentations on the outer tension side or inner compression side of the bending specimen. During the experiments, the bending punch moved by a defined speed of 60 mm/min toward the bottom dead center and deflected the specimen up to 20 mm. At the same time, the force–displacement curve was recorded using the integrated machine load cell and position sensor. Each specimen specification was tested five times consecutively. The curves obtained were averaged taking into account the divergence of measurements. The derivation of the force–displacement curves with respect to displacement (Fds) allowed the determination of extrema such as the maximum force F_{max} which represents the maximum bearable bending force (see Fig. 2b). In general,

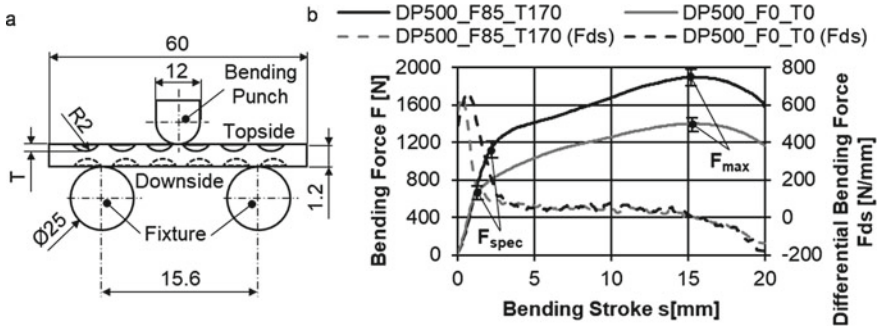


Fig. 2 Illustration of **a** schematic three-point bending test with embossed blank and **b** selected curve characteristics for reference and embossed specimen

measured bending force curves start with a linear increase of force and show a transition between a quasi-elastic and quasi-plastic forming behavior. Simultaneously, the corresponding derived curves (Fds) fall below a minimum value (<200 N/mm) at this point and subsequently tend toward zero. This gradient transition identifies the specific bending force F_{spec}.

3 Results And Discussion

The results gained for specific bending force F_{spec} which represents the switch from elastic to plastic strain and the maximum bending force F_{max} were summarized for selected specimens and plotted in a unified bar chart (see Fig. 3). Untreated specimen made of DP- (DP500_F0_T0) and TRIP-steel (TRIP780_F0_T0) served as reference for the specimen work hardened by embossing. As shown in Fig. 3, the untreated DP500 specimen shows a maximum bending force of 1.41 kN and a specific bending force of 0.67 kN. The untreated high-strength steel TRIP780 exhibits a higher deformation resistance with $F_{max} = 2.18$ kN and $F_{spec} = 1.18$ kN. The embossed specimens generally show an increased bending resistance when exposed to both quasi-elastic and quasi-plastic load conditions. Here, the transition between both load states (F_{spec}) is slightly influenced by the embossing orientation, with marginally higher measured values for blanks embossed on the topside under compressive stresses. Considering measuring divergence, this effect is slightly more pronounced for TRIP780 than for DP500 material. In contrast, maximum bending force F_{max} is not affected by the geometrical orientation of indentations, i.e. regardless of whether top- or downside has been embossed.

The small and near-surface indentations induced by the embossing process lead to work hardening of the material in the surrounded embossed area, which significantly impacts the bending properties of the specimen. For examined parameter space, the specific bending force of the specimens made of DP500 could be increased by

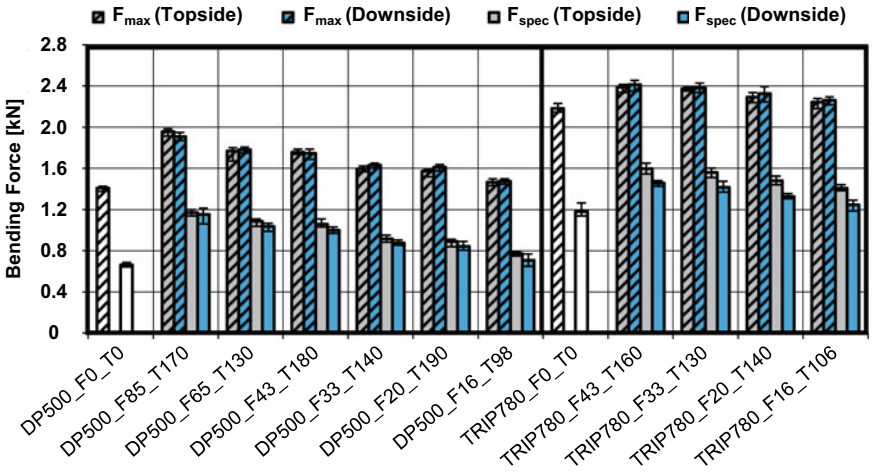


Fig. 3 Experimental results for maximum bending force F_{max} and specific bending force F_{spec} of investigated specimens with distinction between material and orientation of embossing (topside vs. downside). (Color figure online)

the embossing process by 0.046 kN (+7%) up to 0.49 kN (+75%) compared to the reference value of 0.66 kN (DP500_F0_T0). TRIP780 shows a specific bending force increase between 6 and 36% with a maximum increase of F_{spec} from 1.18 to 1.6 kN. The maximum force occurring during bending test (F_{max}) is increased to 1.96 kN (+39%) by embossing DP500 material with high pattern density (F = 85%) and indentation depth (T = 170 μm). Here, the resulting properties are almost comparable to bending properties of the untreated TRIP780 specimen. Minor surface indentations increase the maximum bending force only by 4% compared to the reference of 1.41 kN. The percentage increase of F_{max} for TRIP steel is observed in a range from 3 to 11%, thus showing a minor impact on targeted work hardening of the high-strength material by means of embossing.

In general, the results of the three-point bending test shown in Fig. 3 indicate a significant correlation between the embossing parameters depth T and embossed area F with regard to the bending properties of material DP500. In addition to the increasing F_{spec} and F_{max} values, this can be discerned from the fact that the ratio between F_{spec} and F_{max} as a measure of hardening mechanisms increases from 0.47 to 0.6 with growing embossing depth and density. In this context, further analysis focuses on promising results for DP500 material which is more sensitive to embossing than TRIP780. Therefore, Fig. 4 shows at first a more detailed analysis of the parameter sensitivity for the dual-phase steel. The surface plots exhibit a comparable influence of the parameter embossing depth T and area F on both measured forces F_{spec}, F_{max} and thus the bending properties of the material. Increasing density and/or depth of surface indentations immediately results in an increased resistance of sheet metal part under bending loads. Within investigated parameter range, correlation among

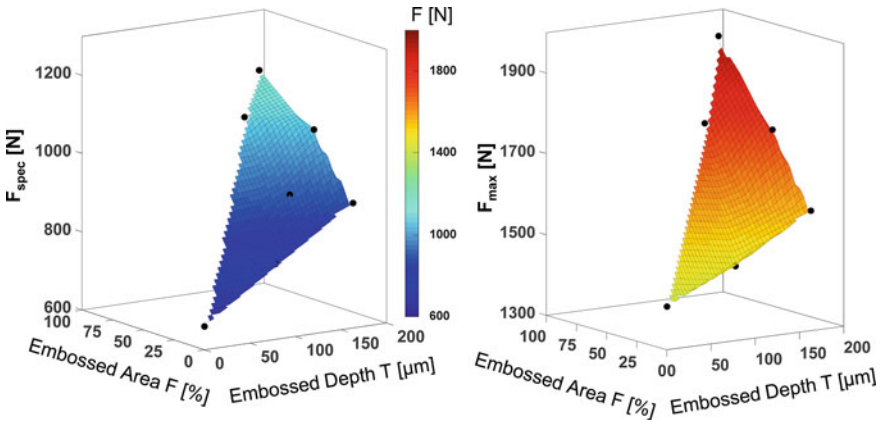


Fig. 4 Evaluation of embossing parameters area ratio F, indentation depth T, and the sensitivity on bending properties F_{spec}, F_{max} of DP500. (Color figure online)

embossing depth T, area F, and bending properties represented by F_{spec}, F_{max} can be described with a linearized response surface (see Fig. 4).

In order to understand the contexts and origins of the observed increased mechanical strength, an analysis of hardness distribution around surface indentions of embossed specimens may provide correlations with work hardening mechanisms. To characterize the increase in the hardness of sheet metal after embossing, microhardness measurements were carried out along thickness direction. For this purpose, four representative DP500 specimens were separated by machining, embedded and polished. Microhardness was measured according to Vickers (MHV) in sheet thickness direction using a pre-defined measuring profile (see Fig. 5). All tests were performed according to the international standard DIN EN ISO 14,577 using the microhardness measuring instrument Picodentor HM500 from Helmut Fischer GmbH. For statistically verified results, 42 hardness measuring points were performed in the field of a single embossed indentation. The measuring distances in horizontal direction amounted to 0.3 mm and in sheet thickness direction 0.2 mm. The maximum applied test load was defined as 300 mN.

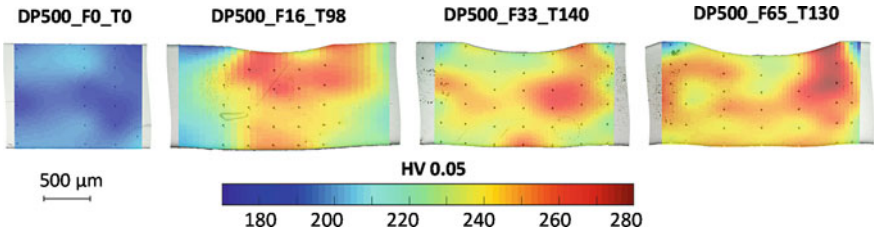


Fig. 5 Microhardness plots of reference specimen and three exemplary embossing setups of DP500 (from left to right). (Color figure online)

As shown in the very left picture of Fig. 5, the reference measurements revealed an averaged hardness value of about 191 HV with a standard deviation of 3.3% for untreated DP500 material without embossings. When comparing these reference measurement values with the measurements of specimen DP500_F65_T130, the considerable impact of embossing on the hardness values becomes more visible. In this case, the detected hardness values amounted to 244 HV with a measured deviation of 5.9%. In average, the difference between the hardness values of the reference specimen and the specimen exhibiting the most indentations amounts to 53 HV, which correspond to an increase of about 28%. In general and contrary to expectations, the highest increase in hardness does not arise below the indentation, but was identified on the highest value (275 HV) in the middle layer of the sheet thickness.

This effect can also be observed with specimen DP500_F33_T140, whose averaged hardness of 239 HV nearly equals the value of highly embossed specimen DP500_F65_T130. The measurements of specimen DP500_F33_T140 indicates an absolute deviation of hardness values by 12.1 HV, respectively 5%, which indicates a reliable comparability between measurements. Specimen DP500_F16_T98 (absolute deviation of 22.8 HV), however, shows a high increase in hardness directly below the punch indentation with a maximum hardness of 268 HV. Additionally, the incremental embossing process and machining sequence of single indentations seem to influence the hardness distribution to be adjusted. Thus, at higher indentation densities, the highest hardness value does not arise below the punch indentation, but is shifted to the mid-level of the sheet metal blank. By contrast, sufficient displacement of the material can be achieved in case of relatively large distances between the individual indentations, causing the highest hardness value to be adjusted directly below the punch indentations. The hardness values on the opposite side of the indentations are very similar even with different specimen setups. No interactions between indentations can be detected here.

The basic research results presented in this paper have shown that embossing of a sheet metal component can significantly increase its strength. Due to this increase in strength, sheet metal size can be reduced, thus leading to new design approaches for sheet metal components in lightweight constructions. In this respect, Fig. 6 illustrates the results of a three-point bending test which shows the potential for weight reduction via the embossing technique. In this investigation, embossed sheet metal blanks with the defined external dimension of 50 × 60 mm and two different embossing patterns were compared to untreated sheet metal blanks that varied in width from 50 to 95 mm and thus differed in weight.

Taking the specimen configuration DP500_F33_T140 as an example, the specific bending force (F_{spec}) of the embossed specimen amounts to 0.9 kN, while the untreated specimen of similar size only provides a bending resistance of 0.64 kN. By iteratively enlarging the specimen width in 5 mm steps, the same specific bending force of 0.9 kN could be achieved with an untreated specimen width of approximately 65 mm. This results in an increase in weight of approximately 32%. Considering the much tighter embossed sample DP500_F85_T170, weight increase even doubles to 64% when comparing the embossed and untreated specimen. The specific bending

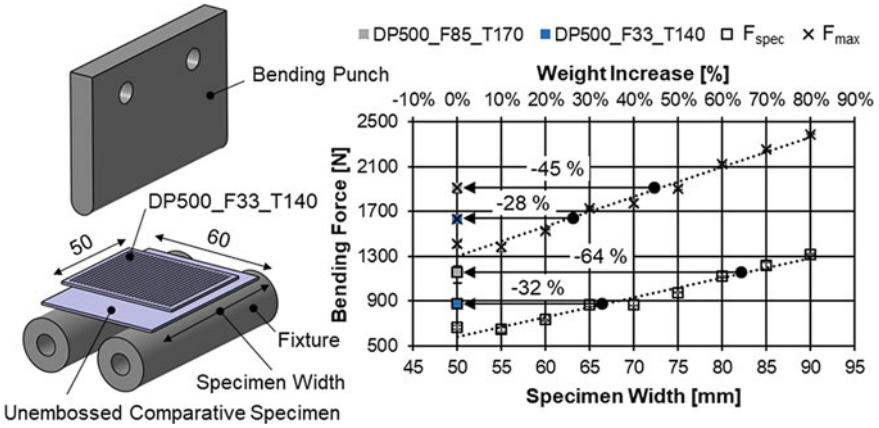


Fig. 6 Investigation of weight-saving potential of embossed DP500 blanks by comparing bending properties of embossed and untreated specimen with different dimensions. (Color figure online)

force for the embossed sample here reaches up to 1.15 kN. To achieve this specific bending force with an untreated specimen, the width must be increased up to 80 mm. Taking into account the absolute force maxima of the three-point bending test (F_{max}), the maximum bending force for the DP500_F33_T140 sample configuration amounts to 1.63 kN. The untreated specimen achieves a comparable maximum bending force with a specimen width of approximately 65 mm, which would correspond to a weight increase of approximately 28%. Similar behavior can be observed with the maximum bending force of specimen DP500_F85_T170. With this specimen configuration, an enlarged width of the untreated specimen compared to the embossed specimen amounts to 22 mm, which corresponds to a weight increase of 45%. Thus, the experimental investigations carried out could demonstrate the enormous potential of weight savings provided by the new embossing approach considered. Looking ahead, the findings obtained will be transferred to load-bearing profiles in the field of battery boxes in e-mobility applications.

The final evaluation of the forming results was carried out by visually inspecting the embossed specimens after bending, thus assessing the deformation behavior of the indentations. In this respect, Fig. 7 shows the embossed specimen DP500_F43_T180 with indentations having a distance of 2 mm in the X- and in Y-direction and a depth T of 180 μm. Bending of the specimen with embossing on the outer tension side (downside) results in an elongation of the spherical indentation diameter from 1.7 to 2.1 mm (+23.5%). On the contrary, bending of the specimen having embossings on the inner compression side (topside) leads to minor compression of the surface indentations in the forming zone of -11.7%. As a conclusion, local deformation of embossing depends on the load direction and occurs higher under tensile than under compressive stress. Based on this assumption, observed tendencies toward marginally higher stiffness and strength of specimens embossed on the topside can be explained

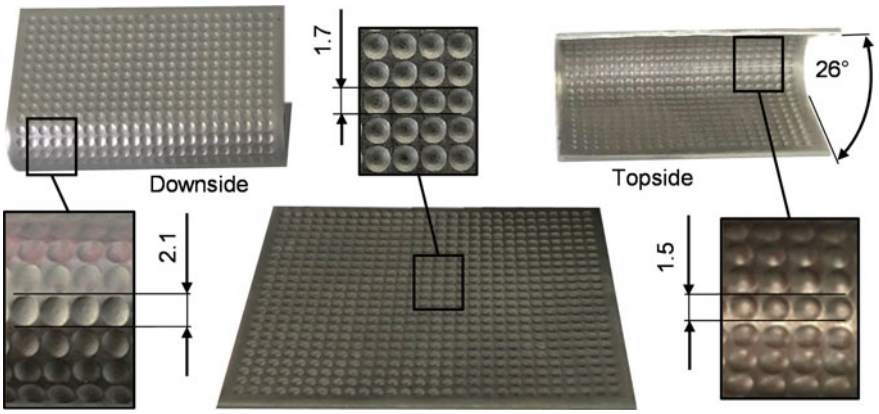


Fig. 7 Visual analysis of three-point bending test results for specimen DP500_F43_T180 on top- or downside. (Color figure online)

(see Fig. 3). Additionally, none of the formed and visually inspected specimens showed any failure such as cracks inside or between the surface indentations.

4 Conclusion and Outlook

The study presented in this paper demonstrates the effect of different embossing patterns on bending behavior of dual- and multi-phase high-strength steels DP500 and TRIP780 with identic sheet thickness. The investigations do reveal increased bending resistance of specimen when increasing pattern density and/or indentation depth, which could be proven by means of the two designated force characteristics (F_{spec}, F_{max}). Especially, dual-phase steel DP500 exhibits an increased sensitivity on work hardening by near-surface indentations with an increased strength of up to 75%. Presented results for dual-phase steel are consistent with observations under uniaxial tensile loads for DP600 [8]. Embossed sheet metal blanks made of TRIP780 steel grade reveal growth rates for elastic-related force F_{spec} of up to 35%. In addition, the study reveals a negligible influence of the localization of the embossing, i.e. whether the indentations are applied on the outer tension side or the inner compression side. Thus, it can be assumed that the occurring work hardening mechanisms may over-compensate geometrically caused effects. In fact that the section modulus is only slightly changed through these very small indentations close to the surface, significant geometric influences with regard to the stiffness can be excluded. Additionally, microhardness measurement of embossed cross sections of DP500 supports these findings by a localization of maximum hardness in the mid-level of the sheet metal blank. As a conclusion, pre-embossing of high-strength sheet metal blanks prior to sheet metal processing significantly influences bending properties of these materials and increases strength under bending loads. Based on these findings, the

developed embossing process allows a tailored adjustment of structural parts and their properties under functional load cases such as crash scenarios. Furthermore, promising new lightweight design possibilities are enabled by tailor embossed sheet metal parts. Exemplary elaborated comparative experiments revealed weight-saving potentials of up to 64% for embossed specimens toward bigger untreated sheet metals with the same bending properties.

Future investigations will address different dual-phase steel grades and sheet thicknesses to exploit further cost and weight-saving potentials for tailor embossed blanks. Besides further developments in the fields of simulation and design of embossing patterns, concept studies for a flexible industrial application of embossing process are necessary for a successful implementation under future technical and economic requirements.

References

1. Shanmugam K, Gadhamshetty V, Yadav P, Athanassiadis D, Tysklind M, Upadhyayula VKK (2019) Advanced high-strength steel and carbon fiber reinforced polymer composite body in white for passenger cars. ACS Sustain Chem Eng 7:4951–4963. https://doi.org/10.1021/acssuschemeng.8b05588
2. Billur E, Altan PDT (2010) Challenges in forming advanced high strength steels. In: International conference on "new developments in sheet metal forming", Stuttgart, pp 285–304. ISBN: 987-3-88355-379-5
3. Merklein M, Johannes M, Lechner M, Kuppert A (2014) A review on tailored blanks—production, applications and evaluation. J Mater Process Technol 214:151–164. https://doi.org/10.1016/j.jmatprotec.2013.08.015
4. Namoco CS, Iizuka T, Hatanaka N, Takakura N, Yamaguchi K (2007) Influence of embossing and restoration on the mechanical properties of aluminum alloy sheets. J Mater Process Technol 192–193:18–26. https://doi.org/10.1016/j.jmatprotec.2007.04.013
5. Namoco CS, Iizuka T, Narita K, Takakura N, Yamaguchi K (2007) Effects of embossing and restoration process on the deep drawability of aluminum alloy sheets. J Mater Process Technol 187–188:202–206. https://doi.org/10.1016/j.jmatprotec.2006.11.182
6. Abe Y, Ichiro MK, Maeno T, Ishihara S, Kato Y (2019) Improvement of sheet metal formability by local work-hardening with punch indentation. Prod Eng 13:589–597. https://doi.org/10.1007/s11740-019-00910-6
7. Jing X (2014) Optimierung von Crashstrukturen mittels lokaler Werkstoffverfestigungen. Dissertation, Leibniz Universität Hannover
8. Walzer S, Liewald M (2019) Studies on the influence of embossing on the mechanical properties of high-strength sheet metal. AIP Conf Proc 2113:160–166. https://doi.org/10.1063/1.5112703
9. DIN EN ISO 7438 (2018) Metallic materials—bend test

On the Determination of the Forming Limits by Necking and Fracture of Polycarbonate Sheet



A. Rosa-Sainz, G. Centeno, M. B. Silva, J. A. López-Fernández, A. J. Martínez-Donaire, and C. Vallellano

Abstract This research evaluates experimental methodologies for determining forming limits by necking and fracture in polycarbonate (PC) sheets by proposing developments of recent methodologies usually used in sheet metal forming. With this purpose, Nakazima tests with different blank geometries are performed on a 1 mm thick polycarbonate (PC) sheet. The experimentation included the use of Digital Image Correlation (DIC) for the evaluation of strains and thickness measurements for the determination of failure strains. The results provided accurate formability limits by necking and fracture, establishing a general framework for analysing specific forming processes (such as incremental forming) on polymeric sheets. Differences in the shaping of the Forming Limit Curve (FLC) and Fracture Forming Limit (FFL) curves for PC compared to those obtained in metal sheet are also discussed.

Keywords Polycarbonate sheet · Forming limits · Necking · Fracture

1 Introduction

Polymers represent a significant part of the raw materials used nowadays in the manufacturing industry, due to their lightweight, high corrosion resistance, good thermal, and electrical isolation properties, among other advantages. The shaping of polymers is commonly performed by means of thermal operations, involving heating, forming, and cooling operations, these being only economically viable for mass production.

However, the industry has currently a trend for low volume, lightweight, high quality, and customization of products that leads to the development of flexible

A. Rosa-Sainz · G. Centeno (✉) · J. A. López-Fernández · A. J. Martínez-Donaire · C. Vallellano
Department of Mechanical and Manufacturing Engineering, University of Seville, Camino de los Descubrimientos s/n, 41092 Sevilla, Spain
e-mail: gaceba@us.es

M. B. Silva
IDMEC, Instituto Superior Técnico, Universidade de Lisboa, Av. Rovisco Pais, 1049-001 Lisboa, Portugal

© The Minerals, Metals & Materials Society 2021

G. Daehn et al. (eds.), *Forming the Future*, The Minerals, Metals & Materials Series,
https://doi.org/10.1007/978-3-030-75381-8_214

processes, short forming cycles, short development, and production times, compatible with rapid prototyping and small-batch production, as it is, for instance, the case of incremental forming of polymeric sheets [1].

Cold forming of polymers remotes to the mid 1960s, where several conventional sheet and bulk metal forming operations were applied to cold plastic deformation of polymers; the review publication of Shaw [2] identifies the most relevant ones. With these works, some advantages of cold forming of polymers were identified such as short time cycles, less energy, better mechanical properties, and simpler and less-expensive tooling. In parallel emerged the need to characterize the polymer's behaviour in cold forming, as the pioneering pressure-dependent yield criteria for polymers by Caddell et al. [3].

Lately, the application of the single point incremental forming process to polymeric sheet [1] raised the interest about cold forming of polymers, its formability, and failure [4, 5].

Marques et al. [6] proposed an experimental methodology to determine the formability limits for four different thermoplastic sheets, polyamide (PA), polycarbonate (PC), polyethylene terephthalate (PET), and polyvinylchloride (PVC). The methodology made use of circle grid analysis (CGA) for the determination of necking limit or forming limit curve (FLC), and the fracture thickness measurements to obtain the "gauge length" strains of fracture limit line (FFL). Results revealed that the FLC and the FFL should be considered as a unique limit, however, the CGA is not the best methodology to determine the necking limit due to the typical stable neck propagation of polymers after the onset of necking as pointed out by Carothers and Hill in [7].

In this scientific and technological framework, this work revisits the methodology for the formability limits by necking and by the fracture of polymer determination, proposing an adaptation of the sheet metal forming procedures. The experimental work is performed by means of experimental Nakazima tests with four different geometries to scan strain paths from pure tension till the equi-biaxial expansion of polycarbonate (PC) sheets with 1 mm thickness.

2 Experimentation

The investigation was carried out on Polycarbonate (PC) sheets with 1 mm thickness, obtained by extrusion. The determination of the formability limits by necking and by fracture of the PC sheets was performed by means of Nakazima tests with a tool following the standard ISO 12,004-2 [8] on a universal sheet testing machine, Erichsen Model 142-20 at room temperature.

The specimens were machined out from the supplied sheets, and four different geometries were considered in order to achieve different strain loading paths, from tensile strain ($\beta = -0.5$) towards equi-biaxial strain ($\beta = 1$). The specimen's geometry was aligned longitudinally with the extrusion direction of the blank. Depending on the geometry and operation conditions, the corresponding strain paths were identified

as tensile strain (TS), plane strain (PS), biaxial strain (BS), and equi-biaxial strain (EBS).

In order to ensure reproducibility of the results, the tests were performed in random order and three repetitions were made for each specimen geometry. In order to minimize the friction, one layer of Polytetrafluoroethylene (PTFE) was sandwiched with two layers of Vaseline between the punch and the polymeric specimen.

The strain measurements on the deformation area, on the vicinity of the zones where cracks are opened, were performed using the digital image correlation (DIC) system ARAMIS v6.2.0-6. The Aramis system was equipped with 2 cameras using an angle between them of 23.6° and lens with 50 mm focal length. The frequency of image acquirement was set to 12 frames/s and a facet size of 13 × 11 pixel. The black and white stochastic pattern on the specimen's surface was defined by a fine spray of matte black on a white background.

3 Methodology

This investigation aims to provide a methodology for the determination of the formability limits by necking and fracture in principal strain space adapting those commonly applied for metals [9, 10] to polymeric sheets.

3.1 Necking Evaluation

Necking is a failure mode that occurs by tension, where relatively large amounts of strain are disproportionately located in a small region of the material. Two different approaches are considered and adapted for the determination of the onset of necking for the PC sheets, a time-dependent and a time-position-dependent approach (also known as "flat-valley") originally proposed by the authors for metal sheet [10].

Figure 1a presents a schematic representation of the Nakazima test tool for a tensile strain geometry. Figure 1b presents a schematic representation of the polymer specimen deformation with the advance of the punch. In this sense, the deformation in polymers is homogeneous along the specimen until a certain reduction of area occurs and local reduction in thickness is achieved (necking). This neck propagates steadily along the length of the specimen, with a cyclic behaviour until the material cannot stand the necking propagation and fracture occurs (refer to Fig. 1b) [11].

Concerning the use of the time-dependent methodology, Fig. 2 presents a schematic evolution of the major strain and the major strain rate with time. The time-dependent approach initially applied to metals is based on the experimental evidence of the necking initiation and its development [10]. The contrast between the localized thinning characteristic of the metals necking, and the necking behaviour for polymers, required some suiting adaptation of the original approach. Further information in this respect can be found elsewhere [12]. The approach makes use of the major

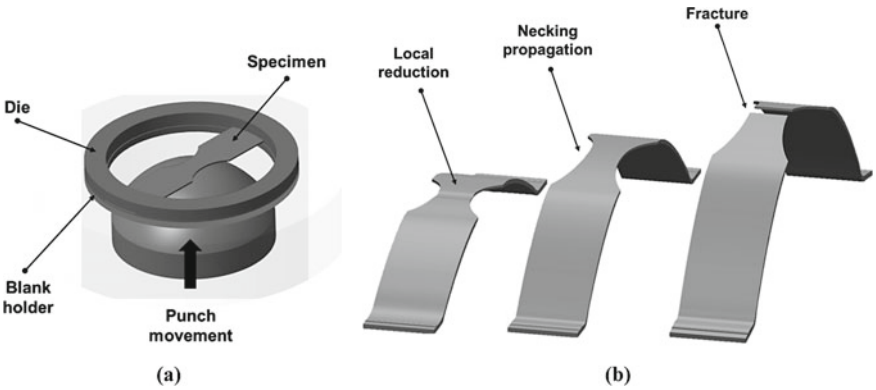


Fig. 1 Schematic representation of (a) Nakazima tool for a tensile strain specimen geometry and **b** deformation evolution of the specimen during the test

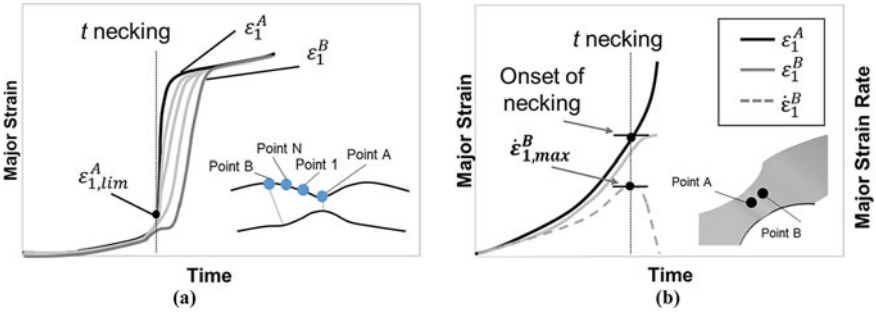


Fig. 2 Schematic representation of time-dependent methodology for a polycarbonate Nakazima test with tensile strain geometry. **a** Evolution of major strains with time for the necking region, and **b** time-dependent approach application adapted from Martinez-Donaire et al. [10]. (Color figure online)

strain temporal analysis and its first time derivative or major strain rate, for a series of points along a section perpendicular to the crack. Figure 1a shows the representation of the major strain with time for several points along a section perpendicular to the site of necking initiation (points A, $P_1 \ldots$, P_N, B). In this sense, point A corresponds to the point where the necking initiates; the points between points A and B also have a monotonical increase of strains, and point B is the first point where the strain starts ceasing (see Fig. 2a, b) temporally identifying the necking region.

On the other hand, the flat-valley approach is based on the direct observation and analysis of the displacements of the superficial layer of the sheet during necking. In this regard, Fig. 3a shows the schematic evolution of the Z-displacement (normal direction to the surface) over the X-position along a section perpendicular to the necking area of a Nakazima specimen, and each profile corresponds to an instant of time. The profile evolution (Z displacement vs. X position) before the onset of necking follows the hemispherical punch geometry (t_1 stage); the onset of necking

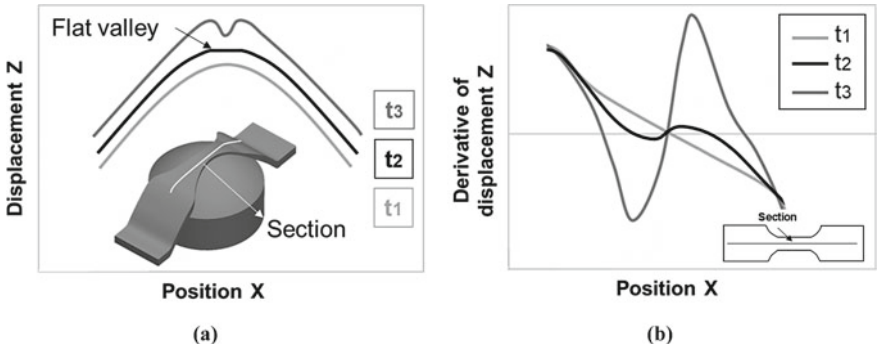


Fig. 3 Schematic representation of flat-valley approach: **a** Z-displacement over the X position and **b** temporal evolution of the Z-displacement spatial derivative on a section perpendicular to the failure area. (Color figure online)

(represented with a dark profile) stage t_2 reveals a flat profile or flat valley corresponding to the inability of the sheet to follow the punch geometry (the top of the profile) as in the previous stage and after the time instant of the onset of necking, the valley is visible (stage t_3). Figure 3b represents the temporal evolution of the Z-displacement spatial derivative for three different stages (t_1, t_2, and t_3) of the same section perpendicular to the necking area (see Fig. 3b for the localization of the section in the specimen). An alternative way to identify the instant of the onset of necking is to consider the first spatial derivative of the Z-displacement and the onset of necking corresponds to the instant where the slope remains locally constant (black curve in Fig. 3b). In polymers, this identification is difficult since the onset of necking and fracture does not occur in the same cross-section, due to the necking propagation along the specimen's length typical of the polymer of [11]. Further details of this methodology applied to polymers can be also found in [12].

3.2 Fracture Limit

The procedure to determine the formability limits by fracture is based on the measurement of the fracture thickness from the fractographies of the fractured specimens, as it is presented in Centeno et al. [9]. The logarithmic strain in the thickness direction is then calculated as follows:

$$\varepsilon_{3f} = \ln \frac{t_f}{t_0} \tag{1}$$

where t_f is the current sheet thickness at fracture and t_0 is the initial sheet thickness.

The general application of this methodology to metals considers that the fracture minor strain gradient in the sheet surface is practically null after necking [13], and it can be estimated as approximately the same as the necking one:

$$\varepsilon_{2f} \cong \varepsilon_{2n} \tag{2}$$

Finally, the fracture major strain is obtained assuming volume constancy [14] as follows:

$$\varepsilon_{1f} = -\varepsilon_{2f} - \varepsilon_{3f} \tag{3}$$

In polymers, due to neck propagation along the specimen, the original methodology developed for determining the fracture forming limit for sheet metal [9] needs to be adjusted for the polymers' behaviour. In this sense, it is more accurate to consider that the minor strain at fracture ε_{2f}^{*} is obtained considering that the local strain loading path slope β^{*} remains constant. The slope β^{*} is obtained at the last measured strains by the DIC system $\left(\varepsilon_1^{DIC}, \varepsilon_2^{DIC}\right)$,

$$\beta^{*} = \frac{d\varepsilon_2^{DIC}}{d\varepsilon_1^{DIC}} \tag{4}$$

Finally, the limit strain pair at fracture $\left(\varepsilon_{1f}^{*}, \varepsilon_{2f}^{*}\right)$ will allow to represent the formability limit by fracture.

4 Results and Discussion

This section presents the determination of the principal strain pairs at the onset of necking and fracture of the experimental plan considered for commercial Polycarbonate sheets with 1 mm thickness by means of the methodology presented in Sect. 3. These principal strain states allow defining the formability limits by necking (FLC) and by fracture (FFL), thus allowing representing the Forming Limit Diagram within the principal strain space.

4.1 Formability Limit by Necking

The methodology described in Sect. 3.1 considered two different approaches to determine the principal strains at the onset of necking, using the time-dependent and the flat-valley approaches [10]. These two approaches were applied to a PC sheet [12] in four different Nakazima specimen geometries to obtain strain paths of tensile strain (TS), plane strain (PS), biaxial strain (BS), and equi-biaxial strain (EBS). As far as the authors are aware, this was the first time that the necking strains were determined in polymeric sheet by these type of approaches, which have been just used in the characterization of necking in sheet metal forming.

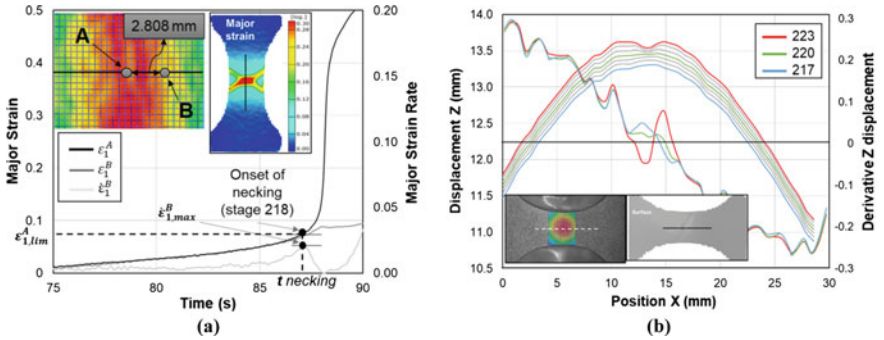


Fig. 4 Application of the methodology to obtain the onset of necking strains for a tensile strain (TS) Nakazima specimen of PC with 1 mm thickness using **a** the time-dependent methodology and **b** the flat-valley approach. (Color figure online)

Figure 4 presents the application of the two approaches to the TS Nakazima specimen of PC sheet. The time-dependent approach allowed to identify points A and B that define the instability region (Fig. 4a), where point B corresponds to the first point where the strain starts ceasing (i.e. onset of necking). The evolution of the strain rate for point B presented in Fig. 4a allows identifying clearly its local maximum $\dot{\varepsilon}^{B}_{1,max}$ and thus the time instant at the onset of necking $t_{necking}$. This approach allowed to obtain the onset of necking which occurs in point A, for the strains $\left(\varepsilon_{1,lim}, \varepsilon_{2,lim}\right)$ at the time instant $t_{necking}$.

The flat-valley approach applied to the TS Nakazima specimen is presented in Fig. 4b. The Z-displacement along a section perpendicular to the necking region presented in Fig. 4b allowed identifying the instant at which the onset of necking initiates (highlighted in green), where the thickness of the central region reduces faster than the adjacent regions and a flatten profile is visible, corresponding to the onset of necking. The spatial derivative of the Z-displacement along the selected section revealed the correspondence for the same instant the occurrence of a greater flatness confirming the onset of necking stage (Fig. 4b highlighted in green), and a sign change for the stages before (Fig. 4b highlighted in blue) and after (Fig. 4b highlighted in red) the onset of necking stage.

Figure 5 presents the application of the two approaches to the PS Nakazima specimen of a PC sheet. Time-dependent methodology is shown in Fig. 5a; the approach allowed identifying the onset of necking delimiting the instability region between point A and point B. In the same way as for TS specimen, the local maximum in the derivative of point B allowed to detect the $t_{necking}$ instant and accordingly, the strains $\left(\varepsilon_{1,lim}, \varepsilon_{2,lim}\right)$ for point A at the onset of necking.

Figure 5b presents the experimental evolutions of the Z-displacement and of the spatial derivative of the Z-displacement of PS Nakazima specimen. The flat-valley approach allowed to identify the onset of necking through the curve evolution; in this sense, highlighted in green corresponds to the instant of the onset of necking due to the slope remaining constant unlike red evolution when the flat is more accused.

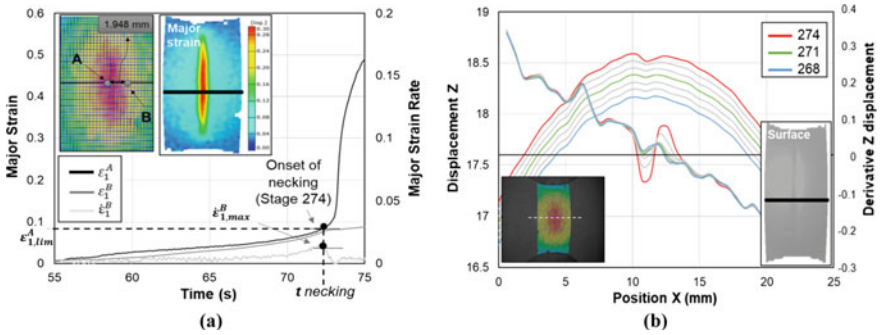


Fig. 5 Application of the methodology to obtain the onset of necking strains for a plane strain (PS) Nakazima specimen of PC with 1 mm thickness using **a** the time-dependent methodology and **b** the flat-valley approach. (Color figure online)

Through the first spatial derivative of the Z-displacement in Fig. 5b, the identification of the onset of necking (highlighted in green) is shown observing a greater flatness and a sign change between previous stages (highlighted in blue) and later stages (highlighted in red).

Figure 6 presents the application of the two approaches to the BS Nakazima specimen of the PC sheet. The time-dependent approach (Fig. 6a), similar to the previous cases (Figs. 4a and 5a), allowed to clearly determine the limit strains at the onset of necking that corresponds to point A strains $(\varepsilon_{1,lim}, \varepsilon_{2,lim})$ at the time instant $t_{necking}$. However, Fig. 6b shows that the flat-valley approach is not as direct, as seen, and the Z-displacement doesn't show a changed slope and the flat valley profile is not visible. As a consequence, the derivative of the Z-displacement does not show a difference in the evolution of the curves. As it was discussed in Rosa et al.[12], it could be necessary to increase the resolution of the DIC system to observe changes at the outer surface topology.

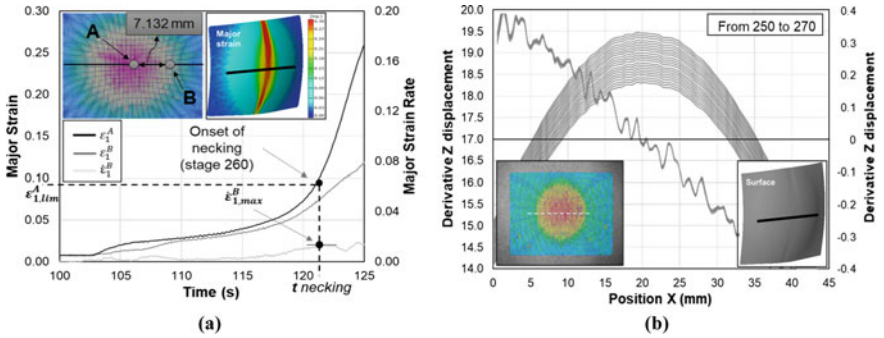


Fig. 6 Application of the methodology to obtain the onset of necking strains for a biaxial strain (BS) Nakazima specimen of PC with 1 mm thickness using **a** the time-dependent methodology and **b** the flat-valley approach. (Color figure online)

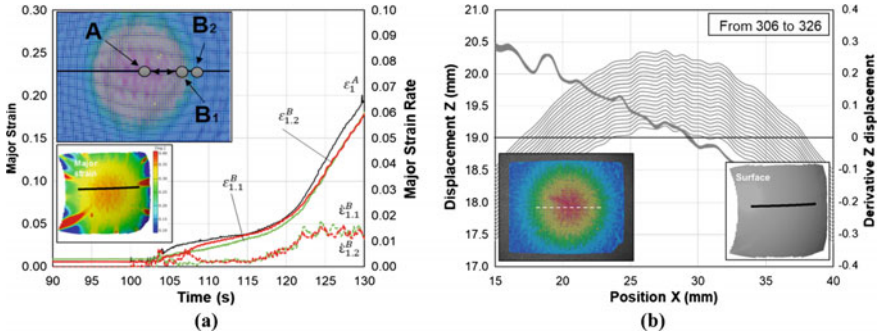


Fig. 7 Application of the methodology to obtain the onset of necking strains for an equi-biaxial strain (EBS) Nakazima specimen of PC with 1 mm thickness using **a** the time-dependent methodology and **b** the flat-valley approach. (Color figure online)

Contrary to the successful application of the presented methodology to the TS, PS, and BS Nakazima specimens, Fig. 7 presents the attempt to apply the two approaches to determine the onset of necking for the EBS Nakazima specimen of the PC sheet. The time-dependent approach revealed that the strain of a series of points along a section perpendicular to the crack showed no ceasing (Fig. 7a). Similarly, the flat-valley approach application in the EBS Nakazima specimen confirmed that the necking is not a failure mode for PC sheet under equi-biaxial strain (Fig. 7b).

4.2 Formability Limit by Fracture

The methodology to determine the fracture strains in metal sheets is based on the measurement of the fracture thickness of the specimens, as described in Sect. 3.2. This procedure, adapted by considering the local strain ratio β^* at the last stages, was applied to the PC for the four different Nakazima specimen geometries. The fractographies of the specimens were obtained with a NIKON® Stereo Microscope SMZ800N, with a magnification of $\times 30$, and allowed the measurement of the fracture thickness. Figure 8 presents the fractographies for a TS Nakazima specimen, where three different areas are clearly identified: transition zone, necking propagation zone, and fracture zone. The transition zone (Fig. 8c) corresponds to the transition between the necked area and the elongated zone, whereas the fracture zone (Fig. 8b) corresponds to the location where the fracture of the specimen occurs. In between these 2 zones, the propagation of the necking zone, typical of polymers, is visible [11].

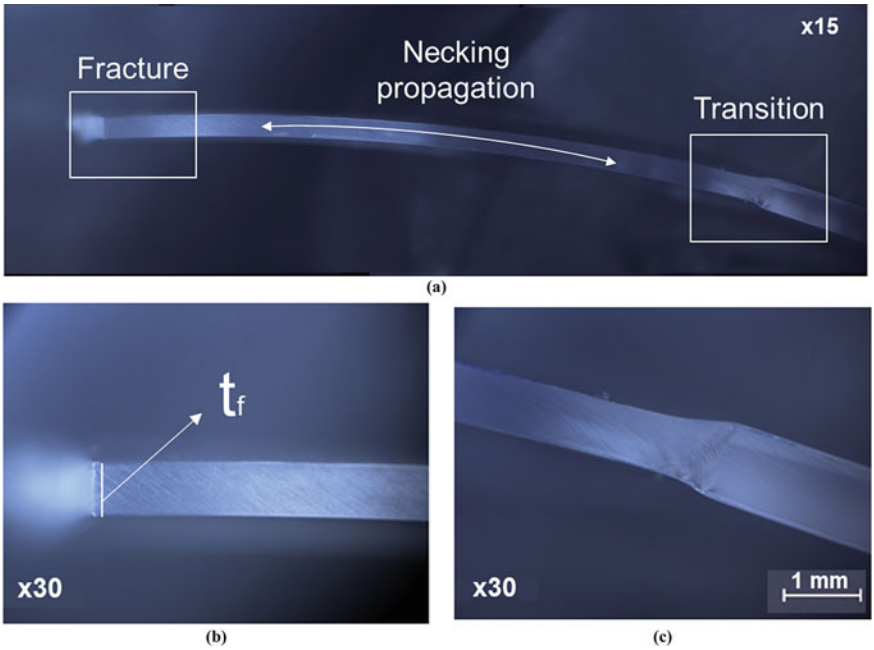


Fig. 8 **a** Fractography of a PT Nakazima specimen in the optical microscope with ×15 augmentation. Detailed view with ×30 augmentation of **b** the fracture zone and **c** the transition zone. (Color figure online)

4.3 Formability Limits in the Principal Strain Space

The formability limits by necking (FLC) and by fracture (FFL) represented in Fig. 9 were determined by means of Nakazima tests using the methodologies previously described in Sect. 3.

On the one hand side, the determination of the forming limit curve followed the methodology presented in Sect. 3.1 is based on the methodology used to determine the FLC for sheet metals. The FLC shows a different behaviour from those previously determined by Silva et al. [4] and Marques et al. [6]. The differences may be related to the use of a DIC system that gives a more accurate definition of the onset of necking due to the steady propagation of the neck than circle grid analysis, which allow measuring the strains only after fracture. The use of a DIC system and the proposed methodology revealed to be adequate to characterize the onset of necking in PC sheets. The resulted FLC can be represented by a straight line in opposition to the typical FLC of metal sheets that typically have a V shape.

On the other hand side, the determination of the fracture limit line (FFL-thickness) followed the methodology presented in Sect. 3.2 based on the procedure used to determine the FFL for sheet metal. This methodology was previously used by the authors [4, 6] and compared with the fracture strains obtained by means of single

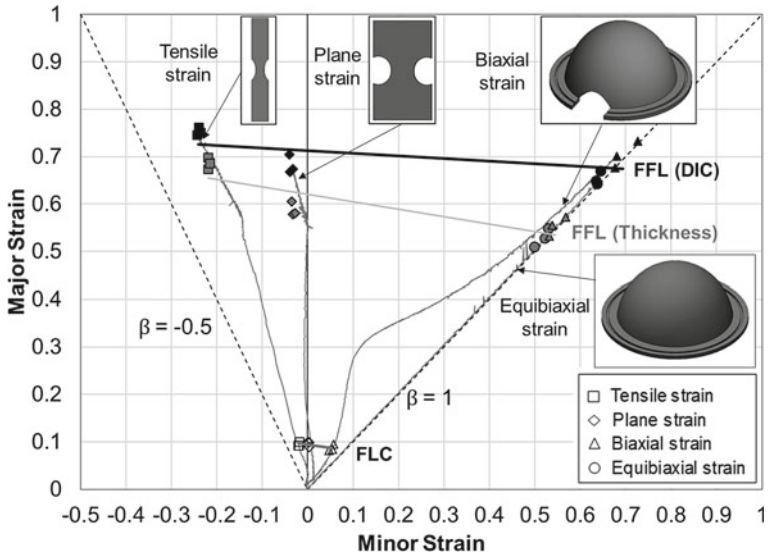


Fig. 9 Formability limits by necking (FLC) and by Fracture (FFL) for PC sheets obtained by means of Nakazima specimens in tensile, plane, biaxial, and equi-biaxial strains

point incremental forming (SPIF) parts. The fracture strains obtained in SPIF and Nakazima tests revealed differences that may be related to the significant springback that polymers experience. As can be seen, the limit strains according to the FFL-thickness are well below of those from FFL-DIC, due to the severe elastic recovery after fracture.

5 Conclusions

The methodologies used to determine the failure limits in sheet metal were adapted to polymeric sheet, allowing the successful determination of necking and fracture limits for PC sheet with 1 mm thickness.

The suiting of the methodology involved, for the first time ever, the determination of necking strains of polymer sheets by means of the time-dependent and flat-valley approaches usually used for sheet metals. The utilization of a DIC system revealed appropriate to obtain the experimental measurements of the strains regardless of the necking propagation typical of polymers, where other techniques like circle grid analysis revealed inappropriate. The resulted FLC for the PC sheet can be represented by a straight line in opposition to the typical FLC V shape for sheet metals.

The determination of the FFL was initially performed using directly the sheet metal methodology and it was verified that the resulting strains were lower than the last strains obtained from the DIC on the instant before fracture. This allowed

concluding that the fracture limit FFL-DIC obtained from the DIC, which can be approximated with a straight line, is the one that should be considered as the fracture limit.

Acknowledgments The authors acknowledge the funding provided by the Grants US-1263138 and P18-RT-3866 within the framework US/JUNTA/FEDER,UE, the Spanish Government under the research project number PGC2018-095508-B-I00 and the Fundação para a Ciência e da Tecnologia of Portugal through the project LAETA-UIDB/50022/2020.

References

1. Franzen V, Kwiatkowski L, Martins PAF, Tekkaya AE (2009) Single point incremental forming of PVC. J Mater Process Technol 209(1):462–469
2. Shaw MT (1980) Cold Forming of polymeric materials. Ann Rev Mater Sci 10:19–42
3. Caddell RM, Raghava RS, Atkins AG (1974) Pressure dependent yield criteria for polymers. Mater Sci Eng 13:113–120
4. Silva MB, Alves LM, Martins PAF (2010) Single point incremental forming of PVC: experimental findings and theoretical interpretation. Eur J Mech A/Solids 29:557–566
5. Bagudanch I, Centeno G, Vallellano C, Garcia-Romeu ML (2017) Revisiting formability and failure of polymeric sheets deformed by single point incremental forming. Polym Degr Stab 144:366–377
6. Marques TA, Silva MB, Martins PAF (2012) On the potential of single point incremental forming of sheet polymer parts. Int J Adv Manuf Technol 60:75–86
7. Carothers WH, Hill JW (1932) Studied of polymerization and ring formation. XV. Artificial fibers from synthetic linear condensation superpolymers. J Am Chem Soc 54(4):1579–1587
8. Standard ISO 12004-2 (2008) Metallic materials—sheet and strip—determination of forming-limit curves—Part 2: Determination of forming-limit curves in the laboratory
9. Centeno G, Martínez-Donaire AJ, Morales-Palma D, Vallellano C, Silva MB, Martins PAF (2015) Novel experimental techniques for the determination of the forming limits at necking and fracture. Materials forming and machining. Woodhead Publishing, United Kingdom, pp 1–24
10. Martínez-Donaire AJ, García-Lomas FJ, Vallellano C (2014) New approaches to detect the onset of localised necking in sheets under through-thickness strain gradients. Mater Des 57:135–145
11. Barenblatt GI (1974) Neck propagation in polymers. Rheol Acta 13(6):924–933
12. Rosa-Sainz A, Centeno G, Silva MB, López-Fernández JA, Martínez-Donaire AJ, Vallellano C (2020) On the determination of forming limits in polycarbonate sheets. Materials (Basel) 13(4):928
13. Embury JD, Duncan JL (1981) Formability maps. Ann Rev Mater Sci 11:505–521
14. Powers JM, Caddell RM (1972) The macroscopic volume changes of selected polymers subjected to uniform tensile deformation. Polym Eng Sci 12(6):432–436

The Effects of Press Ram Vibrations on the Production Quality



Bernd-Arno Behrens, Kai Brunotte, Richard Krimm, and Oliver Commichau

Abstract An indicator for the quality of products that are formed in an embossing process is the contour of the product. Highest contour quality is achieved, if the shape of the forming tool is perfectly imprinted into the material. However, elastic forces and tribological effects, which occur during the forming process, impair the shape-setting progress. In order to improve the embossing process, an electromagnetic actuation unit is presented in this paper, which applies horizontal vibrations into the press ram during the forming process. The actuation unit consists of two strong linear solenoids, which generate oscillating force with variable levels and frequencies. The vibrations improve the shape setting during the embossing process. The concept, design, and the function of the actuators are presented in this paper. Experimental studies on an embossing process in a production environment were performed, to demonstrate the features of the novel system.

Keywords Sheet-bulk forming · Ram vibration · Displacement control

1 Introduction

Sheet-bulk metal forming (SBMF) is a novel process that combines attributes of sheet metal forming and bulk forming operations. This process allows producing sheet metal parts, with very precise functional elements. The ability to merge multiple steps in one operation offers high potential to reduce the manufacturing costs [1,

B.-A. Behrens · K. Brunotte · R. Krimm · O. Commichau (✉)
Leibniz Universität Hannover, Institute of Forming Technology and Machines, An der Universität 2, 30823 Garbsen, Germany
e-mail: commichau@ifum.uni-hannover.de

B.-A. Behrens
e-mail: behrens@ifum.uni-hannover.de

K. Brunotte
e-mail: brunotte@ifum.uni-hannover.de

R. Krimm
e-mail: krimm@ifum.uni-hannover.de

© The Minerals, Metals & Materials Society 2021

G. Daehn et al. (eds.), *Forming the Future*, The Minerals, Metals & Materials Series,
https://doi.org/10.1007/978-3-030-75381-8_215

2]. The SBMF process is defined as a sheet metal operation with a sheet thickness between 1 and 5 mm, combined with a three-dimensional material flow. It is a complex interaction between different forming processes. In order to gain more understanding of the SBMF process, this paper focuses on the appearance of horizontal forces and resulting press displacements occurring during the forming process. SBMF combines many different process steps and therefore depends on many process parameters. Embossing is one process, which can be included in a SBMF operation. The embossing process will be investigated in this paper.

During the embossing process, a topographic geometry is imprinted from the stamp of the tool into a workpiece. Mechanical presses apply high pressure on the part during the embossing process. Usually, the force is directed along the vertical axis of the press frame. Therefore, the rigidity of the press frame is optimized along the vertical axis [3]. However, especially when forming asymmetric parts, the force splits into a vertical as well as a horizontal fraction. The press frame rigidity along the horizontal axes is limited [4] As a result, the horizontal force can cause small amounts of deformation of the press and small displacement of the press ram versus the bolster of the press [5]. One reason for the possible displacement is, that the bearing, which holds the press ram in place, offers small amounts of clearance. The press ram can move horizontally within this horizontal clearance.

2 Superimposed Vibrations

Prior investigations have shown that forming processes can be improved by superimposing oscillations. For instance, the lifetime of a coining tool can be increased, since the vibrations reduced surface pressure peaks, which contribute to the tool wear. In Koch et al. [6], a hydraulic device was added to a sheet-bulk metal forming process. The hydraulic device superimposes vertical vibrations to the process. The results showed that the vibrations reduced the abrasive tool wear during the process. Nonetheless, the study has also proven, that the vibrations do not impair the quality of the tool in terms of accuracy of the geometry imprint into the workpiece. The positive impact of vibrations on the result of embossing processes has also been shown in Behrens et al. [7]. Oscillations have improved the mold filling during the process, allowing to produce within a smaller tolerance band. The paper Müller et al. [8] reports about the reduction of plastic work during the deformation stage by means of overlaying vibrations to the process. Applying vibrations has a number of positive effects on the result. Additionally, it was shown in Kirchner et al. [9] and Osakada et al. [10] that the total necessary force of the process was reduced by means of the vibrations. The reduction of necessary process force could be linked to a better tribological interaction between the tool and the workpiece [11], the reduced friction during the forming process has also been addressed in Siegert and Ulmer [12]. In

Izumi et al. [13], the reduced material strain during the material flow when superimposing ultrasonic vibration has been investigated. Results have shown a significant reduction of such material strains. The reduction of tool wear was studied and experimentally proven in Matsumoto et al. [14].

Overall, the vibrations improve the features of the forming process. However, these investigations focused on oscillations in vertical direction. The effects of horizontal vibrations, perpendicular to the ram travel direction, have not been addressed yet. The limited horizontal stiffness of mechanical servo presses allows to include a system, which is able to force a small-scale horizontal movement of the ram.

3 Horizontal Forces

Horizontal forces are likely to appear during an SBMF process, because many parts are not entirely symmetrical. That leads to an unequal force distribution in horizontal direction. As mentioned before, the forces can cause horizontal displacement of the press ram.

An electromagnetic system, which eliminates horizontal forces that occur during the forming of asymmetric parts by means of electromagnetic counterforce in combination with a control system, was presented in Groene et al. [15]. A numerical study has shown that solenoids with sufficient strength can react in real time to upcoming horizontal forces and hold the press ram in a defined position. In an alternative approach, hydraulic systems were used to reduce horizontal displacement during the forming process [16].

Taking into account, that vibrations of small amplitudes can improve the quality of the embossing process and that solenoids have proven to provide enough force, this paper proposes an actuation unit inducing horizontal vibrations to the press ram.

4 Press Ram Displacement

In order to determine the amount of the press ram displacement under horizontal load, a functional forming tool was designed, which can be used to execute embossing operations under variation of the associated horizontal force. As shown in Fig. 1, the central element of the tool is the stamp, which holds the topographic surface for the embossing. The stamp is held by a bearing. That can be tilted by the angle α between 0° and 10°.

The sheet metal will be placed between the upper and lower tool side, as shown in the figure. The upper tool is rigidly bolted to the press ram, the lower tool side is bolted to the bolster. During the embossing process, horizontal force appears. The maximum of the horizontal force depends on the tilt angle and the applied process force. The experimental study was carried out on a Schuler MSC-2000 press with a nominal force of 2000 kN. The process force in this investigation was set to 500 kN.

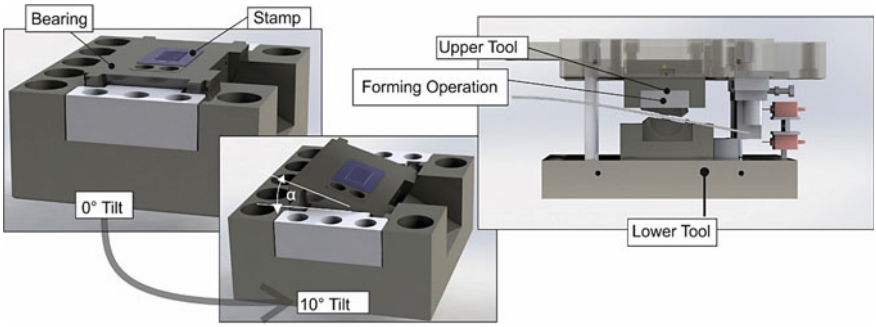


Fig. 1 Adjustable machine tool. (Color figure online)

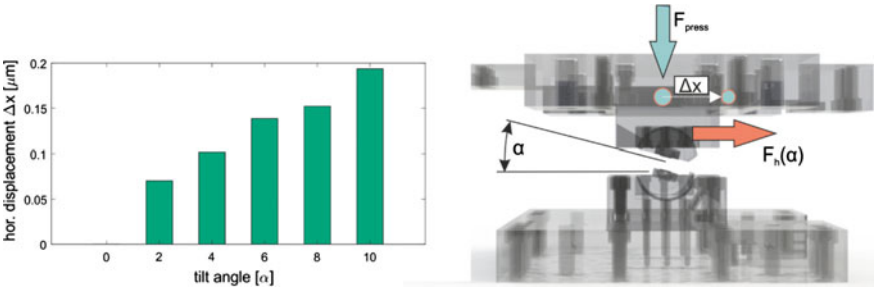


Fig. 2 Ram displacement under variation of the tool tilt angle. (Color figure online)

A Dual-phase steel DP600 with 3 mm thickness was used for the experiment. The measured displacements during the forming process are shown in Fig. 2. As expected, the ram displacement increases, the more the forming tool is tilted. Displacements of almost 0.2 mm have been measured.

The results of the study show that the horizontal displacement during forming asymmetric parts reaches values up to 0.2 mm. Splitting the resulting force into a vertical and a horizontal fraction shows that horizontal forces from 100 kN on are sufficient to trigger horizontal movements of the press ram. In the following section, the device for the application of vibration to the tool is presented.

5 Functional Design of the Actuator

The concept of the system is based on electromagnetic solenoids. The basic components are the magnetic core, a copper wired coil, and the armature. The core and the armature are separated by an air gap. The size of the air gap is adjustable. Both are made of the sheet-metal M400-50A, which has high permittivity. This will improve

the magnetic flux density and the solenoid force accordingly, since there is a proportional relation between those factors. When the coil is excited with a direct current, a magnetic field sets up. The magnetic flux follows the circuit through the magnetic core, passes through the air gap, and returns along the armature. A magnetomotive force appears as a counter effect, trying to close down the air gap for better magnetic flux. The coil is made of 1 × 4 mm flat copper wire with 250 windings. The design allows maximum currents of 20 A. Besides magnetic flux, the size of the pole face impacts the potential force of the magnet. The maximum force also depends on the number of coil windings and the inductivity accordingly. High inductivity leads to high total force on one hand. On the other hand, the inductivity limits the dynamics of the magnet. However, in order to create oscillating force, high dynamics are necessary as well. Therefore, a tradeoff between total force and the dynamics of the force had to be found. With the above-mentioned design parameters, the magnets are able to build up the maximum force of 100 kN in about 50 ms. Therefore, the maximum reachable frequency for this device is 10 Hz. Another limiting factor is the size of the mounting room inside of the press.

The solenoids are designed for use in the tryout press Schuler MSC-2000. A frame was designed which integrates the solenoids in the mounting room of the Servo Press. The designed structure consists of two parts: a frame that holds the armature, which is rigidly attached to the press ram. Another frame is used to connect the magnetic body to the bolster, containing the solenoids and the connectors. The air gap between the magnetic body and the armature is adjustable with a range between 0.5 and 3.5 mm. The non-conductive aluminum alloy EN AW-7075 was used for the mounting plate to avoid magnetization of the framework. There are two actuators integrated on the left side of the forming tool (see Fig. 4). In this setup, the solenoids can frequently pull the press ram to the left side, while the horizontal process force pushed the ram to the right side.

Two frequency converters DCM by Siemens power the solenoids. Both have a nominal current of 29 A. A controlling program was set up that sends the information about the desired frequency and amplitude of the vibration to the converter. This signal is given by a LabVIEW tool, allowing to adjust the amplitude, shape, and frequency of the signal. The LabVIEW tool is connected to the control system of the converter via an I/O-Box, which is connected to the digital and analog I/O ports of the converters. The concept is illustrated in Fig. 3.

The distance between the lower and the upper part of the tool, the ram displacement, respectively, is measured with a laser distance sensor M7L by MEL. The results

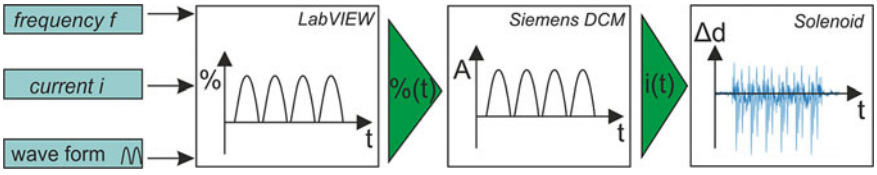


Fig. 3 Connection concept of the actuation unit. (Color figure online)

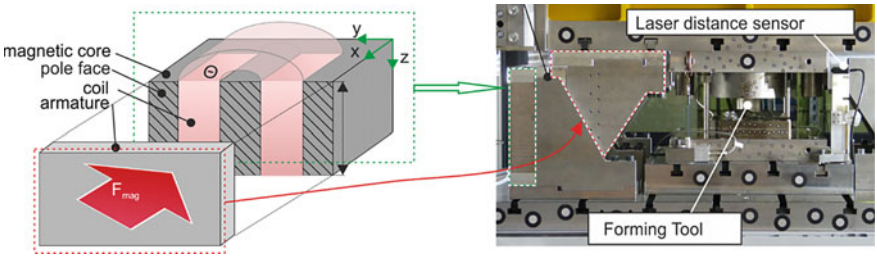


Fig. 4 Experimental setup. (Color figure online)

of the distance measurement are recorded with attached notebooks. Additionally, a height sensor was attached to the tool, measuring the distance between the press ram and the bolster of the press. The height measurement was used to only activate the solenoids, while the forming operation is performed. The solenoids must not operate during the backstroke to avoid unnecessary stressing of the press bearings and overheating of the magnets.

6 Oscillation Potential of Solenoids

The setup described in Fig. 4 was used to determine, whether the proposed device is functional. Firstly, the converter has an internal PI-controller, which needs to be set up with correct parameters, to ensure a stable control behavior. With the LabVIEW tool, the signal of a step function was transmitted to the converter, while evaluating the response of the converter. A set of parameters has been found by using the Ziegler–Nichols Method. This is a common heuristic method for tuning a controller.

In the next step, a sinusoidal signal was used to investigate the oscillation potential of the solenoids. The converter was set to 80% of the nominal current to ensure that the converter nor the solenoids experience any permanent damaging by over-excitation. During the experiment, the signals were recorded by the controlling system of the converter. The signals are shown in Fig. 5 (left). As shown, there is a lag of about 50 ms between the analog signal and the current. The lag appears because of internal processing time between the I/O-Ports and the current controller. However, the only consequence of the lag is a phase difference between the LabVIEW signal and the force generation of the solenoids. The oscillation itself is not impaired by this effect. Besides the phase difference, the current controller shows good controlling behavior, as it replicates the given sinusoidal signal perfectly.

The data was recorded while performing an embossing process with the tool presented in Fig. 1. The ram movement followed a sinusoidal path-time curve, as it is usual for eccentric presses. The vibration effect on the press ram by means of the sinusoidal force pulses is shown in Fig. 5 (right). The displacement is clearly detectable, while the ram oscillates in the same frequency as the solenoids. The

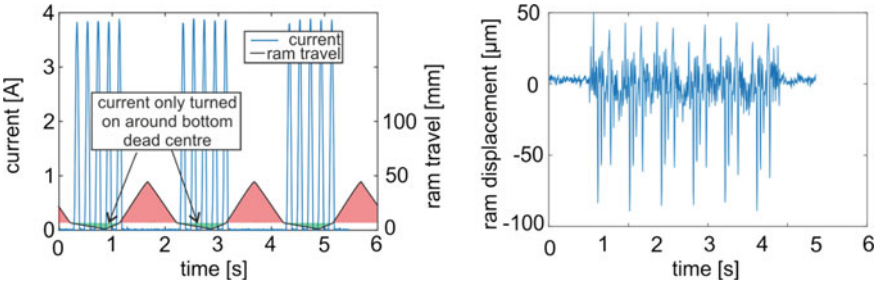


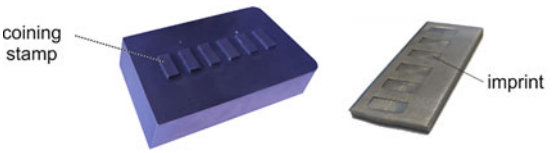
Fig. 5 Current injection in the solenoids and resulting ram vibration. (Color figure online)

amplitude of the oscillation is approximately 60 µm. The displacement graph was recorded while the stamp of the tool touched the workpiece and thus performed the embossing process. This shows that the solenoids are able to induce press ram vibration when the press ram is under load and applies high pressure on the workpiece.

7 Reduction of Abrasive Tool Wear

The production method of coining parts while superimposing the process with horizontal oscillations was tested in an experimental approach. A study was carried out covering the production of 2 × 10.000 coining parts. The experimental setup contains a forming press, a sheet-metal feeding system, and a reel-system. Additionally, the forming tool which was depicted in Fig. 1 was installed in the press. A more detailed description of the forming tool is given in Behrens et al. [17]. The described setup allows fully automated production of coined parts. The geometry of the coining stamp is a rectangular plateau structure, which imprints six plateaus into the sheet metal. The steel type DC04 was used as sheet metal (see Fig. 6).

During the experiments, the forming force was recorded by the press internal strain gauge. Two freshly produced sets of coining stamps were used to ensure comparability between the two production modes mentioned in the table in Fig. 6. A microscopic investigation on the surface of the coining stamps prior to and after the coining operation was performed. The surface roughness was measured along three lines (*left, center, right*) on the plateau (see Fig. 7). Abrasive wear, that leads to



material	DC04
production modes	10.000 - oscillation off 10.000 - oscillation on
geometry	plateau
stroke rate	40 / minute
force	260 kN

Fig. 6 Coining stamp, produced part, and production parameters. (Color figure online)

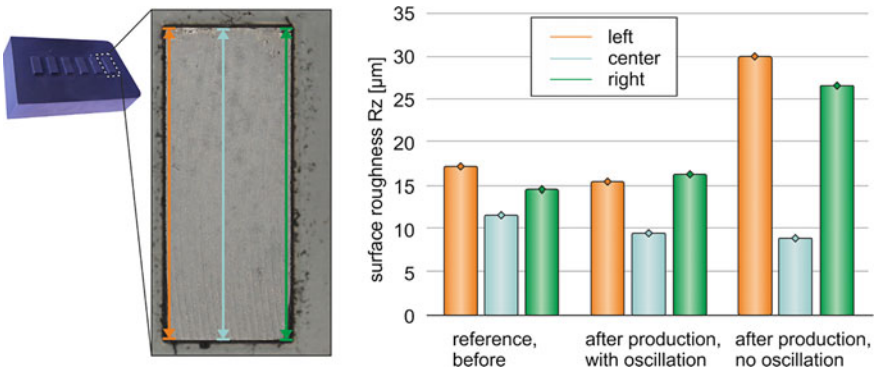


Fig. 7 Results of the microscopic evaluation of a single plateau. (Color figure online)

increased roughness values, was noted. While the coining process without oscillation leads to increased surface roughness, this effect cannot be observed while producing with superimposed oscillation. Further, as shown in the bar diagram, the tool wear seems to appear only on the edges of the plateau structured (orange and green) while the surface roughness remains unaffected on the center line.

The reason for that effect might be, that the material flow, which appears when the coining stamp forces into the sheet metal, always runs across the edges of the stamp. The highly frictional material flow then causes the abrasions. The center line on the other hand does not experience such material flow, since the material extrusion is always directed toward the outer edges of the stamp. Local pressure peaks between the stamp and the sheet could be smoothened by the horizontal oscillation which has the effect that less wear appears.

Although the extend of the study depicts only a small fraction of the lifetime of a coining tool, this study indicates that the abrasive tool wear could be decreased by superimposing the process with horizontal oscillation.

8 Conclusion and Future Work

In the first study, the displacement effect of horizontal force on the press ram position has been shown. Based on these results, an actuation unit was designed. The actuation unit presented in this paper is able to induce horizontal vibrations to the press ram. The development and build-up process were presented, furthermore experimental studies have been performed to determine the functionality of the device. The experiments have shown that solenoids are able to induce oscillating force to the ram and produce oscillating displacement, respectively. A small-scale production study shows indications, that the abrasive wear, that occurs during forming could be decreased by the superimposed oscillation.

Further studies on the potential amplitudes and frequencies are planned in this context. Furthermore, for a full understanding on the impact, a more comprehensive study with more complex coining structure as well as a higher production volume and higher forming force is planned.

Acknowledgments Funded by the Deutsche Forschungsgemeinschaft (DFG, German Research Foundation)—116961331. The authors would like to thank the DFG for their support of the project B7 in the scope of the Transregional Collaborative Research Centre 73 (TCRC73).

References

1. Merklein M, Allwood J, Behrens B-A, Brosius A, Hagenah H, Kuzman K, Mori K, Tekkaya AE, Weckenmann A (2012) Bulk Forming of sheet metal. CIRP Ann Manuf Technol
2. Weckenmann A, Behrens B-A, Reithmeier E, Akkasoglu G, Vucetic M, Cahyono T, Ohrt C, Hübner S, Kästner S (2011) Appliance of the maturity method in the development of endoscopic geometry inspection for sheet bulk metal forming tools. Total Qual Manage Excellence 39:11–16
3. Salfeld V, Matthias T, Krimm R, Behrens B-A (2012) Analysis of machine influence on process stability in sheet bulk metal forming. Proc CIRP 32–36
4. Großmann K, Penter L, Schenke C-C, Hardtmann A, Weber J, Lohse H, Schulze T (2014) FE forming models including press behaviour allow for realistic computation of blankholder forces. Int Deep Draw Res Group 167–169
5. Brecher C, Esser M, Witt S (2009) Interaction of manufacturing process and machine tool. Ann CIRP 58:588–607
6. Koch S, Vucetic M, Hübner S, Bouguecha A, Behrens B-A (2015) Superimposed oscillating and non-oscillating ring compression tests for sheet-bulk metal forming technology. Adv Mater Res 794
7. Behrens B-A, Bouguecha A, Vucetic M, Hübner S, Rosenbusch D, Koch S (2015) Numerical and experimental investigations of multistage sheet-bulk metal forming process with compound press tools. Key Eng Mater 651–653:1153–1158
8. Müller P, Rosenbusch D, Wehmeyer J, Hubner S, Behrens B-A (2019) Investigations of forming force, friction values and surface qualities in ring compression tests using oscillating tools. In: Production at the leading edge of technology, Proceedings of the 9th Congress of thr German academic association for production technology (WGP), pp 73–81
9. Kirchner H, Kromp W, Prinz FB, Trimmel P (1985) Plastic deformation under simultaneous cyclic and unidirectional loading at low and ultrasonic frequencies. Mater Sci Eng 68(2):197–206
10. Osakada K, Wang X, Shinij Hanami S (1997) Precision forging of spline by flashless die forging with axially driven die. Ann CIRP 46(1):209–212
11. Behrens B-A, Biermann D, Menzel A, Tillmann W, Krimm R, Meijer A, Schewe M, Stangier D, Commichau O, Müller P, Rosenbusch D (2019) Untersuchungen strukturierter Werkzeugflächen und der Einfluss auf den Werkzeugverschleiß. 4. Industriekolloquium Blechmassivumformung DFG-Transregio 73
12. Siegert K, Ulmer J (2001) Superimposing ultrasonic waves on the dies in tube and wire drawing. Trans ASME J Eng Mater Technol
13. Izumi O, Oyama K, Suzuki Y (1966) Effects of superimposed ultrasonic vibration on compressive deformation of metals. Trans Jpn Inst Met 7:162–167
14. Matsumoto R, Sawa S, Utsunomiya H, Osakada K (2011) Prevention of galling in forming of deep hole with retreat and advance pulse ram motion on servo press. Ann CIRP 315–318

15. Groene M, Krimm R, Behrens B-A (2017) Electromagnetic system to control the accuracy of ram travel at the presence of horizontal forces. Adv Mater Process
16. Schrobbach H (1995) Kompensation der Stößelkippung an mechanischen Zweipunktpressen unter der Berücksichtigung des Horizontalversatzes im Werkzeugsystem, TU Chemnitz
17. Behrens B-A, Krimm R, Koß J, Commichau O (2019) Charakterisierung von Horizontalbelastungen bei der Blechmassivumformung. Hannover

Localized Contact Pressure of Blankholder for Stamping Irregular Sheet Parts by Configuring the Height of the Supporting Elements



Kuang-Jau Fann, Mathias Liewald, and Kim Rouven Riedmüller

Abstract This paper presents an engineering procedure for stamping irregular sheet metal parts with an elastic blankholder, providing a localized contact pressure to ensure stamped parts without failures of cracks and wrinkles. This is done by arranging the height of the blankholder supporting elements in a die set, which is made using standard manufacturing quality and is implemented in a press line equipped with standard die cushions. However, the contact pressure is very sensitive to the height of supporting elements. To eliminate the inherent noise from the geometric dimension and tolerance of the die set, a finite element model for optimization of the contact pressure must be created according to the actual die set geometry. In this study, the blankholder geometry for stamping a fender-like part was scanned by GOMATOS and the height of cylindrical supporting elements was measured by inserting feeler gauges between the blankholder and the supporting elements according to the outcomes of finite element analysis.

Keywords Sheet forming · Irregular part · Stamping · Blankholder · Die cushion · Blankholder force

1 Introduction

In the past decades, a lot of research has been focused on the improvement of stamping press, die cushion, and die technology for manufacturing sheet metal parts with irregular geometries required by the automotive industry in an attempt to control the metal flow between blankholders by the blankholder force, and thus to produce reliable sheet metal parts. Among them, after the servo motor was introduced into the metal forming press [1], the servo press can form a pulsed pressure plate with its flexibility and programmability, especially in its characteristics of a pulsating ram

K.-J. Fann (✉)
National Chung Hsing University, Kuo Kuang Road 250, Taichung 40227, Taiwan
e-mail: kjfann@nchu.edu.tw

M. Liewald · K. R. Riedmüller
Institute for Metal Forming Technology, Holzgartenstr. 17, 70174 Stuttgart, Germany

© The Minerals, Metals & Materials Society 2021

G. Daehn et al. (eds.), *Forming the Future*, The Minerals, Metals & Materials Series,
https://doi.org/10.1007/978-3-030-75381-8_216

motion, which makes it widely used in sheet metal stamping industry. At the same time, it has attracted many scholars to engage in the related research of servo presses applied to sheet metal forming process [2–6]. Besides, as for the further development of the die cushions, which are implemented in the bed of conventional single-acting presses, some researchers have used the hydraulic cylinders with proportional servo valves onto the die cushion to control the blankholder force in the stamping process [7] or to provide a pulsating blankholder force [8]. Even multiple cylinders are used to form and to regulate the local blankholder force [7], so that the material flow can be more accurately controlled. As for the research of die technology application, it is based on the fact that the line of force formed between the press and the die cushion during the forming process is too long, that there are too many parameters, and that it is not easy to adjust one by one to ensure the accuracy of the forming results. Therefore, changing the blankholder to an elastic body is one of the ways that can form a localized blankholder force by multiple hydraulic cylinders with proportional servo valves configured for the localized blankholder force [9], and using closed-loop control technology is another way that the blankholder force can be controlled by monitoring the side wall stress of the parts during the stamping process [10]. However, this kind of solution is quite expensive. Alternatively, based on the fact that the single-acting presses used in the sheet stamping process are always equipped with die cushions, the idea that a thermal pin can be placed on the die cushion was thus proposed by [9] to change the blankholder force locally. The length of the thermal pin would be adjusted according to its temperature by heating or cooling, so that the material flow between the blankholder can be controlled and the goal of producing precision-stamped sheet metal parts can be achieved in such a cheap way.

To demonstrate the feasibility to convert the existing force control schema to a height control concept initiated by [9], a pre-study has been conducted by using finite element analysis to investigate the influence of the height of individual pins on the contact pressure between the elastic blankholder and the sheet metal from the resultant cushion forces [11]. In that pre-study, it was found that for applications of stamping fender-like irregular parts, there should be two layers of pins, thermal pins (upper layer) and cushion pins (lower layer), separated by an adapter plate, instead of just one layer. Furthermore, the thermal pins should be configured as supporting elements that closely surround the punch and are located underneath the sheet blank. Under this configuration, a sound part could thus be stamped with the pin heights, which is prescribed and correspondingly determined from the existing optimized pin forces. It was further observed that the elastic blankholder along with the supporting pins are quite stiff. The contact pressure is thus very sensitive to the height adjustment of the supporting pins, which is just in the manufacturing tolerance range of the current industry standard. If no extra care is taken to the tolerance between the parts of the die set, it might easily cause the sheet metal part to fail. This article is thus aimed to experimentally validate the previous finite element analysis, as well as to illustrate the implementation of the supporting elements, for a process stamping irregular sheet metal part regarding the geometric dimensioning and tolerancing in manufacturers' daily lives.

2 Elastic Blankholder Geometry and Finite Element Modeling

The fender-like irregular part used in the previous finite element study is the same as that for the study [10]. Its top face is a slender right trapezoid with different radii at the corners. The radii and size on its bottom face are larger than those of the top face. This irregular part has an inclined wall on each side, which easily induce wrinkles on the inclined walls during the stamping process and make this part hard to manufacture.

The die set used to stamp this irregular part with die cushion and elastic blankholder is shown in Fig. 1. It has a base plate to install the punch and to pile up other components. The cushion pins pass the pin holes of the base plate and lift an adapter plate. Ten supporting elements (thermal pins) are installed on the adapter plate to support the elastic blankholder. That means the adapter plate along with the supporting elements and the elastic blankholder move up and down simultaneously during the stamping process.

All the components of the die set are made and assembled with the current shop standard technique. In particular, the elastic blankholder, which needs a hard and polished top face, is manufactured as following: first, it is milled to a certain thickness, then it is case hardened, and finally it is ground and polished to its final thickness. However, the heat treatment during the case hardening might cause permanent deformation of the elastic blankholder. This deformation might not be able to be eliminated later in the grinding process, as it would be straightened by the uniformly distributed load added due to use of the magnetic workholding chuck during grinding. After grinding, when the chuck is off, the deformation would return as the load has been removed.

The deformation of the blankholder can be observed from the relative height distribution of its top face and its thickness distribution as shown in Fig. 2b, which were obtained by scanning both the top and bottom faces of the blankholder with the optical measurement system GOM ATOS 5M. Some outer areas of the faces were not scanned, because some fixtures to hold the blankholder affected the scanning

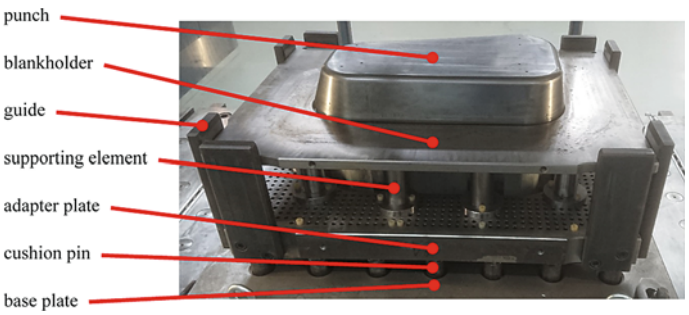


Fig. 1 Lower parts of the die set on a press bed. (Color figure online)

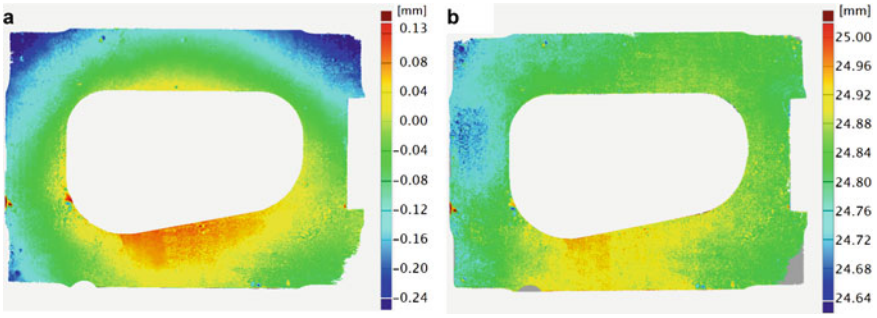


Fig. 2 Geometry of the blankholder **a** relative height of the top face, **b** thickness. (Color figure online)

results. It can be seen that the variation of the thickness is good within the general tolerance range, which is ±0.2 mm for medium tolerance class of a nominal linear measure less than 30 mm according to DIN ISO 2768-1, while the evenness shown in Fig. 2a is within 0.6 mm as the general form tolerance for a specified size less than 1,000 mm according to DIN ISO 2768-2. However, they are far beyond the tolerance for the demand of this application under investigation, in which every individual hundredth mm of the height of the supporting element can cause about 30 kN in the reaction force on the elastic blankholder according to the pre-study via finite element analysis [11]. The same situation also applies to the other components of the die set.

In the pre-study [11], among the components in the die set, only the blankholder is regarded as elastic deformable and modeled just as usual in finite element analysis modeling by directly using the geometry generated from CAD system. To consider the inherent noise attributed to the manufacturing, the actual deformation and thickness should be taken into account during the finite element modeling. This study is thus to investigate if the manufacturing noise affects the results of finite element analysis.

To model this kind of blankholder, the coordinates of the scanned point cloud on the top and bottom faces must be firstly transferred to the existing finite element model by matching all of them around the punch hole with those in the existing model. The point cloud is then transformed, so that the new coordinates of the point cloud can determine a plane by using linear regression, whose normal is the same as that of the existing finite element model and to which the summation of the distance of each point has a minimum. Thereafter, the centroid of the point cloud from the punch hole is preliminarily determined for translation also by linear regressing the point cloud of the long, short, and base side, respectively, while the inclined angle of the slant side is computed for rotation. Once the distance from the point cloud to the existing finite element model has its minimum from the four regarding sides by recursively determining the centroid and the inclined angle, the affine transformation matrix to transfer the whole point cloud is then ascertained. Figure 3a shows that top view of the point cloud on the top face of the blankholder (shown as black area) in comparison with the existing finite element model. It can be noticed that the actual

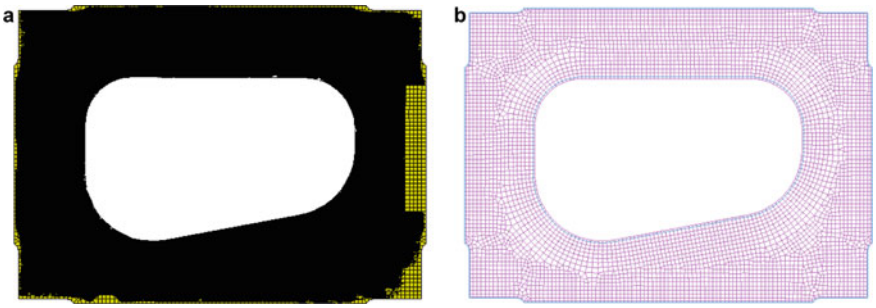


Fig. 3 **a** top view of the point cloud of the top face (*black*) above the existing finite element model (*yellow*), **b** top view of the finite element model for the blankholder in this study (*purple*) above that used in the previous study (*blue*). (Color figure online)

blankholder is smaller than that of the finite element model or as mentioned above from the CAD data. Because the number of the points in the point cloud is too huge to process the further finite element modeling, the faces are approximated and generated with GOM Inspect in a polynomial of degree three for the whole scanned points on the top and bottom faces. By means of projecting the nodes of the existing finite element model to the faces, the finite element model for the approximated actual elastic blankholder is then created, as shown in Fig. 3b. The nodes on the inner and outer edges, which are smaller than the CAD data, are extrapolated and trimmed from the existing finite element model. The blankholder is still modeled with four layers in the thickness. The coordinates of the elements in each layer are interpolated from those of the top and bottom faces.

The other components of the die set were not scanned with GOM ATOS further, because they are regarded as rigid in the previous study and will remain the same in this study. The other concern is that the interaction between the components during the stamping process is quite random, even though the die is driven by the press ram, and the die set is supported by the die cushion, all of which are principally well guided. However, based on the inhomogeneous evenness and thickness, previously observed with GOM ATOS, the base plate must not be exactly flat in order to lift the supporting elements and there should be some clearance between the top face of the supporting elements and the bottom face of the blankholder. The same argument also applies to the other components attached to the press ram and on the press bed. Since the parts are more massive and stiffer than the blankholder, the deformation of those parts are insignificant in this study. In order to get a more accurate description of the contact between the supporting elements and the blankholder, which essentially influences the stiffness of the elastic blankholder, the gap between the supporting elements and the blankholder has been checked with feeler gauges set in a thickness ranging from 0.01 mm. Figure 4a shows the results of the clearance, in which the value represents the minimum of the clearance at that range. That means that the value 0.1 shown for symbol i of #2 indicates the clearance at the inner edge toward to the punch hole has a range larger than 0.1 mm but less than

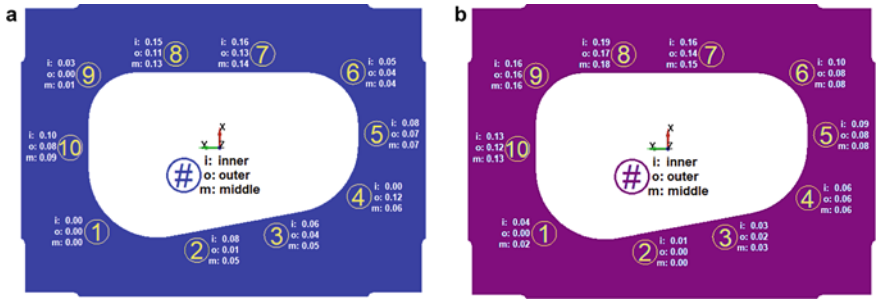


Fig. 4 Clearance from each supporting element to the blankholder measured **a** with feeler gauges, **b** from the finite element model at difference positions related to the punch hole (*o*: outer, *i*: inner, *m*: middle). (Color figure online)

0.11 mm. Correspondingly, the clearances between the rigid supporting elements and the elastic blankholder have been measured from the finite element model and shown in Fig. 4b. The difference of the clearance on each supporting elements can be attributed to that there exist the allowance varying from position to position caused by manufacturing the other components, as well as by assembling the components to the die set. Nevertheless, referring to these clearance results, the finite element model for each supporting element should be correspondingly rotated. This would let the existent contact situation between each supporting element and the blankholder along with the feeler gauges be able to be carried out approximately, because the clearance is significant to the results of this study as mentioned later.

3 Stamping by Elastic Blankholder with Supporting Elements

The finite element analysis of the stiffness of the blankholder with supporting elements has been conducted with LS-DYNA implicit code in the previous study [11], in that, the four elements having a relative lower stiffness are fixed lower than the other six elements and the blankholder is then pressed with the rigid die toward the fixed pins for a given stroke. The blankholder and the supporting elements were modeled as flat. As shown in Fig. 5a, it can be observed that at different position where each supporting element locates, the blankholders have similar stiffness, which is equivalent to the slope of the curves shown in Fig. 5. Furthermore, no gap or backlash-like characteristics can be recognized at the locations of the stiffer supporting elements, while at the positions with less stiff elements a backlash-like characteristic can be recognized. This is because their lower top faces contact the blankholder later. Contrastively, the results from this study shown in Fig. 5b reveal that all positions have a backlash-like characteristics, which shows up as an nonzero

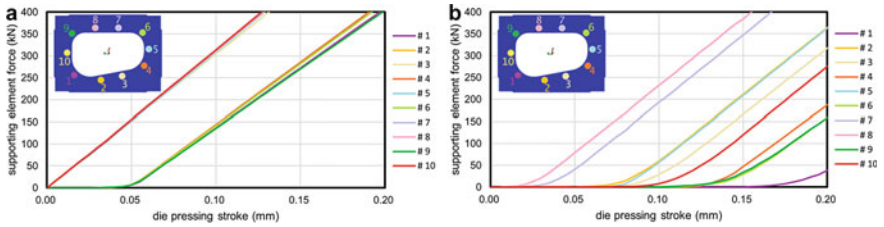


Fig. 5 Stiffness of the blankholder from a finite element model of **a** the previous study [11], **b** this study. (Color figure online)

abscissa intercept on each curve, no matter how high the top face of their corresponding supporting element are. Even the top face of each supporting element is modeled as flat and its maximum clearance to the blankholder is less than 0.0015 mm. The minimum backlash of at least 0.25 mm can be found even at the locations having the strongest stiffness (element #8). This deformation and inhomogeneity in thickness can be attributed to the blankholder being modeled to more or less reflect the actual state after manufacturing.

With such backlash-like characteristics, the distribution of the contact pressure of the blankholder to the blank is then dependent on the total cushion force applied in this study. If the cushion force is small, say 200 kN, there are only two spots popping up on the contact pressure imprint from the supporting elements 7 and 8, because their backlashes are the smallest. If the cushion force reaches 1,110 kN, the backlash of most all supporting elements except the element 1 are eliminated and the corresponding contact pressure appears as shown in Fig. 6b. However, the distribution is quite inhomogeneous in comparison with that from the previous study without regards to the backlash as shown in Fig. 6a. As the backlash is reduced, the contact pressure increases and is spread over a wider area.

Similar results can be observed in the step loading test with LS-DYNA explicit code as shown in Fig. 7, in that, the cushion force stepwise acts on the blankholder from 200 to 800 kN in step of 200 kN, while the die presses and the supporting

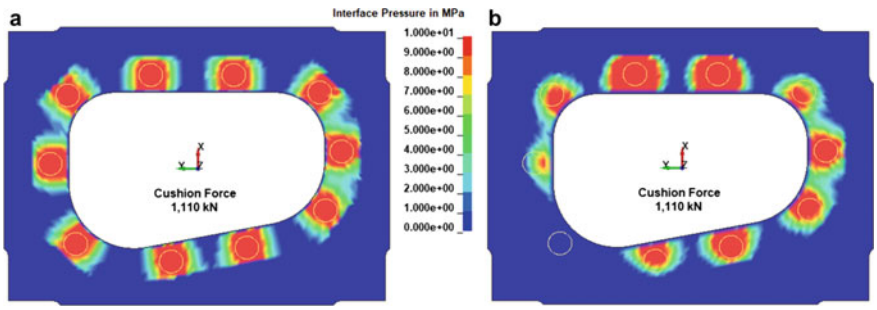


Fig. 6 Contact pressure of the blankholder under the cushion force of 1,110 kN from a finite element model of **a** the previous study [11], **b** this study. (Color figure online)

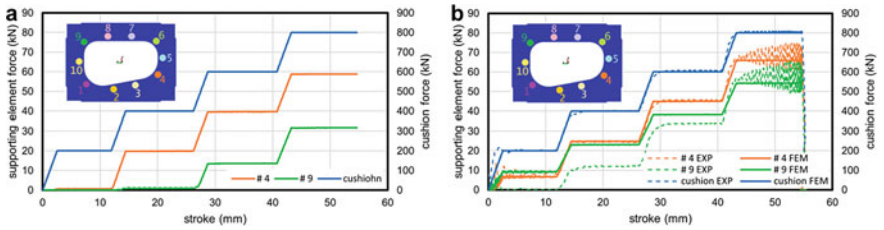


Fig. 7 Force diagram of the supporting element 4 and 9, which is 0.01 mm and 0.02 mm lower than the remaining elements, respectively, from **a** the previous study [11], **b** this study and from experiment. (Color figure online)

elements at position 4 and 9 were positioned 0.01 mm and 0.02 mm lower, respectively, than the remaining elements. The expected results should be those shown in Fig. 7a, in that, the force at position 4 appears first when the cushion force reaches 400 kN and later then the force at position 9 when the cushion force 600 kN. There were no backlash-like characteristics found there due to the intrinsic characteristics of finite element modeling in the previous study, in which the blankholder and the supporting elements are idealized as flat. However, the response shown on the position 9 in the lower loading steps from the results of this study in Fig. 7b can be considered to be the backlash effects from the other elements. It is based on the observation that the blankholder on the position 4 and 9 has similar stiffness there and the curves for the forces there should be parallel to each other, but the force on the position 9 is higher than that on 4 at the beginning and is significantly lower later.

Actually, the step loading test shown in Fig. 7b can be used to determine the backlash on each supporting element in this finite element model, because only the blankholder is modeled as elastic and the superposition method can still be applied. Besides, all available CNC die cushion in the current market can only provide limited number of points to set constant cushion forces for certain cushion stroke range. Therefore, the step loading test actually matches the cushion objective. However, the backlash in the actual die set is very complicated to specify, because all components are elastic and plays always exist among them. Nevertheless, from Fig. 5b, it can be observed that there should no backlash exist for sure, if the applied force is over the threshold, such as 50 kN. This is why the force deviation in Fig. 7b between the results of the finite element analysis and the experiment can be regarded as the backlash effects from the other components. These backlashes cause the results of the finite element analysis shown in Fig. 7 from these two studies to be different to each other. The step loading test with a total cushion force, which can let the force on some supporting elements less than the threshold to detect the backlash characteristics. Depending on the applied step load, the backlash status on each supporting element can be detected with the response force there. The backlash on each supporting element can further determined with the procedure described as follows:

First, the height of each supporting elements is determined, so that all of the supporting elements have the same backlash. According to the needed blankholder force on each supporting element, the further height of each element can be roughly

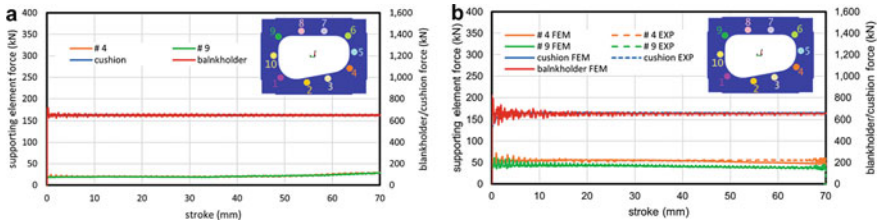


Fig. 8 Force diagram for a stamping irregular sheet part from a finite element model of **a** the previous study [11], **b** this study and from experiment. (Color figure online)

determined by dividing by the stiffness of the blankholder on that element. A first run of the simulation with the height of each element determined by the two previously mentioned steps can then provide the forces on each element. More information of the forces on each element can be provided by further runs of the simulation with the height of each element changed within the range of the feeler gauge, 0.01 mm, in a manner of design of experiment. From the force information obtained by finite element simulation and by the experiments, the backlash on each supporting element can then recursively determined by means of the response surface methodology with the objective of minimum difference of the force between the finite element analysis and the experiments.

Once the backlash on each supporting element has been confirmed, a stamping process can then be conducted. A DC04 sheet in thickness of 1 mm stamped with a constant cushion force of 650 kN for a stroke of 70 mm was conducted in the previous study [11], in that the blankholder force optimized by [6] on each supporting element is approximated by adding the height of the supporting element with feeler gauges. Figure 8a shows the reaction forces on the blankholder and on the supporting elements. The forces on the supporting elements are directly calculated from stiffness about 12 kN, but the results from the finite element analysis shown here are higher as 21 kN. Even though the cushion force stands constant during the stamping process, the force on the blankholder and the supporting elements wobble all the time. It can be attributed to the dynamic nature instincts of explicit finite element code. This phenomenon can also be observed in this study as shown in Fig. 8b. However, those forces from the experiment shown in Fig. 8b, which was executed in an AIDA servo press having the ram capacity of 6,300 kN and the cushion capacity of 1,500 kN along with a centered pattern of 150 mm $\times$ 150 mm for cushion pins of 50 mm diameter each, stay calm. The average force on the supporting element 9 from the finite element analysis is the same as that from experiment, 42 kN, while that on the element 4 is 55 kN and a little bit higher than that from experiment, 53 kN. Figure 9 shows the stamped irregular sheet part, which is made of the first shot and a sound part.

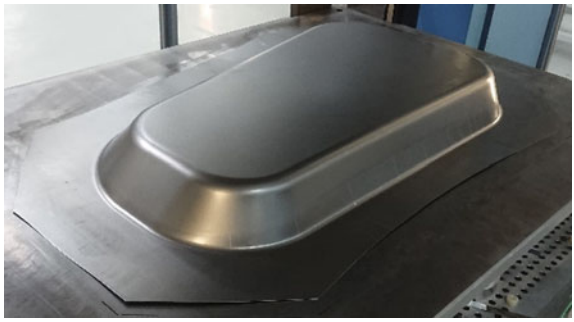


Fig. 9 A stamped irregular sheet part on the elastic blankholder. (Color figure online)

4 Conclusions and Future Works

This study conducts a finite element analysis with a model close to the actual geometry and setup of the blankholder for stamping an irregular sheet metal part. This study investigated the influence of the inherent noise of the geometry induced by current manufacturing processes. These results would be applied in a future study about potential uses of thermal pins to regulate the contact pressure on the blankholder by heating and cooling them to alter their heights. The finite element model of the blankholder is created on the basis of a fitted geometry generated by the optical measurement system GOM ATOS 5M after scanning the blankholder. The clearance between the supporting elements and the blankholder is measured with feeler gauges. Except for the blankholder being modeled as elastic, all other components of the die set including the supporting elements are modeled as rigid in the finite element model.

As a result, the actual blankholder with the supporting elements has backlash-like characteristics. Once the backlash is removed, the blankholder and the supporting elements are all linearly elastic; therefore the superposition method can be applied. However, the present contact pressure built up from the elastic blankholder along with the supporting elements is strongly dependent on the backlash behavior there. Nevertheless, this backlash can be determined by means of a step loading test proposed by this study, when a minimum of force difference between the finite element analysis and the experiments is achieved by recursively modifying the value of the backlash. With this tedious preparation to determine the actual geometry of the blankholder and to confirm the backlash-like behavior related to the supporting elements, a finite element model can be prepared. The model would be used to optimize the process of using an elastic blankholder supported with supporting elements by regulating their heights to adjust the localized contact pressure for stamping irregular sheet parts.

The experiment conducted in this study validates this process, which further makes the process proposed by [9] more feasible, in that, the localized contact pressure of the blankholder would be controlled by regulating the length of thermal pins implemented onto the die set. Therefore, for the future works, it is worth to first develop the process efficiently determining the geometry of the blankholder and

confirming the backlash-like characteristics related to the supporting elements to shorten the preparation period.

Acknowledgments The per diem for the first author working on this research was supported by the Ministry of Science and Technology of the Republic of China with the grant coded MOST 108-2918-I-005-008.

References

1. Osakada K, Mori K, Altan T, Groche P (2011) Mechanical servo press technology for metal forming. CIRP Ann Manuf Technol 60(2):651–672. https://doi.org/10.1016/j.cirp.2011.05.007
2. Xu T, Xia QX, Zhang SJ, Li ZS, Ruan WP (2011) Influence of slide stroke curves on deep drawing of box shaped part. Adv Mat Res 328–330:695–699. https://doi.org/10.4028/scientific.net/AMR.328-330.695
3. Kriechenbauer S, Mauermann R, Muller P (2014) Deep drawing with superimposed low-frequency vibrations onservo-screw presses. Proc Eng 81(2014):905–913. https://doi.org/10.1016/j.proeng.2014.10.116
4. Ju L, Patil S, Dykeman J, Altan T (2015) Forming of Al 5182-O in a servo press at room and elevated temperatures. J Manuf Sci E-T ASME 137:051009. https://doi.org/10.1115/1.4030334
5. Kawamoto K, Ando H, Yamamichi K (2018) Application of servo presses to metal forming processes. Proc Manuf 15(2018):31–38. https://doi.org/10.1016/j.promfg.2018.07.166
6. Del Prete A (2020) Primo T (2020) Sheet metal forming optimization methodology for servo press process control improvement. Metals 10:271. https://doi.org/10.3390/met10020271
7. Siegert K, Doege E (1993) CNC hydraulic multipoint blankholder systems for sheet metal forming presses. CIRP Ann Manuf Technol 42(1):319–322. https://doi.org/10.1016/S0007-8506(07)62452-4
8. Siegert K, Ziegler M (1997) Pulsating blankholder forces in the deep-drawing processes. CIRP Ann Manuf Technol 46(1):205–208. https://doi.org/10.1016/S0007-8506(07)60809-9
9. Liewald M, Barthau M (2018), Adaptive control strategies for deep drawing of high performance sheet metal materials. Paper presented at the International Deep Drawing Research Group 37th Annual Conference, Waterloo, Canada, 3–7 June 2018
10. Liewald M, Blaich C (2009) Approaches for closed-loop control and optimization of deep drawing processes. In: Paper presented at the ANSYS Conference and 27th CADFEM Users' Meeting 2009, Leipzig, Germany, 18–20 November 2009
11. Fann KJ, Liewald M, Riedmüller K, Radonjic R, Karadogan C (2019) Finite element study on sheet metal forming with an elastic blankholder supported by individual length-adjustable pins. In: Paper presented at the 2nd Asian Pacific Symposium on Technology of Plasticity, Tokyo, Japan, 31 July–3 August 2019

Evaluating 980GEN-3 Steel with Tested and Numerical Forming Limit Curves



T. Feister, L. Zoller, J. Gu, and H. Kim

Abstract Forming limit curves (FLC) are widely accepted by industry for predicting necking failure during sheet metal forming. FLCs can be developed directly through material testing or by numerical extrapolation from tensile data. This work evaluates the accuracy of FLCs developed from Nakajima testing using the linear-best-fit method to Keeler, Arcelor V9, and Tata Steel FLC models that are available in the commercial FEM software. Two different stamping shapes and three variations of 980GEN-3 steel were used for physical testing to evaluate the FLC models.

Keywords FLD · FLC · Material variation · Numerical forming limits · FEA

1 Introduction

Using finite element analysis (FEA) has become a standard procedure for determining the formability of a part shape with a given material. Strain-based forming limit diagrams (FLD) remain the most commonly used tool for predicting necking failure during forming. The accuracy of simulation models is directly dependent on the material data that is defined.

Obtaining FLD from experiments would be the more preferable option; however, it can be costly. The problem of accurately predicting part feasibility is made more complex when material variation is considered. FLD changes with material thickness, from one coil to another and even within the same coil.

T. Feister · L. Zoller · J. Gu · H. Kim (✉)
EWI—Forming Center (EWI-FC), Columbus, OH, USA
e-mail: hkim@ewi.org

T. Feister
e-mail: tfeister@ewi.org

© The Minerals, Metals & Materials Society 2021

G. Daehn et al. (eds.), *Forming the Future*, The Minerals, Metals & Materials Series,
https://doi.org/10.1007/978-3-030-75381-8_217

2 Objective

The objective of this study was to establish a cost-effective method of determining FLD limit diagram for high-strength 980GEN-3 steel using only tensile testing data. Tested FLD and numerical FLD were used to predict splits on two different stamping parts with known failure strain paths.

3 Approach

Three variations of 980GEN-3 steel were evaluated with tensile testing (Fig. 1) and Nakajima forming limit testing. The variations of material were selected to provide a large difference in yield strength (YS) and ultimate tensile strength (UTS). Table 1 shows the difference in yield and ultimate stress between the three variations. Tensile samples were machined in each of the 0, 45, and 90 degrees to the rolling direction. Three samples were tested in each orientation. Axial and transverse extensometers were used to measure the anisotropic coefficient r-value during testing.

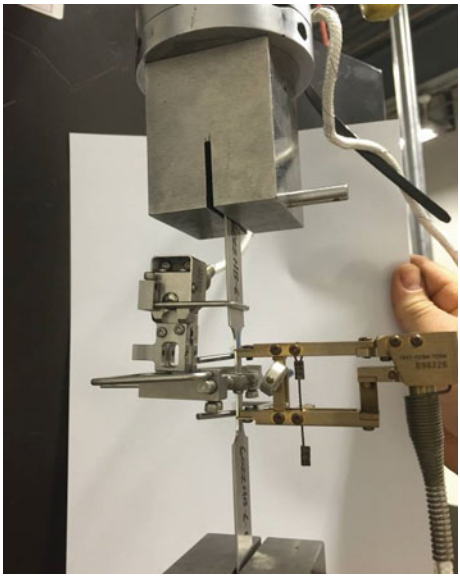


Fig. 1 Tensile testing setup. (Color figure online)

Table 1 Rolling direction mechanical properties for three variations of 980GEN-3 steel

Sample	YS (MPa)	UTS (MPa)
1	620	1046
2	636	1007
3	646	1038

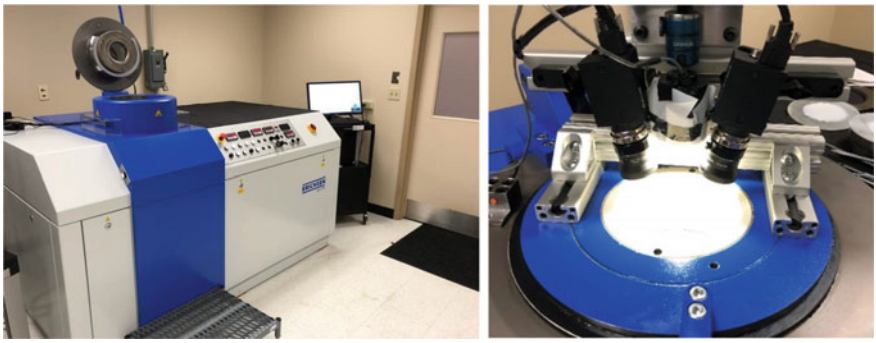


Fig. 2 Erichsen sheet metal forming machine (left) and DIC fixturing (right). (Color figure online)

Nakajima forming limit testing was conducted on an Erichsen sheet metal testing machine (Fig. 2). Five types of Nakajima samples were water jet cut. Digital image correlation (DIC) equipment was used to measure the strain during testing. The linear best fit method (Table 2) [1] was used to establish detecting the necking initiation point.

Forming tests were conducted on a 300 ton AIDA servo mechanical press. A universal forming tool and a cross-form tool were used as shown in Fig. 3. 250 kN blank holding force was required to prevent wrinkles on the parts. The forming stroke was adjusted incrementally until necking was observed in the formed parts. One universal formability part was marked with an ARGUS pattern for subsequent strain measurement.

Forming simulations for the universal forming and cross-form dies were performed using PAM-STAMP. Tensile and FLC testing data were used to create material cards. The Coulomb coefficient of friction of 0.12 was used. The Hill 48 yield criterion was used initially. The simulation stroke was defined to match the forming depth that resulted in necking in the physical parts.

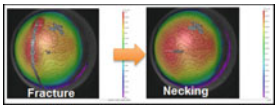
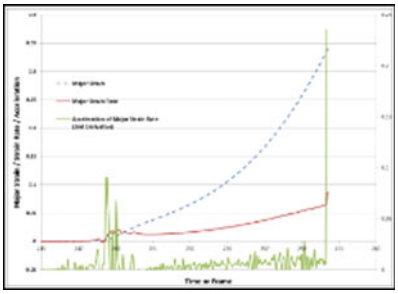
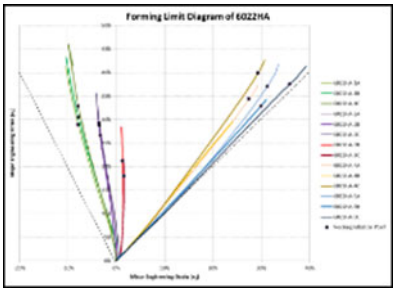
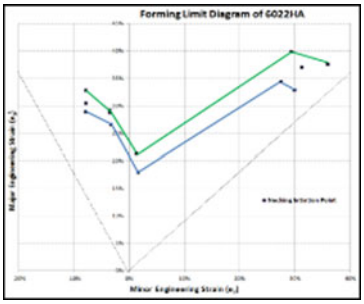
The draw-in of one universal forming part was measured with an ATOS blue light scanner. The strain was measured with ARGUS stain analysis. The draw-in and strain were used to compare with simulation results.

4 Results

The FE-predicted flange draw-in length was well matched with the blue light scan results (Fig. 4 and Table 3). However, the predicted maximum strain (36%) fell short of the 40% ARGUS measurement. Various yield criteria were used and compared against the strain measurement. Vegter Lite yield criterion [2] was shown to have the best correlation with the experiment (Fig. 5).

With the Vegter Lite yield criterion and the tested FLC, the formed part strain is slightly over the FLC for the universal forming part (biaxial) and slightly under

Table 2 A procedure to establish the DIC-based FLC. (Color figure online)

Step no.	Description	Illustrations of each step
1	Conduct the testing of the Nakajima samples using the DIC system	
2	Identify the local necking point using the principle strain plot	
3	Identify the time or frame corresponding to the onset of necking by plotting the history of major strain, strain rate, and acceleration of the major strain	
4	Plot the linear strain path data	
5	Establish the FLC	

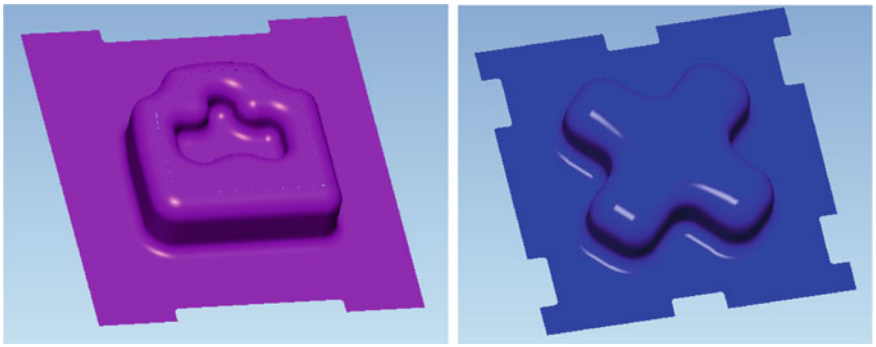


Fig. 3 CAD geometry for the universal forming die (left) and the cross-form die (right). (Color figure online)

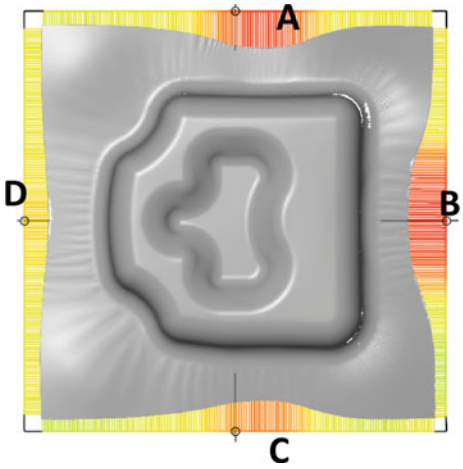


Fig. 4 Draw-in map comparing the FEA result and the scanned part. (Color figure online)

Table 3 Comparison of draw-in distance for scans and simulated parts in four locations

Point A scan (mm)	Point A sim (mm)	Point B scan (mm)	Point B sim (mm)	Point C scan (mm)	Point C sim (mm)	Point D scan (mm)	Point C sim (mm)
39.4	38.9	48.0	49.4	39.3	38.5	29.3	32.3

for the cross-form (uniaxial) part (Figs. 6 and 7 respectively). The correlation was reasonably good.

The experimental FLCs were compared to numerical FLCs extracted from tensile data alone. Keeler FLCs are higher than the tested FLCs and overpredicted the formability (Fig. 8). Figures 9 and 10 show a good comparison of both Tata and Arcelor V9 FLCs with the tested FLCs.

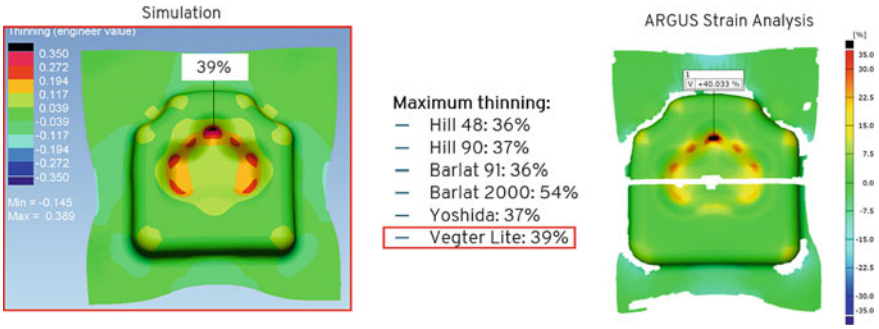


Fig. 5 Maximum thinning as a function of yield criteria compared to the ARGUS strain measurement. (Color figure online)

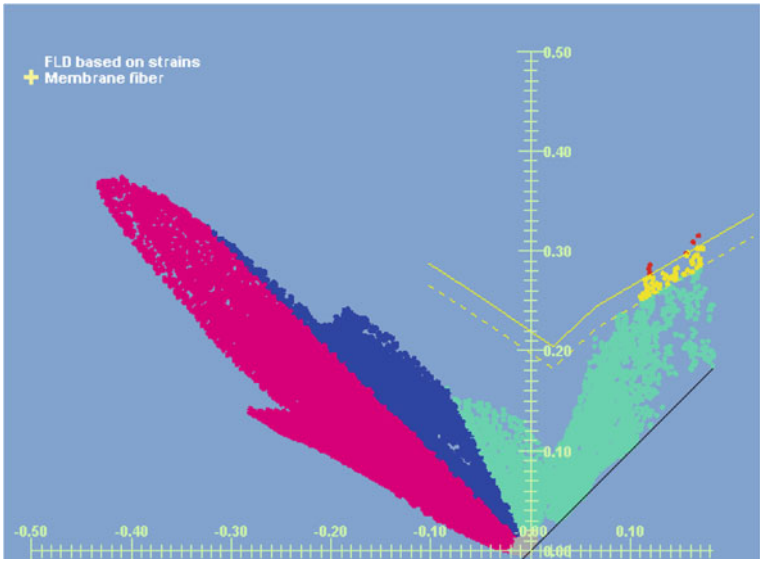


Fig. 6 The universal forming simulation strain path exceeds the forming limit at the end of the stroke. (Color figure online)

5 Conclusions

This work confirmed that the Hill 48 yield criterion is not well suited for modeling sheet forming of high-strength steels. Simulation with the Vegter Lite yield criterion provided a good match of the peak strain when forming 980GEN-3 steel. The linear best fit method gave an accurate forming limit curve that correlated well with biaxial and plane strain failure paths. The Keeler forming limit curve overestimated the formability of the 980GEN-3 steel. Both Tata and Arcelor V9 numerical curves match well with the tested forming limit and the physical necking imitation stroke.

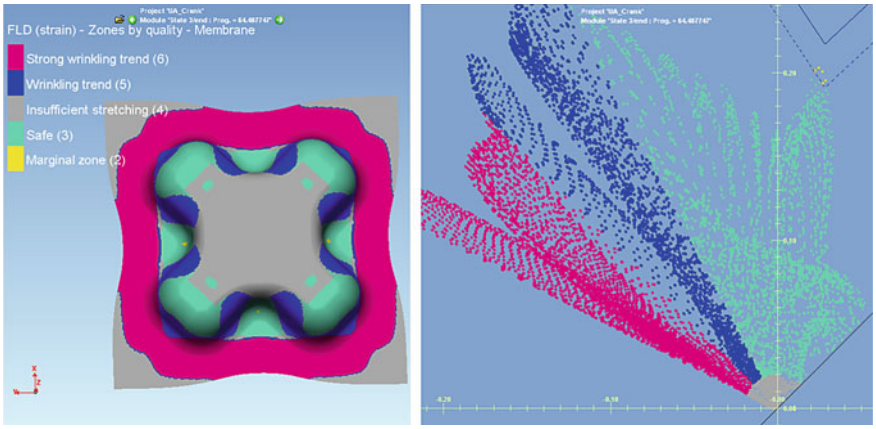


Fig. 7 The cross-form simulation strain path is slightly below the forming limit at the end of the stroke. (Color figure online)

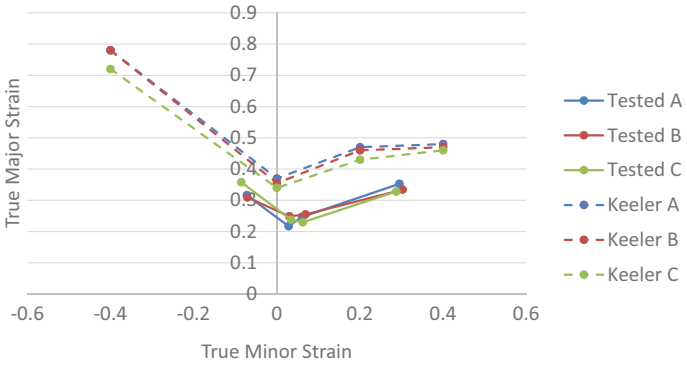


Fig. 8 Tested FLC compared to Keeler FLC. (Color figure online)

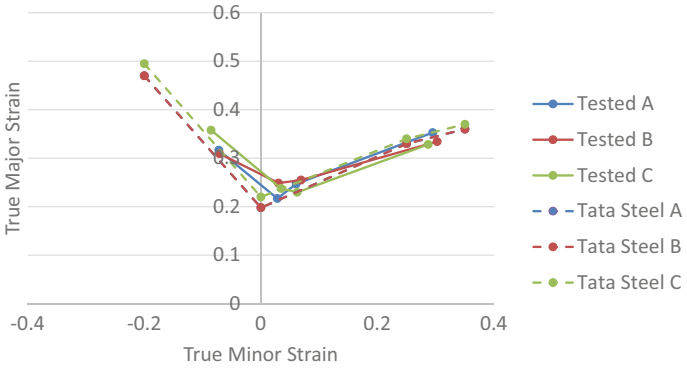


Fig. 9 Tested FLC compared to Tata FLC. (Color figure online)

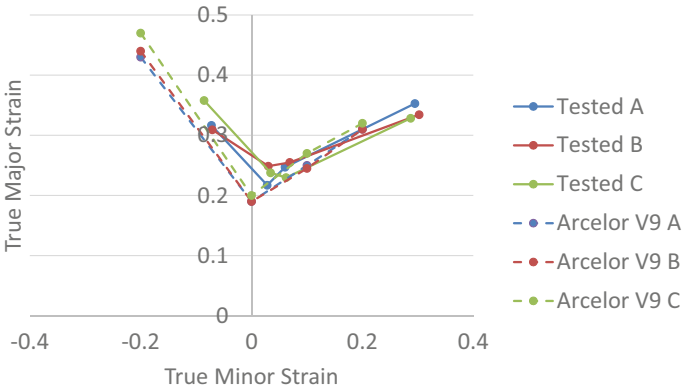


Fig. 10 Tested FLC compared to Arcelor V9 FLC. (Color figure online)

References

1. Rencheck M et al. (2017) Evaluation of DIC based forming limit curve methods at various temperatures of aluminum alloys for automotive applications. SAE International
2. Vegter H et. Al (2009) The Corus-Vegter lite material model: simplifying advanced material modelling. Int J Mater Form 2(1):511–514

Formability of Functional Corrugated Cup



Y. Harada and Y. Nishikubo

Abstract The formability of the corrugated clad cup was investigated to enhance the functionality of the cup. Deep drawing, which is one of press forming, is a plastic processing technology for forming a thin plate into a three-dimensional container. Depending on the application, the functionality of the container itself was required. In the present study, the drawn cup with a corrugated structure on the side wall was formed by deep drawing. In the experiment, the materials were pure titanium TP270, low carbon steel SPCC, and stainless steel SUS304. In the deep drawing process, the composite die combining the roller die was prepared for forming a clad cup. In the side wall of the corrugated cup, the distance between the waves was approximately 8.6 mm. The thickness strain at the bottom of the drawn cup TP270 was no more than 0.06. It was found that the corrugated clad cups were successfully formed by using the composite die combining the roller die.

Keywords Deep drawing · Pure titanium · Corrugated cup

1 Introduction

In the press forming of a metal sheet, there are processes using deep drawing deformation, bulging deformation, stretch-flange deformation, and bending deformation. Process design and die design are often performed for processing methods using these deformations. In the case of deep drawing, experimental and theoretical studies have been conducted on the shape and material of punch and die dies [1], formability of blanks [2], and selection of lubricants [3]. In addition, research on the forming of containers having functions such as high strength and high corrosion resistance has been conducted for a long time. The performance of CrN film coating to reduce adhesion in the forming process of advanced high strength steel sheets was investigated [4]. The hot-rolled Al/Mg/Al laminates were used to conduct deep drawing at

Y. Harada (✉) · Y. Nishikubo
University of Hyogo, Kobe, Japan
e-mail: harada@eng.u-hyogo.ac.jp

© The Minerals, Metals & Materials Society 2021

G. Daehn et al. (eds.), *Forming the Future*, The Minerals, Metals & Materials Series,
https://doi.org/10.1007/978-3-030-75381-8_218

various temperatures, and microstructure evolution of three typical regions including bottom, corner, and wall was investigated [5].

There have been many research reports on ironing, thickening, embossing, etc. to improve the strength of the side wall of the container. A heat treatment cycle, hardening by water quenching followed by prolonged tempering, was proposed for enhancement of strength and formability of Al-killed AISI 1040 graded steel strips [6]. The modeling and the corresponding experimental validation of angular deep drawing parameters on the tensile strength, wall thickness, and height of the square profile cups was investigated [7]. The effects of embossing and restoration process on the deep drawability of aluminum alloy sheets were examined [8]. In addition, research on the forming of clad containers using laminated sheets is also being conducted. The reason for using a laminated sheet is that the functionality is improved beyond the properties of a single sheet. The effects of several parameters on the deep drawing process of laminated sheets are comprehensively studied [9]. On the other hand, in our research group, the formability of highly corrosion-resistant titanium cups was investigated using titanium materials, one of the functional materials [10, 11]. Titanium is a metal that has high corrosion resistance and is lighter than steel. In many products, such as chemical plants and medical applications, the range of use of titanium is expanding [12]. In previous study, deep drawing of clad cup was performed using a laminate of pure titanium and carbon steel sheets [13]. Each sheet was simply in a stacked state, and the sheets were not joined to each other. The clad cup was formed simultaneously with the deep drawing deformation. Furthermore, attempts were made to form a unique cup that developed the method of forming a clad cup [14]. In addition, we focused on a panel having a corrugated shape and attempted to form the cup having corrugated side walls. In the present study, we formed the corrugated clad cup by deep drawing using the composite die incorporating the roller die and investigated mainly the formability.

2 Experimental Procedure

2.1 Materials

The blank for deep drawing was cut from cold rolled metal sheet by shearing and blanking. Three types of blanks, pure titanium TP270 (high purity type), an ultralow-carbon steel (SPCC: Steel Plate Cold Commercial), and austenite stainless steel SUS304, were used. A pure titanium blank was mainly used. Austenite type steel is the most widely used grade of stainless steel due to its excellent formability and corrosion resistance [15]. The initial diameter and thickness of the blank were 80–85 mm and 0.3–0.5 mm. The die and punch were cold-work tool steel JIS-SKD11. They were heat treated under standard conditions.



Fig. 1 Appearance of actual roller die. (Color figure online)

2.2 Deep Drawing

A trial production of the roller die was performed to form the cup having a wavy side wall. Actual appearance of the produced roller die is shown in Fig. 1. The groove was machined at the shoulders of the die. To deform the side wall of the cup into a wave shape, steel balls were placed in the groove without the gap. The steel balls were rotated during drawing. Steel ball was bearing steel, the diameter was 10 mm. The clearance between the punch and die was set to be equal to the thickness of the sheet. Next, the composite die combining the roller die was prepared for forming the clad cup. Figure 2 shows the schematic illustration of the composite die. The composite die is composed of three dies. Each die is provided with a blank. After the first blank is formed by the upper die, it is formed by the roller die and the lower die to finally form the corrugated clad cup. The deep drawing process was performed using an oil hydraulic press at a forming speed of approximately 10 mm/min. A punch diameter was 40 mm, and the drawing ratio was 1.67 at the upper die. A shoulder radius of punch was 3 mm. The lubricant was the solid powders of molybdenum disulfide (ThreeBond 1910 type, specific gravity: 1.6, viscosity: 1.6 Pa-s). The forming conditions of deep drawing are shown in Table 1.

2.3 Measurement of Thickness Strain and Hardness

The thickness of the drawn cup was measured from the center of the bottom of the cup to the side wall using a digital micrometer (Digimatic outside micrometer type, by Mitutoyo Corporation). In the rolled sheets, it is known that anisotropy is caused by a crystalline structure. The thickness strain of the deep drawn cup was measured along a direction parallel to the rolling direction of the blank. Vickers hardness test was also performed to measure hardness of the drawn cup after deep drawing. The measuring instrument used was the micro Vickers hardness tester (by Akashi Seisakusho, Ltd.).

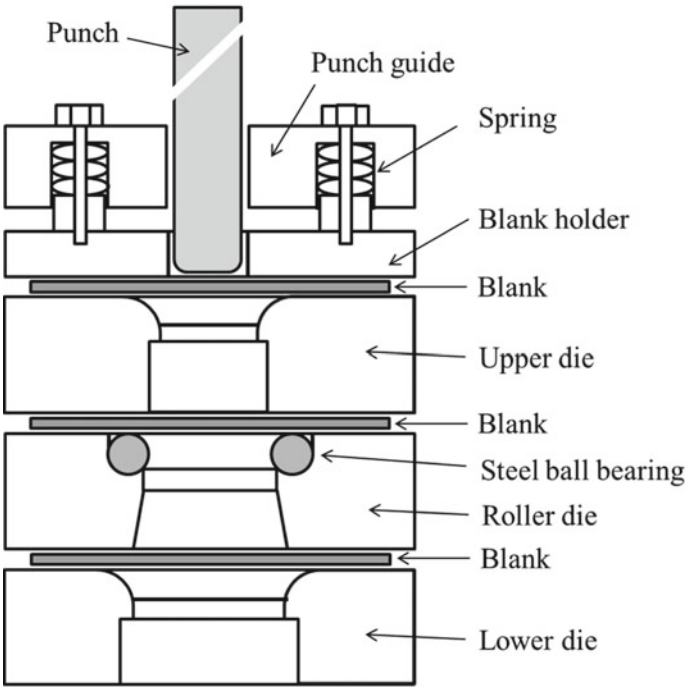


Fig. 2 Deep drawing process by composite die

The hardness of the drawn cup was measured from the center of the bottom of the cup to the side wall. The hardness value was calculated by averaging seven or more measurements.

3 Results and Discussion

3.1 Visual Appearance of Drawn Clad Cup

Using the prototype composite die, a corrugated clad cup was formed. Figure 3 shows the appearance of the corrugated clad cups. The initial blank thickness is 0.3 mm inside the cup and 0.4 mm for the others. The metal constituting the clad cup was the same material. The formability of the drawn cup was sufficient and no fracture at the bottom or wall occurred. Although the outside cup and the inside cup, which were strongly attached to each other, of the clad cup were not bonded to each other, the clad cup could be separated by cutting. In addition, wrinkles were observed at the opening of the drawn cup, as the blank holding force was not sufficient at the opening. In the case of the pure titanium cup, ears were remarkably observed at the

Table 1 Condition of deep drawing

Blank holder force (BHF)		10 kN
Punch	Material	SKD11, 60 HRC
	Diameter	39 mm (0.5 mmt), 40 mm (0.3, 0.4 mmt)
	Corner radius	3 mm
Upper die (flat die)	Material	SKD11, 60 HRC
	Hole diameter	40.0 mm (0.5 mmt), 40.8 mm (0.3 mmt)
	Corner radius	3 mm
Middle die (roller die)	Material	SKD11, 60 HRC
	Hole diameter	41 mm (0.5 mmt), 41.4 mm (0.4 mmt)
Steel ball bearing	Material	SUJ2, 800 HV
	Diameter	10 mm
Lower die (flat die)	Material	SKD11, 60 HRC
	Hole diameter	46.3 mm (0.5 mmt), 46.4 mm (0.4 mmt)
	Corner radius	3 mm
Lubricant		Molybdenum disulfide type oil

cup opening due to the anisotropy. It is well known that planar anisotropy causes ears to form in drawn cups, producing a wavy edge [16]. Earing is defined as formation of waviness on uppermost section of deep drawn cup [17]. Due to the occurrence of ears in the openings, the effect of blank holder was reduced. On the other hand, the outer diameter of the drawn cup was measured to examine the formability of the clad cup. In the case of the drawn cup SPCC, the outer diameter of the cup was 46.2 mm near the bottom and 46.3 mm near the opening. Similarly, the dimensional error of the outer diameter was small in other cups.

3.2 Evaluation of Formability of the Drawn Clad Cup

Since the inner structure was not visible on the side wall of the drawn cup, the cladding cup was cut. Figure 4 shows the structure of the side wall cut near the center of the drawn cup TP270. The initial blank thickness is 0.3 mm inside the cup and 0.4 mm for the others. There was a gap in the side wall, and a regular wave shape was observed. In the side wall of the cup, the distance between the waves was approximately 8.6 mm. Although wrinkles were observed at the opening of all cups, forming was possible. In addition, as a result of observing the cut portion in other cups, a wavy structure was observed (Fig. 5).



Fig. 3 Appearances of drawn clad cup. (Color figure online)

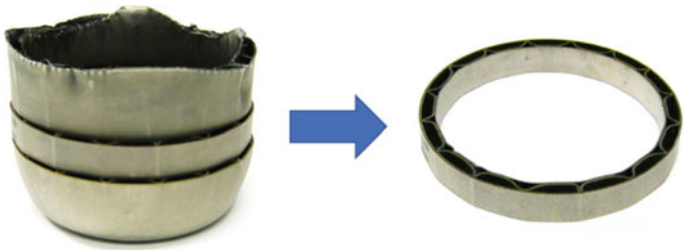


Fig. 4 Cutting near center of side wall of drawn cup TP270. (Color figure online)



Fig. 5 Wavy structure near center of side wall of drawn clad cup

After the cold deep drawing, it is well known that the thickness distribution of formed cups is uneven. The thickness of the wall at the bottom corner tends to decrease, whereas the thickness at the opening tends to increase. The thickness of the drawn clad cup was also measured. Figure 6 shows the thickness strain distribution of the drawn cup TP270. The initial blank thickness is 0.3 mm inside the cup and 0.4 mm for the others. The thickness strain was measured toward the opening from the bottom center of the cup. In the case of corrugated cup, the thickness of the recess on the wavy side wall was measured. In the inside cup, the increase in thickness strain was larger than those in the other cups. Furthermore, the greatest reduction in thickness strain (approximately -0.06) occurred at the bottom corner of the cup. Similarly, for the cup SUS304 and the cup SPCC, the thickness strain was similar to that of the cup TP270.

In the middle cup formed by the roller die, the thickness strain increases near the bottom of the cup. Such a change does not occur in a conventional deep drawing cup [18]. The position showing the increase is an area in contact with a hard ball placed on the shoulder of the roller die. The contact area of the steel ball (red circle)

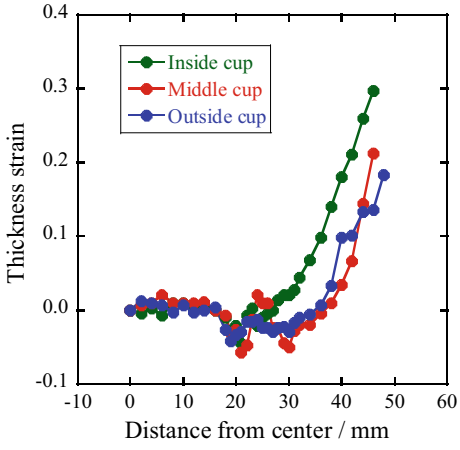


Fig. 6 Distribution of thickness strain of drawn clad cup TP270. (Color figure online)

is shown in Fig. 7. When the material is deformed by the steel ball, the material plastically flows outward. Therefore, the material surface after being brought into contact with the steel ball is in a plastically deformed state. Since the material flows to an unconstrained surface, the thickness strain increases. The mechanism of the increase in the thickness strain is shown in Fig. 8. The material being deformed tends to undergo plastic flow.

The metal sheet after plastic deformation is work-hardened. Work-hardening coefficient (n value) of pure titanium is considerably smaller than other metals. In the case of TP270 type, it is approximately 0.148. Deep drawing was a severe process, however, the hardness of the drawn cup was examined. Hardness of the drawn cup after forming was examined. Figure 9 shows the hardness distribution at the side wall of the drawn cup TP340. In order to measure the hardness, the material was changed from TP270 to TP340. When the sheet thickness was small, it was difficult to measure the hardness. Work-hardening coefficient (n value) of pure titanium TP340 is approximately 0.145. The initial thickness of all blanks is 0.5 mm. Hardness was measured toward the opening from the bottom center of the cup. The measurements were centered on the corners. Hardness of the cup increased from the bottom toward the opening. In each cup, hardness of the opening was approximately 1.3 times that

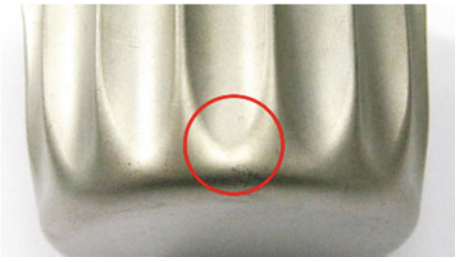


Fig. 7 Contact area of steel ball (red circle). (Color figure online)

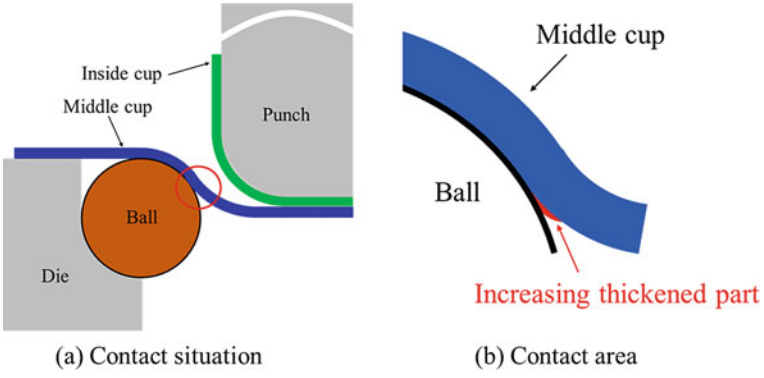


Fig. 8 Mechanism of increase in thickness strain. (Color figure online)

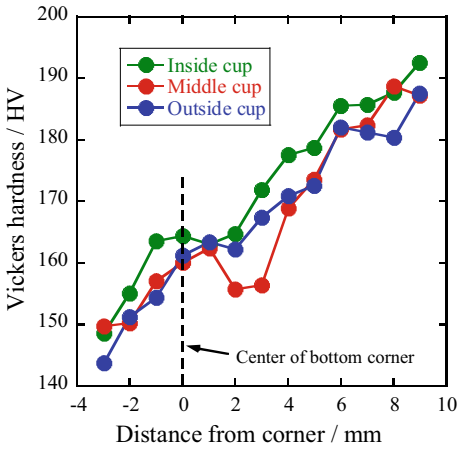


Fig. 9 Vickers hardness of drawn clad cup TP270. (Color figure online)

of the bottom. In the middle cup formed by the roller die, hardness decreases near the bottom of the cup. This reduced area corresponds to the area where the plate thickness strain has increased. Although the plastic flow occurs in this area, the material in no constraint has a small effect of work hardening. For this reason, it is considered that the material having no restraint state did not work harden.

4 Conclusions

The formability of the corrugated clad cup was investigated to enhance the functionality of the cup. The corrugated clad cup was formed using the composite die combining the roller die. The conclusions obtained are as follows:

(1) The corrugated clad cup was formed by using the composite dies including the roller die with steel balls placed on the shoulder of the die.
(2) The cross-section of the side wall of the corrugated clad cup showed a corrugated structure. In addition, the constituent cups were in close contact with each other.
(3) In the drawn cup TP270, the greatest reduction in thickness strain (approximately -0.06) occurred at the bottom corner of the cup.
(4) In the drawn cup TP270, hardness of the cup increased from the bottom toward the opening. In each cup, hardness of the opening was approximately 1.3 times that of the bottom.
(5) In the future, we plan to form corrugated clad cups using different types of blanks. It is considered that the clad cup having functions such as strength and corrosion resistance can be formed.

Acknowledgments The authors would like to thank Mr. T. Fujikami, a former engineering undergraduate at University of Hyogo, for his help in the experimental work. This research was supported in part by a grant from AMADA foundation (AF-2017005).

References

1. Bhatt MR, Buch SH (2017) An expert system of die design for multi stage deep drawing process. Proc Eng 173:1650–1657
2. Yoshihara S, Yamamoto H, Manabe K, Nishimura H (2003) Formability enhancement in magnesium alloy deep drawing by local heating and cooling technique. J Mater Process Technol 143–144:612–615
3. Reichardt G, Liewald M (2019) Investigation on friction behaviour of deep drawing radii using volatile media as lubricant substitutes. Proc Manuf 29:193–200
4. Sresomroeng B, Premanond V, Kaewtatip P, Khantachawana A, Kurosawa A, Koga N (2011) Performance of CrN radical nitrided tools on deep drawing of advanced high strength steel. Surf Coat Technol 205:4198–4204
5. Nie H, Chi C, Chen H, Li X, Liang W (2019) Microstructure evolution of Al/Mg/Al laminates in deep drawing process. J Market Res 8:5325–5335
6. Parida K, Soren S, Jha RN, Sadhukhan S (2016) Formability of Al-killed AISI 1040 medium carbon steel for cylindrical cup formation. ISIJ Int 56(4):610–618
7. Uenal E, Oezek C (2017) A study on the wall thickness in the angular deep drawing process. Mater Test 59(2):178–182
8. Namoco CS, Iizuka T, Narita K, Takakura N, Yamaguchi K (2007) Effects of embossing and restoration process on the deep drawability of aluminum alloy sheets. J Mater Process Technol 187–188:202–206
9. Atrian A, Fereshteh-Saniee F (2013) Deep drawing process of steel/brass laminated sheets. Compos B Eng 47:75–81
10. Harada Y, Ueyama M (2014) Formability of pure titanium sheet in square cup deep drawing. Proc Eng 81:881–886
11. Harada Y, Maeda Y, Ueyama M, Fukuda I (2014) Improvement of formability for multistage deep drawing of Ti-15V-3Cr-3Sn-3Al alloy sheet. Proc Eng 81:819–824
12. Koizumi H, Takeuchi Y, Imai H, Kawai T, Yoneyama T (2019) Application of titanium and titanium alloys to fixed dental prostheses. J Prosthodont Res 63:266–270
13. Harada Y, Ohno H, Nishikubo Y (2018) Deep drawability of Ti/steel/Ti laminated sheets. Mater Sci Forum 920:64–69
14. Harada Y, Nishikubo Y, Tanaka I (2020) Drawability of functional corrugate cup using roller die. Mater Trans 61(2):222–227
15. Brytan Z, Pakieła W (2019) Laser surface treatment of sintered stainless steels for wear resistance enhancement. Key Eng Mater 813:221–227
16. Izadpanah S, Ghaderi SH, Gerdooei M (2016) Material parameters identification procedure for BBC2003 yield criterion and earing prediction in deep drawing. Int J Mech Sci 115–116:552–563
17. Gilormini P, Bacroix B (1997) Simplified approaches for the prediction of deep-drawing ears. Stud Appl Mech 45:331–340
18. Yi S, Bohlen J, Heinemann F, Letzig D (2010) Mechanical anisotropy and deep drawing behaviour of AZ31 and ZE10 magnesium alloy sheets. Acta Mater 58:592–605

Experimental and Numerical Investigations into the Influence of the Process Parameters During the Deep Drawing of Fiber Metal Laminates



T. Heggemann, H. Sapli, and W. Homberg

Abstract Reducing fuel consumption and climate-damaging CO_2 emissions are important challenges for the automotive industry. These goals can be achieved by reducing the weight of the car. Extremely lightweight car bodies can be achieved by using exclusively composite materials, which have the major disadvantage of high costs and unsuitability for a large-scale production. A large-scale production of lightweight car body parts with a high stiffness to weight ratio requires more economic materials and new innovative manufacturing technologies. A very promising approach to meet these requirements investigated at the Paderborn University is the combination of high strength steel alloys and unidirectional CFRP prepregs in a special hybrid material—fiber metal laminate (FML)—which can be processed by specially adapted forming technologies such as deep drawing. The paper presents recent results of the combined curing and forming process. The influence of the process parameters, the process limits, the necessary tool systems, and the process strategies are similarly covered by the paper.

Keywords Multi-material system · Sheet metal · Carbon fiber reinforced plastic (CFRP) · Automotive lightweight design · Integrated forming · Advanced fiber placement · Hybrid forming · Deep drawing · Fiber metal laminate · FML · Combined curing and forming process

1 Introduction

A key goal in the automotive industry is to reduce fuel consumption and thus to reduce the climate-damaging pollutant and CO_2 emissions of future car generations. In the first stage, European legal requirements presupposed a reduction in CO_2 emissions from new vehicles to 130 g CO_2 per km in 2015. In a second stage, the CO_2 emissions from new vehicles will be limited to 95 g per km from 2021 onwards. This goal can be met by reducing the weight of the vehicle, for example, which also leads to

T. Heggemann (✉) · H. Sapli · W. Homberg
Paderborn University, Paderborn, Germany
e-mail: th@luf.uni-paderborn.de

© The Minerals, Metals & Materials Society 2021

G. Daehn et al. (eds.), *Forming the Future*, The Minerals, Metals & Materials Series,
https://doi.org/10.1007/978-3-030-75381-8_219

improved driving characteristics. In addition, the mass-dependent resistances, such as acceleration, ascent, and rolling resistance, are lower when the weight is reduced. A mass reduction of 100 kg leads to a fuel saving of 0.3–0.5 l per 100 km with a concomitant CO_2 reduction of 8.5–15 g per km [1].

In most current mass-produced cars, the body has a weight share of about 20% of the total vehicle mass, which offers a great potential for weight savings [2]. Furthermore, reducing the weight of the body has a positive leverage effect on other components of the car, such as the engine, brakes, and chassis. Extremely lightweight designs can be achieved by using exclusively composite materials [3, 7]. Due to the high material costs and their manual processing, the use of exclusively composite materials is limited, for example, to the aviation industry and to expensive high-performance racing cars.

Large-scale production of lightweight car body parts with a high stiffness to weight ratio requires more economic materials and new innovative manufacturing technologies. A very promising approach to meeting these requirements is the combination of high strength steel alloys and unidirectional CFRP prepregs in a special hybrid material—fiber metal laminate (FML). The FML sheets are structured by having the unidirectional CFRP prepreg patches chambered within two sheet metal layers. With this design, the thermosetting matrix material does not come into contact with the tool surfaces, thus offering a high potential for economical large-scale production with well-established, cost-efficient manufacturing technologies, such as deep drawing. In addition, the mechanical properties of the hybrid components produced can be adjusted by the location of the patch, the patch design, the fiber orientation, and the number of CFRP layers used.

The dissimilar material behavior of the sheet metal components and the CFRP prepregs during the forming process require a suitable material and process design in order to achieve the desired mechanical properties and a high shape and dimensional accuracy. Metals in general have approximately isotropic mechanical properties and deform through elastic and plastic flow. The forming behavior of metallic materials depends in general on the load speed, the stress rate, and the temperature [5, 6].

By contrast to metals, composite materials such as CFRP have a high anisotropy and a divergent forming behavior. As far as the carbon fibers are concerned, the mechanical properties in the fiber direction diverge from those in the transverse fiber direction [4]. CFRPs with thermosetting matrix materials require a curing process to attain their final strength. In general, the curing process of the resin is conditioned by the prevailing pressure, the curing temperature, and the curing time.

Most of the body components of mass-produced cars are currently manufactured by forming processes, such as deep drawing using rigid tools, and have complex geometries with unsteady drawing depths. During the deep drawing process, combined tension-tension stresses and pressure-tension stresses are induced in the flange, which is characterized as the main forming zone. The tangential pressure stresses that develop in the flange area can lead to a wrinkling of the metal sheet, which requires the appropriate countermeasures. In order to inhibit the wrinkling of the sheet in the flange area, normal stresses have to be applied by tool elements such as blank holders. If the normal stress applied by the blank holder exceeds a certain

value, the radial tension forces that develop can lead to a thinning of the material and thus to cracks and bottom tears [5, 6].

With regard to the forming behavior of the hybrid FML sheets, typical defects can be observed during the deep drawing process with non-adapted rigid tools. Pressure stresses can cause hydrostatic conditions to develop inside the uncured thermosetting matrix material within the FML sheet, forcing the resin to flow into neighboring areas. Inhomogeneous wall thickness distributions can be observed at points such as the radii areas of the workpieces where the tools induce high contact pressures [8, 9]. As a result, the shape and dimensional accuracy are negatively affected. The main deformation mechanisms for CFRP patches are draping, interlaminar layer slip, transversal flow of the matrix material, and resin percolation inside the prepreg [10–12]. As a result, wrinkles caused by delamination and buckled and torn off rovings can be observed in the flange and frame areas [13].

This paper focuses on two approaches to improving the shape and dimensional accuracy of the deep-drawn FML parts. To reduce the local thinning of the CFRP in the radii and bottom areas, local pre-curing strategies are investigated. The aim of the second approach is to reduce the wrinkling of the FML sheets during the forming process, and hence the effects of different CFRP patch designs and fiber alignments are investigated.

2 Experimental Setup

Experimental investigations were carried out at the LUF focusing on the development of a suitable advanced tool and process design and the resulting shape and dimensional accuracy for the combined forming and curing process of FML sheets. During the deep drawing process, the different areas of the workpiece are affected by numerous stresses in the course of the forming operation. Bending stresses occur in the feed zone in the frame area and in the radius at the punch. The flange and bottom area are affected by normal stresses caused by the blank holder and the punch. The flange, which is the main forming zone, is additionally affected by combined pressure-tension stresses. In the frame area, tension stresses are additionally applied during the forming process. The effect of the combined tensile pressure stresses mentioned and the normal stresses that occur during the forming operation were investigated using a cup-design specimen geometry.

The FML sheets used for the investigations consisted of two circular sheet metal blanks (HCT490X; $s_0 = 0.55$ mm) with an initial diameter of $D_0 = 180$ mm. The sheet metal blanks were arranged as top and bottom layers so that the CFRP prepregs were chambered inside the hybrid blanks. The FML sheets were stacked with one to three layers of unidirectional CFRP prepregs with an initial diameter of $D_0 = 180$ mm, a fiber weight per unit area of 230 g/m^2 and a resin content of 39% as shown in Fig. 1a). In order to minimize the friction between the tool surfaces and the FML sheet, a temperature-stable ethylene tetrafluoroethylene (ETFE) foil with a thickness

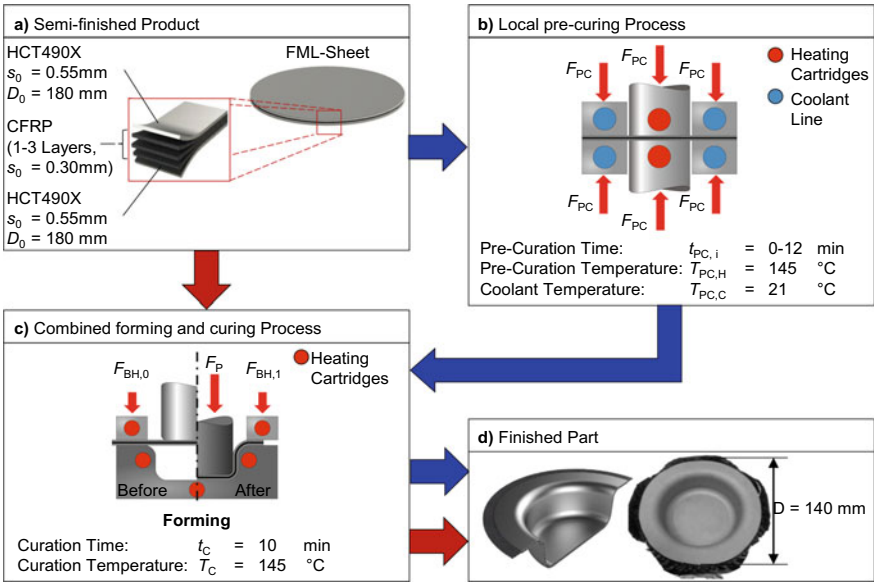


Fig. 1 Schematic image of the semi-finished product (**a**), the pre-curing process (**b**), and the combined forming and curing process (**c**). (Color figure online)

of $s_F = 25$ μm was used. The foil also prevented the resin from contaminating the tools.

In order to investigate the influence of the cross-linking degree of the matrix material on the thickness distribution, in particular in the bottom area and in the radii areas between the bottom and the frame, the specimens were locally pre-cured. The device used for the local pre-curing of the bottom area of the cups consisted of two heated flat circular punches ($T_{PC,H} = 145$ °C) with a diameter of $D_{PC} = 75$ mm and two water-cooled ring tools ($T_{PC,C} = 21$ °C) with an inner diameter of $D_{PC,C} = 79$ mm as shown in Fig. 1b). The pre-curing device was mounted inside a tensile testing machine in order to carry out the pre-curing process under optimal curing conditions for the resin with a defined curing pressure of $p_{PC} = 1$ MPa.

The tool setup for the combined forming and curing operation consisted of a punch, a blank holder, and a die. All the active tool elements can be heated with heating cartridges. The cylindrical punch has a diameter of $D_P = 99$ mm and an edge radius of $R_P = 10$ mm. The die ring has an inner cylindrical diameter of $D_D = 105$ mm and a blanking radius of $R_D = 10$ mm. In the experimental investigations, a drawing depth of $h = 38$ mm was used. The tool setup for the combined forming and curing operation was mounted inside a high precision pillar guide rack in order to achieve a high level of parallelism between the die ring and the blank holder. The whole setup was mounted inside a hydraulic press with a capacity of 1,000 kN. For the experiments, the FML sheets were positioned inside the tool setup. For the combined forming and curing process, the active tools (punch, blank

holder, and die) were heated to a tool temperature of $T_T = 145$ °C. After positioning the FML sheet inside the tool setup, the deep drawing process was started. A blank holder force of $F_{BH,1} = 320$ kN and a punch force of $F_P = 530$ kN were used for the deep drawing process. After the forming process, the FML specimens were cured inside the closed tools for a curing time of $t_C = 10$ min. After the resin of the prepregs had been cured to its final strength, the parts were extracted from the tool setup. The combined forming and curing process and the tool setup are illustrated in Fig. 1c).

For the combined forming and curing process, the FML sheet is positioned on the die. In the next step, the forming process is initiated. The punch force F_{ST} and the blank holder force $F_{BH,1}$ will be set for this, and the FML sheet is formed as the punch moves into the die. The wrinkling of the flange area caused by tangential pressure stresses is suppressed through the normal stresses applied by the blank holder. After the deep drawing process, the FML part remains inside the closed tool until the matrix material is cured to its full strength for a curing time of $t_C = 10$ min. To investigate the influence of the number of CFRP layers on the resulting shape and dimensional accuracy of the FML cups, one to three CFRP layers were used as the core of the hybrid blanks. The semi-finished components used for the first experiments thus consisted of two top-layer circular sheet metal blanks and one to three inner layers of unidirectional CFRP prepregs as shown in Fig. 2. The single-layered FML specimens were arranged with a fiber orientation of 0°. The second layer of CFRP inside the two-layered FML was rotated by 90° compared to the first layer of CFRP, giving the FML sheets an orthotropic design. The third layer inside the three-layered FML sheet was again rotated by 90° compared to the second layer, resulting in a stacking sequence of 0°/90°/0°.

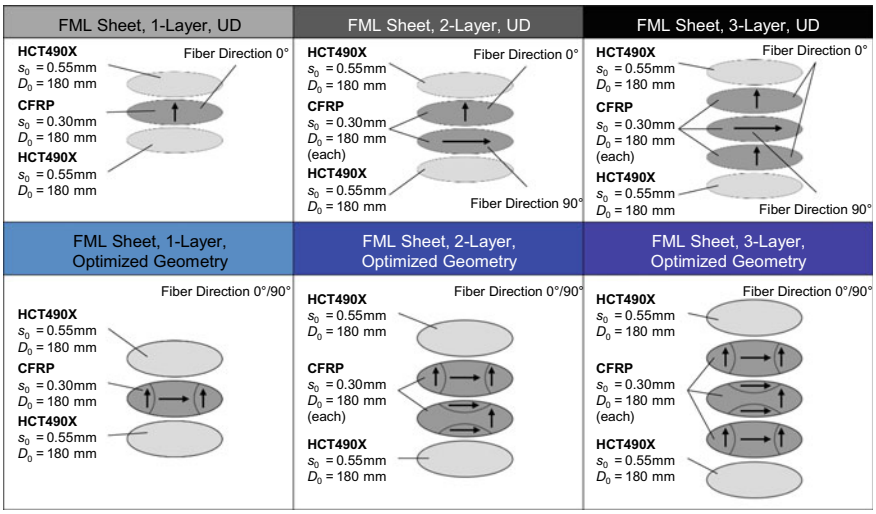


Fig. 2 Schematic image of the FML designs and the layer sequence. (Color figure online)

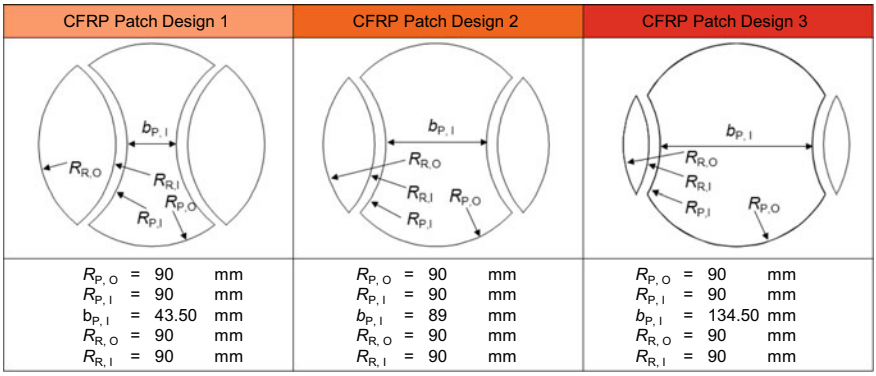


Fig. 3 Schematic image of the CFRP patch Designs. (Color figure online)

In order to investigate the influence of the patch geometries on the forming behavior and on the resulting shape and dimensional accuracy, especially in the frame area of the FML components, three different patch designs were developed for the experimental investigations. The geometries shown in Fig. 3 were thus used.

For every experiment, the circular unidirectional CFRP patch had a constant outer radius of $R_{P,O} = 90$ mm and two circular recesses with constant radii $R_{P,I} = 90$ mm, a varying inner width $b_{P,I}$ at the thinnest point and a fiber direction of 90°. The two recesses were filled by two biconvex UD prepreg patches with radii of $R_{R,O} = R_{R,I} = 90$ mm and a fiber direction rotated by 90° compared to the first patch as shown in Fig. 3. With this patch arrangement, a combined orthotropic 0°/90° fiber orientation results for every prepreg layer of the FML sheets. As a result of this patch alignment, the fibers arranged in the frame and flange area of the specimens are subjected to tangential compressive stresses in the fiber direction during the deep drawing process. Also, with this design, a combination of continuous, long, and short fibers results in the flange and frame area.

In order to analyze the forming result and to evaluate the shape and dimensional accuracy achieved in the FML parts, the specimens were cut in the center and examined by optical and tactile methods such as microscopy and measurements on a coordinate measuring machine.

3 Results

In order to determine the influence of the number of unidirectional CFRP layers used on the resulting shape and dimensional accuracy of the hybrid components, FML sheets with one to three unidirectional CFRP layers were formed and cured inside the tool system developed.

Figure 4 illustrates the correlation between the heights of the wrinkles h_{wr} and the measuring depth z_{md} inside the unidirectional FML specimens that were analyzed.

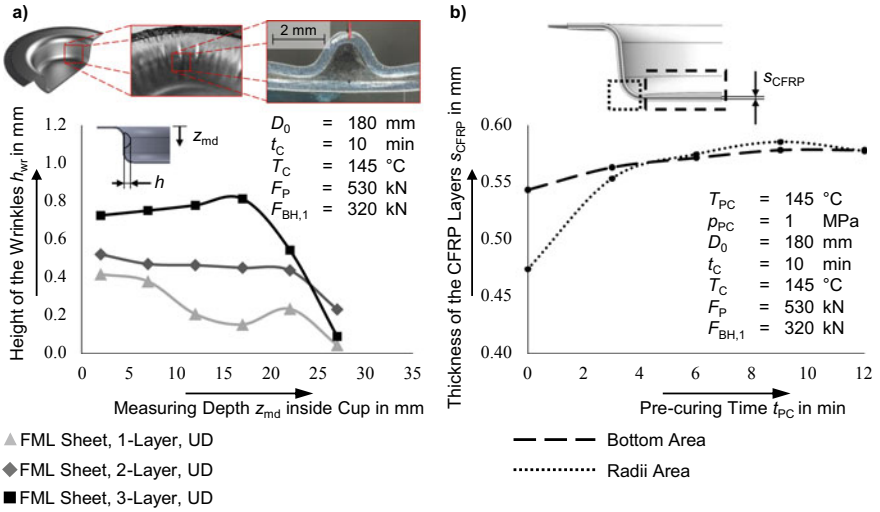


Fig. 4 Wrinkle height h_{wr} inside the specimens as a function of the number of CFRP layers (**a**), thickness of the CFRP layers s_{CFRP} as a function of the pre-curing time t_{PC} (**b**). (Color figure online)

No wrinkles can be determined at the top of the flange area due to the normal force $F_{BH,1}$ applied by the blank holder. Consequently, the first measuring plane for the wrinkle height h_{wr} is in the feed zone and has a depth of $z_{md} = 2.5$ mm from the top surface of the flange. The wrinkles measured at this depth have a wrinkle height of $h_{wr} = 0.42$ mm for an FML sheet with a single-layer unidirectional CFRP patch and they sink steadily up to a measuring depth of $z_{md} = 17$ mm to a value of approximately $h_{wr} = 0.15$ mm. The height of the wrinkles h_{wr} in the frame area then increases up to a measuring depth of $z_{md} = 22$ mm to a value of $h_{wr} = 0.24$ mm. A continuing decrease in the wrinkle height h_{wr} can be determined with an increasing measuring depth z_{md} so that, at a measuring depth of $z_{md} = 27$ mm, wrinkle heights of about $h_{wr} = 0.05$ mm can be detected. No wrinkles can be detected in the radii area between the frame and the bottom of the specimens. Most of the wrinkles occur particularly in areas in which the tangential pressure stresses act almost orthogonally or transversely on the unidirectional fibers. Consequently, most of the wrinkles can be determined around the 0° and 180° directions in one-layered FML components. In FML components with two layers of unidirectional CFRP rotated by 90 degrees to each other, the average wrinkle heights h_{wr} in the feed zone and the frame area are increased by about 79% compared to single-layer FML sheets. Most of the wrinkles can be determined around the 0°, 90°, 180°, and 270° directions. The forming of three-layered FML sheets leads to even higher values for the wrinkle heights h_{wr}, especially in the upper frame area. To sum up, additional FML layers with a unidirectional fiber orientation lead to a significant deterioration in the shape and dimensional accuracy within the FML components. The wrinkles are filled with resin and buckled fibers and hence additional layers of CFRP lead to an increase of the wrinkle height h_{wr}.

During the deep drawing process, the punch induces normal forces at the bottom of the FML parts and high surface pressures at the transition area between the bottom and the frame; this leads to hydrostatic conditions, forcing the resin to flow into neighboring zones. As a result, the wall thickness distribution in these areas is impaired. The pre-curing device as shown in Fig. 1b was used to determine the influence of an upstream pre-curing process on the resulting shape and dimensional accuracy in respect of the thickness of the CFRP layers. Three-layered circular unidirectional CFRP patches were used for the experiments. The pre-curing process was carried out with a pre-curing pressure of $p_{PC} = 1$ MPa, the pre-curing time t_{PC} was varied from $t_{PC} = 0$ min (no pre-curing) to $t_{PC} = 12$ min. The diagram in Fig. 4b shows the relationship between the pre-curing time t_{PC} and the resulting CFRP thickness s_{CFRP} in the bottom and radii areas of the specimens. The forming of specimens without local pre-curing leads to a significant thinning of the CFRP thickness s_{CFRP}, which is especially evident in the radii area. With increasing pre-curing time t_{PC}, the resin gains compressive strength and the resin flow is significantly reduced. With a pre-curing time of at least $t_{PC} = 4$ min, the thinning of the radii and bottom area can be reduced by about 80%, which leads to a distinct improvement in the shape and dimensional accuracy of the FML specimens.

A promising approach to reducing the wrinkle height h_{wr} is to optimize the CFRP patch geometry and the fiber alignment and to adapt the length of the fibers inside the FML sheets. Hence, in further investigations, special prepreg designs as shown in Fig. 3 were used to determine the influence of the CFRP patch geometry in the flange and frame area on the resulting shape and dimensional accuracy of the FML components. The measurement results of the wrinkle heights h_{wr} of the single-layered FML are shown in Fig. 5a. For reference, the gradients of the wrinkle height h_{wr} of the unidirectional FML are marked with a black line and white markers.

The curves marked in light, medium, and dark gray represent the wrinkle heights h_{wr} of those specimens with the patch design under investigation. They tend to absorb compressive forces in fiber direction in the main forming zone and in the frame area during the forming process. The radii $R_{P,O} = R_{P,I} = R_{R,O} = R_{R,I} = 90$ mm were held constant for the investigations. The curve marked in light gray represents the resulting wrinkle height h_{wr} for the investigated patch design 1 with an inner width of $b_{P,I} = 43.50$ mm on the main patch at the thinnest point. The curve marked in medium gray shows the wrinkle heights h_{wr} of the patch design with an inner width of $b_{P,I} = 89.00$ mm, while the dark gray curve represents the patch design with the smallest recesses ($b_{P,I} = 134.50$ mm). For the designs investigated, both short and long and continuous fibers result due to the recess geometry. With regard to the single-layered FML, all the investigated patch designs result in a significant reduction of the wrinkle heights h_{wr} compared to the unidirectional reference specimens up to a measuring depth of $z_{md} = 17.5$ mm. The patches tend to be loaded by compressive stresses in the fiber direction in the edge region of the FML sheets during the forming process, which results in a significant reduction in the wrinkle height.

Compared to the unidirectional reference, the wrinkle height h_{wr} is reduced by almost 74%. Due to the fiber orientation and the shortened fiber length, the fibers can slip into each other in the fiber direction. In addition, flow channels for the resin

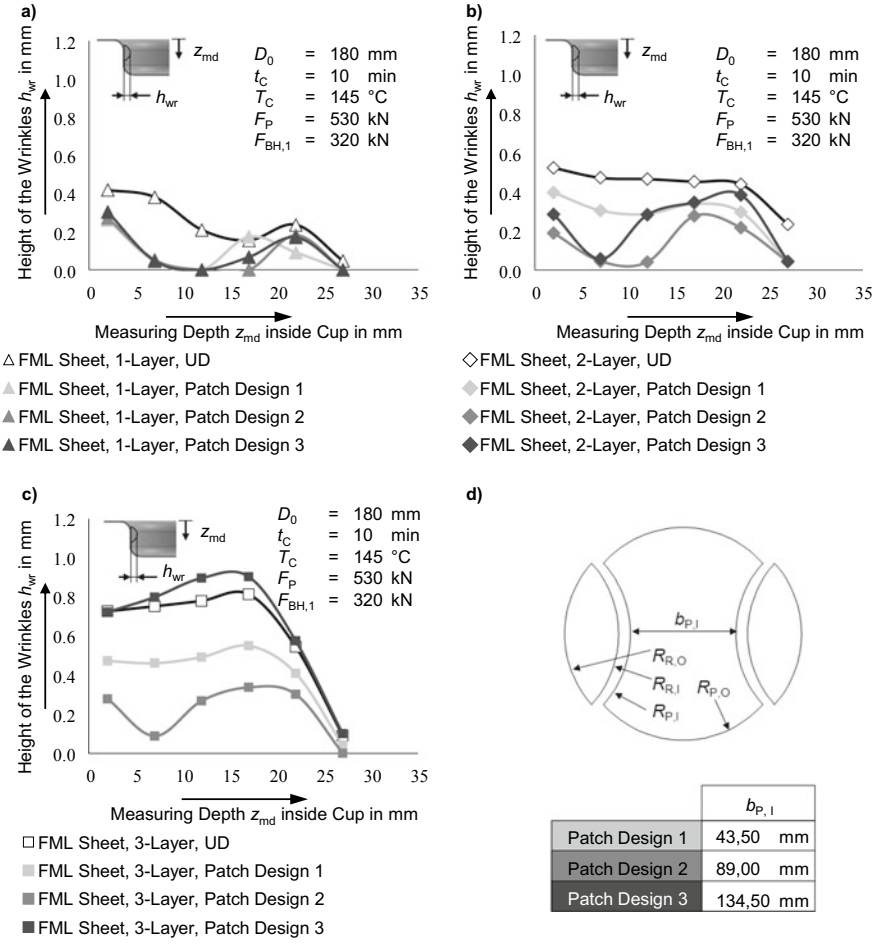


Fig. 5 Wrinkle height h_{wr} inside the specimens as a function of the number of CFRP layers and the patch design (**a**–**c**), schematic image of the patch design (**d**)

are released in the fiber direction. Compared to the transversal fiber direction, the fiber direction offers less flow resistance for the resin. The resin is distributed more homogenously in the frame area and in the feed zone.

The relationship between the measuring depth and the height of the wrinkles h_{wr} for the two-layered FML sheets (the unidirectional references are marked with a black line and white markers, the investigated designs are marked light, medium, and dark gray) is shown in Fig. 5b. The curves of the unidirectional reference and design 1 show a very similar course. A significant reduction in the wrinkle height h_{wr} over the entire frame and feed area can be achieved using patches with a recess of $b_{P,I} = 89.00$ mm. On average, a reduction of the wrinkle height h_{wr} of approximately 70% (h_{wr}) can be achieved.

The wrinkle heights h_{wr} for the three-layered FML specimens are shown in Fig. 5c. A significant reduction in the wrinkle height h_{wr} can be observed for design 2 that was investigated. While the wrinkle heights h_{wr} of the unidirectional reference attain a value of more than 0.70 mm up to a measuring depth of $z_{md} = 20$ mm, the wrinkle heights h_{wr} of design 2 remain below $h_{wr} = 0.35$ mm. On average, a reduction of the wrinkle height h_{wr} of more than 70% can be achieved over the entire frame and feed zone area with design 2. Design 3 does not improve the shape and dimensional accuracy for this stacking sequence, and the height of the wrinkles h_{wr} is even higher than for the reference. A significant improvement can thus be achieved by aligning the patches according to design 2, where the short and long fibers can slip into each other in the forming zone and in the frame area up to the radii area at the bottom of the specimens, thus additionally releasing flow channels. Compared to designs 1 and 3 this fiber arrangement allows a more homogeneous distribution of the resin.

4 Conclusion

In this study, experimental research has been conducted into the development of the process and material design for the production of hybrid components made of FML sheets. The focus of these investigations was to determine the influence of an upstream pre-curing process on the wall thickness distribution, the number of CFRP layers, and the patch geometry, with the aim of improving the shape and dimensional accuracy of the FML parts during the combined forming and curing process. Additional layers of CFRP lead to a significant increase in the measured wrinkle heights h_{wr} inside the FML cups. The local thinning of the bottom area and radii area was reduced through the approach of local pre-curing of the bottom area of the FML sheets. The wrinkle height of the inner metal sheets was reduced by almost 74% on average. For the two and three-layered FML components, the wrinkle heights were reduced by 70%. Future work will investigate the transfer of knowledge from this study to more complex geometries and the development of a numerical model to predict the forming results of FML sheets.

Acknowledgments The authors gratefully acknowledge the financial support from the European Regional Development Fund (ERDF) and the state of North Rhine-Westphalia (NRW).

References

1. Klein B (2007) Leichtbau-Konstruktion. Vieweg-Verlag, Berechnungsgrundlagen und Gestaltung
2. Braess HH, Seiffert U (2013) Vieweg Handbuch Kraftfahrzeugtechnik. Vieweg-Verlag
3. Eversheim W, Erkes K, Kirberg K (1956) Bewertung alternativer Fertigungslinien für Kfz-Pleuel—CFK-Verbund als Stahlsubstitution bietet Vorteile. In: Industrie-Anzeiger / Spezial, Produkt Report, Band 108

4. Spickenheuer A (2013) Zur fertigungsgerechten Auslegung von Faser-Kunststoff-Verbundbauteilen für den extremen Leichtbau auf Basis des variabelaxialen Fadenablageverfahrens Tailored Fiber Placement, Dissertation TU Dresden
5. Johnsin W, Mellor PB (1973) Engineering plasticity. Vand Nostrand Reinhold
6. Doege E, Behrens B-A (2007) Handbuch Umformtechnik. Springer
7. Lutz D (2002) Chassis lightweight design exemplified on a suspension strut—state of the art and potential. In: 11 Aachen Colloquium Automobile and Engine Technology
8. Schmidt HC et al (2013) Manufacturing processes for combined forming of multi-material structures consisting of sheet metal and local CFRP reinforcements. Key Eng Mater 504–506
9. Homberg W, Dau J, Damerow U (2011) Combined forming of steel blanks with local CFRP reinforcement. Steel research international. ICTP 2011
10. McEntee SP, O'Bradaigh CMÓ (1998) Large deformation finite element modelling of single-curvature composite sheet forming with tool contact. Compos Part A Appl Sci Manuf
11. Wang P, Hamila N, Boisse P (2013) Thermoforming simulation of multilayer composites with continuous fibres and thermoplastic matrix. Composites: Part B 52
12. Böhler P, Härtel F, Middendorf P. Identification of forming limits for unidirectional carbon textiles in reality and mesoscopic simulation. Key Eng Mater
13. Heggemann T, Homberg W. Deep drawing of fiber metal laminates for automotive lightweight structures. Compos Struct 216

Experimental Analysis on Granular Media-Based Tube Forming with Active Axial Feed



E. Hoffmann, C. Löbbe, and A. E. Tekkaya

Abstract Production of high strength, high stiffness, and safety-relevant profile parts is feasible through the sequence of media-based forming and in-die quenching. As forming media, solid granular media have been recently introduced. In this work, the granular media tube press hardening process with additional axial feeding is investigated in order to enhance the tube thickness distribution and to enlarge the process window. The experiments show that, compared to the process with frictional feed, the limits for insufficient forming and wrinkling are unaffected by the change of the feeding system, while the area for intolerable thinning is reduced. Additionally, through the new feeding system, a higher degree of design freedom could be achieved, e.g., shoulder angles of 90° are possible. Furthermore, for the design of the process, an advanced FEM simulation has been developed, which is based on the Drucker–Prager cap model and covers also the thermal interactions.

Keywords Hydroforming · Hollow profiles · Press hardening · Granular media

1 Introduction

The demand for high-strength profile parts for automotive body construction is high due to increasing safety regulations and economic demands. Granular media-based hydroforming can serve as an alternative process to conventional liquid-based hydroforming and gas forming to achieve press hardened profiles. Mennecart et al. [1] tested the feasibility of granules as a hydroforming medium. Grüner and Merklein [2] used the Drucker–Prager Cap model to describe the granular media behaviour numerically during a hydroforming process. Typically, zirconia beads are used as this material has been proven to achieve the best forming results [3]. Another possible medium would be quartz sand but the pressure transfer is significantly lower, reducing the possible product complexity [3]. Challenges arise in the behaviour of granular materials. The higher the distance from force initiation area in the medium pillar, the higher is the

E. Hoffmann (✉) · C. Löbbe · A. E. Tekkaya
Institute of Forming Technology and Lightweight Components (IUL), TU Dortmund University, Baroper Str. 303, 44227 Dortmund, Germany
e-mail: eike.hoffmann@iul.tu-dortmund.de

© The Minerals, Metals & Materials Society 2021

G. Daehn et al. (eds.), *Forming the Future*, The Minerals, Metals & Materials Series,
https://doi.org/10.1007/978-3-030-75381-8_220

pressure loss due to internal friction [4]. Additionally, the consolidation pressure of the medium limits the transferred pressure in the volume [5]. Still, in past research, the friction was necessary for the successful production of profile parts. Frictional forces lead to an axial tube feed which negates the tube thinning [6]. To increase the achievable forming limit of the parts produced by this process, a new approach needs to be investigated.

In order to reduce tube thinning while still maintaining low frictional forces in the process, a tool with an active axial feed mechanism was developed. The experiments published in this work using this tool have two objectives. First, the influence of active feed on the process is analysed. A correct adjusted feeding force should stop the tube thinning and enable a better filling of the die cavities [7]. Second, the effect of reducing frictional forces in the process is investigated. Therefore, zirconia beads mixed with boron nitride, a common lubricant which is not carbon-based, are used as the medium. The reduction of frictional forces should lead to a higher possible forming length of the profiles. This effect is investigated through forming of tubes at same forces with different boron nitride fractions in the medium.

2 Experimental Set-Up

For the process tests, a tool for a Müller Weingarten BZE 1000 hydraulic press was developed (Fig. 1). The symmetric tool consists of two independent axial axes for both pressing the granular medium and feeding the tube. The forming force is acting through two hydraulic punches, which can enforce a maximum axial pressure in the medium of 230 MPa, while the feeding axis is driven by servo motors with a

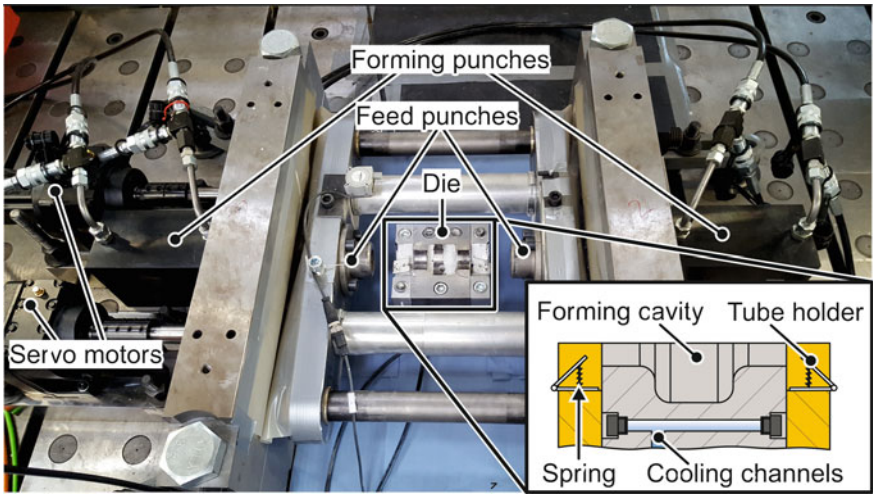


Fig. 1 Granular media-based press hardening tool with active axial feed axis. (Color figure online)

maximum force of 100 kN. The die contains tube holders to reduce the cooling of the tube during closing. Additionally, cooling ducts are drilled into the die to sustain high cooling rates after numerous forming tests. The die closing pressure is applied through the press.

For the tests, 22MnB5 tubes with an outer diameter of $d_{o,d} = 40$ mm, and a thickness of $t_0 = 1.5$ mm (Fig. 2a) are first heated in an oven at 950 °C for 4 min (Fig. 2b). After heating, the tubes are filled with zirconia beads with a diameter of 0.5 mm (Fig. 2c). The filling happens after heating so the medium is still at room temperature, not increasing the necessary cooling rate of the tube for complete martensitic transformation. Afterwards, the tube is inserted into the die and positioned on the tube holders (Fig. 2d). The die closes and, through the closing force, the tube holders are lowered (Fig. 2e). This is timed with the positioning of the form and feed punches to reduce forming time. Consequently, to these steps, the forming process starts. The diameter is increased to 65 mm over a length of 50 mm with a starting temperature of 800 °C. The tube remains in the die for 20 s to reach complete

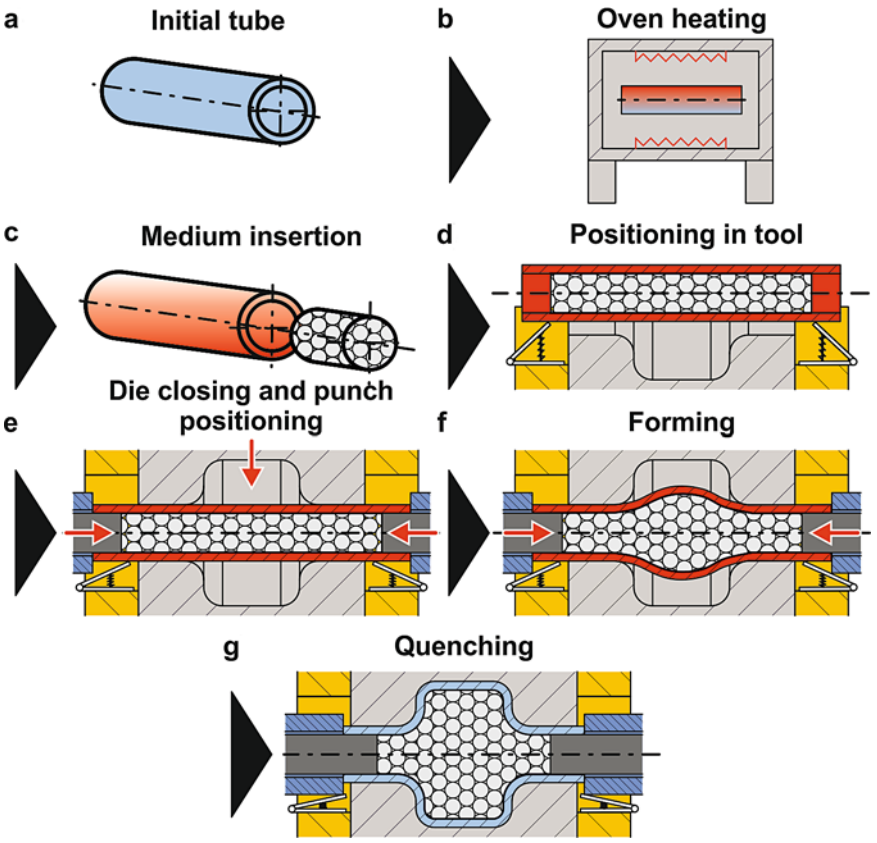


Fig. 2 Forming sequence for the granular media-based press hardening process. (Color figure online)

martensitic transformation (Fig. 2g). The resulting geometry is then measured with an ATOS system and, additionally, the thickness is measured by ultrasonic measurement.

3 Simulation Set-Up

The process simulation is a thermal–mechanical-coupled FEM simulation. The parameters for the simulation are defined in Fig. 3. The granular material is modeled by the Drucker–Prager Cap model, which defines a volume of granular material as a continuum and describes the flow and strain hardening (cap hardening) behaviour

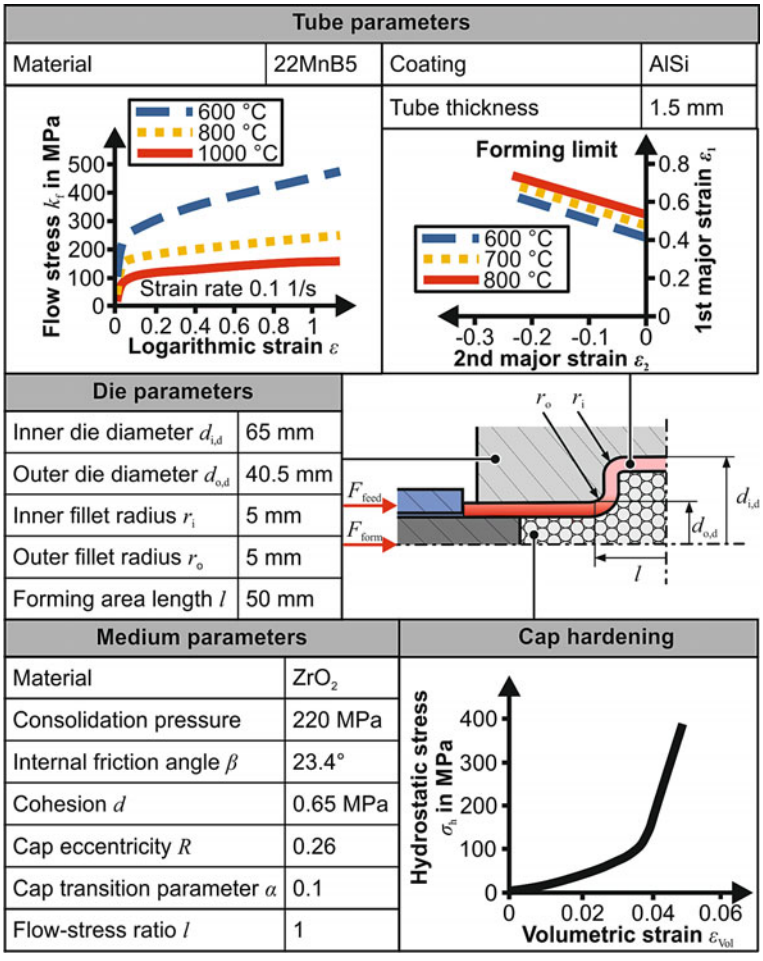


Fig. 3 Simulation parameters for process simulation, also used in [8]. (Color figure online)

of this material [9]. The tube behaves elastoplastic and its properties are influenced by temperature. The temperature dependency of tube properties is achieved by using tabular flow curves for the corresponding temperatures. Temperature-dependent FLC data limits the formability of tube material in the simulation. The die and the punches are mechanical rigid bodies which can transfer temperature.

Friction is defined as a constant value of $\mu = 0.25$ between medium and tube and $\mu = 0.45$ between tube and die [6]. Heat transfer results through conduction between medium, die, and tube. The heat transfer depends on contact pressure. Starting temperature of the tube is 800 °C to compensate for the transfer and loading time from removal of the tube from the oven to insertion into the tool.

While the DPC model for the medium is stable for the case it was characterized for there are still challenges in using this model in metal forming. When adding additives to the medium the internal friction and with this, the flow behavior is changed. Because the medium volume is modelled as a continuum, the medium has to be characterized again after adding additives. Additionally, through the continuum definition, an error on contacts persists, which means that the simulation cannot predict indentations caused by the granular particles. These indentations are a result of the high strength and the dimensions of the medium particles which cause a plastic deformation on the inner tube surface.

4 Discussion

4.1 Influence of Axial Feed

To examine the influence of the axial feed, tests at maximum forming force and at different feeds have been carried out. Feed is defined as

$$f = \frac{v_{\text{feed}}}{v_{\text{form}}} \tag{1}$$

where v_{feed} is the velocity of the axial feed punch and v_{form} the velocity of the forming punch. The active feed has an influence on die cavity filling (Fig. 4). The displayed geometry is measured along the path with the highest cavity filling (Fig. 4a) and the mean curve of the three repetitions is displayed (Fig. 4b). The results are evaluated at a medium pressure of 220 MPa (consolidation pressure of zirconia beads). The press closing force is 1.5 MN. The higher the axial feed, the closer the profile geometry is to the desired geometry. A possible reason for this could be that the axial feed induces bending moments on the tube. These moments might reduce the necessary punch force for the forming process.

For high enough feeds, forming of tubes approximately without thinning is possible (Fig. 5). The values for the experiments are mean values out of the maximum thickness values for three specimens. For a medium pressure of 220 MPa, a feed that

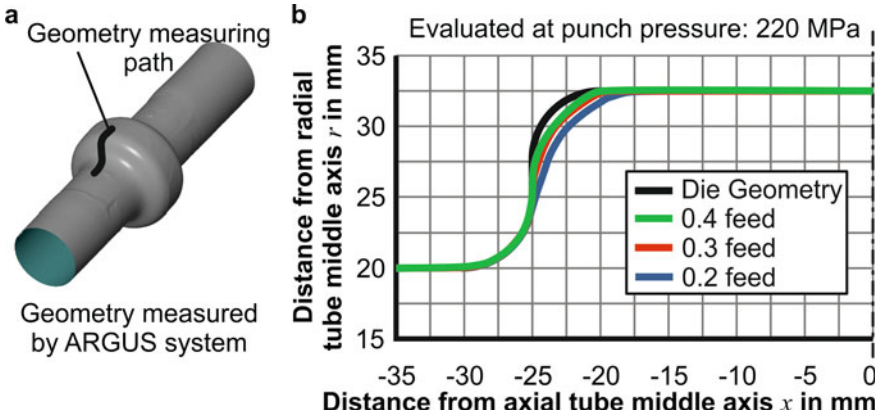


Fig. 4 Influence of axial feed on die cavity filling. **a** Geometry measurement path, **b** resulting part geometry. (Color figure online)

is lower than $f < 0.2$ leads to excessive thinning of the tube. Wrinkling for the evaluated punch pressure occurs at feeds higher than $f > 0.5$. While the thickness strain for $f = 0.2$ is still low the thickness strain for $f = 0.5$, feed is approaching zero showing the effectivity of applying an axial stress.

The results are showing that through the axial feed thickness strain of approximately zero is possible. This effect was discovered in [6] but reached through the friction between tube and medium. One aim in this work is to reduce the media friction so that longer profile products are possible. Through the active feed, minimizing thickness strain while reducing media friction is possible.

With increasing feed, the error between simulation and experiment is increasing. It ranges from +17% to +96% depending on the feeding ratio. A reason for this could be that through the axial feed a bending moment on the tube bulge is initiated. This bending moment may lead to a localization of the strain. Additionally, the number of elements in the simulation is limited. Through the strain localization, the number of elements in the FEM simulation might be too low to accurately predict the strains caused by the bending effects, leading to the error in maximum strain for the high feed cases. While the error is high when measuring the thickness in high feed cases, the failure mode of the tube also changes. In high feed cases, accurately predicting the thickness strain becomes secondary to predicting the actual material failure through wrinkling which is successfully achieved through the model (Fig. 6).

The process window shows the process limits for insufficient forming, excessive thinning and wrinkling of the tube material, and the pressure limit in the medium through the consolidation pressure. The limits from the simulation and from the process tests are depicted. For the tests, the lines are extrapolated from the results of three tests without failure, which consists of three specimens each. To compare to the successful tests, the tests for the first material failure during the forming process are illustrated too.

Insufficient forming occurs when the distance between tube and die is higher than 5 mm. The consolidation pressure limit is the pressure at which the medium forms into a green body, resulting in a case where no more pressure can be transferred through the medium [1]. As can be seen in contrast to Fig. 5, the simulation is in good accordance with the experiments for the process window.

There are two mechanisms leading to the reduction of maximum complexity of profile parts produced by this process. First, the pressure drops over the length of the

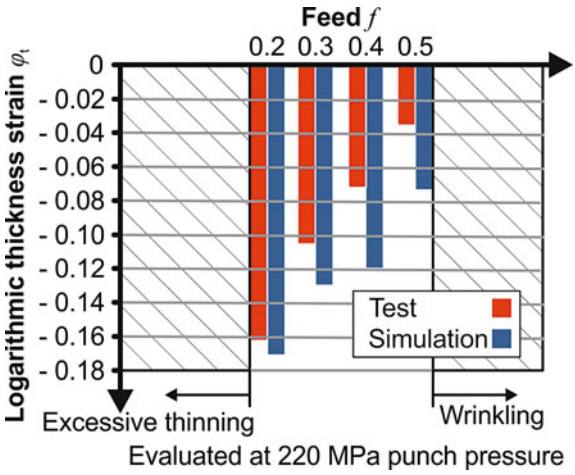


Fig. 5 Influence of axial feed on profile thickness strain. (Color figure online)

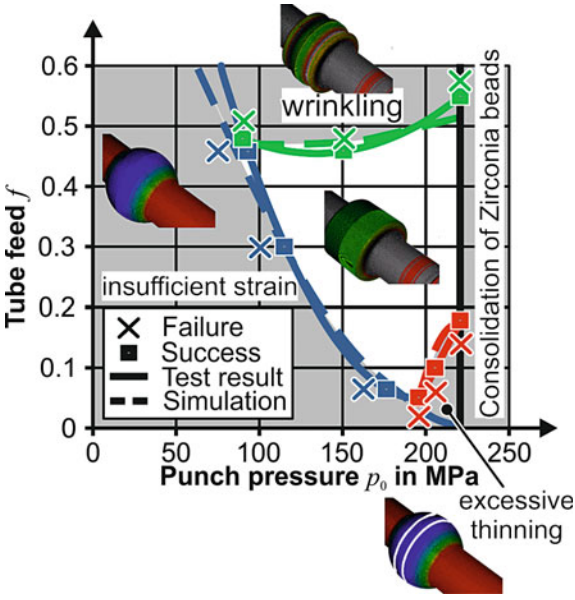


Fig. 6 Process window for zirconia beads as forming medium. (Color figure online)

media pillar due to friction [10]. Second, the maximum pressure transferred by the medium is limited by its consolidation pressure. Thus, to increase profile complexity, a reduction of medium friction is necessary.

4.2 *Influence of Media Friction*

To reduce media friction, the zirconia beads were mixed with different fractions of boron nitride. The boron nitride is evenly distributed in the mixture. Boron nitride is a ceramic material, giving it the high-temperature stability necessary for the press hardening process. The lubrication mechanism of this material is comparable to graphite [11] but as a carbon-based lubricant graphite is not usable as lubrication for steel materials at high temperatures. Even low fractions of boron nitride have a huge influence on forming success (Fig. 7). Depicted is the cross-sectional geometry of the tubes after the forming process and the die geometry as desired geometry. All profiles are evaluated at the feed of $f = 0.2$ and a punch pressure of $p_0 = 150$ MPa. Mean geometry out of three tests is used for each curve. The difference is the mass fraction of boron nitride mixed with the granular medium. As illustrated, a mass fraction of 1% boron nitride (red curve) leads to a reduction of friction and thus an increase in tube formability for the same punch pressure compared to zirconia beads without boron nitride (green curve). Lower fractions of boron nitride reduce the formability.

A higher mass fraction than 1% of boron nitride influences the formability negatively. The reason for this might be the density disparity between the two medium materials. While the zirconium dioxide manifests a density of 6200 kg/m^3, the density for boron nitride is 2250 kg/m^3. This difference leads to the medium mixture consisting of a high volume fraction of boron nitride. Additionally, for the plastic deformation of a volume of granular material, it is necessary for the particles to fill the cavities in the medium pillar meaning the smaller the medium grains, the more force is necessary for the pillar to deform. The high volume of the smaller boron

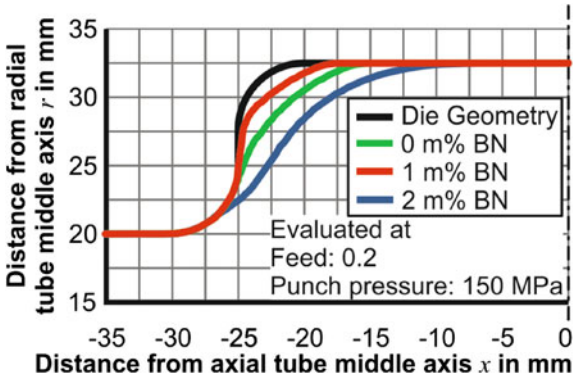


Fig. 7 Geometrical results of the forming process for different mass fractions of boron nitride. (Color figure online)

nitride particles is now filling the cavities influencing the mechanical properties of the medium for mass fractions higher than 1 m%.

5 Conclusion

The objectives of this work were to investigate the influence of axial feed and the influence of media friction on the process. The FEM analysis has proven to predict the failure modes of the tube material during the forming process correctly. While there are still issues in predicting the thickness strains for high feeds and the surface indentations, the model covers typical process errors such as wrinkling and can correctly predict the thinning in low feed cases.

An active feed mechanism was successfully applied in the granular media-based press hardening process. Through the use of the active feed tube, thinning can be prevented. These results grant the basis for increasing the product complexity of the process through the reduction of media friction and thus increasing the transferable forces through the medium.

Lastly, the reduction of friction through using additives such as boron nitride in the medium was shown to improve the formability of the tube at same pressures compared to pure zirconia beads. The amount of additive used may not surpass a certain threshold to achieve a positive effect. With these first results on the reduction of media friction during the granular media-based press hardening process a foundation has been laid for further improvements in product complexity in the process.

Acknowledgments The authors acknowledge funding from the German Research Foundation (DFG) for project TE 508/52-1 “Granular media-based tube press hardening”.

References

1. Mennecart T, Rostek T, Witulski J et al (2011) Presshärten von Rohren und Profilen mittels formlos fester Stoffe. Erlanger Work Warmblechumformung 117–128
2. Grüner M, Merklein M (2010) Numerical simulation of hydro forming at elevated temperatures with granular material used as medium compared to the real part geometry. Int J Mater Form 3:279–282
3. Chen H (2017) Granular medium-based tube press hardening. Dr.-Ing Dissertation. TU Dortmund
4. Mueth DM, Jaeger HM, Nagel SR (1998) Force distribution in a granular medium. Phys Rev E 57:3164–3169
5. Chen H, Güner A, Ben KN et al (2016) Granular media-based tube press hardening. J Mater Process Technol 228:145–159
6. Chen H, Hess S, Haeberle J et al (2016) Enhanced granular medium-based tube and hollow profile press hardening. CIRP Ann 65:273–276
7. Kang BH, Lee MY, Shon SM et al (2007) Forming various shapes of tubular bellows using a single-step hydroforming process. J Mater Process Technol 194:1–6

8. Hoffmann E, Kamaliev M, Löbbe C, et al (2019) Enhanced process limits in the granular media-based tube forming through axial feeding. In Proceedings of 7th international conference on hot sheet metal forming of high performance steel CHS2, pp 95–102
9. Resende L, Martin JB (1985) Formulation of drucker-prager cap model. J Eng Mech 111:855–881
10. Wu C-Y, Ruddy OM, Bentham AC, et al (2005) Modelling the mechanical behaviour of pharmaceutical powders during compaction. Powder Technol 152:107–117
11. Koskilinna JO, Linnolahti M, Pakkanen TA (2006) Friction coefficient for hexagonal boron nitride surfaces from ab initio calculations. Tribol Lett 24:37–41

Finite Element Simulation and Punch Design for Tube Hydro-Piercing



Yeong-Maw Hwang, Wei-Han Dai, and Pin-Chen Lin

Abstract This study is focused on punch shape design in tube hydro-piercing processes of aluminum alloy A6005 tubes. The flow stresses of the aluminum alloy tubes obtained by tensile tests are used in the finite element simulations of tube hydro-piercing process with software "DEFORM 3D." The ductile fracture criterion of normalized Cockcroft and Latham is used during the FE simulations. The critical damage values for the criterion are obtained by comparing simulation results and tensile test data. The effects of various parameters such as the stroke, internal pressure, etc., on hydro-piercing processes and deformation mechanism are discussed. Experiments are conducted and the experimental shearing surface heights are compared with the simulation results to verify the validity of the analytical models. The effects of various parameters on shearing surface heights are also discussed by hydro-piercing experiments.

Keywords Tube hydroforming · Hydro-piercing · Finite element analysis · Punch shape design

1 Introduction

The hydroforming processes have been widely applied to manufacturing parts in various fields, such as automobile, aircraft and aerospace, shipbuilding industry, etc., due to the increasing demands for lightweight parts. Hydraulic punching or piercing is combined with hydroforming processes to save manufacturing costs and raise positional accuracy [1]. Generally, hydro-piercing can be conducted in two ways: outward piercing and inward piercing. In an outward piercing process, a counterpunch moves backward as high internal pressure is reached. The process formability and the hole section characteristics are affected by the internal pressure and the corner shape of the die. The punched scrap is removed out of the tube after the process. In an inward piercing process, a punch moves forward to pierce the tube material and

Y.-M. Hwang (✉) · W.-H. Dai · P.-C. Lin
Department of Mechanical and Electro-Mechanical Engineering, National Sun Yat-Sen University, No. 70 Lein-Hai Rd, Kaohsiung 804, Taiwan
e-mail: ymhwang@mail.nsysu.edu.tw

© The Minerals, Metals & Materials Society 2021

G. Daehn et al. (eds.), *Forming the Future*, The Minerals, Metals & Materials Series,
https://doi.org/10.1007/978-3-030-75381-8_221

make the scrap drop into the tube. The hole section characteristics are affected by the internal pressure and punch shapes. The pierced hole section characteristics are different with inward and outward hydro-piercing processes.

In order to improve the dimensional accuracy of the hole shape in a sheet hydro-piercing process, Shiomi et al. [2] used a hydrostatic pressure to support the sheet. The effects of punch movement types on pierced section surface quality were discussed. Wu et al. [3] used the finite element software ABAQUS with six ductile criteria to predict crack initiation and propagation in the hydro-piercing process of tubes. Some comparisons among the results obtained by simulations using different ductile criteria and the experimental results were also discussed. The model using Rice and Tracey criterion showed good agreement with the experimental data at loading pressure of 60 MPa. Mizumura et al. [4] proposed a nut-inlaying method to join a bolt on a thin-walled tube, in which hydro-piercing and hydro-burring were conducted sequentially. Uchida and Tomsawa [5] investigated the fundamental characteristics of outward hydro-piercing by an internal hydraulic pressure experimentally. The effects of hydraulic pressure, tensile strength, and wall thickness of the tube on the pierced surface shape and shearing resistance during hydro-piercing were discussed. Choi et al. [6] investigated the effects of tube material properties, punch diameter, tube wall thickness, and internal pressure within the tube during hydro-piercing on the deformation behavior experimentally. From the experimental results, empirical equations were developed to predict roll-over height and deformation radius of the punched tube prior to shear fracture in the hydro-piercing process. Korkmaz et al. [7] investigated the effects of the punch movement on the burr formation in a hydro-piercing process of 304 stainless steels using finite element software LS-Dyna and Jonson–Cook hardening and damage model. Their simulation results showed that the burr formation can be eliminated by a two-step movement of the punch through the piercing operation.

Up to now, most researches concerning pierced hole sections after hydro-piercing were experimental works. Few literature investigated the characteristics of the pierced hole sections analytically with different punch shape design during hydro-piercing processes. This paper investigates the effects of the punch shape on the characteristics of the pierced hole section of the tube and discusses the effects of the internal pressure on the residual thickness during hydro-piercing processes of aluminum alloy tubes.

2 Finite Element Modeling

2.1 Tube Material

Aluminum alloys were used as the tube specimens. The flow stresses or the true stress–strain curves of the tube material obtained by tensile tests with an average strain rate of 0.006 s^{-1} are shown in Fig. 1. The corresponding equation best fitted with the flow stress is also shown in the figure. The yield stress is obtained by the

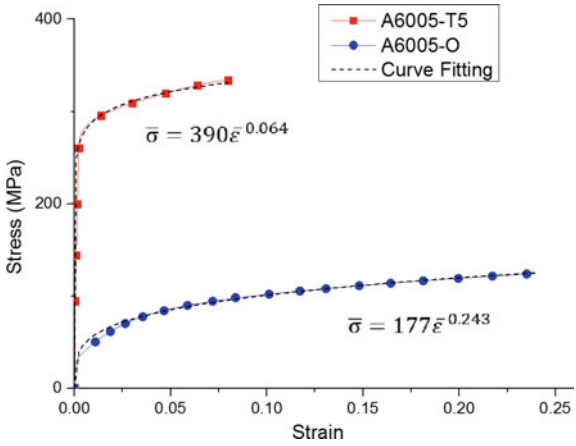


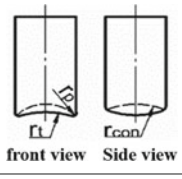
Fig. 1 Flow stress curve of tube materials A6005-T5 and A6005-O. (Color figure online)

0.2% offset method. The obtained yield stress σ_y, for A6005-T5 and A6005-O, are 278 and 69 MPa, respectively.

2.2 Punch Shape Design

Two types of punch shapes were designed as shown in Table 1. (1) Plane punch (PP) exhibits a flat plane at the bottom of the punch. (2) Concave tube surface punch (CTSP) is so designed that the peripheral corner is in contact with the tube surface, whereas the inside is a spherically concave surface. These two types of punches have an identical corner radius of rp at the peripheral corner. The intersection curves or the contact configurations between the punch and tube for type CTSP are shown in Fig. 2.

Table 1 Punch types and corresponding shapes

Punch type	Punch shape
Plane punch (PP)	
Concave tube surface punch (CTSP)	

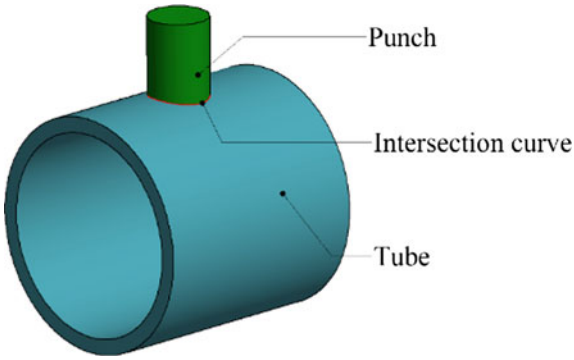


Fig. 2 Contact configurations between punch type CTSP and tube. (Color figure online)

2.3 Forming Conditions

The contact configurations between the punch and tube before and after hydro-piercing are shown in Fig. 3. Initially, a high pressure is imposed on the inner surface of the tube. The punch moves inward with a speed of V. After a stroke of S, the tube exhibits a roll-over height Hr on its top surface and a residual thickness tr at the bottom of the hole section. The scrap does not separate completely with the tube at this moment. If the scrap separates completely with the tube, the scrap will be kept inside the tube and eventually will drop into the oil tank, which is not good for further processes. There is no die or other support structure inside the tube to support the tube, and it is difficult to control the hole quality. Thus, in this paper, a high internal pressure is adopted to improve the characteristics of the pierced hole surface.

The outer diameter and thicknesses of the aluminum alloy tubes are 70 mm and 3.75 mm, respectively. A finite element software "Deform 3D" was used to simulate the tube material deformation and fracture behavior in the hydro-piecing process. The punch diameter Dp is 6.5 mm and the punch speed is set as 1 mm/sec. The punch corner radius rp is 0.2 mm and the spherical radius rcon for type CTSP is 5 mm. The

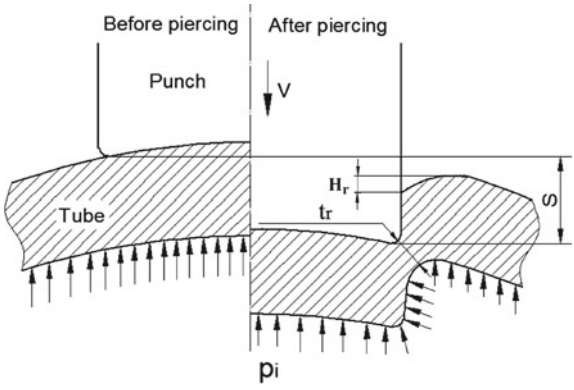


Fig. 3 Contact configurations between punch and tube before and after hydro-piercing

Table 2 Forming parameters used in FE simulations

Material	A6005	Internal pressure	20, 40, 60, 100 MPa
Material model	Rigid-plastic body	Spherical radius r_{con}	5 mm
Tube diameter Dt	70 mm	Punch corner radius rp	0.2 mm
Thickness t0	2.0, 3.75 mm	Temperature T	20 °C
Punch diameter Dp	6.5 mm	Step increment	0.01 mm
Punch velocity V	1 mm/sec	Mesh number	157,000
Coulomb friction coefficient μ	0.1	Minimum element length	0.08 mm

other parameters used in the finite element simulations are summarized in Table 2. The Normalized Cockcroft and Latham (NCL) ductile fracture criterion [8] given in Eq. (1) was used to determine if the tube material reaches the fracture condition and the corresponding element is removed.

$$c = \int_0^{\bar{\varepsilon}_f} \frac{\sigma_1}{\bar{\sigma}} d\bar{\varepsilon} \tag{1}$$

where, $\tilde{\sigma}$ is the effective stress, σ_1 is the maximum tensile stress, $\bar{\varepsilon}_f$ is the effective strain at the fracture point, $\bar{\varepsilon}$ is the effective strain, and c is the critical damage or fracture value. Tensile test simulations with the NCL criterion and real tensile tests were conducted. The critical damage value c is obtained by comparing the elongation and loading curve between the FE simulations and the real tensile tests. The obtained critical damage value for A6005T5 and A6005-O are 0.219and 0.618, respectively.

3 Simulation Results and Discussion

3.1 Punch Load

Figure 4 shows the load variations with punch type CTSP during the hydro-piercing process. The whole process can be divided into three stages: (A) Elastic stage, (B) Plastic stage, and (c) Fracture stage. In stage (A), the tube undergoes elastic deformation and only slight roll-over deformation occurs. In stage (B), the load increases

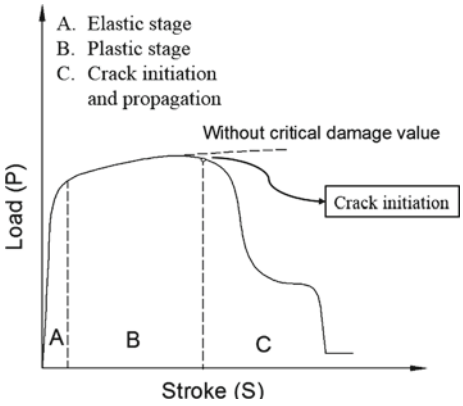


Fig. 4 Punch load variations during hydro-piercing process

monotonically with the stroke, in which the tube undergoes elasto-plastic deformation, the roll-over region expands, and a burnished surface or a slip surface generates. In stage (C), the load drops drastically, in which material fracture initiates and a fracture surface starts to generate. If no critical damage value is set in the FE simulations, the load will continue to increase as showen in Fig. 4.

Figure 5 shows the load variations with different internal pressures during the hydro-piercing process. Clearly, the load increases with the internal pressure, whereas the whole stroke range decreases with the increase in internal pressure. That is because the fracture surface region decreases under a higher hydro-static stress state, however, the roll-over and burr parts are not influenced significantly by the hydro-static stress state.

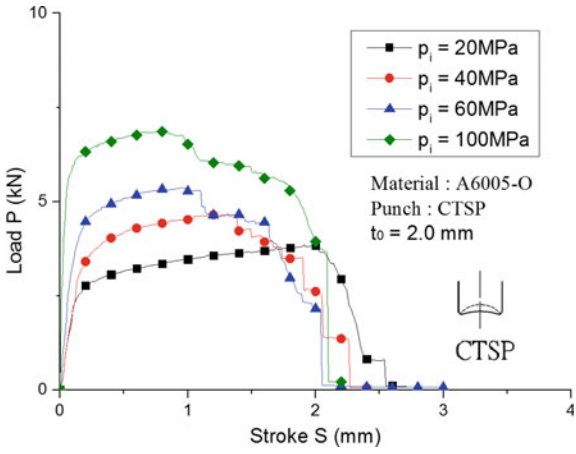


Fig. 5 Punch load variations with different internal pressures during hydro-piercing process. (Color figure online)

3.2 Characteristics at Pierced Hole Section

Figure 6 shows the schematic diagram at the pierced hole section, which is constituted by a roll-over, a burnished surface, a fractured surface, and a burr. The roll-over region results from an inward deflection of the tube in contact with the die. There are shear and tensile stresses existing at the burnished and fracture zones. The burnished surfaces result mainly from shear stresses and fracture surfaces result mainly from tearing of the tube material due to tensile stresses. The burr part results at the free inner surface of the tube. Some simulation results of the extent or quality of each zone affected by punch shapes are discussed in the following figures.

Figure 7 shows the effects of punch shapes on the surface characteristics of the pierced hole section. The forming conditions are internal pressure $P_i = 40$ MPa, initial tube thickness $t_0 = 3.75$ mm, and punch diameter $D_p = 6.5$ mm. From the figure, it is known that a smaller roll-over height Hr can be obtained with punch type of CTSP. For tube material of A5005-O, a smaller burnished surface height is obtained with punch type of CTSP.

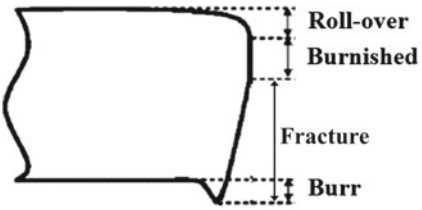


Fig. 6 Schematic at pierced hole section

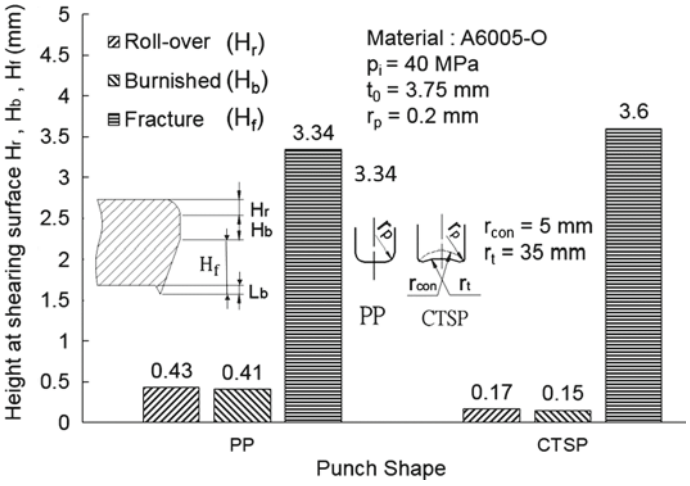


Fig. 7 Effects of punch shapes on characteristics of pierced hole section

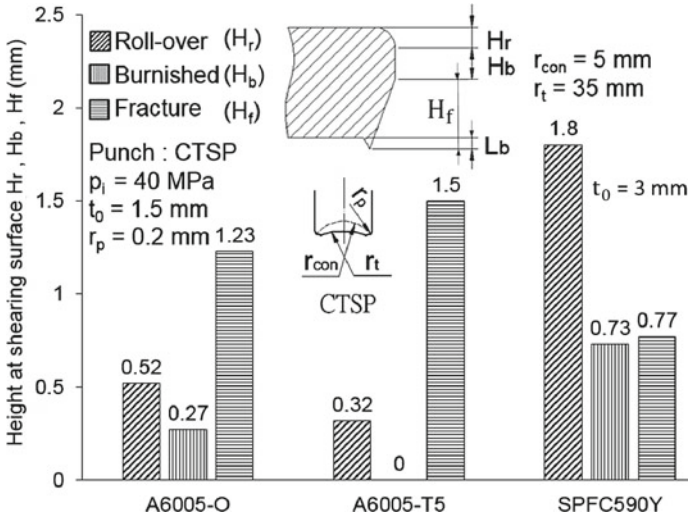


Fig. 8 Effects of different materials on characteristics of pierced hole section

Figure 8 shows the effects of different materials on the heights of roll-over, burnished surface, and fracture surface at the pierced hole section. The initial tube thickness is $t_o = 1.5$ mm and the internal pressure is $p_i = 40$ MPa. Clearly, for tube material of carbon steel SPFC590Y, a larger roll-over was obtained. Because carbon steel SPFC590Y ($t_o = 3$ mm) has a larger critical damage value, a larger burnished surface height and a smaller fracture surface height are obtained. Because of a quite small damage value for aluminum alloy A6005-T5, a quite small burnished surface height was obtained.

3.3 Residual Thickness

In a hydro-piecing process, sometimes the scrap is not pierced off completely because the scrap dropping into the oil tank probably results in some blockage of the oil loop and make the hydraulic system not function normally. A small residual thickness (see Fig. 3) makes the scrap remain on the tube and the scrap is removed manually afterward. Figure 9 shows the effects of internal pressure on the residual thickness with an initial tube thickness of $t_i = 2.0$ mm. Clearly, the residual thickness decreases with the stroke. In other words, as the punch moves forward, the residual thickness decreases from the initial value of 2.0 mm to 0 mm. On the other hand, as the internal pressure increases, the residual thickness decreases. The turning point of the slops of the curves indicates the initiation of the fracture surface. A higher internal pressure can decrease the fracture surface fraction, accordingly, the residual thickness decreases as the internal pressure increases.

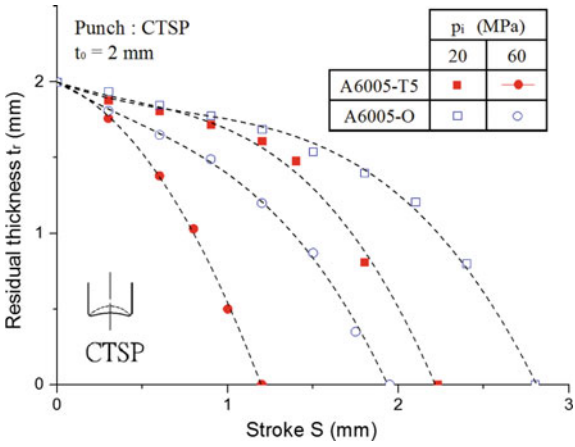


Fig. 9 Effects of internal pressure on residual thickness. (Color figure online)

4 Hydro-Piercing Experiments

4.1 Experimental Apparatus

An experimental apparatus was designed and manufactured by the present authors. The appearance of the die set used in hydro-piercing experiments is shown in Fig. 10. A tube would be placed at the cavity of the bottom die. Two pushing rods move forward for oil sealing at the two ends of the tube. A hydraulic cylinder at the back is used to push the punch forward to implement the hydro-piercing process. A fine-tuning pitch control mechanism is designed to control the stroke of punch accurately. Accordingly, the goal of the residual thickness of the tube can be set easily and accurately. After the top die moves downward to clamp the tube, the left and right pushing rods move forward for oil sealing and then the hydraulic pressure inside the tube is adjusted to the set value. Finally, the hydraulic cylinder combined with the designed punch head moves forward to carry out the hydro-piercing experiments.

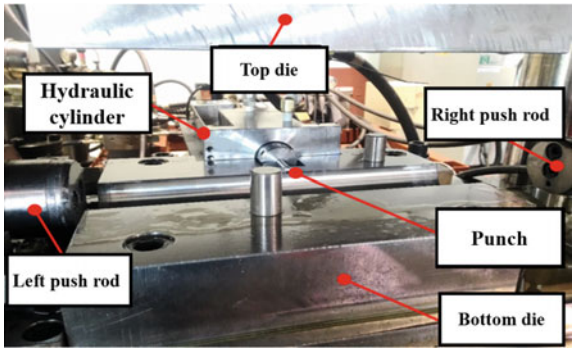


Fig. 10 Appearance of die set and punch used in hydro-piercing experiments. (Color figure online)

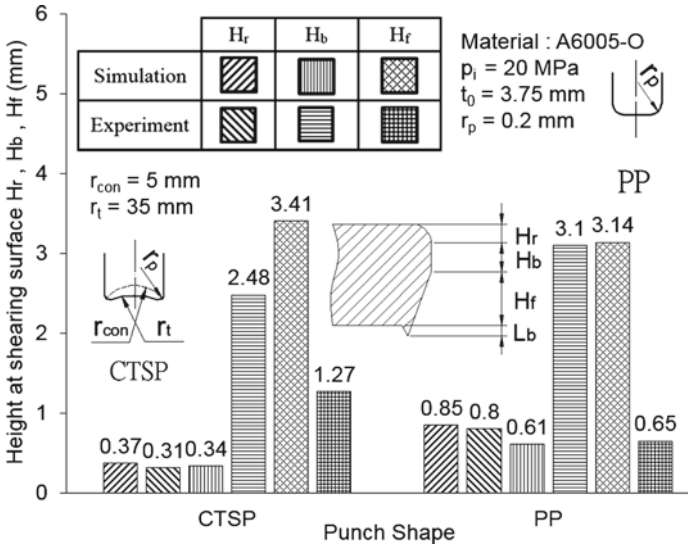


Fig. 11 Effects of punch shape on characteristics of hydro-pierced hole section

4.2 Experimental Results

Figure 11 shows the effects of punch shapes on the characteristics of the hydro-pierced hole section. Clearly, a larger roll-over height, a larger burnished surface height, and a smaller fracture surface height are obtained using punch type of PP compared with those using punch type of CTSP for both simulation and experimental results, which means a better-pierced hole section can be obtained using punch type of PP for tube material of A6005-O. A larger stroke is required using punch type of PP, thus a larger roll-over height is obtained. Generally, the simulation results of roll-over height are coincident with the experimental data. In Fig. 11, there is some discrepancy between simulative and experimental burnished surface heights. That is because the critical damage values in the NCL ductile fracture criterion, which influences greatly the burnished surface height, is difficult to obtain accurately from tensile tests.

Figure 12 shows the effects of punch shapes on the burr length of the hydro-pierced hole section. Clearly, a smaller burr length is obtained using punch type of CTSP compared with those using punch type of PP for both tube materials of A6005-O and A6005-T5, which means a better-pierced hole section can be obtained using punch type of CTSP. A larger stroke is required using punch type of PP, thus a larger burr length is obtained. On the other hand, the burr length for an aluminum alloy of A6005T5 is smaller than that for A6005-O, because A6005T5 is harder than A6005-O.

Figure 13 shows the comparisons of residual thickness between simulation and experimental results with tube thickness of $t_i = 3.75$ mm using punch type of CTSP

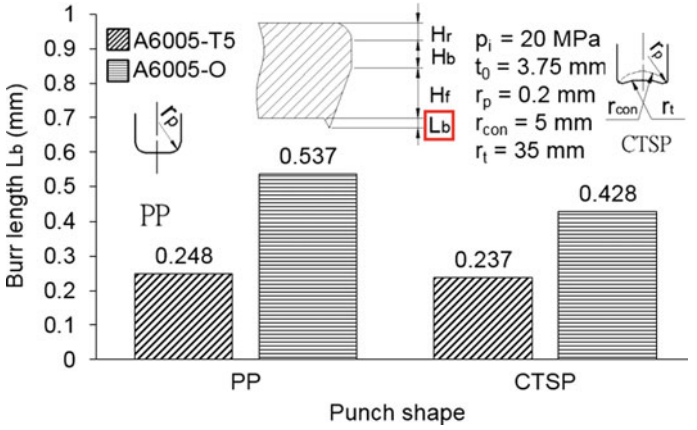


Fig. 12 Effects of punch shape on burr length of hydro-pierced hole section. (Color figure online)

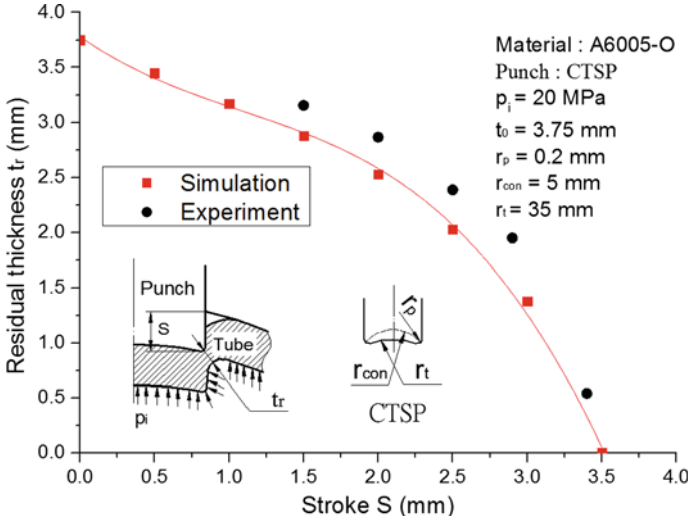


Fig. 13 Comparisons of residual thickness between simulation and experimental results. (Color figure online)

and internal pressure of 20 MPa. Clearly, the residual thickness decreases with the stroke. In other words, as the punch moves forward, the residual thickness decreases from the initial value of 3.75 mm to 0 mm. Generally, the simulation results are quite coincident with the experimental data. The final strokes at tr = 0 mm for simulation and experimental values are 3.50 and 3.60 mm, respectively. Generally, the errors between the simulation and experimental results are about 10%.

5 Conclusions

The finite element software "Deform 3D" was used to analyze the plastic deformation and fracture behavior in tube hydro-piercing processes of aluminum alloys A6005-O and A6005-T5. The effects of various parameters, such as the punch shape, internal pressure, etc., on the characteristics of the pierced hole section after hydro-piercing processes were discussed. Hydro-piercing experiments of aluminum alloys A6005-O and A6005-T5 tubes were conducted. From the simulation and experimental results, it is known that the punch shape of concave tube surface punch (CTSP) is a better design for obtaining a smaller roll-over height and a smaller burr length. Higher internal pressures could reduce the roll-over height and increase the burnished surface fraction on the pierced hole section. The simulation results are generally coincident with the experimental data.

Acknowledgments The authors would like to extend their thanks to the Ministry of Science and Technology of the Republic of China under Grant no. MOST 106-2221-E-110 -029 -MY3. The advice and financial support of MOST are greatly acknowledged.

References

1. Kocanda A, Sadlowska H (2008) Automotive component development by means of hydroforming. Arch Civ Mech Eng 8(3):55–72
2. Shiomi M, Ueda Y, Osakada K (2006) Piercing of steel sheet by using hydrostatic pressure. CIRP Ann Manuf Technol 55(1):255–258
3. Wu ZG, Li SH, Zhang WG, Wang WR (2010) Ductile fracture simulation of hydropiercing process based on various criteria in 3D modeling. Mater Des 31:3661–3671
4. Mizumura M, Sato K, Kuriyama Y (2012) Development of nut-inlaying technique in hydroformed component by hydro-burring. Mater Trans 53:801–806
5. Uchida M, Tomsawa A (2009) Study on outward hydropiercing by internal hydraulic pressure. In: 4th International conference on tube hydroforming, pp 214–219, Kaohsiung, Taiwan, 6–9 September 2009
6. Choi SK, Kim WT, Moon YH (2004) Analysis of deformation surrounding a hole produced by tube hydro-piercing. Proc Instn Mech Engrs Part B: J Eng Manuf 218:1091–1097
7. Korkmaz HG, Toros S, Halkaci M, Halkaci HS (2018) Investigation of hydro-piercing method for stainless steels by finite element method. In: ICMSC proceedings: MATEC web of conferences, p 220. https://doi.org/10.1051/matecconf/201822001003
8. Oh SI, Chen CC, Kobayashi S (1979) Ductile fracture in axisymmetric extrusion and drawing. ASME J Eng Ind 101:36–44

Novel Roll-Bonded Stainless Steel/Boron-Steel Multilayer Under Hot Stamping Conditions



Mike Kamaliev, Marco Teller, Christian Löbbe, Gerhard Hirt, and A. Erman Tekkaya

Abstract Aluminum-silicon-coated (AlSi-) boron-steels are regarded as standard material in direct hot stamping processes. Nevertheless, the material brings along some disadvantages such as the requirement of a long dwell time in the furnace for the generation of a resistant diffusion layer. In this paper, a multilayer steel sheet with a boron-steel core-layer and stainless steel outer-layers is introduced and the manufacturing process by hot roll-bonding is described. Due to the stainless steel surfaces, a coating for hot stamping is no longer necessary. The multilayer is characterized by hot tensile tests and compared with the monolithic multilayer-partners. Hot stamping experiments are conducted on a laboratory scale. Corresponding hardness measurements show that the core-layer is hardened while the outer-layers remain ductile. The new multilayer sheets offer the potential to deliver components with higher formability due to tailored properties along the sheet thickness and the use of rapid heating methods.

Keywords Roll-bonding · Hot stamping · Multilayer

1 Introduction

Due to the high component strengths and the design freedom, hot stamping is an established manufacturing process for safety-relevant components in the automotive industry [1]. Boron-steels with AlSi-coating are still considered as standard materials for this process, with 22MnB5 is the most common alloy [2]. Due to the low melting temperature of the AlSi-layer, the formation of stable Fe/Al/Si diffusion layers is necessary [3]. The required temperature treatment takes place within narrow specifications so that sufficient time is available for the safe development of the protective

M. Kamaliev (✉) · C. Löbbe · A. E. Tekkaya
Institute of Forming Technology and Lightweight Components (IUL), TU Dortmund University, Baroper Str. 303, 44227 Dortmund, Germany
e-mail: mike.kamaliev@iul.tu-dortmund.de

M. Teller · G. Hirt
Institute of Metal Forming (IBF), RWTH Aachen University, Intzestraße 10, 52056 Aachen, Germany

© The Minerals, Metals & Materials Society 2021

G. Daehn et al. (eds.), *Forming the Future*, The Minerals, Metals & Materials Series,
https://doi.org/10.1007/978-3-030-75381-8_222

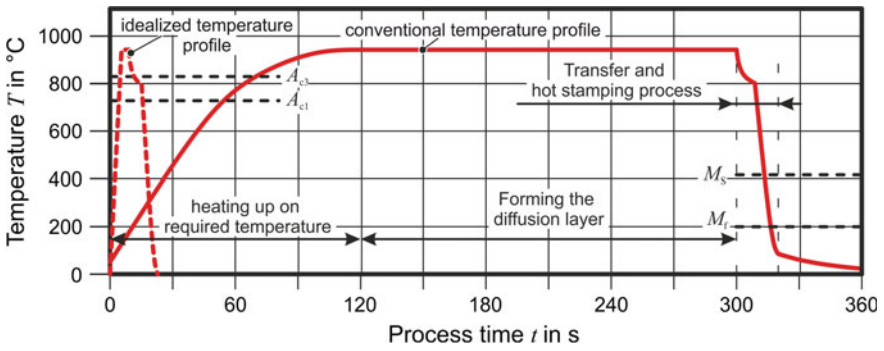


Fig. 1 Typical temperature profile during conventional hot stamping and idealized profile representing processes with rapid heating methods. (Color figure online)

diffusion layers. Like exemplary shown in Fig. 1, a large part of the total process time is attributable to the defined temperature profile. Processes which use rapid heating methods like resistance or induction heating allow temperature profiles from less than 20 s (compare: idealized temperature profile—Fig. 1), shown exemplarily in [4]. With such high heating rates, the use of coating is difficult. On the other hand, the use of uncoated material leads to thin oxide layers which has to be removed after the process—e. g., through blasting or ultrasonic cleaning [5].

A recent developed boron-steel for hot stamping is the roll-bonded three-layer material composite Tribond® from thyssenkrupp Steel Europe AG. The combination of conventional 22MnB5 as core-layer and a microalloyed steel as outer-layers allow for tailored properties over the sheet thickness. AlSi-coatings are still required for this composite in order to protect the material from corrosion [6].

One potential solution to avoid coatings like AlSi is the use of chromium-steels which are offered by different companies (e. g., Aperam—[7]) On the other hand, depended on the exact alloy, an additional thermal treatment is required for these materials. Also the mechanical properties are homogenous over the sheet thickness and the material costs are higher.

The main challenge when plating composite materials is to break-up passivating oxide layers and impurities on the surfaces to be joined so that metallic contact can arise between the composite partners. For this purpose, the surfaces are prepared before the actual plating process [8]. A renewed oxidation of the joining zone must be prevented, especially in hot roll bonding. Therefore, the outer edges of the stacked sheets are often welded [9].

The use of roll-bonded boron-chromium-composites for hot stamping represents a new approach that combines the specific advantages of each alloy. Using a boron-steel as core material and a ductile austenitic stainless steel as outer-layers would lead to tailored products which don't need an AlSi-coating. In order to assess the potential of this composite for hot stamping, the basics of roll-bonding manufacturing, the forming behavior, and the final product properties need to be investigated. This paper will first describe the roll-bonding process to produce such a composite.

Furthermore, the flow stress at elevated temperatures and in the hot-stamped state is investigated. Finally, analytical methods are applied to predict the flow stress, using the characterized separate materials.

2 Experimental Procedure

As core material an industrially produced 27MnCrB5-2 (precidur HLB27, 1.7182) is chosen, which provides the desired strength in the hot-stamped state. For the outer-layers an industrially produced X5CrNi18-10 (1.4301) is used, which brings the required resistance against cinder and corrosion. Furthermore, this austenitic steel is not hardening during hot stamping, whereby the desired tailored properties over the sheet thickness can be reached.

An initial layer ratio of 1:8:1 is chosen, resulting in a core-layer of $s_C = 12$ mm thickness and outer-layers of $s_L/2 = 1.5$ mm thickness (1.5 mm on each site). Different formats with 100 × 250 mm^2 and 175 × 250 mm^2 are cut from the materials. The surfaces are then cleaned by sandblasting and the package is stacked. Due to the low initial thickness of the package and therefore low possible height reduction as well as surface enlargement within rolling, a melter (brazing powder) is applied into the gaps to improve the break-up of the oxide layers. The composite packs, with a total thickness of 15 mm, are welded all around the side faces and on the end faces, leaving a small free space at the head end. The free space allows the melter and the broken oxide layers to leave the contact zones during rolling. The prepared packages are heated in the furnace to 1200 °C within 30 min and afterwards hot-rolled within four passes. After each pass a reheating in the furnace took place and after selected passes, due to the excessive elongation of the semi-finished products, an intermediate cross-cutting after cooling took place. Figure 2 shows the different process steps and the rolling schedule used. After a final cutting, roll-bonded sheets with a length of 1200 mm and a good surface quality are achieved.

In order to characterize the material behavior during the forming process, hot tensile tests with an initial gauge length of $l_0 = 30$ mm are conducted in a Zwick Z250. The complete experimental setup is shown in Fig. 3a. The specimens are heated inductively, using a single-strip face inductor. The traverse velocity of the test is defined as $v = 1$ mm/s. The temperature is measured by a pyrometer Metis M318 and controlled by a PID-controller (co. Sensortherm). The elongation is measured by a high-temperature extensometer PMA-12/V7 with ceramic measurement roods (co. Maytec). The temperature profile is based on a conventional hot stamping process (Fig. 1) with an austenitization temperature of $T_A = 950$ °C and an austenitization time of $t_A = 300$ s (consisting of 120 s heating up and 180 s dwell time). The specimens are cooled for 10 s on forming temperatures T_F between 700 °C and 800 °C, to simulate the transfer during a hot stamping process, before starting the tensile test. In order to be able to compare the flow behavior of the composite material with the individual partners, these are also investigated with the same conditions.

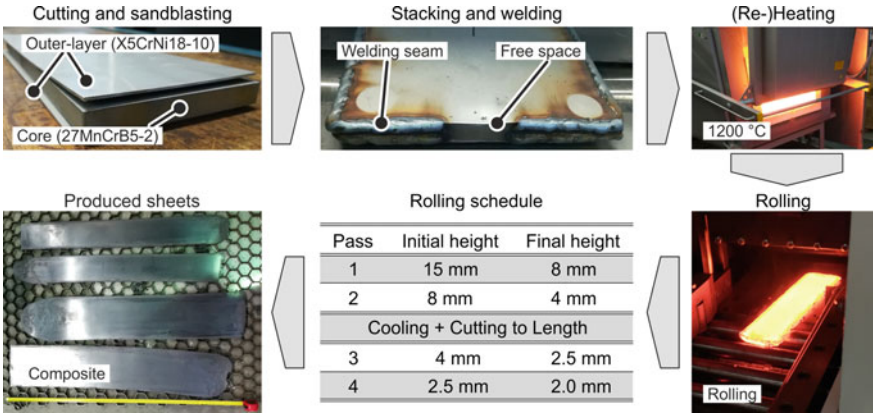


Fig. 2 Process chain and rolling schedule for the production of roll-bonded sheets including the preparation of sheet stacks. (Color figure online)

To estimate the mechanical properties from the roll-bonded composites after the process, sheets are hot stamped without deformation between two cooled plates. The experimental setup is shown in Fig. 4a. Therefore, the specimens are austenitized in a furnace N161 (co. Nabertherm) $T_A = 950$ °C for $t_A = 300$ s. After a manual transfer with the time of $t_T = 10$ s, the specimens are quenched through two cooled plates with a contact pressure of $p_Q = 6$ MPa for $t_Q = 10$ s. For further investigations, specimens for hardness measurements and tensile tests are cut out from the sheets. Tensile tests are conducted in a Zwick Z250 regarding DIN EN ISO 6892–1 with a gauge length of $l_0 = 50$ mm. Microhardness measurements (HV0.1) are conducted over the sheet thickness to determine the hardness and the extent of a boundary layer. Again, the monolithic composite partners are also examined for comparability.

3 Mechanical and Analytical Findings

Sections 3.1 and 3.2 describe the experimental results. These are fundamental for an analytical description in Sect. 3.3 to predict the flow stress of the composite. Various approaches are tested to predict the flow stress of the multilayer at elevated temperatures and after hot stamping.

3.1 Flow Behavior at Elevated Temperatures

The true stress σ as function over the true plastic strain ε_{pl} at temperatures of 700, 750, and 800 °C are shown in Fig. 3b. Table 1 shows the resulting yield points k_{f0} and strain hardening coefficients n. The outer-layers (X5CrNi18-10) have the highest

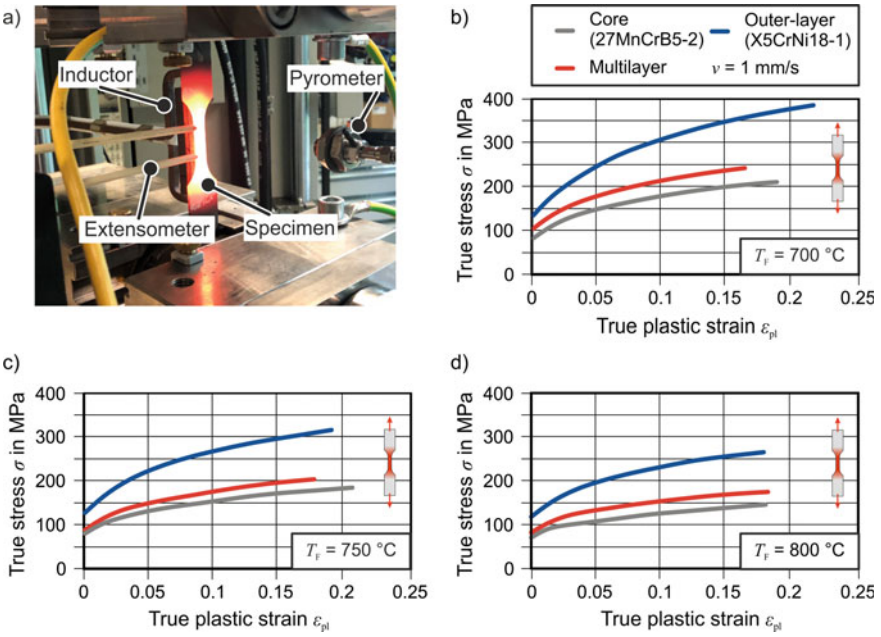


Fig. 3 **a** Experimental setup for tensile tests at elevated temperatures as well as the flow curves of the monolithic steels and the multilayer at **b** 700 °C, **c** 750 °C, and **d** 800 °C. (Color figure online)

Table 1 Results from the tensile tests at elevated temperatures for the monolithic steels and the multilayer

Temperature	700 °C		750 °C		800 °C	
Parameter	k_{f0} in MPa	n	k_{f0} in MPa	n	k_{f0} in MPa	n
Outer-layer (X5CrNi18-10)	130.5	0.31	127.0	0.26	123.7	0.24
Core-layer (27MnCrB5-2)	80.9	0.26	85.3	0.22	83.9	0.18
Multilayer	100.4	0.26	91.0	0.23	86.1	0.20

yield stress at all temperatures. The yield point k_{f0} is on average 43 MPa higher than that of the core material (27MnCrB5-2). Also the measured hardening coefficients are higher. This can be traced back to the alloy elements chrome and nickel.

The flow curves of the multilayer lie between the monolithic partners. The qualitative tendency toward the core material is explained by the layer ratio. This also causes the values for the yield points k_{f0} and the strain hardening coefficients n.

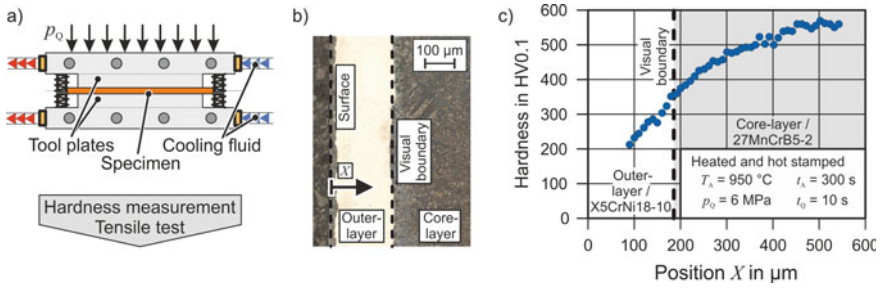


Fig. 4 **a** Experimental setup for hot stamping, **b** optical microscopy of the hot stamped multilayer steel, and **c** hardness in HV0.1 over the visual boundary-layer after hot stamping. (Color figure online)

3.2 Mechanical Properties Under Hot Stamped Conditions

In order to investigate the three different materials after hot stamping, samples were cut out, prepared and microhardness measurements in HV0.1 were carried out. Average values of $HV_L = 186.0$ HV0.1 for the outer-layers and $HV_C = 544.1$ HV0.1 for the core-layer were determined.

In order to investigate the geometrical dimensions of the different composite layers, microhardness measurements are carried out with a distance of $X = 10$ µm. Figure 4c shows the values depending on the distance to the surface. A pronounced transition zone can be recognized, which is probably the result of diffusion processes during the manufacturing process and is regarded as an extra layer. The dimensions from outer-layers and core-layer result from a comparison with the hardness values of the monolithic materials. Due to the required minimum distance to the material surface, the first valid measured values could be determined at $X = 100$ µm. Although a higher hardness compared to 186.0 HV0.1 of approx. 200 HV is determined, the boundary to the outer-layer is defined here. It is assumed that this will have a negligible influence on the following investigations.

The results from the tensile test after hot stamping are shown in Fig. 5. The yield points $R_{p0.2}$ and ultimate tensile strength R_m of the multilayer lie between the values from the monolithic partners. The uniform elongation A_G of the multilayer should

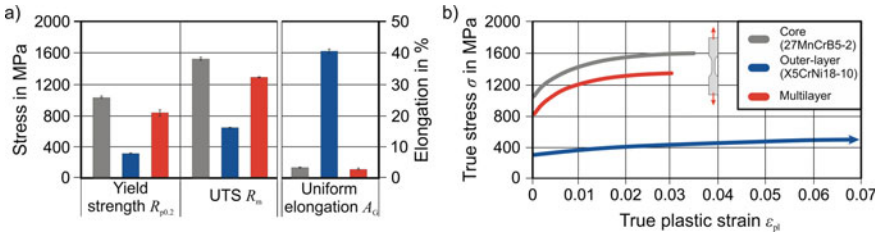


Fig. 5 **a** Parameters from the tensile test regarding DIN EN ISO 6892–1 and **b** Flow curve of the multilayer and the monolithic partners after hot stamping. (Color figure online)

be specified by the brittle partner and is slightly less than expected. The courses of the flow curves are shown in Fig. 5b. While the outer-layers still have high ductility and low strength, the core-layer exhibits a level as expected in hot stamping. The composite material is in terms of strength between the two partners.

3.3 *Analytical Empiric Prediction of Composite Properties*

After the experiments have shown an intermediate flow stress of the bounded material, this section examines different analytical approaches to predict the flow stress of the multilayer material at elevated temperatures and after hot stamping. The aim is to describe the material behavior, although only the separated partners are characterized or to transfer the flow stress to varying layer ratios. In this way, e. g., a required strength of the material after hot stamping can be designed and the flow curve at elevated temperatures can be defined for numerical simulations, without roll-bonding the composite. The experimental results are used to validate the analytics.

Firstly, the dimension of the different layers has to be defined, based on the hardness measurements from Fig. 4c. The values show a clear transition zone where other properties have to be assumed. It follows that the layer ratio before roll-bonding (index 0) and after the roll-bonding together with hot stamping (index 1) must be considered separately, like shown in Fig. 6. While the initial layer ratio is a combination of outer-layer and core-layer

$$\frac{s_{C,0}}{s_0}+\frac{s_{L,0}}{s_0}=R_{L,0}+R_{C,0}=1, \tag{1}$$

the roll-bond and hot-stamped multilayer has to be described with an extra transition zone

$$\frac{s_{C,1}}{s_1}+\frac{s_{B,1}}{s_1}+\frac{s_{L,1}}{s_1}=R_{L,1}+R_{B,1}+R_{C,1}=1 \tag{2}$$

where s is the thickness of the associated layer (C: Core; B: Boundary-layers; L: Outer-layers) and R stands for the ratio to the total composite thickness s_1. The flow

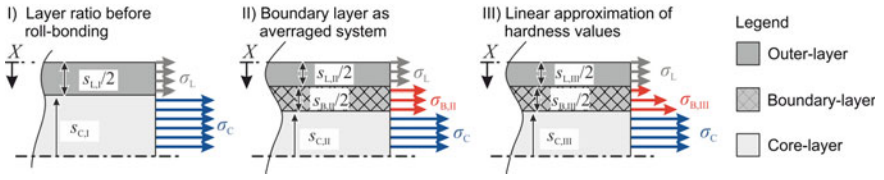


Fig. 6 Different efforts to describe the analytical flow behavior of the multilayer under various conditions. (Color figure online)

stress of the multilayer $\sigma_M(\varepsilon_{pl})$ is assumed to be the sum of these individual parts

$$\sigma_M(\varepsilon_{pl}) = \sigma_L(\varepsilon_{pl}) \cdot R_L + \sigma_B(\varepsilon_{pl}) \cdot R_B + \sigma_C(\varepsilon_{pl}) \cdot R_C \tag{3}$$

where $\sigma_L(\varepsilon_{pl}) \cdot R_L$ stands for the outer-layers, $\sigma_B(\varepsilon_{pl}) \cdot R_B$ for the boundary-layers and $\sigma_C(\varepsilon_{pl}) \cdot R_C$ for core-layer. While the specific flow stress of the outer-layer $\sigma_L(\varepsilon_{pl})$ and core-layer $\sigma_C(\varepsilon_{pl})$ are known from previous experiments, the behavior and dimension from the boundary-layer $\sigma_B(\varepsilon_{pl}) \cdot R_B$ is unknown. This also makes the ratios R_L, R_B, and R_C undefined. Therefore, three approaches I, II, and III are examined with different efforts—visualized in Fig. 6:

I. The ratios $R_{L,0}$ and $R_{C,0}$ before roll-bonding are used. Through this approach, there is no boundary-layer and

$$\sigma_{B,I}(\varepsilon_{pl}) = 0 \tag{4}$$

is valid. The ratios before roll-bonding are used so that $R_{L,I} = R_{L,0}$ and $R_{C,I} = R_{C,0}$ are valid. For this approach, only the flow behavior of the separated partners has to be characterized in advance. In the following, it is checked whether the prediction is sufficiently accurate to give an initial estimate of the properties.

II. The boundaries between the core-layer and the outer-layers are averaged and regarded as homogeneous. Taking into account the hardness measurements, the dimension of the boundary-layer is set between $X = 100$ and 450 µm. The ratios $R_{L,II}$, $R_{B,II}$, and $R_{L,II}$ can now be calculated. The flow behavior of the boundary-layer $\sigma_{B,II}(\varepsilon_{pl})$ is assumed to be the average between the core-layer $\sigma_C(\varepsilon_{pl})$ and the outer-layer $\sigma_L(\varepsilon_{pl})$.

$$\sigma_{B,II}(\varepsilon_{pl}) = \frac{\sigma_C(\varepsilon_{pl}) + \sigma_L(\varepsilon_{pl})}{2}. \tag{5}$$

Hot stamping of the composite and microhardness measurements are required to define the thickness and allow the calculation of the ratios. Transferability to different layer ratios is assumed here.

III. The dimension of the boundary-layers will be defined between $X = 100$ and 450 µm, like in method II. Assuming that the flow behavior is proportional to the hardness, a linear approximation is carried out for each measured value after hot stamping. The number of the increments is defined by the number of hardness measurements n_H in the defined boundary-layer. In this way, the flow stress of each geometric increment is defined as the mixed function of the separated partners. Similar to [10], the relationship between the hardness defines the flow curve of the boundary-layer $\sigma_{B,III}(\varepsilon_{pl})$

$$\sigma_{B,III}(\varepsilon_{pl}) = \sum_{i=1}^{n_H} \frac{1}{n_H} \cdot \left[\left(\frac{HV - HV_L}{HV_C - HV_L} \right) \cdot \sigma_C(\varepsilon_{pl}) + \left(\frac{HV_C - HV}{HV_C - HV_L} \right) \cdot \sigma_L(\varepsilon_{pl}) \right], \tag{6}$$

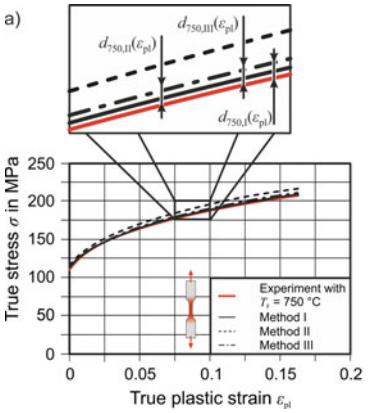
where HV_C is the average hardness of the core, HV_L the average hardness of the outer-layers, and HV the hardness of the associated increment. In this way, each hardness measurement is considered as a separate layer. For this approach, the multilayer has to be hot stamped, hardness measurements have to be conducted and a linear approximation must be performed. Like in method II, a transferability to other layer ratios is assumed.

The approaches are assessed on the basis of the average $|\overline{d}_P|$ and the maximum deviation $|d_{P,max}|$ from the experimental results, where the index P stands for specific material conditions (700, 750, and 800 for elevated temperature at the listed value; HS for hot stamped). For this, the amount of the average deviation for defined process parameters $|\overline{d}_P|$ in every plastic strain increment (here 0.001) is determined

$$|\overline{d}_P| = \left[\frac{1}{n_\varepsilon} \cdot \sum_{i=1}^{n_\varepsilon} \left|d_P(\varepsilon_{pl})\right|\right] \cdot 100\% = \left[\frac{1}{n_\varepsilon} \cdot \sum_{i=1}^{n_\varepsilon} \frac{\left|\sigma_{P,M}(\varepsilon_{pl}) - \sigma_{P,E}(\varepsilon_{pl})\right|}{\left|\sigma_{P,E}(\varepsilon_{pl})\right|}\right] \cdot 100\%, \tag{7}$$

where n_ε is the total amount of plastic strain increments, $\sigma_{P,M}(\varepsilon_{pl})$ is the analytical true stress, and $\sigma_{P,E}(\varepsilon_{pl})$ is the experimental true stress for the associated increment (the index M stands here for the considered analytical method I, II, or III). Figure 7a shows one example at defined process parameters. Furthermore the maximum deviations $|d_{P,max}|$ are listed, which defines the maximum deviation between analytical and experimental true stresses σ at specific plastic strains ε_{pl} for each method. The results for the calculated layer ratios (with $s_1 = 2.04$ mm) and different deviations for various process parameters (700, 750, and 800: tensile tests at elevated temperatures; HS: tensile tests with hot-stamped material) are shown in Fig. 7b.

a)



b)

Parameter			Method I	Method II	Method III
layer ratios	R_L	-	0.2	0.10	0.10
	R_B		0	0.34	0.34
	R_C		0.8	0.56	0.56
700 °C	$\lvert\overline{d}_{700}\rvert$	%	5.00	1.52	3.98
	$\lvert d_{700,max}\rvert$		9.93	3.52	7.70
750 °C	$\lvert\overline{d}_{750}\rvert$	%	0.84	4.87	1.77
	$\lvert d_{750,max}\rvert$		3.52	6.65	4.33
800 °C	$\lvert\overline{d}_{800}\rvert$	%	4.61	0.94	3.55
	$\lvert d_{800,max}\rvert$		7.70	1.10	8.32
Hot stamped	$\lvert\overline{d}_{HS}\rvert$	%	1.54	4.68	1.16
	$\lvert d_{HS,max}\rvert$		7.88	5.55	6.32
Average	$\lvert\overline{d}_{P,Av}\rvert$	%	3.00	3.00	2.62
	$\lvert d_{P,max,Av}\rvert$		7.26	6.46	6.67

Fig. 7 **a** Example: Experimental and analytical flow curves of the multilayer at 750 °C and **b** resulting layer ratios and deviations, based on the methods I, II, and III. (Color figure online)

Comparing the three methods for different material conditions, no clear tendency can be determined. The mean deviations fluctuate between 0.84% and 5.00% while the maximum deviation at defined true plastic strain between 1.10 and 9.93%. To be able to assess the accuracy of the three analytical approaches regardless of the process parameters, $|\overline{d}_{\mathrm{P,Av}}|$ and $|\overline{d}_{\mathrm{P,max,Av}}|$ show the average values of all deviations. Only minor differences between the individual analytical approaches are determined here.

4 Conclusion and Outlook

A multilayer material made of boron-steel precidur HLB 27 (27MnCrB5-2) as core-layer and a chromium-steel (X5CrNi18-10) as outer-layers were successfully manufactured using hot roll-bonding. The flow behavior of the multilayer and the separated partners were characterized at elevated temperatures from 700 to 800 °C through tensile tests. Conventional direct hot stamping processes were conducted with two cooled flat tools. Hardness measurements show that the core-layer hardened by martensitic transformation with 544.1 HV0.1, while the outer-layer with 186.0 HV0.1 stays softer. Tensile tests after hot stamping of the multilayer shows an averaged UTS of 1297 MPa. The uniform elongation of the composite is with averaged 3.1% lower than from the core-layer. This can be attributed to insufficient bond strength of the separated partners [11]. For comparability and analytical approaches, experiments with the monolithic partners have also been conducted. Three different methods were investigated, which should predict the flow stress of the multilayer material, based on an analysis of the separated partners. All three approaches show average deviations of 3% or less, whereby every analytical procedures can be considered suitable. Method I is qualified for providing an estimate of the material properties to be expected before the multilayer is manufactured. Method II and III in combination with hardness measurements provide another option for carrying out the appraisal.

In the following, the manufacturing process of the composites by roll-bonding will be examined further and supplemented by subsequent steps like diffusion annealing. Also different layer ratios and outer-layer materials have to be taken into account to investigate the transferability of the analytical methods. Furthermore, an empirical prediction for the boundary-layer dimension is sensible. This would enable the use of all methods without prior roll-bonding a composite. Forming processes next to tensile tests has to be conducted to investigate the adhesive strength of the multilayer material at different strain states. A combination with rapid heating methods like induction would also reflect the potential reductions in process time. If the roll-bonding of boron-chromium-steels is mastered robustly, an expansion to tailored sheet metal is also possible. One potential design is shown in Fig. 8. Such a material with variable layer ratios over the width would allow the hot stamping of tailored products in conventional process routes.

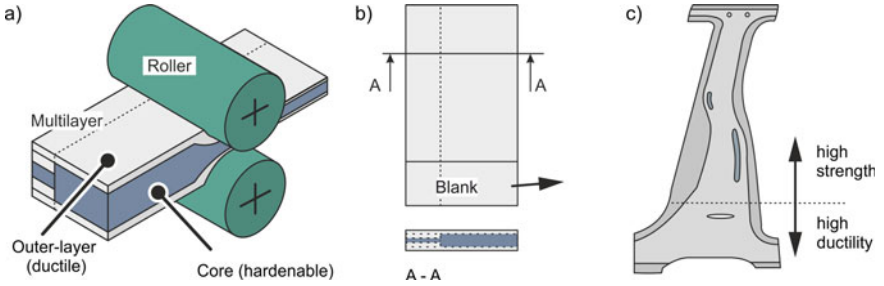


Fig. 8 Potential roll-bonding for sheets with tailored properties—**a** Manufacturing process for **b** sheets with variable layer ratios to produce **c** components with tailored properties. (Color figure online)

Acknowledgments The authors would like to thank the thyssenkrupp Hohenlimburg GmbH for providing the boron-steel precidur HLB 27 (27MnCrB5-2) and the Outokumpu Nirosta GmbH for providing the chromium-steel (X5CrNi18-10).

References

1. Mori K, Bariani PF, Behrens B-A, Brosius A, Bruschi S, Maeno T, Merklein M, Yanagimoto J (2017) Hot stamping of ultra-high strength steel parts. CIRP Ann Manuf Technol 66(2):755–777. https://doi.org/10.1016/j.cirp.2017.05.007
2. Karbasian H, Tekkaya AE (2010) A review on hot stamping. J Mater Process Technol 210(15):2103–2118. https://doi.org/10.1016/j.jmatprotec.2010.07.019
3. Windmann M, Röttger A, Theisen W (2014) Formation of intermetallic phases in Al-coated hot-stamped 22MnB5 sheets in terms of coating thickness and Si content. Surf Coat Techn 246:17–25. https://doi.org/10.1016/j.surfcoat.2014.02.056
4. Kolleck R, Veit R, Merklein M, Lechler J, Geiger M (2009) Investigation on induction heating for hot stamping of boron alloyed steels. CIRP Ann Manuf Technol 58(1):275–278. https://doi.org/10.1016/j.cirp.2009.03.090
5. Maeno T, Mori K, Ogihara T, Fujita T (2019) Removal of thin oxide scale by ultrasonic cleaning with diluted hydrochloric acid in hot stamping of bare 22MnB5 sheet using resistance heating. Procedia Manuf 29:225–231. https://doi.org/10.1016/j.promfg.2019.02.130
6. Rosenstock D, Banik J, Gerber T, Myslowicki S (2019) Hot stamping steel grades with increased tensile strength and ductility - MBW-K 1900, tribond 1200 and tribond 1400. IOP Conf Ser Mater Sci Eng 651. https://doi.org/10.1088/1757-899X/651/1/012040
7. Badinier G, Mithieux J-D, Santacreu P-O, Herbelin J-M (2015) Development of a 1.8 GPa martensitic stainless steel for hot stamping application. 5th CHS^2:715–723
8. Dhib Z, Guermazi N, Gaspérini M, Haddar N (2016) Cladding of low-carbon steel to austenitic stainless steel by hot-roll bonding. Mater Sci Eng A 656:130–141. https://doi.org/10.1016/j.msea.2015.12.088
9. Carreño F, Chao J, Pozuelo M, Ruano OA (2003) Microstructure and fracture properties of an ultrahigh carbon steel–mild steel laminated composite. Scr Mater 48(8):1135–1140. https://doi.org/10.1016/S1359-6462(02)00602-4
10. Eller TK, Ramaker KA, Greve L, Andres MT, Hazrati J, van den Boogaard AH (2017) Plasticity and fracture modeling of three-layer steel composite Tribond 1200 for crash simulation. 36th IDDRG

11. Inoue J, Nambu S, Ishimoto Y, Koseki T (2008) Fracture elongation of brittle/ductile multi-layered steel composites with a strong interface. Scr Mater 59:1055–1058. https://doi.org/10.1016/j.scriptamat.2008.07.020

Effect of Machining Induced Microstructure Changes on the Edge Formability of Titanium Alloys at Room Temperature



J. S. Kwame, E. Yakushina, and P. Blackwell

Abstract The challenges in forming titanium alloys at room temperature are well researched and are linked both to the limitations imposed by the basic crystal structure and their ability to form texture during plastic deformation. One major issue of concern for the sheet forming of titanium alloys is their high sensitivity to surface inhomogeneity. Various machining processes are utilised in preparing sheet hole edges for edge flanging applications. However, the response of edge forming tendencies of titanium to different edge surface finishes is not well investigated. The hole expansion test is used in this project to elucidate the impact of Abrasive Water Jet (AWJ) and Electro-discharge machining (EDM) cutting techniques on the edge formability of CP-Ti (Grade 2) and Ti-3Al-2.5 V alloys at room temperature. The results show that the quality of the edge surface finish has major effect on the edge formability of the materials. The work also found that the variations in the edge forming performance are mainly the result of the influence of machining induced edge surface defects.

Keywords Titanium alloys · Hole expansion test · Edge formability · Non-conventional machining

1 Introduction

Titanium and its alloys have been widely used in the aerospace industry mainly due to their excellent properties such as high temperature strength compared to aluminium, their good strength to weight ratio compared to steels and their good corrosion resistance [1]. However, various issues have been identified to have limited their use. One such is their low formability at room temperature due to limited slip

J. S. Kwame (✉) · P. Blackwell
Department of Design, Manufacturing and Engineering Management, University of Strathclyde, Glasgow, UK
e-mail: james.kwame@strath.ac.uk

E. Yakushina · P. Blackwell
Advanced Forming Research Centre (AFRC), University of Strathclyde, Glasgow, UK

© The Minerals, Metals & Materials Society 2021

G. Daehn et al. (eds.), *Forming the Future*, The Minerals, Metals & Materials Series,
https://doi.org/10.1007/978-3-030-75381-8_223

systems caused by their crystallographic structure and their tendency to develop strong textures with concomitant planar anisotropy [2]. Another limiting factor is their high sensitivity to surface inhomogeneity resulting in reduced fatigue life [3]. These surface inhomogeneities are sometimes introduced during machining processes. Considering the poor machinability of titanium [4], issues relating to the extent of edge defects produced during machining become a major area of research interest. Low heat conductivity coupled with chemical reactivity of titanium are some of the reasons contributing to their poor machinability [5]. Depending on the method used to machine titanium, certain levels of edge surface defects may be introduced onto the part surface. The common edge surface defects produced during machining of titanium include carbide cracking induced cracks, microstructure alteration, white layer formation, and residual stress [6]. Normally, conventional and non-conventional machining methods are adopted in cutting titanium and other metals. Non-conventional machining methods are non-contact techniques widely adopted in industry since they eliminate tool-part contact related issues [7]. Abrasive water jet (AWJ) cutting and Electro-discharge machining (EDM) are used in this work. A standard hole expansion test (HET) is used in this research to examine the hole edge formability of the materials. The extent of edge formability is defined by the hole expansion ratio (HER). The higher the HER value, the higher the edge forming performance of the material. The HER is enumerated by finding the percentage of the ratio of the difference between the final and initial hole diameter to the initial hole diameter [8];

$$HER = \frac{d_f - d_0}{d_0} \times 100\% \tag{1}$$

where d_f—final hole diameter, d_0—initial hole diameter.

Since areas around the hole edge are regions of high stress concentration, the integrity of the fabricated edge becomes a significant factor during HET. However, the impact on forming performance of edge surface micro-features and defects introduced into titanium alloys during machining has not been extensively researched. This work is directed at ascertaining the impact of EDM and AWJ induced edge microstructure alterations on the edge formability of titanium alloys deformed at room temperature. The work seeks to understand how the cutting techniques examined alter the edge related failure modes and failure nucleation process in titanium alloys.

2 Experimental Procedure

2.1 The Materials

The materials studied in this work are commercially pure titanium (CP-Ti) Grade 2 and Ti-3Al-2.5 V alloys. Ti-3Al-2.5 V alloys have intermediate strength and good cold workability. This alloy is mainly utilised in aerospace applications such as hydraulic tubing and light weight honeycomb structures. CP-Ti (Grade 2) possesses a good strength to weight ratio and also has the ability to maintain its strength appreciably during deformation. They are also largely employed in airframe skin applications [9].

2.2 Material Preparation

The edge surface roughness values and micrographs were characterised using an Alicona 3D microscope. The edge surface topography and crack surface fractographs were also examined using a Quanta FEG 250 microscope. AWJ cut edges were prepared with a Calypso water jet machine, operated at 70HP and at a feed rate of 400 g/min. The transverse cutting speed was varied to attain two different edge surface finishes for both materials (250 mm/min: finished edge surface and 600 mm/min: unfinished edge surface). Both materials showed higher edge surface micro-ridge distribution for the unfinished AWJ edges compared to the finished parts. The ratio of the edge surface micro-grooves to micro-ridges was also fairly even for the finished AWJ cut edges compared to the unfinished parts for both materials; Fig. 1a, b, e, f. The EDM cut edges were machined using a GF FI 440 CCS machine fitted with a 0.25 mm diameter brass cutting wire. The EDM cutting parameters were varied to attain two distinct edge surface finishes (1. wire tension ~2 $\times$ 10^1 N, pulse on time

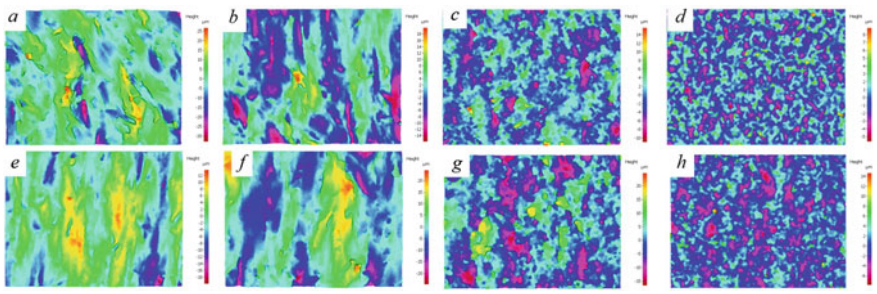


Fig. 1 Alicona micrograph of surface topography and roughness after EDM and AWJ cutting. **a** Unfinished (Ra~5.2 μm) and **b** Finished (Ra~3.2 μm) AWJ for CP-Ti; **c** Unfinished (Ra~2.7 μm) and **d** Finished (Ra~0.8 μm) EDM for CP-Ti; **e** Unfinished (Ra~5.7 μm) and **f** Finished (Ra~3.8) AWJ for Ti-3Al-2.5 V; **g** Unfinished (Ra~2.9 μm) and **h** Finished (Ra~1 μm) EDM for Ti-3Al-2.5 V. (Color figure online)

Table 1 Room temperature tensile properties

Material	Type	Yield strength (0°, 45°, 90°), MPa	Tensile strength (0°, 45°, 90°), MPa
CP-Ti (Grade 2)	α	197.99, 218.19, 250.05	550.31, 489.43, 513.25
Ti-3Al-2.5 V	α/near α	165.97, 188.75, 168.99	605.44, 504.38, 529.42

~0.05 ms, pulse off time ~20 ms: for finished edges and 2. wire tension ~1.3×10^1 N, pulse on time ~0.7 ms pulse off time ~2 ms: for unfinished edges). Both materials showed a finer distribution of surface micro-grooves for the finished EDM edges compared to the unfinished edges; Fig. 1c, d, g, h. The attained surface micro-groove size and distribution for the finished EDM edges for CP-Ti are finer compared to those observed for Ti-3Al-2.5 V; Fig. 1d, h.

2.3 Hole Expansion Test

Hole expansion testing was performed on a Zwick/ Roell BUP 1000 testing machine controlled by testXpert II software. A 60° head conical punch with a die set design consistent with ISO 16,630:2017 was used to deform a 10 mm diameter hole produced with either AWJ or EDM cutting methods. The test trials were done for the two cutting methods as well as their two distinct edge surface finish qualities. A blankholder force of 150 kN was used to prevent the material from drawing-in during the test. The punch was driven at a speed of 1 mm/s through the fabricated hole until an edge crack occurred.

2.4 Mechanical Properties

A Zwick/ Roell Z150 tensile testing machine was used to perform a standard room temperature uniaxial tensile test consistent with ISO 6892–1:2016. The tests were conducted at a constant strain rate of 0.001/s. Both materials exhibited anisotropic behaviour when examined in three sheet processing directions, Table 1.

3 Results and Discussion

3.1 Machined Edge Surface Topography and Defects

The edge surfaces after AWJ machining were characterised by surface mechanical erosion features, produced by the tracks travelled by the abrasive particles during the

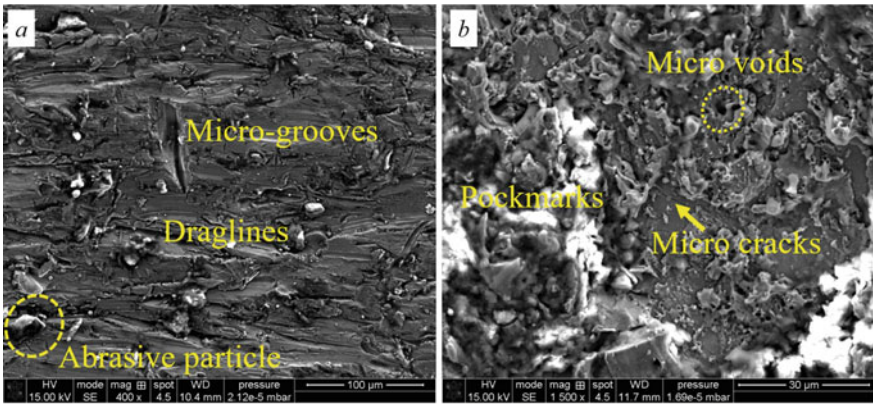


Fig. 2 Surface topography of machined edges. **a** AWJ cut edge surface, **b** EDM cut edge surface. (Color figure online)

cutting process. The surface draglines, micro-grooves, and dents observed are also due to the areas occupied and/or vacated by the abrasive particles during the cutting process, Fig. 2a.

The surface after EDM cutting showed features consistent with its heat erosion attributes. The surface featured micro-voids, micro-cracks, craters, ridges, and pockmarks as the main edge defects, Fig. 2b. The extent of surface pockmarks produced is a function of the ability of the dielectric fluid to wash away debris during the cutting process in the quest to minimise melt solidification.

3.2 Hole Edge Formability

Figure 3 shows the hole edge forming performance of both materials tested for two different edge cutting methods and edge surface finish qualities.

The EDM cut edges showed highest edge formability (CP-Ti: ~195.86% and Ti-3Al-2.5 V: ~78.16%) compared to AWJ cut edges (CP-Ti: ~140.38% and Ti-3Al-2.5 V: ~49.84%). Both materials showed better edge formability for the finished cut edges (CP-Ti: EDM ~195.86%, AWJ ~140.38%, and Ti-3Al-2.5 V: EDM ~78.16%, AWJ ~49.84%) compared to the unfinished edges (CP-Ti: EDM ~148.4%, AWJ ~100.9%, and Ti-3Al-2.5 V: EDM ~69.73%, AWJ ~42.48%) for both cutting techniques. Overall, CP-Ti showed better edge formability compared to Ti-3Al-2.5 V alloy. This trend could be attributed to the nature of the edge microstructures produced after machining of both materials. Generally, the edge micro-features attained for both materials are varied after EDM and AWJ machining. CP-Ti after AWJ cutting showed lower levels of edge surface micro-grooves and defects compared to Ti-3Al-2.5 V, Fig. 4a, b. The EDM microstructure also showed a high volume fraction of machining induced micro-cracks in CP-Ti compared to Ti-3Al-2.5 V, Fig. 4c, d. Pure titanium is predominantly alpha phased alloys and is relatively soft and easier to

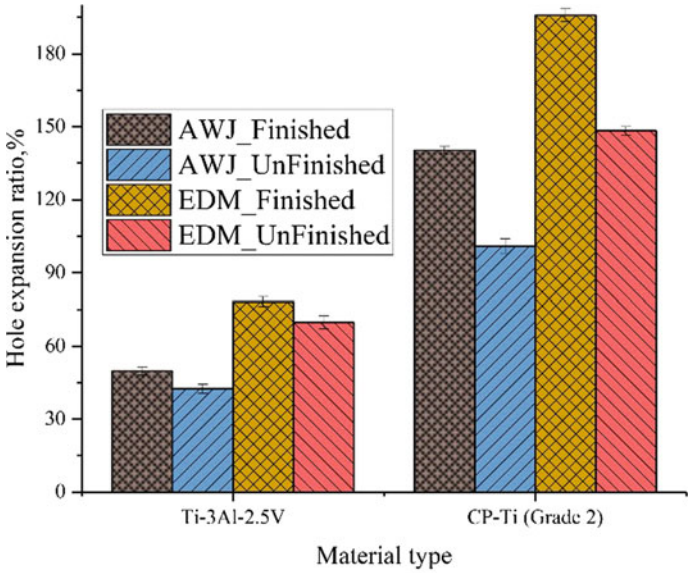


Fig. 3 Edge formability of CP-Ti and Ti-3Al-2.5 V alloys. (Color figure online)

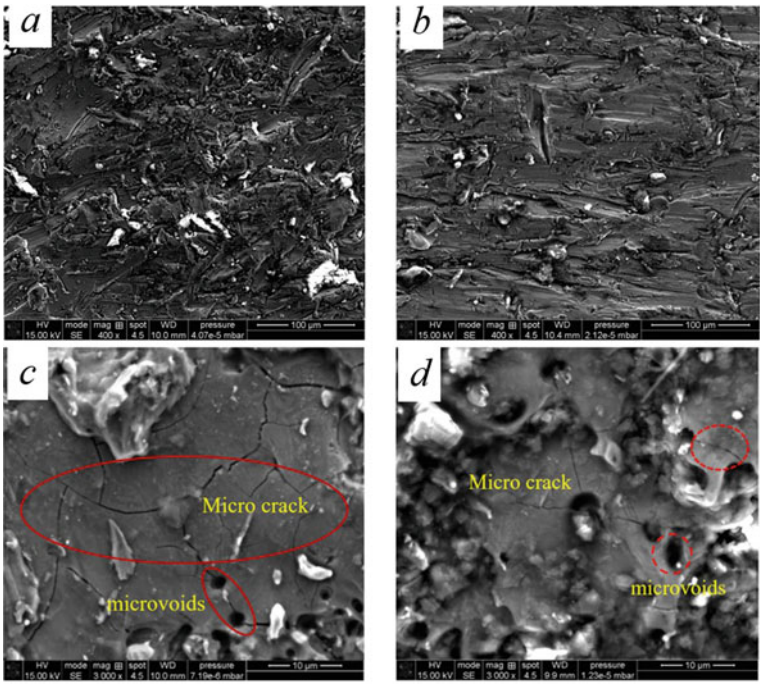


Fig. 4 Machining induced surface microstructure changes. **a** CP-Ti AWJ cut edge, **b** Ti-3Al-2.5 V AWJ cut edge, **c** CP-Ti EDM cut edge, **d** Ti-3Al-2.5 V EDM cut edge. (Color figure online)

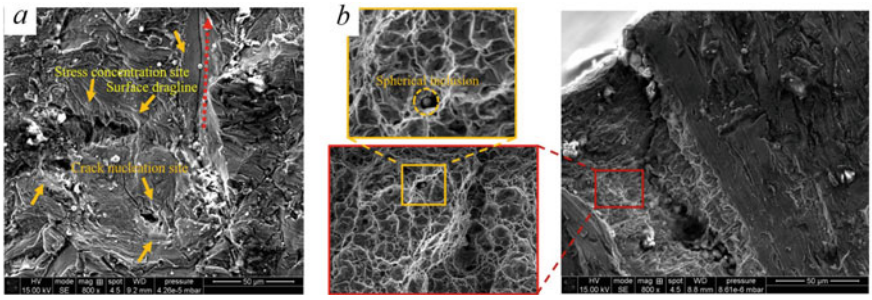


Fig. 5 Failure mode during HET of AWJ cut edge. **a** Crack nucleation site at defect zones, **b** dimpled crack surface of AWJ cut edge. (Color figure online)

machine compared to alloyed titanium [10]. Heat conductivity also plays a massive role in titanium machinability in terms material and heat removal rate. Pure titanium generally exhibits stable heat conductivity with rising temperature during machining compared to its alloyed counterparts [11]. The severity of defects produced during machining is a function of the ease of machinability of the components.

3.3 Failure Nucleation

The edge surface defects observed after AWJ machining are mainly due to the action of the abrasive particles. The severity of the edge defects is a function of the machining parameters and the material's machinability. The surface defects produced on the material surface after AWJ machining act as stress concentration sites (yellow arrow) during HET, Fig. 5a. These defects sites serve as areas of high energy concentration where the cracks begin to grow. The rate of the crack growth is dependent on the defect depth, distribution, and size.

The AWJ fracture surface is characterised by micro-void nucleation sites with dimpled surface at spherical inclusions, Fig. 5b. The growth of these micro-voids around the spherical inclusions (by virtue of interface decohesion) is mainly due to the action of plastic strain and hydrostatic stress which results in major flaws and subsequent failure upon coalescence. Generally, the trajectory of the crack is a function of the stress state at the hole edge. The stress state around the hole edge during HET is pure uniaxial tension [12]. Since the hole edge is subjected to plane strain mode I loading, the optimum plastic strain is obtained at an angle of 45° to the crack axis. From a localised point of view, this angle becomes the favoured trajectory for micro-void growth and coalescence. However, global constraints like edge defects (surface draglines and grooves) have the tendency of redirecting the crack plane path. The zigzag patterns seen at the AWJ cut edge fracture tip is as a result of the corrections made to the deviation by global constraints, reverting back to the optimum plastic strain angle, Fig. 6.

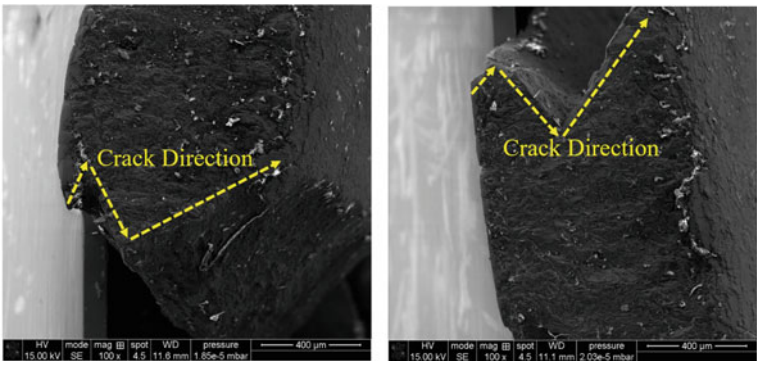


Fig. 6 AWJ edge crack orientation. (Color figure online)

On the other hand, the thermal stresses produced during EDM machining due to plastic deformation or during the cooling process are manifested on the machined surface as micro-cracks. These surface micro-cracks are responsible for distributing the imposed stresses homogenously around the hole edge during HET. This phenomenon delays early failure of the material by preventing the cracks from developing towards the thickness direction of the sheet, Fig. 7a. CP-Ti exhibited higher volume fraction of EDM machining induced surface micro-cracks compared to Ti-3Al-2.5 V cut edge, Fig. 4c, d, hence the higher edge performance. The higher the EDM induced surface micro-cracks, the higher the edge formability of the material. Hasegawa et al. [13] in their research also reported the influence of stress induced surface micro-cracks produced after punching of martensite single phase steels and their role in the restriction of crack extension towards the sheet thickness direction with an accompanying increase in the material's HER performance.

The differences in the attained EDM edge performance observed for CP-Ti and Ti-3Al-2.5 V alloys could also be attributed to the variation in EDM induced residual stress. Normally, metallurgical alterations and thermal gradients produced during EDM machining induce residual stresses [14]. As a consequence, the attained strains

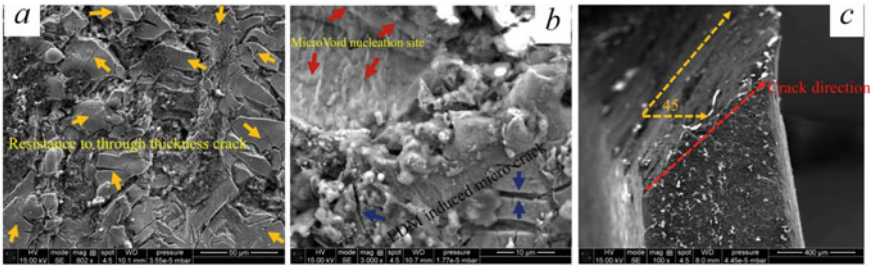


Fig. 7 EDM cut edge failure initiation process during HET. **a** Resistance to through-thickness cracking by EDM induced surface micro-cracks (yellow arrows), **b** free surface formation (red arrow), **c** edge crack orientation. (Color figure online)

result in the inception of tensile residual stresses, which are deleterious in terms of shortened fatigue life and enhanced fatigue crack growth. Fatigue generally emanates from the surface, hence the integrity of component surface is of significant essence. The residual stress values attained after EDM cutting are linked to the attained surface topography and the material yield strength [15].

The crack tip of the EDM samples after HET showed localised necking with ductile shear failure, Fig. 7c. The crack occurred just after the formation of micro-voids on the free surface, Fig. 7b. The shear stresses acting during plastic deformation become highest for a plane of maximum plastic shear strain at 45°. Through-thickness disparity in triaxiality could also be responsible for the shear deformation governed by fracture trajectory at the crack tip orienting at 45° to the optimum principal stress. In such cases, the triaxiality at the crack tip offers an adequate upgrade for micro-void nucleation reminiscent of ductile fracture [16].

4 Conclusions

Varied machining methods are used to cut titanium alloys and these introduce edge surface defects and microstructure alteration into the material. This project sought to examine the impact of AWJ and EDM induced microstructure changes on the edge formability of CP-Ti (Grade 2) and Ti-3Al-2.5 V alloys. The research also examined the nature of the edge surface related failure modes and failure nucleation processes linked to these cutting methods. It was found that

- EDM machined test samples showed higher edge forming performance compared to AWJ cut edges for both materials.
- The high edge formability of the EDM machined edges for CP-Ti was due to the high volume fraction of cutting induced surface micro-cracks compared to those observed in Ti-3Al-2.5 V. CP-Ti also showed a lower volume fraction of edge surface micro-grooves after AWJ cutting compared to Ti-3Al-2.5 V.
- The quality of the edge surface finish has a significant impact on the edge formability of the materials (1. CP-Ti: AWJ finished ~140.38%, unfinished ~100.9%; EDM finished ~195.86%, unfinished ~148.4%, and 2. Ti-3Al-2.5 V: AWJ finished ~49.84%, unfinished ~42.48%; EDM finished ~78.16%, unfinished ~69.73%
- The nature of defects introduced onto the edge surface by virtue of the machining process governs the crack nucleation, growth rate, and orientation in the material
- The failure mechanism in both materials is ductile fracture with the associated growth of micro-voids around spherical inclusions upon increase in plastic strain and hydrostatic stress.

Acknowledgments The authors acknowledge the support of the Advanced Forming Research Centre (AFRC) and the Department of Design, Manufacturing and Engineering Management of the University of Strathclyde, UK. The authors would also like to acknowledge TIMET for material supply.

References

1. Boyer RR (1996) An overview on the use of titanium in the aerospace industry. Mater Sci Eng A 213(1–2):103–114
2. Nasiri-Abarbekoh H, Ekrami A, Ziaei-Moayyed AA, Shohani M (2012) Effects of rolling reduction on mechanical properties anisotropy of commercially pure titanium. Mater Des 34:268–274
3. Yuri T, Ono Y, Ogata T (2003) Effects of surface roughness and notch on fatigue properties for Ti-5Al-2.5Sn ELI alloy at cryogenic temperatures. Sci Technol Adv Mater 4(4):291–299
4. Churi NJ, Pei ZJ, Treadwell C (2007) Rotary ultrasonic machining of titanium alloy (Ti-6Al-4V): effects of tool variables. Int J Precis Technol 1(1):85–96
5. Donachie MJ (1988) Titanium: a technical guide. ASM International, Metals Park, Ohio, OH 44073
6. Pervaiz S, Rashid A, Deiab I, Nicolescu M (2014) Influence of tool materials on machinability of titanium and nickel based alloys: a review. Mater Manuf Process 29(3):219–252
7. Dubey AK, Yadava V (2008) Laser beam machining: a review. Int J Mach Tools Manuf 48(6):609–628
8. Karelova A et al (2009) Hole expansion of dual-phase and complex-phase AHS steels - effect of edge conditions. Mater Technol 80(1):71–77
9. Peters M, Kumpfert J, Ward CH, Leyens C (2003) Titanium alloys for aerospace application. Adv Eng Mater 5(6):419–427
10. Yang X, Liu CR (1999) Machining titanium and its alloys. Mach Sci Technol 3(1):107–139
11. Veiga C, Davim JP, Loureiro AJR (2013) Review on machinability of titanium alloys: the process perspective. Rev Adv Mater Sci 34:148–164
12. Yoon JK, Jung J, Lee HH, Kim G-S, Kim HS (2016) Factors governing hole expansion ratio of steel sheets with sheared edge. Met Mater Int 22(6):1009–1014
13. Hasegawa K, Kawamura K, Urabe T, Hosoya Y (2004) Effects of microstructure on stretch-flange- formability of 980MPa grade cold- rolled ultra-high strength steel sheets. ISIJ Int 44(3):603–609
14. Ekmekci B, Elkoca O, Tekkaya A, Erden A (2005) Residual stress state and hardness depth in electric discharge machining: deionized water as dielectric liquid. Mach Sci Technol 9(1):39–61
15. Cao C, Zhang X, Zha X, Dong C (2014). Surface integrity of tool steels multi-cut by wire electrical discharge machining. Proc Eng 81:1945–1951
16. Anderson TL (2005) Fracture mechanics: fundamentals and applications, 3rd edn. Taylor & Francis Group LLC., Boca Raton

Investigation on Springback Behavior of Multi-intersecting High Stiffened Structure in Die Forming



Qiyuan He, Weidong Li, Min Wan, Cailing Li, and Chao Cui

Abstract Multi-intersecting high stiffened structures have potential application in aerospace components, which are the main load-bearing structure of manned space station. However, its springback behavior is very complicated due to the interaction of multi-intersected ribbons and intersecting patterns during die forming. In this study, for typical spherical shaped multi-intersecting stiffened structures, a new approach is proposed to quantize the influence on flexural neutral layer of multi-intersected ribs. The strain distribution along the thickness at different radial positions of ribs is derived theoretically. Reverse loading method is used to calculate springback radius of each position assisted by Matlab software and the radial profile of the panel after springback is obtained by numerical integration algorithm. To verify the accuracy and effectiveness of the new approach, finite element simulations based on ABAQUS software and experiments were both implemented. Comparison shows that the results are of good agreement, proving the approach is capable of predicting springback of multi-intersecting stiffened structures.

Keywords Multi-intersecting high stiffened integral panel · Neutral layer · Springback prediction

1 Introduction

Spherical integral panel with multi-intersecting high stiffeners is the major load-bearing structure of manned space stations. It has many advantages such as low weight, high structure efficiency, and large rigidity [1, 2]. Because of large curvature of the panel component, die forming is used as the main forming method for its good flexibility and forming ability. However, due to the unevenness of the size and distribution of the stiffened ribs and the interaction between the multi-directional ribs,

Q. He · W. Li (✉) · M. Wan
School of Mechanical Engineering and Automation, Beihang University, Beijing 100191, China
e-mail: space@buaa.edu.cn

C. Li · C. Cui
Beijing Space Craft, China Academy of Space Technology, Beijing 100094, China

© The Minerals, Metals & Materials Society 2021

G. Daehn et al. (eds.), *Forming the Future*, The Minerals, Metals & Materials Series,
https://doi.org/10.1007/978-3-030-75381-8_224

the springback behavior of the panel is especially complicated, affecting the product manufacturing accuracy. Therefore, accurate and efficient prediction of springback is necessary to obtain the final desired shape.

The investigations on springback prediction were mostly focused on 2-D springback of stiffener and 3-D springback of plate. Li [3] derived the shift and rotation of the bending neutral layer with linear hardening model and deduced the springback amounts of single stiffeners with symmetric and asymmetric section in press bending. Wang [4] improved the springback prediction accuracy for Z-section profiles by taking neutral layer shift and power-law hardening model into account. Li and Wu et al. [5] used a cubic non-uniform B-spline to interpolate the die profile with varied curvature, calculated bending moments more accurately by a new formulas of stress and strain, and obtained the final shape of the sheet after springback by proper connecting technologies. As for the 3-D springback problem, in the early stage, Yu and Johnson [6] analyzed the strain distribution of rigid-perfectly plastic circular plates deformed in hemispherical dies, whereby deriving the approximate ratio of the radii of the plate before and after springback according to the edge displacement led by the strain release. An improved approach was proposed by Xue [7–9] who divided the circular plate in stamping into many segments along the meridional direction, each of which had constant strain that was calculated by energy method, then the final profile of the plate was constructed because of the strain release of each segment and the approach was extended to predict springback of a square plate and an unequal double-curvature plate.

Owing to the limitations of theoretical analysis, the finite element method (FEM) was introduced and numerical simulation was applied widely to predict springback of stiffened structures during the forming process. Several researchers had studied the influence of process parameters on the integral panel with FEM models to guide the technology design [10, 11]. But the accuracy and efficiency of simulation were the necessarily concerned problems. The principal factors affecting accuracy were unloading modulus, Bauschinger effect, transient behavior, and permanent softening, which should be modeled more accurately. Zang and Lee [12] evaluated the significance of hardening behavior and unloading modulus in springback prediction for U bending, indicating that unloading modulus is most important but the traditional isotropic hardening scheme with constant initial elastic modulus might be able to predict springback within reasonable accuracy. To improve the efficiency, Li [13] and Yan [14] proposed and built the plastic equivalent FEM models, respectively, achieving acceptable accuracy as well as reducing the simulation time by 70%–80%. Nevertheless, as the integral panels become larger and more complex, the excessive simulation time is still a severe problem.

The present paper proposes an efficient theoretical analysis and numerical approach to predict springback for a typical intersecting high stiffened integral panel in spherical die forming. The approach quantifies the effect between ribs and gets the 3-D springback problem simplified, having excellent efficiency and good reference value in springback prediction.

2 Theoretical Analysis

The typical "*" shaped intersecting stiffened integral panel is shown in Fig. 1. As the panel deforms in spherical die forming (Fig. 2a), its shape can be represented by the bending and springback profiles of the three ribs at the center intersection (Fig. 2b). Define the three ribs as the main ribs whose deformation behavior is affected by others. The effect, when the panel is bent, is reflected in different bending neutral layers at different locations. Such as at the intersection of ribs, the neutral layer is farther away from the skin, suggesting the bending neutral layer can be used to quantize the influence between the ribs. Hence, the complex 3-D springback of the panel is transformed into the 2-D springback of the main ribs.

The main ribs flow with the skin into the die during forming process, so the cross-sectional strain is not only composed of the pure bending component, but also of the component from the deformation of the skin. The deformations proceed simultaneously, superimposed to obtain the total strain. The neutral layer coordinates are required for the bending strain, and the skin deformation displacement is required for the skin strain.

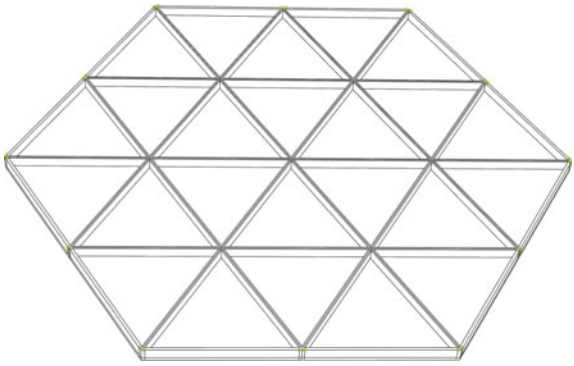


Fig. 1 Typical panel structure. (Color figure online)

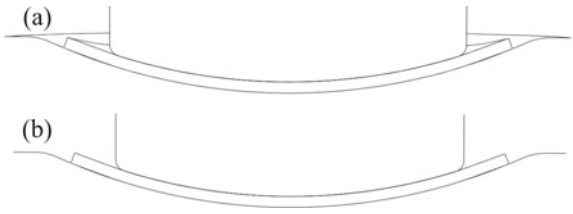


Fig. 2 Deformation of **a** panel and **b** main rib

2.1 Calculation of Bending Neutral Layer

The difference in the coordinates of the neutral layer on the panel is basically caused by the complex geometry. Hereby we define the coordinate of the bending neutral layer at one point as the average value of the neutral layer coordinates of all cross sections passing the point, without considering the shift of the neutral layer during bending. The specific calculation algorithm is as follows.

For any point (x_0, y_0) on the plate and given angle $\theta(0 \leq \theta < \pi)$, the cut line, projected line of the section and depicted in Fig. 3, can be expressed as a parameter form, $x = x_0 + l\cos\theta$, $y = y_0 + l\sin\theta$, in which l is the parameter, and the cross section is shown as the A-A section in Fig. 3 with some rib sections represented by dash lines.

To obtain the section width b and rib width s_i:

(1) Find the boundary of the cut line. Calculate the intersection parameters between cut line and edge line of the panel to obtain the boundary parameters that are marked as l_s and l_e, and $b = l_e - l_s$.
(2) Find the intersection parameters with the rib lines. Calculate the intersection parameters between cut line and projection line of ribs. Put the parameters inside the interval of (l_s, l_e) into a sequence.
(3) Sort the sequence in ascending order. Traverse sorted sequence and calculate the width of each cross section of rib s_i.
(4) Calculate the y-coordinate of the neutral axis of the section. Regarding bottom edge as the reference axis, y-coordinate of the neutral axis satisfies Eq. (1).

$$-bt\left(y_c - \frac{t}{2}\right) + \left(\frac{h}{2} + t - y_c\right)h\sum s_i = 0. \tag{1}$$

Let $s = \sum s_i$, then we obtain

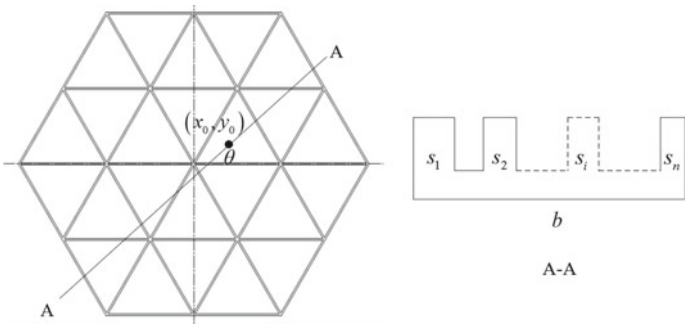


Fig. 3 Schematic diagram of cross section of cut line

$$y_c(\theta) = \frac{bt^2 + sh^2 + 2ths}{2(bt + hs)}. \tag{2}$$

(5) Change the angle θ and repeat steps 1–4.
Then the neutral layer height of the point is

$$\overline{y}_c = \frac{1}{n_d} \sum_{i=1}^{n_d} y_c(\theta_i), \tag{3}$$

in which n_d is the number of θ, that is, the number of the cut lines passing the point, which should be reasonable in accuracy and efficiency. The step size of θ used by the present approach is $\pi/12$, thus n_d is 12. Based on the bending neutral layer, the bending strain can be calculated according to the Kirchhoff assumption.

2.2 Deformation of Skin Component

In die forming, material flowing of the panel's skin can lead to deflection ω and radial displacement u. Adopting finite deformation theory, meridian strain and circumference strain of skin are expressed as:

$$\varepsilon_r = \frac{\partial u}{\partial r} + \frac{1}{2}\left(\frac{\partial \omega}{\partial r}\right)^2, \ \varepsilon_\theta = \frac{u}{r}. \tag{4}$$

When the plate forms a partly spherical surface, $\omega(r) = (r_d^2 - r^2)/2r_p$, where r_d takes the smaller value between the circumferential radius of die and the radius of panel's inscribed circle, r is the radial coordinate, and r_p is radius of the die. The derivation of u is based on the energy method. In axisymmetric die forming of thin plates, there are two energy components presented as follows:

(1) Bending strain energy

$$U_w = \frac{D}{2} \int_0^{2\pi} \int_0^{rd} \left[\left(\frac{\partial^2 \omega}{\partial r^2}\right)^2 + \frac{1}{r^2}\left(\frac{\partial \omega}{\partial r}\right)^2 + \frac{2\nu}{r}\frac{\partial \omega}{\partial r}\frac{\partial^2 \omega}{\partial r^2} \right] r dr d\theta, \tag{5}$$

(2) Membrane strain energy

$$U_m = \frac{\pi E t}{1 - \nu^2} \int_0^{rd} \left(\varepsilon_r^2 + \varepsilon_\theta^2 + 2\nu \varepsilon_r \varepsilon_\theta\right) r dr, \tag{6}$$

in which $D = Et^3/[12(1-v^2)]$ is the bending rigidity of the plate, E is the elastic modulus, t is the plate thickness, and v is the Poisson ratio.

According to variation principle, the real u should lead to the minimum strain energy. The trial function method is used to solve the variation problem. To simplify the answer form, u is approximated by polynomial function of three terms at least. In die forming, due to central radial displacement being zero, assume $u = r(C_1 + C_2 r + C_3 r^2)$ to satisfy the displacement boundary conditions.

Note that only U_m is relative with u; by substituting ω and u into Eq. (6) and solving minimum condition $\partial U_m/\partial C_i = 0 (i = 1, 2, 3)$, u is solved and expressed as

$$u = \frac{1}{16r_p^2} r\left[(1-\upsilon)r_d^2 - (3-\upsilon)r^2\right]. \tag{7}$$

Then the strain distribution function is derived as in Eqs. (8) and (9) by Eq. (4).

$$\varepsilon_r = \frac{1}{16r_p^2}\left[(1-\upsilon)r_d^2 - 3(3-\upsilon)r^2\right] + \frac{r^2}{2r_p^2} \tag{8}$$

$$\varepsilon_\theta = \frac{u}{r} = \frac{1}{16r_p^2}\left[(1-\upsilon)r_d^2 - (3-\upsilon)r^2\right]. \tag{9}$$

When v is 0.33, a typical value for aluminum alloys, ε_r is approximately a constant that is equal to $(1-v)r_d^2/16r_p^2$. The final strain distribution is combined by the bending strain and the meridian strain of the skin.

2.3 Calculation of Springback

Before calculating springback of the main rib, take the springback caused by the release of circumference strain into consideration, which is a relatively small value. The relation between spherical radius r_p and r_d is $r_p = (d^2 + r_d^2)/2d$, derived by arc geometry, where $d = r_p - \sqrt{{r_p}^2 - {r_d}^2}$ is the height of the arc. The differential of r_p with respect to r_d is $\Delta r_p = \Delta r_d \cdot r_d/d$. With the release of circumferential strain, increment of edge radius is $\Delta r_d = r_d|\varepsilon_{\theta r_d}|$, so radius of panel shape is of small variation that is

$$\Delta r_p = \frac{r_d^2}{r_p - \sqrt{r_p^2 - r_d^2}}\left|\varepsilon_{\theta r_d}\right|. \tag{10}$$

Then the springback of the main rib is calculated by the reverse loading method. The rib is divided into n_s segments along the radial direction by Δr; the neutral layer within each segment is regarded as fixed. For the segment with larger rigidity,

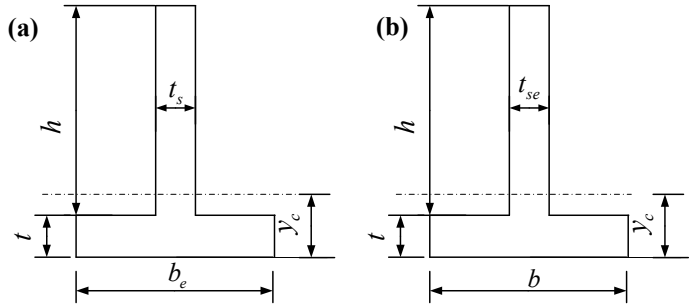


Fig. 4 **a** Equivalent cross section for moment, **b** Equivalent cross section for inertia

its springback amount is smaller for its lower load moment and higher inertia; two equivalent cross sections are devised to calculate equivalent load moment and inertia, respectively.

The equivalent cross section for moment calculation is shown in Fig. 4a, in which b_e can be calculated by Eq. (11).

$$b_e = \left(\frac{h}{2} + t - y_c\right) h t_s \Big/ t\left(y_c - \frac{t}{2}\right). \tag{11}$$

The power-law strain hardening model developed by Wagoner [15] is adopted to consider nonlinear strain hardening, expressed as in Eq. (12).

$$\sigma = \begin{cases} E|\varepsilon|, |\sigma| \le \sigma_s \\ \sigma_s + K\left|\varepsilon_p\right|^n, |\sigma| > \sigma_s \end{cases}, \tag{12}$$

in which σ is the true stress, ε is the true elastic strain, σ_s is the initial yield stress, ε_p is the true plastic strain, K is the hardening coefficient, and n is the hardening exponent.

The coordinate of the elastic–plastic transition point is $y_p = \rho(\varepsilon_e + \varepsilon_r)$, where ε_e is the maximum elastic strain. If$\varepsilon_e > \varepsilon_r$, y_p is on the outer side of the neutral layer; the equivalent load moment on the equivalent section can be calculated by Eq. (13).

$$\begin{aligned} M_e = & t_s \int_{y_p}^{h-\overline{y}_c} \left[\sigma_s + K\left(\varepsilon_r + \frac{y}{\rho} - \varepsilon_e\right)^n\right] y dy + b_e E \int_{-\overline{y}_c}^{-\overline{y}_c+t} \left(\varepsilon_r + \frac{y}{\rho}\right) y dy \\ & + t_s E \int_{-\overline{y}_c}^{y_p} \left(\varepsilon_r + \frac{y}{\rho}\right) y dy. \end{aligned} \tag{13}$$

Otherwise, all of outer sides of the section enter plasticity, y_p is on the inner side, and the M_e is calculated by

$$M_e = t_s \int_0^{h-\bar{y}_c} \left[\sigma_s + K\left(\varepsilon_r + \frac{y}{\rho} - \varepsilon_e\right)^n\right] y dy + b_e E \int_{-\bar{y}_c}^{y_p} \left(\varepsilon_r + \frac{y}{\rho}\right) y dy + b_e E \int_{y_p}^{0} \left[\sigma_s + K\left(\varepsilon_r + \frac{y}{\rho} - \varepsilon_e\right)^n\right] y dy \tag{14}$$

where $\rho = r_p + \Delta r_p + \bar{y}_c$ is the curvature radius of the neutral layer.

Another equivalent section shown in Fig. 4b is to calculate equivalent t_s by Eq. (15) with fixed b that is the maximum value of b_e among all segments.

$$t_{se} = bt\left(y_c - \frac{t}{2}\right) \Big/ \left(\frac{h}{2} + t - y_c\right) h. \tag{15}$$

Then the section is applied to obtain equivalent inertia with the following equation:

$$I_e = \frac{1}{12} b t^3 + bt\left(y_c - \frac{t}{2}\right)^2 + \frac{1}{12} t_{se} h^3 + t_{se} h \left(\frac{h}{2} + t - y_c\right)^2. \tag{16}$$

According to the elastic unloading rule, the springback radius ρ_0 is easily obtained by

$$\frac{1}{\rho} - \frac{1}{\rho_0} = \frac{M_e}{E I_e}. \tag{16}$$

Because the curvature is equal to the second derivative of ω, twice numerical integrations are used to calculate the points on the final profile of the main rib after springback with the boundary conditions presented as $\omega(0) = 0$ and $\omega'(0) = 0$. The formula is

$$\begin{cases} \omega'(i) = \omega'(i-1) + \dfrac{\Delta r}{2}\left(\dfrac{1}{\rho_0(i-1)} + \dfrac{1}{\rho_0(i)}\right) \\ \omega(i) = \omega(i-1) + \dfrac{\Delta r}{2}\left(\omega'(i-1) + \omega'(i)\right) \end{cases} i = 2, 3, \ldots\ldots, n_s. \tag{17}$$

3 FEM Simulations and Experiments

3.1 FEM Simulation Modeling

Material of the integral panel is the H-state 5A06 aluminum alloy and the material properties are shown in Table 1.

ABAQUS software is used to model the die forming process. The contact between the panel and the die is a complex nonlinear problem, so two nonlinear static analysis steps are adopted for the simulation of pressing and springback, in which the loading approach adopts displacement loading. The simulation model consists of an integral panel and upper and lower tools, as shown in Fig. 5. The panel is modeled with solid elements C3D8R, with the plate thickness of 5 mm, the rib height of 15 mm, the rib thickness of 4 mm, and the side length of 400 mm. The global seed size is 5 mm, while the number of the element layers is 3 along the thickness direction of the skin and 4 for the ribs. The tools are discretely rigid with the face radius of 1000 mm, 1200 mm, and 1405 mm, respectively, and the circumference radius of the upper tool being 310 mm. A path is created for acquiring the profile of the panel along the main rib, as depicted in Fig. 6.

Table 1 Material properties of H-state 5A06 aluminum alloy

E(MPa)	σ_s(MPa)	σ_b(MPa)	n	K
72,000	161	420	0.70	1065

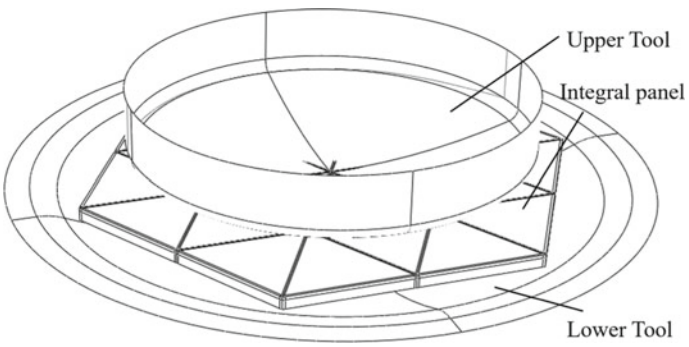


Fig. 5 Simulation model

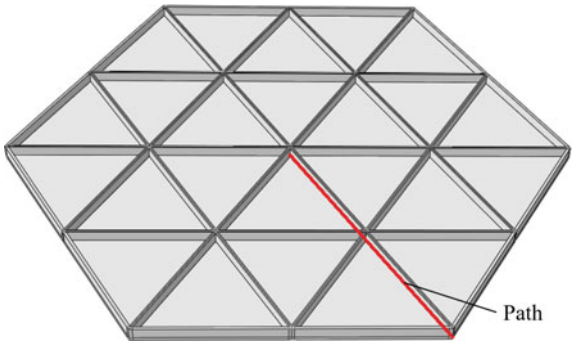


Fig. 6 Path along the main rib. (Color figure online)

3.2 Experiments

Figure 7 is the photo of experimental setup, in which a dial indicator is used to measure the depression height of the punch and the paper clamped by the upper tool and the specimen is to determine the initial contact between them. The experiments with a die radius of 1000, 1200, and 1405 mm are all implemented. Due to the panel not being able to be accurately placed in the center of the tool, the deformation of the adjacent sides of the panel during the forming process is not the same, but the sealing between the sides and the die is better when the punch is fully pressed. After the panel is released, the string length of the main rib is measured with a ruler and the string height with a vernier caliper, through which the springback height is calculated. An experiment specimen after forming is shown in Fig. 8.



Fig. 7 Experimental setup. (Color figure online)



Fig. 8 Experiment specimen after forming. (Color figure online)

4 Results and Discussion

4.1 Simulation Results

For the simulation model, the panel is placed in the center of the die ideally, thus all sides are in the same deformation state during the simulation process and fit the die well after being fully pressed. Figure 9 shows the Mises stress contour and the equivalent plastic strain contour of the simulation results with the die radius of 1000 mm at the end of the pressing step. In Fig. 9a, the maximum stress happens at the rib intersections of the sides that are of intense contact with the die surface. In Fig. 9 b, the whole skin of the panel is almost in elastic state, while the plastic deformation is mainly due to the ribs, which demonstrates the forming principle of the integral panel components. The meridian strain distribution of the main rib is shown in Fig. 10; it can be seen obviously that the neutral layer of the rib intersections is higher than other positons, proving the difference in neutral layers on the panel that is quantitatively considered by the present approach.

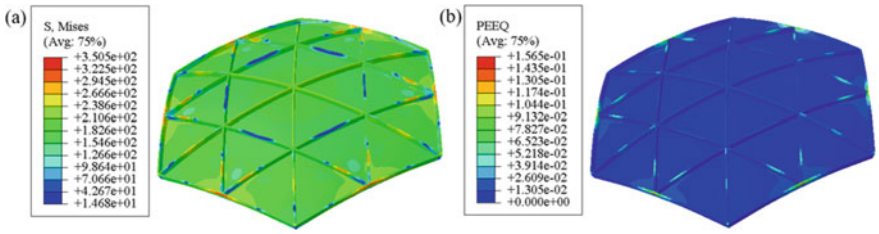


Fig. 9 **a** Mises stress contour **b** Equivalent plastic strain contour of the simulation results with die radius of 1000 mm. (Color figure online)



Fig. 10 The meridian strain distribution of the main rib. (Color figure online)

4.2 Verification of the New Approach

Compare experimental results with corresponding simulation and theoretical calculation results to verify the validity of the simulation model and the numerical approach. The Δr used to divide the main rib is 5 mm. As is shown in Table 2, the finite element model can well simulate the real springback situation. The theoretical calculations, with better computational efficiency, predict slightly larger springback amounts but have relatively small error from the experimental results, proving the effectiveness of the present approach. The calculated and simulated final profiles of the panels are depicted in Fig. 11, where the endpoints of the main ribs on the specimens after springback are also drawn. Great agreement is seen among theoretical predictions, simulation results, and experimental measurements.

Note that the die radius is smaller, and the springback amount is smaller for the reason of the smaller bending radius, which matches the tendency of the springback results of pure bending. Besides, according to the present approach, ε_r is proportional to the square of r_d/r_p, for the certain r_d; ε_r is bigger when r_p is smaller, leading to the bending-tension effect that can further reduce the springback.

Table 2 Comparison of springback amounts among the theoretical predictions and the simulations and experiments results

Die radius/mm	Loading height/mm	Springback amount/mm		
		Calculation	Simulation	Experiment
1000	78.60	9.41	8.59	9.01
1200	68.20	12.17	11.28	11.87
1405	56.20	14.21	13.06	13.72

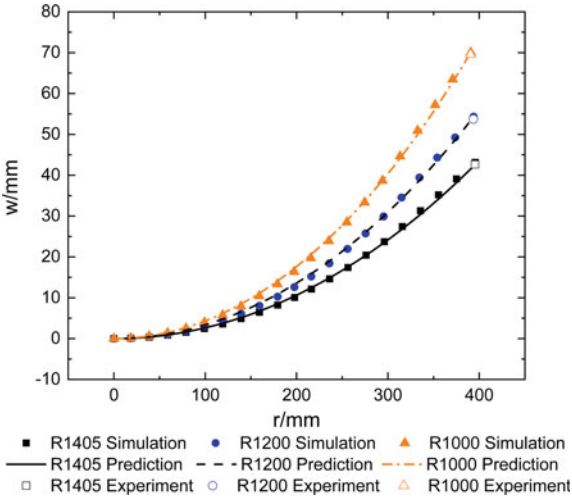


Fig. 11 Comparison of final profiles between theoretical predictions and simulation results. (Color figure online)

5 Conclusions

The paper proposed a theoretical analysis and numerical calculation approach to predict springback for intersecting high-stiffened integral panel in spherical die forming. By comparing with the simulation and experimental results, the present approach is capable of predicting springback accurately and efficiently. The specific conclusions are as follows:

(1) Quantize the influence of the intersecting ribs on the bending and springback behavior by defining neutral layer on the panel and designing algorithm, with which the multi-direction springback problem is transformed into a 2-D springback problem. The difference in bending neutral layer is proved by simulations.

(2) With the consideration of the skin deformation, the power-law hardening model and different elastic–plastic divisions for moment calculation, the approach can accurately describe the springback behavior of the panel in spherical die forming.

(3) Computational results indicate that the r_p is smaller, ε_r is bigger, causing smaller springback amount, which agrees well with simulation and experimental results but is of great calculation efficiency.

Acknowledgments The authors would like to acknowledge the funding support to this research from the project of No.U1737101 from the National Natural Science Foundation of China.

References

1. Ceng YS, Huang X (2008) Forming technology of large integral panel. Chin J Aeronaut 3:721–727
2. Wang XF, Guo X, Chen GN, Jürgen S (2008) Remark of integral panel forming. Mod Manuf Technol Equip 3:1–4
3. Li WD, Wan M, Yan Y (2014) Neutral layer and springback analysis in press bend forming of aircraft integral panels. J Plast Eng 21(5):156–161
4. Wang A, Xue H, Saud S et al (2019) Improvement of springback prediction accuracy for Z-section profiles in four-roll bending process considering neutral layer shift. J Manuf Process 48:218–227
5. Li F, Wu J, Li Y et al (2016) A new calculating method to perform springback predictions for varied curvature sheet bending based on the B-spline function. Int J Mech Sci 113:71–80
6. Yu TX, Johnson W, Stronge WJ (1984) Stamping and springback of circular plates deformed in hemispherical dies. Int J Mech Sci 26(2):131–148
7. Xue P, Yu TX, Chu E (1999) Theoretical prediction of the springback of metal sheets after a double-curvature forming operation. J Mater Process Tech 89:65–71
8. Xue P, Yu TX, Chu E (2001) An energy approach for predicting springback of metal sheets after double-curvature forming, part I: axisymmetric stamping. Int J Mech Sci 43(8):1893–1914
9. Xue P, Yu TX, Chu E (2001) An energy approach for predicting springback of metal sheets after double-curvature forming, part II: unequal double-curvature forming. Int J Mech Sci 43(8):1915–1924
10. Li J (2017) Research on buckling of 7B04 aluminum alloy integral panel using multi-point dies. Master thesis, Jilin University
11. Liao X (2015) Analysis for the stabilization of integral panel ribs under the multistage incremental and aging forming. Master thesis, Wuhan University of Technology
12. Zang S, Lee M, Hoon KJ (2013) Evaluating the significance of hardening behavior and unloading modulus under strain reversal in sheet springback prediction. Int J Mech Sci 77:194–204
13. Li WD, Wan M (2014) Press bending equivalent simulation model of integrally reinforce panel. J Beijing Univ Aeronaut Astronaut 40(11):1537–1542
14. Yan Y, Wan M, Wang HB (2009) FEM equivalent model for press bend forming of aircraft integral panel. Trans Nonferrous Metals Soc China 19(2):414–421
15. Wagoner R, Li M (2007) Simulation of springback: through-thickness integration. Int J Plast 23(3):345–360

Size Effect on Cyclic Deformation Behavior and Springback Prediction of Ultrathin Superalloy Sheet



Weilin He, Bao Meng, Bingyi Song, Rui Zhao, Li Zhang, and Min Wan

Abstract Springback is a challenging issue in the processing of ultrathin superalloy components whose thickness are usually in the range of 0.1 ~ 0.3 mm, and its prediction is affected by the size effect. In this research, the cyclic shearing tests of superalloy sheets with different grain sizes were performed to clarify the relation between size effect and cyclic deformation behavior. The experimental results indicated that it is affected by the geometrical and grain size effects. To explore how the size effect affects the springback of ultrathin superalloy sheet, U-bending tests were performed on specimens with different grain sizes and thicknesses. In addition, different hardening models were compared by multiscale U-bending tests. The results showed that the Yoshida–Uemori (YU) model can well describe the cyclic deformation of superalloy sheet at various scales.

Keywords Size effect · Cyclic deformation behavior · Springback prediction · Superalloy sheet

1 Introduction

In the process of plastic deformation, the metal sheet will produce wrinkling, cracking, springback and other defects. Especially the springback problem is the most difficult to solve. In recent years, the extensive application of high-strength materials such as high-strength steel, superalloy, and titanium alloy has brought more and more challenges to the prediction of forming springback. Especially thin-walled micro-components made of superalloys play an irreplaceable role in reducing the weight and improving the performance of aircraft engine and carrier rocket. In order to study the springback of such ultrathin superalloys, it is essential to investigate the cyclic plastic behavior.

The Bauschinger effect which refers to the phenomenon that the yield stress in the reverse deformation of a material is smaller than the yield stress in the initial

W. He · B. Meng (✉) · B. Song · R. Zhao · L. Zhang · M. Wan
School of Mechanical Engineering and Automation, Beihang University, Beijing 100191, China
e-mail: mengbao@buaa.edu.cn

© The Minerals, Metals & Materials Society 2021

G. Daehn et al. (eds.), *Forming the Future*, The Minerals, Metals & Materials Series,
https://doi.org/10.1007/978-3-030-75381-8_225

direction during cyclic plastic deformation is one of the important characteristics of cyclic plastic deformation. It is caused by residual stress between grain boundaries of polycrystalline materials which reflects the influence of deformation history on material properties. Song et al. [1] investigated the effects of different pre-strains under different loading modes on the Bauschinger effect of AZ31B magnesium alloy. The results revealed that the Bauschinger effect is sensitive to strain rate and pre-strain in tension-unloading-reverse compression loading mode, but not to strain rate in c-u-t loading mode. Mahato et al. [2] explored the effects of forward deformation mode, monotonic and cyclic asymmetry on the Bauschinger phenomenon of annealed polycrystalline copper with different Bauschinger parameters under different uniaxial tensile strains. The results provided that the Bauschinger effect is not obvious under asymmetric cyclic loading compared with uniaxial loading. Kato et al. [3] studied the Bauschinger effect in 1-mm-thick plates by tensile test and four-point bending test. The results showed that this effect does not exist when the pre-strain is less than 4% and exists when the pre-strain is higher than 4%. Unfortunately, there are not sufficient investigation on the influence of the size effect on the Bauschinger effect.

Accurate springback prediction not only needs investigation of the factors influencing cyclic deformation behavior but also of the error sources of springback prediction. U-bending test is considered as the general method to test the springback phenomenon, because the material at the side wall undergoes bending, unloading, and reverse bending and unloading during the forming process with the bending punch and die, which is very suitable for analyzing the factors influencing springback. Among them, the size effect is one of the factors that affects the U-bending test results. There are two size effects existing in micro-scale materials, grain size effect and geometry size effect. The geometry effect is usually reflected in the thickness of the specimen. Wang et al. [4] used copper alloy sheet samples with thickness of 0.1, 0.2, and 0.4 mm to conduct pure micro-bending experiments. The results showed that the springback angle caused by size effect decreases with the increase of sheet thickness and the decrease of grain size. Diehl et al. [5] proposed with the help of bending tests that with the increase of surface grain proportion, the increase of strain gradient, and the decrease of scale factor, the springback behavior of a thin film features different effects.

There are many researches based on the Bauschinger effect and U-bending. However, due to the existence of the size effect, there is a great difference in mechanical properties and forming characteristics of a macroscopic sheet metal and an ultrathin superalloy sheet. Therefore, the superalloy GH4169 was used to perform experimental forming tests in this study. Cyclic shearing and U-bending tests were carried out on samples with different grain sizes. The first aim was to investigate the effect of sample geometry and grain size on the Bauschinger effect and to summarize the influence of grain size on the Bauschinger effect. The second aim was to determine the effect of grain size on the springback parameters in U-bending test. The last aim was to discuss the accuracy of different hardening models in predicting the springback in U-bending of ultrathin sheets.

Table 1 Chemical composition of alloy GH4169

Composition	Ni	Cr	Nb	Mo	Ti	Al	C	Fe
Fraction (wt%)	52.9	19.1	4.7	2.6	0.9	≤ 0.6	≤ 0.05	Balance

Table 2 Obtained grain sizes for different heat treatments

Material	Thickness/mm	Temperature/°C	Grain size/μm	*t/d*
GH4169	0.2	1000	24.2	7.94
	0.2	1030	37.3	5.36
	0.12	1050	32.5	3.69
	0.2	1050	49.3	4.06
	0.3	1050	58.5	5.13
	0.2	1050	70.8	2.82

2 Materials and Methods

2.1 Material Processing and Grain Size Characterization

Ultrathin GH4169 has high-temperature performance, corrosion resistance, pressure resistance, and molding performance. For these reasons, it is widely used in aerospace, nuclear energy, and petroleum industry as well as for extrusion dies. Therefore, GH4169 nickel-based superalloy is selected as the research object whose chemical composition is shown in Table 1.

In order to obtain samples with different grain sizes, the vacuum heat treatment with various temperatures was performed. The holding time was 30 minutes. The grain size of the samples was obtained by metallographic analysis. First, the polished samples were etched in a mixture of HCl solution and H_2O_2 solution with a ratio of 1:1. Then, metallographic pictures were obtained under the Leica microscope. Finally, Image-pro software and the truncation method were used to obtain the average grain size. The results show that the grain size increases with the increase of heat treatment temperature. The different sheet thickness and grain sizes of the material are shown in Table 2, where t represents the thickness of the specimen and d represents the grain size.

2.2 Cyclic Shearing Test

Cyclic shearing tests were performed by installing the shearing test fixture in the uniaxial tensile machine. The experimental equipment is shown in Fig. 1a. The left and right parts of the testing device are symmetrical in the center. During the test, the left part was fixed, and the right part was driven by the testing machine. The relative

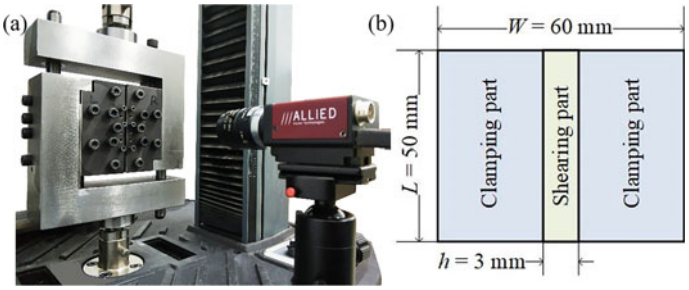


Fig. 1 **a** Cyclic shearing test device; **b** Cyclic shearing test sample. (Color figure online)

motion of the two parts causes forward and reverse shearing strain in the center of the specimen. The DIC system was used to measure the strain of the sample and the output frequency is 2 Hz. Lock nuts were utilized to eliminate device clearance. Compression screws on both sides of the deformation zone were set to avoid slipping and to ensure strain uniformity. The tightening torque of the first-stage compression screw was determined to be 35 Nm and the tightening torque of the second-stage compression screw was determined to be 5 Nm. The shear stress–shear strain curves under cyclic loading were obtained from the testing results of DIC and the load curves of the machine.

In this paper, rectangular samples were selected as shown in Fig. 1b. The length (W) and width (L) of the specimen are 60 mm and 50 mm, respectively. The width (h) of the shearing part is 3 mm. Reducing width of the shearing part can prevent premature wrinkling. But if the width of the deformation zone is too narrow, the recording area of DIC camera is too small and the strain cannot be measured accurately. Therefore, the width of the shearing part was designed to be 3 mm. At the same time, the overall width of the sample was determined to be 60 mm by combining the width of the clamping block. L/h determines the uniformity of stress distribution in shear deformation zone. As L/h increases, the distribution uniformity of shear stress increases. When $L/h \geq 10$, relatively uniform distribution of shear stress and shear strain can be obtained. Therefore, the height of deformation zone L was determined to be 50 mm.

2.3 U-bending Test

The material thickness selected for this test was 0.2 mm. Due to the small sheet thickness, the sample geometry had to be adapted in comparison to samples of larger sheet thicknesses to ensure usable testing results. Therefore, the optimal sample size was determined to be 110 mm and 30 mm (length direction was the rolling direction). The radii of the punch and die were 3 mm. The bending stroke was 28 mm. The bending speed was 10 mm/min. The blank holder force was constant 5 kN. The

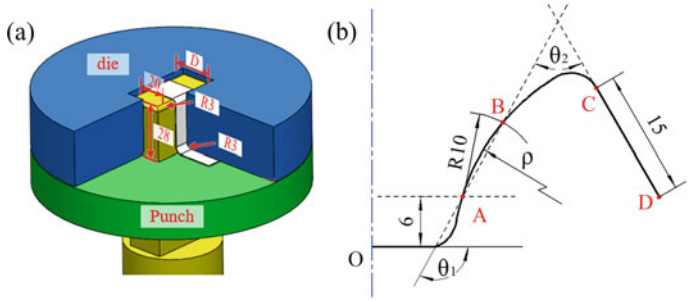


Fig. 2 **a** U-bending test device; **b** Definition of springback parameters in U-bending test. (Color figure online)

punch width was 20 mm and the width of the die was selected 20.5 mm. The test was carried out on the universal sheet metal forming testing machine and the U-bending device is shown in Fig. 2a. After being formed, the U-shaped part was removed from the die and immediately pressed into a printing pad to ink the side. The side outline was then printed on a paper. The method for determining the springback parameters is shown in Fig. 2b. Springback parameters include angle θ_1 between x-axis and AB, angle θ_2 between AB and CD, radius ρ of the circle through A and B.

3 Results and Discussion

3.1 Grain Size and Sheet Thickness Effects on the Bauschinger Effect

The Bauschinger effect can be described with a stress reduction $\Delta\sigma$ due to reverse loading. It is defined as

$$\Delta\sigma = \sigma_{fs} - \sigma_{rs} \tag{1}$$

where σ_{fs} is initial yield stress and σ_{rs} is the reverse yield stress. According to the cyclic shearing test curves of the samples with three grain sizes under different pre-strain conditions, $\Delta\sigma$ was calculated, as shown in Table 3. The relationship between grain size and $\Delta\sigma$ is shown in Fig. 3.

As it can be seen from Fig. 3, softening amount increases with the decrease of grain size, which reveals that the Bauschinger effect becomes more obvious with a decrease of grain size. This can be explained by the Kocks–Mecking dislocation density theory [6]. According to this theory, grain boundaries act as an obstacle for the dislocation movement in the material. This can lead to the generation of a reverse stress opposite to the dislocation movement. Therefore, less stress is needed to start dislocation movement during reverse loading. Smaller grain sizes lead to higher

Table 3 Results for the Bauschinger parameters

Grain size/μm	Pre-strain	σ_{fs}/MPa	σ_{rs}/MPa	σΔ/MPa
24.2	0.02	840.6	449.6	391.0
	0.06	837.9	512.2	325.7
	0.10	844.3	497.5	346.8
	0.14	855.4	491.9	362.5
49.3	0.02	745.0	499.3	245.7
	0.07	747.7	476.3	271.4
	0.11	730.3	514.0	216.3
	0.15	741.3	475.4	265.9
70.8	0.03	680.8	489.0	191.9
	0.07	687.6	426.2	261.5
	0.11	685.1	461.8	223.3
	0.15	691.0	429.5	261.5

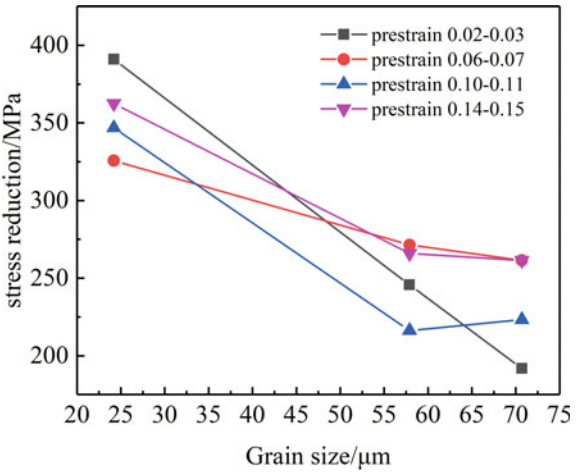


Fig. 3 The relationship between Δσ and grain size. (Color figure online)

densities of grain boundaries, dislocations, and higher reverse stress. Therefore, the Bauschinger effect becomes more obvious.

3.2 Grain Size and Thickness Effect on Springback in U-bending Test

Two analytical theories for springback in sheet metal forming are the Ludwik engineering analytical theory and the Hill precise analytical theory. Due to a relative

bending radius R and material thickness, in this test of $R/t \geq 10$, the state in this test can be considered plane strain. The influence of the inner shift of the neutral layer was ignored to meet the assumption of a flat section. Therefore, the adoption of Ludwik engineering theory can meet the requirements of qualitative analysis. According to the hypothesis, the springback angel $\Delta\alpha$ is calculated with:

$$\Delta\alpha = \left(\frac{3\sigma_c}{E} \cdot \frac{\rho}{t} + \frac{D}{E}\right)\alpha \tag{2}$$

where σ_c is the yield strength of the material, E is the elastic modulus, ρ is the curvature radius of the neutral layer, t is the thickness of the sheet metal, D is the strengthening modulus, and α is the pre-unloading angle.

The U-bending test results for different sheet thicknesses and grain sizes are shown in Fig. 4.

The springback increases with the increase of θ_1 and the decrease of θ_2 and ρ. In all the test results, θ_2, ρ, and θ_1 always show an opposite trend, that is, θ_2 and ρ decrease with the increase of θ_1, while θ_2 and ρ increase with the decrease of θ_1. Therefore, the effects of these three parameters on springback remain consistent.

It can be seen from Fig. 4a that for the same sheet thickness and deformation state, the springback decreases with the increase of the average grain size. This can be explained by the surface layer model and the K-M dislocation density model. With the increase of grain size, the number of grains in sheet thickness direction decreases. The decrease of grain boundary in thickness direction leads to the decrease of dislocation density, which eventually leads to the decline of yield strength and flow stress. According to Eq. (2), the decrease of yield strength and elastic modulus will lead to the decrease of springback. The decrease in yield strength causes a smaller portion of elastic deformation and springback is less obvious.

In addition, it can be seen from Fig. 4b that the springback decreases with the increase of sheet thickness, which is consistent with the conclusion of Eq. (2). On

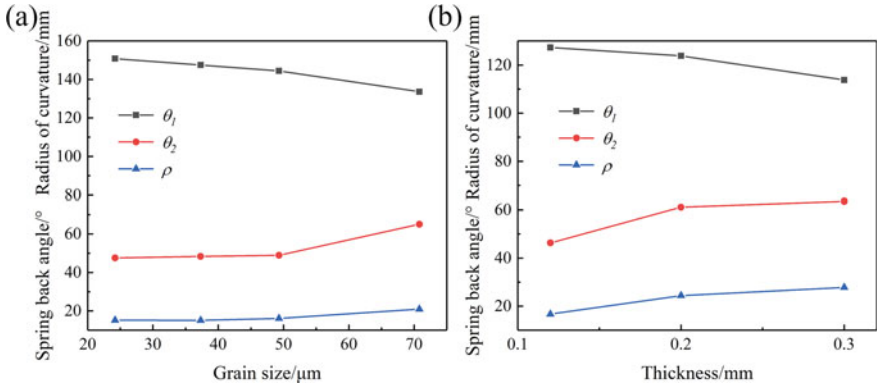


Fig. 4 Influence of **a** grain size and **b** thickness on springback of parameters. (Color figure online)

the other hand, the t/d ratio of the three samples gradually increases as shown in Table 2, which leads to the increase of yield strength and flow stress and thus the springback increases. However, this effect has less influence on springback than the sheet thickness leading to a decrease of springback.

The results of the test indicate that the t/d ratio should be utilized only when the surface layer model and the dislocation density model are characterized simultaneously for the same sheet thickness. This is because the increase of grain size and thickness will lead to the decrease of springback at the same time. If the grain size and thickness are combined as t/d ratio, it is assumed that the two factors have the opposite effect on the springback. This is inconsistent with the test results and caused various contradictory results [7] and the anomaly at the experimental point [8].

3.3 Prediction of Springback with Different Hardening Models

For FE simulation, the special software of dynaform sheet metal forming based on ls-dyna solver was selected for finite element simulation of the springback. Yoshida and Uemori hardening model (Y-U model), isotropic hardening model, and Armstrong and Frederic hardening model (A-F model) were used to predict the springback of a 0.2-mm-thick superalloy sheet. The yield criterion used for three hardening models was Hill48. These three hardening models corresponded to the three material models #125, #37, and #165 in ls-dyna, respectively. The mold mesh size is 1 mm. The mesh size of the specimen is 0.5 mm. Contact definition is FORMING-ONE-WAY-SURFACE-TO-SURFACE. Element formulation is unit 16. Friction coefficient is 0.125. The profiles of the U-bending test samples obtained from simulation and experiment are shown in Fig. 5. The springback parameters obtained from the profiles are shown in Fig. 6.

As it can be seen from Fig. 5b, the predicted profile of Y-U model has the best coincidence degree with the profile obtained from experiment. The prediction accuracy of the isotropic hardening model is worst. Although the prediction accuracy of the A-F model is not as good as that of the Y-U model, it has been improved compared to the isotropic hardening model. The above results are quantified in Fig. 6. It can be seen that the prediction results by the three models are not significantly different and the Y-U model shows the best results in comparison to the experimental values.

Furthermore, the cyclic plastic curves calculated with the three hardening models are shown in Fig. 7. The isotropic hardening model does not take into account the Bauschinger effect, which causes the reverse stress and the stress gradient to be larger, thus overestimating the springback. The A-F model shows significant differences from the experimental curve at the beginning of the reverse loading stage, resulting in deviation of springback prediction. The springback prediction results of the Y-U model are in good agreement with the experimental test results, indicating that it can accurately describe the cyclic loading behavior of materials.

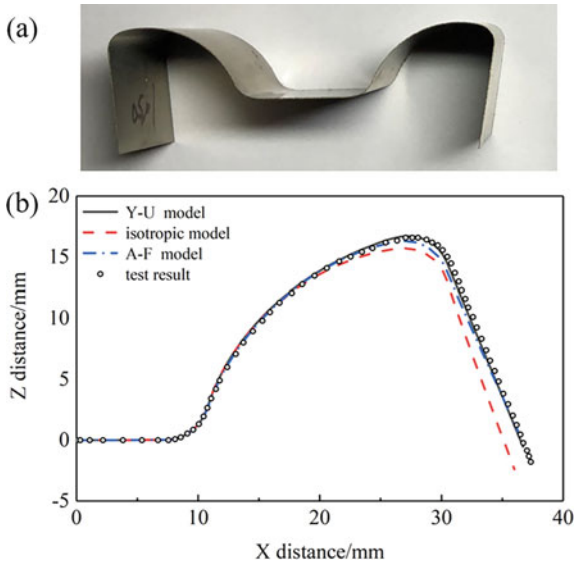


Fig. 5 **a** U-bending experiment sample; **b** Profiles of U-bending test samples from experiment and simulation. (Color figure online)

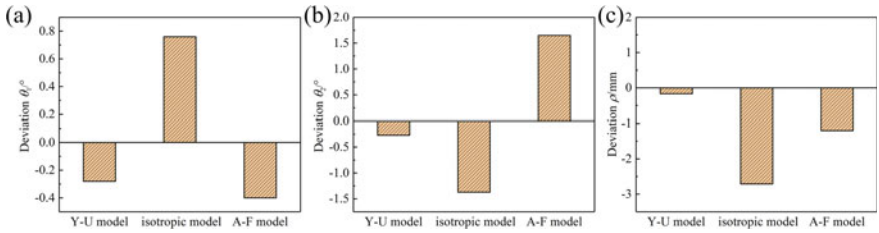


Fig. 6 The deviation of springback parameters with different hardening models: **a** θ_1 **b** θ_2 **c** Radius of curvature ρ. (Color figure online)

4 Summary

In this research, the effect of sheet thickness and grain size on the Bauschinger effect for ultrathin superalloy sheet in cyclic shearing test was investigated. Furthermore the relationship between the effect of sheet thickness and grain size and springback for U-bending was discussed. In addition, different hardening models were compared by multiscale U-bending simulations. The following conclusions are drawn:

(1) Due to the effect of grain size on reverse stress, the Bauschinger effect of ultrathin superalloy sheet becomes more obvious with the increase of grain size.

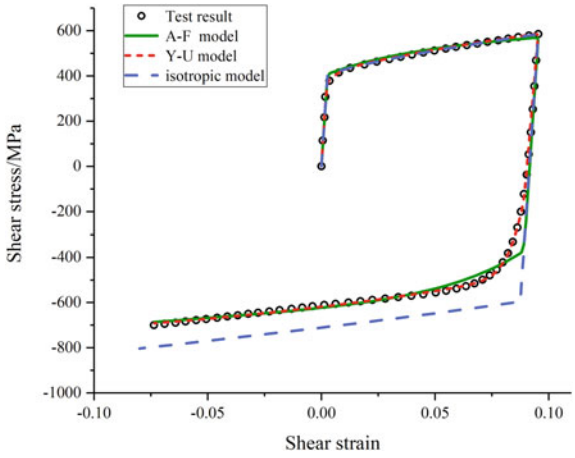


Fig. 7 Cyclic plastic shear curves obtained from experiment and FE simulation. (Color figure online)

(2) With the increase of grain size and the decrease of sheet thickness, the springback is more obvious in U-bending. These results can be explained by surface layer model and K-M dislocation density model.

(3) The Y-U hardening model should be used for the FE simulation of cyclic deformation of ultrathin superalloy sheet at various scales being in good agreement with the experimental results.

Acknowledgments This work was financed and supported by National Natural Science Foundation of China (Grant Nos.: 51975031, 51605018, and 51635005) and Defense Industrial Technology Development Program (No.: JCKY2018601C207).

References

1. Song L, Wu B, Zhang L, Du X, Wang Y, Esling C, Philippe M-J (2019) Detwinning-related Bauschinger effect of an extruded magnesium alloy AZ31B. Mater Charact (2019)
2. Mahato JK, De PS, Sarkar A, Kundu A, Chakraborti PC (2015) Effect of deformation mode and grain size on Bauschinger behavior of annealed copper. Int J Fatigue. S0142112315001395.
3. Kato H, Sasaki K, Mori T (2015) Four-point bending test of the Bauschinger effect in prestrained IF steel thin sheet
4. Wang J, Fu M, Ran J (2014) Analysis of the size effect on springback behavior in micro-scaled U-bending process of sheet metals. Adv Eng Mater 16(4):421–432
5. Diehl A, Engel U, Geiger M (2006) Mechanical properties and bending behaviour of metal foils
6. Mecking H, Kocks UF (1981) Kinetics of flow and strain-hardening. Acta Metall 29(11):1865–1875
7. Chen CC, Jiang CP (2011) Grain size effect in the micro-V-bending process of thin metal sheets. Adv Manuf Process 26(1):78–83
8. Liu JG, Fu MW, Lu J, Chan WL (2011) Influence of size effect on the springback of sheet metal foils in micro-bending. Comput Mater Sci 50(9):2604–2614

Hydro-Mechanical Deep Drawing of Locally Solution-Treated Aluminum Alloy Sheets



Takeshi Nishiwaki, Ryota Sako, and Hideo Tsutamori

Abstract Improvement of formability of aluminum alloy sheets is desired because of their lower drawability than mild steel. Therefore, the special sheet forming methods such as a hydro-mechanical forming and a tailor heat treated blank have been developed for aluminum alloy sheets. In this study, we combined both the methods and investigated the limit of drawing ratio of tailor heat treated blanks in a hydro-mechanical forming process. Tailor heat treated blanks of A6061-T6 sheets were produced by the local solution treatment which was conducted by heat transfer from metal plates heated to a high temperature. Hydro-mechanical deep drawing tests were performed using a cylindrical punch. The limit of drawing ratio of tailor heat treated blanks in a hydro-mechanical forming process was higher than that of simple hydro-mechanical forming and that of simple tailor heat treated blanks.

Keywords Hydro-mechanical deep drawing · Deep drawing · Tailor heat treated blank · Aluminum alloy sheets

1 Introduction

An aluminum alloy sheet has less deep drawability than steel sheet, and it is difficult to form deep cups by conventional deep drawing method (DD). Therefore, the hydro-mechanical deep drawing method (HDD) has been developed and used for manufacturing parts of aircraft and railway vehicles. HDD uses specific dies to apply fluid pressure, therefore multi-stage forming is difficult. It is desired to develop the method of improving deep drawability in one process for complicated products which cannot be produced by conventional HDD.

As one of the ways to improve the drawability of aluminum sheets, the deep drawing of strength graded blanks has been investigated. Tozawa reported the periphery annealing method [1] as strength graded blanks. The periphery over aging

T. Nishiwaki (✉) · R. Sako · H. Tsutamori
Department of Mechanical Engineering, Daido University, 10-3 Takiharu-cho, Minami-ku, Naogoya 457-8530, Japan
e-mail: t-nishi@daido-it.ac.jp

© The Minerals, Metals & Materials Society 2021

G. Daehn et al. (eds.), *Forming the Future*, The Minerals, Metals & Materials Series,
https://doi.org/10.1007/978-3-030-75381-8_226

method [2] and the center aging method [3] have been already examined to make strength graded blanks.

As a method of local heat treatment to produce strength distribution in an aluminum alloy sheet, a steady temperature distribution which was made by contacts with metal heating blocks and cooling blocks was used. A unsteady heat treatment method has also been developed in which metal blocks heated to a high temperature are brought into contact with an aluminum alloy sheet for a short period to give strength distribution [4]. In recent years, laser heat treatment to give strength distribution have been examined mainly. These deep drawing methods of the strength graded blanks are called Tailored Heat Treated Blanks (THTB) [5–9].

The THTB method is a technology for modifying the mechanical property before forming unlike other special forming methods. Therefore, the THTB can be combined with other forming methods. The THTB has been applied for the conventional DD process and could be applied for the HDD process. It is reported that a combination of the THTB and the HDD improves the drawability in numerical analysis [10]. However, there are a few reports that the formability is actually improved in a combination of the THTB and the HDD. In the present work, the improvement of drawability was experimentally examined by the forming method combining both the methods.

2 Experimental Procedure

2.1 Test Material

As a starting material to make the strength graded blanks, the A6061 alloy sheet (1.0 mm thickness) was prepared in T6 heat treated condition. Chemical composition and mechanical properties of A6061 alloy are shown in Tables 1 and 2. Table 2 also shows mechanical properties of A6061-W which is solution-treated in the whole area by the method described later.

Table 1 Chemical composition of A6061 alloy (in wt%)

Si	Fe	Cu	Mn	Mg	Cr	Zn	Ti
0.63	0.3	0.27	0.06	1.0	0.18	0.06	0.03

Table 2 Mechanical properties of A6061 alloy

	YS /MPa	TS /MPa	Elongation / %
A6061-T6	292	315	10.6
A6061-W	99	188	20.3

2.2 Local Solution Treatment

As the method of local solution treatment, the heat transfer by the contact between heating dies and an aluminum sheet was used. Figure 1 shows a schematic diagram of the local solution treatment apparatus. The local solution treatment of the blanks was performed under the condition of heating temperature at 500 °C. The blanks were clamped at 25 kN between heating dies which contained cartridge heaters, held for 0.8 s, and quenched with water. In the center of heating dies, circular grooves were machined to produce a non-contact area. By exchanging these dies, the non-contact area with an aluminum sheet was changed, and it was possible to make various designs of THTB. Four sets of heating dies were prepared in which the ratios between the circular groove diameter D_{in} to the punch diameter D_p were 1.2, 1.4, 1.6, and 1.8. A set of non-grooved heating dies was also prepared for comparison, and the blanks used in this set were solution-treated in the whole area as A6061-W.

Distributions of Vickers hardness in the local solution-treated blanks are shown in Fig. 2. In any distribution, maximum value of hardness is about 110 HV 2 at

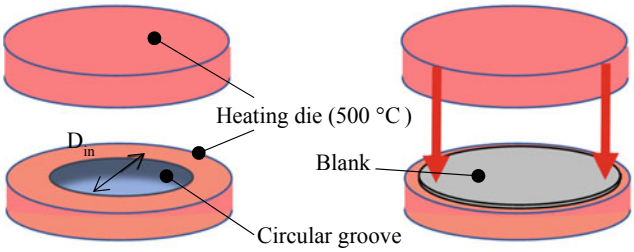


Fig. 1 Schematic diagram of the local solution treatment apparatus. (Color figure online)

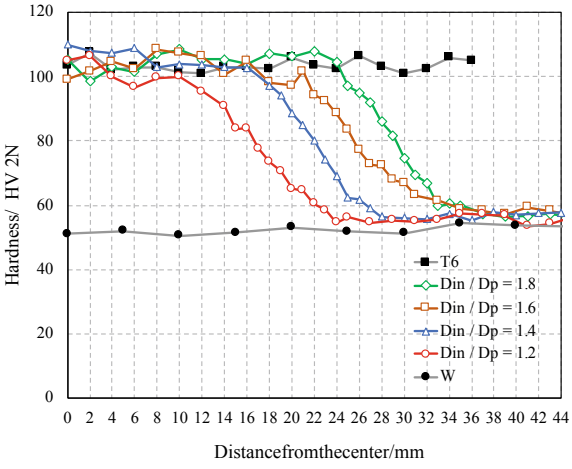


Fig. 2 Hardness distributions of strength graded blanks. (Color figure online)

non-contact area and minimum value of hardness is about 60 HV 2 at contact area. The hardness of the softened part was reduced by over 40%. In addition, a transition region was confirmed around the contact end, where the hardness was continuously reduced by heat conduction from the contact area.

2.3 Forming Test Procedure

2.3.1 Hydro-Mechanical Deep Drawing Process

Our HDD equipment consists of a forming die set, a hydraulic pressure control unit, and a tensile test machine as a driving source. The hydraulic pressure control unit has a relief valve to keep the pressure constant and a hand pump to positively apply hydraulic pressure. Hydraulic pressure increases naturally due to a decrease in the volume of the hydraulic chamber, and extra pressure is added by the pump. Figure 3 shows the hydraulic pressure–punch stroke curve at the condition where holding pressure P_H is 15 MPa and the pressure rise ratio P_H/S_H is 1.0 MPa/mm. Here, S_H is of the holding start stroke. HDD was performed under relatively low blank hold force. Therefore, water leakage was prevented by moving the punch and wrapping the sheet around the die shoulder. Extra pressure is added until 10 MPa which is maximum ability of the pump. In the HDD process, the parameters of the holding pressure P_H and the pressure rise ratio P_H/S_H were controlled.

2.3.2 Hydro-Mechanical Deep Drawing Condition

Cylindrical cups were deeply drawn with tools shown in Table 3. For the drawing test, various strength graded blanks (Hard area ratio D_{in}/D_p is from 1.2 to 1.8) were

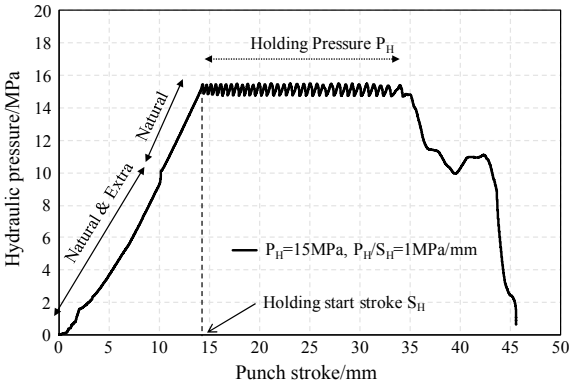


Fig. 3 Hydraulic pressure–punch stroke curve and controlled parameters

Table 3 Dimensions of drawing tools and blanks

Punch	Diameter D_p/mm	33.0
	Profile radius R_p/mm	10.0
Die	Diameter D_d/mm	37.1
	Profile radius R_d/mm	5.0
Blanks	Diameter D_0/mm	ϕ62–85
	Hard area ratio D_{in}/D_p	1.2, 1.4, 1.6, 1.8

used. They were cut into ϕ62 ~ 85 mm circle blanks so that the center of the solution-treated area coincided with the center of the blank. Uniform strength blanks, T6-and W-treated blanks were also drawn as a comparison.

Punch speed of drawing was 6 mm/min. Blank hold forces were 1.3 kN when the blank diameter was less than 66 mm, and 2.4 kN when the blank diameter was more than 68 mm. As a hydraulic condition, the holding pressure P_H was controlled to 4 levels: 5, 10, 15, 20 MPa, and the pressure rise ratio P_H/S_H is controlled to 4 levels: 0.83, 1.0, 1.43, 2.0 MPa/mm. Conventional DD process without hydraulic pressure were also conducted as a comparison.

2.4 Hardness Measurement of Formed Cups

Hardness distribution of cups formed by the DD process and the HDD of the THTB process were measured at a test load of 2.0 N using micro Vickers hardness tester. The cups of THTB were artificially aged at 433 K for 18 h.

3 Results and Discussion

3.1 Effect of the Forming Method

Formability of the DD, the HDD, the THTB, and the HDD of the THTB method are compared in Fig. 4. Figure 5 shows the limit of drawing ratio (LDR) of these forming methods. In the THTB and the HDD of the THTB process, blanks of hard area ratio ($D_{in}/D_p = 1.4$) were used. Common conditions ($P_H = 10$ MPa, $P_H/S_H = 1.0$ MPa/mm) were applied in this HDD process. The formability of A6061-T6 in conventional HDD method is not much improved compared to the DD. However, it was confirmed that the LDR in the HDD of the THTB process was significantly improved by 0.54 compared to the DD.

Figure 6 shows the punch load–stroke curve in the various forming processes of the same blank size. The LDR in the HDD of THTB showed the highest value even though the maximum punch load was higher than the DD and the THTB. This is

	Conventional DD	Conventional HDD	THTB (D_{in}/D_p =1.4)	HDD of THTB (D_{in}/D_p =1.4)
Blank diameter	ϕ62	ϕ64	ϕ74	ϕ80
LDR	1.88	1.94	2.24	2.42
Formed cups				

Fig. 4 Comparison of the forming limit of various forming methods. (Color figure online)

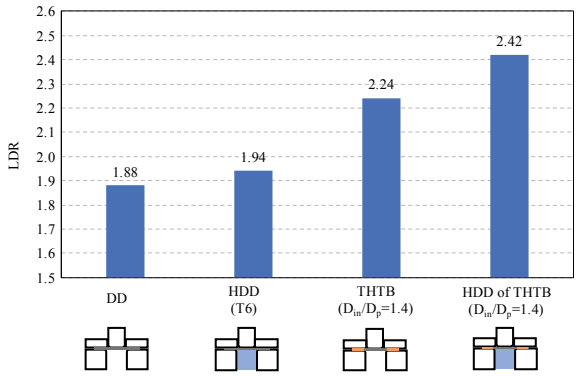


Fig. 5 LDR of various forming methods. (Color figure online)

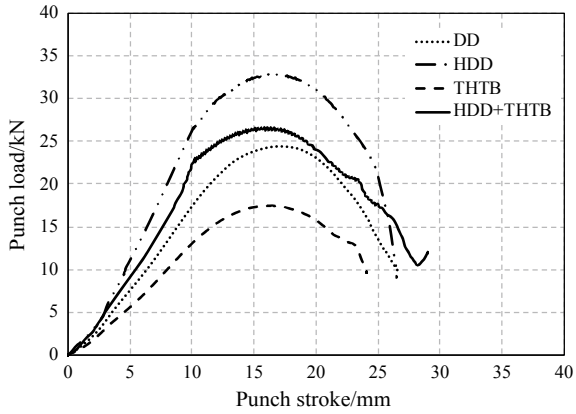


Fig. 6 Punch load–stroke curve in various forming process ($D_0 = \phi 64$)

the reason that the presence of the counter pressure applies a force to the top of the punch. A large maximum load in the HDD does not mean that the deformation resistance of the flange part is large. On the other hand, when results of the HDD and the HDD of THTB were compared, the maximum punch load of the HDD of THTB was lower than the HDD. It is considered that the presence of the softened material reduced the deformation resistance of the flange part.

These results indicate that the HDD of THTB obtained both the counter pressure effect and the periphery softening effect. The former effect reduces the radial stress and friction in the flange area, and the latter one reduces the deformation resistance of the flange part, thereby the formability was greatly improved.

3.2 *Effect of the Local Solution-Treated Region*

The HDD of THTB ($D_{in}/D_p = 1.2, 1.4, 1.6, 1.8$) and the HDD of uniform blanks (T6, W) were conducted to investigate the effect of the locally solution-treated region. Figure 7 shows the LDR of various blanks in the HDD where P_H is 10 MPa and P_H/S_H is 1.0 MPa/mm. It was confirmed that the formability was most improved when THTB ($D_{in}/D_p = 1.4$) was formed by the HDD process, and the LDR was improved by 0.48 compared to the HDD using T6 blanks. However, in the case of narrow softened blank such as THTB ($D_{in}/D_p = 1.8$), the formability is not much improved compared to the DD using T6.

Figure 8 shows the punch load–punch stroke curves for various hard area ratio blanks. As the solution-treated region becomes wider, the punch load decreases, and it is considered that the formability is improved due to the decrease in the deformation resistance of the flange part.

The HDD of the THTB process had two types of fractures as shown in Fig. 9. In the case of hard area ratio of 1.6 and 1.8, fractures occurred at the punch shoulder as the conventional DD or HDD. On the other hand, fractures occurred at the punch side wall in the case of hard area ratio of 1.2 and 1.4. The fracture at the side wall occurred near the boundary between the hard and the softened regions of the blanks.

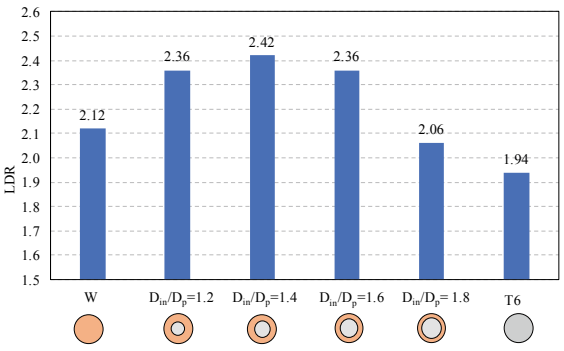


Fig. 7 LDR of various hard area ratio blanks in the HDD ($P_H = 10$ MPa, $P_H/S_H = 1.0$ MPa/mm). (Color figure online)

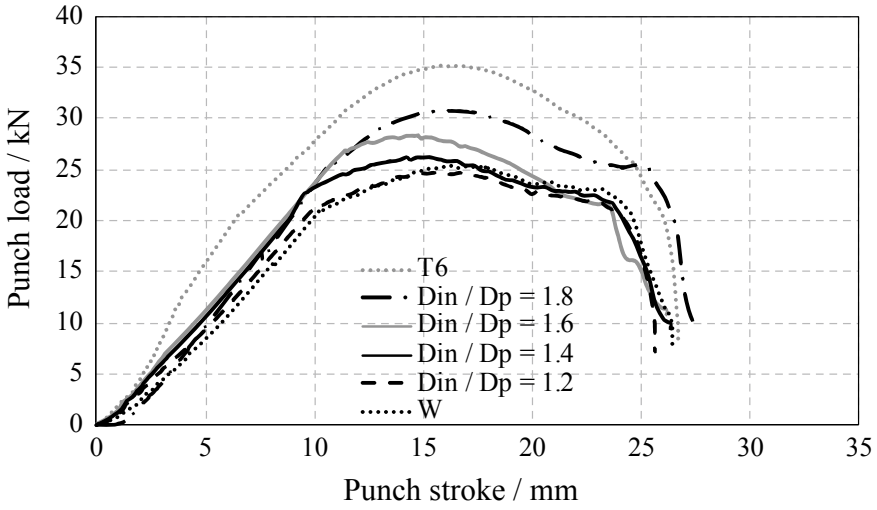


Fig. 8 Punch load–punch stroke curves of the various blanks ($D_0 = \phi 64$)

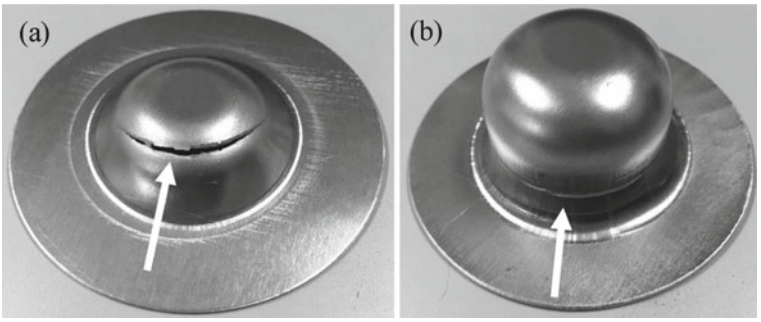


Fig. 9 Two types of fractures **a** fracture at the punch shoulder ($D_{in}/D_p = 1.6$, $D_0 = \phi 80$), **b** fracture at the side wall ($D_{in}/D_p = 1.4$, $D_0 = \phi 82$)

It is considered that the fracture is caused by a decrease in the strength of the wall due to solution treatment. When the softened region is wide, fractures occur at the side wall, and when it is narrow, fractures occur at the punch shoulder. Therefore, the hard area ratio of 1.4, where the softened region is not too wide, was optimal and had the best formability. These two types of fractures occur also in the single THTB process.

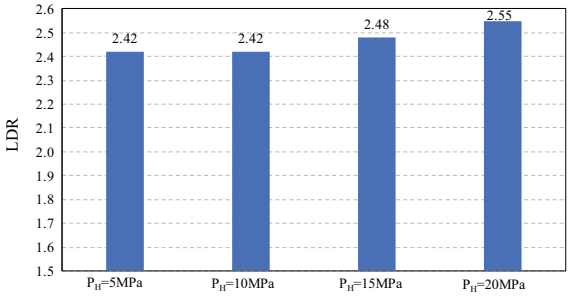


Fig. 10 LDR in various holding pressure of HDD ($P_H/S_H = 1.0$ MPa/mm, $D_{in}/D_p = 1.4$). (Color figure online)

3.3 *Effect of the Holding Pressure*

Figure 10 shows the LDR of the various holding pressure where P_H/S_H is 1.0 MPa/mm and D_{in}/D_p=1.4 in the HDD of the THTB process. The formability was gradually improved by increasing the holding pressure, and it was confirmed that the LDR was improved by 0.13 at 20 MPa compared to 5 MPa. In general, the formability deteriorates when the hydraulic pressure is too high, but no decrease in the LDR was observed at hydraulic pressure up to 20 MPa. The upper limit of LDR was not confirmed.

Although fractures of the THTB ($D_{in}/D_p = 1.4$) occurred at the side wall in low hydraulic pressure, increasing the holding pressure suppressed the side-wall fracture and improved the formability. It is considered that high pressure not only on the punch shoulders, but also on the side walls, activates the friction holding effect, reduces the radial stress, and suppresses fractures.

3.4 *Effect of the Pressure Rise Ratio*

The HDD of THTB tests were performed with the pressure rise rate controlled at 0.83 to 2.0 MPa/mm to investigate the effect on formability. Figure 11 shows the LDR at various pressure rise ratios where P_H is 15 MPa and the hard area ratio of THTB is 1.6. As the pressure rise ratio increased, the LDR gradually improved. It was confirmed that the LDR was improved by 0.12 at 2.0 MPa/mm compared to 0.83 MPa/mm. On the other hand, the pressure rise ratio had no effect on the LDR of the THTB ($D_{in}/D_p = 1.4$).

Holding start stroke S_H depends on pressure rise ratio, and high pressure rise ratio means that S_H is small. The friction holding effect is activated in the early stage of the HDD process and suppresses the deformation of sheets at the punch shoulder. Therefore, it is considered that the LDR was improved at the hard region ratio of 1.6, which reached the forming limit due to the punch shoulder fracture. On the other hand, the pressure rise ratio is independent of the pressure in the middle stage of the

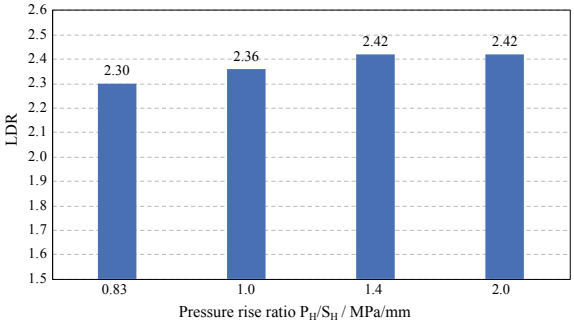


Fig. 11 LDR at various pressure rise ratios of HDD (P_H 15 MPa, $D_{in}/D_p = 1.6$). (Color figure online)

HDD and does not affect the side-wall fracture which occurs in the middle stage. Therefore, the LDR of the THTB ($D_{in}/D_p = 1.4$) was not improved.

3.5 *Hardness Distribution of Formed Cups*

Figure 12 shows the hardness distribution of the formed cups of T6 and the THTB. The hardness of formed cups increased due to strain hardening. Although the initial hardness of the softened periphery region of the blank was low, the hardness after forming increased to 100 HV 2 as well as the original hardness of T6 blank.

The hardness distribution after artificially aging is also shown in Fig. 12. Hardness of softened region and transfer region had increased.

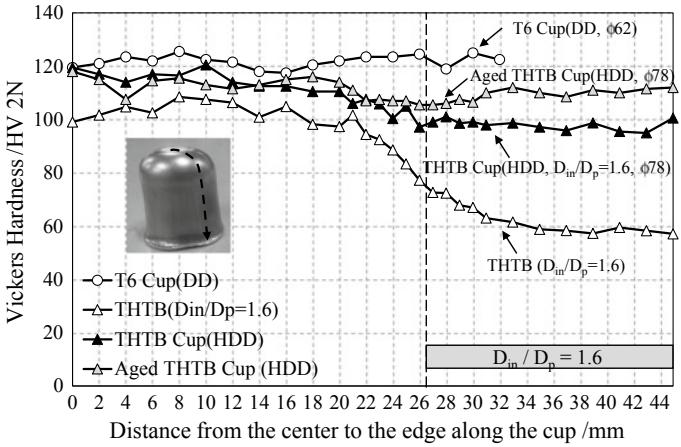


Fig. 12 The hardness distribution of formed cups

4 Conclusions

Combination of the HDD and the THTB methods for 6061-T6 alloy sheets was conducted and improved the LDR compared to a single method. Formability of various hard area ratios of THTB were investigated, and the optimal softened region was found. Fractures occurred at the punch shoulder when the hard region is large, and side-wall fractures occurred when the softened region is large. In addition, it was confirmed that high holding pressure suppressed the wall failure and high pressure rise ration prevented the early fracture at the punch shoulder.

Acknowledgments This work was supported by the AMADA Foundation for metal work technology. This support is gratefully acknowledged.

References

1. Tozawa Y (1960) Japanese title. J Jpn Soc Technol Plast 1(1):23–28
2. Fujioka T, Sugamata M, Kaneko J (1986) Improvement in deep drawability of aluminum and copper alloy sheets by local aging treatment. J Jpn Soc Technol Plast 27(311):1363–1368
3. Bate PS, Schofield H, Barrett DJ (1998) Increasing the drawability of AA2014 Al-Cu by differential heat treatment. Metall Mater Trans A 29A:1405–1414
4. Nishiwaki T, Kanetake N (2004) Partial softening heat treatment of aluminum alloy sheets using the heat transfer between metals. J JILM 54(10):425–429
5. Vollertsen F, Lange K (1998) Enhancement of drawability by local heat treatment. CIRP Ann 47(1):181–184
6. Hofmann A (2001) Deep drawing of process optimized blanks. J Mater Process Technol 119:127–132
7. Nakamura K, Nakamura M, Takahashi A, Yoshioka S (2003) Annealing behavior of local zones of a 1070–H26 aluminum sheet by CO_2 laser irradiation. J. JILM 53(10):421–426
8. Geiger M, Merklein M, Vogt U (2009) Aluminium tailored heat treated blanks. Prod Eng 3:401–410
9. Merklein M, Herrmann J (2016) Effect of a local laser heat treatment on the formability of multi-layered 6000 series aluminum alloys. Phys Proc 83:560–567
10. Piccininni A, Michele GD, Palumbo G, Sorgente D, Tricarico L (2015) Improving the hydromechanical deep-drawing process using aluminum tailored heat treated blanks. Acta Metall Sin (Engl Lett) 28(12):1482–1489

Development of Adhesion Preventing Method During Deep Drawing of Titanium Alloy Sheets



Yusuke Okude, Taku Iwaoka, and Isao Nakamura

Abstract It is necessary to prevent the surface oxide film peeling caused by sliding between workpiece and die material with high surface pressure for reducing punch load and preventing fracture. Hence, we have focused on the method to prevent the titanium surface oxide film peeling during press forming to prevent the adhesion. The workpieces with surface oxide film by atmospheric oxidation were utilized to demonstrate the effect of titanium surface oxide film on formability in deep drawing process. Additionally, the method to prevent adhesion during deep drawing process was developed. In this study, the compressed air was applied to the die and the blank holder force (BHF) with vibration technique was utilized during circular-cup deep-drawing of TP340 sheets. As a result, the occurrence of adhesion was prevented significantly by the application of developed methods.

Keywords Sheet metal working · Deep drawing process · TP340 titanium sheets · Adhesion preventing method

1 Introduction

In recent years, pure titanium has utilized various areas, for example, medical devices and aerospace fields [1]. However, the adhesion easily occurs during press forming. By the occurrence of adhesion, punch load increased and fracture occurs during deep drawing process of pure titanium sheet. So, it is necessary to develop the adhesion preventing method in dry press processing for the global environment. To prevent the adhesion during dry press processing, diamond-like carbon (DLC)-coated die was utilized, but it is difficult to prevent adhesion by using only DLC-coated die. Hence, DLC-coated die and lubrication were applied and 600 times deep drawing process without adhesion were achieved [2]. On the other hand, the ultrasonic vibration was applied to the die during deep drawing process to prevent the adhesion, but it is difficult to prevent the adhesion only by the application of the ultrasonic vibration

Y. Okude (✉) · T. Iwaoka · I. Nakamura
2-4-10, Aomi, Koto-ku, Tokyo, Japan
e-mail: okude.yusuke@iri-tokyo.jp

© The Minerals, Metals & Materials Society 2021

G. Daehn et al. (eds.), *Forming the Future*, The Minerals, Metals & Materials Series,
https://doi.org/10.1007/978-3-030-75381-8_227

[3, 4]. Then, the development of adhesion preventing method for titanium alloy sheets in deep drawing process is necessary. Adhesion occurs easily because the clean metal surface comes in contact with the die due to the peeling off of the oxide film due to the high surface pressure state during deep drawing processing. Therefore, to reduce the adhesion during deep drawing process the TP340 pure titanium with oxide film was utilized [5, 6]. And the effect of the processing conditions on the oxide film was investigated. In this study, the compressed air was applied to the die and the blank holder force (BHF) with vibration technique was utilized during circular-cup deep drawing of TP340 sheets for the reducing of frictional heat and contact between die and blank. As a result, the occurrence of adhesion was prevented significantly by the application of developed methods.

2 Low-Frequency Vibration Applied Crease Suppression-Assisted Cylinder Deep Drawing Test Condition Setting and Adhesion Suppression Method

As the workpiece of experiment, TP340 pure titanium sheet, thickness $t_0 = 0.5$ mm, diameter $\phi = 19.5, 19.95$ mm (Drawing ratio, $DR = 2.0, 2.1$) was utilized. We have focused on the method to prevent the titanium surface oxide film from peeling during press forming to prevent adhesion. Hence, the oxide film was formed on the blank surface by using atmospheric oxidation before deep drawing process. Atmospheric oxidation was maintained for 2 hours at 500 and 600°C using muffle furnace. Figure 1 shows the schematic of experimental apparatus of the cylindrical deep drawing process. Table 1 indicates the dimensions of dies and SKD11 material for die. BHF was loaded in the range of 120–580 N, and the frequency was 0–8 Hz by servo motor control. Punch speed conditions of 1.2, 12, and 120 mm/min were applied. Compressed air was applied in the range of 0–0.8 MPa. After the deep drawing, the die was observed in order to confirm the effect of the peeling of the oxide film on the surface on the adhesion. Figure 2 shows the method of adhesion measurement on die and measurement sample of adhesion after deep drawing of pure titanium sheet. For observation, digital microscope was utilized and adhesion amount was measured at the die shoulder where the most adhesion occurs after deep drawing of TP340 with oxide film.

3 Formability in Cylindrical Deep Drawing of Oxide-Coated TP340 Pure Titanium Sheet

Figure 3 shows the effect of conditions on the peeling of surface oxide film at 500 °C. At the punch speed of 1.2 mm/min, the maximum punch load decreased about 12% compared to 120 mm/min. But the surface oxide film peeling occurs in all punch

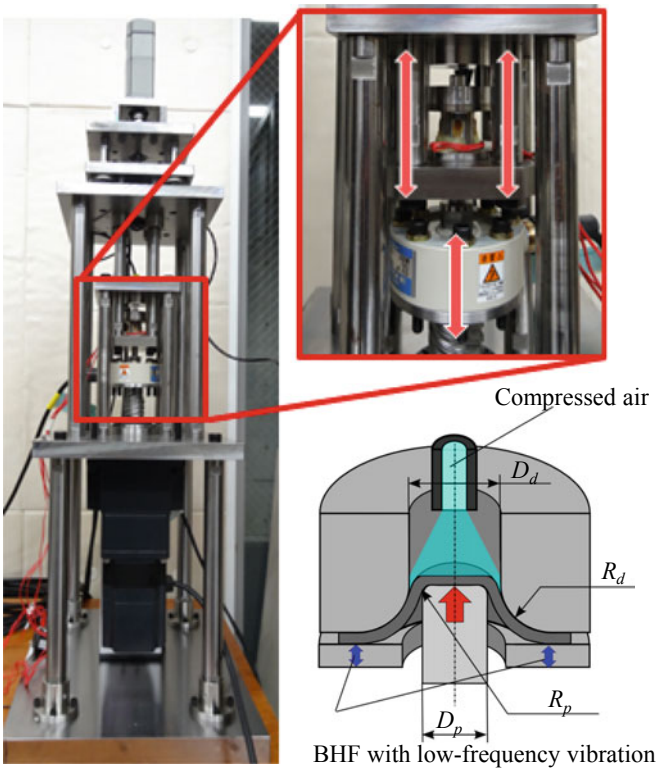


Fig. 1 Experimental apparatus and schematic of deep drawing process with preventing method of adhesion. (Color figure online)

Table 1 Dimension of dies of deep drawing process

Die	Diameter: D_d/mm	11.0
	Shoulder radius: R_d/mm	2.0, 2.5
Punch	Diameter: D_p/mm	9.5
	Shoulder radius: R_p/mm	1.5, 2.0

speed conditions. Figure 4 shows the effect of conditions on peeling of surface oxide film at 600 °C. The maximum punch load of punch speed 1.2 mm/min decreased 6.7% in comparison with 120 mm/min. However, the surface film peeling occurs at the conditions of 1.2 mm/min punch speed as shown in Fig. 4. In the deep drawing of TP340 alloy sheets at held 600 °C, peeling of the surface oxide film was prevented in the conditions of 12 and 120 mm/min. Figure 5 shows the photographs of die and maximum adhesion area after deep drawing of TP340 sheets with oxide film (600 °C). As increasing punch speed, the adhesion of die decreased as shown in the photograph. Hence, the adhesion occurrence was affected by punch speed.

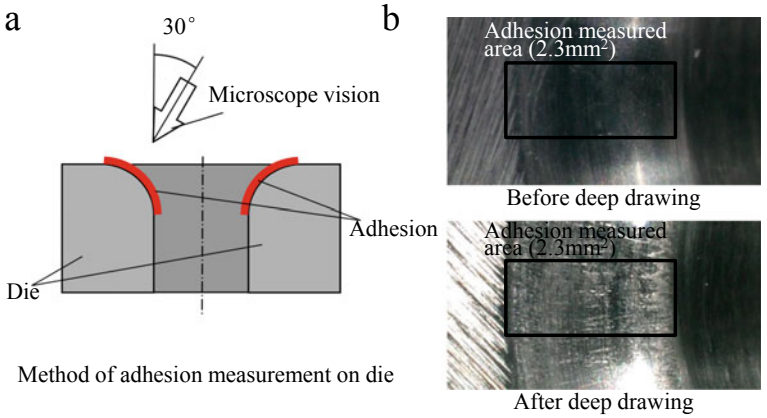
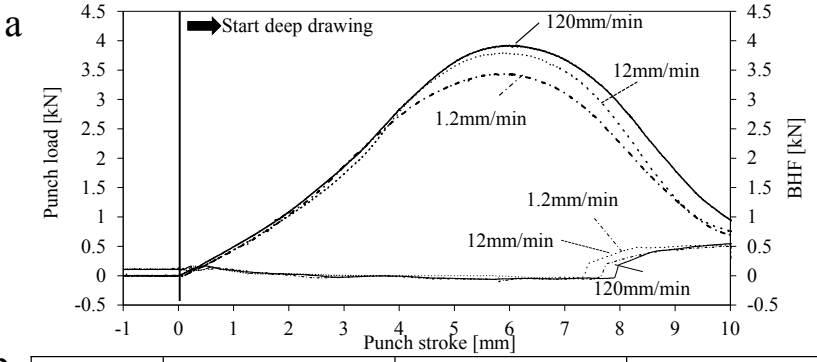


Fig. 2 Method of adhesion measurement on die and measurement sample of adhesion. (Color figure online)



b

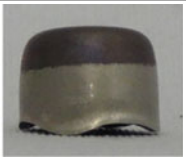
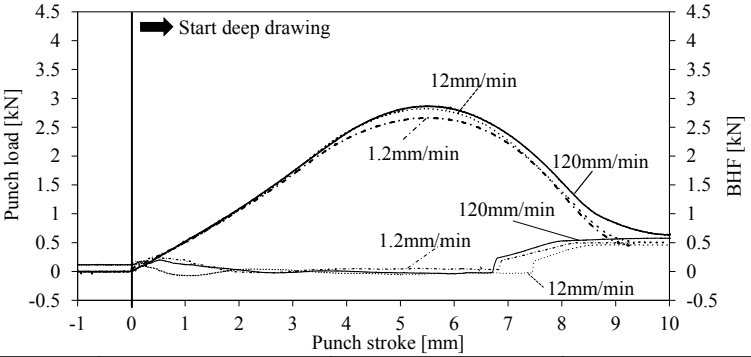
Condition	Punch Speed =1.2mm/min	12mm/min	120mm/min
Photograph of drawn cup			
Max. punch load [kN]	3.47	3.80	3.92

Fig. 3 Effect of conditions on peeling of surface oxide film(500 °C), **a** punch load–punch stroke curve, **b** photograph of drawn cup. (Color figure online)

a



b

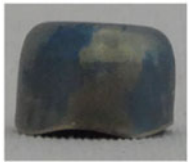
Condition	Punch Speed =1.2mm/min	12mm/min	120mm/min
Photograph of drawn cup			
Max. punch load [kN]	2.68	2.84	2.87

Fig. 4 Effect of conditions on peeling of surface oxide film(600 °C), **a** punch load–punch stroke curve, **b** photograph of drawn cup. (Color figure online)

a b c



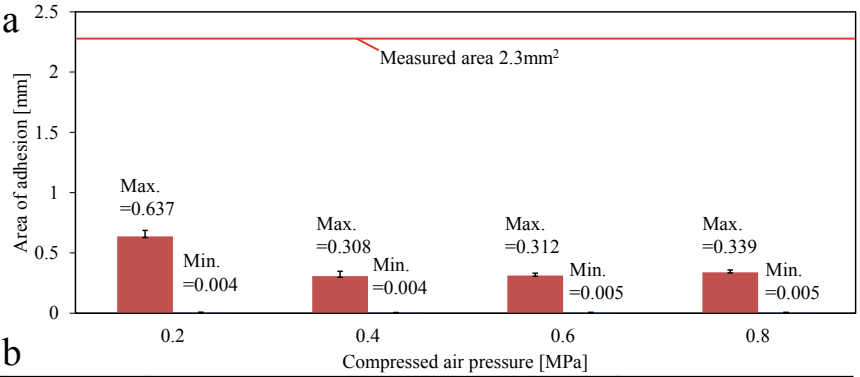
Fig. 5 Photographs of die and maximum adhesion area after deep drawing of TP340 sheets with oxide film (600 °C), **a** punch speed = 1.2 mm/min, **b** 12 mm/min, **c** 120 mm/min. (Color figure online)

4 Development of Preventing Adhesion Method in Deep Drawing Processing

In this study, the compressed air was applied to die and BHF with vibration technique was utilized during deep drawing of TP340 sheets. First of all, to clarify the effect of compressed air on preventing oxide surface film peeling, the deep drawing test with compressed air was carried out for blanks held at 500 °C. Figure 6 indicates the effect of compressed air pressure on peeling of surface oxide film and adhesion on die at TP340 with oxide film at 500 °C. In the 0.4 MPa of compressed air pressure, the measured area of maximum adhesion was 0.308 mm^2 and area minimum adhesion 0.004 mm^2. On the other hand, from a value of 0.4 MPa, the maximum punch load, adhesion of die, and surface film peeling increased as the compressed air increase. From these results, it is considered that a value more than 0.4 MPa has exerted the effect of pressing the workpiece for the punch direction, and thus increased the punch load and increased adhesion. So, 0.4 MPa is a suitable condition of compressed air pressur for decreasing the peeling of surface oxide film and adhesion on die for the reducing of frictional heat during deep drawing process in this experiment.

The low-frequency vibration is applied to the BHF as follows:

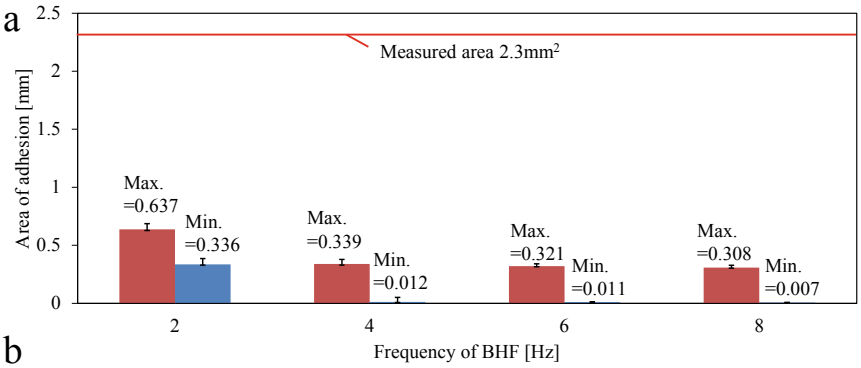
a



b

Condition	0.2MPa	0.4MPa	0.8MPa
Photograph of drawn cup			
Max. punch load [kN]	3.16	3.12	3.21

Fig. 6 Effect of compressed air pressure on peeling of surface oxide film and adhesion on die (500 °C), **a** comparison of max. and min. adhesion area on die, **b** photographs of drawn cup samples. (Color figure online)



b

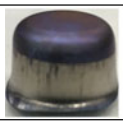
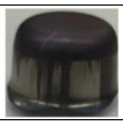
Condition	2Hz	4Hz	8Hz
Photograph of drawn cup			
Max. punch load [kN]	3.76	3.28	3.08

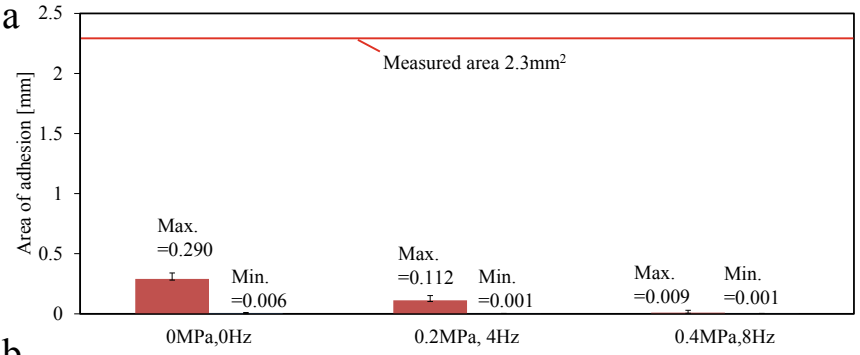
Fig. 7 Effect of frequency of BHF with low-frequency vibration on peeling of surface oxide film and adhesion on die (500 °C), **a** comparison of max. and min. adhesion areas on die, **b** photographs of drawn cup samples. (Color figure online)

$$BHF = A\cos\left(2\pi t\frac{1}{T}\right) = A\cos(2\pi tf) \tag{1}$$

where A is the amplitude of BHF(A is selected from the range of 120 to 580 N), T is the period, t is the time during deep drawing process, and f is the frequency calculated by $1/T$. Hence, in the case of BHF without low-frequency vibration, BHF indicates the value of A. Figure 7 indicates the effect of low-frequency vibration on the peeling of surface oxide film and adhesion on die at TP340 with oxide film at 500 °C. As the frequency of BHF is increased with low-frequency vibration, the area of maximum and minimum adhesions decreased. Because, in the case of frequency less than or equal to 4 Hz, it is considered the surface oxide film peeling occurred by the effect of striking surface oxide film by the die vibration. For frequency of 8 Hz, the effect of reducing of contact time between die and blank has appeared. Hence, the suitable value of frequency BHF with low-frequency vibration prevents the delamination of surface oxide film.

Figure 8 indicates the effect of compressed air and BHF with low-frequency vibration on peeling of surface oxide film and adhesion on die at TP340 with oxide film at 600 °C. By the application of a combination of compressed air and BHF with low-frequency vibration, the surface film peeling and adhesion on die was decrease dramatically as shown in Fig. 8. As the result, the surface film peeling was prevented completely and the area of minimum adhesion decreased to the value 0.009 mm^2 in the compressed air pressure 0.4 MPa and BHF with 8 Hz low-frequency vibration.

a



b

Condition	0MPa,0Hz	0.2MPa, 4Hz	0.4MPa,8Hz
Photograph of drawn cup			
Max. punch load [kN]	3.76	3.42	3.08

Fig. 8 Effect of compressed air and BHF with low-frequency vibration on peeling of surface oxide film and adhesion on die (600 °C), **a** comparison of max. and min. adhesion areas on die, **b** photographs of drawn cup samples. (Color figure online)

5 Conclusion

(1) In the deep drawing process of TP340 sheets with oxide film (600°C), the adhesion of die decreases as increasing punch speed. Hence, the surface film peeling was affected by the punch speed on each thickness of oxide film.

(2) By the application of compressed air pressure during deep drawing process, the surface oxide film peeling of TP340 was decreased. And the measured area of maximum adhesion was 0.308mm^2 and area minimum adhesion 0.004mm^2 in the 0.4 MPa of compressed air pressure.

(3) By the application of BHF with low-frequency vibration during deep drawing process, the surface oxide film peeling of TP340 was decreased. As the frequency of BHF is increased with low-frequency vibration, the area of maximum and minimum adhesions is decreased in the range of 2–8 Hz.

(4) By the application of a combination of compressed air pressure and BHF with low-frequency vibration during deep drawing process, the adhesion of die decreased exponentially. The surface film peeling was prevented completely and the area of minimum adhesion decreased to the value 0.009 mm^2 per measured area 2.3/mm^2 in the compressed air pressure 0.4 MPa and BHF with 8 Hz low-frequency vibration. As a result, the preventing of adhesion was

achieved by the application of a combination of compressed air pressure and BHF with low-frequency vibration without coating dies and lubrication.

Acknowledgments This work was supported by JSPS KAKENHI Grant Number 16K14442.

References

1. Suzuki N, Sano T (2011) J Jpn Soc Technol Plast 52–604:579–583
2. Maeno T, Mori K, Yamashita Y, Nakayama M, Hamedon Z (2011) Proceedings of 2011 Japanese spring conference for the technology of plasticity, pp 345–346
3. Maeno T, Tomobe M, Mori K, Ikeda Y (2018) Proc Manuf 15:1149–1155
4. Suzuki N, Sano T (2010) Proceedings of 16th Japanese spring conference for the technology of plasticity, pp 115–116
5. Okude Y, Iwaoka T, Nakamura I (2018) Proceedings of 69th Japanese spring conference for the technology of plasticity, pp 107–108
6. Okude Y, Iwaoka T, Nakamura I (2018) Proceedings of 135th conference of Japan institute of light metals, pp 335–336

Development of Warm Press Forming Process Method of Ti–6Al–4 V Alloy Sheet



Yusuke Okude, Taku Iwaoka, Isao Nakamura, and Takashi Katagiri

Abstract Because of the low ductility of Ti–6Al–4V alloy at the temperatures between room temperature and 600 °C, fracture easily occurs during press forming. Hence, a method of press forming of Ti–6Al–4V alloy sheets at 300 °C was developed. In this method, the punch motion and blank holding force were applied separately to prevent fracture at the punch radius until the maximum punch load was reached, and the deep drawing process was demonstrated from the maximum punch load until finish forming to prevent the fracture at end of the flange. In addition, by applying the developed method, we were able to prevent the decrease in wall thickness at the punch shoulder, compared with that in press forming. As a result, warm press forming of Ti–6Al–4V alloy sheets at 300 °C was achieved without fracture of the formed cup or local decrease in the wall thickness by applying the developed method.

Keywords Sheet metal working · Warm forming · Ti–6Al–4V alloy · Incremental press forming · Deep drawing process

1 Introduction

Ti–6Al–4V titanium alloy has been actively used in medical equipment and aerospace due to its characteristics of light weight, corrosion resistance, and high specific strength [1]. In general, Ti–6Al–4V alloy sheets are formed by incremental press forming in the temperature range between 600 and 900 °C [2–4]. In this temperature range, the ductility of Ti–6Al–4V alloy is improved, and it has been applied as hot stamping of titanium alloys for aircraft parts in the temperature range of 800–900 °C [5]. Due to the principle of electric heating, the blank material is limited to a rectangular shape. In addition, for high-strength materials with poor formability, continuous resistance heating has been applied to bar rolling, and bar forming of Ti–6Al–4V alloy has been successfully performed with a reduced fracture [6]. Because

Y. Okude (✉) · T. Iwaoka · I. Nakamura · T. Katagiri
2-4-10, Aomi, Koto-ku, Tokyo, Japan
e-mail: okude.yusuke@iri-tokyo.jp

© The Minerals, Metals & Materials Society 2021

G. Daehn et al. (eds.), *Forming the Future*, The Minerals, Metals & Materials Series,
https://doi.org/10.1007/978-3-030-75381-8_228

of the low ductility of Ti–6Al–4V alloy at the temperatures between room temperature and 600 °C, fracture easily occurs during press forming. Hence, a method of press forming of Ti–6Al–4V alloy sheets at 300 °C was developed. In this method, the punch motion and blank holding force were applied separately to prevent fracture at the punch radius until the maximum punch load was reached. As the result, warm press forming of Ti–6Al–4V alloy sheets at 300 °C was achieved without fracture of the formed cup or local decrease in the wall thickness by applying the developed method.

2 Experimental Apparatus and Formability of Ti–6Al–4 V Alloy Sheet at Warm Temperature of Deep Drawing Test

In order to understand the basic formability of circular-cup deep drawing of Ti–6Al–4V alloy sheet, circular-cup deep drawing with a general blank holding force (BHF) was first performed. Figure 1 shows a schematic of deep drawing process, and Table 1 the dimensions of the dies of deep drawing process. The die material used was SKH51. Ti–6Al–4V alloy plate and a blank with a thickness of $t_0 = 0.5$ mm were

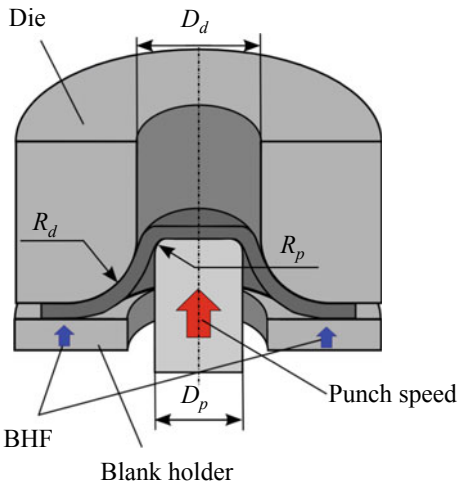


Fig. 1 Schematic of deep drawing process

Table 1 Dimension of dies of deep drawing process

Die	Diameter: D_d/mm	35.0
	Shoulder radius: R_d/mm	3.0
Punch	Diameter: D_p/mm	32.5
	Shoulder radius: R_p/mm	5.0

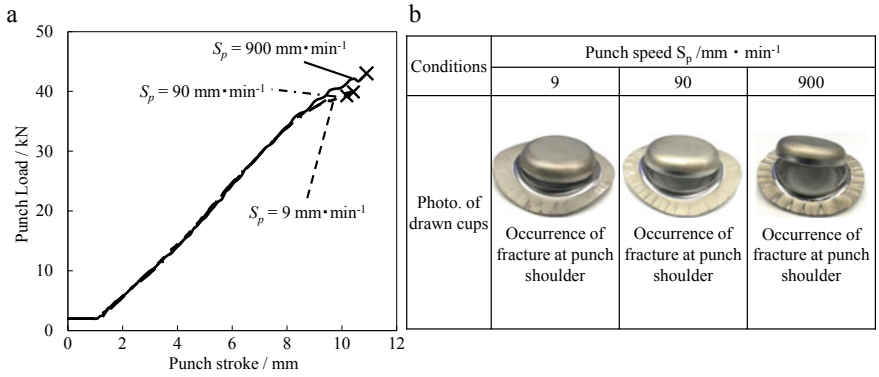


Fig. 2 Effects of punch speed on deformation behavior of Ti–6Al–4V alloy sheet at 300 °C, **a** Punch load–punch stroke curve, **b** Photographs of cups drawn under each set of conditions. (Color figure online)

used as test materials. The test was performed with a blank diameter of $\phi = 60$ mm (Drawing ratio, $DR = 1.85$).

Circular-cup deep drawing was carried out at the condition of 300 °C forming temperature. Test was performed at the same temperature as the blank for the drawing die and the blank holder. The punch was kept at room temperature under all conditions. The punch speed S_p was set to three conditions of 9, 90, and 900 mm/min, and the constant blank holding force BHF_{const} was applied at 4 kN. Figure 2 shows the punch load–punch stroke curve and photographs of cups drawn under each set of conditions. In each condition, fracture occurred at punch shoulder. Therefore, the low formability of Ti–6Al–4V alloy sheet was confirmed.

3 Incremental Press Forming Method and Formability of Ti–6Al–4V Alloy Sheet

In circular-cup deep drawing with constant blank holding force, fracture occurred at the punch shoulder at any punch speed at a forming temperature of 300 °C. In this study, we focused on the fact that in normal cylindrical drawing, wall thinning progressed due to tension due to blank holding force from the start of the punch until the maximum punch load was reached. When the material is pressed into the die with a punch under the condition of applying wrinkle suppressing force, the thickness of the punch shoulder is significantly reduced. Therefore, in order to perform press forming in the incremental forming developed in this study, two processes were separated: a punch motion process and BHF without blank holding force process. Figure 3 shows the schematic of incremental press forming. FORMKOTE T-50 was applied as a lubricant between the blank and the mold. In the incremental forming, press forming was performed under the conditions of $S_{pi} = 9$ mm/min, $P_{si} = 0.2$ mm, and $BHF_i =$

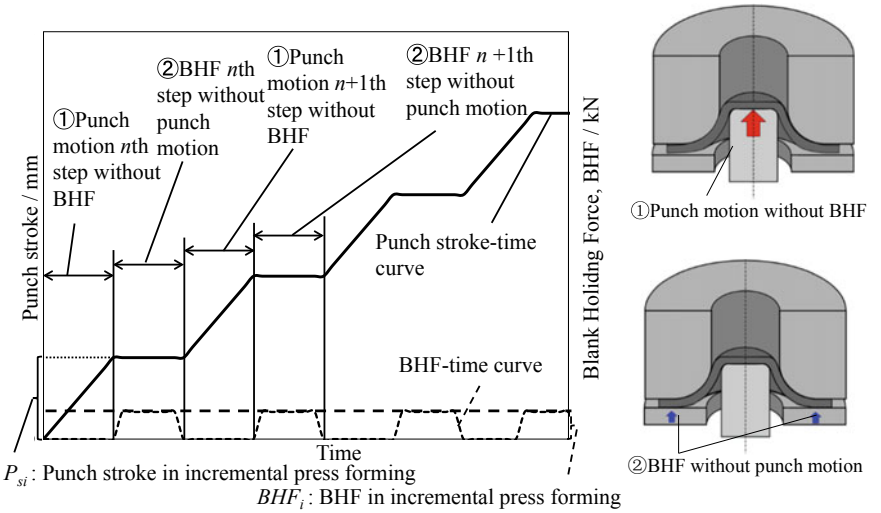


Fig. 3 Schematic of incremental press forming. (Color figure online)

20kN. For comparison, the circular-cup deep drawing was carried out under the same lubricating conditions with a punch speed of 9 mm/min and a blank holding force of 4 kN. Figure 4 shows the effect of incremental forming on formability. However, the fracture occurred at the flange as shown in the figure caused by the compressive deformation of the flange. In addition, the effect of punch feed on the formability was investigated by forming under three conditions of $P_{si} = 0.2$, 0.4, and 0.8 mm,

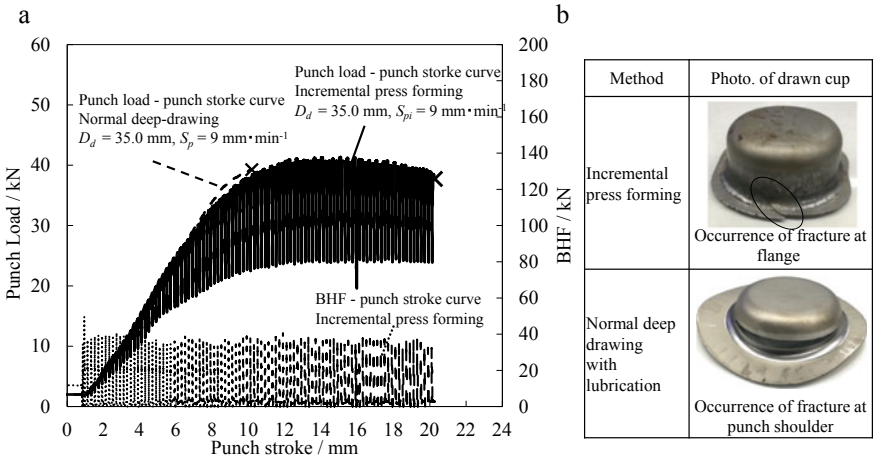


Fig. 4 Effect of incremental forming on deformation behavior at 300 °C, **a** Punch load–punch stroke curve, **b** Photographs of cups drawn under each set of conditions. (Color figure online)

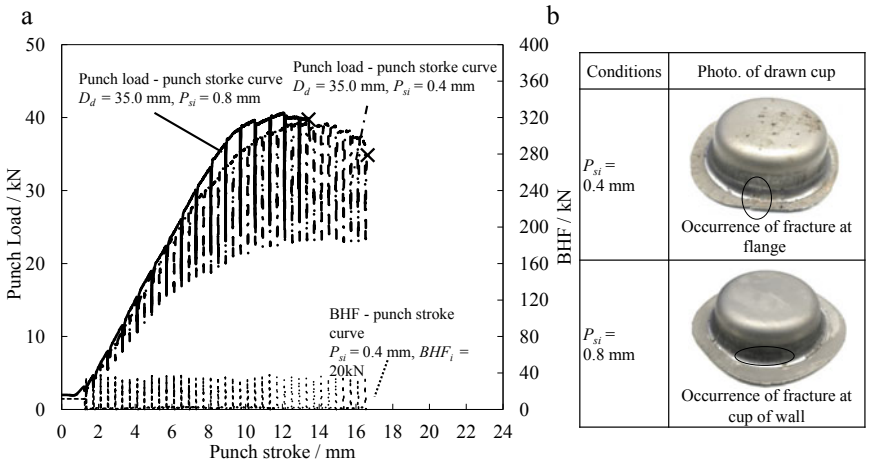


Fig. 5 Effect of punch stroke on deformation behavior during incremental forming at 300 °C, **a** Punch load-punch stroke curve, **b** Photographs of cups drawn under each set of conditions. (Color figure online)

with the punch speed fixed at the condition of $S_{pi} = 9$ mm/min. As in the case of the punch speed, the formability was different depending on the feed amount of the punch. Figure 5 shows the effect of punch feed on formability. As the punch feed increased, the formability decreased, and at a feed of 0.8 mm, the cup wall fractured. The amount of blank flowing into the die increased, as the amount of punch feed increased.

4 Development of Warm Press Forming Process Method for Ti–6Al–4V Alloy Sheet

From the experimental results of incremental press forming, it was difficult to prevent fracture caused by shearing force at the flange, or breaking at the cup wall. For this reason, we developed the method of forming vertical fracture without irregular deformation by combining incremental forming and drawing forming, based on the prediction that fracture by shearing force at the flange is caused by compressive force on the flange part. Concretely, in order to form the cup head where the thin wall progresses especially at the shoulder of the punch, the molding is performed incrementally in the initial stage to the middle stage. In addition, when the blank flows into the mold to form the cup wall, significant compression deformation is applied to the flange part. In the middle to late stages, drawing is performed to reduce the compression deformation. Figure 6 shows the schematic of developed press forming method. In this method, the punch load increment dL for each punch stroke P_{si} was

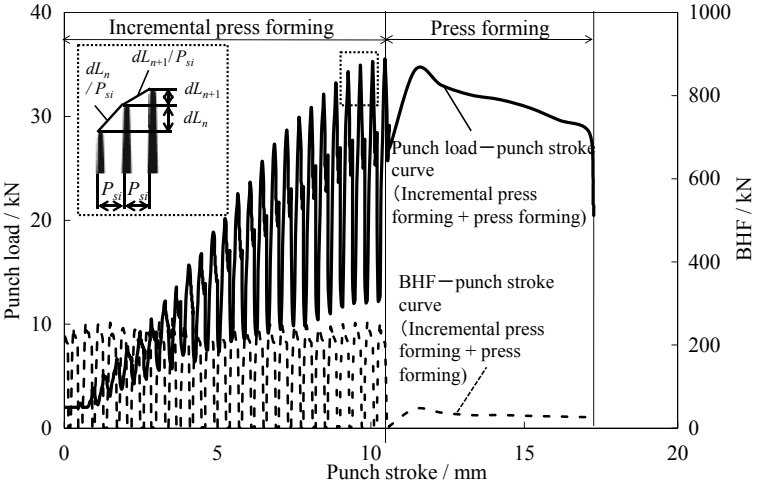


Fig. 6 Schematic of developed press forming method

calculated during incremental forming, and after the value of dL/P_{si} reached 0.2 or less, the process was shifted to drawing.

To achieve press forming of Ti–6Al–4V alloy sheet at 300 °C. $S_{pi} = 9$ mm/min, $P_{si} = 0.2$ mm, $BHF_i = 200$kN in the incremental forming process using FORMKOTE T-50 as the lubrication condition, and $S_{pi} = 900$ mm/min and $BHF = 20$kN in the draw forming. Figure 7 shows the effect of developed forming method on deformation behavior at 300 °C. By application of developed forming method, the press forming

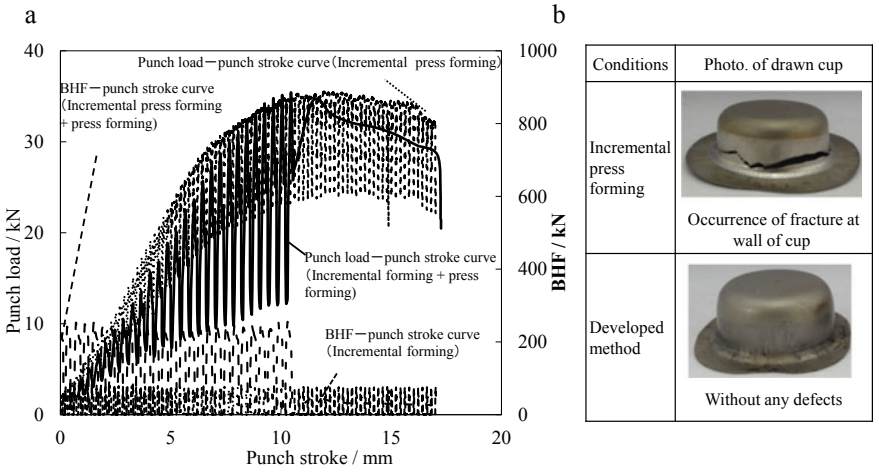


Fig. 7 Effect of developed forming method on deformation behavior at 300 °C, **a** Punch load–punch stroke curve, **b** Photographs of cups drawn under each set of conditions. (Color figure online)

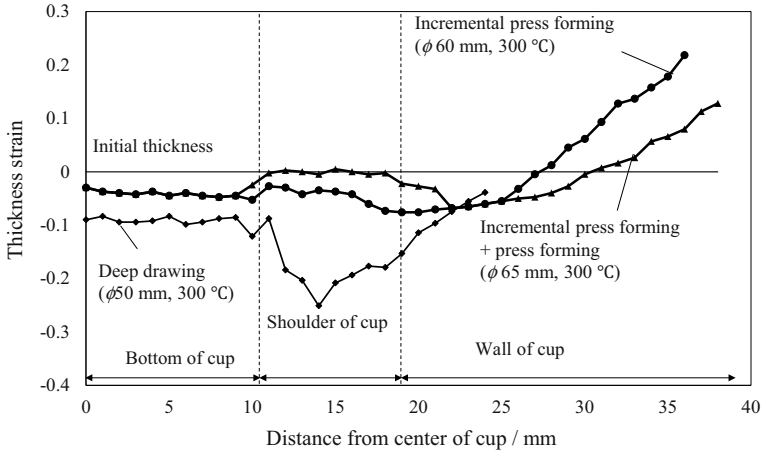


Fig. 8 Effect of developed forming method on thickness strain of drawn cup

of Ti–6Al–4V alloy sheet in the conditions of $DR = 2.0$ at the forming temperature of 300 °C was achieved without fracture and Fig. 8 shows the effect of the forming method on the wall thickness distribution.

5 Conclusion

(1) By applying incremental forming, it was possible to form the Ti–6Al–4V titanium alloy without cracking after reaching the maximum punch load at 300° C, compared to drawing, but drawing was possible. Shortly, before the end of die, fracture caused by shearing force occurred in the flange.

(2) By developing the method of combination of incremental forming and draw forming to prevent the fracture caused by shearing force at the flange part, and the press forming at the condition of $DR = 2.0$ of Ti–6Al–4V alloy was achieved.

(3) With the developed incremental forming and drawing methods, the reduction of the wall thickness distribution was suppressed compared to the constant blank forming force, and the result was that the entire forming cup had a uniform wall thickness.

References

1. Beal DJ, Boyer R, Sanders D (2006) ASM handbook, 14B, metalworking: sheet forming, pp 656–669
2. Maeno T, Mori K, Hamedon Z (2012) Proceedings of manufacturing 14th international conference on metal forming, pp 287–290
3. Maeno T, Mori K, Yamashita Y, Nakayama M, Hamedon Z (2011) Proceedings of 2011 Japanese spring conference for the technology of plasticity, pp 345–346
4. Maeno T, Mori K, Yamashita Y (2012) Proceedings of 2012 Japanese spring conference for the technology of plasticity, pp 67–68
5. Yamazaki K, Yamaguchi T, Murayama Y, Mori K, Maeno T (2014) J Jpn Soc Technol Plast 55–647:1097–1101
6. Yanagimoto J, Izumi R (2009) J Mater Process Technol 209:3060–3068

Research on New Hot Stamping Tool with Low-Cost and High-Efficiency Cooling



Shixin Peng, Jie Zhou, Mengmeng Zhang, Kemin Zhang, and Jie Liu

Abstract Hot stamping technology is widely used to produce car body components with more complex shape, higher strength, and less springback. A pair of optimal hot stamping tool should have a long service life, low manufacturing cost, and good cooling performance simultaneously. Consequently, a new manufacturing method of hot stamping tool with CCC (conformal cooling channels) is introduced in this study. Besides, CuCrZr and Fe-based alloy were welded on the specimens as intermediate layer and surface layer respectively, high-temperature compressive yield strength, the heat conductivity, and thermal expansion coefficient of welding materials were measured. The whole stamping process of the new hot stamping tool is simulated and discussed. The simulation results indicate the maximum stress in each area of the new tool was less than the yield strength of the corresponding welding materials, which demonstrated that the new tool manufactured by surfacing technology could meet the strength requirement and deserve further research.

Keywords Hot stamping tool · Surfacing technology · Surface layer · Intermediate layer · Numerical simulation

1 Introduction

To meet the dual requirement of automotive lightweight and safety improvement, the hot stamping technology of ultra-high-strength steel is widely applied in the automotive industry [1–3]. Hot stamping tools play a key role in the whole stamping process [4]. A set of satisfied hot stamping tools should have three characteristics with long service life and low manufacturing cost and excellent cooling performance simultaneously. However, traditional hot stamping tools with straight holes were integrally manufactured by homogeneous tool materials with high cost, and the partial tool failure would lead to a whole scrap or difficult repair [5–7].

S. Peng (✉) · J. Zhou · M. Zhang · K. Zhang · J. Liu
School of Materials Science and Engineering, Chongqing University, Chongqing 400044, China
e-mail: pengshixing1234@163.com

© The Minerals, Metals & Materials Society 2021

G. Daehn et al. (eds.), *Forming the Future*, The Minerals, Metals & Materials Series,
https://doi.org/10.1007/978-3-030-75381-8_229

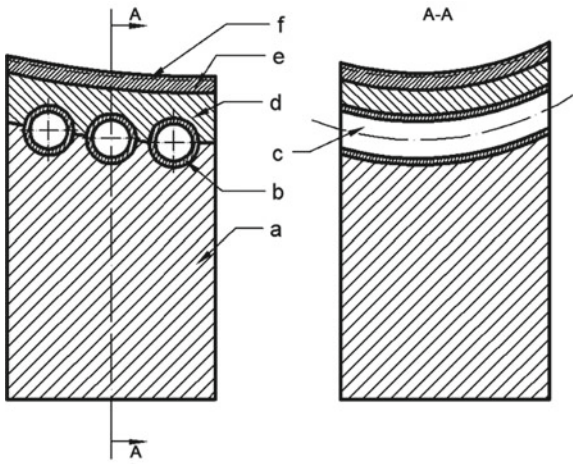


Fig. 1 2D Section diagram of new hot stamping tool insert **a** Matrix; **b**, **c** Copper pipe; **d** Intermediate layer; **e** Surface layer; **f** tool surface

In this paper, a novel design of hot stamping tool with conformal cooling channels (CCC) manufactured by surfacing technology is put forward, as shown in Fig. 1. Firstly, the matrix with a lower half of CCC shape is machined, and then the pre-bended copper pipes are embedded into the cooling channels of the matrix material, so the top half of copper pipes is exposed in the air. Then again, the welding materials with high thermal conductivity are welded on the surface of matrix and copper pipes to form intermediate layer. And then the heat-resisting welding materials are welded on the surface of the intermediate layer to obtain surface layer. Finally, the tool must be heat-treated and machined in order to satisfy the requirements of shape and size and performance. By this method, material properties of the new hot stamping tool can reach the allocation of materials on demand. In other words, the surface layer will withstand severe condition such as high temperature and high stress, and the intermediate layer can improve the cooling efficiency, and the 45 steel matrix will greatly reduce the use of expensive tool materials under the premise of the meeting working conditions.

2 Materials and Methods

In this study, quenched and tempered 45 steel was chosen as the matrix material, Fe-based and CuCrZr alloy were preselected as the surface layer and the intermediate layer, respectively.

The matrix specimens were firstly cleaned and preheated to 400 °C and then the surfacing process was carried out by using an HRWS-3250-type welding machine according to test design requirement. Finally, the specimen was tempered to 500 °C after welding. The 3D model and finished specimens are shown in Fig. 2.

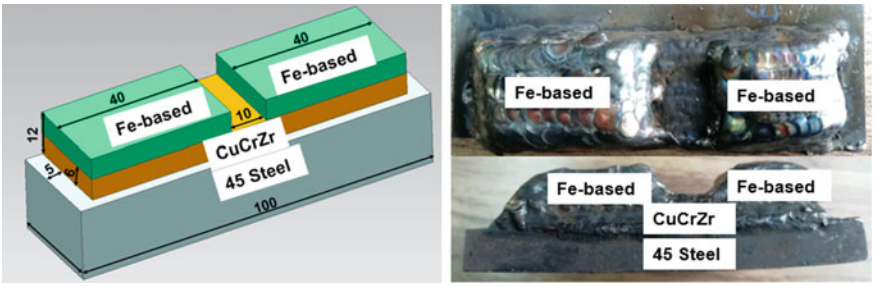


Fig. 2 The surfacing samples. (Color figure online)

3 Performance Test of Surfacing Materials

3.1 Mechanical Properties of Surfacing Materials

The high-temperature compressive yield strength of two single welding materials and two interfaces are shown in Fig. 3. It can be concluded that the yield strength has a downward trend with increasing temperature, but the interface of CuZrCu + Fe-Based exhibits a higher yield strength above 150 °C. The yield strength of Fe-based alloy reduced from 1608 to 1198 Mpa, the yield strength of Cu–Cr–Zr fell from 135 to 90 Mpa, the interface yield strength of 45 + CuCrZr changed from 383 to 361 Mpa, and the interface yield strength of CuCrZr + Fe-Based fluctuated from 343 to 379 Mpa.

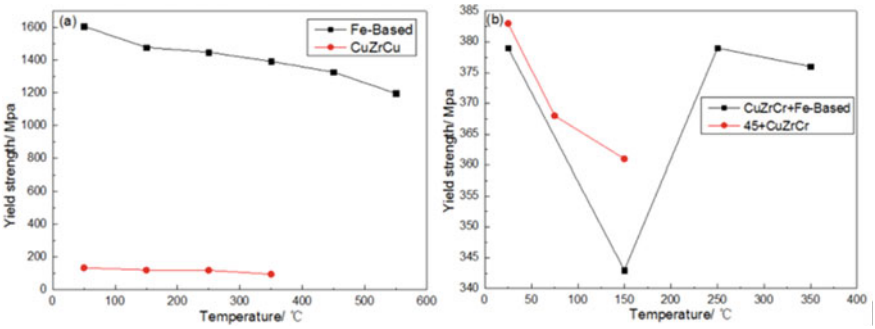


Fig. 3 The high-temperature compressive yield strength of surfacing materials. (Color figure online)

Table 1 Thermal expansion coefficient of two alloy materials (unit in/°C)

Temperature/°C	50	150	250	350	450
Fe-Based	1.50E-5	1.36E-5	1.36E-5	1.34E-5	1.32E-5
CuCrZr	1.63E-5	1.67E-5	1.77E-5	1.76E-5	1.74E-5

Table 2 Heat conductivity of two alloy materials (unit in W/m•°C)

Temperature/°C	25	100	200	300	400
Fe-Based	39	43	48	51	54
CuCrZr	166	154	145	138	134

3.2 Heat Conductivity and Thermal Expansion Coefficient of Surfacing Materials

The heat conductivity and thermal expansion coefficient of Fe-based and CuCrZr are displayed in Tables 1 and 2, respectively. These thermal parameters which directly influence the stress and temperature contribution will be input into ABAQUS software for process simulation.

4 Numerical Simulation of Traditional and New Hot Stamping Tools

4.1 FE Model Establishment

Traditional tools of automotive rear side member were chosen as research object as shown in Fig. 4. Figure 5 presents the structures of traditional and new hot stamping

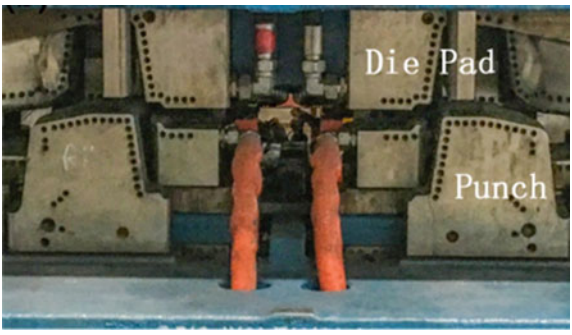


Fig. 4 Traditional hot stamping tool. (Color figure online)

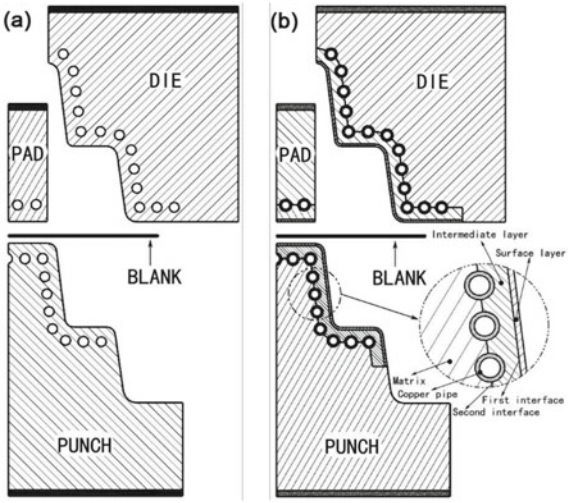


Fig. 5 Two hot stamping tools structures **a** Traditional tool; **b** New tool

tools which both contain die, punch, pad, and rigid tool base; however, the new hot stamping die is divided into surface layer, intermediate layer, matrix, and cooper pipe.

4.2 Temperature Filed Comparison of Traditional and New Tools

In the continuous stamping process, the temperature field of tool will reach dynamic balance after approximately fourth and fifth stamping circles according to trial and error. For both traditional and new tools, the temperature field at the end of pressure holding stage is presented in Figs. 6 and 7. As can be seen from Figs. 6 and 7, the maximum temperature of the traditional tool (TT) is within the range of 110–121 °C, the maximum temperature of the new tool (NT) varies from 70 °C to 74 °C, which indicates that new tool has a higher cooling efficiency due to intermediate layer with high thermal conductivity.

4.3 Stress Filed Comparison of Traditional and New Tools

Figure 8 shows the stress field distribution of traditional and new tools at the end of stamping. The simulation result indicated that new tool will be subjected to lower stress than traditional tool, which is attributed to high heat conductivity and low elastic modulus of intermediate layer. According to the simulation results, the maximum stress of the new tool was less than yield strength under corresponding

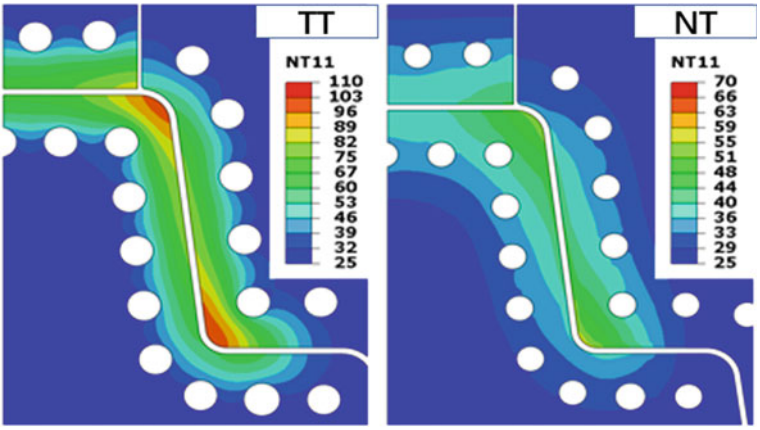


Fig. 6 Temperature field at the end of the pressure holding (the first stamping). (Color figure online)

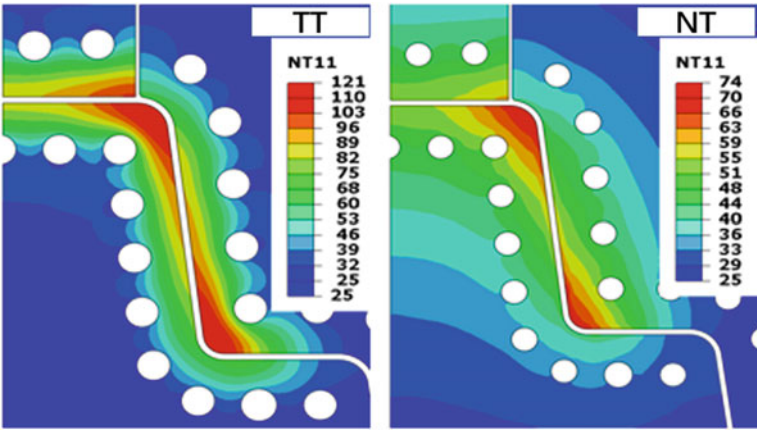


Fig. 7 Temperature field at the end of pressure holding (the sixth stamping). (Color figure online)

temperature, which demonstrated that the new tool manufactured by surfacing technology can satisfy the strength requirement of hot stamping process.

4.4 Cooling Rate Comparison of Traditional and New Tools

Cooling rate above 27 °C/s [8] will lead to hot-stamped part with a fully martensitic structure, a higher cooling rate can improve the production efficiency. Cooling rate comparison of traditional and new tools in the martensitic phase region is shown in Fig. 9. The average cooling rate of the blank in traditional and new tools is about

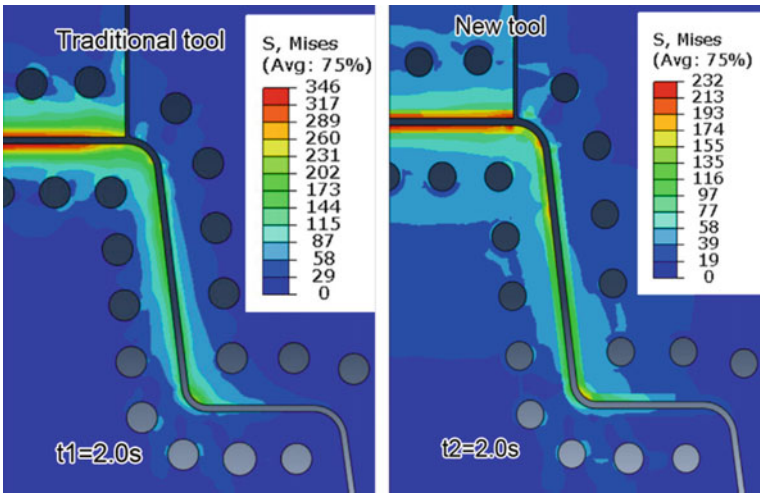


Fig. 8 Stress field comparison of traditional and new tools (the sixth stamping). (Color figure online)

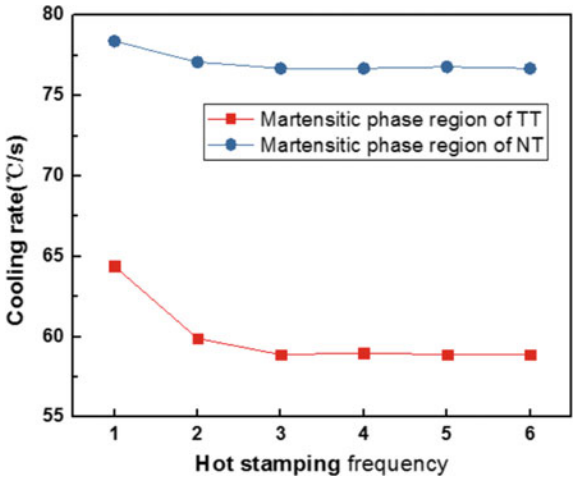


Fig. 9 Cooling rate comparison of traditional and new tools. (Color figure online)

59 °C/s and 77 °C/s, respectively.

5 Conclusions

1. A new manufacturing method of hot stamping tool with CCC is proposed in this study. The temperature of traditional and new tools reached dynamic thermal equilibrium after 4 and 5 stamping circles, respectively.
2. The temperature and stress of new tool were always lower than traditional tool. The maximum stress of new tool was less than the yield strength of the corresponding welding materials, which demonstrated that new tool manufactured by surfacing technology could satisfy the strength requirement and deserve further research.

References

1. Karbasian H, Tekkaya AE (2010) A review on hot stamping. J Mater Proc Technol 210:2103–2118
2. Bok H, Lee M, Pavlina EJ, Barlat F, Kim H (2021) Comparative study of the predictionof microstructure and mechanical properties for a hot-stamped B-pillar
3. Li M, Chiang T, Tseng J, Tsai C (2014) Hot stamping of door impact beam. Proc Eng 81:1786–1791
4. Chokshi P, Dashwood R, Hughes DJ (2017) Artificial Neural Network (ANN) based microstructural prediction model for 22MnB5 boron steel during tailored hot stamping. Comput Struct 190:162–172
5. Merklein M, Lechler J (2006) Investigation of the thermo-mechanical properties of hot stamping steels. J Mater Proc Technol 177:452–455
6. He B, Ying L, Hu P, Yu Y, Zhao X, Zhang LW (2014) Investigation of mechanicalproperty and springback behavior with hot stamping RCP process. Adv Mater Res 1063:186–189
7. He B, Ying L¬ Li XD, Hu P (2016) Optimal design of longitudinal conformal cooling channels in hot stamping tools. Appl Therm Eng 106:1176–1189
8. Lim W, Choi H, Ahn S, Kim B (2014) Cooling channel design of hot stamping tools for uniform high-strength components in hot stamping process. Int J Adv Manuf Technol 70:1189–1203

Formability Analysis of a Local Heat-Treated Aluminium Alloy Thin-Walled Tube



A. Piccininni, J. P. Magrinho, M. B. Silva, and G. Palumbo

Abstract The environmental concerns to save energy are currently driving the attention toward alternative ways to produce lightweight components, matching the most promising light alloys (as in the case of aluminium alloys) with new and innovative manufacturing trends. To address these new requirements the use of tubular structures has increased as a solution to reduce weight. Parallel to the need to increase the material formability local heat treatment of metal sheets has gained some relevance in the last years. The present work is focused on the evaluation of the formability at room temperature of thin-walled aluminium alloy tubes previously overaged in specific zones by laser. The formability limits of the thin-walled tube material in the 'as-received' condition were preliminarily determined by means of tensile tests and tube expansion with elastomer. An initial numerical analysis was performed in order to define laser heating parameters to effectively overage the material. The experimental work (tensile and tube expansion tests) was assisted by the Digital Image Correlation (DIC). On the other hand, the laser treatment to obtain Locally Overaged Tubes (LOTs) was investigated according to the results of the preliminary numerical simulations and such LOTs were subjected to experimental tensile and tube expansion tests. The strain paths and failure strains obtained on LOTs were assessed and compared to the formability limits of the 'as-received' tube, thus allowing to evaluate the effect of the local modification of the material properties on the formability of the tube.

Keywords Thin-walled tubes · Formability limits · Laser heat treatment · Tube forming

A. Piccininni (✉) · G. Palumbo
Department of Mechanics, Mathematics and Management, Politecnico di Bari, Via Orabona, 4, 70125 Bari, Italy
e-mail: antonio.piccininni@poliba.it

J. P. Magrinho · M. B. Silva
IDMEC, Instituto Superior Técnico, Universidade de Lisboa, Av. Rovisco Pais, 1049-001 Lisboa, Portugal

© The Minerals, Metals & Materials Society 2021

G. Daehn et al. (eds.), *Forming the Future*, The Minerals, Metals & Materials Series,
https://doi.org/10.1007/978-3-030-75381-8_230

1 Introduction

Environmental problems have increased in recent years the interest of the research toward energy saving which can be obtained, as discussed in [1], using different approaches such as (i) the design of lightweight components maintaining their mechanical requirements, (ii) the adoption of alternative manufacturing processes, and (iii) materials selection. One of the solutions that has a significant impact on weight and energy reduction is the use of thin-walled tubular structures [2], and this fact might be one of the causes promoting in the last years the increase of tube forming as manufacturing process. Additionally, the use of aluminium (Al) alloys can ensure good mechanical properties combined with low density; however, they are characterized by poor formability at room temperature, when compared to low carbon steel.

Recently, to overcome such a limitation, the scientific community has been developing innovative solutions, among which the local modification of the material properties via short-term heat treatments [3]. These local heat treatments can be performed by laser radiation, conductive [4] or inducting devices according to the complexity of the component as well as the number of parts to be manufactured. Laser heat treatment is therefore highly suitable for complex heating strategies on small series (prototypes) production thanks to its flexibility. The research in this area has been mainly focused on sheet metal parts, whereas only few examples are available in literature regarding the tube properties modification via laser treatment [5].

Under these circumstances, the main contribution of this paper is to provide a systematic methodology to evaluate the effect of laser treatments on the formability of AA6063 tubular samples purchased in the T6 condition. Preliminary numerical simulations were performed to define the process parameters to evaluate the temperature distribution during the laser heating of the tube. According to the numerical results, preliminary experimental laser treatments were carried out on tubular samples; the Locally Overaged Tubes (LOTs) were subsequently subjected to hardness measurements to assess the effectiveness of the laser heating; after the tuning of the treatment to be used for changing the material condition into ‘overaged’, the formability was assessed by means of tensile tests and tube expansion with elastomer.

2 Material and Methodologies

The experimental work was performed on AA6063-T6 Al alloy tubes with an external diameter of 40 mm and an average initial thickness of 1.85 mm. Table 1 presents the chemical composition of the alloy under investigation.

As previously mentioned, the aim of the present work is the evaluation of the effect of a local modification of the material properties on the overall formability at room temperature. In the case of the investigated age-hardenable alloy, the local laser treatment was designed to bring the material in a more formable condition without triggering the natural ageing, i.e. aiming at the overaged condition.

According to what was reported in literature, a fast hardenable Al alloy reaches a more formable condition after being irradiated for few seconds at a temperature between 400 and 450 °C [6–8]. Laser treatments were experimentally carried out using the experimental setup shown in Fig. 1a, mainly composed of an Al cylindrical support on which the tubular sample was mounted; all the tubular samples were preliminarily painted in black to increase the absorption coefficient. Laser heat treatments were carried out adopting a 20 mm square spot.

To properly define the laser heating parameters, the experimental equipment was modelled using the Finite Element (FE) code Abaqus. The tube (initial length:100 mm) and the support were modelled as deformable bodies; the heat exchange between them was considered as conductive whereas a convective heat exchange was considered with the surrounding environment. The laser heating was designed according to a linear path parallel to the tube axis (a DFLUX user subroutine was used to model the laser spot movement). Four different Feed Rate (FR) levels were considered to investigate the effect of the interaction time and the laser

Table 1 Chemical composition (wt%) of the AA6063-T6

Si	Fe	Cu	Mn	Mg	Cr	Zn	Ti	Al
0.2–0.6	< 0.35	< 0.1	< 0.1	0.45–0.9	< 0.1	< 0.1	< 0.1	Bal

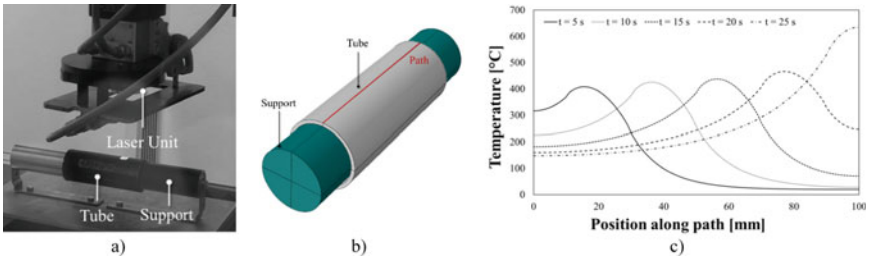


Fig. 1 Tube laser heating: **a** experimental set-up; **b** modelled assembly for the preliminary simulations; **c** distribution of temperature along the longitudinal path. (Color figure online)

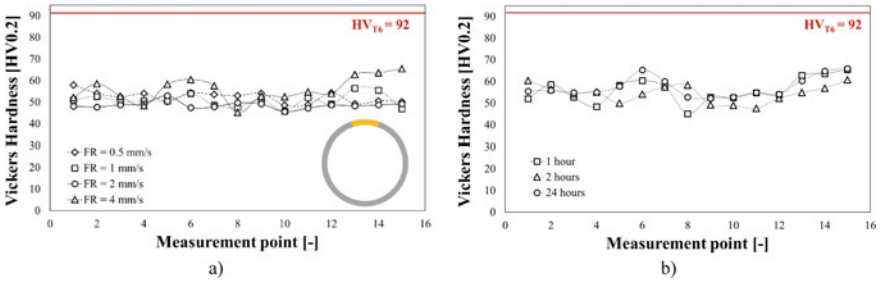


Fig. 2 Hardness measurement: **a** effect of the feed rate, **b** evolution of hardness with time. (Color figure online)

power (LP) was changed accordingly in order to subject the material to the above-mentioned range of temperatures. Results of the thermal simulations were analysed in terms of temperature distribution along a longitudinal path, as shown in Fig. 1b.

Figure 1c, regarding the laser heating setting the LP at 1050 W and the FR at 4 mm/s, shows that, once the initial transient heating was over, most of the tube was subjected to a temperature ranging from 400 to 450 °C. Additionally, as the laser approached the end of the tube, the temperature sensibly increased due to the limited quantity of material available to dissipate the heat.

To evaluate the effectiveness of the laser treatment, a ring sample was extracted from the middle part of the tube; the portion subjected to the laser heating (highlighted in yellow in Fig. 2a) was mounted, grinded, polished, and subjected to Vickers microhardness tests (Qness microhardness tester Q10 A + , setting a load of 200 g and a dwell time of 15 s) at regular interval of time. The hardness of the alloy in the as-received condition (T6) was also measured and resulted equal to 92 HV.

Hardness profiles in Fig. 2a show that all the investigated FR levels were effective in bringing the material to a more formable (and stable) condition: in fact, if focusing the attention on the hardness evolution with time (FR = 2 mm/s) in Fig. 2b, even after 24 h from the heat treatment there was a negligible variation of the hardness. This result confirms that the investigated laser parameters were effective in bringing the material to the overaged condition.

The laser heating for the experimental plan was designed to locally modify the tube properties without affecting the rest of the tube. For this reason, the subsequent treatments, on 200-mm tube samples, were carried out setting the FR at 2 mm/s (material/radiation interaction times equal to 10 s) and, consequently, LP at 800 W. In order to avoid the excessive increase of the temperature in the last part of the laser heating, as previously shown in Fig. 1c, the beam power was reduced by 50% after having completed 75% of the linear track.

Table 2 Summary of the experimental work plan of the tensile tests

Material condition	Geometry dimensions					Number of specimens
	Outer radius (mm)	Thickness (mm)	Gauge length (mm)	Length of the reduced section (mm)	Width (mm)	
T6	20	1.85	50	80	12.5	3
LOT						3

Table 3 Summary of the experimental work plan of the tube expansion with elastomer

Material condition	Geometry dimensions			Operation conditions			Number of specimens
	Outer radius (mm)	Thickness (mm)	Length (mm)	Free length, l_{free} (mm)	Fixing condition	Velocity (mm/min)	
T6	20	1.85	150	20	blocked	5	3
LOT							3

3 Experimentation

The experimental work consisted of (i) the conduction of tensile tests extracted in the longitudinal direction from the tubes and (ii) tube expansion tests using an elastomer. Both the tests were carried out at room temperature condition. The AA6063-T6 tube formability limits by necking and by fracture were determined by the authors in a previous work [9].

3.1 Tensile Tests

The longitudinal tensile test specimens were prepared in accordance to the ASTM E8/E8M standard [10], with a 50 mm gauge length and 12.5 mm of width. The specimens were wire electro-discharge cut and the tensile tests were performed using a universal testing machine (Instron 4507). The experimental work plan for the tensile tests is summarized Table 2 (Table 3).

3.2 Tube Expansion Tests

The elastomer compression was used to expand the tube up to failure. The adopted equipment was assembled on a hydraulic testing machine (Instron Satec 1200) and it is presented in Fig. 3. The main components of the equipment are: punch, dies, rubber plug, and clamping system. The operation of the process is the following: the

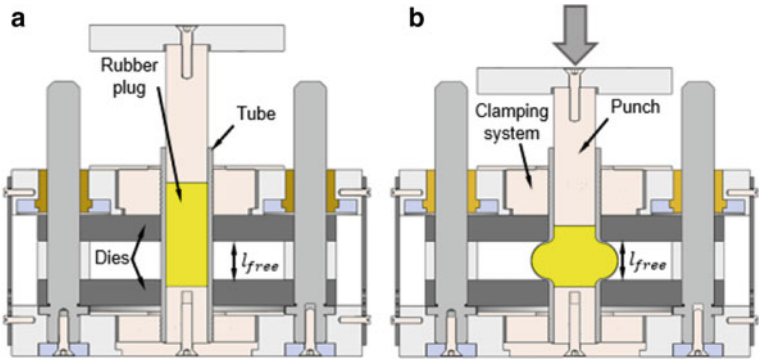


Fig. 3 Schematic representation of the tube expansion tests with elastomer equipment in the **a** initial and **b** final positions [9]. (Color figure online)

tube ends were clamped and the cylindrical rubber plug was placed inside the tube without lubricant and compressed by the punch; the expansion of the tube occurred in the free length, l_{free} between the two dies.

The experimental work plan for the tube expansion tests with elastomer is summarized in Table 2.

3.3 Strain Measurements

The strain distribution on the fracture zone in both tensile and tube expansion with elastomer tests were measured by means of a digital image correlation (DIC) system (Dantec Dynamics model Q-400 3D) equipped with two cameras with 6 megapixels of resolution and 50.2 mm of focal length (aperture: f/11). The frequency of image acquisition was set to ten frames per second and the correlation algorithm was performed with the INSTRA 4D software.

The fracture strains were obtained by measuring the thickness at the cracking (thus calculating the thickness strain ε_3) and combining it with the ε_2 from the last stage of the DIC analysis in order to calculate the major strain ε_1 by the incompressibility condition. The thickness measurements were performed with a stereoscopic microscope Nikon AZ100M with a magnification of 20 $\times$ using the Imaging Software NIS-Elements D 3.21.03.

4 Results and Discussion

The experimental work revealed to be highly replicable thus, to improve the quality of the present section, only results per one condition have been presented.

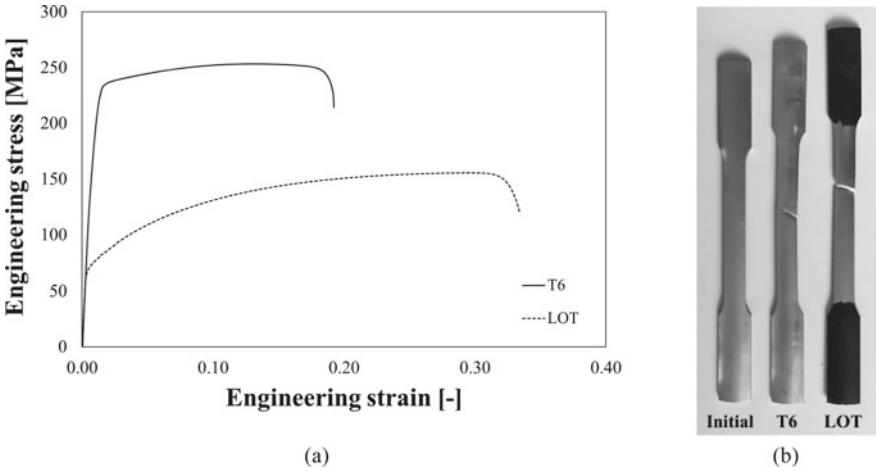


Fig. 4 Tensile tests results: **a** engineering stress–strain curves for the as-received and locally overaged treatment and **b** photograph of the specimens

The stress–strain curves from the tensile tests performed on both the investigated conditions (T6 and LOT) are presented in Fig. 4a, confirming that the overaged condition (characterized by a lower yield point and a remarkable increase in the elongation at failure) was obtained.

The improvement in the material formability was also evident comparing at the end of the tensile test of the undeformed sample with the ones in the T6 and the LOT conditions (please refer to Fig. 4b).

Figure 5 presents the strain loading paths for both experimental tests (tensile and tube expansion) for the two analysed material conditions (T6 and LOT) along with the Fracture Forming Line (FFL) previously determined by the authors [9] for the T6 condition.

The tensile strain loading path, for both conditions, starts from the uniaxial strain condition (slope of −0.5) and the LOT specimen presents a localization in the deformation (plane strain condition, slope 0) before the T6 specimen.

The fracture strain for the T6 condition (labelled as UT T6 in Fig. 5) presents a value in the proximity of the FFL (T6 condition). On the other hand, the fracture strain of the LOT specimen (indicated by the blue square marker in Fig. 5) is characterized by a major strain value which is twice higher than the T6. The difference between the last point of the strain path and the fracture point in all cases is related to localization phenomena [11], which occur in a very short period of time; for this reason, according to the maximum frequency of data acquisition in the DIC system, the number of measurements can differ from case to case. The localization is higher for the LOT specimen because of the more pronounced thickness reduction (as it can be seen in the fractographies detailed in Fig. 5).

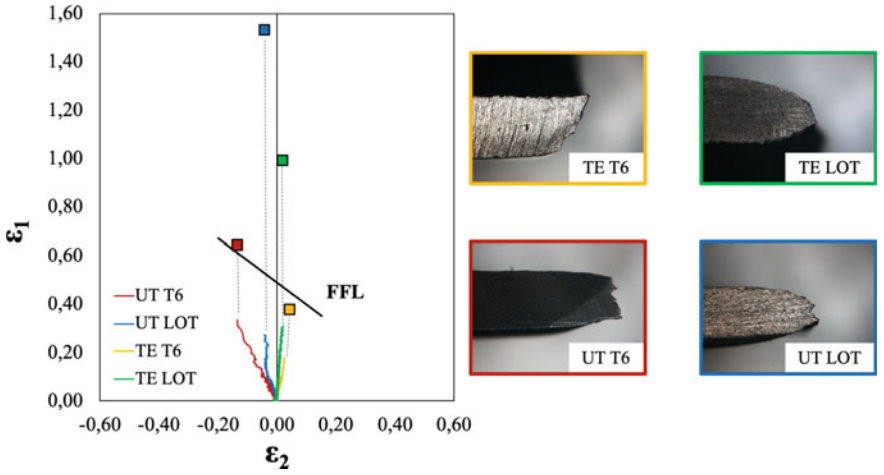


Fig. 5 Strain loading paths, fracture strains, and fractographies for aluminium tube AA6063 in T6 and LOT conditions. (Color figure online)

Similar results were obtained from the tube expansion tests, in particular showing that the local treatment had an influence on the slope of the stain path, moving from the biaxial deformation (slope higher than 0) to an almost plane strain condition.

The results are in accordance with the presented fractographies in Fig. 5 which reveal a more strained condition till fracture for the LOT specimens when compared with the fractographies in the T6 condition.

5 Conclusions

In the present work, a systematic methodology to evaluate the effect of local laser treatments on the formability of AA6063 tube samples has been presented. The designed laser treatment by FE simulations was effective in bringing locally the material in the overaged condition as confirmed by the hardness measurement. Moreover, the stress–strain curve obtained from the tensile tests confirmed these results since the material in the overaged condition showed a remarkable increase of the elongation at fracture along with a reduced yield point.

On the other hand, regarding the formability investigation, the presented fractographies demonstrated that the thinning was much more severe in the LOT samples than the samples in the as-received condition (T6). Consequently, the fracture strains in the principal strain space resulted to be significantly higher for both the experimental tests performed in the LOT conditions.

References

1. Tekkaya AE (2018) Energy saving by manufacturing technology. Proc Manuf 21:392–396
2. Jeswiet J, Geiger M, Engel U, Kleiner M, Schikorra M, Duflou J, Neugebauer R, Bariani P, Bruschi S (2008) Metal forming progress since 2000. CIRP J Manuf Sci Technol 1:2–17
3. Geiger M, Merklein M, Vogt U (2009) Aluminum tailored heat treated blanks. Prod Eng 3:401–410
4. Kahrimanidis A, Lechner M, Degner J, Wortberg D, Merklein M (2015) Process design of aluminum tailor heat treated blanks. Materials (Basel) 8:8524–8538
5. Peixinho N, Soares D, Vilarinho C, Pereira P, Dimas D (2012) Experimental study of impact energy absorption in aluminium square tubes with thermal triggers. Mater Res 15:323–332
6. Merklein M, Böhm W, Lechner M (2012) Tailoring material properties of aluminum by local laser heat treatment. Phys Proc 39:232–239
7. Merklein M, Nguyen H (2011) Adjusting optimized material properties for tailored heat treated blanks. Key Eng Mater 473:420–427
8. Hung N, Marion M (2012) Improved formability of aluminum alloys using laser induced hardening of tailored heat treated blanks. Phys Proc 39:318–326
9. Magrinho JP, Silva MB, Centeno G, Moedas F, Vallellano C, Martins PAF (2019) On the determination of forming limits in thin-walled tubes. Int J Mech Sci 155:381–391
10. 12004–2 ISO (2008) Metallic materials - sheet and strip - determination of forming-limit curves - part 2: determination of forming-limit curves in the laboratory
11. Martins PAF, Bay N, Tekkaya AE, Atkins AG (2014) Characterization of fracture loci in metal forming. Int J Mech Sci 83:112–123

Analysis of Material Work Hardening and Fracture Strains for Sheet Metal Stamping Processes



Sergey Golovashchenko, Srecko Zdravkovic, Natalia Reinberg, Saeid Nasheralahkami, and Weitian Zhou

Abstract Experimental study of sheet material flow curves was performed using combined methods of cold rolling for prestraining material to targeted strain and then tensile testing. Experimental studies revealed that aluminum alloys show a tendency for flow curves saturation which substantially lowers work hardening of the sheet material. Performed numerical simulations of cup drawing illustrated that this effect leads to earlier material wrinkling compared to power law approximation of the flow curve. Examples of numerical simulation with Autoform software comparing the result of cup drawing for various cases of flow curve approximation are discussed in this paper. Analysis of fracture strains was performed by combined gridding and paint spraying on the sheet surface. This approach enabled measurements of local strains in the area closely adjacent to fracture without having continuous access to this area by video camera. This approach was used for sheet hole expansion, sheared edge stretchability along straight cut, hemming, and self-piercing riveting for high-strength steels and aluminum alloys.

Keywords Fracture strain · Work hardening · Wrinkling

1 Introduction

In order to achieve successful prediction of metal forming and joining processes, it is necessary to have knowledge of adequate stress–strain curves and fracture strains, especially where plastic strains substantially exceed those in a traditional tensile test. The risks of trying to define all the parameters via finite element analysis using reverse engineering are associated with a lack of knowledge not only in stress–strain behavior and fracture strains but also in friction behavior which represents an even more significant challenge.

In engineering practice, modelers are often using the power law approximation of stress–strain curves: $\sigma = K\varepsilon^n$. In early studies of diffuse necking by Considere

S. Golovashchenko · S. Zdravkovic · N. Reinberg (✉) · S. Nasheralahkami · W. Zhou
Mechanical Engineering Department, Oakland University, 115 Library Dr, Rochester, MI 48309-4401, USA
e-mail: nataliareinberg@oakland.edu

© The Minerals, Metals & Materials Society 2021

G. Daehn et al. (eds.), *Forming the Future*, The Minerals, Metals & Materials Series,
https://doi.org/10.1007/978-3-030-75381-8_231

[1], this approximation quantified the initiation of diffuse necking when true strain is reaching the n-value. Power law approximation, according to Hollomon and Jaffe [2], worked well for mild steels up to true strains of 0.4. Swift [2] discussed the power law approximation with initial prestrain which provided an additional parameter assisting in more accurate approximation:

$$\sigma = K(\varepsilon_0 + \varepsilon)^n$$

According to Keeler and Kimchi [3] and Davis [4], mild steels and HSLA steels have n-values that are constant with deformation in the tensile test while AHSS steels have n-values that change with deformation. Xu et al. [5] demonstrated that stress–strain curve for AA5754 needs three sets of parameters to achieve a good correlation with experimental stress–strain data obtained from the tensile test where the maximum true strain slightly exceeded 0.2.

Defining the stress–strain behavior beyond uniform elongation in a tensile test represents a challenge. Tensile test experiments performed by Dan et al. [6] for Al alloy extended the stress–strain curve from 0.2 true strain in a standard test to 0.37 by employing Digital Image Correlation. However, it should be indicated that the Lode parameter is substantially different during uniform deformation and necking phases of the tensile test.

Hecker et al. [7] indicated that uniaxial tension with necking correction, biaxial sheet or tube bulging, compression, torsion, wire drawing followed by tension, and rolling followed by tensile testing methodologies are able to extend the range of stress–strain curves substantially. Potential errors during bulging tests were discussed by Ranta-Eskola et al. [8] and by Smith et al. [9].

The compression test does not have the issues of geometric weakening, but it is complicated by friction. Mohebbi et al. [10] studied plane strain compression and observed a change of coefficient of friction (COF) of approximately a factor of four, which serves as an indication that assumptions on constant friction between the tool and the sample may significantly affect the stress–strain results.

A numerical approach to determine the stress–strain curve based upon cold rolling process was developed by Byon et al. [11] using the equation for the roll force and forward slip. However, significant variations of COF admitted by Mohebbi et al. [10] make the stress–strain results less reliable.

Based on the performed review of previous work, the rolling prestrain followed by the uniaxial tensile testing of samples fabricated from prestrained strips was considered the most convenient for the manufacturing processes working with sheet metals and selected for the material testing in this paper.

Defining the fracture strain for sheet metals is also a challenging problem. Bao and Wiezbicki [11] studied fracture strain as a function of hydrostatic pressure. Bai and Wierzbicki [12] emphasized the importance of both hydrostatic pressure and Lode parameter on fracture strains using gridding method. Sriram et al. [14] employed through-thickness strain as a fracture criterion for DP780 and DP980 steels which does not take into account the ratio between two other principal strains. Therefore, gridding method remains the most popular for fracture strain measurements since

early studies of strip compression and extrusion by Nadai [13]. For sheet metal forming applications, the localization of strains was measured by Gensamer [14] where he discovered that the value of maximum strain at localization varies with the strain ratio. The concept of Forming Limit Diagram was developed by Keeler [15] and Goodwin [16] using circular grid analysis for measuring safe and localized strains. The practice of using square grids for material flow analysis was discussed by Wilson [17]. Smith [18] described circular grid analysis as a major experimental tool to define the distribution of strains in stamped sheet metal parts.

The early results on measurement of strain distribution in deformed plane sample using Digital Image Correlation were discussed by Sutton et al. [19]. Garcia et al. [20] discussed strain measurement for Forming Limit Diagram applications. Sutton et al. [21] illustrated DIC capabilities for fracture strain measurement in high-speed plastic deformation. Overall, the DIC method is a powerful tool capable of high resolution of strains which can be employed for measurements of fracture strains. However, the major requirement is to have access for the video camera to the surface of a sheet metal blank and record speckle motions during the deformation process. Due to this circumstance, the grid analysis remains a major tool for measurements of the strain distribution in stamped parts after over 90 years of its initial usage.

The spatial resolution of grid analysis is limited by the size of the applied grid as well as by the quality of the grid pattern (uniform dimensions of individual squares of the applied grid, as well as thickness of lines). Measurement of fracture strain is usually problematic with grid analysis because of cracks propagating through a sequence of grids and not through their boundaries. In this case, the fracture strain is measured as a strain of the nearest grid. When sheared edge stretchability, local strains in processes like hemming, flanging, or self-piercing riveting are of interest, this resolution makes a significant difference. A new method suitable for such applications was proposed by Golovashchenko [22]. The idea of this method is to apply the speckle on top of the etched grid which provides a coordinate system to identify the sprayed dots. The picture of the grid with applied dots is taken before and after the forming process, and finite strains can be calculated based upon the analysis of individual dots stretching. This concept provides the ability to measure the strains in close vicinity to the crack initiation for traditional stamping processes. The applications of this method will be further discussed in this paper.

2 Stress–Strain Curves for Extended Range of Strains and Discussion of Their Effect in Sheet Metal Forming

Stress–strain curve obtained from tensile testing parallel to the initial rolling direction of as-received and prestrained (via cold rolling) AA6111-T4 specimens was compared with Power Law ($\sigma = K(\varepsilon_0 + \varepsilon)^n$) stress–strain curve that is broadly used in numerical simulation of metal forming processes. The chemical composition of AA6111-T4 includes the following elements: Si 0.7–1.1%, Mg 0.5–1%, Fe 0.4%

max, Mn 0.15–0.45%, Zn 0.15% max, Cr 0.1% max, Ti 0.1% max, Other (each) 0.05% max, Al—remainder. The tensile samples were fabricated using wire EDM technology from the strips of AA6111-T4 rolled step-by-step with successive thickness reduction. The geometry of the specimens was selected following ASTM E8 standard [23]. The tensile direction was parallel to the multistep rolling direction, which was parallel to the rolling direction of the as-received AA6111-T4 sheet. The rolled strips were stacked together and clamped between two steel plates 12.7 mm thick, which guided the wire during the EDM process. For AA6111-T4, the results of the tensile test can be approximated using the following parameters: K = 513.92 MPa, $\varepsilon_0 = 0.0001$, and n = 0.24 [26]. These parameters provide the approximation which fits very well the experimental tensile curve obtained in this study. Comparison of stress–strain curves obtained from the tensile testing parallel to the initial rolling direction of prestrained AA6111-T4 with the power law approximation is shown in Fig. 1. From this comparison, it is obvious that both curves are very close to each other up to the true strain of 0.2. For the strains exceeding this level, the rate of work hardening in the experimental curve becomes much slower compared to the power law approximation.

Below is the discussion of manufacturing processes where the difference in material behavior can lead to a visible difference in simulation results if the power law approximation is employed instead of using the extended range curve obtained through rolling tensile testing.

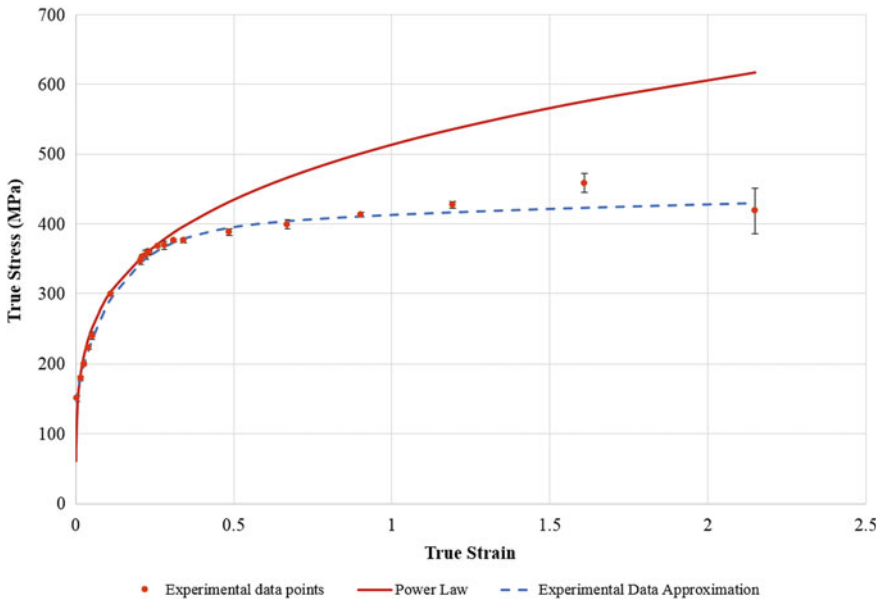


Fig. 1 Comparison of the experimental curve obtained by tensile testing parallel to the initial rolling direction of as-received and prestrained (via cold rolling) AA6111-T4 and power law true stress–true strain curve (K = 513.92 MPa, $\varepsilon_0 = 0.0001$ and n = 0.24). (Color figure online)

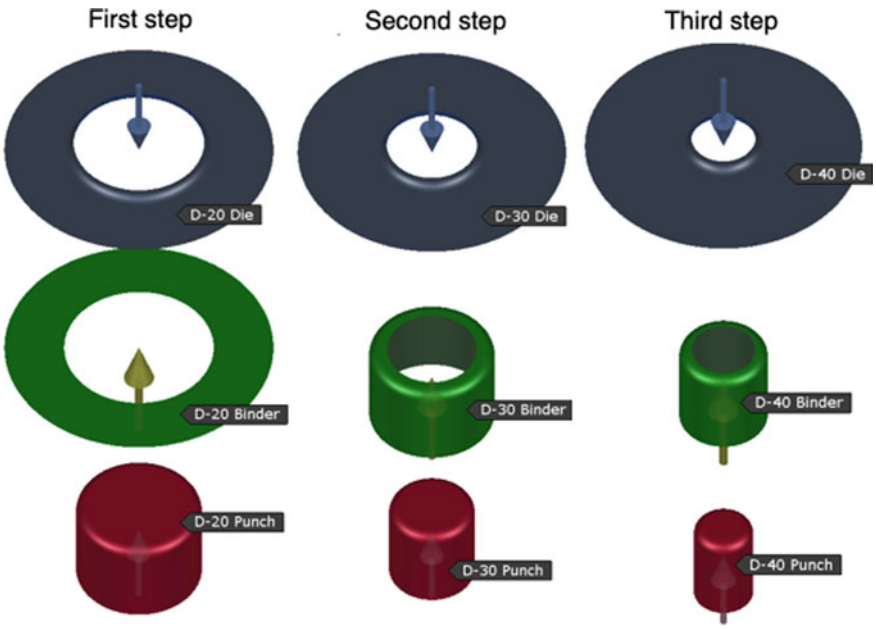


Fig. 2 Multiple-step drawing tool design. (Color figure online)

Deep drawing is the major operation of sheet metal forming technology. In order to illustrate the effect of work hardening on quality of sheet metal drawing, a simple example, drawing of a cylindrical cup, was employed. Computer experiment was performed by using the AutoForm software where the stress–strain curve was varied and the rest of the parameters were kept the same. Multiple-step drawing tools that were used are shown in Fig. 2. At the first step of drawing, the punch of 150 mm in diameter had 33.5 mm displacement for full cup drawing from a flat circular blank 200 mm in diameter and 0.93 mm thick. At the second step of drawing, the punch of 101 mm in diameter made 70 mm displacement to further form the cup initially drawn during the first step from the flat round blank. At the third step of drawing, the punch of 67 mm in diameter mm made 45 mm displacement.

In the analysis, mill oil characteristics were employed for the multistep cup drawing process. The coefficient of friction (COF) used for the contact of the blank with the die and the binder was 0.05 while for the contact with the punch, it was assumed to be 0.5. Higher COF on the punch helps to avoid the material flow from the bottom of the cup. The results of numerical simulation shown in Fig. 3 illustrated that a significant area with wrinkles takes place in case when the experimental stress–strain curve was used for the simulation, and smooth shape without any wrinkles was observed when the power law stress–strain curve was used for the simulation. In case when the experimental curve was used for the analysis, plastic strain value is up to 35% higher than in case when the power law curve was used for the simulation. In the previous studies, Shofman [24] performed analytical derivations indicating

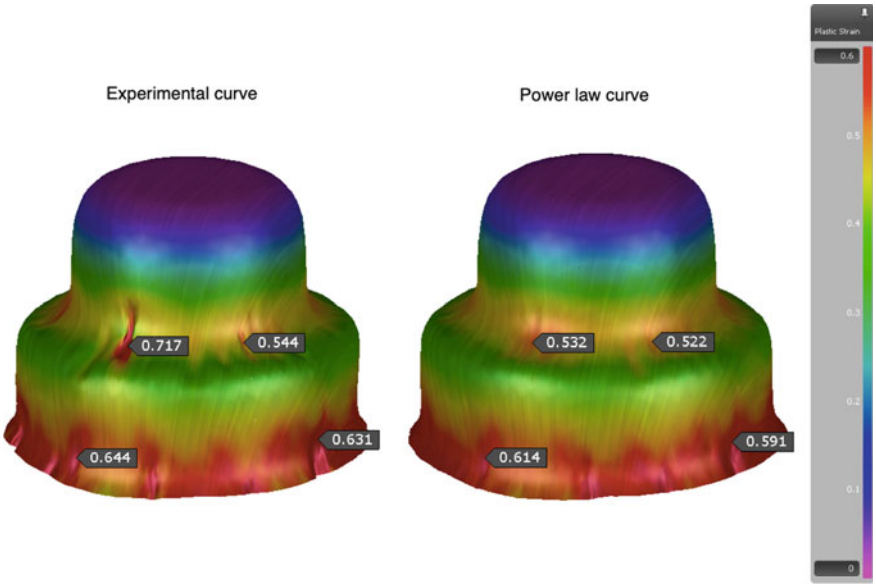


Fig. 3 Plastic strain and wrinkles in multiple-step drawing when experimental stress–strain curve was used for simulation and power law stress–strain curve was used for simulation. (Color figure online)

that materials with lower work hardening exponent n-value have a higher tendency for wrinkling. Later on, Moshnin [25] performed the analysis based upon the sheet buckling being compressed between two rigid surfaces and obtained very similar results: increased work hardening exponent provides better resistance to wrinkling. Cup drawing analysis was studied numerically by Kim et al. [26] where the same trend was confirmed: wrinkling occurs earlier for the materials with lower n-value.

Even though wrinkling is usually suppressed by the binder force, it could be indicated that overestimating work hardening condition might provide misleading information regarding wrinkling. Therefore, while designing the multistep drawing process, it is important to take into account the actual stress–strain curve. It is known from the reference literature [27] that in multistep drawing the drawing ratio can increase up to 6.5 which corresponds to true strain of 1.87. Employment of the power law for the analysis of such a stamping process would lead to substantial overestimation of work hardening and potential errors in the design of the stamping die.

Another important consideration should be taken into account: Hosford and Caddell [28] indicated that the limiting redraw ratio is greater for materials with lower n-value (cold rolled sheets) than for those with higher n-value (annealed sheets). This circumstance is driven by the limitation of the cup drawing process when the stress in the wall of the cup achieves plastic instability limit. It happens earlier for materials with higher n-value because the bottom of the cup wall, which must carry the redrawing force, is not getting work hardened. From this perspective, it becomes

clear that the material work hardening puts two different limitations on the drawing process, and, therefore, should be considered for the processes where the strain level substantially exceeds the range of initial approximation with the power law (n-value).

One more area of sheet metal stamping where knowledge of actual flow stresses is critical is springback prediction and compensation. Even though, a lot of practical efforts illustrate the successful application of springback compensation technology achieved via numerical simulation of the sheet metal blank unloading process, for example, as indicated by Cheng et al. [29]. However, multiple recent studies, for example Xue et al. [30], indicate that the elastic modulus has a tendency to decrease with the increase of plastic deformation, but then stabilize after a certain threshold. This effect partially compensates for the overestimation of the flow stress. However, the discrepancies should tend to grow for a larger level of effective plastic strain, which typically takes place in filling trihedral corners.

3 Fracture Strain Measurements

The examples of fracture strain measurements are provided in this section. In Fig. 4, the results of stretching of the sheared edge are illustrated for the strip sample of DP980 1.45 mm thick sheet. The sample was 127 mm long (in the transverse direction) and 12.7 mm wide (in rolling direction). It was initially sheared with 20% cutting clearance and then subjected to the tensile test to identify the elongation at which fracture initiates on the surface of the edge. The sheared edge had no significant burrs which would be positioned outside the lower plane boundary of the material. However, it can be seen that the burr was initially formed at the bottom, but then broken during the cutting process. During tensile testing, the crack originated from the broken burr. In the observed test of the sheared edge stretching, progression from hairline crack to final failure was rather slow, especially in the tensile test. Cracks could open up to the width nearly a third of the material thickness before

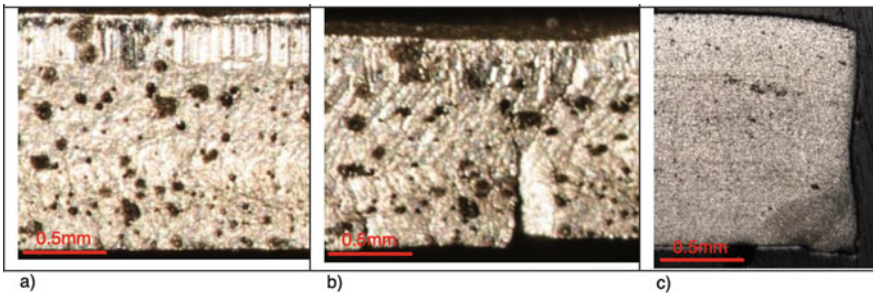


Fig. 4 The views of sheared edge of the trimmed sample: **a** the view of the sheared edge with the dots of paint before the beginning of the tensile test; **b** the view of the sheared edge when fracture crack was propagating; **c** cross section of the sample DP980 sample after cutting with 20% clearance. (Color figure online)

complete failure was detected. The tensile test showed diffuse necking before fracture, but localized necking did not advance before the crack penetrated throughout the thickness. The hairline crack progression was the factor that led to the failure. The fracture strain for the illustrated sample was measured as 0.091 true strain at the initial moment of fracture initiation in the burr area.

The process of fracture strain measurement by bending process is illustrated in Fig. 5. In bending experiment, strain measurement of fifteen samples of DP980 sheet was performed. The experimental procedure included the following steps: (1) cut the samples 76.2 mm in length and 50.8 mm in width to fit the slots on the bending die; (2) draw the lines in the area where fracture occurs; (3) spray black dots on the surface of the sample; (4) take pictures of the selected dots before bending (use a microscope with 20X magnification); (5) clamp the sample in the die positioned in 100 ton hydraulic press; (6) run the press to bend the sample to its final shape shown in Fig. 6; (7) post-process the picture using the software 'ImageJ' to measure the selected dots before and after bending; (8) calculate the local true strain. According to the results, the effective fracture strain is 0.42, which was the average data of the measured results. The standard deviation of the measured fracture strain was 0.08.

The next example was the hole expansion test which was applicable to the self-piercing riveting process (SPR). In order to simulate the SPR process, it was necessary

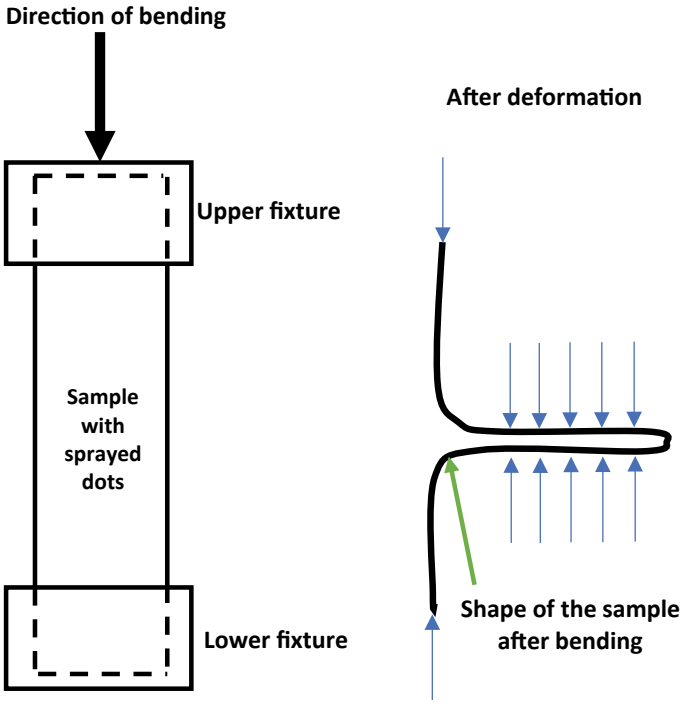


Fig. 5 Schematic of the experiment and the final shape of the sample after bending. (Color figure online)

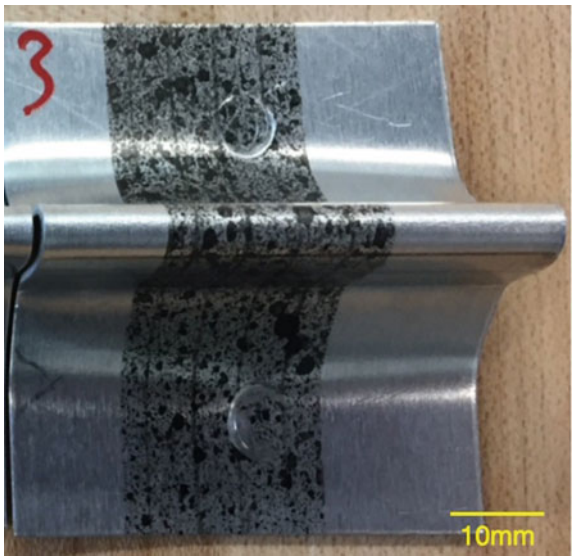


Fig. 6 Pictures of the sample after bending. (Color figure online)

to have a fracture strain for the fracture criterion applicable to the material fracture of joined sheets. The experiment was performed by expanding the hole 5 mm in diameter using hemispherical punch 20 mm in diameter. The selection of the initial hole diameter was dictated by the actual diameter of the rivet. The sequence of steps in the experiment was similar to described above for the folding experiment. The deformed sample of DP590 1 mm steel sheet with the dots of paint is illustrated in Fig. 7, where four quadrants are marked to make it easier to compare the dots before and after fracture. The fracture strains were measured along the perimeter of the hole.

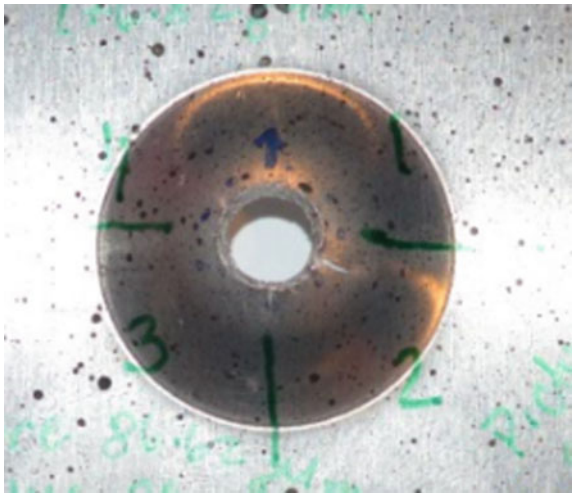


Fig. 7 The sample after hole expansion test using 20 mm in diameter hemispherical punch. (Color figure online)

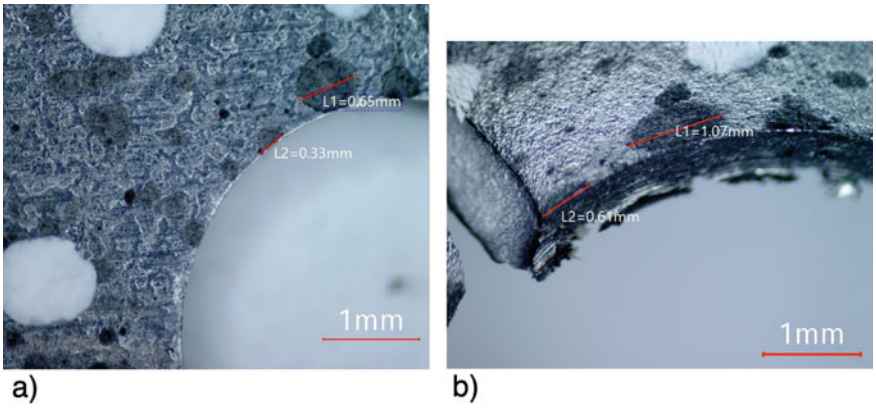


Fig. 8 The tested sample of DP590 steel before **a** and after **b** the hole expansion test. (Color figure online)

The illustration of the sample from DP590 1 mm thick steel sheet with dots before and after the hole expansion process is shown in Fig. 8. The white lines and white dots served to help correlation between the dots at the beginning and at the end of the process. Fracture happened in the area of the white dot, and the white line is used to correlate this area with the initial one. The measured true strain was 0.614 in close vicinity to the crack, while, in some distance from the crack, the true strain was 0.498. Establishing this correlation helped to avoid the necessity to use video camera through the whole process. Instead of a video camera used in traditional digital image correlation measurements, the microscope was utilized in this experiment allowing more accurate measurements of local strains at the very edge of the sample.

4 Conclusions

1. The experimental study of aluminum stress–strain behavior for extended range of strains for aluminum alloy 6111-T4 indicated that power law approximation substantially overestimates the material work hardening outside the range of strains in the tensile test.
2. The performed analysis based upon numerical simulation of cup drawing from sheet metal illustrated that employing power law approximation will likely underestimate potential wrinkling of the blank. In case, when the experimental curve was used for the analysis, the plastic strain value is up to 35% higher than in case, when the power law curve was used for the simulation.
3. Performed measurements of local strains by measurements of changes in the dimensions of the dots of paint provided the capability to measure the fracture strains in close vicinity to fracture initiation without the necessity to have continuous visual access to the surface of the blank.

References

1. Considère A (1885) Mémoire sur l'emploi du fer et de l'acier dans les constructions. Ann Ponts et Chaussées 9, 574–775
2. Hollomon JH, Jaffe LD (1947) Ferrous metallurgical design. Wiley, New York, p 85
3. Swift HW (1952) Plastic instability under plane stress. J Mech Phys Solids 1:1
4. Keeler S, Kimchi M (2014) Advanced High Strength Steel Application Guidelines, Version 5 May, pp 3.5–3.6
5. Davis JR (2004) Tensile testing. ASM International, p 101
6. Xu XH, Jain M, Wilkinson DS, Wilkinson RK, Mishra RK (2008) Microstructure-based finite element analysis of strain localization behavior in AA5754 aluminum sheet. Acta Materialia 56:3187–3201
7. Dan WJ, Zhang WG, Li SH, Lin QN (2007) An experimental investigation of large-strain tensile behavior of a metal sheet. Mater Des 28:2190–2196
8. Hecker SS, Stout MG, Eash DT (1981) Experiments on plastic deformation at finite strains. In: Proceedings of Workshop "Plasticity of metals at finite strain: theory, experiment and computation," Stanford University, CA, June 29–July 1
9. Ranta-Eskola AJ (1979) Use of hydraulic bulge test in biaxial tensile testing. Int J Mech Sci 21:757–465
10. Smith LM, Wanintrudal C, Yang W, Jiang S (2009) A new experimental approach for obtaining diffuse-strain flow stress curves. J Mater Process Technol 209:3830–3839
11. Mohebbi MS, Akbarzadeh A, Yoon YO (2014) Flow stress analysis of ultrafine grained AA1050 by plane strain compression test. Mater Sci Eng A 593:136–144
12. Byon SM, Kimb SI, Lee Y (2008) A numerical approach to determine flow stress–strain curve of strip and friction coefficient in actual cold rolling mill. J Mater Process Technol 201:106–111
13. Bao Y, Wiezbicki T (2012) On the cut-off value of negative triaxiality for fracture. Eng Fract Mech 72:1049–1969
14. Bai Y, Wierzbicki T (2012) A new model of metal plasticity and fracture with pressure and Lode dependence. Int J Plastic 24:1071–1096
15. Sriram S, Yao H, Ramisetti N (2012) Development of an empirical model to Characterize frazture behavior during forming of advanced high strength steels under bending dominated conditions. ASME J Mater Sci Eng 134(3):031003
16. Nadai A (1931) Plasticity. A mechanics of the plastic state of matter. McGraw Hill, 1931, p. 191–192
17. Gensamer M (1946) Strength and Ductility. Transactions of the ASM 36:30–60
18. Keeler SP (1961) Plastic instability and fracture in sheet stretched over rigid punches, PhD Thesis, Massachusetts Institute of Technology, Boston
19. Goodwin G (1968) Application of strain analysis to sheet metal forming in the press shop. SAE Paper No. 680093
20. Wilson FW (1955) Die design handbook, McGraw Hill, 1955, p. 10–3
21. Smith DA Die design handbook. P. 11.14-11.29
22. Sutton MA, Cheng M, Peters WH, Chao YJ, Mcneil SR (1986) Application of an optimized digital correlation method to planar deformation analysis. Image Vision Comput 4:143–150
23. Garcia D, Orteu JJ, Penazzi L (2002) A combined temporal tracking and stereo-correlation technique for accurate measurement of 3D displacements: application to sheet metal forming. J Mater Process Technol 125–126; 736–742
24. Sutton MA, Orteu J-J (2009) Motion and deformation measurements, Springer, H. W. Schreier Image Correlation for Shape, pp 193–196
25. Golovashchenko S (2018) Method of measuring localized strains in sheet metal stampings. US Patent Application Publication No. US 2018/0335296 A1
26. ASTM Standard E8/E8m, Standard Test Methods for Tension Testing of Metallic Materials, ASTM Stand. E8/E8M, 2008, 03.01, pp 743–746
27. Jain M, Lloyd DJ, Macewen SR (1996) Hardening laws, surface roughness and biaxial tensile limit strains of sheet aluminium alloys. Int J Mech Sci 38(2):219–232

28. Shofman A (1952) Elements of theory of cold forming, (Moscow)
29. Moshnin EN (1973) Technology of stamping of large panels, (Moscow)
30. Kim YS, Son YJ, Park JY (1999) Bifurcation analysis of wrinkling formation for anisotropic sheet. KSME Int J 13:221–228
31. Lange K, Pöhlandt K, Raghupathi RS, Saniter JD, Sauer WJ, Schey JA, Weinmann, Widera GEO (1985) Handbook Metal Form 15
32. Hosford WF, Caddell RM (2011) Metal Forming: Mechanics and Metallurgy. Met Form Mech Metall, 1–331
33. Shawn Cheng H, Cao J, Xia ZC (2007) An accelerated springback compensation method. Int J Mech Sci 49(3):267–279
34. Xue X, Liao J, Vincze G, Pereira AB, Barlat F (2016) Experimental assessment of nonlinear elastic behaviour of Dual-Phase Steels and Application to Springback Prediction. Int J Mech Sci 117:1–15

A New Approach for the Production of Burr-Free Sheet Metal Components Having Significantly Increased Residual Formability



Sergei Senn and Mathias Liewald

Abstract Shear cutting induces high strains and work hardening into the shear-affected zone, thus reducing the formability of the sheet metal material during subsequent forming operations. A common method for increasing the residual formability of shear-cut component edges is to shave the surfaces. The shaving process allows for the removal of highly hardened areas from a pre-cut contour, resulting in a comparatively high residual formability of the cutting surface. However, as known from conventional cutting, a burr remains on the shear surface when shaving. Such burr formation is undesirable and therefore usually has to be removed afterward. For this reason, a new process has been developed which combines two processes within the same stroke of punch, the counter-cutting, and shaving process, enabling the production of burr-free shear surfaces showing a high portion of clean-cut proportions and significantly 1.6 times higher hole expansion ratios than conventional cutting surfaces. The present paper deals with numerical and experimental investigations carried out in the course of the process development with the high-strength sheet metal material DP600.

Keywords Shear cutting · Edge crack sensitivity · Work hardening · Counter-shaving · Hole expansion test · Burr-free cutting · Progressive die

1 Introduction

Shear-cut edges can be found at almost every sheet metal component manufactured by sheet metal forming technology. However, shearing induces high strain values onto the cutting edge and thus reduces the residual forming capacity of sheet metal materials with regard to subsequent forming processes [1, 2]. This effect is also

S. Senn (✉) · M. Liewald
Institute for Metal Forming Technology, University of Stuttgart, Holzgartenstraße 17, 70174 Stuttgart, Germany
e-mail: sergei.senn@ifu.uni-stuttgart.de

M. Liewald
e-mail: mathias.liewald@ifu.uni-stuttgart.de

© The Minerals, Metals & Materials Society 2021

G. Daehn et al. (eds.), *Forming the Future*, The Minerals, Metals & Materials Series,
https://doi.org/10.1007/978-3-030-75381-8_232

known as "edge crack sensitivity" and may lead to spontaneous crack initiation and premature failure [3]. A perspective approach for reducing the edge hardening effect of sheared sheet metal components is provided by two-stage shaving [4, 5]. However, this shaving process does not prevent the formation of a shaving burr, which can become detached in subsequent machining processes or during product life cycle and thus leads to pressure marks on the component or on the die surface in case of processing sheet metal components further by subsequent progressive dies. Therefore, shaving is usually followed by a downstream process (e.g., vibratory grinding, troweling, etc.), in which the burr is removed. Due to this processing deficit, methods such as counter-punching [6] or embossing-shearing [7] have been developed in recent research work, which enables burr-free cutting of sheet metal materials. In addition to these processes, the present paper is focusing on the newly developed two-stage counter-shaving process. In particular, the influence of this process on edge hardening effects and edge crack sensitivity of sheet metal materials is numerically and experimentally investigated.

2 Two-Stage Counter-Punching and Shaving

Counter-punching is defined as a shearing process being performed in several stages with at least one reversal of cutting direction. This reversal of cutting direction allows burr formation to be avoided [8]. The counter-punching process was developed by Liebig at the Institute for Metal Forming Technology (IFU), University of Stuttgart, in 1979 as a three-stage process and has been continuously improved during recent years [6, 9–11]. In addition to three-stage counter-punching, [12] and [13] examined a two-stage counter-punching process and showed that robust counter-punching can also be performed by only two tooling operations. In the first stage of two-stage counter-punching, the sheet metal material is embossed from the lower side to a depth t_E by a punch, causing a rollover at the lower side of the sheet metal material to be formed (see Fig. 1). In the second stage, counter-punching is performed in the opposite direction and complete material separation is achieved.

The so-called shaving process belongs to the group of cutting processes with high accuracy, which allow economical production of rectangular cut surfaces with a very high burnish depth. The shaving process is frequently used in industry to significantly improve the cutting surface quality of shear-cut components and thus to enable fitting punching, for example. During shaving, the sheet metal is pre-punched with a smaller cutting diameter in the first stage and cut to size in the same cutting direction with the final contour punch by adding a shaving addition z in the second stage [15–17]. Principle of the second shaving stage is shown in Fig. 2. The separation of a narrow contour (additional shaving) results in changed stress conditions since material separation takes place much later. The shaving process is mainly influenced by the geometric process variables clearance u and shaving addition z, which have been extensively investigated for different materials in [4]. The sensitivity to edge cracking of two-stage recut edges has been tested in [5]. The investigations carried out

by means of hole expansion tests and hole tensile tests clearly show the high potential of recut shaving strategies to reduce edge hardening of shear cut components [5, 18]. Compared to conventionally sheared edges, the sensitivity is significantly lower and the residual forming capacity is higher.

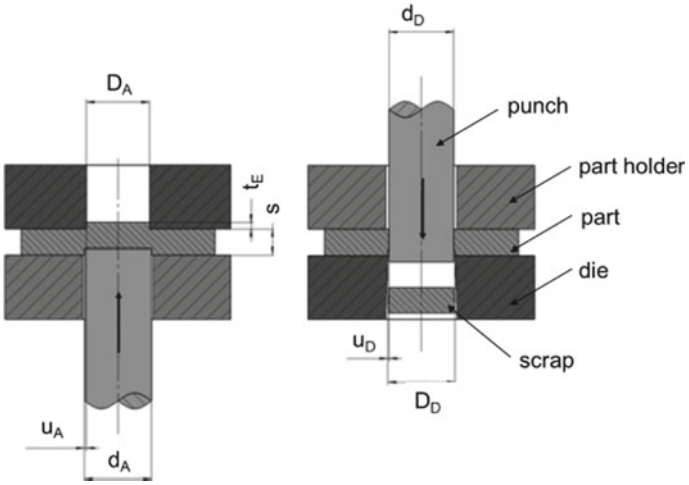
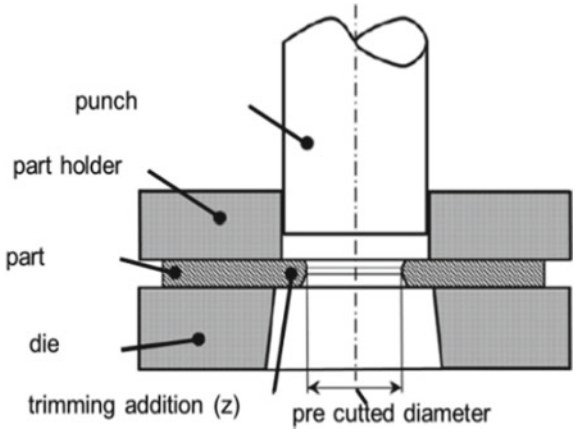


Fig. 1 Principle of two-stage counter-punching [14]

Fig. 2 Principle of a shaving process [18]



Senn and Liewald [27] further developed both cutting processes described above further to achieve a combined counter-shaving process. Counter-shaving leads to an increase in residual formability, a reduction in crack sensitivity, and to a good cutting surface with high clean-cut portions and freedom from burrs, as all advantages of

counter-punching and conventional shaving are combined in this two-stage process (see Fig. 3). Here, pre-piercing and embossing are performed in one stroke. For this purpose, a punch with a step in the diameter is used, which fulfills the function of these two processes. In the second stroke, the shaving step is performed in the counter-direction.

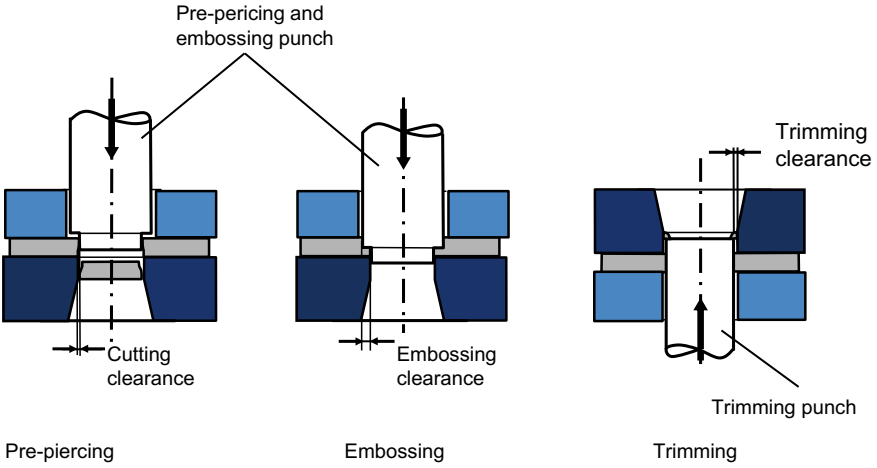


Fig. 3 Functional principle of two-stage counter-shaving [27]. (Color figure online)

3 Simulation Setup and Modeling

For the numerical investigations on the two-stage counter-shaving process, a basic simulation for the first process step with a stepped pre-piercing punch was initially set up using the software environment DEFORM 2D. This simulation provided the basis for all subsequent simulations and for the design of experiments. On this basis, all simulation parameters and boundary conditions were first defined, which were defined as fixed during the investigations and remained constant throughout. The main simulation parameters are listed in the following table (Table 1).

In addition to these basic settings, the punch and die geometries were varied in order to examine the process parameters cutting clearance u_v, embossing clearance u_p, and embossing depth t shown in Fig. 4. This examination was performed by means of a full factorial simulation strategy. For each factor combination, the corresponding geometry of punch and die were created in Dassault Systems Catia, implemented individually in DEFORM, and assigned to each other. The geometric parameters investigated are listed in Table 2 which means that a total of 84 parameter

Table 1 FEM Simulation setup of the combined counter-punching and shearing process with a stepped pre-piercing punch

Shearing parameters		Shearing parameters	
Sheet metal material (workpiece)	DP600(CR330Y590T-DP-GI50/50-U)	Friction model, friction coefficient	Coulomb, 0.1
Material behavior	Elastic–plastic (Hooke's law and von Mises criterion)	Fracture criteria	Normalized Cockroft & Latham
Punching tools modeled	Rigid	Critical value	2.8
Piercing diameter	10 mm	Punch velocity	300 mm/sec
Sheet thickness	1 mm	Yield condition	von Mises
Size of the smallest element	0.006 mm	Part holder force	300 kN
Step size per time step	0.002 mm/step to 0.001 mm/step		

Table 2 Variation of punching parameters

t[%]*	u_v[%]*	u_p[%]*
16	5	−2.5
28	7.5	−5
40	10	−7.5
52		−10
64		
76		
88		

combinations were examined. The values given in percent refer to the sheet thickness. In this study, the piercing of a diameter of D = 10 mm was investigated during counter-shaving process.

The following Figs. 5 and 6 show an exemplary complete simulation of an ideal process cycle in 11 images. In picture 1, the punch with the pre-piercing diameter just engages into the metal sheet. In picture 3, the metal sheet has just been separated. The engagement of the embossing diameter of the punch can be seen in picture 5. After reaching the defined embossing depth t, which is adjusted by the punch stroke, the metal sheet is completely embossed (Picture 6). Immediately afterward, the engagement of the shaving punch is shown on the bottom side of the metal sheet (Picture 7). Pictures 8–10 show the shaving process and the last picture shows the completely trimmed cut surface with the final cut surface shape.

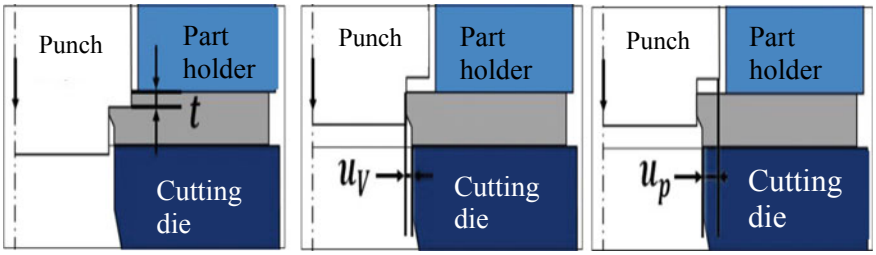


Fig. 4 Explanation of the punching parameters. (Color figure online)

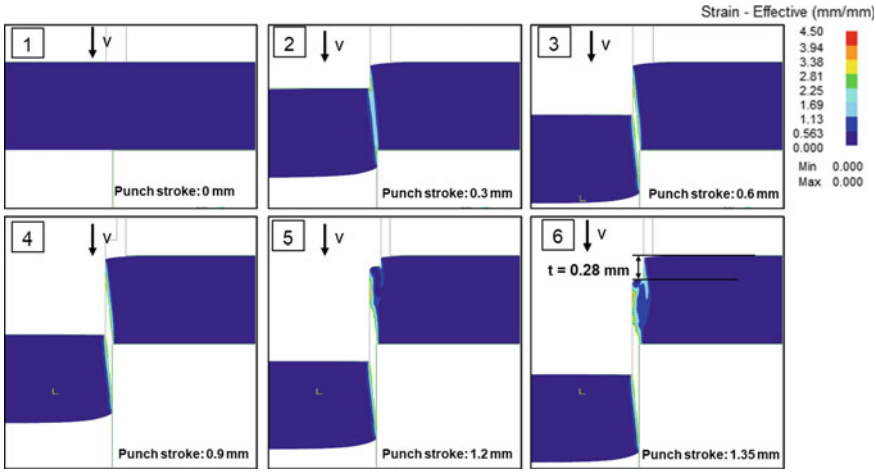


Fig. 5 First stroke: Pre-piercing and embossing, (t = 28%, cutting clearance $u_v = 7.5\%$, embossing clearance $u_p = |-5\%|$). (Color figure online)

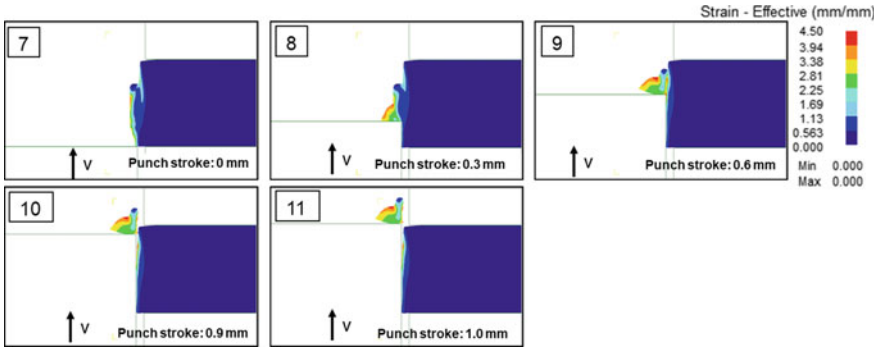


Fig. 6 Second stroke: shaving,; (t = 28%, cutting clearance $u_v = 7.5\%$, embossing clearance $u_p = |-5\%|$. (Color figure online)

After simulating all 84 parameter combinations in sequence, the requested data of the simulation results (after pre-piercing, embossing, and shaving) could be extracted or measured using the measurement tool of the simulation program. The data was collected in tables and subsequently evaluated. All measured data refer to the cutting surface because this is where the highest material load occurs during a cutting process. For the evaluation of the "Strain Effective" as a comparison value between the various simulations, the maximum value occurring at the cut surface was considered. To get this maximum value, 500 measuring points were positioned along the cutting surface. As a result, a sufficiently small distance between the single measuring points could be ensured, which is approximately 1/3 of the smallest element edge length. Figure 7 (left) shows an example of such a punctured cut surface from P0 to P500. For evaluation, the lengths of the two smooth cut portions were measured with the measurement tool which is integrated into DEFORM. The upper clean-cut portion is formed by embossing, the lower clean-cut portion is formed by shaving. The size of the fracture surface could be determined approximately from the data of the clean-cut portions. The areas described are shown in Fig. 7 on the right. In the evaluation, all results of all simulations that were performed for the individual factor combinations were compared with each other according to the full factorial DOE, shown in Table 2.

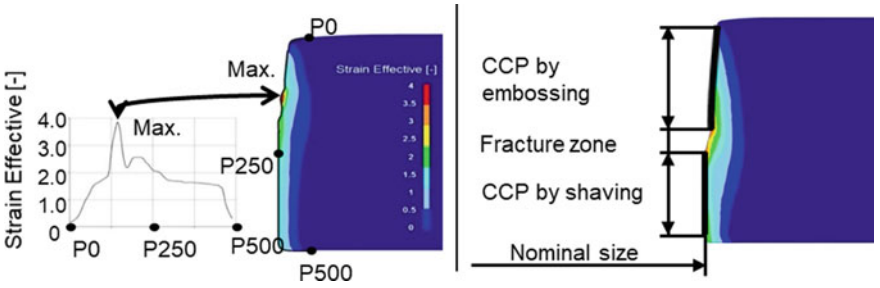


Fig. 7 Strain effective and CCP of counter shaved edge. (Color figure online)

4 Results and Discussion

The counter-shaving process presented in this paper must comply with two main objectives. The first essential objective consists of the production of burr-free component surfaces. The freedom of burrs thereby depends on the cutting parameters embossing depth, embossing clearance, pre-punch clearance, and shaving clearance. The optimum adjustment of these parameters as well as the process limits regarding the production of burr-free components were investigated as part of the research work reported in this paper. The second essential objective of the counter-shaving process is to reduce edge hardening on cutting surfaces. In this respect, the potential of counter-shaving could be demonstrated by means of hole expansion tests.

4.1 Numerical Results

4.1.1 Identifying the Process Limits for Burr-Free Cutting

To determine the numerical limiting process parameters of the counter-shaving process, schematic images of the cutting surface at some intermediate steps of the cutting process are considered. For some parameter combinations, critical process runs occur already during embossing or at the beginning of the shaving process. In this respect, the three main limiting parameters are described in more detail in the following.

1. If embossing is carried out with a depth of more than $t = 64\%$, the sheet metal material flows into the cutting clearance between punch and cutting die, and a material ring is formed on the bottom side of the sheet. On the one hand, this can lead to damage to the surface of the punch and, on the other hand, prevents the shaving punch from touching the sheet metal in a defined way. Thus, the shaving punch does not engage on the underside of the sheet metal but instead folds the material ring. If the material ring breaks, a swarf ring is produced. Furthermore, folding up the material ring hinders the formation of the edge draw-in. Figure 8 shows an example of the formation of the material ring.

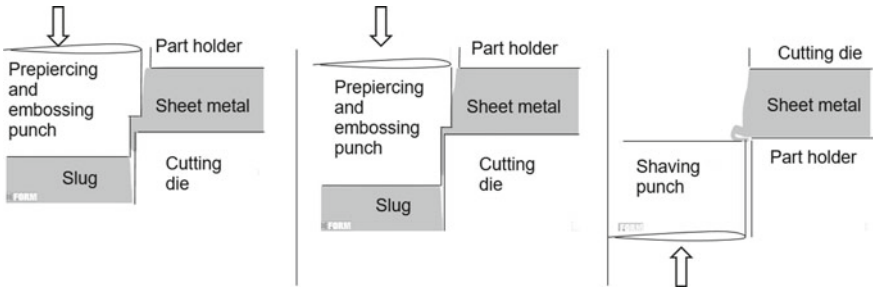


Fig. 8 Material ring formation during embossing and folding during shaving

2. The following Fig. 9 illustrates positioning of the shaving punch on a sheet metal pre-pierced and embossed in the previous step. In the case shown, the previously chosen embossing clearance was too small because the shaving punch does not engage on the bottom side of the sheet metal, but rather on the fracture surface created during pre-piercing. This prevents edge draw-in on the bottom side of the sheet metal and may lead to burrs. This problem does not occur when using larger embossing clearances of over $|-2.5\%|$.
3. Figure 10 shows a counter-shaved sheet metal material. The embossing depth was $t = 16\%$. Due to this low embossing depth, the crack initiation only occurs after a high punch stroke during shaving. As a result, the clean-cut surface due to embossing and the edge draw-in on the top of the sheet metal is lost and a

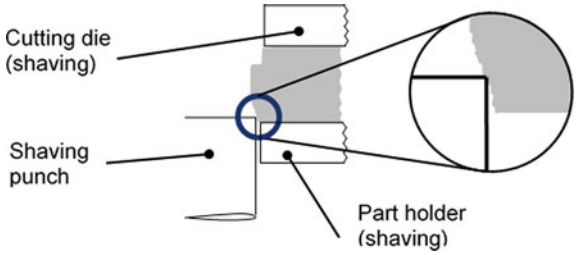


Fig. 9 Shaving punch engagement on the fracture surface. (Color figure online)

cutting burr typically created by normal shaving is formed. For burr-free cutting surfaces, the embossing depth must be at least $t = 28\%$.

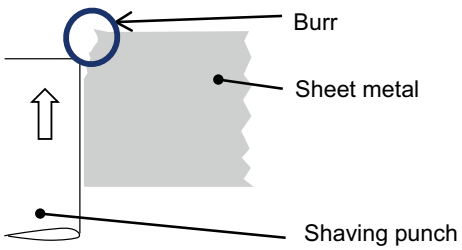


Fig. 10 Burr formation during shaving. (Color figure online)

4.1.2 Effect of Process Parameters on Clean-Cut Portion and Strain Effective

The following sections describe the results of numerical investigations on the combined counter-shaving process with regard to the influence of various process parameters on the cutting result and the occurring interactions. For these investigations, the sheet metal material DP600 with a sheet thickness of 1 mm was used. The following scatter diagrams (Fig. 11 and Fig. 12) do show the influences of the process parameters and the effects of interactions. It can be noticed that the embossing depth affects both the Strain Effective and the clean-cut portions (CCP).

Figure 11 shows the CCP caused only by shaving in relation to the Strain Effective. It can be seen that the CCP correlates with the Strain Effective value and that due to lower embossing depths t, higher clean-cut portions and at the same time lower Strain Effective values can be achieved. So, the investigation on the embossing depths reveals that low embossing depths have a positive effect on both the remaining formability and the geometric cut surface: The smaller the embossing depth, the lower the deformation, and the larger the clean-cut surface created during shaving. This also indicates that there is a correlation between the geometry of the cut surface

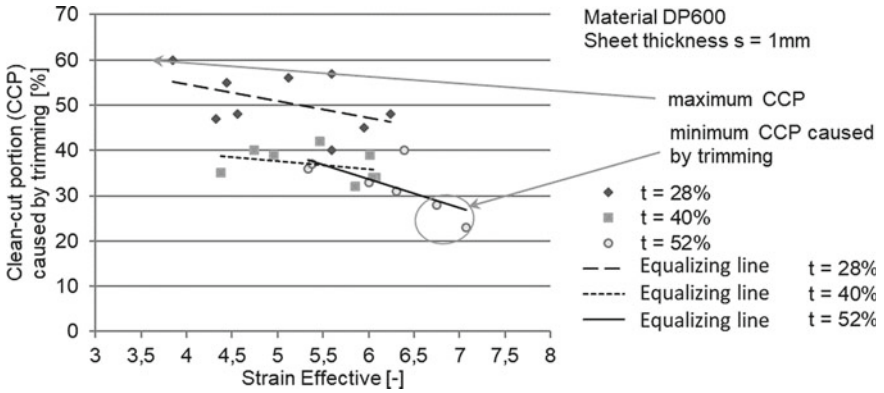


Fig. 11 CCP caused by shaving versus strain effective

and the degree of deformation. Further, the Strain Effective value is influenced by the cutting clearance and the embossing clearance. In the following, only the embossing depth $t = 28\%$ is considered since this embossing depth showed the greatest potential for low Strain Effective values. Figure 12 shows the total CCP (i.e., the sum of the clean-cut portions caused by embossing and shaving) and that the maximum clean-cut portions do not immediately correlate with the Strain Effective, as maximum possible CCP does not correlate with the lowest Strain Effective value.

In Fig. 13, the simulated Strain Effective values are plotted on the ordinate axis and visualized as bars. The considered cutting clearances u_v and the embossing clearances u_p are plotted on the abscissa axis in combination. Neither the increase in the cutting clearance u_v nor the increase in the embossing clearance u_p shows a correlating increase/reduction in the Strain Effective value. Nevertheless, a considerable influence of these process parameters on the result can principally be observed:

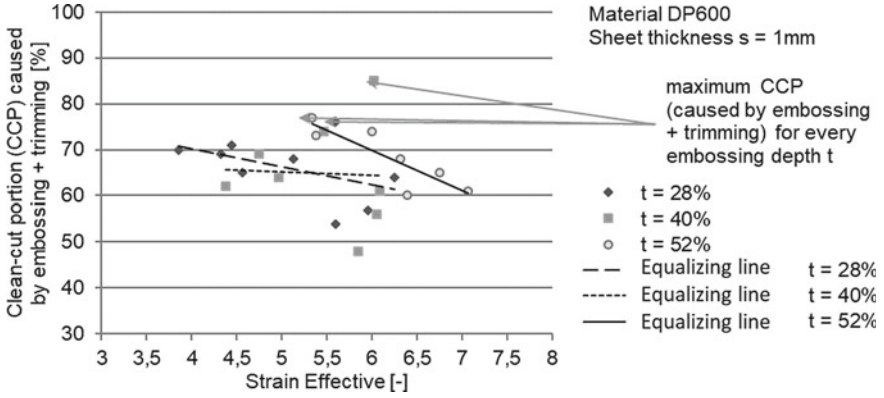


Fig. 12 CCP caused by embossing and shaving

between the largest ($\overline{\varepsilon} = 6.25$) and the lowest Strain Effective value ($\overline{\varepsilon} = 3.85$) is a difference of $\Delta\overline{\varepsilon} = 2.4$, which corresponds to a range of 38%. Based on these investigation results, it is assumed that the influence of cutting clearances and embossing clearances is impaired by varying strengths caused by the further deformation of the cutting surface during shaving. The following combination of parameters can be considered as the best result for achieving low edge crack sensitivity and a suitable cutting surface inside the robust process window: For combined counter-shaving, an embossing depth of $t = 28\%$ with an embossing clearance of $= u_p$|-5%| and a cutting clearance of $= u_v 5\%$ shows the best results.

4.2 Experimental Results

4.2.1 Work Hardening of Shear Cut Edges

In order to quantify edge hardening due to work hardening during the shearing process considered, the hardness test method according to Vickers [19] was used. Vickers hardness testing is standardized in DIN EN ISO 6507–1 and is usually used for small sheet thicknesses such as those considered here. For a microhardness measurement, low test loads (HV0.01) are used. In order to gain meaningful results concerning the hardening of cutting edges, it is important to carry out a hardness gradient measurement with a sufficient number of measuring points. The starting points of the measurement should be close to the cutting edge and extend over the entire sheet thickness. The measuring section must run through the entire solidified area down to the unsolidified one. Thus, it can be determined how deep the influenced cutting edge zone reaches into the material. In addition, it is possible to measure the degree of hardening by comparing the hardness after shearing (HV_1) with the initial hardness of the material (HV_0). Material hardness in that sense can be used as a characteristic value that correlates with the structural change of material. By means of a hardness measurement, conclusions can be drawn about changes in the microstructure caused by the work hardening described above [19]. Figure 14 shows the cutting edge of conventional shearing process according to VDI guideline 2906 with additions for edge hardening. In the influenced marginal zone b_{RZ}, the HV_1/HV_0 ratio is higher than 1, because the hardness after the cutting process (HV_1) is higher than the hardness of the initial material (HV_0). Afterward, when enlarging the distance to the cutting edge, the unaffected area in which HV_1 equals HV_0 follows. The ratio is thus calculated to the value 1 since only the initial hardness of the sheet metal material is available in this area. In order to gain meaningful results, a sufficient number of measuring points must be generated when measuring spatial hardness distribution [19] has illustrated the arrangement of measuring points in a small sketch, which is shown in Fig. 15. The sketch is an example of the arrangement of the measuring points of a sheet thickness of 1 mm. Here, the entire measuring range extends over a width of 0.500 mm. The measuring points are arranged offset over the complete thickness of the sheet metal. The first three vertical measurement

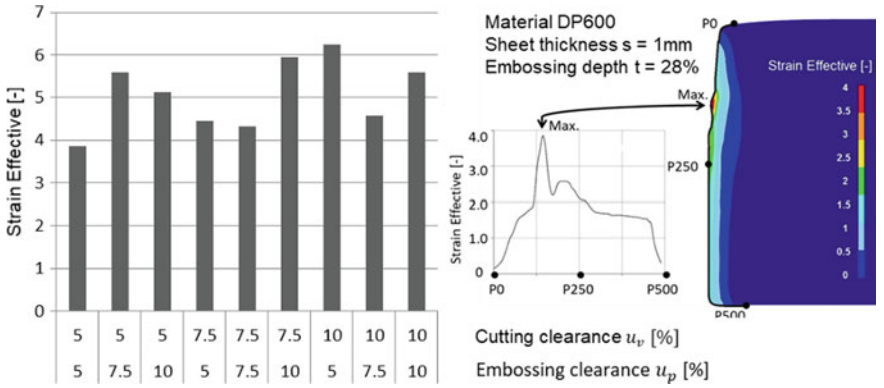


Fig. 13 Effect of cutting clearance $\mathbf{u_v}$ and embossing clearance $\mathbf{u_p}$ on the Strain Effective at embossing depth t = 28%. (Color figure online)

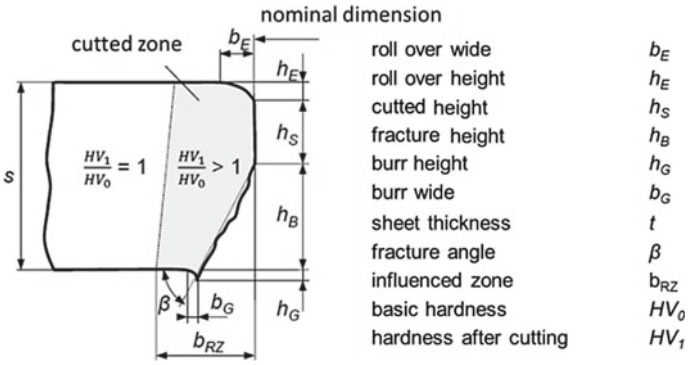


Fig. 14 Hardening of cut edges [20]

series with distances of 0.070 mm, 0.145 mm, and 0.250 mm are used to measure edge hardening. The fourth column, which has a larger distance than the others, is intended for measuring the initial hardness of sheet metal. The distances between the points and rows are selected according to [19] in such a way that the distance rules for hardness indentations according to DIN EN ISO 6507–1 are adhered to.

Figure 16 shows measured microhardness distribution of the conventionally sheared edge of sheet metal material DP600 with thickness s = 1 mm. Cutting clearance was u = 10%. Cutting parameters and cutting process are visualized in the figure. In addition, the small picture of the cut edge shows the distance direction of distances l and d. Distance d indicates the distance of the hardness indentations in the direction of sheet thickness. Distance l shows the distance between the measurement series and the cutting edge. The ratio HV1/HV0 is plotted on the abscissa. This can be used to indicate the degree of hardness. The measuring series in sheet metal thickness direction having a distance of 0.9 mm to hole perimeter represents

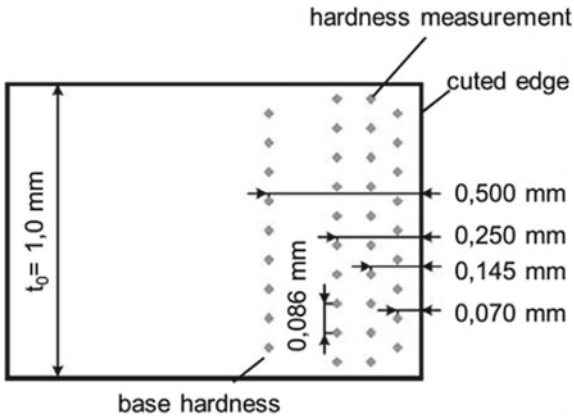


Fig. 15 Arrangement of the measuring points to determine the hardening of an idealized cutting edge [19]

initial material hardness. However, the ratio HV1/HV0 does not correspond exactly to 1.0, as the hardness values of the initial material microstructure also are scattering. The dark blue line, which is the closest to the cutting edge, shows a maximum ratio of 1.65. The following measurement series with a greater distance to the cutting edge (light blue and light gray) cover the whole sheet thickness. The maximum hardening of the edges ranges around 1.65 and all series of measurements, except for the initial material hardness, show an increase in hardening from the starting point. This phenomenon can be justified as follows: The deeper the punch penetrating through the sheet metal during the cutting process, the greater the stress value that emerges in the shearing zone. The material starts to flow plastically as soon as the shear yield point of the material is reached. With progressive deformation, the stresses reach the material-dependent shear fracture limit. No more material can be deformed any further at that stage, the first cracks are formed and therefore the slug breaks through. The stresses are linked with work hardening effects, whereby the cutting edge hardens, too. The work hardening increases with increasing stress, which also increases the hardness at the cutting edge. Thus, the material also shows the greatest edge hardening in the area of the fracture surface.

Figure 17 shows the work hardening of counter-shaving with an embossing clearance of $u_p = -0.5\%$, a precutting clearance of $u_v = 10\%$, and an embossing depth of $t = 0.2$ mm. Similar to shear cutting, the initial material hardness values are 1. Measuring closer to sheared edge shows an increasing hardness distribution. Edge hardening continues to level out over a longer area in a certain scatter band until it finally falls back to the basic level. When shearing, however, edge hardening increases continuously up to the maximum (see Fig. 12). The differences can be explained by [4]. When pre-punching, the first step in the counter-shaving process corresponds to conventional shearing. In the second stage, the actual shaving, the cutting edge of the pre-cut contour is scraped off. This removes the remaining shaving allowance. This process corresponds to machining because a thin chip is unrolled from the upper side of the sheet metal until it breaks off. In [4] it is reported that the cutting forces decrease with declining shaving addition. This is due to the lower stiffness of smaller

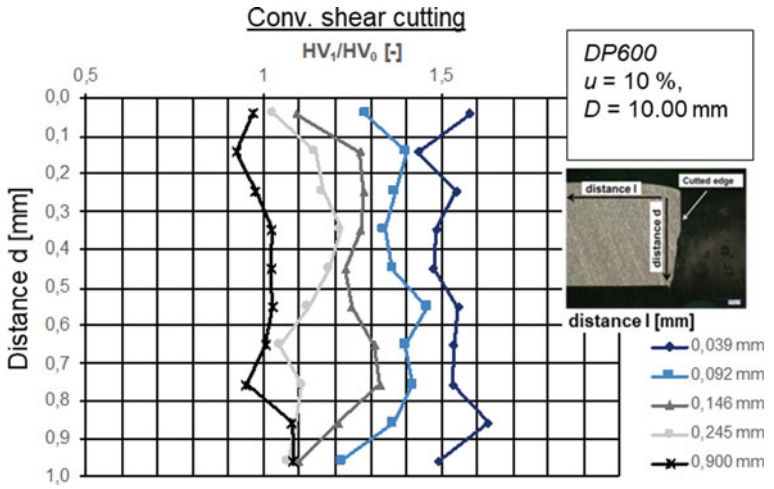


Fig. 16 Measurement of microhardness distribution of shear cut edge. (Color figure online)

shaving addition. The forces and therefore also the tension stress in the cutting edge can be positively influenced by a reduced shaving addition. This correlation also has a positive effect on edge hardening. The maximum measured microhardness distribution values around 1.35, i.e., similar to recut edges. All measurement series show a lower work hardening of counter-shaved edges compared to conventional cut edges.

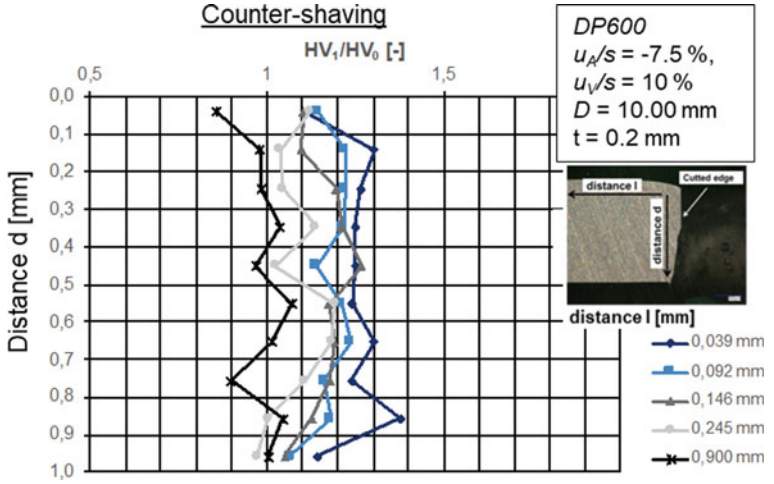


Fig. 17 Measurement of microhardness distribution of counter-shaved edge. (Color figure online)

4.2.2 Crack Edge Sensitivity of Shear Cut Edges

Hardening of cut edges can be measured by spatial hardness measurement strategies as described above. However, the hardness values cannot be used directly to determine the residual formability of the cutting edge [21]. Several methods for determining the sensitivity to edge cracking can be found in literature. For the open cutting line, the diabolo test is usually used [22]. This paper, however, only deals with closed-cutting line conditions. At present, the hole expansion test according to ISO 16,630 is the only standardized test method for determining the sensitivity to edge cracking of closed cutting lines. Prior to the test, a hole with a diameter of 10 mm is punched into a blank. For hole expansion tests according to ISO 16,630, at least three samples should be tested per sample variant. First of all, the sample is placed on a die with the burr pointing upward and centered ahead the punch. A part holder fixes the sample firmly in place thus preventing it from slipping or flowing. A conical punch having a 60° head taper angle moves upwards and expands the hole. The expansion is stopped as soon as a crack has formed through the complete sheet thickness. In [5], the crack detection is carried out visually by the operator. Due to his subjectivity, however, this leads to a range of results. The determination of component failure due to cracks depends very much on the reaction speed and the experience of the operator. In [19], GOM Aramis system is used for crack detection. The exact point of crack initiation can be determined by the system's digital images. This eliminates the influence of the operator's subjectivity. Figure 18 shows the experimental setup of the hole expansion test according to ISO 16,630. Here, the two most important characteristic values are the diameter of punched hole before the test D_0 and the hole diameter after test D_h. Both values are used to calculate hole expansion ratio (HER) by means of the following:

$$\lambda = {(D_h - D_0)}/{D_0} \times 100\%$$

If the cutting edge has a low widening ratio, the material is highly sensitive to edge cracking. Conversely, a high hole expansion ratio indicates a low edge crack sensitivity. According to [24], the hole expansion capability correlates with the tensile strength of the material.

The results of the hole expansion tests carried out for conventionally shear cut and for counter-shaved edges are shown in Fig. 19. For the sheet metal material DP600 having a sheet thickness of t = 2 mm, the hole expansion ratio of conventionally cut edges is 65%. This value is used as a reference value and is compared to the value of the counter-shaved specimens. For this purpose, several specimens counter-shaved with different embossing depths (from t = 40% to t = 70%) were investigated. The results show that the hole expansion ratio can be significantly increased with decreasing depth of embossing. At an embossing depth of t = 60%, the HER is the same as with conventionally shear cutting. However, if the embossing depth is reduced to t = 40%, the HER increases to 104% and thus is significantly higher compared to conventional shear cutting. Fig. 20 presents the influence of the pre-

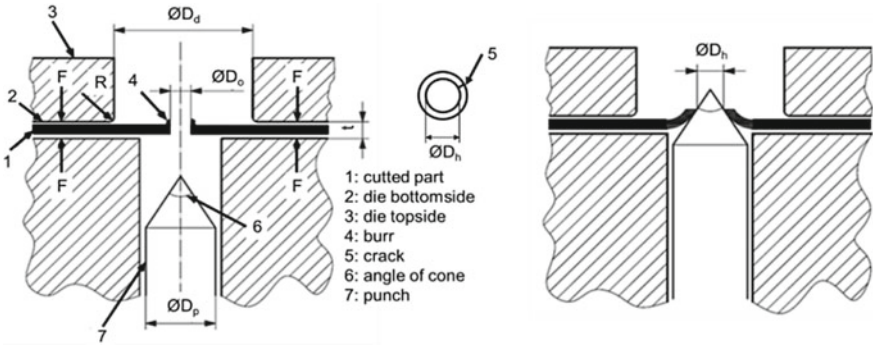


Fig. 18 Experimental setup of the hole expansion test [23]

piercing clearance during counter-shaving. It can be seen that a higher clearance in pre-piercing, here up to 10%, shows better results than a pre-piercing clearance of 5%.

Specimens for counter-shaving were tested in both orientations, as no burr occurs, but according to ISO 16,630 standard the burr should always be directed upwards when testing. Compared to conventional shearing, counter-shaving can be increased the HER by 59%. Thus, it has been demonstrated that counter-shaved components show a lower sensitivity to edge cracking than conventional shear cut edges.

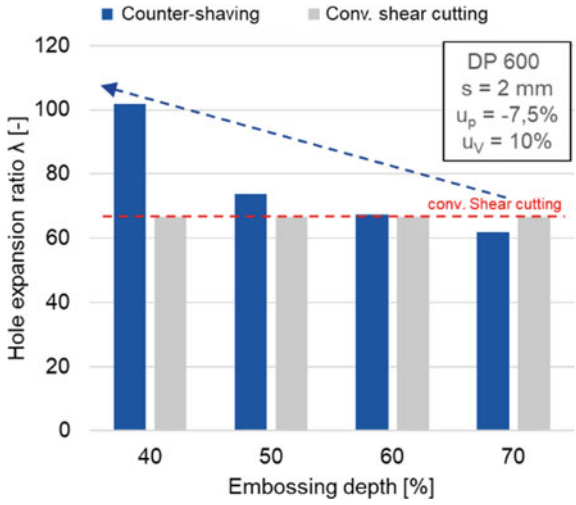


Fig. 19 Effect of embossing depth. (Color figure online)

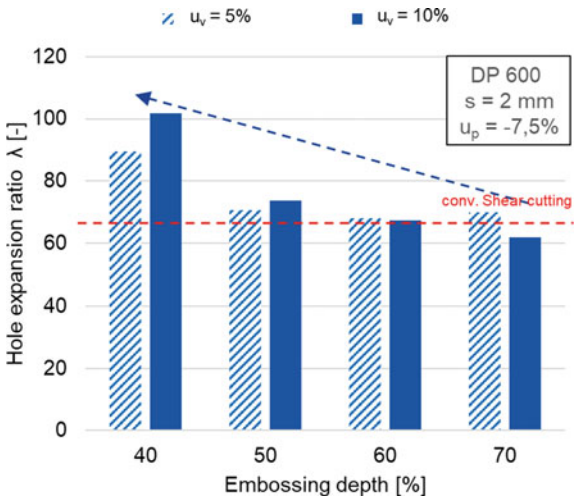


Fig. 20 Effect of pre-piercing clearence. (Color figure online)

5 Conclusion

This paper shows the great potential of the newly developed counter-shaving with regard to the production of burr-free shear cut surfaces having reduced edge hardening and high residual formability compared to conventional shear cutting. Based on the hole expansion test, it could be demonstrated that counter-shaved components are less sensitive to edge cracking than shear cut components. However, when correlating the hole expansion test to edge hardening, it was found that cutting edges achieve different hole widening ratios for comparable edge hardening. As reported in [25, 26], the cut surface quality has an influence on the hole expansion ratio. Thus, a large smooth cut surface increases the forming capacity of a cutting edge. In contrast, microcracks and rough surfaces lead to a large fracture area, which impairs the forming capacity. This means that cutting edges with a lower edge hardening rate in conjunction with a larger smooth cutting surface also have a larger hole expansion ratio. In this respect, shear cutting has the greatest edge hardening and the smallest smooth cut, resulting in the lowest hole expansion ratio of all processes. Furthermore, the results presented in this paper show that counter shaved-components are 59% less sensitive to edge cracking than conventional shear cut components, which enables a significantly higher degree of forming capacity in subsequent forming operations.

References

1. Gall M, Liewald M (2013) Experimental investigation of the influence of shear cutting parameters on the edge crack sensitivity of dual phase steels. IDDRG, Zurich, pp 219–224
2. Wu X, Bahmanpour H, Schmid K (2012) Characterization of mechanically sheared edges of dual phase steels, Elsevier Verlag

3. Matsuno T, Sato K, Okamoto R, Mizumura M, Suehiro M (2016) Synergy effect of shear angle and anisotropic material ductility on hole-expansion ratio of high-strength steels. J Mater Process Technol
4. Kühlewein R (2003) Einfluss der Prozessparameter auf das Nachscheiden schergeschnittener Konturen, Dissertation, TU München
5. Gläsner T, Volk W, Hoffmann H, Golle R (2015) Evaluation eines Verfahrens zur Bestimmung der Kantenrisssensitivität von hochfesten Stählen, utfscience, Verlag Meisenbach
6. Liebing H, Lange K (1978) Erzeugung gratfreier Schnittflächen durch Aufteilen des Schneidvorgangs (Konterschneiden), Dissertation, Universität Stuttgart
7. Sachnik P, Volk W (2017) Methodik für gratfreie Schnittflächen beim Scherschneiden, Disseration, TU München
8. Lange K (1990) Umformtechnik – Handbuch für Industrie und Wissenschaft, Band 3: Blechbearbeitung, 2. völlig neu bearbeitete und erweiterte Auflage; Springer Verlag
9. Erlenmeier W (2010) Stanzwerkzeug und Verfahren zum mehrstufigen Stanzen. Europa-Patent EP 2198988:A1
10. Haack J (1993) Patentschrift: Process for producing burr-free workpieces by blanking, in particular in a counterblanking tool, US Patent No 5247862 A
11. Haack J (1994) Method for manufacture of workpieces by punching, in particular in a precision counter punching tool. Europa Patent No: EP 0418779:B1
12. Kappes J (2010) Schnittgratfreies Scherschneiden mittels Konterschneiden, utfscience, Universität Stuttgart
13. Wörz C, Gall M (2013) Grat- und flitterfreie Aluminiumbleche aus dem Stanzautomaten, MaschinenMarkt
14. Hoffmann H, Neugebauer R, Spur G (2012) Handbuch Umformen. Carl Hanser Verlag, München
15. Guidi A (1965) Nachschneiden und Feinschneiden. Carl Hanser Verlag, München
16. Romanowski WP (1965) Handbuch der Stanzereitechnik. VEB-Verlag, Berlin
17. Weckener H (1975) Werkzeugstähle für Schnittwerkzeuge unter Berücksichtigung der verschiedenen Schneidverfahren, Technischer Bericht
18. Gläsner T, Sunderkötter C, Hoffmann M, Volk W, Hoffmann H, Golle R (2013) Zweistufiges Scherschneiden reduziert die Kantenrissempfindlichkeit, Meisenbach Verlag GmbH
19. Mackensen A (2013) Presswerkorientierte Analyse der Umform- und Scherschneideigenschaften von Mehrphasenstählen, Dissertation, TU München
20. Nothaft K (2013) Scherschneiden höchstfester Blechwerkstoffe im offenen Schnitt, Dissertation, TU München
21. Held C, Schleich R, Sindel M, Liewald M (2009) Untersuchung zum Einfluss der Verfestigung von schergeschnittenen Kanten auf folgende Umformpro-zesse, UTFscience.de
22. Gläsner T, Sunderkötter C, Rommel S, Volk W (2015) Evaluation eines Verfahrens zur Bestimmung der Kantenrisssensitivität von hochfesten Stählen, umformtechnik.net, Meisenbach Verlag GmbH
23. ISO 16630:2009(E), Metallic materials – Sheet and strip – Hole expanding test, 2009
24. Sadagopan S, Urban D (2003) Formability Characterization of a New Generation of High-Strength Steels, AISI/DOE Technology Roadmap Program, Final Report, American Iron and Steel Institute
25. Schneider M, Eggers U (2011) Investigation on punched edge formability, IDDRG 2011, Salzgitter
26. Atzema E et al (2012) A European round robin test for the hole expansion test according to ISO 16630
27. Senn S, Liewald M (2019) Numerical investigation on a new process of combined counter-trimming with regard to improvement of the residual formability of burr-free shear-cut edges, NUMIFORM 2019. Portsmouth, USA

Fine-Piercing of Electrical Steel Sheets by Edge-Sharpened Diamond Punch



Tatsuhiko Aizawa and Tomomi Shiratori

Abstract Femtosecond laser trimming procedure was optimized to reduce the edge curvature of diamond-coated WC (Co) punch as possible and to decrease the maximum roughness of diamond coatings. Bare diamond-coated WC (Co) punches with normal grain size were prepared to have an original film thickness of 9 μm. Through two laser machining steps, the edge width of diamond coating was reduced down to 2 μm. By using the core die with the clearance of 4%, fine piercing experiments were performed to measure the load–stroke relationship and to describe the affected zone formation by shearing. The affected zone area as well as the fractured surface ratio significantly decreased with a reduction of the edge width down to 2 μm.

Keywords Piercing · Electrical steels · Nanostructured diamond punch

1 Introduction

The diamond-coated WC (Co) punches and dies have been developed to put the dry technology of plasticity into practice [1]. Due to the three-dimensional growth of diamond crystals on the WC (Co) tool surface, the normal diamond film has high surface roughness in its maximum up to 3–5 μm [2]. This high maximum surface roughness is not allowed in the precise stamping and forging; a post-treatment of as-coated diamond films is needed to adjust the surface roughness as well as the dimensional inaccuracy in geometry into the tailored surfaces of tools [3]. Plasma oxidation processing was utilized not only to ash the used DLC (Diamond-Like Carbon) films coated onto the tools and dies [4] but also to etch and polish the rough diamond films [5]. Although this process is effective to remove a part of coated films

T. Aizawa
Surface Engineering Design Laboratory, SIT, 3-15-10 Minami-Rokugo, Ota-City, Tokyo 144-0045, Japan
e-mail: taizawa@sic.shibaura-it.ac.jp

T. Shiratori (✉)
Faculty of Engineering, University of Toyama, Gofuku, Toyama City 930-8555, Japan
e-mail: shira@eng.u-toyama.ac.jp

© The Minerals, Metals & Materials Society 2021

G. Daehn et al. (eds.), *Forming the Future*, The Minerals, Metals & Materials Series,
https://doi.org/10.1007/978-3-030-75381-8_233

and to reduce the surface roughness, it is difficult to adjust the geometric inaccuracies within the tolerance of dimensions required for fine embossing and piercing punches of lead frames and fuel-cell separators [6, 7].

High silicon electrical steel sheets as well as amorphous magnetic films were developed to produce the motor cores with a variety of size, geometry, and alignment [8]. The key items common to them are low iron and hysteresis losses and geometric accuracy [9]; how to reduce those losses and how to sustain the dimensional accuracy stand on the high qualification in fine piercing of electrical steel sheets and films into the tailored core component. In particular, the affected zones into cores by piercing must be reduced as possible to lower the core loss [10]. Furthermore, the tool life of piercing punch and die has to be prolonged as possible for significant reduction of production cost [11]. As had been studied in [12, 13], bare WC (Co) punch was easy to be chipped at its edge only after piercing 100 times in continuous. CVD-diamond-coated tools as well as plasma nitrided tools were recognized to prolong the punch and die life in continuous piercing even under nearly zero clearance [14, 15]. The reduction of affected zones in pierced sheets was left as an engineering issue to be solved by trimming these diamond-coated and nitrided tool surfaces.

Authors reconsidered the previous trimming method with the use of the excimer laser processing [16] and proposed the femtosecond laser trimming process to adjust the CVD-diamond-coating geometry and to reduce the edge curvature of diamond-coated punch [17]. In fact, the edge curvature was reduced from 12. 5 μm down to 2.5 μm by this laser trimming. After embossing the AISI304 sheet with a thickness of 0.1 mm, EBSD (Electron Back-Scattering Diffraction) analysis revealed that the affected zone area was significantly reduced by using the trimmed, diamond-coated punch [18].

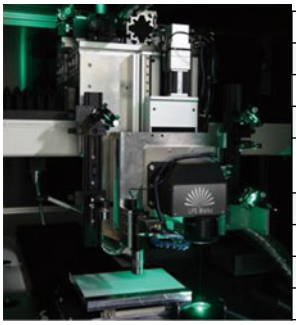
In the present paper, this femtosecond laser trimming procedure is optimized to reduce the edge curvature of diamond-coated WC (Co) punch as possible and to decrease the maximum roughness of diamond coatings. Bare diamond-coated WC (Co) punches with normal WC-grain size are prepared to have an original film thickness of 9 μm. Through two laser machining steps, the edge width of diamond coating was reduced down to 2 μm. With use of the core die with the clearance of 4%, fine piercing experiments are performed to measure the load–stroke relationship and to describe the affected zone formation by shearing. The affected zone area as well as the fractured surface ratio significantly decrease with the reduction of edge width down to 2 μm.

2 Experimental Procedure

Femtosecond laser machining system as well as laser trimming procedure are first stated to explain how to reduce the edge with and surface roughness of diamond coating. CNC (Computer Numerical Control) stamper is used to make fine piercing of electromagnetic steel sheets.

Femtosecond Laser Machining System. Femtosecond or sub-picosecond lasers are developed for innovative research and development; most industrial applications stand on this laser machining in the order of 100 femtoseconds. Since the focused spot of work materials is subjected to ultra-high power irradiation, how to scan the beam spot becomes more important when using this laser machining system. Higher repetition frequency of laser beams as well as higher scanning speed result in fast-rate, dimensionally accurate machining. Our developed system and its configuration are shown in Fig. 1. In the following experiments, the repetition rate was fixed by 400 kHz.

Laser Trimming Program. The laser-trimming and polishing process is instrumented into an experimental setup with notes on the uniform machining and ray pass control. Figure 2 depicts a standard setup for present trimming experiments. The side surface of punch head is first trimmed by using the laser beam controlling mode-1 where the laser is scanned along the central axis of WC (Co)-punch till the total reduction in thickness reaches to 2 μm. The top surface is secondly processed by using mode-2. The laser beam is moved from the center to the end of punch head. In both modes of experiment, the end of punch is held in jig to rotate with the constant velocity; e.g., $\omega = 20$ rps. The fluence (ϕ) for laser irradiation was also fixed to be different between control-I and control-II. In the control-I, $\phi = 0.6$ J/cm^2, while $\phi = 0.265$ J/cm^2.



Wave length	515nm
Pulse duration	180fs～190fs
Average power	8.2W
Repetition	MAX600kHz
Beam spot size	MIN:10μm using Galvanometer MIN:1μm using fixed lens
Stage area	300mm×300mm
Scanning speed	MAX 3000mm/s
Scanning area	MAX 30㎜×30㎜
Sample weight	< 30kg

Fig. 1 A femtosecond laser trimming system with the details on its capacity. (Color figure online)

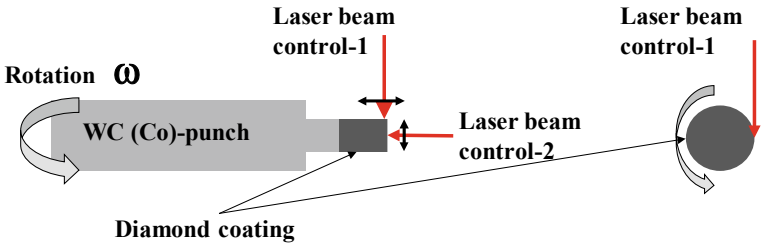


Fig. 2 Two-step laser trimming procedure. (Color figure online)

CNC Fine-Stamper for Piercing. The diamond-coated WC (Co) punch with and without trimming was fixed into a cassette die set for piercing experiment. Figure 3 depicts a typical experimental setup where the stroke is controllable by every 1 μm with in situ measurement of piercing load and punch stroke.

Observation and Measurement. SEM (Scanning Electron Microscopy), EBSD (Electron Back-Scattering Diffraction), and three-dimensional profilometer were employed to make an observation on the untrimmed and trimmed diamond-coated punches as well as the pierced electrical steel sheets and to measure the edge width of punch.

Tooling and Work materials. Bare CVD-diamond-coated WC (Co) punches were prepared in this experiment. The diamond film thickness was constant by 9 μm. Figure 4 shows the SEM image of diamond film prepared for trimming experiments.

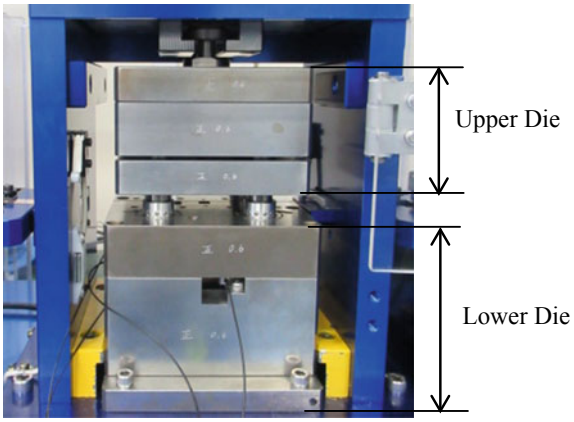


Fig. 3 Precise piercing experiment of electromagnetic steel sheets by using the CNC stamping system. (Color figure online)

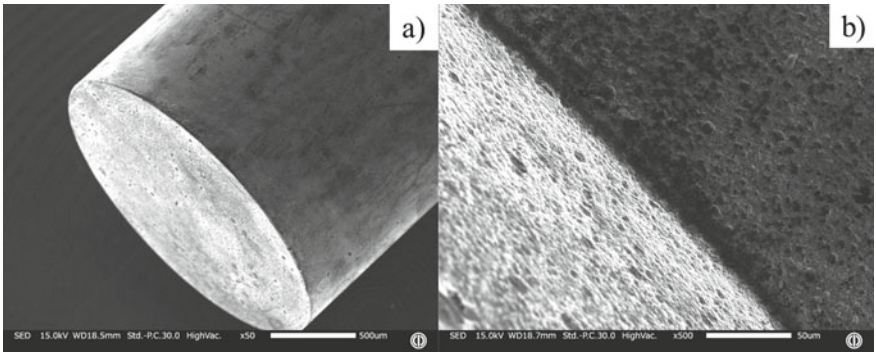


Fig. 4 SEM image on the bare CVD-diamond-coated WC (Co) punch surface. **a** Cylindrical punch with the diameter of 2 mm and **b** rough surface of diamond coating

The diamond film coated the WC (Co) punch surface uniformly. However, the top and side surfaces have high maximum roughness up to 3 μm. In particular, the punch edge becomes an intersection of two diamond films growing respectively on the top and side surfaces of WC (Co) head. As shown in Fig. 4b, the diamond film surface becomes dull at this punch edge.

3 Experimental Results

The diamond-coated WC (Co) punch with the head diameter of 2 mm and head height of 5 mm was laser-trimmed by reduction of diamond from a thickness from 9 μm down to 5 μm. Instead of the curvature radius at the edge of punch, the edge width was measured by SEM and employed as a targeting parameter to optimize the laser trimming conditions. Piercing process was utilized to describe the shearing behavior by using the diamond-coated WC (Co) punch with and without laser trimming.

Femtosecond Laser Trimming. Figure 5 shows the SEM images of trimmed diamond coatings. The top periphery of side surface with a width of 150 μm was trimmed to reduce the diamond film thickness by 5 μm. Comparing the trimmed surface in Fig. 5b with the surface of bare diamond coating in Fig. 4b, the surface condition and roughness are much improved by this laser trimming. Figure 6 shows the enlarged view from the punch head to the punch shoulder surface across the edge of punch. The curvature radius at the punch edge is much reduced from the original radius of 15 μm in the bare diamond-coated punch. Let us precisely describe the geometric configuration across the punch edge.

Optical microscopy is utilized to measure the edge width between the trimmed punch head and side shoulder surface. The laser beam is gradually focused onto the punch edge by changing the position. Figure 6 shows the focused image just on the punch edge; both the punch head and side shoulder surfaces become vague due to

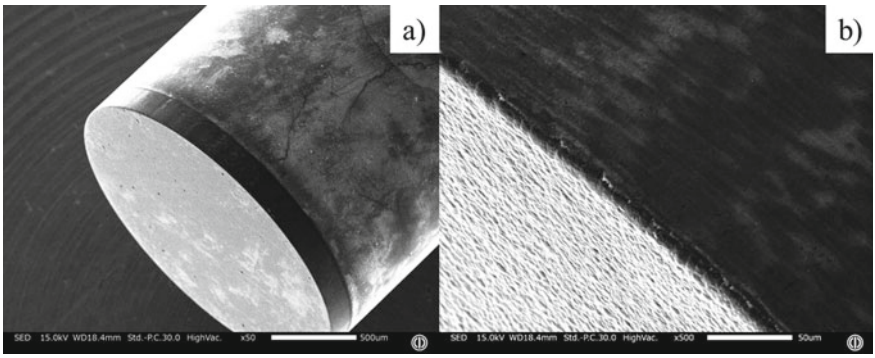


Fig. 5 Trimming results of the CVD-diamond-coated WC (Co) punch. **a** Trimming of diamond coating from surface up to the width of 150 μm, **b** Enlarged punch head and side surface

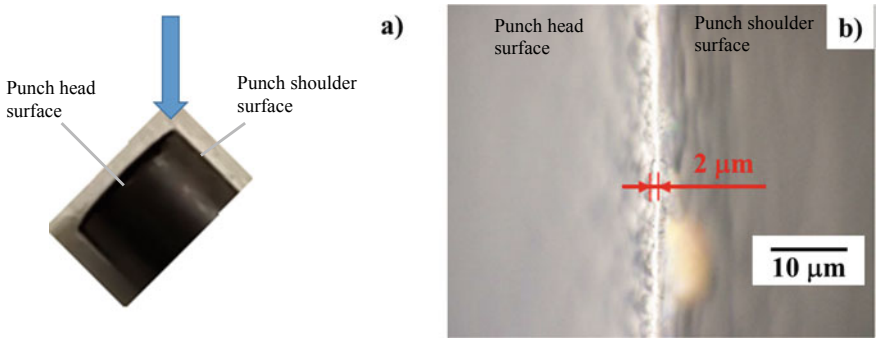


Fig. 6 Optical microscopic image from the punch head to the punch shoulder across the punch edge. **a** Observation field of view, **b** Enlarged punch edge and edge length. (Color figure online)

the focus depth in this laser microscopy. From the focused line width, the edge width is determined to be 2 μm.

Piercing Experiments. Two types of piercing experiments were performed by using the electrical steel sheets with the thickness of 0.5 mm; half and full piercing experiments. In the former, the shearing behavior is mainly governed by indentation of the edge-sharpened punch into worksheet with less influence from the core-die.

As shown in Fig. 7, the fine, fresh surface without local fractures is formed by this

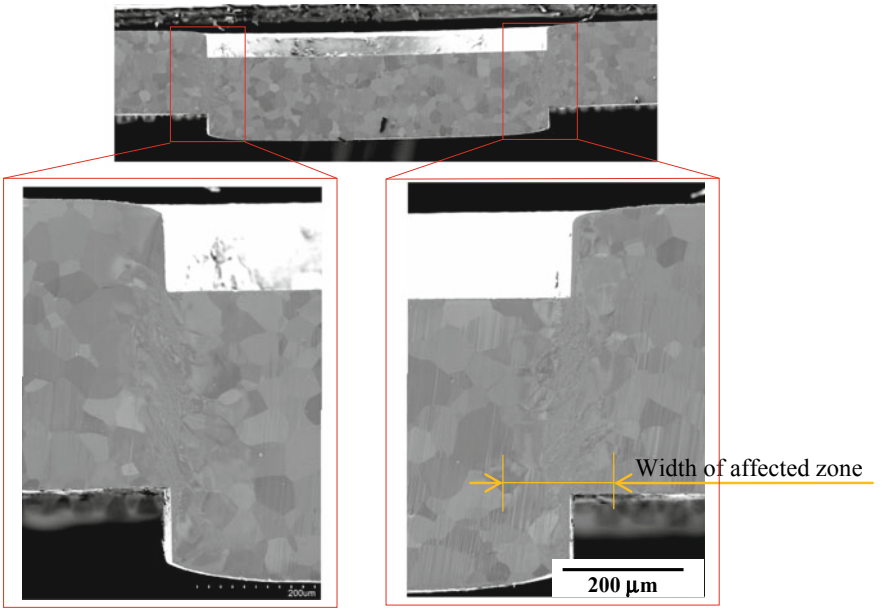


Fig. 7 Plastic flow by shearing process in the half-piercing experiment. (Color figure online)

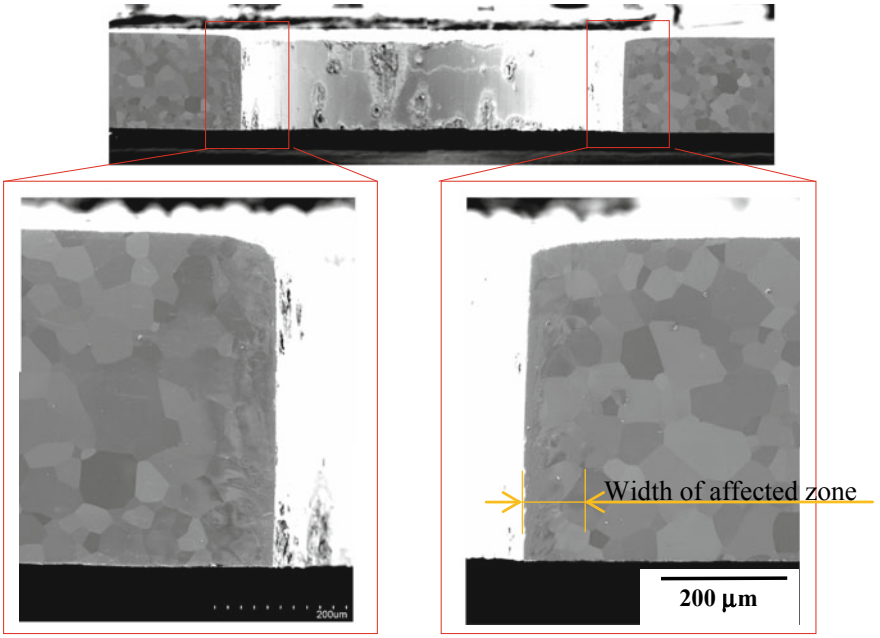


Fig. 8 Plastic flow by shearing process in the full-piercing experiment. (Color figure online)

half-piercing indentation of the trimmed diamond-coated punch. From this SEM observation, the electrical steel grains are severely deformed along the shearing plane. The affected zone width in the circumferential direction of the hole was up to about 180 µm. In case of full-piercing experiments, as shown in Fig. 8, the process affected zone width in the circumferential direction of the hole was decreasing from half-piercing result of 180 µm to full-piercing result of 90 µm. The affected zone width in the circumferential direction of the hole was suppressed to 20% or less of the plate thickness

Figure 9 shows the comparison of the load–stroke relationship in piercing process between the normal WC (Co) punch and the trimmed diamond-coated punch. When changing the punch from the normal WC (Co) punch to the trimmed diamond-coated punch, the maximum punching load was changed from 1765 N to 1654 N. There is 6.3% decreasing of maximum punch load.

Evaluation on Affected Zones in Pierced Sheet by EBSD. Figure 10 shows the EBSD (Electron backscatter diffraction) analysis results of cross section of full-piercing hole that shown in Fig. 8. Figure 10a shows inverse pole figure map. Figure 10b shows the KAM (Kernel Average Misorientation) angle. The measured KAM angle corresponds to equivalent plastic strain [20]. From Fig. 10a, there is a process-affected zone where crystal grains have been refined on the side surfaces of the hole. From Fig. 10b, this process-affected zone was mainly displayed by the

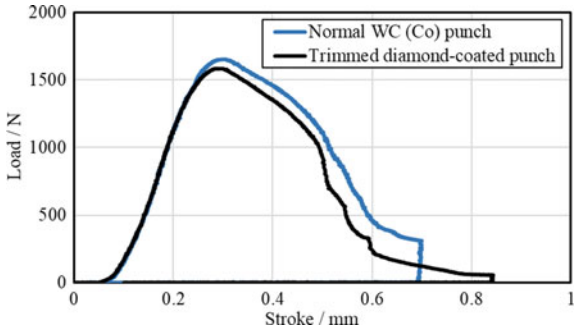


Fig. 9 Comparison of the load–stroke relationship in piercing process between the normal WC (Co) punch and the trimmed diamond-coated punch. (Color figure online)

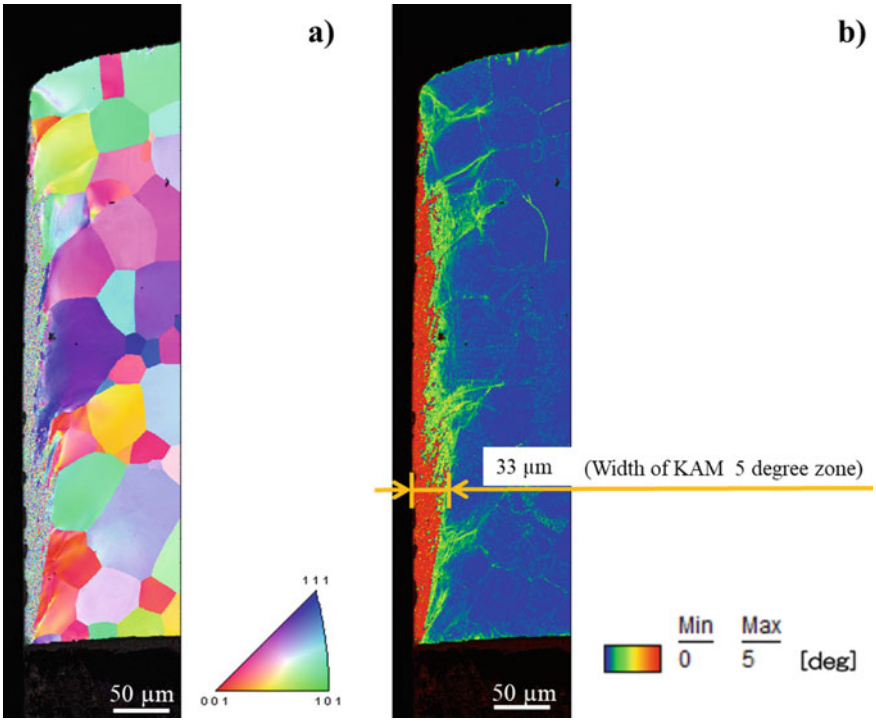


Fig. 10 EBSD analysis on the cross-section of full-pierced electromagnetic steel sheet. **a** Inverse pole figure map, and **b** KAM distribution. (Color figure online)

regions colored in red region with higher KAM degrees than 5. This region was identified as the part with high spin rotation of grains as well as high equivalent plastic strains. The width of this region in the circumferential direction around the hole was 33 μm. The process-affected zone in Fig. 8 was 90 μm. This difference reveals that the highly affected zone with spin rotation and high KAM degrees in Fig. 10 narrows in the plastically strained regions in Fig. 8 [21].

4 Discussion

The edge width or the edge curvature radius could be less than 1 μm if the punch head and side shoulder surfaces were independently trimmed by the femtosecond laser beam. In practice, the laser beam has a finite focusing eye for ablation of work materials, and its energy profile is shaped in Gaussian; there must be mutual interaction between laser trimming processes in control-I and -II in Fig. 2. How to minimize this interaction, becomes a practical issue to significantly reduce the edge width. As suggested by [19], the sacrifice film might be effective to suppress the diffusive beam from the machined surface to its neighboring ones. On the other hand, the edge width of trimmed diamond-coated punch must be tailored to be free from severe damage even after long usage in piercing process. Tool life test by piercing is also necessary to determine the optimum edge width in practice.

The process-affected zone into electrical steel sheets by piercing is observed and measured by various methods. In the above, the process-affected zone width (W) is determined by SEM analysis to have plastically deformed grains; e.g., W = 90 μm. After EBSD analysis, this process-affected zone is redefined to have higher misorientation angles among the neighboring grains in KAM distribution; e.g., W = 33 μm. Furthermore, the detection of local magnetization direction by the Kurr-effect microscopy also becomes a preferable tool to describe the disturbance to spatial magnetization distribution by piercing. As reported in [22], the elastic recovery in the elastoplastically strained grains as well as the affected zones have an influence on this disturbance to increase the iron and hysteresis losses. Mutual comparison among those methods are useful to find a way to minimize these losses by piercing.

In addition to the reduction of the edge width by laser trimming the diamond-coated punch, several approaches must be taken into account to minimize the affected zone width. The friction on the laser-trimmed punch edge and side surface is noticed as the first item. Due to the stress concentration at concentrates the punch edge during piercing, the maximum punching load becomes lower by 6.3% than using the normal WC (Co) punch. The clearance between punch and core-die diameters is the second item. As had been studied in [12–15], nearly zero clearance is effective to narrow the sheared plane in fine piercing. The loading sequence by CNC stamping as well as the loading speed has an influence on the plastic localization along the shearing plane in piercing. A loading program including the high-speed indentation mode might be preferable to narrow the affected zone width.

5 Summary

Femtosecond laser trimming process is effective to reduce the edge width of CVD-diamond-coated WC (Co) punch down to 2 μm. Due to the stress concentration at the edge during piercing, the maximum punching load is significantly decreased together with the reduction of process affected zone width. This edge-sharpened punch as well as the core die with the clearance of 4% is employed for piercing of the electrical steel sheet with a thickness of 0.5 mm.

Acknowledgments The authors would like to express their gratitude to Mr. Y. Suzuki, Mr. T. Yoshino, Mr. T. Aihara (Komatsu-Seiki Kosakusho, Co., Ltd.), and Mr. T. Inohara (LPS-Works, Co., Ltd.) for their help in experiments. This study was financially supported in part by the METI-project on the Supporting Industry Program in 2019.

References

1. Takeuchi S, Yokosawa T (2011) Fabrication and application of diamond films for dry forming die. Surf Eng 62 (3):152–156
2. Tamaoki K, Yokosawa T, Kataoka S (2012) Dry shearing of stainless steel sheets with polycrystalline diamond tools. Proc. 63rd JCTP: 191–192
3. https://www.ykt.co.jp/products/rollomatic/feature_lasersmart500.shtml (20/05/2019)
4. Aizawa T, Masaki E, Sugita Y (2014) Complete ashing of used DLC coating for reuse of the end-milling tools. Manufact Lett 2:1–3
5. Yunata EE, Aizawa T, Yamauchi K (2016) High density oxygen plasma ashing of CVD-diamond coating with minimum damage to WC (Co) tool substrates. Mech Eng JSME (2016) CD-ROM
6. https://www.i-precision.co.jp/rd.shtml (20/05/2019)
7. Watanabe M, Uchida H, Yamashita H, Miyatake K (2015) US-Patent Application 20150295252
8. Kawano M, Okamura S, Fujiyama T (2002) Non-oriented electrical steels having excellent magnetic properties and punchability for high speed micro-motors. Research Report, Kawasaki Steels 34:135–137
9. Weiss HA, Leuning N, Steentjes S, Hameyer K, Andorfer T, Jenner S, Vok W (2017) Influence of shear cutting parameters on the electromagnetic properties of non-oriented electrical steel sheets. J Magn Magn Mater 421:250–259
10. Cao H, Hao L, Yi J, Zhang X, Luo Z, Chen S, Li R (2016) The influence of punching process on residual stress and magnetic domain structure of non-oriented silicon steel. J Magn Magn Mater 406:42–47
11. K.W. Kontz, H. Li, Reducing core loss of segmented laminates, Proc. SMMA Fall Technical Conference (2008). (CD-ROM)
12. E. Katsuta, T. Aizawa, Y. Suzuki, K. Dohda, Effect of Clearance Control on the Micro-piercing Process of Electromagnetic steel sheets. Proc. 2017 Spring Conference for JSTP (2017) pp. 9–10
13. E. Katsuta, T. Aizawam K. Dohda, Micro-piercing of electromagnetic steel sheets by nitrided punch and die with nearly zero clearance. Proc. 10th AWMFT (2018, Pohang, Korea) (CD-ROM)
14. Katsuta E, Aizawa T, Morita H, Dohda K, Anzai M (2018) Fine piercing of electromagnetic steel sheets by micro-punches under nearly zero clearance. Procedia Manufacturing 15:1459–1466

15. E. Katsuta, T. Aizawa, K. Dohda, S-I. Yoshihara, Fabrication of lower temperature plasma nitrided die and development of zero-clearance piercing of electromagnetic steel sheets. J. JSTP 6- (2019) pp. 70–74
16. T. Aizawa, T. Inohara, Geometric adjustment and sizing of CVD-diamond coatings via oxygen plasma etching and laser machining., Proc. 7th SEATUC Conference, (Bandon, 2013) CD-ROM
17. T. Aizawa, T. Shiratori, T. Inohara, Short-pulse laser precise trimming of CVD-diamond coated punch for fine piercing. Proc. 3rd APSP Conference (August, 2019; Tokyo, Japan) pp. 41–46
18. T. Aizawa, T. Shiratori, T, Yoshino, T. Inohara, Femtosecond laser trimming of CVD-diamond coated punch for fine embossing. Mater. Trans. 61 (2020) (in press)
19. Aizawa T, Inohara T (2012) Multi-dimensional micro-patterning onto ceramics by pico-second laser machining. SIT Res. Rep. 56(1):17–26
20. Nomura K, Kubushiro K, Sakakibara Y, Takahashi S, Yoshizawa H (2012) Effect of Grain Size on Plastic Strain Analysis by EBSD for Austenitic Stainless Steels with Tensile Strain at 650°C. J Soc Mater Sci Jpn, 61–4:371–376
21. Aizawa T, Shiratori T, Yoshino T, Dohda K, Shingaki Y (in press) Material characterization on the affected zones by fine piercing into single crystal Fe-3Si steel sheet. Proc. WCMNM2020 (2020, India)
22. Senda K, Ishida M, Nakasu Y, Yagi M (2005) Effect of Shearing Process on Iron Loss and Domain Structure of Non-oriented Electrical Steel. IEE J Trans FM 125–3:241–246

An Investigation on Formability of Ti6Al4V Alloy in the Three-Layer Sheet Hot Stamping Process



Xiaoming Yang, Baoyu Wang, and Chuanbao Zhu

Abstract In the hot stamping process, the sheet will lose a lot of heat which results in poor formability of the sheet. So, a novel hot stamping process for the three-layer sheet is proposed in this paper, which uses two steel sheets to clamp the titanium alloy sheet for transferring and stamping. In this paper, the hot stamping depth is studied by experiments and simulation under the single/three-layer sheet hot stamping condition. The results show that the temperature of the titanium alloy sheet can be controlled effectively by using the three-layer sheet hot stamping process, and the stamping depth can be improved. Compared with the single-layer sheet hot stamping process, the depth of the titanium alloy parts can be increased by 135.7% under the three-layer sheet hot stamping process at 900 °C, and the thickness distribution of titanium alloy parts obtained by three-layer sheet hot stamping process is more uniform. The finite element analysis results show that the temperature and stress distribution of titanium alloy sheet by three-layer sheet stamping process is more uniform, and the temperature difference is small through the sheet. The distribution of thickness obtained by simulation has good consistency with the experimental results. Under the three-layer sheet hot stamping process, the titanium alloy sheet has good deep drawing.

Keywords Three-layer · Sheet hot stamping · Formability · Titanium alloy · Finite element simulation

X. Yang
School of Mechanical Engineering, University of Science and Technology Beijing, Beijing 100083, China

B. Wang (✉)
Beijing Key Laboratory of Metal Lightweight Forming Manufacturing, Beijing, China
e-mail: bywang@ustb.edu.cn

C. Zhu
Shandong Zhongxing Auto Parts Ltd Company, Lixin Town, Laiwu City Shandong Province, 271126, China

© The Minerals, Metals & Materials Society 2021

G. Daehn et al. (eds.), *Forming the Future*, The Minerals, Metals & Materials Series,
https://doi.org/10.1007/978-3-030-75381-8_234

1 Introduction

Titanium alloy is widely used in aerospace due to its high strength, corrosion resistance, and high temperature resistance [1]. Titanium alloy needs high temperature to improve its formability due to its poor plasticity at room temperature [2].

At present, there are many articles about the formability of titanium alloy at high temperature. In order to study the high temperature mechanical properties of titanium alloy, the stress-strain curves and grain growth of Ti6Al4V alloy were studied at the temperature of 650–870 °C and strain rate of 10^{-4}–$10^{-2}s^{-1}$ by Velay et al. [3]. The microstructure of Ti6Al4V titanium alloy under different deformation conditions was observed by Sun et al. [4]. It was found that work hardening occurred mainly at lower deformation temperature, and dynamic recrystallization and dynamic recovery dominated with the increase of deformation temperature. According to the experimental results from Lai et al. [5], the plasticity of Ti6Al4V titanium alloy could be improved at high temperature due to the reduction of yield strength. Li et al. [6]. Used the M-K model to predict the forming limit curves of Ti6Al4V titanium alloy at 700 °C, and then verified the correctness of the model by the hemispherical dome tests at elevated temperature.

The traditional hot forming methods of the titanium alloy sheet include superplastic forming [7], hot creep forming [8] and isothermal forming [9]. However, the forming efficiency of traditional forming method is low, and the tool has a high temperature to protect the heat loss of the sheet. The heating time of the tool is approximately 3 h which reduces the production efficiency. The formability of Ti6Al4V alloy is studied by Kopec et al. [10]. Under the hot stamping and cold die quenching process in order to improve the production efficiency. The results show that Ti6Al4V alloy sheet has a lot heat loss in the transferring and stamping process reducing its formability. Aghchai et al. [11]. Studies the forming limit of Al1100/ST12 composite sheet, and the forming limit curves of double-layer sheet are predicted by the M-K model. The results show that the forming performance of double-layer sheet is better than that of component metal sheet. Therefore, this paper presents a multi-layer sheet hot stamping process to meet the production requirements. The multi-layer sheet hot stamping process is proposed based on the hot stamping and cold die quenching process. In this process, a titanium alloy sheet is clamped by two steel sheets (the sandwich structure) for transferring and stamping to reduce the heat loss of the titanium alloy sheet.

In this paper, the formability of titanium alloy is studied by multi-layer sheet hot stamping process. Both the single-layer and three-layer sheet hot stamping of deep drawing tests were performed and compared for investigating the formability of titanium alloy. The finite element simulation model of titanium alloy multi-layer sheet hot stamping process is established. The distribution of thickness is analyzed and compared by experiment and simulation. The temperature and stress distributions of titanium alloy sheet are analyzed by simulation.

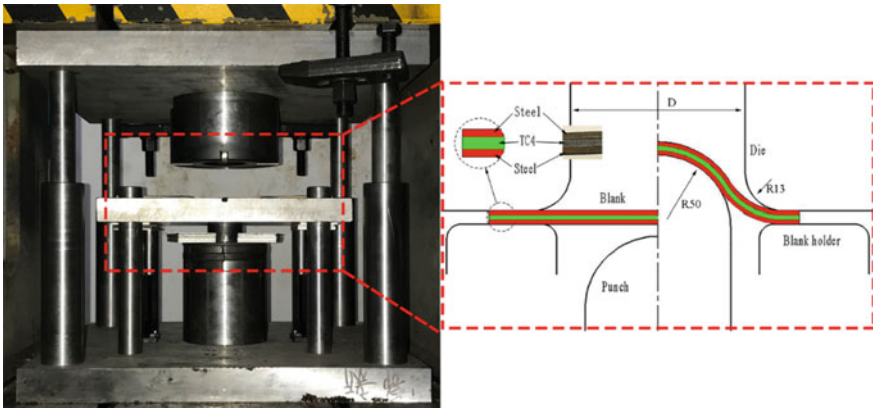


Fig. 1 The experimental tool and geometry size (mm) (**a** One-layer sheet stamping process D = 103.6 mm; **b** Three-layer sheet stamping process D = 110 mm). (Color figure online)

Table 1 The process parameters of experimental tests

Parameters	Values
Sheet temperature/°C	900
Tool temperature/°C	25
Blank holder force/kN	5
Diameter of sheet/mm	100
Stamping speed/mm·s^{-1}	40

2 Experimental Tests

The material used in the tests is the annealing Ti6Al4V titanium alloy with a thickness of 1.6 mm. And the auxiliary sheet is the HC1500HS steel produced by the Shougang steel group with a thickness of 1.4 mm. A 60-ton high speed press is used as the experimental equipment to study the deep drawing of the titanium alloy. The experimental tool and geometry size are shown in Fig. 1. During the tests, the titanium alloy sheet with a diameter of 100 mm is clamped by two steel sheets and put into the furnace for heating 30 min. Then, the three sheets are transferred and stamped when the temperature of the three sheets increases to the required. The process parameters are shown in Table 1.

3 Finite Element Simulation Model

The finite element simulation model shown in Fig. 2 is established to study the formability of titanium alloy by the simulation software Abaqus.

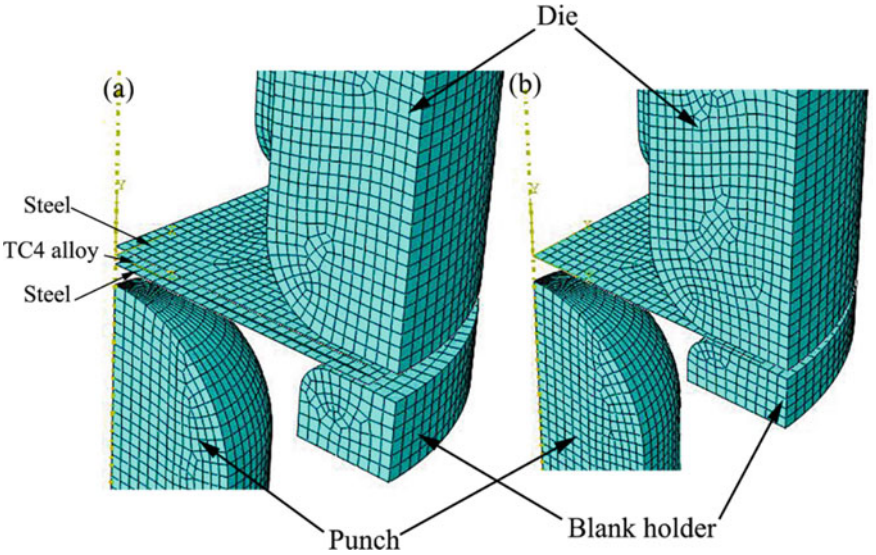


Fig. 2 The finite element simulation model **a** Three-layer sheet hot stamping model, **b** Single-layer sheet hot stamping model. (Color figure online)

In order to ensure the consistency between the simulation results and the experimental results, the material of tool in the simulation model is AISI-H13 which is consistent with the material used in the experiments. The physical parameters of the tool and sheets are shown in Table 2. The true stress-strain curves of the Ti6Al4V titanium alloy and HC1500HS steel are shown in Fig. 3 at a temperature of 900 °C. With the increase of strain rate, the flow stress of the Ti6Al4V titanium alloy and HC1500HS steel shows a rising trend. However, the plastic strain of the Ti6Al4V

Table 2 The physical parameters of the tool and sheets

Parameters		Values					
Temperature (°C)		25	200	400	600	800	1000
Density(kg/m^3)	AISI-H13	7780	–	7670	7580	–	–
	Steel	7848	7790	7722	7644	7616	7519
	Ti6Al4V	4500	–	–	–	–	–
Thermal conductivity (W/(m·K))	AISI-H13	36.5	29.9	29.2	28.3	27.5	–
	Steel	30.7	30	21.7	23.6	25.6	27.6
	Ti6Al4V	6.95	8.87	10.5	12.9	15	17.4
Specific heat (J/(kg·K))	AISI-H13	440	510	548	590	640	–
	Steel	440	520	561	581	590	603
	Ti6Al4V	612	652	691	712	720	725

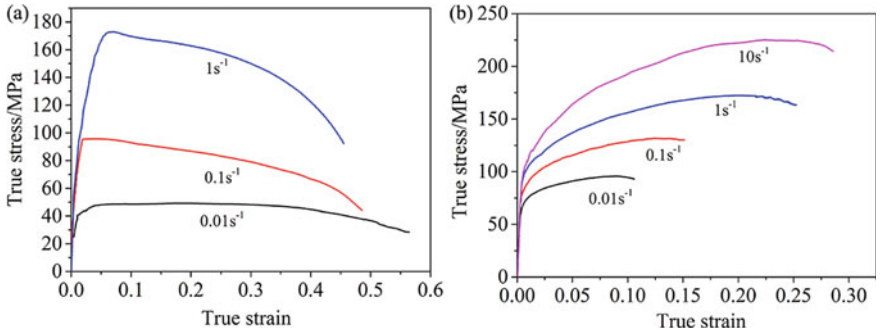


Fig. 3 The true stress-strain curves of the Ti6Al4V titanium alloy and HC1500HS steel at 900 °C **a** Ti6Al4V alloy, **b** HC1500HS steel. (Color figure online)

titanium alloy and HC1500HS steel shows an opposite trend with the strain rate increasing.

Two types of interactions are defined in the simulation model. One is the contact friction, and the other is the interfacial heat transfer between metals. The interfacial heat transfer coefficient of titanium alloy measured by Bai [12] and HC1500HS steel measured by Huang [13] is used in this paper, which is shown in Fig. 4. The friction coefficient between the titanium alloy sheet and HC1500HS steel sheet is 0.1. The friction coefficient between the HC1500HS steel sheet and tool is 0.2. In addition, The friction coefficient between the titanium alloy sheet and tool is 0.12 in the single-layer sheet hot stamping process. The element type of sheet is S4RT coupled with temperature-displacement. And the tools are meshed into C3D8T.

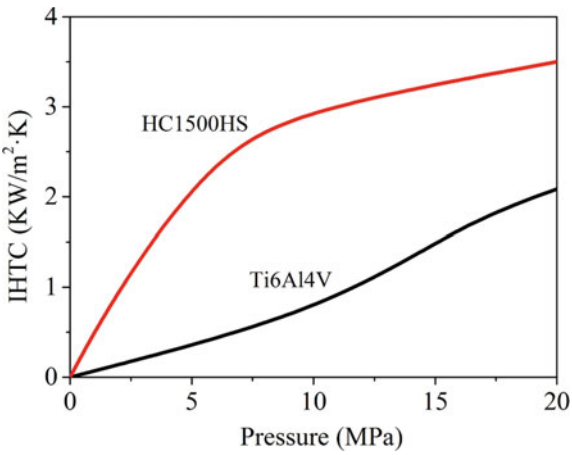


Fig. 4 The interfacial heat transfer coefficient of the Ti6Al4V titanium alloy and HC1500HS steel. (Color figure online)

4 Results and Discussion

4.1 Results of Tests

The titanium alloy parts obtained by different hot stamping methods are shown in Fig. 5. It can be seen that the stamping depth of the titanium alloy sheet increases obviously after the three-layer sheet hot stamping process. Compared with the single-layer sheet hot stamping process, the stamping depth of the titanium alloy parts is 33 mm increased by 135.7% in the three-layer sheet hot stamping process. This is because that the middle titanium alloy sheet clamped by two steel sheets is transferred and stamped, and the temperature of the titanium alloy sheet decreases slowly. In addition, the friction coefficient of the titanium alloy sheet is low, so the sheet is easy to be formed because the three sheets deform simultaneously.

The titanium alloy parts obtained by different stamping methods are cut along the diameter, and the distribution of the thickness is measured. The comparison results of thickness distribution between the simulation and experiments are shown in Fig. 6. The simulation results are in good agreement with the experimental results. The minimum thickness of the titanium alloy sheet is 1.2 mm when the stamping depth is 14 mm in the single-layer sheet hot stamping process. However, There is no thinning

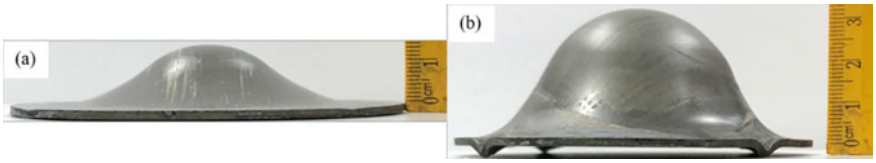


Fig. 5 Forming parts by different stamping processes at 900 °C **a** Single-layer sheet hot stamping process; **b** Three-layer sheet hot stamping process. (Color figure online)

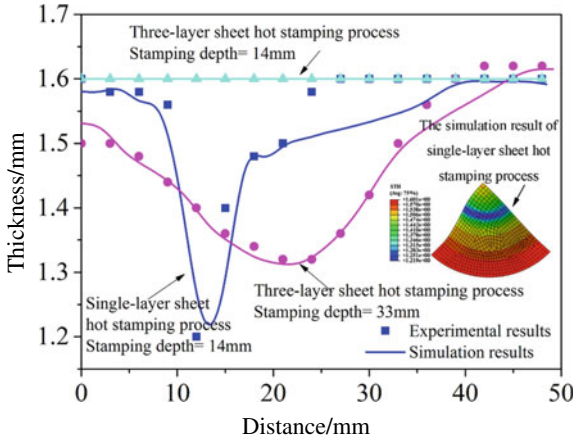


Fig. 6 The change of sheet thickness (Symbols represent experimental results, lines represent simulation results). (Color figure online)

in the three-layer sheet hot stamping process when the stamping depth is 14 mm. The minimum thickness of the titanium alloy parts is 1.32 mm when the stamping depth is 33 mm in the three-layer sheet hot stamping process. The better formability of the titanium alloy sheet can be obtained by using the novel three-layer sheet hot stamping process. It can be seen that the thickness decreases in the side wall region and increases in the blank holder region. The minimum thickness appears in the side wall area. The flow stress in the sidewall region is low because of the higher temperature, so the sheet is easy to be deformed. In the blank holder region, the circumferential compressive stress makes the sheet thickness increase. There is local thinning in the single-layer sheet hot stamping process. Compared with the single-layer sheet hot stamping process, the thickness distribution of the titanium alloy parts obtained by three-layer hot stamping process is more uniform.

4.2 Distribution of Sheet Temperature

The temperature distribution of the titanium alloy parts under different hot stamping conditions is shown in Fig. 7, which is calculated from the simulation results. The highest temperature of the sheet is 634.53 °C at the single-layer sheet hot stamping process and 640.56 °C at the three-layer sheet hot stamping process. Compared with the single-layer sheet hot stamping process, the distribution of temperature is uniform at the three-layer sheet hot stamping process. Under the condition of the single-layer sheet hot stamping, the temperature is 244.42 °C at the central region, which is 399.11 °C lower than the maximum temperature. The heat transfer between the titanium alloy sheet and tool occurs in the single-layer sheet hot stamping process. The cooling rates of the sheet at the contact position are higher than other positions. However, the titanium alloy sheet clamped by two steels is transferred and deformed,

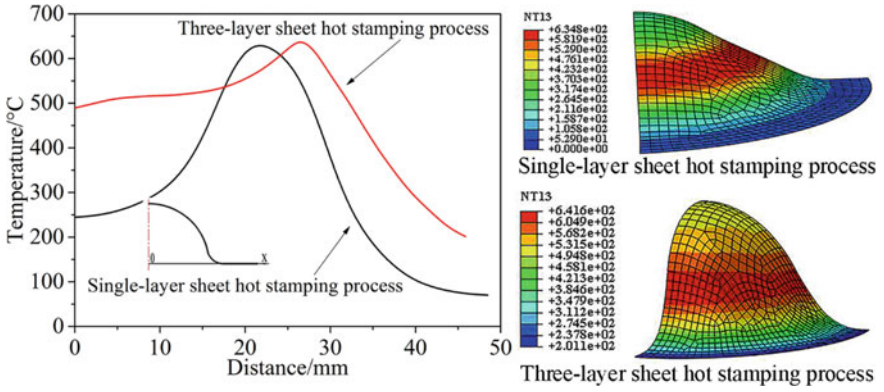


Fig. 7 The distribution of sheet temperature calculated from the FE simulation. (Color figure online)

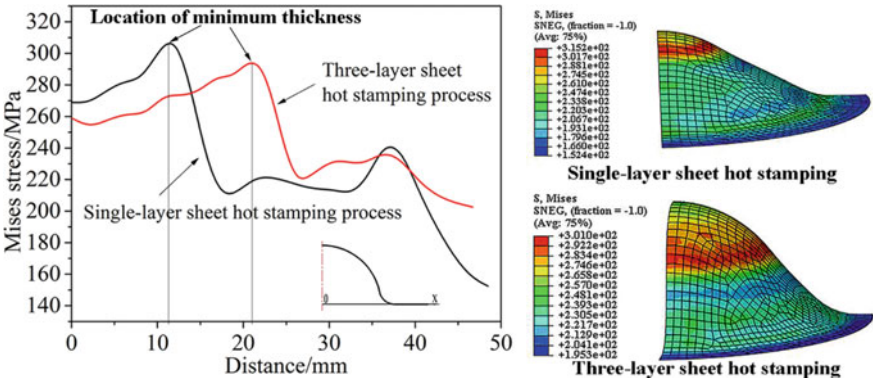


Fig. 8 The distribution of Mises stress calculated from the FE simulation. (Color figure online)

reducing the contact with air and tool in the three-layer sheet hot stamping process. Consequently, the temperature distribution of the titanium alloy parts obtained by the three-layer sheet hot stamping process is uniform.

4.3 Distribution of Mises Stress

The Mises stress distribution of the titanium alloy parts under different stamping conditions is shown in Fig. 8. Compared with the single-layer sheet hot stamping process, the stress distribution of the titanium alloy parts obtained by the three-layer sheet hot stamping process is more uniform. Under the single-layer sheet hot stamping condition, the stress decreased from 311.6 MPa to 208.35 MPa at the distance of 12 mm to 17 mm. And the stress decreased from 294.4 MPa to 218.3 MPa at the distance of 20 mm to 26 mm under the condition of three-layer hot stamping. The smaller stress difference can be obtained in the three-layer sheet hot stamping process. In addition, it can be seen that the position where the stress changes dramatically is the thinning one due to the change of the Mises stress.

5 Conclusion

In this paper, a three-layer sheet hot stamping process is proposed to reduce the heat loss of the titanium alloy sheet in the transferring and stamping process. The formability of Ti6Al4 V titanium alloy is studied by experiment and simulation under the multi-layer sheet hot stamping condition. It can be seen that the simulation results are in good agreement with the experimental results. Compared with the single-layer sheet hot stamping process, the distributions of thickness, temperature and stress are

uniform in the three-layer sheet hot stamping process. And there is deeper stamping depth of Ti6Al4 V alloy in the three-layer sheet hot stamping process.

Acknowledgments This work was supported by the Joint Funds of the National Science Foundation of China (grant number U1564202). This work was also supported by the Beijing Laboratory of Modern Transportation Metal Materials and Processing Technology and the Beijing Key Laboratory of Metal Forming Lightweight.

References

1. Peters CLM (2003) Titanium and titanium alloys. Wiley-VCH, Weinheim
2. Park NK, Yeom JT, Na YS (2002) Charaterization of deformation stability in hot forging of conventional Ti-6Al-4V using processing maps. J Mater Process Technol 130:540–545
3. Velay V, Matsumoto H, Vidal V et al (2016) Behavior modeling and microstructural evolutions of Ti6Al4V alloy under hot forming conditions. Int J Mech Sci 108–109:1–13
4. Sun S-D, Zong Y-Y, Shan D-B et al (2010) Hot deformation behavior and microstructure evolution of TC4 alloy titanium alloy. Trans Nonferrous Metals Soc China 20(11):2181–2184
5. Lai CP, Chan LC, Chow CL et al (2010) Thermal forming of light-weight alloys under a multi-stage forming process. Proc Instn Mech Eng, Part C: J Mech Eng Sci 224:797–803
6. Li X, Guo G, Xiao J et al (2014) Constitutive modeling and the effects of strain-rate and temperature on the formability of Ti6Al4V alloy sheet. Mater Des 55:325–334
7. Franna Pitt and M. Ramulu et al. Influence of grain size and microstructure on oxidation rates in titanium alloy Ti6Al4V under superplastic forming conditions. Journal of Materials Engineering and Performance, 2004, 13(6):727–734
8. Deng T, Liu D, Li X et al (2014) Hot stretch bending and creep forming of titanium alloy profile. Procedia Engineering 81:1792–1798
9. Gao PF, Yang H, Fan XG et al (2012) Microstructural features of TA15 titanium alloy under different temperature routes in isothermal local loading forming. Mater Sci Eng A 540(1):245–252
10. Kopec M, Wang K, Politis DJ et al (2018) Formability and microstructure evolution mechanisms of Ti6Al4V alloy during a novel hot stamping process. Mater Sci Eng A 719:72–81
11. Aghchai A Jalali, Shakeri M, Mollaei-Dariani B (2008) Theoretical and experimental formability study of two-layer metallic sheet. Proceedings of the Insititution of Mechanical Engineers, Part B: Journal of Engineering Manufacture 222:1131–1138
12. Bai Q, Lin J, Zhan L et al (2012) An efficient closed-form method for determining interfacial heat transfer coefficient in metal forming. Int J Mach Tools Manuf 56:102–110
13. Mingdong H (2016) Study on hot stamping process of boron steel HC1500HS and thermos-mechanical-phase transformation modeling and simulation. University of Science and Technology Beijing

The Effects of Servo Press Forming on Various Strain Path Failures



L. Zoller, T. Feister, and H. Kim

Abstract Utilizing a servo press for sheet metal forming provides benefits for users such as a fully adjustable slide motion and blank holder force control during the stroke. These allow users to program unique motion profiles of press slide and cushion based on position and velocity. This paper will discuss how unique servo press motion profiles can avoid various strain path failures that may occur in final formed parts. Standard crank motion, variable blank holder force, and attach-detach slide motion were used to evaluate biaxial and plane strain failures of 980GEN-3 steel. It was determined that different strain failure paths require different servo press programs to improve the overall part quality.

Keywords Servo press · Forming limit diagram · Simulation · 980Gen-3

1 Introduction

The stamping industry is currently increasing the use of servo presses in their production environments. A servo press uses an electric servo motor-driven slide and a hydraulic or pneumatic servo cushion system. The electric servo motor allows for a fully adjustable slide motion. The servo cushion system can be used to freely control the force during forming as well as program multi-drawing steps called attach-detach [1]. It is known that a servo press can be used to improve part quality however there is a lack of understanding how to determine the preferred servo press motion considering the deforming material strain path to avoid necking or wrinkling and the part design [2]. This lack of knowledge creates a need to fully understand how to accurately simulate the servo press motion attach-detach versus a standard crank press motion to study the strain [3].

The strain path-dependent failures are determined from the Forming Limit Diagram (FLD) as shown in Fig. 1 [4]. An FLD is used to evaluate formability with major and minor strains during different strain paths. Deep drawing includes both

L. Zoller (✉) · T. Feister · H. Kim
EWI - Forming Center (EWI-FC), Columbus, OH, USA
e-mail: lzoller@ewi.org

© The Minerals, Metals & Materials Society 2021

G. Daehn et al. (eds.), *Forming the Future*, The Minerals, Metals & Materials Series,
https://doi.org/10.1007/978-3-030-75381-8_235

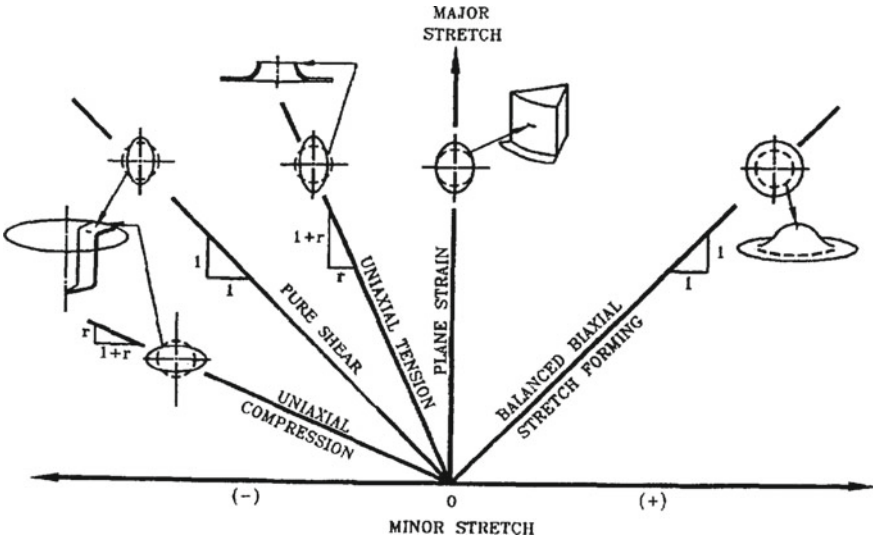


Fig. 1 Strain path failure modes plotted on true strain [M. Karima, N. Chandrasekaran, and W. Tse, Process singatures in metal stamping—basic concepts, J. Mat. Shaping Tech., 7 (3) (1989) 169–183.]

pure shear in the flange area and uniaxial compression in the flange edge. Therefore, thickening occurs in the drawn flange area. For the pure shear strain path, major and minor strain are equal with major strain in tension and minor strain in compression. Uniaxial tension is when major strain is in tension while minor strain is compressing in half the amount of strain as the major. Uniaxial tension behavior is similar to a standard tensile test. Plane strain is the lowest point on the FLD where minor strain is equal to zero. Equi-biaxial strain is when both major and minor strain are equal in tension.

2 Objective

The objective of this study is to determine how failure strain paths change by altering the press slide motion and blank holder force (BHF) profiles. Predicting critical strain paths using Finite Element Method (FEM) helps to identify and avoid any necking failures in the stamped part which is important to reduce scrap and improve productivity.

3 Approach

Two different lab scale die geometries were used in this study. The lab scale dies were chosen due to the type of failures seen in each die. The universal formability testing (UFT) die was designed to create biaxial strain dominant failure on the stamped part and the Crossform testing (CFT) die was designed to create the plane strain dominant failure.

The sheet material used for the both lab scale dies was 980GEN-3 (1.2-mm thick) steel. In order to accurately simulate the UFT and CFT tooling in PAM-STAMP two standard formability tests, uniaxial tensile testing for the flow stress and Limiting Dome Height (LDH) testing for FLD were completed to create the material card for simulations. The material card for each simulation was developed using ESI's material wizard. The hardening curve was developed using the uniaxial tensile test and the yield criteria used was Vegter yield locus as shown in Fig. 2. The coefficient of friction value used was 0.12. The press slide motion and blank holder force measured from experiments were defined in simulations as shown in Fig. 2, standard crank motion with a constant blank holder force, a standard crank motion with a variable blank holder force and an attach-detach motion.

During the attach-detach motion that slide "detaches" two times before completing the stroke. The die position for the first detach was at 15 mm from bottom dead center (BDC) and the die position for the second detach was at 5 mm from BDC and the third one corresponds to BDC. Therefore, the formed part is detached only from the stationary punch while the outer flange area is still constrained with both the upper

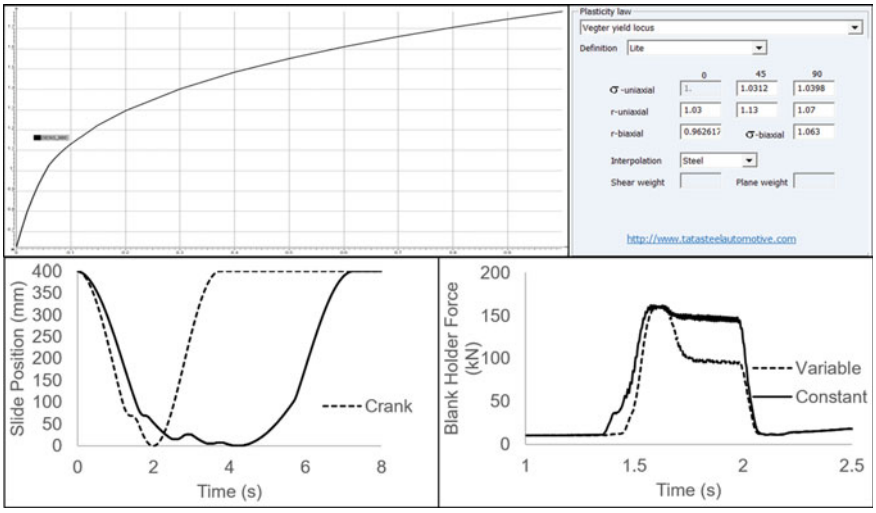


Fig. 2 Hardening curve (top left), yield criterion (top right), slide profile for crank motion and attach-detach (bottom left), and constant and variable blank holder force profiles (bottom right). (Color figure online)

die and blank holder. The crank motion slide profile has a silent deceleration feature that instantaneously slows down the slide speed during the initial contact between the upper die and a flat blank placed on the blank holder surface. The variable BHF profile was selected by preliminary FE simulations. The BHF profile selected is referenced as high-low because the force starts high and ramps down to lower force during forming. Adjusting the BHF is a commonly used method to improve part quality while maintaining the stroke per minute (SPM) in a production environment. Figure 2 shows that attach-detach has a slower SPM compared to crank motion due to the additional die travel during forming.

4 Results

The simulations began with crank motion. The goal for the simulation was to determine the failure stroke based on the FLD tested at EWI. For the UFT die the failure stroke was 68.7 mm for 980GEN-3 steels (Fig. 3). The failure location had a major true strain value of 0.315 and a minor true strain value of 0.168. The failure strain path for the UFT die crank motion was considered to be biaxial stretching conditions due to the positive major and minor strains.

The CFT die failure stroke was 65.5 mm for 980GEN-3 steel (Fig. 4). The failure location had a major true strain value of 0.207 and a minor true strain value of 0.022. The failure strain path location for the CFT die with 980GEN-3 was near plane strain.

With the failure stroke known for each die set, the high-low and attach-detach profile simulations were completed, starting with the high-low profile. The 980GEN-3 failure location (Fig. 5) had a major true strain value of 0.294 (6.6% strain decrease from crank) and a minor true strain value of 0.123 (26.8% strain decrease from crank) with the UFT die. Even though there was a little strain improvement with the 980GEN-3 material, the improvement was not enough to eliminate the failure based on the FLD.

The attach-detach motion with 980GEN-3 (Fig. 6) had a major true strain value

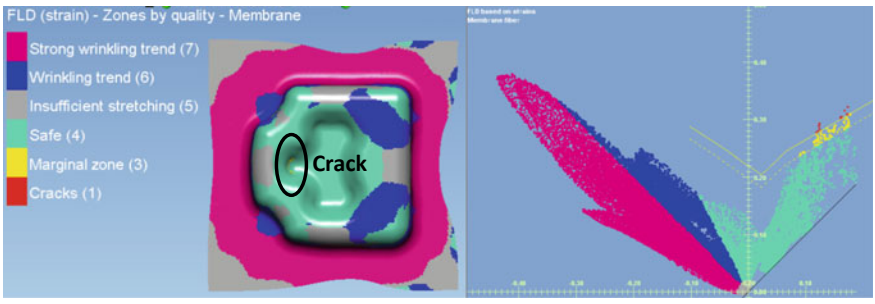


Fig. 3 980GEN-3 Crank Motion Failure using UFT die with Forming Limit Diagram at 68.7 mm die stroke. (Color figure online)

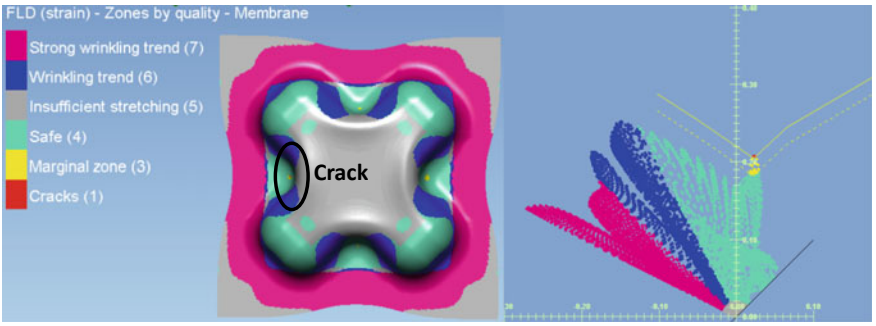


Fig. 4 980GEN-3 Crank Motion using CFT die with Forming Limit Diagram at 65.5 mm die stroke. (Color figure online)

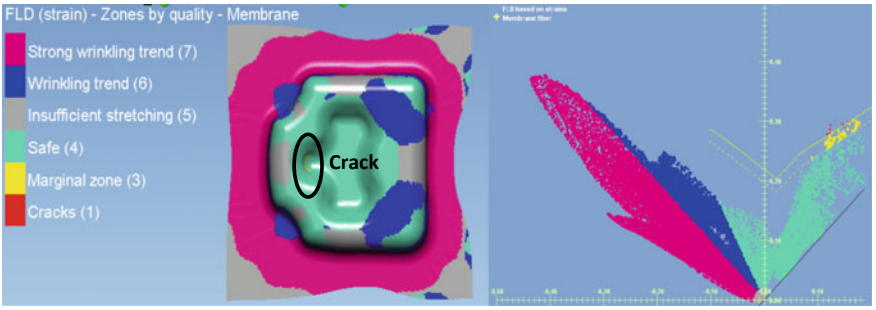


Fig. 5 980GEN3 High-Low Profile using UFT with Forming Limit Diagram at 68.7 mm die stroke. (Color figure online)

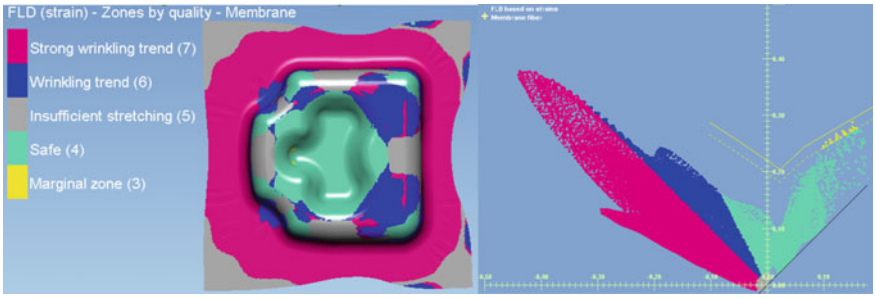


Fig. 6 980GEN-3 Attach-Detach motion using UFT with Forming Limit Diagram at 68.7 mm die stroke. (Color figure online)

of 0.282 (10.5% strain decrease from crank) and a minor true strain value of 0.146 (13.1% strain decrease from crank) with the UFT die. This strain improvement in both major and minor true strain predicted a final part with no failures based on the FLD.

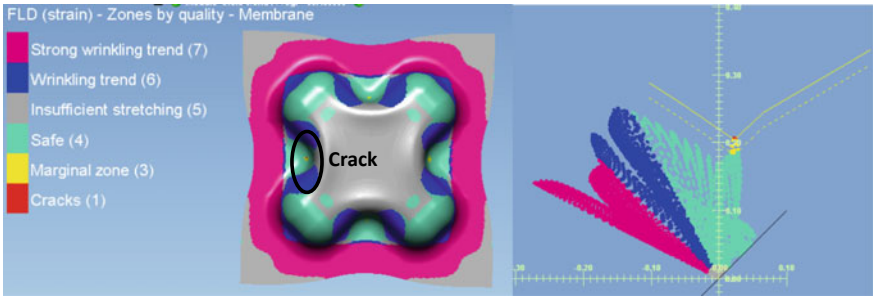


Fig. 7 980GEN-3 Variable Blank Holder Profile using CFT with Forming Limit Diagram at 65.5 mm die stroke. (Color figure online)

The CFT die with 980GEN-3 steel (Fig. 7) using the high-low profile still had the plane strain failure on the final part. The major true strain value was 0.207 (0% strain improvement from crank) and a minor true strain value was 0.024 (9.1% strain increase from crank).

The CFT die with 980GEN-3 steel (Fig. 8) using the attach-detach profile had the same failure location as the crank motion and high-low profiles major true strain value of 0.208 (0.5% strain increase from crank) and a minor true strain value of 0.022 (0% strain improvement from crank).

After the simulations were completed, EWI ran each test in a 300-Ton AIDA servo press. ARGUS strain analysis was also completed on the UFT parts to determine if the attach-detach motion was accurately simulated. The results are summarized in Table 1. The crank motion and the high-low BHF profile cases all failed, and the attach-detach motion improved the UFT part quality in the actual testing however it did not improve the CFT part quality. Figure 9 shows the ARGUS thickness reduction data for crank motion (failure) and attach-detach (good) parts. The ARGUS strain results had good correlation with the simulation results to confirm EWI's initial findings.

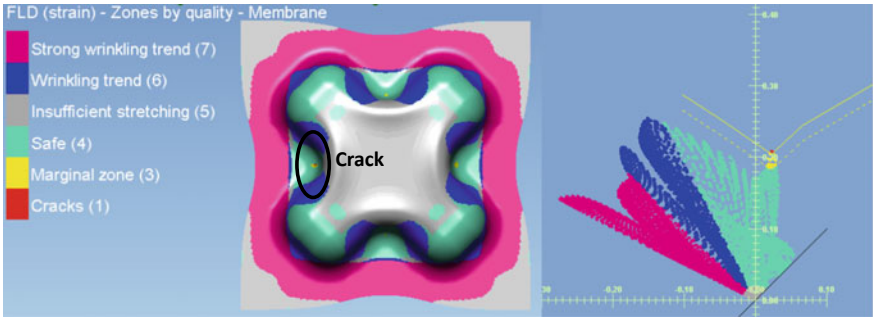


Fig. 8 980GEN-3 Attach-Detach Motion using CFT with Forming Limit Diagram at 65.5 mm die stroke. (Color figure online)

Table 1 Simulation and actual testing results

				Simulation data		ARGUS data	
Die	Material	Stroke	Motion	Major true strain	Minor true strain	Major true strain	Minor true strain
UFT	980GEN-3	68.7 mm	Crank	0.315	0.168	0.32	0.19
			High Low	0.294	0.123	No data	No data
			AD15	0.282	0.146	0.24	0.18
CFT	980GEN-3	65.5 mm	Crank	0.207	0.022	No data	
			High Low	0.207	0.024		
			AD15	0.208	0.022		

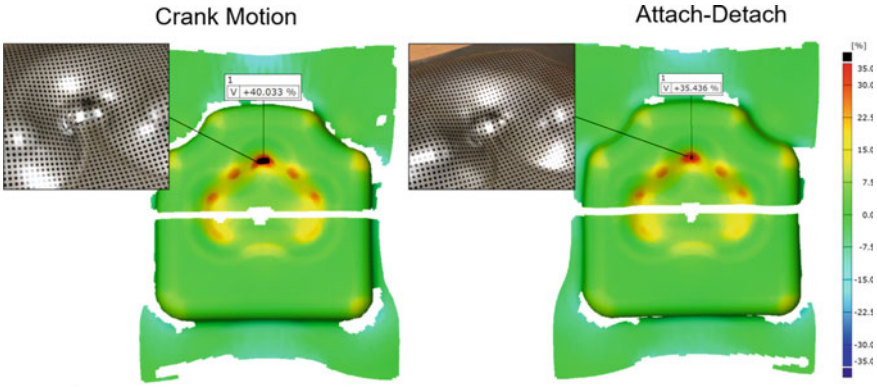


Fig. 9 ARGUS data from testing. Crank motion with failure (left) and attach-detach without a failure (right). (Color figure online)

5 Summary of Major Findings and Conclusions

EWI found that selecting the effective servo press motion is dependent on the type of strain path failure found in the given die geometry based on the simulation and actual testing results. Specifically, the servo motion called attach-detach can improve the part formability of a biaxial part failure; however, it might be limited to improve the part formability of a plane strain failure for advanced high strength steels. Future work after this study will be to implement this process with an industry sized part as well as study different material types with material variation and various "detach" locations for the attach-detach profile.

References

1. Nakagawa (2006) Servo Motor Drive Press and Market Trends in Japan, 56th CIRP GA, Kobe, Japan
2. Nakano T (2010) Press Machine Trends and Servo Press Forming Examples. Steel Res Int 81(9):682–685
3. Osakada K, Mori K, Altan T, Groche P (2011) Mechanical Servo Press Technology for Metal Forming. CIRP Ann Manuf Technol 60:651–672
4. Karima M, Chandrasekaran N, Tse W (1989) Process singatures in metal stamping – basic concepts. J Mat Shaping Tech 7(3):169–183

Part XXIII
Technologies to Speed Innovation

Recent Advances on Modeling Plastic Deformation of Textured Metals with Applications to Metal Forming



Oana Cazacu and Benoit Revil-Baudard

Abstract Due to the ease in calibration from simple tests and the reliability of the parameter identification, generally von Mises isotropic criterion and Hill orthotropic criterion are used in industry. While more advanced 3-D yield criteria have been developed, generally such criteria are written in terms of eigenvalues of transformed stress tensors, and as such the anisotropy coefficients are not directly related to mechanical properties. Therefore, the quality of the F.E. simulations depends on the experience of the analyst in calibrating these parameters. Very recently, it was shown that all advanced non-quadratic yield criteria are in fact polynomials in terms of stress components (see [1]). Moreover, for the 3-D orthotropic criteria involving one linear transformation (e.g. Yld91), the anisotropy coefficients can be determined using analytical formulas, involving only four yield points or three Lankford coefficients, respectively (see [2, 3]). In this paper, the predictive capabilities of the orthotropic criteria of Hill [4], Yld91 [5], and Cazacu [6] calibrated using both analytical and numerical minimization procedures are discussed. Moreover, simulation results of deep drawing of steel alloy DC06 are presented. The influence of the choice of the criterion, the procedure used for identification (analytical vs. numerical), and the type/extent of the data used for identification are analyzed in detail.

Keywords Orthotropic yield criteria · Analytical identification · Cup drawing · DC06 steel

1 Introduction

Due to the fabrication process, most metallic plates and sheets display at the macroscopic scale anisotropy. For example, rolling leads to preferential orientations of the constituent grains (i.e. crystallographic texture), which in turn induces orthotropy of the mechanical properties in the plastic regime of behavior. Modeling of the effects of

O. Cazacu (✉) · B. Revil-Baudard
Department of Mechanical & Aerospace Engineering, University of Florida/REEF, 1350 N. Poquito Rd., Shalimar, FL 32579, USA
e-mail: cazacu@reef.ufl.edu

© The Minerals, Metals & Materials Society 2021

G. Daehn et al. (eds.), *Forming the Future*, The Minerals, Metals & Materials Series,
https://doi.org/10.1007/978-3-030-75381-8_236

orthotropy on the onset of plastic deformation (i.e. yielding) and subsequent evolution of plastic deformation has received a lot of attention. Orthotropy dictates that for 3-D loadings, the yield function should involve at least 6 anisotropy parameters. The most versatile orthotropic yield criteria involve up to 18 parameters (see [1]). For any forming process, the accuracy of the predictions obtained with any orthotropic criterion depends on the experimental database available for parameters identification, the calibration procedure used, as well as the performance of the numerical code. In particular, the identification procedure may strongly influence the quality of the finite-element (F.E.) simulation results (e.g. see discussion on the effects of the numerical identification procedures used for calibration of Hill [4] and Cazacu and Barlat [7] orthotropic criterion for DC06 steel on predictions of the material anisotropy and its behavior during forming presented in [8], and [9]-[10], respectively). Very recently, Cazacu et al. [1] derived new equivalent expressions in terms of stress components for all the 3-D non-quadratic orthotropic yield criteria. Furthermore, Cazacu [2, 3] has demonstrated that for the non-quadratic orthotropic yield criteria Yld91 and Karafillis and Boyce [11], which involve one linear transformation, the parameters identification can be done analytically using formulas involving only four experimental yield points or three Lankford coefficients, respectively. This makes the determination of the anisotropy parameters reliable even in the case when the mechanical data available for identification are limited. Also, it was demonstrated that the 6 anisotropy coefficients involved in either Yld91 or Karafillis and Boyce [11] criteria are not independent. Specifically, as it is the case of Hill [4] yield function, the mathematical form imposes very specific couplings between the yield stresses σ_0 and σ_{90} and the Lankford coefficients r_0 and r_{90} corresponding to the rolling direction (RD), and transverse direction (TD), respectively. Nevertheless, the new explicit expressions of Yld91 and Karafillis and Boyce yield criteria in terms of stress components enable a direct correlation between the anisotropy parameters and mechanical properties and lead to standardization of their use in numerical simulations.

In this paper, the benefits of having for Yld91 an explicit expression in terms of stresses and analytical identification procedures are demonstrated for a strongly anisotropic steel alloy, DC06. Specifically, the influence of the type of data used for identification of Yld91 (i.e. only experimental yield data or only experimental Lankford coefficients) the extent of the data set used for identification (i.e. reduced data set or extended data set), and the identification procedure (analytical vs. numerical) on the accuracy of cup forming predictions for the steel alloy DC06 are analyzed. Hill [4] and Cazacu [6] orthotropic criterion are also applied to DC06 and an in-depth analysis of the influence of the choice of the criterion used for modeling on the accuracy of the predictions is presented. We begin with a brief presentation of the cup drawing test setup for DC06 alloy reported in [8] and [12].

2 Cup Drawing Test Results for DC06 Steel

The geometry of the tools and blank are given in Table 1. The results of the cup

Table 1 Geometry of the tools and blank in the deep drawing test of the DC06 alloy (after [8])

Blank diameter	120 mm
Blank thickness	1 mm
Punch diameter	60 mm
Punch filet radius	5 mm
Die opening diameter	62.4 mm
Die filet radius	10 mm

drawing test were provided for all four quarters of the cup. Assuming that the material is orthotropic, in Fig. 1 is presented the experimental variation of the cup height averaged over the four quarters (i.e. $0 < \theta < 90^o$, with RD corresponding to $\theta = 0^o$). Thus, in Fig. 1 the reported height at θ is the average of the cup height at θ, $180^o - \theta$,$180^o + \theta$, and $360^o - \theta$. Note that this steel alloy exhibits four ears located at RD and TD, the largest height being observed at TD, and the minimum height being at 45^o to the RD.

Concerning the setup for the F.E. simulations, due to geometrical and material symmetries, only a quarter of the cup needs to be modeled. The blank is discretized with 17820 ABAQUS C3D8H elements (8 node brick elements with constant pressure). In all the simulations conducted, the friction coefficient between the blank and the tools is set to 0.03. The blank holder force is of 50 kN. This DC06 alloy is characterized by a Young modulus, E = 200 GPa and a Poisson coefficient $\upsilon = 0.3$. Hardening is considered isotropic. It is modeled with a Swift-type law $\sigma_0 = 529.5(0.0043 + \bar{\varepsilon}^p)^{0.268}$. As expected, if the anisotropy of the material

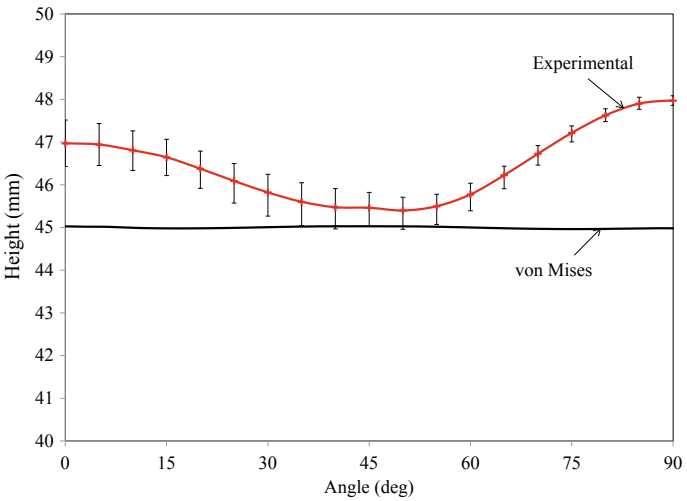


Fig. 1 Experimental cup height versus angle to RD and F. E. predictions according to the isotropic von Mises yield criterion for steel alloy DC06. The data points were averaged over the four quarters of the cup (after [8, 12]). (Color figure online)

is neglected, the earing profile cannot be captured (see Fig. 1). Nevertheless, the cup height according to the von Mises criterion, which is of 44.98 mm, is a good approximation of the experimental average height, $h_{avg}^{\exp} = 46.8$ mm.

3 Predictions of the Orthotropic Yield Criteria Yld91 and Hill Identified Analytically Using a Reduced Data Set

Yld91 yield function is an extension to orthotropy of the isotropic Hershey-Hosford yield function (see [5]). Its expression is given by:

$$\text{YLD91} = \left|\tilde{S}_1 - \tilde{S}_2\right|^m + \left|\tilde{S}_2 - \tilde{S}_3\right|^m + \left|\tilde{S}_3 - \tilde{S}_1\right|^m = 2\bar{\sigma}^m \tag{1}$$

In Eq. (1), $\tilde{S}_k$ are the eigenvalues of a transformed tensor $\tilde{\mathbf{S}}$, defined as

$$\tilde{\mathbf{S}} = \mathbf{C}\sigma \tag{2}$$

with the fourth-order tensor $\mathbf{C}$ being orthotropic, symmetric (i.e. $C_{ijkl} = C_{klij} = C_{jikl}$ for $i, j, k, l = 1\ldots3$), and deviatoric. Relative to the Cartesian coordinate system associated to the orthotropy axes (i.e. RD, TD, ND in the case of a rolled sheet), this tensor is represented by a 6×6 matrix with six non-zero components a, b,$\bar{c}$, f, g, h. For materials with the same behavior in tension and compression, the exponent m should be a positive even integer (see [11]). Specifically, Barlat et al. [5] recommends m =6 for BCC materials, and m =8 for FCC materials. Very recently, the explicit expression of Yld91 in terms of stresses was obtained. It was demonstrated that irrespective of the value of m, Yld91 is a homogeneous polynomial in the components of the Cauchy stress (see [1, 2]). In particular, for $m = 6$:

$$\text{YLD91} = \left(\tilde{S}_1 - \tilde{S}_2\right)^6 + \left(\tilde{S}_2 - \tilde{S}_3\right)^6 + \left(\tilde{S}_1 - \tilde{S}_3\right)^6 = 66\tilde{J}_2^3 - 81\tilde{J}_3^2, \tag{3}$$

where $\tilde{J}_2 = tr\left(\tilde{\mathbf{S}}^2\right)/2$ and $\tilde{J}_3 = tr\left(\tilde{\mathbf{S}}^3\right)/3$ are the second and third-invariant of the transformed stress tensor $\tilde{\mathbf{S}}$, respectively. The expressions of $\tilde{J}_2$ and $\tilde{J}_3$ can be easily obtained by making use of (2) and are given by

$$\tilde{J}_2 = f^2\sigma_{yz}^2 + g^2\sigma_{xz}^2 + h^2\sigma_{xy}^2 + \left[(b+\bar{c})\sigma_{xx} - \bar{c}\sigma_{yy} - b\sigma_{zz}\right]^2/18 + \left[-\bar{c}\sigma_{xx} + (\bar{c}+a)\sigma_{yy} - a\sigma_{zz}\right]^2/18 + \left[-b\sigma_{xx} - a\sigma_{yy} + (a+b)\sigma_{zz}\right]^2/18 \tag{4}$$

$$\tilde{J}_3 = 2(fgh)\,\sigma_{xy}\sigma_{xz}\sigma_{yz} + \frac{1}{27}\begin{bmatrix}\left[(b+\bar{c})\sigma_{xx} - \bar{c}\sigma_{yy} - b\sigma_{zz}\right]\cdot\left[-\bar{c}\sigma_{xx} + (\bar{c}+a)\sigma_{yy} - a\sigma_{zz}\right]\cdot \\ \left[-b\sigma_{xx} - a\sigma_{yy} + (a+b)\sigma_{zz}\right]\end{bmatrix} - \frac{f^2\sigma_{yz}^2}{3}\left[(b+\bar{c})\sigma_{xx} - \bar{c}\sigma_{yy} - b\sigma_{zz}\right] - \frac{g^2\sigma_{xz}^2}{3}\left[-\bar{c}\sigma_{xx} + (\bar{c}+a)\sigma_{yy} - a\sigma_{zz}\right]$$

$$-\frac{h^2\sigma_{xy}^2}{3}\left[-b\sigma_{xx}-a\sigma_{yy}+(a+b)\sigma_{zz}\right] \tag{5}$$

As mentioned, using the polynomial representation of Yld91 given by Eq. (3), Cazacu [2] demonstrated that the anisotropy coefficients are expressible only in terms of experimental yield stresses or experimental r-values. Specifically, it was shown that the anisotropy coefficients a, b, $\bar{c}$ are expressible only in terms of σ_0, σ_{90}, and σ_b the yield stress in equibiaxial tension. The in-plane coefficient h can be easily obtained using a simple formula involving the coefficients a, b, $\bar{c}$ and σ_{45}, the experimental value of the uniaxial yield stress at 45^0 to RD. It was also demonstrated that the same coefficients a, b, $\bar{c}$ can be expressible only in terms of the Lankford coefficients r_0 and r_{90}, while the coefficient h can be expressed in terms of a, b, $\bar{c}$ and r_{45}, the r-value at 45^0 to RD (for more details see [2]). For DC06, the values of the anisotropy coefficients of Yld91 criterion identified using these two analytical procedures are given in Table 2. In the same table are also reported the values of the coefficients involved in Hill criterion, which was also identified with analytical formulas involving only σ_0, σ_{45},σ_{90}, and σ_b (stress-based procedure) and r_0, r_{45} and r_{90} (r-values based procedure), respectively (for these formulas, e.g. see [1]).

3.1 Predictions of the Orthotropic Yield Criteria Yld91 and Hill [4] Identified Analytically Using Four Yield Points

Let us first discuss the predictions obtained with Hill and Yld91 criteria identified analytically using only σ_0, $\sigma_{45}\sigma_{90}$, and σ_b. Figure 2a–b show the theoretical evolution of the yield stress and Lankford coefficients in the plane of the sheet (i.e. (**x**,**y**) or (RD, TD) according to Hill and Yld91 criteria, respectively, in comparison with the experimental yield stresses for the DC06 alloy; the projection of the respective yield surfaces in the $(\sigma_{xx}, \sigma_{yy})$ plane are plotted in Fig. 2c. Note that the predictions of the anisotropy in yield stresses predicted with these criteria are practically the same while the yield surface according to Yld91 is a very slight upper bound of Hill's. Neither criterion captures nor the experimental trends in r-values (see Fig. 2). As concerns the cup drawing predictions, let us note that both models predict an average cup height close to the experimental one. Yld91 criterion predicts $h_{avg} = 45.94$ mm versus $h_{avg} = 45.31$ mm according to Hill, the experimental average height being of 46.08 mm.

However, the improvements in predictions with respect to von Mises criterion concern only average values of the cup height. While data show that the maximum cup height is at TD and the minimum at 45° to the RD, both Yld91 and Hill [4] criteria predict the maximum cup height around 45° to the RD and the minimum at TD. Also, the predicted amplitudes of the ears are much lower than the ones observed experimentally (see Fig. 3).

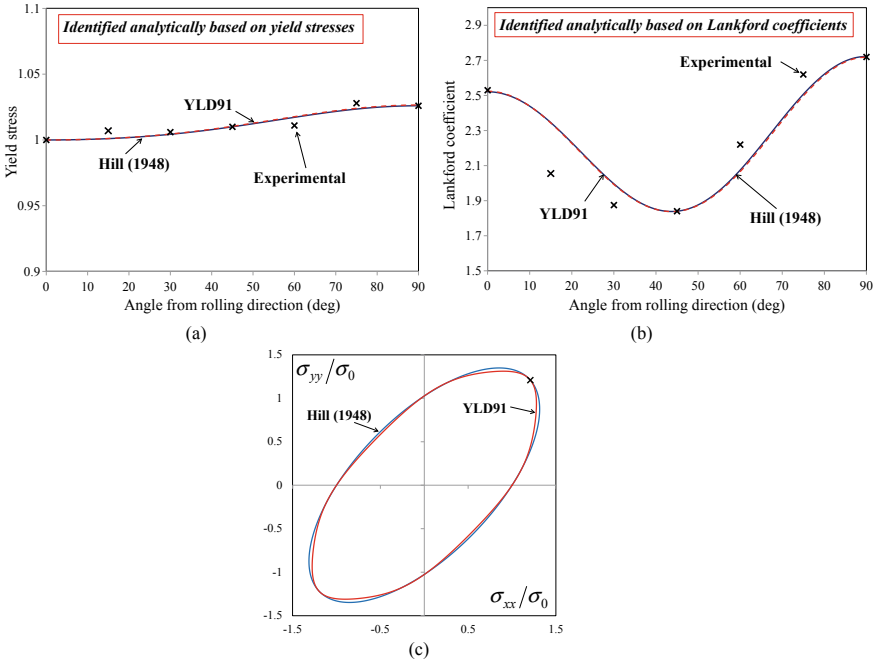


Fig. 2 **a** Evolution of the uniaxial yield stress versus the angle to RD; **b** Variation of the Lankford coefficients; **c** Yield surfaces in the biaxial plane $(\sigma_{xx}, \sigma_{yy})$ for DC06 according to Hill and Yld91. Data after [8, 13, 14]. (Color figure online)

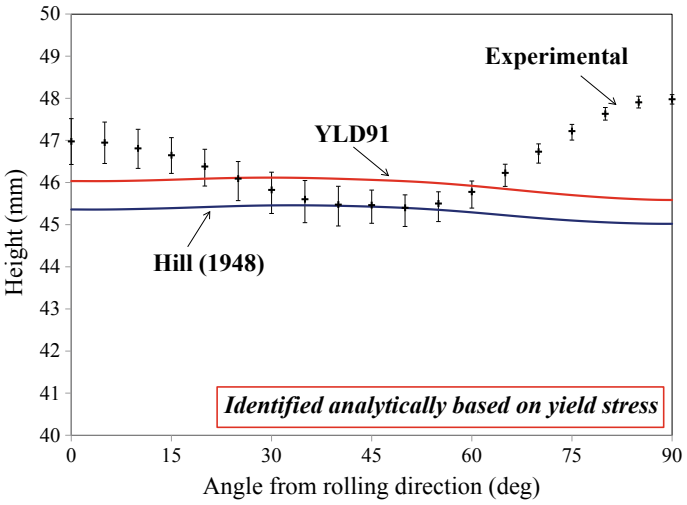


Fig. 3 Earing profile for the DC06 cup according to Yld91 and Hill [4] criteria. Both criteria were identified analytically using only the yield stresses. (Color figure online) σ_0, σ_{45}, σ_{90}, and σ_b. Data after [8, 12]

3.2 *Predictions of the Orthotropic Yield Criteria Yld91 and Hill Identified Analytically Using Only:r_0, r_{45},r_{90}*

The predictions obtained with Hill [4] and Yld91 criteria identified analytically using only the experimental r-values:r_0, r_{45},r_{90} are shown in Figs. 4 and 5.

Let us first note that the predictions of the anisotropy in Lankford coefficients of the steel alloy DC06 are practically the same. Both criteria predict the same variation of the yield stresses in the plane of the sheet, and both criteria greatly overestimate the experimental values. In the biaxial plane the projection of the yield surface according to the Yld91 criterion is interior to the one according to Hill, with Yld91 being in better agreement with the experimental equibiaxial tensile yield stress (see Fig. 4c). Both yield criteria predict the development of four ears at RD and TD, and a minimum height at 45° to the RD (see Fig. 5). In the experiment, the maximum height is at TD whereas either criterion predicts the maximum height at RD.

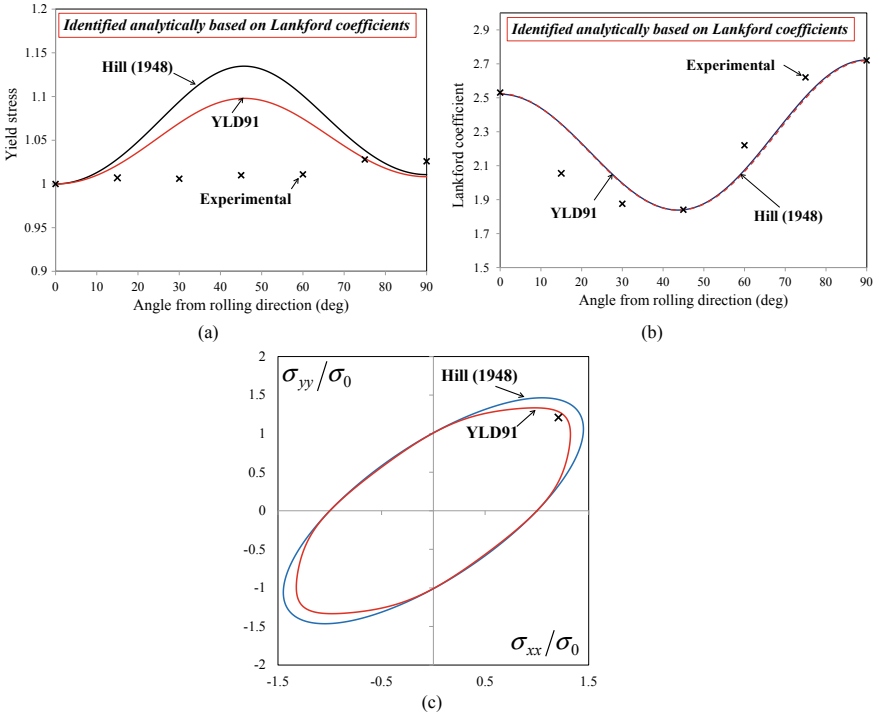


Fig. 4 Comparison between experimental and predicted plastic anisotropy of steel alloy DC06: **a** Evolution of the uniaxial yield stress versus the angle to RD; **b** Variation of the Lankford coefficients; **c** Projection of the yield surfaces in the biaxial plane according to Yld91 and Hill [4] yield criterion. Both criteria were identified analytically using only experimental Lankford coefficients r_0, r_{45},r_{90}. Data reported in [8, 13, 14]. Stresses are normalized by σ_0, the yield stress in uniaxial tension along RD. (Color figure online)

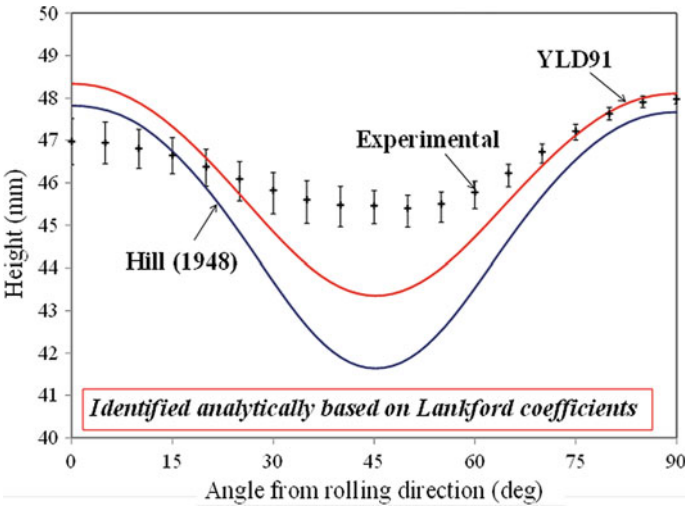


Fig. 5 Earing profile for the DC06 cup according to Yld91 and Hill [4]. Both criteria were identified analytically using experimental Lankford coefficients r_0, r_{45},r_{90}. Data after [8, 12]. (Color figure online)

Although both yield criteria predict the same variation in Lankford coefficients in the plane of the sheet (see Fig. 4b) and match exactly the average experimental r-values at 0^o, 45^o, 90^o to RD, the predictions of the average cup height are different, 44.98 mm according to Hill vs. 45.93 mm according to Yld91. In summary, it can be concluded that these yield criteria do not predict accurately the mechanical behavior of DC06 alloy in cup drawing.

4 Predictions Based on Yld91 and Cazacu [6] Orthotropic Yield Criteria Identified Using All Available Data

4.1 Predictions According to YLD 91 Criterion Calibrated Numerically Using All Available Data

Using the new mathematical results obtained recently in [1–3] for orthotropic yield criteria involving one linear transformation, it becomes now possible to compare the influence of the calibration method, namely, analytical vs. numerical, on the forming predictions. For this purpose, Yld91 was also calibrated numerically using all the available mechanical data for the steel alloy DC06, namely, the experimental r-values and uniaxial yield stresses in seven in-plane orientations, and the equibiaxial stress point. In the cost function all data points were given equal weights.

Note that the optimization algorithm leads to a better description of the experimental Lankford coefficients than that of the yield stresses in the plane of the DC06 sheet. Moreover, the predicted anisotropy in yield stresses and r-values obtained with the set of anisotropy coefficients determined with the numerical calibration procedure is similar to that obtained using the anisotropy coefficients evaluated using analytical formulas and the experimental r_0, r_{45},r_{90} (see Fig. 6b). This is because Yld91 cannot predict at the same time a very weak anisotropy in uniaxial yield stresses and a pronounced anisotropy in r-values. Note that the predicted earing profile obtained using the set of anisotropy coefficients determined with the optimization algorithm is very close to the one obtained using the r-values based identification strategy (see Fig. 6c). Practically, the same average height (45.96 mm vs. 45.93 mm), and the same locations and numbers of ears are obtained. Simulations were also done with Hill's criterion identified numerically using all available dataset. Same conclusions as for

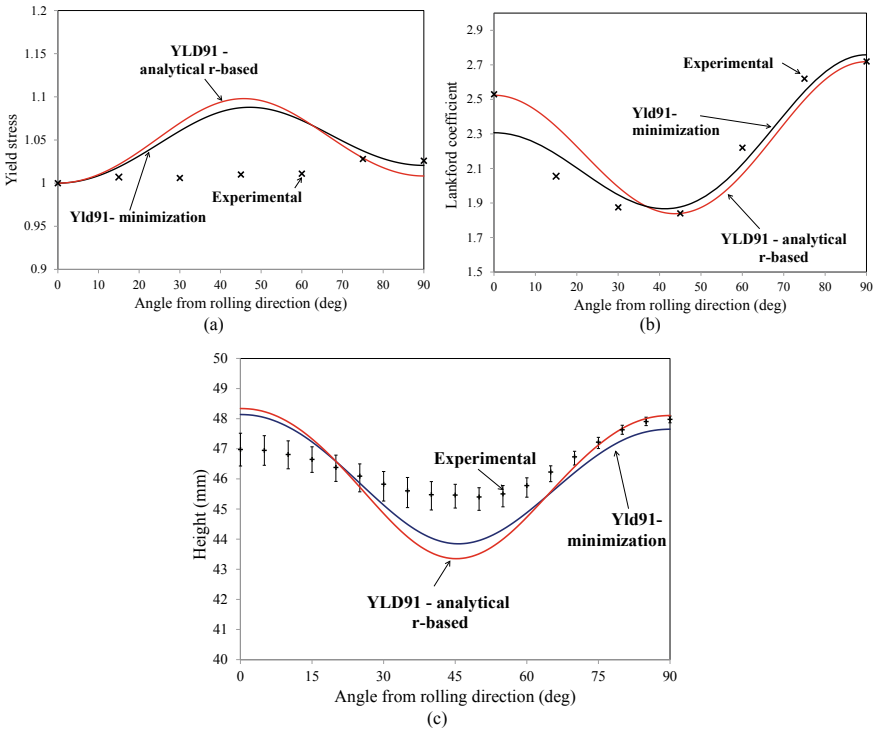


Fig. 6 **a** Evolution of the yield stress versus the angle to RD. **b** Evolution of the Lankford coefficient versus the angle to RD **c** Variation of the cup height versus the angle to RD according to Yld91 yield criterion for two sets of anisotropy coefficients: one determined analytically using only Lankford coefficients (red), and the other obtained by minimization in conjunction with all available data for steel alloy DC06 (black). Stresses are normalized by σ_0, the yield stress in uniaxial tension along RD. Data reported in [8, 13, 14]. (Color figure online)

Yld91 can be drawn concerning the accuracy of the predictions and the influence of the identification procedure and extent/type of data used for identification.

4.2 Predictions According to the Cazacu [6] Criterion

As seen previously the Hill or the Yld91 criteria cannot predict accurately the amplitude of the ears during the cup drawing application. One of the reasons is that the mathematical form of these criteria imposes very specific couplings between the r-values and yield stresses along RD and TD. In the following, the orthotropic criterion of Cazacu [6] will be applied to the same material. This yield criterion is expressed in terms of orthotropic invariants J_2^o, J_3^o as follows:

$$H\left(J_2^0, J_3^0\right) = \left(J_2^0\right)^4 - \alpha\left(J_3^0\right)^2\left(J_2^0\right) \tag{6}$$

where α is a parameter. These orthotropic invariants were developed based on rigorous representation theorems for tensor functions (for more details on the theorems used see Cazacu et al. [1], for the full mathematical proofs and the details concerning the derivation of Eq. (7) and Eq. (8) see Cazacu and Barlat [7]). As a consequence, it was ensured that the combinations of stress components that are involved in their expressions and the number of anisotropy coefficients are such as to fulfill the restrictions associated to orthotropic symmetries. Specifically, the orthotropic second-invariant J_2^o should involve exactly 6 anisotropy coefficients, a_i, $i = 1\ldots6$ and should be of the form:

$$\begin{aligned} J_2^o = {} & \frac{a_1}{6}\left(\sigma_{xx} - \sigma_{yy}\right)^2 + \frac{a_2}{6}\left(\sigma_{yy} - \sigma_{zz}\right)^2 + \frac{a_3}{6}\left(\sigma_{xx} - \sigma_{zz}\right)^2 + a_4\sigma_{xy}^2 \\ & + a_5\sigma_{xz}^2 + a_6\sigma_{yz}^2 \end{aligned} \tag{7}$$

while the third-order orthotropic invariant J_3^o should involve 11 anisotropy coefficients b_k, $k = 1\ldots11$and should be of the form:

$$\begin{aligned} J_3^o = {} & \frac{1}{27}(b_1 + b_2)\sigma_{xx}^3 + \frac{1}{27}(b_3 + b_4)\sigma_{yy}^3 + \frac{1}{27}[2(b_1 + b_4) - b_2 - b_3]\sigma_{zz}^3 \\ & - \frac{1}{9}\left(b_1\sigma_{yy} + b_2\sigma_{zz}\right)\sigma_{xx}^2 - \frac{1}{9}(b_3\sigma_{zz} + b_4\sigma_{xx})\sigma_{yy}^2 \\ & - \frac{1}{9}\left[(b_1 - b_2 + b_4)\sigma_{xx} + (b_1 - b_3 + b_4)\sigma_{yy}\right]\sigma_{zz}^2 + \frac{2}{9}(b_1 + b_4)\sigma_{xx}\sigma_{zz}\sigma_{yy} \\ & - \frac{\sigma_{xz}^2}{3}\left[2b_9\sigma_{yy} - b_8\sigma_{zz} - (2b_9 - b_8)\sigma_{xx}\right] - \frac{\sigma_{xy}^2}{3}\left[2b_{10}\sigma_{zz} - b_5\sigma_{yy} - (2b_{10} - b_5)\sigma_{xx}\right] \\ & - \frac{\sigma_{yz}^2}{3}\left[(b_6 + b_7)\sigma_{xx} - b_6\sigma_{yy} - b_7\sigma_{zz}\right] + 2b_{11}\sigma_{xy}\sigma_{xz}\sigma_{yz} \end{aligned} \tag{8}$$

Cazacu [6] criterion was calibrated numerically using all the available mechanical data for the steel alloy DC06, namely the experimental r-values and uniaxial yield

stresses in seven in-plane orientations and the equibiaxial yield stress point. The predictions according to this criterion are shown in Fig. 7. Note that the criterion describes reasonably well both the anisotropy in yield stresses and r-values in the plane of the sheet. Most importantly, it predicts correctly the earing profile (Fig. 7c). Specifically, it predicts that four ears develop at RD and TD, and that the minimum height is at 45° to the RD. In contrast to Yld91 and Hill criteria, this criterion predicts that the maximum cup height is at TD, as observed experimentally. Moreover, the predicted average height obtained is of 46.11 mm, i.e. very close to the experimental value of 46.8 mm.

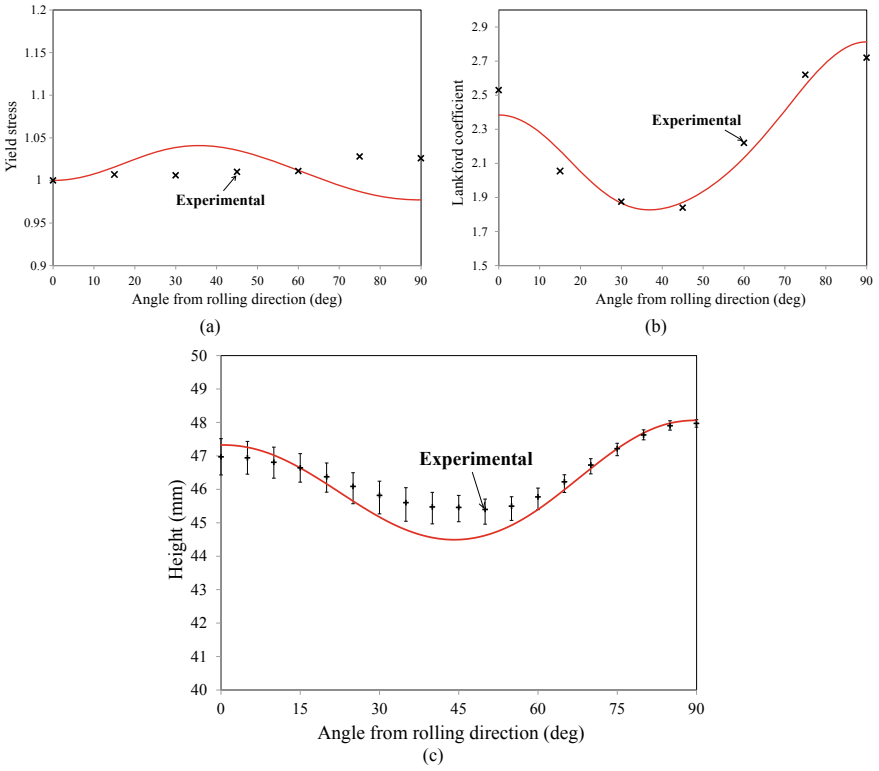


Fig. 7 Comparison between the experimental data and predictions according to Cazacu [6] orthotropic yield criterion for the steel alloy DC06: **a** Evolution of the yield stress vs. the angle to RD. **b** Evolution of the Lankford coefficient versus the angle to RD **c** Variation of the cup height vs. the angle to RD. Data from [8, 12, 14]. (Color figure online)

5 Conclusions

Using the new equivalent representation of Yld91 in terms of stresses (see Eq. (3)), this criterion can be identified analytically using four experimental yield stresses or three experimental Lankford coefficients, respectively (for more details, see [2]). This makes the parametrization of Yld91 very simple and reliable even if the mechanical characterization data set available is limited. Illustrations of the benefits of using the new explicit expression of Yld91 and the analytical identification procedures were presented for a strongly anisotropic steel alloy, DC06. Specifically, the influence of the type of data used for identification (i.e. only experimental yield data or only experimental Lankford coefficients) and the extent of the data set used for identification (i.e. limited data set or all available data set) on the accuracy of cup forming predictions were analyzed. Hill and Cazacu [6] criterion were also applied to DC06 and an in-depth analysis of the influence of the choice of the criterion used for modeling on the accuracy of the predictions was presented. If Yld91 and Hill criteria are identified using a stress-based analytical identification procedure, the predictions of the plastic anisotropy in r-values in the plane of the sheet and the predicted experimental earing profile are incorrect. Only the prediction of the average cup height is an improvement with respect to the von Mises yield criterion. Correct predictions in terms of number and location of ears and location of the minimum height are obtained with parametrizations obtained using analytical expressions involving the Lankford coefficients. It is worth mentioning that if the r-values based analytical identification strategy is used for Yld91, the predictions are slightly more accurate than those obtained with Hill [4]. Also, only a very slight improvement in accuracy is obtained if for the identification of the anisotropy coefficients of Yld91 all the available mechanical data are used. The most accurate predictions for DC06 are obtained using Cazacu [6] yield criterion, which can describe both the weak anisotropy in uniaxial yield stresses and the strong anisotropy in r-values of the material. In contrast to Yld91 [5] and Hill [4] criteria, Cazacu [6] yield criterion captures all the experimentally observed characteristics of the fully drawn cup of DC06 steel, i.e. the average height, the number and location of ears, the location of the maximum height of the fully drawn cup, and the amplitude.

References

1. Cazacu, O., Revil-Baudard, B., Chandola, N. (2019) Plasticity-damage couplings: from single crystal to polycrystalline materials, Springer
2. Cazacu, O. New mathematical results and explicit expressions in terms of the stress components of Barlat, et al (2019) (1991) orthotropic yield criterion. Int J Solids Struct 176–177:86–95
3. Cazacu O (2019) New expressions and calibration strategies for Karafillis and Boyce (1993) yield criterion. Int J Solids Struct 185–186:410–422
4. Hill, R. (1948) A theory of the yielding and plastic flow of anisotropic metals, in: Proc. R. Soc. Lond. Math. Phys. Eng. Sci., The Royal Society; 281–297

5. Barlat F, Lege DJ, Brem JC (1991) A six-component yield function for anisotropic materials. Int J Plast 7:693–712
6. Cazacu O (2018) New yield criteria for isotropic and textured metallic materials. Int J Solids Struct 139–140:200–210
7. Cazacu O, Barlat F (2001) Generalization of Drucker's yield criterion to orthotropy. Mathematics and Mechanics of Solids 6:613–630
8. Aguir H, Alves J, Oliveira M, Menezes L, BelhadjSalah H, Hambli R (2009) Identification of anisotropic parameters using the cylindrical cup deep drawing test and the coupled ANN-inverse method. In: 7th EUROMECH solid mechanics conference. pp 1–11
9. Khalfallah A, Alves JL, Oliveira MC, Menezes LF (2015) Influence of the characteristics of the experimental data set used to identify anisotropy parameters. Simul Model Pract Theory 53:15–44
10. O. Cazacu [2018] Anisotropic yield criteria. Proceedings of Numisheet 2018, the 11th International Conference and Workshop on Numerical Simulation of 3D Sheet Metal Forming Processes, July 30-August 3, 2018, Tokyo, Japan, IOP Conf. Series: Journal of Physics: Conf. Series 1063, pp. 012052
11. Karafillis, A.P., Boyce, M.C. (1993)A general anisotropic yield criterion using bounds and a transformation weighting tensor J. Mech. Phys. Solids. 41: 1859–1886
12. Duarte J, Simões F, Teixeira P, Santos A (2002) Experimental Benchmark# 7-Cylindrical Cup–Earing. In: Digital Die Design System (3DS), IMS 1999 000051, Communication presented in Inter-Regional Meeting, Paris
13. Mattiasson K, Sigvant M (2008) An evaluation of some recent yield criteria for industrial simulations of sheet forming processes. Int J Mech Sci 50(4):774–787
14. Selection and identification of elastoplastic models for the materials used in the benchmarks, Digital Die Design Systems (3DS) Report, 2001

Experimental Investigation of Different WAAM (Wire-Arc Additive Manufacturing) Processes and Their Influence on the Component Properties and Formability



Pascal Colditz, Marcel Graf, André Hälsig, Sebastian Härtel, Keval P. Prajadhiama, Yupiter P. Manurung, and Birgit Awiszus

Abstract Wire-arc additive manufacturing (WAAM) complex components can be built-up layer by layer from metallic construction materials. In this investigation two different WAAM processes with high built-up rates (CMT and pulsed GMAW) were compared in terms of geometry formation and component properties. The reference is a rectangular thin-walled geometry made of the austenitic stainless steel 316LSi (1.4430). During the welding process, the temperature development in the weld layer was measured. The experimental comparison of CMT (R_m = 630MPa) and pulsed GMAW (R_m = 605MPa) is completed by the determination of the mechanical properties using micro-tensile tests. Furthermore, the additive-manufactured walls were cold rolled with a subsequent heat treatment or hot rolled to provide proof of formability and forming induced property improvement.

Keywords WAAM · CMT · Pulsed GMAW · Additive manufacturing · Forming behavior

1 Introduction

Additive manufacturing processes have become much more popular in recent years. Due to various technological developments, metals and metallic composite materials can now also be processed. Additive Manufacturing base on the layer by layer

P. Colditz (✉) · M. Graf · S. Härtel · B. Awiszus
Institute for Machine Tools and Production Processes, Professorship Virtual Production Engineering, Chemnitz University of Technology, Reichenhainer Str. 70, 09126 Chemnitz, Germany
e-mail: pascal.colditz@mb.tu-chemnitz.de

A. Hälsig
Institute of Joining and Assembly, Professorship Welding Engineering, Chemnitz University of Technology, Reichenhainer Str. 70, 09126 Chemnitz, Germany

K. P. Prajadhiama · Y. P. Manurung
Faculty of Mechanical Engineering, UiTM Shah Alam, 40450 Selangor, Malaysia

© The Minerals, Metals & Materials Society 2021

G. Daehn et al. (eds.), *Forming the Future*, The Minerals, Metals & Materials Series,
https://doi.org/10.1007/978-3-030-75381-8_237

structure of components. For this purpose, the starting material is locally melted and solidified by an external energy supply and thus the individual layers are connected with each other. Accordingly, the additive manufacturing processes can be divided into solid, powder, or fluid based. For the processing of metallic materials, wire and powder-based processes are of primary importance. As energy sources, for example, laser technologies or arc processes can be used [1, 2].

With the wire-arc additive manufacturing (WAAM), the first step is to slice the previously created CAD model into layers. Afterward the individual layers are applied using a gas metal arc welding (GMAW) process. The handling of the welding torch to create the 2D contours can be carried out by robotic systems or computer numerical controlled gantries. Compared to powder-based processes, the WAAM is characterized by higher output rates, inexpensive materials, low investment costs, and easy handling. Disadvantages are the significantly lower surface quality and the geometrical accuracy of the components [2]. In addition, the process-related heat input can lead to high internal stresses and thus to component distortion. In order to reduce this heat input during the welding process considerably, corresponding process control variants have been developed from the classic GMAW process [3].

One possibility to reduce the heat input during welding is to use the *Cold Metal Transfer* (CMT) process from *Fronius International GmbH*. While conventional GMAW technologies feed the wire continuously, here the wire is fed oscillating in frequencies up to 130 Hz. The pull back of the wire supports the drop separation. As a result, the short-circuit current is very low and the material transfer takes place almost without electrical current. In addition, the short circuit does not happen in an uncontrolled manner but is timed by the pull back of the wire. These two properties result in a low heat input with nearly spatter-free welding seams. At the same time, the component quality, the build-up rate (1500 cm^3/h) and the output rate (99%) can be increased [4, 5].

Another method to reduce the heat input is to combine the GMAW with a pulsed arc. In this process, the power source is periodically switched between a low basic electrical current and a higher pulse elecrical current. The basic and pulse phases must be adapted to the wire feed. In the initial phase the wire is preheated by the arc. In the subsequent pulse phase the material is melted and afterward transferred. Thus the impulse arc process is a short-circuit free process. This reduces the heat input. In addition, similar high build-up rates can be achieved as with CMT and the macroscopic surface quality is even better. Disadvantages are the lower output and the higher spattering rate [4–6].

The aim of the investigation is to provide proof of formability and forming induced property improvement of the additive-manufactured walls and do compare the two different WAAM processes. Therefore, the components were cold rolled with a subsequent heat treatment or hot rolled, which will be discussed in the following chapters.

2 Experimental Investigation

In order to be able to compare both investigated WAAM processes, a rectangular, thin-walled component made of 316LSi (1.4430) was used as reference geometry with a length of 105mm, a width of 25mm and a height of approximately 42,5mm. (Figs. 1 and 2). This material is usually used as a welding filler for austenitic, stabilized, and unstabilised Cr-Ni-Mo steels. The material was applied to a base plate made of X5CrNi18-10 (1.4301) without pausing between the individual layers.

The following parameters were used for the component manufacturing:

- Wire diameter $d_W = 1,2$mm
- Welding speed $v_{CMT} = 40$cm/min, $v_{pulsed} = 42$cm/min,



Fig. 1 WAAM component, built-up with CMT process with 25 layer (left) and pulsed arc process with 25 layer (right). (Color figure online)

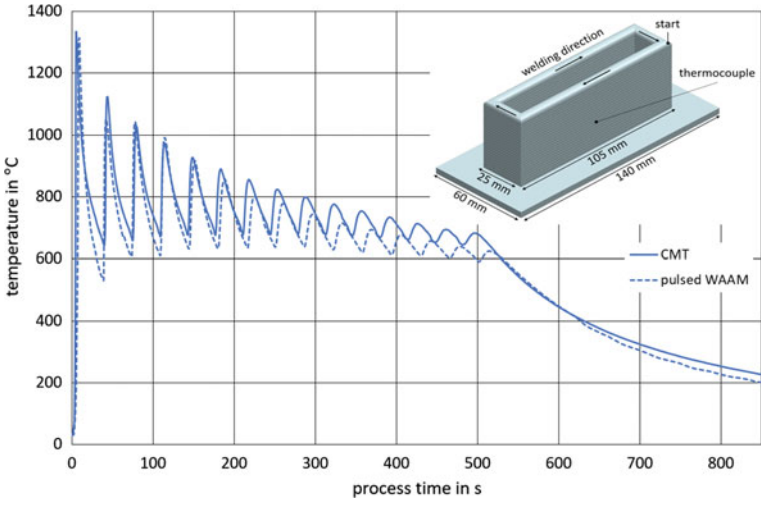


Fig. 2 Temperature curve measured on an additive-manufactured component with 25 layers, measuring on top of layer 10 at the middle of the side wall. (Color figure online)

Table 1 Chemical material composition of 316LSi (1.4430) [7]

	EN ISO 14343	Before welding	After welding
C	<0,03%		
Si	0,65–1,00%	0,76%	0,63%
P	<0,03%		
Nb		0,05%	0,00%
Mo	2,00–3,00%	1,66%	1,63%
S	<0,03%		
Ti		0,34%	0,27%
V		0,38%	0,30%
Cr	18,00–20,00%	17,26%	17,83%
Mn	1,00–2,50%	2,46%	2,43%
Ni	11,00–14,00%	11,36%	10,57%
Cu	<0,75%	0,90%	0,77%
Fe	bal	64,81%	65,53%

- Speed of the wire feed $v_{Wire} = 3$m/min
- Layer height $h_W = 1{,}7$mm
- Initial thickness of the walls $t_W = 6$mm
- Amperage $I_{CMT} = 110$A, $I_{pulsed} = 88$A
- Voltage $U_{CMT} = 13,5$V, $U_{pulsed} = 21$V
- Inert gas CMT 15 l/min; 97, 5% Argon and 2, 5% CO_2;
- Inert gas Pulsed 15l/min; 100% Argon.

In order to document the initial state of the material and to better understand the microstructural changes, the chemical composition of the material before and after the welding process was measured using EDX (Energy Dispersive X-ray Spectroscopy), see Table 1. A wire section was used to measure the material before and a specimen produced by pulsed arc welding to measure the material after welding.

The alloying elements carbon (C), phosphorus (P), and sulfur (S) cannot be reliably detected with the EDX method due to their low atomic mass. The EDX analysis shows a significant decrease in the alloy contents of silicon (Si), nickel (Ni), copper (Cu) due to the arc-related burn off. It can also be assumed that the titanium (Ti) content is reduced by the fusion with carbon to form titanium carbides. During the welding process, the floating of silicate islands can also be seen.

In order to be able to analyze the microstructural changes of the welding filler material during the additive manufacturing, the temperature level in the middle of the side wall were measured, see Fig. 2. For this purpose, a thermocouple type K was welded directly into the component on top of layer 10. The diagram for CMT shows a temperature peak of $\vartheta = 1330$ °C shortly after welding of the wire material and a subsequent cyclical reheating of the welded layer. In the pulsed arc process the temperature after melting is around $\vartheta = 1315$ °C. Both processes show a nearly

similar temperature curve with a low heat input for WAAM processes. In pulsed WAAM the material cools down marginally faster.

To be able to determine and compare the mechanical properties of the additive-manufactured components, hardness measurements, and tensile tests were carried out. For this purpose, the components were separated at the front sides. The respective long sides of the component were machined on both side to a thickness of 2mm, and micro-tensile specimen with an initial cross section of 4mm^2 and a measuring length of 6mm was taken by wire erosion (see Fig. 3). All of the corresponding tensile tests were carried out with the *Galdabini Quasar 50* test press, at a constant forming speed of $\dot{\varphi} = 0{,}1\text{s}^{-1}$ and at room temperature. During the tests, the pulling force and lengthening of the specimen were measured (Fig. 4). Taking into account the specimen geometry, a corresponding stress–strain diagram could then be calculated, see Fig. 5. The end faces were prepared for hardness measurements and microstructure

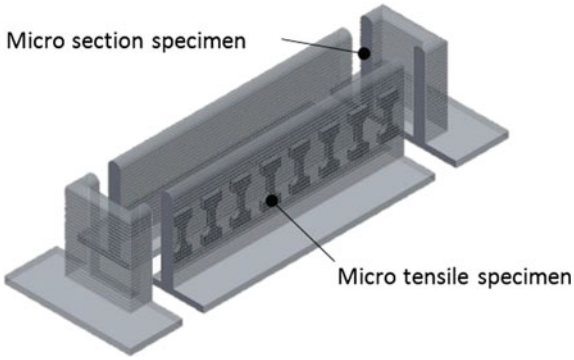


Fig. 3 CAD model of the component geometry to illustrate the specimen orientation. (Color figure online)

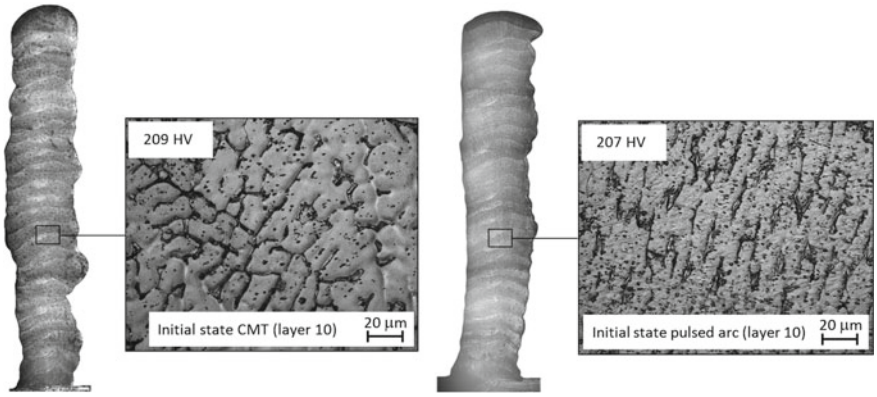


Fig. 4 Microstructure of tenth layer in an additive layer structure of 25 layers, micro-sections of a CMT component (left) and of a pulsed arc component (right)

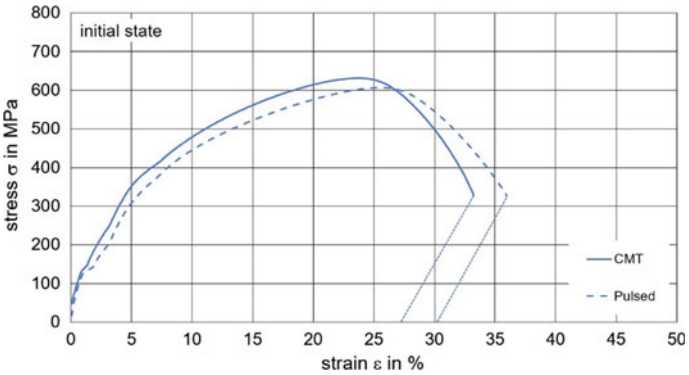


Fig. 5 Stress–strain diagram of the initial state specimens. (Color figure online)

analysis (see Figs. 3 and 4).

The cyclical reheating during both WAAM processes, due to the further layer wise material application is similar to a repeated heat treatment of the material. While a cast structure is occurred immediately after the melting and the application of the wire material, the microstructure is influenced by the following heat treatment. During the investigation of WAAM with low-alloy (G4Si1, 1.5130) welding filler material, a cast structure was occurred after melting and application of the wire material. This structure was strongly globularly shaped by the subsequent repeated heat treatment. With the used material 316LSi no such clear microstructural differences between the individual layers could be detected. The entire specimen cross section shows a microstructure without pronounced grains (see Fig. 4). This indicates that the repeated application of temperature by the welding process does not cause any significant microstructural changes.

This is confirmed by the hardness measurements, which show an almost constant level over the height of the specimen. With the CMT process an average hardness of 209HV could be achieved. The hardness of the sample layer produced by means of the pulsed arc method at 207HV. According to standard ISO 18265 there is a direct relationship between hardness and tensile strength of a material [8]. Based on this relationship, the tensile strength of the two graphs should be significantly higher. The measured tensile strengths also fluctuate over the amount of micro-tensile samples tested. A possible reason for the difference between hardness measurements and tensile tests is the large number of pores in the material, which are created during the welding process (see Fig. 6). The pore creation is favored by the high silicon content in the material [9].

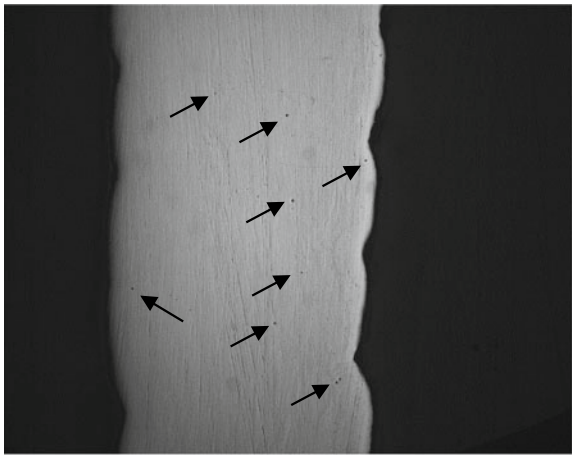


Fig. 6 Microsection specimen with clearly recognizable pores

2.1 Cold Forming and Subsequent Heat Treatment at 850 °C

In order to investigate the influence of cold forming on the additively manufactured components, a side wall was rolled to a thickness of 4mm before sampling. With a layer thickness of about 6mm this corresponds to a plastic strain of $\varphi = 0{,}4$. Afterward the walls were heat treated at 850 °C for one hour to induce static recrystallization effects. As already in the investigations of the initial states of the components, the micro-tensile samples were finally taken by means of machining and wire erosion. In addition, the microstructure was examined again, and hardness measurements were carried out.

Compared to the initial state, the specimen of both WAAM variants show a significantly changed microstructure (see Fig. 7). The cast-like microstructure could be transformed into a more globular structure by forming with subsequent heat treatment due to the static recrystallization.

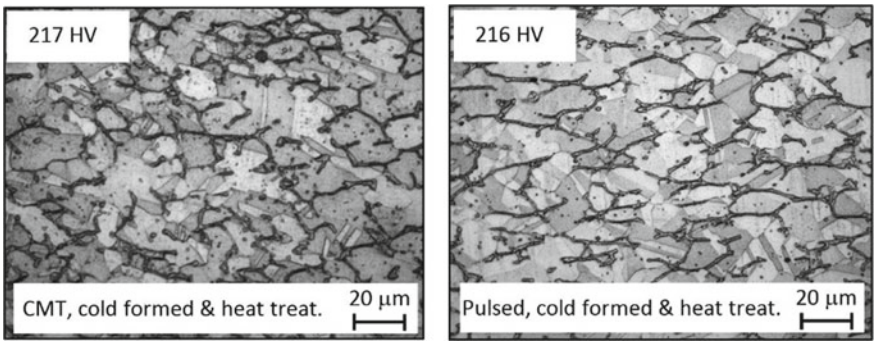


Fig. 7 Microstructure of cold rolled and heat treated (850 °C, 1 h) specimens; $\varphi = 0{,}4$

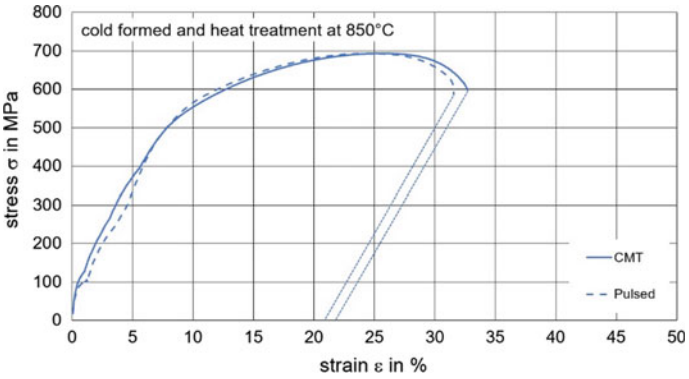


Fig. 8 Stress–strain diagram of the cold rolled $\varphi = 0, 4$ and heat-treated (850 °C, 1 h) specimen. (Color figure online)

It now shows a clearly recognizable grain structure and orientation. Both samples show that there is still a slight elongation of the grains. This indicates that recrystallization has not yet been completely finished. In addition, precipitates collect at the grain boundaries. These could be carbides or locally diffused delta ferrite [10]. The specimen manufactured by the CMT method shows a slightly finer microstructure. Otherwise, both microstructures are very similar. The same applies to the hardness measurements. Both samples achieve a hardness of about 215HV (see Fig. 7).

The stress–strain diagram shows a tensile strength of around $R_m = 690$MPa for both specimen (see Fig. 8). Furthermore, shows a very good agreement between CMT and pulsed WAAM. With the help of cold forming and subsequent recrystallization annealing it was possible to increase the strength of the specimen and to homogenize the mechanical properties. With an appropriately adapted heat treatment at higher temperatures, recrystallization in the material could probably be completed. This could further improve the mechanical properties with regard to higher elongation at break.

2.2 Heat Treatment at 850 °C

In order to be able to prove the influence of cold forming on the microstructural transformations taking place during heat treatment, comparative specimen without previous forming were examined. For this purpose, the additive walls were heat treated at 850 °C for one hour before sampling.

The micro-section specimens prepared for this purpose show clear differences in microstructure (see Fig. 9).

This differs very much from the cold formed and heat-treated specimens. While with these a clear grain structure and orientation was previously visible, the grains now can only be recognized by the precipitates at the grain boundaries. This clearly

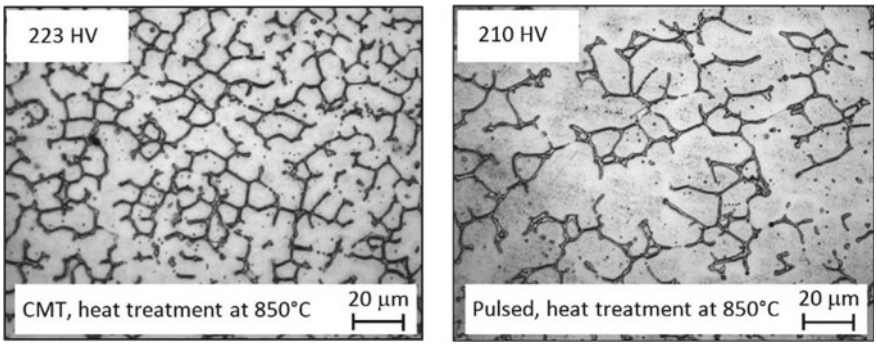


Fig. 9 Microstructure of heat treated (850 °C, 1 h) specimens; $\varphi = 0, 4$

shows that the microstructural transformations necessary for grain formation and growth are strongly dependent on the plastic strain previously introduced.

Here too, the CMT sample has a finer grain structure. Even though the microstructures differ more clearly, the mechanical properties are again almost the same. Due to the more fine-grained structure, the hardness value of the CMT sample at 223HV is slightly higher than that of the specimen produced by means of pulsed arcing (210HV). The curve profiles determined by means of a tensile test, however, are very similar again. As with specimen in their initial state, there is a clear difference between the hardness values and the associated measured tensile strengths (see Fig. 10). Here also the cause could be pores. At the same time, this allows the assumption that these pores could be partially eliminated by the preceding forming in Sect. 2.1.

Compared to the initial state, the mechanical properties of the specimens could not be significantly improved by the heat treatment, neither in terms of strength nor in terms of formability.

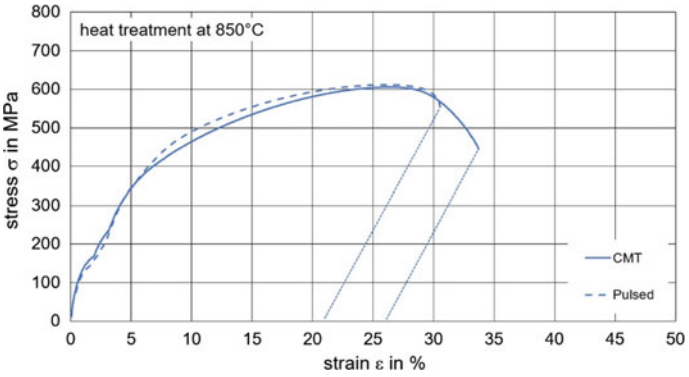


Fig. 10 Stress–strain diagram of the heat-treated (850 °C, 1 h) specimen. (Color figure online)

2.3 Hot Forming at 1150 °C

A further possibility to optimize the mechanical properties of the additive-manufactured components is a subsequent hot forming. For this purpose, the additive-manufactured samples were heated to 1150 °C in a chamber furnace, hot-rolled and then slowly cooled down at room temperature. To ensure comparability with cold forming, the degree of deformation here was also $\varphi = 0,4$.

The microstructural analyses of the hot-formed specimen show a completely different picture from all previous ones (see Fig. 11). Although a grain structure can also be seen here and the precipitates do not collect predominantly at the grain boundaries, as with all previous ones. Both samples show a similar structure independent of the WAAM process. The same applies to the hardness measurement (see Fig. 11). Here both are on a similar level. Compared to the initial state, the hardness could be increased to about 260HV. The increase in the hardness of the material in combination with a coarser grain structure strongly indicates that hot forming is not sufficient to fully complete dynamic recrystallization processes. The remaining hardening of the material, therefore, explains the high measured hardness values.

The stress–strain diagram determined by the tensile tests also shows similar courses for WAAM processes (see Fig. 12).

The strong increase and the low elongation at break of both materials indicate a clear increase in strength of the material achieved by hot forming. The material behaves correspondingly more brittle than in the initial state. The elongation at break was reduced to below $A < 22\%$. This supports the assumption that dynamic recrystallization cannot be completely finished at a plastic strain of $\varphi = 0,4$. A reason for this is the low temperature in the forming zone due to the heat loss when removing from the furnace and the heat transfer into the cold rolls. Similar effects have already been demonstrated in previous investigations on the rolling of weld seams made of G4Si1 (1.5130) [11].

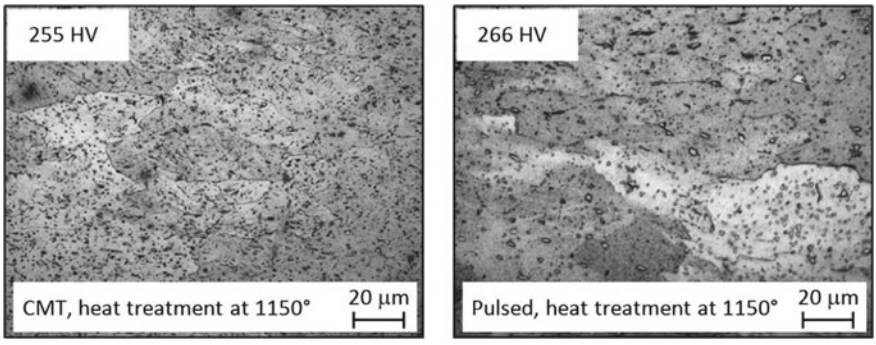


Fig. 11 Microstructure of hot rolled (1150 °C) specimen; $\varphi = 0,4$

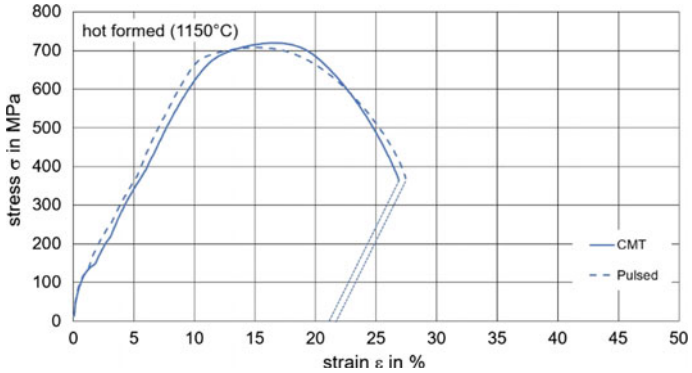


Fig. 12 Stress–strain diagram of the hot rolled $\varphi = 0, 4$ (1150 °C) specimen. (Color figure online)

2.4 Heat Treatment at 1150 °C

Also, for hot forming the influence of forming shall be analyzed by comparison with a simple heat treatment. For this purpose, the additive prepared samples were heated to 1150 °C, the temperature was maintained for 10min (according to the duration of the heat treatment during hot forming) and the samples were then slowly cooled down at room temperature. The components were then machined again, and the micro-tensile samples were taken by wire erosion. The microstructure obtained by heat treatment similar to the hot-formed samples (see Fig. 13). A grain structure with clearly grown grains can also be seen here.

In contrast to the hot-formed samples, however, a significantly lower hardness could be measured for both samples at around 175HV. This is a good approximation of the tensile strength of around $R_m = 560$MPa achieved in the tensile test (see Fig. 14). Regarding the course of the stress–strain curve, the only difference between process variants is the elongation at break. At A = 38% for CMT, the elongation at

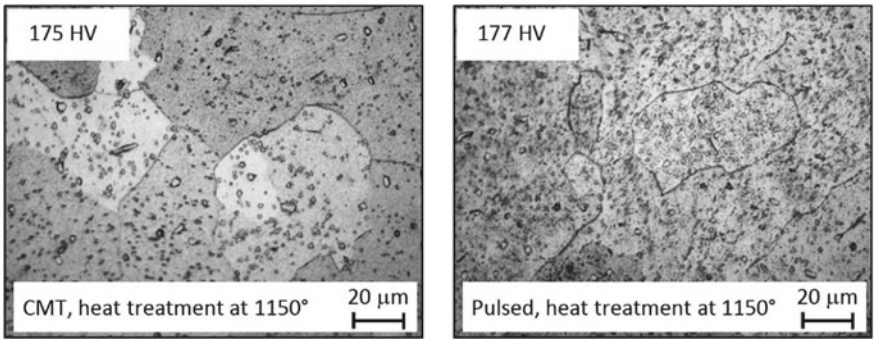


Fig. 13 Microstructure of heat treated (1150 °C, 10 min) specimen

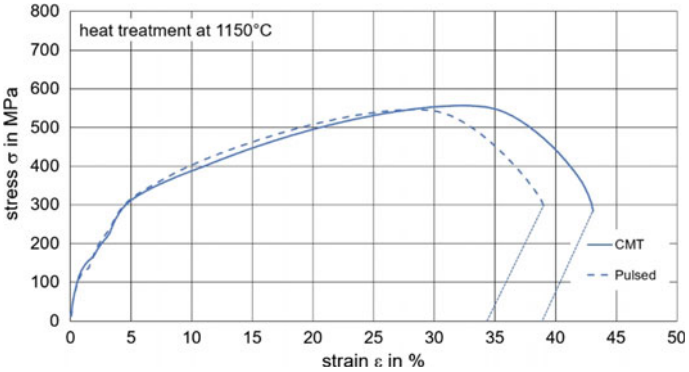


Fig. 14 Stress–strain diagram of the heat treated (1150 °C, 10 min) specimen. (Color figure online)

break is well above A = 34% for pulsed arc welding (see Fig. 14). The analysis of the hardness measurement and the tensile tests clearly shows that it is possible with the help of an appropriate heat treatment to significantly reduce the strength of the additively manufactured components and at the same time significantly increase the forming behavior.

3 Conclusion

With the two process variants CMT and pulsed arc welding process, additive components with slightly different mechanical properties can be produced (without any post-treatment). These differences could be eliminated by subsequent heat treatment and forming. Especially by the forming of the additive-manufactured components a homogenization of the mechanical properties could be achieved.

The degree of deformation of $\varphi = 0,4$ achieved during hot forming was not sufficient to induce complete dynamic recrystallization of the microstructure. This resulted in very high hardness values of around 260HV and a significantly more brittle material behavior with elongations at fracture below A < 22%. A more transformed microstructure with nearly completed recrystallization could be achieved by cold forming ($\varphi = 0,4$) followed by a one-hour heat treatment at 850 °C. As a result, hardness values of around 215HV could be achieved and the tensile strength of both samples was increased to $R_m = 690$MPa.

In order to be able to analyze the influence of the forming process on the microstructural transformations, two heat treatments were also carried out. Firstly, the specimens were heated to 850 °C and tempered for one hour. Due to the absence of a previously introduced forming process, a grain structure was formed and refined, but the mechanical properties could hardly be changed significantly. In contrast, the heat treatment at 1150 °C resulted in significant grain growth. This resulted in a reduction in strength and a significant increase in formability to over A > 34%.

On the basis of the collected data, further interesting investigations could now be set up. For example, cold forming is to be combined with heat treatment at higher temperatures in order to produce components with a completely recrystallized microstructure and significantly improved mechanical properties. Furthermore, the influence of the plastic strain on the course of recrystallization processes taking place during hot forming is to be investigated. Another possible area of investigation could be the influence of pore formation during welding of austenitic steels on their formability.

References

1. Zäh MF (2006) Wirtschaftliche Fertigung mit Rapid-Technologien. Munich: Carl Hanser Verlag. ISBN 978–3–446–22854–2
2. Williams SW, Martina F, Addison AC, Ding J, Pardal G, Colegrove P (2016) Wire + Arc additive manufacturing. Materials science and technology, vol 32, 7th edn. Didcot: Taylor & Francis, pp 641–647
3. Graf M, Härtel S, Hälsig A, Höfer K, Awiszus B, Mayr P (2018) Draht- und Pulverbasierte Additive Fertigung zur Herstellung von Eigenschaftsoptimierten Halbzeugen. In: Scientific Reports; 25th interdisciplinary scientific Conference Mittweida; Mittweida: Hochschule Mittweida—University of Applied Sciences, 480 pp 150–154
4. Dilthey U (2005) Schweißtechnische Fertigungsverfahren 1 – Schweiß- und Schneidtechnologien: Springer Verlag. ISBN 978–3–540–21673–5
5. Nordbruch S (2005) Verfahren zur Optimierung des MSG-Schweißens mit Impulslichtbogen auf der Basis visueller und elektrischer Informationen. PhD Thesis; University Bremen
6. Bruckner J, Egerland S, Himmelbauer K, Millinger A, Schörghuber M, Söllinger D, Waldhör A (2013) Schweißpraxis aktuell: CMT-Technologie. WEKA MEDIA GmbH & Co. KG
7. DIN EN 14343:2017–08, Schweißzusätze - Drahtelektroden, Bandelektroden, Drähte und Stäbe zum Lichtbogenschweißen von nichtrostenden und hitzebeständigen Stählen - Einteilung (ISO 14343:2017)
8. DIN EN ISO 18265:2014–02, Metallische Werkstoffe - Umwertung von Härtewerten (ISO 18265:2013)
9. Dilthey U (2005) Schweißtechnische Fertigungsverfahren 2 – Verhalten der Werkstoffe beim Schweißen: Springer Verlag
10. Häckel P (2013) Entstehung und Stabilität von Delta-Ferrit beim Schweißen von 9% Chromstahlen. Diploma Thesis; Graz University of Technology
11. Härtel S, Adam TE, Hoefer K, Awiszus B, Mayr P (2020) A novel method for improving weld seam properties through inline coupling of welding and forming. Materials, 271:13. https://doi.org/10.3390/ma13020271

Validation of Automatically Generated Forging Sequences by Using FE Simulations



Yorck Hedicke-Claus, Mareile Kriwall, Jan Langner, Malte Stonis, and Bernd-Arno Behrens

Abstract To increase the economic efficiency in the production of geometrically complicated forgings, material efficiency is a determining factor. In this study, a method is being validated to automatically design a multi-staged forging sequence initially based on the CAD file of the forging. The method is intended to generate material-efficient forging sequences and reduce development time and dependence on reference processes in the design of forging sequences. Artificial neural networks are used to analyze the geometry of the forging and classify it into a shape class. Result of the analysis is information on component characteristics, such as bending and holes. From this, special operations such as a bending process in the forging sequence can be derived. A slicer algorithm is used to divide the CAD file of the forging into cutting planes and calculate the mass distribution around the center of gravity line of the forging. An algorithm approaches the mass distribution and cross-sectional contour step by step from the forging to the semi-finished product. Each intermediate form is exported as a CAD file. The algorithm takes less than 10 min to design a four-stage forging sequence. The designed forging sequences are checked by FE simulations. Quality criteria that are evaluated and investigated are form filling and folds. First FE simulations show that the automatically generated forging sequences allow the production of different forgings. In an iterative adaptation process, the results of the FE simulations are used to adjust the method to ensure material-efficient and process-reliable forging sequences.

Keywords Automatic process design · Forging · FEA · Resource efficiency · CAD

Y. Hedicke-Claus (✉) · M. Kriwall · J. Langner · M. Stonis · B.-A. Behrens
IPH-Institut Für Integrierte Produktion Hannover gGmbH, Hollerithallee 6, 30419 Hannover, Germany
e-mail: hedicke-claus@iph-hannover.de
URL: http://www.iph-hannover.de

© The Minerals, Metals & Materials Society 2021

G. Daehn et al. (eds.), *Forming the Future*, The Minerals, Metals & Materials Series,
https://doi.org/10.1007/978-3-030-75381-8_238

1 Introduction

Due to their excellent mechanical properties, forgings are used in highly stressed areas such as automotive and aircraft engines. Because of their high component complexity, forgings are often produced in several process steps (forging sequence) [1]. The most important step toward increasing efficiency in a forging sequence is the reduction of the used material [2]. The quality of the forging sequence and the material efficiency are primarily depending on the design of the individual preforms. For an efficient forging sequence, the mass distribution of the individual preforms must therefore be sensibly approximated to the mass distribution of the finished forging. The cost of designing a material-efficient forging sequence increases significantly with the increasing complexity of the forged part, especially for components with a significant mass distribution in 3D space. One reason for this is the opposite direction between the backward-oriented design of the forging sequence and the forward-oriented FEM simulations, which is used to check the forging sequence. Conventionally used design methods such as the mass distribution diagram according to Mathieu [3] are not suitable for complex forged parts, since an application in 3D space for determining the mass distribution can only be computed by using several complex diagrams. Therefore, in the research project "Efficient Forging Sequence Planning" a method is being developed, which automatically generates a single multi-stage forging sequence based on a CAD file of the finished forged part geometry. The aim is that the method is applicable for forgings of different shape classes. Based on the mass distribution around the center of gravity of the finished forged part, a multi-stage forging sequence is generated step by step by approximating the cross-sectional contour and mass distribution of the forged part and semi-finished product. Without performing FEM simulations, the method is to generate multi-stage forging sequences within a few minutes, instead of several hours or days that are currently required. By using a computer-aided method for efficient forging sequence planning, both material costs and development time can be reduced, thus increasing the economic efficiency of the forging process [4]. There are several projects dealing with a computer-aided design of material-efficient forging processes with the aim to reduce the use of time-consuming FEM simulations during design process. Behrens et al. present an approach for inverse material flow simulation during drop forging. For a rotationally symmetric component, the material movement is modeled via so-called displacement paths, based on the least constraint. By means of this method a backward simulation for the design of intermediate forms during drop forging is possible [5]. However, this approach only applies to 2D space. Guan presents the development of a model for the preform design of a single 3D preform in a multi-stage drop forging process. The approach is based on potential field method and response surface method. Using this approach, a forging can be achieved without defects and a lower flash ratio [6]. Torabi et al. also deal with preform optimization for a turbine blade. The use of extruded elliptical cross section was considered as a blade preform, and then response surface method and multi-objective genetic algorithm was used to optimize this preform. Maximum filling ratio of the final blade

and minimum flash volume, forging force and strain variance of the final blade were considered as objectives of optimization. Results are achieved by simulations and experimental investigations [7]. For rotationally symmetric components, Knust et al. have developed a method that enables preform optimization within a few minutes without the use of FE simulations [8, 9]. The modular description of the component by single cross section allows the optimization of preforms by evolutionary algorithms. The optimized preforms significantly reduced the flash ratio. Alimirzaloo et al. optimize the preforms of a two-stage forging process for a wing blade by using artificial neuronal networks (ANN) and fuzzy logic. A more even strain distribution and a significant reduction of the flash ratio could be achieved [10]. SHAO presents an approach to predict the influence of preform geometry on the forging process for a turbine blade, using genetic algorithms and particle swarm optimization [11, 12].

The presented work on the computer-aided design of forging processes is mainly concerned with the automated design of individual or the optimization of a single multi-stage forging sequence for a defined component. At present, the authors are not aware of any work that allows to automatically generate multi-stage forging sequences for forgings of different shape classes. This study describes the method to achieve this. In the following, we first describe the structure and functionality of the method. Then the results of automatically generated forging sequences for three test components are presented. Subsequently, FE simulations of the forging sequences are carried out and the results of the simulations are discussed.

2 Development of the Method for Efficient Forging Sequence Planning

The method for efficient forging sequence planning consists of several modules and is programmed and implemented in MATLAB. The interaction of the individual modules is outlined in Fig. 1 and the functionalities of the individual modules are presented below.

In the first step, the STL file of the forging is loaded and the geometric dimensions of the component are recorded. An automated classification of the forging into one of the form classes according to SPIES (stocky component, disk form, long form [13]) by an ANN follows [14]. Important information for the automated design of the forging sequence such as bending, holes, and cutting axes for the calculation of the center of gravity line is determined from the analysis and form class classification. For bent components or existing holes, special algorithms are called within the method, which represent a bending operation or close the holes before generating the forging sequence. Parallel to the shape recognition by means of ANN, the complexity of the forging is evaluated by means of a complexity score model. Within this model, various existing evaluation criteria such as envelope volume and fineness factor (cf. [13]) as well as the mass distribution in the cross section (cf. [8, 9]) are combined with each other and in addition combined with further developed evaluation criteria such as the

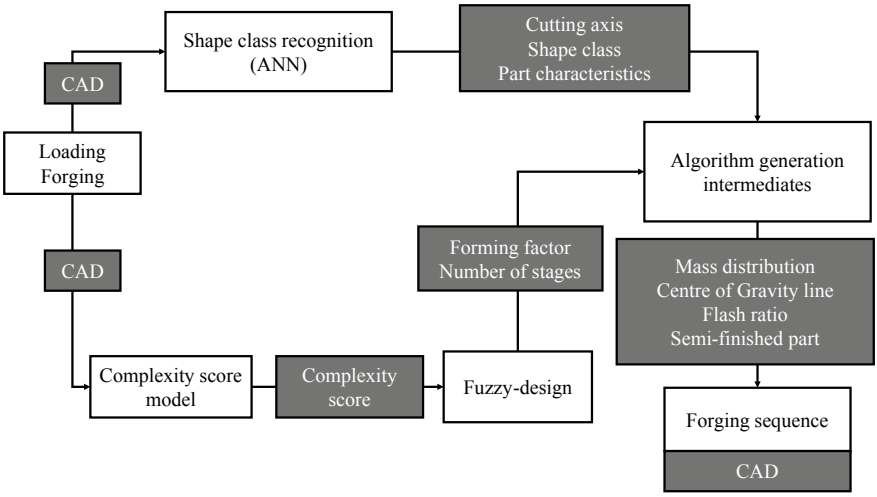


Fig. 1 Flowchart of the method for efficient forging sequence planning

consideration of cross-sectional changes in a forging. The complexity score model can be used to automatically output a statement about the complexity of a forging. The evaluation of the complexity of the forging is done by a numerical value of 0–1 in which all standardized evaluation criteria are added. The value 1 is the maximum complexity and 0 the lowest complexity. The complexity factor of the forging is an important parameter for the automated design of the forging sequence. Depending on the complexity, the flash component in the method is determined according to the approach by Knust [8]. In addition, the number of intermediate forms is initially designed as a function of complexity. A fuzzy control system was developed in order to be able to map the cause–effect relationships of the individual design parameters such as component complexity, number of stages, and forming factors for forging sequences (e.g., "high" component complexity leads to "many" intermediate forms). In addition to the number of stages, the distribution of the deformation per stage is also determined by the fuzzy system. Table 1 shows a possible result for a three-staged forging sequence. However, the user of the method always has the possibility to define input parameters manually. For example, one can specify the number of

Table 1 Exemplary distribution of the forming factors for a three-stage forging sequence from the forging backward to the semi-finished part

Iteration	1	2	3
Forming factor f	0.05	0.8	0.15
Explanation	Small forming, since from the preform to the finished form it is only a matter of the contour shape	Main forming	Small forming, e.g., descaling at the beginning of a forging sequence

stages as a function of one's machine park. As a result, the fuzzy design tool provides the number of stages of the forging sequence as well as the percentage distribution of the forming in the respective stages. The sum of the forming factors f_i over all stages or iterations k must result in one, which is presented in Eq. 1:

$$\sum_{i=1}^{i=k} f_i = 1 \tag{1}$$

The forming factors defined in this method do not correspond to the conventionally defined degree of forming. In the method for efficient forging sequence planning, the forming factors indicate the percentage of the total necessary forming from semi-finished product to finished forged part that is carried out in the respective stage.

The output parameters of the individual modules are then transferred to the algorithm for generating the intermediate forms. The component is divided into n individual cross-sectional planes along the component length L by a slicer algorithm. The distance of the individual section planes is calculated to $d = {}^{L}/_{n}$. The cross-sectional contour of the forged part is represented by a polygon chain P_i. The center of gravity S_i and the area A_i are calculated for each cross section. From this information, the algorithm calculates the mass distribution around the center of gravity line ($\sum_{i=1}^{i=n} S_i$) of the forging [4]. Based on the component complexity and the cross-sectional contour, an adaptive flash ratio is calculated according to KNUST (cf. [8, 9]). However, this calculation approach is only suitable for rotationally symmetric shapes and is extended by a percentage flash addition factor in the method for efficient forging sequence planning. This factor can be set manually by the user of the method. The diameter or length of the semi-finished product can be specified by the user. The cross section of the semi-finished product can be round or square. When automatically calculating the diameter of the semi-finished product, the method is based on the largest cross-sectional area of the forging and the maximum permitted change in length per stage. For each point of the polygon chain in a section plane, target coordinates are assigned on the semi-finished geometry. The corresponding displacement vectors are defined from the start coordinates and the target coordinates of the points as shown in Fig. 2.

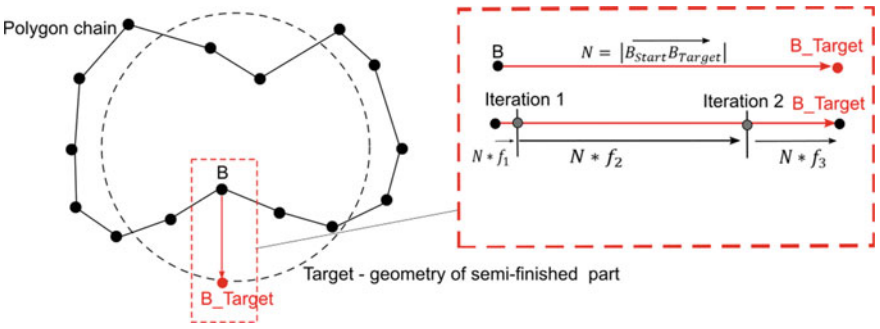


Fig. 2 Iterative procedure for intermediate form generation by point shifting. (Color figure online)

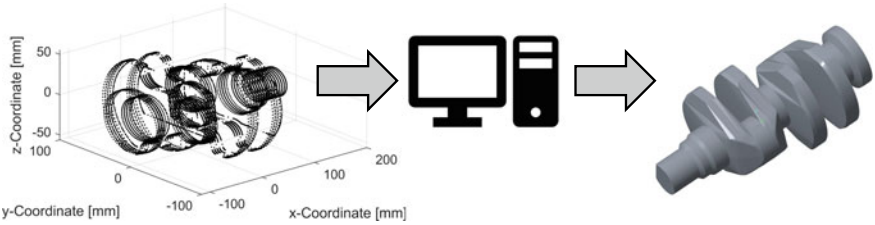


Fig. 3 Creation of the STL file. (Color figure online)

The points are moved step by step along the displacement vectors in order to gradually approximate the mass distribution and center of gravity line of the forging and the semi-finished product. Figure 2 shows the stepwise displacement of a point along the displacement vector for a stage sequence with two intermediate forms between semi-finished product and forging. The point B is moved stepwise to the target point B_{Target} on the semi-finished part geometry. The stepwise displacement along the vector results from the number of stages and the determined percentage deformation (forming factors f_i) per stage. The change in length from intermediate to intermediate within the forging sequence is represented by a change in the distance between the individual cutting planes. Volume constancy must apply to the forging sequence. This means that the volume of the semi-finished product corresponds to the volume of the forging, plus the volume for the calculated adaptive flash ratio, which is presented in Eq. 2:

$$V_{Semi-finishedpart} = V_{Forging} + V_{Flash} \tag{2}$$

After an iteration and thus the change of the cross-sectional areas in all section planes, the volume constancy is checked. If the volume is too high, the distances are reduced; if the volume is too small, the distances between the section planes are increased. After a displacement iteration, the displaced points result in a point cloud of the contour of the respective preform as shown in Fig. 3. A CAD file is then generated from the point cloud using an algorithm and exported thereafter.

3 Results of the Method for Efficient Forging Sequence Planning

In this paper, the validation of the automatically generated forging sequences for different forgings is described. Forged parts of different shape classes (long parts and disk shape) and different complexity will be considered. The following test components are presented in this paper:

- Connecting rod (long part, low complexity; length = 215 mm; volume = 211,638 mm^3);
- Disk (disk shape, low complexity, height = 110 mm; volume = 706,403 mm^3); and
- Crankshaft (long part; high complexity, length = 275 mm; volume = 1,204,704 mm^3).

Table 2 shows the results obtained by the method for each of the components. The class of shape is the result of the ANN. The shape class code in Table 2 corresponds to the classification according to [13]. The form classes according to SPIES consist of the three main shape classes of stocky components (class 1), disk form (class 2), and long form (class 3). Depending on the main axis and the secondary shape elements of the forged part, there are also subclasses in the individual main shape classes. For example, the connecting rod is assigned by the ANN to main class 3 (long forms) with a straight main axis and without secondary form elements (subclass 311). The other meanings of the shape class codes can be found in the literature [13]. The number of steps corresponds to the individual intermediate forms of the forging sequences, i.e., the number of iterations until the forged part has been transferred into the semi-finished product geometry by shifting the cross-sectional points. The deformation factors indicate the percentage deformation for the individual iterations. The specified value for the flash in Table 2 corresponds to the calculated average flash ratio over the entire component. The lengths for the individual intermediate forms are also output by the method.

Figure 4 shows the exported CAD files of the intermediate forms for the forging sequences for the connecting rod (a), the disk (b), and the crankshaft (c). The calculation time for the automated generation of the forging sequence is less than 10 min for each of the three forged parts.

Table 2 Result parameters of the automatically generated forging sequences for the test components

Component	Shape class [13]	Stages	Forming factors	Flash ratio	Length intermediate forms (mm)
Connecting rod	311	3	I1 = 0.1 I2 = 0.6 I3 = 0.3	12%	I1 = 211 I2 = 208 I3 = 183
Disk	211	2	I1 = 0.6 I2 = 0.4	5%	I1 = 64 I2 = 110
Crankshaft	312	4	I1 = 0.1; I2 = 0.4 I3 = 0.35 I4 = 0.15	34%	I1 = 275 I2 = 272 I3 = 246 I4 = 234

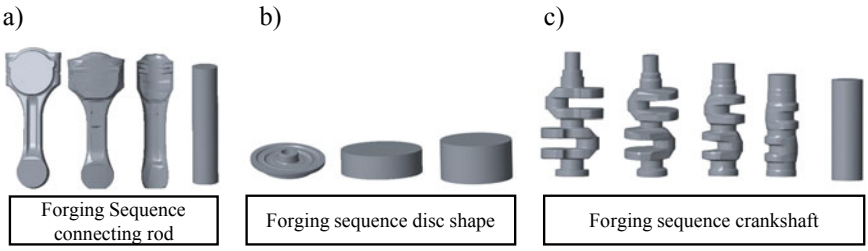


Fig. 4 Forging sequences for the forged parts connecting rod (**a**), disk (**b**), and crankshaft (**c**). (Color figure online)

4 Validation of the Method by Using FE Simulations

When generating the intermediate forms, no characteristics of special preform processes, such as cross-wedge rolling (cf. [14]), are considered when generating the mass distribution and changing the cross-sectional contours. Therefore, in this paper, all intermediate forms are checked for process reliability and freedom from errors by FE simulations of drop forging processes. The dies are first constructed based on the CAD files for the individual intermediate forms of the forging sequence. The simulation of the forging sequences is then carried out using FORGE® NXT 3.0. In validating the method for efficient forging sequence planning, the quality criteria of form filling and freedom from folds are considered in this paper. Based on these quality criteria, it can be checked whether the method is able to design error-free processes and thus suitable for industrial use or whether changes must be made to the algorithm for creating the intermediate forms. Especially the parameter of the form filling is an important assessment parameter for the validation of the forging sequence and a qualitative statement about the generated forging sequences.

The material modeling in the simulations is done with the HENSEL-SPITTEL equation implemented in FORGE® NXT 3.0 [15]. With this equation, the forming behavior is determined by means of a function dependent on the temperature T, the effective strain ε, the flow stress σf, the strain rate $\dot{\varepsilon}$, and the coefficients A and $m1\text{-}4$. The HENSEL-SPITTEL equation used by FORGE® NXT 3.0 is represented in Eq. 3:

$$\sigma_f = A e^{m_1 T} \varepsilon^{m_2} e^{m_4/\varepsilon} \dot{\varepsilon}^{m_3} \tag{3}$$

The flow curve used for hot bulk metal forming processes is sufficiently precise by means of the coefficients A, m_1, m_2, m_3, m_4.The used material in this study is 1.5120. The individual regression coefficients of the HENSEL-SPITTEL equation of 1.5120 are shown in Table 3.

Material modeling will not be the focus of this study, as only qualitative estimation of the results for efficient forging sequence planning will be carried out. For the FE simulations, nondeformable dies and the simulation parameters shown in Table 4 are used.

Table 3 Regression coefficients of Hansel–Spittel equation (Eq. 1.5120)

Coefficient	Dependence of temperature	Dependence of strain hardening	Dependence of equivalent strain rate	Dependence of equivalent strain	Solidity
Value	$m_1 = -0.0029$	$m_2 = -0.14227$	$m_3 = 0.14102$	$m_4 = -0.05764$	$\acute{y}A = 1809 N/mm^2$

Table 4 Simulation parameters for the FE simulations carried out to validate the forging sequences

Simulation parameters	Value
Material	1.5120
Billet temperature	1250 °C
Die temperature	250 °C
Mesh size	4 mm
Press kinematics	Hydraulic press
Ambient temperature	50 °C
Friction μ	0.3
Forming velocity	20 mm/s

Table 5 shows the results of the FE simulations for the forging sequence of the disk. On the one hand, the form filling and, on the other hand, the freedom of folds are considered. The form filling is checked via the contact between billet and die. The results of the form filling can be seen in the top of Table 5. If there is no direct contact between die and billet, this is indicated by red coloring of the billet in those areas. A form filling can be seen in both stages. Only at second iteration (Stage 1), at edge areas no complete form filling is to recognize. The bottom of Table 5 shows that both iterations, the upsetting process (Stage 1) and the final forming (Stage 2), are free of folds. Both quality criteria are fulfilled. Overall, the simulations show

Table 5 FE results for the disk shape (Top: form filling (contact); bottom: Folds)

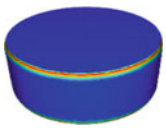
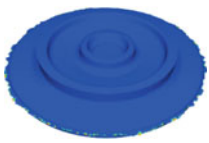
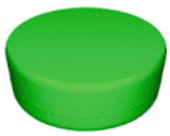
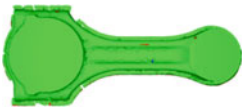
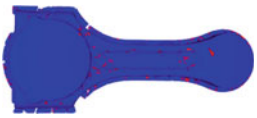
Stage 1	Stage 2
	
Form filling	Form filling
	
No folds	No folds

Table 6 FEM result stage sequence of connecting rod (top form filling; bottom folds)

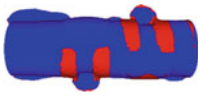
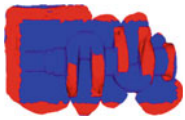
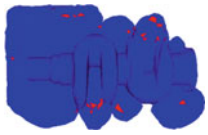
Stage 1	Stage 2	Stage 3
		
Form filling	Form filling	Form filling
		
No folds	Folds	Folds

that the method for efficient forging sequence stadium planning is able to design a material-efficient stadium sequence.

Table 6 shows in the top row the FE results for the contact analysis to check the form filling and in the bottom row the FE results for the monitoring of the fold formation for the connecting rod. The evaluation of the FE results for the forging sequence of the connecting rod shows that form filling is achieved for the individual intermediate forms. During the analysis of the fold formation as seen in the bottom of Table 6, it must be determined that folds are likely to occur on the component in the intermediate forms. This is indicated by FORGE® NXT 3.0 by red coloring of the certain areas. Particularly in the middle area of the connecting rod, many folds occur during the forming process from preform to finished form. This means that the stage sequence is not directly suitable for immediate use in practice yet. The surface quality of the STL files of the intermediate forms can be a possible cause for the folds that occur. In some cases, the surfaces of the STL files from which the dies are constructed exhibit irregularities. In the future, a smoothing algorithm is to be implemented in the method, which will further increase the surface quality of the STL files.

Table 7 shows the simulation results for the crankshaft. The quality factor form filling is considered by the contact between billet and dies. Red areas indicate no contact between workpiece and tool. The largest distance can be identified in the first iteration (Stage 4), with 3 mm between die and billet. When validating the forging sequence for the two-cylinder crankshaft, it must be noted that no form filling is achieved in the cross-sectional area of the crankshaft with large surface contents (area of the crank webs). In the areas of smaller cross sections, on the other hand, there is a clear excess of material. The forging sequence of the crankshaft generated by the method still requires significant changes by the designer before a basic production of the crankshaft with this stage sequence is possible. The FE results show that folds occur in the flash during the forging sequence of the crankshaft. No folds appear in the first stage. Afterward only in the flash. No folds can be identified directly on the crankshaft.

Table 7 FE results for crankshaft forging sequence (form filling (top); folds (bottom))

Stage 1	Stage 2	Stage 3	Stage 4
			
No form filling	No form filling	No form filling	No form filling
			
No folds	Folds in the flash	Folds in the flash	Folds in the flash

Several approaches can be pursued to improve the form filling of the automatically generated forging sequences. One possibility is to change the calculation of the flash ratio so that more material is calculated for the flash ratio. However, this does not meet the requirements for the method to generate material-efficient forging sequences. A further possibility to improve the form filling is to make constructive changes to the dies and to use flash barriers. However, this means increased effort in construction and therefore increased time expenditure.

In order to improve form filling for the crankshaft, adjustments were made to the algorithm for point shifting. The maximum permissible length change in the forging sequence was reduced, resulting in a different calculation of the semi-finished product diameter due to volume constancy. Due to the reduced length change (of approx. 7 percent compared to approx. 15 percent (see Table 2)) in the forging sequence, it was hoped to achieve an improved mass distribution and improved form filling. Figure 5 shows the results of the adapted variant of the algorithm in comparison with the previous state of the algorithm for the crankshaft. In Fig. 5, only the final stage is

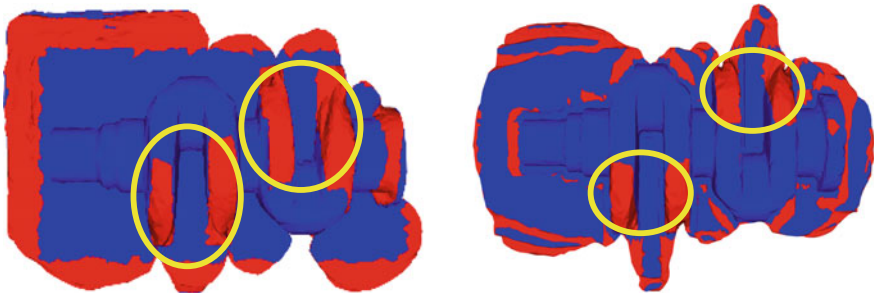


Fig. 5 Results for FE simulations with insufficient form filling in final stage (left) and final stage with adapted algorithm (right). (Color figure online)

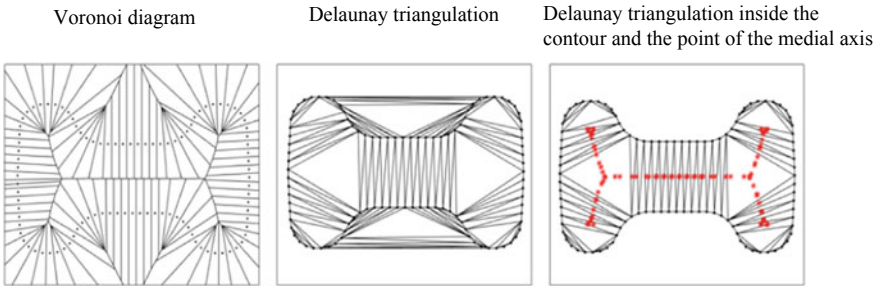


Fig. 6 Schematic representation of the Voronoi diagram, the Delaunay triangulation, and the points of the medial axis from a cross section of a connecting rod. (Color figure online)

presented. The results in terms of form filling for the other stages are comparable and are therefore not shown here. The adjustments have already led to improved form filling in the critical areas. However, there is still no complete form filling. For this reason, the algorithm for the point shift and generation of the individual intermediate form will be fundamentally revised in the future.

The algorithm is to be modified to move the points along the material flow paths in the forging. Determining the material flow paths allows inverse material flow modeling for backward design of the forging sequence. By shifting the points along the material flow paths, the forging sequence can be approximated much closer to the real forging process. Currently, the displacement vectors are defined by the shortest distances of the points on the polygon chains to the semi-finished part geometry. To determine the material flow paths, a Voronoi diagram and a Delaunay triangulation are to be used to determine the medial axis and to derive the material flow paths (see Fig. 6). Subsequently, a new displacement vector is to be determined for the points as a function of the material flow paths. The schematic procedure of this new approach for the point shifting is shown for a cross section from the connecting rod in Fig. 7. Points in the center of the component are shifted perpendicular to the first-order material flow path. Points in the area of the H-contour of the component are displaced along the second-order material flow path. Points in the area of the H-contour of the component are displaced along the second-order material flow path. In the future, a set of rules must be developed that shifts the points depending on the position on the component contour and the calculated material flow paths.

5 Summary and Outlook

The FE simulations of the automatically generated forging sequences show that the developed method partly already delivers very good results and can generate multi-stage forging sequences based on forging geometry for different shape classes. When considering the FE results, it becomes clear that the designer of a forging sequence

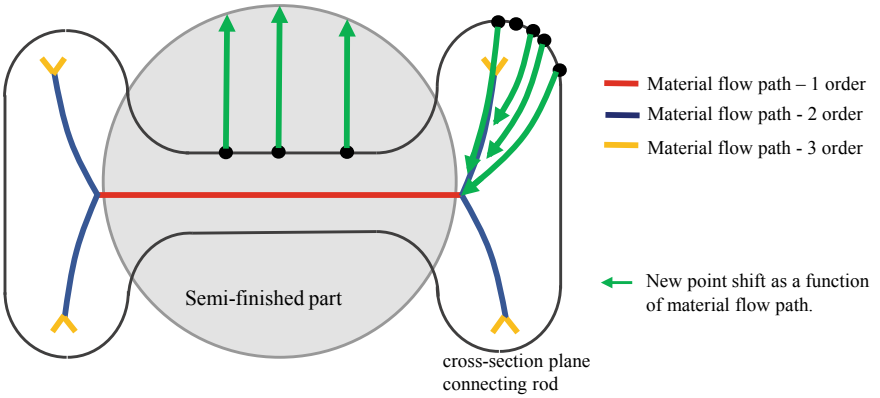


Fig. 7 New approach to shifting the points along the material flow paths. (Color figure online)

using the method already receives an initial very good proposal for a forging sequence in the shortest possible time. The FE results also show that the generated forging sequences do not reliably allow an error-free production of forged parts of different shape classes without corrections yet. The method calculates enough flash to achieve form filling for a connecting rod (24% flash) and a disk (5% flash) and to generate a material-efficient forging sequence. For the crankshaft, no form filling could be achieved in areas with large cross sections, but in small cross-sectional areas there was a large excess of material. In order to improve the form filling for the crankshaft, a smaller change in length within the forging sequence was initially calculated. This resulted in a slight improvement in form filling. However, complete form filling was still not achieved. An approach was presented to calculate the point shifting vectors as a function of the material flow paths in the future. This modification to the algorithm is expected to result in a significantly more process-oriented design of the intermediate forms and the entire forging sequence. In the FE simulations carried out, it was found in some cases that folds occur. In order to avoid the formation of folds in the future, an algorithm is to be implemented in the method, which, after each iteration, checks the generated point cloud based on already existing criteria for the prediction of folds (cf. [9, 16]). The FE simulations are used here for the first validation of the method in order to be able to investigate the first basic quality criteria such as mold filling and freedom from folds without the need for cost-intensive test forging. In the further course of the project, an experimental validation will be performed in addition to the verification of the results by means of FE simulations. Already industrially used forging sequences of different components are to be compared with the forging sequences automatically generated by means of the method. In addition to the quality criteria of form filling and freedom of folds, the forces occurring in the experimental validation, the consumption of material, and the duration of the creation of the design are to be considered. In the future, it will also be possible to combine procedures for preform optimization with evolutionary algorithms (cf. [8, 9]) with the method of

efficient forging sequence planning in order to optimize the individual intermediate forms and further increase the efficiency of the forging sequence.

Acknowledgments The research project "Design of efficient forging sequences with mass distribution around the center of gravity line for forging parts" (IGF project 19752) has been funded by the German Federation of Industrial Research Associations (AiF). The authors thank the AiF for its support.

References

1. Behrens B-A, Nickel R, Müller S (2009) Flashless precision forging of a two-cylinder crankshaft. Prod Eng 3(4–5):381–389
2. Denkena B, Park HS, Behrens BA, Henjes J, Bertys S (2013) Development of a concept to optimize the energy efficiency in forging process chains. Int J Precis Eng Manuf 14(7):1229–1236
3. Mathieu H (1991) Ein Beitrag zur Auslegung von Stadienfolgen beim Gesenkschmieden mit Grat. Fortschritt-Berichte VDI Reihe 2: Fertigungstechnik Nr. 213, VDI-Verlag, Düsseldorf
4. Hedicke Y, Langner J, Stonis M, Behrens BA (2018) Innovativer Ansatz zur effizienten Stadienplanung. ZWF Zeitschrift für wirtschaftlichen Fabrikbetrieb 113(10):668–672
5. Behrens BA, Wolter FE, Blanke P, Santangelo A Inverse 3D-Materialflusssimulation zur Zwischenformauslegung für das Gesenkschmieden. The visual computer, 27, pp 129–139
6. Guan Y, Bai X, Liu M, Song L, Zhao G (2015) Preform design in forging process of complex parts by using quasi-equipotential field and response surface methods. Int J Adv Manuf Technol 79(1–4):21–29
7. Torabi SHR, Alibabaei S, Bonab BB, Sadeghi MH, Faraji G (2017) Design and optimization of turbine blade preform forging using RSM and NSGA II. J Intell Manuf 28(6):1409–1419
8. Knust J, Podszus F, Stonis M, Behrens BA, Overmeyer L, Ullmann G (2016) Preform optimization for hot forging processes using genetic algorithms. Intell J Adv Manuf Technol 89(5–8):1623–1634
9. Knust J, Stonis M, Behrens B-A (2016) Preform optimization for hot forging processes using an adaptive amount of flash based on the cross section shape complexity. Prod Eng Res Devel 10(6):587–598
10. Alimirzaloo V, Biglari FR, Sadeghi MH, Keshtiban PM, Sehat HR (2019) A novel method for preform die design in forging process of an airfoil blade based on La-grange interpolation and meta-heuristic algorithm. Int J Adv Manuf Technol 102(9–12):4031–4045
11. Shao Y, Ou H, Guo P, Yang H (2019) Shape optimization of preform tools in forging of aerofoil using a metamodel-assisted multi-island genetic algorithm. J Chin Inst Eng 42(4):297–308
12. Shao Y, Yan L, Guo P, Yang H, Shi F, Feng D (2019) A comprehensive study on fitness approximation techniques in shape optimization of aerofoil forging preform tools. Metals 9(6):617
13. Spies K (1957) Eine Formenordnung für Gesenkschmiedestücke. Werkstattstechnik und Maschinenbau 47:201–205
14. Hedicke-Claus Y, Langner J, Stonis M, Behrens BA (2019) Klassifizierung von Schmiedeteilen mittels KNN, wt-online 11/12–2019, pp 822–827
15. Blohm T, Mildebrath M, Stonis M, Langner J, Hassel T, Behrens BA (2017) Investigation of the coating thickness of plasma-transferred arc deposition welded and cross wedge rolled hybrid parts. Prod Eng Res Devel 11(3):255–263

16. Hensel A, Spittel T (1978) Kraft- und Arbeitsbedarf bildsamer Formgebungsverfahren, Deutscher Verlag für Grundstoffindustrie
17. Behrens BA, Röhr S, Schäfer F, Hundertmark A (2007) Untersuchungen zur numerischen Ermittlung von Schmiedefalten. UTF-Science, 2

Tube Forming and Fabricating Technologies for Contributing Society by Tackling Problems of Environment and Aging Population



Takashi Kuboki, Atsushi Shirayori, Masaaki Mizumura, Noah Utsumi, and Yeong-Maw Hwang

Abstract Technologies for forming and fabricating tubes have been contributing to the development of society, and should evolve and have great roles in the future societies, considering the problems on environment and population. Global warming is a critical problem and the average temperature in the world is still increasing. The world population number is stopping rapid increase accompanying with decreasing birthrate, resulting in aging society. Tubes have advantages of high rigidity for a unit weight and could manufacture light-weight components for transport equipment. The technologies are utilized for forming parts in medical devices. The technologies on tubes should contribute for solving these problems and realizing sustainable societies. This paper introduces the author's technologies and reviews others' recent technologies on tubes. The technologies include hydro and air forming, rotary forming, bending, micro forming and so on. These technologies are qualitatively evaluated in terms of conflicting characteristics, such as formability, strength, productivity, flexibility and miniaturization. Some technologies are emerging to improve some of the conflicting characteristics at the same time for realizing excellent performances of the formed products.

T. Kuboki (✉)
Department of Mechanical and Intelligent Systems Engineering, The University of Electro-Communications, 1-5-1 Chofu Gaoka, Chofu-Shi, Tokyo 182-8585, Japan
e-mail: kuboki@mce.uec.ac.jp

A. Shirayori
Department of Mechanical and Intelligence Engineering, Utsunomiya University Graduate School of Engineering, 7 Chome-1-2 Yoto, Utsunomiya, Tochigi, Japan

M. Mizumura
Futtsu Unit, Nippon Steel Technology, 20-1 Shintomi, Futtsu-City, Chiba Prefecture 293-0011, Japan

N. Utsumi
Faculty of Education, Saitama University, 255 Shimo-Okubo, Sakura-Ku, Saitama 338-8570, Japan

Y.-M. Hwang
Department of Mechanical and Electro-Mechanical Engineering, National Sun Yat-Sen University, Kaohsiung 804, Taiwan

© The Minerals, Metals & Materials Society 2021

G. Daehn et al. (eds.), *Forming the Future*, The Minerals, Metals & Materials Series,
https://doi.org/10.1007/978-3-030-75381-8_239

Keywords Tube forming · Productivity · Strength · Formability · Flexibility · Light-weight

1 Introduction

Tube forming technologies have been contributing to the development of society, and should evolve and have great roles in the future societies, considering the environmental problems. Global warming is a critical problem and the average temperature in the world is still increasing although many countries are tackling to suppress CO_2 emissions [1]. The CO_2 emissions would be suppressed by the combination of strengthening and lightweight of components of vehicles, and tubes have structural advantages, as the section modulus and second moment of inertia of area are high for a unit cross-sectional area. Realizing these structural advantages requires securement of formability. Some tube forming technologies have been developed for realizing both high formability and strength of material, though they are often conflicting.

The population is another problem, which might be alleviated by the tube forming technologies. The world population number is predicted to stop rapid increase in 2050 accompanying with decreasing birthrate [2], and the proportion of the laboring population would decrease. The tube forming technology should evolve for contributing to the aging society. The tube forming technology would be used for effectively manufacturing the components for medical equipment. The technology would also compensate the lack of the talented engineers and technicians. Many of technologies still depend on the knowledges and skills of the engineers and technicians, many of whom are elderly people in some engineering fields. Therefore, the technical conveyance is urgently needed, and the digitalization of their knowledge with the help of the computational technology would be of great help.

This paper reviews recent technologies and perspectives in tube forming, referring to the recognition of metal forming in the academy. The technologies include hydroforming, air forming, rotary forming, bending, micro forming and so on. These technologies are qualitatively evaluated in terms of conflicting characteristics. Moreover, perspectives and expectation of the tube forming technologies are mentioned, considering environmental problems, ageing societies and development of computational technologies.

2 Trends in Metal Forming

Table 1 shows titles of the keynote papers of STC-F (The Scientific and Technical Committee - Forming) in CIRP (Collége International pour la Recherche en Productique, The International Academy for Production Engineering) for the latest five years. All the papers can be related to tube forming. Prediction and setting product properties (2015) are also important in tube forming. Closed-loop controls (2016)

Table 1 Keynote papers in CIRP annals—manufacturing technology in the latest 5 years

Year	Title	1st author
2019	Models and modelling for process limits in metal forming	W. Volk
2018	Flexibility in Metal Forming	D. Y. Yang
2017	Hot stamping of ultra-high strength steel parts	K. I. Mori
2016	Closed-loop control of product properties in metal forming	J. M. Allwood
2015	Metal forming beyond shaping: predicting and setting product properties	E. Tekkaya

are still difficult, but some technologies are already applied and others are expected to be applied in the industry. One of the examples is TSS bending of tube (Torque Superposed Spatial bending) [3]. Hot stamping (2017) is a superior technology which realizes both formability and strength after forming. Further superior tube forming technology, STAF (Steel Tube Air Forming), is developed in Japan [4]. Flexibility (2018) is also important in tube forming, many tube forming technologies have been developed for realizing flexibility. Prediction of process limits (2019) are also important issue in tube forming, and the prediction method can be expected to evolve with the help of the computational technologies.

Tekkya et al. shows their opinions on innovations and trends in metal forming in "60 Excellent Inventions in Metal Forming" [5]. Technologies and analyses, which would be related or applicable to tube forming technologies, are summarized in Table 2. Some technologies started in advance of the prosperous duration which was recognized in the world. While the duration for hydroforming was 1994–2010

Table 2 Innovations and trends related or applicable to tube forming from "60 Excellent Inventions in Metal Forming [5]"

	Innovations	Prosperous duration
Technology	Hydroforming	1994–2010 (Ogura et al. [6], U.S patent [7])
	Micro forming	1998–2014
	Incremental sheet forming	2002–2020 Matsubara [8, 9]
	Flexible forming	1992–ongoing
	Closed-loop control	2011–ongoing
Analyses	FEM in forming	1977–2005
	Multi scale	2012–ongoing (Matsui et al. [9])
	Damage mechanics	2010–ongoing

in the Table, Ogura et al. showed some results on hydroforming using a purpose-built machine in 1985 [6] after a series of experiments following a U.S. patent in 1940 [7]. While the duration for incremental forming was 2002–2020 in the Table, Matsubara showed some results on incremental forming for tube [8] and sheet metal [9] in 1984. While the duration for Multi-scale analysis started in 2012 in the Table, Matsui et al. showed some results of the analyses on plastic deformation in 2002 [10]. Therefore, some present technologies, which is currently not paid attention to, might be prosperous in the future.

3 Processes in Two Axes of Characteristics

3.1 Hydroforming and Air Forming in Strength and Formability

It might be interesting to analyze processes in terms of different characteristics, which conflict each other. Tube forming processes often enable us to realize some of conflicting characteristics at the same time. Strength and formability conflict each other as shown in Fig. 1, which was qualitatively made depending on the author's impression and interpretation. For example, the flow stress of steels with fine grains is high, but the formability is low, compared to plain carbon steels. Many hydroforming technologies have been developed mainly focusing upon improving formability without concerning strength. The formability was improved by pushing a tool to the point where fracture occurs. Manabe et al. used a counter punch in T-shape hydroforming with the combination of fuzzy theory for improvement of the forming limit [11]. Wada et al. shows the further improvement result of forming limit by applying movable dies [12]. The movable dies utilize the friction affirmatively for

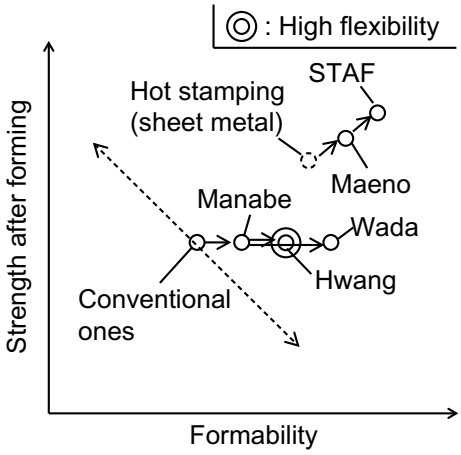


Fig. 1 Hydro and air forming in strength after deformation and formability

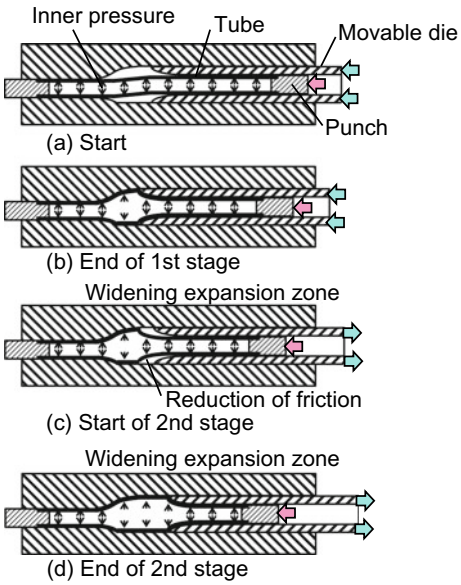


Fig. 2 Enlargement of axial forming area by forward and backward of movable dies [13]. (Color figure online)

supplying the material into where the tube is expanded by the hydro pressure. As the result, the tube periphery-expansion ratio reached 300%. Hwang et al. enhanced the potential ability of the movable dies for high flexibility as shown in Fig. 2 [13]. A movable die pushes the tube end for supplying the material into expansion area as shown in (a)–(b). The movable die moves backward for the enlargement of the axial expansion area. The forward and backward movement of the die improves the flexibility as well as the formability.

Some metal forming processes were developed for improving both strength and formability by controlling the strength during and after deformation as shown in Fig. 1. Hot stamping deforms the sheet metals at high temperature and rapidly cool the metals down for obtain higher strength by utilizing phase transformation [14]. However, hot stamping of sheet metals or tubes still has some disadvantages for manufacturing hollow parts. Hot stamping of sheet metals needs to create flanges and join them together, resulting in low productivity. Hot stamping of tubes is difficult as the inside surfaces of the tubes cannot be supported by tools, resulting in buckling.

Maeno et al. proposed a gas forming process for conquering the problem of hot stamping of tubes [15]. A high-pressured air is enclosed inside the tube, which is heated up by resistance heating. The enclosed air supports the inside surface of the tubes and suppresses buckling. This method improves both formability and strength with realizing lightweight as welding is not needed. Ishizuka et al. (Sumitomo Heavy Industries, Ltd.) developed another gas forming process for commercial use, STAF (Steel Tube Air Forming) as shown in Fig. 3, which utilizes the air pressure more effectively for bulging tubes against the die walls [16]. This method decreases the number of processes from four to two, compared to hot stamping of sheet metals,

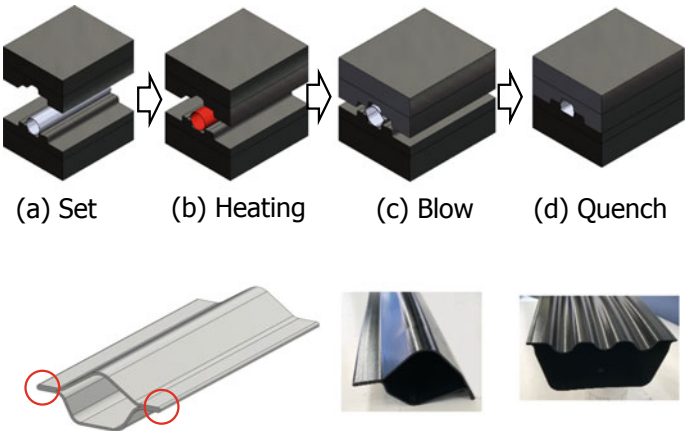


Fig. 3 Steel tube air forming for realizing high forming limit and strength [16]. (Color figure online)

for manufacturing frames of vehicles. Flanges are produced during blow and quench process according to the necessity. The production system is now available in the market.

3.2 Forming for Diameter-Reduction in Productivity and Formability

Figure 4 qualitatively shows forming processes for reducing diameters of tubes in terms of productivity and formability. High flexibility is also denoted by double circle in the figure. Press nosing is commonly used for reducing the diameter of the tube end

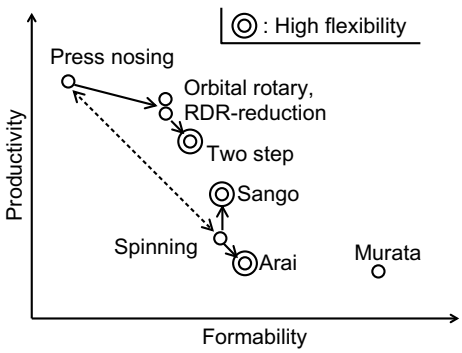


Fig. 4 Forming technologies for diameter-reduction in productivity and formability

when the nosing ratio is not high [17]. While productivity is very high for press nosing, formability is very low. Rotary forming improves the formability, and spinning is an opposite process to nosing in terms of productivity and formability. While formability is very high for spinning, productivity is very low. Murata et al. succeeded to apply spinning to magnesium tube for reducing the tube diameter up to reduction ratio of 95%, using rollers with heaters inside [18]. Sango Co. Ltd. succeeded to develop a spinning machine for mass production for increasing flexibility and improving productivity [19]. The machine evolved on hard and soft wares, and then reduced the diameters of both ends in tilted and eccentric manners within just a few tens of seconds. Arai et al. developed a spinning process, which reduced the tube diameter in an asymmetric manner by synchronizing the rollers position with the rotation angle of the tube [20].

Spinning processes reduces the tube diameter by multi pass formation, where the tools/rollers travel along the tube axis in several times, because the contact area between the tools/rollers and the tube is very small. Other rotary forming processes, which travel tools once, were proposed. They are "orbital rotary forming" by Kitazawa et al. [21, 22] and "RDR-reduction (Relieved Die Rotary reduction, rotary reduction with relieved die)" by Kuboki et al. [23]. These rotary forming have intermediate contact areas between press nosing and spinning.

This paper explains RDR-reduction in a detailed manner. Figure 5 shows a schematic illustration of RDR-reduction. The unique point of this process is to use a relieved die, which is composed of working surfaces and relieves. When the number of working surfaces is three, the highest limit nosing ratio is achieved. The main defects in press nosing is buckling caused by high pushing force and wrinkle caused by high compressive stress in hoop direction. The existence of relieves reduces both pushing force and compressive stresses, leading to higher limit nosing ratio. Adoption of two-step forming is effective for enhancement of limit nosing ratio [24]. The total contact angle γ of 240° gives the highest limit nosing ratio κ_L of 0.49 in the case of one-step forming. Two-step forming elevates κ_L up to 0.75 by adopting the total contact angle for 1st step γ_{1st} of 240° and that of 2nd step γ_{2nd} of 180°. It would be attributed to the difference of defects mechanism between buckling and other

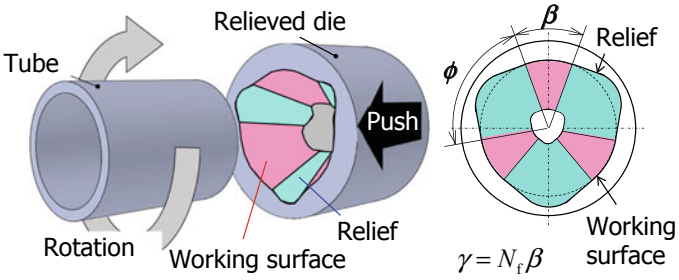


Fig. 5 RDR-reduction (Relieved Die Rotary reduction, rotary reduction with relieved die) [23]. (Color figure online)

defects. Buckling is caused by the temporary value of pushing force, while split and polygonal wrinkle is caused by the accumulation of damage or some unconformity. It is assumed that little damage accumulates during the 1st step of γ_{1st} of 240° and that the damage starts to accumulate during the 2nd step of γ_{2nd} of 180°, leading to higher limit nosing ratio. RDR-reduction should be tried in the industry and its effectiveness should be discussed.

3.3 Tube Bending in Terms of Flexibility

Tube bending processes include many aspects, such as the ratio of bending radius to tube diameter, precision on cross section and radius, flexibility, strength and others. This paper mainly focuses upon the flexibility, sparing other aspects to the next opportunity. Table 3 shows some bending processes in terms of flexibility. Draw bending is one of the most common tube-bending processes, and it can bend tubes in a target radius precisely as bending dies are used considering springback. However, the flexibility is low.

Draw bending is a common process for bending tubes in a precise manner. The process winds the tube around a bending die. The bent radius can easily controlled with evaluation of spring-back in a trial-and-error approach. However, the cross-sectional precision tends to deteriorate due to flattening. Although the mandrel is used for suppression of flattening, there is some limit for its effect. Utsumi et al. proposed a unique mandrel, which is called "laminated elastic mandrel" [25]. The mandrel is a bundle of thin sheets of polyvinyl chloride, stainless steel and acrylic material as shown in Fig. 6. The thin sheets are laminated alternately so that the mandrel might bend flexibly. The laminated elastic mandrel is suitable tube with rectangle cross section and secures the cross-sectional precision while suppressing defects. Further applicability of the laminated elastic mandrel should be discussed and enhanced for circular or smaller tubes.

Dieless U-bend process was developed for bending tubes at various radius from 700 to 2000 mm for atomic power plants [26]. The bending radii can flexibly be set by positioning feeding rolls and a clamp on the bending arms. The bending radii

Table 3 Bending processes on flexibility and unique points

Process	Flexibility			Unique points
	2D	3D	Twist	
Draw bending [25]	–	–	–	Precise bending according to die shape
Dieless U-bend [26]	[✓]	–	–	Precise bending, by open-loop control
MOS bending [27, 28]	[✓]	[✓]	–	Open-loop control
TSS bending [3]	[✓]	[✓]	[✓]	Closed-loop control
3DQ [29]	[✓]	[✓]	[✓]	Strengthen by quenching

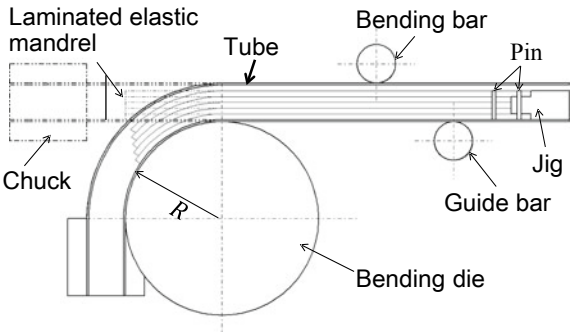


Fig. 6 Draw bending with laminated elastic mandrel [25]

can properly be controlled in an open-loop manner by changing the bending-roller position and the ratio of tube-feeding velocity to travelling velocity of the clamp.

One of the most famous 3-dimensional bending method is MOS bending, which is named after the inventors, Murata, Ohashi and Suzuki [27, 28]. The bending machine is composed of a guide cylinder, a bending die, a spherical-surfaced supporter of the die and a tube-feeding system. Positioning of the bending die according to the tube feeding enables the tube to bend in an arbitrary direction and radius.

Institut für Umformtechnik und Leichtbau (IUL) developed TSS bending, which can bend a tube in a 3-dimensional manner while twisting the tube [3]. The concept is that twisting torque can be superimposed on the bending moment, and then the tube can be twisted as well as bent. One of the unique points of the process is that it uses closed-loop control for controlling bending radius. The target moment is set instead of the target-bending radius. If the target value is set for bending radius, it would inevitably take time for measuring the shape and the bending radius of some portion must be out of the tolerance. On the other hand, the moment can be measured immediately, and the moment is used for the immediate closed-loop control.

Nippon Steel Co. developed 3DQ (3 Dimensional Hot Bending and Quench) as shown in Fig. 7 [29]. The bending system is composed of a robotic manipulator, supporting rollers, a feeding equipment, an induction heater, a cooling system and so on. The bending point of the tube is locally heated by the induction heater while the end of tube is supported by the robotic manipulator. The positioning of the robot hand flexibly determines the bending direction and bending radius. The heated portion was

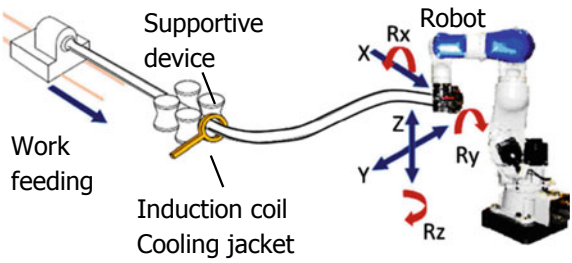


Fig. 7 3-Dimensional Hot Bending and Quench [29]. (Color figure online)

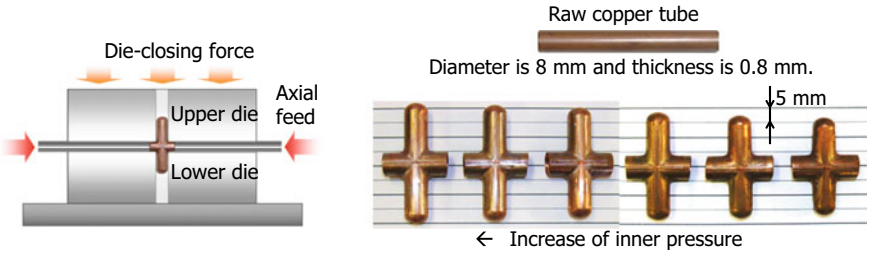
rapidly cooled down after bending, and the strength of the tube is drastically enhanced by the phase transformation.

3.4 *Tube Forming for Medical and Electronic Devices in Terms of Miniaturization*

The tube forming technologies are expected to manufacture small or micro parts in medical and electronic devices. The benefit of the parts would generally increase with decrease of the size when they are used for medical or electronic use. One of the examples for medical use is a joint for a surgical manipulator. Kawashima et al. develop a surgical manipulator which uses a spring joint instead of mechanical joint with gears inside [30]. The concise joint with spring would decrease the diameter of the manipulator, and then reduce the size of holes which are made on the patient's body. The less the hole diameter, the less the burden on the patients would be. The cross section of the spring fiber has a shape of high rectangle ratio, which enables the spring to bend easily and convey heavy twisting torque. The fabricating cost was huge as the spring was made by machining.

Kuboki et al. developed a method for fabricating the spring with a cross section of high rectangle ratio [31]. It is a combination process of coiling and upset using a tube as a raw material. The tube is bent into a spring shape by a conventional coiling process. The positioning of the coiling pin arbitrarily determines the bending radius and the diameter of the spring. The spring is upset and deformed into the spring with a cross section of high rectangle ratio. The usage of a tube instead of a wire as raw material realizes a stable deformation in the upsetting process. However, the process still leaves further improvement to be considered on the dimensional accuracies.

Other tube forming technologies have been developed. Hydroforming technologies for fabrication of cross-shaped tube were developed by Shirayori for tube diameter $D_0 = 8$ mm and thickness $t_0 = 0.5$–0.8 mm as shown in Fig. 8 [32]. A pair of upper and lower half dies are used and the effect of lubrication was clarified. Tubes with a rather thick wall of 0.8 mm were easily deformed into cross shapes with



(a) Experimental set-up (b) Cross-shaped tubes

Fig. 8 Hydroforming for cross-shaped tube with small diameter [32]. (Color figure online)

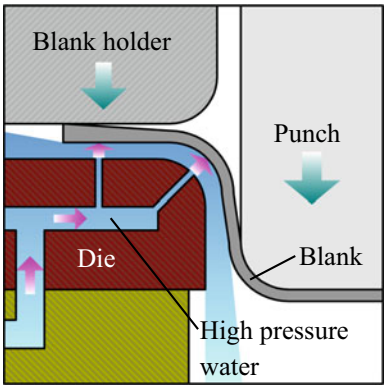


Fig. 9 Deep drawing using high-pressured water [38]. (Color figure online)

very long protrusions by optimization of forming conditions. Furthermore, S. Mori applied the hydroforming technology for micro tubes with diameter $D_0 = 0.5$ mm and thickness $t_0 = 0.1$ mm [33]. The fabricated cross-shaped tubes are expected used for medical, communication and electronic devices in the trend of miniaturization.

Dieless drawing is another prospective technology, and Furushima et al. have been improving the technology [34]. This method reduces the cross section of a hollow tube in a homothetic manner. The portion of tube to be deformed is locally heated by an induction heater or laser, and cooled down immediately after deformation. The tube is stretched at a certain speed and the heating point moves at another speed, and the ratio of the two speeds determines the reduction in area. One of the advantages of this method is that it can reduce the cross section with high area reduction while keeping the similarity. Therefore, once a complicated cross section is fabricated in a macro scale, the same complicated structural cross section can be realized in a micro scale by this method. The method is also applied for magnesium alloy [35] with an expectation that the fabricated magnesium tubes can be used as medical devices in human bodies, such as stents in the near future.

3.5 Supporting Technologies

Computer technologies and information science are rapidly developing. IoT or AI would be used for tube forming technology. Material and products can be tagged and tracked inside works or the preference of customers can be surveyed.

The usage of these science and technologies for conveying technical knowledge to the next generation would be another important aspect in the aging societies. Kuriyama et al. applied design-mapping technology for structuring engineers' knowledge for accumulating technical knowledge for conveying it to the next generation [36]. A few experts have huge amount of implicit knowledge and determine the

processes in many small to medium-sized enterprises. Once they leave the enterprises, it might be difficult to convey their knowledge to other engineers or technicians perfectly. Kuriyama et al. interviewed an expert on tube forming, extract words and classified them. The classified words were put and linked by arrows in a "design mapping". The mapping would tell successors and others the essence of the important knowledge even after an interval of years.

The development of computer technology would help higher analysis methods to become more realistic to be applied in the industry. Multi-scale analyses seem to start to be applied for metal forming around 2000 [10]. Multi-scale analyses should idealistically be conducted in a two-way manner, i.e. from micro to macro scale, and from macro to micro scale. However, the analyses are often conducted in a one-way manner from macro to micro scale due to the limitation of the computer ability. Watanabe et al. succeeded to predict stress-strain diagrams of ferrite-pearlite carbon steels based on the microstructure using the one-way multi-scale method [37]. The developing computer technology will help engineers to conduct two-way multi-scale methods easily and that enhance the benefit of the methods in the industry.

Multi-physics simulations are another possibility in the near future. Some of them started to be used for metal forming. Multi-physics simulation would be useful for evaluation of lubrication, which plays an important role in deformation of metals. Kuboki et al. shows some results on deep drawing using high-pressured water [38]. The deep drawing process is carried out as shown in Fig. 9. The water is supplied between the blank and the die instead of oil for alleviating the damage of oil to the environment. The multi-physic simulation was conducted as shown in Fig. 10. FEM is conducted for blank deformation, and CFD is conducted for lubrication behavior. The geometries after deformation and lubricant pressures are conveyed between the two analyses. The developing computer technologies will make multi-physics simulations easily available for tube forming in the near future.

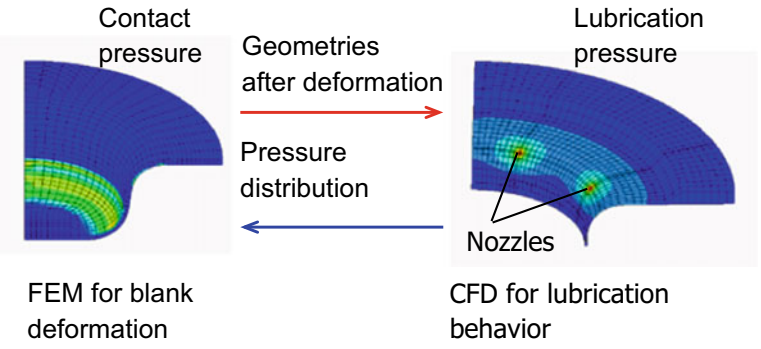


Fig. 10 Multi-physics simulation for deep drawing using high-pressured water [38]. (Color figure online)

3.6 Other Aspects

Thickness control would be another aspect though many research works have been focusing upon precision on bending radius and circularity. Thickness variations are inevitably given by tube forming, leading local weakness when the tubes are mounted into some machines or structures. Some controlling technologies would alleviate the weakness. Studies on thickness of formed tubes started to be reported by a research group under Institute of Steel and Iron Japan (ISIJ). For example, Utsumi et al. tried a unique method for controlling the thickness in tube bending [39]. Tube bending ordinarily causes thinning in extrados and thickening in intrados. Utsumi et al. intentionally gave thickness deviation to the raw tube for cancelling the deviation, which was caused by bending. The research has now started and its effectiveness should be verified by their further study.

Microstructural approaches would be required for tube forming in the future. The tube would be strengthened with decrease of grain size by sever plastic deformation or twin deformation. Anisotropy by texture might be utilized for improvement of the quality of the final products. However, many of present studies for tube forming seem to focus upon the microstructure just for evaluation of the formed products. For example, Wu et al. observed the microstructure of tubes after gas forming for validity of the uniformity [40].

4 Summary

This paper reviews recent technologies and perspectives in tube forming. The technologies include hydroforming, air forming, rotary forming, bending, micro forming and so on. These technologies are qualitatively evaluated in terms of conflicting characteristics, such as formability, strength, productivity, flexibility and miniaturization.

Some technologies are emerging to improve some of the conflicting characteristics. These technologies are expected to contribute for solving problems in environment and aging society. Attainment of both strength and formability will manufacture lightweight parts in vehicles, which will reduce CO_2 emissions. Attainment of both productivity and flexibility will respond the demanding requirements from the diversified societies. Miniaturization will sophisticate the medical devices for helping the society to tackle the problems in aging population.

The developing computer technology and informatics science will boost the tube forming technology. Digitalization of experts' knowledge will help the next generation to realize the sustainable societies. The availability of multi-scale analyses and multi-physics simulations will be improved, and the simulations would help the tube forming technologies to develop rapidly.

References

1. IPCC (Intergovernmental Panel on Climate Change) Climate Report 2018, Global warming of 1.5°
2. Report from Department of Economic and Social Affairs of United Nations, World population prospects 2019
3. Chatti S, Hermes M, Tekkaya A, Kleiner M (2010) The new TSS bending process: 3d bending of profiles with arbitrary cross-sections. CIRP Ann - Manuf Technol 59(1):315–318
4. Nogiwa K, Ishizuka M, Ide A, Ueno N (2017) Proceedings of the 68th Japanese Joint Conference for the Technology of Plasticity, 411–412
5. Tekkaya AE, Brosius A, Homberg, W (2015) 60 excellent inventions in metal forming, vii-ix, Springer
6. Ogura T, Ueda T, Takagi R (1966) On the application of a hydraulic bulging process. Industrie-Anzeige 88(769–772):1001–1004
7. U.S. Patent, 1940, No. 2203868
8. Matsubara S (1994) Incremental nosing of a circular tube with a hemispherical head tool - a study of a numerical control forming system 1 -. J Jpn Soc Technol Plast. 35–398:256–261 in Japanese
9. Matsubara S (1994) Incremental backward bulge forming of a sheet metal with a hemispherical head tool - a study of a numerical control forming system 2 -. J Jpn Soc Technol Plast. 35–406:1311–1316 in Japanese
10. Matsui K, Terada K, Akiyama M, Kuboki T, Kusaka K, Oikawa K (2002) Influence of the micro-structure of carbon steel on the yield stress and the properties of strain hardening, J Jpn Soc Civil Engrs. Appl Mech 5:175–183 in Japanese
11. Manabe K, Chen X, Kobayashi D, Tada K (2014) Development of in-process fuzzy control system for t-shape tube hydroforming. Procedia Engineering 81:2518–2523
12. Manabe K, Chen X, Kobayashi D, Tada K (2013) Weight reduction of axle-housings using high-expansion-ratio hydroforming technology, Proceedings of the 6th International Conference on Tube Hydroforming, Jeju, Korea, 68–72
13. Hwang Y, Hsieh SY, Kuo N (2016) Study of large-expansion-ratio tube hydroforming with movable dies. Key Eng Mater 725:616–622
14. Mori K, Bariani P, Behrens B, Brosius A, Bruschi S, Maeno T, Merklein M, Yanagimoto J (2017) Hot stamping of ultra-high strength steel parts. CIRP Ann - Manuf Technol 66(2):755–777
15. Maeno T, Mori K, Adachi K (2014) Gas forming of ultra-high strength steel hollow part using air filled into sealed tube and resistance heating. J Mater Process Technol 241–1:97–105
16. Manabe K, Chen X, Kobayashi D, Tada K (2019) Development of staf (steel tube air forming) process, Proceedings of 7th International conference on Hot sheet metal forming of high-performance steel, Lulea, Sweden, A7–2nd paper
17. Manabe K (1989) Research trends on tube-end forming. J Jpn Soc Technol Plast. 30–339:481–488 in Japanese
18. Murata M, Kuboki T (2005) Compression spinning of circular magnesium tube using heated roller tool, J Mater Process Technol. 1(162-163):540-545
19. Manabe K, Chen X, Kobayashi D, Tada K (1999) Proceedings of the 50 h Japanese Joint Conference for the Technology of Plasticity, 173-174, in Japanese
20. Oezer A, Sekiguchi A, Arai H (2012) Experimental implementation and analysis of robotic metal spinning with enhanced trajectory tracking algorithms. Robot Comput-Integr Manuf 28–4:539–550
21. Kitazawa K, Kobayashi M, Maruno H (1988) Fitness of circular tube end to tool-envelope-surface in flaring and nosing by orbitally rotary forming. J Jpn Soc Technol Plast. 29–330:767–774 in Japanese
22. Kitazawa K (2015) Prevention of curling in orbital rotary flanging of 1050 and 5052 aluminum alloy tube-ends. J Jpn Inst Light Met. 65–1:2–6 in Japanese

23. Kuboki T, Abe M, Yamada Y, Murata M (2015) Flexible rotary reduction of tube tips by dies with relief surfaces for attaining high forming limit and productivity. CIRP Ann - Manuf Technol 64(1):269–272
24. Oba W, Imaizumi Y, Kajikawa S, Kuboki T (2018) Two-step forming for improvement of forming limit in rotary nosing with relieved die for fabrication of axisymmetric and eccentric nosed tubes. J Mater Process Technol 262:350–358
25. Saito Y, Utsumi N, Yoshida M (2019) Suppression of undesirable phenomenon of thin-walled rectangular tube in rotary draw bending, Proceedings of the 9th International Conference on Tube Hydroforming, 75–80
26. Kuboki, T., Furugen, M., Osaka, S., Ono, T., 1998, Development of die-less bending process for precision u-bent tube, The 7th International Conference on Steel Rolling, Chiba, 981–987
27. Murata M, Ohashi N, Suzuki H (1989) New flexible penetration bending of a tube: 1st report, a study of mos bending method. Trans JSME ser C 55–517:2488–2492 in Japanese
28. Tekkaya, A.E., Brosius, A., Homberg, W., 2015, 60 excellent inventions in metal forming, 363–368, Springer
29. Shimada N, Tomizawa A, Kubota H, Mori H, Hara M, Kuwayama S (2014) Development of three-dimensional hot bending and direct quench technology. Procedia Engineering 81:2267–2272
30. Tadano K, Kawashima K, Kojima K, Tanaka N (2010) Development of a pneumatic surgical manimpulator IBIS IV. J. of Robotics and Mechatronics 22–2:179–188
31. Kuboki T, Muraoka T, Tsubouchi T, Kajikawa S (2017) Upset of bent wire/tube for fabrication of in-plane bent sheet metals with extremely large breadth and small bending radius. CIRP Ann - Manuf Technol 66(1):277–280
32. Shirayori A, Ando T, Narazaki M, Usui M (2013) Effect of initial thickness on cross-shaped-tube hydroforming of small-diameter tubing. J Jpn Soc Technol Plast. 54–634:988–992 in Japanese
33. Mori S, Sato H, Itai K, Manabe K (2017) Development of microtube hydroforming system and its application to cross-shaped microtube. J Jpn Soc Technol Plast. 58–672:72–77 in Japanese
34. Furushima T, Manabe K (2018) Large reduction die-less mandrel drawing of magnesium alloy micro-tubes. CIRP Ann - Manuf Technol 67(1):309–312
35. Milenin A, Kustra P, Furushima T, Du P, Němeček J (2018) Design of the laser dieless drawing process of tubes from magnesium alloy using fem model. J Mater Process Technol 262:65–74
36. Iwasaki K, Kuriyama Y, Kondoh S, Shirayori A (2018) Structuring engineers' implicit knowledge of forming process design by using a graph model. Procedia CIRP 67:563–568
37. Watanabe I, Setoyama D, Iwata N (2011) Influence of the micro-structure of carbon steel on the yield stress and the properties of strain hardening. COMPLAS XI, Barcelona, pp 1–12
38. Horikoshi Y, Kuboki T, Murata M, Matsui K, Tsubokura M (2015) Die design for deep drawing with high-pressured water jet utilizing computer fluid dynamics based on Reynolds' equation. J Mater Process Technol 218:99–106
39. Utsumi N, Saito Y, Yoshida M (2020) Deformation property in bending process of uneven thickness tube. CAMP-ISIJ 52:D21 in Japanese
40. Wu Y, Liu G, Wang K, Liu Z, Yuan S (2017) The deformation and microstructure of Ti-3Al-2.5 V tubular component for non-uniform temperature hot gas forming. Int J Adv Manuf Technol 88:2143–2152

Multi-objective Sizing Optimization of Elbow-Bar Driving Mechanism of Cold Forging Press



Xinyu Dong and Yu Sun

Abstract The kinematics and dynamics characteristics of driving mechanism will directly affect the processing quality and efficiency of multi-link die mechanical press. Based on the structural parameters of a certain type of cold forging press, the dynamic optimal model of elbow-bar driving mechanism is established. Several performance indexes both in the respect of kinematics and dynamics were put forward which were took as the objective functions and constraint functions. Based on virtual prototyping, this paper proposed an improved algorithm method for an elbow-bar driving mechanism, which can also be applied to optimal synthesis of multi-link mechanism. And with this, we find an optimized dimension of elbow-bar driving mechanism. Theoretical and simulation results examine the performance of the optimized mechanism, and demonstrate that its performance parameters are improved obviously.

Keywords Sizing optimization · Elbow-bar mechanism · Multi-objective · Forging press

1 Introduction

Under the background of near-net shape forming, the requirements of press working products have become higher and higher, so it is urgent to improve the working performance [1]. The fluidity of metal under cold forging condition is much lower than that under hot forging condition, and the forming force per unit area is much higher. The forming force of cold forging is sensitive to the forming speed, which requires "forming in accordance with the trend," that is, the forming speed should be as low as possible. The traditional crank press has been unable to meet the needs of the current industrial production. Multi-link presses are widely used in the precision forging of parts, owing to its more reasonable main driving mechanism. The dimension synthesis of the connecting rod is an important part of the design of the

X. Dong · Y. Sun (✉)
School of Mechanical Engineering, Nanjing University of Science and Technology, Nanjing 210094, China
e-mail: sunyu@njust.edu.cn

© The Minerals, Metals & Materials Society 2021

G. Daehn et al. (eds.), *Forming the Future*, The Minerals, Metals & Materials Series,
https://doi.org/10.1007/978-3-030-75381-8_240

press. The dimension parameters of the elbow-bar mechanism determine the main performance of the press [2–4].

The relationship between the rod dimension parameters and the motion lows of the elbow bar press is intricate and nonlinear, so there are still many difficulties in designing a superior mechanism which can satisfy all the requirements and constraints. In the last two decades, several papers on synthesis driving mechanism of mechanical multi-linkage press have been published. In Refs. [5], the kinematic simulation analysis of six link mechanism is carried out by using the simulation software SIMULINK. This method does not need to write tedious programs, reduces the workload, and can easily get the displacement, velocity, and acceleration curves of the pressure mechanism, but this method cannot be used for optimal design. The author makes kinematic analysis on the mechanical characteristics of the linkage mechanism of mechanical press, and studies and compares the mechanical characteristics of traditional driving and new design driving from the aspects of sliding speed, productivity, bearing capacity, and possible workpiece size [6]. In Refs. [7], the optimization model of the six link mechanism was established by using the self-developed universal optimization design software SIPESC. OPT. The optimization software first uses genetic algorithm to get an optimization result, then uses SLP and SQP algorithm to optimize the solution, respectively, compares the optimization results of the three algorithms, and finally gets a satisfactory optimization result. In Refs. [8], the formulas for calculating displacement, velocity, and acceleration of a given motion track are derived by using the theory of Fourier series, and the optimization mathematical model of the mechanism is established. In reference [9], the optimal design of the driving mechanism of the six bar mechanical press is carried out by using the optimization algorithm combining the penalty function and the complex shape, taking the minimum speed fluctuation of the slider and the minimum speed of the contact plate as the optimization objective. Li [10] takes minimum of crack length and maximum of stamping angle as the evaluation index. In the meantime, the optimal model was established with MATLAB.

There are a few studies on multi-objective optimization of the multi-link press both in kinematics and dynamics at once. Researchers always optimize the mechanism for kinematic first, and then check its dynamic performance. In order to improve the working performance of cold forging press both in the kinematics and dynamics, this paper defines the minimum eccentric gear input torque and minimum velocity when the slider first contacts with the workpiece as the objective function. The optimal design model of the press is established by using ADAMS to optimize the size of elbow-bar driving mechanism.

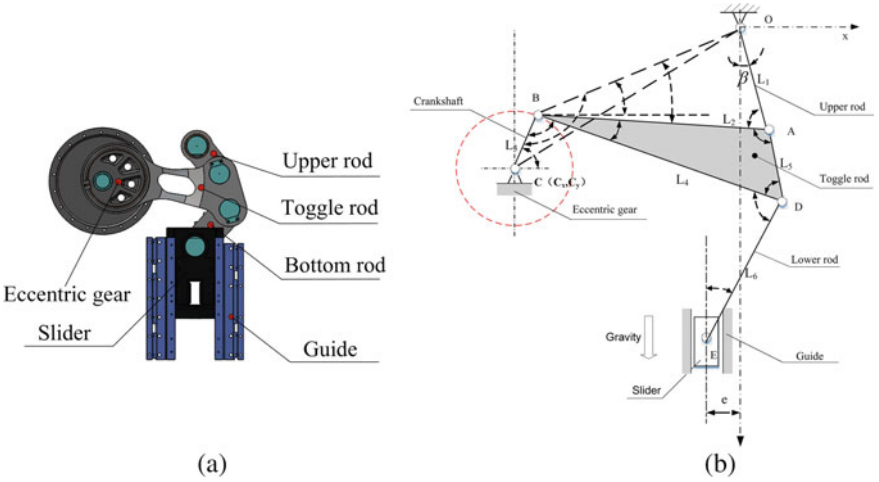


Fig. 1 Configuration of elbow-bar driving mechanism: **a** 3D model of elbow-bar driving mechanism **b** The kinematic sketch and coordinate systems. (Color figure online)

2 Modeling of Elbow-Bar Driving Mechanism

2.1 Introduction of Elbow-Bar Mechanism

Multi-link mechanism presses have become widely used. Compared with the crank press, the elbow-bar press has the other two components: the toggle rod and the upper rod, which can be seen from Fig. 1. The crank is in uniform circular motion during the runtime, the eccentric gear and multi-linkage transfer the circular motion to sliding vertically. Finally, the sliding motion of main slider is achieved along guide rail in vertical direction.

The elbow-bar cold forging press has a more reasonable driving mechanism, which can achieve large slider stroke with small eccentric gear torque; in the plastic deformation area of workpiece, the slider has low working speed to prevent the workpiece from cracking, reduce impact vibration and noise, and improve the service life of die.

2.2 Modeling of Elbow-Bar Mechanism

Adams/view is a commercial software for kinematic and dynamic simulation of mechanical system. A parametric virtual prototyping model was build up using the modeling and analysis function of ADAMS to model. According to the parameterized length of the rod, each component of the model is created. And the corresponding

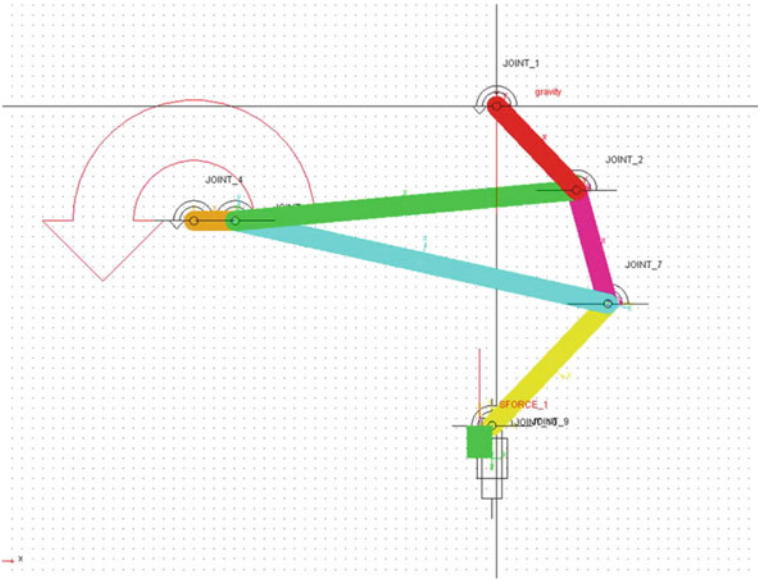


Fig. 2 Parametric virtual prototype model. (Color figure online)

rotating pair and sliding pair are added to the parts according to the actual motion. The established virtual prototype model is shown in Fig. 2.

Based on the parametric virtual prototype model, several parameters can be input or measured. In order to analyze the kinematics and dynamics of the elbow-bar driving mechanism and get the constraint and objective function, it is necessary to input the rotation speed of the crank according to the actual working condition. Nominal pressure is applied to the slider when it is in the nominal stroke. Then, measurement for the speed, acceleration, and displacement of the slider is established. Because the cross-sectional shape and area of the bar system cannot be determined, the friction coefficient and self-weight of the rods and the slider are ignored here. In addition, it can also measure the input torque of the drive shaft, that is, the eccentric gear. Finally, the output performance of the press is calculated when the input torque is obtained. All the physical parameters and notations are listed in Table 1.

3 Optimization Design of Elbow-Bar Driving Mechanism

3.1 Design Variable

The driving mechanism and coordinate system are shown in Fig. 1b, which is used for representing the mechanism easily.

Table 1 Physical parameters (i = 1,…,6)

Parameters	Notation
Length of link	Li
X-coordinate of eccentric gear center	C_x
X-coordinate of eccentric gear center	C_y
Angle between link to horizontal axis	α_i
Angle between L_2 and L_5	θ
Nominal pressure	F
Nominal pressure stroke	S_t
Stroke	H
Slider acceleration	a
Slider velocity	v
Slider displacement	s
Stroke rate	n
Eccentric gear input torque	T

As can be seen from Fig. 1b, we can know that the geometric parameters in the bar system include length of the rods:$L_1, L_2, L_3, L_4, L_5, L_6$, the lateral distance between center of slider and point O, x- and y-coordinates of the center of eccentric gear C_x, C_y. The angle θ between L2 and L5 is a redundant parameter, so the number of parameters which expect to be optimized are 9. The corresponding design variables are defined as follows:

$$X = [x_1, x_2, x_3, x_4, x_5, x_6, x_7, x_8, x_9]^{\mathrm{T}} = [L_1, L_2, L_3, L_5, L_6, \mathrm{e}, C_x, C_y]^{\mathrm{T}} \quad (1)$$

3.2 Objective Function

How to determine the evaluation index of transmission mechanism reasonably is of great significance to improve the overall performance of transmission mechanism. The evaluation index must be relevant with the working performance and process requirement.

Firstly, in the case of a certain nominal force and nominal stroke, the input torque of the press should be as small as possible. This is favorable for the selection of motor, the price of high-power motor is very high, and reducing the power of motor can prove economical. This also ensures that the same power of the motor can produce greater output force, and can produce and form larger products. Besides, the quick-return characteristics can reconcile quality of products and production efficiency. The working speed of the slider of the mechanical press in the forging stage should be less than the maximum speed allowed by the workpiece deformation.

So, this paper sets the optimization goal as minimum eccentric gear input torque and minimum velocity when the slider first contacts with the workpiece.

$$f_1(X) = \min V_{st} \tag{2}$$

V_{st} means the velocity of slider on the nominal stroke.

$$f_2(X) = \min T \tag{3}$$

In order to get the accurate stroke of the slider and improve the quality of the running curve of the slider, the stroke constraint is treated by the outer point penalty function method, and the penalty term is added to the objective function. According to the trade standards, the minimum value of slider travel is set as H_{min}, the maximum value of slider travel is set as H_{max}, generally H_{min}, $H_{max} = H \pm 1\%$.

Therefore, the unified objective function is established as follows:

$$\min f(X) = \min \left\{ \sum_{j=1}^{2} \omega_j f_j(X) + \gamma_k \varphi(X) \right\} \tag{4}$$

where ω_j is the weighting factors of the branch objective function, while γ_k is penalty factor in penalty function method.

Among them, the penalty is

$$\varphi(X) = \left| H(X) - \frac{H\max + H\min}{2} \right| - \frac{H\max - H\min}{2} \tag{5}$$

3.3 Constraint Function

As can be seen from Fig. 1b, there is a crank rock mechanism in the driving mechanism. The constraint conditions for establishing the crank rock mechanism are

$$\begin{cases} g_1(X) = x_3 - x_2 \le 0 \\ g_2(X) = x_3 - x_1 \le 0 \\ g_3(X) = x_3 - L_0 \le 0 \\ g_4(X) = x_3 - x_2 + L_0 - x_1 \le 0 \\ g_5(X) = x_3 - L_0 + x_2 - x_1 \le 0 \\ g_6(X) = x_1 - L_0 - x_2 + x_3 \le 0 \end{cases} \tag{6}$$

L_0 represent the distance between origin of coordinates—point O and the center of eccentric wheel—point C.

In order to ensure the good force transmission effect and prevent the slider from being subjected to excessive lateral force, the constraint conditions of sliding block transmission angle are established as follows.

In order to prevent the sliding block from being subjected to excessive lateral force and ensure that the lateral force does not change direction in the forging process, the constraint condition of sliding block transmission angle is established as follows:

$$\begin{cases} g_7(X) = \arccos\left(\dfrac{L_0^2 + x_1^2 - (x_3 + x_2)^2}{2L_0x_5}\right) - \arctan(-x_8/x_9) - \beta_{\max} \le 0 \\ g_8(X) = -\arccos\left(\dfrac{L_0^2 + x_1^2 - (x_3 + x_2)^2}{2L_0x_5}\right) + \arctan(-x_8/x_9) + \beta_{\min} \le 0 \end{cases} \tag{7}$$

$\beta_{\max}$, $\beta_{\min}$ express the maximum and minimum allowable upper link deflection angles, respectively.

4 Optimization Result

Taking a cold forging press that is used for net-near shape forming, for example. The technical parameters of the press are as follows: nominal pressure, 10000 kN; nominal pressure stroke, 25 mm; main slider stroke, 400 mm; and maximum stroke rate of main slider, 30SPM.

Weighting factors $\gamma_k = 10$, $\gamma_k = 10$, considering the limitation of the structure size of the press frame, the feasible region of design variables is taken as

$$\begin{aligned} X = [x_1, x_2, x_3, x_4, x_5, x_6, x_7, x_8, x_9]^T \in \\ [550, 670, 1650, 1800; 190, 250; 1850, 2000; 600, 800; \\ 750, 950; -25, 5; -1600, -1400; -650, -550]^{\mathrm{T}} \end{aligned}$$

According to the mathematical model of the above optimal design, the optimization program is written by MATLAB. In order to facilitate the manufacturing and accuracy detection of each pole in engineering practice, the optimized results are rounded. The optimal and initial design values are given in Table 2.

Through kinematic analysis, we can get the different curves of the slider. According to the comparison of the curves of the slider before and after optimization, it is obvious that the optimization result is superior to the original parameter, as shown in Fig. 3.

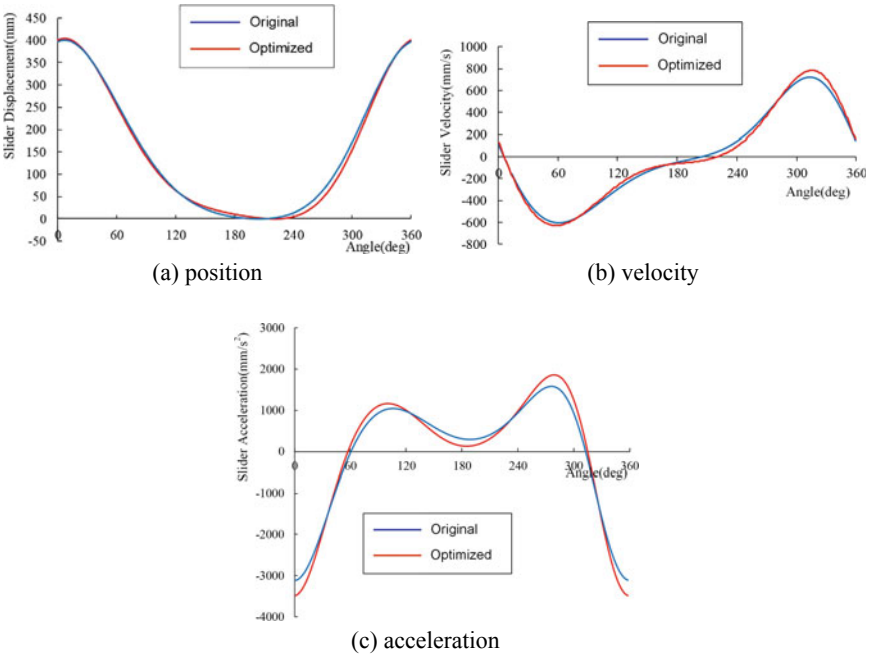
The position of the bottom dead center moves to the right, and the displacement is much more gentle in the forming stage, which shows that the speed of the workpiece forming process is slow and the return speed is fast, with good quick-return characteristics.

Table 2 Initial value and optimal value of design variables

Design variables	Initial variables	Optimal value
L1/mm	610	574
L2/mm	1720	1670
L3/mm	205	220
L4/mm	1930	1882
L5/mm	720	602
L6/mm	845	803
e/mm	−15	−20
Cx	− 1500	−1500
Cy	−615	570

Table 3 Comparison of optimization of the objective function

Objective function	Initial	Optimal
Stroke/mm	400.34	402.4
Crank angle in the down stage/°	198	215
Crank angle in 25 mm Nominal stroke/°	58	68
Velocity on the height of 25 mm/mm/s	−150	106
Total high/mm	2208.8	1972.6
Eccentric gear input torque/N·m	590000	405000



(a) position (b) velocity

(c) acceleration

Fig. 3 Kinematic curve comparison **a** position, **b** velocity, **c** acceleration. (Color figure online)

Then, the dynamic analysis was done by the virtual prototyping mode. The eccentric gear input torque is about 31.3% smaller than initial. The crank angle in 25 mm nominal stroke increases from 58° to 68°, and the crank angle in the down stage increases from 198° to 215°. This means that the time for the slider to return from the top dead point to the bottom dead point is delayed, and the corresponding coefficient of change of the stroke speed of the slider is increased. The quick-return characteristic of the mechanism is significantly enhanced.

5 Conclusion

Based on the parametric modeling in ADAMS, a virtual prototype model of elbow-bar mechanism was established. According to the process performance requirements of near-net forming and the characteristics of the mechanism, the constraint conditions and optimization objectives were set. The correctness and effectiveness of the proposed method are verified by an example. The computer simulation results indicated that the mechanical press with optimized kinematic dimensions can produce better output motion for near-net forming, and the driving torque is also reduced a lot. This paper provides theoretical basis and reference for the optimization design of similar mechanisms. The parameterized optimization results depend on the initial value to a great extent. The selection of the initial value has a great influence on the optimization results. The optimization can be continued on the basis of the given scheme.

References

1. Cominottir G (2008) Near net shape technology: An innovative opportunity for the automotive industry. Robot Comput Integr Manuf 24(6):722–727
2. Osakada K, Mori K, Altan T et al (2011) Mechanical servo press technology for metal forming. CIRP Ann 60(2):651–672
3. Halicioglu R, Dulger LC, Bozdana AT (2016) Structural design and analysis of a servo crank press. Eng Sci Technol Int J 2016:S2215098616304001
4. Huanan Q, Tao JY, Suiran Y (2018) Error modeling and tolerance optimization of double knuckle press. J Donghua Univ: Nat Sci Ed 4:513–519
5. Qu H, Liu Y, Zhou S et al (2014) Kinematic simulation analysis of six bar press mechanism based on Simulink. Forg Equip Manuf Technol 2:20–23
6. Yang C, Zhang S, Li Y et al (2013) Optimization design of six link mechanism of mechanical press. J Dalian Univ Technol 53(1):64–70
7. Ham K, Jang D (2009) Kinematical analysis on the several linkage drives for mechanical presses. J Mech Sci Technol 23(2):512–524
8. Song Q, Li J, Yin W (2012) Design of six-link mechanism of mechanical press based on multi-objective. J Agric Mach 43(4):225–229
9. Li J, Wang J, Yin W et al (2011) Optimization design of driving mechanism of six bar mechanical press. Yizhong Technol 01:11–14
10. Li Y, Sun Y, Wang S (2014) Dimensional Synthesis for Multi-linkage of High-speed Mechanical Press. Procedia Eng 81:1639–1644

Pre-forging Shape Design Using Conformal Mapping Method



Chengshang Liu, Wujiao Xu, and Minyao Liu

Abstract For a forging with complex shape, it is necessary to design one or more pre-forging shapes before the final forging to avoid forging defects and improve forging performance. In this paper, a novel method of using conformal mapping to design the pre-forging shape is proposed to achieve a reasonable three-dimensional (3D) shape of the pre-forging. Firstly, the 3D final forging was two-dimensionally (2D) sliced to simplify the design problem. The new profile of each slice was calculated based on the conformal mapping method. Then, the discrete points on all new profiles were combined into a 3D point cloud for surface reconstruction to obtain 3D model of the pre-forging. Next, four parameters (conformal factor and triaxle scaling factors) were applied to describe the pre-forging shape. Finite element analysis was used to simulate the forging process of the designed pre-forging. Finally, this method was applied to design the pre-forging shapes of different forgings. Through reasonable parameter values, a satisfactory pre-forging shape can be obtained. This method is effective, easy to implement, and has universal adaptation.

Keywords Pre-forging shape design · Conformal mapping · Finite element analysis

1 Introduction

For a forging with complex shape, it is necessary to design one or more pre-forging shapes before the final forging to avoid forging defects and improve forging performance. The design method of the pre-forging shape is mainly to verify the design results by using numerical simulation technology. The basic ideas are usually as follows. First, the design parameters of the pre-forging are selected, such as geometric parameters (length, width, fillet radius, etc. [1–3]), or curve parameters (polynomial curve parameters, Bessel curve parameters, etc. [4, 5]). Next, specific values for each parameter within a reasonable range was set to form a pre-forged shape. Then, the

C. Liu · W. Xu (✉) · M. Liu
College of Material Science and Engineering, Chongqing University, Chongqing 400044, China
e-mail: xuwujiao_cq@163.com

© The Minerals, Metals & Materials Society 2021

G. Daehn et al. (eds.), *Forming the Future*, The Minerals, Metals & Materials Series,
https://doi.org/10.1007/978-3-030-75381-8_241

numerical simulation technology is used to analyze the advantages and disadvantages of this pre-forging shape. And the performance of this pre-forging shape is parameterized to obtain the fitness value. The change of each parameter value will lead to a different pre-forging shape, thus obtaining a different fitness value. Furthermore, the mathematical relationship between design parameters and the fitness can be constructed by using a response surface or a neural network [6, 7]. Finally, the optimization method can be applied to optimize the fitness value to obtain an optimized combination of design parameters [3, 8].

The design parameters of the pre-forging shape are mainly determined by the experience of designers, so the design parameters of different forgings may be completely different. Moreover, the pre-forging shape is complicated for a complex final forging shape, so it is impossible to describe the pre-forging shape with a few simple design parameters. Therefore, poor universality and excessive design parameters are the important reasons that limit the application of the traditional method. In order to improve the above problems in the pre-forging design process, a novel method of conformal mapping for designing the shape of pre-forging was first proposed in this paper.

2 Conformal Mapping Method

2.1 Slice of Final Forging

The 3D design problem can be transformed into a 2D design problem by slicing, which simplifies the design process. Therefore, the slice of a 3D model is an important part of the pre-forging shape design. And a series of 2D closed profiles are the basis for subsequent analysis.

An automobile connecting rod forging is taken as an example. Figure 1a shows the 3D solid model of the final forging. In order to illustrate the slice results clearly, the final forging was cut into slices with thicknesses 20 and 10 mm, respectively, as shown in Fig. 1b, c. In the actual slicing process, the number of slice layers reached 1,000, which minimized the error of the step effect [9]. The conformal mapping method was used to process the 2D slice in the following section.

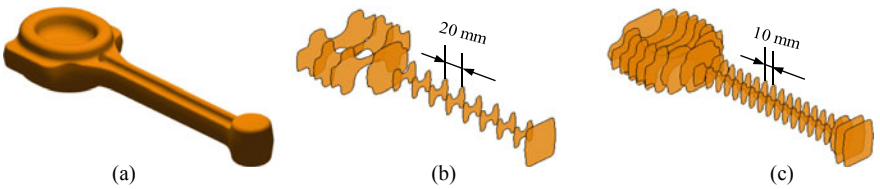


Fig. 1 Slicing results for **a** connecting rod final forging **b** with a thickness of 20 mm and **c** with a thickness of 10 mm. (Color figure online)

2.2 Conformal Mapping Theory

The motion of the continuum can be represented by the initial and instantaneous coordinates of a particle. Set the initial coordinate of the particle at the time t as $\boldsymbol{p}(x, y, z)$, and the instantaneous displacement of the particle is $\Delta \boldsymbol{u}$ after the time Δt. So, the instantaneous coordinate of the particle at the time $t + \Delta t$ is $\boldsymbol{p} + \Delta \boldsymbol{u}$. Set $\Delta t \to 0$, then the velocity vector field of the deformation region can be expressed as

$$\boldsymbol{v}(\boldsymbol{p}, t) = \lim_{\Delta t \to 0} \frac{\Delta \boldsymbol{u}}{\Delta t} \tag{1}$$

Equation (1) represents the instantaneous velocity vector field of all particles in the deformation region. According to the principle of volume invariance of materials during plastic deformation, $\mathrm{div}\boldsymbol{v} = 0$ can be obtained, which can be expressed by the potential function φ as

$$\mathrm{divgrad}\varphi = \nabla \cdot \nabla \varphi = 0 \tag{2}$$

so

$$\nabla^2 \varphi = \frac{\partial^2 \varphi}{\partial x^2} + \frac{\partial^2 \varphi}{\partial y^2} + \frac{\partial^2 \varphi}{\partial z^2} = 0 \tag{3}$$

Besides, the velocity vector field satisfies the irrotational condition, i.e., $\mathrm{rot}\boldsymbol{v} = 0$, which can be expressed as the stream function ψ:

$$\nabla^2 \psi = \frac{\partial^2 \psi}{\partial x^2} + \frac{\partial^2 \psi}{\partial y^2} + \frac{\partial^2 \psi}{\partial z^2} = 0 \tag{4}$$

It can be seen from Eqs. (3) and (4) that the potential function and the stream function of the velocity vector field satisfy Laplace's equation.

In mathematics, conformal mapping has been classically applied to harmonic functions, i.e., solution of Laplace's equation [10]. In physics, it is noted that some physical equations are conformal invariant and thus are equally well suited for conformal mapping, including the advection–diffusion equation for potential flows, the Nernst–Planck equation for bulk electrochemical transport, and Laplace's equation for electrostatic potential.

The equipotential method [11] uses the similarity principle to design the pre-forging shape. However, this method often requires the coupling of multiple software, for example, Ansys software used for solving Laplace's equation to obtain the contours distribution, and Catia software used for surface reconstruction. Repeated data import and export operations reduced the practicality of such a design method. The conformal mapping method uses the numerical method of MATLAB software to solve the contour of the same conformal value, which is called potential value in

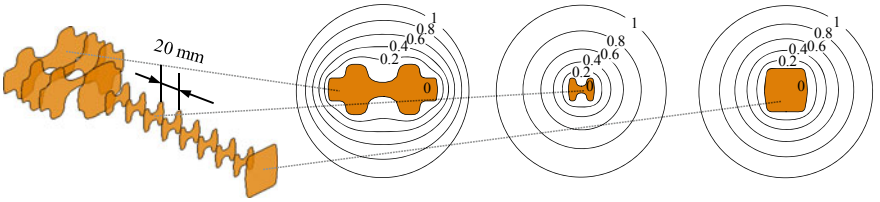


Fig. 2 The conformal mapping results of three representative slices extracted from all slices. (Color figure online)

the equipotential method. There is no need to use other platforms when designing the shape of pre-forging by using the conformal mapping method, which is more convenient and simpler.

The conformal value of the final forging is set as 0 and the conformal value of the initial billet is set as 1. Then the conformal value of the pre-forging is in the range of 0–1. Figure 2 is the conformal mapping results of three representative slices extracted from all slices, where different conformal values correspond to different profiles that do not intersect each other. As shown in Fig. 2, the lower the conformal value, the closer the similarity between the profile and the final forging. The higher the conformal value, the closer the similarity between the profile and the initial billet. Therefore, the conformal value can be adjusted to control the shape of pre-forging.

2.3 Surface Reconstruction

After selecting an appropriate conformal value, the conformal mapping was performed for all slices. Figure 3a shows the mapping result of the conformal value of 0.2 for all slices of Fig. 1c. Next, discrete points were extracted from the mapping profile on the slice. Then the discrete points on all 2D slices were constituted into a 3D point cloud, as shown in Fig. 3b. Finally, surface reconstruction of the point cloud was performed to obtain the 3D model of pre-forging, as shown in Fig. 3c.

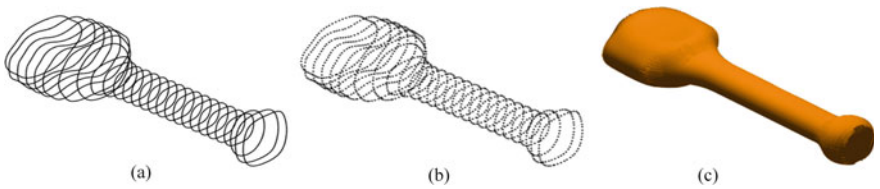


Fig. 3 Construction flow of the pre-forging shape: **a** conformal mapping result; **b** point cloud; **c** surface reconstruction. (Color figure online)

3 Results and Discussion

In the Chap. 2, the conformal mapping method was used to design the pre-forging shape. As a result, the 3D model of the pre-forging shape was successfully obtained. Following this, the influence of some parameters on the shape of the pre-forging was studied, mainly the conformal factor α and scaling factor β.

Firstly, the influence of the conformal factor α on the pre-forging shape was discussed. According to the conformal mapping method, the 3D models of pre-forging with different conformal factors were obtained, as shown in Fig. 4. It can be found that for the 3D shape of pre-forging, the lower the conformal value, the closer the similarity between the pre-forging and the final forging. From the perspective of plastic forming, the physical significance of the conformal factor is to characterize the amount of deformation. The lower the conformal value, the smaller the total deformation. Specifically, the shape of pre-forging is the same as the shape of final forging if the total deformation is 0.

The actual forging process is usually not net-shape forming or near-net-shape forming, so the volume of the pre-forging V_{pre} is not equal to final forging V_{final}, i.e., the flash volume V_{flash} should also be considered. Therefore, the triaxle scaling factors, β_x, β_y , and β_z, were introduced, and satisfying

$$V_{\text{pre}} = V_{\text{final}} + V_{\text{flash}} = \beta_V \cdot V_{\text{final}} = \beta_x \beta_y \beta_z \cdot V_{\text{final}} \tag{5}$$

where β_V is the volume scaling factor, $\beta_V = \beta_x \beta_y \beta_z$, and $\beta_V \geq 1$. For a net-shape forming, $\beta_V = 1$, i.e., $\beta_x \beta_y \beta_z = 1$. For an oblong-shape forming, the metal flow along the axial direction (the axis z) is usually less, i.e., $\beta_z = 1$. The forging of connecting rod can be regarded as an oblong-shape forging, so $\beta_z = 1$. And fixed $\beta_x = 1$ to ensure that the pre-forging can be placed in the mold. In order to ensure that the final forging has a suitable amount of deformation, set $\alpha = 0.2$. Next, the

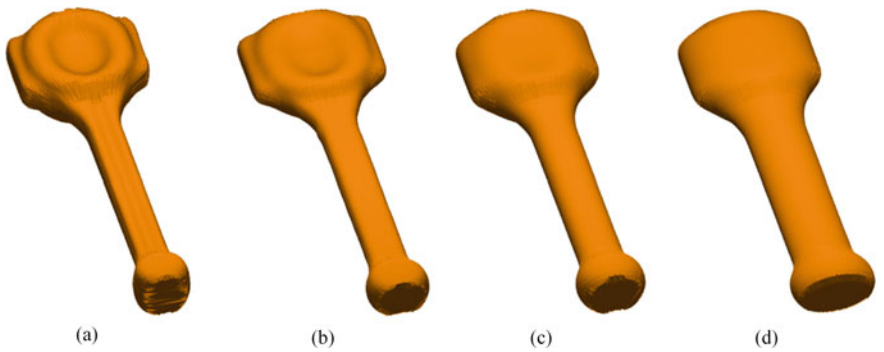


Fig. 4 Effect of conformal factor α on the shape of pre-forging: **a** $\alpha = 0.05$, **b** $\alpha = 0.1$, **c** $\alpha = 0.2$, **d** $\alpha = 0.4$. (Color figure online)

influence of the scaling factor β_y along the axis y on forming quality was discussed, as shown in Fig. 5.

When the scaling factor was small, there were significant unfilled areas on the forging due to insufficient materials, as shown in Fig. 5a, b. When the scaling factor was large, the flash area was also large, which caused material wasting, as shown in Fig. 5c, d. The above two phenomena were consistent with the conclusion of Eq. 5. Thus, it is important to choose an appropriate scaling factor. Finally, the design parameters of the connecting rod in this paper were selected as $\alpha = 0.3$, $\beta_x = 0.9$, $\beta_y = 1.20$, and $\beta_z = 1$. The shape of pre-forging and the forming results are shown in Fig. 6a.

In order to test the universality of designing pre-forging by the conformal mapping method, the pre-forgings design was carried out for different forgings, such as landing gear and transmission bar. As shown in Fig. 6b, c, the desirable forming result can be obtained through the well-designed parameters of pre-forgings.

As shown in Fig. 6, for various forgings with different shapes, four design parameters were reasonably taken to obtain a satisfactory pre-forging shape. The finite

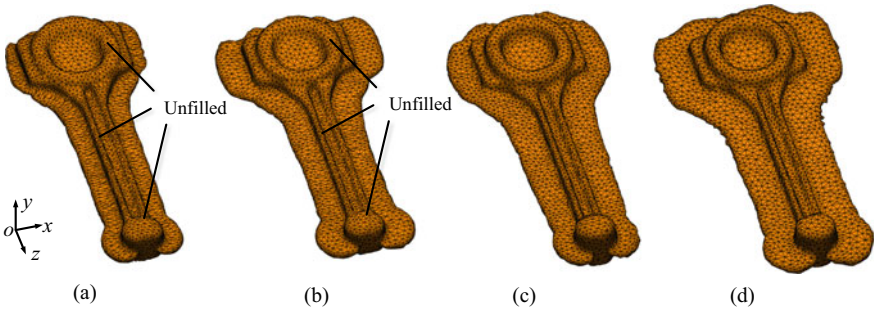


Fig. 5 Effect of the scaling factor β_y on the forming quality: **a** $\beta_y = 1.0$, **b** $\beta_y = 1.1$, **c** $\beta_y = 1.2$, **d** $\beta_y = 1.3$. (Color figure online)

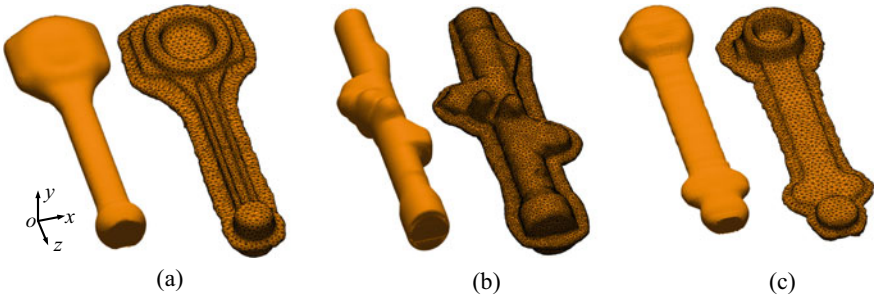


Fig. 6 The shape of pre-forging and forming results for different forgings: **a** connecting rod ($\alpha = 0.3$, $\beta_x = 0.95$, $\beta_y = 1.20$, $\beta_z = 1$); **b** landing gear ($\alpha = 0.2$, $\beta_x = 0.9$, $\beta_y = 1.25$, $\beta_z = 1$); **c** transmission bar ($\alpha = 0.2$, $\beta_x = 0.95$, $\beta_y = 1.20$, $\beta_z = 1$). (Color figure online)

element analysis indicates that the designed pre-forging was well filled and the flash distribution was uniform. Therefore, the conformal mapping method proposed in this paper can be used to design the pre-forging shape of complex forging.

4 Conclusions

In this paper, the main conclusions are as follows:

(1) Physically, the potential function and the stream function of the velocity vector field satisfy Laplace's equation. The conformal mapping has been classically applied to solve Laplace's equation.
(2) The 3D solid model of the pre-forging is reconstructed by the conformal mapping method. This method has the characteristics of high calculation speed and easy implementation.
(3) For various forgings with different shapes, four design parameters were reasonably taken to obtain a satisfactory pre-forging shape. The conformal mapping method has universal adaptability to different forgings.

Acknowledgments This work was supported by the National Natural Science Foundation of China (Grant No. 51975072).

References

1. Kim N, Kobayashi S (1990) Preform design in H-shaped cross section axisymmetric forging by finite element method. Int J Mach Tool Manuf 30(2):243–268
2. Takemasu T, Vazquez V, Painter B, Altan T (1996) Investigation of metal flow and preform optimization in flashless forging of a connecting rod. J Mater Process Technol 59(1–2):95–105
3. Roy S, Ghosh S, Shivpuri R (1997) A new approach to optimal design of multi-stage metal forming processes with micro genetic algorithms. Int J Mach Tool Manuf 37(1):29–44
4. Zhao G, Wright E, Grandhi RV (1997) Sensitivity analysis based preform die shape design for net-shape forging. Int J Mach Tool Manuf 37(9):1251–1271
5. Sedighi M, Tokmechi S (2008) A new approach to preform design in forging process of complex parts. J Mater Process Technol 197(1–3):314–324
6. Ko DC, Kim DH, Kim BM (1999) Application of artificial neural network and Taguchi method to preform design in metal forming considering workability. Int J Mach Tool Manuf 39(5):771–785
7. Guan Y, Bai X, Liu M, Song L, Zhao G (2015) Preform design in forging process of complex parts by using quasi-equipotential field and response surface methods. Int J Adv Manuf Technol 79(1–4):21–29
8. Kampen D, Richter J, Blohm T, Knust J, Langner J, Stonis M, Behrens B (2019) Design of a genetic algorithm to preform optimization for hot forging processes. Int J Mater Form 13:77–89
9. Zhang Z, Joshi S (2015) An improved slicing algorithm with efficient contour construction using STL files. Int J Adv Manuf Technol 80(5–8):1347–1362

10. Bazant MZ (2004) Conformal mapping of some non-harmonic functions in transport theory. Proc R Soc A Math Phys 460(2045):1433–1452
11. Cai J, Li F, Liu T (2011) A new approach of preform design based on 3D electrostatic field simulation and geometric transformation. Int J Adv Manuf Technol 56(5–8):579–588

Part XXIV
Value of, and Limits to, Simulation

Constitutive Law Parameter Identification for Hot Forging Using Compression Experiments on Forging Presses



Gabriel Venet, Cyrille Baudouin, and Tudor Balan

Abstract Constitutive laws for hot forming typically consider the effects of strain, strain rate, and temperature. Their parameter identification requires experiments performed on wide ranges of these three factors. Usually, specialized equipment is utilized to ensure uniform strain, strain rate, and temperature. Alternatively, parameter databases provide parameter sets for various materials and constitutive laws at a low cost. This work explores the potential of using compression experiments on industrial presses for parameter identification of such constitutive models, in order to balance the cost and accuracy of these two existing alternatives. The results are compared with the reference results produced on specialized large temperature/strain rate compression equipment. Two materials are used to prove the usefulness of the proposed methodology.

Keywords Forging · Identification · Constitutive law

1 Introduction

Numerical simulations of the forging process are widely used to prepare the production. In order to have a simulation in line with the reality, a correct modeling of the material rheology is needed. The chosen rheological model must therefore have parameters well identified. Usually, the parametric identification is done by taking as a reference experiments done with specialized equipment (see, for example, [1–4]). However, these specialized equipment aren't cheap and often force the industrial to outsource the testing to a laboratory. This paper's goal is to perform a parametric identification by using industrial presses and therefore present a possible alternative to the specialized devices. The rheological test done here is a compression test. This test was chosen because it is one of the most common tests to identify rheological parameters for the forging process [5–7]. Two presses were used to do the compression: a 600 Ton Loire hydraulic press and a 31.5 kJ Lasco screw press. The hydraulic

G. Venet · C. Baudouin · T. Balan (✉)
Arts Et Metiers Institute of Technology, Université de Lorraine, LCFC, HESAM Université, 57070 Metz, France
e-mail: tudor.balan@ensam.eu

© The Minerals, Metals & Materials Society 2021

G. Daehn et al. (eds.), *Forming the Future*, The Minerals, Metals & Materials Series,
https://doi.org/10.1007/978-3-030-75381-8_242

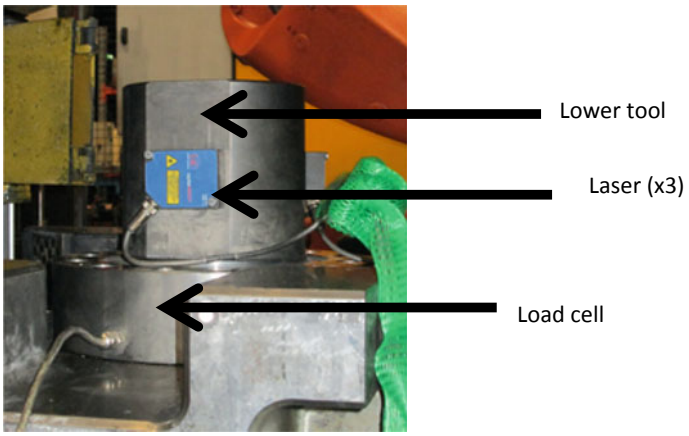


Fig. 1 Tools used for the compression tests on industrial presses. (Color figure online)

press is slow and the screw press is fast. This will help to assess the effect of speed on the rheology of the material. The studied material is a 42CrMo4 steel.

2 Tools

Although the rheological models usually link the stress to the effect of strain, strain rate, and temperature, it is not possible to measure directly the stress and the strain. Instead, the force and the displacement were measured. A specific set of tools was used to do this measurement on any press. It uses three Micro-epsilon optoNCDT 1401 laser sensors to measure the distance between the lower and upper tool at any time of the test. The force is measured with a SCAIME load cell screwed below the lower tool. Fig. 1 is a picture of the lower tool with the sensors attached to it.

3 Thermal Parameters Identification

Since we aim to identify the rheological parameters in the hot forging conditions, the billet must be heated before compression. The billets are heated in a furnace in a controlled atmosphere to prevent oxidation. But as soon the billet is moved out of the furnace, it will cool down. When the compression effectively begun the temperature inside the billet it will be very heterogeneous. To take into account this heterogeneity, a cooling test is made.

Three thermocouples are welded on the billet surface (see Fig. 2). The temperature is recorded as soon as the billet is out of the furnace. The billet is moved to the press

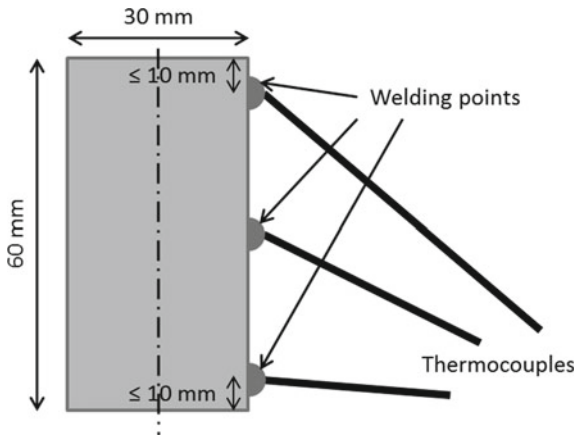


Fig. 2 Thermocouples placement

Table 1 Thermal exchange coefficients

Emissivity	Thermal exchange with air (Wm^{-2} K^{-1})	Thermal exchange with the lower tool (Wm^{-2} K^{-1})	Thermal exchange with the tools under pressure (Wm^{-2} K^{-1})
0.95	10	680	1715

and the upper tool goes down until contact (but not compression) and the temperature recording stops 40 s later.

This experiment is then reproduced with the finite element software FORGE®. Four thermal parameters are changed to simulate the temperature recorded: the billet emissivity, the thermal exchange with air, the thermal exchange with the lower tool when the billet is not under pressure, and the exchange with the two tools when the billet is under pressure. The final parameters are given in Table 1.

4 Friction Coefficient Identification

The ring test [8, 9] was used to evaluate the friction between the billet and the tools. The rings in 42CrMo4 used are 20 mm high. Their inner diameter is 35 mm and their outer diameter is 70 mm. The compressions of the rings are done with the tools presented earlier, and they are made on the screw press and the hydraulic press with two heating temperatures: 950 °C and 1100 °C. These experiments are then reproduced using the finite element software FORGE®. The friction model used is a combined Coulomb-Tresca model with two parameters. These parameters are identified by varying their values in the simulation until the inner diameter of the ring after compression in the simulation is as close as possible to the real ones. The

Table 2 Friction coefficient determined by the ring test

	Hydraulic press (1 s^{-1})	Screw press (10 s^{-1})
μ	0.2	0.125
$\overline{m}$	0.4	0.25

Table 3 Hensel-Spittel parameters for 42CrMo4 steel after identification on industrial presses

A	m_1	m_2	m_3	m_4	m_5	m_7	m_8	m_9	ε_0
1857 MPa	−0.0025	−0.24	0.157	−0.06	0.00059	−0.037	0.00002	−0.069	0.033

hydraulic press and the screw press use different values of friction coefficient due to their different speed. These coefficients are presented in Table 2.

5 Compression on Industrial Presses and Parametric Identification

The compression tests are done on cylindrical billet of 60 mm high and 30 mm wide. Six different testing configurations are done with the hydraulic press (1 s^{-1}) and the screw press (20 s^{-1}) at 950 °C, 1100 °C, and 1250 °C. The force/displacement curves recorded during these tests have served as reference data in the identification. For each configuration, the thermal gradient at the beginning of the compression is simulated, thanks to the thermal exchange coefficients found earlier. Then, the simulation of the compression is made. The rheological model used is the Hensel-Spittel equation [10] (see Eq. 1).

$$\sigma = A e^{m_1 T} (\varepsilon + \varepsilon_0)^{m_2} \dot{\varepsilon}^{m_3} e^{\frac{m_4}{(\varepsilon+\varepsilon_0)}} (1 + (\varepsilon + \varepsilon_0))^{m_5 T + m_6} e^{m_7 (\varepsilon+\varepsilon_0)} \dot{\varepsilon}^{m_8 T} T^{m_9} \quad (1)$$

σ is the stress, ε the equivalent strain, $\dot{\varepsilon}$ the strain rate, and T the temperature. A, ε_0, and the coefficients m_1 to m_9 are the parameters. By using the built-in optimization algorithm of FORGE®, a genetic algorithm helped by a kriging metamodel [11, 12], the rheological parameters of the material are changed until the solution presented in Table 3 and Fig. 3 is found.

6 Discussion and Conclusion

The average difference on all the curves between the simulation and the measure is equal to 13.6%. Although this difference is not negligible, it is in the same order of magnitude as the difference if the simulation is made with the Hensel-Spittel parameters from the FORGE® database (16.9%). Consequently, the identification

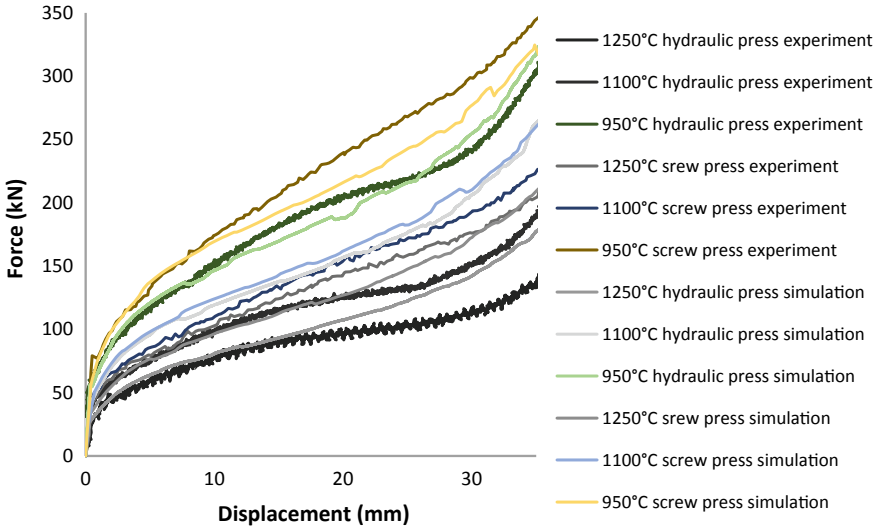


Fig. 3 Force/displacement curves from the experiment and the simulation after optimization. (Color figure online)

on industrial press could serve as an alternative to the specialized devices, in particular if there is no database available. This situation is more and more frequent in industry as new materials are adopted for manufacturing. The advantage is not only the cost but also the availability of the identification procedure onsite and its adaptability to the actual forming conditions (temperature, press speed, etc.).

References

1. Gawad J, Kuziak R, Madej L, Szeliga D, Pietrzyk M (Feb. 2005) Identification of Rheological Parameters on the Basis of Various Types of Compression and Tension Tests. Steel Res Int 76(2–3):131–137
2. Huang Y, Li M, Xiao Z, Liu H, Wang S (2019) A Dynamic Recrystallization (DRX) Constitutive Model for Elevated Temperature Flow Behavior of Cu-0.5Cr-0.1Zr Alloy. Metallogr Microstruct Anal 8(1):45–57
3. Pietrzyk M, Jedrzejewski J (2001) Identification of parameters in the history dependent constitutive model for steels. CIRP Ann-Manuf Technol 50(1):161–164
4. Yu DJ, Xu DS, Wang H, Zhao ZB, Wei GZ, Yang R (2019) Refining constitutive relation by integration of finite element simulations and Gleeble experiments. J Mater Sci Technol 35(6):1039–1043
5. Roebuck B, Lord JD, Brooks M, Loveday MS, Sellars CM, Evans RW (2006) Measurement of flow stress in hot axisymmetric compression tests. Mater High Temp 23(2):59–83
6. Hor A, Morel F, Lebrun J-L, Germain G (2013) Modelling, identification and application of phenomenological constitutive laws over a large strain rate and temperature range. Mech Mater 64:91–110

7. Charpentier PL, Stone BC, Ernst SC, Thomas JF (1986) Characterization and modeling of the high temperature flow behavior of aluminum alloy 2024. Metall Trans A 17(12):2227–2237
8. CETIM, "Test de l'anneau." 01-Jan-1989.
9. Male AT, Cockcroft MG (1964) A Method for the Determination of the Coefficient of Friction of Metals under Conditions of Bulk Plastic Deformation. J Inst Met 93:38–46
10. Hensel A, Spittel T (1978) Kraft und Arbeitsbedarf bildsamer Formgebungsverfahren. VEB Deutscher Verlag für Grundstoffindustrie, Leizig
11. Marie S, Ducloux R, Lasne P, Barlier J, Fourment L (2014) Inverse Analysis of Forming Processes based on FORGE environment. Key Eng Mater 611:1494–1502
12. Emmerich M, Giotis A, Özdemir M, Bäck T, Giannakoglou K (2002) Metamodel—Assisted Evolution Strategies. In: Guervós JJM, Adamidis P, Beyer H-G, Schwefel H-P, Fernández-Villacañas J-L (eds) Parallel Problem Solving from Nature — PPSN VII, vol 2439. Springer, Berlin, Heidelberg, pp 361–370

FE Simulations of Piercing and Trimming of AL and AHSS Alloys



David Diaz-Infante, Advaith Narayanan, Adam Groseclose, and Taylan Altan

Abstract For a given sheet material and thickness, the cutting conditions (punch/die clearance, punch shape, tool corner radii, lubrication, cutting speed, tool wear, and elastic deflection of tool and press) affect the cut edge and the quality of the subsequent forming or flanging operations. Factors such as friction and tool wear are becoming more important as the use of stronger alloys is increasing. This study uses the finite element method to evaluate the effect of these parameters on the edge characteristics and the cutting forces involved (vertical and horizontal). Aluminum 5182-O and CP-W 800 with different sheet thicknesses (1.2 mm and 4.0 mm) were considered. The results indicated that both tool wear and coefficient of friction play a role on the analysis of piercing and trimming and should be accounted for. The effect of each of these variables changes with sheet thickness, material, and process type. This study also illustrates the difficulties and limitations of FE analysis in predicting piercing/trimming variables.

Keywords Critical damage value · FE simulations · Piercing · Trimming · Edge quality · AHSS · Aluminum

1 Introduction

Piercing and trimming are required operations in nearly all sheet metal processes and the characteristics of the edge produced by these operations are influenced by the cutting method. It is well known that mechanical piercing and trimming produce significant damage to the edge, which limits the edge stretchability in subsequent operations. On the other hand, waterjet cutting [1] or laser cutting [2] generate lesser

D. Diaz-Infante (✉)
Nidec Minster Corporation, 240 W 5th St, Minster, OH 45865, USA
e-mail: david.diaz@nidecpa.com

A. Narayanan · T. Altan
Center for Precision Forming, The Ohio State University, Columbus, OH, USA

A. Groseclose
General Motors, Warren, MI, USA

© The Minerals, Metals & Materials Society 2021

G. Daehn et al. (eds.), *Forming the Future*, The Minerals, Metals & Materials Series,
https://doi.org/10.1007/978-3-030-75381-8_243

work hardening and minimal burrs at the cut edge, thus enhancing edge stretchability. However, waterjet cutting and laser cutting may not be practical for mass production due to the tight time constraints involved. Hence, this study will only deal with mechanical cutting processes as it is the most prevalent during production of sheet metal parts.

Some of the variables involved in mechanical trimming and piercing are (a) blank material properties, microstructure and thickness, (b) punch/die alignment, (c) punch/die clearance, (d) elastic deflection and vibrations in the press and tooling, (e) press speed, (f) tool wear and tool edge radii, (g) hardness near the cut edge before and after the cut, (h) coefficient of friction, and (i) possible use of a counter punch. The current trend in the metal forming industry is to move to higher strength and/or lighter alloys. Thus, parameters such as coefficient of friction, tool wear, and tool radii are becoming more important as the operating conditions are getting more severe.

The schematics of piercing and trimming are shown in Fig. 1. The parameters involved in piercing and trimming include sheet material and thickness (t), punch-die clearance (s), punch and die corner radius (r_p and r_d), punch shape, cutting speed (r_p), and blank holder pressure (p_b). Additionally, cutting length (l_c), punch length (l_p) for trimming, and diameter of the punch (d_p) for piercing. Studies conducted on the effect of punch-die clearance (s) on edge stretchability showed that clearances of 15% of sheet thickness or below yielded a good edge in piercing and trimming for aluminum alloys [2, 3] while a clearance in the range of 10–20% of sheet thickness is ideal when cutting advanced high strength steels (AHSS) [4–6].

While the vertical forces involved in trimming and piercing are typically considered, the horizontal forces are often neglected. The literature including horizontal forces in such cutting processes is limited even when these forces may be significant

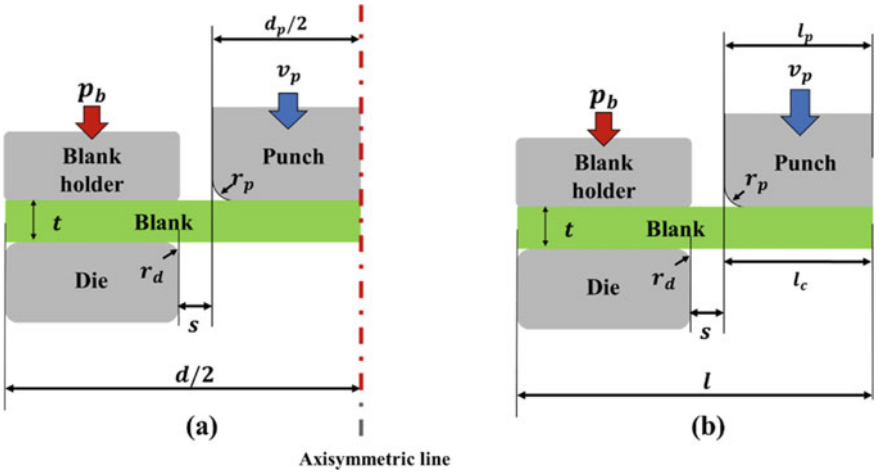


Fig. 1 Schematic of **a** piercing (closed-line cutting) and **b** trimming (open-line cutting). (Color figure online)

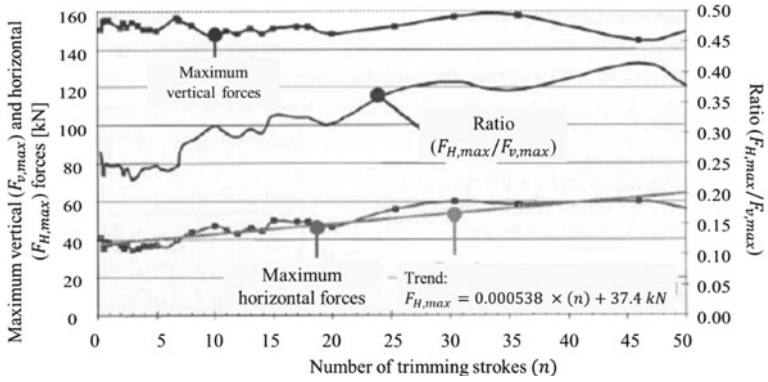


Fig. 2 Variation of the ratio ($F_{H,max}/F_{v,max}$) on tool wear (or number of trimming strokes) for DP600 [7]. (Color figure online)

[7]. This is especially interesting in the presence of worn tools (increased tool radii), which also lead to a significant decrease of the edge stretchability [8, 9]. The findings [7] indicated that the horizontal forces on the punch increase with tool wear (Fig. 2). This study was conducted for a 1.15 mm thick dual-phase (DP) steel with ultimate tensile strength of 600 MPa, and the high cutting forces made the process more prone to elastic deflections and subsequently a non-uniform cutting clearance.

In addition to the horizontal forces, the effect of coefficient of friction (CoF) on the characteristics of the cut edge is also often overlooked. Some FE simulations indicated that the blanking load increased by up to 8% when increasing the coefficient of friction (CoF) from 0.0 to 0.3 for a 1 mm thick mild steel [10]. However, to the best of the authors' knowledge, the effect of CoF on edge quality and forces has not been investigated for AHSS and aluminum. Furthermore, whether a given trend of edge quality and forces hold for sheets of various thicknesses was not investigated previously.

By comparing "thin" 1.2 mm (used in A and B-pillars) and "thick" 4.0 mm (used to make chassis components) sheet metal and using FE simulation, this work aims to approximate the effect of the coefficient of friction and the tool wear (change in tool radii) on the edge quality and cutting forces (vertical and horizontal). Materials included are one aluminum alloy (Al5182-O) and one AHSS (CP-W800). The illustration of the advantages and limitations of FE simulations in predicting the edge quality is also part of the objective.

2 Definition of Edge Quality

There are mixed opinions regarding how to define edge quality or edge stretchability. One of the most common methods is to characterize the cut edge by its geometry (Fig. 3). Previously, the burr height has been related to edge cracking for DP500 and

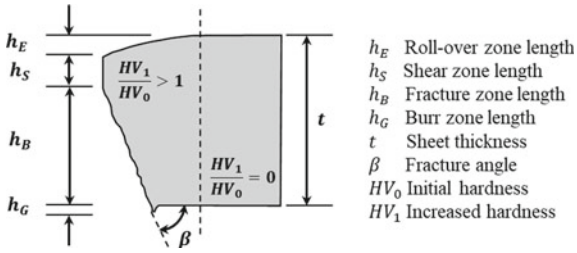


Fig. 3 Cut edge geometry and its characteristics [15]

AA6111-T4 [11]. However, it has been reported that the burr length is practically non-existent for 980 MPa dual-phase (DP) steel for clearances from 5% to 30% [12]. Therefore, the interpretation of edge geometry in terms of what constitutes a good edge quality is wide. Furthermore, it was proposed that the ratio of shear zone length (h_S) and the fracture zone length (h_B) is a good indicator of edge quality for AHSS [12]. Measuring or calculating the stresses at the edge is another method used to estimate edge quality. A study [13] indicated that tensile residual stresses at the edge leads to earlier edge fracture. Certain studies [8, 14, 15] indicated that strain hardening or hardness near the cut edge is the primary factor dictating edge fracture in a material.

Based on the various approaches in the literature, this study will attempt to differentiate the edge quality among cut edges in terms of burr zone length (h_G) and strains, which bear a direct relation to strain hardening or hardness. These strains are calculated near the cut edge and averaged (Fig. 4).

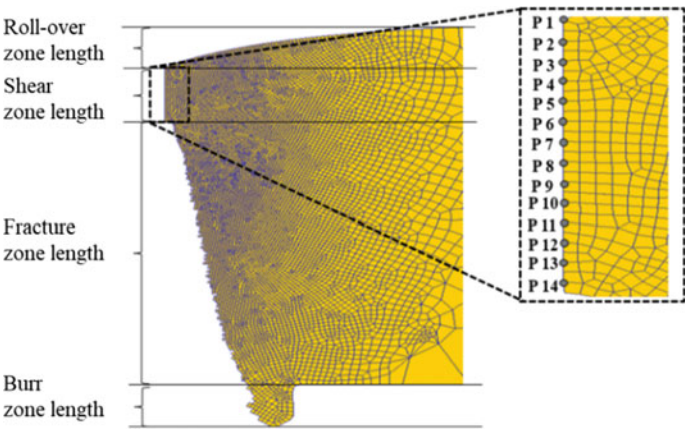


Fig. 4 Calculation of average effective strains at the shear zone of a cut edge by using the points P1-P14 [16]. (Color figure online)

3 Approach

3.1 Finite Element (FE) Model Setup

The piercing conditions used in [14] were replicated by using an axisymmetric model in DEFORM 2D software, similar to the FE model used in [16]. The mesh was generated using brick elements and refined to a size of 1% of sheet thickness near the cutting region. The punch corner radius used in [14] was chosen as 0.05 mm. However, r_p and r_d were modified to a value of 0.1 mm in this study, as previous literature indicates that the use of smaller punch and die corner radii leads to generation of slivers in aluminum. Likewise, sharpening of tools to very small radii (e.g. corner radii = 0.02 mm) may lead to very high contact pressures when piercing AHSS which may lead to chipping of tool. A punch-die clearance of 15% of sheet thickness was chosen for CP-W800 in accordance with the industry consensus that recommends clearance (s) for AHSS to be between 10 and 20% of sheet thickness. A clearance of 12.5% of sheet thickness was chosen for Al5182-O, also as per industry recommendation.

The trimming conditions used were modeled as a plane strain behavior in DEFORM 2D. The mesh size, punch-die clearance (s), and the corner radii (r_p and r_d) were kept the same as piercing. A summary of the conditions used in FE simulations is listed in Table 1.

The flow stress curve for CP-W800 was calculated from its yield strength, ultimate tensile strength, and Young's modulus (values obtained from [14]) by using the procedure described in [17, 18]. The Young's modulus (E) was assumed to be 210 GPa. The flow stress curve was extrapolated using the Holloman's power law to approximately model the behavior of the material at high strains (up to 3). The flow stress curve for Al5182-O was obtained from bulge tests previously conducted at the Center for Precision Forming (CPF)/The Ohio State University and was similarly extrapolated using the power law equation. The dependency of the flow stress curves on the strain rate and temperature was ignored for simplicity. The flow stress curves used in simulation are shown in Fig. 5.

The determination of critical damage value (CDV), which is the parameter that defines the onset of fracture during the FE simulations, was done by comparing the

Table 1 Simulation matrix for both piercing and trimming FE simulations. The clearance (s) for CP-W800 and Al5182-O were 15% and 12.5% of sheet thickness, respectively

	Sheet thickness [mm]	Coefficient of friction (CoF)	Punch/die corner radius [mm]
1		0	0.1
2	4.0	0.1	0.1
3		0.1	0.3
5		0	0.1
6	1.2	0.1	0.1
7		0.1	0.3

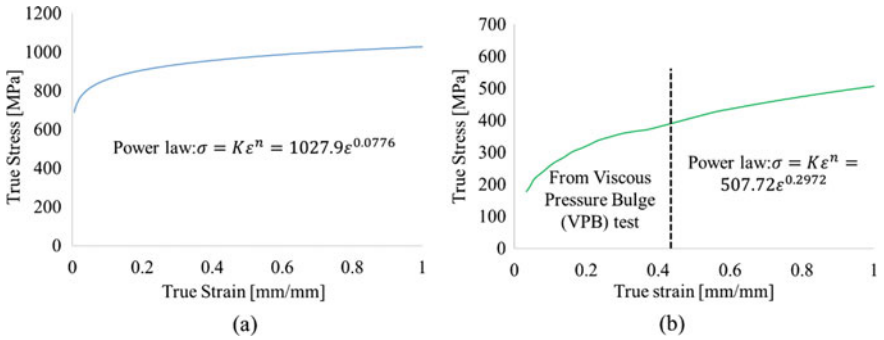


Fig. 5 Flow stress curves for **a** CP-W800 [16] and **b** Al5182-O. (Color figure online)

measured shear zone length in experiments conducted in [14, 19] and the corresponding value calculated in simulations replicating the experimental conditions, through an iterative procedure [20]. 'Adapted Rice & Tracey' fracture criterion was used to define the CDV (Eq. 1) based on observations which compared several fracture criteria in terms of correlation of simulation with experimental cut edge geometry [20].

$$\int_0^{\overline{\varepsilon}_f} e^{\frac{\alpha\sigma_m}{\overline{\sigma}}} d\overline{\varepsilon} = CDV \tag{1}$$

where σ_m = Hydrostatic stress, $\overline{\sigma}$ = effective stress, $\overline{\varepsilon}$ = effective strain and α = 2.9 for Adapted Rice & Tracey criterion. The CDV for CP-W800 and Al5182-O was found to be 1.25 and 1, respectively.

3.2 Simulation Matrix

The FE simulations conducted for piercing and trimming are listed in Table 1. The effect of coefficient of friction (CoF) and tool wear (r_p *and* r_d) on edge quality and cutting forces were investigated. Furthermore, the influence of sheet thickness (1.2 mm and 4.0 mm) on these variables was also considered for both materials. The simulation with CoF = 0.1 and corner radii (r_p, r_d) = 0.1 mm was considered as the base case. The changes in various variables were evaluated with respect to the results obtained in this simulation.

4 Results

4.1 Piercing

4.1.1 Horizontal and Vertical Cutting Forces

The maximum vertical and horizontal cutting forces corresponding to various values of coefficient of friction (CoF) and corner radii (r_p, r_d) in piercing of thick sheets (thickness = 4.0 mm) are shown in Table 2. None of the variables seem to affect the vertical cutting force (< 10% difference). The CoF seems to affect the horizontal cutting forces by up to 20% and 25% for CP-W800/4 mm and Al5182-O/4 mm, respectively, while the effect of tool wear is negligible.

Similarly, the maximum cutting forces in piercing of thin (thickness = 1.2 mm) sheets are shown in Table 3. As expected, none of the variables seem to affect the vertical cutting forces. However, tool wear seems to play a significant role on the horizontal cutting forces, about 80% and 70% increase for CP-W800/1.2 mm and

Table 2 Max. vertical and horizontal forces during piercing of thick (4.0 mm) sheets

	Case	Max. vertical cutting force [kN]	Max. horizontal cutting force [kN]
CP-W800	CoF = 0.0	308.1	116.3
	CoF = 0.1	317.9	136.0
	Worn tools (CoF = 0.1) ($^{r}pi\ ^{r}d$ = 0–3 mm)	331.2	138.0
A15182-O	CoF = 0.0	116.4	46.2
	CoF = 0.1	123.6	58.2
	Worn tools (CoF = 0.1) (r_p, r_d = 0.3 mm)	134.0	64.1

Table 3 Max. vertical and horizontal forces during piercing of thin (1.2 mm) sheets

	Case	Max. vertical cutting force [kN]	Max. horizontal cutting force [kN]
CP-W800	CoF = 0.0	100.3	*25.2*
	CoF = 0.1	101.8	24.4
	Worn tools (CoF = 0.1) (r_v,r_d = 0.3 mm)	108.4	43.4
	CoF = 0.0	39.6	16.1
A15182-O	CoF = 0.1	41.3	17.0
	Worn tools (CoF = 0.1) (r_p,r_d = 0.3 mm)	46.6	24.4

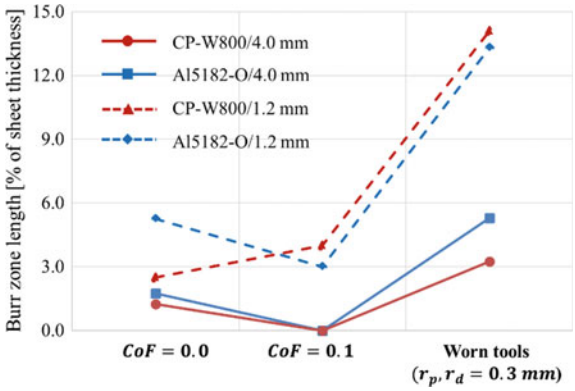


Fig. 6 The burr zone lengths (h_G) after piercing of thick and thin CP-W800 and Al5182-O sheets. (Color figure online)

Al5182-O/1.2 mm, respectively. It is hypothesized that the ratio between the punch corner radius and the sheet thickness influences the effect of the tool wear on the horizontal cutting force. Thus, this effect is more noticeable for thin sheets for similar tool wear assumption (represented by larger punch corner radius).

4.1.2 Cut Edge Geometry

The burr zone length h_g from FE simulations of piercing of thick, as well as thin sheets, is shown in Fig. 6. The burr zone length (h_G) was considered to be the parameter affecting edge quality. Regardless of the sheet material and thickness, tool wear was found to be the most significant parameter affecting the edge quality (based on cut edge geometry), among all the parameters considered in this study. Moreover, the burr length did not change significantly with the sheet thickness, and therefore, this length represents a larger percentage of the thickness for the thin sheets. This idea suggests that an absolute value for the burr length should be used as a limiting factor rather than the ratio to the total sheet thickness. The variation in burr zone lengths with changes in CoF was in the order one to two element sizes (difference of 2–3% of sheet thickness) and was considered negligible.

4.1.3 Strain Hardening Near the Cut Edge

The effective strains in FE simulations were assumed to bear a direct correlation to experimental hardness measurements. As calculations during FE simulations are subject to errors, it is assumed that a given parameter has an influence on strain hardening only if there is a difference of 10% or more in the average effective strains, at both the shear and fracture zones.

The average effective strains after piercing of thick CP-W800 and Al5182-O sheets are shown in Table 4. For thick sheets (4.0 mm thick), the CoF did not affect the edge quality for CP-W800/4 mm. However, the average strains for Al5182-O/4 mm

Table 4 Average effective strains after piercing of thick (4.0 mm) CP-W800 and Al5182-O sheets

Material	Piercing condition	Avg. effective strain at shear zone [mm/mm]	Avg. effective strain at fracture zone [mm/mm]
CP-W800	CoF = 0.0	1.68	0.81
	CoF = 0.1	1.61	0.83
	Worn tools (CoF = 0.1) (r_p, r_d = 0.3 mm)	1.89	1.04
	CoF = 0.0	1.48	0.71
A15182-O	CoF = 0.1	1.65	0.85
	Worn tools (CoF = 0.1) (r_p, r_d = 0.3 mm)	1.78	1.02

Table 5 Average effective strains after piercing of thin (1.2 mm) CP-W800 and Al5182-O sheets

Material	Piercing condition	Avg. effective strain at share zone [mm/mm]	Avg. effective strain at fracture zone [mm/mm]
	CoF = 0.0	1.50	1.00
CP-W800	CoF = 0.1	1.60	1.10
	Worn tools (CoF = 0.1) (r_p,r_d = 0.3 mm)	1.79	1.23
	CoF—0.0	1.45	0.81
A15182-0	CoF = 0.1	1.44	0.91
	Worn tools (CoF = 0.1) (r_p,r_d = 0.3 mm)	1.76	1.30

increased by about 15% with increase in CoF. It is hypothesized that the effect of CoF on edge quality as defined by strain hardening near the cut edge may be a material, as well as thickness dependent. Tool wear increased the effective strains at the edge for CP-W800/4 mm and Al5182-O/4 mm by about 25% and 20%, respectively, during piercing.

For thin (1.2 mm thick) sheets, only the tool wear seemed to increase the strains (by about 20% and 22% for CP-W800/1.2 mm and Al5182-O/1.2 mm, respectively) in piercing, as seen in Table 5.

4.2 Trimming

4.2.1 Horizontal and Vertical Cutting Forces

The maximum vertical and horizontal cutting forces per unit width of the blank for various conditions in trimming of thick sheets (thickness = 4.0 mm) are shown in Table 6. Like what was observed for piercing, none of the variables seem to affect the

Table 6 Max. vertical and horizontal forces during trimming of thick (4.0 mm) sheets

	Case	Max. vertical cutting force [kN/mm]	Max. horizontal cutting force [kN/mm]
CP-W800	CoF = 0.0	1.74	0.52
	CoF = 0.1	1.81	0.74
	Worn tools (CoF = 0.1) (r_p.r_d = 0.3 mm)	1.86	0.83
A15182-O	CoF = 0.0	0.67	0.23
	CoF = 0.1	0.71	0.30

Table 7 Max. vertical and horizontal forces during trimming of thin (1.2 mm) sheets

	Case	Max. vertical cutting force [kN/mm]	Max. horizontal cutting force [kN/mm]
CP-W800	CoF = 0.0	0.55	0.16
	CoF = 0.1	0.57	0.17
	Worn tools (CoF = 0.1) (r_v,r_d = 0.3 mm)	0.60	0.25
A15182-O	CoF = 0.0	0.22	0.09
	CoF = 0.1	0.23	0.10
	Worn tools (CoF = 0.1) (^{r}p > ^{r}d = 0.3 mm)	0.27	0.17

vertical cutting forces. However, the CoF as well as tool wear affected the horizontal cutting forces by up to 30% and 12%, respectively, for CP-W800 and by up to 25% and 25%, respectively for Al5182-O.

For thin (1.2 mm thickness) sheets, the CoF did not affect the horizontal and vertical cutting forces during trimming (Table 7). The tool wear again seems to play a significant role on the horizontal cutting forces, by about 45% and 70% for CP-W800/1.2 mm and Al5182-O/1.2 mm, respectively.

4.2.2 Cut Edge Geometry

Similar to what was observed for piercing, tool wear seemed to generate the worst edge quality for trimming of thick as well as thin Al5182-O and CP-W800 sheets, as seen in Fig. 7.

4.2.3 Strain Hardening Near the Cut Edge

The effective strains corresponding to various conditions during trimming of thick sheets (4.0 mm thick) are shown in Table 8. Contrary to what was observed for

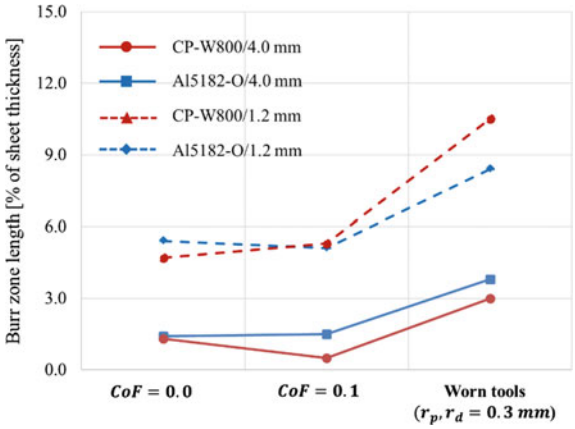


Fig. 7 The burr zone lengths (h_G) after trimming of thick and thin CP-W800 and Al5182-O sheets. (Color figure online)

Table 8 Average effective strains after trimming of thick (4.0 mm) CP-W800 and Al5182-O sheets

	Case	Max. vertical cutting force [kN/mm]	Max. horizontal cutting force [kN/mm]
	CoF = 0.0	1.37	0.50
CP-W800	CoF = 0.1	1.83	0.73
	Worn tools (CoF = 0.1) (^{r}p. ^{r}d = 0.3 mm)	2.04	0.91
	CoF = 0.0	1.72	0.50
A15182-O	CoF = 0.1	1.64	0.58
	Worn tools (CoF = 0.1) (r_p, r_d = 0.3 mm)	2.10	0.77

piercing, the CoF affected the edge quality for CP-W800/4.0 mm by about 25% during trimming, but did not affect the edge quality during trimming of Al5182-O/4 mm. The tool wear affected the edge quality for CP-W800/4 mm and Al5182-O/4 mm by about 20% and 25%, respectively, during trimming.

Similar to what was observed for piercing of thin (1.2 mm thick) sheets, only the tool wear seemed to affect the edge quality (by about 50% and 40% for CP-W800/1.2 mm and Al5182-O/1.2 mm, respectively, at the fracture zone) in trimming, as seen in Table 9.

Table 9 Average effective strains after trimming of thin (1.2 mm) CP-W800 and Al5182-O sheets

Materials	Trimming condition	Avg. effective strain at shear zone [mm/mm]	Avg. effective strain at fracture zone [mm/mm]
CP-W800	CoF = 0.0	1.54	0.60
	CoF = 0.1	1.66	0.66
	Worn tools (CoF = 0.1) (r_p,r_d = 0.3 mm)	1.81	1.04
	CoF = 0.0	1.58	0.52
A15182-O	CoF = 0.1	1.70	0.62
	Worn tools (CoF = 0.1) (r_p,r_d = 0.3 mm)	1.90	1.10

5 Conclusions and Limitations

5.1 Conclusions

In this study, the effects of the coefficient of friction (CoF) and the tool wear (represented by larger punch corner radii) were analyzed for CP-W800 and Al5182-O materials with 1.2 mm and 4.0 mm thicknesses. Based on the results from the FE simulations for piercing and trimming, the following conclusions are drawn:

5.1.1 Vertical Cutting Forces

- The vertical cutting forces increased by less than 10% by any of the process variables or the cutting process (i.e. trimming or piercing).

5.1.2 Horizontal Cutting Forces

- Horizontal forces were influenced the most by CoF on thick sheets and by tool wear on thin sheets.
- The ratio between punch corner radius and sheet thickness seems to influence the effect of tool wear on horizontal cutting forces. The larger the ratio, the larger is the effect.
- The effect of CoF on horizontal cutting forces seems to decrease with decreasing sheet thickness.
- Horizontal forces should be considered when designing tools for piercing and trimming to prevent elastic deflections which can lead to non-uniform cutting clearances. The calculated horizontal forces represented up to 50% of the vertical cutting force. This can be particularly important when dealing with high strength materials.

5.1.3 Edge Quality

- The tool wear worsens the edge quality during cutting (if either burr length or strains at the edge are considered as parameters affecting edge quality), irrespective of the material, the definition of edge quality, the cutting process (i.e. piercing or trimming), and thickness of the material.
- The CoF alone does not affect the edge quality during cutting of thin sheets. However, the effect of CoF on edge quality (defined by strain hardening near the cut edge) in thick sheets depends on the material, thickness, and the cutting process.

5.2 Limitations

- The effect of punch speed (v_p) on the edge quality and the cutting forces was not considered. It is possible that the punch speed influences the edge quality through the combined effect of increase in strain rate and temperature. However, this analysis is outside the scope of this study as the flow stress curves for the above considered materials, in function of strain rate and temperature were not available. This is compounded by the difficulty in quantifying the exact relation between these variables. Furthermore, it is difficult to obtain the heat transfer coefficients between the tools and the workpiece due to variability in the tool materials and workpiece thermal properties.
- The determination of critical damage value (CDV) is dependent on the cutting conditions and the flow stress curve. In this study, the CDV for a given material is assumed to be the same irrespective of the cutting conditions; in reality, this may not be the case. Additionally, batch-to-batch variations in a coil of a given material ensure non-uniformity in its mechanical properties. The value of CDV may affect the results obtained from FE simulations.
- Due to loss of elements and remeshing during FE calculations, it is difficult to quantify the relative effect of each process parameter. Hence, it is not recommended to rely solely on FE simulation results, especially for cutting operations such as trimming or piercing.
- The effect of each of the process parameters mentioned before was considered in isolation. The interaction between these variables and other process parameters (e.g. cutting speed (v_p), if any, cannot be accounted for in these FE simulations.

References

1. Shih HC, Hsiung CK, Wendt B (2014) Optimal Production Trimming Process for AHSS Sheared Edge Stretchability Improvement. SAE Technical Paper 2014–01-0994. https://doi.org/10.4271/2014-01-0994

2. Zhou D, Du C, Siekirk J, McGuire J, Chen X, Levy BS (2010) A practical failure limit for sheared edge stretching of automotive body panels. SAE Technical Paper 2010-01-0986
3. Golovashchenko S, Zhou W, Nasheralahkami S, Wang N (2017) Trimming and sheared edge stretchability of light weight sheet metal blanks. Proc Eng 207:1552–1557
4. Hu XH, Sun X, Golovashchenko SF (2016) An integrated finite element-based simulation framework: from hole piercing to hole expansion. Finite Elem Anal Des 109:1–3
5. SSAB & Uddeholm (2015): Tooling solutions for advanced high strength steels. http://www.uddeholm.com/files
6. Unruh K, Heuse M (2017) New challenges on materials evaluation for advanced high strength steels in automotive seat structures
7. Schaeper EF (2008) Mehr Flexibilität und weniger Verschleiß beim Scherschneiden durch ein neues Werkzeugkonzept mit adaptivem Schneidspalt. PZH, Produktionstechnisches Zentrum. ISBN 978-3-939026-79-2
8. Chiriac C, Shi MF (2013) Studies on edge strain hardening produced by trimming operations. SAE Technical Paper 2013-01-1774
9. Gläsner T, Schaffner T, Sunderkötter C, Volk W, Hoffmann H, Golle R (2015) Studies on the effect of tool wear on the production process in two stage shear cutting. InKey Eng Mater 651:12611270 Trans Tech Publications
10. Maiti SK, Ambekar AA, Singh UP, Date PP, Narasimhan K (2000) Assessment of influence of some process parameters on sheet metal blanking. J Mater Process Technol 102(1–3):249–256
11. Wang N, Golovashchenko SF (2016) Mechanism of fracture of aluminum blanks subjected to stretching along the sheared edge. J Mater Process Technol 233:142–160
12. Horinek H (2015) Variation of cut-edge parameter around the hole circumference for DP- vs. CP1000 steel grades. Bachelor's thesis, University of Applied Sciences Upper Austria
13. Mori K, Abe Y, Kidoma Y, Kadarno P (2013) Slight clearance punching of ultra-high strength steel sheets using punch having small round edge. Int J Mach Tools Manuf 65:41–46
14. Feistle M, Pätzold I, Golle R, Volk W, Frehn A, Ilskens R (2018) Maximizing the expansion ratio through multi-stage shear-cutting process during collar forming. In: IOP conference series: materials science and engineering 2018 Sep (Vol. 418, No. 1, p. 012071). IOP Publishing
15. Paetzold I, Dittmann F, Feistle M, Golle R, Haefele P, Hoffmann H, Volk W (2017) Influence of shear cutting parameters on the fatigue behavior of a dual-phase steel. In: Journal of physics: conference series 2017 Sep (Vol. 896, No. 1, p. 012107). IOP Publishing
16. Diaz-Infante D, Narayanan A, Altan T (2019) Estimation of cutting parameters in two-stage piercing to reduce edge strain hardening. SAE Technical Paper; 2019 Apr 2
17. Kardes N, Choi C, Yang X, Altan T (2011) Determining the flow stress curve with yield and ultimate tensile strengths - Part I. Stamping Journal, p. 12–113, May/June 2011
18. Kardes N, Choi C, Yang X, Altan T (2011) Determining the flow stress curve with yield and ultimate tensile strengths - part ii. stamping journal, p. 14–15, July/August 2011
19. Diaz-Infante D (2019). Prediction and prevention of edge fracture in forming of AHSS. (Electronic Thesis or Dissertation). https://etd.ohiolink.edu/
20. Widenmann R, Sartkulvanich P, Altan T (2009) Finite element analysis on the effect of sheared edge quality in blanking upon hole expansion of advanced high strength steel. In: IDDRG international conference 2009 June

Finite Element Method Based on Space Mesh



Gang Yang and Atsushi Kinoshita

Abstract The finite element method has been widely used because of its powerful calculation since it was proposed. The method has been well developed in many different fields such as civil engineering and the aerospace industry. FEM was also used to simulate the deformation performance of materials in the metal forming process. But one of the critical problems of the conventional FEM is the termination of simulation caused by large deformation of mesh. Many studies are focused on the geographic technical method to solve the problem such as re-mesh. But the method is limited and time consumed. An element called **space mesh** is proposed for the large deformation simulation in this paper. The shape of the space mesh used in the simulation is not changed when the calculation is progressed. And the large deformation can be simulated without termination caused by the shape irregularity of the mesh.

Keywords Space mesh · Finite element method · Large deformation simulation · Boundary condition

1 Algorithm of Finite Element Method Based on Space Mesh

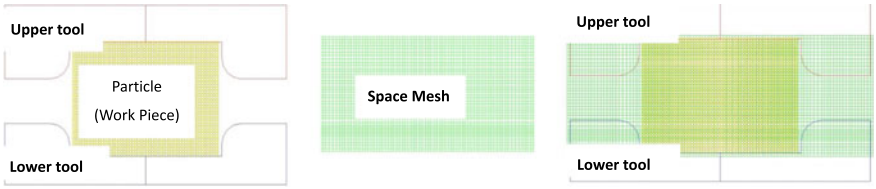
The **space mesh** is a square-shaped element covering the space in which the deformation happens. The nodal values of the space mesh, such as velocities, are calculated by FEM. The deformation of the workpiece is simulated by interpolation from the nodal values of the space mesh in which the workpiece is involved. For the next simulation step, the physical values of the deformed workpiece, such as strain and

G. Yang (✉)
Shanghai Kimeng Information Technology Co., Ltd, Room 604, No. 18, GuFang Road, Shanghai 201102, China
e-mail: yanggang08@vip.163.com

A. Kinoshita
NTT Data Engineering System Corporation, Green Place, Kamata, 37-10, Tokyo 144-860, Japan
e-mail: kinoshita@nttd-es.co.jp

© The Minerals, Metals & Materials Society 2021

G. Daehn et al. (eds.), *Forming the Future*, The Minerals, Metals & Materials Series,
https://doi.org/10.1007/978-3-030-75381-8_244



(a) Work piece and tools (b) Space mesh (c) Combination of space mesh and work piece

Fig. 1 Definition of space mesh and workpiece. (Color figure online)

stress, are transferred from the particles to the space mesh which the particles enter. So the space mesh is not changed from the beginning to the end of the deformation simulation.

1.1 Definition of Space Mesh and Workpiece

The simulation space is divided into a square-shaped **space mesh(green)** as shown in Fig. 1. The workpiece is dispersed into dots called **particles (yellow)** and linked with lines. The space mesh is used for the formulation of FEM and particles are used to simulate the deformation of the workpiece.

1.2 Formulation

The nodal velocities of space mesh are gathered by minimizing the following functional [1]:

$$\Phi = \int_V \overline{\sigma}\dot{\overline{\varepsilon}} dV + \int_S |\tau_f \Delta v| dS + \lambda \int_V \varepsilon dV \tag{1}$$

where $\overline{\sigma}$ is the equivalent stress, $\dot{\overline{\varepsilon}}$ is the equivalent strain-rate, $|\tau_f|$ is the friction shear stress, Δv is the relative velocity, λ is Lagrange coefficient, and $\dot{\varepsilon}$ is the hydrostatic strain rate in the element defined as

$$\dot{\varepsilon} = \dot{\varepsilon}_x + \dot{\varepsilon}_y + \dot{\varepsilon}_z \tag{2}$$

Partial differentiation of formulation (1) with respect to the nodal velocity of the space mesh is expressed as

$$\frac{\partial \Phi}{\partial u_i} = 0 \quad (i = 1 \sim n)$$

$$\frac{\partial \Phi}{\partial \lambda_j} = 0 \quad (j = 1 \sim m) \tag{3}$$

where $\boldsymbol{n}$ is the number of nodes and $\boldsymbol{m}$ is the number of the space mesh which are involved in the calculation.

1.3 Boundary Condition Assignment

As shown in Fig. 2, the particle P(x,y) (yellow circle) is in contact with the tool (red line) within a space mesh (green square). To keep the particle P(x,y) moving along the surface of the tool, the boundary condition is given as follows:

$$ul_2 + vl_1 = a \tag{4}$$

where *l1* and *l2* are the cosine values of the normal vector of the tool at point P(x,y), $\boldsymbol{a}$ is a velocity of the tool in the normal direction, $\boldsymbol{u}$, $\boldsymbol{v}$ are velocities of the particle in the X,Y directions and they can be expressed as follows:

$$\begin{aligned} u &= N_1u_1 + N_2u_2 + N_3u_3 + N_4u_4 \\ v &= N_1v_1 + N_2v_2 + N_3v_3 + N_4v_4 \end{aligned} \tag{5}$$

where $\boldsymbol{N}$*1-4* are the values of interpolation function of the space mesh at point P1, $\boldsymbol{u}_{1\text{-}4}$, $\mathbf{v}$1-*4* are nodal velocities of the space mesh. By substituting formula (5) into formula (4), the boundary condition can be expressed as follows:

$$(N_1u_1 + N_2u_2 + N_3u_3 + N_4u_4)l_2 + (N_1v_1 + N_2v_2 + N_3v_3 + N_4v_4)l_l = a \tag{6}$$

The nodal velocities are calculated by minimizing the formula (1) under the boundary condition expressed in formula (6) with the nodal velocities of the space mesh.

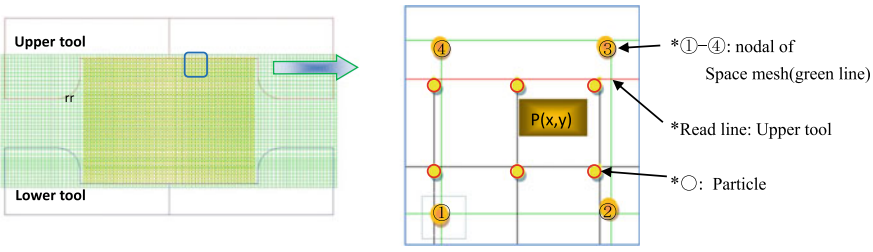


Fig. 2 Boundary condition assignment. (Color figure online)

1.4 Calculation of Workpiece

The velocity of the particle of a workpiece is calculated by interpolation from the 4-node of the space mesh in which the particle is involved.

$$\begin{aligned} u &= a_0 + a_1 x + a_2 y + a_3 xy \\ v &= b_0 + b_1 x + b_2 y + b_3 xy \end{aligned} \tag{7}$$

where ***u,v*** are velocities of particle P(x,y). Parameters ***a0-3, b0-3*** are values related to coordinate values of the particle P(x,y) and decided as follows:

$$\begin{cases} a_0 + a_1 x_1 + a_2 y_1 + a_3 x_1 y_1 = u_1 \\ a_0 + a_1 x_2 + a_2 y_2 + a_3 x_2 y_2 = u_2 \\ a_0 + a_1 x_3 + a_2 y_3 + a_3 x_3 y_3 = u_3 \\ a_0 + a_1 x_4 + a_2 y_4 + a_3 x_4 y_4 = u_4 \end{cases} \tag{8}$$

where ***u1-4,v1-4*** are nodal velocities of the space mesh.

$$[\mathrm{A}]\{\mathrm{a}\} = \{\mathrm{u}\} \tag{9}$$

where $[A] = \begin{bmatrix} 1 & x_1 & y_1 & x_1 y_1 \\ 1 & x_2 & y_2 & x_2 y_2 \\ 1 & x_3 & y_2 & x_3 y_3 \\ 1 & x_4 & y_4 & x_4 y_4 \end{bmatrix}$, $\{a\} = \begin{Bmatrix} a_0 \\ a_l \\ a_2 \\ a_3 \end{Bmatrix}$ $\{u\} = \begin{Bmatrix} u_1 \\ u_2 \\ u_3 \\ u_4 \end{Bmatrix}$

where the parameters ***a0-3*** are computed as

$$\{a\} = [A]^{-1}\{u\} \tag{10}$$

where $[\mathrm{A}]^{-1}$ is the inverse matrix of [A], which is a function of coordinate values of 4-node. So the velocity u of the particle P in the X-direction can be expressed as

$$u = a_0 + a_1 x + a_2 y + a_3 xy = \left\{ 1 \; x \; y \; xy \right\}\{a\} = \left\{ 1 \; x \; y \; xy \right\}[A]^{-1}\{u\} \tag{11}$$

The velocity v of the particle P in the Y-direction can also be expressed in the same way as

$$v = \left\{ 1 \; x \; y \; xy \right\}[A]^{-1}\{v\} \tag{12}$$

Therefore, the strain rate of particle P(x,y) can be calculated from both formulas (11) and (12).

For example, the plane-strain deformation

$$\begin{aligned}\varepsilon_x &= \frac{\partial u}{\partial x} = \{0\ 1\ 0\ y\}[A]^{-1}\{u\} \\ \varepsilon_y &= \frac{\partial v}{\partial y} = \{0\ 0\ 1\ x\}[A]^{-1}\{v\} \\ \varepsilon_x &= \frac{\partial u}{\partial y} + \frac{\partial v}{\partial x} = \{0\ 0\ 1\ x\}[A]^{-1}\{u\} + \{0\ 1\ 0\ y\}[A]^{-1}\{v\}\end{aligned} \tag{13}$$

Stress is calculated as

$$\{\sigma\} = [D]\{\dot{\varepsilon}\} \tag{14}$$

2 Calculation Result

2.1 Calculation Condition

A ring compress process calculation under different friction is carried out to verify the effectiveness of the method [2]. The results in Fig. 3 show that the method is effective even if the compress ratio is bigger than 80%. The calculated data is also used to verify the correctness of the method by comparing it with the experiment data in Fig. 3. They are bigger than the experiment ones (μ is the coefficient of friction between compress tools and ring in Fig. 3).

The property of the material used in the calculation, work condition, and simulation condition are shown in Table 1. A rotational symmetry deformation is assumed

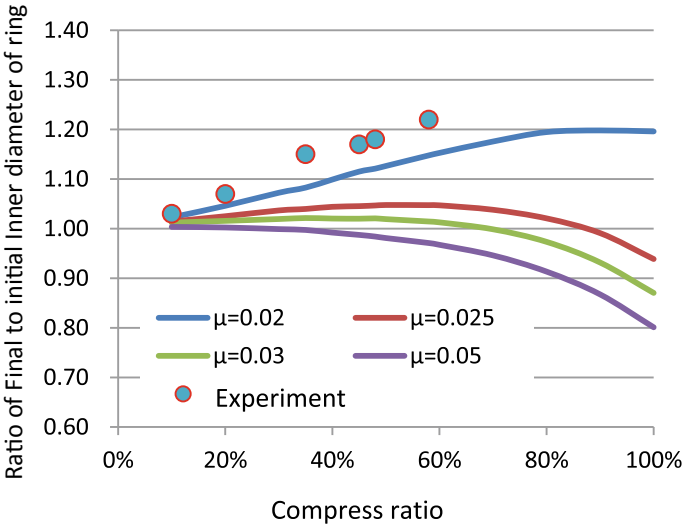


Fig. 3 Ratio of the final and initial inner diameter of a ring with different coefficient of friction (experimental data is used as the data from Reference 2). (Color figure online)

Table 1 Property of material, work condition, and simulation condition

Flow stress / Kgf/mm^2	$\bar{\sigma}23.75\bar{\varepsilon}^{0.127}$
Coefficient of friction	0.05
Stroke /mm	24
Number of space mesh	1598
Number of particle	699

in the calculation.

2.2 Calculation Result

Figure 4 shows the velocity (black arrow) of the particle calculated by interpolation from the 4-node of the space mesh (green square). The shape of the workpiece is deformed with the velocity but the space mesh is not changed.

As shown in Fig. 5, the positions of four particles of the workpiece in each different calculation step are changed greatly. In a conventional FEM, the calculation cannot

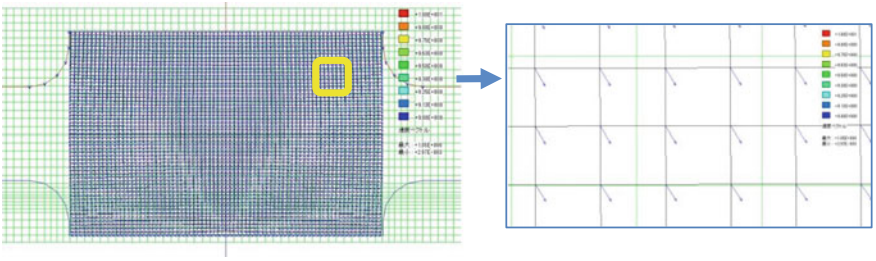


Fig. 4 The velocity of the particle calculated by the space mesh. (Color figure online)

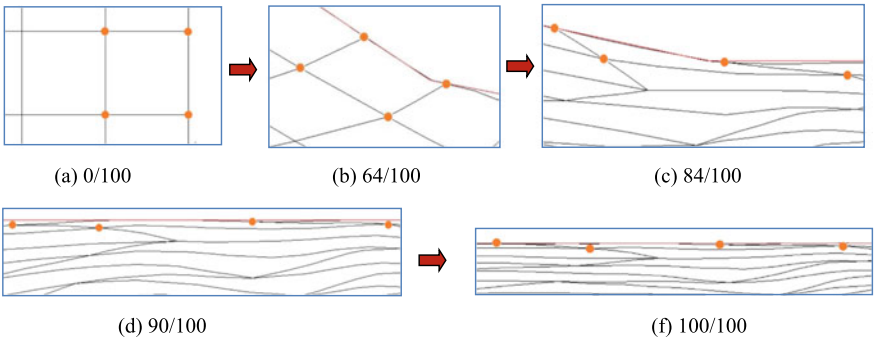


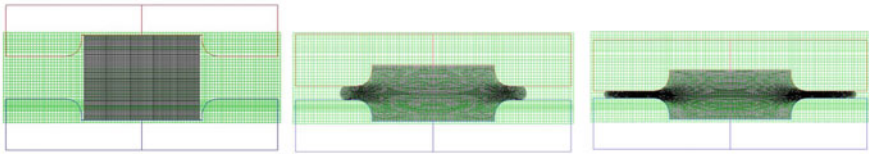
Fig. 5 Large change of positions of a particle in each step. (Color figure online)

be continued when the mesh is changed as shown in Fig. 5c, but the simulation is not terminated because of usage of space mesh.

The simulated deformed shape of the workpiece in each step is shown in Fig. 6, and the same space mesh (green square) is used in each calculation step both in shape and position.

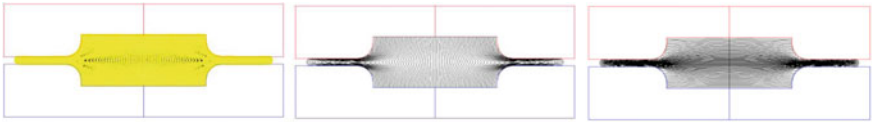
The final shapes are shown in Fig. 7 with particles linked with both vertical and horizontal lines together, respectively. The deformation performance of the material is closer to reality.

The large value of equivalent strain rate appears at cornea as shown in Fig. 8 and the deform force is changed greatly when deformation is close to the final step, as shown in Fig. 9.



(a) 0/100 (b) 80/100 (c) 100/100

Fig. 6 Calculated shape in each step. (Color figure online)



(a) Final shape with particle (b) Final shape with vertical line (c) Final shape with horizontal line

Fig. 7 Final calculated shape. (Color figure online)

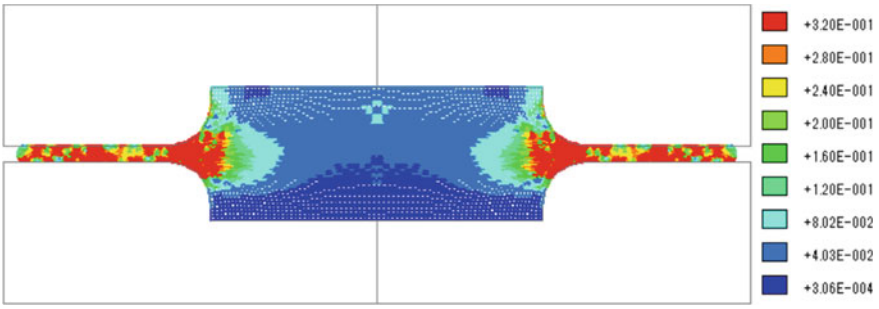


Fig. 8 Equivalent strain rate distribution at the final step. (Color figure online)

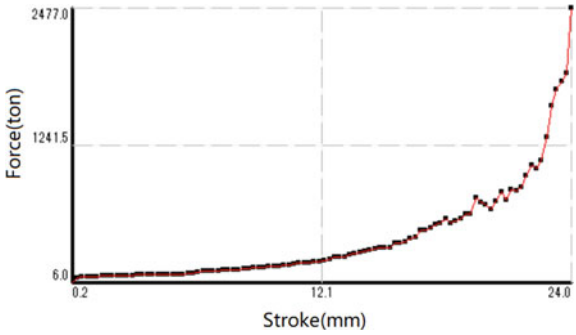


Fig. 9 Calculated deform force. (Color figure online)

3 Conclusion

The space mesh is proposed to be utilized in the FEM. The boundary condition is assigned in a new way. A large deformation simulation is carried out to verify its advantage. The method makes the finite element method more effective and powerful for the large deformation. The large deformation of the metal forming process can be calculated without termination. The performance of the material can be expressed more visibly and more clearly because the same mesh is used in the entire simulation process. By use of space mesh, the FEM becomes easier to be formulated and programmed in many fields, such as hydromechanics, heat transfer, elastic, and plastic deformation simulation.

References

1. Yang G, Mori K-I, Osakada K, Sugyo S (1993) Finite element simulation of three-roll bending of plates. J Jpn Soc Technol Plast 34–392:1034–1039
2. Oyane M (1990) Plastic forming technology, Yokendo

Comparison on the Processing of Height Deviations of Disks from FEM and Real Rollings in Radial-Axial Ring Rolling



Thomas Glaser, Patrick Schwarz, Simon Fahle, Kai Uwe Paffrath, and Bernd Kuhlenkötter

Abstract Transferring insights from simulations to an industrial application is a state-of-the-art procedure. The knowledge of how to design a manufacturing process, e.g. for Radial-Axial Ring Rolling, is mainly taken from two sources: the machine operator's experience and experiments, which are time- and cost-intensive. Therefore, creating results by using finite element method is a valuable alternative. This paper focusses on the shape deviations in the domain of Radial-Axial Ring Rolling. It is a hot forming process to produce, e.g. steel rings, used as blanks for the manufacturing of huge bearings or gear rims. Real Radial-Axial rolled disk-shaped rings will be compared to data of a FEM Simulation Software (QForm 3D) with a focus on the height deviation of the ring. Regarding disk-shaped rings, the production of a constant height is of high importance to save effort and costs of rework.

Keywords Radial-axial ring rolling · Simulation · Quality control

1 Introduction

Simulating a hot forming process like Radial-Axial Ring rolling (RARR) is used to save time and energy, which results in lower expenses [1]. Forecasting an optimized hot forming process design will reduce experimental costs and increase the efficiency [2]. In the domain of Radial-Axial Ring Rolling, the process chain consists of several steps from cutting a piece from an ingot, piercing to forming it into the desired ring-rolling pre-form. After the rolling process itself, the ring in most cases needs to be machined and heat-treated to assure the geometrical and microstructural properties.

T. Glaser (✉) · S. Fahle · B. Kuhlenkötter
Lehrstuhl Für Produktionssysteme, Ruhr-Universität Bochum, Bochum, Germany
e-mail: glaser@lps.rub.de

P. Schwarz
Lehrstuhl Für Neue Fertigungstechnologien Und Werkstoffe, Bergische Universität Wuppertal, Wuppertal, Germany

K. U. Paffrath
TKM GmbH, Remscheid, Germany

© The Minerals, Metals & Materials Society 2021

G. Daehn et al. (eds.), *Forming the Future*, The Minerals, Metals & Materials Series,
https://doi.org/10.1007/978-3-030-75381-8_245

Each of these steps can be simulated. The requirements regarding the accuracy and computational time are high, since the generated data needs to be transferred or processed in further simulations [3]. Assuming that the optimization of an existing production process takes several real world experiments, it needs many resources (staff, material, and energy) and creates lots of scrap material. The same can be said about the feasibility analysis of a new ring geometry. Finite-Element (FE) simulations are an efficient way to get insights on how to reduce the rolling time, avoid form errors or whether to consider a temperature control for specific materials like titanium. Temperature controlled simulations are state of scientific knowledge, since the need to include them into the rolling process goes back to 1997 [4, 5]. The validation of Finite Element Method (FEM) is often based on the behaviour of process parameters such as the growth of the outer diameter, the reduction in height or the axial and radial forces [6–8]. WANG et al. simulated the rolling of a titanium ring with good agreement to the experimental data by comparing the height and thickness plots and the resulting roundness of the ring. Besides that, WANG et al. optimized the initial rolling phase by adjusting the mandrel feeding rate. Thus, by increasing the mandrel feed, the velocity of the ring and the main roll could be adjusted to avoid slip in the radial gap [9].

The further step is the validation of FEM models, which will be presented in this paper. It investigates the comparison of the resulting form deviations like height deflection. The aim is the development of a versatile tool for the geometrical characterization of rings. This paper presents the steps that have been implemented in the geometric characterization tool and shows further developments. Regarding the ring geometry, the focus is set to disk-shaped rings, which due to their extreme shape have a particularly strong tendency to geometrical deviations. Disks are defined by a high wall-thickness-to-height-ratio. This extreme geometry is due to a lower stiffness in axial direction more sensitive for height deviation, which can be caused by an unfavourable distribution of the moments in the axial gap [10]. The disk-shaped rings used here have a ratio of 3:1 in the initial shape and 4:1 in the final dimension. Form deviations can be compensated by adding material. This is not wanted in the high number of industrially produced rings, since it results in higher material costs and reworking costs. The material additions are particularly critical with extreme geometries, for example, disk-shaped rings. Even if no process and thus shape defects occur in the rolling process, the added material must be machined afterwards [11]. In these issues, it can be seen that the geometric characterization of rolled rings with extreme geometries is of great importance. This paper contributes to the measurement, calculation, analysis, and visualization of form deviations. In particular, the topic of the height deviation in the domain of Radial-Axial Ring Rolling is addressed.

1.1 Radial-Axial Ring Rolling

Radial-Axial Ring Rolling has established itself as the most important production process for axial-symmetric parts due to the possibility of manufacturing near-net-shape seamless rings in a wide range of materials and geometries without tool changes and up to a diameter of 16 m [12, 13]. Those rings are used in applications like aerospace, gear manufacturing, and offshore use cases as bearing races and flanges [3, 12, 14, 15]. Other common production processes for rings are forging, casting, and welding. These have negative properties with regard to the possible dimensions, caused casting defects or unfavourable mechanical properties in the welding zone, which can have a negative effect on the fatigue [15]. The principle of the RARR process is based on a diameter growth by synchronous and continuous forming in two oppositely arranged rolling gaps, leading to a reduction of the rings' cross-section because of the variable position of the specific rolls. These two rolling gaps are the radial and axial rolling gap and describe the relevant forming direction. The height of the ring in the rolling process is defined by the position of the upper axial roll in the axial rolling gap towards the lower roll, which is fixed in horizontal position. Both axial rolls are driven. The mandrel roll in the radial gap moves towards the main roll to define the wall thickness. The main roll is driven and by the nearing movement of the mandrel towards the main roll, leading to a compression, the ring rotates. The course of the radial and axial feed rate describes the rolling process. Due to the instability of RARR, deviations from the target process design can occur during forming. This leads to process and form errors, which disturb the forming process and in most cases have a negative effect on quality. The form errors are to be measured and evaluated afterwards using suitable measuring and analysis methods. Another approach is the use of data driven technologies to control or increase quality in the Ring Rolling domain. Appropriate research is done by FAHLE et al. where machine learning in form of time series classification is used to predict the quality of rolled rings [16]. In addition to that innovative method, FAHLE et al. compared different pre-processing methods, resulting in a domain specific approach to use an individual scaling of the log data [17].

1.2 Process and Form Errors in Radial-Axial Ring Rolling

Material additions are used to compensate for example the height deviation, as described in the previous chapter. This stands in contrast to the idea of a near-net-shape process, with which the material is already close to the final geometry. These material surcharges cost companies a lot of effort and money, because in addition to the additional material input during Ring Rolling, there is also additional work in the subtractive post-treatment. This becomes necessary if errors occur during the process. The ring can, for example, move in its height direction or sideways during the process. This instability combined with heavy material weight, high process

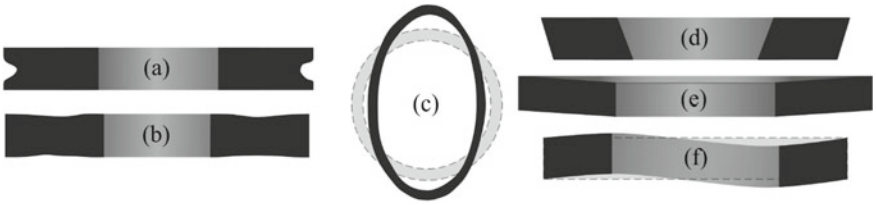


Fig. 1 Form errors in Radial-Axial Ring Rolling. **a** Radial-, **b** axial-cavity, **c** non-circularity, **d** conicity, **e** dishing, and **f** height deviation

forces, and forming speeds leads to inconsistencies in the process sequence, which can result in process and form errors. These errors must be compensated or reduced to ensure a high quality ring and an increased repeatability of the process. By adjusting the rolling process, the system can react immediately when an error occurs. With a suitable adapted rolling strategy, for example, slowing down the roll speeds for a defined period, the process and thus shape errors can be counteracted. Another strategy is to change the axial trim as a reaction or as a standard value from the beginning of the process. The axial trim describes the ratio of the angular speeds of the two axial rolls to each other and can be used to provide a force into the ring that is directed to the rolling table, which leads to a stabilized process. The alternative is a ring that has to be machined afterwards—or is unusable for further processing due to too high deviations. Either way, not counteracting process errors increase the costs of ring production drastically. Six different resulting form errors are described in Ring Rolling related literature. The degree of defects depend, for example, on the geometry of the blank, force and torque ratios and the rolling process itself [10–12]. The focus of the analysis in this paper is on the height deviation of a ring, which is defined as the periodic curvature of the upper and lower face side of a ring. The six form errors are shown in Fig. 1a–f.

1.3 Simulation

FEM software is based on the solution of continuous functions (physical and thermal problems) by the approximation using simpler functions. In the three-dimensional FEM application of Radial-Axial Ring Rolling presented here, the volumes of the tools and the workpiece are divided into smaller elements, which are contacted in the so-called finite element nodes. In forming processes, the rate of deformation of these individual smaller volumes is of high interest. For this purpose, systems of equations are set up based on the FEM model, which are then solved. The solution and thus the forming properties depend strongly on the selected material, the temperature, as well as the boundary conditions. There are several advantages of using simulation methods to design a production process or the process chain from a blank to the final ring. The number of time-consuming and material-intensive test rollings can be reduced

significantly or an optimized rolling strategy can be tested in simulation. Besides simulation, the field of data analysis is growing—also in the domain of hot forming. One advantage of data analysis is the improvement of the Ring Rolling process and to specifically reduce form errors by simulating the rolling. Allegri et al. [18] set up an FEM environment using Deform 3D FEM and initially simulated a standard configuration ring with a constant main roll angular velocity, which leads to a decrease in the ring's angular velocity over time. The approach is to optimize the height and width dispersion, as well as the fishtail defect, by achieving a constant angular velocity of the ring through adapting the main roll's angular velocity over time. The evaluation of the resulting geometry shows the positive influence in comparison to the standard configuration [18]. Another simulation approach to enhance the quality by Giorleo et al. [19] leads to two regression models regarding the rolling ratio (relation between the idle roll feed and the main roll angular velocity) and the idle roll feed.

2 Experimental Setup

The presentation of the experimental part consists of two components. Firstly, real rings are rolled on a Radial-Axial Ring Rolling mill and secondly, the rolling of these rings is simulated in the QForm (QForm Cloud 9.0.9.0) software. The rings of real and simulated rollings are afterwards characterized with respect to their geometry with focus on the height deviation. For this purpose, a coordinate measurement machine (CMM) is used for the real rings, whereas the required measurement data for the simulated rings is drawn directly from the software. The focus of the paper is to present the capabilities of a novel software solution that calculates and clearly visualizes the geometric deviations.

For this study, the Radial-Axial Ring Rolling mill type RAW 20/16-1000/160 from Thyssen Maschinenbau GmbH Wagner Dortmund at the Chair of Production Systems of the Ruhr-University Bochum is used. The mill is capable of rolling rings with dimensions of 200–1000 mm in outer diameter, height between 30 and 160 mm, and wall thickness from 10 to 250 mm. The maximum weight of a ring is 50 kg. Radial forces of 200 kN and axial forces of 160 kN are possible. The used main roll has a diameter of 450 mm and the mandrel roll has a diameter of 130 mm. The rolling force cylinders are modernized to electrohydraulic systems that provide a high precision for the position of the mandrel roll, axial, and centering rolls.

The blanks used for the experiments are made of S355 structural steel with an outer diameter of 380 mm, an inner diameter of 140 mm, a resulting wall thickness of 120 mm, and an initial height of 40 mm. The target height after rolling is 30 mm, while the wall thickness is held constant during the rolling. The final geometry has a wall-thickness-to-height-ratio of 4:1 and is, therefore, declared as a disk-shaped ring. The identification of the real rollings is composed of the prefix Ring_ (for example Ring_2). The rollings differ only in the axial trim, which is varied between 96% (Ring_1, Ring_2, and Ring_3), 100% (Ring_4, Ring_5), and 90% (Ring_6). This is intended to produce a variance in the measurement results to prove the detection

of different height deviations. In each case, the experiments were not repeated, as the focus of this paper is to investigate the capability of the presented tool. Thus, the absolute values and their possible influences are not discussed in the results. A further paper on such an influence analysis is being planned.

With regard to simulation, the FEM Software QForm is used. It offers a high-resolution and fast simulation environment and works with the dual mesh method. The equations of plastic flow are calculated using the computational mesh. In the geometric mesh, the thermo-mechanical fields and the geometry are stored. In the used QForm ring-rolling module, a defined two-dimensional square-shaped equidistant grid is applied to the top and bottom of the ring before simulation. The number of points per side length is user-defined and the grid is placed over the ring. Those points which do not hit the ring surface are ignored for further evaluation. This grid is attached to the nodes of the ring mesh and is carried along accordingly in the simulation/rolling process. The identification of the simulations contains of the prefix Sim_. The plots shown in the result chapters show the pairs of real and simulated rollings. The radial and axial feeds from the real rollings were used for the simulation, so that, for example, simulation Sim_2 uses the input data of the real rolling Ring_2.

To obtain the geometrical data of real rolled rings, a ZEISS Coordinate Measuring Machine in portal design was used. The CALYPSO software of the ZEISS CMM is used to enable the measurement of circular paths on predefined surfaces. In order to prevent the measurements from being influenced by a change in the position of the test specimen, the component is fixed to the test field of the CMM by means of an angle construction so that both end faces of the ring are freely accessible. However, the exact position and orientation of the measurement object is not defined beforehand. To define a circular path, one side of the ring is initially scanned with three points in the first step. The detection of the end faces is done with a T-shaped probe, so that a measurement of both end faces is possible without changing the probe or the position of the ring. This makes it possible to not only measure one face of the ring and calculate the height deviation, but calculate the height of the ring with the same data. The resolution of the measured surface depends on the number and distribution of the measuring points. For this purpose, the theoretical center of the ring is determined by probing the inner diameter with three points. Furthermore, the surface to be measured is defined by probing three points. From the combination of these characteristic values the plane coordinates are determined, on which the circular paths are automatically traced. In the shown case, diameters of 240, 290, 340, 390, and 440 mm as well as 12, 20, 33, 45, and 60 points are used for the measurement. To maintain a constant resolution of the measuring points and a suitable reproduction of the real rings' geometry, the number of measuring points increases the further they are located on the outer diameter.

3 Geometry Characterization Tool

Before the results of the rolling and simulation are presented, the geometry characterization tool is introduced in this chapter. The tool is written in python and uses freely available libraries for calculation and visualization of the data. It is used after a rolling or after a simulation. The point clouds of the geometry resulting from (a) the measurement of the ring or (b) the exported simulation data are processed by the tool. After the processing of the data, a comparison with other rings is then possible, since random influences such as the position of the ring on the measuring table no longer affect the measurement result. The following schematic drawing (Fig. 2) illustrates the point of application of the geometry characterization tool. The input raw data is transformed into the so-called processed data by using the method of least squares or calculations within the covariance matrix.

In the case shown here, the measurement data is available in two varieties: (a) Measuring at the CMM: tangential arranged point clouds for each side of the ring and (b) data from QForm: one measurement file per ring, which is separated into the two surfaces by an additional script. In both cases, the data points are available as x, y, and z coordinates line by line. The measured coordinates of the ring faces are available as point clouds, which are positioned and oriented in space depending on the global CMM or simulation coordinates. Regarding the CMM, in addition to the coordinates of the ring, the measurement data also includes the normalized directions of the force acting on the probe. The measured coordinates correspond to the center of the probe element or the displayed touch point of the probe. For the calculation of the adjusted touch point, an adjustment vector is necessary, which is formed with the help of the normalized force direction and the radius of the used probe elements. The analysis of the unprocessed data would lead to a distorted, wrong result. In this case, processing the data does not lead to an intentional improvement of the measurement result, but only to an evaluable positioning of the ring. To achieve this, the point clouds needs to be rotated and moved. Therefore, a regression plane is needed as a reference for the calculation of the form errors in order to determine the axial positions of the measuring points. The method of calculating the regression plane is crucial for the quality of the results, since the calculation of the key parameter is based on it. The regression plane is a flat plane that is positioned between the two faces of the ring.

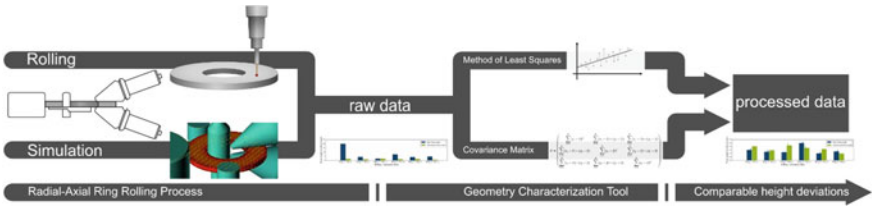


Fig. 2 Sequence of the origin of the raw data via the preparation by the geometry characterization tool to processed data. The graphs illustrate the adjustment of different rollings and simulations. (Color figure online)

For the qualitative evaluation of the axial profile of the rings, a regression plane is calculated where the distances of the measured data to the regression plane are minimal. The covariance matrix and the method of least squares are used in this case so evaluate the regression plane. The methods of vector and matrix calculation enable to move or rotate the measuring points and determine positional relationships. The regression plane can be calculated in the tool by two approaches. First, with the help of the eigenvectors and eigenvalues of the covariance matrix of the point clouds. For this purpose, the covariance matrix is set up and the eigenvalues and eigenvectors are extracted by calculating the roots of the characteristic polynomial. The normalized eigenvector of the smallest eigenvalue corresponds to the surface normal. The second approach is the least squares method. The resulting system of equations is solved using the Gaussian elimination method. After calculating the regression plane, the height deviation is calculated. The method first determines the distance to the regression plane for each data point of both data sets (both sides) using the implemented vector functions. In the following, the minimum and maximum values of the distances of the two data sets are identified. The minimum and maximum values are used to calculate the height deviation of the two sides of the ring. The result of the visualized geometry of the top and bottom side of a ring (simulation Sim_2) is given in Fig. 3.

The following plot in Fig. 4 shows the distance to the regression plane over the angle around the z-axis. An ideal ring would be constant over the whole angle range. From the colour code, the distance of each point to the calculated centre can be read. In this example, the top side of the simulated ring of Sim_2 shows a periodic height deviation, which increases in the direction of the outer diameter. In the first angular range up to about 180°, an increasing height deviation close to the outer diameter of the ring is noticed. This top side of the ring shown here has a calculated height deviation of 1.424 mm, which can be directly read from the plot.

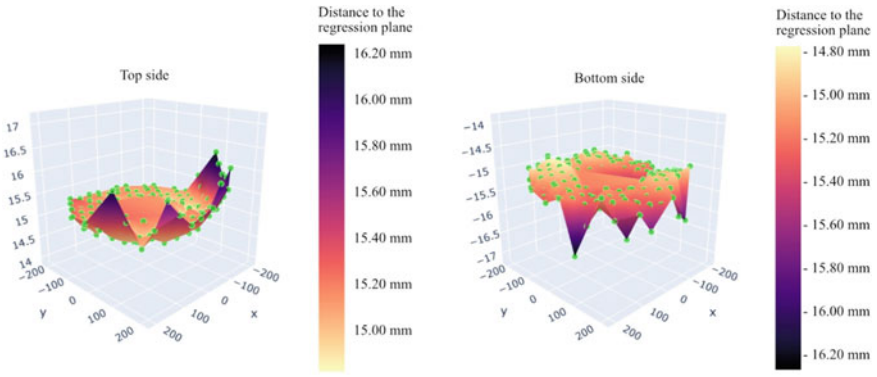


Fig. 3 3D-visualization of the processed upper and lower side of a simulated ring after the rolling (Sim_2). The raw data has been rotated and shifted be the tool. The center of the ring lays on the coordinate origin in the x-y-area. (Color figure online)

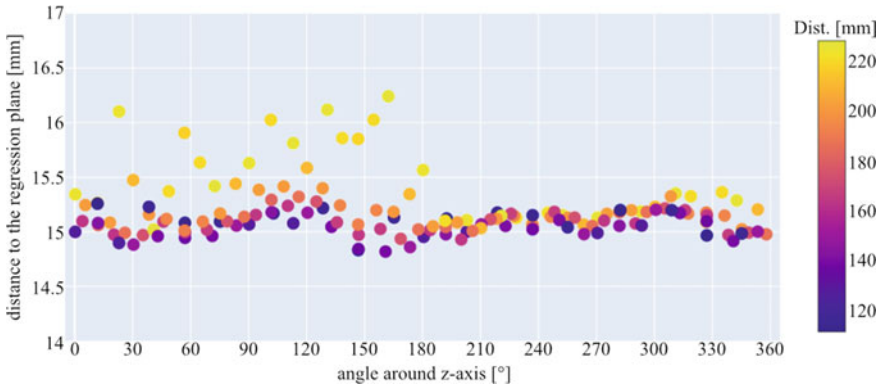


Fig. 4 Example plot of the distance to the regression plane over the angle around the z-axis. (Color figure online)

With the output of these plots, it is quickly possible to classify the ring with respect to the height deviation. Furthermore the calculated values are output. This allows an efficient classification by automated reading and processing of the data.

4 Results

The tool for geometric characterization is the basic component for the evaluation of form deviations, and therefore, important for further research within this subject area. In order to demonstrate the usability of the tool, rolling, and simulations are carried out. The results are shown in pairs, for example, Ring_1 and Sim_1. This is due to the fact that Sim_1 is the simulative reproduction of the rolling Ring_1 and is, therefore, used for direct comparison. Each bar in the following plots represents the mean height deviation of both sides of the referred ring. Within each bar there are two more bars that represent the individual values of the top (left bar) and bottom (right bar) side, giving insights to the deviation between the sides. For further comparison, the mean height deviation will be used in this paper. Raw data in this context means the three-dimensional measurement values from the CMM or simulation that have not been rotated or shifted. Processed as a key word shows the data that went through the calculation of the tool that has been developed and presented in Chap. 3. In the specific coordinate direction, which is orthogonal to the surfaces of the ring, the height deviation can be described as the difference of the minimum and maximum value within this coordinate direction. The comparison of both raw data sets shows the inequality of the data, depending on whether the measurements are from real rings or simulation.

Figure 5 shows that the mean height deviation of the simulation data is rather constant with a mean value of 1.80 mm and a standard deviation of 0.384 mm. The

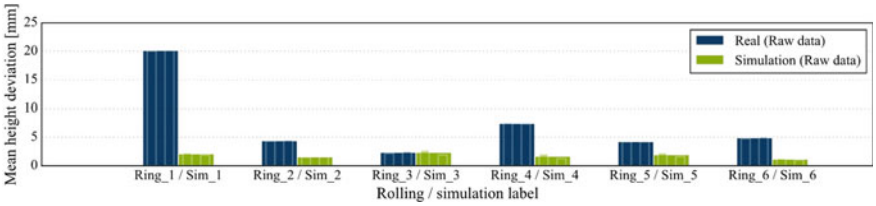


Fig. 5 Mean height deviation of the raw data of real and simulated rollings. Each bar shows the individual values of the top (left bar) and bottom (right bar) side. (Color figure online)

analysis of the time-dependent height deviation is currently researched by the author. Regarding the CMM, an average value of 7.250 mm with a high standard deviation of 5.953 mm is obtained. This is due to the fact, that the rings are positioned and aligned manually on the measuring table which is not possible in any repeatable state. The raw data shows this clearly. The raw data of Ring_1 in particular is about 20 mm and shows, that the ring was tilted strongly on the measuring table. That deviates strongly from the other measurements and, after a first macroscopic examination, does not agree with reality. To avoid this case and to obtain correct, generally valid values, the tool developed here is necessary. Note that the values shown in Fig. 5 do not indicate whether the height deviation is actually high or low. This is only possible after processing by the tool (see Fig. 7).

It can be clearly seen in Fig. 6 that due to the uneven positioning of the rings on the CMM, the height deviation calculated from the raw data varies significantly. This figure shows only the measurements (raw and processed) of the real rollings. Mean values between 2.347 and 20.133 mm are obtained in this way. After processing the data with the presented tool, the height deviation of the processed data differs considerably from the raw data with a factor up to 10. This shows the strongly varying raw measurement results and the capability of the tool.

In the following Fig. 7, the comparison of the processed height deviation of the real and simulated data is shown. For absolute height deviations in the range of 1 to 2.5 mm, the deviations between reality and simulation must be considered strongly. The average deviation is about 0.5 mm. In four of the six data sets the height deviations of the simulation are higher than in the measured reality. This is to be considered positively, as it gives a pessimistic representation of the experiments carried

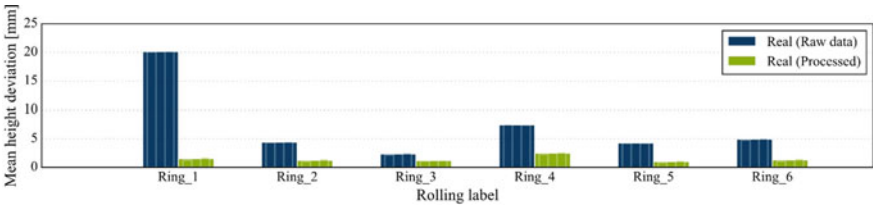


Fig. 6 Raw and processed by the tool data from real ring-rolled rings. Each bar shows the individual values of the top (left bar) and bottom (right bar) side. (Color figure online)

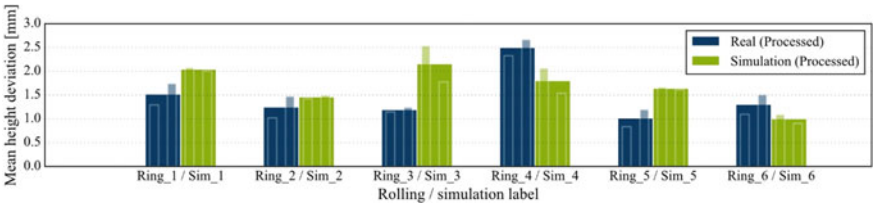


Fig. 7 Mean height deviation of the processed real and simulated rings data. Each bar shows the individual values of the top (left bar) and bottom (right bar) side. (Color figure online)

out. It should be noted here that the height deviations shown in Fig. 7 correspond to the values optimally aligned to the respective regression plane and thus allow comparability.

5 Conclusion

The geometrical characterization of real rolled disk-shaped rings, as well as rings simulated by QForm 3D FEM, are successfully performed with the tool presented in this paper. It is shown that the developed tool is useful for the evaluation of geometric data regarding height deviations. After the pre-processing of the point clouds, vector calculations and mathematical methods (least squares, least variance) are applied to calculate the necessary rotation and displacement of the point clouds. The evaluation of the height deviation considered here is carried out afterwards and aims at the output of the characteristic values as well as visualizations. It is shown that the calculated height deviation scatters strongly without post-processing through the tool. By using the tool and the resulting reorientation of the data points, they are adapted to reality and made comparable. Thus, a clear and constant statement about the quality regarding the height deviation is possible. For further work in the research project, the rolling and simulation of disk-shaped rings will be of high interest. Since the extremely disk-shaped geometries that will be investigated have a strong tendency to height deviation, the tool will be used extensively, also regarding the validation of the simulations.

Further investigations will deal with the robustness of the simulation software itself as well as the stability of the Ring Rolling process in relation to the resulting height deviation. Research specifically related to simulation is currently being carried out. It is of interest here to what extent the results vary when the identical input data is run through several times. The results of the software differ with identical input parameters due to the parallelization and resulting different processing time of the computing operations. A further point is the calculation of the height deviations and other geometric criteria such as roundness over the entire process. For this purpose, the corresponding data can be exported and analyzed at each time step of the simulation (usually about 10–50 ms). The information obtained from this allows

critical points to be defined, which can then be further investigated with regard to possible influencing factors for the occurring form deviation. The corresponding implementation is currently part of the research and is developed by the author.

Acknowledgments This project is funded by European Regional Development Fund (ERDF)/Europäischer Fonds für regionale Entwicklung (EFRE), EFRE-0801521.

References

1. Wang ZW, Zeng SQ, Yang XH et al (2007) The key technology and realization of virtual ring rolling. J Mater Process Technol 182(1–3):374–381
2. Suranuntchai S (2020) Finite element simulation of the yoke spline under hot forging process. Mater Sci Forum 982:106–111
3. Afazov SM, Becker AA, Hyde TH (2012) Development of a finite element data exchange system for chain simulation of manufacturing processes. Adv Eng Softw 47(1):104–113
4. Kluge A (1997) Ringwalzen von Titanlegierungen. Dissertation, RWTH Aachen
5. Liang L, Guo L, Wang Y et al (2019) Towards an intelligent FE simulation for real-time temperature-controlled radial-axial ring rolling process. J Manuf Process 48:1–11
6. Puller S (2003) Simulation des Werkstoffflusses beim Ringwalzen mittels elementarer Plastizitätstheorie. Dissertation, Universität Hannover
7. Xu W, Wang Q, Zhou X et al (2014) Quantitative design methodology for flat ring rolling process. Proc Eng 81:280–285
8. Zhu S, Yang H, Guo L et al (2014) Research on the effects of coordinate deformation on radial-axial ring rolling process by FE simulation based on in-process control. Int J Adv Manuf Technol 72(1–4):57–68
9. Wang ZW, Fan JP, Hu DP et al (2010) Complete modeling and parameter optimization for virtual ring rolling. Int J Mech Sci 52(10):1325–1333
10. Lieb A (1992) Minimierung von Formfehlern beim Ringwalzen. Dissertation
11. Koppers U (1987) Geometrie, Kinematik und Statik beim Walzen von Ringen mit Rechteckquerschnitten. Verlag Stahleisen mbH, Düsseldorf
12. Allwood JM, Tekkaya AE, Stanistreet TF (2005) The development of ring rolling technology. Steel Res Int 76(2/3):111–120
13. Windt K, Lidzba J, Haverkamp M et al. (2019) Herausforderungen und Lösungen der digitalen Transformation im Walzwerk: am Beispiel der virtuellen Inbetriebnahme einer Ringwalzanlage. In: 33. ASK Umformtechnik 2019, pp 7–17
14. Hoffmann H, Spur G, Neugebauer R (2012) Handbuch Umformen. Carl Hanser Fachbuchverlag, s.l.
15. Hua L, Deng J (2017) Recent development of ring rolling theory and technique. Int J Mater Prod Technol 54(1/2/3):65–87
16. Fahle S, Kuhlenkötter B (2020) A framework for data integration and analysis in radial-axial ring rolling. In: CPSL 2020 Proceedings
17. Fahle S, Kneißler A, Glaser T et al. (2021) Research on preprocessing methods for time series classification using machine learning models in the domain of radial-axial ring rolling. In: Behrens B-A, Brosius A, Hintze W et al. (eds) Production at the leading edge of technology, vol 141, pp 487–496. Springer, Berlin
18. Allegri G, Giorleo L, Ceretti E et al (2017) Driver roll speed influence in ring rolling process. Proc Eng 207:1230–1235
19. Giorleo L, Ceretti E, Giardini C (2012) Investigation of the fishtail defect in ring rolling by a FEM approach

PID Controller Integrated with FEM Model to Generate Boundary Conditions for Free Tube Bulging for Tubular Material Characterization



Sobhan Alah Nazari Tiji, Taejoon Park, Hyunki Kim, Amir Asgharzadeh, Madhura Athale, Ji Hoon Kim, and Farhang Pourboghrat

Abstract A PID controller was implemented in FEM platform as a user subroutine instead of a sophisticated and expensive control system implemented in a tube hydroforming machine to numerically generate the required boundary conditions, axial feed, and pressure profiles, based on proportional strain path at the pole of the bulging tube in the FEM simulations. The generated boundary conditions can directly be used in free tube bulging experiments to generate different deformation modes for tubular material characterization based on accumulated plastic work equivalency. It was also shown that the numerical algorithm developed works accurately for isotropic and anisotropic yield functions. In this study von-Mises and Hill's 1948 were used as the material models.

Keywords PID control · FEM · Tubular materials · Characterization

1 Introduction

A few studies have been performed on tubular material characterization [1, 2, 3, 4, 5]. In all these studies, free tube bulging as a process by which biaxial deformation modes can be generated to characterize tubular structures were employed. In most of these studies, a tube hydroforming machine equipped with a sophisticated feedback control system, which is expensive to implement, was used to generate the axial feed and pressure profiles based on stress proportionality at the pole of the tube to characterize the yield surface of the material. For instance, in the study performed by Kuwabara

S. A. N. Tiji · T. Park · H. Kim · A. Asgharzadeh · F. Pourboghrat (✉)
Department of Integrated Systems Engineering, The Ohio State University, 210 Baker Systems, 1971 Neil Avenue, Columbus, OH 43210, USA
e-mail: pourboghrat.2@osu.edu

M. Athale · F. Pourboghrat
Department of Mechanical and Aerospace Engineering, The Ohio State University, 201 W19th Ave, Columbus, OH 43210, USA

J. H. Kim
School of Mechanical Engineering, Pusan National University, 2 Busandaehak-ro 63beon-gil, Geumjeong-gu, Busan 46241, Republic of Korea

© The Minerals, Metals & Materials Society 2021

G. Daehn et al. (eds.), *Forming the Future*, The Minerals, Metals & Materials Series,
https://doi.org/10.1007/978-3-030-75381-8_246

et al. [2], different deformation modes were experimentally generated by controlling the ratio of the true principal stresses by employing a closed-loop, electrical feedback circuit in order to generate the yield surface for extruded 5000 series aluminum alloy tubes. They then used these experimental data to calibrate different yield functions to capture the tubular material's anisotropy. Korkolis and Kyriakides [3, 6] also studied the inflation and burst of anisotropic aluminum tubes during the hydroforming process. They pressurized the tubes under volume control and the axial actuator was run under load control. The generated engineering principal stresses were then controlled through a feedback control system to create linear stress paths. However, stress or strain proportionality is not a necessity when it comes to characterization of the yield surface of the material based on accumulated plastic work equivalency [7].

At the same time, the boundary conditions, axial feed, and pressure profiles, in free tube bulging cannot be randomly generated for the sake of tubular material characterization. But, as long as we can generate a range of biaxial deformation modes with appropriate axial feed and pressure profiles, we will still be able to characterize tubular materials no matter if the generated stress/strain paths will be linear or not.

This study presents the development of a PID controller integrated with a FEM model to numerically generate the required axial feed and pressure profiles for free tube bulging process based on proportional strain path control at the pole of the bulging tube. In order to show that this developed algorithm works accurately for different assumed yield functions in the FEM, two very simple yield functions such as; von-Mises and Hill's 1948 were used in this study. The generated boundary conditions can be later used for free tube bulging experiments for tubular material characterization.

2 Experiments

In order to calibrate the yield functions to be used in the FEM model, uniaxial tensile test and electron backscatter diffraction (EBSD) tests were performed on the AA6061-O tubular material. The uniaxial test data will be enough for the calibration of von-Mises yield function. However, to calibrate the anisotropy coefficients of Hill's 1948, other biaxial and uniaxial tests data are required. Because of the geometrical constrains of the tubular materials it is difficult to acquire these data. Therefore, these results are obtained through crystal plasticity simulations in this study.

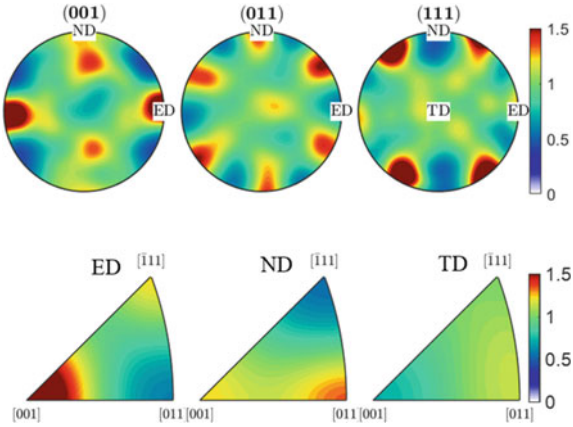


Fig. 1 Pole figure and inverse pole figures of the extruded AA6061-O tube. (Color figure online)

2.1 AA6061-O Tubular Material Characterization

2.1.1 Microstructure Characterization

To characterize the microstructure of the tube, EBSD imaging was performed on two different cross-sections, i.e., axial and hoop of the tube. Figure 1 shows the pole figure and inverse pole figure of the AA6061-O tube microstructure.

2.1.2 Mechanical Characterization

For the mechanical characterization of the tube, uniaxial tensile tests were performed on the specimens cut out of AA6061-O tubular samples along the axial (extrusion) direction based on ASTM E8 standard for uniaxial tensile tests.

The evolution of strain during the uniaxial tensile tests was measured using a Digital Image Correlation (DIC) system.

3 Material Model

3.1 Material Model

A rate-independent [8], dislocation density based hardening crystal plasticity model [9] was used to predict the anisotropy values for Hill's 1948 anisotropy calibration. To calibrate the rate-independent crystal plasticity model, the measured uniaxial stress–strain curve (Fig. 2) along the axial direction, and the measured texture of the tube from the EBSD images (Fig. 1) were used. Detailed explanation of the crystal plasticity model can be found in [8, 9].

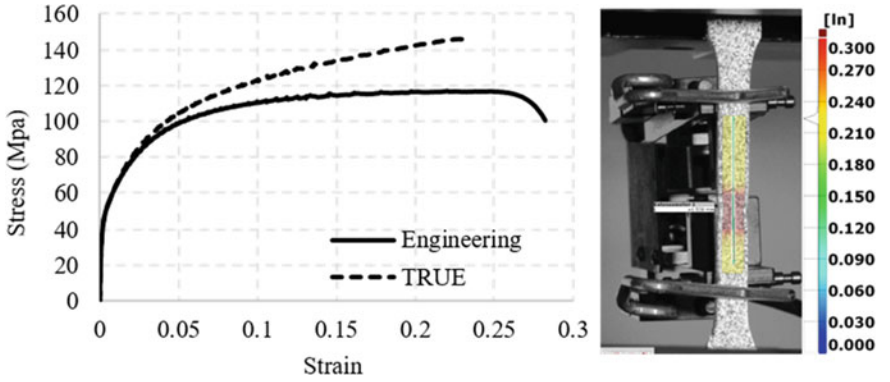


Fig. 2 The stress–strain curve along the axial direction (ED) measured from the uniaxial tensile test utilizing DIC. (Color figure online)

Uniaxial tensile tests for various tensile directions were simulated based on the calibrated crystal plasticity model. Also, the shape of the initial yield surface was predicted as shown in Fig. 3.

Among the crystal plasticity simulation results, the initial yield stress values ofσ_{45},σ_{90}, and σ_{bb}, were utilized to calibrate the Hill's 1948 yield function for AA6061-O tube.

Under the plane stress condition, Hill's 1948 quadratic yield function [10] becomes

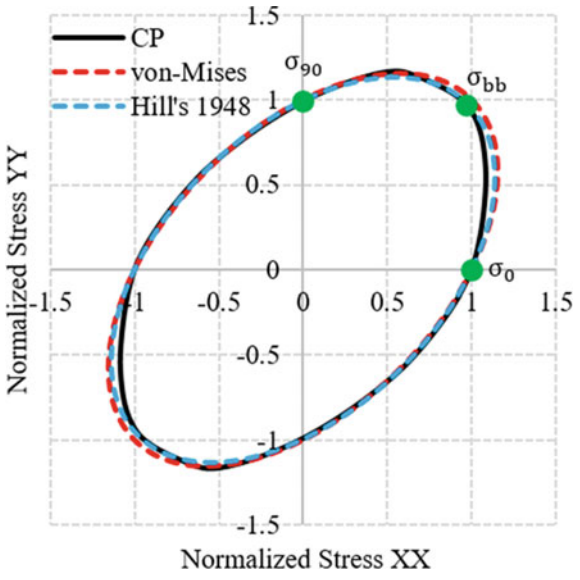


Fig. 3 Calibrated von-Mises and Hill's 1948 yield surfaces based on the uniaxial tensile yield strength and crystal plasticity simulations results, respectively. (Color figure online)

$$f^2 = (G+H)\sigma_{xx}^2 + (H+F)\sigma_{yy}^2 - 2H\sigma_{xx}\sigma_{yy} + 2N\sigma_{xy}^2 = \bar{\sigma}^2 \quad (1)$$

where $\tilde{\sigma}$ is the effective stress, F, G, H, and N are anisotropic coefficients that can be calculated using Eq. (2) [11].

$$\begin{aligned} 2F &= \left(\frac{\sigma_0}{\sigma_{90}}\right)^2 - 1 + \left(\frac{\sigma_0}{\sigma_{bb}}\right)^2;\ 2G = 1 - \left(\frac{\sigma_0}{\sigma_{90}}\right)^2 + \left(\frac{\sigma_0}{\sigma_{bb}}\right)^2 \\ 2H &= 1 + \left(\frac{\sigma_0}{\sigma_{90}}\right)^2 - \left(\frac{\sigma_0}{\sigma_{bb}}\right)^2;\ 2N = \left(\frac{2\sigma_0}{\sigma_{45}}\right)^2 - \left(\frac{\sigma_0}{\sigma_{bb}}\right)^2 \end{aligned} \quad (2)$$

Figure 3 compares the initial yield surface of the tube for the crystal plasticity (CP) model, von-Mises yield function, and Hill's 1948 yield function. It should be noted that all stresses are normalized using the σ_0 value.

4 Finite Element Modeling of Tube Bulging Process

The ABAQUS implicit code was used for the FEM simulations of tube bulging. The FEA simulations of tube bulging were performed with the calibrated von-Mises and Hill's 1948 yield functions and the PID controller to maintain a proportional strain path at the mid-section (pole) of the tube. The outputs from the FEA simulations with these two yield functions were two different sets of axial feed and pressure profiles necessary to maintain the desired proportional strain path. In FEA simulations, the AA6061-O tube was considered to be 75 mm long, 1.651 mm thick, and with an outer diameter of 38.1 mm. Figure 4 shows the boundary conditions applied on the

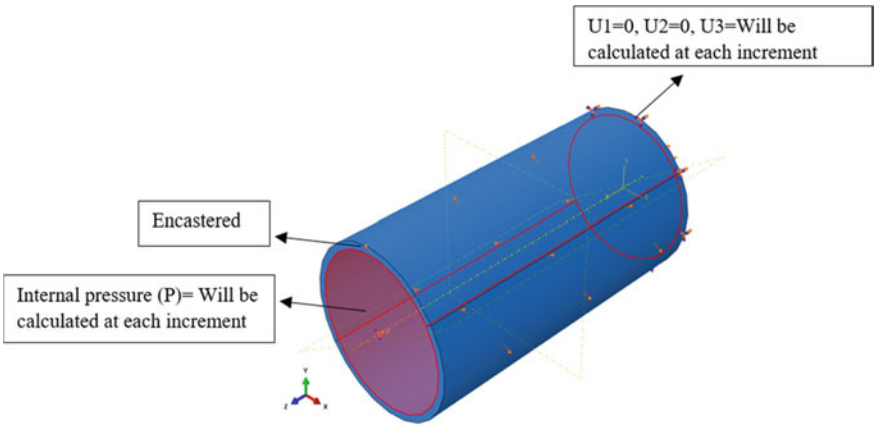


Fig. 4 Applied boundary conditions in FEM. (Color figure online)

tube. The 8-node linear brick element with reduced integration (C3D8R) was used for the tube with a size of 0.7 mm, and three elements were considered through the thickness.

5 PID Algorithm for Boundary Condition Generation for Free Tube Bulging Process Based on Proportional Strain Path Control

Figure 5 shows the flow chart for the PID controller algorithm to generate the axial feed and pressure profiles for free tube bulging based on maintaining a desired strain path during the finite element analysis of tube bulging.

The inputs to the PID algorithm are the desired strain path, β^*, plastic hoop strain rate, $\dot{\varepsilon}^{p^*}_{hoop}$, and the initial internal pressure rate, $\dot{P}_{initial}$. The program starts with the initial internal pressure rate applied as boundary condition in the UAMP user subroutine. Then the first increment of the tube bulging increment will be simulated by ABAQUS implicit code. After that, the principal total and plastic strains along axial (ε_{axial}, ε^p_{axial}) and hoop (ε_{hoop}, ε^p_{hoop}) directions, on the pole element of the tube will be read in UVARM user subroutine and the strain path will be calculated, and afterward, the internal pressure and axial feed are calculated based on the desired strain path, β^*, in the UAMP user subroutine and applied as boundary conditions for the next deformation increment in FEM model in ABAQUS. Tables 1 and 2 show the pressure and axial feed adjustment algorithms.

It is important to mention that the approach taken to calculate the axial feed in the elastic region helps with having a smooth transition from elastic to plastic region in the numerical simulations. This also helps with the PID algorithm to quickly adjust and stabilize the axial feed to obtain the desired strain path during the plastic deformation. In contrast, when elastic strains are ignored and the axial feed is only calculated from when the material goes into the plastic deformation, numerical instability occurs when the PID controller starts to adjust the axial feed.

6 Results and Discussion

FEA simulations were performed for five different strain paths, $\beta = -0.5$ (uniaxial tension), $\beta = -0.2$, $\beta = 0.0$ (plane strain tension), $\beta = 0.5$, and $\beta = 1.0$ (balanced biaxial strain tension), covering a full range of in-plane tensile deformation modes. It must be mentioned that all stresses and strains were recorded for the element at the pole of the tube. The initial internal pressure rate and the plastic hoop strain rate were 0.1 MPa/s, and 0.005/s, respectively. The simulations were performed using both calibrated von-Mises and Hill's 1948 yield functions for all the cases.

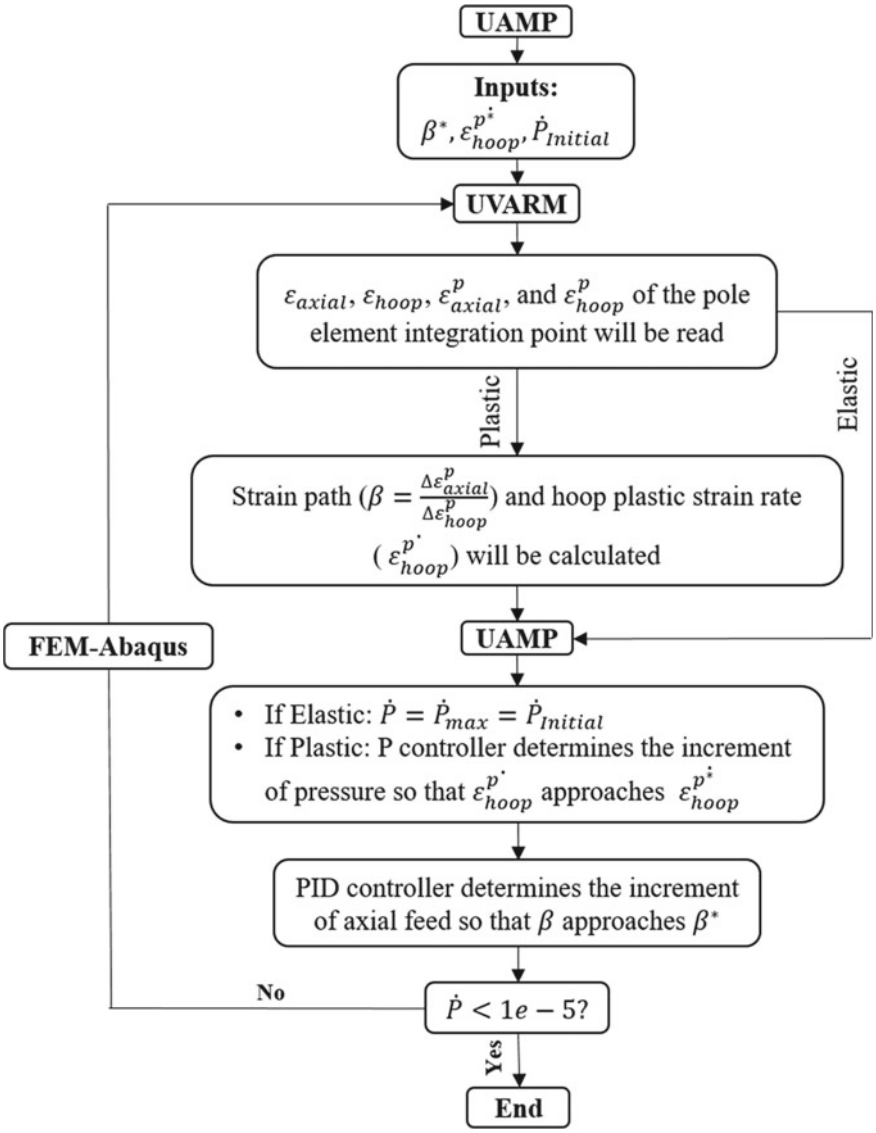


Fig. 5 PID controller algorithm for strain path control in free tube bulging process

Figure 6 shows the five strain paths produced by the PID controller program for von-Mises and Hill's 1948 yield functions. All the strain paths for both yield functions are very well controlled throughout the free tube bulging process.

Figures 7 and 8 also show the boundary conditions generated for three different strain paths generated by von-Mises and Hill's 1948 yield functions.

Table 1 Pressure adjustment algorithm

if $\left(\varepsilon_{hoop}^{p} = 0\right)$ *then*

$\dot{P} = \dot{P}_{Initial}$

elseif $(\dot{P}_{Initial} > \dot{P} * (\frac{\dot{\varepsilon}_{hoop}^{p^*}}{\dot{\varepsilon}_{hoop}^{p}}))$ *then*

$\dot{P} = \dot{P} * \frac{\dot{\varepsilon}_{hoop}^{p^*}}{\dot{\varepsilon}_{hoop}^{p}}$

end if

$P_i = P_{i-1} + \dot{P}dt$

Table 2 Axial feed adjustment algorithm

if $(\varepsilon_{hoop}^{p} = 0)$ *then* (Elastic)

$Axial\ feed = L_0(\beta^* \varepsilon_{hoop} - 1)$ (12)

else (Plastic)

$Error = \beta^* - \beta$ (13)

$Error_{sum} = \sum_i^n Error_i$

$Error_{rate} = Error_i - Error_{i-1}$

if $(-0.2 < \beta^* < 0.2)$ *then*

$\Delta x_i = \Delta x_{i-1} + \left(K_p Error + K_i Error_{sum} + K_d Error_{rate}\right)dt$ (14)

$Axial\ feed_i = Axial\ feed_{i-1} + \Delta x$ (15)

else

$\Delta x = K_p Error + K_i Error_{sum} + K_d Error_{rate}$ (16)

$Axial\ feed_i = Axial\ feed_{i-1}(1 + |\Delta x|)$ (17)

end if

end if

The boundary conditions that were generated can directly be used for free tube bulging tests for tubular material characterization with a tube hydroforming machine that is not equipped with a sophisticated control system. The thing that should be pointed out is that the boundary conditions that were generated were based on very simple yield functions. One can pick the boundary conditions generated using von-Mises yield function or Hill's 1948, but it should be kept in mind that the yield function used for the generation of the boundary conditions may not be an accurate

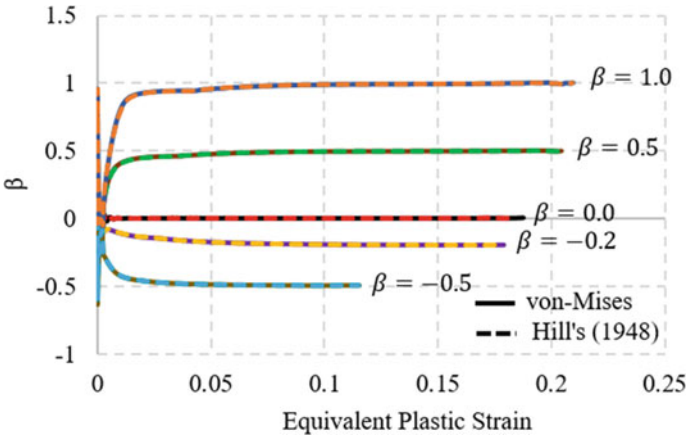


Fig. 6 Controlled strain paths. (Color figure online)

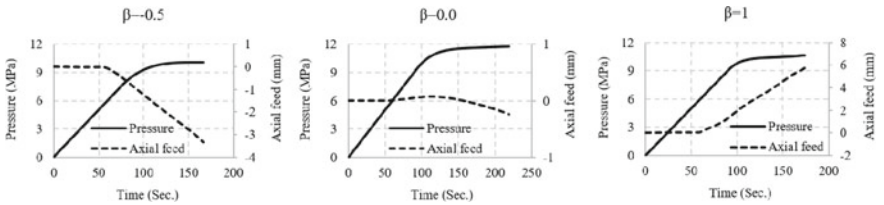


Fig. 7 The axial feed and pressure profiles generated using von-Mises yield function for three different strain paths

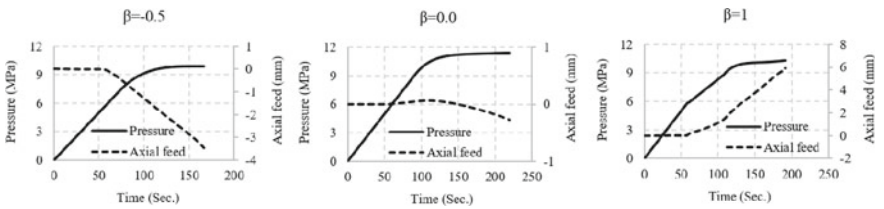


Fig. 8 The axial feed and pressure profiles generated using Hill's 1948 yield function for three different strain paths

representative of the actual material's behavior, therefore, the strain paths that will be obtained in the experiments might not necessarily be similar to the proportional ones generated with the FEM with PID controller. However, the generated boundary conditions will create a range of deformation modes with linear or nonlinear strain/stress paths that can still be used for the characterization of the tubular materials based on accumulated plastic work equivalency.

7 Summary

A PID controller was successfully implemented in FEM platform as a user subroutine to numerically generate appropriate boundary conditions, based on proportional strain path control at the pole of the bulging tube, that can be used for free tube bulging experiments for tubular material characterization based on accumulated plastic work equivalency. It was also shown that the PID controller can generate the boundary conditions based on accurate proportional strain path control using different isotropic or anisotropic yield functions. In this study, von-Mises and Hill's 1948 were employed.

Acknowledgments The authors wish to thank the U.S. Department of Energy for the support of this project through the DOE award DE-FG02-13ER41974 and DOE DE-EE000597, with United States Automotive Materials Partnership LLC (USAMP).

References

1. Koc M (2004) On the characteristics of tubular materials for hydroforming, vol 41, p 12
2. Kuwabara T, Yoshida K, Narihara K, Takahashi S (2005) Anisotropic plastic deformation of extruded aluminum alloy tube under axial forces and internal pressure. Int J Plast 21(1):101–117
3. Korkolis YP, Kyriakides S (2008) Inflation and burst of aluminum tubes. Part II: An advanced yield function including deformation-induced anisotropy. Int J Plast 24(9):1625–1637
4. Khalfallah A, Cristina M, Luís J, Zribi T, Belhadjsalah H, Filipe L (2015) Mechanical characterization and constitutive parameter identi fi cation of anisotropic tubular materials for hydroforming applications. Int J Mech Sci 104:91–103
5. Asgharzadeh A, Alah S, Tiji N, Esmaeilpour R, Park T, Pourboghrat F (2019) Determination of hardness-strength and -flow behavior relationships in bulged aluminum alloys and verification by FE analysis on Rockwell hardness test
6. Korkolis YP, Kyriakides S (2008) Inflation and burst of anisotropic aluminum tubes for hydroforming applications. Int J Plast 24(3):509–543
7. Work P, Rule NF (2019) An evolutionary yield function model based on plastic work and non-associated flow rule
8. Zamiri AR, Pourboghrat F (2010) A novel yield function for single crystals based on combined constraints optimization. Int J Plast 26(5):731–746
9. Park T et al (2019) Crystal plasticity modeling of 3rd generation multi-phase AHSS with martensitic transformation. Int J Plast 120:1–46
10. Hill R (1948) A theory of the yielding and plastic flow of anisotropic metals. Proc R Soc Lond Ser A Math Phys Sci 193:281–297
11. Park T, Chung K (2012) Non-associated flow rule with symmetric stiffness modulus for isotropic-kinematic hardening and its application for earing in circular cup drawing. Int J Sol Struct 49(25):3582–3593

Author Index

A
Abd El-Aty, Ali, 1231
Abedini, A., 667
Abedul, David, 1201
Abe, Eiji, 239
Abirov, R. A., 2009
Agirre, Julen, 773, 1201
Ai, S., 441
Aizawa, Tatsuhiko, 1065, 2807
Akasaka, I., 1043
Akiyama, M., 1043
Alamos, F., 1245
Alamos, Fernando J., 2573
Alaz Erdinc, A., 457
Alimov, Artem, 1715
Allwood, Julian M., 2381
Altan, Taylan, 2925
Alves, José, 1217
Amano, Shuichi, 2155
Aoyagi, Yoshiteru, 253
Arai, Yoshio, 2127
Araki, Wakako, 2127
Argandoña de, Eneko Saenz, 773
Arian, Bahman, 1913
Arnuri, Srinivasulu, 1727
Asakawa, Motoo, 1767
Asgharzadeh, Amir, 283, 681, 1879, 2959
Athale, Madhura, 681, 2959
Atsushi, Danno, 1383
Auer, Peter, 2019
Aue-u-lan, Yingyot, 1519
Awiszus, Birgit, 1411, 1743, 2067, 2853

B
Bader, Fabian, 3
Bailly, David, 507
Bai, Xuepiao, 1623
Baker, Ian, 1853
Bakkal, M., 2077
Balan, Tudor, 2919
Bambach, Markus, 611, 1893
Bansal, Ankush, 383
Barlat, Frédéric, 201
Barlier, Julien, 1217
Barnett, Blake, 1341
Bathelt, Lukas, 3
Baudouin, Cyrille, 1131, 2919
Bauer, Alexander, 1743
Bay, François, 1217
Bay, Niels, 127
Becker, Eric, 1087
Behrens, Bernd-Arno, 959, 1107, 2289, 2345, 2609, 2867
Behrens, S., 959
Bella, P., 729
Ben Khalifa, Noomane, 549, 993
Bergs, Thomas, 1173, 1863
Bertolini, R., 1563
Biba, Nikolay, 1715
Bigot, Régis, 1087, 1131
Bin, Guo, 2547
Blackwell, Paul, 403, 2695
Bo, Hong, 1813
Bonica, Samantha, 1961
Bornhorst, J., 1245
Bouchard, Pierre-Olivier, 493
Bowen, Daniel T., 457
Brückner, Eric, 1411
Bram Kuijer, M., 1853
Brands, Dominik, 2289, 2345
Bremen, Thomas, 507
Bressan, José Divo, 749
Briesenick, David, 2585

© The Minerals, Metals & Materials Society 2021

G. Daehn et al. (eds.), *Forming the Future*, The Minerals, Metals & Materials Series,
https://doi.org/10.1007/978-3-030-75381-8

Brosius, Alexander, 1461
Brunotte, Kai, 2609
Bruschi, Stefania, 67, 1563
Bucek, P., 729
Burik, P., 729
Butcher, C., 667
Butz, Alexander, 935
Bylya, Olga, 403
Byun, J. B., 911

C

Cao, Jian, 271
Cao, Miao, 343
Cao, Quanliang, 1291
Cartier, Elijah, 1469
Cazacu, Oana, 2839
Celal Seyalıoğlu, B., 625
Centeno, G., 2597
Chang, Zhidong, 369
Charni, Dhia, 2233
Chen, Da-Yong, 353
Chen, Dayoung, 1231
Cheng, Randy, 383
Cheng, Sizhu, 1361
Cheng, Xiuquan, 1361
Chen, G. Y., 167
Cheng, Zhe, 2497
Cheng, Zinan, 429
Chen, Hui, 993
Chen, Huiqin, 2371, 2507
Chen, Jun, 369, 441, 867
Chen, Lei, 1691, 1791
Chen, Qiang, 647
Chen, Rui, 2201
Chen, Siyuan, 1291
Chen, Xia, 2179
Chen, Xiaole, 1903
Chen, Xin, 867
Choi, Chang-hwan, 1665
Christopher, Anselm A. A., 1003
Christ, Tyler, 1469
Chung, SukHwan, 1451
Clausmeyer, Till, 635, 691, 2099
Cleaver, Christopher J., 2381
Colditz, Pascal, 2853
Commichau, Oliver, 2609
Conway, Alastair, 403
Cooper, Daniel R., 1003
Cui, Chao, 2705
Cui, Zhenshan, 189
Cui, Z. S., 1757

D

Daehn, Glenn S., 13, 1329, 1341
Dahms, Frederik, 2249
Dai, Wei-Han, 2671
Danno, Atsushi, 25
Dastgiri, Mohammad S., 1573
Davarpanah, Mohammad Ali, 1853
Dean, Trevor, 319
Deng, Jiadong, 2497
Diaz-Infante, David, 2925
Di, Bo-Zhou, 319
Ding, Hongfa, 1373
Ding, Sheng, 739
Djakow, Eugen, 3
Domitner, Josef, 2019
Donadon, Mauricio Vicente, 749
Dong, Wenzheng, 973
Dongsheng, Li, 857
Du, Bing, 1939
Dong, Xinyu, 2899
Durand, Camille, 1131
Dykeman, J., 667

E

Ehmann, Kornel, 271
Emin Tamer, M., 625
Epp, Jérémy, 2233
Ermilova, Evgenia, 1701

F

Félix, Damien, 1087
Fahle, Simon, 589, 2947
Fang, Wenli, 1903
Fang, Xiangfan, 53
Fann, Kuang-Jau, 2619
Feister, T., 2631, 2829
Feng, Wei, 1077, 1099
Feng, Xiawei, 2395
Feng, Zengjie, 1077
Feuerhack, Andreas, 1173, 1863
Fong, Kai Soon, 25, 1383
Franceschi, Alessandro, 2261
Freed, S., 1585
Freund, Ludovic, 1087
Frint, Philipp, 1775
Fujii, Yasuyuki, 2405
Fujii, Yusuke, 763
Fujikawa, Shinichiro, 227
Fukuda, Tatsuya, 1065
Furushima, Tsuyoshi, 801
Furutani, Mika, 227

G
Galdos, Lander, 773, 1201
Gao, Jun, 709
Gebhard, Johannes, 1021
Gehde, Michael, 1411
Gerland, Hendrik, 1107
Ge, Yulong, 1677
Ghiotti, Andrea, 67, 1563
Giannopoulou, Danai, 993
Gibmeier, Jens, 2357
Gilch, Ines, 2303
Girot, F. A., 1269
Glaser, Thomas, 589, 2947
Goede, Martin, 1315
Golle, Roland, 2331
Golovashchenko, Sergey, 2777
Golovko, O., 959
Gondo, Shiori, 1767
Gorji, Maysam B., 601
Graf, Marcel, 2853
Greß, Thomas, 993
Green, Daniel E., 1573
Groche, Peter, 81, 1395, 2261
Groseclose, Adam, 2925
Gruber, Maximilian, 1775
Guan, Ben, 1595, 1633
Guilleaume, Christina, 1461
Gu, J., 1245, 1585, 2631
Gu, Jiahui C., 2573
Gu, Jinbo, 829
Guo, Baofeng, 719, 811, 1791
Guo, Bin, 1351
Guo, Ning, 179
Guo, Xunzhong, 1231
Gurugubelli, Swami Naidu, 1727
Gustschin, Alex, 2303

H
Haguenauer, Victor, 1087
Hahn, M., 2099
Haibo, Wang, 857
Ha, Jinjin, 1805, 1961, 1981, 1991
Hälsig, André, 2853
Hameyer, Kay, 2303
Han, Fei, 1947
Han, Luyi, 2167
Hansen, Niels, 127
Han, Shuting, 719
Han, Xiaotao, 1291
Han, Xinghui, 1099
Hao, Shuo, 1691
Harada, Y., 2639
Harpaz, G., 537
Härtel, Sebastian, 1411, 2067, 2853
Hartmann, Christoph, 1605
Hatta, Akira, 1305
Hayakawa, Kunio, 227
Hebbar, Shreyas, 935
Hedicke-Claus, Yorck, 2867
Heggemann, T., 2649
He, Guoning, 1827, 1841
Heidenreich, Julian N., 601
He, Ming, 2419
Henke, Christian, 3
He, Qiyuan, 2705
Hering, Oliver, 139, 1021
Hermes, Matthias, 395
Herrmann, Marius, 2233
He, Weilin, 2719
He, Wenwu, 2371
Hild, Rafael, 1173
Hirt, Gerhard, 507, 1145, 2319, 2683
Hoche, Holger, 2261
Hoffmann, E., 2661
Holstein, Viktor, 395
Homberg, Werner, 3, 1913, 2115, 2249, 2649
Hongrui, Dong, 857
Horikoshi, Masaya, 2031
Horn, Alexander, 789
Hoshino, Michihiko, 1033
Hou, Wenbin, 1617
Hua, Lin, 1099
Huang, Gaozhu, 333
Huang, Shuo, 891
Huang, Xia, 877
Huang, Yao, 97
Huang, Zhichao, 1423, 1437
Huberth, Frank, 1255
Hu, Bin, 577
Hübner, S., 959
Huh, H., 839
Hu, Jian-Liang, 1813
Hu, Ping, 1617
Husmann, Henning, 1395
Husmann, Simon, 2453
Hu, Xuewen, 1841
Hwang, Yeong-Maw, 2671, 2883

I
Ichimura, Takashi, 1305
Iijima, Takafumi, 2127
Illgen, Christian, 1775
Indhiarto, Ichsan, 801
Iriondo, E., 1269

Isakovic, Jonas, 993
Ishii, Atsushi, 2557
Ishkina, Svetlana, 2233
Ito, Koh-Ichi, 1065
Ito, Yusuke, 1305
Iwaoka, Taku, 2741, 2751

J
Jäckisch, Manuel, 1281
Jaeger, Fabian, 2261
Jagodzinski, Arne, 1107
Jiang, Bo, 1827, 1841
Jiang, Haomin, 1947
Jiang, Yu-Qiang, 1189
Jia, Xiangyang, 1077
Jia, Yinglian, 1423
Jia, Zhe, 1595, 1633
Jin, Miao, 811, 1691, 1791, 1813
Jirathearanat, Suwat, 25, 1383
Jobst, Andreas, 2277
Joo, G., 839
Jost, E., 2099
Jouaffre, D., 1269
Joun, ManSoo, 1451
Joun, M. S., 911

K
Kajikawa, Shohei, 1043, 2031, 2055
Kajino, Satoshi, 1767
Kamaliev, Mike, 2683
Kanayama, Kozo, 2031
Kang, Jiarui, 383
Karadogan, Celalettin, 2041
Katagiri, Takashi, 2751
Katamine, Keiichi, 1161
Kawaguchi, H., 1043
Kawasaki, Keiichiro, 2055
Kaya, Onur, 563
Keray, Viktor, 1145
Kertsch, Lukas, 935
Kiawi, Leo, 1573
Kijima, Hideo, 2467
Kim, H., 1245, 1585, 2631, 2829
Kim, Hyunki, 2959
Kim, Hyunok, 2573
Kim, Ji Hoon, 283, 2959
Kim, JinJae, 1969
Kim, Minki, 1961
Kim, M. K., 839
Kimura, Yukio, 2467
Kim, YoungSuk, 1969
Kinoshita, Atsushi, 2939
Kinsey, Brad L., 1805, 1853, 1981
Kitamura, Kazuhiko, 1529
Kızıltaş, Eda Çapa, 625
Knezevic, Marko, 1805
Kniazkin, Ivan, 1715
Kobayashi, Ryota, 253
Kobayashi, Yoshihiko, 1121
Kock, Christoph, 2289, 2345
Kordtomeikel, Roman, 507
Korkolis, Yannis P., 1805, 1961, 1991, 2127
Kotzyba, Patrick, 1021
Kouyama, Jin, 2127
Kräusel, Verena, 417, 1655
Kraus, Martin, 151
Krimm, Richard, 2609
Krishnamurthy, Bhaskaran, 403
Kriwall, Mareile, 1107, 2867
Kuball, Clara-Maria, 1495
Kuboki, Takashi, 1043, 2031, 2055, 2883
Kuhfuss, Bernd, 2233
Kuhlenkötter, Bernd, 589, 2453, 2947
Kumar, Dharmesh, 25, 1383
Kustra, Piotr, 467
Kuwabara, Toshihiko, 201, 209
Kwame, J. S., 2695

L
Lafarge, Rémi, 1461
Lai, Jiamei, 1423, 1437
Lai, Zhipeng, 1291
Lampke, Thomas, 1743
Langner, Jan, 1107, 2867
Laue, Robert, 2067
Laugwitz, Marvin, 507
Lee, Chang-Whan, 847
Lee, K. H., 911
Lee, Kiyong, 1665
Leem, Dohyun, 271
Leonhardt, André, 417
Lewis, Troy, 1329
Lian, Changwei, 1947
Liang, Junhao, 2221
Liang, Zhenglong, 343
Liao, Shuheng, 271
Li, Cailing, 2705
Li, Dayong, 263, 1903
Liewald, Mathias, 2041, 2357, 2585, 2619, 2789
Li, Fangyi, 429
Li, Fei, 2371
Li, G. J., 167

Li, H., 167
Li, Han, 1939
Lihui, Lang, 983
Li, Huiping, 179
Li, Jianfeng, 429
Li, Jianxiong, 1341
Li, Jingyuan, 829
Li, Liang, 1291
Li, Lihao, 829
Lim, Hojun, 283
Lin, Jianguo, 877, 921
Lin, Jianping, 479
Lin, Longfei, 2521
Lin, Pin-Chen, 2671
Lin, Qiquan, 973
Lin, Y. C., 1189
Li, Qun, 719, 811, 1691, 1791
Liu, Baosheng, 2547
Liu, Chengshang, 2909
Liu, Chongyu, 2507
Liu, Gang, 303
Liu, Jie, 2759
Liu, Jikang, 2497
Liu, Minyao, 2909
Liu, M. X., 1757
Liu, Ning, 1373
Liu, Qi, 901
Liu, Xiao, 2189, 2533
Liu, Xun, 383
Liu, Yazheng, 1827, 1841
Liu, Yi, 479
Liu, Zhao, 2167
Li, Weidong, 1623, 2705
Li, Xiaoxiang, 1291
Li, Xifeng, 867
Li, Xubin, 1055
Li, Yanle, 429
Li, Yantao, 973
Li, Yong, 877, 921
Li, Yongtang, 2507
Li, Y. Q., 1757
Li, Zhiqiang, 709
Löbbe, Christian, 2661, 2683
Long, H., 441
Long, Jinchuan, 333
López-Fernández, J. A., 2597
Loukaides, Evripides G., 457
Lou, Yanshan, 635, 647, 657
Lu, B., 441
Luo, Jun, 2221
Lv, Yiliang, 1291
Lyu, Fenggong, 877

M

Maeda, Yasushi, 2405
Magrinho, J. P., 113, 2767
Ma, J., 167
Makeieva, Hanna, 2115
Ma, Lixia, 1623
Mamros, Elizabeth M., 1853, 1981
Mannens, Robby, 1863
Manurung, Yupiter P., 2853
Mao, Ling, 1077
Mao, Yu, 1329, 1341
Martínez-Donaire, A. J., 2597
Martins, P. A. F., 113
Marx, Sebastian, 935
Masegi, Yusuke, 2211
Matsumoto, Ryo, 217
Matsunaga, Kazuya, 1161
Matsuno, Takashi, 1999
Matumura, Hiromichi, 2055
Ma, Xiang, 97
Ma, Xiaolei, 1827
Ma, Yan, 353
Mayer, Sarah M., 1981
McDowell, David L., 253
Mehner, Thomas, 1743
Mendiguren, Joseba, 773
Meng, Bao, 2719
Meng, Mu, 1055
Merklein, Marion, 151, 563, 789, 1281, 1495, 1537, 2277
Meschut, Gerson, 1495
Milenin, Andrij, 467
Min, Junying, 479
Min, Xinrui, 709
Misiolek, Wojciech Z., 1469
Mitsui, Ryuki, 1767
Mittler, Tim, 993
Miyake, Masaru, 2467
Miyazaki, Makoto, 1305
Mizumura, Masaaki, 2883
Mocellin, Katia, 493
Moghadam, Marcel, 127
Mohr, Dirk, 601
Möhring, Kerstin, 1913
Moser, Newell, 271
Mozaffar, Mojtaba, 601
Mu, Lei, 1595, 1633
Müller, Daniel, 2331
Mull, Jean-François, 1131
Mure, Yuji, 1161
Music, Omer, 457, 2077

N
Nürnberger, F., 959
Nagasawa, Shigeru, 1643
Nagumo, Takaomi, 1643
Nakagiri, Kouta, 1999
Nakamura, Isao, 2741, 2751
Narayanan, Advaith, 2925
Nasheralahkami, Saeid, 2777
Navidirad, Mahsa, 1469
Nazari Tiji, Sobhan Alah, 681, 1879
Neuwirth, Tobias, 2303
Ngaile, Gracious, 37
Nguyen, PhuVan, 1969
Nielsen, Chris Valentin, 127
Ni, Junyan, 709
Nikitin, Alexander, 1701
Ning, Haiqing, 647
Ning, Yongquan, 891, 901
Nishihara, Tadashi, 2089
Nishikubo, Y., 2639
Nishiwaki, Takeshi, 949, 2729
Niu, Liqun, 343
Noder, J., 667
Nomura, Shunya, 209

O
Oberhausen, Gregory J., 1003
Oechsner, Matthias, 2261
Ohashi, Takahiro, 2089
Ohata, Mitsuru, 1999
Okano, Tomoaki, 1529
Okazaki, Toshiro, 2467
Okuda, Kento, 2089
Okude, Yusuke, 2741, 2751
Ong, Wee Kiat, 1383
Onishi, Hiroaki, 949
Ono, Tetushi, 2055
Oruna, Angel, 1201
Osawa, Chihiro, 239
Otake, Izuru, 1033
Otegi, Nagore, 773, 1201
Ou, H., 441
Overhagen, Christian, 2483

P
Pätzold, Isabella, 2331
Packo, Marek, 467
Paffrath, Kai Uwe, 2947
Pal, Arun Kiran, 2135
Palumbo, Gianfranco, 1805, 2767
Pang, Guo-Dong, 1189
Park, Taejoon, 283, 681, 1879, 2959
Pathak, N., 1585
Pavliuchenko, Pavlo, 2319
Peng, Shixin, 2759
Peng, Yinghong, 263, 1903
Piccininni, Antonio, 1805, 2767
Pidvysots'kyy, Valeriy, 467
Poulain, Nicolas, 1217
Pourboghrat, Farhang, 283, 681, 1879, 2959
Prajadhiama, Keval P., 2853
Presz, Wojciech, 1479
Preußner, Johannes, 1255
Psyk, Verena, 935, 1255, 1315

Q
Qian, Dongsheng, 2497
Qi, Haiquan, 2507
Qi, Huiping, 2507
Qi, Lehua, 2221
Qin, Fangcheng, 2507
Qin, Yi, 333

R
Ragupathi, Balaji, 1255
Rautenstrauch, A., 1655
Razali, M. K., 911
Rehm, Matthias, 417
Reinberg, Natalia, 2777
Ren, Peng, 1507
Revil-Baudard, Benoit, 2839
Ridzon, M., 729
Riedmüller, Kim Rouven, 2619
Ripert, Ugo, 1217
Rodriguez-Barrio, N., 1269
Rong, Hai, 1617
Rong, Qi, 921
Rosa-Sainz, A., 2597
Rosenthal, S., 2099
Rostek, Tim, 2115
Roula, Ahmed Mehdi, 493
Roy, Biplov K., 2127
Roy, Sanjib, 2135
Rudolph, Fridtjof, 1145
Rui, Xiao, 983
Ryser, Matthias, 611
Ryzer, Eugene, 1573

S
Sae-eaw, Nuttakorn, 1519
Sajun Prasad, K., 1341
Sakamoto, Azusa, 1643

Sakamoto, Eiji, 1121
Sako, Ryota, 2729
Saldana, C., 2099
Samadian, P., 667
Santiago, Daniel, 37
Sapli, H., 2649
Sarıyarlıoğlu, E. C., 2077
Sarraf, Iman S., 1573
Schauerte, Benedikt, 2303
Scheffler, Christian, 1255, 1315
Schell, L., 81
Schenck, Christian, 2233
Scheunemann, L., 2345
Schlegel, Holger, 417
Schmid, Harald, 1537
Schmidt, R., 1655
Schoch, D., 1245
Schröder, Jörg, 2289, 2345
Schulte, Robert, 563
Schulze, André, 139
Schulz, Michael, 2303
Schwarz, Patrick, 2947
Seimiya, Hikaru, 2055
Senn, Sergei, 2789
Senthil Kumar, A., 25
Shan, Debin, 1351, 2547
Shang, Hongchun, 657
Shang, Xiaoqing, 189
Shao, Jie, 1623
Shen, Jinxia, 2521
Sheu, Jinn-Jong, 523
Shi, Lei, 867
Shim, Dosik, 1665
Shi, Mingxiao, 97
Shimizu, Tetsuhide, 801
Shimura, Jyo, 2155
Shinbutsu, Toshinaka, 2155
Shin, Gwangyong, 1665
Shiratori, Tomomi, 2807
Shirayori, Atsushi, 2883
Shirizly, A., 537
Shi, Zhusheng, 877, 921
Shmuel, A., 537
Shoji, Hiroto, 1999
Shokrani, Alborz, 457
Silva, M. B., 113, 2597, 2767
Simonetto, Enrico, 67
Simon, Nicola, 2357
Sizova, Irina, 1893
Sommitsch, Christof, 2019
Song, Bingyi, 2719
Song, Pengfei, 1939
Son, Jongyoun, 1665
Stahl, Jens, 2331
Stahl, Karsten, 2331
Stalmann, Albrecht, 1315
Stepniowski, Wojciech J., 1469
Stonis, Malte, 1107, 2867
Sun, Yu, 1549, 2899
Suzuki, Shinsuke, 1767
Sviridov, Alexander, 1893

T

Tabatabaei, Hamed Mofidi, 2089
Takatsuka, Seiji, 217
Takemasu, Teruie, 2155
Takemoto, Kosuke, 1767
Takeshita, Tatsumi, 227
Talukder Das, N. K., 2135
Tamai, Yoshikiyo, 763
Tanaka, Soichi, 2031
Tanemura, Rena, 1767
Tang, Bingtao, 179
Tang, Ding, 263, 1903
Tang, Hao-Xing, 2179
Tang, Weiqin, 263
Tanino, Nobuhide, 1529
Tan, Zhanqiu, 709
Tao, Jie, 1231
Tashima, Kenichi, 1767
Taub, Alan, 383
Tekkaya, A. Erman, 139, 635, 691, 1021, 2099, 2661, 2683
Teller, Marco, 2319, 2683
Terashita, Y., 1043
Thiery, Sebastian, 549
Thurston, Brian, 1329
Tian, F., 441
Tiji, Sobhan Alah Nazari, 283, 2959
Tobie, Thomas, 2331
Todorov, E., 1585
Tong, Pengyan, 291
Trân, Ricardo, 935
Trächtler, Ansgar, 3
Traphöner, Heinrich, 691
Tsutamori, Hideo, 949, 2729
Tuffs, Martin, 403

U

Uebing, Sonja, 2289, 2345
Uhe, Benedikt, 1495
Uhlmann, Lars, 1863
Umeda, Masanobu, 1161
Umemoto, Kazuki, 1643
Umemura, Kenji, 2031

Urabe, Masaki, 763
Utsumi, Noah, 2883
Utsunomiya, Hiroshi, 217, 2405

V
Vallellano, C., 2597
Venet, Gabriel, 2919
Vivek, Anupam, 1329, 1341
Vogel, Manfred, 563
Vogt, H., 959
Vogt, Simon, 2303
Voigts, Herman, 1173
Volk, Wolfram, 993, 1605, 1775, 2303, 2331

W
Wagner, Martin F.-X., 1775
Walther, Frank, 1913
Walzer, Stefan, 2357, 2585
Wang, Bao-Shan, 523
Wang, Baoyu, 2521, 2819
Wang, Chunju, 2547
Wang, Guangchun, 2167
Wang, Haibo, 1841
Wang, Hongzhong, 719
Wang, Huamiao, 1903
Wang, Jinliang, 2371
Wang, Leigang, 97
Wang, Li-Liang, 319
Wang, Peng, 1925
Wang, Q., 1563
Wang, Qiang, 1055
Wang, Qiaoling, 179
Wang, Qingjian, 1373
Wang, Xiaochen, 2395
Wang, Xin, 2167
Wang, Yongjun, 291
Wang, You, 1507
Wang, Yu, 2201
Wang, Zhigang, 973
Wan, Min, 1623, 2705, 2719
Watanabe, Atsuo, 227
Watanabe, Masashi, 1469
Watt, Kyle, 403
Weiß, Sabine, 1701
Wei, Chunyu, 577
Weiss, Hannes Alois, 2303
Welo, T., 167
Wen, Huihua, 2371
Wen, Tong, 2179
Wester, Hendrik, 2289, 2345
Wiens, Eugen, 1913
Witt de, Peggy, 417
Wolf, Alexander, 1461
Wolfgarten, Martin, 1145
Worswick, M., 667
Wróbel, Miroslaw, 467
Wu, Fangxing, 179
Wu, Pengfei, 647, 657
Wu, Rongwen, 2497
Wu, Xuze, 1549
Wu, Zedong, 2395

X
Xiao, Hong, 2189, 2533
Xiao, Hua, 867
Xiaoqiang, Li, 857
Xiaoxing, Li, 983
Xia, Qinxiang, 333, 1361
Xia, Yong, 1677
Xie, Bingchao, 901
Xie, Dan, 2201
Xie, Jun, 1939
Xiong, Wei, 1507
Xi, Rui, 2547
Xu, Dongkai, 867
Xue, Shaoxi, 2547
Xu, Jie, 1351
Xu, Shuai, 189
Xu, Wujiao, 2201, 2909
Xu, Yong, 353, 1231
Xu, Zhenhai, 2547

Y
Yagami, Tetsuya, 1121
Yakushina, E., 2695
Yamada, Takayuki, 239
Yamaguchi, Kazuma, 2557
Yamasaki, Yuji, 763
Yanagimoto, Jun, 739
Yan, Chang, 1361
Yanfeng, Yang, 857
Yang, Gang, 2939
Yang, Hao, 901
Yangkai, Chen, 983
Yang, Ming, 801
Yang, Quan, 2395
Yang, Xiaoming, 2819
Yang, Yiheng, 1775
Yan, Ma, 1231
Ying, Liang, 1617
Ying, Pengfei, 1677
Yi, You-Ping, 1813

Yoo, Jaedong, 1451
Yoshikawa, Yasuharu, 2211
Yuan, Shijian, 303
Yuan, Shuai, 333
Yu, Chao, 2189, 2533
Yu, Cheng-Hsien, 523
Yue, Zhenming, 709
Yu, Haiping, 1351
Yu, Hao, 901
Yu, JaeHyeong, 847
Yukawa, Nobuki, 239

Z

Zang, Yong, 1595, 1633
Zdravkovic, Srecko, 2777
Zeng, Yuansong, 877
Zhang, Baohong, 577
Zhang, Baoyun, 891, 901
Zhang, Beijiang, 891
Zhang, Chaolei, 1827, 1841
Zhang, Chengcheng, 1827
Zhang, Chong, 635, 647
Zhang, Haiming, 189
Zhang, Hang, 1373
Zhang, H. M., 1757
Zhang, Jichao, 1947
Zhang, Jie, 709
Zhang, Junhao, 1361
Zhang, Kaifeng, 303
Zhang, Kemin, 2759
Zhang, Li, 2719
Zhang, Mengmeng, 2759
Zhang, Qi, 343
Zhang, Qian, 2221
Zhang, Qifei, 1791
Zhang, Qingling, 811
Zhang, Shi-Hong, 353, 1231
Zhang, Wenyun, 891
Zhang, Xiaodan, 127
zhang, Yi, 1291
Zhang, Yongchao, 1437
Zhang, Zhimin, 1055
Zhao, Changcai, 1939
Zhao, Rui, 2719
Zhao, Shiyan, 719, 1691, 1791
Zhao, Xi, 577
Zheng, Qiu, 801
Zhou, Jia-hua, 1507
Zhou, Jie, 1925, 2759
Zhou, Jiming, 2221
Zhou, Mengjuan, 1077
Zhou, Weitian, 2777
Zhou, Yuting, 1925
Zhuang, Wuhao, 1099
Zhu, Chengxi, 1351
Zhu, Chuanbao, 2819
Zhumagulov, A., 667
Zoller, L., 2631, 2829
Zou, Zongyuan, 719, 1691

Subject Index

A
AA1070-O, 2128
AA2060-T8, 1231–1233, 1236–1240, 1242
AA6061, 1423–1426, 1429, 1430
AA6061-O tubular material characterization, 2961
AA7075, 681–683, 685, 689
AA7075 aluminum alloy, 1617–1621
A bigger vision, 17
A bit of history, 14
Accuracy in terms of tensile test, 912
Acoustic emission, 1173
Acoustoplasticity effect, 393
Activation energy of deformation, 742
Active medium, 549–551, 560
Actuators, 9
Actuators and soft sensors, 1916
ADAMS, 1551, 1553, 1555
Added value, 319, 322–324, 326, 327, 329, 330
Additive manufacturing, 1893–1895, 2100, 2111, 2853, 2856
Adhesion preventing method, 2741, 2742
Advanced High Strength Steel (AHSS), 1245, 1246, 1585, 1586
AE and force analysis of an experimental 2-up compound die fine blanking process, 1178
Age hardening behaviour of Cryo-ECAPed and RT-ECAPed alloys, 1732
Ageing, 877, 878, 880–882, 884, 885, 888, 1727–1729, 1732, 1734, 1736–1739
Agile, 18, 19
AHSS, 1947, 1948, 1950, 1956, 2926–2929
AHSS steels of DQ steel and DP590, 843
AHSS steels of TRIP980 and TWIP980, 841
Aim of press forming technique using in-plane shear deformation, 764
Aircraft industry, 325
AISI H13, 1665–1668
Al alloys, 1805, 1806
Algorithm of finite element method based on space mesh, 2939
Al-Li Alloys, 1231, 1232
Alloy development, 1894, 1901
Al-Mg-Si alloy, 921
Alternate indoor impact welding tools, 1331
Aluminum, 139–141, 144, 146, 2925–2927, 2929
Aluminum AA5083, 1574, 1777, 1778, 1788
Aluminum alloy, 739, 740, 745, 746, 1055–1057, 1060, 1061, 1383, 1385, 1390, 1392–1394, 1715–1717, 1719, 1720, 1723, 1724, 1992
Aluminum Alloy 7075, 384
Aluminum alloy sheets, 2729, 2730
Aluminum plate, 292
Aluminum recycling, 1469
Aluminum sheet, 1305–1309
Al-Zn-Mg alloy, 877, 878
A model for flatness effects, 2494
A modified ductile fracture model, 1596
Analysis method, 1868, 2180
Analysis of Bauschinger effect, 822
Analysis of contionous extrusion, 1026
Analysis of cyclic softening/hardening, 819
Analysis of ratcheting effect, 814
Analysis of the closed backward extrusion, 2176
Analysis of the fatigue test results, 1428
Analysis of the multi-ram radial extrusion process, 2173

© The Minerals, Metals & Materials Society 2021

G. Daehn et al. (eds.), *Forming the Future*, The Minerals, Metals & Materials Series,
https://doi.org/10.1007/978-3-030-75381-8

Analysis of tool loading in typical forging process: Constant Velocity (CV) Joint, 41
Analytical estimation of measurement errors due to strain localization in shear tests, 696
Analytical identification, 2840, 2850
Analytical lateral flow model based on FEM, 2397
Analytical model, 292, 1677, 1678, 1682, 1683, 1686, 1689
Analytical modeling of tailored sheet, 1678
Analytical modeling of THF, 1882
Analytical model of forming force, 372
Analytical model of twisting angle, 375
A neural network-based constitutive model, 607
A new cruciform-like specimen, 1962
Anisotropic damage, 228, 231, 232, 234, 235
Anisotropic plasticity, 681, 682, 688, 689
Anisotropic yield function, 1969–1973, 1979
Anisotropy, 283, 1991–1994, 1997
A physical model for Gen. III sample, 62
Appearance and surface roughness of the outer surface of extruded workpiece, 219
Application and evaluation, 174
Application of constitutive model in solid boss forming by plate forging, 978
Application of IHF on the complex sheet component, The, 363
Application of laser heating to eliminate edge waves in RRF, 488
Application of the proposed yield function to AA6016-T4 sheet, 1975
Application of the proposed yield function to the magnesium sheet, 1977
Application of the proposed yield function to the pure titanium sheet, 1978
Applications of the proposed model, 1975
Approach, 1607, 1865, 2575
Approaches used for sensor modeling in this work, 613
A provoked fracture of a cemented carbide punch due to material overload, 1181
ARAMIS, 1701, 1702, 1704, 1707, 1709, 1710
Arrhenius equation, 1925, 1930, 1931, 1935
Artificial intelligence, 19, 22, 595
Artificial neural networks, 602, 614
Asperity contact, 127, 129
Assistance system, 1145–1147, 1149, 1151, 1155, 1157, 1158
Assumptions, 2144
Asymmetric yield function, 1971
Auger flighting, 2419, 2420, 2422, 2425–2427, 2430, 2434, 2435, 2437, 2439, 2440, 2444, 2445, 2447, 2449, 2450
Auger flighting forwarding velocity and throughput, 2439
Augmentation of laser driven flyers, 1335
Austenite-to-martensite phase transformation, 2346–2348, 2353
Austenitic stainless steel, 2261, 2262, 2274
Autobody sheet metal, 840
Automatic process design, 1122
Automatic thermo-mechanical time-stepping, 1228
Automotive industry, 319
Automotive lightweight design, 2650
Average pressure and dimension of work piece, 2214
Aviation component, 1813–1815, 1823
A vision of metamorphic manufacturing, 16
Axial feed curve, 2208
Axial feed-rate, 2127, 2128, 2131–2133
Axisymmetric welding, 1341, 1342, 1345, 1346, 1348
Axisymmetric welding by tube expansion, 1345
AZ31B, 802

B

Backward extrusion, 219–224, 975, 1055, 1166, 1519, 2167–2169, 2173, 2176, 2177
Ball ironing test, 1519–1521, 1523, 1525, 1526
Ballistic Additive Manufacturing (BAM), 1343, 1346, 1347
Barlat's Yld2000-2d anisotropic yield stress criterion, 750
Barlat's Yld 2000-2d yield criterion, 749, 750, 755
Basic Representation Unit of Forged Products, 1162
Basic principle, 1374
Basic principle and design, 1374
Bauschinger effect, 635, 639, 642, 811, 812, 823–826, 2142, 2143, 2149
Bending, 2099–2102, 2104, 2105, 2110–2112, 2585, 2586, 2588–2595
Bending experiments, 2105

Bending moment, 1643, 1644, 1647–1649, 1651, 1652
Bending under tension, 84, 86, 87, 92
Bending with lateral compression, 85
Bias-variance-tradeoff, 612, 613, 621, 622
Biaxial experiments, 1985
Biaxial loading, 1981, 1982
Biaxial tensile and compression simulations for the prediction of the yield surface, 258
Biaxial tension, 211
Biaxial test, 1962, 1966
Billet flow curve, 1008
Billet-Interface-Machine (BIM) model, 1137
Billet material, 1007
Billet-tool friction condition, 1008
Bimetallic contacts, 1479, 1482, 1485, 1486
Bipolar plates, 1743, 1744, 1752–1755
Bistability, 2319, 2320, 2326–2329
Blankholder, 2619–2628
Blankholder force, 2619, 2620, 2626, 2627
Blanking, 1161, 1162, 1166, 1169, 1170
Bolted joint, 2155, 2156, 2162–2164
Bond strength, 994, 996, 999, 1000
Boron steel, 179, 180, 182–186
Boss forming ability analysis, 980
Boundary condition, 71, 713, 2941, 2946
Boundary condition assignment, 2941
BP neural network, 171
B.Point of care medical manufacturing, 21
Branched tube, 419, 424
Brazing, 1903–1910, 1912
Brazing experiments, 1905
Buckling, 2020, 2023–2025, 2467–2469, 2471–2476, 2479, 2480
Bulge, 383, 385, 390–393
Bulge test, 953
Bulging test, 1238
Bulk microforming, 151–153, 155, 159, 164
Burnishing, 2089
Burr-free cutting, 2790, 2796, 2797
BUT test, 87
Butt-welding fitting, 2019, 2020, 2027, 2028

C

CAD, 2867, 2868, 2872–2874
Cage roll, 523, 524, 526–528, 530, 532–534
Calculation of bending neutral layer, 2708
Calculation of local shear strains, 697
Calculation of measured discrete shear strains, 699
Calculation of springback, 2710
Calculations of roll separating forces, 2430
Calibration model results, 2580
Calibration of multi-axial continuum damage constitutive equations, 1620
Calibration of stress-strain curve in high strain region, 953
Calibration of the model, 884
Calibration plate, 2044
Calibration procedure, 2576
Calibration snapshot, 2045
Carbon fiber reinforced plastic (CFRP), 2649–2651, 2653–2658
Carbon nanotubes, 2221–2224, 2226–2229
Carburization, 789–792, 797, 798
Cassette Dies, 1068
Cedar, 2033
Cellular automata, 1879, 1880, 1885
Cellular automaton simulation, 1813, 1814, 1821, 1823
Cemented carbide, 1173–1177, 1179, 1181–1186
Changes in the roll gap because of the roll offset, 2442
Channel forming, 25
Characteristics of laboratory 4-high rolling mill, 2559
Characterization, 2959–2961, 2966–2968
Chip extrusion, 141, 146
Circumferential metal flowing degree, 1104
Citric acid, 2031–2033, 2035, 2039
Clearance joint, 1549–1553, 1557, 1558
Closed backward extrusion, 2167–2169, 2173, 2176, 2177
Closed backward extrusion process, 2173
Closed die forging, 1121, 1122, 1128, 1129
Cloud based multi-objective FE simulation technology, 329
Cluster-roll straighteners, 2139
CNC Fine-Stamper for Piercing, 2810
CNT/Al composite material model based on Voronoi diagram, 712
Coated strips, 1471, 1472
Co-extrusion, 993, 994, 1000
Cold deformation characteristics of Mn18Cr18N with high nitrogen, The, 2376
Cold drawing, 729, 730, 736
Cold expanding strengthening, 2371, 2372, 2379
Cold forge, 1529, 1530, 1534, 1535
Cold forging, 773–775, 777, 783, 785
Cold forming, 960, 961

Cold forming process route, 960
Cold hydraulic expanding strengthening of thick-wall hollow forgings, The, 2376
Cold Metal Transfer (CMT), 2853–2858, 2860, 2861, 2863, 2864
Cold orbital forging, 1099–1104
Cold rolling, 1903, 1905, 1909, 1910, 1912
Collar forming, 417–419, 421–423, 426–428
Collision point velocity, 1310
Combined curing and forming process, 2649
Combined isotropic-nonlinear kinematic hardening model, 637
Combined tension–shear, 1961–1963, 1965, 1966
Combining the mechanical and thermal roll deformations to a deformed roll barrel and exit strip shape, 2489
Compact casting-rolling forming process, 2508
Compact strip production (CSP), 1841–1843
Comparison between conventional and new tooling designs, 47
Comparison of tangential stress distribution, 2351
Comparison of the crystal plasticity models, 286
Comparison of training duration, 620
Compensation, 167–172, 176, 177
Complex extrusion, 1033, 1034, 1041, 1042
Complex loading, 2009, 2011, 2012, 2014–2016
Complex material behaviors and strain-rate dependent forming limit diagrams, 1221
Composite, 2031–2039
Composite ring, 2497, 2499, 2504
Compound casting, 993–995, 999, 1000
Compression deformation tests, 1792
Compression tests, 1925, 1927
Computational modelling results, 1274
Computation time, 493–495, 497, 500, 506
Computed tomography, 2099–2103
Computer-based production systems, 327
COMSOL, 1373, 1376, 1377
Concave-convex, 549–551, 559, 560
Concept development, 39
Condition for spinner, 2057
Configuration optimization methods, 497
Confocal microscopy after a drawbead passage, 1542
Conformal mapping, 2909–2915
Constant velocity (CV) Joint—Forward Extrusion: Proposed tooling design, 44
Constitutive equations, 894, 2348
Constitutive law, 2919
Constitutive model, 660, 878, 881, 884, 888, 974, 978, 1928
Constitutive modeling, 905, 976
Constitutive modeling of peak stress, 905
Constructive, 2497, 2499, 2504
Contact and friction model, 98, 99
Contact heating, 937, 943–946
Contact model of hot-dip galvanized (GI) sheet, 107
Contact model of hot-dip galvannealed (GA) sheet, 106
Contact tempering, 935, 938, 942, 943, 945
Continous extrusion, 1023
Continuous-bending-under-tension (CBT), 1805, 1806
Continuum damage model, 1617, 1618
Contour of plastic work, 253, 255, 256, 258
Control system and stabilisation, 2150
Conventional shear tests, 698
Convexity condition of yield function, 1973
Cooling rate comparison of traditional and new tool, 2764
Cooling system, 1855
Copper, 467, 469, 470, 472, 473, 475, 477, 537, 538, 543, 546, 547
Correlation of NDE result with HSDT and hardness results, 1591
Corrugated cup, 2639, 2645
Counter-shaving, 2790–2792, 2795–2797, 2799, 2801, 2804, 2805
Crack, 1757, 1764, 1766
Crack edge sensitivity of shear cut edges, 2803
Craft, 457, 458
Creasing, 1643–1649, 1651, 1652
Creep age forming, 921
Critical Damage Value, 2929, 2930, 2937
Cross buckle, 2468
Cross groove CVJ, 2167
Cross-roll straighteners, 2136, 2139, 2144
Cross-roll straightening machines, 2137
Cruciform, 1981–1986, 1988, 1989
Cruciform machine, 1983
Cruciform specimen, 1961, 1962
Cryo ECAP, 1727, 1733–1738
Cryogenic, 1564
Crystal orientation, 1767–1770

Crystal plasticity, 189, 190, 197, 253, 254, 256, 258–261, 283–286, 289, 1757, 1760
Crystal plasticity based constitutive model, 1760
Crystal plasticity finite element simulations, 256
Crystal plasticity models, 284, 711
Cup drawing, 2840, 2841, 2843, 2846, 2848
Cup drawing test results for DC06 steel, 2840
Current role of tribometers in sheet metal forming, The, 83
Curvature, 2059–2065, 2383, 2384
Cut edge geometry, 2932, 2934
Cut-surface characteristics and part bending, 2336
Cutting blades, 2115, 2119
Cyclic bending, 291–298
Cyclic deformation behavior, 2719, 2720
Cyclic hardening/softening, 719, 720, 722, 723, 725, 1691, 1694, 1698
Cyclic loading, 719–723, 725, 1691–1694, 1696
Cyclic shearing test, 2721
Cyclic shear loading, 635
Cyclic softening/hardening, 811, 812, 820
Cyclic stress loading, 813, 817, 826
Cyclic stress-strain curve, The, 719, 723–725
Cyclic torsion tests, 777
Cylindrical parts with inner ribs, 333, 334, 341

D

Damage, 1948, 1952, 1953, 1955, 1956
Damage accumulation and fracture limit characterization, 1952
Damage behavior under complex stress states, 1952
Database, 9
Data set, 592
DC04 steel, 1702
DC06 steel, 2840, 2841, 2850
Decoupling method, 2557, 2559, 2560, 2568
Deep drawing, 81–83, 85, 611–613, 615, 622, 1537, 1539, 1544, 1547, 2639–2641, 2645, 2646, 2649–2651, 2653, 2654, 2656, 2729, 2730, 2732
Deep drawing process, 2742, 2743, 2752
Defect, 2180, 2183–2186
Definition of Edge Quality, 2927
Definition of strain gauge length based on the *n*-value, 703
Definition of the dependent variable, 2461
Deflection of rolls in a four-high mill, 2486
Deformation behavior, 647, 653, 1305, 1306, 1311, 1495, 1498, 1500, 1501, 1503–1505, 1757, 1758, 2110
Deformation behavior of indentation of outer surface of workpiece during extrusion, 221
Deformation characteristics under different forming stages, 1082
Deformation feature of tube wall during dot-denting, 2182
Deformation features of tube wall during incremental grooving, 2183
Deformation-induced α´-martensite, 1914
Deformation measurement, 1608
Deformation mechanism, 369, 370, 375, 1077–1080, 1083, 2085
Deformation mechanism of Ti-55511 alloy, The, 1194
Deformation of skin component, 2709
Deformation path, 1981, 1982, 1988
Deformation twinning, 189, 190, 192, 195, 197
Degeneration of elastic modulus, 7
Degree of deformation and forming temperature, 1917
Delamination process, 1482
Deposition process and experimental specimen preparation, 1667
Derivation of the stabilising rolling strategy, 2458
Description of analytical model, 1682
Description of incremental collar forming process, 419
Description of the powder-fed DED process, 1666
Design and manufacture of high energy-efficiency IHF press, The, 359
Design and manufacture of the pulsating hydroforming machine, The, 356
Design considerations of the main roll assembly, 2446
Design edge, 1318, 1326
Design of main roll shafts, 2446
Design of multidirectional forging process, 2203
Design of reaming process, 2203
Design of ring rolling process, 2205
Design of the process, 2023

Detection methods in the VDA 238-100 tight radius bend test, 671
Determination of cutting performance, 1659
Determination of cutting quality, 1661
Determination of parameters influencing the pre-stress, 1406
Determination of specimen dimensions, 1963
Determination of the maximum cutting force and cutting impact, 1661
Determination of the mechanical properties, 1662
Determination of the roll offset amount for the required thickness of the rolled strip, 2444
Development and verification of FEM model, 335
Development of an ideal stabilising rolling strategy, 2457
Development of FEM model, 335
Development of orbital riveting, 1481
Development of the method for efficient forging sequence planning, 2869
Development of the new specimen for ringing free force measurement, 55
DHTB equipment, 69
DIC, 693, 694, 696, 702, 703, 706
Die angle and friction, 1016
Die clearance, 1247
Die cushion, 2619–2621, 2623, 2626
Die design, 37, 39, 40, 45, 47
Die forging, 1827–1829, 1832, 1837, 1838
Dieless drawing, 467–470, 472, 473, 475–477
Dieless hydro-bulging, 311
Die steel, 829, 830, 832, 836, 837
Die-workpiece contact pressure, 40
Digital image correlation and thermal camera, 1856
Direct energy deposition, 1665–1667, 1671, 1675
Direct hot tube bending (DHTB), 69
Discrete filler, 2179, 2180
Discussion of parameters influencing the residual stress state and effect on the fatigue strength, 2340
Disk-shaped product, 1122, 1128
Dislocation density, 1813, 1817–1820, 1822, 1823
Dissimilar-materials welding, 1270, 1272, 1279
Dissimilar metals welding, 1291
Distorted hardening, 644
Distribution of magnetic pressure and stress, 1297
Distribution of Mises stress, 2826
Distribution of sheet temperature, 2825
Double thread mechanism, 2155, 2156
Double skin panel, 1033, 1034
DP590, 1423–1426, 1429, 1435
Drawbead, 1537–1547
Drawbead preloading, 1541
Drawing with lateral compression (wedge drawing test), 86
DRM-80 mill, 2521, 2525, 2528, 2530
Dry contact model for the translational clearance joint, 1552
Ductibor® 500, 667, 669
Ductile fracture, 179, 180, 183–185, 227–230, 237, 238, 1595–1598, 1600–1602, 1633–1636, 1639–1641, 2000
Ductile fracture criterion, 1635
Ductile fracture criterion to hot-stamped boron steel 22MnB5, 183
Ductile fractures in IRF, 228
Dummy block, 1003, 1004, 1006, 1009, 1010, 1012, 1013, 1015, 1018
Dummy block geometry, 1009
Dummy block profile, 1018
Duplex stainless steel, 1691, 1692, 1694, 1696, 1697
Dynamic, 1132, 1134, 1137, 1142
Dynamic recrystallization, 263, 739–746, 1814, 1817, 1819, 1820, 1822, 1823
Dynamics of joints with clearance, 1552
Dynamic transformation, 1791, 1792, 1795, 1798, 1799, 1802

E

EBSD, 1709, 1710
EBSD analysis, 1770
EC results, 1589
Eddy current, 1585–1588, 1592
Edge cracking, 1245, 1251, 1585, 1586, 1589, 1591
Edge-crack-sensitivity, 2790, 2799, 2804, 2805
Edge formability, 2695, 2696, 2699, 2700, 2702, 2703
Edge fracture, 1633, 1634, 1637, 1641
Edge quality, 2927, 2928, 2930, 2932, 2935, 2937
Edge waves, 479, 480, 482, 484, 485, 487–490
Effective strain, 42
Effective strain distribution, 1102

Effect of ageing on wear behaviour of Cryo-ECAPed and RT-ECAPed alloys, 1734
Effect of α and β on yield surface for the case of plane stress, 1974
Effect of deformation amount on the grain size, 1830
Effect of deformation heat, The, 1797
Effect of laser shock energy *E* on RSH, 1364
Effect of laser spot diameter *D* on RSH, 1365
Effect of main LSP parameters on RSH, 1364
Effect of microalloying elements on the grain size, 1832
Effect of overlap ratio η on RSH, 1366
Effect of part features on formability, 32
Effect of part features on part dimensional accuracy, 33
Effect of preparation method on the total elongation, 1580
Effect of preparation method on the yield stress, 1578
Effect of process parameters on clean-cut portion and strain effective, 2797
Effect of repeated shock times *N* on RSH, 1366
Effect of strain, 1192
Effect of strain rate, 1193
Effect of the holding pressure, 2737
Effect of the pressure rise ratio, 2737
Effect of Y addition on "RE texture" component in terms of twin, The, 267
Effect of Y addition on texture development in terms of DRX mechanisms, The, 268
Effect of Y addition on the formation and growth of DRX grains, The, 266
Effects of holding time on bending relaxation characteristics, 1649
Effects of mass scaling, 276
Ejection load, 40, 42–45, 48
Elastic Blankholder geometry and finite element modelin, 2621
Elastoplastic finite-element method, 1459
Elbow-bar mechanism, 2907
Electrically-assisted, 2547
Electrically-assisted uniaxial tension, 857–862, 864, 865
Electrical steels, 2304–2310, 2314, 2317, 2808, 2810, 2812, 2813, 2815, 2816
Electric drive, 2303–2305
Electromagnetic force, 1373–1375, 1377, 1379
Electromagnetic forming, 1315, 1316, 1318, 1321, 1326
Electromagnetic micro-bulging, 1358
Electromagnetic model, 1220
Electron microscopy, 1711
Electroplastic effect, 857, 858
Electroplasticity, 803
Electropulse, 808
Elementary analysis, 2473
Embossing, 25, 26, 2303–2317, 2357–2360, 2362–2367, 2585–2595
Embossing process, 2587
Energy absorption, 1677, 1678, 1681, 1683, 1684, 1686–1689
Engineering plasticity, 303
English wheel, 457–459, 462
English wheel mechanics, 462
Enhanced PSO-BP based ML model, 173
Enhancement of the VFA technique via chemical augmentation, 1333
Equal-Channel Angular Pressing (ECAP), 1775–1782, 1784, 1786–1788
Equipment and tool geometry, 551
Equivalent strain, 1058–1061
Equivalent strain analysis, 1058
Equivalent von mises stress, 1312
Establishment of 3D FE model, 1079–1081
Establishment of mathematical model of RSH, 1362
Establishment of multi-axial continuum damage constitutive equations, 1618
Estimated friction coefficient at each roll, 2411
Estimation of friction coefficient, 2410
Evaluation indexes of forming quality for SWIR, 338
Evaluation of formability of the drawn clad cup, 2643
Evaluation of high strain rate formability, The, 361
Evaluation of straightness, 2061
Evaluation of suitable models for quality prediction in RARR, 592
Evaluation of the interface bonding, 997
Evaluation of the intervention limit, 2456
Example calculations for the experimental materials, 700
Expansion drawing, 1044, 1050, 1052
Expansion ratio, 1043, 1046, 1048–1053
Experimental setup and test equipment, 2333
Experimental analysis of strain localization in shear tests, 692

Experimental and numerical procedure for thermomechanical processing of cylindrical specimen with eccentric holes, 2294
Experimental and simulation conditions, 336
Experimental conditions, 995, 2407
Experimental description, 1624
Experimental investigation, 721, 1777
Experimental methods, 803
Experimental procedure, 669, 683
Experimental residual stress analysis, 2360
Experimental setup, 153, 385, 840, 1176, 1855, 2043, 2662
Experimental setup and specimen, 693
Experimental setup and testing procedure, 422
Experimental validation, 1275
Experimental validation results, 1277
Experimental verification of friction model, 109
Experimental work, 294
Experimentation, 2598
Experiment procedure, 295
Experiment results, 296
Experiment setup, 294
Experiments for hot-stamped boron steel 22MnB5, 182
Expert interview, 2457
Explosive forming, 1330
Ex-situ EBSD, 189–191, 197
Extraction of sensor data, 616
Extreme value analysis, 253, 254, 259–261
Extreme value analysis of mechanical properties, 259
Extrusion, 39–48, 217–224
Extrusion press, 1021, 1023, 1025, 1027, 1028, 1030
Extrusion process with torsional oscillation and procedures of experiment, 218
Extrusion ratio, 1016

F

Factors affecting the roll separating force, 2431
Failure, 1281, 1282, 1284, 1285, 1288, 1289
Failure mechanism, 1423, 1424
Failure mechanism of AA35 joints, 1431
Failure mechanism of DA32 joints, 1432
Failure mechanism of joints, 1431
Failure mode and fracture analysis, 1444
Failure nucleation, 2701
Fast modelling, 1147
Fast modelling in open-die forging, 1147
Fatigue, 2331–2333, 2335, 2340–2343
Fatigue behavior, 2340
Fatigue characteristics, 1423
Fatigue strength, 1438
Fatigue test, 1427
Fatigue test and analysis, 1440
Fatigue test of single-rivet specimen, 1440
FBRE process of wheel hub, 1056
FEA, 1107, 1112
Feasibility experiment, 2521, 2526, 2528
Feature height, 2550
FEM, 239, 1121, 1124, 2155, 2157–2161, 2959, 2960, 2963, 2964, 2967, 2968
FEM analysis, 2477
FEM analysis conditions, 765
FEM analysis results, 766
FEM modeling, 687
FE model establishment, 2762
FE model of tailored sheet, 1686
FE model verification, 434
FEM simulation model and experimental, 2158
FEM simulations and experiments, 2713
FEM simulations modeling, 2713
FE-simulation, 2347, 2351, 2353
FEM 3d modelling, 1484
Femtosecond laser machining system, 2809
Femtosecond laser trimming, 2811
Ferrite rolling, 1841, 1843
FESEM and TEM analysis, 1834
FE simulation for the determination of the forging load as a function of the billet height, 1137
FE simulations, 611, 921–923, 925, 927, 931, 932, 1131–1133, 1137, 1140, 1142, 1411, 1995, 2927, 2929, 2930, 2932, 2936, 2937
Fiber metal laminate (FML), 2649–2658
Fiber texture, 1767, 1768, 1770–1773
Field shaper, 1373–1375, 1377, 1378
Field transport optimization, 1226
Finding stress relaxation limit, 804
Fineblanking, 1173–1183, 1185, 1186, 2333, 2334, 2336, 2340
Fine-tuning of Process models, 411
Finite Element Analysis (FEA), 209–211, 213–215, 228–231, 235, 2289, 2290, 2307, 2339, 2631, 2635, 2909, 2915
Finite Element Calculation of the straightening process, 7
Finite Element (FE) Model Setup, 2929

Finite element (FE) solution, 542
Finite-element model, 2335
Finite Element Method (FEM), 850, 2056, 2065, 2235, 2939, 2946
Finite element model, 431, 459, 1677
Finite element modeling, 431, 2672
Finite element modeling of the process, 1271
Finite element modeling of tube bulging process, 2963
Finite elements, 271–274, 276, 279, 280, 459, 537, 542, 1220, 1226
Finite elements analysis, 253
Finite element simulation, 482, 2003, 2019, 2021, 2027, 2820–2822
Finite element simulation model, 2821
Finite element type, 274
Fitting scheme for the Swift law's parameters, 2004
Flexible roll forming, 18, 523
5A90, 983, 984, 986–988
5052 aluminum alloy, 973, 974, 976, 977, 981
590R, 667, 669–672, 675, 677, 678
Flange forming, 403, 412, 414
Flatness, 2468, 2483, 2484, 2489, 2494–2496
Flatness of sheet, 2552
Flexibility, 2883, 2885, 2887–2890, 2895
Flexible multi-point forming, 314
Flexible rolling, 563–565, 567, 568, 570, 572, 575
Flexible rolling of tailored blanks and target geometry, 565
Flexible skew rolling, 2521, 2523, 2524, 2531
Flexible skew rolling process (FSR), 2523
Flow behavior, 892–894, 901, 903, 904, 909, 1927
Flow behavior at elevated temperatures, 2686
Flow behavior of 7A85 aluminum alloy, 1816
Flow curve, 692, 693, 697, 700, 704, 1794
Flow forming, 493–501, 503, 505, 1915, 2115–2117, 2120, 2123
Flow rule, 201
Flow stress, 911–915, 917, 919
Flow stresses and microstructures during multi-pass hot compression of Mn18Cr18N, 2372
Folding, 1643, 1644, 1647, 1648, 1651, 1652
Folding over, 668
Force vs displacement results, 1986
Forging, 18–21, 217, 218, 1107–1114, 1117, 1118, 1201–1204, 1208, 1209, 1211, 1213, 1214, 1161, 1162, 1165–1167, 1169, 1170, 2867–2869, 2919, 2920
Forging bimetallic gears, 323
Forging cast preforms, 324
Forging high performance pistons from powder, 323
Forging load and ejection load, 42
Forging net-shape gears, 321
Forging press, 2899–2901, 2905
Forging process by CNC stamper, 1068
Formability, 353–355, 358–364, 441–444, 454, 959–962, 966–970, 1351, 1352, 1805–1807, 1810, 1811, 2819–2821, 2825, 2826, 2883–2889, 2895
Formability in W temper state, 966
Formability limit by fracture, 2605
Formability limit by necking, 2602
Formability limits, 113, 114, 116–121, 124, 2767, 2771
Formability limits in the principal strain space, 2606
Formability of narrow channels, 29
Forming, 1281–1283, 1285, 1286, 1289, 1395–1397, 1743–1755, 1853, 1854, 1981, 1982
Forming apparatus and test platform, 1508
Forming simulation, 1464
Forming behavior, 1411, 1413–1415, 1419, 2864
Forming conditions, 2674
Forming curved complex-shaped profiles, 326
Forming defects, 333, 334, 338, 341
Forming experiments, 1748
Forming for diameter-reduction in productivity and formability, 2888
Forming Limit Curves (FLC), 2631, 2633–2635, 2637, 2638
Forming Limit Diagrams (FLD), 1617, 2631, 2829, 2832
Forming method, 407
Forming pressure, 2167, 2171
Forming process, 1916, 2289–2291, 2293–2296, 2298, 2300
Forming process properties, 2281
Forming quality, 333, 334, 336, 338–341, 2547–2549, 2554
Forward-Backward-Radial Extrusion, 1055–1057, 1061
Forward extrusion, 2277, 2279, 2280, 2285, 2286

Forward extrusion stage, 42
Fractal change of galvanized sheets after friction, 103
Fractal characterization of galvanized sheets, 100
Fractal contact models of galvanized sheets, 104
Fractal theory, 97, 99, 111
Fractography, 113, 121, 122, 124
Fracture, 1947, 1948, 1952–1956
Fracture characterization, 647, 648
Fracture limit, 120, 2601
Fracture limit test and calibration, 1953
Fracture locus, 1563
Fracture mode of the tubes, 1910
Fracture strain, 2777–2779, 2783–2786
Fracture strain measurements, 2783
Fracture strains, 117
Fracture surface, 1563, 1567, 1569, 1571
Fracture toughness, 113–116, 119, 120, 123, 124
Fretting damage, 1437
Friction, 127–131, 133, 136, 218, 223, 1538, 1544–1546
Friction coefficient, 81–93, 2405–2407, 2410–2416
Friction coefficient identification, 2921
Friction coefficient of 45-degree groove roll, 2412
Friction evaluation, 1522, 1525, 1526
Friction model of the hot-dip galvanized (GI) sheet, 109
Friction model of the hot-dip galvannealed (GA) sheet, 109
Friction models of galvanized sheets, 108
Friction of TD groove roll, 2411
Friction-spinning, 2249, 2252
Friction stir forming, 2089
Friction stir processing (FSP), 2221–2223, 2226, 2229
FSR rolling test on DRM-80, 2528
Full explicit scheme model [F-Model], 2058
Full-field, 2041, 2051, 2052
Full-field motion estimation, 1608
Fully connected neural network, 602
Functional design of the actuator, 2612
Further development of an electrodynamic MHP system, 1865

G

Galling free forging, 1074
Galvanized steel, 97, 98, 100, 103
Gears, 2331, 2332
Geometric accuracy, 549, 553, 560
Geometrical accuracy, 507–509, 512
Geometrical features of helicoid auger flighting, 2420
Geometrical modelling based on Voronoi, 712
Geometric comparison, 2106
Geometric deviation, 379, 380
Geometry, 405
Geometry and mesh, 2021
Geometry characterization tool, 2953
Geometry of the elbow, 2024
Geometry reduction, 498
GISSMO damage model calibration and validation, 1955
Global magnetic material behavior, 2313
Grain growth, 1630, 1631, 1903, 1904, 1908, 1909, 1912
Grain orientation, 2507, 2510, 2515–2518
Grain size, 1827–1834, 1837, 1838
Grain size and sheet thickness effects on the Bauschinger effect, 2723
Grain size and thickness effect on springback in U-bending test, 2724
Granular media, 2661–2663, 2669
GS-20Mn5, 719–721, 723, 725

H

Half Specimen Dome Test (HSDT), 1248
Half specimen dome test result, 1251
Hammer, 1201–1205, 1208, 1209, 1211, 1213, 1214
Hardening, 691–693, 695–697, 702, 703, 705, 706, 1947–1952, 1956
Hardening behavior, 839–845
Hardening behavior under large strain, 1949
Hardness, 829, 830, 832, 836, 837, 1727, 1728, 1730, 1732–1735, 1739
Hardness distribution of formed cups, 2738
Hardness measurement of formed cups, 2733
Hardness measurements after drawbead preloading, 1543
Heat transfer, 67, 68, 72, 73, 76
Heat treatment, 1793, 1805–1808, 1810, 1811
Height difference between inner rib and outer rib, 1103
Height of transcribed profile, 2409
Hemispherical shape, 2127, 2131
High carbon steel wire, 1767–1769, 1773

High nitrogen steel, 1498, 1500, 1502, 1504, 1505
High-pressure conditions, 1529, 1530, 1532, 1534, 1535
High-Speed deformation, 1232
High-speed tensile test, 55
High strain rate, 354, 361
High strength steel, 67, 398, 2585–2587, 2589, 2594, 2117
High temperature, 1666, 1671–1673, 1675
High-velocity shearing, 1245, 1253, 1254
Hole-drilling method, 2249, 2250, 2253, 2254
Hole edge formability, 2699
Hole-expansion, 1634, 1991, 1992, 1994–1997
Hole-expansion experiment with prestraining, 1994
Hole expansion forming experiment and FEA simulation, 213
Hole-expansion-test, 2695, 2698, 2791, 2795, 2803, 2805
Homogeneous anisotropic hardening (HAH) model, 639
Homogeneous plane-strain upsetting method, 2430
Horizontal forces, 2611
Hosford–Coulomb fracture criterion, 181
Hot compression, 739–741, 746
Hot cutting, 1655, 1656, 1658, 1661, 1663, 1664
Hot die forging aerofoil blades, 325
Hot extrusion, 1021, 1022, 1025, 1026, 1030, 1031
Hot forming and quenching sheet aluminium alloy, 321
Hot plastic deformation, 891, 892, 894, 897, 899
Hot ring rolling, 2371, 2372, 2372, 2379, 2507, 2508, 2510
Hot ring rolling process of hollow ingots, The, 2372
Hot-roll bonding, 2189, 2190
Hot rolling, 1895, 1897, 1899–1901
Hot stamping, 179, 789–792, 797, 2683–2686, 2688–2690, 2692
Hot stamping tool, 2759, 2760, 2762, 2763, 2766
Hot strip mill, 2559
HSDT and hardness tests, 1588
HTC determination, 75
HTC equipment, 72
Hub bearing unit, 1507
Hybrid concept, 1332
Hybrid experimental-numerical method, 647, 652, 653
Hybrid forming, 2651
Hydraulic-expanding strengthening process of Mn18Cr18N hollow forgings, The, 2377
Hydraulic pressure, 2019–2023, 2027, 2028
Hydroforming, 395–397, 399, 2661
Hydroforming and air forming in strength and formability, 2886
Hydro-mechanical deep drawing, 2729, 2730, 2732, 2733, 2735, 2737–2739
Hydro-mechanical deep drawing condition, 2732
Hydro-mechanical deep drawing process, 2732
Hydro-piercing, 2671, 2672, 2674–2676, 2679, 2682
Hydro-piercing experiments, 2679
Hydrostatic stress, 1595, 1596, 1602
Hypotheses and methodology, 1678
Hysteresis loop, 1694, 1695
Hysteresis loops under cyclic loading, 1694

I

Identification, 2919–2922
Identification of yield function parameters, 953
Identifying of the process limits for burr-free cutting, 2796
Image processing, 2453, 2455, 2456, 2458, 2461
Impact hydroforming, 353, 354, 359–364, 1231, 1242
Implementation of automatic design flow, 1126
Implementation of material model, 925
Implementation of the stabilising control system, 2458
Imprint, 2317
Impulse forming, 1329
Impulse manufacturing, 1341
Incremental bulk forming, 403, 406
Incremental forming, 417, 418, 427, 493, 550, 551, 2067, 2116, 2117, 2237
Incremental grooving, 2180, 2183
Incremental press forming, 2751, 2753–2755
Incremental Sheet Forming (ISF), 375, 441, 507–510, 512, 519
Incremental sheet metal forming, 393

Incremental step cyclic loading test, 723
Indirect extrusion, 1383–1385, 1387, 1393
Induction-heating-assisted spinning, 333, 334, 333
Industrial impact welding tools, 1330
Industrial set-ups of hot and cold strip rolling, 2397
Industrial trials and finite element simulation of the extrusion process, 1717
Influence mechanism, 834
Influence of the die clearance, 2342
Influence of the feed displacement, The, 1512
Influence of air flow and vibrations, 2254
Influence of axial feed, 2665
Influence of ^{Dc} on fatigue property, 1441
Influence of load level on fatigue property, 1442
Influence of lode stress parameter and stress triaxiality ratios, 344
Influence of media friction, 2668
Influence of pre-hole, 427
Influence of process parameters on the weld quality factor, 143
Influence of riveting direction on fatigue property, 1443
Influence of roller feed rate on forming quality, 340
Influence of strain gauge length on strain measurements using DIC, 694
Influence of stress ratio on fatigue property, 1442
Influence of temperature on forming quality, 339
Influence of the feed rate, The, 1513
Influence of the process parameters on the material properties, 1917
Influence of the speckle pattern coating, 2254
Influence of the upper plate on fatigue failure mode, The, 1429
Influence of thinning ratio on forming quality, 340
Inhomogeneous Heating, 1107–1110, 1112, 1114–1118
Initial microstructure, 1626
Initial situation, 1173
Initial situation and motivation, 1863
Injection molding, 2031, 2032, 2034, 2036–2039
Innovative measurement system, 9
In-plane shear deformation, 763–771
In-plane torsion test, 635, 636, 640, 691–693, 695, 696, 698, 699, 701–705
Integral macroscopic analysis, 1260
Integral testing for different process parameters, 1262
Integrated casting and forging process, 343, 348, 349
Intelligent straightening machine, 3, 9
Intelligent straightening process, 4
Interface between CNTs and AZ91D, The, 2228
Interface healing, 2497–2500, 2502, 2504
Interfacial structure of titanium/carbon steel clad plates, 2192
Intermediate layer, 2759, 2760, 2763
Intra-granular ferrite, 1827, 1828, 1833–1836, 1838
Invariant J_2, 1969
Invariant J_3, 1969
Inverse analysis, 949, 950, 1999
Investigated material, 791
Investigated tube material, 421
Investigation methods, 551
Investigation of diagonal cracks in compression tests, 231
Irregular part, 2621
Isothermal compressive tests, 1791
Isothermal forging, 1813–1816, 1820, 1822, 1823
Isotropic hardening (IH) model, 637
Isotropic yield function, 1970–1972, 1974, 1979

J

Joining, 1395, 1397–1400, 1408, 2381, 2383, 2384
Joining and pre-stressing by widening of a FRP-wrapped metal collar, 1398
Joining stress, 1037, 1038, 1040–1042

K

Kinematic hardening, 635–638, 644
Kinematic loading, 2135, 2149
Kinematics, 406, 2419, 2420, 2450
Kinematics of auger flighting rolling, 2435
Knowledge base, 1161, 1162, 1169, 1170

L

Large and complex curvature, 922, 926, 928
Large deformation simulation, 2939, 2946
Large diameter tube, 1292

Laser, 2067, 2068, 2070–2075
Laser heating, 479, 480, 488–490
Laser heat treatment, 2768, 2769
Laser impulse, 1329, 1332, 1333, 1336, 1338
Laser metal deposited material, 1899
Laser shock peening, 1361, 1362
Laser trimming program, 2809
Light-weight, 2883, 2099
Lightweight construction, 1255, 1256
Lightweight design, 1496
Linear strain path, 202
Liquid-solid extrusion, 2221, 2222, 2225, 2226, 2228, 2229
Liquid-solid extrusion process, 2225
Local heat treatment, 1806, 2068, 2070–2073
Local magnetic material behavior, 2311
Local microscopic analysis, 1260
Local solution treatment, 2731
Local strength distribution and process correlation, 1264
Lode parameter, 1077, 1078, 1084, 1085, 1596, 1600
Lode stress parameter, 344–346, 349
Longitudinal buckle, 2468, 2469, 2471–2476, 2479, 2480
Longitudinal peak strain, 479, 484–487, 490
Long-term X-ray analysis and FE-model validation, 2296
Loosening test, 2162–2164
Lower bound, 544
Low load precision bending, 313
Lubricants, 1529, 1530, 1532, 1534, 1535
Lubricated model for the revolute joint, 1553
Lubrication, 1550, 1551, 1555

M

Machine, 406
Machine behavior, 1132
Machine hammer peening, 1863, 1864
Machine learning, 167, 170, 171, 173, 175, 176, 589–592, 595
Machine learning modeling, 171
Macroscopic failure, 1444
Magnesium, 263, 264
Magnesium alloy of AZ31B, 844
Magnesium alloys, 189, 333, 334, 336, 341, 1563–1565, 1568, 1571
Magnesium alloy sheet (AZ31B), 847–851, 855
Magnesium composite, 2221–2223
Magnetic flux barrier, 2305, 2308, 2313
Magnetic pressure seam welding, 1309
Magnetic pulse forming, 1217, 1218, 1229
Magnetic pulse spot welding, 1373
Magnetic pulse welding, 1269, 1270, 1272, 1274, 1278, 1279, 1291, 1292, 1302
Main roll driving power, 2447
Manufacturing aircraft frame part by IHF technology, 1240
Manufacturing of functional components, 573
Manufacturing of Tailored Blanks, 568
Manufacturing process and target geometry, 566
Mapping algorithm, 2046
Martensite content, 1922
Martensite transformation, 1691, 1692, 1697, 1698, 1854, 1857, 1859
Martensitic transformation measurements, 1857
Mass scaling, 272, 273, 276–278
Material, 1905
Material parameters and numerical implementation, 2349
Material and experimental embossing method, 2359
Material and specimen preparation, 802, 1855, 1982
Material Cards, 625, 627–631
Material characterisation of hot forming steels, 2291
Material characterization, 115
Material characterization and parameter identification of constitutive models, 1992
Material Condition, 2278, 2280, 2282, 2286
Material cyclic characterization, 775
Material description, 615
Material efficiency, 1003, 1018
Material flow, 153, 154, 157–160, 162
Material flow behavior, 2171
Material model, 913, 923, 2961
Material modeling, 1780
Material movement, 383, 385, 390, 392, 393
Material optimization interface, 628
Material processing and grain size characterization, 2721
Material properties, 538
Materials and specimen geometry, 2334
Materials and methodology, 99
Materials and process, 1828
Materials anisotropy parameters, 755
Material selection, 669
Materials end methods, 1486

Material, simulation and experiment, 731
Material testing, 444
Material variation, 2631
Mathematical model, 2395
Maximum wall angle, 28–30
Mean stress relaxation, 719, 720, 724, 725
Measurement techniques, 2335
Measurement deviations during elastic–plastic transition, 700
Measurement of thickness strain and hardness, 2641
Measurement technique and local, non-destructive measurement of martensite content, 1922
Mechanical and analytical findings, 2686
Mechanical behaviour, 1567
Mechanical characterization, 625, 626, 2961
Mechanical loading of work and backup rolls, 2486
Mechanical press, 1549–1551, 1553, 1555, 1557
Mechanical properties, 77, 867, 1843, 1919, 2573–2575, 2577, 2578, 2582, 2583
Mechanical properties and tempering stability, 832
Mechanical properties of monotonic loading, 1693
Mechanical properties of the pre-stressed hybrid structures under bending loads, 1407
Mechanical properties of the tubes, 1907
Mechanical properties of titanium/carbon steel clad plates, 2195
Mechanical properties under hot stamped conditions, 2688
Mechanical strength, 1903, 1904, 1910, 2121
Mechanical testing and welding windows, 1299
Mechanical tests, 1906
Mechanics, 2419, 2446, 2450
Mechanics of auger flighting rolling, 2425
Mechanics of bar straightening, 2143
Mechanism of formability improvement, The, 355
Metal expansion, 1475
Metal flow, 1055, 1057, 1058
Metal forming, 271, 272, 278, 319, 321, 327, 330, 457, 458
Metallic composite, 1383
Metallic micro parts, 151, 152, 163, 164
Metallographic analysis, 1301
Metallography, 997
Metallurgical characterization, 1278
Metal-matrix Composite Joining, 1341, 1342, 1348
Metamorphic manufacturing, 16, 18, 21, 22
Methodology, 116, 169, 1175, 2599
Methods, 2157
Methods to influence the roll crown and strip shape, 2489
MHP parameter study, 1867
MHP setup for determination of process kinematics, 1866
Microalloying elements, 1827–1829, 1832–1834, 1836
Micro-forging behavior, 1069
Micro-forming, 1351, 1352
Microhardness, 2285
Microhardness and optical microscopy, 1249
Microhardness measurements, 1252
Micro-magnetic measurement, 1914
Micromagnetic method, 2233–2235, 2238, 2242, 2243, 2245
Microscopic morphology analysis of substrate fracture, 1445
Microscopic observation of the joint, 1037, 1040
Microstructural characterization, 1793, 1843
Microstructural evolution, 885, 1189, 1190, 1192, 1196
Microstructural investigation, 1830
Microstructural model, 1883
Microstructural observation, 1925, 1926
Microstructure, 14, 16, 17, 21, 239, 240, 243, 244, 831, 867–869, 871–874, 901–904, 908, 909, 1715–1717, 1719–1724, 1743, 1746, 1750, 1752, 1755, 1873, 1893–1901, 1921, 2283
Microstructure analysis, 1795
Microstructure and 3D measurement of surfaces, 2095
Microstructure and mechanical properties, 1060
Microstructure and γ' precipitate, 908
Microstructure characterization, 1719, 1897, 2961
Microstructure evolution, 739, 740, 742, 744, 1623, 1624, 1629, 1630, 2372, 2374, 2375
Microstructure evolution analysis, 1822
Microstructure observation, 1907, 1933
Microstructure of the tubes, 1908
Microstructure simulation, 1817

Microstructures of the deposited material, 1670
Microstructure sub-model, 881
Micro Vickers hardness test, 1036
Mild steel sheet, 949, 950
Mill design, 2420, 2443
Millimeter-grade coarse grains (MCGs), 1757–1759, 1762–1766
Mining industry, 324
Mirror-finished surface, 2090, 2091, 2096
Mixed hardening, 773, 774, 783, 786
Miyauchi test, 1775, 1780–1783, 1785–1788
MMC welding, 1344
Mn18Cr18N steel, 2372, 2373, 2375–2377, 2379
Model calibration, 1597
Modelling, 684, 881, 1463
Modelling/numerical modelling, 2149
Modelling of the stress distribution in flat rolling, 2484
Modelling scheme and model parameters, 1885
Model of dynamic transformation of α→β, 1798
Model of numerical simulation, 579
Models and methods, 594
Model specifications, 1272
Modified Mohr–Coulomb fracture criterion, 180
Modified power law hardening model, 1949
Monitoring, 1201, 1203, 1205, 1211, 1214
Monotonic and cyclic material testing. State of the art, 775
Movements design, 2527
Multi-axial continuum damage constitutive equations, 1619
Multiaxial loading, 681
Multi-axial property, 1961
Multi-body metal forming, 1451, 1452, 1459
Multidirectional forging, 2201–2204, 2209
Multi-intersecting high stiffened integral panel, 2706
Multilayer, 2683, 2686–2692
Multi-objective, 2900
Multi-pass, 2127–2132
Multi-phase material, 601, 602, 609
Multi-physical model, 1219
Multi-ram forging, 2167–2169, 2173, 2174, 2177
Multi-ram radial extrusion process, 2170
Multiscale crystal plasticity modeling, 256
Multi-stage, 1605, 1606, 1613
Multi-stage forging process, 1121
Multi-stage incremental forming, 430, 431, 433, 436, 438
Multi-staggered roll types having five, seven or even ten rolls, 2139
Multivariate approach, 593

N

Natural binder, 2031, 2032, 2039
NDE measurement, 1588
NDE measurement setup, 1587
Near-Net-Shape Blanking, 2332
Necking evaluation, 2599
Neural network, 657, 660–663
Neutral layer, 2705–2712, 2715, 2717
Neutron diffraction, 2233, 2235, 2240, 2245
Neutron grating interferometry, 2308
New printing method, 2212
New proposed model, 1971
New variants of ISF, 377
New yield function, 1971
Ni-based superalloy, 901, 909
980Gen-3, 2829, 2831–2835
Nitrogen, 829–832, 834, 836, 837
Non-axisymmetric shape, 1161–1164
Non-conventional machining, 2696
Non-destructive evaluation, 1585
Nondestructive evaluation tool, 2573–2575, 2582, 2583
Non-proportional loading, 1991, 1993, 1994, 1997
Non-proportional monotonic loading, 605
Novel structures and materials (additive plus deformation), 21
NSP modeling, 1510
Numerical analysis, 1037, 1040, 1305, 1307
Numerical analysis of residual stress, 2310
Numerical and experimental study of microstructure evolution of 6XXX aluminum alloy, 1720
Numerical investigations and discussion, 1784
Numerical method, 2362
Numerical model, 73, 131, 1376, 2081
Numerical modelling, 494, 495
Numerical modelling of the flow forming process, 494
Numerical model validation, 2083
Numerical process simulation, 1415
Numerical representation of the Bauschinger effect, 2060
Numerical results, 2796

Numerical simulation, 577, 579, 580, 583, 973, 974, 979, 1131, 1139, 1140, 1142, 1507, 1508, 1939, 1941, 1943, 1945, 2100, 2101, 2103, 2106, 2108, 2111, 2112, 2762
Numerical simulation for thermal forming limit prediction of AA7075, 1621

O
Objective, 1175, 1864
Objective products and design of die, The, 2168
Occurrence conditions of the prism-shape distortion, 2185
Off-centering, 2557–2561, 2564, 2566–2568
OM analysis, 1833
OM microstructure, 1844
1.4307, 2261–2263, 2265–2267, 2269, 2270, 2273, 2274
1.4404, 2261–2268, 2270–2274
On the bias-variance-tradeoff in modeling, 612
Open-die forging, 16–18, 21, 537–539, 547, 1145–1148, 1151–1153, 1155, 1157, 1158
Optical, 2041, 2043, 2046
Optical measurement and analysis of incrementally formed collars, 424
Optical microscopy, 1254
Optical micro-strain measurements, 2252
Optimization, 493, 494, 497, 499–501, 505, 506, 625, 626, 628, 629, 631
Optimization algorithm, 1121
Optimization of forming angle increment and moving direction of roller to eliminate edge waves in RRF, 482
Optimization of forming parameters, 484
Optimization results of coil and FS, 1298
Orbital riveting, 1479, 1481, 1482
Orbital riveting of electric contacts, 1482
Orthotropic yield criteria, 2840, 2842, 2843, 2845, 2846
Oscillation potential of solenoids, 2614
Oven-heating uniaxial tension, 857–860, 862, 864, 865
Overshoot, 1050–1052
Overview of ML-based modeling for springback, 169

P
Paperboard, 1643, 1644, 1649, 1651, 1652
Parallel roller straightening, 2140
Parameter study, 1113
Parametric Study, 464
Penalty method, 1455, 1459
Performance test of surfacing materials, 2761
Permanent softening, 839, 840, 842, 844, 845
Phase transformation, 792
Phase transition, 1529, 1530, 1532, 1534, 1535
Phenomenological material modeling, 2348
Phenomenological models, 636
Photographic performance, 2049
Physical process modelling, 1025
PID control, 2959, 2963–2965, 2967, 2968
Piercing, 2807, 2808, 2810–2816, 2925, 2926, 2929–2937
Pillow effect, 26, 32, 33
Pin extrusion, 162
Pipe bending, 2019, 2020, 2027
Pipe bending process, 2020
Piping system, 2019, 2020
Plane strain structure, 1678
Plastic, 1412, 1413, 1415
Plastic anisotropy, 750, 751, 755–758, 760
Plastic deformation, 2142, 2420, 2425, 2427
Plasticity, 201–206, 602, 603, 2009
Plasticity flow behaviour, 1626
Plasticity improve, 2221
Plastic waves, 127–130, 133–135
Plastic work, 667–669, 675, 678
Plate forging, 973–975, 978, 979, 981
Pneumatic press, 1245–1247, 1249–1251, 1253, 1254
Porosity closure model, 343, 345, 346
Post-form mechanical properties sub-model, 883
Post-form mechanical property, 877, 878, 881, 883, 888
Post-processing and dataset preparation, 606
Powder-fed DED equipment, 1667
Power spinning, 2080
Precision forging, 1077–1085
Precision forging methods, 2170
Precision metal forming, 2167, 2168
Prediction model for porosity closure, 344
Prediction of in-plane shear deformation by FEM analysis, 765
Prediction of springback with different hardening models, 2726
Pre-forging, 2909–2915
Pre-forming, 577, 578, 580–583, 585, 764

Pre-forming of RF, 581
Preform operation, 1108, 1110
Pre-processing of specimen, 1644
Press forming technique, 763, 764, 771
Press-hardened steels, 1655, 1656
Press hardening, 2661–2663, 2668, 2669
Press peak load at shearing, 1251
Press ram displacement, 2611
Pre-strained material, 204
Pre-stress, 1395, 1396, 1398–1400, 1403, 1405, 1406, 1408, 1409
Prevention of measurement errors due to strain localization in shear tests, 702
Prevention of strain localization using a new grooved specimen for in-plane torsion tests, 703
Principal stresses calculation, 684
Principle of impact hydroforming, The, 359
Principle of roll forming, 578
Procedure to identify the fracture strain, 1566
Profile bending, 18
Process and form errors in radial-axial ring rolling, 2949
Process planning, 1161, 1162, 1164, 1170
Process and process parameters, 1256
Process conditions, 2022
Process design, 1110
Process design using fast models, 1148
Process effects, 1255
Process force, 1490
Processing map, 891, 892, 897–899, 1925, 1926, 1930, 1932–1935
Process instabilities, 404
Process investigation of pulsating hydroforming, The, 357
Process kinematics and impact energies, 1868
Process mechanics, 2084
Process monitoring, 1148
Process optimization, 1149, 1412
Process principles, 1914
Process scrap, 1016, 1018
Process strategy and resulting geometry, 568
Process time, 76
Process understanding, 519
Process window, 379
Producible rolling thickness, 2533–2535, 2542, 2544, 2545
Productivity, 2883, 2887–2889, 2895
Profile shape, 1017
Progressive die, 2790
Properties, 2189–2191, 2195, 2198, 2199
Properties of an incrementally formed collar, 425
Property control, 1923
PSO algorithm, 172
Pulsating hydroforming, 353–357
Pulse current, 867–875
Pulsed GMAW, 2853
Pulse straightening, 2140
Punching, 1161, 1162, 1166, 1169, 1170
Punching tool and measurement concept, 1657
Punch load, 2675
Punch shape design, 2671–2673
Pure iron interlayer, 2189, 2190, 2194–2199
Pure titanium, 1351, 1353, 1356, 1358, 2639, 2640, 2642, 2646

Q

QForm, 1717–1719, 1724
Quality control, 2949
Quality prediction, 590–592, 595, 598
Quantitative analysis, 1369
Quasi-beta deformation behavior, The, 1191
Quasi-beta forging, 1189, 1190
Quenched microstructure investigation, 1830
Quenching, 790–793, 797, 798

R

Radial-Axial ring rolling, 591, 2947–2951
Radial feed curve, 2205
Radial Rotation Profile-Forming, 2067, 2069, 2071
Railway and architectural industries, 326
Ram vibration, 2615
Rare earth, 263
Ratcheting, 811, 812, 814, 815, 817–819, 826
Rate dependency, 839, 841–845
Rate-dependent tension–compression hardening behaviors of sheet metals, 841
Reaming, 2201–2205, 2209
Recent developments using the VFA technique, 1344
Recrystallization, 239–249
Recurrent neural network, 601, 602, 609
Reduction of abrasive tool wear, 2615
Reduction of residual contact pressure in extrusion by manipulating die elastic strain field, 44
Regarded forming task, 1318
Regression, 611–614, 617, 619, 620, 622

Relation between estimated friction and transcribed profile, 2415
Relationship between RD and TD groove roll, 2414
Relaxation, 1643, 1644, 1648, 1649, 1651, 1652
Relaxation resistance, 808
Repair, 1665
Representation of Totally Non-Axisymmetric Forged Products, 1164
Requirements, 595
Research process and methods, 1940
Residual stresses, 2331–2333, 2335, 2337–2343, 2345, 2346, 2351, 2352
Residual curvature, 2144, 2145, 2151
Residual pressure, 43
Residual stresses, 4–6, 9, 1872, 2261–2274, 2277–2283, 2286, 2287, 2303–2311, 2315–2317, 2319, 2328, 2330, 2357–2367
Residual stresses in the process and measurements, 2148
Residual stress hole, 1361, 1362, 1369
Residual stress measurement, 2249, 2252, 2254, 2255, 2257, 2258
Residual stress stability, 2289, 2290
Residual thickness, 2678
Resource efficiency, 1108
Results and discussion of waveforms of AE and process forces, 1178
Results of the method for efficient forging sequence planning, 2872
Ring climbing, 2453–2455, 2463, 2464
Ring rolling, 589, 591, 593, 2201–2203, 2205–2209, 2381–2384, 2387, 2388, 2390, 2391, 2393, 2453–2458, 2460, 2463–2465, 2497–2501, 2504
Ring rolling forming process with Mn18Cr18N thick-wall hollow ingot, The, 2375
Rivet and die, 1425
Riveting assembly, 1507–1509, 1511–1513
Riveting direction, 1437–1440, 1443, 1444, 1449
Robotic roller forming, 479–481, 490
Robust 2nd order time-stepping , 1224
Role of rollers and straightening processes, 2147
Roll-bonding, 1469, 1471, 2684, 2689, 2690, 2692, 2693
Rollers, 2136, 2139, 2141, 2144, 2145, 2147, 2148, 2150–2152
Rollers design, 2526
Roll forming, 577, 578, 585
Rolling, 983, 984, 986, 2419–2428, 2431–2434, 2437–2442, 2444–2451, 2467–2472, 2474, 2476–2478, 2480, 2548–2550, 2553
Rolling contact area, 2427
Rolling experiments, 1905, 2405, 2406
  microstructure evolution and mechanical properties, 1899
Rolling experiments and heat treatment, 1896
Rolling mill (DRM-80), 2524
Rolling process, 984
Rolling theory, 2484
Rolling torque on main roll shafts, 2432
Roll offset, 2442
Roll separating force, 2428
Rotary draw bending and springback, 170
Rotary forging, 1451, 1452, 1456, 1459, 1507
Rotary Forming, 227, 228, 403–406, 408, 411, 414
Rotary hub-straightening, 2140
Rotary swaging, 2261–2272, 2274
Rotational Swing-Folding, 2067, 2069
Rotation speed and contact pressure between container and workpiece, 223
Roughness, 467, 469, 476, 1753
Roughness evaluation, 1575
Round hole staggered perforated plate, 603
RRF with local laser heating, 488
RVEs and representative microstructures, 1760

S

Samples manufacturing by laser metal deposition, 1895
Sandwich sheets, 2100–2102, 2105, 2111
Scanning electron microscopy, 1575
Scheme of texture development during drawing with the fixed plug, 735
Scheme of texture development during hollow sinking process, 736
Screw thread structure of modified DTB-II, 2157
Section straightening machines, 2137
Selection of alloys, 1656
Self-piercing riveting, 1424–1426, 1438, 1441, 1444, 1495, 1496
Self-piercing riveting test, 1425
SEM, 1423, 1424, 1432, 1433

SEM analysis, 998
SEM analysis and correlation with hardness behaviour, 1735
SEM and EDX analysis of the alloy during age hardening, 1733
Sensors, 5
Servo-hydraulic testing machine, 53
Servo press, 2829, 2834, 2835
Setup of boundary value problem, 2347
Setup for dieless drawing and experiments, 470
Setup for joining and pre-stressing of the hybrid structures, 1400
Setup for the bending test, 1403
Setup for the numerical investigations, 1401
Setup of stochastic finite element simulation, 615
7xxx Aluminum Alloys, 959, 970
7xxx series aluminum, 935–937
Shape design, 2910
Shape transformation rules, 1165
Shaping, 577, 578, 580, 583
Shaping of RF, 582
Shear, 1652
Shear affected zone, 1605, 1606, 1611–1613
Shear cutting, 1605–1607, 1610–1613, 2331–2333, 2336, 2789, 2801, 2803, 2805
Shear cutting setup, 2333
Shearing, 1585–1587, 1589
Shearing speed, 1250
Shear punching test, 1999–2001, 2003, 2004, 2006
Shear test, 691–703, 706, 1246
Sheet and tube, 353
Sheet-bulk forming, 2609
Sheet forming, 97, 564, 1939, 2620
Sheet metal, 151–155, 157–160, 162–164, 2048, 2357–2360, 2362, 2363, 2365, 2650, 2651, 2653
Sheet metal forming, 81–85, 87, 90, 92, 93, 2574, 2583
SiC coated dies, 1065–1069
Similarity of plasticine and aluminum, 1025
Simulation, 271–280, 1057, 1715–1719, 1723, 1724, 2831, 2832, 2834, 2835, 2947, 2948, 2950–2957
Simulation/numerical simulation, 2149
Simulation matrix, 2930
Simulation results, 928, 2715
Simulation setup, 614, 2664
Simulation setup and modelling, 2792
$\sin^{2}2\ \Psi$, 2261, 2263–2265
Single point incremental forming, 25–30, 32, 34, 35
Single sheet tests, 2309
Single step cyclic loading test, 722
Six-roll straighteners, 2138
6063 aluminium alloy, 1727–1729, 1739
Size effect, 151–155, 158–164, 190, 194, 1351, 1352, 1355–1358, 2719, 2720
Skew-roll straightening machine, 2140
Skin pass, 2470
Slab analysis, 539
Slice of final forging, 2910
Slow cooled microstructure investigation, 1833
Soft material, 2211, 2212, 2214–2216, 2219
Solid boss forming by plate forging process, 975
Solid state bonding, 140, 141
Solution approach, 2070
Space mesh, 2939–2942, 2944–2946
Spatial discretization, 1220
Specimen and equipment, 720
Specimen design, 1961, 1966
Specimen geometry, 54, 55, 57, 59, 65
Specimen geometry and preparation, 1399
Specimen manufacturing process, 2305
Specimen preparation, 1439, 1574
Spectrum analysis, 2089–2091, 2094, 2098
SPHE, 1841–1843, 1847, 1849–1851
Spinner, 2055–2060, 2062–2065
Spinner straighteners, 2139
Spinning process, 1913, 1915
Springback, 167–172, 174–177, 2179, 2180, 2183, 2184, 2186
Springback simulation, 1464
Springback prediction, 2706, 2720, 2726
Spur gears, 1077–1082, 1085
Square plate diagonal stretching, 1939, 1942, 1943
SRAF test verification, 930
Stainless steel, 27, 29, 749, 750, 755, 756, 759, 1383–1386, 1389, 1392–1394, 1495, 1498, 1500, 1502, 1504, 1505, 1853, 1854, 1864–1867, 1868, 1870, 1874–1876, 1981, 1982, 2277–2280, 2285, 2286
Stainless steel pipe, 2019, 2020, 2022, 2027
Staking, 1411–1417, 1421
Stamping, 2619–2621, 2623, 2624, 2627
Stamping by elastic Blankholder with supporting elements, 2624
State of the art, 53, 417, 1109, 1462, 1174, 1863, 2279, 2455

Static recrystallization, 1715, 1716, 1718–1720, 1723, 1724, 1879, 1883, 1884, 1890
Static recrystallization model of 6XXX aluminum alloy based on industrial experiments, 1719
Static transformation during heat treatment, 1795
Steel, 1281–1283, 1288, 2189–2197, 2199
Steel sheet, 209, 210, 215
Steering control, 2557, 2559–2563, 2568
Step shafts forming, 2526
Stone formula, 2533, 2534
Straightener, 2055–2057, 2059, 2065
Straightness, 2055, 2061, 2135, 2136, 2139–2141, 2147–2149, 2151, 2152
Strain, 1605–1607, 1609, 1611–1613, 2009–2016
Strain distribution in conventional shear tests, 694
Strain distribution in in-plane torsion tests, 695
Strain gauge, 1701, 1702, 1704, 1705, 1707, 1710
Strain hardening, 911–913, 915, 1915
Strain hardening near the cut edge, 2932, 2934
Strain hardening rate, 60, 62, 63
Strain localization, 692, 696, 702–704, 706
Strain measurements, 2772
Strain penetration, 2371, 2374, 2375, 2379
Strain penetration during ring rolling forming, 2374
Strain rate, 657–660, 662, 663, 1605, 1606, 1609, 1613
Strain-rate potential, 284, 286–289
Strain results, 1988
Strain state of different forming stages, The, 1084
Strength, 2883–2888, 2890, 2892, 2895
Strengthening mechanism, 1850
Stress, 2009–2011, 2014
Stress deviator, 1970, 1972
Stress exponent, 807
Stress exponent of creep strain, 851
Stress filed comparison of traditional and new tool, 2763
Stress loss ratio, 1361, 1363–1369
Stress metric, 668, 674–678
Stress ratio, 1437, 1438, 1440–1443, 1449
Stress relaxation, 801–809, 847, 848, 850, 853–855, 877–882, 885, 886, 888
Stress-relaxation age forming, 921, 925, 932
Stress relaxation ageing sub-model, 882
Stress relaxation behaviour, 885
Stress state of different forming stages, The, 1083
Stress-strain analysis, 437
Stress-strain behavior, 1236
Stress-strain curve, 60–62, 949, 950, 953
Stress-strain curve of AA 6016-T6, The, 1597
Stress–strain curves, 1858
Stress-strain relationship of auger flighting rolling, 2425
Stress-train curve, 292
Stress triaxiality, 1596, 1600
Stress triaxiality ratio, 343–346, 349
Stress wave, 53–55, 57, 62–65
Stress wave propagation and system ringing analysis, 55
Stress wave simulation, 1464
Stretch straightening machines, 2137
Strip deviation angles, 2445
Strip drawing test, 81, 84, 89, 90, 93
Strip drawing tests and retention forces, 1541
Strip drawing with flat dies (FD test), 90
Strip feeding (bite) condition, 2439
Stripping off, 1173–1185
Strip rolling, 2483, 2487, 2489
Strip steel, 2421, 2425, 2430
Strip velocity in forming zone, 2435
Structured Sheet Metals (SSM), 1701–1703, 1710
Structure of bimetallic microcontact, 1491
Sucrose, 2031–2033, 2035, 2037, 2039
Superalloy sheet, 2719, 2720, 2726–2728
Superimposed vibrations, 2610
Superplastic forming (SPF), 1573, 1574, 1578, 1582
Superplasticity, 983, 984, 986, 988, 1623, 1624, 1628
Supporting technologies, 2893
Surface, 217–224
Surface asperity, 2211
Surface integrity, 1863–1865, 1867, 1868, 1874
Surface layer, 2759, 2760, 2763
Surface morphology, 1576
Surface profiles and textures, 2092
Surface profiles and 3D topographies of galvanized sheets, 100
Surface quality, 377–379, 2120, 2553
Surface reconstruction, 2912
Surface roughness, 1573, 1575, 1576, 1581–1583, 2405, 2406

Surface roughness and hardness, 1870
Surface strengthening, 1362
Surface texture, 2547–2551, 2554
Surfacing technology, 2759, 2760, 2764, 2766
Surface topographies and fractal features of galvanized sheets, 99
Surrogate modeling, 617, 619, 622
Surrogate modeling of drawing aid forces, 619
Surrogate modeling of draw-ins, 617
Surrogate modeling of sensor signals, 617

T

Tailored blank, 563–575
Tailored sheet, 1677, 1678, 1684, 1686–1689
Tailored tempering, 964, 968, 970
Tailored tempering of EN AW 7075, 968
Tailor heat treated blank, 2729
Taylor-Quinney coefficient, 1775, 1776
TCBC experiment and results discussion, 448
TCBC test concept development, 444
TCBC test rig design and manufacturing, 447
Temperature, 1857, 2041, 2042, 2046, 2051, 2052
Temperature filed comparison of traditional and new tool, 2763
Tempering stability, 829, 830, 832–834, 837
Temper rolling, 2467–2470, 2477, 2480
Tensile strength, 2155–2158, 2162–2164
Tensile strength tests, 2162
Tensile experiment and results, 986
Tensile properties, 1665, 1666
Tensile test, 1426, 1574–1576, 1579–1583, 1701–1703, 1705–1707, 1709, 1710, 1898
Tensile testing results, 2578
Tensile test of extruded products, 1035
Tensile tests, 1672, 2771
Tension and compression, 839, 840, 844, 845
Test and calibration of QP1180-EL, 1950
Test cases, 1221
Testing methods and instruments, 1916
Texture, 263, 264, 266–269, 729, 730, 733–736
Texture evolution, 2508, 2509, 2513, 2515, 2517, 2518
Texture rolling, 2406
Theoretical analysis, 2707
Theoretical aspects, 2141
Theoretical model, 2535
Theory of the producible rolling thickness, 2535
Thermal cycle, 70
Thermal flow, 1617
Thermal loading of work rolls during a strip rolling campaign, 2487
Thermal model, 1884
Thermal parameters identification, 2920
Thermal profile, 74
Thermal softening, 657, 660, 662
Thermal strain, 2255, 2256
Thermal treatment, 1656, 1658
Thermographic performance, 2050
Thermomechanical analysis, 1775–1777, 1779–1781, 1783, 1786
Thermomechanical model, 1219
Thickness distribution, 436
Thickness evolution, 429, 431, 436, 438
Thickness profile, 2484, 2493–2496
Thickness reduction, 1043, 1044, 1046, 1048, 1049, 1052
Thin part with high circular ribs, 1099
Thin-walled tubes, 113–115, 120, 123, 124, 2179, 2180, 2767
Thread rolling, 2155–2160
Thread rolling FEM simulation and experiments, 2159
3D-DIC optical residual stress measuring system, 2250
3D digital-image-correlation, 2249
Three-layer sheet hot stamping, 2819, 2820, 2822, 2824–2827
3MA, 2573–2577, 2580–2583
316L, 1743–1745, 1747–1749, 1749–1753
316LN austenitic stainless steel, 1757
Three-point bending test, 2588
Thrust force, 2557–2562, 2567, 2568
Ti-55511 alloy, 1189, 1190, 1192–1194, 1196
Ti–5Al–5Mo–5V–3Cr–1Zr alloy, 1925
Ti-6Al-2Zr-1Mo-1V alloy, 1791–1794, 1802
Ti-6Al-4V alloy, 2751–2753
Time series classification, 591
Titanium, 1065–1074, 2189–2193, 2195–2197, 2199
Titanium alloys, 2695, 2696, 2703, 2819–2826
Titanium wire work, 1068
TNW700 titanium alloy, 1623–1631
Tool design, 1319

Tool force, 465
Tool geometry, 551, 559, 560
Tooling setup, 1522
Tool kinematics, 403, 404
Tool life, 37, 40, 41, 44–46, 48, 49
Tool materials, 2000, 2214
Tool path, 369, 370, 381
Tool path algorithm, 370
Tool path design, 553
Torsion, 217, 220, 224
Toughness, 829, 830, 832, 836, 837
TP340 titanium sheets, 2741, 2742
Transfer printing, 2212
Transverse weld, 1003–1006, 1008, 1013, 1016, 1018
Tribological test methods, 82
Tribology, 81–84, 90, 93
Tribometer, 81–85, 87, 90–93
Tribo-test, 1519–1521
Trimming, 2925–2927, 2929, 2930, 2933–2937
TRIP effect, 1691, 1694, 1698
True stress-strain curve, 741, 903, 976
Tselikov's method, 2428
Tube bending, 167–171, 175, 177
Tube bending in terms of flexibility, 2890
Tube bulging, 682, 683
Tube draw bending, 67–69
Tube expansion tests, 2771
Tube formability tests, 116
Tube forming, 113, 114, 124, 397, 402, 524, 2020, 2768, 2884–2886, 2892–2895
Tube hydroforming, 1880, 1881
Tube material, 2672
Tube spinning, 2077–2080, 2082–2084, 2086, 2087, 2127–2130, 2133
Tube welding, 1291, 1292
Tubular materials, 2959–2961, 2966–2968
Two-roll bar straighteners or reeling machines, 2138
Two-stage counter punching and shaving, 2790
Types of straighteners, 2136

U

U-bending test, 2722
Ultimate strain limit, 291
Ultrahigh strength steel, 867, 875
Ultra-large forgings, 21
Ultrasonic, 1281–1285, 1287–1289
Ultrasonic assisted, 384, 385
Ultrasonic processing, 2224
Ultrasonic riveting, 1479
Ultrasonic vibration, 429, 430
Ultra-thin strip rolling, 2533–2535, 2539, 2540, 2542
Uncoupled model, 1635
Uniaxial tensile creep, 849, 850, 855
Uniaxial tensile creep test, 849
Uniaxial tensile simulation for determination of material parameters, 257
Uniaxial tensile test, 949, 950, 952, 953
Uniaxial tensile testing, 974
Uniaxial tensile tests at elevated temperatures, 791, 793
Uniaxial tension, 1853–1855, 1861
Uniaxial tension test, 721
Universal tensile, 983, 986
Unregularized and regularized linear regression, 613
Upper bound, 537, 538, 540–542, 544, 545, 547
Upper bound solution, 540

V

Validation and evaluation of the results after the collar widening process, 1404
Validation of s-s curve in high strain region obtained by proposed method, 956
Validation of the calibration function, 2577, 2580
Validation of the method by using FE simulations, 2874
Validation of the porosity closure model, 346
Validation of the predictive capacity of the model for copper cylinder upsetting, 1136
Validation of the 6XXX aluminum alloy static recrystallization model, 1722
Validation of the temperature compensation method, 2256
Validation via design of experiments, 2461
Vaporizing Foil Actuator (VFA), 1341, 1342, 1345, 1346, 1348
Vaporizing foil method, 1329, 1330, 1332, 1339
Various loading states, 647
V-bending process, 854
V-Bend mechanics, 671
VDA 238-100 tight radius bend test, 671, 673
Verification, 271, 273–276, 278, 279
Verification target, 1125
Verification of finite element model, 336

Verification of the new approach, 2716
Vibration loosening tests, 2162
Vibration assisted, 385
Visco-plastic constitutive model, 1617
Visual appearance of drawn clad cup, 2642
Visualization of model quality dependent on model complexity, 621
VUMAT, 1617, 1618, 1621

W

Wall thickness measurement, 2107
Warm forming, 847, 848, 2751, 2752, 2755
Wear, 1727, 1729, 1730, 1734–1740
Wear analysis, 1447
Weight reduction versus cost effectiveness, 319
Welding device design, 1378
Welding platform, 1373
Welding principle, 1306
Weld quality prediction and experimental validation, 144
Whole forming process of ring, The, 2201, 2202
Wire, 467–473, 475–477
Wire-Arc Additive Manufacturing (WAAM), 2853–2855, 2857–2860, 2862
Wire drawing, 1768, 1769, 1771, 1773
Wood, 2031–2033, 2036, 2037, 2039
Workability, 467–469, 473, 475, 477
Work hardening, 1537, 1538, 1543, 1544, 1546, 1623, 1624, 1626, 1628, 1629, 1631, 2116, 2117, 2277, 2278, 2777, 2285, 2286, 2780–2783, 2786, 2789, 2799, 2801, 2802
Work-hardening and strain rate sensitivity exponent, 1628
Work hardening behaviour, 886
Work hardening of shear cut edges, 2799
Work roll contour, 2395–2397, 2400–2402
Work roll flattening, 2487
Wrinkle instability, 1939, 1940
Wrinkling, 2067, 2069–2072, 2075, 2777, 2782, 2786
W-temper, 935–939, 942, 943, 945

X

X-ray diffraction, 2233–2235, 2238, 2241, 2242, 2245, 2246, 2261, 2264, 2265, 2289, 2295, 2300

Y

Yield condition, 201–205
Yield function, 209, 210, 212–215
Yield functions calibration, 685
Yield strength, 1842, 1847–1851
Yield strength behaviour, 886
Yield stress surface, 284, 286–289
Yield surface, 201–206
Yoshida-Uemori (YU) model, 638